

Volume I-VI

DEKKER  
Encyclopedia of  
Nanoscience  
and  
Nanotechnology

Second Edition



# Encyclopedias from Taylor & Francis Group

## Agriculture Titles

- Dekker Agropedia Collection (Eight Volume Set)**  
ISBN: 978-0-8247-2194-7      Cat. No.: DK803X
- Encyclopedia of Agricultural, Food, and Biological Engineering**  
Edited by Dennis R. Heldman  
ISBN: 978-0-8247-0938-9      Cat. No.: DK9381
- Encyclopedia of Animal Science**  
Edited by Wilson G. Pond and Alan Bell  
ISBN: 978-0-8247-5496-9      Cat. No.: DK2206
- Encyclopedia of Pest Management**  
Edited by David Pimentel  
ISBN: 978-0-8247-0632-6      Cat. No.: DK6323
- Encyclopedia of Pest Management, Volume II**  
Edited by David Pimentel  
ISBN: 978-1-4200-5361-6      Cat. No.: 53612
- Encyclopedia of Plant and Crop Science**  
Edited by Robert M. Goodman  
ISBN: 978-0-8247-0944-0      Cat. No.: DK1190
- Encyclopedia of Soil Science, Second Edition (Two Volume Set)**  
Edited by Rattan Lal  
ISBN: 978-0-8493-3830-4      Cat. No.: DK830X
- Encyclopedia of Water Science, Second Edition (Two Volume Set)**  
Edited by Stanley W. Trimble  
ISBN: 978-0-8493-9627-4      Cat. No.: DK9627

## Chemistry Titles

- Encyclopedia of Chromatography, Second Edition (Two Volume Set)**  
Edited by Jack Cazes  
ISBN: 978-0-8247-2785-7      Cat. No.: DK7851
- Encyclopedia of Supramolecular Chemistry (Two Volume Set)**  
Edited by Jerry L. Atwood and Jonathan W. Steed  
ISBN: 978-0-8247-5056-5      Cat. No.: DK056X
- Encyclopedia of Surface and Colloid Science, Second Edition (Eight Volume Set)**  
Edited by P. Somasundaran  
ISBN: 978-0-8493-9615-1      Cat. No.: DK9615

## Engineering Titles

- Encyclopedia of Chemical Processing (Five Volume Set)**  
Edited by Sunggyu Lee  
ISBN: 978-0-8247-5563-8      Cat. No.: DK2243
- Encyclopedia of Corrosion Technology, Second Edition**  
Edited by Philip A. Schweitzer, P.E.  
ISBN: 978-0-8247-4878-4      Cat. No.: DK1295
- Encyclopedia of Energy Engineering and Technology (Three Volume Set)**  
Edited by Barney L. Capehart  
ISBN: 978-0-8493-3653-9      Cat. No.: DK653X
- Dekker Encyclopedia of Nanoscience and Nanotechnology, Second Edition (Six Volume Set)**  
Edited by Cristian I. Contescu and Karol Putyera  
ISBN: 978-0-8493-9639-7      Cat. No.: DK9639
- Encyclopedia of Optical Engineering (Three Volume Set)**  
Edited by Ronald G. Driggers  
ISBN: 978-0-8247-0940-2      Cat. No.: DK9403

## Business Titles

- Encyclopedia of Library and Information Science, Second Edition (Four Volume Set)**  
Edited by Miriam Drake  
ISBN: 978-0-8247-2075-9      Cat. No.: DK075X
- Encyclopedia of Library and Information Science, First Update Supplement**  
Edited by Miriam Drake  
ISBN: 978-0-8493-3894-6      Cat. No.: DK8948
- Encyclopedia of Public Administration and Public Policy, Second Edition (Three Volume Set)**  
Edited by Evan M. Berman  
ISBN: 978-0-4200-5275-6      Cat. No.: AU5275
- Encyclopedia of Wireless and Mobile Communications (Three Volume Set)**  
Edited by Borko Furht  
ISBN: 978-0-4200-4326-6      Cat. No.: AU4326

These titles are available both in print and online. To order, visit:

[www.crcpress.com](http://www.crcpress.com)

Telephone: 1-800-272-7737

Fax: 1-800-374-3401

E-Mail: [orders@taylorandfrancis.com](mailto:orders@taylorandfrancis.com)

Volume I-VI

DEKKER  
Encyclopedia of  
Nanoscience  
and  
Nanotechnology

Second Edition

Edited by  
Cristian I. Contescu  
Karol Putyera

Founding Editor James A. Schwarz



CRC Press  
Taylor & Francis Group  
Boca Raton London New York

CRC Press is an imprint of the  
Taylor & Francis Group, an **informa** business

CRC Press  
Taylor & Francis Group  
6000 Broken Sound Parkway NW, Suite 300  
Boca Raton, FL 33487-2742

© 2009 by Taylor & Francis Group, LLC  
CRC Press is an imprint of Taylor & Francis Group, an Informa business

No claim to original U.S. Government works  
Printed in the United States of America on acid-free paper  
10 9 8 7 6 5 4 3 2 1

International Standard Book Number-13: 978-0-8493-9639-7 (Six Volume Print Set)  
International Standard Book Number-13: 978-0-8493-9636-6 (Volume 1)  
International Standard Book Number-13: 978-0-8493-9635-9 (Volume 2)  
International Standard Book Number-13: 978-0-8493-9634-2 (Volume 3)  
International Standard Book Number-13: 978-0-8493-9633-5 (Volume 4)  
International Standard Book Number-13: 978-0-8493-9632-8 (Volume 5)  
International Standard Book Number-13: 978-0-8493-9629-8 (Volume 6)

This book contains information obtained from authentic and highly regarded sources. Reasonable efforts have been made to publish reliable data and information, but the author and publisher cannot assume responsibility for the validity of all materials or the consequences of their use. The authors and publishers have attempted to trace the copyright holders of all material reproduced in this publication and apologize to copyright holders if permission to publish in this form has not been obtained. If any copyright material has not been acknowledged please write and let us know so we may rectify in any future reprint.

Except as permitted under U.S. Copyright Law, no part of this book may be reprinted, reproduced, transmitted, or utilized in any form by any electronic, mechanical, or other means, now known or hereafter invented, including photocopying, microfilming, and recording, or in any information storage or retrieval system, without written permission from the publishers.

For permission to photocopy or use material electronically from this work, please access [www.copyright.com](http://www.copyright.com) (<http://www.copyright.com/>) or contact the Copyright Clearance Center, Inc. (CCC), 222 Rosewood Drive, Danvers, MA 01923, 978-750-8400. CCC is a not-for-profit organization that provides licenses and registration for a variety of users. For organizations that have been granted a photocopy license by the CCC, a separate system of payment has been arranged.

**Trademark Notice:** Product or corporate names may be trademarks or registered trademarks, and are used only for identification and explanation without intent to infringe.

---

#### Library of Congress Cataloging-in-Publication Data

---

Dekker encyclopedia of nanoscience and nanotechnology / editors, Cristian Contescu, Karol Putyera. -- 2nd ed.

p. cm.  
"A CRC title."

Includes bibliographical references and index.

ISBN 978-0-8493-9639-7 (six volume print set : alk. paper) -- ISBN 978-0-8493-9636-6 (volume 1 : alk. paper) -- ISBN 978-0-8493-9635-9 (volume 2 : alk. paper) -- ISBN 978-0-8493-9634-2 (volume 3 : alk. paper) -- ISBN 978-0-8493-9633-5 (volume 4 : alk. paper) -- ISBN 978-0-8493-9632-8 (volume 5 : alk. paper) -- ISBN 978-0-8493-9629-8 (volume 6 : alk. paper)

I. Contescu, Cristian I., 1948- II. Putyera, Karol. III. Title: Encyclopedia of nanoscience and nanotechnology.

QC176.8.N35D43 2009  
620'.5--dc22

2008034137

---

Visit the Taylor & Francis Web site at  
<http://www.taylorandfrancis.com>

and the CRC Press Web site at  
<http://www.crcpress.com>

*To the lasting memory of the Founding Editor,  
Professor James A. Schwarz,  
who shaped our lives;  
and to the enduring patience of our wives,  
Adriana and Ildiko, who understood so  
well and always supported us.*

*Cristian I. Contescu  
Karol Putyera  
Oak Ridge, TN and Syracuse, NY  
July 2008*

**Cristian I. Contescu**

*Materials Science and Technology Division,  
Oak Ridge National Laboratory, Oak Ridge, Tennessee, U.S.A.*

**Karol Putyera**

*EAG New York Shiva Technologies, Syracuse, New York, U.S.A.*

**Founding Editor James A. Schwarz**

*Syracuse University, Syracuse, New York, U.S.A.*

***Editorial Advisory Board***

**Frank Armatis**

*Advanced Materials Technology Center,  
3M Corporation, St. Paul,  
Minnesota, U.S.A.*

**R. Terry K. Baker**

*Catalytic Materials Ltd., Holliston,  
Massachusetts, U.S.A.*

**Robert Birge**

*Department of Chemistry,  
University of Connecticut, Storrs,  
Connecticut, U.S.A.*

**Vijoleta Braach-Maksvytis**

*CSIRO Executive Management Council,  
Australian Government, Lindfield,  
New South Wales, Australia*

**Gianfranco Cerofolini**

*Department of Materials Science,  
University of Milano-Bicocca,  
Milan, Italy*

**Stephen Y. Chou**

*Department of Electrical Engineering,  
Princeton University, Princeton,  
New Jersey, U.S.A.*

**Morinobu Endo**

*Faculty of Engineering, Shinshu University,  
Nagano-city, Japan*

**Toshiaki Enoki**

*Department of Chemistry,  
Tokyo Institute of Technology,  
Tokyo, Japan*

**Gerhard Ertl**

*Department of Physical Chemistry,  
Fritz Haber Institute of the Max Planck  
Society, Berlin, Germany*

**Robert Glass**

*Lawrence Livermore National Laboratory,  
Livermore, California, U.S.A.*

**D. Wayne Goodman**

*Department of Chemistry,  
Texas A&M University,  
College Station, Texas, U.S.A.*

**Elias Greenbaum**

*Chemical Sciences Division,  
Oak Ridge National Laboratory,  
Oak Ridge, Tennessee, U.S.A.*

**Hans-Joachim Güntherodt**

*Institut für Physik der Universität Basel,  
Basel, Switzerland*

**Norbert Hampp**

*Department of Chemistry,  
Philipps Universität,  
Marburg, Germany*

**Tim Harper**

*CMP-Cientifica S.L., Madrid, Spain*

**Arthur Hubbard**

*Santa Barbara Science Project,  
Santa Barbara, California, U.S.A.*

**Enrique Iglesia**

*Department of Chemical Engineering,  
University of California, Berkeley,  
California, U.S.A.*

**Mietek Jaroniec**

*Department of Chemistry,  
Kent State University, Kent,  
Ohio, U.S.A.*

**Andy Kaldor**

*ExxonMobil Research and Engineering,  
Annandale, New Jersey, U.S.A.*

**Jürgen Kirschner**

*Max-Planck-Institut für  
Mikrostrukturphysik,  
Halle, Germany*

**Laszlo B. Kish**

*Department of Electrical Engineering,  
Texas A&M University,  
College Station, Texas, U.S.A.*

**Kenneth Klabunde**

*Department of Chemistry,  
Kansas State University,  
Manhattan, Kansas, U.S.A.*

**James Leckie**

*Department of Civil and Environmental  
Engineering, School of Engineering,  
Stanford University, Stanford,  
California, U.S.A.*

**Charles M. Lieber**

*School of Engineering and Applied Science,  
Harvard University, Cambridge,  
Massachusetts, U.S.A.*

**Chad Mirkin**

*Department of Chemistry,  
Northwestern University,  
Evanston, Illinois, U.S.A.*

**Shuming Nie**

*Department of Biomedical Engineering,  
Emory University School of Medicine,  
Atlanta, Georgia, U.S.A.*

**Jens K. Norskov**

*Department of Physics,  
Technical University of Denmark,  
Lyngby, Denmark*

**Mark Reed**

*Department of Electrical Engineering and  
Applied Physics, Yale University,  
New Haven, Connecticut, U.S.A.*

**David C. Rees**

*Astex Technology Ltd., Cambridge, U.K.*

**Stacey L. Ristinmaa-Sörensen**

*Department of Physics,  
University of Lund,  
Lund, Sweden*

**John A. Rogers**

*Department of Chemistry, University of  
Illinois at Urbana-Champaign,  
Urbana, Illinois, U.S.A.*

**Debra R. Rolinson**

*Advanced Electrochemical Materials,  
Naval Research Laboratory, Washington,  
District of Columbia, U.S.A.*

**Jurgen Ruhe**

*Institute for Microsystem Technology,  
Albert-Ludwig University,  
Freiburg, Germany*

**Purnesh Seegopaul**

*Pangaea Ventures, Jersey City,  
New Jersey, U.S.A.*

**Stu Soled**

*ExxonMobil Research and  
Engineering, Annandale,  
New Jersey, U.S.A.*

**Stephan J. Stranick**

*National Institute of Standards and  
Technology (NIST), Gaithersburg,  
Maryland, U.S.A.*

**Arthur ten Wolde**  
*Confederation of Netherlands  
Industry and Employers VNO-NCW,  
The Hague, The Netherlands*

**Frederick Tepper**  
*Argonide Corp., Sanford, Florida, U.S.A.*

**Gary Tompa**  
*Structured Materials Industries, Inc.,  
Piscataway, New Jersey, U.S.A.*

**Robert Trew**  
*Department of Electrical and Computer  
Engineering, North Carolina*

*State University, Raleigh,  
North Carolina, U.S.A.*

**Etienne F. Vansant**  
*Department of Chemistry, University of  
Antwerp (UIA), Wilrijk, Belgium*

**Younan Xia**  
*Department of Biomedical Engineering,  
Washington University, Saint Louis,  
Missouri, U.S.A.*

**Peidong Yang**  
*Department of Chemistry,  
University of California, Berkeley,  
California, U.S.A.*

# Contributors

- Nehal I. Abu-Lail** / *Department of Chemical Engineering, Worcester Polytechnic Institute, Worcester, Massachusetts, U.S.A.*
- R. Shane Addleman** / *Pacific Northwest National Laboratory, Richland, Washington, U.S.A.*
- Rigoberto C. Advincula** / *Department of Chemistry, University of Alabama at Birmingham, Birmingham, Alabama, U.S.A., and Department of Chemistry, University of Houston, Houston, Texas, U.S.A.*
- Sean R. Agnew** / *Department of Materials Science and Engineering, University of Virginia, Charlottesville, Virginia, U.S.A.*
- J. P. Aimé** / *Centre de Physique Moléculaire Optique et Hertzienne (CPMOH), Université Bordeaux I, Talence, France*
- Brahim Akdim** / *Materials and Manufacturing Directorate, Air Force Research Laboratory, Wright-Patterson Air Force Base, Ohio, U.S.A.*
- Joseph Akkara** / *National Science Foundation, Arlington, Virginia, U.S.A.*
- Tomoyuki Akutagawa** / *Research Institute for Electronic Science, Hokkaido University, Sapporo, Japan*
- Markus Albrecht** / *RWTH-Aachen, Institut für Organische Chemie, Aachen, Germany*
- A. Paul Alivisatos** / *Department of Chemistry, University of California–Berkeley, Berkeley, California, U.S.A.*
- Charles W. Allen** / *Materials Science Division, Argonne National Laboratory, Argonne, Illinois, U.S.A.*
- Tsuneya Ando** / *Department of Physics, Tokyo Institute of Technology, Tokyo, Japan*
- Ronald P. Andres** / *Purdue University, West Lafayette, Indiana, U.S.A.*
- Mikhail A. Anisimov** / *Department of Chemical Engineering and Institute for Physical Science and Technology, University of Maryland, College Park, Maryland, U.S.A.*
- Masakazu Aono** / *Nanomaterials Laboratory, National Institute for Materials Science, Ibaraki, Japan*
- Silvia Ardizzone** / *Department of Physical Chemistry and Electrochemistry, University of Milan, Milan, Italy*
- Eduard Arzt** / *Leibniz-Institut für Neue Materialien (INM), Saarbrücken, Germany*
- Hajime Asahi** / *Institute of Scientific and Industrial Research, Osaka University, Osaka, Japan*
- K. Asakawa** / *Femtosecond Technology Research Association (FESTA), Ibaraki, Japan*
- B. J. Ash** / *Sandia National Laboratories, Albuquerque, New Mexico, U.S.A.*
- Masafumi Ata** / *Materials Laboratories, Sony Corporation, Yokohama, Japan*
- Plamen B. Atanassov** / *Chemical and Nuclear Engineering, University of New Mexico, Albuquerque, New Mexico, U.S.A.*
- Elizabeth K. Auty** / *Department of Chemistry, University of Bristol, Bristol, U.K.*
- Eric Ayars** / *Department of Physics, California State University–Chico, Chico, California, U.S.A.*
- George Bachand** / *Biomolecular Materials and Interfaces, Sandia National Laboratories, Albuquerque, New Mexico, U.S.A.*
- Ganesh Balasubramanian** / *Department of Civil and Environmental Engineering, University of Cincinnati, Cincinnati, Ohio, U.S.A.*
- Kannan Balasubramanian** / *Max Planck Institut für Festkörperforschung, Stuttgart, Germany*



- Anna C. Balazs** / *Department of Chemical Engineering, University of Pittsburgh, Pittsburgh, Pennsylvania, U.S.A.*
- Tommaso Baldacchini** / *Eugene F. Merkert Chemistry Center, Boston College, Chestnut Hill, Massachusetts, U.S.A.*
- Ioan Balint** / *Institute of Physical Chemistry, Romanian Academy, Bucharest, Romania*
- S. Bandyopadhyay** / *Department of Electrical Engineering, Virginia Commonwealth University, Richmond, Virginia, U.S.A.*
- Rajarshi Banerjee** / *Department of Materials Science and Engineering, Ohio State University, Columbus, Ohio, U.S.A.*
- Sarbajit Banerjee** / *Department of Chemistry, State University of New York at Stony Brook, Stony Brook, New York, U.S.A.*
- Paul F. Barbara** / *Department of Chemistry and Biochemistry, University of Texas at Austin, Austin, Texas, U.S.A.*
- Maria C. Bartelt** / *Lawrence Livermore National Laboratory, Livermore, California, U.S.A.*
- Bahar Basim** / *Intel Co., Santa Clara, California, U.S.A.*
- James D. Batteas** / *Surface and Microanalysis Science Division, National Institute of Standards and Technology (NIST), Gaithersburg, Maryland, U.S.A.*
- Jan Becher** / *Department of Chemistry, University of Southern Denmark, Odense, Denmark*
- Paul D. Beer** / *Inorganic Chemistry Laboratory, Department of Chemistry, University of Oxford, Oxford, U.K.*
- Silke Behrens** / *Forschungszentrum Karlsruhe, Institute of Technical Chemistry, Karlsruhe, Germany*
- Elena Bekyarova** / *University of California–Riverside, Riverside, California, U.S.A.*
- G. Benedek** / *Dipartimento di Scienza dei Materiali, Università di Milano Bicocca, Milan, Italy*
- Yaakov Benenson** / *Department of Computer Science and Applied Mathematics, Weizmann Institute of Science, Rehovot, Israel*
- M. Bernasconi** / *Dipartimento di Scienza dei Materiali, Università di Milano Bicocca, Milan, Italy*
- Steven L. Bernasek** / *Department of Chemistry, Princeton University, Princeton, New Jersey, U.S.A.*
- Alexey Bezryadin** / *Department of Physics, University of Illinois at Urbana–Champaign, Urbana, Illinois, U.S.A.*
- Ajay Kumar Bhagi** / *Department of Chemistry, University of Delhi, Delhi, India*
- Dhruba Jyoti Bharali** / *Institute of Laser Photonics and Biophotonics, State University of New York at Buffalo, Buffalo, New York, U.S.A.*
- Claudia L. Bianchi** / *Department of Physical Chemistry and Electrochemistry, University of Milan, Milan, Italy*
- T. A. Birks** / *Department of Physics, University of Bath, Bath, U.K.*
- Jerome C. Birnbaum** / *Pacific Northwest National Laboratory, Richland, Washington, U.S.A.*
- Harvey W. Blanch** / *Department of Chemical Engineering, University of California–Berkeley, Berkeley, California, U.S.A.*
- Alexandre Blumstein** / *Center for Advanced Materials, University of Massachusetts–Lowell, Lowell, Massachusetts, U.S.A.*
- Andrew B. Bocarsly** / *Department of Chemistry, Princeton University, Princeton, New Jersey, U.S.A.*
- Michael R. Bockstaller** / *Massachusetts Institute of Technology, Cambridge, Massachusetts, U.S.A.*
- A. Bogicevic** / *Ford Motor Company, Dearborn, Michigan, U.S.A.*
- R. Boisgard** / *Centre de Physique Moléculaire Optique et Hertzienne (CPMOH), Université Bordeaux I, Talence, France*
- Anthony Bollinger** / *University of Illinois at Urbana–Champaign, Urbana, Illinois, U.S.A.*
- Olga V. Boltalina** / *Chemistry Department, M.V. Lomonosov Moscow State University, Moscow, Russia*
- Mila Boncheva** / *Department of Chemistry and Chemical Biology, Harvard University, Cambridge, Massachusetts, U.S.A.*
- Helmut Bönemann** / *Department of Heterogeneous Catalysis, Max Planck Institut für Kohlenforschung, Mülheim an der Ruhr, Germany*

- Paul Borm** / *Centre of Expertise in Life Sciences, Zuyd University, Heerlen, The Netherlands*
- Rüdiger Bormann** / *Institute of Materials Research, GKSS Research Centre GmbH, Geesthacht, Schleswig-Holstein, Germany*
- Arijit Bose** / *Department of Chemical Engineering, University of Rhode Island, Kingston, Rhode Island, U.S.A.*
- Eduardo J. Bottani** / *Instituto de Investigaciones Fisicoquímicas Teóricas y Aplicadas, La Plata, Argentina*
- Laurent Bouteiller** / *Laboratoire de Chimie Macromoléculaire, Université Pierre et Marie Curie, Paris, France*
- Charles Brands** / *Department of Physics Engineering, Virginia Technical Institute, Blacksburg, Virginia, U.S.A.*
- Paul S. Braterman** / *Department of Chemistry, University of North Texas, Denton, Texas, U.S.A.*
- Roberto J. Brea** / *Department of Organic Chemistry, Universidad de Santiago de Compostela, Santiago de Compostela, Spain*
- Lyudmila M. Bronstein** / *Department of Chemistry, Indiana University, Bloomington, Indiana, U.S.A.*
- E.A. Martijn Brouwer** / *Solid State Physics, University of Twente, Enschede, The Netherlands*
- Ronald C. Brown** / *Department of Chemistry, Mercyhurst College, Erie, Pennsylvania, U.S.A.*
- Scott C. Brown** / *University of Florida, Gainesville, Florida, U.S.A.*
- Nigel D. Browning** / *Department of Chemical Engineering and Materials Science, University of California–Davis, Davis, California, U.S.A.*
- Dmitri A. Bulushev** / *Swiss Federal Institute of Technology, Lausanne, Switzerland*
- Marko Burghard** / *Max Planck Institut für Festkörperforschung, Stuttgart, Germany*
- Daryle H. Busch** / *Department of Chemistry, University of Kansas, Lawrence, Kansas, U.S.A.*
- Harshala Butala** / *Department of Chemical Engineering, University of Mississippi, University, Mississippi, U.S.A.*
- Gavin A. Buxton** / *Department of Chemical Engineering, University of Pittsburgh, Pittsburgh, Pennsylvania, U.S.A.*
- Scott Buzby** / *Department of Materials Science and Engineering, University of Delaware, Newark, Delaware, U.S.A.*
- Mark E. Byrne** / *Department of Chemical Engineering, Auburn University, Auburn, Alabama, U.S.A.*
- Valérie Cabuil** / *Université Pierre et Marie Curie, Paris, France*
- Tahir Cader** / *Isothermal Systems Research, Clarkston, Washington, U.S.A.*
- Nathaniel Cady** / *College of Nanoscale Science and Engineering, State University of New York at Albany, Albany, New York, U.S.A.*
- Yuguang Cai** / *Department of Chemistry, Princeton University, Princeton, New Jersey, U.S.A.*
- Terri A. Camesano** / *Department of Chemical Engineering, Worcester Polytechnic Institute, Worcester, Massachusetts, U.S.A.*
- Giuseppe Cappelletti** / *Department of Physical Chemistry and Electrochemistry, University of Milan, Milan, Italy*
- Autumn T. Carlsen** / *College of Nanoscale Science and Engineering, State University of New York at Albany, Albany, New York, U.S.A.*
- Efraín Carreño-Morelli** / *Design and Materials Unit, University of Applied Sciences of Western Switzerland, Sion, Switzerland*
- Andrew D.W. Carswell** / *Department of Chemical Engineering and Materials Science, University of Oklahoma, Norman, Oklahoma, U.S.A.*
- Alessandro Casnati** / *Dipartimento di Chimica Organica e Industriale, Università di Parma, Parma, Italy*
- Mehmet S. Celik** / *Mineral and Coal Processing Section, Istanbul Technical University, Istanbul, Turkey*
- Gianfranco Cerofolini** / *Post-Silicon Technology, STMicroelectronics, Agrate Brianza, Italy, and Department of Materials Science, University of Milano–Bicocca, Milan, Italy*
- Neil R. Champness** / *School of Chemistry, University of Nottingham, Nottingham, U.K.*

- Selena Chan** / *The Center for Future Health, University of Rochester, Rochester, New York, U.S.A.*
- Christophe Chassenieux** / *Laboratoire de Physico-Chimie Macromoléculaire, Université Pierre et Marie Curie, Paris, France*
- James R. Chelikowsky** / *Chemical Engineering and Materials Science, University of Minnesota, Minneapolis, Minnesota, U.S.A.*
- Bin Chen** / *National Aeronautics and Space Administration (NASA), Moffett Field, California, U.S.A.*
- Chenggang Chen** / *Nonmetallic Division, University of Dayton Research Institute, Dayton, Ohio, U.S.A.*
- Zhan Chen** / *Department of Chemistry, University of Michigan, Ann Arbor, Michigan, U.S.A.*
- W.C.D. Cheong** / *Materials Science and Characterisation Laboratory, Institute of Materials Research and Engineering, Singapore, Singapore*
- Lifeng Chi** / *Department of Physics, Westfälische Wilhelms-Universität Münster, Münster, Germany*
- Russell R. Chianelli** / *Chemistry Department, University of Texas at El Paso, El Paso, Texas, U.S.A.*
- Po-Wen Chiu** / *Max Planck Institut für Festkörperforschung, Stuttgart, Germany*
- Jeong-Min Cho** / *Materials Science and Engineering Department, University of Florida, Gainesville, Florida, U.S.A.*
- Seung Il Cho** / *Department of Chemistry and Biochemistry, University of Maryland, College Park, Maryland, U.S.A.*
- Kwang-Min Choi** / *Department of Chemical Science and Engineering, Osaka University, Osaka, Japan*
- Thomas Clifford** / *Department of Chemistry, University of Kansas, Lawrence, Kansas, U.S.A.*
- Luise S. Couchman** / *Naval Research Laboratory, Washington, District of Columbia, U.S.A.*
- Christophe Coudret** / *Centre d'Elaboration de Matériaux et d'Etudes Structurales (CEMES), Centre National de la Recherche Scientifique (CNRS), Toulouse, France*
- G. Couturier** / *Centre de Physique Moléculaire Optique et Hertzienne (CPMOH), Université Bordeaux I, Talence, France*
- Alexander Couzis** / *Department of Chemical Engineering, City College of City University of New York, New York, New York, U.S.A.*
- Mercedes Crego-Calama** / *Laboratory of Supramolecular Chemistry and Technology, University of Twente, Enschede, The Netherlands*
- Brian M. Cullum** / *Department of Chemistry and Biochemistry, University of Maryland, Baltimore County, Baltimore, Maryland, U.S.A.*
- Peter T. Cummings** / *Department of Chemical Engineering, Vanderbilt University, Nashville, Tennessee, U.S.A., and Chemical Sciences Division, Oak Ridge National Laboratory, Oak Ridge, Tennessee, U.S.A.*
- Joan E. Curry** / *Department of Soil, Water and Environmental Science, University of Arizona, Tucson, Arizona, U.S.A.*
- Lars Dähne** / *Capsulation Nanoscience AG, Berlin, Germany*
- Sheng Dai** / *Chemical Sciences Division, Oak Ridge National Laboratory, Oak Ridge, Tennessee, U.S.A.*
- Enrico Dalcanele** / *Dipartimento di Chimica Organica e Industriale, Università di Parma, Parma, Italy*
- Jayanta Das** / *FG Physikalische Metallkunde, Technische Universität Darmstadt, Darmstadt, Germany*
- Anthony P. Davis** / *Department of Chemistry, University of Bristol, Bristol, U.K.*
- Jason J. Davis** / *Inorganic Chemistry Laboratory, Department of Chemistry, University of Oxford, Oxford, U.K.*
- Richey M. Davis** / *Department of Chemical Engineering, Virginia Technical Institute, Blacksburg, Virginia, U.S.A.*
- Robert J. Davis** / *Department of Chemical Engineering, University of Virginia, Charlottesville, Virginia, U.S.A.*
- A. Prasanna de Silva** / *School of Chemistry, Queen's University, Belfast, Northern Ireland*
- James J. De Yoreo** / *Lawrence Livermore National Laboratory, Livermore, California, U.S.A.*
- Thomas F. Degnan, Jr.** / *Research Laboratory, ExxonMobil Research and Engineering Company, Annandale, New Jersey, U.S.A.*

- Aránzazu del Campo** / *Max-Planck-Institut für Metallforschung, Stuttgart, Germany, and Functional Surfaces, Leibniz-Institut für Neue Materialien (INM), Saarbrücken, Germany*
- Thierry Delair** / *CNRS-bioMérieux, École Normale Supérieure de Lyon, Lyon, France*
- F. Delogu** / *Department of Chemical Engineering and Materials, University of Cagliari, Cagliari, Italy*
- Linette M. Demers** / *NanoInk Inc., Chicago, Illinois, U.S.A.*
- Pedro A. Derosa** / *Department of Electrical Engineering, University of South Carolina, Columbia, South Carolina, U.S.A.*
- Roland Dersch** / *Philipps-Universität Marburg, Marburg, Germany*
- Stephan Diekmann** / *Abteilung Molekularbiologie, Institut für Molekulare Biotechnologie, Jena, Germany*
- João C. Diniz da Costa** / *Nanomaterials Centre, School of Engineering, University of Queensland, Brisbane, Queensland, Australia*
- Dionysios D. Dionysiou** / *Department of Civil and Environmental Engineering, University of Cincinnati, Cincinnati, Ohio, U.S.A.*
- Mark M. Disko** / *Corporate Strategic Research, ExxonMobil Research and Engineering, Annandale, New Jersey, U.S.A.*
- Sukanta Dolai** / *City University of New York, New York, New York, U.S.A.*
- Ken Donaldson** / *Queens Medical Research Institute, University of Edinburgh, Edinburgh, Midlothian, U.K.*
- Stephen K. Doorn** / *Chemistry Division, Los Alamos National Laboratory, Los Alamos, New Mexico, U.S.A.*
- Bogdan Dragnea** / *Department of Chemistry, Indiana University, Bloomington, Indiana, U.S.A.*
- Charles Michael Drain** / *Department of Chemistry and Biochemistry, Hunter College, City University of New York, and Rockefeller University, New York, New York, U.S.A.*
- Jaroslav Drelich** / *Department of Metallurgical and Materials Engineering, Michigan Technological University, Houghton, Michigan, U.S.A.*
- G. Dresselhaus** / *Francis Bitter Magnet Laboratory, Massachusetts Institute of Technology, Cambridge, Massachusetts, U.S.A.*
- Mildred S. Dresselhaus** / *Department of Electrical Engineering and Computer Science, Massachusetts Institute of Technology, Cambridge, Massachusetts, U.S.A.*
- Xiangfeng Duan** / *Advanced Research Center, Nanosys Inc., Palo Alto, California, U.S.A.*
- Xiaofeng F. Duan** / *Materials and Manufacturing Directorate, Air Force Research Laboratory, Wright-Patterson Air Force Base, Ohio, U.S.A.*
- Geraud Dubois** / *IBM Almaden Research Center, San Jose, California, U.S.A.*
- Yves F. Dufrêne** / *Unite de Chimie des Interface, Université catholique de Louvain, Louvain-la-Neuve, Belgium*
- Etienne Duguet** / *Institut de Chimie de la Matière Condensée de Bordeaux, CNRS, Pessac Cedex, France*
- Kathleen A. Dunn** / *College of Nanoscale Science and Engineering, State University of New York at Albany, Albany, New York, U.S.A.*
- R. D. Dupuis** / *Microelectronics Research Center, University of Texas at Austin, Austin, Texas, U.S.A.*
- Anne-Sophie Duwez** / *Research Center in Micro and Nanoscopic Materials and Electronic Devices (CERMIN), Université catholique de Louvain, Louvain-la-Neuve, Belgium*
- Kohki Ebitani** / *Department of Chemical Science and Engineering, Osaka University, Osaka, Japan*
- Jürgen Eckert** / *FG Physikalische Metallkunde, Technische Universität Darmstadt, Darmstadt, Germany*
- A. Eitan** / *Department of Materials Science and Engineering, Rensselaer Polytechnic Institute, Troy, New York, U.S.A.*
- Jeremiah Ejirofor** / *Department of Biomedical Engineering, Purdue University, West Lafayette, Indiana, U.S.A.*
- Vladimir I. Elokhin** / *Boreskov Institute of Catalysis, Novosibirsk, Russia*

- Todd Emrick** / *Department of Polymer Science and Engineering, University of Massachusetts, Amherst, Massachusetts, U.S.A.*
- Morinobu Endo** / *Shinshu University, Nagano, Japan*
- Douglas S. English** / *Department of Chemistry and Biochemistry, University of Maryland, College Park, Maryland, U.S.A.*
- Jonah Erlebacher** / *Department of Materials Science and Engineering, Johns Hopkins University, Baltimore, Maryland, U.S.A.*
- Bahri Ersoy** / *Iscehisar Vocational School, Afyon Kocatepe University, Afyon, Turkey*
- Lars-Oliver Essen** / *Department of Chemistry, Philipps University, Marburg, Germany*
- Louise S. Evans** / *School of Chemistry, University of Southampton, Southampton, U.K.*
- Jeffrey D. Evanseck** / *Center for Computational Sciences and Department of Chemistry and Biochemistry, Duquesne University, Pittsburgh, Pennsylvania, U.S.A.*
- Andrew G. Ewing** / *Department of Chemistry, Pennsylvania State University, University Park, Pennsylvania, U.S.A.*
- Rodney C. Ewing** / *Departments of Geological Sciences, Material Science and Engineering, and Nuclear Engineering and Radiological Science, University of Michigan, Ann Arbor, Michigan, U.S.A.*
- D. Howard Fairbrother** / *Johns Hopkins University, Baltimore, Maryland, U.S.A.*
- Xiaowu Fan** / *Department of Chemistry, University of Alabama at Birmingham, Birmingham, Alabama, U.S.A.*
- Jiyu Fang** / *Advanced Materials Processing and Analysis Center, University of Central Florida, Orlando, Florida, U.S.A.*
- Zhigang Zak Fang** / *Department of Metallurgical Engineering, University of Utah, Salt Lake City, Utah, U.S.A.*
- Tarek R. Farhat** / *Department of Chemical Engineering, Massachusetts Institute of Technology, Cambridge, Massachusetts, U.S.A.*
- Philippe M. Fauchet** / *Department of Electrical and Computer Engineering, University of Rochester, Rochester, New York, U.S.A.*
- H.-J. Fecht** / *Materials Division, University of Ulm, Ulm, Germany*
- X. Feng** / *Ferro Corporation, Independence, Ohio, U.S.A.*
- Ben L. Feringa** / *Department of Organic and Molecular Inorganic Chemistry, University of Groningen, Groningen, The Netherlands*
- Shaun F. Filocamo** / *Department of Chemistry, Duke University, Durham, North Carolina, U.S.A.*
- Paul D.I. Fletcher** / *Department of Chemistry, University of Hull, Hull, U.K.*
- Robert E. Fontana, Jr.** / *Research Staff Member, IBM Almaden Research Center, San Jose, California, U.S.A.*
- Christy Ford** / *Chemistry Department, Tulane University, New Orleans, Louisiana, U.S.A.*
- John T. Fourkas** / *Eugene F. Merkert Chemistry Center, Boston College, Chestnut Hill, Massachusetts, U.S.A.*
- Elzbieta Frackowiak** / *Institute of Chemistry and Technical Electrochemistry, Poznan University of Technology, Poznan, Poland*
- Thomas Franklin** / *Department of Electrical Engineering and Computer Science, Massachusetts Institute of Technology, Cambridge, Massachusetts, U.S.A.*
- Hamish L. Fraser** / *Department of Materials Science and Engineering, Ohio State University, Columbus, Ohio, U.S.A.*
- Wolfgang Fritzsche** / *Department of Biotechnical Microsystems, Institute for Physical High Technology (IPHT), Jena, Germany*
- Glen E. Fryxell** / *Pacific Northwest National Laboratory, Richland, Washington, U.S.A.*
- Jürgen-Hinrich Fuhrhop** / *Institut für Organische Chemie, Freie Universität Berlin, Berlin, Germany*
- T. A. Fulton** / *Bell Laboratories, Lucent Technologies, Murray Hill, New Jersey, U.S.A.*
- Kunio Furusawa** / *Department of Chemistry, University of Tsukuba, Ibaraki, Japan*
- Charles-André Fustin** / *Max Planck Institute for Polymer Research, Mainz, Germany*

- Anand Gadre** / *College of Nanoscale Science and Engineering, State University of New York at Albany, Albany, New York, U.S.A.*
- Aurelian C. Gálca** / *University of Twente, Enschede, The Netherlands*
- Philip A. Gale** / *School of Chemistry, University of Southampton, Southampton, U.K.*
- Nidia C. Gallego** / *Carbon Materials Technology Group, Materials Science and Technology Division, Oak Ridge National Laboratory, Oak Ridge, Tennessee, U.S.A.*
- Giulia Galli** / *Lawrence Livermore National Laboratory, Livermore, California, U.S.A.*
- Ignacio L. Garzón** / *Instituto de Física, Universidad Nacional Autónoma de México, Mexico City, Mexico*
- J. Gaudioso** / *Sandia National Laboratories, Albuquerque, New Mexico, U.S.A.*
- Andrew J. Gellman** / *Department of Chemical Engineering, Carnegie Mellon University, Pittsburgh, Pennsylvania, U.S.A.*
- Andre J. Gesquiere** / *Nanoscience Technology Center and Department of Chemistry, University of Central Florida, Orlando, Florida, U.S.A.*
- Bruce C. Gibb** / *Department of Chemistry, University of New Orleans, New Orleans, Louisiana, U.S.A.*
- Jeffrey C. Gibeling** / *Department of Chemical Engineering and Materials Science, University of California–Davis, Davis, California, U.S.A.*
- Harry W. Gibson** / *Department of Physics Engineering, Virginia Technical Institute, Blacksburg, Virginia, U.S.A.*
- M. Lane Gilchrist** / *New York Center for Biomedical Engineering, City College of New York, New York, New York, U.S.A.*
- David S. Ginley** / *National Renewable Energy Laboratory (NREL), Golden, Colorado, U.S.A.*
- Anit Giri** / *Nanomats, Inc., North Huntingdon, Pennsylvania, U.S.A.*
- Michael Gleiche** / *Physikalisches Institut, Westfälische Wilhelms-Universität Münster, Münster, Germany*
- William A. Goddard III** / *Department of Chemistry, California Institute of Technology, Pasadena, California, U.S.A.*
- George W. Gokel** / *Departments of Molecular Biology and Pharmacology and Chemistry, Washington University School of Medicine, St. Louis, Missouri, U.S.A.*
- Shun-ichi Gonda** / *Fukui University of Technology, Fukui, Japan*
- D. Wayne Goodman** / *Department of Chemistry, Texas A&M University, College Station, Texas, U.S.A.*
- Lionel Goodman** / *Department of Chemistry, Rutgers University, New Brunswick, New Jersey, U.S.A.*
- Brian P. Grady** / *University of Oklahoma, Norman, Oklahoma, U.S.A.*
- Juan R. Granja** / *Department of Organic Chemistry, Universidad de Santiago de Compostela, Santiago de Compostela, Spain*
- Christine S. Grant** / *Chemical Engineering Department, North Carolina State University, Raleigh, North Carolina, U.S.A.*
- Vicki H. Grassian** / *Department of Chemistry, University of Iowa, Iowa City, Iowa, U.S.A.*
- Jay W. Grate** / *Pacific Northwest National Laboratory, Richland, Washington, U.S.A.*
- Elias Greenbaum** / *Chemical Sciences Division, Oak Ridge National Laboratory, Oak Ridge, Tennessee, U.S.A., and Center for Environmental Biotechnology, Graduate School of Genome Science and Technology, University of Tennessee, Knoxville, Tennessee, U.S.A.*
- Andreas Greiner** / *Philipps–Universität Marburg, Marburg, Germany*
- Mark W. Grinstaff** / *Departments of Chemistry and Biomedical Engineering, Boston University, Boston, Massachusetts, U.S.A.*
- Edward Grochowski** / *IBM Almaden Research Center, San Jose, California, U.S.A.*
- Gwen M. Gross** / *Department of Chemistry, University of Washington, Seattle, Washington, U.S.A.*
- Joanna R. Groza** / *Department of Chemical Engineering and Materials Science, University of California–Davis, Davis, California, U.S.A.*
- Dirk M. Guldi** / *Radiation Laboratory, University of Notre Dame, Notre Dame, Indiana, U.S.A.*

- Jianchang Guo** / *Department of Chemistry, Emory University, Atlanta, Georgia, U.S.A.*
- Vinay K. Gupta** / *Department of Chemical Engineering, University of Illinois at Urbana–Champaign, Urbana, Illinois, U.S.A.*
- Alexandr I. Gusev** / *Institute of Solid State Chemistry, Ural Division, Russian Academy of Sciences, Yekaterinburg, Russia*
- Matthew Guzy** / *Department of Chemical Engineering, Virginia Technical Institute, Blacksburg, Virginia, U.S.A.*
- Kwon-Soo Ha** / *Department of Molecular and Cellular Biochemistry, Kangwon National University School of Medicine, Chunchon, South Korea*
- Robert C. Haddon** / *Center for Nanoscale Science and Engineering, University of California–Riverside, Riverside, California, U.S.A.*
- Hamidou Haidara** / *Institut de Chimie des Surfaces et Interfaces-ICSI-CNRS, Mulhouse, France*
- Wolfgang Haiss** / *Department of Chemistry, University of Liverpool, Liverpool, U.K.*
- Kimberly Hamad-Schifferli** / *Department of Mechanical Engineering and Division of Biological Engineering, Massachusetts Institute of Technology, Cambridge, Massachusetts, U.S.A.*
- Bing Q. Han** / *Department of Chemical Engineering and Materials Science, University of California–Davis, Davis, California, U.S.A.*
- Jingmin Han** / *Department of Mechanical Engineering, University of Alberta, Edmonton, Alberta, Canada*
- Encai Hao** / *Department of Chemistry, Northwestern University, Evanston, Illinois, U.S.A.*
- Atsushi Harada** / *Department of Applied Chemistry, Graduate School of Engineering, Osaka Prefecture University, Osaka, Japan*
- J. W. Harrell** / *Department of Physics and Astronomy, University of Alabama, Tuscaloosa, Alabama, U.S.A.*
- Stephen J. Haswell** / *Department of Chemistry, University of Hull, Hull, U.K.*
- Bryan C. Hathorn** / *Division of Computer Science and Mathematics, Oak Ridge National Laboratory, Oak Ridge, Tennessee, U.S.A.*
- Takuya Hayashi** / *Shinshu University, Nagano, Japan*
- Jibao He** / *Chemistry Department, Tulane University, New Orleans, Louisiana, U.S.A.*
- J. R. Heflin** / *Department of Physics Engineering, Virginia Technical Institute, Blacksburg, Virginia, U.S.A.*
- James M. Helt** / *Graduate Center, City University of New York, New York, New York, U.S.A.*
- Joshua A. Henry** / *Department of Chemistry, Cornell University, Ithaca, New York, U.S.A.*
- Hans-Peter Hentze** / *Department of Chemical Engineering, University of Delaware, Newark, Delaware, U.S.A.*
- Henry Hess** / *Department of Bioengineering, University of Washington, Seattle, Washington, U.S.A.*
- Daniel A. Higgins** / *Department of Chemistry, Kansas State University, Manhattan, Kansas, U.S.A.*
- Alexander Hillisch** / *Structural Bioinformatics and Drug Design, EnTec GmbH, Jena, Germany*
- J. Zachary Hilt** / *Department of Chemical and Materials Engineering, University of Kentucky, Lexington, Kentucky, U.S.A.*
- Melissa A. Hines** / *Department of Chemistry, Cornell University, Ithaca, New York, U.S.A.*
- Satoshi Hirose** / *Research and Development Division, Sumitomo Special Metals Company, Ltd., Osaka, Japan*
- Andreas Hirsch** / *Institut für Organische Chemie, Universität Erlangen-Nürnberg, Erlangen, Germany*
- Richard G. Hoagland** / *Materials Science and Technology Division, Los Alamos National Laboratory, Los Alamos, New Mexico, U.S.A.*
- Eric M.V. Hoek** / *Department of Chemical and Environmental Engineering, University of California–Riverside, Riverside, California, U.S.A.*
- Peter M. Hoffmann** / *Department of Physics, Wayne State University, Detroit, Michigan, U.S.A.*
- J. Hone** / *Department of Mechanical Engineering, Columbia University, New York, New York, U.S.A.*

- Louisa J. Hope-Weeks** / *Chemistry and Chemical Engineering Directorate, Lawrence Livermore National Laboratory, Livermore, California, U.S.A.*
- David Hopkins** / *University of Illinois at Urbana–Champaign, Urbana, Illinois, U.S.A.*
- Scott R. Horner** / *Department of Biochemistry and Biophysics, University of Rochester, Rochester, New York, U.S.A.*
- Yanwen Hou** / *Kansas State University, Manhattan, Kansas, U.S.A.*
- Hui Hu** / *University of California–Riverside, Riverside, California, U.S.A.*
- Zhibing Hu** / *Departments of Physics and Chemistry, University of North Texas, Denton, Texas, U.S.A.*
- Yu Huang** / *Massachusetts Institute of Technology, Cambridge, Massachusetts, U.S.A.*
- Yu-Wen Huang** / *Department of Chemical Engineering, University of Illinois at Urbana–Champaign, Urbana, Illinois, U.S.A.*
- Dale L. Huber** / *Nanostructures and Advanced Materials Chemistry Department, Sandia National Laboratories, Albuquerque, New Mexico, U.S.A.*
- Mark Hughes** / *Department of Materials Science and Metallurgy, University of Cambridge, Cambridge, U.K.*
- Deborah E. Hunka** / *Sandia National Laboratories, Albuquerque, New Mexico, U.S.A.*
- Ho Jung Hwang** / *Institute of Technology and Science, Chung-Ang University, Seoul, South Korea*
- Akihisa Inoue** / *Institute for Materials Research, Tohoku University, Sendai, Japan*
- Yasushi Inouye** / *Osaka University, Osaka, Japan*
- Stephan Irlle** / *Department of Chemistry, Emory University, Atlanta, Georgia, U.S.A.*
- Kelvin Isaacson** / *Department of Mechanical Engineering, University of Alberta, Edmonton, Alberta, Canada*
- Toshihiro Ishikawa** / *Functional Materials Research Department, Ube Research Laboratory, Yamaguchi, Japan*
- Hiroyuki Isobe** / *Department of Chemistry, University of Tokyo, Tokyo, Japan*
- Mikhail E. Itkis** / *University of California–Riverside, Riverside, California, U.S.A.*
- Takashi Ito** / *Akiruno Technology Center, Fujitsu Ltd., Tokyo, Japan*
- Kenji Iwahori** / *CREST, Japan Science and Technology Agency (JST), Kawaguchi, Japan*
- Heinrich M. Jaeger** / *Department of Physics, University of Chicago, Chicago, Illinois, U.S.A.*
- Dustin K. James** / *Chemistry Department, Rice University, Houston, Texas, U.S.A.*
- David B. Janes** / *School of Electrical and Computer Engineering, Purdue University, West Lafayette, Indiana, U.S.A.*
- Andrés Jaramillo-Botero** / *School of Engineering, Pontificia Universidad Javeriana, Cali, Colombia*
- Anna Jawor** / *Department of Chemical and Environmental Engineering, University of California–Riverside, Riverside, California, U.S.A.*
- Karthik Jayaraman** / *Department of Chemistry and Biochemistry, University of Maryland, College Park, Maryland, U.S.A.*
- Andreas Jentys** / *Institut für Technische Chemie, Technische Universität München, Garching, Germany*
- Z. Q. Jin** / *Department of Physics, University of Texas at Arlington, Arlington, Texas, U.S.A.*
- Christian Joachim** / *Centre d'Elaboration de Matériaux et d'Etudes Structurales (CEMES), Centre National de la Recherche Scientifique (CNRS), Toulouse, France*
- Vijay T. John** / *Chemistry Department, Tulane University, New Orleans, Louisiana, U.S.A.*
- Katrina A. Jolliffe** / *Department of Chemistry, University of Sydney, Sydney, New South Wales, Australia*
- Ulrich Jonas** / *Max Planck Institute for Polymer Research, Mainz, Germany*
- Clinton D. Jones** / *School of Chemistry and Biochemistry, Georgia Institute of Technology, Atlanta, Georgia, U.S.A.*
- A. Jorio** / *Departamento de Física, Universidade Federal de Minas Gerais, Belo Horizonte, Brazil*
- Leonid Kaledin** / *Argonide Corporation, Sanford, Florida, U.S.A.*



- Alain E. Kaloyeros** / *College of Nanoscale Science and Engineering, State University of New York at Albany, Albany, New York, U.S.A.*
- Toshiya Kamikado** / *Communications Research Laboratory, Kobe, Japan*
- Kiyotomi Kaneda** / *Department of Chemical Science and Engineering, Osaka University, Osaka, Japan*
- Jeong Won Kang** / *Computational Semiconductor Laboratory, Chung-Ang University, Seoul, South Korea*
- David Kaplan** / *Chemical Engineering Department, Tufts University, Medford, Massachusetts, U.S.A.*
- Ifat Kaplan-Ashiri** / *Materials and Interfaces Department, Weizmann Institute of Science, Rehovot, Israel*
- Pramesh N. Kapoor** / *Department of Chemistry, University of Delhi, Delhi, India*
- Kazunori Kataoka** / *Department of Materials Science, Department of Materials Engineering, Tokyo, Japan*
- Hiromichi Kataura** / *Department of Physics, Tokyo Metropolitan University, Tokyo, Japan*
- Satoshi Kawata** / *Department of Applied Physics, Osaka University, Osaka, Japan*
- Mark A. Keane** / *Department of Chemistry and Materials Engineering, University of Kentucky, Lexington, Kentucky, U.S.A.*
- Christine D. Keating** / *Department of Chemistry, Pennsylvania State University, University Park, Pennsylvania, U.S.A.*
- Klaus Kern** / *Max Planck Institut für Festkörperforschung, Stuttgart, Germany*
- Miklos Kertesz** / *Department of Chemistry, Georgetown University, Washington, District of Columbia, U.S.A.*
- Abbas Khaleel** / *Department of Chemistry, United Arab Emirates University, Al-Ain, United Arab Emirates*
- Aleksandr Khitun** / *Electrical Engineering Department, University of California–Los Angeles, Los Angeles, California, U.S.A.*
- Sakhrat Khizroev** / *Electrical and Computer Engineering, Florida International University, Miami, Florida, U.S.A.*
- David T. Kim** / *Department of Chemical Engineering, University of California–Berkeley, Berkeley, California, U.S.A.*
- Dong Wook Kim** / *Advanced Materials Division, Korea Research Institute of Chemical Technology, Taejeon, South Korea*
- Ho-Cheol Kim** / *IBM Almaden Research Center, San Jose, California, U.S.A.*
- Jungbae Kim** / *Pacific Northwest National Laboratory, Richland, Washington, U.S.A.*
- Ki Buem Kim** / *FG Physikalische Metallkunde, Technische Universität Darmstadt, Darmstadt, Germany*
- Kwang S. Kim** / *Department of Chemistry, Pohang University of Science and Technology, Pohang, South Korea*
- Sungsoo Kim** / *Department of Chemical and Biomolecular Engineering, University of Illinois at Urbana–Champaign, Champaign, Illinois, U.S.A.*
- Yoong Ahm Kim** / *Shinshu University, Nagano, Japan*
- R. Allen Kimel** / *Materials Science and Engineering Department, Pennsylvania State University, University Park, Pennsylvania, U.S.A.*
- Laszlo B. Kish** / *Department of Electrical Engineering, Texas A&M University, College Station, Texas, U.S.A.*
- Kenneth J. Klabunde** / *Department of Chemistry, Kansas State University, Manhattan, Kansas, U.S.A.*
- Jennifer E. Klare** / *Lawrence Livermore National Laboratory, Livermore, California, U.S.A.*
- Paul G. Klemens** / *Department of Physics, University of Connecticut, Storrs, Connecticut, U.S.A.*
- Robert F. Klie** / *Brookhaven National Laboratory, Upton, New York, U.S.A.*
- J. C. Knight** / *Department of Physics, University of Bath, Bath, U.K.*

- Spomenka Kobe** / *Department for Nanostructured Materials, Jožef Stefan Institute, Ljubljana, Slovenia*
- Carl C. Koch** / *Department of Materials Science and Engineering, North Carolina State University, Raleigh, North Carolina, U.S.A.*
- Andraž Kocjan** / *Department for Nanostructured Materials, Jožef Stefan Institute, Ljubljana, Slovenia*
- Kenichiro Koga** / *Department of Chemistry, Okayama University, Okayama, Japan*
- Punit Kohli** / *Department of Chemistry, University of Florida, Gainesville, Florida, U.S.A.*
- S. Kohmoto** / *Femtosecond Technology Research Association (FESTA), Ibaraki, Japan*
- Toshihiro Kondo** / *Hokkaido University, Sapporo, Japan*
- E. Stefan Kooij** / *Faculty of Science and Technology, Department of Solid State Physics, University of Twente, Enschede, The Netherlands*
- Nicholas A. Kotov** / *Department of Chemical Engineering, University of Michigan, Ann Arbor, Michigan, U.S.A.*
- Vladimír Král** / *Department of Analytical Chemistry, Institute of Chemical Technology, Prague, Czech Republic*
- Xiomara C. Kretschmer** / *Department of Geological Sciences, University of Texas at El Paso, El Paso, Texas, U.S.A.*
- Ilna Kretschmar** / *Department of Electrical Engineering, Yale University, New Haven, Connecticut, U.S.A.*
- Arthur Jerome Kropf** / *Argonne National Laboratory, Argonne, Illinois, U.S.A.*
- Bon-Cheol Ku** / *Department of Chemistry, University of Massachusetts–Lowell, Lowell, Massachusetts, U.S.A.*
- Clifford P. Kubiak** / *Department of Chemistry, University of California–San Diego, La Jolla, California, U.S.A.*
- Debasish Kuila** / *Department of Chemistry, Louisiana Tech University, Ruston, Louisiana, U.S.A.*
- G. U. Kulkarni** / *Chemistry and Physics of Materials Unit, Jawaharlal Nehru Center for Advanced Scientific Research, Bangalore, India*
- Jayant Kumar** / *Department of Physics, University of Massachusetts–Lowell, Lowell, Massachusetts, U.S.A.*
- Nitin Kumar** / *Institute of Soldier Nanotechnology, Massachusetts Institute of Technology, Cambridge, Massachusetts, U.S.A.*
- Daniel Y. Kwok** / *Department of Mechanical Engineering, University of Alberta, Edmonton, Alberta, Canada*
- Soon-Bark Kwon** / *Department of Environmental Science and Engineering, Kwangju Institute of Science and Technology, Gwangju, South Korea*
- Dominique Larcher** / *Chemistry, Université de Picardie–Jules Verne, Amiens, France*
- Sarah C. Larsen** / *Department of Chemistry, University of Iowa, Iowa City, Iowa, U.S.A.*
- Jean-Pierre Launay** / *Centre d'Elaboration de Matériaux et d'Etudes Structurales (CEMES), Centre National de la Recherche Scientifique (CNRS), Toulouse, France*
- Enrique J. Lavernia** / *Department of Chemical Engineering and Materials Science, University of California–Davis, Davis, California, U.S.A.*
- Valentina Lazarescu** / *I.G. Murgulescu Institute of Physical Chemistry, Bucharest, Romania*
- Nikolai N. Ledentsov** / *Institut für Festkörperphysik, Technische Universität Berlin, Berlin, Germany*
- Haiwon Lee** / *Department of Chemistry, Hanyang University, Seoul, South Korea*
- Han Myoung Lee** / *Department of Chemistry, Pohang University of Science and Technology, Pohang, South Korea*
- Ken Won Lee** / *Department of Environmental Science and Engineering, Kwangju Institute of Science and Technology, Gwangju, South Korea*
- Sang Bok Lee** / *Department of Chemistry and Biochemistry, University of Maryland, College Park, Maryland, U.S.A.*
- Seunghyun Lee** / *Department of Chemistry, Hanyang University, Seoul, South Korea*

- Young Jong Lee** / *Polymers Division, National Institute of Standards and Technology (NIST), Gaithersburg, Maryland, U.S.A.*
- Graham J. Leggett** / *Department of Chemistry, University of Sheffield, Sheffield, S. Yorkshire, U.K.*
- Zoltán Lenčič** / *Institute of Inorganic Chemistry, Slovak Academy of Sciences, Bratislava, Slovakia*
- Steven Lenhert** / *Physikalisches Institut, Westfälische Wilhelms-Universität Münster, Münster, Germany*
- Kam W. Leong** / *Department of Biomedical Engineering, Johns Hopkins University School of Medicine, Baltimore, Maryland, U.S.A.*
- Johannes A. Lercher** / *Institut für Technische Chemie, Technische Universität München, Garching, Germany*
- Marat I. Lerner** / *Design Technology Center, Russian Academy of Sciences, Tomsk, Russia*
- Rastislav Levicky** / *Department of Chemical Engineering, Columbia University, New York, New York, U.S.A.*
- Guangtao Li** / *Institut für Organische Chemie, Freie Universität Berlin, Berlin, Germany*
- Liang-shi Li** / *Department of Chemistry, University of California–Berkeley, Berkeley, California, U.S.A.*
- Tianquan Lian** / *Department of Chemistry, Emory University, Atlanta, Georgia, U.S.A.*
- Chengdu Liang** / *Oak Ridge National Laboratory, Oak Ridge, Tennessee, U.S.A.*
- Xuemei Liang** / *Department of Chemical Engineering and Materials Science, Wayne State University, Detroit, Michigan, U.S.A.*
- Charles M. Lieber** / *Department of Chemistry and Chemical Biology, Harvard University, Cambridge, Massachusetts, U.S.A.*
- Yeshayahu Lifshitz** / *Center of Super-Diamond and Advanced Films, City University of Hong Kong, Hong Kong, China, and Soreq Nuclear Research Center, Yavne, Israel*
- Peter T. Lillehei** / *Langley Research Center, National Aeronautics and Space Administration (NASA), Hampton, Virginia, U.S.A.*
- Chwee Teck Lim** / *Division of Bioengineering and Department of Mechanical Engineering, National University of Singapore, Singapore, Singapore*
- Xiao-Min Lin** / *Material Science Division, Chemistry Division and Center for Nanoscale Materials, Argonne National Laboratory, Argonne, Illinois, U.S.A.*
- Yuehe Lin** / *Pacific Northwest National Laboratory, Richland, Washington, U.S.A.*
- Jeffrey A. Lindeman** / *Nixon Peabody LLP, Washington, District of Columbia, U.S.A.*
- Leonard F. Lindoy** / *Department of Chemistry, University of Sydney, Sydney, New South Wales, Australia*
- Dmitri Litvinov** / *Center for Nanomagnetic Systems, University of Houston, Houston, Texas, U.S.A.*
- Hongjie Liu** / *Department of Chemical Engineering, City College of New York, New York, New York, U.S.A.*
- J. Liu** / *Sandia National Laboratory, Albuquerque, New Mexico, U.S.A.*
- Jian Liu** / *Department of Chemistry, Michigan Technological University, Houghton, Michigan, U.S.A.*
- Jianlin Liu** / *Department of Electrical Engineering, University of California–Riverside, Riverside, California, U.S.A.*
- Jingyue Liu** / *Monsanto Company, St. Louis, Missouri, U.S.A.*
- Zhen Liu** / *Department of Chemical Engineering, Columbia University, New York, New York, U.S.A.*
- Jason Locklin** / *Department of Chemistry, University of Houston, Houston, Texas, U.S.A.*
- Yueh-Lin Loo** / *Department of Chemical Engineering, University of Texas at Austin, Austin, Texas, U.S.A.*
- Gabriel P. López** / *Chemical and Nuclear Engineering, University of New Mexico, Albuquerque, New Mexico, U.S.A.*
- Dmitri Valentinovich Louzguine** / *Institute for Materials Research, Tohoku University, Sendai, Japan*
- J. Christopher Love** / *Department of Chemistry and Chemical Biology, Harvard University, Cambridge, Massachusetts, U.S.A.*

- Fang Lu** / *Pacific Northwest National Laboratory, Richland, Washington, U.S.A.*
- Gao Qing (Max) Lu** / *Nanomaterials Centre, Department of Chemical Engineering, University of Queensland, Brisbane, Queensland, Australia*
- Nan Lu** / *Physikalisches Institut, Westfälische Wilhelms-Universität Münster, Münster, Germany*
- Yan-Yeung Luk** / *Department of Chemical Engineering, University of Wisconsin–Madison, Madison, Wisconsin, U.S.A.*
- Simon O. Lumsdon** / *Particle Science and Technology, DuPont Central Research and Development, Wilmington, Delaware, U.S.A.*
- Andrew R. Lupini** / *Materials Science and Technology Division, Oak Ridge National Laboratory, Oak Ridge, Tennessee, U.S.A.*
- Yuri M. Lvov** / *Institute for Micromanufacturing, Louisiana Tech University, Ruston, Louisiana, U.S.A.*
- L. Andrew Lyon** / *School of Chemistry and Biochemistry, Georgia Institute of Technology, Atlanta, Georgia, U.S.A.*
- Alexander Lyubartsev** / *Division of Physical Chemistry, Stockholm University, Stockholm, Sweden*
- Jeffrey D. Madura** / *Department of Chemistry and Biochemistry, Duquesne University, Pittsburgh, Pennsylvania, U.S.A.*
- Kenzo Maehashi** / *Institute of Scientific and Industrial Research, Osaka University, Osaka, Japan*
- Thomas F. Magnera** / *University of Colorado, Boulder, Colorado, U.S.A.*
- Amitesh Maiti** / *Materials Science, Accelrys Inc., San Diego, California, U.S.A.*
- Amarnath Maitra** / *Department of Chemistry, University of Delhi, Delhi, India*
- T. L. Makarova** / *Department of Experimental Physics, Institute of Physics, Umeå University, Umeå, Sweden*
- Sergey A. Maksimenko** / *Institute of Nuclear Problems, Belarus State University, Minsk, Belarus*
- Charles Maldarelli** / *Department of Chemical Engineering and the New York Center for Biomedical Engineering, City College of New York, New York, New York, U.S.A.*
- Arif A. Mamedov** / *Oklahoma State University and Nomadics, Inc., Stillwater, Oklahoma, U.S.A.*
- Nataliya N. Mamedova** / *Department of Chemistry, Oklahoma State University, Stillwater, Oklahoma, U.S.A.*
- Guangzhao Mao** / *Department of Chemical Engineering and Materials Science, Wayne State University, Detroit, Michigan, U.S.A.*
- Gabriela Marinescu** / *Institute of Physical Chemistry, I.G. Murgulescu Institute of the Romanian Academy, Bucharest, Romania*
- S. Marsaudon** / *Centre de Physique Moléculaire Optique et Hertzienne (CPMOH), Université Bordeaux I, Talence, France*
- C. L. Marshall** / *Argonne National Laboratory, Argonne, Illinois, U.S.A.*
- Charles R. Martin** / *Department of Chemistry, University of Florida, Gainesville, Florida, U.S.A.*
- Shinro Mashiko** / *Communications Research Laboratory, Kobe, Japan*
- Hiroshi Matsui** / *Department of Chemistry, Hunter College, City University of New York, New York, New York, U.S.A.*
- Hideo Matsumura** / *National Institute of Advanced Industrial Science and Technology, Tsukuba, Japan*
- Hideki Matsuoka** / *Department of Polymer Chemistry, Kyoto University, Kyoto, Japan*
- S. V. Mattigod** / *Pacific Northwest National Laboratory, Richland, Washington, U.S.A.*
- F. Maurigh** / *Department of Engineering, DIEGM University of Udine, Udine, Italy*
- Mikhail V. Maximov** / *Ioffe Physico-Technical Institute, St. Petersburg, Russia*
- Ursula Mazur** / *Department of Chemistry and Materials Science, Washington State University, Pullman, Washington, U.S.A.*
- James R. McBride** / *Department of Chemistry, Vanderbilt University, Nashville, Tennessee, U.S.A.*

- Clare McCabe** / *Colorado School of Mines, Golden, Colorado, U.S.A.*
- Nathan D. McClenaghan** / *School of Chemistry at Queen's University, Belfast, Northern Ireland*
- E. W. McFarland** / *Chemical Engineering Department, University of California–Santa Barbara, Santa Barbara, California, U.S.A.*
- Duncan J. McGillivray** / *Physical and Theoretical Chemistry Laboratory, Oxford University, Oxford, U.K.*
- Paul McGuinness** / *Department for Nanostructured Materials, Jožef Stefan Institute, Ljubljana, Slovenia*
- Gary McPherson** / *Chemistry Department, Tulane University, New Orleans, Louisiana, U.S.A.*
- Michael J. McShane** / *Biomedical Engineering Program, Louisiana Tech University, Ruston, Louisiana, U.S.A.*
- Claude F. Meares** / *Department of Chemistry, University of California–Davis, Davis, California, U.S.A.*
- Mark S. Meier** / *Department of Chemistry, University of Kentucky, Lexington, Kentucky, U.S.A.*
- Latika Menon** / *Department of Physics and the Center for Nanotechnology, Texas Tech University, Lubbock, Texas, U.S.A.*
- Curtis W. Meuse** / *Biomolecular Materials Group, National Institute of Standards and Technology (NIST), Gaithersburg, Maryland, U.S.A.*
- Agnes A. Mewe** / *Faculty of Applied Physics, University of Twente, Enschede, The Netherlands*
- F. Miani** / *Department of Engineering, DIEGM University of Udine, Udine, Italy*
- Weifang Miao** / *Nanommat, Inc., North Huntingdon, Pennsylvania, U.S.A.*
- Carsten Michaelson** / *Incoatec GmbH, Geesthacht, Schleswig-Holstein, Germany*
- Josef Michl** / *University of Colorado, Boulder, Colorado, U.S.A.*
- Laszlo Mihaly** / *Department of Physics and Astronomy, State University of New York at Stony Brook, Stony Brook, New York, U.S.A.*
- Abigail E. Miller** / *Lawrence Livermore National Laboratory, Livermore, California, U.S.A.*
- Benjamin L. Miller** / *Department of Dermatology, University of Rochester, Rochester, New York, U.S.A.*
- Jeffrey T. Miller** / *British Petroleum (BP), Naperville, Illinois, U.S.A.*
- Robert D. Miller** / *Advanced Organic Materials, IBM Almaden Research Center, San Jose, California, U.S.A.*
- Scott A. Miller** / *Department of Chemistry, University of Florida, Gainesville, Florida, U.S.A.*
- Ioana Mindru** / *I.G. Murgulescu Institute of the Romanian Academy, Bucharest, Romania*
- Christophe Mingotaud** / *Laboratoire des IMRCP, Université Paul Sabatier, Toulouse, France*
- John W. Mintmire** / *Department of Physics, Oklahoma State University, Stillwater, Oklahoma, U.S.A.*
- Francis M. Mirabella, Jr.** / *Analytical Department, Equistar Chemicals, LP, Cincinnati, Ohio, U.S.A.*
- Amit Misra** / *Materials Science and Technology Division, Los Alamos National Laboratory, Los Alamos, New Mexico, U.S.A.*
- Susmita Mitra** / *Department of Chemistry, University of Delhi, Delhi, India*
- Akane Miyazaki** / *Department of Environmental Chemistry and Engineering, Tokyo Institute of Technology, Yokohama, Japan*
- Tomoo Mizugaki** / *Department of Chemical Science and Engineering, Osaka University, Osaka, Japan*
- Peter Moeck** / *Department of Physics, Portland State University, Portland, Oregon, U.S.A.*
- Carlo D. Montemagno** / *Department of Bioengineering, University of California–Los Angeles, Los Angeles, California, U.S.A.*
- Keiji Morokuma** / *Department of Chemistry, Emory University, Atlanta, Georgia, U.S.A.*
- Brij M. Moudgil** / *Department of Materials Science and Engineering, University of Florida, Gainesville, Florida, U.S.A.*
- Karine Mougini** / *Institut de Chimie des Surfaces et Interfaces-ICSI-CNRS, Mulhouse, France*
- Emiko Mouri** / *Nanostructured Composites and Fibers, Kyoto University, Kyoto, Japan*

- Douglas Mulhall** / *Marsh Harbour, Bahamas*
- Thomas Müller** / *Veeco Metrology Group, Santa Barbara, California, U.S.A.*
- Ravichandra S. Mulukutla** / *Nanoscale Materials, Inc., Manhattan, Kansas, U.S.A.*
- Kei Murakoshi** / *Department of Chemistry, Osaka University, Osaka, Japan*
- Makoto Murata** / *Osaka University, Osaka, Japan*
- Michael Murphey** / *University of Illinois at Urbana–Champaign, Urbana, Illinois, U.S.A.*
- Mustafa Musameh** / *Department of Chemistry and Biochemistry, New Mexico State University, Las Cruces, New Mexico, U.S.A.*
- Aleksandr V. Myshlyavtsev** / *Omsk State Technical University, Omsk, Russia*
- Edward M. Nadgorny** / *Department of Physics, Michigan Technological University, Houghton, Michigan, U.S.A.*
- K. S. Nagabhushana** / *Department of Heterogeneous Catalysis, Max Planck Institut für Kohlenforschung, Mülheim an der Ruhr, Germany*
- Eiichi Nakamura** / *Department of Chemistry, University of Tokyo, Tokyo, Japan*
- H. Nakamura** / *Advanced Technology Research and Development Center, Femtosecond Technology Research Association (FESTA), Ibaraki, Japan*
- Takayoshi Nakamura** / *Research Institute for Electronic Science, Hokkaido University, Sapporo, Japan*
- Hisao Nakashima** / *Institute of Scientific and Industrial Research, Osaka University, Osaka, Japan*
- Yoshihiro Nakato** / *Department of Chemistry, Osaka University, Osaka, Japan*
- Dario Narducci** / *CNISM and Department of Materials Science, University of Milano–Bicocca, Milan, Italy*
- Richard M. Narske** / *Department of Chemistry, Augustana College, Rock Island, Illinois, U.S.A.*
- Chaitanya Kumar Narula** / *Physical Chemistry of Materials, Materials Science and Technology Division, Oak Ridge National Laboratory, Oak Ridge, Tennessee, U.S.A.*
- Alexandra Navrotsky** / *Department of Chemical Engineering and Materials Science, University of California–Davis, Davis, California, U.S.A.*
- David A. Nelson** / *Pacific Northwest National Laboratory, Richland, Washington, U.S.A.*
- Sarah A. Nespolo** / *Department of Chemical and Biomolecular Engineering, University of Melbourne, Melbourne, Victoria, Australia*
- Piers Newbery** / *Department of Chemical Engineering and Materials Science, University of California–Davis, Davis, California, U.S.A.*
- M. K. Neylon** / *Chemical Technology Division, Argonne National Laboratory, Argonne, Illinois, U.S.A.*
- Patrick J. Neyman** / *Department of Physics Engineering, Virginia Technical Institute, Blacksburg, Virginia, U.S.A.*
- K.Y. Simon Ng** / *Department of Chemical Engineering and Materials Science, Wayne State University, Detroit, Michigan, U.S.A.*
- Richard J. Nichols** / *Department of Chemistry, University of Liverpool, Liverpool, U.K.*
- Marc Nicklaus** / *National Cancer Institute, National Institutes of Health (NIH), Frederick, Maryland, U.S.A.*
- David E. Nikles** / *Department of Chemistry, University of Alabama, Tuscaloosa, Alabama, U.S.A.*
- S. Nishikawa** / *Advanced Technology Research and Development Center, Femtosecond Technology Research Association (FESTA), Ibaraki, Japan*
- Sandip Niyogi** / *University of California–Riverside, Riverside, California, U.S.A.*
- Ijeoma M. Nnebe** / *Department of Chemical Engineering, Carnegie Mellon University, Pittsburgh, Pennsylvania, U.S.A.*
- Donald W. Noid** / *Division of Computer Science and Mathematics, Oak Ridge National Laboratory, Oak Ridge, Tennessee, U.S.A.*
- Tyler B. Norsten** / *Department of Chemistry, University of Massachusetts, Amherst, Massachusetts, U.S.A.*

- Aleksandr Noy** / *Lawrence Livermore National Laboratory, Livermore, California, U.S.A.*
- Stacie Nunes** / *Department of Physics, State University of New York, New Paltz, New York, U.S.A.*
- Kenji Okamoto** / *Department of Chemistry and Biochemistry, University of Maryland, College Park, Maryland, U.S.A.*
- Masayuki Okamura** / *Physical Chemistry Laboratory, Hokkaido University, Sapporo, Japan*
- Yuji Okawa** / *Nanomaterials Laboratory, National Institute for Materials Science, Ibaraki, Japan*
- S. Oktyabrsky** / *College of Nanoscale Science and Engineering, State University of New York at Albany, Albany, New York, U.S.A.*
- Masahiko Ooe** / *Department of Chemical Science and Engineering, Osaka University, Osaka, Japan*
- Sara G. Ostrowski** / *Department of Chemistry, Pennsylvania State University, University Park, Pennsylvania, U.S.A.*
- Neil S. Oxtoby** / *School of Chemistry, University of Nottingham, Nottingham, U.K.*
- Ruth Pachter** / *Materials and Manufacturing Directorate, Air Force Research Laboratory, Wright-Patterson Air Force Base, Ohio, U.S.A.*
- Christopher S. Palenik** / *Department of Geological Sciences, University of Michigan, Ann Arbor, Michigan, U.S.A.*
- Chandra Sekhar Palla** / *Department of Chemical Engineering, University of Delaware, Newark, Delaware, U.S.A.*
- So-Jung Park** / *Department of Chemistry, Nanoscale Materials and Surface Chemistry, University of Pennsylvania, Philadelphia, Pennsylvania, U.S.A.*
- Raghuv eer Parthasarathy** / *James Franck Institute, University of Chicago, Chicago, Illinois, U.S.A., and University of California–Berkeley, Berkeley, California, U.S.A.*
- Sandeep Patel** / *Department of Chemistry and Biochemistry, Hunter College, City University of New York, New York, New York, U.S.A.*
- Luminita Patron** / *I.G. Murgulescu Institute of the Romanian Academy, Bucharest, Romania*
- Derek Patton** / *Department of Chemistry, University of Houston, Houston, Texas, U.S.A.*
- Stephen J. Pennycook** / *Materials Science and Technology Division, Oak Ridge National Laboratory, Oak Ridge, Tennessee, U.S.A.*
- Sandrine Pens ec** / *Laboratoire de Chimie Macromoléculaire, Université Pierre et Marie Curie, Paris, France*
- John H. Perepezko** / *Materials Science and Engineering, University of Wisconsin, Madison, Wisconsin, U.S.A.*
- Myriam Perez de la Rosa** / *Materials Research and Technology Institute, University of Texas at El Paso, El Paso, Texas, U.S.A.*
- Christopher C. Perry** / *Johns Hopkins University, Baltimore, Maryland, U.S.A.*
- Claire S. Peyratout** / *Max Planck Institute of Colloids and Interfaces, Potsdam, Germany*
- M. P. Pileni** / *Laboratoire des Matériaux Mésoscopiques et Nanométriques, Université Pierre et Marie Curie, Paris, France*
- M. A. Pimenta** / *Departamento de Física, Universidade Federal de Minas Gerais, Belo Horizonte, Brazil*
- Frédéric Pincet** / *Laboratoire de Physique Statistique de l'Ecole Normale Supérieure, Paris, France*
- Laura Pirondini** / *Dipartimento di Chimica Organica e Industriale, Università di Parma, Parma, Italy*
- Bene Poelsema** / *Faculty of Applied Physics, University of Twente, Enschede, The Netherlands*
- Karsten Pohl** / *Department of Physics, University of New Hampshire, Durham, New Hampshire, U.S.A.*
- Vojislava Pophristic** / *Center for Molecular Modeling, Department of Chemistry, University of Pennsylvania, Philadelphia, Pennsylvania, U.S.A.*
- Daniel Portinha** / *Laboratoire de Chimie Macromoléculaire, Université Pierre et Marie Curie, Paris, France*
- B.L.V. Prasad** / *Materials Chemistry Division, National Chemical Laboratory, Pune, India*
- Maurizio Prato** / *Dipartimento di Scienze Farmaceutiche, Università di Trieste, Trieste, Italy*

- Aaron Puzder** / *Lawrence Livermore National Laboratory, Livermore, California, U.S.A.*
- Georgios Pyrgiotakis** / *Materials Science and Engineering Department, University of Florida, Gainesville, Florida, U.S.A.*
- Clayton J. Radke** / *Department of Chemical Engineering, University of California–Berkeley, Berkeley, California, U.S.A.*
- Srikanth Raghunathan** / *Nanomat, Inc., North Huntingdon, Pennsylvania, U.S.A.*
- Krishnaswami S. Raja** / *Department of Chemistry, Scripps Research Institute, La Jolla, California, U.S.A.*
- G. V. Rama Rao** / *Chemical and Nuclear Engineering, University of New Mexico, Albuquerque, New Mexico, U.S.A.*
- Subramanian Ramakrishnan** / *Department of Chemical and Biomolecular Engineering, University of Illinois at Urbana–Champaign, Urbana, Illinois, U.S.A.*
- David M. Rampulla** / *Department of Chemical Engineering, Carnegie Mellon University, Pittsburgh, Pennsylvania, U.S.A.*
- C.N.R. Rao** / *Chemistry and Physics of Materials Unit and CSIR Centre of Excellence in Chemistry, Jawaharlal Nehru Center for Advanced Scientific Research, Bangalore, India*
- Lev Rapoport** / *Tribology Laboratory, Holon Academic Institute of Technology, Holon, Israel*
- Jean-Yves Raty** / *Charge de Recherches du FNRS, University of Liège, Sart-Tilman, Belgium*
- Serge Ravaine** / *Centre de Recherche Paul Pascal, CNRS, Pessac, France*
- Stéphane Reculosa** / *Centre de Recherche Paul Pascal, CNRS, Pessac, France*
- Mark A. Reed** / *Department of Electrical Engineering, Yale University, New Haven, Connecticut, U.S.A.*
- David N. Reinhoudt** / *Laboratory of Supramolecular Chemistry and Technology, University of Twente, Enschede, The Netherlands*
- Mikas Remeika** / *University of Illinois at Urbana–Champaign, Urbana, Illinois, U.S.A.*
- Maja Remskar** / *Jozef Stefan Institute, Ljubljana, Slovenia*
- Zhifeng Ren** / *Boston College, Chestnut Hill, Massachusetts, U.S.A.*
- Paulo Ricardo** / *Department of Nanotechnology, Institute of Materials Research, GKSS Research Centre GmbH, Geesthacht, Schleswig-Holstein, Germany*
- Ryan M. Richards** / *Department of Chemistry, International University of Bremen, Bremen, Germany*
- Carlos Rinaldi** / *Department of Chemical Engineering, University of Puerto Rico, Mayagüez, Puerto Rico*
- P. J. Roberts** / *BlazePhotonics Ltd., Bath, U.K.*
- Ian Robinson** / *Department of Chemistry and School of Biological Sciences, University of Liverpool, Liverpool, U.K.*
- Jose A. Rodriguez** / *Chemistry Department, Brookhaven National Laboratory, Upton, New York, U.S.A.*
- Miguel Rodriguez, Jr.** / *Life Sciences Division, Oak Ridge National Laboratory, Oak Ridge, Tennessee, U.S.A.*
- Andrey Rogachev** / *University of Illinois at Urbana–Champaign, Urbana, Illinois, U.S.A.*
- John A. Rogers** / *Department of Materials Science and Engineering and Beckman Institute, University of Illinois at Urbana–Champaign, Urbana, Illinois, U.S.A.*
- B. Roldan Cuenya** / *Chemical Engineering Department, University of California–Santa Barbara, Santa Barbara, California, U.S.A.*
- Harry W. Rollins** / *Chemistry Department, Idaho National Engineering and Environmental Laboratory, Idaho Falls, Idaho, U.S.A.*
- Elisabetta Romano** / *CNISM and Department of Materials Science, University of Milano–Bicocca, Milan, Italy*
- Sandra J. Rosenthal** / *Department of Chemistry and Physics, Vanderbilt University, Nashville, Tennessee, U.S.A.*
- Björn T. Rosner** / *NanoInk Inc., Chicago, Illinois, U.S.A.*



- Vincent M. Rotello** / *Department of Chemistry, University of Massachusetts, Amherst, Massachusetts, U.S.A.*
- Siegmar Roth** / *Max Planck Institut für Festkörperforschung, Stuttgart, Germany*
- Wielsaw J. Roth** / *ExxonMobil Research and Engineering Company, Annandale, New Jersey, U.S.A.*
- Jason H. Rouse** / *Langley Research Center, National Aeronautics and Space Administration (NASA), Hampton, Virginia, U.S.A.*
- James F. Rusling** / *Department of Chemistry, University of Connecticut, Storrs, Connecticut, U.S.A.*
- P. St. J. Russell** / *Department of Physics, University of Bath, Bath, U.K.*
- Ajit Sadana** / *Department of Chemical Engineering, University of Mississippi, University, Mississippi, U.S.A.*
- R. Saito** / *Department of Electronic Engineering, University of Electro-Communications, Tokyo, Japan*
- Pavol Šajgalík** / *Institute of Inorganic Chemistry, Slovak Academy of Sciences, Bratislava, Slovakia*
- Mark R. Sambrook** / *Inorganic Chemistry Laboratory, Department of Chemistry, University of Oxford, Oxford, U.K.*
- Anna Cristina Samia** / *Chemistry Division, Argonne National Laboratory, Argonne, Illinois, U.S.A.*
- Lynne A. Samuelson** / *Research, Development and Engineering Command (RDECOM), U.S. Army, Natick, Massachusetts, U.S.A., and Center for Advanced Materials, University of Massachusetts–Lowell, Lowell, Massachusetts, U.S.A.*
- Charlene A. Sanders** / *Chemical Sciences Division, Oak Ridge National Laboratory, Oak Ridge, Tennessee, U.S.A.*
- Francesco Sansone** / *Dipartimento di Chimica Organica e Industriale, Università di Parma, Parma, Italy*
- Venugopal Santhanam** / *Institut für Anorganische Chemie, Universität Duisburg-Essen, Essen, Germany*
- Amitav Sanyal** / *Department of Chemistry, University of Massachusetts, Amherst, Massachusetts, U.S.A.*
- D. Y. Sasaki** / *Biomolecular Materials and Interfaces, Sandia National Laboratories, Albuquerque, New Mexico, U.S.A.*
- Daniel M. Schaadt** / *Department of Electrical and Computer Engineering, University of California–San Diego, La Jolla, California, U.S.A.*
- L. S. Schadler** / *Department of Materials Science and Engineering, Rensselaer Polytechnic Institute, Troy, New York, U.S.A.*
- David J. Schiffrin** / *Department of Chemistry, University of Liverpool, Liverpool, U.K.*
- Jacob J. Schmidt** / *Department of Bioengineering, University of California–Los Angeles, Los Angeles, California, U.S.A.*
- James W. Schneider** / *Department of Chemical Engineering, Carnegie Mellon University, Pittsburgh, Pennsylvania, U.S.A.*
- Holger Schönherr** / *Department of Materials Science and Technology of Polymers, University of Twente, Enschede, The Netherlands*
- Christian Schüller** / *Institut für Angewandte Physik und Zentrum für Mikrostrukturforschung, Universität Hamburg, Hamburg, Germany*
- Adam M. Schwartzberg** / *Department of Chemistry and Biochemistry, University of California–Santa Cruz, Santa Cruz, California, U.S.A.*
- Purnesh Seegopaul** / *Technology and Business Development, Umicore USA Inc., Hillsborough, New Jersey, U.S.A.*
- Gotthard Seifert** / *Institut für Physikalische Chemie, Technische Universität Dresden, Dresden, Germany*
- Jorge M. Seminario** / *Department of Electrical Engineering, University of South Carolina, Columbia, South Carolina, U.S.A.*
- Deborahnyaa Sengupta** / *Department of Chemistry, Cornell University, Ithaca, New York, U.S.A.*
- Mamoru Senna** / *Department of Applied Chemistry, Keio University, Yokohama, Japan*
- Jonathan L. Sessler** / *Department of Chemistry and Biochemistry, University of Texas at Austin, Austin, Texas, U.S.A.*

- Kay Severin** / *Institut de Chimie Moléculaire et Biologique, École Polytechnique Fédérale de Lausanne, Lausanne, Switzerland*
- S. Ismat Shah** / *Department of Materials Science and Engineering, Department of Physics and Astronomy, University of Delaware, Newark, Delaware, U.S.A.*
- Sean E. Shaheen** / *National Renewable Energy Laboratory (NREL), Golden, Colorado, U.S.A.*
- Ehud Shapiro** / *Department of Computer Science and Applied Mathematics, Weizmann Institute of Science, Rehovot, Israel*
- Yury E. Shapiro** / *Department of Life Sciences, Bar-Ilan University, Ramat-Gan, Israel*
- P. C. Sharma** / *Electrical Engineering Department, University of California–Los Angeles, Los Angeles, California, U.S.A.*
- Pramod K. Sharma** / *Nanomats, Inc., North Huntingdon, Pennsylvania, U.S.A.*
- Roy Shenhar** / *Department of Chemistry, University of Massachusetts, Amherst, Massachusetts, U.S.A.*
- Peter M.A. Sherwood** / *Department of Chemistry, Kansas State University, Manhattan, Kansas, U.S.A.*
- Wei Shi** / *City University of New York, New York, New York, U.S.A.*
- Masashi Shiraishi** / *Pi-electron Materials Research Lab, Sony Corporation, Yokohama, Japan*
- Tatiana V. Shishkanova** / *Department of Analytical Chemistry, Institute of Chemical Technology, Prague, Czech Republic*
- Young-Seok Shon** / *Department of Chemistry, Western Kentucky University, Bowling Green, Kentucky, U.S.A.*
- Ulrich Siggel** / *Max Volmer Institut für Physikalische Chemie, Technischen Universität Berlin, Berlin, Germany*
- Wolfgang M. Sigmund** / *Materials Science and Engineering Department, University of Florida, Gainesville, Florida, U.S.A.*
- Richard Silberglitt** / *RAND Corporation, Arlington, Virginia, U.S.A.*
- Kevin Sill** / *Department of Polymer Science and Engineering, University of Massachusetts, Amherst, Massachusetts, U.S.A.*
- Amit Singhal** / *NEI Corporation, Piscataway, New Jersey, U.S.A.*
- Rhonda Skaggs** / *Pacific Northwest National Laboratory, Richland, Washington, U.S.A.*
- Ganesh Skandan** / *NEI Corporation, Piscataway, New Jersey, U.S.A.*
- Gregory Ya. Slepyan** / *Institute of Nuclear Problems, Belarus State University, Minsk, Belarus*
- Gabriela Smeureanu** / *Department of Chemistry and Biochemistry, Hunter College, City University of New York, New York, New York, U.S.A.*
- James N. Smith** / *Atmospheric Chemistry Division, National Center for Atmospheric Research, Boulder, Colorado, U.S.A.*
- Damian Sobrevilla** / *NEI Corporation, Piscataway, New Jersey, U.S.A.*
- Karl Sohlberg** / *Department of Chemistry, Drexel University, Philadelphia, Pennsylvania, U.S.A.*
- Glenn S. Solomon** / *Department of Electrical Engineering, Stanford University, Stanford, California, U.S.A.*
- Michael J. Solomon** / *Chemical Engineering, University of Michigan, Ann Arbor, Michigan, U.S.A.*
- Anongnat Somwangthanaroj** / *Macromolecular Science and Engineering Program, University of Michigan, Ann Arbor, Michigan, U.S.A.*
- Sang Jun Son** / *Department of Chemistry and Biochemistry, University of Maryland, College Park, Maryland, U.S.A.*
- Wenbo Song** / *Hokkaido University, Sapporo, Japan*
- A. G. Souza Filho** / *Universidade Federal do Ceará, Fortaleza, Brazil*
- Patrick T. Spicer** / *Complex Fluids Research, Procter & Gamble Company, West Chester, Ohio, U.S.A.*
- Ivan Stensgaard** / *Department of Physics and Astronomy, University of Aarhus, Aarhus, Denmark*
- Geoffrey W. Stevens** / *Department of Chemical and Biomolecular Engineering, University of Melbourne, Melbourne, Victoria, Australia*
- Rebecca L. Stoermer** / *Department of Chemistry, Pennsylvania State University, University Park, Pennsylvania, U.S.A.*

- Savka I. Stoeva** / *Department of Chemistry, Kansas State University, Manhattan, Kansas, U.S.A.*
- Peter K. Stoimenov** / *Department of Chemistry, Kansas State University, Manhattan, Kansas, U.S.A.*
- Michael Störmer** / *Department of Nanotechnology, Institute of Materials Research, GKSS Research Centre GmbH, Geesthacht, Schleswig-Holstein, Germany*
- Steven H. Strauss** / *Department of Chemistry, Colorado State University, Fort Collins, Colorado, U.S.A.*
- Pieter Stroeve** / *Department of Chemical Engineering and Materials Science, University of California–Davis, Davis, California, U.S.A.*
- Makram T. Suidan** / *Department of Civil and Environmental Engineering, University of Cincinnati, Cincinnati, Ohio, U.S.A.*
- Gleb B. Sukhorukov** / *Max Planck Institute of Colloids and Interfaces, Potsdam/Golm, Germany*
- Bobby G. Sumpter** / *Division of Computer Science and Mathematics, Oak Ridge National Laboratory, Oak Ridge, Tennessee, U.S.A.*
- Guangyu Sun** / *National Cancer Institute, National Institutes of Health (NIH), Frederick, Maryland, U.S.A.*
- Kai Sun** / *Department of Physics, University of Illinois at Chicago, Chicago, Illinois, U.S.A.*
- Xiangcheng Sun** / *Center for Materials for Information Technology, University of Alabama, Tuscaloosa, Alabama, U.S.A.*
- Yugang Sun** / *Department of Materials Science and Engineering, University of Illinois at Urbana–Champaign, Urbana, Illinois, U.S.A.*
- Aydin K. Sunol** / *Chemical Engineering Department, University of South Florida, Tampa, Florida, U.S.A.*
- Sermin G. Sunol** / *University of South Florida, Tampa, Florida, U.S.A.*
- Robert E. Synovec** / *Department of Chemistry, University of Washington, Seattle, Washington, U.S.A.*
- Makoto Tadokoro** / *Department of Chemistry, Osaka City University, Osaka, Japan*
- Atsushi Takahara** / *Institute for Fundamental Research of Organic Chemistry, Kyushu University, Fukuoka, Japan*
- Taishi Takenobu** / *Institute of Materials Research, Sony Corporation, Yokohama, Japan*
- Eunice Phay Shing Tan** / *Division of Bioengineering, National University of Singapore, Singapore, Singapore*
- Hideki Tanaka** / *Department of Chemistry, Okayama University, Okayama, Japan*
- Zhiyong Tang** / *Department of Chemical Engineering, University of Michigan, Ann Arbor, Michigan, U.S.A.*
- P. Tarakeshwar** / *Department of Chemistry, Pohang University of Science and Technology, Pohang, South Korea*
- Jean-Marie Tarascon** / *Faculté des Sciences, Université de Picardie–Jules Verne, Amiens, France*
- Vandana R. Tarigopula** / *Department of Electrical Engineering, University of South Carolina, Columbia, South Carolina, U.S.A.*
- Juan Manuel Diez Tascón** / *Instituto Nacional del Carbón, CSIC, Oviedo, Spain*
- Boyd R. Taylor** / *Chemistry and Chemical Engineering Directorate, Lawrence Livermore National Laboratory, Livermore, California, U.S.A.*
- Reshef Tenne** / *Materials and Interfaces Department, Weizmann Institute of Science, Rehovot, Israel*
- Frederick Tepper** / *Argonide Corporation, Sanford, Florida, U.S.A.*
- Roger Terrill** / *San Jose State University, San Jose, California, U.S.A.*
- Mauricio Terrones** / *Department of Advanced Materials, Institute Potosino of Scientific and Technological Research (IPICYT), San Luis Potosí, Mexico*
- V. A. Tertykh** / *Institute of Surface Chemistry, National Academy of Sciences of Ukraine, Kiev, Ukraine*
- N. N. Thadhani** / *School of Materials Science and Engineering, Georgia Institute of Technology, Atlanta, Georgia, U.S.A.*

- Nguyen T.K. Thanh** / *Department of Chemistry and School of Biological Sciences, University of Liverpool, Liverpool, U.K.*
- Edwin L. Thomas** / *Massachusetts Institute of Technology, Cambridge, Massachusetts, U.S.A.*
- P. John Thomas** / *Chemistry and Physics of Materials Unit, Jawaharlal Nehru Center for Advanced Scientific Research, Bangalore, India*
- Gregory B. Thompson** / *Department of Materials Science and Engineering, Ohio State University, Columbus, Ohio, U.S.A.*
- Steven M. Thornberg** / *Sandia National Laboratories, Albuquerque, New Mexico, U.S.A.*
- Bernd Tieke** / *Institut für Physikalische Chemie, Universität zu Köln, Köln, Germany*
- Tia Benson Tolle** / *Plastic Composites/Military Organic Matrix Composites, Air Force Research Laboratory, Wright-Patterson Air Force Base, Ohio, U.S.A.*
- Anna W. Topol** / *IBM T.J. Watson Research Center, Yorktown Heights, New York, U.S.A.*
- Jessica Torres** / *Johns Hopkins University, Baltimore, Maryland, U.S.A.*
- Naoki Toshima** / *Department of Materials Science and Engineering, Tokyo University of Science, Yamaguchi, Japan*
- James M. Tour** / *Chemistry Department, Rice University, Houston, Texas, U.S.A.*
- Ali Toutianoush** / *Universität zu Köln, Köln, Germany*
- Günter E.M. Tovar** / *Fraunhofer Institute for Interfacial Engineering and Biotechnology, University of Stuttgart, Stuttgart, Germany*
- Costas Tsouris** / *Separations and Materials Research Group, Oak Ridge National Laboratory, Oak Ridge, Tennessee, U.S.A.*
- Yi Tu** / *Boston College, Chestnut Hill, Massachusetts, U.S.A.*
- Le Duc Tung** / *Department of Physics, University of Liverpool, Liverpool, U.K.*
- Royale S. Underhill** / *Emerging Materials Section, Defence Research and Development Canada–Atlantic, Dartmouth, Nova Scotia, Canada*
- Rocco Ungaro** / *Dipartimento di Chimica Organica e Industriale, Università di Parma, Parma, Italy*
- Eberhard Unger** / *Institute of Molecular Biotechnology, Jena, Germany*
- Kohei Uosaki** / *Physical Chemistry Laboratory, Hokkaido University, Sapporo, Japan*
- Satoshi Utsunomiya** / *Department of Nuclear Engineering and Radiological Sciences, University of Michigan, Ann Arbor, Michigan, U.S.A.*
- Stefan Vajda** / *Chemical Sciences and Engineering Division, Center for Nanoscale Materials, Argonne National Laboratory, Argonne, Illinois, U.S.A., and Department of Chemical Engineering, Yale University, New Haven, Connecticut, U.S.A.*
- Ivan U. Vakarelski** / *Department of Chemical Engineering, Kyoto University, Kyoto, Japan*
- Martin Valík** / *Department of Analytical Chemistry, Institute of Chemical Technology, Prague, Czech Republic*
- Klaus van Benthem** / *Center for Nanophase Materials Sciences, Oak Ridge National Laboratory, Oak Ridge, Tennessee, U.S.A., and Department of Chemical Engineering and Materials Science, University of California–Davis, Davis, California, U.S.A.*
- Kevin E. Van Cott** / *Department of Chemical Engineering, Virginia Technical Institute, Blacksburg, Virginia, U.S.A.*
- Richard A. van Delden** / *Department of Organic and Molecular Inorganic Chemistry, University of Groningen, Groningen, The Netherlands*
- Daniel W. van der Weide** / *Department of Electrical and Computer Engineering, University of Wisconsin, Madison, Wisconsin, U.S.A.*
- Paul R. Van Tassel** / *Department of Chemical Engineering, Yale University, New Haven, Connecticut, U.S.A.*
- G. Julius Vancso** / *Department of Materials Science and Technology of Polymers, University of Twente, Enschede, The Netherlands*
- Natalia Varaksa** / *University of Colorado, Boulder, Colorado, U.S.A.*
- James C. Vartuli** / *ExxonMobil Research and Engineering Company, Annandale, New Jersey, U.S.A.*

- Stephanie Butler Velegol** / *Department of Civil and Environmental Engineering, Pennsylvania State University, State College, Pennsylvania, U.S.A.*
- Orlin D. Velev** / *Department of Chemical Engineering, North Carolina State University, Raleigh, North Carolina, U.S.A.*
- Alexei Yu. Vinogradov** / *Department of Intelligent Materials Engineering, Osaka City University, Osaka, Japan*
- Viriya Vithayaveroj** / *Georgia Institute of Technology, Atlanta, Georgia, U.S.A.*
- Viola Vogel** / *Institute for Biologically Oriented Materials, Department of Materials, Swiss Federal Institute of Technology, Zurich, Switzerland*
- Pete Vukusic** / *School of Physics, Exeter University, Exeter, U.K.*
- Anthony J. Wagner** / *Johns Hopkins University, Baltimore, Maryland, U.S.A.*
- H. Daniel Wagner** / *Materials and Interfaces Department, Weizmann Institute of Science, Rehovot, Israel*
- Chien M. Wai** / *Department of Chemistry, University of Idaho, Moscow, Idaho, U.S.A.*
- Joseph Wang** / *Department of Chemistry and Biochemistry, New Mexico State University, Las Cruces, New Mexico, U.S.A.*
- Kang L. Wang** / *Electrical Engineering Department, University of California–Los Angeles, Los Angeles, California, U.S.A.*
- Qian Wang** / *Department of Chemistry and Biochemistry, University of Southern Carolina, Columbia, South Carolina, U.S.A.*
- Shaopeng Wang** / *Nomadics Inc., Stillwater, Oklahoma, U.S.A.*
- Zhong Lin Wang** / *Center for Nanoscience and Nanotechnology, Georgia Institute of Technology, Atlanta, Georgia, U.S.A.*
- Paul Watts** / *Department of Chemistry, University of Hull, Hull, U.K.*
- Achim Weber** / *Fraunhofer Institute for Interfacial Engineering and Biotechnology, University of Stuttgart, Stuttgart, Germany*
- Thomas J. Webster** / *Department of Biomedical Engineering, Purdue University, West Lafayette, Indiana, U.S.A.*
- Brandon L. Weeks** / *Biosecurity Support Laboratory, Lawrence Livermore National Laboratory, Livermore, California, U.S.A.*
- Alexander Wei** / *Department of Chemistry, Purdue University, West Lafayette, Indiana, U.S.A.*
- Jie Wen** / *Department of Biomedical Engineering, Johns Hopkins University School of Medicine, Baltimore, Maryland, U.S.A.*
- Joachim H. Wendorff** / *Philipps–Universität Marburg, Marburg, Germany*
- Carter T. White** / *Naval Research Laboratory, Washington, District of Columbia, U.S.A.*
- George M. Whitesides** / *Department of Chemistry and Chemical Biology, Harvard University, Cambridge, Massachusetts, U.S.A.*
- James Wicksted** / *Department of Physics, Oklahoma State University, Stillwater, Oklahoma, U.S.A.*
- Jörg Wiesmann** / *Incoatec GmbH, Geesthacht, Schleswig-Holstein, Germany*
- J. P. Wilcoxon** / *Nanostructures and Advanced Materials Chemistry, Sandia National Laboratories, Albuquerque, New Mexico, U.S.A.*
- Andrew Williamson** / *Lawrence Livermore National Laboratory, Livermore, California, U.S.A.*
- Nicholas Winograd** / *Department of Chemistry, Pennsylvania State University, University Park, Pennsylvania, U.S.A.*
- Marc Wirtz** / *PPG Industries, Inc., Monroeville, Pennsylvania, U.S.A.*
- David Witkin** / *Department of Chemical Engineering and Materials Science, University of California–Irvine, Irvine, California, U.S.A.*
- Daniel B. Wolfe** / *Department of Chemistry and Chemical Biology, Harvard University, Cambridge, Massachusetts, U.S.A.*
- Glenn M. Wolfe** / *Johns Hopkins University, Baltimore, Maryland, U.S.A.*

- Stanislaus S. Wong** / *Materials and Chemical Sciences Department, Brookhaven National Laboratory, Upton, New York, U.S.A., and Department of Chemistry, State University of New York at Stony Brook, Stony Brook, New York, U.S.A.*
- Bruce W. Woods** / *Lawrence Livermore National Laboratory, Livermore, California, U.S.A.*
- Herbert Wormeester** / *Faculty of Science and Technology, University of Twente, Enschede, The Netherlands*
- Ludger Wöste** / *Institut für Experimentalphysik, Freie Universität Berlin, Berlin, Germany*
- Fanxin Wu** / *Department of Chemistry and Biochemistry, University of California–Santa Cruz, Santa Cruz, California, U.S.A.*
- H. Wu** / *Pacific Northwest National Laboratory, Richland, Washington, U.S.A.*
- Jianzhong Wu** / *Department of Chemical and Environmental Engineering, University of California–Riverside, Riverside, California, U.S.A.*
- Xianxian Wu** / *Carbon Materials Technology Group, Materials Science and Technology Division, Oak Ridge National Laboratory, Oak Ridge, Tennessee, U.S.A.*
- You-Ting Wu** / *Chemical Engineering Department, North Carolina State University, Raleigh, North Carolina, U.S.A.*
- Chuanjun Xia** / *Department of Chemistry, University of Alabama at Birmingham, Birmingham, Alabama, U.S.A.*
- Younan Xia** / *Department of Chemistry, University of Washington, Seattle, Washington, U.S.A.*
- Wei Xing** / *Nanomaterials Centre, School of Engineering, University of Queensland, Brisbane, Queensland, Australia*
- Zhi Ping Xu** / *Department of Chemistry, University of North Texas, Denton, Texas, U.S.A.*
- Dalia G. Yablon** / *Corporate Research Strategies, ExxonMobil Research and Engineering, Annandale, New Jersey, U.S.A.*
- Boris I. Yakobson** / *Department of Mechanical Engineering and Materials Science, Rice University, Houston, Texas, U.S.A.*
- Ichiro Yamashita** / *Graduate School of Material Science, Nara Institute of Science and Technology (NAIST), Ikoma, Japan*
- Juchao Yan** / *Department of Physical Sciences, Eastern New Mexico University, Portales, New Mexico, U.S.A.*
- Z. F. Yan** / *Institute of Catalysis, University of Petroleum, Dongying, China*
- Bai Yang** / *College of Chemistry, Jilin University, Changchun, China*
- Chao Yang** / *National Energy Research Science Computer Center, Lawrence Berkeley National Laboratory, Berkeley, California, U.S.A.*
- Jun Yang** / *Department of Mechanical Engineering, University of Alberta, Edmonton, Alberta, Canada*
- Kun-Lin Yang** / *Georgia Institute of Technology, Atlanta, Georgia, U.S.A.*
- T. Yang** / *Nanoelectronics Collaborative Research Center (NCRC), Femtosecond Technology Research Association (FESTA), Ibaraki, Japan*
- Wassana Yantasee** / *Pacific Northwest National Laboratory, Richland, Washington, U.S.A.*
- Xiang-Rong Ye** / *Department of Chemistry, University of Idaho, Moscow, Idaho, U.S.A.*
- Sotira Yiacoymi** / *School of Civil and Environmental Engineering, Georgia Institute of Technology, Atlanta, Georgia, U.S.A.*
- Shiyoshi Yokoyama** / *Communications Research Laboratory, Kobe, Japan*
- Takashi Yokoyama** / *Graduate School of Integrated Science, Yokohama City University, Yokohama, Japan, and National Institute for Materials Science, Tsukuba, Japan*
- Seunghoo Yoo** / *Department of Polymer Science and Engineering, University of Massachusetts, Amherst, Massachusetts, U.S.A.*
- Yi Yu** / *Key Laboratory of Excited Process of Physics, Chinese Academy of Sciences, Changchun, China*
- Igor Yuranov** / *Swiss Federal Institute of Technology, Lausanne, Switzerland*

- Markus Zahn** / *Department of Electrical Engineering and Computer Science, Massachusetts Institute of Technology, Cambridge, Massachusetts, U.S.A.*
- Mondona Zangeneh** / *Department of Chemistry, San Jose State University, San Jose, California, U.S.A.*
- Stefan Zauscher** / *Department of Mechanical Engineering and Materials Science, Duke University, Durham, North Carolina, U.S.A.*
- T. S. Zemanian** / *Pacific Northwest National Laboratory, Richland, Washington, U.S.A.*
- Hua Chun Zeng** / *Department of Chemical and Environmental Engineering, National University of Singapore, Singapore, Singapore*
- Dajie Zhang** / *Center for Nondestructive Evaluation, Johns Hopkins University, Baltimore, Maryland, U.S.A.*
- Gang Zhang** / *Department of Chemistry, Jilin University, Changchun, China*
- Jin Z. Zhang** / *Department of Chemistry and Biochemistry, University of California–Santa Cruz, Santa Cruz, California, U.S.A.*
- Junhu Zhang** / *Department of Chemistry, Jilin University, Changchun, China*
- Kai Zhang** / *Key Lab of Supramolecular Structure and Materials, Jilin University, Changchun, China*
- X. B. Zhang** / *Microelectronics Research Center, University of Texas at Austin, Austin, Texas, U.S.A.*
- Xunli Zhang** / *Department of Chemistry, University of Hull, Hull, U.K.*
- Zongtao Zhang** / *Oak Ridge National Laboratory, Oak Ridge, Tennessee, U.S.A.*
- Bin Zhao** / *Departments of Chemistry and Chemical and Environmental Engineering, University of California–Riverside, Riverside, California, U.S.A.*
- Genady Zhavnerko** / *Institute of Chemistry of New Materials, National Academy of Sciences of Belarus, Minsk, Belarus*
- Xiang Zheng** / *Department of Chemistry, Drexel University, Philadelphia, Pennsylvania, U.S.A.*
- N. B. Zhitenev** / *Bell Laboratories, Lucent Technologies, Murray Hill, New Jersey, U.S.A.*
- Zhigang Zhou** / *Center for Computational Sciences and Department of Chemistry and Biochemistry, Duquesne University, Pittsburgh, Pennsylvania, U.S.A.*
- Shu Zhu** / *Business Development, PLIVA Inc., East Hanover, New Jersey, U.S.A.*
- Charles F. Zukoski** / *Department of Chemical and Biomolecular Engineering, University of Illinois at Urbana–Champaign, Urbana, Illinois, U.S.A.*

# Contents

<i>Topical Table of Contents</i> .....	xlvii
<i>Preface</i> .....	lxxxiii
<i>Preface to the First Edition</i> .....	lxxxv
<i>Acknowledgment</i> .....	lxxxvii
<i>A Note on Terminology</i> .....	lxxxix
<i>About the Editors-in-Chief</i> .....	xc

---

## Volume I

<b>Aberration-Corrected Z-Contrast STEM: Semiconducting Nanocrystals</b> / James R. McBride, Andrew R. Lupini, Stephen J. Pennycook, and Sandra J. Rosenthal .....	1
<b>Adhesion: Cell on a Substrate</b> / Frédéric Pincet .....	22
<b>Adhesion: Coated Surfaces, Effect of Humidity</b> / Joan E. Curry and Sungsoo Kim .....	32
<b>Adsorption on Heterogeneous Surfaces</b> / Vinay K. Gupta and Yu-Wen Huang .....	41
<b>Aerosol Nanoparticles: Coagulation Theory</b> / Ken Won Lee and Soon-Bark Kwon .....	53
<b>AFM: Biopolymers</b> / Nehal I. Abu-Lail and Terri A. Camesano .....	63
<b>AFM: Hydrogen-Bonded Nanostructures</b> / Holger Schönherr, Mercedes Crego-Calama, G. Julius Vancso, and David N. Reinhoudt .....	76
<b>AFM: Imaging Artifacts</b> / Stephanie Butler Velegol .....	88
<b>AFM: Imaging and Force Spectroscopy on Cell Surfaces</b> / Yves F. Dufrêne .....	99
<b>AFM: Metal Ion Sorption</b> / Viriya Vithayaveroj, Sotira Yiacoumi, and Costas Tsouris .....	109
<b>AFM: Nanolithography on Organized Films</b> / Seunghyun Lee and Haiwon Lee .....	119
<b>AFM: Protein Adsorption</b> / David T. Kim, Harvey W. Blanch, and Clayton J. Radke .....	129
<b>AFM: Simulation of Interaction Forces</b> / Ivan U. Vakarelski, Scott C. Brown, Bahar Basim, and Brij M. Moudgil .....	153
<b>Amphiphilic Block Copolymer Monolayer at Air–Water Interface</b> / Emiko Mouri and Hideki Matsuoka .....	168
<b>Anion-Templated Self-Assembly: Inorganic Compounds</b> / Louise S. Evans and Philip A. Gale .....	178
<b>Anion-Templated Self-Assembly: Organic Compounds</b> / Paul D. Beer and Mark R. Sambrook .....	191
<b>Anodization Patterned on Aluminum Surfaces</b> / Juchao Yan, G. V. Rama Rao, Plamen B. Atanassov, and Gabriel P. López .....	203
<b>Antidot Lattices: Chaotic Transport</b> / Tsuneya Ando .....	210
<b>Atmospheric Nanoparticles: Formation and Physicochemical Properties</b> / James N. Smith .....	228
<b>Automotive Parts: Impact of Nanotechnology</b> / Ganesh Skandan, Amit Singhal, and Damian Sobrevilla .....	241
<b>Axle Molecules Threaded through Macrocycles</b> / Daryle H. Busch and Thomas Clifford .....	249
<b>Barcoded Nanowires</b> / Rebecca L. Stoermer and Christine D. Keating .....	259
<b>Barrier Properties of Ordered Polymer Nanocomposites</b> / Bon-Cheol Ku, Alexandre Blumstein, Jayant Kumar, Lynne A. Samuelson, and Dong Wook Kim .....	267



<b>Basic Nanostructured Catalysts</b> / Robert J. Davis	278
<b>Bimetallic Layered Nanocomposites</b> / Amit Misra and Richard G. Hoagland	288
<b>Bio-Microarrays</b> / Günter E.M. Tovar and Achim Weber	298
<b>Biocatalytic Single-Enzyme Nanoparticles</b> / Jay W. Grate and Jungbae Kim	307
<b>Biological and Chemical Decontamination</b> / Peter K. Stoimenov and Kenneth J. Klabunde	312
<b>Biomaterials: Mechanical Characterization</b> / Eunice Phay Shing Tan and Chwee Teck Lim	317
<b>Biomedical Applications: Implants</b> / Jeremiah Ejiolor and Thomas J. Webster	327
<b>Biomedical Applications: Novel Materials and Devices</b> / J. Zachary Hilt and Mark E. Byrne	339
<b>Biomedical Magnetic Nanoparticles</b> / Ian Robinson, Le Duc Tung, and Nguyen T.K. Thanh	354
<b>Biomimetic Design of Self-Assembling Systems</b> / Mila Boncheva and George M. Whitesides	364
<b>Biomimetic Receptors for Carboxylate Recognition</b> / Rocco Ungaro, Alessandro Casnati, and Francesco Sansone	372
<b>Bionanoparticles</b> / Krishnaswami S. Raja, Sukanta Dolai, Wei Shi, and Qian Wang	386
<b>Bioremediation of Environmental Contaminants</b> / Xiomara C. Kretschmer and Russell R. Chianelli	397
<b>Biosensor Applications: Porous Silicon Microcavities</b> / Benjamin L. Miller, Philippe M. Fauchet, Scott R. Horner, and Selena Chan	408
<b>Biosensor Applications: Surface Engineering</b> / Genady Zhavnerko and Kwon-Soo Ha	416
<b>Biosensors Based on Carbon Nanotubes</b> / Yuehe Lin, Wassana Yantasee, Fang Lu, Joseph Wang, Mustafa Musameh, Yi Tu, and Zhifeng Ren	428
<b>Biosensors: Fractal Analysis of Binding Kinetics</b> / Harshala Butala and Ajit Sadana	441
<b>Biosurfaces: Water Structure at Interfaces</b> / Yan-Yeung Luk	453
<b>Block Copolymer Nanoparticles</b> / Sandrine Pensec, Daniel Portinha, Laurent Bouteiller, and Christophe Chassenieux	467
<b>Cadmium Selenide Quantum Dots</b> / Kenzo Maehashi and Hisao Nakashima	477
<b>Cadmium Selenide Quantum Rods: Anisotropy</b> / Liang-shi Li and A. Paul Alivisatos	487
<b>Cadmium Sulfate Nanocrystals: Computational Analysis</b> / Stacie Nunes, Zhigang Zhou, Jeffrey D. Evanseck, and Jeffry D. Madura	498
<b>Capsules: Polymer Microcapsules</b> / Gleb B. Sukhorukov	508
<b>Capsules: Specific Layer Structures</b> / Lars Dähne and Claire S. Peyratout	522
<b>Carbon-Based Nanostructures: Hydrogen Storage</b> / Xianxian Wu and Nidia C. Gallego	535
<b>Carbon Forms Structured by Energetic Species</b> / Yeshayahu Lifshitz	553
<b>Carbon Nanotransistors</b> / Po-Wen Chiu and Siegmund Roth	563
<b>Carbon Nanotube-Conducting Polymer Composites in Supercapacitors</b> / Mark Hughes	574
<b>Carbon Nanotube Electrodes</b> / Valentina Lazarescu	586
<b>Carbon Nanotube Interconnects</b> / Alain E. Kaloyeros, Kathleen A. Dunn, Autumn T. Carlsen, and Anna W. Topol	596
<b>Carbon Nanotube-Metal Matrix Composites</b> / Efraín Carreño-Morelli	611
<b>Carbon Nanotubes: Electrochemical Modification</b> / Kannan Balasubramanian, Marko Burghard, and Klaus Kern	620
<b>Carbon Nanotubes: Flow Control in Membranes</b> / Scott A. Miller and Charles R. Martin	630
<b>Carbon Nanotubes: Functionalization</b> / Bin Zhao, Hui Hu, Elena Bekyarova, Mikhail E. Itkis, Sandip Niyogi, and Robert C. Haddon	640
<b>Carbon Nanotubes: Gas Adsorption Properties</b> / Juan Manuel Diez Tascón and Eduardo J. Bottani	653
<b>Carbon Nanotubes: Hydrogen Storage</b> / Masashi Shiraishi, Taishi Takenobu, Hiromichi Kataura, and Masafumi Ata	662
<b>Carbon Nanotubes: Modeling of Hydrogen Chemisorption</b> / Ronald C. Brown	671

<b>Carbon Nanotubes: Optical Properties</b> / R. Saito, Mildred S. Dresselhaus, G. Dresselhaus, A. Jorio, A. G. Souza Filho, and M. A. Pimenta . . . . .	679
<b>Carbon Nanotubes and Other Carbon Materials</b> / Morinobu Endo, Yoong Ahm Kim, Takuya Hayashi, Mauricio Terrones, and Mildred S. Dresselhaus . . . . .	691
<b>Carbon Nanotubes for Storage of Energy: Supercapacitors</b> / Elzbieta Frackowiak . . . . .	707
<b>Carbon Nanotubes: Supramolecular Mechanics</b> / Boris I. Yakobson and Luise S. Couchman . . . . .	722
<b>Carbon Nanotubes: Thermal Properties</b> / J. Hone . . . . .	736
<b>Catalysis by Supported Gold Nanoclusters</b> / D. Wayne Goodman . . . . .	744

---

## Volume II

<b>Catalyst Nanostructures: X-Ray Absorption</b> / Jeffrey T. Miller, M. K. Neylon, C. L. Marshall, and Arthur Jerome Kropf . . . . .	753
<b>Catalysts by Nanoscale Design</b> / Chaitanya Kumar Narula . . . . .	772
<b>Catalytic Processes: Nanoscale Simulations</b> / Vladimir I. Elokhin and Aleksandr V. Myshlyavtsev . . . . .	782
<b>Ceramic Nanocomposites: Self-Diagnostic Ability of Catastrophic Damage</b> / Pavol Šajgalík and Zoltán Lenčés . . . . .	794
<b>Charge Carrier Dynamics of Nanoparticles</b> / Fanxin Wu and Jin Z. Zhang . . . . .	804
<b>Charge Transfer in Metal–Molecule Heterostructures</b> / Debasish Kuila, David B. Janes, and Clifford P. Kubiak . . . . .	819
<b>Charge Transport in Multilayer Nanostructures</b> / Daniel M. Schaadt . . . . .	834
<b>Chemical Warfare Agents: Biosensors for Detection</b> / Elias Greenbaum, Miguel Rodriguez, Jr., and Charlene A. Sanders . . . . .	842
<b>Colloid Systems: Micelles and Nanocrystals</b> / B.L.V. Prasad and Savka I. Stoeva . . . . .	856
<b>Colloidal Nanometals as Fuel Cell Catalyst Precursors</b> / Helmut Bönnemann and K. S. Nagabhushana . . . . .	863
<b>Colloidal Nanoparticles: Aggregation Patterns at Surfaces</b> / Hamidou Haidara and Karine Mougín . . . . .	882
<b>Colloidal Nanoparticles: Electrokinetic Characterization</b> / Kunio Furusawa and Hideo Matsumura . . . . .	893
<b>Colloidal Structures on Patterned Surfaces</b> / Aránzazu del Campo, Anne-Sophie Duwez, Charles-André Fustin, and Ulrich Jonas . . . . .	907
<b>Computational Analysis Using Normal and Multibody Modes</b> / Bryan C. Hathorn, Donald W. Noid, Bobby G. Sumpter, Chao Yang, and William A. Goddard III . . . . .	921
<b>Computational Analysis of Switchable Catenanes</b> / Xiang Zheng and Karl Sohlberg . . . . .	930
<b>Computational Analysis of Switchable Rotaxanes</b> / Xiang Zheng and Karl Sohlberg . . . . .	939
<b>Conducting Polymer Nanopatterns</b> / Shaun F. Filocamo and Mark W. Grinstaff . . . . .	954
<b>Conducting Polymer Nanotubes</b> / Seung Il Cho and Sang Bok Lee . . . . .	965
<b>Controlled Size and Shape Supramolecular Aggregates on Solid Surfaces</b> / Takashi Yokoyama, Toshiya Kamikado, Shiyoshi Yokoyama, and Shinro Mashiko . . . . .	974
<b>Coordination Framework Topology</b> / Neil R. Champness and Neil S. Oxtoby . . . . .	984
<b>Core–Shell Hydrogel Nanoparticles</b> / Clinton D. Jones and L. Andrew Lyon . . . . .	993
<b>Core–Shell Nanospheres, Hollow Capsules, and Bottles</b> / Gang Zhang, Kai Zhang, Yi Yu, and Bai Yang . . . . .	1003
<b>Cubosomes: Bicontinuous Liquid Crystalline Nanoparticles</b> / Patrick T. Spicer . . . . .	1018
<b>Cyanogels: Processing by Spin Coating</b> / Shu Zhu and Andrew B. Bocarsly . . . . .	1029
<b>Cyclic Peptides: Self-Assembly in Hydrogen-Bonded Nanotubes</b> / Roberto J. Brea and Juan R. Granja . . . . .	1037
<b>Dendritic Nanocatalysts</b> / Kiyotomi Kaneda, Masahiko Ooe, Makoto Murata, Tomoo Mizugaki, and Kohki Ebitani . . . . .	1054

<b>Dimensionally Graded Semiconductor Nanoparticle Films</b> / Arif A. Mamedov, Nicholas A. Kotov, and Nataliya N. Mamedova	1062
<b>Dip-Pen Nanolithography: Applications and Functional Extensions</b> / Björn T. Rosner and Linette M. Demers	1070
<b>Dip-Pen Nanolithography: Optical Inks</b> / Brandon L. Weeks, Aleksandr Noy, Abigail E. Miller, Jennifer E. Klare, Bruce W. Woods, and James J. De Yoreo	1084
<b>Dissymmetrical Nanoparticles</b> / Stéphane Reculosa, Christophe Mingotaud, Etienne Duguet, and Serge Ravaine	1093
<b>DNA-Based Nanoinstrument Design</b> / Alexander Hillisch and Stephan Diekmann	1102
<b>DNA-Conjugated Metal Nanoparticles: Chip Detection Applications</b> / Wolfgang Fritzsche	1114
<b>DNA Hybridization: Electronic Control</b> / Kimberly Hamad-Schifferli	1122
<b>DNA Interactions with Functionalized Emulsions</b> / Thierry Delair	1134
<b>Dynamic AFM on Heterogeneous Surfaces</b> / Ijeoma M. Nnebe and James W. Schneider	1144
<b>Electrical Double-Layer Formation</b> / Kun-Lin Yang, Sotira Yiacoumi, and Costas Tsouris	1157
<b>Electrically Functional Nanostructures</b> / Orlin D. Velev and Simon O. Lumsdon	1171
<b>Electrochemical Langmuir Trough</b> / Natalia Varaksa, Thomas F. Magnera, and Josef Michl	1189
<b>Electrochemical Sensors: Functionalized Silica</b> / Yuehe Lin, Wassana Yantasee, and Glen E. Fryxell	1196
<b>Electrochemical Toxicity Sensors</b> / James F. Rusling	1207
<b>Electron Microscopy at Very High Resolution</b> / Klaus van Benthem and Stephen J. Pennycook	1217
<b>Electronic Switches</b> / Richard J. Nichols, David J. Schiffrin, and Wolfgang Haiss	1230
<b>Enantioselectivity on Surfaces</b> / David M. Rampulla and Andrew J. Gellman	1242
<b>Environmental Electron Microscopy Imaging</b> / Satoshi Utsunomiya, Christopher S. Palenik, and Rodney C. Ewing	1252
<b>Environmental Nanoparticles</b> / Alexandra Navrotsky	1262
<b>Enzymatic Synthesis of Nanostructured Polymers and Composites</b> / Christy Ford, Vijay T. John, Gary McPherson, Jibao He, Joseph Akkara, David Kaplan, and Arijit Bose	1271
<b>Epoxy-Layered Silicate Nanocomposites</b> / Chenggang Chen and Tia Benson Tolle	1284
<b>Ethane-Preferred Conformation</b> / Lionel Goodman and Vojislava Pophristic	1294
<b>Fluorescence-Voltage Single Molecule Spectroscopy</b> / Young Jong Lee, Andre J. Gesquiere, So-Jung Park, and Paul F. Barbara	1300
<b>Fluorofullerenes</b> / Olga V. Boltalina and Steven H. Strauss	1307
<b>Fullerenes and Carbon Nanotubes</b> / Laszlo Mihalý	1322
<b>Fullerenes: Chemistry</b> / Mark S. Meier	1331
<b>Fullerenes: Isomer Identification</b> / Guangyu Sun	1340
<b>Fullerenes: Magnetic Behavior</b> / T. L. Makarova	1352
<b>Fullerenes: Topology and Structure</b> / G. Benedek and M. Bernasconi	1360
<b>Functionalization of Surface Layers on Ceramics</b> / Toshihiro Ishikawa	1375
<b>Gecko-Inspired Adhesives: Nanofabrication</b> / Aránzazu del Campo and Eduard Arzt	1384
<b>Gene Delivery via Polymer Nanoparticles</b> / Jie Wen and Kam W. Leong	1394
<b>Germanium Nanoparticles</b> / Boyd R. Taylor and Louisa J. Hope-Weeks	1405
<b>Gold Nanoclusters: Structural Disorder</b> / Ignacio L. Garzón	1412
<b>Gold Nanoparticles on Titania: Activation and Behavior</b> / Jose A. Rodriguez	1422
<b>Guests within Hydrophobic Pockets: Conventional Synthesis</b> / Bruce C. Gibb	1429
<b>Guests within Hydrophobic Pockets: Self-Assembly</b> / Bruce C. Gibb	1451
<b>Halide Transport through Biological Membranes</b> / Lars-Oliver Essen	1476

## Volume III

<b>Heterogeneous Catalysts: Atomic Scale Studies</b> / Robert F. Klie, Kai Sun, Mark M. Disko, Jingyue Liu, and Nigel D. Browning	1491
<b>Heterogeneous Catalytic Reactions by Mass Spectrometry</b> / Steven M. Thornberg and Deborah E. Hunka	1505
<b>Heterogeneous Surfaces with Nanosized Channel Lattices</b> / Lifeng Chi, Michael Gleiche, Steven Lenhart, and Nan Lu	1515
<b>Hierarchically Imprinted Nanostructures for Separation</b> / Sheng Dai, Zongtao Zhang, and Chengdu Liang	1525
<b>High-Strength Alloys: Nanogranular Phases</b> / Dmitri Valentinovich Louzguine and Akihisa Inoue	1536
<b>Hydrogel Nanoparticles Made of Cross-Linked Polyvinylpyrrolidone</b> / Susmita Mitra, Dhruva Jyoti Bharali, and Amarnath Maitra	1546
<b>Ice Nanotubes inside Carbon Nanotubes</b> / Kenichiro Koga and Hideki Tanaka	1558
<b>In-Situ Electron Microscopy</b> / Charles W. Allen	1568
<b>Indium Arsenide Islands on Silicon</b> / P. C. Sharma and Kang L. Wang	1582
<b>Infrared Spectroscopy: Biomolecular Structure at Interfaces</b> / Curtis W. Meuse	1590
<b>Inorganic Nanotubes</b> / Reshef Tenne	1598
<b>Inorganic Nanotubes: Synthesis by Chemical Transport Reaction</b> / Maja Remskar	1606
<b>Inorganic Sulfide Nanotubes: Mechanical Behavior</b> / Ifat Kaplan-Ashiri, H. Daniel Wagner, Gotthard Seifert, and Reshef Tenne	1617
<b>Integrated Methods in Quantum Chemistry</b> / Stephan Irle and Keiji Morokuma	1627
<b>Intercalated Polypropylene Nanocomposites</b> / Michael J. Solomon and Anongnat Somwangthanaroj	1642
<b>Interfacial Forces: Colloidal Particle-Liquid</b> / Sarah A. Nespolo and Geoffrey W. Stevens	1650
<b>Interfacial Phenomena: Chemical Selectivity</b> / Vinay K. Gupta	1662
<b>Ionic Strength Effects: Tunable Nanocrystal Distribution in Colloidal Gold Films</b> / E. Stefan Kooij, E.A. Martijn Brouwer, Herbert Wormeester, and Bene Poelsema	1672
<b>Iron Nanoparticles</b> / Dale L. Huber	1681
<b>Iron Oxide Nanoparticles</b> / Mamoru Senna	1688
<b>Island Nucleation: Predictions</b> / Maria C. Bartelt	1696
<b>Island Surfaces: Fabrication on Self-Assembled Monolayers</b> / Hongjie Liu, Charles Maldarelli, M. Lane Gilchrist, and Alexander Couzis	1708
<b>Lab-on-a-Chip Microreactors</b> / Paul D.I. Fletcher, Stephen J. Haswell, Paul Watts, and Xunli Zhang	1721
<b>Langmuir-Blodgett Films</b> / Ursula Mazur	1738
<b>Laser-Based Deposition: Patterning</b> / Edward M. Nadgorny and Jaroslaw Drelich	1749
<b>Layer-by-Layer Assembly of Electroactive Thin Films to Layered Carbon Electrodes</b> / Tarek R. Farhat	1764
<b>Layer-by-Layer Assembly of Gold Nanoclusters with Self-Assembled Monolayers</b> / Kohei Uosaki, Wenbo Song, Masayuki Okamura, and Toshihiro Kondo	1773
<b>Layer-by-Layer Assembly of Polyelectrolyte Films: Membranes and Catalysts</b> / Bernd Tieke and Ali Toutianoush	1784
<b>Layer-by-Layer Assembly of Semiconducting and Photoreactive Bolaform Amphiphiles</b> / Jason Locklin, Derek Patton, Chuanjun Xia, Xiaowu Fan, and Rigoberto C. Advincula	1798
<b>Layer-by-Layer Assembly of Thin Films of Mixed Nanoparticles</b> / Jianchang Guo, Encai Hao, and Tianquan Lian	1813
<b>Layer-by-Layer Electrostatic Self-Assembly</b> / Michael J. McShane and Yuri M. Lvov	1823
<b>Layered Double Hydroxides: Self-Assembly and Multiple Phases</b> / Zhi Ping Xu and Paul S. Braterman	1841

<b>Ligand–Receptor Systems with Infinite Binding Affinity</b> / <i>Claude F. Meares</i> . . . . .	1853
<b>Lipid Membranes: Nanostructure and Dynamic Organization</b> / <i>J. Gaudioso and D. Y. Sasaki</i> . . . . .	1859
<b>Liposomes: Direct Force Measurement by AFM</b> / <i>Guangzhao Mao, Xuemei Liang, and K.Y. Simon Ng</i> . . . . .	1869
<b>Liquid Crystals and Nanostructured Surfaces: Detecting Protein Binding</b> / <i>Yan-Yeung Luk</i> . . . . .	1878
<b>Litho-to-Nano Link</b> / <i>Gianfranco Cerofolini, Dario Narducci, and Elisabetta Romano</i> . . . . .	1890
<b>Low-Dielectric Constant Materials</b> / <i>Robert D. Miller</i> . . . . .	1901
<b>Luminescence of Nanoparticle-Labeled Antibodies and Antigens</b> / <i>Shaopeng Wang and Nicholas A. Kotov</i> . . . . .	1915
<b>Magnetic Ferrofluids</b> / <i>Carlos Rinaldi, Thomas Franklin, Markus Zahn, and Tahir Cader</i> . . . . .	1922
<b>Magnetic Nanocarbon</b> / <i>T. L. Makarova</i> . . . . .	1939
<b>Magnetic Nanomaterials: Conventional Synthesis and Properties</b> / <i>Dajie Zhang</i> . . . . .	1951
<b>Magnetic Nanomaterials: Nonconventional Synthesis and Chemical Design</b> / <i>Luminita Patron, Ioana Mindru, and Gabriela Marinescu</i> . . . . .	1968
<b>Magnetic Nanoparticles</b> / <i>Valérie Cabuil</i> . . . . .	1985
<b>Magnetic Nanoparticles for Granular Recording Media</b> / <i>David E. Nikles and J. W. Harrell</i> . . . . .	2001
<b>Membrane-Coated Nanoparticles: Photochemistry</b> / <i>Ulrich Siggel, Guangtao Li, and Jürgen-Hinrich Fuhrhop</i> . . . . .	2012
<b>Mesoporous Materials</b> / <i>James C. Vartuli, Wielsaw J. Roth, and Thomas F. Degnan, Jr.</i> . . . . .	2029
<b>Metal Clusters on Oxides</b> / <i>Ivan Stensgaard</i> . . . . .	2044
<b>Metal Nanoparticle Catalysts</b> / <i>Naoki Toshima</i> . . . . .	2052
<b>Metal Nanoparticle Ensembles: Collective Optical Properties</b> / <i>Alexander Wei</i> . . . . .	2064
<b>Metal Nanoparticles Prepared in Supercritical Carbon Dioxide</b> / <i>Harry W. Rollins</i> . . . . .	2072
<b>Metal Nanoparticles: Self-Assembly into Electronic Nanostructures</b> / <i>Venugopal Santhanam and Ronald P. Andres</i> . . . . .	2079
<b>Metal Nanostructures: Synthesis Controlled by Photoexcitation</b> / <i>Kei Murakoshi and Yoshihiro Nakato</i> . . . . .	2091
<b>Metal Nanostructures: Synthesis by Soft Chemical Methods</b> / <i>Yugang Sun and Younan Xia</i> . . . . .	2105
<b>Metal–Oxide Interfaces: Design via Control of Defect Density</b> / <i>A. Bogicevic</i> . . . . .	2116
<b>Metal Oxide Nanoparticles</b> / <i>Ryan M. Richards</i> . . . . .	2126
<b>Metal Oxide Nanoribbons and Carbon Nanotubes: Modeling</b> / <i>Amitesh Maiti</i> . . . . .	2140
<b>Metallic Nanopowders</b> / <i>Frederick Tepper, Marat I. Lerner, and David S. Ginley</i> . . . . .	2153
<b>Metallic Nanopowders: Rocket Propulsion</b> / <i>Leonid Kaledin and Frederick Tepper</i> . . . . .	2165
<b>Metallic Quantum Dots</b> / <i>J. P. Wilcoxon</i> . . . . .	2176
<b>Metallomacrocyclic Selective Ion Receptors</b> / <i>Kay Severin</i> . . . . .	2202

---

## Volume IV

<b>Mica Surfaces: Charge Nucleation and Wear</b> / <i>James M. Helt and James D. Batteas</i> . . . . .	2211
<b>Micro- and Mesoporous Nanomaterials: Catalytic Properties</b> / <i>Johannes A. Lercher and Andreas Jentys</i> . . . . .	2229
<b>Microgel Dispersions: Colloidal Forces and Phase Behavior</b> / <i>Jianzhong Wu and Zhibing Hu</i> . . . . .	2243
<b>Microweighing in Supercritical Carbon Dioxide</b> / <i>You-Ting Wu and Christine S. Grant</i> . . . . .	2253
<b>Mineral Nanoparticles: Electrokinetics</b> / <i>Mehmet S. Celik and Bahri Ersoy</i> . . . . .	2266
<b>Mixed Metal Oxide Nanoparticles</b> / <i>Pramesh N. Kapoor, Ajay Kumar Bhagi, Ravichandra S. Mulukutla, and Kenneth J. Klabunde</i> . . . . .	2280
<b>Molecular Computing Machines</b> / <i>Yaakov Benenson and Ehud Shapiro</i> . . . . .	2291
<b>Molecular Electronics: Logic and Memory</b> / <i>Dustin K. James and James M. Tour</i> . . . . .	2303



<b>Molecular Electronics: Models of Switchable and Programmable Devices</b> / <i>Pedro A. Derosa, Vandana R. Tarigopula, and Jorge M. Seminario</i> . . . . .	2317
<b>Molecular Manipulator: Dynamic Design Criteria</b> / <i>Andrés Jaramillo-Botero</i> . . . . .	2336
<b>Molecular Motor-Powered Nanodevices: Control Mechanisms</b> / <i>Jacob J. Schmidt and Carlo D. Montemagno</i> . . . . .	2347
<b>Molecular Orientation at Interfaces: Vibrational Spectroscopy</b> / <i>Zhan Chen</i> . . . . .	2357
<b>Molecular Probes of Cation–Arene Interactions</b> / <i>George W. Gokel</i> . . . . .	2369
<b>Molecular Receptor-Modified Metal Nanoparticles</b> / <i>Jian Liu</i> . . . . .	2377
<b>Molecular Self-Assembly: Environmental and Sensing Applications</b> / <i>Glen E. Fryxell, R. Shane Addleman, S. V. Mattigod, Yuehe Lin, T. S. Zemanian, H. Wu, Jerome C. Birnbaum, J. Liu, and X. Feng</i> . . . . .	2387
<b>Molecular Simulations of DNA Counterion Distributions</b> / <i>Alexander Lyubartsev</i> . . . . .	2398
<b>Molecular Switches</b> / <i>Jean-Pierre Launay, Christophe Coudret, and Christian Joachim</i> . . . . .	2411
<b>Molecular Switches and Motors</b> / <i>Richard A. van Delden and Ben L. Feringa</i> . . . . .	2424
<b>Molecular Wires</b> / <i>Dustin K. James and James M. Tour</i> . . . . .	2441
<b>Monolayer-Protected Metal Nanoparticles: Chemical Sensing and Gas Chromatography</b> / <i>Jay W. Grate, David A. Nelson, Rhonda Skaggs, Robert E. Synovec, and Gwen M. Gross</i> . . . . .	2460
<b>Monolayer-Protected Metal Nanoparticles: Synthesis</b> / <i>Young-Seok Shon</i> . . . . .	2469
<b>Moore’s Law: Performance and Power Dissipation</b> / <i>Laszlo B. Kish</i> . . . . .	2480
<b>Motor Proteins in Synthetic Materials and Devices</b> / <i>Henry Hess, George Bachand, and Viola Vogel</i> . . . . .	2484
<b>Nano–Mesoscopic Interface: Hybrid Devices</b> / <i>Gianfranco Cerofolini</i> . . . . .	2493
<b>Nanoarrays: Electrochemically Self-Assembled</b> / <i>S. Bandyopadhyay</i> . . . . .	2502
<b>Nanobiological Sensors</b> / <i>Nathaniel Cady, Anand Gadre, and Alain E. Kaloyeros</i> . . . . .	2514
<b>Nanobridges: Thermal Properties</b> / <i>Jeong Won Kang and Ho Jung Hwang</i> . . . . .	2522
<b>Nanoceramics</b> / <i>Abbas Khaleel</i> . . . . .	2531
<b>Nanoceramics: Thermal Conductivity</b> / <i>Paul G. Klemens</i> . . . . .	2539
<b>Nanocolloidal Gold Films: Self-Assembly</b> / <i>E. Stefan Kooij, E.A. Martijn Brouwer, Agnes A. Mewe, Herbert Wormeester, and Bene Poelsema</i> . . . . .	2545
<b>Nanocomposite Magnetic Materials: Shock-Induced Synthesis</b> / <i>N. N. Thadhani and Z. Q. Jin</i> . . . . .	2556
<b>Nanocrystal Arrays: Self-Assembly and Physical Properties</b> / <i>Xiao-Min Lin, Raghuv eer Parthasarathy, and Heinrich M. Jaeger</i> . . . . .	2568
<b>Nanocrystals Synthesized in Colloidal Self-Assemblies</b> / <i>M. P. Pileni</i> . . . . .	2581
<b>Nanocrystalline Magnesia and Alumina: Surface Chemistry</b> / <i>Richard M. Narske</i> . . . . .	2592
<b>Nanocrystalline Materials: Fatigue</b> / <i>Alexie Yu. Vinogradov and Sean R. Agnew</i> . . . . .	2602
<b>Nanocrystalline Materials: Synthesis and Properties</b> / <i>Alexandr I. Gusev</i> . . . . .	2621
<b>Nanocrystalline Oxides: Surfactant-Assisted Growth</b> / <i>Claudia L. Bianchi, Silvia Ardizzone, and Giuseppe Cappelletti</i> . . . . .	2637
<b>Nanocrystalline Zeolites</b> / <i>Vicki H. Grassian and Sarah C. Larsen</i> . . . . .	2646
<b>Nanocrystallization</b> / <i>John H. Perepezko</i> . . . . .	2655
<b>Nanocrystals: Size-Dependent Properties and Emerging Applications</b> / <i>G. U. Kulkarni, P. John Thomas, and C.N.R. Rao</i> . . . . .	2665
<b>Nanocrystals: Synthesis and Mesoscalar Organization</b> / <i>G. U. Kulkarni, P. John Thomas, and C.N.R. Rao</i> . . . . .	2676
<b>Nanodiamonds</b> / <i>Jean-Yves Raty and Giulia Galli</i> . . . . .	2697
<b>Nanoencapsulation of Bioactive Substances</b> / <i>Yury E. Shapiro</i> . . . . .	2707
<b>Nanofibers and Carbon Nanotubes: Novel Metal Catalyst Supports</b> / <i>Mark A. Keane</i> . . . . .	2723

<b>Nanofilms in Giant Magnetoresistance Heads</b> / Edward Grochowski and Robert E. Fontana, Jr. . . . .	2737
<b>Nanofiltration Separations</b> / Eric M.V. Hoek and Anna Jawor . . . . .	2749
<b>Nanofriction and Nanowear of Sliding Systems: Simulations</b> / W.C.D. Cheong . . . . .	2763
<b>Nanolithography: Length Scale Limitations</b> / Takashi Ito . . . . .	2779
<b>Nanomaterials: Advances in Technology and Industry</b> / Ganesh Skandan and Amit Singhal . . . . .	2788
<b>Nanomaterials: Manufacturing, Processing, and Applications</b> / Pramod K. Sharma, Weifang Miao, Anit Giri, and Srikanth Raghunathan . . . . .	2799
<b>Nanomaterials and Molecular Devices: De Novo Design Theory</b> / Kwang S. Kim, P. Tarakeshwar, and Han Myoung Lee . . . . .	2815
<b>Nanomaterials and Nanodevices: Ion-Beam Technology</b> / Dmitri Litvinov and Sakhrat Khizroev . . . . .	2825
<b>Nanomaterials: Trends</b> / Richard Silbergliitt . . . . .	2836
<b>Nanomechanical Resonant Devices: Surface Chemistry</b> / Joshua A. Henry, Debodhonyaa Sengupta, and Melissa A. Hines . . . . .	2848
<b>Nanoparticle Arrays: Optical and Electronic Applications</b> / Ilona Kretschmar and Mark A. Reed . . . . .	2856
<b>Nanoparticle Assemblies: Magnetic Properties</b> / Xiangcheng Sun . . . . .	2868
<b>Nanoparticle Suspensions: Phase Behavior</b> / Subramanian Ramakrishnan and Charles F. Zukoski . . . . .	2878
<b>Nanoparticle Synthesis: Biological Path</b> / Kenji Iwahori and Ichiro Yamashita . . . . .	2890
<b>Nanoparticles: Generation, Functionalization, and Ion Sensing</b> / Jason J. Davis and Paul D. Beer . . . . .	2898
<b>Nanoparticles: Synthesis in Polymer Substrates</b> / Bai Yang and Junhu Zhang . . . . .	2912

## Volume V

<b>Nanophase Powders: Mechanosynthesis</b> / F. Miani, F. Maurigh, and F. Delogu . . . . .	2923
<b>Nanoporosity Evolution on Dealloying</b> / Jonah Erlebacher . . . . .	2938
<b>Nanoporous Anodic Alumina: Structural and Optical Anisotropy</b> / E. Stefan Kooij, Aurelian C. Gâlcă, Herbert Wormeester, and Bene Poelsema . . . . .	2947
<b>Nanostructured Alloys: Cryomilling Synthesis and Behavior</b> / David Witkin, Piers Newbery, Bing Q. Han, and Enrique J. Lavernia . . . . .	2958
<b>Nanostructured Catalysts</b> / Ravichandra S. Mulukutla . . . . .	2967
<b>Nanostructured Catalysts: Design and Synthesis</b> / Hua Chun Zeng . . . . .	2974
<b>Nanostructured Composites: Carbon-Derived Fibers</b> / Peter M.A. Sherwood . . . . .	2986
<b>Nanostructured Composites: Titanium-Based Alloys</b> / Jürgen Eckert, Jayanta Das, and Ki Buem Kim . . . . .	2996
<b>Nanostructured Materials: Metals on Microtubule Supports</b> / Silke Behrens and Eberhard Unger . . . . .	3012
<b>Nanostructured Materials: Synthesis by Mechanical Attrition</b> / Carl C. Koch . . . . .	3019
<b>Nanostructured Materials: Synthesis by Mechanical Means</b> / H.-J. Fecht . . . . .	3030
<b>Nanostructured Materials: Synthesis in Supercritical Fluids</b> / Yuehe Lin, Xiang-Rong Ye, and Chien M. Wai . . . . .	3040
<b>Nanostructured Multilayers: Applications in X-Ray Optics</b> / Michael Störmer, Carsten Michaelsen, Jörg Wiesmann, Paulo Ricardo, and Rüdiger Bormann . . . . .	3052
<b>Nanostructured Silica and Silica-Derived Materials</b> / Ho-Cheol Kim and Geraud Dubois . . . . .	3063
<b>Nanostructured Ultrastrong Materials</b> / Nicholas A. Kotov, Arif A. Mamedov, Dirk M. Guldi, Zhiyong Tang, Maurizio Prato, James Wicksted, and Andreas Hirsch . . . . .	3072

<b>Nanostructures Based on Layered Transition-Metal Chalcogenides</b> / <i>Russell R. Chianelli and Myriam Perez de la Rosa</i> .....	3080
<b>Nanostructures Derived from Phase-Separated Polymers</b> / <i>Michael R. Bockstaller and Edwin L. Thomas</i> .....	3093
<b>Nanotube Sensors</b> / <i>Marc Wirtz and Charles R. Martin</i> .....	3109
<b>Nanotubes: Functionalization</b> / <i>Stanislaus S. Wong and Sarbajit Banerjee</i> .....	3119
<b>Nanowires: Molecular Assembly</b> / <i>Tomoyuki Akutagawa, Takayoshi Nakamura, and Jan Becher</i> .....	3136
<b>Nanowires and Nanobelts: Mechanical Properties</b> / <i>Zhong Lin Wang</i> .....	3146
<b>Near-Field Microscopy</b> / <i>Björn T. Rosner and Daniel W. van der Weide</i> .....	3159
<b>Near-Field Raman Spectroscopy</b> / <i>Eric Ayars</i> .....	3169
<b>Near-Field Raman Spectroscopy: Resolution Enhancement</b> / <i>Satoshi Kawata and Yasushi Inouye</i> .....	3177
<b>Near-Field Scanning Optical Microscopy: Chemical Imaging</b> / <i>Bogdan Dragnea</i> .....	3185
<b>Noble Metal Nanoparticles on Carbon Fibers</b> / <i>Dmitri A. Bulushev and Igor Yuranov</i> .....	3195
<b>Nonlinear Optical Materials from Self-Assembled Organic Films</b> / <i>Matthew Guzy, Richey M. Davis, Patrick J. Neyman, Charles Brands, J. R. Heflin, Harry W. Gibson, and Kevin E. Van Cott</i> .....	3206
<b>Nucleoside- and Nucleobase-Substituted Oligopyrrolic Macrocycles</b> / <i>Vladimír Král, Martin Valík, Tatiana V. Shishkanova, and Jonathan L. Sessler</i> .....	3216
<b>Oil-Filled Nanocapsules</b> / <i>Royale S. Underhill</i> .....	3234
<b>One-Dimensional Electrically Conducting Polymeric Nanostructures</b> / <i>Andrew D.W. Carswell and Brian P. Grady</i> .....	3243
<b>Optical Molecular Devices</b> / <i>A. Prasanna de Silva and Nathan D. McClenaghan</i> .....	3251
<b>Optical Nanosensors and Nanobiosensors</b> / <i>Brian M. Cullum</i> .....	3258
<b>Ordered Vesicles at the Silicon–Water Interface</b> / <i>Duncan J. McGillivray</i> .....	3269
<b>Organofullerenes in Water</b> / <i>Eiichi Nakamura and Hiroyuki Isobe</i> .....	3277
<b>Organosilanes: Molecular Assembly</b> / <i>Atsushi Takahara</i> .....	3287
<b>Oxide Nanoparticles: Electrochemical Performance</b> / <i>Dominique Larcher and Jean-Marie Tarascon</i> .....	3299
<b>Palladium Nanoclusters</b> / <i>Kiyotomi Kaneda, Kwang-Min Choi, Tomoo Mizugaki, and Kohki Ebitani</i> .....	3309
<b>Patents and Inventions</b> / <i>Jeffrey A. Lindeman</i> .....	3318
<b>Permanent Magnets Based on Nanostructured Intermetallic Alloys</b> / <i>Paul McGuinness, Andraž Kocjan, and Spomenka Kobe</i> .....	3328
<b>Permanent Nanocomposite Magnets</b> / <i>Satoshi Hirosawa</i> .....	3336
<b>Phase Transfer of Monosaccharides through Noncovalent Interactions</b> / <i>Elizabeth K. Auty and Anthony P. Davis</i> .....	3347
<b>Photonic Crystal Fibers</b> / <i>P. St. J. Russell, J. C. Knight, T. A. Birks, and P. J. Roberts</i> .....	3356
<b>Photovoltaics: Organic-Based Solar Cells</b> / <i>Sean E. Shaheen and David S. Ginley</i> .....	3370
<b>Platinum Nanoparticles: Synthesis and Catalytic Properties</b> / <i>Ioan Balint and Akane Miyazaki</i> .....	3386
<b>Polyelectrolyte Films with Incorporated Carbon Nanotubes</b> / <i>Jason H. Rouse and Peter T. Lillehei</i> .....	3396
<b>Polyelectrolyte–Surfactant Complex Nanoparticles</b> / <i>Hans-Peter Hentze</i> .....	3403
<b>Polyion Complex Micelles</b> / <i>Atsushi Harada and Kazunori Kataoka</i> .....	3409
<b>Polymer–Clay Nanocomposites and Polymer Brushes</b> / <i>Xiaowu Fan, Chuanjun Xia, and Rigoberto C. Advincula</i> .....	3417
<b>Polymer Colloids and Their Metallation</b> / <i>Lyudmila M. Bronstein</i> .....	3430
<b>Polymer-Mediated Self-Assembly of Nanoparticles</b> / <i>Tyler B. Norsten, Amitav Sanyal, Roy Shenhar, and Vincent M. Rotello</i> .....	3443



<b>Polymer Molding: Nanostructure Replication</b> / Daniel B. Wolfe, J. Christopher Love, and George M. Whitesides . . . . .	3456
<b>Polymer Nanocomposites with Nanoparticle and Carbon Nanotube Fillers</b> / B. J. Ash, A. Eitan, and L. S. Schadler . . . . .	3466
<b>Polymer Nanofibers Prepared by Electrospinning</b> / Roland Dersch, Andreas Greiner, and Joachim H. Wendorff . . . . .	3480
<b>Polymer–Nanoparticle Composites</b> / Kevin Sill, Seunghoo Yoo and Todd Emrick . . . . .	3487
<b>Polymer Nanowires Conjugated by Controlled Chain Polymerization</b> / Yuji Okawa and Masakazu Aono . . . . .	3501
<b>Polypropylene and Thermoplastic Olefins Nanocomposites</b> / Francis M. Mirabella, Jr. . . . .	3509
<b>Porous Alumina Templates for Nanofabrication</b> / Latika Menon . . . . .	3525
<b>Porphyric Materials: Self-Assembly on Surfaces</b> / Charles Michael Drain, James D. Batteas, Gabriela Smeureanu, and Sandeep Patel . . . . .	3539
<b>Printed and Molded Nanostructures: Photonic Applications</b> / John A. Rogers . . . . .	3559
<b>Protein Adsorption Kinetics under an Applied Electric Field</b> / Paul R. Van Tassel . . . . .	3569
<b>Protein Nanotubes as Building Blocks</b> / Hiroshi Matsui . . . . .	3578
<b>Proteins: Structure and Interaction Patterns to Solid Surfaces</b> / Thomas J. Webster . . . . .	3590
<b>Quantum Dot Arrays: Electromagnetic Properties</b> / Sergey A. Maksimenko and Gregory Ya. Slepyan . . . . .	3606
<b>Quantum Dot Lasers</b> / Mikhail V. Maximov and Nikolai N. Ledentsov . . . . .	3617
<b>Quantum Dots: Electronic Coupling and Structural Ordering</b> / Glenn S. Solomon . . . . .	3634
<b>Quantum Dots: Inelastic Light Scattering from Electronic Excitations</b> / Christian Schüller . . . . .	3661
<b>Quantum Dots: Phonons in Self-Assembled Multiple Germanium Structures</b> / Jianlin Liu, Aleksandr Khitun, and Kang L. Wang . . . . .	3673
<b>Raman Spectroscopy of Carbon Nanotube–Polymer Composites</b> / Bin Chen . . . . .	3682
<b>Ring Structures from Nanoparticles and Other Nanoscale Building Blocks</b> / Zhen Liu and Rastislav Levicky . . . . .	3694
<b>Risk Assessment and Benefits</b> / Douglas Mulhall . . . . .	3702

---

## Volume VI

<b>Scanning Near-Field Photolithography</b> / Graham J. Leggett . . . . .	3709
<b>Scanning Probe Lithography: Polymeric and Biomolecular Nanostructures</b> / Stefan Zauscher . . . . .	3721
<b>Scanning Single-Electron Transistor Microscopy</b> / N. B. Zhitenev and T. A. Fulton . . . . .	3731
<b>Self-Assembled Monolayers: Adsorption and Desorption from Alkanethiols on Gold</b> / Pieter Stroeve . . . . .	3738
<b>Self-Assembled Monolayers: Chemical and Physical Modification under Vacuum</b> / Jessica Torres, Anthony J. Wagner, Christopher C. Perry, Glenn M. Wolfe, and D. Howard Fairbrother . . . . .	3747
<b>Self-Assembled Monolayers: Surface Nanostructure Effect on Wetting</b> / Jun Yang, Jingmin Han, Kelvin Isaacson, and Daniel Y. Kwok . . . . .	3762
<b>Self-Assembled Quantum Dots: Atomic Scale Engineering</b> / S. Oktyabrsky and Alain E. Kaloyeros . . . . .	3775
<b>Self-Assembled Quantum Dots: Electronic Structures and Optical Properties</b> / Andrew Williamson . . . . .	3789
<b>Self-Assembled Silane Monolayers: Cyano-to-Carboxylic Termination Conversion</b> / Chandra Sekhar Palla and Alexander Couzis . . . . .	3801
<b>Self-Assembled Structures</b> / Anna Cristina Samia and Xiao-Min Lin . . . . .	3816
<b>Self-Assembled Thin Films: Optical Characterization</b> / Herbert Wormeester, E. Stefan Kooij, and Bene Poelsema . . . . .	3829

<b>Self-Assembly and Chirality of Molecules at Interfaces</b> / <i>Dalia G. Yablon</i> . . . . .	3840
<b>Self-Assembly of Coordination Cages</b> / <i>Laura Pironcini and Enrico Dalcanale</i> . . . . .	3848
<b>Self-Assembly Directed by NH-O Hydrogen Bonding</b> / <i>Katrina A. Jolliffe and Leonard F. Lindoy</i> . . . . .	3864
<b>Self-Formed Quantum Dots: Structural and Optical Characterization</b> / <i>Shun-ichi Gonda and Hajime Asahi</i> . . . . .	3877
<b>Self-Organized Superstructures: Molecular Design</b> / <i>Makoto Tadokoro</i> . . . . .	3886
<b>Semiconductor Nanowires: Macroelectronics Applications</b> / <i>Yugang Sun and John A. Rogers</i> . . . . .	3896
<b>Semiconductor Nanowires: Nanoscale Electronics and Optoelectronics</b> / <i>Yu Huang, Xiangfeng Duan, and Charles M. Lieber</i> . . . . .	3910
<b>Semiconductor Nanowires: Rational Synthesis</b> / <i>Xiangfeng Duan and Charles M. Lieber</i> . . . . .	3941
<b>Semiconductor Quantum Dots: Atomic Ordering over Time</b> / <i>Peter Moeck</i> . . . . .	3954
<b>Semiconductor Quantum Dots: Site-Controlled Self-Organization</b> / <i>S. Kohmoto, H. Nakamura, S. Nishikawa, T. Yang, and K. Asakawa</i> . . . . .	3965
<b>Sensors Based on Chemicurrents</b> / <i>B. Roldan Cuenya and E. W. McFarland</i> . . . . .	3973
<b>Silane Self-Assembled Monolayers: Nanoscale Domains by Sequential Adsorption</b> / <i>Nitin Kumar</i> . . . . .	3984
<b>Silica Nanotubes: Wetting and Diffusion</b> / <i>Kenji Okamoto, Karthik Jayaraman, Sang Jun Son, Sang Bok Lee, and Douglas S. English</i> . . . . .	3995
<b>Silica Surfaces Functionalization</b> / <i>V. A. Tertykh</i> . . . . .	4001
<b>Silicon Functionalization for Molecular Electronics</b> / <i>Gianfranco Cerofolini, Dario Narducci, and Elisabetta Romano</i> . . . . .	4009
<b>Silicon Nanoclusters: Simulations</b> / <i>Aaron Puzder</i> . . . . .	4021
<b>Silicon Nanocrystals: Quantum Confinement</b> / <i>James R. Chelikowsky</i> . . . . .	4033
<b>Single-Cell Level Mass Spectrometric Imaging</b> / <i>Sara G. Ostrowski, Andrew G. Ewing, and Nicholas Winograd</i> . . . . .	4046
<b>Single Molecule Spectroscopy for Nanomaterials Characterization</b> / <i>Daniel A. Higgins and Yanwen Hou</i> . . . . .	4057
<b>Single-Walled Carbon Nanotubes: Field Emission Properties</b> / <i>Xiaofeng F. Duan, Brahim Akdim, and Ruth Pachter</i> . . . . .	4078
<b>Single-Walled Carbon Nanotubes: Geometries, Electronic Properties, and Actuation</b> / <i>Guangyu Sun, Marc Nicklaus, and Miklos Kertesz</i> . . . . .	4085
<b>Single-Walled Carbon Nanotubes: Separation Using Capillary Electrophoresis</b> / <i>Stephen K. Doorn</i> . . . . .	4096
<b>Single-Walled Carbon Nanotubes: Structures and Symmetries</b> / <i>Carter T. White and John W. Mintmire</i> . . . . .	4108
<b>Small Amplitude AFM</b> / <i>Peter M. Hoffmann</i> . . . . .	4119
<b>Smallest Size Regime: Control of Ultrafast Dynamics</b> / <i>Stefan Vajda and Ludger Wöste</i> . . . . .	4132
<b>Smart Nanotubes for Biotechnology and Biocatalysis</b> / <i>Charles R. Martin and Punit Kohli</i> . . . . .	4147
<b>Soft Materials: AFM Investigations and Nanophysics</b> / <i>J. P. Aimé, R. Boisgard, S. Marsaudon, and G. Couturier</i> . . . . .	4158
<b>Stability of Nanostructures on Surfaces</b> / <i>Karsten Pohl</i> . . . . .	4167
<b>STEM of Chiral Pair Self-Assembled Monolayers</b> / <i>Yuguang Cai and Steven L. Bernasek</i> . . . . .	4176
<b>STEM: Self-Assembly on Graphite</b> / <i>Thomas Müller</i> . . . . .	4185
<b>Structural Color</b> / <i>Pete Vukusic</i> . . . . .	4195
<b>Structural Nanomaterials</b> / <i>Joanna R. Groza and Jeffrey C. Gibeling</i> . . . . .	4205
<b>Structural Transitions in Thin Films</b> / <i>Rajarshi Banerjee, Gregory B. Thompson, and Hamish L. Fraser</i> . . . . .	4217
<b>Superconductor Nanowires: Templated by Single Molecules</b> / <i>Alexey Bezryadin, Anthony Bollinger, David Hopkins, Michael Murphey, Mikas Remeika, and Andrey Rogachev</i> . . . . .	4228

<b>Supramolecular Networks Synthesized in Nanoparticle–Polymer Mixtures</b> / <i>Anna C. Balazs and Gavin A. Buxton</i> . . . . .	4240
<b>Surface-Enhanced Raman Scattering</b> / <i>Adam M. Schwartzberg and Jin Z. Zhang</i> . . . . .	4250
<b>Surface Forces on Nanoparticles Determined by Direct Measurement</b> / <i>Jeong-Min Cho, Georgios Pyrgiotakis, and Wolfgang M. Sigmund</i> . . . . .	4260
<b>Surface Plasmon Spectra of Silver and Gold Nanoparticle Assemblies</b> / <i>Mondona Zangeneh and Roger Terrill</i> . . . . .	4271
<b>Template-Directed Assembly of Dinuclear Triple-Stranded Helicates</b> / <i>Markus Albrecht</i> . . . . .	4283
<b>Templating Aerogels for Tunable Nanoporosity</b> / <i>Aydin K. Sunol and Sermin G. Sunol</i> . . . . .	4294
<b>Templating Polymer Crystal Growth Using Block Copolymers</b> / <i>Yueh-Lin Loo</i> . . . . .	4303
<b>Thermal Effect on the Luminescence Properties of Quantum Dots</b> / <i>X. B. Zhang and R. D. Dupuis</i> . . . . .	4316
<b>Thermodynamics at the Meso- and Nanoscale</b> / <i>Mikhail A. Anisimov</i> . . . . .	4326
<b>Three-Dimensional Nanofabrication Using Multiphoton Absorption</b> / <i>John T. Fourkas and Tommaso Baldacchini</i> . . . . .	4338
<b>Titania Coatings on Stainless Steel</b> / <i>Ganesh Balasubramanian, Dionysios D. Dionysiou, and Makram T. Suidan</i> . . . . .	4348
<b>Titania Nanoparticles: Photocatalytic Properties</b> / <i>Scott Buzby and S. Ismat Shah</i> . . . . .	4356
<b>Toxicological Effects and Screening of Engineered Nanoparticles</b> / <i>Paul Borm and Ken Donaldson</i> . . . . .	4363
<b>Tribology of Inorganic Nanoparticles</b> / <i>Lev Rapoport</i> . . . . .	4375
<b>Tribology at the Nanoscale</b> / <i>Peter T. Cummings and Clare McCabe</i> . . . . .	4385
<b>Tungsten Carbide–Cobalt Nanocomposites</b> / <i>Purnesh Seegopaul and Zhigang Zak Fang</i> . . . . .	4390
<b>Ultrathin Polymer Films: Nanoparticle Nucleation</b> / <i>Pieter Stroeve</i> . . . . .	4400
<b>Virus Nanoparticles: Adsorption and Organization on Substrates</b> / <i>Jiyu Fang</i> . . . . .	4407
<b>Yttria-Tetragonally Stabilized Zirconia</b> / <i>R. Allen Kimel</i> . . . . .	4414
<b>Zeolite Membranes</b> / <i>Wei Xing, João C. Diniz da Costa, Gao Qing (Max) Lu, and Z. F. Yan</i> . . . . .	4421

# Topical Table of Contents

---

## Analytical Methods and Characterization Techniques

---

### *Atomic Force Microscopy*

<b>AFM: Biopolymers</b> / Nehal I. Abu-Lail and Terri A. Camesano . . . . .	63
<b>AFM: Hydrogen-Bonded Nanostructures</b> / Holger Schönherr, Mercedes Crego-Calama, G. Julius Vancso, and David N. Reinhoudt . . . . .	76
<b>AFM: Imaging and Force Spectroscopy on Cell Surfaces</b> / Yves F. Dufrêne . . . . .	99
<b>AFM: Imaging Artifacts</b> / Stephanie Butler Velegol . . . . .	88
<b>AFM: Metal Ion Sorption</b> / Viriya Vithayaveroj, Sotira Yiacoumi, and Costas Tsouris . . . . .	109
<b>AFM: Nanolithography on Organized Films</b> / Seunghyun Lee and Haiwon Lee . . . . .	119
<b>AFM: Protein Adsorption</b> / David T. Kim, Harvey W. Blanch, and Clayton J. Radke . . . . .	129
<b>AFM: Simulation of Interaction Forces</b> / Ivan U. Vakarelski, Scott C. Brown, Bahar Basim, and Brij M. Moudgil . . . . .	153
<b>Biomaterials: Mechanical Characterization</b> / Eunice Phay Shing Tan and Chwee Teck Lim . . . . .	317
<b>Dip-Pen Nanolithography: Applications and Functional Extensions</b> / Björn T. Rosner and Linette M. Demers . . . . .	1070
<b>Dynamic AFM on Heterogeneous Surfaces</b> / Ijeoma M. Nnebe and James W. Schneider . . . . .	1144
<b>Liposomes: Direct Force Measurement by AFM</b> / Guangzhao Mao, Xuemei Liang, and K.Y. Simon Ng . . . . .	1869
<b>Mica Surfaces: Charge Nucleation and Wear</b> / James M. Helt and James D. Batteas . . . . .	2211
<b>Self-Formed Quantum Dots: Structural and Optical Characterization</b> / Shun-ichi Gonda and Hajime Asahi . . . . .	3877
<b>Small Amplitude AFM</b> / Peter M. Hoffmann . . . . .	4119
<b>Soft Materials: AFM Investigations and Nanophysics</b> / J. P. Aimé, R. Boisgard, S. Marsaudon, and G. Couturier . . . . .	4158
<b>Surface Forces on Nanoparticles Determined by Direct Measurement</b> / Jeong-Min Cho, Georgios Pyrgiotakis, and Wolfgang M. Sigmund . . . . .	4260

---

### *Electron Microscopy*

<b>Aberration-Corrected Z-Contrast STEM: Semiconducting Nanocrystals</b> / James R. McBride, Andrew R. Lupini, Stephen J. Pennycook, and Sandra J. Rosenthal . . . . .	1
<b>Catalysts by Nanoscale Design</b> / Chaitanya Kumar Narula . . . . .	772
<b>Controlled Size and Shape Supramolecular Aggregates on Solid Surfaces</b> / Takashi Yokoyama, Toshiya Kamikado, Shiyoshi Yokoyama, and Shinro Mashiko . . . . .	974
<b>Electron Microscopy at Very High Resolution</b> / Klaus van Benthem and Stephen J. Pennycook . . . . .	1217

---

**Analytical Methods and Characterization Techniques (*cont'd.*)**


---

**Electron Microscopy (*cont'd.*)**

<b>Environmental Electron Microscopy Imaging</b> / Satoshi Utsunomiya, Christopher S. Palenik, and Rodney C. Ewing	1252
<b>Heterogeneous Catalysts: Atomic Scale Studies</b> / Robert F. Klie, Kai Sun, Mark M. Disko, Jingyue Liu, and Nigel D. Browning	1491
<b>In-Situ Electron Microscopy</b> / Charles W. Allen	1568
<b>Molecular Switches</b> / Jean-Pierre Launay, Christophe Coudret, and Christian Joachim	2411
<b>Nanoparticle Assemblies: Magnetic Properties</b> / Xiangcheng Sun	2868
<b>Nanostructures Based on Layered Transition-Metal Chalcogenides</b> / Russell R. Chianelli and Myriam Perez de la Rosa	3080
<b>Nanowires: Molecular Assembly</b> / Tomoyuki Akutagawa, Takayoshi Nakamura, and Jan Becher	3136
<b>Polymer Nanowires Conjugated by Controlled Chain Polymerization</b> / Yuji Okawa and Masakazu Aono	3501
<b>Scanning Single-Electron Transistor Microscopy</b> / N. B. Zhitenev and T. A. Fulton	3731
<b>Semiconductor Quantum Dots: Atomic Ordering over Time</b> / Peter Moeck	3954
<b>Semiconductor Quantum Dots: Site-Controlled Self-Organization</b> / S. Kohmoto, H. Nakamura, S. Nishikawa, T. Yang, and K. Asakawa	3965
<b>Stability of Nanostructures on Surfaces</b> / Karsten Pohl	4167
<b>STEM of Chiral Pair Self-Assembled Monolayers</b> / Yuguang Cai and Steven L. Bernasek	4176
<b>STEM: Self-Assembly on Graphite</b> / Thomas Müller	4185

---

**Mass Spectrometry**

<b>Fluorofullerenes</b> / Olga V. Boltalina and Steven H. Strauss	1307
<b>Heterogeneous Catalytic Reactions by Mass Spectrometry</b> / Steven M. Thornberg and Deborah E. Hunka	1505
<b>Single-Cell Level Mass Spectrometric Imaging</b> / Sara G. Ostrowski, Andrew G. Ewing, and Nicholas Winograd	4046

---

**Near-Field Microscopy Techniques**

<b>Near-Field Microscopy</b> / Björn T. Rosner and Daniel W. van der Weide	3159
<b>Near-Field Raman Spectroscopy</b> / Eric Ayars	3169
<b>Near-Field Raman Spectroscopy: Resolution Enhancement</b> / Satoshi Kawata and Yasushi Inouye	3177
<b>Near-Field Scanning Optical Microscopy: Chemical Imaging</b> / Bogdan Dragnea	3185
<b>Scanning Near-Field Photolithography</b> / Graham J. Leggett	3709

---

**Optical Characterization Methods**

<b>Barcoded Nanowires</b> / Rebecca L. Stoermer and Christine D. Keating	259
<b>Nanoporous Anodic Alumina: Structural and Optical Anisotropy</b> / E. Stefan Kooij, Aurelian C. Gâlcă, Herbert Wormeester, and Bene Poelsema	2947
<b>Self-Assembled Silane Monolayers: Cyano-to-Carboxylic Termination Conversion</b> / Chandra Sekhar Palla and Alexander Couzis	3801
<b>Self-Assembled Thin Films: Optical Characterization</b> / Herbert Wormeester, E. Stefan Kooij, and Bene Poelsema	3829
<b>Smallest Size Regime: Control of Ultrafast Dynamics</b> / Stefan Vajda and Ludger Wöste	4132

<b>Structural Color</b> / <i>Pete Vukusic</i> . . . . .	4195
<b>Surface Plasmon Spectra of Silver and Gold Nanoparticle Assemblies</b> / <i>Mondona Zangeneh and Roger Terrill</i> . . . . .	4271

### **Other Techniques**

<b>Colloidal Nanoparticles: Electrokinetic Characterization</b> / <i>Kunio Furusawa and Hideo Matsumura</i> . . . . .	893
<b>Fluorescence-Voltage Single Molecule Spectroscopy</b> / <i>Young Jong Lee, Andre J. Gesquiere, So-Jung Park, and Paul F. Barbara</i> . . . . .	1300
<b>Fullerenes: Isomer Identification</b> / <i>Guangyu Sun</i> . . . . .	1340
<b>Single Molecule Spectroscopy for Nanomaterials Characterization</b> / <i>Daniel A. Higgins and Yanwen Hou</i> . . . . .	4057
<b>Single-Walled Carbon Nanotubes: Separation Using Capillary Electrophoresis</b> / <i>Stephen K. Doorn</i> . . . . .	4096

### **Vibrational Spectroscopy**

<b>Infrared Spectroscopy: Biomolecular Structure at Interfaces</b> / <i>Curtis W. Meuse</i> . . . . .	1590
<b>Molecular Orientation at Interfaces: Vibrational Spectroscopy</b> / <i>Zhan Chen</i> . . . . .	2357
<b>Raman Spectroscopy of Carbon Nanotube–Polymer Composites</b> / <i>Bin Chen</i> . . . . .	3682
<b>Surface-Enhanced Raman Scattering</b> / <i>Adam M. Schwartzberg and Jin Z. Zhang</i> . . . . .	4250

### **X-Ray Spectroscopy Techniques**

<b>Biomedical Magnetic Nanoparticles</b> / <i>Ian Robinson, Le Duc Tung, and Nguyen T.K. Thanh</i> . . . . .	354
<b>Catalyst Nanostructures: X-Ray Absorption</b> / <i>Jeffrey T. Miller, M. K. Neylon, C. L. Marshall, and Arthur Jerome Kropf</i> . . . . .	753
<b>Nanostructured Composites: Carbon-Derived Fibers</b> / <i>Peter M.A. Sherwood</i> . . . . .	2986
<b>Nanostructured Multilayers: Applications in X-Ray Optics</b> / <i>Michael Störmer, Carsten Michaelsen, Jörg Wiesmann, Paulo Ricardo, and Rüdiger Bormann</i> . . . . .	3052
<b>Self-Assembled Monolayers: Chemical and Physical Modification under Vacuum</b> / <i>Jessica Torres, Anthony J. Wagner, Christopher C. Perry, Glenn M. Wolfe, and D. Howard Fairbrother</i> . . . . .	3747

## **Bionanotechnology and Biomedical Nanotechnology**

### **Adsorption, Adhesion, and Binding at Interfaces**

<b>Adhesion: Cell on a Substrate</b> / <i>Frédéric Pincet</i> . . . . .	22
<b>AFM: Biopolymers</b> / <i>Nehal I. Abu-Lail and Terri A. Camesano</i> . . . . .	63
<b>AFM: Imaging Artifacts</b> / <i>Stephanie Butler Velegol</i> . . . . .	88
<b>AFM: Protein Adsorption</b> / <i>David T. Kim, Harvey W. Blanch, and Clayton J. Radke</i> . . . . .	129
<b>Bio-Microarrays</b> / <i>Günter E.M. Tovar and Achim Weber</i> . . . . .	298
<b>Biosurfaces: Water Structure at Interfaces</b> / <i>Yan-Yeung Luk</i> . . . . .	453
<b>Electrochemical Sensors: Functionalized Silica</b> / <i>Yuehe Lin, Wassana Yantasee, and Glen E. Fryxell</i> . . . . .	1196
<b>Halide Transport through Biological Membranes</b> / <i>Lars-Oliver Essen</i> . . . . .	1476
<b>Infrared Spectroscopy: Biomolecular Structure at Interfaces</b> / <i>Curtis W. Meuse</i> . . . . .	1590
<b>Liposomes: Direct Force Measurement by AFM</b> / <i>Guangzhao Mao, Xuemei Liang, and K.Y. Simon Ng</i> . . . . .	1869
<b>Liquid Crystals and Nanostructured Surfaces: Detecting Protein Binding</b> / <i>Yan-Yeung Luk</i> . . . . .	1878



---

## Bionanotechnology and Biomedical Nanotechnology (*cont'd.*)

---

### *Adsorption, Adhesion, and Binding at Interfaces (cont'd.)*

<b>Protein Adsorption Kinetics under an Applied Electric Field</b> / Paul R. Van Tassel . . . . .	3569
<b>Proteins: Structure and Interaction Patterns to Solid Surfaces</b> / Thomas J. Webster . . . . .	3590
<b>Virus Nanoparticles: Adsorption and Organization on Substrates</b> / Jiyu Fang . . . . .	4407

---

### *Biomimetic Devices and Sensors*

<b>Biomimetic Receptors for Carboxylate Recognition</b> / Rocco Ungaro, Alessandro Casnati, and Francesco Sansone . . . . .	372
<b>Biosensor Applications: Porous Silicon Microcavities</b> / Benjamin L. Miller, Philippe M. Fauchet, Scott R. Horner, and Selena Chan . . . . .	408
<b>Biosensor Applications: Surface Engineering</b> / Genady Zhavnerko and Kwon-Soo Ha . . . . .	416
<b>Biosensors Based on Carbon Nanotubes</b> / Yuehe Lin, Wassana Yantasee, Fang Lu, Joseph Wang, Mustafa Musameh, Yi Tu, and Zhifeng Ren . . . . .	428
<b>Biosensors: Fractal Analysis of Binding Kinetics</b> / Harshala Butala and Ajit Sadana . . . . .	441
<b>Motor Proteins in Synthetic Materials and Devices</b> / Henry Hess, George Bachand, and Viola Vogel . . . . .	2484
<b>Nanobiological Sensors</b> / Nathaniel Cady, Anand Gadre, and Alain E. Kaloyeros . . . . .	2514
<b>Nanoparticle Synthesis: Biological Path</b> / Kenji Iwahori and Ichiro Yamashita . . . . .	2890
<b>Nucleoside- and Nucleobase-Substituted Oligopyrrolic Macrocycles</b> / Vladimír Král, Martin Valík, Tatiana V. Shishkanova, and Jonathan L. Sessler . . . . .	3216
<b>Optical Nanosensors and Nanobiosensors</b> / Brian M. Cullum . . . . .	3258

---

### *Biomolecular Substrates*

<b>Biocatalytic Single-Enzyme Nanoparticles</b> / Jay W. Grate and Jungbae Kim . . . . .	307
<b>Bionanoparticles</b> / Krishnaswami S. Raja, Sukanta Dolai, Wei Shi, and Qian Wang . . . . .	386
<b>Nanostructured Materials: Metals on Microtubule Supports</b> / Silke Behrens and Eberhard Unger . . . . .	3012
<b>Nanostructured Silica and Silica-Derived Materials</b> / Ho-Cheol Kim and Geraud Dubois . . . . .	3063
<b>Scanning Probe Lithography: Polymeric and Biomolecular Nanostructures</b> / Stefan Zauscher . . . . .	3721
<b>Single-Cell Level Mass Spectrometric Imaging</b> / Sara G. Ostrowski, Andrew G. Ewing, and Nicholas Winograd . . . . .	4046
<b>Smart Nanotubes for Biotechnology and Biocatalysis</b> / Charles R. Martin and Punit Kohli . . . . .	4147

---

### *DNA-Based Technologies*

<b>DNA Hybridization: Electronic Control</b> / Kimberly Hamad-Schifferli . . . . .	1122
<b>DNA-Conjugated Metal Nanoparticles: Chip Detection Applications</b> / Wolfgang Fritzsche . . . . .	1114
<b>Electrochemical Toxicity Sensors</b> / James F. Rusling . . . . .	1207
<b>Gold Nanoclusters: Structural Disorder</b> / Ignacio L. Garzón . . . . .	1412
<b>Molecular Computing Machines</b> / Yaakov Benenson and Ehud Shapiro . . . . .	2291

---

### *Drug and Gene Delivery*

<b>Biomedical Magnetic Nanoparticles</b> / Ian Robinson, Le Duc Tung, and Nguyen T.K. Thanh . . . . .	354
<b>Capsules: Specific Layer Structures</b> / Lars Dähne and Claire S. Peyratout . . . . .	522
<b>Gene Delivery via Polymer Nanoparticles</b> / Jie Wen and Kam W. Leong . . . . .	1394
<b>Ligand-Receptor Systems with Infinite Binding Affinity</b> / Claude F. Meares . . . . .	1853

<b>Lipid Membranes: Nanostructure and Dynamic Organization</b> / <i>J. Gaudioso and D. Y. Sasaki</i> . . . . .	1859
<b>Luminescence of Nanoparticle-Labeled Antibodies and Antigens</b> / <i>Shaopeng Wang and Nicholas A. Kotov</i> . . . . .	1915
<b>Nanoencapsulation of Bioactive Substances</b> / <i>Yury E. Shapiro</i> . . . . .	2707
<b>Polyelectrolyte–Surfactant Complex Nanoparticles</b> / <i>Hans-Peter Hentze</i> . . . . .	3403

### ***Environmental and Health Implications***

<b>Atmospheric Nanoparticles: Formation and Physicochemical Properties</b> / <i>James N. Smith</i> . . . . .	228
<b>Biological and Chemical Decontamination</b> / <i>Peter K. Stoimenov and Kenneth J. Klabunde</i> . . . . .	312
<b>Bioremediation of Environmental Contaminants</b> / <i>Xiomara C. Kretschmer and Russell R. Chianelli</i> . . . . .	397
<b>Chemical Warfare Agents: Biosensors for Detection</b> / <i>Elias Greenbaum, Miguel Rodriguez, Jr., and Charlene A. Sanders</i> . . . . .	842
<b>Electrochemical Toxicity Sensors</b> / <i>James F. Rusling</i> . . . . .	1207
<b>Environmental Nanoparticles</b> / <i>Alexandra Navrotsky</i> . . . . .	1262
<b>Nanomaterials: Manufacturing, Processing, and Applications</b> / <i>Pramod K. Sharma, Weifang Miao, Anit Giri, and Srikanth Raghunathan</i> . . . . .	2799
<b>Toxicological Effects and Screening of Engineered Nanoparticles</b> / <i>Paul Borm and Ken Donaldson</i> . . . . .	4363

### ***Supramolecular Chemistry***

<b>Biomimetic Design of Self-Assembling Systems</b> / <i>Mila Boncheva and George M. Whitesides</i> . . . . .	364
<b>Cyclic Peptides: Self-Assembly in Hydrogen-Bonded Nanotubes</b> / <i>Roberto J. Brea and Juan R. Granja</i> . . . . .	1037
<b>Hierarchically Imprinted Nanostructures for Separation</b> / <i>Sheng Dai, Zongtao Zhang, and Chengdu Liang</i> . . . . .	1525
<b>Nanomaterials: Trends</b> / <i>Richard Silbergliitt</i> . . . . .	2836
<b>Phase Transfer of Monosaccharides through Noncovalent Interactions</b> / <i>Elizabeth K. Auty and Anthony P. Davis</i> . . . . .	3347
<b>Protein Nanotubes as Building Blocks</b> / <i>Hiroshi Matsui</i> . . . . .	3578

### ***Tissue Engineering***

<b>Biomaterials: Mechanical Characterization</b> / <i>Eunice Phay Shing Tan and Chwee Teck Lim</i> . . . . .	317
<b>Biomedical Applications: Implants</b> / <i>Jeremiah Ejiofor and Thomas J. Webster</i> . . . . .	327
<b>Biomedical Applications: Novel Materials and Devices</b> / <i>J. Zachary Hilt and Mark E. Byrne</i> . . . . .	339
<b>Layer-by-Layer Electrostatic Self-Assembly</b> / <i>Michael J. McShane and Yuri M. Lvov</i> . . . . .	1823

## **Catalysts and Catalytic Properties at the Nanoscale**

### ***Metal Clusters and Nanoparticles on Supports***

<b>Catalysis by Supported Gold Nanoclusters</b> / <i>D. Wayne Goodman</i> . . . . .	744
<b>Catalyst Nanostructures: X-Ray Absorption</b> / <i>Jeffrey T. Miller, M. K. Neylon, C. L. Marshall, and Arthur Jerome Kropf</i> . . . . .	753
<b>Catalysts by Nanoscale Design</b> / <i>Chaitanya Kumar Narula</i> . . . . .	772
<b>Catalytic Processes: Nanoscale Simulations</b> / <i>Vladimir I. Elokhin and Aleksandr V. Myshlyavtsev</i> . . . . .	782



---

**Catalysts and Catalytic Properties at the Nanoscale (cont'd.)**


---

**Metal Clusters and Nanoparticles on Supports (cont'd.)**

<b>Colloidal Nanometals as Fuel Cell Catalyst Precursors</b> / Helmut Bönnemann and K. S. Nagabhushana .....	863
<b>Dendritic Nanocatalysts</b> / Kiyotomi Kaneda, Masahiko Ooe, Makoto Murata, Tomoo Mizugaki, and Kohki Ebitani .....	1054
<b>Gold Nanoparticles on Titania: Activation and Behavior</b> / Jose A. Rodriguez .....	1422
<b>Heterogeneous Catalysts: Atomic Scale Studies</b> / Robert F. Klie, Kai Sun, Mark M. Disko, Jingyue Liu, and Nigel D. Browning .....	1491
<b>Metal Clusters on Oxides</b> / Ivan Stensgaard .....	2044
<b>Metal Nanoparticle Catalysts</b> / Naoki Toshima .....	2052
<b>Nanofibers and Carbon Nanotubes: Novel Metal Catalyst Supports</b> / Mark A. Keane .....	2723
<b>Noble Metal Nanoparticles on Carbon Fibers</b> / Dmitri A. Bulushev and Igor Yuranov .....	3195
<b>Palladium Nanoclusters</b> / Kiyotomi Kaneda, Kwang-Min Choi, Tomoo Mizugaki, and Kohki Ebitani .....	3309
<b>Platinum Nanoparticles: Synthesis and Catalytic Properties</b> / Ioan Balint and Akane Miyazaki .....	3386

---

**Molecular Sieves and Mesoporous Materials**

<b>Basic Nanostructured Catalysts</b> / Robert J. Davis .....	278
<b>Heterogeneous Catalytic Reactions by Mass Spectrometry</b> / Steven M. Thornberg and Deborah E. Hunka .....	1505
<b>Mesoporous Materials</b> / James C. Vartuli, Wielsaw J. Roth, and Thomas F. Degnan, Jr. ....	2029
<b>Micro- and Mesoporous Nanomaterials: Catalytic Properties</b> / Johannes A. Lercher and Andreas Jentys .....	2229
<b>Nanocrystalline Zeolites</b> / Vicki H. Grassian and Sarah C. Larsen .....	2646
<b>Zeolite Membranes</b> / Wei Xing, João C. Diniz da Costa, Gao Qing (Max) Lu, and Z. F. Yan .....	4421

---

**Nanotechnology Methods for Catalyst Synthesis**

<b>Biocatalytic Single-Enzyme Nanoparticles</b> / Jay W. Grate and Jungbae Kim .....	307
<b>Enzymatic Synthesis of Nanostructured Polymers and Composites</b> / Christy Ford, Vijay T. John, Gary McPherson, Jibao He, Joseph Akkara, David Kaplan, and Arijit Bose .....	1271
<b>Layer-by-Layer Assembly of Polyelectrolyte Films: Membranes and Catalysts</b> / Bernd Tieke and Ali Toutianoush .....	1784
<b>Mixed Metal Oxide Nanoparticles</b> / Pramesh N. Kapoor, Ajay Kumar Bhagi, Ravichandra S. Mulukutla, and Kenneth J. Klabunde .....	2280
<b>Nanocrystalline Oxides: Surfactant-Assisted Growth</b> / Claudia L. Bianchi, Silvia Ardizzone, and Giuseppe Cappelletti .....	2637
<b>Nanostructured Catalysts</b> / Ravichandra S. Mulukutla .....	2967
<b>Nanostructured Catalysts: Design and Synthesis</b> / Hua Chun Zeng .....	2974
<b>Polymer-Mediated Self-Assembly of Nanoparticles</b> / Tyler B. Norsten, Amitav Sanyal, Roy Shenhar, and Vincent M. Rotello .....	3443
<b>Polymer-Nanoparticle Composites</b> / Kevin Sill, Seunghoo Yoo, and Todd Emrick .....	3487
<b>Titania Coatings on Stainless Steel</b> / Ganesh Balasubramanian, Dionysios D. Dionysiou, and Makram T. Suidan .....	4348

<b>Titania Nanoparticles: Photocatalytic Properties</b> / Scott Buzby and S. Ismat Shah .....	4356
--------------------------------------------------------------------------------------------------	------

## Colloidal Phenomena

### *Adsorption, Adhesion, Surface Interactions*

<b>Aerosol Nanoparticles: Coagulation Theory</b> / Ken Won Lee and Soon-Bark Kwon .....	53
<b>AFM: Metal Ion Sorption</b> / Viriya Vithayaveroj, Sotira Yiacoymi, and Costas Tsouris .....	109
<b>AFM: Simulation of Interaction Forces</b> / Ivan U. Vakarelski, Scott C. Brown, Bahar Basim, and Brij M. Moudgil .....	153
<b>Colloidal Nanoparticles: Aggregation Patterns at Surfaces</b> / Hamidou Haidara and Karine Mougín .....	882
<b>Colloidal Structures on Patterned Surfaces</b> / Aránzazu del Campo, Anne-Sophie Duwez, Charles-André Fustin, and Ulrich Jonas .....	907
<b>Heterogeneous Surfaces with Nanosized Channel Lattices</b> / Lifeng Chi, Michael Gleiche, Steven Lenhert, and Nan Lu .....	1515
<b>Ionic Strength Effects: Tunable Nanocrystal Distribution in Colloidal Gold Films</b> / E. Stefan Kooij, E.A. Martijn Brouwer, Herbert Wormeester, and Bene Poelsema .....	1672
<b>Nanocolloidal Gold Films: Self-Assembly</b> / E. Stefan Kooij, E.A. Martijn Brouwer, Agnes A. Mewe, Herbert Wormeester, and Bene Poelsema .....	2545
<b>Protein Adsorption Kinetics under an Applied Electric Field</b> / Paul R. Van Tassel .....	3569
<b>Self-Assembled Monolayers: Surface Nanostructure Effect on Wetting</b> / Jun Yang, Jingmin Han, Kelvin Isaacson, and Daniel Y. Kwok .....	3762
<b>Surface Forces on Nanoparticles Determined by Direct Measurement</b> / Jeong-Min Cho, Georgios Pyrgiotakis, and Wolfgang M. Sigmund .....	4260
<b>Yttria-Tetragonally Stabilized Zirconia</b> / R. Allen Kimel .....	4414

### *Electrically Charged Particles*

<b>Carbon Nanotubes: Flow Control in Membranes</b> / Scott A. Miller and Charles R. Martin .....	630
<b>Colloidal Nanoparticles: Electrokinetic Characterization</b> / Kunio Furusawa and Hideo Matsumura .....	893
<b>DNA Interactions with Functionalized Emulsions</b> / Thierry Delair .....	1134
<b>Electrical Double-Layer Formation</b> / Kun-Lin Yang, Sotira Yiacoymi, and Costas Tsouris .....	1157
<b>Electrically Functional Nanostructures</b> / Orlin D. Velev and Simon O. Lumsdon .....	1171
<b>Electrochemical Langmuir Trough</b> / Natalia Varaksa, Thomas F. Magnera, and Josef Michl ...	1189
<b>Hierarchically Imprinted Nanostructures for Separation</b> / Sheng Dai, Zongtao Zhang, and Chengdu Liang .....	1525
<b>Hydrogel Nanoparticles Made of Cross-Linked Polyvinylpyrrolidone</b> / Susmita Mitra, Dhruba Jyoti Bharali, and Amarnath Maitra .....	1546
<b>Mineral Nanoparticles: Electrokinetics</b> / Mehmet S. Celik and Bahri Ersoy .....	2266
<b>Molecular Simulations of DNA Counterion Distributions</b> / Alexander Lyubartsev .....	2398
<b>Polyion Complex Micelles</b> / Atsushi Harada and Kazunori Kataoka .....	3409
<b>Polymer Colloids and Their Metallation</b> / Lyudmila M. Bronstein .....	3430

### *Nucleation and Crystal Growth*

<b>Atmospheric Nanoparticles: Formation and Physicochemical Properties</b> / James N. Smith .....	228
<b>Germanium Nanoparticles</b> / Boyd R. Taylor and Louisa J. Hope-Weeks .....	1405
<b>Interfacial Forces: Colloidal Particle-Liquid</b> / Sarah A. Nespolo and Geoffrey W. Stevens .....	1650

---

**Colloidal Phenomena (cont'd.)**


---

***Nucleation and Crystal Growth (cont'd.)***

- Nanocrystals Synthesized in Colloidal Self-Assemblies** / *M. P. Pileni* . . . . . 2581
- Nanoparticle Suspensions: Phase Behavior** / *Subramanian Ramakrishnan and Charles F. Zukoski* . . . . . 2878
- 

***Spontaneous Organization of Matter***

- Adhesion: Coated Surfaces, Effect of Humidity** / *Joan E. Curry and Sungsoo Kim* . . . . . 32
- Amphiphilic Block Copolymer Monolayer at Air–Water Interface** / *Emiko Mouri and Hideki Matsuoka* . . . . . 168
- Biomimetic Design of Self-Assembling Systems** / *Mila Boncheva and George M. Whitesides* . . . . . 364
- Capsules: Polymer Microcapsules** / *Gleb B. Sukhorukov* . . . . . 508
- Colloid Systems: Micelles and Nanocrystals** / *B.L.V. Prasad and Savka I. Stoeva* . . . . . 856
- Cubosomes: Bicontinuous Liquid Crystalline Nanoparticles** / *Patrick T. Spicer* . . . . . 1018
- Enzymatic Synthesis of Nanostructured Polymers and Composites** / *Christy Ford, Vijay T. John, Gary McPherson, Jibao He, Joseph Akkara, David Kaplan, and Arijit Bose* . . . . . 1271
- Microgel Dispersions: Colloidal Forces and Phase Behavior** / *Jianzhong Wu and Zhibing Hu* . . . . . 2243
- Self-Assembled Structures** / *Anna Cristina Samia and Xiao-Min Lin* . . . . . 3816
- Self-Assembled Thin Films: Optical Characterization** / *Herbert Wormeester, E. Stefan Kooij, and Bene Poelsema* . . . . . 3829
- 

**Computational Analysis, Simulations, and Theoretical Modeling**


---

***Electronic Structures, Optical, and Transport Properties***

- Antidot Lattices: Chaotic Transport** / *Tsuneya Ando* . . . . . 210
- Carbon Nanotransistors** / *Po-Wen Chiu and Siegmur Roth* . . . . . 563
- Carbon Nanotubes: Gas Adsorption Properties** / *Juan Manuel Diez Tascón and Eduardo J. Bottani* . . . . . 653
- Carbon Nanotubes: Optical Properties** / *R. Saito, Mildred S. Dresselhaus, G. Dresselhaus, A. Jorio, A. G. Souza Filho, and M. A. Pimenta* . . . . . 679
- Carbon Nanotubes: Thermal Properties** / *J. Hone* . . . . . 736
- Fullerenes and Carbon Nanotubes** / *Laszlo Mihaly* . . . . . 1322
- Fullerenes: Topology and Structure** / *G. Benedek and M. Bernasconi* . . . . . 1360
- Photonic Crystal Fibers** / *P. St. J. Russell, J. C. Knight, T. A. Birks, and P. J. Roberts* . . . . . 3356
- Self-Assembled Quantum Dots: Electronic Structures and Optical Properties** / *Andrew Williamson* . . . . . 3789
- Silicon Nanocrystals: Quantum Confinement** / *James R. Chelikowsky* . . . . . 4033
- Supramolecular Networks Synthesized in Nanoparticle–Polymer Mixtures** / *Anna C. Balazs and Gavin A. Buxton* . . . . . 4240
- Thermodynamics at the Meso- and Nanoscale** / *Mikhail A. Anisimov* . . . . . 4326
- 

***First Principles Analysis and Density Functional Theory***

- Carbon Nanotubes: Modeling of Hydrogen Chemisorption** / *Ronald C. Brown* . . . . . 671
- Ethane-Preferred Conformation** / *Lionel Goodman and Vojislava Pophristic* . . . . . 1294

<b>Metal Oxide Nanoribbons and Carbon Nanotubes: Modeling</b> / Amitesh Maiti . . . . .	2140
<b>Metal–Oxide Interfaces: Design via Control of Defect Density</b> / A. Bogicevic . . . . .	2116
<b>Molecular Electronics: Models of Switchable and Programmable Devices</b> / Pedro A. Derosa, Vandana R. Tarigopula, and Jorge M. Seminario . . . . .	2317
<b>Silicon Nanoclusters: Simulations</b> / Aaron Puzder . . . . .	4021
<b>Single-Walled Carbon Nanotubes: Field Emission Properties</b> / Xiaofeng F. Duan, Brahim Akdim, and Ruth Pachter . . . . .	4078
<b>Single-Walled Carbon Nanotubes: Geometries, Electronic Properties, and Actuation</b> / Guangyu Sun, Marc Nicklaus, and Miklos Kertesz . . . . .	4085
<b>Single-Walled Carbon Nanotubes: Structures and Symmetries</b> / Carter T. White and John W. Mintmire . . . . .	4108

---

### ***Molecular Dynamics, Monte Carlo, and Hybrid Simulation Methods***

<b>Cadmium Sulfate Nanocrystals: Computational Analysis</b> / Stacie Nunes, Zhigang Zhou, Jeffrey D. Evanseck, and Jeffrey D. Madura . . . . .	498
<b>Catalytic Processes: Nanoscale Simulations</b> / Vladimir I. Elokhin and Aleksandr V. Myshlyavtsev . . . . .	782
<b>Computational Analysis of Switchable Catenanes</b> / Xiangge Zheng and Karl Sohlberg . . . . .	930
<b>Computational Analysis of Switchable Rotaxanes</b> / Xiangge Zheng and Karl Sohlberg . . . . .	939
<b>Computational Analysis Using Normal and Multibody Modes</b> / Bryan C. Hathorn, Donald W. Noid, Bobby G. Sumpter, Chao Yang, and William A. Goddard III . . . . .	921
<b>Electrical Double-Layer Formation</b> / Kun-Lin Yang, Sotira Yiaccoumi, and Costas Tsouris . . . . .	1157
<b>Integrated Methods in Quantum Chemistry</b> / Stephan Irle and Keiji Morokuma . . . . .	1627
<b>Island Nucleation: Predictions</b> / Maria C. Bartelt . . . . .	1696
<b>Molecular Simulations of DNA Counterion Distributions</b> / Alexander Lyubartsev . . . . .	2398
<b>Nanofriction and Nanowear of Sliding Systems: Simulations</b> / W.C.D. Cheong . . . . .	2763
<b>Tribology at the Nanoscale</b> / Peter T. Cummings and Clare McCabe . . . . .	4385

---

## **Design Methods at the Nanoscale**

---

### ***Bioinspired Materials***

<b>Biomimetic Design of Self-Assembling Systems</b> / Mila Boncheva and George M. Whitesides . . . . .	364
<b>DNA-Based Nanoinstrument Design</b> / Alexander Hillisch and Stephan Diekmann . . . . .	1102
<b>Gecko-Inspired Adhesives: Nanofabrication</b> / Aránzazu del Campo and Eduard Arzt . . . . .	1384
<b>Nanomaterials: Trends</b> / Richard Silbergliitt . . . . .	2836
<b>Nanoparticle Synthesis: Biological Path</b> / Kenji Iwahori and Ichiro Yamashita . . . . .	2890
<b>Nanostructured Materials: Metals on Microtubule Supports</b> / Silke Behrens and Eberhard Unger . . . . .	3012

---

### ***Controlled Assembly Strategies***

<b>Layer-by-Layer Assembly of Semiconducting and Photoreactive Bolaform Amphiphiles</b> / Jason Locklin, Derek Patton, Chuanjun Xia, Xiaowu Fan, and Rigoberto C. Advincula . . . . .	1798
<b>Layer-by-Layer Assembly of Thin Films of Mixed Nanoparticles</b> / Jianchang Guo, Encai Hao, and Tianquan Lian . . . . .	1813
<b>Layered Double Hydroxides: Self-Assembly and Multiple Phases</b> / Zhi Ping Xu and Paul S. Braterman . . . . .	1841
<b>Molecular Probes of Cation–Arene Interactions</b> / George W. Gokel . . . . .	2369
<b>Nanocrystals Synthesized in Colloidal Self-Assemblies</b> / M. P. Pileni . . . . .	2581

---

**Design Methods at the Nanoscale (cont'd.)**


---

**Controlled Assembly Strategies (cont'd.)**

<b>Nanostructured Ultrastrong Materials</b> / Nicholas A. Kotov, Arif A. Mamedov, Dirk M. Guldi, Zhiyong Tang, Maurizio Prato, James Wicksted, and Andreas Hirsch	3072
<b>Self-Assembly Directed by NH-O Hydrogen Bonding</b> / Katrina A. Jolliffe and Leonard F. Lindoy	3864
<b>Self-Assembly of Coordination Cages</b> / Laura Pirondini and Enrico Dalcanale	3848
<b>Semiconductor Nanowires: Macroelectronics Applications</b> / Yugang Sun and John A. Rogers	3896
<b>Semiconductor Nanowires: Nanoscale Electronics and Optoelectronics</b> / Yu Huang, Xiangfeng Duan, and Charles M. Lieber	3910
<b>Surface Plasmon Spectra of Silver and Gold Nanoparticle Assemblies</b> / Mondona Zangeneh and Roger Terrill	4271
<b>Template-Directed Assembly of Dinuclear Triple-Stranded Helicates</b> / Markus Albrecht	4283
<b>Templating Aerogels for Tunable Nanoporosity</b> / Aydin K. Sunol and Sermin G. Sunol	4294
<b>Templating Polymer Crystal Growth Using Block Copolymers</b> / Yueh-Lin Loo	4303

---

**Interfacial Engineering**

<b>Carbon Nanotubes: Functionalization</b> / Bin Zhao, Hui Hu, Elena Bekyarova, Mikhail E. Itkis, Sandip Niyogi, and Robert C. Haddon	640
<b>Metal-Oxide Interfaces: Design via Control of Defect Density</b> / A. Bogicevic	2116
<b>Nanolithography: Length Scale Limitations</b> / Takashi Ito	2779
<b>Nano-Mesoscopic Interface: Hybrid Devices</b> / Gianfranco Cerofolini	2493
<b>Nanostructured Catalysts: Design and Synthesis</b> / Hua Chun Zeng	2974
<b>Nanostructured Multilayers: Applications in X-Ray Optics</b> / Michael Störmer, Carsten Michaelsen, Jörg Wiesmann, Paulo Ricardo, and Rüdiger Bormann	3052
<b>Nanostructured Silica and Silica-Derived Materials</b> / Ho-Cheol Kim and Geraud Dubois	3063
<b>Nanotube Sensors</b> / Marc Wirtz and Charles R. Martin	3109
<b>Polyelectrolyte Films with Incorporated Carbon Nanotubes</b> / Jason H. Rouse and Peter T. Lillehei	3396
<b>Ultrathin Polymer Films: Nanoparticle Nucleation</b> / Pieter Stroeve	4400

---

**Structure Control**

<b>Colloidal Nanometals as Fuel Cell Catalyst Precursors</b> / Helmut Bönnemann and K. S. Nagabhushana	863
<b>Coordination Framework Topology</b> / Neil R. Champness and Neil S. Oxtoby	984
<b>Metal Oxide Nanoparticles</b> / Ryan M. Richards	2126
<b>Nanomaterials and Molecular Devices: De Novo Design Theory</b> / Kwang S. Kim, P. Tarakeshwar, and Han Myoung Lee	2815
<b>Organofullerenes in Water</b> / Eiichi Nakamura and Hiroyuki Isobe	3277
<b>Polymer Nanowires Conjugated by Controlled Chain Polymerization</b> / Yuji Okawa and Masakazu Aono	3501
<b>Self-Organized Superstructures: Molecular Design</b> / Makoto Tadokoro	3886
<b>Semiconductor Nanowires: Rational Synthesis</b> / Xiangfeng Duan and Charles M. Lieber	3941
<b>Structural Transitions in Thin Films</b> / Rajarshi Banerjee, Gregory B. Thompson, and Hamish L. Fraser	4217

<b>Superconductor Nanowires: Templated by Single Molecules</b> / Alexey Bezryadin, Anthony Bollinger, David Hopkins, Michael Murphey, Mikas Remeika, and Andrey Rogachev .....	4228
<b>Zeolite Membranes</b> / Wei Xing, João C. Diniz da Costa, Gao Qing (Max) Lu, and Z. F. Yan .....	4421

---

## Energy Storage Devices and Energy-Directed Applications

<b>Automotive Parts: Impact of Nanotechnology</b> / Ganesh Skandan, Amit Singhal, and Damian Sobrevilla .....	241
<b>Carbon Nanotube Electrodes</b> / Valentina Lazarescu .....	586
<b>Carbon Nanotube–Conducting Polymer Composites in Supercapacitors</b> / Mark Hughes .....	574
<b>Carbon Nanotubes for Storage of Energy: Supercapacitors</b> / Elzbieta Frackowiak .....	707
<b>Carbon Nanotubes: Electrochemical Modification</b> / Kannan Balasubramanian, Marko Burghard, and Klaus Kern .....	620
<b>Carbon Nanotubes: Gas Adsorption Properties</b> / Juan Manuel Diez Tascón and Eduardo J. Bottani .....	653
<b>Carbon Nanotubes: Hydrogen Storage</b> / Masashi Shiraishi, Taishi Takenobu, Hiromichi Kataura, and Masafumi Ata .....	662
<b>Carbon Nanotubes: Modeling of Hydrogen Chemisorption</b> / Ronald C. Brown .....	671
<b>Carbon-Based Nanostructures: Hydrogen Storage</b> / Xianxian Wu and Nidia C. Gallego .....	535
<b>Nanomaterials: Advances in Technology and Industry</b> / Ganesh Skandan and Amit Singhal .....	2788
<b>Oxide Nanoparticles: Electrochemical Performance</b> / Dominique Larcher and Jean-Marie Tarascon .....	3299
<b>Photovoltaics: Organic-Based Solar Cells</b> / Sean E. Shaheen and David S. Ginley .....	3370
<b>Porous Alumina Templates for Nanofabrication</b> / Latika Menon .....	3525

---

## Environmental Applications and Societal Implications

<b>Atmospheric Nanoparticles: Formation and Physicochemical Properties</b> / James N. Smith .....	228
<b>Automotive Parts: Impact of Nanotechnology</b> / Ganesh Skandan, Amit Singhal, and Damian Sobrevilla .....	241
<b>Biological and Chemical Decontamination</b> / Peter K. Stoimenov and Kenneth J. Klabunde .....	312
<b>Bioremediation of Environmental Contaminants</b> / Xiomara C. Kretschmer and Russell R. Chianelli .....	397
<b>Chemical Warfare Agents: Biosensors for Detection</b> / Elias Greenbaum, Miguel Rodriguez, Jr., and Charlene A. Sanders .....	842
<b>Electrochemical Toxicity Sensors</b> / James F. Rusling .....	1207
<b>Environmental Nanoparticles</b> / Alexandra Navrotsky .....	1262
<b>Gold Nanoparticles on Titania: Activation and Behavior</b> / Jose A. Rodriguez .....	1422
<b>Molecular Self-Assembly: Environmental and Sensing Applications</b> / Glen E. Fryxell, R. Shane Addleman, S. V. Mattigod, Yuehe Lin, T. S. Zemanian, H. Wu, Jerome C. Birnbaum, J. Liu, and X. Feng .....	2387
<b>Moore's Law: Performance and Power Dissipation</b> / Laszlo B. Kish .....	2480
<b>Nanocrystalline Zeolites</b> / Vicki H. Grassian and Sarah C. Larsen .....	2646
<b>Nanofiltration Separations</b> / Eric M.V. Hoek and Anna Jawor .....	2749
<b>Nanomaterials: Advances in Technology and Industry</b> / Ganesh Skandan and Amit Singhal .....	2788
<b>Patents and Inventions</b> / Jeffrey A. Lindeman .....	3318



---

**Environmental Applications and Societal Implications (*cont'd.*)**

<b>Photovoltaics: Organic-Based Solar Cells</b> / Sean E. Shaheen and David S. Ginley . . . . .	3370
<b>Platinum Nanoparticles: Synthesis and Catalytic Properties</b> / Ioan Balint and Akane Miyazaki . . . . .	3386
<b>Risk Assessment and Benefits</b> / Douglas Mulhall . . . . .	3702
<b>Titania Nanoparticles: Photocatalytic Properties</b> / Scott Buzby and S. Ismat Shah . . . . .	4356
<b>Toxicological Effects and Screening of Engineered Nanoparticles</b> / Paul Borm and Ken Donaldson . . . . .	4363
<b>Zeolite Membranes</b> / Wei Xing, João C. Diniz da Costa, Gao Qing (Max) Lu, and Z. F. Yan . . . . .	4421

---

**Fullerenes and Carbon Nanotubes**


---

**Chemistry and Functionalization**

<b>Biosensors Based on Carbon Nanotubes</b> / Yuehe Lin, Wassana Yantasee, Fang Lu, Joseph Wang, Mustafa Musameh, Yi Tu, and Zhifeng Ren . . . . .	428
<b>Carbon Nanotubes: Electrochemical Modification</b> / Kannan Balasubramanian, Marko Burghard, and Klaus Kern . . . . .	620
<b>Carbon Nanotubes: Flow Control in Membranes</b> / Scott A. Miller and Charles R. Martin . . . . .	630
<b>Carbon Nanotubes: Functionalization</b> / Bin Zhao, Hui Hu, Elena Bekyarova, Mikhail E. Itkis, Sandip Niyogi, and Robert C. Haddon . . . . .	640
<b>Fullerenes: Chemistry</b> / Mark S. Meier . . . . .	1331
<b>Ice Nanotubes inside Carbon Nanotubes</b> / Kenichiro Koga and Hideki Tanaka . . . . .	1558
<b>Nanotubes: Functionalization</b> / Stanislaus S. Wong and Sarbajit Banerjee . . . . .	3119
<b>Organofullerenes in Water</b> / Eiichi Nakamura and Hiroyuki Isobe . . . . .	3277
<b>Smart Nanotubes for Biotechnology and Biocatalysis</b> / Charles R. Martin and Punit Kohli . . . . .	4147

---

**Composite Materials**

<b>Nanoceramics: Thermal Conductivity</b> / Paul G. Klemens . . . . .	2539
<b>Nanofibers and Carbon Nanotubes: Novel Metal Catalyst Supports</b> / Mark A. Keane . . . . .	2723
<b>Nanostructured Composites: Carbon-Derived Fibers</b> / Peter M.A. Sherwood . . . . .	2986
<b>Nanostructured Materials: Synthesis in Supercritical Fluids</b> / Yuehe Lin, Xiang-Rong Ye, and Chien M. Wai . . . . .	3040
<b>Nanostructured Ultrastrong Materials</b> / Nicholas A. Kotov, Arif A. Mamedov, Dirk M. Guldi, Zhiyong Tang, Maurizio Prato, James Wicksted, and Andreas Hirsch . . . . .	3072
<b>Noble Metal Nanoparticles on Carbon Fibers</b> / Dmitri A. Bulushev and Igor Yuranov . . . . .	3195
<b>Polyelectrolyte Films with Incorporated Carbon Nanotubes</b> / Jason H. Rouse and Peter T. Lillehei . . . . .	3396
<b>Polymer Nanocomposites with Nanoparticle and Carbon Nanotube Fillers</b> / B. J. Ash, A. Eitan, and L. S. Schadler . . . . .	3466
<b>Raman Spectroscopy of Carbon Nanotube–Polymer Composites</b> / Bin Chen . . . . .	3682

---

**Energy-Related Applications**

<b>Carbon Nanotube Electrodes</b> / Valentina Lazarescu . . . . .	586
<b>Carbon Nanotubes for Storage of Energy: Supercapacitors</b> / Elzbieta Frackowiak . . . . .	707
<b>Carbon Nanotubes: Gas Adsorption Properties</b> / Juan Manuel Diez Tascón and Eduardo J. Bottani . . . . .	653

<b>Carbon Nanotubes: Hydrogen Storage</b> / Masashi Shiraishi, Taishi Takenobu, Hiromichi Kataura, and Masafumi Ata	662
<b>Carbon Nanotubes: Modeling of Hydrogen Chemisorption</b> / Ronald C. Brown	671
<b>Carbon-Based Nanostructures: Hydrogen Storage</b> / Xianxian Wu and Nidia C. Gallego	535

### **Structures and Properties**

<b>Carbon Forms Structured by Energetic Species</b> / Yeshayahu Lifshitz	553
<b>Carbon Nanotube Interconnects</b> / Alain E. Kaloyeros, Kathleen A. Dunn, Autumn T. Carlsen, and Anna W. Topol	596
<b>Carbon Nanotubes and Other Carbon Materials</b> / Morinobu Endo, Yoong Ahm Kim, Takuya Hayashi, Mauricio Terrones, and Mildred S. Dresselhaus	691
<b>Carbon Nanotubes: Optical Properties</b> / R. Saito, Mildred S. Dresselhaus, G. Dresselhaus, A. Jorio, A. G. Souza Filho, and M. A. Pimenta	679
<b>Carbon Nanotubes: Supramolecular Mechanics</b> / Boris I. Yakobson and Luise S. Couchman	722
<b>Carbon Nanotubes: Thermal Properties</b> / J. Hone	736
<b>Fluorofullerenes</b> / Olga V. Boltalina and Steven H. Strauss	1307
<b>Fullerenes and Carbon Nanotubes</b> / Laszlo Mihaly	1322
<b>Fullerenes: Isomer Identification</b> / Guangyu Sun	1340
<b>Fullerenes: Magnetic Behavior</b> / T. L. Makarova	1352
<b>Fullerenes: Topology and Structure</b> / G. Benedek and M. Bernasconi	1360
<b>Integrated Methods in Quantum Chemistry</b> / Stephan Irle and Keiji Morokuma	1627
<b>Magnetic Nanocarbon</b> / T. L. Makarova	1939
<b>Nanodiamonds</b> / Jean-Yves Raty and Giulia Galli	2697
<b>Single-Walled Carbon Nanotubes: Field Emission Properties</b> / Xiaofeng F. Duan, Brahim Akdim, and Ruth Pachter	4078
<b>Single-Walled Carbon Nanotubes: Geometries, Electronic Properties, and Actuation</b> / Guangyu Sun, Marc Nicklaus, and Miklos Kertesz	4085
<b>Single-Walled Carbon Nanotubes: Separation Using Capillary Electrophoresis</b> / Stephen K. Doorn	4096
<b>Single-Walled Carbon Nanotubes: Structures and Symmetries</b> / Carter T. White and John W. Mintmire	4108
<b>Superconductor Nanowires: Templated by Single Molecules</b> / Alexey Bezryadin, Anthony Bollinger, David Hopkins, Michael Murphey, Mikas Remeika, and Andrey Rogachev	4228

### **Functional Nanomaterials**

#### **Catalysts and Adsorbents**

<b>Catalysis by Supported Gold Nanoclusters</b> / D. Wayne Goodman	744
<b>Dendritic Nanocatalysts</b> / Kiyotomi Kaneda, Masahiko Ooe, Makoto Murata, Tomoo Mizugaki, and Kohki Ebitani	1054
<b>Layer-by-Layer Assembly of Polyelectrolyte Films: Membranes and Catalysts</b> / Bernd Tieke and Ali Toutianoush	1784
<b>Mesoporous Materials</b> / James C. Vartuli, Wielsaw J. Roth, and Thomas F. Degnan, Jr.	2029
<b>Mixed Metal Oxide Nanoparticles</b> / Pramesh N. Kapoor, Ajay Kumar Bhagi, Ravichandra S. Mulukutla, and Kenneth J. Klabunde	2280
<b>Molecular Receptor-Modified Metal Nanoparticles</b> / Jian Liu	2377
<b>Nanocrystalline Magnesia and Alumina: Surface Chemistry</b> / Richard M. Narske	2592



---

**Functional Nanomaterials (cont'd.)**


---

**Catalysts and Adsorbents (cont'd.)**

- Silica Surfaces Functionalization** / V. A. Tertykh ..... 4001
- Titania Coatings on Stainless Steel** / Ganesh Balasubramanian, Dionysios D. Dionysiou,  
and Makram T. Suidan ..... 4348
- 

**Electronic and Photonic Materials**

- Carbon Nanotransistors** / Po-Wen Chiu and Siegmund Roth ..... 563
- Carbon Nanotube Electrodes** / Valentina Lazarescu ..... 586
- Carbon Nanotube Interconnects** / Alain E. Kaloyeros, Kathleen A. Dunn, Autumn T. Carlsen,  
and Anna W. Topol ..... 596
- Charge Carrier Dynamics of Nanoparticles** / Fanxin Wu and Jin Z. Zhang ..... 804
- Conducting Polymer Nanopatterns** / Shaun F. Filocamo and Mark W. Grinstaff ..... 954
- Conducting Polymer Nanotubes** / Seung Il Cho and Sang Bok Lee ..... 965
- Electrically Functional Nanostructures** / Orlin D. Velev and Simon O. Lumsdon ..... 1171
- Low-Dielectric Constant Materials** / Robert D. Miller ..... 1901
- Membrane-Coated Nanoparticles: Photochemistry** / Ulrich Siggel, Guangtao Li and  
Jürgen-Hinrich Fuhrhop ..... 2012
- Nanofilms in Giant Magnetoresistance Heads** / Edward Grochowski and  
Robert E. Fontana, Jr. .... 2737
- One-Dimensional Electrically Conducting Polymeric Nanostructures** / Andrew D.W. Carswell  
and Brian P. Grady ..... 3243
- Oxide Nanoparticles: Electrochemical Performance** / Dominique Larcher and  
Jean-Marie Tarascon ..... 3299
- Photonic Crystal Fibers** / P. St. J. Russell, J. C. Knight, T. A. Birks, and  
P. J. Roberts ..... 3356
- Photovoltaics: Organic-Based Solar Cells** / Sean E. Shaheen and David S. Ginley ..... 3370
- Semiconductor Nanowires: Macroelectronics Applications** / Yugang Sun and  
John A. Rogers ..... 3896
- Semiconductor Nanowires: Rational Synthesis** / Xiangfeng Duan and Charles M. Lieber ..... 3941
- Silicon Functionalization for Molecular Electronics** / Gianfranco Cerofolini,  
Dario Narducci, and Elisabetta Romano ..... 4009
- 

**Functionalized Surfaces and Molecular Recognition**

- Anodization Patterned on Aluminum Surfaces** / Juchao Yan, G. V. Rama Rao,  
Plamen B. Atanassov, and Gabriel P. López ..... 203
- Capsules: Specific Layer Structures** / Lars Dähne and Claire S. Peyratout ..... 522
- Core-Shell Nanospheres, Hollow Capsules, and Bottles** / Gang Zhang, Kai Zhang,  
Yi Yu, and Bai Yang ..... 1003
- Dip-Pen Nanolithography: Applications and Functional Extensions** / Björn T. Rosner and  
Linette M. Demers ..... 1070
- Dip-Pen Nanolithography: Optical Inks** / Brandon L. Weeks, Aleksandr Noy, Abigail E. Miller,  
Jennifer E. Klare, Bruce W. Woods, and James J. De Yoreo ..... 1084
- Dissymmetrical Nanoparticles** / Stéphane Reculosa, Christophe Mingotaud, Etienne Duguet,  
and Serge Ravaine ..... 1093
- Gecko-Inspired Adhesives: Nanofabrication** / Aránzazu del Campo and Eduard Arzt ..... 1384
- Gene Delivery via Polymer Nanoparticles** / Jie Wen and Kam W. Leong ..... 1394

<b>Monolayer-Protected Metal Nanoparticles: Chemical Sensing and Gas Chromatography</b> / <i>Jay W. Grate, David A. Nelson, Rhonda Skaggs, Robert E. Synovec, and Gwen M. Gross</i> . . .	2460
<b>Nanoporous Anodic Alumina: Structural and Optical Anisotropy</b> / <i>E. Stefan Kooij, Aurelian C. Gâlcă, Herbert Wormeester, and Bene Poelsema</i> . . . . .	2947
<b>Polymer Colloids and Their Metallation</b> / <i>Lyudmila M. Bronstein</i> . . . . .	3430
<b>Self-Assembled Monolayers: Chemical and Physical Modification under Vacuum</b> / <i>Jessica Torres, Anthony J. Wagner, Christopher C. Perry, Glenn M. Wolfe, and D. Howard Fairbrother</i> . . . . .	3747

### ***Magnetism-Based Utilization***

<b>Iron Oxide Nanoparticles</b> / <i>Mamoru Senna</i> . . . . .	1688
<b>Magnetic Ferrofluids</b> / <i>Carlos Rinaldi, Thomas Franklin, Markus Zahn, and Tahir Cader</i> . . . . .	1922
<b>Magnetic Nanomaterials: Conventional Synthesis and Properties</b> / <i>Dajie Zhang</i> . . . . .	1951
<b>Magnetic Nanomaterials: Nonconventional Synthesis and Chemical Design</b> / <i>Luminita Patron, Ioana Mindru, and Gabriela Marinescu</i> . . . . .	1968
<b>Magnetic Nanoparticles</b> / <i>Valérie Cabuil</i> . . . . .	1985
<b>Magnetic Nanoparticles for Granular Recording Media</b> / <i>David E. Nikles and J. W. Harrell</i> . . . . .	2001
<b>Nanoparticle Assemblies: Magnetic Properties</b> / <i>Xiangcheng Sun</i> . . . . .	2868

### ***Nanopowders and Nanocomposites***

<b>Automotive Parts: Impact of Nanotechnology</b> / <i>Ganesh Skandan, Amit Singhal, and Damian Sobrevilla</i> . . . . .	241
<b>Bimetallic Layered Nanocomposites</b> / <i>Amit Misra and Richard G. Hoagland</i> . . . . .	288
<b>Carbon Nanotube–Conducting Polymer Composites in Supercapacitors</b> / <i>Mark Hughes</i> . . . . .	574
<b>Carbon Nanotube–Metal Matrix Composites</b> / <i>Efraín Carreño-Morelli</i> . . . . .	611
<b>Carbon Nanotubes: Flow Control in Membranes</b> / <i>Scott A. Miller and Charles R. Martin</i> . . . . .	630
<b>Carbon Nanotubes: Functionalization</b> / <i>Bin Zhao, Hui Hu, Elena Bekyarova, Mikhail E. Itkis, Sandip Niyogi, and Robert C. Haddon</i> . . . . .	640
<b>Ceramic Nanocomposites: Self-Diagnostic Ability of Catastrophic Damage</b> / <i>Pavol Šajgalík and Zoltán Lenčéš</i> . . . . .	794
<b>Functionalization of Surface Layers on Ceramics</b> / <i>Toshihiro Ishikawa</i> . . . . .	1375
<b>Intercalated Polypropylene Nanocomposites</b> / <i>Michael J. Solomon and Anongnat Somwangthanaroj</i> . . . . .	1642
<b>Iron Nanoparticles</b> / <i>Dale L. Huber</i> . . . . .	1681
<b>Metallic Nanopowders</b> / <i>Frederick Tepper, Marat I. Lerner, and David S. Ginley</i> . . . . .	2153
<b>Metallic Nanopowders: Rocket Propulsion</b> / <i>Leonid Kaledin and Frederick Tepper</i> . . . . .	2165
<b>Metallic Quantum Dots</b> / <i>J. P. Wilcoxon</i> . . . . .	2176
<b>Nanotubes: Functionalization</b> / <i>Stanislaus S. Wong and Sarbjit Banerjee</i> . . . . .	3119

### ***Inorganic Nanowires***

<b>Barcoded Nanowires</b> / <i>Rebecca L. Stoermer and Christine D. Keating</i> . . . . .	259
<b>Inorganic Nanotubes</b> / <i>Reshef Tenne</i> . . . . .	1598
<b>Inorganic Nanotubes: Synthesis by Chemical Transport Reaction</b> / <i>Maja Remskar</i> . . . . .	1606
<b>Inorganic Sulfide Nanotubes: Mechanical Behavior</b> / <i>Ifat Kaplan-Ashiri, H. Daniel Wagner, Gotthard Seifert, and Reshef Tenne</i> . . . . .	1617
<b>Molecular Wires</b> / <i>Dustin K. James and James M. Tour</i> . . . . .	2441
<b>Nanobridges: Thermal Properties</b> / <i>Jeong Won Kang and Ho Jung Hwang</i> . . . . .	2522

---

**Inorganic Nanowires (*cont'd.*)**

<b>Nanostructured Materials: Metals on Microtubule Supports</b> / <i>Silke Behrens and Eberhard Unger</i> .....	3012
<b>Nanostructures Based on Layered Transition-Metal Chalcogenides</b> / <i>Russell R. Chianelli and Myriam Perez de la Rosa</i> .....	3080
<b>Nanowires and Nanobelts: Mechanical Properties</b> / <i>Zhong Lin Wang</i> .....	3146
<b>Nanowires: Molecular Assembly</b> / <i>Tomoyuki Akutagawa, Takayoshi Nakamura, and Jan Becher</i> .....	3136
<b>Semiconductor Nanowires: Rational Synthesis</b> / <i>Xiangfeng Duan and Charles M. Lieber</i> .....	3941
<b>Silica Nanotubes: Wetting and Diffusion</b> / <i>Kenji Okamoto, Karthik Jayaraman, Sang Jun Son, Sang Bok Lee, and Douglas S. English</i> .....	3995
<b>Superconductor Nanowires: Templated by Single Molecules</b> / <i>Alexey Bezryadin, Anthony Bollinger, David Hopkins, Michael Murphey, Mikas Remeika, and Andrey Rogachev</i> .....	4228

---

**Magnetic Nanoparticles**

<b>Antidot Lattices: Chaotic Transport</b> / <i>Tsuneya Ando</i> .....	210
<b>Biomedical Magnetic Nanoparticles</b> / <i>Ian Robinson, Le Duc Tung, and Nguyen T.K. Thanh</i> .....	354
<b>Charge Transport in Multilayer Nanostructures</b> / <i>Daniel M. Schaadt</i> .....	834
<b>Fullerenes: Magnetic Behavior</b> / <i>T. L. Makarova</i> .....	1352
<b>Iron Oxide Nanoparticles</b> / <i>Mamoru Senna</i> .....	1688
<b>Magnetic Ferrofluids</b> / <i>Carlos Rinaldi, Thomas Franklin, Markus Zahn, and Tahir Cader</i> .....	1922
<b>Magnetic Nanocarbon</b> / <i>T. L. Makarova</i> .....	1939
<b>Magnetic Nanomaterials: Conventional Synthesis and Properties</b> / <i>Dajie Zhang</i> .....	1951
<b>Magnetic Nanomaterials: Nonconventional Synthesis and Chemical Design</b> / <i>Luminita Patron, Ioana Mindru, and Gabriela Marinescu</i> .....	1968
<b>Magnetic Nanoparticles</b> / <i>Valérie Cabuil</i> .....	1985
<b>Magnetic Nanoparticles for Granular Recording Media</b> / <i>David E. Nikles and J. W. Harrell</i> .....	2001
<b>Nanocomposite Magnetic Materials: Shock-Induced Synthesis</b> / <i>N. N. Thadhani and Z. Q. Jin</i> ..	2556
<b>Nanocrystals: Size-Dependent Properties and Emerging Applications</b> / <i>G. U. Kulkarni, P. John Thomas, and C.N.R. Rao</i> .....	2665
<b>Nanofilms in Giant Magnetoresistance Heads</b> / <i>Edward Grochowski and Robert E. Fontana, Jr.</i> .....	2737
<b>Nanomaterials and Nanodevices: Ion-Beam Technology</b> / <i>Dmitri Litvinov and Sakhrat Khizroev</i> .....	2825
<b>Nanoparticle Assemblies: Magnetic Properties</b> / <i>Xiangcheng Sun</i> .....	2868
<b>Permanent Magnets Based on Nanostructured Intermetallic Alloys</b> / <i>Paul McGuinness, Andraž Kocjan, and Spomenka Kobe</i> .....	3328
<b>Permanent Nanocomposite Magnets</b> / <i>Satoshi Hirosawa</i> .....	3336
<b>Porous Alumina Templates for Nanofabrication</b> / <i>Latika Menon</i> .....	3525

---

**Mechanical Properties at the Nanoscale**
***Alloys and Composites***

<b>Bimetallic Layered Nanocomposites</b> / <i>Amit Misra and Richard G. Hoagland</i> .....	288
<b>Carbon Nanotube–Metal Matrix Composites</b> / <i>Efraín Carreño-Morelli</i> .....	611

<b>Ceramic Nanocomposites: Self-Diagnostic Ability of Catastrophic Damage</b> / Pavol Šajgalík and Zoltán Lenčés . . . . .	794
<b>Epoxy-Layered Silicate Nanocomposites</b> / Chenggang Chen and Tia Benson Tolle . . . . .	1284
<b>High-Strength Alloys: Nanogranular Phases</b> / Dmitri Valentinovich Louzguine and Akihisa Inoue . . . . .	1536
<b>Intercalated Polypropylene Nanocomposites</b> / Michael J. Solomon and Anongnat Somwangthanaroj . . . . .	1642
<b>Nanostructured Alloys: Cryomilling Synthesis and Behavior</b> / David Witkin, Piers Newbery, Bing Q. Han, and Enrique J. Lavernia . . . . .	2958
<b>Nanostructured Composites: Titanium-Based Alloys</b> / Jürgen Eckert, Jayanta Das, and Ki Buem Kim . . . . .	2996
<b>Polypropylene and Thermoplastic Olefins Nanocomposites</b> / Francis M. Mirabella, Jr. . . . .	3509

**Friction, Deformations, and Wear**

<b>AFM: Simulation of Interaction Forces</b> / Ivan U. Vakarelski, Scott C. Brown, Bahar Basim, and Brij M. Moudgil . . . . .	153
<b>Mica Surfaces: Charge Nucleation and Wear</b> / James M. Helt and James D. Batteas . . . . .	2211
<b>Nanocrystalline Materials: Fatigue</b> / Alexie Yu. Vinogradov and Sean R. Agnew . . . . .	2602
<b>Nanofriction and Nanowear of Sliding Systems: Simulations</b> / W.C.D. Cheong . . . . .	2763
<b>Nanophase Powders: Mechanosynthesis</b> / F. Miani, F. Maurigh, and F. Delogu . . . . .	2923
<b>Nanostructured Materials: Synthesis by Mechanical Attrition</b> / Carl C. Koch . . . . .	3019
<b>Nanostructured Materials: Synthesis by Mechanical Means</b> / H.-J. Fecht . . . . .	3030
<b>Structural Nanomaterials</b> / Joanna R. Groza, and Jeffrey C. Gibeling . . . . .	4205
<b>Tribology at the Nanoscale</b> / Peter T. Cummings and Clare McCabe . . . . .	4385
<b>Tribology of Inorganic Nanoparticles</b> / Lev Rapoport . . . . .	4375

**Nanomechanical Devices**

<b>Magnetic Ferrofluids</b> / Carlos Rinaldi, Thomas Franklin, Markus Zahn, and Tahir Cader . . . . .	1922
<b>Microweighing in Supercritical Carbon Dioxide</b> / You-Ting Wu and Christine S. Grant . . . . .	2253
<b>Molecular Motor-Powered Nanodevices: Control Mechanisms</b> / Jacob J. Schmidt and Carlo D. Montemagno . . . . .	2347
<b>Nanomechanical Resonant Devices: Surface Chemistry</b> / Joshua A. Henry, Deborahonyaa Sengupta, and Melissa A. Hines . . . . .	2848

**Soft Materials and Weak Interfacial Forces**

<b>AFM: Biopolymers</b> / Nehal I. Abu-Lail and Terri A. Camesano . . . . .	63
<b>AFM: Imaging Artifacts</b> / Stephanie Butler Velegol . . . . .	88
<b>Biomaterials: Mechanical Characterization</b> / Eunice Phay Shing Tan and Chwee Teck Lim . . . . .	317
<b>Dynamic AFM on Heterogeneous Surfaces</b> / Ijeoma M. Nnebe and James W. Schneider . . . . .	1144
<b>Interfacial Forces: Colloidal Particle-Liquid</b> / Sarah A. Nespolo and Geoffrey W. Stevens . . . . .	1650
<b>Langmuir-Blodgett Films</b> / Ursula Mazur . . . . .	1738
<b>Liposomes: Direct Force Measurement by AFM</b> / Guangzhao Mao, Xuemei Liang, and K.Y. Simon Ng . . . . .	1869
<b>Small Amplitude AFM</b> / Peter M. Hoffmann . . . . .	4119
<b>Soft Materials: AFM Investigations and Nanophysics</b> / J. P. Aimé, R. Boisgard, S. Marsaudon, and G. Couturier . . . . .	4158
<b>Surface Forces on Nanoparticles Determined by Direct Measurement</b> / Jeong-Min Cho, Georgios Pyrgiotakis, and Wolfgang M. Sigmund . . . . .	4260

---

**Mechanical Properties at the Nanoscale (*cont'd.*)**


---

***Supramolecular Mechanics of Nanotubes and Nanowires***

<b>Carbon Nanotubes: Supramolecular Mechanics</b> / Boris I. Yakobson and Luise S. Couchman . . . . .	722
<b>Inorganic Nanotubes</b> / Reshef Tenne . . . . .	1598
<b>Inorganic Sulfide Nanotubes: Mechanical Behavior</b> / Ifat Kaplan-Ashiri, H. Daniel Wagner, Gotthard Seifert, and Reshef Tenne . . . . .	1617
<b>Nanostructured Ultrastrong Materials</b> / Nicholas A. Kotov, Arif A. Mamedov, Dirk M. Guldi, Zhiyong Tang, Maurizio Prato, James Wicksted, and Andreas Hirsch . . . . .	3072
<b>Nanowires and Nanobelts: Mechanical Properties</b> / Zhong Lin Wang . . . . .	3146
<b>Nanowires: Molecular Assembly</b> / Tomoyuki Akutagawa, Takayoshi Nakamura, and Jan Becher . . . . .	3136

---

**Molecular Electronics and Nanoscale Devices**


---

***Molecular Electronics and Nanocomputing***

<b>Barcoded Nanowires</b> / Rebecca L. Stoermer and Christine D. Keating . . . . .	259
<b>Carbon Nanotransistors</b> / Po-Wen Chiu and Siegmund Roth . . . . .	563
<b>Charge Transfer in Metal–Molecule Heterostructures</b> / Debasish Kuila, David B. Janes, and Clifford P. Kubiak . . . . .	819
<b>DNA Hybridization: Electronic Control</b> / Kimberly Hamad-Schifferli . . . . .	1122
<b>DNA-Conjugated Metal Nanoparticles: Chip Detection Applications</b> / Wolfgang Fritzsche . . . . .	1114
<b>Electronic Switches</b> / Richard J. Nichols, David J. Schiffrin, and Wolfgang Haiss . . . . .	1230
<b>Litho-to-Nano Link</b> / Gianfranco Cerofolini, Dario Narducci, and Elisabetta Romano . . . . .	1890
<b>Metal Nanoparticles: Self-Assembly into Electronic Nanostructures</b> / Venugopal Santhanam and Ronald P. Andres . . . . .	2079
<b>Molecular Computing Machines</b> / Yaakov Benenson and Ehud Shapiro . . . . .	2291
<b>Molecular Electronics: Logic and Memory</b> / Dustin K. James and James M. Tour . . . . .	2303
<b>Molecular Electronics: Models of Switchable and Programmable Devices</b> / Pedro A. Derosa, Vandana R. Tarigopula, and Jorge M. Seminario . . . . .	2317
<b>Molecular Switches</b> / Jean-Pierre Launay, Christophe Coudret, and Christian Joachim . . . . .	2411
<b>Molecular Wires</b> / Dustin K. James and James M. Tour . . . . .	2441
<b>Nano–Mesoscopic Interface: Hybrid Devices</b> / Gianfranco Cerofolini . . . . .	2493
<b>Optical Molecular Devices</b> / A. Prasanna de Silva and Nathan D. McClenaghan . . . . .	3251
<b>Semiconductor Nanowires: Nanoscale Electronics and Optoelectronics</b> / Yu Huang, Xiangfeng Duan, and Charles M. Lieber . . . . .	3910
<b>Silicon Functionalization for Molecular Electronics</b> / Gianfranco Cerofolini, Dario Narducci, and Elisabetta Romano . . . . .	4009

---

***Molecular Mechanical Devices***

<b>Computational Analysis of Switchable Catenanes</b> / Xiang Zheng and Karl Sohlberg . . . . .	930
<b>Computational Analysis Using Normal and Multibody Modes</b> / Bryan C. Hathorn, Donald W. Noid, Bobby G. Sumpter, Chao Yang, and William A. Goddard III . . . . .	921
<b>Molecular Manipulator: Dynamic Design Criteria</b> / Andrés Jaramillo-Botero . . . . .	2336
<b>Molecular Motor-Powered Nanodevices: Control Mechanisms</b> / Jacob J. Schmidt and Carlo D. Montemagno . . . . .	2347

<b>Molecular Switches and Motors</b> / <i>Richard A. van Delden and Ben L. Feringa</i> . . . . .	2424
<b>Motor Proteins in Synthetic Materials and Devices</b> / <i>Henry Hess, George Bachand, and Viola Vogel</i> . . . . .	2484
<b>Protein Nanotubes as Building Blocks</b> / <i>Hiroshi Matsui</i> . . . . .	3578

---

## Nanocomposites

<b>Barrier Properties of Ordered Polymer Nanocomposites</b> / <i>Bon-Cheol Ku, Alexandre Blumstein, Jayant Kumar, Lynne A. Samuelson, and Dong Wook Kim</i> . . . . .	267
<b>Carbon Nanotube–Conducting Polymer Composites in Supercapacitors</b> / <i>Mark Hughes</i> . . . . .	574
<b>Carbon Nanotube–Metal Matrix Composites</b> / <i>Efraín Carreño-Morelli</i> . . . . .	611
<b>Epoxy-Layered Silicate Nanocomposites</b> / <i>Chenggang Chen and Tia Benson Tolle</i> . . . . .	1284
<b>High-Strength Alloys: Nanogranular Phases</b> / <i>Dmitri Valentinovich Louzguine and Akihisa Inoue</i> . . . . .	1536
<b>Layer-by-Layer Assembly of Thin Films of Mixed Nanoparticles</b> / <i>Jianchang Guo, Encai Hao, and Tianquan Lian</i> . . . . .	1813
<b>Nanocomposite Magnetic Materials: Shock-Induced Synthesis</b> / <i>N. N. Thadhani and Z. Q. Jin</i> . . . . .	2556
<b>Nanocrystals: Synthesis and Mesoscale Organization</b> / <i>G. U. Kulkarni, P. John Thomas, and C.N.R. Rao</i> . . . . .	2676
<b>Nanofiltration Separations</b> / <i>Eric M.V. Hoek and Anna Jawor</i> . . . . .	2749
<b>Nanomaterials: Trends</b> / <i>Richard Silbergli</i> . . . . .	2836
<b>Nanostructured Composites: Carbon-Derived Fibers</b> / <i>Peter M.A. Sherwood</i> . . . . .	2986
<b>Nanotubes: Functionalization</b> / <i>Stanislaus S. Wong and Sarbajit Banerjee</i> . . . . .	3119
<b>Permanent Nanocomposite Magnets</b> / <i>Satoshi Hirosawa</i> . . . . .	3336
<b>Polymer Nanocomposites with Nanoparticle and Carbon Nanotube Fillers</b> / <i>B. J. Ash, A. Eitan, and L. S. Schadler</i> . . . . .	3466
<b>Polymer–Clay Nanocomposites and Polymer Brushes</b> / <i>Xiaowu Fan, Chuanjun Xia, and Rigoberto C. Advincula</i> . . . . .	3417
<b>Polymer–Nanoparticle Composites</b> / <i>Kevin Sill, Seunghoo Yoo, and Todd Emrick</i> . . . . .	3487
<b>Polypropylene and Thermoplastic Olefins Nanocomposites</b> / <i>Francis M. Mirabella, Jr.</i> . . . . .	3509
<b>Tungsten Carbide–Cobalt Nanocomposites</b> / <i>Purnesh Seegopaul and Zhigang Zak Fang</i> . . . . .	4390

---

## Nanofabrication and Controlled Synthesis of Nanoparticles

### *Chemical Synthesis Methods*

<b>Conducting Polymer Nanotubes</b> / <i>Seung Il Cho and Sang Bok Lee</i> . . . . .	965
<b>DNA-Conjugated Metal Nanoparticles: Chip Detection Applications</b> / <i>Wolfgang Fritzsche</i> . . . . .	1114
<b>Inorganic Nanotubes: Synthesis by Chemical Transport Reaction</b> / <i>Maja Remskar</i> . . . . .	1606
<b>Lab-on-a-Chip Microreactors</b> / <i>Paul D.I. Fletcher, Stephen J. Haswell, Paul Watts, and Xunli Zhang</i> . . . . .	1721
<b>Metal Nanostructures: Synthesis by Soft Chemical Methods</b> / <i>Yugang Sun and Younan Xia</i> . . . . .	2105
<b>Nanoarrays: Electrochemically Self-Assembled</b> / <i>S. Bandyopadhyay</i> . . . . .	2502
<b>Nanoceramics</b> / <i>Abbas Khaleel</i> . . . . .	2531
<b>Three-Dimensional Nanofabrication Using Multiphoton Absorption</b> / <i>John T. Fourkas and Tommaso Baldacchini</i> . . . . .	4338



---

**Nanofabrication and Controlled Synthesis of Nanoparticles (*cont'd.*)**


---

**Colloidal Chemistry Methods**

<b>Colloid Systems: Micelles and Nanocrystals</b> / B.L.V. Prasad and Savka I. Stoeva . . . . .	856
<b>Colloidal Structures on Patterned Surfaces</b> / Aránzazu del Campo, Anne-Sophie Duwez, Charles-André Fustin, and Ulrich Jonas . . . . .	907
<b>Dimensionally Graded Semiconductor Nanoparticle Films</b> / Arif A. Mamedov, Nicholas A. Kotov, and Nataliya N. Mamedova . . . . .	1062
<b>Enzymatic Synthesis of Nanostructured Polymers and Composites</b> / Christy Ford, Vijay T. John, Gary McPherson, Jibao He, Joseph Akkara, David Kaplan, and Arijit Bose . . . . .	1271
<b>Gecko-Inspired Adhesives: Nanofabrication</b> / Aránzazu del Campo and Eduard Arzt . . . . .	1384
<b>Germanium Nanoparticles</b> / Boyd R. Taylor and Louisa J. Hope-Weeks . . . . .	1405
<b>Hydrogel Nanoparticles Made of Cross-Linked Polyvinylpyrrolidone</b> / Susmita Mitra, Dhruba Jyoti Bharali, and Amarnath Maitra . . . . .	1546
<b>Ionic Strength Effects: Tunable Nanocrystal Distribution in Colloidal Gold Films</b> / E. Stefan Kooij, E.A. Martijn Brouwer, Herbert Wormeester, and Bene Poelsema . . . . .	1672
<b>Island Surfaces: Fabrication on Self-Assembled Monolayers</b> / Hongjie Liu, Charles Maldarelli, M. Lane Gilchrist, and Alexander Couzis . . . . .	1708
<b>Layer-by-Layer Assembly of Electroactive Thin Films to Layered Carbon Electrodes</b> / Tarek R. Farhat . . . . .	1764
<b>Layered Double Hydroxides: Self-Assembly and Multiple Phases</b> / Zhi Ping Xu and Paul S. Braterman . . . . .	1841
<b>Monolayer-Protected Metal Nanoparticles: Synthesis</b> / Young-Seok Shon . . . . .	2469
<b>Nanocrystalline Materials: Synthesis and Properties</b> / Alexandr I. Gusev . . . . .	2621
<b>Nanomaterials: Advances in Technology and Industry</b> / Ganesh Skandan and Amit Singh . . . . .	2788
<b>Nanomaterials: Manufacturing, Processing, and Applications</b> / Pramod K. Sharma, Weifang Miao, Anit Giri, and Srikanth Raghunathan . . . . .	2799
<b>Nanoparticles: Synthesis in Polymer Substrates</b> / Bai Yang and Junhu Zhang . . . . .	2912

---

**Dissolution and Etching**

<b>Anodization Patterned on Aluminum Surfaces</b> / Juchao Yan, G. V. Rama Rao, Plamen B. Atanassov, and Gabriel P. López . . . . .	203
<b>Metal Nanostructures: Synthesis Controlled by Photoexcitation</b> / Kei Murakoshi and Yoshihiro Nakato . . . . .	2091
<b>Nanoporosity Evolution on Dealloying</b> / Jonah Erlebacher . . . . .	2938
<b>Nanotube Sensors</b> / Marc Wirtz and Charles R. Martin . . . . .	3109
<b>Porous Alumina Templates for Nanofabrication</b> / Latika Menon . . . . .	3525

---

**Lithography**

<b>AFM: Nanolithography on Organized Films</b> / Seunghyun Lee and Haiwon Lee . . . . .	119
<b>Conducting Polymer Nanopatterns</b> / Shaun F. Filocamo and Mark W. Grinstaff . . . . .	954
<b>Dip-Pen Nanolithography: Optical Inks</b> / Brandon L. Weeks, Aleksandr Noy, Abigail E. Miller, Jennifer E. Klare, Bruce W. Woods, and James J. De Yoreo . . . . .	1084
<b>Laser-Based Deposition: Patterning</b> / Edward M. Nadgorny and Jaroslaw Drelich . . . . .	1749
<b>Litho-to-Nano Link</b> / Gianfranco Cerofolini, Dario Narducci, and Elisabetta Romano . . . . .	1890
<b>Nanolithography: Length Scale Limitations</b> / Takashi Ito . . . . .	2779

<b>Nanomaterials and Nanodevices: Ion-Beam Technology</b> / Dmitri Litvinov and Sakhrat Khizroev	2825
<b>Polymer Molding: Nanostructure Replication</b> / Daniel B. Wolfe, J. Christopher Love, and George M. Whitesides	3456
<b>Printed and Molded Nanostructures: Photonic Applications</b> / John A. Rogers	3559
<b>Scanning Near-Field Photolithography</b> / Graham J. Leggett	3709
<b>Scanning Probe Lithography: Polymeric and Biomolecular Nanostructures</b> / Stefan Zauscher	3721

### ***Mechanosynthesis***

<b>Nanocrystallization</b> / John H. Perepezko	2655
<b>Nanophase Powders: Mechanosynthesis</b> / F. Miani, F. Maurigh, and F. Delogu	2923
<b>Nanostructured Alloys: Cryomilling Synthesis and Behavior</b> / David Witkin, Piers Newbery, Bing Q. Han, and Enrique J. Lavernia	2958
<b>Nanostructured Materials: Synthesis by Mechanical Attrition</b> / Carl C. Koch	3019
<b>Nanostructured Materials: Synthesis by Mechanical Means</b> / H.-J. Fecht	3030

### ***Sol-Gel Synthesis***

<b>Cyanogels: Processing by Spin Coating</b> / Shu Zhu and Andrew B. Bocarsly	1029
<b>Metal Oxide Nanoparticles</b> / Ryan M. Richards	2126
<b>Mixed Metal Oxide Nanoparticles</b> / Pramesh N. Kapoor, Ajay Kumar Bhagi, Ravichandra S. Mulukutla, and Kenneth J. Klabunde	2280
<b>Nanomaterials: Manufacturing, Processing, and Applications</b> / Pramod K. Sharma, Weifang Miao, Anit Giri, and Srikanth Raghunathan	2799
<b>Polymer Nanofibers Prepared by Electrospinning</b> / Roland Dersch, Andreas Greiner, and Joachim H. Wendorff	3480

### ***Synthesis in Supercritical Fluids***

<b>Metal Nanoparticles Prepared in Supercritical Carbon Dioxide</b> / Harry W. Rollins	2072
<b>Microweighing in Supercritical Carbon Dioxide</b> / You-Ting Wu and Christine S. Grant	2253
<b>Nanostructured Materials: Synthesis in Supercritical Fluids</b> / Yuehe Lin, Xiang-Rong Ye, and Chien M. Wai	3040
<b>Templating Aerogels for Tunable Nanoporosity</b> / Aydin K. Sunol and Sermin G. Sunol	4294

## **Nanostructures and Nanophase Structures**

### ***Advanced Ceramics***

<b>Functionalization of Surface Layers on Ceramics</b> / Toshihiro Ishikawa	1375
<b>Iron Oxide Nanoparticles</b> / Mamoru Senna	1688
<b>Magnetic Nanomaterials: Nonconventional Synthesis and Chemical Design</b> / Luminita Patron, Ioana Mindru, and Gabriela Marinescu	1968
<b>Nanoceramics</b> / Abbas Khaleel	2531
<b>Nanoceramics: Thermal Conductivity</b> / Paul G. Klemens	2539
<b>Nanostructured Silica and Silica-Derived Materials</b> / Ho-Cheol Kim and Geraud Dubois	3063
<b>Tungsten Carbide–Cobalt Nanocomposites</b> / Purnesh Seegopaul and Zhigang Zak Fang	4390
<b>Ytria-Tetragonally Stabilized Zirconia</b> / R. Allen Kimel	4414



---

**Nanostructures and Nanophase Structures (*cont'd.*)**


---

**Arrays and Superlattices**

<b>Bio-Microarrays</b> / Günter E.M. Tovar and Achim Weber	298
<b>Colloidal Nanoparticles: Aggregation Patterns at Surfaces</b> / Hamidou Haidara and Karine Mougin	882
<b>Conducting Polymer Nanopatterns</b> / Shaun F. Filocamo and Mark W. Grinstaff	954
<b>Nanocrystals: Synthesis and Mesoscale Organization</b> / G. U. Kulkarni, P. John Thomas, and C.N.R. Rao	2676
<b>Nanoparticle Arrays: Optical and Electronic Applications</b> / Ilona Kretzschmar and Mark A. Reed	2856
<b>Printed and Molded Nanostructures: Photonic Applications</b> / John A. Rogers	3559
<b>Quantum Dot Arrays: Electromagnetic Properties</b> / Sergey A. Maksimenko and Gregory Ya. Slepyan	3606
<b>Quantum Dots: Phonons in Self-Assembled Multiple Germanium Structures</b> / Jianlin Liu, Aleksandr Khitun, and Kang L. Wang	3673
<b>Supramolecular Networks Synthesized in Nanoparticle–Polymer Mixtures</b> / Anna C. Balazs and Gavin A. Buxton	4240

---

**Core–Shell and Asymmetric Nanostructures**

<b>Capsules: Polymer Microcapsules</b> / Gleb B. Sukhorukov	508
<b>Capsules: Specific Layer Structures</b> / Lars Dähne and Claire S. Peyratout	522
<b>Core–Shell Hydrogel Nanoparticles</b> / Clinton D. Jones and L. Andrew Lyon	993
<b>Core–Shell Nanospheres, Hollow Capsules, and Bottles</b> / Gang Zhang, Kai Zhang, Yi Yu, and Bai Yang	1003
<b>Dissymmetrical Nanoparticles</b> / Stéphane Reculosa, Christophe Mingotaud, Etienne Duguet, and Serge Ravaine	1093
<b>Metal Nanostructures: Synthesis by Soft Chemical Methods</b> / Yugang Sun and Younan Xia	2105
<b>Nanobridges: Thermal Properties</b> / Jeong Won Kang and Ho Jung Hwang	2522
<b>Nanoencapsulation of Bioactive Substances</b> / Yury E. Shapiro	2707
<b>Oil-Filled Nanocapsules</b> / Royale S. Underhill	3234

---

**Layered Nanostructures**

<b>Bimetallic Layered Nanocomposites</b> / Amit Misra and Richard G. Hoagland	288
<b>Charge Transport in Multilayer Nanostructures</b> / Daniel M. Schaadt	834
<b>Dimensionally Graded Semiconductor Nanoparticle Films</b> / Arif A. Mamedov, Nicholas A. Kotov, and Nataliya N. Mamedova	1062
<b>Epoxy-Layered Silicate Nanocomposites</b> / Chenggang Chen and Tia Benson Tolle	1284
<b>Nanostructures Based on Layered Transition-Metal Chalcogenides</b> / Russell R. Chianelli and Myriam Perez de la Rosa	3080
<b>Structural Transitions in Thin Films</b> / Rajarshi Banerjee, Gregory B. Thompson, and Hamish L. Fraser	4217

---

**Metal Nanoparticles**

<b>Catalysis by Supported Gold Nanoclusters</b> / D. Wayne Goodman	744
<b>Colloidal Nanometals as Fuel Cell Catalyst Precursors</b> / Helmut Bönnemann and K. S. Nagabhushana	863
<b>Gold Nanoclusters: Structural Disorder</b> / Ignacio L. Garzón	1412

<b>Iron Nanoparticles</b> / Dale L. Huber	1681
<b>Metal Nanoparticle Catalysts</b> / Naoki Toshima	2052
<b>Metal Nanoparticles Prepared in Supercritical Carbon Dioxide</b> / Harry W. Rollins	2072
<b>Metallic Nanopowders</b> / Frederick Tepper, Marat I. Lerner, and David S. Ginley	2153
<b>Nanoporosity Evolution on Dealloying</b> / Jonah Erlebacher	2938
<b>Nanostructured Composites: Titanium-Based Alloys</b> / Jürgen Eckert, Jayanta Das, and Ki Buem Kim	2996
<b>Noble Metal Nanoparticles on Carbon Fibers</b> / Dmitri A. Bulushev and Igor Yuranov	3195
<b>Palladium Nanoclusters</b> / Kiyotomi Kaneda, Kwang-Min Choi, Tomoo Mizugaki, and Kohki Ebitani	3309

---

### ***Nanocrystals and Nanopowders***

<b>Cubosomes: Bicontinuous Liquid Crystalline Nanoparticles</b> / Patrick T. Spicer	1018
<b>Metal Oxide Nanoparticles</b> / Ryan M. Richards	2126
<b>Nanocrystal Arrays: Self-Assembly and Physical Properties</b> / Xiao-Min Lin, Raghuvver Parthasarathy, and Heinrich M. Jaeger	2568
<b>Nanocrystalline Materials: Fatigue</b> / Alexei Yu. Vinogradov, and Sean R. Agnew	2602
<b>Nanocrystalline Materials: Synthesis and Properties</b> / Alexandr I. Gusev	2621
<b>Nanocrystallization</b> / John H. Perepezko	2655
<b>Nanocrystals Synthesized in Colloidal Self-Assemblies</b> / M. P. Pileni	2581
<b>Nanodiamonds</b> / Jean-Yves Raty and Giulia Galli	2697
<b>Nanomaterials: Advances in Technology and Industry</b> / Ganesh Skandan and Amit Singhal	2788
<b>Nanomaterials: Manufacturing, Processing, and Applications</b> / Pramod K. Sharma, Weifang Miao, Anit Giri, and Srikanth Raghunathan	2799
<b>Nanoparticles: Generation, Functionalization, and Ion Sensing</b> / Jason J. Davis and Paul D. Beer	2898
<b>Permanent Magnets Based on Nanostructured Intermetallic Alloys</b> / Paul McGuinness, Andraž Kocjan, and Spomenka Kobe	3328

---

## **Optical Properties and Optoelectronic Devices**

---

### ***Photonic Crystals and Nonlinear Optical Media***

<b>Nanoparticle Arrays: Optical and Electronic Applications</b> / Ilona Kretschmar and Mark A. Reed	2856
<b>Nanoporous Anodic Alumina: Structural and Optical Anisotropy</b> / E. Stefan Kooij, Aurelian C. Gâlcă, Herbert Wormeester, and Bene Poelsema	2947
<b>Nanostructures Derived from Phase-Separated Polymers</b> / Michael R. Bockstaller and Edwin L. Thomas	3093
<b>Nonlinear Optical Materials from Self-Assembled Organic Films</b> / Matthew Guzy, Richey M. Davis, Patrick J. Neyman, Charles Brands, J. R. Heflin, Harry W. Gibson, and Kevin E. Van Cott	3206
<b>Photonic Crystal Fibers</b> / P. St. J. Russell, J. C. Knight, T. A. Birks, and P. J. Roberts	3356
<b>Porphyritic Materials: Self-Assembly on Surfaces</b> / Charles Michael Drain, James D. Batteas, Gabriela Smeureanu, and Sandeep Patel	3539
<b>Printed and Molded Nanostructures: Photonic Applications</b> / John A. Rogers	3559
<b>Structural Color</b> / Pete Vukusic	4195

---

**Optical Properties and Optoelectronic Devices (*cont'd.*)**


---

**Quantum Confinement Effects**

<b>Cadmium Selenide Quantum Dots</b> / Kenzo Maehashi and Hisao Nakashima . . . . .	477
<b>Cadmium Selenide Quantum Rods: Anisotropy</b> / Liang-shi Li and A. Paul Alivisatos . . . . .	487
<b>Core-Shell Hydrogel Nanoparticles</b> / Clinton D. Jones and L. Andrew Lyon . . . . .	993
<b>Indium Arsenide Islands on Silicon</b> / P. C. Sharma and Kang L. Wang . . . . .	1582
<b>Luminescence of Nanoparticle-Labeled Antibodies and Antigens</b> / Shaopeng Wang and Nicholas A. Kotov . . . . .	1915
<b>Membrane-Coated Nanoparticles: Photochemistry</b> / Ulrich Siggel, Guangtao Li, and Jürgen-Hinrich Fuhrhop . . . . .	2012
<b>Metallic Quantum Dots</b> / J. P. Wilcoxon . . . . .	2176
<b>Optical Molecular Devices</b> / A. Prasanna de Silva and Nathan D. McClenaghan . . . . .	3251
<b>Quantum Dot Lasers</b> / Mikhail V. Maximov and Nikolai N. Ledentsov . . . . .	3617
<b>Quantum Dots: Electronic Coupling and Structural Ordering</b> / Glenn S. Solomon . . . . .	3634
<b>Self-Assembled Quantum Dots: Electronic Structures and Optical Properties</b> / Andrew Williamson . . . . .	3789
<b>Self-Formed Quantum Dots: Structural and Optical Characterization</b> / Shun-ichi Gonda and Hajime Asahi . . . . .	3877
<b>Semiconductor Nanowires: Nanoscale Electronics and Optoelectronics</b> / Yu Huang, Xiangfeng Duan, and Charles M. Lieber . . . . .	3910
<b>Silicon Nanoclusters: Simulations</b> / Aaron Puzder . . . . .	4021
<b>Silicon Nanocrystals: Quantum Confinement</b> / James R. Chelikowsky . . . . .	4033
<b>Thermal Effect on the Luminescence Properties of Quantum Dots</b> / X. B. Zhang and R. D. Dupuis . . . . .	4316

---

**Surface Plasmons and Raman Scattering**

<b>Carbon Nanotubes: Optical Properties</b> / R. Saito, Mildred S. Dresselhaus, G. Dresselhaus, A. Jorio, A. G. Souza Filho, and M. A. Pimenta . . . . .	679
<b>Metal Nanoparticle Ensembles: Collective Optical Properties</b> / Alexander Wei . . . . .	2064
<b>Metal Nanostructures: Synthesis Controlled by Photoexcitation</b> / Kei Murakoshi and Yoshihiro Nakato . . . . .	2091
<b>Nanocrystals: Size-Dependent Properties and Emerging Applications</b> / G. U. Kulkarni, P. John Thomas, and C.N.R. Rao . . . . .	2665
<b>Optical Nanosensors and Nanobiosensors</b> / Brian M. Cullum . . . . .	3258
<b>Quantum Dots: Inelastic Light Scattering from Electronic Excitations</b> / Christian Schüller . . . . .	3661
<b>Surface-Enhanced Raman Scattering</b> / Adam M. Schwartzberg and Jin Z. Zhang . . . . .	4250
<b>Surface Plasmon Spectra of Silver and Gold Nanoparticle Assemblies</b> / Mondona Zangeneh and Roger Terrill . . . . .	4271

---

**Polymer Nanomaterials**


---

**Electronic Materials and Nanocomposites**

<b>Conducting Polymer Nanotubes</b> / Seung Il Cho and Sang Bok Lee . . . . .	965
<b>Fluorescence-Voltage Single Molecule Spectroscopy</b> / Young Jong Lee, Andre J. Gesquiere, So-Jung Park, and Paul F. Barbara . . . . .	1300

<b>Litho-to-Nano Link</b> / Gianfranco Cerofolini, Dario Narducci, and Elisabetta Romano . . . . .	1890
<b>Low-Dielectric Constant Materials</b> / Robert D. Miller . . . . .	1901
<b>Polymer Nanocomposites with Nanoparticle and Carbon Nanotube Fillers</b> / B. J. Ash, A. Eitan, and L. S. Schadler . . . . .	3466
<b>Polymer–Clay Nanocomposites and Polymer Brushes</b> / Xiaowu Fan, Chuanjun Xia, and Rigoberto C. Advincula . . . . .	3417
<b>Polypropylene and Thermoplastic Olefins Nanocomposites</b> / Francis M. Mirabella, Jr. . . . .	3509
<b>Raman Spectroscopy of Carbon Nanotube–Polymer Composites</b> / Bin Chen . . . . .	3682
<b>Semiconductor Nanowires: Macroelectronics Applications</b> / Yugang Sun and John A. Rogers . . . . .	3896

### ***Polymer Networks and Self-Assembled Structures***

<b>Adsorption on Heterogeneous Surfaces</b> / Vinay K. Gupta and Yu-Wen Huang . . . . .	41
<b>Amphiphilic Block Copolymer Monolayer at Air–Water Interface</b> / Emiko Mouri and Hideki Matsuoka . . . . .	168
<b>Anion-Templated Self-Assembly: Organic Compounds</b> / Paul D. Beer and Mark R. Sambrook . . . . .	191
<b>Barrier Properties of Ordered Polymer Nanocomposites</b> / Bon-Cheol Ku, Alexandre Blumstein, Jayant Kumar, Lynne A. Samuelson, and Dong Wook Kim . . . . .	267
<b>Block Copolymer Nanoparticles</b> / Sandrine Pensec, Daniel Portinha, Laurent Bouteiller, and Christophe Chassenieux . . . . .	467
<b>Coordination Framework Topology</b> / Neil R. Champness and Neil S. Oxtoby . . . . .	984
<b>Cyanogels: Processing by Spin Coating</b> / Shu Zhu and Andrew B. Bocarsly . . . . .	1029
<b>Guests within Hydrophobic Pockets: Conventional Synthesis</b> / Bruce C. Gibb . . . . .	1429
<b>Hydrogel Nanoparticles Made of Cross-Linked Polyvinylpyrrolidone</b> / Susmita Mitra, Dhruva Jyoti Bharali, and Amarnath Maitra . . . . .	1546
<b>Layer-by-Layer Assembly of Gold Nanoclusters with Self-Assembled Monolayers</b> / Kohei Uosaki, Wenbo Song, Masayuki Okamura, and Toshihiro Kondo . . . . .	1773
<b>Layer-by-Layer Assembly of Polyelectrolyte Films: Membranes and Catalysts</b> / Bernd Tieke and Ali Toutianoush . . . . .	1784
<b>Layer-by-Layer Assembly of Semiconducting and Photoreactive Bolaform Amphiphiles</b> / Jason Locklin, Derek Patton, Chuanjun Xia, Xiaowu Fan, and Rigoberto C. Advincula . . . . .	1798
<b>Polymer Colloids and Their Metallation</b> / Lyudmila M. Bronstein . . . . .	3430
<b>Polymer Nanofibers Prepared by Electrospinning</b> / Roland Dersch, Andreas Greiner, and Joachim H. Wendorff . . . . .	3480
<b>Supramolecular Networks Synthesized in Nanoparticle–Polymer Mixtures</b> / Anna C. Balazs and Gavin A. Buxton . . . . .	4240
<b>Templating Polymer Crystal Growth Using Block Copolymers</b> / Yueh-Lin Loo . . . . .	4303

### ***Polymerization and Structure Control***

<b>Capsules: Polymer Microcapsules</b> / Gleb B. Sukhorukov . . . . .	508
<b>Core–Shell Hydrogel Nanoparticles</b> / Clinton D. Jones and L. Andrew Lyon . . . . .	993
<b>Fullerenes: Magnetic Behavior</b> / T. L. Makarova . . . . .	1352
<b>Intercalated Polypropylene Nanocomposites</b> / Michael J. Solomon and Anongnat Somwangthanaroj . . . . .	1642
<b>Polymer Molding: Nanostructure Replication</b> / Daniel B. Wolfe, J. Christopher Love, and George M. Whitesides . . . . .	3456
<b>Polymer Nanowires Conjugated by Controlled Chain Polymerization</b> / Yuji Okawa and Masakazu Aono . . . . .	3501
<b>Polymer-Mediated Self-Assembly of Nanoparticles</b> / Tyler B. Norsten, Amitav Sanyal, Roy Shenhar, and Vincent M. Rotello . . . . .	3443

---

**Polymer Nanomaterials (cont'd.)**


---

**Polymerization and Structure Control (cont'd.)**

<b>Polymer–Nanoparticle Composites</b> / Kevin Sill, Seunghoo Yoo, and Todd Emrick . . . . .	3487
<b>Scanning Probe Lithography: Polymeric and Biomolecular Nanostructures</b> / Stefan Zauscher . . .	3721
<b>Three-Dimensional Nanofabrication Using Multiphoton Absorption</b> / John T. Fourkas and Tommaso Baldacchini . . . . .	4338
<b>Ultrathin Polymer Films: Nanoparticle Nucleation</b> / Pieter Stroeve . . . . .	4400

---

**Quantum Dots**


---

**Architecture and Growth Modes**

<b>Cadmium Selenide Quantum Dots</b> / Kenzo Maehashi and Hisao Nakashima . . . . .	477
<b>Cadmium Selenide Quantum Rods: Anisotropy</b> / Liang-shi Li and A. Paul Alivisatos . . . . .	487
<b>Cadmium Sulfate Nanocrystals: Computational Analysis</b> / Stacie Nunes, Zhigang Zhou, Jeffrey D. Evanseck, and Jeffry D. Madura . . . . .	498
<b>Electron Microscopy at Very High Resolution</b> / Klaus van Benthem and Stephen J. Pennycook . . . . .	1217
<b>Indium Arsenide Islands on Silicon</b> / P. C. Sharma and Kang L. Wang . . . . .	1582
<b>Ionic Strength Effects: Tunable Nanocrystal Distribution in Colloidal Gold Films</b> / E. Stefan Kooij, E.A. Martijn Brouwer, Herbert Wormeester, and Bene Poelsema . . . . .	1672
<b>Layer-by-Layer Assembly of Thin Films of Mixed Nanoparticles</b> / Jianchang Guo, Encai Hao, and Tianquan Lian . . . . .	1813
<b>Membrane-Coated Nanoparticles: Photochemistry</b> / Ulrich Siggel, Guangtao Li, and Jürgen-Hinrich Fuhrhop . . . . .	2012
<b>Nanoarrays: Electrochemically Self-Assembled</b> / S. Bandyopadhyay . . . . .	2502
<b>Quantum Dots: Electronic Coupling and Structural Ordering</b> / Glenn S. Solomon . . . . .	3634
<b>Self-Assembled Quantum Dots: Atomic Scale Engineering</b> / S. Oktyabrsky and Alain E. Kaloyeros . . . . .	3775
<b>Self-Formed Quantum Dots: Structural and Optical Characterization</b> / Shun-ichi Gonda and Hajime Asahi . . . . .	3877
<b>Semiconductor Quantum Dots: Atomic Ordering over Time</b> / Peter Moeck . . . . .	3954
<b>Semiconductor Quantum Dots: Site-Controlled Self-Organization</b> / S. Kohmoto, H. Nakamura, S. Nishikawa, T. Yang, and K. Asakawa . . . . .	3965

---

**Size-Dependent Properties**

<b>Charge Carrier Dynamics of Nanoparticles</b> / Fanxin Wu and Jin Z. Zhang . . . . .	804
<b>Luminescence of Nanoparticle-Labeled Antibodies and Antigens</b> / Shaopeng Wang and Nicholas A. Kotov . . . . .	1915
<b>Metallic Quantum Dots</b> / J. P. Wilcoxon . . . . .	2176
<b>Nanocrystals: Size-Dependent Properties and Emerging Applications</b> / G. U. Kulkarni, P. John Thomas, and C.N.R. Rao . . . . .	2665
<b>Nanoparticles: Generation, Functionalization, and Ion Sensing</b> / Jason J. Davis and Paul D. Beer . . . . .	2898
<b>Quantum Dot Arrays: Electromagnetic Properties</b> / Sergey A. Maksimenko and Gregory Ya. Slepyan . . . . .	3606

<b>Quantum Dot Lasers</b> / Mikhail V. Maximov and Nikolai N. Ledentsov . . . . .	3617
<b>Quantum Dots: Inelastic Light Scattering from Electronic Excitations</b> / Christian Schüller . . . . .	3661
<b>Quantum Dots: Phonons in Self-Assembled Multiple Germanium Structures</b> / Jianlin Liu, Aleksandr Khitun, and Kang L. Wang . . . . .	3673
<b>Self-Assembled Quantum Dots: Electronic Structures and Optical Properties</b> / Andrew Williamson . . . . .	3789
<b>Silicon Nanoclusters: Simulations</b> / Aaron Puzder . . . . .	4021
<b>Silicon Nanocrystals: Quantum Confinement</b> / James R. Chelikowsky . . . . .	4033
<b>Thermal Effect on the Luminescence Properties of Quantum Dots</b> / X. B. Zhang and R. D. Dupuis . . . . .	4316

## Sensors and Actuators

### *Biosensors and Biomimetic Chemistry*

<b>Biomedical Applications: Novel Materials and Devices</b> / J. Zachary Hilt and Mark E. Byrne . . . . .	339
<b>Biomimetic Receptors for Carboxylate Recognition</b> / Rocco Ungaro, Alessandro Casnati, and Francesco Sansone . . . . .	372
<b>Biosensor Applications: Porous Silicon Microcavities</b> / Benjamin L. Miller, Philippe M. Fauchet, Scott R. Horner, and Selena Chan . . . . .	408
<b>Biosensor Applications: Surface Engineering</b> / Genady Zhavnerko and Kwon-Soo Ha . . . . .	416
<b>Biosensors Based on Carbon Nanotubes</b> / Yuehe Lin, Wassana Yantasee, Fang Lu, Joseph Wang, Mustafa Musameh, Yi Tu, and Zhifeng Ren . . . . .	428
<b>Biosensors: Fractal Analysis of Binding Kinetics</b> / Harshala Butala and Ajit Sadana . . . . .	441
<b>Chemical Warfare Agents: Biosensors for Detection</b> / Elias Greenbaum, Miguel Rodriguez, Jr., and Charlene A. Sanders . . . . .	842
<b>DNA-Based Nanoinstrument Design</b> / Alexander Hillisch and Stephan Diekmann . . . . .	1102
<b>Layer-by-Layer Electrostatic Self-Assembly</b> / Michael J. McShane and Yuri M. Lvov . . . . .	1823
<b>Ligand–Receptor Systems with Infinite Binding Affinity</b> / Claude F. Meares . . . . .	1853
<b>Lipid Membranes: Nanostructure and Dynamic Organization</b> / J. Gaudioso and D. Y. Sasaki . . . . .	1859
<b>Liquid Crystals and Nanostructured Surfaces: Detecting Protein Binding</b> / Yan-Yeung Luk . . . . .	1878
<b>Nanobiological Sensors</b> / Nathaniel Cady, Anand Gadre, and Alain E. Kaloyeros . . . . .	2514
<b>Optical Nanosensors and Nanobiosensors</b> / Brian M. Cullum . . . . .	3258

### *Chemical Imaging and Molecular Sensing*

<b>Near-Field Raman Spectroscopy: Resolution Enhancement</b> / Satoshi Kawata and Yasushi Inouye . . . . .	3177
<b>Near-Field Scanning Optical Microscopy: Chemical Imaging</b> / Bogdan Dragnea . . . . .	3185
<b>Optical Molecular Devices</b> / A. Prasanna de Silva and Nathan D. McClenaghan . . . . .	3251
<b>Surface-Enhanced Raman Scattering</b> / Adam M. Schwartzberg and Jin Z. Zhang . . . . .	4250

### *Chemical Sensors*

<b>Electrically Functional Nanostructures</b> / Orlin D. Velev and Simon O. Lumsdon . . . . .	1171
<b>Metallomacrocyclic Selective Ion Receptors</b> / Kay Severin . . . . .	2202
<b>Molecular Probes of Cation–Arene Interactions</b> / George W. Gokel . . . . .	2369
<b>Molecular Receptor-Modified Metal Nanoparticles</b> / Jian Liu . . . . .	2377



---

**Sensors and Actuators (cont'd.)**


---

**Chemical Sensors (cont'd.)**

- Molecular Self-Assembly: Environmental and Sensing Applications** / Glen E. Fryxell,  
R. Shane Addleman, S. V. Mattigod, Yuehe Lin, T. S. Zemanian, H. Wu,  
Jerome C. Birnbaum, J. Liu, and X. Feng . . . . . 2387
- Monolayer-Protected Metal Nanoparticles: Chemical Sensing and Gas Chromatography** /  
Jay W. Grate, David A. Nelson, Rhonda Skaggs, Robert E. Synovec, and  
Gwen M. Gross . . . . . 2460
- Phase Transfer of Monosaccharides through Noncovalent Interactions** / Elizabeth K. Auty  
and Anthony P. Davis . . . . . 3347
- Sensors Based on Chemicurrents** / B. Roldan Cuenya and E. W. McFarland . . . . . 3973
- 

**Electrochemical Sensors**

- Carbon Nanotubes: Electrochemical Modification** / Kannan Balasubramanian,  
Marko Burghard, and Klaus Kern . . . . . 620
- Electrochemical Sensors: Functionalized Silica** / Yuehe Lin, Wassana Yantasee, and  
Glen E. Fryxell . . . . . 1196
- Electrochemical Toxicity Sensors** / James F. Rusling . . . . . 1207
- Nanoparticles: Generation, Functionalization, and Ion Sensing** / Jason J. Davis and  
Paul D. Beer . . . . . 2898
- Nanotube Sensors** / Marc Wirtz and Charles R. Martin . . . . . 3109
- 

**Molecular Motors, Switches and Actuators**

- Electronic Switches** / Richard J. Nichols, David J. Schiffrin, and Wolfgang Haiss . . . . . 1230
- Molecular Motor-Powered Nanodevices: Control Mechanisms** / Jacob J. Schmidt and  
Carlo D. Montemagno . . . . . 2347
- Motor Proteins in Synthetic Materials and Devices** / Henry Hess, George Bachand, and  
Viola Vogel . . . . . 2484
- Single-Walled Carbon Nanotubes: Geometries, Electronic Properties, and Actuation** /  
Guangyu Sun, Marc Nicklaus, and Miklos Kertesz . . . . . 4085
- 

**Spontaneous Self-Organization of Matter**


---

**Architecture and Growth Modes**

- Indium Arsenide Islands on Silicon** / P. C. Sharma and Kang L. Wang . . . . . 1582
- Nanoarrays: Electrochemically Self-Assembled** / S. Bandyopadhyay . . . . . 2502
- Nanocrystalline Zeolites** / Vicki H. Grassian and Sarah C. Larsen . . . . . 2646
- Nanocrystals: Synthesis and Mesoscale Organization** / G. U. Kulkarni,  
P. John Thomas, and C.N.R. Rao . . . . . 2676
- Porphyritic Materials: Self-Assembly on Surfaces** / Charles Michael Drain,  
James D. Batteas, Gabriela Smeureanu, and Sandeep Patel . . . . . 3539
- Ring Structures from Nanoparticles and Other Nanoscale Building Blocks** /  
Zhen Liu and Rastislav Levicky . . . . . 3694
- 

**Arrays and Superlattices**

- Bio-Microarrays** / Günter E.M. Tovar and Achim Weber . . . . . 298
- Colloid Systems: Micelles and Nanocrystals** / B.L.V. Prasad and Savka I. Stoeva . . . . . 856

<b>Metal Nanoparticle Ensembles: Collective Optical Properties</b> / Alexander Wei	2064
<b>Molecular Electronics: Logic and Memory</b> / Dustin K. James and James M. Tour	2303
<b>Nanocolloidal Gold Films: Self-Assembly</b> / E. Stefan Kooij, E.A. Martijn Brouwer, Agnes A. Mewe, Herbert Wormeester, and Bene Poelsema	2545
<b>Nanocrystal Arrays: Self-Assembly and Physical Properties</b> / Xiao-Min Lin, Raghuvver Parthasarathy, and Heinrich M. Jaeger	2568
<b>Nanoparticle Arrays: Optical and Electronic Applications</b> / Ilona Kretzschmar and Mark A. Reed	2856
<b>Self-Assembled Thin Films: Optical Characterization</b> / Herbert Wormeester, E. Stefan Kooij, and Bene Poelsema	3829
<b>Stability of Nanostructures on Surfaces</b> / Karsten Pohl	4167
<b>Virus Nanoparticles: Adsorption and Organization on Substrates</b> / Jiyu Fang	4407

### **Host-Guest Chemistry**

<b>Guests within Hydrophobic Pockets: Conventional Synthesis</b> / Bruce C. Gibb	1429
<b>Guests within Hydrophobic Pockets: Self-Assembly</b> / Bruce C. Gibb	1451
<b>Interfacial Phenomena: Chemical Selectivity</b> / Vinay K. Gupta	1662
<b>Metallomacrocyclic Selective Ion Receptors</b> / Kay Severin	2202

### **Intermolecular Association and Phase Behavior**

<b>Block Copolymer Nanoparticles</b> / Sandrine Pensec, Daniel Portinha, Laurent Bouteiller, and Christophe Chassenieux	467
<b>Microgel Dispersions: Colloidal Forces and Phase Behavior</b> / Jianzhong Wu and Zhibing Hu	2243
<b>Nanoparticle Suspensions: Phase Behavior</b> / Subramanian Ramakrishnan and Charles F. Zukoski	2878
<b>Nanostructures Derived from Phase-Separated Polymers</b> / Michael R. Bockstaller and Edwin L. Thomas	3093

### **Langmuir-Blodgett Films**

<b>AFM: Nanolithography on Organized Films</b> / Seunghyun Lee and Haiwon Lee	119
<b>Biosensor Applications: Surface Engineering</b> / Genady Zhavnerko and Kwon-Soo Ha	416
<b>Electrochemical Langmuir Trough</b> / Natalia Varaksa, Thomas F. Magnera, and Josef Michl	1189
<b>Heterogeneous Surfaces with Nanosized Channel Lattices</b> / Lifeng Chi, Michael Gleiche, Steven Lenhart, and Nan Lu	1515
<b>Langmuir-Blodgett Films</b> / Ursula Mazur	1738
<b>Nanowires and Nanobelts: Mechanical Properties</b> / Zhong Lin Wang	3146
<b>Organosilanes: Molecular Assembly</b> / Atsushi Takahara	3287
<b>Polyelectrolyte Films with Incorporated Carbon Nanotubes</b> / Jason H. Rouse and Peter T. Lillehei	3396
<b>Self-Assembled Silane Monolayers: Cyano-to-Carboxylic Termination Conversion</b> / Chandra Sekhar Palla and Alexander Couzis	3801

### **Layer-by-Layer Assembly**

<b>Barrier Properties of Ordered Polymer Nanocomposites</b> / Bon-Cheol Ku, Alexandre Blumstein, Jayant Kumar, Lynne A. Samuelson, and Dong Wook Kim	267
<b>Layer-by-Layer Assembly of Electroactive Thin Films to Layered Carbon Electrodes</b> / Tarek R. Farhat	1764



---

**Spontaneous Self-Organization of Matter (cont'd.)**


---

**Layer-by-Layer Assembly (cont'd.)**

<b>Layer-by-Layer Assembly of Gold Nanoclusters with Self-Assembled Monolayers</b> / <i>Kohei Uosaki, Wenbo Song, Masayuki Okamura, and Toshihiro Kondo</i> . . . . .	1773
<b>Layer-by-Layer Assembly of Semiconducting and Photoreactive Bolaform Amphiphiles</b> / <i>Jason Locklin, Derek Patton, Chuanjun Xia, Xiaowu Fan, and Rigoberto C. Advincula</i> . . . . .	1798
<b>Layer-by-Layer Assembly of Thin Films of Mixed Nanoparticles</b> / <i>Jianchang Guo,</i> <i>Encai Hao, and Tianquan Lian</i> . . . . .	1813
<b>Layer-by-Layer Electrostatic Self-Assembly</b> / <i>Michael J. McShane and Yuri M. Lvov</i> . . . . .	1823
<b>Layered Double Hydroxides: Self-Assembly and Multiple Phases</b> / <i>Zhi Ping Xu and</i> <i>Paul S. Braterman</i> . . . . .	1841
<b>Metal Nanostructures: Synthesis by Soft Chemical Methods</b> / <i>Yugang Sun and Younan Xia</i> . . . . .	2105
<b>Nanoparticles: Synthesis in Polymer Substrates</b> / <i>Bai Yang and Junhu Zhang</i> . . . . .	2912

---

**Self-Assembled Monolayers**

<b>Adhesion: Coated Surfaces, Effect of Humidity</b> / <i>Joan E. Curry and Sungsoo Kim</i> . . . . .	32
<b>Magnetic Nanoparticles for Granular Recording Media</b> / <i>David E. Nikles and J. W. Harrell</i> . . . . .	2001
<b>Metal Nanoparticles: Self-Assembly into Electronic Nanostructures</b> / <i>Venugopal Santhanam</i> <i>and Ronald P. Andres</i> . . . . .	2079
<b>Monolayer-Protected Metal Nanoparticles: Synthesis</b> / <i>Young-Seok Shon</i> . . . . .	2469
<b>Nonlinear Optical Materials from Self-Assembled Organic Films</b> / <i>Matthew Guzy,</i> <i>Richey M. Davis, Patrick J. Neyman, Charles Brands, J. R. Heflin,</i> <i>Harry W. Gibson, and Kevin E. Van Cott</i> . . . . .	3206
<b>Scanning Near-Field Photolithography</b> / <i>Graham J. Leggett</i> . . . . .	3709
<b>Self-Assembled Monolayers: Adsorption and Desorption from Alkanethiols on Gold</b> / <i>Pieter Stroeve</i> . . . . .	3738
<b>STEM of Chiral Pair Self-Assembled Monolayers</b> / <i>Yuguang Cai and Steven L. Bernasek</i> . . . . .	4176

---

**Self-Assembled Quantum Dots**

<b>Cadmium Selenide Quantum Dots</b> / <i>Kenzo Maehashi and Hisao Nakashima</i> . . . . .	477
<b>Quantum Dots: Inelastic Light Scattering from Electronic Excitations</b> / <i>Christian Schüller</i> . . . . .	3661
<b>Quantum Dots: Phonons in Self-Assembled Multiple Germanium Structures</b> / <i>Jianlin Liu,</i> <i>Aleksandr Khitun, and Kang L. Wang</i> . . . . .	3673
<b>Self-Assembled Quantum Dots: Atomic Scale Engineering</b> / <i>S. Oktyabrsky and</i> <i>Alain E. Kaloyeros</i> . . . . .	3775
<b>Self-Assembled Quantum Dots: Electronic Structures and Optical Properties</b> / <i>Andrew Williamson</i> . . . . .	3789
<b>Thermal Effect on the Luminescence Properties of Quantum Dots</b> / <i>X. B. Zhang and</i> <i>R. D. Dupuis</i> . . . . .	4316

---

**Supramolecular Structure Control**

<b>AFM: Hydrogen-Bonded Nanostructures</b> / <i>Holger Schönherr, Mercedes Crego-Calama,</i> <i>G. Julius Vancso, and David N. Reinhoudt</i> . . . . .	76
<b>Biomimetic Design of Self-Assembling Systems</b> / <i>Mila Boncheva and George M. Whitesides</i> . . . . .	364
<b>Controlled Size and Shape Supramolecular Aggregates on Solid Surfaces</b> / <i>Takashi Yokoyama,</i> <i>Toshiya Kamikado, Shiyoshi Yokoyama, and Shinro Mashiko</i> . . . . .	974
<b>Cyclic Peptides: Self-Assembly in Hydrogen-Bonded Nanotubes</b> / <i>Roberto J. Brea and</i> <i>Juan R. Granja</i> . . . . .	1037

<b>Inorganic Nanotubes: Synthesis by Chemical Transport Reaction</b> / Maja Remskar	1606
<b>Nanoencapsulation of Bioactive Substances</b> / Yury E. Shapiro	2707
<b>Polyelectrolyte–Surfactant Complex Nanoparticles</b> / Hans-Peter Hentze	3403
<b>Polymer-Mediated Self-Assembly of Nanoparticles</b> / Tyler B. Norsten, Amitav Sanyal, Roy Shenhar, and Vincent M. Rotello	3443
<b>Self-Assembled Structures</b> / Anna Cristina Samia and Xiao-Min Lin	3816
<b>Self-Assembly Directed by NH–O Hydrogen Bonding</b> / Katrina A. Jolliffe and Leonard F. Lindoy	3864
<b>Self-Assembly of Coordination Cages</b> / Laura Pirondini and Enrico Dalcanale	3848
<b>Self-Organized Superstructures: Molecular Design</b> / Makoto Tadokoro	3886

### **Surface-Mediated Assembly**

<b>Adsorption on Heterogeneous Surfaces</b> / Vinay K. Gupta and Yu-Wen Huang	41
<b>Biosurfaces: Water Structure at Interfaces</b> / Yan-Yeung Luk	453
<b>Charge Transfer in Metal–Molecule Heterostructures</b> / Debasish Kuila, David B. Janes, and Clifford P. Kubiak	819
<b>Colloidal Structures on Patterned Surfaces</b> / Aránzazu del Campo, Anne-Sophie Duwez, Charles-André Fustin, and Ulrich Jonas	907
<b>Island Surfaces: Fabrication on Self-Assembled Monolayers</b> / Hongjie Liu, Charles Maldarelli, M. Lane Gilchrist, and Alexander Couzis	1708
<b>Liquid Crystals and Nanostructured Surfaces: Detecting Protein Binding</b> / Yan-Yeung Luk	1878
<b>Molecular Self-Assembly: Environmental and Sensing Applications</b> / Glen E. Fryxell, R. Shane Addleman, S. V. Mattigod, Yuehe Lin, T. S. Zemanian, H. Wu, Jerome C. Birnbaum, J. Liu, and X. Feng	2387
<b>Self-Assembled Monolayers: Chemical and Physical Modification under Vacuum</b> / Jessica Torres, Anthony J. Wagner, Christopher C. Perry, Glenn M. Wolfe, and D. Howard Fairbrother	3747
<b>Self-Assembled Monolayers: Surface Nanostructure Effect on Wetting</b> / Jun Yang, Jingmin Han, Kelvin Isaacson, and Daniel Y. Kwok	3762
<b>Self-Assembly and Chirality of Molecules at Interfaces</b> / Dalia G. Yablon	3840
<b>Silane Self-Assembled Monolayers: Nanoscale Domains by Sequential Adsorption</b> / Nitin Kumar	3984
<b>STEM: Self-Assembly on Graphite</b> / Thomas Müller	4185

### **Templated Assembly**

<b>Oil-Filled Nanocapsules</b> / Royale S. Underhill	3234
<b>Protein Nanotubes as Building Blocks</b> / Hiroshi Matsui	3578
<b>Template-Directed Assembly of Dinuclear Triple-Stranded Helicates</b> / Markus Albrecht	4283
<b>Templating Aerogels for Tunable Nanoporosity</b> / Aydin K. Sunol and Sermin G. Sunol	4294

## **Supramolecular Chemistry**

### **Molecular Recognition**

<b>Biosensor Applications: Porous Silicon Microcavities</b> / Benjamin L. Miller, Philippe M. Fauchet, Scott R. Horner, and Selena Chan	408
<b>DNA Hybridization: Electronic Control</b> / Kimberly Hamad-Schifferli	1122
<b>Interfacial Phenomena: Chemical Selectivity</b> / Vinay K. Gupta	1662
<b>Ligand–Receptor Systems with Infinite Binding Affinity</b> / Claude F. Meares	1853

---

**Supramolecular Chemistry (cont'd.)**


---

**Molecular Recognition (cont'd.)**

<b>Lipid Membranes: Nanostructure and Dynamic Organization</b> / J. Gaudioso and D. Y. Sasaki . . . . .	1859
<b>Molecular Probes of Cation–Arene Interactions</b> / George W. Gokel . . . . .	2369
<b>Molecular Receptor-Modified Metal Nanoparticles</b> / Jian Liu . . . . .	2377
<b>Nanomaterials and Molecular Devices: De Novo Design Theory</b> / Kwang S. Kim, P. Tarakeshwar, and Han Myoung Lee . . . . .	2815
<b>Nucleoside- and Nucleobase-Substituted Oligopyrrolic Macrocycles</b> / Vladimír Král, Martin Valík, Tatiana V. Shishkanova, and Jonathan L. Sessler . . . . .	3216
<b>Phase Transfer of Monosaccharides through Noncovalent Interactions</b> / Elizabeth K. Auty and Anthony P. Davis . . . . .	3347

---

**Selective Self-Assembly**

<b>AFM: Hydrogen-Bonded Nanostructures</b> / Holger Schönherr, Mercedes Crego-Calama, G. Julius Vancso, and David N. Reinhoudt . . . . .	76
<b>Anion-Templated Self-Assembly: Inorganic Compounds</b> / Louise S. Evans and Philip A. Gale . . . . .	178
<b>Controlled Size and Shape Supramolecular Aggregates on Solid Surfaces</b> / Takashi Yokoyama, Toshiya Kamikado, Shiyoshi Yokoyama, and Shinro Mashiko . . . . .	974
<b>Cyclic Peptides: Self-Assembly in Hydrogen-Bonded Nanotubes</b> / Roberto J. Brea and Juan R. Granja . . . . .	1037
<b>Porphyric Materials: Self-Assembly on Surfaces</b> / Charles Michael Drain, James D. Batteas, Gabriela Smeureanu, and Sandeep Patel . . . . .	3539
<b>Self-Assembly Directed by NH–O Hydrogen Bonding</b> / Katrina A. Jolliffe and Leonard F. Lindoy . . . . .	3864
<b>Template-Directed Assembly of Dinuclear Triple-Stranded Helicates</b> / Markus Albrecht . . . . .	4283

---

**Supramolecular Networks and Templates**

<b>Anion-Templated Self-Assembly: Organic Compounds</b> / Paul D. Beer and Mark R. Sambrook . . . . .	191
<b>Axle Molecules Threaded through Macrocycles</b> / Daryle H. Busch and Thomas Clifford . . . . .	249
<b>Block Copolymer Nanoparticles</b> / Sandrine Pensec, Daniel Portinha, Laurent Bouteiller, and Christophe Chassenieux . . . . .	467
<b>Carbon Nanotubes: Supramolecular Mechanics</b> / Boris I. Yakobson and Luise S. Couchman . . . . .	722
<b>Coordination Framework Topology</b> / Neil R. Champness and Neil S. Oxtoby . . . . .	984
<b>Guests within Hydrophobic Pockets: Conventional Synthesis</b> / Bruce C. Gibb . . . . .	1429
<b>Guests within Hydrophobic Pockets: Self-Assembly</b> / Bruce C. Gibb . . . . .	1451
<b>Metallomacrocyclic Selective Ion Receptors</b> / Kay Severin . . . . .	2202
<b>Organofullerenes in Water</b> / Eiichi Nakamura and Hiroyuki Isobe . . . . .	3277
<b>Self-Assembled Structures</b> / Anna Cristina Samia and Xiao-Min Lin . . . . .	3816
<b>Self-Assembly of Coordination Cages</b> / Laura Pirondini and Enrico Dalcanale . . . . .	3848
<b>Self-Organized Superstructures: Molecular Design</b> / Makoto Tadokoro . . . . .	3886
<b>Supramolecular Networks Synthesized in Nanoparticle–Polymer Mixtures</b> / Anna C. Balazs and Gavin A. Buxton . . . . .	4240

---

## Surface and Interfacial Chemistry

---

### *Adhesion and Interfacial Forces*

<b>Adhesion: Cell on a Substrate</b> / <i>Frédéric Pincet</i> . . . . .	22
<b>Dynamic AFM on Heterogeneous Surfaces</b> / <i>Ijeoma M. Nnebe and James W. Schneider</i> . . . . .	1144
<b>Interfacial Forces: Colloidal Particle–Liquid</b> / <i>Sarah A. Nespolo and Geoffrey W. Stevens</i> . . . . .	1650
<b>Self-Assembled Monolayers: Surface Nanostructure Effect on Wetting</b> / <i>Jun Yang, Jingmin Han, Kelvin Isaacson, and Daniel Y. Kwok</i> . . . . .	3762
<b>Tribology of Inorganic Nanoparticles</b> / <i>Lev Rapoport</i> . . . . .	4375

---

### *Adsorption and Porous Materials*

<b>Adsorption on Heterogeneous Surfaces</b> / <i>Vinay K. Gupta and Yu-Wen Huang</i> . . . . .	41
<b>AFM: Metal Ion Sorption</b> / <i>Viriya Vithayaveroj, Sotira Yiacoumi, and Costas Tsouris</i> . . . . .	109
<b>AFM: Protein Adsorption</b> / <i>David T. Kim, Harvey W. Blanch, and Clayton J. Radke</i> . . . . .	129
<b>Biological and Chemical Decontamination</b> / <i>Peter K. Stoimenov and Kenneth J. Klabunde</i> . . . . .	312
<b>Biosurfaces: Water Structure at Interfaces</b> / <i>Yan-Yeung Luk</i> . . . . .	453
<b>Hierarchically Imprinted Nanostructures for Separation</b> / <i>Sheng Dai, Zongtao Zhang, and Chengdu Liang</i> . . . . .	1525
<b>Interfacial Phenomena: Chemical Selectivity</b> / <i>Vinay K. Gupta</i> . . . . .	1662
<b>Micro- and Mesoporous Nanomaterials: Catalytic Properties</b> / <i>Johannes A. Lercher and Andreas Jentys</i> . . . . .	2229
<b>Microweighing in Supercritical Carbon Dioxide</b> / <i>You-Ting Wu and Christine S. Grant</i> . . . . .	2253
<b>Nanoporosity Evolution on Dealloying</b> / <i>Jonah Erlebacher</i> . . . . .	2938
<b>Protein Adsorption Kinetics under an Applied Electric Field</b> / <i>Paul R. Van Tassel</i> . . . . .	3569
<b>Proteins: Structure and Interaction Patterns to Solid Surfaces</b> / <i>Thomas J. Webster</i> . . . . .	3590
<b>Self-Assembled Monolayers: Adsorption and Desorption from Alkanethiols on Gold</b> / <i>Pieter Stroeve</i> . . . . .	3738
<b>Single-Walled Carbon Nanotubes: Field Emission Properties</b> / <i>Xiaofeng F. Duan, Brahim Akdim, and Ruth Pachter</i> . . . . .	4078
<b>Virus Nanoparticles: Adsorption and Organization on Substrates</b> / <i>Jiyu Fang</i> . . . . .	4407

---

### *Catalysts and Catalytic Processes*

<b>Catalytic Processes: Nanoscale Simulations</b> / <i>Vladimir I. Elokhin and Aleksandr V. Myshlyavtsev</i> . . . . .	782
<b>Metal Clusters on Oxides</b> / <i>Ivan Stensgaard</i> . . . . .	2044
<b>Nanofibers and Carbon Nanotubes: Novel Metal Catalyst Supports</b> / <i>Mark A. Keane</i> . . . . .	2723
<b>Nanostructured Catalysts</b> / <i>Ravichandra S. Mulukutla</i> . . . . .	2967
<b>Nanostructured Catalysts: Design and Synthesis</b> / <i>Hua Chun Zeng</i> . . . . .	2974

---

### *Electrically Charged Surfaces*

<b>Electrical Double-Layer Formation</b> / <i>Kun-Lin Yang, Sotira Yiacoumi, and Costas Tsouris</i> . . . . .	1157
<b>Electrochemical Langmuir Trough</b> / <i>Natalia Varaksa, Thomas F. Magnera, and Josef Michl</i> . . . . .	1189
<b>Mica Surfaces: Charge Nucleation and Wear</b> / <i>James M. Helt and James D. Batteas</i> . . . . .	2211
<b>Mineral Nanoparticles: Electrokinetics</b> / <i>Mehmet S. Celik and Bahri Ersoy</i> . . . . .	2266
<b>Oxide Nanoparticles: Electrochemical Performance</b> / <i>Dominique Larcher and Jean-Marie Tarascon</i> . . . . .	3299

---

**Surface and Interfacial Chemistry (cont'd.)**


---

**Phase Separation and Self-Organization**

<b>Metal–Oxide Interfaces: Design via Control of Defect Density</b> / A. Bogicevic	2116
<b>Nanocrystalline Oxides: Surfactant-Assisted Growth</b> / Claudia L. Bianchi, Silvia Ardizzone, and Giuseppe Cappelletti	2637
<b>Nanoparticles: Synthesis in Polymer Substrates</b> / Bai Yang and Junhu Zhang	2912
<b>Nanostructures Derived from Phase-Separated Polymers</b> / Michael R. Bockstaller and Edwin L. Thomas	3093
<b>Ordered Vesicles at the Silicon–Water Interface</b> / Duncan J. McGillivray	3269
<b>Polyelectrolyte–Surfactant Complex Nanoparticles</b> / Hans-Peter Hentze	3403
<b>Polyion Complex Micelles</b> / Atsushi Harada and Kazunori Kataoka	3409
<b>Templating Polymer Crystal Growth Using Block Copolymers</b> / Yueh-Lin Loo	4303

---

**Surface Reactivity**

<b>Biosensors: Fractal Analysis of Binding Kinetics</b> / Harshala Butala and Ajit Sadana	441
<b>Enantioselectivity on Surfaces</b> / David M. Rampulla and Andrew J. Gellman	1242
<b>Lab-on-a-Chip Microreactors</b> / Paul D.I. Fletcher, Stephen J. Haswell, Paul Watts, and Xunli Zhang	1721
<b>Molecular Orientation at Interfaces: Vibrational Spectroscopy</b> / Zhan Chen	2357
<b>Nanocrystalline Magnesia and Alumina: Surface Chemistry</b> / Richard M. Narske	2592
<b>Nanomechanical Resonant Devices: Surface Chemistry</b> / Joshua A. Henry, Debodhonyaa Sengupta, and Melissa A. Hines	2848
<b>Nano–Mesoscopic Interface: Hybrid Devices</b> / Gianfranco Cerofolini	2493
<b>Nanotubes: Functionalization</b> / Stanislaus S. Wong and Sarbajit Banerjee	3119
<b>Sensors Based on Chemicurrents</b> / B. Roldan Cuenya and E. W. McFarland	3973
<b>Silica Surfaces Functionalization</b> / V. A. Tertykh	4001
<b>Stability of Nanostructures on Surfaces</b> / Karsten Pohl	4167
<b>Yttria-Tetragonally Stabilized Zirconia</b> / R. Allen Kimel	4414

---

**Symmetry and Patterns on Solid Surfaces**

<b>Anodization Patterned on Aluminum Surfaces</b> / Juchao Yan, G. V. Rama Rao, Plamen B. Atanassov, and Gabriel P. López	203
<b>Colloidal Nanoparticles: Aggregation Patterns at Surfaces</b> / Hamidou Haidara and Karine Mougin	882
<b>Dissymmetrical Nanoparticles</b> / Stéphane Reculosa, Christophe Mingotaud, Etienne Duguet, and Serge Ravaine	1093
<b>Heterogeneous Surfaces with Nanosized Channel Lattices</b> / Lifeng Chi, Michael Gleiche, Steven Lenhart, and Nan Lu	1515
<b>Laser-Based Deposition: Patterning</b> / Edward M. Nadgorny and Jaroslaw Drelich	1749
<b>Self-Assembly and Chirality of Molecules at Interfaces</b> / Dalia G. Yablon	3840
<b>Silica Nanotubes: Wetting and Diffusion</b> / Kenji Okamoto, Karthik Jayaraman, Sang Jun Son, Sang Bok Lee, and Douglas S. English	3995

---

**Thin Films and Monolayers at Surfaces**

<b>AFM: Nanolithography on Organized Films</b> / Seunghyun Lee and Haiwon Lee	119
<b>Amphiphilic Block Copolymer Monolayer at Air–Water Interface</b> / Emiko Mouri and Hideki Matsuoka	168

<b>Biosensor Applications: Surface Engineering</b> / <i>Genady Zhavnerko and Kwon-Soo Ha</i> . . . . .	416
<b>Charge Transfer in Metal–Molecule Heterostructures</b> / <i>Debasish Kuila, David B. Janes, and Clifford P. Kubiak</i> . . . . .	819
<b>Cyanogels: Processing by Spin Coating</b> / <i>Shu Zhu and Andrew B. Bocarsly</i> . . . . .	1029
<b>Functionalization of Surface Layers on Ceramics</b> / <i>Toshihiro Ishikawa</i> . . . . .	1375
<b>Infrared Spectroscopy: Biomolecular Structure at Interfaces</b> / <i>Curtis W. Meuse</i> . . . . .	1590
<b>Island Nucleation: Predictions</b> / <i>Maria C. Bartelt</i> . . . . .	1696
<b>Island Surfaces: Fabrication on Self-Assembled Monolayers</b> / <i>Hongjie Liu, Charles Maldarelli, M. Lane Gilchrist, and Alexander Couzis</i> . . . . .	1708
<b>Langmuir-Blodgett Films</b> / <i>Ursula Mazur</i> . . . . .	1738
<b>Layer-by-Layer Assembly of Electroactive Thin Films to Layered Carbon Electrodes</b> / <i>Tarek R. Farhat</i> . . . . .	1764
<b>Organosilanes: Molecular Assembly</b> / <i>Atsushi Takahara</i> . . . . .	3287
<b>Polyelectrolyte Films with Incorporated Carbon Nanotubes</b> / <i>Jason H. Rouse and Peter T. Lillehei</i> . . . . .	3396
<b>Self-Assembled Silane Monolayers: Cyano-to-Carboxylic Termination Conversion</b> / <i>Chandra Sekhar Palla and Alexander Couzis</i> . . . . .	3801
<b>Silane Self-Assembled Monolayers: Nanoscale Domains by Sequential Adsorption</b> / <i>Nitin Kumar</i> . . . . .	3984
<b>STEM: Self-Assembly on Graphite</b> / <i>Thomas Müller</i> . . . . .	4185
<b>Titania Coatings on Stainless Steel</b> / <i>Ganesh Balasubramanian, Dionysios D. Dionysiou, and Makram T. Suidan</i> . . . . .	4348

# Preface

The science of the “ultra small”—nanoscience—has dramatically exploded during the last few years, and the technologies operating with “ultra small things”—the nanotechnologies—acquired quickly a firm position in today’s world of business, technological development, and public perception. Several factors contributed to the acceleration of scientific knowledge and technological progress in the last decades, among which the rapid development of fast computers, availability of high-resolution analytical techniques, and the progress of molecular biology and genetics are probably the most important. The result was an unprecedented expansion of the frontiers of science, which empowered the human genius with unlimited options of top-down and bottom-up methods for manipulation of materials structure and control of properties at multiple levels, from atomic to molecular, supramolecular, and biomolecular. Already a distinctive mark of 21st century, nanoscience and nanotechnology will certainly have a steadily increasing influence on the quality of life and the environment of this Planet for centuries to come.

*Dekker Encyclopedia of Nanoscience and Nanotechnology, Second Edition* provides a comprehensive and detailed review, from multiple angles, of major developments in the human’s quest for understanding and mastering of physical, chemical and biological objects and structures having at least one dimension smaller than about 100 nm.

Under the expert supervision of the late Professor James A. Schwarz, Marcel Dekker, Inc. published the first edition in 2004 to great acclaim. The success of first edition, the development of the title through online updates, and the dynamics of this continuously growing field has created a high demand for a second edition only four years after the first edition. The second edition offers updated and revised entries, along with many additions that reflect the focus towards energy and environmental issues currently in the news. The new edition is expanded to six volumes. All entry titles have been revised to better reflect to the entry’s content, while optimized for alphabetical listing. In addition, a comprehensive (though not exhaustive) topical table of contents has been designed, structured on 24 major topics and almost 100 subtopics. With a robust and efficient indexing system and staggered bleed tabs, this second print edition will be a useful reference tool for scientists in academia and national laboratories, engineers, students, as well as entrepreneurs, policy makers, and opinion builders. The online version of the Encyclopedia offers quick access to individual entries in HTML or PDF format, enriched graphical content, hundreds of color illustrations and photographs, and an efficient keyword search engine.

Cristian I. Contescu

*Oak Ridge National Laboratory, Oak Ridge, Tennessee, USA*

Karol Putyera

*EAG-NY Shiva Technologies, Syracuse, New York, USA*

July 2008



# Preface to the First Edition

Nanoscience encompasses all scientific phenomena that transpire in dimensions spanning the range of multiple atom clusters, molecular aggregates, supermolecular structures, polymers and biomolecules. In other words, nanoscience is the science of the nanoscale—or the very, very minute. Nanotechnology, the technological use of these properties and phenomena, has the potential to revolutionize a breathtaking range of fields, across practically all domains of human activity. The intense interest in using nanostructures stems from the promise that they boast superior electrical, optical, mechanical, chemical, or biochemical properties. There is little doubt that the use of these new materials and systems will lay the ground for the new technological revolution of 21st century. Research in nanoscience is exploding as scientists from chemistry, physics, and biology, including colloid and polymer chemistry, materials and surface science, and biochemistry, biophysics and molecular biology have begun to examine the superior properties that characterize materials and phenomena at the nanoscale.

The Dekker Encyclopedia of Nanoscience and Nanotechnology is a vehicle by which scientists and the interested public can explore the most recent developments in today's nanomaterials, and preview several of their foreseen applications of tomorrow. The subject areas of this five volume collective work include, but are not limited to, chemistry, physics, molecular and quantum biology, materials science and engineering and computer science. The topics include fullerenes and carbon nanotubes, quantum dots and inorganic nanowires, interfacial chemistry, nanostructures, analytical and characterization methods, design and fabrication techniques of nanocomposites, properties of functional nanomaterials, nanostructured catalysts, molecular electronics, optical devices, bionanotechnology, colloidal phenomena—even future and environmental considerations about nanotechnology. In short, the reference strives to encompass, document, and organize the enormous proliferation of information that has emerged from the revolution at the nanoscale.

It is the editors' hopes that the Dekker Encyclopedia of Nanoscience and Nanotechnology will help researchers, graduate students, undergraduate students, and non-professionals all better understand and participate in this remarkable emerging field. To keep the reference accessible, the Encyclopedia is published in both online and print formats. The print version consists of multiple traditional hardbound volumes with articles arranged alphabetically. The front matter to each volume provides an alphabetical Table of Contents and a Topical Table of Contents. An index at the back of each volume is intended as a further guide.

The online version of the Encyclopedia has been created by coupling the content of the print edition with a powerful search engine and user-friendly interface. The online database is dynamic, with additional articles added each quarter. As with the print edition, users will be able to browse the alphabetical and topical Table of Contents, but they will also be able to search for entries by keywords.

The editors of the Dekker Encyclopedia of Nanoscience and Nanotechnology could not have accomplished their feat without the help of many. We first thank the authors of more than 300 articles which, as recognized experts in their fields, lend their credibility and prestige to the Encyclopedia. In addition, the editors were joined by an esteemed International Editorial Advisory Board whose input was crucial to shaping the reference. Success in the coordination of the activities that has resulted in this final product is due to the remarkable staff at Marcel Dekker, Inc. We are indebted to the direction provided to us by Ellen Lichtenstein, Carolyn Hall, Oona Schmid, Susan Lee, Joanne Jay, and Jeeran Ok.



In particular, the creative ideas and boundless energy that Oona Schmid has demonstrated is greatly acknowledged by the three of us. We also thank Anita Lekhwani for her confidence in us as editors and Russell Dekker for his support and encouragement.

James A. Schwarz  
*Syracuse University, Syracuse, New York*

Cristian I. Contescu  
*Material Methods LLC, Newport Beach, California*

Karol Putyera  
*EAG-NY Shiva Technologies, Syracuse, New York*

# Acknowledgment

This Encyclopedia is the result of a relentless and enthusiastic effort of hundreds of scientists from all over the world. Although from different backgrounds—physicists and chemists, biologists and software engineers, mathematicians and materials scientists—and speaking different languages, they all share a devouring passion for discovery and scientific knowledge, and an immense dedication to their profession. We cannot be more grateful to all and every one of the reputed scientists who wrote this Encyclopedia, chapter by chapter, almost “layer by layer”. Our thanks go also to all members of the Editorial Advisory Board who improved this collective work. Built upon the first edition published at Marcel Dekker, Inc., this Second Edition could not be finalized without the dedication and professionalism of the staff at Taylor & Francis Group. In particular we appreciate the remarkable direction and creativity of Claire Miller, Director of Encyclopedia Programs at Taylor & Francis, and of her assistants, Alasdair Denvil, Elif Kaynak, Susan Lee, and Laura Sylvest.

Cristian I. Contescu

*Oak Ridge National Laboratory, Oak Ridge, Tennessee, USA*

Karol Putyera

*Shiva Technologies, Syracuse, New York, USA*

July 2008

## A Note on Terminology

New terms, based on the prefix nano, have gained broad circulation, unified the older terminology, and defined the topics of newly found disciplines. Just as the research community has struggled to restrict when and where the prefix nano can be appropriately used, we too struggled with the *Dekker Encyclopedia of Nanoscience and Nanotechnology* to avoid puncturing every sentence with the prefix nano. As this terminology develops, the online edition of the Encyclopedia will be able to incorporate these new conventions.

But at the time of publication of the first edition of the Encyclopedia these questions are still unresolved. One definition that has been proposed in order to remove the ambiguity would limit the use of the nano prefix to research and development of objects having the key property that they have at least one dimension in the range of 1 to 100 nanometers. New advances in synthetic methods for making such structures, combined with new analytical and manipulation tools, made it possible to refine methods to the point where de novo designed objects with nanoscopic dimension can, in many cases, be assembled in molecule-pure form or spatially organized structures. These systems, designed through processes that exhibit fundamental control over the physical and chemical attributes of molecular-scale structures, can be combined to form larger structures.

However, the *Dekker Encyclopedia of Nanoscience and Nanotechnology* has numerous entries that include the words micro and meso. Thus the use of the term nano, which, according to one broadly circulated definition, only limits research and technology to development in the length scale of approximately 1–100 nanometer range, is not simply a metric of length. Science at the nanoscale does not accept rigid limits on dimensionality. Indeed the very utility of nanoscience may be compromised by arbitrarily circumscribing its reach. After all, for ancient Greeks, the term “nanos” meant a dwarf. Keeping this in mind, we attempted in this reference to use the term nano to refer to objects and their subsequent processing into newly created structures, devices, or systems that have novel properties and functions because of their small and/or intermediate size. In other words, size and performance are the critical parameters that provide the requisite conditions to justify the use of the term nano.

By adopting a more elastic definition, which on one hand spans sizes from a few nanometer(s) to one (or a few) hundred(s) nanometers, but at the same time recognizes that the properties and performance of nanoobjects are rooted in their nanoscopic size, we believe that we made justice to all views that currently shape this field of continuous development and hope that other investigators—at universities, state laboratories, and in industries—will follow our lead.

## About the Editors-in-Chief

**Cristian I. Contescu** is Senior Staff Member of Materials Science and Technology Division at Oak Ridge National Laboratory, in Oak Ridge, Tennessee (USA). A former Senior Scientist of the Institute of Physical Chemistry in Bucharest, Romania (1971–1992), he later became an Adjunct Assistant Professor at Syracuse University, Syracuse NY, and served as Senior Scientist at HITCO Carbon Composites (Gardena, CA) and Material Methods, LLC (Newport Beach, CA). His scientific interests include surface and interface processes, adsorption and catalysis, gas and energy storage. Dr. Contescu is author or coauthor of over 50 peer-reviewed publications, book chapters, and patents. He is member of the Editorial Board of CARBON journal, and served as co-chair of the Colloid and Surface Chemistry Division of the American Chemical Society symposia on nanoscience and nanotechnology. He is a member of the American Carbon Society and the American Chemical Society. He received the M.Sc. degree (1971) in physical chemistry from Bucharest University, Romania, and the Ph.D. degree (1979) in physical chemistry from Bucharest Polytechnic Institute, Romania.

- Editorial Board, CARBON journal (2007)
- “Gheorghe Spacu” National Award of the Romanian Academy Division of Chemical Sciences (1991)
- International Research & Exchanges Board (IREX) fellowship (1990)
- Special Merit Diploma (Summa cum Laudae) from Bucharest University (1971)

**Karol Putyera** is Director of Analytical Services, Evans Analytical Group (EAG) Shiva Technologies, Syracuse, New York (USA). He started to work for Shiva Technologies, Inc. in 1992 as a part-time GDMS analyst while being a Research Associate in the L.C. Smith College of Chemical Engineering and Materials Science at Syracuse University NY, from 1992-1995. After completing his JSPS fellowship at Chiba University in Japan Dr. Putyera joined Shiva full-time as Technical Manager and subsequently held positions in the company as Director of Advanced Technology Group, General Manager Shiva West, Laboratory Director, Vice President for Business and Technology Development and most recently President of Shiva Technologies, Inc. and Shiva Technologies Europe. Dr. Putyera completed his BS and M.S. degrees in Physical Chemistry at Charles University, Prague, Czech Republic in 1983 and 1985, respectively. He received his Ph.D. degree in Inorganic Chemistry in 1991 at the Institute of Inorganic Chemistry, Slovak Academy of Sciences, Slovak Republic.

- Japanese Society for Promotion of Science Fellowship (1996)
- Slovak Academy of Sciences “Golden Plaque” for young research scientists from the Slovak Academy of Sciences (1990)

**Founding Editor James A. Schwarz** (deceased, 2004) was Professor of Chemical Engineering and Materials Science at Syracuse University, Syracuse, New York (USA). The author or coauthor of numerous professional publications, presentations, and patents, Prof. Schwarz had unanimously recognized contributions in surface science, catalysis, carbon science, and colloid science. He was President of the California Catalysis Society and a member of the American Vacuum Society, the American Chemical Society, and the American Institute of Chemical Engineers. He was the 2004 Chair of the Colloid and Surface Chemistry Division of the American Chemical Society. He received the

B.S. degree (1965) in science and the M.S. degree (1966) in chemistry from Stevens Institute of Technology, Hoboken, New Jersey, and the Ph.D. degree (1969) in chemistry from Stanford University, California.

- Chair of Colloid Division of the American Chemical Society (2004)
- Senior Fulbright Fellow to Romania (1997)
- American Chemical Society Langmuir Award (2001)
- Chancellor's Citation for Academic Excellence at Syracuse University (2002)

*Encyclopedia of*

# **Nanoscience and Nanotechnology**

*Second Edition*

## **Volume I**

*Pages 1 through 752*

*Aberration – Catalysis*

Aberration –  
Aerosol

AFM – AFM

Amphiphilic  
– Axle

Barcoded –  
Biomimetic

Bionanoparticles  
– Block

Cadmium –  
Capsules

Carbon-Based –  
Carbon Nanotube

Carbon Nanotubes  
– Catalysis

# Aberration-Corrected Z-Contrast STEM: Semiconducting Nanocrystals

**James R. McBride**

*Department of Chemistry, Vanderbilt University, Nashville, Tennessee, U.S.A.*

**Andrew R. Lupini**

**Stephen J. Pennycook**

*Materials Science and Technology Division, Oak Ridge National Laboratory, Oak Ridge, Tennessee, U.S.A.*

**Sandra J. Rosenthal**

*Department of Chemistry and Physics, Vanderbilt University, Nashville, Tennessee, U.S.A.*

## Abstract

The development of aberration-corrected scanning transmission electron microscopy (STEM) has provided new insight in the development of nanomaterials. Specifically, atomic number contrast STEM, or Z-STEM, has been applied to elucidate the structure of cadmium-based semiconductor nanocrystals. With sub-angstrom detail, the images obtained elucidated the effects of surfactants on the nanocrystal shape, showed the precise coverage of epitaxial shells for core/shell quantum dots, as well as provided the first images of the atomic structure of alloy nanocrystals.

Semiconducting nanocrystals are one of the most beautiful examples of how new and fascinating physical properties arise in the nano-regime. As first demonstrated by Louis Brus, the band gap, and in essence, the color of a semiconductor becomes size-dependent when the diameter is reduced to below the bulk Bohr exciton diameter.<sup>[1]</sup> This allows for precise tuning of the absorption and emission properties by simply controlling the nanocrystal's diameter. In 1993, Murray, Norris, and Bawendi published the synthesis that would form the basis of the production of monodisperse, colloidal nanocrystals.<sup>[2]</sup> This has become the foundation of the nanocrystal field, which has since grown to not only include fundamental investigations into the properties of the nanocrystals themselves, but also the development of practical applications. Efforts are currently focused on the use of colloidal nanocrystals or “quantum dots” for the development of fluorescent probes for biological imaging, phosphors for solid-state lighting, and light harvesters for photovoltaics.<sup>[3–10]</sup> Although great strides have been made towards the development of these applications, much more basic research is needed to develop them into powerful, reliable, and competitive technologies.

One of the most useful properties of nanocrystals is their large surface-to-volume ratio. For example, in a 1.2 nm diameter nanocrystal, nearly all of the atoms are surface atoms. This results in the surface dominating the chemical and physical properties of the nanocrystal. The surface consists of a mixture of unpassivated atoms with dangling bonds and atoms that are passivated with surfactants. The electronic, optical, and physical

properties of the nanocrystal are extremely sensitive to the surface conditions. Dangling bonds can act as charge traps, reducing the emission efficiency. They are also able to easily take part in chemical reactions. For example, oxygen can bind to the unpassivated atoms forming an oxide, which can cause photo-brightening and eventually quenching.<sup>[11]</sup> The presence and type of passivating ligand can also be chosen to tailor the properties of the nanocrystal in controlled ways, such as improving the emission efficiency, or quenching the emission completely, if desired. The surface can also be affected by “shelling”; core/shell quantum dots have an outer coating of a wide bandgap semiconductor to passivate the surface and confine electrons and holes to the core. The thickness and total coverage of the shell dictates the quantum yield and resistance to photobleaching of core/shell quantum dots.

The importance of the surface structure has driven the application of aberration-corrected, atomic number contrast scanning transmission electron microscopy (Z-STEM) to characterize nanocrystals. This technique allows for direct imaging the nanocrystal's core and surface structure with sub-angstrom resolution. Additionally, the image intensity is dependent on chemical composition and thickness affording an unparallel view of the nanocrystal. This entry will review our recent work in utilizing this technique to study colloidal cadmium-based semiconductor nanocrystals. Specifically, Z-STEM was used for (1) observing the effect of surfactant on the nanocrystal shape; (2) guiding the development of near unity quantum

yield core/shell nanocrystals; and (3) the characterization of homogeneous nanocrystal alloys. These applications rely on the unique capability of Z-STEM to simultaneously provide sub-angstrom resolution, allowing individual atoms to be imaged, and chemical identification of the elements present.

## SYNTHESIS OF CdSe NANOCRYSTALS

The current methods for synthesizing CdSe nanocrystals follow procedures similar to those of Bowen-Katari, Colvin, and Alivisatos, which eliminated the need for size-selective precipitation to produce monodisperse samples.<sup>[12]</sup> In this preparation, 99% trioctylphosphine oxide (TOPO) and tri-*n*-butylphosphine (TBP) is used as received from Aldrich. Se (60 mesh powder) is dissolved in TBP and followed by the addition of dimethylcadmium. The injection solution of cadmium and selenium in TBP is then diluted 4:1 with TBP and injected into the reaction vessel of TOPO at ~350°C. The solution is removed from heat and allowed to cool under argon, which prevents oxidation of the nanocrystal surface. To recover nanocrystals from the solid, room temperature TOPO mixture, methanol is added to dissolve the TOPO and precipitate the nanocrystals, which are then recovered by filtration. To make nanocrystals with an absorption maximum larger than 580 nm, the reaction is cooled from 350°C to 320°C and the nanocrystals are allowed to grow while the size is monitored by drawing aliquots from solution and monitoring the absorption spectra. Using this growth method, the initial tight size distribution is lost. This can be overcome by the addition of additional reagent solution to “focus” the size distribution.

The use of dimethylcadmium to produce high-quality nanocrystals is still common. However, Peng and Peng demonstrated the use of CdO as a benign source of cadmium.<sup>[13]</sup> In this one-pot approach, CdO, TOPO and either hexylphosphonic acid (HPA) or tetradecylphosphonic acid (TDPA) are loaded into a three-neck flask. At temperatures above 270°C, the phosphonic acid complexes with the CdO forming a clear and colorless solution. After the formation of the colorless cadmium phosphonate complex, Se:TBP is injected into the reaction, which initiates the formation of nanocrystals. This method can also be used to produce high-quality CdS and CdTe nanocrystals by replacement of the anion solvated by TBP.<sup>[14]</sup>

Weller and co-workers developed a similar synthetic methodology using cadmium acetate  $\text{Cd}(\text{CH}_3\text{CO}_2)_2$  as the precursor.<sup>[15]</sup> In this method, a stock selenium solution of trioctylphosphine:Se (TOP:Se) is added to a mixture of TOPO:hexadecylamine (HDA):TDPA at 120°C. This is then heated to 300°C to which a stock solution of cadmium acetate and selenium dissolved in

TOP is rapidly injected. Both the cadmium and selenium stock solutions are stored inside a glove box under nitrogen atmosphere. Additionally, efforts to reduce the use of phosphine in the chemistry has led to the development of the use of oleic acid and octadecene as the surfactants, in place of TOPO and the phosphonic acids.<sup>[16]</sup>

## TEM EXPERIMENTAL

Nanocrystal sample preparation for electron microscopy is, in general, simple. The as-synthesized nanocrystal powder or liquid need to be purified to remove any excess starting materials and surfactants. It is critical to develop a methodology that removes the unbound surfactants as they will deposit with the nanocrystals onto the TEM grid, making the overall sample thicker than desired, and they may also cause contamination. Contamination is believed to be beam-induced polymerization of carbonaceous materials on the carbon support. This polymer can continue to grow until the beam can no longer penetrate the specimen. The cleaning steps typically used to remove this unwanted material depend on the surfactants used during synthesis. TOPO-coated nanocrystals need only three methanol washes, TOPO-HDA nanocrystals require an inverse precipitation step in octanol, while oleic acid-coated nanocrystals require three washes with a careful mixture of chloroform and acetone.<sup>[17]</sup> Once clean, the powdered nanocrystals should be brought into solution with an appropriate solvent. For TOPO-coated nanocrystals, toluene or hexanes work well. Ultrathin carbon on formvar TEM grids purchased from Ted Pella, Inc. (part no. 01822-F) are ideal for imaging nanocrystal samples. They have an average thickness of 30 nm and are fairly resilient to sample preparations due to the formvar support. The formvar support can be removed to minimize the film thickness and subsequently the carbon background in the TEM images. For Z-STEM, lacey carbon coated with ultrathin carbon, also from Ted Pella, is used to provide the least amount of background for imaging.

After the film is cleaned, a drop of a nanocrystal solution with an optical density of less than 0.1 is placed onto the grid. Anticapillary tweezers should prevent premature drawing up of, or wicking, of the solution. A Kimwipe™ can be used to “wick” the solvent off in a controllable fashion, leaving the nanocrystals on the carbon film. Alternatively, the solvent can be allowed to evaporate, helping the nanocrystals to array and limit nanocrystal stacking and bunching. The higher the boiling point of the solvent, the longer the nanocrystals will have to order themselves on the grid. However, leaving the solvent to dry also allows for



more of the excess surfactants to accumulate on the grid, increasing the chance for contamination under the electron beam.

Since the electron beam is focused to a point in STEM, it is more susceptible to contamination and requires extra care during sample preparation. Even samples that do not contaminate under conventional TEM conditions can be problematic in STEM. To combat this, samples on ultra-thin carbon grids can be plasma cleaned for up to 20 sec in an argon/oxygen plasma cleaner. More effectively, yet more damaging to the nanocrystals, the sample can be exposed to a high intensity light bulb, either outside the microscope, or in the air lock under vacuum. Twenty minutes of the “light bulb” treatment can effectively eliminate contamination and allow for sustained imaging over a single area for an extended period of time.

## THE MICROSCOPES

Conventional high-resolution transmission electron microscopy (HRTEM) images were obtained using a Phillips CM20 operating at 200 kV, located at Vanderbilt University. Z-STEM images were taken using the VG HB603u 300 kV aberration-corrected STEM located at Oak Ridge National Laboratories, in collaboration with Stephen J. Pennycook. Fitted with a Nion  $C_s$  corrector, the HB603u has a record-setting 0.78 Å resolution, allowing for several pixels in an image to be devoted to a single angstrom.<sup>[18]</sup> Images are collected using a high-angle annular dark field detector (HAADF), which allows for simultaneous collection of dark field (Z-STEM) and bright field images. The dark field images are formed by the highly scattered electrons, resulting in image intensities that are dependent on sample thickness and the atomic number ( $Z$ ) of the atom or atomic column being imaged. Images are collected and processed using Gatan’s Digitalmicrograph software. Unless otherwise noted, images are “smoothed” to remove any high frequency shot noise from the images. Color has been added to emphasize that the intensity is important in image interpretation.

## CONVENTIONAL HIGH-RESOLUTION TRANSMISSION ELECTRON MICROSCOPY (HRTEM) FOR CHARACTERIZATION OF NANOCRYSTALS

Conventional HRTEM is the standard technique for measuring the size, dispersity, and overall quality of a nanocrystal sample. Owing to the ability of nanocrystals to freely rotate under the electron beam, obtaining lattice resolved images of them requires quick reflexes and often a bit of luck. Unlike thin films of solids, whose crystallographic orientation is dependent on how it is sliced, nanocrystals are free to rotate on the carbon film and align themselves randomly. Fringe patterns in phase contrast imaging are used to determine the size, shape, and the crystal structure of the object being imaged. Because of the relatively small number of properly aligned nanocrystals, finding nanocrystals that are not in contact with others and facing with the zone axis towards the electron beam can be a difficult task. Using solutions with a low concentration of nanocrystals and allowing the solvent to evaporate, allowing the nanocrystals to array, is best for producing the highest number of isolated nanocrystals per area of carbon film. The difference between evaporating and “wicking” the nanocrystal solution can be seen in the TEM images in Fig. 1. The nanocrystals in the wicked sample, Fig. 1A, are clumped together, while those of the evaporated sample, Fig. 1B, are evenly separated into a two-dimensional array, with the distance between them dictated by sample concentration and surfactant. Highly concentrated solutions of nanocrystals form extremely dense arrays that are not useful for imaging individual nanocrystals, as shown in Fig. 1C. Figure 2 shows the three distinct fringe patterns that can be assigned to different orientations of the nanocrystal.<sup>[19]</sup> The pattern labeled “B” is consistent with the [100] orientation. This is the most common orientation found, since the largest face of the nanocrystal is in contact with the carbon film. The zigzag pattern labeled “C” is that of the [010] orientation. To achieve this orientation, the nanocrystal must be resting on a corner

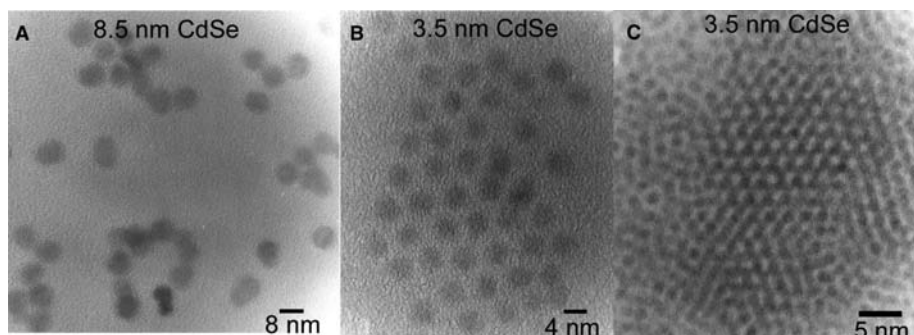


**Fig. 1** TEM sample preparation. TEM images of samples that were wicked (A), not wicked (B) and overcrowded (C) are shown.

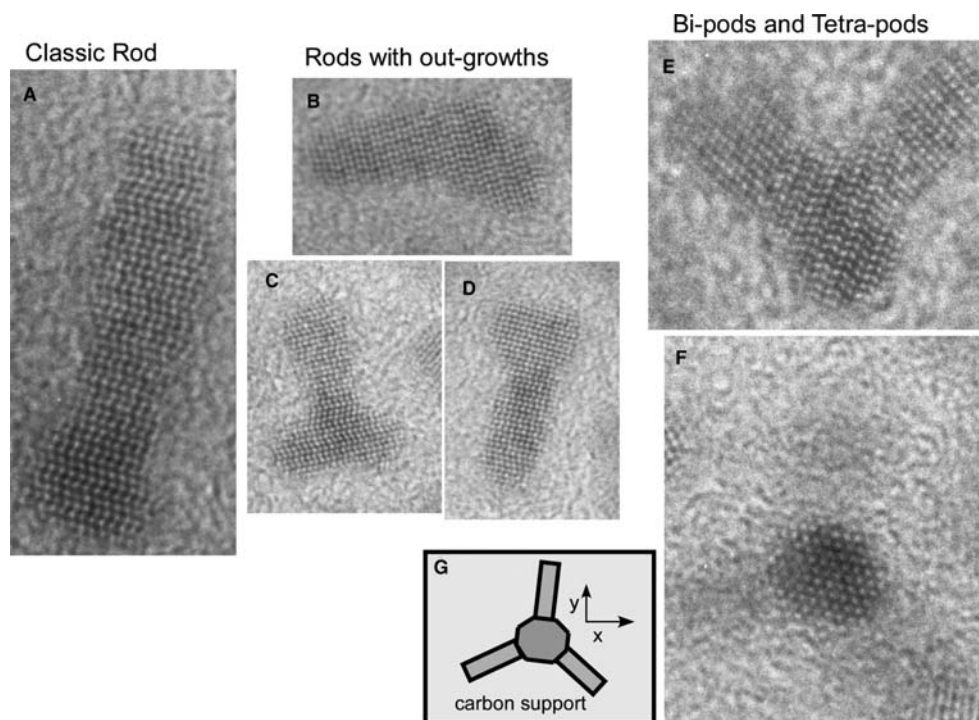


**Fig. 2** Fringe patterns. (A) TEM image of randomly orientated CdSe nanocrystals. (B–D) [100], [010], [001] fringe patterns and their associated lattice spacing.

facet. The orientation labeled “D” corresponds to [001] direction and requires the nanocrystal to be sitting on end. This orientation clearly shows the hexagonal shape of wurtzite CdSe. From images like these, it is not only possible to determine the average nanocrystal size but also determine the average shape. The size of the nanocrystal can be determined either by counting the number of lattice fringes and multiplying that number times the fringe spacing or by simply determining the scale of the image and then measuring the diameter of the particle. The latter, however, requires that the microscope be precisely calibrated. Approximately 200 measurements of individual nanocrystals are needed to determine a size distribution.<sup>[19]</sup>

Large shape morphologies can be easily seen under HRTEM conditions. Fig. 3 contains HRTEM images of CdSe nanocrystal prepared under different reaction conditions. Fig. 3A is a CdSe nanorod. Figure 3D are images of nanorods with small outgrowths, and Fig. 3E and F are TEM images of a bipod and tetrapod, respectively. The odd shapes of the nanocrystals in Fig. 3 could be the result of the large number of stacking faults [a stacking fault is a break in the regular crystal pattern,<sup>[20]</sup>] or the result of the mixture of surfactants used in the synthesis. Wurtzite CdSe nanocrystals often have zinc blende stacking faults in them due to the small energetic difference between the two phases. The nanocrystal in 3A shows several sections of zinc blende in the top half while the bottom half

exhibits the normal alternating pattern of a wurtzite crystal lattice oriented in the [010] direction. From the fringes, it can be presumed that the growth is along the *c*-axis, since this is the long axis of the nanocrystal. It is also known from the CdSe nanocrystal structure that there are Cd and Se rich facets, which should create surfaces with different chemical reactivities. However, in which direction growth occurs, whether towards the Se face or the Cd face, cannot be determined. This unidirectional growth, if understood, could lead to control of facet-specific growth mechanisms such as those that formed the tetrapods in Fig. 3E and F.<sup>[14,21]</sup> Unfortunately, phase contrast imaging does not yield enough detail to differentiate the Cd- and Se-terminated facets.<sup>[11,22,23]</sup> However, Z-STEM can directly probe the chemical structure with atomic level precision. A general description of the technique is described in the following section.

### ATOMIC NUMBER CONTRAST SCANNING TRANSMISSION ELECTRON MICROSCOPY (Z-STEM)

Atomic number contrast scanning transmission electron microscopy uses an atom-sized probe that scans across the sample to form an image. The electrons scattered at low angles are used to form a bright field image while those scattered at high angles are used to

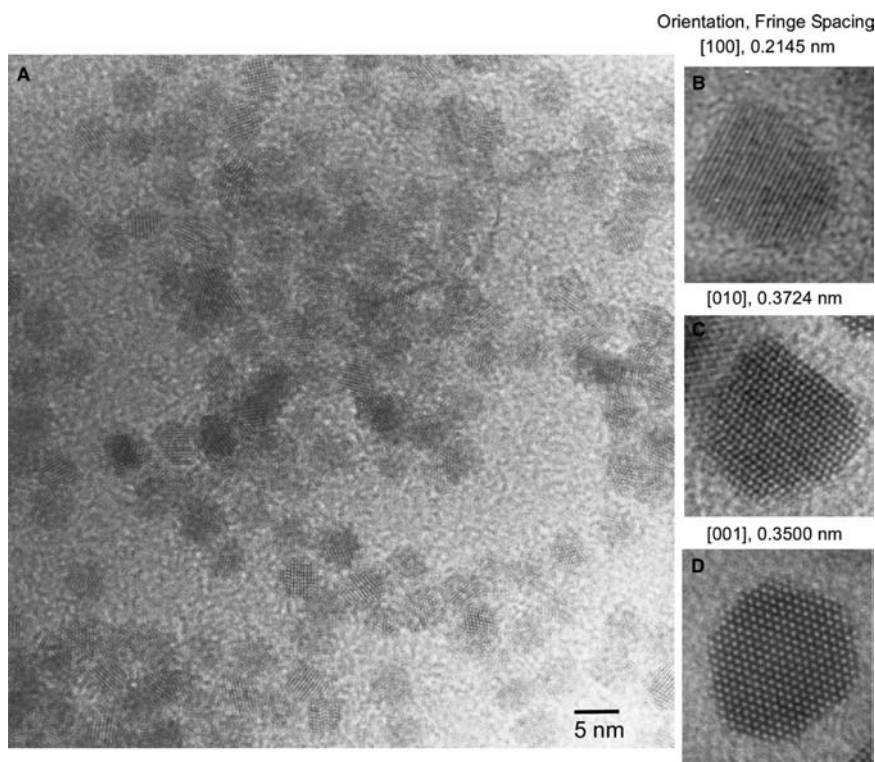


**Fig. 3** TEM images of various shapes of CdSe nanocrystals. Depending on the growth conditions, nanocrystals can form shapes such as rods (A), rods with growths (B–D) and bi-pods and tetrapods (E and F). G is a cartoon illustrating the tetrapod in (F) with the fourth arm pointing in the Z direction, out of the sample plane.

form a dark field image. The bright field image is a coherent phase contrast image, similar to that formed in a comparable high-resolution TEM. High-angle scattering is generated incoherently, and leads to an incoherent image, the resolution of which is directly related to electron probe diameter. The electron probe size in STEM is limited by the beam energy, its energy spread, and by aberrations in probe-forming lenses.<sup>[24]</sup> Also, high-angle scattered electrons show a strong atomic number contrast, hence the term Z-STEM, or Z-contrast imaging, also known as HAADF imaging.<sup>[25–27]</sup> These electrons can be compared with the He ions in Rutherford Backscattering in that their energy and intensity are dependent on the material with which they interact. Electrons impinging upon a heavy atom will scatter more frequently to higher angles than those that encounter a lighter atom. Therefore, scattered electrons detected from atoms with differing atomic weights appear as intensity variations in the image, yielding elemental information directly from the image. Unlike coherent imaging techniques such as phase contrast imaging (conventional HRTEM), there are no complicated contrast changes with focus or specimen thickness.<sup>[28]</sup> This allows for direct interpretation of the images; a bright spot in the image plane corresponds directly to a scattering center in the object plane, i.e. an atom. Additionally, the intensity of the scattered electrons depends on the square of the atomic number of the scattering atom, yielding spatially resolved chemical information.<sup>[25]</sup>

As a result of the sub-angstrom probe and its imaging design, Z-STEM provides an unmatched ability to achieve structural and chemical information from individual nanostructures at the atomic level.<sup>[18,29]</sup> For example, Z-STEM tomography was recently used to determine the 3D structure of less than 10 nm Sn quantum dots embedded in Si with cubic nanometer resolution.<sup>[30]</sup> Z-STEM has been used for many years to directly image the atomic structure of grain boundaries and interfaces, even revealing specific impurity segregation sites.<sup>[31–33]</sup> A key advantage of Z-STEM is that it can be easily combined with electron energy loss spectroscopy (EELS) to achieve elemental identification with atomic resolution.<sup>[34]</sup> Today, with the successful correction of lens aberrations, Z-STEM has demonstrated 0.78 Å spatial resolution by directly imaging Si [112] atomic dumbbells.<sup>[18]</sup> The higher resolution and image contrast also results in a greatly improved sensitivity for EELS, opening many opportunities for materials science research.<sup>[35]</sup> For example, it was shown using these two techniques that rare earth dopant atoms, such as La, preferentially segregate to the amorphous crystal interfaces of Si<sub>3</sub>N<sub>4</sub>.<sup>[36]</sup> This level of precise information is critical for the development of nanomaterials where the placement of a single atom can drastically affect the desired properties.

A comparison between two similarly orientated CdSe nanocrystals, imaged under HRTEM and Z-STEM, is shown in Fig. 4. False color has been added to the Z-STEM image to emphasize the



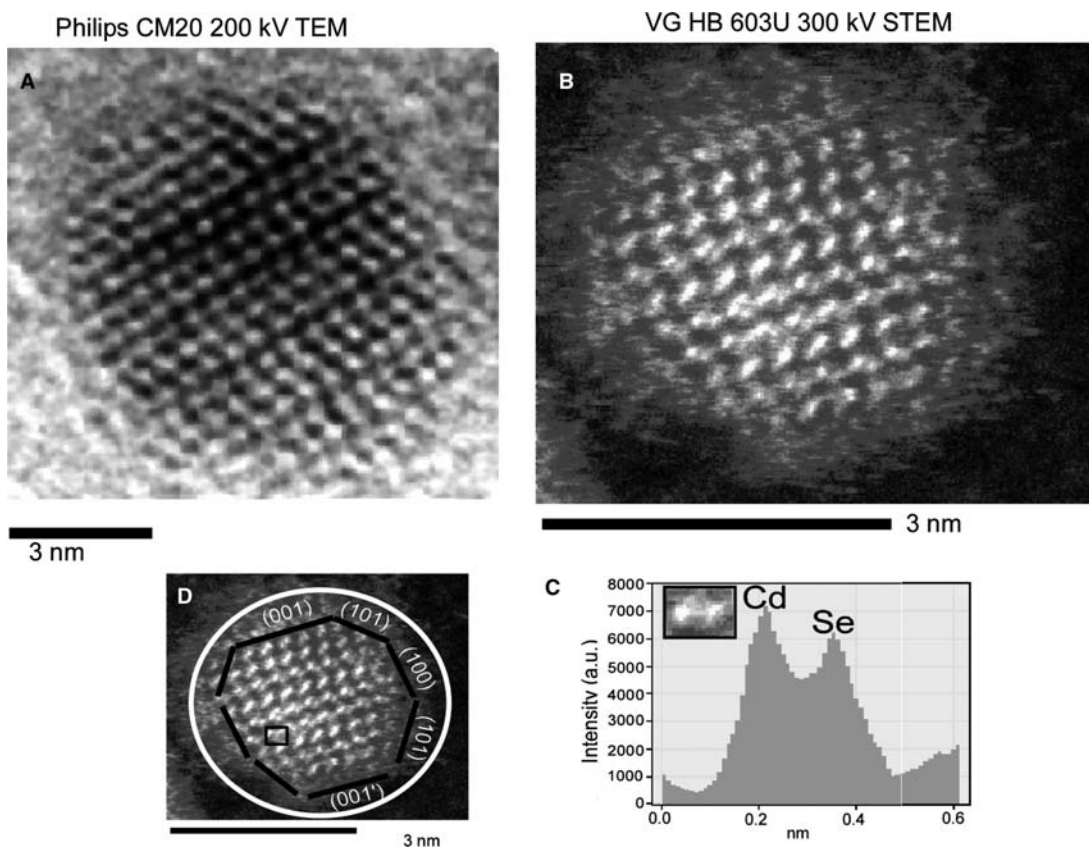


**Fig. 4** TEM-Z-STEM comparison. (A) and (B) are TEM and Z-STEM images of similarly orientated CdSe nanocrystals. (C) is a line profile taken from (D) (black box) showing intensity contrast from the Cd and Se atomic columns. The intensity contrast can be used to assign specific facets in the image (D). The white circle in (D) highlights the amorphous oxide coating. *Source:* Reprinted with permission from *Nano Lett.*, **2004**, 4 (7) 1279–1283. © 2004 American Chemical Society.

importance of the image intensity. Unlike the conventional HRTEM image in Fig. 4A, chemical and structural information can be obtained directly from the intensities in the raw Z-STEM image. For example, the Cd and Se columns in Fig. 4B can be assigned from the intensity difference found in the raw image, as indicated by the intensity profile in Fig. 4C. With this information, the Cd-rich (001) and the Se-rich (001') surfaces can be then assigned by following the alternating intensities to the surface, as shown in Fig. 4D. Additionally, since the electrons that are detected are incoherently scattered, phase contrast that produces the speckle pattern in bright field images of amorphous carbon is not present. As a result, single atoms can be imaged on the surface of an amorphous carbon film, and nanocrystal edges are clearly visible in cases where the nanocrystal is not susceptible to oxidation.<sup>[37]</sup> In the images in Fig. 4, the nanocrystal edges are oxidized owing to exposure to air, and the resultant amorphous oxide layer, which has been enclosed by a white circle, can be clearly seen in the Z-STEM image in Fig. 4D. The spots seen in the oxide are the remains of the outer surface of the nanocrystal. Individual atoms and

atomic clusters can readily be found in this region; these atoms and clusters would not be visible using conventional HRTEM since there is no contrast between amorphous materials and the amorphous carbon support.

Besides the smaller probe size, an additional advantage of aberration correction is that the STEM Bright Field (BF) has about two orders of magnitude more current, enhancing the signal-to-noise resolution, making it a practically useful additional channel of information. It is obtained simultaneously with the Z-STEM image, and is equivalent to an aberration-corrected HRTEM image by the principle of reciprocity (reversing ray directions). Fig. 5 shows the simultaneous BF and Z-STEM images of a triangular shaped CdSe/CdS core/shell nanocrystal taken after the installation of the aberration corrector.<sup>[38]</sup> The BF image shows the edge of the nanocrystal more clearly, because of the reduced image delocalization, but it is still not able to detect individual atoms on the amorphous carbon support because of the lack of strong Z-contrast. The Z-STEM image does show individual atoms and small clusters on the carbon film. The

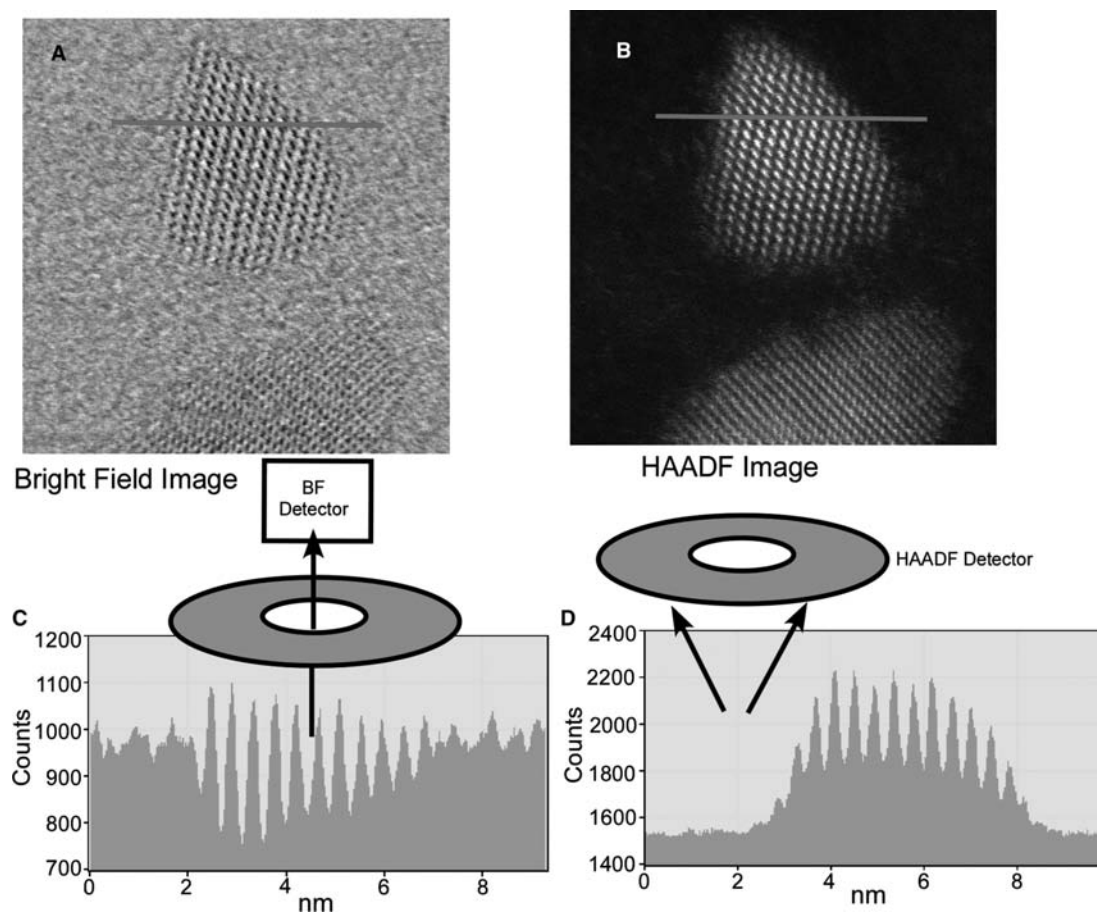


**Fig. 5** Bright field vs. dark field STEM. The STEM images A (bright field) and B (dark field) are obtained simultaneously during imaging. The line profiles (C and D) show the reduction in back ground intensity afforded by dark field imaging. *Source:* Reprinted with permission from *Surf. Sci. Rep.*, **2007**, 62, 111–157. © 2007 Elsevier B. V.

line profiles in Figs. 5C and D illustrate how the bright field image is formed by constructive and destructive interference on top of the contrast from the carbon support, whereas the Z-STEM image exhibits a sharp increase in intensity between the carbon film and the nanocrystal, indicating the precise location of the surface. However, the bright field image is still particularly useful for finding focus and for manually adjusting for astigmatism, although it should be noted that optimum focus for a bright field image is not exactly the same as optimum focus for the Z-STEM image.<sup>[28]</sup>

### Z-STEM OF CdSe NANOCRYSTALS

The following figures show how easily Z-STEM images can be interpreted. There are three main orientations that allow lattice-resolved images. Examples of these are shown in Figs. 6 and 7. The images can be interpreted simply by comparison to a computer generated “ball-and-stick” CdSe nanocrystal model and rotating it in three dimensions to match the atomic arrangement

in the Z-STEM image. This particular model was developed by Andreas Kadavanich using Crystal Maker.<sup>[39]</sup> It is interesting to note that in the image of the nanocrystal in the [100] orientation, Fig. 6A, the Cd and Se columns are nearly resolved. The spacing between the atomic columns in this orientation is 0.67 Å, just beyond the resolution of the microscope. The nanocrystal in Fig. 6B is in the [001] orientation, showing no mass contrast as the Se and Cd atomic columns are overlapped. Alternatively, the nanocrystal in Fig. 7A is in the [010] orientation where the Cd and Se atomic columns are separated, showing mass contrast. Also, a new orientation that had not been resolved prior to use of the aberration corrector is seen in Fig. 7B; it is the [111] orientation with a column separation of 2.75 Å.

Figs. 8A and B show two Z-STEM images of the TOPO/HDA nanocrystals with a zinc blende crystal structure. These nanocrystals do not exhibit the alternating “zigzag” pattern of a wurtzite nanocrystal. Also, these images exhibit a larger coating of the oxide layer, probably due to the light bulb treatment applied

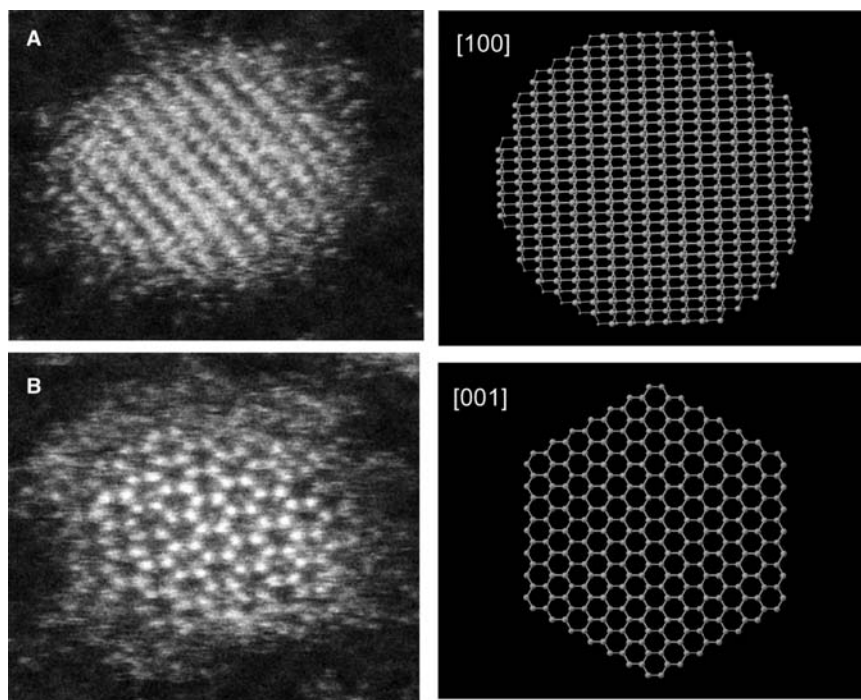


**Fig. 6** Z-STEM images and model. The images obtained (A and B) can be directly compared to a traditional ball and stick model to determine orientation. The larger, orange atoms represent Cd while the smaller, blue atoms are Se. *Source:* Reprinted with permission from *Surf. Sci. Rep.*, **2007**, 62, 111–157. © 2007 Elsevier B. V.

prior to imaging. Fig. 8A is a CdSe nanocrystal in the [010] orientation. This position shows the clearest mass contrast between the Cd and Se columns. However, a crystallographic defect can be seen in the image as there is an extra intensity source in between the atomic columns, probably indicating a stacking fault or twin boundary in the nanocrystal. The nanocrystal in Fig. 8B is also in the [010] orientation, but has a stacking fault parallel to the beam direction, indicated by the black line. In the case of the nanocrystal in Fig. 8B, two zinc blende phases are separated by a wurtzite stacking fault, forming a twin boundary. These low-energy defects in the crystal lattice are common for semiconducting nanocrystal systems.<sup>[40–42]</sup>

The nanocrystal in Fig. 8C shows the typical [001] pattern, but with faint “spots” situated directly in the center of the hexagons, as can be seen in the intensity profile (8F). The intensity profile shows that these peaks, marked by black arrows, are above the noise level in the image and appear perfectly spaced between the other atomic columns. This particular pattern is the result of a stacking fault midway through the nanocrystal that causes a shift of half of the crystal lattice. Figs. 8D and E show a model CdSe nanocrystal with a stacking fault that can reproduce the experimental image from the [001] and [010] orientations, respectively. The yellow arrow indicates the direction of the stacking fault.

The nanocrystal shown in Fig. 9A shows a relatively symmetrical intensity along its C-axis as would be expected for a traditional nanocrystal. The 3D cartoon

(Fig. 9B) is helpful for visualizing the 3D shape of the nanocrystal. However, the nanocrystal in Fig. 9C clearly shows a large decrease in intensity for half of the nanocrystal, giving the impression that it is only partially completed or that a possible defect formation prevented further growth. An artist’s conception of the approximate 3D shape is shown in Fig. 9D. From the 3D shape, it appears that the growth occurs in a stepwise manner, starting at a surface edge and then moving across while building upward along the C-axis. This most likely occurs due to the higher number of dangling bonds on the edges of the nanocrystal. With the surface clearly visible in these images, it should be feasible to observe subtle differences in surface structure caused by varying the surfactants, as illustrated in the following section.

## SURFACTANT EFFECTS ON NANOCRYSTAL SURFACE STRUCTURE

It has been reported previously that CdSe nanocrystals prepared by the TOPO-only method are Cd rich.<sup>[43]</sup> It is believed that the excess Cd found in the TOPO-only nanocrystals resides in the elongated [101] facets, where there are two Se dangling bonds at each Se surface site. However, when an HDA was used as a co-surfactant, improvements in fluorescence quantum yield and narrower size distribution were also accompanied by a reduction in the excess cadmium measured. Z-STEM was used to image the CdSe



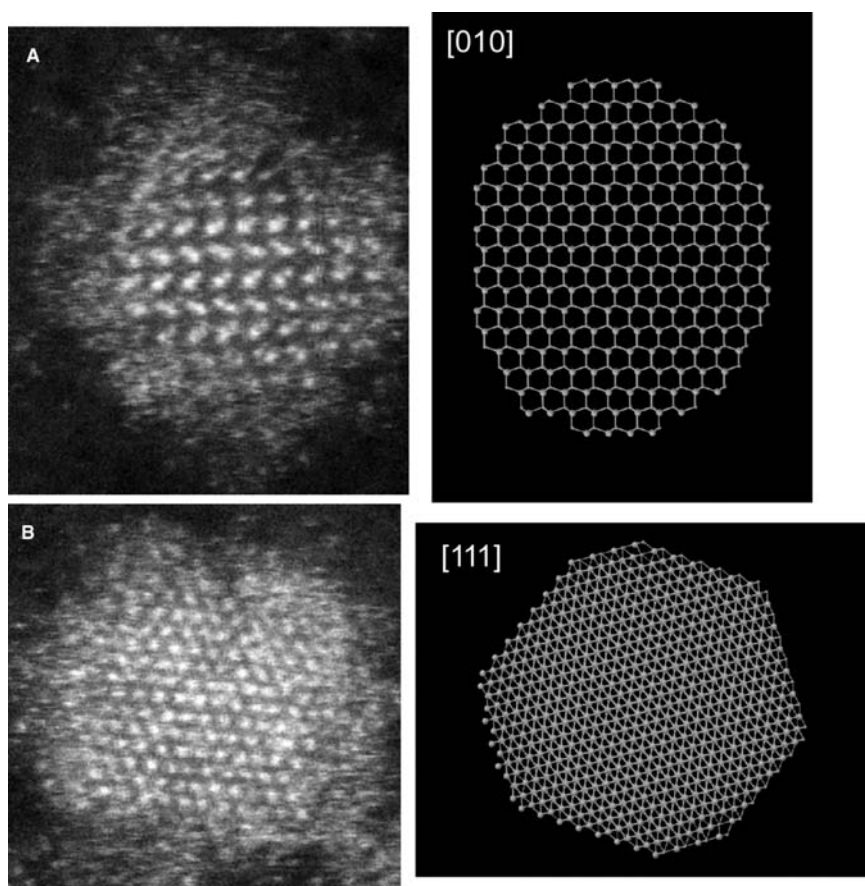


**Fig. 7** Z-STEM images and model. (A) is a Z-STEM image of a CdSe nanocrystal showing atomic contrast with its associated model. (B) shows a peculiar spot pattern that can be obtained by tilting a nanocrystal to the [111] orientation. *Source:* Reprinted with permission from *Surf. Sci. Rep.*, **2007**, *62*, 111–157. © 2007 Elsevier B. V.

nanocrystals produced under these two conditions and to determine any difference in surface structure.

The images in Fig. 10 are the first aberration-corrected Z-STEM images of CdSe nanocrystals ever taken, obtained shortly after the installation of the spherical aberration ( $C_s$ ) corrector. The optimum probe size just after installation was around 0.8 Å, later demonstrated with the direct imaging of the 0.78 Å spacing in an Si [112] foil.<sup>[18]</sup> The striking detail of the surface of these nanocrystals prepared with TOPO as the only surfactant clearly shows the precise shape of the nanocrystals. Several of the nanocrystals in Fig. 10A appear elongated, while most exhibit an ovoid shape. The Z-STEM images clearly show a lack of shape distribution control. It was proposed that this might be the result of a “magic” impurity that exists in technical grade TOPO causing an increase in growth along the  $C$ -axis.<sup>[44]</sup> However, CdSe nanocrystals with a good size distribution cannot be grown without this “magic” impurity. Additionally, having too much of this impurity leads to uncontrolled growth. Prior to the Z-STEM reported here, it was determined by Peng and Peng that the magic ingredient was a phosphonic acid impurity in the TOPO that was necessary to control the shape and growth of the nanocrystals.<sup>[14]</sup> In addition to the phosphonic acid, a long-chain, primary

amine, such as HDA, was also added to obtain superb size distribution without the need for size selective precipitation.<sup>[23]</sup> Atomic number contrast scanning transmission electron microscopy images of CdSe nanocrystals prepared with the mixture of TOPO/HDA and dodecylphosphonic acid, are shown in Fig. 10B. In both images, the large number of lattice-resolved nanocrystals illustrates the benefit of the  $C_s$  corrector and the small probe size. Since the nanocrystals are free to rotate, obtaining a good lattice-resolved image is dependent on the orientation of the nanocrystal during image capture. As the probe size decreases, the number of lattice-resolved nanocrystals increases due to improved ability to image nanocrystals off axis, and the higher number of zone-axis orientations that are resolvable. The small features seen near the surface would be very difficult to detect using conventional HRTEM.

Interestingly, a striking difference between the two images can be seen. Although the sizes of the nanocrystal samples differ only by 0.3 nm on average, their overall shape is markedly different. The TOPO-prepared CdSe nanocrystals in Fig. 10A appear to be elongated, compared with those of the TOPO/HDA-prepared nanocrystals in Fig. 10B. For example, the nanocrystal circled in Fig. 10C shows a definite

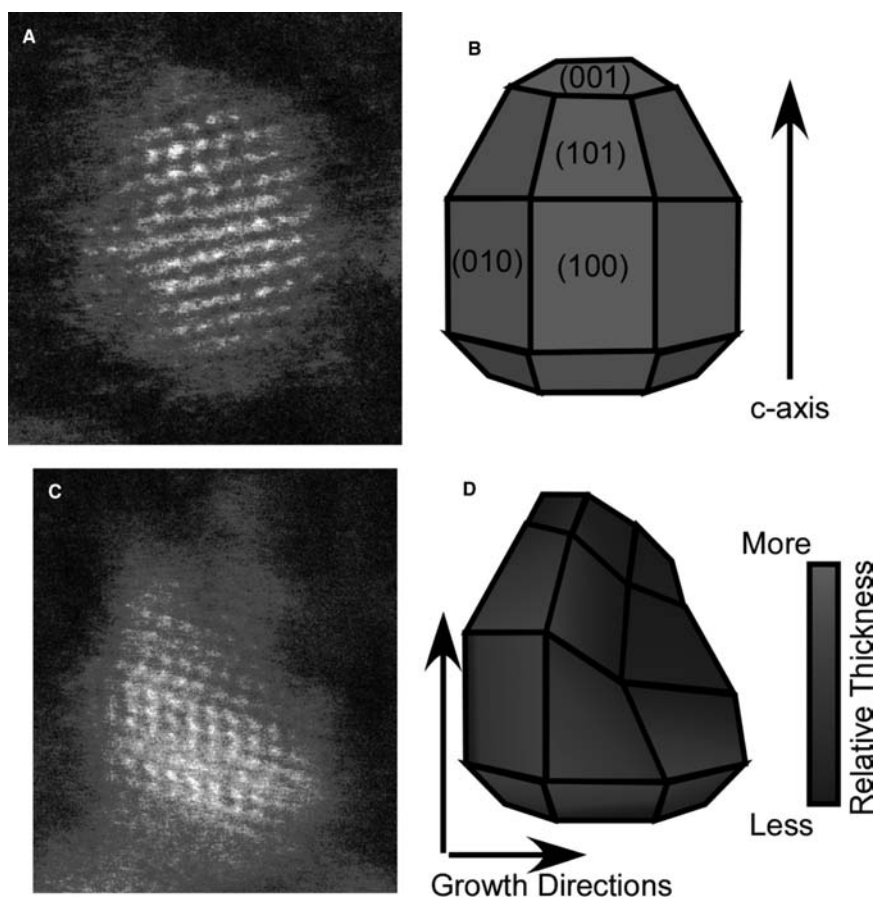


**Fig. 8** (A) and (B) show Z-STEM images of CdSe nanocrystals with stacking faults perpendicular to the image plane. (C) is a Z-STEM image of a CdSe nanocrystal with a stacking fault in the image plane, adding intensity in the center of hexagons (D–F). *Source:* Reprinted with permission from *Surf. Sci. Rep.*, **2007**, *62*, 111-157. © 2007 Elsevier B. V.

narrowing along the  $c$ -axis, which is parallel to the surface plane. The inhomogeneous faceting of this sample is most likely the result of preferential growth along this axis. From this image, the orientation of the Cd and Se dumbbells can be determined, illustrated by the line profile in Fig. 10D, allowing us to assign the narrow end of the nanocrystal as the Se-rich (001') face. This directly assigns the Se-rich face as the primary growth face and allows the direct determination of the remaining faces as shown in Fig. 10C. The growth direction and growth mode matches what was seen in more detail in the Z-STEM image of an “incomplete” nanocrystal in Fig. 9.

### CHARACTERIZATION OF THE SHELL STRUCTURE OF CdSe-BASED CORE/SHELL NANOCRYSTALS

The ability of Z-STEM to simultaneously collect chemical information with structural position makes it an ideal tool for studying core/shell nanocrystals. The mass difference between the core and shell material manifests itself as a clear change in intensity in the raw images. Core-less, or “dark,” particles are

easily identified in the same manner. We chose to study CdSe-based cores/shell systems since they have been previously characterized extensively. The purpose of the shell material is to passivate surface trap sites and to energetically confine the electron and hole. For high photoluminescence yields, ideally every absorbed photon will lead to the emission of a photon. To ensure radiative electron and hole recombination, a material with a wider band gap than the core is used to coat the surface. ZnS satisfies this requirement for CdSe cores, and is typically used as the shell material due. CdSe/ZnS is also an ideal test-bed for Z-STEM because of the large mass difference between the ZnS shell and the CdSe core. This work was performed in collaboration with Quantum Dot Corporation (now part of Invitrogen) to develop core/shell nanocrystals into commercially viable fluorescent probes.

Fig. 11A shows the first Z-STEM image of a CdSe/ZnS core/shell nanocrystal, prepared using the standard literature preparation by Quantum Dot Corp. with a core size of 3.0 nm and a measured fluorescence quantum yield of 34%.<sup>[11]</sup> The nanocrystal in the center of the raw Z-STEM image features a bright core, with a fainter shell encircling it. Lattice fringes seen on the shell indicate that it is crystalline; however,



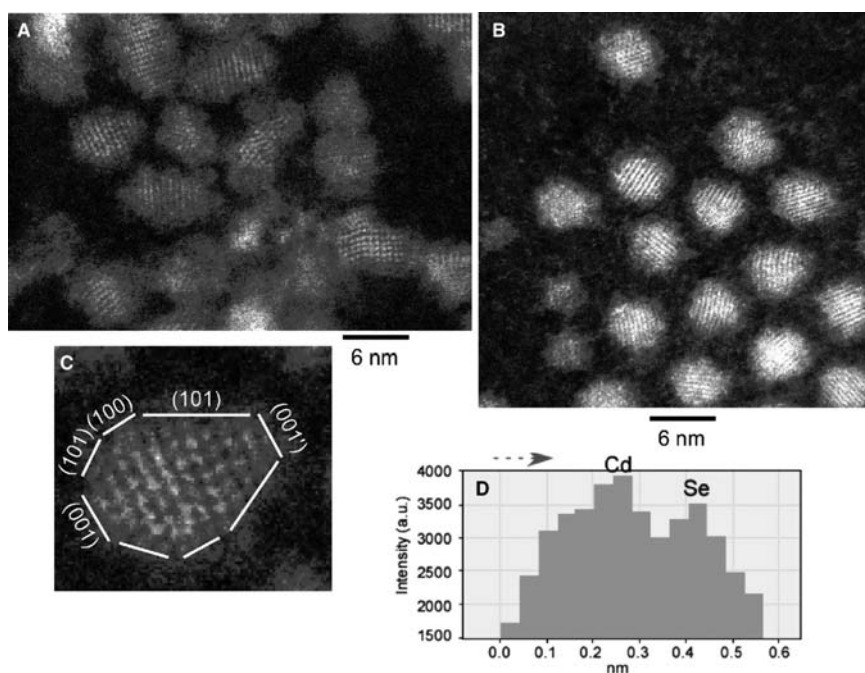


**Fig. 9** Z-STEM and shape. The intensity contrast can be used to judge the overall nanocrystal shape. (A) is a regularly shaped nanocrystal with uniform intensity, illustrated by the cartoon (B). 7C shows a drastic decrease in intensity suggesting that the nanocrystal may not be complete, as illustrated by the cartoon (D). *Source:* Reprinted with permission from *Surf. Sci. Rep.*, **2007**, *62*, 111–157. © 2007 Elsevier B. V.

the shell is not spherical in shape and coats the core unevenly. From this image, the existence of core-less particles, presumably ZnS nanocrystals that nucleated during shell growth, are also seen. These dark particles can be clearly identified by their uniform intensity across the particle. Additionally, a large amount of excess starting material can be seen associated with the core/shell nanocrystals. This is surprising to find, given that the nanocrystals were washed several times. Finally, an amorphous or semicrystalline shell can be seen on the outermost surface of the core/shells, which is most likely an oxide coating on the ZnS shell.

**Fig. 11B** shows an extreme case where the ZnS shell only grew in one direction. This could be the result of the 11% lattice mismatch between CdSe and ZnS.<sup>[20]</sup> However, a more likely cause is the varied reactivity of the different nanocrystal surfaces. The Se rich, (001') face of CdSe is unpassivated and typically the most reactive, and therefore it is the most likely place for shell growth to initiate. It is quite likely that this surface remains the most chemically reactive, since as the shell grows it remains the least passivated. This leads to a competitive growth process that often leaves the remainder of the core with little or no shell coverage, **Fig. 11C** shows a line profile along the *C*-axis of the core/shell in **Fig. 11B**, illustrating the intensity change going from shell to core due to the mass difference between the CdSe core and the ZnS shell. The interface between core and shell has been marked with a black arrow. The shell can be seen only covering one surface of the core. The large number of ZnS particles found is most

likely due to the extreme excess of ZnS precursors that were used in an attempt to force the shell to grow on all the surfaces.

In general, the problem of growing a lattice-mismatched material onto a surface has been addressed before.<sup>[45–47]</sup> When a material is grown onto another material with different lattice spacing, strain energy is created as the chemical bonds are bent and stretched. For a cubic system, the strain energy areal density,  $E_e$ , is given by Eq. (1).

$$E_e = \varepsilon^2 B h \quad (1)$$

$\varepsilon$  is defined as the in-plane strain,  $B$  is the bulk modulus for a thin film (for bulk CdSe,  $B$  is  $5.5 \times 10^{11}$  dyn/cm<sup>2</sup> at room temperature), and  $h$  is the film thickness. This thickness dependence leads to an important parameter called the critical thickness,  $h_c$ . In equilibrium, there is a maximum thickness of material that can be grown on a lattice-mismatched substrate before a dislocation forms. For growth on (100) cubic substrates,  $h_c$  is defined by Eq. (2).

$$h_c = \frac{b(1 - \nu \cos^2 \Theta_{db}) [\ln(\frac{h_c}{b}) + 1]}{8\pi(1 + \nu)f(\cos \lambda)} \quad (2)$$

In this equation,  $b$  is the Burgers vector, or the lattice constant of the defect,  $\nu$  is Poisson's ratio,  $f$  is the lattice mismatch,  $\Theta$  is the angle between the dislocation and its Burgers vector, and  $\lambda$  is the angle between the slip direction, the direction that the defect propagates

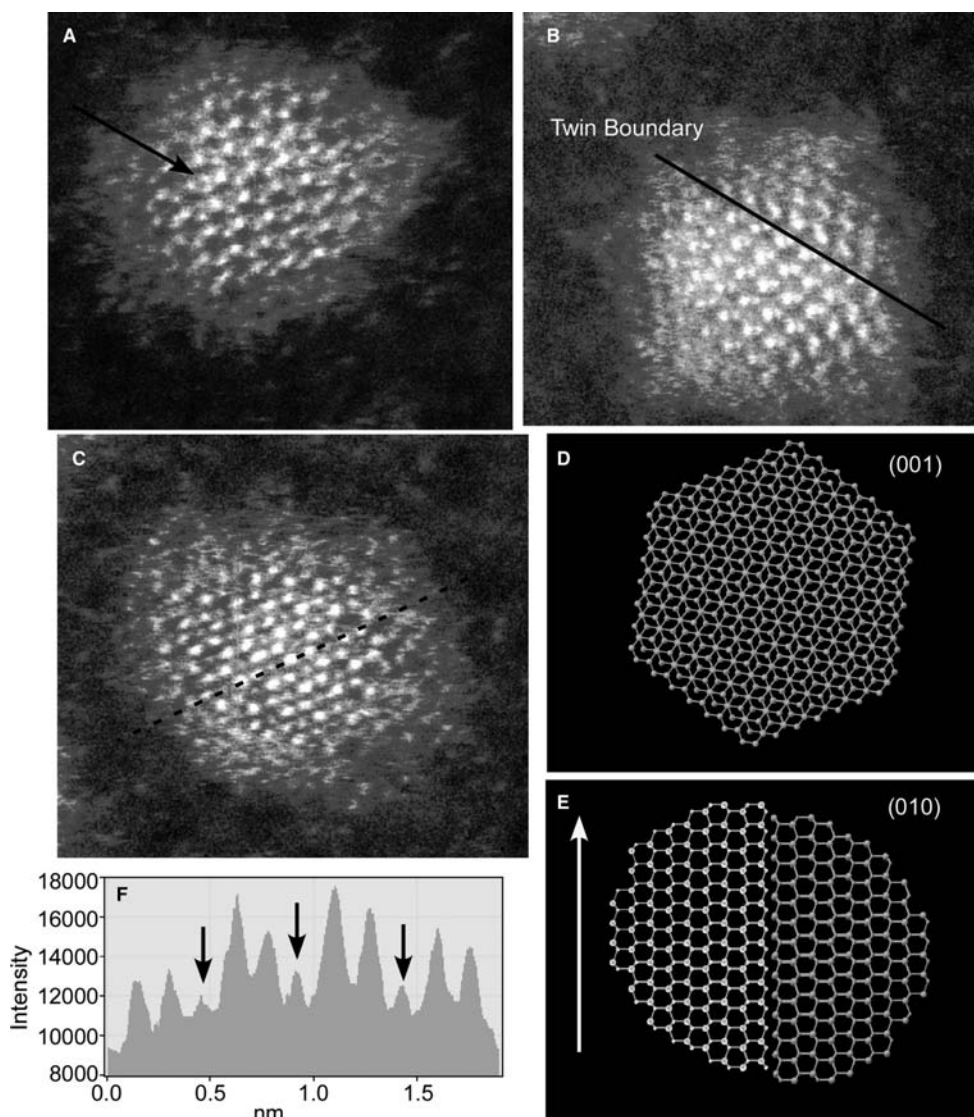


**Fig. 10** TOPO vs. TOPO/HDA. (A) and (B) are Z-STEM images of CdSe nanocrystals prepared with TOPO and a mixture of TOPO and HDA, respectively. The TOPO only nanocrystals exhibit elongated facets (C). The relative intensity differences between atomic columns (D) seen in the images was used to identify the elongated facet as the (101) facet. *Source:* Reprinted with permission from *Nano Lett.*, **2004**, 4 (7) 1279–1283. © 2004 American Chemical Society.

and a line in the interface plane.<sup>[20]</sup> The important result of this relationship is that the critical thickness is inversely related to the lattice mismatch between the materials. Since the lattice mismatch between ZnS and CdSe is nearly 11%,  $h_c$  is less than 1 nm, so only a very thin ZnS shell can be grown before dislocations form. These dislocations could act as potential recombination centers, degrading the effectiveness of the shell. To obtain thicker shells, a shell material that has a smaller lattice mismatch with CdSe can be grown initially, followed by a thin coating of the material with a larger lattice mismatch. Two potential intermediate shell materials for the CdSe/ZnS core/shell system are CdS and ZnSe, which have lattice constants that reside between those of CdSe and ZnS.

Quantum Dot Corporation chose to introduce Cd in the shelling process to “dope” the shell to improve shell coverage. This method could produce either a  $Zn_{(1-x)}Cd_xS$  shell or a CdSe/CdS/ZnS graded-shelled nanocrystal. Rutherford backscattering spectroscopy (RBS). RBS was used to confirm the addition of Cd to the shell, with an atomic ratio of Zn to Cd of 3:1, reduced from the 8:1 ratio found in the literature prepared sample.<sup>[44]</sup> This indicates that the majority of the shell contains Cd. Although the images (such as Fig. 11D) obtained do not clearly indicate an outer ZnS shell, owing to the varied reactivities of the cation precursors, it is quite likely that the majority of the zinc is coating the surface. Atomic number contrast scanning transmission electron microscopy images were

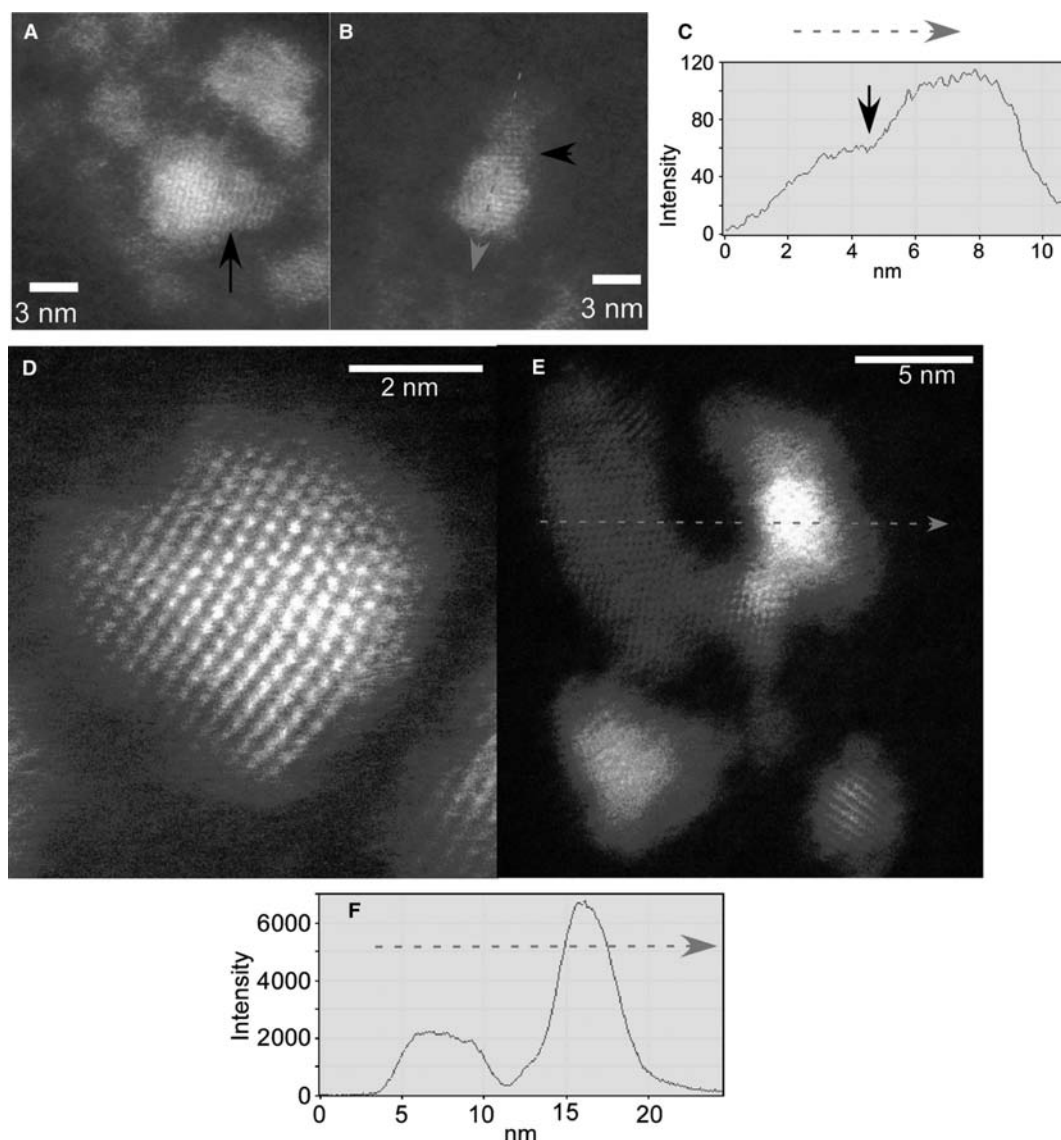


**Fig. 11** Z-STEM of core/shell nanocrystals. (A) and (B) are images of CdSe/ZnS core/shell nanocrystals showing intensity contrast between core and shell (C). The black arrow in B and C indicates the interface between core and shell. (D) has cadmium doped into the shell, which improved shell coverage but reduced the amount of intensity contrast between core and shell. (E) shows a ZnS nanocrystal along side a core/shell nanocrystal with the associated intensity profile (F). Since the ZnS nanocrystal does not have a shell, the intensity remains uniform over its entirety. The dashed arrows indicate the position where the intensity profiles (C and F) were obtained. Reprinted with permission from *Nano Lett.*, **2006**, 6 (7) 1496–1501. Source: © 2006 American Chemical Society.

obtained from the 3 nm core/shell/shell sample. This was the first core/shell/shell sample examined after the microscope was fitted with the  $C_s$  corrector. Fig. 11D shows the first lattice resolved image of a graded core/shell nanocrystal.

The square shape of the core/shell nanocrystal in 11D suggests that all sides are being coated. In comparison with the CdSe/ZnS quantum dot in Fig. 11B, the mass contrast between core and shell has diminished. This is most likely due to the structure being that of a core with a double shell of CdS/ZnS. The CdS acts

as an intermediate layer, which improved total shell coverage when compared with that of a shell consisting of only ZnS. The increased ease of coating the quantum dot surface with CdS is manifested in the fact that the majority of the nanocrystals imaged in this sample are core/shells and not CdS or ZnS nanoparticles. Although the image in Fig. 11E was not typical of the sample, it does afford a unique opportunity to show the mass contrast difference between a core/shell nanocrystal and ZnS nanocrystal. This image features a core/shell nanocrystal associated with a long ZnS

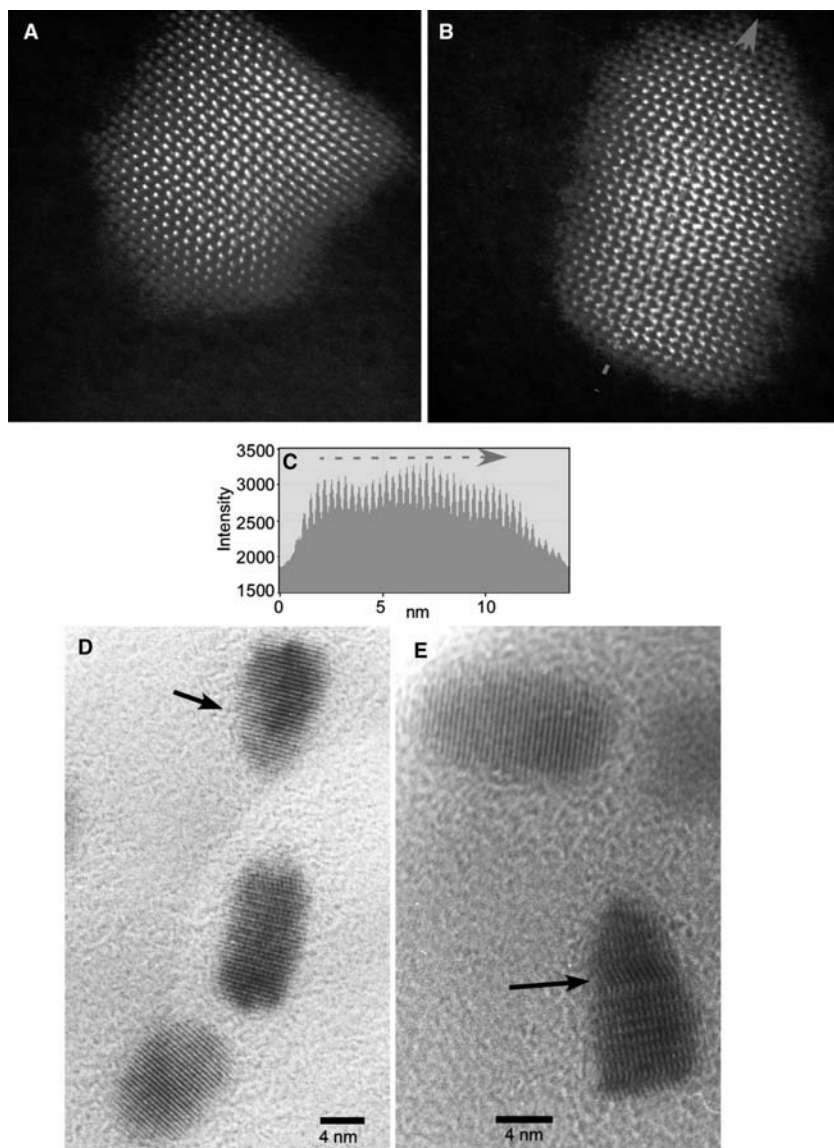


**Fig. 12** Z-STEM of Qdot 655 core/shell nanocrystals. The core/shells (A and B) have a graded CdS/ZnS shell coating and exhibit a “nano-bullet” shape. Despite the graded shell, the overall coverage continues to prefer one particular surface over the others. 12C is the intensity profile taken along the c-axis showing a fairly uniform intensity profile until it begins to decrease near the tip. (D and E) are conventional TEM images of the same material with markers indicating contrast that can be misinterpreted as the result of the core/shell structure and is typical for nanocrystal rods. *Source:* Reprinted with permission from *Nano Lett.*, **2006**, 6 (7) 1496–1501. © 2006 American Chemical Society and from *Surf. Sci. Rep.*, **2007**, 62, 111–157. © 2007 Elsevier B. V.

nanocrystal. The line profile, Fig. 11F, illustrates how easily ZnS particles can be identified by the image intensity. Since there is no change in the chemical composition, the ZnS particle has a nearly flat intensity profile, while the neighboring core/shell nanocrystal has a gaussian intensity profile. The intensity changes dramatically across the core/shell nanocrystal since the intensity is not only affected by the change in the amount of material but also by the change in chemical composition.

The double-shell method was also applied to the coating of CdSe nanorods with aspect ratios (length : width) near 2 : 1. The resulting core/shell/shell rods routinely have quantum efficiencies of 100% and are now commercially available from Invitrogen under the product names 655 and 605 AMP Quantum Dots. The initial number is the wavelength in nanometers of the emission maximum. These core/shells were coated with an AMP

polymer that makes them water-soluble.<sup>[48]</sup> AMP stands for a generalized group of amphiphilic polymers, which have hydrophobic and hydrophilic end groups. The hydrophobic tails are used to interact with the hydrophobic surfactants on the surface of the nanocrystal. In the presence of water, the polymer forms a micelle around the quantum dot with the hydrophilic head groups forming the outer surface. These groups can then be cross-linked, essentially sealing the quantum dot in a “plastic bag.”

The Z-STEM images in Fig. 12A and B show very little contrast between core and shell, since the shell is nearly all CdS. However, clear contrast can be seen between the intensities of the selenium and sulfur from the atomic dumbbells in the images. This is illustrated by the noticeable change in the appearance of the alternating dumbbells going from the center of the particle to the tip. The lesser intensity of the peaks in the atomic



dumbbell is from the anion, which in this case is the Se and S atomic columns. As the material transitions from predominantly CdSe/CdS to CdS, the anion intensity decreases to the point where only intensity from the Cd column can be seen. The abruptness of the loss of the anion intensity suggests that these particular nanorods may have a layered structure and are not an alloy.

Interestingly, the overall morphology deviates strongly from a homogeneous shell coating. The core/shell shape is that of a “bullet,” capped with a flat surface on one end while forming a point on the other. The line profile in Fig. 12C indicates very little intensity difference between core and shell. The sloping nature of the intensity profile near the tip of the nanorod is most likely due to a convolution of the lower atomic number of the shell material and the nanorod narrowing to a point. For comparison, Fig. 12D and E show two HRTEM images of the 655 AMP nanorods. The core/shell rod marked with an arrow in Fig. 12D appears to have some intensity

contrast that could be attributed to the core/shell structure. However, none of the other rods in the same image show similar of contrast. This suggests that the contrast change is more likely a chromatic aberration effect, or the result of lattice strain, than actual contrast between different materials. Further evidence that the contrast change is not related to a core/shell structure is that similar contrast changes have been seen in nanorods that do not have a shell. The arrow in Fig. 12E points to a zinc blende stacking fault similar to the ones seen in the Z-STEM images (Fig. 12A and B).

Surprisingly, the Z-STEM images of the 605 AMP core/shell nanorods, Fig. 13A and B, appear narrower and more elongated in comparison with the 655 AMP “nano-bullets.” The shell covering the (001') facet is nearly as thick as the core nanocrystal, as illustrated by the intensity profile in Fig. 13C. Additionally, this intensity profile shows a three-tiered structure that suggests three different chemical compositions. We can

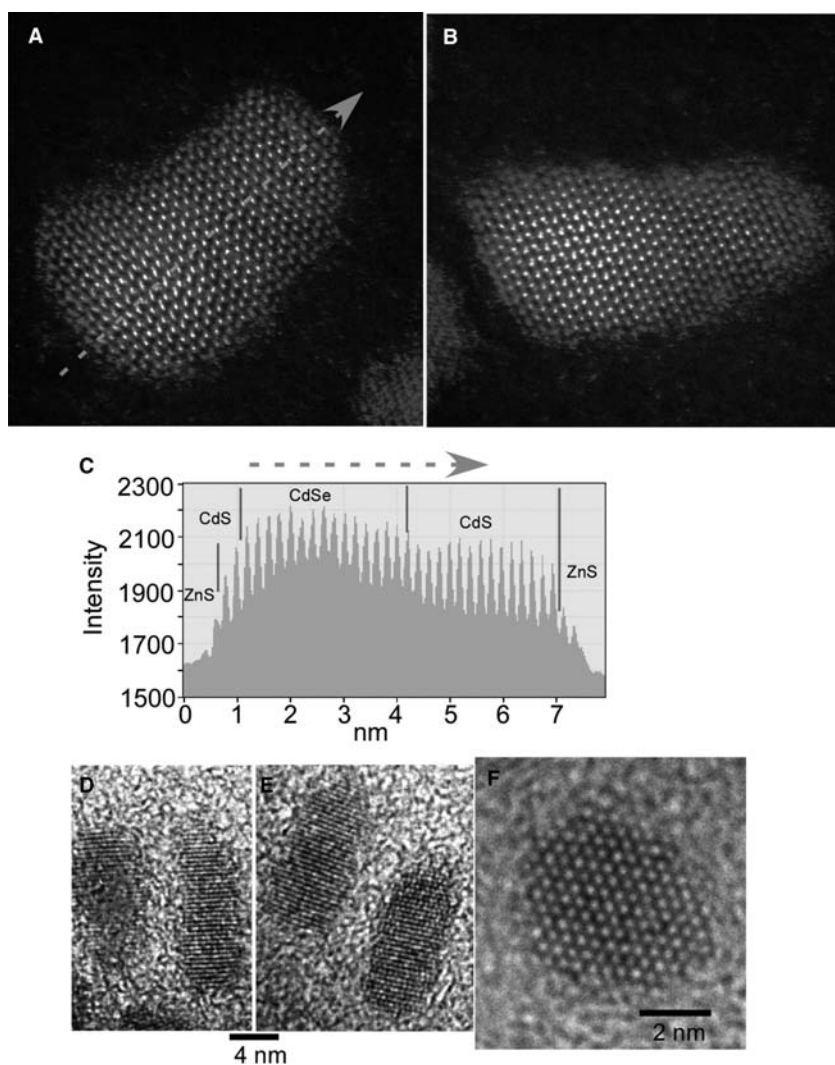


**Fig. 13** Z-STEM of 605 Qdots. (A) and (B) are Z-STEM images of graded core/shell nanocrystals with the shell material predominantly coating one surface. The graded structure can be seen in the intensity profile (C). (D–F) are conventional TEM images of the same material, with F having the c axis perpendicular to the image plane. *Source:* Reprinted with permission from *Nano Lett.*, **2006**, 6 (7) 1496–1501. © 2006 American Chemical Society and from *Surf. Sci. Rep.*, **2007**, 62, 111–157. © 2007 Elsevier B. V.

assign the highest-intensity region to the CdSe core, the intermediate region to the CdS inner shell and the edges to the ZnS outer shell. The other possibility is that the final two rows are also CdS but only covering a small portion of the surface. The filling of the  $\{101\}$  facets is not as evident in the majority of the 605 emitting core/shell rods; however, the shell material still covers the Se-rich faces preferentially. For comparison, Fig. 13D–F shows three HRTEM images of the 605 AMP core/shell nanorods. Figure 13D and E are typical TEM images of this nanorod sample, showing a rounded end and a pointed end on each of the core/shell rods. Fig. 13F is a HRTEM image of a 605 AMP nanorod aligned with the (001) face perpendicular to the TEM grid. Although the surface is not well defined, the overall shape appears asymmetrical, which is most likely due to the shell coating certain surfaces preferentially. Unfortunately, no Z-STEM images of an on-end core/shell rod have been obtained owing to the extremely low occurrence of this orientation for rod-shaped nanocrystals.

Fig. 14 shows Z-STEM images of the 605 AMP core/shell rods whose shell surfaces are clearly resolved. Several gaps and outgrowths, marked with a white oval can be seen, showing that the shell is not perfect at its surface. If tunneling of charges through the shell occurs, these defects would serve as potential trap sites due to the presence of unsatisfied bonds. However, this sample has a quantum yield of nearly 100%, indicating that the ability of an electron

or hole to tunnel to the shell surface is limited. This means that the shell surface need not be perfect, but instead that the shell only needs to cover the entire surface of the core, to effectively passivate the core.

The level of atomic detail afforded by Z-STEM can be used to identify specific nanocrystal faces of core/shell nanocrystals. This is important because the CdSe nanocrystal facets are not chemically equivalent, which may explain why the coating of the shell is not uniform. As illustrated by the cartoon in Fig. 15, once the alternating intensity pattern of the Cd and Se dumbbells is identified (Fig. 15B), we can then assign one end of the rod as the Se-rich (001') face and the other as the Cd-rich (001) face. A comparison of the image to a model of the CdSe core (Fig. 15C) can then be used to identify the remaining surfaces. The image in Fig. 15D exhibits the typical "nano-bullet" shape, with a near perfectly flat end opposite a pointed end. Using the atomic dumbbells, we can definitively assign the pointed end of the nanorod as the anion rich (001') face. This supports predictions in the literature stating that the Se-rich face is the primary growth face for the CdSe core.<sup>[23]</sup> The facets with the next highest concentration of Se surface sites are the (101') facets, located near the flat end of the "nano-bullet" (marked with a blue arrow). Interestingly, to achieve the unique bullet shape, these corner (101') facets must also grow at a faster rate than the side (100) faces. The shell appears to be at its thinnest on the Cd-rich (001) and the  $\{100\}$  surfaces, with an average coverage of a

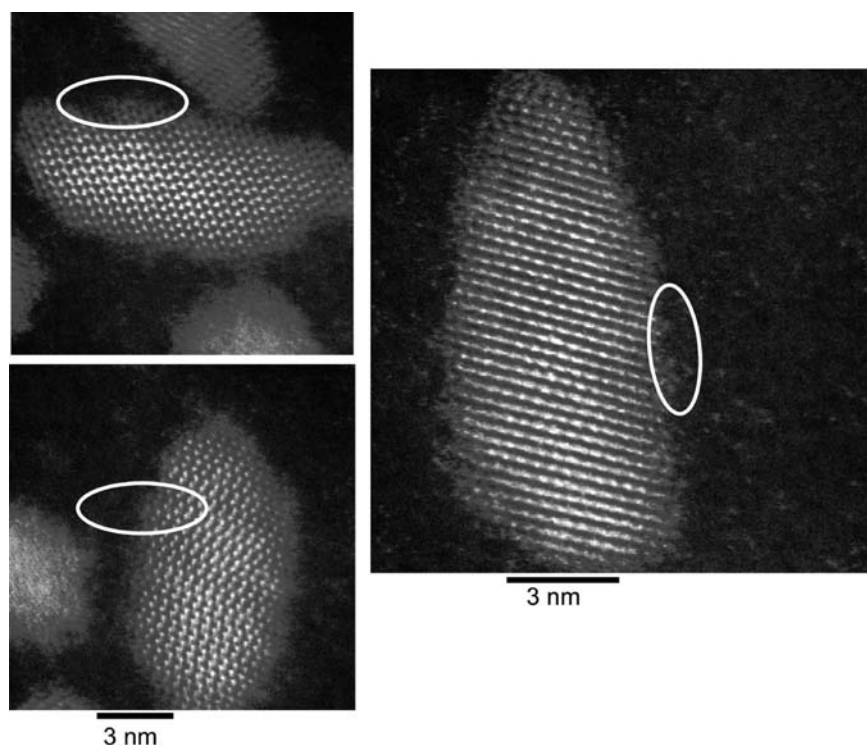


**Fig. 14** Z-STEM images of core/shell surface. Defects such as missing atomic columns can be seen on the shell surface (circled). *Source:* Reprinted with permission from *Surf. Sci. Rep.*, **2007**, *62*, 111–157. © 2007 Elsevier B. V.

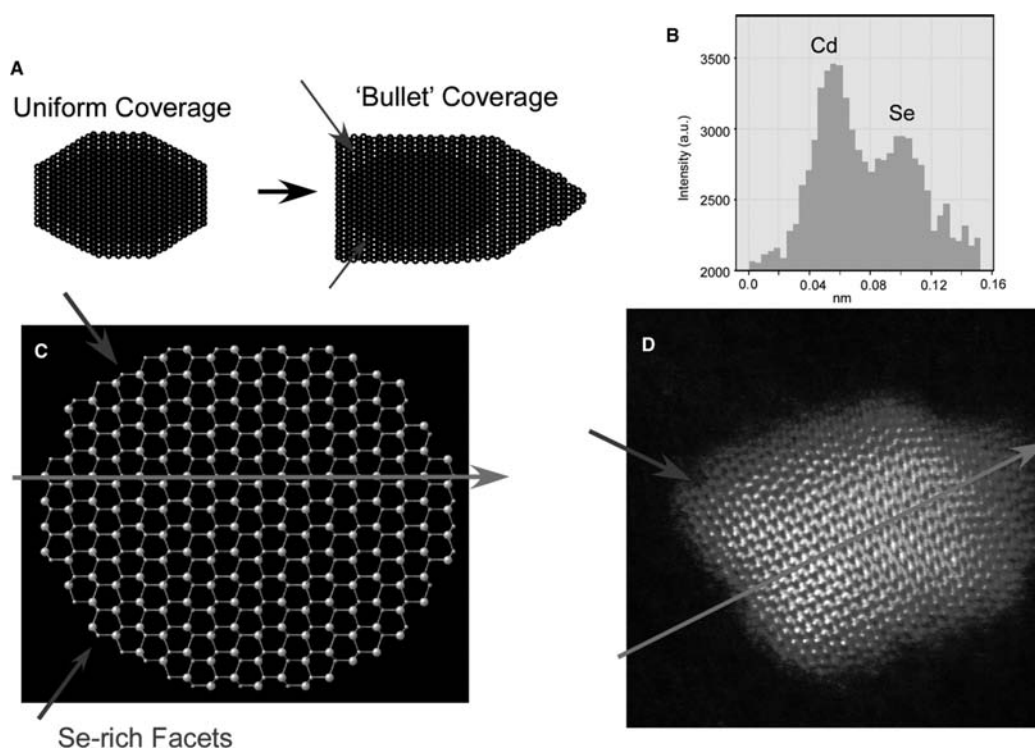


**Fig. 15** Shell Growth Model. (A) shows a cartoon illustration of the difference between the predicted core/shell structure and the obtained “nano-bullet” shape. From atomic dumbbell contrast (B) one can orientate a model (C) to an image of a core/shell nanocrystal (D). With this simple comparison, it would appear that the shell is preferentially growing on the anion rich surfaces. *Source:* Reprinted with permission from *Nano Lett.*, **2006**, 6 (7) 1496–1501. © 2006 American Chemical Society.

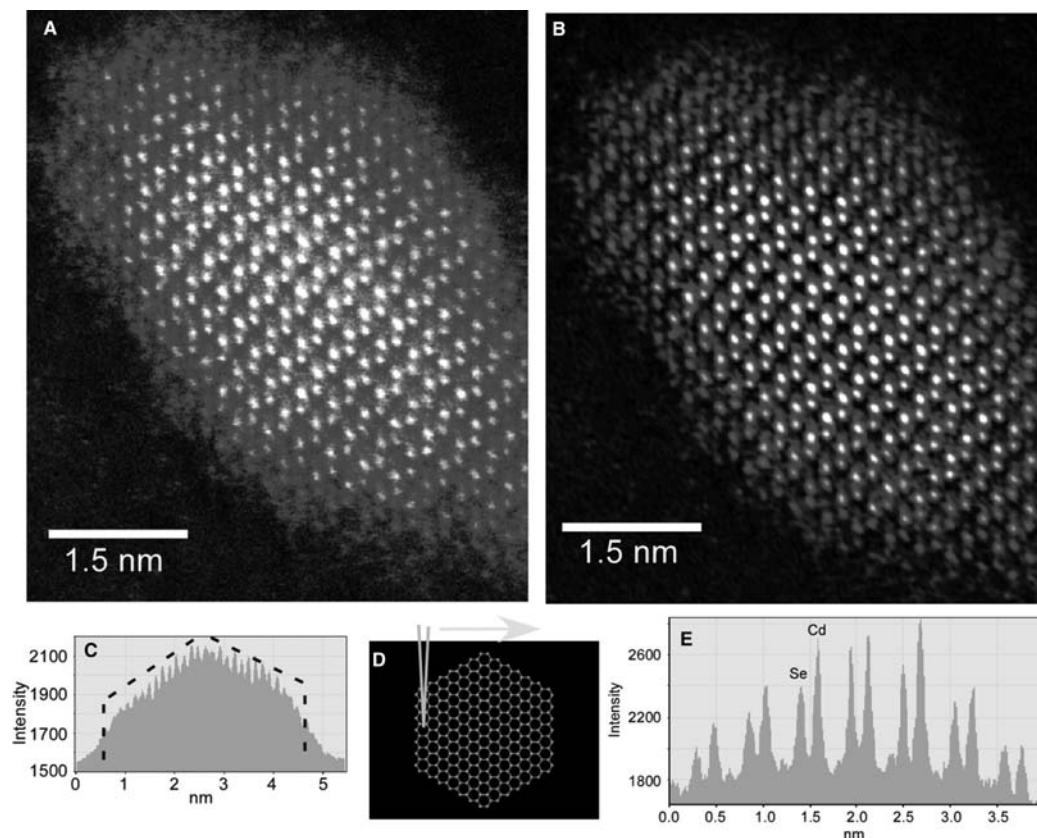
monolayer or two, while the Se-rich  $\{101'\}$  facets have about 4–5 monolayers and the  $(001')$  facet has anywhere from 6 to 15 monolayers. Thus, the shell-growth mechanism appears to select the anion surface sites preferentially.

Fig. 16 shows a CdSe/CdS core/shell nanorod oriented with the  $(010)$  face parallel to the TEM grid. The atomic dumbbells are clearly resolved in the raw image and can easily be assigned by their mass contrast. In Fig. 16B, a Fourier filter has been used to reduce the amount of noise in the image to better show the mass contrast. This rod was resting on an edge, as illustrated by the model in Fig. 16D and provides a unique opportunity to illustrate how structure in the  $z$ -direction (out of the image plane) can be obtained from the raw image. The intensity profile in Fig. 16C beautifully outlines the faceted shape of the nanocrystal surface that coincides with this orientation. Lastly, the intensity profile in Fig. 16E shows how cleanly the individual atomic columns are resolved in the image. In this single image, we can see the atomic structure, identify specific facets, and determine the core/shell rod's 3D shape.

The Z-STEM images and the near unity quantum yield of the AMP-coated core/shell nanorods suggest that shell coverage free of interfacial defects is more important than electron and hole confinement.

Presumably, in the case of ZnS, defects in the shell or a lack of complete shell coverage provide tunneling sites or surface sites for non-radiative recombination. This is supported by the result that the largest improvement in fluorescence quantum yield was realized by choosing a better lattice-matched material at the expense of electron confinement. Elimination of dark particles is also important, resulting in another 20% increase in fluorescence quantum yield. However, the role of Zn in the core/shell/shell system remains important. Core/shell rods made with only a CdS shell were found to be far less photostable than those containing Zn. The role of ZnS as a photostabilizing layer has been supported by previous work, in which CdSe cores with ZnS shells demonstrated an improved photostability over cores with a CdS shell.<sup>[22]</sup> This is most likely due to the CdS shell absorbing at 366 nm, which is the wavelength commonly used for fluorescence imaging. Since bulk ZnS absorbs at 345 nm and below, a ZnS shell should only absorb at even lower wavelengths (due to quantum confinement), making it less susceptible to photodegradation under typical experimental conditions. In this system, the benefit of a lattice-matched CdS shell has been combined with the photostability of the ZnS shell to make very bright and stable core/shell nanocrystals.





**Fig. 16** Nanocrystal Hand-stand. (A) (raw) and (B) (Fourier filtered) are Z-STEM images of a core/shell rod in the (010) orientation. The intensity profile (C) shows the shape of the nanocrystal with a facet rising out of the image plane. (D) illustrates the nanocrystal orientation relative to the electron beam (green) and scan direction (green arrow). (E) is an intensity profile from B showing atomic contrast and thickness contrast simultaneously. *Source:* Reprinted with permission from *Nano Lett.*, **2006**, 6 (7) 1496–1501. © 2006 American Chemical Society.

### Z-STEM OF $\text{CdSe}_x\text{S}_{(1-x)}$ ALLOYS

$\text{CdSe}_x\text{S}_{(1-x)}$  alloys have the potential for use as fluorescent probes when multiple emission colors are needed without resorting to changing the diameter of the nanocrystals. For example, work by Bawendi et al. illustrates the need to consider the effects of the nanocrystal's hydrodynamic radius when conducting a fluorescence imaging experiment in vivo.<sup>[49]</sup> By changing the relative amounts of the two anions, the band gap can be adjusted while maintaining the nanocrystal diameter.

Alloy nanocrystals were synthesized by using the method of Swafford, where the composition was controlled by adjusting the relative amounts of the anions found in the injection solution.<sup>[17]</sup> The composition of the nanocrystal was determined by RBS analysis on purified aliquots pulled during growth. However, although the RBS data suggests that the relative amounts of sulfur and selenium remained constant during growth, sequestering of one the anions or the nucleation of non-alloyed nanocrystals could not be

ruled out from the RBS analysis alone. Z-STEM was employed to demonstrate uniform distribution of the anions throughout the nanocrystals. If the nanocrystals exhibited a core/shell structure in the Z-STEM images, this would indicate that the elements were sequestering during growth.

Figure 17A and B show the Z-STEM images of  $\text{CdS}_{0.55}\text{Se}_{0.45}$ . Unlike the core/shell images shown earlier, there is no noticeable change in intensity across the nanocrystal. However, the nanocrystals exhibit a zinc blende structure with a large number of stacking faults that can be seen on nearly every nanocrystal. To determine whether this was a result of the alloying process or an affect of the oleic acid surfactant, CdSe nanocrystals prepared using oleic acid as the surfactant were also imaged. Figure 17C shows Z-STEM images of CdSe prepared in oleic acid. The CdSe nanocrystals are also zinc blende, unlike those produced in TOPO and appear to have the same large number of stacking faults as seen for the alloys. This suggests that the zinc blende structure and number of stacking faults is the result of the surfactant and not the alloying process.



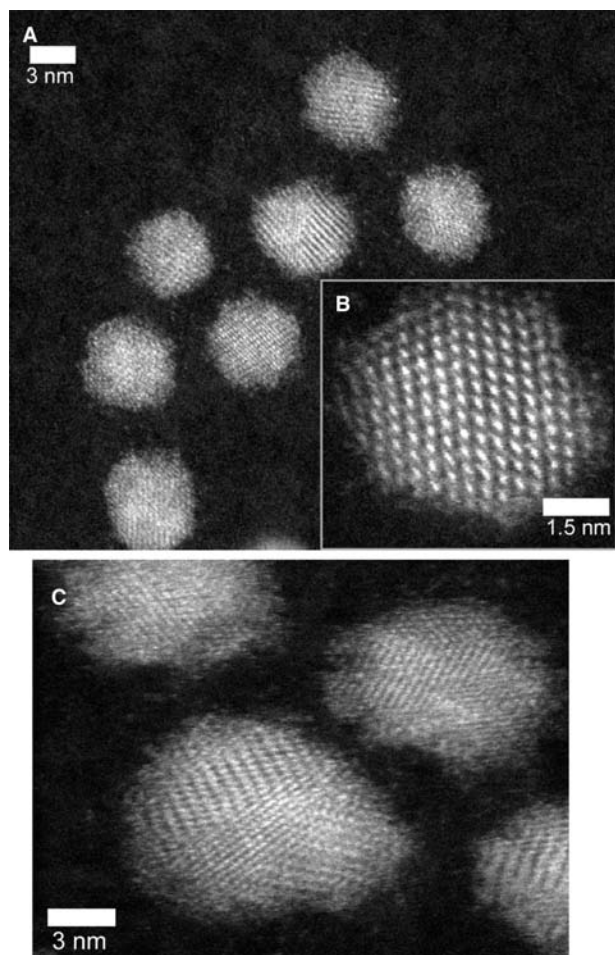


**Fig. 17** Z-STEM of CdS<sub>0.55</sub>Se<sub>0.45</sub> alloyed nanocrystal. (A) and (B) are Z-STEM images of alloyed nanocrystals showing large number of stacking fault but no contrast due to sequestering or core/shell structures. (C) is an image of CdSe nanocrystals prepared using oleic acid. In contrast to nanocrystals synthesized in TOPO/HDA, there are a large number of stacking faults and twinning, the result of the oleic acid surfactant.

## CONCLUSION

The use of aberration-corrected Z-STEM has provided a clearer understanding of the surface structure of nanocrystals and its importance in growth. For the first time, it was possible to image, with atomic-scale precision, the surface of a nanocrystal. The result of this has allowed for the accurate assignment of the nanocrystal surfaces and uses that to formulate a mechanism for nanocrystal growth and, in a similar fashion, shell growth.

From the Z-STEM images obtained and the chemistry employed, our current understanding of nanocrystal growth involves a dynamic competition between the different reactivities of the nanocrystal surface. Growth is predominantly along the C-axis

from the anion terminated surface, with a rate dependent on the amount of phosphonic acid and aliphatic amine used in the reaction. The growth of a symmetrical epitaxial shell is also hindered by the highly reactive anion-rich facets leading to certain surfaces with very little shell and others with a large excess. Homogeneous nanocrystal alloys are possible; however, the use of oleic acid produces nanocrystals with large numbers of stacking faults.

## ACKNOWLEDGEMENTS

This research was sponsored by the Office of Basic Energy Sciences, Division of Materials Sciences and Engineering, DOE grant FG02-02ER45957 and NIH RO1 EB003728-02.

## REFERENCES

1. Brus, L.E. Electron-electron and electron-hole interaction in small semiconductor crystallites: the size dependence of the lowest excited electronic state. *J. Chem. Phys.* **1984**, *80* (9), 4403–4408.
2. Murray, C.B.; Norris, D.J.; Bawendi, M.G. Synthesis and characterization of nearly monodisperse CdE (E = S, Se, Te) semiconductor nanocrystallites. *J. Am. Chem. Soc.* **1993**, *115*, 8706–8715.
3. Bruchez, M.; Moronne, M.; Gin, P.; Weiss, S.; Alivisatos, A.P. Semiconductor nanocrystals as fluorescent biological labels. *Sci. Rep.* **1998**, *281*, 2013–2015.
4. Colvin, V.L.; Schlamp, M.C.; Alivisatos, A.P. Light-emitting diodes made from cadmium selenide nanocrystals and a semiconducting polymer. *Nature* **1994**, *370* (4), 354–357.
5. Gao, X.; Cui, Y.; Levenson, R.M.; Chung, L.W.K.; Nie, S. In vivo cancer targeting and imaging with semiconductor quantum dots. *Nat. Biotechnol.* **2004**, *22* (8), 969–976.
6. Gao, X.; Yang, L.; Petros, J.A.; Marshall, F.F.; Simons, J.W.; Nie, S. In vivo molecular and cellular imaging with quantum dots. *Curr. Opin. Biotechnol.* **2005**, *16*, 63–72.
7. Goldman, E.R.; Clapp, A.R.; Anderson, G.P.; Uyeda, H.T.; Mauro, J.M.; Medintz, I.L.; Mattoussi, H. Multiplexed toxin analysis using four colors of quantum dot fluororeagents. *Anal. Chem.* **2004**, *76* (3), 684–688.
8. Huynh, W.U.; Dittmer, J.J.; Alivisatos, A.P. Hybrid nanorod-polymer solar cell. *Science* **2002**, *295*, 2425–2427.
9. Rosenthal, S.J.; Tomlinson, I.; Adkins, E.M.; Schroeter, S.; Adams, S.; Swafford, L.; McBride, J.; Wang, Y.; DeFelice, L.J.; Blakely, R.D. Targeting cell surface receptors with ligand-conjugated nanocrystals. *J. Am. Chem. Soc.* **2002**, *124*, 4586–4594.
10. Schlamp, M.C.; Peng, X.; Alivisatos, A.P. Improved efficiencies in light emitting diodes made with CdSe(CdS) core/shell type nanocrystals and a semiconducting polymer. *J. Appl. Phys.* **1997**, *82* (11), 5837–5842.

11. Manna, L.; Scher, E.; Li, L.; Alivisatos, A.P. Epitaxial growth and photochemical annealing of graded CdS/ZnS shells on colloidal CdSe nanorods. *J. Am. Chem. Soc.* **2002**, *124* (24), 7136–7145.
12. Bowen-Katari, J.E.; Colvin, V.L.; Alivisatos, A.P. X-ray photoelectron spectroscopy of CdSe nanocrystals with applications to studies of the nanocrystal surface. *J. Phys. Chem.* **1994**, *98*, 4109–4117.
13. Peng, Z.A.; Peng, X. Formation of high-quality CdTe, CdSe, and CdS nanocrystals using CdO as precursor. *J. Am. Chem. Soc.* **2001**, *123*, 183–184.
14. Peng, Z.A.; Peng, X. Mechanisms of the shape evolution of CdSe nanocrystals. *J. Am. Chem. Soc.* **2001**, *123*, 1389–1395.
15. Qu, L.; Peng, A.Z.; Peng, X. Alternative routes toward high quality CdSe nanocrystals. *Nano Lett.* **2001**, *1* (6), 333–337.
16. Yu, W.W.; Peng, X. Formation of high-quality CdS and other II-VI semiconductor nanocrystals in noncoordinating solvents: tunable reactivity of monomers. *Angew. Chem. Int. Ed.* **2002**, *41* (13), 2368–2371.
17. Swafford, L. Homogeneously alloyed cadmium sulfoselenide nanocrystals. In *Chemistry*; Vanderbilt University: Nashville, 2006.
18. Nellist, P.D.; Chisholm, M.F.; Dellby, N.; Krivanek, O.L.; Murfitt, M.F.; Szilagy, Z.S.; Lupini, A.R.; Borisevich, A.; Sides, W.H., Jr.; Pennycook, S.J. Direct sub-angstrom imaging of a crystal lattice. *Science* **2004**, *305*, 1741.
19. Shiang, J.J.; Kadavanich, A.V.; Grubbs, R.K.; Alivisatos, A.P. Symmetry of annealed wurtzite CdSe nanocrystals: Assignment to the  $C_{3v}$  point group. *J. Phys. Chem.* **1995**, *99*, 17,417–17,422.
20. Tu, K.; Mayer, J.W.; Feldman, L.C. *Electronic Thin Film Science*; Macmillan Publishing Company: New York City, 1992.
21. Peng, X.; Manna, L.; Yang, W.; Wickham, J.; Scher, E.; Kadavanich, A.; Alivisatos, A.P. Shape control of CdSe nanocrystals. *Nature* **2000**, *404* (2), 59–61.
22. Mekis, I.; Talapin, D.V.; Kornowski, A.; Haase, M.; Weller, H. One-pot synthesis of highly luminescent CdSe/CdS core-shell nanocrystals via organometallic and “greener” chemical approaches. *J. Phys. Chem. B* **2003**, *2003* (107), 7454–7462.
23. Talapin, D.V.; Koeppel, R.; Gotzinger, S.; Kornowski, A.; Lupton, J.M.; Rogach, A.L.; Benson, O.; Feldmann, J.; Weller, H. Highly emissive colloidal CdSe/CdS heterostructures of mixed dimensionality. *Nano Lett.* **2003**, *3* (12), 1677–1681.
24. Krivanek, O.L.; Nellist, P.D.; Dellby, N.; Murfitt, M.F.; Szilagy, Z. Towards sub-0.5 angstrom electron beams. *Ultramicroscopy* **2003**, *96*, 229–237.
25. Kadavanich, A.V.; Kippeny, T.C.; Erwin, M.M.; Pennycook, S.J.; Rosenthal, S.J. Sublattice resolution structural and chemical analysis of individual CdSe nanocrystals using atomic number contrast scanning transmission electron microscopy. *J. Phys. Chem. B* **2001**, *105* (2), 361–369.
26. Nellist, P.D.; Pennycook, S.J. Incoherent imaging using dynamically scattered coherent electrons. *Ultramicroscopy* **1999**, *78* (1–4), 111–124.
27. Pennycook, S.J.; Nellist, P.D. Z-contrast scanning transmission electron microscopy. In *Impact of Electron Scanning Probe Microscopy on Materials Research*; Rickerby, D., Valdre, G., Valdre, U., Eds.; Kluwer Academic Publishers: The Netherlands, 1999.
28. Borisevich, A.Y.; Lupini, A.R.; Travaglini, S.; Pennycook, S.J. Depth sectioning of aligned crystals with the aberration-corrected scanning transmission electron microscope. *J. Elect. Microsc.* **2006**, *55* (1), 7–12.
29. Varela, M.; Findlay, S.D.; Lupini, A.R.; Christen, H.M.; Borisevich, A.Y.; Dellby, N.; Krivanek, O.L.; Nellist, P.D.; Oxley, M.P.; Allen, L.J.; Pennycook, S.J. Spectroscopic imaging of single atoms within a bulk solid. *Phys. Rev. Lett.* **2004**, *92* (9), 095502.
30. Arslan, I.; Yates, T.J.V.; Browning, N.D.; Midgley, P.A. Embedded nanostructures revealed in three dimensions. *Science* **2005**, *309*, 2195–2198.
31. Yan, Y.; Chisholm, M.F.; Duscher, G.; Maiti, A.; Pennycook, S.J.; Pantelides, S.T. Impurity-induced structural transformation of a MgO grain boundary. *Phys. Rev. Lett.* **1998**, *81* (17), 3675–3678.
32. Chisholm, M.F.; Maiti, A.; Pennycook, S.J.; Pantelides, S.T. Atomic configurations and energetics of arsenic impurities in a silicon grain boundary. *Phys. Rev. Lett.* **1998**, *81* (1), 132135.
33. McGibbon, M.M.; Browning, N.D.; Chisholm, M.F.; McGibbon, A.J.; Pennycook, S.J.; Ravikumar, V.; Dravid, V.P. Direct determination of grain boundary atomic structure in SrTiO<sub>3</sub>. *Science* **1994**, *266*, 102–104.
34. Browning, N.D.; Chisholm, M.F.; Pennycook, S.J.; Norton, D.P.; Lowndes, D.H. Correlation between hole depletion and atomic structure at high-angle grain boundaries in YBa<sub>2</sub>Cu<sub>3</sub>O<sub>7-d</sub>. *Physica C* **1993**, *212* (1–2), 185–190.
35. Varela, M.; Lupini, A.R.; Benthem, K.V.; Borisevich, A.Y.; Chisholm, M.F.; Shibata, N.; Abe, E.; Pennycook, S.J. Materials characterization in the aberration-corrected scanning transmission electron microscope. *Ann. Rev. Mater. Res.* **2005**, 539–569.
36. Shibata, N.; Pennycook, S.J.; Gosnell, T.R.; Painter, G.S.; Shelton, W.A.; Becher, P.F. Observation of rare-earth segregation in silicon nitride ceramics at subnanometer dimensions. *Nature* **2004**, *428*, 730–733.
37. Borisevich, A.Y.; Lupini, A.R.; Pennycook, S.J. Depth sectioning with the aberration-corrected scanning transmission electron microscope. *Proc. Natl Acad. Soc.* **2006**, *103* (9), 3044–3048.
38. Rosenthal, S.J.; McBride, J.; Pennycook, S.J.; Feldman, L.C. Synthesis, surface studies, composition and structural characterization of CdSe, core/shell and biologically active nanocrystals. *Surf. Sci. Rep.* **2007**, *62*, 111–157.
39. Palmer, D. *Crystal Maker*; Crystal Maker Software, 1994.
40. Manna, L.; Scher, E.C.; Alivisatos, A.P. Synthesis of soluble and processable rod-, arrow-, teardrop-, and tetrapod-shaped CdSe nanocrystals. *J. Am. Chem. Soc.* **2000**, *122*, 12,700–12,706.
41. Rogach, A.L.; Kornowski, A.; Gao, M.; Eychmuller, A.; Weller, H. Synthesis and characterization of a size series of extremely small thiol-stabilized CdSe. *J. Phys. Chem. B* **1999**, *103*, 3065–3069.

42. Wei, S.; Zhang, S.B. Structure stability and carrier localization in CdX (X = S, Se, Te) semiconductors. *Phys. Rev. B* **2000**, *62* (11), 6944–6946.
43. Taylor, J.; Kippeny, T.; Rosenthal, S.J. Surface stoichiometry of CdSe nanocrystals determined by Rutherford backscattering spectroscopy. *J. Clust. Sci.* **2001**, *12* (4), 571–582.
44. McBride, J.; Treadway, J.; Feldman, L.C.; Pennycook, S.J.; Rosenthal, S.J. Structural basis for near unity quantum yield core/shell nanocrystals. *Nano Lett.* **2006**, *6* (7), 1496–1501.
45. Amano, H.; Sawaki, N.; Akasaki, I. Metalorganic vapor phase epitaxial growth of a high quality GaN film using an AlN buffer layer. *Appl. Phys. Lett.* **1985**, *48* (5), 353–355.
46. Lincot, D.; Kampmann, A.; Mokili, B.; Vedel, J. Epitaxial electrodeposition of CdTe films on InP from aqueous solutions: role of a chemically deposited CdS intermediate layer. *Appl. Phys. Lett.* **1995**, *67* (16), 2355–2357.
47. Wu, X.; Peng, Z.; Yuan, S. Interface structure of CdSe/ZnSe epilayers. *J. Appl. Phys.* **1995**, *77* (8), 3818–3822.
48. Pellegrino, T.; Manna, L.; Kudera, S.; Liedl, T.; Koktysh, D.; Rogach, A.L.; Keller, S.; Radler, J.; Natile, G.; Parak, W.J. Hydrophobic nanocrystals coated with an amphiphilic polymer shell: a general route to water soluble nanocrystals. *Nano Lett.* **2004**, *4* (4), 703–707.
49. Zimmer, J.P.; Kim, S.; Ohnishi, S.; Tanaka, E.; Frangioni, J.V.; Bawendi, M.G. Size series of small indium arsenide-zinc selenide core-shell nanocrystals and their application to in vivo imaging. *J. Am. Chem. Soc.* **2006**, *128*, 2526–2527.

# Adhesion: Cell on a Substrate

Frédéric Pincet

Laboratoire de Physique Statistique de l'Ecole Normale Supérieure, Paris, France

## INTRODUCTION

Life would not exist if the molecules involved did not interact in a very dynamical way. An equilibrium situation must not be reached and evolution has to be continual. This implies that life originates from interactions and bonds that are weak and have a short lifetime (1  $\mu$ sec to several days) because of thermal fluctuations. Living systems endure a constant competition among these molecules that bind to each other. These molecular bonds, called ligand–receptor bonds or keylock bonds, define what is known as specific interactions. All molecules interact with each other, but, if possible, will form the strongest possible bond. It can be considered that two molecules that tend to bind in many situations are able to recognize each other. This can be observed in cell adhesion when two cells adhere because of specific molecules that they express at their surfaces. In real cells, this adhesion is usually difficult to quantify because of their complex physical properties and the high number of molecules that are present at their surfaces. However, for model cells, it is possible to quantify the adhesion and to deduce molecular properties of the bonds, even for very weak bonds. Here such a model of a cell adhering to a substrate will be presented. This model will be experimentally checked by the vesicle micromanipulation technique and applied to a bond involved in embryogenesis.

## MODEL OF A CELL ADHERING ON A SUBSTRATE

Let us consider the following model where a “cell” of constant total area  $A_t$  will be seen as a capsule bearing  $N$  freely diffusing recognition sites (ligands) on its surface (Fig. 1). This cell adheres to a substrate containing complementary sites (receptors) that are not able to diffuse. The density of receptors is therefore fixed and will be called  $\rho_0$ . Apart from the ligand–receptor interactions, the cell and the substrate do not exhibit either significant repulsion (polymer-like, for instance) or attraction (van der Waals, for instance). During the adhesion process, the ligands tend to move toward the contact region to bind to receptors on the substrate.

This leads to an enrichment of ligands in the contact area  $A_c$ , where their density becomes higher than in the rest of the cell, therefore creating a bidimensional osmotic pressure that pushes the ligands away from the contact. Qualitatively, equilibrium will be reached when the attraction of the sites toward the contact zone is perfectly balanced by this osmotic repulsion.

More quantitatively, when the cell adheres to the substrate, the mechanical equilibrium represents the balance between the specific energy associated with contact formation and the cellular deformation work. For a variation  $\delta A_c$  of the contact area, it can be written:

$$W_{\text{adh}}\delta A_c + \delta w = 0 \quad (1)$$

where  $\delta w$ ,  $W_{\text{adh}}$  is the adhesion energy (positive), namely, the free energy to create a unit contact area, and  $\delta w$  is the cellular deformation work associated with the variation of contact  $\delta A_c$ . One has to be aware that the  $W_{\text{adh}}$  is not the energy necessary to bring one unit area of the initial cell surface to contact. It is more subtle: it represents the energy gained by taking an adapted area of the part of the cell that is not in contact with the substrate, concentrating the ligands to their final concentration in the contact area (this must give a unit final area), and bringing it to contact with the substrate where bonds can form.

Because the differential of the free energy  $F$  is  $dF = \delta w - SdT$  and the reaction is isothermic, one obtains  $dF = \delta w$ .

This means that at mechanical equilibrium:

$$W_{\text{adh}} = \left( \frac{\partial F}{\partial A_c} \right)_{v,T} = k_B T \left( \frac{\partial \ln Z}{\partial A_c} \right)_{v,T} \quad (2)$$

where  $Z$  is the partition function.

To obtain the value of the adhesion energy, it is therefore required to differentiate the free energy as a function of  $A_c$ .<sup>[1]</sup>

In the contact area, the ligands can be in two states, unbound or bound to a receptor. As they are energetically in the same configurations, the unbound ones and the ligands in the rest of the cell must have the same concentration,<sup>[2]</sup>  $n_u$ . The concentration of bound ligands will be noted  $n_b$ .

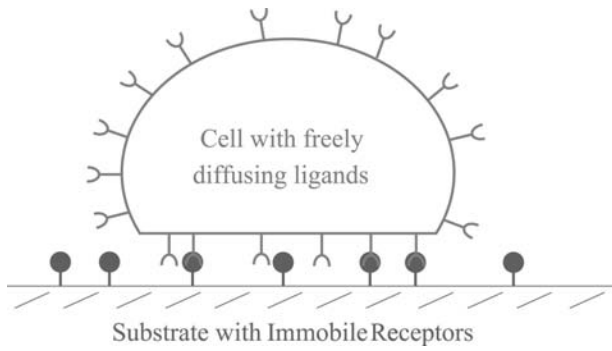


**Fig. 1** Schematic view of the model of a cell adhering to a substrate: the cell is a capsule containing freely diffusing sites, ligands, on its membrane. These sites can bind to complementary sites, receptors, on the substrate, where they are immobile.

### ADHESION ENERGY AND BIDIMENSIONAL OSMOTIC PRESSURE AT EQUILIBRIUM

To relate the adhesion energy and the bidimensional osmotic pressure, the same approach as that taken by Evans<sup>[3]</sup> will be used. The Gibbs free energy can be written  $G = \mu_b N_b + \mu_u N_u$ , where  $\mu_b$  and  $N_b$  ( $\mu_u$  and  $N_u$ ) are the chemical potential and number of the bound (unbound) ligands.

This leads directly to:

$$\delta G = \mu_b \delta N_b + N_b \delta \mu_b + \mu_u \delta N_u + N_u \delta \mu_u \quad (3)$$

Since  $\mu_b = \mu_b^0 + k_B T \ln(n_b/n_0)$  and  $\mu_u = \mu_u^0 + k_B T \ln(n_u/n_0)$ , where  $n_b = N_b/A_c$ ,  $n_u = N_u/A_t$  and  $n_0 = N/A_t$ ,

$$N_b \delta \mu_b = k_B T N_b (\delta n_b)/n_b = k_B T A_c \delta n_b \quad (4)$$

and, similarly,

$$N_u \delta \mu_u = k_B T N_u (\delta n_u)/n_u = k_B T A_t \delta n_u \quad (5)$$

Also, the chemical equilibrium can be written:

$$\mu_u = \mu_b \quad (6)$$

and the conservation of the total number of ligands  $N = N_u + N_b = A_t n_u + A_c n_b$ . Differentiating these last two expressions gives

$$\delta N_u = -\delta N_b \quad (7)$$

and

$$n_b \delta A_c + A_c \delta n_b + A_t \delta n_u = 0 \quad (8)$$

Inserting Eqs. (4)–(8) into Eq. (3) considerably simplifies  $\delta G$ :  $\delta G = -n_b k T \delta A_c$ . The expression of  $W_{adh}$  follows:

$$W_{adh} = n_b k T \quad (9)$$

This relation was derived in the mid-80s<sup>[3,4]</sup> and means that the adhesion energy equals the bidimensional osmotic pressure. This kind of relation between these two quantities could be expected because, as mentioned above, the adhesion energy tends to pull the ligands toward the contact area and the osmotic pressure (entropy) pushes them away. At equilibrium, the induced incoming and outgoing fluxes must balance each other and therefore the adhesion energy must be related to the osmotic pressure.

From Eq. (6), one gets

$$n_f = n_b \exp((\mu_b^0 - \mu_u^0)/kT) \quad (10)$$

$(\mu_b^0 - \mu_u^0)$  has to depend on the binding energy  $e_b$ . Thus, it would seem at first sight that using Eq. (9), one can deduce  $e_b$  from  $W_{adh}$ . This turns out to be incorrect because to know the exact expression of  $(\mu_b^0 - \mu_u^0)$ , other information about the interaction is needed. For instance, the naive approach where  $\mu_b^0 - \mu_u^0 = e_b$  is wrong (it can be seen that Eqs. (9) and (10) are then not compatible for  $e_b = 0$ ).

To circumvent this problem, a simple model of the ligand–receptor interaction is needed.

### MACROSCOPIC ADHESION ENERGY AND MOLECULAR BINDING ENERGY

To schematize the interaction, it will be considered that around each receptor of the substrate, there is a molecular trapping area  $\alpha$ , meaning that a ligand will be bound only if it is within this area  $\alpha$  surrounding the receptor (Fig. 2).<sup>[5]</sup> It will also be assumed that the trapping areas of the different receptors cannot overlap. The total number of receptors in the contact zone is  $\rho_0 A_c$ , which means that the area of the total trapping zone is  $A_b = \alpha \rho_0 A_c$ . The ligands within  $A_b$  are bound to a receptor, those in the rest of the cell, no matter whether or not they are in the contact zone, are unbound. The internal energy of a given configuration

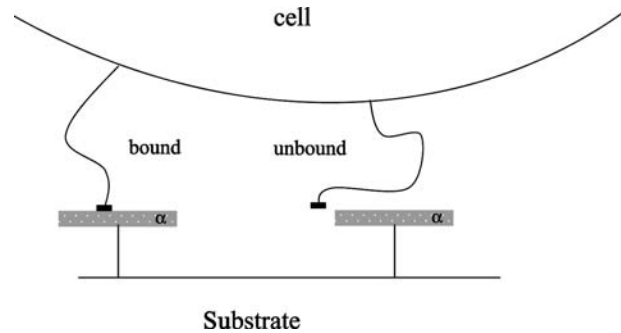


**Fig. 2** Model of the ligand–receptor interaction: if the ligand is within the attraction area  $\alpha$  of the receptor, it is bound (left ligand). Otherwise, it is unbound (right ligand).

with  $n$  ( $0 \leq n \leq N$ ) ligands in the trapping zone and  $N - n$  ligands in the rest of the cell is  $-ne_b$ . Therefore, the partition function of the system can be written:

$$\begin{aligned}
 Z &= \sum_{n=0}^N \frac{N!}{n!(N-n)!} A_b^n (A_t - A_b)^{N-n} e^{ne_b/k_B T} \\
 &= (A_t + A_b(e^{e_b/k_B T} - 1))^N \quad (11)
 \end{aligned}$$

where  $k_B T$  is the thermal energy.

Hence, the free energy is:

$$F = -Nk_B T \ln(A_t + A_b(e^{e_b/k_B T} - 1)) \quad (12)$$

$W_{adh}$  is directly derived from Eq. (2):

$$W_{adh} = N\alpha\rho_0 k_B T \frac{(e^{e_b/k_B T} - 1)}{(A_t + \alpha\rho_0 A_c(e^{e_b/k_B T} - 1))} \quad (13)$$

Results that could have been intuitively anticipated can be deduced from Eq. (13):

1.  $W_{adh}$  decreases when the contact zone increases because the “reservoir” made by the outer part of the cell becomes relatively smaller as compared to  $A_c$ .
2. When the number of receptors in the contact zone is small,  $W_{adh}$  is independent of  $A_c$ . This is the linear regime where the fraction of bound ligands is small.
3. When  $e_b$  is large, all the ligands are bound to receptors and, as expected from Eq. (9),  $W_{adh} = Nk_B T/A_c$ .

One may note that there is a strong limitation of this model, which is to allow several ligands to be bound to the same receptor. In practice, this is usually not a problem, but it can happen that when there are too few receptors and the binding energy is large, the number of bound ligands and therefore  $W_{adh}$  will be overestimated. Also, any cooperative effects among the ligand molecules have been neglected. In a system where these problems arise, numerical simulations seem to be the best way to relate  $W_{adh}$  and  $e_b$ .

This second approach (model of a trapping area) is compatible with Eq. (9) because the latter can be derived from Eq. (13). The average number of bound ligands  $\langle n \rangle$  is:

$$\begin{aligned}
 \langle n \rangle &= \frac{\left( \sum_{n=0}^N n \frac{N!}{n!(N-n)!} A_b^n (A_t - A_b)^{N-n} e^{ne_b/k_B T} \right)}{Z} \\
 &= \frac{NA_b e^{e_b/k_B T}}{A_t + A_b(e^{e_b/k_B T} - 1)} = \frac{A_c W_{adh}}{k_B T} \quad (14)
 \end{aligned}$$

Since  $n_b = \langle n \rangle/A_c$ , Eq. (14) is the same as Eq. (9).

Therefore, Eqs. (9) and (13) give a complete description of the ligand distribution at equilibrium and allow one to directly deduce the molecular binding energy from the total adhesion energy if the trapping area  $\alpha$ , the total number of ligands  $N$ , and the density of receptors  $\rho_0$  are known.

## EXPERIMENTAL VERIFICATION OF THE MODEL

To test this model, a suitable technique is based on vesicle adhesion measurement by micromanipulation.<sup>[6]</sup> It consists in holding a slightly deflated 10- to 30- $\mu\text{m}$  vesicle in a micropipette with a controlled aspiration. At the start of the experiment, the shape of the vesicle is a segment of sphere outside of the pipette and a cylindrical portion inside the pipette (which ends in an hemisphere of radius equal to the inner radius of the pipette,  $r_p$ ). The knowledge of the initial diameter of the vesicle, the length of cylindrical part, and the pipette inner diameter allows one to determine the surface and volume of the vesicle. Facing the vesicle is the substrate with a known geometry. For instance, in Fig. 3 is shown the case of a vesicle facing a bead. The vesicle is then moved and placed in tangential contact with the substrate. If adhesion occurs, e.g., through weak ligand–receptor bonds, the vesicle will stretch following the shape of the substrate in order to increase the contact area. The volume and surface of the vesicle remain essentially constant throughout the whole process. Therefore, adhesion requires the volume and surface of the vesicle outside the pipette to be larger than it originally was. This is achieved by a decrease of the projected length inside the pipette. The adhesion energy can then be deduced through the Young–Dupr  equation:

$$W_{adh} = \gamma(1 - \cos \theta) \quad (15)$$

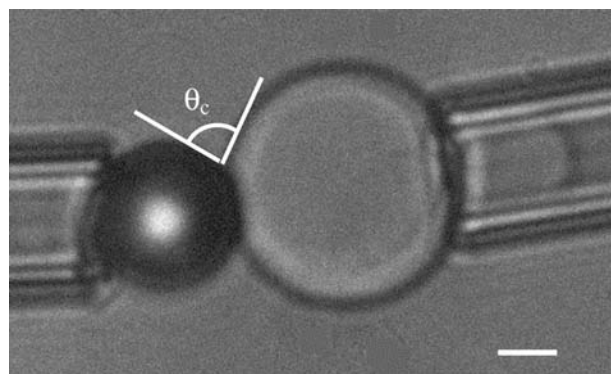


**Fig. 3** Micromanipulated vesicle in contact with a bead held by a micropipette. The bar represents 5  $\mu\text{m}$ . The measurement of the contact angle  $\theta$  directly gives the adhesion energy through the Young–Dupr  equation [Eq. (15)].

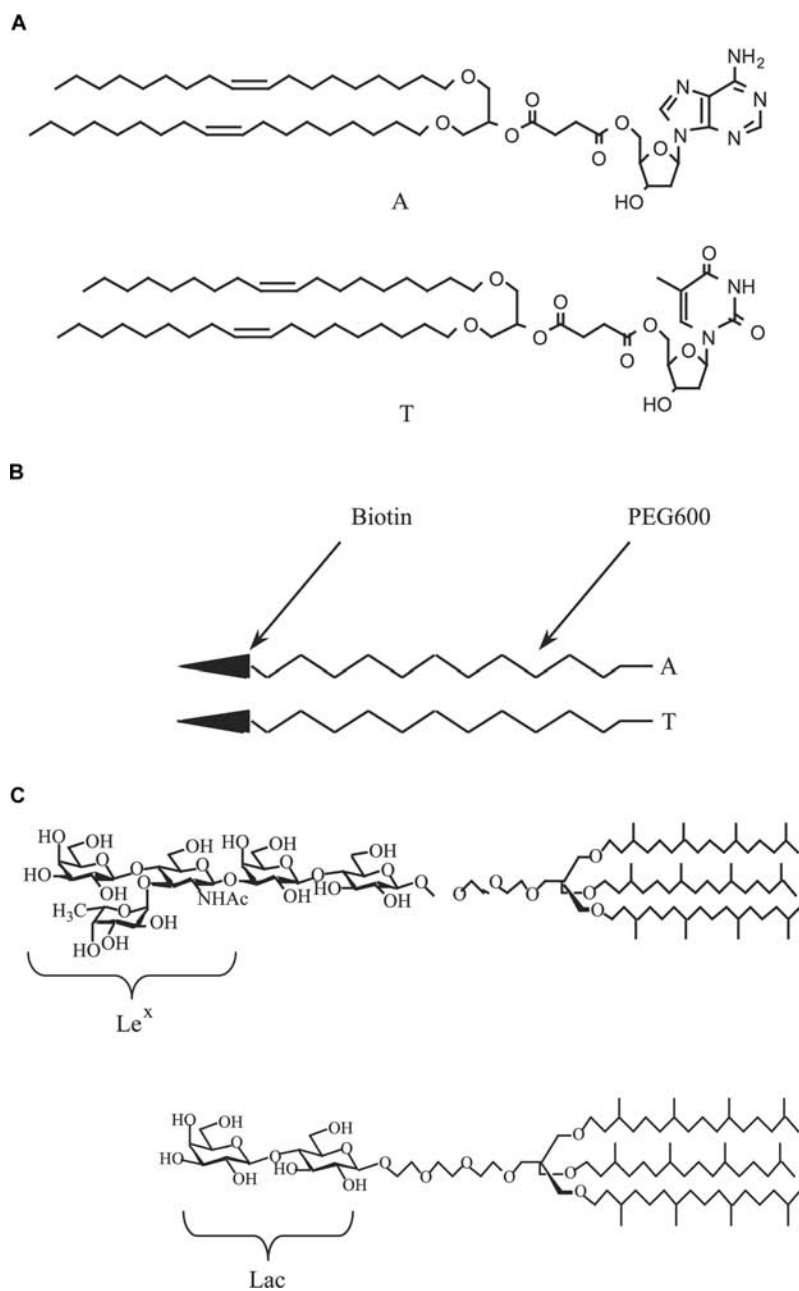


**Fig. 4** Structures of the functionalized molecules used in the adhesion experiments. (A) Lipids with two unsaturated chains with 18 carbons to ensure the fluidity of the vesicle membranes and either adenosine (top) or thymidine (bottom) in the polar head. Vesicles containing 10% of either of these lipids and 90% of a common neutral lipid (SOPC) were used in the vesicle-bead adhesion experiments. (B) Heterofunctional molecules containing a PEG chain with a biotin at one end and either adenosine (top) or thymidine (bottom) at the other end. These molecules were grafted on superavidin-coated beads that were used for the vesicle-bead adhesion experiments. (C) Top: The Lewis X ( $Le^x$ ) determinant is a trisaccharide ( $Gal\beta 1 \rightarrow 4 [Fuc\alpha 1 \rightarrow 3] GlcNAc$ ). In this lipid, it is covalently bound to three hydrophobic chains. To ensure good accessibility of the  $Le^x$  groups for interaction, they were provided with translational and orientational mobilities by branching the chains (this keeps the layers in a fluid state by hindering their crystallization) and by means of a flexible spacer between the chains and the  $Le^x$ . Bottom: the same lipid without the  $Le^x$  group.

where  $\theta$  is the contact angle,  $W_{adh}$  is the adhesion energy as defined above, and  $\gamma$  is the tension of the vesicle, which is obtained by applying the Laplace equation to the outer part of the vesicle and to the hemisphere at the tip of the cylinder inside the pipette:

$$\gamma = \frac{r_p \Delta P}{2(1 - r_p c)} \quad (16)$$

Here  $c$  is the average curvature of the vesicle and  $\Delta P$  is the aspiration (i.e., the difference in pressure between the outside and inside of the pipette).

Combining Eqs. (15) and (16) gives:

$$W_{adh} = \frac{r_p \Delta P}{2(1 - r_p c)} (1 - \cos \theta) \quad (17)$$

It is possible to obtain an accurate value of  $W_{adh}$  by plotting  $\Delta P$  as a function of  $G$ :

$$G = \frac{r_p (1 - \cos \theta)}{2(1 - r_p c)} \quad (18)$$

The slope of the graph is then exactly  $W_{adh}$ . To make sure the adhesion process is reversible, it is necessary to make cycles of decreasing-increasing aspiration

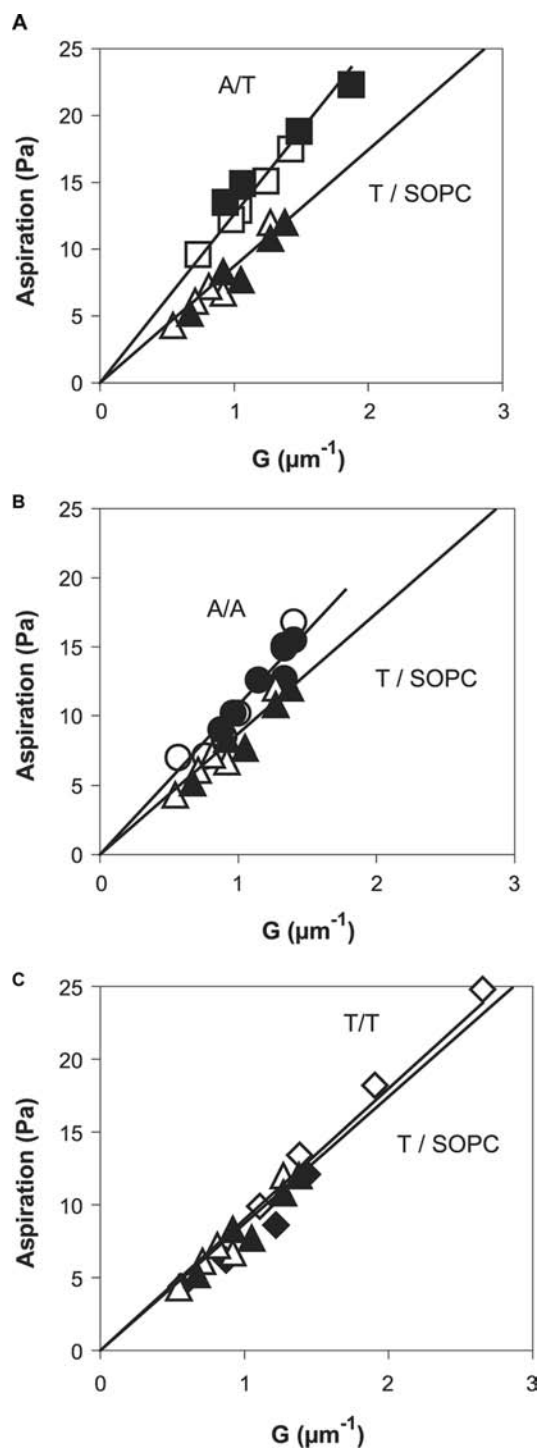


**Fig. 5** Aspiration pressure as a function of  $G$  [cf. Eq. (18)] for a specific interaction and comparison with the non-specific case T/SOPC (control). According to Eq. (3), the slopes are equal to  $W_{adh}$ . The solid lines are fits forced through zero and they roughly represent the adhesion energy. However, the values reported in Table 1 are averages from fits not forced through zero and in which the increasing pressure is treated separately from the decreasing one. Closed (open) symbols correspond to the increase (decrease) of the aspiration pressure. (A) A bead–T vesicle, (B) A bead–A vesicle, (C) T bead–T vesicle.

pressure. It will not work in the case of strong bonds with lifetimes longer than the experimental characteristic time: the membrane is then pinned on the substrate and the receding contact angle will be larger than the advancing one. Therefore, to test the model, it is necessary to use weak bonds with well-known binding energies. Nucleosides such as adenosine and thymidine are good examples of such bonds.<sup>[7,8]</sup> For this purpose, lipids carrying one nucleoside (adenosine, A, or thymidine, T) as a polar headgroup were synthesized (Fig. 4A). Giant vesicles were formed by hydrating a lipid mixture of stearyl-oleoylphosphatidylcholine (SOPC)/nucleoside lipid (9/1) (after evaporation from chloroform solution) in 320 mOsm sucrose solution.<sup>[9]</sup> The vesicle suspension was added to an aqueous glucose solution chamber of a slightly higher osmolarity (360 mOsm) than that of the vesicle in order to deflate it and make it micromanipulable.

The substrates were superavidin-coated polystyrene beads purchased from Bangs Labs. The average area per attachment site for biotin was of a few hundreds of nanometers squared per effective binding site. To coat them with nucleosides, a polyethylene glycol (PEG) spacer arm was dissymmetrically functionalized at one end with biotin, and at the other end with a nucleoside (A or T) (Fig. 4B). The beads were incubated in water (50  $\mu\text{g}/\text{ml}$ ) with one of these heterobi-functionalized PEG arms (1 mg/mL) for 1 day. The contact angle was measured for several tension values of the flaccid vesicle membrane by decreasing the aspiration and then increasing it to check for the reversibility of the adhesion. This decreasing/increasing aspiration process was repeated several times on the same vesicle/bead couple, and, as expected, it was observed that this adhesion was reversible within the experimental error.

Four adhesion situations were investigated: A bead–A vesicle, T bead–T vesicle, T bead–A vesicle, and A bead–T vesicle. A control experiment was performed in which the vesicle was made of only SOPC and adhered to a T-coated bead. It turns out that the adhesion measured in the control experiment cannot be neglected, meaning that there is a non-specific adhesion that has to be subtracted from the measurements to obtain the actual value of  $W_{adh}$  due to the bonds. Fig. 5 shows the aspiration pressure as a function of  $G$  for the different cases. The resulting values for  $W_{adh}$ , reported in Table 1, are independent of the vesicle size.

Given the experimental error, the A bead–T vesicle and T bead–A vesicle systems have the same adhesion energy, as expected. It may be observed that the specific adhesion energies follow the increasing order:  $W_{adh}(T/T) < W_{adh}(A/A) < W_{adh}(A/T)$ . This is consistent with the data reported in the literature.<sup>[7,8]</sup>



**Table 1** Adhesion energy values ( $W$ ) averaged, as indicated in Fig. 5, from at least two separate experiments and six cycles

	A bead–T vesicle	T bead–A vesicle	A bead–A vesicle	T bead–T vesicle	T bead–SOPC vesicle
$W$ ( $\mu\text{J}/\text{m}^2$ )	12.0	12.9	9.9	9.3	8.6
$W_{\text{adh}}$ ( $\mu\text{J}/\text{m}^2$ )	3.4	4.3	1.3	0.7	

The error is  $\pm 1 \times 10^{-6} \text{ J m}^{-2}$ .  $W_{\text{adh}}$  is equal to  $W - W_{\text{nspe}}$ , where  $W_{\text{nspe}}$  is the T bead–SOPC vesicle adhesion energy.

The short lifetime of the bonds is illustrated by the small fraction of occupied bead sites (5%) that can be estimated from the specific adhesion energy, the known bond energy, and the bead site density.

By using Eq. (13) one directly obtains  $e_b$  from the measured specific adhesion energy values if  $\rho_o\alpha$  is known. As the same grafting technique was used for the A and T beads,  $\rho_o\alpha$  should also be the same in all the cases and is expected to be of the order of  $10^{-4}$ . We can therefore try to find a value that conciliates the four types of adhesion data (A/T, T/A, A/A, T/T).  $\rho_o\alpha = 2.4 \times 10^{-4}$  gives values that are in closest agreement with the known binding energy values.<sup>[7,8]</sup> This value for  $\rho_o\alpha$  seems reasonable because the  $\alpha$  should be of the order of a fraction of the polar head of the lipid (a few tenths of nanometers squared) and of the  $\rho_o$  order of  $10^{15}$  molecules/ $\text{nm}^2$ . The accuracy on  $\rho_o\alpha$  can be estimated from Table 2 where the binding energy values assuming different values of  $\rho_o\alpha$  near the best one are given.

Experimentally, the equilibrium seems to be reached in less than a minute for each change of aspiration pressure. This result may seem surprising because it generally takes about 15 min for lipids to diffuse around a giant vesicle. Given  $W_{\text{adh}}$  and Eq. (10), the enrichment is around 1% at the true equilibrium obtained within 15 min. This negligible amount is within the experimental error of  $W_{\text{spe}}$ . This was fully checked experimentally as the measured contact angle did not vary significantly for 20 min at a given aspiration pressure. In this approximation, equilibrium can be obtained locally because of the excess of sites on the vesicle, and lateral diffusion does not bring significant change. The local equilibrium time is typically the one needed for a lipid to explore an area  $1/\rho_o$ , which is less than a second. This explains the fast

equilibrium and why the observed hysteresis is not stronger than for non-functionalized vesicles.<sup>[10]</sup> In contrast, if there were more sites on the bead or less sites on the vesicle, the diffusion of the vesicle sites toward the contact region would noticeably change the equilibrium time.

Therefore, the description relating adhesion energy measurements to binding energies through Eq. (13) is satisfactory and can be applied to other systems. The main limitation is the requirement to know  $\rho_o\alpha$  because it is not easy to obtain, but numerical simulations may provide good estimates in some cases. The vesicle micromanipulation technique is also a good approach to measure binding energies in this way. The precision of the technique is given by the dispersion of the adhesion energy data. In the case of weak bonds like A/T where this dispersion is seen in Table 2, the error is about  $0.5k_B T$ .

## A BIOLOGICALLY RELEVANT APPLICATION OF THE APPROACH

Molecular features governing the selectivity in cell–cell recognition and adhesion are key elements to understand morphogenesis and organogenesis. All living organisms are characterized by the presence of glycoproteins and glycosphingolipids (GSLs) on the cytoplasmic membrane. Carbohydrate chains, being exposed structures at the cell surface, should play an essential role in early events of cell–cell recognition. Indeed, they have firmly been recognized as interaction sites in cell adhesion processes such as leukocyte recruitment or host–pathogen interaction. Such events are commonly attributed to lectin or lectinlike proteins and the corresponding specific carbohydrate ligands. It has been suggested only a decade ago that specific carbohydrate–carbohydrate interactions may also play this important role.<sup>[11]</sup> Several direct measurements of adhesion between surfaces decorated with glycolipids have been reported in the past.<sup>[12–18]</sup> These strong adhesions, obtained through various techniques (surface force apparatus, osmotic stress method, and vesicle micromanipulation), were due to van der Waals or other non-specific forces. However, some carbohydrate–carbohydrate interactions found in biological processes, have been proposed to be specific.<sup>[11,19,20]</sup> One of them, the Lewis<sup>x</sup> determinant

**Table 2** Binding energy values ( $e_b$ ) as deduced from Eq. (17) for different values of  $\rho_o\alpha$ 

$\rho_o\alpha$	$1.9 \times 10^{-4}$	$2.4 \times 10^{-4}$	$3.1 \times 10^{-4}$	Literature values
A/T	2.9	3.2	3.4	3.6
T/A	3.1	3.4	3.6	3.6
A/A	2.0	2.3	2.5	1.9
T/T	1.5	1.7	1.9	1.5

The binding energy values can be compared to the literature values (right column).

(Le<sup>x</sup>) has been identified as presumably playing a biological role by means of intermembrane interactions. According to current hypothesis, it has a calcium-mediated specific interaction with itself.

Le<sup>x</sup> has been shown to be involved in murine and human embryogenesis. This carbohydrate is present on the cell membrane in the polar headgroup of glycolipids. It is not expressed at the cell surface until the eight-cell stage, shows maximal expression at the morula stage of mouse embryogenesis, and declines after compaction.<sup>[21,22]</sup> This compaction stage could be inhibited either by anti-Le<sup>x</sup> antibodies, Le<sup>x</sup> itself, or by inactivating the calcium with Ethylenediaminetetraacetic Acid (EDTA). As Le<sup>x</sup> is not charged, the role of the calcium is not of an electrostatic nature. These results<sup>[23,24]</sup> led the authors to propose a calcium-mediated Le<sup>x</sup>–Le<sup>x</sup> specific homotypic interaction as a basis of cell adhesion in preimplantation embryos and in various tumour cells. Other observations also strongly suggest that Le<sup>x</sup>–Le<sup>x</sup> interactions exist in the presence of Ca<sup>2+</sup>.<sup>[25–28]</sup>

The approach described above made it possible to conduct the first direct quantitative measurements of this putative interaction in a physicochemically well-defined system and in conditions similar to the natural environment of the glycolipid, i.e., lipid bilayers. This was done through the adhesion between two giant vesicles functionalized with synthetic glycolipids.

The Le<sup>x</sup> determinant is a trisaccharide, which, in classical natural sphingolipids, is attached to the ceramide through a lactose group. For this study, a lipid<sup>[29]</sup> with a Le<sup>x</sup> headgroup attached to hydrophobic chains via a “spacer” group to ensure its mobility was synthesized (Fig. 4C). In this synthetic glycolipid, a rather low solubility in water together with good bilayer cohesion was obtained by using three hydrophobic chains instead of two as in ceramide. To ensure good accessibility of the Le<sup>x</sup> groups for interaction, they were provided with translational mobility by branching the chains. This hinders the bidimensional crystallization of the chains and keeps the layers in a fluid state. Orientational mobility was provided by a flexible spacer between the chains and the Le<sup>x</sup>. This allowed the Le<sup>x</sup> groups to take the exact orientation and position for which the specific interaction can occur.

For the controls, a glycolipid with the same features but without Le<sup>x</sup> was synthesized (Fig. 4C) that will be referred to as Lac lipid.

Giant vesicles were formed exactly in the same way as for the A and T vesicles by lipid hydration (after evaporation from chloroform solution) in 320 mOsm sucrose solution. The Le<sup>x</sup>-functionalized vesicles, hereinafter referred to as Le<sup>x</sup> vesicles, were made from a mixture of SOPC and the synthetic Le<sup>x</sup> lipid (90 : 10 mol ratio). Control vesicles were made of SOPC and Lac lipid (90 : 10 mol ratio) and will be called Lac vesicles.

Two vesicles were transferred into another chamber filled with salt solution (either NaCl or CaCl<sub>2</sub> at 360 mOsm). As in the previous experiment, both vesicles were micromanipulated into tangential contact. One of the vesicles represents the substrate. It is strongly aspirated so that its spherical shape is not modified throughout the whole process. The contact angle was measured for several tension values of the other vesicle membrane by decreasing the aspiration and then increasing it to check the reversibility of the adhesion.

The experiments consisted in comparing the adhesion of two Le<sup>x</sup> vesicles in NaCl and in CaCl<sub>2</sub> (Le<sup>x</sup>/Le<sup>x</sup> experiments). As calcium is sometimes known to produce peculiar effects on bilayer interactions,<sup>[30]</sup> it was necessary to compare Le<sup>x</sup>/Le<sup>x</sup> experiments with experiments in which the Le<sup>x</sup> groups from one of the vesicles were absent (Le<sup>x</sup>/Lac experiments).

Fig. 6 shows the aspiration pressure as a function of  $G$  [cf. Eq. (17)] for the controls and Le<sup>x</sup>/Le<sup>x</sup> experiments. As before, the slopes are equal to the vesicle adhesion free energies and are independent of the vesicle size. Adhesion energy values for the controls and for the Le<sup>x</sup>/Le<sup>x</sup> experiments are given in Table 3. The effect of adding calcium on the Le<sup>x</sup> vesicles is clearly seen in Table 3 and in Fig. 6. The adhesion energy in CaCl<sub>2</sub> is 2.5 times higher than in NaCl whereas the Le<sup>x</sup>/Lac experiments showed a small decrease of the adhesion energy with calcium ( $3 \times 10^{-6} \text{ J m}^{-2}$ ). These results unambiguously show that Le<sup>x</sup> groups are necessary on both vesicles for the calcium-induced adhesion enhancement to occur. This is in agreement with the specific interaction scheme advocated by Hakomori.<sup>[11]</sup>

The adhesion, in the case of NaCl and for both types of vesicles, is the result of a balance between van der Waals attractions and short-range repulsions that include entropic and structural contributions.<sup>[15,31]</sup> Therefore, the higher adhesion in NaCl in the Le<sup>x</sup>/Lac system as compared to Le<sup>x</sup>/Le<sup>x</sup> may seem surprising. However, one may note that the sugar groups are bound to the lipid chains by a flexible spacer (Fig. 4C). The thermal fluctuations of this spacer can cause steric repulsions as polymer brushes do.<sup>[32]</sup> This difference between Le<sup>x</sup>/Le<sup>x</sup> and Le<sup>x</sup>/Lac experiments is not relevant for our purpose because van der Waals forces do not play a significant role in cell membrane interactions. Usually, the adhesions are governed by cell adhesion molecules such as proteins or lipids given that there are many steric repulsions produced by the glycocalix. For this reason, two biomembranes will not adhere in the absence of specific adhesion sites.

The specific contribution  $W_{\text{adh}}$  of the Le<sup>x</sup> groups to the adhesion energy of our vesicles is equal to the difference between the effects of calcium on adhesion

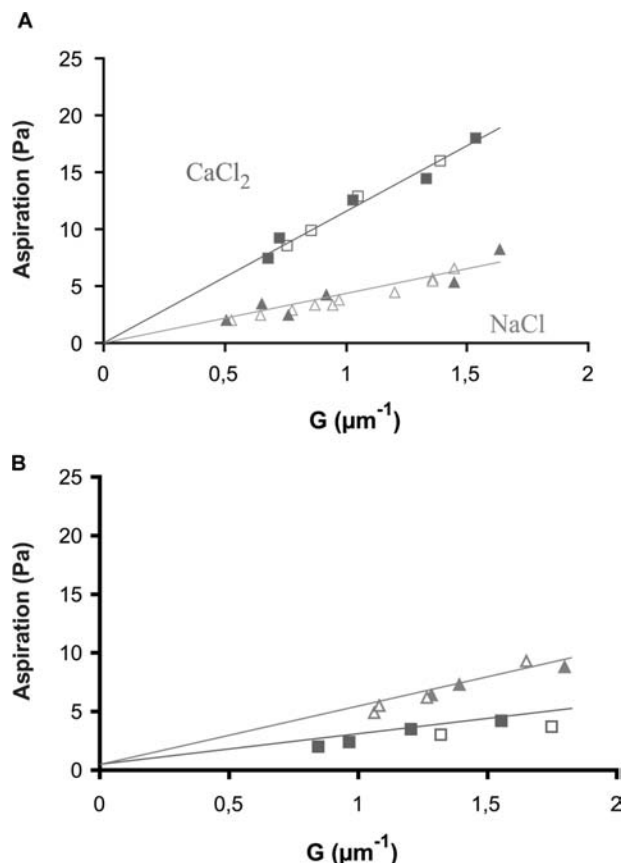


**Fig. 6** Aspiration pressure as a function of parameter  $G$  given in Eq. (18): (A)  $\text{Le}^x/\text{Le}^x$  experiment (two vesicles with SOPC/ $\text{Le}^x$ , 90:10); (B)  $\text{Le}^x/\text{Lac}$  experiment (one vesicle is SOPC/ $\text{Le}^x$ , 90:10, and the other is SOPC/Lac, 90:10); The closed symbols represent decreasing aspiration, and open ones are for increasing aspiration. Triangles are for NaCl solution and squares for  $\text{CaCl}_2$ . The straight lines are least square fits.

energy in the  $\text{Le}^x/\text{Le}^x$  and in the  $\text{Le}^x/\text{Lac}$  experiments. Table 3 shows that  $W_{\text{adh}} = 10 \pm 5 \mu\text{J m}^{-2}$ . This adhesion is weak for the density of sugar that was used. This indicates that the interactions must be weak and therefore that the lifetime of the bonds is small. Thus, the case of  $\text{Le}^x$  is favorable for the use of the model of

**Table 3** Adhesion energy of vesicles ( $10^{-6} \text{J/m}^2$ ) in aqueous media between  $\text{Le}^x$ - or Lac-functionalized vesicles in NaCl and in  $\text{CaCl}_2$

Left vesicle/right vesicle	Adhesion energy ( $\mu\text{J/m}^2$ )	
	In 0.2 M NaCl	In 0.11 M $\text{CaCl}_2$
$\text{Le}^x/\text{Le}^x$	$4.5 \pm 2$	$11 \pm 2$
$\text{Le}^x/\text{Lac}$	$5.4 \pm 2$	$2.5 \pm 2$

$\text{Le}^x$  means that the vesicle composition is SOPC/ $\text{Le}^x$  90:10; same for Lac.

a cell adhering to a substrate. This is confirmed by the fact that a single slope for the contact formation and separation of the vesicles are identical, meaning that the adhesion is continuous and reversible. Eq. (9) gives an enrichment smaller than 2%. Therefore, the density can be considered as constant. This has the consequence that the density of sites on the substrate can be taken as the initial density of  $\text{Le}^x$  in the vesicles, which is  $1.4 \times 10^{17}$  molecules/ $\text{m}^2$ . In addition,  $\alpha\rho_0A_c$  will be much smaller than  $A_t$ . Therefore, Eq. (13) can be rewritten here:

$$W_{\text{adh}} = A_t\rho_0^2\alpha k_B T(e^{e_b/k_B T} - 1) \quad (19)$$

Because the  $\text{Le}^x$  are in the polar head of the lipids,  $\alpha$  should be of the order of the polar head of the lipid. A good estimate seems to take the same value as that measured with two membranes made of A and T lipids:<sup>[33]</sup>  $0.3 \times 10^{-18} \text{m}^2$ . With these values,  $e_b$  ranges between  $0.17$  and  $0.5k_B T$  (i.e.,  $0.1$  and  $0.3$  kcal/mol). Previous glycolipid studies showed strong van der Waals interactions.<sup>[12–16,18]</sup> In the present work, the calcium-induced interaction is specific and comes in addition to van der Waals forces. Note that these molecules are neutral and therefore this interaction is not intrinsically electrostatic.

This ultraweak interaction energy validates the assumption that the binding energy is substantially below  $k_B T$ . A rough estimate of the bond lifetime can be obtained by comparison with the streptavidin/biotin system ( $30k_B T$  bond energy and lifetime of several days) and assuming an Arrhenius law. It is well below  $1 \mu\text{sec}$ . It is most unusual to measure molecular interaction energies well below the thermal energy. This only shows that cell–cell adhesion will require a large number of these molecules as is indeed observed during the morula stage of mouse embryogenesis. The molecular mechanism of the  $\text{Le}^x$  interaction still remains mysterious. The mediation by  $\text{Ca}^{2+}$  could result from the setting up of an appropriate coordination shell around the cation.<sup>[34]</sup>

These measurements with synthetically tailored  $\text{Le}^x$  containing neoglycolipids could be analyzed with the model of a cell adhering to a substrate presented above. It directly confirms the involvement of neutral cell surface oligosaccharides in cell–cell adhesion and illustrates why, when the  $\text{Le}^x$  sites are blocked, the compaction stage of the embryo does not occur.<sup>[23]</sup>  $\text{Le}^x$  is capable, in the presence of  $\text{Ca}^{2+}$ , to substantially enhance the deformation and adhesion of lipid vesicles, i.e., objects with mechanical features akin to those of the cell membranes. The interaction scaled down to one molecule is well below thermal energy. It produces transient and dynamic adhesion that is indeed what cell differentiation requires.

This direct measurement of biologically relevant carbohydrate/carbohydrate interaction shows that it is now possible to quantify such ultraweak bonds with the presented model. It opens up a new promising field in biology.

## CONCLUSION

The simple model that describes cell adhesion on a substrate gives quantitatively good results and allows one to relate the adhesion energy to the excess of ligand in the contact zone and to the molecular binding energy. The experimental approach that is presented can be used to describe the properties of adhesion molecules that produce weak bonds. In contrast, for vesicles bearing stronger binding sites, Eq. (9) is not valid anymore. However, some information about the ligand receptor information can still be obtained.<sup>[35]</sup> The adhesion molecules are expected to diffuse toward the contact zone, which therefore should contain a higher density of adhesion molecules, leaving the non-contacting part of the vesicle depleted, especially for large contact areas.

Also, this model deals only with adhesion at equilibrium. With the same kind of approach, it is possible to try to understand the formation dynamics of the contact zone. More precisely, the nucleation of patches can appear during the spreading of the contact. This has been discussed elsewhere.<sup>[36]</sup>

Finally, the case of real biological cells is much more complicated to quantify, as there are many more parameters involved such as the glycocalyx, the cytoskeleton, and many adhesion molecules acting at the same time. The role of the glycocalyx has been included in another approach by Bell, Dembo, and Bongrand<sup>[4]</sup> The mechanical properties of a cell are very different from that of a vesicle and, although it has been tried in the past,<sup>[37,38]</sup> the measurement of the contact angle does not give very satisfactory results.

## REFERENCES

- Evans, E.; Kukan, B. Free energy potential for aggregation of erythrocytes and phosphatidylcholine/phosphatidylserine vesicles in dextran (36,500 MW) solutions and in plasma. *Biophys. J.* **1983**, *44*, 255–260.
- Bell, G.I. A theoretical framework for adhesion mediated by reversible bonds between cell surface molecules. *Science* **1978**, *200*, 618–627.
- Evans, E. Detailed mechanics of membrane–membrane adhesion and separation. I. Continuum of molecular bridges. *Biophys. J.* **1985**, *48*, 175–183.
- Bell, G.I.; Dembo, M.; Bongrand, P. Cell adhesion: competition between non-specific repulsion and specific binding. *Biophys. J.* **1984**, *45*, 1051–1064.
- Pincet, F.; Perez, E.; Loudet, J.-C.; Lebeau, L. From macroscopic adhesion energy to molecular bonds: a test of the theory. *Phys. Rev. Lett.* **2001**, *87*, 178101-1-4.
- Evans, E. Equilibrium “wetting” of surfaces by membrane-covered vesicles. *Adv. Colloid Interface Sci.* **1992**, *39*, 103–128.
- Pincet, F.; Perez, E.; Bryant, G.; Lebeau, L.; Mioskowski, C. Specific forces between DNA bases. *Mod. Phys. Lett. B* **1996**, *10*, 81–99.
- Pincet, F.; Rawicz, W.; Perez, E.; Lebeau, L.; Mioskowski, C.; Evans, E. Electrostatic nanotitration of weak biochemical bonds. *Phys. Rev. Lett.* **1997**, *79*, 1949–1952.
- Needham, D.; Evans, E. Structure and mechanical properties of giant lipid (DMPC) vesicle bilayers from 20°C below to 10°C above the liquid crystal–crystalline phase transition at 24°C. *Biochemistry* **1988**, *27*, 8261–8269.
- Evans, E.; Needham, D. Attraction between lipid bilayer membranes in concentrated solutions of non-adsorbing polymers: comparison of mean-field theory with measurements of adhesion energy. *Macromolecules* **1988**, *21*, 1822–1831.
- Hakomori, S. Carbohydrate–carbohydrate interaction as an initial step in cell recognition. *Pure Appl. Chem.* **1991**, *63*, 473–482.
- Marra, J. Controlled deposition of lipid monolayers onto mica and direct force measurements between galactolipid bilayers in aqueous electrolyte solutions. *J. Colloid Interface Sci.* **1985**, *107*, 446–455.
- Marra, J. Direct measurements of attractive van der Waals and adhesion forces between uncharged lipid bilayers in aqueous solutions. *J. Colloid Interface Sci.* **1988**, *109*, 11–20.
- Evans, E. Physical properties of surfactant bilayer membranes: thermal transitions, elasticity, rigidity, cohesion and colloidal interactions. *J. Phys. Chem.* **1987**, *91*, 4219–4228.
- Rand, R.P.; Parsegian, V.A. Hydration forces between phospholipid saccharide bilayers. *BBA* **1989**, *988*, 351–376.
- Luckham, P.; Wood, J.; Swart, R. The surface properties of gangliosides. *J. Colloid Interface Sci.* **1993**, *156*, 173–183.
- Yu, Z.W.; Calvert, T.L.; Leckband, D. Molecular forces between membranes displaying neutral glycosphingolipids: evidence for carbohydrate attraction. *Biochemistry* **1998**, *37*, 1540–1550.
- Ricoul, F.; Dubois, M.; Belloni, L.; Zemb, T.; André-Barrès, C.; Rico-Lattes, I. Phase equilibria and equation state of a mixed cationic surfactant–glycolipid lamellar system. *Langmuir* **1998**, *14*, 2645–2655.
- Sharon, N.; Lis, H. Carbohydrates in cell recognition. *Sci. Am.* **1993**, *268*, 74–81.
- Bovin, N.V. Carbohydrate–carbohydrate interactions: a review. *Biochemistry (Moscow)* **1996**, *61*, 694–704.
- Solter, D.; Knowles, B. Monoclonal antibody defining a stage-specific mouse embryonic antigen (SSEA-1). *Proc. Natl. Acad. Sci. U. S. A.* **1978**, *75*, 5565–5569.
- Fenderson, B.A.; Holmes, E.H.; Fukushi, Y.; Hakomori, S. Coordinate expression of X and Y haptens during murine embryogenesis. *Dev. Biol.* **1986**, *114*, 12–21.

23. Eggens, I.; Fenderson, B.; Toyokuni, T.; Dean, B.; Stroud, M.; Hakomori, S. Specific interaction between Le<sup>x</sup> and Le<sup>x</sup> determinants, a possible basis for cell recognition in preimplantation embryos and in embryonal carcinoma cells. *J. Biol. Chem.* **1989**, *264*, 9476–9484.
24. Kojima, N.; Fenderson, B.A.; Stroud, M.R.; Goldberg, R.I.; Habermann, R.; Toyokuni, T.; Hakomori, S. Further studies on cell adhesion based on Le<sup>x</sup>–Le<sup>x</sup> interaction, with new approaches: embryoglycan aggregation of F9 teratocarcinoma cells, and adhesion of various tumour cells based on Le<sup>x</sup> expression. *Glycoconj. J.* **1994**, *11*, 238–248.
25. Boubelik, M.; Floryk, D.; Bohata, J.; Draberova, L.; Macak, J.; Smid, F.; Draber, P. Le<sup>x</sup> glycosphingolipids-mediated cell aggregation. *Glycobiology* **1998**, *8*, 139–146.
26. Siuzdak, G.; Ichikawa, Y.; Caulfield, T.J.; Munoz, B.; Wong, C.-H.; Nicolaou, K.C. Evidence of Ca<sup>2+</sup>-dependent carbohydrate association through ion spray mass spectrometry. *J. Am. Chem. Soc.* **1993**, *115*, 2877–2881.
27. Henry, B.; Desvaux, H.; Pristchepa, M.; Berthault, P.; Zhang, Y.; Mallet, J.-M.; Esnault, J.; Sinaÿ, P. NMR study of a Lewis<sup>x</sup> pentasaccharide derivative: solution structure and interaction with cations. *Carbohydr. Res.* **1999**, *315*, 48–62.
28. Geyer, A.; Gege, C.; Schmidt, R.R. Calcium dependent carbohydrate–carbohydrate recognition between Lewis<sup>x</sup> blood group antigens. *Angew. Chem., Int. Ed.* **2000**, *39*, 3246–3249.
29. Esnault, J.; Mallet, J.M.; Zhang, Y.; Sinay, P.; Le Bouar, T.; Pincet, F.; Perez, E. New highly hydrophobic Lewis<sup>x</sup> glycolipids: synthesis and monolayer behaviour. *Eur. J. Org. Chem.* **2001**, *2001*, 253–260.
30. Marcelja, S. Electrostatics of membrane adhesion. *Biophys. J.* **1992**, *61*, 1117–1121.
31. Israelachvili, J.N.; Wennerström, H. Hydration or steric forces between amphiphilic surfaces. *Langmuir* **1990**, *6*, 873–876.
32. Taunton, H.J.; Toprakcioglu, C.; Fetters, L.J.; Klein, J. Interaction between surfaces bearing end-adsorbed chains in a good solvent. *Macromolecules* **1990**, *23*, 571–580.
33. Pincet, F.; Perez, E.; Bryant, G.; Lebeau, L.; Mioskowski, C. Long-range attraction between nucleosides with short-range specificity. *Phys. Rev. Lett.* **1994**, *73*, 2780–2783.
34. Bugg, C.E. Calcium binding to carbohydrates. Crystal structure of a hydrated calcium bromide complex of lactose. *J. Am. Chem. Soc.* **1973**, *95*, 908–913.
35. Noppl-Simson, D.A.; Needham, D. Avidin–biotin interactions at vesicle surfaces: adsorption and binding, cross-bridge formation, and lateral interactions. *Biophys. J.* **1996**, *70*, 1391–1401.
36. Brochard-Wyart, F.; de Gennes, P.G. Adhesion induced by mobile binders: dynamics. *Proc. Natl. Acad. Sci. U.S.A.* **2002**, *99*, 7854–7859.
37. Sung, K.L.; Sung, L.A.; Crimmins, M.; Burakoff, S.J.; Chien, S. Determination of junction avidity of cytolytic T cell and target cell. *Science* **1986**, *234*, 1405–1408.
38. Tozeren, A.; Sung, K.L.; Chien, S. Theoretical and experimental studies on cross-bridge migration during cell disaggregation. *Biophys. J.* **1989**, *55*, 479–487.

# Adhesion: Coated Surfaces, Effect of Humidity

**Joan E. Curry**

*Department of Soil, Water and Environmental Science, University of Arizona, Tucson, Arizona, U.S.A.*

**Sungsoo Kim**

*Department of Chemical and Biomolecular Engineering, University of Illinois at Urbana–Champaign, Champaign, Illinois, U.S.A.*

## INTRODUCTION

Self-assembled monolayers (SAMs) are monomolecular layers that are spontaneously formed on immersing a solid substrate into a solution containing active surfactant molecules. The best studied examples are silanes, which are used to modify, for example, silica and mica surfaces, and alkylthiols, which have an affinity for coinage metals.<sup>[1]</sup> Organic SAMs can be used to alter and control the chemical nature of surfaces. For instance, SAMs provide a robust base layer for immobilizing biological molecules in biosensors. The bonding of enzymes to alkanethiol SAMs on gold has received attention as a method of constructing enzyme electrodes.<sup>[2]</sup> Lee et al.<sup>[3]</sup> are developing a surface plasmon resonance-based monosaccharide sensor by immobilizing a small thiol-based receptor molecule on gold containing a boronic acid group that is known to covalently bind the 1,2 or 1,3-diol of sugars. The success of SAM-based sensor applications depends on the stability of the underlying SAM as a function of aging and on environmental conditions such as humidity and temperature.

Self-assembly is simple and widely applicable in areas such as coatings, lubrication, templating, optoelectronics, and microelectromechanical systems/nanoelectromechanical systems (MEMS/NEMS). MEMS offers great promise for system integration of sensors, actuators, and signal processing. The miniaturization and integration offered by MEMS devices is attractive in applications where smaller size and weight are desirable. However, as devices become smaller, the surface area-to-volume ratio becomes larger and surface forces become more important. Factors determining the performance, reliability, and durability of MEMS devices are not well understood. In many applications, it will be impractical or impossible to protect MEMS devices from the operating environment. For instance, robust MEMS actuators must operate in a variety of conditions, some of which may be extreme (e.g., high temperature, a wide range of climatic conditions, and

high vacuum).<sup>[4]</sup> In MEMS, nanoscale dimensions potentially separate device components where water can capillary condense, giving rise to stiction. Many applications for MEMS/NEMS are not really practical, as many studies have revealed the profound negative influence of stiction, friction, and wear on the efficiency, power output, and steady-state speed of microdynamic/nanodynamic devices.<sup>[5,6]</sup> Komvopoulos and Yan<sup>[7]</sup> have shown that liquid bridging at intermediate humidity is the dominating short-range attraction mechanism prevailing at MEMS interfaces. It is also known that head/disk stiction occurs at humidities greater than 80%.<sup>[8]</sup> The ubiquitous presence of water vapor makes the study of the effect of relative humidity (RH) on the performance and reliability of MEMS devices crucial. Depositing a hydrophobic SAM on a hydrophilic surface can reduce surface wettability. Organosilane SAMs are being investigated as boundary lubricants and antiwetting coatings in MEMS devices to reduce the effect of humidity on friction and wear.

In order for SAMs to be useful as boundary lubricants, in biosensors, as MEMS coatings, and in a variety of other applications, it is important to understand the effect of environmental conditions such as humidity and temperature on SAM robustness and stability. In this entry, we present current research on the effect of humidity on the adhesiveness of alkyl-based SAM coatings on gold, silica, and mica. The wide variety of SAMs designed to be immersed in water (for instance functionalized SAMs for sensor applications) is not specifically discussed here, but this information should be pertinent for those interested in the effect of water on underlying SAM stability and adhesion.

## CAPILLARY CONDENSATION AND ADHESION

In studies of physisorbed surfactant monolayers on mica, Chen and Israelachvili<sup>[9]</sup> found that adhesion increased with RH and was dependent on the

hydrophilicity of headgroups and the phase state of hydrocarbon chains. Humidity has also been shown to increase the mobility of surfactant molecules on the surface by penetrating into the headgroup region and by weakening the attraction between the surfactant molecules and the mica.<sup>[10,11]</sup> Humidity affects adhesion between surfaces because when the surfaces are close enough, water capillary condenses around the contact zone as long as the sum of the water contact angles on the two surfaces is less than  $180^\circ$ .<sup>[12]</sup> This annulus gives rise to an attractive capillary force in addition to any direct solid–solid adhesion that must be overcome to separate the surfaces. The capillary pressure depends on the relative vapor pressure according to the Kelvin equation:

$$\frac{kT}{v_m} \ln \frac{p}{p_0} = \gamma_{LV} \left( \frac{1}{r_1} + \frac{1}{r_2} \right) \quad (1)$$

where  $r_1$  and  $r_2$  are the meniscus radii of curvature,  $k$  is the Boltzmann constant,  $T$  is the temperature,  $\gamma_{LV}$  is the liquid–vapor surface tension,  $p/p_0$  is the vapor pressure, and  $v_m$  is the molar volume of the condensed liquid. It is assumed that the vapor is ideal, the liquid is incompressible, and the molar volume of the vapor is much larger than the molar volume of the liquid. More complicated expressions can be used to account for these assumptions.<sup>[13,14]</sup>

The adhesive force because of capillary condensation is simply:

$$F_{\text{cap}} = \Delta p A \quad (2)$$

where  $\Delta p$  is the pressure difference across a curved interface acting on an area  $A$ . The Young–Laplace equation relates the Laplace pressure to the surface tension and local meniscus curvature as follows:

$$\Delta p = \gamma_{LV} \left( \frac{1}{r_1} + \frac{1}{r_2} \right) \quad (3)$$

Considering the general case of a rigid sphere of radius  $R$  interacting with a rigid, flat plate (no surface deformations because of adhesive forces), the capillary pressure is given by:

$$F_{\text{cap}} = \Delta p A = 2\pi\gamma_{LV} \left( \frac{1}{r_1} + \frac{1}{r_2} \right) R^2 \sin^2 \phi \quad (4)$$

where  $\phi$  is the filling angle, as shown in Fig. 1A.<sup>[12]</sup> In the limit of vanishing filling angle, the capillary pressure is given by:

$$F_{\text{cap}} = 2\pi R \gamma_{LV} (\cos \theta_1 + \cos \theta_2) \quad (5)$$

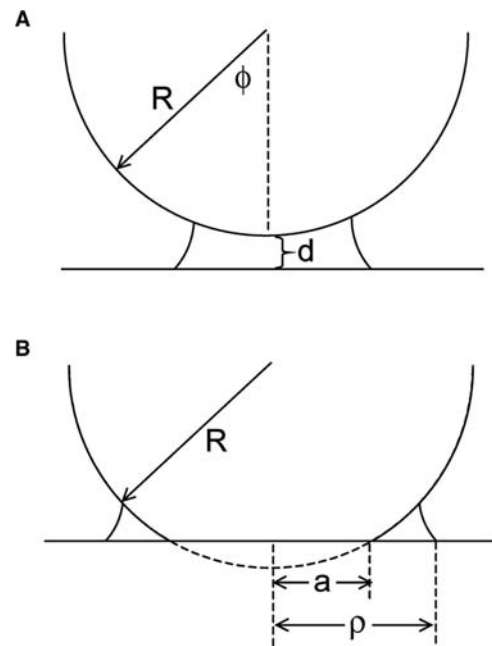


**Fig. 1** Schematic illustration of capillary condensation between a sphere of radius  $R$  and a flat plate. In panel (A), both the sphere and the flat are rigid.  $\phi$  is the filling angle and  $d$  is the sphere–plate separation. In panel (B), the sphere is deformable.  $a$  is the radius of the flattened contact zone and  $\rho$  is the distance from the contact center to the edge of the capillary condensate.

where  $\theta_1$  and  $\theta_2$  are the water contact angles on the two surfaces. If the filling angle is large, such as the tip of an atomic force microscope (AFM) in contact with a surface at high humidity, more complicated expressions are required, as detailed by Orr, Scriven, and Rivas.<sup>[12]</sup> If the meniscus is assumed to be circular, the capillary force can be approximated as:<sup>[15]</sup>

$$F_{\text{cap}} = \pi R \gamma_{LV} \times \left( -\sin \phi + \frac{\cos(\theta_1 + \phi) + \cos \theta_2}{\frac{d}{R} + 1 - \cos \phi} \sin^2 \phi \right) \quad (6)$$

where the filling angle is fixed by the vapor pressure according to the Kelvin equation:

$$\begin{aligned} \frac{kT}{\gamma_{LV} v_m} \ln \frac{p}{p_0} &= \frac{\Delta p}{\gamma_{LV}} = \left( \frac{1}{r_1} + \frac{1}{r_2} \right) \\ &= \frac{1}{R \sin \phi} - \frac{\cos(\theta_1 + \phi) + \cos \theta_2}{d + R(1 - \cos \phi)} \end{aligned} \quad (7)$$

and  $d$  is the sphere–flat separation at the point of closest approach. In the case of an AFM tip, the resolved surface tension force may also be important



and should be added. It is given as:

$$F_S = 2\pi\gamma_{LV}R \sin \phi \sin(\theta_1 + \phi) \quad (8)$$

If the sphere and flat are elastic and adhesive, the theory of Johnson, Kendall, and Roberts (JKR)<sup>[16]</sup> is frequently used to explain surface deformation and adhesion in dry conditions. The JKR theory predicts a finite contact diameter even under zero load. The adhesive force is given by:

$$F = \frac{3}{2}\pi RW = 3\pi R\gamma \quad (9)$$

where  $W$  is the Dupré energy of adhesion given by:

$$W = \gamma_1 + \gamma_2 - \gamma_{12} \quad (10)$$

where  $\gamma_1$  and  $\gamma_2$  are the surface energies of the contacting materials, and  $\gamma_{12}$  is the interfacial energy between the two surfaces. If the materials are identical, then  $\gamma_{12} = 0$  and  $W = 2\gamma$ . The JKR theory only takes into account the adhesive interactions inside the contact zone and neglects interactions between the surfaces outside the contact zone. Derjaguin, Muller, and Toporov (DMT)<sup>[17]</sup> approached the problem from a different point of view by treating the contact as Hertzian but taking into account the interactions outside the contact zone. Their theory predicts an adhesive force of:

$$F = 2\pi RW = 4\pi R\gamma \quad (11)$$

Maugis<sup>[18]</sup> showed that these two theories are actually special cases of a theory derived using linear elastic fracture mechanics with an adhesive “Dugdale” zone outside the contact area. In the Dugdale model, a constant adhesive stress is assumed to act between the surfaces in a region just outside the contact zone. Outside this region, the adhesive force falls to zero.

Maugis and Gauthier-Manuel<sup>[19]</sup> pointed out that capillary condensation is the perfect example of a Dugdale zone outside the contact area. The condensate occupies an annulus in which the adhesive stress is constant and is given by the Laplace pressure. Maugis took the stress outside the contact zone to be:

$$\begin{aligned} \sigma_0 &= \Delta p & a > r > \rho \\ &= 0 & r > \rho \end{aligned} \quad (12)$$

where  $a$  is the radius of the contact zone,  $\rho$  is the radius of the area covered by the condensate, and  $r$  is the radial coordinate (Fig. 1B). Maugis derived the

following equations:

$$\begin{aligned} \frac{W}{\sigma_0} &= \frac{a^2}{\pi R} ((x^2 - 1)^{1/2} + (x^2 - 2) \tan^{-1} \\ &\quad \times (x^2 - 1)^{1/2}) + \frac{16\sigma_0 a}{3\pi K} ((x^2 - 1)^{1/2} \tan^{-1} \\ &\quad \times (x^2 - 1)^{1/2} - x + 1) \end{aligned} \quad (13)$$

$$\begin{aligned} F &= \frac{a^3 K}{R} - 2\sigma_0 a^2 ((x^2 - 1)^{1/2} + x^2 \tan^{-1} \\ &\quad \times (x^2 - 1)^{1/2}) \end{aligned} \quad (14)$$

where  $x = \rho/a$  and  $F$  is the load on the system. Although it is not possible to simplify these equations further to obtain one equation that gives the load as a function of the contact radius, it is possible to solve these two equations using an iterative procedure. As shown in Maugis,<sup>[18]</sup> as  $p/p_0 \rightarrow 0$ , JKR results are recovered and as  $p/p_0 \rightarrow 1$ , DMT results are recovered.

The effect of humidity on the stability, wettability, and adhesion of SAM-coated surfaces depends on the ability of water to favorably interact with the monolayer. The contact angle of water on a SAM surface gives a good indication of SAM wettability. SAMs with hydrophilic terminal groups have low contact angles and adhesion is strongly affected by humidity because of capillary condensation. On highly hydrophobic SAMs, advancing contact angles are generally very high ( $\sim 110^\circ$ ) with receding angles slightly lower.<sup>[20]</sup> The hysteresis between advancing and receding angles provides a measure of the degree of surface roughness or heterogeneity.<sup>[1]</sup> Large contact angle hysteresis or contact angles that decrease with time indicate that water interacts somewhat favorably with the SAM. In the case of alkylsilane SAMs, it is likely that water changes the monolayer by penetrating to the SAM–substrate interface and by hydrolyzing the siloxane bonds. In these cases, humidity will affect adhesion near saturation.

## ALKYLTHIOL SAMs ON GOLD

SAMs that are particularly effective in repelling water are alkanethiol SAMs deposited on gold. These SAMs are packed very tightly and are covalently bound to the gold substrate through the metal–sulfur bond. The alkyl chains of the thiols are in the all-trans conformation, tilted at an angle of  $\sim 20\text{--}30^\circ$  from normal to the metal surface.<sup>[21]</sup> In general, these SAMs have very high advancing and receding contact angles, indicating that water is unable to disrupt the layer at least on the time scale of the experiment. Liu and Bhushan<sup>[5]</sup> used the AFM to measure adhesion between a silicon nitride tip and SAMs with different



terminal groups deposited on Au(111) and Si(111) as a function of humidity up to 60% RH. Fig. 2 shows the adhesive force as a function of RH for bare gold and silicon, a carboxylic acid-terminated SAM (16-mercapto-hexadecanoic acid) on gold (MHA), a hydroxyl-terminated biphenyl SAM (4,4'-dihydroxybiphenyl) on silicon (DHBp), a biphenyl SAM (1,1'-biphenyl-4-thiol) on gold (BPT), a cross-linked version of the biphenyl SAM (BPTC), and a hydrophobic SAM (hexadecane thiol) (HDT). Adhesion increases with RH for the uncoated and the hydrophilic SAM-coated surfaces. It increases less dramatically for phenyl-terminated SAM coatings and it is independent of humidity for the hydrophobic coating. This suggests that at least for humidities up to 60%, the methyl-terminated thiol SAM affords protection against capillary-induced adhesion.

Li, Chen, and Jiang<sup>[22]</sup> found that the friction of a silicon nitride AFM tip on an alcohol-terminated

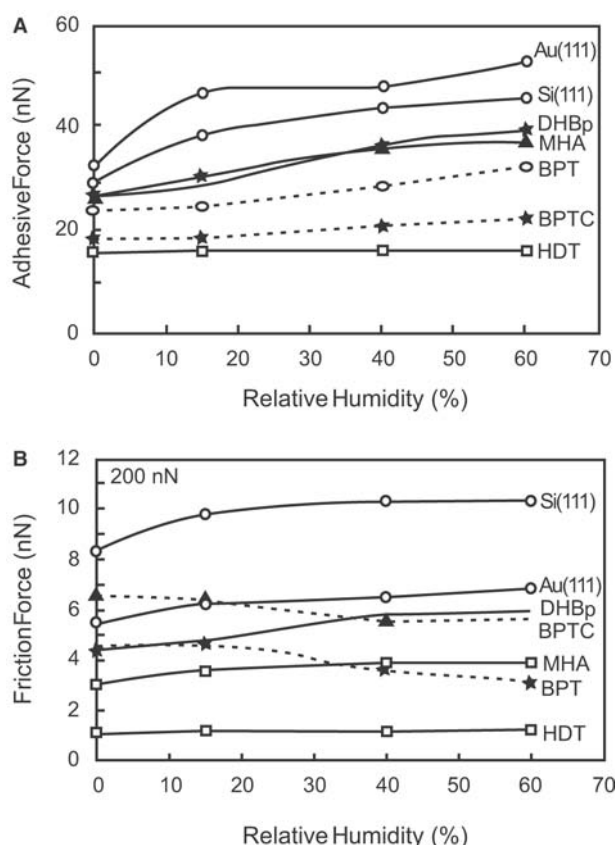


**Fig. 2** The influence of RH on the adhesive force between a silicon nitride AFM tip and Si(111), Au(111), and five SAMs: a carboxylic acid-terminated SAM (16-mercapto-hexadecanoic acid) on gold (MHA), a hydroxyl-terminated biphenyl SAM (4,4'-dihydroxybiphenyl) on silicon (DHBp), a biphenyl SAM (1,1'-biphenyl-4-thiol) on gold (BPT), a cross-linked 1,1'-biphenyl-4-thiol (BPTC), and a hydrophobic SAM (hexadecane thiol) (HDT). *Source:* From Fig. 9 of Ref.<sup>[5]</sup>.

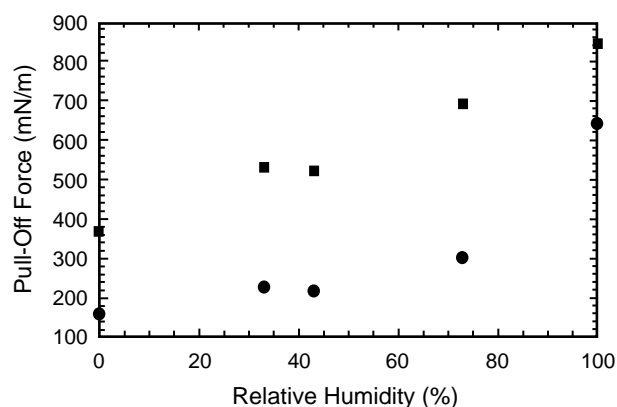


**Fig. 3** Pull-off forces (mN/m) as a function of RH. Separate SAMs were prepared for each data point: square symbols are for the alcohol-terminated SAM; circles are for the methyl-terminated SAM. *Source:* From Fig. 1 of Ref.<sup>[24]</sup>.

SAM ( $C_{11}OH$ ) on gold is high at 10% RH but decreases with increasing humidity because water acts as a lubricant. Friction on a methyl-terminated SAM ( $C_{12}$ ) is independent of humidity even for immersion in pure water. However, as pointed out by Yoshizawa, Chen, and Israelachvili<sup>[23]</sup> there is no fundamental relationship between friction and adhesion even though they are sometimes highly correlated.

In contrast to AFM studies, Quon, Ulman, and Vanderlick<sup>[24]</sup> measured the effect of humidity on the adhesion between a SAM-coated gold surface [root mean square (rms) roughness 20 Å] and a molecularly smooth mica surface using a surface forces apparatus (SFA).<sup>[25]</sup> In the SFA, the force is measured between cross-cylinders with radii of curvature of approximately 2 cm. Because water wets mica ( $\theta = 0$ ), according to Eq. (5), it is expected that humidity will affect adhesion through capillary condensation. As shown in Fig. 3, for both alcohol- and methyl-terminated alkylthiol SAMs, adhesion increased with increasing RH. The magnitude of the adhesion at a particular RH was always higher for the alcohol-terminated SAM because the water contact angle is very small. Interestingly, near saturation, the adhesive force for the methyl-terminated SAM is much greater (643 mN/m) than is predicted by Eq. (5) (335 mN/m) if the SAM is assumed to be very hydrophobic ( $\theta \sim 105^\circ$ ). The reason for this unexpectedly large adhesion is not clear. However, it suggests that water interacts with the hydrophobic surface to a greater extent than expected for an alkanethiol on gold.

## ALKYLSILANE SAMs ON SILICA

The effect of humidity on the adhesion of alkylsilane SAMs deposited on Si/SiO<sub>2</sub> surfaces has been more thoroughly investigated compared with alkylthiols on

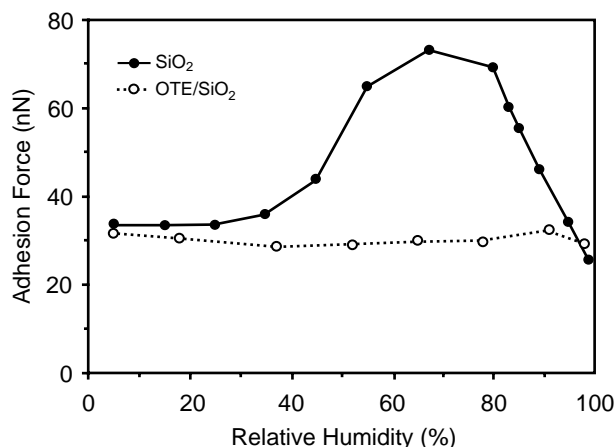


**Fig. 4** Measured adhesion force as a function of humidity for SiO<sub>2</sub> and OTE/SiO<sub>2</sub> against a Si<sub>3</sub>N<sub>4</sub> AFM tip. Source: From Fig. 2 of Ref.<sup>[15]</sup>.

gold in part because of the importance of antiadhesive coatings in silicon-based MEMS devices. An important difference between SAMs formed by alkylthiols and organosilanes is the possibility for the formation of cross-linked siloxane bridges (Si–O–Si) between adjacent molecules. It is commonly assumed that this cross-linking stabilizes these SAMs.<sup>[26]</sup> However, it is not clear as to what extent this actually occurs because the cross-linking should be sterically hindered.<sup>[27]</sup> Zhang et al.<sup>[28]</sup> investigated the effect of humidity (up to 80%) on the adhesive force between an AFM silicon nitride tip and organosilane SAMs with different terminal groups (–CH<sub>3</sub>, –COOCH<sub>3</sub>, and –COOH) deposited on hydrogen-terminated silica Si(111). Adhesion to hydrophilic SAMs increased at the highest humidities because of capillary condensation, whereas there was no change in the adhesive force between the tip and the methyl-terminated SAM. He et al.<sup>[29]</sup> also found that the adhesive force between an AFM tip rendered hydrophobic by coating with *n*-octadecyltrichlorosilane (OTS) and a silicon surface did not change for humidities up to 80%. Xiao and Qian<sup>[15]</sup> examined the adhesion between an AFM silicon nitride tip and an *n*-octadecyltriethoxysilane (OTE)-coated silicon surface, and found essentially no dependence on humidity up to 98%, as shown in Fig. 4. Interestingly, adhesion between the tip and a bare hydrophilic silica surface first increases with increasing humidity because of capillary condensation and then decreases close to saturation. Because the tip radius is small, the filling angle becomes large near saturation. According to Eq. (6), the effect of an increasing filling angle is a decreasing adhesive force, as is observed. The net effect is that the adhesive forces on the bare silica surface and the OTE-coated silicon surface are the same near saturation. For practical purposes, the AFM experiments discussed here show that the hydrophobic SAM affords

protection against capillary-induced adhesion even at high humidity.

With a specific focus on MEMS, some workers have developed an in situ microcantilever beam technique for measuring adhesion using an as-fabricated MEMS test structure constructed from polycrystalline silicon (polysilicon) that exhibits nanometer-scale rms roughness.<sup>[30–32]</sup> Capillary condensation complicates the fabrication as well as the operation of MEMS, so much effort is being directed at antiadhesive strategies. Hydrophobic SAMs are being investigated as coatings for MEMS devices as these coatings reduce adhesion. De Boer et al.<sup>[30]</sup> studied the effect of humidity on the adhesion of perfluorotrichlorosilane (FDTS)-coated (from solution in isooctane) cantilever beams to an FDTS-coated substrate. For humidities up to 80%, adhesion of the beams was not observed to change significantly. After a 4-hr exposure at 90% RH, a mild adhesion increase was observed, and a much more significant increase was observed after 7 hr of exposure (Fig. 5). AFM topographic images showed mounds, strongly suggesting that increased adhesion correlates with this structural change of the surface. The authors hypothesized that the mounds are the result of humidity-induced restructuring from a surface monolayer phase to a lyotropic bulk phase. Mayer et al.<sup>[32]</sup> coated cantilever beams with monolayer films of tridecafluoro-1,1,2,2-tetrahydrooctyltrichlorosilane (FOTS) in a chemical vapor deposition process. These coatings are hydrophobic, and adhesion tests on coated and uncoated MEMS test structures demonstrate superior performance of FOTS coatings. Cleaned, uncoated, cantilever beam structures exhibit high adhesion energies in a high-humidity environment (100 mJ/m<sup>2</sup> for >90% RH) because of capillary condensation. FOTS-coated beams exhibit negligible adhesion at low humidity and ≤20 mJ/m<sup>2</sup> adhesion energy at >90% RH. No obvious film degradation was observed for films exposed to >90% RH at room temperature for ~24 hr. The authors suggest that chemical vapor deposition of FOTS affords greater stability in high-humidity environments compared with solution-based deposition.

Patton et al.<sup>[4]</sup> evaluated the effect of an OTS SAM coating on the tribological performance of a MEMS electrostatic lateral output motor. For uncoated motors, excessive wear of sliding contacts and permanent adhesion of static contacts were observed at 0.1% RH. Degradation of electrostatic force and high stiction forces limited dynamic performance and reliability, and caused device sticking at and above 70% RH because of capillary condensation. Around 50% RH, uncoated motors exhibited negligible wear, low adhesion, and a wear life at least three orders of magnitude longer than in dry conditions. Water vapor behaved as a gas-replenishable lubricant. The OTS

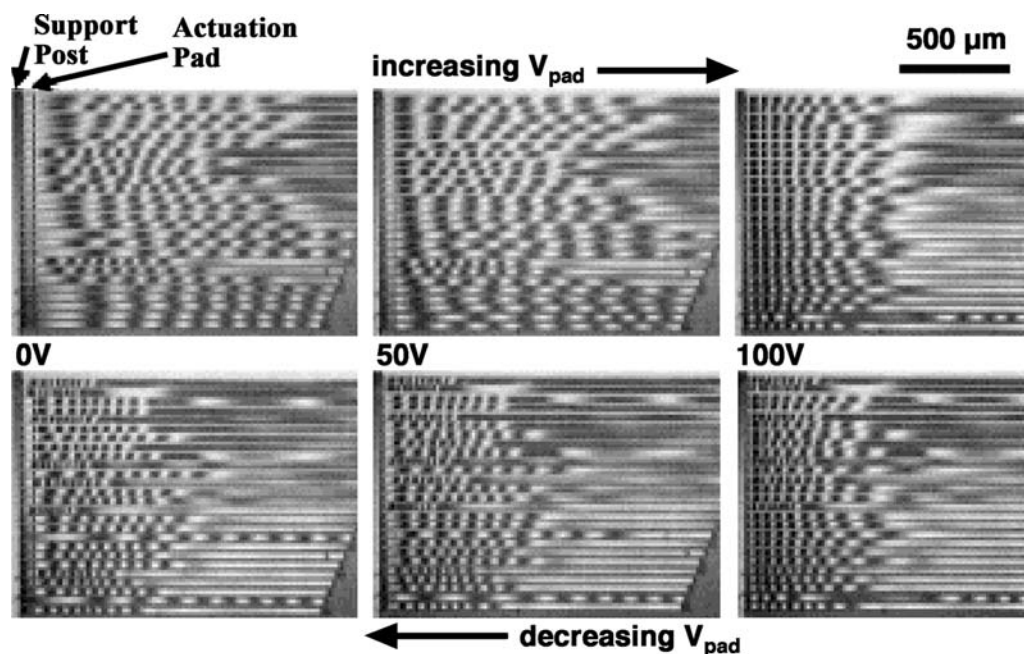


**Fig. 5** Interferograms of adhesion hysteresis observed at RH = 90% after a 7-hr exposure. The images are compressed by a factor of three in the horizontal direction relative to the vertical. Twenty-five beams run horizontally, are 10  $\mu\text{m}$  wide, and are spaced 5  $\mu\text{m}$  apart. Their lengths are from 1500  $\mu\text{m}$  (bottom of each image) to 2000  $\mu\text{m}$  (top). Beams longer than 1700  $\mu\text{m}$  are cut off because of the charge-coupled device (CCD) camera field limit. The voltage was increased up to 160 V before decreasing. *Source:* From Fig. 5 of Ref.<sup>[30]</sup>.

coating broadened the operating envelope to 30–50% RH and reduced stiction, which allowed better dynamic performance at high RH. At high RH, stiction problems recurred when the OTS coating was worn away. By controlling and optimizing the amount of adsorbed water with the OTS coating, excellent performance, low friction and wear, and excellent durability were attained with the lateral output motor.

It is generally thought that organosilane SAMs covalently bind to silica, imparting enhanced stability.<sup>[33]</sup> However, infrared spectroscopic studies indicate that few, if any, bonds are formed and that with exposure to water over time, siloxane bonds hydrolyze.<sup>[34]</sup> It is difficult to determine how water vapor interacts with the SAM on the molecular level from the AFM and cantilever beam studies. Ohnishi, Yaminsky, and Christenson<sup>[35]</sup> measured the force between heptadecafluoro-1,1,2,2,-tetrahydrodecyltriethoxysilane (FTE) SAMs deposited on identical fused glass surfaces (radius of curvature  $\sim 2\text{mm}$ ) using the interfacial gauge.<sup>[36]</sup> The force as a function of surface separation was measured in dry conditions, near saturation, and in water. In humid air, the force curve obtained as the surfaces were brought together was shifted toward larger distances compared with dry conditions, presumably because layers of water were adsorbed between the substrate and the

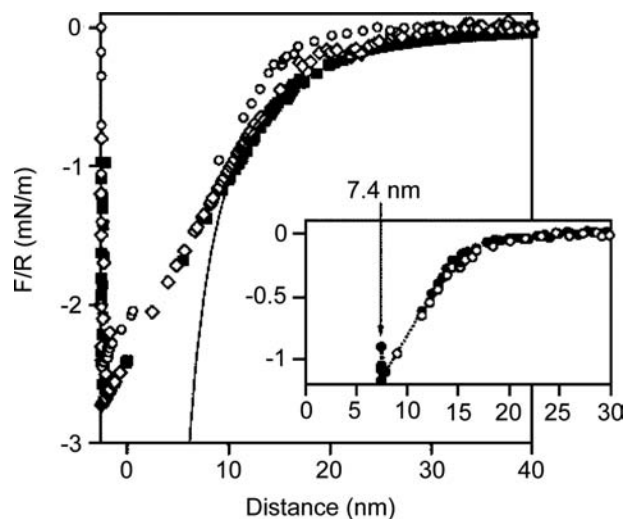


**Fig. 6** Measured forces on approach to saturated water vapor of fluorinated surfaces prepared by three different methods: ( $\circ$ ) Langmuir–Blodgett deposition; ( $\diamond$ ) FTE adsorbed from  $\text{CHCl}_3$ ; ( $\blacksquare$ ) FTE adsorbed from the neat solution. In the inset of the lower figure, the force profile of Langmuir–Blodgett in humid air (shifted to larger distances) is compared with that in dry air ( $\cdots \cdots \bullet \cdots \cdots$ ). The solid line is a fit obtained with the equation for the capillary force [Eq. (4)] *Source:* From Ref.<sup>[35]</sup>, with  $V = 3 \times 10^{-15} \text{ cm}^3$ . From Fig. 5 of Ref.<sup>[37]</sup>.

fluorocarbon layer (Fig. 6). No capillary condensation forces were detected with increasing humidity even though SAM thickness increased.<sup>[37]</sup> This suggests that in this case, the silane SAM is not covalently bound to the silica surface. The response to humidity is reversible in that if the water vapor is removed, the forces measured in dry conditions are recovered.

## ALKYLSILANE SAMS ON MICA

Alkylsilanes have attracted attention because they are capable of cross-polymerization and covalent attachment to SiO<sub>2</sub>-based oxide surfaces such as oxidized silicon wafers. Mica also contains Si–O bonds, but there are no inherent functional groups on the surface to serve as attachment sites. SAMs on mica are potentially useful in non-linear optics because mica can be prepared as relatively large, molecularly smooth sheets.<sup>[1]</sup>

Several research groups have investigated the deposition of alkylsilanes, mostly OTS and OTE, on mica.<sup>[38–42]</sup> These monolayers are hydrophobic as judged by the contact angle of water, but in some cases, the contact angle decreases with prolonged exposure to water.<sup>[42,43]</sup> Tian et al.<sup>[39]</sup> investigated the effect of humidity on the friction force on OTE SAMs on mica. On bare mica, water acts as a lubricant and the friction force decreases gradually as humidity increases. At low humidities, an OTE SAM coating also serves as a good lubricant, reducing friction. As humidity increases, friction increases, indicating that water in contact with the OTE SAM decreases its lubricating effectiveness. Above ~30% RH, the film breaks down at a critical load and the tip contacts bare mica. The load required to cause breakdown decreases as humidity increases, indicating that the presence of water makes it easier to remove the SAM. Because the OTE SAM is not fully compact because of long-range disordering, condensed water can penetrate through the film to the OTE–mica interface. The accumulation of water at the interface weakens the OTE–mica links as well as the links between OTE molecules; therefore the film quality deteriorates.

Kim, Christernson, and Curry<sup>[42]</sup> used the SFA to study OTE SAMs on mica. In this case, the OTE SAM was deposited on both bare mica and plasma-pretreated mica. Because mica has no functional groups to which the OTE can bond covalently, plasma treatment was used to break surface Si–O–Si bonds to create an opportunity for covalent attachment between the OTE SAM and mica. In this work, OTE SAMs deposited on both untreated and plasma-treated mica were initially highly hydrophobic, but contact angle hysteresis indicated that water interacts favorably with the monolayers on prolonged exposure. Defects in the monolayer most likely make it possible for the water to

reach the hydrophilic region between the silane head-groups and the mica. More water was adsorbed by the monolayers on untreated mica compared with the plasma-treated case. This work strongly indicated that if the SAM is not firmly anchored to the substrate, water can accumulate in the region between the SAM and the substrate. Near saturation, water droplets also condensed on the surface presumably as monolayer defects regardless of how well the SAM was anchored. At very high humidities, a capillary condensed annulus of water was observed around the contact zone.

In a further study, Kim, Christernson, and Curry<sup>[44]</sup> used the SFA to investigate the effect of humidity on surface deformation and adhesion of untreated and plasma-treated mica surfaces coated with OTE SAMs. In general, when two solid bodies come into contact, they deform in a way that is determined by their elastic or viscoelastic properties, by the surface forces between them, and by any externally applied load.<sup>[45]</sup> Because of the practical importance of understanding interparticle adhesion, the relationship between surface deformation and adhesion has been studied extensively.<sup>[18]</sup> Capillary condensation acts outside the contact area and modifies the adhesive force in two interrelated ways: first, by altering the surface deformation; and, second, by increasing the adhesive force because of the Laplace pressure in the annulus. In the presence of a capillary condensed liquid bridging the two surfaces, the measured adhesive force has contributions both from the direct solid–solid adhesion and from the Laplace pressure arising from the liquid–vapor interface.<sup>[46]</sup> In this study, the size of the contact area was measured as a function of applied load and the contact mechanics-based Maugis model outlined in Eqs. (12–14) was applied to extract the capillary condensation and solid–solid contributions to the adhesive force. The SFA is particularly well suited for these experiments because the interferometric technique allows direct observation of the surface shape and size of the contact zone. Pulloff forces were also measured by pulling the surfaces apart. Fig. 7 shows adhesive forces obtained from both methods. From load-vs.-contact area measurements, it is clear that the adhesive force because of capillary condensation depends on humidity. It decreases from the highest values near saturation to zero in dry conditions. This is not unexpected and has been shown previously.<sup>[47]</sup> However, Eq. (5) predicts that the adhesive force because of capillary condensation is independent of humidity. There is agreement with Eq. (5) at high humidities. At low humidities before capillary condensation is detectable, pulloff forces agree well with predicted adhesive forces determined from force-vs.-contact area measurements and the Maugis model. At high humidity, force-vs.-contact area values are generally higher than the pulloff force measurements. It is

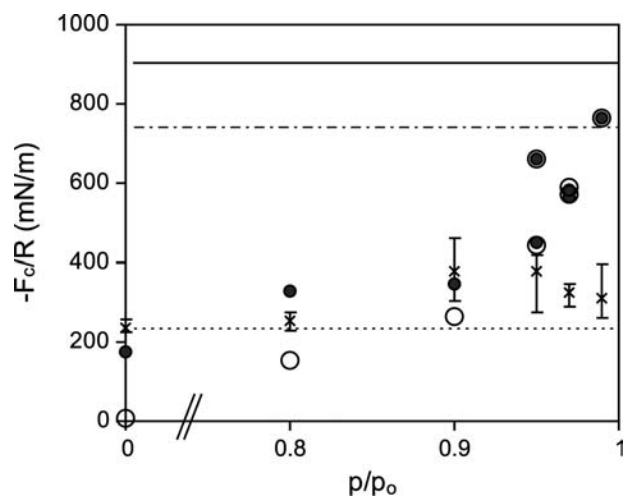


**Fig. 7** Normalized adhesive force for OTE on untreated mica as a function of RH. The open and closed circles denote the Laplace pressure contribution to the adhesive force and the total adhesive force predicted from the Maugis model. Experimental pulloff force measurements are denoted by x symbols, with error bars indicating the range of measured values. Horizontal lines denote the normalized adhesive force due to capillary condensation as calculated from Eq. (5) with  $\theta_1 = \theta_2 = 0^\circ$  (—),  $35^\circ$  (---), and  $75^\circ$  (- - -). Source: From Fig. 5 of Ref.<sup>[44]</sup>.

suggested that the difference is because of the history of the surfaces prior to pulloff. In force-vs.-area measurements, a load is applied to push the surfaces together before pulling them apart slowly, whereas in pulloff force measurements, the surfaces are separated more rapidly without applying an extra load. This work suggests that adhesion between OTE SAMs on mica is not dominated by capillary condensation below  $\sim 80\%$  RH. At higher RH, the effect of capillary condensation on the adhesive force is significant and depends on the amount of compression prior to detachment.

## CONCLUSION

Capillary condensation increases adhesion between contacting surfaces in humid environments. Hydrophobic SAMs reduce this effect by reducing surface wettability. SAMs must be resistant to water-induced degradation to effectively reduce adhesion in the long term. There are relatively few studies that address the effect of humidity on SAMs despite the importance of this effect in practical applications. Among these studies, there is substantial variability in the reported effectiveness of hydrophobic SAMs in reducing adhesion in humid environments. This depends on the particular SAM, the substrate, and the SAM deposition method. Even for initially hydrophobic

SAMs, exposure to humidity over long time periods is shown to reduce SAM stability and effectiveness in some cases. Further work in this area is needed to fully understand the effect of humidity on SAM stability and adhesion.

## ACKNOWLEDGMENTS

This work has been supported by the American Chemical Society Petroleum Research Fund.

## REFERENCES

1. Ulman, A. *An Introduction to Ultrathin Organic Films from Langmuir-Blodgett to Self-Assembly*; Academic Press: London, 1991.
2. Gooding, J.J.; Hibbert, D.B. The application of alkanethiol self-assembled monolayers to enzyme electrodes. *Trends Anal. Chem.* **1999**, *18* (8), 525–533.
3. Lee, M.; Kim, T.I.; Kim, K.H.; Kim, J.H.; Choi, M.S.; Choi, H.J.; Koh, K. Formation of a self-assembled phenylboronic acid monolayer and its application toward developing a surface plasmon resonance-based monosaccharide sensor. *Anal. Biochem.* **2002**, *310* (2), 163–170.
4. Patton, S.T.; Cowan, W.D.; Eapen, K.C.; Zabinski, J.S. Effect of surface chemistry on the tribological performance of a MEMS electrostatic lateral output motor. *Tribol. Lett.* **2000**, *9* (3–4), 199–209.
5. Liu, H.; Bhushan, B. Investigation of nanotribological properties of self-assembled monolayers with alkyl and biphenyl spacer chains. *Ultramicroscopy* **2002**, *91* (1–4), 185–202.
6. Bhushan, B. *Handbook of Micro/Nanotribology*, 2nd Ed. CRC Press: Boca Raton, FL, 1999.
7. Komvopoulos, K.; Yan, W. A fractal analysis of stiction in microelectromechanical systems. *J. Tribol.* **1997**, *119* (4), 391–400.
8. Stanley, H.M.; Etsion, I.; Bogy, D.B. Adhesion of contacting rough surfaces in the presence of subboundary lubrication. *J. Tribol.* **1990**, *112* (1), 98–104.
9. Chen, Y.L.; Israelachvili, J.N. Effects of ambient conditions on adsorbed surfactant and polymer monolayers. *J. Phys. Chem.* **1992**, *96* (19), 7752–7760.
10. Chen, Y.L.E.; Gee, M.L.; Helm, C.A.; Israelachvili, J.N.; McGuiggan, P.M. Effects of humidity on the structure and adhesion of amphiphilic monolayers on mica. *J. Phys. Chem.* **1989**, *93* (20), 7057–7059.
11. Berman, A.D.; Cameron, S.D.; Israelachvili, J.N. Mobility of surfactants in and between adsorbed monolayers. *J. Phys. Chem., B* **1997**, *101* (29), 5692–5697.
12. Orr, F.M.; Scriven, L.E.; Rivas, A.P. Pendular rings between solids—Meniscus properties and capillary force. *J. Fluid Mech.* **1975**, *Feb.* **25**, 67, 723–742.
13. Defay, R.; Prigogine, I.; Bellemans, A. *Surface Tension and Adsorption*; Wiley: New York, 1966.
14. Melrose, J.C. Model calculations for capillary condensation. *AIChE J.* **1966**, *12* (5), 986–994.
15. Xiao, X.; Qian, L. Investigation of humidity dependent capillary force. *Langmuir* **2000**, *16* (21), 8153–8158.

16. Johnson, K.L.; Kendall, K.; Roberts, A.D. Surface energy and contact of elastic solids. *Proc. R. Soc. Lond., A* **1971**, *324* (1558), 301–313.
17. Derjaguin, B.V.; Muller, V.M.; Toporov, Y.P. Effect of contact deformations on adhesion of particles. *J. Colloid Interface Sci.* **1975**, *53* (2), 314–326.
18. Maugis, D. Adhesion of spheres—the JKR–DMT transition using a Dugdale model. *J. Colloid Interface Sci.* **1992**, *150* (1), 243–269.
19. Maugis, D.; Gauthier-Manuel, B. JKR–DMT transition in the presence of a liquid meniscus. *J. Adhes. Sci. Technol.* **1994**, *8* (11), 1311–1322.
20. Miura, Y.F.; Takenaga, M.; Koini, T.; Graupe, M.; Garg, N.; Graham, R.L., Jr.; Lee, T.R. Wettabilities of self-assembled monolayers generated from CF<sub>3</sub>-terminated alkanethiols on gold. *Langmuir* **1998**, *14* (20), 5821–5825.
21. Gooding, J.J.; Mearns, F.; Yang, W.; Liu, J. Self-assembled monolayers into the 21st century: recent advances and applications. *Electroanalysis* **2003**, *15* (2), 81–96.
22. Li, L.; Chen, S.; Jiang, S. Nanoscale frictional properties of mixed alkanethiol self-assembled monolayers on Au(111) by scanning force microscopy: humidity effect. *Langmuir* **2003**, *19* (3), 666–671.
23. Yoshizawa, H.; Chen, Y.L.; Israelachvili, J. Fundamental mechanisms of interfacial friction: 1. relation between adhesion and friction. *J. Phys. Chem.* **1993**, *97* (16), 4128–4140.
24. Quon, R.A.; Ulman, A.; Vanderlick, T.K. Impact of humidity on adhesion between rough surfaces. *Langmuir* **2000**, *16* (8), 8912–8916.
25. Israelachvili, J.N.; Adams, G. Measurement of forces between 2 mica surface in aqueous–electrolyte solutions in the range 0–100 nm. *J. Chem. Soc., Faraday Trans., I* **1978**, *74*, 975–1001.
26. Ulman, A. Formation and structure of self-assembled monolayers. *Chem. Rev.* **1996**, *96* (4), 1533–1554.
27. Stevens, M.J. Thoughts on the structure of alkylsilane monolayers. *Langmuir* **1999**, *15* (8), 2773–2778.
28. Zhang, L.; Li, L.; Chen, S.; Jiang, S. Measurements of friction and adhesion for alkyl monolayers on Si(111) by scanning force microscopy. *Langmuir* **2002**, *18* (14), 5448–5456.
29. He, M.; Szuchmacher Blum, A.; Aston, D.E.; Buenviaje, C.; Overney, R.M.; Luginbuhl, R. Critical phenomena of water bridges in nanoasperity contacts. *J. Chem. Phys.* **2001**, *114* (3), 1355–1360.
30. De Boer, M.P.; Knapp, J.A.; Michalske, T.A.; Srinivasan, U.; Maboudian, R. Adhesion hysteresis of silane coated microcantilevers. *Acta Mater.* **2000**, *48* (18–19), 4531–4541.
31. Howe, R.T. Surface micromachining for microsensors and microactuators. *J. Vac. Sci. Technol., B* **1988**, *6* (6), 1809–1813.
32. Mayer, T.M.; De Boer, M.P.; Shinn, N.D.; Clews, P.J.; Michalske, T.A. Chemical vapor deposition of fluoroalkylsilane monolayer films for adhesion control in microelectromechanical systems. *J. Vac. Sci. Technol., B* **2000**, *18* (5), 2433–2440.
33. Feng, X.; Fryxell, G.E.; Wang, L.Q.; Kim, A.Y.; Liu, J.; Kemner, K.M. Functionalized monolayers on ordered mesoporous supports. *Science* **1997**, *276* (5314), 923–926.
34. Tripp, C.P.; Hair, M.L. Direct observation of the surface bonds between self-assembled monolayers of octadecyltrichlorosilane and silica surfaces: a low-frequency IR study at the solid / liquid interface. *Langmuir* **1995**, *11* (4), 1215–1219.
35. Ohnishi, S.; Yaminsky, V.V.; Christenson, H.K. Measurements of the force between fluorocarbon monolayer surfaces in air and water. *Langmuir* **2000**, *16* (22), 8360–8367.
36. Yaminsky, V.V.; Ninham, B.W.; Stewart, A.M. Surface activity and ion exchange. A study via surface tension, wetting tension, and surface force techniques. *Langmuir* **1996**, *12* (3), 836–850.
37. Ohnishi, S.; Ishida, T.; Yaminsky, V.V.; Christenson, H.K. Characterization of fluorocarbon monolayer surfaces for direct force measurements. *Langmuir* **2000**, *16* (6), 2722–2730.
38. Peanasky, J.; Schneider, H.M.; Granick, S.; Kessel, C.R. Self-assembled monolayers on mica for experiments utilizing the surface forces apparatus. *Langmuir* **1995**, *11* (3), 953–962.
39. Tian, F.; Xiao, X.; Loy, M.M.T.; Wang, C.; Bai, C. Humidity and temperature effect on frictional properties of mica and alkylsilane monolayer self-assembled on mica. *Langmuir* **1999**, *15* (1), 244–249.
40. Parker, J.L.; Claesson, P.M.; Cho, D.L.; Ahlberg, A.; Tidblad, J.; Blomberg, E. Plasma modification of mica. *J. Colloid Interface Sci.* **1990**, *134* (2), 449–458.
41. Wood, J.; Sharma, R. Interaction forces between hydrophobic mica surfaces. *Langmuir* **1995**, *11* (12), 4797–4802.
42. Kim, S.; Christenson, H.K.; Curry, J.E. The effect of humidity on the stability of an octadecyltriethoxysilane monolayer self-assembled on untreated and plasma-treated mica. *Langmuir* **2002**, *18* (6), 2125–2129.
43. Xiao, X.D.; Liu, G.; Charych, D.H.; Salmeron, M. Preparation, structure, and mechanical stability of alkylsilane monolayers on mica. *Langmuir* **1995**, *11* (5), 1600–1604.
44. Kim, S.; Christenson, H.K.; Curry, J.E. *N*-octadecyltriethoxysilane monolayer coated surfaces in humid atmospheres: Influence of capillary condensation on surface deformation and adhesion. *J. Phys. Chem., B* **2003**, *107* (16), 3774–3781.
45. Horn, R.G.; Israelachvili, J.N.; Pribac, F. Measurement of the deformation and adhesion of solids in contact. *J. Colloid Interface Sci.* **1987**, *115* (2), 480–492.
46. Israelachvili, J.N. *Intermolecular and Surface Forces*, 2nd Ed. Ed.; Academic Press: New York, 1991.
47. Christenson, H.K. Adhesion between surfaces in undersaturated vapors—a reexamination of the influence of meniscus curvature and surface forces. *J. Colloid Interface Sci.* **1988**, *121* (1), 170–178.



# Adsorption on Heterogeneous Surfaces

Vinay K. Gupta

Yu-Wen Huang

*Department of Chemical Engineering, University of Illinois at Urbana–Champaign, Urbana, Illinois, U.S.A.*

## INTRODUCTION

In this review, we focus on the role of surface heterogeneity in polymer adsorption and discuss novel experiments that clarify the impact of topographical and chemical heterogeneity on adsorption of flexible polymers and globular proteins. The comparison of the experimental results with existing theoretical predictions provides valuable insights into the adsorption process and guides future development of theory and experiments. Furthermore, these results provide a starting point for more sophisticated design and control of polymer adsorption at the nanoscale and in engineering of surfaces to achieve specific tasks.

The importance of polymer and protein adsorption stems from its critical role in a host of industrial applications such as adhesion, biocompatibility, colloidal stabilization, and chromatography. Scientifically, the interfacial behavior of globular proteins and long, flexible macromolecules and the accompanying balance of enthalpic and entropic effects from surface–segment interactions provide a system replete with interesting static and dynamic phenomena. Consequently, adsorption of polymers and biopolymers at a solid–liquid interface has been the subject of intense investigation over the last decade.

Despite the advances in characterization and theoretical understanding of near-equilibrium properties of adsorbed polymer layers, several aspects of the adsorption process remain elusive.<sup>[1–3]</sup> Among these elusive aspects is the effect of nanometer scale compositional and topographical heterogeneity of surfaces (Fig. 1A) on the process of adsorption and the structural properties of the adsorbed layer. Because adsorption frequently occurs on real surfaces such as minerals, pigments, colloidal particles, and biological membranes that are inherently heterogeneous, understanding the impact of surface heterogeneity is an essential prerequisite to controlling the adsorption process.

## BACKGROUND

### Modeling of Transport and Adsorption of Macromolecules

Adsorption at a surface occurs from a bulk polymer solution if the net change of free energy is negative. The surface–segment contacts of the polymer provide a gain of adsorption energy to balance the loss of translational and conformational entropy from the confinement at the interface. The properties of the adsorbed layer depend not only on the thermodynamic details of the system but also on the adsorption history.<sup>[4]</sup> Therefore control of adsorption requires a complete understanding of adsorption kinetics and the role of the surface.

Three main steps are typically involved in polymer adsorption: mass transport toward the surface, surface attachment, and spreading or conformational rearrangement toward equilibrium configurations.<sup>[1–3]</sup> The driving force for transport from bulk solution is the gradient between the bulk solution concentration ( $C_b$ ) and the subsurface concentration ( $C_s$ ). Because the gradient is established rapidly in most cases, the flux of the polymer can be

$$J(t) = \frac{C_b - C_s(\Gamma)}{R_m} \quad (1)$$

where the mass transfer resistance ( $R_m$ ) depends on the convection–diffusion in bulk solution.  $R_m$  can be expressed as  $1/k_m$ , where  $k_m$  is the mass transfer coefficient.  $C_s$  depends on the surface excess ( $\Gamma$ ) of the polymer and its temporal evolution

$$\frac{d\Gamma(t)}{dt} = \frac{C_s(\Gamma) - C_{eq}}{R_b(\Gamma)} \quad (2)$$

The processes of penetration of a chain through an already adsorbed layer of polymer, attachment to the



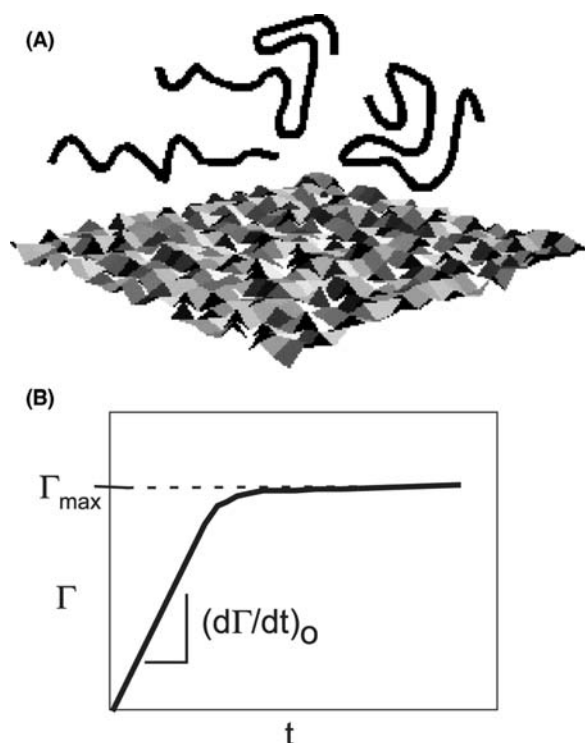


**Fig. 1** Schematic of (A) a heterogeneous surface and (B) evolution of the surface excess ( $\Gamma$ ).

surface, and spreading on the surface determine the barrier resistance  $R_b$ .<sup>[5]</sup>

At pseudo-steady state, the flux and the rate of adsorption are equal, which gives

$$\frac{d\Gamma(t)}{dt} = \frac{C_b - C_{eq}}{R_m + R_b(\Gamma)} \quad (3)$$

During the formative stages of an adsorbed layer,  $R_m$  should dominate and for high-affinity adsorption,  $C_{eq} \sim 0$ . Therefore the initial rate of adsorption becomes

$$\left(\frac{d\Gamma(t)}{dt}\right)_0 = \frac{C_b}{R_m} \quad (4)$$

and  $\Gamma(t)$  typically shows a linear rise (Fig. 1B). Over a longer period equilibrium is established and  $\Gamma(t)$  reaches a plateau, which is determined by parameters such as solvency,  $C_b$ , surface-segment interaction, and molecular weight.

### Adsorption on Heterogeneous Surfaces: Theoretical and Simulation Studies

In previous theoretical studies on the role of physical heterogeneity, rough surfaces were modeled as random, fractal, and periodically structured.<sup>[6–10]</sup>

Most of these studies came to the conclusion that adsorption is enhanced with surface roughness. Ji and Hone<sup>[11]</sup> predicted that the enhancement is most significant when amplitudes and spatial size of roughness are of the order of a polymer chain or Kuhn length, which is of nanometer dimensions. The enhancement occurs as larger adsorption energy is gained by increasing probability of polymer-surface intersections in comparison to a smooth planar interface. Consequently, a polymer chain undergoes smaller distortion and configurational entropy penalty is also predicted to be less relative to adsorption on flat surfaces. These studies predicted that a polymer can adsorb on a rough surface and not on a flat surface even if the chemical interface is identical.

More recent investigations<sup>[12]</sup> have explored the role of polymer architecture in adsorption on rough surfaces. Striolo and Prausnitz predicted that adsorption occurs readily for branched polymers compared to linear polymer chains because a smaller entropic penalty is involved for adsorption of globular polymers. However, when the interaction between polymer segments and surface becomes strong enough, it was predicted that a linear polymer chain can spread more than the globular polymer as the entropic loss is overcome by the gain in adsorption energy from spreading. Thus for highly attractive segment-surface interactions, linear polymers are believed to adsorb strongly compared to globular polymers.

In previous theoretical studies, the influence of chemical heterogeneity on adsorption varied with the systems. The chemical heterogeneity of the surfaces was manipulated by changing the distribution, size, and shape of the heterogeneity.<sup>[13–18]</sup> Meanwhile, several types of polymers such as a homopolymer, a block-copolymer, and an end-sticking polymer were employed in simulations. Heterogeneous interaction between polymer and surfaces was predicted to be a larger weighing factor than physical heterogeneity in polymer adsorption.<sup>[19]</sup> Several remarkable effects were found in these studies. First, the heterogeneity on the surfaces induced adsorption even when the average surface was neutral. It was predicted that adsorption was enhanced for homopolymers because of the presence of heterogeneity. Second, most studies pointed out that the distribution and size of adsorbing sites and nonadsorbing sites play a crucial role. Again, the domain size was required to be commensurate to that of polymer chains. When a threshold value of either the distribution or the size of domains was reached, polymers responded to the surface in dramatically different ways. This was reflected in the adsorption behavior, the amount, and the arrangement of polymers on the surfaces. In the case of homopolymers, van der Linden and coworkers showed that a mere change in the distribution of sites could cause a

nonadsorbing surface to become adsorbing. Sumithra and Sebastian observed a sudden change in the size of an adsorbed polymer. In the case of block copolymers and end-sticking polymers, change of domain sizes on the surface caused segregation of polymers in a uniform adsorbed layer.

In addition to the focus on homopolymers and copolymers, recent studies have used Monte Carlo simulation and replica field theory to explore the adsorption behavior of random heteropolymers (RHPs) on chemically heterogeneous surfaces.<sup>[20,21]</sup> Striking recognition between polymers and random surfaces has been predicted. A sharp transition from weak to strong adsorption was seen when the statistical sequence of chain segments and the randomness of sites on surfaces were related. Similar instances of pattern matching have also been predicted during adsorption of charged polyelectrolytes on surfaces with a pattern of charges.<sup>[22]</sup> Recently, Genzer developed a three-dimensional self-consistent field lattice model to study adsorption of copolymers and showed that architecture as well as composition is important in the pattern recognition.<sup>[23]</sup> By using different copolymers such as alternating, diblock, and triblock copolymers with various ratio of adsorbing segments, chemical heterogeneity on surfaces could either be masked or amplified and recognition could be extended into the third dimension normal to the surface.

Thus theory and simulation based on statistical physics has explored extensively the influence of both chemical and physical heterogeneity on the adsorption behavior of polymeric chains. However, corroboration by systematic and well-defined experiments to test and exploit these predictions has been nonexistent. The bottleneck for realizing actual systems lies in the difficulty of manipulating heterogeneity on a size scale that is commensurate with that of a polymer chain (typical radius of gyration of 10–100 nm). By modifying and characterizing surfaces at a molecular level, we have carried out the first studies to overcome the experimental challenges. The next few sections review these experimental results.

## IMPACT OF NANOMETER SCALE PHYSICAL HETEROGENEITY

In recent years, synthesis of surfaces and control of interfacial properties has been transformed by the use of self-assembled monolayers (SAMs).<sup>[24]</sup> Their excellent chemical stability, low defect density, and spontaneous formation permit the preparation of a well-defined interface on a molecular level, easily and reproducibly. We have addressed the challenge of preparing physically heterogeneous surfaces that are commensurate with the typical dimensions of a

polymer chain and are chemically homogeneous.<sup>[25]</sup> The approach exploits ultraflat, template-stripped gold films and rough, evaporated gold films supporting self-assembled monolayers. In addition, a surface plasmon resonance technique that permits in situ measurements at the solid–liquid interface with high time resolution is used to investigate the kinetics of adsorption. With these two tools, we have studied in detail the adsorption of a flexible, uncharged polymer such as poly(ethylene oxide) (PEO) and established the interplay between physical heterogeneity, the polymer flux to the surface, and the polymer chain length.<sup>[26]</sup>

Fig. 2 shows the typical surface plot and cross-section analysis of a rough and an ultraflat gold substrate. When compared to cases considered by past theoretical studies of adsorption on physically heterogeneous surfaces, the images show that the experimental system here represents a case of polymer adsorption onto a random surface rather than a periodically structured surface. Both substrates possess a grainy but distinct surface texture, which indicates that the spatial distribution of surface roughness differs for the two surfaces. The evaporated rough gold substrate shows a larger range of feature heights compared to ultraflat template-stripped substrate.

Because the surfaces are characterized by small vertical deviations in surface topography with high spatial complexity, the variation of root-mean-square roughness  $R_{\text{rms}}$  with the lateral length-scale was analyzed. The variational  $R_{\text{rms}}$  for the rough and ultraflat gold substrates increases as the lateral length scale increases above 10 nm and becomes independent beyond a spatial scale of 60 nm. This macroscopic value is  $R_{\text{rms}} \sim 8 \text{ \AA}$  for the rough gold substrate and  $R_{\text{rms}} \sim 3 \text{ \AA}$  for the ultraflat surface, which is perceived in the real-space images as a difference in vertical heights. Between 10 and 60 nm, the geometric complexity of the surfaces is fractal-like and the fractal dimension ( $D_F$ ) for rough gold substrate is approximately 2.25 and for ultraflat substrate is approximately 2.15. Because of this fractal-like nature, the relative area of peaks and valleys on the surfaces shown in Fig. 2 changes with the image size for lateral length scales below 60 nm. This length scale is commensurate with the typical dimensions of a polymer chain. Furthermore, the vertical deviations in height for both surfaces are comparable to the size of a few monomers along the polymer chain over a wide spatial extent. The topography of these surfaces is well suited to test the predictions of theoretical studies.

In order to ensure that the two gold substrates have identical chemical interface, a self-assembled monolayer of dodecanethiol ( $\text{CH}_3(\text{CH}_2)_{11}\text{SH}$ ) was formed on both substrates. The advancing contact angle ( $\theta_a$ ) of hexadecane on the resulting surfaces was 46–47°,

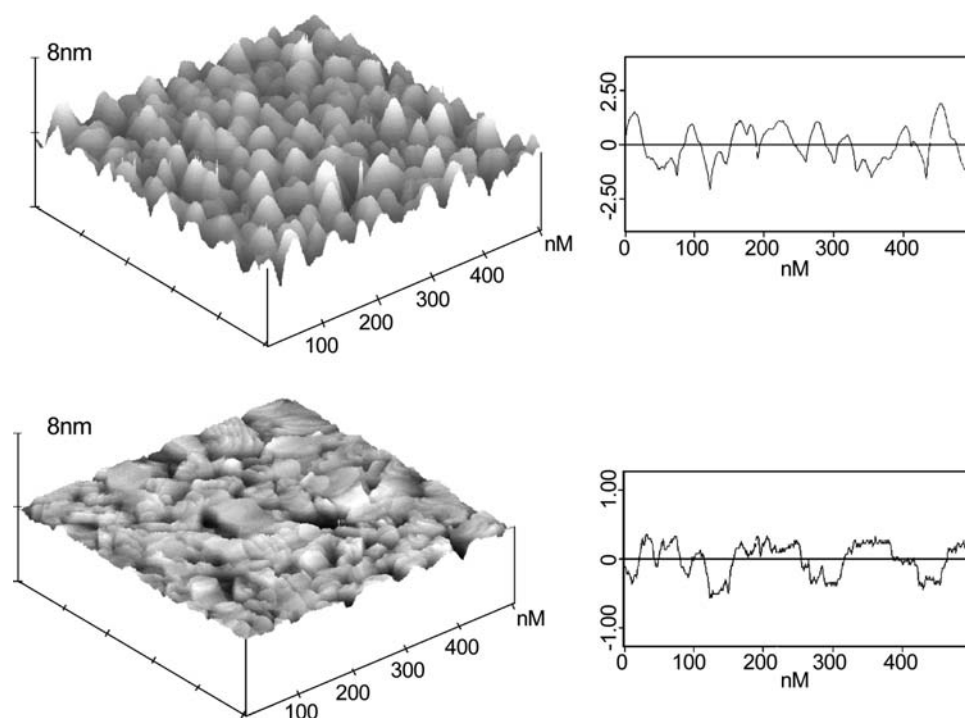


**Fig. 2** STM image and cross section of a rough gold substrate (top) and an ultra-flat gold substrate (bottom).

which is consistent with an interface of densely packed  $\text{CH}_3$  groups. The receding contact angles ( $\theta_r$ ) for the monolayers supported on the rough gold substrate showed a contact angle hysteresis of  $4^\circ$  and the monolayers on the ultraflat substrate gave a hysteresis of  $1^\circ$ . These different values of hysteresis reflect the differences in the topography of the substrates supporting the monolayers.

Fig. 3A shows the adsorption isotherm for PEO with a molecular weight ( $M_w$ ) of 53.5 kDa. PEO has similar maximum surface excess ( $\Gamma_{\max}$ ) at low and high bulk concentrations, which indicates high affinity adsorption behavior on both surfaces [Eq. (4)]. Fig. 3B shows the effect of molecular weight on the adsorption amount in the plateau regime for a bulk concentration of 1 ppm. Higher  $M_w$  gives slightly larger adsorption amounts. This is generally because longer polymer chains can form longer loops and tails than shorter chains, as predicted by the Scheutjens–Fleer model.<sup>[1]</sup> The dependency of adsorption amount on molecular weight is stronger for shorter chains and approaches a limit for longer chains. Rough gold surfaces and ultraflat surfaces possess the same degree of hydrophobicity but different extents of surface roughness. Interestingly, plateau adsorption amounts on ultraflat surfaces are 20–30% lower than that on rough surfaces for the various molecular weights investigated. These results indicate that the maximum surface excess of the polymer increases because of the presence of physical heterogeneity. This is the first experimental

corroboration of the theoretical predictions that adsorbed amount of a polymer increases with surface roughness.

The surface area occupied by a PEO chain on the surface can be estimated from

$$A = \frac{M_w}{\Gamma_{\max} N_A} \quad (5)$$

The lower values of  $\Gamma_{\max}$  in Fig. 3B for the ultraflat surfaces lead to higher area per chain and indicate that the adsorbed polymer chains flatten slightly more on the smooth substrates relative to the rough surfaces. Because the spreading of chains on ultraflat surfaces will occur on time-scales that are characteristic of the polymeric system and the adsorption conditions, it is useful to analyze the evolution of  $\Gamma(t)$ . Fig. 3C shows the evolution of  $\Gamma(t)$  for a PEO chain ( $M_w = 230.7$  kDa) on rough and ultraflat surfaces. Both adsorption curves resemble the schematic  $\Gamma(t)$  shown in Fig. 1B. However, the effect of physical heterogeneity is clearly revealed in the initial adsorption rate, which is higher on rough surfaces. Except for a very short PEO ( $\sim 10$  kDa), the difference  $\Delta(d\Gamma/dt)_0$  is manifested in the adsorption of several different PEO ranging from 53.5 to 624 kDa.

Because the adsorption occurs under the same flow and concentration conditions (i.e.,  $R_m$  and  $C_b$ ), the simplified Eq. (4) cannot be used to interpret the

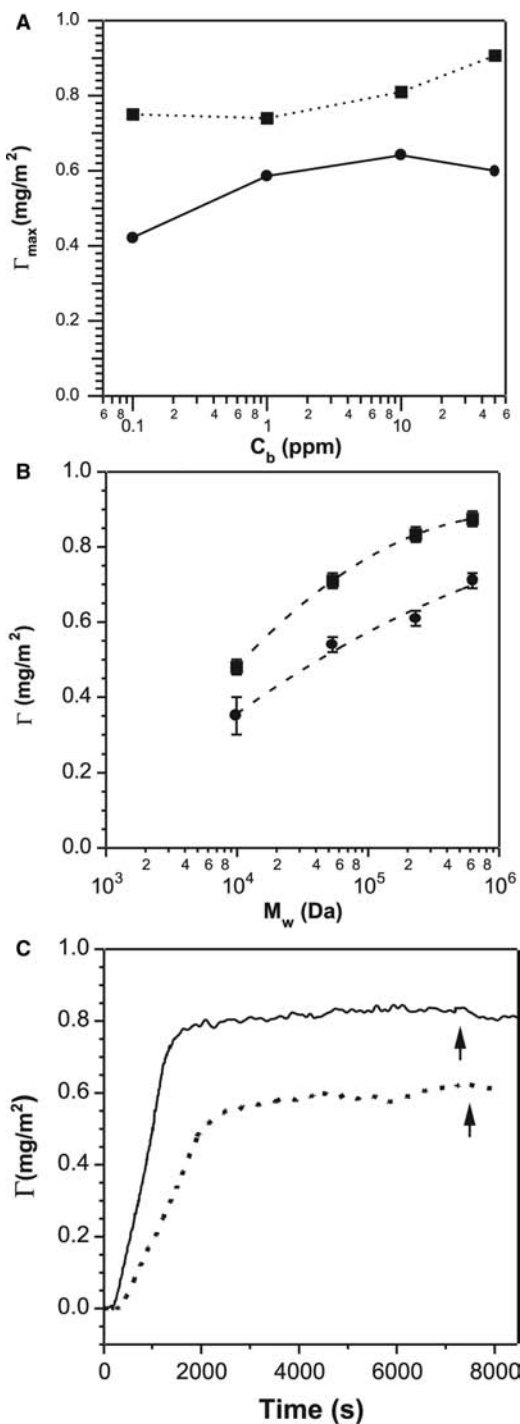


**Fig. 3** Adsorbed amount of PEO as a function of bulk concentration in solution (A) and molecular weight (B) on rough surfaces (squares) and ultra-flat surface (circles). (C) An illustration of  $\Gamma(t)$  for PEO adsorption on rough (solid line) and ultra-flat (dashed line) surfaces.

difference  $\Delta(d\Gamma/dt)_o$ . Instead, the experimental results suggest that

$$\left(\frac{d\Gamma(t)}{dt}\right)_o = \frac{C_b}{R_m + R_b(\Gamma)} \quad (6)$$

is more appropriate for the ultraflat surface and that a finite resistance  $R_b$  due to spreading, attachment, and penetration of polymer chains leads to a lower initial rate of adsorption. This conclusion is supported by a disappearance of the difference in initial rate of adsorption as the bulk concentration  $C_b$  and the bulk flow velocity is increased (Fig. 4). Physically, the polymer flux increases as  $J \propto C_b$  and  $k_m \propto v^{1/3}$ . As a consequence of the rapid transport of chains to the surface, the spreading of the chains on ultraflat gold during the initial stages of adsorption is suppressed and no difference in initial rate is observed. Fig. 4 shows that this interplay between transport effects and reorganization of polymer chains on the surface is a function of the length of the polymer chain. In contrast to PEO of  $M_w = 53.5$  kDa, it is significantly harder to suppress the difference in  $(d\Gamma/dt)_o$  by increasing the convective flux via  $C_b v^{1/3}$  for long chains. On the other hand, for low molecular weight materials, the difference in the rate of adsorption is not observed because of the progressive difficulty in accessing very low values of  $C_b v^{1/3}$  in the experimental window.

As chain length impacts the structure of the adsorbed layer, at this stage it is not possible to attribute the variation in kinetic effects with  $M_w$  to either the interaction potential between the polymer and the surface or the time scale of spreading. While the experiments on physically heterogeneous surfaces corroborate

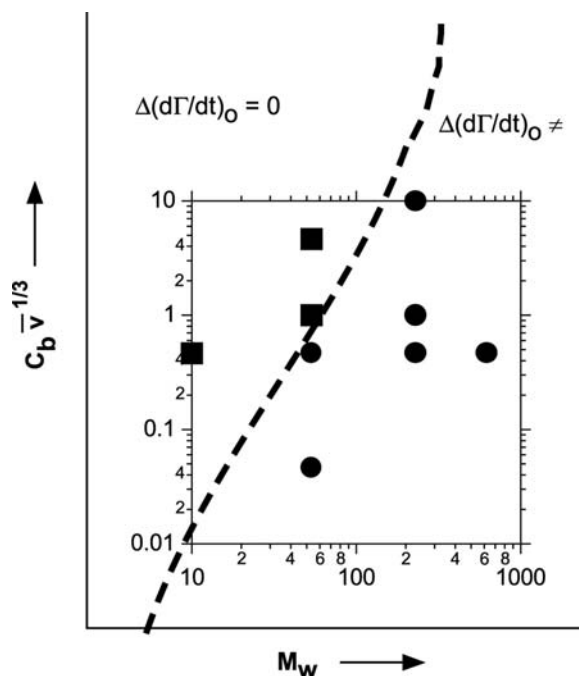


**Fig. 4** Plot showing interplay between  $M_w$  and convective flux on the difference in initial rate of adsorption for rough and ultra-flat surfaces (see text for discussion). Experimental points are shown as symbols.

theoretical predictions, they also underscore the need for development of new kinetic models that will not only aid in interpreting results such as those presented here but also guide newer experiments for understanding polymer adsorption at an interface that is heterogeneous on the nanometer scale.

### IMPACT OF CHEMICAL HETEROGENEITY

Design of surfaces using SAMs provides a hitherto unexplored approach to experimentally understand the effects of chemical heterogeneity of surfaces on polymer adsorption.<sup>[27,28]</sup> It is well known that millimeter- or micrometer-sized patterns in self-assembled monolayers can be created using techniques such as UV photooxidation, microcontact printing, and micromachining.<sup>[29]</sup> However, these patterns are large compared to the typical dimensions of a polymer chain and not predicted to dramatically alter the adsorption behavior. Patterning on length scales smaller than 200 nm using nano-lithography is possible but impractical for areas as large as 1 cm<sup>2</sup> that are necessary for noninvasive optical measurements of adsorption.

In contrast, mixed SAMs formed by coadsorption from a mixture of long and short chains [e.g., CH<sub>3</sub>(CH<sub>2</sub>)<sub>9</sub>SH (DT) and HOOC(CH<sub>2</sub>)<sub>3</sub>SH (MPA)] can produce quenched heterogeneous surfaces with a statistical distribution of nanometer-sized domains when the relative proportion of the two species and the time of formation is carefully controlled.<sup>[30–32]</sup>

Fig. 5A shows a low-current STM image of the typical mixed monolayer used in the polymer adsorption. Bright domains correspond to areas dominated by a longer methyl-terminated alkanethiol (DT) while the rest of the gold surface corresponds to regions that are rich in the carboxylic acid terminated MPA. The STM image shows that the surface consists of isolated DT areas that are as small as a few nanometer in dimension and also regions where the DT domains cluster into larger patches. It is evident that the domains on the surface fall predominantly between 10 and 100 nm<sup>2</sup> in area and that the heterogeneous surface is well suited to study polymer adsorption. Because SAMs of MPA are known<sup>[33]</sup> to exhibit a pK<sub>a</sub> greater than 5, variation of the solution pH can also be used to control the state of ionization of the acid groups on the surface and create a patchy

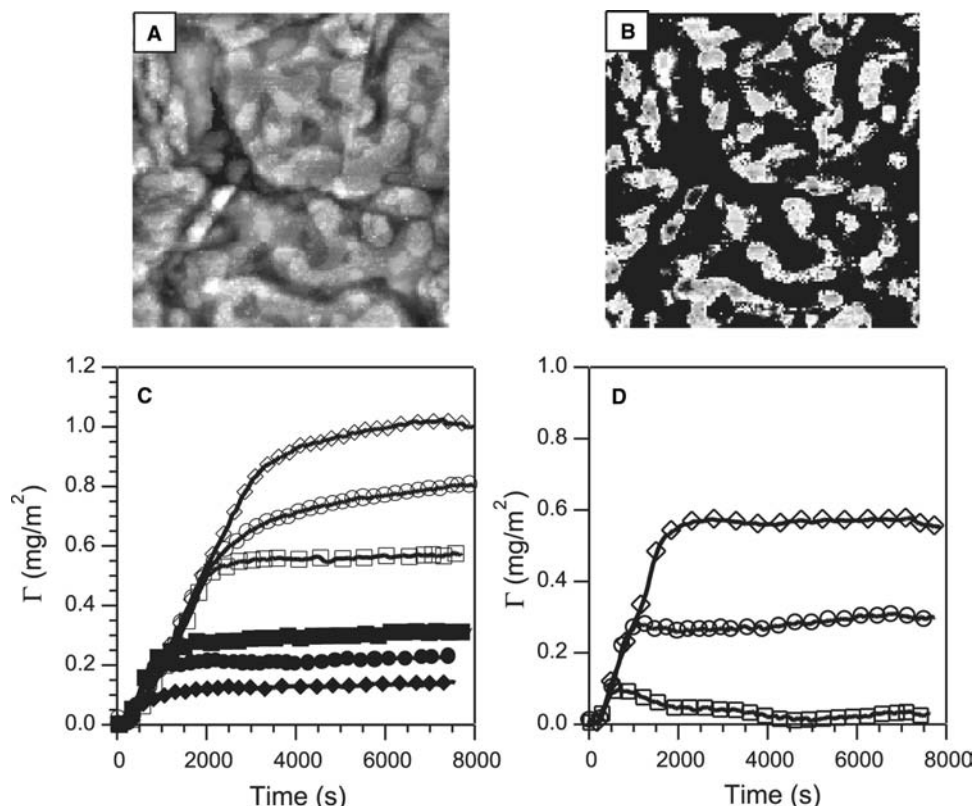


**Fig. 5** A mixed SAM showing patchy domains of DT in the STM image before (A) and after image processing (B). The size of the image is 200 × 200 nm. Adsorption of (C) P2VP and (D) PEO on homogeneous surfaces of DT (diamonds) and MPA (squares) compared to adsorption on a patchy surface (circles). Open symbols correspond to pH = 4.5 and filled symbols to pH = 2.

distribution of charges on the surface. Using the heterogeneous SAMs we have studied the influence of chemical heterogeneity of the surface on adsorption of two broad classes of polymers: flexible, linear polymers and globular proteins.

### Adsorption of Flexible Polymers on Chemically Heterogeneous Surfaces

A number of polymer–surface combinations are realizable and therefore experiments have focused on a subset using nonionic or ionic polymers. The experiments have explored the adsorption of an uncharged polymer [e.g., nonionic PEO or neutral poly(2-vinylpyridine) (P2VP) or neutral poly(acrylic acid)(PAA)] or a charged polymer (e.g., positively charged P2VP) on a largely neutral heterogeneous surfaces and a neutral polymer (e.g., PEO) on a surface with heterogeneous distribution of charge.<sup>[27,28]</sup> Physically, these combinations represent simplified cases where no electrostatic contributions to the surface–segment interaction exist.

Fig. 5C and D shows the typical  $\Gamma(t)$  for P2VP and PEO on the chemically heterogeneous surface containing both DT and MPA sites. A comparison with  $\Gamma(t)$  on homogeneous surfaces of either MPA or DT is also shown. The kinetic curves show a characteristic shape of a constant initial rate of adsorption followed by a slow approach to a plateau. For P2VP adsorption on each type of homogeneous surface (MPA or DT) the value of  $\Gamma_{\max}$  is almost four times larger at pH 4.5 ( $\sim 0.6$ – $1.2$  mg/m<sup>2</sup>) when compared to the lower pH of 2.0 ( $\sim 0.15$ – $0.35$  mg/m<sup>2</sup>). P2VP becomes ionized at the low pH and electrostatic repulsion between neighboring segments of a charged polymer chain leads to lower  $\Gamma$  as accumulation of charge within the surface layer is not favorable. In contrast, no effect of pH is observed on the adsorption of PEO and the  $\Gamma(t)$  shown in Fig. 5D remains unchanged.

At low pH, the largely hydrophobic backbone of P2VP is shielded by the hydrophilic (protonated) pyridine group, which decreases the adsorption affinity to the hydrophobic methyl DT surface and results in a  $\Gamma_{\max}$  that is lower than the value observed on MPA. Thus at pH 2.0 the domains of DT in the heterogeneous surfaces correspond to sites that are less attractive to P2VP relative to the surrounding regions of MPA on the surface. In contrast, at pH 4.5 the DT sites are more attractive relative to the MPA sites.

The adsorption curves clearly show the effect of chemical heterogeneity. For both P2VP and PEO the initial rate of adsorption on the heterogeneous surface is the same as that observed on the homogeneous surfaces. Adsorption of either a charged polymer (P2VP at pH2) or an uncharged polymer (P2VP at pH4.5 and PEO) on a neutral surface shows that the adsorbed

amount  $\Gamma_{\max}$  lies in between the value observed on the two types of homogeneous surfaces. Thus although the initial kinetics are not altered dramatically by the presence of heterogeneity, the surface heterogeneity does impact later stages of adsorption. Physically, the intermediate value of  $\Gamma_{\max}$  indicates that the effective surface adsorption energy of the polymer chain represents some average of the interactions with the two different sites. The experiments also suggest that in these simplified physical situations it does not matter if the minority domains are more or less attractive than the surrounding areas. Other recent experiments by Chun and coworkers<sup>[28]</sup> have shown that beyond a threshold density of DT sites on the surface, the adsorbed amount of the polymer depends on the fraction of heterogeneous sites on the surface.

These first experimental results on compositionally heterogeneous surface verify theoretical predictions regarding polymer adsorption on chemically heterogeneous surfaces. Van der Linden and coworkers used a self-consistent lattice model to study the influence of the degree of clustering of attractive and repulsive sites. On a surface with a patchwise distribution of chemical sites, which is similar to the experiments reported here, the lattice model predicted that the homopolymer adsorption was proportional to the fraction of adsorbing sites. Fig. 5 demonstrates that the adsorption behavior in a real system closely matches the lattice model. Zajac and Chakrabarti used a Monte Carlo simulation to explore the adsorption of a homopolymer on chemically heterogeneous surfaces containing 30–50% of sites that were either repulsive to the polymer or were simply inactive. They predicted that during the early stages the presence of surface impurities did not alter the growth kinetics of the adsorbed layer. However, as chains spread on the surface and competed for sites, there was a net decrease in the number of chains that were adsorbed and that the decrease was proportional to the fraction of inactive or repulsive surface sites. The kinetic curves of  $\Gamma(t)$  measured in Fig. 5 corroborate the predictions from the simulations.

### Adsorption of Globular Proteins on Chemically Heterogeneous Surfaces

Protein adsorption at a surface is ubiquitous in biology and a critical component of synthetic implants and biocompatibility. Because of the intrinsic chemical heterogeneity of a globular protein and its nanometer size, the role of surface heterogeneity in protein adsorption is significant. Therefore we have focused on the adsorption behavior and morphology of a common protein–bovine serum albumin (BSA). To better understand the impact of surface heterogeneity, we also review the adsorption of BSA on homogeneous



surfaces and illustrate the changes in adsorption as chemical heterogeneity is introduced into the surface.

Fig. 6A shows adsorption kinetics on chemically homogeneous surfaces formed using single-component SAMs of DT, MPA, and MUA ( $\text{HOOC}(\text{CH}_2)_{10}\text{SH}$ ).  $\Gamma(t)$  shows that the protein is irreversibly adsorbed on those model surfaces and that the surface chemical properties clearly affect the adsorption amount. The hydrophobicity of each homogeneous surface in Fig. 6A was probed using contact angle measurement with water, which gave  $\theta_{\text{advancing}}$  as  $107^\circ$ ,  $35^\circ$ , and  $25^\circ$  for SAMs of DT, MPA, and MUA, respectively. The plateau values ( $\Gamma_{\text{max}}$ ) therefore follow a trend and increase with the hydrophobic nature of the surface, which is consistent with previous studies that have reported that the adsorption amount of BSA is dependent on the hydrophobicity of surfaces.<sup>[34,35]</sup>

The initial short span of time magnified in Fig. 6A shows that the chemical properties of the surface influence not only the adsorption amount but also the adsorption kinetics, which contrasts with the adsorption behavior of linear flexible polymers. Fig. 6A also shows that despite the identical carboxylic acid (COOH) terminal group of MUA and MPA, the rates of adsorption BSA are vastly different. These

differences in  $\Gamma(t)$  result from the combined influence of electrostatic forces and hydrophobic interactions that are an intimate part of protein adsorption. Bovine serum albumin has an isoelectric point of  $\text{pH} \sim 5$  and at the experimental  $\text{pH}$  of 7.5 the protein is negatively charged because of the presence of three domains that have a net charge of  $-10$ ,  $-8$ , and  $0$ , respectively.<sup>[36]</sup> The SAMs of MPA and MUA ionize at  $\text{pH} > 5$  and can be considered to be largely deprotonated at a  $\text{pH}$  of 7.5.<sup>[37]</sup> In contrast, DT remains neutral in charge. The slow adsorption rate on deprotonated MUA SAMs is therefore attributable to the electrostatic repulsion between the surface and the charged domains of BSA molecules. Because of the shorter chain length of MPA, the self-assembled monolayer is more disordered than the monolayer formed from the longer MUA, where intermolecular interactions between the alkanethiol chain lead to more conformational order. The disorder in the SAMs formed from MPA causes the exposure of methylene groups at the interface and this is manifested in the higher advancing contact angles. We believe that the gradual increase in the adsorption amount over time to  $\Gamma_{\text{max}}$  that is close to the hydrophobic DT surface results from the exposure of the methylene groups, which allows

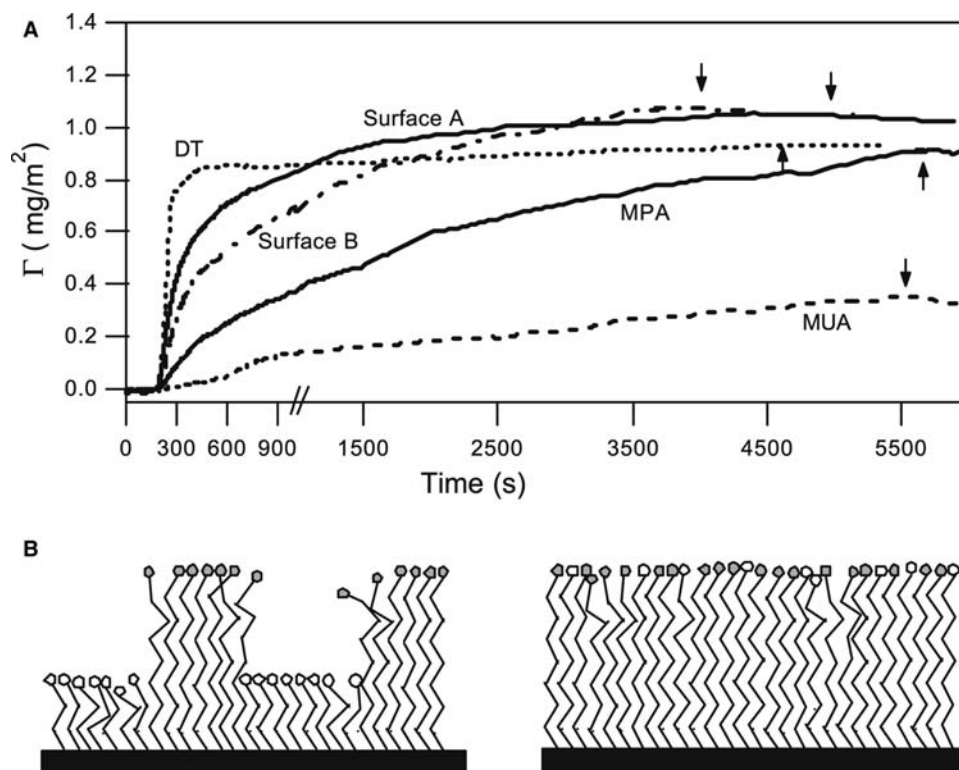


**Fig. 6** (A) Comparison of the kinetics of BSA adsorption on homogeneous surfaces of DT, MPA, and MUA with the adsorption on heterogeneous surfaces A and B. Arrow indicates time when washing with pure buffer solution was begun. The time scale at the beginning of adsorption has been magnified in the plot. (B) Schematic illustration of heterogeneous surfaces with a well-mixed and a nanometer scale, patch-wise distribution of heterogeneity.



hydrophobic interaction between the hydrophobic residues on BSA and the SAMs even with the presence of electrostatic repulsion. The adsorption of BSA occurs when the molecule arrives in a preferred orientation, which overcomes the electrostatic repulsion from the surfaces and the adsorbed neighboring molecules but results in a slower rate of adsorption.

Aside from single-component SAMs as model homogeneous surfaces, several recent studies have used binary SAMs to investigate the specific and nonspecific binding of proteins and DNA.<sup>[38-40]</sup> In these studies, the surfaces were heterogeneous on a “molecular level” with each component being uniformly dispersed in the “well-mixed” binary SAMs. Fig. 6B illustrates schematically the differences between the well-mixed SAMs and the phase-separated SAMs that contain nanometer-sized heterogeneous sites distributed in a patchwise manner. The adsorption of BSA was studied on both types of heterogeneous surfaces to establish the role of the length-scale of surface heterogeneity. For comparison with the patchy heterogeneous surfaces (surface A), well-mixed SAMs (surface B)

were prepared from DT and MUA, which are similar in chain length and lead to uniformly dispersed monolayers.<sup>[41,42]</sup> The advancing contact angles are 87° and 85° for surfaces A and B, respectively, which lie in between the values measured on the corresponding single-component surfaces.

Fig. 6A shows the kinetics of BSA adsorption on surfaces A and B. Surprisingly, the plateau value ( $\Gamma_{\max}$ ) exceeds that on DT suggesting that adsorption can be enhanced by the presence of two well-mixed functional groups of CH<sub>3</sub> and COO<sup>-</sup> on the surface. The initial rate of adsorption on the well-mixed heterogeneous surfaces falls in between the rates on chemically homogeneous surfaces and once again illustrates the difference in adsorption behavior of a globular protein from that of a flexible polymer.

The morphology of the protein (Fig. 7) is one of many interesting aspects in the study of adsorption. Tapping mode AFM (TM-AFM) is a common scanning probe microscopy technique for visualization of biomaterials, cells, and proteins. Use of TM-AFM minimizes the force exerted on the surface during

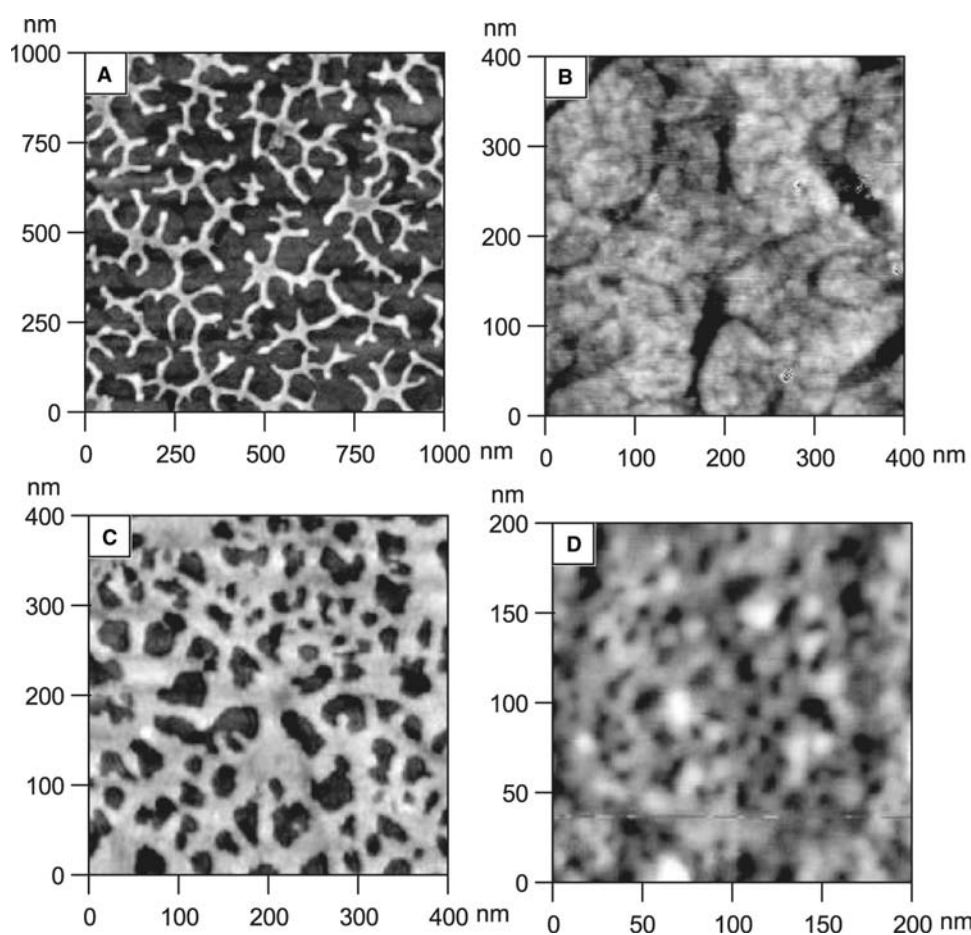


**Fig. 7** Tapping mode AFM images of adsorbed BSA on SAMs of homogeneous surfaces of DT (A) and MPA (B) compared with the adsorbed BSA on well-mixed (C) and patch-wise (D) heterogeneous surfaces.

imaging, which avoids possible damage and distortion of the proteins. Fig. 7A shows that the adsorbed BSA on a DT surface has a dendrite-like structure of approximately 5 nm in height and 20 nm in width. A similar morphology was also observed by Ge and coworkers.<sup>[43]</sup> In past studies, it was found that a hydrophobic surface generally causes protein to unfold or denature upon adsorption and the unfolding can expose internal hydrophobic sites of the BSA. The preadsorbed BSA, in turn, provides preferential sites for adsorption of BSA from bulk solutions. Our experiments show that the dendrite-like structures form in an extremely short time (within seconds), which supports the hypothesis that proteins rapidly unfold upon adsorption. Kim and coworkers have proposed a different mechanism for a protein such as lysozyme, where clusters of proteins on the surface are believed to form by diffusion of adsorbed proteins on the surface.<sup>[44]</sup> Clearly, more experiments are needed to reach a definitive conclusion.

The adsorption morphology on surfaces formed by MPA and MUA (Fig. 7B) shows fluffy and relatively featureless morphology. Bovine serum albumin is a globular protein with approximate dimensions of  $4 \times 4 \times 14$  nm, which indicates that  $\Gamma_{\max}$  should be  $2.5 \text{ mg/m}^2$  for a closely packed protein monolayer in a side-on orientation and  $8.8 \text{ mg/m}^2$  in an end-on orientation. The adsorption amounts on MPA and MUA range from 0.3 to  $0.9 \text{ mg/m}^2$  (Fig. 6), which are much lower than these estimates of  $\Gamma_{\max}$ . The adsorbed BSA layers are therefore not continuous when one considers the rigidity of the BSA molecule resisting total unfolding on hydrophilic surfaces.<sup>[45,46]</sup> However, the individual BSA molecules or clusters of BSA cannot be clearly imaged due to the effects of tip-broadening and the chemical interplay between the SAMs and the BSA layers in tip-surface forces.<sup>[47]</sup> In these AFM images, nevertheless, the deep boundaries of gold grains/terraces can be roughly mapped out, which suggests that the BSA is likely adsorbed in a distributed manner on the hydrophilic surfaces.

The AFM images of adsorbed BSA on each type of heterogeneous surfaces are shown in Fig. 7C and D. While the adsorption amounts on the well-mixed and patchy heterogeneous surfaces do not differ significantly, the morphology of adsorbed BSA layer is strikingly different although the SAMs possess similar surface energy (reflected in the comparable values of  $\theta_{\text{advancing}}$ ). Comparison between Fig. 7A and Fig. 7C shows that when the surface changes from a hydrophobic ( $\theta_a \sim 107$ ), methyl-terminated interface to an interface where  $\text{CH}_3$  and  $\text{COO}^-$  are well mixed ( $\theta_a \sim 86$ ), the morphology of adsorbed BSA changes from a dendrite-like structure to a network-like structure. Surprisingly, the TM-AFM image of the adsorbed BSA on patchy surfaces indicates breakdown of both

dendrite and network structure. Instead, the layer of BSA shows few distinct features but appears as a continuous layer (Fig. 7D). When compared to the BSA layer on a MPA surface (Fig. 7B) where the morphology was featureless, the image in Fig. 7D shows the presence of a few holes/depression and occasional high spots. Results in Fig. 7 underscore the importance of the nanometer scale of the heterogeneity in surfaces. Recent studies<sup>[43,48,49]</sup> have reported adsorption of BSA on phase-separated Langmuir–Blodgett films where micrometer circular domains of a methyl  $\omega$ -functionalized organosilane were formed in a matrix of perfluoryl  $\omega$ -functionalized organosilanes. The morphology of the adsorbed BSA on each domain was found to be more or less similar to the corresponding single component LB film. Fig. 7C and D demonstrates that the adsorption characteristics of the BSA are strongly affected by the patchwise distribution of hydrophobic domains only when the surface heterogeneity is commensurate in size with the nanometer-sized, globular protein.

## CONCLUSION

The experiments reported here and the agreement with theoretical studies demonstrate that, in addition to fundamental insights into adsorption on heterogeneous surfaces, we can now pursue experimental systems that exploit the interactions between lateral nanoscale morphology of a surface and an adsorbing polymer chain. For example, recent simulations have shown that a pattern of distributed charges on a surface can be recognized during the adsorption of an oppositely charged polyelectrolyte chain. Similarly others have predicted that the nanoscale morphology of a surface and the heterogeneous chemical interactions with a polymer chain can be used to direct segregation or patterning within adsorbed layers. The present strategy of using molecularly designed self-assembled surfaces for polymer adsorption enables the exploration of physical phenomena such as biomimetic recognition and segregation in polymer adsorption on heterogeneous surfaces and promises both scientific and technological advances.

## ACKNOWLEDGMENT

The research reviewed here is based upon work performed with the support of the U.S. Department of Energy, Division of Materials Sciences under Award No. DEFG02-ER9145439, through the Frederick Seitz Materials Research Laboratory at the University of Illinois. Support from the University of Illinois and National Science Foundation is also acknowledged.

## REFERENCES

- Fleer, G.J.; Stuart, M.A.C.; Scheutjens, J.M.H.M.; Cosgrove, T.; Vincent, B. *Polymers at Interfaces*; Chapman and Hall: London, 1993.
- Stuart, M.A.C.; Fleer, G.J. Adsorbed polymer layers in nonequilibrium situations. *Annu. Rev. Mater. Sci.* **1996**, *26*, 463–500.
- Ramsden, J.J. Kinetics of protein adsorption. *Surfactant Sci. Ser.* **1998**, *75*, 321–361. (Biopolymers at Interfaces).
- Frantz, P.; Granick, S. Exchange kinetics of adsorbed polymer and the achievement of conformational equilibrium. *Macromolecules* **1994**, *27* (9), 2553–2558.
- Semenov, A.N.; Joanny, J.F. Kinetics of adsorption of linear homopolymers onto flat surfaces: Rouse dynamics. *J. Phys. II* **1995**, *5* (6), 859–876.
- Blunt, M.; Barford, W.; Ball, R. Polymer adsorption and electron binding on rough and fractal surfaces. *Macromolecules* **1989**, *22* (3), 1458–1466.
- Douglas, J.F. How does surface roughness affect polymer–surface interactions?. *Macromolecules* **1989**, *22* (9), 3707–3716.
- Edwards, S.F.; Muthukumar, M. The size of a polymer in random media. *J. Chem. Phys.* **1988**, *89* (4), 2435–2441.
- Sumithra, K.; Baumgaertner, A. Polymer adsorption on planar random surfaces. *J. Chem. Phys.* **1998**, *109* (4), 1540–1544.
- Baumgaertner, A.; Muthukumar, M. Effects of surface roughness on adsorbed polymers. *J. Chem. Phys.* **1991**, *94* (5), 4062–4070.
- Ji, H.; Hone, D. Polymer adsorption on rough surfaces: 2. Good solvent conditions. *Macromolecules* **1988**, *21* (8), 2600–2605.
- Striolo, A.; Prausnitz, J.M. Adsorption of branched homopolymers on a solid surface. *J. Chem. Phys.* **2001**, *114* (19), 8565–8572.
- Balazs, A.C.; Gempe, M.C.; Zhou, Z. Polymer adsorption on chemically heterogeneous substrates. *Macromolecules* **1991**, *24* (17), 4918–4925.
- Andelman, D.; Joanny, J.F.R. Polymer adsorption on surfactant monolayers and heterogeneous solid surfaces. *J. Phys. II* **1993**, *3* (1), 121–138.
- Halperin, A.; Sommer, J.U.; Daoud, M. Copolymers at striped surfaces: Coupling effects. *Europhys. Lett.* **1995**, *29* (4), 297–302.
- Odijk, T. Adsorption of a polymer to a randomly interacting surface. *Macromolecules* **1990**, *23* (6), 1875–1876.
- Sumithra, K.; Sebastian, K.L. Polymer molecules at chemically random surfaces. *J. Phys. Chem.* **1994**, *98* (37), 9312–9317.
- van der Linden, C.C.; van Lent, B.; Leermakers, F.A.M.; Fleer, G.J. Adsorption of polymers on heterogeneous surfaces. *Macromolecules* **1994**, *27* (7), 1915–1921.
- Huber, G.; Vilgis, T.A. Polymer adsorption on heterogeneous surfaces. *Eur. Phys. J., B Cond. Matter Phys.* **1998**, *3* (2), 217–223.
- Zajac, R.; Chakrabarti, A. Effects of chemical impurities on the adsorption of polymer chains from a semi-dilute solution. *J. Chem. Phys.* **1997**, *107* (20), 8637–8653.
- Bratko, D.; Chakraborty, A.K.; Shakhnovich, E.I. Recognition between random heteropolymers and multifunctional disordered surfaces. *Chem. Phys. Lett.* **1997**, *280* (1,2), 46–52.
- Muthukumar, M. Pattern recognition by polyelectrolytes. *J. Chem. Phys.* **1995**, *103* (11), 4723–4731.
- Genzer, J. Copolymer adsorption on planar substrates with a random distribution of chemical heterogeneities. *J. Chem. Phys.* **2001**, *115* (10), 4873–4882.
- Ulman, A. Formation and structure of self-assembled monolayers. *Chem. Rev.* **1996**, *96* (4), 1533–1554.
- Huang, Y.-W.; Gupta, V.K. Effects of physical heterogeneity on the adsorption of poly(ethylene oxide) at a solid–liquid interface. *Macromolecules* **2001**, *34* (11), 3757–3764.
- Huang, Y.-W.; Gupta, V.K. Influence of polymer flux and chain length on adsorption of poly(ethylene oxide) on physically heterogeneous surfaces. *Langmuir* **2002**, *18* (6), 2280–2287.
- Huang, Y.-W.; Chun, K.-Y.; Gupta, V.K. Adsorption of a polyelectrolyte on surfaces with nanometer sized chemical patchiness. *Langmuir* **2003**, *19* (6), 2175–2180.
- Chun, K.-Y.; Huang, Y.-W.; Gupta, V.K. Polymer adsorption on nanoheterogeneous surfaces: Impact of size and density of heterogeneous sites. *J. Chem. Phys.* **2003**, *118* (7), 3252–3257.
- Kumar, A.; Abbott, N.L.; Kim, E.; Biebuyck, H.A.; Whitesides, G.M. Patterned self-assembled monolayers and meso-scale phenomena. *Acc. Chem. Res.* **1995**, *28* (5), 219–226.
- Tamada, K.; Hara, M.; Sasabe, H.; Knoll, W. Surface phase behavior of *N*-alkanethiol self-assembled monolayers adsorbed on Au(111)—an atomic force microscope study. *Langmuir* **1997**, *13* (6), 1358–1366.
- Imabayashi, S.-I.; Hobara, D.; Kakiuchi, T.; Knoll, W. Selective replacement of adsorbed alkanethiols in phase-separated binary self-assembled monolayers by electrochemical partial desorption. *Langmuir* **1997**, *13* (17), 4502–4504.
- Hobara, D.; Ota, M.; Imabayashi, S.-I.; Niki, K.; Kakiuchi, T. Phase separation of binary self-assembled thiol monolayers composed of 1-hexadecanethiol and 3-mercaptopropionic acid on Au(111) studied by scanning tunneling microscopy and cyclic voltammetry. *J. Electroanal. Chem.* **1998**, *444* (1), 113–119.
- Hu, K.; Bard, A.J. Use of atomic force microscopy for the study of surface acid–base properties of carboxylic acid-terminated self-assembled monolayers. *Langmuir* **1997**, *13* (19), 5114–5119.
- Sigal, G.B.; Mrksich, M.; Whitesides, G.M. Effect of surface wettability on the adsorption of proteins and detergents. *J. Am. Chem. Soc.* **1998**, *120* (14), 3464–3473.
- Silin, V.; Weetall, H.; Vanderah, D.J. Spr studies of the nonspecific adsorption kinetics of human Igg and Bas on gold surfaces modified by self-assembled monolayers (SAMs). *J. Colloid Interface Sci.* **1997**, *185* (1), 94–103.

36. Peters, J.T. *All About Albumin: Biochemistry, Genetics, and Medical Applications*; Academic Publishers: San Diego, CA, 1995.
37. Dai, Z.; Ju, H. Effect of chain length on the surface properties of omega-carboxy alkanethiol self-assembled monolayers. *Phys. Chem., Chem. Phys.* **2001**, *3* (17), 3769–3773.
38. Higashi, N.; Takahashi, M.; Niwa, M. Immobilization of DNA through intercalation at self-assembled monolayers on gold. *Langmuir* **1999**, *15* (1), 111–115.
39. Patel, N.; Davies, M.C.; Hartshorne, M.; Heaton, R.J.; Roberts, C.J.; Tendler, S.J.B.; Williams, P.M. Immobilization of protein molecules onto homogeneous and mixed carboxylate-terminated self-assembled monolayers. *Langmuir* **1997**, *13* (24), 6485–6490.
40. Spinke, J.; Liley, M.; Schmitt, F.J.; Guder, H.J.; Angermaier, L.; Knoll, W. Molecular recognition at a self-assembled monolayers: Optimization of surface functionalization. *J. Chem. Phys.* **1993**, *99* (9), 7012–7019.
41. Stranick, S.J.; Atre, S.V.; Parikh, A.N.; Wood, M.C.; Allara, D.L.; Winograd, N.; Weiss, P.S. Nanometer-scale phase separation in mixed composition self-assembled monolayers. *Nanotechnology* **1996**, *7* (4), 438–442.
42. Creager, S.E.; Clarke, J. Contact-angle titrations of mixed omega-mercaptoalkanoic acid/alkanethiol monolayers on gold. Reactive vs nonreactive spreading, and chain length effects on surface  $pK_a$  values. *Langmuir* **1994**, *10* (10), 3675–3683.
43. Ge, S.; Kojio, K.; Takahara, A.; Kajiyama, T. Bovine serum albumin adsorption onto immobilized organotrichlorosilane surface: Influence of the phase separation on protein adsorption patterns. *J. Biomater. Sci., Polym. Ed.* **1998**, *9* (2), 131–150.
44. Kim, D.T.; Blanch, H.W.; Radke, C.J. Direct Imaging of Aqueous Lysozyme Adsorption onto Mica by Atomic Force Microscopy. Abstracts of Papers, 224th ACS National Meeting, Boston, MA, 2002.
45. Morrissey, B.W.; Stromberg, R.R. Conformation of adsorbed blood proteins by infrared bound fraction measurements. *J. Colloid Interface Sci.* **1974**, *46* (1), 152–164.
46. Tarasevich, Y.I.; Monakhova, L.I. Interaction between globular proteins and silica surfaces. *Colloid J.* **2002**, *64* (4), 482–487.
47. Brandsch, R.; Bar, G.; Whangbo, M.H. On the factors affecting the contrast of height and phase images in tapping mode atomic force microscopy. *Langmuir* **1997**, *13* (24), 6349–6353.
48. Fang, J.; Knobler, C.M. Phase-separated two-component self-assembled organosilane monolayers and their use in selective adsorption of a protein. *Langmuir* **1996**, *12* (5), 1368–1374.
49. Takahara, A.; Ge, S.; Kojio, K.; Kajiyama, T. In situ atomic force microscopic observation of albumin adsorption onto phase-separated organosilane monolayer surface. *J. Biomater. Sci., Polym. Ed.* **2000**, *11* (1), 111–120.

# Aerosol Nanoparticles: Coagulation Theory

Ken Won Lee

Soon-Bark Kwon

*Department of Environmental Science and Engineering, Kwangju Institute of Science and Technology, Gwangju, South Korea*

## INTRODUCTION

Many important physical properties of natural or man-made aerosol particles such as light scattering, electrostatic charges, and toxicity, as well as their behavior involving physical processes such as diffusion, condensation, and thermophoresis, depend strongly on their size distribution. An important aerosol behavior mechanism affecting the size distribution of aerosol particles is coagulation. Aerosol particles suspended in a fluid may come into contact because of their Brownian motion, or as a result of their relative motion produced by external forces (e.g., gravity, hydrodynamic forces, electrical forces, etc.). The result is a continuous decrease in number concentration and an increase in particle size. The theory of coagulation was originally devised for particles in liquids and was later extended to aerosols. In the case of solid particles, the process is sometimes called agglomeration, and the resulting particle clusters are known as agglomerates. Therefore in many basic and applied fields (e.g., synthesis of nanostructured material via gas-phase synthesis), the evolution of the particle size distribution because of coagulation is of fundamental importance and interest.

Aerosol coagulation is caused by relative motion among particles. When the relative motion is because of Brownian motion, the process is called Brownian coagulation. Brownian coagulation is a spontaneous and ever-present phenomenon for aerosols. When the relative motion arises from external forces such as gravity or electrical forces, or from aerodynamic effects, the process is called kinematic coagulation. Kinematic coagulation includes gravitational coagulation, turbulent coagulation, electrostatic coagulation, etc.

The objective of this entry is to review the theories of coagulation describing how particle number concentration and particle size change as a function of time. To do that, first, an overview of some important coagulation mechanisms is presented. Next, various solution techniques for the coagulation equation are comparatively reviewed.

## COAGULATION OF MONODISPERSE AEROSOLS

When an aerosol contains particles of the same size, it is called monodisperse, whereas if particles are present in a variety of sizes, the aerosol is polydisperse. Coagulation of a monodisperse aerosol was developed for Brownian coagulation by Smoluchowski.<sup>[1]</sup> Smoluchowski derived the monodisperse coagulation equation by solving the diffusion equation around a single particle, and by obtaining the flux of other particles toward it. He assumed that particles adhere at every collision and that particle size changes slowly. The change in particle number concentration is represented by the following equation:

$$\frac{dN}{dt} = -2K_{co}N^2 \quad (1)$$

where  $N$  is the number concentration of the particles,  $t$  is the time,  $K_{co}$  ( $=2\pi d_p D$ ) is the Brownian coagulation coefficient in the continuum regime,  $d_p$  is the diameter of the particles, and  $D$  is the diffusion coefficient of the particles. The diffusion coefficient  $D$  is given by the following Stokes–Einstein equation:

$$D = \frac{k_B T}{3\pi\mu d_p} \quad (2)$$

where  $k_B$  is the Boltzmann constant,  $T$  is the absolute temperature, and  $\mu$  is the gas viscosity. Using Eq. (2),  $K_{co}$  in Eq. (1) can be expressed as follows:

$$K_{co} = \frac{2k_B T}{3\mu} \quad (3)$$

By integrating Eq. (1), the number concentration is determined as a function of time as follows:

$$\frac{N}{N_0} = \frac{1}{1 + 2K_{co}N_0 t} \quad (4)$$

where  $N_0$  is the initial value for  $N$ .

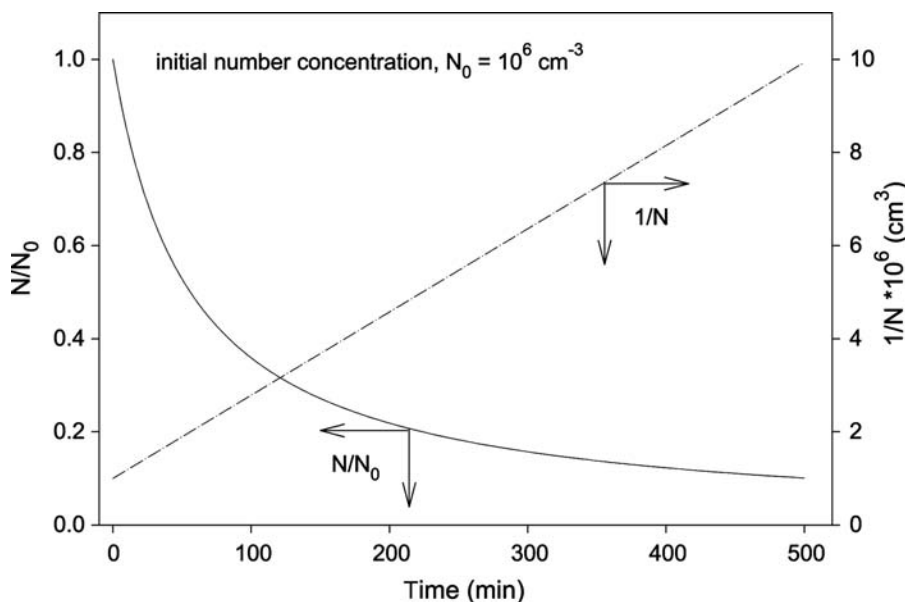


**Fig. 1** Coagulation of monodisperse aerosol particles.

Because the rate of coagulation is proportional to  $N^2$ , it is rapid at high concentrations but decreases as coagulation reduces the concentration of particles. This relationship is shown in Fig. 1, which presents a plot of the number concentration of a monodisperse aerosol as a function of time. When the data are replotted as  $1/N$  vs.  $t$ , a straight line is obtained. The quantity  $1/N$  is in units of cubic centimeters and represents the average gas volume per particle. The slope of the line is the coagulation coefficient  $K_{co}$ .

volumes between  $v$  and  $(v + dv)$  from the combination of particles of volume  $v - \bar{v}$  and  $\bar{v}$ . The second term in the right-hand side of this equation represents the loss of particles with volumes between  $v$  and  $(v + dv)$  resulting from the coagulation of particles of volume  $v$  and  $\bar{v}$ . Thus this equation gives an expression for the net rate of change of particles whose volumes lie between  $v$  and  $(v + dv)$ . The collision kernel  $\beta(v, \bar{v})$  is dependent on the collision mechanism as well as on the particle size of two colliding particles.

## GENERAL COAGULATION EQUATION

In “Coagulation of Monodisperse Aerosols,” the equations describing coagulation were introduced for a monodisperse aerosol. We now consider the more complicated situation of polydisperse aerosols where a range of particle sizes is present. Because the rate of coagulation depends on the range of sizes present, the mathematics become much more complicated and no explicit solution exists.

The change in the particle size distribution of a polydisperse aerosol by coagulation is represented by the following population balance equation:<sup>[2]</sup>

$$\frac{\partial n(v, t)}{\partial t} = \frac{1}{2} \int_0^v \beta(v - \bar{v}, \bar{v}) n(v - \bar{v}, t) n(\bar{v}, t) \times d\bar{v} - n(v, t) \int_0^\infty \beta(v, \bar{v}) n(\bar{v}, t) d\bar{v} \quad (5)$$

where  $n(v, t)$  is the particle size distribution function at time  $t$ , and  $\beta(v, \bar{v})$  is the collision kernel for two particles of volume  $v$  and  $\bar{v}$ . The first term in the right-hand side of Eq. (5) represents the increase in particles with

## COLLISION KERNELS

### Brownian Coagulation

The Brownian collision kernel can be derived by either the kinetic theory of gases, or by the continuum diffusion theory according to particle size. Particles much smaller than the mean free path length of the gas molecules behave like molecules, and the kinetic theory of gases must be used to derive the collision kernel. In the meanwhile, for the particles much larger than the mean free path of the gas molecules, the continuum diffusion theory should be used. Generally, the Knudsen number  $Kn (= \lambda/r)$ , with  $\lambda$  as the mean free path length of the surrounding gas molecules and  $r$  as the particle radius, is used to define the particle size regime.

In the free molecule regime, where the Knudsen number is larger than about 50,  $\beta_{fm}(v, \bar{v})$  results from the kinetic theory of gases and is given as:<sup>[3]</sup>

$$\beta_{fm}(v, \bar{v}) = K_{fm}(v^{1/3} + \bar{v}^{1/3})^2 \sqrt{\frac{1}{v} + \frac{1}{\bar{v}}} \quad (6)$$

where  $K_{\text{fm}} = (3/4\pi)^{1/6}(6k_{\text{B}}T/\rho)^{1/2}$  is the Brownian coagulation coefficient for the free molecule regime and  $\rho$  is the particle density.

In the continuum regime, where the Knudsen number is smaller than about 1,  $\beta_{\text{co}}(v, \bar{v})$  is derived by the continuum diffusion theory as follows:

$$\beta_{\text{co}}(v, \bar{v}) = K_{\text{co}}(v^{1/3} + \bar{v}^{1/3}) \left( \frac{C(v)}{v^{1/3}} + \frac{C(\bar{v})}{\bar{v}^{1/3}} \right) \quad (7)$$

where  $C = 1 + Kn\{1.142 + 0.558 \exp(-0.999/Kn)\}$  is the gas slip correction factor.<sup>[4]</sup>

The entire transition regime is characterized by Knudsen numbers in the range of  $\sim 1 < Kn < \sim 50$ . In the transition regime, the coagulation rate is described neither by the continuum diffusion theory nor by the simple kinetic theory. Fuchs<sup>[5]</sup> found a semi-empirical solution of the collision kernel by assuming that outside of a certain distance, namely, an average mean free path of an aerosol particle, the transport of particles is described by the continuum diffusion theory including the slip correction, and that inside the distance, the particles behave like in a vacuum and the transport is described by the kinetic theory. The two theories were brought together by matching the fluxes at the absorbing sphere radius.

This so-called flux matching was the basis for most of the following theories because of its phenomenological approach and the guarantee that the collision kernel is valid over the entire size regime. All theories dealing with an absorbing sphere use a correction function first calculated by Fuchs. This function is mainly expressed as an enhancement of the collision kernel for the continuum regime including the slip correction:

$$\beta_{\text{B}}(v, \bar{v}) = K_{\text{co}}(v^{1/3} + \bar{v}^{1/3}) \times \left( \frac{C(v)}{v^{1/3}} + \frac{C(\bar{v})}{\bar{v}^{1/3}} \right) f(Kn_{\text{D}}) \quad (8)$$

where  $Kn_{\text{D}} = \frac{\beta_{\text{co}}(v, \bar{v})}{2\beta_{\text{fm}}(v, \bar{v})}$  and the subscripts ‘‘co’’ and ‘‘fm’’ designate the continuum regime including the slip correction and the free molecule regime, respectively. Dahneke<sup>[6]</sup> described the diffusion process as a mean free path phenomenon. To obtain the coagulation coefficient, Dahneke also matched the two fluxes but at a distance which is the mean free path of the particles. To compare the different theories, the following general enhancement function  $f(Kn_{\text{D}})$  is used:

$$f(Kn_{\text{D}}) = \frac{1 + B_1 Kn_{\text{D}}}{1 + B_2 Kn_{\text{D}} + B_3 Kn_{\text{D}}^2} \quad (9)$$

The coefficients  $B_1$ ,  $B_2$ , and  $B_3$  are given for some theories in Table 1. By comparing various theories on the collision kernel in the transition regime, Otto et al.<sup>[8]</sup>

**Table 1** Coefficients for enhancement function  $f(Kn_{\text{D}})$

	$B_1$	$B_2$	$B_3$
Fuchs <sup>[5]</sup>	$\frac{3}{2} \cdot \frac{\Delta_{12}}{\lambda_p}$	2	$3 \cdot \frac{\Delta_{12}}{\lambda_p}$
Fuchs and Sutugin <sup>[7]</sup>	$\frac{3}{2}$	2.566	3
Dahneke <sup>[6]</sup>	1	2	2
Harmonic mean	0	2	0

recommended Dahneke’s theory to be used partially for its simplicity and partially for its accuracy.

## Gravitational Coagulation

Kinematic coagulation is coagulation that occurs as a result of relative particle motion caused by mechanisms other than Brownian motion. From this section through ‘‘Electrostatic Coagulation,’’ various kinematic coagulations are introduced.

Particles of different sizes will settle at different rates under the influence of gravity and thereby create relative motion between them, which leads to collision and coagulation. This mechanism is called gravitational coagulation. The collision kernel by gravitational coagulation is expressed as the following equation when the slip correction factor is neglected:<sup>[9]</sup>

$$\beta_{\text{G}}(v, \bar{v}) = K_{\text{G}}\varepsilon(r, \bar{r})(r + \bar{r})^2|r^2 - \bar{r}^2| \quad (10)$$

where  $K_{\text{G}} (= \frac{2\pi g \rho}{9\mu})$  is the gravitational coagulation constant,  $g$  is the gravity constant,  $\rho$  is the particle density,  $\mu$  is the gas viscosity, and  $r [= (\frac{3v}{4\pi})^{1/3}]$  and  $\bar{r} [= (\frac{3\bar{v}}{4\pi})^{1/3}]$  are the radii of the colliding particles.  $\varepsilon(r, \bar{r})$  is the collision efficiency, which can be expressed as follows:

$$\varepsilon(r, \bar{r}) = \frac{3y_c^2}{2(r + \bar{r})^2} \quad \text{if } r \leq \bar{r}, y_c = r \text{ and if } r > \bar{r}, y_c = \bar{r} \quad (11)$$

When both the Brownian and gravitational coagulations are significant, the two collision kernels  $\beta_{\text{B}}$  and  $\beta_{\text{G}}$  are commonly added to predict the behavior of aerosols. This simple addition would appear to be based on a physical picture of each of the mechanisms acting independently with neither affecting the other, but it would seem that this is not the case. Thus the combined kernel was suggested by Simon, Williams, and Cassel<sup>[10]</sup> and their kernel is plotted in Fig. 2 with the sum kernel and each kernel of the Brownian and gravitational coagulations. Their kernel describing the combined effect of Brownian and gravitational coagulations increases the rate of coagulation compared with the sum kernel in the size range of 0.1–1  $\mu\text{m}$ . On the contrary, Qiao, Li, and Wen<sup>[12]</sup> reported that weak Brownian diffusion, the effect of which is



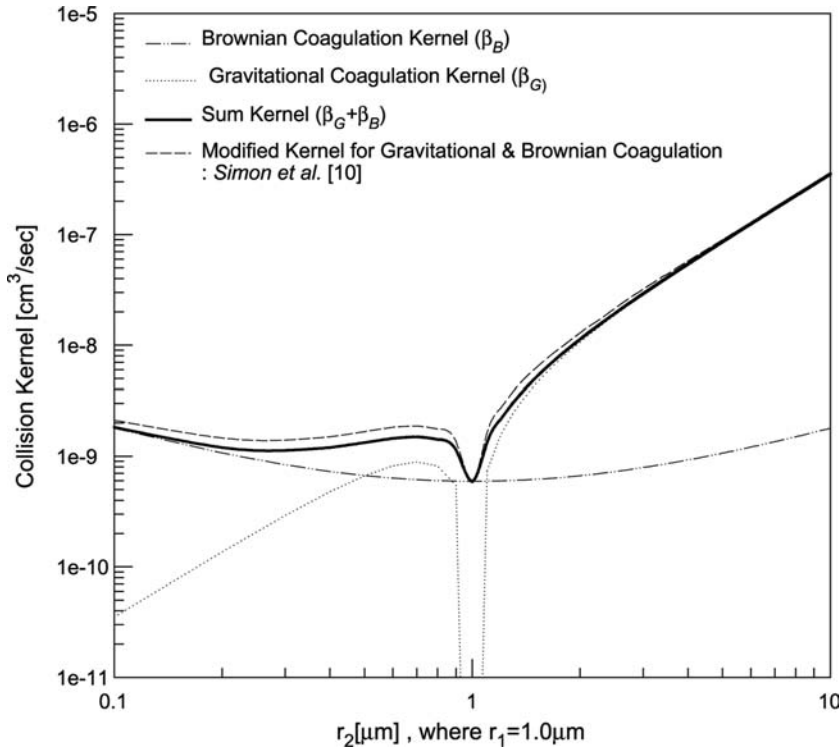


**Fig. 2** Comparison of Brownian and gravitational coagulation kernels. *Source:* From Ref.<sup>[11]</sup>.

non-linearly coupled with gravity, can act to decrease the coagulation rate.

### Turbulent Coagulation

In many physical situations, the flow field in a fluid is turbulent. There are two ways in which turbulence causes collisions between neighboring particles. First, there are spatial variations of the turbulent motion. Because of this process, collision mechanism is conventionally called “shear mechanism.” Second, each particle moves relative to the air surrounding it, owing to the fact that the inertia of a particle is different from that of an equal volume of air. Because the inertia of a particle depends on its size, neighboring particles of unequal size will have different velocities and this will also lead to collisions. This mechanism is called “accelerative mechanism.” Saffman and Turner<sup>[13]</sup> derived the following collision kernel by combining the shear mechanism and the accelerative mechanism:

$$\begin{aligned} \beta_T(v_1, v_2) &= \left(\frac{8\pi}{3}\right)^{1/2} (r_1 + r_2)^2 (w_a^2 + w_s^2)^{1/2} \\ &= \left(\frac{8\pi}{3}\right)^{1/2} (r_1 + r_2)^2 \left[ 3 \left(1 - \frac{\rho_f}{\rho_p}\right)^2 (\tau_1 - \tau_2)^2 \right. \\ &\quad \left. \times \left[ \left(\frac{Dv_f}{Dt}\right)^2 + \frac{1}{5}(r_1 + r_2)^2 \frac{\varepsilon}{\nu} \right]^{1/2} \right] \end{aligned} \quad (12a)$$

where  $r_i = [(3v_i/4\pi)^{1/3}]$  is the particle radius,  $\rho_f$  is the fluid density,  $\rho_p$  is the particle density,  $\varepsilon$  is the turbulent energy dissipation rate, and  $\nu$  is the kinematic viscosity of the fluid. The particle relaxation time  $\tau_i$  including the Cunningham slip correction factor  $C_{c,i}$  is defined as:

$$\tau_i = \frac{C_{c,i}(2\rho_p + \rho_f)r_i^2}{9\mu} \quad (12b)$$

where  $\mu$  is the dynamic viscosity of the fluid. The average acceleration of eddies in the dissipation range  $(Dv_f/Dt)^2$  is defined as:<sup>[14]</sup>

$$\left(\frac{Dv_f}{Dt}\right)^2 = 1.16\varepsilon^{3/2}\nu^{-1/2} \quad (12c)$$

The first and second terms in the square root term on the right-hand side of Eq. (12a) represent the accelerative mechanism and shear mechanism, respectively. However, under more vigorous turbulence or with larger particles, the approaching particles may no longer be entrained completely by the smallest eddies, so they will have less correlated velocities.

Recently, Kruis and Kusters<sup>[15]</sup> analyzed this problem using a turbulence spectrum, which describes both the viscous subrange and the inertial subrange. In their work, the relative particle velocity  $w$  is represented by

the following equations:

$$w_a^2 = 3(1-b)^2 v_f^2 \frac{\gamma}{\gamma-1} \times \frac{(\theta_1 + \theta_2)^2 - 4\theta_1\theta_2 \sqrt{\frac{1+\theta_1+\theta_2}{(1+\theta_1)(1+\theta_2)}}}{(\theta_1 + \theta_2)} \times \left\{ \frac{1}{(1+\theta_1)(1+\theta_2)} - \frac{1}{(1+\gamma\theta_1)(1+\gamma\theta_2)} \right\} \quad (13)$$

$$w_s^2 = 0.238bv_f^2 \left( \frac{v_1^2}{v_f^2} \frac{\theta_1}{C_{c,1}} + \frac{v_2^2}{v_f^2} \frac{\theta_2}{C_{c,2}} + 2 \frac{\overline{v_1 v_2}}{v_f^2} \sqrt{\frac{\theta_1 \theta_2}{C_{c,1} C_{c,2}}} \right) \quad (14)$$

The root mean square (rms) fluid velocity  $v_f$  is expressed as:

$$v_f^2 = \frac{\gamma(\varepsilon\nu)^{1/2}}{0.183} \quad (15)$$

where  $\gamma$  is the spectrum constant, which usually has a value between 10 and 100. The turbulent energy  $k$  ( $k = 3/2v_f^2$ ) and the dissipation rate  $\varepsilon$  are obtained mostly from fluid dynamic simulations. The added mass coefficient  $b$  is defined as:

$$b = \frac{3\rho_f}{2\rho_p + \rho_f} \quad (16)$$

The dimensionless particle relaxation time  $\theta_i$  is defined as:

$$\theta_i = \frac{\tau_i}{T_L} \quad (17)$$

where  $T_L$  is the Lagrangian time scale:

$$T_L = \frac{0.4v_f^2}{\varepsilon} \quad (18)$$

The rms particle velocity  $v_i$ , valid in both the viscous and the inertial subranges of turbulence, is represented as:

$$\frac{v_i^2}{v_f^2} = \frac{\gamma}{\gamma-1} \left\{ \frac{1+b^2\theta_i}{1+\theta_i} - \frac{1+b^2\gamma\theta_i}{\gamma(1+\gamma\theta_i)} \right\} \quad (19)$$

whereas the velocity correlation is:

$$\frac{\overline{v_1 v_2}}{v_f^2} = \frac{\gamma}{\gamma-1} \left\{ \frac{(\theta_1 + \theta_2 + 2\theta_1\theta_2) + b(\theta_1^2 + \theta_2^2 - 2\theta_1\theta_2) + b^2(\theta_1^2\theta_2 + \theta_1\theta_2^2 + 2\theta_1\theta_2)}{(\theta_1 + \theta_2)(1 + \theta_1)(1 + \theta_2)} - \frac{(\theta_1 + \theta_2 + 2\gamma\theta_1\theta_2) + b\gamma(\theta_1^2 + \theta_2^2 - 2\theta_1\theta_2) + b^2(\gamma^2\theta_1^2\theta_2 + \gamma^2\theta_1\theta_2^2 + 2\gamma\theta_1\theta_2)}{\gamma(\theta_1 + \theta_2)(1 + \gamma\theta_1)(1 + \gamma\theta_2)} \right\} \quad (20)$$

## Electrostatic Coagulation

Charged particles may experience either enhanced or retarded coagulation rates depending on their charges. For a unipolar aerosol, it is necessary to consider electrostatic dispersion (i.e., the tendency of charged particles of the same sign to move away from each other). This dispersion tends to reduce the concentration of an aerosol, for example, by causing particles to deposit on the walls of any containing vessel or nearby surface. In the presence of particle charging, the collision kernel of particles must be corrected by:

$$\beta_E(v_1, v_2) = \frac{\beta_n(v_1, v_2)}{W} \quad (21)$$

where the subscript “n” designates neutral particles. The Fuchs stability function  $W$  is given by:<sup>[16]</sup>

$$W = \frac{\exp(\kappa) - 1}{\kappa}, \quad \kappa = \frac{z_1 z_2 e^2}{(r_1 + r_2)k_B T} \quad (22)$$

where  $z_1$  and  $z_2$  are the numbers of unit charges contained in particles, and  $e$  is the electron charge. For  $\kappa > 0$  (like charge),  $W > 1$  and coagulation is retarded from that for neutral particles. Conversely, for  $\kappa < 0$  (unlike charge),  $W < 1$  and coagulation is enhanced.

## SOLUTIONS TO THE COAGULATION EQUATION

Methods of solving a coagulation equation were summarized by Williams and Loyalka.<sup>[17]</sup> These methods range from the discrete (computationally intensive) and sectional models in which Eq. (5) is transformed into a number of differential equations, to the less accurate monodisperse models. Approximate solutions can be found using the method of moments. Exact solutions for asymptotic limiting cases can be obtained with the self-preserving theory.

### Sectional Method

Because solving the coagulation equation with a direct numerical method is impractical owing to its time-consuming property, several approximate methods have been developed. The sectional method developed by Gelbard, Tambour, and Seinfeld<sup>[18]</sup> is known as a

very accurate but comparatively time-efficient tool. Their model solved a one-dimensional form of the aerosol general dynamic equation by dividing the particle size domain into a finite number of sections by particle volume, and by calculating the addition and subtraction of particle mass to each section. The model assumed that particles kept their spherical shape during growth; therefore the volume sections corresponded to sections of particle size. However, as irregular particles have become omnipresent in nanoparticle production (e.g., generation of titanic or silica particles by gas-phase reaction), substantial progress has been made in developing models that account for irregular particle shape through fractal dimensions. The volume and surface area of irregularly shaped particles were chosen as the two particle size dimensions because these are the most commonly employed powder properties in engineering applications. Then the two-dimensional aerosol dynamic equations were solved by extending a one-dimensional sectional technique to the two-dimensional space.<sup>[19]</sup> A two-dimensional particle size distribution function is defined as  $n_t(v, a)$ , where  $n_t(v, a) da dv$  is the number density of particles having a volume between  $v$  and  $v + dv$  and a surface area between  $a$  and  $a + da$  at time  $t$ . For an aerosol that is formed by gas-phase reaction at high temperatures, the rate of change in  $n_t(v, a)$  is given by the rate of simultaneous coagulation and coalescence (by sintering) among aerosol particles.<sup>[19,20]</sup>

$$\frac{\partial n_t(v, a)}{\partial t} = \left[ \frac{\partial n_t(v, a)}{\partial t} \right]_{\text{coag}} + \left[ \frac{\partial n_t(v, a)}{\partial t} \right]_{\text{sint}} \quad (23)$$

The coagulation term in Eq. (23) can be obtained by extending the classical collision theory to the two-dimensional space  $v, a$  as:

$$\begin{aligned} & \left[ \frac{\partial n_t(v, a)}{\partial t} \right]_{\text{coag}} \\ &= \frac{1}{2} \int_0^v \theta \left( a > \left( \frac{\bar{v}}{v_0} \right)^{2/3} a_0 + \left( \frac{v - \bar{v}}{v_0} \right)^{2/3} a_0 \right) \\ & \quad \times \int_{\left( \frac{\bar{v}}{v_0} \right)^{2/3} a_0}^{\frac{v}{v_0} a_0} \beta_{\bar{v}, v - \bar{v}}(\bar{a}, a - \bar{a}) n_t(\bar{v}, \bar{a}) \\ & \quad \times n_t(v - \bar{v}, a - \bar{a}) d\bar{a} d\bar{v} - n_t(v, a) \int_0^\infty \\ & \quad \times \int_{\left( \frac{\bar{v}}{v_0} \right)^{2/3} a_0}^{\frac{v}{v_0} a_0} \beta_{v, \bar{v}}(a, \bar{a}) n_t(\bar{v}, \bar{a}) d\bar{a} d\bar{v} \end{aligned} \quad (24)$$

where  $v_0$  and  $a_0$  are the volume and surface area, respectively, of the primary particle, which is the smallest possible particle (e.g., a molecule or a monomer).

The sintering contribution in Eq. (23) is related to the particle sintering rate through the continuity:<sup>[20]</sup>

$$\left[ \frac{\partial n_t(v, a)}{\partial t} \right]_{\text{sint}} = - \frac{\partial}{\partial a} \left[ \frac{da}{dt} n_t(v, a) \right] \quad (25)$$

The sintering of solid particles or highly viscous fluids can be the result of various sintering mechanisms such as solid-state surface or volume diffusion and viscous flow. For the mechanism of viscous flow coalescence beyond a small initial time scale, Hiram and Nir<sup>[21]</sup> found that the neck size approaches the radius of the resulting sphere exponentially. For longer times, this leads to a similar behavior for the particle surface:<sup>[20]</sup>

$$\frac{da}{dt} = - \frac{1}{\tau_f} (a - a_{\text{final}}) \quad (26)$$

where  $a_{\text{final}}$  is the surface area of the completely fused sphere of volume  $v$ , and  $\tau_f$  is the characteristic coalescence time. The characteristic time for coalescence or sintering  $\tau_f$  is the time needed to reduce by 63% the excess agglomerate surface area over that of a spherical particle with the same mass.

Therefore by combining Eqs. (23) and (24) and Eqs. (25) and (26), the overall aerosol population balance equation can be written as:

$$\begin{aligned} & \frac{\partial n_t(v, a)}{\partial t} - \frac{1}{\tau_f} \frac{\partial}{\partial a} \left( \left[ a - \left( \frac{v}{v_0} \right)^{2/3} a_0 \right] n_t(v, a) \right) \\ &= \frac{1}{2} \int_0^v \theta \left( a > \left( \frac{\bar{v}}{v_0} \right)^{2/3} a_0 + \left( \frac{v - \bar{v}}{v_0} \right)^{2/3} a_0 \right) \\ & \quad \times \int_{\left( \frac{\bar{v}}{v_0} \right)^{2/3} a_0}^{\frac{v}{v_0} a_0} \beta_{\bar{v}, v - \bar{v}}(\bar{a}, a - \bar{a}) n_t(\bar{v}, \bar{a}) n_t(v - \bar{v}, a - \bar{a}) \\ & \quad \times d\bar{a} d\bar{v} - n_t(v, a) \int_0^\infty \int_{\left( \frac{\bar{v}}{v_0} \right)^{2/3} a_0}^{\frac{v}{v_0} a_0} \beta_{v, \bar{v}}(a, \bar{a}) n_t(\bar{v}, \bar{a}) d\bar{a} d\bar{v} \end{aligned} \quad (27)$$

Equation (27) is a two-dimensional partial integro-differential equation that needs to be solved numerically. In solving the conventional one-dimensional coagulation equation, a sectional model has been developed. The sectional method proves to be both computationally efficient and numerically robust, especially in dealing with aerosols having an extremely large size spectrum. Xiong and Pratsinis<sup>[19]</sup> presented a set of  $M$  ordinary differential equations (ODEs) using an efficient ODEs solver.

### Self-Preserving Solution

One of the interesting features of coagulation known to date is that the shape of the size distribution of suspended particles undergoing coagulation often does not change after a long time and the distribution becomes *self-preserving*.<sup>[22-24]</sup>

Conventionally, in the self-preserving formulation, the dimensionless particle volume is defined as:

$$\eta = \frac{N(t)v}{\phi(t)} \tag{28}$$

and the dimensionless size distribution density function is defined as:

$$\Psi(\eta) = \frac{n(v, t)\phi(t)}{N^2(t)} \tag{29}$$

Friedlander and Wang<sup>[24]</sup> obtained the following equation for the Brownian coagulation in the continuum regime:

$$\begin{aligned} (1 + ab)\eta \frac{\partial \Psi(\eta)}{\partial \eta} + (2ab - b\eta^{1/3} - a\eta^{-1/3})\Psi(\eta) \\ + \int_0^\eta \Psi(\eta - \bar{\eta})\Psi(\bar{\eta}) \left\{ 1 + \left( \frac{\eta - \bar{\eta}}{\bar{\eta}} \right)^{1/3} \right\} d\bar{\eta} = 0 \end{aligned} \tag{30}$$

where  $a = \int_0^\infty \eta^{1/3}\Psi(\eta)d\eta$  and  $b = \int_0^\infty \eta^{-1/3}\Psi(\eta)d\eta$ . Friedlander and Wang derived analytical solutions of Eq. (30), shown in Eqs. (31) and (32), for small  $\eta$  regime and for large  $\eta$  regime, respectively:

$$\Psi(\eta) = \frac{0.5086}{\eta^{1.06}} \exp(1.758\eta^{1/3} - 1.275\eta^{-1/3}) \tag{31}$$

$$\Psi(\eta) = 0.915 \exp(-0.95\eta) \tag{32}$$

Equation (30) can be solved numerically for the entire  $\eta$  range. The results obtained by Friedlander and Wang are shown in Fig. 3 together with the results of numerical simulations by Vemury, Kusters, and Pratsinis,<sup>[25]</sup> who solved the coagulation equation [Eq. (5)] using the sectional method of Landgrebe and Pratsinis.<sup>[26]</sup> Lai et al.<sup>[27]</sup> used the above technique to derive the self-preserving size distribution for the free molecule regime.

Wang and Friedlander<sup>[28]</sup> applied the same method to the Brownian coagulation either with slip correction or with simultaneous shear flow. However, in their work, they had to introduce an unrealistic assumption that some parameters are special functions of time. Pich, Friedlander, and Lai<sup>[29]</sup> obtained the self-preserving particle size distribution for the problem of simultaneous coagulation and condensation, but the similar constraint confined the application of the solution obtained.

### Moment Method

Although the self-preserving size distribution theory played a very important role for researchers in understanding the coagulation mechanism, one shortcoming of the theory is its inability to resolve the size distribution for the time period before an aerosol attains the self-preserving size distribution. Therefore it was still necessary to resort to numerical calculations. However, during coagulation, the size distribution of particles changes by the interaction of particles in so many size classes at each time step that the computing time becomes excessive for the calculation of the change of size distribution of particles. To overcome this problem and to accelerate the computations, much effort has been made. Cohen and Vaughan<sup>[30]</sup> succeeded in reducing the coagulation equation to a set

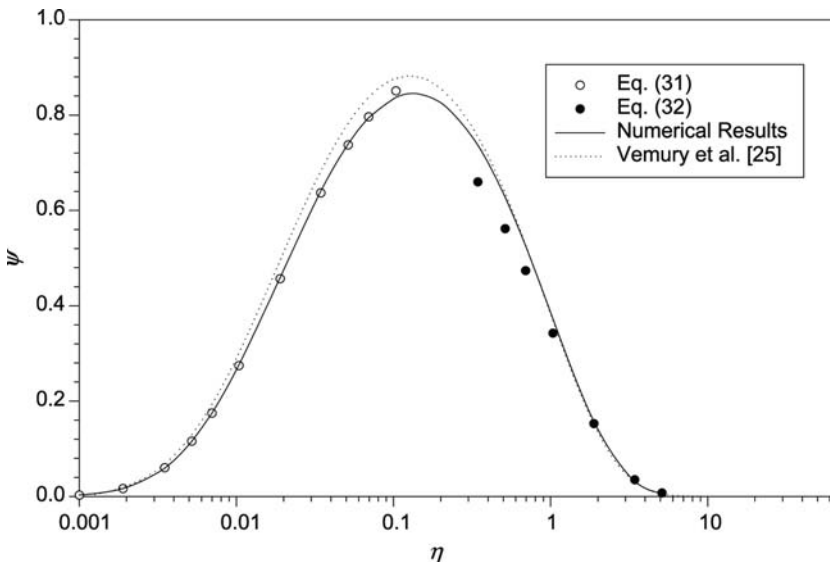


Fig. 3 Self-preserving size distribution for Brownian coagulation.

of ODEs for the moments of size distribution. By choosing a specific functional form for the distribution of the particle size, they were able to calculate the parameters of the size distribution as a function of the three leading moments. This method, known as the moment method, has the advantage of simplicity while providing important information on the change of the size distribution of aerosol.<sup>[31]</sup> Therefore the moment method has been widely applied in the simulation of aerosol coagulation.<sup>[32,33]</sup> Here, the application of the moment method to Brownian coagulation of fractal agglomerates,<sup>[34]</sup> which are often involved in the synthesis of nanoparticles, is addressed as an example for the continuum regime where the slip correction factor is equal to 1.

In the moment method, to represent a polydisperse aerosol size distribution, the log-normal function (one of the most commonly used mathematical forms for the study of the dynamics of particles) is used. The size distribution density function for particles whose radius is  $r$  for the log-normal distribution is written as:

$$n(r, t) = \frac{1}{r} \frac{N(t)}{\sqrt{2\pi \ln \sigma(t)}} \exp \left[ \frac{-\ln^2 \{r/r_g(t)\}}{2 \ln^2 \sigma(t)} \right] \quad (33)$$

where  $N(t)$  is the total number concentration of particles,  $\sigma(t)$  is the geometric standard deviation based on particle radius, and  $r_g(t)$  is the geometric number mean particle radius. For studying the coagulation problem in which two particles collide to become a particle whose volume is the sum of the two volumes, it is convenient to rewrite Eq. (33) in terms of particle volume:

$$n(v, t) = \frac{1}{3v} \frac{N(t)}{\sqrt{2\pi \ln \sigma(t)}} \exp \left[ \frac{-\ln^2 \{v/v_g(t)\}}{18 \ln^2 \sigma(t)} \right] \quad (34)$$

where  $v_g$  is the geometric number mean particle volume. If one obtains the time evolution of the three parameters  $N(t)$ ,  $\sigma(t)$ , and  $v_g(t)$ , the particle size distribution of the coagulating aerosol of interest for any time  $t$  can be constructed using Eq. (34).

The  $k$ th moment of the particle size distribution is written as:

$$M_k = \int_0^\infty v^k n(v, t) dv \quad (35)$$

where  $k$  is an arbitrary real number. According to the properties of a log-normal function, any moment can be written in terms of  $M_0$ ,  $v_g$ , and  $\sigma$  as follows:

$$M_k = M_0 v_g^k \exp \left( \frac{9}{2} k^2 \ln^2 \sigma \right) \quad (36)$$

If Eq. (36) is written for  $k = 0, 1$ , and  $2$ , and subsequently solved for  $v_g$  and  $\sigma$  in terms of  $M_0$ ,  $M_1$ , and

$M_2$ , we have:

$$\ln^2 \sigma = \frac{1}{9} \ln \left( \frac{M_0 M_2}{M_1^2} \right) \quad (37)$$

$$v_g = \frac{M_1^2}{M_0^{3/2} M_2^{1/2}} \quad (38)$$

The collision kernel of fractal agglomerates  $\beta_F(v, \bar{v})$  covering the continuum regimes is represented by the following expression:<sup>[35]</sup>

$$\beta_F(v, \bar{v}) = K_{co} (v^{1/D_f} + \bar{v}^{1/D_f}) \left( \frac{1}{v^{1/D_f}} + \frac{1}{\bar{v}^{1/D_f}} \right) \quad (39)$$

where  $K_{co}$  is defined by Eq. (3), and  $D_f$  is the mass fractal dimension, which varies between 1 and 3.<sup>[36]</sup> Substituting Eq. (39) into Eq. (5) and integrating from 0 to  $\infty$ , one can obtain the following equations using Eq. (35):

$$\frac{dM_0}{dt} = -K_{co} (M_0^2 + M_{-1/D_f} M_{1/D_f}) \quad (40)$$

$$\frac{dM_1}{dt} = 0 \quad (41)$$

$$\frac{dM_2}{dt} = 2K_{co} \{ M_1^2 + M_{(D_f-1)/D_f} M_{(D_f+1)/D_f} \} \quad (42)$$

Equation (41) merely indicates that  $M_1 = \text{const}$ . Substituting Eq. (36) for the moments appearing in the right-hand side of Eqs. (40) and (42), and substituting Eqs. (37) and (38) thereafter, we have the following two equations for  $k = 0$  and  $2$ , respectively:

$$\frac{dM_0}{dt} = -K_{co} \left( M_0^2 + M_0^{(2+(1/D_f^2))} M_1^{-2/D_f^2} M_2^{1/D_f^2} \right) \quad (43)$$

$$\frac{dM_2}{dt} = 2K_{co} \left\{ M_1^2 + M_0^{1/D_f^2} M_1^{(2-(2/D_f^2))} M_2^{1/D_f^2} \right\} \quad (44)$$

The governing equation has just been converted into a set of three first-order ODEs. Eqs. (41), (43), and (44) can be solved using any standard numerical package for solving first-order ODEs. After  $M_0$ ,  $M_1$ , and  $M_2$  are solved from Eqs. (43), (41), and (44), respectively,  $\sigma$  and  $v_g$  can be computed using Eqs. (37) and (38). Subsequently, the size distribution of the fractal agglomerates for any time can be constructed using Eq. (34).

## Coagulation in Nanoparticle Synthesis

Among the most recent developments in the theoretical description of gas-to-particle conversion process is the simultaneous modeling of precursor decomposition, coagulation, and sintering processes in the aerosol, originally reported by Koch and Friedlander<sup>[20]</sup> and

Kobata, Kusakabe, and Morooka<sup>[37]</sup> and refined further by Xiong and Pratsinis,<sup>[19]</sup> Xiong, Pratsinis, and Mastrangelo<sup>[38]</sup> and Tsantilis and Pratsinis<sup>[39]</sup> using elaborate two-dimensional sectional models of the population balance equation. In chemical vapor synthesis (CVS), particles pass through the complete temperature profile of a hot wall reactor together with the gas stream. The CVS technique is based on the process of chemical vapor deposition (CVD), which is widely employed to prepare coatings at a high level of control of the growth parameter and, consequently, of the microstructure. As the process is very important for basic research and industrial production, the conditions for CVD growth have been determined for many material systems. The formation process of nanoparticles in the gas phase has been studied intensively both experimentally and theoretically. Many kinetic models exist to describe the dependence of the particle size on various synthesis parameters such as partial and total pressure, temperature, etc. It is of particular interest to study the particle formation on an atomic scale to understand the diffusional processes that lead to coagulation and particle rearrangement on the short time scale of their formation. Molecular dynamics (MD) simulation is used to study the particle formation and the coagulation/sintering processes.

## CONCLUSION

Therefore the coagulation of particles suspended in a gas or a liquid strongly influences the particle size distribution and is of fundamental interest in a wide range of applications in science and engineering. In this entry, some theories of coagulation are reviewed.

The coagulation of a monodisperse aerosol was studied for Brownian coagulation by Smoluchowski<sup>[1]</sup> and the change of particle number concentration with respect to time was provided. The general coagulation equation of polydisperse aerosol particles was introduced and the collision kernels for Brownian, gravitational, laminar shear, turbulent, and electrostatic coagulations were presented. In case of Brownian coagulation, the kinetic theory and the continuum diffusion theory were used to derive the collision kernel for the free molecule regime and the continuum regime, respectively, and the two theories were brought together by flux matching to produce the kernel for transition regime. At the end of this entry, various solution techniques were introduced including the sectional method, the self-preserving solution, and the moment method. The sectional method provides the most accurate prediction on the size distribution changes. The self-preserving size distribution theory presents the asymptotic size distribution. The moment method has the advantage of simplicity while

providing important information on the change of the size distribution of aerosol.

## ACKNOWLEDGMENTS

We are grateful to Dr. Sung-Hoon Park (University of British Columbia) and Mr. Xiang Rongbiao for their valuable comments on the manuscript.

## REFERENCES

1. Smoluchowski, M.V. Versuch zur mathematischen Theorie der Koagulationskinetik kolloider Lösungen. *Z. Phys. Chem.* **1917**, *92*, 129–168.
2. Müller, H. Zur allgemeinen Theorie der raschen Koagulation. *Kolloidbeihfte* **1928**, *27*, 223–250.
3. Hidy, G.M.; Brock, J.R. *The Dynamics of Aerocolloidal Systems*; Pergamon Press: New York, 1970.
4. Allen, M.D.; Raabe, O.G. Slip correction measurements of spherical solid aerosol particles in an improved Millikan apparatus. *Aerosol Sci. Technol.* **1985**, *4*, 269–286.
5. Fuchs, N.A. Zur Theorie der Koagulation. *Z. Phys. Chem.* **1934**, *171A*, 199–208.
6. Dahneke, B. Simple kinetic theory of Brownian diffusion in vapors and aerosols. In *Theory of Dispersed Multiphase Flow*; Meyer, R.E., Ed.; Academic Press: New York, 1983; 97–133.
7. Fuchs, N.A.; Sutugin, A.G. High-dispersed aerosols. In *Topics in Current Aerosol Research*; Hidy, G.M., Brock, J.R., Eds.; Pergamon Press: New York, 1971; 1–60.
8. Otto, E.; Fissan, H.; Park, S.H.; Lee, K.W. The log-normal size distribution theory of Brownian aerosol coagulation for the entire particle size range: part II. Analytical solution using Dahneke's coagulation kernel. *J. Aerosol Sci.* **1999**, *30*, 17–34.
9. Reed, L.D.; Lee, K.W.; Gieseke, J.A. The behavior of contained radioactive suspensions. *Nucl. Sci. Eng.* **1980**, *75*, 167–180.
10. Simon, S.; Williams, M.M.R.; Cassel, J.S. A kernel for combined Brownian and gravitational coagulation. *J. Aerosol Sci.* **1986**, *17*, 789–793.
11. Kwon, S.B.; Lee, K.W. Experimental and numerical study on aerosol coagulation by gravitation. Part. Part. Syst. Charact. **2002**, *19*, 103–110.
12. Qiao, R.L.; Li, Z.; Wen, C.S. Effect of weak Brownian motion on gravitational coagulation. *J. Colloid Interface Sci.* **1998**, *202*, 205–207.
13. Saffman, P.G.; Turner, J.S. On the collision of drops in turbulent clouds. *J. Fluid Mech.* **1956**, *1*, 16–30.
14. Hinze, J.O. *Turbulence*, 2nd Ed.; McGraw-Hill: New York, 1975.
15. Kruijs, F.E.; Kusters, K.A. The collision rate of particles in turbulent flow. *Chem. Eng. Commun.* **1997**, *158*, 201–230.
16. Fuchs, N.A. *The Mechanics of Aerosols*; Pergamon Press: New York, 1964.

17. Williams, M.M.R.; Loyalka, S.K. *Aerosol Science Theory and Practice*; Pergamon Press: New York, 1991.
18. Gelbard, F.; Tambour, Y.; Seinfeld, J.H. Sectional representations for simulating aerosol dynamics. *J. Colloid Interface Sci.* **1980**, *76*, 541–556.
19. Xiong, Y.; Pratsinis, S.E. Formation of agglomerate particles by coagulation and sintering: part I. A two-dimensional solution of the population balance equation. *J. Aerosol Sci.* **1993**, *24*, 283–300.
20. Koch, W.; Friedlander, S.K. The effect of particle coalescence on the surface area of a coagulating aerosol. *J. Colloid Interface Sci.* **1990**, *140*, 419–427.
21. Hiram, Y.; Nir, A. A simulation of surface tension driven coalescence. *J. Colloid Interface Sci.* **1983**, *95*, 462–470.
22. Swift, D.L.; Friedlander, S.K. The coagulation of hydrosols by Brownian motion and laminar shear flow. *J. Colloid Sci.* **1964**, *19*, 621–647.
23. Hidy, G.M. On the theory of the coagulation of non-interacting particles in Brownian motion. *J. Colloid Sci.* **1965**, *20*, 123–144.
24. Friedlander, S.K.; Wang, C.S. The self-preserving size distribution for coagulation by Brownian motion. *J. Colloid Interface Sci.* **1966**, *22*, 126–132.
25. Vemury, S.; Kusters, K.A.; Pratsinis, S.E. Time lag for attainment of the self-preserving particle size distribution by coagulation. *J. Colloid Interface Sci.* **1994**, *165*, 53–59.
26. Landgrebe, J.D.; Pratsinis, S.E. A discrete-sectional model for powder production by gas phase chemical reaction and aerosol coagulation in the free-molecular regime. *J. Colloid Interface Sci.* **1990**, *139*, 63–86.
27. Lai, F.S.; Friedlander, S.K.; Pich, J.; Hidy, G.M. The self-preserving particle size distribution for Brownian coagulation in the free-molecule regime. *J. Colloid Interface Sci.* **1972**, *39*, 395–405.
28. Wang, C.S.; Friedlander, S.K. The self-preserving particle size distribution for coagulation by Brownian motion: II. Small particle slip correction and simultaneous shear flow. *J. Colloid Interface Sci.* **1967**, *24*, 170–179.
29. Pich, J.; Friedlander, S.K.; Lai, F.S. The self-preserving particle size distribution for coagulation by Brownian motion: III. Smoluchowski coagulation and simultaneous Maxwellian condensation. *J. Aerosol Sci.* **1970**, *1*, 115–126.
30. Cohen, E.R.; Vaughan, E.U. Approximate solution of the equation for aerosol agglomeration. *J. Colloid Interface Sci.* **1971**, *25*, 612–623.
31. Pratsinis, S.E.; Kodas, T.T.; Dudukovic, M.P.; Friedlander, S.K. Aerosol reactor design: effect of reactor type and process parameters on product aerosol characteristics. *Ind. Eng. Chem. Process Des. Dev.* **1986**, *25*, 634–642.
32. Pratsinis, S.E. Simultaneous nucleation, condensation, and coagulation in aerosol reactors. *J. Colloid Interface Sci.* **1988**, *124*, 416–427.
33. Whitby, E.R.; McMurry, P.H.; Shankar, U.; Binkowski, F.S. *Modal Aerosol Dynamics Modeling*, EPA Report 600/3-91/020, 1991.
34. Park, S.H.; Xiang, R.; Lee, K.W. Brownian coagulation of fractal agglomerates: analytical solution using the log-normal size distribution assumption. *J. Colloid Interface Sci.* **2000**, *231*, 129–135.
35. Mountain, R.D.; Mulholland, G.W.; Baum, H. Simulation of aerosol agglomeration in the free molecular and continuum flow regimes. *J. Colloid Interface Sci.* **1986**, *114*, 67–81.
36. Schaefer, D.W.; Hurd, A.J. Growth and structure of combustion aerosols: fumed silica. *Aerosol Sci. Technol.* **1990**, *12*, 876–890.
37. Kobata, A.; Kusakabe, K.; Morooka, S. Growth and transformation of TiO<sub>2</sub> crystallites in aerosol reactor. *AIChE J.* **1991**, *37*, 347–359.
38. Xiong, Y.; Pratsinis, S.E.; Mastrangelo, S.U.R. The effect of ionic additives on aerosol coagulation. *J. Colloid Interface Sci.* **1992**, *153*, 106–117.
39. Tsantilis, S.; Pratsinis, S.E. Evolution of primary and aggregate particle-size distributions by coagulation and sintering. *AIChE J.* **2000**, *46*, 407–415.



# AFM: Biopolymers

Nehal I. Abu-Lail

Terri A. Camesano

Department of Chemical Engineering, Worcester Polytechnic Institute,  
Worcester, Massachusetts, U.S.A.

## INTRODUCTION

Biopolymers are macromolecules of biological origin, which include nucleic acids (DNA and RNA), proteins, peptides, and polysaccharides. Although these macromolecules influence biological processes in different ways, most biological processes are associated to some extent with the physical properties of biopolymers (chain structure, flexibility, and excluded volume interactions). For example, the conformation of bacterial surface biopolymers affects their adhesion to host tissue in the establishment of infection. In other biological processes such as protein synthesis, the specific structural units of the biopolymers (nucleic acids and proteins) control the biological function.<sup>[1]</sup>

Interest in analyzing the physical properties and structural features of biopolymers stems from the wide variety of functions they can perform in living systems of humans,<sup>[2]</sup> animals,<sup>[2,3]</sup> plants,<sup>[4]</sup> bacteria,<sup>[5]</sup> and fungi<sup>[6,7]</sup> or the important roles they play in industrial operations. The ultimate aim behind the characterization of biopolymer properties is to provide a better understanding and control of their behavior in biological, medical, and/or industrial processes. Examples of applications affected by biopolymer properties are environmental bioremediation,<sup>[8–10]</sup> biomedical applications such as wound healing,<sup>[11–13]</sup> gene therapy,<sup>[14]</sup> growth mechanisms of macromolecular crystals,<sup>[15]</sup> food technology,<sup>[16,17]</sup> and bacterial adhesion.<sup>[18]</sup>

## OVERVIEW

A wide range of techniques and instruments have been used to characterize biopolymer properties. Examples include the use of vibrational circular dichroism (VCD) to investigate DNA condensation,<sup>[19]</sup> fluorescence correlation spectroscopy (FCS) to study the diffusion properties, size, and conformation of native and denatured *schizophyllan* in dilute solutions,<sup>[20]</sup> size exclusion chromatography (SEC) to characterize *Pseudomonas putida* KT2442 surface biopolymers,<sup>[21]</sup>

X-ray diffraction (XRD) to study the ordered conformation of gel-forming polysaccharides,<sup>[22]</sup> transmission electron microscopy (TEM) to image well-characterized algal cellulose microfibrils,<sup>[23]</sup> scanning electron microscopy (SEM) to study the extracellular matrix of nutrient-limited adherent bacterial populations,<sup>[24]</sup> Fourier transform infrared (FTIR) spectroscopy to study the effect of protein immobilization on birnessite,<sup>[25]</sup> and laser light scattering (LLS) to investigate the effect of pH on gelatin self-association in dilute solutions.<sup>[26]</sup> Other techniques such as optical tweezers<sup>[27]</sup> and the surface-force apparatus<sup>[28]</sup> have also been used to measure the interactions between biopolymers and surfaces.

Because of the accelerating developments made in atomic force microscopy (AFM) as a surface characterization technique, AFM is now a preferred instrument in the study of biological macromolecules. Atomic force microscopy is characterized by high lateral (6 Å) and vertical (1 Å) resolutions<sup>[29,30]</sup> and a high signal-to-noise ratio.<sup>[31]</sup> These features give rise to the AFM's ability to image detailed structures of individual or groups of delicate biopolymers.<sup>[31]</sup> In contrast to conventional biological imaging methods such as SEM and TEM, AFM can be used to image biopolymers in their native state without the need for staining,<sup>[3]</sup> labeling,<sup>[31]</sup> or coating with a conducting gold layer.<sup>[8]</sup> In addition, AFM can be used to probe biopolymers in ambient air or liquid without the need to operate under vacuum.<sup>[3]</sup> In particular, the ability to image biopolymers in liquid with AFM allows for investigation of macromolecules under native conditions for several hours or even days without damage.<sup>[31,32]</sup> Although AFM can be used to image biopolymers in air, precautionary measures have to be taken to ensure that the sample is not damaged and that artifacts are not created. When samples are allowed to air-dry, there is the possibility of coagulation or rearrangement of the molecules on the substrate during the drying process.<sup>[33]</sup>

Interaction forces between biopolymers and surfaces should be measured in a liquid environment to

minimize the presence of large capillary forces that are present in air ( $\sim 30$  nN).<sup>[34]</sup> The high adhesive forces caused by capillary forces are destructive to many biological samples and mask other interaction forces of lesser magnitudes, such as van der Waals forces and electrostatic interactions.

Atomic force microscopy has evolved from an imaging technique to a versatile tool that also allows for investigation of molecular forces at interfaces with great detail. Atomic force microscopy can also be used to probe the chemical nature,<sup>[35]</sup> elasticity,<sup>[36]</sup> roughness,<sup>[13]</sup> and surface charge<sup>[37]</sup> of biopolymers. We review the use of AFM as a state-of-the-art tool to characterize biopolymers. Examples will be provided on the use of AFM to characterize DNA, proteins, and polysaccharides.

## PROBING DNA WITH ATOMIC FORCE MICROSCOPY

### Earlier Efforts to Establish High-Resolution DNA Imaging

Since the invention of AFM, continuous improvements have been made in the ability to image and characterize deoxyribonucleic acid (DNA), which carries the genetic code of all living organisms. Most early attempts to image DNA were performed in air<sup>[38]</sup> because early attempts to image DNA in liquid (especially water) showed that if the molecules were not fixed properly, they could move during the imaging process. Their movement limited the ability to obtain reproducible results.<sup>[39]</sup> This challenge was overcome by stable binding of double-stranded DNA molecules to flat mica using chemical modification of the mica with 3-aminopropyltriethoxysilane. DNA molecules were bound to mica by this technique and molecules with contour lengths of 20–80 nm were stably imaged under repetitive scanning.<sup>[40]</sup> With techniques available at that time, the highest resolution achievable in DNA imaging was 2–3 nm. Because this was an order of magnitude less than the resolution required for DNA sequencing,<sup>[41]</sup> better substrate and sample preparation methods were required. Continuous and accelerated efforts were focused on reaching high-resolution AFM imaging of DNA. For example, Bensimon et al.<sup>[42]</sup> invented a technique for alignment of DNA on a silanated mica substrate, known as “molecular combing.” With this preparation technique, DNA could be elongated and even minute quantities ( $10^3$  molecules) could be imaged, which opened the way for faster physical mapping of the genome and increased detection abilities. Many variations of DNA immobilization based on coating of a surface with an

aminosilane compound or a self-assembled monolayer can be found in the literature.<sup>[43–45]</sup>

### Imaging of DNA Structure

Although there are numerous successful examples of high-resolution DNA imaging, we will focus on selected examples. Atomic force microscopy imaging has been widely used to discern the structure of DNA. Single- and double-stranded DNA were each imaged in propanol, butanol, and air. Measured molecular lengths were  $\sim 1$   $\mu\text{m}$ .<sup>[46]</sup> From imaging DNA on mica, single- and double-stranded DNA could be differentiated.<sup>[47]</sup> The images of the double-stranded DNA showed an open circular shape without drastic contortions and a contour length within 7% of the calculated length. Single-stranded DNA was present as compact open circles with nodes or lumps almost uniformly distributed or as highly elongated circles with a few nodes, the latter being more common.<sup>[47]</sup>

Because of much effort, rapid characterization of the structure of DNA by tapping mode AFM imaging in ambient conditions has become a relatively routine technique.<sup>[48]</sup> Examples on the use of tapping mode AFM imaging to discern differences between linear double-stranded  $\lambda$ -DNA, circular double-stranded plasmid DNA, and supercoiled double-stranded DNA plasmids with twists and writhes are shown in Fig. 1. DNA supercoiling has also been observed. The intramolecular triplex H-DNA formed by mirror-repeated purine–pyrimidine repeats and stabilized by negative DNA supercoiling was imaged. These images showed that the H-DNA is a protrusion with a different thickness than the DNA duplex (Fig. 2).<sup>[49]</sup> The conformation of DNA can be also studied with AFM imaging. For example, pH was shown to affect DNA conformation because  $\lambda$ -DNA could be denatured by HCl addition and renatured upon NaOH addition.<sup>[50]</sup>

### Characterization of DNA Molecular Properties

Analyzing AFM images provides a wealth of information on the size and conformation of DNA. For example, DNA imaged under ambient conditions using near-contact mode showed width values up to four times smaller than values measured in non-contact mode, even with the same tip.<sup>[51]</sup> The discrepancy was attributed to the greater resolution achievable through near contact compared with non-contact mode imaging. Estimation of the length of double-stranded DNA molecules as short as 100–200 base pairs from AFM images in air was considered an advance in DNA characterization. The measurements gave lengths consistent with the known dimensions of A-DNA.<sup>[52]</sup> It was not possible to image shorter

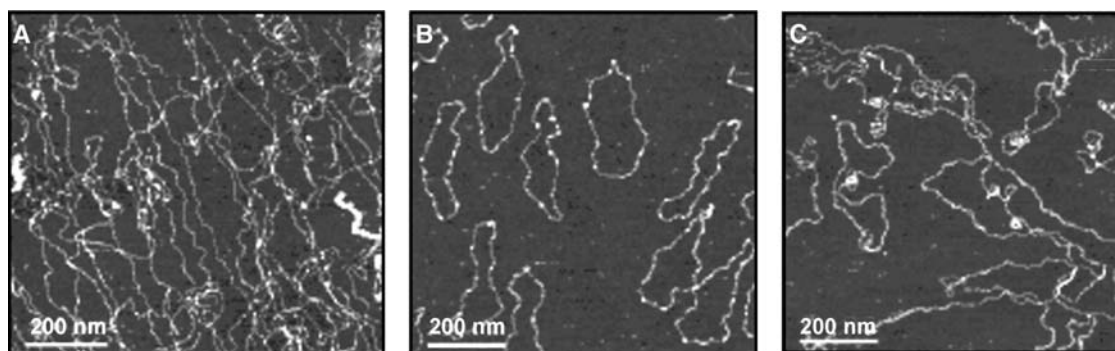


**Fig. 1** Top-view AFM images of different double-stranded (ds) DNA topologies on amino-terminated mica (vertical color scale = 3 nm) taken in AFM tapping mode under ambient conditions. (A) Linear  $\lambda$ -DNA (with 48.5 kbp), (B) non-twisted circular DNA plasmids (vector with 3.2 kbp) and (C) circular supercoiled DNA with twists and writhes due to internal supercoiling (supercoiled DNA ladder 2–16 kbp). The measured width of dsDNA of all geometrical topologies was  $\sim 3$ –7 nm and affected by the tip geometry. The molecular height was  $\sim 1$  nm. Source: From Ref.<sup>[48]</sup> with permission from Wiley & Sons Inc.

DNA molecules (25–50 base pairs) because intermolecular cross-bridging and base pairing in the molecules caused only globular forms to be viewed.<sup>[52]</sup>

In a revolutionary development, carbon nanotube AFM tips are starting to provide a new dimension in AFM imaging. These tips are ideal for AFM work because of their small diameter, high aspect ratio, large Young's modulus, mechanical robustness, well-defined structure, and unique chemical properties.<sup>[53]</sup> With the use of carbon nanotube tips, high-resolution images of RecA-double stranded DNA complexes were obtained (Fig. 3). The images revealed the 10-nm pitch of RecA-double stranded DNA complexes and RecA filaments as three-dimensional surface topographical features, without reconstruction analysis. The depth of the notch between two pitches was  $< 1$  nm.<sup>[54]</sup>

New imaging modes also helped improve DNA characterization. In a recent study, magnetic-mode AFM was used to characterize the process of DNA

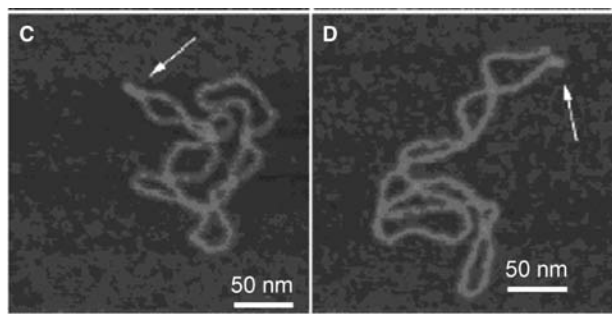


**Fig. 2** Atomic force microscopy images of DNA deposited at pH = 5.0. These images represent high-resolution images of H-DNA. The two images are schematics of the height and width. Source: From Ref.<sup>[49]</sup>. © 2001, with permission from Elsevier.

adsorption on a highly oriented pyrolytic graphite (HOPG) electrode surface. The images of single- and double-stranded DNA molecules showed that both types have the tendency to self-assemble from solution onto the HOPG surface (Figs. 4 and 5). The adsorbed film heights were dependent on the DNA concentration and were held to the surface with non-covalent interactions such as hydrogen bonding, base stacking, and electrostatic, van der Waals, and hydrophobic interactions.<sup>[55]</sup>

### Stretching DNA to Study Biomechanical Properties

The biomechanical properties of DNA can be obtained through stretching these molecules in a technique known as single molecule force spectroscopy (SMFS). DNA molecules are tethered to a surface at one end and stretched through application of an external force, which may be magnetic,<sup>[56]</sup> caused by hydrodynamic flow,<sup>[56]</sup> or result from the AFM cantilever stiffness<sup>[57]</sup> or an electrical field.<sup>[58]</sup> Typically, one DNA molecule is picked up from an adsorbed layer of DNA molecules by the AFM tip because of an applied contact force of several nanoNewtons. Upon retraction of the tip from the layer, the DNA strand is stretched. The resulting force from this stretching is measured as cantilever deflection, which can be converted to force by accounting for the spring constant of the cantilever. Several methods exist for determining these spring constants, as reviewed in Ref.<sup>[59]</sup>. Stretching experiments provide important information about the mechanical properties of DNA. We will discuss three examples: probing DNA elasticity, quantifying interactions between complementary strands of DNA, and DNA sequencing.

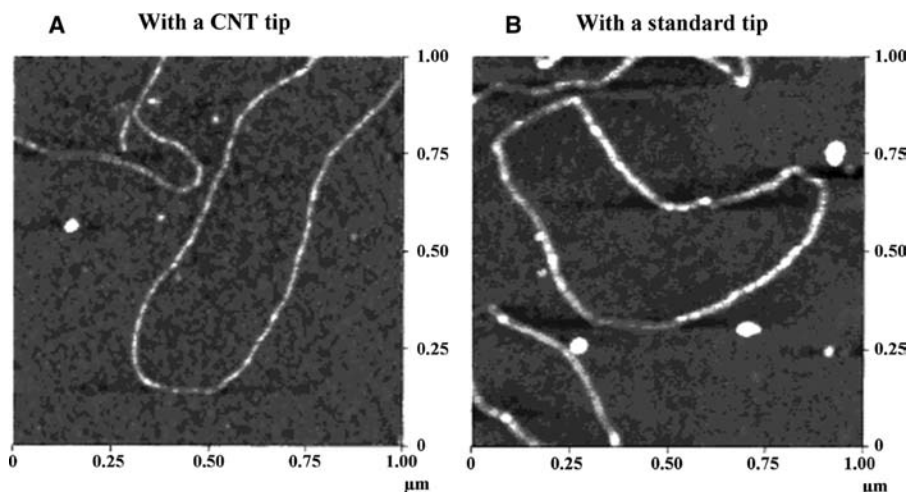


**Fig. 3** Topographic AFM images of RecA-dsDNA filaments observed with (A) a CNT tip and (B) with a standard tip (TESP-type tip). *Source:* From Ref.<sup>[54]</sup>. © 2001, with permission from Elsevier.

### Elasticity of DNA

The elasticity of single molecules can be estimated directly from force-extension measurements by applying random-walk statistical mechanical-based models. The most frequently used models are the freely jointed chain (FJC), extensible freely jointed chain (FJC+), and wormlike chain (WLC) models.<sup>[36]</sup> The elasticity of DNA molecules was first estimated by applying the FJC model to force-extension data between single DNA molecules (chemically attached by one end to a glass surface and by the other end to a magnetic bead) and an AFM tip under three different salt concentrations.<sup>[56]</sup> The FJC model failed to explain the force-extension data because of the fact that it does not account for the extensibility of the molecules. It appeared that the DNA molecules could deform when exposed to stress. The authors discounted the WLC model because they speculated that the latter model

would also fail due to the inability to account for the extensibility of DNA.

However, in some cases, the WLC model was appropriate for explaining DNA's mechanical properties. For example, the elasticity of  $\lambda$ -phage DNA was explained well with the WLC model, although the FJC model showed a large deviation from the experimental data.<sup>[58]</sup> The WLC model provided a contour length of  $32.8 \pm 0.1 \mu\text{m}$  and a persistence length of  $53.4 \pm 2.3 \text{ nm}$ .<sup>[58]</sup> An additional difference between the FJC and WLC models is that the FJC model accounts for entropic effects only, while the WLC model also accounts for enthalpic interactions.

In another example, the elasticity of a single supercoiled DNA molecule was probed via SMFS. Sharp

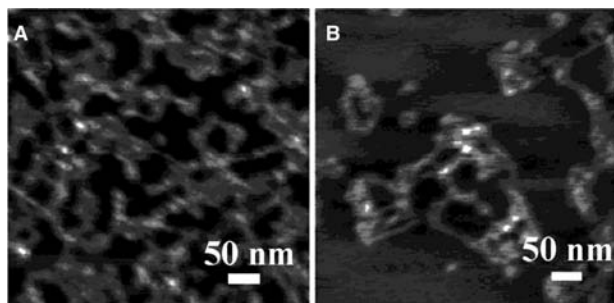


**Fig. 4** Magnetic alternating contact (MAC) mode AFM topographical images in air of the DNA biosensor surface prepared by 3 min of free adsorption onto HOPG from (A)  $10 \mu\text{g/ml}$  and (B)  $5 \mu\text{g/ml}$  dsDNA in phosphate buffer (pH 7.0, 0.1 M). *Source:* From Ref.<sup>[55]</sup>. © 2001 American Chemical Society.

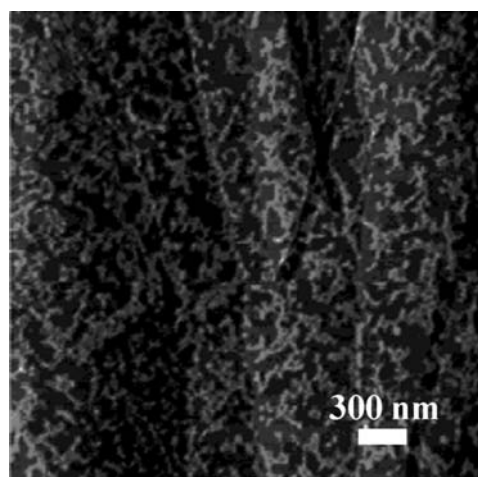


**Fig. 5** Magnetic alternating contact mode AFM topographical images in air of the DNA biosensor surface prepared by 3 min of free adsorption onto HOPG from a  $5 \mu\text{g/ml}$  single-stranded DNA in phosphate buffer (pH 7.0, 0.1 M). *Source:* From Ref.<sup>[55]</sup>. © 2001 American Chemical Society.)

transitions were observed in the elasticity of the molecules at  $\sim 0.45$  and  $\sim 3$  pN for underwound and overwound molecules, respectively. These transitions were attributed to the possibility of the formation of alternative DNA superstructures or because of DNA transcription and replication.<sup>[60]</sup>

### Interaction Forces between Complementary Strands of DNA

Understanding the intermolecular forces within the DNA double helix is important to control the behavior of DNA in various applications, such as DNA sequencing. In the first effort to measure the forces between single DNA strands, DNA oligonucleotides were covalently attached to a spherical probe and to a silica surface.<sup>[57]</sup> Force measurements between these strands showed three distinct force regimes, centered at 1.52, 1.11, and 0.83 nN. The forces were directly associated with the rupture of the interaction between a single pair of molecules involving 20, 16, and 12 base pairs, respectively. This study demonstrated the importance of AFM in detecting the presence of, and relative positions of, specific base sequences with angstrom resolution.<sup>[57]</sup>

In a study on double-stranded  $\lambda$ -phage DNA, the split of the molecule into single strands was observed via force microscopy.<sup>[61]</sup> Stretching experiments revealed a transition in the force-extension measurement at 65 pN attributed to the conversion of B-DNA to a new overstretched conformation called S-DNA. This transition was followed by a nonequilibrium melting transition at 150 pN (Fig. 6). The melting transition is the part of the curve at which the double-stranded DNA split into single strands that fully recombined upon relaxation.<sup>[61]</sup>

### DNA Sequencing

Because of the continuous increase in the resolution of AFM to the angstrom level, sequencing of DNA became possible. The principle behind this application is that the force-extension curve that arises when DNA is stretched is sequence-dependent. In one of the first studies to address DNA sequencing, a comparison was made between the force measurements on poly(dG-dC) and poly(dA-dT), where “d” represents the deoxynucleotide.<sup>[61]</sup> With knowledge of the melting transition for  $\lambda$ -phage DNA,<sup>[62]</sup> single strands of poly(dG-dC) and poly(dA-dT) were prepared. Upon relaxation, these strands reannealed into hairpin structures as a result of their self-complementary sequences.<sup>[61]</sup> Studying the unzipping of these hairpins with AFM directly revealed the base pair unbinding forces for G-C and for A-T, which were  $20 \pm 3$  and  $9 \pm 3$  pN, respectively. In another study of DNA unzipping, the force needed to open the double strands upon tip retraction was measured as a function of extension of the DNA molecule (Fig. 7). The required force was between 10 and 20 pN on a length scale of 10 bases. The force profiles were characteristic for each specific DNA sequence.<sup>[63]</sup>

### PROBING PROTEINS WITH ATOMIC FORCE MICROSCOPY

#### High-Resolution Imaging of Proteins

High-resolution protein imaging with AFM is a well-established technique. Proteins are often bound to mica for imaging because their tight binding facilitates imaging.<sup>[64]</sup> Alternately, proteins are covalently bound

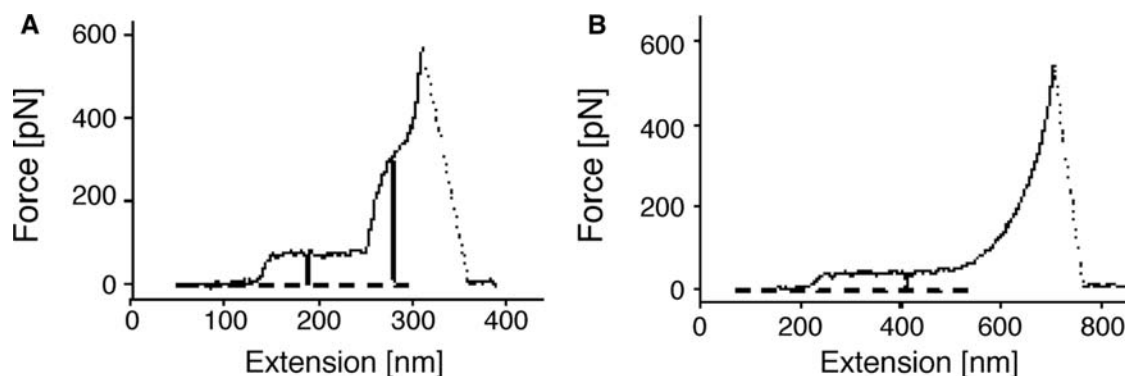


**Fig. 6** The mechanical compliance of DNA strongly depends on the specific base pairing in the double helix. (A) For double-stranded poly(dG-dC) DNA, there was a transition from B-DNA to a new overstretched form (S-DNA) that occurred at 65 pN (see arrows), similar to the transition observed in  $\lambda$ -DNA. The melting transition occurred at 300 pN for this DNA, compared to 150 pN in  $\lambda$ -DNA. (B) In duplex poly(dA-dT) DNA, the force of the B to S transition is reduced to 35 pN and the strands melt during this transition, so that no separate melting transition can be observed. *Source:* From Ref.<sup>[61]</sup>. © 1999 Nature Publishing Group (<http://www.nature.com/>).



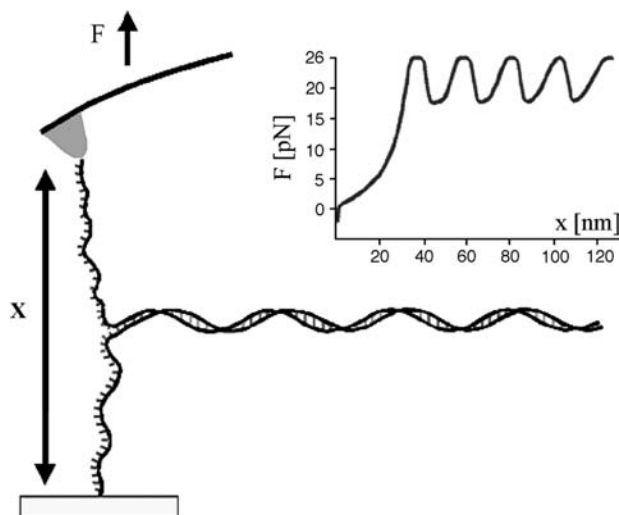


**Fig. 7** Complementary DNA oligonucleotides are chemically attached to an AFM tip and a glass surface. As the tip is brought in contact with the surface, a double strand forms, which can subsequently be unfolded upon retraction of the tip. *Source:* From Ref.<sup>[63]</sup>. © 2003 American Chemical Society.

to chemically modified surfaces.<sup>[65]</sup> Examples of AFM imaging studies on proteins are too numerous and diverse to be contained in this entry. We focus on two illustrative examples: 1) imaging of ligand–receptor interactions between cholera toxin B-oligomers bound to bilayers of biologically relevant lipids<sup>[66]</sup> and 2) imaging microtubules, protein structures of eukaryotic cells.<sup>[67]</sup>

In the first example, the interactions between cholera toxin B-oligomers (CTX-B) and a dipalmitoylphosphatidylcholine (DPPC) bilayer containing 10 mol% GM1 (the membrane receptor for CTX-B) were characterized. Images taken before and after the CTX-B oligomers were added to the lipid bilayer confirmed the high binding affinity of CTX-B to the receptor GM1 (Fig. 8). The high quality of the images revealed the ability of AFM to image membrane proteins without the need for cross-linking.

As a second example, a comparison was made between AFM, scanning tunneling microscopy (STM), and transmission electron microscopy (TEM) for their abilities to image microtubules isolated from pig brains. Atomic force microscopy was the easiest to use and most reproducible imaging technique.<sup>[67]</sup> The AFM images revealed the linear structure of the microtubules (Fig. 9) and the possibility of crossing of various tubules.

The capabilities of AFM imaging of proteins were extended to many other interesting applications such as capturing the conformational changes of proteins under physiological conditions<sup>[68]</sup> and visualization of DNA–protein complexes.<sup>[69]</sup>

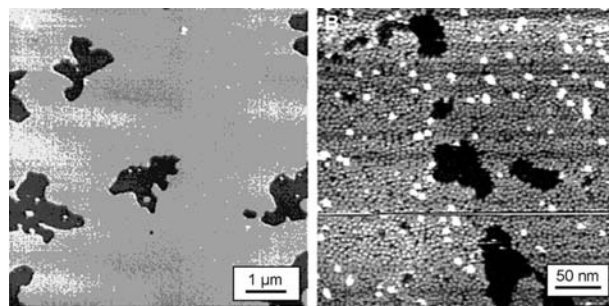


**Fig. 8** (A) A typical AFM image of a DPPC bilayer with 10 mol% GM1 before CTX-B was added. (B) The CTX-B bound to the ganglioside in the bilayer is clearly seen. The coverage is complete indicating that the distribution of the ganglioside is uniform. *Source:* From Ref.<sup>[66]</sup>. © 1995, with permission from Elsevier.

### Folding and Unfolding of Proteins

Proteins are molecules that are composed of a sequence of amino acids. This sequence of amino acids determines the complex helical shape that the protein will assume. The protein helix can be denatured under special conditions (chemical or thermal) and refold to its native state upon the removal of the denaturing source.<sup>[70]</sup> Each protein has a unique structure and a specific folding pattern for its polypeptide chain that

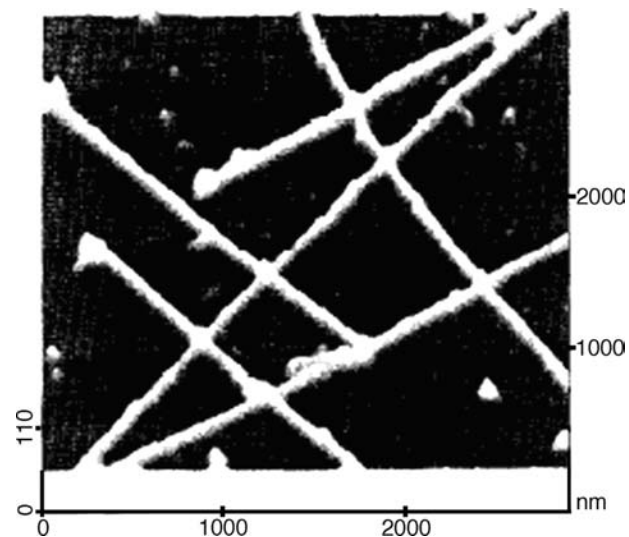


**Fig. 9** Atomic force microscopy top-view image of chemically immobilized microtubules (MTs) on silicon imaged under buffer solution (MES buffer with 0.7 M glycerol). Protein concentration was 2.0 mg/ml at the start of polymerization. Microtubules fixed with 5% glutaraldehyde before immobilization and imaged without damage under liquid, demonstrating an improved resistance to tip pressure. *Source:* From Ref.<sup>[67]</sup>. © 1995, with permission from Elsevier.

is required for proper biological function.<sup>[71,72]</sup> Understanding the process of folding and unfolding of proteins can help in controlling protein function for many applications.

The force-extension curves measured with AFM can characterize protein folding and unfolding.<sup>[73,74]</sup> For example, the mechanical properties of titin immunoglobulin (a giant sarcomeric protein of striated muscle) were studied by repetitive stretching of an individual titin molecule with AFM.<sup>[71]</sup> The stretching force was recorded as a function of molecule elongation. At large extensions, the force extensions exhibited a sawtooth-like pattern, with a periodicity that varied between 25 and 28 nm. These peaks were attributed to unfolding of individual domains of the protein. The forces required to unfold these domains were 150–300 pN and were dependent on the pulling speed. Refolding of protein was observed upon relaxation.

In a similar study, the folding and unfolding of fibronectin (a modular extracellular matrix protein) was investigated via AFM.<sup>[75]</sup> Statistical analysis of the force-extension curves clearly revealed the unfolding of three different types of fibronectin. The unfolding of fibronectin was irreversible within the timescale of one extension-relaxation cycle. The folding and unfolding of other proteins such as human tenascin-C<sup>[72]</sup> (Fig. 10), titin Ig,<sup>[76]</sup> and barnase<sup>[77]</sup> were also studied with AFM.

### Probing Ligand–Receptor Interactions

Ligand–receptor interactions can occur during the formation of double-stranded DNA, in enzymatic reactions, and in antigen–antibody recognition.<sup>[78]</sup> To measure these interactions, the AFM tip is functionalized with either the ligand or the receptor and the surface is functionalized with the other component.<sup>[79]</sup> In the first AFM study to measure the interactions between ligands and receptors, the interactions between a model receptor, streptavidin, and its ligand, biotin, were probed under physiological conditions.<sup>[80]</sup> The adhesion forces between the two functionalized surfaces were 3–8 times higher than the non-specific interactions measured between blocked streptavidin and biotinylated surfaces. Statistical analysis of the adhesive forces revealed the maximum number of streptavidin–biotin interactions and the force required to rupture the ligand–receptor bond. In another study of the interactions between avidin and biotin, the unbinding forces of discrete complexes were proportional to the enthalpy change of the complex formation, but independent of the free energy.<sup>[81]</sup> As another example, the interactions between P-selectin and P-selectin glycoprotein ligand-1 were probed with SMFS.<sup>[82]</sup> By modeling the resulting intermolecular

forces, knowledge of the rupture forces, elasticity, and kinetics of the interactions of the P-selectin/P-selectin glycoprotein ligand-1 interactions were obtained.

### PROBING POLYSACCHARIDES WITH ATOMIC FORCE MICROSCOPY

Polysaccharides are a large group of molecules that exist as components of plant, animal, algal, bacterial, and yeast cells. They provide structural support and act as an energy reservoirs in plants and animals.<sup>[23]</sup> Polysaccharides also play an important role in microbial activity, including evasion of host defense systems and attachment to host tissue in infections. Polysaccharides are important in biofilm formation, which affects such diverse microbial processes as the uptake of trace metals in soil,<sup>[83]</sup> failure of medical implants such as artificial heart valves,<sup>[84]</sup> the success of bioremediation,<sup>[85]</sup> and the virulence of pathogenic infections.<sup>[86]</sup> Polysaccharides are also linked with cancer pathology.<sup>[87]</sup> In many of these fields, the mechanisms by which polysaccharides control the biological processes are not well known. A better understanding of the properties of polysaccharides and their subsequent biological functions can be obtained by high-resolution studies using AFM imaging and force measurements.

### Quantitative Characterization of Polysaccharide Morphology by Atomic Force Microscopy Imaging

Atomic force microscopy imaging of polysaccharides can be used to obtain quantitative information on the molecule's height,<sup>[88]</sup> thickness,<sup>[88]</sup> width,<sup>[89]</sup> contour length,<sup>[33]</sup> persistence length,<sup>[34]</sup> end-to-end distance,<sup>[88]</sup> and the polydispersity and distribution of polysaccharides on the surfaces of living microbial cells.<sup>[90]</sup>

Conformational transitions of polysaccharides can be investigated with AFM imaging. For example, the denaturation/renaturation process for the xanthan triple helix was observed with tapping mode AFM imaging under ambient conditions. The triple helix denatured upon heating and renatured when cooled only if sufficient salt was present in solution.<sup>[88]</sup> The effect of different solvent chemistries (pH and ionic strength) on polysaccharide conformation was also investigated with tapping mode AFM. For example, the conformation of succinoglycan deposited on mica was observed in the presence and absence of salt. When there was no salt in the aqueous solution, a combination of rigid and flexible chains was observed, while



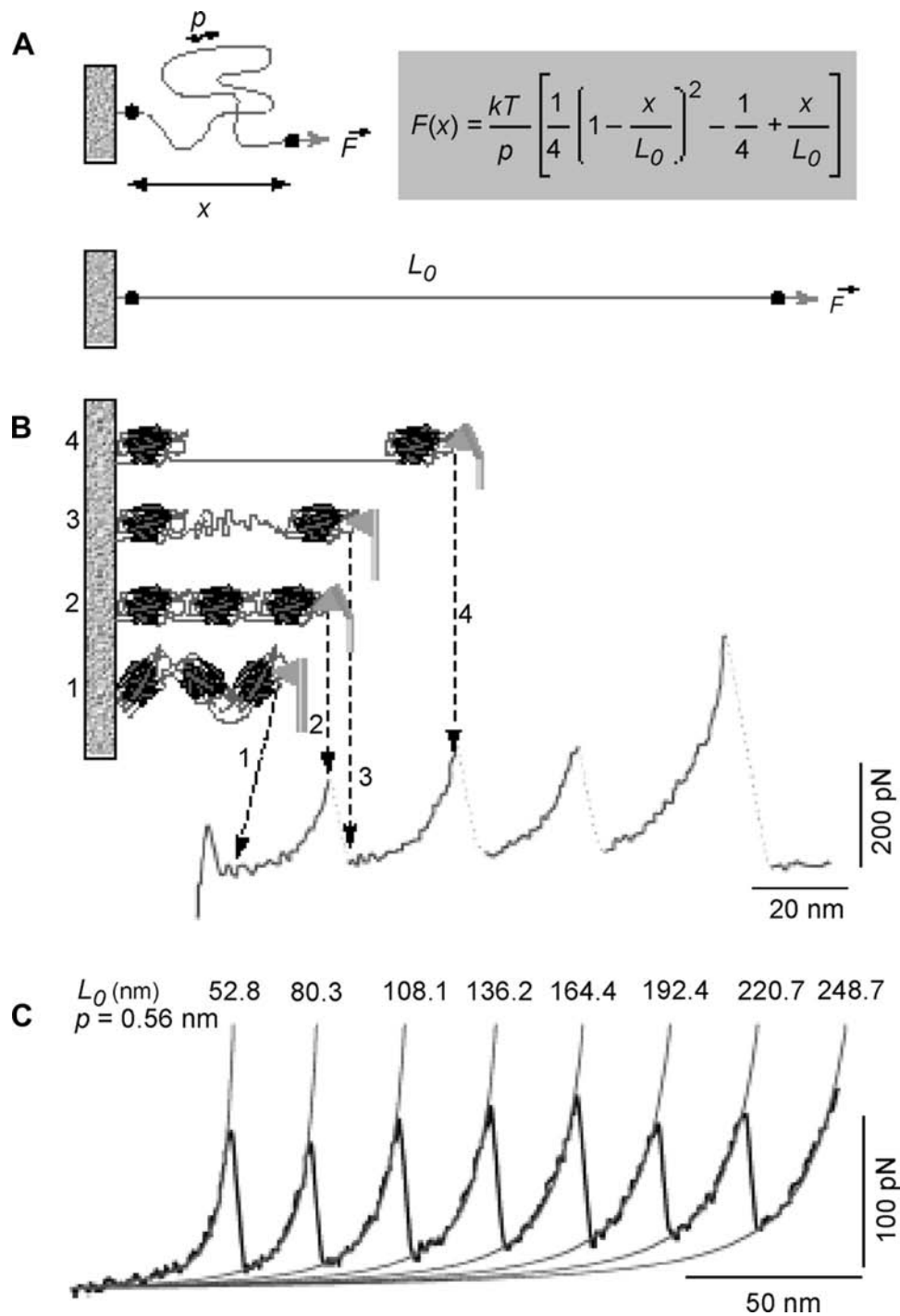


**Fig. 10** The entropic elasticity of proteins and domain unfolding. (A) The entropic elasticity of proteins can be described by the WLC model, which expresses the relationship between force ( $F$ ) and extension ( $x$ ) of proteins using its persistence length ( $p$ ) and its contour length ( $L_0$ );  $k$  is Boltzmann constant and  $T$  is temperature. (B) The sawtooth pattern of peaks observed when force was applied to extend the protein corresponds to sequential unraveling of individual domains of modular proteins. As the distance between the substrate and the cantilever increases (from state 1 to state 2), the protein elongates, generating a restoring force that bends the cantilever. When a domain unfolds (state 3), the free length of the protein increases, returning the force of the cantilever to near zero. Further extension results in force on the cantilever (state 4). The last peak represents the final extension of the unfolded protein prior to detachment from the AFM tip. (C) Consecutive unfolding peaks of recombinant human tenascin-C were fit using WLC model. The contour length ( $L_0$ ) for each fit is shown; the persistence length ( $p$ ) was fixed at 0.56 nm. *Source:* From Ref.<sup>[72]</sup>. © 1999, with permission from Elsevier.

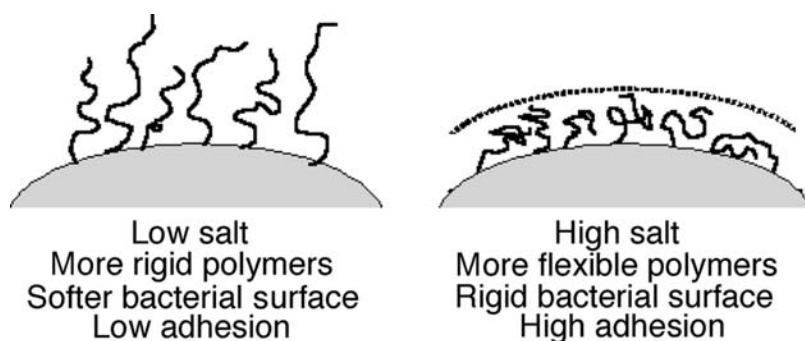


Fig. 11 Conceptual representation of the conformation of bacterial surface biopolymers at low and high salt concentrations.

only flexible single chains were observed in the presence of 0.01 M KCl.<sup>[89]</sup>

Another exciting application of AFM with respect to polysaccharide research is the imaging of dynamic biological processes. Gunning et al.<sup>[91]</sup> imaged molecular motion of a water-soluble wheat pentosan polysaccharide extracted from wheat flour. Parts of the molecules desorbed and reabsorbed onto the mica surface during tapping mode imaging in 10-mM HEPES buffer. Loops, trains, and tails were directly observed, confirming that polymer chains were desorbing and reabsorbing. The use of AFM to study other dynamic biological processes, including enzymatic breakdown of polysaccharides, is therefore not far from being realizable.

### Force Microscopy for Mechanical Characterization of Polysaccharides

Studying the force spectra recorded on polysaccharides (pure polysaccharides or polysaccharides on a microbial surface) provides useful information on the elastic, mechanical, and sometimes chemical nature of the macromolecules. Examples of the types of information that can be deduced from SMFS are the following: quantitative information about polysaccharide elasticity, estimated by applying polymer statistical models;<sup>[92]</sup> identifying the components of a mixture of pure polysaccharides;<sup>[93]</sup> probing the elasticity of polysaccharides on microbial cells;<sup>[7,36,94]</sup> and qualitative prediction of the conformation of microbial biopolymers.<sup>[95]</sup> We will discuss some of these examples in detail.

In the first study to quantify the elasticity of macromolecules on a microbial surface, surface macromolecules of dormant spores of *Aspergillus oryzae* were probed via SMFS.<sup>[94]</sup> The elongation forces were well described by the FJC + model, with estimated values of the Kuhn length and the segment elasticity in agreement with reported values for the structural properties of the polysaccharides dextran and amylose.

Single molecule force spectroscopy was also used to qualitatively predict the conformation of biopolymers,

predominately polysaccharides, on the surface of the bacterium *P. putida* KT2442. Forces were measured on individual bacterial cells in solutions with varying added salt concentrations (water–1 M KCl). The biopolymers on the microbial surface adopted a more flexible conformation with increasing solution salt concentration.<sup>[95]</sup> The flexibility of the molecules was quantified using the FJC model for polymer elasticity. Because of the increased flexibility of the biopolymers in high salt solutions, the biopolymers collapsed onto the surface of the bacterium, leading to a more rigid surface when in high salt (Fig. 11). The transition in polysaccharide conformation was related to the slope of the compliance region of the approach curves measured between the bacterial cells and the AFM silicon nitride tip (Fig. 12). Changes in biopolymer conformation and the biomechanical properties of the bacterium were related to bioadhesion.<sup>[95]</sup>

Atomic force microscopy can also be used as a spectroscopic technique for chemical fingerprinting of polysaccharides. Transitions in the flexibility of

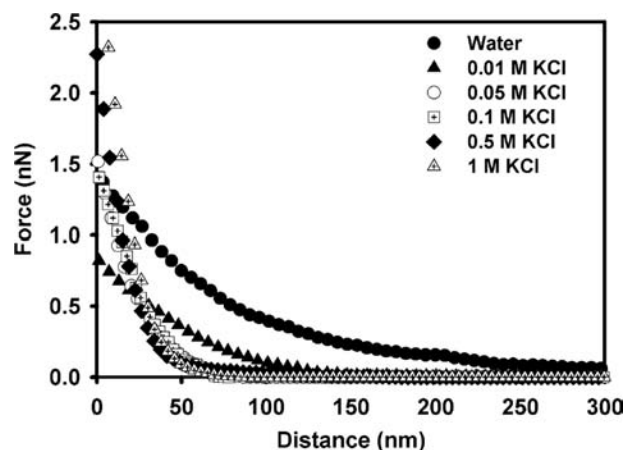
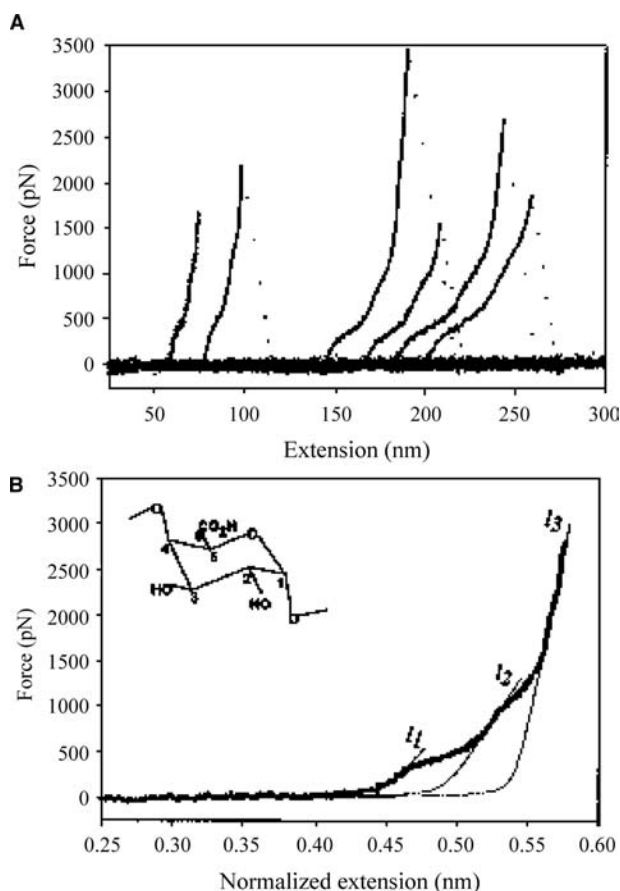


Fig. 12 A comparison between average approach curves (each curve is an average of 25 individual force measurements) for *P. putida* KT2442 in various solutions. Slopes of the compliance region of these curves are  $-0.014$ ,  $-0.010$ ,  $-0.054$ ,  $-0.035$ ,  $-0.109$ , and  $-0.114$  nN/nm, from water to 1 M KCl, respectively.

xanthan, amylose, and dextran upon the cleavage of the pyranose ring were observed by AFM and linked with the chemical structure of the molecules.<sup>[96]</sup> Specifically, the pyranose ring was identified as the structural unit controlling the molecules' elasticities. Cleavage of the pyranose ring with 5 mM sodium metaperiodate eliminated the extra enthalpic component of the elasticity and made the force transition disappear. The transitions were attributed to force-induced elongations of the ring structure and, for some molecules, to transitions in the pyranose ring from a chair to boat structure. These transitions produced fingerprints in the extension-force spectrum that were characteristic of the ground-energy conformations of the pyranose ring and the type of glycosidic linkage present in each polysaccharide<sup>[93,97]</sup> (Fig. 13).



**Fig. 13** Force-extension curves for single-pectin molecules reveal a two-step transition. (A) The shape of the curves for molecules with varying lengths reveals two enthalpic extensions at  $\sim 300$  and  $\sim 800$ – $900$  pN. (B) High-resolution normalized plot of the force-extension relationship for a single-pectin molecule. The thin lines are fits of the FJC model modified to include the extensibility of the monomers. *Source:* From Ref.<sup>[97]</sup> (PNAS, vol. 96) © 1999 by the National Academy of Sciences, Courtesy of the National Academics Press, Washington, D.C.

## CONCLUSION

The use of AFM and SMFS to characterize the physicochemical properties of biopolymers was reviewed. Atomic force microscopy is preferred over other surface characterization techniques because of several unique advantages, including 1) high lateral and vertical resolutions, 2) high signal-to-noise ratio, 3) ability to probe biopolymers in their native environment with minimal sample preparation, 4) ability to measure interaction forces at interfaces, and 5) ability to obtain quantitative information about the chemical structure of macromolecules.

High-resolution imaging of single molecules of DNA, proteins, and polysaccharides, including polysaccharides on microbial surfaces, can now be routinely performed with AFM. Images can provide quantitative information on molecular properties and can be used to elucidate biopolymer conformation. Among the more interesting examples of probing biopolymers with SMFS are DNA sequencing, quantifying ligand-receptor interactions between proteins and lipids, protein folding and unfolding, identifying polysaccharide components from mixtures, and probing the distribution of macromolecules on living cells.

New advancements continue to be made in the formulation of more sensitive AFM probes, improved instrumentation, less-invasive sample preparation techniques, and facilitated data analysis. Undoubtedly, AFM will continue to be a key tool for probing the properties of delicate biopolymers at the nanoscale. Knowledge of the relationships between molecular structure and function of biopolymers will benefit such diverse fields as biotechnology, food safety, environmental science, pharmaceuticals, and medicine.

## ACKNOWLEDGMENTS

This publication was made possible in part by a CAREER Award to TAC from the National Science Foundation (Grant Number BES-0238627).

## REFERENCES

1. Grosberg, A.Y.; Khokhlov, A.R. *Statistical Physics of Macromolecules. Polymers and Complex Materials*; Larson, R., Pincus, P.A., Eds.; American Institute of Physics: New York, 1994.
2. Gunning, A.P.; Morris, V.J.; Al-Assaf, S.; Phillips, G.O. AFM studies of hylan and hyaluronan. *Carbohydr. Polym.* **1996**, *30*, 1–8.
3. Hanssen, E.; Franc, S.; Garrone, R. AFM and modeling of natural elastic fibrillin polymers. *Biol. Cell* **1998**, *90* (3), 223–228.

4. Morris, V.J.; Gunning, A.P.; Kirby, A.R.; Round, A.; Waldron, K.; Ng, A. AFM of plant cell walls, plant cell wall polysaccharides and gels. *Int. J. Biol. Macromol.* **1997**, *21*, 61–66.
5. Kirby, A.R.; Gunning, A.P.; Morris, V.J.; Ridout, M.J. Observation of the helical structure of bacterial polysaccharide acetan by AFM. *Biophys. J.* **1995**, *68*, 360–363.
6. Dufrêne, Y.F.; Boonaert, C.J.P.; Gerin, P.A.; Asther, M.; Rouxhet, P.G. Direct probing of the surface ultrastructure and molecular interactions of dormant and germinating spores of *Phanerochaete chrysosporium*. *J. Bacteriol.* **1999**, *181*, 5350–5354.
7. Van der Aa, B.C.; Asther, M.; Dufrêne, Y.F. Surface properties of *Aspergillus oryzae* spores investigated by atomic force microscopy. *Colloids Surf., B Biointerfaces* **2002**, *24*, 277–284.
8. Wilkinson, K.J.; Balnois, E.; Leppard, G.G.; Buffle, J. Characteristic features of the major components of freshwater colloidal organic matter revealed by transmission electron and atomic force microscopy. *Colloids Surf., A Physicochem. Eng. Asp.* **1999**, *155*, 287–310.
9. Stoll, S.; Starchev, K.; Wilkinson, K.J.; Chodanowski, P.; Balnois, E.; Leng, X.; Buffle, J. The study of environmental biopolymers by mathematical modeling and single molecule detection techniques. *Chimia* **2001**, *55* (3), 190–195.
10. Santschi, P.H.; Balnois, E.; Wilkinson, K.J.; Zhang, J.; Buffle, J. Fibrillar polysaccharides in marine macromolecules organic matter as imaged by AFM and TEM. *Limnol. Oceanogr.* **1998**, *43* (5), 896–908.
11. Jandt, K.D.; Finke, M.; Cacciafesta, P. Aspects of the physical chemistry of polymers, biomaterials, and mineralised tissues investigated with AFM. *Colloids Surf., B Biointerfaces* **2000**, *19*, 301–314.
12. Andrew, R.; Argyrios, M. Production and mass transfer characteristics of non-Newtonian biopolymers for biomedical applications. *Crit. Rev. Biotechnol.* **2002**, *22* (4), 355–374.
13. Kayirhan, N.; Denizli, A.; Hasirci, N. Adsorption of blood proteins on glow-discharge-modified polyurethane membranes. *J. Appl. Polym. Sci.* **2001**, *81* (6), 1322–1332.
14. Yokota, H.; Sunwoo, J.; Sarikaya, M.; Engh, G.; Aebersold, R. Spin-stretching of DNA and protein molecules for detection by fluorescence and AFM. *Anal. Chem.* **1999**, *71*, 4418–4422.
15. Kuznetsov, Y.G.; Malkin, A.J.; McPherson, A. AFM studies of the nucleation and growth mechanisms of macromolecular crystals. *J. Cryst. Growth* **1999**, *196*, 489–502.
16. Round, A.N.; MacDougall, A.J.; Ring, S.G.; Morris, V.J. Unexpected branching in pectin observed by AFM. *Carbohydr. Res.* **1997**, *303*, 251–253.
17. Morris, V.J.; Mackie, A.R.; Wilde, P.J.; Kirby, A.R.; Mills, E.C.N.; Gunning, A.P. AFM as a tool for interpreting the rheology of food biopolymers at the molecular level. *Lebensm.-Wiss. Technol.* **2001**, *34*, 3–10.
18. Jucker, B.A.; Zehnder, A.J.B.; Harms, H. Quantification of polymer interactions in bacterial adhesion. *Environ. Sci. Technol.* **1998**, *32*, 2909–2915.
19. Andrushchenko, V.; Leonenko, Z.; Cramb, D.; van de Sande, H.; Wieser, H. Vibrational CD (VCD) and atomic force microscopy (AFM) study of DNA interaction with Cr<sup>+3</sup> ions: VCD and AFM evidence of DNA condensation. *Biopolymers* **2002**, *61*, 243–260.
20. Leng, X.; Starchev, K.; Buffle, J. Applications of fluorescence correlation spectroscopy: Measurements of size–mass relationship of native and denatured schizophyllan. *Biopolymers* **2001**, *59*, 290–299.
21. Camesano, T.A.; Abu-Lail, N.I. Heterogeneity in bacterial surface polysaccharides, probed on a single-molecule basis. *Biomacromolecules* **2002**, *3* (661–667).
22. Arnott, S. Ordered conformations of gel forming polysaccharides obtained by X-ray diffraction analysis of oriented fibers. *Dev. Food Carbohydr. Ser.* **1977**, *1*, 43–60.
23. Hanely, S.J.; Giasson, J.; Revol, J.-F.; Gray, D.G. Atomic force microscopy of cellulose microfibrils: Comparison with TEM. *Polymer* **1992**, *33* (21), 4639–4642.
24. Gilbert, P.; Allison, D.G.; Evans, D.J.; Handley, P.S.; Brown, M.R. Growth rate control of adherent bacterial populations. *Appl. Environ. Microbiol.* **1989**, *55* (5), 1308–1311.
25. Naidja, A.; Liu, C.; Huang, P.M. Formation of protein–birnessite complex: XRD, FTIR, and AFM analysis. *J. Colloid Interface Sci.* **2002**, *251*, 46–56.
26. Lin, W.; Yan, L.; Mu, C.; Li, W.; Zhang, M.; Zhu, Q. Effect of pH on gelatin self-association investigated by laser light scattering and AFM. *Polym. Int.* **2002**, *51*, 233–238.
27. Sun, Y.; Luo, Z.; An, K. Stretching short biopolymers using optical tweezers. *Biochem. Biophys. Res. Commun.* **2001**, *286* (4), 826–830.
28. Hartley, P.G.; Bailey, A.I.; Luckham, P.F.; Batts, G. Non-specific interactions between heparin and poly(L-lysine) surfaces. *Colloids Surf., A Physicochem. Eng. Asp.* **1993**, *77* (3), 191–198.
29. Scheuring, S.; Fotiadis, D.; Moller, C.; Muller, S.A.; Engel, A.; Muller, D.J. Single proteins observed by AFM. *Single Mol.* **2001**, *2*, 59–67.
30. Binning, G.; Quate, C.F.; Gerber, C.H. Atomic force microscope. *Phys. Rev. Lett.* **1986**, *56* (9), 930–933.
31. Muller, D.J.; Anderson, K. Biomacromolecular imaging using atomic force microscopy. *Trends Biotechnol.* **2002**, *20* (8), S45–S49.
32. Brant, D.A. Conformation Behavior of Polysaccharides in Solution. In *The Biochemistry of Plants*; Academic Press, Inc., 1980; 425–469.
33. Balnois, E.; Wilkinson, K.J. Sample preparation techniques for the observation of environmental biopolymers by AFM. *Colloid Surf., A Physicochem. Eng. Asp.* **2002**, *207*, 229–242.
34. Vuppu, A.K.; Garcia, A.A.; Vernia, C. Tapping mode AFM of scleroglucan networks. *Biopolymers* **1997**, *42*, 89–100.
35. McMaster, T.J.; Miles, M.J.; Wannerberger, L.; Eliasson, A.-C.; Shewry, P.R.; Tatham, A.S. Identification of microphases in mixed alpha and omega gliadin protein films investigated by AFM. *J. Agric. Food Chem.* **1999**, *47*, 5093–5099.
36. Abu-Lail, N.I.; Camesano, T.A. Elasticity of *Pseudomonas putida* KT2442 biopolymers probed with single-molecule force microscopy. *Langmuir* **2002**, *18*, 4071–4081.

37. Muller, D.J.; Engel, A. The height of biomolecules measured with the atomic force microscope depends on electrostatic interactions. *Biophys. J.* **1997**, *73* (3), 1633–1644.
38. Hansma, H.G.; Sinsheimer, R.L.; Groope, J.; Bruice, T.C.; Elings, V.; Gurley, G.; Bezanilla, M.; Mastrangelo, I.A.; Hough, P.V.C.; Hansma, P.K. Recent advances in AFM of DNA. *Scanning* **1993**, *15* (5), 296–299.
39. Hansma, H.G.; Weisenhorn, A.L.; Gould, S.A.C.; Sinsheimer, R.L.; Gaub, H.E.; Stucky, G.D.; Zaremba, C.M.; Hansma, P.K. Progress in sequencing deoxyribonucleic acid with AFM. *J. Vac. Sci. Technol., B Microelectron. Nanometer Struct.* **1991**, *9* (2. Pt.2), 1282–1284.
40. Yuri, L.L.; Alexander, A.G.; Lyuda, S.S.; Rodney, E.H.; Bertram, L.J.; Patrick, I.O.; Stuart, M.L. AFM imaging of double stranded DNA and RNA. *J. Biomol. Struct. Dyn.* **1992**, *10* (3), 589–606.
41. Hansma, H.G.; Hansma, P.K. Potential applications of AFM of DNA to the human genome project. *Proc. SPIE Int. Soc. Opt. Eng.* **1993**, *1891*, 66–70.
42. Bensimon, A.; Simon, A.; Chiffaudel, A.; Croquette, V.; Heslot, F.; Bensimon, D. Alignment and sensitive detection of DNA by a moving interface. *Science* **1994**, *265*, 2096–2098.
43. Rivetti, C.; Guthold, M.; Bustamante, C. Scanning force microscopy of DNA deposited onto mica: Equilibration versus kinetic trapping studied by statistical polymer chain analysis. *J. Mol. Biol.* **1996**, *264* (5), 919–932.
44. Lyubchenko, Y.; Shlyakhtenko, L.; Harrington, R.; Oden, P.; Lindsay, S. Atomic force microscopy of long DNA—Imaging in Air and under water. *Proc. Natl. Acad. Sci. U. S. A.* **1993**, *90* (6), 2137–2140.
45. Hansma, H.G.; Golan, R.; Hsieh, W.; Lollo, C.P.; Mullen-Ley, P.; Kwoh, D. DNA condensation for gene therapy as monitored by atomic force microscopy. *Nucleic Acids Res.* **1998**, *26*, 2481–2487.
46. Hansma, H.G.; Sinsheimer, R.L.; Li, M.Q.; Hansma, P.K. AFM of single and double stranded DNA. *Nucleic Acids Res.* **1992**, *20* (14), 3585–3590.
47. Thundat, T.; Allison, D.P.; Warmack, R.J.; Doktycz, M.J.; Jacobson, K.B.; Brown, G.M. AFM of single and double stranded deoxyribonucleic acid. *J. Vac. Sci. Technol., A, Vac. Surf. Films* **1993**, *11* (4, Pt.1), 824–828.
48. Dario, A.; Jurgen, F.; Benjamin, S.; Xavier, F.-B. Single molecule DNA biophysics with AFM. *Single Mol.* **2000**, *1* (1), 53–58.
49. Tiner, W.J.; Potaman, V.N.; Sinden, R.R.; Lyubchenko, Y.L. The structure of intramolecular triplex DNA: AFM study. *J. Mol. Biol.* **2001**, *314* (3), 353–357.
50. Wei, L.J.; Fang, T.; Chen, W.; Li, B.C.; Hua, C.E. Possible multistranded DNA induced by acid denaturation–renaturation. *J. Vac. Sci. Technol., B, Microelectron. Nanometer Struct.* **1997**, *15* (5), 1637–1640.
51. Frank, N.; Bernd, G.; Norbert, H. Improvement of DNA-visualization in dynamic mode AFM in air. *Scanning* **2001**, *23* (3), 175–181.
52. Hansma, H.G.; Irene, R.; Kerry, K.; Daniel, L.E. AFM of long and short double stranded and triple stranded nucleic acids. *Nucleic Acids Res.* **1996**, *24* (4), 713–720.
53. Hafner, J.H.; Cheung, C.-L.; Woolley, A.T.; Lieber, C.M. Structural and functional imaging with carbon nanotube AFM probes. *Prog. Biophys. Mol. Biol.* **2001**, *77* (1), 73–110.
54. Kazuo, U.; Jun, K.; Takayuki, U.; Nami, C.; Shukuko, I.; Taro, N.; Takehiko, S.; Yoshikazu, N.; Shinji, K.; Akira, M.; Hiroshi, T.; Mitsuru, I.; Reiko, K. AFM of RecA–DNA complexes using a carbon nanotube tip. *Biochem. Biophys. Res. Commun.* **2001**, *281* (2), 390–395.
55. Oliveira, B.A.M.; Ana-Maria, C. AFM of DNA immobilized onto a highly oriented pyrolytic graphite electrode surface. *Langmuir* **2003**, *19* (9), 3830–3839.
56. Smith, S.B.; Finzi, L.; Bustamante, C. Direct mechanical measurements of the elasticity of single DNA molecules by using magnetic beads. *Science* **1992**, *258*, 1122–1126.
57. Lee, G.U.; Chrisey, L.A.; Colton, R.J. Direct measurement of the forces between complementary strands of DNA. *Science* **1994**, *266*, 771–773.
58. Marko, J.F.; Siggia, E.D.; Smith, S. Entropic elasticity of lambda-phage DNA. *Science* **1994**, *265*, 1599–1600.
59. Burnham, N.A.; Chen, X.; Hodges, C.S.; Matei, G.A.; Thoreson, E.J.; Roberts, C.J.; Davies, M.C.; Tendler, S.J.B. Comparison of calibration methods for atomic-force microscopy cantilevers. *Nanotechnology* **2003**, *14*, 1–6.
60. Strick, T.R.; Allemand, J.-F.; Bensimon, D.; Bensimon, A.; Croquette, V. The elasticity of a single supercoiled DNA molecule. *Science* **1996**, *271*, 1835–1837.
61. Rief, M.; Clausen-Schaumann, H.; Gaub, H.E. Sequence-dependent mechanics of single DNA molecules. *Nat. Struct. Biol.* **1999**, *6* (4), 346–349.
62. Smith, S.B.; Cui, Y.; Bustamante, C. Overstretching B-DNA: The elastic response of individual double-stranded DNA molecules. *Science* **1996**, *271*, 795–799.
63. Rupert, K.; Rief, M.; Gaub, H.E. Unzipping DNA oligomers. *Nano Lett* **2003**, *3* (4), 493–496.
64. Czajkowski, D.M.; Shao, Z. Submolecular resolution of single macromolecules with AFM. *FEBS Lett.* **1998**, *430*, 51–54.
65. Wadu-Mesthrige, K.; Amro, N.A.; Liu, G.Y. Immobilization of proteins on self-assembled monolayers. *Scanning* **2000**, *22* (6), 380–388.
66. Mou, J.; Yang, J.; Shao, Z. AFM of cholera toxin B-oligomers bound to bilayers of biologically relevant lipids. *J. Mol. Biol.* **1995**, *248*, 507–512.
67. Vinckier, A.; Heyvaert, I.; D’Hoore, A.; McKittrick, T.; Haesendonck, C.V.; Engelborghs, Y.; Hellemans, L. Immobilizing and imaging microtubules by AFM. *Ultramicroscopy* **1995**, *57*, 337–343.
68. Muller, D.J.; Sass, H.J.; Muller, S.; Buldt, G.; Engel, A.J. Surface structures of native bacteriorhodopsin depend on the molecular packing arrangement in the membrane. *J. Mol. Biol.* **1999**, *285* (5), 1903–1909.
69. Ohad, M.; Joseph, E.; Reinhard, G.; Joseph, S. AFM imaging in solution of protein–DNA complexes formed on DNA anchored to a gold surface. *Ultramicroscopy* **2002**, *90* (2/3), 103–112.
70. Stanier, R.; Ingraham, J.L.; Wheelis, M.L.; Painter, P.R. *The Microbial World*, 5th Ed.; Prentice-Hall: New Ed. Jersey, 1986.
71. Rief, M.; Gautel, M.; Oesterhelt, F.; Fernandez, J.M.; Gaub, H.E. Reversible unfolding of individual titin

- immunoglobulin domains by AFM. *Science* **1997**, *276*, 1109–1111.
72. Fisher, T.E.; Oberhauser, A.F.; Carrion-Vazquez, M.; Marszalek, P.E.; Fernandez, J.M. The study of protein mechanics with AFM. *Trends Biochem. Sci.* **1999**, *24*, 379–384.
  73. Fernandez, J.M.; Rief, G.M.; Gaub, H.E. Single molecule force spectroscopy with individual proteins. *NATO Sci. Ser. Ser. C, Math. Phys. Sci.* **1999**, *519*, 319–336.
  74. Carrion-Vazquez, M.; Oberhauser, A.F.; Fisher, T.E.; Marszalek, P.E.; Li, H.; Fernandez, J.M. Mechanical design of proteins studied by single-molecule force spectroscopy and protein engineering. *Biophys. Mol. Biol.* **2000**, *74* (1–2), 63–91.
  75. Oberdorfer, Y.; Fuchs, H.; Janshoff, A. Conformational analysis of native fibronectin by means of force spectroscopy. *Langmuir* **2000**, *16* (26), 9955–9958.
  76. Fowler, S.B.; Best, R.B.; Jose, L.T.H.; Trevor, J.R.; Annette, S.; Emanuele, P.; Martin, K.; Jane, C. Mechanical unfolding of a titin Ig domain: structure of unfolding intermediate revealed by combining AFM, molecular dynamic simulations, NMR and protein engineering. *J. Mol. Biol.* **2002**, *322* (4), 841–849.
  77. Best, R.B.; Li, B.; Steward, A.; Daggett, V.; Clarke, J. Can non-mechanical proteins withstand force? Stretching barnase by AFM and molecular dynamic simulations. *Biophys. J.* **2001**, *81* (4), 2344–2356.
  78. Janshoff, A.; Neitzert, M.; Oberdorfer, Y.; Fuchs, H. Force spectroscopy of molecular systems—Single molecule spectroscopy of polymers and biomolecules. *Angew. Chem., Int. Ed.* **2000**, *39*, 3212–3237.
  79. Lisa, W.M.; Stephanie, A.; Martyn, C.D.; Saul, J.B.T.; Philip, W.M.; Clive, R.J. Bifunctional AFM probes for molecular screening applications. *Anal. Chim. Acta* **2003**, *479* (1), 77–85.
  80. Lee, G.U.; Kidwell, D.A.; Colton, R.J. Sensing discrete streptavidin–biotin interactions with atomic force microscopy. *Langmuir* **1994**, *10*, 354–357.
  81. Moy, V.T.; Florin, E.-L.; Gaub, H.E. Intermolecular forces and energies between ligands and receptors. *Science* **1994**, *266*, 257–259.
  82. Fritz, J.A.D.; Katopodis, A.G.; Kolbinger, F.; Anselmetti, D. Force-mediated kinetics of single P-selectin/ligand complexes observed by AFM. *Proc. Natl. Acad. Sci. U. S. A.* **1998**, *95* (21), 12283–12288.
  83. Brantley, S.L.; Liermann, L.; Bau, M.; Wu, S. Uptake of trace metals and rare earth elements from hornblende by a soil bacterium. *Geomicrobiol. J.* **2001**, *18*, 37–61.
  84. Verheyen, C.C.P.M.; Dhert, W.J.A.; de Bleeck-Hogervorst, J.M.A.; van der Reijen, T.J.K.; Petit, P.L.C.; de Groot, K. Adherence to a metal, polymer and composite by *Staphylococcus aureus* and *Staphylococcus epidermidis*. *Biomaterials* **1993**, *14*, 383–391.
  85. Caccavo, F.J.; Das, A. Adhesion of dissimilatory Fe(III)-reducing bacteria to Fe(III) minerals. *Geomicrobiol. J.* **2002**, *19*, 161–177.
  86. Mecsas, J.; Strauss, E.J. Molecular mechanisms of bacterial virulence: Type III secretion and pathogenicity islands. *Emerg. Infect. Dis.* **1996**, *2*, 271–288.
  87. Kwakman, J.M.; Freihofer, H.P.; van Waas, M.A. Needs for implant therapy in cancer patients, a retrospective study. *Ned. Tijdschr. Tandheelkd.* **2000**, *107* (8), 318–321.
  88. Camesano, T.A.; Wilkinson, K.J. Single molecule study of xanthan conformation using atomic force microscopy. *Biomacromolecules* **2001**, *2*, 1184–1191.
  89. Balnois, E.; Stoll, S.; Wilkinson, K.J.; Buffle, J.; Rinaudo, M.; Milas, M. Conformations of succinoglycan as observed by atomic force microscopy. *Macromolecules* **2000**, *33*, 7440–7447.
  90. Gad, M.; Itoh, A.; Ikai, A. Mapping cell wall polysaccharides of living microbial cells using atomic force microscopy. *Cell Biol. Int.* **1997**, *21*, 697–706.
  91. Gunning, P.A.; Mackie, A.R.; Kirby, A.R.; Kroon, P.; Williamson, G.; Morris, V.J. Motion of a cell wall polysaccharide observed by AFM. *Macromolecules* **2000**, *33* (15), 5680–5685.
  92. Li, H.; Rief, M.; Oesterhelt, F.; Gaub, H.; Zhang, X.; Shen, J. Single-molecule force spectroscopy on polysaccharides by AFM nanomechanical fingerprint of alpha- (1–4) linked polysaccharides. *Chem. Phys. Lett.* **1999**, *305*, 197–201.
  93. Marszalek, P.E.; Li, H.; Fernandez, J.M. Fingerprinting polysaccharides with single-molecule force spectroscopy. *Nat. Biotechnol.* **2001**, *19*, 258–262.
  94. Van der Aa, B.C.; Michel, R.M.; Asther, M.; Zamora, M.T.; Rouxhet, P.G.; Dûfrene, Y.F. Stretching cell surface macromolecules by atomic force microscopy. *Langmuir* **2001**, *17*, 3116–3119.
  95. Abu-Lail, N.I.; Camesano, T.A. Role of ionic strength on the relationship of biopolymer conformation, DLVO contributions, and steric interactions to bioadhesion of *Pseudomonas putida* KT2442. *Biomacromolecules* **2003**, *4*, 1000–1012.
  96. Marszalek, P.E.; Oberhauser, A.F.; Pang, Y.-P.; Fernandez, J.M. Polysaccharide elasticity governed by chair-boat transitions of the glucopyranose ring. *Nature* **1998**, *396*, 661–666.
  97. Marszalek, P.E.; Pang, Y.-P.; Li, H.; El Yazal, J.; Oberhauser, A.F.; Fernandez, J.M. Atomic levers control pyranose ring conformation. *Proc. Natl. Acad. Sci. U. S. A.* **1999**, *96*, 7894–7898.

# AFM: Hydrogen-Bonded Nanostructures

## Holger Schönherr

Department of Materials Science and Technology of Polymers, University of Twente, Enschede, The Netherlands

## Mercedes Crego-Calama

Laboratory of Supramolecular Chemistry and Technology, University of Twente, Enschede, The Netherlands

## G. Julius Vancso

Department of Materials Science and Technology of Polymers, University of Twente, Enschede, The Netherlands

## David N. Reinhoudt

Laboratory of Supramolecular Chemistry and Technology, University of Twente, Enschede, The Netherlands

## INTRODUCTION

Bottom-up strategies in molecular nanotechnology, including the self-assembly of small molecular building blocks into supramolecular aggregates based on non-covalent interactions, are regarded as a viable route to realize molecular devices, as well as to fabricate and template well-defined nanometer-scale structures and objects.<sup>[1]</sup> Recent progress in nanostructuring has enabled several groups to control the arrangement of molecules and supramolecular aggregates on surfaces by exploiting designed intermolecular interactions and/or scanning probe microscopy (SPM) approaches at variable temperatures.<sup>[2–5]</sup> This work, which is based on the profound knowledge in the fields of supramolecular chemistry<sup>[6–9]</sup> and intermolecular (surface) forces,<sup>[10,11]</sup> will ultimately lead to a general strategy to develop hierarchical functional nanostructures with molecular precision.

We have designed and investigated rosette nanostructures, which are based on multiple hydrogen bonding<sup>[12]</sup> between the basic building blocks—melamine-substituted calix[4]arenes and 5,5-diethylbarbiturate (DEB). These thermodynamically stable nanostructures can be ordered on solid substrates in highly regular, chiral 2-D assemblies, or immobilized as individual entities in self-assembled monolayers (SAM). In this entry, we review our recent progress in the formation, and in particular in the real-space structural analysis, of nanometer-sized supramolecular rosette nanostructures and their aggregates in 2-D via atomic force microscopy (AFM).

## SELF-ASSEMBLY OF HYDROGEN-BONDED NANOSTRUCTURES

The non-covalent synthesis of well-defined structures with nanoscale dimensions has recently been receiving increasing attention.<sup>[12,13]</sup> The components in these structures, termed *supramolecular aggregates*,<sup>[6]</sup> are connected to each other via reversible and weak non-covalent interactions, comprising, for instance, forces based on the hydrophobic effect, as well as electrostatic,  $\pi - \pi$  stacking, hydrogen bonding, or metal–ligand coordination interactions.<sup>[14–17]</sup> These interactions are distinctly different from the non-reversible and more stable interactions in covalently linked molecules and offer a number of important advantages. For instance, in our synthesis of nanoscale self-assembled aggregates,<sup>[18]</sup> hydrogen bonds are utilized that form spontaneously under thermodynamically controlled conditions. The thermodynamic control together with the reversibility of the individual interactions provide the assemblies with their ability to “proof-read” and correct mistakes. Hence carefully designed molecules assemble into well-defined, error-free motifs because they are encoded with the correct H-bonding information and geometry.

One well-known H-bonded system is based on isocyanuric acid (CA) and melamine. The three orthogonal acceptor–donor–acceptor (ADA) hydrogen bonding arrays of isocyanuric acid (CA) are complementary to the three DAD hydrogen bonding arrays of melamine (M). Mixing both components in a 1:1 ratio leads to an infinite 2-D lattice held together by hydrogen bonds (Fig. 1).



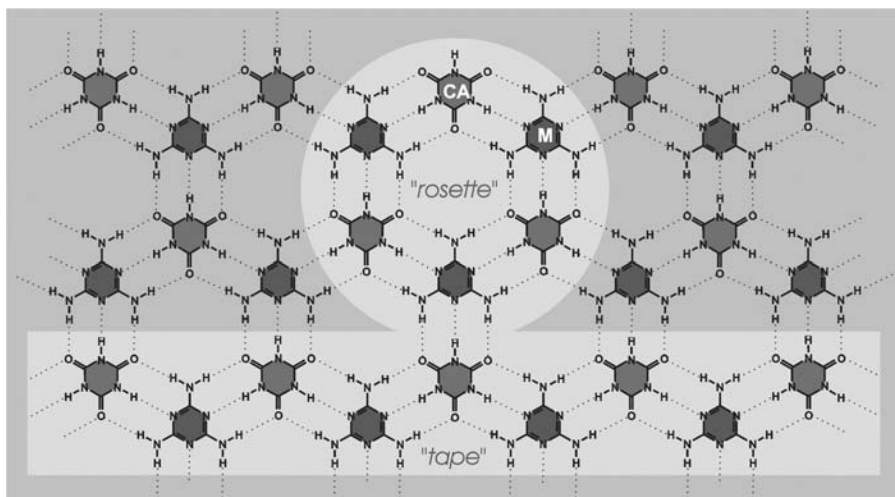


**Fig. 1** 2-D melamine–isocyanuric acid lattice.

Lehn et al.<sup>[19]</sup> and Whitesides et al.<sup>[20,21]</sup> identified this complementary hydrogen bonding motif in the melamine–isocyanuric lattice and showed that, depending on the preorganization of the melamines and the steric interactions between the building blocks, cyclic *rosettes* instead of *tapes* could be formed *selectively* (Fig. 1). Recently, our group showed, based on model calculations, that it is indeed possible to promote the rosette formation over tape formation by steric repulsion in the linear tapes, but the effect is not as large as was earlier believed.<sup>[22]</sup>

As an extension of the rosette motif, our group has shown that calix[4]arenes diametrically substituted with two melamine units at the upper rim form *double rosette* assemblies  $\mathbf{1a}_3 \cdot (\text{DEB})_6$  or  $\mathbf{1b}_3 \cdot (\text{DEB})_6$  in the presence of two equivalents of 5,5-diethylbarbiturate (DEB) (or isocyanuric acid) (Fig. 2).<sup>[23,24]</sup> These assemblies comprise 9 different components held together by 36 hydrogen bonds. The synthetic strategy involves the sideways connection via the calix[4]arene units of two rosette layers, which gives additionally improved stability to the non-covalent assemblies. The assemblies are stable even at  $10^{-4}$  M concentration in apolar solvents, such as chloroform, benzene, and toluene.

X-ray diffraction studies of similar double rosettes showed that the two rosette layers are tightly stacked on top of each other with an interatomic separation of 3.5 Å at the edges and 3.2 Å at the center of the rosette.<sup>a</sup> The assemblies  $\mathbf{1a}_3 \cdot (\text{DEB})_6$  have a height of 1.2 nm and a width of  $\sim 3.0$  nm.

These double rosettes can easily be extended to *tetrorosettes* by using *tetramelamine* as a building block. In this unit, two calix[4]arene dimelamines are

connected by a flexible linker unit X (Fig. 3).<sup>[25]</sup> A tetrorosette consists of 15 components (three tetramelamines and twelve 5,5-diethylbarbiturates) held together by 72 hydrogen bonds forming a nanostructure  $\mathbf{2}_3 \cdot (\text{DEB})_{12}$  with four parallel rosette “floors.” The thermodynamic equilibrium for this type of assembly is reached within seconds after mixing the corresponding building blocks, but the rate of exchange of the components decreases in comparison with the double rosette.<sup>b</sup> In addition, we have reported on the extension of this series of double and tetrorosettes to higher-order complex structures, such as hexa- and octarosettes.<sup>[26]</sup>

The isolation, manipulation, and characterization of non-covalent nanostructures require special consideration, because these assemblies are less robust than the corresponding covalent structures in solution. Nevertheless, conventional proton nuclear magnetic resonance ( $^1\text{H}$  nmR) can be used for the structural identification of the above-described hydrogen-bonded assemblies, because they are very well defined structures and the exchange between the assembly and components is relatively slow.<sup>c</sup> Furthermore, matrix-assisted laser desorption ionization time-of-flight (MALDI-TOF) mass spectrometry using the  $\text{Ag}^+$ -labeling technique<sup>[29,30]</sup> gives additional evidence for the formation of the hydrogen-bonded nanostructures. Positively charged assemblies are generated in a nondestructive way by, for example, coordination of  $\text{Ag}^+$  to a cyano group or by complexation of  $\text{Ag}^+$  between two phenyl rings.

<sup>b</sup>Formation of the first double rosette disfavors the formation of the second double rosette.

<sup>c</sup>More detailed information about the characterization of double rosette assemblies can be found in Refs.<sup>[27,28]</sup>

<sup>a</sup>Interatomic separations of 3.5 Å at the edges and 3.2 Å at the center of the rosette were determined, see Ref.<sup>[24]</sup>.

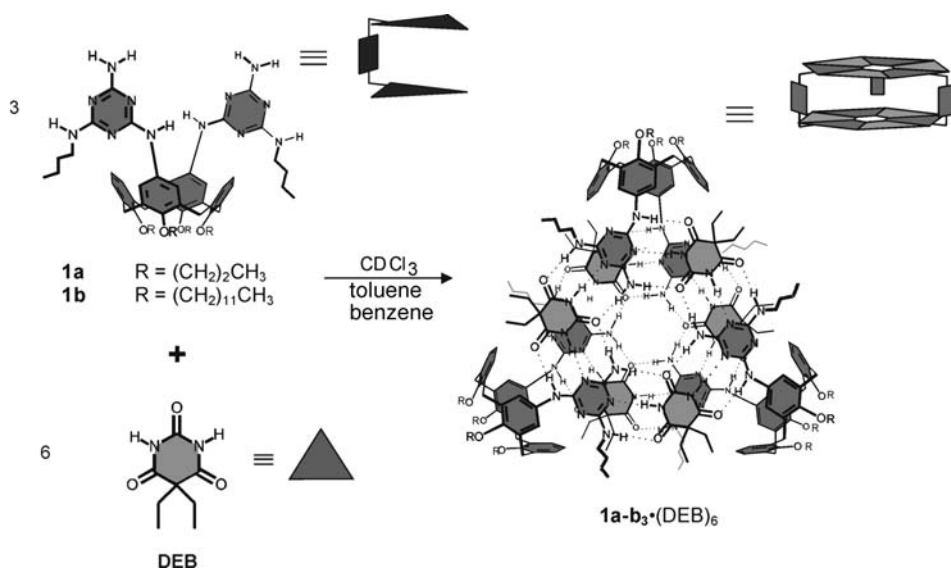


**Fig. 2** Formation of the double rosette assemblies **1a<sub>3</sub>·(DEB)<sub>6</sub>** and **1b<sub>3</sub>·(DEB)<sub>6</sub>**.

The multicomponent nature of hydrogen-bonded nanostructures based on rosette motifs, as well as the multiple sites available for further chemical derivatization,<sup>[31]</sup> make these structures a very interesting alternative for the precise spatial arrangement of functional diversity on solid supports, for instance, using metal nanoparticles and peptide chains. In this context, the immobilization of rosette nanostructures on solid supports and the control over the spatial arrangement in 2-D are key issues for the development of supramolecular platforms. Given

the nanometer-scale dimensions of individual rosettes, atomic force microscopy (AFM)<sup>[32]</sup> proved to be a particularly well-suited tool to study the higher-order assemblies obtained by various approaches, as will be discussed below.

### ATOMIC FORCE MICROSCOPY

Soon after its invention,<sup>[32]</sup> AFM was developed as a characterization technique for real-space structure

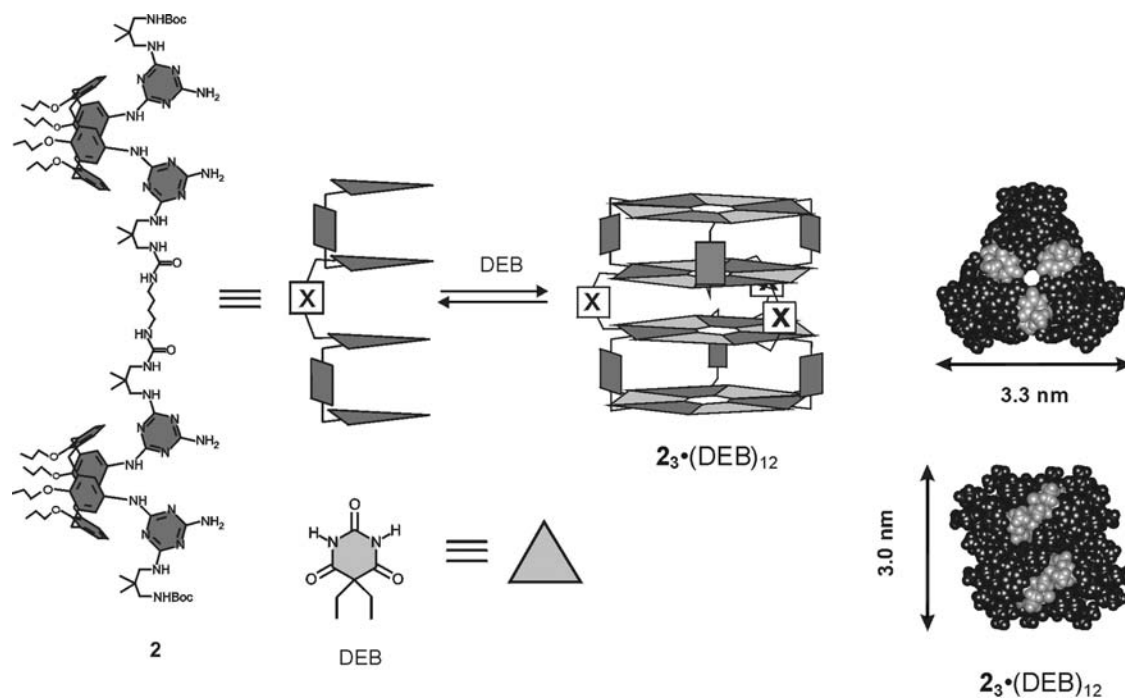


**Fig. 3** Formation of tetra-rosette assemblies **2<sub>3</sub>·(DEB)<sub>12</sub>** (left) and gas phase minimized structure (right). *Source:* From Ref.<sup>[55]</sup>. © 2002 National Academy of Sciences, U.S.A.

determination at surfaces of non-conductors on micrometer- as well as subnanometer-length scales.<sup>[33–36]</sup> The general scanning probe microscopy approach as enabling technology is regarded as one of the workhorses of emerging (molecular) nanotechnology.

In contrast to scanning tunneling microscopy (STM), which is inherently limited to conductive substrates or conductive substrates covered with an insulating layer of, e.g., molecules less than  $\sim 1.0$ – $1.5$  nm thick,<sup>[37]</sup> AFM is generally applicable to the study of virtually any surface.<sup>[32–36]</sup> Different modes, including contact mode, force modulation mode,<sup>[38]</sup> and intermittent contact (or tapping) mode,<sup>[39]</sup> have been developed to elucidate surface structure, but also spatial composition in a variety of systems.<sup>[40–43]</sup> The potential of the technique to follow dynamic processes in real-time, especially under temperature control, has been attracting increasing attention in recent years.<sup>[44–46]</sup>

In particular, thin organized films of organic matter have been the focus of many AFM investigations. High-resolution images of ultraviolet (UV)-photopolymerized films of Langmuir films comprising diacetylene units were among the first molecularly resolved *contact mode* AFM images of soft matter.<sup>[47]</sup> While contact mode AFM performed in ambient conditions or in liquid typically yields lattice resolution, such as for self-assembled monolayers on solid substrates<sup>[48–51]</sup> or thin organic films,<sup>[52]</sup> in several cases true molecular resolution has been obtained.<sup>[53]</sup> For the study of delicate assemblies, such as the 2-D arrays of rosette nanostructures discussed in this review, tapping mode atomic force microscopy (TM-AFM) proved to be superior to contact mode AFM, because lateral (shear) forces are absent<sup>[34]</sup> and the normal forces can be controlled by careful selection of suitable imaging parameters (*vide infra*). The resolution in these experiments is limited by the shape and sharpness of the probe tip.

## 2-D ARRANGEMENTS OF ROSETTE NANOSTRUCTURES ON HOPG

Highly ordered, highly regular 2-D arrays of rosette nanostructures can be obtained by deposition of the rosettes from a suitable solvent, such as chloroform or toluene, on freshly cleaved highly oriented pyrolytic graphite (HOPG) surfaces, as unveiled by AFM approaches (*vide infra*).<sup>[54,55]</sup> The concentration of the solution, the temperature, the rate of solvent evaporation, the presence of defects, such as step edges, on the graphite substrates and possible reorganization of the adsorbate molecules are among the factors that influence the formation of the 2-D assemblies. In particular, the slow evaporation of the solvent in a near-saturated atmosphere of the solvent helps to suppress 3-D (bulk) crystallization of the rosettes.<sup>[55]</sup>

### Double Rosettes $1a_3$ ·(DEB)<sub>6</sub> on HOPG

Deposition of double rosettes  $1a_3$ ·(DEB)<sub>6</sub> onto HOPG leads to the formation of typical 2-D arrays, so-called nanorod domains. These domains and their internal structure can be conveniently analyzed via TM-AFM, as shown in Fig. 4. To avoid possible damage of the soft organic layer, the AFM is operated slightly off resonance, the amplitude is minimized, and very soft tapping conditions are employed.<sup>[56–61]</sup>

Tightly packed rows with an interrow distance of  $3.8 \pm 0.2$  nm can be observed in two adjacent domains in all three basic TM-AFM image channels, i.e., height (constant amplitude), amplitude (error signal), as well as phase angle shift. The clear observation of the domain boundary shows that the true resolution of the experiment is  $\leq 1$  nm. The apparent height of the domains varied between  $\sim 0.5$  and  $\sim 1.5$  nm. However, the absolute determination of feature heights in heterogeneous systems with spatially different

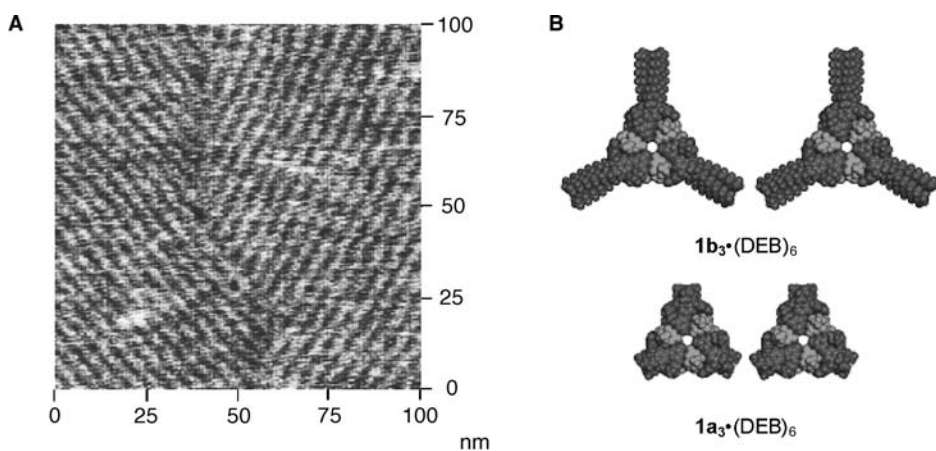


**Fig. 4** (A) TM-AFM image of  $1a_3$ ·(DEB)<sub>6</sub> on HOPG. *Source:* From Ref.<sup>[54]</sup>. © 1999 Am. Chem. Soc. (B) Gas phase minimized structures of *n*-dodecyl-substituted double rosettes  $1b_3$ ·(DEB)<sub>6</sub> (top) and *n*-propyl-substituted double rosettes  $1a_3$ ·(DEB)<sub>6</sub>.

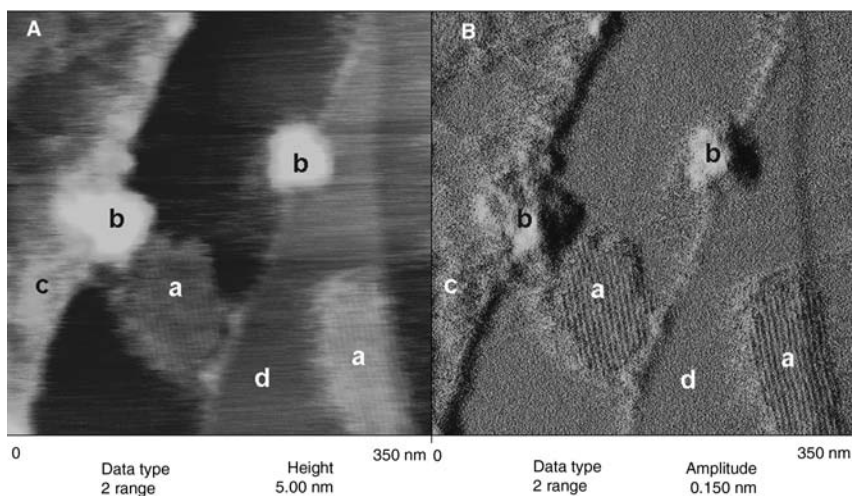


**Fig. 5** Dual height (A) and amplitude (B) TM-AFM images of the multiphase film structure in films of  $2_3:(DEB)_{12}$  on HOPG [nanorod (a), crystal (b), granular (c), and gas/liquid phase (d)].

tip-sample interactions must be regarded with some reservation.<sup>[62,63]</sup>

The angle between the directions of the rows observed in Fig. 4 is  $\sim 73^\circ$ . This angle deviates significantly from the  $60^\circ$  angle anticipated for a simple epitaxial layer structure on graphite ( $C_3$  symmetry), in which the nanorods or domains are oriented along the underlying graphite lattice. If we take more recent data on related tetra-rosettes  $2_3:(DEB)_{12}$  into account, the origin of this mismatch may be attributed to the presence of a chiral layer structure (vide infra).<sup>[55]</sup>

The observed interrow distances ( $3.8 \pm 0.2$  nm) can be attributed to a face-to-face stacking of the double rosettes based on the interrow spacings observed for double rosettes with different substituents on the calix[4]arene unit. As mentioned, for *n*-propyloxy substituents, an interrow distance of  $3.8 \pm 0.2$  nm was measured based on the cross-sectional analysis of many AFM images, while *n*-dodecyloxy-substituted rosettes show a spacing of  $5.3 \pm 0.2$  nm.<sup>[54]</sup> This observation, together with the gas phase minimized structures (Fig. 4B), implies that the rows are composed of rows of rosettes, in which the nanostructures are arranged such that the calix[4]arene units point outward to the neighboring row, and that the rosettes are stacked approximately face-to-face. In addition, a detailed study showed that, for both *n*-propyloxy-substituted and *n*-dodecyloxy-substituted double rosettes, little to no interdigitation of the protruding *n*-alkane chains exists in the 2-D arrays on HOPG.<sup>[54]</sup>

### Tetra-rosettes $2_3:(DEB)_{12}$ on HOPG

The morphology of  $2_3:(DEB)_{12}$  on HOPG resembles the morphology of  $1a_3:(DEB)_6$  on HOPG and typical

domains with parallel rows are observed by TM-AFM (Fig. 5). The appearance of the domains, as well as the other phases (vide infra), is similar to the mentioned double rosettes. The interrow spacing of  $4.6 \pm 0.1$  nm is comparable to the double rosettes discussed above, which implies a similar arrangement as the one shown in Fig. 4B. Before the internal structure is elucidated in more detail, the different phases present on the samples will be discussed.

The different phases present on the HOPG surface can be identified based on their appearance in the TM-AFM micrographs, as well as the temporal development of the layer morphology at elevated temperatures (Figs. [5–7]). In addition to the nanorod domains (denoted “a” in Fig. 5), a 3-D crystal phase

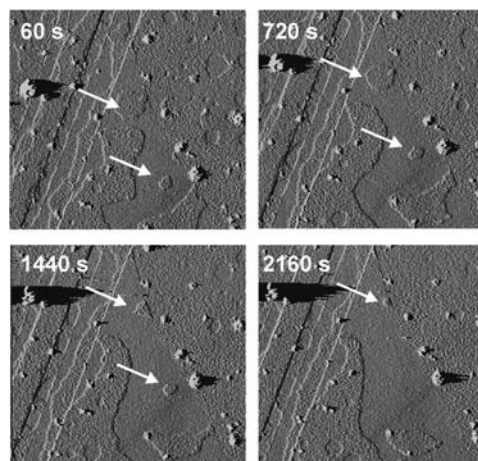


**Fig. 6** TM-AFM amplitude images (scan size,  $5 \times 5 \mu\text{m}^2$ ) recorded during the restructuring of multiphase film of  $2_3:(DEB)_{12}$  on HOPG at  $34^\circ\text{C}$  (every 5th frame). The arrows point to diffusing and shrinking domains of the granular phase.

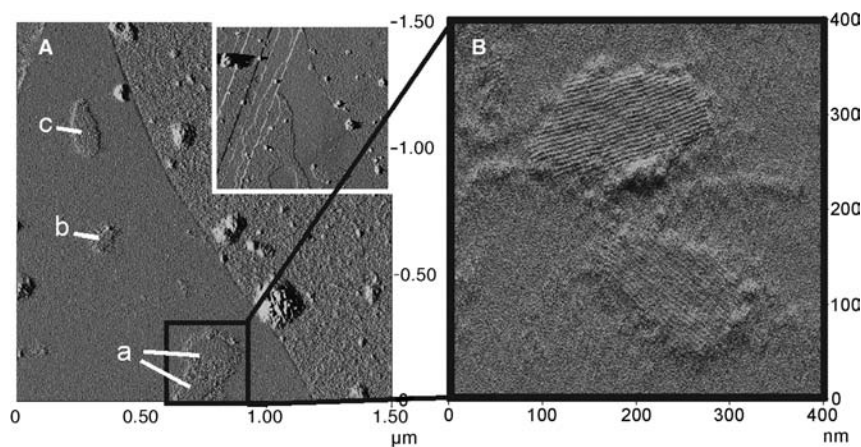


**Fig. 7** TM-AFM amplitude images acquired after storage of the film shown in Fig. 6 (right) for 60 hr at 34°C: (A) multiphase film structure including four nanorod domains labeled a–c (left, inset:  $5 \times 5 \mu\text{m}^2$  scan of the same region before storage) and (B) higher-resolution image of two nanorod domains labeled a in (A). Note that the nanorod domains have been formed in an area that was initially covered by the featureless gas or liquid-like phase.

(b), a granular phase (c), and a gas/liquid phase (d) can be distinguished. The 3-D crystal phase appeared elevated ( $>5 \text{ nm}$ ) and did not change in time, even at elevated temperatures (40°C) or after annealing at  $>60^\circ\text{C}$ . The granular phase also appeared elevated in TM-AFM height images, but became mobile upon increasing the temperature to  $>30^\circ\text{C}$ , while the gas/liquid phase was identified based on the fuzzy image contrast on flat HOPG terraces.

All phases are reminiscent of those reported by Loi et al.<sup>[64–66]</sup> of polyphenylene dendrimers on HOPG. In contrast to this dendrimer system, the tetra-rosette  $2_3\cdot(\text{DEB})_{12}$  nanostructures were found to be (meta)-stable in a limited temperature range. At temperatures  $>40^\circ\text{C}$ , the ordered arrays of tetra-rosettes disappeared and did not reform upon lowering the temperature to  $<20^\circ\text{C}$ .

The morphology of the layers deposited onto HOPG following a brief vacuum treatment (to remove residual solvent) was observed to change during the AFM measurements. As shown in Fig. 6, the granular phase was mobile at 34°C and several islands decreased in size or changed position relative to the immobile crystalline phase. This mobility can be attributed to a rearrangement of the layer structure during the AFM experiment at controlled temperature.<sup>[44–46,67,68]</sup>

At this stage, nanorod domains were *not* observed on this particular sample. However, after prolonged storage at 34°C, nanorod domains formed in areas that appeared featureless in the TM-AFM amplitude images shown in Fig. 6. In Fig. 7, TM-AFM images of the same area of the specimen are shown. Four nanorod domains can be observed.

The observed changes in the size of isolated islands of the granular phase (Fig. 6) and the formation of nanorod domains in previously apparently uncovered areas of HOPG after storage of the sample film for 60 hr at 34°C (Fig. 7) support the presence of a gas/liquid phase, as well as the surface diffusion of *intact* rosette nanostructure  $2_3\cdot(\text{DEB})_{12}$ .

The ordered arrays of supramolecular nanostructures are formed *spontaneously* by a self-assembly process at the HOPG surface. The formation of nanorod domains in areas where the gas/liquid phase had been previously observed indicates that the assembly is truly a supramolecular assembly of supramolecular nanostructures, i.e., an ordered 2-D array of individual rosette entities. Further, it indicates that surface diffusion of intact rosettes and subsequent nucleation and growth are one pathway to the formation of the nanorod domain of rosettes on HOPG surfaces. This pathway is well-known for, e.g., self-assembled monolayers of alkanethiols on gold.<sup>[69–71]</sup>

In addition to the intermolecular interactions between individual rosette assemblies, the adsorption energy of these supramolecules to HOPG plays an important role in this process. This can be concluded from the correlation of the nanorod structures with the  $C_3$  symmetry directions of the underlying substrate (vide infra). For methylene groups (in *n*-alkanes) and phenyl groups on HOPG, adsorption energies of  $E_{\text{ad}}(\text{CH}_2) \sim 7 \text{ kJ/mol}$ <sup>[72]</sup> and  $E_{\text{ad}}(\text{phenyl}) \sim 15 \text{ kJ/mol}$ , respectively,<sup>[73]</sup> have been reported. The tetra-rosette adsorbates  $2_3\cdot(\text{DEB})_{12}$  do not possess long alkyl-substituents; thus the adsorption energies will be modest. This feature is responsible for the observed dynamic behavior of the multiphase films even at temperatures between room temperature and  $\leq 40^\circ\text{C}$ , as revealed by real-time AFM experiments at controlled temperature (Fig. 6), which clearly indicates that the individual tetra-rosette assemblies can diffuse on HOPG at these temperatures.

### Chirality of Tetra-rosette Assemblies in 2-D

For the tetra-rosette  $2_3\cdot(\text{DEB})_{12}$ , domain boundaries can be clearly imaged and isolated defects are well-resolved (Fig. 8). The orientation of the rods appeared to be related by the underlying HOPG substrate. As



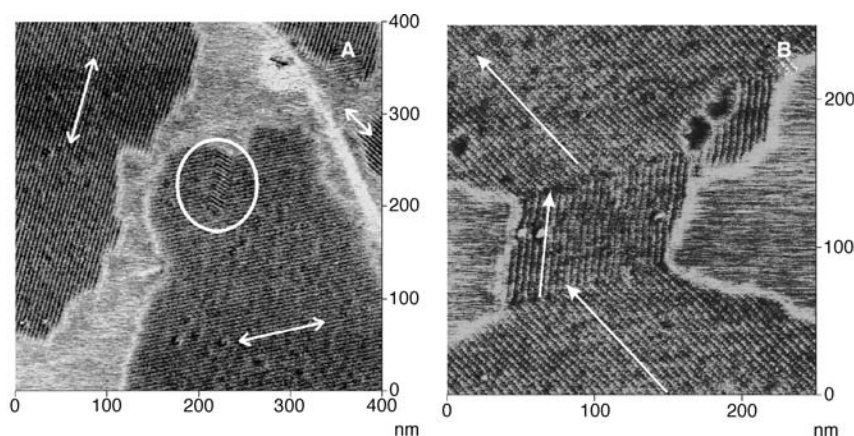


**Fig. 8** (A) TM-AFM phase images of nanorod domains of tetra-rosettes  $2_3\bullet(\text{DEB})_{12}$  on HOPG: The orientation of several nanorod domains is related to the threefold symmetry of the HOPG substrate as shown by the three arrows; within the distinct defect in the largest domain (inside circle), a different orientation can be recognized. *Source:* From Ref.<sup>[55]</sup>. © 2002 National Academy of Sciences, U.S.A. (B) The angle between different domains on the same sample can be estimated as  $46^\circ$ , as shown by the arrows.

shown by the arrows in Fig. 8A, three distinct orientations are observed in this micrograph.

Because the domains possess a mutual orientation of  $60^\circ$ , an orientation along the lattice of graphite seems plausible. However, upon close inspection of Fig. 8A, a deviating subdomain orientation can be observed for the “defect” in the center of the AFM nanograph. The rods in this subdomain are oriented at an angle of  $\sim 45^\circ$  with respect to the orientation of the surrounding domain. The interpretation of this peculiar orientation is complicated by the fact that the orientation of the underlying graphite remains unknown; in contrast with contact mode AFM,<sup>[74]</sup> it is impossible to resolve the corresponding lattice structure with TM-AFM. A similar angle of  $46^\circ$  between different domains is shown in Fig. 8B, which indicates that there are two sets of orientation of the nanorods.

The origin of the different orientations was unraveled by elucidating the nanometer-scale arrangement of the rosettes in high-resolution TM-AFM images (Fig. 9). Here a *chiral* superstructure with smaller periodicity is clearly present. The raw data shown in Fig. 9A suggests the presence of inclined elongated features along the rows.

The quantitative analysis of the 2-D fast Fourier transforms (inset in Fig. 9A) reveals an oblique lattice structure with  $a = 2.5 \pm 0.3$  nm,  $b = 5.0 \pm 0.1$  nm,  $\gamma = 122 \pm 3^\circ$ . This unit cell, which has an area of  $10.6 \text{ nm}^2$  and contains probably one tetra-rosette nanostructure, is indicated in the Fourier filtered section shown in Fig. 9B. In different domains, the same structure is found; however, the inclination of the elongated features is directed to the complementary direction, i.e., the angle is  $-122 \pm 3^\circ$ .

In the absence of elements of chirality, the rosette assemblies form as a racemic mixture of P and M enantiomers in solution.<sup>[75,76]</sup> However, the lattice structures formed on HOPG are clearly chiral with two types of domains that display opposite inclination angles with respect to the nanorod direction. The

observation of these two sets of domains that differ in orientation by  $46^\circ$ , while each set exists in domains with mutual angles of  $60^\circ$ , is consistent with a spontaneous chiral resolution of the P and M rosettes into enantiopure (homochiral) domains on HOPG. Consequently, the orientation of the nanorod domains appears to be  $\pm 23^\circ$  with respect to the orientation of the underlying HOPG. The same orientation is probably present for the double rosettes discussed above. Such behavior has been observed before for *molecular* adsorbates.<sup>d</sup> Hence the observation of chiral resolution indicates that the rosette nanostructures behave as individual entities and can form higher-order hierarchical structures in two dimensions.

The observed nanorods in the chiral structure consist of rows of tetra-rosette assemblies, as concluded from a comparison of the AFM data and the known crystal structure of the corresponding double rosette assemblies<sup>[24]</sup> and the gas phase minimized structure of the tetra-rosettes (Fig. 3).<sup>[80]</sup> The area requirement for such an arrangement is ca.  $8.6\text{--}9.9 \text{ nm}^2$ , depending on the orientation. This value compares well with the experimentally observed  $10.6 \text{ nm}^2$  (vide supra). In this simplified analysis, the possible spreading of the alkyl side chains of the rosettes due to the strong interaction of the methylene units with the graphite and the concomitant flattening of the nanostructures was not taken into consideration; hence the estimated area requirement can be regarded as a lower limit. The precise orientation of the  $2_3\bullet(\text{DEB})_6$  nanostructure within the rows remains unknown at this point because the height and width of the tetra-rosettes are essentially the same (Fig. 3); thus no definite assignment of the orientation of this assembly in the nanorod domains on HOPG can be made based on the presently available AFM data.

<sup>d</sup>For a discussion of chirality in 2-D, see e.g., Refs.<sup>[77–79]</sup>.

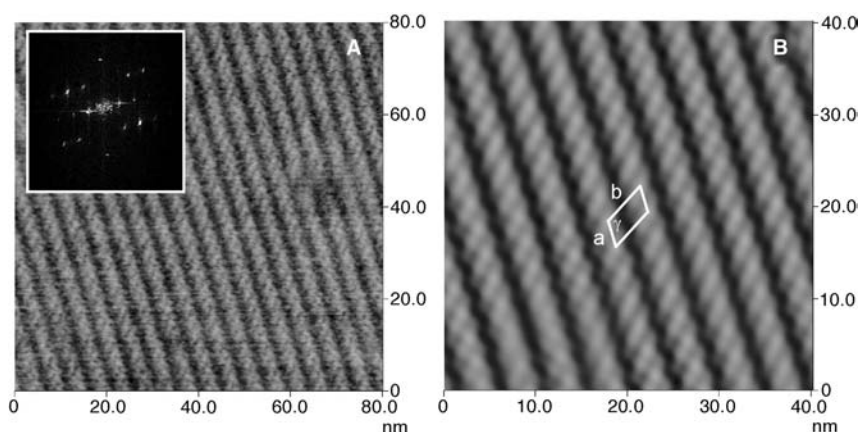


**Fig. 9** (A) High-resolution tapping mode AFM image of tetra-rosette nanorod domain structure resolved for  $2_3\bullet(\text{DEB})_{12}$  on HOPG (left, inset: 2-D FFT); (B) Fourier filtered AFM image and unit cell of the lattice structure (right). This chiral structure can be described by an oblique lattice with  $a = 2.5 \pm 0.3$  nm,  $b = 5.0 \pm 0.1$  nm, and  $\gamma = 122 \pm 3^\circ$ . Source: From Ref.<sup>[55]</sup>. © 2002 National Academy of Sciences, U.S.A.

### GROWTH OF INDIVIDUAL ROSETTE NANOSTRUCTURES AT SURFACES

One of the ultimate challenges in nanotechnology is the controlled growth and positioning of *individual* nanostructures onto solid supports. As a first step, the growth of single double rosette nanostructures on gold monolayers has been studied.<sup>[81]</sup> For this purpose, calix[4]arene dimelamine **3**, bearing a thioether functionality, is embedded into a hexanethiol self-assembled monolayer (SAM) on gold,<sup>[82–84]</sup> followed by the growth of single assemblies on the monolayer. The insertion process is based on the general approach for dendrimer insertion into SAMs and interfacial reaction at SAMs developed in our groups.<sup>[85–88]</sup> Similarly to the exchange reaction in solution, the growth of rosettes occurs via an exchange reaction between dimelamines **3** and the dimelamines constituting a preformed double rosette assembly  $1a_3\cdot(\text{DEB})_6$  in

solution. The exchange, and consequently the growth process, are the result of the high thermodynamic stability of the H-bonded assemblies combined with a relatively low kinetic stability (Fig. 10).<sup>[89]</sup>

The SAMs formed by insertion of calix[4]arene dimelamine **3** and subsequently by growth of the assembly  $1a_2\cdot 3\cdot(\text{DEB})_6$  were studied via TM-AFM. In the first case, TM-AFM images show single isolated features with an average height of  $1.1 \pm 0.2$  nm, in good agreement with the height obtained from the Corey–Pauling–Koltun (CPK) model of the adsorbate **3** (0.9 nm). By contrast, the TM-AFM images acquired subsequent to the growth of the rosette assemblies show two differently sized features (Fig. 11).

The height of the larger features (3.5 nm, Fig. 11C) agrees well with the expected size for the assembly  $1a_2\cdot 3\cdot(\text{DEB})_6$ , considering the crystal structure of a similar double rosette assembly. Therefore these features are attributed to mixed assemblies  $1a_2\cdot 3\cdot(\text{DEB})_6$

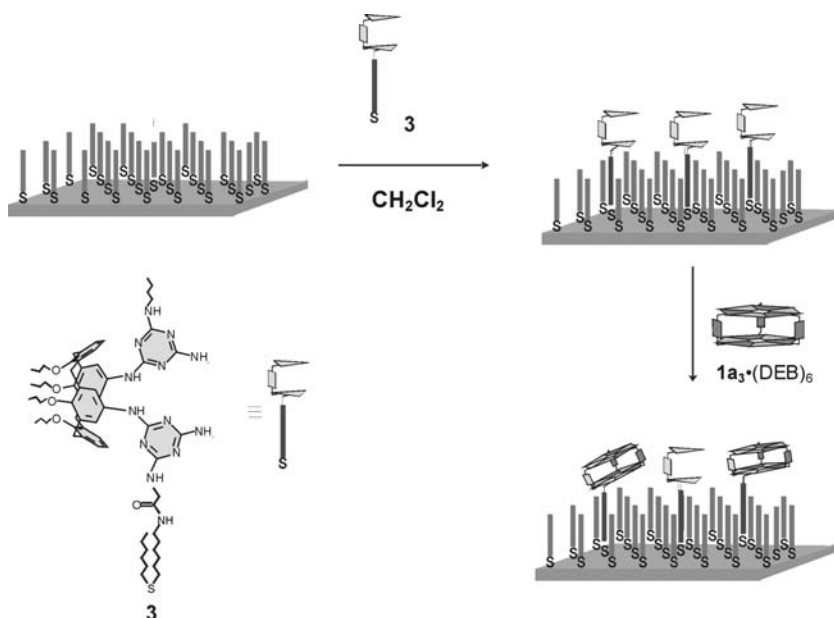


**Fig. 10** Schematic representation of the methodology followed for the growth of assemblies  $1a_2\cdot 3\cdot(\text{DEB})_6$  in SAMs on gold.



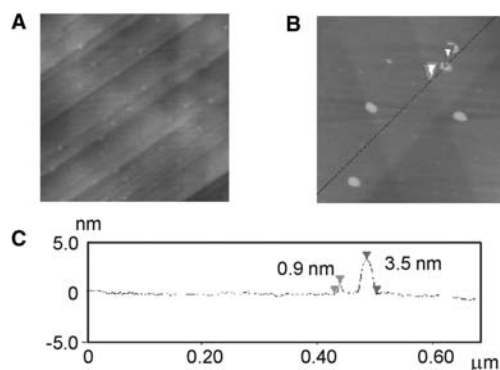


**Fig. 11** (A) TM-AFM image ( $500 \times 500 \text{ nm}^2$ ) of hexanethiol monolayers on Au(111) containing calix[4]arene dimelamine **3** acquired in air. (B) TM-AFM image ( $500 \times 500 \text{ nm}^2$ ) after treatment with a solution of assembly  $\mathbf{1a}_3 \bullet (\text{DEB})_6$ . (C) Comparison of heights. The height profile corresponds to the line drawn in the AFM image (B). Color scale from dark to bright:  $z = 10 \text{ nm}$ . Source: From Ref.<sup>[81]</sup>. Reproduced with permission from The Royal Society of Chemistry.)

obtained through reversible exchange of components **1a** and **3**. The height of the smaller features (0.9 nm, Fig. 11C) corresponds to single isolated molecules of **3**, which were not involved in exchange reactions with assemblies  $\mathbf{1a}_3 \bullet (\text{DEB})_6$ .

## CONCLUSION

We have shown that well-defined nanometer-sized structures can be formed from individual low molecular mass components in a bottom-up strategy. Highly regular 2-D arrays of these rosette nanostructures are formed at the HOPG–air interface, thus establishing a second hierarchical level. Based on the successful elucidation of the orientation of individual rosettes within the nanorods, novel approaches that allow one to control the chirality of 2-D structures formed by assembly of rosettes on HOPG, as well as the syntheses and assembly of novel *functionalized* rosettes, we develop a strategy that will enable us to position supramolecular nanostructures comprising functions with molecular precision in space. The obtained assemblies are hierarchical in nature and thus open pathways to increased complexity. The anticipated functionalized 2-D arrays of rosettes will be useful as, e.g., templates for the deposition of metals and other materials, sensor arrays, etc. In addition, individual rosette nanostructures can be successfully “synthesized” in suitably functionalized self-assembled monolayers on gold. The incorporation of functions will open the way toward surface-immobilized molecular nanotechnology. To realize the ultimate challenge of the controlled

growth and positioning of *individual* nanostructures on solid supports, different positioning strategies, including scanning probe approaches, are currently being pursued in our laboratories.

## ACKNOWLEDGMENTS

The authors thank C. W. Frank, J. J. García-López, K. A. Jolliffe, H.-A. Klok, M. Möller, V. Paraschiv, L. J. Prins, C. L. Schauer, J. P. Spatz, P. Timmerman, F. C. J. M. van Veggel, and S. Zapotoczny for stimulating discussions and their invaluable contributions to the work reviewed here. This work has been financially supported by the Council for Chemical Sciences of the Netherlands Organization for Scientific Research (CW-NWO) and the Deutscher Akademischer Austauschdienst (DAAD) in the framework of the “Hochschulsonderprogramm III” (H.S.). The research of M.C.-C. has been made possible by a fellowship of the Royal Netherlands Academy of Arts and Sciences.

## REFERENCES

1. Lehn, J.-M. *Supramolecular Chemistry: Concepts and Perspectives*; VCH: Weinheim, 1995.
2. Yokoyama, T.; Yokoyama, S.; Kamikado, T.; Okuno, Y.; Mashiko, S. Selective assembly on a surface of supramolecular aggregates with controlled size and shape. *Nature* **2001**, *413*, 619–621.
3. Neu, B.; Meyer, G.; Rieder, K.H. Controlled vertical and lateral manipulation of single atoms and molecules with the scanning tunneling microscope. *Mod. Phys. Lett.* **1995**, *9*, 963–969.
4. Jung, T.A.; Schlittler, R.R.; Gimzewski, J.K.; Tang, H.; Joachim, C. Controlled room-temperature positioning of individual molecules: Molecular flexure and motion. *Science* **1996**, *271*, 181–184.
5. Gimzewski, J.K.; Joachim, C. Nanoscale science of single molecules using local probes. *Science* **1999**, *283*, 1683–1688.
6. Lehn, J.-M. Supramolecular chemistry—scope and perspectives. Molecules, supermolecules and molecular devices (Nobel lecture). *Angew. Chem., Int. Ed. Engl.* **1988**, *27*, 89–112.
7. Cram, D.J. The design of molecular hosts, guests, and their complexes (Nobel lecture). *Angew. Chem., Int. Ed. Engl.* **1988**, *27*, 1009–1020.
8. Pedersen, C.J. The discovery of crown ethers (Nobel lecture). *Angew. Chem., Int. Ed. Engl.* **1988**, *27*, 1021–1027.
9. Reinhoudt, D.N., Ed.; *Supramolecular Materials and Technologies*; Wiley: New York, 1999.
10. Israelachvili, J. *Intermolecular and Surface Forces*; Academic Press: London, 1991.
11. Schönherr, H.; Beulen, M.W.J.; van Veggel, F.C.J.M.; Bügler, J.; Huskens, J.; Reinhoudt, D.N.; Vancso, G.J.

- Individual supramolecular host–guest interactions studied by dynamic single molecule force spectroscopy. *J. Am. Chem. Soc.* **2000**, *122*, 4963–4967.
12. Prins, L.J.; Reinhoudt, D.N.; Timmerman, P. Noncovalent synthesis using hydrogen bonding. *Angew. Chem., Int. Ed.* **2001**, *40*, 2383–2426.
  13. Brunsveld, L.; Folmer, B.J.B.; Meijer, E.W.; Sijbesma, R.P. Supramolecular polymers. *Chem. Rev.* **2001**, *101*, 4071–4097.
  14. Cooke, G.; Rotello, V.M. Methods of modulating hydrogen bonded interactions in synthetic host–guest systems. *Chem. Soc. Rev.* **2002**, *31*, 275–286.
  15. Lehn, J.M. Toward self-organization and complex matter. *Science* **2002**, *295*, 2400–2403.
  16. Ikkala, O.; ten Brinke, G. Functional materials based on self-assembly of polymeric supramolecules. *Science* **2002**, *295*, 2407–2409.
  17. Whitesides, G.M.; Grzybowski, B. Self-assembly at all scales. *Science* **2002**, *295*, 2418–2421.
  18. Reinhoudt, D.N.; Crego-Calama, M. Synthesis beyond the molecule. *Science* **2002**, *295*, 2403–2407.
  19. Lehn, J.-M.; Mascial, M.; DeCian, A.; Fischer, J. Molecular recognition directed self-assembly of ordered supramolecular strands by cocrystallization of complementary molecular components. *J. Chem. Soc., Chem. Commun.* **1990**, 479–481.
  20. Seto, C.T.; Whitesides, G.M. Self-assembly based on the cyanuric acid melamine lattice. *J. Am. Chem. Soc.* **1990**, *112*, 6409–6411.
  21. Zerkowski, J.A.; Seto, C.T.; Wierda, D.A.; Whitesides, G.M. Design of organic structures in the solid state-hydrogen-bonded molecular tapes. *J. Am. Chem. Soc.* **1990**, *112*, 9025–9026.
  22. Bielejewska, A.G.; Marjo, C.E.; Prins, L.J.; Timmerman, P.; de Jong, F.; Reinhoudt, D.N. Thermodynamic stabilities of linear and crinkled tapes and cyclic rosettes in melamine–cyanurate assemblies: A model description. *J. Am. Chem. Soc.* **2001**, *123*, 7518–7533.
  23. Vreekamp, R.H.; van Duynhoven, J.P.M.; Hubert, M.; Reinhoudt, D.N. Molecular boxes based on calix[4]arene double rosettes. *Angew. Chem., Int. Ed. Engl.* **1996**, *35*, 1215–1218.
  24. Timmerman, P.; Vreekamp, R.; Hulst, R.; Verboom, W.; Reinhoudt, D.N.; Rissanen, K.; Udachin, K.A.; Ripmeester, J. Noncovalent assembly of functional groups on calix[4]arene molecular boxes. *Chem. Eur. J.* **1997**, *3*, 1823–1832.
  25. Jolliffe, K.A.; Timmerman, P.; Reinhoudt, D.N. Noncovalent assembly of a fifteen-component hydrogen-bonded nanostructure. *Angew. Chem., Int. Ed.* **1999**, *38*, 933–937.
  26. Paraschiv, V.; Crego-Calama, M.; Fokkens, R.H.; Padberg, C.J.; Timmerman, P.; Reinhoudt, D.N. Nanostructures via noncovalent synthesis: 144 hydrogen bonds bring together 27 components. *J. Org. Chem.* **2001**, *66*, 8297–8301.
  27. Reinhoudt, D.N.; Timmerman, P.; Cardullo, F.; Crego-Calama, M. Synthesis and Characterization of Hydrogen-Bonded Assemblies: Towards the Generation of Binding Site Diversity. In *Supramolecular Science: Where It Is and Where It Is Going*; Ungaro, R., Dalcanale, E., Eds.; Kluwer Academic Publishers: Dordrecht, 1999; NATO, pp. 181–195.
  28. Timmerman, P.; Prins, L.J. Noncovalent synthesis of melamine–cyanuric/barbituric acid derived nanostructures: Regio- and stereoselection. *Eur. J. Org. Chem.* **2001**, 3191–3205.
  29. Jolliffe, K.A.; Crego-Calama, M.; Fokkens, R.; Nibbering, N.M.M.; Timmerman, P.; Reinhoudt, D.N. Characterization of hydrogen-bonded supramolecular assemblies by MALDI-TOF mass spectrometry after Ag<sup>+</sup> labeling. *Angew. Chem., Int. Ed.* **1998**, *37*, 1247–1251.
  30. Timmerman, P.; Jolliffe, K.A.; Crego-Calama, M.; Weidmann, J.-L.; Prins, L.J.; Cardullo, F.; Snellink-Ruël, B.H.M.; Fokkens, R.; Nibbering, N.M.M.; Shin-kai, S.; Reinhoudt, D.N. Ag<sup>+</sup> labeling: A convenient new tool for the characterization of hydrogen-bonded supramolecular assemblies by MALDI-TOF mass spectrometry. *Chem. Eur. J.* **2000**, *6*, 4104–4115.
  31. Kerckhoffs, J.M.C.A.; Crego-Calama, M.; Luyten, I.; Timmerman, P.; Reinhoudt, D.N. Self-assembly of polar functionalities using noncovalent platforms. *Org. Lett.* **2000**, *2*, 4121–4124.
  32. Binnig, G.; Quate, C.F.; Gerber, Ch. Atomic force microscope. *Phys. Rev. Lett.* **1986**, *56*, 930–933.
  33. Sarid, D. *Scanning Force Microscopy, with Applications to Electric, Magnetic and Atomic Forces*; Oxford University Press: Oxford, 1991.
  34. Magonov, S.N.; Whangbo, M.-H. *Surface Analysis with STM and AFM*; VCH: New York, 1996.
  35. Frommer, J. Scanning tunneling microscopy and atomic force microscopy in organic chemistry. *Angew. Chem., Int. Ed. Engl.* **1992**, *31*, 1298–1328.
  36. Hamers, R.J. Scanned probe microscopies in chemistry. *J. Phys. Chem.* **1996**, *100*, 13103–13120.
  37. Bonnell, D.A. *Scanning Tunneling Microscopy and Spectroscopy: Theory, Techniques and Applications*; VCH: New York, 1993.
  38. Chi, L.-F.; Anders, M.; Fuchs, H.; Johnston, R.R.; Ringsdorf, H. Domain structures in Langmuir–Blodgett films investigated by atomic force microscopy. *Science* **1993**, *259*, 213–216.
  39. Zhong, Q.; Inniss, D.; Kjoller, K.; Elings, V.B. Fractured polymer silica fiber surface studied by tapping mode atomic force microscopy. *Surf. Sci.* **1993**, *290*, L688–L692.
  40. Overney, R.M.; Meyer, E.; Frommer, J.; Brodbeck, D.; Lüthi, R.; Howald, L.; Güntherodt, H.-J.; Fujihira, M.; Takano, H.; Gotoh, Y. Friction measurements on phase-separated thin films with a modified atomic force microscope. *Nature* **1992**, *359*, 133–135.
  41. Frisbie, C.D.; Rozsnyai, L.F.; Noy, A.; Wrighton, M.S.; Lieber, C.M. Functional group imaging by chemical force microscopy. *Science* **1994**, *265*, 2071–2074.
  42. Noy, A.; Vezenov, D.V.; Lieber, C.M. Chemical force microscopy. *Annu. Rev. Mater. Sci.* **1997**, *27*, 381–421.
  43. Schönherr, H.; Hruska, Z.; Vancso, G.J. Toward high resolution mapping of functional group distributions at surface-treated polymers by AFM using modified tips. *Macromolecules* **2000**, *33*, 4532–4537.

44. Sikes, H.D.; Schwartz, D.K. Two-dimensional melting of an anisotropic crystal observed at the molecular level. *Science* **1997**, *278*, 1604–1607.
45. Pearce, R.; Vancso, G.J. Imaging of melting and crystallization of poly(ethylene oxide) in real-time by hot-stage atomic force microscopy. *Macromolecules* **1997**, *30*, 5843–5848.
46. Schönherr, H.; Bailey, L.E.; Frank, C.W. Analyzing the surface temperature depression in hot stage atomic force microscopy with unheated cantilevers: Application to the crystallization of poly(ethylene oxide). *Langmuir* **2002**, *18*, 490–498 and reference cited.
47. Marti, O.; Ribi, H.O.; Drake, B.; Albrecht, T.R.; Quate, C.F.; Hansma, P.K. Atomic force microscopy of an organic monolayer. *Science* **1988**, *239*, 50–52.
48. Alves, C.A.; Smith, E.L.; Porter, M.D. Atomic scale imaging of alkanethiolate monolayers at gold surfaces with atomic force microscopy. *J. Am. Chem. Soc.* **1992**, *114*, 1222–1227.
49. Jaschke, M.; Schönherr, H.; Wolf, H.; Butt, H.-J.; Bamberg, E.; Besocke, M.K.; Ringsdorf, H. Structure of alkyl and perfluoroalkyl disulfide and azobenzethiol monolayers on gold(111) revealed by atomic force microscopy. *J. Phys. Chem.* **1996**, *100*, 2290–2301.
50. Schönherr, H.; Vancso, G.J. Lattice imaging of self-assembled monolayers of partially fluorinated disulfides and thiols on sputtered gold by atomic force microscopy. *Langmuir* **1997**, *13*, 3769–3774.
51. Schönherr, H.; Vancso, G.J.; Huisman, B.-H.; van Veggel, F.C.J.M.; Reinhoudt, D.N. An atomic force microscopy study of self-assembled monolayers of calix[4]resorcinarene adsorbates on Au(111). *Langmuir* **1997**, *13*, 1567–1570.
52. Schönherr, H.; Kenis, P.J.A.; Engbersen, J.F.J.; Harkema, S.; Hulst, R.; Reinhoudt, D.N.; Vancso, G.J. Scanning force microscopy studies on molecular packing and friction anisotropy in thin films of tetranitrotetrapropoxycalix[4]arene. *Langmuir* **1998**, *14*, 2801–2809.
53. Overney, R.M.; Takano, H.; Fujihira, M.; Paulus, W.; Ringsdorf, H. Anisotropy in friction and molecular stick slip motion. *Phys. Rev. Lett.* **1994**, *72*, 3546–3549.
54. Klok, H.-A.; Jolliffe, K.A.; Schauer, C.L.; Prins, L.J.; Spatz, J.P.; Möller, M.; Timmerman, P.; Reinhoudt, D.N. Self-assembly of rodlike hydrogen-bonded nanostructures. *J. Am. Chem. Soc.* **1999**, *121*, 7154–7155.
55. Schönherr, H.; Paraschiv, V.; Zapotoczny, S.; Crego-Calama, M.; Timmerman, P.; Frank, C.W.; Vancso, G.J.; Reinhoudt, D.N. Unraveling the nanostructure of supramolecular assemblies of hydrogen-bonded rosettes on graphite: An atomic force microscopy study. *Proc. Natl. Acad. Sci. U. S. A.* **2002**, *99*, 5024–5027.
56. Magonov, S.N.; Elings, V.; Whangbo, M.-H. Phase imaging and stiffness in tapping-mode atomic force microscopy. *Surf. Sci.* **1997**, *375*, L385–L391.
57. Spatz, J.P.; Sheiko, S.; Möller, M.; Winkler, R.G.; Reincker, P.; Marti, O. Forces affecting the substrate in resonant tapping force microscopy. *Nanotechnology* **1995**, *6*, 40–44.
58. Burnham, N.A.; Behrend, O.P.; Oulevey, F.; Gremaud, G.; Gallo, P.-J.; Gourdon, D.; Dupas, E.; Kulik, A.J.; Pollock, H.M.; Briggs, G.A.D. How does a tip tap? *Nanotechnology* **1997**, *8*, 67–75.
59. Spatz, J.P.; Sheiko, S.; Möller, M.; Winkler, R.G.; Reincker, P.; Marti, O. Tapping scanning force microscopy in air—Theory and experiment. *Langmuir* **1997**, *13*, 4699–4703.
60. Winkler, R.G.; Spatz, J.P.; Sheiko, S.; Möller, M.; Reincker, P.; Marti, O. Imaging material properties by resonant tapping-force microscopy: A model investigation. *Phys. Rev., B* **1996**, *54*, 8908–8912.
61. Tamayo, J.; García, R. Deformation, contact time, and phase contrast in tapping mode scanning force microscopy. *Langmuir* **1996**, *12*, 4430–4435.
62. Eberstein, Y.; Nahum, E.; Banin, U. Tapping mode atomic force microscopy for nanoparticle sizing: Tip-sample interaction effects. *Nano. Lett.* **2002**, *2*, 945–950.
63. van Noort, S.J.T.; van der Werf, K.O.; De Grooth, B.G.; van Hulst, N.F.; Greve, J. Height anomalies in tapping mode atomic force microscopy in air caused by adhesion. *Ultramicroscopy* **1997**, *69*, 117–127.
64. Loi, S.; Wiesler, U.-M.; Butt, H.-J.; Müllen, K. Formation of nanorods by self-assembly of alkyl-substituted polyphenylene dendrimers on graphite. *J. Chem. Soc., Chem. Commun.* **2000**, 1169–1170.
65. Loi, S.; Wiesler, U.M.; Butt, H.-J.; Müllen, K. Self-assembly of alkyl-substituted polyphenylene dendrimers on graphite. *Macromolecules* **2001**, *34*, 3661–3671.
66. Loi, S.; Butt, H.-J.; Hampel, C.; Bauer, R.; Wiesler, U.M.; Müllen, K. Two-dimensional structure of self-assembled alkyl-substituted polyphenylene dendrimers on graphite. *Langmuir* **2002**, *18*, 2398–2405.
67. Schönherr, H.; Frank, C.W. Ultrathin films of poly(ethylene oxides) on oxidized silicon: 2. In situ study of crystallization and melting by hot stage AFM. *Macromolecules* **2003**, *36*, 1199–1208.
68. Schönherr, H.; Waymouth, R.M.; Frank, C.W. Nucleation and crystallization of low-crystallinity polypyrrole followed in situ by hot stage atomic force microscopy. *Macromolecules* **2003**, *36*, 2412–2418.
69. Poirier, G.E.; Pylant, E.D. The self-assembly mechanism of alkanethiols on Au(111). *Science* **1996**, *272*, 1145–1148.
70. Yamada, R.; Uosaki, K. In situ, real time monitoring of the self-assembly process of decanethiol on Au(111) in liquid phase. A scanning tunneling microscopy investigation. *Langmuir* **1997**, *13*, 5218–5221.
71. Tamada, K.; Hara, M.; Sasabe, H.; Knoll, W. Surface phase behavior of *n*-alkanethiol self-assembled monolayers adsorbed on Au(111): An atomic force microscope study. *Langmuir* **1997**, *13*, 1558–1566.
72. Martin, D.S.; Weightman, P.; Gauntlett, J.T. The evaporation of *n*-hexadecane from highly oriented pyrolytic graphite studied by atomic force microscopy. *Surf. Sci.* **1998**, *417*, 390–405.
73. Vernov, A.; Steele, W.A. Computer simulations of benzene adsorbed on graphite (2): 298 K. *Langmuir* **1991**, *7*, 2817–2820.
74. Marti, O.; Drake, B.; Gould, S.; Hansma, P.K. Atomic resolution atomic force microscopy of graphite and native oxide on silicon. *J. Vac. Sci. Technol., A* **1988**, *6*, 287–290.

75. Prins, L.J.; Huskens, J.; de Jong, F.; Timmerman, P.; Reinhoudt, D.N. Complete asymmetric induction of supramolecular chirality in a hydrogen-bonded assembly. *Nature* **1999**, *398*, 498–502.
76. Prins, L.J.; de Jong, F.; Timmerman, P.; Reinhoudt, D.N. An enantiomerically pure hydrogen-bonded assembly. *Nature* **2000**, *408*, 181–184.
77. De Feyter, S.; Gesquiere, A.; Wurst, K.; Amabilino, D.B.; Veciana, J.; De Schryver, F.C. Homo- and hetero-chiral supramolecular tapes from achiral, enantiopure, and racemic promesogenic formamides: Expression of molecular chirality in two and three dimensions. *Angew. Chem., Int. Ed.* **2001**, *40*, 3217–3220 and references cited.
78. Lahav, M.; Leiserowitz, L. Spontaneous resolution: From three-dimensional crystals to two-dimensional magic nanoclusters. *Angew. Chem., Int. Ed.* **1999**, *38*, 2533–2536.
79. Weissbuch, I.; Kuzmenko, I.; Berfeld, M.; Leiserowitz, L.; Lahav, M. Stereochemical studies on chiral systems in two dimensions. *J. Phys. Org. Chem.* **2000**, *13*, 426–434.
80. Timmerman, P.; Weidmann, J.-L.; Jolliffe, K.A.; Prins, L.J.; Reinhoudt, D.N.; Shinkai, S.; Frish, L.; Cohen, Y. NMR diffusion spectroscopy for the characterization of multicomponent hydrogen-bonded assemblies in solution. *J. Chem. Soc., Perkin Trans. 2* **2000**, 2077–2089.
81. García-López, J.J.; Zapotoczny, S.; Timmerman, P.; van Veggel, F.C.J.M.; Vancso, G.J.; Crego-Calama, M.; Reinhoudt, D.N. Growth of individual hydrogen-bonded nanostructures on gold monolayers. *J. Chem. Soc., Chem. Commun.* **2003**, 352–353.
82. Ulman, A. *An Introduction to Ultrathin Organic Films: From Langmuir–Blodgett to Self-Assembly*; Academic Press: New York, 1991.
83. Dubois, L.H.; Nuzzo, R.G. Synthesis, structure, and properties of model organic surfaces. *Annu. Rev. Phys. Chem.* **1992**, *43*, 437–463.
84. Ulman, A. Formation and structure of self-assembled monolayers. *Chem. Rev.* **1996**, *96*, 1533–1554.
85. Huisman, B.-H.; Schönherr, H.; Huck, W.T.S.; Friggeri, A.; van Manen, H.-J.; Menozzi, E.; Vancso, G.J.; van Veggel, F.C.J.M.; Reinhoudt, D.N. Surface-confined metallodendrimers: Isolated nanosize molecules. *Angew. Chem., Int. Ed. Engl.* **1999**, *38*, 2248–2251.
86. Friggeri, A.; Schönherr, H.; van Manen, H.-J.; Huisman, B.-H.; Vancso, G.J.; Huskens, J.; van Veggel, F.C.J.M.; Reinhoudt, D.N. Insertion of individual dendrimer molecules into self-assembled monolayers on gold: A mechanistic study. *Langmuir* **2000**, *16*, 7757–7763.
87. Friggeri, A.; van Manen, H.-J.; Auletta, T.; Li, X.-M.; Zapotoczny, S.; Schönherr, H.; Vancso, G.J.; Huskens, J.; van Veggel, F.C.J.M.; Reinhoudt, D.N. Chemistry on surface-confined molecules: An approach to anchor isolated functional units to surfaces. *J. Am. Chem. Soc.* **2001**, *123*, 6388–6395.
88. van Manen, H.-J.; Auletta, T.; Dordi, B.; Schönherr, H.; Vancso, G.J.; van Veggel, F.C.J.M.; Reinhoudt, D.N. Non-covalent chemistry on surface-confined, isolated dendrimers. *Adv. Funct. Mater.* **2002**, *12*, 811–818.
89. Crego-Calama, M.; Hulst, R.; Fokkens, R.; Nibbering, N.M.M.; Timmerman, P.; Reinhoudt, D.N. Libraries of non-covalent hydrogen-bonded assemblies; combinatorial synthesis of supramolecular systems. *J. Chem. Soc., Chem. Commun.* **1998**, 1021–1022.

# AFM: Imaging Artifacts

Stephanie Butler Velegol

Department of Civil and Environmental Engineering, Pennsylvania State University,  
State College, Pennsylvania, U.S.A.

## INTRODUCTION

The invention of the atomic force microscope (AFM; also known as scanning probe microscope, SPM) in 1986<sup>[1]</sup> has revolutionized the way researchers study surfaces.<sup>[2]</sup> Material surfaces such as metallic or polymeric thin films can be imaged under ambient conditions (air, liquids) with nanometer resolution. Furthermore, it is now possible to image biological species such as DNA, proteins, and bacteria in their natural environment. However, researchers using the AFM for imaging must do so with great care to avoid the many artifacts that can be present during imaging. It is the purpose of this entry to identify these artifacts and to present ways to avoid these artifacts while using the AFM. Interestingly, the discovery of many of these artifacts has opened doors to new uses of the AFM. This will be discussed as well.

## OVERVIEW

Before discussing the artifacts present in the AFM, a brief discussion of the AFM mechanism is warranted. Fig. 1 shows the mechanism of a typical AFM. The primary components are: 1) helium–neon laser; 2) AFM probe; 3) piezoelectric scanner; and 4) photodiode detector. Laser light is reflected off the top of a probe and is detected by a photodiode detector. The probe consists of a sharp tip attached to a flexible cantilever beam. The piezoelectric scanner controls either the vertical position of the surface (Fig. 1), or the vertical position of the probe. The piezoelectric scanner is able to move in three dimensions with angstrom-level precision. When the surface and the tip are brought closer together, the interaction between them causes the tip to be deflected either toward the surface (because of attractive forces), or away from the surface (because of repulsive forces). This deflection of the tip is recorded as the change in the position of the laser on the detector. The piezo responds to this change by increasing or decreasing the height of the sample to maintain a constant distance between the tip and the surface. Images can be recorded as either the deflection on the detector (deflection image), or the vertical

distance of the piezo (height image). The vertical resolution of AFM images is dictated by the interaction between the tip and the surface. The lateral resolution is determined by the size of the tip, as will be discussed below.

Fig. 2 shows a diagram of a typical pyramidal AFM tip on a cantilever. In most systems, the cantilever is tilted approximately  $12^\circ$  toward the surface. At a  $0^\circ$  scan angle, the tip moves across the surface in the direction of the arrow in Fig. 2. The AFM tips have traditionally been pyramidal in shape, but can also be of other shapes, such as a nanowire or a colloidal sphere.

Because the functionality of the AFM depends on the interaction between the tip and the surface, most of the artifacts that exist with the AFM are because of the size, shape, and cleanliness of the tip. Artifacts are also introduced when the tip interacts with the surface in a way that changes the surface itself. Finally, there are artifacts that exist because of the electronics of the control system. Table 1 shows a summary of each artifact along with the solution to the problem. Details of each artifact are discussed below.

## ARTIFACTS BECAUSE OF FINITE SIZE AND PYRAMIDAL SHAPE OF TIP

The image produced by the AFM is a convolution of both the shape of the surface being imaged and the tip geometry. The rule of thumb is that the image will accurately reflect the surface structure if the difference in the image of the radius of curvature of the tip is one-tenth the radius of the imaged structure.<sup>[3]</sup> The exception to this rule occurs if the height of the imaged structure is comparable to the height of the tip.

### Broadening of Surface Features

For any object on the surface with a finite height, the side of the tip will interact with the side of the surface feature. For the surface structures shown in Fig. 3, the side of the tip interacts with the surface structure when it is a distance of  $b$  away from the edge of the object. This will produce a broadening of the object in the

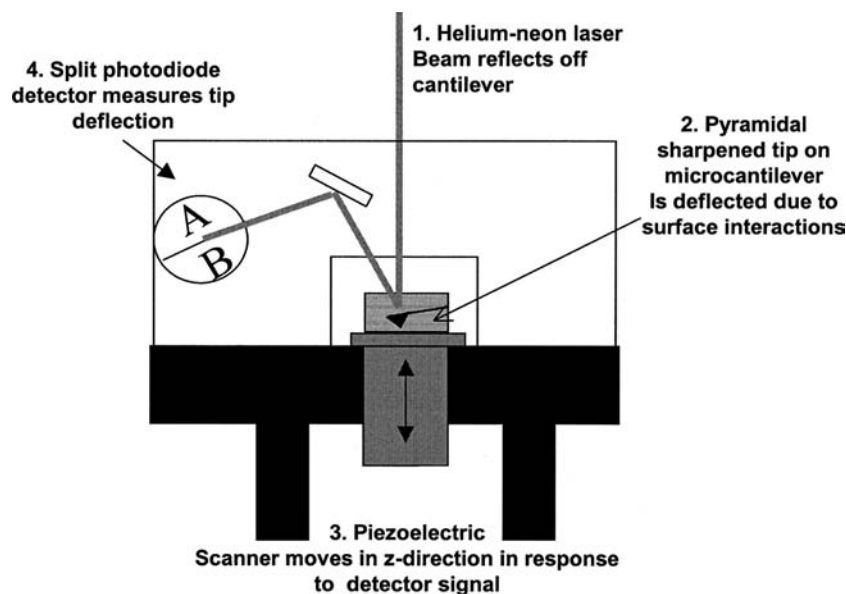


Fig. 1 Schematic of AFM.

image by a distance of  $b$  on both sides of the surface structure. If the lateral dimension  $a$  of the object is large and the height of the object is small (Fig. 3A), this effect is small. However, if the lateral dimension of the surface structure is small, or the height of the surface structure is large (Fig. 3B and C, respectively), the interaction of the side of the tip with the surface structure will result in significant broadening of the object in the image. For these reasons, this artifact will be predominant in images of nanoparticles (including proteins or DNA) as well as images of large particles such as bacteria.

An experimental example of the broadening of a small object because of the tip size (similar to Fig. 3B) has been observed when imaging DNA. Images obtained with a tip, with a radius of 30–50 nm, indicate that the diameter of the DNA strand is 14 nm whereas the true diameter is 2 nm.<sup>[4,5]</sup> In this case, the height of the image (as determined by the line plot) will be correct and only the width will be distorted.

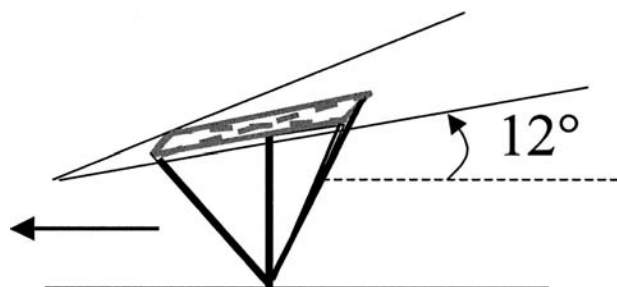


Fig. 2 Typical shape of AFM tip and cantilever relative to the surface. The tip is square pyramidal and the cantilever is tilted toward the surface at an angle of 12°. The arrow indicates the direction of scan (at 0° scan angle).

An effect similar to Fig. 3C can be observed while imaging large bacteria in aqueous media (Fig. 4). Although the radius of the bacteria (500 nm) is much larger than the radius of curvature of the AFM tip (5–40 nm), the object is also very tall compared to the tip. The diagonal lines represent the interaction of the diagonal edges of the tip with the side of the bacterium or sphere. Note that the lines appear mostly on one side because of the 12° tilt of the cantilever.<sup>[6]</sup> Similar effects have been observed in tapping-mode images of *P. chrysosporium* spores<sup>[7]</sup> and images of a fixed liver endothelial cell (LEC).<sup>[8]</sup>

There have been many attempts to correct this image artifact. One way is to use a standard tip and then reconstruct the image to determine the true size of the surface structure.<sup>[9–15]</sup> In most cases, these reconstruction techniques require knowledge of the shape and size of the AFM tip. Information such as the radius of curvature of the AFM tip can be obtained from the manufacturer but is best determined experimentally by the technique of reverse imaging. In this technique, the surface structure is smaller than the tip itself, so that the image reflects mostly the shape of the tip. The surface structure can be a grading of spikes,<sup>[15]</sup> circular depressions,<sup>[13]</sup> or close-packed spheres.<sup>[10]</sup> Digital Instruments® also has a Tip Estimation software program that can be used to determine the shape of the tip. Blind restoration, or blind reconstruction, can also be used to deconvolute the images without information about the tip shape.<sup>[4,16]</sup> This is performed via mathematical morphology operations (e.g., dilation and erosion) that can estimate the shape of the tip from the image.<sup>[4]</sup>

Another solution to the broadening effect is to use a tip with a high aspect ratio such as a nanowire (Fig. 5).

**Table 1** How to identify and avoid common AFM imaging artifacts

Artifact	Cause	Solution
Broadening of features	Interaction of surface with side of tip (structure above surface is too small laterally, or too high vertically)	Use deconvolution techniques
	Contamination on tip	Use sharpened tip (higher aspect ratio) Clean tip with UV/ozone or piranha solution Test for cleanliness by taking a force curve before and after imaging Image tip with SEM before and after imaging
	Bluntness of tip	Use new tip image tip Image tip with SEM to ascertain shape Use deconvolution techniques to determine actual surface structure
Smaller features	Interaction of surface with side of tip (surface structure below surface is too small laterally, or too deep)	Use deconvolution techniques
Surface structures that disappear while imaging	Lateral forces between tip and surface are too large and objects are pushed away via AFM tip	Use sharpened tip (higher aspect ratio) Use tapping mode
		Minimize force during imaging Bond surface structures to surface
Destruction of soft surfaces	Vertical forces between tip and surface are too high	Use tapping mode
		Use smaller force during imaging Use cantilever with smaller spring constant Stiffen surface
Appearance of “shadows” on opposite side of tip movement	Overshoot of control system	Slow down imaging speed
Distortion after image zoom	Drift in piezoelectric scanner	Change scan direction Rescan area of interest
Periodic “noise” in image	Mechanical or electrical noise	Remove vibrations from room Decrease gains on control system

The high aspect ratio reduces the interaction of the side of the tip with the surface structure, but one must be cautious when using a sharpened tip because it can create large pressures on the surface that are more likely to damage soft samples. For large objects on the surface, adjusting the angle between the cantilever and the surface so that they are parallel can minimize artifacts because of high vertical dimensions.

### Features Appear Too Small

If the probe needs to go into a feature that is below the surface, the surface structure in the image may appear too small because of the interaction between the tip and the inside of the structure. This artifact

has been observed in images of germanium surfaces bombarded by ions.<sup>[9]</sup> Atomic force microscope images showed the presence of columnar structures present because of the shape of the tip and did not appear in electron microscopy images. In this case, the tip may not be able to image the corner of the feature (Fig. 6A), or may not be able to reach the bottom of the structure (Fig. 6B). This will be particularly noticeable if the hole is small laterally (Fig. 6A) and/or deep (Fig. 6B).

Again, this artifact may be removed by using a tip with a higher aspect ratio (such as a sharpened tip, or a nanowire). Reconstruction of the image can also be performed, although the deconvolution algorithm cannot reconstruct parts of the tip that did not make contact with the sample.<sup>[12]</sup>



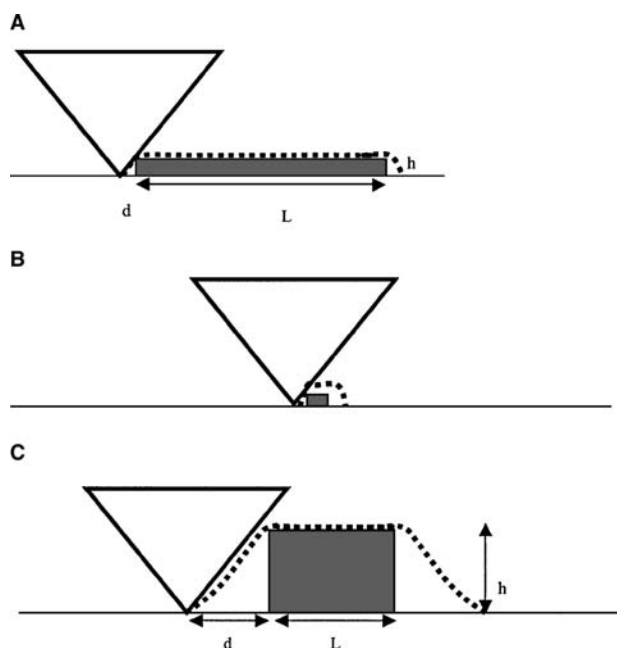


**Fig. 3** Schematic of image artifacts because of the size and shape of the tip. In all cases, the side of the tip interacts with the surface object with a lateral dimension of  $L$  and a height of  $h$  at a distance of  $d$  away from the object. This causes a distortion in the image, indicated by the dotted line. In (A), the radius of the tip is much smaller than the radius of the object being imaged, and the artifact is minimized. In (B)  $L$  is small and the distortion is more noticeable. In (C), the height of the object  $h$  causes a greater distortion of the image.

### Artifacts Because of Contamination of Tip or Misshapen Tips

Because the lateral resolution of the image depends on the radius of the tip, any change to the tip that causes the tip to become broader will sacrifice this resolution. These changes to the tip may be because of contaminants on the tip, or because of tip damage.

Scanning electron microscopy has shown that many tips have defects and have been contaminated before they are even used (Fig. 7).<sup>[17]</sup> These contaminants may include silicone oils from packaging,<sup>[18]</sup> or irregular apices. More commonly, the tip can pick up contamination during imaging.<sup>[17]</sup> The presence of these contaminants, or defects, can change the shape of the image and result in an irregularly shaped image, or a broadening of the image. The presence of contaminants is particularly problematic for AFM applications where the tip is chemically modified because these techniques rely on a clean tip surface.

There are multiple suggestions for cleaning tips before using them. The most common cleaning procedure is to use UV/ozone cleaning.<sup>[18]</sup> This destroys organics on the tip and can be performed easily using an UV/ozone cleaner. Another more rigorous

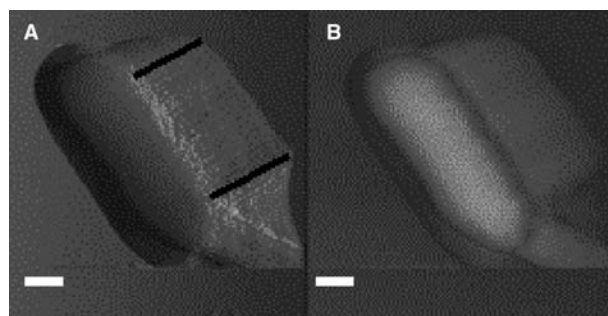


**Fig. 4** Atomic force microscope line artifacts because of the interaction of the side of the tip with a tall surface structure (Fig. 3C). (A) and (B) are tapping-mode amplitude and phase images of 1-mm-high *E. coli*. The white bar represents 1 mm. The vertical scale for the height images is 1 mm. The scan direction is from right to left, with a  $0^\circ$  scan angle. The lines highlighted in black show the artifact, which appears as lines  $\pm 27^\circ$  to the scan direction. The line artifacts appear on the right side of the image because of the tilt of the cantilever relative to the surface. *Source:* ©American Chemical Society.

approach is to soak the tips for 30 min in piranha solution (70:30  $\text{H}_2\text{SO}_4/\text{H}_2\text{O}_2$ ).<sup>[17]</sup> These cleaning procedures ensure only that the tip is clean before it is used, but does not prevent the tip from becoming contaminated during imaging.

One suggestion to test for the cleanliness of the tip during imaging is to measure the force between the tip and a clean surface (such as clean glass or mica) before and after imaging your surface of interest. A change in force indicates a chemical change in the tip.<sup>[17]</sup> Another suggestion is to image the tip via SEM before and after use. Although this is a



Veeco Metrology

**Fig. 5** Multiwall nanotube attached to a silicon tip as an example of a high aspect ratio AFM tip. *Source:* From World Wide Web page at <http://www.veeco.com>, Veeco Instruments, Santa Barbara, CA.

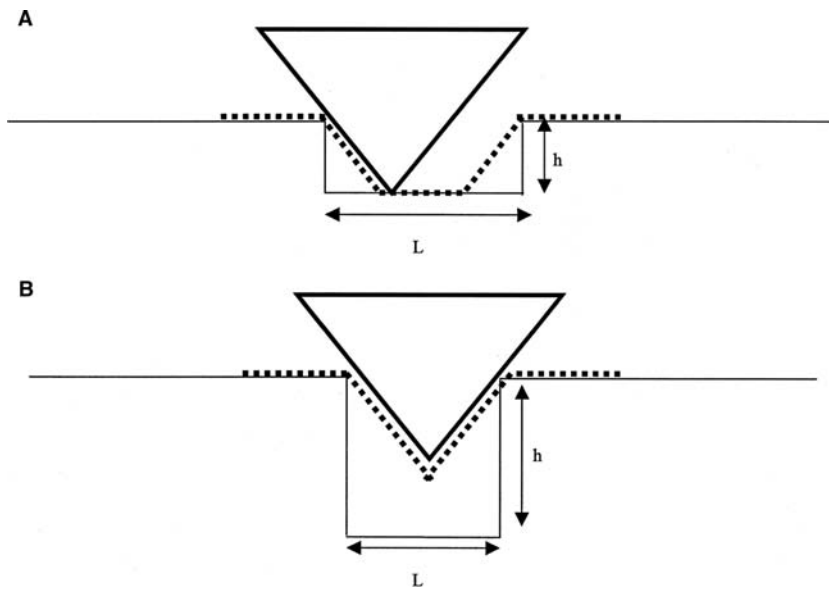


**Fig. 6** Schematic of image artifacts because of imaging a surface structure with a lateral dimension of  $L$  and a depth of  $h$  below the surface. In (A), the tip is not able to image the corner of the structure, whereas in (B), the tip is not able to image the bottom of the structure. The dotted line represents the image produced by the AFM.

time-consuming step, it will identify any contaminant that adheres while imaging.

A tip may become misshapen either during manufacturing of the tip, or during imaging. This effect is

similar to the presence of a contaminant and will result in a strangely shaped image. The new shape of the tip can be identified by using a deconvolution program (discussed above), or by imaging with an SEM.

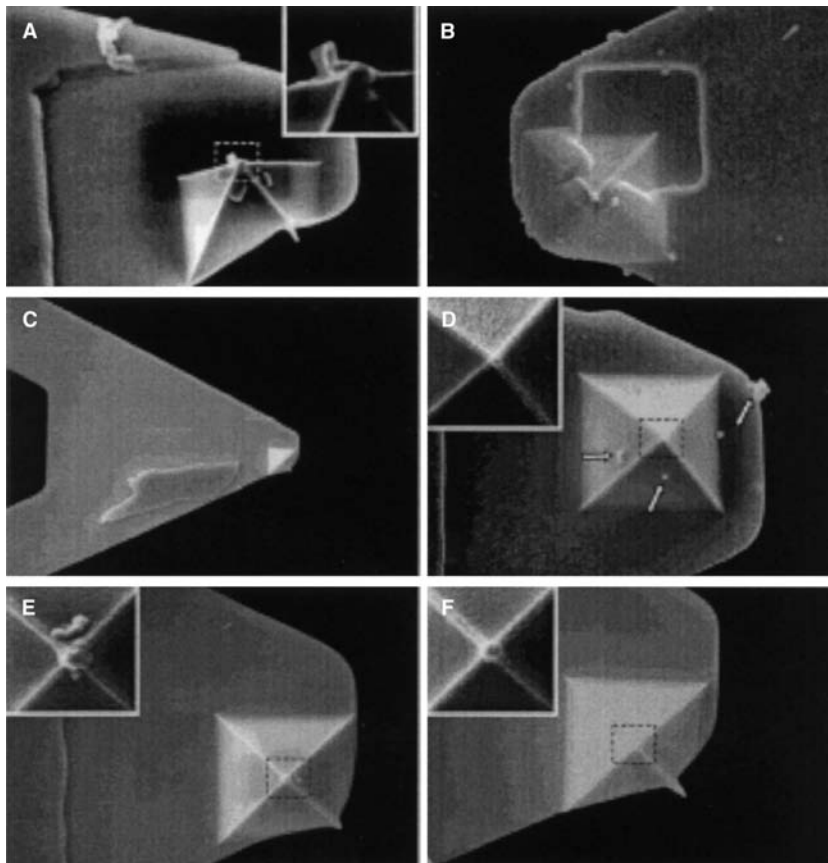


**Fig. 7** Scanning electron micrographs of impurities on AFM tips. (A) Multiple contaminants and imperfections. (B) Cantilever tip located under cantilever coating. (C) Off-centered probe. (D) Unused probe showing particulate contamination with protein-like globules (arrows). (E) Contaminated probe with protein. (F) Used probe showed doubling images. *Source:* ©John Wiley & Sons.

## CHANGING SURFACE STRUCTURES DURING IMAGING

Unlike optical microscopy or electron microscopy, atomic force microscopy uses physical force to image the surface “by feel” and not by electromagnetic radiation or electrons. This mechanical force can often be destructive to the surface itself. Lateral forces because of the rastering of the tip over the surface can cause surface objects to be displaced during imaging, whereas vertical forces can cause indentation of soft surfaces.

### Displacement during Imaging

As the tip is rastered across the surface, there is a lateral force applied to the object being imaged. This lateral force can remove the object from the surface if the object is not adhered strongly to the surface. If the object is removed during imaging, the structure will suddenly disappear from the image. The image may show just part of the surface structure (imaged before it disappears). It is possible to observe this more clearly by first imaging a small area at a high force for some time and then imaging a larger area with a smaller force. The middle of Fig. 8 shows an area that has been imaged for some time. All the particles in this area have been removed because of imaging.<sup>[19]</sup>

The lateral interaction between the tip and the surface can be minimized by imaging with tapping-mode atomic force microscopy instead of contact-mode atomic force microscopy, or by decreasing the amount of force used while imaging. In tapping-mode atomic force microscopy, the tip is not in constant contact with the sample surface. Instead, the tip is vibrated close to the resonance frequency of the AFM probe. When the vibrating tip strikes the surface, some of the energy is absorbed by the surface. This causes a decrease in the vibrational amplitude of the probe. The piezo adjusts the distance between the surface and the tip to maintain constant vibrational amplitude.

Although tapping-mode atomic force microscopy will reduce lateral forces on the surface objects, it is often necessary to take more steps to ensure that the objects are not displaced. One approach is to ensure that the objects are strongly anchored to the surface. This is particularly important for imaging negatively charged objects on a negatively charged surface, which is the case for most biological species on silica or mica. For example, Shibata-Seki et al.<sup>[19]</sup> showed that liposomes can be pushed out of the way at a force  $>4.2$  nN. Similarly, SK-N-SH (human neuroblastoma cells) and AV12 (Syrian hamster cells) can be moved during imaging, especially if they are alone.<sup>[20]</sup>

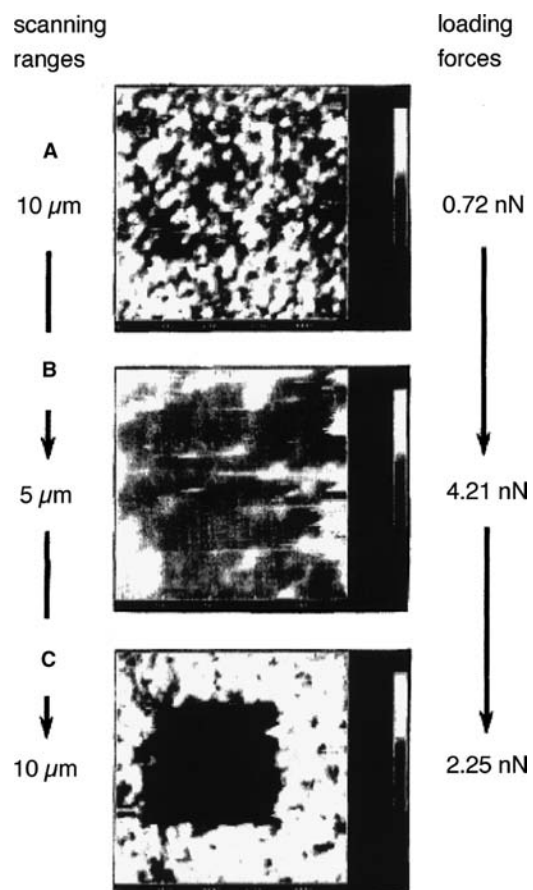


**Fig. 8** Demonstration of AFM artifacts because of high forces. In situ AFM images of liposomes on substrates taken at different load forces over the same region. Images were taken with a standard  $\text{Si}_3\text{N}_4$  cantilever tip (spring constant of  $0.12$  N/m). (A) Load force was approximately  $0.72$  nN. (B) Load force was approximately  $4.2$  nN. (C) Load force was approximately  $2.2$  nN. Source: From Ref.<sup>[19]</sup>; ©Elsevier.

One solution is to modify the surface so that it can covalently bond with the object. This can be accomplished by using amino-silanization<sup>[21,22]</sup> on silica. In this method, silane trimethoxysilyl-propyl-diethylenetriamine functionalizes the glass. The object can then bond to the functionalized surface via an amide bond linkage.

Another solution is to render the surface cationic using a cationic polymer. These polymers include spermine,<sup>[23]</sup> polylysine,<sup>[24]</sup> polyethyleneimine (PEI),<sup>[25,26]</sup> chitosan,<sup>[25]</sup> and diethyl-aminoethyl dextran (DEAE—dextran).<sup>[25]</sup> A complete study of the adhesion of *Escherichia coli* as well as polystyrene spheres via the above surface modification showed that PEI is the most effective adhesion mechanism.<sup>[25]</sup> When using cationic polymers, care should be taken to remove all the non-adhered polymers, as non-adhered polymers may stick to and contaminate the tip during imaging.

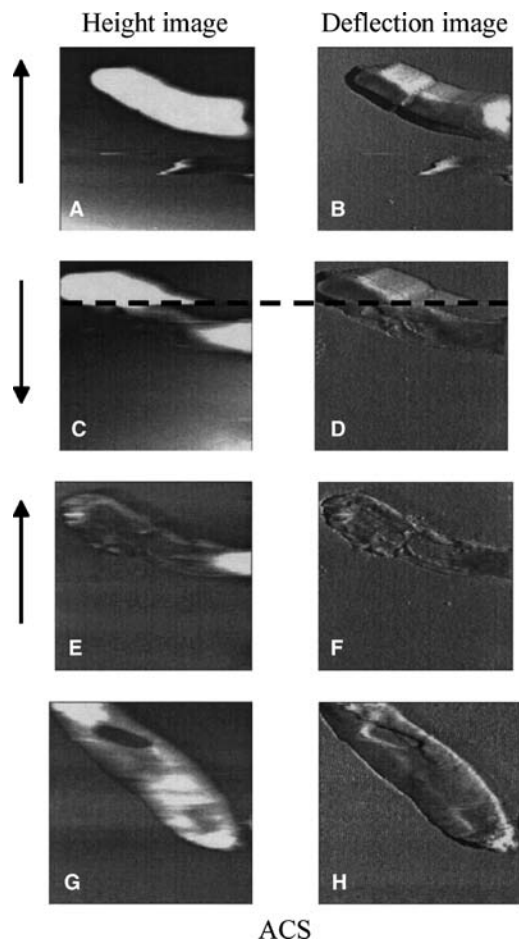


**Fig. 9** Creation of a deflated bacterium because of high vertical forces. (A), (C), (E), and (G) are height images, whereas (B), (D), (F), and (H) are deflection images. The bacterium is deflated in (C) and (D) at the dotted line. A similar deflated bacterium is shown in (G) and (H). *Source:* ©American Chemical Society.

Another option for imaging bacteria is to trap them in holes in a filter to prevent them from moving around.<sup>[27]</sup> You et al.<sup>[20]</sup> showed that bacteria adhered to the surface via cell–EPS interactions or cell–cell

interactions may be strong enough to prevent displacement. Finally, studies on DNA have shown that imaging in air<sup>[23]</sup> or propanol<sup>[28]</sup> prevents water–tip interactions and makes imaging easier.

### Indenting During Imaging

Tips can cause not only lateral forces but also vertical forces that can deform the surface. This is particularly seen on soft surfaces such as polymers, and biomaterials such as bacteria. Fig. 9 shows a bacterium in an aqueous solution being irreversibly “deflated” because of tapping-mode atomic force microscopy imaging. The arrows indicate the direction of scanning.<sup>[6]</sup> At first, the image of the bacterium shows a height of 1 μm (Fig. 9A and B). As scanning continues, the height of the image suddenly decreases, as shown on the top of Fig. 9C and D. Finally, in Fig. 9E and F, the bacterium has been completely deflated. Another deflated bacterium shown in Fig. 9G and H shows a rectangular indent in the top left corner of the image. Other biological species such as tobacco mosaic virus (TMV)<sup>[23]</sup> and human neuroblastoma cells (SK-N-SH)<sup>[20]</sup> have been irreversibly damaged during imaging.

This indentation will occur if the effective spring constant of the object is similar to the spring constant of the cantilever. If the surface is a Hookian elastic material, the deformation, or indentation, of the surface  $i$  and the deflection of the cantilever  $d$  can be expressed by Eq. (1):

$$i = \frac{k_c d}{k_s} \quad (1)$$

where  $k_c$  is the spring constant of the cantilever and  $k_s$  is the spring constant of the surface.

The first step to avoid this indentation is to use tapping-mode atomic force microscopy. However, as shown in Fig. 10, this does not completely eliminate the indentation. Another solution is to use a cantilever

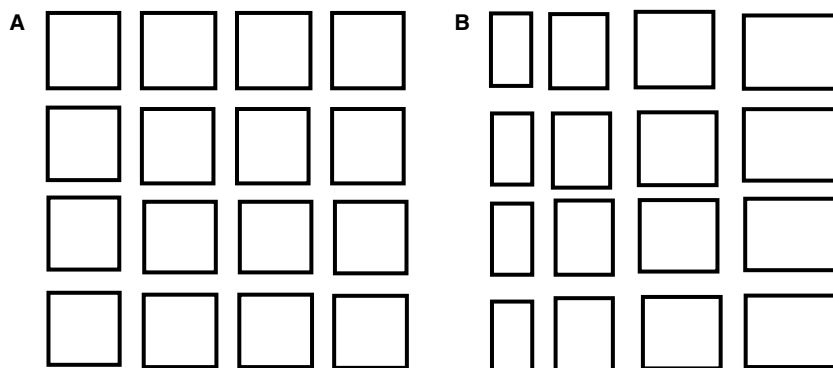


**Fig. 10** Linearity and  $x$ – $y$  calibration of the AFM piezo. (A) Test pattern. (B) Image produced when the piezoelectric scanner is not linear. *Source:* From *Microscopy Today*.

with a smaller spring constant. This will decrease  $k_c$  and decrease  $i$  in Eq. (1) but may also sacrifice some resolution. In both contact-mode atomic force microscopy and tapping-mode atomic force microscopy, it is possible to image with a lower force, which can decrease the indentation.

Finally, in some cases, it may be possible to “stiffen” the surface structure. In the case of biological cells, this can be performed by exposing the cells to glutaraldehyde.<sup>[26,29,30]</sup> This makes imaging easier because the spring constant of the bacteria increases; however, the procedure may render the cells more hydrophobic.<sup>[31]</sup> Another option is to image the soft surface in a media other than water, such as air<sup>[28]</sup> or propanol.<sup>[29,32]</sup> These techniques will provide better images but may not accurately represent the image topography in an aqueous solution.

## SCANNER ARTIFACTS

The scanner head on the AFM can introduce artifacts while imaging. These artifacts result from non-linearity in the horizontal and vertical movements of the scanner, vertical overshoot because of the control system, and scanner drift.

The piezoelectric scanner moves the tip across the surface in both horizontal ( $x$ - $y$ ) and vertical ( $z$ ) planes. It is critical that the scanner is moving linearly with time and that it is calibrated. If the scanner is not moving linearly, features on one side of the image will

appear smaller than the other side (Fig. 10).<sup>[33]</sup> If the scanner is moving linearly but not calibrated, the dimensions in the horizontal dimension will not be accurate. Most AFM packages come with a standard grid that can be used to check the linearity and accuracy of the scanner. Similar compensation software tools can be used to calibrate the scanner in the vertical plane.

Another common artifact because of the scanner is the presence of “shadows” on the opposite side of the direction of scanning (Fig. 11). These shadows are because of hysteresis in the vertical control of the piezoscanner. The scanner overshoots the edge and shows a decrease in height, even in the line profile. Decreasing the scan speed can reduce this effect, whereas reversing the scan direction can reveal the true edge of the object.

The scanner is sensitive to temperature changes. These temperature changes can cause drifts in the scanner and distortions of the image. This most commonly appears at the beginning of a scan of a zoomed-in region of an image (Fig. 12).<sup>[33]</sup> For this reason, an area should be scanned multiple times to make sure there are no changes.

## ELECTRONIC ARTIFACTS

While imaging with the AFM, it is important that the equipment is isolated from external vibrations. These can include acoustic vibrations from sound or

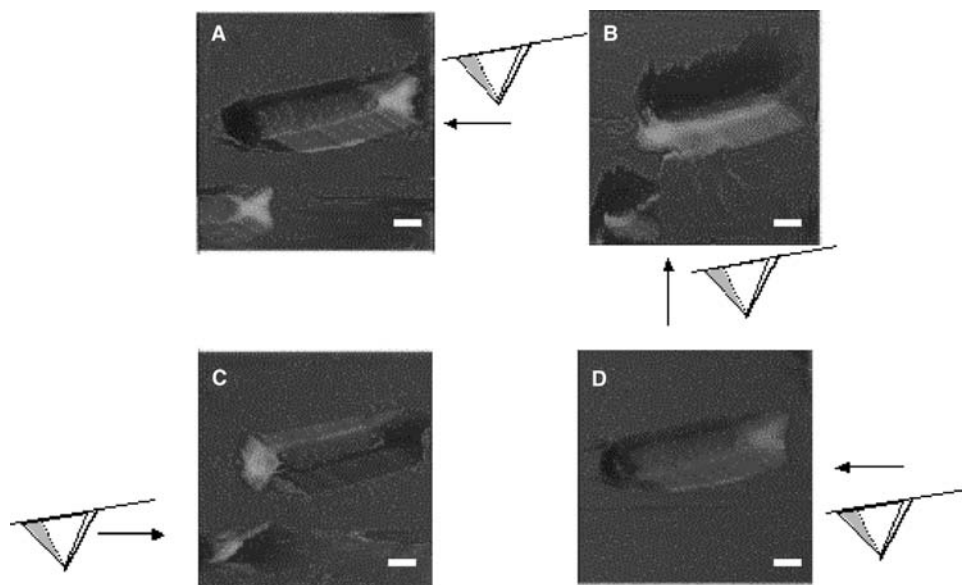


**Fig. 11** Tapping-mode atomic force microscopy images of *E. coli* bacteria with a scan angle of 0° (A), 180° (B), and 90° (C). In (D), the scan angle is 180° and the tip direction is from left to right. The dark spots of the image are always on the back side of the scanning probe direction. This is because of an overshoot in the feedback control system. *Source:* ©American Chemical Society.

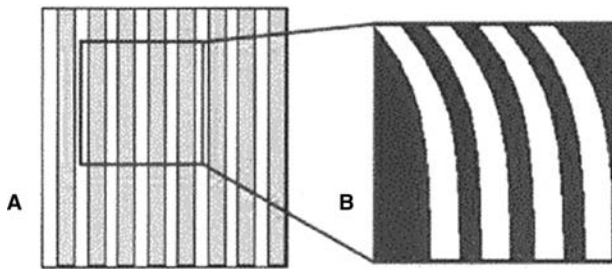


**Fig. 12** Artifact caused by scanner drift. (B) A zoomed-in area of (A). The pattern is distorted because of scanner drift. Source: From *Microscopy Today*.

mechanical vibrations of the floor. These artifacts typically appear as periodic patterns in the image. The equipment can be isolated from the room by using an isolation table, or by suspending the apparatus from a tripod.

Electronic noise can also cause periodic patterns in the image. If the gains of the control system are set too high, the system control system will become unstable. Reducing the gains can eliminate this problem. Similar effects can be observed with faulty electronics.

## USING ARTIFACTS TO YOUR ADVANTAGE

Although the artifacts discussed should be avoided to obtain the most accurate image possible, the identification of many of these artifacts has led to breakthroughs in new ways of using the AFM. These breakthroughs include nanomanipulation and nanoindentation.

Although it is often not desired to move the object to be imaged, researchers have recently taken advantage of the interaction between the tip and the objects on the surface to manipulate surface objects. The ability of the AFM tip to move with angstrom-level precision makes it ideal for nanomanipulation. The surface can be imaged using weak attractive forces. The tip can then be brought into stronger contact with individual objects to manipulate them.<sup>[34]</sup> This technique has been used to build two-dimensional and three-dimensional structures of nanoparticles,<sup>[34,35]</sup> as well as to manipulate biomolecules such as DNA and proteins.<sup>[36–38]</sup>

Researchers have also taken advantage of vertical forces applied during imaging using the AFM for nanoindentation. Nanoindentation allows measurements of mechanical properties of various surfaces including polymers surfaces<sup>[39–42]</sup> and biological surfaces.<sup>[8,21,26,43–46]</sup> For polymeric surfaces, the indentations

made with a high spring constant cantilever (100–300 N/m) made at various forces are imaged via tapping mode. The depth of the indentations is used to determine the spring constant of the surface according to Eq. (1). For more elastic surfaces, such as biological surfaces, the mechanical properties of the surface can be determined by analyzing the AFM force curves.<sup>[8,21,26,43–46]</sup>

## CONCLUSION

The AFM is a powerful tool for imaging surfaces. With proper care, accurate images can be obtained and can provide important quantitative information about surfaces on the nanometer scale. However, it is imperative that researchers using this tool are aware of the many artifacts that can be present in the created images. These artifacts may be because of the shape and size of the AFM tip, the lateral or vertical interaction between the tip and the surface, or the electronics of the AFM system. Once aware of these artifacts, corrections can be made to create more accurate images of the surface structures of interest.

## REFERENCES

1. Binnig, G.; Quate, C.F. Atomic force microscopy. *Phys. Rev. Lett.* **1986**, *56*, 930–933.
2. Louder, D.R.; Parkinson, B.A. Scanning probe microscopy. *Anal. Chem.* **1994**, *66* (12), 84R–105R.
3. Westra, K.L.; Thomson, D.J. *J. Vac. Sci. Technol., B* **1994**, *12*, 3176.
4. Dongmo, S.; Troyon, M.; Vautrot, P.; Delain, E.; Bonnet, N. Blind reconstruction method of scanning tunneling and atomic force microscopy images. *J. Vac. Sci. Technol., B* **1996**, *14* (2), 1552.
5. Thundat, T.; Zheng, X.-Y.; Sharp, S.L.; Allison, D.P.; Warmack, R.J.; Joy, D.C.; Ferrell, T.L. Calibration of atomic force microscope tips using biomolecules. *Scanning Microsc.* **1992**, *6* (4), 903–910.
6. Velegol, S.B.; Pardi, S.T.; Li, X.; Velegol, D.; Logan, B.E. AFM imaging artifacts due to bacterial cell height and AFM tip geometry. *Langmuir* **2003**, *19* (3), 851–857.
7. Boonaert, C.J.P.; Rouxhet, P.G.; Dufrene, Y.F. Surface properties of microbial cells probed at the nanometre scale with atomic force microscopy. *Surf. Interface Anal.* **2000**, *30*, 32–35.
8. Braet, F.; Rotsch, C.; Wisse, E.; Radmacher, M. Comparison of fixed and living liver endothelial cells by atomic force microscopy. *Appl. Phys., A Mater. Sci. Process.* **1998**, *66*, S575–S578.
9. Chen, Y.J.; Wilson, I.H.; Lee, C.S.; Xu, J.B.; Yu, M.L. Tip artifacts in atomic force microscope imaging of

- ion bombarded nanostructures on germanium surfaces. *J. Appl. Phys.* **1997**, *82* (11), 5859.
10. Odin, C.; Aime, J.P.; El Kaakour, Z.; Bouhacina, T. Tip's finite size effects of atomic force microscopy in the contact mode: Simple geometrical considerations for rapid estimation of apex radius and tip angle based on the study of polystyrene latex balls. *Surf. Sci.* **1994**, *317*, 321–340.
  11. Wilson, D.L.; Dalal, P.; Kump, K.S.; Benard, W.; Xue, P.; Marchant, R.E.; Eppell, S.J. *J. Vac. Sci. Technol., B* **1996**, *4* (14), 2407.
  12. Markiewicz, P.; Goh, M.C. Simulation of atomic force microscope tip-sample/sample-tip reconstruction. *J. Vac. Sci. Technol., B* **1995**, *13* (3), 1115.
  13. Markiewicz, P.; Goh, M.C. Atomic force microscope tip convolution using calibration arrays. *Rev. Sci. Instrum.* **1995**, *66* (5), 3186.
  14. Keller, D.J.; Franke, F.S. Envelope reconstruction of probe microscope images. *Surf. Sci.* **1993**, *294*, 409–419.
  15. Neto, C.; Craig, V.S.J. *Langmuir* **2001**, *17*, 2097–2099.
  16. Williams, P.M.; Shakesheff, K.M.; Davies, M.C.; Jackson, D.E.; Roberts, C.J.; Tendler, S.J.B. Blind reconstruction of scanning probe image data. *J. Vac. Sci. Technol., B* **1995**, *14* (2), 1557.
  17. Taatjes, D.J.; Quinn, A.S.; Lewis, M.R.; Bovill, E.G. Quality assessment of atomic force microscopy probes by scanning electron microscopy probes by scanning electron microscopy: Correlation of tip structure with rendered images. *Microsc. Res. Tech.* **1999**, *44*, 312–326.
  18. Lo, Y.-S.; Huefner, N.D.; Chan, W.S.; Dryden, P.; Hagenhoff, B.; Beebe, T.P. Organic and inorganic contamination on commercial AFM cantilevers. *Langmuir* **1999**, *15*, 6522–6526.
  19. Shibata-Seki, T.; Masai, J.; Tagawa, T.; Sorin, T.; Kondo, S. In-situ atomic force microscopy study of lipid vesicles adsorbed on a substrate. *Thin Solid Films* **1996**, *273*, 297–303.
  20. You, H.X.; Lau, J.M.; Xhang, S.; Yu, L. Atomic force microscopy imaging of living cells: A preliminary study of the disruptive effect of the cantilever tip on cell morphology. *Ultramicroscopy* **2000**, *82*, 297–305.
  21. Arnoldi, M.; Kacher, C.M.; Bauerlein, E.; Radmacher, M.; Fritz, M. Elastic properties of the cell wall of *Magnetospirillum gryphiswaldense* investigated by atomic force microscopy. *Appl. Phys., A* **1998**, *66*, S613–S617.
  22. Camesano, T.A.; Logan, B.E. Probing bacterial electrostatic interactions using atomic force microscopy. *Environ. Sci. Technol.* **2000**, *34*, 3354–3362.
  23. Vesenka, J.; Manne, S.; Giberson, R.; Marsh, T.; Henderson, E. Colloidal gold particles as an incompressible atomic force microscope imaging standard for assessing the compressibility of biomolecules. *Biophys. J.* **1993**, *65*, 995–997.
  24. Bolshakova, A.V.; Kiselyova, O.I.; Filonov, A.S.; Frolova, O.Y.; Lyubchenko, Y.L.; Yaminsky, I.V. Comparative studies of bacteria with an atomic force microscopy operating in different modes. *Ultramicroscopy* **2001**, *86*, 121–128.
  25. Pardi, S.T. Investigation of Bacterial Extracellular Polymeric Substances Utilizing an Atomic Force Microscope with a Newly Developed Deflection Curve Acquisition and Analysis Protocol. In *Civil and Environmental Engineering*; Pennsylvania State University: University Park, PA, 2002.
  26. Velegol, S.B.; Logan, B.E. Contribution of bacterial surface polymers, electrostatics and cell elasticity to the shape of AFM force curves. *Langmuir* **2002**, *18*, 5256–5262.
  27. Kasas, S.; Ikai, A. A method for anchoring round shaped cells for atomic force microscope imaging. *Biophys. J.* **1995**, *68*, 1678–1680.
  28. Hansma, H.G.; Laney, D.E.; Bezanilla, M.; Sinsheimer, R.L.; Hansma, P.K. Applications for atomic force microscopy of DNA. *Biophys. J.* **1995**, *68*, 1672–1677.
  29. Radmacher, M.; Fritz, M.; Hansma, P.K. Imaging soft surfaces with the atomic force microscope: Gelatin in water and propanol. *Biophys. J.* **1995**, *69*, 264–270.
  30. Razatos, A.; Ong, Y.-L.; Sharma, M.M.; Georgiou, G. Molecular determinants of bacterial adhesion monitored by atomic force microscopy. *Proc. Natl. Acad. Sci. U.S.A.* **1998**, *95*, 11059–11064.
  31. Bowen, W.R.; Lovitt, R.W.; Wright, C.J. Atomic force microscopy of the adhesion of *Saccharomyces cerevisiae*. *J. Colloid Interface Sci.* **2001**, *237*, 54–61.
  32. Amro, N.A.; Kotra, L.P.; Wadu-Mesthrige, K.; Bulychew, A.; Mobashery, S.; Lui, G.-y. High-resolution atomic force microscopy studies of *Escherichia coli* outer membrane: Structural basis for permeability. *Langmuir* **2000**, *16*, 2789–2796.
  33. West, P.; Starostina, N. How to recognize and avoid AFM image artifacts. *Microsc. Today* May/June **2003**, 20–24.
  34. Junno, T.; Deppert, K.; Montelius, L.; Samuelson, L. Controlled manipulation of nanoparticles with an atomic force microscope. *Appl. Phys. Lett.* **1995**, *66* (26), 3627–3629.
  35. Resch, R.; Baur, C.; Bugacov, A.; Koel, B.E.; Madhukar, A.; Requicha, A.A.G.; Will, P. Building and manipulating three-dimensional and linked two-dimensional structures of nanoparticles using scanning force microscopy. *Langmuir* **1998**, *14* (23), 6613–6616.
  36. Wadu-Mesthrige, K.; Amro, N.A.; Garno, J.C.; Xu, S.; Liu, G.-y. Fabrication of nanometer-sized protein patterns using atomic force microscopy and selective immobilization. *Biophys. J.* **2001**, *80*, 1891–1899.
  37. Agarwal, G.; Sowards, L.A.; Naik, R.R.; Stone, M.O. Dip-pen nanolithography in tapping mode. *J. Am. Chem. Soc.* **2003**, *125*, 580–583.
  38. Bruckbauer, A.; Ying, L.; Rothery, A.M.; Zhou, D.; Shevchuk, A.I.; Abell, C.; Korchev, Y.E.; Klenerman, D. Writing with DNA and protein using a nanopipet for controlled delivery. *J. Am. Chem. Soc.* **2002**, *124*, 8810–8811.
  39. Cleveland, J.P.; Manne, S.; Bocek, D.; Hansma, P.K. *Rev. Sci. Instrum.* **1993**, *64*, 403–405.
  40. VanLandingham, M.R.; McKnight, S.H.; Palmese, G.R.; Elings, J.R.; Huang, X.; Bogetti, T.A.; Eduljee, R.F.; Gillespie, J.W. Nanoscale indentation of polymer systems using the atomic force microscope. *J. Adhes.* **1997**, *64* (1–4), 31–59.



41. VanLandingham, M.R.; Villarrubia, J.S.; Guthrie, J.S.; Meyers, G.F. Nanoindentation of polymers: An overview. *Macromol. Symp.* **2001**, *167*, 15–43.
42. Du, B.Y.; Tsui, O.K.C.; Zhang, Q.L.; He, T.B. Study of elastic modulus, yield strength of polymer thin films using atomic force microscopy. *Langmuir* **2001**, *17* (11), 3286–3291.
43. Arnoldi, M.; Fritz, M.; Bauerlein, E.; Radmacher, M.; Sackmann, E.; Boulbitch, A. Bacterial turgor pressure can be measured by atomic force microscopy. *Phys. Rev., E* **2000**, *62* (1), 1034–1044.
44. A-Hassan, E.; Hienz, W.F.; Antonik, M.D.; D'Costa, N.P.; Nageswaran, S.; Schoenenberger, C.-A.; Hoh, J.H. Relative microelastic mapping of living cells by atomic force microscopy. *Biophys. J.* **1998**, *74*, 1564–1578.
45. Boulbitch, A.; Quinn, B.; Pink, d. Elasticity of rod-shaped gram negative eubacteria. *Phys. Rev. Lett.* **2000**, *85* (24), 5246–5249.
46. Hoh, J.H.; Schoenenberger, C.-A. Surface morphology and mechanical properties of MDCK monolayers by atomic force microscopy. *J. Cell Sci.* **1994**, *107*, 1105–1114.

# AFM: Imaging and Force Spectroscopy on Cell Surfaces

Yves F. Dufrêne

*Unite de Chimie des Interface, Université catholique de Louvain, Louvain-la-Neuve, Belgium*

## INTRODUCTION

Characterization of the structural and physical properties of microbial cell surfaces is a continuously expanding field of microbiology.<sup>[1–10]</sup> Studying cell surfaces is important not only in basic research to elucidate their functions (cell shape, protection, molecular sieve, molecular recognition, cell adhesion, and cell aggregation), but also in medicine (fouling of implants, microbial infections) and biotechnology (cellular interactions in fermentation technology, removal of heavy metals). Electron microscopy has long been the technique of choice for probing cell surface structure down to the molecular level.<sup>[1,2,4,6,7]</sup> Yet the requirement of vacuum conditions may raise the question of whether the information obtained is always relevant to the real, hydrated state. In parallel, a variety of approaches have been developed to probe the cell surface physical properties, including chemical analysis of wall constituents, specific binding studies, selective degradation by enzymes, cell wall mutants, modifications by antibiotics, and surface analysis using various physical techniques.<sup>[1,4,5,10]</sup> Many of these techniques provide averaged information obtained on a large ensemble of cells; that is, they are not suited for mapping the nanoscale distribution of physical properties on individual cells.

Since the late 1980s, atomic force microscopy (AFM)<sup>[11]</sup> has been increasingly used in biology and it is now established as a versatile tool to address the structure, properties, and functions of biological structures, going from single molecules to lipid membranes and living cells.<sup>[12–17]</sup> Basically, AFM offers two main advantages over conventional microscopy techniques. First, it provides images of the specimen with nanometer (subnanometer) resolution, in real-time and under physiological conditions. Second, because the instrument works by sensing the force between a very sharp tip and the sample surface, this principle can be exploited to measure molecular interactions and physical properties on a local scale. These capabilities provide a range of novel opportunities in microbiology.<sup>[18]</sup> For example, the following questions can

now be addressed with AFM. Does the surface nanostructure of untreated living cells correlate with that observed by electron microscopy? How does surface structure change with time during dynamic processes such as cell growth and cell division? How do external agents such as enzymes and antibiotics affect the cell surface architecture? Do surface properties such as hydrophobicity, charge, and elasticity vary across the surface of a single cell? What are the intermolecular forces involved in molecular recognition and cellular interactions? What is the elasticity of single-cell surface macromolecules? The intent of this article is to survey recent achievements brought by AFM in microbiology, particularly emphasizing studies on whole cells. Rather than providing an exhaustive review of the literature in the area, the paper discusses imaging and force spectroscopy applications using a selection of recent data.

## IMAGING

### Image Recording and Sample Preparation

Atomic force microscopy images are created by raster-scanning a sharp tip across the sample, while sensing the force experienced by the tip. To this end, the sample is mounted on a piezoelectric scanner that ensures three-dimensional positioning with high resolution. The force is monitored by attaching the tip to a soft cantilever and by measuring the bending or “deflection” of the cantilever. The larger the cantilever deflection, the higher the force that will be experienced by the tip. Nowadays, most instruments use an optical method to measure the cantilever deflection with high resolution. A laser beam is focused on the free end of the cantilever and the position of the reflected beam is detected by a position-sensitive photodiode.

In contact mode, the most common imaging mode, images can be acquired in two ways, i.e., either in the constant-height mode in which the cantilever deflection is recorded while the sample is horizontally scanned, or in the constant-deflection mode in which the sample height is adjusted to keep the deflection of the

cantilever constant using a feedback loop. In the latter case, the feedback output can be used to display a true height image, which gives calibrated height information about the sample morphology. Alternatively, the error signal can also be employed to generate a so-called deflection image that does not provide quantitative height information but is more sensitive to fine surface details. Besides contact mode, several other imaging modes have been developed. Among these, tapping mode atomic force microscopy in which the tip is oscillated at a given frequency is very useful for imaging soft samples.

After the first AFM images of biological structures were published, it was soon realized that a crucial factor for successful imaging is specimen preparation. This led to the development of a number of immobilization methods. For single molecules, two-dimensional protein crystals, lipid membranes, and animal cells, immobilization protocols are generally based on physical adsorption onto flat substrates such as mica, glass, and silicon oxide (for a detailed description of these procedures, see Ref. [19]). However, for microbial cells, sample preparation is often challenging because of the cell geometry. Indeed, a microbial cell must be viewed as a fairly rigid spherical or rod-like particle of 1–5  $\mu\text{m}$  size. This geometry usually leads to a very small cell–substrate contact area and therefore to cell detachment by the scanning tip. Presumably, this is the main reason why the potential of AFM in cellular microbiology had been neglected in the early age. However, the past few years have seen tremendous progress in the application of AFM to microbiological specimens owing to improvements in imaging conditions and sample immobilization procedures.

The selection of an appropriate imaging environment is critical for high-resolution imaging because it directly influences the force acting between tip and sample. In air, high-resolution imaging is often difficult as a result of strong adhesion forces resulting from the presence of a water layer on both tip and sample. This problem is eliminated when imaging in aqueous solution, which is actually the most relevant environment for microbiological specimens. By selecting appropriate buffer conditions (nature of electrolytes, ionic strength, pH), it is generally possible to maintain a very low applied force, typically in the range of 0.1–0.5 nN.<sup>[20]</sup> Hence it is certainly very useful to investigate the effect of salt composition, pH, and ionic strength on the image quality when high resolution is desired.

### Imaging of Living Cells

By combining high spatial resolution with the possibility to work in liquids, AFM enables researchers to

visualize the surface morphology of untreated living cells, thus providing information that is complementary to data obtained with classical microscopy techniques. As mentioned above, an important requirement is that the cells must be firmly attached to a solid substrate. This can be achieved by mechanically trapping the cells into a porous polymer membrane. Fig. 1 presents a three-dimensional height image showing a single *Saccharomyces cerevisiae* cell protruding from a pore of a polymer membrane. In these conditions, images could be repeatedly obtained in aqueous solution without detaching the cell or altering the surface morphology. Generally, the entire cell surface was very smooth, an observation that was consistent with previous chemical and electron microscopy studies. However, some cells showed circular protrusions, about 1  $\mu\text{m}$  in diameter, which reflected the bud scars left on the surface after cell division.<sup>[21]</sup>

Provided that the cell is well attached, it is possible to acquire high-resolution images at different locations. For *S. cerevisiae*, topographic images were recorded to a lateral resolution of 2 nm, without significant modification of the surface morphology. The surface roughness (on  $250 \times 250 \text{ nm}$  areas) was found to be smaller than 1 nm.<sup>[21]</sup> Interestingly, a very different surface architecture was observed for fungal spores. Fig. 2A shows that the surface of *Aspergillus oryzae* spores was covered by a layer of regularly arranged nanostructures, referred to as rodlets, that were several hundred nanometers in length and had a periodicity of 10 nm.<sup>[22]</sup> Presumably, these crystalline-like nanostructures play an important role in determining the biological functions of the spore (i.e., dispersion, protection).

Accordingly, AFM is a valuable technique for probing the surface architecture of native microbial cells. However, researchers must realize that high-resolution

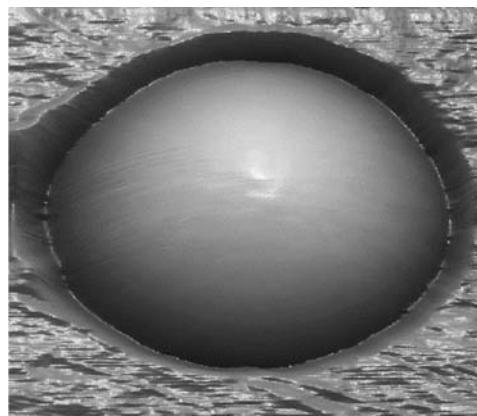


**Fig. 1** Atomic force microscopy height image ( $6 \times 6 \mu\text{m}$ ;  $z$  range: 1  $\mu\text{m}$ ) of a living *S. cerevisiae* cell immobilized in a porous polymer membrane.

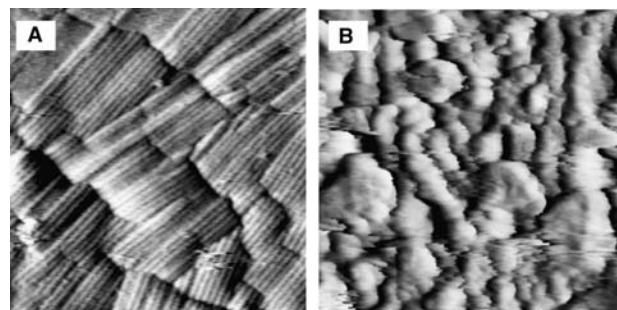


**Fig. 2** High-resolution deflection images acquired under water for the surface of *A. oryzae* spores: (A) dormant spore ( $500 \times 500$  nm); (B) spore after  $\sim 10$  h of germination ( $1 \times 1 \mu\text{m}$ ). *Source:* From Ref.<sup>[22]</sup>. © 2001 American Chemical Society.

imaging often remains difficult, especially for bacterial surfaces. A first source of problems is related to sample softness. The above images were obtained on cells that possess thick, mechanically strong cell walls. In comparison, bacterial walls are thinner and more fragile, meaning that imaging may be destructive, especially in contact mode. For instance, the image contrast obtained for the surface of *Lactococcus lactis* was dominated by tip-sample interactions; that is, grooves oriented along the scanning direction were created by the scanning tip.<sup>[23]</sup> For some bacteria, the presence of flexible, loosely bound macromolecules or appendages at the surface may further limit the image resolution. The immobilization procedure may also be an issue. The porous membrane approach described here is only suited for spherical cells, indicating that alternative strategies must be used for other geometries. Consequently, further developments are necessary (non-destructive dynamic imaging modes, novel immobilization procedures) before researchers can achieve molecular resolution and perhaps monitor molecular conformational changes as is already the case with isolated cell surface layers made of two-dimensional protein crystals.<sup>[14]</sup>

### Following Dynamic Processes

Of particular interest is the possibility to study the changes of cell surface structure associated with dynamic processes such as cell growth and germination. An example of this is the germination of fungal spores. For *A. oryzae* spores,<sup>[22]</sup> high-resolution images revealed that dramatic changes of the surface morphology occurred upon germination, the rodlet layer (Fig. 2A) changing into a layer of soft material (Fig. 2B). On close examination, this material showed streaks oriented in the scanning direction, suggesting

that soft, loosely bound material was interacting with the scanning tip. These direct observations were in good agreement with previous structural and chemical studies showing that germination results in the disruption of the proteinaceous rodlet layer and reveals inner spore walls that are rich in polysaccharides. As we shall see below, morphological changes were directly correlated with profound modifications of molecular interactions as measured by force spectroscopy.

Real-time imaging also enables to follow the progressive effect of external agents such as solvents, ions, chemicals, enzymes, and antibiotics on the cell surface. In this context, the surface morphology of yeast cells was investigated at fixed time intervals following addition of protease and amyloglucosidase solutions.<sup>[21]</sup> Progressive changes of the cell surface topography were clearly observed after protease addition (Fig. 3). With time, the surface became eroded and showed large depressions, about 500 nm in diameter, surrounded by protruding edges, about 50 nm in height (estimated from height images). By contrast, no modification of the cell surface was noted upon addition of amyloglucosidase, which was consistent with the cell wall biochemical composition. These real-time experiments have a strong potential in cell wall enzyme digestion studies as well as in medicine, where they may be used to investigate the effect of antibiotics on microbial cell walls.

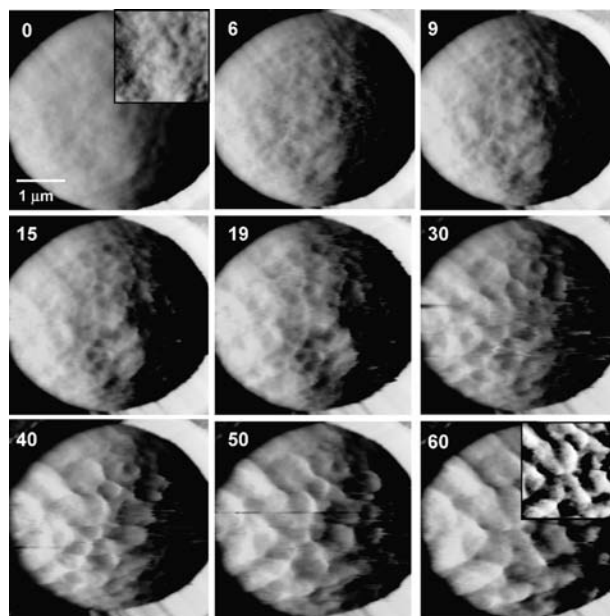


**Fig. 3** Series of deflection images ( $4.2 \times 4.2 \mu\text{m}$ ; insets:  $2.5 \times 2.5 \mu\text{m}$ ) recorded in real time for a single *S. cerevisiae* cell prior to and after contact with a protease solution for 6, 9, 15, 19, 30, 40, 50, and 60 min. *Source:* From Ref.<sup>[21]</sup>. © 2003 John Wiley & Sons, Inc.

## FORCE SPECTROSCOPY

### Principle of Force Spectroscopy

The basic idea behind force spectroscopy is that rather than scanning the tip in the  $x$  and  $y$  directions, the cantilever deflection is recorded as a function of the vertical displacement of the sample, i.e., as the sample is pushed toward the tip and retracted from it. Using appropriate corrections, the raw voltage vs. displacement curve is converted into a force vs. distance curve, which then enables the measurement of molecular interactions and physical properties.<sup>[24,25]</sup> Interestingly, spatially resolved information can be obtained by recording a so-called “force–volume image” consisting of arrays of force–distance curves.<sup>[25]</sup>

A typical force–distance curve obtained for a non-deformable surface in liquid is shown in Fig. 4. When the tip is far away from the sample surface, there is no force acting on the tip and the cantilever is not deflected (label 1). As the tip approaches the surface, the cantilever may bend upward as a result of repulsive forces (label 2) until the tip jumps into contact when the gradient of attractive forces exceeds the spring constant plus the gradient of repulsive forces (label 3). When the force is increased in the contact region, different behaviors may be observed depending on the sample stiffness. On a hard, nondeformable surface, the plot is a vertical line (label 3), while on a soft surface, elastic indentation will occur, leading to a different shape. In the latter case, analyzing the in-contact part of the curve with appropriate theoretical models enables quantitative determination of the sample elasticity. Upon retracting the tip from the surface, the curve often shows a hysteresis referred to as the adhesion “pull-off” force (label 4), which can be used to estimate the surface energy of solids or the binding forces between complementary biomolecules. In the presence of long, flexible macromolecules, elongation

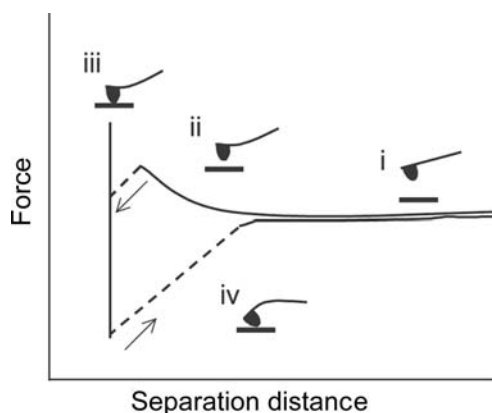


**Fig. 4** Example of force–distance curve (see text for details).

forces usually develop nonlinearly as a result of the deformation of the molecules. In this case, it is common to present the force curve as the positive pulling force vs. extension. Theoretical models from statistical mechanics enable the elasticity of the molecules to be deduced from the force–extension profile. In the next sections, the various applications offered by force spectroscopy in microbial cell surface research are surveyed.

### Spatially Resolved Force Spectroscopy

The microbial surface is rarely of homogeneous composition, but is rather made of a complex mixture of macromolecules. As a result, a single cell can show important lateral variations of physical properties. Until recently, such local variations of properties were very difficult to measure, especially on hydrated, living cells. With spatially resolved force spectroscopy, it is possible to map the distribution of parameters such as adhesion and elasticity at the subcellular level.<sup>[25]</sup> The power of this approach is illustrated in Fig. 5. During cell growth, disruption of cell wall layers may

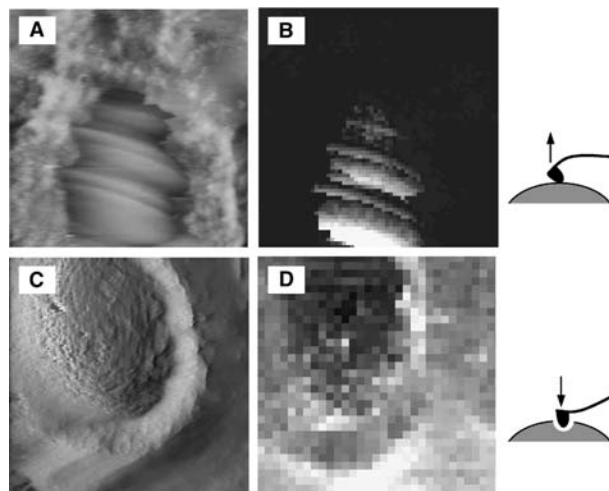


**Fig. 5** Mapping adhesion forces and cell wall elasticity using spatially resolved force spectroscopy. (A) Deflection image ( $2 \times 2 \mu\text{m}$ ) and (B) adhesion map ( $z$  range = 10 nN) acquired on the same area of a germinating spore of *P. chrysosporium*; the adhesion map was obtained by recording  $64 \times 64$  force–distance curves, calculating the adhesion force for each force curve, and displaying adhesion force values as grey levels (brighter contrast means larger adhesion forces). (C) Deflection image ( $1.5 \times 1.5 \mu\text{m}$ ) and (D) force map obtained for a *S. cerevisiae* cell after cell division; the force map, qualitatively reflecting the sample mechanical properties, was generated by recording  $32 \times 32$  force–distance curves and taking a slice of the force volume at a given sample height in the contact region of the curves (brighter contrast means softer properties).

occur and newly formed material may accumulate in localized regions, leading to heterogeneous surface properties. For germinating spores of *Phanerochaete chrysosporium*,<sup>[26]</sup> the heterogeneous surface morphology (Fig. 5A) was directly correlated with differences in adhesion forces (Fig. 5B). The strong adhesion forces measured on localized zones were suggested to be responsible for cell aggregation observed during germination.

Another example of surface physical heterogeneity is found in yeast during budding. While chitin is usually not found in the cell walls of *S. cerevisiae*, it accumulates in the very localized region of the wall involved in budding where it may act as a stiffening agent. In this context, force–volume images were recently recorded in parallel with topographic images on the surface of budding yeast cells.<sup>[27]</sup> In Fig. 5C,D, it can be seen that the force map was highly contrasted, the bud scar region being clearly darker compared to the surrounding cell surface. These data indicated that the bud scar was qualitatively stiffer than the surrounding cell wall, a finding that was further supported by theoretical treatment of the force curves (see next section).

### Elasticity of Cell Walls

The mechanical properties of microbial layers can be addressed on a local scale using AFM force measurements. A first approach consists in pressing isolated cell wall material into a groove in a solid surface with the AFM tip and then deducing the elastic modulus from the applied force vs. depression distance curve. In a pioneering study, this “depression technique” was used to measure the elastic modulus of the sheath of the archeon *Methanospirillum hungatei* GP1.<sup>[28]</sup> The large modulus values (20–40 GPa) indicated that this single-layered structure of unusual strength could withstand an internal pressure of 400 atm. For murein sacculi of Gram-negative bacteria in the hydrated state, elastic moduli of 25 MPa were measured, which are in excellent agreement with theoretical calculation of the elasticity of the peptidoglycan network.<sup>[29]</sup>

For whole cells, quantitative information on sample elasticity is obtained by converting force curves into force vs. indentation curves and analyzing them with theoretical models.<sup>[30]</sup> Using this “nanoindentation method,” the wall compressibility of whole *Magneto-spirillum gryphiswaldense* cells was determined to be about 42 mN/m.<sup>[31]</sup> Interestingly, local nanoindentation measurements on *S. cerevisiae* revealed significant variation of elasticity across the cell surface: Young’s modulus was 6 MPa on the bud scar and 0.6 MPa on the surrounding cell surface.<sup>[27]</sup> These measurements provided the first direct evidence that the chitinous

bud scar in yeast is about 10 times stiffer than the surrounding nonchitinous cell wall.

### Chemically Functionalized Tips

Because commercial AFM tips usually have a poorly defined surface chemistry, they are not suited for quantitative surface force measurements. Tips of well-defined chemical composition can be created by functionalizing the surface with organic monolayers (alkanethiols or silanes) terminated by specific functional groups.<sup>[32]</sup> In doing so, researchers can measure local surface forces and physicochemical properties such as surface charge and surface hydrophobicity. Ahimou et al.<sup>[33]</sup> used AFM tips functionalized with ionizable carboxyl groups (COO<sup>-</sup>/COOH) to probe the surface charges of *S. cerevisiae* at the nanometer level (Fig. 6). Force–distance curves were strongly influenced by pH: While no adhesion was measured at neutral/alkaline pH, multiple adhesion forces were recorded at acidic pH. Adhesion maps always showed fairly homogeneous contrast, indicating that the cell surface properties were homogeneous. The change of adhesion forces as a function of pH was interpreted as resulting from a change of cell surface electrostatic properties, a claim that was supported by the correlation obtained between the AFM titration curve constructed by plotting the adhesion force vs. pH

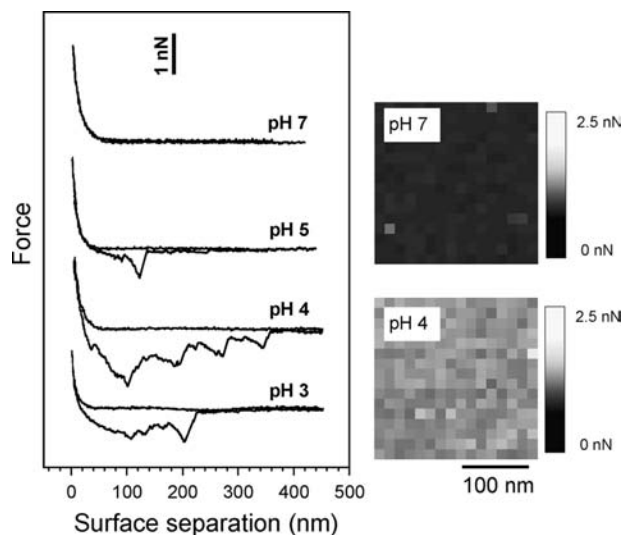


**Fig. 6** Use of chemically functionalized tips for mapping cell surface charges. The left panel presents force–distance curves recorded in solutions of varying pH between the surface of *S. cerevisiae* and an AFM tip functionalized with carboxyl groups. The right panel shows adhesion force maps recorded at pH 7 and pH 4. The differences in adhesion forces observed with pH were related to a change of ionization state of the cell surface. Source: From Ref.<sup>[33]</sup>. © 2002 American Chemical Society.

and the electrophoretic mobility vs. pH curve obtained by classical microelectrophoresis. Using a similar approach, it has been shown that hydrophilic (OH) and hydrophobic (CH<sub>3</sub>) tips can be used to map cell surface hydrophobicity.<sup>[34]</sup> These studies demonstrate that chemically functionalized tips enable quantitative measurement of surface properties at the subcellular level.

### Biologically Functionalized Tips

Atomic force microscopy tips can also be functionalized with biomolecules to measure receptor–ligand interactions. A typical experiment consists in attaching ligands to the AFM tip and receptors to a solid substrate, or vice versa, bringing the modified surfaces in contact, and then measuring the unbinding force by pulling the tip away from the substrate. Successful measurements require that the binding of the biomolecules to the tip and substrate is much stronger than the intermolecular force. This is typically achieved by

using the chemisorption of alkanethiols on gold or the covalent binding of silanes on silicon oxide. Using this technique, a variety of intermolecular forces have been measured in recent years, among which the forces between biotin–avidin, antibody–antigen, complementary strands of DNA, carbohydrate–carbohydrate, and lectin–carbohydrate.<sup>[16,35,36]</sup>

Although they are not yet widely used in microbiology, AFM tips modified with biomolecules have a promising potential to measure receptor–ligand interaction forces associated with cell surfaces. This approach was recently applied to measure the specific interactions involved in yeast flocculation, an aggregation event of crucial importance in fermentation technology.<sup>[37]</sup> The yeast *Saccharomyces carlsbergensis* is known to flocculate according to a lectin-mediated mechanism in which active lectin receptors appear at the cell surface in the stationary phase and bind mannose residues of adjacent cells (Fig. 7). Atomic force microscopy tips functionalized with oligoglucose carbohydrates were used to record force–distance curves on yeast cells. While nonflocculating

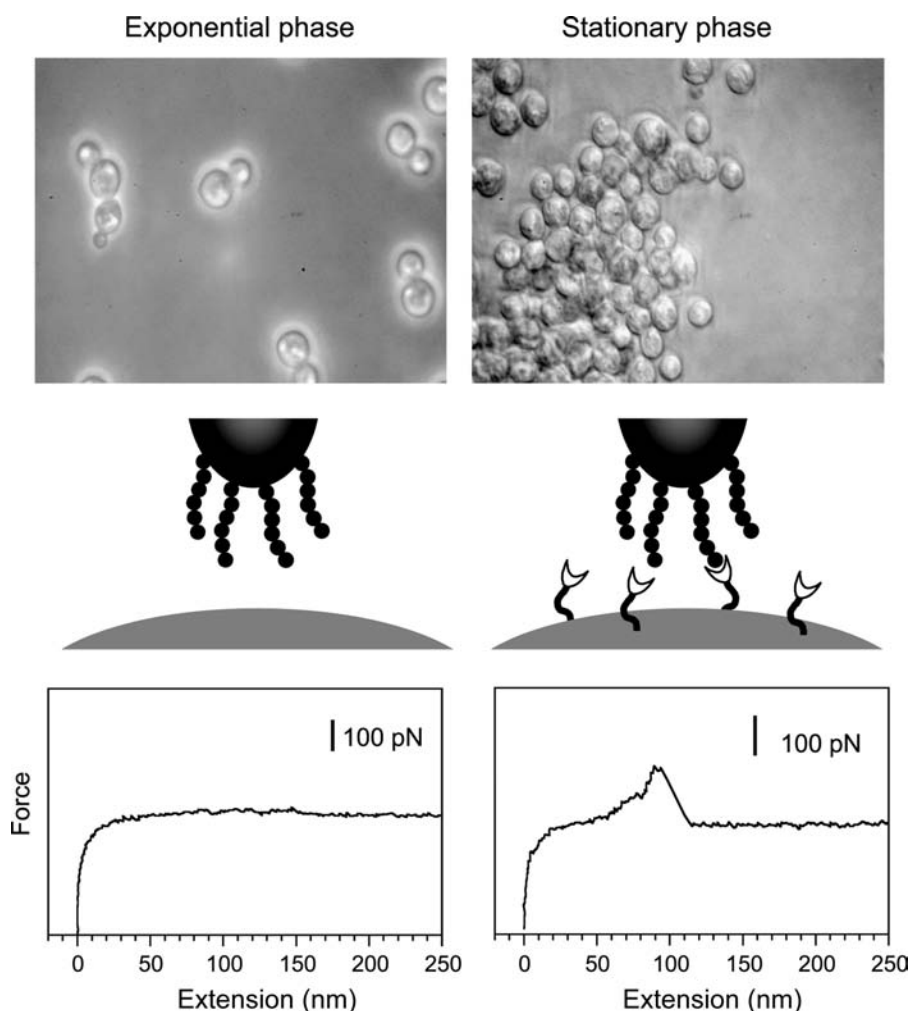


**Fig. 7** Use of biologically functionalized tips for probing cell surface receptors. Optical micrographs of *S. carlsbergensis* cells in the exponential phase (left) and in the stationary phase (right). Force curves recorded between exponential (left) or stationary (right) cells and AFM tips functionalized with oligoglucose carbohydrates. The adhesion force measured on stationary cells was attributed to the specific interaction between cell surface lectins and glucose residues on the AFM tip.



exponential cells showed no or poor adhesion, stationary cells showed adhesion forces of 121 pN (Fig. 7). Control experiments (blocking with mannose, use of a nonfloculating strain) lead to the conclusion that the measured adhesion forces reflected individual lectin-carbohydrate interactions involved in yeast flocculation. This type of experiments should have an important impact on medicine because they may be used to measure the interaction forces between pathogens and host cells.

“Cell probes” represent another type of biologically modified tips that are useful for measuring interaction forces between cells and solid substrata. Here a crucial issue is to ensure that both the metabolic activity and natural surface architecture are preserved during immobilization procedures. In this context, Bowen and coworkers developed an approach in which a single living cell is glued on the apex of a tipless cantilever using a micromanipulator. In doing so, the adhesion between fungal spores,<sup>[38]</sup> yeast cells,<sup>[39]</sup> and various solid surfaces was directly quantified. Another non-destructive strategy consists in coating an amino-functionalized bead with living bacterial cells and then attaching it to an AFM cantilever. This approach enabled the forces between *Shewanella oneidensis* bacteria and mineral surfaces to be quantitatively measured;<sup>[40]</sup> an important finding was that stronger adhesion energies were measured under anaerobic conditions. Accordingly, AFM-based force spectroscopy measurements provide a means to study a variety of cellular interactions at the molecular level.

### Mechanical Properties of Single Molecules

Remarkably, AFM can also be used to probe intramolecular forces associated with individual molecules, thereby providing quantitative information on the elasticity of the molecules, on conformational transitions along the chains, on the mechanical stability of chemical bonds, and on secondary structures. In recent years, these single-molecule force spectroscopy experiments have been applied to a variety of biomolecules, including DNA, proteins, and polysaccharides.<sup>[16,35,36,41–43]</sup> Outstanding work has also been carried out on isolated microbial cell surface layers. In the first such study, Müller, Baumeister, and Engel<sup>[44]</sup> combined AFM imaging and force spectroscopy to unzip proteins from the hexagonally packed intermediate (HPI) layer of *Deinococcus radiodurans*. Force-extension curves recorded for the inner surface of the HPI layer showed saw-tooth patterns with six force peaks of about 300 pN. This behavior was attributed to the sequential pulling out of the protomers of the hexameric HPI protein complex. After recording the force curve, a molecular defect the size of a hexameric complex was clearly visualized by

means of high-resolution imaging. In another study, Oesterhelt et al.<sup>[45]</sup> unraveled the unfolding pathways of individual bacteriorhodopsins. Molecules were individually extracted from the membrane, anchoring forces of 100–200 pN being found for the different helices. Upon retraction, the helices were found to unfold and the force spectra revealed the individuality of the unfolding pathways. Scheuring et al.<sup>[46]</sup> combined AFM imaging and single-molecule force spectroscopy to gain insight into the mechanical properties of the *Corynebacterium glutamicum* S-layer. The results provided a basis for understanding the extraordinary stability of these protein networks that protect microorganisms from hostile environment. The above studies demonstrate that AFM imaging and force spectroscopy is a powerful approach to address the structure-function relationships of microbial cell surface layers at the single molecule level.

Single-molecule elasticity experiments on living cells are very challenging in view of the complex and dynamic nature of their surface architecture. Recent studies indicate that progress is being made in this area. Atomic force microscopy was used to pull on macromolecules exposed at the surface of living *A. oryzae* spores with the aim to gain insight into their elasticity.<sup>[22]</sup> As mentioned earlier, topographic imaging revealed that, upon germination, the crystalline-like surface of dormant spores changed into a layer of soft granular material attributed to cell surface polysaccharides. This structural modification was correlated with a change of molecular interactions: While dormant spores showed poor adhesion, germinating spores showed attractive forces of 400 pN magnitude along with elongation forces that were attributed to the stretching of the cell surface polysaccharides (Fig. 8). This interpretation was supported by the finding that fitting the curves with a theoretical model from statistical mechanics yielded parameters similar to those reported for individual amylose and dextran molecules. It was concluded that the stickiness and flexibility of cell surface polysaccharide chains may promote spore aggregation via macromolecular bridging interactions between opposing cells.

Single-molecule force spectroscopy has also been applied to bacterial cells. The elasticity and adhesion of surface polymers from *Pseudomonas putida* was measured in solvents spanning a range of polarity and ionic strengths.<sup>[47]</sup> Adhesion forces in water and formamide were about the same and smaller than forces observed in methanol. Different models from statistical mechanics were used to analyze the force-extension profiles. Although biopolymer contour lengths varied over a wide range in all solvents, shorter lengths were observed when salt was present, indicating that the polymer chains were less extended in the presence of salt. In a related study, the heterogeneity

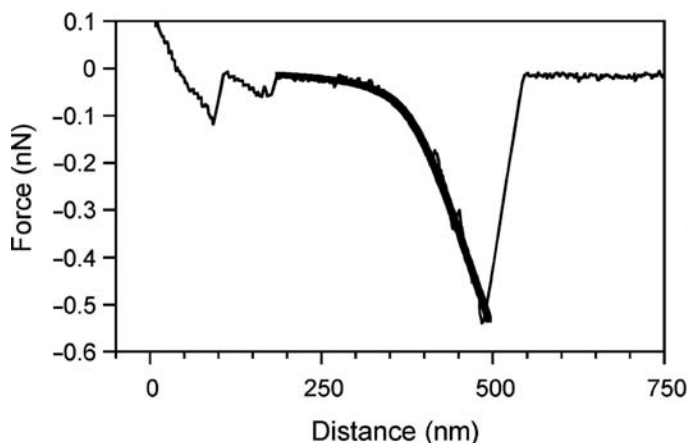


**Fig. 8** Pulling on cell surface macromolecules. Force–distance curve recorded under water between a silicon nitride tip and the surface of a germinating *A. oryzae* spore (thin line). The elongation force was well described by an extended freely jointed chain model (thick line) with parameters consistent with the stretching of a single polysaccharide chain.

in bacterial surface macromolecules was probed on the surface of *P. putida*.<sup>[48]</sup> Force measurements on different bacterial cells showed a range of adhesion affinities and polymer lengths, but substantial heterogeneity was also observed in the curves on a single bacterium. These experiments indicated that heterogeneity in biopolymer properties on an individual bacterium and within a population of bacterial cells may be much greater than previously believed and should be incorporated into models of bacterial adhesion. Summarizing, the above studies indicate that single-molecule force measurements should be very useful in future microbiological research for elucidating the properties of cell surface macromolecules.

## CONCLUSION

Atomic force microscopy imaging and force spectroscopy have recently opened a wide spectrum of novel applications for microbiologists and biophysicists. Using imaging in aqueous solution, microscopists can visualize cell surface nanostructures (surface layers, appendages), follow physiological changes (germination, growth), and monitor the effect of external agents (antibiotics, metals) in real time. By recording force–distance curves on cell surfaces, researchers can learn about local biomolecular interactions and physical properties. Spatially resolved force mapping offers a means to determine physical/chemical heterogeneities at the subcellular level, thereby providing complementary information to classical characterization methods. Force spectroscopy can be used to quantitatively probe the elasticity of cell wall components and whole cells. Functionalizing the AFM tip with chemical groups, biomolecules, and living cells enables quantitative measurements of surface charge, surface hydrophobicity, receptor–ligand interactions, and cell–material interactions. Finally, single-molecule force

spectroscopy can be applied to cell surface molecules to gain insight into their mechanical properties. Clearly, these AFM-based experiments contribute to improve our understanding of the structure–function relationships of microbial cell surfaces and will have considerable impact on biotechnology and medicine.

## ACKNOWLEDGMENTS

The author is a Research Associate of the Belgian National Foundation for Scientific Research (FNRS). The support of the FNRS, the Foundation for Training in Industrial and Agricultural Research (FRIA), the Federal Office for Scientific, Technical and Cultural Affairs (Interuniversity Poles of Attraction Program), and the Research Department of Communauté Française de Belgique (Concerted Research Action) is gratefully acknowledged. The author thanks all the people who were involved in the experiments discussed here, especially C. Boonaert, B. van der Aa, F. Ahimou, A. Touhami, F. Denis, M. Asther, A. Vasella, B. Nysten, and P. Rouxhet.

## REFERENCES

1. Beveridge, T.J.; Graham, L.L. Surface layers of bacteria. *Microbiol. Rev.* **1991**, *55* (4), 684–705.
2. Beveridge, T.J. Structures of gram-negative cell walls and their derived membrane vesicles. *J. Bacteriol.* **1999**, *181* (16), 4725–4733.
3. Busscher, H.J.; Handley, P.S.; Bos, R.; van der Mei, H.C. Physico-chemistry of Microbial Adhesion—From an Overall Approach to the Limits. In *Physical Chemistry of Biological Interfaces*; Baszkin, A., Norde, W., Eds.; Marcel Dekker, Inc.: New York, 2000; 431–458.
4. Mozes, N.; Handley, P.S.; Busscher, H.J.; Rouxhet, P.G. *Microbial Cell Surface Analysis: Structural and*

- Physicochemical Methods*; VCH Publishers: New York, 1991.
5. Pembrey, R.S.; Marshall, K.C.; Schneider, R.P. Cell surface analysis techniques: What do cell preparation protocols do to cell surface properties? *Appl. Environ. Microbiol.* **1999**, *65* (7), 2877–2894.
  6. Sleytr, U.B.; Messner, P.; Pum, D. Analysis of Crystalline Bacterial Surface Layers by Freeze-Etching, Metal Shadowing, Negative Staining and Ultrathin Sectioning. In *Methods in Microbiology*; Mayer, F., Ed.; Academic Press: London, 1988; Vol. 20, 29–60.
  7. Sleytr, U.B.; Beveridge, T.J. Bacterial S-layers. *Trends Microbiol.* **1999**, *7* (6), 253–260.
  8. Sleytr, U.B.; Sara, M.; Pum, D.; Schuster, B. Characterization and use of crystalline bacterial cell surface layers. *Prog. Surf. Sci.* **2001**, *68* (7–8), 231–278.
  9. Stoodley, P.; Sauer, K.; Davies, D.G.; Costerton, J.W. Biofilms as complex differentiated communities. *Annu. Rev. Microbiol.* **2002**, *56*, 187–209.
  10. van der Mei, H.C.; de Vries, J.; Busscher, H.J. X-ray photoelectron spectroscopy for the study of microbial cell surfaces. *Surf. Sci. Rep.* **2000**, *39* (1), 3–24.
  11. Binnig, G.; Quate, C.F.; Gerber, C. Atomic force microscope. *Phys. Rev. Lett.* **1986**, *56* (9), 930–933.
  12. Shao, Z.; Mou, J.; Czajkowsky, D.M.; Yang, J.; Yuan, J.-Y. Biological atomic force microscopy: What is achieved and what is needed. *Adv. Phys.* **1996**, *45* (1), 1–86.
  13. Colton, R.J.; Baselt, D.R.; Dufrêne, Y.F.; Green, J.-B.D.; Lee, G.U. Scanning probe microscopy. *Curr. Opin. Chem. Biol.* **1997**, *1*, 370–377.
  14. Engel, A.; Gaub, H.E.; Müller, D.J. Atomic force microscopy: A forceful way with single molecules. *Curr. Biol.* **1999**, *9* (4), R133–R136.
  15. Morris, V.J.; Kirby, A.R.; Gunning, A.P. *Atomic Force Microscopy for Biologists*; Imperial College Press: London, 1999.
  16. Clausen-Schaumann, H.; Seitz, M.; Krautbauer, R.; Gaub, H.E. Force spectroscopy with single biomolecules. *Curr. Opin. Chem. Biol.* **2000**, *4*, 524–530.
  17. Hansma, H.G. Surface biology of DNA by atomic force microscopy. *Annu. Rev. Phys. Chem.* **2001**, *52*, 71–92.
  18. Dufrêne, Y.F. Atomic force microscopy, a powerful tool in microbiology. *J. Bacteriol.* **2002**, *184* (19), 5205–5213.
  19. Colton, R.J.; Engel, A.; Frommer, J.E.; Gaub, H.E.; Gewirth, A.A.; Guckenberger, R.; Rabe, J.; Heckel, W.M.; Parkinson, B. *Procedures in Scanning Probe Microscopies*; John Wiley & Sons Ltd.: Chichester, 1998.
  20. Müller, D.J.; Fotiadis, D.; Scheuring, S.; Müller, S.A.; Engel, A. Electrostatically balanced subnanometer imaging of biological specimens by atomic force microscope. *Biophys. J.* **1999**, *76* (2), 1101–1111.
  21. Ahimou, F.; Touhami, A.; Dufrêne, Y.F. Real-time imaging of the surface topography of living yeast cells by atomic force microscopy. *Yeast* **2003**, *20* (1), 25–30.
  22. van der Aa, B.C.; Michel, R.M.; Asther, M.; Zamora, M.T.; Rouxhet, P.G.; Dufrêne, Y.F. Stretching cell surface macromolecules by atomic force microscopy. *Langmuir* **2001**, *17* (11), 3116–3119.
  23. Boonaert, C.J.P.; Toniazzo, V.; Mustin, C.; Dufrêne, Y.F.; Rouxhet, P.G. Deformation of *Lactococcus lactis* surface in atomic force microscopy study. *Colloids Surf., B Biointerfaces* **2002**, *23* (2–3), 201–211.
  24. Butt, H.-J.; Jaschke, M.; Ducker, W. Measuring surface forces in aqueous electrolyte solution with the atomic force microscope. *Bioelectrochem. Bioenerg.* **1995**, *38* (1), 191–201.
  25. Heinz, W.F.; Hoh, J.H. Spatially resolved force spectroscopy of biological surfaces using the atomic force microscope. *Tibtech* **1999**, *17* (4), 143–150.
  26. Dufrêne, Y.F.; Boonaert, C.J.P.; Gerin, P.A.; Asther, M.; Rouxhet, P.G. Direct probing of the surface ultrastructure and molecular interactions of dormant and germinating spores of *Phanerochaete chrysosporium*. *J. Bacteriol.* **1999**, *181* (17), 5350–5354.
  27. Touhami, A.; Nysten, B.; Dufrêne, Y.F. Nanoscale mapping of the elasticity of microbial cells by atomic force microscopy. *Langmuir* **2003**, *19* (11), 4539–4543.
  28. Xu, W.; Mulhern, P.J.; Blackford, B.L.; Jericho, M.H.; Firtel, M.; Beveridge, T.J. Modeling and measuring the elastic properties of an archaeal surface, the sheath of *Methanospirillum hungatei*, and the implication for methane production. *J. Bacteriol.* **1996**, *178* (11), 3106–3112.
  29. Yao, X.; Jericho, M.; Pink, D.; Beveridge, T. Thickness and elasticity of gram-negative murein sacculi measured by atomic force microscopy. *J. Bacteriol.* **1999**, *181* (22), 6865–6875.
  30. Radmacher, M. Measuring the elastic properties of living cells by the atomic force microscope. *Methods Cell Biol.* **2002**, *68*, 67–90.
  31. Arnoldi, M.; Kacher, C.M.; Bäuerlein, E.; Radmacher, M.; Fritz, M. Elastic properties of the cell wall of *Magnetospirillum gryphiswaldense* investigated by atomic force microscopy. *Appl. Phys., A* **1998**, *66*, S613–S617.
  32. Frisbie, C.D.; Rozsnyai, L.F.; Noy, A.; Wrighton, M.S.; Lieber, C.M. Functional group imaging by chemical force microscopy. *Science* **1994**, *265* (5181), 2071–2074.
  33. Ahimou, F.; Denis, F.A.; Touhami, A.; Dufrêne, Y.F. Probing microbial cell surface charges by atomic force microscopy. *Langmuir* **2002**, *18* (25), 9937–9941.
  34. Dufrêne, Y.F. Direct characterization of the physicochemical properties of fungal spores using functionalized AFM probes. *Biophys. J.* **2000**, *78* (6), 3286–3291.
  35. Janshoff, A.; Neitzert, M.; Oberdörfer, Y.; Fuchs, H. Force spectroscopy of molecular systems—Single molecule spectroscopy of polymers and biomolecules. *Angew. Chem., Int. Ed.* **2000**, *39* (18), 3213–3237.
  36. Zlatanova, J.; Lindsay, S.M.; Leuba, S.H. Single molecule force spectroscopy in biology using the atomic force microscope. *Prog. Biophys. Mol. Biol.* **2000**, *74* (1–2), 37–61.
  37. Touhami, A.; Hoffmann, B.; Vasella, A.; Denis, F.A.; Dufrêne, Y.F. Aggregation of microbial cells: Direct measurement of discrete lectin–carbohydrate interactions. *Microbiology* **2003**, *149* (10), 2873–2878.
  38. Bowen, W.R.; Lovitt, R.W.; Wright, C.J. Direct quantification of *Aspergillus niger* spore adhesion in liquid

- using an atomic force microscope. *J. Colloid Interface Sci.* **2000**, *228* (2), 428–433.
39. Bowen, W.R.; Lovitt, R.W.; Wright, C.J. Atomic force microscopy study of the adhesion of *Saccharomyces cerevisiae*. *J. Colloid Interface Sci.* **2001**, *237* (1), 54–61.
40. Lower, S.K.; Hochella, M.F.; Beveridge, T.J. Bacterial recognition of mineral surfaces: Nanoscale interactions between *Shewanella* and  $\alpha$ -FeOOH. *Science* **2001**, *292* (5520), 1360–1363.
41. Bustamante, C.; Smith, S.B.; Liphardt, J.; Smith, D. Single-molecule studies of DNA mechanics. *Curr. Opin. Struct. Biol.* **2000**, *10* (3), 279–285.
42. Carrion-Vazquez, M.; Oberhauser, A.F.; Fisher, T.E.; Marszalek, P.E.; Li, H.B.; Fernandez, J.M. Mechanical design of proteins—Studied by single-molecule force spectroscopy and protein engineering. *Prog. Biophys. Mol. Biol.* **2000**, *74* (1–2), 63–91.
43. Hugel, T.; Seitz, M. The study of molecular interactions by AFM force spectroscopy. *Macromol. Rapid Commun.* **2001**, *22* (13), 989–1016.
44. Müller, D.J.; Baumeister, W.; Engel, A. Controlled unzipping of a bacterial surface layer with atomic force microscopy. *Proc. Natl. Acad. Sci. U. S. A.* **1999**, *96* (23), 13170–13174.
45. Oesterhelt, F.; Oesterhelt, D.; Pfeiffer, M.; Engel, A.; Gaub, H.E.; Müller, D.J. Unfolding pathways of individual bacteriorhodopsin. *Science* **2000**, *288* (5463), 143–146.
46. Scheuring, S.; Stahlberg, H.; Chami, M.; Houssin, C.; Rigaud, J.L.; Engel, A. Charting and unzipping the surface layer of *Corynebacterium glutamicum* with the atomic force microscope. *Mol. Microbiol.* **2002**, *44* (3), 675–684.
47. Abu-Lail, N.I.; Camesano, T.A. Elasticity of *Pseudomonas putida* KT2442 surface polymers probed with single-molecule force microscopy. *Langmuir* **2002**, *18* (10), 4071–4081.
48. Camesano, T.A.; Abu-Lail, N.I. Heterogeneity in bacterial surface polysaccharides, probed on a single-molecule basis. *Biomacromolecules* **2002**, *3* (4), 661–667.

# AFM: Metal Ion Sorption

**Viriya Vithayaveroj**

*Georgia Institute of Technology, Atlanta, Georgia, U.S.A.*

**Sotira Yiacoumi**

*School of Civil and Environmental Engineering, Georgia Institute of Technology, Atlanta, Georgia, U.S.A.*

**Costas Tsouris**

*Separations and Materials Research Group, Oak Ridge National Laboratory, Oak Ridge, Tennessee, U.S.A.*

## INTRODUCTION

Sorption plays an important role both in natural waters and in water treatment processes, and is one of the techniques used to remove metal ions from aqueous solutions. However, the uptake of metal ions from aqueous solutions is limited by interactions between ions and surfaces in contact with the solution. Moreover, the fate and transport of metal ions are controlled by their reactions with surfaces at the solid–liquid interface. For example, inorganic colloids such as clays, metal oxides, and carbonates have been reported as effective sorbents of metal ions through ion exchange and surface complexation reactions.<sup>[1–4]</sup> It has also been noted that surface properties of sorbents, such as surface charge and electrical double layer, change continuously during sorption of metal ions.<sup>[5,6]</sup> As a result, physical transport, chemical reactivity, and/or bioavailability of the pollutants is altered during the sorption process.

Earlier studies have shown that sorption of ions from aqueous solutions by colloidal particles affects colloidal stability, mobility, and reactivity.<sup>[2,7–11]</sup> This sorption process also has significant influences on interparticle forces and the zeta potential of the colloidal sorbent. In most cases, reactions of metal ions with functional groups on the surface of particles are time-dependent.<sup>[12]</sup> A quantitative understanding of the changes in surface properties caused by chemical interactions between the particles and the ions present in the surrounding environment is critical to the prediction and control of the behavior of the colloidal system. This knowledge can be obtained by using atomic force microscopy (AFM), which provides direct and real-time measurements of colloidal forces during sorption of ions. However, the extent of metal ion sorption by colloidal particles is strongly influenced by several factors such as solution pH, ionic strength,

size and type of the substrate, concentration of metal ions and particles, reaction time, and temperature.<sup>[6]</sup> Atomic force microscopy is employed here to elucidate the influence of solution ionic strength and concentration of metal ions on sorption and colloidal behavior. The AFM cantilever with an attached colloidal particle can be regarded as a sensor in water/wastewater systems.

## ATOMIC FORCE MICROSCOPY

Atomic force microscopy was developed from scanning tunneling microscopy by Binnig, Quate, and Gerber<sup>[13]</sup> in 1986. In addition to rendering images of surfaces with nanoscale resolution, AFM has been used extensively in direct measurements of interaction forces between approaching similar surfaces and dissimilar surfaces such as particle–particle,<sup>[14–27]</sup> particle–plate,<sup>[19,25,28]</sup> and particle–bubble<sup>[29–37]</sup> surfaces.

The influences of solution conditions such as pH and ionic strength were investigated.<sup>[5,14–19,25]</sup> The measured force was discovered to decay exponentially with distance when the ionic strength increases and the pH decreases. The comparison between experimental data and the prediction of the Poisson–Boltzman equation<sup>[14,18]</sup> as well as the Derjaguin–Landau–Verwey–Overbeek (DLVO) theory was performed in some cases (e.g., Refs.<sup>[5,15–17,19,25]</sup>). Such studies clearly showed good agreement. The type of solution also plays a role in interfacial forces. For example, with increasing weight fraction, alcohol was found to suppress the long-range electrostatic repulsive force and to enhance the attractive force.<sup>[20]</sup>

Atomic force microscopy has been used to explore non-DLVO as well as DLVO forces.<sup>[21–24,28,38]</sup> For instance, the interaction between bacteria and the silicon nitride surface of the AFM tip was dominated

by steric force.<sup>[38]</sup> The steric force and the thickness of polymer layers on the surface of bacteria were affected by the solution pH. In solutions of high ionic strength, a repulsive hydration force was found to exist between similarly charged hydrophilic particles, whereas attractive forces were found to exist between oppositely charged hydrophilic particles.<sup>[21]</sup> Both short-range and long-range hydrophobic attractive forces were analyzed by Rabinovich and Yoon<sup>[23]</sup> and Nalaskowski et al.<sup>[24]</sup> for different types of systems.

Atomic force microscopy can be used to evaluate surface charge density. Based on force measurements between silica and  $\alpha$ -alumina surfaces for different values of solution pH, the zeta potential was found to be in agreement with the values obtained from direct electrokinetic measurements.<sup>[17]</sup> A similar study was conducted by Butt,<sup>[39]</sup> who used AFM to determine local surface charge densities of the plasma membranes of *Halobacterium halobium* in electrolyte solutions. Butt's previous work<sup>[40]</sup> revealed that the electrostatic force increases with increasing surface charge density and decreases roughly exponentially with distance. It can be reduced by imaging in high salt concentrations. Electrical double layers were also examined.<sup>[26,41]</sup> A repulsive force resulting from the overlapping of electrical double layers of similar approaching surfaces in intermediate-pH aqueous electrolyte solutions was observed.<sup>[18]</sup>

Information obtained from AFM measurements, including surface charge densities,<sup>[27,39]</sup> steric interactions,<sup>[28,38]</sup> and functional groups on surfaces,<sup>[41,42]</sup> is helpful in determining the structure of biological macromolecules and in understanding their functions through interparticle forces. In addition, AFM has been successfully employed to determine the Hamaker constant in various systems<sup>[15,16,27]</sup> and to evaluate the roughness of interfaces.<sup>[24,43]</sup>

The study of surface forces between colloidal probes and air–bubble interfaces has received increased attention in the past decade. A repulsive force was observed between a hydrophilic particle and a bubble, whereas a force between a hydrophobic particle and a bubble exhibited strong attraction.<sup>[29,30]</sup> The dependence of particle–bubble interactions on surfactant molecules was studied.<sup>[31,32]</sup> The force between a hydrophobic particle and an air–bubble interface was found to become repulsive when surfactants were added to the aqueous solution. Contact angle and adhesion also decreased simultaneously. For hydrophilic particles, different behaviors were observed depending on the adsorption of surfactants on the particle surface.

Besides particle–bubble interactions, surface interaction forces of oil–particle,<sup>[34]</sup> oil–water,<sup>[35]</sup> and protein inclusion bodies–bubble<sup>[36]</sup> systems were determined as well. Atomic force microscopy was also applied to measure the contact angle.<sup>[32,37]</sup>

The use of AFM to study changes in topography and surface forces as a result of sorption was recently reported. The type and concentration of both electrolyte solutions and surfactants were shown to have an effect on the structure of surfactants adsorbed onto the surface and also on the sorption behavior.<sup>[15,23,24,44–52]</sup> The structural transformation of the mixture between two surfactants that have different surface aggregate structures was investigated by Ducker and Wanless.<sup>[53]</sup> The shape of the aggregate at interfaces can be controlled by the mole fraction of surfactants in bulk solution. The establishment of changes in electrokinetic properties of surfaces because of the adsorption of surfactants was performed quantitatively.<sup>[54]</sup>

Temperature is also an important parameter in determining the adsorbed surfactant structure.<sup>[55,56]</sup> The binding site competition between cations in the electrolyte solution and cationic surfactant was observed.<sup>[57]</sup> Protons were found to produce more defects in the aggregates of surfactants than potassium ions do. Although surfactants slow the adsorption of hydrogen ions, it has no effect on that of potassium ions.

Atomic force microscopy provides not only information on force measurements because of sorption of surfactants, but also images of the structure of surfactants such as copolymer<sup>[56]</sup> and blend components.<sup>[58]</sup>

## SORPTION OF METAL IONS

The sorption of metal ions has been widely studied by flame atomic absorption spectrometry (FAAS), voltammetric techniques, potentiometric titrations, time-resolved laser fluorescence spectroscopy (TRLFS), X-ray absorption fine structure (XAFS) spectroscopy, X-ray absorption spectroscopy, extended X-ray absorption fine structure (EXAFS) spectroscopy, biosorption, etc.<sup>[6,59–66]</sup> Most of the experimental studies of metal sorption by particles have been described by distribution ratios or isotherm equations such as the Langmuir and Freundlich models.

In recent studies, AFM has been used to investigate the sorption of metal ions. For example, the adsorption of copper ions onto a silicon nitride probe was qualitatively studied by Larson and Pugh.<sup>[67]</sup> Chin, Yiacoymi, and Tsouris<sup>[5]</sup> used AFM to measure colloidal surface forces between a silica particle and a smooth glass plate in an aqueous solution, both with and without the presence of copper ions. The adsorption of metal ions on oxide surfaces was found to include specific interactions between ions and surface hydroxyl groups.<sup>[5,6]</sup> Under acidic conditions, copper ions have a low sorption affinity for oxide surfaces. Furthermore, the surface charge of silica is positive at low pH (lower than pH 2) and copper also has a

positive charge. Therefore silica and copper repel. During the experiment, the surface charge density of the silica particle remained the same because no sorption occurred. The experiment also showed that the interaction force between the silica particle and the glass plate was similar to that measured in solutions without copper ions.<sup>[5]</sup>

The sorption of metal ions by oxide surfaces was found to increase as the pH of the solution increases.<sup>[2,12,68–70]</sup> Tenorite (CuO) and metastable copper hydroxide are the dominant copper species at high pH. The removal of copper ions is attributed to the precipitation of tenorite.<sup>[6]</sup> If copper precipitates accumulate on silica particles, the forces are expected to change because the zeta potential of copper precipitates is different from that of silica.

Typically, each metal ion species has a critical pH range in which sorption competence increases from close to zero to 100%. Silica particles have OH<sup>−</sup> groups on the surface. The isoelectric point of silica occurs at approximately pH 2.<sup>[6]</sup> Above this pH, silica exhibits a negative zeta potential. However, silica shows a positive zeta potential at lower pH values. Therefore at the experimental pH of 5.5, silica has a negative charge. The force between the silica and the glass plate is repulsive because the plate also has a negative charge. For negatively charged colloids, charge reversal from negative to positive is usually observed with the presence of hydrolyzable metal ions above the pH of zero charge of colloids.<sup>[5]</sup>

At neutral pH, the sorption of copper ions causes the charge reversal of silica particles, thus changing the force between the silica particle and the glass plate from repulsive to attractive. Experimental data agreed well with calculations based on the DLVO theory for the case of constant surface charge. Electrostatic repulsion was found to decrease with increasing ionic strength and decreasing pH.

In addition to other sorption mechanisms, the formation of surface precipitates may also be a factor in changes in force profiles with time because the dissolution of silica can lead to the formation of metal ion surface precipitates.

By conducting the same experiment but using non-sorptive polystyrene particles instead of silica, Chin, Yiacomí, and Tsouris<sup>[5]</sup> also proved that no sorption of copper ions onto the glass surface occurs at experimental pH. The force between the tip and the glass was found to be repulsive; therefore Chin et al. concluded that no sorption of copper ions onto the glass plate had occurred.

Changes in the surface charge and the adjacent electrical double layer caused by the sorption of ions have been previously demonstrated.<sup>[5,6]</sup> If sorption occurs on the external surface of colloidal particles suspended in an aqueous solution, the resulting modification of

the electrical double layer is reflected in the interaction force between two particles. Therefore by measuring this interaction force as a function of time during sorption, it is possible to extract information on the sorption kinetics of ions by particles. The concept is employed in this work to investigate the effect of copper ion sorption by a silica particle on the interaction force between the particle and the glass plate. Note that in this study, the term *sorption* generally refers to various mechanisms of metal ion accumulation on silica particles.

## PRINCIPLE OF ATOMIC FORCE MICROSCOPY AND DATA ANALYSIS

Atomic force microscopy controls the movement of samples by applying a voltage to the piezoelectric tube, whereas the deflection of the cantilever is monitored using a laser beam. This beam was focused on the end of the cantilever and reflected to a photodiode. Deflection-vs.-displacement data were converted to ASCII format by the NanoScope software (Digital Instruments, Santa Barbara, CA) and imported into a spreadsheet program. To achieve a force-vs.-separation curve, zero values for force and distance were defined. The zero value for force was set at the point at which the deflection was constant. Zero distance was determined to be the position at which the deflection of the tip was the same as the displacement of the sample. The force was then calculated by means of Hooke's law:

$$F = kx \quad (1)$$

where  $F$  is the force,  $k$  is the spring constant, and  $x$  is the tip deflection. The separation distance is the sum of the tip deflection and the sample displacement.

## DERJAGUIN–LANDAU–VERWEY–OVERBEEK THEORY

According to the theory of colloidal stability (DLVO), the interaction force can be separated into two contributions: a repulsive electrostatic interaction, and an attractive van der Waals force.<sup>[71]</sup> The total interaction force  $F_{DLVO}$  is taken as a sum of these two terms:

$$F_{DLVO} = F_{\text{electrostatic}} + F_{\text{vdW}} \quad (2)$$

where  $F_{\text{electrostatic}}$  and  $F_{\text{vdW}}$  refer to the electrostatic and van der Waals components, respectively.

Although the system geometry is for sphere–flat plate interactions, the radius of the AFM tip was small relative to the flat plate and can be simplified. To



describe the electrostatic interaction force, a linearized form of the Poisson–Boltzmann equation and the Derjaguin approximation was used. The electrostatic interaction force is calculated from:

$$F_{\text{electrostatic}} = \frac{4\pi\sigma_{\text{silica}}\sigma_{\text{glass}}R}{\epsilon\kappa} e^{-\kappa D} \quad (3)$$

where  $\sigma_{\text{silica}}$  and  $\sigma_{\text{glass}}$  are the charge densities of a silica particle and a glass plate, respectively;  $R$  is the radius of the particle tip;  $\epsilon$  is the permittivity of water;  $\kappa$  is the inverse of double-layer thickness; and  $D$  is the separation distance. The inverse of the double-layer thickness is described as:

$$\kappa \equiv 5.552 \times 10^{-6} \sqrt{I/\epsilon kT} \quad (4)$$

where  $k$  is the Boltzmann constant,  $T$  is the absolute temperature, and  $I$  is the ionic strength.

Within the Derjaguin approximation, a simple expression for the non-retarded van der Waals forces is given by:

$$F_{\text{vdW}} = -\frac{AR}{6D^2} \quad (5)$$

where  $A$  is the Hamaker constant. Based on Lifshitz theory, the Hamaker constant ( $A$ ) for silica and glass in water was found to be  $5.4 \times 10^{-21}$  J.

The total force is:

$$F_{\text{DLVO}} = \frac{4\pi\sigma_{\text{silica}}\sigma_{\text{glass}}R}{\epsilon\kappa} e^{-\kappa D} - \frac{AR}{6D^2} \quad (6)$$

The measured zeta potentials of the sphere and the substrate were converted to surface charge densities by using the Grahame equation<sup>[72]</sup> and by assuming that the zeta potential is the same as the surface potential:

$$\sigma = 0.117[I]^{1/2} \sinh(\psi_0/51.4) \quad (7)$$

where  $\psi_0$  is the surface potential [mV] and  $\sigma$  is the surface charge density [C/m<sup>2</sup>]. This model is based on the assumption that the surface charge remains constant as the two surfaces approach each other. Previous studies<sup>[11,16,19]</sup> showed that the assumption of constant surface charge is more accurate than the assumption of constant surface potential because of large changes in surface potential as the two double layers interpenetrate.

## MATERIALS AND METHODS

### Colloidal Probe Preparation

In this study, 3- $\mu\text{m}$  silica particles from Bangs Laboratories, Inc. (Fishers, IN) were used as colloidal probes. The particles were non-porous and had hydroxyl (–OH) surface groups. A silica particle was glued to the end of a tipless contact-mode cantilever (Digital Instruments) with epoxy (ITWDevcon, Danvers, MA) by means of a micromanipulator and a camera/monitor system. Two sharp-tip needles were attached to the micromanipulator. The first was used to transfer epoxy glue to the end of the cantilever, and the second was used to pick up a silica particle and place it on top of the epoxy. Consequently, the free surface of the colloidal probe is glue-free.

The spring constant is a critical factor in the conversion of deflection data to force and can be estimated from the geometry, mass, and Young's modulus of a cantilever.<sup>[17,21,23]</sup> To have more accurate force data, the spring constants of cantilevers were verified by using the “cantilever tune” function in AFM. Because the resonant frequency of a cantilever changes after an additional mass is loaded, frequencies were measured before and after a particle was glued on the cantilever. The mass of the added particle  $M$  was calculated from its density, as reported by the manufacturer. Particle size was determined by scanning electron microscopy (SEM). The spring constant of the cantilever  $k$  was then calculated by the method of Cleveland and Manne:<sup>[73]</sup>

$$k = (2\pi)^2 \frac{M}{(1/\nu^2) - (1/\nu_0^2)} \quad (8)$$

where  $\nu_0$  and  $\nu$  are the resonant frequencies of a cantilever before and after the loading of particle, respectively. The cantilever with a 3- $\mu\text{m}$  silica particle tip is shown in Fig. 1.

### Sample Preparation

The substrate was a non-sorptive borosilicate glass coverslip. The coverslips (Ted Pella, Inc., Redding, CA) were cleaned by soaking them overnight in a 1 N HCl solution (Fisher Scientific, Fair Lawn, NJ). They were then immersed in acetone (Aldrich, Milwaukee, WI) for 30 min, boiled in a mixture of 5H<sub>2</sub>O:1H<sub>2</sub>O<sub>2</sub>:1NH<sub>4</sub>OH at 85°C for 25 min, washed with chromic acid (LabChem, Inc., Pittsburgh, PA) for 25 min, and then reimmersed in water. Glass substrates underwent plasma cleaning (model PDC-32G; Harrick Scientific Corp., Ossining, NY) before being used to remove any residual organic contaminants. The smoothness of the surface was determined by

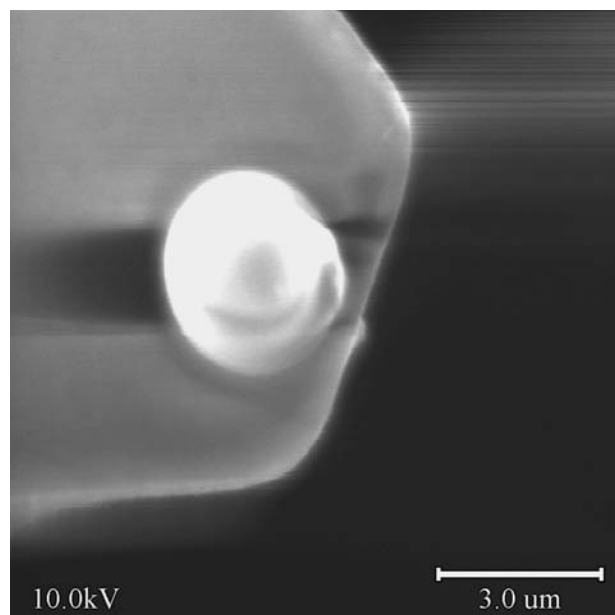


**Fig. 1** A SEM photomicrograph of a 3- $\mu\text{m}$  silica particle tip.

AFM images obtained using a silicon nitride tip (Digital Instruments). Water of 18 M $\Omega$ /cm resistivity at 25°C was prepared by an E-pure system (model D4631; Barnstead Thermolyne Co., Dubuque, IA).

Measurements of zeta potential were carried out using a ZetaPlus zeta potential analyzer (Brookhaven Instrument Corp., Holtsville, NY). These values were then used for theoretical calculations of interparticle forces.

### Force Measurements

Interaction forces between the small probe and the substrate were measured using AFM (model MMAFM-2; Digital Instruments). Fresh solutions at different values of ionic strength (as NaCl) and copper concentration [as Cu(NO<sub>3</sub>)<sub>2</sub>] were prepared by using triply distilled 18 M $\Omega$  deionized water. Because the sorption of copper ions onto silica particles occurs at intermediate pH values,<sup>[5,6]</sup> all solutions were prepared at pH 5.5. An O-ring was used to seal the fluid cell of the AFM to prevent flooding and to isolate the cell from possible contamination from the ambient environment. Initially, the colloidal probe was immersed in NaCl solution. Then, at the beginning of the sorption experiment, the metal ion solution was manually injected into the cell.

## RESULTS AND DISCUSSION

Both the equilibrium and the dynamics of copper ion uptake by silica particles under various solution conditions were studied. A repulsive force was initially observed in all experiments. This force is attributed

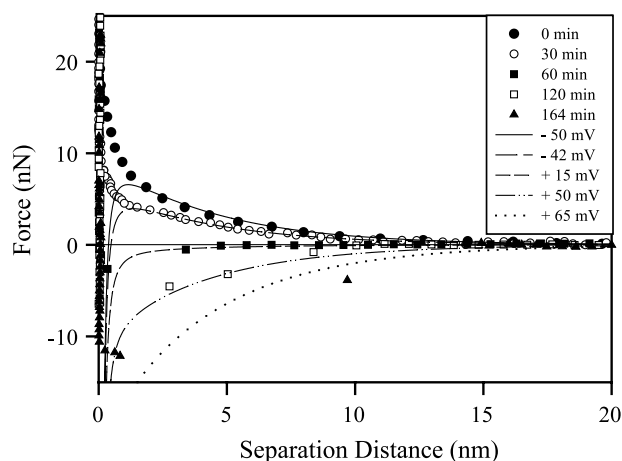


**Fig. 2** Dynamic force-profile measurements during the adsorption of copper ions by a silica tip for a copper concentration of  $7.6 \times 10^{-6}$  M. Ionic strength = 0.005 M NaCl, pH = 5.5,  $A = 5.43 \times 10^{-21}$  J. Data points represent direct force measurements by AFM. Lines represent predictions of the DLVO theory for the corresponding values of the zeta potential.

to an electrostatic repulsion between the negatively charged silica particle tip and the negatively charged glass surface. After copper ions were introduced into the system, they began to be adsorbed onto the surface of the silica particle. Consequently, the surface charge of silica was converted from negative to positive, and the repulsive force was gradually changed to an attractive force. The zeta potential of silica particles was a variable parameter that was used in calculations based on the DLVO theory to fit the experimental data. In Figs. 2 through 9, symbols represent force measurements at different times during sorption, and calculated results are represented by lines.

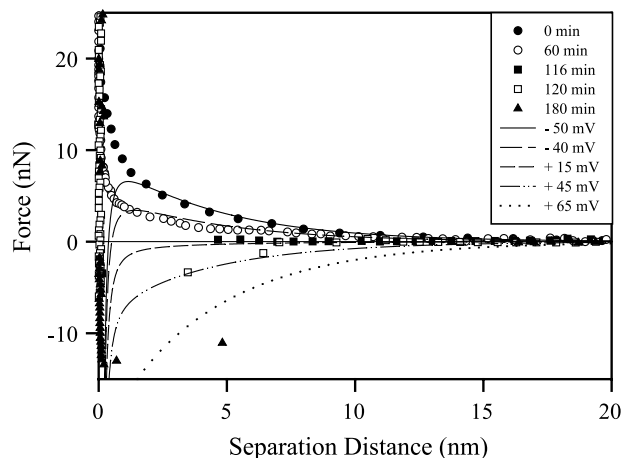


**Fig. 3** Dynamic force-profile measurements during the adsorption of copper ions by a silica tip for a copper concentration of  $1.5 \times 10^{-6}$  M. Ionic strength = 0.005 M NaCl, pH = 5.5,  $A = 5.43 \times 10^{-21}$  J.

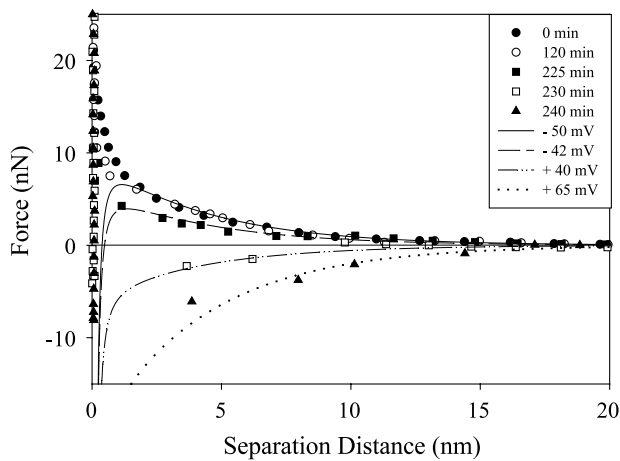


**Fig. 4** Dynamic force-profile measurements during the adsorption of copper ions by a silica tip for a copper concentration of  $7.6 \times 10^{-7}$  M. Ionic strength = 0.005 M NaCl, pH = 5.5,  $A = 5.43 \times 10^{-21}$  J.

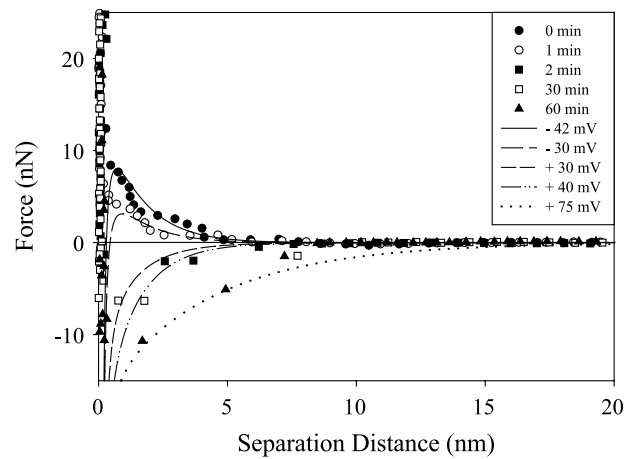


**Fig. 7** Dynamic force-profile measurements during the adsorption of copper ions by a silica tip for an ionic strength of 0.05 M NaCl. pH = 5.5, copper concentration =  $7.6 \times 10^{-5}$  M,  $A = 5.43 \times 10^{-21}$  J.

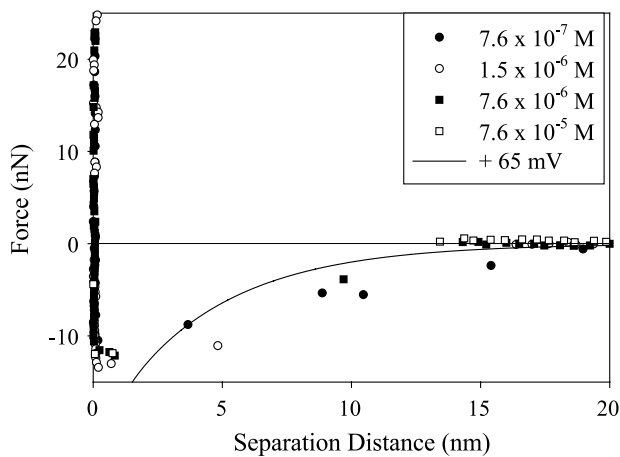


**Fig. 5** Equilibrium state of adsorption of copper ions by a silica tip. Ionic strength = 0.005 M NaCl, pH = 5.5,  $A = 5.43 \times 10^{-21}$  J.

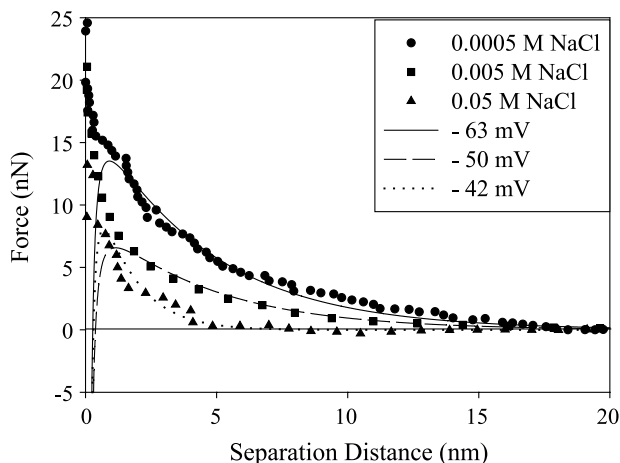


**Fig. 6** Effect of ionic strength on force-profile measurements at equilibrium.

### Effect of Metal Ion Concentration

The effect of copper concentration on the interaction force between a colloidal silica probe and a glass substrate was investigated. The forces were measured for solutions of various copper ion concentrations at a background electrolyte concentration of 0.005 M and at a pH of 5.5. In the previous study, Chin, Yiacoumi, and Tsouris<sup>[5]</sup> observed an immediate change in the measured force because of sorption of copper ions, with the surface charge of the silica particle being reversed from negative ( $-48$  mV) to positive (2 mV) in 10 min.

Fig. 2 presents the total measured force for  $7.6 \times 10^{-6}$  M copper concentration, which is 10 times lower than the concentration used by Chin, Yiacoumi,

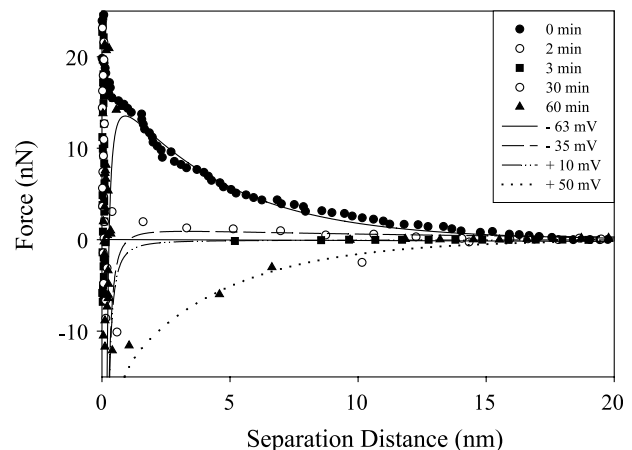


**Fig. 8** Dynamic force-profile measurements during the adsorption of copper ions by a silica tip for an ionic strength of 0.0005 M NaCl. pH = 5.5, copper concentration =  $7.6 \times 10^{-5}$  M,  $A = 5.43 \times 10^{-21}$  J.

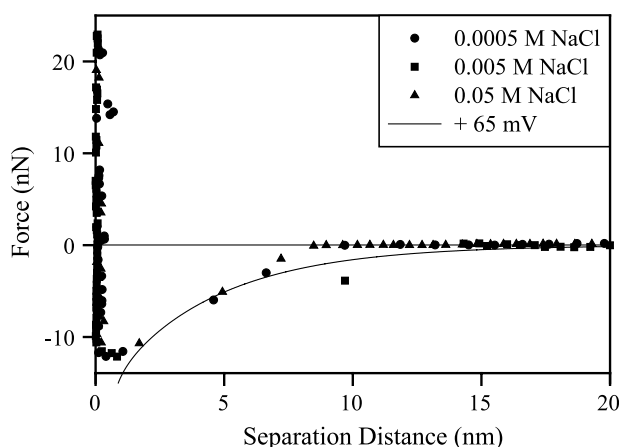


**Fig. 9** Equilibrium state of adsorption of copper ions by a silica tip. pH = 5.5, copper concentration =  $7.6 \times 10^{-5}$  M,  $A = 5.43 \times 10^{-21}$  J.

and Tsouris<sup>[5]</sup> As shown in this figure, sorption progressed more slowly than in the previous study, with the charge reversal occurring in 60 min. Because the concentration gradient was lower, a longer period of time was required for the surface of the silica particle to be fully covered by copper ions. The interaction force reached equilibrium after approximately 164 min. Similar experiments were repeated at the same pH and ionic strength with  $1.5 \times 10^{-6}$  and  $7.6 \times 10^{-7}$  M copper concentrations, as shown in Figs. 3 and 4, respectively. The sorption of copper ions onto a silica tip took place at a slower rate because of the lower concentration gradient. Approximately 180 min was required for the interaction force to reach equilibrium when the concentration of copper was  $1.5 \times 10^{-6}$  M, whereas 240 min was required when the concentration of copper was  $7.6 \times 10^{-7}$  M. These results indicate that as the metal ion concentration is decreased, more time is required for the interaction force to reach equilibrium.

Metal ion sorption equilibrium using various metal ion concentrations is shown in Fig. 5. At equilibrium, a strong attractive force was found in all solution conditions, indicating that the surface of the silica particle was fully covered by copper ions. The surface charge was positive in all cases. Therefore at equilibrium, the surface charges of a silica sphere and a glass plate have opposite signs, which lead to an attractive force. The measured forces for all solution conditions demonstrated the same behavior. The zeta potential of the silica particle at equilibrium was estimated to be +65 mV, which matched the calculated result according to the DLVO theory based on Eq. (6). This behavior shows that for the concentration range used in these experiments, the metal ion concentration had no effect on sorption at equilibrium, which can be explained by the full coverage of sorption sites.

## Effect of Ionic Strength

All sorption experiments were conducted at  $7.6 \times 10^{-5}$  M copper concentration and at a pH of 5.5, using different ionic strengths. The force–distance profiles between a silica sphere and a glass plate in a variety of NaCl solutions without copper ions (Fig. 6) indicate that the magnitude of electrostatic repulsion decreases with increasing ionic strength. This behavior can be explained by Eq. (4), in which decay length is reduced as ionic strength is increased because of the compression of the electrical double layer. As the ionic strength is increased, as shown in Eq. (7), this value overcomes the repulsion caused by an increase in the surface charge density.

Figs. 7 and 8 present the curves for force-vs.-separation distance for the silica–glass system at a copper concentration of  $7.6 \times 10^{-5}$  M in 0.05 and 0.0005 M NaCl solutions, respectively. These figures show that sorption is a relatively fast process. In the case of high ionic strength, surface charge reversal occurred 2 min after the copper ion solution was introduced into the system. However, at a much lower ionic strength, a repulsive force was still observed after the same period of time. Although the latter system required a longer period of elapsed time before reversal of the surface charge occurred, both systems reached equilibrium within approximately the same time (1 hr).

Equilibrium measurements of the same copper concentration but performed with solutions of different ionic strength are illustrated in Fig. 9. All force curves exhibited a strong attractive force at equilibrium, confirming the findings of Subramaniam, Yiacoumi, and Tsouris<sup>[6]</sup> that ionic strength has no significant effect on sorption equilibria.

## CONCLUSION

Atomic force microscopy was used to investigate the effect of metal concentration and ionic strength on metal ion sorption. Changes in interaction forces as a function of time demonstrated surface charge reversal and the occurrence of sorption. This study also showed that metal concentration has an effect on sorption dynamics (e.g., charge reversal occurs more slowly and the system requires a longer period of time to reach equilibrium at a lower concentration). However, ionic strength has no significant effect on sorption kinetics. Moreover, neither metal concentration nor ionic strength exhibits any effect on sorption equilibria, indicating that surface sites of the silica particle are fully covered by copper ions under the experimental conditions in this study.

## ACKNOWLEDGMENTS

Support for this research was provided by the National Science Foundation through a Career Award (BES-9702356 to S.Y.) and by the Division of Chemical Sciences, Office of Basic Energy Sciences, U.S. Department of Energy, under contract DE-AC05-00OR22725 with UT-Battelle, LLC. The authors are also thankful to Dr. Marsha K. Savage for editing the manuscript.

## REFERENCES

- Dzombak, D.A.; Morel, F.M.M. Adsorption of inorganic pollutants in aquatic systems. *J. Hydraul. Eng.* **1987**, *113*, 430–475.
- Dzombak, D.A.; Morel, F.M.M. *Surface Complexation Modeling: Hydrous Ferric Oxide*; Wiley: New York, 1990.
- Shuman, L.M. Effect of removal of organic matter and iron- or manganese-oxides on zinc adsorption by soil. *Soil Sci.* **1988**, *146* (4), 248–254.
- Zachara, J.M.; Ainsworth, C.C.; Cowan, C.E.; Resch, C.T. Adsorption of chromate by subsurface soil horizons. *Soil Sci. Soc. Am. J.* **1989**, *53*, 418–428.
- Chin, C.J.; Yiacoumi, S.; Tsouris, C. Influence of metal ion sorption on colloidal surface forces measured by atomic force microscopy. *Environ. Sci. Technol.* **2002**, *36* (3), 343–348.
- Subramaniam, K.; Yiacoumi, S.; Tsouris, C. Copper uptake by inorganic particles—equilibrium, kinetics, and particle interactions: experimental. *Colloids Surf., A* **2001**, *177* (2–3), 133–146.
- James, R.O.; Healy, T.W. Adsorption of hydrolyzable metal ions at the oxide–water interface: II. Charge reversal of SiO<sub>2</sub> and TiO<sub>2</sub> by adsorbed Co(II), La(III), and Th(IV) as model systems. *J. Colloid Interface Sci.* **1972**, *40*, 42–52.
- Crawford, R.J.; Harding, I.H.; Mainwaring, D.E. The zeta potential of iron and chromium hydrous oxides during adsorption and coprecipitation of aqueous heavy metals. *J. Colloid Interface Sci.* **1996**, *181* (2), 561–570.
- Liang, L.; Morgan, J.J. Chemical aspects of iron oxide coagulation in water: laboratory studies and implications for natural systems. *Aquat. Sci.* **1990**, *52*, 33–55.
- Stumm, W.; Morgan, J.J. The solid–solution interface. In *Aquatic Chemistry: Chemical Equilibria and Rates in Natural Waters*, 3rd Ed. Wiley: New York, 1996; 516–599.
- Colic, M.; Fisher, M.L.; Fuerstenau, D.W. Electro-phoretic behaviour and viscosities of metal oxides in mixed surfactant systems. *Colloid Polym. Sci.* **1998**, *276* (1), 72–80.
- Yiacoumi, S.; Tien, C. Adsorption of metal ions from aqueous solutions: model application. In *Kinetics of Metal Ion Sorption from Aqueous Solutions: Models, Algorithms, and Applications*; Kluwer Academic Publishers: Boston, 1995; 151–197.
- Binnig, G.; Quate, C.F.; Gerber, C.H. Atomic force microscopy. *Phys. Rev. Lett.* **1986**, *56* (9), 930–933.
- Ducker, W.A.; Senden, T.J. Measurement of forces in liquids using a force microscope. *Langmuir* **1992**, *8* (7), 1831–1836.
- Biggs, S.; Mulvaney, P. Measurement of the forces between gold surfaces in water by atomic force microscopy. *J. Chem. Phys.* **1994**, *100* (11), 8501–8505.
- Larson, I.; Drummond, C.J.; Chan, D.Y.C.; Grieser, F. Direct force measurements between TiO<sub>2</sub> surfaces. *J. Am. Chem. Soc.* **1993**, *115*, 11,885–11,890.
- Veeramasuneni, S.; Yalamanchilli, M.R.; Miller, J.D. Measurement of interaction forces between silica and  $\alpha$ -alumina by atomic force microscopy. *J. Colloid Interface Sci.* **1996**, *184* (2), 594–600.
- Toikka, G.; Hayes, R.A. Direct measurement of colloidal forces between mica and silica in aqueous electrolyte. *J. Colloid Interface Sci.* **1997**, *191* (1), 102–109.
- Larson, I.; Drummond, C.J.; Chan, D.Y.C.; Grieser, F. Direct force measurements between dissimilar metal oxides. *J. Phys. Chem.* **1995**, *99* (7), 2114–2118.
- Kanda, Y.; Nakamura, T.; Higashitani, K. AFM studies of interaction forces between surfaces in alcohol–water solutions. *Colloids Surf., A* **1998**, *139*, 55–62.
- Veeramasuneni, S.; Yalamanchilli, M.R.; Miller, J.D. Interactions between dissimilar surfaces in high ionic strength solutions as determined by atomic force microscopy. *Colloids Surf., A* **1998**, *131*, 77–87.
- Adler, J.J.; Rabinovich, Y.I.; Moudgil, B.M. Origins of the non-DLVO force between glass surfaces in aqueous solution. *J. Colloid Interface Sci.* **2001**, *237*, 249–258.
- Rabinovich, Y.I.; Yoon, R.-H. Use of atomic force microscope for the measurements of hydrophobic forces. *Colloids Surf., A* **1994**, *93*, 263–273.
- Nalaskowski, J.; Veeramasuneni, S.; Hupka, J.; Miller, J.D. AFM measurements of hydrophobic forces between a polyethylene sphere and silanated silica plates—The significance of surface roughness. *J. Adhes. Sci. Technol.* **1999**, *13* (12), 1519–1533.
- Li, Y.Q.; Tao, N.J.; Pan, J.; Gracia, A.A.; Lindsay, S.M. Direct measurement of interaction forces between colloidal particles using the scanning force microscope. *Langmuir* **1993**, *9* (3), 637–641.
- Hüttl, G.; Beyer, D.; Müller, E. Investigation of electrical double layers on SiO<sub>2</sub> surfaces by means of force vs. distance measurements. *Surf. Interface Anal.* **1997**, *25*, 543–547.
- Hartley, P.; Matsumoto, M.; Mulvaney, P. Determination of the surface potential of two-dimensional crystals of bacteriorhodopsin by AFM. *Langmuir* **1998**, *14* (18), 5203–5209.
- Considine, R.F.; Dixon, D.R.; Drummond, C.J. Laterally-resolved force microscopy of biological microspheres—Oocysts of *Cryptosporidium parvum*. *Langmuir* **2000**, *16* (3), 1323–1330.
- Butt, H.J. A technique for measuring the force between a colloidal particle in water and bubble. *J. Colloid Interface Sci.* **1994**, *166*, 109–117.
- Fielden, M.L.; Hayes, R.A.; Ralston, J. Surface and capillary forces affecting air bubble–particle interactions

- in aqueous electrolyte. *Langmuir* **1996**, *12* (15), 3721–3727.
31. Preuss, M.; Butt, H.J. Direct measurement of particle–bubble interactions in aqueous electrolyte: dependence on surfactant. *Langmuir* **1998**, *14* (12), 3164–3174.
  32. Ducker, W.A.; Xu, Z.; Israelachvili, J.N. Measurement of hydrophobic and DLVO forces in bubble–surface interactions in aqueous solutions. *Langmuir* **1994**, *10* (9), 3279–3289.
  33. Considine, R.F.; Drummond, C.J. Long-range force of attraction between solvophobic surfaces in water and organic liquids containing dissolved air. *Langmuir* **2000**, *16* (2), 631–635.
  34. Snyder, B.A.; Aston, D.E.; Berg, J.C. Particle–drop interactions examined with an atomic force microscope. *Langmuir* **1997**, *13* (3), 590–593.
  35. Hartley, P.G.; Grieser, F.; Mulvaney, P.; Stevens, G.W. Surface forces and deformation at the oil–water interface probed using AFM force measurement. *Langmuir* **1999**, *15* (21), 7282–7289.
  36. Wangsa-Wirawan, N.D.; Ikai, A.; O’Neill, B.K.; Middelberg, A.P.J. Measuring the interaction forces between protein inclusion bodies and an air bubble using an atomic force microscope. *Biotechnol. Prog.* **2001**, *17* (5), 963–969.
  37. Preuss, M.; Butt, H.J. Measuring the contact angle of individual colloidal particles. *J. Colloid Interface Sci.* **1998**, *208*, 468–477.
  38. Camesano, T.A.; Logan, B.E. Probing bacterial electrostatic interactions using atomic force microscopy. *Environ. Sci. Technol.* **2000**, *34* (16), 3354–3362.
  39. Butt, H.-J. Measuring local surface charge densities in electrolyte solutions with a scanning force microscope. *Biophys. J.* **1992**, *63*, 578–582.
  40. Butt, H.-J. Electrostatic interaction in atomic force microscopy. *Biophys. J.* **1991**, *60*, 777–785.
  41. Ishino, T.; Hieda, H.; Tanaka, K.; Gemma, N. Measurements of electrostatic double-layer forces due to charged functional groups on Langmuir–Blodgett films with an atomic force microscope. *Jpn. J. Appl. Phys., Part 1* **1994**, *33* (8), 4718–4722.
  42. Frisbie, C.D.; Rozsnyai, L.F.; Noy, A.; Wrighton, M.S.; Lieber, C.M. Functional group imaging by chemical force microscopy. *Science* **1994**, *265*, 2071–2074.
  43. Crossley, A.; Sofield, C.J.; Goff, J.P.; Lake, A.C.I.; Hutchings, M.T.; Menelle, A. A study comparing measurements of roughness of silicon and SiO<sub>2</sub> surfaces and interfaces using scanning probe microscopy and neutron reflectivity. *J. Non-Cryst. Solids* **1995**, *187*, 221–226.
  44. Subramanian, V.; Ducker, W.A. Counterion effects on adsorbed micellar shape: experimental study of the role of polarizability and charge. *Langmuir* **2000**, *16* (10), 4447–4454.
  45. Liu, J.-F.; Min, G.; Ducker, W.A. AFM study of adsorption of cationic surfactants and cationic polyelectrolytes at the silica–water interface. *Langmuir* **2001**, *17* (16), 4895–4903.
  46. Kramer, G.K.; Estel, K.; Schmitt, F.-J.; Jacobasch, H.-J. Laterally resolved measurement of interaction forces between surfaces that are partly covered with electrolytes. *J. Colloid Interface Sci.* **1998**, *208* (1), 302–309.
  47. Wanless, E.J.; Ducker, W.A. Organization of sodium dodecyl sulfate at the graphite–solution interface. *J. Phys. Chem.* **1996**, *100* (8), 3207–3214.
  48. Ducker, W.A.; Senden, T.J. Measurement of forces in liquids using a force microscope. *Langmuir* **1992**, *8* (7), 1831–1836.
  49. Xu, Z.; Ducker, W.; Israelachvili, J. Forces between crystalline alumina (sapphire) surfaces in aqueous sodium dodecyl sulfate surfactant solutions. *Langmuir* **1996**, *12* (9), 2263–2270.
  50. Subramanian, V.; Ducker, W. Proximal adsorption of cationic surfactant on silica at equilibrium. *J. Phys. Chem., B* **2001**, *105* (7), 1389–1402.
  51. Bremmell, K.E.; Jameson, G.J.; Biggs, S. Forces between surfaces in the presence of a cationic polyelectrolyte and an anionic surfactant. *Colloids Surf., A* **1999**, *155*, 1–10.
  52. McNamee, C.E.; Matsumoto, M.; Hartley, P.G.; Mulvaney, P.; Tsujii, Y.; Nakahara, M. Interaction forces and zeta potentials of cationic polyelectrolyte coated silica surfaces in water and in ethanol: Effects of chain length and concentration of perfluorinated anionic surfactants on their binding to the surface. *Langmuir* **2001**, *17* (20), 6220–6227.
  53. Ducker, W.A.; Wanless, E. Surface-aggregate shape transformation. *Langmuir* **1996**, *12* (24), 5915–5920.
  54. Whitby, C.P.; Scales, P.J.; Grieser, F.; Healy, T.W. The adsorption of dodecyltrimethylammonium bromide on mica in aqueous solution studied by x-ray diffraction and atomic force microscopy. *J. Colloid Interface Sci.* **2001**, *235*, 350–357.
  55. Liu, J.F.; Ducker, W.A. Surface-induced phase behavior of alkyltrimethylammonium bromide surfactants adsorbed to mica, silica, and graphite. *J. Phys. Chem., B* **1999**, *103* (40), 8558–8567.
  56. Gadegaard, N.; Almdal, K.; Larsen, N.B.; Mortensen, K. The lamellar period in symmetric diblock copolymer thin films studied by neutron reflectivity and AFM. *Appl. Surf. Sci.* **1999**, *142*, 608–613.
  57. Ducker, W.A.; Wanless, E. Adsorption of hexadecyltrimethylammonium bromide to mica: Nanometer-scale study of binding-site competition effects. *Langmuir* **1999**, *15* (1), 160–168.
  58. Karim, A.; Douglas, J.F.; Satija, S.K.; Han, C.C.; Goyette, R.J. Frustrated coalescence in a chemically reactive polymer blend film. *Macromolecules* **1999**, *32* (4), 1119–1127.
  59. Tewari, P.K.; Singh, A.K. Synthesis, characterization and applications of pyrocatechol modified amberlite XAD-2 resin for preconcentration and determination of metal ions in water samples by flame atomic absorption spectrometry (FAAS). *Talanta* **2001**, *53* (4), 823–833.
  60. Palmqvist, U.; Ahlberg, E.; Lövgren, L.; Sjöberg, S. Competitive metal ion adsorption in goethite systems using in situ voltammetric methods and potentiometry. *J. Colloid Interface Sci.* **1999**, *218* (2), 388–396.
  61. Stumpf, Th.; Rabung, Th.; Klenze, R.; Geckeis, H.; Kim, J.I. Spectroscopic study of Cm(III) sorption onto  $\gamma$ -alumina. *J. Colloid Interface Sci.* **2001**, *238* (1), 219–224.

62. Trainor, T.P.; Fitts, J.P.; Templeton, A.S.; Grolimund, D.; Brown, G.E., Jr. Grazing-incidence XAFS study of aqueous Zn(II) sorption on  $\alpha$ -Al<sub>2</sub>O<sub>3</sub> single crystals. *J. Colloid Interface Sci.* **2001**, *244* (2), 239–244.
63. Chen, C.-C.; Hayes, K.F. X-ray absorption spectroscopy investigation of aqueous Co(II) and Sr(II) sorption at clay–water interfaces. *Geochim. Cosmochim. Acta* **1999**, *63* (19–20), 3205–3215.
64. Schlegel, M.L.; Charlet, L.; Manceau, A. Sorption of metal ions on clay minerals: Mechanism of Co sorption on hectorite at high and low ionic strength and impact on the sorbent stability. *J. Colloid Interface Sci.* **1999**, *220*, 392–405.
65. Chen, J.P.; Yiacoumi, S. Biosorption of metal ions from aqueous solutions. *Sep. Sci. Technol.* **1997**, *32*, 51–69.
66. Xia, K.; Mehadi, A.; Taylor, R.W.; Bleam, W.F. X-ray adsorption and electron paramagnetic resonance studies of Cu(II) sorbed to silica: surface-induced precipitation at low surface coverages. *J. Colloid Interface Sci.* **1997**, *185*, 252–257.
67. Larson, I.; Pugh, R.J. Qualitative adsorption measurements with an atomic force microscope. *Langmuir* **1998**, *14* (20), 5676–5679.
68. Schindler, P.W.; Fürst, B.; Dick, R.; Wolf, P.U. Ligand properties of silanol groups: I. Surface complex formation with Fe(III), Cu(II), Cd(II), and Pb(II). *J. Colloid Interface Sci.* **1976**, *55*, 469–475.
69. Benjamin, M.M.; Leckie, J.O. Multiple-site adsorption of Cd, Cu, Zn, and Pb on amorphous iron oxyhydroxide. *J. Colloid Interface Sci.* **1981**, *79* (1), 209–221.
70. James, R.O.; Healy, T.W. Adsorption of hydrolyzable metal ions at the oxide–water interface: I. Co(II) adsorption on SiO<sub>2</sub> and TiO<sub>2</sub> as model systems. *J. Colloid Interface Sci.* **1972**, *70* (1), 42–52.
71. Israelachvili, J.N. Contrasts Between Intermolecular, Interparticle and Intersurface Forces. In *Intermolecular and Surface Forces*, 2nd Ed. Academic Press: London, 1992; 161–270.
72. Hiemenz, P.C.; Rajagopalan, R. The electrical double layer and double-layer interaction. In *Principles of Colloid and Surface Chemistry*, 3rd Ed. Marcel Dekker, Inc.: New York, 1997; 516–520.
73. Cleveland, J.P.; Manne, S. A nondestructive method for determining the spring constant of cantilevers for scanning force microscopy. *Rev. Sci. Instrum.* **1993**, *64* (2), 403–405.



# AFM: Nanolithography on Organized Films

Seunghyun Lee

Haiwon Lee

*Department of Chemistry, Hanyang University, Seoul, South Korea*

## INTRODUCTION

The ongoing miniaturization in size and integrity of electronic and mechanic devices has led to an interest in fabrication of nanometer-sized uniform structures on surfaces. With the device downscaling dimensions to the nanometer range, current interest is focused on the state-of-the-art lithographic development such as electron beam lithography, extreme UV lithography, imprint lithography, and scanning probe microscope (SPM) lithography. Binnig et al.<sup>[1]</sup> first developed the scanning probe microscope in 1982, and since then, SPM have been primarily used to obtain topographic and electronic surface maps. Nowadays, SPM is also being used to fabricate patterns and structures in nanometer scale, as well as to directly modify chemical or physical structure of surfaces.

Among several nanolithographic methods, scanning probe lithography (SPL) is one of the best lithographic techniques for forming nanostructures. Scanning probe lithography using a sharpened tip of an atomic force microscope (AFM) or a scanning tunneling microscope (STM) with the highest spatial resolution has demonstrated outstanding capabilities for atomic-level manipulation, and also wide varieties of potential applications such as electronic devices,<sup>[2,3]</sup> biochips, and biosensors<sup>[4,5]</sup> using different approaches—a direct method of writing patterns consisting of relatively small molecules on solid state surface, an exposure of organic thin films such as self-assembled monolayers (SAMs) and a selective anodic oxidation of various substrates. In particular, AFM lithography is the most promising method for fabricating organic thin films or the substrate itself in nanometer scale. Whereas STM-based lithography is mainly carried out in ultrahigh vacuum (UHV), fabrication using AFM lithography can be performed in liquid state as well as in ambient environment. Also, several novel methods using AFM as a lithographic tool have been developed in the past 10 years. This is a very active research area because of the flexibility and simplicity of the technique. In this technique, an AFM tip may be used to carry catalysts to selectively induce surface reactions, to attach molecules on surfaces as a pen,

and to direct local oxidation on surfaces as an electrode.

Subsequently, several principal AFM nanolithography techniques on organized molecular films such as self-assembled monolayers, Langmuir–Blodgett (LB) monolayer, and spin-coated polymer films will be illustrated.

## AFM-BASED NANOLITHOGRAPHY

### Dip-Pen Nanolithography

Mirkin et al.<sup>[6,7]</sup> introduced a dip-pen nanolithography (DPN) to construct patterns of molecules on a substrate in a positive printing by using an AFM tip as a “pen,” Au substrate as a “paper,” and alkanethiols with chemical affinity for Au substrate as “molecular inks.” In DPN, molecules are moved from the AFM tip to the solid substrate via capillary action to perform nanoscale patterns directly. The schematic diagram of patterning process in a DPN is shown in Fig. 1, and Fig. 2 represents the nanopatterns of alkanethiol on gold substrate via DPN.

Although DPN resolution relies on some parameters such as grain size of Au substrate, the contact time of tip–substrate, and relative humidity, this technique is a simple method for transporting molecules from AFM tip to substrate to control the architecture of a surface on the sub-100 nm.

Recently, DPN has been improved to generate nanoarray with dot-and-line pattern of biomolecules such as proteins, oligonucleotides, and magnetic nanoparticles. In case of fabricating magnetic nanostructures, 16-mercaptohexadecanoic acid (MHA) is used to make nanopatterns on Au substrate via DPN at the first stage, and then this patterned Au substrate is dipped into 1-octadecanethiol solutions to form passivated layer. Then, this sample is immersed into the iron oxide nanoparticles suspension solution once more. After going through these procedures, nanoarray with almost identical magnetic dots and lines composed of nanoparticles is prepared.<sup>[8]</sup>

To investigate a various surface-mediated biological recognition phenomenon, the construction of biomaterial

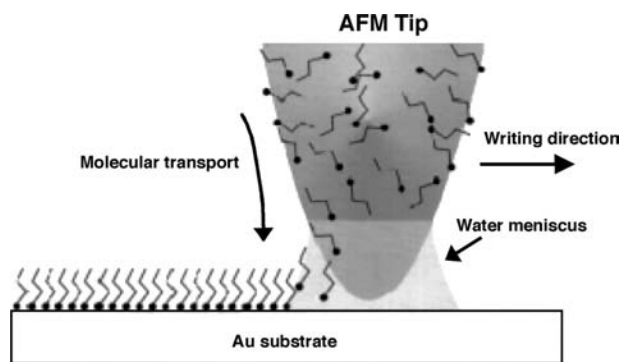


**Fig. 1** Schematic representation of DPN. A water meniscus forms between the AFM tip coated with alkanethiol and the Au substrate. *Source:* Prof. Chad A. Mirkin.

nanoarray is needed. DPN is useful not only to fabricate nanopatterns for differentiating active area from non-specific binding site of the substrate, but also to recognize specific binding properties. DPN forms nanopatterns on Au substrate using alkanethiols coated on AFM tips, and initially, the system of organothiol-gold substrate was used to fabricate nanopatterns because it was simple to use. However, the electrical conductivity of the gold substrate interferes with the observation of charge transport and near-field optical properties in building up nanostructures on surfaces like this, and also quenches the emission from any surface-bound materials with fluorescence.<sup>[9,10]</sup> Thus oxidized silicon substrate, as well as gold substrate, are used to generate nanoarray of proteins, oligonucleotides. In the case of oxidized

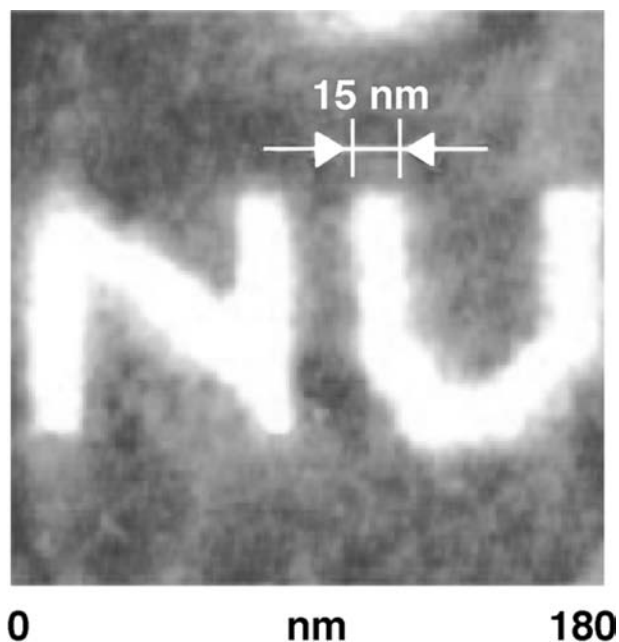


**Fig. 2** Nanoscale molecular letters written on an Au(111) surface with 16-mercaptohexadecanoic acid (MHA) molecules by DPN. *Source:* Prof. Chad A. Mirkin.

silicon wafers as substrate, there are two ways to modify the substrate to form nanoarray through DPN. One is to charge the silicon oxide surfaces negatively by treatment of base, and the other is to modify the surface with aldehyde functional group. AFM tip is modified by organosilane that forms a biocompatible and hydrophilic surface layer. Next, proteins are attached to the modified silicon oxide surface via DPN with AFM tip coated by immersing the tip in protein solution because of electrostatic interaction between the positively charged sites of the proteins and the negatively charged surface or covalent bonding between the surface with aldehyde functional head group and amine group on the proteins.<sup>[11]</sup> In a similar manner, DPN can be extended to useful direct-write methods to fabricate nanoarray of proteins using silicon oxide substrate and gold substrate.

### Nanografting Lithography

Liu et al.<sup>[12-14]</sup> have reported the nanografting technique for fabricating a patterned self-assembled monolayer (SAM) by combining mechanical displacement of selected molecular resist by an AFM tip and backfilling of new adsorbates.

In this case, SAM alkanethiol molecules at selected areas of the gold surface are removed by an AFM tip with a force greater than the threshold displacement force to fabricate desired patterns within the SAM. Next, new alkanethiol molecules having different alkyl chains from the contacting solution are immediately adsorbed onto the exposed regions by an AFM tip. **Fig. 3** shows the procedure for the nanografting lithography.

Using nanografting, the fabricated patterns can be quickly obtained in situ without changing the mask or repeating the entire fabrication procedure.

A nanopen reader and writer (NPRW), an improved nanografting technique, was introduced to produce nanopatterns on gold surface.<sup>[15]</sup> This technique combines the advantage of both nanografting and DPN. Compared to the existing nanografting technique, the NPRW technique has several advantages. In contrast to DPN, the resolution of NPRW is not influenced by the texture of the paper and the humidity of the experimental surroundings. Also, nanopatterns are easily fabricated and characterized in both solution and ambient environments, as well as solution phase in NPRW experiments. This technique is useful for producing nanopatterned arrays of biomolecules such as DNA and proteins.<sup>[16-18]</sup>

### Constructive Nanolithography

More recently, nanopatterning techniques using applied bias between the scanning probe microscope tip and the sample were reported. Sagiv et al. suggested a constructive nanolithography<sup>[19-21]</sup> that can be adapted

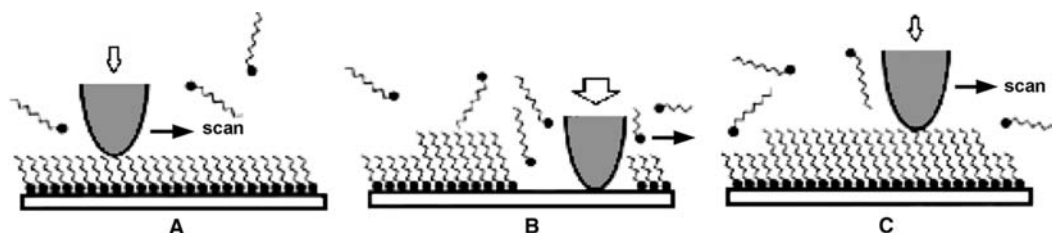


Fig. 3 Schematic diagram of the nanografting process. Source: Prof. Gang-Yu Liu.

to construct hybrid metal–organic nanostructures on silicon surface. In the constructive nanolithography, an electrically conducting AFM tip composes non-destructive chemical information on the exposed outer surface of self-assembled monolayers, and converts modified surface into a nanopatterned template for spatial control of the surface self-assembly of various selected organic and inorganic nanostructures.

Metallic silver nanoparticles are generated at selected surface regions by AFM tip-induced electrochemical reduction of the surface-bound metal ions on a thiol-top-functionalized silane monolayer (TFSM).<sup>[19]</sup> They also take the shape of the organic bilayer template on spatially modified,<sup>[20]</sup> non-destructive *n*-octadecyltrichlorosilane (OTS) SAMs via an electrically biased AFM tip, and then build various inorganic particle or layer. The scheme of constructive nanolithography is summarized in Fig. 4.

### Nanolithography Using Current Sensing AFM

Zhao and Uosaki<sup>[22,23]</sup> prepared well-defined nanopatterns of alkanethiol SAMs on gold substrate by using

current sensing atomic force microscopy (CS-AFM). When the conducting tip with a sufficient bias was scanned over a SAM in inert solvent containing alkanethiols with different chain length, the original SAM underneath the tip was removed and a new nanometer-sized spatial SAM of the alkanethiol was formed. In this method, toluene was chosen as the medium because of its non-polarity and low dielectric constant. A leak of current can be avoided, and the amount of water contained in toluene also has a crucial effect on lithographic performance. The mechanism of CSAFM-based lithography is as follows:

For positive bias condition,

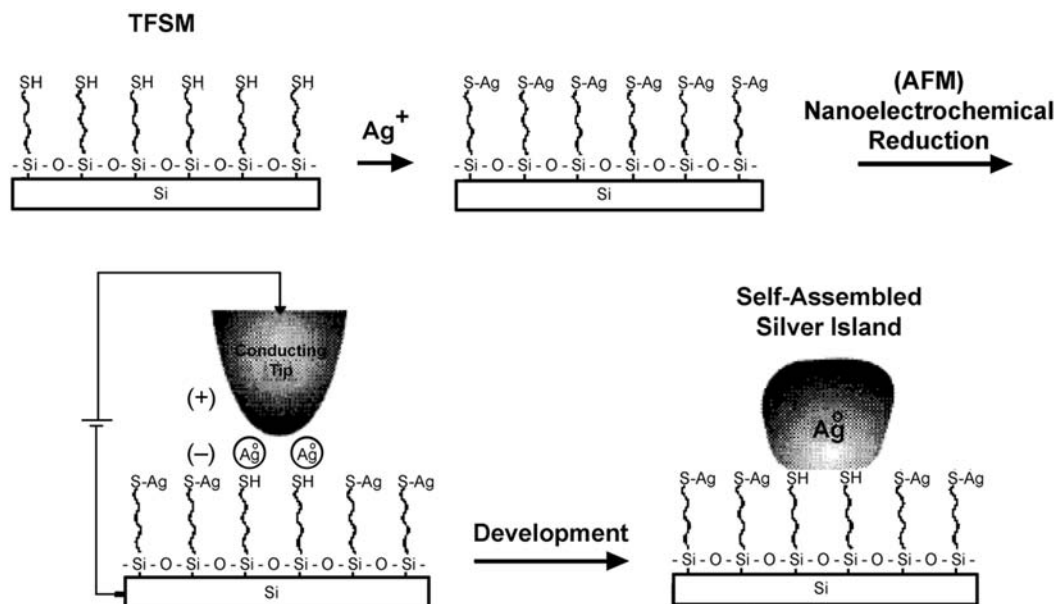
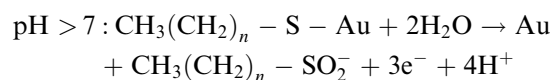
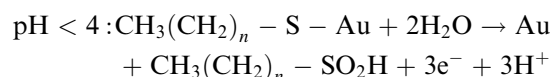
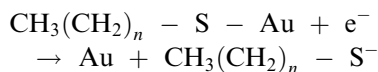


Fig. 4 Scheme of the constructive nanolithography: the site-defined self-assembly of silver metal on a thiol-top-functionalized silane monolayer preassembled on silicon. Source: Prof. Jacob Sagiv.

For negative bias condition,



### Anodization AFM Nanolithography

Some AFM-based nanolithographic methods are not practical because their lithographic speed is only in the order of nanometer/second, and both nanografting and current sensing AFM lithography are usually accomplished under liquid–solid interface.

However, the anodization lithographic technique, one of the most promising methods to prepare nanopattern with AFM, is accomplished by the reaction on the substrate surface.

AFM anodization lithography has also been reported elsewhere for producing protruded oxide patterns on a substrate by faradaic current from the cathode tip to the anode substrate.<sup>[24–37]</sup> Anodic patterning can be mainly accomplished on silicon<sup>[33,34]</sup> or titanium substrate<sup>[38,39]</sup> by electrochemical reactions mediated by the scanning probe tip. Electrochemical anodization occurs by emitted electrons from the tip at the locally scanned area on a silicon substrate in the presence of an atmospheric water column between the tip and the scanned area of the sample. This direct modification of silicon or metal surfaces by the anodization process using the electric field from an AFM tip is one promising method of accomplishing direct-writing lithography for the electronic device fabrication.

The first report of tip-induced oxidation of silicon was the STM study by Dagata et al.<sup>[40]</sup> They used an H-passivated silicon surface with a positively biased tip for generating oxide features on the surface. They suggested that the electrochemical oxidation reaction, which is locally induced beneath the tip in an adsorbed water column on the sample surface, is responsible for metal and semiconductor surfaces.

As shown in Fig. 5, the emitted electrons flow from the tip to the substrate through an organic resist, and they cause the anodization process with water on

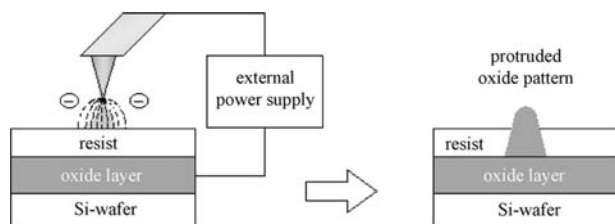
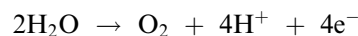


**Fig. 5** Schematic description of AFM anodization nanolithography on silicon substrate.

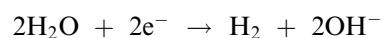
the silicon substrate. Accordingly, a protruded oxide pattern is newly formed at the local area of the substrate as a result of the anodization process.

Sugimura and Nakagiri<sup>[25]</sup> have suggested an electrochemical reaction between the tip and the sample for the anodization lithography as follows:

Anode reactions at sample surface:



Cathode reaction at AFM tip:



As the AFM anodization nanolithography is closely related to the magnitude of current, the size of the protruded pattern strongly depends on the amount of accepted electrons on the substrate. Also, it has been reported that the geometric factors of the nanopattern, such as the protruding height and the line-width, are affected by scan speed or duration time of the cathode AFM tip,<sup>[26,33,37,38]</sup> surface group, environmental relative humidity,<sup>[30,34,35,37]</sup> and the applied voltage between the tip and the sample.<sup>[33,34]</sup> Even the operational mode of AFM, both contact mode and noncontact mode, also influences on anodization patterning.<sup>[41]</sup>

The key to reach high resolution and precision is to selectively modify the surface either by breaking chemical bonds or through direct chemical reactions using local tip–surface interactions. The selection of high-performance resist materials is one of the important factors in the successful application of AFM lithography.

In the case of resist, the resist film should be prepared in a thin and uniform layer to attain high resolution in nanometer scale. Langmuir–Blodgett (LB) films<sup>[28,29,42]</sup> and self-assembled monolayers<sup>[27,30,43–46]</sup> have been used as resists and patterned with nanometer precision. These films are well-organized molecular assemblies formed by layer-by-layer deposition via either van der Waals force or covalent bonding.<sup>[47]</sup> The size of the molecule determines the layer thickness and can be carefully controlled to produce layers of uniform coverage. SAM films, consisting of organosilane, bipolar amphiphiles, and alkanethiol molecules, show a great potential as ultrathin resist films. Such SAM films, formed through the chemisorption onto oxide and metal surfaces, have excellent uniformity in molecular order and resistivity to various types of chemical reagents. As most of the lithographic works

with organic resists have been exclusively carried out on silicon surface for practical application, several organic resists with different functional groups have been studied in order to investigate the surface group effect on the anodic anodization using AFM.

### Anodization AFM nanolithography on self-assembled monolayers (SAMs)

Achieving fast lithographic scan speed is an important task to apply AFM to electronic devices. Because organic resist on silicon substrate can affect to the lithographic speed, it raises considerable interest in AFM anodization lithography.

In the case of AFM anodization, the electronic feature of terminal group of a resist on the surface is very important, because electrons are transferred from a tip to a substrate via the resist molecules and affects the line-width and the height of protruded oxide nanopatterns. An effective AFM lithographic process can be affected by the functional groups of self-assembled molecules. Lee and coworkers prepared the mixed SAMs of the 1,12-diaminododecane · dihydrochloride (DAD · 2HCl) and *n*-tridecylamine · hydrochloride (TDA · HCl) with the same alkyl chain on charged silicon substrate to observe effects of the surface of groups of the organic resists on lithographic AFM anodization.<sup>[27,30]</sup> Both DAD · 2HCl and TDA · HCl have an ammonium chloride on their headgroups to bind electrostatically onto charged silicon surface. In contrast to the head-group, they have different terminal groups at their air–molecule interfaces.

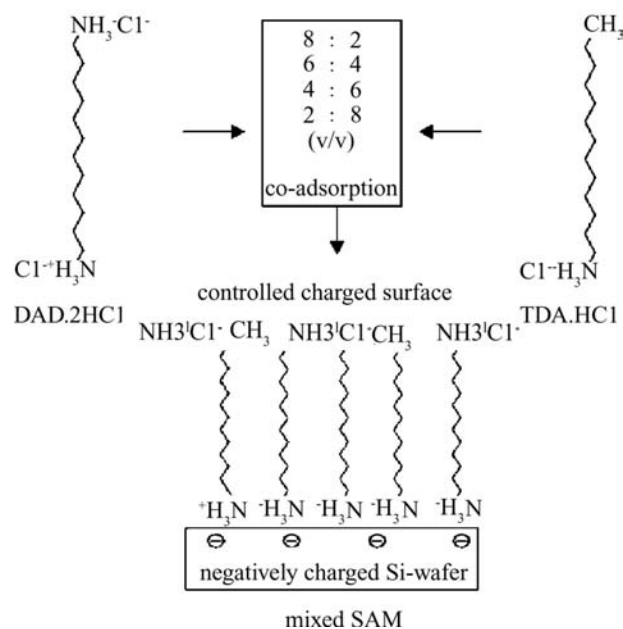


**Fig. 6** Preparation of the mixed SAM of DAD and TDA on a negatively charged Si wafer.

The schematic diagram of preparing mixed SAMs of DAD · 2HCl with a cationic surface group and TDA · HCl with a methyl surface group is shown in Fig. 6.

The difference of the mixing ratio of the two molecules has a great influence on the wetting property of SAM surface. The ammonium chloride ionic pair, the terminal functional group of DAD · 2HCl increases the hydrophilicity of the SAM resist, and so enlarges the size of water column between the AFM tip and the substrate interfaces related to contact angle. This characteristic causes the line-width and the height of the grown up oxide nanopattern to be expanded and the threshold voltage for protruding an oxide pattern decreases.

The results of contact angle measurement and AFM anodization lithography according to mixing ratio of DAD · 2HCl and TDA · HCl are shown in Fig. 7.

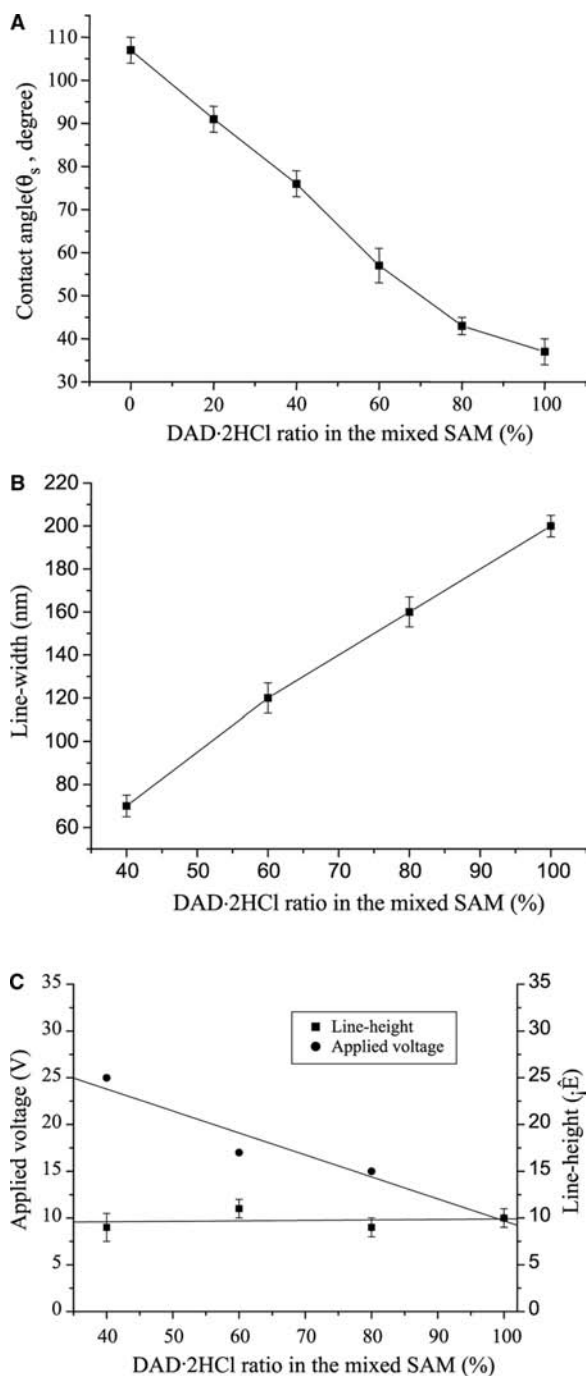
### Anodization AFM nanolithography on Langmuir–Blodgett (LB) films

Several research groups reported that the resist films could be adapted to the AFM anodization lithography to fabricate the high-resolution patterns. Pattern with tens of nanometer line-width were easily obtained when an appropriate resist was selected. Although there are many reports about the kinetics and the mechanism of silicon oxide growth in anodization process, the detailed anodization processes on the well-oriented organic resist system has yet to be clearly presented.

Lee and coworkers<sup>[28,29]</sup> used the easily obtainable Langmuir–Blodgett film of palmitic acid and hexadecylamine to elucidate the mechanism of AFM anodization process. A series of AFM images containing the lithographic stages at various bias voltage ranging from 4.00 to 8.00 V are shown in Fig. 8.

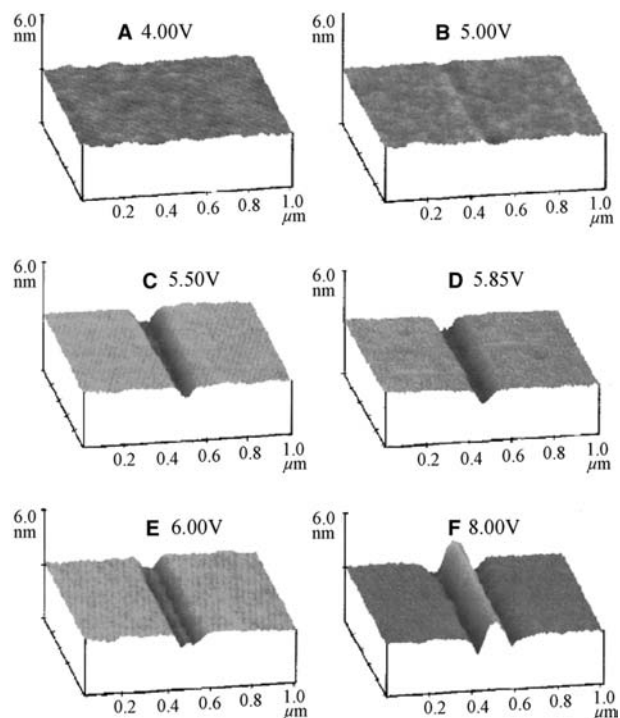
In the case of 4.00 V bias voltage in Fig. 8(A), no visible change of surface topography is observed. However, as the applied voltage increases, the growing protruded oxide patterns are sufficiently observed. To confirm the nature of the degraded surface, measured frictional force compared with the morphology changes are shown in Fig. 9.

Fig. 10A shows the AFM images patterned at 5.50 V and tip speed of 1.0 μm/sec. The degradation pattern with 202 ± 5 nm of line-width and 0.7 ± 0.3 nm of degradation depth is specified by difference between B and C points. The stripped substrate does not have the pattern of degradation but the protruded pattern with 212 ± 4 nm of line-width and 0.8 ± 0.3 nm of line-height as revealed in Fig. 10(B). The complete stripping of the resist was confirmed by the topographical change of the landmark from 1.2 ± 0.1 nm of vertical difference between B and D in Fig. 10A to 3.3 ± 0.1 nm in Fig. 10B.



**Fig. 7** (A) Water contact angle changes of the mixed SAMs at the various compositions of DAD · 2HCl and TDA · HCl. (B) Line-width changes of mixed SAMs at the various compositions of DAD · 2HCl and TDA · HCl. (C) Required applied voltages for protruding an oxide pattern with  $10 \pm 1 \text{ \AA}$  line-height using mixed SAMs at the various compositions.

This experimental result shows the direct evidence that degradation and anodization are simultaneously preceded in the AFM anodization nanolithography by a two-step mechanism: 1) a partial degradation of the resist was first achieved and 2) silicon oxide started



**Fig. 8** Lithographic pattern at constant lithographic speed at the specified voltage: (A) 4.00 V, (B) 5.00 V, (C) 5.50 V, (D) 5.85 V, (E) 6.00 V, and (F) 8.00 V.

to be grown at the presence of a resist, as shown in Figs. 8 and 9.

Among the number of factors influenced on AFM anodization lithography, the effect on polarity change of the bias potential applied between the cantilever and a

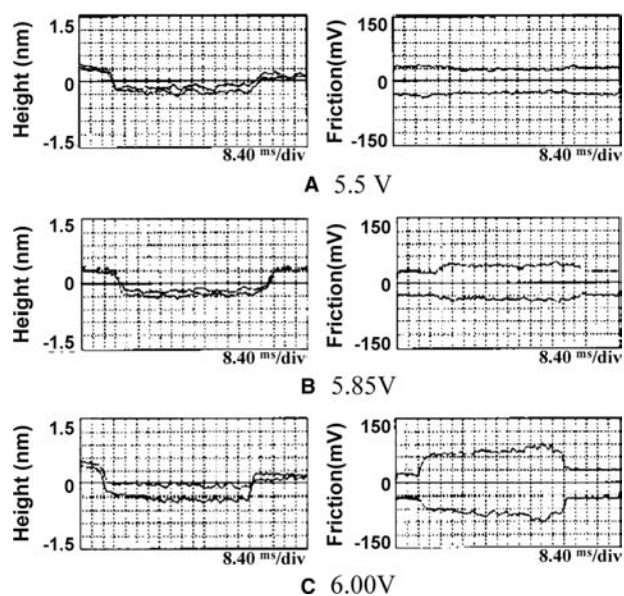


**Fig. 9** Oscilloscope mode of topographies and friction at the specified bias voltage: (A) 5.50 V, (A) 5.85 V, and (C) 6.00 V.



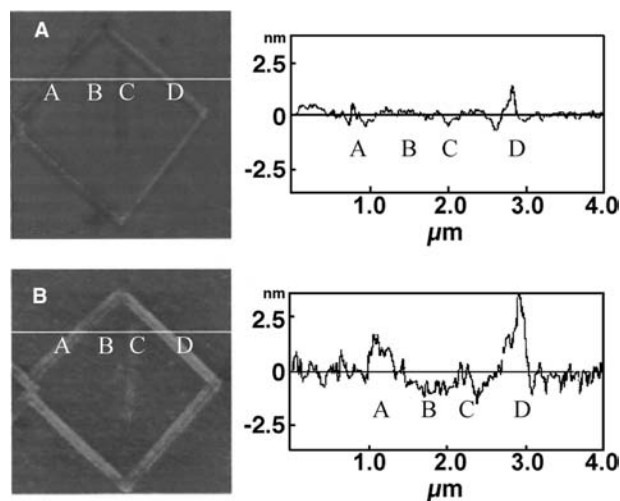


**Fig. 10** Topological views and cross sectional views of the patterned surface at 5.50 V bias voltage: (A) before stripping a resist film, (B) after stripping a resist film.

sample affects to generate patterned shape. Langmuir–Blodgett (LB) film composed of palmitic acid is used to investigate the polarity effect of AFM anodization lithography.<sup>[29]</sup> Lithographic result obtained at  $-10$  V of tip bias (tip negative; the normal polarity for AFM anodization lithography) shows the protruded pattern with  $1.5 \pm 0.1$  nm height and  $80 \pm 10$  nm width in Fig. 11(A). And then, as shown in Fig. 11(B), the result acquired at 10 V of tip bias (tip positive) has a grooved pattern with  $2 \pm 0.2$  nm height and  $80 \pm 10$  nm width.

This methodology, using polarity change of bias potential, will expand the application of AFM anodization lithography.

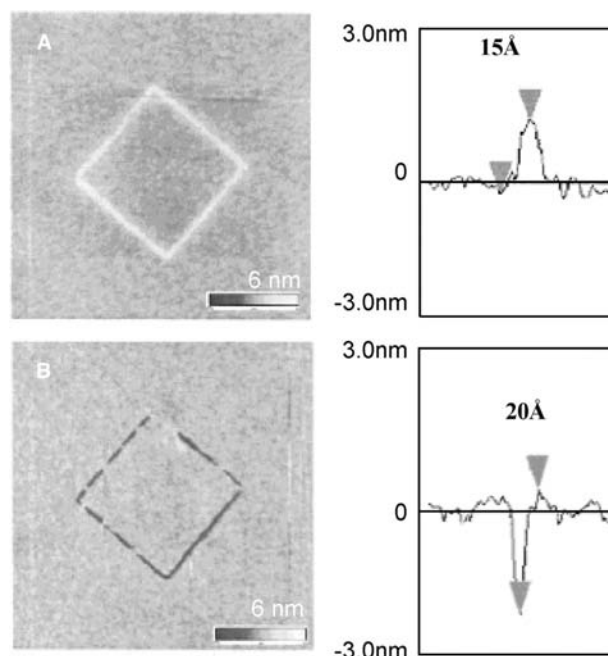


**Fig. 11** Lithographic pattern obtained at (A)  $-10$  V and (B) 10 V with section analysis.

### Anodization AFM nanolithography on the spin-coated polymer films

The preparation of ultrathin resist film is one of the key factors in the successful application of AFM lithography. From this viewpoint, spin-coated polymer film is usually easy to prepare, thermally stable, and more resistant to etching solution than organic self-assembled layer.

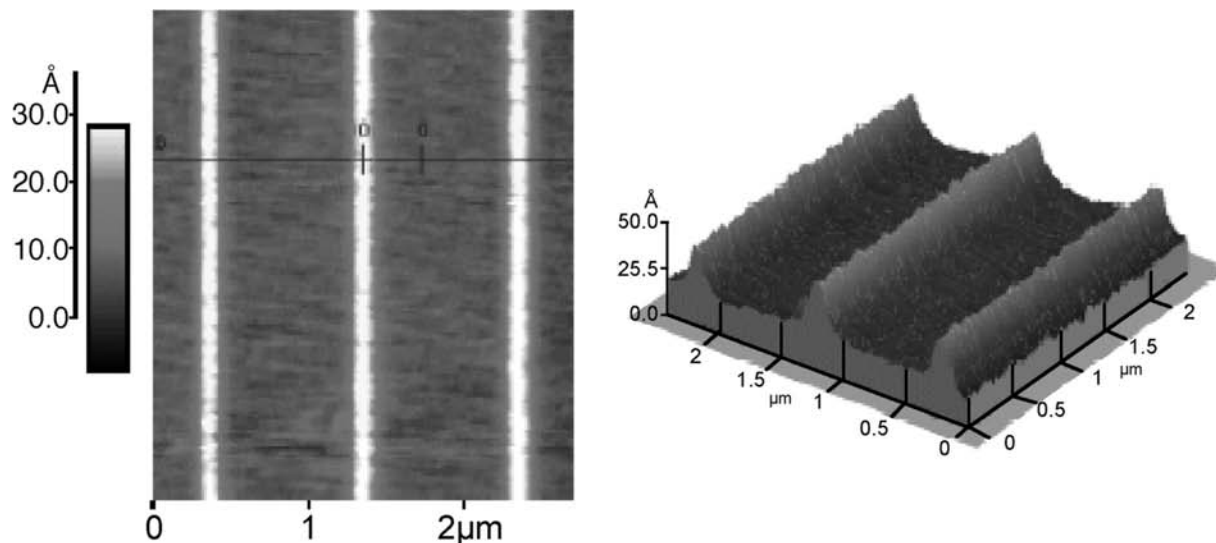


**Fig. 12** Topographic AFM images of the protruded lines.



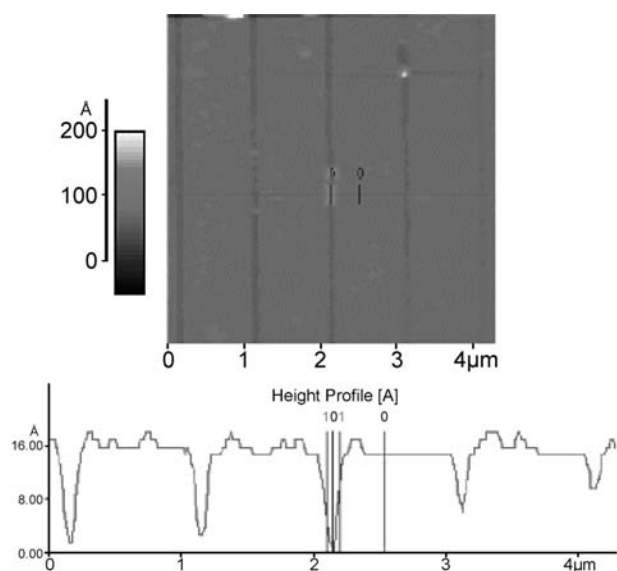


**Fig. 13** Topographic AFM image of grooved line pattern after etching process.

As shown in Fig. 12, the protruded lines by AFM anodization lithography on spin-coated methacrylate-based polymer film are about 60–80 nm.<sup>[48]</sup>

Methacrylate-based polymer has a unique molecular structure of acid labile silicon whose side groups enhance the thermal stability and the etching resistance of terpolymer. Also, an organic solvent easily strips this polymer.

Fig. 13 shows the AFM image of line pattern on silicon substrate after etching of the protruded pattern of methacrylate-based polymer with appropriate hydrofluoric acid (HF) solution. The obtained line pattern is about 90 nm of line-width and 15 Å of the etched depth. After the etching process, the polymer resist

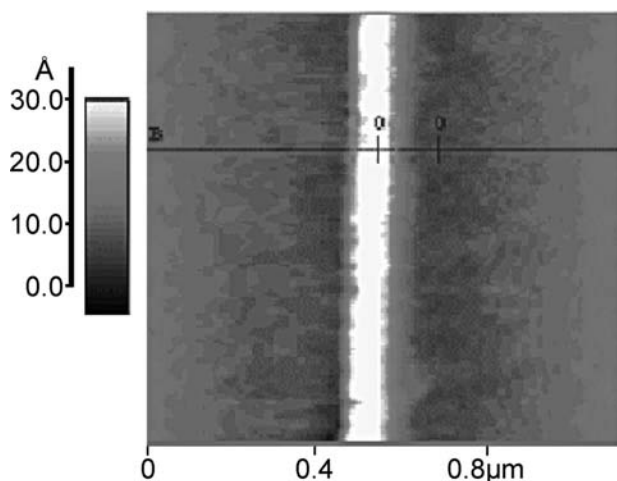


**Fig. 14** Topographic AFM image of line pattern after stripping process.

was completely removed by using a stripping process with tetrahydrofuran (THF) solvent. The AFM image of stripped line patterns having line-width of 100 nm and line-height of 28 Å is shown in Fig. 14.

Because of these characteristics, polymers can be used as practical resists in AFM anodization lithography.

## CONCLUSION

Various AFM-based nanolithography techniques are highlighted in this entry. These approaches using molecular assemblies are clearly the combination of the “bottom-up” methodology and “top-down” process to fabricate nanostructures of materials.

AFM nanolithography exhibits the highest spatial precision and resolution to reach fundamental scientific issues such as molecular fabrication, and quantum properties of specific system. These advantages make AFM a promising lithographic tool for future molecular electronics such as terabit nanostorage, and biotechnology, especially in biochips and sensors.

## ACKNOWLEDGMENT

This work was supported by both the National Research Laboratory program and the Tera-level Nanodevices of the Ministry of Science and Technology of Korea.

## REFERENCES

1. Binnig, G.; Rohrer, H.; Gerber, Ch.; Weibel, E. Surface studies by scanning tunneling microscopy. *Phys. Rev. Lett.* **1982**, *49* (1), 57–61.
2. Cooper, E.B.; Manalis, S.R.; Fang, H.; Dai, H.; Matsumoto, K.; Minne, S.C.; Hunt, T.; Quate, C.F. Terabit-per square-inch data storage with the atomic force microscope. *Appl. Phys. Lett.* **1999**, *75* (22), 3566–3568.
3. Chien, F.S.-S.; Hsieh, W.-F.; Gwo, S.; Vladar, A.E.; Dagata, J.A. Silicon nanostructures fabricated by scanning probe oxidation and tetra-methyl ammonium hydroxide etching. *J. Appl. Phys.* **2002**, *91* (12), 10,044–10,050.
4. Green, J.D.; Lee, G.U. Atomic force microscopy with patterned cantilevers and tip arrays: force measurements with chemical arrays. *Langmuir* **2000**, *16* (8), 4009–4015.
5. Wilson, D.L.; Martin, R.; Hong, S.; Cronin-Golomb, M.; Mirkin, C.A.; Kaplan, D.L. Surface organization and nanopatterning of collagen by dip-pen lithography. *Proc. Natl. Acad. Sci. U.S.A.* **2001**, *98* (24), 13,660–13,664.

6. Piner, R.D.; Zhu, J.; Xu, F.; Hong, S.; Mirkin, C.A. "Dip-pen" nanolithography. *Science* **1999**, *283* (5402), 661–663.
7. Hong, S.; Zhu, J.; Mirkin, C.A. Multiple ink nanolithography: toward a multiple-pen nano-plotter. *Science* **1999**, *286* (5439), 523–525.
8. Liu, X.; Fu, L.; Hong, S.; Dravid, V.P.; Mirkin, C.A. Array of magnetic nanoparticles patterned via "dip-pen" nanolithography. *Adv. Mater.* **2002**, *14* (3), 231–234.
9. Lee, K.-B.; Park, S.-J.; Mirkin, C.A.; Smith, J.C.; Mrksich, M. Protein nanoarrays generated by dip-pen nanolithography. *Science* **2002**, *295* (5560), 1702–1705.
10. Demers, L.M.; Ginger, D.S.; Park, S.-J.; Li, Z.; Chung, S.-W.; Mirkin, C.A. Direct patterning of modified oligonucleotides on metals and insulators by dip-pen nanolithography. *Science* **2002**, *296* (5574), 1836–1838.
11. Lim, J.-H.; Ginger, D.S.; Lee, K.-B.; Heo, J.; Nam, J.-M.; Mirkin, C.A. Direct-write dip-pen nanolithography of proteins on modified silicon oxide surfaces. *Angew. Chem., Int. Ed.* **2003**, *42* (20), 2309–2312.
12. Xu, S.; Liu, G.Y. Nanometer-scale fabrication by simultaneous nanoshaving and molecular self-assembly. *Langmuir* **1997**, *13* (2), 127–129.
13. Xu, S.; Miller, S.; Laibinis, P.E.; Liu, G.Y. Fabrication of nanometers scale patterns within self-assembled monolayers by nanografting. *Langmuir* **1999**, *15* (21), 7244–7251.
14. Liu, J.F.; Cruchon-Dupeyrat, S.; Garmo, J.C.; Frommer, J.; Liu, G.Y. Three-dimensional nanostructure constructive via nanografting: positive and negative pattern transfer. *Nano Lett.* **2002**, *2* (9), 937–940.
15. Armo, N.A.; Xu, S.; Liu, G.Y. Patterning surfaces using tip-directed displacement and self-assembly. *Langmuir* **2000**, *16* (7), 3006–3009.
16. Wadu-Mesthrige, K.; Xu, S.; Armo, N.A.; Liu, G.Y. Fabrication and imaging of nanometer-sized protein patterns. *Langmuir* **1999**, *15* (25), 8580–8583.
17. Wadu-Mesthrige, K.; Armo, N.A.; Garmo, J.C.; Xu, S.; Liu, G.Y. Fabrication of nanometer-sized patterns using atomic force microscopy and selective immobilization. *Biophys. J.* **2001**, *80* (4), 1891–1899.
18. Liu, M.; Armo, N.A.; Chow, C.S.; Liu, G.Y. Production of nanostructures of DNA on surfaces. *Nano Lett.* **2002**, *2* (8), 863–867.
19. Maoz, R.; Frydman, E.; Cohen, S.R.; Sagiv, J. Constructive nanolithography: site-defined silver self-assembly on nanoelectrochemically patterned monolayer templates. *Adv. Mater.* **2000**, *12* (6), 424–429.
20. Maoz, R.; Frydman, E.; Cohen, S.R.; Sagiv, J. "Constructive nanolithography"; inert monolayers as patternable templates for in-situ nanofabrication of metal–semiconductor–organic surface structures—a generic approach. *Adv. Mater.* **2000**, *12* (10), 725–731.
21. Hoepfner, S.; Maoz, R.; Sagiv, J. Constructive microlithography: electrochemical printing of monolayer template patterns extends constructive nanolithography to the micrometer–millimeter dimension range. *Nano Lett.* **2003**, *3* (6), 761–767.
22. Zhao, J.; Uosaki, K. A novel nanolithography technique for self-assembled monolayers using a current sensing atomic force microscope. *Langmuir* **2001**, *17* (25), 7784–7788.
23. Zhao, J.; Uosaki, K. Formation of nanopatterns of a self-assembled monolayer (SAM) within a SAM of different molecules using a current sensing atomic force microscope. *Nano Lett.* **2002**, *2* (2), 137–140.
24. Gordon, A.E.; Fayfield, R.T.; Litfin, D.D.; Higman, T.K. Mechanisms of surface anodization produced by scanning probe microscopes. *J. Vac. Sci. Technol., B* **1995**, *13* (6), 2805–2808.
25. Sugimura, H.; Nakagiri, N. Scanning probe anodization: nanolithography using thin films of anodically oxidizable materials as resists. *J. Vac. Sci. Technol., A* **1996**, *14* (3), 1223–1227.
26. Legrand, B.; Stievenard, D. Nanooxidation of silicon with an atomic force microscope: a pulsed voltage technique. *Appl. Phys. Lett.* **1999**, *74* (26), 4049–4051.
27. Lee, W.; Oh, Y.; Kim, E.R.; Lee, H. Nanopatterning of self-assembled monolayers on Si-surfaces with AFM lithography. *Synth. Met.* **2001**, *117*, 305–306.
28. Ahn, S.J.; Jang, Y.K.; Lee, H.; Lee, H. Mechanism of atomic force microscopy anodization lithography on a mixed Langmuir–Blodgett resist of palmitic acid and hexadecylamine on silicon. *Appl. Phys. Lett.* **2002**, *80* (14), 2592–2594.
29. Lee, H.; Kim, S.A.; Ahn, S.J.; Lee, H. Positive and negative patterning on a palmitic acid Langmuir–Blodgett monolayer on Si surface using bias-dependent atomic force microscopy lithography. *Appl. Phys. Lett.* **2002**, *81* (1), 138–140.
30. Lee, W.; Kim, E.R.; Lee, H. Chemical approach to high-resolution patterning on self-assembled monolayers using atomic force microscope lithography. *Langmuir* **2002**, *18* (22), 8375–8380.
31. Zheng, J.; Zhu, Z.; Chen, H.; Liu, Z. Nanopatterned assembling of colloidal gold nanoparticles on silicon. *Langmuir* **2000**, *16* (10), 4409–4412.
32. Zheng, J.; Chen, Z.; Liu, Z. Atomic force microscopy-based nanolithography on silicon using colloidal Au nanoparticles as a nanooxidation mask. *Langmuir* **2000**, *16* (24), 9673–9676.
33. Stievenard, D.; Fontaine, P.A.; Dubois, E. Nanooxidation using a scanning probe microscope: an analytical model based on field induced oxidation. *Appl. Phys. Lett.* **1997**, *70* (24), 3272–3274.
34. Avouris, P.; Hertel, T.; Martel, R. Atomic force microscope tip-induced local oxidation of silicon: kinetics, mechanism, and nanofabrication. *Appl. Phys. Lett.* **1997**, *71* (2), 285–287.
35. Avramescu, A.; Ueta, A.; Uesugi, K.; Suemune, I. Atomic force microscope based patterning of carbonaceous masks for selective area growth on semiconductor surfaces. *J. Appl. Phys.* **2000**, *88* (6), 3158–3165.
36. Hattori, T.; Ejiri, Y.; Saito, K.; Yasutake, M. Fabrication of nanometer-scale structures using atomic force microscope with conducting probe. *J. Vac. Sci. Technol., A* **1994**, *12* (4), 2586–2590.

37. Snow, E.S.; Campbell, P.M.; Perkins, F.K. High speed patterning of a metal silicide using scanned probe lithography. *Appl. Phys. Lett.* **1999**, *75* (10), 1476–1478.
38. Dubois, E.; Bubbendorff, J. Nanometer scale lithography on silicon, titanium and PMMA resist using scanning probe microscopy. *Solid-State Electron.* **1999**, *43* (6), 1085–1089.
39. Huh, C.; Park, S.-J. Atomic force microscope tip-induced anodization of titanium film for nanofabrication of oxide patterns. *J. Vac. Sci. Technol., B* **2000**, *18* (1), 55–59.
40. Dagata, J.A.; Schneir, J.; Harary, H.H.; Evans, C.J.; Postk, M.T.; Bennett, J. Modification of hydrogen-passivated silicon by a scanning tunneling microscope operation in air. *Appl. Phys. Lett.* **1990**, *56* (20), 2001–2003.
41. Tello, M.; Garcia, R. Nano-oxidation of silicon surfaces: comparison of noncontact and contact atomic-force microscopy methods. *Appl. Phys. Lett.* **2001**, *79* (3), 424–426.
42. Bourgoïn, J.P.; Sudiwala, R.V.; Palacin, S. High speed layer by layer patterning of phthalocyanine Langmuir–Blodgett films by the atomic force microscope. *J. Vac. Sci. Technol., B* **1996**, *14* (5), 3381–3385.
43. Lee, H.; Bae, E.; Lee, W. Fabrication of nanometer scale patterns with organized molecular films. *Thin Solid Films* **2001**, *393*, 237–242.
44. Kim, S.M.; Ahn, S.J.; Lee, H.; Kim, E.R.; Lee, H. A study of positive charge effect on AFM anodization lithography using phosphate monolayers. *Ultramicroscopy* **2002**, *91*, 165–169.
45. Lee, H.; Jang, Y.K.; Bae, E.; Lee, W.; Kim, S.M.; Lee, S. Organized molecular assemblies for scanning probe microscope lithography. *Curr. Appl. Phys.* **2002**, *2* (1), 85–90.
46. Kramer, S.; Fuierer, R. *Chem. Rev.* **2003**, *103* (11), 4367–4418.
47. Ulman, A. *An Introduction to Ultrathin Organic Films from Langmuir–Blodgett to Self-Assembly*; Academic Press: San Diego, 1991.
48. Son, M.-S.; Kim, E.R.; Lee, H. Nanofabrication of a methacrylate-based polymer on a silicon substrate by using atomic force microscope lithography. *J. Korean Phys. Soc.* **2002**, *41* (6), 949–952.

# AFM: Protein Adsorption

David T. Kim  
Harvey W. Blanch  
Clayton J. Radke

*Department of Chemical Engineering, University of California–Berkeley,  
Berkeley, California, U.S.A.*

## INTRODUCTION

Non-specific protein adsorption onto solid surfaces occurs in many important applications. These include drug storage, where adsorption of a therapeutic protein onto the container walls may denature and render the drug inactive, as well as change its solution concentration, posing a major problem when exact dosing is required.<sup>[1]</sup> Protein adsorption can contribute to blood clotting and heart disease;<sup>[2]</sup> the biocompatibility of materials used in medical implants, food processing, and chromatographic media depends on the interaction of proteins with the surface.<sup>[3–8]</sup> Newly developed biosensors and immunoassay methods depend on the immobilization of proteins.<sup>[9]</sup> Fouling of contact lenses is due, in part, to the non-specific adsorption of protein on the lens surface.<sup>[10]</sup> In all of these applications, a fundamental understanding of protein adsorption is required to control the interaction between the protein and the solid.

This entry discusses the role of atomic force microscopy (AFM) in elucidating protein adsorption mechanisms onto solid surfaces. After a brief review of other experimental techniques, we outline the advantages and disadvantages of AFM for in situ study of protein adsorption and summarize findings for AFM available to date. We conclude with a brief discussion of the protein adsorption process.

## OVERVIEW

### Measurement Techniques

A wide range of techniques provides information on protein adsorption onto solid surfaces. Vibrational sum frequency spectroscopy (VSFS)<sup>a</sup> is a surface-specific

non-linear optical technique in which a sum frequency signal is obtained from an ordering of dipoles at surfaces. Moieties that are well aligned at the surface can be observed by VSFS. Using this technique, information on protein organization in addition to water structure and organization can be obtained. In particular, Kim et al.<sup>[11]</sup> used this technique to study the organization of lysozyme at the water/quartz interface at various pH values.

The interaction force between two solid surfaces can be measured as a function of distance by the surface force apparatus (SFA). Claesson et al.<sup>[12]</sup> employed SFA to study a wide range of proteins (globular, unordered, fibrous) and determined protein conformation, orientation, and the operative forces. Small compact globular and soft globular proteins could be distinguished by measuring their compressibility. Blomberg et al.<sup>[13]</sup> used SFA to study the adsorption of lysozyme on mica as a function of protein concentration, determining the protein's adsorption orientation, ability to form multilayers, and adsorption irreversibility.

Conformation information on adsorbed protein is also available from several spectroscopic methods. Circular dichroism spectroscopy (CD), Fourier transform infrared spectroscopy (FTIR), and Raman spectroscopy all probe protein secondary structure. These techniques have been useful in demonstrating how proteins alter their structure upon adsorption. Proteins have been shown to have greater structural perturbation on hydrophobic surfaces, compared to hydrophilic surfaces using CD,<sup>[14,15]</sup> FTIR,<sup>[7]</sup> and Raman spectroscopy.<sup>[8,16]</sup>

A significant amount of literature on protein adsorption is concerned with the kinetics and total mass of protein adsorbed onto a solid surface. The quartz crystal microbalance (QCM) measures the changes in resonance frequency and dissipation factor of an oscillating quartz crystal and can provide information on the adsorbed mass and temporal variations in surface viscoelastic properties. Otzen, Oliveberg, and Hook<sup>[17]</sup> employed QCM to study the adsorption of

<sup>a</sup>A glossary of abbreviations appears at the end of this entry.

protein S6 onto a methyl-terminated quartz surface and found that the adsorption kinetics of protein S6 depends on the equilibrium fraction of denatured protein in the bulk, rather than on the kinetics of bulk denaturation. Upon comparison with optical techniques, such as ellipsometry and optical waveguide light-mode spectroscopy (OWLS), Hook et al.<sup>[18]</sup> showed that QCM reports higher adsorbed mass, this being attributed to water bound to the adsorbed protein.

Total internal reflection fluorescence (TIRF) measures the fluorescence emission of fluorescent-tagged protein triggered by an evanescent wave arising from a totally internally reflected light beam inside an adjacent optically clear adsorption substrate. This method permits adsorption isotherms and adsorption kinetics to be measured. It has also been used to show that proteins reorient and/or undergo conformational change at the surface, depending on the surface concentration,<sup>[19]</sup> the rate of adsorption to the surface,<sup>[19]</sup> and the hydrophobicity of the surface.<sup>[20,21]</sup> These factors all affect the final surface loading.<sup>[22]</sup>

Other optical methods exist to determine adsorption kinetics and isotherms. Ellipsometry gauges the change in polarization of light that is reflected from the surface of a sample. This technique requires a reflecting surface. In OWLS, light is totally internally reflected within an optical waveguide, setting up an evanescent wave in the nearby solution. The electric and transverse magnetic modes of the evanescent wave are then measured. In surface plasmon resonance (SPR), a laser beam undergoes total internal reflection at the adsorption glass/metal interface. Coupling between the photon and a surface plasmon causes excitation of surface plasmon at the interface and a reduction in intensity of the internally reflected light. Scanning angle reflectometry (SAR) is another optical method that is used to determine protein adsorption isotherms and kinetics. All these techniques measure the adsorption thickness and the refractive index of the layer above the adsorption interface, which can then be used to calculate adsorbed mass. Surface plasmon resonance<sup>[23]</sup> and ellipsometry<sup>[24]</sup> show how adsorption packing and kinetics vary for proteins of various dimensions and conformations. Ellipsometry has shown that more protein adsorbs onto hydrophobic surfaces compared to hydrophilic surface.<sup>[25]</sup> Ellipsometry also has been used to show that more protein is irreversibly adsorbed on hydrophobic surfaces<sup>[26]</sup> and that the degree of irreversibility is time dependent.<sup>[25,26]</sup> Time-dependent spreading of protein at the interface has been studied using OWLS<sup>[27]</sup> and ellipsometry.<sup>[25]</sup> Multilayer formation for lysozyme has been observed using ellipsometry.<sup>[24,28]</sup> Optical techniques have been used to study how ionic strength affects protein adsorption area,<sup>[29]</sup> adsorption isotherms,<sup>[28,30]</sup> kinetics,<sup>[28]</sup> and irreversibility.<sup>[28]</sup>

## Atomic Force Microscopy Techniques

All of the above experimental techniques provide information on length scales much larger than the dimensions of a single protein molecule. Hence they cannot provide data on the spatial distribution of proteins on a surface. Conversely, atomic force microscopy (AFM) enables direct observation of real-space topographic surfaces on a nanometer scale and can, in principle, detect the spatial distribution of adsorbed protein. Atomic force microscopy can image surfaces in solution, so that proteins remain in an aqueous environment. By imaging in situ, adsorption dynamics are observable. By combining the real-time and real-space resolution of AFM, one obtains information on the spatial and temporal distribution of adsorbed protein. The literature on AFM studies of proteins is vast. However, most studies are primarily concerned with imaging large, isolated single-protein molecules<sup>[31–33]</sup> and not on adsorption patterns and mechanisms. We review studies on the fundamentals of the protein adsorption process. Table 1 contains a listing of AFM research that we mention in this entry, along with the particular properties studied.

Access to lateral spatial information on protein adsorption enables supramolecular organization on the surface to be observed in real time. This includes the ability to directly observe clustering and multilayer formation. Height differences across the surface provide information on the adsorbed protein conformation and orientation and their changes in time. Non-uniform surfaces can be imaged, allowing comparison between protein adsorption on differing surface chemistry and on patterned interfaces. Atomic force microscopy provides information on the interaction forces between the protein-covered surface and the scanning probe and mechanical properties using the force-distance-curve feature.

## ATOMIC FORCE MICROSCOPY

### Features

Originally designed to measure the topography of surfaces, AFM has the potential to obtain atomic-scale spatial resolution. Although specific designs differ, AFM generally operates by raster scanning a fine, cantilevered tip over a solid surface while measuring tip deflection with a laser. As the tip encounters features on the surface, the tip deflects; the feedback mechanism moves the sample closer or farther from the cantilever-tip assembly in response. This height movement, in addition to the raster scanning movement, is controlled to angstrom precision by a piezoelectric crystal. It is the height of the sample surface (rather

**Table 1** Atomic force microscopy studies highlighted in this entry

First author	Protein	Surface	Real time	Multilayer	Protein structure and orientation	Non-uniform surfaces	Force curves	Comments	Reference
Chen, X. et al.	BSA, BFG	PS					×	Change in adhesion as protein film forms, breakthrough force to surface increases with time	[67]
Coen, M.C. et al.	Protein A	Silicon		×	×			Multilayer formation over time, subsequent layers become less structurally perturbed	[55]
Cullen, D.C. et al.	IgG and GOx	HOPG	×		×			Comparison of adsorption mechanisms for two structurally different proteins	[56]
Galli, G. et al.	Protein A and F-actin	Si and Ti, nanostructures				×		Effects of nanostructures on protein adsorption	[62]
Kim, D.T. et al.	Lysozyme	Mica	×	×	×		×	Complete monolayer formation monitoring, multilayer formation, tip contamination issues	[45]
Mueller, H. et al.	Cytochrome c, MBP	Lipid bilayers	×					Adsorption behavior on mixed acidic, basic, and zwitterionic lipid bilayers	[54]
Radmacher, M. et al.	Lysozyme	Mica					×	Classic force curve work on lysozyme, analysis of adhesion, estimation of viscosity and Young's modulus	[66]
Raghavachari, M. et al.	VWF	Mica and OTS/glass			×			Hydrophobicity determines adsorbed protein structure	[59]
Sheller, N.B. et al.	HAS	CH <sub>3</sub> SAMs			×			Protein coverage at surface determines adsorbed protein structure	[48]
Ta, T.C. et al.	BFG	HOPG and mica	×		×			Hydrophobicity determines adsorbed protein structure	[37]
Ta, T.C. et al.	BFG	CH <sub>3</sub> and COOH SAMs	×		×	×		Hydrophobicity determines adsorbed protein structure	[44]
Takahara, A. et al.	BSA	OTS/FOETS mixed monolayer	×			×		Adsorption behavior on mixed monolayer at different pH conditions	[51–53]

See [Abbreviation Glossary](#).

than the tip deflection) that is reported as the height of features on the surface.

Two main methods for imaging topographical features exist. In “contact mode,” the tip is kept in constant contact with the surface while maintaining a constant force (or deflection). The instrument feedback loop operates by raising or lowering the sample surface to maintain a constant tip force. This is the original method of operation for the AFM; it has the advantage of high resolution. Continuous improvements in preparation techniques and imaging conditions make it possible to image proteins with lateral resolution of  $\sim 0.5$  nm and vertical resolution of  $\sim 0.1$  nm in this mode.<sup>[34,35]</sup> “Tapping-mode” imaging was developed to reduce possible damage to the sample that results from the tip “dragging” along the surface. This is especially relevant for “soft” biomolecules such as proteins. Tips can damage protein structure and sweep away loosely adsorbed biomolecules. In tapping-mode imaging, the cantilevered tip oscillates at resonance frequency and only intermittently “taps” the surface at the bottom of its oscillation. In this imaging mode, the feedback loop maintains a constant oscillation amplitude, rather than the tip force. Using tapping mode, proteins that are loosely adsorbed can be imaged without being swept away by the scanning tip.<sup>[31]</sup> The lateral resolution suffers somewhat in this mode, but is still sufficient to monitor protein adsorption.

A major advantage of AFM is that imaging can be performed in liquid solution. Thus protein can be imaged in aqueous solution. With a fluid flow cell, the liquid environment can be changed while the sample remains on the surface. Thus protein solution, surfactant solution, or different buffer solutions can be introduced. Imaging adsorbed proteins after drying the surface is a common application. Although sample preparation and imaging in open air tends to be easier and faster, we caution that the drying process may distort protein structure and pattern formation. In most, but all of the images presented in “Atomic Force Microscopy and Protein Adsorption,” the tapping mode in aqueous environment is employed.

Other imaging variations for the AFM exist. One mode, known as lateral- (or friction-) force mode can “image” a force map by detecting differences in chemistry and mechanical properties at the surface. This is possible by operating the AFM in contact mode and measuring the “twisting” of the cantilever as the tip moves over different regions of the sample. Twisting of the cantilever is a result of the tip adhering to the surface as it is scanned; the amount of twisting is a function of the adhesion between the tip and surface. A resulting friction map distinguishes parts of the surface with different chemistry and/or mechanical properties.

In addition to imaging, AFM is able to measure the interaction normal force between the tip and the surface. This occurs by measuring the tip deflection as the surface approaches the probe tip, comes into contact, slightly pushes the tip, then retracts and separates from the tip. Information is garnered on the physical and mechanical properties of surfaces and the interaction forces between the tip and surface. When the interaction between the surface and tip material is not of direct interest, tips can be coated with proteins or monolayers that expose a specific chemical functionality to probe-specific interactions. This is sometimes referred to as chemical force microscopy.<sup>[36]</sup> If force curves are taken at regular distances over a surface, a so-called force-volume (actually force-area) map can be created. In a force-volume map, the tip deflection from a force curve at a defined tip-sample distance is mapped into a two-dimensional array. This discloses the tip interactions with the surface over various regions of the surface. The force-volume map can be compared to the topographical surface images and physical features on the surface can be correlated to the force interactions.

### Imaging Artifacts

Care should be taken when interrogating AFM images. Interpreting images without cognizance of possible artifacts can lead to misinterpretation. Because AFM is an intrusive process, the probe tip may mechanically induce protein adsorption patterns on the surface, possibly contributing to the overall adsorption process. Many researchers have reported the “sweeping” action of the tip. Ta, Sykes, and McDermott<sup>[37]</sup> and McMaster et al.<sup>[38]</sup> both reported streaky images attributable to tip mechanical influence. Denis et al.<sup>[39]</sup> found that elongated structures were bent toward the left or right depending on the scanning direction of the tip. Johnson, Yuan, and Lenhoff<sup>[40]</sup> attributed bare patches devoid of adsorbed molecules to the tip sweeping away protein molecules. Immunoglobulin G (IgG)<sup>[41]</sup> and immunoglobulin M (IgM)<sup>[42]</sup> are known to aggregate on mica as a result of tip mechanical influence.

Contamination of the AFM tip by unwanted particles in solution or particles garnered from the surface is a common problem and is difficult to avoid. Depending on the scanning size, the effects on imaging may be significant. Tip contamination alters the tip-surface interaction force and may have a significant effect on the height information obtained.<sup>[43]</sup> In Ta and McDermott's<sup>[44]</sup> studies with friction-force microscopy, the authors observed that tip contamination probably occurred and affected the magnitude of the tip friction. Fortunately, their studies were directed at friction contrast, rather than absolute values. In our



work with in situ lysozyme adsorption onto mica, tip contamination distorted the apparent size of the protein adsorbed onto the surface, compounding the problem of tip broadening.<sup>[45]</sup>

With tip broadening, the AFM image is enlarged as a result of a convolution of the imaged particle and the imaging tip.<sup>[46,47]</sup> Tip broadening is significant when the size of the imaged particle is of the same length scale of the tip point, which is the case for proteins. Enlargement of the image causes overestimation of the amount of protein adsorbed onto the surface, making quantitative assessment of adsorption amounts problematic. Sheller, Petrash, and Foster<sup>[48]</sup> have shown that a grain size analysis of the unmodified image of albumin adsorption yielded a value of 10–15% coverage. However, after taking into account tip broadening, the coverage was reduced to 3–4%. In Ta, Sykes, and McDermott<sup>[37]</sup> studies with fibrinogen adsorption, it is difficult to identify early adsorption features as single molecules or clusters. Thus these researchers considered the adsorbed particles to be clusters of protein. In the work of Kim et al.<sup>[45]</sup> with lysozyme and mica, tip contamination contributed to the tip-broadening problem. This can be seen in Fig. 1. We initially interpreted the observed enlargement of the protein features on the surface as a result

of cluster growth over time. However, this was disproved when after 19 hr (Fig. 1D), smaller clusters were again observed, presumably after the tip was inadvertently “cleaned” of debris. There exist methods to characterize the shape of the tip so that the amount of broadening can be estimated.<sup>[49,50]</sup> However, the amount of contamination can change at any time during imaging or exposure to protein solution, as documented in Kim et al.<sup>[45]</sup>

Finally, we remark that AFM is limited to surfaces that are smooth on the length scale of the protein molecules or aggregates. Accordingly, solid surfaces studied to date include mica, graphite, silicon (i.e., actually a SiO<sub>2</sub> overgrowth), selected polymers, and coated monolayers on these surfaces.

### ATOMIC FORCE MICROSCOPY AND PROTEIN ADSORPTION

One of the main advantages of AFM over other techniques is its ability to gather information on the supramolecular organization of adsorbed protein. Atomic force microscopy, unlike optical techniques such as OWLS, SPR, TIRFS, or ellipsometry, has superb lateral spatial resolution. Further, unlike electron

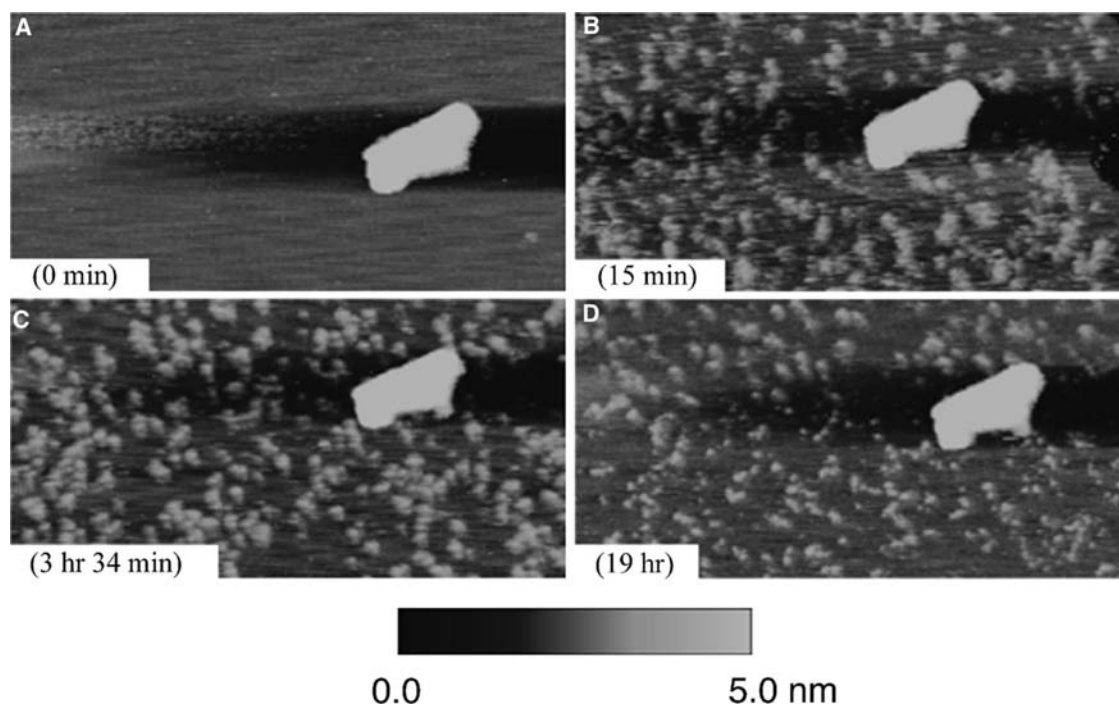


**Fig. 1** Effect of tip contamination on AFM imaging. Atomic force microscopy images of adsorption of HEWL on mica in 10 mM acetate buffer, pH 4.0, under stopped-flow conditions. Initial bulk concentration of HEWL is 2  $\mu\text{g}/\text{mL}$ . Each image was taken at the exact same location. A large prominent white feature (i.e., debris) marks the same location on the mica surface. (A) Bare mica before exposure to protein solution. (B) Lysozyme adsorption after 15 min, (C) 3 hr 34 min, and (D) 19 hr. Note that in this last scan, the particles below the large feature are much smaller than those above the feature and those scanned at earlier times. All images are 250 nm  $\times$  500 nm. *Source:* Reprinted From Ref.<sup>[45]</sup> with permission from The American Institute of Physics.

microscopy, sample preparation is relatively easy. Protein adsorption events can be observed in situ in aqueous environments and in real time.

## Supramolecular Organization

### Real-time imaging

Takahara et al.<sup>[51–53]</sup> observed a real-time increase of bovine serum albumin (BSA) coverage on surfaces covered with *n*-octadecyltrichlorosilane (OTS) islands surrounded by 2-perfluorooctyltrichlorosilane (FOETS) at both pH 4.7 and 7.5. Complete monolayer coverage can be obtained with sufficient protein in solution. Mueller, Butt, and Bamberg<sup>[54]</sup> imaged myelin basic protein (MBP) adsorption onto negatively charged, acidic lipid bilayers supported on mica and observed that protein elevations on the surface grew laterally and eventually fused with neighboring protein elevations to form a complete monolayer. As reported in Fig. 2, hen egg white lysozyme (HEWL) formed clusters on mica that increased in number until a complete monolayer was formed.<sup>[45]</sup> Coen et al.<sup>[55]</sup> saw similar adsorption patterns for protein A adsorbing onto silicon.

Because of its excellent lateral resolution, AFM can distinguish between different adsorption patterns. Cullen and Lowe<sup>[56]</sup> examined how protein and surface structures dictate adsorption patterns by adsorbing IgG and glucose oxidase (GOx) onto highly oriented pyrolytic graphite (HOPG), as shown in Figs. 3 and 4. Within minutes, patches of IgG containing 300–500 molecules were observed across the HOPG plane (Fig. 3B). Over time, more patches at random locations appeared on the surface until a complete monolayer formed (Fig. 3D). Conversely, in Fig. 4, GOx nucleated initially at HOPG defects. Subsequent adsorption occurred at locations adjacent to protein already adsorbed, forming “sheets” of protein and leaving regions of bare HOPG. In both cases, the protein appeared to aggregate on the surface, which is likely a result of hydrophobic residues exposed during adsorption conformation change leading to favorable intraprotein interaction at the surface. The differences in adsorption patterns arise from physicochemical differences between the two proteins, which we will discuss later.

Conversely, Ta et al.<sup>[37,44]</sup> demonstrated how differences in the hydrophobicity of the solid surface affect protein adsorption patterns. Fig. 5 displays consecutive

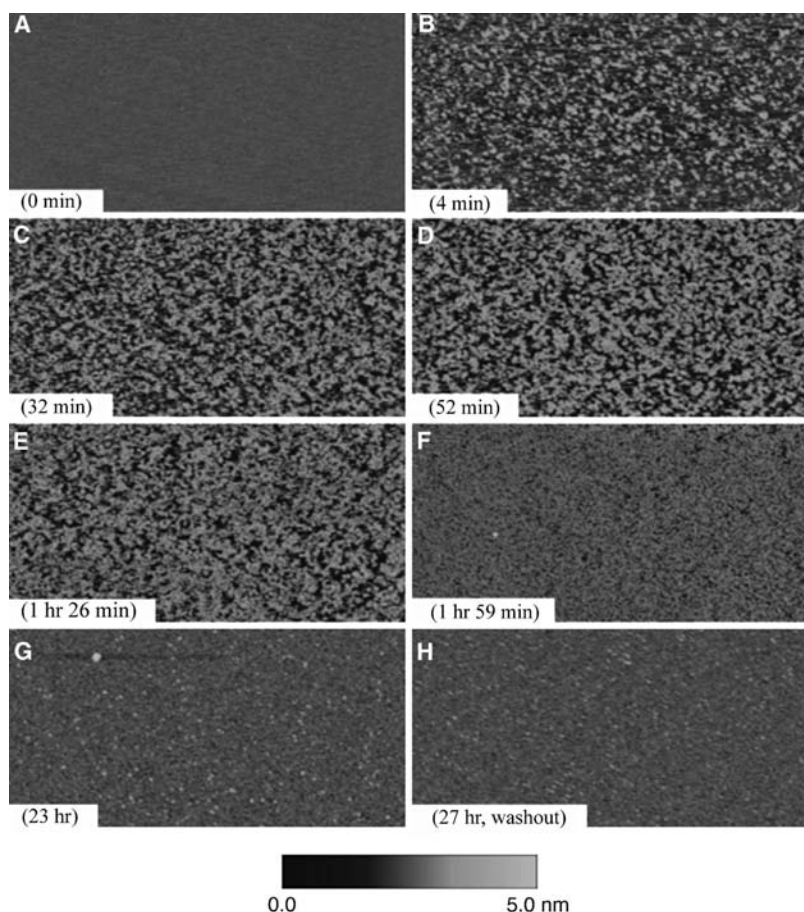


**Fig. 2** Lysozyme adsorption onto mica. Atomic force microscopy images of adsorption of HEWL on mica in 10 mM acetate buffer, pH 4.0, under stopped-flow conditions. The initial bulk concentration of HEWL is 5  $\mu\text{g}/\text{mL}$ . Each image is 500 nm  $\times$  100 nm. The light areas are clusters of protein molecules and the dark areas represent the bare mica surface. (A) Bare mica surface before contact with the protein solution. (B) Lysozyme adsorption after 4 min, (C) 32 min, (D) 52 min, (E) 1 hr 26 min, (F) 1 hr 59 min, and (G) 23 hr. (H) Washout with buffer after 27 hr. *Source:* Reprinted from Ref.<sup>[45]</sup> with permission from The American Chemical Society.

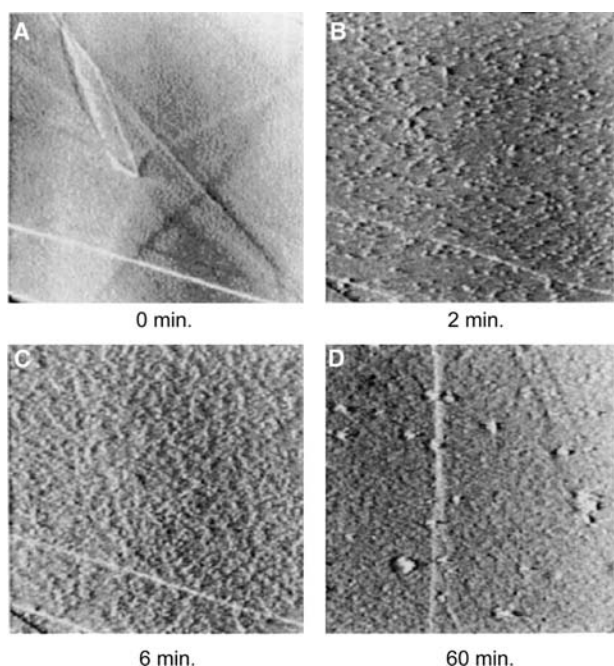


**Fig. 3** Immunoglobulin G adsorption onto HOPG. Time-resolved AFM images of the adsorption of IgG from a phosphate-buffered saline (PBS) solution with a bulk concentration of  $50 \mu\text{g/mL}$  of protein to a freshly cleaved HOPG surface. Image size: (A–C)  $5.3 \mu\text{m} \times 5.3 \mu\text{m}$ , (D)  $5 \mu\text{m} \times 5 \mu\text{m}$ . All images were obtained with an applied repulsive force of  $\sim 1 \text{ nN}$  and presented as left-shaded topographic images. *Source:* Reprinted from Ref.<sup>[56]</sup> with permission from Elsevier.

AFM images of bovine fibrinogen (BFG) film growth on HOPG. At 75 sec (Fig. 5C), a network of branched strands can be observed extending across the HOPG plane with no apparent preference for step defects. After 125 sec (Fig. 5E), more networks of branched strands are apparent. A complete monolayer is formed after 225 sec (Fig. 5G). Fig. 5H shows a friction image of the complete monolayer, indicating that the frictional forces between the tip and protein film are low and constant, meaning that the protein structure is robust and crystalline-like.

On mica, as depicted in Fig. 6, BFG homogeneously adsorbed across the surface until a full monolayer was formed. This adsorption process is very similar to that of lysozyme on mica shown in Fig. 2. The authors also compared BFG adsorption onto octadecanethiol (ODT;  $\text{CH}_3$ -terminated) and mercaptohexadecanoic acid (MHA;  $\text{COOH}$ -terminated) self-assembled monolayers (SAMs) supported on gold-covered glass.<sup>[44]</sup> The hydrophobic,  $\text{CH}_3$ -terminated surface showed similar adsorption behavior to that of the HOPG surface, with strand-like surface features gradually filling in the surface to form a smooth, well-packed, uniform monolayer. Friction-force images showed that the friction properties across the surface did not significantly

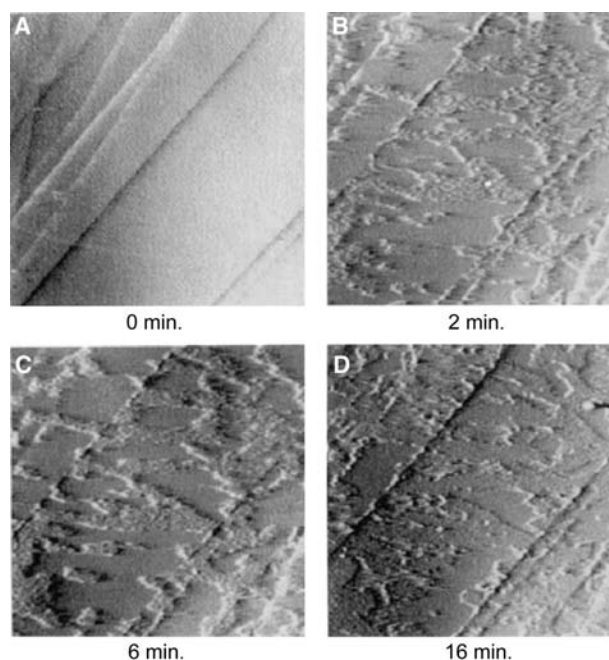


**Fig. 4** Glucose oxidase adsorption onto HOPG. Time-resolved AFM images of the adsorption of GOx from a phosphate-buffered saline (PBS) solution with a concentration of  $50 \mu\text{g/mL}$  of protein to a freshly cleaved HOPG surface. All images are  $5 \mu\text{m} \times 5 \mu\text{m}$  in area, imaged with an applied repulsive force of  $\sim 1 \text{ nN}$  and presented as left-shaded topographic images. *Source:* Reprinted from Ref.<sup>[56]</sup> with permission from Elsevier.

change during the adsorption process. However, the hydrophilic,  $\text{COOH}$ -terminated surface showed different adsorption behavior to that of the mica surface. Instead of homogeneously filling the surface as in Fig. 6, on the  $-\text{COOH}$  surface, circular, island-like domains 4-nm in height appeared on the surface and grew laterally, ultimately forming a complete, well-packed layer. Friction-force images in this case showed friction contrast between the adsorbed protein and bare surface. The discrepancy between the adsorption patterns on the hydrophilic mica and the  $\text{COOH}$ -terminated surface may be because of the specific chemical differences at the interface such as polarity and charge density and distribution.

#### Multilayer formation

With AFM, one can visually determine the existence of multilayers and when and how they occur. Kim et al.<sup>[45]</sup> showed that lysozyme formed a second layer of adsorption (Fig. 2G), only after the first monolayer was complete (Fig. 2F). In addition, formation of the second layer was significantly slower than the first. Coen et al.<sup>[55]</sup> showed that protein A, when adsorbed on silicon, also formed multilayers as pictured in Figs. 7 and 8. Fig. 7A shows an incomplete monolayer



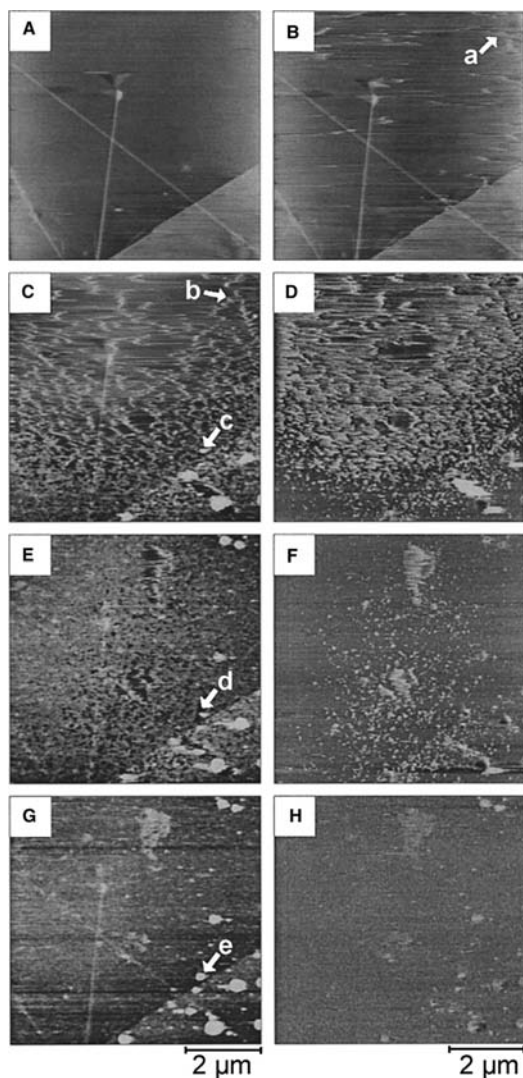


**Fig. 5** Bovine fibrinogen adsorption onto HOPG.  $6.6\ \mu\text{m} \times 6.6\ \mu\text{m}$  consecutive AFM images of BFG film growth on HOPG monitored in real time with continuous flow. Parts A and B are topographic images ( $z$ -scale = 10 nm). Parts C, E, and G are sequential topographic images ( $z$ -scale = 10 nm) while parts D, F, and H are the corresponding lateral force images ( $z$ -scale = 0.2 V). For timing purposes, the center of the scan in part B is defined as  $t = 0$ , as this is the point initial adsorption is observed. C and D were captured 75 sec after initial adsorption. E and F correspond to 125 sec, and G and H correspond to 225 sec. Arrow a highlights a BFG strand that elongates to a branching point shown in arrow b. Arrow c demarks the growth of a single aggregate later fully formed and highlighted by arrow e. Arrow d indicates a defect site on the HOPG plane. Source: Reprinted from Ref.<sup>[37]</sup> with permission from the American Chemical Society.

of protein A, with the dark spots indicating locations of bare silicon. The existence of a single incomplete monolayer in Fig. 7 was confirmed using X-ray photoelectron spectroscopy (XPS). As with lysozyme

adsorption on mica, subsequent protein layers seen in Fig. 8A did not form until the previous monolayer was complete. The cases of lysozyme on mica and protein A on silicon differ in their electrostatic conditions. At pH 4.0, mica is negatively charged while the lysozyme is positively charged. For the protein A/silicon system, at pH values between 5 and 6, the protein is slightly negatively charged and the surface is also negatively charged. Despite differences in charge conditions, both systems displayed multilayer formation. The role of electrostatics in protein adsorption is covered later.

### Adsorbed Protein Structure and Orientation

Using AFM, it is possible to ascertain adsorbed protein structure and orientation. Although height information (i.e., adsorbate layer thickness) is available from other experimental techniques, AFM has the advantage of directly imaging differences in terrain height with nanometer lateral resolution. Optical techniques average over hundreds of nanometers.

Several researchers have shown with AFM that proteins exhibit structural changes and lateral spreading at the surface. Bovine fibrinogen adsorbed onto ODT ( $\text{CH}_3$ -terminated) SAMs displays an adsorbed AFM height of 1–1.5 nm that is in contrast to the adsorbed height of 4 nm on MHA ( $\text{COOH}$ -terminated) SAMs.<sup>[44]</sup> The smallest dimension of the BFG molecule obtained from X-ray crystallography is 4–6 nm. The lower height on the  $\text{CH}_3$ -terminated SAMs is indicative of more extensive conformational spreading on that surface, which is a result of its more hydrophobic nature. Glucose oxidase was also shown to have a lower adsorbed height of 5–8 Å on HOPG<sup>[56]</sup> compared to the dimensions of the native protein ( $7.0 \times 5.5 \times 8.0\ \text{nm}$ ).<sup>[57]</sup> However, not all proteins show extensive lateral spreading on hydrophobic surfaces. The thickness of IgG films on HOPG was shown to be 3 nm, compared to the dimensions of the protein given by X-ray crystallography ( $14.2 \times 8.5 \times 3.8\ \text{nm}$ ).<sup>[58]</sup> In fact, using AFM, Raghavachari et al.<sup>[59]</sup> have shown an apparently opposite behavior. Fig. 9 illustrates the hydrophilic mica surface after 1 hr of exposure to von Willebrand factor (VWF) followed by protein-free phosphate buffer saline (PBS) wash-out. The VWF on this surface adopted a spread-out conformation. On the hydrophobic OTS surface, shown in Fig. 10, VWF maintained a “ball of yarn” configuration.

Different amounts of spreading were observed for subsequent layers in the multilayer adsorption of protein A on silicon.<sup>[55]</sup> The first monolayer exhibited a height of approximately 1 nm. This is shown in Fig. 7B by the section line of the silicon surface after

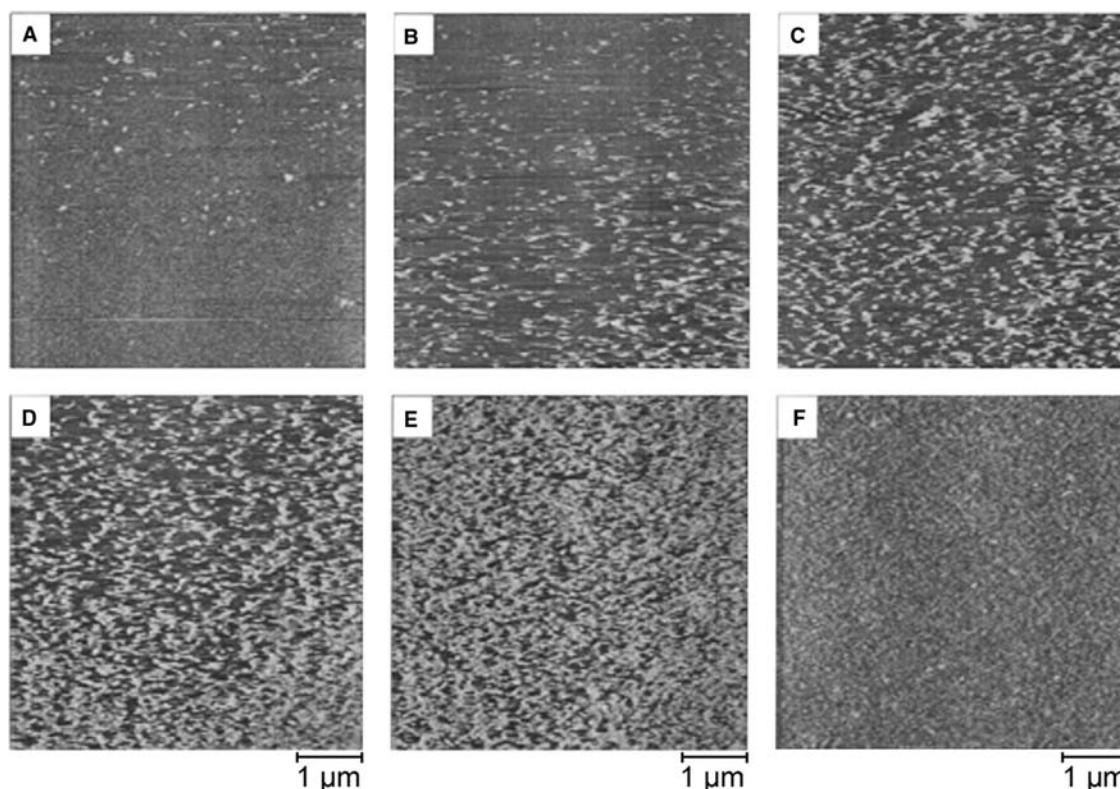


**Fig. 6** Bovine fibrinogen adsorption onto mica. Atomic force microscopy images,  $5\ \mu\text{m} \times 5\ \mu\text{m}$ , of BFG film growth on mica monitored in real time with continuous flow. All images are topographic with a  $z$  scale = 10 nm except for part A, where the  $z$  scale = 5 nm. (A) Upward scan  $t = 0$  sec is defined at halfway through the scan. (B) Successive downward scan, with an elapsed time of 75 sec. (C) Successive upward scan with an elapsed time of 125 sec. (D) Successive downward scan with an elapsed time of 175 sec. (E) Successive upward scan with an elapsed time of 225 sec. (F) Upward scan with an elapsed time of 325 sec. *Source:* Reprinted from Ref.<sup>[37]</sup> with permission from The American Chemical Society.

15 sec of adsorption. The size of native protein A is roughly 3 nm.<sup>[55]</sup> Thus a significant amount of lateral spreading (and likely unfolding) occurred in the first layer of adsorbed protein, assignable to direct contact with the silicon surface. The height of the second monolayer was considerably larger at 2–3 nm (Fig. 8B), indicating less structural perturbation. The height on the third monolayer was approximately 3 nm (not shown.) Thus Coen et al.<sup>[55]</sup> concluded that the protein in the third layer was not conformationally altered. Each new monolayer adsorbs onto a different surface. Therefore it is not surprising that the adsorbed protein structure differs in each layer. However, given very long time exposure to the surface, protein in the multilayers may continue to rearrange, slowly unfolding and aggregating into the sublayer.

In many cases, protein molecules were observed to adsorb in a side-on orientation on solid surfaces. Kim et al.<sup>[45]</sup> showed that the height of adsorbed lysozyme on mica was approximately 2.5 nm while the native protein dimensions from X-ray crystallography are  $3 \times 3 \times 4.5$  nm.<sup>[60]</sup> The height of adsorbed C hordein on mica is 2–3 nm<sup>[38]</sup> while the dimensions of

the protein are 1.9 nm in width by 28.2 nm in length.<sup>[61]</sup> By adsorbing in a side-on fashion, the protein maximizes contact with the surface.

There are cases where protein does not adsorb in a side-on fashion. Sheller, Petrash, and Foster<sup>[48]</sup> examined human serum albumin (HSA) adsorption onto hexadecyltrichlorosilane (HTS;  $\text{CH}_3$ -terminated) SAMs and found that the adsorbed orientation depends on surface concentration. For low submonolayer coverage, as shown in Fig. 11C,D, the height profile of protein adsorbed onto the surface measured by AFM was 3.6–3.7 nm. Protein films of a full monolayer, as shown in Fig. 11A,B, had a thickness of 16–17 Å as measured by X-ray reflectivity. Sheller et al. suggested that for higher surface coverage of protein, there is a significant net removal of weakly adsorbed protein from the surface by adjacent, strongly adsorbed protein spreading on the surface. This implies that the stronger adsorbed protein undergoes structural changes to a greater extent giving more contacts with the surface. When the surface coverage is low, the exchange process is not significant, and proteins adsorb in any configuration. Thus both strongly and weakly bound protein

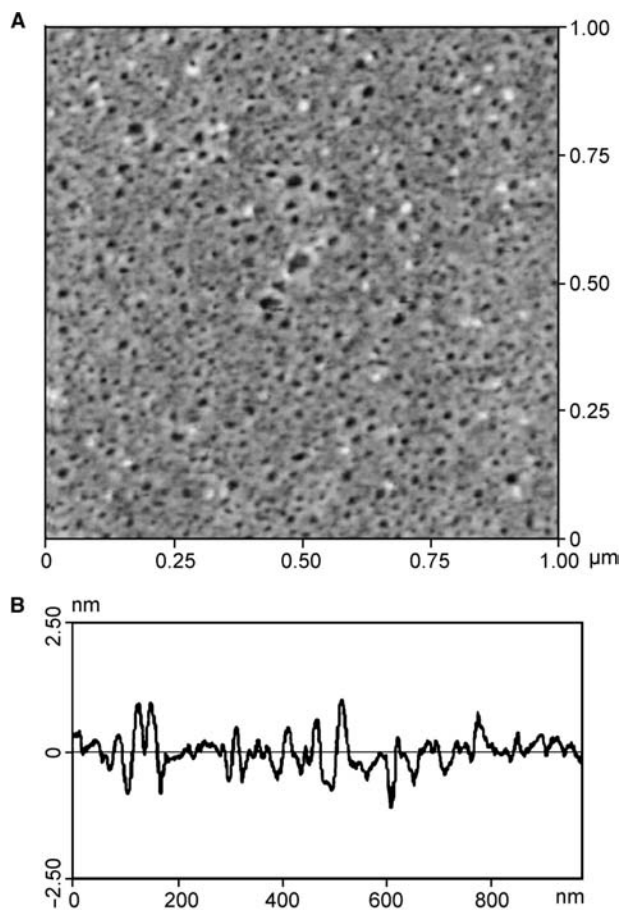


**Fig. 7** Protein A adsorption onto silicon. (A) Atomic force microscopy picture of the silicon surface after a 15-sec adsorption of protein A from a 0.1 mg/mL solution. The first monolayer of protein A is almost complete. Bare mica is evidenced by the black spots in the image. The vertical scale is 5 nm. (B) Line section of the AFM image displaying the height of features. *Source:* Reprinted from Ref.<sup>[55]</sup> with permission from Elsevier.

adhere to the surface with varying degrees of conformation change. Sheller et al. do not provide experimental evidence that weakly bound protein remains on the surface for long exposure times.

### Non-uniform Surfaces

The exceptional lateral resolution of AFM allows study of non-uniform and patterned surfaces and of the differences in protein adsorption as a direct result of surface non-uniformities. Patterned surfaces presenting both hydrophobic and hydrophilic regions highlight the differences in the degree of hydrophobicity on protein adsorption.<sup>[44]</sup> Fig. 12 shows a topographical (A) and friction image (B) of a protein-free surface, patterned with ODT and MHA SAMs. These images illustrate that the two SAMs are topographically

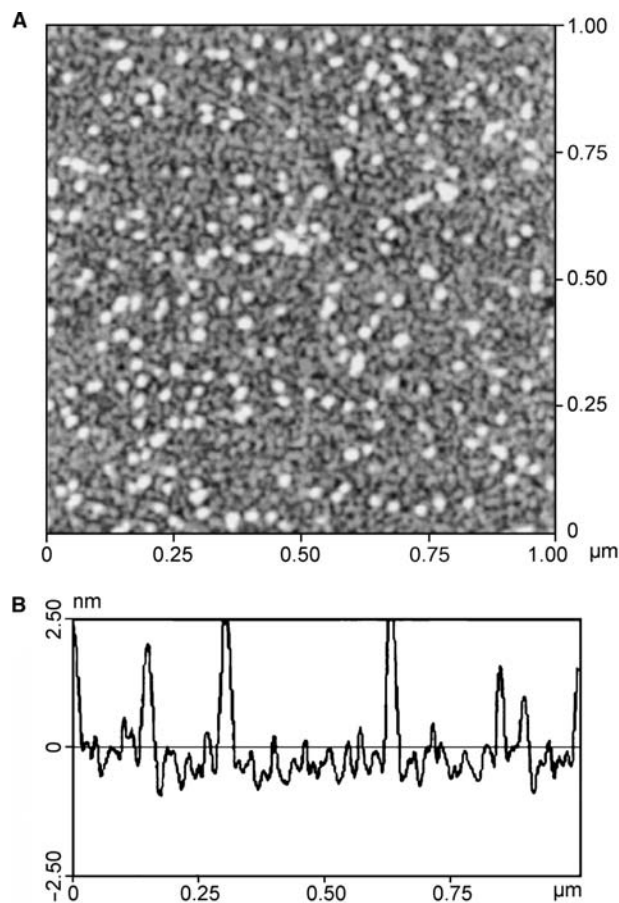


**Fig. 8** Protein A multilayer adsorption onto silicon. (A) Atomic force microscopy picture of the silicon surface after an 8-min adsorption of protein A from a 0.1 mg/mL solution. A second layer of adsorbed protein is evident as the brightest spots. The vertical scale is 5 nm. (B) Line section of the AFM image displaying the height of features. *Source:* Reprinted from Ref.<sup>[55]</sup> with permission from Elsevier.

rather similar, but the friction-force image establishes that the tip experiences different adhesive forces on the two SAMs. Fig. 13 presents friction images of the patterned surface before (Fig. 13A) and during exposure to bovine fibrinogen (BFG) solution (Fig. 13B–D). Image D was collected after 22 min of exposure to the protein solution and again shows that the tip experiences different adhesive forces now on the fibrinogen layers of each type of SAM. This result indicates that the protein adsorbs on both surface regions, but in a different conformation or orientation on the hydrophobic (CH<sub>3</sub>-terminated) and hydrophilic (COOH-terminated) surfaces.

Patterned surfaces also highlight differences in adsorption behaviors on different surfaces with varying electrostatic conditions.<sup>[51–53]</sup> Fig. 14A shows a mixed monolayer consisting of OTS surrounded by FOETS supported on a silicon substrate. When



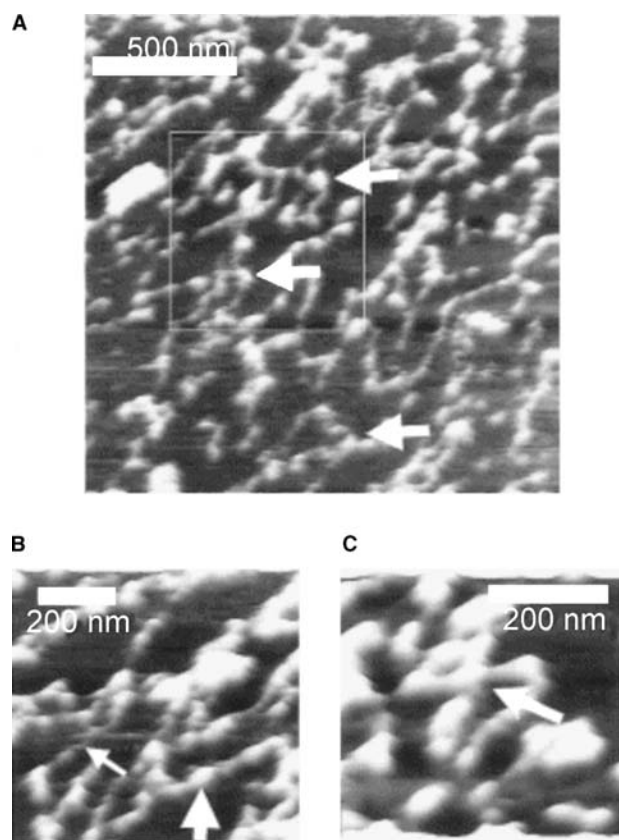


**Fig. 9** von Willebrand factor adsorption onto mica. A is an AFM image ( $2\mu\text{m} \times 2\mu\text{m}$  scan) of VWF multimers adsorbed on hydrophilic mica and imaged under PBS. Most of the VWF molecules are extended and are not ball of yarn structures. Extended VWF multimer chains overlap with themselves and with neighboring chains (arrows). Intramolecular structural features in the VWF multimer chain are discernible. Individual chains of multimers are not clearly distinguishable because of the high surface density of VWF. Mean lateral dimensions of the VWF multimers are  $640 \pm 161\text{ nm} \times 303 \pm 113\text{ nm}$ . B and C are expanded AFM images of VWF on mica, showing intramolecular structural features of individual chain VWF multimers. VWF chains are composed of globular domains (B, large arrow) joined by thin rod-like interconnecting sections (B, small arrow). C contains an example of a crossover (see arrow) of the VWF multimer chain within the same VWF chain. *Source:* Reprinted from Ref.<sup>[59]</sup> with permission from Elsevier.

exposed to a BSA solution at pH 7.5, only the FOETS regions demonstrated significant adsorption, as illustrated in Fig. 14B. However, at pH 4.7, the isoelectric point of BSA, the protein adsorbed to both phases, as demonstrated in Fig. 14C. Although BSA adsorbed onto both OTS and FOETS surfaces when uncharged, it has an apparently higher affinity for FOETS, which is, apparently, more hydrophobic than OTS. At pH 7.5, the protein carries a net negative charge and readily adsorbed on FOETS. Adsorption onto the

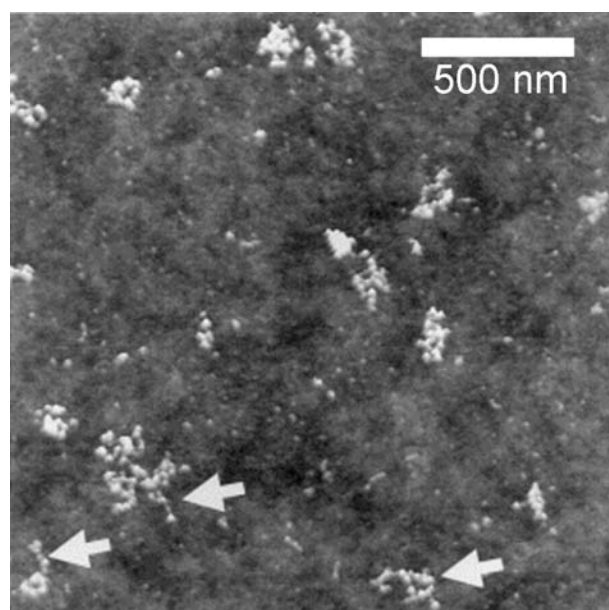


**Fig. 10** von Willebrand factor adsorption onto OTS. Atomic force microscopy image ( $2\mu\text{m} \times 2\mu\text{m}$  scan) of VWF multimers adsorbed on hydrophobic OTS and imaged under PBS. Most VWF multimers display the characteristic compact ball of yarn structures observed by electron microscopy. Each VWF multimer is closely packed with intramolecular overlap and crossover of chains. Intramolecular structural features of the VWF multimer chain are resolved. However, the compact arrangement of the chain makes it difficult to discern the structural features belonging to neighboring repeat units. In some multimer chains, short sections are not as compact and appear extended (arrows). Completely extended chains are rare. None are seen in this image area. The average lateral dimensions of the VWF multimers are  $256 \pm 74\text{ nm} \times 152 \pm 62\text{ nm}$ . *Source:* Reprinted from Ref.<sup>[59]</sup> with permission from Elsevier.

OTS phase was possibly prevented by electrostatic repulsion from already adsorbed negatively charged protein on the FOETS phase.<sup>[51–53]</sup>

The effects of the physical differences in terrain on protein adsorption can also be elucidated by AFM. Galli et al.<sup>[62]</sup> examined the effect of nanostructures created by local anodic oxidation on protein adsorption. They created elevated lines 30–40 nm in width and 1–3 nm in height on silicon (Si) and titanium (Ti) surfaces (actually  $\text{SiO}_2$  and  $\text{TiO}_2$  overgrowths, respectively). Fig. 15 shows an AFM image of the 1-nm high lines on Si. Fig. 16 shows that the lined nanostructures (highlighted with arrows) made no difference to protein A (a globular protein with a size of 3 nm) adsorption in terms of adsorbed amount. In contrast, F-actin, a filamentous protein with a diameter between 6.5 and 8.2 nm, had a tendency to adsorb along the 1-nm-high nanostructured lines, whereas no preferential orientation occurred on the flat surfaces. Fig. 17 shows F-actin adsorbed on the Si surface containing



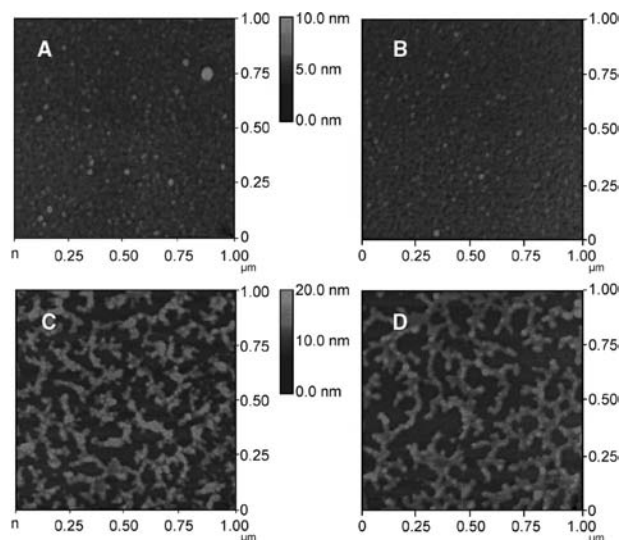


**Fig. 11** Human serum albumin adsorption onto HTS. Atomic force microscopy images of substrates covered with HTS SAMs with HSA layer adsorbed at different bulk protein concentrations: (A) 0.5 mg/mL; (B) 0.1 mg/mL; (C) 0.05 mg/mL; (D) 0.01 mg/mL. Note that the  $z$  range in images a and b is one-half that in images C and D. Images A and B represent full monolayer coverage while images C and D show incomplete monolayer coverage. Source: Reprinted from Ref.<sup>[48]</sup> with permission from The American Chemical Society.

nanostructures 1 nm in height. Fig. 18 shows F-actin adsorption on Ti with 1- and 3-nm nanostructures and with no nanostructures. Thus on Si and Ti, F-actin had a tendency to adsorb along 1-nm-high nanostructured lines, whereas no preferential orientation occurred on the planar surfaces. Galli et al. speculated that the reason for preferential orientation is that the contact area between the surface and protein is

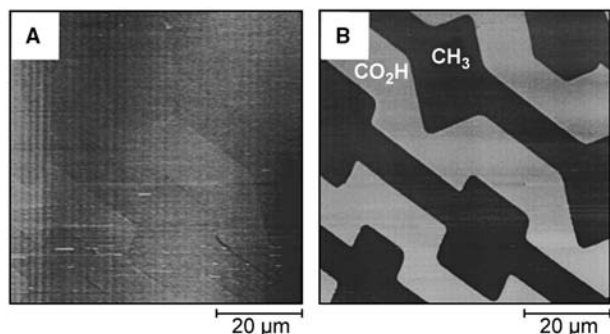


**Fig. 12** Octadecanethiol and mercaptohexadecanoic acid nanopatterns on gold. Images, 70 μm × 70 μm, collected in ambient air, of a patterned monolayer prepared by micro-contact printing ODT and back-filling with MHA. (A) Topography ( $z$  scale 5 nm). (B) Friction image ( $z$  scale 0.5 V). Source: Reprinted from Ref.<sup>[44]</sup> with permission from The American Chemical Society.

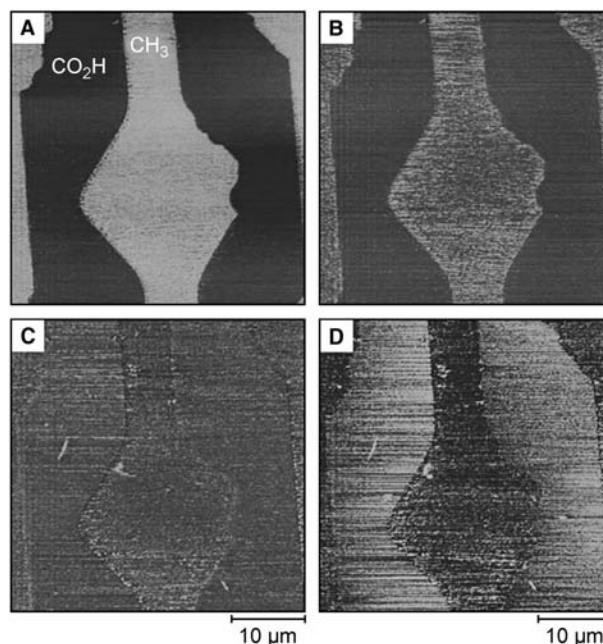


**Fig. 13** Bovine fibrinogen adsorption onto nanopatterned ODT/MHA SAMs. Friction images, 40 μm × 40 μm, depicting the real-time adsorption of BFG to a patterned monolayer. All images were collected under flowing solution. (A) Initial surface under flowing PBS. Methyl groups show higher contrast in images A ( $z$  scale 0.7 V), B ( $z$  scale 0.7 V), and C ( $z$  scale 0.4 V) during the adsorption of BFG. (D) Completed BFG film ( $z$  scale 0.3 V). Image D was collected 22 min after initial addition of BFG to the fluid cell. Source: Reprinted from Ref.<sup>[44]</sup> with permission from the American Chemical Society.

increased along the lines. However, on Ti, 3–4-nm-high lined nanostructures garnered very low F-actin adsorption. This height corresponds to half the diameter of F-actin. These authors cite similar height dependencies for a variety of cells.<sup>[63–65]</sup> It is possible that F-actin is not sufficiently labile to adsorb across these higher nanostructures and maintain enough contacts with the surface to adsorb.

### Force Interactions

A major strength of AFM is the probing of interactions between the protein-coated surface and the tip. Force interactions can be mapped across different regions of the surface. Radmacher et al.<sup>[66]</sup> illustrated the utility of force–distance curves for protein adsorption. Fig. 19A and B present force curves on bare mica and on aggregates of lysozyme on mica in 10 mM KH<sub>2</sub>PO<sub>4</sub> (pH 6.4), respectively. Force curves report the cantilever deflection (which can readily be translated into force) as a function of the sample height as the tip approaches, and then retracts from the surface. The

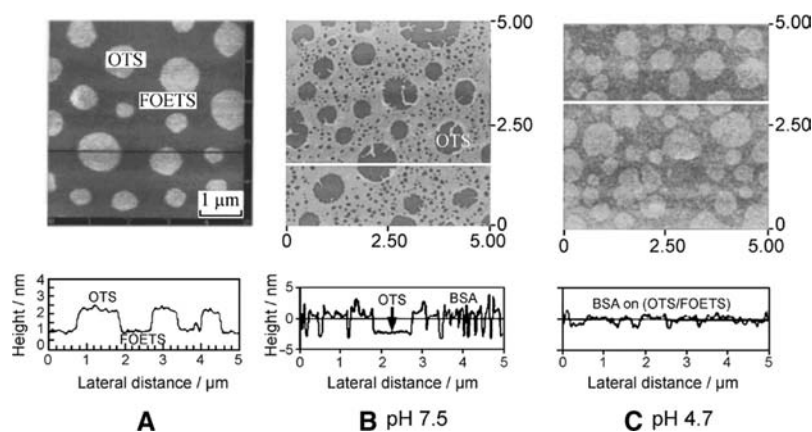


**Fig. 14** Bovine serum albumin adsorption on OTS/FOETS supported monolayers. Atomic force microscopy image of the mixed (OTS/FOETS) monolayer (A) before exposure to BSA, (B) after exposure to a 0.1 g/L BSA solution in PBS (0.01M) at pH 7.5 and (C) pH 4.7 for 10 min. Line sections are shown below each AFM image. *Source:* Reprinted from Ref.<sup>[53]</sup> with permission from Elsevier.

large ( $\sim 25$  nm) negative deflection of the retract curve on bare mica indicates that the tip is highly attracted to the surface, whereas the smaller ( $\sim 8$  nm) negative deflection over lysozyme indicates a smaller attraction. An identical result was found by Kim et al.<sup>[45]</sup> The deviation in linearity on the contact region of the force–distance curve for lysozyme is a result of the elastic deformation of the protein. By fitting to a Hertzian model, Radmacher et al.<sup>[66]</sup> estimated the Young’s modulus for adsorbed lysozyme on mica to be  $0.5 \pm 0.2$  MPa. In addition, the time for liftoff, the region of the retract force curve when the tip loses contact with the surface, is longer for lysozyme compared to that of the bare mica surface. This is related to the viscosity of lysozyme on the surface, estimated to be  $800 \pm 400$  Pa sec.<sup>[66]</sup>

Clearly, AFM can detect mechanical properties of protein films. Given a high-enough applied force, the tip can break through protein films. Thus by examining the force curves, one can uncover protein assembly at the surface. On myelin basic protein (MBP) clusters adsorbed at both acidic (30 wt.% cholesterol, 56% egg phosphatidylcholine, 14% dioleoylphosphatidylserine) and basic (30 wt.% cholesterol, 56% egg phosphatidylcholine, 14% dioleoyl trimethyl-ammonium salt) lipid bilayers supported on mica, Mueller et al.<sup>[54]</sup> observed a “jump-in” on the initial approach curve that disappeared for subsequent force curves at the same location. The adhesion force between the tip and the cluster was approximately 0.5 nN as measured by tip deflection upon retraction. Fig. 20B shows a typical set of consecutive force curves on an acidic lipid

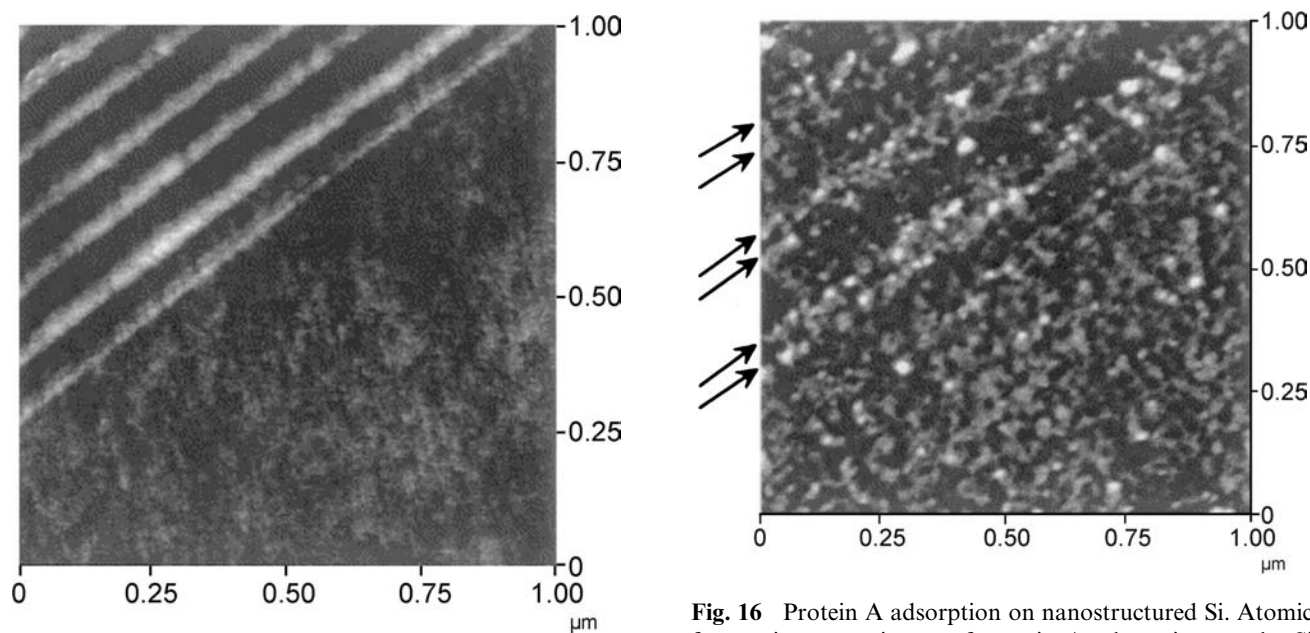


**Fig. 15** Nanostructured Si. Atomic force microscopy image of Si surface with 1-nm high lines. The vertical scale is 5 nm. *Source:* Reprinted from Ref.<sup>[62]</sup> with permission from Elsevier.

**Fig. 16** Protein A adsorption on nanostructured Si. Atomic force microscopy image of protein A adsorption on the Si nanostructures shown in Fig. 15. The vertical scale is 5 nm. Arrows highlight placement of lines. *Source:* Reprinted from Ref.<sup>[62]</sup> with permission from Elsevier.



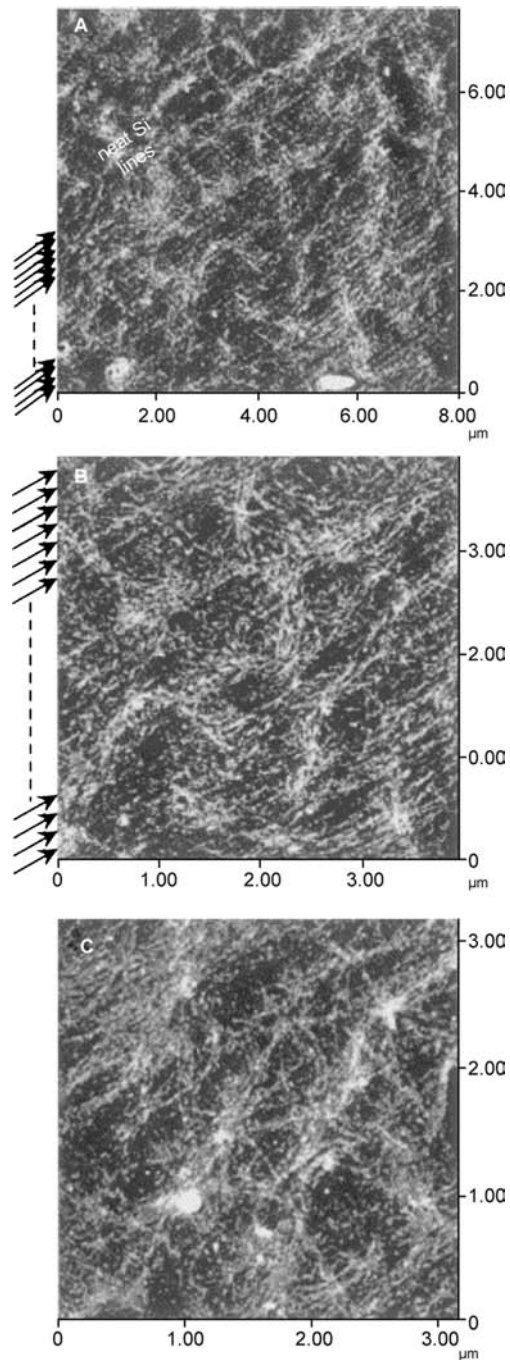


**Fig. 17** F-actin adsorption on Si nanostructures. Adsorption of F-actin on surface displaying both Si nanostructures and planar Si as shown in Fig. 15. The vertical scales are 10 nm. (A) General view of the adsorbed F-actin. (B) Enlargement of the nanostructure area. (C) Enlargement of the planar Si area. Arrows highlight placement of lines. Source: Reprinted from Ref.<sup>[62]</sup> with permission from Elsevier.

bilayer. Force–distance curves consistently displayed a characteristic “jump-in” upon approach at 5 nN and a negligible adhesion force. The “jump-in” indicates the moment when the tip breaks through the lipid bilayer and protein layer (if present) to the solid surface.

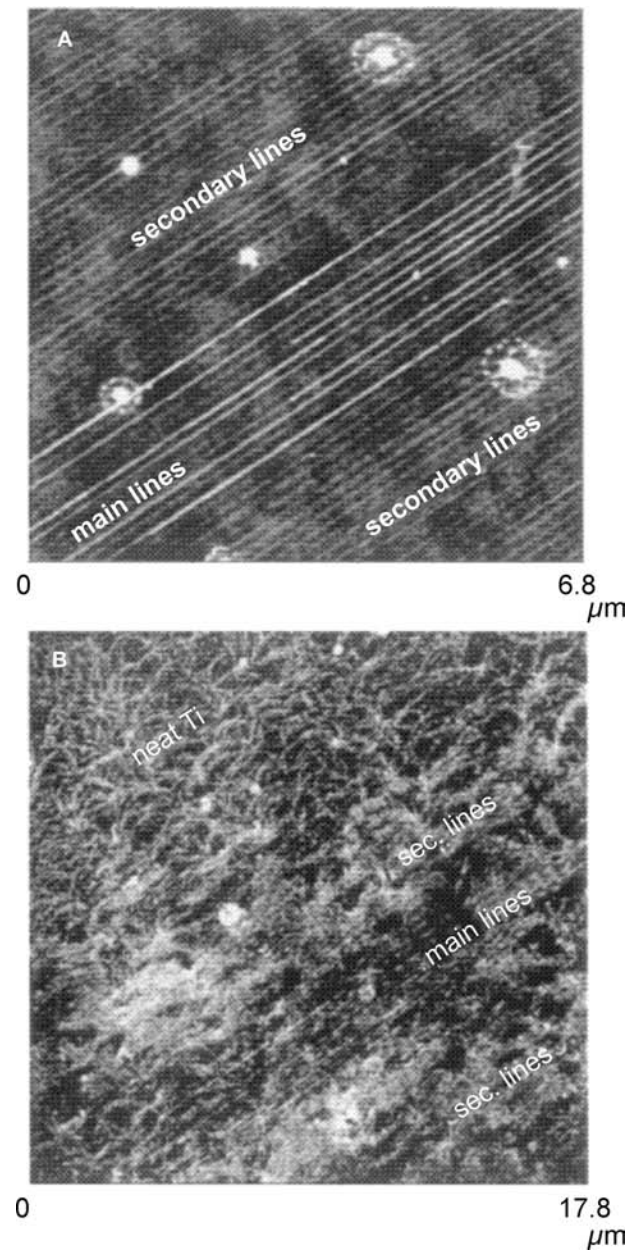


**Fig. 18** F-actin adsorption on Ti nanostructures. (A) Nanostructures created on Ti. Main lines are 3–4 nm high. Secondary lines are 1 nm high. (B) F-actin adsorbed on nanostructured Ti. The vertical scales are 8 nm. Source: Reprinted from Ref.<sup>[62]</sup> with permission from Elsevier.

Fig. 20C also gives four consecutive force–distance curves but now for a MBP cluster adsorbed on the acidic lipid bilayer. The disappearance of the jump after the first force curve in Fig. 20C indicates that the tip locally destroyed the protein structure and that the original structure did not recover. The tip may irreversibly compress and break apart the protein aggregate structure, leaving behind a permanently damaged protein–lipid bilayer complex and expose the bare surface. On the bare lipid layer, as shown in

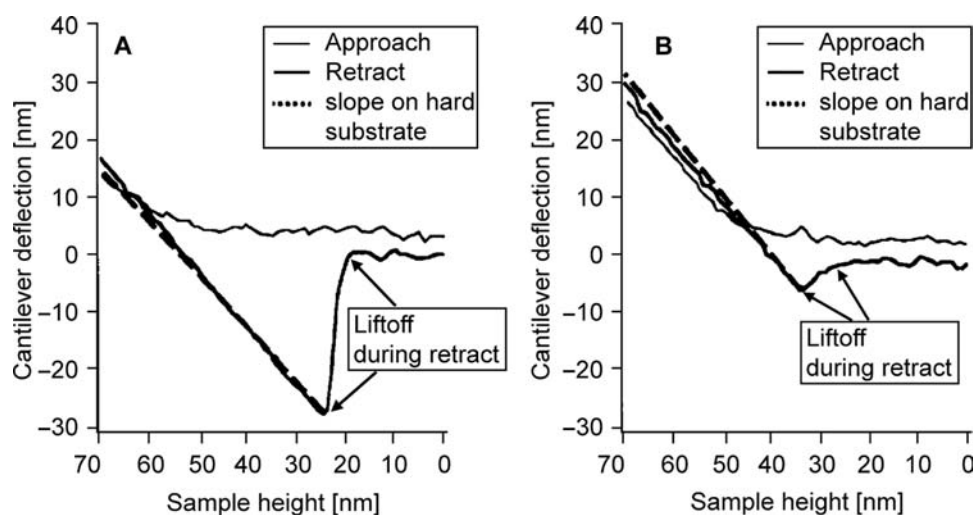


**Fig. 19** Force-distance curves on mica and lysozyme. (A) Force curve on the substrate mica. (B) Force curve on an aggregated cluster of lysozyme adsorbed onto mica. Note that the hysteresis during retract is larger on mica, indicating a higher adhesion force. However, liftoff over the lysozyme cluster is gradual in comparison to mica. This effect is probably due to damping of the cantilever by the lysozyme. As a result of elastic indentation, the contact region of the force curve is not just a straight line, but shows some deviation in the case of lysozyme (see fitted dashed contact lines in parts A and B). *Source:* Reprinted from Ref.<sup>[66]</sup> with permission from The American Chemical Society.

Fig. 20B, the jump-in consistently occurred and the recovery after tip breakthrough occurred fast, probably because of the high mobility of the lipid molecules. On zwitterionic bilayers (not shown), protein clusters showed inconsistent behavior. This is not surprising because the protein aggregates on zwitterionic bilayers were irregular in height and two-dimensional morphology.<sup>[54]</sup>

Chen et al.<sup>[67]</sup> found long-term structural changes in BSA films adsorbed on polystyrene (PS) surfaces. Albumin-coated probes exhibited high adhesion forces on bare PS, but only small adhesion forces on protein-exposed surfaces. When high probe forces were exerted on the BSA films, high adhesion forces were observed, indicating that the albumin-coated probe was able to penetrate the protein layer to the bare PS surface. These authors found that the contact-force limit increases with protein adsorption time. Hence after adsorption, protein continues to undergo structural changes that increase the mechanical strength (or integrity) of the film.

Force interactions between the tip and the surface at a fixed distance away from the surface can allow presentation of a two-dimensional array or a force-volume image. Fig. 21A shows a force-volume map and the corresponding topograph (Fig. 21B) of a BSA film adsorbed onto PS.<sup>[67]</sup> The brighter shades on the force-volume map indicate higher adhesion energy. These correspond to the low area of the topograph corresponding to bare PS. Kim et al.<sup>[45]</sup> employed force-volume imaging for a lysozyme submonolayer on mica

to distinguish between areas that corresponded to bare mica and to lysozyme.

Force-distance curves can be used to detect differences in adsorbed protein structure. Denis et al.<sup>[39]</sup> studied collagen adsorption on CH<sub>3</sub>- and OH-terminated SAMs using force-distance curves. Approach interaction curves for protein adsorbed onto CH<sub>3</sub>-terminated SAMs exhibited significant curvature, whereas the approach curves for protein adsorbed onto-OH-terminated SAMs demonstrated no curvature. This result indicates that collagen adsorbed on the hydrophobic CH<sub>3</sub>-terminated SAMs was “softer” than that adsorbed on the hydrophilic OH-terminated SAMs. Differences in protein adsorption behavior on hydrophobic and hydrophilic surfaces are addressed below.

## PROTEIN ADSORPTION MECHANISMS

### Electrostatic Effects

Electrostatic interactions between the protein and surface in addition to those between proteins can play an important role in the adsorption onto solid surfaces. Many adsorption processes are driven in part by electrostatic attraction between the surface and protein. For example, lysozyme at pH 4.0 is positively charged, whereas mica is negatively charged; protein adsorption occurs quite readily as shown in Fig. 2.<sup>[31,45,66]</sup>

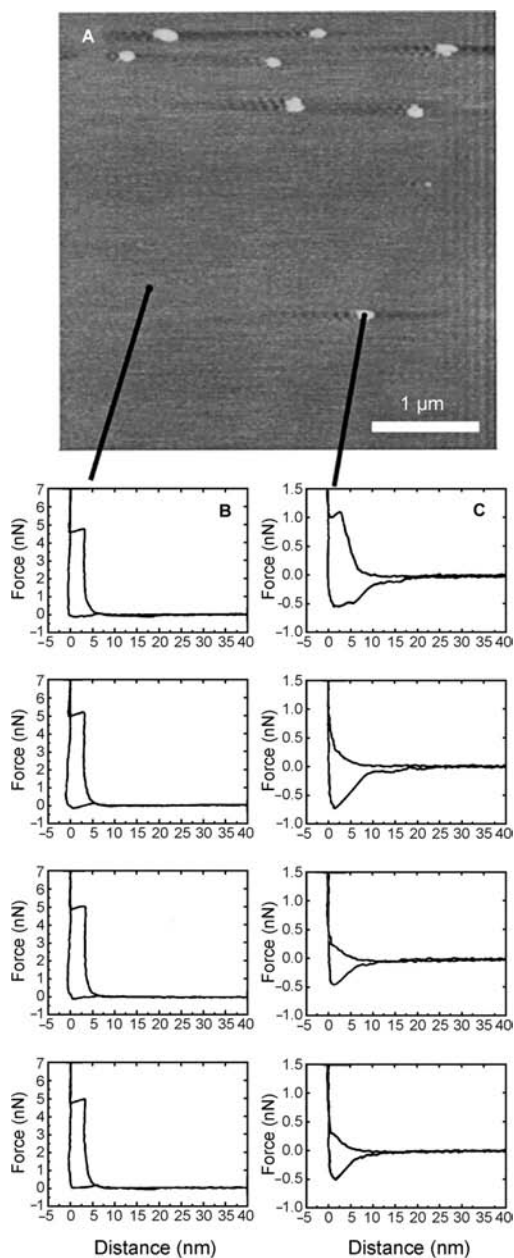


**Fig. 20** Sequential, spatially resolved force spectroscopy on an acidic bilayer with adsorbed MBP aggregates. (A) Height image of an acidic lipid bilayer 15 min after injection of 2  $\mu\text{g}/\text{mL}$  MBP solution. (B) Column of four consecutive force curves take at the indicated position in the flat area of the image. (C) Column of four consecutive force curves taken on the indicated MBP aggregate. The penetration force was smaller than in b, the jump vanished during the force scans, and an adhesion of approximately 0.5 nN was observed. *Source:* Reprinted from Ref.<sup>[54]</sup> with permission from The American Chemical Society.

Cytochrome *c* at pH 7.4 is positively charged and significantly adsorbs on negatively charged bilayers, minimally on neutral bilayers, and not at all on positively charged bilayers.<sup>[54]</sup> In addition, cytochrome

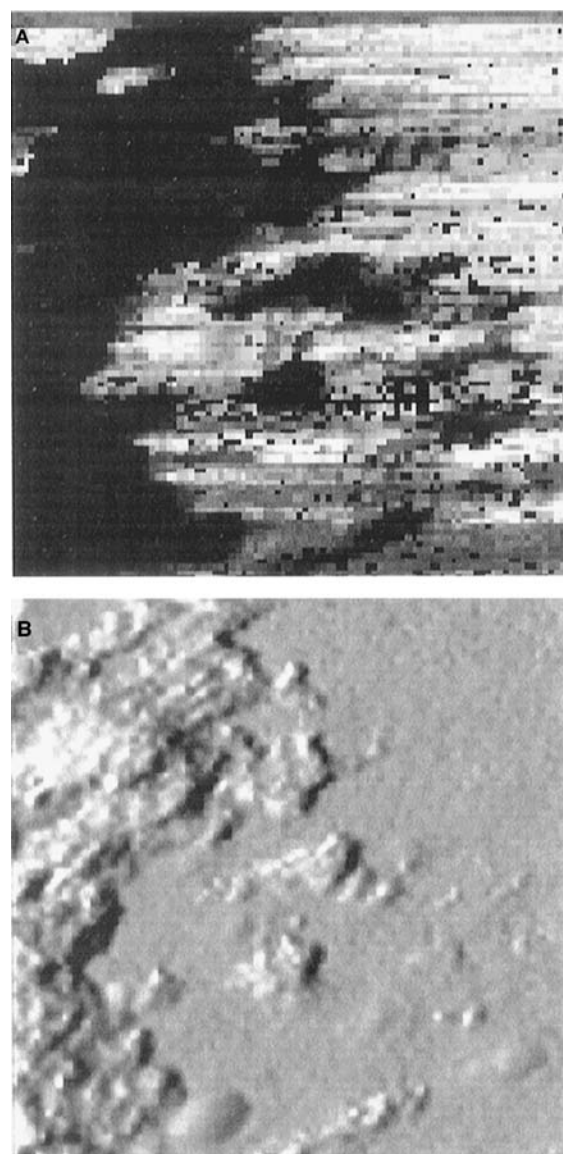


**Fig. 21** Force-volume map of BSA adsorbed onto polystyrene. (A) Two-dimensional distribution of the adhesion energy between a BSA-coated probe and a polystyrene surface preadsorbed with BSA, with (B) a simultaneous recorded surface topography ( $2\ \mu\text{m} \times 2\ \mu\text{m}$ ). Only the left portion of the surface was exposed to the protein solution. The measurements were performed in pH 7 phosphate buffer at the boundary region between the BSA-free and BSA-covered polystyrene surfaces. The adhesion energies are extracted from force–distance curves measured at each sampling point, with brighter shades indicating higher adhesion energy. The topographic image is artificially shadowed for a better presentation. *Source:* Reprinted from Ref.<sup>[67]</sup> with permission from The American Chemical Society.

*c* adsorption was reversible under high salt conditions (5 M NaCl) whereas the protein appeared to be irreversibly adsorbed at lower salt conditions (150 mM NaCl). In some cases, protein can still adsorb onto



surfaces even when they are similarly charged. MBP at pH 7.4 is positively charged and adsorbs onto a positively charged bilayer.<sup>[54]</sup> Patel et al.<sup>[68]</sup> have shown that negatively charged catalase at pH 8.0 adsorbs onto negatively charged SAMs. Likewise, HSA can adsorb to both positively and negatively charged polymer surfaces.<sup>[30]</sup> There are several reasons why this can occur. First, a protein of a particular net charge still presents oppositely charged residues on its structure and those residues can favorably interact with the charged solid surface. Second, as discussed later, the driving force for adsorption usually involves hydrophobic forces. These can overcome a net electrostatic repulsion with the surface.

High-ionic-strength solutions shield electrostatic repulsions between charged proteins resulting in increased protein adsorption. Johnson, Yuan, and Lenhoff<sup>[40]</sup> illustrated this with ferritin adsorption onto trimethoxysilylpropyldiethylenetriamine (DETA) coated glass. However, adsorption amount does not monotonically increase with ionic strength because of the competition between surface-protein interactions and surface protein-protein interactions.<sup>[40]</sup> Protein-protein repulsion can also be minimized by adjusting the solution pH to the isoelectric point ( $pI$ ) of the protein, where the protein has a zero net charge, but may have a large dipole moment. Several researchers have reported that adsorption is increased or maximized at the  $pI$ .<sup>[40,51-53,69,70]</sup> Kajiyama et al. observed that BSA adsorbed on both OTS and FOETS phases only at the  $pI$  (Fig. 14C). But when BSA carried a net charge, it only adsorbed only onto the FOETS phase (Fig. 14B) as a result of the electrostatic repulsion between adsorbed protein and protein in solution.<sup>[51-53]</sup> Johnson, Yuan, and Lenhoff<sup>[40]</sup> reported that at the  $pI$ , ferritin adsorption approached the random sequential adsorption (RSA) jamming limit. This increased adsorption could be attributed to the fact that at the  $pI$ , intramolecular charge repulsions are minimized and the protein adopts its most compact shape.<sup>[69]</sup> Thus the protein requires less space on the surface to adsorb as compared to a more elongated structure that exists when the protein carries a net charge. However, this reasoning must be tempered by the observation that denatured and random-coil-like proteins adsorb more quickly<sup>[17]</sup> most likely because the surface unfolding kinetic step is hastened.

### Kinetics of Adsorption

General trends have been observed in the kinetics of protein adsorption. Almeida, Salvadori, and Petri<sup>[70]</sup> divided the process into four stages, assuming a continuous supply of protein. The first stage is a mass-transfer-limited stage where proteins rapidly adsorb

onto the surface. Feng et al.<sup>[2]</sup> described this initial step as a “fast process.” In our work with lysozyme, protein on the surface could be imaged within minutes of exposure to an unstirred protein solution.<sup>[45]</sup> The second stage is a non-linear reduction of the adsorption rate until a monolayer plateau is established. During the second stage, the slowing down of adsorption may be explained by lower availability of free adsorption sites on the surface while the protein diffuses, structurally rearranges, and aggregates on the surface. The third stage represents completion of monolayer coverage followed by the fourth stage, where slow multilayer growth begins. The slow growth of a second layer of lysozyme on mica has been reported (Fig. 2).<sup>[45]</sup> It is thought that the slower kinetics of multilayer adsorption is possibly because the proteins in the bulk solution are largely in their native conformation and do not readily interact with protein that is minimally unfolded at the surface. As the monolayer remains longer on the surface and unfolds more, interactions with bulk native protein is likely enhanced.

Currently, the kinetics of protein adsorption at solid surfaces cannot be reliably predicted. This is because of the complicated collection of possible behaviors including irreversibility of protein adsorption, slow conformational changes, and aggregation both within a given layer and between multilayers. The onset of irreversibility can occur in the first and second stages of adsorption. For example, the surface concentration of cytochrome *c* leveled off at a non-zero value when washout began at this second stage.<sup>[27]</sup> The initial lysozyme clusters observed after 4 min of exposure to mica in Fig. 2 are already irreversibly adsorbed.<sup>[45]</sup> Subsequent lateral migration and surface aggregation strongly affects the kinetics of adsorption.<sup>[27]</sup>

### Growth Mechanisms: Surface Diffusion/Lateral Migration

Many proteins have been found to diffuse laterally on the surface. Tilton, Gast, and Robertson<sup>[71,72]</sup> have shown using fluorescence recovery after photobleaching (FRAP) that even proteins that are irreversibly adsorbed undergo lateral motion. These workers report surface diffusion coefficient values for bovine serum albumin (BSA) irreversibly adsorbed on poly(methyl methacrylate) (PMMA) and poly(dimethylsiloxane) (PDMS) of  $1.2 \pm 0.3 \times 10^{-9}$  and  $2.6 \pm 0.1 \times 10^{-9}$  cm<sup>2</sup>/sec, respectively. We explained the clustering of lysozyme molecules on mica as arising from surface diffusion and aggregation of irreversibly adsorbed protein molecules.<sup>[45]</sup> The irreversible adsorption of lysozyme onto mica probably disturbs the protein conformation sufficiently to expose hydrophobic residues giving rise to surface cluster formation through



interprotein aggregation at the surface. Mueller, Butt, and Bamberg<sup>[54]</sup> reported a similar mechanism of adsorption, diffusion, and aggregation resulting in clusters of MBP adsorbed onto lipid bilayers. The adsorption patterns shown in Figs. 3 and 4 of IgG and GOx on HOPG also imply surface mobility and aggregation of proteins. Denis et al.<sup>[39]</sup> attributed the elongated structures of collagen on solids to surface mobility. Collagen formed elongated structures on smooth surfaces exposing  $-CH_3$  moieties, but not on rough surfaces or surfaces exposing  $-OH$  moieties. This was ascribed to the diminished mobility on the rough surfaces. In Hook et al.'s<sup>[18]</sup> ellipsometry and OWLS studies with serum proteins, it was found that the adsorption saturation mass frequently exceeds the mass predicted by the RSA model. The explanation lies in the ability of protein on the surface to move laterally, clearing space for additional protein to adsorb. Calonder, Tie and Van Tassei<sup>[27]</sup> reported that the kinetics of additional protein adsorption depends on the amount of time protein has to rearrange and move to form clusters.

### Multilayer Formation

Some proteins have the ability to form multilayers. We ascertained that lysozyme forms a second layer, but only after establishing a first monolayer on mica (Fig. 2).<sup>[45]</sup> The growth of the second layer occurred on a slower time scale than that for the first monolayer, indicating that the adsorption mechanism must be different. This is not surprising considering that once the first monolayer is established, subsequent proteins must adsorb onto a completely different interface. We speculate that the driving force for adsorption on a second layer is exposed, hydrophobic residues resulting from protein conformational changes, occurring in the first layer, that interact with protein in the bulk solution. Hydrophobic interactions may also explain the irreversibility of the second layer of adsorbed lysozyme. Wahlgren, Arnebrant and Lundstrom<sup>[28]</sup> and Malmsten<sup>[73]</sup> likewise reported multilayer adsorption of lysozyme using ellipsometry. Coen et al.<sup>[55]</sup> also documented multilayer adsorption for protein A onto silicon. As was observed with lysozyme, formation of subsequent layers of protein A did not occur until the previous layer was saturated with protein (Figs. 7 and 8). It was observed that protein in the first monolayer was significantly unfolded (Fig. 7), whereas protein in the second layer was less structurally altered (Fig. 8). Protein in the third layer had no significant structural perturbations.<sup>[55]</sup> Hook et al.,<sup>[18]</sup> using OWLS and ellipsometry, found that hemoglobin formed multilayers on titanium oxide surfaces, and Ladam et al.,<sup>[30]</sup> using SAR, showed that HSA forms

multilayers on a positively charged polyallylamine surface.

Nevertheless, not all proteins have the ability to form multilayers. Green et al.<sup>[23]</sup> found that albumin does not form multilayers on negatively charged polystyrene and neither did HSA.<sup>[30]</sup> However, multilayer formation can occur over long time scales and most studies do not investigate adsorption beyond a few minutes. Thus it is important to extend the time scale of investigation over several hours or days before eliminating possible irreversible and multilayer adsorption behavior. Also, these phenomena are clearly protein and surface specific.

### Protein Structure and Adsorption Behavior

Several studies directly compare different adsorption patterns on different solid surfaces. Immunoglobulin G has been observed to adsorb randomly on HOPG surfaces, forming clusters, whereas GOx prefers to adsorb at HOPG step defects forming “sheets” that eventually grow from these initial nucleation sites (Figs. 3 and 4).<sup>[56]</sup> Bovine fibrinogen adsorbs onto HOPG in a strand network (Fig. 5), whereas on mica, it adsorbs homogeneously (Fig. 6).<sup>[37]</sup> This variety of adsorption behavior is most likely related to specific protein structure. The location and the number of hydrophobic and hydrophilic residues can play a large part in the final adsorption pattern. Glucose oxidase is heavily glycosylated and, at pH 7.2, is more negatively charged than is IgG.<sup>[74]</sup> Thus it is not surprising that GOx nucleates preferentially at higher energy step defects on HOPG rather than on the basal planes. In contrast, IgG is more hydrophobic and can interact more strongly with the hydrophobic surface. Ta, Sykes, and McDermott<sup>[37]</sup> explained the discrepancy in the adsorption patterns for BFG on mica and on HOPG based on the native protein structure. The BFG molecule is known to have two distal D domains connected to a central E domain.<sup>[75]</sup> The D domains are hydrophobic with low structural stability. From each D domain extends an  $\alpha C$  domain with both hydrophobic and hydrophilic regions.  $\alpha C$  domains are known to have a tendency to interact intra- and intermolecularly with other  $\alpha C$  domains. Ta, Sykes, and McDermott<sup>[37]</sup> proposed that on HOPG, the D domains hydrophobically bind to the surface while the  $\alpha C$  domains interact with other  $\alpha C$  domains. In contrast, on negatively charged mica surfaces, the positively charged  $\alpha C$  domains likely interact strongly with the surface and unavailable for intermolecular binding.

The particular protein structure clearly affects the final adsorbed conformation. The von Willebrand factor has a native structure where the termini are

extensively disulfide bonded and, therefore, structurally very stable.<sup>[76]</sup> The termini are also very hydrophilic. The remainder of the molecule is balanced in its hydrophobic and hydrophilic character. On mica, VWF is thought to be more loosely bound; thus, the extended structure of the protein and the high coverages, as shown in Fig. 9, may be a result of a combination of repulsive hydration, electrostatic, and attractive van der Waals interactions.<sup>[59]</sup> On HOPG, evidence of spreading is shown by its smaller height compared to the native structure (Fig. 10). However, both the amount of lateral spreading and the surface coverage under similar conditions are much smaller than for VWF on mica (compare Figs. 9 and 10). The origin of this difference is not transparent. The authors suggest that on HOPG, “the spreading stresses [of VWF] may be transmitted via the structurally rigid termini causing the VWF to adopt compact structures.” Structural stability of the protein is a key factor in determining the extent of conformational change upon adsorption. This was illustrated by Billsten et al.,<sup>[77]</sup> who measured the extent of change in secondary structure by CD of T4 lysozyme mutants adsorbed onto silica nanoparticles (average diameter ~15 nm). Not unexpectedly, it was found that the less structurally sound, native structures lost more secondary conformation upon adsorption.

### Protein Structural Changes

Protein molecules adsorbed on a non-specific surface tend to undergo conformational change. Structural alteration results from the interaction forces between the hydrated surface and the hydrated protein, which disturb the delicate balance of energy and entropy that maintains the protein in a particular conformation in solution. Conformation rearrangement is seen widely in many experiments. Height measurements and antibody-binding experiments by Coen et al.<sup>[55]</sup> demonstrated that the first layer of protein A adsorbed at the silicon surface is denatured (Fig. 7). Height profiles of both GOx (Fig. 4)<sup>[56]</sup> and IgG (Fig. 3)<sup>[37]</sup> on HOPG suggest that the proteins are structurally reconfigured at the surface. Circular dichroism spectroscopy has been used to show that  $\alpha$ -chymotrypsin and cutinase change their  $\alpha$ -helix content when adsorbed on either Teflon or silica.<sup>[14,15]</sup> Interleukin-2, upon exposure to silicone rubber tubing for 24 hr, lost 99.5% of its bulk activity. Experimentation with FTIR revealed that the protein adopts a non-native conformation in which the  $\alpha$ -helix,  $\beta$ -sheet, and turn content changes.<sup>[7]</sup> Sane, Cramer, and Przybycien<sup>[8]</sup> also found that lysozyme's secondary structure is disturbed after adsorption onto reversed-phase chromatographic supports.

The extent of conformational change is related to many factors including the relative hydrophobicity of the surface, the exposure time of adsorption, and the adsorption density or surface packing of protein. The hydrophobic residues of a protein are usually more concentrated in the core. Upon contact with a hydrophobic surface, the free energy of the system decreases as water molecules that were adjacent to the hydrophobic areas on the protein and on the solid surface are driven out to allow the hydrophobic residues to reside next to the surface. One can imagine that the more hydrophobic a surface is, the greater is the structural rearrangement that will occur. Ta, and McDermott<sup>[44]</sup> confirmed this assertion in AFM studies of BFG adsorption onto CH<sub>3</sub>- and COOH-terminated SAMs. On the hydrophobic -CH<sub>3</sub> surface, the height profile indicates that the protein flattened out, whereas on the more hydrophilic -COOH surface, BFG did not change shape to the same degree. Norde et al.<sup>[14,15]</sup> established that  $\alpha$ -chymotrypsin and cutinase retain some enzymatic activity on hydrophilic silica while losing all activity on hydrophobic Teflon. In a study of BSA adsorption, Norde and Giacconelli<sup>[78]</sup> showed that irreversible structural changes occurred on polystyrene, but not on silica. Wahlgren and Arnebrant<sup>[25]</sup> reported that  $\beta$ -lactoglobulin underwent more significant structural changes on methylated silica and polysulfone than on silica. Fibrinogen and albumin were shown to leave larger “footprints” on hydrophobic surfaces as compared to a hydrophilic surface.<sup>[21,79]</sup> However, proteins do not unfold and denature solely on hydrophobic surfaces. Coen et al.<sup>[55]</sup> reported a highly denatured monolayer of protein A on hydrophilic silicon.

The structural rearrangement of the protein at a surface is thought to be a “slow” process. Over time, the number of residue contacts with the surface increases, making the surface-protein interaction stronger. The amount of high-density lipoprotein (HDL) that can be desorbed from polyethylene surfaces by surfactant exposure is significantly decreased after 24 hr of storage.<sup>[2]</sup> In addition to making more and stronger bonds with the surface, the unfolding protein is thought to change its packing structure, possibly aggregating to form intertwining networks. In force-distance curve experiments, Chen et al.<sup>[67]</sup> discovered that the force required to penetrate through a layer of albumin adsorbed on polystyrene increased over time. Friction-force microscopy of BFG on patterned CH<sub>3</sub>- and COOH-terminated SAMs revealed that the friction behavior of the adsorbed protein on this surface changes over time, as in Fig. 13.<sup>[44]</sup> Almeida, Salvadori, and Petri<sup>[70]</sup> have shown that the contact angles for monolayers of enolase adsorbed onto both hydrophilic silicon wafers and (aminopropyl)-trimethoxysilane (APS) and hydrophobic PS change

with time, indicating structural rearrangements are occurring well after the protein is initially adsorbed to the surface.

The amount of crowding on the surface affects the amount of structural rearrangement that can occur. If the average nearest neighbor distance is relatively large, then the protein has a greater opportunity to spread. However, if the surface is more crowded, there is only limited space for the protein to spread. Using CD, Norde et al.<sup>[14,15]</sup> showed that a higher fraction of  $\alpha$ -chymotrypsin and cutinase adsorbed on silica remain in their native state if the surface coverage was higher. Of course, with time, structural reconfiguration is still likely to occur, but at a slow rate. For BSA on silica and PS, Norde and Giacconelli<sup>[78]</sup> reported similar findings. However, Sane, Cramer and Przybycien<sup>[8]</sup> showed that the secondary structure of lysozyme is more disturbed on more crowded surfaces. They attributed this finding to lateral interactions between the adsorbed lysozyme.

Irreversible adsorption of protein on a surface is most likely to result from significant structural changes occurring on the surface. As unfolding proceeds, more contacts are created with the surface. In analogy to polymer adsorption, it becomes difficult for the partially denatured protein to be removed. Wahlgren, Arnebrant, and Lundstrom<sup>[28]</sup> showed that the longer lysozyme was adsorbed on silicon oxide, the larger was the fraction of protein irreversibly adsorbed. This is true for  $\beta$ -lactoglobulin on silicon oxide as well.<sup>[26]</sup> Given more time to unfold, both the number of contacts with the surface and their strength increases. Foster showed that the irreversibility of albumin adsorption was higher for hydrophobic CH<sub>3</sub>-terminated SAMs than for bare silica. Both Wahlgren and Arnebrant<sup>[25]</sup> and Marsh, Jones, and Sferrazza<sup>[26]</sup> confirmed this with  $\beta$ -lactoglobulin adsorption onto hydrophilic and hydrophobic surfaces. This was attributed to hydrophobic surfaces being more likely to denature protein to a greater extent than hydrophilic surfaces. However, given the tendency of proteins to reconfigure at long times, the distinction in the amount of protein irreversibly adsorbed on hydrophilic and hydrophobic surfaces is likely to decrease. Wertz and Santore<sup>[79]</sup> showed that adsorbed protein layers were more susceptible to washout at higher coverage because the increased crowding on the surface limited the amount of solid surface area available per protein molecule.

Fig. 22 shows a general kinetic picture of protein adsorption onto a non-specific solid surface (i.e., a solid surface without designed specific binding sites for the protein). Particular proteins on particular surfaces may not visit all the listed steps. Initially, in Fig. 22A, protein is in its native conformation (labeled as “N” with a shaded hydrophobic core and a more

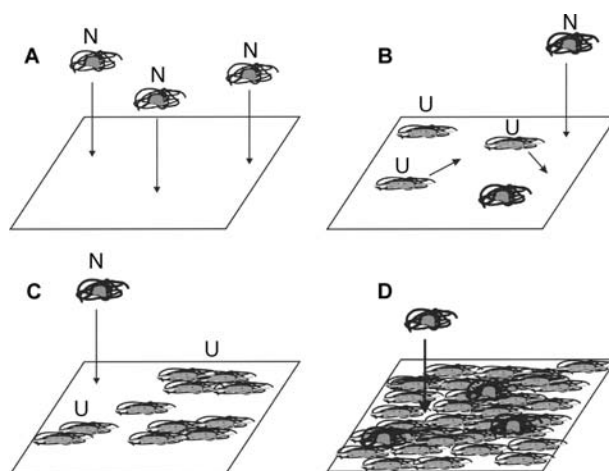


**Fig. 22** Generalized illustration of protein adsorption. (A) At early times, protein in its native “N” state rapidly adsorbs onto bare surface. (B) Once adsorbed, protein begins slow unfolding and spreading on the surface (labeled as “U”), rendering them irreversibly adsorbed, but yet mobile on the surface. Additional protein adsorbs onto the surface on available bare surface. (C) Protein aggregates on the surface to form clusters. The rate of protein adsorption onto the surface decreases as less bare surface is available. (D) A complete monolayer is eventually established. Multilayer adsorption and reconfiguration occurs on a slow time scale.

diffuse hydrophilic corona) in the bulk aqueous environment. Mass transfer processes bring the native protein particle to the surface where it quickly adsorbs onto the mostly empty surface via a combination of van der Waals, electrostatic, and hydrophobic forces. At this stage, interaction forces between the surface and the protein can be weak, and reversible desorption is possible. Once adsorbed at the surface, the protein undergoes structural rearrangement as it is no longer completely surrounded by bulk water. Replacement of surface water by protein segments can be favorable leading to partial unfolding (labeled as “U” in Fig. 22B). The time for and extent of unfolding depends both on surface chemistry (e.g., hydrophobic vs. hydrophilic) and quite importantly on the stability of the native protein. Typically, surface conformation change gives rise to unburying of hydrophobic residues and to lateral “spreading” of the protein adsorbate as more residues can now contact the surface. The amount of spreading depends on the surrounding coverage. Irreversible adsorption and partial denaturation develops at this point. Simple model calculations indicate the conformation change can be extensive creating loops and trains, quite analogous to polymer adsorption from solution.<sup>[80,81]</sup> Although irreversibly attached to the surface, the individual protein monomers participate in lateral diffusion, as shown in Fig. 22B. Collisions between adsorbate protein molecules permit surface aggregation via interprotein

exposed hydrophobic residues. Clusters result, as shown in Fig. 22C, similar to bulk aggregation of partially denatured protein. Upon clustering, the surface aggregates are likely to be immobile because of the increased number of contacts with the surface. As slow reconfiguration and clustering continues, more protein arrives at the surface, but the rate of adsorption slows because of the decreasing availability of bare surface area. It may be possible for protein to adsorb onto already adsorbed protein but this apparently occurs on a longer time scale compared to that onto the unoccupied surface. Typically, the surface fills into a monolayer before multilayers begin forming in Fig. 22D. If the rate of protein arrival to the surface is fast compared to the time scale for lateral diffusion, formation of clusters is bypassed and monolayer coverage is directly reached. Additional protein may adsorb onto the first layer by interaction with hydrophobic residues exposed as a result of the conformation changes induced in the underlying layer. Initially, the multilayer protein might be reversibly adsorbed. However, irreversible incorporation and aggregation is later anticipated. Slow cooperative reconfiguration of the multilayer protein film may continue for very extended times.

## CONCLUSION

Atomic force microscopy is a powerful technique to study protein adsorption. With nanometer lateral resolution of height and force interactions, AFM provides information that optical and spectroscopic techniques cannot. This includes elucidation of the supramolecular assembly of adsorbed protein and of multilayer formation. It can also provide information on of the structure and orientation of the protein as it adsorbs onto the surface. Because of its excellent lateral resolution, non-uniform surfaces can be studied to compare the adsorption behavior of proteins when presented with various surfaces at the same time. Through its ability to measure forces on a piconewton scale, AFM can measure force interactions between the protein-coated surface and the tip. This gives insight into the forces arising between the protein-coated surface and tip material and the mechanical properties of protein films.

In conjunction with optical and spectroscopic instruments, AFM provides insight into the mechanisms of aqueous protein adsorption onto a solid surface. Electrostatics play a significant role in the amount of protein adsorbed, protein structure, and packing structure. The kinetics of adsorption can be broken down into several stages to reveal kinetic details such as conformation change, surface crowding, monolayer establishment, and multilayer growth.

Multilayer growth does not appear to be a universal phenomenon and probably depends on the particular chemical composition and adsorption configuration of a protein. However, we caution that there are only a few long-term (several hours to days) experiments on multilayer formation with a sufficiently wide range of proteins. Once adsorbed on the surface, some proteins exhibit lateral movement, and can form clusters, affecting the total mass adsorbed and the final adsorption patterns. Typically, the particular adsorption patterns observed at the surface can be explained on the basis of the specific protein structure and chemistry. In general, an adsorbed protein undergoes structural perturbation. Structural rearrangement can be minimal or dramatic depending on the system. The extent of unfolding is thought to be related to the hydrophobicity of the surface, although instances of irreversible adsorption on hydrophilic surfaces are legion. Highly unfolded and, therefore, denatured proteins may have many points of contact with the surface and are, thus, more likely to be irreversibly adsorbed. Atomic force microscopy has contributed considerably to the understanding of protein adsorption on non-specific solid surfaces and will undoubtedly continue to play an important role.

## GLOSSARY OF ABBREVIATIONS

AFM	atomic force microscopy
APS	(aminopropyl)-trimethoxysilane
BFG	bovine fibrinogen
BSA	bovine serum albumin
CD	circular dichroism spectroscopy
DETA	trimethoxysilylpropyldiethenetriamine
FOETS	[2-(perfluorooctyl)ethyl]trichlorosilane
FRAP	fluorescence recovery after photobleaching
FTIR	Fourier-transform infrared spectroscopy
GOx	glucose oxidase
HDL	high-density lipoprotein
HEWL	hen egg white lysozyme
HOPG	highly oriented pyrolytic graphite
HAS	human serum albumin
HTS	hexadecyltrichlorosilane
IgG	immunoglobulin G
IgM	immunoglobulin M
MBP	myelin basic protein
MHA	mercaptophexadecanoic acid
ODT	octadecanethiol
OTS	<i>n</i> -octadecyltrichlorosilane
OWLS	optical waveguide lightmode spectroscopy
PBS	phosphate-buffered saline
pI	isoelectric point
PDMS	poly(dimethylsiloxane)
PMMA	poly(methyl methacrylate)
PS	polystyrene

QCM	quartz crystal microbalance
RSA	random sequential adsorption
SAM	self-assembled monolayer
SAR	scanning angle reflectometry
SFA	surface force apparatus
SPR	surface plasmon resonance
TIRF	total internal reflection fluorescence
VSFS	vibrational sum frequency spectroscopy
VWF	von Willebrand factor
XPS	X-ray photoelectron spectroscopy

## REFERENCES

- Brange, J.; Langkaer, L. Insulin Structure and Stability. In *Stability and Characterization of Protein and Peptide Drugs*; Wang, Y., Pearlman, R., Eds.; Plenum Press: New York, 1993; 315–348.
- Feng, M.; Morales, A.B.; Beugeling, T.; Bantjes, A.; Vanderwerf, K.; Gosselink, G.; Degrooth, B.; Greve, J. Adsorption of high density lipoproteins (HDL) on solid surfaces. *J. Colloid Interface Sci.* **1996**, *177* (2), 364–371.
- Horbett, T.; Brash, J. Proteins at Interfaces: Current Issues and Future Prospects. In *Proteins at Interfaces—Physicochemical and Biochemical Studies*; Brash, J., Horbett, T., Eds.; American Chemical Society: Washington, DC, 1987; 1–33.
- Andrade, J.D.; Hlady, V. Protein adsorption and materials biocompatibility—A tutorial review and suggested hypotheses. *Adv. Polym. Sci.* **1986**, *79*, 1–63.
- Ivarsson, B.; Lundstrom, I. Physical characterization of protein adsorption on metal and metaloxide surfaces. *Crit. Rev. Biocompat.* **1986**, *2* (1), 1–96.
- Norde, W. Adsorption of proteins from solution at the solid–liquid interface. *Adv. Colloid Interface Sci.* **1986**, *25* (4), 267–340.
- Tzannis, S.T.; Hrushesky, W.J.M.; Wood, P.A.; Przybycien, T.M. Adsorption of a formulated protein on a drug delivery device surface. *J. Colloid Interface Sci.* **1997**, *189* (2), 216–228.
- Sane, S.U.; Cramer, S.M.; Przybycien, T.M. Protein structure perturbations on chromatographic surfaces. *J. Chromatogr., A* **1999**, *849* (1), 149–159.
- Benmakroha, Y.; Zhang, S.; Rolfe, P. Haemocompatibility of invasive sensors. *Med. Biol. Eng. Comput.* **1995**, *33* (6), 811–821.
- Tighe, B.; Franklin, V. Lens Deposition and Spoliation. In *The Eye in Contact Lens Wear*; Larke, J.R., Ed.; Butterworth-Heinemann: Oxford, England, 1997; 49–100.
- Kim, G.; Gurau, M.; Kim, J.; Cremer, P.S. Investigations of lysozyme adsorption at the air/water and quartz/water interfaces by vibrational sum frequency spectroscopy. *Langmuir* **2002**, *18* (7), 2807–2811.
- Claesson, P.M.; Blomberg, E.; Froberg, J.C.; Nylander, T.; Arnebrant, T. Protein interactions at solid surfaces. *Adv. Colloid Interface Sci.* **1995**, *57*, 161–227.
- Blomberg, E.; Claesson, P.M.; Froberg, J.C.; Tilton, R.D. Interaction between adsorbed layers of lysozyme studied with the surface force technique. *Langmuir* **1994**, *10* (7), 2325–2334.
- Zoungrana, T.; Findenegg, G.H.; Norde, W. Structure, stability, and activity of adsorbed enzymes. *J. Colloid Interface Sci.* **1997**, *190* (2), 437–448.
- Norde, W.; Zoungrana, T. Surface-induced changes in the structure and activity of enzymes physically immobilized at solid/liquid interfaces. *Biotechnol. Appl. Biochem.* **1998**, *28*, 133–143.
- Sane, S.U.; Cramer, S.M.; Przybycien, T.M. A holistic approach to protein secondary structure characterization using amide I band Raman spectroscopy. *Anal. Biochem.* **1999**, *269* (2), 255–272.
- Otzen, D.E.; Oliveberg, M.; Hook, F. Adsorption of a small protein to a methyl-terminated hydrophobic surface: Effect of protein-folding thermodynamics and kinetics. *Colloids Surf., B Biointerfaces* **2003**, *29* (1), 67–73.
- Hook, F.; Voros, J.; Rodahl, M.; Kurrat, R.; Boni, P.; Ramsden, J.J.; Textor, M.; Spencer, N.D.; Tengvall, P.; Gold, J.; Kasemo, B. A comparative study of protein adsorption on titanium oxide surfaces using in situ ellipsometry, optical waveguide lightmode spectroscopy, and quartz crystal microbalance/dissipation. *Colloids Surf., B Biointerfaces* **2002**, *24* (2), 155–170.
- Wertz, C.F.; Santore, M.M. Adsorption and relaxation kinetics of albumin and fibrinogen on hydrophobic surfaces: Single-species and competitive behavior. *Langmuir* **1999**, *15* (26), 8884–8894.
- Buijs, J.; Britt, D.W.; Hlady, V. Human growth hormone adsorption kinetics and conformation on self-assembled monolayers. *Langmuir* **1998**, *14* (2), 335–341.
- Wertz, C.F.; Santore, M.M. Effect of surface hydrophobicity on adsorption and relaxation kinetics of albumin and fibrinogen: Single-species and competitive behavior. *Langmuir* **2001**, *17* (10), 3006–3016.
- Robeson, J.L.; Tilton, R.D. Spontaneous reconfiguration of adsorbed lysozyme layers observed by total internal reflection fluorescence with a pH-sensitive fluorophore. *Langmuir* **1996**, *12* (25), 6104–6113.
- Green, R.J.; Davies, J.; Davies, M.C.; Roberts, C.J.; Tendler, S.J.B. Surface plasmon resonance for real time in situ analysis of protein adsorption to polymer surfaces. *Biomaterials* **1997**, *18* (5), 405–413.
- Malmsten, M.; Lassen, B.; Westin, J.; Golander, C.G.; Larsson, R.; Nilsson, U.R. Adsorption of complement protein c3 at polymer surfaces. *J. Colloid Interface Sci.* **1996**, *179* (1), 163–172.
- Wahlgren, M.; Arnebrant, T. Adsorption of  $\beta$ -lactoglobulin onto silica, methylated silica, and polysulfone. *J. Colloid Interface Sci.* **1990**, *136* (1), 259–265.
- Marsh, R.J.; Jones, R.A.L.; Sferrazza, M. Adsorption and displacement of globular protein on hydrophilic and hydrophobic surfaces. *Colloids Surf., B Biointerfaces* **2002**, *23* (1), 31–42.
- Calonder, C.; Tie, Y.; van Tassel, P.R. History dependence of protein adsorption kinetics. *Proc. Natl. Acad. Sci. U. S. A.* **2001**, *98* (19), 10664–10669.
- Wahlgren, M.; Arnebrant, T.; Lundstrom, I. The adsorption of lysozyme to hydrophilic silicon oxide surfaces—Comparison between experimental data and

- models for adsorption kinetics. *J. Colloid Interface Sci.* **1995**, *175* (2), 506–514.
29. Ramsden, J.J.; Prenosil, J.E. Effect of ionic strength on protein adsorption kinetics. *J. Phys. Chem.* **1994**, *98* (20), 5376–5381.
  30. Ladam, G.; Gergely, C.; Senger, B.; Decher, G.; Voegel, J.-C.; Schaaf, P.; Cuisinier, F.J.G. Protein interactions with polyelectrolyte multilayers: Interactions between human serum albumin and polystyrene sulfonate/polyallylamine multilayers. *Biomacromolecules* **2000**, *1* (4), 674–687.
  31. Fritz, M.; Radmacher, M.; Cleveland, J.P.; Allersma, M.W.; Stewart, R.J.; Gieselmann, R.; Janmey, P.; Schmidt, C.F.; Hansma, P.K. Imaging globular and filamentous proteins in physiological buffer solutions with tapping mode atomic force microscopy. *Langmuir* **1995**, *11* (9), 3529–3535.
  32. Bustamante, C.; Rivetti, C. Visualizing protein–nucleic acid interactions on a large scale with the scanning force microscope. *Annu. Rev. Biophys. Biomol. Struct.* **1996**, *25*, 395–429.
  33. Bergkvist, M.; Carlsson, J.; Karlsson, T.; Oscarsson, S. TM–AFM threshold analysis of macromolecular orientation: A study of the orientation of IgG and IgE on mica surfaces. *J. Colloid Interface Sci.* **1998**, *206* (2), 475–481.
  34. Muller, D.J.; Sass, H.-J.; Muller, S.A.; Buldt, G.; Engel, A. Surface structures of native bacteriorhodopsin depend on the molecular packing arrangement in the membrane. *J. Mol. Biol.* **1999**, *285* (5), 1903–1909.
  35. Muller, D.J.; Engel, A. pH and voltage induced structural changes of porin ompf explain channel closure. *J. Mol. Biol.* **1999**, *285* (4), 1347–1351.
  36. Smith, D.A.; Connell, S.D.; Robinson, C.; Kirkham, J. Chemical force microscopy: Applications in surface characterization of natural hydroxyapatite. *Anal. Chim. Acta* **2003**, *479* (1), 39–57.
  37. Ta, T.C.; Sykes, M.T.; McDermott, M.T. Real-time observation of plasma protein film formation on well-defined surfaces with scanning force microscopy. *Langmuir* **1998**, *14* (9), 2435–2443.
  38. McMaster, T.J.; Miles, M.J.; Shewry, P.R.; Tatham, A.S. In situ surface adsorption of the protein c hordein using atomic force microscopy. *Langmuir* **2000**, *16* (4), 1463–1468.
  39. Denis, F.A.; Hanarp, P.; Sutherland, D.S.; Gold, J.; Mustin, C.; Rouxhet, P.G.; Dufrene, Y.F. Protein adsorption on model surfaces with controlled nanotopography and chemistry. *Langmuir* **2002**, *18* (3), 819–828.
  40. Johnson, C.A.; Yuan, Y.; Lenhoff, A.M. Adsorbed layers of ferritin at solid and fluid interfaces studied by atomic force microscopy. *J. Colloid Interface Sci.* **2000**, *223* (2), 261–272.
  41. Lin, J.N.; Drake, B.; Lea, A.S.; Hansma, P.K.; Andrade, J.D. Direct observation of immunoglobulin adsorption dynamics using the atomic force microscope. *Langmuir* **1990**, *6* (2), 509–511.
  42. Lea, A.S.; Pungor, A.; Hlady, V.; Andrade, J.D.; Herron, J.N.; Voss, E.W. Manipulation of proteins on mica by atomic force microscopy. *Langmuir* **1992**, *8* (1), 68–73.
  43. Gunning, A.P.; Mackie, A.R.; Wilde, P.J.; Morris, V.J. In situ observation of the surfactant-induced displacement of protein from a graphite surface by atomic force microscopy. *Langmuir* **1999**, *15* (13), 4636–4640.
  44. Ta, T.C.; McDermott, M.T. Mapping interfacial chemistry induced variations in protein adsorption with scanning force microscopy. *Anal. Chem.* **2000**, *72* (11), 2627–2634.
  45. Anderson, R.E.; Pande, V.S.; Radke, C.J. Dynamic lattice Monte Carlo simulation of a model protein at an oil/water interface. *J. Chem. Phys.* **2000**, *112* (20), 9167–9185.
  46. Howald, L.; Haefke, H.; Luthi, R.; Meyer, E.; Gerth, G.; Rudin, H.; Guntherodt, H.-J. Ultrahigh-vacuum scanning force microscopy—Atomic scale resolution at monatomic cleavage steps. *Phys. Rev., B* **1994**, *49* (8), 5651–5656.
  47. Grutter, P.; Zimmermann-Edling, W.; Brodbeck, D. Tip artifacts of microfabricated force sensors for atomic force microscopy. *Appl. Phys. Lett.* **1992**, *60* (22), 2741–2743.
  48. Sheller, N.B.; Petrash, S.; Foster, M.D. Atomic force microscopy and x-ray reflectivity studies of albumin adsorbed onto self-assembled monolayers of hexadecyltrichlorosilane. *Langmuir* **1998**, *14* (16), 4535–4544.
  49. Villarrubia, J.S. Morphological estimation of tip geometry for scanned probe microscopy. *Surf. Sci.* **1994**, *321* (3), 287–300.
  50. Villarrubia, J.S. Algorithms for scanned probe microscope image simulation, surface reconstruction, and tip estimation. *J. Res. Natl. Inst. Stand.* **1997**, *102* (4), 425–454.
  51. Takahara, A.; Ge, S.R.; Kojio, K.; Kajiyama, T. In situ atomic force microscopic observation of albumin adsorption onto phase-separated organosilane monolayer surface. *J. Biomater. Sci., Polym. Ed.* **2000**, *11* (1), 111–120.
  52. Takahara, A.; Hara, Y.; Kojio, K.; Kajiyama, T. Scanning force microscopic study of protein adsorption on the surface of organosilane monolayers prepared by the Langmuir–Blodgett method. *Macromol. Symp.* **2001**, *167*, 271–284.
  53. Takahara, A.; Hara, Y.; Kojio, K.; Kajiyama, T. Plasma protein adsorption behavior onto the surface of phase-separated organosilane monolayers on the basis of scanning force microscopy. *Colloids Surf., B Biointerfaces* **2002**, *23* (2–3), 141–152.
  54. Mueller, H.; Butt, H.J.; Bamberg, E. Adsorption of membrane-associated proteins to lipid bilayers studied with an atomic force microscope: Myelin basic protein and cytochrome *c*. *J. Phys. Chem., B* **2000**, *104* (18), 4552–4559.
  55. Coen, M.C.; Lehmann, R.; Groning, P.; Biemann, M.; Galli, C.; Schlapbach, L. Adsorption and bioactivity of protein A on silicon surfaces studied by AFM and XPS. *J. Colloid Interface Sci.* **2001**, *233* (2), 180–189.
  56. Cullen, D.C.; Lowe, C.R. AFM studies of protein adsorption: 1. Time-resolved protein adsorption to highly oriented pyrolytic graphite. *J. Colloid Interface Sci.* **1994**, *166* (1), 102–108.



57. Hecht, H.J.; Kalisz, H.M.; Hendle, J.; Schmid, R.D.; Schomburg, D. Crystal structure of glucose-oxidase from *Aspergillus niger* refined at 2.3 angstrom resolution. *J. Mol. Biol.* **1993**, *229* (1), 153–172.
58. Silverton, E.W.; Navia, M.A.; Davies, D.R. 3-Dimensional structure of an intact human immunoglobulin. *Proc. Natl. Acad. Sci. U. S. A.* **1977**, *74* (11), 5140–5144.
59. Raghavachari, M.; Tsai, H.M.; Kottke-Marchant, K.; Marchant, R.E. Surface dependent structures of von Willebrand factor observed by AFM under aqueous conditions. *Colloids Surf., B Biointerfaces* **2000**, *19* (4), 315–324.
60. Blake, C.C.F.; Koenig, D.F.; Mair, G.A.; North, A.C.T.; Phillips, D.C.; Sarma, V.R. Structure of hen egg-white lysozyme—A 3-dimensional Fourier synthesis at 2 angstrom resolution. *Nature* **1965**, *206* (4986), 757.
61. Field, J.M.; Tatham, A.S.; Baker, A.M.; Shewry, P.R. The structure of c hordein. *FEBS Lett.* **1986**, *200* (1), 76–80.
62. Galli, C.; Coen, M.C.; Hauert, R.; Katanaev, V.L.; Groning, P.; Schlapbach, L. Creation of nanostructures to study the topographical dependency of protein adsorption. *Colloids Surf., B Biointerfaces* **2002**, *26* (3), 255–267.
63. Clark, P.; Connolly, P.; Curtis, A.S.G.; Dow, J.A.T.; Wilkinson, C.D.W. Topographical control of cell behavior: 2. Multiple grooved substrata. *Development* **1990**, *108* (4), 635–644.
64. Clark, P.; Connolly, P.; Curtis, A.S.G.; Dow, J.A.T.; Wilkinson, C.D.W. Cell guidance by ultrafine topography in vitro. *J. Cell Sci.* **1991**, *99*, 73–77.
65. Curtis, A.; Wilkinson, C. Topographical control of cells. *Biomaterials* **1997**, *18* (24), 1573–1583.
66. Radmacher, M.; Fritz, M.; Cleveland, J.P.; Walters, D.A.; Hansma, P.K. Imaging adhesion forces and elasticity of lysozyme adsorbed on mica with the atomic force microscope. *Langmuir* **1994**, *10* (10), 3809–3814.
67. Chen, X.; Davies, M.C.; Roberts, C.J.; Tendler, C.J.B.; Williams, P.M. Recognition of protein adsorption onto polymer surfaces by scanning force microscopy and probe surface adhesion measurements with protein-coated probes. *Langmuir* **1997**, *13* (15), 4106–4111.
68. Patel, N.; Davies, M.C.; Heaton, R.J.; Roberts, C.J.; Tendler, S.J.B.; Williams, P.M. A scanning probe microscopy study of the physisorption and chemisorption of protein molecules onto carboxylate terminated self-assembled monolayers. *Appl. Phys., A* **1998**, *66* (PT1 SUPPS), S569–S574.
69. Lee, S.H.; Ruckenstein, E. Adsorption of proteins onto polymeric surfaces of different hydrophilicities—A case-study with bovine serum-albumin. *J. Colloid Interface Sci.* **1988**, *125* (2), 365–379.
70. Almeida, A.T.; Salvadori, M.C.; Petri, D.F.S. Enolase adsorption onto hydrophobic and hydrophilic solid substrates. *Langmuir* **2002**, *18* (18), 6914–6920.
71. Tilton, R.D.; Gast, A.P.; Robertson, C.R. Surface diffusion of interacting proteins—Effect of concentration on the lateral mobility of adsorbed bovine serum albumin. *Biophys. J.* **1990**, *58* (5), 1321–1326.
72. Tilton, R.D.; Robertson, C.R.; Gast, A.P. Lateral diffusion of bovine serum albumin adsorbed at the solid liquid interface. *J. Colloid Interface Sci.* **1990**, *137* (1), 192–203.
73. Malmsten, M. Ellipsometry studies of protein layers adsorbed at hydrophobic surfaces. *J. Colloid Interface Sci.* **1994**, *166* (2), 333–342.
74. Wilson, R.; Turner, A.P.F. Glucose-oxidase—An ideal enzyme. *Biosens. Bioelectron.* **1992**, *7* (3), 165–185.
75. Feng, L.; Andrade, J.D. *Proteins at Interfaces II: Fundamentals and Applications*; Brash, J.L., Horbett, T.A., Eds.; American Chemical Society: Washington, DC, 1995; Chapter 5.
76. Titani, K.; Kumar, S.; Takio, K.; Ericsson, L.H.; Wade, R.D.; Ashida, K.; Walsh, K.A.; Chopek, M.W.; Sadler, J.E.; Fujikawa, K. Amino-acid-sequences of human von Willebrand-factor. *Biochemistry* **1986**, *25* (11), 3171–3184.
77. Billsten, P.; Wahlgren, M.; Arnebrant, T.; McGuire, J.; Elwing, H. Structural changes of t4 lysozyme upon adsorption to silica nanoparticles measured by circular dichroism. *J. Colloid Interface Sci.* **1995**, *175* (1), 77–82.
78. Norde, W.; Giacomelli, C.E. BSA structural changes during homomolecular exchange between the adsorbed and the dissolved states. *J. Biotechnol.* **2000**, *79* (3), 259–268.
79. Wertz, C.F.; Santore, M.M. Fibrinogen adsorption on hydrophilic and hydrophobic surfaces: Geometrical and energetic aspects of interfacial relaxations. *Langmuir* **2002**, *18* (3), 706–715.
80. Anderson, R.E. *Dynamic Monte Carlo Simulation of Protein Interaction with an Oil/Water Interface*; University of California: Berkeley, CA, 2000; Masters thesis.
81. Castells, V.; Yang, S.X.; Van Tassel, P.R. Surface-induced conformational changes in lattice model proteins by Monte Carlo simulation. *Phys. Rev., E* **2002**, *65* (3). Art. No. 031912.

# AFM: Simulation of Interaction Forces

**Ivan U. Vakarelski**

*Department of Chemical Engineering, Kyoto University, Kyoto, Japan*

**Scott C. Brown**

*University of Florida, Gainesville, Florida, U.S.A.*

**Bahar Basim**

*Intel Co., Santa Clara, California, U.S.A.*

**Brij M. Moudgil**

*Department of Materials Science and Engineering, University of Florida, Gainesville, Florida, U.S.A.*

## INTRODUCTION

Chemical mechanical polishing (CMP), otherwise known as chemical mechanical planarization, has been an enabling catalyst for rapid technological advancements in microelectronic fabrication and design over the last decade. Although now a multibillion-dollar business in the microelectronics industry, besides patents, there is a dearth of scientific publications on the subject. After initially touching on the significance of CMP, this entry reviews the literature on the versatility of atomic force microscopy (AFM) as a means to probe and simulate the CMP process at the single-particle level.

## IMPORTANCE OF CHEMICAL MECHANICAL POLISHING

Chemical mechanical polishing has become the preferred technology for achieving wafer-level global planarization in ultra-large-scale integration circuits.<sup>[1–5]</sup> In this process, the creation and subsequent controlled abrasion of angstrom- to nanometer-thick chemically modified surface layers is used to remove topographic variations from the surface of microelectronic wafers enabling layer-by-layer device construction. The success and versatility of CMP technologies have been realized largely through the formulation of submicron to nanoscale particulate slurries, which provide both the mechanical and chemical action required for effective and efficient “flattening” of wafer surfaces for subsequent multilayer metallization.<sup>[3–11]</sup> Chemical mechanical polishing is now a multibillion-dollar industry and the fastest-growing unit operation in the microelectronic

manufacturing.<sup>[4]</sup> Yet the fundamental science behind CMP is not well understood. The numerous process variables (>20) as well as the lack of publications outside patent literature have led to a jumbled picture of the essential processes that dictate CMP performance.

Conventional approaches to academic and industrial CMP research have focused on studies in which ensemble endpoints, such as material removal rate, surface roughness, and maximum defect size, are measured subsequent to the use of benchtop or industrial-scale polishing devices to access slurry performance. These studies typically provide comparative results and evidence toward the utility of a particular slurry formulation but generally lack information about the fundamental molecular and nanoscale interactions that control polishing performance. This article discusses the versatility of AFM as a means to probe and simulate the CMP process. The characterization and integration of self-assembled surfactant systems into effective CMP slurries are used to exemplify the utility of the AFM for the elucidation of elementary parameters critical for optimal slurry design. As devices become smaller, more intricate, and incorporate new materials for enhanced electronic properties, the technology-driven slurries of the past may not provide the performance necessary for the continued large-scale production of latest-generation microelectronic devices. To advance manufacturing techniques, a sound scientific understanding of the fundamental nanoscale to microscale interfacial interactions and mechanisms present in the CMP process must be developed.<sup>[3]</sup> The integration of AFM-based single particle measurements in fundamental CMP studies may provide an added level of insight necessary for

the design of “smart” and “tunable” slurries that support the manufacture of future electronic devices.

## DISCUSSION

### Fundamental Issues in Slurry Design

Chemical mechanical polishing utilizes both chemical and mechanical interactions to essentially flatten, or planarize, dielectric and metal surfaces using a slurry composed of chemicals and submicron particles.<sup>[1–11]</sup> As illustrated in Fig. 1, the CMP process has three main components: 1) the wafer surface (onto which the device is built), 2) the polymeric polishing pad (which entraps and holds the abrasive particles), 3) the polishing slurry composed of submicron particles and reactive chemical agents. Slurry is dosed onto a rotating polymeric pad onto which the wafer is pressed while rotating, causing attrition of unwanted asperities. The overall aim of the process is to remove topographic features from the surface such that multilayer metallization, or layer-by-layer construction of devices, can occur. The general strategy for this is to engineer slurries that provide a pressure-sensitive material removal response. This is desired such that the higher asperities are preferentially removed and the end product is a planarized surface.

Chemical mechanical polishing slurry solutions often contain multiple chemical reagents at high ionic strength and high pH values at the time of polishing to provide the necessary reactivity with the wafer surface. Although these conditions favor the formation of a chemically modified layer, they complicate strategies for maintaining slurry stability. The presence of less than 1 ppm of aggregates in a slurry can cause deleterious deformation of the wafer surface;<sup>[6–8]</sup> therefore an optimally polishing

CMP slurry must be aggregate-free. Stable suspensions provide more repeatability, lower surface defectivity, and better consistency in polishing.<sup>[4]</sup>

Because of the difficulties in adequately dispersing CMP slurries in the presence of the necessary chemical reagents, some manufacturers have resorted to the mixing of particulate slurries with the salts and reactive chemicals at the point of use.<sup>[4]</sup> This technique effectively reduces the time for particulate coagulation and may aid in slurry handling. However, problematic aggregation and slurry particle deposition onto the wafer surface still occur. The next generation of particulate slurries should possess more advanced approaches such as the incorporation of robust steric dispersants.<sup>[5]</sup>

To assess whether or not the stability requirements for a slurry have been met, one typically performs a number of particle sizing or turbidity tests. These measurements provide evidence of whether or not a system will coagulate under the given chemical environment; however, the extent or magnitude of the barrier to coagulation is not directly revealed. Because of this shortcoming, AFM normal force measurements to simulate particle–particle interactions have gained considerable attention in the fields of colloid and interfacial science over the last decade.<sup>[12]</sup> An AFM with an attached liquid cell or suitable liquid reservoir provides a readily accessible means of directly measuring nano-scale surface force interactions in numerous solution environments. These force–distance curves can be further evaluated to derive parameters such as the surface charge,<sup>[13–15]</sup> the mechanical properties of surface layers,<sup>[16]</sup> and the mode and potential mechanism behind the observed surface forces.<sup>[17]</sup> The advent of colloidal probes has further advanced this approach by extending the measurement beyond the typical silicon or silicon nitride tip materials toward real particle systems.

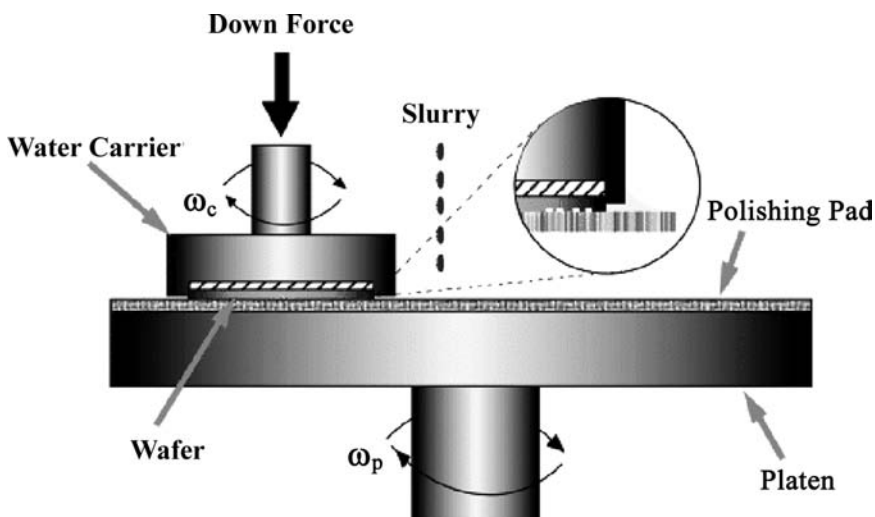


Fig. 1 Schematic representation of chemical mechanical polishing process.

In CMP, chemical reagents not only facilitate the formation and passivation of chemically modified surface layers, but also modulate dispersion within the particle system.<sup>[3–11]</sup> Therefore care must be taken to ensure that the system to be measured by AFM adequately represents the real system at hand. Slight changes, for instance, in surface chemistry, crystalline structure, and morphology, can alter the adsorption behavior of species from solution as well as the bare interaction forces between surfaces, thereby obscuring the appropriate interpretation. Because CMP slurries are formulated with submicron or nanosized particles that are nearly impossible to singly attach at the tip apex, bare AFM tips or larger-sized particles are used for simulating the CMP process. Recently, AFM tips with attached nanotubes have been procured that may be further functionalized with the appropriate nanoparticle at the free end.<sup>[18]</sup> Unfortunately, a large degree of uncertainty remains with respect to the appropriate treatment of mechanical response of these “nanoprobes” under compression and lateral motion.<sup>[19]</sup>

### Interpreting Slurry Stability

When focused on particle–particle interactions, a flat substrate may be chosen to simulate a particle surface, and either a bare tip or an attached larger particle may be used to probe the system. The former is applicable when no appreciable interference from the AFM tip material, apart from the real particle system, is expected. The utilization of AFM normal force–distance curves to interpret slurry stability has been well documented.<sup>[13–15]</sup> Intuitively, if solely attractive or repulsive forces are measured between a representative probe–substrate system, then the corresponding particulate system will be unstable or stable, respectively. If both types of forces are present, there will exist critical forces or distances in the system that define stability. As a general rule of thumb, slurry stability typically ensues if repulsive force barriers greater than 10 kT are present.<sup>[20]</sup>

At solution ionic strengths on the order of 0.1 M, purely electrostatic mechanisms for particulate stability are ineffective because of extensive double-layer compression. Hence other measures such as the addition of dispersants are needed to prevent coagulation. Recently, self-assembled alkyl trimethyl ammonium surfactants have been shown to provide robust stability in silica suspension slurries under saturated salt solutions, extremes in pH,<sup>[21,22]</sup> and under high shear<sup>[23]</sup>—conditions where traditional polymeric or inorganic dispersants are often ineffective. These findings prompted fundamental investigations into the properties of these self-assembled surfactant structures at the solid–liquid interface for the formulation

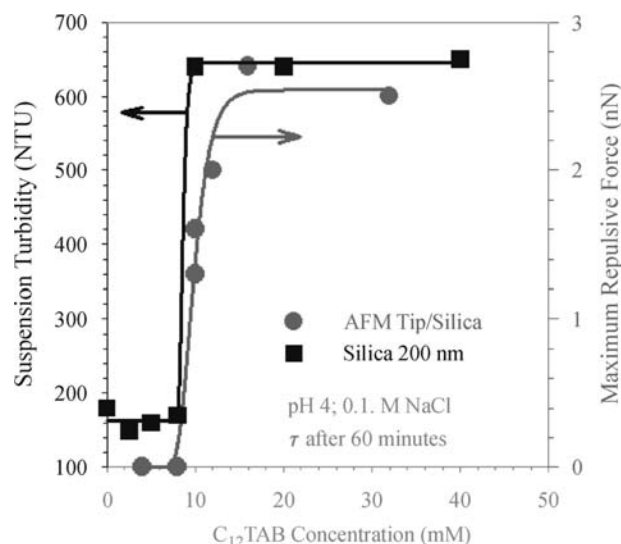


**Fig. 2** Turbidity in nephelometric turbidity units (NTU) of silica particles after 60 min in a solution of 0.1 M NaCl at pH 4 as a function of C<sub>12</sub>TAB concentration, and the measured interaction forces between an AFM tip and silica substrate under identical solution conditions. *Source:* From Ref.<sup>[21]</sup>.

of silica dielectric CMP slurries.<sup>[5,8]</sup> Atomic force microscopy has uncovered fundamental mechanisms and key relationships for CMP slurry and dispersant system design in this system.

>The onset of silica slurry stability at high ionic strengths as discussed above has been linked to the onset of repulsive force barrier.<sup>[21]</sup> Fig. 2 illustrates the excellent agreement between ensemble turbidity measurements and the AFM normal force measurements for the silica wafer–silicon nitride tip system at pH 4.0 and 0.1 M NaCl as a function of dodecyl trimethyl ammonium bromide surfactant (C<sub>12</sub>TAB) concentration. The mechanism behind C<sub>12</sub>TAB-induced stabilization was subsequently investigated through zeta potential, contact angle, adsorption isotherms, and Fourier transform infrared spectroscopy–attenuated total internal reflection (FTIR–ATR) analysis.<sup>[21,22]</sup> These experiments illustrated that the repulsive barrier was induced via hydrophilic adsorbed surfactant assemblies that were micelle-like in origin. Ref.<sup>[25]</sup> reviews the adsorption of cationic surfactants from solution to oxide surfaces.

The general mechanisms by which micellar interfacial surfactant structures physically intervene in the engagement process of approaching surfaces have been documented.<sup>[16,26]</sup> Fig. 3 illustrates a typical force–distance curve between two approaching surfactant-coated oxide surfaces, under low electrolyte conditions. The depicted force profile was measured between a 7.5- $\mu$ m silica colloidal probe and a planar silica substrate at twice the bulk critical micelle concentration (CMC) concentration (32 mM) of C<sub>12</sub>TAB. Under

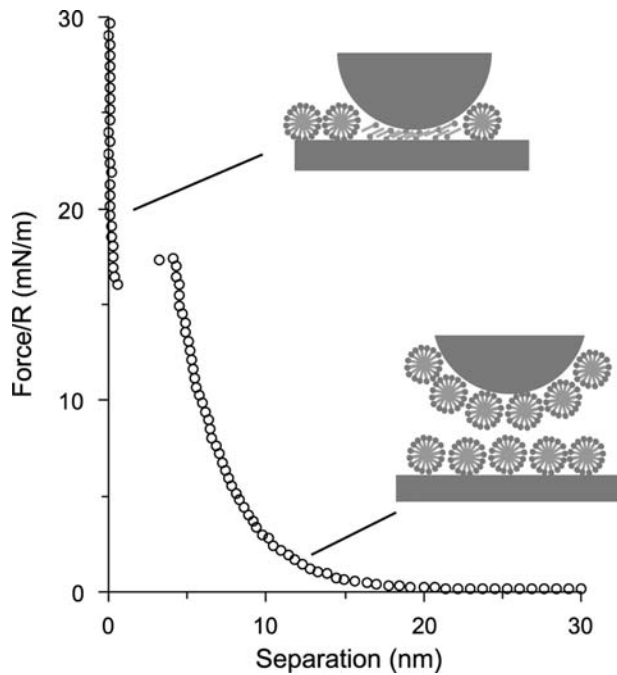


**Fig. 3** A typical force-separation curve for the interaction of a 7.5- $\mu\text{m}$  silica sphere and a flat silica substrate in a solution of 32 mM  $\text{C}_{12}\text{TAB}$ . Data from several runs are presented. *Source:* From Ref.<sup>[24]</sup>.

these solution conditions, a saturated layer of micelles is adsorbed to both the colloidal probe and the flat interface. As the surfaces are brought together, the positively charged micelles begin to interact through long-range electrostatic forces. At shorter distances, just before and during the initial contact, a combination of electrostatics and short-range hydration forces between surfactant headgroups contributes to the interaction profile. As the intervening micelles are further pressed together, a sharp pseudo-linear increase in repulsion occurs from steric contributions resulting from the elastic deformation of the surface aggregates. Then at a critical applied load, these aggregates break apart and the surfaces jump into contact. After this point, the measured interaction is in constant compliance, and no further deformation of the adsorbed surfactant structures is measured. A thin layer of surfactant monomers still resides between the approaching surfaces as indicated in Fig. 3; however, this layer is not mechanically detectable by AFM normal force measurements because of the sensitivity limits of the experimental configuration. Moreover, the apparent modulus of molecular-scale organic layers is largely impacted by the underlying surface, and the existence of a rigid underlayer is known to lead to effective mechanical properties orders-of-magnitude larger than those of the film alone.<sup>[26,27]</sup>

Because of the potential for these surfactant systems to provide stability in CMP slurry formulations in the

presence of harsh additives, alkyl trimethyl ammonium surfactants were added to silica slurries and tested for polishing performance. Two-hundred-nanometer monodisperse Stober silica particles were used as the abrasive particles at a loading of 12 wt.% to closely resemble conventional CMP slurries while still maintaining a certain degree of idealness for fundamental interaction studies. The pH in the slurries was maintained at 10.5 such that the “gel-like” chemically modified layer formation could occur at the wafer surface, and 0.6 M NaCl was added to simulate the ionic strength induced by industrial CMP additives. Experiments performed on a benchtop polishing device illustrated that the robust dispersion provided by the surfactant systems exhibiting an appreciable repulsive force barrier at post-CMC concentrations (Fig. 4A) led to excellent surface finish and low surface defectivity (Fig. 4B). However, at the same time, negligible polishing rates occurred. For optimally polishing CMP slurry, both high removal rates ( $>600$  nm/min) and

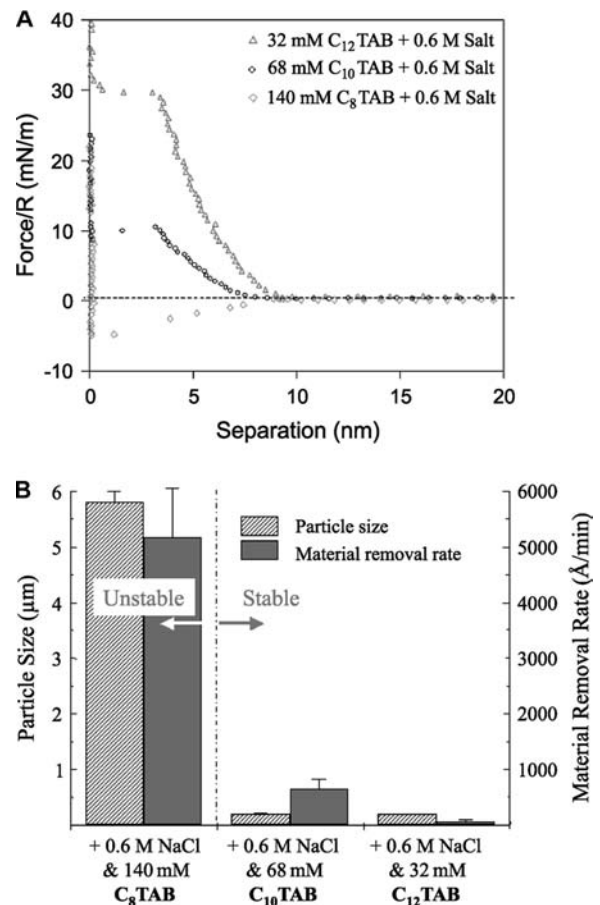


**Fig. 4**  $\text{C}_{12}\text{TAB}$ ,  $\text{C}_{10}\text{TAB}$ , and  $\text{C}_8\text{TAB}$  surfactants at 32, 68, and 140 mM concentrations in the presence of 0.6 M NaCl at pH 10.5 (a) Maximum repulsive force responses obtained with AFM; (b) slurry particle size (stability) and material removal rate responses. *Source:* From Ref.<sup>[30]</sup>.

low surface defectivity [ $>2$  nm root-mean-square (RMS) and maximum defect sizes  $<20$  nm] must be achieved simultaneously.<sup>[3,5,8]</sup> An important conclusion from the above finding is that that dispersion is a necessary but not a sufficient component for CMP slurry design; this emphasizes the importance of particle–wafer interactions in CMP processes.

### Particle–Substrate Interactions

Although particle–particle interaction can be simulated by AFM to ensure adequate slurry stability—which translates into lower surface defectivity and fewer wafers lost to large-scale surface deformations (scratches)—particle–surface interactions drive the material removal and planarization processes. Hence the overall effectiveness of the CMP process largely depends on these interactions. Not surprisingly, the majority of AFM studies involving CMP focus on these interactions almost in entirety.

At the nanoscale, one can envision the CMP process as a single particle phenomenon. This is depicted in Fig. 5 where an abrasive particle is entrapped by a polymeric pad asperity as it transverses across the wafer surface. The particle–surface interactions incurred by the applied normal and lateral loads ( $F_N$  and  $F_L$ , respectively) result in the removal of the thin chemically modified layer. As the bare wafer surface is exposed to the solution environment, chemical reagents form a new chemically modified surface layer. This process repeats itself as subsequent particles are brought into contact with the wafer surface.

From this perspective, the CMP process can be effectively simulated by rastering an AFM probe against a wafer surface. Recently, several authors have performed this experiment to simulate the CMP of metal materials by scratching metal substrates with an unmodified AFM tip.<sup>[28–30]</sup> In metal CMP, a brittle oxide layer is formed on the more ductile metal surface, which is thought to be removed, almost in

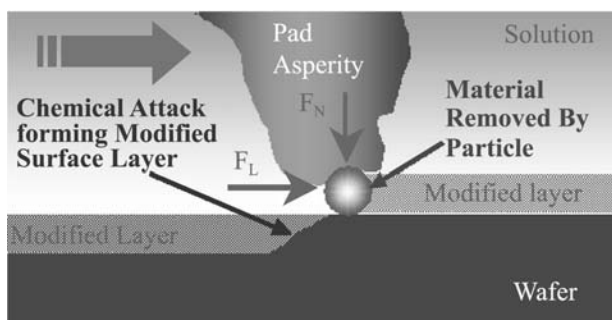


**Fig. 5** Schematic illustrating a single particle material removal event during CMP.

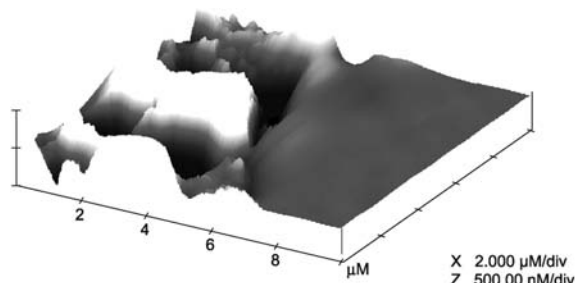
entirety, via the mechanical normal and shear stresses imposed by the abrasive particles.<sup>[3]</sup> Contrary to silica polishing, in these systems, an AFM tip may provide an adequate surrogate for an abrasive particle. However, it should be stressed that this assumption is speculation because no definitive studies have been conducted yet to verify the brittle fracture/film delamination mechanisms for metal CMP.<sup>[3]</sup> Nonetheless, bare AFM tips have been reported to adequately simulate an abrasive particle in metal CMP.

Deveecchio, Schametz, and Frankel<sup>[28]</sup> used a silicon AFM tip and a pure alumina substrate to simulate the polishing of a metallized wafer. By rastering the tip over a known area on the metal surface for a given time and applied load, they were able to derive nominal material removal rates from AFM experiments. The material volume losses from “scratched” areas were determined by subsequent imaging at low applied loads. This value was normalized by the rastering time to obtain a nominal removal rate. Using this approach, the nominal material removal rates were studied under a range of conditions including varying tip/sample forces, solution pH, and electrode potentials (used to imitate an oxidizing agent). Baseline experiments performed in air had a negligible removal rate, illustrating that the observed phenomenon results from both the mechanical abrasion and the solution chemistry. As with ensemble CMP experiments, the removal rate was found to be strongly dependent on the solution pH, the relative amount of oxidation, and the applied load.

A standard silicon nitride AFM tip was used by Lim et al.<sup>[29]</sup> to measure frictional and topographic changes at the copper surface in the presence of nitric acid and neutral solution with benzotriazole (BTA), a corrosion inhibitor. No significant changes were found to occur in neutral solutions with BTA. However, under acidic conditions where isotropic dissolution of the copper surface is known to occur, BTA acted as a passivation agent. Moreover, the BTA-passivated chemically modified layers could be removed via abrasion with the AFM tip, resulting in preferential material removal at the contacting asperities. The presence of higher interfacial friction with BTA-passivated copper surfaces as well as tip-mediated, localized dissolution of copper interface was observed. Similarly, Berdyeva, Emery, and Sokolov<sup>[30]</sup> also used a silicon nitrate tip to simulate the CMP of copper surfaces oxidized in aqueous solutions of peroxide and glycine at varying pH values. The material removal rate and observed indentation depth as a function of pH was consistent with the previous CMP results. The friction force between the tip and the surface was measured, and, in general, it was shown that the lower friction coefficients correspond to the slower removal rates.

Maw et al.<sup>[31]</sup> recently proposed an alternative approach for studying CMP processes. Single surface





10 x 10 μm Image (z = ± 1 μm)

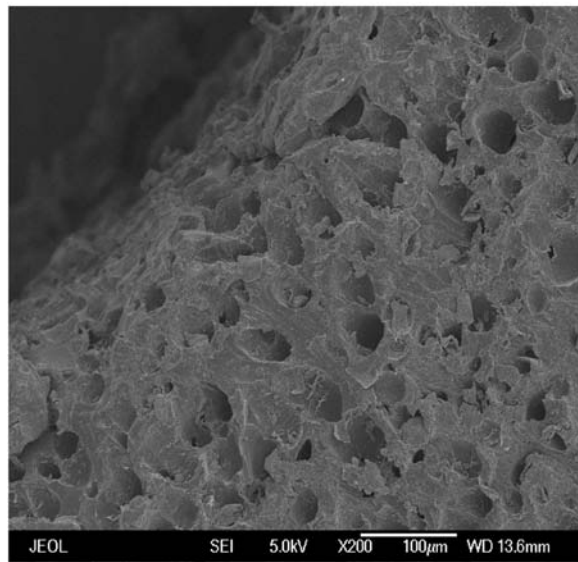


**Fig. 6** IC-1000 polishing pad surface as imaged by AFM (top image) and SEM (bottom image) showing the macro-porosity and microporosity. *Source:* From Ref.<sup>[30]</sup>.

asperity wear was simulated by measuring the dulling or material removal from a silicon nitride AFM tip rastered against a variety of substrates in aqueous solution. The chemical nature of the substrate was shown to play a critical role in the wear of dielectric oxide materials—significant material removal was observed only when the surface was populated with the appropriate metal-hydroxide bonds. These results suggest that pressure-induced bridging between oxide bonds on the substrate may assist in CMP processes.

The investigation described above further illustrates the importance of the selection of an appropriate probe material when attempting to simulate a CMP process via AFM. A bare AFM tip should be used only to simulate another material on which the probe is not expected to significantly react with the solution environment, wafer surface, or otherwise facilitate the adsorption of solution species that would interfere with the measurement process. These criteria may not be applicable in silica CMP especially if the abrasive particle material is also silica. Although a significant fraction of the silicon nitride surface may contain silica

because of hydrolysis in water, the surfaces are nevertheless different in charge, hydroxyl site density, and modulus.<sup>[31]</sup> Under such situations, an attached larger-sized particle (colloidal probe) with nearly identical surface chemistry with respect to the primary slurry particles may provide the best simulation. For reasons of sensitivity, reproducibility, and scalability with radius, smooth particles are generally preferred unless an adequate surface morphology match can be made or specific morphological features are investigated.

The range of normal loading forces required for simulation must also be known. This requires an approximation of the pressure per particle experienced in the CMP process. The applied tool pressures in CMP operations can range from less than 1 to over 7 psi. Because of the corrugation (Fig. 6) of the polishing pad, only a fraction of the pad surface transfers this loading force. Hence the localized forces transferred by pad asperities can be appreciably higher, and the pressure per particle will depend on the pad characteristics such as its effective surface morphology and elastic modulus.

Recently, FTIR-ATR was used to measure the effective pad contact area as a function of applied pressure.<sup>[9]</sup> The IR spectra of the IC 1000 pad sample were collected with applied download forces ranging from 23 to 79 kPa. As the applied load was increased, the signal intensity also increased, indicating that more pad contact was achieved with the ATR crystal. To obtain the percent pad coverage, the same analyses were also conducted on a piece of polyurethane without corrugation, identical in composition to the pad. The results represented in Fig. 7A and B evidence that only a fraction of the pad surface was in contact with the wafer surface or with the ATR crystal. Indeed, the percent pad contact values varied between 0.25% and

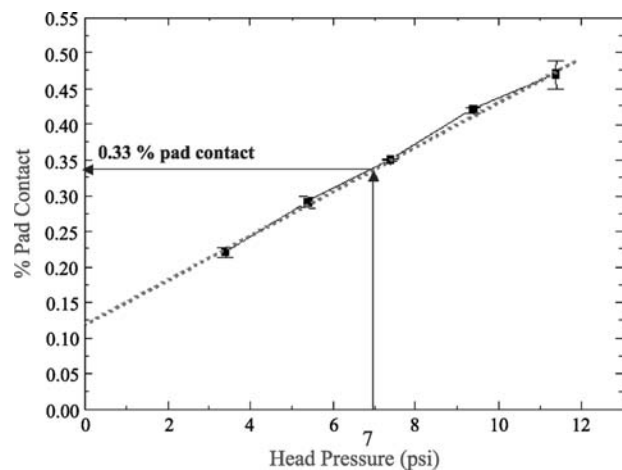


**Fig. 7** Percent IC-1000 pad contact as a function of applied load. *Source:* From Ref.<sup>[30]</sup>.

0.5% in the selected pressure range. These results agree with the literature findings, which have reported the pad contacts between 0.05% (hard pad with elastic modulus value  $E = 100$  MPa) and 0.54% (soft pad with  $E = 10$  MPa) at 7 psi.<sup>[32]</sup> Through scanning electron microscope (SEM) and subsequent image analysis of the particle-laden pad after polishing, the number of 200-nm particles in contact with the pad at 12 wt.% solids loading was estimated to be  $42 \times 10^6$  per in.<sup>2</sup>, and the interpreted applied load was then found to be 750 nN per particle. Through these approximations, it became evident that the steric force barriers imposed by micellar aggregates on the silica surface in Fig. 3 were exceeded during the polishing process. Therefore micelles were not present on the wafer surface during CMP and could not be responsible for the lack of material removal. Hence the presence of surfactant monomer was found to impede the polishing process.

To investigate this anomalous polishing behavior, rectangular tipless cantilevers (MikroMasch) were selected with a normal spring constant in the range of  $K_N = 2.8 \pm 0.3$  N/m to ensure that normal forces comparable to those experienced in CMP could be accessed. Sol-gel silica particles (7.5  $\mu\text{m}$ ) were attached to the end of the cantilevers using a small amount of high-temperature melting epoxy (Shell Epikote 1009) to ideally simulate the slurry particles. As with the previous normal force measurements, the frequency method<sup>[33]</sup> was used to determine the exact values of the normal spring constants, and forces normal to the flat surface were measured according to the method introduced by Ducker, Senden, and Pashley<sup>[13,14]</sup> As will become evident, the utility of colloidal probes and AFM, in general, for CMP simulations offers multiple routes to probe the fundamental interactions that define the CMP process.

### Lateral Forces and Surfactant Adsorption

Atomic force microscopy lateral force measurements have been used to investigate the loss of material attrition in the surfactant-based slurry system. The lateral interaction force between a silica colloidal particle and an atomically smooth flat silica surface was measured to simulate particle-wafer system interactions. Fig. 8 illustrates representative lateral force vs. loading force curves for the case of silica surfaces interacting across pure water and a 32-mM solution of  $\text{C}_{12}\text{TAB}$ . Data from several experiments are presented to illustrate the reproducibility of the measurements. Each experimental series was taken at a fixed position on the sample. Subsequent to each increase in the normal force, 10 friction force cycles were allowed to transpire to allow the lateral force magnitude to stabilize prior to taking a reading. Consecutive runs taken over

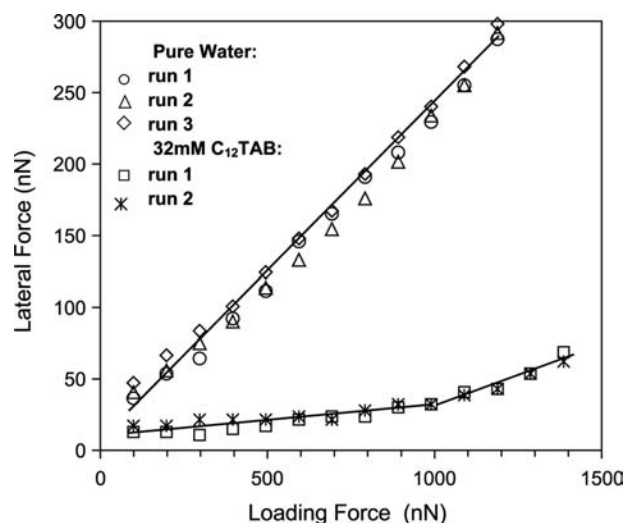


**Fig. 8** Lateral force as a function of the applied load for a 7.5- $\mu\text{m}$  silica sphere interacting with a smooth silica surface in pure water and in solution 32mM  $\text{C}_{12}\text{TAB}$ . Data from several runs are presented. *Source:* From Ref.<sup>[24]</sup>.

different areas show good reproducibility with a maximum deviation of about  $\pm 5\%$ . This suggests that there was no significant wearing of the probe during measurement. It is important to mention that the experimental results from different probes have similar features with regards to lateral and adhesive force interactions under the given solution conditions; however, slight differences in magnitude might appear because of variations in the local roughness of the probe surface.<sup>[34]</sup> For consistency, the data presented have been obtained using the same colloidal probe, unless otherwise noted. The lateral force measurements presented were also taken at a constant lateral scan velocity of 2  $\mu\text{m}/\text{sec}$ . However, it should be noted that contrary to studies on chemisorbed self-assembled monolayers<sup>[35–37]</sup> and adsorbed polyelectrolytes,<sup>[38]</sup> no significant dependence of the frictional force was found when the scan rate was varied between 1 and 20  $\mu\text{m}/\text{sec}$ . The measurements in surfactant solutions were systematically performed 30 min after the solution injection to prevent variations in the extent of consolidation or the packing and morphological state of the adsorbed layers.<sup>[39,40]</sup>

The lateral force measurements were performed using the “friction-force” mode of the AFM, in which the colloidal probe is pressed against the substrate at a constant applied load while the substrate slides horizontally underneath the cantilever. Further details of the measurement procedure are given elsewhere.<sup>[41–47]</sup>

In lateral force microscopy (LFM), a micron-sized colloidal probe significantly improves the reproducibility of lateral force measurements by reducing the relative impact of probe wear on the experimental results; surprisingly, however, attached particles have

only been incorporated in a few AFM/LFM studies.<sup>[38,40,41]</sup> The friction force, as measured between bare silica surfaces in deionized water, was found to increase linearly with the applied load in agreement with the Amontons' law. Accordingly, the data for these conditions can be fitted to a linear function of the type  $F_L = a + \mu F_N$ , where  $F_N$  is the applied load,  $\mu$  is the frictional coefficient, and  $a$  is the adhesive force contribution. The average friction coefficient obtained for pure water was found to be  $\mu = 0.22$  and is in the range of the literature values (0.1–1.0) measured between quartz surfaces.<sup>[48]</sup>

It has been established that  $\text{CH}_3\text{-CH}_3$  group interactions result in a significant reduction in friction when compared with the interactions of higher-energy functional groups<sup>[49,50]</sup> from previous studies of monomolecular films adsorbed at interfaces. The presence of surfactant at the solid–liquid interface is thought to prevent material removal by inhibiting bare surface contact or by acting as boundary layer lubricants. The interactions between intervening surfactant hydrocarbon tails and the silica surface replace the pure  $\text{SiOH}$  and  $\text{SiO}^-$  interactions found in the pure water. From this perspective, the extent of lubrication should therefore depend on the number of surfactant residing between the interface, which was found to be the case, as illustrated in Fig. 9. As free surfactant concentration increased, the lubrication between the interfaces also increases. The maximum amount of lubrication is a plateau value that occurs at and above the bulk CMC (16 mM), representing an order-of-magnitude decrease in the frictional interactions. These measurements confirm that surfactant monomer actively participates in mitigating the particle–wafer surface

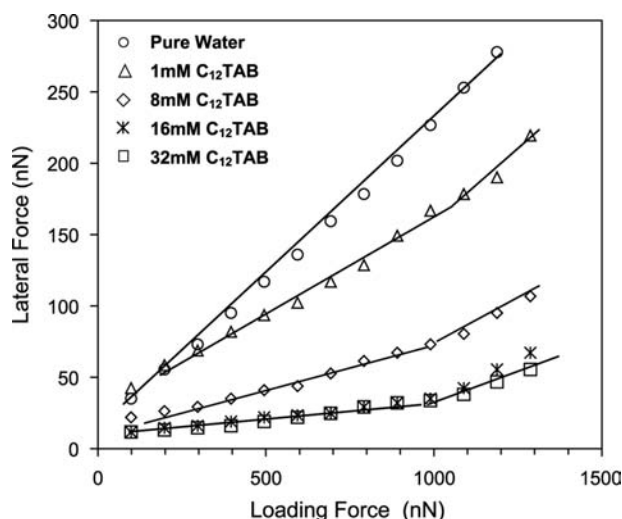


**Fig. 9** Lateral force as a function of the applied load for a 7.5-mm silica sphere interacting with a smooth silica surface in pure water and  $\text{C}_{12}\text{TAB}$  solutions of various concentration. Source: From Ref.<sup>[24]</sup>.

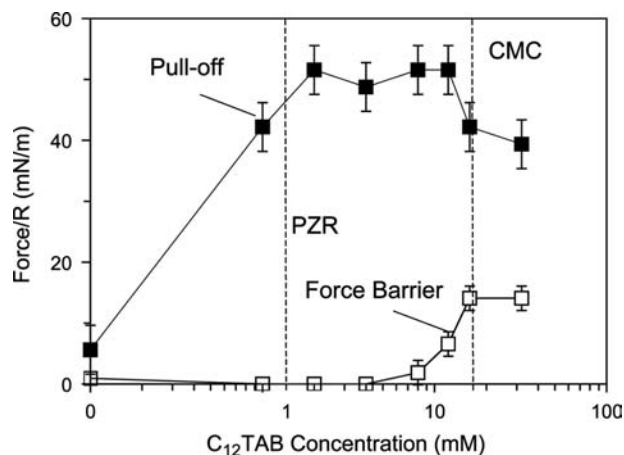


**Fig. 10** Repulsive force barrier and pull-off force as measured between a 7.5-mm silica sphere and a flat silica surface as function of the  $\text{C}_{12}\text{TAB}$  concentration. Source: From Ref.<sup>[24]</sup>.

engagement. As noted earlier, the experiments were performed at high loading forces at which the micellar structures have already been broken.

The enhanced lubrication at and above the CMC may be caused by the relative number of surfactant in the local vicinity of the interface. This is indicated in Fig. 10, where the extents of the repulsive force barrier at the surfactant concentrations of 16 and 32 mM are shown to be nearly identical, indicating that saturation adsorption has been reached as previously demonstrated through experimental adsorption isotherms.<sup>[21,25]</sup> Hence under these conditions, the probable number of entrapped surfactant monomers should be the highest and identical, resulting in equivalent frictional interactions. Similarly, at lower free surfactant concentrations, the extent of lubrication should be lower, resulting from fewer surfactant residing between the interfaces. These trends have been verified in Fig. 9, which illustrates that the lubrication efficacy of surfactant solution increases with free surfactant concentration until the bulk CMC is reached. Both electrostatically bound and hydrophobically associated surfactant monomers are thought to participate in the surfactant-mediated lubrication phenomena. The lowest concentration of amine shown in Fig. 9, 1 mM  $\text{C}_{12}\text{TAB}$ , corresponds to the point of zeta-potential reversal (PZR) at which the surfactant molecules are primarily electrostatically bound to the interface. The surfactant adsorption is still as low as 20–25% of that of the saturation value at the PZR.<sup>[51,52]</sup> At higher concentrations, adsorption primarily takes place through hydrophobic association. These additional hydrophobically bound surfactant monomers participate in a further decrease of the frictional force until saturation adsorption.

### Pull-Off Force Measurements—Deciphering Dispersant Molecule Adhesion Mechanisms

To design surfactant-dispersed slurries with appreciable polishing rates, the dominant mechanism leading to the presence of residual monomer at the solid–liquid interface needed to be determined. Pull-off force measurements—the force required to detach the colloidal probe from the planar substrate—were performed in an attempt to gain additional information on the origins and strength of adhesion of the residual surfactant layer. As with the lateral force microscopy measurements, the magnitude of the pull-off force is also strongly influenced by the existence of the intervening molecular films. In the presence of surfactant, the value of typical pull-off forces between the probe used in this investigation and the planar silica substrate increased by an order of magnitude in comparison to the pure state as indicated in Fig. 10. This additional adhesive component between the surfaces is attributed to the hydrophobic interactions between strongly bound surfactant molecules adsorbed to the opposing silica surfaces. However, whether these interaction forces represent the detachment of the adsorbed headgroups from the interface or the disengagement of the interacting hydrophobic surfactant groups themselves remains unknown. These two proposed scenarios are illustrated in Fig. 11. By monitoring the maximum pull-off force as a function of concentration, some clues are given. As indicated in Fig. 10, the adhesive force reaches a plateau value in the vicinity of the PZR and not at the maximum monolayer coverage, which occurs just

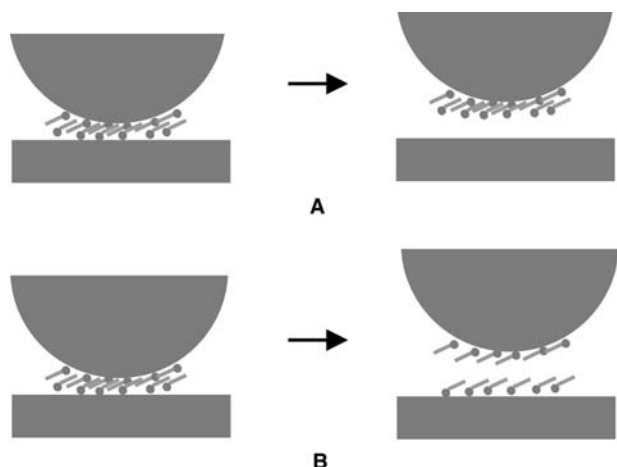


**Fig. 11** Schematic representation of the two proposed scenarios for surfactant-mediated detachment of the silica surfaces in this study. (A) The surfactants remain in hydrophobic association and detach at the head–surface interface. (B) The surfactants remain adsorbed at the opposing interfaces and detach through breaking of hydrophobic chain–chain interactions. *Source:* From Ref.<sup>[24]</sup>.

prior to 8 mM  $C_{12}TAB$ .<sup>[21]</sup> This suggests that force required to separate the engaged surfaces is largely electrostatic and not caused by the detachment of hydrophobic bonds. To verify this, the relative magnitude of the interfacial energies expected for the two scenarios depicted in Fig. 11 was investigated and compared with the values calculated from experimental results.

To estimate the energy required for electrostatic detachment, the contribution of the coulombic interaction to the interfacial separation energy  $\gamma_{el}$  was estimated by:<sup>[53,54]</sup>

$$\gamma_{el} = \frac{1}{2} \Gamma_{el} z e \psi_i \quad (1)$$

where  $\Gamma_{el}$  represents the adsorption density of the electrostatically adsorbed surfactant monomers to the substrate,  $z$  is the valency of the headgroups,  $e$  is the electronic charge, and  $\psi_i$  is the potential of the inner Helmholtz plane of the surface prior to surfactant adsorption. For simplicity, it was assumed that  $\psi_i \approx \zeta$ , the zeta potential of the silica surface in pure water, and that  $\Gamma_{el} = \Gamma_{PZR}$ , the amount of surfactant adsorbed at the PZR. Taking typical values<sup>[25,51,52]</sup> of  $\zeta = -60$  mV and  $\Gamma_{PZR} = 1 \mu\text{M}/\text{m}^2$ , the magnitude of  $\gamma_{el}$  was found to be approximately  $3.8 \text{ mJ}/\text{m}^2$ .

To estimate the amount of energy required to separate the surfaces through purely hydrophobic interactions between the hydrocarbon tails (Fig. 11B), the interfacial separation energy,  $\gamma_h$ , was estimated as:

$$\gamma_h = \Gamma_h n \theta_h \quad (2)$$

where  $\Gamma_h$  is the density of strongly bound surfactant molecules that mediate the separation event,  $n$  is the number of  $\text{CH}_2$  groups that effectively interact between the individual surfactant molecules, and  $\theta_h$  is the energy per  $\text{CH}_2$ – $\text{CH}_2$  group interaction. For this estimate, it was assumed that  $\Gamma_h = \Gamma_{el}$  (or the lower limiting case in which only the electrostatically adsorbed molecules are detached), and that full interpenetration of the hydrocarbon chains ( $n = 12$ ) occurs. By employing a typical value<sup>[17]</sup> for  $\theta_h$  as  $6.3 \times 10^{-21}$  J,  $\gamma_h$  was calculated to be approximately  $45 \text{ mJ}/\text{m}^2$ .<sup>[55]</sup> Alternatively, the magnitude of the interfacial separation energy for hydrophobic detachment can be estimated to be close to the experimental values of the adhesion force between chemisorbed  $\text{CH}_3$  group-terminated surfactant monolayers interacting across an aqueous medium. From both force and contact angle measurements, the range of this interfacial energy  $\gamma_{ch}$  is found to be between 40 and  $100 \text{ mJ}/\text{m}^2$ ,<sup>[55]</sup> which compares to the above result and 1 order-of-magnitude greater than  $\gamma_{el}$ .

To further compare these values with the experimental pull-off force measurements in this study, the Johnson–Kendall–Roberts (JKR)<sup>[56]</sup> (upper limiting value) or Derjaguin–Muller–Toporov (DMT)<sup>[57]</sup> (lower limiting value) theories were employed. Accordingly, the effective experimental interfacial separation energies were given by:

$$\gamma(\text{JKR}) = \frac{F_{\text{pull-off}}}{3\pi R}, \text{ or } \gamma(\text{DMT}) = \frac{F_{\text{pull-off}}}{4\pi R} \quad (3)$$

By incorporating values of  $F_{\text{pull-off}}$  from Fig. 10, it was found that  $\gamma \approx 3\text{--}4\text{ mJ/m}^2$ , which is in the range of  $\gamma_{\text{el}}$ . This is an order-of-magnitude less than that speculated for purely hydrophobic-mediated detachment. Hence although the adsorption of surfactant at the solid–liquid interface mediates by both chain–chain and head–surface interactions, contributions from the adsorption affinity of the surfactant headgroup to the surface appear to dominate the overall resilience of the remaining films at the interface. For the surfactant system in this investigation, the chain–chain interactions appear much greater than the head–surface affinity (assumed purely electrostatic), causing the latter to dictate the extent of adhesion (pull-off force) and possibly the extent of lubrication. Accordingly, the scenario depicted in Fig. 11a was determined to be more plausible when the two surfaces are pulled apart. Hence to modulate the material removal rate in these surfactant-based slurries, the electrostatic attraction of the surfactant to the wafer and particle surfaces needs to be manipulated.

Although evidence in the preceding section suggested that the resilience of residual surfactant moieties depends largely on the extent of head–surface engagement, the utility of this for the control of the extent of particle–surface engagement mediated by physisorbed surfactant systems has not been illustrated. It is well established that quaternary amine surfactants adsorb to silica interfaces through a combination of electrostatic, hydrogen-bonding, and hydrophobic interactions.<sup>[58]</sup> However, the relative importance of these interactions in maintaining surface attachment and lubrication is not well understood.

If one assumes that the extent of lubrication is mediated by intervening molecular films attached to the solid–liquid interface primarily by electrostatic interactions, then there should be a large dependence on the lateral force with solution pH. It is well documented that the number of deprotonated (negatively charged) silanol groups at silica interfaces increases with pH causing an increase in the net surface charge. The isoelectric point of silica is near pH 2.5; the zeta potential is about  $-50.0\text{ mV}$  at pH 5.6 and  $-70\text{ mV}$  at pH 9.0.<sup>[59]</sup> Hence the extent of lubrication caused by electrostatically adsorbed surfactant structures

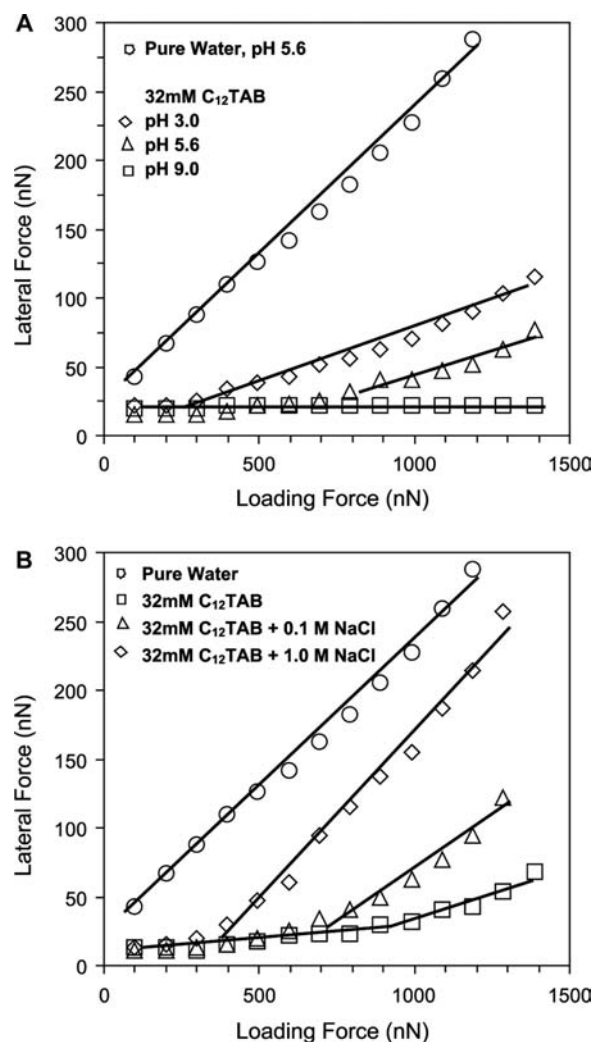


**Fig. 12** Lateral force as a function of the applied load for a 7.5-mm silica sphere interacting with a smooth silica surface in solutions of 32 mM  $\text{C}_{12}\text{TAB}$  at (A) various pH values and (B) at various concentrations of NaCl given in logarithmic scale. *Source:* From Ref.<sup>[24]</sup>.

should increase with pH. This is indeed the case, as Fig. 12 indicates. For all solution pH values, the lateral forces at low loading forces (100–300 nN) were found to be identical; however, a deviation in lubrication performance occurred at higher normal forces indicated by the variant of Amontons’ law and potentially a non-Prestonian polishing response.<sup>[3]</sup> This experimental evidence suggests that at a critical load, the adsorbed surfactant structures begin to detach from the surface as marked by the increase in the apparent friction coefficient. This “activation energy” for surfactant detachment shifts to higher energies (loads) with pH. At a pH of 9.0, the transition was not observed for loads up to 1400 nN and was attributed to the strong electrostatic interactions between the surfactant and the silica surface at high pH.



The above illustrates that electrostatic interactions could be used to modulate friction, which physically can be interpreted as the extent of silica-silica engagement; however, for silica CMP, a high pH is generally fixed to ensure the formation of a gel-like layer. This prompted investigations into an alternative approach for modulating the extent of particle engagement and material removal in CMP systems. The influence of co-ion competition with respect to the surfactant molecule for negatively charged surface sites was investigated to suit this purpose. The frictional force between silica surfaces in the presence of post-CMC surfactant solutions at a pH of 5.6 and various ionic strength NaCl solutions were measured and are depicted in Fig. 12B. A significant increase in frictional engagement occurs at high  $\text{Na}^+$  concentrations, further indicating that the electrostatic binding efficacy to the silica interface largely controls the extent of bare surface engagement in these surfactant systems. These findings also suggested for the first time that competitive adsorption strategies may be used to tailor the frictional properties and possibly the material removal rates in slurries dispersed by physisorbed surfactants. Fig. 12B further shows that as the number of competing ions increases, the transition load at which higher friction coefficients appear becomes lower and the magnitude of the friction coefficient becomes higher.

### Optimizing Slurry Formulation Through Systematic Atomic Force Microscopy Measurements

The strategies suggested above focused on diminishing the extent of surfactant surface affinity to allow for greater engagement of the bare particle with the substrate surfaces. It has not been clearly demonstrated, however, whether or not this loss in surfactant surface affinity will result in aggregation of the silica particulate system, which would be deleterious to CMP operations. Pull-off force and repulsive force barrier measurements were conducted as a function of pH and electrolyte concentration to further develop the correlations between stability, surfactant surface affinity, and lubrication. The pull-off force indicates the relative strength of attachment of surfactants to the solid-liquid interface, whereas the presence of a repulsive force barrier indicates that particle stability still exists.<sup>[21]</sup>

Fig. 13A presents the pull-off and repulsive force barrier measurements as a function of pH for the same experimental conditions as in Fig. 12a. At twice the CMC surfactant concentrations, both the repulsive barrier and the pull-off force increase with increasing pH. These trends are attributed to both the greater

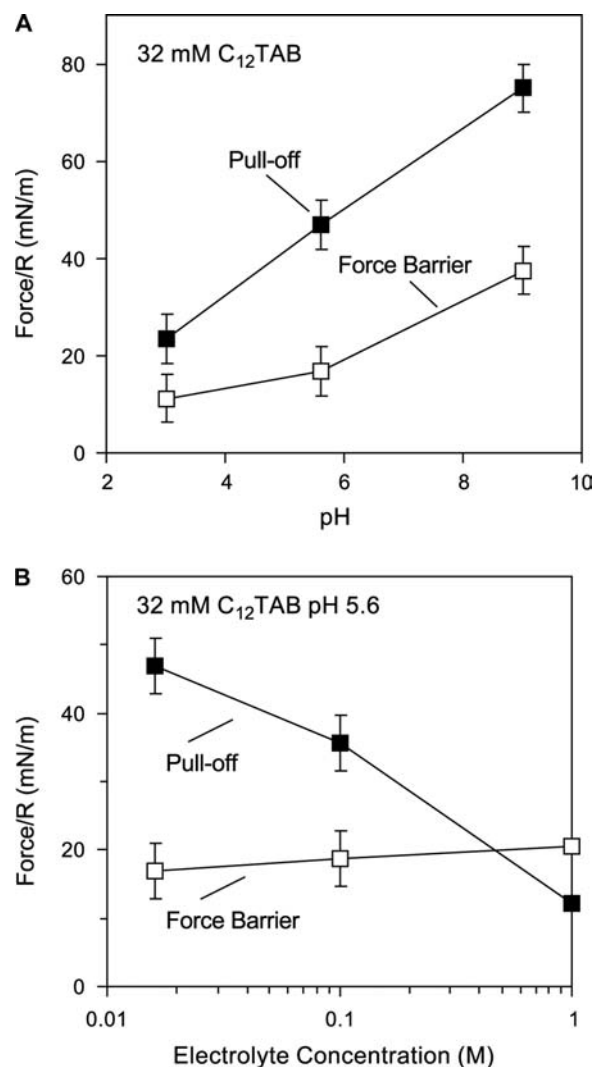


**Fig. 13** Force barrier and pull-off force between a 7.5-mm silica sphere and flat silica surface in solutions of 32 mM C<sub>12</sub>TAB as function of (a) solution pH and (b) solution electrolyte concentration. *Source:* From Ref.<sup>[24]</sup>.

electrostatic affinity and perhaps the greater localized concentration of surfactant at the silica-solution interface at higher pH values. Both the enhancement of the barrier and the pull-off forces correlate well with the increased lubrication observed with pH as demonstrated in Fig. 12A.

However, as indicated in Fig. 13b, the extent of the repulsive barrier does not primarily depend on the magnitude of surfactant surface affinity. Although both the lubrication and the pull-off force decrease by nearly an order of magnitude with a 1-M increase in ionic strength, the repulsive force barrier remains nearly constant. This counterintuitive resilience of the surfactant-mediated repulsion under high electrolyte concentrations was first demonstrated in a previous study,<sup>[21]</sup> in which the primary factor for establishing



an effective force barrier was the extent of surfactant–surfactant cohesion in the three-dimensional surface structures. The relationship between the surfactant force barrier and the surfactant surface affinity has been inferred recently.<sup>[24]</sup> Fig. 13B demonstrates that the relative number of strongly bound surfactant monomers at the solid–liquid interface has little bearing on the mechanical properties, or the extent of the repulsive force barrier, imparted by adsorbed micelles or bilayer-like structures. Hence to some extent, it is possible to control the degree of lubrication imbibed by adsorbed surfactants without significantly altering the suspension stability. The above discussion indicates that multifunctional and tailored pressure-sensitive surfactant-based lubricants are plausible through the use of competitive adsorption and surface affinity concepts.

In another study<sup>[8]</sup> utilizing an alternative colloidal probe, it was found that modifying the cohesion between surfactant chain length does not significantly induce a modification in the lubrication, or surface engagement, behavior in the absence of salt as depicted in Fig. 14A. However, with the addition of 0.6 M NaCl, the induced ion competition resolves the difference in surface affinity between C<sub>8</sub>TAB, C<sub>10</sub>TAB, and C<sub>12</sub>TAB surfactants as illustrated in Fig. 14B. A similar result has been previously shown in studies concerning lateral force measurements of monomolecular chemisorbed or deposited films.<sup>[60,61]</sup> These investigations depict a reduction in lubrication with a reduction of the hydrocarbon chain length for intervening films.

As the extent of chain–chain cohesion increases with amphiphile chain length, a reduction in friction occurs because these molecules can more effectively mask the underlying surface because of their higher mutual affinity. Although it is possible to modify surfactant chain length to decrease surfactant surface affinity and thereby induce surface engagement and material removal, maintaining slurry stability at the same time presents an issue. The normal force–distance interaction curves between a silica sphere and a silica wafer in the presence at post-CMC concentrations in the presence of 0.6 M NaCl were previously given in Fig. 4. Under pseudo-CMP conditions, the lower chain surfactant (C<sub>8</sub>TAB) is unable to provide a steric barrier; however, it is able to incur significant surface engagement. The benchmark polishing studies collaborate with these results illustrating a material removal rate of over 5000 Å/min for C<sub>8</sub>TAB compared with removal rates of over 500 and approximately 50 Å/min, respectively, for the C<sub>10</sub>TAB and C<sub>12</sub>TAB slurries in the presence of 0.6 M electrolyte. However, as predicted by the normal force measurements, the C<sub>8</sub>TAB slurries result in an unacceptable surface finish with a root-mean-squared surface roughness near 1 nm and defect diameters on the order of 50 nm.

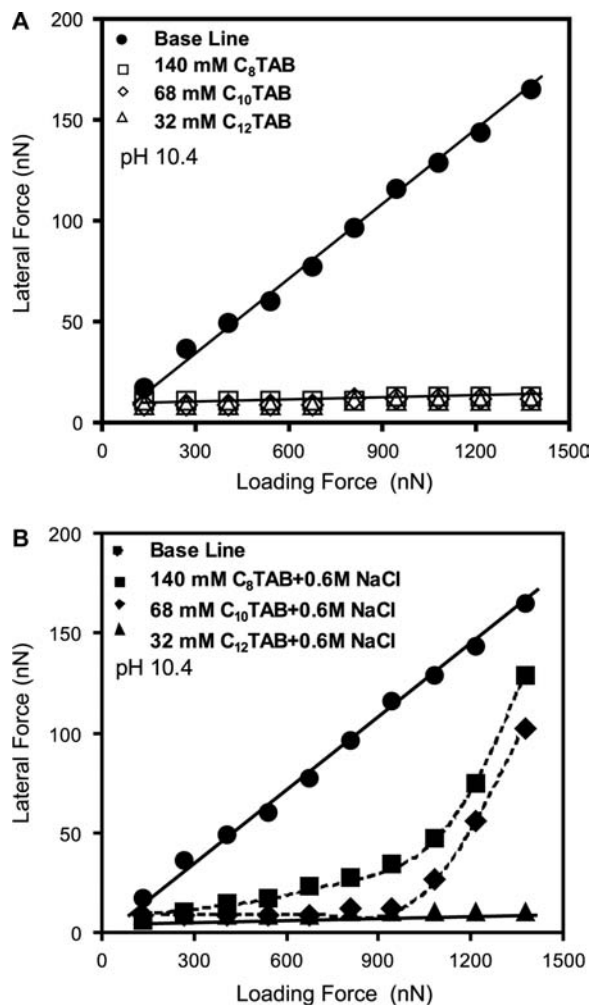


**Fig. 14** Atomic force microscopy friction force measurements between a silica wafer and a 7.5- $\mu\text{m}$  silica particle for solutions containing C<sub>12</sub>TAB, C<sub>10</sub>TAB, and C<sub>8</sub>TAB surfactants at post-CMC concentrations in the absence (A) and the presence (B) of 0.6 M NaCl. *Source:* From Ref.<sup>[30]</sup>.

Because of the inadequacy of the above results to provide for both good surface quality and adequate material removal, an alternative approach was attempted. It was hypothesized that by modifying the strength of the competing ion from solution, the affinity of the surfactant to the surface could be modulated resulting in a potentially tunable material removal. Moreover, as shown with the lateral force measurements with alternative salt concentrations, the kink or the sudden increase in surface engagement after a certain load in the loading curves tends to shift toward lower loads with increasing salt and indicates that non-Prestonian polishing responses<sup>[3]</sup> may be achieved through ion competition strategies with the appropriate formulation.

To test whether modifying the surfactant surface affinity via alternative competing species could be a

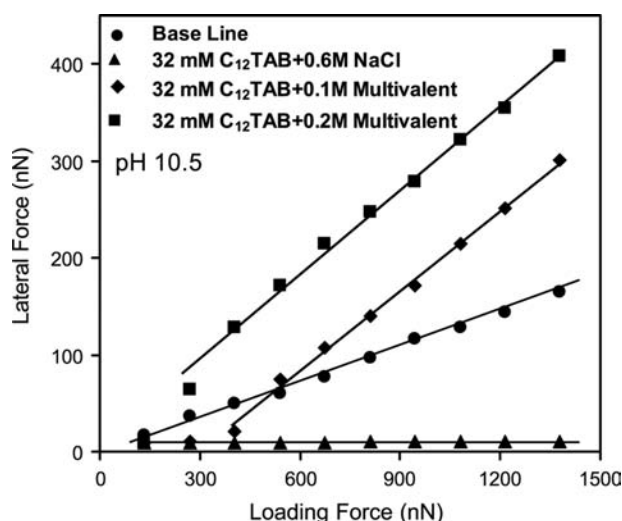


**Fig. 15** Atomic force microscopy friction force measurements between a silica wafer and a 7.5- $\mu\text{m}$  silica particle in DI water at pH 10.5 (baseline), with 32 mM  $\text{C}_{12}\text{TAB}$  with 0.6 M NaCl and 0.1 or 0.2 M  $\text{CaCl}_2$ .

valid approach for achieving both high material removal rates and good surface quality after polishing,  $\text{CaCl}_2$  was added to the silica slurries in the presence of 32 mM  $\text{C}_{12}\text{TAB}$ . Equivalent ionic strengths were maintained in the solutions containing surfactant. The lateral force measurements are displayed in Fig. 15, which illustrates that the surface engagement between the silica surface and the silica particle significantly increased in comparison to the NaCl surfactant solutions and the baseline (pH 10.5, no salt) conditions. Approaching normal force measurements in all three cases (not shown) as well as direct particle sizing indicated that all three slurries were stable. The corresponding polishing results (200-nm sol-gel silica at 12 wt.%) confirmed the LFM experiments and showed that the  $\text{CaCl}_2$ -based surfactant slurries could achieve higher removal rates ( $\sim 1000 \text{ \AA}/\text{min}$  greater) and improved surface quality (nearly identical to the non-polishing surfactant slurries) when compared with the baseline slurry. Hence by changing the magnitude of interaction of competing ions in solution, the polishing behavior of surfactant-based slurries can be modulated, resulting in improved material removal, enhanced surface finish, and potentially tunable polishing responses with the competing ion concentration in solution.

## CONCLUSION

The AFM is a powerful tool for simulating nanoscale CMP processes. Through a systematic study of both normal force (approaching and pull-off) and lateral

force interactions, fundamental mechanisms resulting in modified polishing behavior can be investigated. In CMP operations, the behavior of the slurry is often the defining parameter for overall polishing performance. The integration and effectiveness of dispersants in CMP processes can provide an improved nanoscale surface finish as well as an alternative means to control the extent of material removal.

In this entry, the use of AFM to probe quaternary ammonium surfactant systems for the purpose of the integration and the optimization in silica dielectric polishing slurries was reviewed. Approaching AFM normal force measurements were shown to effectively predict slurry stability and subsequent surface defectivity from benchtop polishing tests. Pull-off force measurements in conjunction with systematic lateral force measurements were found to be effective for deciphering key mechanisms behind modulated polishing performance. The influence of intervening surfactant moieties on the frictional interactions between oxide surfaces was also examined in detail.

As new, softer, and more fragile materials are introduced into microelectronic device fabrication, more intricate slurry formulations will be needed to provide for efficient material removal while maintaining adequate levels of surface defectivity and selectivity in polishing. The AFM is expected to grow more important in future CMP slurry development investigations as well as in fundamental investigations into nanoscale CMP processes. The ion competition strategies and dispersant strategies discussed within may also play a significant role in the development of novel “smart” slurries for future CMP processes.

## ACKNOWLEDGMENTS

The authors acknowledge the financial support of the Particle Engineering Research Center (PERC) at the University of Florida, the National Science Foundation (NSF) (Grant EEC-94-02989), and the Industrial Partners of the ERC for support of this research. Any opinions, findings, and conclusions or recommendations expressed in this material are those of the author(s) and do not necessarily reflect those of the National Science Foundation.

## REFERENCES

- Steigerwald, J.; Murarka, S.; Gutmann, R. *Chemical-Mechanical Planarization of Microelectronic Material*; John Wiley & Sons: New York, 1997.
- Shon-Roy, L. CMP: Market trends and technology. *Solid State Technol.* **2000**, *43*, 67–75.

3. Singh, R.; Lee, S.; Choi, K.; Basim, G.; Choi, W.; Chen, Z.; Moudgil, B. Fundamentals of slurry design for CMP of metal and dielectric materials. *MRS Bull.* **2002**, *27*, 752–760.
4. Singh, R.; Bajaj, R. Advances in chemical mechanical planarization. *MRS Bull.* **2002**, *27*, 743–747.
5. Basim, G.; Brown, S.; Vakarelski, I.; Moudgil, B. Strategies for optimal chemical mechanical polishing (CMP) slurry design. *J. Dispers. Sci. Technol.* **2003**, *24*, 499–515.
6. Basim, G.; Moudgil, B. Effect of soft agglomerates on CMP slurry performance. *J. Colloid Interface Sci.* **2002**, *256*, 137–142.
7. Basim, G.; Adler, J.; Mahajan, U.; Singh, R.; Moudgil, B. Effect of particle size of chemical mechanical polishing slurries for enhanced polishing with minimal defects. *J. Electrochem. Soc.* **2000**, *147*, 3328–3523.
8. Basim, G.; Vakarelski, I.; Moudgil, B. Role of interaction forces in controlling the stability and polishing performance of CMP slurries. *J. Colloid Interface Sci.* **2003**, *263*, 506–515.
9. Basim, G.; Moudgil, B. Slurry design for chemical mechanical polishing. *Kona* **2003**, *21*, 178–184.
10. Qin, K.; Moudgil, B.; Park, C. A chemical mechanical polishing model incorporating both the chemical and mechanical effects. *Thin Solid Films* **2004**, *446*, 277–286.
11. Rajan, K.; Singh, R.; Adler, J.; Mahajan, U.; Rabinovich, Y.; Moudgil, B. Surface interaction forces in chemical-mechanical planarization. *Thin Solid Films* **1997**, *308–309*, 529–532.
12. Larson, I.; Ralston, J. Atomic Force Microscopy and Colloid Interaction Forces. In *Encyclopedia of Surface and Colloid Science*, 1st Ed.; Hubbard, A., Ed.; Marcel Dekker, Inc.: New York, 2002; 653–663.
13. Ducker, W.; Senden, T.; Pashley, R. Direct measurement of colloidal forces using an atomic force microscope. *Nature* **1991**, *353*, 239–241.
14. Ducker, W.; Senden, T.; Pashley, R. Measurement of forces in liquids using a force microscope. *Langmuir* **1992**, *8*, 1831–1836.
15. Butt, H. Measuring electrostatic, van der Waals, and hydration forces in electrolyte solutions with an atomic force microscope. *Biophys. J.* **1991**, *60*, 1438–1444.
16. Rabinovich, Y.; Vakarelski, I.; Brown, S.; Singh, P.; Moudgil, B. Mechanical and thermodynamic properties of surfactant aggregates at the solid–liquid interface. *J. Colloid Interface Sci.* **2004**, *270*, 29–36.
17. Israelachvili, J. *Intermolecular and Surface Forces*, 2nd Ed.; Academic Press Inc.: San Diego, 1992.
18. Dai, H.; Hafner, J.; Rinzler, A.; Colbert, D.; Smalley, R. Nanotubes as nanopropes in scanning probe microscopy. *Nature* **1996**, *384*, 147–150.
19. Falvo, M.; Clary, G.; Taylor, R.; Chi, V.; Brooks, F., Jr.; Washburn, S.; Superfine, R. Bending and buckling of carbon nanotubes under large strain. *Nature* **1997**, *389*, 582–584.
20. Fuchs, N. Über die stabilität und aufladung der aerosole. *Z. Phys.* **1934**, *89* (5), 736–743.
21. Adler, J.; Singh, P.; Patist, A.; Rabinovich, Y.; Shah, D.; Moudgil, B. Correlation of particulate dispersion stability with the strength of self-assembled surfactant films. *Langmuir* **2000**, *16*, 7255–7262.
22. Singh, P.; Adler, J.; Rabinovich, Y.; Moudgil, B. Investigation of self-assembled surfactant structures at the solid–liquid interface using FT-IR/ATR. *Langmuir* **2001**, *17*, 468–473.
23. Zaman, A.; Singh, P.; Moudgil, B. Impact of self-assembled surfactant structures on rheology of concentrated nanoparticle dispersions. *J. Colloid Interface Sci.* **2002**, *251*, 381–387.
24. Vakarelski, I.; Brown, S.; Rabinovich, Y.; Moudgil, B. Lateral force microscopy investigation of surfactant mediated aqueous adsorption from solution. *Langmuir* **2004**, *20*, 1724–1731.
25. Atkin, R.; Craig, V.; Wanless, E.; Biggs, S. Mechanism of cationic surfactant adsorption at the solid–aqueous interface. *Adv. Colloid Interface Sci.* **2003**, *103*, 219–304.
26. Shull, K.R.; Ahn, D.; Mowery, C.L. Finite-size corrections to the JKR technique for measuring adhesion: Soft spherical caps adhering to flat, rigid surfaces. *Langmuir* **1997**, *13*, 1799–1804.
27. Shull, K.R.; Dongchan, A.; Chen, W.C.; Flanigan, C.M.; Crosby, A. Axisymmetric adhesion tests of soft materials. *J. Macromol. Chem. Phys.* **1998**, *199*, 489–511.
28. Devecchio, D.; Schumtz, P.; Frankel, G.S. A new approach for the study of chemical mechanical polishing. *Electrochem. Solid-State Lett.* **2000**, *3*, 90–92.
29. Lim, M.S.; Perry, S.S.; Galloway, H.C.; Koeck, D.C. Microscopic studies of friction and wear at the benzotriazole/copper interface. *Tribol. Lett.* **2003**, *14*, 261–268.
30. Berdyeva, T.K.; Emery, S.B.; Sokolov, I.Yu. In situ AFM study of surface layer removal during copper CMP. *Electrochem. Solid-State Lett.* **2003**, *6*, G91–G94.
31. Maw, W.; Stevens, F.; Langford, S.C.; Dickinson, J.T. Single asperity tribochemical wear of silicon nitride studied by atomic force microscopy. *J. Appl. Phys.* **2002**, *92*, 5103–5109.
32. Yu, T.; Yu, C.; Orlowski, M. A Statistical Polishing Pad Model for Chemical-Mechanical Polishing, Electron Devices Meeting Technical Digest., International, Washington, DC, USA, Dec. 5–8, 1993; IEEE Publications: Washington, DC, 1993, 865–868. 4805299.
33. Cleveland, J.P.; Manne, S.; Bockec, D.; Hansma, P.K. A nondestructive method for determining the spring constant of cantilevers for scanning force microscopy. *Rev. Sci. Instrum.* **1993**, *64*, 403–405.
34. Vakarelski, I.U.; Ishimura, K.; Higashitani, K. Adhesion between silica particle and mica surfaces in water and electrolyte solutions. *J. Colloid Interface Sci.* **2000**, *227*, 111–118.
35. Liu, Y.; Wu, T.; Evans, D.F. Lateral force microscopy study on the shear properties of self-assembled monolayers of dialkylammonium surfactant on mica. *Langmuir* **1994**, *10*, 2241–2245.
36. Liu, G.; Salmeron, B. Reversible displacement of chemisorbed n-alkanethiol molecules on Au(111) surface: An atomic force microscopy study. *Langmuir* **1994**, *10*, 367–370.
37. Liu, Y.; Evans, F.D.; Song, Q.; Grainger, D.W. Structure and frictional properties of self-assembled surfactant monolayers. *Langmuir* **1996**, *12*, 1235–1244.
38. Feiler, A.; Plunkett, M.A.; Rutland, M.W. Atomic force microscopy measurements of adsorbed polyelectrolyte

- layers 1. Dynamics of forces and friction. *Langmuir* **2003**, *19*, 4173–4179.
39. Ducker, W.A.; Wanless, E.J. Adsorption of hexadecyltrimethylammonium bromide to mica: Nanometer-scale study of binding-site competition effects. *Langmuir* **1999**, *15*, 160–168.
40. Drummond, C.J.; Sender, T.J. Examination of the geometry of long-range tip-sample interaction in atomic force microscopy. *Colloids Surf. A* **1994**, *87*, 217–234.
41. Feiler, A.; Larson, I.; Attard, P. Quantitative study of interaction forces and friction in aqueous colloidal systems. *Langmuir* **2000**, *16*, 10269–10277.
42. Meurk, A.; Larson, I.; Bergstrom, L. Tribological Properties of Iron Powder Subjected to Various Surface Treatments. In *Fundamentals in Nanoindentation and Nanotribology*, Mater. Res. Soc. Symp. Proc. Spring 1998, San Francisco, CA, USA, April 13–17, 1998; Session, T., Ed.; MRS: San Francisco, 1998, 427–430.
43. Bogdanovic, G.; Meurk, A.; Rutland, M.W. Tip friction-torsional spring constant determination. *Colloids Surf. B* **2000**, *19*, 397–405.
44. Gibson, T.C.; Watson, G.S.; Myhra, S. Lateral force microscopy—A quantitative approach. *Wear* **1997**, *213*, 72–79.
45. Hess, P. Laser diagnostics of mechanical and elastic properties of silicon and carbon films. *Appl. Surf. Sci.* **1996**, *106*, 429–437.
46. Cain, R.G.; Page, N.W.; Biggs, S. Force calibration in lateral force microscopy. *J. Colloid Interface Sci.* **2000**, *227*, 55–65.
47. Cain, R.G.; Reitsma, M.G.; Biggs, S. Quantitative comparison of three calibration techniques for the lateral force microscope. *Rev. Sci. Instrum.* **2001**, *72*, 3304–3312.
48. Weast, R.C. Coefficient of Friction. In *Handbook of Chemistry and Physics*, 56th Ed.; CRC Press: Cleveland, OH, 1975; F-14.
49. Overney, R.; Meyer, E. Tribological investigations using friction force microscopy. *MRS Bull.* **1993**, *18*, 26–35.
50. Clear, S.C.; Nealey, P.F. Lateral force microscopy study of the frictional behavior of self-assembled monolayers of octadecyltrichlorosilane on silicon/silicon dioxide immersed in *n*-alcohols. *Langmuir* **2001**, *17*, 720–732.
51. Whitby, C.P.; Scales, P.J.; Grieser, F.; Healy, T.W.; Nishimura, S.; Tateyama, H. The adsorption of dodecyltrimethylammonium bromide on mica in aqueous solution studied by X-ray diffraction and atomic force microscopy. *J. Colloid Interface Sci.* **2001**, *235*, 350–357.
52. Chorro, M.; Chorro, C.; Dolladille, O.; Partyka, S.; Zana, R. Adsorption mechanism of conventional and dimeric cationic surfactants on silica surface: Effect of the state of the surface. *J. Colloid Interface Sci.* **1999**, *210*, 134–143.
53. Somasundaran, P.; Healy, T.W.; Fuerstenau, D.W. Surfactant adsorption at the solid-liquid interface—dependence of mechanism on chain length. *J. Phys. Chem.* **1964**, *68*, 3562–3566.
54. Hunter, J.R. Adsorption at Charged Interfaces. In *Foundation of the Colloid Science*, 2nd Ed.; Oxford University Press Inc.: New York, 2001; 522–525.
55. Warszynski, P.; Papastavrou, G.; Wantke, K.-D.; Mohwald, H. Interpretation of adhesion force between self-assembled monolayers measured by chemical force microscopy. *Colloids Surf. A* **2003**, *214*, 61–75.
56. Johnson, K.L.; Kendall, K.; Roberts, A.D. Surface energy and the contact of elastic solids. *Proc. R. Soc. Lond., A* **1971**, *453*, 136–179.
57. Derjaguin, B.V.; Muller, V.M.; Toporov, V. Effect of contact deformations on the adhesion of particles. *J. Colloid Interface Sci.* **1975**, *53*, 318–326.
58. Ducker, W.A.; Grant, L.M. Effect of substrate hydrophobicity on surfactant surface-aggregate geometry. *J. Phys. Chem.* **1996**, *100*, 11507–11511.
59. Hardley, P.G.; Larson, I.; Scales, M.; Scales, P.J. Electrokinetic and direct force measurements between silica and mica surfaces in dilute electrolyte solutions. *Langmuir* **1997**, *13*, 2207–2214.
60. Xiao, X.; Hu, J.; Charych, D.H.; Salmeron, M. Chain length dependence of the frictional properties of alkylsilane molecules self-assembled on mica studied by atomic force microscopy. *Langmuir* **1996**, *12*, 235–237.
61. Lee, S.; Shon, Y.-S.; Colorado, R., Jr.; Guenard, R.L.; Lee, T.R.; Perry, S.S. The influence of packing densities and surface order on the frictional properties of alkanethiol self-assembled monolayers (SAMs) on gold: A comparison of SAMs derived from normal and spiroalkanedithiols. *Langmuir* **2000**, *16*, 2220–2224.

# Amphiphilic Block Copolymer Monolayer at Air–Water Interface

Emiko Mouri

*Nanostructured Composites and Fibers, Kyoto University, Kyoto, Japan*

Hideki Matsuoka

*Department of Polymer Chemistry, Kyoto University, Kyoto, Japan*

## INTRODUCTION

Amphiphilic diblock copolymers,<sup>[1,2]</sup> which have hydrophilic and hydrophobic chains, self-assemble to form a monolayer at the air/water interface and a micelle in selective solvents. The diblock copolymer monolayer system is of great importance and interest from the scientific and technological points of view. The relationship between the fundamental molecule structure and properties, such as length and stiffness of each chain, hydrophilicity–hydrophobicity balance, and the nanostructure of monolayer formed, is an important aspect in establishing a tailor-made polymer assembly at the surface and interface. Furthermore, the hydrophilic chain in the polymer monolayer is an excellent model system of the “polymer brush,”<sup>[3]</sup> which is useful in surface modification, colloid stabilization, etc.

## OVERVIEW

We have been studying amphiphilic diblock copolymer monolayers at the air/water interface by in situ X-ray<sup>[4–9]</sup> and neutron reflectometry.<sup>[10]</sup> In recent years, our interest has been focused on ionic amphiphilic diblock copolymer monolayer systems that form an ionic polymer brush in water subphase.<sup>[6,8,9]</sup> The long-range electrostatic interaction and osmotic pressure inside the ionic polymer brush are important for the monolayer nanostructure, in addition to short-range steric forces and conformational effects that are usually seen in the neutral brush. This situation causes a large variety of brush structures. Elucidation of the polymer brush nanostructure will enable on-demand control of surface structure and a wide-range application of the polymer brush system.

The diblock copolymer chosen for the investigation is composed of a fluid-like, very flexible hydrophobic chain and a weak polyacid chain, poly(1,1-diethylsilacyclobutane)<sub>m</sub>-*block*-poly(methacrylic acid)<sub>n</sub> [poly(Et<sub>2</sub>SB-*b*-MAA)].<sup>[11]</sup> The fluid-like nature of Et<sub>2</sub>SB makes it

possible to form a polymer monolayer with smooth interface between air and hydrophobic layer with 3–5 Å roughness.<sup>[6]</sup> Furthermore, the electron density contrast between Et<sub>2</sub>SB and MAA is larger than that in the general diblock copolymer system. Merited by these two, a suitable system for X-ray reflectivity measurement could be achieved by this diblock copolymer.

The nanostructure of the polymer monolayer has been systematically investigated as a function of hydrophilic chain length, surface pressure, and pH.<sup>[6,8,9]</sup> Interesting features are as follows: 1) The hydrophobic layer thickness takes a minimum as a function of hydrophilic chain length at any surface pressure studied.<sup>[6]</sup> 2) The hydrophilic layer under the water is not a simple layer but is divided into two layers, i.e., a “carpet”-like dense MAA layer near the water surface and a polyelectrolyte brush layer.<sup>[9]</sup> 3) The thickness of this dense layer is about 10–20 Å independent of surface pressure and polymerization degree of PMAA in the range studied.<sup>[9]</sup> Phenomenon 1) can be explained by reasonable speculation based on 2) and 3).

The above-mentioned phenomena (1–3) have not been predicted or reported before except for one case.<sup>[31,32]</sup> By combining precision synthesis of diblock copolymers, in situ and high-resolution X-ray reflectivity (XR) measurement, and highly quantitative analysis, we have clarified the nanostructure of polymer self-assembly at the interfaces.

## IN SITU X-RAY REFLECTIVITY EXPERIMENT

The X-ray reflectivity (XR) technique has been attracting attention as a useful tool for the in situ investigation of the surface nanostructure in laboratory-scale experiments.<sup>[12–14]</sup> The usefulness and powerfulness of the neutron reflectivity (NR) technique have also been widely recognized, and novel NR instruments have been constructed<sup>[10]</sup> although NR is still regarded as a special technique because of the limitation of experimental facilities.

X-ray reflectivity measurements were performed with an RINT-TTR-MA (Rigaku Corp., Tokyo, Japan) apparatus in which the X-ray generator and detector vertically rotate around the sample stage. The Langmuir–Blodgett (LB) trough (length 130 mm  $\times$  width 60 mm), made of aluminum coated with Teflon<sup>®</sup> (USI System, Fukuoka, Japan), was mounted on the sample stage to study the water surface system. Details of the XR apparatus and data treatment have been fully described elsewhere.<sup>[15–17]</sup> Data analysis is based on the theory of Parrat<sup>[18]</sup> and Sinha et al.<sup>[19]</sup> The measurements were performed under specular conditions; that is, the incident and reflection angles were kept equal. The specular reflectivity of X-ray provides information on an electron-density variation normal to the surface in the order of angstroms. The scattering vector  $q$  in specular reflectivity is defined by  $q = 4\pi\sin\theta/\lambda$ , where  $\theta$  is the incident or reflection angle from the sample surface, and  $\lambda$  is the wavelength of the incident X-rays, which was 1.5406 Å (Cu K<sub>α1</sub>).

## AMPHIPHILIC DIBLOCK COPOLYMER AND POLYMER BRUSH

Amphiphilic diblock copolymers have both hydrophilic and hydrophobic chains in one molecule. It is possible to design diblock copolymer amphiphiles with large hydrophilic and hydrophobic parts in contrast with amphiphilic small molecules whose hydrophilic and hydrophobic parts are both short. Because of the large hydrophobicity due to the long hydrophobic chain, the diblock copolymer forms a polymer monolayer on water with dangling hydrophilic chain. The long hydrophilic chain in the monolayer forms a “polymer brush” in the water subphase.

The brush structure is mainly characterized by brush thickness, brush density, and density profile in the brush. Theoretical predictions, especially for charged brush, have been made since the early 1990s.<sup>[20–22]</sup> In the past two decades, experimental studies on the polymer brush have been greatly promoted by advances in reflectometry<sup>[12–14]</sup> and methods of surface graft polymerization.<sup>[23]</sup>

The polymer brush in water has been mainly studied on either the hydrophilic chain in diblock copolymer monolayer at air/water interface or grafted polymer chain from a solid substrate immersed in water. The advantages of the monolayer at the air/water interface are as follows: 1) The graft length and polydispersity can be precisely controlled and characterized in the polymerization procedure of a diblock copolymer. 2) The graft density can be easily and freely controlled by changing the surface pressure after spreading a diblock copolymer on a water surface if the sample is insoluble to the subphase. On the other hand, if the sample is not perfectly insoluble, it might be anticipated that the  $\pi$ -A

isotherm gives only apparent graft density. An estimation of the solubility and its effect on the monolayer is needed. The solubility problem in our case can be solved by a simple calculation from density and thickness of the hydrophobic layer.<sup>[6]</sup> For a grafted polymer chain from a solid substrate, once a well-characterized sample is prepared, the same graft density is always maintained regardless of subphase condition, i.e., pH and salt concentration. However, simultaneous control of graft density and chain length is still difficult, and special instruments and efforts are needed for their characterization.

In the course of polymer brush studies, a neutral diblock copolymer system has been studied by reflectometry from the preliminary stage.<sup>[24–29]</sup> The polyethyleneoxide (PEO) brush in the water subphase is a well-studied representative system.<sup>[26–29]</sup> Many investigations on the polyelectrolyte brush have been performed since the late 1990s.<sup>[6,30–37]</sup> In the polyelectrolyte brush systems, the grafted polymer system is often introduced instead of the monolayer system at the air/water interface.<sup>[33–36]</sup> This trend owes much to the progress of living radical polymerization.<sup>[23]</sup> However, as described above, the diblock copolymer system has many advantages. Furthermore, the diblock copolymer system is suitable for investigating the relationships between the monolayer structure and the hydrophilic–hydrophobic balance that has not yet been systematically studied either experimentally or theoretically. We believe that detailed discussions on the monolayer structure at the air/water interface and the interesting features related to the hydrophilic–hydrophobic balance are possible only when the diblock copolymer system is utilized.

## MONOLAYER STRUCTURE INVESTIGATED BY X-RAY REFLECTOMETRY

### Monolayer Preparation

Three polymer samples with different MAA (hydrophilic) chain lengths and a constant Et<sub>2</sub>SB (hydrophobic)

**Table 1** Characterization of poly(Et<sub>2</sub>SB)<sub>m</sub>-b-poly(MAA)<sub>n</sub>

Et <sub>2</sub> SB:MAA ( <i>m</i> <sup>a</sup> : <i>n</i> <sup>b</sup> )	<i>M</i> <sub>n</sub> <sup>c</sup>	<i>M</i> <sub>w</sub> / <i>M</i> <sub>n</sub> <sup>d</sup>
40:10	6,300	1.16
45:60	11,200	1.18
43.81	12,800	1.12

<sup>a</sup>Number-average degree of polymerization of the poly (Et<sub>2</sub>SB) segment determined by <sup>1</sup>H-NMR.

<sup>b</sup>Number-average degree of polymerization of the poly (*t*BMA) segment (before hydrolysis) determined by <sup>1</sup>H-NMR.

<sup>c</sup>Number-average molecular weight of the block copolymer determined by <sup>1</sup>H-NMR.

<sup>d</sup>Polydispersity index determined by gel permeation chromatography (GPC) relative to polystyrene standard before hydrolysis.

Source: Ref. [6]. © 2002 by the American Chemical Society.



chain length were synthesized by anionic polymerization.<sup>[6,11]</sup> The characteristics of the samples are summarized in Table 1. A polymer monolayer was prepared by spreading the sample solution [1 mg/mL tetrahydrofuran (THF) solution] on the water surface in a Langmuir trough. After solvent evaporation, the surface was compressed to reach the desired surface pressure at which XR measurements were carried out.

### Nanostructure of Polymer Monolayer—Carpet/Polymer Brush Double-Layer Formation in Hydrophilic Layer

The XR profiles of poly(Et<sub>2</sub>SB-*b*-MAA) monolayer on water surface are shown in Fig. 1. The profiles had clear, high-order Kiessig fringes that were rarely observed in profiles on water surface systems mainly because of surface roughness and low contrast. Such clear profiles enabled highly quantitative data analysis and detailed discussion on the monolayer structure in the Å scale.<sup>[6,9]</sup>

In principle, if the monolayer is composed of two discrete layers with a thickness of  $d_1$  and  $d_2$ , the reflectivity profile should be represented as a superimposition of three cosine curves with a frequency of  $d_1$ ,  $d_2$ , and  $(d_1 + d_2)$ , on the decay of  $-4$  power governed by Fresnel's law. The cosine curve is amplified by each electron density contrast between layers. The sufficient density contrast between each layer enables us to detect three kinds of frequencies. However, in a poly(Et<sub>2</sub>SB-*b*-MAA) system, the Et<sub>2</sub>SB hydrophobic layer is more enhanced in the reflectivity curves because this layer has larger electron density contrast than the MAA hydrophilic layer. As a result, the frequency of fringes in the observed curves reflects the thickness of the Et<sub>2</sub>SB layer, but the profile contains a contribution from the MAA layer. In fact, the small fringes that originated from the whole layer including the MAA layer were found in a  $m:n = 43:81$  sample around  $q = 0.05 \text{ \AA}^{-1}$ .

The monolayer structure was determined by model fitting of the XR profiles. The amphiphilic diblock copolymer monolayer on water is supposed to be composed of hydrophobic and hydrophilic layers. Therefore a two-box model, which has two discrete layers with interface roughness between layers, is applied first to reproduce experimental data. A three-box model was applied if there was not sufficient agreement by the two-box model.<sup>[8,9]</sup>

As is indicated in Fig. 1 by lines, a three-box model was needed to reproduce the XR profiles for the  $m:n = 43:81$  monolayer above 20 mN/m. The small fringe at a lower  $q$  pointed above could not be reproduced by the two-box model. Profiles for the other two samples were well reproduced by a two-box model at any surface pressure studied.

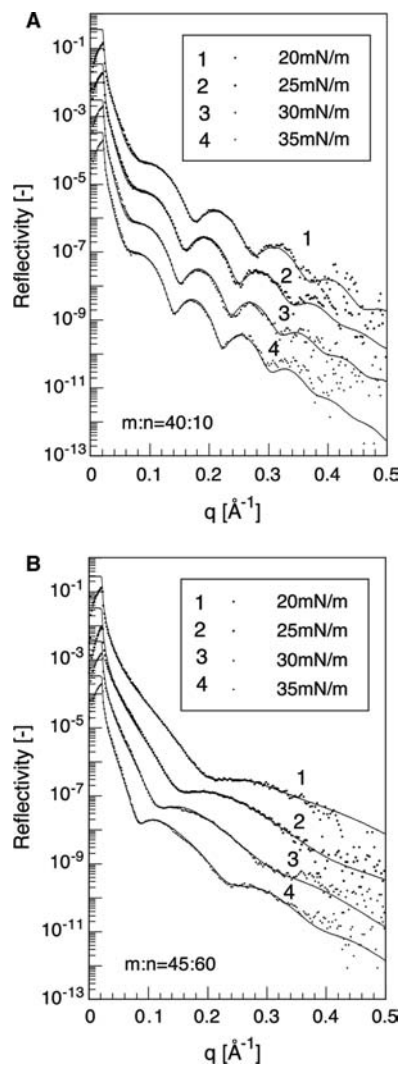


**Fig. 1** X-ray reflectivity profiles for poly(Et<sub>2</sub>SB)<sub>*m*</sub>-*b*-poly(MAA)<sub>*n*</sub> monolayer on water. (A)  $m:n = 40:10$ , (B)  $m:n = 45:60$ , (C)  $m:n = 43:81$ . Each profile was shifted downward by one decade for clarity. The solid lines are the best-fit curves by the two-box model ( $m:n = 40:10$ ,  $45:60$ ) and the three-box model ( $m:n = 43:81$ ). Source: A,B—From Ref.<sup>[6]</sup>. © 2002 by the American Chemical Society. C—From Ref.<sup>[9]</sup>. © 2003 by John Wiley & Sons, Inc.

The density profiles obtained by the three-box model fitting are shown in Fig. 2. The  $m:n = 43:81$  monolayer (Fig. 2C) above 20 mN/m was found to be composed of an Et<sub>2</sub>SB layer and two MAA layers: The MAA layer was divided into two MAA layers, an upper MAA layer and a lower MAA layer. The upper MAA layer just beneath the Et<sub>2</sub>SB layer has a higher density than the lower MAA layer. The lower layer has a lower density and has a large roughness at the interface with a water subphase. This means that this MAA layer has a diffuse structure like a polymer brush. So we call the former a *dense MAA layer* and the latter a *diffuse MAA layer*. The diffuse layer is, in principle, the

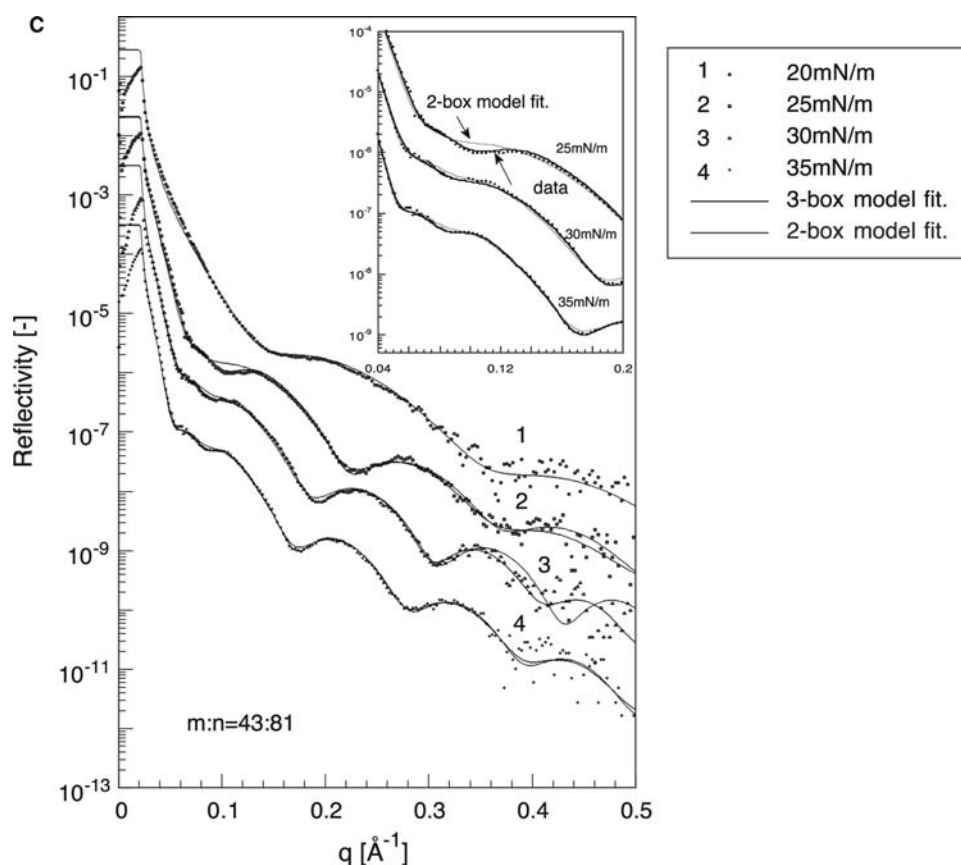


Fig. 1 (Continued).

“brush layer.” A schematic figure of the monolayer structure is also shown in Fig. 3. The thickness of the dense MAA layer is about 15 Å and its density is almost the same as the bulk density of MAA. The surface pressure and chain length dependence of the monolayer structure will be discussed in the following section.

### Effect of Surface Pressure—Transition from Carpet Layer to Carpet/Polymer Brush Double Layer

X-ray reflectivity measurements were carried out at different surface pressures, i.e., at different grafting densities (number of polymer chains per unit area), by compressing the monolayer. Brush density was from 0.1 to 0.8 nm<sup>-2</sup> in the surface pressure range studied.<sup>[6,9]</sup>

The distinguishing feature shown in Fig. 2 is that the existence of the MAA dense layer with 10–20 Å thickness is independent of surface pressure. The maximum density of the dense MAA layer in contact with water surface, i.e., contact with a hydrophobic Et<sub>2</sub>SB layer, is almost the same as the bulk MAA density. The dense layer seems to have an important role in determining the monolayer structure as discussed in the following section.

In Fig. 2C, the transition from a carpet-like dense layer to a dense/diffuse double layer as the surface pressure increases is clearly visualized. At a low surface pressure (20 mN/m), the brush layer cannot be seen by XR; that is, almost no brush layer exists. By an increase of the surface pressure, the MAA brush layer was formed in addition to the dense layer, and the thickness of the diffused brush layer increased with a further increase of surface pressure.

The density difference between the dense MAA layer and the diffuse MAA layer was largest at 25 mN/m, at which the density of the dense MAA layer was also at maximum. The MAA fraction that contributed to the dense MAA layer was calculated to be 40% at 25 mN/m with an assumption that the MAA bulk density was 1.22 g/cm<sup>3</sup>. The density difference became smaller as surface pressure increased beyond this point. At the same time, the brush layer formed and its thickness increased as the surface pressure increased.

From these observations, a possible interpretation of the structural change is that a part of the MAA chains is no longer necessary in dense layer above 20 mN/m and they are pushed out to the water sub-phase and then joined to make a polyelectrolyte brush. In this sense, the dense layer plays a role similar to a

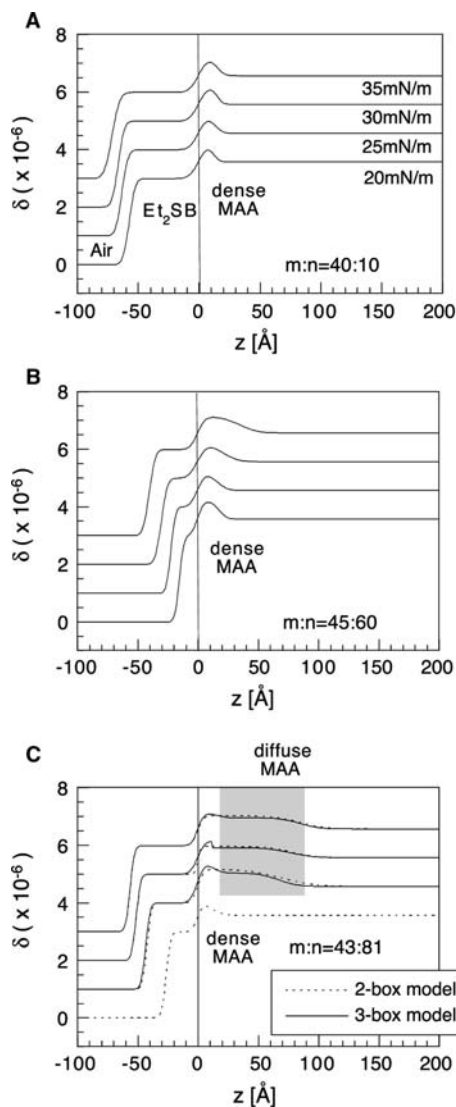


**Fig. 2** Density ( $\delta$ ) profiles for poly(Et<sub>2</sub>SB)<sub>*m*</sub>-*b*-poly(MAA)<sub>*n*</sub> on water. (A) *m*:*n* = 40:10, (B) *m*:*n* = 45:60, (C) *m*:*n* = 43:81.  $\delta$  is proportional to electron density, and defined by  $\text{r.i.} = 1 - \delta - i\beta$ , where r.i. is the refractive index. Each profile was shifted upward by one decade for clarity. The order of the profiles is consistent from (A) to (C). *Source*: A,B—From Ref. [6]. © 2002 by the American Chemical Society. C—From Ref. [9]. © 2003 by John Wiley & Sons, Inc.

“carpet” or “cushion” for the Et<sub>2</sub>SB hydrophobic layer on water.

### Effect of Hydrophilic Chain Length—Minimum Hydrophobic Layer Thickness and Discrete Layers in the Hydrophilic Layer

The XR profiles for all three samples at 30 mN/m are compared in Fig. 4. As mentioned above, the period of the fringe corresponds to the hydrophobic Et<sub>2</sub>SB layer

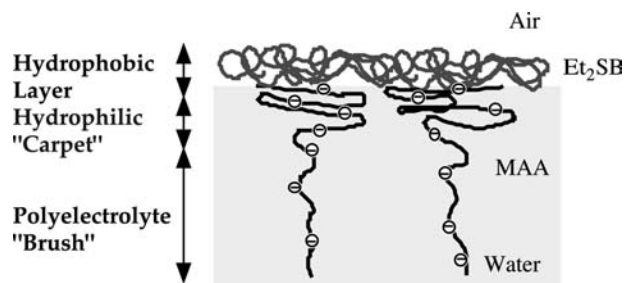


**Fig. 3** Schematic representation of the “carpet” layer and the brush layer in poly(Et<sub>2</sub>SB)<sub>43</sub>-*b*-poly(MAA)<sub>81</sub> monolayer.

thickness. It is obvious that the period of the profile for *m*:*n* = 45:60 (middle MAA length) is the longest, which means that the Et<sub>2</sub>SB layer for the sample is the thinnest. The same tendency was observed at any other surface pressure studied.<sup>[6,9]</sup>

In Fig. 5, the MAA chain length dependence of each layer thickness is shown. The Et<sub>2</sub>SB layer showed an interesting phenomenon: The Et<sub>2</sub>SB thickness at the same surface pressure takes a minimum at a medium MAA length at every surface pressure studied (Fig. 5A). The variation of MAA layer thickness with

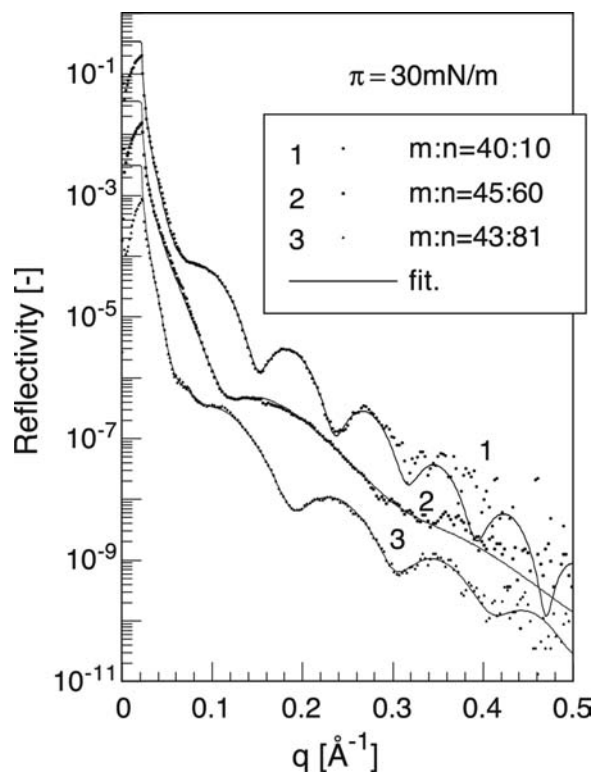


**Fig. 4** X-ray reflectivity profiles for poly(Et<sub>2</sub>SB)<sub>*m*</sub>-*b*-poly(MAA)<sub>*n*</sub> on water at 30 mN/m. (1) *m*:*n* = 40:10, (2) *m*:*n* = 45:60, (3) *m*:*n* = 43:81. Each profile was shifted downward by one decade for clarity. The solid lines are the best-fit curves obtained by the two-box model (*m*:*n* = 40:10, 45:60) and the three-box model (*m*:*n* = 43:81).

MAA unit length is also interesting. The thickness variation of the three samples with different hydrophilic chain length ( $m:n = 40:10, 45:60, 43:81$ ) in Fig. 5 showed that the thickness of this dense layer is 10–20 Å independent of surface pressure and polymerization degree of PMAA in the range studied. It is also confirmed in the density profiles in Fig. 2. For  $m:n = 45:60$  sample, slightly larger thickness, i.e., 18–35 Å, was observed. It is fair to say that we could not distinguish the dense and the short diffuse MAA layers from the XR profiles in this case.

The independence of the thickness in MAA layer just beneath the Et<sub>2</sub>SB layer, i.e., dense layer, is interesting because the number of MAA units largely varies from 10 to 80 units. Although the data are not shown here, our newly synthesized samples with different chain lengths ( $m:n = 30:20$  to  $30:90$ ) also have a dense layer with a thickness of 10–20 Å.<sup>[32]</sup> A thickness of about 15 Å might be the “critical thickness” for a dense layer, or for a dense layer–brush layer transition.

On the other hand, a well-established polyelectrolyte brush is formed only for the  $m:n = 43:81$  polymer monolayer. For  $m:n = 40:10$  and  $m:n = 45:60$  polymer monolayer, only dense MAA layer is formed.

The minimum hydrophobic layer thickness can be related to the double-layer formation in the hydrophilic

layer. To explain the Et<sub>2</sub>SB layer thickness variation, it is reasonable to consider that the MAA layer has two opposite effects, positive and negative, on surface pressure, and that the formation of a dense MAA layer and diffuse MAA layer in  $m:n = 43:81$  monolayer is the key point. For a small  $n$  sample,  $m:n = 40:10$ , because the MAA contribution to surface pressure is small, much surface compression is needed to achieve the surface pressure desired. This results in the largest thickness of Et<sub>2</sub>SB layer. For the medium  $n$  sample,  $m:n = 45:60$ , a *positive* contribution of MAA chain due to its layer size to the surface pressure appears. Hence at the same surface pressure, the Et<sub>2</sub>SB layer becomes thinner. For the large  $n$  sample,  $m:n = 43:81$ , a *negative* contribution due to brush formation appears in addition to the *positive* contribution mentioned above. An increase in Et<sub>2</sub>SB layer thickness should be observed to compensate for the negative contribution. At this stage, it is not clear whether the dense and the diffuse MAA layers directly correspond to the positive and the negative contributions to surface pressure, respectively. However, it is reasonable to think that the layer near the surface should contribute to a larger increase in surface pressure (a decrease in surface energy) than the brush layer in the subphase.

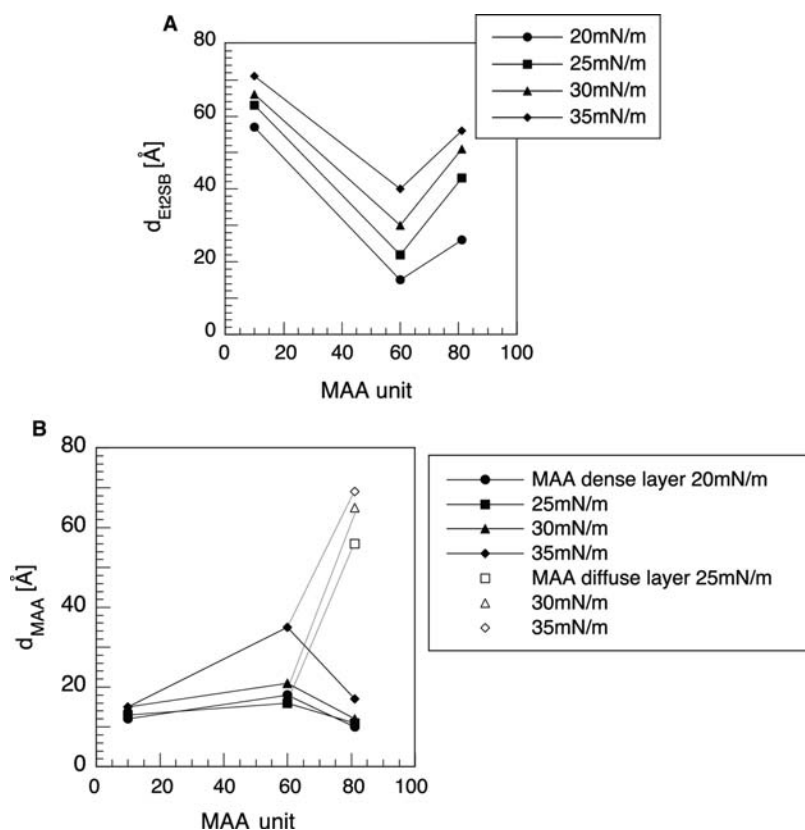


**Fig. 5** Thickness variation of the hydrophobic and hydrophilic layers with MAA length. (A) Et<sub>2</sub>SB layer and (B) MAA layer. The MAA layer in the  $m:n = 43:81$  sample was well reproduced by two discrete layers, a dense MAA layer and a diffuse MAA layer. Source: From Ref.<sup>[9]</sup>. © 2003 by John Wiley & Sons, Inc.



### Effect of pH on the Monolayer Structure—Anomalous $pK_a$ at the Surface

The hydrophilic chain of the diblock copolymer is a weak polyacid, which enabled us to control the monolayer structure by pH. Hence the pH dependence of the monolayer nanostructure was investigated by changing the pH of the subphase.<sup>[6,8]</sup>

A marked structural change by pH was observed especially for the  $m:n = 43:81$  monolayer. Fig. 6 shows the XR profiles for  $m:n = 43:81$  monolayer at different pHs. The fringe with a short period, which was notable for pH 2 and 7 (pure water), was not observed for the profile on the subphase of pH 10. Density profiles (Fig. 7) obtained by model fitting of the XR profiles indicate that the brush layer was not detected for the  $m:n = 43:81$  sample on pH 10 subphase (dotted line) at 25 mN/m, at which the carpet/brush layer formation was detected for acid (solid line) and neutral (dashed line) conditions. Taking the block ratio into consideration, a highly diffused brush should be formed by alkaline condition. Because of the low contrast between the brush layer and water subphase coming from the low volume fraction of the polymer chain in the brush layer, the brush layer could not be detected by XR measurements.

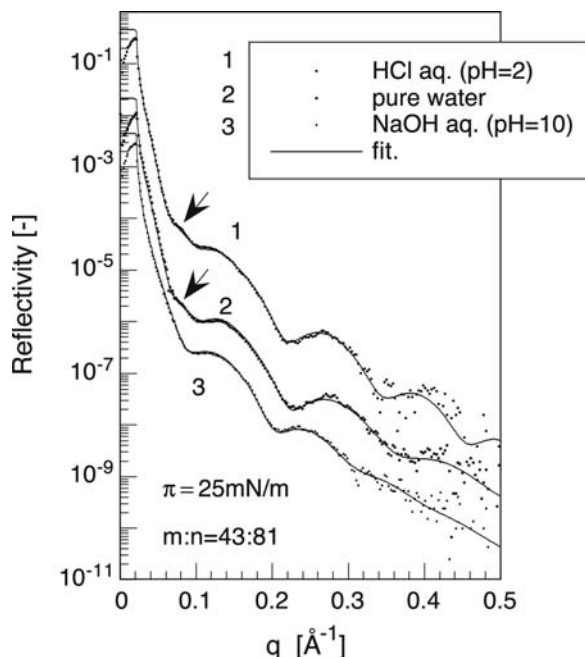


**Fig. 6** X-ray reflectivity profiles for poly(Et<sub>2</sub>SB)<sub>43</sub>-*b*-poly(MAA)<sub>81</sub> monolayer on various pH subphases at 25 mN/m. (1) pH 2, (2) pH 7 (pure water), (3) pH 10. Each profile was shifted downward by one decade for clarity. The solid lines are the best-fit curves obtained by the two-box model (pH 10) and the three-box model (pH 2, pH 7). *Source:* From Ref.<sup>[8]</sup>. © 2003 by IUCr.

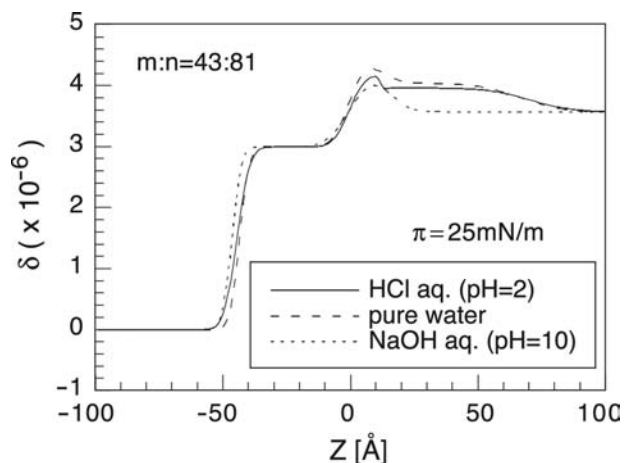


**Fig. 7** Density ( $\delta$ ) profiles for poly(Et<sub>2</sub>SB)<sub>43</sub>-*b*-poly(MAA)<sub>81</sub> monolayer on various pH subphases at 25 mN/m. (1) pH 2 (solid line), (2) pH 7 (dashed line), (3) pH 10 (dotted line). *Source:* From Ref.<sup>[8]</sup>. © 2003 by IUCr.

The variation in hydrophobic and hydrophilic layer thickness with pH for all three samples is summarized in Fig. 8. Almost the same monolayer structure was obtained at acidic (pH 2) and neutral (pure water) conditions, but significant differences were found on the monolayer on subphase of pH 10. For the shortest MAA chain samples, the thickness of the Et<sub>2</sub>SB layer in monolayer at pH 10 is explicitly larger than those in acidic and neutral conditions at the same surface pressure. For the long MAA polymer, the carpet/brush structure in the monolayer was not observed and only a dense carpet layer was detectable. Obviously, the observed change of nanostructure with pH is a result of the change of the degree of ionization of carboxylic acid on the hydrophilic chain.

In general, a drastic change is expected at the pH around  $pK_a$ , which is  $pH = 4-5$  in bulk solution for carboxylic acids. However, in this system, at the air/water interface, the change occurs between neutral pH and  $pH = 10$ . This means that the  $pK_a$  value of the carboxylic groups on the polymer chain in the monolayer is higher than that for bulk state, and it should be located between 7 and 10. This is one of the special characteristics of the surface. The possible origin of this anomalous  $pK_a$  at the surface might be an anomalous structure of water, which shows two-dimensional packing of molecules such that the density of polymer chain in the brush is high. This should be clarified in future works.

### Comparison with Proposed Theory

Theoretical studies on the structure of the polyelectrolyte brush with variable charges (e.g., weak polyacid) have been carried out as a function of grafting density

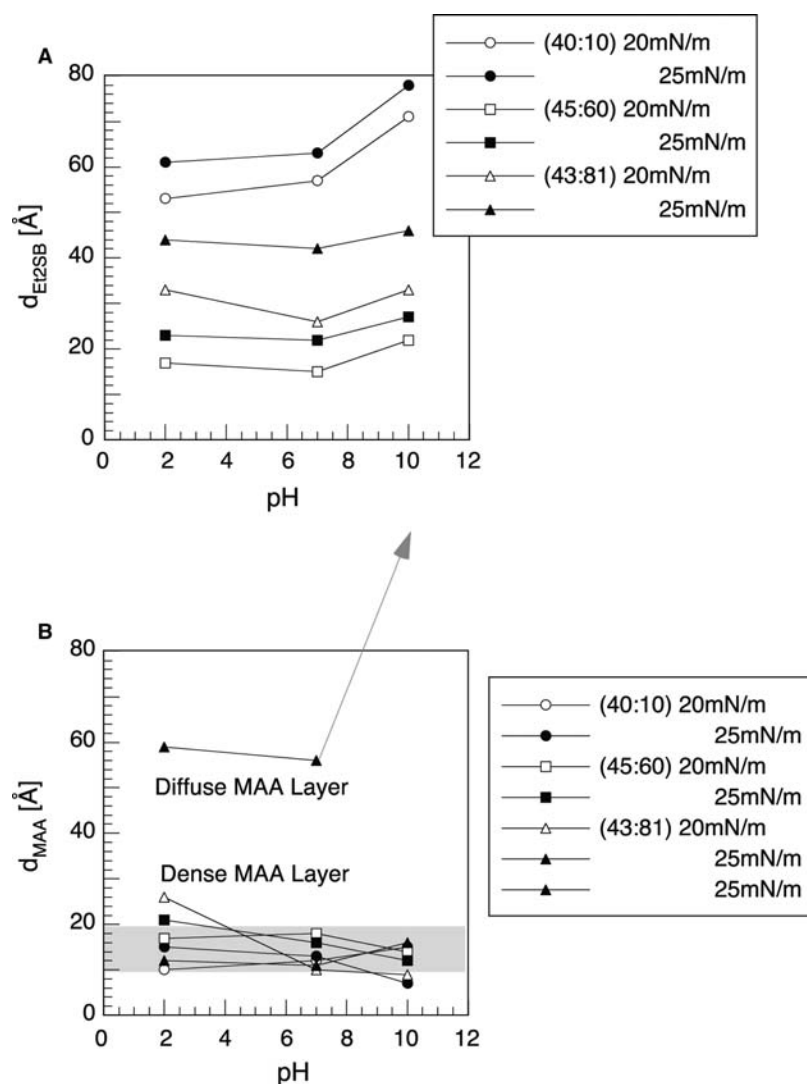


**Fig. 8** Thickness variation of the hydrophobic and hydrophilic layers with pH at 20 and 25 mN/m. (A) Et<sub>2</sub>SB layer and (B) MAA layer. The  $m:n = 43:81$  monolayer was well described by a three-box model at pH 2 and pH 7 but well reproduced by a two-box model at pH 10. Considering the  $m:n$  block ratio, the diffuse MAA layer should exist at pH 10 in a very diffused form as indicated by the arrow.

and ionic strength.<sup>[20–22]</sup> The variation of brush thickness with grafting density and ionic strength is not monotonic and is categorized into several regimes. The regimes are characterized by the ratio  $\alpha/\alpha_b$ , where  $\alpha$  is the degree of dissociation in brush and  $\alpha_b$  is the degree of dissociation in bulk. For a brush of weak polyacid in a salt-free solution as in our system,  $\alpha$  is considered to be very small compared to  $\alpha_b$ , and categorized into neutral brush regime. In this regime, the brush is expected to behave like a neutral brush.<sup>[21,22]</sup> However, our observation of the two discrete MAA layers seems to be characteristic of the polyelectrolyte brush. In addition, the two discrete layers have not been observed in a neutral brush system. These discrepancies are simply because of the oversimplification of the theoretical model: To theoretically describe the polymer brush, the interaction between the brush and the substrate surface (grafted surface) should be taken into account.

### The “Real” Nanostructure of Polymer Monolayer and Polymer Brush

The surface pressure and chain length dependencies of the monolayer structure are schematically summarized in Fig. 9.<sup>[6,9]</sup> The density profiles are described besides drawings. As also indicated in Fig. 9, the value of the area per molecule is largest for middle  $n$  sample. Similarly, the hydrophobic layer thickness is thinnest for the middle  $n$  sample. The polymer monolayer formed by the samples with a shorter MAA length is composed of a hydrophilic layer and a dense MAA layer, i.e., without a well-established brush layer at any surface pressure. For the monolayer of a longer MAA sample, a similar situation is observed at a lower surface pressure. With increasing surface pressure, long MAA chains extend to the sub-phase to form a brush layer that has a lower density than the dense layer.



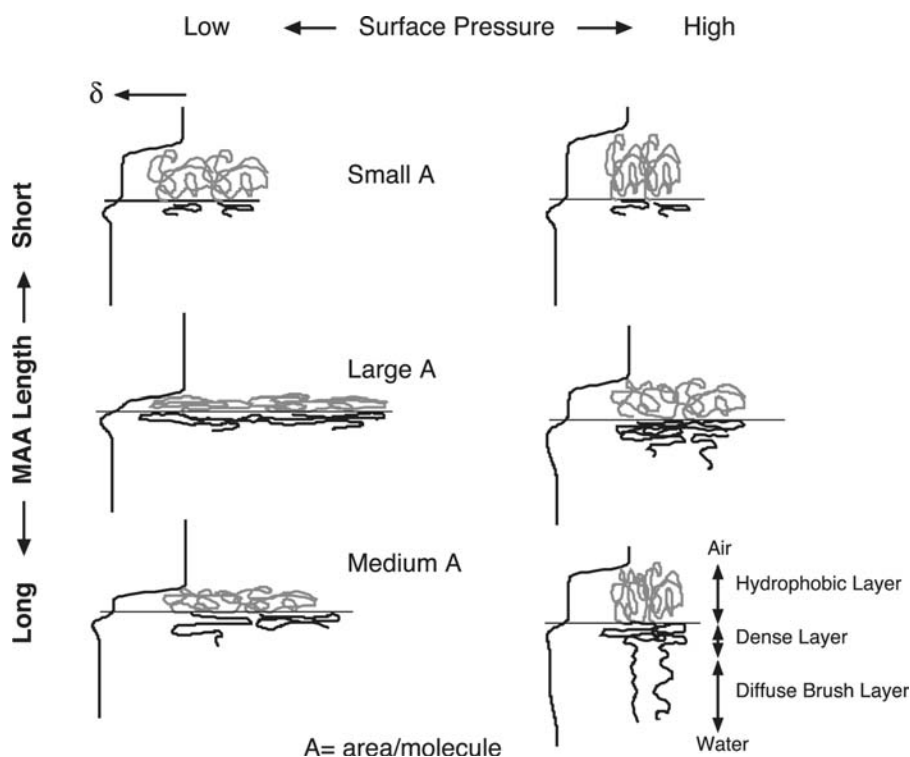


**Fig. 9** Schematic representation of the dense layer and the brush layer in  $\text{poly}(\text{Et}_2\text{SB})_m\text{-}b\text{-poly}(\text{MAA})_n$  monolayer on water surface as functions of the surface pressure and the hydrophilic PMAA length. Density profiles are also shown beside the drawings. Source: From Ref.<sup>[9]</sup>. © 2003 by John Wiley & Sons, Inc.

## CONCLUSION

The nanostructure of a monolayer of the ionic amphiphilic diblock copolymer, poly(1,1-diethylsilacyclobutane)-*block*-poly(methacrylic acid) [ $\text{poly}(\text{Et}_2\text{SB-}b\text{-MAA})$ ], at the air/water interface was investigated by in situ XR as a function of surface pressure, MAA chain length, and pH. The MAA brush under the water surface was found to be composed of two parts: a dense layer with a higher density and a diffuse layer with a lower density. The dense layer is always formed independent of MAA chain length, surface pressure, and pH. By contrast, the diffuse layer is formed in addition to the carpet layer only when the hydrophilic chain length is long enough and the surface pressure, i.e., the brush density, is also high enough at lower pHs. At pH 10, the diffuse layer was not observed in the studied range. The dense layer thickness was found to be almost constant at 10–20 Å, independent of surface pressure and MAA chain length. Furthermore, the discrete MAA structure could be an explanation for the interesting observation that the MAA chain length dependence of the thickness of  $\text{Et}_2\text{SB}$  layer showed a minimum at a critical MAA chain length. Either dense or diffuse layer structure and minimum thickness has never been expected in a theoretical study, which indicate the great importance of the in situ experimental study.

We found several new aspects of the diblock copolymer monolayer structure in this study. In situ studies

are essential for identifying the carpet/brush double-layer structure and anomalous  $\text{p}K_a$ . Systematical in situ investigation should clarify the nature of polyelectrolyte brush and make it possible to design and control its structure totally by chain length, chain length ratio, pH, and salt concentration. These findings are expected to contribute to the development of fundamental polymer surface chemistry and of polymer surface nanomaterials.

## REFERENCES

1. Hamley, I.W. *The Physics of Diblock Copolymers*; Oxford University Press, 1998; 131–220.
2. Alexandridis, P.; Lindman, B. *Amphiphilic Block Copolymers*; Elsevier: Amsterdam, 2000; 57–190.
3. Milner, S.T. Polymer brushes. *Science* **1991**, *251*, 905–914.
4. Kago, K.; Matsuoka, H.; Yoshitome, R.; Mouri, E.; Yamaoka, H. The importance of a direct in situ evaluation of an amphiphilic diblock copolymer monolayer. The similarity and difference between its nanostructures on water and on solid substrates examined by x-ray reflectometry and atomic force microscopy. *Langmuir* **1999**, *15* (12), 4295–4301.
5. Nakano, M.; Deguchi, M.; Endo, H.; Matsumoto, K.; Matsuoka, H.; Yamaoka, H. Self-assembly of poly(1,1-diethylsilabutane)-*block*-poly(2-hydroxyethyl methacrylate) block copolymer. 2. Monolayer at the air–water interface. *Macromolecules* **1999**, *32* (19), 6088–6092.

6. Mouri, E.; Wahnes, C.; Matsuomoto, K.; Matsuoka, H.; Yamaoka, H. X-ray reflectivity study of anionic amphiphilic carbosilane block copolymer monolayers on a water surface. *Langmuir* **2002**, *18* (10), 3865–3874.
7. Matsumoto, K.; Mizuno, U.; Matsuoka, H.; Yamaoka, H. Synthesis of novel silicon-containing amphiphilic diblock copolymers and their self-assembly formation in solution and at air/water interface. *Macromolecules* **2002**, *35* (2), 555–565.
8. Mouri, E.; Matsumoto, K.; Matsuoka, H. Effect of pH on the nanostructure of an amphiphilic carbosilane/methacrylic acid block copolymer at air/water interface. *J. Appl. Crystallogr.* **2003**, *36* (3), 722–726.
9. Mouri, E.; Matsumoto, K.; Matsuoka, H. “Carpet”-like dense layer formation in polyelectrolyte brush at air/water interface. *J. Polym. Sci., B* **2003**, *41* (16), 1921–1928.
10. Torikai, N.; Furusaka, M.; Matsuoka, H.; Matsushita, Y.; Shibayama, M.; Takahara, A.; Takeda, M.; Tasaki, S.; Yamaoka, H. Instrumental design and performance of a new pulsed-neutron reflectometer (ARISA) at KENS for studying free surfaces. *Appl. Phys., A* **2002**, *74*, S264–S266.
11. Matsumoto, K.; Wahnes, C.; Mouri, E.; Matsuoka, H.; Yamaoka, H. Synthesis of anionic amphiphilic carbosilane block copolymer: Poly(1,1-diethylsilylacetylene-block-methacrylic acid). *J. Polym. Sci., A* **2001**, *39* (1), 86–92.
12. Daillant, J.; Gibaud, A.; Eds. *X-ray and Neutron Reflectivity: Principles and Applications*; Springer, 1999; 3–194.
13. Tolan, M. *X-ray Scattering from Soft-Matter Thin Films: Materials Science and Basic Research*; Springer Tracts in Modern Physics; Springer, 1999; Vol. 148, 33–86.
14. Als-Nielsen, J.; McMorrow, D. *Element of Modern X-ray Physics*; Wiley, 2000; 61–103.
15. Yamaoka, H.; Matsuoka, H.; Kago, E.; Eckelt, J. X-ray reflectivity study of fine structure of thin polymer films and polymer assembly at interface. *Physica, B* **1998**, *248*, 280–283.
16. Kago, K.; Matsuoka, H.; Endo, H.; Eckelt, J.; Yamaoka, H. X-ray reflectivity study of polymer assembly at air–water interface. *Supramol. Sci.* **1998**, *5*, 349–355.
17. Matsuoka, H.; Mouri, E.; Matsuomoto, K. Direct in situ investigation of the nanostructure of molecular and macromolecular assemblies at air/water interface by x-ray reflectometry. *Rigaku J.* **2001**, *18*, 54–68.
18. Parratt, L.G. Surface studies of solids by total reflection of X-rays. *Phys. Rev.* **1954**, *95* (2), 359–369.
19. Sinha, S.K.; Sirota, E.B.; Garoff, S.; Stanley, H.B. X-ray and neutron scattering from rough surfaces. *Phys. Rev., B* **1988**, *38* (4), 2297–2311.
20. Wittmer, J.; Joanny, J.F. Charged diblock copolymers at interfaces. *Macromolecules* **1993**, *26* (11), 2691–2697.
21. Israëls, R.; Leermakers, F.A.M.; Fleer, G.J. On the theory of grafted weak polyacids. *Macromolecules* **1994**, *27* (11), 3087–3093.
22. Zhulina, E.B.; Birshtein, T.M.; Borisov, O.B. Theory of ionizable polymer brushes. *Macromolecules* **1995**, *28* (5), 1491–1499.
23. Patten, T.E.; Xia, J.; Abernathy, T.; Matyjaszewski, K. Polymers with very low polydispersities from atom transfer radical polymerization. *Science* **1996**, *272*, 866–868.
24. Auroy, P.; Auvray, L.; Leager, L. Structures of end-grafted polymer layers: a small-angle neutron scattering study. *Macromolecules* **1991**, *24* (9), 2523–2528.
25. Kent, M.S.; Lee, L-T.; Farnoux, B.; Rondelez, F. Characterization of diblock copolymer monolayers at the liquid–air interface by neutron reflectivity and surface tension measurement. *Macromolecules* **1992**, *25* (23), 6240–6247.
26. Bijsterbosch, H.D.; de Haan, V.O.; de graaf, A.W.; Mellema, M.; Leermakers, F.A.M.; Stuart, M.A.C.; van Well, A.A. Tethered adsorbing chains: Neutron reflectivity and surface pressure of spread diblock copolymer monolayers. *Langmuir* **1995**, *11* (11), 4467–4473.
27. Dewhurst, P.F.; Lovell, M.R.; Jones, J.L.; Richards, R.W.; Webster, J.R.P. Organization of dispersions of a diblock copolymer of polystyrene and poly(ethylene oxide) at the air–water interface. *Macromolecules* **1998**, *31* (22), 7851–7864.
28. Faure, M.C.; Bassereau, P.; Lee, L.T.; Menelle, A.; Lheveder, C. Phase transitions in monolayers of PS–PEO copolymer at the air–water interface. *Macromolecules* **1999**, *32* (25), 8538–8550.
29. Wesemann, A.; Ahrens, H.; Steitz, R.; Förster, S.; Helm, C.A. Internal interface of a compressed PEE–PEO diblock copolymer monolayer. *Langmuir* **2003**, *19* (3), 709716.
30. Su, T.J.; Styrkas, D.A.; Thomas, R.K.; Baines, F.L.; Billingham, N.C.; Armes, S.P. Neutron and x-ray reflectivity studies of water-soluble block and statistical copolymers adsorbed at the air–water interface. *Macromolecules* **1996**, *29* (21), 6892–6900.
31. Ahrens, H.; Förster, S.; Helm, C.A. Polyelectrolyte brushes grafted at the air/water interface. *Macromolecules* **1997**, *30* (26), 8447–8451.
32. Ahrens, H.; Förster, S.; Helm, C.A. Charged polymer brushes: Counterion incorporation and scaling relations. *Phys. Rev. Lett.* **1998**, *81* (19), 4172–4175.
33. Tran, Y.; Auroy, P.; Lee, L.T. Determination of the structure of polyelectrolyte brushes. *Macromolecules* **1999**, *32* (26), 8952–8964.
34. Tran, Y.; Auroy, P.; Lee, L.T.; Stamm, M. Polyelectrolyte brushes: Counterion distribution and complexation properties. *Phys. Rev., E* **1999**, *60* (6), 6984–6990.
35. Currie, E.P.K.; Sieval, A.B.; Fleer, G.J.; Stuart, M.A.C. Polyacrylic acid brushes: surface pressure and salt-induced swelling. *Langmuir* **2000**, *16* (22), 8324–8333.
36. Biesalski, M.; Rühle, J. Scaling laws for the swelling of neutral and charged polymer brushes in good solvents. *Macromolecules* **2002**, *35* (2), 499–507.
37. Mouri, E.; Matsumoto, K.; Matsuoka, H. to be submitted.

# Anion-Templated Self-Assembly: Inorganic Compounds

Louise S. Evans

Philip A. Gale

School of Chemistry, University of Southampton, Southampton, U.K.

## INTRODUCTION

The use of anions to template the formation of new supramolecular entities is a relatively new approach to self-assembly, but one that is expanding the available number of non-covalent and coordinate bonding motifs for the construction of new interlocked materials and new supramolecular nanoarchitectures.<sup>[1–5]</sup> Transition metal directed approaches (e.g., using a transition metal to template catenane formation) rely on the directionality of the coordination sphere of the metal to define the geometry of the new self-assembled entity. Hydrogen bonds to anions are also directional in nature,<sup>[6]</sup> and this, combined with the range of geometries that anions possess, allows them to be used to template a variety of new organic supramolecular species. The range of anion geometries has also allowed anionic species to be employed in templating roles in the formation of inorganic clusters and new materials.

This entry focuses on “inorganic” systems, subdivided by the type of metal cation used. Readers interested in organic systems are directed to the entry on “Anion-Templated Self Assembly: Organic Compounds,” keeping in mind that there are many overlaps between these categories and this division is intended only as an aid to the reader.

## INORGANIC ANION-TEMPLATED SYSTEMS

### Vanadium

Müller et al. have extensively investigated the roles anions can play in templating the formation of structures from linked  $V^{n+}O_x$  polyhedra.<sup>[7]</sup> Specifically, Müller et al. have shown that anionic templates such as nitrate and acetate can control the linking of these species.<sup>[8,9]</sup> For example, different shell-like clusters were shown to form by reduction of vanadate (V) or oxidation of vanadate (IV)/vanadate (V) species in water in the presence of anions such as  $NO_3^-$  (1),  $SCN^-$  (2), and  $CH_3COO^-$  (3) (Fig. 1).

Oxo-vanadium species can be templated by ion-pairs.<sup>[10]</sup> In the central cavity of the system  $[V_{14}O_{22}(OH)_4(H_2O)_2-$

$(C_6H_5PO_3)_8]^{6-}$  (4), Müller and coworkers have shown that two chloride ions and two ammonium ions reside, the templation of this cluster being reliant upon the presence of the ion-pair (Fig. 2).

Salta et al. have also shown the templating ability of chloride ions to assist the formation of oxovanadium–organophosphate cluster structures. They have synthesized a number of cage structures containing differing numbers of templating chlorides. For example, cluster 5 shown in Fig. 3 contains a single chloride template (Fig. 3).<sup>[11]</sup>

### Iron

Hasenknopf et al. have used iron bipyridyl complexes to form a pentameric circular helicate around a chloride anion. The formation of this circular species was found to be dependent on the nature of the iron salt present. Complexation of iron chloride by the tris(bipyridine) ligand (6) produced the pentameric structure  $[Fe_5L_5Cl]^{9+}$  (7), templated around a chloride ion locked at the center of the structure (Scheme 1). Attempts to use bromide as the templating anion produced a mixture of the penta- and hexameric structures, while the use of non-halide iron salts, such as iron sulfate or tetrafluoroborate, produced only the untemplated hexameric structure 8.<sup>[12,13]</sup> Further work revealed that the above reaction of  $FeCl_2$  (and also the analogous one using nickel) progressed first through a linear helicate, which then progressively transformed into the circular structures.<sup>[14]</sup> Use of the longer ligand produced a tetrameric double helicate, irrespective of the type of iron salt used.

### Cobalt

Cobalt-based tetrahedral supramolecular arrays have been reported by Fleming et al.<sup>[15]</sup> Cage complexes have been synthesized from a pyrazoyl–pyridine ligand by reaction of the ligand with the appropriate metal acetate hydrate in methanol followed by addition of aqueous sodium tetrafluoroborate (resulting in the complex precipitating from solution). As shown in Fig. 4, a  $BF_4^-$  anion is located at the center of the

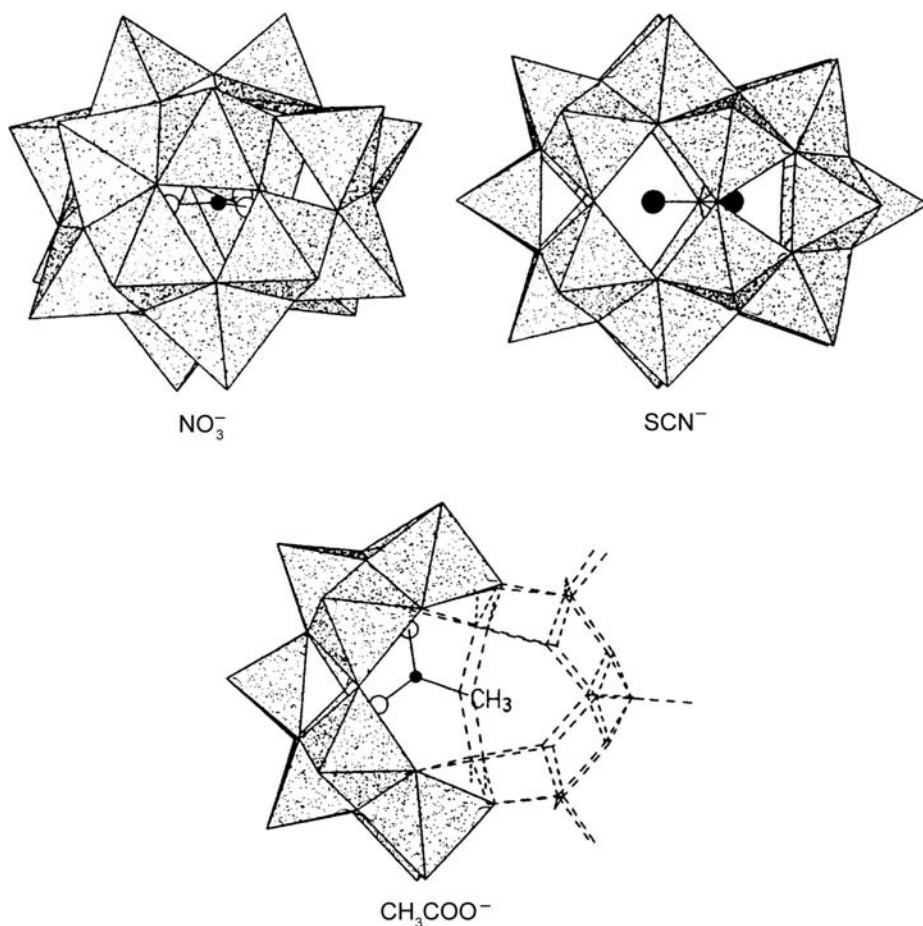


**Fig. 1** Anion-templated polyhedral V–O structures **1** (top left), **2** (top right) and **3** (below). *Source:* From Ref.<sup>[8]</sup>.

tetrahedral cage<sup>[9]</sup> formed by the four cobalt(II) metal ions at the vertices and six bridging ligands, thus each cobalt is octahedrally complexed. Each of the fluorines of the encapsulated anion is directed toward the triangular faces of the cluster rather than the metal

ions, implying electrostatic interactions are the driving force for this templation process, the anion partially balancing the  $8^+$  charge of the ring. Presumably, the anion has adopted an orientation dictated by

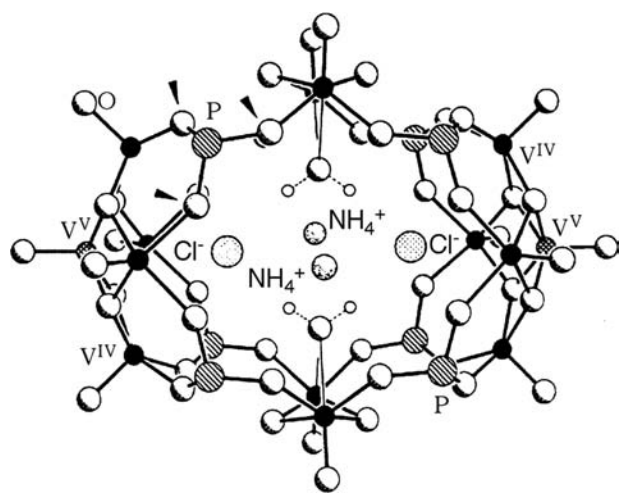


**Fig. 2** Structure of the oxo-vanadium cluster **4** showing templating ammonium and chloride ion-pairs in the center of the cavity. *Source:* From Ref.<sup>[10]</sup>.

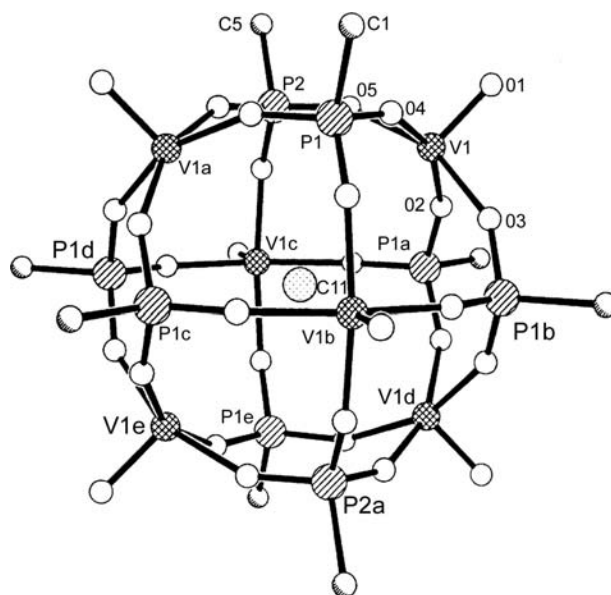
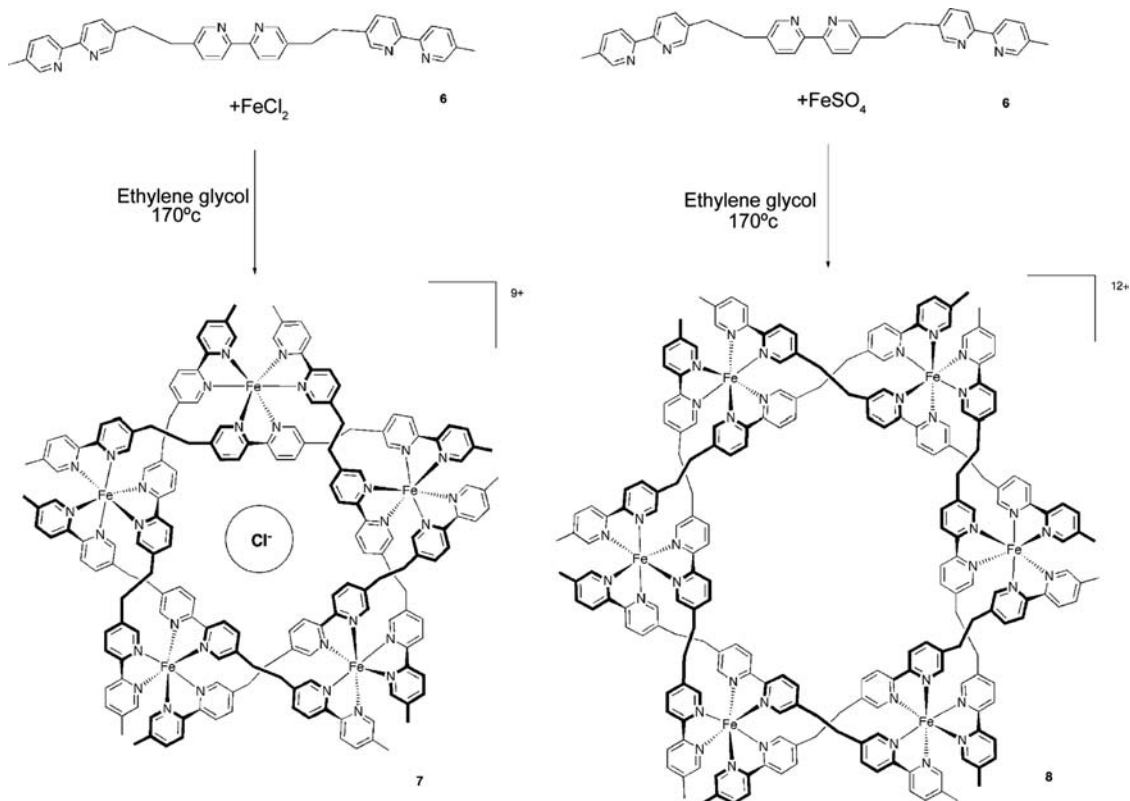


**Fig. 3** A view of the structure of **5** showing chloride template. *Source:* From Ref.<sup>[11]</sup>.



**Scheme 1** Chloride-templated assembly of a pentameric circular helicate.

the geometry of the internal cavity. Multiple  $\pi$ -stacking interactions between the ligands also assist the assembly of the structure. Such a configuration can also be templated by  $\text{ClO}_4^-$ , but in the absence of any template anion the cage does not form. Interestingly

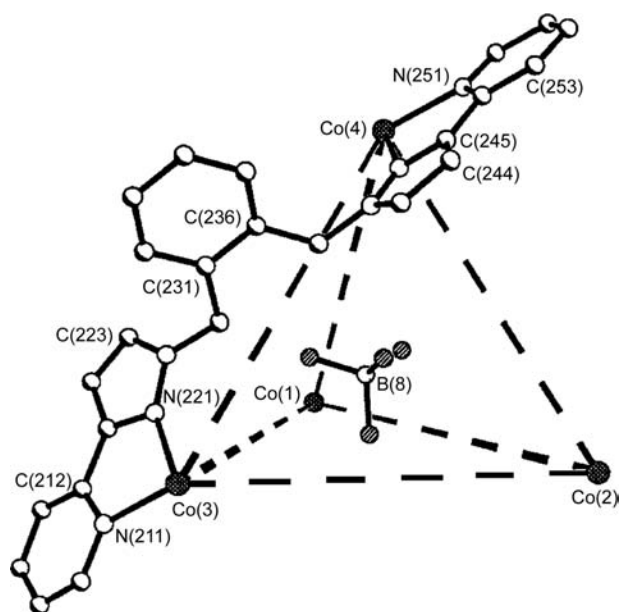


**Fig. 4** Part view of the tetrahedral cage structure **9**, with the central templating  $\text{BF}_4^-$  anion. *Source:* From Ref.<sup>[15]</sup>.

when nickel is used a different structure is formed (a dinuclear structure species with no templating anion). If an analogous ligand containing a biphenyl spacer is used, then a larger tetrahedral complex forms; however, the central cavity is empty, i.e., the system is not templated by an anion.<sup>[16]</sup> In solution it has been shown that the  $\text{BF}_4^-$  ions diffuse in and out of this cavity. This example illustrates how delicately balanced these systems are, and how changing only one aspect of the system in a small way can have a dramatic impact on the assembled structure.

The same research group have used cobalt in combination with a bis{3-(2-pyridyl)pyrazol-1-yl}dihydroborate ligand to form a cyclic structure encapsulating a perchlorate anion.<sup>[17]</sup> Reaction of [bis{3-(2-pyridyl)pyrazol-1-yl}dihydroborate] with cobalt(II) produced the cycle **10** shown in Fig. 5. Each ligand acts as a bridge between two adjacent metal ions, with an alternating pattern of one and then two ligands. The isostructural octanuclear ring is also formed if Ni(II) is used.

## Nickel

Mingosnet al. have synthesized metallamacrocycles and metallacages, by reacting  $\text{NiCl}_2$  with atu (Hatu = amidinothiourea) to produce the monomer  $[\text{Ni}(\text{atu})_2]$ ,

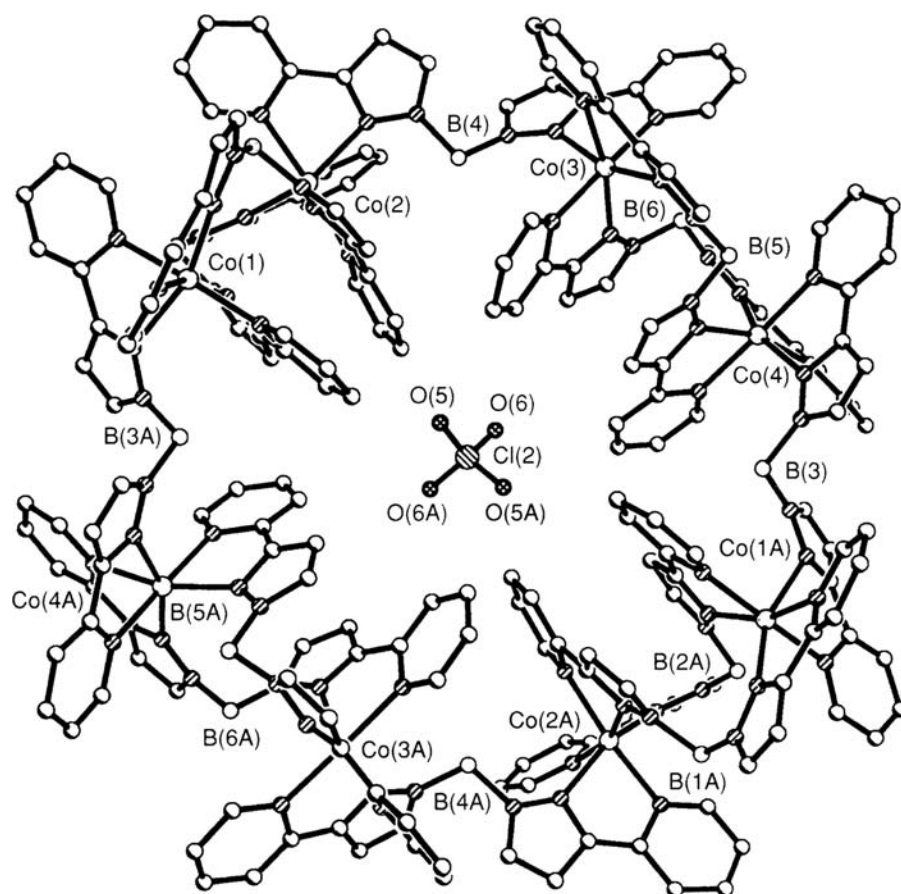


**Fig. 5** Crystal structure of the cobalt cage **10** with the central  $\text{ClO}_4^-$  ion. Source: From Ref.<sup>[17]</sup>.

with further reaction yielding the metallacage  $[\text{Ni}_6(\text{atu})_8\text{Cl}]\text{Cl}_3$  (**11**).<sup>[18]</sup> The eight amidinothiourea units coordinate to the six nickel ions through the nitrogen and sulfur atoms via hydrogen bond interactions (Fig. 6). A single chloride ion was identified as being bound at the center of the cage, through eight  $\text{N-H}\cdots\text{Cl}$  hydrogen bonds and Lewis acid/base interactions utilizing the two  $\text{NiS}_4$  units. The analogous bromide species  $[\text{Ni}_6(\text{atu})_8\text{Br}]\text{Br}_3$  has been synthesized. Confirmation of the templating role of the halide anion was provided by the failure of nitrate, acetate, or perchlorate to produce the desired cage, and instead monomer salts  $[\text{Ni}(\text{Hatu})_2]^{2+}$  were formed. However, subsequent addition of halide ions to the salt was found to generate the cage complex.

Campos-Fernandez, Clerac, and Koomen have also used nickel in anion-templated complex formation.<sup>[19]</sup> When solutions of  $[\text{Ni}(\text{CH}_3\text{CN})_6][\text{BF}_4]_2$  and bptz (3,6-bis(2-pyridyl)-1,2,4,5-tetrazine) were mixed in a 1:1 molar ratio the molecular square  $[\text{Ni}_4(\text{bptz})_4(\text{CH}_3\text{CN})_8][\text{BF}_4]_8$  (**12**) was produced (Fig. 7). One  $\text{BF}_4^-$  anion is held in the internal cavity of the square. A similar assembly is also produced when zinc is used instead of nickel, and in both these cases the templating ion can be either the tetrafluoroborate or perchlorate. However, if the larger anion  $\text{SbF}_6^-$  is used (by starting from

$[\text{Ni}(\text{CH}_3\text{CN})_6][\text{SbF}_6]$ ), a pentameric compound is obtained as the major product  $[\text{Ni}_5(\text{bptz})_5(\text{CH}_3\text{CN})_{10}][\text{SbF}_6]_{10}$ .<sup>[20]</sup>

## Molybdenum

A number of supramolecular structures using second-row transition metals have been reported. Chen et al. have employed metal-metal bonded molybdenum species to form the cyclic hexanuclear structure  $\{[\text{trans-Mo}_2(\text{O}_2\text{CCF}_3)_2(\mu\text{-dppa})]_3(\mu\text{-CO}_3)(\mu\text{-X})_3\text{F}\}$  ( $\text{X} = \text{Cl}, \text{Br}, \text{I}$ ) (**13**). This complex is the product of the reaction between  $[\text{trans-Mo}_2(\text{O}_2\text{CCF}_3)_2(\text{MeCN})_6][\text{BF}_4]_2$ ,  $\text{K}_2\text{CO}_3$  and dppa (*N,N'*-bis(diphenylphosphine)amine).<sup>[21]</sup> The quadruply bonded  $\text{Mo}_2$  units are held in position by the central carbonate ion. It is assumed that the chloride ions present in the complex originate from the solvent as the analogous Br and I complexes are formed during the reaction in acetonitrile and the subsequent addition of  $\text{ZnX}_2$  ( $\text{X} = \text{Br}$  or  $\text{I}$ ) (Fig. 8).

## Palladium and Platinum

Fujita and coworkers have recently reported the synthesis of palladium(II) cage complexes around



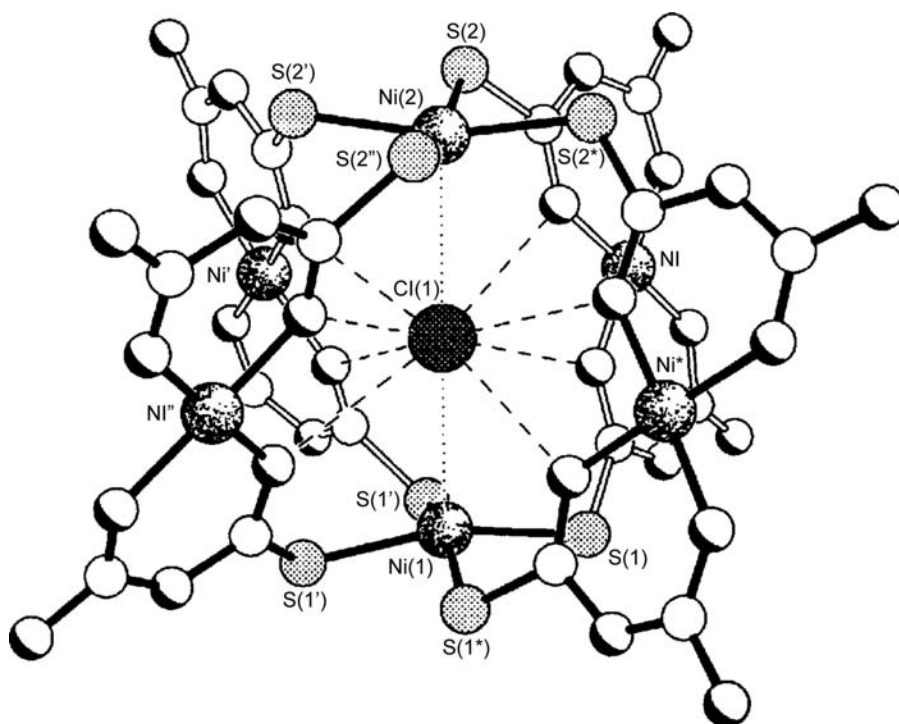


**Fig. 6** Structure of the nickel cage **11** showing the central chloride. *Source:* From Ref.<sup>[18]</sup>.

hydrophobic anions.<sup>[22]</sup>  $[\text{enPd}(\text{NO}_3)_2]$  was added to the tridentate ligand 1,3,5-tris(4-pyridylmethylbenzene) in the presence of sodium 4-methoxyphenylacetate producing the cage structure **14** shown in Fig. 9. A variety of carboxylate salts containing phenyl, naphthyl, or adamantyl groups were used as templates. NMR studies of the complexes suggest that the hydrophobic part of the

anion is located within the cavity of the cage while the polar group protrudes from the structure. Neutral linear ligands such as *p*-xylene were also able to template these systems, but in the absence of a templating anion no cage was produced.

More recently, the formation of anion-templated nanotubes has been reported.<sup>[23]</sup> Reaction of  $[\text{Pd}(\text{en})_2(\text{NO}_3)_2]$  with pentakis(3,5-pyridine) **15** in the presence of a rod-like anionic template, e.g., 4,4'-biphenylenedicar-

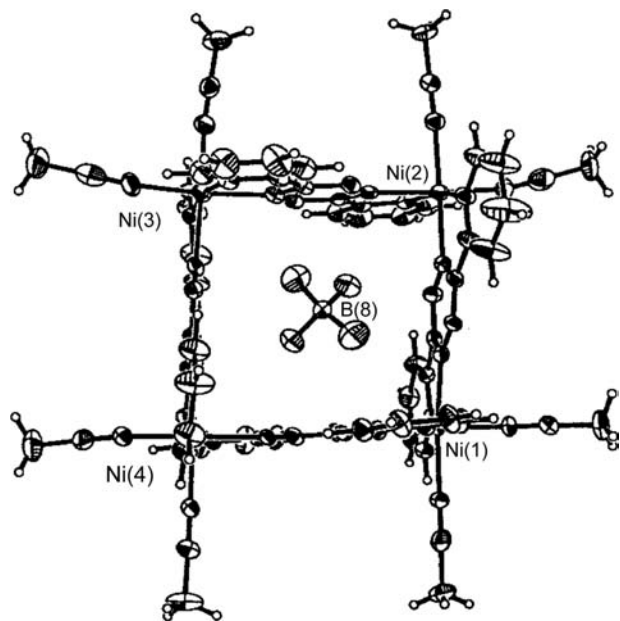


**Fig. 7** Dunbar's tetrafluoroborate templated nickel square **12**. *Source:* From Ref.<sup>[19]</sup>.

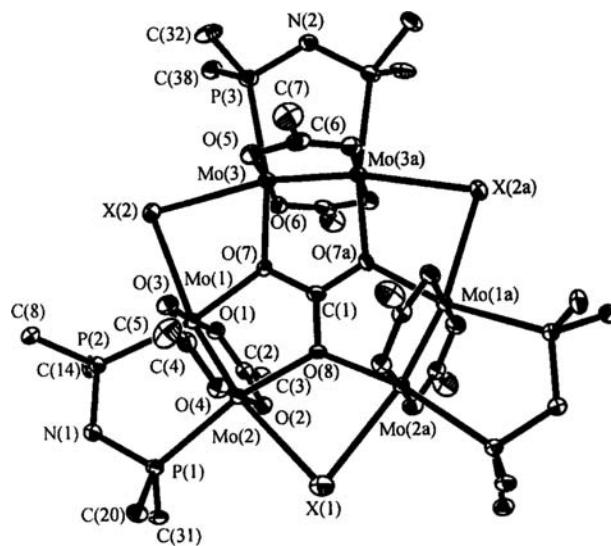


**Fig. 8** The hexa-molybdenum-based complex **13**. *Source:* From Ref.<sup>[21]</sup>.

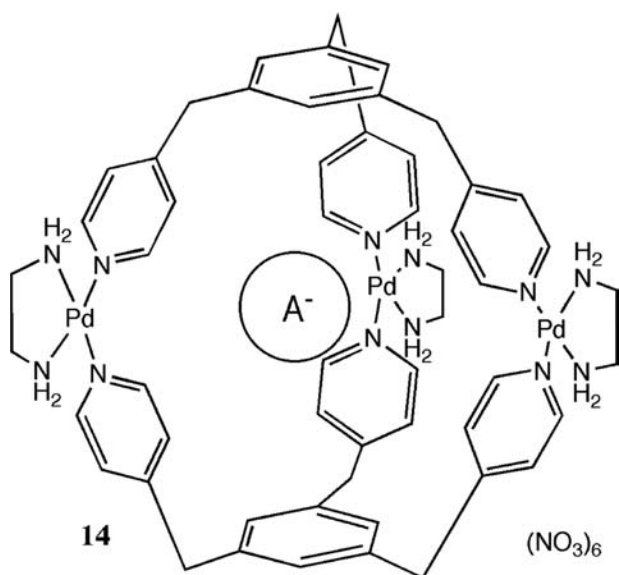
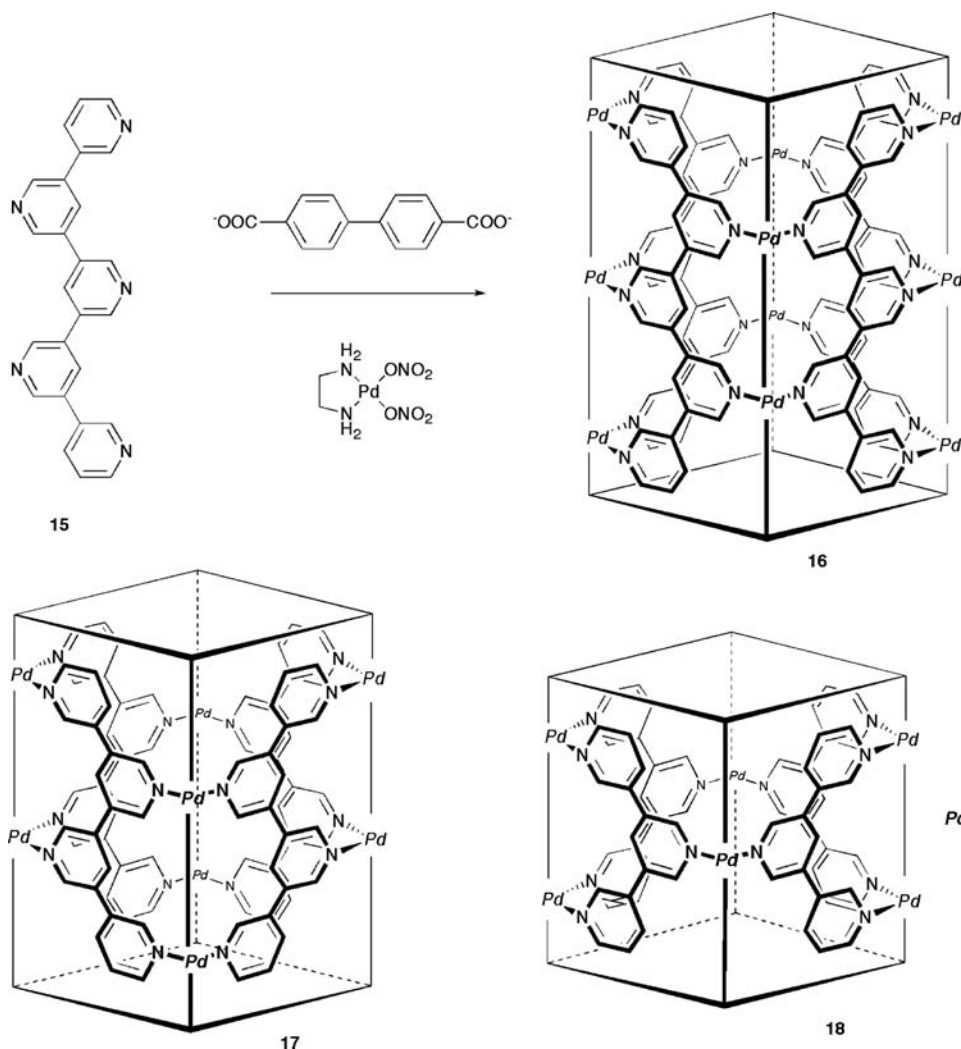


Fig. 9 Anion templated palladium cage 14.

boxylate, quantitatively yielded the coordination channels **16–18** (Scheme 2). The reaction is reversible, with the extraction of the template possible at high temperatures. This results in the destruction of the nanotubes, which reassemble upon the re-introduction of the template molecule. Elucidation of the crystal structures of both the cages and nanotubes revealed the linear templates to be bound via combinations of  $\pi$ - $\pi$  stacking, CH- $\pi$  interactions, and hydrophobic effects.

Schnebeck, freisinger, and Lippert have reported a synthetic solid-state ion channel which incorporates both palladium and platinum.<sup>[24]</sup> The reaction of  $[\text{Pt}(\text{en})(\text{H}_2\text{O}_2)]^{2+}$  and 2,2'-bipyrazine (bpz), and subsequent reaction with  $[\text{Pd}(\text{en})]^{2+}$  afforded the hexametallic molecular triangle **19** with one of the palladium corner sites displaying a 50% occupancy:  $[\{(\text{en})\text{Pd}\}_{2.5}(\text{2,2}'\text{-bpz})_3\{\text{NH}_3\}_2\text{Pt}_3][\text{ClO}_4]_6(\text{NO}_3)_5 \cdot 5\text{H}_2\text{O}$  (en = ethylenediamine, bpz = 2,2'-bipyrazine) (Fig. 10A). The molecular triangle hosts within its center one  $\text{ClO}_4^-$  ion (Fig. 10B), and in the solid state uses



Scheme 2 Formation of the nanotubes **16–18** from pentakis(3,5-pyridine).

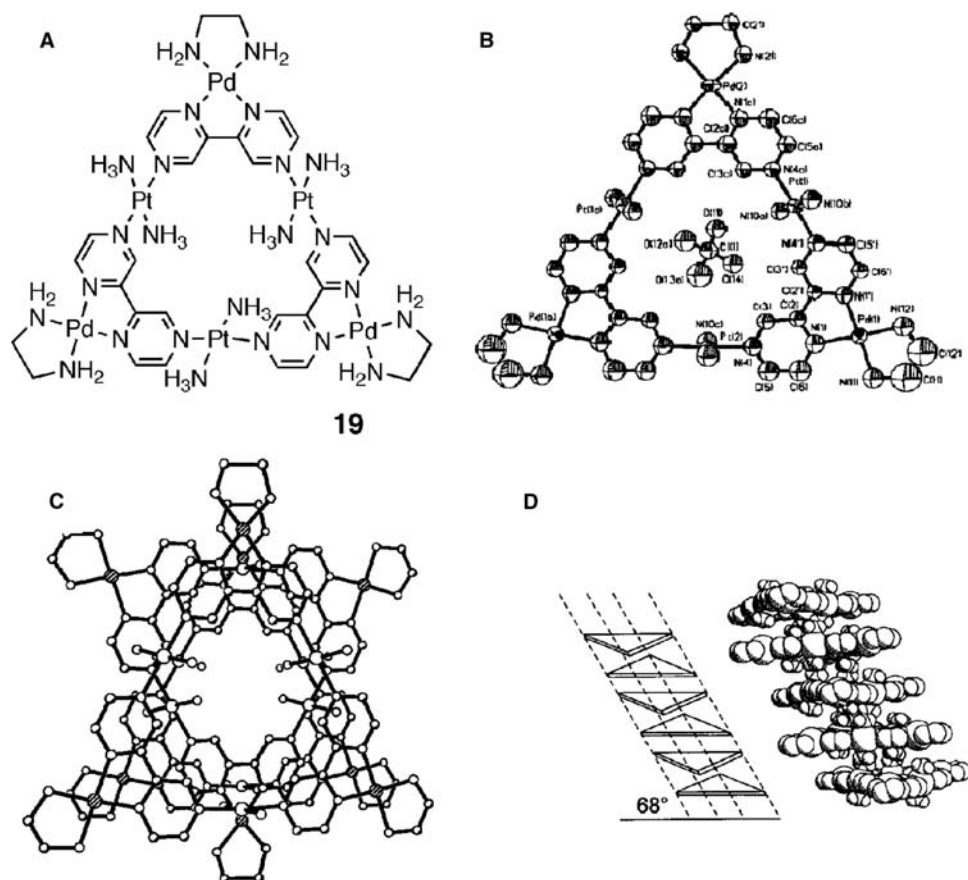


**Fig. 10** Crystal structure of the palladium-based molecular triangle, and schematic representation of its stacking in solid state. *Source:* From Ref. [24].

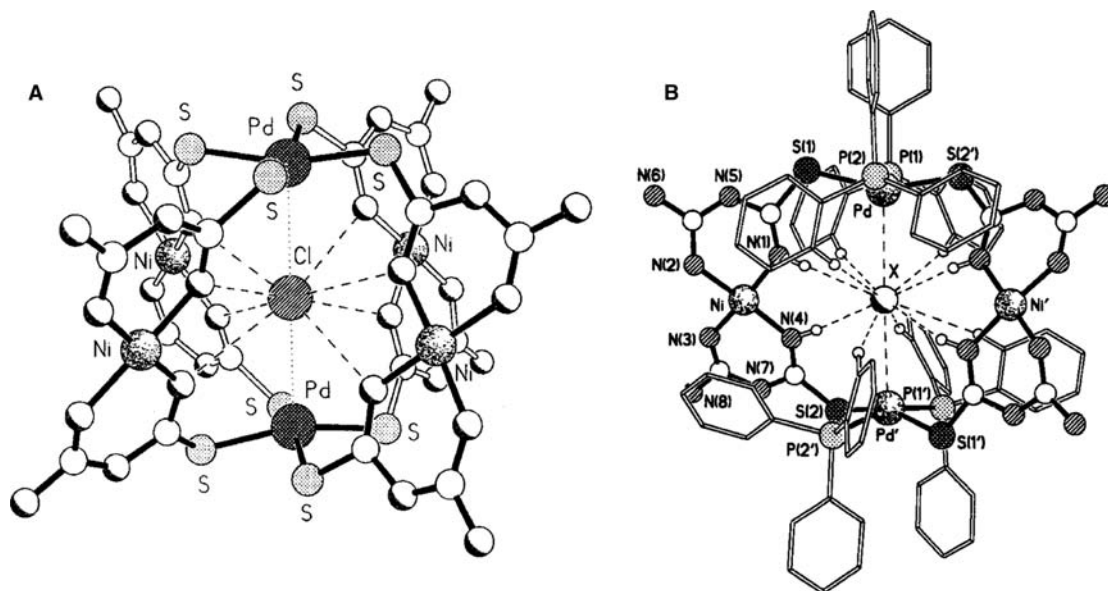
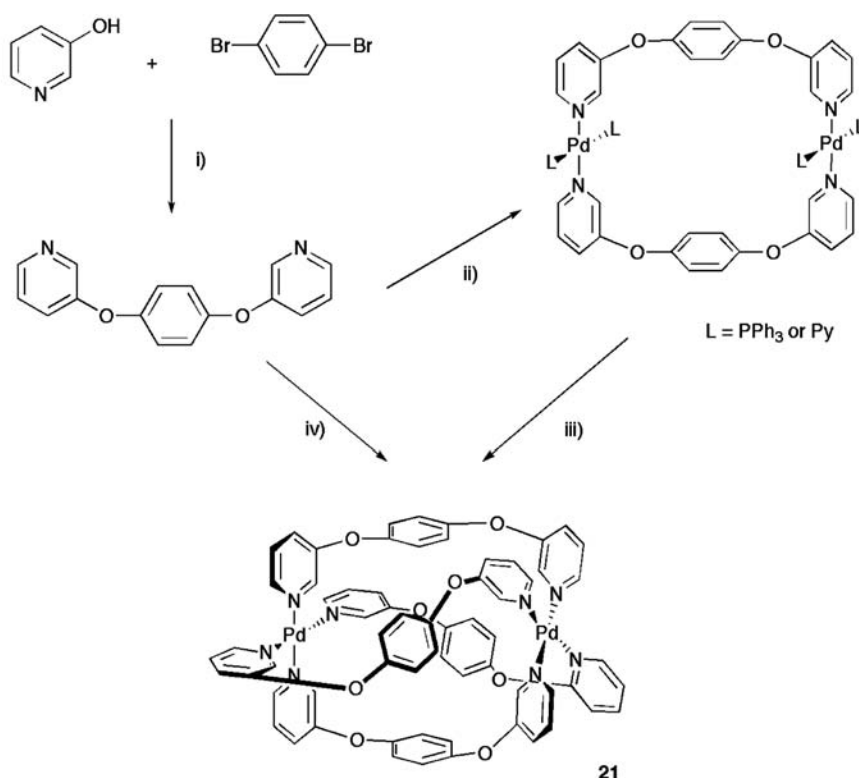


**Fig. 11** The molecular structures of the mixed metal nickel and palladium cages  $[\text{Ni}_4\text{Pd}_2(\text{atu})_8\text{X}]\text{X}_3$  and  $[\text{Pd}_2\text{Ni}_2(\text{atu})_4(\text{PPh}_3)_4\text{Cl}][\text{ClO}_4]_2$ . *Source:* From Refs. [26,27].



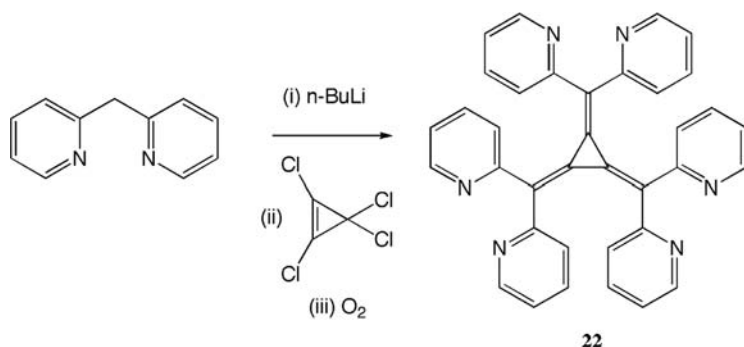
i)  $\text{K}_2\text{CO}_3$ ,  $\text{Cu}^0$ , dimethylacetamide, heat; ii)  $\text{L} = \text{PPh}_3$ :  $[\text{PdCl}_2(\text{PPh}_3)_2]$ ,  $\text{AgOTf}$ ,  $\text{CH}_2\text{Cl}_2$ ,  $\text{L} = \text{Py}$ :  $[\text{PdI}_2(\text{Py})_2]$ ,  $\text{AgOTf}$ , acetone,  $\text{NH}_4\text{PF}_6$ ; iii)  $\text{MeCN}/\text{Et}_2\text{O}$ ; iv) 0.5 equiv  $[\text{PdI}_2(\text{Py})_2]$ ,  $\text{AgOTf}$ ,  $\text{MeCN}$ ,  $\text{NH}_4\text{PF}_6$ ,  $\text{OTf} = \text{Trifluoromethanesulfonate (triflate)}$ .

**Scheme 3** Route of formation of the palladium cage, and a schematic showing the association of two of the fluorines with the metal centers.

$\text{NO}_3^-$  ions and  $\text{H}_2\text{O}$  molecules sandwiched between adjacent triangles to “glue” the structure together (Fig. 10C and D), the glue in part being a balancing of the cationic charge on each triangle. Thus this structure is templated by the  $\text{ClO}_4^-$  anion at an individual unit level and at the macromolecular level is held together by  $\text{NO}_3^-$  ions and the water molecules. The similar structure  $[\{(\text{en})\text{Pt}(\text{bpz})\text{Pd}(\text{en})\}_3](\text{NO}_3)_4(\text{PF}_6)_8$  was formed by the addition of chelating metal entities such as  $(\text{en})\text{Pd}^{\text{II}}$  to  $[\{(\text{en})\text{Pt}(\text{bpz})\}_3](\text{NO}_3)_6$ . It has been demonstrated that this molecule simultaneously encapsulates a  $\text{NO}_3^-$  ion and a  $\text{PF}_6^-$  ion at its center.<sup>[25]</sup>

In solution the host demonstrates an affinity for anions such as  $\text{PF}_6^-$ ,  $\text{ClO}_4^-$ ,  $\text{BF}_4^-$ , and  $\text{SO}_4^{2-}$ .

Mingos and coworkers have used palladium in conjunction with nickel to generate mixed metal systems similar to compound **11** above. Adding a solution of  $[\text{Pd}(\text{PhCN})_2\text{Cl}_2]$  to the nickel monomer  $\text{Ni}(\text{atu})_2$  produced the mixed metal cage  $[\text{Ni}_4\text{Pd}_2(\text{atu})_8\text{X}]\text{X}_3$  (Fig. 11A).<sup>[26]</sup> Once again a halide ion is encapsulated at the center of the cage. Either chloride or bromide may be used as the template. The metallamacrocycle  $[\text{Pd}_2\text{Ni}_2(\text{atu})_4(\text{PPh}_3)_4\text{Cl}][\text{ClO}_4]_2$  was formed via a very similar route: reaction of one equivalent of *trans*



**Scheme 4** Route to the hexanuclear silver array.



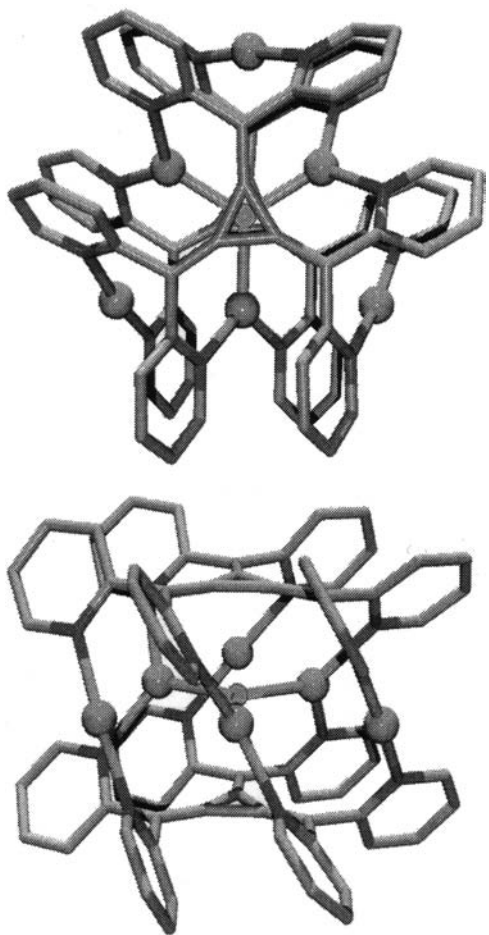


**Fig. 12** Two perspective views of the  $\text{Ag}_6(22)_2\text{F}$ . Source: From Ref.<sup>[30]</sup>.

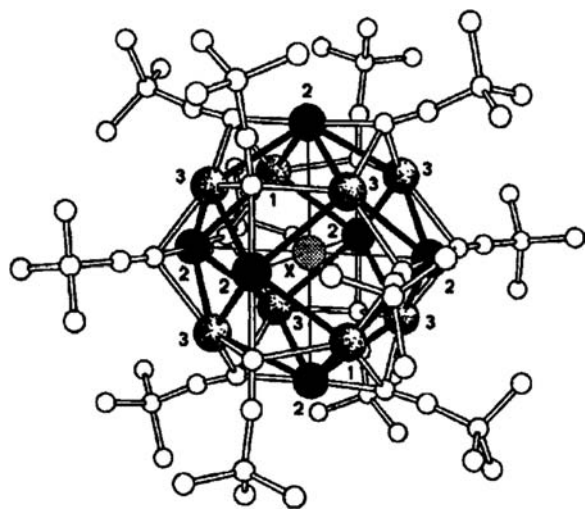


**Fig. 13** Structure of the silver cage complex **23**. Source: Reproduced with permission from *Angew. Chem. Int. Ed. Engl.* **2001** *40* (18) 3464. © 2001, Wiley-VCH.

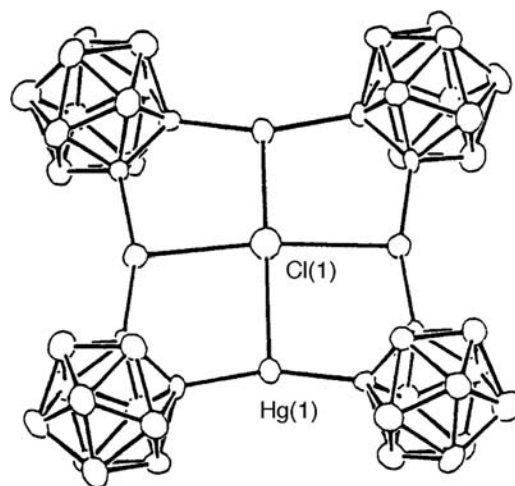
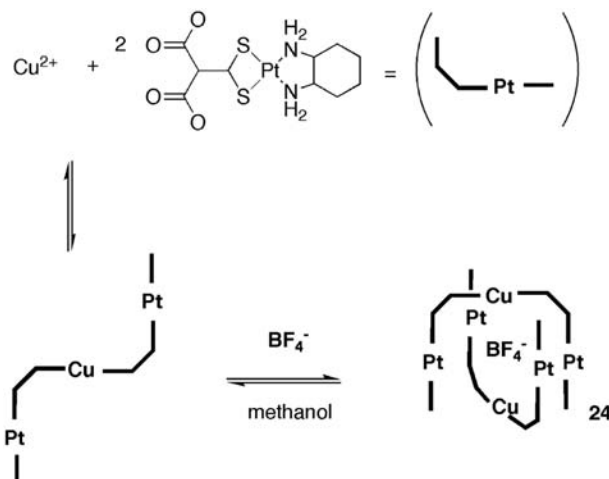


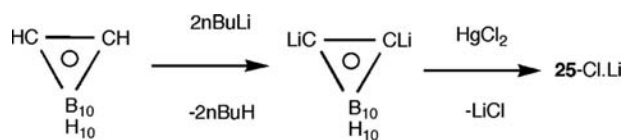
**Fig. 14** X-ray crystal structure of the chloride complex of  $25\text{-Cl}^-$ . Source: From Ref.<sup>[36]</sup>.

$\text{Pd}(\text{Ph}_3)_2\text{Cl}_2$  with one equivalent of  $\text{Ni}(\text{atu})_2$ .<sup>[27]</sup> Two of the  $\text{Ni}(\text{atu})_2$  groups have been replaced by the four inward pointing  $\text{PPh}_3$  ligands in the solid-state structure. Once again a chloride ion was found to have templated the formation of the cage by being at the center of the metallacycle (Fig. 11B). The bromide analogue displays the same characteristics; however, in the absence of a halide, monomeric units are produced.

McMorran and Steel have investigated the treatment of the ligand 1,4-bis(3-pyridyloxy)benzene with  $[\text{PdCl}_2(\text{PPh}_3)_2]$  and  $[\text{PdI}(\text{py})_2]$  in the presence of silver triflate producing dimeric complexes.<sup>[28]</sup> Crystallization of the dimeric species in the presence of ammonium hexafluorophosphate resulted in a reorganization of components to give a  $\text{M}_2\text{L}_4$  helical cage **21** as shown in Scheme 3, at the center of which was a  $\text{PF}_6^-$  anion. The anion



**Scheme 5** A schematic representation of the arrangement of the platinum, copper, and  $\text{BF}_4^-$  components.



Scheme 6 Synthesis of [12]mercuracarborand-4 **25**.

forms weak  $F \cdots Pd$  interactions, bridging between the two metals in the helical structure.

## Silver

Steel and Sumbly have recently reported the formation of cages and polymers with silver as the metallic component.<sup>[29,30]</sup> Using hexa(2-pyridyl)[3]radialene (**22**), prepared from reaction of diarylmethyl anions with tetrachlorocyclopropene<sup>[31,32]</sup> and reaction of this with silver tetrafluoroborate produces  $[Ag(\mathbf{22})F(BF_4)_5 \cdot 11H_2O]$ , a hexametallc cage, with each **22** acting in a hexapodal-hexadentate mode (Scheme 4). Within the cavity is a fluoride ion bound in a trigonal arrangement to three silver atoms with the other three arranged symmetrically away from this (Fig. 12). Reaction of this same ligand with silver nitrate yields a coordination polymer with each ligand coordinated to four silver atoms, in a twisted helical arrangement.

Further examples of the use of silver are provided by Rais et al. These researchers have reported the synthesis of  $[Ag_{14}(C \equiv C^tBu)_{12}Cl]OH$ , from a solution of  $AgBF_4$  being mixed with  $tBuC \equiv CH$  and  $NEt_3$  to form the initially insoluble polymeric  $[Ag(C \equiv C^tBu)]_n$ , which upon the addition of chloride is transformed into the metallacage **23** (Fig. 13).<sup>[33]</sup> More recently, the more direct route from  $AgBF_4$ ,  $tBuC \equiv CH$ ,  $NEt_3$ , and  $NMe_4Cl$  has been developed.<sup>[34]</sup> Via this same route  $[Ag_{14}(C \equiv C^t-$

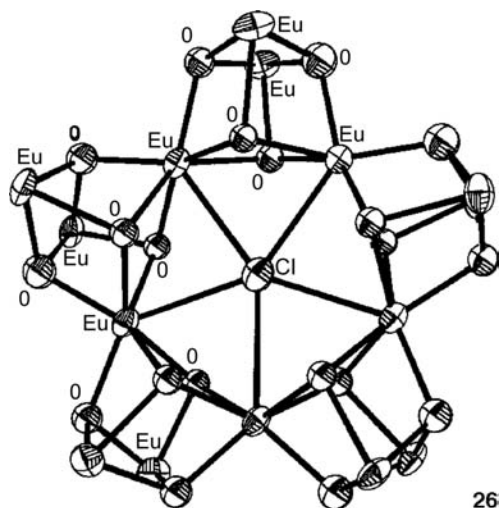


Fig. 15 The europium-based cubane structure. Source: From Ref.<sup>[39]</sup>.

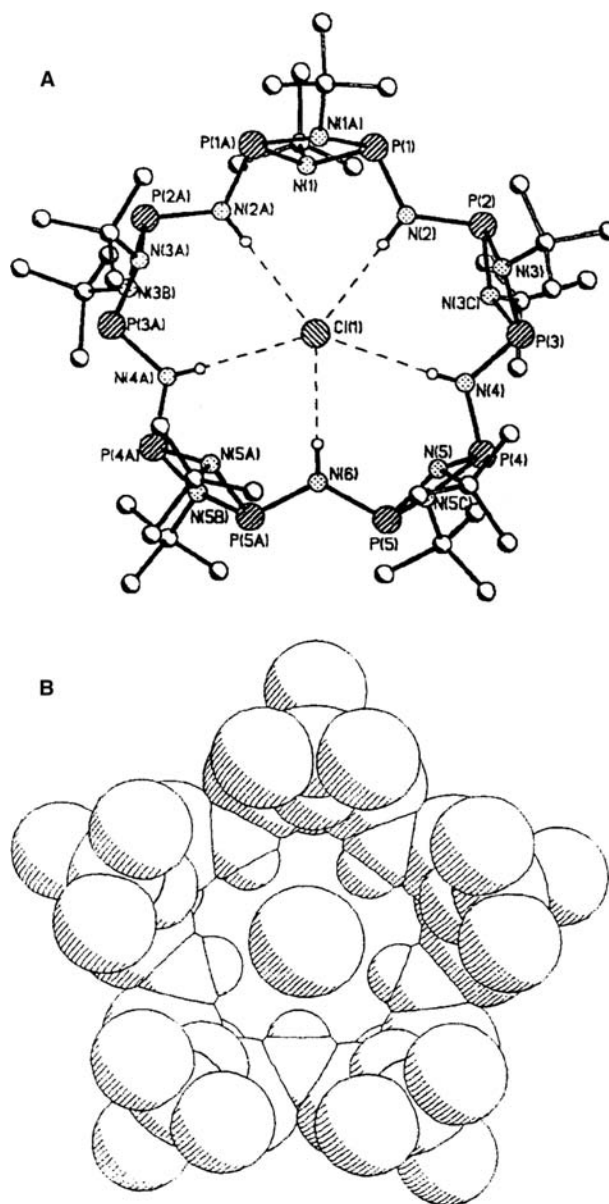
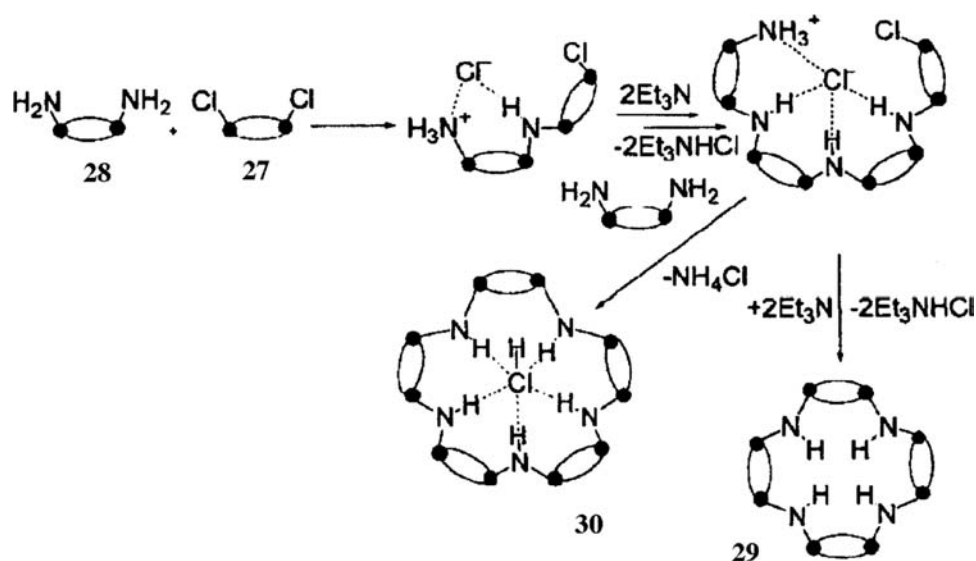


Fig. 16 The X-ray crystal structure of complex **30**. Source: From Ref.<sup>[41]</sup>.

$Bu)_{12}X][BF_4]$  ( $X = F, Cl, Br$ ) has also been prepared. Each cage has a single halide at its center and is formed through halide templation and metallophilic interactions (Fig. 14). The use of the alternative silver salts  $AgTos$  and  $AgNO_3$  produced only polymeric compounds ( $Tos = p$ -toluenesulfonate).

The first example of an inorganic “tennis ball” motif encapsulating an anion has been reported by Kim et al.<sup>[35]</sup> Dissolution of the complex  $\{(dach)Pt(BETMP)\}_2 - Cu(BF_4)_2$  ( $dach = trans(\pm)$ -1,2-diaminocyclohexane,  $BETMP = Bis(ethylthio)methylenepropanedioate$ ) resulted in the formation of complex **24** shown in Scheme 5. The starting material contains hydrogen bond acceptors (carboxylate) and donor (amine)





**Scheme 7** Preparation of both the tetra and pentameric forms of  $\{[P(\mu\text{-N}^t\text{Bu})_2](\mu\text{-NH})\}_{2n}$ . Source: From Ref.<sup>[41]</sup>.

groups, allowing the complex to dimerize around a central  $\text{BF}_4$  anion giving the tennis ball motif.

One of the first examples of work in this area is the mercuracarborand macrocycles reported by Hawthorne et al.<sup>[36–38]</sup> Preparation of tetraphenyl [12]mercuracarborand-4 (**25**) was achieved via the reaction of mercuric chloride with 1,2-dilithiocarborane (Scheme 6). Addition of mercury chloride templated the lithiated carboranes into a tetrameric cycle around a chloride template (Fig. 14). Synthesis of the iodide analogue was successfully performed, but instead of the anion being incorporated into the plane of the cycle, it was perched 1.25 Å above the plane. Use of nonspherical anions resulted in the formation of acyclic compounds instead of the desired macrocycles.

Very few examples of lanthanide clusters templated by anions have been reported. The exception is the series of lanthanide (III)-tyrosine metallamacrocycles synthesized by Wang et al.<sup>[39,40]</sup> The clusters were prepared by L-tyrosine-controlled hydrolysis of the appropriate lanthanide perchlorate, where  $\text{Ln} = \text{La}, \text{Pr}, \text{Nd}, \text{Sm}, \text{Eu}, \text{Gd}, \text{and Dy}$ . In all cases an isostructural pentanuclear structure resulted. Below, as an example, is the europium (III)-tyrosine metallamacrocycle **26** (Fig. 15), with core formula  $[\text{Eu}_{15}(\mu_3\text{-OH})_{20}(\mu_5\text{-X})]^{24+}$ .

Its pentameric structure is clearly demonstrated with the Eu ions forming three layers, each containing five ions. At the center is a chloride ion, which simultaneously coordinates the five inner-layer  $\text{Eu}^{\text{III}}$  atoms. The formation of this complex can best be described as a chloride-induced self-assembly, i.e., the chloride is acting as a template. When a lanthanide perbromate was used the equivalent pentameric complex with a bromate at the center was produced. Yet when iodide was used as the templating agent an alternative

dodecanuclear lanthanide complex was formed, with a core formula of  $[\text{Ln}_{12}(\mu_3\text{-OH})_{16}(\text{I})_2]^{18+}$  ( $\text{Ln} = \text{Dy}, \text{Er}$ ). Such complexes have a square cyclic arrangement with an iodide on either side of the square plane. Syntheses that do not use halides as the templating agent do not produce these penta and dodecanuclear species.

### Main Group

Wright et al. have investigated the formation of a series of macrocycles, from the reaction of  $[\text{CIP}(\mu\text{-N}^t\text{Bu})]_2$  (**27**) with  $[\text{NH}_2\text{P}(\mu\text{-N}^t\text{Bu})]_2$  (**28**) in the presence of a base to produce a  $\{[P(\mu\text{-N}^t\text{Bu})_2](\mu\text{-NH})\}_{2n}$  framework.<sup>[41]</sup> In the absence of a templating anion, the tetrameric species **29** is formed (i.e.,  $n = 4$ ), but when the same reaction is performed in the presence of an excess of  $\text{LiCl}_2$  then the major product is the pentameric form  $\{[P(\mu\text{-N}^t\text{Bu})_2](\mu\text{-NH})\}_5(\text{HCl})$  **30** (Fig. 16; Scheme 7). The templating chloride ion is found at the center of the macrocycle, held in position by five hydrogen bond interactions between it and the NH groups.

### CONCLUSION

We believe that the recent advances in the use of anions in self-assembly processes will lead to their employment in the templating of both inorganic and organic supramolecular nanoarchitectures in the future. This area of chemistry is yet to be fully explored and in particular the exploitation of the geometry of the anionic guest to guide the assembly process has untapped potential for the construction of new supramolecular species. We look forward to advances in this area of chemistry in years to come.

## ACKNOWLEDGMENTS

We would like to thank the Royal Society for a University Research Fellowship (P.A.G.) and the EPSRC for a DTA studentship (L.S.E.).

## REFERENCES

- Vilar, R. Anion-templated synthesis. *Angew. Chem. Int. Ed. Engl.* **2003**, *42*, 1460–1477.
- Gale, P.A. Anion coordination and anion directed assembly: highlights from 1997 and 1998. *Coord. Chem. Rev.* **2000**, *119* (1), 181–233.
- Gale, P.A. Anion receptor chemistry: highlights from 1999. *Coord. Chem. Rev.* **2001**, *213* (1), 79.
- Gale, P.A. Anion and ion pair receptor chemistry: highlights from 2000 and 2001. *Coord. Chem. Rev.* **2003**, *240* (1–2), 191–221.
- Gale, P.A.; Beer, P.D. Anion recognition and sensing: the state of the art and future perspectives. *Angew. Chem. Int. Ed. Engl.* **2001**, *40*, 486–516.
- Hay, B.P.; Dixon, D.A.; Bryan, J.C.; Moyer, B.A. Crystallographic evidence for oxygen acceptor directionality in oxanion hydrogen bonds. *J. Am. Chem. Soc.* **2002**, *124* (2), 182–183.
- Müller, A.; Pank, M.; Rohlfing, P.; Krickemeyer, E.; Doring, J. Topologically interesting cages for negative ions with extremely high “Coordination number”: an unusual property of V–O clusters. *Angew. Chem. Int. Ed.* **1990**, *29* (8), 926–927.
- Müller, A.; Rohlfing, R.; Krickemeyer, E.; Bogge, H. Control of the linkage of inorganic fragments of V–O compounds: from cluster shells as carcerands via cluster aggregates to solid-state structures. *Angew. Chem. Int. Ed.* **1993**, *32* (6), 909–912.
- Müller, A.; Reuter, H.; Dillinger, S. Supramolecular inorganic chemistry: small guests in small and large hosts. *Angew. Chem. Int. Ed.* **1995**, *34*, 2328–2361.
- Müller, A.; Hovemeier, K.; Rohlfing, R. A novel host/guest system with a nanometer large cavity for anions and cations  $[2\text{NH}_4^+, 2\text{Cl}^-, \text{cV}_{14}\text{O}_{22}(\text{OH})_4(\text{H}_2\text{O})_2^-(\text{C}_6\text{H}_5\text{PO}_3)_8]^{6-}$ . *Angew. Chem. Int. Ed.* **1992**, *31* (9), 1192–1195.
- Salta, J.; Chen, Q.; Chang, Y.-D.; Zubieta, J. The oxovanadium–organophosphonate system complex cluster structures. *Angew. Chem. Int. Ed. Engl.* **1994**, *33* (7), 757–760.
- Hasenknopf, B.; Lehn, J.-M.; Boumediene, N.; Dupont-Gervais, A.; Dorsselaer, A.-V.; Kneisel, D. Self-assembly of tetra- and hexanuclear circular helicates. *J. Am. Chem. Soc.* **1997**, *119* (45), 10,956–10,962.
- Hasenknopf, B.; Lehn, J.-M.; Kneisel, B.O.; Baum, G.; Fenske, D. Self-assembly of a circular double helicate. *Angew. Chem. Int. Ed. Engl.* **1996**, *35* (16), 1838.
- Hasenknopf, B.; Lehn, J.-M.; Boumediene, N.; Lieze, E.; Dorsselaer, A.V. Kinetic and thermodynamic control in self-assembly: sequential formation of linear and circular helicates. *Angew. Chem. Int. Ed. Engl.* **1998**, *37* (23), 3265–3266.
- Fleming, J.S.; Mann, K.L.V.; Carraz, C.-A.; Psillakis, E.; Jeffery, J.C.; McCleverty, J.A.; Ward, M.D. Anion-templated assembly of a supramolecular cage complex. *Angew. Chem. Int. Ed. Engl.* **1998**, *37* (9), 1279–1281.
- Paul, R.L.; Couchman, S.M.; Jeffery, J.C.; McCleverty, J.A.; Reeves, Z.R.; Ward, M.D. Effects of metal co-ordination geometry on self-assembly: a dinuclear double helicate and a tetranuclear cage complex of a new bis-bidentate bridging ligand. *J. Chem. Soc., Dalton Trans.* **2000**, (10), 845–851.
- Jones, P.L.; Byrom, K.J.; Jeffery, J.C.; McCleverty, J.A.; Ward, M.D. A cyclic supramolecular complex containing eight metal ions, twelve bridging ligands and an anion encapsulated in the central cavity. *Chem. Commun.* **1997**, (15), 1361.
- Vilar, R.; Mingos, D.M.P.; White, A.J.P.; Williams, D.J. Anion control in the self-assembly of a cage coordination complex. *Angew. Chem. Int. Ed. Engl.* **1998**, *37* (9), 1258–1261.
- Campos-Fernandez, C.S.; Clerac, R.; Dunbar, K.R. A one-pot, high-yield synthesis of a paramagnetic nickel square from divergent precursors by anion template assembly. *Angew. Chem. Int. Ed. Engl.* **1999**, *38* (23), 3477–3479.
- Campos-Fernandez, C.S.; Clerac, R.; Koomen, J.M.; Russell, D.H.; Dunbar, K.R. Fine-tuning the ring size of metallacyclophanes: a rational approach to molecular pentagons. *J. Am. Chem. Soc.* **2001**, *123* (4), 773–774.
- Suen, M.-C.; Tseng, G.-W.; Chen, J.-D.; Keng, T.-C.; Wang, J.-C. Novel cyclic hexanuclear complexes containing quadruply bonded units joined by  $\mu_6$ -carbonate ions. *Chem. Commun.* **1999**, (13), 1185–1186.
- Fujita, M.; Nagao, S.; Ogura, K. Guest-induced organisation of a three-dimensional palladium(II) cagelike complex. A prototype for “Induced-Fit” molecular recognition. *J. Am. Chem. Soc.* **1995**, *117* (5), 1649–1650.
- Aoyagi, M.; Biradha, K.; Fujita, M. Quantitative formation of coordination nanotubes templated by rodlike guests. *J. Am. Chem. Soc.* **1999**, *121* (32), 7457–7458.
- Schnebeck, R.-D.; Freisinger, E.; Lippert, B. Anion pore structure through packing of molecular triangles. *Chem. Commun.* **1999**, (8), 675–676.
- Schnebeck, R.-D.; Freisinger, E.; Lippert, B. A novel highly charged (+12) anion receptor that encapsulates simultaneously  $\text{NO}_3^-$  and  $\text{PF}_6^-$  ions. *Angew. Chem. Int. Ed. Engl.* **1999**, *38* (1/2), 168–171.
- Vilar, R.; Mingos, D.M.P.; White, A.J.P.; Williams, D.J. Aufbau synthesis of a mixed-metal anion receptor cage. *Chem. Commun.* **1999**, (3), 229–230.
- Cheng, S.-T.; Doxiadi, E.; Vilar, R.; White, A.J.P.; Williams, D.J. Anion templated synthesis of Ni/Pd containing metallamacrocycles. *J. Chem. Soc., Dalton Trans.* **2001**, (15), 2239–2244.
- McMorran, D.A.; Steel, P.J. The first coordinatively saturated, quadruply stranded helicate and its encapsulation of a hexafluorophosphate salt. *Angew. Chem. Int. Ed. Engl.* **1998**, *37* (23), 3295–3297.
- Steel, P.J.; Sumby, C.J. Anion-directed self assembly of metallosupramolecular coordination polymers of the

- radialene ligand hexa(2-pyridyl)[3]radialene. *Inorg. Chem Commun.* **2002**, *5* (5), 323–327.
30. Steel, P.J.; Sumbly, C.J. Hexa(2-pyridyl)[3]radialene: self assembly of a hexanuclear silver array. *Chem. Commun.* **2002**, (4), 322–323.
  31. Enomoto, T.; Nishigaki, N.; Kurato, H.; Kawase, T.; Oda, M. Synthesis, structure, and properties of hexaaryl[3]radialenes. *Bull. Chem. Soc. Jpn.* **2000**, *73* (No. 9), 2109–2114.
  32. Enomoto, T.; Kawaso, T.; Kurato, H.; Oda, M. Hexaaryl[3]radialenes. *Tetrahedron Lett.* **1997**, *38* (15), 2693.
  33. Rais, D.; Yau, J.; Mingos, D.M.P.; Vilar, R.; White, A.J.P.; Williams, D.J. Anion-templated synthesis of rhombohedral silver-alkenyl cage compounds. *Angew. Chem. Int. Ed.* **2001**, *40* (18), 3464–3467.
  34. Rais, D.; Mingos, D.M.P.; Vilar, R.; White, A.J.P.; Williams, D.J. Directing role of anions in the synthesis of the silver-alkynyl cages  $[Ag_{14}(C-C'Bu)_{12}X][BF_4]$  ( $X = F, Cl, Br$ ) and silver-alkynyl polymers  $[Ag_3(C-C'Bu)_2(X)]_n$  ( $X = Tos, NO_3$ ) in all cases is a triple bond. *J. Organomet. Chem.* **2002**, *652* (1–2), 87–93.
  35. Kim, K.M.; Park, J.S.; Kim, Y.-S.; Jun, Y.J.; Kang, T.Y.; Sohn, Y.S.; Jun, M.-J. The first inorganic “Tennis Ball” encapsulating an anion. *Angew. Chem. Int. Ed. Engl.* **2001**, *40* (13), 2458–2460.
  36. Yang, X.; Knobler, C.B.; Hawthorne, M.F. “[12]-Mercuracarborand-4,” the first representative of a new class of rigid macrocyclic electrophiles: the chloride ion complex of a charge-reversed analogue of [12]crown-4. *Angew. Chem. Int. Ed.* **1991**, *30* (11), 1507–1508.
  37. Zheng, Z.; Knobler, C.B.; Hawthorne, M.F. Stereoselective anion template effects: Syntheses and molecular structures of tetraphenyl [12]mercuracarborand-4 complexes of halide ions. *J. Am. Chem. Soc.* **1995**, *117* (18), 5105–5113.
  38. Wedge, T.J.; Hawthorne, M.F. Multidentate carborane-containing Lewis acids and their chemistry: Mercuracarborands. *Coord. Chem. Rev.* **2003**, *240* (1–2), 111–128.
  39. Wang, R.; Zheng, Z.; Jin, T.; Staples, R.J. Coordination chemistry of lanthanides at “High” pH: synthesis and structure of the pentadecanuclear complex of europium(III) with tyrosine. *Angew. Chem. Int. Ed. Engl.* **1999**, *38* (12), 1813–1815.
  40. Wang, R.; Selby, H.D.; Liu, H.; Carducci, M.D.; Jin, T.; Zheng, Z.; Anthis, J.W.; Staples, R.J. Halide-templated assembly of polynuclear lanthanide-hydroxo complexes. *Inorg. Chem.* **2002**, *41* (2), 278–286.
  41. Bashall, A.; Bond, A.D.; Doyle, E.L.; Garcia, F.; Kidd, S.; Lawson, G.T.; Parry, M.C.; McPartlin, M.; Woods, A.D.; Wright, D.S. Templating and selection in the formation of macrocycles containing  $[P(m-Nt-Bu)_2](m-NH)]_n$  frameworks: observation of halide ion coordination. *Chem. Eur. J.* **2002**, *8* (15), 3377–3385.

# Anion-Templated Self-Assembly: Organic Compounds

Paul D. Beer

Mark R. Sambrook

*Inorganic Chemistry Laboratory, Department of Chemistry, University of Oxford, Oxford, U.K.*

## INTRODUCTION

The field of self-assembly is an increasingly attractive area of supramolecular chemistry. With many principles derived from biological systems, it often enables the synthesis of large, complex structures that would be far too demanding using conventional covalent techniques.<sup>[1–3]</sup> Utilizing weak, reversible, non-covalent interactions, self-assembly can, through rational design of simple ligands, help minimize the amount of information inherent in the building blocks for the system and allow for error checking and self-correction.<sup>[4–6]</sup> To date, the range of non-covalent interactions used in self-assembly processes includes hydrogen bonding, metal coordination, hydrophobic, and  $\pi$ – $\pi$  donor–acceptor interactions.<sup>[7–18]</sup> The range of structures prepared via templated self-assembly continues to become increasingly diverse and intricate.<sup>[7–18]</sup>

Interest in the binding and recognition of anionic guest species has increasingly grown in the last decade or so, such that the field is now considered an important area of supramolecular chemistry. Anions often play key roles in biological processes; many enzyme substrates and cofactors are anionic and DNA itself is a polyanion. The fields of medicine and catalysis also help illustrate the diverse areas in which anions play key roles. Some anions are of environmental concern (e.g., there is a need to sense and remove nitrate and phosphate pollutants from natural waterways). In the past two decades, progress in the binding and recognition of anions has advanced considerably, and there are now many reviews dedicated entirely to this specific area of supramolecular chemistry.<sup>[19–22]</sup>

In light of this, it is surprising that investigations into the use of anions as templates in the self-assembly of supramolecular architectures has, until recently, been limited. Reasons for this may stem from the anion's small charge-to-radius ratio (more diffuse nature), pH sensitivity, and high solvation energy. The large geometrical diversity found in anions indicates the possibilities for predefining a wide range of supramolecular structures.

At the time of writing, we are unaware of any reviews dedicated solely to anion-templated self-assembly and are thus led to believe that this encyclopedia offers the first reviews of this topic.<sup>a</sup> Readers interested in anion-templated self-assembly of inorganic based frameworks are directed to the entry “Anion-Templated Self-Assembly: Inorganic Compounds.” This entry focuses solely on the anion-templated self-assembly of organic compounds.

## ANION-TEMPLATED SELF-ASSEMBLY OF ORGANIC FRAMEWORKS

The range of organic supramolecules prepared via anion-templated self-assembly is highly varied. Examples given in this review include solid-state polymers, helicates, pseudorotaxanes, and rotaxanes. Although nuclear magnetic resonance (NMR) and mass spectrometry data provide solution evidence of assembly in many examples, X-ray crystallography remains an invaluable tool for confirmation of the role of anions in many of the early reports.

The first example of anion templation in organic systems is in the rational design of organic solid-state structures reported by Geib et al.<sup>[24]</sup> in 1991. In contrast to traditional *endo* hydrogen bonding sites that form discrete 1:1 complexes with complementary receptors, they illustrate that by utilizing an *exo* configuration, the same components can be made to assemble into an alternating polymeric structure.

By simple protonation of the pyridine ring in 2,6-dibutyramidopyridine, repulsive interactions force rotation about the pyridine–amide bond, leading to the formation of two intramolecular hydrogen bonds to the carbonyl oxygen. Therefore the amide–NH groups are outwardly (or *exo*) directed and thus available for intermolecular hydrogen bonding. Addition of bis(4-nitrophenyl)hydrogenphosphate not only results

<sup>a</sup>Since the submission of this review article, Ref.<sup>[23]</sup> has appeared in the literature.

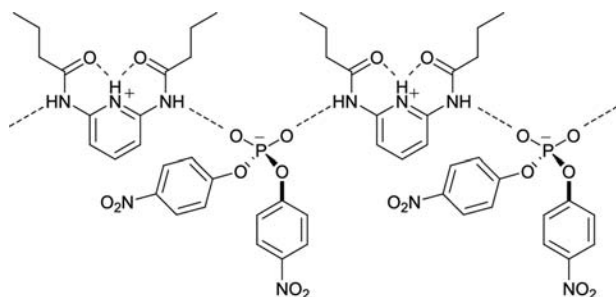


**Fig. 1** Ribbon arrangement of Hamilton's self-assembled solid-state hydrogen-bonded structure.

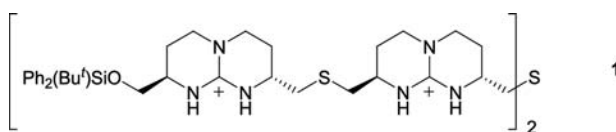


**Fig. 2** Mendoza's tetraguanidinium strand self-assembles into a double helicate structure.

in protonation but leads to the self-assembly of a polymeric alternating ribbon structure. The diaryl hydrogen phosphate plays two key roles in this assembly: protonation of the pyridine ring and provision of an anionic hydrogen bond acceptor of suitable geometry. The ribbon arrangement has hydrogen bonds in its core, with the anionic and cationic components segregated onto opposite sides of the structure in parallel alignment to each other (Fig. 1). A further structure was assembled using diphenyl hydrogen phosphate, indicating the generality of this assembling strategy.

The first example of an anion-templated helicate was reported by Sánchez-Quesada et al.<sup>[25]</sup> in 1996. A tetraguanidinium strand **1** was prepared, in which the spacer unit is too short for it to be able to wrap around one sulphate anion (Fig. 2). Consequently, two strands are forced to self-assemble into a double helicate structure, the handedness of which is imposed by the chiral receptor. Evidence for the helical nature of the anion-templated structure is provided by ROESY

(Rotational nuclear Overhauser Effect Spectroscopy) NMR techniques. In addition and in contrast to many helicates assembled by coordination chemistry, these organic helicates are overall neutral.

In 1996, Sessler et al.<sup>[26]</sup> reported on the self-assembly of polypyrrolic macrocycles. Based on the anion binding properties of sapphyrins and calix[4]pyrroles, zwitterionic carboxylate-appended structures **2** and **3** (Fig. 3) were synthesized. The ability to bind intramolecularly is absent because of the choice of spacer; with the sapphyrin compound methylene, carboxylate groups are positioned at either R<sup>2</sup> or R<sup>4</sup>, with the other R groups being hydrogen or methyl groups, and on the calixpyrrole, R is a propylene carboxylate.

It was found that these structures assemble into dimers; the carboxylate group of one molecule is chelated by the pyrrole core of another (Fig. 4). The tail of this second molecule is subsequently bound by the first molecule.

Protonated sapphyrins are known to have a high affinity for fluoride anions. Addition of fluoride ions is shown to inhibit the dimer assembly, thus providing further evidence for the assembly process. This example demonstrates how known anion binding sites can be exploited in the self-assembly of discrete supramolecular species.

Sessler et al.<sup>[27]</sup> have also reported on the possible templating effect of anionic nitrates in the synthesis of an oligopyrrolic macrocycle. An unusual example of large polynuclear anions as templates in organic synthesis is provided by Kim, Calabrese, and McEwen<sup>[28]</sup> who utilized the [CaCl<sub>3</sub>(DMAc)<sub>3</sub>]<sup>-</sup> (DMAc = dimethyl acetamide) pseudo-octahedral anion in a directing role in the preparation of cyclic aromatic amides.

The use of anions in the synthesis of [L<sub>4</sub>]imidazoliophanes was reported by Alcalde et al.<sup>[29,30]</sup> in 1999. Based on a [3 + 1] convergent cyclization (Scheme 1), yields are significantly enhanced by the presence of certain anions (e.g., 42% yield in the absence of anions, to 83% for chloride and 88% for bromide). Templating is postulated to be because of the formation of

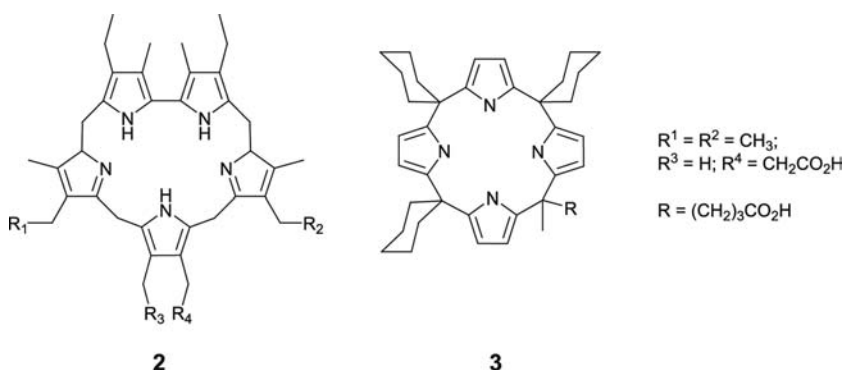


**Fig. 3** Carboxylate-appended sapphyrins and calix[4]pyrroles.

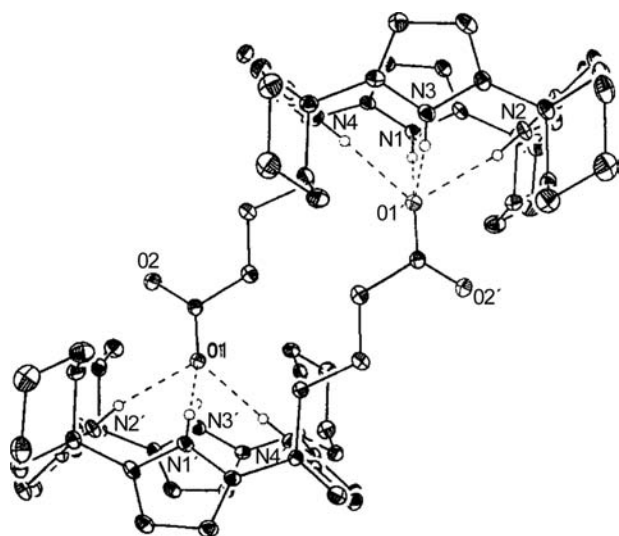
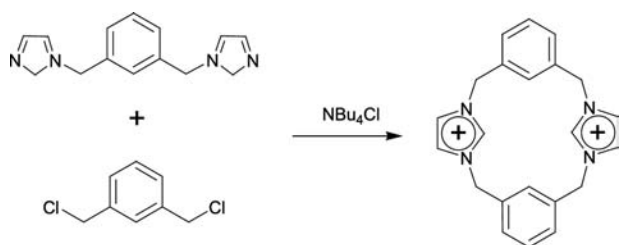


**Fig. 4** Side view of the non-covalent calix[4]pyrrole dimer where  $R = (\text{CH}_2)_3\text{CO}_2\text{H}$ . Source: From Ref.<sup>[26]</sup>. *Angewandte Chemie International Edition English*.

an intermediate in which  $\text{C-H}\dots\text{Cl}^-$  hydrogen bonds force a conformation that favors subsequent cyclization.

In recent years, interest in the preparation of mechanically interlocked supramolecules, such as catenanes and rotaxanes, has grown immensely. Rotaxanes are systems where a threadlike molecule is encircled by a macrocycle. Large stopper groups prevent the macrocycle from slipping off the ends of the thread. These molecules present a great challenge to the synthetic chemist because of their unusual nature and the possibilities for unusual molecular properties.<sup>[31–37]</sup> An extension of rotaxane work is the ever-expanding field of molecular shuttles and machines.<sup>[31–37]</sup> To date, the majority of rotaxane preparations have involved the use of hydrogen bonds, metal cation coordination chemistry, and  $\pi$ - $\pi$  donor-acceptor interactions to mediate the assembly.<sup>[38–42]</sup> More recently, some research groups have started to look into the possibility of using anions to template the formation of these interlocked, complex structures.



**Scheme 1** Alcalde's convergent synthesis of [4]imidazoliophanes.

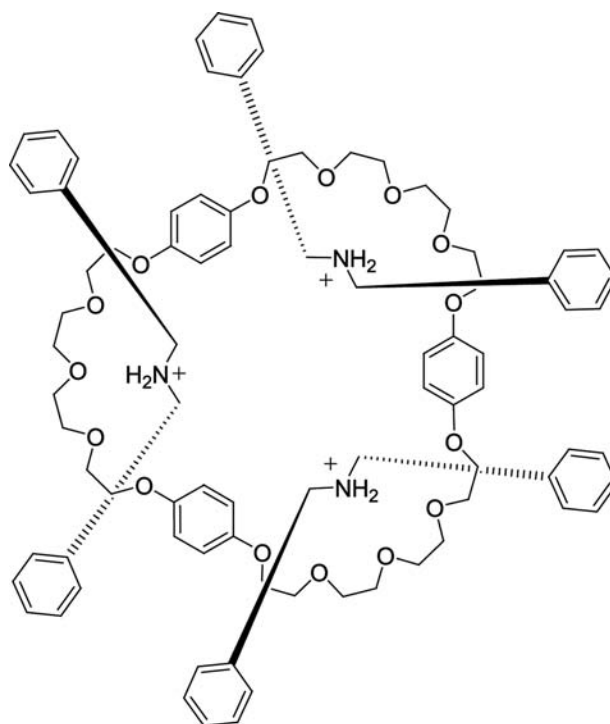


**Fig. 5** Stoddart's [4]pseudorotaxane.

In 1997, Fyfe et al.<sup>[43]</sup> reported what they describe as “anion-assisted self-assembly” of polypseudorotaxanes. Pseudorotaxanes are supramolecular complexes in which one molecule is threaded through another, but the absence of stopper groups means they can subsequently dissociate. These equilibrium complexes are important as they not only provide a great deal of information on the assembling motif but are precursors to both rotaxanes and catenanes. Earlier work by Montalti and Prodi<sup>[44]</sup> and Ashton et al.<sup>[45,46]</sup> established a strategy for pseudorotaxane formation constructed from macrocyclic polyethers and dibenzylammonium ions. Favorable  $[\text{N}^+\text{-H}\dots\text{O}]$  and  $[\text{C-H}\dots\text{O}]$  hydrogen bonds and  $\pi$ - $\pi$  stacking interactions help thread the ammonium ions through the macrocycles. Extension of this work to higher-order pseudorotaxanes hinted at the organizational role of an encapsulated  $\text{PF}_6^-$  ion within the interior of the supramolecule.

With tri-*p*-phenylene[51]crown-15, there lies the possibility of incorporating three ammonium ions into the cavity, thus forming a [4]pseudorotaxane (Fig. 5). Each ammonium ion interacts independently with a single polyether loop by the expected  $[\text{N}^+\text{-H}\dots\text{O}]$  and  $[\text{C-H}\dots\text{O}]$  interactions. Crystal structure evidence reveals that a single  $\text{PF}_6^-$  anion is located centrally and partially encapsulated within a cleft generated by the saddlelike conformation of the complex. A series of  $[\text{C-H}\dots\text{F}]$  hydrogen bonds to the hydroquinone rings on the polyether macrocycle



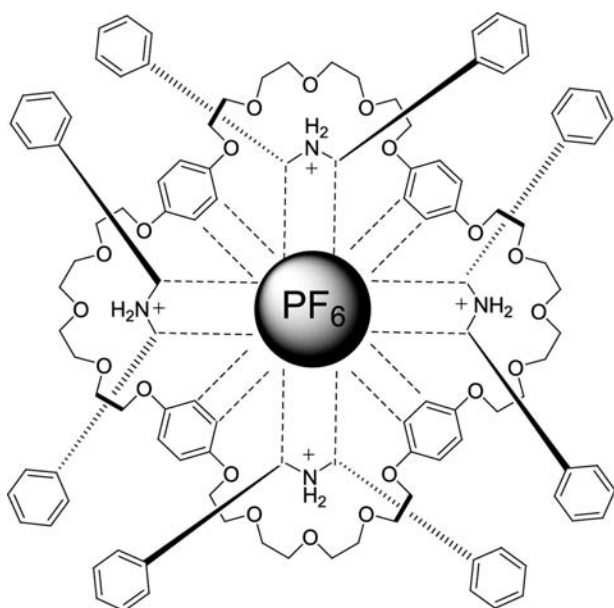


Fig. 6 Stoddart's [5]pseudorotaxane.

and to the ammonium benzylic methylene groups stabilizes and imposes order on the  $\text{PF}_6^-$  ion.

The larger [5]pseudorotaxane formed between four ammonium threads and tetrakis-*p*-phenylene[68]-crown-20 also features an ordered  $\text{PF}_6^-$  ion (Fig. 6). In this case, the anion is completely encapsulated by the four tetrahedrally arranged ammonium ions and by the four hydroquinone rings of the macrocycle. Order is imposed on the octahedral anion by a series of [C–H...F] hydrogen bonds involving the methylene hydrogen atoms of the threads and the hydroquinone protons of the polyether ring.

Stoddart et al. conclude that the  $\text{PF}_6^-$  anion “programs” the geometry of both complexes. However, although the anion undoubtedly plays a role in the assembly of these complexes and the final geometry

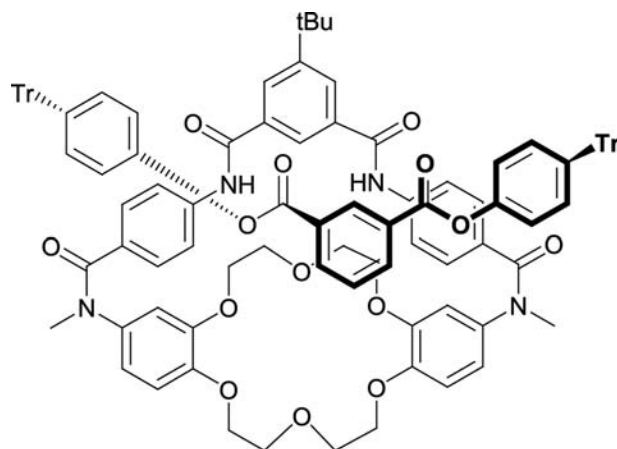
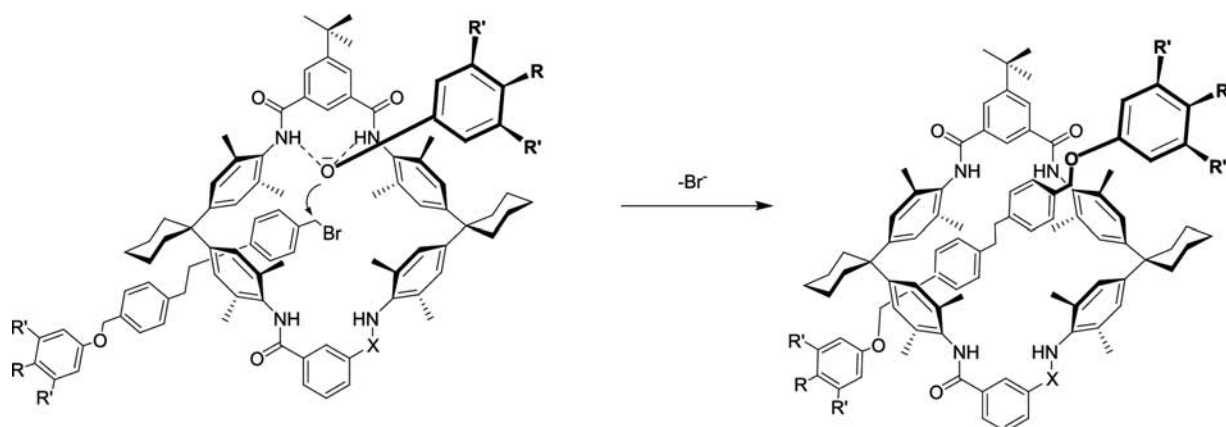


Fig. 7 Schematic of Smith's ion pair binding rotaxane indicating the predominant co-conformation of axle and wheel orientation in  $\text{CDCl}_3$ . Tr = Trityl.

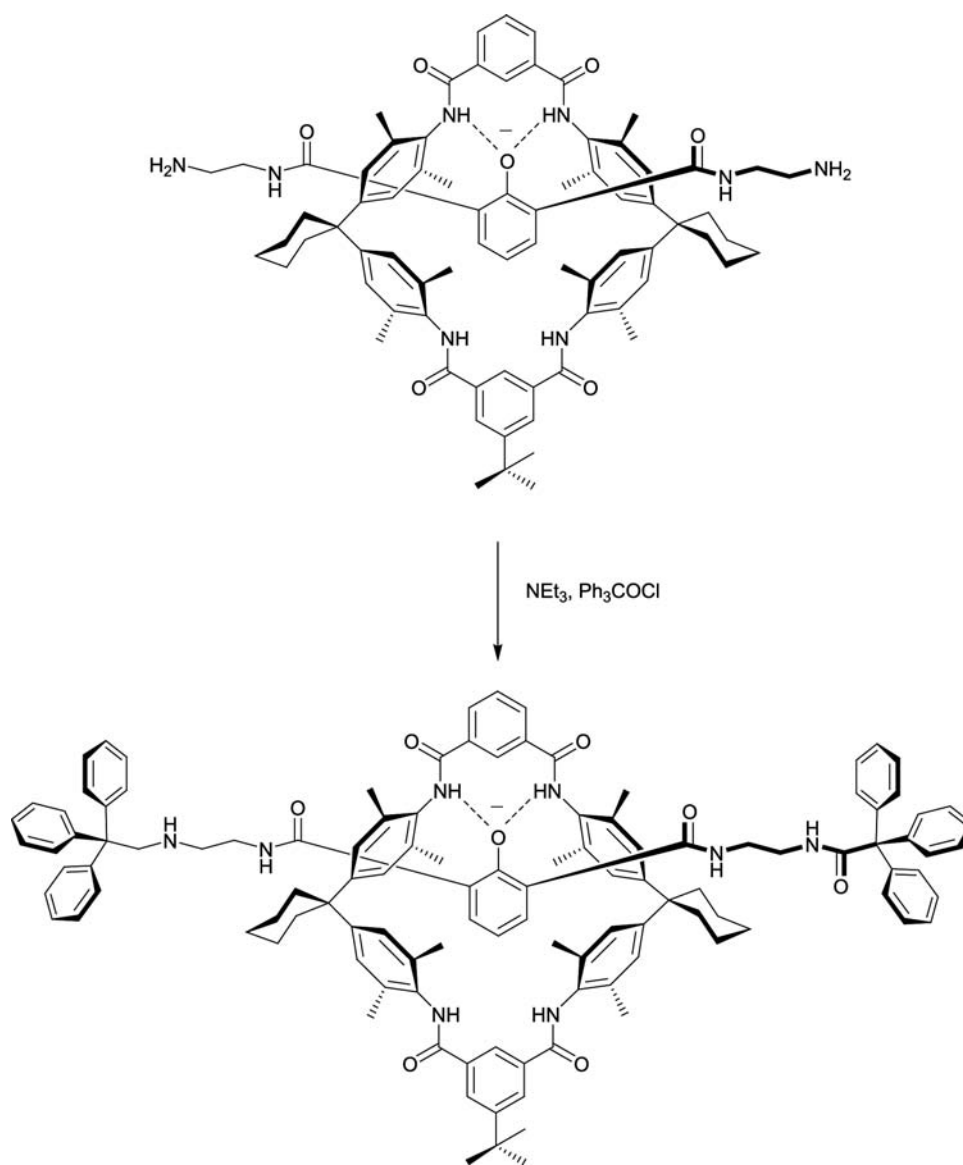
of the system, it is worth noting that secondary ammonium threads have been shown to assemble with polyether chains, especially dibenzo[24]crown[8], where the counter-anion is found to play no role in the assembly.

The first example of anion-templated synthesis of rotaxanes was reported by Hübner et al.<sup>[47]</sup> in 1999. Relying on the anion recognition properties of macrocyclic lactams, the synthesis proceeds via a “supramolecular nucleophile” or “wheeled phenoxide.” The hydrogen bond-donating ability of the lactam wheel is used to complex an organic anion, which can then serve as a nucleophile in an  $\text{S}_{\text{N}}2$  reaction. The reaction of *p*-tritylphenolate bound inside the lactam wheel with the suitable axle component gives the [2]rotaxane (Scheme 2) in a remarkably high yield of 95%. It is worth noting that the rotaxane product is neutral; the anion template is “used up” in the synthesis.<sup>[48]</sup>

Further reports have demonstrated the versatility of this so-called “trapping” methodology using a wide



Scheme 2 Vogtle's anion-templated rotaxane synthesis.



**Scheme 3** Schalley's "stopping" rotaxane synthesis using an anion template.

variety of axle building blocks. Rotaxanes with carbonate, acetal, and ester centerpieces have been prepared in varying yields.<sup>[49]</sup> Attempts to extend the synthesis to proceed via carboxylate anions have proven problematic and demonstrate that phenolate formation is essential in the preparation of these rotaxanes.

Smith et al. have tried to exploit the trapping technique developed by Vögtle in the preparation of ion pair binding [2]rotaxanes. Earlier ion pair binding macrocycles developed by Smith et al. incorporate an anion binding isophthalamide cleft that bridges a cation binding crown region and a close structural analogue has now been used to form the wheel of new rotaxanes.<sup>[50,51]</sup> In these macrocyclic systems, it was found that not only could an alkali

metal cation and an anion be bound simultaneously, but that the anion affinity is enhanced by the presence of suitable cations. It has been shown that the new host is capable of binding the potassium salt of 4-tritylphenolate and that subsequent reaction of the "wheeled phenolate" with isophthaloyl dichloride yields a thermodynamically stable [2]rotaxane in 20% yield (Fig. 7).

Evidence for rotaxane formation is provided by fast atom bombardment (FAB) mass spectrometry and  $^1\text{H}$  NMR assignments carried out by a combination of homonuclear correlation spectroscopy (COSY) and ROESY methods. ROESY evidence also suggests that the presence of  $\text{K}^+$  cations freezes out a single co-conformation. In the absence of  $\text{K}^+$  cations, broad signals that sharpen on heating, indicating a number of

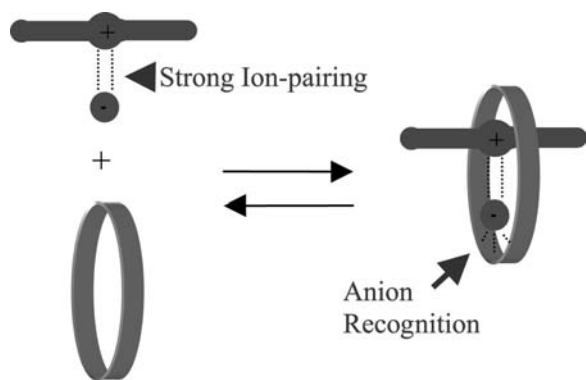


**Fig. 8** Wisner et al.<sup>[59]</sup> have developed a powerful and versatile anion-templated assembling motif for interlocked molecules.

axle–wheel orientations, are observed at room temperature. This cation-dependent behavior hints at future work whereby molecular motion could be controlled. The binding of chloride has been found to have an effect on the dynamic behavior of the rotaxane, although the combined effect of  $K^+/Cl^-$  binding produces the most rigid structure.<sup>[52,53]</sup>

Since this initial report, Deetz et al.<sup>[53]</sup> have embarked on a systematic study of their ion pair binding rotaxanes including rotaxanes with larger anion binding cavities and longer acetal-based threads, which could potentially be used in molecular shuttle devices.

Schalley et al.<sup>[54]</sup> have ascertained that low yields are often obtained with these rotaxane “snapping” syntheses because the nucleophilic anion required for rotaxane formation is often buried within the wheel and thus protected against attack of the semiaxle. To circumvent this problem, Ghosh, Mermagen, and Schalley<sup>[55]</sup> have designed a centerpiece, which contains a phenolate group and two sites for stopper attachment. Complete deprotonation of the phenolate using Schweisinger’s  $P_1$  base forms a supramolecular complex with the axle bound within the wheel. The final step is the attachment of the stopper units via amide bond formation to yield [2]rotaxanes in 20–30% yield

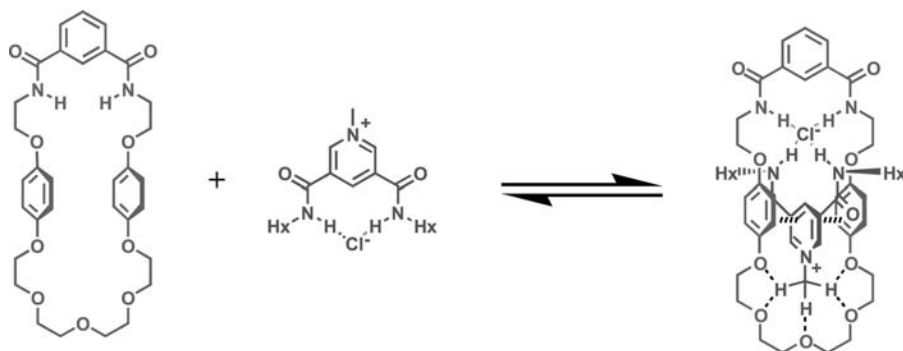


**Fig. 9** The chloride anion templates the self-assembly of the threadlike and macrocyclic components giving an interlocked structure.

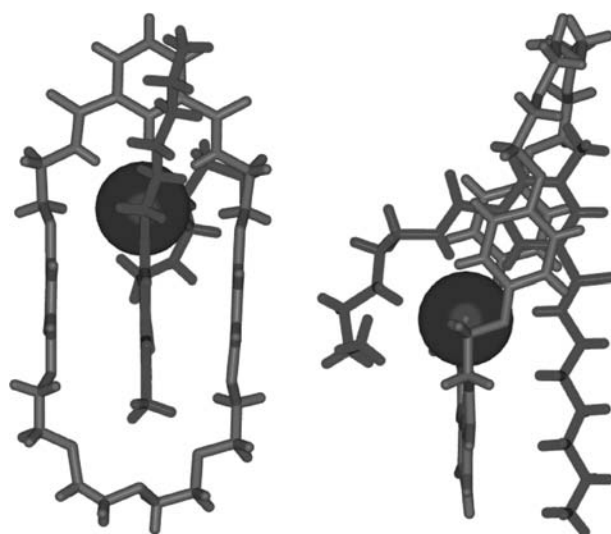


**Fig. 10** Stick representation of the pseudorotaxane crystal structure. Left: View through the annulus of the macrocyclic ring. Right: View in the plane of the macrocyclic ring. Chloride represented as CPK sphere for clarity. *Source:* From Ref.<sup>[59]</sup>. Angewandte Chemie International Edition English.

(Scheme 3). Rotaxane formation is confirmed by both  $^1H$  NMR and matrix-assisted laser desorption ionization (MALDI) mass spectrometry.

However, computer modelling results suggest that a phenolate–wheel complex can form in which the components are not threaded, with both arms of the axle on the same side. This is primarily because of the flexibility of the centerpiece; therefore the addition of stoppers can result in a non-interlocked axle–wheel complex. Increased rigidity in the axle may lead to higher rotaxane yields. The functionalized centerpiece raises the possibility of inducing molecular motion within related systems, especially if phenol-to-phenolate interconversion can easily be achieved.<sup>[55]</sup>

Recent reports from Li et al.<sup>[56]</sup> have been concerned with the anion-templated synthesis of related rotaxanes using modified tetralactam wheels that have *exo*-oriented bipyridine functionalities capable of complexing metal ions.

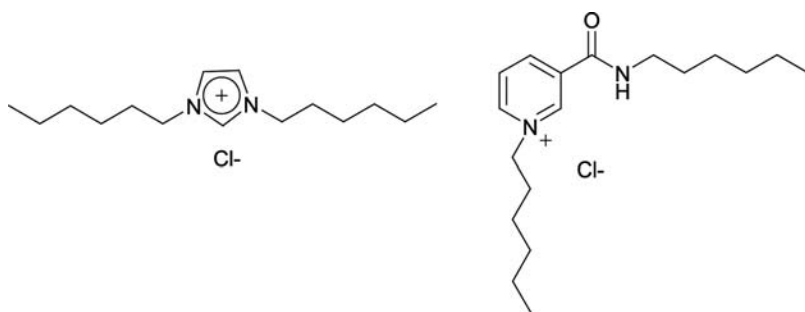
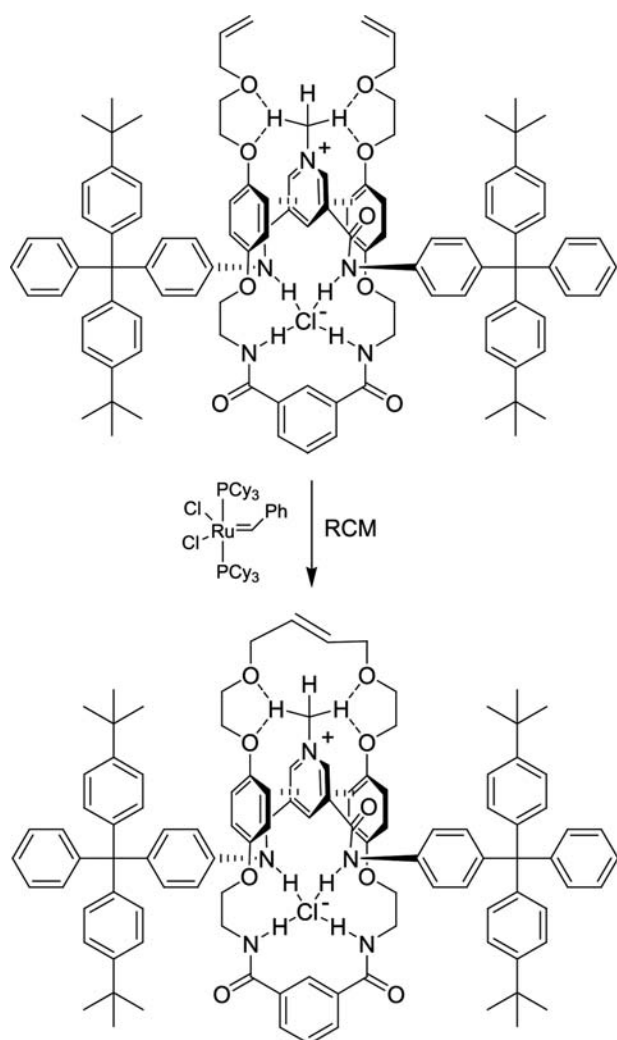


**Fig. 11** Imidazolium (left) and nicotinamide (right) threads used by Beer et al. in the assembly of pseudorotaxanes.

Beer et al. have since begun exploiting anions in the templated synthesis of pseudorotaxanes and rotaxanes. Inspired by the demonstration of anion recognition by simple isophthalamide molecules by Kavallieratos et al.<sup>[57,58]</sup> they have designed a novel assembling motif consisting of two amide clefts orthogonally disposed about a central chloride anion core. Neutral isophthalamide receptors bind chloride in 1:1 stoichiometry and so are unsuitable for assembly purposes. However, the

use of a cationic molecule as one of the ligands enables two receptors to bind to the halide anion.<sup>[59]</sup> As a consequence of increased amide acidity because of the cationic nature of the pyridinium ring, the chloride counter-anion is bound much more tightly compared with an analogous isophthalamide neutral compound. The tight ion pair leaves the chloride anion coordinatively unsaturated in non-competitive solvents, with an empty meridian exposed, which is capable of coordinating with another suitable hydrogen bonding ligand. Incorporation of a neutral isophthalamide fragment into a macrocyclic structure provides the



**Scheme 4** Beer et al.'s anion-templated rotaxane synthesis.

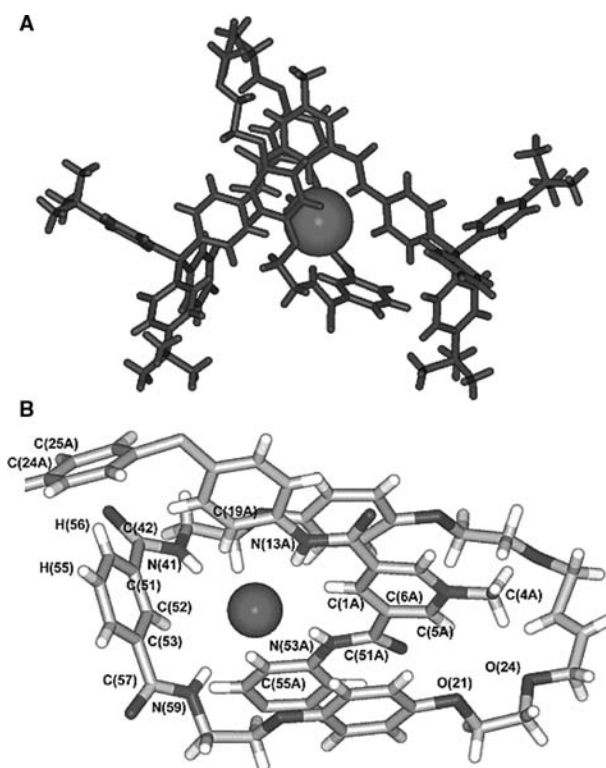


**Fig. 12.** Crystal structure of Beer et al.'s [2]rotaxane. (A) Stick representation of the solid-state structure illustrating the interlocked nature of the components (solvent is omitted and only one occupancy of the *tert*-butyl groups is shown). (B) Solid-state structure of the [2]rotaxane showing the enclosed cavity. Chloride anion shown as CPK for clarity. *Source:* From Ref.<sup>[61]</sup>. American Chemical Society.

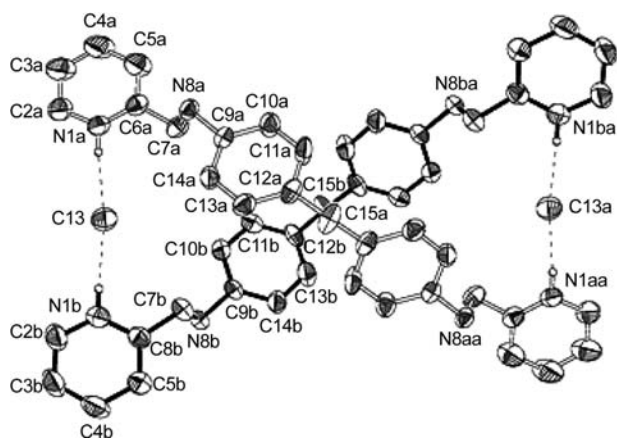


**Fig. 13** Molecular structure of a Kruger's double helicate. Source: From Ref.<sup>[62]</sup>. The Royal Society of Chemistry.

wheel component of the pseudorotaxane through which the cationic component can be threaded in non-competitive solvents. The general strategy adopted by Beer et al. is illustrated in Fig. 8.

For the pyridinium pseudorotaxanes first reported, additional stability is provided by  $\pi$ - $\pi$  interactions and hydrogen bonding (Fig. 9).<sup>[59]</sup> A high degree of selectivity was exhibited in these systems, with the pyridinium threads binding in the order  $\text{Cl}^- > \text{Br}^- > \text{I}^- > \text{PF}_6^-$ . Therefore the system not only self-assembles but also displays a high degree of anion-specific recognition.

The crystal structure of the pyridinium-based pseudorotaxane reveals the threaded nature of the components (Fig. 10) and provides evidence of  $\pi$ - $\pi$  acceptor-donor interactions and hydrogen bonding between the pyridinium methyl group and the polyether chain.

Further work has demonstrated the versatility of this assembling motif by the formation of pseudorotaxanes based on nicotinamide and imidazolium cationic threads (Fig. 11).<sup>[60]</sup> Neither of the threads have hydrogen bond donors capable of binding to the polyether ring and although the former has one

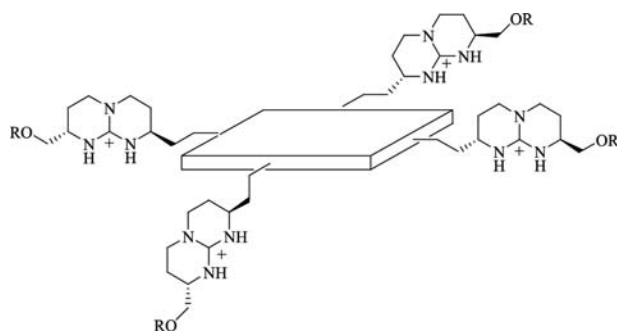


**Fig. 14** Guanidinium-appended porphyrins (R = H,  $\text{SiPh}_2\text{Bu}'$ ).

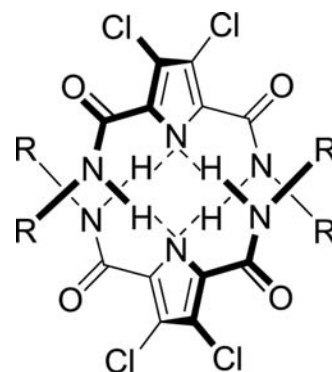


**Fig. 15** Hydrogen bonding between 2,5-diamidopyrrole anions (R = Ph).

amide group capable of anion binding, the latter has none and threads simply by virtue of being an ion pair.<sup>[60]</sup> The chloride anion can be seen to “drag” the cationic thread into the macrocycle, and further stabilization is provided by second-sphere acceptor-donor interactions. With nicotinamide and imidazolium, selective macrocycle binding for chloride threads over hexafluorophosphate threads was demonstrated.

Wisner et al.<sup>[61]</sup> have also reported on the extension of this work to the anion-templated formation of [2]rotaxane. An acyclic chloride anion template based on simple pyridinium pseudorotaxane threads has been designed, which acts as the “axle” of the rotaxane. The second component is a neutral acyclic molecule incorporating an isophthaloyl anion binding cleft and has two long side chains terminating in allyl groups capable of ring closing metathesis (RCM). The side chains each possess a hydroquinone group, as with the original pseudorotaxane macrocycle (to facilitate donor-acceptor interaction), and polyether chains capable of hydrogen bonding. The two components associate strongly in non-competitive solvents, and rotaxane formation facilitates ring closing metathesis of the neutral component about the ion pair using Grubbs' catalyst with yields up to 47% obtained (Scheme 4).<sup>[61]</sup> No rotaxane formation occurs with pyridinium bromide or hexafluorophosphate salts, indicating the templating nature of the chloride anion.

An impressive feature of this method of rotaxane assembly is that the resultant product retains a degree

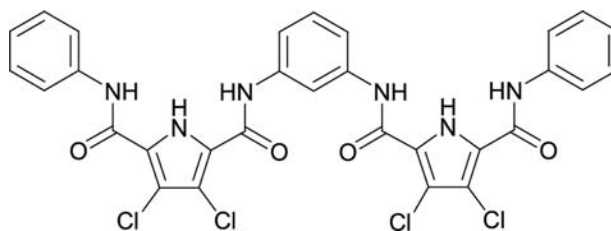


**Fig. 16** Gale's diamidopyrrole ligand.



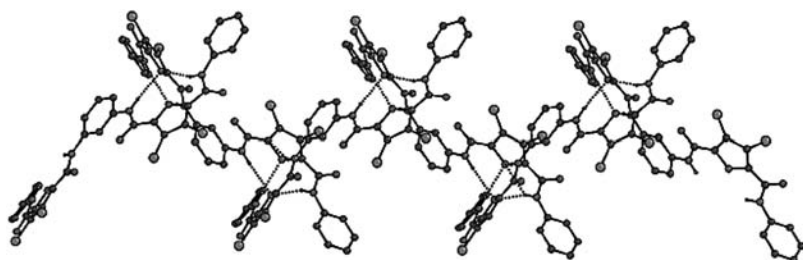


**Fig. 17** X-ray crystal structure of Gale's "anion-anion" assembled solid-state polymer. *Source:* From Ref.<sup>[65]</sup>. American Chemical Society.

of functionality based on the anion template itself. Exchange of the templating chloride anion for the non-competitive hexafluorophosphate anion leaves a highly selective binding site within the rotaxane. Binding studies have shown that although the pyridinium  $\text{PF}_6^-$  thread alone binds anions with a selectivity trend  $\text{AcO}^- \gg \text{H}_2\text{PO}_4^- > \text{Cl}^-$ , the pyridinium  $\text{PF}_6^-$  rotaxane exhibits a complete selectivity reversal and a high selectivity for chloride (i.e., the templating anion). Beer et al. assign this binding selectivity to the creation of a unique hydrogen bond donating pocket within the [2]rotaxane superstructure, which possesses a complementary topology to chloride (Fig. 12). Larger anions cannot penetrate this diamide cleft and bind at the periphery of the rotaxane, or via a large displacement of the pyridinium thread from the macrocyclic cavity. Therefore this example demonstrates not only anion templation for the synthesis of mechanically interlocked components but also shows how a rigorous design procedure has led, via self-assembly, to a functional supramolecule whose properties are dependent on the templation process.<sup>[57,58]</sup>

Keegan et al.<sup>[62]</sup> have reported the first structurally characterized anion-directed assembly of a dinuclear double helicate. The di-ammonium-bis-pyridinium salt  $[(\text{H}_4\text{LCl})_2] \cdot 6\text{HCl} \cdot \text{H}_2\text{O}$ , where L is a diamino-bis-pyridine ligand, assembles into a double helical structure, featuring a major and a minor groove, with two ligands wrapping around two chloride anions (Fig. 13). The chloride anions are coordinated by two pyridinium moieties and interact weakly with methylene and aromatic CH groups.

Camiolo et al.<sup>[63]</sup> have demonstrated the anion-controlled assembly of porphyrin-bicyclic guanidinium conjugates in aqueous solution. Exploiting the cooperative interaction of porphyrin and guanidinium moieties with anions, they have reported the assembly of structures in which chirality is controlled by the anion template used (Fig. 14).

Detailed investigations using, primarily, circular dichroism indicate that the assembly process is achieved by the presence of small achiral anions. The authors propose that the anions serve as linkers that diminish repulsive forces between the porphyrin units.

Gale et al. have been investigating the use of pyrroles in anion-templated self-assembly. In 2002,

they reported on the deprotonation and subsequent dimerization of a series of simple 2,5-diamidopyrrole compounds. It was shown that the anionic diamidopyrrolate ion can recognize another diamidopyrrolate ion through hydrogen bonding.<sup>[64]</sup>

The components arrange themselves orthogonally to each other (Fig. 15). Not only is  $\text{NH} \dots \text{N}^-$  (pyrrole) hydrogen bonding observed in this case, but  $\pi$ -H interactions are also present.<sup>[64]</sup>

The first extension of this work was the so-called "anion-anion" assembly of a supramolecular polymer.<sup>[65]</sup> These polymers are based on two pyrrole units linked together and are the first example of interlocked materials based on hydrogen bonding where both components are anionic. One of the ligands developed is shown in Fig. 16.

Crystallization of this ligand from acetonitrile in the presence of excess TBA fluoride gave the doubly

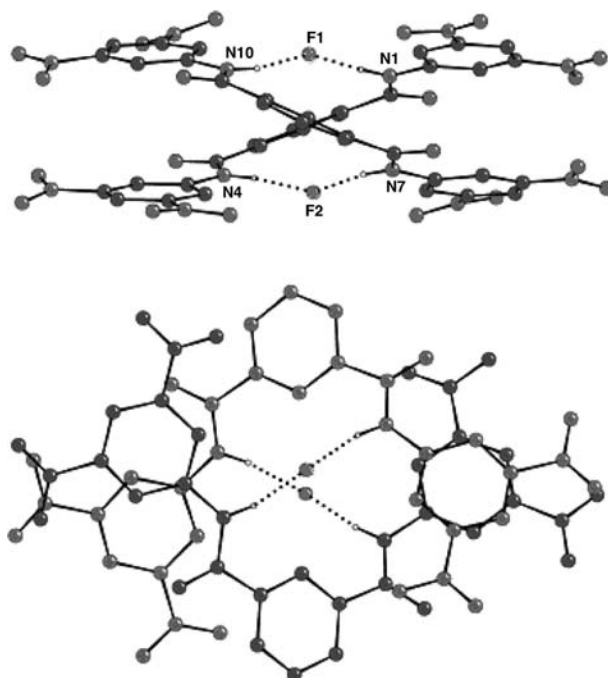


**Fig. 18** Crystal structure of Gale's fluoride templated helix. Top: Side view. Bottom: Top view showing  $\pi$ -stacking interactions. TBA salts and some hydrogens omitted. *Source:* From Ref.<sup>[66]</sup>. The Royal Society of Chemistry.



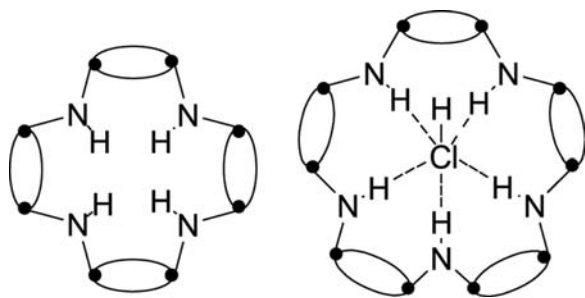


Fig. 19 Wright's tetrameric macrocycle (left) and chloride anion-templated macrocycle (right).

deprotonated anions forming interlocked chains of anions via  $\text{NH} \dots \text{N}^-$  hydrogen bonding (Fig. 17).<sup>[65]</sup>

Coles et al.<sup>[66]</sup> have also extended their self-assembly interests to the use of isophthalamide clefts in the formation of a double helix. This is the first reported use of neutral ligands forming anion-templated helicates. A ligand is designed featuring an anion binding amide cleft and electron-withdrawing groups to enhance ligand–anion interactions. A crystal structure of the ligand in the presence of fluoride anions was obtained and shows the double helix structure formed around two fluoride anions, again via  $\text{N-H} \dots \text{F}$  hydrogen bonds (Fig. 18). Further stabilization is provided by  $\pi$ – $\pi$  interactions between terminal nitroaromatic groups.

Bashall et al.<sup>[67]</sup> have recently reported the synthesis of a series of macrocycles containing  $\{[\text{P}(\mu\text{-N}^t\text{Bu})_2](\mu\text{-NH})\}_n$  frameworks. A tetrameric macrocycle is formed on the reaction of  $[\text{ClP}(\mu\text{-N}^t\text{Bu})_2]$  with  $[\text{NH}_2\text{P}(\mu\text{-N}^t\text{Bu})_2]$  in the presence of a base (THF/Net<sub>3</sub>). However, addition of an excess of LiCl results in the formation of a pentameric macrocycle  $\{[\text{P}(\mu\text{-N}^t\text{Bu})_2](\mu\text{-NH})\}_5(\text{HCl})$ , with the ratio of tetrameric to pentameric being influenced strongly by excess chloride (Fig. 19).

Structural characterization of the pentamer indicates that the chloride anion is positioned at the center of the macrocycle and is hydrogen-bonded to the five NH groups of the ring.

## CONCLUSION

This review is intended to provide a general discussion of the emerging field of anion-templated self-assembly in organic systems. It can be seen that the range of organic compounds self-assembled by anion templates is highly diverse. Rational design has been employed from the start, and the field has rapidly developed to the stage at which topologically complex structures, such rotaxanes, are being prepared.

As with self-assembly as a whole, the range of complex molecules prepared by self-assembly techniques,

which would otherwise be practically impossible using covalent synthesis, is becoming increasingly diverse. A bright future for anion-templated self-assembly seems highly likely, with the above results illustrating the rapid progress made in such a short time span. There is no doubt that even on a short-term basis, many more impressive results will be seen within the literature and it remains the authors' view that anions will have a key role to play in the future of self-assembly.

## REFERENCES

1. Menger, F.M. Supramolecular chemistry and self-assembly. *PNAS* **2002**, *99* (8), 4818–4822.
2. Greig, L.M.; Philp, D. Applying biological principles to the assembly and selection of synthetic superstructures. *Chem. Rev.* **2001**, *30*, 287–302.
3. Lindoy, L.F.; Atkinson, I.M. *Self-Assembly in Supramolecular Systems*; RSC: Cambridge, UK, 2000.
4. Wu, A.; Isaacs, L. Self-sorting: The exception or the rule. *J. Am. Chem. Soc.* **2003**, *125* (16), 4831–4835.
5. Davis, A.V.; Yeh, R.M.; Raymond, K.N. Supramolecular assembly dynamics. *PNAS* **2002**, *99* (8), 4793–4796.
6. Furlan, R.L.E.; Otto, S.; Sanders, J.K.M. Supramolecular templating in thermodynamically controlled synthesis. *PNAS* **2002**, *99* (8), 4801–4804.
7. Raymo, F.M., Stoddart, J.F., Eds.; *Templated Organic Synthesis*; Wiley: Weinheim, Germany, 2000.
8. Steed, J.W.; Atwood, J.L. *Supramolecular Chemistry*; Wiley, 2000.
9. Krische, M.J.; Lehn, J.-M. The utilization of persistent H-bonding motifs in the self-assembly of supramolecular architectures. *Struct. Bond.* **2000**, *96*, 3–29.
10. Brancato, G.; Coutrot, F.; Leigh, D.A.; Murphy, A.; Wong, J.K.Y.; Zerbetto, F. From reactants of products via simple hydrogen-bonding networks: Information transmission in chemical reactions. *PNAS* **2002**, *99* (8), 4967–4971.
11. Cooke, G.; Rotello, V.M. Methods of modulating hydrogen bonded interactions in synthetic host–guest systems. *Chem. Soc. Rev.* **2002**, *31*, 272–286.
12. Seidel, S.R.; Stang, P.J. High symmetry coordination cages via self-assembly. *Acc. Chem. Res.* **2002**, *35* (11), 972–983.
13. Johnson, D.W.; Raymond, K.N. The role of guest molecules in the self-assembly of metal–ligand clusters. *Supramol. Chem.* **2001**, *13* (6), 639–659.
14. Sun, W.-Y.; Yoshizawa, M.; Kusukawa, T.; Fujita, M. Multicomponent metal–ligand self-assembly. *Curr. Opin. Chem. Biol.* **2002**, *6* (6), 757–764.
15. Childs, L.J.; Alcock, N.W.; Hannon, M.J. Assembly of a nanoscale chiral ball through supramolecular aggregation of bowl-shaped triangular helicates. *Angew. Chem., Int. Ed. Engl.* **2002**, *41* (22), 4244–4247.
16. Stoddart, J.F.; Tseng, H.R. Chemical synthesis gets a fillip from molecular recognition and self-assembly processes. *PNAS* **2002**, *99* (8), 4797–4800.
17. Gillard, R.R.; Raymo, F.M.; Stoddart, J.F. Controlling self-assembly. *Chem. Eur. J.* **1997**, *3* (12), 1933–1940.

18. Try, A.C.; Harding, M.M.; Hamilton, D.G.; Sanders, J.K.M. Reversible five-component assembly of a [2]catenane from a chiral metallocycle and a dinaphtho-crown ether. *Chem. Commun.* **1998**, 723–724.
19. Beer, P.D.; Gale, P.A. Anion recognition and sensing: The state of the art and future perspectives. *Angew. Chem., Int. Ed. Engl.* **2001**, *40* (3), 486–516.
20. Beer, P.D.; Cadman, J. Electrochemical and optical sensing of anions by transition metal based receptors. *Coord. Chem. Rev.* **2000**, *205*, 131–155.
21. Berger, M.; Schmidtchen, F.P. Artificial organic host molecules for anions. *Chem. Rev.* **1997**, *97* (5), 1609–1646.
22. Bianchi, A.; Bowman-James, K.; Garcia-España, E., Eds.; *Supramolecular Chemistry of Anions*; Wiley-VCH: New York, 1997.
23. Vilar, R. Anion-templated synthesis. *Angew. Chem., Int. Ed. Engl.* **2003**, *42* (13), 1460–1477.
24. Geib, S.J.; Hirst, S.C.; Vicent, C.; Hamilton, A.D. Molecular recognition and the design of solid state structures: Protonation-induced conformational change and self-assembly of 2,6-diamidopyridinium phosphates. *J. Chem. Soc., Chem. Commun.* **1991**, 1283–1285.
25. Sánchez-Quesada, J.; Seel, C.; Prados, P.; de Mendoza, J. Anion helicates: Double strand helical self-assembly of chiral bicyclic guanidinium dimers and tetramers around sulfate templates. *J. Am. Chem. Soc.* **1996**, *118* (1), 277–278.
26. Sessler, J.L.; Andrievsky, A.; Gale, P.A.; Lynch, V. Anion-binding: Self-assembly of polypyrrolic macrocycles. *Angew. Chem., Int. Ed. Engl.* **1996**, *35* (23/24), 2782–2785.
27. Sessler, J.L.; Mody, T.D.; Lynch, V. Synthesis and X-ray characterization of a uranyl(VI) Schiff base complex derived from a 2:2 condensation product of 3,4-diethylpyrrole-2,5-dicarbaldehyde and 1,2-diamino-4,5-dimethoxybenzene. *Inorg. Chem.* **1992**, *31* (4), 529–531.
28. Kim, Y.H.; Calabrese, J.; McEwen, C.  $\text{CaCl}_3^-$  or  $\text{Ca}_2\text{Cl}_4^{4-}$  complexing cyclic aromatic amide. template effect on cyclization. *J. Am. Chem. Soc.* **1996**, *118* (6), 1545–1546.
29. Alcalde, E.; Ramos, S.; Pérez-García, L. Anion template-directed synthesis of dicationic [4]imidazoliophanes. *Org. Lett.* **1999**, *1* (7), 1035–1038.
30. Alcalde, E.; Alvarez-Rúa, C.; García-Granda, S.; García-Rodríguez, E.; Mequida, N.; Pérez-García, L. Hydrogen bonded driven anion binding by dicationic [4]imidazoliophanes. *Chem. Commun.* **1999**, 295–296.
31. Sauvage, J.-P.; Dietrich-Buchecker, C., Eds.; *Molecular Catenanes, Rotaxanes and Knots*; Wiley-VCH: Weinheim, Germany, 1999.
32. Panova, I.G.; Topchieva, I.N. Rotaxanes and polyrotaxanes. Their synthesis and the supramolecular devices based on them. *Russ. Chem. Rev.* **2001**, *70* (1), 23–44.
33. Sauvage, J.-P. Transition metal-containing rotaxanes and catenanes in motion: Toward molecular machines and motors. *Acc. Chem. Res.* **1998**, *31* (10), 611–619.
34. Raymo, F.M.; Stoddart, J.F. Interlocked macromolecules. *Chem. Rev.* **1999**, *99* (7), 1643–1663.
35. Hubin, T.J.; Busch, D.H. Template routes to interlocked molecular structures and orderly molecular entanglements. *Coord. Chem. Rev.* **2000**, *200–202*, 5–52.
36. Blanco, M.-J.; Jiménez, M.C.; Chambron, J.-C.; Heitz, V.; Linke, M.; Sauvage, J.-P. Rotaxanes as new architectures for photoinduced electron transfer and molecular motions. *Chem. Soc. Rev.* **1999**, *28*, 293–305.
37. Balzani, V.; Credi, A.; Raymo, F.M.; Stoddart, J.F. Artificial molecular machines. *Angew. Chem., Int. Ed. Engl.* **2000**, *39*, 3348–3391.
38. Gatti, F.G.; Leigh, D.A.; Nepogodiev, S.A.; Slawin, A.M.; Teat, S.J.; Wong, J.K. Stiff and sticky in the right places: The dramatic influence of preorganising guest binding sites on the hydrogen bond-directed assembly of rotaxanes. *J. Am. Chem. Soc.* **2001**, *123* (25), 5983–5989.
39. Hunter, C.A.; Low, C.M.R.; Packer, M.J.; Spey, S.E.; Vinter, J.G.; Vysotsky, M.O.; Zonta, C. Noncovalent assembly of [2]-rotaxane architectures. *Angew. Chem., Int. Ed. Engl.* **2001**, *40* (14), 2678–2682.
40. Hambron, J.C.; Heitz, V.; Sauvage, J.P. A rotaxane with two rigidly held porphyrins as stoppers. *Chem. Commun.* **1992**, *16*, 1131–1133.
41. Jeppesen, J.O.; Perkins, J.; Becher, J.; Stoddart, J.F. *Org. Lett.* **2000**, *2* (23), 3547–3550.
42. Loeb, S.J.; Wisner, J.A. 1,2-Bis(4,4'-dipyridinium) ethane: A versatile dication for the formation of [2]rotaxanes with dibenzo-24-crown-8 ether. *Chem. Commun.* **1998**, *24*, 2757–2758.
43. Fyfe, M.C.T.; Glink, P.T.; Menzer, S.; Stoddart, J.F.; White, A.J.P.; Williams, D.J. Anion-assisted self-assembly. *Angew. Chem., Int. Ed. Engl.* **1997**, *36* (19), 2068–2070.
44. Montalti, M.; Prodi, L. A supramolecular assembly controlled by anions: Threading and unthreading of a pseudorotaxane. *Chem. Commun.* **1998**, 1461–1462.
45. Ashton, P.R.; Chrystal, E.J.T.; Glink, P.T.; Menzer, S.; Schia'vo, C.; Spencer, N.; Stoddart, J.F.; Tasker, P.A.; White, A.J.P.; Williams, D.J. Pseudorotaxanes formed between secondary dialkylammonium salts and crown ethers. *Chem. Eur. J.* **1996**, *2* (6), 709–728.
46. Ashton, P.R.; Glink, P.T.; Stoddart, J.F.; Tasker, P.A.; White, A.J.P.; Williams, D.J. Self-assembling [2]- and [3]rotaxanes from secondary dialkylammonium salts and crown ethers. *Chem. Eur. J.* **1996**, *2* (6), 729–736.
47. Hübner, G.M.; Gläser, J.; Seel, C.; Vögtle, F. High-yielding rotaxane synthesis with an anion template. *Angew. Chem., Int. Ed. Engl.* **1999**, *38* (3), 383–386.
48. Seel, C.; Vögtle, F. Templates, “wheeled reagents,” and a new route to rotaxanes by anion complexation: The trapping method. *Chem. Eur. J.* **2000**, *6* (1), 21–24.
49. Reuter, C.; Wienand, W.; Hübner, G.M.; Seel, C.; Vögtle, F. High-yield synthesis of ester, carbonate and acetal rotaxanes by anion template assistance and their hydrolytic dethreading. *Chem. Eur. J.* **1999**, *5* (9), 2692–2697.
50. Shukla, R.; Deetz, M.J.; Smith, B.D. [2]Rotaxane with a cation-binding wheel. *Chem. Commun.* **1999**, 2397–2398.
51. Deetz, M.J.; Shang, M.; Smith, B.D. A macrobicyclic receptor with versatile recognition properties: Simultaneous binding of an ion pair and selective complexation of dimethylsulfoxide. *J. Am. Chem. Soc.* **2000**, *122* (26), 2397–2398.

52. Mahoney, J.M.; Shukla, R.; Marshall, A.; Beatty, A.M.; Zajicek, J.; Smith, B.D. Templated conversion of a crown ether-containing macrobicycle into [2]rotaxanes. *J. Org. Chem.* **2002**, *67* (5), 1436–1440.
53. Deetz, M.J.; Shukla, R.; Smith, B.D. Recognition-directed assembly of salt-binding [2]rotaxanes. *Tetrahedron* **2002**, *58*, 799–805.
54. Schalley, C.A.; Silva, G.; Nising, C.F.; Linnartz, P. Analysis and improvement of an anion-templated rotaxane synthesis. *Helv. Chim. Acta* **2002**, *85*, 1578–1596.
55. Ghosh, P.; Mermagen, O.; Schalley, C.A. Novel template effect for the preparation of [2]rotaxanes with functionalised centre pieces. *Chem. Commun.* **2002**, 2628–2629.
56. Li, X.; Illigen, J.; Nieger, M.; Michel, S.; Schalley, C.A. Tetra- and octalactam macrocycles and catenanes with exocyclic metal coordination sites: Versatile building blocks for supramolecular chemistry. *Chem. Eur. J.* **2003**, *9* (6), 1332–1347.
57. Kavallieratos, K.; Bertao, C.M.; Crabtree, R.H. Hydrogen bonding in anion recognition: A family of versatile, nonpreorganized neutral and acyclic receptors. *J. Org. Chem.* **1999**, *64* (5), 1675–1683.
58. Kavallieratos, K.; de Gala, S.R.; Austin, D.J.; Crabtree, R.H. Readily available non-preorganized neutral acyclic halide receptor with an unusual nonplanar binding conformation. *J. Am. Chem. Soc.* **1997**, *119* (9), 2325–2326.
59. Wisner, J.A.; Beer, P.D.; Drew, M.G.B. A demonstration of anion templation and selectivity in pseudorotaxane formation. *Angew. Chem., Int. Ed. Engl.* **2001**, *40* (19), 3606–3609.
60. Wisner, J.A.; Beer, P.D.; Berry, N.G.; Tomapatanaget, B. Anion recognition as a method for templating pseudorotaxane formation. *PNAS* **2002**, *99* (8), 4983–4986.
61. Wisner, J.A.; Beer, P.D.; Drew, M.G.B.; Sambrook, M.R. Anion-templated rotaxane formation. *J. Am. Chem. Soc.* **2002**, *124* (42), 12469–12476.
62. Keegan, J.; Kruger, P.E.; Nieuwenhuyzen, M.; O'Brien, J.; Martin, N. Anion directed assembly of a dinuclear double helicates. *Chem. Commun.* **2001**, 2192–2193.
63. Král, V.; Schmidtchen, F.P.; Lang, K.; Berger, M. Anion-controlled assembly of porphyrin–bicyclic guanidine conjugates. *Org. Lett.* **2002**, *4* (1), 51–54.
64. Camiolo, S.; Gale, P.A.; Hursthouse, M.B.; Light, M.E.; Shi, A.J. Solution and solid-state studies of 3,4-dichloro-2,5-diamidopyrroles: Formation of an unusual anionic narcissistic dimer. *Chem. Commun.* **2002**, 758–759.
65. Gale, P.A.; Navakhun, K.; Camiolo, S.; Light, M.E.; Hursthouse, M.B. Anion–anion assembly: A new class of anionic supramolecular polymer containing 3,4-dichloro-2,5-diamido-substituted pyrrole anion dimers. *J. Am. Chem. Soc.* **2002**, *124* (38), 11228–11229.
66. Coles, S.J.; Frey, J.G.; Gale, P.A.; Hursthouse, M.B.; Light, M.E.; Navakhun, K.; Thomas, G.L. Anion-directed assembly: The first fluoride-directed double helix. *Chem. Commun.* **2003**, 568–569.
67. Bashall, A.; Bond, A.D.; Doyle, E.L.; García, F.; Kidd, S.; Lawson, G.T.; Parry, M.C.; McPartlin, M.; Woods, A.D.; Wright, D.S. Templating and selection in the formation of macrocycles containing  $\{[P(\mu-N^tBu)_2]\{\mu-NH\}_n\}$  frameworks: Observation of halide ion coordination. *Chem. Eur. J.* **2002**, *8* (15), 3377–3385.

# Anodization Patterned on Aluminum Surfaces

Juchao Yan

*Department of Physical Sciences, Eastern New Mexico University,  
Portales, New Mexico, U.S.A.*

G. V. Rama Rao

Plamen B. Atanasov

Gabriel P. López

*Chemical and Nuclear Engineering, University of New Mexico,  
Albuquerque, New Mexico, U.S.A.*

## INTRODUCTION

Novel nanofabrication techniques are being explored as alternatives to conventional lithographic techniques to mass produce structures with feature sizes smaller than 100 nm and to minimize costs.<sup>[1]</sup> Porous anodic aluminum oxide (AAO) is a self-ordered, hexagonal array of straight cylindrical pores with high densities ( $10^8$ – $10^{11}$  pores/cm<sup>2</sup>), tunable diameters (5–250 nm), and depths (a few nanometers to hundreds of micrometers).<sup>[2–5]</sup> It can be fabricated through electrochemical anodization of aluminum at moderate and constant temperatures of 0–10°C in aqueous acidic electrolytes.<sup>[6–8]</sup> Anodic aluminum oxide is optically transparent in the fingerprint UV/vis and IR regions<sup>[9]</sup> and thermally stable up to 1000°C.<sup>[10]</sup> Moreover, it has recently been demonstrated to have unique advantages in several technological applications, including nanotemplating,<sup>[3,4]</sup> membrane transport,<sup>[11]</sup> and photonic crystals.<sup>[12]</sup> Through-hole AAO membranes have been used as evaporation masks to fabricate nanodot arrays<sup>[13,14]</sup> and as etching masks to transfer patterns into several substrates including diamond,<sup>[15]</sup> silicon,<sup>[16,17]</sup> and other semiconductors.<sup>[18]</sup>

The high fragility of through-hole AAO membranes<sup>[19]</sup> limits their integration into established microfabrication processes where robust membranes are needed. Although an elastic polypropylene support ring that runs around the circumference of AAO membrane permits one to pick up the membrane with membrane tweezers without shattering the membrane,<sup>[20]</sup> this approach fails when the membrane undergoes a high-temperature and/or an ultrahigh vacuum. To provide additional supports to fragile AAO, one could pattern aluminum surfaces with an anodization barrier prior to anodization. During anodization of the patterned surfaces, the anodization barrier prevents

anodization in the patterned areas while the oxide grows in the unpatterned areas. Recently, Huang et al.<sup>[21]</sup> have reported the first anodization barrier of polymethylmethacrylate deposited on aluminum films. Because of the penetration of the electrolyte through this polymeric layer, the underlying surface was partially anodized to form AAO up to 10-nm deep. In addition, the procedure required optical lithography, polymer nanoprinting, ion-beam exposure, and milling. Because of its excellent adhesion to aluminum surfaces and electrical insulation as well as its inertness to acidic electrolytes,<sup>[22]</sup> a SiO<sub>2</sub> layer prepatterned on aluminum surfaces could provide a good anodization barrier. The patterning of aluminum surfaces with a SiO<sub>2</sub> layer can be achieved through a sol–gel coating or a dielectric evaporation.

This entry describes a patterned anodization of bulk aluminum sheets and evaporated aluminum films prepatterned with an anodization barrier of SiO<sub>2</sub> through a sol–gel process or a dielectric evaporation. Using a two-step anodization process,<sup>[6–8]</sup> we formed highly ordered, uniform, and straight nanopores of AAO in the unpatterned areas, and did not observe any pores in the patterned areas before and after SiO<sub>2</sub> was removed. This approach provides intermittent aluminum supports to fragile AAO membranes, allowing facile incorporation of AAO in a robust form into microdevices for microelectronics, microfluidics, and integrated optics.

## ANODIZATION CELL

In most of the reported anodization processes, the whole aluminum sheet has been exposed to the anodizing electrolyte to fabricate ordered AAO. This results in a complete conversion of an aluminum surface into

fragile AAO, and thus limits the integration of AAO into microfabrication technologies that require robust AAO at specifically defined sample areas. To address this issue, Li and Metzger<sup>[23]</sup> coated one side of aluminum sheet with an insulating layer. To further address this, we prepared a custom-built novel anodization cell and used it in our experiments (Fig. 1). This jacketed cell is specifically designed for general temperature-controlled electrochemical experiments where film and/or membrane electrodes are used, and is compatible with a commercially available cell stand (BAS Inc., Indiana). The samples to be anodized, aluminum sheets or vacuum-evaporated aluminum films on glass slides, serve as the anode. The anode is clamped down against a Teflon-coated rubber O-ring in the anodization cell. Another piece of aluminum sheet serves as the cathode. Alligator clips are used to connect the power supply to the electrodes.

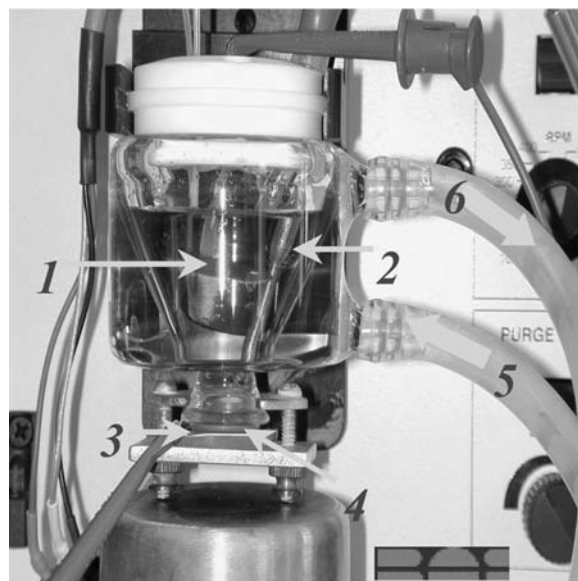


**Fig. 1** Custom-built anodization cell: (1) aluminum cathode; (2) thermocouple thermometer; (3) aluminum anode; (4) Teflon-coated O-ring; (5) water inlet; and (6) water outlet.

## PATTERNED ANODIZATION ON BULK ALUMINUM SHEETS

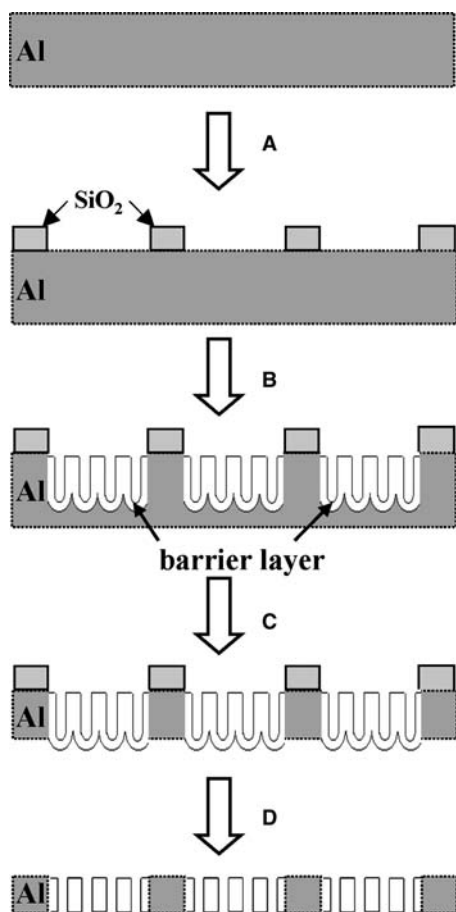
**Scheme 1** shows our procedure to fabricate freestanding and through-hole AAO membranes with intermittent aluminum supports on bulk aluminum sheets. Sol-gel coating<sup>a</sup> or dielectric evaporation forms the SiO<sub>2</sub>-patterned surfaces. The patterned surfaces were anodized using a two-step anodization process as previously described.<sup>[6–8]</sup> Briefly, the patterned surface was degreased in a 5 wt.% sodium hydroxide solution at 60°C for 30 sec, neutralized in a 50% (wt/wt) nitric acid solution for 5 sec, and then rinsed with deionized water. The pretreated surface was first anodized at a voltage of 40 V in a 0.3 M oxalic acid solution at 0°C for 20 min to eliminate large ridges and to texture the surface. The oxide was removed in a mixed solution of 0.2 M chromic acid and 0.4 M phosphoric acid at 60°C for 5 min. The surface was then anodized for 2 hr to create long-range ordering, with the newly formed oxide being removed again under the same conditions as used in the first anodization. Finally, the thus-treated surface was anodized again under the same conditions for 30 min to grow highly ordered pores. The postetching treatment of the resulting AAO consists of three steps: 1) removal of the remaining aluminum in a saturated mercury(II) chloride solution;

2) removal of the barrier layer at the bottom in a 5 wt.% phosphoric acid solution at 30°C; and 3) removal of the patterned SiO<sub>2</sub> on the top in a 5 wt.% sodium hydroxide solution at room temperature.

Aluminum sheets (99.999%, 0.25-mm thick) were purchased from Aldrich. Before use, they were cut into small pieces (20 × 20 mm). The SiO<sub>2</sub> sol used for patterning was prepared by adopting a two-step, acid-catalyzed sol-gel process. In a typical preparation, tetraethylorthosilicate (TEOS), ethanol, deionized water (18.2 MΩ cm) and dilute hydrochloric acid solution (HCl) were mixed in a molar ratio of 1:3.8:1:0.0005. The resulting solution was refluxed at 60°C for 90 min to provide the stock sol. Before use, 1 mL of stock sol was diluted with ethanol, followed by addition of water and dilute HCl solution, to provide a final overall molar ratio of TEOS/ethanol/water/HCl to be 1:22:5:0.0053. The SiO<sub>2</sub> sol was introduced into Marsmatic technical pens (0.13-mm tip, Staedtler) and was used to pattern the aluminum sheets.

**Fig. 2A** shows an illustrative scanning electron microscope (SEM) cross-sectional micrograph of AAO on a bulk aluminum sheet prepatterned with SiO<sub>2</sub> circular dots (ca. 1-mm diameter). Highly ordered, uniform, and straight pores are evident in the unpatterned areas. The average pore diameter, depth, and density are determined by SEM images to be 43 ± 7 nm, ~10 μm, and 1.7 × 10<sup>10</sup> pores/cm<sup>2</sup>, respectively. No pores appear in the areas beyond the O-ring, indicating no electrolyte leak from the inside to the outside of the O-ring. No pores are

<sup>a</sup>Although sol-gel processes have been widely used as one of the major template synthetic strategies to fabricate nanostructures (tubules, fibrils, and wires) of semiconductors and other inorganic materials in porous membranes including AAO,<sup>[24,25]</sup> there is no report on the application of sol-gel to obtain an anodization barrier on aluminum surfaces for patterned anodization. Advantages of sol-gel processes include simplicity of the procedure, stability of sol-gel films in acidic environments, and plausibility of composite coatings.



**Scheme 1** Schematic diagram for the micropatterning process of aluminum foils through a sol-gel resist. (A) Micropatterning of anodization barriers using various techniques including microwriting, screen printing, and chemical vapor deposition; (B) patterned anodization; (C) removal of the remaining aluminum in a saturated mercury(II) chloride solution; (D) removal of the barrier layer at the bottom in a 5 wt.% phosphoric acid solution and removal of the patterned SiO<sub>2</sub> on the top in a 5 wt.% sodium hydroxide solution.

observed in the patterned areas. Appearing visible as a thin overhang around the periphery of the AAO membrane, the patterned SiO<sub>2</sub> layer shows no cracking and/or peeling against the applied voltage and anodizing electrolytes. Shown in Fig. 2B, no pores are observed beneath the SiO<sub>2</sub> layer if it is removed using a 5 wt.% sodium hydroxide solution at room temperature for 5 min. The pores were also widened to be about 60 nm as a result of base etching. This demonstrates an excellent inhibition of the SiO<sub>2</sub> layer in preventing the electrolyte from penetrating into the SiO<sub>2</sub>/aluminum interface. The inhibition ability of the SiO<sub>2</sub> layer, together with the good adhesion to aluminum and the capability of undergoing long-time anodization, makes SiO<sub>2</sub> an ideal resist for patterned anodization of aluminum.

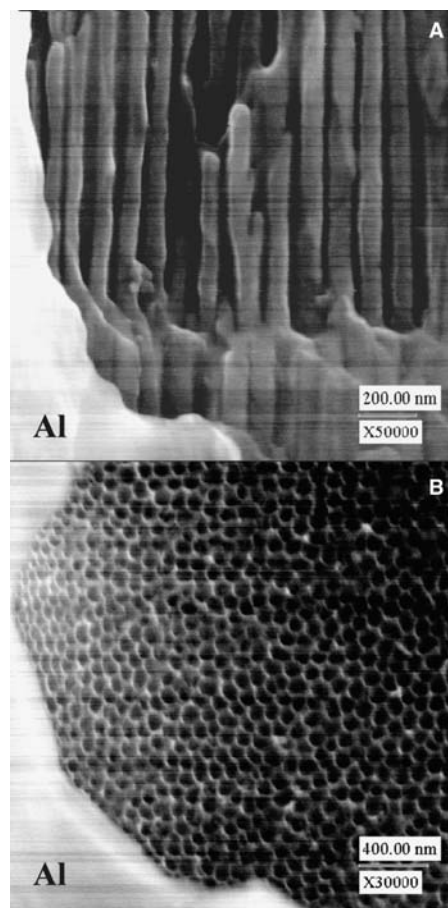


**Fig. 2** Scanning electron micrographs of ordered AAO on an aluminum sheet prepatterned with SiO<sub>2</sub> circular spots (ca. 1-mm diameter) through a sol-gel process: (A) cross-sectional view of the AAO/Al interface; (B) surface view of the AAO/Al interface. B was obtained by dissolving SiO<sub>2</sub> in a 5 wt.% sodium hydroxide solution.

After carefully removing the remaining aluminum, the bottom-barrier layer, and the patterned SiO<sub>2</sub> layer, a freestanding, highly ordered, through-pore AAO membrane with intermittent aluminum supports is obtained. In our control experiments, we anodized patterned aluminum sheets under the same conditions, except for the different anodization times in the final step (from 30 min up to 11 h). We then measured the membrane thickness by SEM for the resulting freestanding and through-hole AAO membranes. We found that the membrane thickness increased almost linearly with the anodization time in the final step up to 9 h, after which it increased slightly with the anodization time in the final step. For example, the membrane thicknesses are  $13.2 \pm 1.3$ ,  $23.6 \pm 0.4$ , and  $24.3 \pm 0.4 \mu\text{m}$  for a 5, 9, and 10 hr anodization in the final step, respectively, with the aspect ratio of the nanopores in the membranes being  $307 \pm 58$ ,  $549 \pm 90$ , and  $565 \pm 92$ , respectively. Because the



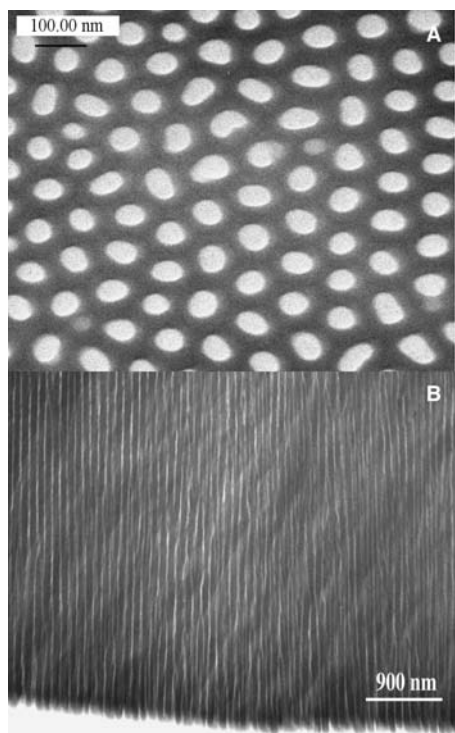


**Fig. 3** Transmission electron micrographs of surface (A) and cross section (B) of freestanding and through-hole AAO membranes.

pH value of the electrolyte mainly defines the nanopore diameter,<sup>[26]</sup> during the two-step anodization process in a given polyprotic acid, the nanopore diameter is held almost constant. One can control the anodization time in the final step to control the depth of the nanopores. This offers a unique advantage to tailor the aspect ratio of the nanopores. Huang et al.<sup>[21]</sup> found that sub-100-nm AAO pores with aspect ratios 1000:1 can easily be formed without elaborate processing.

Fig. 3 shows the transmission electron microscopic (TEM) surface (A) and cross section (B) of a cutout of the freestanding and through-hole AAO membranes. Highly ordered, uniform, and hexagonal pores are evident in Fig. 3A. The average pore diameter became larger than that shown in Fig. 2A. This is because of the pore widening from the phosphoric acid solution used to remove the bottom-barrier layer. Through-hole nanopores oriented normal to the aluminum surface are also clearly shown in Fig. 3B.

### ANODIZATION ON EVAPORATED ALUMINUM FILMS ON GLASS

Although irregular pore arrays of AAO were obtained through a single-step anodization process of bulk aluminum foils at the beginning of 1950s,<sup>[27]</sup> regular

pore arrays were not fabricated until 1995 when Masuda and Fukuda<sup>[6]</sup> demonstrated that a two-step anodization process can dramatically improve the periodicity of the pores. During the past several years, almost all reported works have been using bulk aluminum instead of thin aluminum films. This greatly limits the integration of AAO into potential technologies because of the inherent fragility of AAO membranes<sup>[19]</sup> and the practical need of many technologies to have materials in thin-film forms. Very few reports are available on anodization of vacuum-evaporated aluminum films,<sup>[13,17,21,28,29]</sup> in which single-step anodization processes with short anodization times (5–13 min) were used, resulting in a low ordering of pore arrangement. To improve the ordering of the pore arrangement, one should use the two-step anodization process with longer anodization times, as for bulk aluminum foils.<sup>[30]b</sup> To the best of our knowledge, there has been no report on the application of two-step anodization process to the evaporated aluminum films.

Thin aluminum films ( $\sim 2.2 \mu\text{m}$ ) were obtained by electron beam evaporation of 99.99% aluminum at a rate of 2.0 nm/sec in a vacuum of  $2 \times 10^{-7}$  Torr on microscopic glass slides (Baxter Scientific, M6145). The glass slides were cleaned in freshly prepared “piranha solution” (7:3 concentrated  $\text{H}_2\text{SO}_4$  and 30%  $\text{H}_2\text{O}_2$ ), thoroughly washed with water, and blown dry with nitrogen. The films were stored under vacuum in a drying chamber or were immediately used.

Prior to use, the aluminum film was degreased by sonicating in ethanol for 10 min, and blown dry under a stream of nitrogen. The two-step anodization process that was established for bulk aluminum<sup>[6–8]</sup> was used to anodize aluminum films. Typically, the film was first anodized at a voltage of 40 V in a 0.3 M oxalic acid solution at  $0^\circ\text{C}$  for 15 min to texture the surface. After removing the oxide in a mixed solution of 0.2 M chromic acid and 0.4 M phosphoric acid at  $60^\circ\text{C}$  for 5 min, the surface was anodized again for 15 min to create long-range ordering. The newly formed oxide was removed again under the same conditions as used in the first anodization. Finally, the thus-treated surface was anodized under the same conditions to grow highly ordered pores. The final anodization was stopped at a point when the anodizing current significantly dropped. At this point, all the aluminum is consumed. For a  $\sim 2\text{-}\mu\text{m}$ -thick film, the anodizing time in the final step is usually about 12 min.

Using the two-step anodization process, we repeatedly observed a circular disk of oxide (ca. 8-mm diameter) locating in the center of the area defined by the

<sup>b</sup>For bulk aluminum sheets, it is reported that longer anodization times lead to greater pore regularity through self-organization processes that occur during anodization.

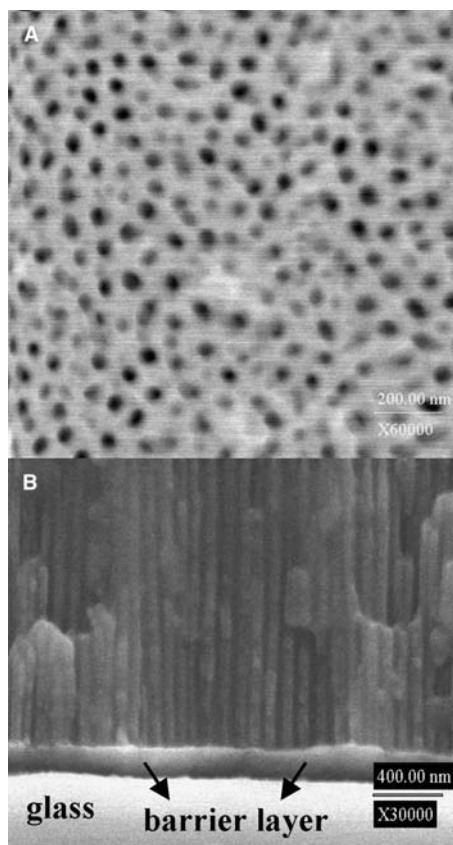


**Fig. 4** Scanning electron micrographs of surface (A) and cross section (B) obtained on vacuum-evaporated aluminum films on glass.

O-ring (12-mm diameter). No oxide was present beyond this disk. Huang et al.<sup>[21]</sup> observed similar delamination behavior. They attributed it to the stress generated as a result of volume expansion when aluminum is anodized to porous alumina. Depositing an adhesion layer between aluminum and glass substrates may eliminate delamination. Fig. 4A shows a scanning electron microscope (SEM) surface micrograph of AAO obtained on the central disk. Highly ordered, uniform, and straight pores can be seen. The average pore diameter, depth, and density are determined by SEM images to be  $60 \pm 8$  nm,  $\sim 3 \mu\text{m}$ , and  $1.3 \times 10^{10}$  pores/cm<sup>2</sup>, respectively. This membrane thickness results in a volume expansion of alumina to aluminum of about 1.3, which is in good agreement with the mechanical stress model<sup>[31,32]</sup> and the 10% porosity rule.<sup>[26]</sup> Fig. 4B shows the SEM cross-sectional micrograph. There is a thin oxide barrier layer on which parallel, straight-through pores are evident. There are voids of alumina below the barrier layer. Similar voids were previously observed for anodization of aluminum thin films on silicon,<sup>[13,17]</sup> with the formation being attributed to a localized temperature increase or electric-field-enhanced dissolution near

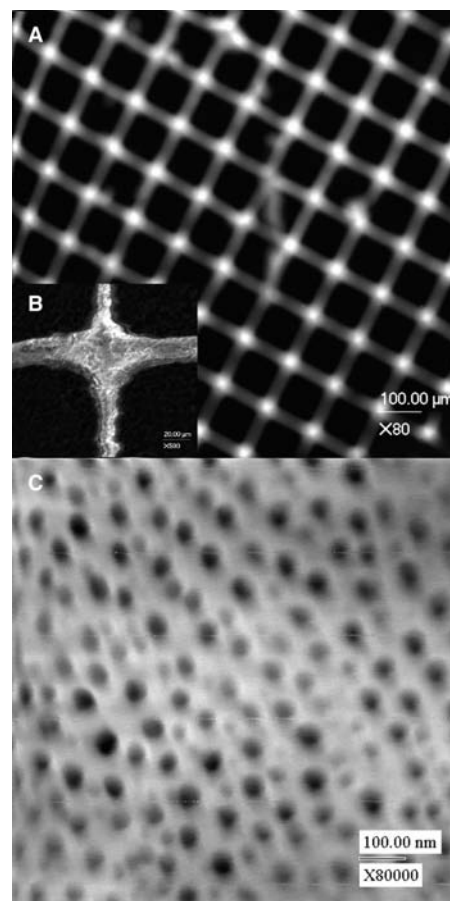


**Fig. 5** Scanning electron micrographs of the surface of ordered AAO on an evaporated aluminum film prepatterned with SiO<sub>2</sub> microgrids ( $75 \times 75 \mu\text{m}$ ): (A) low-magnification image; (B and C) high-magnification images.

the interface. Because of this unique structure, the bottom part of the oxide layer can be easily removed by postetching treatment with phosphoric acid solution. This allows for the alumina to be directly used as an etch mask for pattern transfer into other substrates.<sup>[17]</sup>

#### PATTERNED ANODIZATION ON EVAPORATED ALUMINUM FILMS

The SiO<sub>2</sub> pattern ( $\sim 4.0\text{-}\mu\text{m}$  thick)<sup>c</sup> was dielectrically deposited on the freshly evaporated aluminum films on glass at a rate of  $2 \text{ \AA}/\text{sec}$  by electron beam

<sup>c</sup>Control experiments demonstrated that a relatively thick layer of SiO<sub>2</sub> is required for complete inhibition of electrolyte from penetrating into the SiO<sub>2</sub>/aluminum interface. For example, when anodizing bulk aluminum sheets and evaporated aluminum films with a thickness of  $\sim 2 \mu\text{m}$  for the patterned SiO<sub>2</sub> layer, we have observed pore formation in the patterned areas although no cracking and/or peeling of SiO<sub>2</sub> is observed.

evaporation at a base pressure of  $1.5 \times 10^{-5}$  Torr, using a TEM copper grid ( $75 \times 75 \mu\text{m}$ ) as an evaporation mask. The thus-patterned surfaces were anodized using the two-step anodization process as for the evaporated aluminum films on glass.

Fig. 5 shows SEM surface micrographs of the patterned surface after anodization. Parts A and B correspond to low-magnification and high-magnification images, respectively. No pores appear in the patterned areas while highly ordered and uniform pores appear in the unpatterned areas, i.e., the borders of the  $\text{SiO}_2$  microgrids (Fig. 5C).

## CONCLUSION

In summary, we have developed an efficient, inexpensive procedure to fabricate highly ordered, through-hole nanoporous AAO with intermittent aluminum supports from patterns of controlled size and shape. The use of patterned  $\text{SiO}_2$  layer as anodization barriers in the patterned anodization provides the required structural robustness, electrical insulation, and excellent adhesion to aluminum surfaces, and constitutes the basis of a method for the direct assembly of novel nanodevices, especially for nanoelectronic manufacturing. Our ongoing investigation is centered on scaling down the patterned features to the micron and submicron dimensions, development of methods for use of micropatterned AAO in fluidic and electronic nanovias, and construction of heterostructural nanowires using patterned AAO as a template through chemical vapor deposition and/or pulsed electrodeposition.

## ACKNOWLEDGMENTS

We are grateful to the Army Research Office and the Ceramic and Composite Materials Center for financial support. We thank Mr. Marcos Barela and Dr. Huifang Xu for their assistance with the SEM and TEM measurements, and Dr. Michael J. O'Brien for his assistance with aluminum evaporation.

## REFERENCES

- Xia, Y.; Rogers, J.A.; Paul, K.; Whitesides, G.M. Unconventional methods for fabricating and patterning nanostructures. *Chem. Rev.* **1999**, *99*, 1823–1848.
- Despić, A.; Parkhutik, V.P. Electrochemistry of Aluminum in Aqueous Solutions and Physics of Its Anodic Oxide. In *Modern Aspects of Electrochemistry*; Bockris, J.O., White, R.E., Conway, B.E., Eds.; Plenum Press: New York, 1989; Vol. 20, 401–503.
- Martin, C.R. Membrane-based synthesis of nanomaterials. *Chem. Mater.* **1996**, *8*, 1739–1746.
- Huczko, A. Template-based synthesis of nanomaterials. *Appl. Phys., A* **2000**, *70*, 365–376.
- Schmid, G. Materials in nanoporous alumina. *J. Mater. Chem.* **2002**, *12*, 1231–1238.
- Masuda, H.; Fukuda, K. Ordered metal nanohole arrays made by a two-step replication of honeycomb structures of anodic alumina. *Science* **1995**, *268*, 1466–1468.
- Masuda, H.; Satoh, M. Fabrication of gold nanodot array using anodic porous alumina as an evaporation mask. *Jpn. J. Appl. Phys.* **1996**, *35*, L126–L129. Part 2.
- Li, F.Y.; Zhang, L.; Metzger, R.M. On the growth of highly ordered pores in anodized aluminum oxide. *Chem. Mater.* **1998**, *10*, 2470–2480.
- Sawitowski, T.; Miquel, Y.; Heilmann, A.R.; Schmid, G. Optical properties of quasi one-dimensional chains of gold nanoparticles. *Adv. Funct. Mater.* **2001**, *11* (6), 435–440.
- Braunstein, P.; Kormann, H.-P.; Meyer-Zaika, W.; Pugin, R.; Schmid, G. Strategies for the anchoring of metal complexes, clusters, and colloids inside nanoporous alumina membranes. *Chem. Eur. J.* **2000**, *6* (24), 4637–4646.
- Martin, C.R.; Nishizawa, M.; Jirage, K.; Kang, M.; Lee, S.B. Controlling ion-transport selectivity in gold nanotubule membranes. *Adv. Mater.* **2001**, *13* (18), 1351–1362.
- Nakao, M.; Oku, S.; Tanaka, H.; Shibata, Y.; Yokoo, A.; Tamamura, T.; Masuda, H. Fabrication of GaAs hole array as a 2D-photon crystal and their application to photonic bandgap waveguide. *Opt. Quantum Electron.* **2002**, *34*, 183–193.
- Masuda, H.; Yasui, K.; Sakamoto, Y.; Nakao, M.; Tamamura, T.; Nishio, K. Ideally ordered anodic porous alumina mask prepared by imprinting of vacuum-evaporated Al on Si. *Jpn. J. Appl. Phys.* **2001**, *40*, L1267–L1269. Part 2.
- Kouklin, N.; Menon, L.; Bandyopadhyay, S. Room-temperature single-electron charging in electrochemically synthesized semiconductor quantum dot and wire array. *Appl. Phys. Lett.* **2002**, *80* (9), 1649–1651.
- Masuda, H.; Yasui, K.; Watanabe, M.; Nishio, K.; Nakao, M.; Tamamura, T.; Rao, T.N.; Fujishima, A. Fabrication of through-hole diamond membranes by plasma etching using anodic porous alumina mask. *Electrochem. Solid-State Lett.* **2001**, *4* (11), G101–G103.
- Kanamori, Y.; Hane, K.; Sai, H.; Yugami, H. 100 nm period silicon antireflection structures fabricated using a porous alumina membrane mask. *Appl. Phys. Lett.* **2001**, *78* (2), 142–143.
- Crouse, D.; Lo, Y.-H.; Miller, A.E.; Crouse, M. Self-ordered pore structure of anodized aluminum on silicon and pattern transfer. *Appl. Phys. Lett.* **2000**, *76* (1), 49–51.
- Liang, J.Y.; Chik, H.; Yin, A.J.; Xu, J. Two-dimensional lateral superlattices of nanostructures: Nonlithographic formation by anodic membrane template. *J. Appl. Phys.* **2002**, *91* (4), 2544–2546.
- Li, Y.; Holland, E.R.; Wilshaw, P.R. Synthesis of high density arrays of nanoscaled gridded field emitters based

- on anodic alumina. *J. Vac. Sci. Technol.*, B **2000**, *18* (2), 994–996.
20. [http://www.2spi.com/catalog/spec\\_prep/supp-ring.html](http://www.2spi.com/catalog/spec_prep/supp-ring.html).
  21. Huang, Q.Y.; Lye, W.-K.; Longo, D.M.; Reed, M.L. Submicron patterned anodic oxidation of aluminum thin films. *Mater. Res. Soc. Symp. Proc.* **2001**, *636*, D9.49.
  22. [http://www.ri.cmu.edu/pubs/pub\\_3590.html](http://www.ri.cmu.edu/pubs/pub_3590.html).
  23. Li, F.Y.; Metzger, R.M. Activation volume of  $\alpha$ -Fe particles in alumite films. *J. Appl. Phys.* **1997**, *81* (8), 3806–3808.
  24. Lakshmi, B.B.; Patrissi, C.J.; Martin, C.R. Sol-gel template synthesis of semiconductor oxide micro- and nanostructures. *Chem. Mater.* **1997**, *9*, 2544–2550.
  25. Chu, S.Z.; Wade, K.; Inoue, S.; Todoroki, S. Synthesis and characterization of titania nanostructures on glass by AI anodization and sol-gel process. *Chem. Mater.* **2002**, *12*, 266–272.
  26. Niles, K.; Choi, J.; Schwarz, K.; Wehrspohn, R.B.; Gösele, U. Self-ordering regimes of porous alumina: The 10% porosity rule. *Nano Lett.* **2002**, *2* (7), 677–680.
  27. Keller, F.; Hunter, M.S.; Robinson, D.L. Structural features of oxide coatings on aluminum. *J. Electrochem. Soc.* **1953**, *100*, 411–419.
  28. Behnke, J.F.; Sands, T. Bimodal spatial distribution of pores in anodically oxidized aluminum thin films. *J. Appl. Phys.* **2000**, *88* (11), 6875–6880.
  29. Chu, S.-Z.; Wada, S.; Inoue, S.; Todoroki, S. Formation of microstructures of anodic alumina films from aluminum sputtered on glass substrate. *J. Electrochem. Soc.* **2002**, *149* (7), B321–B327.
  30. Almawlawi, D.; Bosnick, K.A.; Osika, A.; Moskovits, M. Fabrication of nanometer-scale patterns by ion-milling with porous anodic alumina masks. *Adv. Mater.* **2000**, *12*, 1252–1257.
  31. Jessensky, O.; Müller, F.; Gösele, U. Self-organized formation of hexagonal pore arrays in anodic alumina. *Appl. Phys. Lett.* **1998**, *72* (10), 1173–1175.
  32. Li, A.-P.; Müller, F.; Birner, A.; Nielsch, K.; Gösele, U. Hexagonally pore arrays with a 50–420 nm interpore distance formed by self-organization in anodic alumina. *J. Appl. Phys.* **1998**, *84* (11), 6023–6026.

# Antidot Lattices: Chaotic Transport

Tsuneya Ando

Department of Physics, Tokyo Institute of Technology, Tokyo, Japan

## INTRODUCTION

Advances in microfabrication and crystal growth technology have enabled the preparation of lateral superlattices with submicron structures on top of a two-dimensional (2-D) electron system with mean free path as large as 100  $\mu\text{m}$ . The 2-D system modulated by a periodic strong repulsive potential is called antidot lattice. The transport in this system is ballistic (i.e., electrons are scattered from the antidot potential itself rather than from impurities). The purpose of this entry is to give a brief review on chaotic transport in antidot lattices in the presence of magnetic fields mainly from a theoretical point of view.

Various interesting phenomena have been observed in antidot lattices in magnetic fields: quenching of the Hall effect,<sup>[1,2]</sup> Altshuler–Aronov–Spivak oscillation near vanishing fields,<sup>[3–6]</sup> the so-called commensurability peaks in magnetoresistance,<sup>[1,7–16]</sup> and fine oscillations around them.<sup>[17,18]</sup>

Antidot lattices are introduced in “Antidot Lattices.” In “Commensurability Peaks,” the origin of commensurability peaks is discussed with emphasis on the roles of classical chaotic motion. In “Aharonov–Bohm-Type Oscillation,” the Aharonov–Bohm-type oscillation superimposed on the commensurability peak is analyzed based on semiclassical quantization of periodic orbits existing in the chaotic sea. Triangular lattices are discussed in “Triangular Antidot Lattices” with emphasis on differences from square lattices. In “Altshuler–Aronov–Spivak Oscillation,” a kind of the Altshuler–Aronov–Spivak oscillation appearing in weak magnetic fields is discussed in relation to the roles of inherent disorder in the antidot potential arising during the fabrication process. A new method based on a scattering matrix to calculate electronic states and transport properties is introduced in “Scattering Matrix Formalism,” together with some examples of the results obtained. A summary and conclusions are given in “Conclusion.”

## ANTIDOT LATTICES

Fig. 1 shows an illustration of the potential of a square antidot lattice. It is characterized by the period  $a$  and

the diameter  $d$  of the antidot. We have typically  $d \gtrsim 1000 \text{ \AA}$ , larger than the Fermi wavelength of the 2-D electron system ( $\lambda_F \sim 500 \text{ \AA}$ ) for a typical electron concentration less than  $5 \times 10^{11} \text{ cm}^{-2}$  in a GaAs/AlGaAs heterostructure. Correspondingly, the period of the antidot is usually  $a \geq 2000 \text{ \AA}$ . This means that the system is in the boundary between the quantum regime and the classical regime. In classical mechanics, electron motion is fully chaotic and, in fact, the antidot lattice is a kind of a Sinai billiard, which is a typical system where chaotic motion has been intensively studied.

The model antidot potential used often for a square antidot is given by:

$$U(\mathbf{r}) = U_0 \left| \cos\left(\frac{\pi x}{a}\right) \cos\left(\frac{\pi y}{a}\right) \right|^{2\beta} \quad (1)$$

where  $U_0$  is the potential maximum and the parameter  $\beta$  characterizes its steepness. The antidot diameter can be defined as  $d/2 = |\mathbf{r}|$ , with  $U(\mathbf{r}) = E_F$ , where  $E_F$  is the Fermi energy and  $\mathbf{r}$  is chosen in the direction of a nearest neighbor. In a triangular lattice, the corresponding potential is given by:

$$U(\mathbf{r}) = U_0 \left| \cos\left(\frac{\pi \mathbf{a}_1 \cdot \mathbf{r}}{a^2}\right) \cos\left(\frac{\pi \mathbf{a}_2 \cdot \mathbf{r}}{a^2}\right) \times \cos\left(\frac{\pi(\mathbf{a}_1 - \mathbf{a}_2) \cdot \mathbf{r}}{a^2}\right) \right|^{4\beta/3} \quad (2)$$

with  $\mathbf{a}_1 = (\sqrt{3}a/2, a/2)$  and  $\mathbf{a}_2 = (0, a)$ .

Sometimes, we use the following model potential:

$$U(\mathbf{r}) = E_F \left( \frac{d/2 + \Delta - r}{\Delta} \right)^2 \theta(d/2 + \Delta - r) \quad (3)$$

where  $r$  is the distance from the center of an antidot,  $\Delta$  is the parameter characterizing the steepness of the potential, and  $\theta(t)$  is the step function defined by  $\theta(t) = 1$  for  $t > 0$  and 0 for  $t < 0$ .

A self-consistent calculation in quantum wires at GaAs/AlGaAs heterostructures<sup>[19,20]</sup> suggests that the potential is nearly parabolic for a wire with small width, and consists of a flat central region and a parabolic increase near the edge for a wider wire. The width



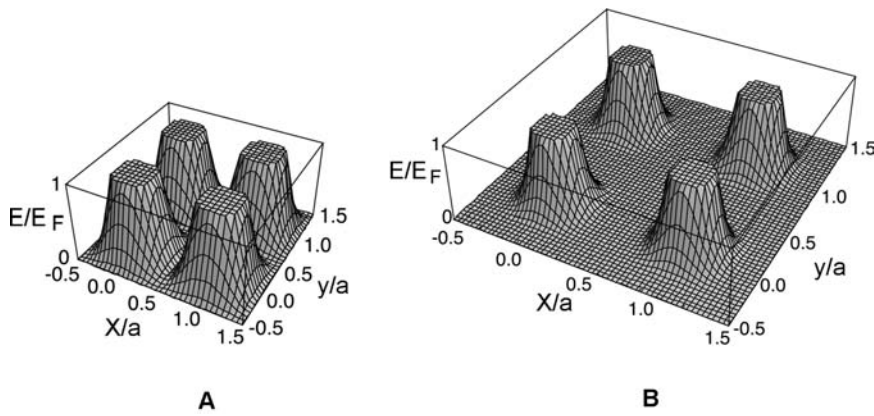


**Fig. 1** A model antidot potential in a square lattice. (A)  $d/a = 0.5$  and  $\beta = 1$ . (B)  $d/a = 0.3$  and  $\beta = 4$ . The potential is cut off at the Fermi energy.

$\Delta$  of the region where the potential increases from the bottom to the Fermi energy is of the same order as the Fermi wavelength  $\lambda_F$  for typical electron concentrations. This leads to roughly  $\beta \sim 1$  for  $d/a \sim 0.5$ ,  $\beta \sim 2$  for  $d/a \sim 0.4$ , and  $\beta \sim 4$  for  $d/a \sim 0.3$  in the case  $d \sim 1000 \text{ \AA}$ .

**COMMENSURABILITY PEAKS**

Fig. 2 shows an example of observed diagonal and Hall resistivity in a square antidot lattice.<sup>[1]</sup> Two prominent peaks appear in the diagonal resistivity  $\rho_{xx}$  in weak magnetic fields and, correspondingly, some steplike structures are present for the off-diagonal Hall resistivity  $\rho_{xy}$ . Cyclotron orbits can be classified into those affected and not affected by antidots.<sup>[1]</sup> At certain magnetic fields, electrons can move on the commensurate classical orbit encircling a specific number of antidots, as shown in Fig. 3 (pinned orbits). Magnetoresistance was expected to increase at this magnetic field.

However, a numerical simulation based on classical electron motion showed that the change in the volume of the pinned orbits in the phase space is not enough to cause commensurability oscillation, and suggested that chaotic orbits that have a character close to the periodic orbits give larger contribution.<sup>[21]</sup> The importance of the “runaway” orbit, which skips regularly from an antidot to its neighboring antidot in the same direction, was also proposed.<sup>[22]</sup> Experiments on rectangular and/or disordered antidots<sup>[23–27]</sup> and numerical simulations<sup>[27–29]</sup> provided pieces of evidences showing the importance of such orbits.

A better way of understanding the origin of commensurability peaks is through diffusive orbits and magnetic focusing. Consider first the limit of a small aspect ratio  $d/a \ll 1$ . In this case, the electron loses its previous memory of the direction of the velocity when it collides with an antidot; therefore successive

scattering with antidots can be approximately regarded as independent of each other.<sup>[30]</sup> This means that antidots are nothing but independent scatterers.

In magnetic fields, transport is possible through the migration of the center of the cyclotron motion; therefore conductivity vanishes in the absence of scattering. When  $2R_c < a$ , where  $R_c$  is the classical cyclotron radius, the scattering of an electron from an antidot cannot give rise to diffusion or conduction because the electron is trapped by the antidot.

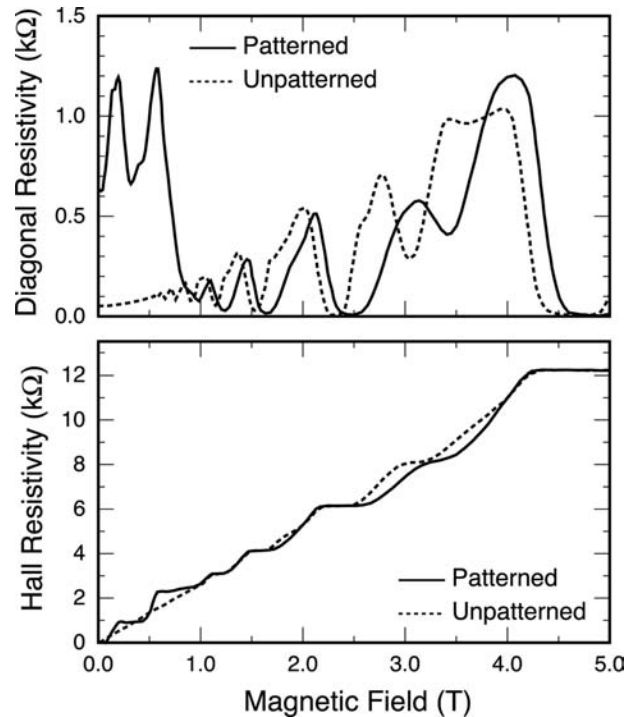


**Fig. 2** An example of  $\rho_{xx}$  and  $\rho_{xy}$  observed in patterned (solid lines) and unpatterned (dotted lines) 2-D systems. Source: From Ref.<sup>[1]</sup>. Two prominent peaks and step structures appear in the diagonal and Hall resistivity, respectively, at  $\sim 0.2$  and  $\sim 0.6$  T in antidot lattices.

Amphiphilic  
– Axle



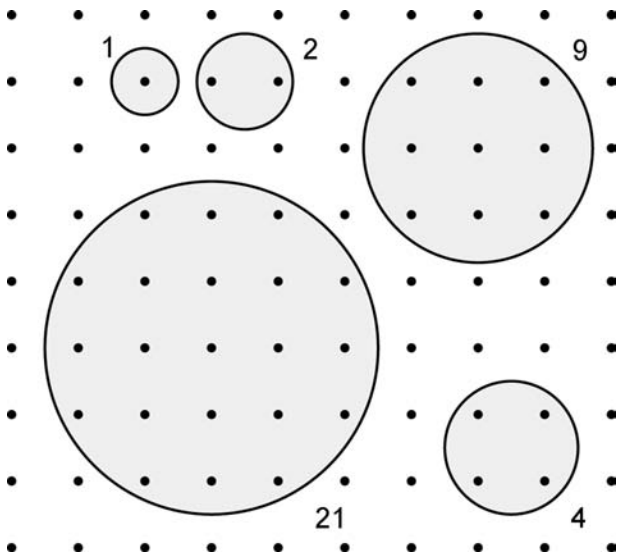


**Fig. 3** Some examples of pinned orbits. It was suggested that the resistivity exhibits a peak at the magnetic fields where the classical cyclotron orbit encircles 1, 2, 4, 9, 21, etc., antidots.

Scattering from antidots starts to contribute to conductivity when  $2R_c > a - d$ . The migration of the center of the cyclotron orbit occurs most frequently because of successive scattering from nearest-neighbor antidots at the magnetic field corresponding to  $2R_c = a$ . At this magnetic field, the measure of such orbits becomes maximum in the phase space because of a kind of magnetic focusing effect. In fact, a slight change  $\theta$  in the direction from the direction normal to the line connecting neighboring antidot leads to a change only on the order of  $2R_c\theta^2$  in position when the electron collides with a neighboring antidot, as shown in Fig. 4. This leads to an increase of the phase space volume of the orbits contributing to the increase of the diffusion coefficient at  $2R_c \approx a$ . This magnetic

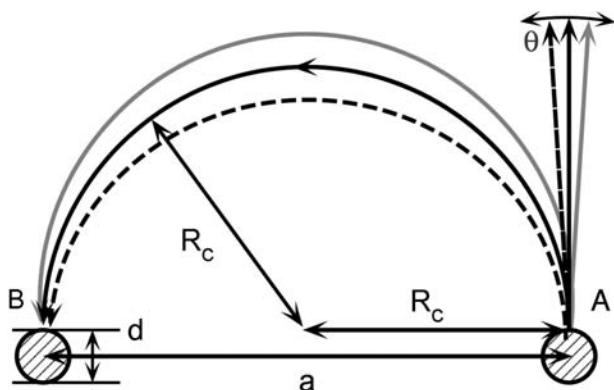


**Fig. 4** Schematic illustration of magnetic focusing leading to the fundamental commensurability peak.

focusing is different from mechanisms suggested in other works.<sup>[25,27,31]</sup>

As shown in Fig. 5, the orbit corresponding to  $2R_c = a$  can be denoted as  $(n_x, n_y) = (\pm 1, 0)$  or  $(0, \pm 1)$ , where the line segment connecting the point  $(n_x, n_y)$  and the origin constitutes the diameter of the circle. With a further decrease in the magnetic field, successive scattering with next nearest-neighbor antidots becomes possible and the conductivity has a peak around  $2R_c = \sqrt{2}a$  corresponding to  $(\pm 1, \pm 1)$ . However, this contribution becomes less prominent because the orbit passes through the position of a nearest-neighbor antidot. The next peak arises from  $(\pm 2, 0)$  or  $(0, \pm 2)$ , and  $(\pm 2, \pm 1)$  or  $(\pm 1, \pm 2)$ , which lie close to each other. The latter contribution should be larger because its measure is twice as large as that of the former; therefore the peak occurs roughly around  $2R_c \sim \sqrt{5}a$ . However, this peak should be weaker as these orbits also pass through the position of other antidots. The next prominent peak is expected to be given by  $(\pm 2, \pm 2)$ ,  $(\pm 3, 0)$ ,  $(0, \pm 3)$ ,  $(\pm 3, \pm 1)$ , and  $(\pm 1, \pm 3)$ . The peak is expected to be at  $2R_c \approx 3a$  because the orbits  $(\pm 3, 0)$  and  $(0, \pm 3)$  are not disturbed by other antidots. Most of the commensurability peaks observed experimentally can be explained qualitatively in this way.

When the diameter  $d$  is no longer negligible in comparison with the period  $a$ , the commensurability peak in the diagonal conductivity  $\sigma_{xx}$  deviates from the condition  $2R_c = (n_x^2 + n_y^2)^{1/2}a$ . In the following, we confine ourselves to the fundamental peak given by  $(\pm 1, 0)$  and  $(0, \pm 1)$ . A cyclotron orbit starting at an

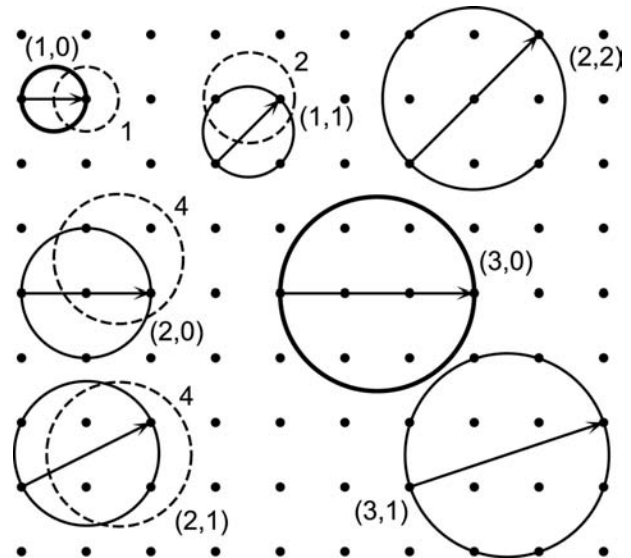


**Fig. 5** Some examples of diffusive cyclotron orbits contributing to the migration of the guiding center. The dashed circles correspond to pinned orbits (the number denotes antidots in the orbit).

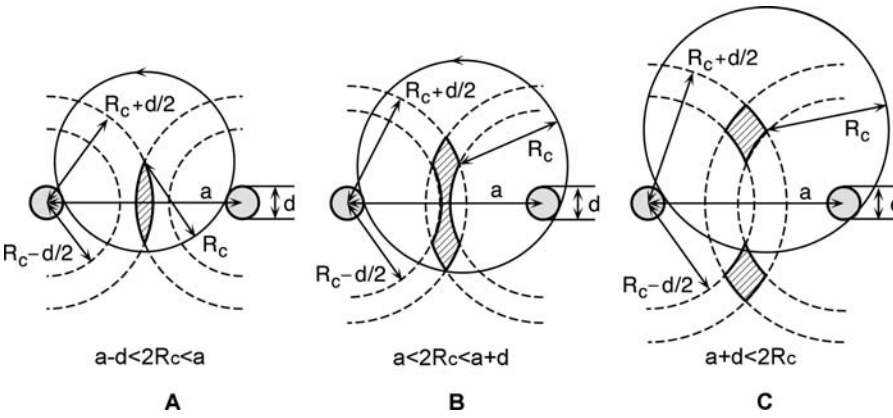


**Fig. 6** The region (shaded) of the center of cyclotron orbits passing through two nearest-neighbor antidots.

antidot and colliding with a neighboring antidot has a center in the region schematically illustrated in Fig. 6, to which the phase space volume of such orbits is proportional. Fig. 7 shows the area as a function of the magnetic field. The area has a maximum at  $2R_c = a + fd$ , where  $f \sim 0.3$  is a constant weakly dependent on  $d/a$ . This means that the commensurability peak is shifted to the weak-field side roughly in proportion to  $d/a$ .

For a non-negligible  $d/a$ , the correlation among successive scattering from antidots becomes important. In fact, it manifests itself most directly in the Hall conductivity. As illustrated in Fig. 8, it tends to enhance the left circular motion of electrons in the weak-field region  $2R_c \gtrsim a$  and reduce it in the high-field region  $2R_c \lesssim a$ . This leads to an enhancement of  $|\sigma_{xy}|$  for  $2R_c \gtrsim a$  and a reduction for  $2R_c \lesssim a$ , giving rise to a steplike structure around  $2R_c \approx a$ .

With the increase of  $d/a$ , the measure of the diffusive orbits increases, as shown in Fig. 7, and the diagonal conductivity becomes larger and comparable to  $\sigma_{xy}$  (numerical calculations show that  $\sigma_{xx} \sim |\sigma_{xy}|$

around  $d/a \sim 0.5$ <sup>[30]</sup>). Therefore the commensurability peaks in the resistivity become different from those in the diagonal conductivity. Let  $\Delta\sigma_{xx}$  and  $\Delta\sigma_{xy}$  be small changes around the field corresponding to the commensurability peak and let  $\bar{\sigma}_{xx}$  and  $\bar{\sigma}_{xy}$  be the average ( $\Delta\sigma_{xx} \ll \bar{\sigma}_{xx}$ ,  $|\Delta\sigma_{xy}| \ll |\bar{\sigma}_{xy}|$ ). Then, we have:

$$\Delta\rho_{xx} = \frac{(\bar{\sigma}_{xy}^2 - \bar{\sigma}_{xx}^2)\Delta\sigma_{xx} - 2\bar{\sigma}_{xx}\bar{\sigma}_{xy}\Delta\sigma_{xy}}{(\bar{\sigma}_{xx}^2 + \bar{\sigma}_{xy}^2)^2} \quad (4)$$

This means that  $\Delta\sigma_{xy}$  determines the structure of  $\rho_{xx}$  when  $\bar{\sigma}_{xx} \sim |\bar{\sigma}_{xy}|$  (i.e., the reduction of  $|\sigma_{xy}|$  in the high-field side gives the peak in  $\rho_{xx}$  for a large  $d/a$ ).

Fig. 9 shows an example of the results of numerical simulations in classical mechanics<sup>[30]</sup> It shows that the peak in  $\sigma_{xx}$  is broadened considerably with the increase of  $d/a$  and, at the same time, shifted to the lower magnetic field side. A step structure corresponding to the first derivative of  $\sigma_{xx}$  with the magnetic field appears in  $\sigma_{xy}$ . However, it is interesting that the

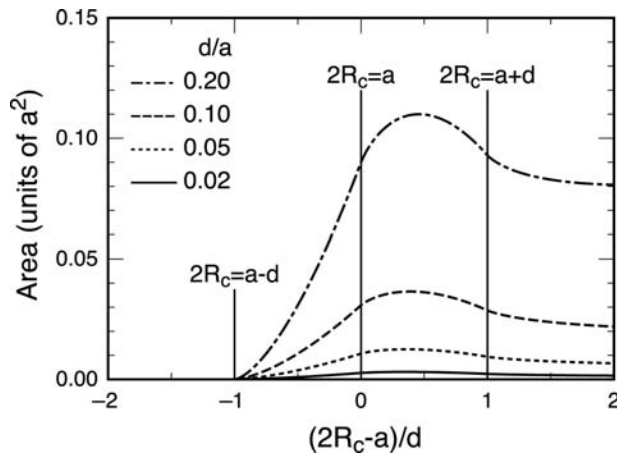


**Fig. 7** The area of the region where cyclotron orbits pass through two nearest-neighbor antidots. The diagonal conductivity is roughly proportional to the area at  $2R_c \sim a$ .

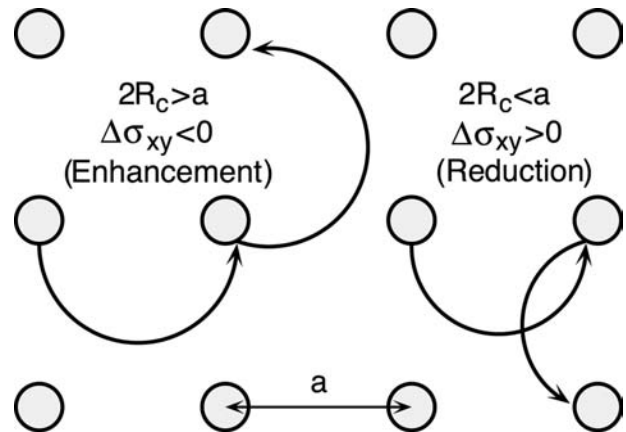


**Fig. 8** A schematic illustration of scattering from two adjacent antidots. This leads to an enhancement of  $|\sigma_{xy}|$  for  $2R_c \lesssim a$  and a reduction for  $2R_c \gtrsim a$ .

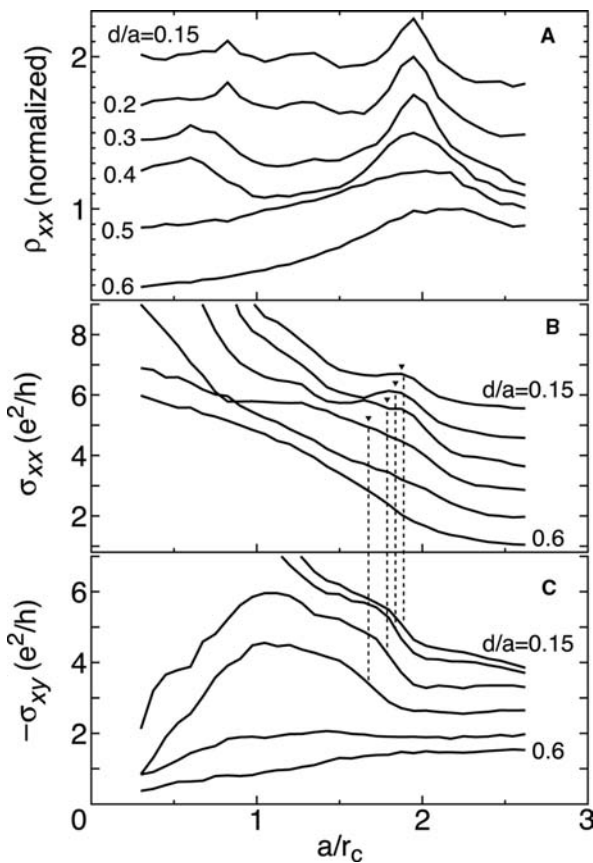


**Fig. 9** Some examples of (A)  $\rho_{xx}$ , (B)  $\sigma_{xx}$ , and (C)  $\sigma_{xy}$  calculated in classical mechanics. Each curve of  $\rho_{xx}$  is normalized by its maximum value and shifted successively. The results for  $\sigma_{xx}$  are shifted successively by  $e^2/h$ . The peak positions of  $\sigma_{xx}$  are indicated by triangles and vertical dotted lines. The mean free path is  $\Lambda = 3.3a$ . Source: From Ref.<sup>[30]</sup>.

commensurability peak in the resistivity  $\rho_{xx}$  remains around  $2R_c = a$ , independent of  $d/a$ . This results from the fact that the resistivity is rather a complicated function of  $\sigma_{xx}$  and  $\sigma_{xy}$ . For  $d/a \geq 0.5$ , the structures in  $\sigma_{xx}$  and  $\sigma_{xy}$  disappear almost completely and  $\rho_{xx}$  does not show a clear commensurability peak.

A large aspect ratio usually corresponds to a small antidot period  $a$  and to a narrow spacing between the nearest-neighbor antidot comparable to the Fermi wavelength  $\lambda_F$ . Therefore quantum effects can be important for antidot lattices with large  $d/a$  for a fixed value of  $a$ . In fact, a quantum mechanical calculation<sup>[32]</sup> in a self-consistent Born approximation<sup>[33,34]</sup> shown in Fig. 10 gave the result for  $d/a = 0.5$  that the diagonal conductivity  $\sigma_{xx}$  exhibits essentially no structure and the off-diagonal Hall conductivity has a small dip at  $2R_c \sim a$ , leading to the fundamental commensurability peak at  $2R_c \sim a$ . Some experiments have shown that  $\sigma_{xx}$  has a dip at  $2R_c \sim a$  for antidot lattices with larger  $d/a$ .<sup>[27,35]</sup> The structure appearing in the off-diagonal Hall resistivity at the fundamental

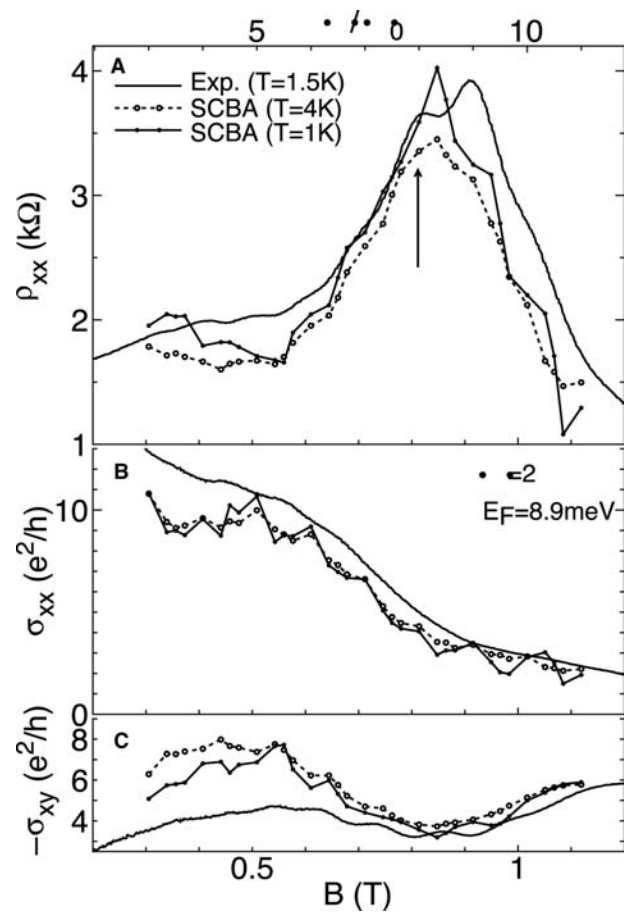


**Fig. 10** (A)  $\rho_{xx}$ , (B)  $\sigma_{xx}$ , and (C)  $\sigma_{xy}$  calculated in a self-consistent Born approximation as a function of the magnetic field for  $\beta = 2$ . Source: The experimental data From Ref.<sup>[17]</sup>, are also shown for comparison. From Ref.<sup>[32]</sup>.

commensurability peak was analyzed experimentally and theoretically.<sup>[36]</sup>

In high magnetic fields, the structure of the energy bands is relatively simple and can be understood as combinations of Landau bands, which have non-zero dispersion in the presence of antidot lattices and quantized edge states localized along an antidot boundary. With the decrease of the magnetic field, these magnetic minibands start getting mixed with each other. This mixing gives rise to many bands having a large quantized value of the Hall conductivity, both negative and positive.<sup>[37]</sup> Extremely large values are usually canceled out if they are summed over adjacent minibands. Actual calculations seem to show that this cancellation is not complete and the Hall conductivity tends to have a dip around a certain magnetic field, giving rise to a peak in the resistivity. The Hall conductivity is sensitive to parameters such as the Fermi energy and sometimes exhibits even a signature change. Therefore the origin of commensurability peaks becomes unclear when quantum effects become important.

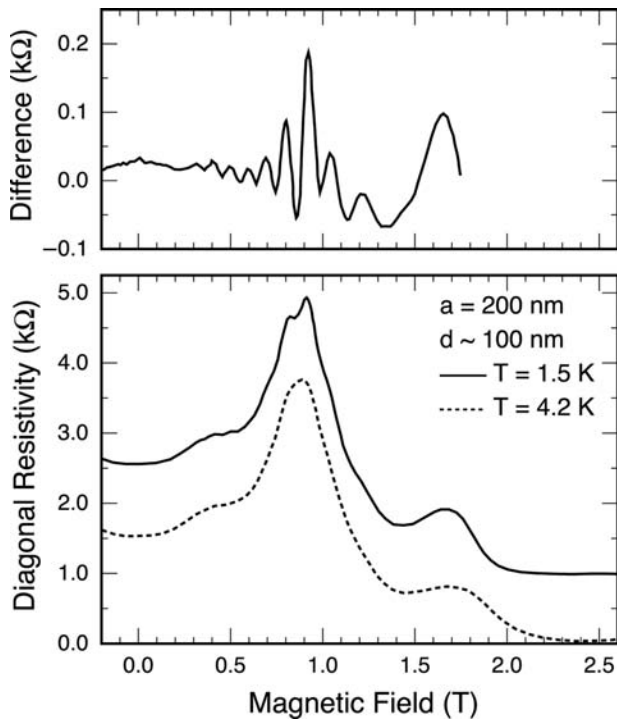


**Fig. 11** Observed quantum oscillation superimposed on the fundamental commensurability peak. The oscillation becomes clear in the difference of the resistivity at  $T = 4.2$  K and that at  $T = 1.5$  K (shifted vertically by 1 kΩ). *Source:* From Ref.<sup>[17]</sup>.

### AHARONOV–BOHM-TYPE OSCILLATION

A fine oscillation was observed to be superimposed on commensurability peaks of the magnetoresistance.<sup>[5,17,18]</sup> Figs. 11 and 12 give examples of such Aharonov–Bohm-type oscillation reported in Refs.<sup>[17]</sup> and<sup>[18]</sup>. The period is roughly given by  $\Delta B \sim \Phi_0/a^2$ , where  $\Phi_0 = ch/e$  is the magnetic flux quantum. Numerical calculations have been performed on this Aharonov–Bohm-type oscillation.<sup>[32,38,39]</sup> In the following, some of the results<sup>[32,40]</sup> obtained in a self-consistent Born approximation are reviewed briefly.

The calculated diagonal and Hall conductivity at  $T = 4$  K, shown in Fig. 10, oscillate with period  $\Phi_0$  over the range of magnetic fields considered. This oscillation originates from the butterfly band structure of Hofstadter,<sup>[41]</sup> as suggested theoretically.<sup>[42–44]</sup> In fact, the band structure exhibits a quasi-periodic oscillation as a function of the magnetic flux passing through a unit cell with period given by the magnetic flux quantum. At a lower temperature ( $T = 1$  K), another kind of oscillation appears in addition to this butterfly

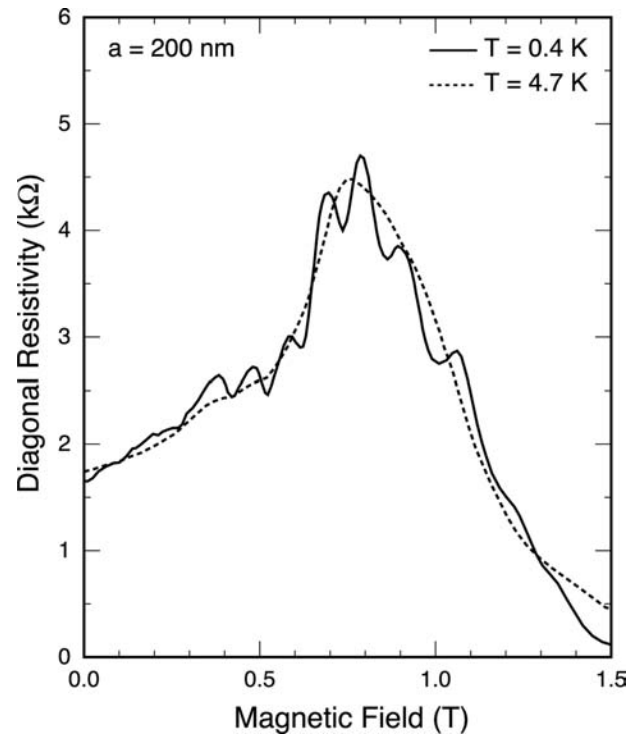


**Fig. 12** An example of observed quantum oscillations superimposed on the fundamental commensurability peak. *Source:* From Ref.<sup>[18]</sup>.

oscillation. Actually, these oscillations are sensitive to the antidot potential and the difference between this new oscillation and the butterfly oscillation becomes much clearer for the more realistic parameter  $\beta = 1$ , although not shown here.

The density of states in classically chaotic systems can be calculated semiclassically using the so-called periodic orbit theory.<sup>[45–47]</sup> According to the trace formula, the density of states is given by the sum of a classical contribution and a quantum correction. The latter is given by semiclassically quantized energy levels associated with periodic orbits and the former is proportional to the classical phase space volume at the energy. The contribution of a particular periodic orbit can be written as the summation of  $\delta$  functions for a stable orbit:

$$D_{\text{osc}}^{\text{po}}(E) = \frac{T}{\hbar} \sum_{m=0}^{\infty} \left[ \sum_{n=-\infty}^{\infty} \delta \left( \frac{S_c}{\hbar} - \left( m + \frac{1}{2} \right) v - 2n\pi \right) - \frac{1}{2\pi} \right] \quad (5)$$

and the summation of Lorentzian functions for an unstable orbit:

$$D_{\text{osc}}^{\text{po}}(E) = \frac{T}{\hbar} \sum_{m=0}^{\infty} (\pm 1)^m \left[ \sum_{n=-\infty}^{\infty} \frac{1}{\pi} \times \frac{(2m+1)u/2}{[S_c/\hbar - 2\pi(\mu/4 + n)]^2 + [(2m+1)u/2]^2} - \frac{1}{2\pi} \right] \quad (6)$$

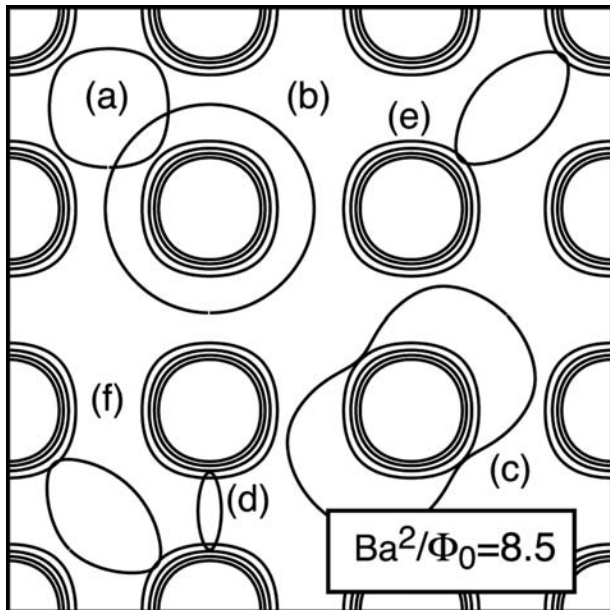
where  $S_c$  is the classical action,  $T$  is the period, and  $v$  is the stability angle. For unstable orbits,  $u$  is the Lyapunov exponent,  $\mu$  is the Maslov index, and the sign becomes  $\pm$  accordingly as the neighborhood of a periodic orbit is hyperbolic or inverse hyperbolic. The integer  $m$  is considered as a quantum number for a motion transverse to the periodic orbit.<sup>[48]</sup> The quantization conditions are:

$$S_c = \begin{cases} 2\pi\hbar \left[ n + \frac{1}{2\pi} \left( m + \frac{1}{2} \right) v \right] & \text{for stable orbit} \\ 2\pi\hbar \left( n + \frac{\mu}{4} \right) & \text{for unstable orbit} \end{cases} \quad (7)$$

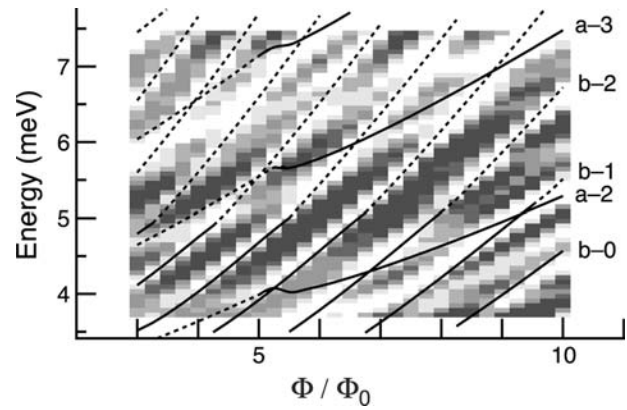
with integer  $n$  and non-negative integer  $m$ .

Fig. 13 shows some examples of periodic orbits having a short trajectory.<sup>[49,50]</sup> The orbit (a) is localized in the potential well region surrounded by four neighboring antidots. It turns continuously into a normal cyclotron orbit in sufficiently high magnetic fields. The orbit (b) circling around an antidot is considered to be most important in giving rise to the quantum oscillation.

Fig. 14 shows an example of the calculated density of states together with quantized energy levels associated with the orbits (a) and (b) for  $m = 0$ .<sup>[32,40]</sup> The density of states is correlated well with semiclassical energy levels, although many features remain to be explained.



**Fig. 13** Some examples of periodic orbits having a short trajectory in a square antidot in a magnetic field  $Ba^2/\Phi_0 = 8.5$  roughly corresponding to the main commensurability peak. The parameters are  $a/\lambda_F = 4.31$ ,  $U_0/E_F = 8.4$ ,  $d/a = 0.6$ , and  $\beta = 2$ . *Source:* From Ref.<sup>[49]</sup>.



**Fig. 14** The density of states calculated in a self-consistent Born approximation for  $\hbar/\tau = 0.18$  meV and  $\beta = 1$ . It is large in the light region and small in the dark region. The energy levels for the orbits (a) and (b) are given by lines (solid lines for stable orbits and dotted lines for unstable orbits). *Source:* From Ref.<sup>[40]</sup>.

A semiclassical expression can be obtained for the conductivity tensor,<sup>[32,51,52]</sup> but has proved to be unsuccessful for the parameter range corresponding to the experiments mentioned above.<sup>[32]</sup> As discussed in “Commensurability Peaks,” diffusive orbits have a dominant contribution to transport in the magnetic field region near the commensurability peak. These orbits are perturbed by the presence of quantized periodic orbits, which is likely to lead to a quantum oscillation. The semiclassical expression for the conductivity does not take into account such effects.

## TRIANGULAR ANTIDOT LATTICES

Commensurability peaks have been observed also in triangular antidot lattices. Their origin is the same as in square lattices and is understood in terms of diffusive orbits and magnetic focusing. Fig. 15 shows some examples of diffusive orbits contributing to the migration of guiding centers of cyclotron orbits. They are specified by two integers  $(n_1, n_2)$  such that  $n_1 a_1 + n_2 a_2$  corresponds to a vector whose length is equal to the cyclotron diameter (i.e.,  $2R_c/a = \sqrt{n_1^2 + n_2^2 + n_1 n_2}$ ).

There are some important differences from the square lattice. First, diffusive orbits are strongly disturbed by the presence of other antidots with increasing antidot diameter. As schematically illustrated in Fig. 16, diffusive orbits start to be severely influenced for  $d/a > (\sqrt{3} - 1)/2 \approx 0.37$  in the triangular case, in contrast to  $d/a > 2/3 \approx 0.67$  in the square case. Therefore commensurability peaks are much more sensitive to the aspect ratio.



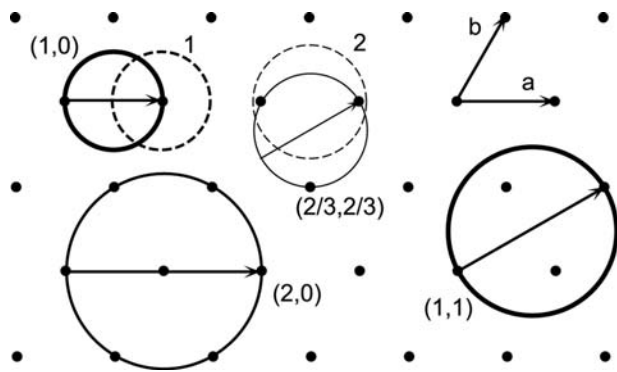


**Fig. 15** Some examples of diffusive cyclotron orbits contributing to the migration of the guiding center in a triangular lattice. The dashed circles correspond to pinned orbits (the number denotes antidots in the orbit). The measure of the diffusive orbits has a dip around the field corresponding to  $(n_1, n_2) = (2/3, 2/3)$ .

Second, there is a wide gap in the magnetic field between the fundamental peak given by  $a/R_c = 2$  [ $(n_1, n_2) = (\pm 1, 0)$  or  $(0, \pm 1)$ ] and the next peak given by  $a/R_c = 2/\sqrt{3}$  [ $(n_1, n_2) = (\pm 1, \pm 1)$ ]. As shown in Fig. 17, the area of the region corresponding to a guiding center of a cyclotron orbit passing through a pair of nearest-neighbor antidots starts to overlap with that of another pair at a magnetic field given by the condition  $R_c + d/2 = a/\sqrt{3}$ . This leads to a reduction in the measure of the diffusive orbits around  $a/R_c \sim \sqrt{3}$ , giving rise to a small dip in the diffusion coefficient at this magnetic field (see below).

Fig. 18 shows some examples of results of quantum and classical calculations.<sup>[37,53]</sup> The commensurability peaks are rapidly shifted to the lower magnetic field side with increasing  $d/a$ , which is more appreciable in quantum results. In fact, the peak is shifted down to the vanishing magnetic field; therefore only a large

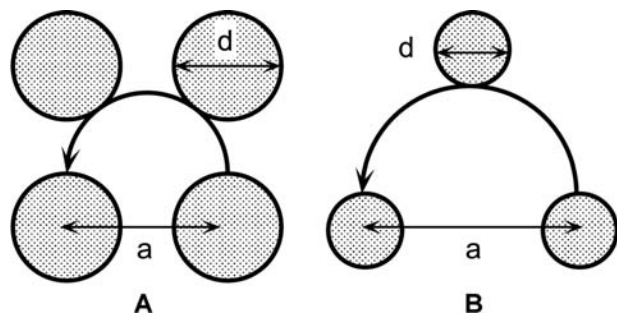


**Fig. 16** Schematic illustration of diffusive orbits giving rise to a fundamental commensurability peak in (A) square and (B) triangular lattices. The orbit starts to be disturbed by other antidots for smaller  $d/a$  in the triangular case.

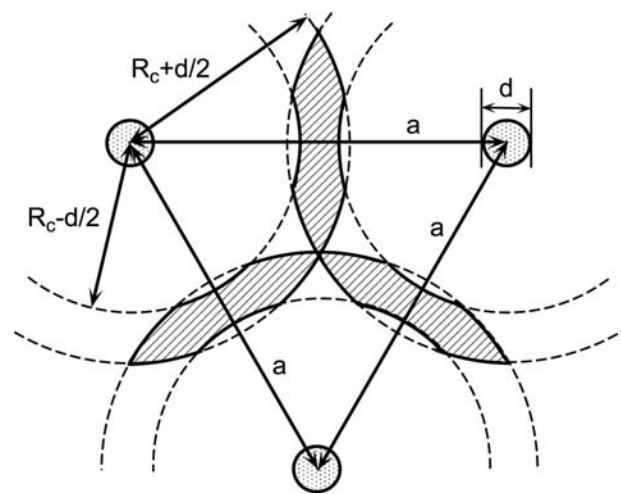


**Fig. 17** The region (shaded) of the guiding center of cyclotron orbits passing through two nearest-neighbor antidots in a triangular lattice when  $R_c + d/2 \approx a/\sqrt{3}$ .

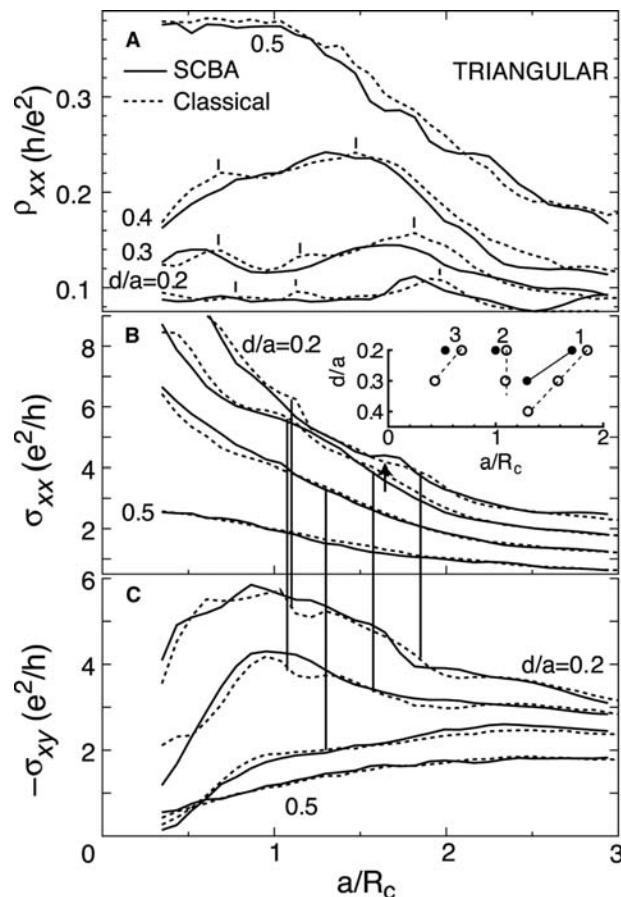


**Fig. 18** Calculated resistivity and conductivities in triangular antidot lattices. Quantum and classical results are shown by solid and dotted lines, respectively. The peak positions of  $\sigma_{xx}$  (closed and open circles for quantum and classical, respectively) are shown in the inset. The upward arrow indicates a small dip at  $a/R_c = \sqrt{3}$ . Source: From Ref.<sup>[37]</sup>.



negative magnetoresistance can be seen for  $d/a \geq 0.5$ . These results can be well understood in terms of the differences between the square and triangular lattices mentioned above (a weak dip may be identified in the diagonal conductivity at the magnetic field given by  $a/R_c = \sqrt{3}$  for  $d/a = 0.2$ ).

The strong disturbance of diffusive orbits in triangular lattices with a large aspect ratio suggests that the number of events that an electron is scattered by the same antidot is larger than that in square lattices. This means that the electron trajectory is much more complicated in triangular lattices than in square lattices, explaining the reason that the conductivity itself is considerably smaller in triangular lattices and that the amplitude of the Altshuler–Aronov–Spivak oscillation is much larger, as will be discussed in “Altshuler–Aronov–Spivak Oscillation.”<sup>[54,55]</sup> This also explains the similar behavior of the Altshuler–Aronov–Spivak oscillation of the localization length, which was observed experimentally<sup>[56]</sup> and also demonstrated theoretically.<sup>[57,58]</sup>

### ALTSHULER–ARONOV–SPIVAK OSCILLATION

The conductance of a conductor in the form of a hollow cylinder oscillates as a function of the magnetic flux passing through its cross section with a period given by half of the flux quantum  $\Phi_0 = ch/e$ . This oscillation is a result of interference effects and is called the Altshuler–Aronov–Spivak oscillation.<sup>[59]</sup> This oscillation was experimentally observed in cylindrical metal films<sup>[60]</sup> and networks of thin metallic wires<sup>[61]</sup> in the diffusive regime, where the mean free path is much smaller than the sample size or the wire width.

Similar oscillations have been observed also in antidot lattices.<sup>[3–6]</sup> Fig. 19 shows an example.<sup>[6]</sup> The essential features of the experiments can be summarized as follows: 1) the oscillations are observed clearly in triangular lattices but are almost invisible in square lattices;<sup>[5,6]</sup> and 2) the negative magnetoresistance is observed together with the oscillation. In the following, a numerical study<sup>[54,55]</sup> is reviewed briefly.

Real antidot lattices have inherent randomness arising from fabrication processes, in addition to impurities whose strength is characterized by the mean free path  $\Lambda$ . This disorder is introduced through fluctuations in antidot diameters around the mean value  $d$ . The amount of fluctuations is characterized by the root mean square deviation  $d_f$ . The conductance is calculated by Green’s function technique<sup>[62]</sup> for systems with length  $L_x$  and width  $L_y$  containing a finite number of antidots ( $\sim 25$ ).

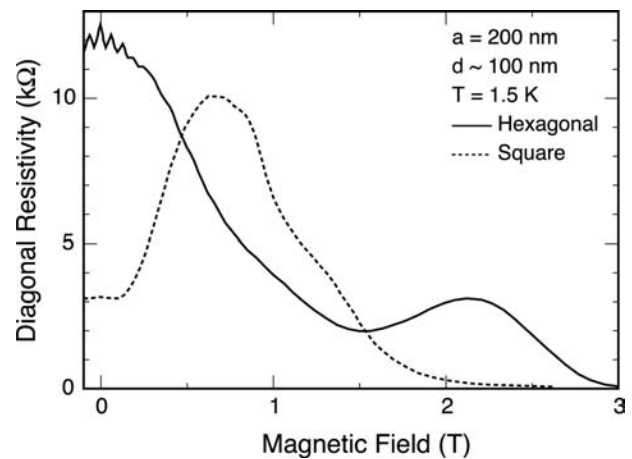


**Fig. 19** Comparison of the resistivity in a triangular (solid line) and a square (dotted line) antidot lattice observed experimentally. A prominent oscillation with a period determined by  $\Phi_0/2$  appears in the triangular lattice.

Fig. 20 gives calculated conductance of a triangular antidot lattice with  $a/\lambda_F = 4$  in the absence of disorder in the antidot potential. In the ballistic regime  $\Lambda/\lambda_F = 16$ , where  $\Lambda$  is larger than the antidot period, the conductance exhibits an irregular oscillation. This is a consequence of the fact that an irregular oscillation with period  $\Phi_0$  caused by interference

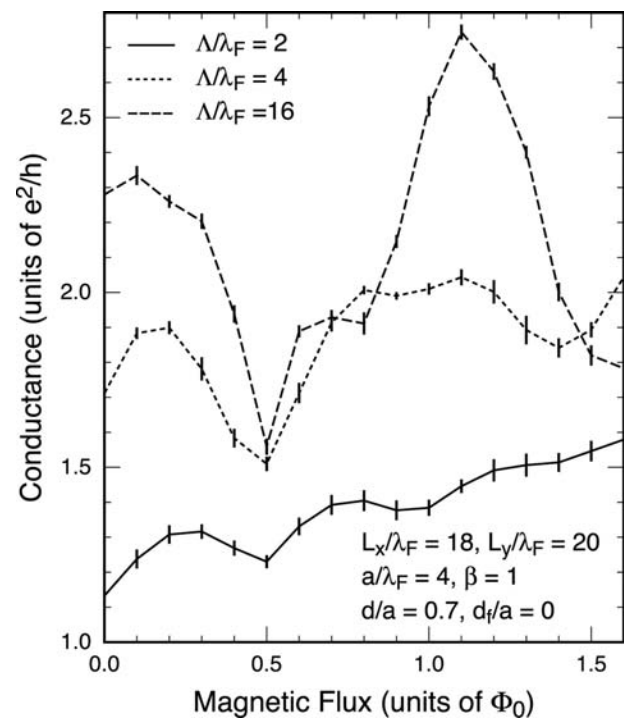


**Fig. 20** Conductance of a triangular antidot lattice with size  $L_x \times L_y$  as a function of magnetic flux passing through a unit cell. Source: From Refs.<sup>[54]</sup> and<sup>[55]</sup>.

effects has a dominant contribution. In fact, both phase and form of the oscillation vary sensitively depending on parameters such as  $d/a$ ,  $a/\lambda_F$ , and  $\beta$ . With the decrease in the mean free path, the amplitude of the irregular oscillation becomes smaller and that of the Altshuer–Aronov–Spivak oscillation characterized by period  $\Phi_0/2$  becomes more and more dominant. In particular, a beautiful oscillation manifests itself in the diffusive regime where  $\Lambda/\lambda_F = 2$  or  $\Lambda/a = 1/2$ .

Similarly, the contribution of the irregular oscillation diminishes with the increase of disorder in the antidot potential, as shown in Fig. 21. The oscillation with period  $\Phi_0/2$  becomes dominant for a disorder as large as  $d_f/a = 0.07$ . Fig. 21 shows that the oscillation is accompanied by a weak negative magnetoresistance, or a slight increase in the conductance as a function of a magnetic field. This is in agreement with one of the features of the experiments discussed above. The amplitude of the oscillations saturates for  $d_f/a > 0.07$ .

In the square lattice, the oscillation has a smaller amplitude than that in the triangular lattice, again in excellent agreement with experiments not shown here explicitly. Note that the conductance of the triangular lattice is much smaller than that of the square

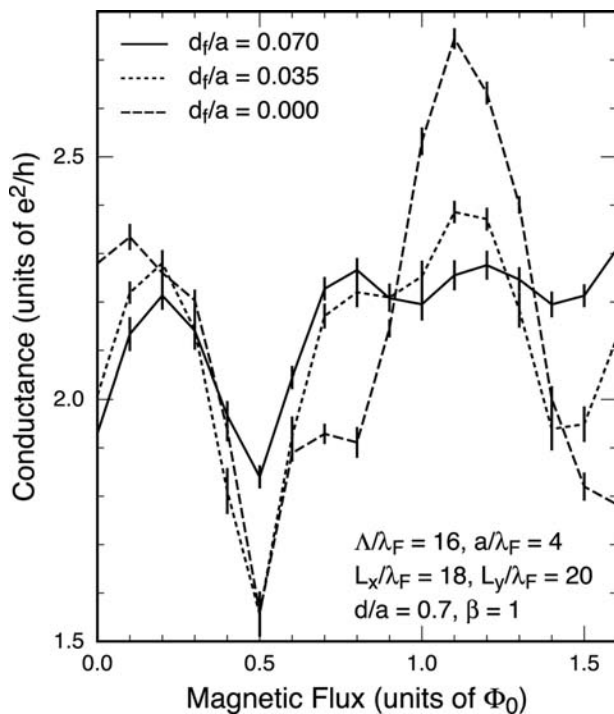


**Fig. 21** Conductance of a triangular antidot lattice in the presence of fluctuations in antidot diameter. Source: From Refs.<sup>[54]</sup> and<sup>[55]</sup>.

lattice. Electrons perform more complicated motion and stay longer in the triangular lattice than in the square lattice.<sup>[5,6]</sup> This is presumably the main origin of the enhancement of oscillation in the triangular lattice, as has been discussed in “Triangular Antidot Lattices.”

## SCATTERING MATRIX FORMALISM

### Quantum Wire Junction

Difficulties of quantum mechanical calculations of energy levels and transport coefficients in antidot lattices lie in the fact that we have to consider a magnetic unit cell that can become very large, depending on the magnetic flux passing through a unit cell. In this section, a new method of full quantum calculations of energy bands and transport quantities<sup>[63,64]</sup> is reviewed.

We shall replace an antidot lattice by a 2-D array of quantum wire junctions with width  $W_x$  in the  $x$  direction and  $W_y$  in the  $y$  direction, as illustrated in Fig. 22. Each junction is connected to neighboring junctions through a quantum wire with length  $L_x$  and  $L_y$  in the  $x$  and  $y$  directions, respectively. The lattice period in the  $x$  direction is  $a$  and that in the  $y$  direction is  $b$ . For the calculation of an  $S$  matrix, we consider the model shown in Fig. 23. We divide this system into five regions (i.e., four wires and a junction).

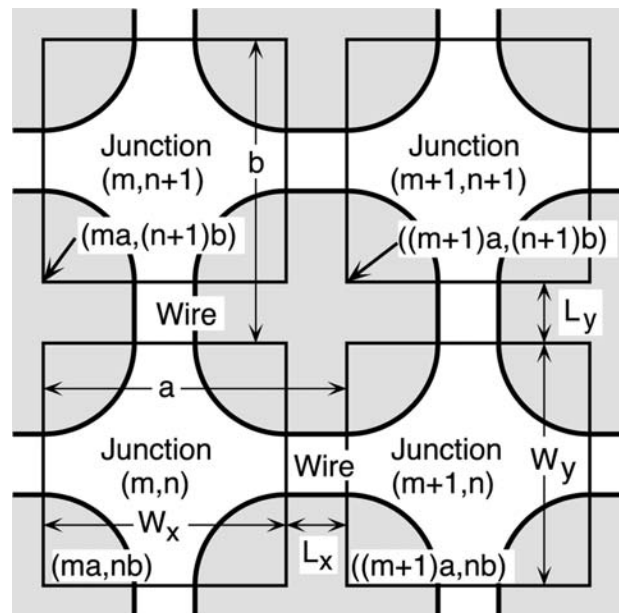


**Fig. 22** Two-dimensional array of quantum wire junctions.

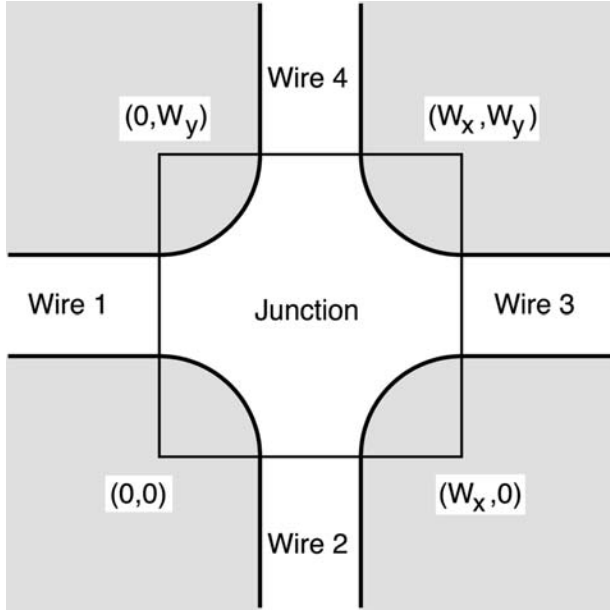


**Fig. 23** A quantum wire junction for calculation of an  $S$  matrix.

The vector potential is chosen as  $\mathbf{A} = (-By, 0)$ . The modes in wires 1–4 are given by:

$$\begin{aligned}
 \psi_{1\nu}^{\pm}(x, y) &= (v_{\nu}^x)^{-1/2} \eta_{\nu\pm}(y) \exp[i(\pm\kappa_{\nu}^x + W_y/2l^2) \\
 &\quad \times (x + L_x/2)] \\
 \psi_{2\nu}^{\pm}(x, y) &= (v_{\nu}^y)^{-1/2} \xi_{\nu\pm}(x) \exp(-ixy/l^2) \\
 &\quad \times \exp[i(\pm\kappa_{\nu}^y - W_x/2l^2)(y + L_y/2)] \\
 \psi_{3\nu}^{\pm}(x, y) &= (v_{\nu}^x)^{-1/2} \eta_{\nu\pm}(y) \exp[i(\pm\kappa_{\nu}^x + W_y/2l^2) \\
 &\quad \times (x - W_x - L_x/2)] \\
 \psi_{4\nu}^{\pm}(x, y) &= (v_{\nu}^y)^{-1/2} \xi_{\nu\pm}(x) \exp(-ixy/l^2) \\
 &\quad \times \exp[i(\pm\kappa_{\nu}^y - W_x/2l^2) \\
 &\quad \times (y - W_y - L_y/2)] \quad (8)
 \end{aligned}$$

where  $l = \sqrt{eB/\hbar c}$  is the magnetic length,  $\nu$  denotes modes,  $v_{\nu}$  corresponds to velocities,  $\eta(y)$  is an eigenfunction for a wire in the  $x$  direction, and  $\xi(x)$  is that for a wire in the  $y$  direction for the vector potential  $\mathbf{A} = (0, Bx)$ .

There are two kinds of modes. One of them is a traveling mode whose wave number  $\kappa$  is real and the other is an evanescent mode whose wave number has an imaginary part. The sign  $+(-)$  denotes a mode traveling or decaying in the positive (negative) direction. The wave function in a wire region is represented using expansion coefficients  $C$  with respect to modes in the wires:

$$\Psi_i(x, y) = \sum_{\nu} [C_{i\nu}^+ \psi_{i\nu}^+(x, y) + C_{i\nu}^- \psi_{i\nu}^-(x, y)] \quad (9)$$

The  $S$  matrix gives the following relation between incoming and outgoing waves:

$$\begin{pmatrix} C_1^- \\ C_2^- \\ C_3^+ \\ C_4^+ \end{pmatrix} = \mathbf{S}(E) \begin{pmatrix} C_1^+ \\ C_2^+ \\ C_3^- \\ C_4^- \end{pmatrix} \quad (10)$$

where  $\mathbf{C}$  consists of expansion coefficients  $C$ ; therefore its dimension is the number of modes.

### Energy Bands and Density of States

We can calculate the energy bands of an infinitely large array of junctions using Bloch's theorem. In the following, we confine ourselves to the case in the absence of the magnetic field for simplicity. The extension to the case in magnetic fields is discussed in Ref.<sup>[64]</sup>. The Bloch condition for  $\Psi_i(x, y)$  gives the conditions for expansion coefficients  $C_{1\nu} = \exp(-ik_x a) C_{3\nu}$  and  $C_{2\nu} = \exp(-ik_y b) C_{4\nu}$ . These are rewritten as the following relation between incoming and outgoing waves:

$$\begin{pmatrix} C_1^- \\ C_2^- \\ C_3^+ \\ C_4^+ \end{pmatrix} = P(k_x, k_y) \begin{pmatrix} C_1^+ \\ C_2^+ \\ C_3^- \\ C_4^- \end{pmatrix} \quad (11)$$

where:

$$P(k_x, k_y) = \begin{pmatrix} 0 & 0 & P_x^{-1} & 0 \\ 0 & 0 & 0 & P_y^{-1} \\ P_x & 0 & 0 & 0 \\ 0 & P_y & 0 & 0 \end{pmatrix} \quad (12)$$

with  $P_x = \exp(ik_x a)$  and  $P_y = \exp(ik_y b)$ . Energy bands are given with the condition that Eqs. (10) and (11) have non-trivial solutions for  $\mathbf{C}$ :

$$\det[P(k_x, k_y) - \mathbf{S}(E)] = 0 \quad (13)$$

This equation gives energy bands as equi-energy lines in the  $\mathbf{k}$  space at the energy  $E$ .

**Fig. 24** shows some examples of calculated energy bands for a square lattice ( $b = a$ ). The parameters are  $a/\lambda_F = 4.31$ ,  $U_0/E_F = 8.4$ ,  $d/a = 0.6$ , and  $\beta = 2$  (this choice of  $\beta$  is likely to be too large for realistic antidots). The corresponding equipotential lines are given in **Fig. 13**. The magnetic field  $Ba^2/\Phi_0 = 4$  corresponds to about 0.4 T for a typical antidot lattice with  $a \sim 2000 \text{ \AA}$ . The bands are calculated by including all traveling modes and a single evanescent mode having the smallest imaginary wave vector. The horizontal dotted lines denote the bottom of one-dimensional subbands in the wire region.

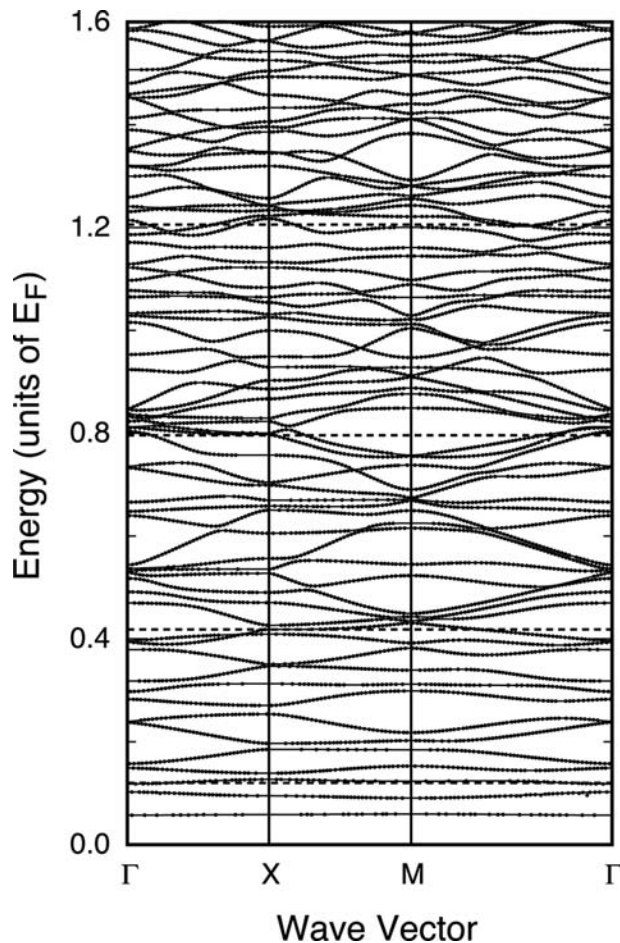


**Fig. 24** Calculated energy bands in a magnetic field  $Ba^2/\Phi_0 = 4$ . In the  $S$  matrix method, all traveling modes and only a single evanescent mode are taken into account. *Source:* From Ref.<sup>[64]</sup>.

The results using the  $S$  matrix formalism with only a single evanescent mode agree quite well with the exact results in which all the evanescent modes are included. This shows that the inclusion of a few evanescent modes is sufficient for an accurate description of energy bands of antidot lattices. The bands for  $Ba^2/\Phi_0 = 4$  corresponding to  $2R_c/a \sim 2$  may be regarded as a mixture of a band with a large dispersion (run-away orbit) and those having a small dispersion for  $0.4 \lesssim E/E_F \lesssim 1.0$ .<sup>[32]</sup> The energy bands become more complicated for higher energies.

Fig. 25 shows the corresponding energy dependence of the density of states and the conductivity calculated using the Boltzmann transport equation. The density of states is measured in units of the 2-D value  $m^*/\pi\hbar^2$  and the conductivity in units of  $ne^2\tau/m^*$ , where  $n$  is the electron concentration in the absence of the antidot potential and  $m^*$  is the effective mass. They are averaged over the Gaussian distribution with broadening  $\Gamma/E_F = 0.02$ . Some structures of the conductivity

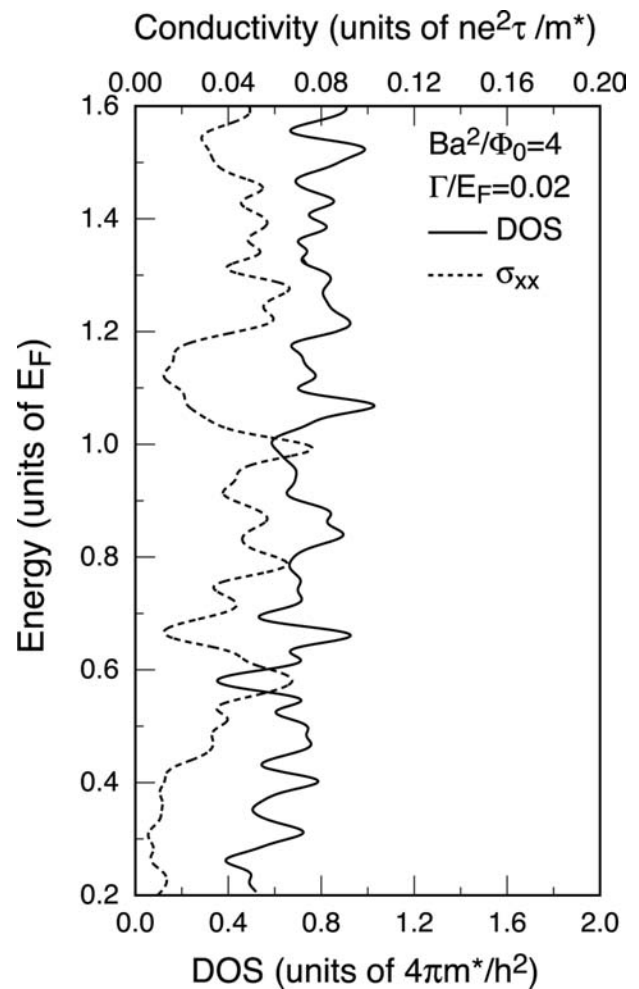


**Fig. 25** The energy dependence of the density of states (solid line) and conductivity (dotted line) in the magnetic field  $Ba^2/\Phi_0 = 4$ . *Source:* From Ref.<sup>[64]</sup>.

correspond to those of the density of states, but most of them do not.

A semiclassical analysis has been made for the density of states by considering six periodic orbits (a)–(f) given in Fig. 13.<sup>[49,64,65]</sup> As a cutoff of a quantum number  $m$  in Eq. (5), the factor  $\exp(-\alpha m)$  has been introduced, where  $m$  is the quantum number for a motion transverse to each periodic orbit. Fig. 26 shows some examples in the magnetic field corresponding to  $Ba^2/\Phi_0 = 8.5$ , where the condition of the fundamental commensurability peak is nearly satisfied (i.e.,  $2R_c \sim a$  at the Fermi level).

The orbit (a) is stable in the energy region  $E/E_F \leq 0.43$ , the orbit (b) in  $0.72 \leq E/E_F \leq 1.41$  and  $E/E_F \leq 0.52$ , the orbit (c) in  $0.7 \leq E/E_F \leq 0.74$ , and the orbit (e)  $E/E_F \leq 0.68$ . Orbit (c) merges into orbit (b) and disappears at  $E/E_F = 0.7$ . The quantized levels associated with such stable orbits give clear peaks in the semiclassical density of states, many of which are in agreement with those of the

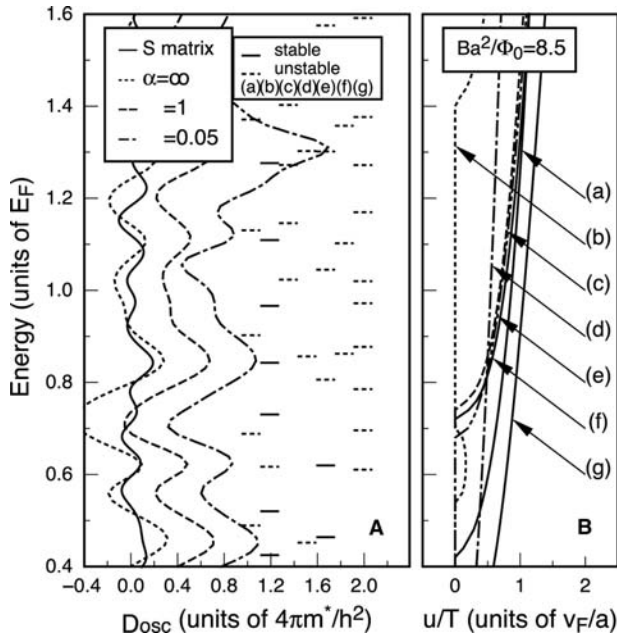


**Fig. 26** (A) The oscillatory part of the density of states at  $Ba^2/\Phi_0 = 8.5$  corresponding to  $2R_c/a \approx 2$ . The dashed line is shifted to the right by 0.4 and the dot-dashed line is shifted by 0.8. (B) The corresponding Lyapunov exponents. *Source:* From Ref.<sup>[49]</sup>.

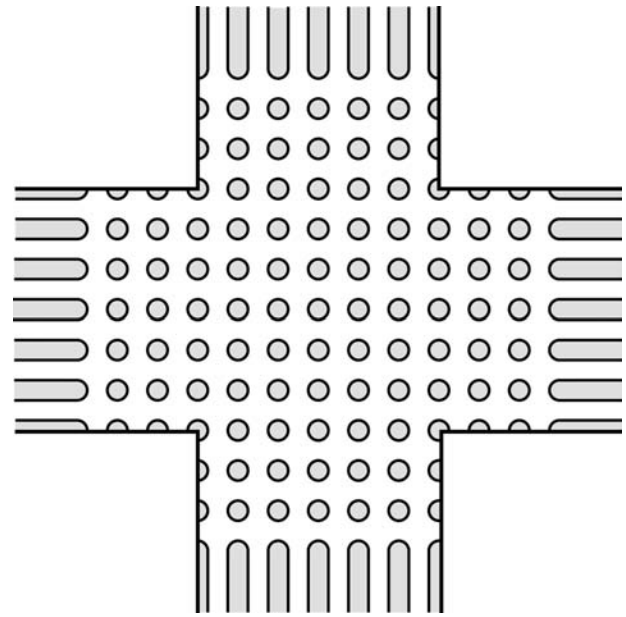


**Fig. 27** Schematic illustration of a finite antidot lattice for which the numerical calculation is performed. It has eight sites in the direction of the wire width and 16 sites in the direction of the wire length.

quantum-mechanical density of states. Particularly, near the Fermi energy, the orbit (b) circling around an antidot gives a major contribution in agreement with the analysis mentioned in “Aharonov–Bohm-Type Oscillation.” Inclusion of higher transverse modes does not considerably affect the structures of the semiclassical density of states. However, peaks at  $E/E_F = 0.97$  and 1.1, which roughly correspond to peaks of quantum-mechanical density of states, are shifted to the higher-energy side including higher transverse modes and the agreement becomes worse. A more elaborate work in which many periodic orbits are taken into account is necessary for a full understanding of the correspondence between the quantum-mechanical and semiclassical results for the density of states.

**Aharonov–Bohm Oscillation**

To calculate transport quantities, we take a quantum wire junction array as a model of an antidot lattice, as shown in Fig. 27.<sup>[39]</sup> This is a kind of four-terminal system where constrictions at edges are connected, respectively, to four reservoirs through ideal leads. Transport coefficients are calculated based on the Büttiker–Landauer formula<sup>[66–68]</sup> from an *S* matrix for a junction array obtained by connecting *S* matrices for a single junction.

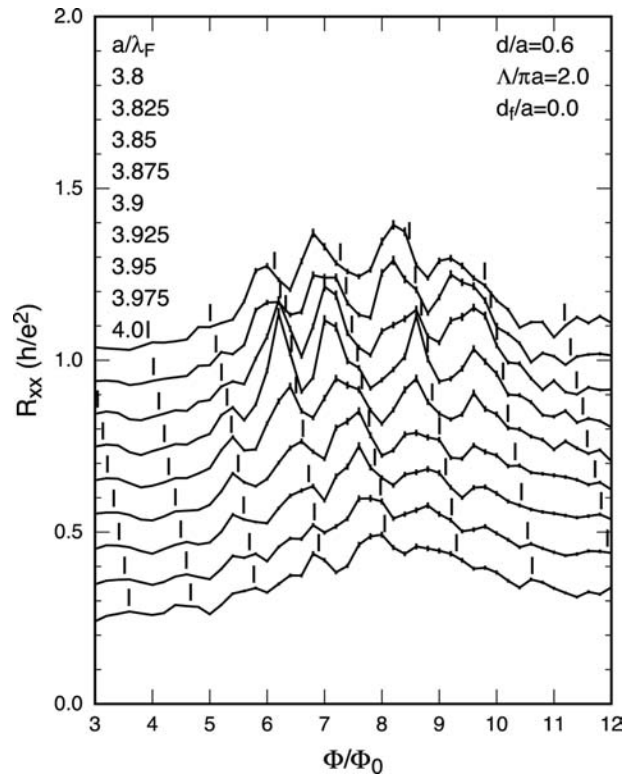


**Fig. 28** Diagonal resistance as a function of the magnetic field for  $d/a = 0.6$  and the mean free path  $\Lambda/\pi a = 2$ . *Source:* From Ref.<sup>[65]</sup>.

Amphiphilic  
– Axle



In the following, square antidot lattices are considered and parameters are chosen as  $d/a = 0.5$ . The parameter  $\Delta$  for the model potential given by Eq. (3) characterizing the steepness of the potential is chosen as  $\Delta/a = 0.24$ . This model potential becomes close to that given by Eq. (1) for  $\beta = 1$  and  $d/a \sim 0.5$ . Effects of impurities are introduced through random short-range scatterers, and fluctuations in the diameter of antidots are also introduced.

First, we consider the commensurability peak and the superimposed Aharonov–Bohm oscillation. Fig. 28 shows the dependence of the calculated magnetoresistance on the Fermi wavelength  $\lambda_F$  for the mean free path  $\Lambda/\pi a = 2$  in the absence of the antidot disorder.<sup>[65]</sup> The Aharonov–Bohm-type oscillation is clearly seen to be superimposed on the commensurability peak. The vertical solid and dashed lines indicate semiclassical quantized levels of the stable and unstable periodic orbits, respectively, encircling a dot, which are calculated based on Eq. (7). The Aharonov–Bohm-type oscillation varies with the Fermi

energy in a somewhat irregular manner, but is correlated quite well with semiclassical levels.

For the model potential (Eq. (3)), the periodic orbit encircling an antidot is quite sensitive to the aspect ratio  $d/a$  and disappears when  $d/a$  exceeds a critical value depending on the magnetic field. Fig. 29 shows the boundary of the existence of the periodic orbit encircling an antidot for a model potential given by Eq. (3).<sup>[69]</sup> The insets in the right-hand side of the figure show the periodic orbit (solid line) for  $d/a = 0.6$  and  $0.677$ . With the increase of  $d/a$ , it merges into another orbit (dotted line), which is unstable and has a longer trajectory, and disappears. It contains the boundary in the case of  $\Delta/a = 0.18$  and  $0.36$  as well. The critical aspect ratio becomes smaller with the increase of  $\Delta/a$  (i.e., as the antidot potential becomes broader).

Fig. 30 shows the calculated results of magnetoresistance for various values of the aspect ratio in the case of dominant impurity scattering.<sup>[69]</sup> The Aharonov–Bohm-type oscillation changes as a function of the magnetic field in an irregular manner, but the

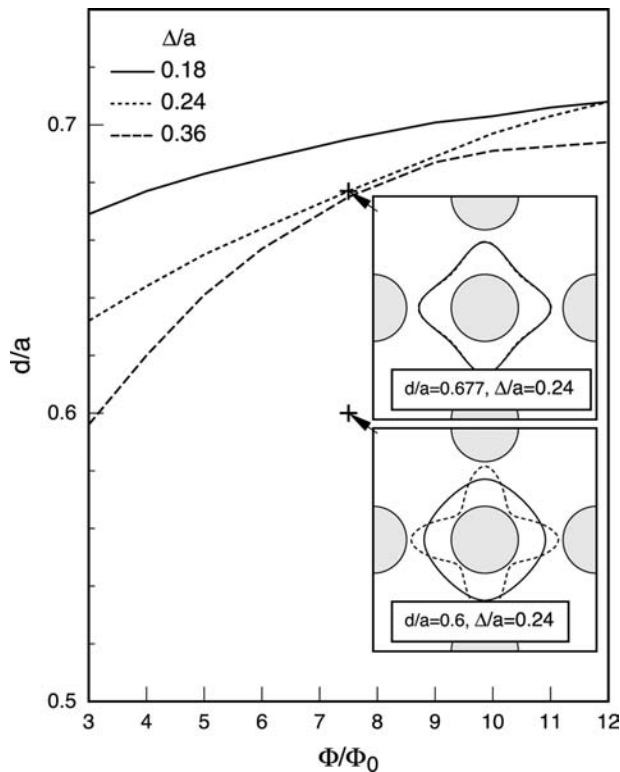


**Fig. 29** Critical values of the aspect ratio at which the periodic orbit encircling an antidot disappears.  $\Delta/a = 0.18$  (solid line),  $0.24$  (dotted line, realistic), and  $0.36$  (dashed line). The right upper and lower insets show the periodic orbit (solid line) giving the Aharonov–Bohm-type oscillation and the other (dotted line) that is unstable. These orbits merge and disappear when the aspect ratio approaches a critical value. *Source:* From Ref.<sup>[69]</sup>.

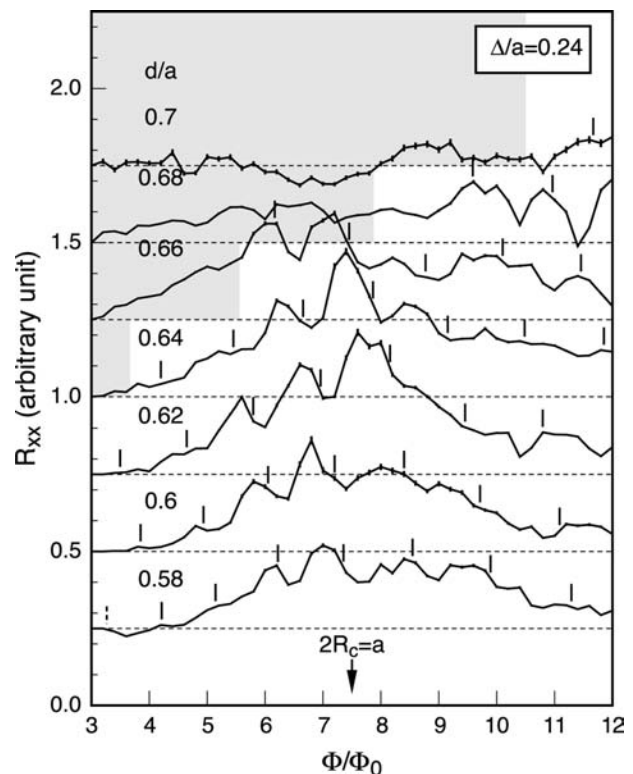


**Fig. 30** Calculated resistance as a function of the total flux  $\Phi$  passing through a unit cell divided by the flux quantum  $\Phi_0$  for varying Fermi wavelengths. Short vertical lines represent semiclassically quantized energy levels associated with the periodic orbit encircling an antidot (solid and dotted lines for stable and unstable orbits, respectively). *Source:* From Ref.<sup>[69]</sup>.



dependence on the field is, on the whole, in good agreement with that of the position of quantized levels of the periodic orbit. The oscillation disappears or becomes unrecognizable near the field corresponding to  $2R_c = a$  for a large aspect ratio  $d/a = 0.7$ . This field corresponds to the disappearance of the periodic orbit. In fact, the periodic orbit is absent in the hatched region, where no clear Aharonov–Bohm-type oscillation is visible. This provides a clear evidence that the Aharonov–Bohm-type oscillation is caused by the specific periodic orbit (b) in Fig. 13 encircling an antidot.

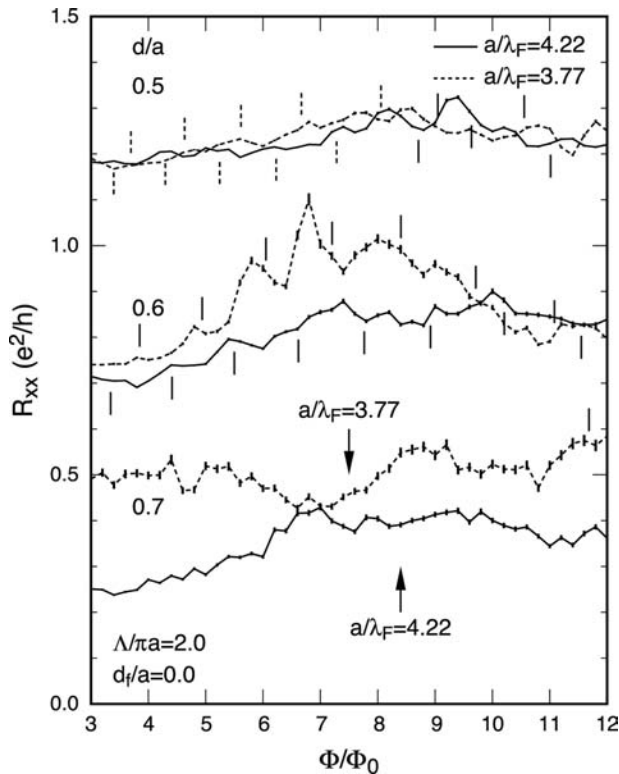
Fig. 31 shows the resistivity for the mean free path  $\Lambda/\pi a = 2$  in the absence of the antidot disorder at several values of  $d/a$  and  $a/\lambda_F$ .<sup>[70]</sup> Both commensurability peak and Aharonov–Bohm-type oscillation vary in an irregular manner with the change in the Fermi energy and the aspect ratio. This can be understood in terms of the anomalous behavior of the Hall conductivity because of the complicated band mixing, as mentioned in “Commensurability Peaks.”

Fig. 32 shows the resistivity in the presence of disorder  $d_f/a = 0.07$  in the antidot diameter without

impurities.<sup>[70]</sup> The irregular dependence of the commensurability peak and the Aharonov–Bohm-type oscillation on the Fermi energy and the aspect ratio has disappeared completely. In particular, the resistivity shows a smooth Aharonov–Bohm-type oscillation much closer to experiments. This suggests that such a band structure is destroyed almost completely by the presence of the antidot disorder.

Many periodic orbits can contribute to the Aharonov–Bohm-type oscillation in ideal antidot lattices. In the presence of disorder in the antidot potential, the shortest orbit encircling a single antidot is expected to be less influenced and its quantized energy levels can survive, whereas those of other orbits are strongly disturbed and smeared out. In other words, the antidot disorder tends to enhance the contribution of the energy levels of this orbit relative to those of other orbits. This explains the fact that the Aharonov–Bohm-type oscillation is sensitive to the Fermi energy for impurity scattering but not for scattering from antidot disorder.

The present formalism is quite effective in the study of insulator–quantum Hall transition and the localization oscillation observed experimentally.<sup>[56]</sup> In fact, a numerical study demonstrated the presence of quantum oscillations of the localization length with periods of  $\Phi_0/2$  and  $\Phi_0$ , and also an insulator–quantum Hall



**Fig. 31** Calculated magnetoresistance in the case of dominant impurity scattering. The arrows indicate the field corresponding to  $2R_c/a = 1$ . Short vertical lines represent energy levels associated with the orbit encircling an antidot (solid and dotted lines for stable and unstable orbits, respectively). Source: From Ref.<sup>[70]</sup>.

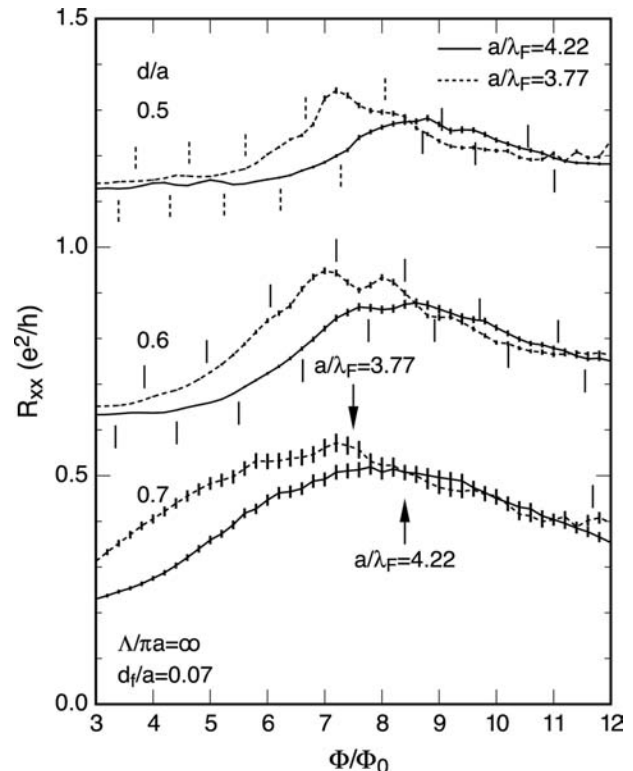


**Fig. 32** Calculated resistance in the case of dominant scattering by antidot disorder. Source: From Ref.<sup>[70]</sup>.

transition point where the Fermi level crosses extended states.<sup>[71]</sup> It showed also that extended states float in energy and disappear at a critical magnetic field. This problem is outside the scope of this entry; therefore this will not be discussed further.

## CONCLUSION

A review of magnetotransport in antidot lattices has been given mainly from a theoretical point of view. The commensurability peaks appearing in magnetoresistivity can be understood in terms of an enhancement in the measure of diffusive orbits contributing to the diffusion coefficients caused by a magnetic focusing effect. Differences existing between square and triangular lattices and roles of quantum effects have been understood by the same mechanism. It has also been shown that realistic antidot lattices have a large amount of disorder in the potential, which accounts for the appearance of the Altshuler–Aronov–Spivak oscillation and manifests itself in the commensurability peak and the superimposed Aharonov–Bohm-type oscillation. The disorder in the antidot potential also gives rise to localization of electron wave functions oscillating as a function of a magnetic field and the insulator–quantum Hall transition in high magnetic fields.

## ACKNOWLEDGMENTS

I would like to acknowledge the collaboration with Dr. T. Nakanishi, Dr. S. Ishizaka, and Dr. S. Uryu.

## REFERENCES

- Weiss, D.; Roukes, M.L.; Menschig, A.; Grambow, P.; von Klitzing, K.; Weimann, G. Electron pinball and commensurate orbits in a periodic array of scatterers. *Phys. Rev. Lett.* **1991**, *66*, 2790.
- Fleischmann, R.; Geisel, T.; Ketzmerick, K. Quenched and negative Hall effect in periodic media: Application to antidot superlattices. *Europhys. Lett.* **1994**, *25*, 219.
- Gusev, G.M.; Kvon, Z.D.; Litvin, L.V.; Nastaushev, Yu.V.; Kalagin, A.K.; Toropov, A.I. Aharonov–Bohm oscillations in a 2D electron gas with a periodic lattice of scatterers. *JETP Lett.* **1992**, *55*, 123.
- Gusev, G.M.; Basmaji, P.; Kvon, Z.D.; Litvin, L.V.; Nastaushev, Yu.V.; Toropov, A.I. Negative differential magnetoresistance and commensurability oscillations of two-dimensional electrons in a disordered array of antidots. *J. Phys., Condens. Matter* **1994**, *6*, 73.
- Nakamura, K.; Ishizaka, S.; Nihey, F. Anisotropic mobilities of low-dimensional electrons at stepped n-AlGaAs / GaAs interfaces with 15 nm periodicity on vicinal (111)B substrates. *Physica, B* **1994**, *197*, 144.
- Nihey, F.; Hwang, S.W.; Nakamura, K. Observation of large  $h/2e$  oscillations in semiconductor antidot lattices. *Phys. Rev., B* **1995**, *51*, 4649.
- Lorke, A.; Kotthaus, J.P.; Ploog, K. Magnetotransport in two-dimensional lateral superlattices. *Phys. Rev., B* **1991**, *44*, 3447.
- Yamashiro, T.; Takahara, J.; Takagaki, Y.; Gamo, K.; Namba, S.; Takaoka, S.; Murase, K. Commensurate classical orbits on triangular lattices of anti-dots. *Solid State Commun.* **1991**, *79*, 885.
- Takahara, J.; Kakuta, T.; Yamashiro, T.; Takagaki, Y.; Shiokawa, T.; Gamo, K.; Namba, S.; Takaoka, S.; Murase, K. Ballistic electron transport on periodic and quasi-periodic triangular lattices of scatterers. *Jpn. J. Appl. Phys.* **1991**, *30*, 3250.
- Deruelle, T.; Ensslin, K.; Petroff, P.M.; Efros, A.L.; Pikus, F.G. Effective size of scattering centers in a two-dimensional electron gas. *Phys. Rev., B* **1992**, *45*, 9082.
- Berthold, G.; Smoliner, J.; Rosskopf, V.; Gornik, E.; Böhm, G.; Weimann, G. Magnetoresistance and temperature effects in dotlike lateral surface superlattices. *Phys. Rev., B* **1993**, *47*, 10383.
- Schuster, R.; Ensslin, K.; Kotthaus, J.P.; Holland, M.; Stanley, C. Selective probing of ballistic electron orbits in rectangular antidot lattices. *Phys. Rev., B* **1993**, *47*, 6843.
- Schuster, R.; Ensslin, K.; Wharam, D.; Kühn, S.; Kotthaus, J.P.; Böhm, G.; Klein, W.; Tränkle, T.; Weimann, G. Phase-coherent electrons in a finite antidot lattice. *Phys. Rev., B* **1994**, *49*, 8510.
- Weiss, D.; Richter, K.; Vasiliadou, E.; Lütjering, G. Magnetotransport in antidot arrays. *Surf. Sci.* **1994**, *305*, 408.
- Deruelle, T.; Meurer, B.; Guldner, Y.; Vieren, J.P.; Riek, M.; Weiss, D.; von Klitzing, K.; Eberl, K.; Ploog, K. Influence of the depletion length on the commensurability effects in tunable antidots. *Phys. Rev., B* **1994**, *49*, 16561.
- Tsukagoshi, K.; Wakayama, S.; Oto, K.; Takaoka, S.; Murase, K.; Gamo, K. Transport properties in artificial lateral superlattice. *Superlattices Microstruct.* **1994**, *16*, 295.
- Nihey, F.; Nakamura, K. Aharonov–Bohm effect in antidot structures. *Physica, B* **1993**, *184*, 398.
- Weiss, D.; Richter, K.; Menschig, A.; Bergmann, R.; Schweizer, H.; von Klitzing, K.; Weimann, G. Quantized periodic orbits in large antidot arrays. *Phys. Rev. Lett.* **1993**, *70*, 4118.
- Kumar, A.; Laux, S.E.; Stern, F. Electron states in a GaAs quantum dot in a magnetic field. *Phys. Rev., B* **1990**, *42*, 5166.
- Suzuki, T.; Ando, T. Subband structure of quantum wires in magnetic fields. *J. Phys. Soc. Jpn.* **1993**, *62*, 2986.
- Fleischmann, R.; Geisel, T.; Ketzmerick, R. Magnetoresistance due to chaos and nonlinear resonances in lateral surface superlattices. *Phys. Rev. Lett.* **1992**, *68*, 1367.

22. Baskin, E.M.; Gusev, G.M.; Kvon, Z.D.; Pogosov, A.G.; Entin, M.V. Stochastic dynamics of 2D electrons in a periodic lattice of antidots. *JETP Lett.* **1992**, *55*, 678.
23. Ensslin, K.; Sasa, S.; Deruelle, T.; Petroff, P.M. Anisotropic electron transport through a rectangular antidot lattice. *Surf. Sci.* **1992**, *263*, 319.
24. Takahara, J.; Nomura, A.; Gamo, K.; Takaoka, S.; Murase, K.; Ahmed, H. Magnetotransport in hexagonal and rectangular antidot lattices. *Jpn. J. Appl. Phys.* **1995**, *34*, 4325.
25. Tsukagoshi, K.; Wakayama, S.; Oto, K.; Takaoka, S.; Murase, K.; Gamo, K. Magnetotransport through disordered and anisotropic antidot lattices in GaAs/AlGaAs heterostructures. *Phys. Rev., B* **1995**, *52*, 8344.
26. Tsukagoshi, K.; Haraguchi, M.; Oto, K.; Takaoka, S.; Murase, K.; Gamo, K. Current-direction-dependent commensurate oscillations in GaAs/AlGaAs antidot superlattice. *Jpn. J. Appl. Phys.* **1995**, *34*, 4335.
27. Tsukagoshi, K.; Haraguchi, M.; Takaoka, S.; Murase, K. On the mechanism of commensurability oscillations in anisotropic antidot lattices. *J. Phys. Soc. Jpn.* **1996**, *65*, 811.
28. Nagao, T. Effect of anisotropy on magnetotransport through antidot lattices. *J. Phys. Soc. Jpn.* **1995**, *64*, 4097.
29. Nagao, T. Magnetotransport through random antidot lattices. *J. Phys. Soc. Jpn.* **1996**, *65*, 2606.
30. Ishizaka, S.; Ando, T. Detailed analysis of the commensurability peak in antidot arrays with various periods. *Phys. Rev., B* **1997**, *55*, 16331.
31. Lu, W.-C.; Anderson, O.K. Transport Properties in Finite Antidot System. In Proceedings of the 23rd International Conference on Physics of Semiconductors; Scheffler, M., Zimmermann, R., Eds.; World Scientific: Singapore, 1996; 1497.
32. Ishizaka, S.; Nihey, F.; Nakamura, K.; Sone, J.; Ando, T. Numerical studies on quantum transport in antidot arrays in magnetic fields. *Jpn. J. Appl. Phys.* **1995**, *34*, 4317.
33. Ando, T.; Uemura, Y. Theory of quantum transport in a two-dimensional electron system under magnetic fields: I. Characteristics of level broadening and transport under strong fields. *J. Phys. Soc. Jpn.* **1974**, *36*, 959.
34. Ando, T. Theory of quantum transport in a two-dimensional electron system under magnetic fields: II. Single-site approximation under strong fields. *J. Phys. Soc. Jpn.* **1974**, *36*, 1521.
35. Schuster, R.; Ernst, G.; Ensslin, K.; Entin, M.; Holland, M.; Böhm, G.; Klein, W. Experimental characterization of electron trajectories in antidot lattices. *Phys. Rev., B* **1994**, *50*, 8090.
36. Tsukagoshi, K.; Nagao, T.; Haraguchi, M.; Takaoka, S.; Murase, K.; Gamo, K. Investigation of Hall resistivity in antidot lattices with respect to commensurability oscillations. *J. Phys. Soc. Jpn.* **1996**, *65*, 1914.
37. Ishizaka, S.; Ando, T. Quantum transport in square and triangular antidot arrays with various periods. *Phys. Rev., B* **1997**, *56*, 15195.
38. Silberbauer, H.; Rössler, U. Quantum study of magnetotransport in antidot superlattices. *Phys. Rev., B* **1994**, *50*, 11911.
39. Uryu, S.; Ando, T. Magnetotransport in Antidot Lattices. In Proceedings of the 23rd International Conference on Physics of Semiconductors; Scheffler, M., Zimmermann, R., Eds.; World Scientific: Singapore, 1996; 1505.
40. Ishizaka, S.; Nihey, F.; Nakamura, K.; Sone, J.; Ando, T. Quantum transport in antidot arrays in magnetic fields. *Phys. Rev., B* **1995**, *51*, 9881.
41. Hofstadter, D. Energy levels and wave functions of Bloch electrons in rational and irrational magnetic fields. *Phys. Rev., B* **1976**, *14*, 2239.
42. Oakshott, R.B.S.; MacKinnon, A. Bandstructure of two-dimensional periodic potentials in a magnetic field: A recursive Green-function approach. *J. Phys., Condens. Matter* **1993**, *5*, 6971.
43. Oakshott, R.B.S.; MacKinnon, A. On the conductivity of lateral-surface superlattices. *J. Phys., Condens. Matter* **1993**, *5*, 6983.
44. Oakshott, R.B.S.; MacKinnon, A. On the conductivity of antidot lattices in magnetic fields. *J. Phys., Condens. Matter* **1994**, *6*, 1519.
45. Gutzwiller, M.C. Phase-integral approximation in momentum space and the bound states of an atom. *J. Math. Phys.* **1967**, *8*, 1979.
46. Gutzwiller, M.C. *Path Integrals*; Papadopoulos, G.J., Devreese, J.T., Eds.; Plenum: New York, 1978; 163 pp.
47. Gutzwiller, M.C. *Chaos in Classical and Quantum Mechanics*; Springer: New York, 1990.
48. Miller, W.H. Semiclassical quantization of nonseparable systems: A new look at periodic orbit theory. *J. Chem. Phys.* **1975**, *63*, 996.
49. Uryu, S.; Ando, T. Analysis of antidot lattices with periodic orbit theory. *Physica, B* **1996**, *227*, 138.
50. Richter, K. Phase coherence effects in antidot lattices: A semiclassical approach to bulk conductivity. *Europhys. Lett.* **1995**, *29*, 7.
51. Wilkinson, M. A semiclassical sum rule for matrix elements of classically chaotic systems. *J. Phys., A* **1987**, *20*, 2415.
52. Hackenbroich, G.; von Oppen, F. Periodic-orbit theory of quantum transport in antidot lattices. *Europhys. Lett.* **1995**, *29*, 151.
53. Ishizaka, S.; Ando, T. Commensurability peak in square and triangular antidot arrays. *Solid State Electron.* **1998**, *42*, 1147.
54. Nakanishi, T.; Ando, T. Quantum interference effects in antidot lattices in magnetic fields. *Phys. Rev., B* **1996**, *54*, 8021.
55. Nakanishi, T.; Ando, T. AAS oscillation in antidot lattices. *Physica, B* **1996**, *227*, 127.
56. Nihey, F.; Kastner, M.A.; Nakamura, K. Insulator-to-quantum-Hall-liquid transition in an antidot lattice. *Phys. Rev., B* **1997**, *55*, 4085.
57. Uryu, S.; Ando, T. Localization oscillation in antidot lattices. *Physica, B* **1998**, *249–251*, 308.
58. Uryu, S.; Ando, T. Numerical study of localization in antidot lattices. *Phys. Rev., B* **1998**, *58*, 10583.
59. Altshuler, B.L.; Aronov, A.G.; Spivak, B.Z. The Aaronov–Bohm effect in disordered conductors. *JETP Lett.* **1981**, *33*, 94.

60. Sharvin, D.Yu.; Sharvin, Yu.V. Magnetic-flux quantization in a cylindrical film of a normal metal. *JETP Lett.* **1981**, *34*, 272.
61. Dolan, G.J.; Licini, J.C.; Bishop, D.J. Quantum interference effects in lithium ring arrays. *Phys. Rev. Lett.* **1986**, *56*, 1493.
62. Ando, T. Quantum point contacts in magnetic fields. *Phys. Rev., B* **1991**, *44*, 8017.
63. Uryu, S.; Ando, T. Scattering-matrix formalism for antidot lattices. *Jpn. J. Appl. Phys.* **1995**, *34*, 4295.
64. Uryu, S.; Ando, T. Electronic states in antidot lattices: Scattering-matrix formalism. *Phys. Rev., B* **1996**, *53*, 13613.
65. Uryu, S. Antidot Lattices in Magnetic Fields. In *Doctoral Thesis*; University of Tokyo, 1998.
66. Landauer, R. Spatial variation of currents and fields due to localized scatterers in metallic conduction. *IBM J. Res. Dev.* **1957**, *1*, 223.
67. Landauer, R. Electrical resistance of disordered one-dimensional lattices. *Philos. Mag.* **1970**, *21*, 863.
68. Büttiker, M. Four-terminal phase-coherent conductance. *Phys. Rev. Lett.* **1986**, *57*, 1761.
69. Uryu, S.; Ando, T. Aharonov–Bohm oscillation and periodic orbits in antidot lattices. *Physica, B* **1998**, *256–258*, 388.
70. Uryu, S.; Ando, T. Aharonov–Bohm type oscillation in antidot lattices. *Solid State Electron.* **1998**, *42*, 1141.
71. Uryu, S.; Ando, T. Insulator–quantum Hall transition in antidot lattices. *Phys. Rev., B* **2001**, *65*, 35322.

# Atmospheric Nanoparticles: Formation and Physicochemical Properties

James N. Smith

Atmospheric Chemistry Division, National Center for Atmospheric Research,  
Boulder, Colorado, U.S.A.

## INTRODUCTION

Atmospheric nanoparticles, defined as particles with spherical equivalent diameters smaller than 50 nm, are either directly emitted from combustion sources, or are formed in the atmosphere by a process called nucleation. They then quickly grow by the condensation of gas monomers or clusters, or by coagulation with other particles, to become a critical participant in a number of important atmospheric processes such as heterogeneous chemistry, cloud formation, precipitation, and the scatter and absorption of solar radiation. An understanding of nanoparticles has increased dramatically in recent years because of significant advances in instrumentation to detect, size, and determined their chemical composition. Recent observations now show us that atmospheric nanoparticles are ubiquitous: Measurements carried out in city centers, isolated islands and forests, and the remote troposphere have never failed to encounter periods characterized by concentrations of up to  $10^6$  nanoparticles/cm<sup>3</sup>. Theoretical advances in nucleation and growth, at present, have not made the same sort of progress as observation, but this is an area of rapid progress.

The goal of this entry is to provide an overview of the role that nanoparticles play in the atmosphere, the observational and theoretical tools currently being employed in their study, and recent observations that continue to direct progress in understanding their formation and fate. Although much is known about these transient particles, researchers appear to be at the cusp of huge scientific advances that will make it possible to predict their formation and behavior in the atmosphere.

## BACKGROUND

Excellent texts are available on the subject of atmospheric particulate matter,<sup>[1,2]</sup> which is commonly referred to as atmospheric aerosol. These texts are also adequate references on atmospheric nanoparticles; however, recently, a review chapter<sup>[3]</sup> and a special

journal issue<sup>[4]</sup> have focused specifically on this area. The goal of this section is to provide a broad overview of the distribution, sources, and lifetimes of atmospheric aerosol. This is followed by a review of relevant atmospheric process involving nanoparticles.

## Atmospheric Particle Size Distributions

Close to the Earth's surface, continental air typically contains from  $10^3$  to  $10^5$  particles/cm<sup>3</sup>. These particles have spherical equivalent diameters  $d_p$  ranging from 1 nm to 100  $\mu$ m. A plot of particle number concentration, surface area, or volume *vs.*  $d_p$ , such as those shown in Fig. 1 for typical rural settings, usually shows that these particles are distributed over three or more modes. Most particles are smaller than 100 nm in diameter (Fig. 1A), in a mode referred to as the Aitken mode. The term *ultrafine aerosol* is often used for those with diameters smaller than 100 nm. The other two predominant modes are the accumulation mode ( $0.1 < d_p < 2.5 \mu$ m) and the coarse mode ( $d_p > 2.5 \mu$ m). Within the Aitken mode, for  $d_p < 50$  nm, many properties of the condensed phase, most notably vapor pressure, become quite different from those of the bulk phase: Thus particles smaller than 50 nm have come to be known as nanoparticles. The implications of the distributions in Fig. 1 on atmospheric processes can be generalized as follows: For phenomena that depend on the particle number concentration, it is the Aitken mode that contributes the most; for those processes that are surface area dependent, the accumulation mode is most influential; for those that depend on total aerosol volume or mass, the coarse mode dominates.

## Atmospheric Particle Sources and Sinks

The different modes in aerosol size distribution reflect differences in the atmospheric sources, transformations, and sinks Fig. 2. Particles in the coarse mode are generated by mechanical processes such as wind and friction. The accumulation mode contains particles that have grown in the atmosphere by condensation

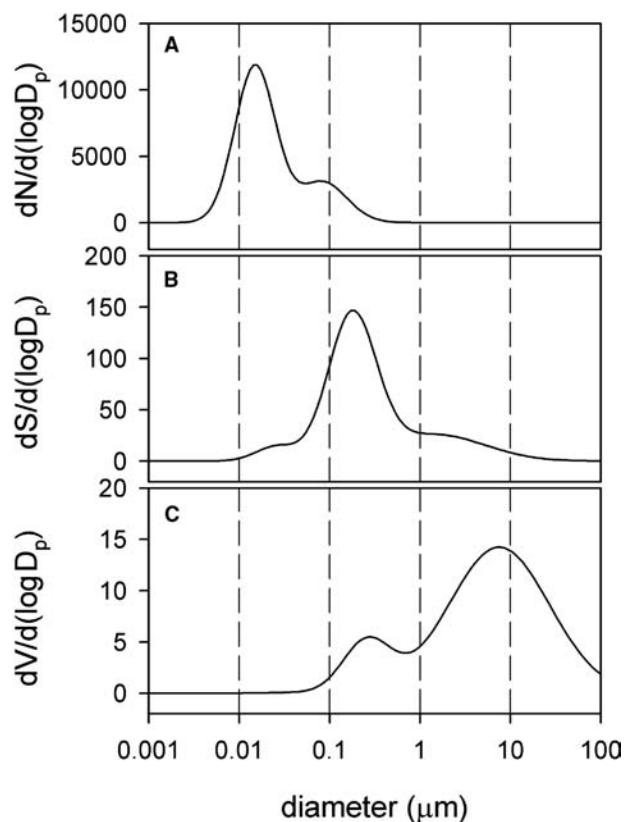


**Fig. 1** Particle (A) number, (B) surface area, and (C) volume distributions for typical rural conditions, generated using the parameterization of Jaenicke.<sup>[6]</sup>

of gases, or coagulation with other particles. The Aitken mode contains particles that are generated chemically, either directly emitted from a source (primary aerosol) or are created or grown from gas phase reactions in the atmosphere (secondary aerosol). The dominant loss mechanisms for Aitken mode particles are coagulation and condensation growth. Particles in the accumulation mode leave the atmosphere by adhering onto wetted surfaces, most commonly rain and cloud drops, through a process called wet deposition. Coarse mode particles eventually settle to the ground in a process called dry deposition. Fig. 3 shows the typical timescales for these removal processes. Dry deposition, coagulation, and condensational growth are relatively rapid processes, whereas wet deposition is the least efficient means of particle removal. The result is that particles in the accumulation mode are the longest-lived particles, having lifetimes that may span several days. Therefore these particles are commonly spatially homogeneous, and number distributions in this size range do not change rapidly with time. In contrast, Aitken mode particles have lifetimes of a few minutes to an hour. Therefore these particles commonly exist close to their source (e.g., near busy freeways) and their number distributions usually change rapidly with time.

## Nanoparticles in the Atmosphere

Nanoparticles, as a subset of the Aitken mode, are generated chemically either as primary emissions or through gas phase reactions in the atmosphere. The latter process is, in fact, nucleation and will be the focus of much of the discussion that follows. It is also true that nanoparticles are some of the most transient in the atmosphere, with a corresponding heterogeneous spatial distribution that depends on source distribution and meteorological conditions. Additionally nanoparticles may frequently dominate an aerosol number distribution, but usually not distributions of surface area and almost never of volume (Fig. 1). In view of these observations, it is reasonable to ask if nanoparticles play an important role in atmospheric processes, outside of their crucial role as the primary source of new particles. A question of equal importance, although outside the scope of this article, is whether atmospheric nanoparticles play a deleterious role in human health through respiration. The answer to this question is a qualitative “yes,” although the mechanism and magnitude of this effect are far from clear.<sup>[3,8,9]</sup>

The contribution of nanoparticles to scattering and absorption of solar radiation, which controls processes such as visibility reduction and climate, is understood to be negligible.<sup>[2]</sup> This is because of the low efficiency with which nanoparticles interact with solar radiation.<sup>[10]</sup> Perhaps the most important contribution of nanoparticles on climate is to influence the optical properties, abundance, and persistence of clouds.<sup>[11]</sup> An abundance of new particles could increase the number of cloud condensation nuclei (CCN), which are water-soluble aerosols on which water vapor condenses to form cloud droplets. The overall result of this so-called “indirect effect of aerosols on climate” is an issue of active research and debate, but is generally thought to be a reduction in incoming solar radiation.<sup>[11]</sup>

At the time of this writing, very little is known about whether nanoparticles may play a unique role in the chemistry of the atmosphere. It is certainly true that chemical reactions occur on atmospheric nanoparticles, just as they occur on all aerosol;<sup>[1]</sup> however, in most circumstances, the minimal contribution of nanoparticles to overall aerosol surface area (e.g., Fig. 1B) decreases the likelihood that these particles may influence the chemistry of the gas phase. The exception to this may be during “nucleation bursts,” which are periods of intense new particle production that can dominate the surface area distribution.<sup>[12]</sup> Although it may be true that the concentrations of certain reactive compounds may be enhanced in nanoparticles through the processes of nucleation and condensational growth, a simple analysis has



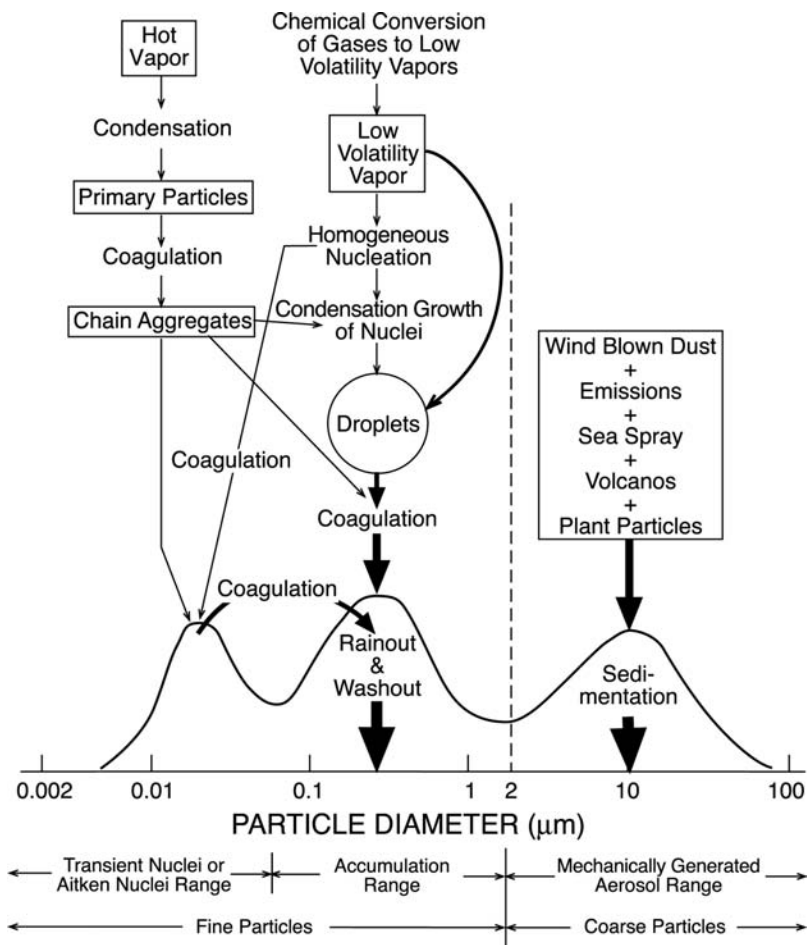


**Fig. 2** Schematic of the distribution of particle surface area in the atmosphere. Modes, sources, and sinks are indicated. *Source:* From Ref.<sup>[7]</sup>. ©IEEE, 2003.

shown that, even during nucleation burst periods, this enhancement would need to be a factor of  $10^6$  greater than reactant concentrations in typical cloud droplets to have a similar effect.<sup>[3]</sup>

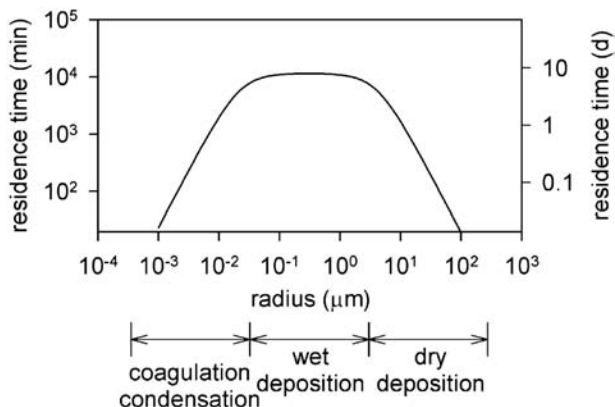


**Fig. 3** Residence time of particles in the lower 1.5 km of the atmosphere as a function of particle radius, generated using data from Jaenicke.<sup>[19]</sup> Also shown are approximate size ranges for predominant removal mechanisms.

### OBSERVATIONS OF ATMOSPHERIC NANOPARTICLE PHYSICOCHEMICAL PROPERTIES

Most of the important advances in our understanding of atmospheric nanoparticles have resulted from dramatic improvements in instrumentation for characterizing their size, number, and composition. As we will see later, these observations have challenged our theoretical understanding of both aerosol nucleation and growth. This section will provide an overview of these instruments, and some representative measurements.

#### Physical Characterization

Advances in the physical characterization of atmospheric nanoparticles now allow us to size and detect them when they are less than an hour old, corresponding to diameters of about 3 nm. It is now possible to characterize nanoparticle growth rates; thus we can start to make links between the presence of these nanoparticles and the variety of phenomena that they

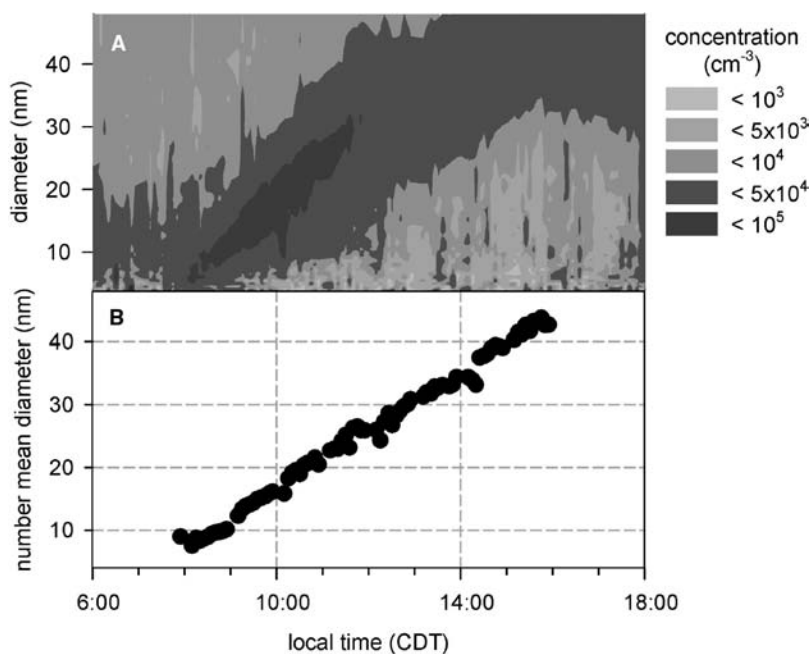


**Fig. 4** (A) Particle size distribution vs. local time for a nucleation event in St. Louis, MO. (B) Number mean diameter vs. local time for distributions in (A), showing a linear nanoparticle growth rate. *Source:* From Ref.<sup>[60]</sup> Courtesy of Q. Shi, University of Minnesota.

control. The current section briefly summarizes these physical characterization techniques.

The condensation nucleus counter (CNC)<sup>[13]</sup> can detect particles as small as 3 nm in diameter.<sup>[14]</sup> It accomplishes this by flowing the sample air first through a region that is saturated with a condensing vapor, usually *n*-butanol, and then through a cooled region. The gas then becomes supersaturated with the vapor, which causes the particles to grow to a size that can be detected by light scattering. The minimum detectable particle size is a function of vapor supersaturation; thus two CNCs with different supersaturations (or different transmission characteristics) can be operated in parallel and, by subtracting their readings, can be used to determine the concentration of particles within a certain size range. This subtraction technique is the most frequently used way of observing atmospheric nanoparticles.<sup>[15]</sup> Recent advances have been reported in the development of particle size magnifiers,<sup>[16]</sup> which are similar to CNCs but are being developed with the goal of detecting particles at diameters of 1 nm and below.

Size classification of nanoparticles is now possible using a number of techniques. The differential mobility analyzer (DMA)<sup>[17]</sup> is an “electrical mobility classifier” device that can size-classify particles down to 3 nm in diameter.<sup>[18]</sup> It does this by charging particles and passing them through a region where a sheath gas and an electric field are combined in such a way that only particles of a certain surface area-to-charge ratio can pass through the exit aperture. These instruments are commonly combined with CNCs to obtain nanoparticle size distributions. Fig. 4A shows an example of a continuous record of particle size distributions

from an urban site (St. Louis, MO), which features a new particle formation event that reached detectable levels at 8:00 A.M. Subsequent growth of the mean diameter of the spectrum is quite linear (Fig. 4B). This can be equated with aerosol growth if one assumes that the aerosol was homogeneous in a large-scale air mass.

Two additional methods for obtaining nanoparticle size distributions are the pulse height analysis (PHA) and the ion mobility spectrometer (IMS) techniques. PHA<sup>[20]</sup> operates on the principle that particles smaller than 10 nm grow by condensation in the CNC to reach a unique final diameter, which can be sized by optical techniques. The IMS can measure the size spectra of charged nanoparticles down to diameters below 1 nm, by measuring their drift velocity in a constant electric field.<sup>[21]</sup> IMS measurements have shown that, under certain conditions, nanoparticle formation is correlated with bursts of atmospheric ion clusters.<sup>[21]</sup>

### Chemical Composition

Until recently, the chemical characterization of atmospheric nanoparticles has not seen the same sort of progress as physical characterization. However, currently, several techniques have been developed for obtaining chemical composition information by: 1) indirectly inferring it by measuring some other behavior; 2) using off-line collection and analysis techniques; 3) using on-line real-time mass spectrometry-based techniques. In this section, these various methods will be briefly described.

Some of the earliest measurements of the chemical properties of nanoparticles were performed by using

a DMA to size-select particles, then exposing these particles to a controlled environment and acquiring a particle size distribution on the result to observe any changes in aerosol size.<sup>[22]</sup> Most of these instruments, called tandem differential mobility analyzers (TDMAs), expose size-selected particles to high humidity to investigate their hygroscopic properties, but others characterize volatility by applying high temperatures<sup>[23]</sup> or organic composition by using a gas saturated with various organic vapors.<sup>[24]</sup> In a related application, the growth characteristics of aerosol in a CNC have been investigated using the PHA technique, which was used to infer that nanoparticles in a boreal forest region were composed primarily of organic acids.<sup>[25]</sup>

Off-line sampling techniques involve collecting particles on a substrate, often in a size-segregated manner, for later chemical analysis. Such analysis might involve extraction of the constituents from the substrate and analysis of the integrated composition by techniques such as ion chromatography and inductively coupled plasma mass spectrometry (ICP-MS), illuminating the substrate with a light source to investigate optical absorption, or the study of isolated particles on the substrate by microanalytical techniques such as secondary ion mass spectrometry (SIMS) and Fourier transform infrared spectroscopy (FTIR).<sup>[26]</sup> The application of off-line techniques to nanoparticle composition is challenged by an inability to collect sufficient mass of these particles; nonetheless, most of what is known about the composition of the smallest particles in the atmosphere is derived from off-line techniques. Low-pressure impactors are often employed for collecting size-segregated ultrafine particles,<sup>[27–30]</sup> but these devices do not usually extend into the sub-50 nm diameter range. Observations of ultrafine urban aerosol from low-pressure impactors show particles to be composed of 50–70% (by weight) organic compounds and 6–14% (by weight) of each of the following: elemental carbon, sulfate, nitrate, and trace metals.<sup>[27,28]</sup> Recently, a particle concentrator that allows the collection of particles as small as 10 nm in diameter, requiring integration times of 3 hr or more, has been described.<sup>[31]</sup> That study found a distinct mode in the 36–50-nm diameter range, affected primarily by combustion processes; however, correlations between elemental and organic carbon compositions also suggested that these particles contained secondary organic compounds.<sup>[31]</sup> Dimethylamine has been identified by the chemical analysis of newly formed particles collected in a low-pressure impactor in a boreal forest.<sup>[30]</sup> One recent example of the use of off-line microanalytical techniques has been reported in the study of recently formed particles in a coastal setting. That study observed both iodine and sulfur in particles with diameters below 10 nm,<sup>[32]</sup> suggesting

that biogenic iodine species emitted from seaweeds may be responsible for new particle formation or growth.

On-line chemical analysis techniques directly analyze particles in real time, usually by vaporizing particles through lasers or heated surfaces, ionizing the resulting gas, and injecting the ions into a mass spectrometer for analysis.<sup>[33]</sup> These techniques are highly desirable for the study of nanoparticle composition, as they have capabilities of both high sensitivity and short sampling times. Most current on-line techniques rely on improving the nanoparticle sampling efficiency of existing instruments (e.g., Phares, Rhoads, and Wexler.)<sup>[34]</sup> This has been accomplished primarily by the use of aerodynamic focusing lens systems<sup>[35]</sup> whose transmission efficiency degrades significantly for particle diameters smaller than 20 nm. Most of these instruments are very new—field measurements have only just started; therefore very little published data are available. One example of published results comes from the 1999 Atlanta Southern Oxidant Study, which found that particles as small as 14 nm are almost completely organic.<sup>[36]</sup> The authors point out the ability to analyze nanoparticles is based, to some degree, on particle composition. For example, sulfate was not identified in any particles with their instrument, whereas other measurements during the same field campaign identified sulfate as a major constituent.<sup>[37]</sup>

New instruments that have been designed specifically for the on-line characterization of nanoparticles

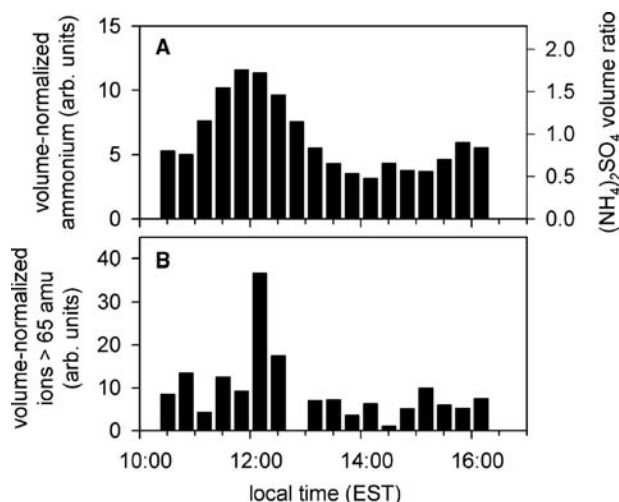


**Fig. 5** Measurements of the chemical composition of sub-20 nm diameter aerosol performed outside of the author's laboratory in Boulder, CO, on June 6, 2002. (A) Ammonium ion concentration, normalized by collected aerosol volume (left axis) and as the ratio to the ion signal from an equivalent volume of ammonium sulfate aerosol. (B) Integrated volume-normalized concentration of ions with molecular weight greater than 65 amu.

have also been introduced. Most of these new devices are limited to obtaining atomic, rather than molecular, composition of the aerosol, and usually employ high-power lasers<sup>[38]</sup> and plasmas<sup>[39]</sup> to desorb and ionize aerosols smaller than 20 nm in diameter. The author has recently reported the development of the thermal desorption chemical ionization mass spectrometer (TDCIMS), an instrument capable of on-line measurements of the molecular composition of nanoparticles as small as 5 nm in diameter at time resolutions of ca. 20 min.<sup>[40,41]</sup> The TDCIMS operates by charging and then collecting nanoparticles on a metal filament, then resistively heating the filament and analyzing the desorbed gas by chemical ionization mass spectrometry (CIMS). Fig. 5 shows an example of continuous TDCIMS measurements of sub-20-nm-diameter aerosols performed outside our laboratories in Boulder, CO, in the spring of 2002. The major ion observed is ammonium (Fig. 5A); however, the integrated concentration of ions larger than 65 amu varies greatly during the day (Fig. 5B). The TDCIMS has also performed measurements of the composition of freshly nucleated particles at the 2002 Aerosol Nucleation and Real-time Characterization Experiment (ANARChE) in Atlanta, GA. Preliminary results from that experiment suggest that freshly nucleated

aerosols in Atlanta are composed almost entirely of sulfate with variable degrees of neutralization by ammonium.<sup>[42]</sup>

## ATMOSPHERIC NANOPARTICLE FORMATION AND GROWTH: MODELS AND OBSERVATIONS

Given the current understanding of the atmospheric impact of nanoparticles, it is clear that the ability to predict the physicochemical properties of nanoparticles requires equal effort placed on understanding the growth of nanoparticles and their formation. Because instruments are, thus far, unable to directly observe newly formed aerosol in the atmosphere, the interpretation of observations of nucleation also requires an understanding of the mechanism and dynamics of condensational growth. The goal of the present section is to review the current theoretical basis for nucleation and growth.

Fig. 6 shows a schematic of the formation and growth of atmospheric nanoparticles. The primary formation process is homogeneous nucleation, which is defined as the formation of thermodynamically stable particles from the condensation of gaseous precursors. Primary sources, such as diesel

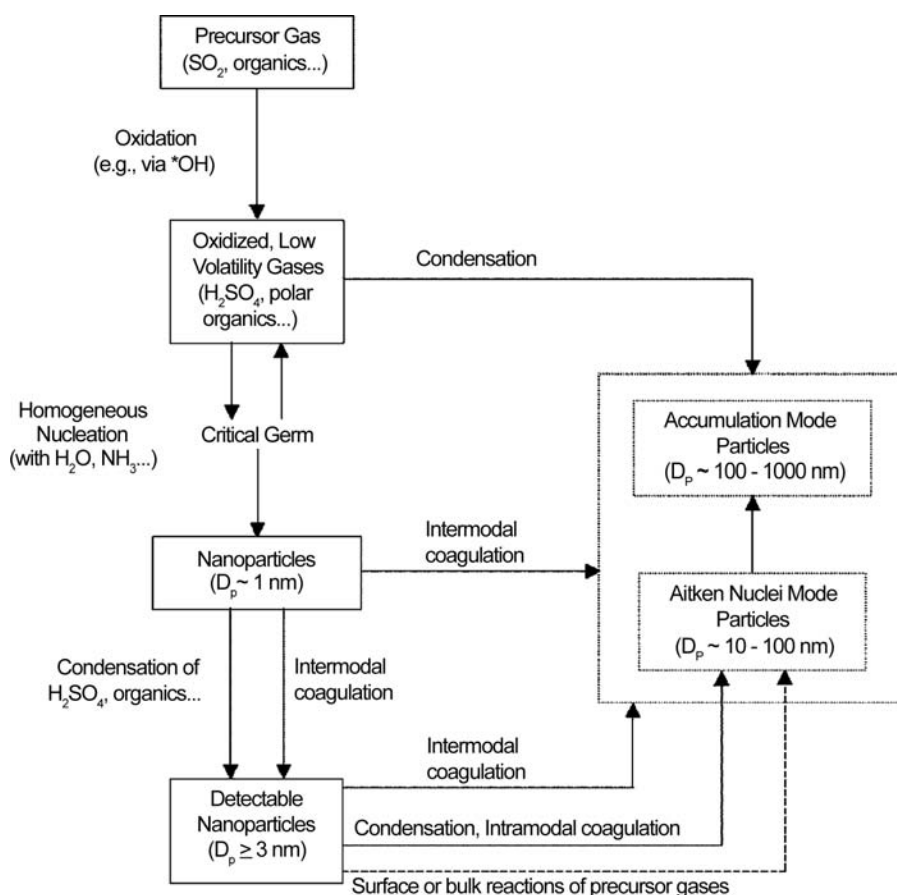


**Fig. 6** Schematic of nucleation and growth processes. *Source:* From Ref.<sup>[3]</sup>. Mineralogical Society of America.

engines,<sup>[43,44]</sup> can be significant sources of nanoparticles in urban settings but will not be discussed in this entry. Heterogeneous nucleation, defined as condensation of gases on foreign media such as gas phase ions, might also lead to the formation of atmospheric nanoparticles. It is important to note that, in the atmosphere, homogeneous nucleation is in competition with scavenging of the low-volatility gas by preexisting aerosol. Because of this, new particle formation in the atmosphere tends to occur in bursts (Fig. 4), either when the total aerosol surface area is suddenly dropped, or when a sudden meteorological or chemical change modifies the concentration of condensable vapor.

### Condensational Growth

One of the most unique properties of nanoparticles involves their evaporation and condensation behavior. As the curvature of a particle surface decreases, the separation between adjacent surface molecules increases leading to an overall decrease in the attractive forces between them. The result of this is that, at equilibrium, the partial pressure surrounding the curved surface will exceed the saturation vapor pressure for the flat surface. The equation that describes this effect is known as the Kelvin, or Thomson–Gibbs, equation:

$$S = \frac{p_d}{p_s} = \exp\left(\frac{4\sigma M_w}{\rho R T d^*}\right) \quad (1)$$

Here the vapor saturation ratio  $S$  is defined as the ratio of the vapor pressure surrounding the particle  $p_d$  to the saturation vapor pressure of the flat surface  $p_s$ . The surface tension, molecular weight, and density of the liquid are given by  $\sigma$ ,  $M_w$ , and  $\rho$ , respectively.  $R$  is the universal gas constant,  $T$  is temperature, and  $d^*$  is the diameter of a particle that will neither grow nor evaporate at  $S$ . Fig. 7A shows the relationship between  $S$  and  $d^*$ . The line given by Eq. (1) can be thought of as the boundary between condensational growth (region A in Fig. 7A) and evaporation (region B). If a particle's diameter and saturation ratio place it on the line and  $S$  were suddenly lowered, then the particle will completely evaporate; if, conversely,  $S$  were raised, then the droplet will grow indefinitely. The Kelvin equation predicts that a pure 10-nm-diameter water particle would require a minimum relative humidity of 125% to prevent evaporation.

In reality, there are no pure particles in the atmosphere. If the particle contains a soluble material, then during evaporation it will experience two competing effects: the Kelvin effect, which would require an increase in vapor pressure to stop evaporation, and the solute effect, in which the increase in solute

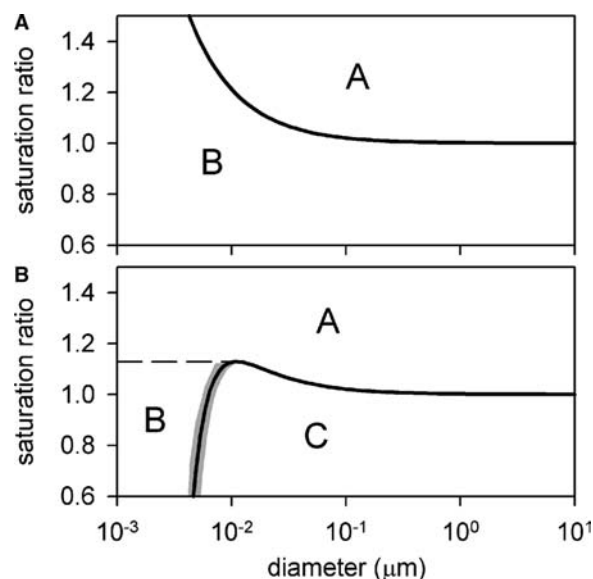


**Fig. 7** Saturation ratio vs. particle size for (A) pure water, using Eq. (1), and (B) water with NaCl added, assuming a dry particle diameter of 4 nm. Shaded line in (B) indicates line of stable equilibrium. Capital letters indicate regions of condensational growth and evaporation (see text).

concentration in the particle reduces the saturation ratio required for droplet stability. As the particle shrinks, the solute effect dominates over the Kelvin effect. The Köhler equation describes this competition:

$$\frac{p_d}{p_s} = \left(1 + \frac{6imM_w}{M_s\rho\pi d_p^3}\right)^{-1} \exp\left(\frac{4\sigma M_w}{\rho R T d^*}\right) \quad (2)$$

In Eq. (2),  $i$  is the solute van't Hoff factor and  $m$  is the mass of the dissolved solute with molecular weight  $M_s$ , and  $\rho$  is the density of the solvent. As Fig. 7B shows, the effect of this is dramatic. A nanoparticle in a gas at a saturation ratio that places it in region A will grow indefinitely. A particle in region B will grow until it reaches the shaded part of the curve, where it equilibrates with its surroundings. A particle in region C will evaporate until it reaches the shaded part of the curve, where it again forms a stable particle. The shaded part of the curve in Fig. 7B defines a true equilibrium, unlike the remaining part of the curve and the entire Kelvin equation curve shown in Fig. 7A, both of which define points of unstable equilibrium. This equilibrium particle size will change only if the saturation ratio changes, which will move it up or down the shaded line. If a particle were to grow until it reaches the curve maximum, then it will enter region A and proceed to grow into a cloud particle. However, if the saturation ratio were continuously lowered, the particle dries to form a solid residue. For a particle containing insoluble materials, the effect is to increase the solute

effect. Effectively, the insoluble material displaces the equivalent volume of solvent. Thus for the same diameter particle, the solute concentration is larger and the solute effect is greater. It is important to note the assumptions that are used to derive Eqs. (1) and (2). These are the capillarity assumption, in which bulk thermodynamic properties (e.g., surface tension  $\sigma$ ) are assigned to particles of all sizes, and the incompressibility approximation, which states that the overall particle volume can be calculated by summing the volumes of the individual species.

Once a stable nanoparticle is formed, the rate at which it grows by condensation is determined by the number of random collisions of vapor molecules with the particle. The kinetic theory of gases can be applied for particle diameters smaller than the mean free path of the vapor, resulting in:

$$\frac{dd_p}{dt} = \frac{2M_w(p - p_d)}{\rho N_a \sqrt{2\pi m k T}} \quad (3)$$

In Eq. (3),  $m$  is the mass of the vapor molecule;  $p$  is the partial pressure of the surrounding vapor;  $N_a$  is Avogadro's number;  $k$  is the Boltzmann constant; and  $p_d$  is the partial pressure of the vapor given by the Kelvin equation [Eq. (1)]. [Eq. (3)] states that nanoparticle growth is independent of particle size—precisely the observation provided by the particle growth measurements shown in Fig. 4.

### Homogeneous Nucleation

If homogeneous nucleation were to start on an individual water molecule ( $d^* = 0.4$  nm), then, according to the Kelvin equation, a saturation ratio of 220 would be required. Yet experiments with pure water at 20°C have shown that the process occurs at saturation ratios greater than 3.5.<sup>[45]</sup> Clearly, homogeneous nucleation in the atmosphere does not occur by condensation of vapor on individual molecules. In reality, intermolecular forces such as van der Waals forces lead to the formation of molecular clusters. As these clusters form and fall apart, some portions of these will reach the critical cluster size, which, for pure materials, is given by the Kelvin equation [Eq. (1)], and become stable nanoparticles. This is the microscopic view of homogeneous nucleation. Theoretical treatments of homogeneous nucleation fall into three categories: purely molecular theories, which apply only to simple molecules (e.g., Senger et al.);<sup>[46]</sup> phenomenological theories, which predict nucleation rates using measurable fluid properties as input; and intermediate theories, which share characteristics of each (e.g., Zeng and Oxtoby).<sup>[47]</sup> The focus of the current section will be on the phenomenological treatment classical

nucleation theory (CNT) since most of our current understanding is rooted in this theory. A good reference for recent progress in models and observations of nucleation can be found in the published proceedings of a recent conference devoted to this.<sup>[48]</sup>

As in the discussion of condensation, we start with the case of homogeneous nucleation by a single species. In CNT, the energy change associated with the spontaneous formation of a critical embryo  $\Delta G_{\text{embr}}$  is the sum of the energy change associated with molecules leaving the vapor phase and entering the embryo and the energy associated with the curved embryo surface:

$$\Delta G_{\text{embr}} = n^* \Delta \mu + \pi d^{*2} \sigma \quad (4)$$

where  $n^*$  is the number of molecules in the embryo,  $\Delta \mu$  is the difference in chemical potential for the molecule between solution and vapor, and  $\sigma$  is the surface tension, which is again approximated by the bulk surface tension (capillarity assumption). The nucleation rate, defined as the number of embryos nucleated per unit volume per unit time, is collision rate between molecules and embryos of the critical cluster size, multiplied by the number of critically sized embryos as given by the Boltzmann distribution. The result is:

$$J = \frac{p_v}{\sqrt{2\pi m k T}} \pi d^{*2} n_1 \exp\left(-\frac{\Delta G_{\text{embr}}}{kT}\right) \quad (5)$$

where  $n_1$  is the monomer concentration in the gas phase and  $m$  is the mass of the vapor molecule.

The chemical composition of the critical embryo can be determined by applying the nucleation theorem,<sup>[49]</sup> which relates the saturation ratio dependence on  $\Delta G_{\text{embr}}$  and  $n^*$ :

$$\frac{d\Delta G_{\text{embr}}}{d(kT \ln S)_T} = -n^* \quad (6)$$

The nucleation theorem is generally applicable to either molecular, phenomenological, or intermediate theory of nucleation. Combining Eqs. (5) and (6), one finds:

$$\frac{dJ}{d(\ln S)_T} = n^* + \frac{d(\ln K)}{d(\ln S)_T} \quad (7)$$

where  $K$  is the preexponential factor in Eq. 5. The  $d(\ln K)/d(\ln S)_T$  term can be generally neglected,<sup>[50]</sup> leaving a simple way of determining the critical cluster size  $n$  from observations of  $J$  and  $S$ .

The extension of CNT to multicomponent nucleation is straightforward<sup>[51]</sup> and involves solving



the simultaneous equations:

$$\frac{\ln S_{1,\text{sol}}}{v_1} = \frac{\ln S_{2,\text{sol}}}{v_2} = \dots = \frac{\ln S_{i,\text{sol}}}{v_i} \quad (8)$$

where  $S_{i,\text{sol}}$  is the saturation ratio of species  $i$  with respect to the liquid solution and  $v_i$  is the partial molecular volume of species  $i$ . Once the mole fraction of each compound  $x_i$  in the critical cluster is found from  $v_i$ , the embryo diameter is calculated from:

$$d^* = \frac{4\sigma \sum x_i v_i}{\sum x_i \Delta\mu_i} \quad (9)$$

$\Delta G_{\text{embr}}$  can then be found by substituting  $d^*$  into the multicomponent form of Eq. (4), in which  $n\Delta\mu$  is replaced by the sum of all  $n_i\Delta\mu_i$ . This can then be used to calculate  $J$  by using a multicomponent form of Eq. (5).<sup>[52]</sup>

The principal limitation of CNT is its reliance on the capillarity assumption. For binary nucleation, it has been found that the predictions of CNT are reasonable when the nucleating species form ideal solutions,<sup>[50]</sup> however, when one of the components tends to concentrate on the surface, the theory can yield unphysical results.<sup>[53]</sup> Most intermediate nucleation theories address this issue by retaining most of CNT while introducing correction factors for the nonideal behavior of molecular clusters. Another modification to CNT is required when the nucleating species readily hydrates (i.e., binds with one or more water vapor molecules). The most important example of this in the atmosphere is sulfuric acid/water binary nucleation, which will be discussed later.

## Coagulation

A brief discussion shall be devoted to coagulation, as it is one of the primary loss mechanisms for nanoparticles (Fig. 6). Coagulation is the process by which particles collide with one another and adhere to form larger particles. Nanoparticles are particularly susceptible to loss by Brownian coagulation, in which collisions are caused by relative Brownian motion. A simplified theory of coagulation<sup>[45]</sup> states that the rate of change of the number concentration,  $N$ , for particles of a given size is expressed as

$$\frac{dN}{dt} = -K_0 N^2 \quad (10)$$

$K_0$  is the coagulation coefficient, and is a function of diffusion coefficients and diameters of each particle in the mixture. Two interesting observations emerge from coagulation theory: First, the  $N^2$  dependence in

Eq. (10) means that coagulation is rapid when particle number concentrations are large. The second observation, which comes from the analysis of  $K_0$ , is that coagulation rate is at its minimum when particles are all of the same size, and rises rapidly when larger particles are added to the mixture.

## Observations of Atmospheric Nanoparticle Nucleation and Growth

In a recent review of more than 100 investigations of particle nucleation and growth rates, it was found that the formation rates of 3 nm diameter particles (The minimum detectable size) are in the range of  $0.01 - 10 \text{ cm}^{-3} \text{ sec}^{-1}$  in the clean remote troposphere, but can be up to  $100 \text{ cm}^{-3} \text{ sec}^{-1}$  in urban areas and as high as  $10^5 \text{ cm}^{-3} \text{ sec}^{-1}$  in certain coastal areas and in industrial plumes.<sup>[15]</sup> Sulfuric acid is the species most commonly associated with nucleation in the atmosphere, although there is still no direct proof of this because the chemical composition of nucleating clusters has, thus far, not been measured. Observations at a remote site in Colorado Fig. 8, show clear correlations between increases in sulfuric acid vapor and nucleation. This frequently observed phenomenon and sulfuric acid's extremely low volatility have made it the most likely candidate for study. Sulfuric acid forms hydrates that tend to decrease its effectiveness as a nucleating agent by a factor of  $10^5 - 10^6$ , compared with the absence of hydrates.<sup>[1]</sup> Models that account for hydrate formation do so by treating hydrates as small liquid droplets.<sup>[55]</sup> When these models are applied to observations of nucleation, results such as those shown in Fig. 9 are commonly observed. In Fig. 9, conditions that initiated nucleation are plotted for a variety of sites in the troposphere. These observations are compared with two different CNTs that included corrections for hydrate formation. The plot shows basic agreement with binary nucleation theory for events observed in and around clouds, and discrepancies of two to three orders of magnitude for terrestrial locations. In this locations, not only does binary CNT inadequately predict the concentrations needed for nucleation, it also cannot model the functional dependence of nucleation rate on sulfuric acid and water concentration. Weber et al.<sup>[56]</sup> found that the formation rate is proportional to the first to second power of  $\text{H}_2\text{SO}_4$  concentration, which, according to Eq. (7), indicates that the critical embryo contains only one or two sulfuric acids.

The current understanding of atmospheric nucleation, which has evolved from measurements such as those shown in Figs. 8 and 9, is that, with the exception of a small set of observations from very clean locales, binary nucleation theory does not

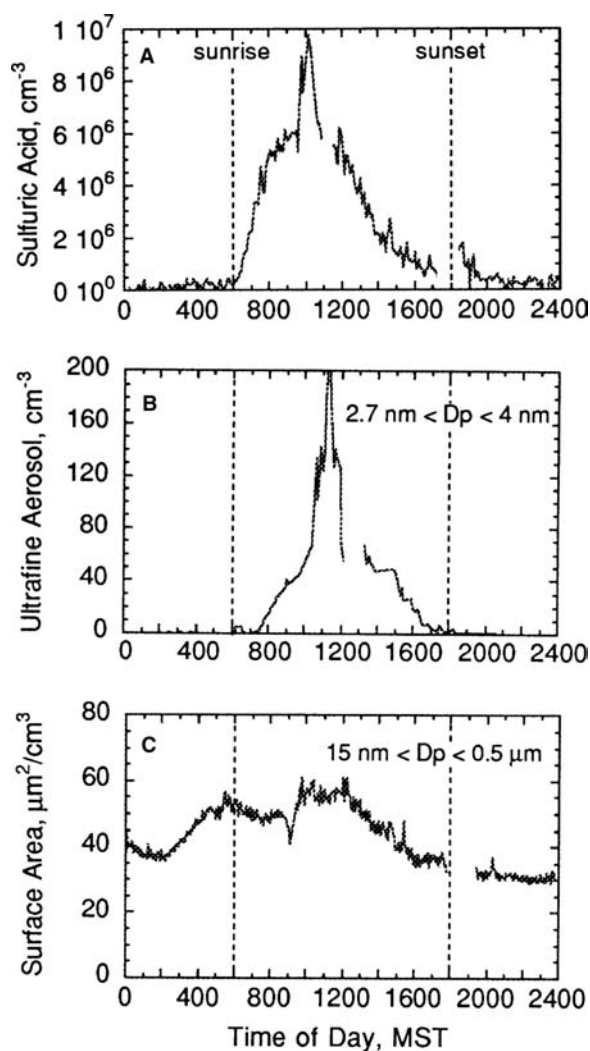


**Fig. 8** Measured (A)  $\text{H}_2\text{SO}_4$ , (B) nanoparticle concentration, and (C) aerosol surface area concentrations at Idaho Hill, CO, a remote forest site. *Source:* From Ref.<sup>[54]</sup>. American Geophysical Union.

adequately model the observed sulfuric acid concentrations that initiated nucleation. Because the observations where the discrepancy occurs were at or near ground level, this suggests that one or more of the following may be occurring: 1) nucleation is occurring as a ternary process, perhaps including ammonia or an organic compound; 2) some other compound in addition to, or instead of, sulfuric acid is participating in binary nucleation; and 3) a heterogeneous process, perhaps involving nucleation of vapor onto ion centers, is occurring. Although none of the above three possibilities can be categorically eliminated, the ternary theory of sulfuric acid/ammonia/water is increasingly viewed as the most likely mechanism.<sup>[57]</sup> This view is aided by the observation that the presence of ammonia in sulfuric acid/water solutions considerably decreases the vapor pressure of sulfuric acid.<sup>[58]</sup> In addition,

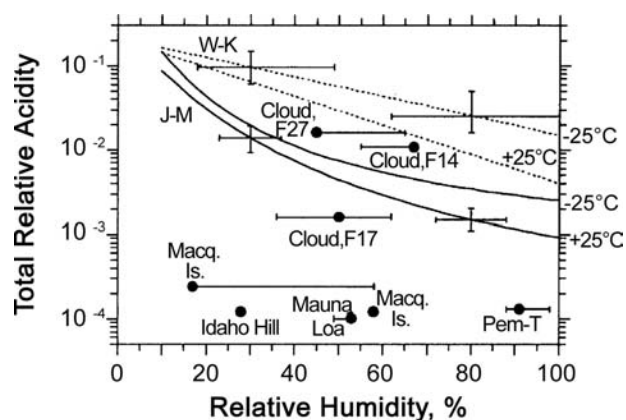


**Fig. 9** Comparison of conditions that resulted in nucleation events at various sites in the remote troposphere to predictions of the onset of sulfuric acid/water binary nucleation using two CNT models that include hydrate effects (solid and dashed lines). *Source:* From Ref.<sup>[53]</sup>. American Geophysical Union.

laboratory studies have shown that very low levels of tens of parts per trillion of ammonia can boost nucleation substantially.<sup>[59]</sup> A heterogeneous process of nucleation on ion centers might also explain current observations of nucleation.<sup>[54]</sup> Laboratory investigations have shown that the presence of gaseous ions can enhance nucleation rates.<sup>[61]</sup> Yet, to date, there have been no measurements of the composition of atmospheric ions during nucleation events to validate this hypothesis.

In the review of observations mentioned above, observed particle diameter growth rates are typically in the range of 1–26 nm/hr in midlatitudes, and depend heavily on the presence of condensable vapors and temperature. Attempts to interpret these observations by using Eq. (3) for the condensation of sulfuric acid and water generally underpredict growth by a factor of 5–10.<sup>[5]</sup> Either other species are contributing to particle growth, or growth is occurring by other processes in addition to monomer addition. The former option is quite likely to occur, as many oxidized organic compounds have sufficiently low vapor pressure to contribute to aerosol growth. Unfortunately, the property that makes such compounds candidates for condensational growth also makes them extremely difficult to study. For the latter option, preliminary results from the ANARChE study suggest that growth can be accounted for by including cluster condensation in Eq. (3).

## CONCLUSION

Atmospheric nanoparticles, which are defined here as particles with a spherical equivalent diameter smaller

than 50 nm, are now understood to be important atmospheric constituents that can dominate a particle number distribution spectrum. They can be directly emitted from combustion sources, but on a global scale, the most important formation process is by homogeneous nucleation. Nanoparticle growth, which in some locales can be as rapid as 26 nm/hr, can occur as a result of coagulation and physical uptake of compounds into the aerosol. Such growth links the presence of nanoparticles to a variety of phenomena such as climate, health, visibility degradation, and chemical transformations in the atmosphere. Measurement techniques are already able to detect and size nanoparticles at sizes as small as 3 nm. Future advances may include the ability to detect postnucleation clusters, which would require detection sensitivity to about 1 nm particles. Chemical composition techniques are undergoing rapid progress, with on-line instruments now capable of characterizing the composition of particles in the 5–20 nm diameter range. Modeling of the formation and growth of nanoparticles has traditionally relied on CNT and approximations to key nanoparticle physical properties such as the capillarity assumption. These have found some success at predicting formation rates in some parts of the atmosphere, but for the majority of locales, theories based on binary CNT are overpredicting the chemical environment required for nucleation by several orders of magnitude. Ternary nucleation of sulfuric acid, ammonia, and water may be the solution to this discrepancy, and is expected to be an important component of future theoretical advances.

## ACKNOWLEDGMENTS

The author gratefully acknowledges the following individuals for their assistance in assembling this manuscript: P. H. McMurry, P. Y. Chuang, Q. Shi, K. F. Moore, C. Anastasio, G. Tyndall, and R. J. Weber. This work was supported by funding from the NSF through its support of NCAR.

## REFERENCES

- Seinfeld, J.H.; Pandis, S.N. *Atmospheric Chemistry and Physics*; John Wiley and Sons: New York, 1998.
- Finlayson-Pitts, B.J.; Pitts, J.N.J. *Chemistry of the Upper and Lower Atmosphere: Theory, Experiments and Applications*; Academic Press: London, 2000.
- Anastasio, C.; Martin, S.T. Atmospheric nanoparticles. In *Nanoparticles and the Environment*; Mineralogical Society of America: Washington, DC, 2000; 293–349.
- Brown, L.M.; Collings, N.; Harrison, R.M.; Maynard, A.D.; Maynard, R.L. Ultrafine particles in the atmosphere: introduction. *Philos. Trans. R. Soc. Lond. Ser. A: Math. Phys. Eng. Sci.* **2000**, *358*, 2563–2565.
- Weber, R.J.; Marti, J.J.; McMurry, P.H.; Eisele, F.L.; Tanner, D.J.; Jefferson, A. Measurements of new particle formation and ultrafine particle growth rates at a clean continental site. *J. Geophys. Res. Atmos.* **1997**, *102*, 4375–4385.
- Jaenicke, R. Atmospheric aerosol size distribution. In *Atmospheric Particles*; John Wiley and Sons: West Sussex, 1978; 1–28.
- Whitby, K.T.; Cantrell, B. Fine particles. In *International Conference on Environmental Sensing and Assessment*; Institute of Electrical and Electronic Engineers, Inc.: Las Vegas, NV, 1976.
- Oberdorster, G.; Gelein, R.M.; Weiss, B. Association of particulate air pollution and acute mortality: Involvement of ultrafine particles? *Inhal. Toxicol.* **1995**, *7*, 111–124.
- Peters, A.; Wichmann, H.E.; Tuch, T.; Heinrich, J.; Heyder, J. Respiratory effects are associated with the number of ultrafine particles. *Am. J. Respir. Crit. Care Med.* **1997**, *155*, 1376–1383.
- Bohren, C.F.; Huffman, D.R. *Absorption and Scattering of Light by Small Particles*; Wiley-Interscience: New York, 1983.
- Intergovernmental Panel on Climate Change (IPCC). *Climate Change 2001: The Scientific Basis*; Cambridge University Press: Cambridge, 2001.
- Woo, K.S.; Chen, D.R.; Pui, D.Y.H.; McMurry, P.H. Measurement of Atlanta aerosol size distributions: Observations of ultrafine particle events. *Aerosol Sci. Technol.* **2001**, *34*, 75–87.
- McMurry, P.H. The history of condensation nucleus counters. *Aerosol Sci. Technol.* **2000**, *33*, 297–322.
- Stolzenburg, M.R.; McMurry, P.H. An ultrafine aerosol condensation nucleus counter. *Aerosol Sci. Technol.* **1991**, *14*, 48–65.
- Kulmala, M.; Vehkamäki, H.; Petaja, T.; dal Maso, M.; Lauri, A.; Kerminen, V.-M.; Birmili, W.; McMurry, P.H. Formation and growth rates of ultrafine atmospheric particles: a review of observations. *J. Aerosol Sci.* **2004**, *35*, 143–175.
- Chan, S.K.; Okuyama, K.; Fernandez de la Mora, J. Performance evaluation of an improved particle size magnifier (PSM) for single nanoparticle detection. *Aerosol Sci. Technol.* **2003**, *37*, 791–803.
- Flagan, R.C. History of electrical aerosol measurements. *Aerosol Sci. Technol.* **1998**, *28*, 301–380.
- Chen, D.R.; Pui, D.Y.H.; Hummes, D.; Fissan, H.; Quant, F.R.; Sem, G.J. Design and evaluation of a nanometer aerosol differential mobility analyzer (Nano-DMA). *J. Aerosol Sci.* **1998**, *29*, 497–509.
- Jaenicke, R. Physical aspects of the atmospheric aerosol. In *Chemistry of the Polluted and Unpolluted Troposphere*; D. Reidel Publishing Co.: Dordrecht, 1982; 341–373.
- Saros, M.T.; Weber, R.J.; Marti, J.J.; McMurry, P.H. Ultrafine aerosol measurement using a condensation nucleus counter with pulse height analysis. *Aerosol Sci. Technol.* **1996**, *25*, 200–213.

21. Horrak, U.; Salm, J.; Tamm, H. Bursts of intermediate ions in atmospheric air. *J. Geophys. Res. Atmos.* **1998**, *103*, 13,909–13,915.
22. Rader, D.J.; McMurry, P.H. Application of the tandem differential mobility analyzer to studies of droplet growth or evaporation. *J. Aerosol Sci.* **1986**, *17*, 771–787.
23. Sakurai, H.; Tobias, H.J.; Park, K.; Zarling, D.; Docherty, K.S.; Kittelson, D.B.; McMurry, P.H. On-line measurements of diesel nanoparticle composition and volatility. *Atmos. Environ.* **2003**, *37*, 1199–1210.
24. Joutsensaari, J.; Vaattovaara, P.; Vesterinen, M.; Hameri, K.; Laaksonen, A. A novel tandem differential mobility analyzer with organic vapor treatment of aerosol particles. *Atmos. Chem. Phys.* **2001**, *1*, 51–60.
25. O'Dowd, C.D.; Aalto, P.; Hameri, K.; Kulmala, M.; Hoffmann, T. Aerosol formation—atmospheric particles from organic vapours. *Nature* **2002**, *416*, 497–498.
26. Solomon, P.A.; Norris, G.; Landis, M.; Tolocka, M. Chemical analysis methods for atmospheric aerosol Components. In *Aerosol Measurement*, 2nd Ed.; Wiley-Interscience: New York, 2001; 261–291.
27. Pakkanen, T.A.; Kerminen, V.M.; Korhonen, C.H.; Hillamo, R.E.; Aarnio, P.; Koskentalo, T.; Maenhaut, W. Urban and rural ultrafine (PM<sub>0.1</sub>) particles in the Helsinki area. *Atmos. Environ.* **2001**, *35*, 4593–4607.
28. Cass, G.R.; Hughes, L.A.; Bhawe, P.; Kleeman, M.J.; Allen, J.O.; Salmon, L.G. The chemical composition of atmospheric ultrafine particles. *Philos. Trans. R. Soc. Lond. Ser. A: Math. Phys. Eng. Sci.* **2000**, *358*, 2581–2592.
29. Chung, A.; Herner, J.D.; Kleeman, M.J. Detection of alkaline ultrafine atmospheric particles at Bakersfield, California. *Environ. Sci. Technol.* **2001**, *35*, 2184–2190.
30. Makela, J.M.; Yli-Koivisto, S.; Hiltunen, V.; Seidl, W.; Swietlicki, E.; Teinila, K.; Sillanpaa, M.; Koponen, I.K.; Paatero, J.; Rosman, K.; Hameri, K. Chemical composition of aerosol during particle formation events in boreal forest. *Tellus, Ser. B Chem. Phys. Meteorol.* **2001**, *53*, 380–393.
31. Geller, M.D.; Kim, S.; Misra, C.; Sioutas, C.; Olson, B.A.; Marple, V.A. A methodology for measuring size-dependent chemical composition of ultrafine particles. *Aerosol Sci. Technol.* **2002**, *36*, 748–762.
32. Makela, J.M.; Hoffmann, T.; Holzke, C.; Vakeva, M.; Suni, T.; Mattila, T.; Aalto, P.P.; Tapper, U.; Kauppinen, E.I.; O'Dowd, C.D. Biogenic iodine emissions and identification of end-products in coastal ultrafine particles during nucleation bursts. *J. Geophys. Res. Atmos.* **2002**, *107*.
33. Wexler, A.S.; Johnston, M.V. Real-time single-particle analysis. In *Aerosol Measurement: Principles, Techniques, and Applications*, 2nd Ed.; Wiley-Interscience: New York, 2001; 365–386.
34. Phares, D.J.; Rhoads, K.P.; Wexler, A.S. Performance of a single ultrafine particle mass spectrometer. *Aerosol Sci. Technol.* **2002**, *36*, 583–592.
35. Liu, P.; Ziemann, P.J.; Kittelson, D.B.; McMurry, P.H. Generating particle beams of controlled dimensions and divergence: 1. Theory of particle motion in aerodynamic lenses and nozzle expansions. *Aerosol Sci. Technol.* **1995**, *22*, 293–313.
36. Rhoads, K.P.; Phares, D.J.; Wexler, A.S.; Johnston, M.V. Size-resolved ultrafine particle composition analysis: 1. Atlanta. *J. Geophys. Res. Atmos.* **2003**, *108*.
37. Solomon, P.A.; Chameides, W.; Weber, R.; Middlebrook, A.; Kiang, C.S.; Russell, A.G.; Butler, A.; Turpin, B.; Mikel, D.; Scheffe, R.; Cowling, E.; Edgerton, E.; St. John, J.; Jansen, J.; McMurry, P.; Hering, S.; Bahadori, T. Overview of the 1999 Atlanta Supersite Project. *J. Geophys. Res. Atmos.* **2003**, *108*.
38. Reents, W.D.; Schabel, M.J. Measurement of individual particle atomic composition by aerosol mass spectrometry. *Anal. Chem.* **2001**, *73*, 5403–5414.
39. Okada, Y.; Yabumoto, J.; Takeuchi, K. Aerosol spectrometer for size and composition analysis of nanoparticles. *J. Aerosol Sci.* **2002**, *33*, 961–965.
40. Smith, J.N.; Moore, K.F.; McMurry, P.H.; Eisele, F.L. Atmospheric measurements of sub-20 nm diameter particle chemical composition performed using thermal desorption chemical ionization mass spectrometry. *Aerosol Sci. Technol.* **2004**, *38*, 100–110.
41. Voisin, D.; Smith, J.N.; Sakurai, H.; McMurry, P.H.; Eisele, F.L. Thermal desorption chemical ionization mass spectrometer for ultrafine particle chemical composition. *Aerosol Sci. Technol.* **2003**, *37*, 471–475.
42. Smith, J.N.; Moore, K.F.; Eisele, F.L.; Ghimire, A.K.; Sakurai, H.; McMurry, P.H. Recent insights into the formation and chemical composition of atmospheric nanoparticles from the aerosol nucleation and real-time characterization experiment. In *Proceedings of the ACS Nanotechnology and the Environment Symposium*; 2003, *in press*.
43. Kittelson, D.B. Engines and nanoparticles: A review. *J. Aerosol Sci.* **1998**, *29*, 575–588.
44. Collings, N.; Graskow, B.R. Particles from internal combustion engines—what we need to know. *Philos. Trans. R. Soc. Lond., A* **2000**, *358*, 2611–2622.
45. Hinds, W.C. *Aerosol Technology: Properties, Behavior, and Measurement of Airborne Particles*, 2nd Ed.; John Wiley and Sons: New York, 1999.
46. Senger, B.; Schaaf, P.; Corti, D.S.; Bowles, R.; Voegel, J.C.; Reiss, H. A molecular theory of the homogeneous nucleation rate: I. Formulation and fundamental issues. *J. Chem. Phys.* **1999**, *110*, 6421–6437.
47. Zeng, X.C.; Oxtoby, D.W. Binary homogeneous nucleation theory for the gas–liquid transition—a non-classical approach. *J. Chem. Phys.* **1991**, *95*, 5940–5947.
48. Hale, B.N.; Kulmala, M. *Nucleation and Atmospheric Aerosols 2000*; American Institute of Physics: New York, 2000.
49. Oxtoby, D.W.; Kashchiev, D. A general relation between the nucleation work and the size of the nucleus in multicomponent nucleation. *J. Chem. Phys.* **1994**, *100*, 7665–7671.
50. Strey, R.; Viisanen, Y. Measurement of the molecular content of binary nuclei—use of the nucleation rate surface for ethanol–hexanol. *J. Chem. Phys.* **1993**, *99*, 4693–4704.
51. Wilemski, G. Composition of the critical nucleus in multicomponent vapor nucleation. *J. Chem. Phys.* **1984**, *80*, 1370–1372.
52. Trinkhaus, H. Theory of the nucleation of multicomponent precipitates. *Phys. Rev., B* **1983**, *27*, 7372–7378.

53. Laaksonen, A.; McGraw, R.; Vehkamäki, H. Liquid drop formalism and free-energy surfaces in binary homogeneous nucleation theory. *J. Chem. Phys.* **1999**, *99*, 2019–2027.
54. Yu, F.; Turco, R.P. Ultrafine aerosol formation via ion-induced nucleation. *Geophys. Res. Lett.* **2000**, *27*, 883–886.
55. Jaeger-Voirol, A.; Mirabel, P.; Reiss, H. Hydrates in supersaturated binary sulfuric acid–water vapor: a reexamination. *J. Chem. Phys.* **1987**, *87*, 4849–4852.
56. Weber, R.J.; Marti, J.J.; McMurry, P.H.; Eisele, F.L.; Tanner, D.J.; Jefferson, A. Measured atmospheric new particle formation rates: implications for nucleation mechanisms. *Chem. Eng. Commun.* **1996**, *151*, 53–64.
57. Kulmala, M.; Korhonen, P.; Napari, I.; Karlsson, A.; Berresheim, H.; O’Dowd, C.D. Aerosol formation during PARFORCE: ternary nucleation of H<sub>2</sub>SO<sub>4</sub>, NH<sub>3</sub> and H<sub>2</sub>O. *J. Geophys. Res. Atmos.* **2002**, *107*, PAR 15-11-11.
58. Scott, W.D.; Cattell, F.C.R. Vapor pressure of ammonium sulfates. *Atmos. Environ.* **1979**, *13*, 307–317.
59. Ball, S.M.; Hanson, D.R.; Eisele, F.L.; McMurry, P.H. Laboratory studies of particle nucleation: initial results for H<sub>2</sub>SO<sub>4</sub>, H<sub>2</sub>O, and NH<sub>3</sub> vapors. *J. Geophys. Res. Atmos.* **1999**, *104*, 23,709–23,718.
60. Shi, Q. Continuous Measurements of 3 nm to 10 μm aerosol size distributions in St. Louis. In *Department of Mechanical Engineering*; University of Minnesota: Minneapolis, 2003.
61. Katz, J.L.; Fisk, J.A.; Chakarov, V.M. Condensation of a supersaturated vapor: IX. Nucleation on ions. *J. Chem. Phys.* **1994**, *52*, 4733–4748.

# Automotive Parts: Impact of Nanotechnology

Ganesh Skandan

Amit Singhal

Damian Sobrevilla

NEI Corporation, Piscataway, New Jersey, U.S.A.

## INTRODUCTION

This article explores the present impact of nanotechnology (mostly nanomaterials so far) on the consumer automotive market. Our attempt throughout the paper has been to situate technical aspects of nanotechnology as they pertain to the automotive market in a business context. The initial part of the paper describes some early successes of nanomaterials embraced by the industry, bearing in mind that the market entrants are few and far apart. This includes a description of technology developments in the area of *coatings*, particularly the outer body *clearcoat*, and a summary of *bulk* nanostructured materials, specifically polymer-clay nanocomposites for non-critical automotive body parts. Even though the aftermarket is a smaller component of the overall market, several new products for the aftermarket have begun to appear, ostensibly incorporating nanotechnology. The section, Potential Applications, briefly describes a number of research and development activities that are in various stages of testing and qualification. Fig. 1 depicts the present and future possible applications of nanotechnology in an automobile. Concluding thoughts and the road ahead for nanotechnology as it relates to the automotive market are presented in the final section.

## BACKGROUND

A discussion of nanotechnology in the context of automotive applications is timely because the acceptance of a new enabling technology into the mainstream market can be gauged by its acceptance in the automotive industry, and nanotechnology is by and large an enabling technology. In fact, approval by the automotive industry is a test of the robustness of any technology, particularly in the area of advanced materials.

The automotive sector has been the backbone of the US economy for most of the past 100 years. The health of the overall economy is often measured by the “health” of the automakers. Until a few years ago,

the three US automakers, General Motors (GM), Ford Motor Company, and Chrysler dominated the world market. With the purchase of Chrysler by Daimler-Benz and the decision by Japanese and European car-makers to assemble cars in the U.S.A., the dominance by US-based automakers has quite noticeably diminished. Despite the disparate performance in the recent times of GM and Ford on one hand and foreign-based automakers on the other, and owing to company-specific issues coupled with changes in the landscape of the consumer economy, new car sales continue to be an important lagging indicator that US economists watch for. Considering the hype surrounding nanotechnology and the huge amount of research sponsored by governments worldwide, it is worth taking a reality check of the payoffs to date.

Nanotechnology either adds value to an existing application, or enables the creation of new applications. The acceptance criteria (technical as well as economic) set by the automotive industry for any technology is more stringent than anywhere else. Therefore, one measure of commercial success and societal impact of nanotechnology can be measured in terms of the level of penetration in the automotive market. A report by the firm Frost & Sullivan, entitled “Global Analysis of Nanotechnology in the Automotive Market,” estimates that revenues arising out of nanotechnology will be ~\$6.46 billion by 2015, with the maximum impact being made in the areas of paints and coatings, catalytic converters, and fuel additives.<sup>[1]</sup>

Although nanotechnology is a burgeoning field, there are already a number of components that use nanomaterials. In some cases, such as carbon black used in tires and catalyst particles used in catalytic converters, they have been in use prior to being recognized and termed as nanostructured materials. All the same, the total dollar value of newly developed nanomaterials in use today in a vehicle as a fraction of the cost of an automobile is too small to even measure. Nonetheless, as outlined in this entry, the potential for nanomaterials to be ubiquitous in automobiles is huge. Because the authors themselves are actively involved



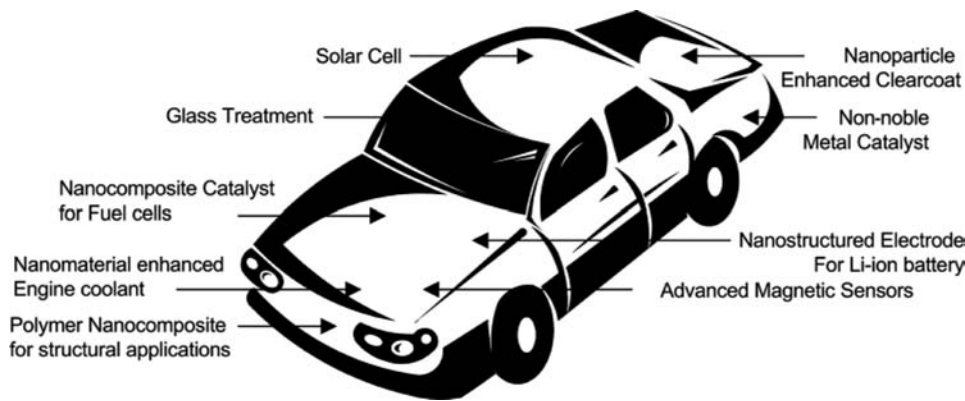


**Fig. 1** Potential nanotechnology applications to modern automobile.

in various aspects of nanotechnology as they relate to the automotive market, some bias toward a positive outlook is unavoidable (mention of the authors' activities is made in various sections of the article). This article will concentrate on the payoffs as revealed on the modern automobile.

## NANOSTRUCTURED COATING TECHNOLOGIES

One of the concerns that faze researchers is the long time it takes for a product to be introduced in the primary automotive market. For example, it took several years of concerted effort to develop nanoparticle-enhanced *clearcoats* by Pittsburgh Plate Glass Company for Mercedes-Benz.<sup>[2,3]</sup> Successful launch of this product has been one of the most recent success stories involving nanotechnology in automotive applications. The clear lacquer contains nanoscale particles, which beneficially alter the three-dimensional cross-linked polymer network. The scratch resistance of the nanoparticle containing coating is reported to be increased threefold, with the gloss being extended for substantially longer periods of use. The chemical resistance of the coating has been preserved because of the nanoparticle addition.

The paintwork in automobiles is complex, and is composed of multiple steps and many layers of coatings, each one having a specific feature. The multilayered coating used by Mercedes-Benz, as described by Kimberley,<sup>[4]</sup> consists of five layers with a combined thickness of  $\sim 100\ \mu\text{m}$ . The first layer is a zinc phosphate coating, which protects the metal from corrosion. A subsequent dip coating in a primer paint coats the edges and grooves, thereby providing additional protection against corrosion. The anticorrosion layers together are about  $\sim 25\ \mu\text{m}$  thick. A coat ( $\sim 25\ \mu\text{m}$ ) of the base paint, which contains the desired color is then applied. The addition of aluminum flakes in this layer leads to paints with a metallic finish. The top *clearcoat* is

the final coating layer, and is about  $40\ \mu\text{m}$  thick. The top coat provides the gloss and protection against the elements. The demands on the performance of the clearcoat are significant as it should protect against such things as bird droppings, acid precipitation, dust, chipping, sunlight, fluctuations in temperature, and automatic car wash swipes. The complex nature of these coatings perhaps explains the long lead times from conception to implementation of a new product, and nanotechnology is no exception.

Based upon the extensive amount of ongoing work on ultraviolet (UV) light cured polymers, it is likely that the next innovation employing nanotechnology will be in *clearcoat* polymers cured by UV light. The current industrial practice for curing the clearcoat during production is by heating the automotive body to  $\sim 60^\circ\text{C}$ . It has been argued that UV-curable clearcoats possess many potential advantages such as excellent scratch and mar resistance, and improved initial appearance.<sup>[5]</sup> Further, the volatile organic compound content could also be substantially reduced. The authors are quick to point out that the UV curing process should make use of current automotive paint application infrastructure, and should allay common concerns that automotive manufacturers have, such as ozone production, power consumption, shadow zones, and worker safety. Accordingly, the authors demonstrated that the UV curable clearcoats can be cross-linked not only by using conventional high intensity lamps, but also by using diffuse fluorescent radiation and xenon flash lamps.

Antireflection coatings, which are multilayered coatings with the thickness of each layer being well below  $100\ \text{nm}$ , have been in commercial production for quite sometime.<sup>[6]</sup> An example is an antireflection coating on glass with a trade name Schott Conturan.<sup>[7,8]</sup> Saint Gobain produces a grade of glass that has nanoscale layers of sun protecting and infrared reflecting material embedded within.<sup>[8,9]</sup>

In contrast to exterior coatings, much less commercial implementation has occurred in the area of

nanostructured coatings for interior components in an automobile, and in particular, aluminum engine blocks. This is not to say that there is lack of potential, but perhaps because the issues involved are fairly complex and the coating has to simultaneously satisfy a multitude of functional performance requirements. As Dahotre and Nayak<sup>[10]</sup> have outlined in a recent review article, the coating must possess a low coefficient of friction, good corrosion resistance, good scuffing resistance, amenability to honing to create a surface topography with many small recesses that can store oil, good thermal insulation to prevent heat from being lost through the engine block, and affinity for oil coating. The scientific basis by which nanostructured coatings could improve the engine efficiency is shown in Fig. 2. It turns out that the mechanical properties of interest (e.g., hardness, modulus, and plasticity) reach a maximum value when the microstructure of the material transitions from being a coarse-grained structure to an amorphous structure. Candidate materials that are being investigated for possible replacement of cast iron liners in the cylinder bores of aluminum alloy engine blocks include nickel-based coatings deposited using atmospheric plasma deposition techniques, diamond-like carbon coatings, and laser-annealed iron oxide coatings.

## NANOMATERIALS FOR STRUCTURAL APPLICATIONS

Bulk polymer nanocomposites, particularly for automotive applications, have been synonymous with dispersed clay-polymer nanocomposites. After about 10 years of intense R&D, both in academia and industry, GM and Toyota Motor Company were among the first

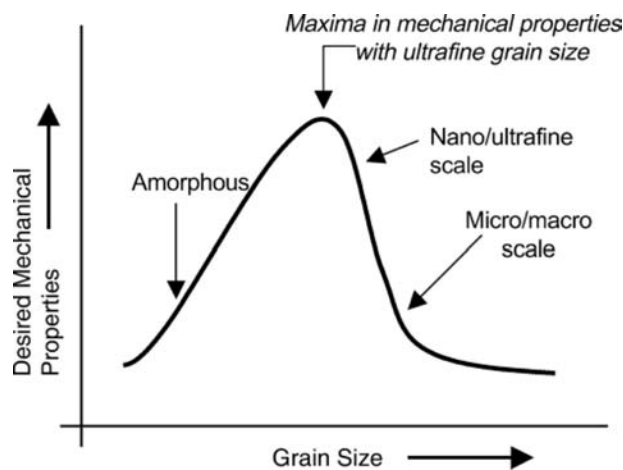


**Fig. 2** Schematic depiction of mechanical properties as a function of grain size.

to introduce nanocomposite products.<sup>[11]</sup> The exterior step-assist in GM's 2002 Safari and Astro vans are made of nanoclay/thermoplastic polyolefin nanocomposites,<sup>[12]</sup> manufactured by Bassell, utilizing clay particles from Southern Clay Products. The dispersion of the nanoparticles increases the flexural modulus by ~75%, compared to the neat resin. A more recent polymer nanocomposite product is the side molding on the 2004 Chevrolet Impala.<sup>[13]</sup> It is estimated that GM can use ~500,000 lbs/yr of nanocomposites. From a nanoparticle supplier's standpoint, this represents a potential sale of 25,000 lbs/yr because clay-based nanocomposites are typically composed of ~5 wt.% dispersion of either exfoliated or intercalated platelet-shaped clay particles in a thermoplastic resin (Fig. 3).<sup>[14]</sup>

Ever since the beginning, the driving force for developing polymer nanocomposites has been to replace metals with lighter weight materials that are low-cost and provide adequate performance. This in turn would

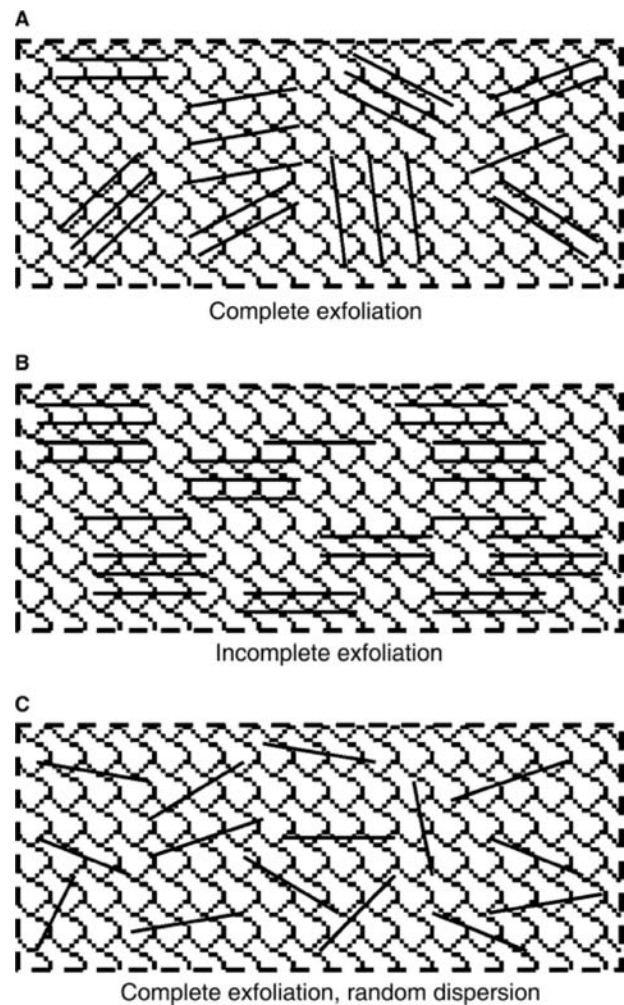


**Fig. 3** Different exfoliation and dispersion schemes for montmorillonite organoclay reinforced polymer nanocomposites. *Source:* Adapted from Ref.<sup>[14]</sup>.

lead to enormous savings in energy consumption through reduced use of fuel during the automobile's life cycle. Garces et al.<sup>[15]</sup> of Dow Chemical Company estimated that using polymer nanocomposites for just the non-critical structural parts in an automobile, such as front and rear fascia, cowl vent grills, valve/timing covers, and truck beds, would lead to billions of kilograms in weight saved per year. This is because polymer nanocomposites offer an estimated 25% weight savings over glass and carbon fiber filled plastics, and as much as 80% over steel. Expanding their use to other parts such as body panels, could lead to further savings in weight.

In a broad sense, materials advances in automotive applications have centered on using structural plastics, lightweight metals instead of steel and cast iron, and reinforcing polymers with fillers such as glass fibers, talc, mica, and calcium carbonate. Unfortunately, none of these approaches is a panacea. Conventional fillers add too much weight and compromise on the toughness and surface finish. Lightweight metals are expensive and suffer from the same processing limitations of steel and iron. Similarly, structural plastics cost more and require postforming modifications of the surface and long cycle times.<sup>[14]</sup>

As with any other technology, there have already been a few marketplace casualties despite stunning technical results. Toyota Motor Company had been a pioneer in the area of polymer nanocomposites, and was the first to develop an alternative production process to the conventional method of dispersing and exfoliating into polymers by melt compounding. They developed Nylon 6-clay hybrid (NCH) nanocomposites by the in situ intercalation polymerization method, where the monomer was first intercalated in the clay, and subsequently polymerized in situ.<sup>[16]</sup> The tensile modulus of NCH containing only 1.6 wt.% clay was twice that of Nylon 6, and the coefficient of linear thermal expansion was reduced by half. The initial target for the nanocomposite material was a timing-belt cover. Cost and other considerations prevented successful commercial introduction.<sup>[17]</sup>

Over the past several decades, the automobile industry has found itself at the crosshairs of environmental groups, who demand more fuel-efficient vehicles. Reducing the weight automatically leads to improved fuel efficiency. However, reducing the weight through the use of advanced materials invariably ends up increasing the cost, which is often not commensurate with the improved performance offered by the new material. Because bulk polymer nanocomposites undoubtedly possess certain mechanical properties that are better than in heavier traditional materials, cost is the major stumbling block for widespread acceptance. In a seminal study, Lloyd and Lave<sup>[14]</sup> lay out an economic case for using polymer nanocomposites

in automotive applications. On the basis of detailed financial and statistical assessment, the authors present a compelling case for using polymer nanocomposites in automobiles. Because of the uncertainty involved with a relatively new technology, they have estimated the value of this material as a function of its efficiency and the amount of steel it can replace. At the upper bound 67% efficiency, the nanocomposite substitution will be worth a little more than \$8/lb in materials and processing cost. At a lower bound 38% efficiency, the substitution will be worth slightly below \$4/lb. Given that the market price for filled polymer nanocomposites is between \$1 and \$2, these materials present a persuasive value proposition. It should be noted that although vehicles with greater fuel economy lead to potentially large economic and environmental benefits, US consumers have been traditionally indifferent to fuel economy. With crude oil prices in the range of \$50–60 per barrel as of the writing of this entry, and speculation that it might touch \$100 per barrel in the foreseeable future, change in the US consumers' attitude toward fuel economy could come sooner rather than later. One could hazard a guess that polymer nanocomposite manufacturers are eagerly awaiting higher gas prices. A combination of mounting social–environmental concerns and rising oil prices might lessen the current cost obstacle for more pervasive introduction of nanotechnology into the behemoth automotive industry.

## NANOTECHNOLOGY-ENABLED PRODUCTS FOR THE AFTERMARKET

Recognizing that it is easier to get a product into the automotive aftermarket as opposed to the primary market, Nanofilm Ltd., a 20-year old thin film developer, started selling an auto glass treatment product into the retail market.<sup>[18]</sup> The Clarity Defender, as it is called, repels rain, snow, mud, bugs, bird dropping, spray paint, and most liquids that come in contact with the windshield. The windshield coating from Nanofilm is expected to last a lot longer than competing products. It is not clear as to what component of the treatment solution is made of a nanomaterial, but then in almost all cases the consumer is concerned more with a new and improved end-product rather than a nano-enabled product.

Along the same vein, the NanoBreeze™ Car Air Purifier, produced and marketed by NanoTwin Technologies, is said to clean and purify the air inside the passenger compartment of any motor vehicle.<sup>[19]</sup> When placed over a dashboard vent, the air circulating inside the car is cleaned by reduction and oxidation through a photocatalytic reaction. The heart of the NanoBreeze

is a nano-TiO<sub>2</sub>-coated fiberglass wrapping on a fluorescent tube. The inside of the tube is coated with a phosphor that generates UV-A radiation.

## POTENTIAL APPLICATIONS

Presting and Konig,<sup>[7]</sup> researchers at Daimler Chrysler in Germany have written an aptly titled article “Future nanotechnology developments for automotive applications,” because the list of current applications is rather small. This goes to show that the automotive industry, despite being a \$2000 billion worldwide industry at retail [including both original equipment manufacturer (OEM) and aftermarket], is conservative and extremely cost conscious. As with many new and exciting fields of science and technology, the list of potential applications is invariably a lot larger than that of current applications. Nanotechnology in the context of automobiles is not immune to this trend.

An emerging theme is that nanotechnology, particularly nanomaterials, is likely to be an enabler in a number of different components and subsystems in the automobile. This can pan out as envisioned, provided the materials manufacturers come to grips with cost and reproducibility issues. If nanotechnology lives up to its promise, many parts of a car could contain a variety of nanostructured materials. Some of these potential applications are described below.

### Catalysts

Noble metal catalysts, including those based on platinum, are used to decompose the combustion products in a catalytic converter into relatively less harmful emissions. Catalysts have always been particles at the nanoscale—they just were not called nanoparticles. The enormously high surface area is used for efficient gas–solid reactions. A company called Nanostellar Inc.<sup>[20]</sup> has started developing nanocomposite catalysts, which it says will substantially reduce the amount of platinum that is presently used. Platinum-based catalysts are also used in the electrodes of a fuel cell. Because the catalyst is expensive and accounts for a large part of the cost in a fuel cell, there is an interest in developing alternative non-noble metal catalysts. If QuantumSphere<sup>[21]</sup> has its way, its nanonickel could replace platinum-based catalysts. It is not clear though how the surfaces of non-noble metals can be passivated and prevented from complete oxidation. A third company, Catalytic Solutions, is an active player in this market as well.<sup>[22]</sup> The use of oxide-based compositions has also been investigated as potential replacements for noble metal catalysts.<sup>[23]</sup>

## Nanotechnology-Based Magnetic Sensors

A modern automobile uses a multitude of sensors, many of them magnetic sensors that are based on the Hall Effect (or inductive effect), and more recently anisotropic magnetoresistance. A magnetic sensor allows contactless, and hence, wear-free determination of mechanical parameters such as angle of rotation and angular speed.<sup>[24]</sup> A new phenomenon called Giant Magnetoresistance (GMR), discovered in 1988,<sup>[25,26]</sup> offers the possibility of increasing the output signal, the opportunity to miniaturize, and the ability to sense in 360°. The sensor element essentially consists of multilayers of metals, each layer only a nanometer or two thick. The GMR effect is unique to the multilayered magnetically inhomogeneous nanostructured material (Fig. 4). Giebeler et al.<sup>[24]</sup> have shown that the GMR effect, which has been in commercial use in hard disc drives for about 10 years, can be used in automotive applications to determine many functions such as valve position, and chassis height and position. Extensive research at Robert Bosch GmbH and Mitsubishi<sup>[27]</sup> has led to the development of commercial magnetic sensors based on the GMR effect.

### Nanomaterial-Based Engine Coolants

Researchers at the Argonne National Laboratory created a sudden burst of excitement in the engine coolant (i.e., antifreeze) business in the mid-1990s by demonstrating that the thermal conductivity (and hence the heat transfer coefficient with a constant or greater heat capacity) of nanoparticle containing fluids is greater than that of the neat fluid.<sup>[28,29]</sup> The experiments were conducted with nanoparticles dispersed in ethylene glycol, which is the major component of an engine coolant. A few companies, such as Valvoline, picked up on this and research was carried out where nanotubes were dispersed in heat transfer fluids.<sup>[30]</sup>

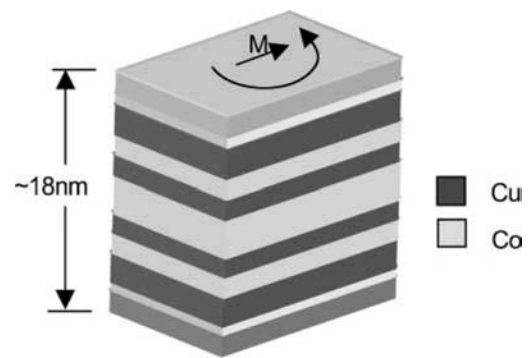


**Fig. 4** GMR sensor sample layer configuration: hard magnetic layer of artificial antiferromagnet with soft magnetic detection layers (top and bottom, Fe/Co).

NEI Corporation, the employer of the authors, has advanced the state-of-the-art to a commercially viable fluid, both from a technical and a commercial standpoint. Working in concurrence with an OEM customer, tests are underway by an engine coolant manufacturer to qualify the fluid for use in aftermarket and OEM applications.

### Nanomaterials-Enabled Lithium-Ion Batteries

Cathode and anode materials determine the fundamental performance of a battery, and the role of a battery in an automobile is changing as we see more and more hybrid electric vehicles on the road. The hybrid can range from a micro-hybrid, where the engine shuts off when the vehicle stops at say a traffic light and the integrated starter/alternator assists the gasoline engine in accelerating the vehicle, to a full-hybrid where an electric motor powered by a large battery drives the vehicle by itself.<sup>[31]</sup> The gasoline engine in a full-hybrid is relatively small as its primary function is to recharge the battery. The hybrid has taken the emphasis away from the all-electric vehicle, which for the time being is restricted to golf carts and off-road vehicles of the like. The unavailability of a cost-effective and low-weight battery technology has prevented the all-electric vehicle from becoming a reality. Nevertheless, the Nickel Metal Hydride (NiMH) battery of a hybrid electric vehicle is an important component and weighs substantially (e.g., Cobasys NiMHax HEV 288-60, weighs 75 kg).<sup>[32]</sup> Lead-acid batteries, which have been the 12 V power supply in modern automobiles, simply do not have sufficient energy density and cycle life for use in a hybrid electric vehicle. In contrast, NiMH has good power capability. In terms of energy density and cycle life, the lithium-ion (Li-ion) battery reigns supreme, however, obtaining batteries of the size required for use in an automobile has been an elusive target. Apart from cost, which is a huge limiting factor, the large size poses safety concerns that have not been fully resolved to date. Cost considerations are staggering—the target price by the US Department of Energy for cathode materials for hybrid electric vehicles is \$8/kg.<sup>[33]</sup> Few materials synthesis technologies are currently available that can meet this target. Pasquier et al.<sup>[34]</sup> have proposed a cell chemistry that utilizes nanostructured lithium titanate (LTO). The charge-discharge capabilities of the proposed chemistry are better than conventional Li-ion chemistries, which utilize carbon anode and lithium cobalt oxide (LCO) cathode, and the energy density is much higher than that of a carbon-carbon double-layer supercapacitor (Fig. 5). The cycle life of Pasquier et al.'s proposed device is far better than that of any competing Li-ion battery. Work done at NEI Corporation has

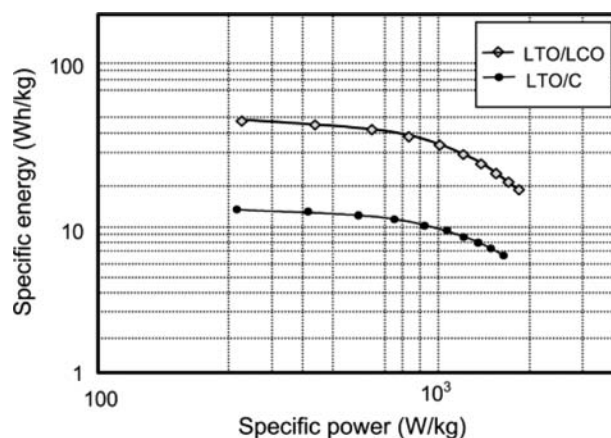


Fig. 5 Energy-Power Ragone plot comparison of LTO/C and LTO/LCO batteries. Source: Adapted from Ref.<sup>[34]</sup>.

unequivocally demonstrated that nanostructured anode and cathode materials have higher capacity and/or better rate capability than their coarse-grained counterparts.<sup>[35]</sup> In one particular case, for a given rate of charge, the capacity is higher by 100%.<sup>[36]</sup> As with any other technology, the economics and life cycle cost will determine if a hybrid electric vehicle will utilize advanced Li-ion devices with nanostructured electrodes.

### Improved Fuel Cells through Use of Nanomaterials

A discussion on automobiles is always incomplete without reference to the “coming” hydrogen economy. It is envisioned that fuel cells will someday deliver the power for driving the motor in all vehicles, and therefore we will need an infrastructure for producing, storing, and delivering hydrogen safely at ambient temperature and pressure, as well as at low cost. On recognition of its large surface or interfacial area, as the case may be, the nanostructured material became a subject of intense investigation in the mid-1990s for use as a medium of hydrogen storage. In particular, early reports indicated that single-walled carbon nanotubes (SWNTs) could store up to 10 wt.%<sup>[37]</sup> of H<sub>2</sub>, which exceeded the target of 6.5% set by the US Department of Energy<sup>[38]</sup> for a commercially viable technology. However, careful experiments in trying to reproduce these initial reports revealed that the absorption mechanism is by and large physisorption. As yet, it has not been successful to reproduce the early reports and consequently meet the Department of Energy target using SWNTs. On the other hand, a well-known class of materials called “alanates” (e.g., NaAlH<sub>4</sub> and LiAlH<sub>4</sub>) adsorb hydrogen reversibly and some reports have shown that a nanocomposite

material has an increased efficacy for hydrogen adsorption.<sup>[39,40]</sup>

Oddly enough, the heart of a fuel cell has generated relatively less number of opportunities for utilizing nanotechnology. Perhaps the biggest area of research in enabling a better performing fuel cell has been the Nafion<sup>®</sup> separator membrane in a polymer electrolyte membrane fuel cell. The ideal membrane should satisfy the following requirements: 1) low cost and ready availability; 2) a high proton conductivity of over  $10^{-2}$  S/cm at room temperature; 3) chemical and thermal stability at an operating temperature of 150°C; 4) enough water uptake above 100°C; 5) good mechanical properties (strength, flexibility, and processability); 6) low gas permeability; 7) low water drag; 8) minimal fuel crossover in case of direct methanol fuel cell; and 9) fast kinetics for electrode reactions.<sup>[41]</sup> Some studies<sup>[42]</sup> have shown that dispersing exfoliated clay nanoparticles with appropriately engineered end-groups can improve the performance of neat Nafion.

## Solar Power and Nanotechnology

Harnessing energy by the use of either solar cells or thermoelectric modules that convert heat released by the engine to electricity has taken the fancy of some automakers. For example, Mercedes-Benz and Audi offer a line of cars with solar cells on the roof to provide power to a ventilation system that keeps the interior of the car cool when the engine is off.<sup>[8]</sup> This is akin to sail boats equipped with a few large solar panels that generate electricity and store in a battery. Ge nanostructures embedded in a Si matrix is a variation of the conventional crystalline Si solar cell, and can provide improved conversion efficiencies.<sup>[43]</sup> One needs to only stretch one's imagination (as Presting and Koning<sup>[7]</sup> have done) to somehow integrate a dye-sensitized solar cell, which uses nanoparticles of TiO<sub>2</sub> as an active constituent of the photovoltaic cell, on to the surface of a car body. In all fairness, given the conservative nature of the automotive industry, only a very small fraction of vehicles on the road will see solar cells in the foreseeable future.

## CONCLUSIONS

The lure of a huge market in the automotive sector is clearly a driving force for researchers and developers to come up with new materials and technologies that can be of value to a consumer who is willing and able to pay additional money for the added benefit. Even though the modern automobile still has four tires and a steering wheel, much like the cars from more than a 100 years ago, each and every component goes

through a steady metamorphosis. This offers opportunities for new technologies that offer new functionalities to be incorporated into the design. All the same, introducing nanomaterials and nanotechnology-based products into either the aftermarket or the OEMs is replete with challenges. As with anything else, this includes identifying the value chain and being able to deliver on the promised value proposition. Additionally, issues pertaining to manufacturability and robustness need to be addressed early in the development phase of the product. Last, but not the least, cost considerations take center stage when it comes to the automotive market.

## ACKNOWLEDGMENTS

The authors are grateful to Mr. John Blair of Executive Strategies for stimulating discussions, helpful comments, and suggestions.

## REFERENCES

1. <http://www.nanoinvestornews.com/modules.php?name=News&file=article&sid=3810> (accessed April 2005).
2. <http://www.abrn.com/abrn/issue/issueDetail.jsp?id=3163> (accessed August 2005).
3. <http://www.auto123.com/en/info/news/news.view.spy?artid=21942&pg=1> (accessed August 2005).
4. Kimberley, W. Taking a shine to Mercedes. *Automot. Eng.* **2004**, March, 44–46.
5. Seubert, C.M.; Nichols, M.E. Alternative curing methods of UV curable automotive clearcoats. *Prog. Org. Coat.* **2004**, *49*, 218–224.
6. [www.denglas.com](http://www.denglas.com) (accessed April 2005).
7. Presting, H.; Konig, U. Future nanotechnology developments for automotive applications. *Mat. Sci. Eng.* **2004**, *23*, 737.
8. <http://www.us.schott.com/english/index.html> (accessed April 2005).
9. <http://www.saint-gobain-sekurit-transport.com/bus/comfort/index.htm#1/> (accessed April 2005).
10. Dahotre, N.B.; Nayak, S. Nanocoatings for engine applications. *Surf. Coat. Technol.* **2005**, *194*, 58–67.
11. <http://www.plasticstechnology.com/articles/200110fa3.html> (accessed August 2005).
12. <http://www.autofieldguide.com/columns/gary/1001mat.html> (accessed August 2005).
13. [http://www.findarticles.com/p/articles/mi\\_m3012/is\\_3\\_184/ai\\_n6047552](http://www.findarticles.com/p/articles/mi_m3012/is_3_184/ai_n6047552) (accessed August 2005).
14. Lloyd, S.; Lave, L. Life cycle economic and environmental implications of using nanocomposites in automobiles. *Environ. Sci. Technol.* **2003**, *37* (15), 3458–3466.
15. Garces, J.; Moll, D.; Bicerano, J.; Fibiger, R.; McLeod, D. *Adv. Mat.* **2000**, *12* (23), 1835.



16. Kurauchi, T.; Okada, A.; Nomura, T.; Nishio, T.; Saegusa, S.; Deguchi, R. SAE Technical Paper Ser. **1991**, 910, 584.
17. <http://www.plasticstechnology.com/articles/200110fa3.html> (accessed August 2005).
18. [http://www.findarticles.com/p/articles/mi\\_go1575/is\\_200412/ai\\_n9756207](http://www.findarticles.com/p/articles/mi_go1575/is_200412/ai_n9756207) (accessed August 2005).
19. [www.nanotwin.com](http://www.nanotwin.com) (accessed April 2005).
20. [www.nanostellar.com](http://www.nanostellar.com) (accessed April 2005).
21. <http://www.qsinano.com/> (accessed April 2005).
22. <http://www.wpherald.com/storyview.php?StoryID=20050325-123219-4868r> (accessed April 2005).
23. Tschöpe, A.; Liu, W.; Flytzanistephanopoulos, M.; Ying, J.Y. Redox activity of nonstoichiometric cerium oxide-based nanocrystalline catalysts. *J. Catal.* **1995**, 157 (1), 42–50.
24. Giebeler, C.; Adelerhof, D.J.; Kuiper, A.; von Zon, J.; Oelgeschlager, D.; Schulz, G. Robust GMR sensors for angle detection and rotation speed sensing. *Sens. Actuators A* **2001**, 91, 16–20.
25. Binash, G.; Grunberg, B.; Saurenbach, F.; Zinn, W. Enhanced magnetoresistance in layered magnetic structures with antiferromagnetic interlayer exchange. *Phys. Rev. B* **1989**, 39, 4828–4830.
26. Baibich, M.; Broto, J.; Fert, A.; Nguyen van Dau, F.; Petroff, F. Giant magnetoresistance of Fe/Cr magnetic superlattices. *Phys. Rev. Lett.* **1988**, 61, 2472–2475.
27. [http://www.just-auto.com/news\\_detail.asp?art=38683](http://www.just-auto.com/news_detail.asp?art=38683) (accessed April 2005).
28. Ahmed, S.; Lee, S.; Carter, J.; Krumpelt, M. Methods for generating hydrogen for fuel cells. 6,713,040, March 30, 2004.
29. Keblinski, P.; Philpot, S.; Choi, S.; Eastman, J. Mechanisms of heat flow in suspensions of nano-sized particles. *Int. J. Heat Mass Transfer* **2002**, 45, 855–863.
30. Xue, L.; Keblinski, P.; Philpot, S.; Choi, S.; Eastman, J. Effect of liquid-solid interface on thermal transport. *Int. J. Heat Mass Transfer* **2004**, 47, 4277–4284.
31. Uhrig, R. Using plug-in hybrid vehicles. *The Bent of Tau Beta Pi* **2005**, Spring 31.
32. [http://www.cobasys.com/pdf/transportation/NiMhaxHEV/NiMhax\\_HEV\\_Brochure.html](http://www.cobasys.com/pdf/transportation/NiMhaxHEV/NiMhax_HEV_Brochure.html) (accessed April 2005).
33. Henriksen, G. Materials cost model. In *Advanced Technology Development Program*, Annual Merit Review Meeting, Argonne, IL, July 23, 2004; Department of Energy.
34. Pasquier, A.; Plitz, I.; Menocal, S.; Amatucci, G. A comparative study of Li-ion battery, supercapacitor and nonaqueous asymmetric hybrid devices for automotive applications. *J. Power Sources* **2003**, 115 (1), 171–178.
35. Singhal, A.; Skandan, G.; Amatucci, G.; Badway, F.; Ye, N.; Manthiram, A.; Ye, H.; Hu, J. Nanostructured electrodes for next generation rechargeable electrochemical devices. *J. Power Sources* **2004**, 129, 38.
36. Singhal, A.; Skandan, G.; Khij, F. Nanostructured Electrodes for Next Generation Rechargeable Electrochemical Devices, 41st Power Sources Conference, Philadelphia, PA, June 14, 2004.
37. Dillon, A.C.; Jones, K.M.; Bekkedahl, T.A.; Kiang, C.H.; Bethune, D.; Heben, M.J. *Nature* **1997**, 386, 377.
38. Hynek, S.; Fuller, W.; Bentley, J. *Int. J. Hydrogen Energy* **1997**, 22, 601.
39. [www.csun.edu/~wpg08917/Hydrogen%20Storage.ppt](http://www.csun.edu/~wpg08917/Hydrogen%20Storage.ppt) (accessed April 2005).
40. <https://engineering.purdue.edu/ChE/webpublications/ericjri/Nanotechnology.htm> (accessed April 2005).
41. Jung, D.; Cho, S.; Peck, D.; Shin, D.; Kim, J. Preparation and performance of nafion/montmorillonite nanocomposite membrane for direct methanol fuel cell. *J. Power Sources* **2003**, 118, 205–211.
42. Kim, H. Nanostructured Materials, The Knowledge Foundation's 4th Annual International Conference on Nanostructure Materials, Miami Beach, November 9–10, 2003.
43. Konle, J.; Presting, H.; Kibbel, H.; Banhart, F. Growth studies of Ge-islands for enhanced performance on thin film solar cells. *Mat. Sci. Eng. B* **2002**, 89 (1–3), 160.

# Axle Molecules Threaded through Macrocycles

Daryle H. Busch

Thomas Clifford

Department of Chemistry, University of Kansas, Lawrence, Kansas, U.S.A.

## INTRODUCTION

Interlocked structures exploit a mode of interaction that is old beyond history with everyday objects, but is relatively new in the molecular sciences.<sup>[1–3]</sup> Just as interlocking iron rings make chains for pulling or suspending heavy loads and as two-dimensional arrays of interlocked iron rings were used to make chain mail for the armor of knights of yore, one-dimensional and two-dimensional interlocking molecular rings may provide exciting, new materials for the future. If chains can be made, then why not molecular braiding, knitting, or weaving? A molecular cloth composed of linear polymer molecules, woven at the molecular level, would certainly have unanticipated properties. For example, the behavior might appear at first to resemble a live object. At room temperature, each molecular strand in the cloth would likely have some of its vibrational modes activated, so that the cloth would constantly be subject to motions that would tend to unravel it. This unraveling could be prevented, probably by having large groups on the ends of each strand, so that they could not pass through the openings in the weave, a subject of this entry.

One reason interlocked molecular structures are not yet available in multitudes of shapes and sizes, including the familiar forms just described, is that they are difficult to make. Unlike ordinary thread, string, or rope, it is difficult to get a hold on a molecular strand, so it is more difficult to put them through the motions that would create a needle work product—and that is precisely what this brief missive is about. It is about one of the simplest of tasks that has to be overcome if one wants to make chains, or knit, or weave on the molecular level. The subject is the threading of a, more or less, linear molecule through a molecular ring. One of the two simplest interlocked molecules is the *rotaxane* and it is composed of an axle molecule, inserted through a ring molecule and held there by its own end groups that are simply too big to permit the axle to be propelled easily out of the ring (Fig. 1).

## OVERVIEW

Actually, to a very small extent, linear molecules will spontaneously insert themselves into ring molecules in condensed phases.<sup>[4,5]</sup> However, if the axle and the ring contain atomic groupings that can bind to each other, then a so-called templating interaction may occur and the threading of the axle through the ring may occur extensively.<sup>[6,7]</sup> Such templates have been used extensively by chemists to make chains with several interlocked rings<sup>[3]</sup> and to tie knots, including the overhand knot, the square knot, and the granny.<sup>[8]</sup> Two structural designs have been suggested, and partially demonstrated, for the formation of polymers by rotaxane formation. They are shown in Fig. 2. The first, the *daisy-chain polyrotaxane*, uses molecules that contain both a ring and an axle so that they are able to self-assemble into polymer forms. The second, the *riveted polyrotaxane*, is formed by riveting together molecules that have two rings, similar in construction to one side of a bicycle drive chain.

If the molecular axle and the ring of a rotaxane are not locked in place by big blocking end groups on the axles, they are called pseudo-rotaxanes, to acknowledge their temporary nature. In fact, it is the pseudo-rotaxanes that are of interest here because, whatever the ultimate goal may be, the threading process does indeed initially produce a pseudo-rotaxane. Fig. 1 shows the progression from independent axle and ring molecules to pseudo-rotaxane, and then to rotaxane for a simple example. Focusing on the real issue that is at hand, chemists would like to be able to make molecular cloth, but they are, metaphorically, just learning how to thread the needle—and that is the current subject.

## THE BEGINNINGS OF MOLECULAR THREADING

About half a century ago, Wasserman<sup>[9]</sup> proposed the formation of rotaxanes and calculated the extent to

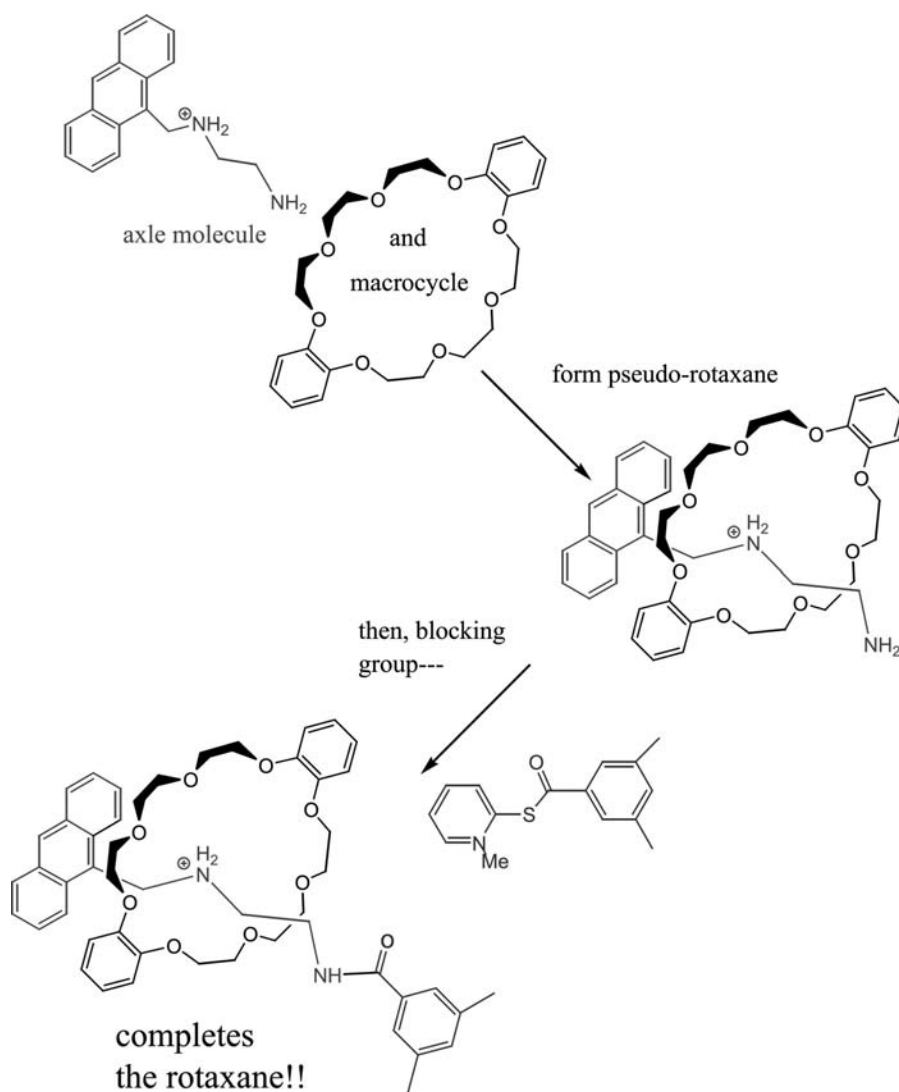


**Fig. 1** Progression from axle and macrocycle to pseudo-rotaxane and then to rotaxane.

which a pseudo-rotaxane should form if there were no particular intervening force to stabilize the interlocked molecule. Under Wasserman's defined conditions, about 0.01% pseudo-rotaxane formation might be expected. Some years later, Harrison and Harrison<sup>[5]</sup> performed elaborate experiments to determine the extent of spontaneous threading. Their results strongly supported the earlier conclusion that only a small fraction of the axle and ring molecules undergoes threading in the absence of some intervening force.

In their strikingly original templating studies, Chambron, Dietrich-Buchecker, and Sauvage<sup>[8]</sup> created a number of interlocked molecules along pathways that required threading. In these studies, the copper(I) ion served as the anchor for the template, locking axle molecules into rings both in final product rotaxanes and in intermediates in the synthesis of more complicated structures. Even with templates based on robust metal-ligand interactions, yields were low in the early studies of rotaxane or pseudo-rotaxane formation.

This offered a major challenge to the more ambitious goals of researchers because high levels of threading would be necessary to make materials that require many sequential steps as, for example, in polymer formation. Furthermore, it is essential that the interlocked materials not contain equivalents of hazardous materials. For that reason and because they have opened the way to a quantitative study of intermolecular threading, attention has more recently focused on weaker templating forces arising from hydrogen bonding and  $\pi$ - $\pi$  stacking interactions. From the standpoint of eventual development of useful products, templates using these supramolecular modes of interaction are most promising. Earlier studies judged success in threading based on the yields of rotaxanes that were formed. For example, in 1992, Wenz and Keller<sup>[10]</sup> showed that high threading yields occurred with polyamines going through cyclodextrins. This suggested that multiple hydrogen bonds could generally produce high levels of threading. Yields of 30–40% were

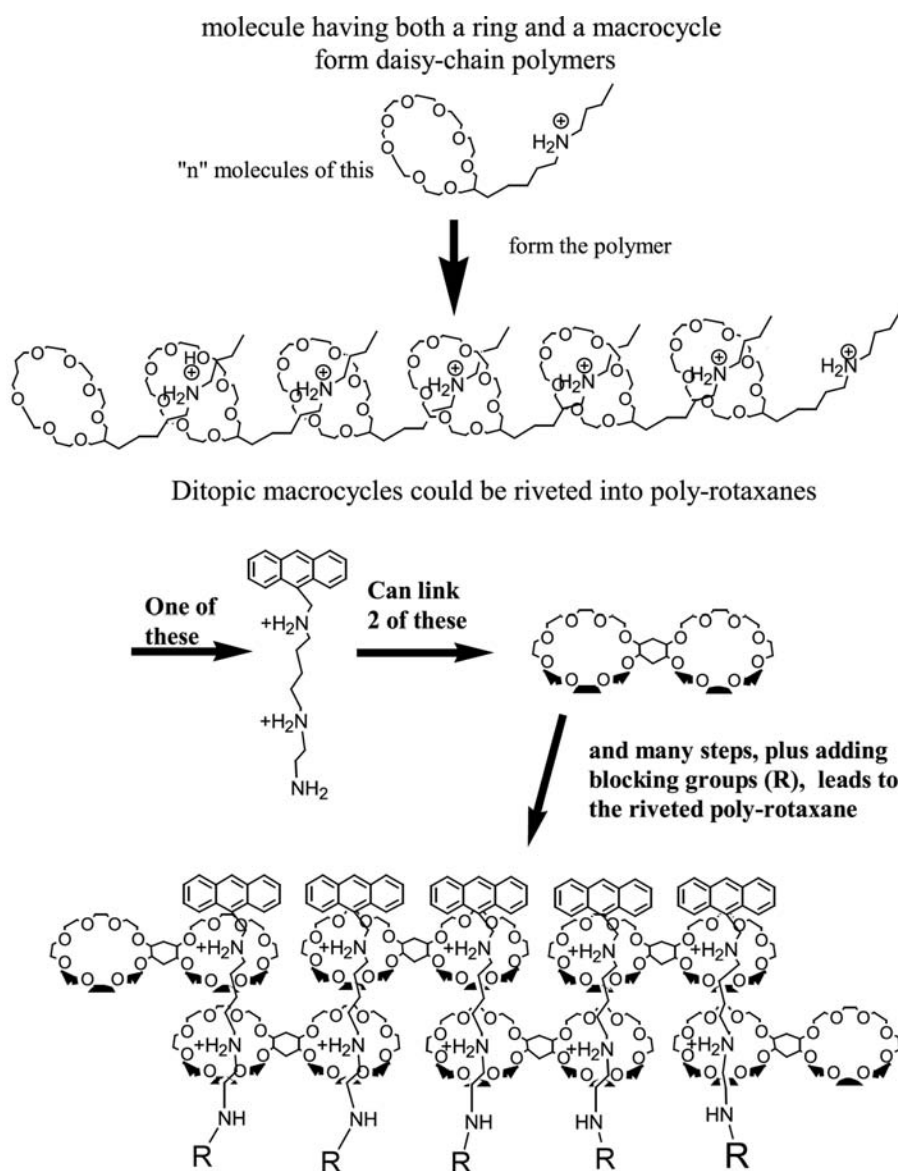


Fig. 2 Polymers based on rotaxane formation.

heralded as substantial achievements.<sup>[11,12]</sup> Furthermore, the synthesis of a [3]-rotaxane in 84% yield by coupling two molecules of a pseudo-[2]-rotaxane was considered as strong evidence of threading at least at the 90% level (Fig. 3).<sup>[13]</sup> Equilibrium constants for pseudo-rotaxane formation are at the center of developing and understanding how threading occurs on the molecular level.

### EQUILIBRIUM CONSTANTS FOR PSEUDO-[2]-ROTAXANE FORMATION

Traditional nuclear magnetic resonance (NMR) techniques (Fig. 4) have dominated the determination of equilibrium constants for the molecular threading process, with much less literature on values obtained from diffusion methods (NMR) and from direct

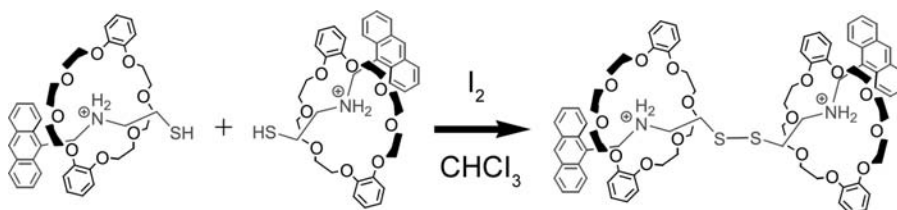
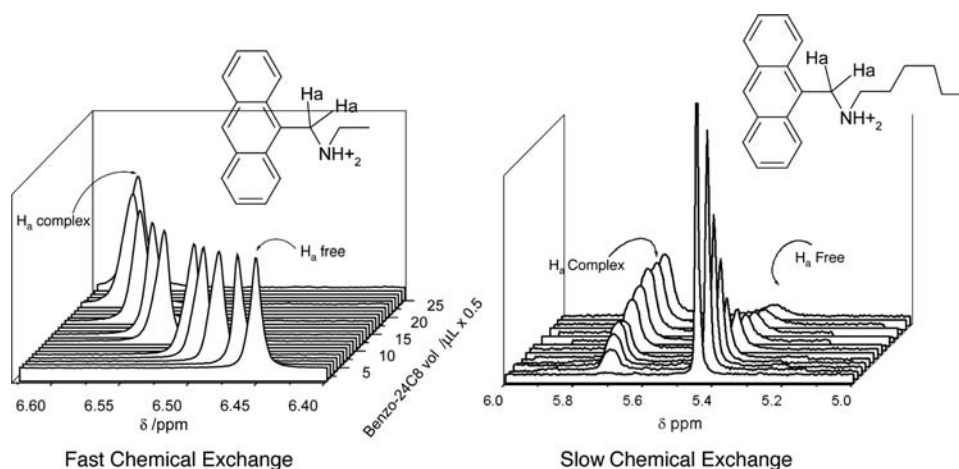


Fig. 3 Coupling of pseudo-[2]-rotaxanes to produce a [3]-rotaxane.



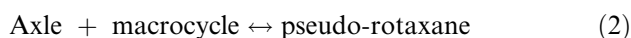
**Fig. 4** Nuclear magnetic resonance measurements for the determination of equilibrium constants.

thermodynamic measurements. Detailed measurements yield relatively reliable values, but estimates are often made from single measurements.<sup>[14]</sup> Analysis of these equilibrium measurements reveals the present state of knowledge with regard to the threading of axle molecules through macrocyclic molecules. Significant amounts of data exist only for templated formation of pseudo-rotaxanes, and the templating can, as indicated above, involve a variety of interactions. The most powerful templates involve covalent bonds such as those formed in ordinary organic compounds, but the metal–ligand equivalent, the coordinate bond, is more often used. Of greatest importance are the weaker linkages collectively called *supramolecular interactions* because the individual molecular partners retain their individualities while working together, like a fireman on a ladder, rather than being fused into a single entity, like a branch from a pear tree grafted onto a quince tree stalk. Outstanding among these are hydrogen bonding, which is the subject that has been most studied;  $\pi$ – $\pi$  stacking, which is second in importance; and hydrophobic force, which is notable among the oligocyclic sugars called cyclodextrins.

### FACTORS AFFECTING EQUILIBRIUM CONSTANTS FOR MOLECULAR THREADING

Equilibrium constant is defined in its traditional form by Eq. (1). The subscript in  $K_a$  indicates that the corresponding chemical equation has been written in the associative direction, rather than in the dissociative direction (Eq. (2)):

$$K_a = [\text{pseudo-rotaxane}]/[\text{axle}][\text{macrocycle}] \quad (1)$$



For supramolecular interactions of this kind (generally called complex formation), a simple relationship exists between the equilibrium constant  $K_a$ , and the rate constants for the associative (threading) reaction  $k_a$  and the dissociative (unthreading) reaction  $k_d$  (Eq. (3)):

$$K_a = k_a/k_d \quad (3)$$

Equilibrium constant data are presented in Tables 1 and 2 and the molecular partners, the ring and the axle, are identified by abbreviations. The abbreviations are identified with the correct molecular structures in Figs. 5 and 6. For the most part, the names from which the abbreviations have been constructed appear in the related text.

### Effect of Solvent

Both the diversity of molecular partners that can be united in the threading process and the effect of solvents on the threading equilibria are well illustrated by the first 10 entries in Table 1. The macrocycle used in the first five entries, symmetrical dibenzo-24-crown-8 (s-DB24Cr8), and the axle, dibenzylammonium ion, are prototypical for studies of this class, and Ashton et al.<sup>[15]</sup> used them to show the great impact of solvents that compete for hydrogen binding interactions that template the threading process. A relatively large equilibrium constant is found for the equilibrium in deuterio-chloroform ( $27,000 \text{ M}^{-1}$ ), but the value decreases markedly when the solvent is changed to acetonitrile ( $460 \text{ M}^{-1}$ ) or acetone ( $360 \text{ M}^{-1}$ ), and no threading occurs when dimethyl sulfoxide is used as the solvent. The monotonic effect of mixing the solvents is shown by the datum for the mixed solvent chloroform/acetonitrile ( $1700 \text{ M}^{-1}$ ).<sup>[16]</sup>

A dramatic solvent effect has been observed with the system consisting of the axle, bis(cyclohexylmethyl)-ammonium hexafluorophosphate (DCHXMA), and

**Table 1** Factors affecting molecular threading

Line	Macrocycle	Axle	Solvent	$T$ [°C]	$K_a$ [ $M^{-1}$ ]	Reference
1	s-DB24Cr8	DBA	$CDCl_3$	25	27,000	[15]
2	s-DB24Cr8	DBA	$CD_3CN$	25	460	[15]
3	s-DB24Cr8	DBA	$CD_3COCD_3$	25	360	[15]
4	s-DB24Cr8	DBA	$CD_3SOCD_3$	25	X	[15]
5	s-DB24Cr8	DBA	$CDCl_3/CD_3CN$	25	1,700	[16]
6	CR7	$MV^{2+}$	$H_2O$	25	200,000	[18]
7	TMe- $\beta$ -CD	TPPOC3PS	$H_2O$	25	Too high	[19]
8	TMe- $\beta$ -CD	TPPOC3PS	EG	25	8,700	[19]
9	TMe- $\beta$ -CD	TPPOC3PS	MeOH	25	290	[19]
10	TMe- $\beta$ -CD	TPPOC3PS	DMSO	25	0	[19]
11	s-DB24Cr8	<i>p,p'</i> -Me <sub>2</sub> DBA	$CDCl_3/CD_3CN$	31	960	[16]
12	s-DB24Cr8	DBA	$CDCl_3/CD_3CN$	31	1,110	[16]
13	s-DB24Cr8	<i>p,p'</i> -Cl <sub>2</sub> DBA	$CDCl_3/CD_3CN$	31	1,890	[16]
14	s-DB24Cr8	<i>p,p'</i> -Br <sub>2</sub> DBA	$CDCl_3/CD_3CN$	31	2,010	[16]
15	s-DB24Cr8	<i>p,p'</i> -(CO <sub>2</sub> H) <sub>2</sub> DBA	$CDCl_3/CD_3CN$	31	2,520	[16]
16	s-DB24Cr8	<i>p,p'</i> -(NO <sub>2</sub> ) <sub>2</sub> DBA	$CDCl_3/CD_3CN$	31	5,940	[16]
17	s-DB24Cr8	DBDXA	$CD_3CN$	25	352	[20]
18	u-DB24Cr8	DBA	$CD_3CN$	25	360	[21]
19	DPy <sub>2</sub> 4Cr8	DBDXA	$CD_3CN$	25	1,100	[22]
20	s-DB24Cr8	D- <i>i</i> -PrDBA	$CDCl_3/CD_3CN$	40	2,470	[23]
21	s-DB24Cr8	DCPMA	$CDCl_3/CD_3CN$	40	110	[23]
22	s-DB24Cr8	DCHXMA	$CDCl_3/CD_3CN$	40	110	[23]
23	s-DB24Cr8	DtBuPhMeAMAC1	$CD_3CN$	25	104	[24]
24	s-DB24Cr8	DtBuPhMeAMAC2	$CD_3CN$	25	70	[24]
25	s-DB24Cr8	DtBuPhMeAMAC3	$CD_3CN$	25	220	[24]
26	s-DB24Cr8	DtBuPhMeAMAC4	$CD_3CN$	25	250	[24]

ICE = intermediate chemical exchange; X = no threading detected.

the ring, DB24Cr8. After reflux (40°C) in  $CH_2Cl_2$  for 32 days with a 6:1 excess of macrocycle, ~98% of the axle molecule exists as pseudo-rotaxane. Subsequently, the material showed no evidence of dissociation in 3:1  $CDCl_3/CD_3CN$  on standing at room temperature for weeks. However, the crystalline rotaxane dissociated completely when dissolved in perdeuterated DMSO in 18 hr or less at 25°C.<sup>[17]</sup> These observations dramatize both the great variation in threading equilibrium constants in different solvents and the fact that the kinetics of equilibrations can be very slow. Reflecting on the collision event that must occur between the axle molecule and the macrocyclic molecule, it is a little like throwing a stiff thread at the hole in a needle during a wind storm. It may not be quite that bad, but the specific conformational, orientational, and trajectory requirements for threading and unthreading are quite limited, compared with the complete portfolios of orientations and motions available to the axle

and the macrocycle. Clearly, the events of interest here may be expected to be of low probability.

The influence of markedly different templating forces is evident from studies with more exotic systems. The distinctly polar environment within *cucubit[7]juril* (CR7) binds the dimethylviologen cation,  $MV^{2+}$ , very strongly in water (Table 1, line 6).<sup>[18]</sup> The contrasting relatively nonpolar environment within the hydrophobic cavity of a cyclodextrin (lines 7–10) provides a distinctly parallel behavior for reasons that might be considered opposite to those of the CR7. Kano et al.<sup>[19]</sup> report that the equilibrium constant in water for binding to tetramethyl- $\beta$ -cyclodextrin (TMe- $\beta$ -CD) of the long, negatively charged, sulfonate-terminated arm of the tetrasubstituted porphyrin, TPPOC3PS, is too large to measure by their methods. However, values of 8700 and 290  $M^{-1}$  were determined in ethylene glycol and methanol, respectively. No binding was observed in DMSO. For related axle molecules and the same



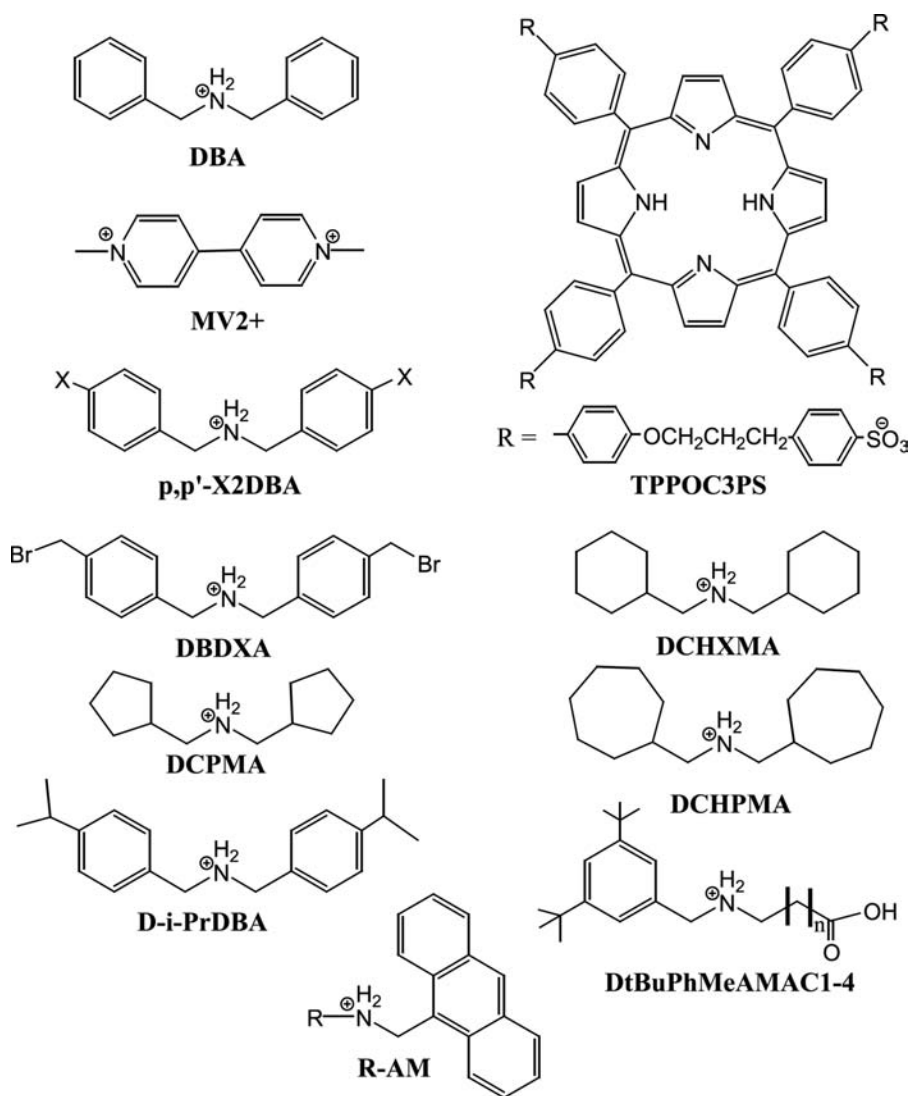


Fig. 5 Axle molecules cited in the text.

cyclodextrin, the equilibrium constant increased as water was mixed with the ethylene glycol solvent.

### Substituent Effects

The prototypic combination of s-DB24Cr8 and dibenzylammonium ion was used to evaluate the effects of axle substituents on the equilibrium constants for threading (Table 1, entries 11–16).<sup>[16]</sup> The affinity of the axle for the macrocycle ( $K_a$ ) increases smoothly as the electron-withdrawing capability of the substituents increases. This is consistent with the stabilization of hydrogen bonding to ether oxygen atoms of the macrocycle DB24Cr8 as the acidity of the protons of the substituted dibenzyl ammonium ion increases. Replacing the protons at the *para* positions on the phenyl groups with methyl groups has the opposite effect, as expected. Moving the substituent (Br) to a *para* methyl group (DBDXA) leaves a small effect.<sup>[20]</sup>

The position of the benzo groups on DB24Cr8 has little impact (lines 2 and 18),<sup>[21]</sup> but replacing ether oxygens with pyridine nitrogens more than doubles the binding constant (lines 17 and 19).<sup>[22]</sup> The more basic nitrogen donors on the macrocycle form stronger hydrogen bonds to the protons of the axle ammonium function.

### Steric Effects

The beginnings of an understanding of steric effects came with the investigation of the equilibria and rates of reaction of the common macrocycle DB24CR8 with various axle molecules related to dibenzylammonium ion by replacing the phenyl groups with cyclopentyl, cyclohexyl, and cycloheptyl rings. Both rate and equilibrium data are reported.<sup>[23]</sup> The bis-*para*-*i*-propyl-phenyl ammonium ion, used for reference purposes, gives association and dissociation rate constants of

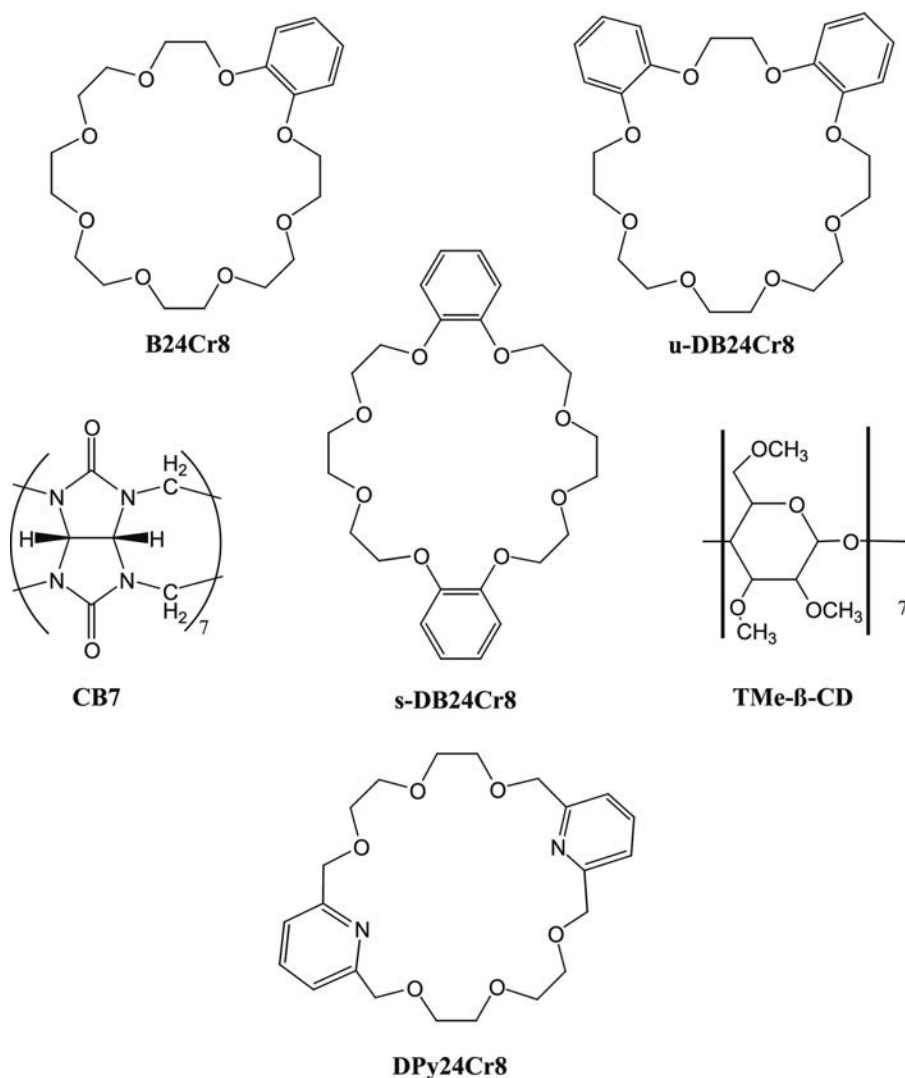


Fig. 6 Macrocycles cited in the text.

$3.2 \times 10^{-3} \text{ M}^{-1} \text{ sec}^{-1}$  and  $1.3 \times 10^{-6} \text{ sec}^{-1}$ , respectively, and a  $K_a$  value of  $2470 \text{ M}^{-1}$  at  $40^\circ\text{C}$ . Remarkably, the rates of association and dissociation for the two saturated ring derivatives, cyclopentyl and cyclohexyl, bracket those for the reference axle (*D-i*-PrDBA), but exhibit identical equilibrium constants at  $40^\circ\text{C}$ ; that value is  $K_a = 110 \text{ M}^{-1}$ . As described above in “Effect of Solvent,” the cyclohexyl derivative reacts at an astoundingly low rate (weeks), whereas the smaller cyclopentyl derivative threads on the second-to-minute time scale. The cycloheptyl derivative gave no evidence for binding at all.

### Effects of Chain Length and Branching

Using an interesting family of axle molecules that are blocked on one end and have a carboxylic acid on the other end, Zehnder and Smithrud<sup>[24]</sup> found a small increase in affinity with longer chains. Clifford et al.

explored chain length and a number of other factors affecting the threading process with monobenzo-24-crown-8, B24Cr8, and 29 axle molecules (R-AM) having an anthracen-9-ylmethyl group in common.<sup>[14]</sup> Their results are summarized in Table 2. The normal linear alkyl groups methyl through *n*-nonyl, plus octadecyl, made up a thorough exploration of the influence of chain length on threading. The equilibrium constants ranged from  $120$  to  $180 \text{ M}^{-1}$ , with a mean of  $160 \pm 20 \text{ M}^{-1}$ . No systematic variation was found for the seven  $K_a$  values available for *n*-alkyl threading groups. Within the range of uncertainty, the  $K_a$  values changes vary randomly as chain length. There is no hint of an even-odd hydrocarbon variation.

In contrast to the insensitivity of the equilibrium constant to chain length, the axles are readily separated into two groups based on the rates at which they undergo threading. Axles shorter than pentyl equilibrate rapidly on the NMR time scale, whereas those longer than pentyl equilibrate slowly. The pentyl group

**Table 2** Factors affecting threading

Line	Threading group	$K_a$ [ $M^{-1}$ ]	NMR method
<i>Linear alkyl groups</i>			
1	Methyl	IS	
2	Ethyl	180	Fast
3	<i>n</i> -Butyl	127	Fast
4	<i>n</i> -Pentyl	ICE	
5	<i>n</i> -Hexyl	177	Slow
6	<i>n</i> -Heptyl	161	Slow
7	<i>n</i> -Octyl	151	Slow
8	<i>n</i> -Nonyl	120	Slow
9	<i>n</i> -Octadecyl	179	Slow
<i>Branched alkyl groups</i>			
10	<i>i</i> -Propyl	17	Fast
11	<i>i</i> -Butyl	43	Fast
12	<i>i</i> -Pentyl	164	Fast
13	2-MeHexyl	27	Slow
14	Cyclohexyl	17	Slow
15	Cyclohexylmethyl	X	
<i>Butyl isomers</i>			
3	<i>n</i> -Butyl	127	Fast
16	<i>i</i> -Butyl	43	Fast
17	<i>s</i> -Butyl	13	Fast
18	<i>t</i> -Butyl	X	
<i>Phenyl-substituted alkyls</i>			
19	Benzyl	94	Slow
20	2-Phenylethyl	194	Slow
21	3-Phenylpropyl	282	Slow
<i>Hydroxyl-substituted alkyls</i>			
22	2-Hydroxyethyl	93	Fast
23	3-Hydroxypropyl	82	Fast
24	5-Hydroxypentyl	ICE	
25	$\alpha$ -Hydroxy- <i>p</i> -xylyl	100	Slow
<i>Terminal carboxylic acid group</i>			
26	Pentanoic acid group	280	Slow
27	Hexanoic acid group	223	Slow
28	Toluic acid group	221	Slow
29	Ethyl acetate group	ICE	

ICE = intermediate chemical exchange; X = no threading detected; IS = insoluble.

exchanges on an intermediate time scale that prevented the determination of  $K_a$  with the tools available to these researchers. The general conclusion is that the equilibrium constant for threading is essentially insensitive to the length of the chain, but the rates at which threading and unthreading occur depend strongly on chain length. It is interesting that long chains give the same effect on rate as increased bulk, as represented by

increased ring sizes for the saturated rings cyclopentyl and cyclohexyl substituents on axle molecules (vide supra).

Branched alkyl axle components show a distinctive behavior. For the axle groups *i*-propyl, *i*-butyl, and *i*-pentyl (Table 2, lines 10–12), branching moves regularly to greater distance from the ammonium binding site. Correspondingly,  $K_a$  increases from a very low value of  $17 M^{-1}$  at *i*-propyl to  $164 M^{-1}$  for *i*-pentyl, essentially the average value noted above for linear ligands. This suggests that the steric effect because of alkyl branching greatly weakens threading, but that it is only effective when the branching occurs near the ammonium binding site. Similarly, comparing the isomers of the butyl group,  $K_a$  decreases markedly from *n*-butyl through *i*-butyl and *s*-butyl, finally disappearing at *t*-butyl. Furthermore, all of the branched structures described up to this point equilibrate on the rapid NMR time scale, a performance completely consistent with their linear isomers. The 2-methylhexyl-substituted R-AM axle molecule gives an equilibrium constant between those for the *i*-propyl and *i*-butyl derivatives, but reacts on the slow NMR time scale.

The cyclohexyl derivative (Table 2, line 14) binds with a  $K_a$  identical to that of an *i*-propyl group, but the binding rate is slow, a feature already discussed for saturated ring derivatives. Based on the work of others, the failure of these studies to produce a  $K_a$  value for the cyclohexylmethyl derivative may be attributed to either insufficient reaction time, or to the specific properties of the solvent acetone.<sup>[17]</sup>

### Influence of Terminal Groups

Hydroxyl, carboxylic acid, and phenyl groups were studied as terminal groups on the threading components of the anthracen-9-ylmethyl blocked axle molecules (R-AM) of Clifford, Abushamleh, and Busch<sup>[14]</sup> B24Cr8 was used as the macrocycle. For hydroxyalkyl derivatives (Table 2, lines 22–25), the  $K_a$  values all fall in the range around and just below  $100 M^{-1}$ , suggesting that the OH group substantially weakens the binding compared with a simple alkyl thread. In contrast, a carboxylic acid group at the terminal site (lines 26–28) definitely enhances  $K_a$ , giving values in the range between 200 and  $300 M^{-1}$ . Interestingly, the alcohol functional group does not affect the rates (i.e., hydroxypentyl falls in the intermediate rate region, just like pentyl itself). In contrast, pentanoic acid equilibrates on the slow NMR time scale, acting as if both the carboxyl carbon and oxygens contribute to the “effective” chain length.

Phenyl terminal groups on the threading arm of the axle molecule (Table 2, lines 19–21) show a behavior that parallels that of both the carboxylic acid derivatives

and the branched alkyl groups. Like branched alkyls,  $K_a$  increases substantially for each methyl group placed between it and the ammonium group, proceeding to a value of  $282 \text{ M}^{-1}$  for 3-phenylpropyl. However, unlike the branched alkyls, the highest value for  $K_a$  found for the phenyl derivatives is almost double that for *n*-alkyls. In this enhancement of threading affinity, the phenyl group resembles the carboxylic acid group. It is reasonable to suggest that the enhanced affinities associated with terminal carboxylic acids and phenyl substituents arise from additional intermolecular attractions, and that these interactions are facilitated by the increasing flexibility that comes with a small increase in chain length. It is also conceivable that the weakened binding of alcohol functions may be because of competitive binding with the solvent, externally, as well as within the macrocycle. Competition between threading and binding outside the macrocycle has been observed.<sup>[25]</sup>

## CONCLUSION

The threading of axle molecules through macrocyclic molecules is but one of several elementary steps that must be controlled if scientists are eventually to learn to manipulate the interlocking of molecules to produce new materials, such as fabrics, only one molecule thick. Threading produces pseudo-rotaxanes and, in the absence of templating forces, the random threading of axle molecules through rings occurs to only a very small extent (hundredths of a percent). However, through the use of intermolecular forces, the axle may be selectively templated inside the ring in high yields. Examples of binding sources for templating include metal ion complexation, hydrogen bonding, and  $\pi$ - $\pi$  stacking of aromatic rings. Like polymers in general, new materials based on molecular interlocking will require large numbers of sequential steps. If such steps involve threading, that process must be accomplished with high efficiency.

Much has been learned about threading using hydrogen bonding templates, based mainly on macrocyclic polyethers with (as axles) secondary ammonium groups having one or two, more or less, linear arms that actually perform the threading. Therefore the equilibrium constant and the fraction of the axle and ring that are in the pseudo-rotaxane form increase with increased macrocycle basicity and with increased acidity of the ammonium ion axle (for the types of interactions described here, the opposite is possible). Hydrogen bonding sites outside the ring compete with threading, and terminal hydroxyl groups on axle molecules weaken threading. For linear alkyl groups, affinity is insensitive to chain length. However, branched alkyls show variable steric effects; branching inside the  $\gamma$ -position of the axle lowers the threading affinity. However, threading is favored by carboxylic acid groups and by phenyl groups

at the ends of alkyls (also at the  $\gamma$ -position or greater).  $K_a$  is strongly favored by nonpolar solvents having poor hydrogen bonding abilities. In contrast, strongly hydrogen-bonding solvents greatly weaken the interactions. The solvent effects are dramatically different in systems based on cyclodextrins—large cyclic molecules that bind their axle molecules through hydrophobic interactions. They bind most strongly in water and  $K_a$  is decreased by the addition of organic solvents. Remarkably, cucubituril selectively binds cationic axles, and the binding is extremely strong in water.

Returning to the hydrogen-bonded templates, steric effects and chain length effects all dramatically affect the rate of the equilibration process, in some cases, with no change in equilibrium constant. Saturated rings appended to ammonium ions through methylene groups exhibit extreme behavior. The cyclopentyl derivative equilibrates in  $\sim 10$  min under conditions where the cyclohexyl derivative requires over a month. For simple *n*-alkyl groups, chains shorter than pentyl react on the fast NMR time scale, whereas those longer than pentyl react on the slow NMR time scale, despite the fact that there is no assignable change in affinity with chain length. Seemingly, neither branching nor the presence of functional groups has a substantial effect on the rate pattern of linear alkyl groups.

The increased understanding of the elemental process of threading an axle molecule through a large molecular ring should fuel research on interlocked molecular species of high molecular weights. Polymerization in one, two, or three dimensions by rotaxane formation or by interlocked rings (*catenane* formation) will lead to new and exciting materials. Expectations include materials of great strength and unusual flexibility. How the abilities of the individual interlocked molecular units to move independently will affect the various properties of molecularly interlocked materials remains unclear. Expectations continue to grow that such structures will have information-related applications, in the limit, as integral parts of a *molecular computer*. If history is our guide, it is the unexpected applications that will eventually be the most important and will change people's lives.

## REFERENCES

1. Busch, D.H. *Transition Metal Ions in Supramolecular Chemistry*; Fabbrizzi, L., Ed.; Kluwer: Dordrecht, The Netherlands, 1994; 55–80.
2. Hubin, T.J.; Busch, D.H. Template routes to interlocked molecular structures and orderly molecular entanglements. *Coord. Chem. Rev.* **2000**, *200–202*, 5–52.
3. Amabilino, D.B.; Ashton, P.R.; Balzani, V.; Boyd, S.E.; Credi, A.; Lee, J.Y.; Menzer, S.; Stoddart, J.F.; Venturi, M.; Williams, D.G. Oligocatenanes made to order. *J. Am. Chem. Soc.* **1998**, *120*, 4295–4307.

4. Frisch, H.L.; Wasserman, E. Chemical topology. *J. Am. Chem. Soc.* **1961**, *83*, 3789–3795.
5. Harrison, L.T.; Harrison, S. Synthesis of a stable complex of a macrocycle and a threaded chain. *J. Am. Chem. Soc.* **1967**, *89*, 5723–5724.
6. Hubin, T.J.; Kolchinski, A.G.; Vance, A.L.; Busch, D.H. Template control of supramolecular architecture. *Adv. Supramol. Chem.* **1999**, *5*, 237–357.
7. Busch, D.H.; Vance, A.L.; Kolchinski, A.G. Molecular template effect: Historical view, principles, and perspectives. *Compr. Supramol. Chem.* **1996**, *9*, 1–43.
8. Chambron, J.-C.; Dietrich-Buchecker, C.; Sauvage, J.-P. Transition metals as assembling and templating species: Synthesis of catenanes and molecular knots. *Compr. Supramol. Chem.* **1996**, *9*, 43–83.
9. Wasserman, E. The preparation of interlocking rings: A catenane. *J. Am. Chem. Soc.* **1960**, *82*, 4433–4434.
10. Wenz, G.; Keller, G. Threading cyclodextrin rings on polymer chains. *Angew. Chem.* **1992**, *31*, 197.
11. Kolchinskii, A.G.; Busch, D.H.; Alcock, N.W. Gaining control over molecular threading—Benefits of second coordination sites and aqueous/organic interfaces in rotaxane synthesis. *Chem. Commun.* **1995**, 1289–1291.
12. Ashton, P.R.; Glink, P.T.; Stoddart, J.F.; Tasker, P.A.; White, A.J.P.; Williams, D.J. Self-assembling [2]- and [3]-rotaxanes from secondary dialkylammonium salts and crown ethers. *Chem. Eur. J.* **1996**, *2*, 729.
13. Kolchinski, A.G.; Alcock, N.W.; Roesner, R.A.; Busch, D.H. Molecular riveting: High yield preparation of a [3]-rotaxane. *Chem. Commun.* **1998**, 1437.
14. Clifford, T.; Abushamleh, A.; Busch, D.H. Factors affecting the threading of axle molecules through macrocycles: Binding constants for semi-rotaxane formation. *PNAS* **2002**, *99*, 4830–4836.
15. Ashton, P.R.; Campbell, P.J.; Chrystal, E.J.T.; Glink, P.T.; Menzer, S.; Philip, D.; Spencer, N.; Stoddart, J.F.; Tasker, P.A.; Williams, D.J. Dialkylammonium ion/crown ether complexes: The forerunners of a new family of interlocked molecules. *Angew. Chem., Int. Ed. Engl.* **1995**, *34*, 1865–1869.
16. Ashton, P.R.; Fyfe, M.C.T.; Hickingbottom, S.K.; Stoddart, J.F.; White, A.J.P.; Williams, D.J. Hammett correlations beyond the molecule. *J. Chem. Soc., Perkin Trans.* **1998**, *2*, 2117–2128.
17. Elizarov, A.R.; Chang, T.; Chiu, S.-H.; Stoddart, J.F. Self-assembly of dendrimers by slippage. *Org. Lett.* **2002**, *4*, 3565–3568.
18. Kim, H.-J.; Jean, W.S.; Ko, Y.H.; Kim, K. Inclusion of methylviologen in cucubit[7]uril. *PNAS* **2002**, *99*, 5007–5011.
19. Kano, K.; Nishiyabu, R.; Asada, T.; Kuroda, Y. Static and dynamic behavior of 2:1 inclusion complexes of cyclodextrins and charged porphyrins in aqueous organic media. *J. Am. Chem. Soc.* **2002**, *124*, 9937–9944.
20. Rowan, S.J.; Cantrill, S.J.; Stoddart, J.F. Triphenylphosphonium-stoppered [2]rotaxanes. *Org. Lett.* **1999**, *1*, 129–132.
21. Ashton, P.R.; Chrystal, E.J.T.; Glink, P.T.; Menzer, S.; Schiaro, C.; Spencer, N.; Stoddart, J.F.; Tasker, P.A.; White, A.J.P.; Williams, D.J. Pseudorotaxanes formed between secondary dialkylammonium salts and crown ethers. *Chem. Eur. J.* **1996**, *2*, 709–729.
22. Chang, T.; Heiss, A.M.; Cantrill, S.J.; Fyfe, M.C.T.; Pease, A.R.; Rowan, S.J.; Stoddart, J.F.; White, A.J.P.; Williams, D.J. Ammonium ion binding with pyridine-containing crown ethers. *Org. Lett.* **2000**, *2*, 2947–2950.
23. Ashton, P.R.; Baxter, I.; Fyfe, M.C.T.; Raymo, F.M.; Spencer, N.; Stoddart, J.F.; White, A.J.P.; Williams, D.J. Rotaxane or pseudorotaxane? That is the question. *J. Am. Chem. Soc.* **1998**, *120*, 2297–2307.
24. Zehnder, D.W.; Smithrud, D.B. Facile synthesis of rotaxanes through condensation reactions of DCC-[2]rotaxanes. *Org. Lett.* **2001**, *3*, 2485–2487.
25. Ghosh, P.; Mermagen, O.; Schalley, C.A. Novel template effect for the preparation of [2]rotaxanes with functionalised centre pieces. *Chem. Commun.* **2002**, 2628–2629.

# Barcoded Nanowires

Rebecca L. Stoermer

Christine D. Keating

*Department of Chemistry, Pennsylvania State University,  
University Park, Pennsylvania, U.S.A.*

## INTRODUCTION

Metal nanowires have been prepared with segments of different materials along their lengths. These particles can be synthesized in a large number of optically distinguishable striping patterns, and thus have been referred to as barcoded nanowires. These barcoded wires can be used for encoding information such as the type of biological assay being performed on the surface of the particle. Thus they have application in multiplexed bioanalysis.

A variety of methods exist for metal and semiconductor nanowire synthesis. Of these, few are capable of producing wires with segments of different materials along the length of the wire. Templated electrodeposition has been used for production of striped metal nanowires tens to hundreds of nanometers in diameter and several microns in length. The length of each segment can be as small as tens of nanometers or as long as the entire wire. The resulting nanowires have potential application as components in self-assembled functional electronic devices. Segments of differing electronic properties (e.g., conductors, semiconductors, and even monolayers) can be incorporated to prepare building blocks for the bottom-up assembly of electronic devices.

Optically encoded (barcoded) particles also have potential applications analogous to barcodes in the retail industry, where the products are tracked by the barcode pattern. Typically, the barcode labels used on retail products are readily identifiable to the human eye. In addition to these overt tags, there is also interest in microscopic barcodes invisible to the naked eye. Striped nanowires can serve as such microscopic identifiers, and have enormous potential for use in biological sensing applications where many different bioassays must be simultaneously followed. In this last application, the barcoded nanowires perform a function analogous to the individual spots of a DNA microarray, encoding the identity of biomolecules attached to their surface.

## SYNTHESIS OF NANOWIRES

A variety of synthetic methods have been reported for the preparation of nanowires of carefully regulated composition, size, and aspect ratio. They include electrochemical<sup>[1–3]</sup> and photochemical<sup>[4]</sup> reduction methods in various media including aqueous surfactant,<sup>[5]</sup> porous alumina templates,<sup>[6,7]</sup> polycarbonate membranes,<sup>[8]</sup> and carbon nanotube templates.<sup>[9,10]</sup> Nanowires have also been prepared by catalytic synthesis,<sup>[11,12]</sup> electroless deposition,<sup>[13–15]</sup> seeding growth methods,<sup>[16–19]</sup> vapor–liquid–solid growth,<sup>[20,21]</sup> and photochemical synthesis.<sup>[22]</sup> Magnetic wires have also been made via metal electrodeposition.<sup>[23]</sup>

Other types of fabricated nanowires include nanocables having coaxial structures generated with silver centers coated with silica,<sup>[24]</sup> electrochemically prepared gold-core, silver-shell nanowires,<sup>[25]</sup> metal oxide wires made using either a mild, solution-based colloidal approach,<sup>[26]</sup> solvothermal methods,<sup>[27]</sup> sonochemistry,<sup>[28]</sup> thermal evaporation,<sup>[29]</sup> or gas-phase catalytic growth methods,<sup>[12]</sup> and nanowire diodes created by coating polymer films on metal nanowires.<sup>[30]</sup>

## SYNTHESIS OF STRIPED NANOWIRES

Although a number of synthetic methods are available for creating nanowires, only a few methods exist that allow for the creation of nanowires with stripes of different materials along their lengths. One such method is the vapor–solid–liquid (VSL) growth technique, which has primarily been used to create semiconductor nanowires and superlattices.<sup>[21,31,32]</sup> Another involves electrochemical synthesis whereby metal ions are reduced into membrane templates.<sup>[6,33–36]</sup>

In VSL nanowire synthesis, a catalyst nanoparticle, which defines the diameter of the wire, is used to initiate wire growth from a reactant vapor. As more vapor is introduced, wire growth continues. An equilibrium phase diagram is used to select a catalyst that



can form a liquid alloy with the nanowire material. For example, gold nanoparticles have been used as catalysts for the VSL growth of silicon wires.<sup>[12]</sup> To obtain striped heterostructured nanowires, different vapor sources are consecutively fed into the system.<sup>[21,31,32]</sup> For example, semiconductor superlattices have been prepared in which photoluminescence from the wires is patterned based on the position of GaP and GaAs segments.<sup>[32]</sup>

Striped metal nanowires are typically prepared by electrochemically reducing metal ions into the pores of a template. Porous aluminum oxide or track-etch membranes are commonly used.<sup>[3,37–41]</sup> Alumina membranes are prepared by anodizing Al at constant potential to give a nanoporous membrane.<sup>[39,41]</sup> Pore diameters can be varied (from tens to several hundred nanometers) by controlling the anodization potential.<sup>[40]</sup> Track-etch membranes are prepared by using nuclear fission fragments to attack a non-porous sheet of desired material (e.g., polycarbonate or polyester), to yield indentations in the material that are further chemically etched into pores.<sup>[41]</sup>

To electrochemically produce barcoded nanowires, one side of a template membrane (e.g., Al<sub>2</sub>O<sub>3</sub>) is coated with a silver film to serve as a cathode for reducing metal ions from solution into the pores of the membrane template. This can be accomplished by vapor deposition or sputtering. The opposite side of the template is then immersed in a plating solution of a desired metal for electrochemical deposition. The length of the metal stripe created is dictated by the amount of current passed and the amount of time the plating is allowed to deposit. Once a stripe of a desired length has been created, the plating solution is simply changed such that the next metal segment can be added. The thickness of each individual stripe can in principle be controlled with great accuracy during the electrodeposition process.<sup>[42,43]</sup> Indeed, repeating Cu and Co segments only 8-nm-thick have been prepared from a solution containing both metal ions.<sup>[31]</sup> Selective electrodeposition of each metal from this solution is accomplished by careful control over plating solution composition (i.e., relative concentrations of the two metal ions) and the electrode potential, which is switched between values favoring Cu deposition to those favoring Co deposition during synthesis.<sup>[44–46]</sup>

The aspect ratio ( $l/d$ , where  $l$  is the length and  $d$  is the diameter of the nanowires) of the wires is controlled by the membrane pore diameter (which dictates wire width), and the deposition time (which determines the length). The maximum wire length is limited by the thickness of the template (which is roughly 50–60  $\mu\text{m}$  for commercial alumina membranes) and to breakage for wires with high aspect ratios (over 25:1 aspect ratio). Once the electrochemical deposition is complete, the silver backing and membrane are

dissolved away, leaving behind a suspension of striped metal nanowires.

To date, barcoded nanowires have been prepared with Au, Ag, Pt, Pd, Ni, Co, and Cu metal segments.<sup>[33]</sup> Fig. 1A shows a reflectance image of a 320-nm AuAgPd striped nanowire imaged at 430 nm. At this wavelength, Au has the lowest reflectivity, followed by Pd and then Ag. Fig. 1 shows that these metals can be optically distinguished based on reflectivity difference. The number of possible distinctive patterns or permutations available to the barcoded metal wires is  $m^s$ , where  $m$  is the number of metal types and  $s$  is the number of stripes in each wire. For example, wires consisting of four metals (i.e., Au, Pt, Co, and Ag) with six stripes leads to 4096 possible striping patterns ( $4^6 = 4096$ ). Ag/Au striped wires having 13 distinguishable stripes have been reported,<sup>[47]</sup>  $2^{13} = 8192$  possible patterns. Addition of a third metal leads to over 1.5 million possible patterns. To account for patterns that repeat in the forward and reverse direction, the following equation should be used: possibilities =  $m^s + m^{\text{ceil}(s/2)}/2$ , where  $m$  is the number of metals in the rod,  $s$  is the number of stripes, and  $\text{ceil}$

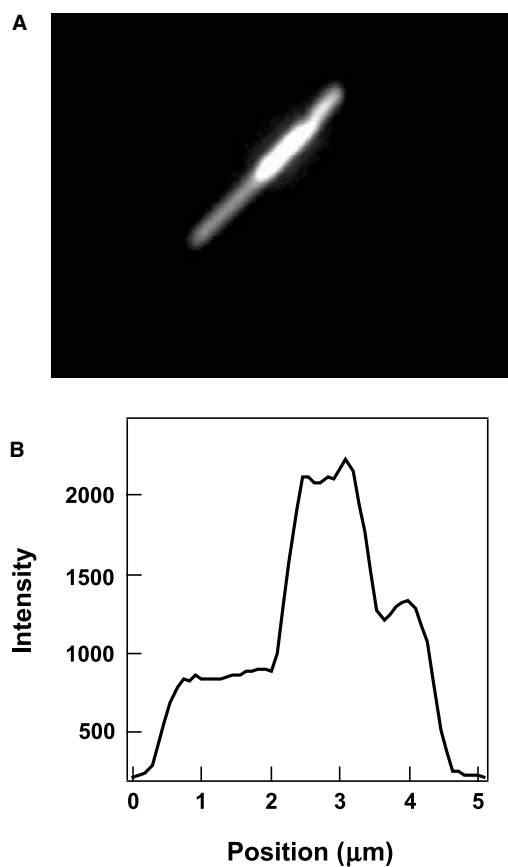


**Fig. 1** (A) Reflectance image of an AuAgPd nanowire taken at 430-nm wavelength. (B) Line scan profile of intensity vs. distance across the nanowire length.

stands for ceiling function, which rounds the exponent of  $n$  to the next highest integer (i.e.,  $3/2$  rounds up to 2). Using this equation, the actual number of different patterns that could be obtained from a 4-metal, 6-stripe wire is 2080, and for a 3-metal, 13-segment particle is  $7.98 \times 10^5$ .

## CHARACTERIZATION

Once nanowires are fabricated, they are characterized via many methods to determine their actual compositions, sizes, shapes, optical, and electrical properties. Transmission electron microscopy (TEM) is used to determine the size and shape of nanowires. Scanning electron microscopy (SEM) is used to examine the stripes and the metal-metal interfaces between segments. With SEM, striping patterns of heterostructured nanowires and surface defects can be identified, which cannot be detected using TEM. Fig. 2 is an example of a field emission (FE) SEM image of a 5- $\mu\text{m}$ -long, 320-nm-diameter AuAuAgAu striped nanowire. Energy dispersive X-ray spectroscopy is used to determine the average chemical composition of nanowires, including the microstructure of single metal and multilayered wires.<sup>[12,48,49]</sup>

In identifying the striping pattern in barcoded nanowires, optical reflectance microscopy is used. The striping pattern is deciphered based on reflectance differences of adjacent metal stripes. For optical resolution using reflectance detection, the different metal segments have to be separated by a distance greater than  $\lambda/2\text{NA}$ , where NA is the numerical aperture of the objective lens (a typical oil immersion lens has  $\text{NA} = 1.4$ ). The optical properties of 320-nm-diameter



**Fig. 2** Field emission SEM image of a AuAuAgAu nanowire, acquired with backscattered electron detection. The Ag segment appears darker as compared to the Au.

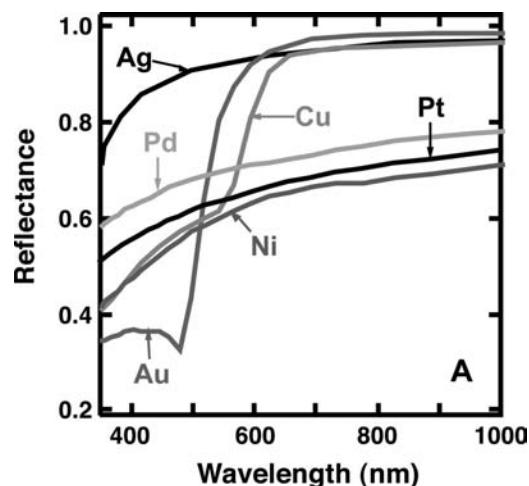


**Fig. 3** Reflectance values for various bulk metals. Source: From Ref.<sup>[81]</sup> ©American Chemical Society.

nanowire segments resemble those of their bulk counterparts.<sup>[40,50–54]</sup> Reflectance values for various bulk metals, plotted over a range of wavelengths, are shown in Fig. 3.<sup>[55]</sup> The differences in reflectivity of the various metal types allows for the detection of multiple metal stripes in a single barcoded nanowire. Fig. 1B shows a line scan of the AuAgPd striped nanowire pictured in Fig. 3A. This scan illustrates the changes in reflectance intensity across the length of the wire. Freeman et al.<sup>[56]</sup> have demonstrated a 100-particle library of barcoded nanowires in which more than 70 of the patterns could be identified with greater than 90% accuracy. These authors developed software for rapid readout of barcode striping pattern.

## POTENTIAL USES FOR BARCODED NANOWIRES

### Nanoelectronics

Striped metal nanowires have potential application as primary components for nanoscale electronic devices.<sup>[57–59]</sup> Current-voltage responses of nanowires can be altered by incorporating either semiconductor, particulate, or molecular segments into the wires during fabrication.<sup>[30,60]</sup> Thus far, nanowire conductors, rectifiers, switches, and photoconductors have been created and characterized.<sup>[61–63]</sup> These electrically functional nanowires are promising as building blocks in the bottom-up assembly of electronic devices. Nanowire assembly into parallel, raft-like structures has been investigated for developing bottom-up nanoscale patterning.<sup>[64,65]</sup> Biomolecular recognition processes such as DNA hybridization have also been used for directing such assembly.<sup>[66]</sup> Further application, for

which techniques are still being developed, includes assembling nanowires into cross-point arrays for memory and logic devices.

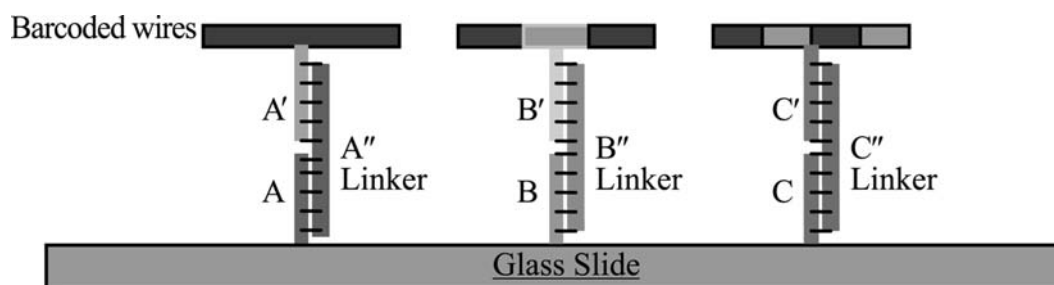
### Biological Multiplexing

Performing many simultaneous experiments (i.e., multiplexing) has become an important theme in bioanalysis. For example, functional genomics experiments often follow mRNA expression levels for many—or even all—genes in an organism's genome simultaneously. These experiments employ fluorescence on planar microarrays in which spots of DNA corresponding to the different genes of an organism's genome are positioned on a planar glass slide.<sup>[67,68]</sup> The  $x,y$  coordinates of each spot correlate to its identity. Microarrays permit the detection of thousands to tens of thousands of species at once, saving both time and reagents. However, there are some drawbacks of using microarrays, which include limitations in the dynamic range of analyte detection, long diffusion times for analyte binding, and variations in fluorescence signals between arrays.<sup>[69]</sup> Encoded particles have been introduced to address issues of diffusion and increase flexibility in microarray design.<sup>[70,71]</sup> Polystyrene microbeads incorporating red and infrared fluorescent dyes in different intensity ratios are one type of encoded particle introduced for use in multiplexing applications.<sup>[72–74]</sup> Although microbeads offer improved diffusion as compared to two-dimensional arrays, the use of fluorescence limits the number of species that can be simultaneously detected, as the spectral bandwidths of the fluorescent peaks are large and oftentimes overlap. Semiconductor quantum dots, which have reduced spectral bandwidths as compared to molecular dyes, have been used in place of organic fluorophores in encoded beads as well as other applications.<sup>[75–80]</sup> These particles are very promising for multiplexing, and are resistant to photobleaching; however, the detection still relies on fluorescence, which ultimately limits the number of species that are

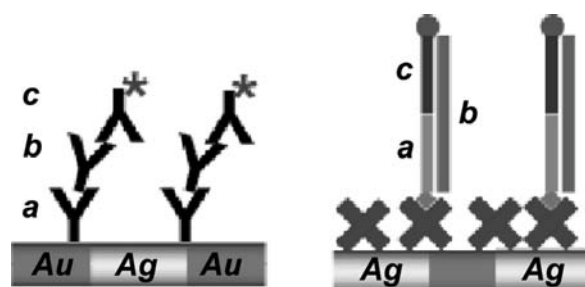
possible to detect simultaneously (i.e., only one color of fluorophore can typically be used in detection, as other channels are occupied with encoding the particle identity).

Barcoded nanowires are a promising alternative to fluorescent tags in some applications. The barcode striping pattern will not photobleach, reflective read-out is simple and does not require expensive excitation sources or detectors, and many patterns can be synthesized and are optically detectable. These particles can be employed as encoded substrates for biosensing, analogous to DNA chips, or as tags for simultaneous detection and identification, analogous to fluorescent molecules or nanocrystals. Scheme 1 illustrates the second approach, where barcoded nanowires may potentially be used as tags to detect and identify specific DNA hybridization events. In this example, a glass slide is spotted with several different capture sequences of DNA selective to the 5' (or 3') region of the target sequence. Target sequences, labeled double prime (") in the figure, bind to the surface via hybridization to these capture strands. They are then detected by hybridization-driven assembly of barcoded nanowires that carry a third strand of DNA, complementary to the 3' (or 5') region of the target sequence. Optical reflectance microscopy can then be used to count and identify the wires bound to each spot on the surface, giving the amount and identity of target molecules present in the initial solution. This approach is conceptually simple, and does not require fluorescence for detection. Improvements in the selectivity of nanoparticle attachment will be important for the ultimate use of this approach in multiplexed analysis.<sup>[66]</sup>

Barcoded nanowires not only serve as identifying markers, but can also serve as easily detectable substrates on which binding events take place.<sup>[34]</sup> Scheme 2 illustrates how barcoded nanowires can serve as encoded substrates for antigen and DNA detection.<sup>[81]</sup> Scheme 2 (left) illustrates a standard sandwich immunoassay performed on the nanowire surface. The striped particles are first derivatized with a capture antibody (a) that is specific for an analyte, which in



**Scheme 1** Overview of nonfluorescent bioassay using barcoded rods. DNA strands labeled A–C are not complementary to their primed counterparts (A'–C'); however, the strands labeled as double prime (") link the respective sequences to their primed counterparts via complementary DNA hybridization. (Not drawn to scale.)



**Scheme 2** Schematic of assays using barcoded nanowires as substrates. (Left) For immunoassays, the striped particles are first derivatized with a capture antibody (A) that is specific for the analyte (B), which is also an antibody. Following incubation of the capture antibody with the analyte, the fluorescently labeled detection antibody (C) is added. (Right) For DNA hybridization assays, particles are derivatized with NeutrAvidin (NA) followed by reaction with a biotinylated capture sequence (A) that is specific for a solution phase analyte (B). Fluorescently labeled oligonucleotides (C) were then added for detection. *Source:* From Ref.<sup>[81]</sup>. ©American Chemical Society.

this case is also an antibody. Following incubation of the capture antibody with the analyte (b), a fluorescently labeled detection antibody (c) is added. Scheme 2 (right) shows the analogous experiment for DNA detection. Here the barcoded nanowire serves as the substrate on which a DNA probe sequence (a) is attached. Probe sequences are designed to be complementary to one half of the target sequence, as in the previous example (Scheme 1). The target DNA sequence (b) binds to the probe from solution via hybridization, and is subsequently detected by hybridization to a fluorescently tagged third DNA strand (c). In either of these two types of bioassay, target detection and quantification is made possible by the fluorescence intensity of the labeled probe molecules, while target identification (i.e., DNA sequence) is determined by the nanowire barcode pattern as observed in reflectivity optical microscopy.<sup>[34,81]</sup>

Both immunoassays and DNA hybridization assays have been performed on barcoded nanowires.<sup>[34,81]</sup> Nicewarner-Pena et al.<sup>[34]</sup> demonstrated two simultaneous immunoassays in which two different fluorescent dyes were employed. Keating et al.<sup>[81]</sup> have also reported three simultaneous DNA assays using a single fluorescent probe for all three assays. Under some conditions, it proved possible to observe the barcode-stripping pattern in the fluorescence image,<sup>[81]</sup> such that acquisition of a single image enabled both identification and detection. Barcoded nanowire libraries of 100 particles have already been reported,<sup>[56]</sup> and could be combined with these types of biological assays for increased multiplexing. Ultimately, it should be possible to perform thousands or tens of thousands of different DNA hybridizations simultaneously on different particles in

the same suspension, similar to the level of multiplexing now possible only with planar DNA microarrays.

## Nonbiological Tagging

Finally, barcoded nanowires have potential application as covert tags in non-biological materials. Macroscopic barcodes are currently largely used in manufacturing to track materials. These tags are visible to the naked eye. There is also a desire to create hidden, or covert, tags for use in some applications such as in paper currency, stock certificates, and passports. The hidden tags currently incorporated into such documents include near-IR fluorescent dyes or particles, chemical isotopes, and sometimes even biological molecules. A problem with some of these internal tags lies in their durability.<sup>[33]</sup> Striped metal nanowires are too small to see with the naked eye, and can serve as robust and easily identifiable covert tags. They have been incorporated into inks, paper, explosives, glass, metals, bulk polymers, and textiles, where they could still be identified via optical microscopy.<sup>[33]</sup>

## CONCLUSION

Striped metal nanowires can be readily prepared via templated electrodeposition, and have promise not only in future electronic devices built from the bottom-up, but also as optically encoded, microscopic barcodes. Optical encoding is accomplished by incorporating segments of different wavelength-dependent reflectivities, which are then read out in an optical microscope. Very large numbers of distinguishable barcode patterns can in principle be synthesized and optically detected. Such particles are attractive in both nonbiological and biological tagging applications. When coated with proteins or DNA oligonucleotides, these barcoded nanowires can serve as encoded supports for biomolecule detection. Many simultaneous bioassays can in principle be performed using suspensions of barcoded nanowires, each particle pattern corresponding to a different bioassay.

## REFERENCES

1. Yu, Y.; Chang, S.; Lee, C.; Wang, C.R. Gold nanorods: Electrochemical synthesis and optical properties. *J. Phys. Chem., B* **1997**, *101* (34), 6661–6664.
2. Chang, S.S.; Shih, C.W.; Chen, C.D.; Lai, W.C.; Wang, C.R.C. The shape transition of gold nanorods. *Langmuir* **1999**, *15* (3), 701–709.
3. Brumlik, C.J.; Menon, V.P.; Martin, C.R.J. Template synthesis of metal microtubule ensembles utilizing

- chemical, electrochemical, and vacuum deposition techniques. *J. Mater. Res.* **1994**, *9*, 1174–1183.
4. Esumi, K.; Matsuhisa, K.; Torigoe, K. Preparation of rodlike gold particles by UV irradiation using cationic micelles as a template. *Langmuir* **1995**, *11* (9), 3285–3287.
  5. Murphy, C.J.; Jana, N.R. Controlling the aspect ratio of inorganic nanorods and nanowires. *Adv. Mater.* **2002**, *14* (1), 80–82.
  6. Martin, B.R.; Dermody, D.J.; Reiss, B.D.; Fang, M.M.; Lyon, L.A.; Natan, M.J.; Mallouk, T.E. Orthogonal self-assembly on colloidal gold–platinum nanorods. *Adv. Mater.* **1999**, *11* (12), 1021–1025.
  7. van der Zande, B.M.; Bohmer, M.R.; Fokkink, L.G.; Schonenberger, C. Colloidal dispersions of gold rods: synthesis and optical properties. *Langmuir* **2000**, *16* (2), 451–458.
  8. Cepak, V.M.; Martin, C.R. Preparation and stability of template-synthesized metal nanorod sols in organic solvents. *J. Phys. Chem., B* **1998**, *102* (49), 9985–9990.
  9. Govindaraj, A.; Satishkumar, B.C.; Nath, M.; Rao, C.N.R. Metal nanowires and intercalated metal layers in single walled carbon nanotube bundles. *Chem. Mater.* **2000**, *12* (1), 202–205.
  10. Fullam, S.; Cottell, D.; Rensmo, H.; Fitzmaurice, D. Carbon nanotube templated self-assembly and thermal processing of gold nanowires. *Adv. Mater.* **2000**, *12* (19), 1430–1432.
  11. Huang, Y.; Duan, X.; Cui, Y.; Lieber, C.M. Gallium nitride nanowire devices. *Nano Lett.* **2002**, *2*, 101–104.
  12. Hu, J.; Odom, T.W.; Lieber, C.M. Chemistry and physics in one dimension: synthesis and properties of nanowires and nanotubes. *Acc. Chem. Res.* **1999**, *32*, 435–445.
  13. Tanori, J.; Pileni, M.P. Control of the shape of copper metallic particles by using a colloidal system as template. *Langmuir* **1997**, *13* (4), 639–646.
  14. Wirtz, M.; Martin, C.R. Template-fabricated gold nanowires and nanotubes. *Adv. Mater.* **2003**, *15* (5), 455–458.
  15. Zhang, Z.; Dai, S.; Blom, D.A.; Shen, J. Synthesis of ordered metallic nanowires inside ordered mesoporous materials through electroless deposition. *Chem. Mater.* **2002**, *14*, 965–968.
  16. Busbee, B.D.; Obare, S.O.; Murphy, C.J. An improved synthesis on high-aspect-ratio gold nanorods. *Adv. Mater.* **2003**, *15* (5), 414–416.
  17. Jana, N.R.; Gearheart, L.; Murphy, C.J. Wet chemical synthesis of high aspect ratio cylindrical gold nanorods. *J. Phys. Chem., B* **2001**, *105*, 4065–4067.
  18. Gai, P.L.; Harmer, M.A. Surface atomic defect structures and growth of gold nanorods. *Nano Lett.* **2002**, *2* (7), 771–774.
  19. Brown, K.R.; Walter, D.G.; Natan, M.J. Seeding of colloidal Au nanoparticle solutions. 2. Improved control of particle size and shape. *Chem. Mater.* *12* (2), 306–313.
  20. Wu, Y.; Yang, P. Direct observation of vapor–liquid–solid nanowire growth. *J. Am. Chem. Soc.* **2001**, *123*, 3165–3166.
  21. Bjork, M.T.; Ohlsson, B.J.; Sass, T.; Persson, A.I.; Thelander, C.; Magnusson, M.H.; Deppe, K.; Wallenberg, L.R.; Samulson, L. One dimensional steeplechase for electrons realized. *Nano Lett.* **2002**, *2* (2), 87–89.
  22. Kim, F.; Song, J.H.; Yang, P. Photochemical synthesis of gold nanorods. *J. Am. Chem. Soc.* **2002**, *124*, 14,316–14,317.
  23. Park, S.; Kim, S.; Lee, S.; Khim, Z.G.; Char, K.; Hyeon, T. Synthesis and magnetic studies of uniform iron nanorods and nanospheres. *J. Am. Chem. Soc.* **2000**, *122*, 8581–8582.
  24. Yin, Y.; Lu, Y.; Sun, Y.; Xia, Y. Silver nanowires can be directly coated with amorphous silica to generate well-controlled coaxial nanocables of silver/silica. *Nano Lett.* **2002**, *2* (4), 427–430.
  25. Ah, C.S.; Hong, S.D.; Jang, D. Preparation of Au<sub>core</sub>Ag<sub>shell</sub> nanorods and characterization of their surface plasmon resonances. *J. Phys. Chem., B* **2001**, *105* (33), 7871–7873.
  26. Lee, K.; Seo, W.S.; Park, J.T. Synthesis and optical properties of colloidal tungsten oxide nanorods. *J. Am. Chem. Soc.* **2003**, *125*, 3408–3409.
  27. Wang, X.; Li, Y. Selected-control hydrothermal synthesis of  $\alpha$ - and  $\beta$ -MnO<sub>2</sub> single crystal nanowires. *J. Am. Chem. Soc.* **2002**, *124* (12), 2880–2881.
  28. Zhu, Y.; Li, H.; Kolytyn, Y.; Rosenfeld, Y.; Gedanken, A. Sonochemical synthesis of titania whiskers and nanotubes. *Chem. Commun.* **2001**, *24*, 2616–2617.
  29. Pan, Z.W.; Dai, Z.R.; Wang, Z.L. Nanobelts of semiconducting oxides. *Science* **2001**, *291*, 1947–1949.
  30. Kovtyukhova, N.I.; Martin, B.R.; Mbindyo, J.K.N.; Smith, P.A.; Razavi, B.; Mayer, T.S.; Mallouk, T.E. Layer-by-layer assembly of rectifying junctions in and on metal nanowires. *J. Phys. Chem., B* **2001**, *105*, 8762–8769.
  31. Wu, Y.; Fan, R.; Yang, R.P. Block-by-block growth of single-crystalline Si/SiGe superlattice nanowires. *Nano Lett.* **2002**, *2*, 83–86.
  32. Gudiksen, M.S.; Lauhon, L.J.; Wang, J.; Smith, D.C.; Lieber, C.M. Growth of nanowire superlattice structures for nanoscale photonics and electronics. *Nature* **2002**, *415*, 617–620.
  33. Keating, C.D.; Natan, M.J. Striped metal nanowires as building blocks and optical tags. *Adv. Mater.* **2003**, *15* (5), 451–454.
  34. Nicewarner-Pena, S.R.; Freeman, G.; Reiss, B.D.; He, L.; Pena, D.J.; Walton, I.D.; Cromer, R.; Keating, C.D.; Natan, M.J. Submicrometer metallic barcodes. *Science* **2001**, *294*, 137–141.
  35. Al-Mawlawi, D.; Liu, C.Z.; Moskovits, M. Nanowires formed in anodic oxide nanotemplates. *J. Mater. Res.* **1994**, *9* (4), 1014.
  36. Hulteen, J.C.; Martin, C.R. A general template-based method for the preparation of nanomaterials. *J. Mater. Chem.* **1075**, *7* (7), 1075–1087.
  37. Yi, G.; Schwarzacher, W. Single crystal superconductor nanowires by electrodeposition. *Appl. Phys. Lett.* **2000**, *74*, 1746–1748.
  38. Dubois, S.; Michel, A.; Eymery, J.P.; Duvail, J.L.; Piroux, L.J. Fabrication and properties of arrays of superconducting nanowires. *J. Mater. Res.* **1999**, *14*, 665–671.



39. Masuda, H.; Nishio, K.; Baba, N. Preparation of micro-porous metal membranes by two step replication of the microstructure of anodic alumina. *Thin Solid Films* **1993**, *223*, 1–3.
40. Hornyak, G.L.; Patrissi, C.J.; Martin, C.R. Fabrication, characterization, and optical properties of gold nanoparticle/porous alumina composites: the non-scattering Maxwell–Garnett limit. *J. Phys. Chem., B* **1997**, *101*, 1548–1555.
41. Martin, C.R. Nanomaterials: a membrane-based synthetic approach. *Science* **1994**, *266*, 1961–1966.
42. Paunovic, M.; Schlesinger, M. *Fundamentals of Electrochemical Deposition*; John Wiley & Sons, Inc.: New York, 1998.
43. Schlesinger, M.; Paunovic, M. *Modern Electroplating*; John Wiley & Sons, Inc.: New York, 2000.
44. Liu, K.; Nagodawithana, K.; Searson, P.C.; Chien, C.L. Perpendicular giant magnetoresistance of multi-layered Co/Cu nanowires. *Phys. Rev., B* **1995**, *51* (11), 7381–7384.
45. Fert, A.; Piraux, L. Magnetic nanowires. *J. Magn. Magn. Mater.* **1999**, *200*, 338–358.
46. Hong, K.; Yang, F.Y.; Liu, K.; Reich, D.H.; Searson, P.C.; Chein, C.L. Giant positive magnetoresistance of Bi nanowire arrays. *J. Appl. Phys.* **1999**, *85* (8), 6184–6186.
47. Reiss, B.D.; Freeman, R.G.; Walton, I.D.; Norton, S.M.; Smith, P.C.; Stonas, W.G.; Keating, C.D.; Natan, M.J. Electrochemical synthesis and optical readout of striped metal rods with submicron features. *J. Electroanal. Chem.* **2002**, *522*, 95–103.
48. Lui, B.; Zeng, H.C. Hydrothermal synthesis of ZnO nanorods in the diameter regime of 50 nm. *J. Am. Chem. Soc.* **2003**, *125*, 4430–4431.
49. Piraux, L.; Dubois, S.; Duvail, J.L.; Ounadjela, K.; Fert, A. Arrays of nanowires of magnetic metals and multi-layers: Perpendicular GMR and magnetic properties. *J. Magn. Magn. Mater.* **1997**, *175*, 127–136.
50. Link, S.; El-Sayed, M.A. Spectral properties and relaxation dynamics of surface plasmon electronic oscillations in gold and silver nanodots and nanorods. *J. Phys. Chem., B* **1999**, *103*, 8410–8426.
51. Foss, C.A.; Hornyak, G.L.; Stockert, J.A.; Martin, C.R. Template-synthesized nanoscopic gold nanoparticles: optical spectra and the effects of particle size and shape. *J. Phys. Chem.* **1994**, *98*, 2963–2971.
52. Preston, C.K.; Moskovits, M. Optical characterizations of anodic aluminum oxide films containing electrochemically deposited metal particles. 1. Gold in phosphoric acid anodic aluminum oxide films. *J. Phys. Chem.* **1993**, *97*, 8495–8503.
53. Hulteen, J.C.; Patrissi, C.J.; Miner, D.L.; Crosthwait, E.R.; Oberhauser, E.B.; Martin, C.R. Changes in the shape and optical properties of gold nanoparticles contained within alumina membranes due to low-temperature annealing. *J. Phys. Chem., B* **1997**, *101*, 7727–7731.
54. Link, S.; Mohamed, M.B.; El-Sayed, M.A. Simulation of the optical absorption spectra of gold nanorods as a function of their aspect ratio and the effect of the medium dielectric constant. *J. Phys. Chem., B* **1999**, *103*, 3073–3077.
55. *CRC Handbook of Chemistry and Physics*, 71st Ed.; CRC Press: Cleveland, OH, 1990.
56. Walton, I.D.; Norton, S.M.; Balasingham, A.; He, L.; Oviso, D.F.; Gupta, D.; Raju, P.A.; Natan, M.J.; Freeman, R.G. Particles for multiplexed analysis in solution: detection and identification of striped metallic particles using optical microscopy. *Anal. Chem.* **2002**, *74*, 2240–2247.
57. Huang, Y.; Duan, X.; Wei, Q.; Lieber, C.M. Directed assembly of one-dimensional nanostructures into functional networks. *Science* **2001**, *291*, 630–633.
58. Huang, Y.; Duan, X.; Cui, Y.; Lauhon, L.J.; Kim, K.H.; Lieber, C.M. Logic gates and computation from assembled nanowire building blocks. *Science* **2001**, *294*, 1313–1317.
59. Zhong, Z.; Wang, D.; Cui, Yi.; Bockrath, M.W.; Lieber, C.M. Nanowire crossbar arrays as address decoders for integrated nanosystems. *Science* **2003**, *302*, 1377–1379.
60. Mbindyo, J.K.N.; Mallouk, T.E.; Mattzela, J.B.; Kratochvilova, I.; Razavi, B.; Jackson, T.N.; Mayer, T.S. Template synthesis of metal nanowire containing monolayer molecular junctions. *J. Am. Chem. Soc.* **2002**, *124*, 4020–4026.
61. Kovtyukhova, N.I.; Mallouk, T.E. Nanowires as building blocks for self-assembling logic and memory circuits. *Chem. Eur. J.* **2002**, *8*, 4354–4363.
62. Smith, P.A.; Nordquist, C.D.; Jackson, T.N.; Mayer, T.S.; Martin, B.R.; Mbindyo, J.; Mallouk, T.E. Electric-field assisted assembly and alignment of metallic nanowires. *Appl. Phys. Lett.* **2000**, *77*, 1399–1401.
63. Pena, D.J.; Mbindyo, J.K.N.; Carado, A.J.; Mallouk, T.E.; Keating, C.D.; Razavi, B.; Mayer, T.S. Template growth of photoconductive metal–CdSe–metal nanowires. *J. Phys. Chem., B* **2002**, *106*, 7458–7462.
64. Whang, D.; Jin, S.; Leiber, C.M. Nanolithography using hierarchically assembled nanowire masks. *Nano Lett.* **2003**, *3* (7), 951–954.
65. Tao, A.; Kim, F.; Hess, C.; Goldberger, J.; He, R.; Sun, Y.; Xia, Y.; Yang, P. Langmuir–Blodgett silver nanowire monolayers for molecular sensing using surface-enhanced Raman spectroscopy. *Nano Lett.* **2003**, *3* (9), 1229–1233.
66. Mbindyo, J.K.N.; Reiss, B.D.; Martin, B.R.; Keating, C.D.; Natan, M.J.; Mallouk, T.E. DNA-directed assembly of gold nanowires on complementary surfaces. *Adv. Mater.* **2001**, *13* (4), 249–254.
67. Shena, M. *DNA Arrays: A Practical Approach*; University Press: Oxford, 1999.
68. McBeath, G.; Schreiber, S.L. Printing proteins as microarrays for high-throughput function determination. *Science* **2000**, *289*, 1760–1762.
69. Shena, M. *Microarray Biochip Technology*; TelChem International Inc.: Sunnydale, CA, 2000.
70. Nolan, J.P.; Sklar, L.A. Suspension array technology: evolution of the flat array paradigm. *Trends Biotechnol.* **2002**, *20*, 9–12.
71. Braeckmans, K.; De Smedt, S.C.; Leblans, M.; Pauwels, R.; Demeester, J. Encoding microcarriers: present and



- future technologies. *Nature Rev. Drug Dis.* **2002**, *1*, 447–456.
72. Walt, D.R. Molecular biology: Bead based fiber optic arrays. *Science* **2000**, *287*, 451–452.
73. McBride, M.T.; Gammon, S.; Pitesky, M.; O'Brien, T.W.; Smith, T.; Aldrich, J.L.; Anglois, R.G.; Colston, B.; Venkateswaran, K.S. Multiplexed liquid arrays for simultaneous detection of simulants of biological warfare agents. *Anal. Chem.* **2003**, *75*, 1924–1930.
74. Stitzel, S.E.; Sein, D.R.; Walt, D. Enhancing vapor sensor discrimination by mimicking a canine nasal cavity flow environment. *J. Am. Chem. Soc.* **2003**, *125*, 3684–3685.
75. Bruchez, M.; Moronne, M.; Gin, P.; Weiss, S.; Alivisatos, A.P. Semiconductor nanocrystals as fluorescent biological labels. *Science* **1998**, *281*, 2013–2018.
76. Han, M.; Gao, X.; Su, J.Z.; Nie, S. Quantum-dot-tagged microbeads for multiplexed optical coding of biomolecules. *Nat. Biotechnol.* **2001**, *19*, 631–635.
77. Alivisatos, A.P. Perspectives on the physical chemistry of semiconductor nanocrystals. *J. Phys. Chem.* **1996**, *100*, 13,226–13,239.
78. Colvin, V.L.; Schlamp, M.C.; Alivisatos, A.P. Light-emitting diodes made from cadmium selenide nanocrystals and a semiconducting polymer. *Nature* **1994**, *370*, 354–357.
79. Alivisatos, A.P. Semiconductor clusters, nanocrystals, and quantum dots. *Science* **1996**, *271*, 933–937.
80. Gerion, D.; Pinaud, F.; Williams, S.C.; Parak, W.J.; Zanchet, D.; Weiss, S.; Alivisatos, A.P. Synthesis and properties of biocompatible water-soluble silica-coated CdSe/ZnS semiconductor quantum dots. *J. Phys. Chem., B* **2001**, *105*, 8861–8871.
81. Nicewarner-Pena, S.R.; Carado, A.J.; Shale, K.E.; Keating, C.D. Barcoded metal nanowires: optical reflectivity and patterned fluorescence. *J. Phys. Chem., B* **2003**, *107*, 7360–7367.

# Barrier Properties of Ordered Polymer Nanocomposites

## Bon-Cheol Ku

*Department of Chemistry, University of Massachusetts–Lowell, Lowell, Massachusetts, U.S.A.*

## Alexandre Blumstein

*Center for Advanced Materials, University of Massachusetts–Lowell, Lowell, Massachusetts, U.S.A.*

## Jayant Kumar

*Department of Physics, University of Massachusetts–Lowell, Lowell, Massachusetts, U.S.A.*

## Lynne A. Samuelson

*Research, Development and Engineering Command (RDECOM), U.S. Army, Natick, Massachusetts, U.S.A., and Center for Advanced Materials, University of Massachusetts–Lowell, Lowell, Massachusetts, U.S.A.*

## Dong Wook Kim

*Advanced Materials Division, Korea Research Institute of Chemical Technology, Taejeon, South Korea*

## INTRODUCTION

During the last decade, the development of a novel type of composite material led to a significant improvement of mechanical, thermal, and vapor transport properties of films and coatings. Such materials are based on finely dispersed or interspersed organic–inorganic components down to their nanodimensions and are characterized by an intimate contact of their components and their nanodimensionality, whereas their specific architecture (crystal structure, morphology, etc.) is often preserved in the material. This results in a particularly strong interaction between components and an optimal summation of their properties. Especially interesting are nanocomposites in which one or more components have been oriented because orientation often results in additional strengthening and enhancement of properties. Coatings and films from such materials are endowed with exceptional mechanical and thermal stability, allowing for small thicknesses and making them very interesting for various applications. In this entry, we describe the resistance to the vapor penetration of multilayer nanocomposites with a focus on the resistance to gas/vapor diffusion, rather than on their separation ability (permselectivity). Such properties acquire a special importance in the packaging of materials such as food, beverages, chemical and medical packaging, etc.

### Permeability of Polymers

The permeation of a gas/vapor (permeant) through a polymeric membrane/film is driven by the

concentration gradient of the permeant dissolved in the membrane.<sup>[1–3]</sup> If the concentration gradient is kept constant throughout the membrane and if Henry’s law is applied, the amount of gas/vapor diffusing through the film/unit area and per unit time  $Q$  can be expressed quantitatively:

$$Q = \frac{P(P_2 - P_1)}{\ell} \quad (1)$$

in which  $\ell$  is the thickness of the membrane/film  $P_2 - P_1$  is the differential gas/vapor pressure across the membrane and  $P$  is the permeability coefficient of the material of the film with

$$P = D \times S \quad (2)$$

where  $D$  is the translational diffusion coefficient of the gas and  $S$  is the solubility coefficient of Henry’s law. It is given by the amount of permeant (expressed in cubic centimeters or cubic meters of gas at standard temperature and pressure) divided by the amount of polymer (often given as volume) and by the pressure gradient across the film. Thus  $Q$  expresses the transmission rate of a permeant and is often used in assessing the quality of a packaging material as a barrier to vapor/gas permeation. Units are expressed and converted in Table 1.<sup>[2]</sup>

Permselectivity is another important characteristic of a membrane giving the relative barrier properties vis-à-vis different permeants. Such selectivity is expressed as a ratio of permeabilities. For two

**Table 1** Units for diffusivity, solubility, and permeability

	Units	
Diffusivity ( $D$ )	$\text{cm}^2/\text{sec}$	$\text{m}^2/\text{sec}$
Solubility ( $S$ )	$[\text{cm}^3 \text{ (STP)}]/[(\text{cm}^3) \text{ (atm)}]$	$[\text{m}^3 \text{ (STP)}]/[(\text{m}^3) \text{ (Pa)}]$
Permeability ( $P$ )	$[(\text{cm}^3) \text{ (cm)}]/[(\text{m}^2) \text{ (day) (atm)}]$	$[(\text{cm}^3) \text{ (mil)}]/[(\text{cm}^2) \text{ (day) (cm Hg)}]$

permeants A and B, the permselectivity  $\alpha_{A/B}$  is:

$$\alpha_{A/B} = \frac{P_A}{P_B} = \frac{S_A D_A}{S_B D_B} \quad (3)$$

For a binary system where one component is nonporous (filler), the solubility of the filled polymer  $S$  in a given vapor can be determined<sup>[4]</sup> and barrier properties (permeabilities) for different permeants can be calculated.<sup>[2]</sup>

### Factors Influencing Permeability

As can be seen from Eq. (2), the permeability of polymers with respect to a given permeant depends on both the translational diffusion ( $D$ ) and solubility constants ( $S$ ).<sup>[2,3]</sup> As is well known,  $D$  increases with temperature and with the strength of attractive interactions between the polymer and the permeant. Permeability decreases with an increase in the size of the permeant and with the decrease in the free volume of the polymer. Thus glasses are less permeable than rubbers. Consequently, the increase in the degree of crystallinity of a polymer, the increase in chain order, the increase in the degree of cross-linking, and the increase in the packing density and compact morphology of the polymer are all structural factors decreasing permeability and enhancing the barrier properties of a polymer. The solubility coefficient of Henry's law of the permeant  $S$  in a given polymer can be estimated from the solubility parameter, which in turn can be obtained from the tables.<sup>[2]</sup> Polymers that interact strongly with permeants will favor permeability and, conversely, polymers interacting poorly with a given permeant will decrease permeation and thus enhance the barrier properties of the composite vis-à-vis a given permeant. Thus inorganic fillers reducing the free volume of the composite system and/or interacting poorly with a given permeant (such as talc, titanium dioxide, calcium carbonate, etc.) will enhance barrier properties vis-à-vis a number of compounds. Organic fillers may act in the same direction if they repel the particular gas/vapor (e.g., hydrophobic fillers vis-à-vis water vapor). If the composite is obtained by macroscopical or even microscopical blending of components, many desirable properties of the polymer may deteriorate. This is especially true of mechanical properties.

Such deterioration may compromise the mechanical integrity of a separation membrane. The advantage of nanocomposites resides in their intimate nanoscale mixing and a very high interface between the polymer and the added ingredients. The improvement of particular properties of the polymer component is obtained with a far smaller amount of additives. In contrast to ordinary composite materials, nanocomposites, although heterophase on a molecular scale, can be considered homogeneous on a macroscale. Therefore the nanocomposite combines the advantageous properties of its components without the decrease in the properties of the polymer because of the existence of a large heterophase and large amounts of additives. In what follows, we will focus our attention on barrier properties of various layered nanocomposite systems with a special emphasis on the preparation and the properties of polymer-layered aluminosilicate nanocomposites.

## POLYMER-LAYERED ALUMINOSILICATE NANOCOMPOSITES

### General Considerations

Polymer-layered aluminosilicate nanocomposites have recently attracted much attention in many applications.<sup>[5-9]</sup> Such nanocomposites can provide significant improvements in various properties of polymers such as mechanical,<sup>[10]</sup> thermal,<sup>[11,12]</sup> barrier,<sup>[9,13]</sup> and flame retardancy.<sup>[14]</sup> The applications of such materials extend to the automotive, electrical, biomedical, and packaging industries.<sup>[5]</sup> The remarkable properties of aluminosilicate nanocomposites are due not only to their chemical structure but to the particular properties of the lattice expanding layered clays allowing for relatively easy formation of nanocomposite materials and films. Layered aluminosilicates are semicrystalline materials consisting of 1-nm-thick lamellae and are structurally composed of sheets of octahedrally coordinated aluminum atoms sandwiched between two layers of tetrahedrally coordinated silicon atoms, such as those shown in Fig. 1.<sup>[6]</sup>

The lamellae are associated along their edges and are also stacked disorderly in the vertical direction, forming aggregates which, for the in situ clay, can have an average dimension of several micrometers.

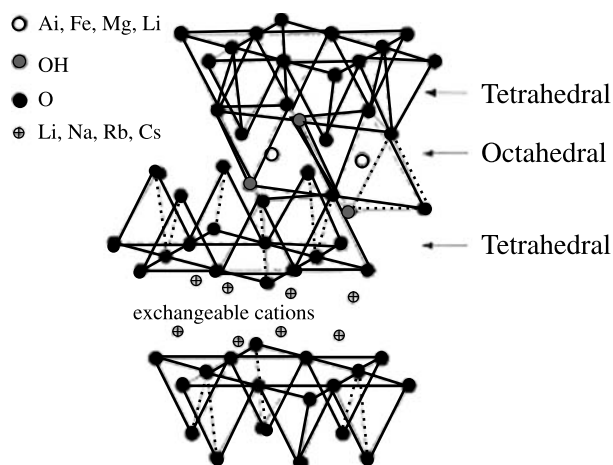


**Fig. 1** Structure of 2:1 phyllosilicates. *Source:* From Ref.<sup>[6]</sup>; © Springer-Verlag, 1999.

The lamellae are negatively charged because of occasional internal substitutions of higher-valence atoms within the layers such as Al by lower-valence atoms such as Mg or others. This results in a diffusive negative surface charge on the lamella. The negative charge is compensated by exchangeable cations, most commonly  $\text{Na}^+$  or  $\text{Ca}^{2+}$ , that hold the structure together. The weakening of these cohesive coulombic forces by solvation leads to the expansion of the lattice. Therefore the interlamellar spaces (often called galleries) can be filled with polar molecules of different nature and sizes, including polymers. The electrostatic cohesive forces can be experimentally weakened to a point of complete dissociation of the aggregate (or particle), leaving a totally dispersed lamellae 1 nm thick and 20–50 nm in transversal length (exfoliation and delamination). Conversely, the in situ sample is often characterized by a wide distribution of aggregate sizes that can reach macroscopical dimensions. The most commonly used layered, expanding clay minerals are, among others, montmorillonites (MMTs), saponites, and hectorites, all of dioctahedral structure, often called 2:1 phyllosilicates. Their general structural formula, upper exchange capacity, and the typical average transversal dimension of the lamellar aggregate are given in Table 2.<sup>[15,33]</sup> Several methods for the preparation of polymer-layered aluminosilicate

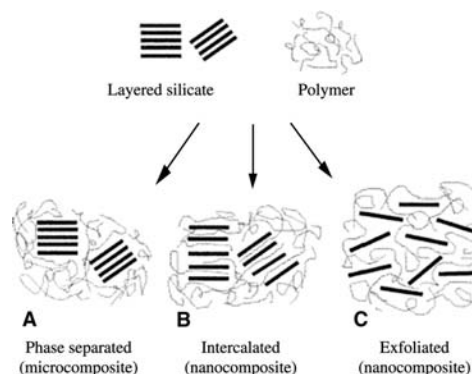


**Fig. 2** Scheme of different types of composite arising from the interaction of layered silicates and polymers: (A) phase-separated microcomposite; (B) intercalated nanocomposite; and (C) exfoliated nanocomposite. *Source:* From Ref.<sup>[7]</sup>; © Elsevier Science, 2001.

composites are described in the literature.<sup>[5–9]</sup> Generally, there are two basic ways of proceeding (Fig. 2).<sup>[7]</sup>

One involves the use of an in situ hydrophilic aluminosilicate; the other involves the use of a structurally modified clay rendered organophilic (“organic clay”) by the insertion of alkyl chain derivatives into the expandable galleries of the pristine, hydrophilic clay. This is often accomplished by exchanging  $\text{Na}^+$  or  $\text{Ca}^{2+}$  ions against organic cations containing long alkyl chains. To form polymer–aluminosilicate composites, one or the other form of clay can be mixed with the polymer in a solution or with a polymer melt. It can also be obtained by polymerizing the monomer previously intercalated into the expanding lattice. Both ways of proceeding can lead, under proper circumstances, to exfoliation of the aluminosilicate. However, the use of the “organic” clay to obtain exfoliated systems is more frequent. As pointed out above, polymer-layered silicate nanocomposites (PLSNs) are characterized by properties vastly superior to those of ordinary microcomposites (non-lamellar non-porous systems) including barrier properties. The enhanced barrier properties of PLSNs can be explained by the so-called “tortuous path model”<sup>[16]</sup> given schematically in Fig. 3.

In this, model the “tortuosity” of the molecular trajectory of the permeant is determined by several

**Table 2** Commonly used 2:1 phyllosilicates<sup>a</sup>

2:1 Phyllosilicate	General formula	CEC <sup>[33]</sup> (mEq/100 g)	Average length <sup>b</sup> (nm)
Montmorillonite	$\text{M}_x(\text{Al}_{4-x}\text{Mg}_x)\text{Si}_8\text{O}_{20}(\text{OH})_4$	119	218
Saponite	$\text{M}_x\text{Mg}_6(\text{Si}_{8-x}\text{Al}_x)\text{O}_{20}(\text{OH})_4$	100	165
Hectorite	$\text{M}_x(\text{Mg}_{6-x}\text{Li}_x)\text{Si}_8\text{O}_{20}(\text{OH})_4$	55	46

<sup>a</sup>M = monovalent cation;  $x$  = degree of isomorphous substitution ( $0.5 \leq x \leq 1.3$ ).

<sup>b</sup>Average length of a delaminated clay particle.

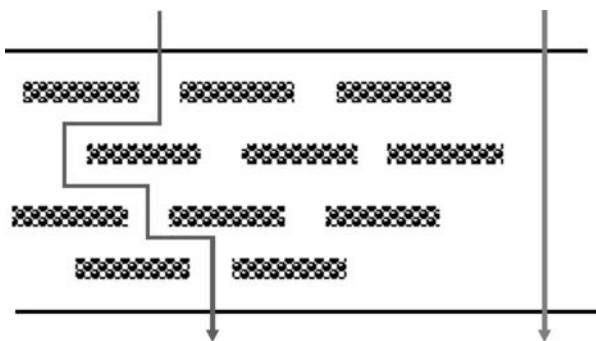


Fig. 3 The tortuous path model.

parameters such as the length  $L$  of the lamellae and its state of aggregation expressed by the transversal dimension of the particle  $W$ , concentration of the delaminated clay  $\phi$ , and the mutual orientation of the lamellar planes expressed by the order parameter  $S$  defined below:<sup>[17]</sup>

$$\frac{P_s}{P_p} = \frac{1 - \phi_s}{1 + \frac{L}{2W}\phi_s\left(\frac{2}{3}\right)\left(S + \frac{1}{2}\right)} \quad (4)$$

$$S = \frac{1}{2}\langle 3 \cos^2 \theta - 1 \rangle \quad (5)$$

where  $P_s$  and  $P_p$  represent the permeabilities of the polymer-silicate nanocomposite and pure polymer, respectively;  $L$  and  $W$  are the average length and width of a delaminated clay particle, respectively; and  $\theta$  is the average angle between the normal direction  $n$  to the barrier membrane and the normal direction to the surface of the lamellar plane  $p$ , as shown in Fig. 4.

It follows from this model that for a given concentration  $\phi$  of the aluminosilicate, barrier properties are maximized for a composite with highly delaminated aggregates (high  $L/W$  ratio) and a high degree of lamellar orientation ( $S \rightarrow 1$ ).

### Preparation of Polymer-Layered Silicate Nanocomposites

As pointed out earlier, several preparation methods of PLSNs exist. One method frequently used is based on an in situ intercalative polymerization of an inserted monomer.

#### In situ intercalative polymerization

A monomer in the form of a vapor, liquid, or solution in a poorly adsorbing solvent is brought into contact with the layered silicate.<sup>[18-27]</sup> The monomer interacting strongly with the exchangeable cations can then

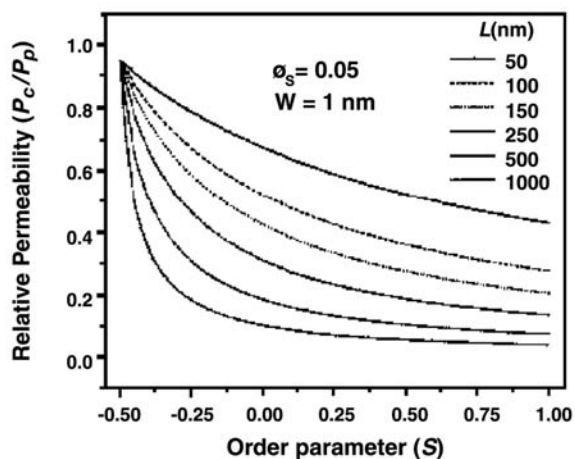
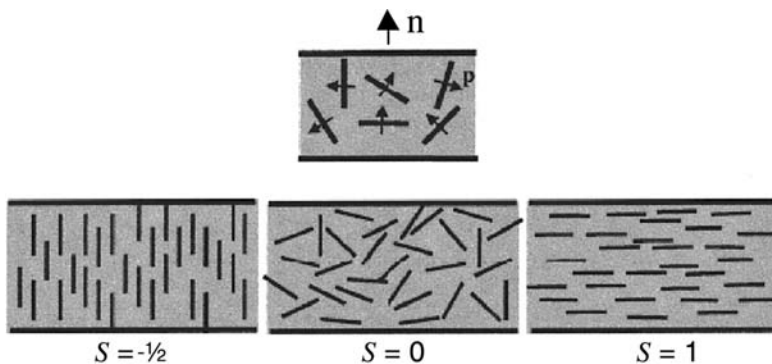


Fig. 4 Effect of sheet orientation on the relative permeability in exfoliated nanocomposites  $\phi_s = 0.05$  and  $W = 1$  nm. Source: From Ref.<sup>[17]</sup>; © American Chemical Society, 2001.

be polymerized by means of initiators, which may be deposited on the clay or dissolved in the liquid phase. The polymerization can also be brought about by gamma radiation. This method does not lead to completely exfoliated nanocomposites. It produces aggregated particles with a high silicate content and an intergallery polymer in which the stereostructure may keep a “memory” of its polymerization matrix.<sup>[19,20]</sup>

#### Intercalation by a molten polymer

In this method, the polymer is heated to a melt and blended with the clay mineral.<sup>[28–32]</sup> The mineral may be of a pristine hydrophilic nature or a modified “organic” hydrophobic clay. The blending may be assisted by hydrodynamic shear forces (shear produced by mixing, extrusion, etc.). Under such circumstances, the polymer is likely to diffuse into the interstices and galleries of the aluminosilicate particles. In the case of strong interactive forces between segments of the polymer chain and the lamellae of the aluminosilicate, exfoliation of clay particles may take place, leading to polymer–clay hybrid nanocomposites. The effectiveness of blending will depend on parameters such as the melt viscosity, molecular mass, segmental structure of the polymer, and its softening temperature. The advantages of this approach are its simplicity, effectiveness, and the possibility of using a variety of large-scale formulations.<sup>[13]</sup> The disadvantage resides in the possibility of thermal degradation of the polymer in the blend.

#### Exfoliation–adsorption from solvent

The clay mineral (often in its “organic” form) is treated by a (relatively volatile) solvent with a high affinity for both the polymer and the clay mineral.<sup>[33–35]</sup> The solvent intercalates into the galleries of the aluminosilicate under conditions leading to exfoliation. It is then blended with a solution of the polymer. The polymer chain, through strong segmental interactions with the surface of the individual lamellae, replaces the solvent through cooperative segmental diffusion. The elimination of the solvent through evaporation leads then to formation of an ordered multilayer nanocomposite. This approach to the formation of multilayered nanocomposites is not favored in industries because of the high cost of solvents and of their disposal.

#### Electrostatic layer-by-layer self-assembly

In this technique, a clay mineral (“organic” or pristine) is deposited from a solution (or suspension) on a smooth substrate (glass, mica, polymer, etc.) by dipping the substrate into a solution of a positively

charged polyelectrolyte.<sup>[36–40]</sup> Thus a positively charged surface is developed on the substrate on which negatively charged, ordered lamellae of aluminosilicate can be easily deposited by dipping the now positively charged substrate into a suspension of a finely dispersed aluminosilicate preferentially in a highly exfoliated state. An ordered, negatively charged lamellar layer is formed on top of the positively charged polymer. If necessary, the underlying substrate can be disposed off, generating free-standing nanocomposite films.<sup>[41,42]</sup> The process of dipping can be repeated and varied to build ordered multilayered systems with several components, leading to a variety of film-forming and membrane-forming nanocomposite materials, which can be used for the separation of gases and vapors and other barrier applications. This approach to forming organic/inorganic nanocomposites has many advantages—it is simple, economical, and flexible. A variety of high-performance materials can be produced because of the synergistic effects of individual organic and inorganic components. It can be used directly in industries for coating various substrates such as cellulose acetate,<sup>[42]</sup> PET,<sup>[43,44]</sup> Nafion™,<sup>[45]</sup> etc.

### Barrier Properties of Polymer-Layered Silicate Nanocomposites

Messersmith and Giannelis<sup>[25,26]</sup> have reported on the permeability to water vapor of nanocomposite films based on poly( $\epsilon$ -caprolactone) (PCL) and delaminated organic aluminosilicates prepared by in situ intercalative polymerization. An 80% reduction in water vapor permeability compared to the unfilled PCL was observed for only a 4.8% volume of the aluminosilicate in the composite films due probably to the increased tortuosity path length (Fig. 5).<sup>[25]</sup>

Nanocomposites prepared by melt extrusion have attracted much industrial attention because of the simplicity of the preparation process and the possibility of using a variety of large-scale formulations. Recently, barrier properties of melt extruded clay nanocomposites for ethylene-co-vinyl alcohol (EVOH),<sup>[28]</sup> polyethylene,<sup>[29]</sup> and polyamide<sup>[30]</sup> have been reported. Furthermore, property improvements for such nanocomposites were observed in tensile strength and Young’s modulus. In melt extrusion, it should be noted that the formation of strong barrier membranes requires not only a good organoclay–polymer compatibility but also optimum processing conditions.<sup>[31]</sup>

Yano et al.<sup>[33,34]</sup> have reported the effects of the average length of the exfoliated clay particles on gas (O<sub>2</sub>, H<sub>2</sub>O, and He) permeabilities for polyimide nanocomposites prepared by the exfoliation–adsorption



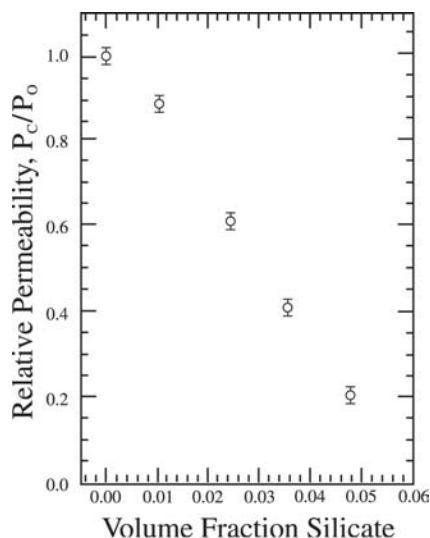


**Fig. 5** Relative permeability ( $P_c/P_o$ ) vs. volume fraction silicate for nanocomposite films. Source: From Ref.<sup>[25]</sup>; © Wiley Interscience, 1995.

method. According to Eq. (4), the permeability depends on the length  $L$  of the exfoliated clay particle (see Table 2 and Fig. 6).<sup>[33]</sup>

It should be also noted that a 2 wt.% concentration of MMT in polyimide membranes reduced the permeability coefficients of various gases by 50%.<sup>[34]</sup> Although the barrier properties of polymer films containing conventional fillers decrease linearly with the filler content, the polyimide nanocomposites showed a much more pronounced decrease of permeability as a function of the filler content and of the aspect ratio of the particle, as shown in Fig. 7.<sup>[35]</sup>

The technique of ELBL formation of barrier materials was only very recently described. As pointed out earlier, this method has a significant potential to form highly ordered nanocomposites. The ordering of

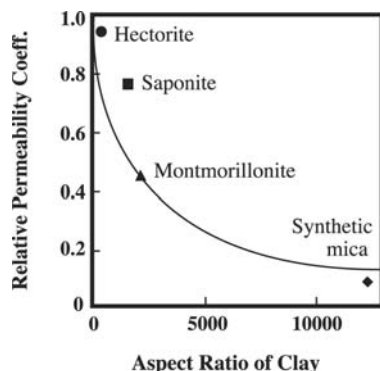


**Fig. 6** Relative permeability with respect to water vapor as a function of the average length of the exfoliated clay particle (aspect ratio) in polyimide–clay nanocomposites. Source: From Ref.<sup>[33]</sup>; © Wiley Interscience, 1997.

aluminosilicates is an important factor in enhancing the barrier properties of nanocomposite membranes. The first ELBL nanocomposite film was reported by Kleinfeld and Ferguson<sup>[40]</sup> An example of materials and a schematic of the procedure for an alternate layer-by-layer adsorption process are shown in Fig. 8.<sup>[46]</sup>

In this process, exfoliated aluminosilicate nanoparticles are prepared by means of extensive shaking, sonication, and centrifugation of their water suspensions.<sup>[47]</sup> The exfoliated particles of the aluminosilicates are then deposited on a substrate and a nanolayer of a cationic polyelectrolyte is deposited on top of the exfoliated clay. The thickness control of the nanofilm is maintained by a repetition of steps described above. Kotov et al.<sup>[43]</sup> studied the barrier properties of nanocomposite films of MMT and cationic polyelectrolytes such as poly(vinylpyridinium) (Fig. 9) and others using an untreated PET substrate.

The permeation rate of  $O_2$  decreased linearly with the number of deposition cycles, as shown in Fig. 10.<sup>[43]</sup>

However, the permeation rate for water vapor did not change regardless of the number of deposited layers because of the intrinsic hydrophilic nature of the polyelectrolytes and of the clay. Kim et al.<sup>[45]</sup> achieved a substantial reduction in water vapor permeation rate using cationic polyacetylenes substituted with a long alkyl chain such as poly(*N*-octadecyl-2-ethynylpyridinium bromide) and saponite nanoplatelets on Nafion<sup>TM</sup> substrate (Fig. 11).

Such systems displayed an increase of barrier properties with the number of deposited layers and a very substantial decrease of permeability with respect to the substrate. For example, the water vapor permeability of this nanocomposite decreased by 95% when compared to the pristine Nafion<sup>®</sup> film.<sup>[45]</sup> This rather dramatic effect may be explained by the

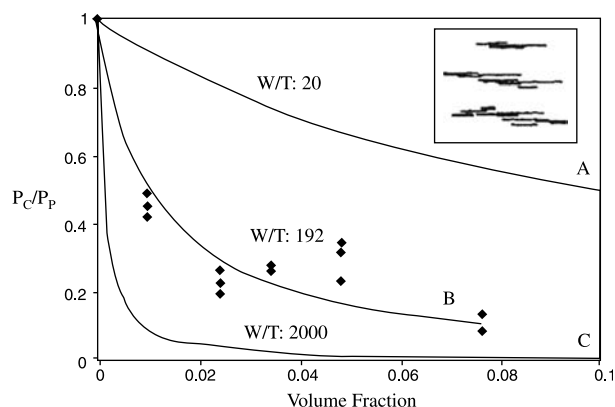


**Fig. 7** Relative permeability of  $CO_2$  as a function of clay concentration in the polyimide–clay nanocomposites. The inset illustrates a possible self-similar aggregation mechanism for the clay platelets. Source: From Ref.<sup>[35]</sup>; © American Chemical Society, 2001.

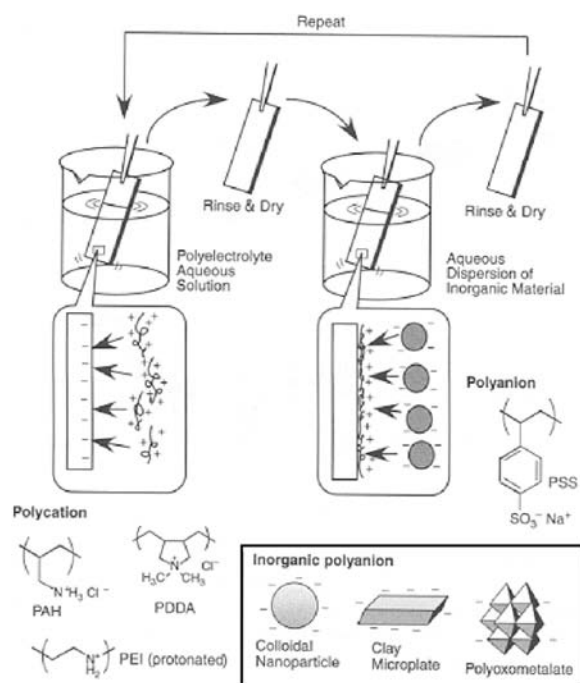


**Fig. 8** Procedure for alternate layer-by-layer adsorption. *Source:* From Ref.<sup>[46]</sup>; © Elsevier Science, 2001.

formation of an ordered micellar structure of polyacetylene furthered by the long hydrocarbon substituent when adsorbed on the surface of the clay platelet. In this respect, one can think that the partial crystallinity of the polymer film, because of chain order on surfaces (epitaxial or otherwise), can contribute to enhancing the barrier properties of polymer-clay nanocomposites. Electrostatic layer-by-layer nanocomposite films can be deposited on various substrates such as PET, cellulose acetate, EVOH, etc. The technique of

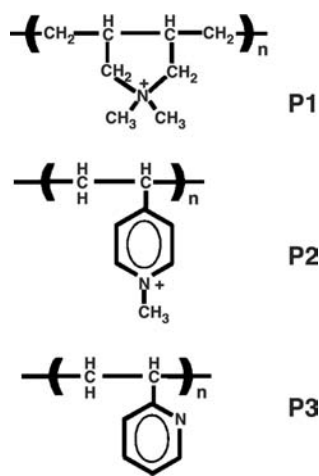


**Fig. 9** Structure of polyelectrolytes used for the preparation of MMT-polyelectrolyte LBL assemblies. *Source:* From Ref.<sup>[43]</sup>; © American Chemical Society, 2001.

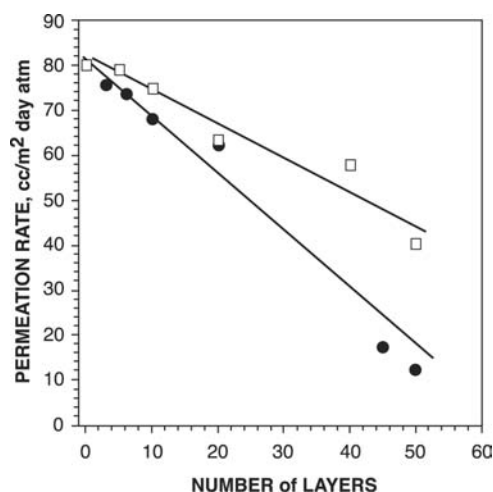


**Fig. 10** Dependence of the permeation rate of oxygen through PET substrate coated with  $(P_1/M)_n$  (●) and  $(P_2/M)_n$  (□) film on the number of deposition cycles  $n$ . *Source:* From Ref.<sup>[43]</sup>; © American Chemical Society, 2001.

cross-linking of polyelectrolyte films has also been reported to contribute to the increase in vapor and gas barrier properties of nanocomposite films while simultaneously improving their pH stability, heat resistance, and mechanical properties.<sup>[44,48]</sup> This effect was illustrated in the case of heat-induced amide formation. Ku et al.<sup>[44]</sup> have prepared electrostatically layered aluminosilicate nanocomposites by sequential deposition of poly(allylamine hydrochloride) (PAH)/poly(acrylic acid)/poly(allylamine hydrochloride)/saponite on PET film. The oxygen permeability of cross-linked nanocomposites decreased with the heating temperature (i.e., the degree of cross-linking). Composite films prepared by 10 deposition cycles followed by heating at 190°C for 2 hr produced films with one third of the permeability of the uncoated PET film. Therefore cross-linking of the multilayer components may enhance water vapor and gas barrier properties. As mentioned above, such properties depend also on the crystallinity of the polymer layer and, in some cases, both factors may contribute simultaneously to the increase of barrier properties. Cross-linking also improves the mechanical properties of the film. In some applications, it is needed to avoid food contact with inorganic materials in nanocomposite packaging containers. Multilayered nanocomposites produced by using existing dies may be an

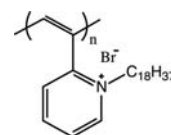


**Fig. 11** Structure of poly(*N*-octadecyl-2-ethynylpyridinium bromide).

alternative for these applications. In this process, nanocomposite materials form an internal layer and are sandwiched between two other unfilled polymer layers. Nylon is a suitable material for a barrier layer because it is an effective gas barrier and has good adhesion to PET. The clay content of the central Nylon layer was reported to range between 1% and 3 wt%.<sup>[49]</sup> This approach can improve recyclability and optical transparency.<sup>[13]</sup> In spite of several advantages, it should be noted that barrier properties of such nanocomposite films will be adversely affected by the unfilled polymer layers.

### MULTILAYERED POLYMER-POLYMER NANOCOMPOSITES

Multilayered polymer-polymer nanocomposites (MPPNs) are formed through nanolayers of different pristine polymers deposited successively on top of each other. The most direct method leading to the formation of MPPNs is the electrostatic layer-by-layer (ELBL) self-assembly described above. Multilayered polymer-polymer nanocomposites are used in the formation of protective barriers in which the advantageous properties of its nanolayer components are combined to give effective protection from various gases and vapors. Here as in previously described nanocomposite films, because of the nanodimensional thickness of such coatings and films, a number of deleterious properties such as opacity, thermal resistance, and lack of flexibility leading to mechanical failure can be avoided. It was reported that the ordered nanolayered or microlayered coextrusion could provide

higher barrier properties when compared to the conventional melt blends.<sup>[50]</sup> After coextrusion, the permeability was measured and related to the number of layers and morphology. Multilayered polymer nanocomposite films prepared by layer-by-layer self-assembly without additives have been also investigated<sup>[51]</sup> for gas, alcohol/water, ion, and proteins separation. Zhou et al.<sup>[52,53]</sup> prepared poly(*N*-octadecyl-2-ethynylpyridinium bromide) and PSS nanocomposite films on a Nafion<sup>TM</sup> substrate using ELBL assembly and Langmuir-Blodgett (LB) techniques. The membranes displayed a high permselectivity for oxygen ( $\alpha = 3.5-4.7$ ) because of the strong affinity of conjugated double bonds to oxygen.<sup>[54]</sup> Sullivan and Bruening<sup>[55]</sup> recently reported polyimide membranes on porous alumina supports obtained through electrostatic deposition of poly(amic acid) salts and PAH followed by heating at 250°C for 2 hr. These are shown in Fig. 12. Such polyimide membranes displayed high-flux permselectivities ( $O_2/N_2$  up to 6.9 and  $CO_2/CH_4$  up to 68).

### MISCELLANEOUS SYSTEMS

Thin film metal oxide on polymer substrates can be used as barrier coatings and films in various applications such as, for example, in protecting pharmaceuticals and food products from oxygen.<sup>[56-60]</sup> In this process, many attempts to optimize oxygen barrier properties have been carried out with respect to adhesion, internal stress, and nanoscopy and microscopical defects. The polymer/metal oxide nanocomposites were also used as gas separation membranes. Poly(amide-imide)/TiO<sub>2</sub> nanocomposite membranes

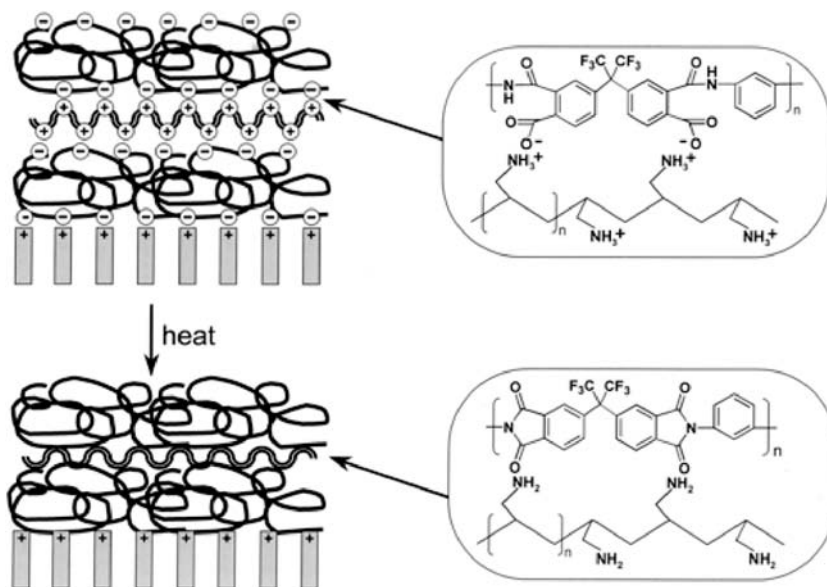


**Fig. 12** Heat-induced imidization of a poly(amic acid)/PAH film on a porous support. Neutralization of PAH occurs when it contributes a proton for the formation of water. *Source:* From Ref.<sup>[55]</sup>; © American Chemical Society, 2001.

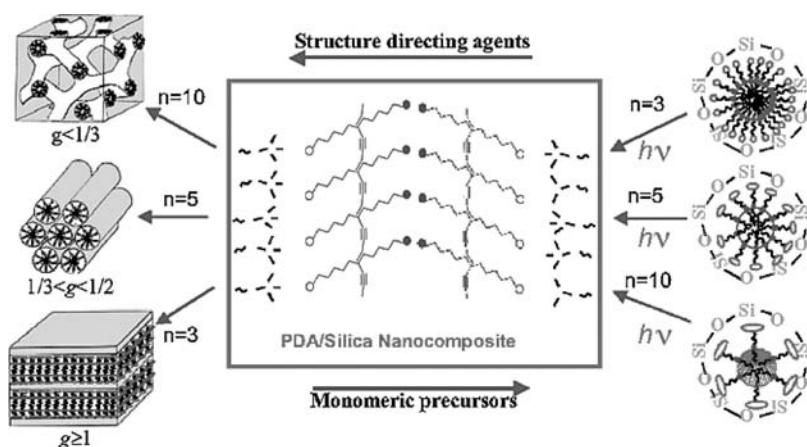


**Fig. 13** The variety of micellar mesostructures obtained with monomers and polymers of diacetylene substituted with ethylene oxide (EO) side groups of different lengths ( $n$ ). Source: From Ref.<sup>[60]</sup>, © American Chemical Society, 2001.

were also described.<sup>[58]</sup> The permselectivities of such membranes attained 50.8 in the case of  $H_2/CH_4$  by using only 7.3% of the incorporated  $TiO_2$ . In contrast to the conventional concept, Merkel et al.<sup>[59]</sup> recently reported on the preparation of ultrapermeable nanocomposite membranes using glassy amorphous poly(4-methyl-2-pentyne) (PMP) and fumed silica particles. Although conventional, size-selective, polymer membranes allow small molecules to preferentially permeate, the reverse-selective membranes allow larger species to diffuse preferentially. The reverse selectivity of such membranes results from inefficient chain packing, producing an increase in the free volume of the polymer. The nanosized filler particles such as fumed silica play an important function as nanospacers, preventing rigid PMP chains from orderly packing and thus increasing the reverse selectivity. The nanocomposite structure of polydiacetylene (PDA) and silicic acid can be tuned by different hydrophilic head groups  $(EO)_n$ , as shown in Fig. 13. The hexagonally ordered PDA ( $n = 5$ )/silica nanocomposites showed significantly lower permeabilities when compared to pure polymers.<sup>[60]</sup>

## CONCLUSION

During the last decade, nanocomposite membranes were extensively used in the formation of coatings, films, and separation membranes. This field is characterized by vigorous research in the area of barriers and permselectivity. Exfoliation and ordering of aluminosilicate nanoparticles are key factors for enhancing the barrier properties of polymer–mineral nanocomposites. Among various methods of membrane formation, ELBL self-assembly was shown to be a promising technique. In addition to synthetic and structural improvement of such barrier materials, cost and production effectiveness still have to be enhanced in the future.

## ACKNOWLEDGMENTS

We gratefully acknowledge the financial support of the U.S. Army. We thank D. Steeves, P. W. Gibson, D. Froio, J. Lucciarini, and J. A. Ratto of the U.S. Army for the measurements of barrier properties and helpful comments. We also appreciate the PET film gift of Bobby Reekers of Dupont Co.

## REFERENCES

1. Rabek, J.F. Diffusion in Polymers. In *Experimental Methods in Polymer Chemistry*; John Wiley and Sons, Inc.: New York, 1980; 606–615.
2. Pauly, S. Permeability and Diffusion Data. In *Polymer Handbook*, 4th Ed.; Brandrup, J., Immergut, E.H.L., Grulke, E.A., Eds.; John Wiley and Sons, Inc.: New York, 1999; 543–569.
3. Sperling, L.H. Diffusion and Permeability in Polymer. In *Introduction to Physical Polymer Science*, 3rd Ed.; John Wiley and Sons, Inc.: New York, 2001; 148–154.
4. Barrer, R.M. *Diffusion in Polymers*; Crank, J., Park, G.S., Eds.; Academic Press: London, 1968; 165–217.
5. Pinnavaia, T.J., Beal, G.W., Eds.; *Polymer–Clay Nanocomposites*; John Wiley and Sons, Inc.: New York, 2001.
6. Giannelis, E.P.; Krishnamoorti, R.; Manias, E. Polymer–silicate nanocomposites: Model systems for confined polymers and polymer brushes. *Adv. Polym. Sci.* **1999**, *138*, 107–147.
7. Alexandre, M.; Dubois, P. Polymer-layered silicate nanocomposites: Preparation, properties and uses of a new class of materials. *Mater. Sci. Eng., R Rep.* **2000**, *28*, 1–63.
8. LeBaron, P.C.; Wang, Z.; Pinnavaia, T.J. Polymer-layered silicate nanocomposites: An overview. *Appl. Clay Sci.* **1999**, *15*, 11–29.
9. Giannelis, E.P. Polymer layered silicate nanocomposites. *Adv. Mater.* **1996**, *8*, 29–35.

10. Kojima, Y.; Usuki, A.; Kawasumi, M.; Okada, A.; Fukushima, Y.; Kurauchi, T.; Kamigaito, O. Mechanical properties of Nylon 6–clay hybrid. *J. Mater. Sci.* **1993**, *6*, 1185–1189.
11. Blumstein, A. Polymerization in adsorbed layers. *Bull. Soc. Chim. Fr.* **1961**, *5*, 899–914.
12. Blumstein, A. Polymerization of adsorbed monolayers: II. Thermal degradation of the inserted polymer. *J. Polym. Sci., Part A* **1965**, *3*, 2665–2672.
13. Matayabas, J.C., Jr.; Turner, S.R. Nanotechnology for Enhancing the Gas Barrier of Polyethylene Terephthalate. In *Polymer–Clay Nanocomposites*; Pinnavaia, T.J., Beal, G.W., Eds.; John Wiley and Sons, Inc.: New York, 2001; 207–226.
14. Gilman, J.W. Flammability and thermal stability studies of polymer layered-silicate (clay) nanocomposites. *Appl. Clay Sci.* **1999**, *15*, 31–49.
15. Grim, R.E. *Clay Mineralogy*, 2nd Ed.; McGraw-Hill Inc.: New York, 1968.
16. Nielsen, L.E. Models for the permeability of filled polymer systems. *J. Macromol. Sci., Part A* **1967**, *1*, 929–942.
17. Bharadwaj, R.K. Modeling the barrier properties of polymer-layered silicate nanocomposites. *Macromolecules* **2001**, *34*, 9189–9192.
18. Blumstein, A. Polymerization of adsorbed monolayers: I. Preparation of the clay–polymer complex. *J. Polym. Sci., Part A* **1965**, *3*, 2653–2664.
19. Blumstein, A.; Malhotra, S.L.; Watterson, A.C. Polymerization of monolayers: V. Tacticity of the insertion poly(methyl methacrylate). *J. Polym. Sci., A-2* **1970**, *8*, 1599–1615.
20. Blumstein, A. *Polymerization in Preoriented Media*; Advances in Macromolecular Chemistry; Pasika, M., Ed.; Academic Press: New York, 1970; Vol. 2, 123–148.
21. Usuki, A.; Kojima, Y.; Kawasumi, M.; Okada, A.; Fukushima, Y.; Kurauchi, T.; Kamigaito, O. Synthesis of Nylon 6–clay hybrid. *J. Mater. Res.* **1993**, *8*, 1179–1183.
22. Usuki, A.; Kawasumi, M.; Kojima, Y.; Okada, A.; Fukushima, Y.; Kurauchi, T.; Kamigaito, O. Swelling behavior of montmorillonite cation exchanged for  $\omega$ -amino acid by  $\epsilon$ -caprolactam. *J. Mater. Res.* **1993**, *8*, 1174–1178.
23. Kojima, Y.; Usuki, A.; Kawasumi, M.; Okada, A.; Kurauchi, T.; Kamigaito, O. Synthesis of Nylon-6–clay hybrid by montmorillonite intercalated with  $\epsilon$ -caprolactam. *J. Polym. Sci., A* **1993**, *31*, 983–986.
24. Kojima, Y.; Usuki, A.; Kawasumi, M.; Okada, A.; Kurauchi, T.; Kamigaito, O. One-pot synthesis of Nylon-6–clay hybrid. *J. Polym. Sci., A* **1993**, *31*, 1755–1758.
25. Messersmith, P.B.; Giannelis, E.P. Synthesis and barrier properties of poly( $\epsilon$ -aprolactone)-layered silicate nanocomposites. *J. Polym. Sci., A* **1995**, *33*, 1047–1057.
26. Messersmith, P.B.; Giannelis, E.P. Polymer-layered silicate nanocomposites: in situ intercalative polymerization of  $\epsilon$ -caprolactone in layered silicates. *Chem. Mater.* **1993**, *5*, 1064–1066.
27. Weimer, M.W.; Chen, H.; Giannelis, E.P.; Sogah, D.Y. Direct synthesis of dispersed nanocomposites by in situ living free radical polymerization using a silicate-anchored initiator. *J. Am. Chem. Soc.* **1999**, *121*, 1615–1616.
28. Lucciarini, J.M.; Ratto, J.A.; Koene, B.E.; Powell, B. Nanocomposites study of ethylene co-vinyl alcohol and montmorillonite clay. *Antec* **2002**, *2*, 1514–1518.
29. McConaughy, S.D. Effects of nanocomposites on the oxygen barrier properties of polyethylene. *Antec* **2002**, *2*, 3587–3588.
30. Bonner, S.; Sabandith, D.; Swannack, C.; Zhou, W. Nanocomposite polymer film technology. *Antec* **2001**, *3*, 3256–3260.
31. Anderson, P.G. Twin screw extrusion guidelines for compounding nanocomposites. *Antec* **2002**, *1*, 219–223.
32. Paul, M.-A.; Alexandre, M.; Degée, P.; Henrist, C.; Rulmont, A.; Dubois, P. New nanocomposite materials based on plasticized poly(L-lactide) and organo-modified montmorillonites: thermal and morphological study. *Polymer* **2003**, *44*, 443–450.
33. Yano, K.; Usuki, A.; Okada, A. Synthesis and properties of polyimide–clay hybrid films. *J. Polym. Sci., A* **1997**, *35*, 2289–2294.
34. Yano, K.; Usuki, A.; Okada, A.; Kurauchi, T.; Kamigaito, O. Synthesis and properties of polyimide–clay hybrid. *J. Polym. Sci., A* **1993**, *31*, 2493–2498.
35. Lan, T.; Kaviratna, P.D.; Pinnavaia, T.J. On the nature of polyimide–clay hybrid composites. *Chem. Mater.* **1994**, *6*, 573–575.
36. Ariga, K. Layered nanohybrids of polyelectrolytes and inorganic materials prepared by alternate layer-by-layer adsorption. In *Handbook of Polyelectrolytes and Their Applications*; Tripathy, S.K., Kumar, J., Nalwa, H.S., Eds.; American Scientific Publishers: California, 2002; Vol. 1, 127–148.
37. Hammond, P.T. Recent explorations in electrostatic multilayer thin film assembly. *Curr. Opin. Colloid Interface Sci.* **2000**, *4*, 430–442.
38. Decher, G. Fuzzy nanoassemblies: Toward layered polymeric multicomposites. *Science* **1997**, *77*, 1232–1237.
39. Lvov, Y.; Ariga, K.; Ichinose, I.; Kunitake, T. Formation of ultrathin multilayer and hydrated gel from montmorillonite and linear polycations. *Langmuir* **1996**, *12*, 3038–3044.
40. Kleinfeld, E.R.; Ferguson, G.S. Stepwise formation of multilayered nanostructural films from macromolecular precursors. *Science* **1994**, *265*, 370–373.
41. Sharpe, W.N., Jr.; Hemker, K.J. Mechanical testing of free-standing thin films. *Mater. Res. Soc. Symp. Proc.* **2002**, *697*, 215–226.
42. Mamedov, A.A.; Kotov, N.A. Free-standing layer-by-layer assembled films of magnetite nanoparticles. *Langmuir* **2000**, *16*, 5530–5533.
43. Kotov, N.A.; Magonov, S.; Tropsha, E. Layer-by-layer self-assembly of aluminosilicate–polyelectrolyte composites: Mechanism of deposition, crack resistance, and perspectives for novel membrane materials. *Chem. Mater.* **1998**, *10*, 886–895.
44. Ku, B.-C.; Froio, D.; Ratto, J.A.; Steeves, D.; Kim, D.W.; Blumstein, A.; Kumar, J.; Samuelson, L.A. Cross-linked polymer-layered silicate nanocomposites and their oxygen barrier properties. *ACS New Orleans-March 23–27* **2003**.

45. Kim, D.W.; Ku, B.-C.; Steeves, D.; Yun, J.; Nagarajan, R.; Blumstein, A.; Kumar, J.; Gibson, P.W.; Ratto, J.A.; Samuelson, L.A. Ordered multilayer nanocomposites: Molecular self-assembly of amphiphilic polyacetylenes on aluminosilicate nanoparticles and their water vapor barrier properties. submitted for publication.
46. Ariga, K.; Lvov, Y.; Ichinose, I.; Kunitake, T. Ultrathin films of inorganic materials prepared by alternate layer-by-layer assembly with organic polyions. *Appl. Clay Sci.* **1999**, *15*, 137–152.
47. Kim, D.W.; Blumstein, A.; Kumar, J.; Samuelson, L.A.; Kang, B.; Sung, C. Ordered multilayer nanocomposites prepared by electrostatic layer-by-layer assembly between aluminosilicate nanoplatelets and substituted ionic polyacetylenes. *Chem. Mater.* **2002**, *14*, 3925–3929.
48. Harris, J.J.; De Rose, P.M.; Bruening, M.L. Synthesis of passivating, nylon-like coatings through crosslinking of ultrathin polyelectrolyte films. *J. Am. Chem. Soc.* **1999**, *121*, 1978–1979.
49. Harrison, A.G.; Meredith, W.N.E.; Higgins, D.E. Polymeric Packaging Film Coated with a Composition Comprising a Layer Mineral and a Cross-Linked Resin. US Patent 5,571,614, November 5, 1996
50. Jarus, D.; Hiltner, A.; Baer, E. Barrier properties of polypropylene/polyamide blends produced by micro-layer coextrusion. *Polymer* **2002**, *43*, 2401–2408.
51. Tieke, B. Polyelectrolyte multilayer membranes for materials separation. In *Handbook of Polyelectrolytes and Their Applications*; Tripathy, S.K., Kumar, J., Nalwa, H.S., Eds.; American Scientific Publishers: California, 2002; Vol. 3, 115–124.
52. Blumstein, A.; Samuelson, L. Highly conjugated ionic polyacetylenes. Thin-film processing and potential applications. *Adv. Mater.* **1998**, *10*, 173–176.
53. Zhou, P.; Samuelson, L.A.; Alva, K.S.; Chen, C.-C.; Blumstein, R.; Blumstein, A. Ultrathin films of amphiphilic ionic polyacetylenes. *Macromolecules* **1997**, *30*, 1577–1581.
54. Masuda, T.; Higashimura, T. Polyacetylenes with substituents. Their synthesis and properties. *Adv. Polym. Sci.* **1986**, *81*, 121–165.
55. Sullivan, D.M.; Bruening, M.L. Ultrathin gas-selective polyimide membranes prepared from multilayer polyelectrolyte films. *Chem. Mater.* **2003**, *15*, 281–287.
56. Leterrier, Y. Durability of nanosized oxygen-barrier coatings on polymers. *Prog. Mater. Sci.* **2003**, *48*, 1–55.
57. Chatham, H. Oxygen diffusion barrier properties of transparent oxide coatings on polymeric substrates. *Surf. Coat. Technol.* **1996**, *78*, 1–9.
58. Hu, Q.; Marand, E.; Dhingra, S.; Fritsch, D.; Wen, J.; Wilkes, G. Poly (amide-imide)/TiO<sub>2</sub> nanocomposite gas separation membranes: Fabrication and characterization. *J. Membr. Sci.* **1997**, *135*, 65–79.
59. Merkel, T.C.; Freeman, B.D.; Spontak, R.J.; He, Z.; Pinnau, I.; Meakin, P.; Hill, A.J. Ultraparpermeable, reverse-selective nanocomposite membranes. *Science* **2002**, *296*, 519–522.
60. Yang, Y.; Lu, Y.; Lu, M.; Huang, J.; Haddad, R.; Xomeritakis, G.; Liu, N.; Malanoski, A.P.; Sturmayer, D.; Fan, H.; Sasaki, D.Y.; Assink, R.A.; Shelnut, J.A.; van Swol, F.; Lopez, G.P.; Burns, A.R.; Brinker, C.J. Functional nanocomposites prepared by self-assembly and polymerization of diacetylene surfactants and silicic acid. *J. Am. Chem. Soc.* **2003**, *125*, 1269–1277.



# Basic Nanostructured Catalysts

Robert J. Davis

Department of Chemical Engineering, University of Virginia, Charlottesville, Virginia, U.S.A.

## INTRODUCTION

Solid bases catalyze a wide variety of chemical transformations (e.g., condensations, alkylations, cyclizations, and isomerizations). However, compared with their solid acid analogues, they have received relatively little attention from the industrial and academic communities. The search for novel solid bases that catalyze reactions with high product selectivity, high reaction rate, and low deactivation rate is an ongoing process. The following text describes current research trends in the design and utilization of nanostructured solid bases composed mainly of supported metals and metal oxides.

## HISTORICAL PERSPECTIVE

The earliest use of alkalis was probably about 4000 B.C. during the New Stone Age period in the production of quicklime (CaO) by roasting limestone (CaCO<sub>3</sub>).<sup>[1]</sup> The early uses of quicklime were for the removal of fat and hair from leather and in the production of cement. Around 3000 B.C., a dilute solution of potash (K<sub>2</sub>CO<sub>3</sub>) produced by leaching ashes from wood fires was found to have cleaning powers.<sup>[1]</sup> Adding fat to the solution likely formed the first soap. At about the same time, evidence shows that glass containing sodium carbonate was also being produced. These early uses of bases preceded the common uses of acids by several thousand years. The first commonly used acid was probably acetic acid because it was used to prepare white lead pigment around 300–400 B.C.<sup>[1]</sup>

Despite the tremendous lead time in technology with bases, applications in catalysis by solid bases lag far behind that by solid acids. Tanabe and Holderich<sup>[2]</sup> recently performed a statistical survey of industrial processes using solid acids, solid bases, and acid–base bifunctional catalysts and have counted 103, 10, and 14 industrial processes for these types of catalysts, respectively. The number of acid-catalyzed processes outnumbers those catalyzed by solid bases by an order of magnitude. However, as novel base materials are discovered and new base-catalyzed reactions are found to be commercially relevant, new processes are sure to appear.

## DEFINITION AND EVALUATION OF BASICITY

Basicity, in the context of the following discussion, can be defined in the Lewis sense as the donation of electrons from a solid surface to an acceptor species. Thus for a typical solid base such as a metal oxide, the exposed metal cation is regarded as a Lewis acid site and the exposed oxygen atom is regarded as a Lewis base site, as illustrated in Fig. 1. Because basicity is related to the electronic charge on the oxygen atom, it is important to understand how this charge depends on composition. One very simple method that is often used to compare structurally similar compounds is based on the intermediate electronegativity principle of Sanderson. The Sanderson intermediate electronegativity ( $S_{E,int}$ ) of a solid is calculated from the mean of the individual electronegativities of the elements present according to Eq. (1), where  $S_{E,Z}$  is the individual electronegativity of element  $Z$  and  $x$  is the atomic ratio of element  $Z$  present. The general idea is that an equalization of the electronegativities in a compound results from electron transfer that occurs in the formation of the compound.<sup>[3]</sup> The calculation of the intermediate electronegativity takes into account only the composition of the compound, ignoring the effect of structure and surface composition. From the Sanderson intermediate electronegativity, the partial negative charge on oxygen ( $\delta_q)_O$  can be calculated from Eqs. (2) and (3). A high partial negative charge on oxygen indicates strong basicity of the oxide surface:

$$S_{E,int} = \left( \prod S_{E,Z}^x \right) (\sum x)^{-1} \quad (1)$$

$$\Delta S_{E,O} = 2.08(S_{E,O})^{1/2} \quad (2)$$

$$(\delta_q)_O = \frac{(S_{E,int} - S_{E,O})}{\Delta S_{E,O}} \quad (3)$$

Typical measurements of basicity are obtained by titration with indicators having a wide range of  $pK_a$  values. For a reaction of an acid indicator BH with a solid base B\* (Eq. (4)), the Hammett basicity function  $H_-$  is defined by Eq. (5), where [BH] is the concentration of the indicator and [B<sup>-</sup>] is the concentration of its conjugate form. One problem with using adsorbed indicators to evaluate basicity is the interference of

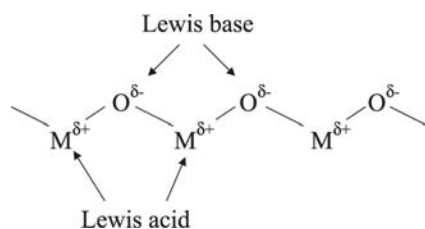


**Fig. 1** Schematic illustration of Lewis acid and Lewis base sites on a metal oxide surface. M represents a surface metal cation and O represents a surface oxygen anion.

indicator reactions that are not because of acid–base chemistry. In addition, evidence of reaction is often provided by a color change, which requires the use of colorless catalysts. Clearly, there is a need for other methods to probe surface base sites:



$$\text{H}_- = \text{p}K_a + \log \frac{[\text{B}^-]}{[\text{BH}]} \quad (5)$$

One commonly used method to study solid base sites involves adsorption of a probe molecule followed by examination with infrared (IR) spectroscopy. Infrared spectrometric studies of various probe molecules adsorbed on solid bases have been reviewed by Lavalley.<sup>[4]</sup> One of the major problems with this technique is that many of the commonly used probe molecules decompose or react on interaction with the basic site, and thus do not effectively interrogate the catalyst surface. For example, pyrrole has been found to dissociatively chemisorb on highly basic metal oxides such as  $\text{ThO}_2$  and  $\text{CeO}_2$ , forming the  $\text{C}_4\text{H}_4\text{N}^-$  pyrrolate anion.<sup>[4]</sup> A probe molecule should undergo specific chemical interactions with the base sites without dramatically altering the catalyst surface. Therefore the search for a unique, widely applicable adsorbate molecule to probe the surface base sites of heterogeneous catalysts is a daunting process. No single probe is universally adept at characterizing the active sites on all basic solids. Carbon dioxide is probably the most widely used probe for surface basicity because of its stability and ease of handling. Because carbon dioxide is a weakly acidic molecule, it selectively adsorbs on base sites. However, carbon dioxide adsorption on metal oxides results in many different types of surface species, which can complicate interpretation.

Temperature-programmed desorption (TPD) of adsorbed probe molecules can also be used to measure the number and strength of sites found on solid base catalysts. Because strongly bound probe molecules have high adsorption energies, increased temperatures are necessary to desorb these species. Experiments are typically performed under identical experimental conditions (carrier gas flow, heating rate, and sample size)

so that a qualitative comparison can be made between samples. During a TPD experiment, the amount of desorbed molecules is often monitored by mass spectrometry and the surface interactions are explored with IR spectroscopy.

## NANOSTRUCTURED MATERIALS AS SUPPORTS FOR BASES

Alkali metals and metal oxides are among the strongest bases known. However, these materials typically have a very low surface area that limits their ability to be effective catalysts. New material processing technology can be used to create bulk materials with very high surface-to-volume ratios (i.e., very small crystallite sizes), but the resulting fine powders become very difficult to use as heterogeneous catalysts. Therefore basic metals and metal oxides are often supported on high surface area carriers to achieve high dispersion of the base sites without sacrificing ease of handling.

To illustrate the concept of supporting alkali metal oxides on supports, Dorskocil, Bordawekar, and Davis<sup>[5]</sup> loaded rubidium onto magnesia, titania, alumina, carbon, and silica by decomposition of an impregnated acetate precursor at 773 K. Results from x-ray absorption spectroscopy indicated that the local structure around Rb was highly dependent on the support composition. For example, the Rb–O distance was significantly shorter on carbon and silica compared with more basic carriers. Results from  $\text{CO}_2$  stepwise TPD showed that Rb/MgO possessed strongly basic sites that were not present on pure MgO. However, the basic sites formed by Rb addition to the other supports were weaker than those on Rb/MgO. The TPD experiments were complemented by adsorption microcalorimetry of both ammonia (titrates acid sites) and carbon dioxide (titrates base sites) on the same samples.<sup>[6]</sup> Microcalorimetry revealed that incorporation of rubidium onto the supports neutralized acid sites and created new base sites. Decomposition of 2-propanol at 593 K was used as a probe reaction to relate catalytic activity to surface basicity.<sup>[5]</sup> As anticipated, Rb/MgO and MgO were highly active and selective for dehydrogenation of alcohol. The addition of Rb to alumina and titania significantly decreased the activity of the support oxides for the acid-catalyzed dehydration of 2-propanol. Both reactivity and characterization results on Rb/SiO<sub>2</sub> were consistent with the formation of a highly disordered, weakly basic, surface silicate phase that exhibited little activity for alcohol decomposition. Evidently, highly basic rubidium oxide reacted with the silica surface, probably through surface hydroxyl groups, to form rubidium silicate. Because the overall rate of acetone formation from 2-propanol correlated with the ranking of support

basicity, as evaluated from the Sanderson intermediate electronegativity principle, strongly basic alkali-containing catalysts should utilize basic carriers to minimize alkali-support interactions that lower base strength.

It has become clear that to have strongly basic catalysts on conventional supports, the carrier should be preconditioned with a base to create a surface phase that can accommodate a strong base. Another strategy used to support bases involves incorporation into the nanopores of a crystalline material such as a zeolite. The following discussion focuses on the most commonly studied nanostructured materials that have been explored as supports for base catalysts.

## Zeolites

Zeolites are highly porous aluminosilicates that are constructed from  $\text{TO}_4$  tetrahedra (T = tetrahedral atom, e.g., Si, Al), with each apical oxygen atom shared with an adjacent tetrahedron. When tetrahedra containing  $\text{Si}^{4+}$  and  $\text{Al}^{3+}$  are connected to form a three-dimensional zeolite framework, a negative charge is associated with each  $\text{Al}^{3+}$  atom. The negative framework charge is balanced by an exchangeable cation to achieve electrical neutrality. Some of the counterions in the zeolite pores can be readily exchanged with other cations, altering the acid-base character of the zeolite framework. Exchanging zeolites with a less electronegative charge-balancing cation such as cesium creates a more basic zeolite. An excellent review of basic zeolites was written by Barthomeuf.<sup>[7]</sup>

The main feature that makes zeolites very interesting nanostructured supports is that their pores are uniform in size and are in the same size range as small molecules. Zeolites are molecular sieves because they discriminate molecules based on size. Molecules smaller than the pore size are adsorbed in the crystal interior, whereas those that are larger are excluded. This feature of zeolites creates a unique reaction environment for supported base catalysts, if the base sites are located in the micropores.

## Alkali Metal Oxides in Zeolite Pores

Fig. 2 illustrates a typical procedure for incorporating alkali metal oxide clusters into the pores of zeolite X. Zeolite X is of the faujasite type with a Si/Al ratio ranging from 1 to 1.5. The rather high content of aluminum in the structure indicates that the framework has a substantial negative charge that is balanced by exchangeable cations. The exchangeable cations are usually replaced with heavy alkali metal cations prior to impregnating an alkali metal compound. In Fig. 2, an aqueous solution of cesium acetate is impregnated into the micropores of Cs-exchanged X zeolite. Thermal treatment in air is sufficient to decompose the acetate precursor and leave behind alkali metal oxide in the pores of the zeolite.

The basic properties of cesium oxide occluded in the pores of zeolite X have been characterized by a wide variety of methods, including  $\text{CO}_2$  adsorption microcalorimetry,<sup>[8,9]</sup>  $\text{CO}_2$  TPD,<sup>[9-14]</sup> IR spectroscopy of adsorbed  $\text{CO}_2$ ,<sup>[10,15]</sup> nuclear magnetic resonance (NMR) spectroscopy,<sup>[10,16,17]</sup> and x-ray absorption spectroscopy.<sup>[15]</sup> For basic zeolites containing occluded Cs oxide that have been thermally activated at about 773 K, most of the  $\text{CO}_2$  desorbed with a peak temperature less than 573 K. This result suggests a rather moderate base strength for the occluded Cs species. In fact, results from  $\text{CO}_2$  adsorption microcalorimetry indicated that most of the adsorption sites at 373 K are characterized by an adsorption enthalpy of about  $-100 \text{ kJ mol}^{-1}$ , which is hundreds of kilojoules lower in magnitude than that anticipated for adsorption of  $\text{CO}_2$  on a stoichiometric alkali metal oxide.

The stoichiometry of the occluded alkali metal oxide cluster is still an open question. Lasperas et al.<sup>[13,14]</sup> used TPD of  $\text{CO}_2$  from cesium oxide loaded onto CsX zeolite to measure an adsorption stoichiometry of one  $\text{CO}_2$  desorbed per occluded pair of Cs atoms. Because that ratio matches the ideal reaction stoichiometry of  $\text{Cs}_2\text{O}$  plus  $\text{CO}_2$  to form  $\text{Cs}_2\text{CO}_3$ , they concluded that the oxide in the zeolite pores was likely  $\text{Cs}_2\text{O}$ . In contrast, Bordawekar and Davis<sup>[8]</sup> reported results from  $\text{CO}_2$  adsorption microcalorimetry that

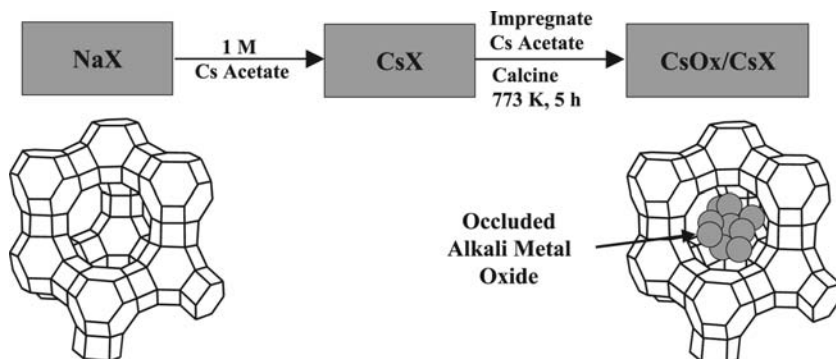


**Fig. 2** Synthesis procedure for preparing cesium oxide species in the supercages of Cs-exchanged zeolite X.

indicated an adsorption stoichiometry of one  $\text{CO}_2$  adsorbed per four occluded Cs atoms. An explanation for the difference is not readily apparent. What appears to be consistent from the various works is that cesium is fairly well distributed throughout the zeolite pores at loadings below about two cesium atoms per supercage. At higher loadings, cesium deposits on the external surface of the zeolite.

The rather moderate base strength evaluated by  $\text{CO}_2$  adsorption microcalorimetry suggests that the occluded Cs is not in a form that is typical of a stoichiometric alkali oxide. Krawietz, Murray, and Haw<sup>[18]</sup> recently reported that they could not successfully prepare bulk-phase  $\text{Cs}_2\text{O}$  by conventional chemical methods, whereas stoichiometric lighter alkali metal oxides could be prepared. The heavy alkali preferred instead to form higher oxides. Their intriguing result points to the possibility that higher oxides such as cesium peroxide and cesium superoxide might be present in zeolite-supported cesium oxide samples. Indeed, higher oxides of Cs should exhibit less base strength than the stoichiometric oxide  $\text{Cs}_2\text{O}$ . Yagi and Hattori<sup>[19]</sup> have shown that dioxygen retains its molecular identity when adsorbed on thermally activated cesium oxide clusters occluded in zeolite X. In other words, exposure of the material to  $^{18}\text{O}_2$  yields both  $^{18}\text{O}_2$  and  $^{16}\text{O}_2$  in the gas phase, with only traces of  $^{18}\text{O}^{16}\text{O}$  being observed. A mechanism involving the formation of peroxides was invoked to explain the isotopic distribution. Although the authors of that study speculate that the zeolite initially contained  $\text{Cs}_2\text{O}$  clusters, the presence of peroxides should not be ruled out.

Intrazeolitic clusters of cesium oxide species are active in a variety of base-catalyzed reactions. For example, the decomposition of 2-propanol to acetone was catalyzed by cesium oxide species in Y zeolite at a rate (based on surface area) comparable to  $\text{MgO}$ .<sup>[20]</sup> In general, solid bases catalyze the dehydrogenation of 2-propanol to acetone, whereas solid acids typically catalyze dehydration to propene. Another reaction catalyzed by basic materials is the cycloaddition of  $\text{CO}_2$  to an oxirane such as ethylene oxide. The rather moderate adsorption strength of  $\text{CO}_2$  on zeolites containing occluded alkali metal oxides indicates that  $\text{CO}_2$  might be useful as a reagent in catalytic reactions on these solids.

Reactions of  $\text{CO}_2$  with ethylene oxide and epoxypropylbenzene were studied over a series of base catalysts, including alkali-loaded X zeolites, Cs-loaded alumina, magnesia, and a homogeneous catalyst, tetraethylammonium bromide.<sup>[21]</sup> Interestingly, the site time yield (defined here as the total number of product molecules formed divided by the number of  $\text{CO}_2$  adsorption sites divided by the total reaction time) of the homogeneous catalyst was only three to four times greater than that of the basic zeolite catalysts containing occluded alkali metal oxide for the cycloaddition of  $\text{CO}_2$  to ethylene oxide. Perhaps the most important part of that study was the demonstration that the porosity of the catalyst influenced the conversion of epoxides. A schematic illustration of the concept is presented in Fig. 3. Ideally, the nonmicroporous base  $\text{MgO}$  should catalyze  $\text{CO}_2$  addition to ethylene oxide regardless of the presence of larger molecules because  $\text{MgO}$  exposes very accessible catalytic surface sites. However, steric restrictions in the pores of a zeolite should affect ethylene oxide conversion in the presence of large molecules. Table 1 summarizes the site time yields measured during the various runs with pure and mixed feeds. Pure ethylene oxide reacted at about the same rate over the zeolite and  $\text{MgO}$  catalysts. For mixed epoxide experiments, both epoxypropylbenzene and its cyclic carbonate retarded the diffusion of ethylene oxide into the zeolite pores and severely reduced (by almost an order of magnitude) the rate of ethylene carbonate production. However, the bulky reactant and product negligibly affected (less than a factor of 2) the rate of ethylene carbonate production over non-microporous  $\text{MgO}$ . These results indicate that most of the basic sites of the zeolite catalysts containing occluded alkali metal oxide species were located within the micropore network and suggest their use as shape-selective base catalysts. Future work with these materials should exploit the molecular sieving property of the zeolite support. Of course, care must be utilized with highly polar solvents and products because the alkali metal oxides would be expected to leach with time in those liquid systems.

Zeolites containing occluded cesium oxide species are also active catalysts in the double-bond isomerization of 1-butene,<sup>[8–12]</sup> even at temperatures as low as 273 K.<sup>[11,12]</sup> The *cis/trans* ratio of the product

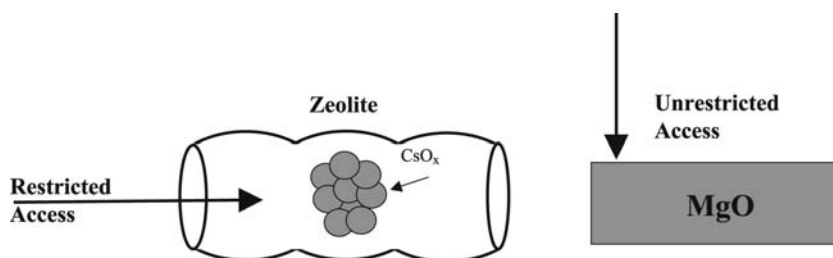


Fig. 3 Comparison of accessibility of the base sites on alkali-loaded zeolite and  $\text{MgO}$ .

**Table 1** Addition of CO<sub>2</sub> to epoxides over microporous Cs-Loaded zeolite X and nonmicroporous MgO

Catalyst <sup>a</sup>	Reactant <sup>b</sup>	Product <sup>c</sup>	Site time yield <sup>d</sup> (hr <sup>-1</sup> )
CsOx/KX	EO	EC	250
	EO + EPBz	EC	31
		BzD	14
MgO	EO	EC	309
	EO + EPBz	EC	189
		BzD	29

<sup>a</sup>CsOx/KX is a catalyst prepared by impregnation of cesium acetate into K-exchanged X zeolite followed by calcination at 773 K.

<sup>b</sup>EO = ethylene oxide; EPBz = 2,3-epoxypropylbenzene.

<sup>c</sup>EC = ethylene carbonate; BzD = 4-benzyl-1,3-dioxolan-2-one.

<sup>d</sup>Defined as (molecules of product) × (number of CO<sub>2</sub> adsorption sites)<sup>-1</sup> × (total reaction time)<sup>-1</sup>.

Source: From Ref.<sup>[21]</sup>.

2-butenes typically ranges from about 10 to 20, indicating a base-catalyzed reaction path. Given the rather moderate base strength of the catalysts as determined by CO<sub>2</sub> microcalorimetry, the high activity of the occluded cesium is quite impressive. Because the active sites for butene isomerization are readily poisoned by CO<sub>2</sub>, the active site density can be measured by selective regeneration of the poisoned catalyst at various temperatures. Using this method, Li and Davis<sup>[9]</sup> discovered that about 5% of the base sites titrated by CO<sub>2</sub> adsorption at 373 K is responsible for butene isomerization on CsOx/CsX. Evidently, most of the basic sites counted by CO<sub>2</sub> adsorption do not play any role in the butene isomerization reaction. Similar conclusions were reported by Yagi et al.<sup>[12]</sup> Only very few strong basic sites account for the high activity of the catalysts.

### Alkali metal clusters in zeolite pores

Zeolites containing alkali metals in the pores are strong base catalysts. Martens et al.<sup>[22–25]</sup> have reported a unique method for synthesizing zeolite-supported alkali metals via azide precursors. Unlike their alkali metal counterparts, the azides themselves are stable at ambient conditions. Decomposition of the alkali azide in the pores of the zeolite forms either ionic or neutral alkali metal clusters, depending primarily on the heating rate used to decompose the supported azide. As determined by electron spin resonance (ESR) spectroscopy, a fast heating rate of 25 K min<sup>-1</sup> formed ionic clusters, whereas a slow heating rate of 1 K min<sup>-1</sup> formed primarily neutral metal clusters.<sup>[23]</sup>

In separate studies, ESR spectroscopy of the alkali metal-loaded KX zeolites indicated the formation of potassium clusters, despite using other alkali azides

as precursors.<sup>[15,26]</sup> Apparently, the zeolite cations exchanged with the impregnated alkali either during azide impregnation or thermal treatment. The reduction of potassium ions by cesium metal makes sense thermodynamically, but the reduction of potassium ions by sodium metal is harder to rationalize. Perhaps the large amount of potassium in the zeolite facilitates the transformation. Quantitative work clearly needs to be done in this area. Interestingly, some of the zeolites also exhibited broad ESR lines at high *g*-values, indicating the presence of additional extra lattice alkali metal clusters. The relative importance of extra framework metal clusters in catalytic reactions must be determined.

The microcalorimetry of O<sub>2</sub> adsorption on thermally activated zeolite samples containing occluded alkali metals revealed very high initial enthalpies of –300 to –400 kJ mol<sup>-1</sup>, possibly indicating the formation of alkali metal oxides and peroxides.<sup>[8]</sup> However, the uptake of O<sub>2</sub> was always orders of magnitude lower than the content of alkali metal azide that was loaded into the zeolites. Therefore the active site density in these materials was probably very low. Because adsorption of small molecules such as O<sub>2</sub> and CO<sub>2</sub> is irreversible, poisoning of these catalysts can be problematic if impure feeds are used.

The side-chain alkylation of aromatics with olefins is catalyzed by strong solid bases such as alkali metals. Thus Martens et al.<sup>[25]</sup> studied the side-chain alkylation of alkylaromatics with ethylene over zeolites containing occluded alkali metals. They observed that the alkylation activity of Na metal in NaX zeolite was higher than that of Na metal in NaY zeolite. In addition, the alkylation activity for isopropylbenzene was lower than that of ethylbenzene, possibly because of steric effects.

The liquid-phase alkenylation reaction of *o*-xylene with butadiene to form 5-*o*-tolyl-2-pentene (OTP) is also catalyzed by zeolite-supported alkali metals.<sup>[15]</sup> Like toluene alkylation with ethylene, the alkenylation reaction requires a stronger base site than that associated with supported alkali metal oxides. The selectivity to OTP, based on the total amount of monoalkenylated, dialkenylated, and trialkenylated products, was greater than 85% for *o*-xylene conversions ranging from 1% to 14%. However, extra lattice metal clusters were evident on each of the alkali-metal-loaded zeolites that were effective catalysts for the alkenylation reaction, suggesting that these clusters might be the active species. For each reaction in which OTP was produced, the solution color indicated that alkali metal formed from the decomposition of the supported azide may have leached into solution to form an organoalkali complex. Thus catalytic activity was likely because of metal species in the solution as well as those associated with the zeolite (possibly through reaction with the

zeolite). Shape-selective reactions on these catalysts might be problematic in the liquid phase.

Zeolites containing alkali metals also catalyze reactions such as butene isomerization<sup>[8,22]</sup> and aldol condensation of acetone.<sup>[25]</sup> However, these reactions do not require the alkali to be in metallic form to be catalytic. It is very likely that the alkali metal clusters are converted into supported oxides or hydroxides during aldol condensation because the ESR signal of the alkali metal disappeared on exposure to acetone.<sup>[25]</sup> Nevertheless, the selectivity of the aldol condensation reaction over various zeolite catalysts indicates that the shape-selective environment in the micropore can be important.

#### Amide and imide clusters supported in zeolites

Baba et al.<sup>[27,28]</sup> reported on the synthesis and catalytic activity of low-valent ytterbium (Yb) and europium (Eu) in the cages of Y zeolite. In their method, Yb or Eu metal ingots were placed together with dehydrated zeolite Y under a nitrogen atmosphere. Then, liquid ammonia was introduced to the reactor that was cooled with dry ice and ethanol. The metal dissolved in the ammonia and subsequently impregnated into the zeolite pores. Ammonia was removed from the sample by heating under vacuum. The resulting materials catalyzed the selective conversion of 1-butene at 273 K to *cis*-2-butene, which is consistent with base catalysis. The *cis/trans* ratio of the product 2-butene was ~10 for the Eu-loaded sample and ~4.5 for the Yb-loaded sample.<sup>[27]</sup> The counteraction of the zeolite affected the activity of the catalysts according to  $K > Rb > Cs > Na > Li$ . Potassium was the best cation, presumably because only low levels of cation exchange were achieved with the heavier alkalis.<sup>[27]</sup> The activity of the catalysts also increased linearly with loading of Eu on Y zeolite until ~8 wt.% Eu was achieved.<sup>[27]</sup> At lower levels, the Eu was apparently well dispersed in the zeolite pores. The new materials were also effective in the Michael reaction of 2-cyclopent-2-enon with dimethyl malonate, another base-catalyzed reaction.<sup>[28]</sup> A very important feature of these catalysts is that maximum activity was achieved in base-catalyzed reactions after evacuation pretreatment at 490 K.<sup>[28]</sup> Higher temperatures caused a rapid decline in catalytic activity.

Characterization of the lanthanide-loaded zeolites revealed some insights into the possible base sites involved in the catalysis. Infrared spectroscopy of the initial Yb-loaded zeolite Y before thermal treatment showed the presence of amide species.<sup>[28]</sup> The amide peaks in the IR spectrum decreased with evacuation temperature and nearly disappeared by 473 K, which is consistent with decomposition of the amide species. The x-ray absorption spectrum associated with the Yb  $L_2$  edge was also recorded for Yb-loaded zeolite

as a function of evacuation temperature.<sup>[28]</sup> The shape of the absorption edge was used to derive the relative amounts of  $Yb^{2+}$  and  $Yb^{3+}$  in the sample. Interestingly, the temperature at which the maximum in activity occurred for base catalysis (~490 K) almost coincided with the highest level of  $Yb^{2+}$  in the sample. Heating to higher temperatures increased the relative amount of  $Yb^{3+}$  compared with  $Yb^{2+}$ <sup>[28]</sup> and lowered the dispersion of Yb throughout the zeolite.<sup>[29]</sup> A reasonable model for the thermal evolution of these materials involves occluded amides  $(NH_2)_2$  and  $(NH_2)_3$  at low temperature, occluded imide NH at moderate temperature, and occluded nitrides at the highest temperature. The imide is the likely species responsible for base catalysis on these materials.

#### Mesoporous (Alumino)Silicates

The aluminosilicate form of MCM-41 is a mixed oxide that is templated with large surfactant molecules during synthesis to yield a solid with highly oriented, unidimensional mesopores in a nanometer size range that depends on the surfactant size.<sup>[30]</sup> Although the pores are packed in a regular hexagonal array, the local structure of the aluminosilicate wall is amorphous. A pure silica form of MCM-41 can also be synthesized. As discussed earlier, the charge imbalance because of the presence of  $Al^{3+}$  in a silicate framework requires extra framework cations for electrical neutrality. Alkali metal cations can be used to form a basic mesoporous solid, similar to a zeolite. Although the ion-exchanged MCM-41 materials are weakly basic, base strength can be improved by incorporation of occluded cesium in the mesopores by an impregnation method similar to that depicted in Fig. 2.

Kloetstra and van Bekkum<sup>[31]</sup> reported that Na-exchanged and Cs-exchanged MCM-41 are selective, water-stable, recyclable catalysts for the base-catalyzed Knoevenagel condensation of benzaldehyde and ethyl cyanoacetate. The same group also reported on the base catalysis of occluded Cs species in the pores of MCM-41 for the Michael addition of diethyl malonate to chalcone<sup>[31]</sup> and to neopentyl glycol diacrylate.<sup>[32]</sup> Results from TPD of adsorbed  $CO_2$  and catalytic activity for the Michael addition showed that basicity increased with occluded Cs loading. The researchers also noted an unfortunate problem with the stability of the support to repeated thermal cycles, presumably because of the formation of cesium silicate. However, the framework stability of the MCM-41 was observed to increase with increasing aluminum content. More recently, Kloetstra, Van Laren, and Van Bekkum<sup>[33]</sup> have added La to Cs-loaded MCM-41 materials and demonstrated their activity in both Knoevenagel condensation and Michael addition



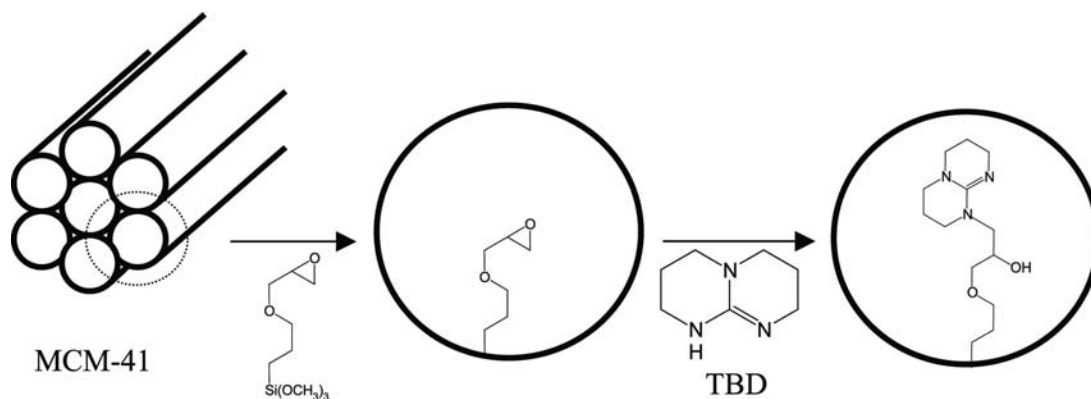


Fig. 4 Synthesis procedure for anchoring organic strong base in the pores of MCM-41 mesoporous silica.

reactions. The combined results from these studies revealed that the base sites formed by occlusion of basic compounds in the pores of MCM-41 are not significantly different than those formed on other amorphous (alumino)silicates. The major advantage of these catalysts appears to be the high surface area of the support oxide that is exposed in the mesopores. The large pores of MCM-41, compared with those of zeolite molecular sieves, permit the adsorption and reaction of relatively large molecules that are relevant to fine chemicals synthesis.

A unique approach to synthesizing stronger base sites in MCM-41 involves the immobilization of a strong organic base on the pore wall. For example, Rao, De Vos, and Jacobs<sup>[34]</sup> reported recently the synthesis and reactivity of a strong base catalyst in which a guanidine base is covalently coupled to the silicate wall of pure silica MCM-41. Their synthetic strategy is schematically illustrated in Fig. 4. The pore walls of MCM-41 were first treated with 3-(trimethoxysilyl)propyl oxirane to provide a reactive tether to the silica. Next, 1,5,7-triazabicyclo[4.4.0]dec-5-ene (TBD) was put in contact with the oxirane-derivatized MCM-41 to react with the NH group and to couple the strong base to the solid. The materials appeared to be much more effective solid base catalysts in Michael addition reactions than Cs-containing MCM-41 because milder reaction temperatures and shorter reaction times were used to achieve high product yield.

### Carbogenic Molecular Sieves

Carbogenic molecular sieves (CMS) formed by pyrolysis of a poly(furfural alcohol)–poly(ethylene glycol) mixture are chemically inert, nanoporous supports that can host Cs atoms to form strong base catalysts.<sup>[35]</sup> The nanopores are narrowly distributed about a mode of 0.5 nm. Stevens and Foley<sup>[35]</sup> prepared Cs/CMS material by a vapor-phase deposition method in which

Cs metal was heated together with CMS in vacuum. A unique feature of this material is its lack of pyrophoricity, which offers a strong advantage over cesium metal and graphite Cs compounds. Despite their non-pyrophoric nature, the Cs/CMS materials still reduce liquid water to produce H<sub>2</sub>. Results from magnetic susceptibility measurements and EPR spectroscopy indicate that a significant number of unpaired electrons resided in Cs/CMS. Interestingly, the value of the *g*-factor for Cs/CMS suggests that the electrons from Cs were actually donated to the carbon support.<sup>[36]</sup>

The Cs/CMS materials were shown to be active in a variety of base-catalyzed reactions, including those requiring strong basicity typically associated with alkali metals. For example, side-chain alkylation of toluene with propene was observed at 4 bar and temperatures ranging from 423 to 673 K.<sup>[37]</sup> In addition, benzene coupling to biphenyl was measured over these materials at 2 bar and 723 K.<sup>[36]</sup> The catalysts have also demonstrated catalytic activity in double-bond isomerization of 1-butene at temperatures as low as 298 K.<sup>[35]</sup> It is important to note that a second pore system, with a center of distribution at ~10 nm, was needed to facilitate the transport of reactant molecules to the active sites in the nanopores.<sup>[35]</sup> Catalysts without this “transport porosity” were not very active.

Stevens, Chen, and Foley<sup>[38]</sup> purposefully exposed Cs/CMS to air to create a highly dispersed alkali metal oxide or hydroxide in carbon nanopores. They discovered new peaks in x-ray diffraction pattern that were attributed to a crystalline form of cesium hydrous oxide, but the pattern did not match known cesium oxides or hydroxides. These materials were also tested as catalysts in the aldol condensation of acetone to isophorone. Compared with an analogous catalyst prepared by wet impregnation of CsOH solution, the oxidized Cs/CMS was more active and more selective to isophorone. Apparently, a higher dispersion of active material was achieved with the vapor deposition method followed by oxidation.

**Table 2** Turnover frequencies of 2-propanol and 1-butene reactions over MgO, thermally treated hydrotalcites, and Al<sub>2</sub>O<sub>3</sub><sup>a</sup>

Catalyst <sup>b</sup>	TOF of acetone formation <sup>c</sup> (10 <sup>-3</sup> sec <sup>-1</sup> )	TOF of propene formation <sup>c</sup> (10 <sup>-4</sup> sec <sup>-1</sup> )	TOF of 1-butene isomerization <sup>d</sup> (sec <sup>-1</sup> )
MgO	2.6	0.82	0.22
Mg:Al, 5:1	3.3	2.1	0.18
Mg:Al, 3:1	2.3	4.4	0.10
Mg:Al, 2:1	2.7	11.5	0.093
Al <sub>2</sub> O <sub>3</sub>	1.9	750	0.0071

<sup>a</sup>Turnover frequency is the rate of product formation divided by the number of surface sites counted by CO<sub>2</sub> adsorption.

<sup>b</sup>Calcined for 4 hr at 823 K in flowing He.

<sup>c</sup>2-Propanol decomposition temperature was 593 K.

<sup>d</sup>Reaction temperature was 340 K.

Source: From Ref.<sup>[45]</sup>.

## Hydrotalcite

Hydrotalcite is an anionic clay mineral with the structural formula Mg<sub>6</sub>Al<sub>2</sub>(OH)<sub>16</sub>(CO<sub>3</sub>) · 4H<sub>2</sub>O.<sup>[39]</sup> The structure consists of brucite-like layers (Mg(OH)<sub>2</sub>) that are positively charged because of the partial substitution of Al<sup>3+</sup> for Mg<sup>2+</sup>. To balance the positive layer charge, carbonate anions are located in the interlayer spaces, together with waters of hydration. The synthetic form of hydrotalcite can be prepared with a variable Al content and a variety of charge-compensating anions.<sup>[40]</sup> An interesting feature of hydrotalcite for base catalysis is the nature of the solid after thermal treatment. Reichle, Kang, and Everhardt<sup>[41]</sup> reported that heating hydrotalcite to about 723 K caused the loss of interlayer water and carbon dioxide, as well as dehydroxylation of the brucite-type layers. However, this thermal treatment neither changed crystal morphology, nor caused exfoliation of the layered structure. A large increase in surface area with heating was a result of the creation of small pores (2–4 nm radius) perpendicular to the crystal surface. Additionally, Rey, Fornes, and Rojo<sup>[42]</sup> reported that thermal treatment of hydrotalcite creates a substantial number of micropores with radius smaller than 1.75 nm.

Thermally-treated hydrotalcite is known to be active in a variety of base-catalyzed reactions.<sup>[39,43,44]</sup> The compositional variability that hydrotalcites afford suggests that these solid base catalysts can be “tuned” by direct synthesis methods. For example, Fishel and Davis<sup>[45]</sup> studied the reactions of 2-propanol and 1-butene over thermally activated hydrotalcites having different amounts of Al in the structure. Table 2 summarizes the turnover frequencies (TOFs), or rates of product formation normalized by the number of surface sites, for the various reactions. Because the TOFs were based on the adsorption capacity of carbon dioxide, the TOF of a structure-insensitive base-catalyzed reaction should be relatively constant at a given temperature and pressure. Indeed, the invariance of

the TOF for acetone formation from 2-propanol over MgO, Mg:Al mixed oxides (from thermal treatment of hydrotalcite) and Al<sub>2</sub>O<sub>3</sub> supports the idea of structure insensitivity. In contrast to the dehydrogenation results, the turnover rate for 2-propanol dehydration increased by three orders of magnitude as the catalyst was changed from magnesia to alumina. Apparently, the surface sites counted by CO<sub>2</sub> adsorption did not function equally well for alcohol dehydration. This trend is expected because dehydration is usually considered an acid-catalyzed reaction. In addition, the mechanism for secondary alcohol dehydration over basic oxides differs from that over alumina. It is of interest to note that the TOF of base-catalyzed isomerization of 1-butene (Table 2) was also a strong function of composition, with magnesia being the most active. As discussed earlier, adsorption of CO<sub>2</sub> does not provide an accurate measure of the active base sites for olefin isomerization. Nevertheless, the results in Table 2 clearly show the adjustability of catalytically active surfaces on thermally treated hydrotalcites.

## CONCLUSION

In a recent review of industrial processes catalyzed by solid acids and bases, Tanabe and Holderich<sup>[2]</sup> showed that commercial base catalysts consist mainly of alkali metal and alkaline earth metal oxides, hydroxides, and carbonates in bulk form, or supported on a common carrier such as alumina. In several cases, alkali metals are also supported on a basic carrier.

The porous nanostructure of zeolites, MCM-41, and CMS provides a unique, shape-selective reaction environment in which novel base catalysts can be prepared. Recently, Merck and Co. created a pilot plant scale process to synthesize 4-methyl thiazol using a catalyst composed of cesium sulfate impregnated into ZSM-5 zeolite.<sup>[46]</sup> As research progresses on basic species located on nanostructured supports, additional

base-catalyzed commercial processes that utilize these advanced materials will appear.

The compositional variability of hydrotalcites offers a tremendous opportunity to adjust the acid–base properties of Mg:Al mixed oxide surfaces for base catalysis. Indeed, Henkel KGaA developed a new heterogeneous catalyst, formed by roasting synthetic hydrotalcite at 773 K, for the production of narrow molecular weight distribution ethoxylates from etherification of ethylene oxide in the presence of fatty alcohols.<sup>[2]</sup> The presence of both acid and base sites on the materials introduces the concept of acid–base bifunctional catalysis, which is beyond the scope of this entry.

For additional information on base catalysis, the reader is referred to Refs.<sup>[47–50]</sup>.

## ACKNOWLEDGMENTS

This work was supported by the Department of Energy—Basic Energy Sciences (DEFG02-95ER14549).

## REFERENCES

- Schofield, H.; Dwyer, J. Historical Perspectives of Acidity and Basicity: Part 1. 4000 B.C.–1800 A.D.. In *Acidity and Basicity of Solids, Theory, Assessment and Utility*; Fraissard, J., Petrakis, L., Eds.; Kluwer: Dordrecht, 1994; 1–12.
- Tanabe, K.; Holderich, W.F. Industrial application of solid acid–base catalysts. *Appl. Catal., A Gen.* **1999**, *181* (2), 399–434.
- Sanderson, R. *Chemical Bonds and Bond Energy*; Academic Press: New York, 1976; 218.
- Lavalley, J.C. Infrared spectrometric studies of the surface basicity of metal oxides and zeolites using adsorbed probe molecules. *Catal. Today* **1996**, *27*, 377–401.
- Doskocil, E.J.; Bordawekar, S.V.; Davis, R.J. Alkali–support interactions on rubidium base catalysts determined by XANES, EXAFS, CO<sub>2</sub> adsorption, and IR spectroscopy. *J. Catal.* **1997**, *169*, 327–337.
- Bordawekar, S.V.; Doskocil, E.J.; Davis, R.J. Microcalorimetric study of CO<sub>2</sub> and NH<sub>3</sub> adsorption on Rb- and Sr-modified catalyst supports. *Langmuir* **1998**, *14*, 1734–1738.
- Barthomeuf, D. Basic zeolites: Characterization and uses in adsorption and catalysis. *Catal. Rev., Sci. Eng.* **1996**, *38*, 521–612.
- Bordawekar, S.V.; Davis, R.J. Probing the basic character of alkali-modified zeolites by CO<sub>2</sub> adsorption microcalorimetry, butene isomerization, and toluene alkylation with ethylene. *J. Catal.* **2000**, *189*, 79–90.
- Li, J.; Davis, R.J. On the use of 1-butene double bond isomerization as a probe reaction on cesium-loaded zeolite X. *Appl. Catal., A Gen.* **2003**, *239*, 59–70.
- Kim, J.C.; Li, H.-X.; Chen, C.-Y.; Davis, M.E. Base catalysis by intrazeolitic cesium oxides. *Microporous Mater.* **1994**, *2*, 413–423.
- Tsuji, H.; Yagi, F.; Hattori, H. Basic sites on alkali ion-added zeolite. *Chem. Lett.* **1991**, 1881–1884.
- Yagi, F.; Tsuji, H.; Hattori, H. IR and TPD (temperature-programmed desorption) studies of carbon dioxide on basic site active for 1-butene isomerization on alkali-added zeolite X. *Microporous Mater.* **1997**, *9*, 237–245.
- Lasperas, M.; Cambon, H.; Brunel, D.; Rodriguez, I.; Geneste, P. Characterization of basicity in alkaline cesium-exchanged X zeolites post-synthetically modified by impregnation: A TPD study using carbon dioxide as a probe molecule. *Microporous Mater.* **1993**, *1*, 343–351.
- Lasperas, M.; Cambon, H.; Brunel, D.; Rodriguez, I.; Geneste, P. Cesium oxide encapsulation in faujasite zeolites effect of framework composition on the nature and basicity of intrazeolitic species. *Microporous Mater.* **1996**, *7*, 61–72.
- Doskocil, E.J.; Davis, R.J. Spectroscopic characterization and catalytic activity of zeolite X containing occluded alkali species. *J. Catal.* **1999**, *188*, 353–364.
- Hunger, M.; Schenk, U.; Burger, B.; Weitkamp, J. Synergism between guest compound and the host framework in zeolite CsNaY after impregnation with cesium hydroxide. *Angew. Chem., Int. Ed. Engl.* **1997**, *36* (22), 2504–2506.
- Yagi, F.; Kanuka, N.; Tsuji, H.; Nakata, S.; Kita, H.; Hattori, H. <sup>133</sup>Cs and <sup>23</sup>Na MAS NMR studies of zeolite X containing cesium. *Microporous Mater.* **1997**, *9*, 229–235.
- Krawietz, T.R.; Murray, D.K.; Haw, J.F. Alkali metal oxides, peroxides, and superoxides: A multinuclear MAS NMR study. *J. Phys. Chem., A* **1998**, *102*, 8779–8785.
- Yagi, F.; Hattori, H. Oxygen exchange between adsorbed oxygen and cesium-added zeolite X. *Microporous Mater.* **1997**, *9*, 247–251.
- Hathaway, P.E.; Davis, M.E. Base catalysis by alkali-modified zeolites: I. Catalytic activity. *J. Catal.* **1989**, *116*, 263–278.
- Tu, M.; Davis, R.J. Cycloaddition of CO<sub>2</sub> to epoxides over solid base catalysts. *J. Catal.* **2001**, *199*, 85–91.
- Martens, L.R.M.; Grobet, P.J.; Jacobs, P.A. Preparation and catalytic properties of ionic sodium clusters in zeolites. *Nature* **1985**, *315*, 568–570.
- Martens, L.R.M.; Grobet, P.J.; Vermeiren, W.J.M.; Jacobs, P.A. Sodium clusters in zeolites as active sites for carbanion catalyzed reactions. *Stud. Surf. Sci. Catal.* **1986**, *28*, 935–941.
- Martens, L.R.M.; Vermeiren, W.J.M.; Grobet, P.J.; Jacobs, P.A. Parameters influencing the preparation and characterization of sodium on zeolite catalysts. *Stud. Surf. Sci. Catal.* **1987**, *31*, 531–542.
- Martens, L.R.M.; Vermeiren, W.J.M.; Huybrechts, D.R.; Grobet, P.J.; Jacobs, P.A. Sodium Clusters in Large Pore Zeolites as Basic Catalysts. In *Proceedings of the 9th International Congress on Catalysis*; Phillips, M.J., Ternan, M., Eds.; Chem. Institute of Canada: Ottawa, 1988; 1, 420–428.

26. Xu, B.; Kevan, L. Formation of alkali-metal particles in alkali-metal cation exchanged X-zeolite exposed to alkali-metal vapor—Control of metal-particle identity. *J. Phys. Chem.* **1992**, *96*, 2642–2645.
27. Baba, T.; Kim, G.J.; Ono, Y. Catalytic properties of low-valent lanthanide species introduced into Y-zeolite. *J. Chem. Soc., Faraday Trans.* **1992**, *88*, 891–897.
28. Baba, T.; Hikita, S.; Kolde, R.; Ono, Y.; Hanada, T.; Tanaka, T.; Yoshida, S. Physico-chemical and catalytic properties of ytterbium introduced into Y-zeolite. *J. Chem. Soc., Faraday Trans.* **1993**, *89*, 3177–3180.
29. Yoshida, T.; Tanaka, T.; Yoshida, S.; Hikita, S.; Baba, T.; Ono, Y. EXAFS study of Yb species encapsulated in Y-type zeolite. *Solid State Commun.* **2000**, *114*, 255–259.
30. Beck, J.S.; Vartuli, J.C.; Roth, W.J.; Leonowicz, M.E.; Kresge, C.T.; Schmidt, K.D.; Chu, C.T.-W.; Olson, D.H.; Sheppard, E.W.; McCullen, S.B.; Higgins, J.B.; Schlenker, J.L. A new family of mesoporous molecular-sieves prepared with liquid-crystal templates. *J. Am. Chem. Soc.* **1992**, *114*, 10834–10843.
31. Kloetstra, K.R.; van Bekkum, H. Base and acid catalysis by the alkali-containing MCM-41 mesoporous molecular sieve. *J. Chem. Soc., Chem. Commun.* **1995**, 1005–1006.
32. Kloetstra, K.R.; van Bekkum, H. Solid mesoporous base catalysts comprising of MCM-41 supported intraporous cesium oxide. *Stud. Surf. Sci. Catal.* **1997**, *105*, 431–438.
33. Kloetstra, K.R.; van Laren, M.; van Bekkum, H. Binary caesium-lanthanum oxide supported on MCM-41: A new stable heterogeneous basic catalyst. *J. Chem. Soc., Faraday Trans.* **1997**, *93*, 1211–1220.
34. Rao, Y.V.S.; De Vos, D.E.; Jacobs, P.A. 1,5,7-Triazabicyclo[4.4.0]dec-5-ene immobilized in MCM-41: A strongly basic porous catalyst. *Angew. Chem., Int. Ed. Engl.* **1997**, *36*, 2661–2663.
35. Stevens, M.G.; Foley, H.C. Alkali metals on nanoporous carbon: New solid-base catalysts. *Chem. Commun.* **1997**, 519–520.
36. Stevens, M.G.; Sellers, K.M.; Subramoney, S.; Foley, H.C. Catalytic benzene coupling on caesium/nanoporous carbon catalysts. *Chem. Commun.* **1998**, 2679–2680.
37. Stevens, M.G.; Anderson, M.R.; Foley, H.C. Side-chain alkylation of toluene with propene on caesium/nanoporous carbon catalysts. *Chem. Commun.* **1999**, 413–414.
38. Stevens, M.G.; Chen, D.; Foley, H.C. Oxidized caesium/nanoporous carbon materials: Solid base catalysts with highly-dispersed active sites. *Chem. Commun.* **1999**, 275–276.
39. Cavani, F.; Trifiro, F.; Vaccari, A. Hydrotalcite-type anionic clays: Preparation, properties and applications. *Catal. Today* **1991**, *11*, 173–301.
40. Miyata, S. Physico-chemical properties of synthetic hydrotalcites in relation to composition. *Clays Clay Miner.* **1980**, *28*, 50–56.
41. Reichle, W.T.; Kang, S.Y.; Everhardt, D.S. The nature of the thermal decomposition of a catalytically active anionic clay mineral. *J. Catal.* **1986**, *101*, 352–359.
42. Rey, F.; Fornes, V.; Rojo, J.M. Thermal decomposition of hydrotalcites. *J. Chem. Soc., Faraday Trans.* **1992**, *88*, 2233–2238.
43. Reichle, W.T. Catalytic reactions by thermally activated, synthetic, anionic clay minerals. *J. Catal.* **1985**, *94*, 547–557.
44. Sels, B.F.; De Vos, D.E.; Jacobs, P.A. Hydrotalcite-like anionic clays in catalytic organic reactions. *Catal. Rev.* **2001**, *43*, 443–488.
45. Fishel, C.T.; Davis, R.J. Use of catalytic reactions to probe Mg–Al mixed oxide surfaces. *Catal. Lett.* **1994**, *25*, 87–95.
46. Dartt, C.B.; Davis, M.E. Applications of zeolites to fine chemicals synthesis. *Catal. Today* **1994**, *19*, 151–186.
47. Hattori, H. Heterogeneous basic catalysts. *Chem. Rev.* **1995**, *95*, 537–558.
48. Ono, Y.; Baba, T. Selective reactions over solid base catalysts. *Catal. Today* **1997**, *38*, 321–337.
49. Hattori, H. Solid base catalysts: Generation of basic sites and application to organic synthesis. *Appl. Catal., A Gen.* **2001**, *222*, 247–259.
50. Weitkamp, J.; Hunger, M.; Ryma, U. Base catalysis on microporous and mesoporous materials: Recent progress and perspectives. *Microporous Mater.* **2001**, *48*, 255–270.

# Bimetallic Layered Nanocomposites

Amit Misra

Richard G. Hoagland

*Materials Science and Technology Division, Los Alamos National Laboratory,  
Los Alamos, New Mexico, U.S.A.*

## INTRODUCTION

Bimetallic layered nanocomposites, composed of alternating layers of soft metals, are shown to possess ultrahigh yield strengths, often approaching the theoretical limits defined for perfect crystals. For example, nanolayered composites made from ordinary soft metals such as Cu, Ni, Nb, etc. each with strength on the order of a few tens of MPa in the bulk can achieve strengths in excess of 2–3 GPa. More importantly, the conventional descriptions relating mechanical properties to the microstructural dimensions do not extrapolate to nanometer dimensions. The mechanisms that determine strength and failure limits of nanoscale materials lie within new realms of behavior. This overview starts with a description of the synthesis methods and the microstructures of bimetallic layered nanocomposites. The layer thickness dependence of the yield strengths of the nanocomposites, in the length scale range of submicrometer to  $\sim 1$  nm, is shown for a variety of material systems. Different functional dependences of layer thickness on strength are interpreted using dislocation models of strengthening. Dislocation pileup based Hall–Petch (H–P) model is applicable at submicrometer to a few tens of nanometer length scales. At smaller thicknesses, confined layer slip (CLS) of single dislocations provides the strength increase with decreasing layer thickness. A peak in strength is usually achieved at layer thickness of around 2–5 nm. This peak is determined by the stress needed for single-dislocation transmission across interfaces. Atomistic modeling results that explore the slip transmission stress for unit dislocations across coherent and incoherent interfaces are described. We show that the mechanical properties of bimetallic layered composites can be tailored via length scales as well as interface properties.

## BACKGROUND

The ability to refine the microstructural length scales, such as grain size, twin spacing, or interphase spacing,

of materials creates opportunities to develop ultrahigh strength materials without suffering a corresponding loss in toughness.<sup>[1]</sup> Nanoscale design may allow the synthesis of materials with strengths approaching the theoretical limit. Although the theoretical strength limit may be determined in various ways, the theoretical shear strength for perfect crystals is estimated to be in the range of  $\mu/2\pi$  to  $\mu/30$ , where  $\mu$  is the shear modulus.<sup>[2]</sup> For many metals, this theoretical limit corresponds to stresses of 1–5 GPa. In contrast, the experimentally measured critical resolved shear strengths are about 5–50 MPa for pure, single crystal metals. This huge difference arises from the fact that perfect crystals contain no dislocations, the defects that transmit slip at very low applied stresses in typical metals.<sup>[2]</sup> Indeed, yield strengths in excess of 1 GPa have been observed in carefully synthesized metallic whiskers that are near-perfect crystals with no glide dislocations.<sup>[3]</sup> However, the initial yield of such whiskers is followed by catastrophic nucleation of many glide dislocations resulting in large drops in the stress needed to sustain plastic flow. Furthermore, whiskers have severe limitations with regard to the shapes and sizes that can be synthesized. Therefore, the traditional approaches to strengthen metals, have involved methods that impede the motion of dislocations by means of obstacles such as grain or phase boundaries, rather than attempting to produce dislocation-free materials. Grain size refinement to the micrometer range by thermomechanical treatments is effective in increasing the strength of typical metals above 100 MPa. Further increases in strength, of pure metals at room temperature, are achievable by reducing grain dimensions to the 100 nm ranges by severe plastic deformation (SPD) approaches such as equal-channel angular pressing or high-pressure torsion. Such methods are capable of producing high purity metals with yield strengths of several hundred MPa,<sup>[4,5]</sup> but microstructures with a uniform grain size in the nanometer range has not yet been achieved by SPD methods. For a discussion of mechanical properties of three-dimensional structural nanomaterials the reader is directed to another review entry of this Encyclopedia.<sup>[6]</sup>

Bimetallic layered nanocomposites, produced by deposition methods (described in the following section), serve as good model systems to investigate the mechanical behavior of metallic materials where the layer dimension can be refined, in a well-controlled manner, from hundreds of nanometers down to below 1 nm. The synthesis methods, microstructures and mechanical properties of this class of nanocomposites are reviewed in this article, with emphasis on correlating mechanical behavior with bimetallic interface properties and layer thickness.

## SYNTHESIS AND MICROSTRUCTURES

There are two commonly used synthesis methods that are discussed here. First, is a “top down” approach involving SPD of bulk sheets.<sup>[7–9]</sup> The starting materials are tens or hundreds of micrometers thick individual metal sheets that are alternately stacked and subjected to repeated hot pressing–cold rolling–annealing cycles to produce bulk nanolaminate sheets. A typical processing cycle employed for Fe/Ag multilayers<sup>[7,8]</sup> is described below. Hundred sheets (13 mm × 18 mm) each of 50 μm thick Fe and 30 μm thick Ag were stacked together and pressed in a controlled temperature and atmosphere to bond the metal sheets. The bonded stacked was then rolled in ambient atmosphere to reduce the thickness of the layers. The rolled sheets were then annealed at 873 K to reduce the hardness, while maintaining the layered microstructure, before the next pressing–rolling cycle. After the second pressing–rolling step, the average Ag layer thickness was 20 nm. Since annealing after cold rolling leads to some coarsening, an alternate procedure eliminating the annealing step, results in an average Ag layer thickness of 4 nm. Similar results were obtained for Fe–Cu<sup>[8]</sup> and Cu–Al<sup>[9]</sup> multilayers as well. This press–rolling synthesis approach could effectively reduce the metal layer thickness from tens of micrometers to a few nanometers (a factor of 10<sup>4</sup>), although the resulting nanolaminates do not have very uniform interlamellar spacing.

Deposition methods, either electrodeposition or physical vapor deposition (PVD) such as magnetron sputtering or electron-beam evaporation, are more commonly used to synthesize bimetallic layered nanocomposites. These “bottom-up” synthesis methods offer several advantages. First, any two (or more) metals (or ceramics) can be alternately deposited to produce a layered composite. Second, the individual layer thicknesses can be controlled to within an atomic layer (unlike many techniques that produce a distribution in grain sizes). Third, the products have high purity, and are porosity free. Fourth, self-supported samples with total thicknesses of tens of micrometers,

or more, are readily synthesized so that a variety of nanomechanical characterization may be performed such as nanoindentation, microtensile testing, and large strain deformation via cold rolling.

Electrodeposition synthesis of nanolaminates is accomplished by using an electrolyte from which two different metals can be deposited by varying the applied voltage.<sup>[10–12]</sup> For example, Cu–Ni nanolaminates with a total foil thickness of 50 μm and individual layer thickness down to ~1 nm are electrodeposited from a nickel sulfamate bath containing Cu.<sup>[11]</sup> The constraint of finding an electrolyte from which two different metals can be electrodeposited limits the number of nanolaminate systems that can be synthesized by electrodeposition.

Magnetron sputtering, ion-beam sputtering, and electron-beam evaporation are widely used to synthesize nanolaminates.<sup>[13–16]</sup> To synthesize a multilayered film, shutters are alternated, typically through a computer-controlled stepper motor, between two different sputtering targets or e-beam melted sources. In another design, the sample stage can be rotated to alternately face the two (or more) sputtering targets for sequential deposition of the individual layers that make up the multilayer stack. The typical deposition rates vary from 2 to 20 Å/sec. Thousands of bilayers can be easily deposited to produce samples with total thickness >10 μm in a few hours. To sputter metal nitride layers, reactive sputtering is used in an Ar/N<sub>2</sub> gas mixture while sputtering from the metal target. For sputtering of insulating materials, rf power instead of dc is applied to the target. In both evaporation and sputtering, the substrate can be either heated or cooled. Often elevated temperature deposition, at least of the seed layer, is needed to produce single crystal growth of deposited layers. Energetic particle bombardment of the growing film, at any temperature, provides an additional way to control the density, residual stress, and texture of the films. A separate ion-gun added in the evaporator can be used to bombard the growing film (ion-beam assisted deposition). For sputtering, a negative dc bias can be applied to the substrate (which is otherwise kept at ground potential) to induce Ar<sup>+</sup> bombardment of the growing film. Both sputtering<sup>[17]</sup> and evaporation<sup>[18,19]</sup> techniques have been used to prepare nanolaminates with total thicknesses of several hundred micrometers.

Typical microstructures of bimetallic layered composites synthesized via sputter deposition techniques are shown in Figs. 1 and 2. Using shadow masks during sputtering allows the synthesis of self-supported dog-bone shaped tensile samples (Fig. 1A) that are more than 10 μm thick but consist of thousands of nanometer thick alternating layers of the two constituent metals. An example of 1 nm thick Cu/Nb multilayer is shown in Fig. 1B. Room temperature



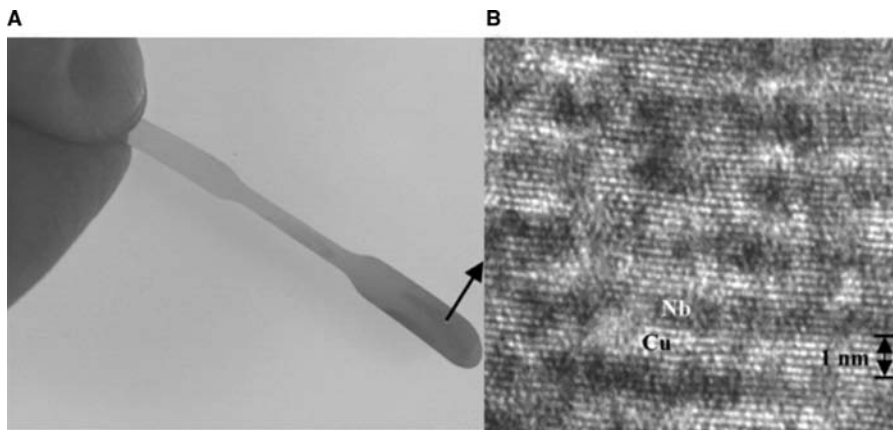


**Fig. 1** (A) Photograph of a 20  $\mu\text{m}$  thick sputter-deposited tensile sample of a Cu–Nb multilayer; (B) high-resolution TEM image showing the internal nanostructure of the bulk tensile sample, consisting of alternating 1 nm thick Cu and Nb layers.

deposition on substrates such as Si with an oxide layer typically produces a textured, nanocrystalline structure within the layers. An example of such a polycrystalline microstructure is shown in Fig. 2A for a 75 nm thick Cu/Nb multilayer, with the corresponding selected area diffraction pattern shown in Fig. 2B. For fcc/bcc systems such as Cu/Nb, the crystal of one layer is oriented relative to the adjacent layers by the Kurdjumov–Sachs orientation relationship:  $\{110\}\text{Nb} // \{111\}\text{Cu}$ ,  $\langle 111 \rangle \text{Nb} // \langle 110 \rangle \text{Cu}$ ,<sup>[20]</sup> and the interface plane is  $\{110\}\text{Nb} // \{111\}\text{Cu}$ . Elevated temperature deposition or room temperature deposition on carefully cleaned substrates such as HF etched Si is typically needed to produce single crystalline multilayer structures.<sup>[14,15,21–23]</sup>

### LAYER THICKNESS DEPENDENCE OF STRENGTH

The general trends in the dependence of strength on: 1) microstructural length scales; and 2) the physical properties of the constituents layers may be discerned

by studying a variety of model multilayered systems. Table 1 lists the systems investigated by the authors' team that largely form the basis of the following discussion. In all these multilayers, the individual layer thicknesses of the two constituents were equal. Thus, the mechanical behavior could be interpreted in terms of a single length scale: layer thickness ( $h$ ) that is one-half of the bilayer period. Note that two categories, fcc/fcc and fcc/bcc, of material systems are studied. For each category, systems were selected so as to cover a wide range of elastic moduli and lattice parameter mismatches.

Hardness, based on nanoindentation measurements, of the systems listed in Table 1 is shown in Fig 3. For all systems, hardness scales linearly with  $1/\sqrt{h}$  for  $h > \sim 50$  nm. This observation is consistent with slip involving groups of dislocations such as the dislocation pileup on which the H–P model<sup>[24]</sup> is based. Such pileups possess a mechanical advantage in which the stress available to transmit slip through a barrier is equal to the applied stress times the number of dislocations in the pileup. Equivalently, the  $1/\sqrt{h}$  dependence is clearly an indication that the stress near the head of

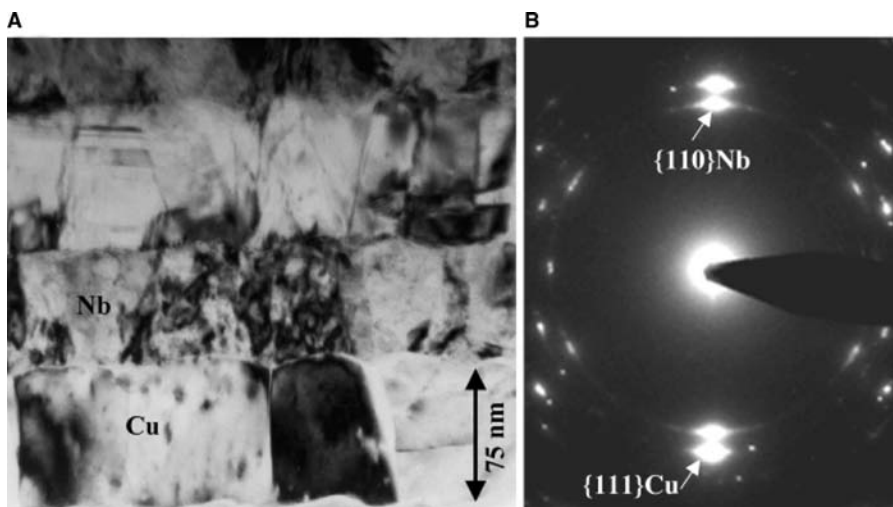


**Fig. 2** (A) Bright field TEM image and (B) corresponding selected area diffraction pattern of a 75 nm layer thickness Cu–Nb multilayer. Note the polycrystalline,  $\{110\}\text{Nb} // \{111\}\text{Cu}$  textured microstructure.

**Table 1** Summary of the multilayered systems for which mechanical properties are reported in Fig. 3

System (production method)	Crystal structure	Orientation relationship	Modulus ratio <sup>a</sup> , $E_X/E_{Cu}$	Lattice mismatch <sup>b</sup> (%)
Cu–Ag (evaporation)	fcc/fcc	$\langle 111 \rangle$ texture	0.64	12.1
Cu–Ni (evaporation)	fcc/fcc	$\langle 100 \rangle$ single crystalline	1.54	2.66
Cu–330SS (sputtering) <sup>c</sup>	fcc/fcc	$\langle 111 \rangle$ texture	1.51	0.92
Cu–Nb (sputtering)	fcc/bcc	Kurdjumov–Sachs <sup>d</sup>	0.80	11.1
Cu–Cr (sputtering)	fcc/bcc	Kurdjumov–Sachs	2.15	2.33
Cu–304SS (sputtering)	fcc/bcc	Kurdjumov–Sachs	1.5	2.9

<sup>a</sup>Ratio of the Young's modulus of the second phase to the modulus of Cu.

<sup>b</sup>Lattice mismatch =  $(d_1 - d_2)/\{(d_1 + d_2)/2\}$  where  $d_1$  and  $d_2$  are the spacings of planes forming the interface.

<sup>c</sup>330SS and 304SS are austenitic stainless steels 330 and 304 respectively; 304SS adopts a bcc structure when sputter deposited.

<sup>d</sup> $\{110\}bcc//\{111\}fcc$ ;  $\langle 111 \rangle bcc//\langle 110 \rangle fcc$ .

the pileup is proportional to the square root of the length of the pileup, a result that holds as long as there are many dislocations in the pileup. For smaller layer thicknesses (typically,  $h < \sim 50$  nm), the pileups contain too few dislocations for this scaling law to be applicable and critical slip events involve a very few or single dislocations. From Fig. 3, as the layer thickness is reduced below the H–P range, three kinds of functional dependence of hardness on  $h$  are observed: 1) at  $5 \text{ nm} < h < 50 \text{ nm}$  range, hardness increases with decreasing  $h$  but more slowly than  $1/\sqrt{h}$  scaling; 2) a peak in hardness is reached when  $h$  is on the order of 2 nm; and 3) at  $h < 2$  nm, some systems exhibit a small drop in hardness. The maximum strength achieved in all these systems, estimated from hardness divided by a factor of 3, are typically greater than 10 times the rule-of-mixtures estimates based on bulk properties.<sup>a</sup> In addition to establishing the functional dependence of strength on length scale, Fig. 3 also allows comparison of strengths of different systems at equal layer thicknesses. Such comparisons reveal significant differences in the maximum achievable strengths. These differences are elucidated in the molecular dynamics (MD) simulations described later.

The data shown in Fig. 3 are summarized in Table 2 along with information on other metallic multilayers.<sup>[26–38]</sup> The data compiled in Table 2 show that the peak strength for most systems is typically on the order of 1.5–2.5 GPa. When expressed as a fraction of the Young's modulus of the composite ( $E_c$ ), the peak strength is typically within a factor of 2–4 of a

lower-bound estimate of the theoretical strength of perfect crystals ( $\sim E_c/25$ ). For systems where data are available at larger bilayer periods where H–P behavior is observed, the H–P slope is calculated and shown in Table 2. For a given type of material systems, e.g., polycrystalline fcc-fcc such as Ag–Cu, Cu–Ni, and Cu–SS330, note that the H–P slope increases with  $E_c$ . Similar trend is observed in polycrystalline fcc-bcc systems (Cu–Nb, Cu–Cr, and Pt–Fe). A high H–P slope indicates a strong resistance of interfaces to transmission of piled-up dislocations. For a given layer thickness, material systems with a higher H–P slope have higher strength. The intrinsic resistance of interfaces to slip transmission is discussed in the section on atomistic modeling.

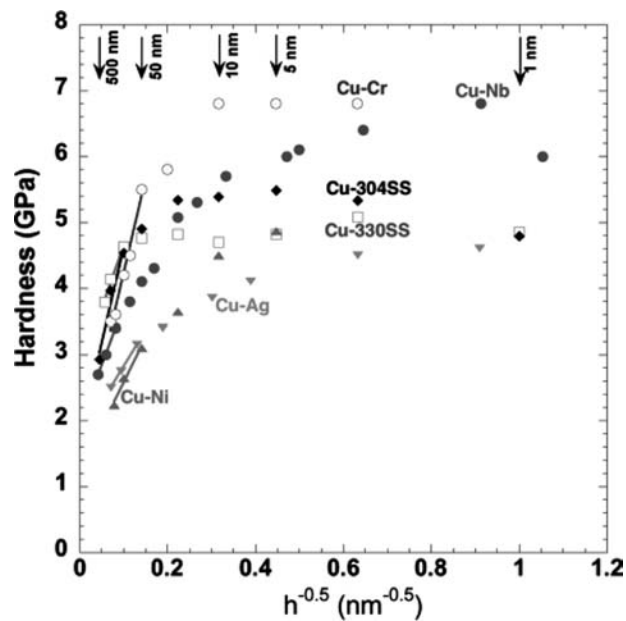


**Fig. 3** Nanoindentation measured hardness of a variety of Cu-based multilayers. Linear fit to the hardness vs.  $1/\sqrt{h}$  data, at  $h > \sim 50$  nm, is consistent with Hall–Petch model.

<sup>a</sup>The ratio,  $H/\sigma_y \sim 3$ , is a commonly used rule-of-thumb relating hardness ( $H$ ) to strength ( $\sigma_y$ ). For Cu–Nb we measured tensile strengths of  $\sim 1.1$  and  $\sim 1.4$  GPa for  $h = 75 \text{ nm}$ <sup>[25]</sup> and  $h = 40 \text{ nm}$ , respectively. The corresponding hardness of these composites were  $3.6 \pm 0.2$  and  $4 \pm 0.2$  GPa, respectively, consistent with the factor of 3 rule. We do not, however, espouse the universality of this rule as systems with very weak interfaces may exhibit a significantly different ratio.

**Table 2** Mechanical properties of bimetallic layered nanocomposites

Multilayer system	$\sigma_{\max}$ (GPa)	$h$ (nm) at $\sigma_{\max}$	$\sigma_{\max}$ as a fraction of $E_c$	H-P slope (MPa $\sqrt{m}$ )	Reference
fcc-fcc					
Cu–Ni	1.6	5	$E_c/100$	0.14 0.10 <sup>a</sup>	[21,26] [1,27]
Ag–Cu	1.5	1.2	$E_c/70$	0.11 0.11 <sup>a</sup>	[28] [29]
Au–Ni	2.1	1–2	$E_c/70$	nr	[30]
Ag–Ni	2.08	5	$E_c/70$	nr	[31,32]
Cu–SS330	1.7	5	$E_c/100$	0.204	[33]
Al–Al <sub>3</sub> Sc <sup>b</sup>	1	1.5 (Al <sub>3</sub> Sc); 50 (Al)	$E_c/75$	nr	[34]
fcc-bcc					
Ag–Cr	1.63	2.5	$E_c/100$	nr	[35]
Cu–Nb	2.2	2.5	$E_c/55$	0.18	[26,36]
Cu–Cr	2.3	2.5–10	$E_c/80$	0.30	[26,36]
Pt–Fe	3.2	2	$E_c/65$	0.23	[35]
Cu–304SS	1.8	5	$E_c/95$	0.30	[37]
bcc-bcc					
Fe–Cr (sc)	2.8	2	$E_c/80$	nr	[35]
Mo–W	6.5	5	$E_c/55$	nr	[38]

$\sigma_{\max}$  is the maximum strength for that system estimated from nanoindentation measured hardness divided by a factor of 3.

$E_c$  is the rule-of-mixtures Young's modulus for the multilayer.

H–P slope refers to the Hall–Petch slope obtained from data where hardness scales with  $h^{-0.5}$ . nr (not reported).

<sup>a</sup>Slope from tensile data.

<sup>b</sup>Al<sub>3</sub>Sc is fcc-based ordered L1<sub>2</sub> structure.

## SINGLE-DISLOCATION-BASED DEFORMATION MECHANISMS

As discussed above, at nanometer length scales when the dislocation pileup based mechanisms do not apply, three kinds of functional dependence of strength on layer thickness are observed: 1) strength increase with decreasing layer thickness; 2) a strength maximum independent of layer thickness; and 3) a drop in strength with decreasing layer thickness. The single-dislocation-based mechanisms that give rise to these behaviors are discussed below.

### Confined Layer Slip

Strength increase with decreasing layer thickness at length scales where dislocation pileups do not form is interpreted in terms of the confined layer slip mechanism that involves propagation of single-dislocation loops parallel to the interfaces.<sup>[36,39–45]</sup> For macroscopic yielding of the composite, both metallic layers must co-deform by CLS of Orowan loops, as shown in Fig. 4A. An example of CLS is the formation of misfit dislocations during coherency loss of very thin

epitaxial Ni layers on a thick Cu under layer. The misfit dislocation formation mechanism is the glide of existing threading dislocations, confined to the Ni layer. As a glide loop propagates, it deposits an interface dislocation in the Ni/Cu bilayer.<sup>[44]</sup> Such CLS was inferred from TEM studies<sup>[46]</sup> for Ni layer thickness  $\geq 3$  nm, while at lower thicknesses Ni was coherently matched with Cu. Glide on four  $\{111\}$  planes in the Ni layer produces two orthogonal sets of misfit dislocations at the  $\{001\}$  Ni–Cu interface [Fig. 4B]. The stress needed to glide a dislocation in the configuration shown in Fig. 4A depends on the self-energy of the deposited interface dislocations, and hence, for CLS, strength scales with layer thickness as:  $\sigma_{ys} \propto h^{-1} \ln(h)$ . An implication of this relation is that strength will continue increasing with decreasing  $h$ , but experimental results (Fig. 3) suggest that all multilayer systems exhibit a maximum strength at layer thickness on the order of 1–2 nm. At the very smallest  $h$ , the CLS stress exceeds the critical stress for dislocation transmission across the interface. Hence, dislocations cannot propagate as loops confined to individual layers, rather a dislocation loop must be transmitted across the interface first before it can spread in a direction parallel to the interfaces. The stress to transmit a single

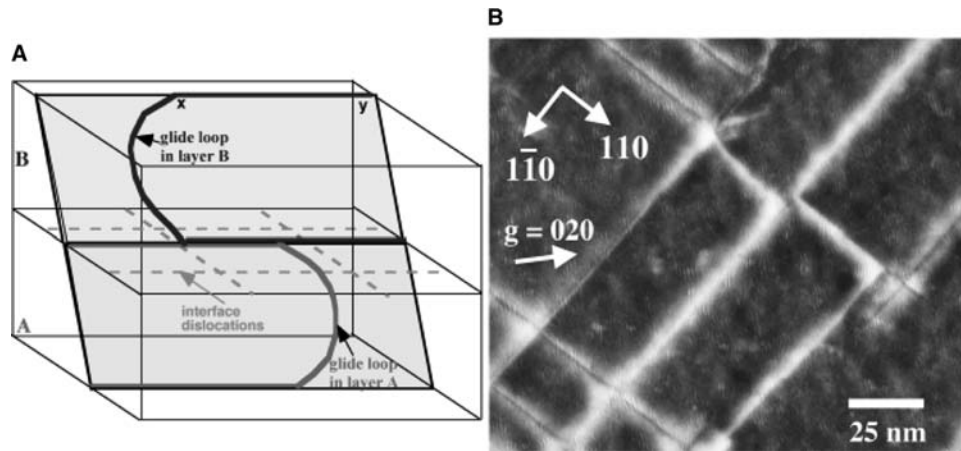


**Fig. 4** (A) Schematic illustration of the confined layer slip in bimetallic layered nanocomposites. Glide of a dislocation loop confined to an individual layer results in deposition of dislocation segments (shown as dotted line) at the two interfaces confining the loop. (B) Plan view TEM image of a 5 nm thick Ni layer on a 100 nm (0 0 1) Cu. Confined layer slip in the Ni layer to partially relieve the coherency strain has resulted in a cross-grid of  $60^\circ$  misfit dislocations at the interface with Burgers vectors in the  $\{111\}$  glide plane.

dislocation across the interface is, therefore, the critical event that defines the nanolaminate yield strength, and this is discussed next.

### Atomistic Modeling of Glide Dislocation Transmission across Interfaces

In our discussion of the stress needed for single-dislocation transmission across interfaces, we consider two kinds of interfaces: *transparent* and *opaque*. The characteristic feature of interfaces in the fcc-fcc, Cu–Ni and Cu–Ag composites is that slip planes and slip directions are nearly continuous across the interfaces and both layers have the same crystal structure. Therefore, because of the continuity in slip across these interfaces, we refer to them as *transparent interfaces*. The second kind, *opaque interfaces*, apply to systems where the slip planes and slip directions are discontinuous across the interfaces and the two layers have different crystal structures, e.g., fcc-bcc Cu–Nb systems.

#### Transparent interfaces

For the coherent Cu–Ni case, in spite of the continuity of slip, dislocations are not able to easily move from one layer to the next because of coherency stresses. Fig. 5 shows the results of a MD simulation of slip transmission across  $\{001\}$  Cu–Ni interface under applied in-plane tension. A  $1/2\langle 011 \rangle$  dislocation on a  $\{111\}$  glide plane in the Cu layer, denoted BD in Thompson tetrahedron notation in Fig. 5A, dissociates into Shockley partials ( $\gamma D$  and  $B\gamma$  in Fig. 5B). In the simulation, the magnitude of the in-plane applied tensile stress needed to cause the lead partial  $B\gamma$  to

transmit across the coherent Cu–Ni interface into the Ni layer was 2.6 GPa.<sup>[47,48]</sup> Comparing this stress to the biaxial in-plane coherency stress in the Cu and Ni that are  $-2.4$  and  $+2.4$  GPa, respectively, we find that the critical applied stress to cross the interface is very nearly equal to the coherency stress. The small difference arises from contributions from non-linear elastic effects, dislocation image forces due to elastic moduli mismatch between the layers, and creation of a step at the interface during slip transmission. Assuming that we can neglect these small contributions, a very simple relation that predicts the dependence of the peak strength attainable in such multilayers on elastic moduli and misfit strain is obtained as

$$\sigma_f = \frac{C^A C^B}{C^A + C^B} \varepsilon_m \quad (1)$$

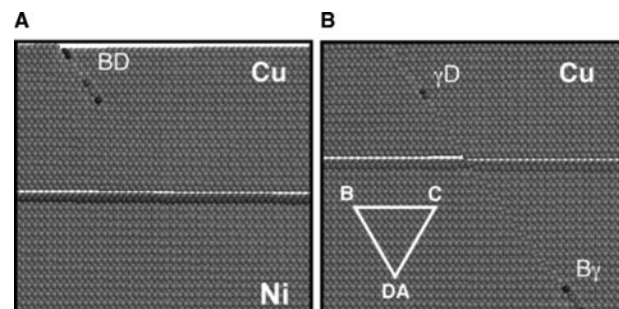


**Fig. 5** MD simulation of slip transmission across Ni–Cu interface. (A) A glide dislocation (labeled BD in Thompson tetrahedron notation) is placed in the Cu layer and the bilayer loaded in tension parallel to the interface plane. (B) At an applied stress of 2.6 GPa, the leading partial has transmitted to the Ni layer.

where  $C^A$  and  $C^B$  are the effective biaxial elastic constants for layers A and B respectively, and  $\varepsilon_m$  is the lattice mismatch strain between the two materials. For the Cu/Ni embedded atom method (EAM) potentials,  $C^{Cu} = 133$  GPa,  $C^{Ni} = 212$  GPa,  $\varepsilon_m = 0.0266$ , a strength of 2.2 GPa is calculated from Eq. (1) in reasonable agreement with the MD simulation results and in fair agreement with the experimentally observed (Fig. 3) peak strength values of 1.7 GPa for Cu/Ni at  $h \sim 5$  nm. Our TEM observations, Fig. 4B, of Ni–Cu interfaces at  $h = 5$  nm revealed a partial coherency loss that would result in a lower  $\sigma_f$ . Eq. (1) shows that higher strengths should be achieved in higher modulus materials, and combinations of materials with higher misfit strains. However, there are limits to the applicability of Eq. (1). For Cu/Ag the misfit strain is 0.12, significantly larger than for Cu/Ni. However, this misfit is too large to achieve coherency in this system because the misfit dislocations are so close together that the cores of the adjacent dislocations at the interface overlap. Consequently, coherency is lost and the maximum strength in Cu/Ag is less than that of Cu/Ni. Consistent with experiments that show a drop in strength as  $h$  is reduced below  $\sim 2$  nm, MD simulation results obtained from models with very thin layers also show a corresponding decrease in the stress needed to transmit slip across the interface as the layer thickness is reduced.<sup>[47–50]</sup> There are two explanations for this behavior: 1) the image forces on glide dislocations due to modulus mismatch decrease with layer thickness, and 2) the dislocation core size becomes a significant fraction of the layer thickness.

### Opaque interfaces

The transfer of slip across an interface between two different phases or between two misoriented crystals must, in general, involve dislocation multiplication because of discontinuity of slip planes and directions. Furthermore, the interface may have limited shear strength, a property that leads to attraction of glide dislocations to the interface and core spreading for dislocations in the interface. Such interfaces are typically incoherent, and, although periodic structures might occur, they may not be able to sustain the large coherency stresses that can develop in the transparent

interface systems. Consequently, in such materials, the interface itself is a barrier to slip, and we identify these interfaces as opaque.

Fig. 6A shows results from an unstressed Cu/Nb model in which a dissociated glide dislocation was placed in the Cu layer near the interface. In this particular case, the model is oriented such that one set of slip planes in the Cu and another set in the Nb are misoriented by a small tilt (although there is a large change in slip vector) and their traces on the interface are normal to the page. The lead partial of a dissociated glide dislocation in the Cu was attracted to the interface while the trailing partial remained some distance away. At a relatively small applied stress of about 0.2 GPa, the trailing dislocation also entered the interface. Disregistry analysis shows that the in-plane components of these dislocations spread significantly in the interface. Very large strains are required for the slip to transfer into the Nb. Fig. 6B shows a glide dislocation emerging in the Nb on a  $\{110\}$  slip plane at an in-plane strain of 3.5% (equal in both layers), producing an applied tensile stress of about 7 GPa in the Cu and 4.5 GPa in the Nb.<sup>[48]</sup> There is also evidence of a dislocation emerging on another  $\{111\}$  plane in the Cu layer at this huge stress. The results shown here derive from calculations near 0 K and it is very likely that at higher temperatures, thermal activation would assist dislocation nucleation into the Nb layer at lower stresses. In a different simulation, the shear strength of the interface in the Cu/Nb system was measured by applying an increasing homogeneous shear strain accompanied by energy minimization. The shear stress at which irreversible slip on the interface occurred was found to be about 0.55 GPa, much less than the stress to transmit slip across the interface. We have shown that this relative “weakness” of the interface is a key factor in core spreading of the glide dislocation along the interface.

### SUMMARY

The length scale dependence of strength of bimetallic nanolayered composites discussed in this article is shown schematically in Fig. 7.<sup>[36,51]</sup> As the layer thickness is decreased below around 200  $\mu\text{m}$ , strength becomes dependent on the length scale of the material

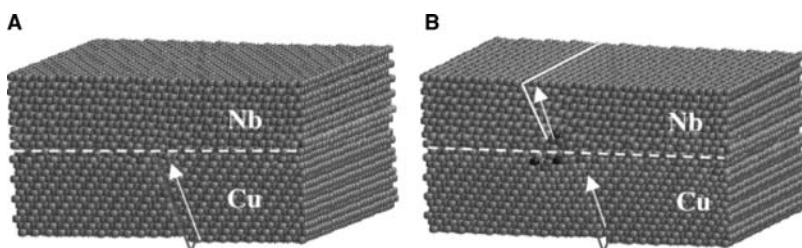


**Fig. 6** MD simulation of slip transmission across Nb–Cu interface. (A) A glide dislocation in Cu is approaching the Cu/Nb interface under applied in-plane tension. (B) The glide dislocation in Cu is absorbed, with its core spread, in the interface plane, and a glide dislocation is emerging on the Nb side.



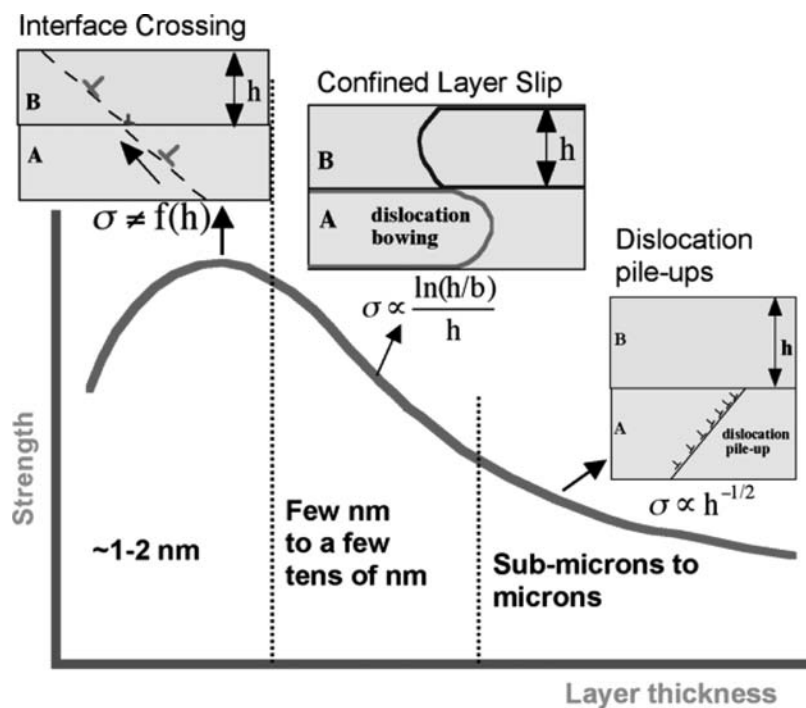


Fig. 7 Schematic illustration of the length scale dependent deformation mechanisms in bimetallic layered nanocomposites.

via the H-P model,  $\sigma \propto h^{-1/2}$ . Dislocations pile up at the interfaces that are barriers to slip transmission and the stress concentration from the pileup eventually overcomes the interface barrier to propagate slip through the composite. With reducing layer thickness, the pileup length gets shorter and so does the stress concentration at the tip of the pileup, thereby resulting in a higher applied stress for slip transmission. This continuum model is applicable to submicrometer length scales. As the layer thickness in a bimetallic laminate is decreased below a few tens of nanometers, the H-P scaling law is no longer applicable implying that continuum-scale dislocation pileups cannot form in nanoscale multilayers, and the deformation behavior must be interpreted in terms of the nucleation and motion of single dislocations. For such nanolaminates, strength increase with decreasing layer thickness in the few to a few tens of nanometers range is interpreted as CLS of single Orowan loops (Fig. 7). As the layer thickness is decreased to a couple nanometers, the strength reaches a peak value independent of layer thickness. This peak strength is interpreted as the stress needed to transmit a single glide dislocation across the interface, and can be as high as  $\sigma_{th}/2$  where  $\sigma_{th}$  is the theoretical limit of strength for perfect crystals. The peak strength can be tailored by interface properties. For example, for coherent systems, the peak strength is determined by the magnitude of coherency stress. For incoherent interfaces between metals of dissimilar crystal structures, the crucial interface property is the interface shear strength. A weak interface shears in response to the glide

dislocation stress field leading to trapping of the dislocation in the interface plane via core spreading. Finally, as the layer thickness decreases below the typical dislocation core dimensions of  $\sim 1$  nm, the interface stress to single-dislocation transmission decreases.

The mechanical properties of bimetallic layered composites can thus be tailored by both length scales and by interface properties to achieve strengths approaching the theoretical limit for perfect crystals.

Structural transitions in bimetallic layered composites at layer thickness of a few atomic layers are not covered in this entry and the reader is referred to another review<sup>[52]</sup> on this topic published in the Dekker Encyclopedia of Nanoscience and Nanotechnology.

## ACKNOWLEDGMENTS

Authors acknowledge discussions and collaboration with H. Kung, J.P. Hirth, J.D. Embury, F. Spaepen, P.M. Anderson, M. Nastasi, T.E. Mitchell, X. Zhang, D. Mitlin, and J.G. Swadener. This research is supported by DOE, Office of Science, Office of Basic Energy Sciences.

## REFERENCES

- Misra, A.; Kung, H.; Embury, J.D. Preface to the viewpoint set on: deformation and stability of nanoscale metallic multilayers. *Scripta Mater.* **2004**, *50* (6), 707–710.



2. Hirth, J.P.; Lothe, J. *Theory of Dislocations*; Krieger: Malabar, FL, 1992.
3. Brenner, S.S. *Growth and Perfection of Crystals*; Doremus, R.H., Roberts, B.W., Turnbull, D., Eds.; Wiley: New York, 1958; 3 pp.
4. Valiev, R.Z.; Kozlov, E.V.; Ivanov, Y.F.; Lian, J.; Nazarov, A.A.; Baudalet, B. Deformation behaviour of ultra-fine-grained copper. *Acta Metall. Mater.* **1994**, *42* (7), 2467–2475.
5. Valiev, R.Z.; Islamgaliev, R.K.; Alexandrov, IV. Bulk nanostructured materials from severe plastic deformation. *Prog. Mater. Sci.* **2000**, *45* (2), 103–189.
6. Groza, J.R.; Gibeling, J.C. Structural nanomaterials. In *Dekker Encyclopedia of Nanoscience and Nanotechnology*, 2E; Schwarz, J.A., Contescu, C.I., Putyera, K., Eds.; Taylor & Francis: New York, NY, 2009; Vol. 6, 4205–4216.
7. Yasuna, K.; Terauchi, M.; Otsuki, A.; Ishihara, K.N.; Shingu, P.H. Formation of nanoscale Fe/Ag multilayer by repeated press-rolling and its layer thickness dependence of magnetoresistance. *Mater. Sci. Eng. A* **2000**, *A285* (1–2), 412–417.
8. Shingu, P.H.; Ishihara, K.N.; Otsuki, A.; Hashimoto, M.; Hasegawa, N.; Daigo, I.; Huang, B. Nano-scaled multilayered bulk materials manufactured by repeated pressing and rolling in the Ag–Fe and Cu–Fe systems. *Mater. Sci. Forum* **1999**, *312–314*, 293–298.
9. Bordeaux, F.; Yavari, R. Multiple necking and deformation behaviour of multilayer composites prepared by cold rolling. *Zeitschrift fur Metallkunde* **1990**, *81* (2), 130–135.
10. Foecke, T.; Lashmore, D.S. Mechanical behavior of compositionally modulated alloys. *Scripta Metall. Mater.* **1992**, *27*, 651.
11. Tench, D.M.; White, J.T. Tensile properties of nano-structured Ni–Cu multilayered materials prepared by electrodeposition. *J. Electrochem. Soc.* **1991**, *138*, 3757.
12. Menezes, S.; Anderson, D.P. Wavelength-property correlation in electrodeposited ultrastructured Cu–Ni multilayers. *J. Electrochem. Soc.* **1990**, *137*, 440.
13. Sproul, W.D. New routes in the preparation of mechanically hard films. *Science* **1996**, *273* (5277), 889–892.
14. Barnett, S.A. *Physics of Thin Films: Mechanic and Dielectric Properties*; Francombe, M.H., Vossen, J.L., Eds.; 1993; Vol. 17, 1 pp.
15. Daniels, B.J.; Nix, W.D.; Clemens, B.M. Enhanced mechanical hardness in compositionally modulated Fe/Pt and Fe/Cr epitaxial thin films. *Thin Solid Films* **1994**, *253* (1–2), 218–222.
16. Misra, A.; Kung, H.; Hammon, D.; Hoagland, R.G.; Nastasi, M. Damage mechanisms in nanolayered metallic composites. *Int. J. Damage Mech.* **2003**, *12* (4), 365–376.
17. Dahlgren, S.D. Columnar grains and twins in high-purity sputter-deposited copper. *J. Vacuum Sci. Technol.* **1974**, *11* (4), 832–826.
18. Bunshah, R.F.; Nimmagadda, R.; Doerr, H.J.; Movchan, B.A.; Grechanuk, N.I.; Dabizha, E.V. Structure and property relationships in microlaminate Ni–Cu and Fe–Cu condensates. *Thin Solid Films* **1980**, *72* (2), 261–275.
19. Bickerdike, R.L.; Clark, D.; Easterbrook, J.N.; Hughes, G.; Mair, W.N.; Partridge, P.G.; Ranson, H.C. Microstructures and tensile properties of vapour deposited aluminium alloys. I. Layered microstructures. *Int. J. Rapid Solidification* **1985**, *1* (4), 305–325.
20. Misra, A.; Hirth, J.P.; Hoagland, R.G.; Embury, J.D.; Kung, H. Dislocation mechanisms and symmetric slip in rolled nano-scale metallic multilayers. *Acta Mater.* **2004**, *52* (8), 2387–2394.
21. Verdier, M.; Niewczas, M.; Embury, J.D.; Hawley, M.; Nastasi, M.; Kung, H. Plastic behaviour of Cu Ni multilayers. *Mater. Res. Soc. Symp. Proc.* **1998**, *522*, 77–82.
22. Harp, G.R.; Parkin, S.S.P. Epitaxial growth of metals by sputter deposition. *Thin Solid Films* **1996**, *288* (1–2), 315–324.
23. Sperling, E.A.; Banerjee, R.; Thompson, G.B.; Fain, J.P.; Anderson, P.M.; Fraser, H.L. Processing and microstructural characterization of sputter-deposited Ni/Ni<sub>3</sub>Al multilayered thin films. *J. Mater. Res.* **2003**, *18* (4), 979–987.
24. Hall, E.O. The deformation and ageing of mild steel 3. Discussion of results. *Proc. Phys. Soc. Lond. Sect. B* **1951**, *64* (381), 747–753.
25. Mara, N.; Sergueeva, A.; Misra, A.; Mukherjee, A.K. Structure and high-temperature mechanical behavior relationship in nano-scaled multilayered materials. *Scripta Mater.* **2004**, *50* (6), 803–806.
26. Misra, A.; Verdier, M.; Lu, Y.C.; Kung, H.; Mitchell, T.E.; Nastasi, N.; Embury, J.D. Structure and mechanical properties of Cu–X (X = Nb, Cr, Ni) nanolayered composites. *Scripta Mater.* **1998**, *39*, 555.
27. Tench, D.; White, J. Enhanced tensile strength for electrodeposited nickel-copper multilayer composites. *Metall. Trans. A* **1984**, *15*, 2039.
28. McKeown, J.; Misra, A.; Kung, H.; Hoagland, R.G.; Nastasi, M. Microstructures and strength of nanoscale Cu–Ag multilayers. *Scripta Mater.* **2002**, *46*, 593.
29. Huang, H.B.; Spaepen, F. Tensile testing of free-standing Cu, Ag and Al thin films and Ag/Cu multilayers. *Acta Mater.* **2000**, *48*, 3261.
30. Baker, S.P.; Nix, W.D. Mechanical properties of compositionally modulated Au–Ni thin films: nanoindentation and microcantilever deflection experiments. *J. Mater. Res.* **1994**, *9*, 3131–3144.
31. Geisler, H.; Schweitz, K.O.; Chevallier, J.; Bottiger, J.; Samwer, K. Hardness enhancement and elastic modulus behaviour in sputtered Ag/Ni multilayers with different modulation wavelengths. *Phil. Mag. A* **1999**, *79*, 485.
32. Schweitz, K.O.; Chevallier, J.; Bottiger, J.; Matz, W.; Schell, N. Hardness in Ag/Ni, Au/Ni and Cu/Ni multilayers. *Phil. Mag. A* **2001**, *81*, 2021–2032.
33. Zhang, X.; Misra, A.; Wang, H.; Shen, T.D.; Nastasi, M.; Mitchell, T.E.; Hirth, J.P.; Hoagland, R.G.; Embury, J.D. Enhanced hardening in Cu/330 stainless steel multilayers by nanoscale twinning. *Acta Mater.* **2004**, *52*, 995–1002.

34. Phillips, M.A.; Clemens, B.M.; Nix, W.D. Microstructure and nanoindentation hardness of Al/Al<sub>3</sub>Sc multilayers. *Acta Mater.* **2003**, *51*, 3171–3184.
35. Clemens, B.M.; Kung, H.; Barnett, S.A. Structure and strength of multilayers. *MRS Bull.* **1999**, *24*, 20–26.
36. Misra, A.; Hirth, J.P.; Kung, H. Single-dislocation-based strengthening mechanisms in nanoscale metallic multilayers. *Philos. Mag.* **2002**, *82* (16), 2935–2951.
37. Zhang, X.; Misra, A.; Wang, H.; Shen, T.D.; Swadener, J.G.; Embury, J.D.; Kung, H.; Hoagland, R.G.; Nastasi, M. Strengthening mechanisms in nanostructured copper/304 stainless steel multilayers. *J. Mater. Res.* **2003**, *18*, 1600–1606.
38. Geyang, L.; Junhua, X.; Liuqiang, Z.; Liang, W.; Mingyuan, G. Growth, microstructure, and microhardness of W/Mo nanostructured multilayers. *J. Vac. Sci. Technol. B* **2001**, *19* (1), 94–97.
39. Anderson, P.M.; Foecke, T.; Hazzledine, P.M. Dislocation-based deformation mechanisms in metallic nanolaminates. *MRS Bull.* **1999**, *24*, 27–33.
40. Embury, J.D.; Hirth, J.P. On dislocation storage and the mechanical response of fine scale microstructures. *Acta Metall. Mater.* **1994**, *42*, 2051–2056.
41. Nix, W.D. Yielding and strain hardening of thin metal films on substrates. *Scripta Mater.* **1998**, *39*, 545–554.
42. Nix, W.D. Elastic and plastic properties of thin films on substrates: nanoindentation techniques. *Mater. Sci. Eng.* **1997**, *A234–236*, 37–44.
43. Freund, L.B. The driving force for glide of a threading dislocation in a strained epitaxial layer on a substrate. *J. Mech. Phys. Solids* **1990**, *38*, 657–679.
44. Chu, X.; Barnett, S.A. Model of superlattice yield stress and hardness enhancements. *J. Appl. Phys.* **1995**, *77* (9), 4403–4411.
45. Phillips, M.A.; Clemens, B.M.; Nix, W.D. A model for dislocation behavior during deformation of Al/Al<sub>3</sub>Sc (fcc/L1<sub>2</sub>) metallic multilayers. *Acta Mater.* **2003**, *51* (11), 3157–3170.
46. Mitlin, D.; Misra, A.; Radmilovic, V.; Nastasi, M.; Hoagland, R.; Embury, D.J.; Hirth, J.P.; Mitchell, T.E. Formation of misfit dislocations in nanoscale Ni–Cu bilayer films. *Philos. Mag.* **2004**, *84* (7), 719–736.
47. Hoagland, R.G.; Mitchell, T.E.; Hirth, J.P.; Kung, H. On the strengthening effects of interfaces in multilayer fcc metallic composites. *Philos. Mag. A* **2002**, *82* (4), 643–664.
48. Hoagland, R.G.; Kurtz, R.J.; Henager, C.H. Slip resistance of interfaces and the strength of metallic multilayer composites. *Scripta Mater.* **2004**, *50* (6), 775–779.
49. Rao, S.I.; Hazzledine, P.M. Atomistic simulations of dislocation-interface interactions in the Cu–Ni multilayer system. *Philos. Mag. A* **2000**, *80* (9), 2011–2040.
50. Henager, C.H.; Kurtz, R.J.; Hoagland, R.G. Interactions of dislocations with disconnections in fcc metallic nanolayered materials. *Philos. Mag.* **2004**, *84* (22), 2277–2303.
51. Misra, A.; Verdier, M.; Kung, H.; Embury, J.D.; Hirth, J.P. Deformation mechanism maps for polycrystalline metallic multilayers. *Scripta Mater.* **1999**, *41* (9), 973–979.
52. Banerjee, R.; Thompson, G.B.; Fraser, H.L. Structural transitions in thin films. *Dekker Encyclopedia of Nanoscience and Nanotechnology.* **2004**, 3737–3747.

# Bio-Microarrays

Günter E.M. Tovar

Achim Weber

*Fraunhofer Institute for Interfacial Engineering and Biotechnology,  
University of Stuttgart, Stuttgart, Germany*

## INTRODUCTION

Microarray technology is a key factor in today's biotechnology research. There already exists a variety of chip-based polynucleic acids analysis systems. DNA microchips are already commercially available and are widely used in laboratories worldwide. In contrast, new methods are needed for the starting era of proteomics—the investigation of function, structure, and molecular interaction among proteins. Protein microarrays are widely expected to play an outstanding role in this new field of research.

The change of scope from nucleic acids to proteins needs, by far, more than a little change in the technology to be applied. Especially, there is a tremendous need to develop new microarrays with a flexible surface chemistry. Proteins are, by far, more complex in their material properties than polynucleic acids. Whereas DNA is composed of only four different nucleotides, which are chemically quite closely related to one another, proteins consist of 21 different amino acids that can differ drastically in their chemical functionality. Additionally, posttranslational modifications on proteins within organisms create an even larger variety in the chemical properties of naturally occurring proteins and polypeptides. Therefore, intending to establish a protein-oriented microarray technology, there is an immense need for a large variety of different tailor-made surface chemistries.

In our approach described here, we provide a pre-structured microarray for the immobilization of proteins. By adsorbing a patterned layer of nanoparticles with various surface modifications to a substrate, we separate the two steps of chemical tailoring of the surface on a molecular level and the subsequent microstructuring of the chip in two fundamentally independent processes. Thereby, an extremely efficient microarray preparation is realized while providing notably high flexibility in chemical surface structures. In the first step, by means of chemical nanotechnology, tailor-made nanoparticles are prepared. The particle's surface is customized to match the specific demands for the immobilization of a certain kind or class of proteins. In a second step, the nanoparticles are deposited

on a chip to render a microstructured monolayer array of nanoparticles. This microstructure can be achieved by a choice of different lithographic processes. Either photolithography,<sup>[1]</sup> microcontact printing,<sup>[2–4]</sup> or micro-spotting<sup>[5]</sup> is applied for nanoparticle deposition only at well-defined areas of the substrate. The resulting system is a nanoparticle-based microarray ready for the selective binding of protein ligands.

## GENERAL SCHEME OF THE MICROSTRUCTURED SURFACE PREPARATION

To understand the flexibility of the practical approach of preparing nanoparticle-based microarrays, the overall process can be regarded as being composed of four different processes: 1) synthesis of functional nanoparticles; 2) substrate surface activation step; 3) nanoparticle deposition; and 4) lithographic process. Combining these processes in different ways provides the possibility to achieve the patterned deposition of nanoparticles in a direct or an indirect way. The performance of steps (2)–(4) will be described in “Surface Activation.” Subsequently, we will introduce a selection of functional nanoparticles (step 1), which are designed to determine the surface chemistry of the resulting microarray. Finally, we will give an example of a microarray based on functional nanoparticles.

### Surface Activation

The surface of the solid substrate has to be prepared to bind particles strong enough to withstand common washing procedures. In this approach, charged particles were fixed to an oppositely charged surface. Surface activation was achieved by self-assembly of ultrathin polyelectrolyte monolayers or multilayers on the substrate by applying a simple dipping process. The method used is referred to as layer-by-layer (LbL) technique<sup>[6,7]</sup> and was also used to deposit nanoparticles.<sup>[8–11]</sup>

According to the LbL technique, solid substrates were coated with ultrathin layers of positively and

negatively charged polyions by an alternating adsorption process. This process, in principle, can be repeated indefinitely; the only condition is a proper alternation of positively and negatively charged components [e.g., here, poly(diallyl-dimethyl ammonium chloride) (PDADMAC) was used as a polycation and the sodium salt of poly(styrene sulfonate) (SPS) was used as a polyanion]. The resulting polyelectrolyte layers then give rise to adhesive binding of charged nanoparticles by electrostatic forces. Most importantly, surface charge density is increased and homogenized by the LbL procedure (for experimental details, see “[Materials and Methods](#)”).

### Lithographic Microstructuring and Particle Deposition

Patterned nanoparticle deposition on the activated surface can be achieved either in a direct or an indirect way: Spotting or stamping the particles onto an activated surface directly generates a nanoparticle pattern on a homogeneous polyelectrolyte layer.

The photoablation of certain regions of polyelectrolyte layers by deep ultraviolet (DUV) irradiation through a mask leads to well-defined particle deposition only onto undamaged parts of the polyelectrolyte coating. Both methods to prepare a microstructured chip surface will be described in the following.

### Microstructuring of the Activated Surface by Photoablation

In structuring the activated surface, a photolithographic technique is employed (e.g., a homogeneously

activated surface is covered with a microstructured mask and is then irradiated with DUV light).<sup>[12]</sup> Thereby, the irradiated areas of the LbL film are transformed to become nonadhesive to the nanoparticles during the later nanoparticle adsorption step.

To characterize this photoablation process, first, irradiation of differently activated surfaces was performed without using a mask. The ablation kinetics and the change of the chemical composition of the polyelectrolyte layers during the photoablation process were monitored by ellipsometry and X-ray photoelectron spectroscopy (XPS), respectively.

Ellipsometric measurements showed that material degradation during DUV treatment depends on the duration of radiation. The layer thickness of the LbL polyelectrolyte film  $d_{\text{LbL}}$  decreased exponentially with the time of DUV irradiation  $t_{\text{DUV}}$ .

Here, three different samples were prepared: silica substrates coated with one layer of PDADMAC, with a double layer of PDADMAC/SPS, or with a triple layer of PDADMAC/SPS/PDADMAC, and then were exposed to DUV irradiation. Fig. 1 shows the decrease of the thickness of these polyelectrolyte layers plotted against the duration of radiation. In all cases, a simple exponential decrease of layer thickness with the duration of radiation was observed. After 45 min, the depth of the layers depreciated to about 20% of the starting value in each layer system.<sup>[13]</sup>

The chemical layer composition before and after exposure to DUV light was determined by XPS measurements (Fig. 2 and Table 1). After DUV irradiation for 45 min, the carbon measurement signal broadened significantly and shifted to a higher bonding energy (286.4–289.2 eV; Fig. 2). This higher bonding energy is the result of the chemical modification of carbon

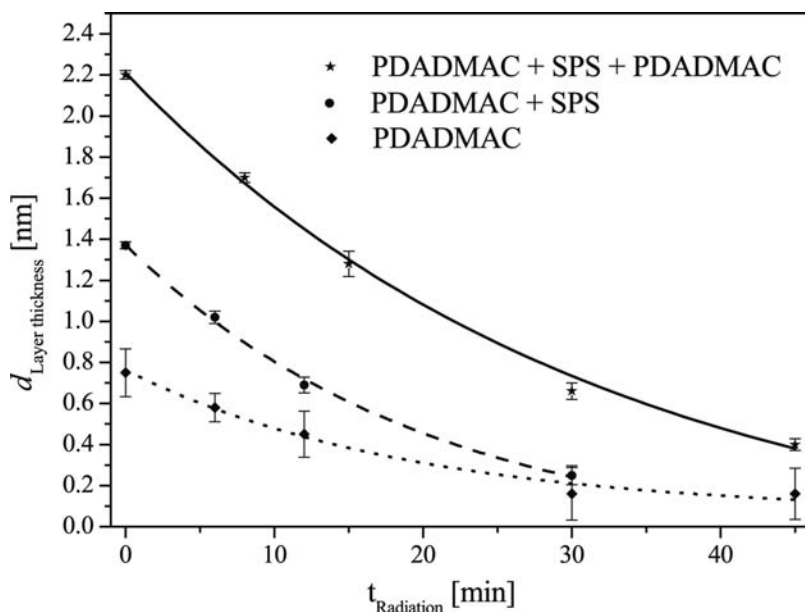


**Fig. 1** Decrease of the layer thickness of polyelectrolyte layers on silicon wafer with DUV irradiation time. (★) Triple layer (PDADMAC/SPS/PDADMAC). (●) Double layer (PDADMAC/SPS). (◆) Monolayer (PDADMAC). Source: From Ref.<sup>[13]</sup>.

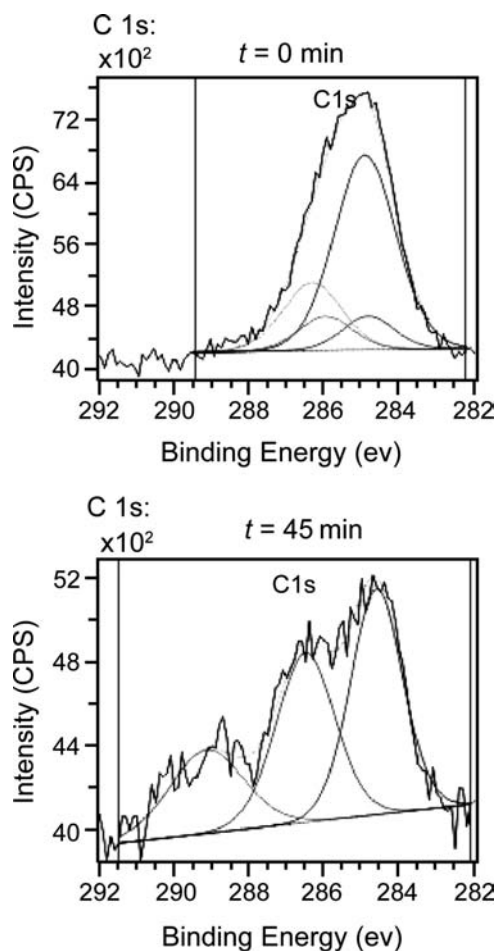


**Fig. 2** High-resolution carbon spectra of the XPS of a PDADMAC-coated silicon wafer before (above) and after (below) irradiation with DUV.

atoms via oxygen atoms. The broadening and displacement of the nitrogen signal (402.0–400.8 eV) originated both from the partial loss of quarternary nitrogen compounds and the loss of positive charges from polyelectrolytes (Table 1).<sup>[13]</sup>

Irradiation with DUV in our simple experimental setup does not result in a complete ablation of the polyelectrolyte film. However, the structuring of polyelectrolyte layers on silica functions excellently: Because of the combination of material ablation and chemical modification, the overall charge density

in the irradiated sectors of polyelectrolyte layers decreased substantially and thus electrostatic interactions (essential for the immobilization of particles) diminished decisively.

### Nanoparticle Monolayer Array by Dip Coating of Nanoparticles on a Microstructured Activated Substrate

A microstructured activated surface can be used as a substrate for the microstructured deposition of particles by a simple dipping process. Therefore, subsequent to the photolithographic treatment, the chip is dipped in a nanoparticle suspension, taken out, and simply rinsed with water. A microstructured nanoparticle array is thereby formed effectively. Fig. 3 shows a PDADMAC-pretreated and photolithographically patterned silica wafer after coating with silica nanoparticles. After the attachment of particles, a precise cutoff between the irradiated and nonirradiated sectors of the PDADMAC-coated silica surface was observed.

### Nanoparticle Monolayer Array by Microspotting or Microcontact Printing on a Nonstructured Activated Substrate

For direct or mask-free structuring of nanoparticle layers, a drop of particle suspension is deposited by a microarrayer at a defined position of the surface (microspotting), or a patterned particle layer is transferred by means of an elastomeric stamp (microcontact printing).

After vaporescence of the liquid phase, the particles stay as a microstructured film at the initially homogeneously coated substrate. Examples for both routes are described in the following sections.

### Microcontact Printing of the Nanoparticle Layer

Microcontact printing is a soft lithographic structuring method. In this technique, a microstructured elastomeric stamp is used to transfer a chemical “ink” to

**Table 1** Quantitative analysis of the XPS of a PDADMAC-coated silicon wafer for elements in question before and after DUV irradiation.

Silicon wafer	Element $E_B$ [eV]	Composition [at.%]							
		C 289.2	C 286.4	C 286.2	C 284.6	O 531.8	N 402.1	N 400.8	N 397.4
Hydroxylated and coated with PDADMAC		Tr	3.1	1.4	10.7	29.9	1.4	–	1.0
Hydroxylated with PDADMAC and UV-radiated (45 min)		1.8	2.9	–	3.6	35.8	0.7	0.5	1.1

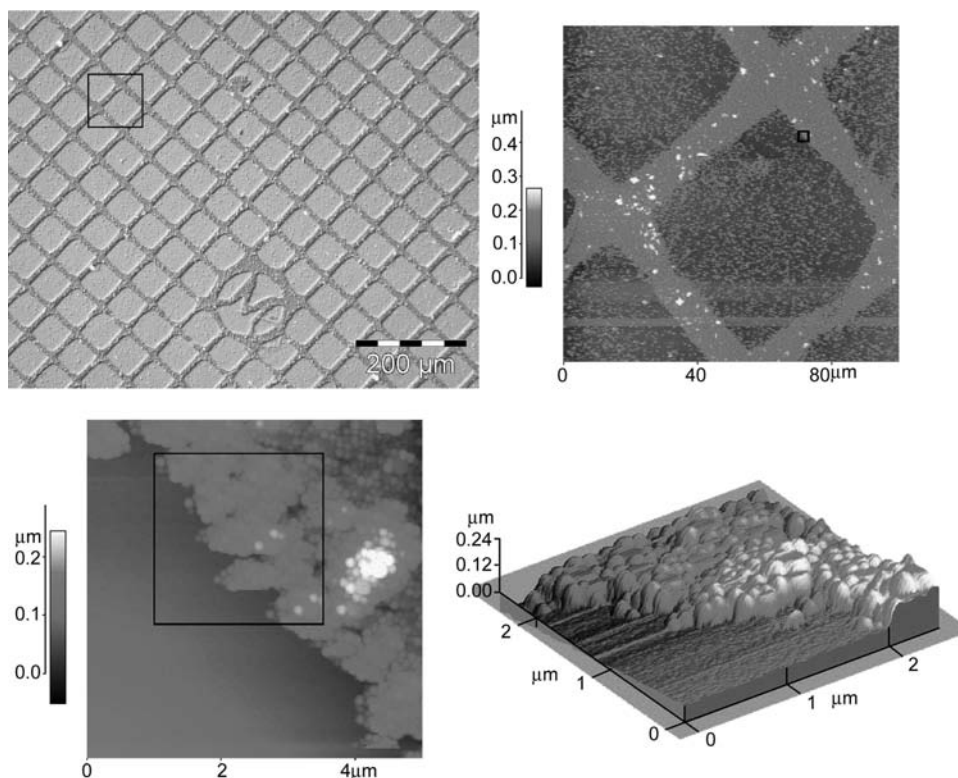


**Fig. 3** Light micrograph (upper left) and atomic force microscopy (AFM) images (upper right, lower left and right) of a photo-lithographically structured PDADMAC layer on a silicon wafer with deposited silica nanoparticles.

some parts of a surface, which is so subdivided into areas of different chemical properties.

The stamps used here are made from polydimethylsiloxane (PDMS) (Fig. 4). According to the hydrophobic properties of the stamp material, the aqueous particle suspension does not spread uniformly over the surface of a freshly prepared stamp. Therefore the surface of the stamp was hydrophilized by an oxygen low-pressure plasma.<sup>[14]</sup> By this treatment, hydroxyl groups were generated at the PDMS surface, and the interaction of the stamp with water dipoles was substantially increased. The stamp was then coated with one layer of polyelectrolytes by a simple dipping

process in a polyelectrolyte solution, rinsed with water, and subsequently dipped into the particle suspension. When the stamp was brought into contact with the activated substrate surface, the particles were effectively transferred to the chip because of the stronger interaction of the charged particles with the activated surface of the substrate.<sup>[15]</sup>

### Microspotting of the Nanoparticle Layer

Microarrays are computer-driven robots that transfer dropwise a solution or a nanoparticle suspension

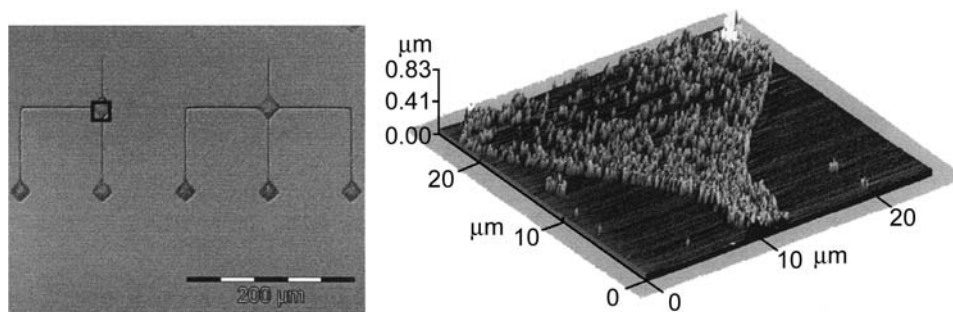


**Fig. 4** Light micrograph (left) and AFM image (right) of microcontact-printed silica nanoparticles on a PDADMAC-coated glass slide.



to precisely defined positions on a substrate. Herewith, any pattern composed of circular spots can be appointed on a planar surface.

The presented structures were printed with a pin-ring spotter. Here, a probe of a nanoparticle suspension was collected from a microtiter plate by dipping a steel ring in the suspension. Thus a thin film of the nanoparticle suspension was spread inside the ring, forming a reservoir for the subsequent spotting process. A steel needle (pin) passed through the liquid film is wetted by the nanoparticle suspension. At a defined position according to the coordinates chosen by the operator, the pin came in contact with the surface of the substrate, and thus a drop of the nanoparticle suspension was deposited. The evaporated liquid and a defined amount of nanoparticles were transferred to the activated substrate (Fig. 5).

### Nanoparticles Applied in the Microarray Preparation

A large variety of spherical nanoparticles, with a diameter from 50 to 300 nm and a molecularly defined surface, were generated and employed in microarray preparation e.g., surface-modified silica nanoparticles,<sup>[16,17]</sup> molecularly imprinted nanoparticles based on the monomer methacrylic acid (MAA) and the cross-linker ethylene glycol dimethacrylate (EGDMA),<sup>[18–20]</sup> or polymer nanoparticles providing an active ester surfmer for easy bioconjugation reactions.<sup>[21,22]</sup>

Surface-modified silica nanoparticles are receiving increasing attention in modern biotechnical and biomedical applications.<sup>[23–25]</sup> They provide an excellent model system for the development of nanoparticulate carrier systems as they are relatively simple tunable in particle size<sup>[17,23,26]</sup> and provide high flexibility in surface modification reactions by silanization (Fig. 6) (e.g., silica nanoparticles with a diameter of 100 nm were covalently modified at their surfaces by adjustable amounts of amine and carboxyl functional groups) (Fig. 7). The protein streptavidin was then conjugated

with nanoparticles, thus resulting in biofunctional hybrid particles with optimized protein density at the surface of nanoparticles.<sup>[27]</sup> Now the simple biotinylation of a protein prepares it for immobilization at the surface of silica particles, often conserving their full bioactivity.<sup>[28]</sup> In contrast, molecularly imprinted polymer nanospheres are examples of fully synthetic receptor nanoparticles. Here, highly crosslinked polymer nanospheres composed of poly(methacrylic acid)-co-(ethylene glycol dimethacrylate) were synthesized by miniemulsion polymerization in the presence of a chiral molecular template, L-Boc-phenylalanine anilid or D-Boc-phenylalanine anilid. By simple extraction of the template, polymer nanoparticles were obtained, which provided binding sites for the recognition of template molecules because of an imprinting process during polymerization. Because of the MAA content in copolymer particles, negative charges are disposed for attachment to polyelectrolyte layer systems. The present paper focuses on polymer nanoparticles composed of a copolymer formed by methylmethacrylate (MMA) with a special polymerizable surfactant bearing an active ester group.

### Protein Binding Polymer Nanoparticles Using Activated Ester Surfmers

Polymer nanoparticles with bioconjugation capabilities are an attractive solid-phase carrier system. For bioconjugation with a protein, the particles must provide a specific reactive function on their surface. These functions are traditionally introduced by surface modification of a preformed latex, often by formation of an activated ester.<sup>[21]</sup> Activated esters are valuable in bioconjugate chemistry as they react with nucleophilic groups of biomolecules (in proteins, peptides, or dyes) under mild conditions, hence usually preserving biomolecule activity. Here, we used a specific trifunctional active ester surfmer molecule to introduce the active ester function already during the formation of the polymer particle. A surfmer molecule is a

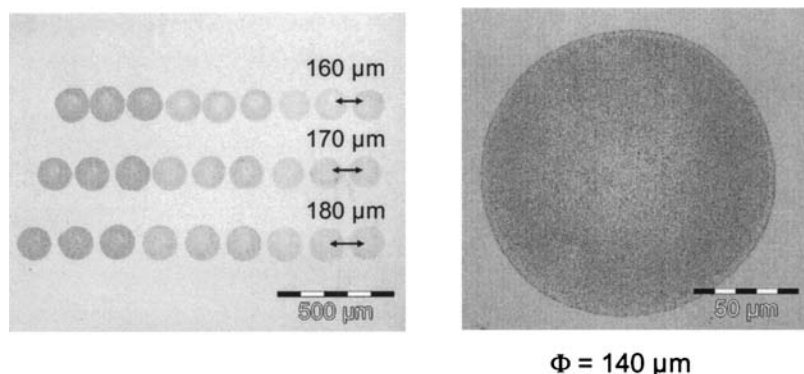


**Fig. 5** Left: Light micrograph of silica nanoparticle spots, deposited by a microarrayer on a glass slide. Lines: Different gap widths. Columns: 5, 2, and 1 droplet per spot. Right: Magnified image of a single spot with a diameter of 140  $\mu\text{m}$ .

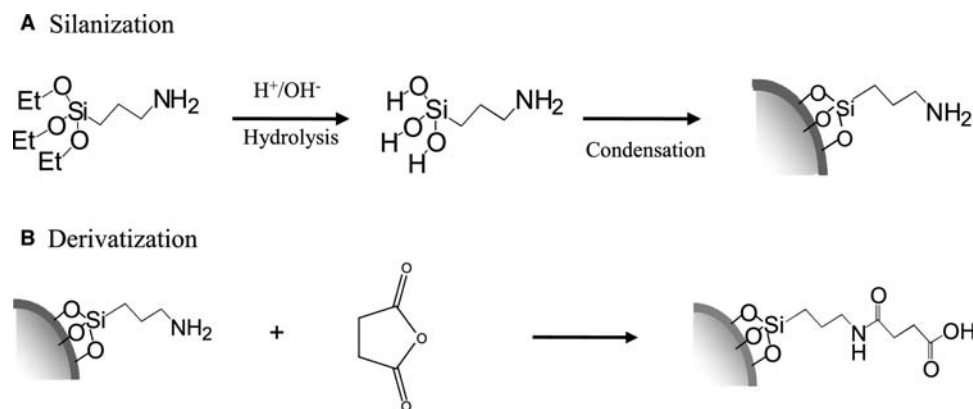


**Fig. 6** Schematic of exemplary silanization (A) and derivatization (B) of silica nanoparticles.

polymerizable surfactant. In addition to the copolymerization of the molecule and its surface activity, here, active ester function is also disposed with the molecule *p*-(11(acrylamido)undecanoyloxy)phenyl dimethylsulfonium methylsulfate (AUPDS, **1**; Fig. 8). Thus nanoscopic polymer particles with a tunable diameter in the range from 120 to 160 nm with an activated ester surface were prepared by copolymerization with MMA (**2**; Fig. 8) in a one-stage reaction using emulsion polymerization.<sup>[22,29]</sup>

### Microarray Based on Patterned Monolayers of Functional Nanoparticles

The functionality of nanoparticles after deposition determines also the overall performance of the microarray. Qualitative assays of the functional properties of nanoparticles after microarraying were exemplarily performed with active ester surfmer nanoparticles deposited on glass substrates. In biochip technology, fluorescent labels are often used as markers and are detected with a fluorescence scanner. Thus for the

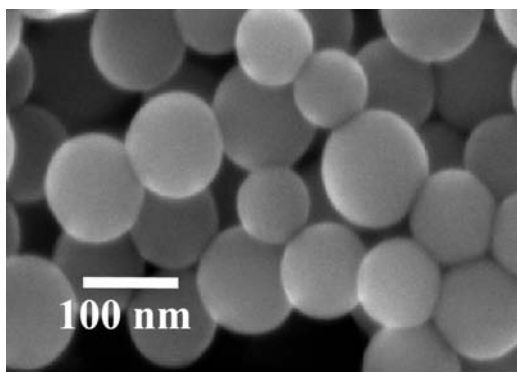


**Fig. 7** Scanning electron micrograph of silica nanoparticles. Bar, 100 nm.

demonstration of the reactivity of the active ester function of nanoparticles, a fluorescent dye (5,6-amino-fluorescein) was reacted with nanoparticles before or after deposition in a microarray.<sup>[13]</sup>

Glass slides were homogeneously activated by a double layer of polyanion and polycation, and the positively charged surfmer nanoparticles were deposited by a microspotter. The microarray was then incubated with a solution containing the fluorescent dye. Thereby, the amine group of the dye reacted covalently with the active ester group of the assembled surfmer nanoparticles. By scanning the microarray with a fluorescence scanner, the microstructure appeared very clearly, thus indicating effective binding of the marker (Fig. 9). The binding of the dye originated exclusively from the covalent binding of the dye, and the non-specific binding of the dye was negligible as was shown by a simple control experiment: When the active ester function was hydrolyzed and the microarray was incubated with the fluorescent dye solution in the same way, no fluorescence was observed.

In contrast, when surfmer ester nanoparticles were reacted with the fluorescent dye prior to deposition in a microarray, fluorescence activity was found again. The fluorescence scanner micrograph of the microarray formed with the fluorescently labeled nanoparticles appears the same as those reacted at the microarray surface (Fig. 9). Thus it was demonstrated that the (bio)conjugation reactivity of active ester surfmer nanoparticles was effectively conserved during the deposition in microarray.

When, instead of the fluorescence dye, for example, a protein receptor is immobilized by reaction with the active ester, or a protein biochip is realized by this simple bioconjugation reaction, all the surface chemistry for conserving the bioactivity of any protein receptor can be developed with the nanoparticles in solution and then a protein biochip can easily be prepared by the new route shown here.

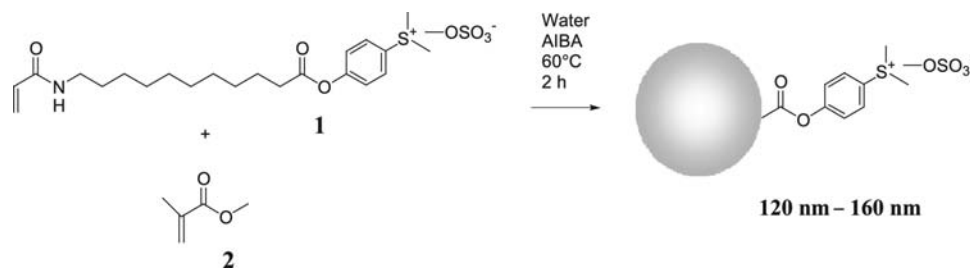


**Fig. 8** Reaction scheme of nanoscopic polymer particles (diameter: 120–160 nm) with an optimized ester surface. AUPDS (1) is converted with MMA (2) as copolymer in a one-stage reaction using emulsion polymerization.

## MATERIALS AND METHODS

### Layer-by-Layer Technique

The substrates used for the immobilization of nanoparticles are glass slides (76 × 26 × 1 mm in size; Carl Roth, Germany), silica wafers, and gold-coated silica wafers. The polyions used are PDADMAC (low molecular weight) as polycation (Aldrich) and the sodium salt of SPS as polyanion (Sigma).

The slides were cleaned in 2 vol.% glass cleaner (Hellmanex, Germany) at 40°C for 90 min and placed in MilliQ water for ultrasonication for 5 min. Afterward, hydrolyzation took place in a 3:1 (vol/vol) mixture of ammonia (NH<sub>3</sub>, 25%; Fluka) and hydrogen peroxide (H<sub>2</sub>O<sub>2</sub>, 30%; Merck) for 20 min at 70°C. The hydrophilic surface of slides was rinsed with MilliQ water and cleaned in MilliQ water in an ultrasonic bath for 5 min. The slides were now dipped into a solution of 0.02 M poly(diallyldimethyl ammonium chloride) and 0.1 M NaCl in MilliQ water for 20 min and rinsed with MilliQ water. To obtain a negatively charged surface, the glass slides were immersed into a solution of 0.02 M SPS and 0.1 M NaCl in MilliQ water for 20 min after the adsorption of the positively charged polycation. Finally, the slides were placed in MilliQ water in an ultrasonic bath for 5 min to homogenize the polyelectrolyte surface and again rinsed with MilliQ water.

### Photolithography

Photoablation of polyelectrolyte layers was performed using a mercury vapor UV lamp (UVP Ultra-Violet Products Limited, Cambridge, UK). The mask used was a copper transmission electron microscopy (TEM) grid “Identigrid M”: 400 mesh (400 bars per 25.4 mm; PLANO, Wetzlar, Germany).

After irradiation, the wafers were rinsed with MilliQ water and then incubated with a 0.5% particle suspension.

### Microcontact Printing

The elastomeric stamps were made from Sylgard 184 (Dow Corning GmbH, Wiesbaden, Germany). The stamps (line width: 2 μm; squares: 20 μm; gaps: 100 μm) used were from A. Offenhäuser of the Max-Planck Institute for Polymer-Research (Mainz, Germany; now Research Center Jülich, Germany).

### Microarrayer

The microarrayer used is the GMS 417 (MWG Biotech AG, Ebersberg, Germany). It has a fourfold pin-ring unit. The distance between pins is 9 mm. The diameter of the pintip is 125 μm. The spotter has a lateral error of 10 μm.

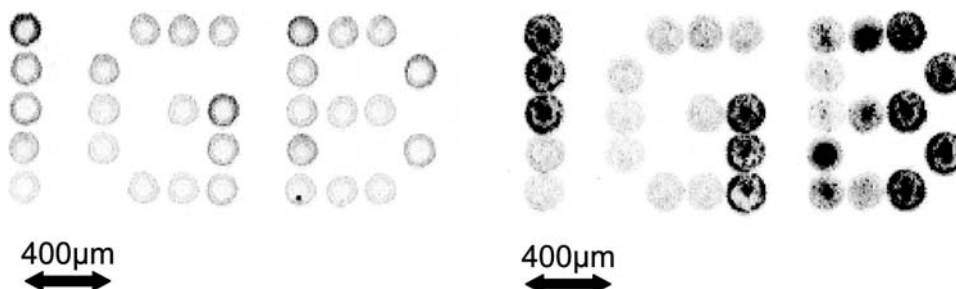


**Fig. 9** Illustration of structured and fluorescein–amine conjugated active ester surfmer nanoparticles on a PDADMAC/SPS-coated glass slide; here, cutouts from the 16-bit grayscale picture of the microarray laser scanner (GMS 417 Array Scanner) are shown as 256-color bitmap after color reverse. Left: Dye labeling of beads after spotted deposition. Right: Dye labeling of particles before spotted deposition. Bar, 400 μm.

## Analytical Methods

### Optical and atomic force microscopy

Optical micrographs are taken using a digital camera mounted on an optical microscope (Olympus BX 60). Scanning force microscopy is performed in noncontact mode with an Autoprobe cp (Park Scientific Instruments, USA).

### Photon correlation spectroscopy

Particle size is determined by dynamic light scattering using a Zetasizer 3000 HSA (Malvern Instruments, Herrenberg, Germany).

### Ellipsometer

The thickness of polyelectrolyte layers is detected with a computer-supported Multiscopie equipped with a HeNe laser (632.8 nm; Optrel GbR, Berlin, Germany).<sup>[30]</sup>

### X-ray photoelectron spectroscopy measurements

The atomic composition of layers is measured with the Axis Ultra system (Kratos Analytical Ltd., Manchester, UK; monochromatic Al K<sub>α</sub> pass energy: 160 eV for survey spectra, 40 eV for detail spectra). For peak integration and fitting, the shipped software is used.<sup>[31,32]</sup>

## CONCLUSION

A large variety of possible options and best fitting procedures were introduced to match the demands of an envisaged protein microarray structure in a most flexible way by employing functional nanoparticles. For a stable linkage of charged particles, the substrates were coated with polyelectrolytes by the LbL technique. For this purpose, hydrophilic or charged surfaces proved to be suitable.

The flexible route to a variety of nanoparticle-based microarrays allows for choosing the appropriate method for a certain kind of application. Spotting particles using a microarrayer allows for placing nanoparticles with different functionalities in different spots of the chip. Using the photolithographic or soft lithographic method, only one kind of particle can be transferred in one process, but user-defined and more complex structures can be generated more easily. However, multifunctional chips can be generated by step-and-repeat processes.

Each of the introduced methods generated microstructured monolayers of nanoparticles with high packing densities and homogenous distribution of

nanoparticles. The functional groups at the surface of the nanoparticles thus arrayed keep their functionality after deposition in a microstructure. Thus the large variety of nanoparticles optimized for the binding of a certain kind or class of proteins or peptides can be used for the relatively simple preparation of a biochip. Protein biochips allow for screening of complex interactions and are expected to play an outstanding role in upcoming proteome research (proteomics). One specific example of using these new kinds of protein biochips is to use them as substrates in affinity matrix-assisted laser desorption initiation turnover frequency (MALDI-TOF) mass spectrometry.<sup>[33]</sup>

## ACKNOWLEDGMENTS

G. E. M. T. thanks the German Federal Ministry BMBF, the Land Baden-Württemberg, and the Fraunhofer-Gesellschaft for financial support of a Junior Research Group ("Nachwuchsforschergruppe") on "Biomimetic Surfaces" (FKZ 0312180). We thank M. Herold (IGVT), N. Reinhardt, and Th. Schiestel (both IGB) for the preparation of nanoparticles; B. Steitz and S. Knecht (both IGVT) for help with nanoparticle deposition; K. Borchers for help with microstructuring; U. Vohrer (IGB) for XPS measurements; and A. Offenhäusser (Research Center Jülich) for providing microcontact printing stamps.

## REFERENCES

1. Prucker, O.; Schimmel, M.; Tovar, G.E.M.; Knoll, W.; Rühle, J. Microstructuring of molecularly thin polymer layers by photolithography. *Adv. Mater.* **1998**, *10* (14), 1073–1076.
2. Xia, Y.; Whitesides, G.M. Softlithographie. *Angew. Chem.* **1998**, *110* (5), 568–594.
3. Kane, R.S.; Takayama, S.; Ostuni, E.; Ingber, D.E.; Whitesides, G.M. Patterning proteins and cells using soft lithography. *Biomaterials* **1999**, *20* (23–24), 2363–2376.
4. Michel, B.; Bernard, A.; Bietsch, A.; Delamarque, E.; Geissler, M.; Juncker, D.; Kind, H.; Rnault, J.-P.; Rothuizen, H.; Schmid, H.; Schmidt-Winkel, P.; Stutz, R.; Wolf, H. Printing meets lithography: Soft approaches to high-resolution patterning. *IBM J. Res. Develop.* **2001**, *45* (5), 697–719.
5. Schena, M.; Shalon, D.; Davis, R.W.; Brown, P.O. Quantitative monitoring of gene expression patterns with a complementary DNA microarray. *Science* **1995**, *270* (5235), 467–470.
6. Decher, G. Fuzzy nanoassemblies: Toward layered polymeric multicomposites. *Science* **1997**, *277* (5330), 1232–1237.
7. Bertrand, P.; Jonas, A.; Laschewsky, A.; Legras, R. Ultrathin polymer coatings by complexation of

- polyelectrolytes at interfaces: Suitable materials, structure and properties. *Macromol. Rapid Commun.* **2000**, *21* (7), 319–348.
8. Chen, K.M.; Jiang, X.; Kimerling, L.C.; Hammond, P.T. Selective self-organization of colloids on patterned polyelectrolyte templates. *Langmuir* **2000**, *16* (20), 7825–7834.
  9. Hua, F.; Shi, J.; Lvov, Y.; Cui, T. Patterning of layer-by-layer self-assembled multiple types of nanoparticle thin films by lithographic technique. *Nano Lett.* **2002**, *2* (11), 1219–1222.
  10. Hua, F.; Cui, T.; Lvov, Y. Lithographic approach to pattern self-assembled nanoparticle multilayers. *Langmuir* **2002**, *18* (17), 6712–6715.
  11. Zheng, H.; Rubner, M.F.; Hammond, P.T. Particle assembly on patterned “plus/minus” polyelectrolyte surfaces via polymer-on-polymer stamping. *Langmuir* **2002**, *18* (11), 4505–4510.
  12. Tovar, G.E.M.; Paul, S.; Knoll, W.; Prucker, O.; R uhe, J. Patterning molecularly thin films of polymers—New methods for photolithographic structuring of surfaces. *Supramol. Sci.* **1995**, *2* (2), 89–98.
  13. Weber, A.; Knecht, S.; Brunner, H.; Tovar, G.E.M. Modularer aufbau von biochips durch mikrostrukturierte abscheidung von funktionellen nanopartikeln. *Chem. Eng. Technol.* **2003**, *75*, 437–441.
  14. Hegemann, D.; Oehr, C.; Brunner, H. Plasma treatment of polymers for surface and adhesion improvement. *Nucl. Instrum. Methods Phys. Res., B* **2003**, *208*, 281–286.
  15. Weber, A.; Knecht, S.; Schiestel, T.; Brunner, H.; Tovar, G.E.M. Bioaktive mikroarrays durch mikrostrukturierte anlagerung von funktionellen nanopartikeln. *Technische Systeme f ur Biotechnologie und Umwelt-11. Heiligenst adter Kolloq.* **2003**, *11*, 57–64.
  16. Tovar, G.E.M.; Scheurich, P. Nanotechnologische werkzeuge f ur die immunologie. *Bioworld* **2002**, *2002-1*, 6–7.
  17. St ober, W.; Fink, A. Controlled growth of monodisperse silica spheres in the micron size range. *J. Colloid Interface Sci.* **1968**, *8*, 62.
  18. Vaihinger, D.; Landfester, K.; Kr auser, I.; Brunner, H.; Tovar, G.E.M. Molecularly imprinted polymer nanospheres as synthetic affinity receptors obtained by mini-emulsion polymerisation. *Macromol. Chem. Phys.* **2002**, *203* (13), 1965–1973.
  19. Tovar, G.E.M.; Gruber, C.; Kr auser, I. Molecularly imprinted polymer nanospheres as fully synthetic affinity receptors. *Top. Curr. Chem.—Colloid Chem.* **2003**, *227*, 125–144.
  20. Weber, A.; Dettling, M.; Brunner, H.; Tovar, G.E.M. Isothermal titration calorimetry of molecularly imprinted polymer nanospheres. *Macromol. Rapid Commun.* **2002**, *23* (14), 824–828.
  21. Herold, M.; Brunner, H.; Tovar, G.E.M. Synthesis of novel activated ester surfmers for use in preparation of latexes for bioconjugation. *Polym. Prep.* **2002**, *43-2*, 1003–1004.
  22. Herold, M.; Brunner, H.; Tovar, G.E.M. Polymer nanoparticles with activated-ester surface by using functional surfmers. *Macromol. Chem. Phys.* **2003**, *204*, 770–778.
  23. Kneuer, C.; Sameti, M.; Haltner, E.G.; Schiestel, T.; Schirra, H.; Schmidt, H.; Lehr, C.-M. Silica nanoparticles modified with aminosilanes as carriers for plasmid DNA. *Int. J. Pharm.* **2000**, *196* (2), 257–261.
  24. Qhobosheane, M.; Santra, S.; Zhang, P.; Tan, W. Biochemically functionalized silica nanoparticles. *Analyst* **2001**, *126* (8), 1274–1278.
  25. Santra, S.; Zhang, P.; Wang, K.; Tapeç, R.; Tan, W. Conjugation of biomolecules with luminophore-doped silica nanoparticles for photostable biomarkers. *Anal. Chem.* **2001**, *73*, 4988–4993.
  26. Kneuer, C.; Sameti, M.; Bakowsky, U.; Schiestel, T.; Schirra, H.; Schmidt, H.; Lehr, C.-M. Surface modified silica-nanoparticles can enhance transfection in vitro: A novel class of non-viral DNA vectors. *Bioconjug. Chem.* **2000**, *11* (6), 926–932.
  27. Schiestel, T.; Brunner, H.; Tovar, G.E.M. Controlled surface functionalization of silica nanospheres by covalent conjugation chemistry and preparation of high density streptavidin nanoparticles. *J. Nanosci. Nanotechnol.* **2003**, *in press*.
  28. Flad, T.; Schiestel, T.; Brunner, H.; Tolson, J.; Ouyang, Q.; Pawelec, G.; Tovar, G.; M uller, G.A.; M uller, C.A.; Beck, H. Development of an MHC-class I peptide selection assay combining nanoparticle technology and MALDI mass spectrometry. *J. Immunol. Methods* **2003**, submitted for publication.
  29. Tovar, G.E.M.; Herold, M.; Weber, A.; Brunner, H. Herstellung und charakterisierung von aktivesternanopartikeln. *Chem. Eng. Technol.* **2002**, *74*, 717.
  30. Harke, M.; Teppner, R.; Schulz, O.; Orendi, H.; Motschmann, H. Description of a single modular optical setup for ellipsometry, surface plasmons, waveguide modes, and their corresponding imaging techniques including Brewster angle microscopy. *Rev. Sci. Instrum.* **1997**, *68* (8), 1–5.
  31. Vohrer, U.; Hegemann, D.; Oehr, C. XPS, AES, and AFM as tools for study of optimized plasma functionalization. *Anal. Bioanal. Chem.* **2003**, *375*, 929–934.
  32. Vohrer, U.; Hegemann, D.; Oehr, C.; Brunner, H. Charakterisierung plasmamodifizierter polymere mittels SSXPS und XPS-imaging. *Vak. Forsch. Prax.* **2000**, *2*, 118–121.
  33. Tovar, G.E.M.; Schiestel, T.; Hoffmann, C.; Schmucker, J. Protein biochips for affinity—MALDI-TOF-mass spectrometry. *Bioforum Int.* **2001**, *5*, 235–237.

# Biocatalytic Single-Enzyme Nanoparticles

Jay W. Grate

Jungbae Kim

*Pacific Northwest National Laboratory, Richland, Washington, U.S.A.*

## INTRODUCTION

Enzymes are useful biocatalysts of nanometer scale that regulate the chemistry of cells and organisms.<sup>[1]</sup> The potential application of enzymes as practical biocatalysts is well recognized and also growing.<sup>[2,3]</sup> The uses of enzymes have been realized in various fields, and are also being expanded in new fields: fine chemical synthesis, pharmaceuticals, commodity catalysts in food processing and detergent applications, biosensing, bioremediation, polymerase chain reaction, and protein digestion in proteomic analysis. The unique activities and specificities of enzymes play a key role in yielding a wide range of applications. However, the widespread application of enzymes is generally limited by their short lifetimes. As an innovative way of enzyme stabilization, we recently developed a new enzyme composite of nanometer scale that we call "single-enzyme nanoparticles (SENs)."<sup>[4]</sup> Each enzyme molecule is surrounded with a porous composite organic/inorganic network of less than a few nanometers thick. This approach represents a new type of enzyme-containing nanostructure. In this entry, we will describe the synthesis, characterization, and catalytic activity of SENs containing  $\alpha$ -chymotrypsin (CT).

## BACKGROUND

Many different approaches have been taken to stabilize enzyme activities, including various enzyme immobilization methods, enzyme modification, genetic modification, and medium engineering.<sup>[5–14]</sup> Genetic modification involves changing the amino acid sequence of an enzyme protein to yield an intrinsically more stable structure using molecular biology techniques such as directed evolution or random mutagenesis. However, medium engineering involves making the enzyme structure more stable by the effect of the medium around it, either by changing the salt composition of an aqueous solution, or by the use of non-aqueous solvents.

Chemically changing the structure of the enzyme through covalent reactions to the protein molecule defines enzyme modification. These reactions often

occur on the surface of the enzyme molecule. Covalent reactions have also been used to crosslink the peptide chains of enzyme molecules to reduce protein unfolding and denaturation. Addition of surface groups or polymers may be used to change the hydrophilicity or hydrophobicity of the molecule, and may result in an improvement in stability under certain solvent conditions. Alternatively, reactions may modify surface amino acids so that they no longer serve as the recognition site for proteolytic enzymes.

Enzyme immobilization entails attaching or incorporating enzyme molecules onto or into larger structures, including immobilization on surfaces, attachment within porous solids, or encapsulation in polymer, sol-gel, or composite materials. Especially in the case of multipoint attachment, immobilization reduces protein unfolding and hence improves stability. These conventional enzyme immobilization approaches often result in a final immobilization of micrometer scale, and the mass of support compared to that of the enzyme is often quite large. Encapsulating enzymes causes serious limitations on mass transfer of the substrate from the reaction medium to the enzyme active site.

The preparation of SENs represents a new approach that is distinct from immobilizing enzymes on the surfaces of solids, or from encapsulating them in sol-gels, polymers, or bulk composite structures. Converting free enzymes to SENs can result in significantly more stable catalytic activity, as we shall demonstrate for CT, whereas the nanoscale structure of the SEN does not impose a serious mass transfer limitation on substrates. At the same time, the synthesis of SENs is also different from conventional enzyme modifications such as surface amino acid modifications or polymer attachments, which generally do not provide as great a long-term enzyme stabilization. Fig. 1 provides a schematic comparison of various enzyme modification and immobilization approaches.

## SENS

### Synthesis

The process for the preparation of SENs begins from the surface of the enzyme molecule, with covalent



reactions to anchor, grow, and crosslink a composite organic/inorganic network around each separate enzyme molecule. The chemistry is shown in Fig. 2.<sup>[4]</sup> A vinyl group functionality is grafted onto the enzyme surface by covalently modifying the amino groups on the enzyme surface with acryloyl chloride. These modified enzymes are then solubilized in an organic solvent such as hexane. The solubilized enzymes are mixed with silane monomers containing both vinyl groups and trimethoxysilyl groups, such as methacryloxypropyltrimethoxysilane (MAPS) or vinyltrimethoxysilane (VTMS). Under suitable conditions, free radical-initiated vinyl polymerization yields linear polymers that are covalently bound to the enzyme surface. This represents the first polymerization. Careful hydrolysis of the pendant trimethoxysilyl groups, followed by condensation of the resulting silanols, yields a cross-linked composite network around each separate enzyme molecule. Hydrolysis and silanol condensation represent the second orthogonal polymerization.

The reactions are carried out so that crosslinking is largely confined to individual enzyme surfaces, yielding discrete nanoparticles, rather than the bulk solids that result from interparticle reactions. These enzyme-containing nanostructures are the structures we have called SENs. Using MAPS as the vinyl monomer, SENs containing CT (SEN-CT) as the enzyme have been prepared in synthetic yields of 38–73%.<sup>[4]</sup>

In the SEN structure, the enzyme is attached to the hybrid polymer network by multiple attachment points limited by the total number of amino groups on the

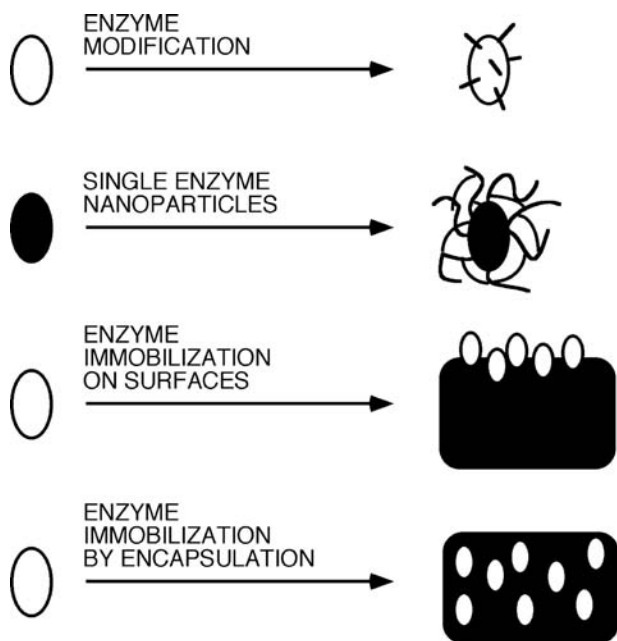
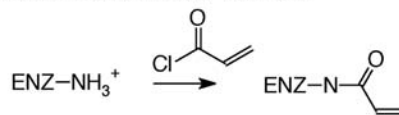
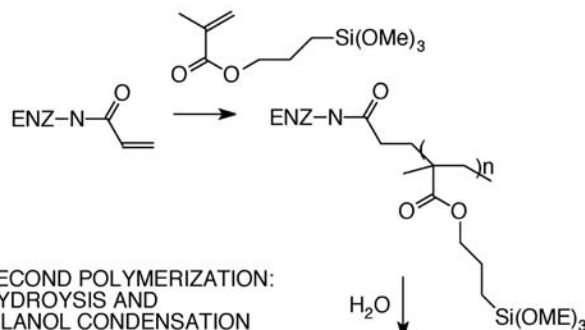


**Fig. 1** Schematic comparison of various enzyme stabilization approaches.

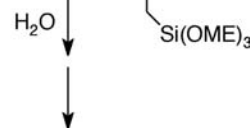
#### INITIAL ENZYME MODIFICATION



#### FIRST POLYMERIZATION: FREE RADICAL VINYL POLYMERIZATION



#### SECOND POLYMERIZATION: HYDROLYSIS AND SILANOL CONDENSATION



*Single Enzyme Nanoparticles (SENs)*

**Fig. 2** Synthesis of SENs. ENZ represents enzyme and it is understood that there are multiple amino groups around the enzyme that are modified as shown.

original enzyme surface. In addition, the thickness of the network around the enzyme is less than a few nanometers. The network is sufficiently porous to allow substrates to have access to the active site, as demonstrated in the catalytic studies below.

The synthetic parameters can be varied to control the thickness of the network and the likelihood of obtaining individual nanoparticles. Using VTMS as the vinyl monomer, which is less reactive to vinyl polymerization than MAPS, nanoparticles are obtained with thinner networks around the enzyme. The addition of vinyl crosslinkers such as trimethylpropane trimethacrylate (TMA) during the vinyl group polymerization with MAPS results in a thicker and denser network structure. The addition of crosslinker can also increase the formation of aggregates, rather than discrete nanoparticles containing single-enzyme molecules.

### Transmission Electron Microscopy

SENs were observed using high-resolution transmission electron microscopy (TEM). Individual nanoparticles with seemingly hollow centers and a contrasting outer structure could be resolved, as shown in Fig. 3A. The dimensions of the transparent core containing the protein are 4–8 nm across, which is consistent with the size and shape of CT (4 × 3 × 8 nm). The presence of silicon in the dark structure around

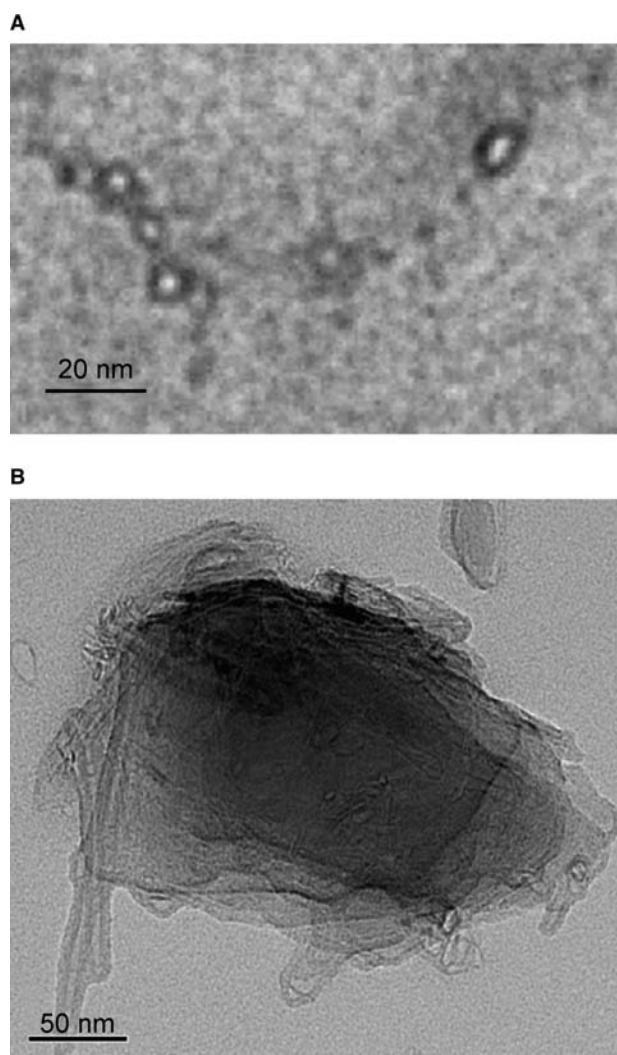


**Fig. 3** TEM images of SEN-CT (A) and biocatalytic silicates (B). The scale bars are 20 and 50 nm respectively.

the cores was confirmed by energy-dispersive X-ray analysis in the TEM instrument. In some images, nanoparticles are observed with sizes corresponding to two protein molecules, and in others, nanoparticles rest next to one another, either by chance or because of linkage during the synthesis. The use of crosslinkers under some conditions leads to larger size aggregates.

### Catalytic Stability

The activities of SEN-CT and free CT were measured by the hydrolysis of *N*-succinyl-Ala-Ala-Pro-Phe-*p*-nitroanilide (TP) in a buffer solution (10 mM phosphate buffer, pH 7.8). Whereas free CT is inactivated very rapidly by autolysis at 30°C, SEN-CT did not show any decrease in CT activity in a buffer solution for 4 days at the same temperature. Inactivations of

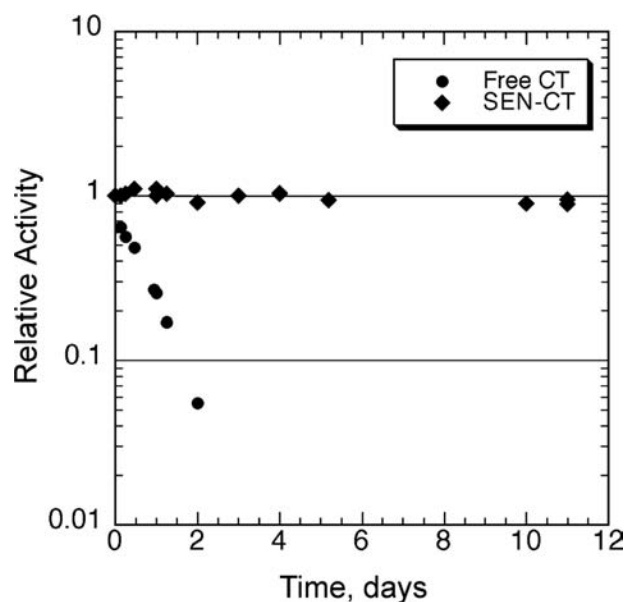


**Fig. 4** Kinetic results showing the inactivation of free CT and stability of SEN-CT at 30°C.

free CT and SEN-CT are compared in Fig. 4. Slight decreases in SEN-CT activity are observed in extended experiments, leading to an estimated half-life of up to 143 days.<sup>[4]</sup> Stored in buffer solution at 4°C, a sample of SEN-CT solution showed negligible decrease in CT activity over 5 months. Thus these enzyme-containing nanoparticles offer significant stabilization for this initial test case using the protease CT. It has also been demonstrated that trypsin can be stabilized in the SEN form.<sup>[4]</sup>

Modified CT, representing a preparation after vinyl group polymerization and before the second orthogonal polymerization, showed a marginal stabilization of CT activity. However, it did not come close to the impressive stability of SEN-CT prepared using sequential orthogonal polymerizations. For example, the relative activities after 1-day incubation, defined as the ratio of the residual activity to the initial activity, were 27%, 54%, and 100% for free CT, modified CT, and SEN-CT, respectively (Table 1). Thus the second orthogonal polymerization creating a hybrid network around the enzyme molecule is essential for achieving the observed high stability of SENs.

Although it is conceivable that the network surrounding the enzyme may interfere with biomolecular proteolysis, the fact that the CT molecules within SEN-CT retain their catalytic activity over extended periods of time also demonstrates that they are not losing activity by denaturation within the nanoparticle structure. Proteolysis of free CT by other active CT molecules is believed to occur by a mechanism entailing rate-limiting denaturation followed by

**Table 1** Stability of free CT, modified CT, immobilized CT (biocatalytic silicates), and SEN-CT<sup>a</sup>

CT preparation	Relative activity (%) after one-day incubation at 30°C
Free CT	27%
Modified CT <sup>b</sup>	54%
Immobilized CT <sup>c</sup>	≈100%
SEN-CT	≈100%

<sup>a</sup>The CT activity was determined by the hydrolysis of N-succinyl-Ala-Ala-Pro-Phe p-nitroanilide in an aqueous buffer (10 mM phosphate, pH 7.8) at room temperature (22°C). Each sample was incubated at 30°C in a standing position. After one-day incubation, the residual CT activity was measured, and the relative activity (%) was calculated from the ratio of the residual activity to the initial activity of each sample.

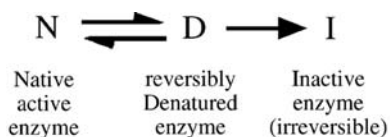
<sup>b</sup>Modified CT represent the preparation after the first vinyl-group polymerization and before the orthogonal silicate polymerization.

<sup>c</sup>Immobilized CT represents biocatalytic silicates. (From Ref.<sup>[15]</sup>.)

irreversible proteolysis of the denatured form.<sup>[15]</sup> In this mechanism, the observed rate of activity loss corresponds to the denaturation rate.

Stabilization of the SEN-CT against inactivation by denaturation likely results from multiple covalent attachment points within the nanostructure. Enzyme inactivation is usually considered as a two-step process,<sup>[16]</sup> as shown in Scheme 1.

In this mechanism, the species N, D, and I represent the active native, inactive reversibly denatured, and irreversibly inactivated forms of enzymes, respectively. Inactivation usually starts with a reversible unfolding of proteins (N → D) followed by secondary irreversible processes (D → I). Many strategies of enzyme stabilization generally aim at slowing down or inhibiting the first step (i.e., unfolding of enzyme molecule). To this end, enzyme immobilization, endowing the enzyme molecule with additional resistance to unfolding by attachment to a surface or encapsulation within a composite, seems to be one of the most promising methods for enzyme stabilization.<sup>[10,13]</sup> The use of multiple covalent attachment points is recognized as a method for improving stabilization.<sup>[13,17]</sup> Thus it is reasonable to expect that the multiple covalent attachment points created in the synthesis of SENs will lead to stabilization in the present test case, and also for other enzyme species that may be prepared as SENs in the future.

**Scheme 1**

## Kinetics and Mass Transfer Issues

In general, mass transfer effects are a fundamental issue in enzyme immobilization methods. Many immobilization methods, especially those that encapsulate the enzyme within a polymer, silica gel, or composite matrix, result in a serious mass transfer limitation of substrates and lowered volumetric activity because of the large mass of supports (in general, >90% by weight).<sup>[10]</sup>

Kinetic constants for the hydrolysis of TP by SEN-CT ( $k_{\text{cat}}$ ,  $K_m$ , and  $k_{\text{cat}}/K_m$ ) were determined.<sup>[4]</sup> The apparent binding constant ( $K_m$ ) of SEN-CT was 40 μM, which is almost the same as that of free CT (39 μM). This suggests that the nanostructure surrounding the enzyme did not cause a significant mass transfer limitation for the substrate (TP).<sup>[18]</sup>

These results can be compared with those for biocatalytic silicates previously prepared by Kim, Delio, and Dordick<sup>[19]</sup> These immobilized enzyme preparations yielded solid composites of micrometer scale (20–250 μm) (Fig. 3B) by a seemingly similar approach using two orthogonal polymerization steps. The stability of the CT activity in these biocatalytic silicates was also impressive (Table 1). However, the catalytic efficiency ( $k_{\text{cat}}/K_m$ ) of the enzyme in these bulk composites was lowered by a factor of 10, indicating a significant limitation on mass transfer of the substrate through the composite matrix.<sup>[19]</sup> Similarly, biocatalytic plastics isolated as micrometer-scale solids are subject to significant mass transfer limitations in an aqueous buffer.<sup>[20]</sup> The SEN nanostructures of single-enzyme scale significantly reduced the mass transfer limitation compared to these other microscale enzyme stabilization methods.

## CONCLUSION

We have developed a new nanostructure containing active and stable enzyme molecules. Dramatic activity stabilization was achieved with minimal substrate mass transfer limitation compared to enzymes entrapped in larger-scale particles. The development of stabilized enzymes as soluble individual enzyme particles provides the opportunity to further process these new nanomaterials, in contrast to enzymes entrapped in bulk solids. The SENs can be deposited as films or immobilized on solid supports. Given their small size, they can penetrate and be immobilized within nanostructured or nanoporous matrices, creating hierarchical architectures. They can potentially be linked with other nanoparticles or molecules as part of multifunctional nanoassemblies.

We are also optimistic that other enzymes may also be stabilized as SENs, using the approach described

above or other synthetic routes yielding crosslinked porous network nanostructures around them. Such hybrid enzyme nanostructures offer great potential to be used as prepared, or processed into other forms for a wide variety of applications such as biosensors, bioremediation, and bioconversions.

## ACKNOWLEDGMENTS

We thank A. Dohnalkova and C. Wang for the electron microscopy. This work was supported by Battelle Memorial Institute, U.S. Department of Energy (DOE) LDRD funds administered by the Pacific Northwest National Laboratory (PNNL), and the DOE Office of Biological and Environmental Research under the Environmental Management Science Program. The research was performed at the W. R. Wiley Environmental Molecular Sciences Laboratory, a national scientific user facility sponsored by the DOE's Office of Biological and Environmental Research and located at the Pacific Northwest National Laboratory. PNNL is operated for the DOE by the Battelle Memorial Institute.

## REFERENCES

1. Walsh, C. Enabling the chemistry of life. *Nature* **2001**, *409*, 226–231.
2. Robert, S.M.; Turner, N.J.; Willets, A.J.; Turner, M.K. *Introduction to Biocatalysis Using Enzymes and Microorganisms*; Cambridge University Press: New York, 1995.
3. Ball, P. Biocatalysis. *Nature* **2001**, *409*, 225.
4. Kim, J.; Grate, J.W. Single-enzyme nanoparticles armored by a nanometer-scale organic/inorganic network. *Nano Lett.* **2003**, *3*, 1219–1222.
5. Tischer, W.; Wedekind, F. *Biocatalysis—From Discovery to Application*; Fessner, D., Ed.; Springer-Verlag: Berlin, 1999; Vol. 200, 95–126.
6. Tischer, W.; Wedekind, F. Immobilized enzymes: Methods and applications. *Top. Curr. Chem.* **1999**, *200*, 95–126.
7. Gianfreda, L.; Scarfi, M.R. Enzyme stabilization: state of the art. *Mol. Cell. Biochem.* **1991**, *100*, 97–128.
8. Livage, J.; Coradin, T.; Roux, C. Encapsulation of biomolecules in silica gels. *J. Phys. Chem., Condens. Mater.* **2001**, *13*, 673–691.
9. DeSantis, G.; Jones, J.B. Chemical modification of enzymes for enhanced functionality. *Curr. Opin. Biotechnol.* **1999**, *10*, 324–330.
10. Govardhan, C.P. Crosslinking of enzymes for improved stability and performance. *Curr. Opin. Biotechnol.* **1999**, *10*, 331–335.
11. Mozhaev, V.V.; Berezin, I.V.; Martinek, K. Structure–stability relationship in proteins: fundamental tasks and strategy for the development of stabilized enzyme catalysts for biotechnology. *Crit. Rev. Biochem.* **1988**, *23*, 235–281.
12. Mozhaev, V.V. Mechanism-based strategies for protein thermostabilization. *Trends Biotechnol.* **1993**, *11*, 88–95.
13. Mozhaev, V.V.; MelikNubarov, N.S.; Sergeeva, M.V.; Siksnis, V.; Martinek, K. Strategy for stabilizing enzymes: part 1. Increasing stability of enzymes via their multi-point interaction with a support. *Biocatalysis* **1990**, *3*, 179–187.
14. Mozhaev, V.V.; MelikNubarov, N.S.; Siksnis, V.; Martinek, K. Strategy for stabilizing enzymes: part 2. Increasing enzyme stability by selective chemical modification. *Biocatalysis* **1990**, *3*, 189–196.
15. Jaswal, S.S.; Sohl, J.L.; Davis, J.H.; Agard, D.A. Energetic landscape of alpha-lytic protease optimizes longevity through kinetic stability. *Nature* **2002**, *415*, 343–346.
16. Lumry, R.; Eyring, H. Conformational changes of proteins. *J. Phys. Chem.* **1954**, *58*, 110–120.
17. Wang, P.; Dai, S.; Waezsada, S.D.; Tsao, A.Y.; Davison, B.H. Enzyme stabilization by covalent binding in nanoporous sol–gel glass for nonaqueous biocatalysis. *Biotechnol. Bioeng.* **2001**, *74*, 249–255.
18. Blanch, H.; Clark, W.; Eds. *Biochemical Engineering*; Marcel Dekker: New York, 1997; 103–161.
19. Kim, J.; Delio, R.; Dordick, J.S. Protease-containing silicates as active antifouling materials. *Biotechnol. Prog.* **2002**, *18*, 551–555.
20. Wang, P.; Sergeeva, M.V.; Dordick, L.; Lim, J.S. Biocatalytic plastics as active and stable materials for biotransformations. *Nat. Biotechnol.* **1997**, *15*, 789–793.



# Biological and Chemical Decontamination

Peter K. Stoimenov  
Kenneth J. Klabunde

*Department of Chemistry, Kansas State University, Manhattan, Kansas, U.S.A.*

## INTRODUCTION

A great deal of interest has been focused on nanomaterials in the last decade because of their unusual physical, mechanical, and chemical properties. They have found numerous applications, or are expected to find such applications in electronics, catalysis, composite materials, etc. The differences in their chemical properties, in particular, compared with the corresponding bulk material are mostly because of a largely increased surface area and a great increase in the number of active sites on the surface, such as corners, edges, and dislocations. Furthermore, nanomaterials are usually less thermodynamically stable than the corresponding bulk materials, which contributes to their enhanced chemical activity.

Decontamination of chemical and biological warfare is of considerable interest not only for eliminating the hazard of warfare agents on a battlefield, but also in cases of terrorist attacks, industrial accidents, demilitarization of warfare stockpiles, etc. The application of solid materials as decontaminants for both chemical and biological warfare agents has been severely limited by the incomplete and generally slow interaction of solid materials with warfare agents. Nanoparticles with their high surface area, enhanced chemical reactivity, and easy deployment allow the development of new perspectives regarding decontamination. In addition, generally, the products of these decontamination reactions are benign, mineral-like solids.

## CHEMICAL WARFARE AGENTS DECONTAMINATION

A component of a filtration system is always a high surface area solid, usually activated carbon, which adsorbs warfare agents physically but does not destroy them. The sorbed material is still highly toxic and the decontamination of the contaminated carbon is a problem. Nanoparticles offer surface areas comparable with active carbon, but at the same time high chemical reactivity toward the warfare agents, allowing their chemical decomposition and detoxification.

Several chemical warfare agents are noted as most important because of their very high toxicity, persistence, and large existing stockpiles.<sup>[1]</sup> Mustard gas or HD is a blistering agent, which can be lethal in high concentrations. It irreversibly alkylates key amines in organisms such as proteins, enzymes, and especially DNA, which causes cell malfunction and death. Another warfare agent with similar action and chemical structure is the arsine analog, Lewisite (Fig. 1).

Another large class of chemical warfare agents is the nerve agents class, which is based on phosphonic acid derivatives. Some of them feature a relatively stable bond with fluorine-like sarin (GB agent) or soman (GD agent) (Fig. 1). The later generation, such as VX, contains a more stable ester bond, which contributes to higher persistence, slower hydrolysis, and decontamination, which is more difficult. The VX generation of warfare agents is more toxic as well. The action of the nerve agent is based on its ability to selectively bind to the active centers of key phosphatase enzymes (such as acetylcholinesterases), which are responsible for nerve impulse propagation. Similar to nerve gases are certain widely used pesticides, such as paraoxon (Fig. 1).

## Physical Action

There are several requirements for successful decontamination,<sup>[1]</sup> the most important of which is that non-toxic by-products must be formed and the decontamination should be quick and complete. There is a requirement that the decontamination agent should not be corrosive to the surfaces to which it is applied. Nanoparticles do have excellent properties in this respect, as they are very easy to deploy and to clean up. In general, they are not corrosive, or not as corrosive as typical developed decontamination compositions and solutions. As such, nanoparticulate formulations should be applicable to all kind of surfaces, including the skin, metals, and sensitive equipment, including electronics. Most decontaminating compositions are liquids, which contain organic liquid, electrolytes, as well as corrosive oxidants.

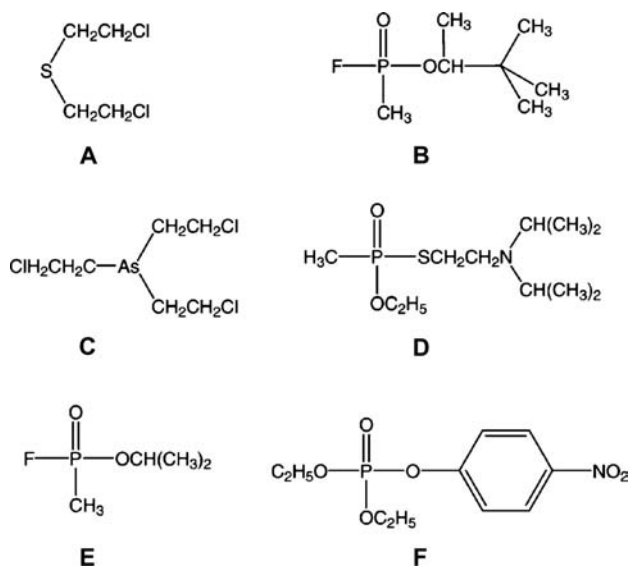


**Fig. 1** Structures of the most common chemical warfare agents. (A) 2,2'-Dichloroethyl sulfide (mustard gas or HD); (B) soman or GD; (C) Lewisite; (D) VX agent; (E) sarin or GB; and (F) paraoxon (pesticide).

Nanoparticles are in the form of fine powder, which can be deployed by an inert solvent suspension such as freon or just by carrier gas under pressure. They can be removed by standard vacuum cleaning procedures. Alternatively, if an air-filtering or water-filtering approach is needed, nanoparticles can be used in the form of porous reactive pellets.

## CHEMICAL ACTION

It has already been mentioned that chemical warfare agents are usually alkylating agents. Usually their hydrolysis renders them non-toxic or much less toxic than warfare agents because the chemical groups that determine toxicity are usually the most reactive parts of the molecule.<sup>[1]</sup> Similarly, detoxification can be achieved by their oxidation<sup>[1-3]</sup> because both HD and nerve gases contain relatively easy-to-oxidize sulfur (HD and VX) and/or phosphorus atoms, which have a large contribution to their extreme toxicity.

Metal oxide nanoparticles are apparently a very good choice for detoxification of warfare agents because of the presence of a huge number of basic Lewis and Bronsted sites, as well as acidic sites, which can very significantly accelerate hydrolysis process. By-products, in the form of phosphonates and alcohols, have the tendency to bind strongly to solid surfaces and be retained there. Taking into consideration the high surface area of nanomaterials, this corresponds to a large amount of decomposed warfare agent and rapid reactions compared with bulk metal oxide surfaces because the rate of the interaction is

proportional to the contact area. It is additionally strongly facilitated on corners and edges, which have higher activity and lower activation energy barriers compared with normal surface sites.

Most interesting for this type of application are certain metal oxides that have high melting points and chemical stability. The nanomaterial form is thermodynamically less stable than the corresponding bulk material. The higher the melting point is (higher lattice energy), the more stable the nanomaterial will be. Based on this reaction, the best metal oxide nanoparticle systems are magnesium oxide and aluminum oxide nanoparticles,<sup>[4-9]</sup> although activity has also been found for other oxides, such as calcium oxide.<sup>[10]</sup>

## Detoxification of HD (Mustard Gas)

The toxicity of mustard gas (Fig. 1) is because of its capability to attach simultaneously and irreversibly to two biomolecules. The reaction takes place by an  $S_N^1$  mechanism with an intermediate sulfonium cation as a key reaction species.

Magnesium oxide has a considerable number of basic sites that interact with the HD by hydrohalogen elimination, forming vinyl chloroethyl sulfide, or by exchange of chlorine with a hydroxyl group from the magnesium oxide surface.<sup>[6]</sup> The reaction proceeds further to divinylsulfide and in the other case to the corresponding glycol. The final ratio between the two major products was found to be approximately 50:50. The half-life of HD in this first-order reaction is 17.8 hr.<sup>[6]</sup> According to a careful kinetic examination, the reaction actually starts much faster. However, it slows down when part of the surface becomes clogged with residues of the reaction, which are permanently bound to the surface. Thus the limiting step in the reaction is the diffusion of the viscous and relatively low-volatility HD among magnesium oxide aggregates. This study has shown that the half-life of warfare agents is proportional to their vapor pressure—the higher the vapor pressure is, the higher the diffusion rate and hence the reactions leading to decontamination will be.<sup>[6]</sup> When calcium oxide was tested instead of magnesium oxide, the ratio of the products changed significantly to 80:20 elimination/hydrolysis products.<sup>[10]</sup> Elimination was the preferred route for the reaction, although it depended significantly on the way the sample was pretreated: When the nanoparticles were dried in advance before their contact with HD, elimination to hydrolysis products changed completely to 5:95 elimination/hydrolysis products.<sup>[10]</sup> It is particularly important to note that a catalytic decomposition process was found for CaO nanoparticles.<sup>[10]</sup>

Additional experiments have shown<sup>[7]</sup> that dispersion of nanoparticulate magnesium oxides in a variety



of solvents with/without addition of small amounts of water can alter the rate as well as the product types and their ratio. The most prominent effect observed was that the solvent speeds up the reactions because it eliminates the diffusion problem caused by the relatively high viscosity of warfare agents. Another important feature is that Lewis and Bronsted acid sites work simultaneously with Lewis base sites to decompose HD and HD stimulants.<sup>[7]</sup>

Another oxide that can be synthesized with high surface area using an aerogel procedure is aluminum oxide (AP- $\text{Al}_2\text{O}_3$ ). Although aluminum oxide is not as basic as magnesium and calcium oxides, it possesses a large number of Lewis acid sites, which accelerate hydrolysis processes.<sup>[5]</sup> Because nucleophilic centers are much less abundant, elimination is less prominent and the ratio of the elimination/hydrolysis products is 17:83, with the major product being dithioglycol, as observed by solid-state nuclear magnetic resonance (NMR).<sup>[5]</sup>

#### Detoxification of nerve agents (VX, GD, GB, and paraoxon)

The interaction of nerve agents such as VX and GD (soman) (Fig. 1) with nanosized magnesium oxide particles (AP-MgO) was tracked by solid-state NMR.<sup>[6]</sup> It allowed the kinetics of interaction as well as the intermediate products to be determined. The width of the peaks was used to judge whether a particular product or intermediate was attached to the surface: Species attached to the surface have broader peaks because of anisotropic effects. In the case of GD, hydrolysis was the major process that took place, yielding GD acid (pinacolylmethylphosphonic acid) as a major product and methylphosphonic acid as a secondary product. According to NMR data, both products strongly interact with the surface, most probably by strong ionic interaction.<sup>[6]</sup> The basic surface of the magnesium oxide nanocrystals most certainly converts the products to their respective anions, which bind with the positively charged surface. A quick start of the reaction, followed by a slowing down to a constant rate of  $t_{1/2} = 28$  min, is observed, as in all cases of interactions of nanomaterials with viscous warfare agents.

The VX agent is a thioester with high viscosity and lower volatility compared with GD. It slowly hydrolyses to ethyl methylphosphonic acid and methylphosphonic acid. It is noteworthy to mention that the toxic hydrolysis product, EA-2192 (the VX toxin with the ethyl group replaced by hydrogen), which usually forms by hydrolysis in water, is not observed when contacted with AP-MgO nanoparticles. A very similar behavior was found in the interaction of VX and GD with nanosized calcium oxide.<sup>[10]</sup>

Nanoscale-sized aluminum oxide interacts with nerve agents with a very different rate: Although the

reactive and relatively volatile GD has a  $t_{1/2} = 1.8$  hr after a quick start-up, the VX agent's  $t_{1/2}$  is above 6 days. The difference from the MgO case is that the interaction with the warfare agents erodes the surface, allowing the "bulk" of  $\text{Al}_2\text{O}_3$  nanoparticles to participate in the detoxification process. This makes aluminum oxide a very promising material for warfare agent cleaning because this erosion behavior, coupled with its high surface area, allows a very high reaction capacity.

### BIOLOGICAL WARFARE DECONTAMINATION USING NANOMATERIALS

Biological warfare agents could be several completely different types: bacteria, fungi, viruses, or toxins. All these have major differences in their behavior, and their decontamination procedures can vary significantly. This makes creating a single total decontaminating material practically impossible.

There are several methods recognized so far in decontaminating biological warfare agents. The most widely applied method is disinfecting solutions, such as diluted bleach or chloramine T solution. They have the advantage of quick and complete disinfection of bacteria, viruses, and certain fungi. However, it has very significant disadvantages, such as aging, which deteriorates disinfecting activity. Another disadvantage is that the bleach solution exhibits a strong smell, is corrosive, and is safely applicable only for the most durable surfaces. There are studies which reveal that in some respects, bleach effectiveness can be overrated,<sup>[11]</sup> especially for aged solutions.

A limited method for decontamination is applying a gas such as chlorine or chlorine dioxide. It cannot be applied in open spaces and on sensitive equipment, and can permanently damage many surface types.

Another approach is the use of oil-in-water microemulsions, developed by Hamouda et al.<sup>[12,13]</sup> and Hamouda and Baker.<sup>[14]</sup> They have demonstrated good activity against certain spores and bacteria, but they have the disadvantage of being difficult to remove after the decontamination procedure. In addition, they cannot be used for filtering airborne pathogens.

An alternative to the aforementioned approaches is the application of very fine solid powders in the form of nanoparticles. They are advantageous for a decontamination procedure because they can be easily collected from surfaces by simple vacuum cleaning, and they can be applied on sensitive electronic and other equipment because no liquid is present; they are much less corrosive than any of the aforementioned methods as well.

Nanoparticles such as AP-MgO, ZnO, or CaO have limited bactericidal activity against most biological warfare agents, although they have decent activity

against vegetative bacteria such as *Escherichia coli*, *Bacillus cereus*, and *B. subtilis*.<sup>[15]</sup> An outstanding property of nanoparticles is the demonstration of their capability to remove powerful biological toxins such as aflatoxins.<sup>[15]</sup>

As was discussed in the “Introduction,” nanoparticles feature huge surface areas and higher surface reactivity compared with bulk materials. Thus nanoparticles have very high adsorption activity per mass adsorbent, which allows adsorption of potent bactericides such as elemental chlorine, bromine, or iodine. Halogens are excellent bactericides in general. However, their use is restricted because of their high volatility, corrosive action, and toxicity.

Nanoparticles are capable of adsorbing as much as 6–10 wt.% free chlorine, 13–15 wt.% bromine, and 20–30 wt.% iodine. The adsorbates are preserved as halogens on the surface, preserving their properties as oxidizers, including their excellent bactericidal and sporicidal properties.<sup>[16]</sup>

The halogen-loaded magnesium oxide nanoparticles were found to preserve their activity even in water suspension,<sup>[16]</sup> or in the dry state. If suspended, all types of halogen-loaded nanoparticles become positively charged, thus being attracted to the negatively charged (in general) bacteria or spores.<sup>[16]</sup> It was demonstrated by laser confocal microscopy that AP-MgO/X<sub>2</sub> (X = Cl, Br, none) coagulates spontaneously with the bacteria in clumps composed of both bacteria and nanoparticle aggregates. When observed with transmission electron microscopy (TEM) and atomic force microscopy (AFM), microbial spores (*B. subtilis*) and vegetative cells (*E. coli*) were severely damaged (Fig. 2). In the case of more vulnerable vegetative cells, nanoparticles were found to enter the cells through holes developed in the membrane, thus bringing the adsorbed halogen inside the cell. The cell membrane and the spore coat were significantly damaged and eventually killed the cell by allowing its internal content out of the cell envelope.

An important feature of nanoparticles for their sporicidal activity is their basicity: It was demonstrated that pretreatment of spores with basic solution removes partially or completely the thin outermost layer composed of base-sensitive proteins, which is a strong barrier for conventional sporicides, including free halogens.<sup>[17]</sup> Apparently, the nanoparticles of magnesium oxide have several properties, which render them as highly active bactericides and sporicides. They are abrasive (which is important for damaging the cell membrane), basic (important for partial spore coat removal), oppositely charged to the bacteria and spore cells, and carry a significant amount of oxidizing potential in the form of a potent bactericide (chlorine or bromine). For example, chlorine-loaded magnesium oxides carry as much as 10 wt.% active chlorine,

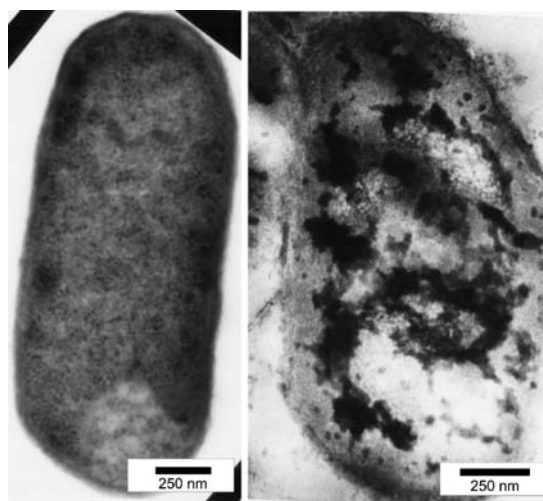


**Fig. 2** Nontreated *E. coli* (left) and *E. coli* treated with AP-MgO/Cl<sub>2</sub> nanoparticles (right). The dark matter in the right micrograph represents nanoparticles that penetrated inside the cell.

whereas in comparison, undiluted bleach contains 6 wt.% active chlorine.

## CONCLUSION

Nanoparticles constitute a new realm of the matter, which has properties very different from those of the bulk material. Because of higher surface-to-bulk ratios for the constituting atoms or ions and the much higher overall surface per unit weight, they exhibit outstanding chemical, physical, and biological properties. Their high surface area and activity may find use in “hasty” decontamination of warfare agents. Nanoparticles of metal oxides can be pelletized and used as an additional protective layer for standard activated carbon filters. Furthermore, nanoparticles detoxify adsorbed warfare agents. Nanoparticulate magnesium oxide and its halogen-loaded derivatives, in particular, were found to possess bactericidal, viricidal, and sporicidal properties as well as capabilities to adsorb and deactivate complex toxins such as aflatoxins.

Nanoparticles have the potential to be used as an “all-in-one” solution for both chemical and biological warfare decontamination.

## REFERENCES

1. Yang, Y.; Baker, J.A.; Ward, J.R. Decontamination of chemical warfare agents. *Chem. Rev.* **1992**, *92* (8), 1729–1743.
2. Yang, Y.; Szafraniec, L.L.; Beaudry, W.T. Perhydrolysis of nerve agent VX. *J. Org. Chem.* **1993**, *58* (25), 6964–6965.

- Yang, Y. Chemical detoxification of nerve agent VX. *Acc. Chem. Res.* **1999**, *32* (2), 109–115.
- Klabunde, K.J. *Nanoscale Materials in Chemistry*; Klabunde, K.J., Ed.; John Wiley and Sons, 2001.
- Wagner, G.; Procel, L.R.; O'Connor, R.J.; Munavalli, S.; Carnes, C.L.; Kapoor, P.N.; Klabunde, K.J. Reactions of VX, GB, GD, and HD with nanosize Al<sub>2</sub>O<sub>3</sub>. Formation of aluminophosphonates. *J. Am. Chem. Soc.* **2001**, *123* (8), 1636–1644.
- Wagner, G.; Bartam, P.W.; Koper, O.; Klabunde, K.J. Reactions of VX, GD, and HD with nanosize MgO. *J. Phys. Chem., B* **1999**, *103* (16), 3225–3228.
- Narske, R.M.; Klabunde, K.J.; Fultz, S. Solvent effects of the heterogenous adsorption and reactions of (2-chloroethyl)ethyl sulfide on nanocrystalline magnesium oxide. *Langmuir* **2002**, *18* (12), 4819–4825.
- Lucas, E.M.; Klabunde, K.J. Nanocrystals as destructive adsorbents for mimics of chemical warfare agents. *Nanostruct. Mater.* **1999**, *12* (1), 179–182.
- Rajagopalan, S.; Koper, O.; Decker, S.; Klabunde, K.J. Nanocrystalline metal oxides as destructive adsorbents for organophosphorous compounds at ambient temperatures. *Eur. J. Chem.* **2002**, *8* (11), 2602–2607.
- Wagner, G.W.; Koper, O.; Lucas, E.; Decker, S.; Klabunde, K.J. Reactions of VX, GD, and HD with nanosize CaO: autocatalytic dehydrohalogenation of HD. *J. Phys. Chem., B* **2000**, *104* (21), 5118–5123.
- Sagripani, J.; Bonifacino, A. Bacterial spores survive treatment with commercial sterilants and disinfectants. *Appl. Environ. Microbiol.* **1999**, *65* (9), 4255–4260.
- Hamouda, T.; Myc, A.; Donovan, B.; Shih, A.; Reuter, J.; Baker, J., Jr. A novel surfactant nanoemulsion with a unique non-irritant topical antimicrobial activity against bacteria, enveloped viruses and fungi. *Microbiol. Res.* **2001**, *156* (1), 1–7.
- Hamouda, T.; Hayes, M.; Cao, Z.; Tonda, R.; Johnson, K.; Craig, W.; Brisker, J. A novel surfactant nanoemulsion with broad band sporicidal activity against *Bacillus* species. *J. Infect. Dis.* **1999**, *180* (6), 1939–1949.
- Hamouda, T.; Baker, J., Jr. Antimicrobial mechanism of action of surfactant lipid preparations in enteric Gram-negative bacilli. *J. Appl. Microbiol.* **2000**, *89*, 397–403.
- Koper, O.; Klabunde, K.J.; Marchin, G.L.; Klabunde, K.J.; Stoimenov, P.; Bohra, L. Nanoscale powder and formulations with biocidal activity toward spores and vegetative cells of *Bacillus* species, viruses, and toxins. *Curr. Microbiol.* **2002**, *44* (1), 49–55.
- Stoimenov, P.K.; Klinger, R.L.; Marchin, G.L.; Klabunde, K.J. Metal oxide nanoparticles as bactericidal agents. *Langmuir* **2002**, *18* (17), 6679–6686.
- Russel, A.D. *Disinfection, Sterilization and Preservation*, 4th Ed.; Block, S.S., Ed.; Lea and Febiger, 1991.

# Biomaterials: Mechanical Characterization

**Eunice Phay Shing Tan**

*Division of Bioengineering, National University of Singapore, Singapore, Singapore*

**Chwee Teck Lim**

*Division of Bioengineering and Department of Mechanical Engineering,  
National University of Singapore, Singapore, Singapore*

## INTRODUCTION

Nanoscale biomaterials, in the form of nanostructures such as nanofibers and nanoparticles, have been extensively used in biomedical applications such as tissue engineering and drug delivery. As these nanostructures are subjected to physical stresses within the body during application, it is important to ensure that their structural integrity remains intact and that they do not fail in vivo. Thus, there is a need to mechanically characterize these nanoscale biomaterials. Here, techniques for characterizing these nanobiomaterials using tensile test, nanoscale bend test, and nanoindentation will be presented and the challenges involved highlighted. Most of these techniques involve the use of atomic force microscopy (AFM) or AFM cantilevers as a means to apply or measure force and displacement in the nanometer range. The current limitations in the mechanical characterization of nanoscale biomaterials and future work required will be briefly mentioned.

## BACKGROUND

Biomaterials can be defined as any biological or man-made materials that are used to construct prosthetics or medical devices for implantation in a human body for the purpose of performing, augmenting, or replacing a natural function.<sup>[1,2]</sup> Biomaterials in the form of nanostructures are often fabricated to mimic the body's extracellular matrix in the area of tissue engineering<sup>[3]</sup> and/or as drug delivery devices in the area of pharmaceuticals.<sup>[4]</sup> These nanostructures normally come in the form of nanofibers and nanoparticles. When the nanostructures are implanted in the body, it is essential that they do not buckle, deform permanently, or fracture when subjected to various stresses in the human body. Therefore it is important to obtain the mechanical properties of individual nanofibers and nanoparticles to ensure that these nanostructures are able to perform their designated functions in vivo.

In this entry, various mechanical characterization techniques of these nanostructures will be presented. These techniques include tensile test, bend test, and indentation done at the nanoscale for the characterization of nanofibers. Owing to the shape of nanoparticles, only nanoindentation or compression tests have been performed. The challenges of each technique and the methods of overcoming them will be mentioned in each section. Finally, the current limitations and future directions will be discussed.

## NANOFIBERS

The most common type of nanofibers used for biomedical applications are the biodegradable polymeric nanofibers. These fibers have been used to form tissue engineering scaffolds for the regeneration of tissues such as cartilage,<sup>[5]</sup> blood vessel,<sup>[6]</sup> and nerve.<sup>[7]</sup> The preferred method of fabricating such nanofibers is by electrospinning as it is simple and able to produce continuous nanofibers (Fig. 1A).<sup>[3]</sup> Phase separation has also been used to produce nanofibers in the form of a nanofibrous foam (Fig. 1B).<sup>[7,8]</sup>

Owing to the small size of the nanofibers, conventional testing methods of characterizing larger fibers cannot be directly applied to nanofibers. The difficulties of testing single nanofibers include preparing and handling single strand nanofibers, finding force transducers and actuators with nanoscale and subnanoscale resolutions, and finding a way to observe the deformation of nanofibers. Although methods for testing nanoscale materials have been established for materials such as carbon nanotubes (CNTs),<sup>[9–11]</sup> these methods cannot be easily applied to polymeric nanofibers as the tests have to be carried out inside a scanning electron microscope (SEM) or transmission electron microscope. Owing to the nonconductive nature of most polymeric nanofibers, such methods are not suitable. However, by modifying existing techniques for testing microscale fibers and CNTs, feasible methods of testing single polymeric nanofibers have been developed.

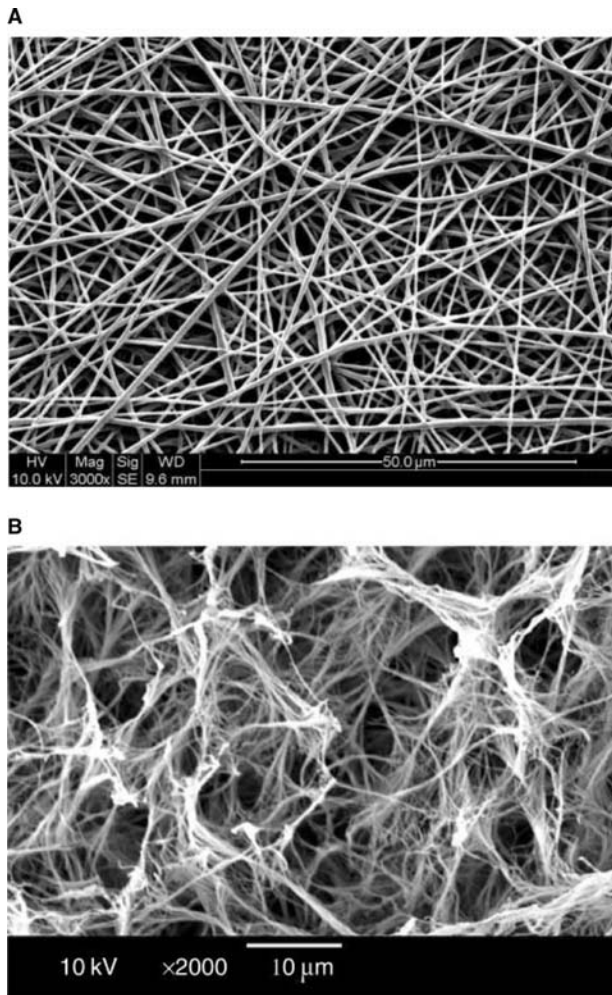


**Fig. 1** SEM images of biodegradable nanofibers. (A) Electrospun polycaprolactone (PCL) nanofibers and, (B) poly(L-lactic acid) (PLLA) nanofibrous scaffold produced by phase separation.

### Tensile Test

Some challenges unique to tensile tests in addition to those mentioned in the previous section include sample

gripping and fiber alignment. Conventional mechanical gripping methods may not be suitable for nanofibers owing to the small size of the fibers.<sup>[12]</sup> Fiber alignment is necessary as misalignment between fiber axis and loading direction may result in unwanted bending moment, which may lead to premature sample failure.<sup>[12]</sup> Two methods of performing tensile test of nanofibers are presented with these factors in mind.

AFM cantilevers have been used for tensile tests of CNTs within the SEM chamber.<sup>[11,13]</sup> Although this method is not suitable for nonconductive samples, it can be adapted for testing polymeric nanofibers. Tan et al.<sup>[14]</sup> performed tensile test of electrospun polyethylene oxide (PEO) nanofibers using a piezo-resistive AFM cantilever. Aligned electrospun nanofibers were produced<sup>[15]</sup> to obtain several aligned fibers across two parallel strings mounted on a wooden frame. One end of a selected nanofiber was attached to a motorized optical microscope stage and the other end to a piezo-resistive AFM cantilever tip (Fig. 2). The nanofiber was stretched by moving the microscope stage in the X-direction and the force was measured by the cantilever deflection. The stress-strain characteristics of the nanofiber can be obtained from this test. Although this method is feasible, it is time consuming and requires practice for successful attachment of nanofiber to the AFM tip and the microscope stage.

The conventional method of preparing tensile test samples of microfibers is to mount single fibers onto a paper or plastic frame with the fiber spanning across a hole in the frame.<sup>[16,17]</sup> A similar method of preparing single nanofibers for tensile test can be done for electrospun nanofibers.<sup>[18]</sup> Currently, a commercial nano tensile testing system (Nano Bionix System, MTS, U.S.A.) has the capability of testing polymeric nanofibers of as small as few hundred nanometers.<sup>[18,19]</sup> Electrospun polycaprolactone (PCL)<sup>[18]</sup> and poly(L-lactic acid) (PLLA)<sup>[19]</sup> nanofibers have been tested using this method. Polycaprolactone nanofibers were electrospun by directly depositing nanofibers across a cardboard frame (Fig. 3). After mounting the sample on the nano tensile tester, the cardboard frame was cut along the

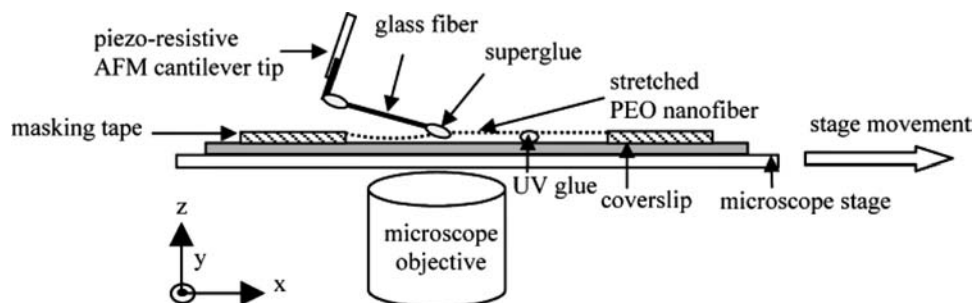


**Fig. 2** Schematic diagram of the tensile test of a polyethylene oxide (PEO) nanofiber using a piezo-resistive AFM tip. *Source:* From Ref.<sup>[14]</sup>.

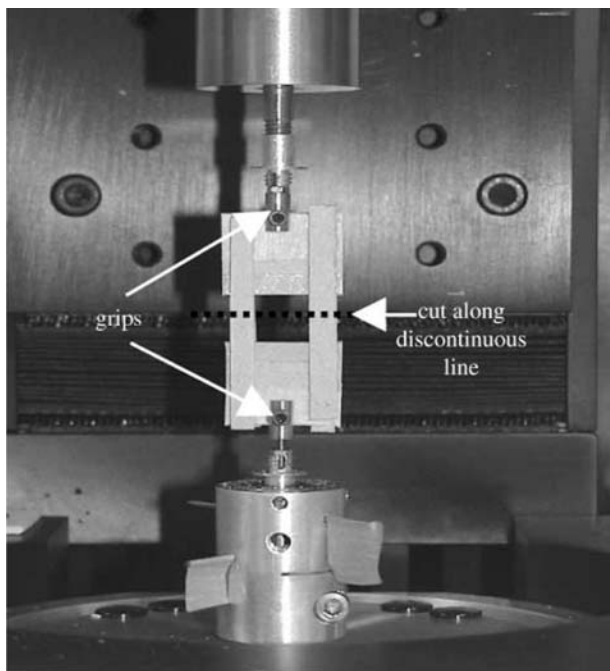


**Fig. 3** A single nanofiber sample (not visible) is first mounted vertically across a cardboard partition or frame. This cardboard frame is then mounted onto a nano tensile tester for the nano tensile testing of a single polymer nanofiber. (NanoBionix, MTS, U.S.A.). *Source:* From Ref.<sup>[18]</sup>.

discontinuous lines at the two sides of the frame before the fiber was stretched (Fig. 3). The stress–strain curves for the PCL fibers at different fiber diameters are shown in Fig. 4.

The mechanical properties were observed to vary with fiber diameter owing to the higher “draw ratio” that was applied during the electrospinning process for fibers with smaller diameter. Although many samples can be tested conveniently with this method, observation of the nanofibers during the tensile test is

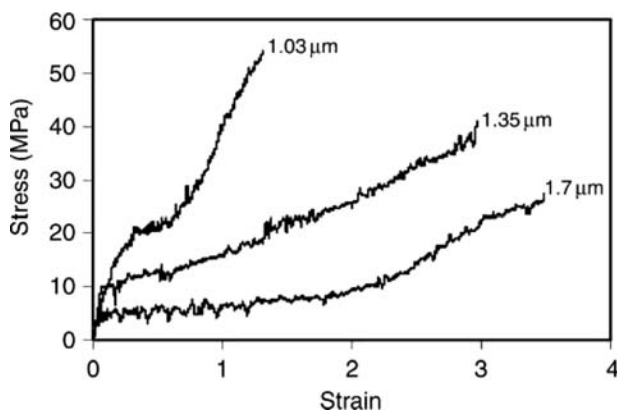


**Fig. 4** Plot of stress vs. strain for electrospun polycaprolactone (PCL) ultrafine fibers with varying fiber diameters. *Source:* From Ref.<sup>[18]</sup>.

difficult as this system does not provide a suitable observation system to investigate the deformation and mode of failure.

### Bend Test

The AFM is able to apply forces in the nano- and pico-Newton range and measure deformation in the subnanometer range. Thus it is a very useful tool for mechanical testing of nanostructures. The AFM has been used for three-point bend tests of CNTs<sup>[20–22]</sup> by using the AFM tip to apply a point load at the mid-span of a CNT suspended over a hole or groove. Three-point bend test of nanofibers such as  $\beta$ -chitin,<sup>[23]</sup> PEO,<sup>[24]</sup> and PLLA<sup>[25]</sup> can be performed in the same way as the sample does not need to be conductive.

PLLA nanofibers produced by phase separation will be used to illustrate three-point bend test of single nanofibers.<sup>[25]</sup> The bend test was performed by using an AFM tip to apply a point load at the mid-span of a suspended nanofiber over an etched groove on the silicon wafer (Fig. 5).

The adhesion between the sample and substrate is usually sufficient for the bend test to be conducted successfully without slippage at the fixed ends. Young’s

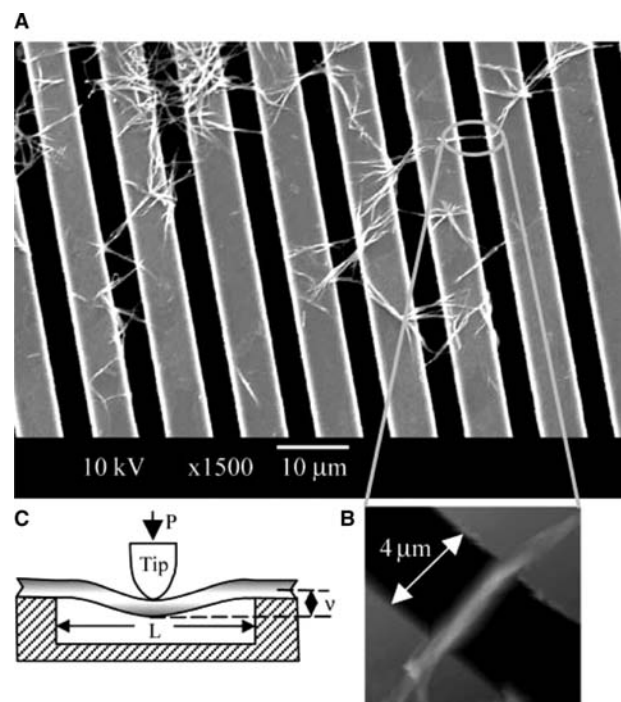


**Fig. 5** Nanofibers suspended over etched grooves of silicon wafer. (A) SEM image of poly(L-lactic acid) PLLA nanofibers deposited onto the silicon wafer; (B) AFM contact mode image of a single nanofiber (300 nm diameter) suspended over an etched groove; and (C) schematic diagram of a nanofiber with mid-span deflected by an AFM tip. *Source:* From Ref.<sup>[25]</sup>.



modulus,  $E$ , is found from beam bending theory<sup>[26]</sup> for a beam with two ends fixed as

$$E = \frac{PL^3}{192\nu I} \quad (1)$$

where  $P$  is the maximum force applied,  $L$  is the suspended length,  $\nu$  is the deflection of the beam at mid-span, and  $I$  is the second moment of area of the beam (where  $I = \pi D^4/64$  and  $D$  is the beam diameter). The method of obtaining  $\nu$  from the force curves using AFM is shown in Fig. 6.  $E$  is found to be  $1.0 \pm 0.2$  GPa for PLLA nanofibers assuming that the fibers undergo pure bending.

The nanofiber was assumed to be an elastic string instead of a rigid elastic beam for the bend test of electrospun PEO nanofibers<sup>[24]</sup> as the force curves for suspended PEO nanofibers were best fitted with a cubic equation. In this case, the Young's modulus is given by

$$E = \frac{P}{8A(\nu/L)^3} \quad (2)$$

where  $A$  is the cross-sectional area of the fiber. It is necessary to ensure that there is no indentation made on the nanofiber by the AFM tip for the bend tests as this will result in underestimating the Young's modulus. This can be done by ensuring that no indentation is made when applying the same maximum force to portions of nanofiber on the substrate. This technique is useful for testing both continuous nanofibers and nanofibrous networks.

A novel way of performing bend test of single nanofibers was proposed by Gu et al.<sup>[27]</sup> Single electrospun

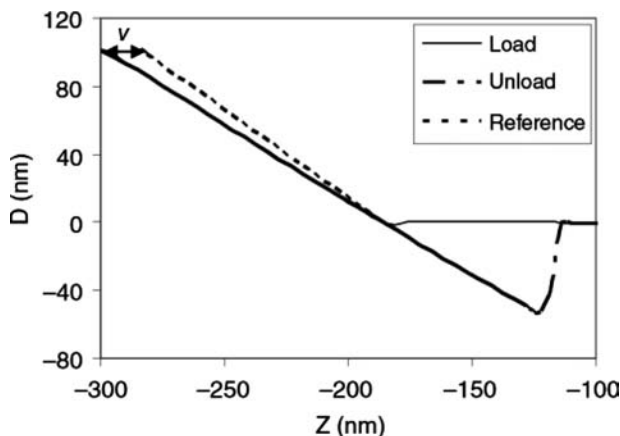


**Fig. 6** Plot of cantilever deflection ( $D$ ) vs. vertical displacement of the  $z$ -piezo ( $Z$ ). A reference curve is obtained by measuring the cantilever deflection over the  $Z$  piezo displacement on a silicon wafer. The loading and unloading curves are obtained by using the AFM tip to deflect the mid-span of the nanofiber. The deflection of the fiber,  $\nu$  is the difference between the loading and the reference curve. *Source:* From Ref.<sup>[25]</sup>.

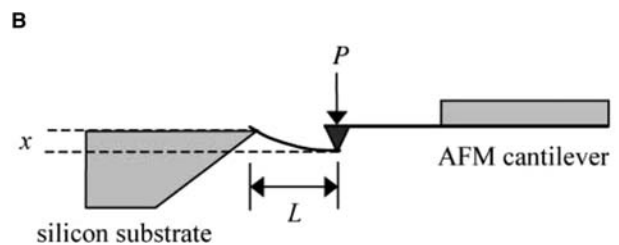
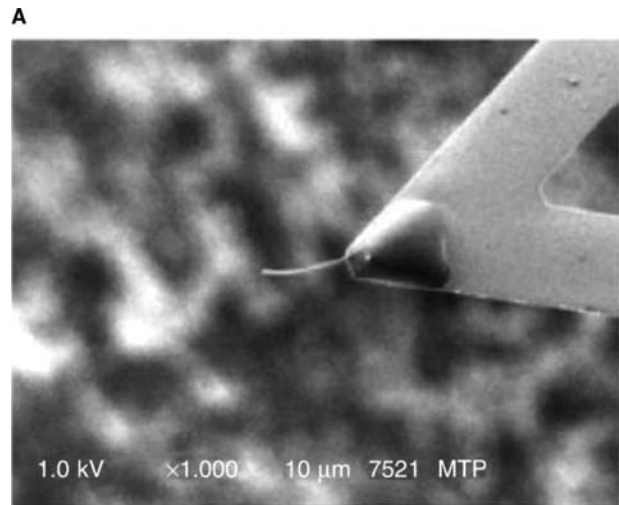


**Fig. 7** (A) SEM image of a polyacrylonitrile (PAN) fiber attached to a contact mode cantilever and (B) schematic diagram of a nanofiber with one end attached to AFM tip and the other end deflected by silicon substrate. *Source:* From Ref.<sup>[27]</sup>.

polyacrylonitrile (PAN) nanofibers were cut before attaching one end to an AFM tip with epoxy (Fig. 7A). The free ends of the nanofibers were bent on the sharp edge of a silicon substrate (Fig. 7B). The dimensions of the nanofiber are obtained from SEM observation without coating the sample. The nanofiber was considered to be an ideal spring over the whole length and the Young's modulus is given by

$$E = \frac{4}{3\pi} \times \frac{P}{x} \times \frac{L^3}{r^4} \quad (3)$$

where  $r$  is the radius of the nanofiber and  $P/x$  is the product of the spring constant of cantilever and the slope of the approaching line of the force curve. This method may not be suitable for fibers that are sensitive to thermal treatments as the fibers need to be first cooled in liquid nitrogen before cutting them and then subsequently get heated up by electron beam in the SEM.

## Nanoindentation

Nanoindentation of nanofibers is performed by using an AFM tip to apply a load on the curved or sectioned

surface of the nanofiber, such that the nanofiber deforms elastically or elastic-plastically. Although the sample can be prepared for testing by simply depositing the nanofibers on a hard and flat substrate with sufficient adhesion between the substrate and the nanofiber, interpretation of nanoindentation results may vary based on the assumptions used.

### Elastic nanoindentation

The elastic modulus of the material is obtained during elastic nanoindentation, whereby the deformation of the sample by the AFM tip is recoverable. The use of AFM for nanoindentation requires careful consideration of the following factors:

1. The elastic modulus values can be overestimated if the diameter of the nanofiber is too small (<200 nm).<sup>[28]</sup> However, this can be overcome by using small penetration depths.
2. Actual tip radius and cantilever spring constants usually deviate from the nominal values provided by the manufacturer.
3. Surface roughness of the nanofiber will result in the reduction of contact pressure for a given load,<sup>[29]</sup> thereby resulting in an underestimated value of elastic modulus.
4. If nanoindentation is performed on the curve surface of the nanofiber, the curved surface of the nanofiber has to be taken into account especially when the radius of curvature of the AFM tip and the fiber diameter are of comparable size.
5. As the AFM tip is not perpendicular to the sample surface, slip and friction between the AFM tip and the sample surface may occur during indentation.<sup>[30]</sup> However, the non-perpendicular load factor is not significant.<sup>[31]</sup>
6. In a high-humidity environment (>70% relative humidity), the effects of adhesion owing to capillary effect of water condensation between tip and sample can be significant.<sup>[32]</sup>

AFM was used to perform nanoindentation of electrospun PAN nanofibers.<sup>[33,34]</sup> It was assumed that the indentation depth was of comparable size to the AFM tip, and the tip radius (5 nm) was small compared to nanofiber diameter (50–500 nm) such that the nanofiber curvature can be ignored. The reduced modulus is given by

$$\frac{P}{\delta} = 2\sqrt{\frac{A}{\pi}}E_r \quad (4)$$

where  $P$  is the normal force,  $\delta$  is the indentation depth,  $A$  is the contact area, and  $E_r$  is the reduced modulus,

which is given by

$$\frac{1}{E_r} = \frac{1 - \nu^2}{E} + \frac{1 - \nu_i^2}{E_i} \quad (5)$$

where  $E$  and  $\nu$  are the elastic modulus and Poisson's ratio, respectively, for the sample and  $E_i$  and  $\nu_i$  are the same quantities for the AFM tips. As the AFM tip is much stiffer than polymeric samples ( $E_i \gg E$ ), the last term in Eq. (5) is assumed to be zero.

A different assumption was used for the nanoindentation of PLLA nanofibers produced by the phase separation method.<sup>[35]</sup> Hertz's theory of normal contact of elastic solids was used to analyze the force-indentation data.<sup>[36]</sup> The nanofiber was assumed to be a cylinder and the AFM tip a sphere. The reduced modulus,  $E_r$ , is given by

$$E_r = \sqrt{\frac{9P^2}{16R_e\delta^3}} \quad (6)$$

where  $P$  is the force applied,  $\delta$  is the indentation depth, and  $R_e$  is the equivalent radius for a spherical indenter in contact with an infinitely long cylinder.  $R_e$  is given by

$$R_e = \sqrt{\frac{R_t^2 R_f}{R_t + R_f}} \quad (7)$$

where  $R_t$  is the AFM tip radius and  $R_f$  is the radius of the nanofiber. The elastic modulus of the nanofiber was then calculated assuming that  $\nu$  is 0.33.<sup>[37]</sup>

The root mean square (RMS) roughness<sup>[29]</sup> ( $R_q = 1.1 \pm 0.6$  nm) was taken from the AFM image of the nanofiber surface and used to determine the correction required for the calculated modulus values. The elastic modulus of PLLA nanofiber was found to be  $0.7 \pm 0.2$  GPa for fibers with diameter >250 nm. Higher values were obtained for fibers with smaller diameter owing to the effect of the underlying substrate. To determine if the effect of surface roughness on the calculated elastic modulus was significant, a nondimensional parameter,  $\alpha$ , has to be determined where

$$\alpha = \sigma_s \left( \frac{16R_e E_r^2}{9P^2} \right)^{1/3} \quad (8)$$

and  $\sigma_s$  is the RMS roughness. The Hertz's theory for smooth surfaces can be used with a few percentage of error if the parameter  $\alpha$  is less than 0.05.<sup>[29]</sup> Because  $\alpha$  for this study was calculated to be 0.28, correction has to be made to the elastic modulus values. A second nondimensional parameter,  $\mu$ , defined by Greenwood

and Tripp<sup>[38]</sup> is given by

$$\mu = \frac{8}{3} \eta_s \sigma_s (2R/\kappa_s)^{1/2} \quad (9)$$

where  $\eta_s$  is the asperity density and  $\kappa_s$  is the mean curvature of the summits of the asperities. Greenwood and Tripp obtained a range of  $\mu$  between 4 and 17, which encompass a wide range of practical rough surfaces. The two parameters,  $\alpha$  and  $\mu$ , are then used to determine the correction required. The ratio of effective contact radius  $a^*$  (experimental) to the Hertz radius  $a_0$  (theoretical) are influenced by the surface roughness as shown in Fig. 8. For  $\alpha = 0.28$  and  $4 < \mu < 17$ , the ratio of  $a^*/a_0$  is between 1.14 and 1.18. As  $E$  is proportional to  $1/a^3$ , the elastic modulus after roughness correction was found to be approximately 1 GPa. This result after roughness correction for the PLLA nanofibers agrees well with that of the three-point bend test.<sup>[25]</sup>

### Elastic–plastic nanoindentation

The elastic modulus can also be obtained from elastic–plastic nanoindentation. However, this type of nanoindentation is not suitable for very thin sections or very small fibers owing to the larger penetration depth. Typically, the elastic modulus from elastic–plastic indentation is obtained from the slope of the initial portion of the unloading curve ( $S$ ), which has been fitted by a power-law relation. This was first formulated by Oliver and Pharr<sup>[39]</sup> as shown in Eq. (10)

$$S = 2\beta \sqrt{\frac{A}{\pi}} E_r \quad (10)$$

where  $\beta$  is a constant that depends on the geometry of the indenter and  $A$  is the projected area of the indent. This model assumes that the nanofiber diameter is much larger than the AFM tip.

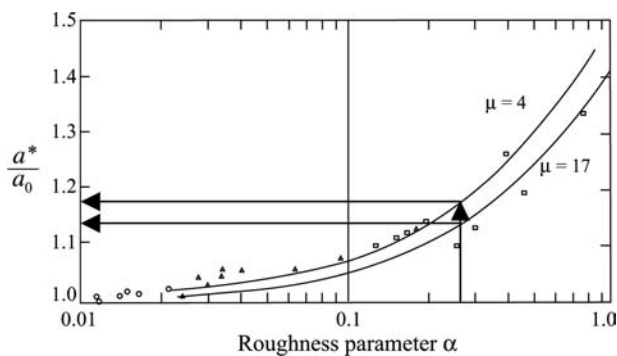


**Fig. 8** Influence of the surface roughness on the effective contact radius  $a^*$  compared with the Hertz radius  $a_0$ . Source: Adapted from Ref.<sup>[29]</sup>.

Elastic–plastic nanoindentation has been performed on electrospun silk nanofibers.<sup>[40]</sup> The uncertainties of cantilever stiffness and tip geometry of the AFM tip make it difficult to determine the exact value of modulus from Eq. (10). This problem was overcome by first making an indent on epoxy, which has a known value of elastic modulus ( $E_1$ ). The contact radius of the plastic indent ( $r_1$ ) and slope of unloading curve at maximum load for epoxy ( $S_1$ ) were then obtained. Another indent is made with the same loading force on the nanofiber using the same tip. The contact radius of the plastic indent ( $r_2$ ) and slope of unloading curve at maximum load for the nanofiber ( $S_2$ ) were obtained. All these values are substituted into Eq. (11) to calculate the modulus of the nanofiber ( $E_2$ ).

$$\frac{S_1}{S_2} = \frac{r_1 E_1}{r_2 E_2} \quad (11)$$

Viscoelastic creep may be significant for polymeric samples, which results in overestimation of modulus values. This is owing to the increase in the initial slopes of the unloading curves.<sup>[41]</sup>

### NANOPARTICLES

Nanoparticles such as polymeric and ceramic nanoparticles, polymeric micelles, liposomes, and dendrimers have been used as drug delivery devices.<sup>[42]</sup> An example of nanoparticles is shown in Fig. 9. Most nanoparticles used for drug delivery are in the form of nanocapsules or vesicles in which the drug is confined to a cavity surrounded by a membrane. Fabrication methods include microemulsification, supercritical fluids, aerosols, and reactive precipitation.<sup>[44]</sup> Owing to the size

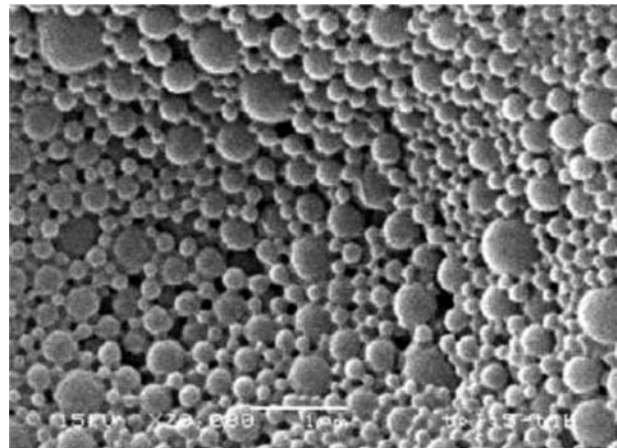


**Fig. 9** SEM image of paclitaxel-loaded vitamin E D- $\alpha$ -tocopheryl polyethylene glycol 1000 succinate (TPGS) emulsified poly(lactic-co-glycolic acid) (PLGA) nanoparticles (bar = 1  $\mu$ m). Source: From Ref.<sup>[43]</sup>.

and geometry of nanoparticles, nanoindentation or compression using the AFM is the most suitable technique for probing the mechanical properties of single nanoparticles. Although other techniques such as micropipette aspiration have been used<sup>[45,46]</sup> to characterize microparticles, it cannot be easily applied to nanoparticles as it is challenging to fabricate pipettes with nano-sized openings. Mechanical properties such as elastic modulus, bending modulus, and buckling instability can be obtained from the AFM studies.

Hertz's theory of normal contact of elastic solids has been used to obtain the elastic modulus of egg yolk phosphatidylcholine (EggPC) liposome in the form of vesicles.<sup>[47–49]</sup> The size of the vesicles range from 40 to 70 nm in diameter. The aim of these studies was to investigate effects of modification on the stability and rigidity of the vesicles. The elastic modulus of the vesicles were found using Eq. (6). After substituting the relevant parameters for the reduced modulus  $E_r$ , the force applied  $P$ , and the equivalent radius for a spherical indenter in contact with a spherical object  $R_e$ , the indentation depth  $\delta$  is given by

$$\delta = 0.825 \left[ \frac{k^2 (R_{\text{tip}} + R_{\text{ves}}) (1 - \nu_{\text{ves}}^2)^2}{E_{\text{ves}}^2 R_{\text{tip}} R_{\text{ves}}} \right]^{1/3} \times (d - d_0)^{2/3} \quad (12)$$

where  $E_{\text{ves}}$  is the elastic modulus of the vesicle,  $R_{\text{tip}}$  and  $R_{\text{ves}}$  are the radius of the tip and vesicle, respectively,  $\nu_{\text{ves}}$  is the Poisson's ratio of the vesicle,  $k$  is the cantilever spring constant,  $d$  is the deflection of the AFM tip, and  $d_0$  is the noncontact deflection. The bending modulus of the vesicle  $k_c$  is deduced from the elastic modulus as

$$k_c = \frac{E_{\text{ves}} h^3}{12(1 - \nu_{\text{ves}}^2)} \quad (13)$$

where  $h$  is the bilayer thickness.

Owing to the small size of the vesicles, the force curves have to be interpreted carefully. Fig. 10 shows a typical force curve on a cholesterol-containing EggPC liposome.<sup>[48]</sup> Region I represents the non-contact region whereby the tip is far away from vesicle and the force between the tip and the vesicle is zero. Region II shows the elastic deformation of the vesicle under tip compression, which can be used to calculate the elastic properties. Region III corresponds to further tip compression after the tip penetrates the top bilayer of the vesicle. Region IV reflects the cantilever deflection when it is in contact with the hard mica substrate after penetrating through the vesicle's bottom bilayer. As mentioned in the section "Elastic Nanoindentation," elastic nanoindentation of thin

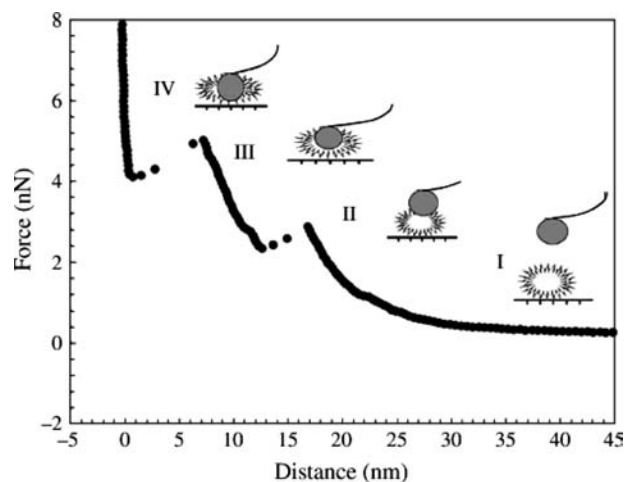


**Fig. 10** Force curve on an egg yolk phosphatidylcholine (EggPC)/cholesterol liposome. *Source:* From Ref.<sup>[48]</sup>.

samples requires the penetration depth to be shallow to avoid the influence of the hard substrate on the mechanical properties obtained. Therefore only data obtained in region II was used to deduce the elastic properties. It was found that addition of cholesterol<sup>[48]</sup> or Pluronic<sup>®</sup><sup>[49]</sup> copolymer resulted in a significant increase in bending modulus of EggPC vesicles. This increases the viability of this liposome as a drug carrier.

Mechanical properties of polyelectrolyte-multilayer capsules were studied using AFM in a similar

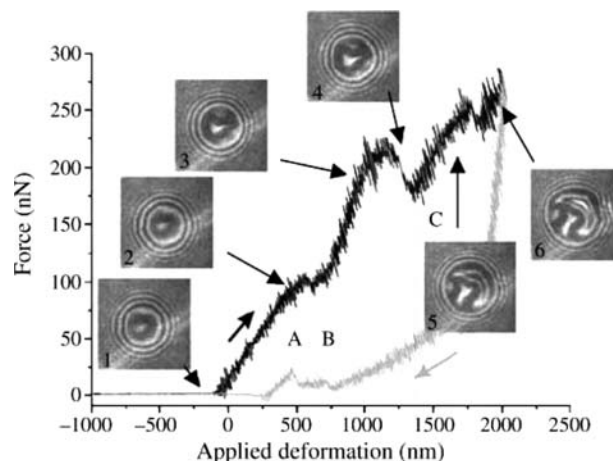


**Fig. 11** Typical force–deformation curve of a 20  $\mu\text{m}$  diameter capsule. Loading and unloading curves are shown in black and gray, respectively. Inset pictures are 11.4  $\mu\text{m} \times 11.4 \mu\text{m}$ . Reflection interference contrast microscopy (RICM) images were taken at different intervals during the experiment that can be separated in three parts: (A) small-deformation regime; (B) large deformations with an increase in contact area; and (C) buckling of capsule with an increase in contact area. The fringes inside the contact area show the buckling of the capsule (Box 4). *Source:* From Ref.<sup>[50]</sup>.

**Table 1** Summary of mechanical testing techniques for nanoscale biomaterials

Nanostructure	Test method	Instruments and techniques	Materials	References
Nanofiber	Tensile test	Atomic force microscope cantilevers	Polyethylene oxide (PEO)	[14]
		Commercial nano tensile tester	Polycaprolactone (PCL)	[18]
	Bend test	Three-point bend test using AFM	Poly(L-lactic acid) (PLLA)	[19]
			PEO	[24]
		Deflection of free end of nanofiber with fixed end attached to AFM tip	PLLA	[25]
	Nanoindentation	Elastic nanoindentation using AFM	Polyacrylonitrile (PAN)	[27]
PAN			[33,34]	
Nanoparticle	Nanoindentation	Elastic-plastic nanoindentation using AFM	PLLA	[35]
			Silk	[40]
		Nanoindentation/compression using AFM	Egg yolk phosphatidylcholine (EggPC) liposome	[47–49]
			Sodium poly(styrene sulfonate)/poly(allylamine hydrochloride) (PSS/PAH) capsule	[50,51]

manner.<sup>[50,51]</sup> These capsules consist of alternating layers of sodium poly(styrene sulfonate) and poly(allylamine hydrochloride). Although these particles are microscale in size, nanoscale particles can be fabricated using the same layer-by-layer method.<sup>[51]</sup> Therefore, this characterization technique can be applied for smaller particles. The indentation experiments were carried out with a micro-sized glass bead attached to the end of an AFM cantilever and under an inverted microscope operating in reflection interference contrast microscopy (RICM). The buckling behavior of the capsules could be observed under the microscope. The particles were assumed to be shells of radius  $R$ , of thickness  $h$ , and were made of an isotropic elastic material with Young's modulus  $E$  given by

$$E = SR/Ah^2 \quad (14)$$

where  $S$  is the slope of the force–displacement curve and  $A$  is a numerical prefactor around 0.6. The onset of buckling instability could be observed from both force curves of the AFM and from RICM (Fig. 11).

## CONCLUSIONS

Developing techniques for mechanical characterization of nanoscale biomaterials is essential for the design of the materials that match the *in vivo* requirement. The range of techniques presented here for nanofibers and nanoparticles are summarized in Table 1. It can be seen that most techniques involve the use of AFM or AFM cantilevers for imaging and/or force measurement. The main advantage of the characterization

methods presented is in most cases, direct manipulation of single nanofiber or nanoparticle is minimal, thus allowing nanomechanical characterization to be performed easily. Tensile test, bend test, and nanoindentation are used to characterize the mechanical properties of nanofibers. Only nanoindentation has been used to characterize nanoparticles.

Although nanostructured materials can be characterized using various methods, an effective mode of observing deformation is yet to be found. Most of the measurements also did not take into account the viscoelastic nature of the polymers used. In some techniques such as tensile test and bend test, it is difficult to perform the test in *in vivo* conditions as only dry samples can be tested conveniently. Therefore, future work would involve developing devices or methods of observing the deformation behavior of the various nanostructures and means of performing dynamic material characterization. A means of characterizing the nanostructures in *in vivo* conditions is required. It would also be interesting to determine the actual mechanism of deformation and failure of nanofibers or nanoparticles in relation to their nano and molecular structures.

## REFERENCES

1. Brown, S. Biomaterials. In *Introduction to Biomedical Engineering*; Enderle, J.D., Blanchard, S.M., Bronzino, J.D., Eds.; Academic Press: USA, 2000; 538 pp.
2. Martin, R.B. Biomaterials. In *Introduction to Bioengineering*; Berger, S.A., Goldsmith, W., Lewis, E.R., Eds.; Oxford University Press: New York, 2000; 339 pp.

3. Zhang, Y.Z.; Lim, C.T.; Ramakrishna, S.; Huang, Z.M. Recent development of polymer nanofibers for biomedical and biotechnological applications. *J. Mat. Sci. Mat. Med.* **2005**, *16* (10), 933–946.
4. Brannon-Peppas, L. Recent advances on the use of biodegradable microparticles and nanoparticles in controlled drug delivery. *Int. J. Pharmaceut.* **1995**, *116*, 1–9.
5. Li, W.-J.; Tuli, R.; Okafor, C.; Derfoul, A.; Danielson, K.G.; Hall, D.J.; Tuan, R.S. A three-dimensional nanofibrous scaffold for cartilage tissue engineering using human mesenchymal stem cells. *Biomaterials* **2005**, *26*, 599–609.
6. Xu, C.Y.; Inai, R.; Kotaki, M.; Ramakrishna, S. Aligned biodegradable nanofibrous structure: a potential scaffold for blood vessel engineering. *Biomaterials* **2004**, *25*, 877–886.
7. Yang, F.; Murugan, R.; Ramakrishna, S.; Wang, X.; Ma, Y.-X.; Wang, S. Fabrication of nano-structured porous PLLA scaffold intended for nerve tissue engineering. *Biomaterials* **2004**, *25*, 1891–1900.
8. Ma, P.X.; Zhang, R. Synthetic nano-scale fibrous extracellular matrix. *J. Biomed. Mater. Res.* **1999**, *46*, 60–72.
9. Demczyk, B.G.; Wang, Y.M.; Cumings, J.; Hetman, M.; Han, W.; Zettl, A.; Ritchie, R.O. Direct mechanical measurement of the tensile strength and elastic modulus of multiwalled carbon nanotubes. *Mat. Sci. Eng. A Struct. Mat. Properties Microstruct. Process.* **2002**, *334* (1–2), 173–178.
10. Poncharal, P.; Wang, Z.L.; Ugarte, D.; Heer, W.A.D. Electrostatic deflections and electromechanical resonances of carbon nanotubes. *Science* **1999**, *283*, 1513–1516.
11. Yu, M.F.; Lourie, O.; Dyer, M.J.; Moloni, K.; Kelly, T.F.; Ruoff, R.S. Strength and breaking mechanism of multiwalled carbon nanotubes under tensile load. *Science* **2000**, *287*, 637–640.
12. Haque, M.A.; Saif, M.T.A. A review of MEMS-based microscale and nanoscale tensile and bending testing. *Exp. Mech.* **2003**, *43* (3), 248–255.
13. Yu, M.F.; Dyer, M.J.; Skidmore, G.D.; Rohrs, H.W.; Lu, X.K.; Ausman, K.D.; Ehr, J.R.V.; Ruoff, R.S. Three-dimensional manipulation of carbon nanotubes under a scanning electron microscope. *Nanotechnology* **1999**, *10*, 244–252.
14. Tan, E.P.S.; Goh, C.N.; Sow, C.H.; Lim, C.T. Tensile test of a single nanofiber using an atomic force microscope tip. *Appl. Phys. Lett.* **2005**, *86* (6), 073115.
15. Li, D.; Wang, Y.L.; Xia, Y.N. Electrospinning of polymeric and ceramic nanofibers as uniaxially aligned arrays. *Nano Lett.* **2003**, *3* (8), 1167–1171.
16. ASTM Committee D-30 on High Modulus Fibers and Their Composites. ASTM D3379-75. Standard Test Method for Tensile Strength and Young's Modulus for High-Modulus Single-Filament Materials. In *Test Methods and Design Allowables for Fibrous Composites*; Chamis, C.C., Ed.; ASTM: Philadelphia, PA, 1989; Vol. 2, 127–130.
17. Perez-Rigueiro, J.; Viney, C.; Llorca, J.; Elices, M. Silk worm silk as an engineering material. *J. Appl. Polym. Sci.* **1998**, *70*, 2439–2447.
18. Tan, E.P.S.; Ng, S.Y.; Lim, C.T. Tensile testing of a single ultrafine polymeric fiber. *Biomaterials* **2005**, *26*, 1453–1456.
19. Inai, R.; Kotaki, M.; Ramakrishna, S. Structure and properties of electrospun PLLA single nanofibres. *Nanotechnology* **2005**, *16*, 208–213.
20. Salvetat, J.-P.; Briggs, G.A.D.; Bonard, J.-M.; Bacsá, R.R.; Kulik, A.J.; Stockli, T.; Burnham, N.A.; Forro, L. Elastic and shear moduli of single-walled carbon nanotube ropes. *Phys. Rev. Lett.* **1999**, *82* (5), 944–947.
21. Tomblér, T.W.; Zhou, C.; Alexseyev, L.; Kong, J.; Dai, H.; Liu, L.; Jayanthi, C.S.; Tang, M.; Wu, S.-Y. Reversible electromechanical characteristics of carbon nanotubes under local-probe manipulation. *Lett. Nat.* **2000**, *405*, 769–772.
22. Kim, G.-T.; Gu, G.; Waizmann, U.; Roth, S. Simple method to prepare individual suspended nanofibers. *Appl. Phys. Lett.* **2002**, *80* (10), 1815–1817.
23. Xu, W.; Mulhern, P.J.; Blackford, B.L.; Jericho, M.H.; Templeton, I. A new atomic force microscopy technique for the measurement of the elastic properties of biological materials. *Scanning Microsc.* **1994**, *8* (3), 499–506.
24. Bellan, L.M.; Kameoka, J.; Craighead, H.G. Measurement of the Young's moduli of individual polyethylene oxide and glass nanofibres. *Nanotechnology* **2005**, *16*, 1095–1099.
25. Tan, E.P.S.; Lim, C.T. Physical properties of a single polymeric nanofiber. *Appl. Phys. Lett.* **2004**, *84* (9), 1603–1605.
26. Ugural, A.C. Stresses in beams. In *Mechanics of Materials*, 2nd Ed.; McGraw-Hill, Inc., 1993; 152–213.
27. Gu, S.-Y.; Wu, Q.-L.; Ren, J.; Vansco, G.J. Mechanical properties of a single electrospun fiber and its structures. *Macromol. Rapid Commun.* **2005**, *26*, 716–720.
28. Domke, J.; Radmacher, M. Measuring the elastic properties of thin polymer films with the atomic force microscope. *Langmuir* **1998**, *14* (12), 3320–3325.
29. Johnson, K.L. Rough surfaces. In *Contact Mechanics*; Cambridge University Press: Cambridge, 1992; 397–423.
30. Li, X.; Gao, H.; Murphy, C.J.; Caswell, K.K. Nanoindentation of silver nanowires. *Nano Lett.* **2003**, *3* (11), 1495–1498.
31. Bischel, M.S.; Vanlandingham, M.R.; Eduljee, R.F.; Gillespie, J.W.; Schultz, J.M. On the use of nanoscale indentation with the AFM in the identification of phases in blends of linear low density polyethylene and high density polyethylene. *J. Mat. Sci.* **2000**, *35* (1), 221–228.
32. Sumomogi, T.; Hieda, K.; Endo, T.; Kuwahara, K. Influence of atmosphere humidity on tribological properties in scanning probe microscope observation. *Appl. Phys. A Mat. Sci. Process.* **1998**, *66*, 299–303.
33. Ko, F.; Gogotsi, Y.; Ali, A.; Naguib, N.; Ye, H.H.; Yang, G.L.; Li, C.; Willis, P. Electrospinning of continuous carbon nanotube-filled nanofiber yarns. *Adv. Mat.* **2003**, *15* (14), 1161–1165.
34. Mack, J.J.; Viculis, L.M.; Ali, A.; Luoh, R.; Yang, G.; Hahn, H.T.; Ko, F.K.; Kaner, R.B. Graphite nanoplatelet reinforcement of electrospun polyacrylonitrile nanofibers. *Adv. Mat.* **2005**, *17* (1), 77–80.



35. Tan, E.P.S.; Lim, C.T. Nanoindentation study of nanofibers. *Appl. Phys. Lett.* **2005**, *87* (12), 123106.
36. Johnson, K.L. Normal contact of elastic solids: hertz theory. In *Contact Mechanics*; Cambridge University Press: Cambridge, 1992; 84–106.
37. Garlotta, D. A literature review of poly (Lactic acid). *J. Polym. Environ.* **2001**, *9* (2), 63–84.
38. Greenwood, J.A.; Tripp, J.H. The elastic contact of rough spheres. *Trans. ASME E J. Appl. Mech.* **1967**, *34* (153), 417–420.
39. Oliver, W.C.; Pharr, G.M. An improved technique for determining hardness and elastic-modulus using load and displacement sensing indentation experiments. *J. Mat. Res.* **1992**, *7* (6), 1564–1583.
40. Wang, M.; Jin, H.-J.; Kaplan, D.L.; Rutledge, G.C. Mechanical properties of electrospun silk fibers. *Macromolecules* **2004**, *37*, 6856–6864.
41. VanLandingham, M.R.; Villarrubia, J.S.; Guthrie, W.F.; Meyers, G.F. Nanoindentation of polymers: an overview. *Macromol. Symp.* **2001**, *167*, 15–43.
42. Sahoo, S.K.; Labhasetwar, V. Nanotech approaches to drug delivery and imaging. *Drug Discov. Today* **2003**, *8* (24), 1112–1120.
43. Feng, S.S.; Mu, L.; Win, K.Y.; Huang, G.F. Nanoparticles of biodegradable polymers for clinical administration of paclitaxel. *Curr. Med. Chem.* **2004**, *11*, 413–424.
44. Date, A.A.; Patravale, V.B. Current strategies for engineering drug nanoparticles. *Curr. Opin. Coll. Interf. Sci.* **2004**, *9*, 222–235.
45. Kwok, R.; Evans, E. Thermoelasticity of large lecithin bilayer vesicles. *Biophys. J.* **1981**, *35*, 637–652.
46. Evans, E.; Kwok, R. Mechanical calorimetry of large dimyristoylphosphatidylcholine vesicles in the phase transition region. *Biochemistry* **1982**, *21*, 4874–4879.
47. Liang, X.; Mao, G.; Ng, K.Y.S. Probing small unilamellar EggPC vesicles on mica surface by atomic force microscopy. *Coll. Surf. B Biointerfaces* **2004**, *34*, 41–51.
48. Liang, X.; Mao, G.; Ng, K.Y.S. Mechanical properties and stability measurement of cholesterol-containing liposome on mica by atomic force microscopy. *J. Coll. Interf. Sci.* **2004**, *278*, 53–62.
49. Liang, X.; Mao, G.; Ng, K.Y.S. Effect of chain lengths of PEO-PPO-PEO on small unilamellar liposome morphology and stability: an AFM investigation. *J. Coll. Interf. Sci.* **2005**, *285*, 360–372.
50. Dubreuil, F.; Elsner, N.; Fery, A. Elastic properties of polyelectrolyte capsules studied by atomic-force microscopy and RICM. *Eur. Phys. J. E* **2003**, *12*, 215–221.
51. Dubreuil, F.; Shchukin, D.G.; Sukhorukov, G.B., et al. Polyelectrolyte capsules modified with YF<sub>3</sub> nanoparticles: an AFM study. *Macromol. Rapid Commun.* **2004**, *25*, 1078–1081.

# Biomedical Applications: Implants

Jeremiah Ejiófor  
Thomas J. Webster

*Department of Biomedical Engineering, Purdue University, West Lafayette, Indiana, U.S.A.*

## INTRODUCTION

Over the past nine decades of administering bioimplants to humans, most of the synthetic prostheses consist of material particles and/or grain sizes with conventional dimensions (approximately 1 to  $10^4 \mu\text{m}$ ).<sup>[1]</sup> Most of these early implants were made out of the following: vanadium steel (in the 1920s), stainless steel, cobalt alloys, titanium (in the 1930s), gold, and amalgams (a metal alloy containing mercury).<sup>[1]</sup> However, the lack of sufficient bonding of synthetic implants to surrounding body tissues and the inability to obtain mechanical characteristics (such as flexural strength, bending strength, modulus of elasticity, toughness and, ductility) as well as electrical characteristics (such as resistivity and even piezoelectricity) that simulate their human tissue equivalents have, in recent years, led to the investigations of nanomaterials.<sup>[2–12]</sup> Consequently, improving the biocompatibility of these implants remains the focus of many research groups around the world. Several nanobiomedical implants are being investigated, and are likely to gain approvals for clinical use. The critical factor for this drive is the increasingly documented, special, non-biological improved material properties of nanophase materials when compared to conventional grain-size formulations of the same material chemistry.<sup>[2–12]</sup>

This entry seeks to add another property of nanophase materials that makes them attractive for use as implants: bio- and cytocompatibility. Active works are focused in the domains of orthopedic, dental, bladder, neurological, vascular, and cardiovascular graft applications. The present level of advances was previously unimaginable with conventional materials possessing large micron-sized particulates. This entry will briefly articulate the seeming revolutionary changes and the potential gains of nanostructured implants in medical technology.

## RATIONALE AND DEVELOPMENTS

### The Problem—Fibrous Encapsulation of Newly Implanted Materials

For the replacement of dysfunctional and diseased tissues, millions of biomedical implants are used each

year around the globe. The characteristics vital for the effective functioning of these implants in the host animal tissue (usually, humans) include lack of any toxicity tendencies, resistance to corrosion by surrounding tissue fluids, sufficient strength against involuntary and normal physical motion or loading, resistance to bodily fatigue forces, ability to promote cellular adhesion that may lead to tissue regeneration, and, finally, biocompatibility (or cytocompatibility) with the host tissue or organs.

The healing response immediately following biomaterial implantation determines the long-term functionality of the device. This response is primarily affected by the chemical and physical characteristics of the bioimplant. Healing characteristics common of unsuccessful biomaterial wound healing include fibrous encapsulation and chronic inflammation. Inflammation and the subsequent processes involve recruitment of a variety of body fluids, proteins, and unwanted cell types to the tissue–implant interface.<sup>[13–15]</sup> Fibrous encapsulation—or callus formation, in the case of bone implants—at the interface or implant–body tissue site decreases the bonding effectiveness and often results in clinical failures.<sup>[13]</sup> Fig. 1 depicts the sequential events of cellular responses of soft tissues following an injury.<sup>[14–22]</sup> There exists a latent period for the collagen molecules to polymerize and align according to the principal direction of stress. This slows rapid attainment of the physical strength in the region that would be juxtaposed to that of normal tissue. Currently, most of the medical devices for cardiovascular or neural treatments, such as pacemakers, defibrillators, neural probes, etc., are routinely coated with parylene, a polymer with increased dielectric constant and coating depth, for better compatibility with body tissues. However, parylene degrades at temperatures above 125–140°C in the presence of oxygen, and a special grade of the polymer loses its optical clarity, becoming hazy at thickness levels above 5  $\mu\text{m}$ . Therefore, modulating the healing response may improve biomaterial compatibility to decrease unwanted fibrous tissue formation, and this is the role envisaged of nanostructured implants.<sup>[2,6–8,17]</sup>

### A Potential Solution—Nanostructured Implants

Nanotechnology embraces a system whose core of materials is in the range of nanometers ( $10^{-9}$  m). The

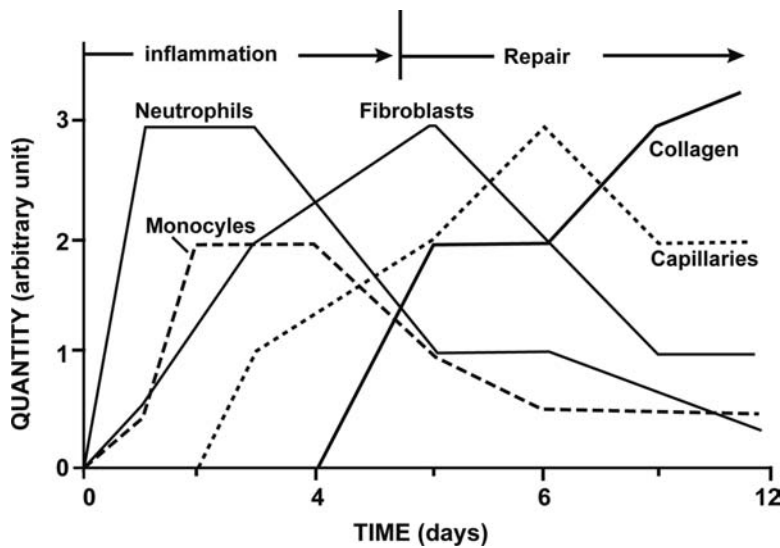


Fig. 1 Sequential events of soft tissue wound healing. Source: From Ref.<sup>[14]</sup>.

application of nanomaterials for medical diagnosis, treatment of failing organ systems, or prevention and cure of human diseases can generally be referred to as nanomedicine. The branch of nanomedicine devoted to the development of biodegradable or non-biodegradable prostheses or implants fall within the purview of nanobiomedical science and engineering. Although various definitions are attached to the word “nanomaterial” by different experts,<sup>[23]</sup> the commonly accepted concept refers to nanomaterials as that material with the basic structural unit in the range 1–100 nm (nanostructured), crystalline solids with grain sizes 1–100 nm (nanocrystals), individual layer or multi-layer surface coatings in the range 1–100 nm (nanocoatings), extremely fine powders with an average particle size in the range 1–100 nm (nanopowders), and fibers with a diameter in the range 1–100 nm (nanofibers).

Nanostructure science and technology create materials and products that potentially outperform, at several boundaries, the existing advanced materials (such as advanced/fine ceramics, advanced polymers and composites, and electronic and photonic materials).<sup>[24]</sup> For example, with the development of macromolecular complexes, modern technology enhances the secrets of biology and communicates to it. High-resolution instruments, such as scanning tunneling microscope, atomic force microscope, and high-resolution transmission electron microscope, are capable of atom-by-atom resolution in the structure of solids. Atom layer by atom layer structures can now be built using ion beam or molecular beam. Advanced instruments can also monitor processes in materials at atomic or subatomic levels on real time scales.

Assisted by these developments emerges, concurrently, nanotechnology, an endeavor able to work at the molecular level atom by atom to create large structures with fundamentally new molecular organization,

with at least one characteristic dimension measured in nanometers.<sup>[9]</sup> The commonly known nanostructures include carbon nanotubes, proteins, DNA-based structures, thin film and laser emitters, quantum wire and dots, and single-electron transistors that operate at room temperatures. The substances in the list that are significantly relevant to designing future implants are proteins and DNA-based structures. Scientific activities on nanobiomedical implants seek to mimic the nanomorphology that proteins create in natural tissue, mainly for efficient and effective cytocompatibility.<sup>[16]</sup> Clearly, cells in our body are accustomed to interacting with nanostructured surfaces. It is evident that nanotechnology-enabled increases in computation power will permit the characterization of macromolecular networks in realistic environments. Such simulation will be essential in developing biocompatible implants to mimic these novel topographies.

## CHARACTERISTICS, DEVELOPMENTS, AND POTENTIALS

### Characteristics

Functions of implants can benefit immensely from the manifold increase in size reduction, bonding potential, and mechanical and electrical characteristics of consolidated nanoparticles or nanofibers. The specific properties relevant for the synthesis and efficacy of these nanobiomedical implants are high surface energy of the discrete substances, increased surface roughness of the bulk material, strength, elastic modulus, ductility, and electrical conductivity.<sup>[5,6,16]</sup>

Surface properties (such as area, charge, and morphology) depend on the particulate (such as grain) or fiber size of a material.<sup>[10–12]</sup> The increased surface

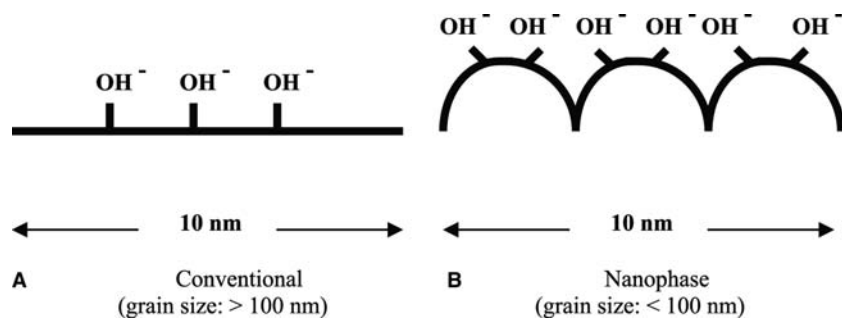


**Fig. 2** Schematic representation of surface properties of (A) conventional materials and (B) nanophase materials. Nanophase materials have higher surface areas, possess greater numbers of atoms at the surface, and less acidic OH<sup>-</sup> groups (because of an increase in electron delocalization) in the hydroxide layer. *Source:* From Ref.<sup>[35]</sup>.

defects (such as at the edge/corner sites) and the high number of grain boundaries<sup>[10,11]</sup> in nanophase materials have special advantageous properties that are being exploited in the development of biocompatible implants. Because of their small size (1–100 nm), bioceramic or metallic particulates require less severe sintering conditions (temperature and pressure) to become fully consolidated. Thus, for complex inorganic ceramics, the likelihood of phase separation is reduced. For the particulate or hybrid composites, excessive interfacial reactions between the matrix and filler phases are reduced because process temperature is lower. Kinetics of reactions in the various systems are shorter. Thus, there are promises for nanophase materials from a material processing point of view.

To date, the increased surface reactivity of nanomaterials has been used for catalytic applications almost exclusively,<sup>[10,11]</sup> for example, compared with conventional (>100 nm average grain size) magnesium oxide (MgO), nanophase (4 nm average grain size) MgO possessed increased numbers of atoms at the surface, higher surface area (100–160 m<sup>2</sup>/g compared to 200–500 m<sup>2</sup>/g, respectively), less acidic OH<sup>-</sup> groups (because of a much higher proportion of edge sites for the nanophase MgO to cause delocalization of electrons) (Fig. 2), increased adsorption of acidic ions (such as SO<sub>3</sub><sup>2-</sup> and CO<sub>3</sub><sup>2-</sup>), and increased destructive adsorption of organophosphorous and of chlorocarbons.<sup>[10,11]</sup>

### Proteins—Control of Implant Biocompatibility

Living systems are governed by molecular behavior at nanometer scales.<sup>[5,6,16]</sup> The molecular building blocks of life—proteins, nucleic acids, lipids, carbohydrates, and their non-biological mimics—are examples of materials that possess unique properties determined by the size, folding, and patterns at the nanoscale. Most current in vivo implants are used for orthopedics (bone therapy or replacement), their fixation, or for dental (tooth therapy) purposes. An increasing number is also applied in vascular and cardiovascular organ systems. These implants are known to be of the

conventional structure (average grain size is in microns). Being in-body prostheses, most implants (such as orthopedic or vascular) are initially interfaced with soluble proteins (through biological fluids), as against insoluble proteins (which usually occurs through synthesis and deposition by cells after initial adhesion to implants).<sup>[13,14]</sup>

Protein interaction with surfaces is mainly by adsorption and orientation (conformation). Significant protein adsorption leads progressively—but not always—to an appropriate conformation (or orientation) and for subsequent cell adhesions.<sup>[15,16]</sup> These molecular activities, however, depend on the relative bulk concentration of each protein in solution and the properties of the surface that control protein reactivity.<sup>[15]</sup> As shown in Table 1,<sup>[13,17–22]</sup> solid surface features (such as specific surface, roughness, charge, chemistry, wettability, etc.) and the specific properties of each amino acid influence protein adsorption (ultimately affecting implant biocompatibility with host tissue). Fig. 3 presents the schematics on how cells interact with adsorbed proteins on a substrate.<sup>[15]</sup> For nanostructured substrate formulations (or nanoimplants), the surface grain size increases the number of grain boundaries at the surface to enhance material surface wettability for protein adsorption that, subsequently, promotes select cell function. Note, however, that proteins will adsorb to a material surface seconds after implantation. Thus, their interactions are imperative to controlling subsequent cell function and eventual implant success/failure.

The dimensions of proteins are at the nanometer level.<sup>[5,6,16]</sup> In addition, other inorganic constituents in natural bone, such as hydroxyapatite (HAP) fibers, possess nanometer dimensions between 2 and 5 nm in width, and lengths around 50 nm.<sup>[1]</sup> Several studies have positively correlated the adhesion and functions of various proteins with the nanoscale surface features of potential implants.<sup>[16,25–33]</sup> In fact, some of the best examples of how nanophase, compared with conventional, materials alter interactions with proteins are provided in the investigations of the potential use of nanostructured materials as the next generation of bone implants.<sup>[6,25–33]</sup> Following are presented the

**Table 1** Structural categories and specific properties of amino acids contained in proteins

Amino acid (three and one-letter abbreviation)	Charge	Hydrophobicity (values as kcal/mol to transfer from hydrophobic to more hydrophilic phase; increase positive value means more hydrophobic)	Surface tension (values as ergs/cm <sup>2</sup> /mol per liter lowering of the surface tension of water)
Isoleucine (Ile or I)	Neutral	0.73	-15.2
Phenylalanine (Phe or F)	Neutral	0.61	-17.3
Valine (Val or V)	Neutral	0.54	-3.74
Leucine (Leu or L)	Neutral	0.53	-21.9
Tryptophan (Trp or W)	Neutral	0.37	-9.6
Methionine (Met or M)	Neutral	0.26	-3.01
Alanine (Ala or A)	Neutral	0.25	0.96
Glycine (Gly or G)	Neutral	0.16	1.12
Cysteine (Cys or C)	0 to -1	0.04	0.69
Tyrosine (Tyr or Y)	0 to -1	0.02	-15.1
Proline (Pro or P)	Neutral	-0.07	-0.49
Threonine (Thr or T)	Neutral	-0.18	0.59
Serine (Ser or S)	Neutral	-0.26	0.76
Histidine (His or H)	0 to 1	-0.40	1.03
Glutamic acid (Glu or E)	0 to -1	-0.62	0.86
Asparagine (Asn or N)	Neutral	-0.64	1.17
Glutamine (Gln or Q)	Neutral	-0.69	1.21
Aspartic acid (Asp or D)	0 to -1	-0.72	0.96
Lysine (Lys or K)	0 to 1	-1.1	0.92
Arginine (Arg or R)	0 to 1	-1.8	1.03

Because of a wide range of amino acid properties, proteins have diverse properties.

Source: Refs.<sup>[13,17-22]</sup>.

significant milestones from current activities on protein or cellular interactions with ceramics, metals/alloys, polymers, or their composites.

### Developments and Potentials of Nanophase Ceramics as Nanobiomedical Implants

Ceramic materials have been used for sometime in dentistry for dental crowns. Their high compressive strength, good esthetic appearance, and inertness to body fluids were responsible. Investigations of underlying mechanisms on tissue-implant interaction revealed that the initial adsorbed concentration,<sup>[27]</sup> conformation,<sup>[31]</sup> and bioactivity<sup>[31]</sup> of proteins contained in blood serum were responsible for the select, enhanced functions of osteoblasts (bone-forming cells). Notably, cumulative adsorption of proteins contained in serum was significantly higher on smaller, nanometer, grain-size ceramics.<sup>[27]</sup> In particular, the interaction of four proteins—fibronectin, vitronectin, laminin, and collagen—known to enhance osteoblast function, increased greatly on nanophase compared to conventional (micron-sized grains) ceramics.

Furthermore, a novel adaptation of the standard surface-enhanced Raman scattering (SERS) technique

has provided evidence of increased unfolding of the aforementioned proteins adsorbed on nanophase vs. conventional ceramics (Fig. 4).<sup>[31]</sup> This is important because unfolding of these proteins promotes availability of specific cell-adhesive epitopes that increased bone-cell adhesion and function.<sup>[34,35]</sup> In addition, nanophase ceramics have much greater surface reactivity because of increased numbers of atoms at the surface, greater amounts of grain boundaries at the surface, and higher proportions of edge sites (Fig. 2).<sup>[35]</sup>

Clearly, these novel properties of nanophase ceramics may be influencing interactions with proteins. In particular, nanophase ceramics have also been reported to have increased surface wettability over conventional ones.<sup>[26]</sup> Because proteins assume a tertiary structure with mostly hydrophilic amino acid residues on the exterior of globular shapes, it is believed that a material surface with increased wettability (or hydrophilic) properties should increase protein adsorption and possibly enhance unfolding of that protein to expose interior amino acids important for cell adhesion. Because of protein dimension being in the nanometer regime, biomedical implants with nanophase surfaces can now be engineered to manipulate adsorbed protein conformation for increased implant

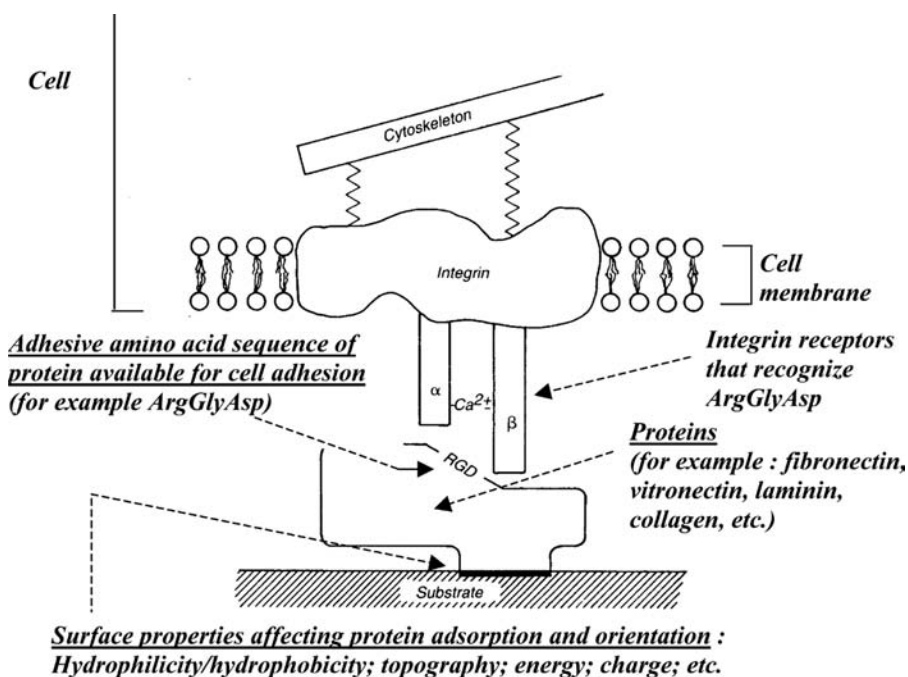


**Fig. 3** Schematic representation of the interaction of cells with proteins adsorbed on a substrate such as an implant. *Source:* From Ref.<sup>[15]</sup>.

efficacies over a long time. For instance, compared to conventional (micron-size) ceramic formulations, nanostructured substrates made from spherical particles of alumina, titania, and hydroxyapatite provided evidence of enhanced adhesion of osteoblasts (bone-forming cells), decreased adhesion of fibroblasts (cells that contribute to fibrous encapsulation and callus formation events that may lead to implant loosening and failure), and decreased adhesion of endothelial cells (cells that line the vasculature of the body).<sup>[26]</sup> In addition, consolidated substrates formulated from nanofibrous alumina (diameter 2 nm, length >50 nm) have demonstrated a significant adhesion and proliferation of the bone-forming cells (osteoblasts) in comparison with similar alumina substrates formulated from nanospherical particles.<sup>[16]</sup> The study further reported enhanced calcium deposition (calcium deposition is an index of mineralization of the bone matrix) by osteoblasts as well as increased functions of osteoclasts (bone-resorbing cells) on the alumina nanoparticles. In a comparative study, Price et al. has determined a twofold increased adhesion cell density of the osteoblasts on alumina nanofiber vs. conventional titanium, following a 2-hr culture.<sup>[52]</sup> These findings consistently testify to unprecedented and excellent cytocompatibility of nanobioceramics with physiological bone.

Furthermore, other studies have reported the detrimental influences of wear particles (or debris) resulting from articulating components of conventional orthopedic implants that are subjected to physiological loading forces (such as friction).<sup>[36–38]</sup> These particles induce bone loss, which leads to implant loosening, and sometimes results in clinical failure of bone

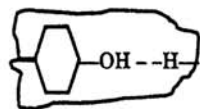
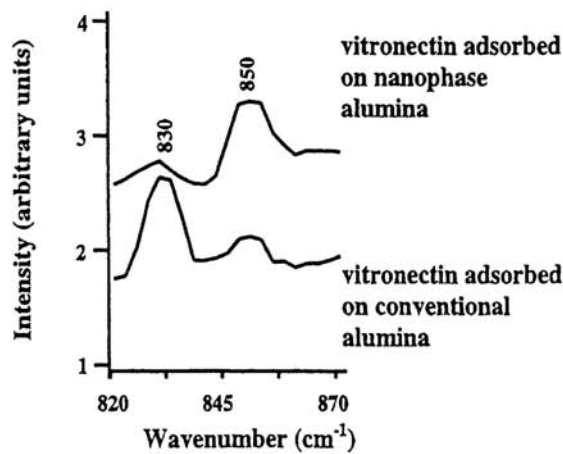
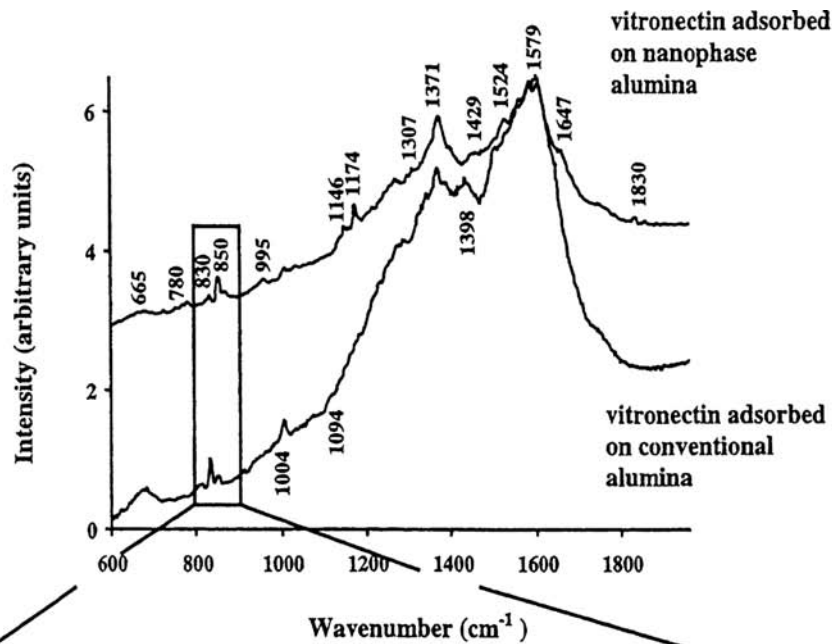
prostheses (such as hip, elbow, knee, ankle, etc.). In a recent report, however, results of a more well spread morphology and increased cell proliferation in the presence of nanophase particles have demonstrated that wear debris resulting from bone prostheses composed of nanophase ceramics affects bone and cartilage cell functions less adversely in comparison to larger conventional ceramic wear particles.<sup>[39]</sup> In addition, the ductility and superplastic-forming capabilities of nanoceramic particles have now been demonstrated as favorable to initial cellular activities, indicating their potential for orthopedic nanobiomaterials.<sup>[16,39]</sup>

Following these significant discoveries, extremely fine bioceramic powders can be used as components in a wide range of biomedical implants, from hard sintered ceramic disk implants to porous bone grafts (bone replacement), controllable-setting calcium-phosphate-based bone cements (for implant fixation), and nanocomposites that have superior mechanical and biological properties in vitro. Phase-stabilized zirconia is used to make femoral heads of the implants in hip-replacement operations. With the improved ductility of nanoceramics, the synthesis of polycrystalline phase-stabilized zirconia from nanoparticles will allow the material to be made even stronger, with better fracture toughness and improved wear-resistance properties, compared to current-generation zirconia materials.<sup>[40]</sup>

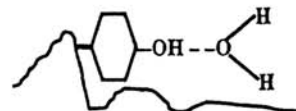
### Developments and Potentials of Nanophase Metals as Nanobiomedical Implants

Whereas for dental applications conventional silver-tin amalgam is selected because of its plasticity and





**Protein Folding**  
 $I_{830} > I_{850}$



**Protein Unfolding**  
 $I_{850} > I_{830}$

**Fig. 4** Surface-enhanced Raman scattering technique illustrating increased unfolding of proteins (specifically, vitronectin) adsorbed on nanophase alumina in comparison with conventional alumina. *Source:* From Ref.<sup>[31]</sup>.

cold-setting property, and micron-grain-sized gold often chosen because of its corrosion resistance as well as malleability and durability,<sup>[1]</sup> the conventional metallic materials—titanium, titanium alloys (such as Ti-6Al-4V), Co-Cr-Mo, and 316L stainless steel—are

selected for orthopedic implants based on their mechanical properties and ability to remain inert in vivo.<sup>[1]</sup> [Table 2](#) compares the elastic modulus property of select conventional metallic and ceramic materials currently applied in orthopedics with compact

**Table 2** Comparison of elastic modulus ( $E$ ) of major internal bone structures with select conventional metallic and ceramic materials currently used as orthopedic implants

	Material	Modulus of elasticity (GPa)
	Bone	12–18
	Trabecular bone	0.1
Ceramic/carbon	Calcium phosphate	40–117
	Carbon (pyrolytic) <sup>a</sup>	28
Metal/alloys	Titanium and Ti–6Al–4V	110
	Tantalum (cold-worked)	190
	Cobalt alloys	220–234
	316L stainless steel	193–200
	Aluminum alloy	70–77

<sup>a</sup>1.0 wt.% Si-alloyed pyrolytic carbon, Pyrolite (Carbomedics, Austin, TX).

and spongy bones. The choice of these materials as implants only satisfied physiological loading conditions but did not duplicate the mechanical, chemical, and morphological properties of the bone.<sup>[1,16]</sup>

Most importantly, to date the failures of conventional orthopedic and dental implant materials is often due to insufficient bonding with juxtaposed bone or tissue. Timely and desirable responses from surrounding cells and tissues are required to enhance deposition of the mineralized matrix at the tissue–implant interface, which provides crucial mechanical stability to implants. This requirement, in addition to the hardness and strength of metallic implants, can be greatly increased by nanostructuring. Metallic implants coated with conventional HAP have been tried with little success, causing stress shielding of the surrounding bone and experiencing a reduced durability of the HAP coatings over time.<sup>[1]</sup> It is therefore intriguing to ponder an alternative approach using nanostructured metals to promote interactions with juxtaposed bone to increase implant success. This objective remains largely uninvestigated to date.

## Developments and Potentials of Nanophase Polymers as Nanobiomedical Implants

Several micron-grain-sized polymers [such as hyaluronan-based polymer, Dacron, and poly(lactic-*co*-glycolic acid) (PLGA)] investigated as potential implants have been reported as either causing defects or unsuitable.<sup>[1]</sup> Solchaga et al. observed cracks and fissures in some biodegradable materials, e.g., hyaluronan-based polymers, within 12 weeks that followed implantation.<sup>[41]</sup> This investigation studied the polymer as a potential implant for the treatment of osteochondral defects on femoral condyles of rabbits. Messner had earlier reported improper cartilage morphology, early-stage debris formation, and synovitis when he implanted polyethylene terephthalate (Dacron), a non-degradable synthetic material in rabbits for similar treatment.<sup>[42]</sup>

Although much scientific activity is focused on it, the Food and Drug Administration (FDA)-approved PLGA does not mimic the nanometer morphology of biological tissues they are intended to replace. Fig. 5 shows the scanning electron images distinguishing the surface roughness of nanostructured from conventional PLGA. As could be observed, the nano-PLGA exhibits a finer surface morphology than the conventional PLGA. While the latter registers a roughness of 100 nm–1  $\mu$ m, the former has a surface roughness value within the range 50–100 nm. Recently, a synthesized nanostructured PLGA has been shown to lead to significant proliferation of chondrocytes in comparison with the conventional FDA-approved PLGA.<sup>[43]</sup> The study further provided evidence of preferred growth of chondrocytes along the aligned portions in the nanostructure. This discovery is of practical significance because articular cartilage has aligned nanostructures (i.e., the collagen fiber). Thus, by simulating the nanostructure and alignment topography of cartilage tissue in monolithic PLGA or in PLGA–matrix composite formulations, a more natural environment is created for chondrocytes to regenerate cartilage.

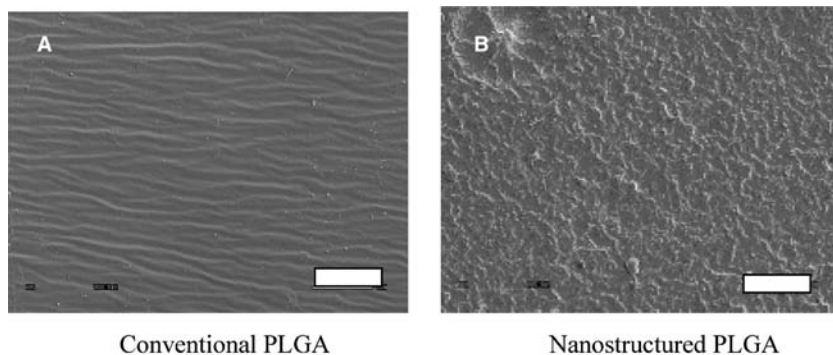


**Fig. 5** Scanning electron images depicting (A) surface roughness of conventional PLGA (100 nm–1  $\mu$ m) in comparison with (B) fine surface roughness of nanophase PLGA (50–100 nm). Bar represents 100  $\mu$ m in dimensions. Source: From Ref.<sup>[46]</sup>.

Also, a related study found a 23% and 76% increase in adhesion of both vascular and bladder smooth muscle cells on nanophase PLGA (average surface roughness: approx. 50 nm) and nanostructured polyurethane (PU), respectively, vs. their conventional formulations.<sup>[44]</sup> The potential application of these formulations as vascular graft implants was further demonstrated by the enhanced long-term biofunction (such as proliferation) of cells on the substrates and the “controllable” degradation rate of PLGA, within 1- to 5-day culture range.<sup>[44]</sup> These exciting and improved characteristics of the nanopolymers would very shortly form the basis for reducing health-related costs due to implant removals. Their commercial importance is further elevated by earlier conclusion that micron-sized tubular scaffolds of poly(glycolic acid) (PGA) physically support vascular smooth muscle and endothelial cell growth in vitro.<sup>[45]</sup>

Nanostructured topography of bioimplants may not always be the desired morphology for effective regeneration of human tissues. Miller et al. have recently demonstrated that in comparison with conventional PLGA, rat aortic endothelial cells adhered and proliferated less on PLGA substrates whose surface was transformed to nanodimensions through treatment with sodium hydroxide.<sup>[46]</sup> They concluded that the residual hydroxyl radical on the surface, and not the nanoscale roughness, might be responsible for decreased endothelial cell function on the nanophase polymer. This apparent anomaly can be of significance if scientists attempt to engineer vascular implants to influence cell localization in the host environment. However, once surface chemistry changes were eliminated using cast-mold procedures,<sup>[46]</sup> a greater endothelial cell function was achieved on the nanophase PLGA in comparison to the conventional one. Generally speaking, therefore, the different cellular responses elicited from varied surface features of current and potential implants can pave the way to modulating wound healing in relation to immunoactivity of the surrounding tissue.

### Developments and Potentials of Nanostructured Composites as Nanobiomedical Implants

Composites, as tissue scaffolds, are emerging owing to the need to engineer the high strength of monolithic ceramics or metals with known biocompatible polymers, notably, PLGA and poly(L-lactic acid) (PLLA).<sup>[47]</sup> On another note, some carbons have earlier found use in implants especially for blood interfacing applications such as heart valves. Hitherto, because of their anisotropic mechanical, surface, and electrical properties and relative biocompatibility, conventional-size carbon fibers are used in orthopedic

implants.<sup>[48–53]</sup> Combined with the prominent electrical conductivity of the fibers (reaching up to 2000 W/m K), these studies suggest a strong potential for the use of carbon nanofibers as neural prostheses. Not long ago, clinical studies have demonstrated that these micron-size fibers provide insufficient bonding to juxtaposed tissue, which leads to clinical failures.<sup>[50]</sup> This concern of biocompatibility prompted in vitro studies using multiwalled carbon nanotubes functionalized with a bioactive molecule, 4-hydroxynonenal. The functionalized nanosized carbon tubes resulted in increased extension of neurites in rat brain neurons.<sup>[51]</sup> Long neurites improve transmission and coordination of nerve responses to stimuli. In an effort to develop an efficient and effective material capable of minimizing gliotic scar tissue formation around regions of neural implants, a formulation of polycarbonate urethane (PCU) reinforced with 10–25 wt.% high-surface-energy carbon nanotubes (carbon tubes with no pyrolytic layer) was studied by McKenzie et al.<sup>[54]</sup> They reported a decreased adhesion of astrocytes by 50% on the composite in comparison with only PCU,<sup>[54]</sup> after a 1-hr culture. Astrocytes are neuroglial cells that, among other functions, respond to injury of brain tissue, forming a special type of scar tissue, which fills spaces and closes gaps in the central nervous system. A gliotic response that is mediated largely by astrocytes forms at implant/injury sites, impeding axonal regeneration<sup>[55–57]</sup> and electrical signaling between neurons and implanted probes.<sup>[58]</sup> Although silicon has good electrical properties, inhibited neural function is often reported with neural probes made out of micron-size structures of silicon.<sup>[58]</sup> The report by McKenzie et al. followed a previous study by the same group of scientists in which they demonstrated decreased astrocyte cell densities on nanophase carbon fibers (size: approx. 60 nm) in comparison with conventional ones (size: approx. 0.125  $\mu$ m), following adhesion and proliferation studies for 1 hr and up to 5 days, respectively. These carbon fibers in compact form are presented in Fig. 6.

Another study mimicked the nanometer dimensions of hydroxyapatite crystals (which are present in bones) in carbon fibers. The investigators used unfunctionalized carbon nanofibers (diameter: 60–200 nm), and they observed the first evidence of increased adhesion<sup>[52]</sup> as well as enhanced long-term functions (specifically, proliferation, synthesis of alkaline phosphatase, and concentration of calcium in the extracellular matrix) of osteoblasts in relation to the conventional fibers.<sup>[53]</sup> The positive behaviors, combined with the high specific strength of carbon nanotubes, can readily be exploited in using the fiber as a reinforcing component for composite implant materials and tensile loading applications, such as artificial tendon and ligaments. The clinical benefits from their desirable qualities and the ease of the fabrication of

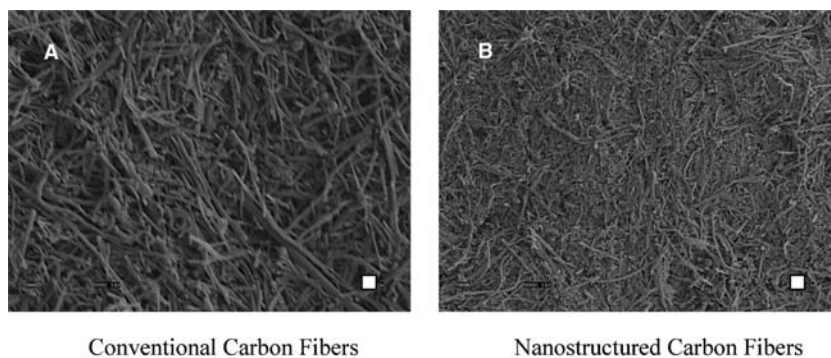


**Fig. 6** Scanning electron images depicting (A) conventional carbon fibers (0.125  $\mu\text{m}$  diameter) in comparison with (B) nanophase carbon fibers (60 nm diameter). Bar represents 10  $\mu\text{m}$  in dimensions. *Source:* From Ref.<sup>[53]</sup>.

their composites make them attractive candidates for orthopedic and dental implants.

Nanostructured surface topography of PLGA substrates, in both aligned and non-aligned arrangements, significantly increased adhesion and proliferation of chondrocytes (cartilage-synthesizing cells) over the conventional substrate.<sup>[59]</sup> There was preferred alignment of the cells along the nanoscale ridges on the aligned surfaces of the polymer. Other investigators have observed increased adhesion and proliferation of chondrocytes on nanostructured synthetic ceramic/PLGA composites.<sup>[60,61]</sup> More recently, Ejiofor and coworkers studied the adhesion and long-term functions of chondrocytes and osteoblasts on conventional and nanophase titania/PLGA composites for use as bone prostheses.<sup>[43]</sup> Of the various size-classified titania/PLGA composites studied, nanostructured titania/nanophase PLGA demonstrated the highest adhesion of both bone-producing cells (by 150%) and cartilage-synthesizing cells (twofold) compared to their conventional composite equivalent. These composites are pictured in Fig. 7. In addition, following a 4- to 7-day culture, the total intracellular protein synthesized by chondrocytes on the nanocomposite was significant (>400%) vs. the conventional titania/conventional PLGA composite substrate. The increased surface roughness and specific surface area were thought to be responsible for the favorable results.<sup>[43]</sup> The above developments lend credence to

the positive influences of nanostructured composites on the synthesis of cartilage tissues.

On further investigations of the same material system, the researchers attributed fine grain size of nanocomposites as the major potential cause of the enlargement of the developing cartilage tissue, as indexed by their alkaline phosphatase activity. The activity level on the nanostructured titania/nanophase PLGA composites yielded 1.4 activity units/ $\text{cm}^2$  whereas the rest of the substrates investigated leveled off to 0.85 activity units/ $\text{cm}^2$ . Although further mechanical characterization is needed, materials such as this may allow for exciting alternatives in the design of more effective cartilage tissue engineering prostheses.

## POTENTIAL RISKS

Since the research on and the use of nanobiomedical implants using nanopowders or nanofibers is still at its infancy, risks to human health and environment must not be overlooked. Many issues relating to safe and healthy fabrication of nanobiomedical implants still need to be addressed. For example, small nanoparticles can enter the human body through pores and may accumulate in the cells of the respiratory or integumentary organ system, and the health effects are yet to be known. This would happen during commercial-scale processing of the nanoparticles as

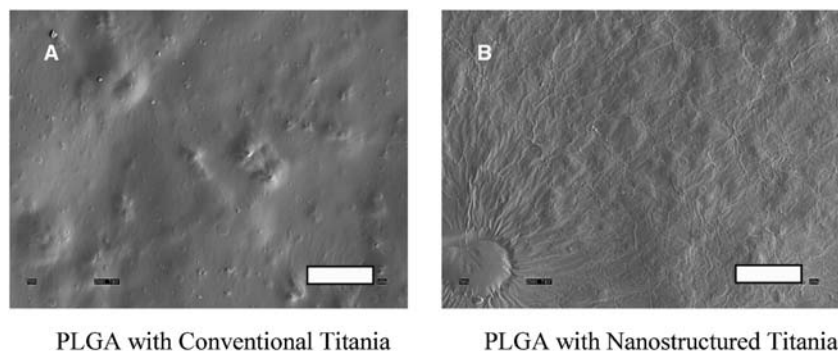


**Fig. 7** Scanning electron images depicting PLGA composites containing: (A) conventional titania (4.120  $\mu\text{m}$  grain size) in comparison with (B) nanophase titania (32 nm grain size). 70/30 wt.% PLGA/titania. Bar represents 100  $\mu\text{m}$  in dimensions. *Source:* From Ref.<sup>[61]</sup>.

well as through the use of these materials as implants. According to Debra Rolison of Naval Research Laboratory (Washington, DC), because of humankind's history with viruses—and viruses are already nanobiotechnological—there should be a need for continuous monitoring of potential effects of newly designed and fabricated nanomaterials.

## FUTURE ACTIVITY

According to the U.S. government's research agenda, the current and future broad interests in nanobiomedical activity can be categorized as given in Table 3.<sup>[24,62]</sup> Marsch<sup>[62]</sup> further grouped the entire activity in three broad related fronts:

1. Development of pharmaceuticals for inside-the-body applications—such as drugs for anticancer and gene therapy.
2. Development of diagnostic sensors and lab-on-a-chip techniques for outside-the-body applications—such as biosensors to identify bacteriological infections in biowarfare.
3. Development of prostheses and implants for inside-the-body uses.

Whereas the European governments emphasize commercial applications in all three fronts above according to Marsch, the U.S. government—as can be seen in Table 3—tends to gear toward fundamental research on biomedical implants and biodefense, leaving commercial applications to industry. Both classifications identify nanobiomedical implants (item 8 in Table 3 and the third classification by Marsch) as potential interests. The biological and biomimetic nanostructures to be used as an implant involve some sort of an assembly in which smaller materials later assume the shape of a body part, such as hipbone.

**Table 3** U.S. government current and future broad interests in nanobiomedical research activity

U.S. Government Research Interests for Nanobiomedical Research
1 Synthesis and use of nanostructures
2 Applications of nanotechnology in therapy
3 Biomimetic nanostructures
4 Biological nanostructures
5 Electronic–biological interface
6 Devices for early detection of diseases
7 Instruments for studying individual molecules
8 Nanotechnology for tissue engineering

Source: Refs.<sup>[24]</sup> and<sup>[62]</sup>.

These final, biomimetic, bulk nanostructures can start with a predefined nanochemical (such as an array of large reactive molecules attached to a surface) or nano-physical (such as a small crystal) structure. It is believed that by using these fundamental nanostructured building blocks as seed molecules or crystals, a larger bulk material will self-assemble or keep growing by itself. Further research is needed in self-assembly of nanostructured materials.

Several developments on implants for clinical uses are ongoing, while just a few are at various clinical testing stages.<sup>[63,64]</sup> For instance, peripheral vascular grafts made out of polytetrafluoroethylene (PTFE) have been developed to serve as artificial arteries to restore blood flow to peripheral limbs of the body, and is already under clinical test.<sup>[63]</sup> Coronary artery bypass grafts made out of expanded polytetrafluoroethylene (ePTFE) is a potential material for supplying blood to the heart tissue, and this has been developed.<sup>[63]</sup> In addition, biologically hybridized polymeric immunoisolation devices are considered a biocompatible substitute capable of preventing rejection responses following immunosuppressant therapy. Clearly, nanomaterials as mentioned in this chapter are at their infancy and much more testing must be conducted before their full potential is realized.

## CONCLUSIONS

We would like to note that the scientific developments reported above do not exhaust the current global beehive research efforts on the biological potentials of nanoparticulates as implants. It is believed, however, that following the trends of these impressive application properties of the nanomaterials in the biomedical domain, there exists a bright future for therapies and treatments through prosthetic implantation.

Recent developments in modifying existing conventional materials to possess nanoscale dimensions without altering their chemistry would build upon the existing implant materials or clinical approvals by the various responsible agencies (for instance, the FDA in the United States). This is a much easier route to exploiting the beneficial properties of nanostructured materials as nanobiomedical implants than creating new chemistries that have not yet been recommended for inside-the-body use.

## REFERENCES

1. Kaplan, F.S.; Hayes, W.C.; Keaveny, T.M.; Boskey, A.; Einhorn, T.A.; Iannotti, J.P. Form and function of bone. In *Orthopedic Basic Science*; Simon, S.P., Ed.; American Academy of Orthopedic Surgeons: Columbus, OH, 1994; 127–185.

2. Roco, M.S., Williams, R.S., Alivisatos, P., Eds.; *Nano-Technology Research Directions: IWGN Workshop Report*; NSF: Washington, DC, 1999.
3. Siegel, R.W.; Fougere, G.E. Mechanical properties of nanophase materials. In *Nanophase Materials: Synthesis-Properties-Applications*; Hadjipanayis, G.C., Siegel, R.W., Eds.; Kluwer: Dordrecht, 1994; 233 pp.
4. Siegel, R.W.; Fougere, G.E. Mechanical properties of nanophase metals. *Nanostruct. Mater.* **1995**, *6*, 205.
5. Siegel, R.W. Creating nanophase materials. *Sci. Am.* **1996**, *275*, 42–47.
6. Webster, T.J.; Siegel, R.W.; Bizios, R. Design and evaluation of nanophase alumina for orthopedic/dental applications. *Nanostruct. Mater.* **1999**, *12*, 983–986.
7. Webster, T.J.; Siegel, R.W.; Bizios, R. Osteoblast adhesion on nanophase ceramics. *Biomaterials* **1999**, *20*, 1221–1227.
8. Webster, T.J.; Schadler, L.S.; Siegel, R.W.; Bizios, R. Mechanisms of enhanced osteoblast adhesion on nanophase alumina involve vitronectin. *Tissue Eng.* **2001**, *7*, 291–302.
9. Siegel, R.W., Hu, E., Roco, M.C., Eds.; *Nano-Structure Science and Technology*; Kluwer Academic Press: Boston, 1999.
10. Baraton, M.I.; Chen, X.; Gonsalves, K.E. FTIR study of nanostructured alumina nitride powder surface: Determination of the acidic/basic sites by CO, CO<sub>2</sub>, and acetic acid adsorptions. *Nanostruct. Mater.* **1999**, *8*, 435.
11. Klabunde, K.J.; Strak, J.; Koper, O.; Mohs, C.; Park, D.; Decker, S.; Jiang, Y.; Lagadic, I.; Zhang, D. Nanocrystals as stoichiometric reagents with unique surface chemistry. *J. Phys. Chem.* **1996**, *100*, 12141.
12. Wu, S.J.; DeJong, L.C.; Rahaman, M.N. Sintering of nanophase  $\gamma$ -Al<sub>2</sub>O<sub>3</sub> powder. *J. Am. Ceram. Soc.* **1996**, *79*, 2207.
13. Horbett, T.A. Proteins: Structure, Properties and Adsorption to surfaces. In *Biomaterials Science: An Introduction to Materials in Medicine*; Ratner, B.D., Hoffman, A.S., Schoen, A.S., Lemmons, J.E., Eds.; Academic Press: New York, 1996; 133–140.
14. Hench, L.L.; Ethridge, E.C. Biomaterial—The interfacial problem. *Adv. Biomed. Eng.* **1975**, *5*, 35–150.
15. Schakenraad, J.M. Cell: Their Surfaces and Interactions with Materials. In *Biomaterials Science: An Introduction to Materials in Medicine*; Ratner, B.D., Hoffman, A.S., Schoen, A.S., Lemmons, J.E., Eds.; Academic Press: New York, 1996; 141–147.
16. Webster, T.J. Nanophase Ceramics: The Future of Orthopedic and Dental Implant Material. In *Nanostructured Materials*; Ying, J.Y., Ed.; Academic Press: New York, 2001; 125–166.
17. Eisenberg, D. Three-dimensional structure of membrane and surface proteins. *Annu. Rev. Biochem.* **1984**, *53*, 595–623.
18. Peters, T. Serum Albumin. In *Advances in Protein Chemistry, Vol. 37*; Anfinsen, C.B., Edsall, J.T., Richards, F.M., Eds.; Academic Press: New York, 1985; 161–245.
19. Stryer, L. *Biochemistry*, 2nd Ed.; W. H. Freeman: San Francisco, 1981.
20. Loeb, W.F.; Mackey, W.F. A “cuvette method” for the determination of plasma fibrinogen. *Bull. Am. Soc. Vet. Clin. Pathol.* **1972**, *1*, 5–8.
21. Norde, W.; Lyklema, J. Why proteins prefer interfaces. *J. Biomater. Sci., Polym. Ed.* **1991**, *2*, 183–202.
22. Yutani, K.; Ogasahara, K.; Tsujita, T.; Sugino, Y. Dependence of conformational stability on hydrophobicity of the amino acid residue in a series of variant proteins substituted at a unique position of tryptophan synthase alpha subunit. *Proc. Natl. Acad. Sci. U.S.A.* **1987**, *84*, 4441–4444.
23. Grinder, O. Consultants corner: Question and answer. *Int. J. Powder Metall.* **June 2002**, *38* (4), 33–35.
24. Malsch, I. The Nano-body: Sense and Non-sense on Biomedical Applications of Nanotechnology, Lecture for COST and NanoSTAG Conference, Leuven, Oct. 29, 2001.
25. Webster, T.J.; Siegel, R.W.; Bizios, R. Design and evaluation of nanophase alumina for orthopaedic/dental applications. *Nanostruct. Mater.* **1999**, *12*, 983.
26. Webster, T.J.; Siegel, R.W.; Bizios, R. Osteoblast adhesion on nanophase ceramics. *Biomaterials* **1999**, *20*, 1221.
27. Webster, T.J.; Ergun, C.; Doremus, R.H.; Siegel, R.W.; Bizios, R. Specific proteins mediate enhanced osteoblast adhesion on nanophase ceramics. *J. Biomed. Mater. Res.* **2000**, *51* (3), 475.
28. Webster, T.J.; Siegel, R.W.; Bizios, R. Enhanced functions of osteoblasts on nanophase ceramics. *Biomaterials* **2000**, *21*, 1803.
29. Webster, T.J.; Siegel, R.W.; Bizios, R. Enhanced Surface and Mechanical Properties of Nanophase Ceramics for Increased Orthopaedic/Dental Implant Efficacy. In *Bioceramics 13: 13th International Symposium on Ceramics in Medicine Conference Proceedings*; Giannini, S., Moroni, A., Eds.; Zurich, Switzerland, 2000; 321 pp.
30. Webster, T.J. Nanophase Ceramics: The Future Orthopedic and Dental Implant Material. In *Advances in Chemical Engineering, Vol. 27*; Ying, J.Y., Ed.; Academic Press: New York, 2001; 125–166.
31. Webster, T.J.; Schadler, L.S.; Siegel, R.W.; Bizios, R. Mechanisms of enhanced osteoblast adhesion on nanophase alumina involve vitronectin. *Tissue Eng.* **2001**, *7* (3), 291–301.
32. Webster, T.J.; Ergun, C.; Doremus, R.H.; Siegel, R.W.; Bizios, R. Enhanced functions of osteoclast-like cells on nanophase ceramics. *Biomaterials* **2001**, *22* (11), 1327–1333.
33. Webster, T.J.; Siegel, R.W.; Bizios, R. Nanoceramic surface roughness enhances osteoblast and osteoclast functions for improved orthopaedic/dental implant efficacy. *Scr. Mater.* **2001**, *44*, 1639–1642.
34. Horbett, T.A. Techniques for Protein Adsorption Studies. In *Techniques of Biocompatibility Testing*; Williams, D.F., Ed.; CRC Press: Boca Raton, FL, 1986; 183–214.
35. Klabunde, K.J.; Strak, J.; Koper, O.; Mohs, C.; Park, D.; Decker, S.; Jiang, Y.; Lagadic, I.; Zhang, D. Nanocrystals as stoichiometric reagents with unique surface chemistry. *J. Phys. Chem.* **1996**, *100*, 12141.
36. Oparaugo, P.C.; Clarke, I.C.; Malchau, H.; Herberts, P. Correlation of wear debris-induced osteolysis and



- revision with volumetric wear-rate of polyethylene: A survey of 8 reports in the literature. *Acta Orthop. Scand.* **2001**, *72*, 22–28.
37. Urban, R.M.; Jacobs, J.J.; Tomlinson, M.J.; Gavriloic, J.; Black, J.; Peoc'h, M. Dissemination of wear particles to the liver, spleen, and abdominal lymph nodes of patients with hip or knee replacement. *Am. J. Bone Joint Surg.* **2000**, *82*, 457–476.
  38. Lerouge, S.; Huk, O.; Yahia, L.H.; Sedel, L. Characterization of in vitro wear debris from ceramic–ceramic total hip arthroplasties. *J. Biomed. Mater. Res.* **1996**, *32*, 627–633.
  39. Gutwein, L.G.; Webster, T.J. Osteoblast and chondrocyte proliferation in the presence of alumina and titania nanoparticles. *J. Nanopart. Res.* **2002**, *4*, 231–238.
  40. Litsy, A.S.; Spector, M. Form and function of cartilage. In *Orthopedic Basic Science*; Simon, S.P., Ed.; American Academy of Orthopedic Surgeons: Columbus, OH, 1994; 482.
  41. Solchaga, L.A.; Yoo, J.U.; Lundberg, M.; Dennis, J.E.; Huibregtse, B.A.; Goldberg, V.M.; Caplan, A.I. Hyaluronan-based polymers in the treatment of osteochondral defects. *J. Orthop. Res.* **2000**, *18*, 773–780.
  42. Messner, K. Durability of artificial implants for repair of osteochondral defects of the medial femoral condyle in rabbits. *Biomaterials* **1994**, *15*, 657–664.
  43. Ejiofor, J.U.; Kay, S.; Thapa, A.; Haberstroh, K.M.; Webster, T.J. Novel titania/PLGA nanocomposite for bone and cartilage applications. *Composites, Part B Paper* **2003**, *in press*.
  44. Miller, D.C.; Thapa, A.; Haberstroh, K.M.; Webster, T.J. An In Vitro Study of Nanofiber Polymers for Guided Vascular Regeneration. Paper presented at the 2002 Annual Meeting of American Institute of Chemical Engineers, Indianapolis, IN, Nov. 3–8, 2002.
  45. Nikolovski, J.; Mooney, D.J. Smooth muscle cell adhesion to tissue engineering scaffolds. *Biomaterials* **2000**, *21*, 2025–2032.
  46. Miller, D.C.; Thapa, A.; Haberstroh, K.M.; Webster, T.J. Increased Vascular Cell Function on Nano-Rough Poly(lactic-co-glycolic acid) Films. Paper presented at the 2002 Annual Meeting of American Institute of Chemical Engineers, Indianapolis, IN, Nov. 3–8, 2002.
  47. Zhang, R.; Ma, P.X. Porous poly(L-lactic acid)/apatite composites created by biomimetic process. *J. Biomed. Mater. Res.* **1999**, *45* (4), 285–293.
  48. Morris, D.M.; Hindman, J.; Marino, A.A. Repair of fascial defects in dogs using carbon fibers. *J. Surg. Res.* **1998**, *80*, 300–303.
  49. Kus, W.M.; Gorecki, A.; Strzelczyk, P.; Swiader, P. Carbon fiber scaffolds in the surgical treatment of cartilage lesions. *Ann. Transp.* **1999**, *4*, 101–102.
  50. Mortier, J.; Engelhardt, M. Foreign body reaction in carbon fiber prosthesis implantation in the knee joint—Case report and review of the literature. *Z. Orthop. Ihre Grenzgeb.* **2000**, *138*, 390–394.
  51. Mattson, M.P.; Haddon, R.C.; Rao, A.M. Molecular functionalization of carbon nanotubes and use as substrates for neuronal growth. *J. Mol. Neurosci.* **2000**, *14*, 175–182.
  52. Price, R.L.; Gutwein, L.G.; Haberstroh, K.M.; Webster, T.J. Nanometer Carbon and Alumina Fiber Structure Enhances Osteoblast Adhesion. Paper presented at the 2002 Annual Meeting of American Institute of Chemical Engineers, Indianapolis, IN, Nov. 3–8, 2002.
  53. Elias, K.E.; Price, R.L.; Webster, T.J. Enhanced functions of osteoblasts on nanometer diameter carbon fibers. *Biomaterials* **2000**, *23*, 3279–3287.
  54. McKenzie, J.L.; Waid, M.C.; Shi, R.; Webster, T.J. Functions of Astrocyte on Carbon Nanofibers. Paper presented at the 2002 Annual Meeting of American Institute of Chemical Engineers, Indianapolis, IN, Nov. 3–8, 2002.
  55. Webb, K.; Budko, E.; Neuberger, T.J.; Chen, S.; Schachner, M.; Tresco, P.A. Substrate-bound human recombinant L1 selectively promotes neuronal attachment and outgrowth in the presence of astrocytes and fibroblasts. *Biomaterials* **2001**, *22*, 1017–1028.
  56. Kam, L.; Shain, W.; Turner, J.N.; Bizios, R. Correlation of astroglial cell function on micropatterned surfaces. *Biomaterials* **1999**, *20*, 2343–2350.
  57. Geisert, E.E., Jr.; Bidanset, D.J.; del Mar, N.; Robson, J.A. Up-regulation of a keratin sulfate proteoglycan following cortical injury in neonatal rats. *Int. J. Dev. Neurosci.* **1996**, *14*, 257–267.
  58. Edell, D.J.; Toi, V.V.; McNeil, V.M.; Clark, L.D. Factors influencing the biocompatibility of insertable silicon microshafts in cerebral cortex. *IEEE Trans. Biomed. Eng.* **1992**, *39*, 635–643.
  59. Park, G.E.; Ward, B.C.; Park, K.; Webster, T.J. Functions of Chondrocytes on Nanostructured and Aligned PLGA Surfaces, Paper presented at the 2002 Annual Meeting of American Institute of Chemical Engineers, Indianapolis, IN, Nov. 3–8, 2002.
  60. Park, G.E.; Savaiano, J.K.; Park, K.; Webster, T.J. *An In Vitro Study of Chondrocyte Function on Nanostructured Polymer/Ceramic Formulations to Improve Cartilage Repair*, NANO 2002 Conference Abstract Book, Orlando, FL, 2002.
  61. Kay, S.; Thapa, A.; Haberstroh, K.M.; Webster, T.J. Nanostructured polymer/nanophase ceramic composites enhance osteoblast and chondrocyte adhesion. *Tissue Eng.* **2002**, *8*, 753–761.
  62. Malsch, I. Biomedical applications of nanotechnology. *Ind. Phys.* **June/July 2002**, *51*, 15–17.
  63. Williams, S.K.; Jarrell, B.E. Tissue engineered vascular grafts. *Nat. Med.* **1996**, *2*, 32–34.
  64. Ogiso, M.; Yamashita, Y.; Matsumoto, T. Differences in microstructural characteristics of dense HA and HA coating. *J. Biomed. Mater. Res.* **1998**, *41* (2), 296–303.

# Biomedical Applications: Novel Materials and Devices

**J. Zachary Hilt**

*Department of Chemical and Materials Engineering, University of Kentucky,  
Lexington, Kentucky, U.S.A.*

**Mark E. Byrne**

*Department of Chemical Engineering, Auburn University,  
Auburn, Alabama, U.S.A.*

## INTRODUCTION

The emergence of nanoscale science and the materialization of consequent technologies have provided new avenues for engineering materials and devices that will revolutionize the way health care is administered. In particular, the ability to engineer with molecular to macromolecular precision has led to the creation of nanoscale materials and devices with inherent advantages relative to macroscale-structured counterparts.

In biological and medical applications, controlling interactions at the level of natural building blocks, from proteins to cells, facilitates the novel exploration, manipulation, and application of living systems and biological phenomena. Nanoengineered tissue scaffolds and nanostructured biomaterials and coatings for implants and prostheses are leading to better solutions in tissue design, reconstruction, and reparative medicine. Synthetic nanopores of tailored dimensions are probing, characterizing, and sequencing biological macromolecules. Nano- and microarrays are accelerating drug discovery and assessment of drug candidates. Self-assembly is creating new biomaterials with well-ordered structures at the nanoscale such as nanofiber peptide and protein scaffolds. Also, nanostructured materials and nanoparticulate delivery systems enable a wide range of materials for imaging and/or therapeutic purposes to be easily introduced or injected in the body.

Application of these techniques to create novel materials and devices for tissue engineering, diagnostics, and therapeutics will profoundly impact the practice of medicine. This entry reviews and discusses the emerging field of nanomedicine, where nanoscale science and technology are sculpting future innovations in medicine, and outlines the enormous potential of the field.

## FABRICATION, ASSEMBLY, AND VISUALIZATION AT THE NANOSCALE

In a recent perspective on nanobiotechnology, Whitesides<sup>[1]</sup> emphasizes the value of the microscale in the current enthusiasm of nanoscale science and technology. The scales encountered in biology, medicine, and biotechnology range from the micro- to nanometer and developments will continue to progress and expand on both levels. This overview is presented in much the same manner, with an analysis of exciting and novel technologies that are equally relevant to nanotechnology, but are not strictly classified as nanoscale.

The development of fabrication processes capable of manipulation at the micro- and nanoscale, such as electron-beam and ion-beam lithography,<sup>[2]</sup> nanoimprint lithography,<sup>[3]</sup> microcontact printing ( $\mu$ CP),<sup>[4]</sup> and dip-pen nanolithography (DPN),<sup>[5]</sup> enabled the creation of novel devices. In addition, self-assembly has been demonstrated to be a powerful method for creating well-defined nanostructures.<sup>[6–8]</sup> At the same time, visualization with submicron resolution has been essential in the implementation and utilization of these fabrication techniques. The development of nanoscale visualization techniques, such as scanning tunneling microscopy<sup>[9]</sup> and atomic force microscopy,<sup>[10]</sup> has facilitated manipulating and imaging at the atomic level. In recent years, micro- and nanoscale fabrication techniques have been utilized to construct micro-/nanoelectromechanical systems (MEMS/NEMS), microarrays, microfluidic devices, micro total analysis systems (i.e., lab-on-a-chip), and other micro-/nanodevices.

## NANOMEDICINE

Within the last century, technology has revolutionized the practice of medicine and drastically improved

quality of life. Two entries listed within the top 20 greatest achievements of the 20th century by the National Academy of Engineering were related to the field of medicine: imaging and health technologies, ranked at number 14 and 16, respectively.<sup>[11]</sup> The list included a number of technologies such as X-rays, the electron microscope, radioactive tracers, ultrasound and ultrasonic imaging, computer-aided topography, magnetic resonance imaging, endoscopy, pacemakers, the ventricular defibrillator, the blood-heat exchanger, contact lenses, heart valves, artificial kidney, etc. Slightly before the century began, W.C. Roentgen discovered X-rays in 1895, which dramatically changed medicine and allowed visualization inside the human body as never before.

At the transition into the 21st century, technology is becoming progressively controlled at the molecular level. Molecular understanding is driving the next generation of commercial diagnostic and therapeutic devices (Fig. 1).<sup>[12]</sup> The application of micro-/nano-

devices for biological and medical applications is leading to fundamental insights about the behavior and function of tissues,<sup>[13]</sup> intra- and intercellular communication,<sup>[13–15]</sup> forces and flows and the effects on individual cells,<sup>[16]</sup> the structure, function, and behavior of proteins, DNA, and other biological molecules;<sup>[17]</sup> and pharmacogenetics and genetic predisposition toward disease, etc. Similarly to X-rays in 1895, the two decades before the beginning of the 21st century had the discoveries of the atomic force and scanning tunneling microscopes, which allowed visualization and manipulation on a molecular and atomic level as never before. It is in this regard that nanoscale science and engineering has an unlimited potential to affect the diagnosis and etiology of a number of diseases with enhanced prognosis and rational treatment. Therefore this century is anticipated to be unparalleled in the progress of medical science and technology and lead to more technological innovation in medicine than any other in history.

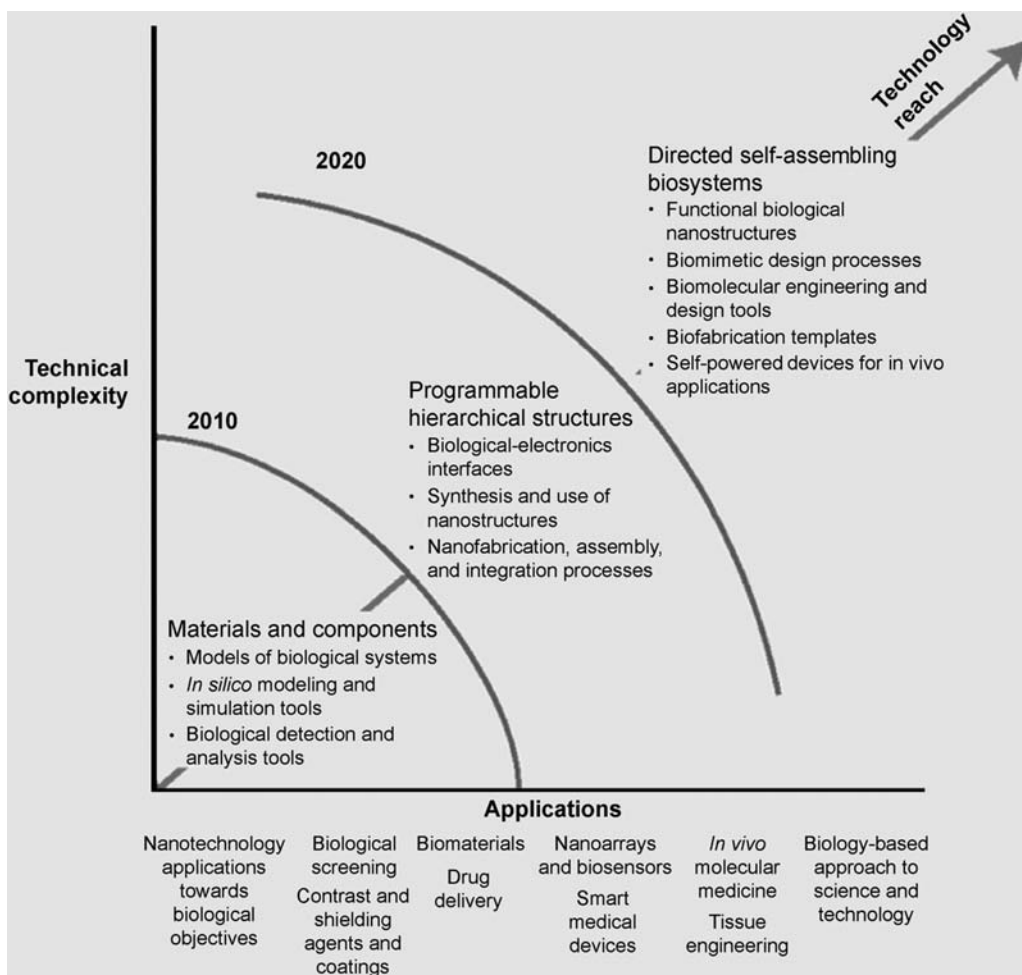


**Fig. 1** Nanobiotechnology: A continuum of opportunity for nanotechnology in the life sciences. *Source:* From Ref.<sup>[12]</sup>, SRI Consulting Business Intelligence (SRIC-BC; Menlo Park, CA, U.S.A.)—permission pending.

## NANOTECHNOLOGY IN CELLULAR AND TISSUE ENGINEERING: REPARATIVE MEDICINE

Tissue engineering is a diverse and evolving field that focuses upon the regeneration, modification, and assembly of functional tissue, tissues, or organs using specific combinations of cells, extracellular scaffolds, and temporal supporting mechanisms (i.e., biochemical, mechanical, electrical signals, etc.) for tissue synthesis events.<sup>[18–20]</sup> The field can be classified into two main areas of relevance: *therapeutic relevance*, which covers tissue regeneration and organ replacement (in vivo or in vitro); and *diagnostic relevance*, where tissue is formed in vitro and used for toxicology studies, metabolism, drug discovery, etc.<sup>[21]</sup>

Based on a recent commentary by Yannas<sup>[22]</sup> and an overview by Sipe,<sup>[23]</sup> six methods have been practiced to address the problem of organ or tissue replacement: 1) transplantation (allograft or xenograft), which depends on a supply of available organs or tissue and appropriate histocompatibility; 2) autografting, removing a viable tissue or organ and placing it elsewhere in the body than the original site; 3) replacement with permanent prosthesis (synthetic material or device); 4) use of an external device to substitute or augment a poorly functioning organ; 5) in vitro synthesis (organ or tissue synthesized in culture and then implanted); and 6) in vivo synthesis (implantation of minimum constituents to induce organ or tissue regeneration in situ). The last two (5 and 6), and 7, when it includes cellular machinery in a bioartificial device, describe the field of tissue engineering.

The essential elements of tissue engineering as outlined in a recent NIH symposium<sup>[23]</sup> are as follows: 1) cells, 2) signaling, 3) extracellular matrix scaffold, 4) design principles, 5) vascular assembly, 6) bioreactors, 7) storage and translation, and 8) host remodeling and immune response. We direct the reader to the following reviews for a discussion on the challenges and obstacles within each element as well as the road ahead in the field.<sup>[19,20,23]</sup>

The hierarchical structure of human anatomy begins with the building block of cells. A collection of cells similar in structure and function form tissues (epithelial, connective, muscle, and nervous) and a collection of tissues that perform physiological tasks are organs. Consequently, multiple organs form systems such as the cardiovascular, respiratory, musculoskeletal, digestive, endocrine, reproductive, etc.

Each tissue and tissue system has unique biochemical composition, cellular components, mechanical/physiochemical properties, and extracellular matrix, etc., which vary over length scales. Of particular importance within the tissue or cellular framework (i.e., scaffold), as outlined by Griffith,<sup>[20]</sup> are the macroscopic shape and composition; the size, orientation, and surface chemistry of pores and interconnected pores or

channels (microscale); and the local substrate surface roughness, texture, and porosity (micro- to nanoscale).<sup>[24–27]</sup> Therefore the success of scaffold-based strategies depends highly on the substrate materials and material physiochemical properties, determined fundamentally by the material micro-/nanostructure and design.

This section will focus on scaffolds for cellular and tissue engineering, specifically highlighting micro- and nanofabricated surfaces, matrices, and scaffolds; cellular spatial and function regulation by micro- and nanoscale features; and novel nanoscale science and engineering developments toward tissue regeneration.

### Micro- and Nanotechnology for Cellular Spatial and Function Regulation

Most mammalian cells are anchorage-dependent and therefore must adhere and spread on a substrate in order to live and remain functional. Cell spreading, locomotion, and active migration are primarily influenced by the physiochemical characteristics of the surface (substratum surface free energy and surface topography).<sup>[28]</sup> However, protein adsorption always precedes cellular adhesion<sup>[24]</sup> and extracellular matrix proteins regulate and promote cell adhesion, spreading, and motility (Fig. 2). Binding strength, conformation, and orientation of proteins on a biomaterial surface particularly influence subsequent cellular binding and motility. Functional cell behaviors include proliferation, differentiation (i.e., cellular specialization), migration, and secretion of their own extracellular matrix. For further information, we direct the reader to an excellent review of cell surfaces and interactions with materials.<sup>[24]</sup>

To induce cells to attach to certain areas or patterns of a particular biomaterial, one must alter the underlying substrate chemistry. The underlying surface chemistry has been modified to include hydrophilic or hydrophobic molecules or polymers,<sup>[29,30]</sup> polysaccharides,<sup>[31,32]</sup> stimuli-sensitive and responsive materials,<sup>[33–35]</sup> and proteins or growth factors.<sup>[36–39]</sup> The ability to pattern has enabled control over the adsorption or immobilization of adhesive proteins and, thus, the patterning or selective adhesion of cells on substrates.<sup>[40]</sup> These modifications change the ability of a cell to attach, but to some extent, regulate cellular functions such as growth, differentiation, and apoptosis.<sup>[41]</sup>

In order for a surface to be patterned in micro- or nanoscale dimensions, a means to spatially control a chemical modification of the surface is required at the resolution necessary to fit the design of the application or device. By patterning a surface, domains of a few microns or nanometers can be created, each able

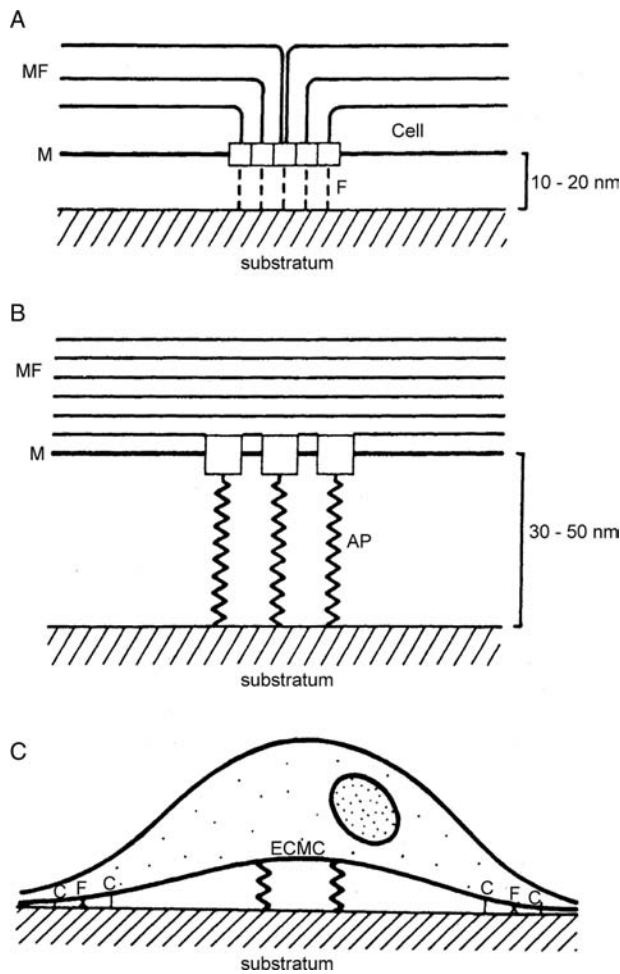


**Fig. 2** Schematic of cell-substratum contact sites. In (A), focal adhesion sites are demonstrated. These are predominantly found at cell extension boundaries. The integrin connects the cytoskeleton with the substratum via fibronectin. In (B), close contacts, which are weaker adhesion sites, are illustrated. In (C), the localization of the different adhesion sites is demonstrated. MF, microfilaments; M, cell membrane; AP, adhesive protein; F, fibronectin; ECMC, extracellular matrix contact; C, close contact; F, focal adhesion. *Source:* From Ref.<sup>[24]</sup>—permission pending.

to maintain different interactions with the environment. Various techniques have been developed to achieve a fine level of control, which include lithographic techniques (e.g., UV, electron-beam, ion-beam lithography,<sup>[2]</sup> nanoimprint lithography,<sup>[3]</sup>), and soft lithographic techniques (e.g., microcontact printing ( $\mu$ CP),<sup>[4]</sup> micromolding in capillaries (patterning using microfluidic channels),<sup>[42]</sup> dip-pen nanolithography (DPN),<sup>[5]</sup> laminar flow patterning).<sup>[43,44]</sup> By integrating microcontact printing with microfluidics<sup>[42,45]</sup> a surface was patterned by pumping solution through channels formed when stamp and substrate were brought into contact. Reviews of these soft lithographic techniques discussing patterned surface creation<sup>[45,46]</sup> and also

their application for microfluidics devices<sup>[47]</sup> were recently published.

While the approaches above are adequate for a number of tissue types, the fabrication of thick complex tissues with complex vascularization remains difficult due to a limited diffusion distance of nutrients, gases, and waste products.<sup>[48,49]</sup> Various forms of three-dimensional (3-D) work are beginning to address these concerns.

Three-dimensional printing (3DP<sup>TM</sup>), which is a solid free-form fabrication method, creates physically joined structures in desired, very complex micro- and macroarchitecture.<sup>[50]</sup> Also, 3-D micromolding in capillaries (3D MIMIC) has been shown to pattern multiple cells and proteins in complex, discontinuous structures with close proximity and in well-defined structures.<sup>[51]</sup> Each allows understanding of tissue architecture at the resolution of individual cells.

Three-dimensional peptide scaffolds<sup>[52]</sup> and artificial amphiphilic protein scaffolds<sup>[8,53,54]</sup> have also shown promise to maintain functional, mature differentiated cells,<sup>[52]</sup> as well as to support the differentiation of progenitor cells.<sup>[55,56]</sup> For example, Zhang et al. recently demonstrated primary rat neuronal cells projecting axons along the contours of the peptide surface with active synaptic connections as well as neuronal progenitor cell migration.<sup>[52,56]</sup>

In a recent paper by Vacanti et al., a mold of a branched network of vascular channels (with capillary channels 10  $\mu$ m in diameter) was formed in silicon and Pyrex utilizing photolithographic and micromachining techniques (Fig. 3).<sup>[57]</sup> Three-dimensional units of tissue could be lifted from the mold after seeding and proliferation of endothelial cells. Including these branched vascular networks within layers of tissue has the potential to form 3-D conformations of living tissue for implantation.

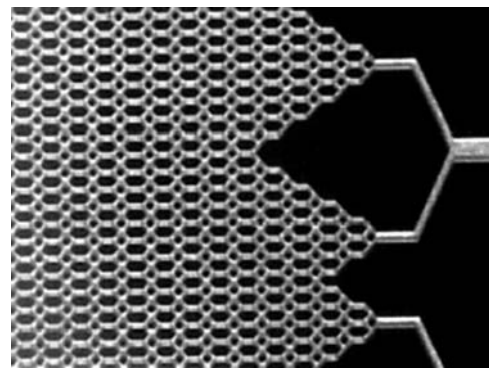


**Fig. 3** Optical micrograph of a portion of a capillary network etched into a silicon wafer. *Source:* From Ref.<sup>[57]</sup>—permission pending.

## Micro- and Nanotopography: Structured Biomaterials

Experimental evidence exists that surface topography and texture of implanted materials have a large effect on the rate of success. It has been known for many years that grooved substrata of particular dimensionality induced cellular orientation, locomotion, and cell guidance.<sup>[58–60]</sup> It has also been shown that fibrous capsule formation and foreign body response can be greatly reduced by using microtextured materials.<sup>[61]</sup> For orthopedic and dental implants, a decrease in the grain size of ceramic formulations into the nanometer regime has demonstrated improved efficacy.<sup>[62]</sup> However, as discussed in the previous section, the underlying surface chemistry is a determining factor in cellular adhesion and function, and it is unclear as to the extent that chemical or topographical clues control.<sup>[63]</sup>

The length scale of basement membranes (i.e., the extracellular matrix in epithelium and endothelium) is of nanoscale dimension with a complex mixture of pores, fibers, and ridges.<sup>[25,27,64]</sup> For example, the corneal basement membrane of the Macaque monkey has average feature heights between 147 and 191 nm, average fiber width of 77 nm, and pores with an average diameter of 72 nm.<sup>[27]</sup> Recently, by matching of synthetic nanoscale topographies with feature dimensions similar to basement membrane, cell behavior and function was affected.<sup>[25]</sup> The authors demonstrate that endothelial cells respond strongly to topography in orientation, elongation, and cytoskeletal organization and that focal adhesions are narrower on substrates with regions of nanoscale dimensions than on smooth substrates. It has been demonstrated that focal adhesion assembly contributes significantly to cellular adhesion strengthening independent of cell morphology changes and redistribution of adhesive structures.<sup>[65]</sup> In this study, micropatterning methods were used to control focal adhesion size and position and to decouple integrin and focal adhesion assembly from gross changes in cell morphology.

An excellent review exists on the topic of micro- and nanoscale-substrate interactions, which highlights that micro- and nanoscale topographical cues, independent of biochemistry, generated by the extracellular matrix may have significant effects upon cellular behavior.<sup>[26]</sup> The effects of textured surfaces on cell behavior are listed for a number of systems, which includes a variety of cell types and substratum features such as grooves, ridges, steps, pores, wells, nodes, and adsorbed protein fibers.

Typically, grooves, ridges, and other shapes are fabricated in similar ways as discussed in the last section, but that various isotropic or anisotropic etching steps are added. Depending on the type of substrate and the corresponding etching scheme, a number

of different shapes of varying sizes can be produced. Recently, engineered surface textures such as micro- and nanoscale patterns (pillars, ridges, and complex shapes) were only superimposed on microscale features using nanolithography.<sup>[66]</sup> Pillars and ridges ranging in height from 1.5 to 5  $\mu\text{m}$  and separated by 5, 10, and 20  $\mu\text{m}$  were prepared. Nanoscale pillars and ridges ranged from 12 to 300 nm.

## NANOTECHNOLOGY IN DIAGNOSTIC SYSTEMS

In medical diagnostics, the speed and precision with which a condition is detected determines patient prognosis. With the development of lab-on-a-chip and other miniature point-of-care (POC) devices, the speed and precision with which health care is administered can be radically enhanced. In addition, novel analysis techniques allowing for acquisition of previously unattainable information and, consequently, leading to improved diagnosis have been enabled by micro- and nanoscale technologies. For instance, DNA arrays have enabled for individual genetic analysis to become a reality, which can allow for early detection of diseases.<sup>[67]</sup> Furthermore, diagnostics by means of molecular imaging and profiling has been enabled with the maturation of quantum dot technologies.<sup>[68–72]</sup>

The administration of health care will always require a human provider, who is naturally subjective yet invaluable for the treatment of a patient. The role of this physician will likely be reduced with the advancement of diagnostic techniques, and patient outcomes will be greatly enhanced by eliminating much of the guesswork in diagnosing a condition. The ability to accurately assess the levels of specific analytes that are indicators for a disease or condition is the foundation of successful diagnostics. Therefore the sensitivity, selectivity, response time, and other key characteristics that define the quality of a sensor profoundly impact the quality of a diagnosis.

## Nanoscale Sensor Platforms—Fundamentals and Applications

A sensor is characterized by two key components, a sensing element, which has a specific interaction with an analyte or environmental condition, and a transducing element, which converts this interaction into a measurable effect (Fig. 4). For biomedical applications, the sensing element is designed to interact specifically with biologically significant conditions or target molecules. Natural receptors, such as antibody/antigen, enzymes, nucleic acids/DNA, cellular structures/cells, are the most common choice for sensing elements in biosensors, because of their evolved high affinity and specificity.<sup>[73,74]</sup> Biomimetic sensing



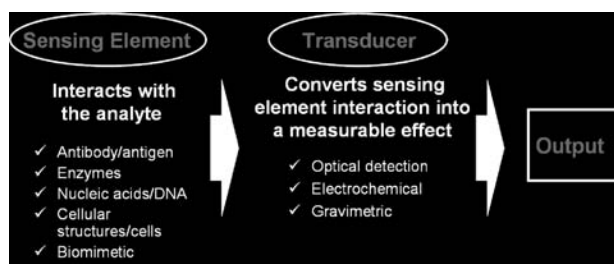


**Fig. 4** Illustration of the key components of a biosensor platform.

elements, such as biorecognitive polymer networks, can be advantageous over their biological counterparts because they can be designed to mimic biological recognition pathways and at the same time exhibit other abiotic properties that are more favorable, such as greater stability in harsh environments.<sup>[75,76]</sup> Common transducing elements, such as optical, electrochemical, gravimetric, and micromechanical, have been highlighted in recent reviews.<sup>[77–82]</sup>

By minimizing the sensor size, diagnostic devices can be fabricated that not only have a significant impact in *ex vivo* sensing applications, but can also be applied to *in vivo* and *in vitro* applications, where micro- or nanoscale dimensionality is imperative. These miniaturized sensors require small sample and/or reagent volumes, tend to be less invasive, and can be faster and more sensitive relative to macroscale technologies. Micro- and nanoscale sensor platforms, such as the ones that are discussed in the following paragraphs, will replace current laboratory methods and facilitate novel diagnostic analysis.

### Micro-/nanoelectromechanical sensors

In a seminal paper,<sup>[83]</sup> Peterson described the early efforts in developing MEMS that were based on the exceptional mechanical properties of silicon, which had been neglected relative to its well-established

electrical properties. In the years that have followed, MEMS have been successfully developed and made commercially available, such as pressure and acceleration sensors for medical and automobile applications.<sup>[84]</sup> In recent years, NEMS devices have received more attention, particularly with a focus on the creation of novel sensor devices.<sup>[85]</sup>

Microcantilevers, an example of a MEMS transducing element, have been integrated with a wide variety of sensing elements, such as intelligent polymer networks<sup>[86,87]</sup> and single-stranded DNA,<sup>[88]</sup> for application as ultrasensitive sensing devices. Recently, researchers have focused on developing techniques to fabricate nanocantilevers,<sup>[89–91]</sup> enabling for the enhancement of the inherent advantages associated with diminishing size.

### Nanopore sensors

Once knowledge of the genetic code of humans, bacteria, viruses and other organisms can easily be attained, diagnosis of many illnesses and diseases can be completed in a rapid and accurate manner. While microarrays, dubbed DNA arrays, DNA chips, and GeneChips, have been established as the preferred method for carrying out genetic analysis on a massive scale,<sup>[67]</sup> novel technologies, such as nanopore sequencing, have demonstrated the possibility to make the analysis faster and cheaper.<sup>[92]</sup>

Nanopores have been applied as a novel method for probing and characterizing the molecular structure of macromolecules (Fig. 5). A translocating molecule alters the ionic current through the pore relative to its open state, and this current change is monitored vs. time and then correlated to the specific characteristics of the target macromolecule. For the majority of studies,<sup>[93,94]</sup>  $\alpha$ -hemolysin has been applied as a model natural ion channel, and these promising results have been highlighted in a recent review.<sup>[95]</sup> Recently, nanofabrication methods have been applied to

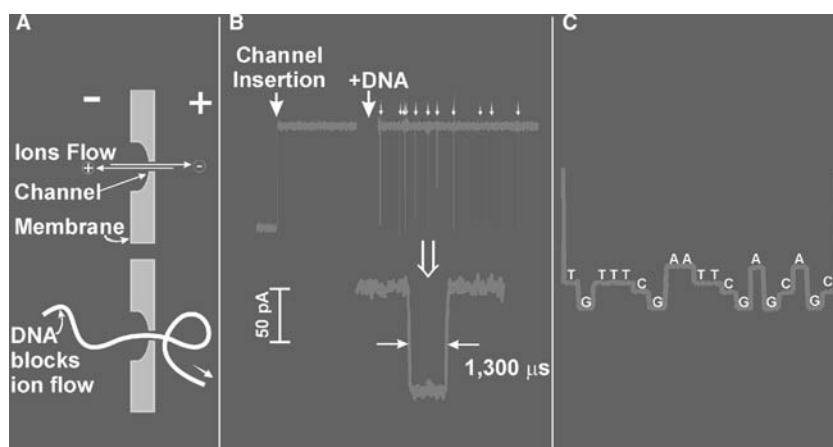


**Fig. 5** Illustration of the principles and components of a high-speed device based on a nanopore for probing single molecules of DNA. Source: <http://www.mcb.harvard.edu/branton/>—permission pending.

reproducibly create more robust, synthetic nanopores that can be tailored to have desired dimensions.<sup>[96–100]</sup> With further progress in fabrication and analysis, this simple, yet powerful technique, will sequence biomacromolecules, such as proteins, nucleic acids, and polysaccharides, with molecular precision for cheaper and faster technologies.

### Optical nanosensors

Optical nanosensors, which are devices that transduce a chemical or biological event using an optical signal, have been shown to be an enabling technology for making quantitative measurements in the intracellular environment, demonstrating again the advantages of nanoscale sensors. In a recent review, the impact of this rapidly growing field was highlighted.<sup>[101]</sup> Probes encapsulated by biologically localized embedding (PEBBLEs), with diameters on order of 40 nm, have been utilized to measure intracellular values of pH, calcium, magnesium, potassium, and oxygen.<sup>[102,103]</sup> In other work, optical nanofibers, with a tip diameter of approximately 50 nm, were fabricated and then functionalized with antibodies, allowing for nanometer resolved spatial measurements of a target analyte.<sup>[15]</sup> In addition, other researchers have created a nanoscale optical biosensor based on monitoring the localized surface plasmon resonance (LSPR) spectrum of functionalized silver nanoparticles and demonstrated the ability to apply this device as a real-time immunoassay in physiological buffer.<sup>[104]</sup> In considering the above successes demonstrated with nanoscale optical biosensors, the near future technologies based on these platforms will be utilized for real-time quantitative measurement and imaging within single living cells.

### Point-of-Care Diagnostic Devices

The clinical diagnostics field presents numerous opportunities where micro- and nanoscale biosensor technology can be exploited.<sup>[105,106]</sup> In particular, POC diagnostic devices, which enable diagnostic testing (in vivo or ex vivo) at the site of care, can enhance patient outcomes by substantially abbreviating analysis times as a result of the intrinsic advantages of the miniature device and by eliminating the need for sample transport to an onsite or off-site laboratory for testing. These POC diagnostic devices rely on miniature biosensors as a fundamental component. In addition, the novel information that nanoscale sensors are able to probe provides a superior knowledge base, allowing the physician to accurately diagnose a condition. In critical care medicine, the need for rapid diagnosis and, thus, POC diagnostic devices is magnified, because a delay of even a minute or second can mean

the difference between patient survival and death.<sup>[107,108]</sup>

The development of micro or miniaturized total analysis systems ( $\mu$ S), also referred to as lab-on-a-chip devices, has profoundly impacted the corresponding development of POC diagnostic devices. These  $\mu$ -TAS devices integrate microvalves, micropumps, microseparations, microsensors, and other components to create miniature systems capable of analysis that typically requires an entire laboratory of instruments. Since introduced as a novel concept for chemical sensing devices,<sup>[109]</sup> reviews have been published illustrating the widespread applicability of  $\mu$ -TAS devices.<sup>[110,111]</sup> Of particular interest, other reviews have focused on the application of  $\mu$ -TAS devices as innovative biological devices<sup>[112]</sup> and POC diagnostic devices.<sup>[113,114]</sup> The advancements facilitating the creation of the micro- and nanosensor platforms introduced above have led to the corresponding maturation of POC diagnostic devices. Micro- and nanoscale sensors enable improved and novel analysis, and the consequent POC diagnostic devices will be fundamental to the future of medical diagnostics.

A number of medical conditions or treatments require the sensing and control of a particular biomolecule. In the insulin-dependent diabetes mellitus market, a wide array of sensors are available that operate in a variety of ways in the management of the disease (e.g., small sample sizes, multiple day averages, event markers, diabetes management software, data ports/access to transfer readings). However, many diseases still require a clinic visit to properly monitor the disease or adequately manage medication levels. The technology either does not exist for these sensors or cannot be technically or economically scaled down for POC use.

With nanotechnology and novel material design, the future of medical management will involve small, POC, and possibly disposable sensors that intermittently or continuously monitor the biological molecule of interest. This will translate into an informed patient with better overall hands-on control for disease management. Also, it may alert and aid patients in determining when a low-risk environment or high-risk situation exists and offer greater control. As such, the quality of life and term of life of a person with a chronic disease can be enhanced. Also, with the increase in wireless technology, data can be processed and transmitted to a variety of systems, as well as a family or specialist physician.

### NANOTECHNOLOGY IN THERAPEUTICS

In addition to the intrinsic activity of a drug, the delivery of it in a specific, controlled manner to the desired

site of action is critical to its overall therapeutic effect. For instance, the optimum therapeutic effect depends on a drug getting to the right place at the right time and then staying active for a certain time period. Consequently, advanced drug delivery formulations have been developed over the past 20 years that do not simply release a drug at a specific rate, but release the drug in a way that the pharmaceutical scientist and molecular designer have designed.<sup>[115,116]</sup> Additionally, because drug delivery can improve safety, efficacy, convenience, and patient compliance, novel delivery methods are a major focus of pharmaceutical companies.<sup>[117]</sup> Also, novel methods of delivery are prolonging patent protection.<sup>[118]</sup>

### Drug Development and Discovery

In the field of drug discovery, about half of drug development candidates fail due to problems with absorption, distribution, metabolism, elimination, or toxicity.<sup>[119]</sup> Recent technologies have not had much impact on reducing the cost of drug discovery within the pharmaceutical industry.<sup>[120]</sup> Rather than present an exhaustive history, we direct the reader to an excellent review on the history of drug discovery technologies.<sup>[120]</sup>

In the early 1990s, genomics became a commercial enterprise with high-throughput sequencing on an industrial scale.<sup>[67,121]</sup> As the automation, speed, and accuracy of sequencing results increased, it dramatically decreased the time to complete the Human Genome Project (HGP), which determined the sequences of the 3 billion chemical base pairs and identified approximately 30,000 genes in human DNA as well as patterns of variation across the genome. This was a tremendous accomplishment, but work is now beginning to probe the potential of the sequence code (Table 1).<sup>[122]</sup> This work is expected to have a profound influence on the genetic and mechanistic basis for disease and will lead to genotype- or phenotype-specific therapeutics.

With the knowledge of genome sequences and new high-throughput technologies (nanoarrays and nanoliter systems of increasingly smaller volumes and high degrees of parallelization),<sup>[123]</sup> problems can be attacked on a much larger scale than ever before (e.g., fast screening of focused chemical libraries for target molecules,<sup>[120]</sup> studying all the genes in a genome, and discovering how genes and proteins function in interconnected networks, etc.). The demand for increased sensitivity and throughput for genomics and proteomics<sup>[14]</sup> has companies such as Affymetrix (Santa Clara, CA) and Nanogen (San Diego, CA) looking for solutions at the nanoscale.<sup>[12]</sup>

Tissue microarrays have been developed that can have high-throughput validation of drug targets and

**Table 1** Research challenges that remain after sequencing the genome

---

#### Post-sequencing research challenges

---

Gene number, exact locations, and functions
Gene regulation
DNA sequence organization
Chromosomal structure and organization
Noncoding DNA types, amount, distribution, information content, and functions
Coordination of gene expression, protein synthesis, and post-translational events
Interaction of proteins in complex molecular machines
Predicted vs. experimentally determined gene function
Evolutionary conservation among organisms
Protein conservation (structure and function)
Proteomes (total protein content and function) in organisms
Correlation of SNPs (single-base DNA variation among individuals) with health and disease
Disease-susceptibility prediction based on gene sequence variation
Genes involved in complex traits and multigene diseases
Complex systems biology including microbial consortia useful for environmental restoration
Developmental genetics, genomics

---

Source: From Ref.<sup>[122]</sup>.

evaluation of efficiency, distribution, and toxicity.<sup>[38]</sup> Using laminar microfluidic flows, delivery of membrane-permeable molecules into selective regions of a single cell and differential manipulation of regions within a single cell have been demonstrated. Specifically, Takayama et al. were able to selectively label subpopulations of mitochondria as well as disrupt actin filaments in selected cellular regions (Fig. 6).<sup>[14]</sup> The authors speculate that the technique may allow for the probing and manipulation of cellular metabolic and structural machinery and major applications include chemotaxis, spatially regulated signaling, drug screening, and toxicity studies.

### Miniaturization of Controlled Drug Delivery Devices

Advances in micro- and nanotechnologies have accelerated the development of new drug delivery vehicles that will transform biological potential into medical reality.<sup>[124]</sup> For instance, micro- and nanofabrication techniques have enabled the development of novel drug delivery devices that can improve the therapeutic effect of a drug, such as micro- and nanoscale needles, pumps, valves, and implantable drug delivery devices. The field of micro- and nanofabricated drug delivery

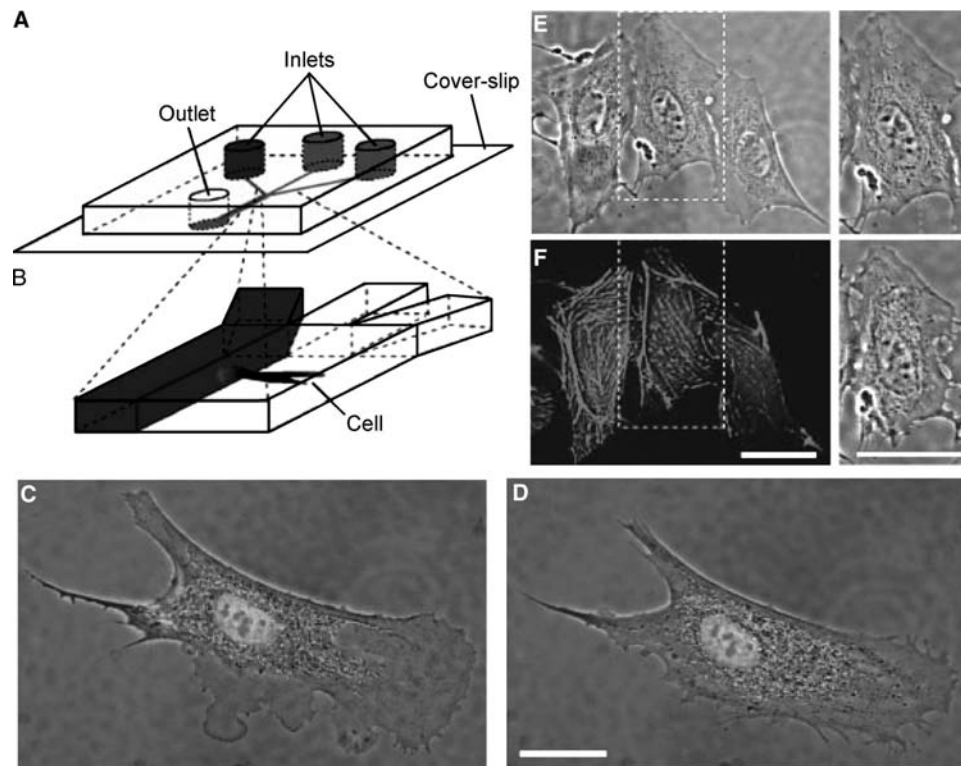


**Fig. 6** Differential manipulation of regions of a single bovine capillary endothelial cell using multiple laminar flows. *Source:* From Ref.<sup>[14]</sup>—permission pending.

devices, which is still in its infancy, has unlimited potential.

#### Micro-/nanoscale needles for cellular and transdermal delivery

For over 150 years, syringes and hypodermic needles have been utilized for the delivery of drugs bypassing the transport barriers that exist in other delivery routes. Currently, the smallest needles that are commercially available for injections are 30 gauge for conventional syringes and 31 gauge for pen injectors, having outer diameters of 305 and 254  $\mu\text{m}$ , respectively.<sup>[125]</sup> Microfabrication techniques have been utilized to create miniature needles, which are orders of magnitude smaller in diameter and capable of localized and painless delivery of drugs into cells or tissues. Recently, novel methods have been developed to fabricate nanoneedles, which have been proposed to enhance performance even further.<sup>[126,127]</sup>

Microscale needles have been applied for cellular delivery of membrane impermeable molecules. For example, arrays of microneedles were fabricated and utilized to deliver DNA into plant and mammalian cells, as a method for transforming cells.<sup>[128,129]</sup> Additionally, microneedles have been utilized to target

drug delivery to a specific region or tissue in the body, thus avoiding detrimental effects that can result from administering certain drugs systemically. This targeting can reduce side effects, minimize the dose of an expensive drug, and/or provide a means of delivery to a location that is difficult to treat.<sup>[117]</sup> For instance, a multichannel silicon microneedle has been microfabricated to deliver bioactive compounds into neural tissue while simultaneously monitoring and stimulating the neurons *in vivo*.<sup>[130]</sup> In addition, microneedles have been used to penetrate vessel walls of normal and atherosclerotic rabbit arteries *in vitro* demonstrating potential use for targeted delivery of antirestenosis drugs.<sup>[129]</sup>

Furthermore, microscale needles have been applied for transdermal drug delivery. In conventional transdermal drug delivery, the outer 10–20  $\mu\text{m}$  of skin, the stratum corneum, acts as a barrier to the diffusion of the drug molecules, thus limiting its applicability to small drug molecules. Because the stratum corneum does not have any nerves, needles that are long enough and robust enough to penetrate across this layer, but short enough to not stimulate the nerves in the deeper tissue, have the potential to make transdermal delivery a painless and much more viable option.<sup>[125,131]</sup>

**Table 2** Selected nanobiotechnology companies developing drug delivery and therapeutic applications

Focus	Company	Platform
Therapeutics	Alnis Biosciences (Emeryville, CA)	Polyfunctional nanoparticles
	ALZA (Mountain View, CA)	Lipid nanoparticles with PEG coating; Doxil on the market
	NanoCrystal Technologies (King of Prussia, PA)	NanoMill technology for creating nanocrystals
	NanoMed Pharmaceuticals (Kalamazoo, MI)	Nanotemplate engineering for drug and vaccine delivery systems
	StarPharma (Melbourne, Australia)	VivaGel anti-HIV dendrimer (phase I)
Drug Delivery	Advectus Life Sciences (British Columbia, Canada)	NanoCure system for delivery of anticancer drugs across the blood–brain barrier
	BioDelivery Sciences (Newark, NJ)	BioOral nanocochleates cigar-shaped structures composed of lipid bilayers
	BioSante Pharmaceuticals (Lincolnshire, IL)	Nanoparticulate platform (CAP) for drug delivery (phase I)
	C-Sixty (Houston, TX)	Fullerene-based drug delivery
	Cytimmune Sciences (College Park, MD)	Tumor necrosis factor bound to colloidal gold nanocrystals for targeting tumors; vector with docking site for gene therapy
	NanoCarrier (Chiba, Japan)	NanoCap micellar nanoparticle for water-insoluble drugs (under development)
	NanoBio (Ann Arbor, MI)	Antimicrobial nanoemulsions (phase II)
	NanoSpectra Biosciences (Houston, TX)	Nanoshells for optical therapies
	Targesome (Palo Alto, CA)	Injectable nanospheres for therapeutic or diagnostic agents

Source: From Ref.<sup>[12]</sup>—pending permission.

### Nanoscale polymer carriers for controlled drug delivery

Polymer nanoparticle and nanosphere carriers are very attractive for biomedical and pharmaceutical applications, because of their unique and tailorable properties. In the case of polymer networks, the release profile can be precisely controlled through the design of its molecular structure, such as degree of cross-linking and ionic characteristics of the pendent functional groups.<sup>[132,133]</sup>

Polymer nanospheres have been molecularly designed to be responsive to the pH of their environment, enabling for the protection of fragile therapeutic peptides and proteins in the harsh, acidic stomach environment and then release in the more amiable environment of the upper small intestine.<sup>[134–136]</sup> In addition, nanoparticle carriers have been designed to have stealth properties, allowing extended residence time without being recognized by the immune system.<sup>[137,138]</sup> In other efforts, synthetic delivery systems, including polymeric nanoparticles, have been developed for application in gene delivery.<sup>[139,140]</sup> By creating polymer drug delivery systems that are biodegradable, the need for removal of the system post-delivery is eliminated, as the polymer can be naturally resorbed by the body.<sup>[141]</sup> Also, a number of companies are reformulating insoluble drugs as nanoparticles and nanocrystals to control uptake through cellular

membranes.<sup>[12]</sup> Table 2 lists a few selected nanobiotechnology companies and platforms.

### Microchip-based delivery systems

Microchips have been created for the storage and then delivery of multiple drugs in a controlled manner. For instance, a solid-state silicon microchip that can provide controlled release of single or multiple chemical substances on demand was fabricated and demonstrated.<sup>[142,143]</sup> The release is achieved via electrochemical dissolution of the thin anode membranes covering the microreservoirs filled with chemicals in solid, liquid, or gel form. The advantages of this microdevice include that it has a simple release mechanism, very accurate dosing, ability to have complex release patterns, potential for local delivery, and possible biological drug stability enhancement by storing in a microvolume that can be precisely controlled. Recently, multipulse drug delivery from a resorbable polymeric microchip device was demonstrated.<sup>[144]</sup>

The aforementioned microdevices demonstrate only a few examples of the wide variety of novel applications that exist for integration of micro- and nanofabrication technologies with drug delivery, revealing the immaturity of the field. These novel drug delivery devices can enable efficient delivery that was unattainable with conventional drug delivery techniques, resulting in the enhancement of the therapeutic activity of a

drug. The future of drug delivery is assured to be significantly influenced by micro- and nanofabrication technologies.

## CONCLUSION

Nanoscale science and engineering has an unlimited potential to affect the diagnosis and etiology of a number of diseases with enhanced prognosis and rational treatment. Although this field is in its infancy, the unlimited potential is clear, especially for application in medical science and technology leading to technological innovations in medicine. In the near future, micro- and nanodevices will be created that will combine the diagnostic and therapeutic actions described in this review, enabling for comprehensive devices that can monitor conditions and administer therapy. As the interest and investment in this maturing field continues to grow, it is impossible to identify the full breadth and reach of the resulting technologies, yet it is unmistakable that the developments will dramatically influence the nature and practice of medicine.

## ACKNOWLEDGMENTS

We would like to acknowledge Prof. Nicholas A. Peppas and Prof. Rashid Bashir for insightful discussions regarding the subject matter. We would also like to acknowledge NSF and NIH for funding.

## REFERENCES

- Whitesides, G.M. The right size in nanobiotechnology. *Nat. Biotechnol.* **2003**, *21* (10), 1161–1165.
- Chen, Y.; Pepin, A. Nanofabrication: conventional and nonconventional methods. *Electrophoresis* **2001**, *22*, 187–207.
- Chou, S.Y.; Krauss, P.R.; Renstrom, P.J. Imprint of sub-25 nm vias and trenches in polymers. *Appl. Phys. Lett.* **1995**, *67*, 3114–3116.
- Jackman, R.J.; Wilbur, J.L.; Whitesides, G.M. Fabrication of submicrometer features on curved substrates by microcontact printing. *Science* **1995**, *269*, 664–666.
- Piner, R.D.; Zhu, J.; Xu, F.; Hong, S.; Mirkin, C.A. “Dip-Pen” nanolithography. *Science* **1999**, *283*, 661–663.
- Whitesides, G.M.; Boncheva, M. Beyond molecules: self-assembly of mesoscopic and macroscopic components. *Proc. Natl. Acad. Sci. U. S. A.* **2002**, *99* (8), 4769–4774.
- Zhang, S. Fabrication of novel biomaterials through molecular self-assembly. *Nat. Biotechnol.* **2003**, *21* (10), 1171–1178.

- Nowak, A.P.; Breedveld, V.; Pakstis, L.; Ozbas, B.; Pine, D.J.; Pochan, D.; Deming, T.J. Rapidly recovering hydrogel scaffolds from self-assembling diblock copolypeptide amphiphiles. *Nature* **2002**, *417*, 424–428.
- Binnig, G.; Rohrer, H.; Gerber, Ch.; Weibel, E. Surface studies by scanning tunneling microscopy. *Phys. Rev. Lett.* **1982**, *49*, 57–61.
- Binnig, G.; Quate, C.F.; Gerber, Ch. Atomic force microscope. *Phys. Rev. Lett.* **1986**, *56*, 930–933.
- (accessed October 13, 2003); <http://www.greatachievements.org>.
- Mazzola, L. Commercializing nanotechnology. *Nat. Biotechnol.* **2003**, *21* (10), 1137–1143.
- Deutsch, J.; Desai, T.A.; Russell, B. Microfabricated in vitro cell culture systems for investigating cellular interactions: fabricating a model system for cardiac myocytes. *Proc. SPIE Int. Soc. Opt. Eng.* **2000**, *3912*, 105–113.
- Takayama, S.; Ostuni, E.; LeDuc, P.; Naruse, K.; Ingber, D.E.; Whitesides, G.M. Subcellular positioning of small molecules. *Nature* **2001**, *411*, 1016–1017.
- Vo-Dinh, T. Nanobiosensors: Probing the sanctuary of individual cells. *J. Cell. Biochem., Suppl.* **2002**, *39*, 154–161.
- Bao, G. Mechanics of biomolecules. *J. Mech. Phys. Solids* **2002**, *50*, 2237–2274.
- Misevic, G.N. Atomic force microscopy measurements: binding strength between a single pair of molecules in physiological solution. *Mol. Biotechnol.* **2001**, *18*, 149–154.
- Caplan, A.I.; Bruder, S.P. Mesenchymal stem cells: building blocks for molecular medicine in the 21st century. *Trends Mol. Med.* **2001**, *7* (6), 259–264.
- Saltzman, W.M.; Olbricht, W.L. Building drug delivery into tissue engineering. *Nat. Rev., Drug Discov.* **2002**, *11*, 177–186.
- Griffith, L.G. Emerging design principles in biomaterials and scaffolds for tissue engineering. *Ann. N.Y. Acad. Sci.* **2002**, *961*, 83–95.
- Haruyama, T. Micro- and nanobiotechnology for biosensing cellular responses. *Adv. Drug Deliv. Rev.* **2003**, *55*, 393–401.
- Yannas, I.V. Synthesis of organs: in vitro or in vivo? *Proc. Natl. Acad. Sci. U. S. A.* **2000**, *97* (17), 9354–9356.
- Sipe, J.D. Tissue engineering and reparative medicine. *Ann. N.Y. Acad. Sci.* **2002**, *961*, 1–9.
- Schakenraad, J.M. Cells: their surfaces and interactions with materials. In *Biomaterials Science*; Ratner, B.D., Hoffman, A.S., Schoen, F.J., Lemons, J.E., Eds.; Academic Press: San Diego, 1996; 141–147.
- Teixeira, A.I.; Abrams, G.A.; Murphy, C.J.; Nealey, P.F. Cell behavior on lithographically defined nanostructured substrates. *J. Vac. Sci. Technol., B* **2003**, *21* (2), 683–687.
- Flemming, R.G.; Murphy, C.J.; Abrams, G.A.; Goodman, S.L.; Nealey, P.F. Effects of synthetic micro- and nano-structured surfaces on cell behavior. *Biomaterials* **1999**, *20*, 573–588.
- Abrams, G.A.; Goodman, S.L.; Nealey, P.F.; Franco, M.; Murphy, C.J. Nanoscale topography of the



- basement membrane underlying the corneal epithelium of the rhesus macaque. *Cell Tissue Res.* **2000**, *299* (1), 39–46.
28. Schakenraad, J.M.; Busscher, H.J.; Wildevuur, C.R.H.; Arends, J. The influence of substratum surface free energy on growth and spreading of human fibroblasts in the presence and absence of serum proteins. *J. Biomed. Mater. Res.* **1986**, *20*, 773–784.
  29. Singhvi, R.; Kumar, A.; Lopez, G.; Stephanopoulos, G.; Wang, D.; Whitesides, G.; Ingber, D. Engineering cell shape and function. *Science* **1994**, *264*, 696–698.
  30. Tan, J.; Tien, J.; Chen, C. Microcontact printing of proteins on mixed self-assembled monolayers. *Langmuir* **2002**, *18*, 519–523.
  31. Griffith, L.G.; Lopina, S. Microdistribution of substratum-bound ligand affects cell function: hepatocyte spreading on PEO-tethered galactose. *Biomaterials* **1998**, *19*, 979–986.
  32. Bos, G.W.; Scharenborg, N.M.; Poot, A.A.; Engbers, G.H.M.; Beugeling, T.; van Aken, W.G.; Feijen, J. Proliferation of endothelial cells on surface-immobilized albumin-heparin conjugate loaded with basic fibroblast growth factor. *J. Biomed. Mater. Res.* **1999**, *44*, 330–340.
  33. Yamato, M.; Konno, C.; Utsumi, M.; Kikuchi, A.; Okano, T. Thermally responsive polymer-grafted surfaces facilitate patterned cell seeding and co-culture. *Biomaterials* **2002**, *23*, 561–567.
  34. Nandkumar, M.A.; Yamato, M.; Kushida, A.; Konno, C.; Hirose, M.; Kikuchi, A.; Okano, T. Two-dimensional cell sheet manipulation of heterotypically co-cultured lung cells utilizing temperature-responsive culture dishes results in long-term maintenance of differentiated epithelial cell functions. *Biomaterials* **2002**, *23*, 1121–1130.
  35. Chen, G.; Imanishi, Y.; Ito, Y. Effect of protein and cell behavior on pattern-grafted thermoresponsive polymer. *J. Biomed. Mater. Res.* **1998**, *42*, 38–44.
  36. Blawas, A.S.; Reichert, W.M. Protein patterning. *Biomaterials* **1998**, *19*, 595–609.
  37. Ito, Y. Regulation of cellular gene expression by artificial materials immobilized with biosignal molecules. *Jpn. J. Artif. Org.* **1998**, *27*, 541–544.
  38. Park, A.; Wu, B.; Griffith, L.G. Integration of surface modification and fabrication techniques to prepare patterned poly(L-lactide) substrates allowing regionally selective cell adhesion. *J. Biomater. Sci. Polymer Ed.* **1998**, *9* (2), 89–110.
  39. Sorribas, H.; Padeste, C.; Tiefenauer, L. Photolithographic generation of protein micropatterns for neuron culture applications. *Biomaterials* **2002**, *23*, 893–900.
  40. Mrksich, M.; Dike, L.E.; Tien, J.; Ingber, D.E.; Whitesides, G.M. Using microcontact printing to pattern the attachment of mammalian cells to self-assembled monolayers of alkanethiolates on transparent films of gold. *J. Am. Chem. Soc.* **1997**, *235*, 305–313.
  41. Ito, Y. Surface micropatterning to regulate cell functions. *Biomaterials* **1999**, *20*, 2333–2342.
  42. Kim, E.; Xia, Y.; Whitesides, G.M. Polymer microstructures formed by molding in capillaries. *Nature* **1995**, *376*, 581–584.
  43. Takayama, S.; McDonald, J.; Ostuni, E.; Liang, M.; Kenis, P.; Ismagilov, R.; Whitesides, G. Patterning cells and their environments using multiple laminar fluid flows in capillary networks. *Proc. Natl. Acad. Sci. U. S. A.* **1999**, *96*, 5545–5548.
  44. Kenis, P.; Ismagilov, R.; Whitesides, G. Microfabrication inside capillaries using multiphase laminar flow patterning. *Science* **1999**, *285*, 83–85.
  45. Kane, R.; Takayama, S.; Ostuni, E.; Ingber, D.E.; Whitesides, G.M. Patterning protein and cells using soft lithography. *Biomaterials* **1999**, *20*, 2363–2376.
  46. Jackman, R.; Wilbur, J.; Whitesides, G.M. Fabrication of submicron features on curved substrates by microcontact printing. *Science* **1995**, *269*, 664–666.
  47. McDonald, J.C.; Duffy, D.C.; Anderson, J.R.; Chiu, D.T.; Wu, H.; Schueller, O.J.; Whitesides, G.M. Fabrication of microfluidics systems in poly(dimethylsiloxane). *Electrophoresis* **2000**, *21*, 27–40.
  48. Folkman, J.; Hochberg, M.M. Self regulation of growth in three dimensions. *J. Exp. Med.* **1973**, *138*, 745–753.
  49. Lalan, S.; Pomerantseva, I.; Vacanti, J.P. Tissue engineering and its potential impact on surgery. *World J. Surg.* **2001**, *25*, 1458–1466.
  50. Griffith, L.G.; Wu, B.; Cima, J.; Powers, M.J.; Chaignavo, B.; Vacanti, J.P. In vitro organogenesis of liver tissue. *Ann. N.Y. Acad. Sci.* **1997**, *831*, 382–397.
  51. Chiu, D.T.; Jeon, N.L.; Huang, S.; Kane, R.S.; Wargo, C.J.; Choi, I.S.; Ingber, D.E.; Whitesides, G.M. Patterned deposition of cells and proteins onto surfaces by using three-dimensional microfluidic systems. *Proc. Natl. Acad. Sci. U. S. A.* **2000**, *97* (6), 2408–2413.
  52. Holmes, T.; Delacalle, S.; Su, X.; Rich, A.; Zhang, S. Extensive neurite outgrowth and active neuronal synapses on peptide scaffolds. *Proc. Natl. Acad. Sci. U. S. A.* **2000**, *97*, 6728–6733.
  53. Hartgerink, J.D.; Beniash, E.; Stupp, S.I. Self-assembly and mineralization of peptide-amphiphile nanofibers. *Science* **2001**, *294*, 1684–1688.
  54. Niece, K.L.; Hartgerink, J.D.; Donners, J.; Stupp, S.I. Self-assembly combining two bioactive peptide-amphiphile molecules into nanofibers by electrostatic attraction. *J. Am. Chem. Soc.* **2003**, *125*, 7146–7147.
  55. Semino, C.E.; Merok, J.R.; Crane, G.G.; Panagiotakos, G.; Zhang, S. Functional differentiation of hepatocyte-like spheroid structures from putative liver progenitor cells in three-dimensional peptide scaffolds. *Differentiation* **2003**, *71*, 262–270.
  56. Semino, C.E.; Kasahara, J.; Hayashi, Y.; Zhang, S. Entrapment of hippocampal neural cells in self-assembling peptide scaffold. *Tissue Eng. in press*.
  57. Kaihara, S.; Borenstein, J.; Koka, R.; Lalan, S.; Ochoa, E.; Ravens, M.; Pien, H.; Cunningham, B.; Vacanti, J.P. Silicon micromachining to tissue engineer branched vascular channels for liver fabrication. *Tissue Eng.* **2000**, *6*, 105–117.

58. Brunette, D.M. Spreading and orientation of epithelial cells on grooved substrata. *Exp. Cell Res.* **1986**, *167*, 203–217.
59. Brunette, D.M. Fibroblasts on micromachined substrata orient hierarchically to grooves of different dimensions. *Exp. Cell Res.* **1986**, *16*, 11–26.
60. Brunette, D.M.; Kenner, G.S.; Gould, T.R.L. Grooved titanium surfaces orient growth and migration of cells from human gingival explants. *J. Dent. Res.* **1983**, *62*, 1045–1048.
61. Chehroudi, B.; McDonnell, D.; Brunette, D.M. The effects of micromachined surfaces on formation of bone-like tissue on subcutaneous implants as assessed by radiography and computer image processing. *J. Biomed. Mater. Res.* **1997**, *34*, 279–290.
62. Webster, T.J.; Ergun, C.; Doremus, R.H.; Siegel, R.W.; Bizios, R. Enhanced functions of osteoclast-like cells on nanophase ceramics. *Biomaterials* **2001**, *22* (11), 1327–1333.
63. Tirrell, M.; Kokkoli, E.; Biesalski, M. The role of surface science in bioengineered materials. *Surf. Sci.* **2002**, *500*, 61–83.
64. Abrams, G.A.; Goodman, S.L.; Nealey, P.F.; Murphy, C.J. Nanoscale topography of the extracellular matrix underlying the corneal epithelium of the non-human primate. *IOVS* **1997**, *38*, 350–354.
65. Gallant, N.D.; Capadona, J.R.; Frazier, A.B.; Collard, D.M.; Garcia, A.J. Micropatterned surfaces to engineer focal adhesions for analysis of cell adhesion strengthening. *Langmuir* **2002**, *18* (14), 5579–5584.
66. Feinberg, A.W.; Seegert, C.A.; Gibson, A.L.; Brennan, A.B. Engineering micrometer and nanometer scale features in polydimethylsiloxane elastomers for controlled cell function. *Mater. Res. Soc. Symp. Proc.* **2002**, *3711*, 181–186.
67. Gershon, D. Microarray technology an array of opportunities. *Nature* **2002**, *416*, 885–891.
68. Gao, X.; Nie, S. Molecular profiling of single cells and tissue specimens with quantum dots. *Trends Biotechnol.* **2003**, *21* (9), 371–373.
69. Seydel, C. Quantum dots get wet. *Science* **2003**, *300*, 80–81.
70. Jaiswal, J.K.; Mattoussi, H.; Mauro, J.M.; Simon, S.M. Long-term multiple color imaging of live cells using quantum dot bioconjugates. *Nat. Biotechnol.* **2003**, *21*, 47–51.
71. Akerman, M.E.; Chan, W.C.; Laakkonen, P.; Bhatia, S.N.; Ruoslahti, E. Nanocrystal targeting in vivo. *Proc. Natl. Acad. Sci. U. S. A.* **2002**, *99* (20), 12,617–12,621.
72. Klarreich, E. Biologists join the dots. *Nature* **2001**, *413*, 450–451.
73. Subrahmanyam, S.; Piletsky, S.; Turner, A. Application of natural receptors in sensors and assays. *Anal. Chem.* **2002**, *74* (16), 3942–3951.
74. Byfield, M.; Abuknesha, R. Biochemical aspects of biosensors. *Biosens. Bioelectron.* **1994**, *9*, 373–400.
75. Byrne, M.E.; Park, K.; Peppas, N.A. Molecular imprinting within hydrogels. *Adv. Drug Deliv. Rev.* **2002**, *54* (1), 149–161.
76. Hilt, J.Z.; Byrne, M.E.; Peppas, N.A. Configurational biomimesis in drug delivery. *Adv. Drug Deliv. Rev.* *in press*.
77. Wolfbeis, O. Fiber-optic chemical sensors and biosensors. *Anal. Chem.* **2002**, *74* (12), 2663–2678.
78. Bakker, E.; Telting-Diaz, M. Electrochemical sensors. *Anal. Chem.* **2002**, *74* (12), 2781–2800.
79. Schoning, M.; Poghossian, A. recent advances in biologically sensitive field-effect transistors (BioFETs). *Analyst* **2002**, *127*, 1137–1151.
80. O'Sullivan, C.; Guilbault, G. Commercial quartz crystal microbalances—theory and applications. *Biosens. Bioelectron.* **1999**, *14*, 663–670.
81. Benes, E.; Groschl, M.; Burger, W.; Schmid, M. Sensors based on piezoelectric resonators. *Sens. Actuators, A, Phys.* **1995**, *48*, 1–21.
82. Sepaniak, M.; Datskos, P.; Lavrik, N.; Tipple, C. Microcantilever transducers: A new approach in sensor technology. *Anal. Chem.* **2002**, *74* (21), 68A–575A.
83. Peterson, K. Silicon as a mechanical material. *Proc. IEEE* **1982**, *70* (5), 420–457.
84. Bryzek, J.; Petersen, K.; McCulley, W. Micromachines on the march. *IEEE Spectrum* **1994**, *31* (5), 20–31.
85. Voss, D. NEMS: Machines get tiny—nanoelectromechanical systems begin to flex their muscles. *Technol. Rev.* **2001**, *104* (3), 35
86. Hilt, J.Z.; Gupta, A.K.; Bashir, R.; Peppas, N.A. Ultrasensitive biomems sensors based on microcantilevers patterned with environmentally responsive hydrogels. *Biomed. Microdev.* **2003**, *5* (3), 177–184.
87. Bashir, R.; Hilt, J.Z.; Elibol, O.; Gupta, A.; Peppas, N.A. Micromechanical cantilever as an ultrasensitive pH microsensor. *Appl. Phys. Lett.* **2002**, *81* (16), 3091–3093.
88. Wu, G.; Ji, H.; Hansen, K.; Thundat, T.; Datar, R.; Cote, R.; Cote, M.; Hagan, M.; Chakraborty, A.; Majumdar, A. Origin of nanomechanical cantilever motion generated from biomolecular interactions. *Proc. Natl. Acad. Sci. U. S. A.* **2001**, *98*, 1560–1564.
89. Gupta, A.; Denton, J.; McNally, H.; Bashir, R. Novel fabrication method for surface micromachined thin single-crystal silicon cantilever beams. *J. Microelectromech. S.* **2003**, *12* (2), 185–192.
90. Hughes, W.; Wang, Z. Nanobelts as nanocantilevers. *Appl. Phys. Lett.* **2003**, *82* (17), 2886–2888.
91. Li, X.; Ono, T.; Wang, Y.; Esashi, M. Ultrathin single-crystalline-silicon cantilever resonators: fabrication technology and significant specimen size effect on Young's modulus. *Appl. Phys. Lett.* **2003**, *83* (15), 3081–3083.
92. Wang, H.; Branton, D. Nanopores with a spark for single-molecule detection. *Nat. Biotechnol.* **2001**, *19*, 622–623.
93. Kasianowicz, J.; Brandon, E.; Branton, D.; Deamer, D. Characterization of individual polynucleotide molecules using a membrane channel. *Proc. Natl. Acad. Sci. U. S. A.* **1996**, *93*, 13770–13773.
94. Meller, A.; Nivon, L.; Bransin, E.; Golovchenko, J.; Branton, D. Rapid nanopore discrimination between single polynucleotide molecules. *Proc. Natl. Acad. Sci. U. S. A.* **2000**, *97* (3), 1079–1084.
95. Bayley, H.; Cremer, P. Stochastic sensors inspired by biology. *Nature* **2001**, *413*, 226–230.

96. Nakane, J.; Akeson, M.; Marziali, A. Nanopore sensors for nucleic acid analysis. *J. Phys., Condens. Matter* **2003**, *15*, R1365–R1393.
97. Austin, R. Nanopores: the art of sucking spaghetti. *Nat. Mater.* **2003**, *2*, 567–568.
98. Li, J.; Gershow, M.; Stein, D.; Brandin, E.; Golovchenko, J. DNA molecules and configurations in a solid-state nanopore microscope. *Nat. Mater.* **2003**, *2*, 611–615.
99. Storm, A.; Chen, J.; Ling, X.; Zandbergen, H.; Dekker, C. Fabrication of solid-state nanopores with single-nanometre precision. *Nat. Mater.* **2003**, *2*, 537–540.
100. Li, J.; Stein, D.; McMullan, C.; Branton, D.; Aziz, M.; Golovchenko, J. Ion-beam sculpting at nanometre length scales. *Nature* **2001**, *412*, 166–169.
101. Aylott, J. Optical nanosensors—an enabling technology for intracellular measurements. *Analyst* **2003**, *128*, 309–312.
102. Park, E.; Brasuel, M.; Behrend, C.; Philbert, M.; Kopelman, R. Ratiometric optical PEBBLE nanosensors for real-time magnesium ion concentrations inside viable cells. *Anal. Chem.* **2003**, *75* (15), 3784–3791.
103. Clark, H.; Barker, S.; Brasuel, M.; Miller, M.; Monson, E.; Parus, S.; Shi, Z.; Song, A.; Thorsrud, B.; Kopelman, R.; Ade, A.; Meixner, W.; Athey, B.; Hoyer, M.; Hill, D.; Lightle, R.; Philbert, M. Subcellular optochemical nanobiosensors: probes encapsulated by biologically localized embedding (PEBBLEs). *Sens. Actuators, B, Chem.* **1998**, *51*, 12–16.
104. Riboh, J.; Haes, A.; McFarland, A.; Yonzon, C.; Van Duyne, R. A nanoscale optical biosensor: real-time immunoassay in physiological buffer enabled by improved nanoparticle adhesion. *J. Phys. Chem., B* **2003**, *107*, 1772–1780.
105. McGlennen, R. Miniaturization technologies for molecular diagnostics. *Clin. Chem.* **2001**, *47* (3), 393–402.
106. Vo-Dinh, T.; Cullum, B. Biosensors and biochips: advances in biological and medical diagnostics. *Freseenius' J. Anal. Chem.* **2000**, *366*, 540–551.
107. Okorodudu, A.; Jacobs, E.; Fogh-Anderson, N. Critical care testing in the new millennium: the integration of point-of-care testing. *Clin. Chim. Acta* **2001**, *307*, 1–2.
108. Drenck, N. Point of care testing in critical care medicine: the clinician's view. *Clin. Chim. Acta* **2001**, *307*, 3–7.
109. Manz, A.; Graber, N.; Widmer, H. Miniaturized total chemical analysis systems: A novel concept for chemical sensing. *Sens. Actuators, B, Chem.* **1990**, *1*, 244–248.
110. Reyes, D.; Iossifidis, D.; Auroux, P.; Manz, A. Micro total analysis systems: 1. Introduction, theory, and technology. *Anal. Chem.* **2002**, *74* (12), 2623–2636.
111. Auroux, P.; Iossifidis, D.; Reyes, D.; Manz, A. Micro total analysis systems: 2. Analytical standard operations and applications. *Anal. Chem.* **2002**, *74* (12), 2637–2652.
112. Jakeway, S.; de Mello, A.; Russell, E. Miniaturized total analysis systems for biological analysis. *Freseenius' J. Anal. Chem.* **2000**, *366*, 525–539.
113. Tudos, A.; Besselink, G.; Schasfoort, R. Trends in miniaturized total analysis systems for point-of-care testing in clinical chemistry. *Lab Chip* **2001**, *1*, 83–95.
114. Liu, Y.; Garcia, C.; Henry, C. Recent progress in the development of  $\mu$ TAS for clinical analysis. *Analyst* **2003**, *128*, 1002–1008.
115. Peppas, N.; Bures, P.; Leobandung, W.; Ichikawa, H. Hydrogels in pharmaceutical formulations. *Eur. J. Pharm. Biopharm.* **2000**, *50*, 27–46.
116. Langer, R. Drug delivery and targeting. *Nature* **1998**, *392*, 5–10.
117. Henry, C. Special delivery: alternative methods for delivering drugs improve performance, convenience, and patient compliance. *CEN Sept. 18* **2000**, *78* (38), 49–65.
118. Leong, K.W.; Langer, R. Polymeric controlled drug delivery. *Adv. Drug Deliv. Rev.* **1987**, *1*, 199–233.
119. Hodgson, J. ADMET-turning chemicals into drugs. *Nat. Biotechnol.* **2001**, *19*, 722–726.
120. Gershell, L.J.; Atkins, J.H. A brief history of novel drug discovery technologies. *Nat. Rev., Drug Discov.* **2003**, *2*, 321–327.
121. Kononen, J.; Bubendorf, L.; Kallioniemi, A.; Barlund, M.; Schraml, P.; Leighton, S.; Torhorst, J.; Mihatsch, M.J.; Sauter, G.; Kallioniemi, O.P. Tissue microarrays for high-throughput molecular profiling of tumor specimens. *Nat. Med.* **1998**, *4*, 844–847.
122. Human Genome Program, U.S. Department of Energy Post-sequencing research challenges. *Hum. Genome News* **2000**, *11* (1–2), 7.
123. Hong, J.W.; Quake, S.R. Integrated nanoliter systems. *Nat. Biotechnol.* **2003**, *21* (10), 1179–1183.
124. LaVan, D.; Lynn, D.; Langer, R. Moving smaller in drug discovery and delivery. *Nat. Rev., Drug Discov.* **2002**, *1*, 77–84.
125. McAllister, D.; Allen, M.; Prausnitz, M. Microfabricated microneedles for gene and drug delivery. *Annu. Rev. Biomed. Eng.* **2000**, *2*, 289–313.
126. Mani, R.; Li, X.; Sunkara, M.; Rajan, K. Carbon nanopipettes. *Nano Lett.* **2003**, *3* (5), 671–673.
127. Prinz, A.; Prinz, V.; Seleznev, V. Semiconductor micro- and nanoneedles for microinjections and ink-jet printing. *Microelectron. Eng.* **2003**, *67–68*, 782–788.
128. Trimmer, W.; Ling, P.; Chee-Kok Chin Orton, P.; Gaugler, R.; Hashmi, S.; Hashmi, G.; Brunett, B.; Reed, M. Injection of DNA into Plant and Animal Tissues with Micromechanical Piercing Structures, Proc. IEEE MicroElectroMech. Syst. Workshop, Amsterdam, Jan. 29–Feb. 2, 1995, 111–115.
129. Reed, M.; Wu, C.; Kneller, J.; Watkins, S.; Vorp, D.; Nadeem, A.; Weiss, L.; Rebello, K.; Mescher, M.; Smith, A.; Rosenblum, W.; Feldman, M. Micromechanical devices for intravascular drug delivery. *J. Pharm. Sci.* **1998**, *87*, 1387–1394.
130. Chen, J.; Wise, K. A multichannel neural probe for selective chemical delivery at the cellular level. *IEEE Trans. Biomed. Eng.* **1997**, *44*, 760–769.
131. Kaushik, S.; Hord, A.H.; Denson, D.D.; McAllister, D.V.; Smitra, S.; Allen, M.G.; Prausnitz, M.R. Lack of pain associated with microfabricated microneedles. *Anesth. Analg.* **2001**, *92*, 502–504.
132. Peppas, N.; Khare, A. Preparation, structure and diffusional behavior of hydrogels in controlled release. *Adv. Drug Deliv. Rev.* **1993**, *11*, 1–35.

133. Peppas, N.; Bures, P.; Lerbandung, W.; Ichikawa, H. Hydrogels in pharmaceutical formulations. *Eur. J. Pharm. Biopharm.* **2000**, *50*, 27–46.
134. Torres-Lugo, M.; Peppas, N. Preparation and characterization of p(MAA-g-EG) nanospheres for protein delivery applications. *J. Nanopar. Res.* **2002**, *4*, 73–81.
135. Donini, C.; Robinson, D.; Colombo, P.; Giordano, F.; Peppas, N. Preparation of poly(methacrylic acid-g-poly(ethylene glycol)) nanospheres from methacrylic monomers for pharmaceutical applications. *Int. J. Pharm.* **2002**, *245*, 83–91.
136. Robinson, D.; Peppas, N. Preparation and characterization of pH-responsive poly(methacrylic acid-g-ethylene glycol) nanospheres. *Macromolecules* **2002**, *35*, 3668–3674.
137. Gref, R.; Minamitake, Y.; Peracchia, M.; Trubetskoy, V.; Torchilin, V.; Langer, R. Biodegradable long-circulating polymeric nanospheres. *Science* **1994**, *263*, 1600–1603.
138. Peracchia, M.T. Stealth nanoparticles for intravenous administration. *S.T.P. Pharm. Sci.* **2003**, *13* (3), 155–161.
139. Cohen, H.; Levy, R.; Fishbein, I.; Kousaev, V.; Sosnowski, S.; Slomkowski, S.; Golomb, G. Sustained delivery and expression of DNA encapsulated in polymeric nanoparticles. *Gene Ther.* **2000**, *7*, 1896–1905.
140. Luo, D.; Saltzman, W. Synthetic DNA delivery systems. *Nat. Biotechnol.* **2000**, *18*, 33–37.
141. Brannon-Peppas, L. Recent advances on the use of biodegradable microparticles and nanoparticles in controlled drug delivery. *Int. J. Pharm.* **1995**, *116*, 1–9.
142. Santini, J., Jr.; Cima, M.; Langer, R. A controlled-release microchip. *Nature* **1999**, *397*, 335–338.
143. Santini, J., Jr.; Richards, A.; Scheidt, R.; Cima, M.; Langer, R. Microchips as controlled drug-delivery devices. *Angew. Chem., Int. Ed.* **2000**, *39*, 2396–2407.
144. Grayson, A.C.; Choi, I.S.; Tyler, B.M.; Wang, P.P.; Brem, H.; Cima, M.J.; Langer, R. Multi-pulse drug delivery from a resorbable polymeric microchip device. *Nat. Mater.* *in press*.

# Biomedical Magnetic Nanoparticles

**Ian Robinson**

*Department of Chemistry and School of Biological Sciences,  
University of Liverpool, Liverpool, U.K.*

**Le Duc Tung**

*Department of Physics, University of Liverpool, Liverpool, U.K.*

**Nguyen T.K. Thanh**

*Department of Chemistry and School of Biological Sciences,  
University of Liverpool, Liverpool, U.K.*

## INTRODUCTION

Interest in nanoparticles has grown rapidly in recent years because of their diverse applications in biomedicine and as novel materials for engineering and devices. Magnetic nanoparticles are of particular interest because of their potential application in areas such as magnetic separation, magnetic resonance imaging (MRI), targeted drug delivery, hyperthermia treatment of solid tumors, and high-density magnetic storage.

In this entry, we cover some of the synthesis methods (chemical reduction in reverse micelle, and solution, fabrication in hydrogels, thermal decomposition, seed-mediated growth, and precipitation from aqueous solution) and characterization of magnetic nanoparticles (transmission electron microscopy (TEM), X-ray diffraction (XRD), X-ray absorption spectroscopy (XAS), superconducting quantum interference device (SQUID), Mössbauer spectroscopy, and small angle neutron scattering (SANS)). We will also explore some of the biomedical applications such as magnetic separation, targeted drug delivery, hyperthermia cancer treatment, and MRI contrast agents.

## METHODS OF SYNTHESIS

Fabrication of nanoparticles can be grouped into three main synthetic methods: solid, gas, and solution.<sup>[1]</sup> The solid route involves the mechanical milling or the mechanochemical synthesis of raw powder to produce nanoparticles. This method has the disadvantage of introducing contamination to the products from the milling equipment as well as producing particles with wide size distribution. In gas and chemical routes, the synthesis can be considered as either “phase-transformation” or “phase-build-up.” The “phase-transformation” can be described as

the conversion of finely divided metal compounds into metals through thermal decomposition (see later) or chemical reduction. On the other hand, in “phase-build-up,” particles are “constructed” from building blocks (metal atoms). This process can take place from the gas phase (chemical or physical vapor deposition) or from the liquid phase (chemical precipitation). Gas-phase synthesis involves the formation of a supersaturated vapor of condensable gaseous species as a result of a chemical reaction that produces a new species or as a result of a physical process such as cooling that will reduce the vapor pressure of the condensable species. There are also several methods that use the solution route and are discussed in further detail later. These techniques produce uniform nanoparticles of different shapes by using appropriate precursors and by adding a surfactant or a capping ligand during the transformation. The addition of a surfactant/capping ligand can also prevent aggregation of the particles.

In the liquid phase, the chemical precipitation usually occurs from homogeneous solution. When the concentration of the constituent precursor reaches critical supersaturation, there is short burst of nucleation. This is followed by a period of uniform growth as the solutes diffuse from the solution to the surface of the nuclei until the final size is reached. To achieve monodisperse nanoparticles, this process requires the separation of the nucleation and growth phases, with no further nucleation occurring during the growth period. Multiple nucleation events can result in small particles aggregating to form much larger particles.<sup>[2,3]</sup> This process is known as Ostwald ripening and typically leads to the coarsening of the size distribution of the particles. Nucleation, particle growth, and particle interaction can be better controlled in a liquid medium, making chemical precipitation a more favorable method for producing uniform particles with well-controlled features (see Fig. 1).

## Chemical Reduction in Solution

Reduction is the transfer of electrons from reducing agent to oxidized metal species in a process driven by redox potential of the reaction,  $\Delta E^0$ . The value of  $\Delta E^0$  will indicate the likelihood of the reduction proceeding and can predict the rate of the chemical reaction. An increase in its value is associated with faster generation of atoms in the liquid phase. This leads to a higher supersaturation concentration of atoms and therefore faster nucleation. Thus, finely controlling the redox potential of the reacting species and the overall reaction is vitally important in controlling the properties of the metal particle produced. Complexing or precipitating the oxidized metallic species can alter their electrochemical potential. The degree of change is dependent on the stability constants or the solubility products of the resulting compounds.<sup>[4]</sup>

The reducing agent can form an intermediate with the oxidized metal species without altering its oxidation state. In this situation, the reduction process can be initiated by increasing the temperature, for example, and it can be conducted very slowly, producing conditions that lead to the formation of highly crystalline structures of regular shape.

An example of this is the reduction of iron (II) chloride and platinum acetylacetonate using superhydride ( $\text{LiBEt}_3\text{H}$ ) at high temperature ( $263^\circ\text{C}$ ) to produce 4 nm FePt magnetic nanoparticles.<sup>[5]</sup> Alternatively, 5 nm CoPt nanoparticles can be produced by coreduction of cobalt and platinum acetylacetonate in trimethylene glycol.<sup>[6]</sup> These particles are ferromagnetic at room temperature and by annealing above  $550^\circ\text{C}$ , the magnetic properties of the nanoparticles can be enhanced, owing to the induction of ordering.

## Redox Transmetalation

This process involves metal ions of the reactant metal complexes being reduced on the surface of metal (Me) nanoparticles with the simultaneous oxidation of the neutral  $\text{Me}^0$  to  $\text{Me}^{n+}$  via ligand migration to form a metal–ligand complex as a reaction by-product.<sup>[7–9]</sup> This process also means that the particle size remains the same during the reaction. Using redox transmetalation, Lee et al.<sup>[9]</sup> fabricated cobalt core nanoparticles with shells of gold, palladium, platinum, and copper. Of particular interest are Co@Au core-shell nanoparticles, because they can be transferred to the aqueous phase without losing any magnetism and the gold shell layer is very versatile.<sup>[9]</sup>

## Reduction in Reverse Micelles

Reverse micelles are spherical aggregates formed by surfactants dissolved in organic solvent. In the presence of small amount of water, which is readily solubilized in the polar core, monodisperse aggregates can be formed.<sup>[10]</sup> In contrast, microemulsions are formed with a larger amount of water. The reverse micelles can be used as microreactors for the synthesis of nanoparticles. Briefly, aqueous solutions of metal salts containing elements that formed the desired nanoparticle are added to the reverse micelle suspension. A reductant (e.g.,  $\text{NaBH}_4$ ) is added to the mixture and once the metallic nanoparticles are formed, the micelle solution is disrupted by the addition of an excess amount of polar solvent (e.g.,  $\text{CHCl}_3$ ; methanol) and the particles are collected.<sup>[11–15]</sup>

Reverse micelles provide unique reaction media as they can solubilize, concentrate, localize, and even

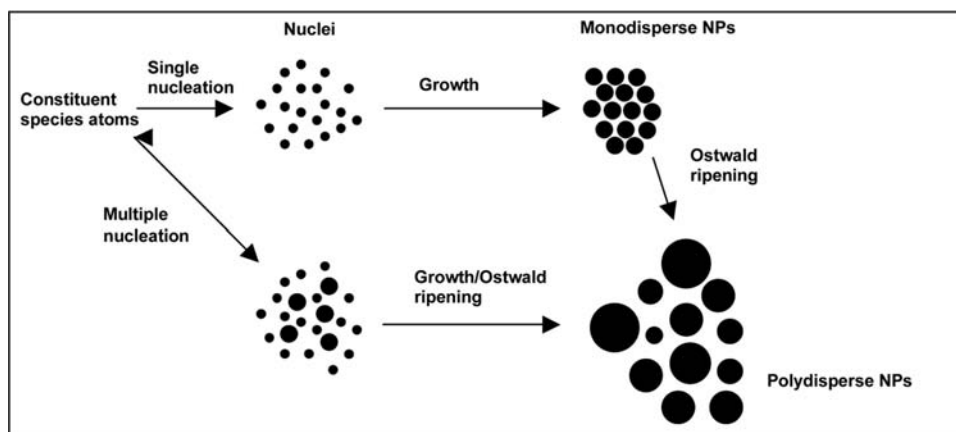


**Fig. 1** Formation mechanism of nanoparticles where, following a single burst of nucleation, a period of uniform growth leads to the formation of monodisperse nanoparticles by diffusion. Multiple nucleation events and growth via Ostwald ripening can lead to polydisperse suspensions of nanoparticles.



organize reactants. They also allow the nanoparticle synthesis to take place in aqueous solution. However, control of the size and shape of nanoparticles synthesized by this method is difficult as it reflects the interior of the micelles.

## Hydrogels

A hydrogel is a gel that will expand greatly in aqueous solution. They are usually composed of a hydrophilic organic polymer component that is cross-linked through either covalent or non-covalent interactions.<sup>[16]</sup> They can be synthesized to contain magnetic nanoparticles by using a two-step emulsifier-free emulsion polymerization. For example, bovine serum albumin (BSA) can be covalently attached to the particles to form thermosensitive magnetic immunospheres, which can be very useful in the immunoaffinity purification of anti-BSA antibodies from antiserum.<sup>[17]</sup>

## Thermal Decomposition

In this process, organometallic complexes are rapidly broken down in hot solvent containing surfactant, which can form a protecting layer around the nanoparticle, whilst acting as a dispersant. For example, the rapid pyrolysis of  $\text{Co}_2(\text{CO})_8$  in *o*-dichlorobenzene, in the presence of trioctyl phosphine oxide (TOPO) and oleic acid at  $185^\circ\text{C}$  will produce cobalt nanoparticles, whose size and shape can be controlled by varying the molar ratios of precursor and surfactant.<sup>[18,19]</sup> The protective layer can also consist of polymers, which can be tailored to improve the biocompatibility of the nanoparticles. For example, Stevenson et al.<sup>[20]</sup> used a poly[dimethylsiloxane-*b*-(3-cyanopropyl)methylsiloxane-*b*-dimethylsiloxane] (PDMS-PCPMS-PDMS) family of triblock polymers with controlled length to coat Co nanoparticles. The central block (PCPMS) is absorbed onto the nanoparticle surface and the hydrophobic end-blocks protrude into the carrier fluid (poly[dimethylsiloxane]), providing suspension stability. Alternatively, one can also use peptides as capping ligands for *in situ* synthesis of water-soluble Co nanoparticles with the aim to use these particles for biological applications.<sup>[21]</sup> The ability to tune the properties of the peptides (by varying the length, and sequence of amino acids) makes them a unique class of ligands for combinatorial nanomaterial synthesis. In addition to the 20 amino acids that occur naturally in proteins, over 100 unnatural amino acids are available for peptide synthesis, which provide access to a huge chemical combinatorial space. Like metallic nanoparticles, 13 nm monodisperse maghemite particles have been synthesized by injecting  $\text{Fe}(\text{CO})_5$  into

a solution containing surfactants and a mild oxidant (trimethylamine oxide).<sup>[22]</sup> Moreover, Park et al.,<sup>[23]</sup> using the same method, have been able to synthesize monodisperse iron oxide nanoparticles with extremely fine size control, producing particles with diameters of 6, 7, 9, 10, 12, 13, and 15 nm.

## Seed-Mediated Growth

Introducing “seeds” to a reaction mixture can increase the nucleation rate and thus the properties of the resulting nanoparticles.<sup>[4]</sup> The catalytic or surface properties of the small solid entities can trigger the reduction of the species and the nucleation process. This is of particular use in systems in which nucleation would otherwise not take place or would be too slow. It also has the advantage of artificially separating the nucleation and growth phases of the particle formation.

Seeds can be produced “in situ” by the rapid reduction of a different, more electropositive element or be in the form of a stable dispersed preformed nanosized particle of the same element. To form monodisperse nanoparticles, it is necessary for the nucleation process to be uniform throughout the entire solution, a condition that is difficult to achieve in rapid reductions. This has an effect upon reproducibility and scale up of the process.

To avoid this, it is favorable to use systems in which the electron transfer is inhibited when the reactant species are brought into contact, but can be induced by changing the conditions (e.g., pH, temperature, etc.) after the system is already homogenized. For example, the solvent used to dissolve the metal salts will become the reducing agent on changing the conditions. Wang et al.<sup>[24]</sup> used  $\text{Fe}_3\text{O}_4$  nanoparticles as seeding materials for the reduction of gold precursors to synthesize gold-coated  $\text{Fe}_3\text{O}_4$  nanoparticles ( $\text{Fe}_3\text{O}_4@\text{Au}$ ).

## Precipitation from Aqueous Solution

Precipitation routes from aqueous solution are widely used for the synthesis of iron oxide nanoparticles.<sup>[25]</sup> One method involves ferrous hydroxide suspensions that are partially oxidized, using a variety of oxidizing agents. The amorphous ferrous hydroxide is first precipitated and the aqueous gel is aged at  $90^\circ\text{C}$  over various time periods in the presence of a mild oxidant (e.g., nitrate ions). A study of the evolution of the precipitation with time has shown that minute primary particles, nucleated in the ferrous hydroxide gel, aggregate and then larger particles form by a contact-recrystallization mechanism. The aggregation of the primary iron oxide particles results from the Van der Waals and magnetic forces acting under the

conditions of weak repulsion, close to the isoelectric point, giving rise to spherical crystalline particles.<sup>[26]</sup>

An example of this is using an iron (II) chloride and iron (III) nitrate mixture (at a ratio of 1 : 1) in a basic aqueous solution to precipitate spherical magnetite ( $\text{Fe}_3\text{O}_4$ ) nanoparticles with an average diameter of 7 nm.<sup>[27]</sup> Alternatively, by adding polyelectrolytes, again at basic pH, to the iron salts during the precipitation, ferrite nanoparticles of nearly uniform size can be produced.<sup>[28]</sup> By varying the polyelectrolyte concentration in the solution, the size of the resulting iron oxide nanoparticles can be easily controlled.

## CHARACTERIZATION METHODS

For sample characterization, it is important to know the phase, morphology (size and shape), as well as the physical properties of the as-prepared magnetic nanoparticles. In the following, we will cover some of the most common techniques for this purpose.

### Phase and Morphology Characterization

#### Transmission electron microscopy

Transmission electron microscopy (TEM) is one of the most common techniques used to visualize and determine the morphology of the particles. In this technique, the specimen is illuminated by a beam of monochromatic electrons, some of which are

transmitted through the objective lens and then projected onto a viewing screen (for example, a layer of electron fluorescent material) to produce an image. In TEM, one can “see” particles as small as a few angstroms ( $10^{-10}$  m), which is near atomic levels. As an example, in Fig. 2 is shown the TEM image of a self-assembled sample of Co nanoparticles with the mean particle size of 4.5 nm; the particle size distribution is also shown in the left panel.

High-resolution transmission electron microscopy (HRTEM) can sometimes be used for complex structures such as core-shell or those consisting of an alloy. The HRTEM allows us to obtain information on the crystal planes of the particles and measure the lattice distance.

#### Scanning electron microscopy

A scanning electron microscope (SEM), like TEM, uses a beam of electrons aimed at a specimen; therefore, both instruments have similar features such as an electron gun, condenser lenses, and a vacuum system. However, the images are produced and magnified in different ways and while TEM provides information about the morphology of the nanoparticles, SEM is mainly used to study the surface or near surface structure of bulk specimens. The spatial resolution of SEM is approximately 15 nm, and therefore, not as good as TEM, which can have spatial resolutions in the sub-nanometer range; however, SEM images are generally much easier to interpret. Also SEM has the ability to

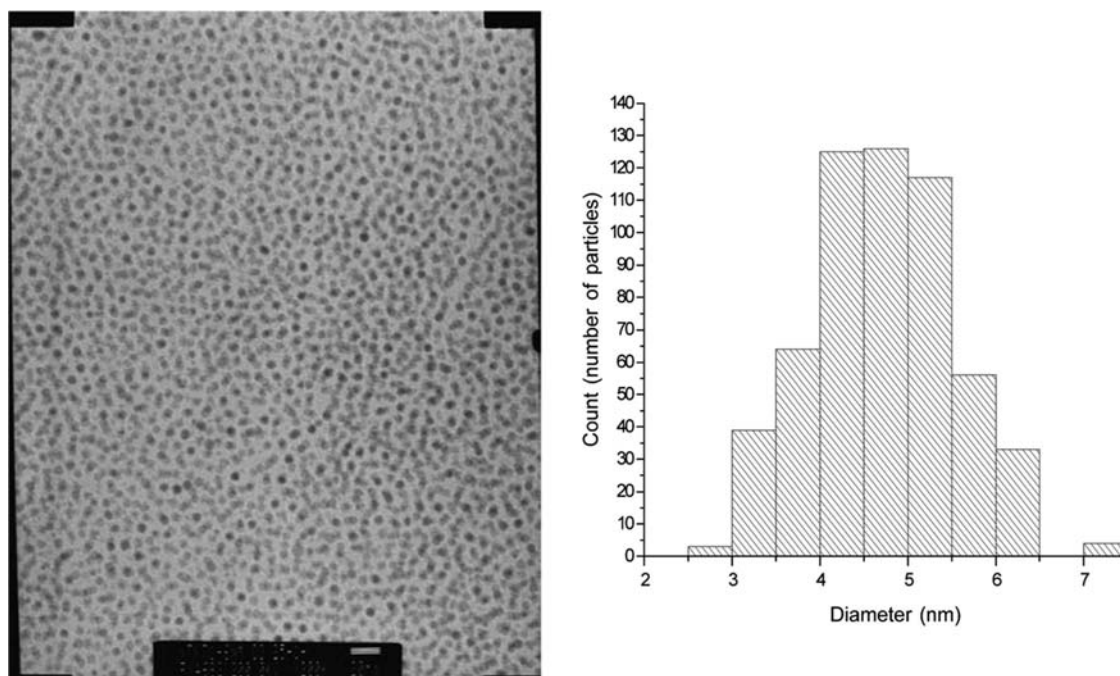


**Fig. 2** TEM micrograph of 4.5 nm Co nanoparticles with the size distribution graph (Bar 50 nm).

image a comparatively large area of the specimen; the ability to image bulk materials (not just thin films or foils); and the variety of analytical modes available for measuring the composition and nature of the specimen.

Field-emission SEM (FESEM) uses a field-emission cathode in the electron gun of a scanning electron microscope and provides narrower probing beams both at low and high electron energy; this results in both improved spatial resolution and minimized sample charging and damage. FESEM produces clearer, less electrostatically distorted images with spatial resolution down to 1.5 nm or better, i.e., several times better than the conventional SEM. High-quality, low-voltage images are obtained with negligible electrical charging of samples (accelerating voltages range from 0.5 to 30 kV).

### X-ray diffraction

Powder X-ray diffraction (XRD) is the most conventional technique that can be used to determine the structure, phases, and average size of the particles. In this technique, the structure and the lattice parameters are determined by fitting the X-ray patterns by means of the Rietveld profile procedure,<sup>[29]</sup> several software programs are available, such as FULLPROF.<sup>[30]</sup> The size of the particles can also be determined from the width of the X-ray peaks using the Scherrer formula.<sup>[31]</sup> The particle size estimated from the XRD is often found to be larger than that from TEM estimates because of the broadening of X-ray diffraction lines, which can be affected by many factors. In addition, the X-ray coherence length does not allow the technique to be applied to the study of particles that are too small (say less than 1 nm).

### X-ray absorption spectra

When a beam of X-rays passes a sample, it can be absorbed. A certain amount of energy of the incident X-ray photons is sufficient to cause excitation of a core electron of an absorbing atom, which causes it to pass into a continuum state, thus producing a photoelectron. This results in a drastic increase in the absorption, giving rise to an absorption edge. If one defines the electron binding energy as  $E_0$ , an X-ray absorption spectrum (XAS) is generally divided into four sections: (1) pre-edge ( $E < E_0$ ); (2) X-ray absorption near edge structure (XANES), where the energy of the incident X-ray beam is  $E = E_0 \pm 10$  eV; (3) near edge X-ray absorption fine structure (NEXAFS), in the region between 10 eV up to 50 eV above the edge; and (4) extended X-ray absorption fine structure (EXAFS), which starts approximately from 50 eV and continues up to

1000 eV above the edge. The analysis of the different spectrum sections is particularly useful. The XANES contains information about the electronic state of the X-ray absorbing atom and the local structure around it. The NEXAFS can give information relating to bond angles, bond lengths, and the presence of adsorbates. Finally, the EXAFS can give information on the atomic number, distance, and coordination number of the atoms surrounding the element.

### Magnetization Characterization

Magnetic particles with size smaller than few tens of nanometers can be considered as single magnetic domains, which display properties markedly different from the bulk. One of the interesting features of nano-size magnetic materials is the presence of the magnetic relaxation process that is due to the thermal effect and the existence of the energy barriers separating the local minima for different equilibrium states of the system. As a result, the magnetic behavior of a small particle depends on its relaxation time ( $\tau$ ),

$$\tau = \tau_0 \exp[KV/(k_B T)],$$

where  $\tau_0$  is of the order of  $10^{-9}$ – $10^{-13}$  s and weakly depends on temperature,  $k_B$  the Boltzmann constant,  $T$  the temperature; and  $K$  and  $V$  are the anisotropy and (average) volume of the particle, respectively. When  $\tau$  is smaller than the experimental time window ( $\tau_{\text{ex}}$ ), the magnetization vector is seen to change quickly between different states, i.e., the system is in a superparamagnetic state. By contrast, when  $\tau > \tau_{\text{ex}}$ , the thermal dynamic equilibrium state is very difficult to observe, since the energy barriers arising from the anisotropy obstruct the magnetization vector from switching to a lower energy state. This case is generally called the blocked state. The temperature at which  $\tau = \tau_{\text{ex}}$  is defined as the blocking temperature.

For magnetization characterization, it is important to determine the blocking temperature of the nanoparticle sample. From this, sometimes one can also obtain complementary information such as the monodispersity of the sample; size and anisotropy of the particles; formation of an oxide layer on the intermetallic sample, and the magnetic (dipole–dipole) interaction between particles.

One of the most common devices used in magnetization characterization is the superconducting quantum interference device (SQUID) in which the magnetization can be measured within an experimental window  $\tau_{\text{ex}}$  of about 20 s. Here, one can determine the blocking temperature  $T_B$  of the sample from a standard zero-field-cooled (ZFC) and field-cooled (FC)

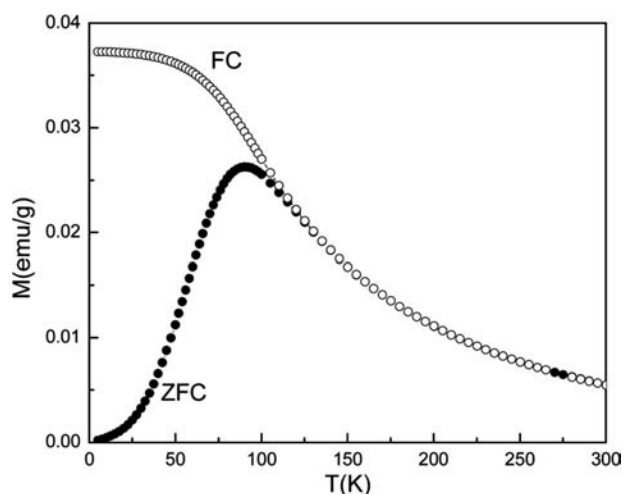


**Fig. 3** Temperature dependence of the magnetization of 3.3 nm  $\text{CoFe}_2\text{O}_4$  nanoparticles measured in zero-field cooled (ZFC) and field-cooled (FC) conditions with an applied field  $H = 10$  Oe.

measurement of the magnetization. As an example, Fig. 3 shows the results measured on 3.3 nm  $\text{CoFe}_2\text{O}_4$  nanoparticles. The ZFC curve shows a peak at about 90.5 K, which corresponds to the blocking temperature  $T_B$ . This sample shows a good monodispersity with the sharp peak at  $T_B$  and the splitting between ZFC and FC curves occurs very close to the peak's position.

Another useful magnetization characterization can be realized on measuring the a.c. susceptibility at different frequencies ( $f$ ). Here, the experimental time window  $\tau_{\text{ex}} = 1/f$ . Fig. 4 shows an example for 3.3 nm  $\text{CoFe}_2\text{O}_4$  nanoparticles. It can be seen that

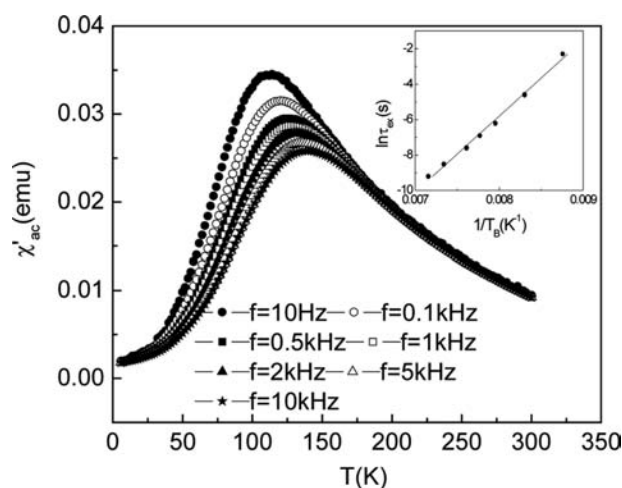


**Fig. 4** Temperature dependence of the in-phase component of the a.c. susceptibility of 3.3 nm  $\text{CoFe}_2\text{O}_4$  nanoparticles ( $\chi'_{\text{ac}}$ ) at different frequencies. The inset shows the logarithm of the experimental time window  $\tau_{\text{ex}}$  as a function of inverse blocking temperature ( $1/T_B$ ).

the blocking temperature  $T_B$  at the peak of the a.c. susceptibility shifts toward higher temperatures with increasing frequencies. The slope of the plot  $\ln \tau_{\text{ex}}$  vs.  $1/T_B$  in the inset of Fig. 4 gives information on the anisotropy ( $K$ ) and the volume of the particles ( $V$ ) through the relationship  $\ln \tau_{\text{ex}} = \ln \tau_0 + KV/k_B T_B$ .<sup>[32]</sup>

## Other Techniques for Characterization of Magnetic Nanoparticles

### Mössbauer spectroscopy

Mössbauer technique is a very useful tool for probing the properties of materials although it can be applied only to those consisting of elements (more than 40) that are Mössbauer-active of which  $^{57}\text{Fe}$  is the most prominent “Mössbauer nuclide.” For magnetic nanoparticles, the magnetic hyperfine field splitting in the Mössbauer spectra begins right below the blocking temperature  $T_B$  where the relaxation rate of particles has slowed down sufficiently for the reversal energy to exceed the thermal energy.<sup>[33]</sup> Note that because of very small experimental time window ( $\tau_{\text{ex}}$ ) in Mössbauer ( $\approx 10^{-9}$  s) when compared with other techniques such as SQUID ( $\approx 20$  s), the blocking temperature derived from the technique is higher. The analysis of the spectra close to  $T_B$  would give information on the size distribution of the particles. Spectra below  $T_B$  can give different information on the phase(s) of the sample, oxidation state, magnetic structure, dynamics effects as well as the interaction between the particles.

### Small angle neutron scattering

Small angle neutron scattering (SANS) is a useful tool to study magnetic nanoparticles. In contrast to light and X-rays, which are scattered by the electrons surrounding atomic nuclei, neutrons are scattered by the nucleus itself. In this technique, one can “see” the particle in the range between 1 and 500 nm. Several parameters can be evaluated from SANS data, including the radius of gyration, the particle surface area, shape of the scattering particles, magnetic structure, magnetic correlation, alignment of nanoparticles as well as their response to an external magnetic field.<sup>[34,35]</sup>

## BIOMEDICAL APPLICATIONS

### Magnetic Separation

Since magnetic nanoparticles can be quickly separated by magnetic forces, they are excellent candidates for purification and reuse in biotechnology. The special

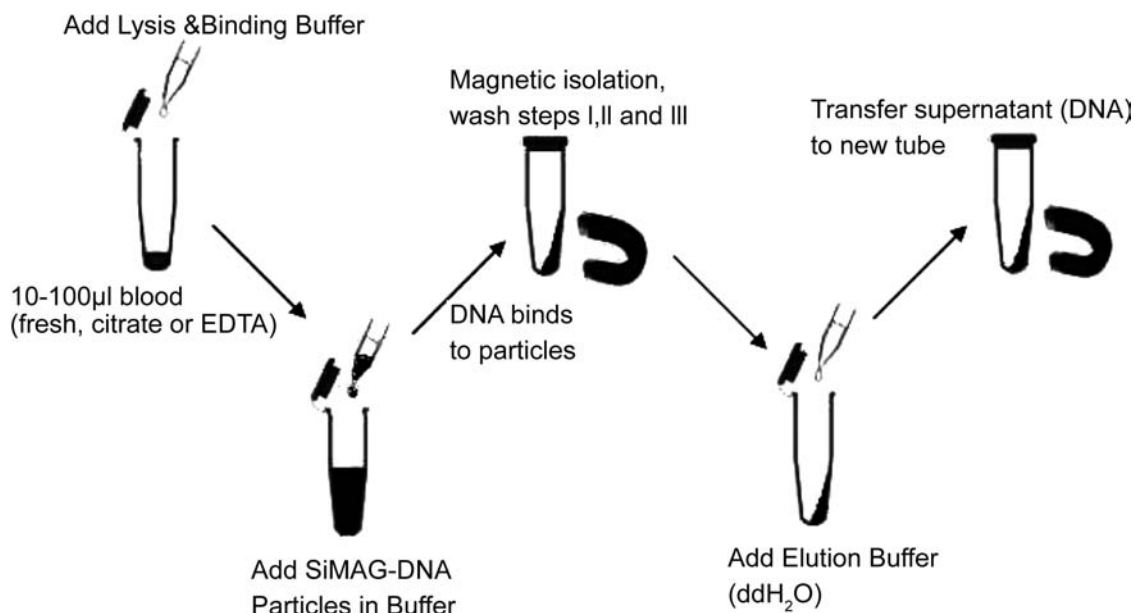


**Fig. 5** Schematic view of the use of magnetic nanoparticles to separate the DNA from blood sample. *Source:* From <http://www.chemicell.com>.

advantages of magnetic separation techniques are the fast and simple handling of a sample vial and the opportunity to deal with large sample volumes. This is because intensive steps of centrifugation can be omitted. Therefore, biomagnetic separation is highly compatible for labor automatization systems that will play a very important role in the near future.

In magnetic separation, first the magnetic nanoparticles have to be tagged with a desired biological entity such as proteins, DNA, RNA, enzymes, blood cells, and cancer cells in the native solution. This tagging can be made possible by chemical coating of magnetic nanoparticles with biocompatible molecules such as dextran, peptides, and phospholipids. The magnetically labeled entities can then be separated using a permanent magnet and washed with water. Finally, the magnetic particles can be untagged and removed again by a magnetic field to obtain the desired biological product. An example of the use of magnetic nanoparticles for the separation of DNA from a blood sample is illustrated in Fig. 5.

### Drug Delivery

Most current chemotherapies are relatively non-specific and tend to attack normal healthy tissue leading to unwanted side effects that can lead to the discontinuation of their use. However, if such treatments could be localized, e.g., anti-inflammatory drug to arthritic joints, the dose and thus the side effects

could be minimized allowing prolonged use of these agents (see Fig. 6).<sup>[36]</sup>

One particular method of achieving this would be to attach a therapeutic drug to a biocompatible magnetic nanoparticle carrier that is injected into the patient via the circulatory system. Once in the blood stream, the drug-carrier complex can be concentrated at a specific site by applying a high-gradient, external magnetic field; the drug released via enzymatic activity or changes in the physiological conditions.<sup>[37]</sup>

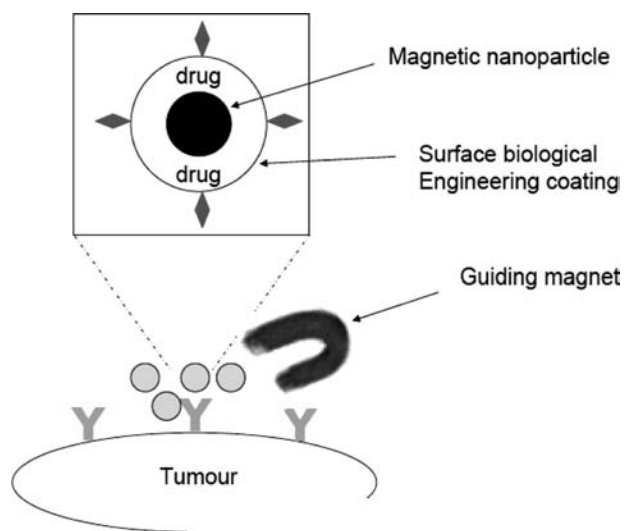


**Fig. 6** Schematic view of the use of magnetic nanoparticles for guided drug delivery.

There are several physical parameters that govern the effectiveness of the therapy, including field strength, gradient, and volumetric and magnetic properties of the particles. Hydrodynamic factors, such as blood flow rate, carrier concentration, and infusion route and circulation time, will also play a major role if the carriers are administered via the circulatory system. Finally, physiological parameters such as tissue depth to the target site (i.e., distance from the magnetic field source), reversibility, and strength of the drug/carrier binding and, in cancer treatments, tumor volume are also very important.<sup>[38]</sup>

Generally, the carriers are magnetic particles coated with a biocompatible molecule (e.g., polymer, peptide, silica), which can be functionalized by adding carboxyl groups, biotin, avidin, and other molecules.<sup>[39–41]</sup> These molecules can then act as attachment points for the coupling of therapeutic drugs.<sup>[42]</sup>

### Therapeutic Hyperthermia

Hyperthermia treatment of cancers involves using a device to heat malignant cells. However, the majority of devices are restricted in their use owing to coincidental damage to surrounding healthy tissue. Magnetic nanoparticle hyperthermia provides a possible solution to this problem. Generally, magnetic particles can be dispersed into the target tissue and an AC magnetic field of sufficient strength and frequency is applied resulting in the heating of the particles. The heat is then transferred to the surrounding diseased tissue and if the temperature can be maintained above the therapeutic threshold of 42°C for a minimum of 30 min, the tumor is destroyed.<sup>[42]</sup>

However, to date, most laboratory and animal model based studies have used magnetic field strengths that would have deleterious effects on humans, such as peripheral and skeletal muscle stimulation, cardiac stimulation, and arrhythmia and non-specific heating of tissue. This may be overcome by direct administration of the magnetic material directly into the target site rather than via the circulatory system. This would allow far greater quantities of the material to be used, and therefore, lower field strengths could be applied.

### MRI Contrast Enhancement

Magnetic resonance imaging (MRI) utilizes the vast number of protons present in biological tissue as each has an extremely small magnetic moment, which together lead to a measurable response in a large magnetic field. The response is derived from the net magnetic moment of the protons in a radio frequency transverse field applied in a pulsed sequence. Pick-up coils within the MRI scanner measure induced currents

caused by the relaxation of the response from the instant when the pulse is switched off.

By using magnetic contrast agents, the relaxation times  $T_1$  (longitudinal or spin–lattice) and  $T_2$  (transverse or spin–spin) can be shortened. Paramagnetic gadolinium ion complexes are the most commonly used contrast agents, while superparamagnetic (SPM) iron oxide particles are available for the organ specific targeting of liver lesions. In the field strengths normally used in MRI scanners, SPM particles become magnetically saturated, leading to a considerable locally perturbing dipolar field, which has the effect of shortening the relaxation times.

Magnetic nanoparticles are selectively taken up by the reticuloendothelial system of cells lining blood vessels, which remove foreign substances from the body, the differential up-take of different tissues in the body is vital for MRI.<sup>[43]</sup> Particle size is also of great importance; smaller particles have a longer half life in the blood stream, accumulating in the reticuloendothelial cells throughout the body.<sup>[44,45]</sup> One of the drawbacks of using iron oxide nanoparticles as contrast agents is their relatively low saturation magnetization, requiring the use of larger particles. Transition metal nanoparticles, e.g., those made from cobalt, have a much higher saturation magnetization value, allowing the use of smaller particles (<8 nm), without compromising sensitivity, and research is currently ongoing to assess their effectiveness.

### CONCLUSIONS

We have attempted to present an up-to-date review of the synthesis, characterization, and biological application of magnetic nanoparticles. The synthetic methods currently used have to surmount the problem of producing particles that are not only soluble in aqueous solution but also able to withstand the specific environments present in a biological system (e.g., powerful electrolytes, etc.). Nanoparticles can be produced in aqueous solution, but tend to be polydisperse aggregates, whilst those produced in organic solvent are monodispersed but they do not readily dissolve in aqueous solution. In the future, new syntheses methods need to be developed that are designed with a specific biological application as the focus to overcome the problem of technology transfer as this is one of the major challenges in the biomedical application of magnetic nanoparticles.

### ACKNOWLEDGMENTS

The authors thank the Royal Society, the EPSRC, and the North West Cancer Research fund for financial support. They also thank Drs. J. Goff, S. Lee, A. Cervellino, P. Murray, I. Prior, L. Parkes, R. Hodgson, and



Professors D. Walton, D. Fernig, P. Rudland, and D. Edgar for their collaborative research and useful discussion.

## REFERENCES

- Tartaj, P.; Morales, M.P.; Veintemillas-Verdaguer, S.; Gonzalez-Carreno, T.; Serna, C.J. *Handbook of Magnetic Materials*; Elsevier: Amsterdam, 2006; 403–482.
- Morales, M.P.; Gonzalez-Carreno, T.; Serna, C.J. The formation of alpha-Fe<sub>2</sub>O<sub>3</sub> monodispersed particles in solution. *J. Mater. Res.* **1992**, *7*, 2538–2545.
- Ocana, M.; Rodriguezclemente, R.; Serna, C.J. Uniform colloidal particles in solution—formation mechanisms. *Adv. Mater.* **1995**, *7*, 212–216.
- Goia, D.V. Preparation and formation mechanisms of uniform metallic particles in homogeneous solutions. *J. Mater. Chem.* **2004**, *14*, 451–458.
- Sun, S.H.; Anders, S.; Thomson, T.; Baglin, J.E.E.; Toney, M.F.; Hamann, H.F.; Murray, C.B.; Terris, B.D. Controlled synthesis and assembly of FePt nanoparticles. *J. Phys. Chem. B* **2003**, *107*, 5419–5425.
- Chinnasamy, C.N.; Jayadevan, B.; Shinoda, K.; Tohji, K. Polyol-process-derived CoPt nanoparticles: structural and magnetic properties. *J. Appl. Phys.* **2003**, *93*, 7583–7585.
- Park, J.I.; Cheon, J. Synthesis of “solid solution” and “core-shell” type cobalt-platinum magnetic nanoparticles via transmetalation reactions. *J. Am. Chem. Soc.* **2001**, *123*, 5743–5746.
- Park, J.I.; Kim, M.G.; Jun, Y.W.; Lee, J.S.; Lee, W.R.; Cheon, J. Characterization of superparamagnetic “core-shell” nanoparticles and monitoring their anisotropic phase transition to ferromagnetic “solid solution” nanoalloys. *J. Am. Chem. Soc.* **2004**, *126*, 9072–9078.
- Lee, W.R.; Kim, M.G.; Choi, J.R.; Park, J.I.; Ko, S.J.; Oh, S.J.; Cheon, J. Redox-transmetalation process as a generalized synthetic strategy for core-shell magnetic nanoparticles. *J. Am. Chem. Soc.* **2005**, *127*, 16,090–16,097.
- Pileni, M.P. Reverse micelles as microreactors. *J. Phys. Chem.* **1993**, *97*, 6961–6973.
- Carpenter, E.E.; Sangregorio, C.; O'Connor, C.J. Effects of shell thickness on blocking temperature of nanocomposites of metal particles with gold shells. *IEEE Trans. Magnetics* **1999**, *35*, 3496–3498.
- Lin, J.; Zhou, W.L.; Kumbhar, A.; Wiemann, J.; Fang, J.Y.; Carpenter, E.E.; O'Connor, C.J. Gold-coated iron (Fe@Au) nanoparticles: synthesis, characterization, and magnetic field-induced self-assembly. *J. Solid State Chem.* **2001**, *159*, 26–31.
- Cho, S.J.; Idrobo, J.C.; Olamit, J.; Liu, K.; Browning, N.D.; Kauzlarich, S.M. Growth mechanisms and oxidation resistance of gold-coated iron nanoparticles. *Chem. Mater.* **2005**, *17*, 3181–3186.
- Mikhaylova, M.; Kim, D.K.; Bobrysheva, N.; Osmolowsky, M.; Semenov, V.; Tsakalakos, T.; Muhammed, M. Superparamagnetism of magnetite nanoparticles: dependence on surface modification. *Langmuir* **2004**, *20*, 2472–2477.
- Mandal, M.; Kundu, S.; Ghosh, S.K.; Panigrahi, S.; Sau, T.K.; Yusuf, S.M.; Pal, T. Magnetite nanoparticles with tunable gold or silver shell. *J. Colloid Interface Sci.* **2005**, *286*, 187–194.
- Nayak, S.; Lyon, L.A. Soft nanotechnology with soft nanoparticles. *Angewandte Chemie-International Edition* **2005**, *44*, 7686–7708.
- Kondo, A.; Kamura, H.; Higashitani, K. Development and application of thermosensitive magnetic immunomicrospheres for antibody purification. *Appl. Microbiol. Biotechnol.* **1994**, *41*, 99–105.
- Puntes, V.F.; Krishnan, K.M.; Alivisatos, A.P. Colloidal nanocrystal shape and size control: the case of cobalt. *Science* **2001**, *291*, 2115–2117.
- Ma, W.W.; Yang, Y.; Chong, C.T.; Eggeman, A.; Piramanayagam, S.N.; Zhou, T.J.; Song, T.; Wang, J.P. Synthesis and magnetic behavior of self-assembled Co nanorods and nanoballs. *J. Appl. Phys.* **2004**, *95*, 6801–6803.
- Stevenson, J.P.; Rutnakornpituk, M.; Vadala, M.; Esker, A.R.; Charles, S.W.; Wells, S.; Dailey, J.P.; Riffle, J.S. Magnetic cobalt dispersions in poly(dimethylsiloxane) fluids. *J. Magn. Magn. Mater.* **2001**, *225*, 47–58.
- Thanh, N.T.K.; Puntes, V.F.; Tung, L.D.; Fernig, D.G. Peptides as capping ligands for *in situ* synthesis of water soluble Co nanoparticles for bioapplications. *J. Phys.: Confer. Ser.* **2005**, *17*, 70–76.
- Hyeon, T.; Lee, S.S.; Park, J.; Chung, Y.; Bin Na, H. Synthesis of highly crystalline and monodisperse maghemite nanocrystallites without a size-selection process. *J. Am. Chem. Soc.* **2001**, *123*, 12798–12801.
- Park, J.; Lee, E.; Hwang, N.M.; Kang, M.S.; Kim, S.C.; Hwang, Y.; Park, J.G.; Noh, H.J.; Kim, J.Y.; Park, J.H.; Hyeon, T. One-nanometer-scale size-controlled synthesis of monodisperse magnetic iron oxide nanoparticles. *Angewandte Chemie-International Edition* **2005**, *44*, 2872–2877.
- Wang, L.Y.; Luo, J.; Fan, Q.; Suzuki, M.; Suzuki, I.S.; Engelhard, M.H.; Lin, Y.H.; Kim, N.; Wang, J.Q.; Zhong, C.J. Monodispersed core-shell Fe<sub>3</sub>O<sub>4</sub>@Au nanoparticles. *J. Phys. Chem. B* **2005**, *109*, 21, 593–21, 601.
- Tartaj, P.; Morales, M.D.; Veintemillas-Verdaguer, S.; Gonzalez-Carreno, T.; Serna, C.J. The preparation of magnetic nanoparticles for applications in biomedicine. *J. Phys. D-Appl. Phys.* **2003**, *36*, R182–R197.
- Ocana, M.; Morales, M.P.; Serna, C.J. The growth-mechanism of alpha-Fe<sub>2</sub>O<sub>3</sub> ellipsoidal particles in solution. *J. Colloid Interface Sci.* **1995**, *171*, 85–91.
- Gee, S.H.; Hong, Y.K.; Erickson, D.W.; Park, M.H.; Sur, J.C. Synthesis and aging effect of spherical magnetite (Fe<sub>3</sub>O<sub>4</sub>) nanoparticles for biosensor applications. *J. Appl. Phys.* **2003**, *93*, 7560–7562.
- Si, S.; Kotal, A.; Mandal, T.K.; Giri, S.; Nakamura, H.; Kohara, T. Size-controlled synthesis of magnetite nanoparticles in the presence of polyelectrolytes. *Chem. Mater.* **2004**, *16*, 3489–3496.
- Rietveld, H.M. A profile refinement method for nuclear and magnetic structures. *J. Appl. Crystallography* **1969**, *2*, 65–71.

30. Rodriguez-Carvajal, J. FullProf: a program for rietveld refinement and profile matching analysis of complex powder diffraction patterns (ILL, unpublished).
31. Klug, H.P.; Alexander, L.E. *X-ray diffraction procedures for polycrystalline and amorphous materials*, 2nd Ed.; Wiley-Interscience: New York, 1974.
32. Tung, L.D.; Kolesnichenko, V.; Caruntu, D.; Chou, N.H.; O'Connor, C.J.; Spinu, L. Magnetic properties of ultrafine cobalt ferrite particles. *J. Appl. Phys.* **2003**, *93*, 7486–7488.
33. Johnson, C.E. Characterization of magnetic materials by Mössbauer spectroscopy. *J. Phys. D: Appl. Phys.* **1996**, *29*, 2266–2273.
34. Bellouard, C.; Mirebeau, I.; Hennion, M. Magnetic correlations of fine ferromagnetic particles studied by small-angle neutron scattering. *Phys. Rev. B* **1996**, *53*, 5570–5578.
35. Ijiri, Y.; Kelly, C.V.; Borchers, J.A.; Rhyne, J.J.; Farrell, D.F.; Majetich, S.A. Detection of spin coupling in iron nanoparticles with small angle neutron scattering. *Appl. Phys. Lett.* **2005**, *86*, 1–3, 243102.
36. Schutt, W.; Gruttner, C.; Hafeli, U.; Zborowski, M.; Teller, J.; Putzar, H.; Schumichen, C. Applications of magnetic targeting in diagnosis and therapy—possibilities and limitations: a mini-review. *Hybridoma* **1997**, *16*, 109–117.
37. Alexiou, C.; Arnold, W.; Klein, R.J.; Parak, F.G.; Hulin, P.; Bergemann, C.; Erhardt, W.; Wagenpfeil, S.; Lubbe, A.S. Locoregional cancer treatment with magnetic drug targeting. *Can. Res.* **2000**, *60*, 6641–6648.
38. Lubbe, A.S.; Bergemann, C.; Brock, J.; McClure, D.G. Physiological aspects in magnetic drug-targeting. *J. Magn. Magn. Mater.* **1999**, *194*, 149–155.
39. Mehta, R.V.; Upadhyay, R.V.; Charles, S.W.; Ramchand, C.N. Direct binding of protein to magnetic particles. *Biotechnol. Techniques* **1997**, *11*, 493–496.
40. Koneracka, M.; Kopcansky, P.; Antalik, M.; Timko, M.; Ramchand, C.N.; Lobo, D.; Mehta, R.V.; Upadhyay, R.V. Immobilization of proteins and enzymes to fine magnetic particles. *J. Magn. Magn. Mater.* **1999**, *201*, 427–430.
41. Koneracka, M.; Kopcansky, P.; Timko, M.; Ramchand, C.N.; de Sequeira, A.; Trevan, M. Direct binding procedure of proteins and enzymes to fine magnetic particles. *J. Mol. Catal. B-Enzymatic* **2002**, *18*, 13–18.
42. Pankhurst, Q.A.; Connolly, J.; Jones, S.K.; Dobson, J. Applications of magnetic nanoparticles in biomedicine. *J. Phys. D: Appl. Phys.* **2003**, *36*, R167–R181.
43. Lawaczeck, R.; Bauer, H.; Frenzel, T.; Hasegawa, M.; Ito, Y.; Kito, K.; Miwa, N.; Tsutsui, H.; Volger, H.; Weinmann, H.J. Magnetic iron oxide particles coated with carboxydextran for parenteral administration and liver contrasting—Pre-clinical profile of SH U555A. *Acta Radiologica* **1997**, *38*, 584–597.
44. Weissleder, R.; Elizondo, G.; Wittenberg, J.; Rabito, C.A.; Bengel, H.H.; Josephson, L. Ultrasmall superparamagnetic iron-oxide—characterization of a new class of contrast agents for MR imaging. *Radiology* **1990**, *175*, 489–493.
45. Ruehm, S.G.; Corot, C.; Vogt, P.; Kolb, S.; Debatin, J.F. Magnetic resonance imaging of atherosclerotic plaque with ultrasmall superparamagnetic particles of iron oxide in hyperlipidemic rabbits. *Circulation* **2001**, *103*, 415–422.

# Biomimetic Design of Self-Assembling Systems

Mila Boncheva

George M. Whitesides

*Department of Chemistry and Chemical Biology, Harvard University,  
Cambridge, Massachusetts, U.S.A.*

## INTRODUCTION

Successful solutions to many problems in science and technology have emerged by extracting design or strategy from biology, and applying it in a nonbiological context.<sup>[1–16]</sup> The use of biomimetic approaches is particularly well suited when designing self-assembling functional systems because life—from single cells to complex, multicellular organisms—demonstrates an enormous number of successful, functional designs and because living systems assemble themselves. Cells and organisms consist of collections of molecular and supramolecular structures that perform a range of complex functions, including molecular recognition, ligand binding, signal transduction, information storage and processing, and energy conversion. The molecular organization of biological structures also underpins their mechanical properties. In addition, certain of these structures can self-heal, self-repair, and self-replicate.

## OVERVIEW

There are two reasons for studying self-assembly. First, self-assembly is centrally important for life. Biological systems form and are sustained as a result of self-organization. Therefore understanding life requires, among other things, understanding self-assembly. Second, self-assembly can generate ordered three-dimensional (3-D) aggregates of components, ranging in size from the molecular to the macroscopic. These structures often cannot be generated by any other procedure.

In the past, self-assembly has been best known as a synthetic strategy in the molecular size regime.<sup>[17]</sup> New examples of its application to nanoscale and microscale components are now beginning to emerge.<sup>[18,19]</sup> As a consequence, self-assembly is becoming increasingly important as a strategy for the formation of useful nanoscale and microscale structures.<sup>[20]</sup>

We discuss the characteristics of self-assembly in living systems and review self-assembled functional systems designed according to biological principles.

The examples include only systems that self-assemble from preexisting components larger than molecules; synthetic biomimetic approaches to molecular aggregates are reviewed elsewhere.<sup>[21–25]</sup>

## SELF-ASSEMBLY IN LIVING SYSTEMS

Self-assembly in living organisms has four distinct characteristics:

1. Programmed (coded) self-assembly: Self-assembly in living systems is based on information that is encoded into the components themselves (e.g., as sequences of nucleic acids in the genome, or of amino acid residues at the active sites of proteins). The order of monomers in these sequences and the environments they experience determine their “shape” (i.e., their 3-D atomic surfaces), patterns of electrostatic charge, hydrogen bonds, hydrophobicity, and other characteristics that determine their functions. Both these encoded instructions *and* features of the environment determine the outcome of self-organization in living organisms. For example, during embryonic development, cell differentiation is governed by the cell origin and by a multitude of environmental signals and cues. Neural circuits also assemble themselves from individual components (cells) following a combination of internal program and external guidance.<sup>[26]</sup>
2. Constrained (templated) self-assembly: Order and asymmetry in self-assembled aggregates of biological molecules are often achieved by imposing constraints (e.g., by “templating” the process of self-assembly). One mechanism that introduces constraints and is found throughout biology consists in using chains of monomers. The order of monomers in these sequences is fixed, and this constraint restricts possible 3-D structures that can form. Another mechanism that imposes constraints on biological self-assembly involves geometrical restrictions to self-assembly.<sup>[27]</sup>

Undesired contacts with other molecules that might occur during the folding of linear precursors into correctly folded 3-D structures can be prevented by geometrically restricting the volume in which the folding process takes place, as happens, for example, during chaperonin-assisted protein folding.<sup>[28]</sup> Local geometrical factors are also important at the supramolecular level (e.g., for templating crystal growth during biomineralization,<sup>[29]</sup> for regulation of cell growth and viability,<sup>[30]</sup> and for exchange of materials between cells and their environment).<sup>[31]</sup>

- Hierarchical self-assembly: Living organisms form by bottom-up, hierarchical self-assembly—the primary building blocks (molecules) associate into larger, more complex secondary structures, which are, in turn, integrated into increasingly more complex structures in hierarchical designs. Thus, the organization of biological structures is integrated across length scales from the molecular to the organismic. For example, tendons have six discrete levels of hierarchical organization, starting from the triple helices of tropocollagen, and proceeding through microfibriles, subfibriles, fibrils, fascicles, and tendons.<sup>[32]</sup>
- Static and dynamic self-assembly: Self-assembly in biological systems may generate equilibrium structures; examples include molecular recognition and folding of globular proteins. Other biological processes and systems are dynamic, that is, they exist out-of-equilibrium, and the systems maintain their characteristic order only

while dissipating energy.<sup>[19,33]</sup> Living cells and organisms are examples of such systems—they die when the flow of energy through them stops. In many animate systems, new properties and patterns emerge as a result of interactions between autonomously moving components (e.g., bacteria in swarming colonies, fish in schools, and birds in flocks).

## ARTIFICIAL SELF-ASSEMBLING SYSTEMS DESIGNED USING BIOLOGICAL PRINCIPLES

In analogy to biological self-assembled structures, the shape and functionality of artificial self-assembled aggregates are governed by the shapes of their components, by the interactions between them, and by the environments and constraints imposed on them (e.g., the degree of order and the symmetry of a crystalline lattice of microspheres determine its optical properties, and the shape and connectivity in aggregates that form electrical circuits determine the type of electronic functionality that they exhibit). Control over the structure—and, thereby, the properties—of self-assembled aggregates has been achieved in several ways by borrowing strategies from biological systems.

### Constrained Self-Assembly

Figure 1 illustrates templating of the structure of self-assembled aggregates using geometric restrictions. In

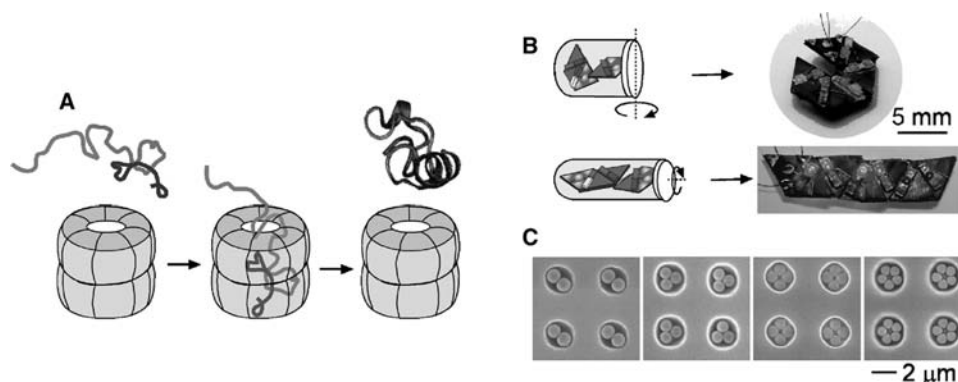


**Fig. 1** Templating of the structure of biological (A) and artificial (B, C) self-assembled aggregates using geometric restrictions. (A) Scheme illustrating chaperonin-assisted protein folding. The limited volume within a chaperonin molecule in which the folding process takes place ensures the correct folding of a polypeptide chain into a functional 3-D protein by preventing undesired contacts with other molecules. (B) Geometric templating of the structure and function of 3-D aggregates self-assembled from millimeter-sized components. Self-assembly in containers of different shapes generated topologically different 3-D structures—helices (top) or zigzags (bottom); these structures had different patterns of electrical connections among LEDs carried by the components. *Source:* From Ref.<sup>[34]</sup>. ©Wiley-VCH, 2003. (C) Geometric templating of the morphology of aggregates self-assembled from micrometer-sized spherical colloids. The structure of the aggregates was determined by the ratio between the dimensions of the colloids and the cylindrical holes templating their self-assembly. From Ref.<sup>[35]</sup>. ©American Chemical Society, 2001.

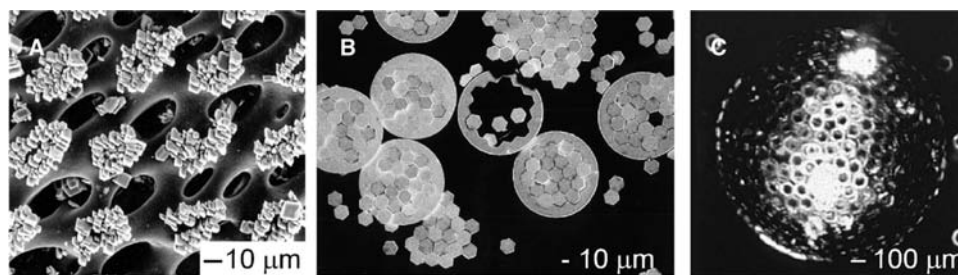


**Fig. 2** Templating of the structure of biological (A) and artificial (B, C) self-assembled aggregates using preformed templates. (A) Epitaxial overgrowth of calcite crystals on the spine surface of the brittle star *Ophiocoma wendtii*. Source: From Ref.<sup>[39]</sup>. Nucleation of the newly formed calcite crystals occurs at and is templated by specific sites on the surface. (Courtesy of J. Aizenberg.) (B) Two-dimensional, close-packed arrays of metal hexagons. The size and the shape of the assemblies were determined by the boundaries of the metal cavities used as templates. Source: From Ref.<sup>[40]</sup>. ©American Chemical Society, 2002. (C) Three-dimensional, spherical structure formed by self-assembly of hexagonal metal plates on the surface of a drop of perfluorodecalin in water. The surface of the liquid drop acts as a template for the structure. From Ref.<sup>[41]</sup>. ©American Chemical Society, 1998.

these systems, the geometry of the volume available for the self-assembly of components determined the morphology and the pattern of functional connections formed between self-assembled components. The same principle has been used in colloidal<sup>[36,37]</sup> and macroscopic<sup>[38]</sup> systems.

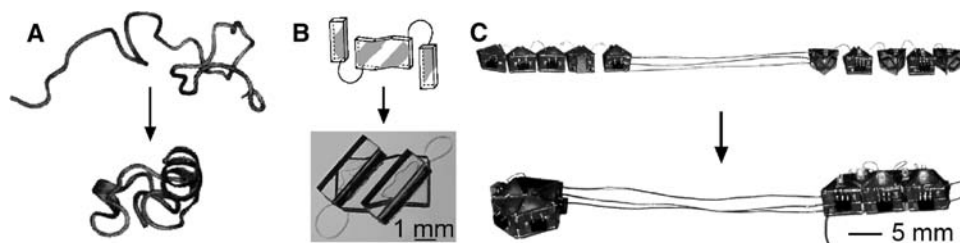
Figure 2 illustrates templating of the structure of self-assembled aggregates by preformed templates. In a system without constraints, self-assembly of micron-sized hexagonal plates resulted in the formation of sheetlike aggregates containing undefined numbers of components (plates). Self-assembly of the same plates in the presence of templates (holes with complementary shapes,<sup>[40]</sup> or drops of immiscible liquid),<sup>[41–44]</sup> led to the formation of new types of structures: planar aggregates with defined shapes, or spherical aggregates. In other examples, pre-assembled colloidal structures<sup>[45]</sup> chiral kernels,<sup>[38]</sup> encapsulating host molecules,<sup>[46]</sup> and micropatterned Scanning Auger Microscopy (SAM)<sup>[30,47,48]</sup> have also been used as templates.

Figure 3 illustrates templating of the structure of self-assembled aggregates by using sequence-restricted folding of linear precursors,<sup>[49–51]</sup> in analogy to the sequence-restricted folding of proteins and RNA into

3-D structures. In these examples, the sequence of millimeter-sized components in a chain and the properties (e.g., topology and flexibility) of the connections between them templated the structure and function of the self-assembled aggregates.

### Self-Assembly Based on Multiple Driving Forces

Biomolecular systems usually self-assemble by the concerted action of multiple types of weak interactions. In most artificial systems, self-assembly of the components involves not more than two types of interactions: fluidic and gravitational,<sup>[52]</sup> vibrational and gravitational,<sup>[53]</sup> magnetic and hydrodynamic,<sup>[54]</sup> or magnetic and electrostatic.<sup>[55]</sup> By using several types of interactions between the components, it is possible to form independently different types of connections between the components: structural connections, functional connections, or connections combining both tasks. Figure 4 shows one such system, modeled on the structure of tobacco mosaic virus.<sup>[56]</sup> The millimeter-sized components forming the helical aggregate interacted via two orthogonal capillary interactions: a



**Fig. 3** Templating of the structure of biological (A) and artificial (B, C) self-assembled aggregates by using sequence-restricted folding of linear precursors. (A) Scheme illustrating the formation of the functional 3-D structure of a protein molecule by folding of a linear chain of amino acid residues. (B) Compact 3-D structure formed by folding of a string of tethered, polymeric polyhedra. Source: From Ref.<sup>[50]</sup>. ©American Chemical Society, 2002. (C) Self-assembled, asymmetric device formed by folding of a linear string of electronic components. From Ref.<sup>[51]</sup>. ©National Academy of Sciences, USA, 2002.

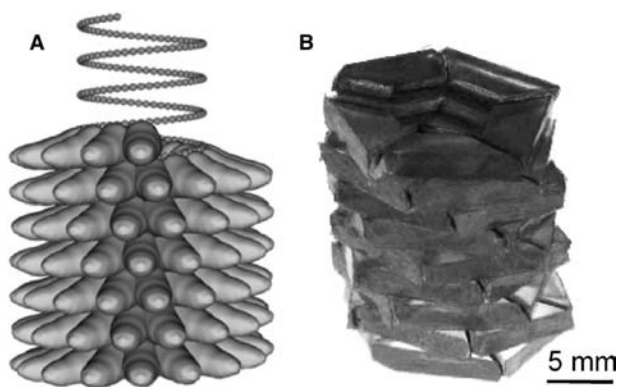


**Fig. 4** Biological (A) and artificial (B) aggregates self-assembled by the concerted action of multiple types of weak interactions between molecular or millimeter-sized components. (A) The structure of tobacco mosaic virus. Protein molecules and a strand of RNA assemble into a right-handed helical structure via hydrogen bonds, electrostatic interactions, and hydrophobic interactions. (B) Helical aggregate formed by millimeter-sized polyurethane polyhedra interacting via two orthogonal capillary interactions acting in parallel. *Source:* From Ref.<sup>[56]</sup>. ©American Institute of Physics, 2002.

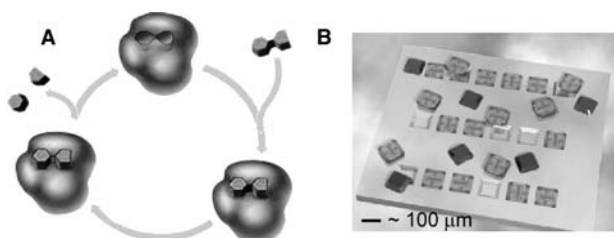


**Fig. 5** Biological (A) and artificial (B) self-assembling systems in which the components interact by 3-D complementary surfaces. (A) Scheme of interaction between an enzyme and its substrate. The binding pocket of the enzyme molecule adopts a geometrical shape complementary to the shape of the substrate. (B) Silicon chips self-assemble into indentations of complementary shapes on a substrate. *Source:* From Ref.<sup>[60]</sup>.

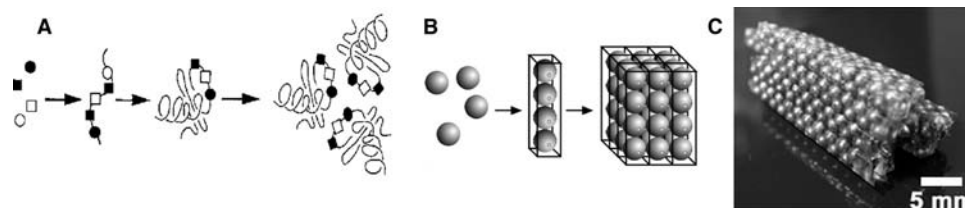


**Fig. 6** Biological (A) and artificial (B, C) self-assembling systems in which the components are organized at several hierarchical levels of structural complexity. (A) Hierarchical self-assembly of a viral capsid. Amino acids (shown as squares and circles) form a disordered polypeptide chain; the chain folds (self-assembles) into a functional protein; several protein molecules aggregate into the viral capsid. *Source:* From Ref.<sup>[66]</sup>. ©Wiley-VCH, 1999. (B) Hierarchical self-assembly of millimeter-sized spheres. The spheres are packed into rods, which subsequently self-assemble into 3-D structures (C). From Ref.<sup>[67]</sup>.

strong interaction based on drops of liquid solders was responsible for the growth of the aggregates and resulted in electrical connectivity between the components, and a weaker interaction based on drops of hydrophobic liquid stabilized the aggregates laterally.

### Recognition by Shape Complementarity

This principle has been used to design components that interact in both molecular<sup>[57]</sup> and mesoscale<sup>[58–60]</sup> self-assembling systems. Three-dimensional surfaces enable high specificity in recognition, and contribute to the structural stability of self-assembled aggregates. Figure 5 shows a mesoscale system in which polyhedral, micron-sized electronic components self-assemble onto a common substrate by shape recognition and shear forces.

### Hierarchical Self-Assembly

Bottom-up, hierarchical self-assembly has been used to build nanostructures for application as optical and magnetic materials,<sup>[61]</sup> tunable nanoporous<sup>[62]</sup> and microporous<sup>[63]</sup> materials, nanomaterials with anisotropic properties,<sup>[64]</sup> metal nanostructures on diblock copolymer scaffolds,<sup>[65]</sup> and extended arrays of polymeric objects at a fluid–fluid interface.<sup>[66]</sup> Figure 6 illustrates the use of hierarchical self-assembly to form three-dimensional lattices of spheres.<sup>[67]</sup> Unrestricted and templated self-assemblies of spheres have been shown to give access to only a limited range of structures. The use of a hierarchical approach (i.e., the confinement of spheres in rods, followed by assembly of these rods) makes it possible to generate 3-D structures with a variety of 3-D lattices.

### Self-Healing Structures

Designing materials and structures that can self-repair in ways modeled on living systems is an emerging goal for materials science.<sup>[68]</sup> Self-healing in living systems



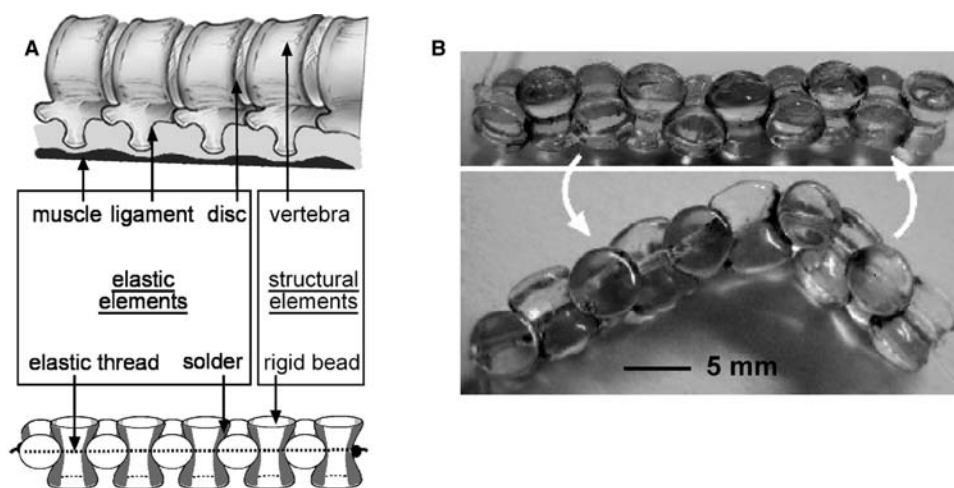


**Fig. 7** Self-healing structures in biology and engineering. (A) Common features of the design of a vertebrate spine (top) and a self-assembling system of millimeter-sized components (bottom). Both systems consist of rigid structural elements connected by elastomeric elements. (B) The structure loosely mimicking the organization of vertebrate spine spontaneously realigns and heals after breaking and dislocation. *Source:* From Ref.<sup>[69]</sup>. ©Wiley-VCH, 2003.

involves complex cascades of out-of-equilibrium processes that are impossible to reproduce in current man-made systems. However, self-assembly may offer an interesting alternative for the design of self-healing, steady-state systems. After disruption, equilibrium self-assembled systems return to their ordered state, provided that this state corresponds to a thermodynamic minimum. Figure 7 shows a self-healing system loosely mimicking the spine of vertebrates, based on self-assembly of a string of millimeter-sized components interacting via capillary forces.<sup>[69]</sup>

### Dynamic Self-Assembling Systems

The central importance of dynamic systems for life has prompted the development of simple out-of-equilibrium systems with which to model complex behavior and emergence.<sup>[54,55,70,71]</sup> Figure 8 shows two examples of dynamic, mesoscopic self-assembling systems. The first system consists of millimeter-sized metallic objects rotating at the liquid–air interface. The objects self-organize into a variety of patterns. The second system consists of polymer plates floating at the surface of an aqueous solution of hydrogen peroxide. The individual components can move autonomously and can interact with one another. Obviously, these systems are too primitive to mimic the complex biological dynamic systems; the studies of dynamic self-assembly are just beginning.

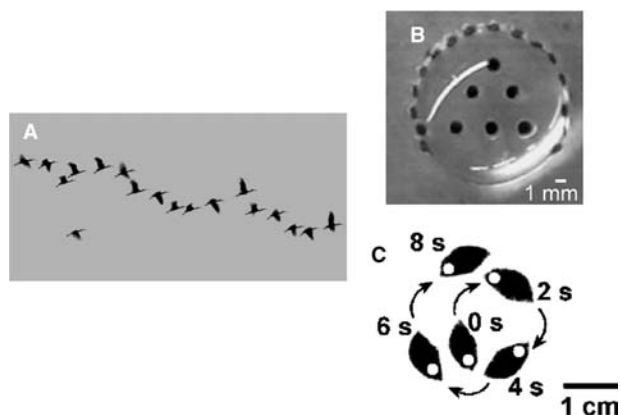


**Fig. 8** Biological (A) and artificial (B, C) dynamic self-assembling systems. (A) A flock of ibises (Image J. -M. Bettex). (B) Magnetized disks rotating on the top surface of a droplet of perfluorodecalin covered with water. *Source:* From Ref.<sup>[70]</sup>. ©Macmillan Magazines Limited, 2000. (C) A system of millimeter-scale objects that move autonomously across the surface of a liquid powered by the catalytic decomposition of hydrogen peroxide. The numbers indicate time elapsed during change between two positions of the objects at the fluid–air interface. From Ref.<sup>[71]</sup>. ©Wiley-VCH, 2002.

### CONCLUSION

Self-assembly is an efficient, and often, practical way to organize components ranging in size from molecular to macroscopic into functional aggregates. Biomimetic approaches to the design of self-assembling systems have been immensely stimulating in solving critical problems in the design of artificial self-assembling systems; they might be the key to many of the unsolved problems facing the future of self-assembled functional systems in different size regimes.

In the molecular size regime, supramolecular self-assembly based on biomimetic principles has delivered many types of complex molecules<sup>[17,46]</sup> and useful materials.<sup>[5,22,72]</sup> The synthesis and assembly of large molecules and molecular aggregates with intricate

structure and functionality (e.g., analogs of integrated circuits or viruses) remain unsolved problems.<sup>[73]</sup> Templated and hierarchical self-assembly—concepts familiar from many biological instances—may offer a solution.<sup>[46]</sup>

In the nanoscale size regime, principles extracted from biology have been applied to the fabrication of functional materials (e.g., photonic bandgap crystals and self-healing materials). Much of the current research in the nanoscale is focused on achieving electronic functionality, notably on the problems of electrically connecting the components, organizing them into arrays, and establishing the best architectures for nanoscale devices.<sup>[74]</sup> Biological systems have demonstrated the utility of templating and hierarchical self-assembly in ordering components of similar sizes (macromolecules and organelles) into functional entities (cells). Dynamic, reconfigurable biological systems offer examples of a different approach to self-assembly: dynamic systems are currently of purely academic interest, but may become useful in the future.<sup>[75]</sup>

In the microscale and macroscale size regimes, self-assembly can generate functions that are not possible at smaller scales (e.g., electric connectivity and electronic functionality).<sup>[20]</sup> In addition, self-assembling systems may be useful in solving problems in robotics and microfabrication. Biomimicry might help to solve the most significant problem in this size range—the fabrication of small, functionalized components. Self-folding and hierarchical self-assembly—two strategies widely used by biological systems—are among the most promising approaches to this problem.<sup>[76,77]</sup>

Some of the most important problems in current technology include: 1) better systems for information processing (i.e., systems that are fast, cheap, and can be cooled efficiently); 2) systems that use and store energy efficiently; 3) materials and structures with internal organization leading to valuable properties (e.g., capability to self-repair, self-heal, and self-replicate); and 4) small, three-dimensional, functional structures. All of the materials and functions in this list are found in biological systems.<sup>[78]</sup> The self-assembled, living world provides examples of some of the most efficient functional systems known. To the extent that one can understand and model the designs and strategies used in these systems, the biomimetic approach will stimulate new designs for self-assembled functional systems.

## ACKNOWLEDGMENTS

This work was supported by the NSF (CHE-0101432) and DARPA. We thank D.A. Bruzewicz for many insightful comments.

## REFERENCES

1. Clegg, W.J.; Kendall, K.; Alford, N.M.; Button, T.W.; Birchhall, J.D. A simple way to make tough ceramics. *Nature* **1990**, *347*, 455–457.
2. Gordon, J.E.; Jeronimidis, G. Composites with high work of fracture. *Philos. Trans. R. Soc. Lond., A* **1980**, *294*, 545–550.
3. Li, S.H.; Zang, R.H. A biomimetic model of fibre reinforced composite materials. *J. Miner. Met. Mater. Soc.* **1993**, *March*, 24–27.
4. Simmons, A.H.; Michal, C.A.; Jelinski, L.W. Molecular orientation and two-component nature of the crystalline fraction of spider dragline silk. *Science* **1996**, *271*, 84–87.
5. Cubberley, M.S.; Iverson, B.L. Models of higher-order structure: foldamers and beyond. *Curr. Opin. Struct. Biol.* **2001**, *5*, 650–673.
6. Bechert, D.W.; Bruse, M.; Hage, W.; Meyer, R. Fluid mechanics of biological surfaces and their technological application. *Naturwissenschaften* **2000**, *87*, 157–171.
7. Dickinson, M.H.; Farley, C.T.; Full, R.J.; Koehl, M.A.R.; Kram, R.; Lehman, S. How animals move: an integrative view. *Science* **2000**, *288*, 100–106.
8. Mirkin, C.A.; Letsinger, R.L.; Mucic, R.C.; Storhoff, J.J. A DNA-based method for rationally assembling nanoparticles into macroscopic materials. *Nature* **1996**, *382*, 607–609.
9. Alivisatos, A.P.; Peng, X.; Wilson, T.E.; Johnson, K.P.; Loweth, C.J.; Bruchez, M.P., Jr.; Schultz, P.G. Organization of nanocrystal molecules using DNA. *Nature* **1996**, *382*, 609–611.
10. Braun, E.; Eichen, Y.; Sivan, U.; Ben-Yosef, G. DNA-templated assembly and electrode attachment of a conducting silver wire. *Nature* **1998**, *391*, 775–778.
11. Bashir, R. DNA-mediated artificial nanobiostructures: state of the art and future directions. *Superlattices Microstruct.* **2001**, *29*, 1–16.
12. Lee, S.W.; McNally, H.A.; Guo, D.; Pingle, M.; Bergstrom, D.E.; Bashir, R. Electric-field-mediated assembly of silicon islands coated with charged molecules. *Langmuir* **2002**, *18*, 3383–3386.
13. Mertig, M.; Ciacchi, L.C.; Seidel, R.; Pompe, W.; De Vita, A. DNA as a selective metallization template. *Nano Lett.* **2002**, *2*, 841–844.
14. Smith, B.L.; Schaeffer, T.E.; Viani, M.; Thompson, J.B.; Frederick, N.A.; Kindt, J.; Belcher, A.; Stucky, G.D.; Morse, D.E.; Hansma, P.K. Molecular mechanistic origin of the toughness of natural adhesives, fibres and composites. *Nature* **1999**, *399*, 761–763.
15. Whaley, S.R.; English, D.S.; Hu, E.L.; Barbara, P.F.; Belcher, A.M. Selection of peptides with semiconductor binding specificity for directed nanocrystal assembly. *Nature* **2000**, *405*, 665–668.
16. Yamashita, I. Prospects of bio-nanotechnology. *Oyo Buturi* **2002**, *71*, 1014–1019.
17. Lehn, J.M.; Ball, P. *Supramolecular Chemistry*. In *The New Chemistry*; Hall, N., Ed.; Cambridge University Press: Cambridge, UK, 2000; 300–351.
18. Whitesides, G.M.; Boncheva, M. Beyond molecules: self-assembly of mesoscopic and macroscopic

- components. *Proc. Natl. Acad. Sci. U. S. A.* **2002**, *99*, 4769–4774.
19. Whitesides, G.M.; Grzybowski, B. Self-assembly at all scales. *Science* **2002**, *295*, 2418–2421.
  20. Boncheva, M.; Bruzewicz, D.A.; Whitesides, G.M. Millimeter-scale self-assembly and its applications. *Pure Appl. Chem.* **2003**, *75*, 621–630.
  21. Alivisatos, A.P.; Barbara, P.F.; Castelman, A.W.; Chang, J.; Dixon, D.A.; Klein, M.L.; McLendon, G.L.; Miller, J.S.; Ratner, M.A.; Rossky, P.J.; Stupp, S.I.; Thompson, M.E. From molecules to materials: current trends and future directions. *Adv. Mater.* **1998**, *10*, 1297–1336.
  22. Tolles, W.M. Self-assembled materials. *MRS Bull.* **2000**, *25*, 36–38.
  23. Ball, P. Natural strategies for the molecular engineer. *Nanotechnology* **2002**, *13*, R15–R28.
  24. van Bommel, K.J.C.; Friggeri, A.; Shinkai, S. Organic templates for the generation of inorganic materials. *Angew. Chem., Int. Ed. Engl.* **2003**, *42*, 980–999.
  25. *Biological and Biomimetic Materials—Properties to function*, Proceedings of the Material Research Society Symposium, San Francisco, CA, April, 1–5, 2002; Aizenberg, J., McKittrick, J.M., Orme, C.A., Eds.; MRS: Warrendale, PA, 2002.
  26. Kostyuk, P. *Plasticity in Nerve Cell Function*; Oxford University Press: Oxford, UK, 1998.
  27. Alberts, B.; Bray, D.; Lewis, J.; Raff, M.; Roberts, K.; Watson, J.D. *Molecular Biology of the Cell*; Garland: New York, NY, 1994.
  28. Grantcharova, V.; Alm, E.J.; Baker, D.; Horwich, A.L. Mechanisms of protein folding. *Curr. Opin. Struct. Biol.* **2001**, *11*, 70–82.
  29. Aizenberg, J.; Muller, D.A.; Grazul, J.L.; Hamann, D.R. Direct fabrication of large micropatterned single crystals. *Science* **2003**, *299*, 1205–1208.
  30. Chen, C.S.; Mrksich, M.; Huang, S.; Whitesides, G.M.; Ingber, D.E. Geometric control of cell life and death. *Science* **1997**, *276*, 1425–1428.
  31. Johnson, J.E.; Speir, J. Quasi-equivalent viruses: a paradigm for protein assemblies. *J. Mol. Biol.* **1997**, *269*, 665–675.
  32. Kastelic, J.; Palley, I.; Baer, E. A structural mechanical model for tendon crimping. *J. Biomech.* **1980**, *13*, 887–893.
  33. Ball, P. *The Self-Made Tapestry: Pattern Formation in Nature*; Oxford University Press: Oxford, UK, 1999.
  34. Boncheva, M.; Ferrigno, R.; Bruzewicz, D.A.; Whitesides, G.M. Plasticity in self-assembly: templating generates functionally different circuits from a single precursor. *Angew. Chem., Int. Ed. Engl.* **2003**, *42*, 3368–3371.
  35. Yin, Y.; Lu, Y.; Gates, B.; Xia, Y. Template-assisted self-assembly: a practical route to complex aggregates of monodispersed colloids with well-defined sizes, shapes and structures. *J. Am. Chem. Soc.* **2001**, *123*, 8718–8729.
  36. van Blaaderen, A.; Rene, R.; Wiltzius, P. Template-directed colloidal crystallization. *Nature* **1997**, *385*, 321–324.
  37. Xia, Y.; Gates, B.; Yin, Y.; Sun, Y. Self-Assembly of monodispersed spherical colloids into complex structures. In *Handbook of Surface and Colloid Chemistry*, 2nd Ed.; Birdi, K.S., Ed.; CRC Press LLC: Boca Raton, FL, 2003; 555–579.
  38. Boncheva, M.; Bruzewicz, D.A.; Whitesides, G.M. Formation of chiral, three-dimensional aggregates by self-assembly of helical components. *Langmuir* **2003**, *19*, 6066–6071.
  39. Aizenberg, J. Patterned crystallization of calcite in vivo and in vitro. *J. Cryst. Growth* **2000**, *211*, 143–148.
  40. Clark, T.D.; Ferrigno, R.; Tien, J.; Paul, K.; Whitesides, G.M. Template-directed self-assembly of 10- $\mu\text{m}$ -sized hexagonal plates. *J. Am. Chem. Soc.* **2002**, *124*, 5419–5426.
  41. Huck, W.T.S.; Tien, J.; Whitesides, G.M. Three-dimensional mesoscale self-assembly. *J. Am. Chem. Soc.* **1998**, *120*, 8267–8268.
  42. Velev, O.D.; Furusawa, K.; Nagayama, K. Assembly of latex particles by using emulsion droplets as templates: 1. microstructured hollow spheres. *Langmuir* **1996**, *12*, 2374–2384.
  43. Velev, O.D.; Lenhoff, A.M.; Kaler, E.W. A class of microstructured particles through colloidal crystallization. *Science* **2000**, *287*, 2240–2243.
  44. Dinsmore, A.D.; Hsu, M.F.; Nikolaidis, M.G.; Marquez, M.; Bausch, A.R.; Weitz, D.A. Colloidosomes: selectively permeable capsules composed of colloidal particles. *Science* **2002**, *298*, 1006–1009.
  45. Yin, Y.; Xia, Y. Self-assembly of monodispersed spherical colloids into complex aggregates with well-defined sizes, shapes, and structures. *Adv. Mater.* **2001**, *13*, 267–271.
  46. Hof, F.; Craig, S.L.; Nuckolls, C.; Rebek, J., Jr. Molecular encapsulation. *Angew. Chem., Int. Ed. Engl.* **2002**, *41*, 1488–1508.
  47. Aizenberg, J.; Black, A.J.; Whitesides, G.M. Control of crystal nucleation by patterned self-assembled monolayers. *Nature* **1999**, *398*, 495–498.
  48. Bernard, A.; Fitzli, D.; Sonderegger, P.; Delamarche, E.; Michel, B.; Bosshard, H.R.; Biebuyck, H. Affinity capture of proteins from solution and their dissociation by contact printing. *Nat. Biotechnol.* **2001**, *19*, 866–869.
  49. Choi, I.S.; Weck, M.; Jeon, N.L.; Whitesides, G.M. Mesoscale folding: A physical realization of an abstract, 2D lattice model for molecular folding. *J. Am. Chem. Soc.* **2000**, *122*, 11997–11998.
  50. Clark, T.D.; Boncheva, M.; German, J.M.; Weck, M.; Whitesides, G.M. Design of three-dimensional, millimeter-scale models for molecular folding. *J. Am. Chem. Soc.* **2002**, *124*, 18–19.
  51. Boncheva, M.; Gracias, D.H.; Jacobs, H.O.; Whitesides, G.M. Biomimetic self-assembly of a functional asymmetrical electronic device. *Proc. Natl. Acad. Sci. U.S.A.* **2002**, *99*, 4937–4940.
  52. Yeh, H.-J.J.; Smith, J.S. Fluidic self-assembly for the integration of GaAs light-emitting diodes on Si substrates. *IEEE Photonics Technol. Lett.* **1994**, *6*, 706–708.
  53. Cohn, M.; Kim, C.J.; Pisano, A. In: *Self-Assembling Electrical Networks: An Application of Micromachining Technology*, Proceedings of Transducers '91 International Conference on Solid-State Sensors

- and Actuators, San Francisco, June, 24–27, 1991; IEEE: New York, 1991, 493pp.
54. Grzybowski, B.; Whitesides, G.M. Dynamic aggregation of chiral spinners. *Science* **2002**, *296*, 718–721.
  55. Grzybowski, B.A.; Winkelman, A.; Wiles, J.A.; Brumer, Y.; Whitesides, G.M. Electrostatic self-assembly of macroscopic crystals using contact electrification. *Nat. Mater.* **2003**, *2*, 241–245.
  56. Gracias, D.H.; Boncheva, M.; Omoregie, O.; Whitesides, G.M. Biomimetic self-assembly of helical electrical circuits using orthogonal capillary interactions. *Appl. Phys. Lett.* **2002**, *80*, 2802–2804.
  57. Martin, T.; Obst, U.; Rebek, J., Jr. Molecular assembly and encapsulation by hydrogen-bonding preferences and the filling of space. *Science* **1998**, *281*, 1842–1845.
  58. Choi, I.S.; Bowden, N.; Whitesides, G.M. Shape-selective recognition and self-assembly of mm-scale components. *J. Am. Chem. Soc.* **1999**, *121*, 1754–1755.
  59. Terfort, A.; Whitesides, G.M. Self-assembly of an operating electrical circuit based on shape complementarity and the hydrophobic effect. *Adv. Mater.* **1998**, *10*, 470–473.
  60. Alien Technology Morgan Hill CA. <http://www.alien-technology.com/technology/overview.html>.
  61. Drain, C.M.; Batteas, J.D.; Flynn, G.W.; Milic, T.; Chi, N.; Yablon, D.G.; Sommers, H. Designing supramolecular porphyrin arrays that self-organize into nanoscale optical and magnetic materials. *Proc. Am. Chem. Soc.* **2002**, *99*, 6498–6502.
  62. Boal, A.K.; Ilhan, F.; DeRouchey, J.E.; Thurn-Albrecht, T.; Russel, T.P.; Rotello, V.M. Self-assembly of nanoparticles into structured spherical and network aggregates. *Nature* **2000**, *404*, 746–748.
  63. Jenekhe, S.A.; Chen, X.L. Self-assembly of ordered microporous materials from rod-coil block copolymers. *Science* **1999**, *283*, 372–375.
  64. Ikkala, O.; ten Brinke, G. Functional materials based on self-assembly of polymeric supramolecules. *Science* **2002**, *295*, 2407–2409.
  65. Lopez, W.A.; Jaeger, H.M. Hierarchical self-assembly of metal nanostructures on diblock copolymer scaffolds. *Nature* **2001**, *414*, 735–738.
  66. Choi, I.S.; Bowden, N.; Whitesides, G.M. Macroscopic, hierarchical two-dimensional self-assembly. *Angew. Chem., Int. Ed. Engl.* **1999**, *38*, 3078–3081.
  67. Wu, H.; Thalladi, V.R.; Whitesides, S.; Whitesides, G.M. Using hierarchical self-assembly to form three-dimensional lattices of spheres. *J. Am. Chem. Soc.* **2002**, *124*, 14495–14502.
  68. White, S.R.; Sottos, N.R.; Geubelle, P.H.; Moore, J.S.; Kessler, M.R.; Sriram, S.R.; Brown, E.N.; Viswanathan, S. Autonomic healing of polymer composites. *Nature* **2001**, *409*, 794–797.
  69. Boncheva, M.; Whitesides, G.M. Self-healing systems having a design stimulated by the vertebrate spine. *Angew. Chem., Int. Ed. Engl.* **2003**, *42*, 2644–2647.
  70. Grzybowski, B.; Stone, H.A.; Whitesides, G.M. Dynamic self-assembly of magnetized, millimeter-sized objects rotating at the liquid–air interface. *Nature* **2000**, *405*, 1033–1036.
  71. Ismagilov, R.F.; Schwartz, A.; Bowden, N.; Whitesides, G.M. Autonomous movement and self-assembly. *Angew. Chem., Int. Ed. Engl.* **2002**, *41*, 652–654.
  72. Whitesides, G.M. Self-assembling materials. *Sci. Am.* **1995**, *273*, 146–149.
  73. Stupp, S.I.; LeBonheur, V.; Walker, K.; Li, L.S.; Huggins, K.E.; Keser, M.; Amstutz, A. Supramolecular materials: self-organized nanostructures. *Science* **1997**, *276*, 384–389.
  74. Lieber, C.M. The incredible shrinking circuit. *Sci. Am.* **2001**, *285*, 58–64.
  75. Heath, J.R.; Kuekes, P.J.; Snider, G.S.; Williams, R.S. A defect-tolerant computer architecture: opportunities for nanotechnology. *Science* **1998**, *280*, 1716–1721.
  76. Gracias, D.H.; Kavthekar, V.; Love, J.C.; Paul, K.E.; Whitesides, G.M. Fabrication of micron-scale, patterned polyhedra by self-assembly. *Adv. Mater.* **2002**, *14*, 235–238.
  77. Smela, E.; Inganäs, O.; Lundstrom, I. Controlled folding of micrometer-sized structures. *Science* **1995**, *268*, 1735–1738.
  78. Whitesides, G.M. The once and future nanomachine. *Sci. Am.* **2001**, *285*, 70–75.

# Biomimetic Receptors for Carboxylate Recognition

Rocco Ungaro  
Alessandro Casnati  
Francesco Sansone

Dipartimento di Chimica Organica e Industriale,  
Università di Parma, Parma, Italy

## INTRODUCTION

Carboxylate anions are ubiquitous in nature and are involved in several biological processes. For example, the carboxylate group of the D-alanyl-D-alanine terminal part of the cell wall peptidoglycan is selectively recognized by the binding pocket of vancomycin-type antibiotics.<sup>[1]</sup> di- and tricarboxylates are involved in several metabolic processes,<sup>[2]</sup> and other carboxylate anions are known to be substrates or inhibitors of enzymes.<sup>[3]</sup> Moreover, chiral propionic acid derivatives are widely used in therapy as non-steroidal anti-inflammatory drugs<sup>[4]</sup> and carboxylate polyanions can form well-ordered self-assembled structures when mixed with complementary polycations or hydrogen bonding donor groups.<sup>[5]</sup> For all these reasons the synthesis of biomimetic receptors for carboxylate anions have been recently pursued in supramolecular chemistry,<sup>[6–8]</sup> with the aim of obtaining 1) useful models of the biological processes, 2) biologically active molecules, 3) selective chemosensors, and 4) selective separation systems.

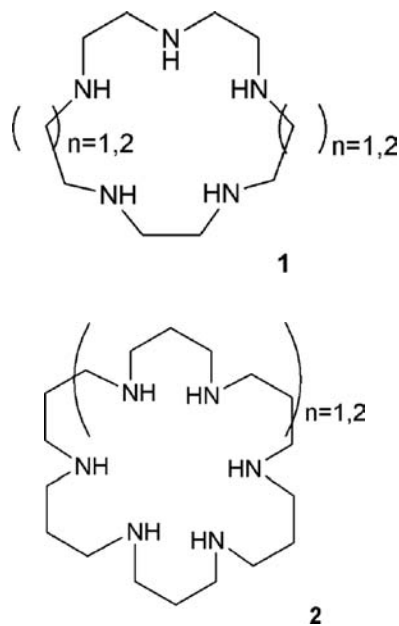
The objective of this entry is to highlight the most successful approaches followed in the design and synthesis of biomimetic receptors for carboxylate anion recognition, with major emphasis on the results achieved in the last 5 years with macrocyclic compounds, and on our own work.

## CHARGED RECEPTORS

The most obvious way to bind anions, and therefore also carboxylates, is to use positively charged receptors that can cause strong electrostatic ion–ion interactions with the guests.<sup>[9]</sup> Quite often in positively charged receptors, besides electrostatic forces, also hydrogen bonds and hydrophobic interaction are exploited, especially to increase substrate selectivity.

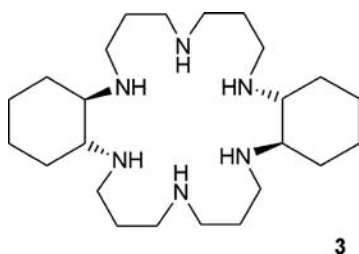
The first examples of receptors for carboxylate anions were presented by Kimura et al.<sup>[10]</sup> and Dietrich et al.<sup>[11]</sup> in 1981. They showed that polyazamacrocycles

(e.g., **1** and **2**), when protonated, are able to form complexes with polycarboxylated guests in water solution. In some way they mimic the action of biogenic linear polyamines, such as spermine and spermidine, which are known to interact with the phosphate backbone of nucleic acid and with polycarboxylates.<sup>[12,13]</sup>

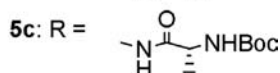
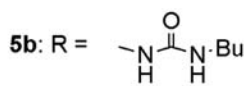
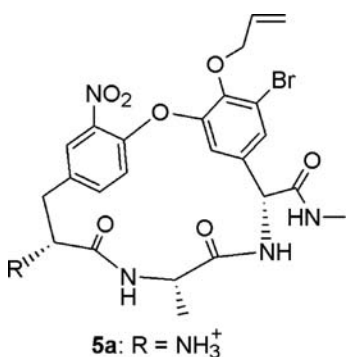
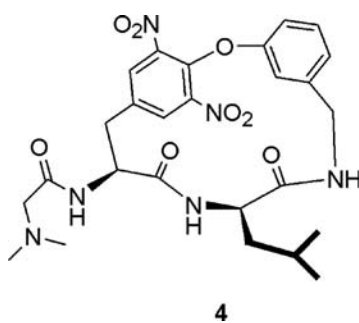


For protonated polyazamacrocycles the formation of hydrogen bonds with the anions strongly complements the most important electrostatic ion–ion interactions, because quaternary ammonium receptors (vide infra) usually show weaker binding.

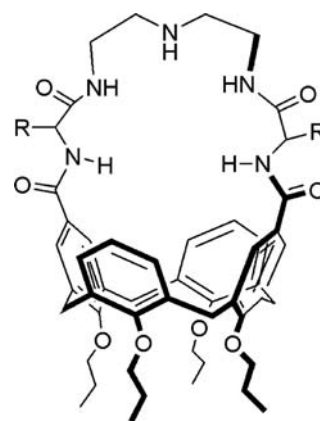
Incorporation of one or two chiral (*R,R*)-1,2-diaminocyclohexyl units into a hexazamacrocyclic structure gives rise to receptors (e.g., **3**), which exhibit enantioselective discrimination toward dicarboxylates. They show clear selectivity for D-tartrate, *N*-Ac-D-aspartate and *N*-Ac-D-glutamate over their L-enantiomers.<sup>[14]</sup> However, this selectivity is strongly dependent on the degree of protonation of the receptor.<sup>[15]</sup>



The properties of vancomycin family of antibiotics are linked to their ability to bind the terminal part of L-Lys-D-Ala-D-Ala-COO<sup>-</sup> of the cell wall mucopeptide precursor of gram-positive bacteria via a combination of hydrogen bonds and hydrophobic interactions, which act cooperatively.<sup>[1]</sup> Hamilton tried to mimic the action of vancomycin carboxylate binding pocket,<sup>[16]</sup> synthesizing receptor **4**, which is able to bind carboxylic acid via a proton transfer from guest to host and the formation of a salt bridge. Carboxylates are held inside the cavity by hydrogen bonds with all free peptide NHs. The binding constant of cyanoacetic acid in CDCl<sub>3</sub> was estimated to be ca. 580 M<sup>-1</sup>. A similar system (**5a**) reported by Pieters, binds *N*-Ac-D-Ala in CDCl<sub>3</sub>, with association constants  $K_{\text{ass}} \approx 3 \times 10^4 \text{ M}^{-1}$ .<sup>[17]</sup> As in vancomycin, the protonated amino group does not seem to be essential for binding because **5b** or **5c** show approximately the same association constants.



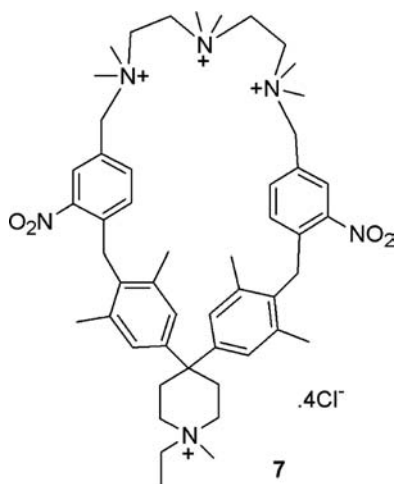
With a quite different approach, we synthesized a series of macrobicyclic ligands **6** belonging to the class of *upper rim* *N*-linked peptidocalix[4]arenes and having  $\alpha$ -amino acids of different structure (Gly, Ala, Phe) and configuration (LL, DD, or DL).<sup>[18,19]</sup> The minimum inhibitory concentrations (MICs) of these macrocycles against gram-positive bacterial strands show that biological activity increases as the steric hindrance of *R* groups decreases. The L-Ala,L-Ala (**6**: R = CH<sub>3</sub>) receptor shows activity quite close to that of vancomycin and ability to bind carboxylate guests in organic solvents, as demonstrated by nuclear magnetic resonance (NMR) and electrospray ionization mass spectrometry (ESI-MS). Stability constants ( $K_{\text{ass}}$ ) increase in CDCl<sub>3</sub> from lauric acid (log  $K_{\text{ass}} = 3.0$ ) to *N*-lauroyl-D-Ala (log  $K_{\text{ass}} = 4.1$ ) and to *N*-lauroyl-D-Ala-D-Ala (log  $K_{\text{ass}} > 5.0$ ). NMR diffusion experiments in CDCl<sub>3</sub> + 3% dimethyl sulfoxide (DMSO-*d*<sub>6</sub>) show that *N*-Ac-L-Ala-L-Ala is bound more strongly (log  $K_{\text{ass}} = 3.4$ ) than *N*-Ac-L-Ala (log  $K_{\text{ass}} = 2.4$ ).<sup>[20]</sup> These data indicate that besides the most important electrostatic interaction between carboxylate and the ammonium headgroup, additional H bonding and possibly CH- $\pi$  interaction between the alanine methyl group of the guest and the calixarene cavity stabilize the complexes.



The water-soluble polyquaternary ammonium receptor **7** synthesized by Diederich is able to recognize mono- and dicarboxylates in D<sub>2</sub>O.<sup>[21]</sup> It binds *N*-Ac-D-Ala ( $K_{\text{ass}} = 74 \text{ M}^{-1}$ ) and less strongly *N*-Ac-D-Ala-D-Ala ( $K_{\text{ass}} = 51 \text{ M}^{-1}$ ) essentially through electrostatic interactions that take place outside the cavity. However, the cyclophane structure seems important for the efficiency of the anion binding, as the hexamethylammonium salt of 1,4,7-triazaheptane is not able to bind alanines under the same conditions.

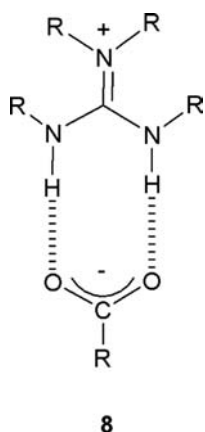
The use of quaternary ammonium salts instead of protonated amines for anion recognition has the





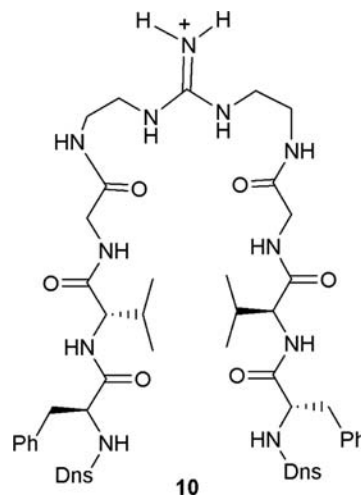
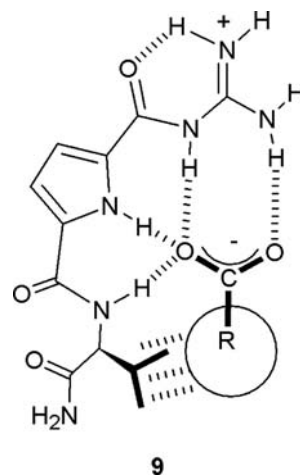
advantage of rendering complexation independent from the pH of the solution, but also has the disadvantage of removing hydrogen bond contributions to the binding. In the complexation of a series of dicarboxylates to bisquaternary ammonium anion receptors, Schneider found a value of 8 kJ/mol in H<sub>2</sub>O for a single carboxylate–ammonium interaction, independently of the rigidity of the two partners.<sup>[22]</sup>

Guanidinium salts offer the great advantage of being protonated over a wide pH range and to bind carboxylates via a combination of electrostatic forces and bidentate H-bonding interactions (**8**).<sup>[23]</sup> The importance of the formation of hydrogen bonds for carboxylate recognition in DMSO is highlighted by the fact that the change from NH to NCH<sub>3</sub> groups causes a remarkable drop in the stability of the carboxylate–guanidinium complexes (**8**).<sup>[24]</sup>



Also in the case of guanidinium-based receptors, the most interesting results in terms of efficiency and selectivity have been obtained when this carboxylate binding group is used in cooperation with additional interactions (hydrogen bonding, hydrophobic, van der Waals, etc.). The 2-guanidiniocarbonyl pyrrole

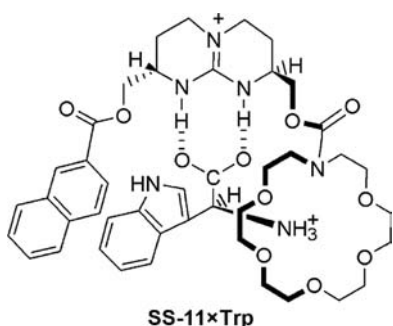
receptors (e.g., **9**) bind carboxylates in 40% H<sub>2</sub>O/DMSO ( $K_{\text{ass}} \approx 10^3 \text{ M}^{-1}$ ), more than 30 times stronger than a simple acylguanidinium cation. This significant increase is due to the formation of additional H bonding with the pyrrole and amide protons, whereas selectivity is mainly given by steric repulsion or attractive cation– $\pi$  interaction between substituents on the host and on the guest. A fair enantioselectivity was found for *N*-Ac-L/D-Ala ( $K_{\text{ass}}$  1610 and 730 M<sup>-1</sup>, respectively).<sup>[25,26]</sup> Kilburn prepared a tweezer receptor having a guanidinium moiety in the middle and two arms made up of an N-protected tripeptide. By using a combinatorial library it was shown that **10** is able to complex N-protected tripeptides possibly via hydrophobic interactions and  $\beta$ -sheets like hydrogen bonds. Calorimetric titration allowed one to determine a  $K_{\text{ass}} = 4 \times 10^5 \text{ M}^{-1}$  in DMSO/H<sub>2</sub>O for *N*-Cbz-Glu(O<sup>t</sup>Bu)-Ser(O<sup>t</sup>Bu)-Val-OH.<sup>[27]</sup>



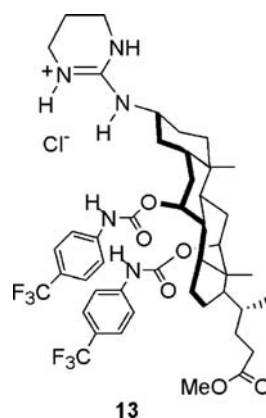
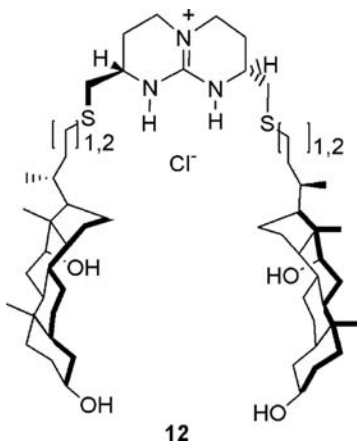
Bicyclic guanidinium salts, offering the advantage to protrude NH groups in only one direction, are particularly efficient in carboxylate binding. Chiral bicyclic guanidinium salts have been prepared by Schmidtchen,<sup>[28]</sup> de Mendoza,<sup>[29]</sup> and Davis<sup>[30]</sup> and

included in receptor structures especially with the aim to reach enantioselective binding.

de Mendoza proposed a receptor for  $\alpha$ -amino acids where a naphthalene unit and a crown ether moiety are linked to a chiral bicyclic guanidinium ion. The crown ether and guanidinium ion provide the two anchoring groups for ammonium and carboxylate ions, respectively, whereas the naphthalene ring, giving rise to stabilizing  $\pi$ - $\pi$  interaction with aromatic side chains, determines the observed selectivity for Phe  $\approx$  Trp  $\gg$  Val in extraction experiments (e.g., **SS-11**  $\times$  Trp). High enantioselectivity was observed in extraction into  $\text{CH}_2\text{Cl}_2$ , as no D-enantiomer could be detected in the organic phase, whereas the RR stereoisomer extracts D-Phe and D-Trp but not their L-enantiomers.<sup>[31]</sup>

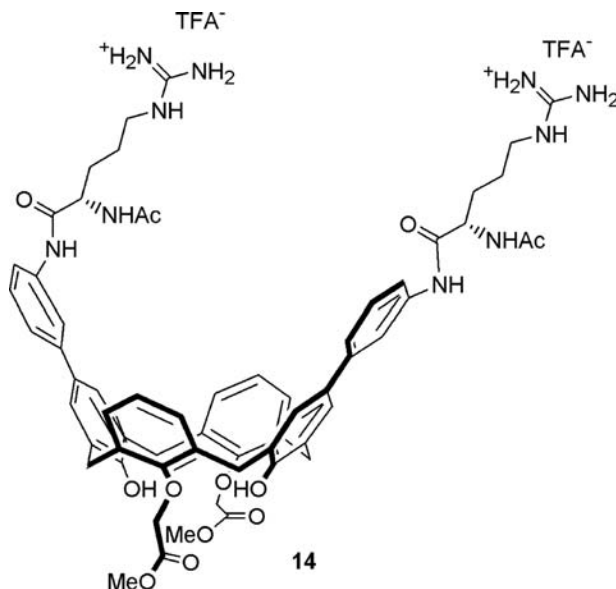
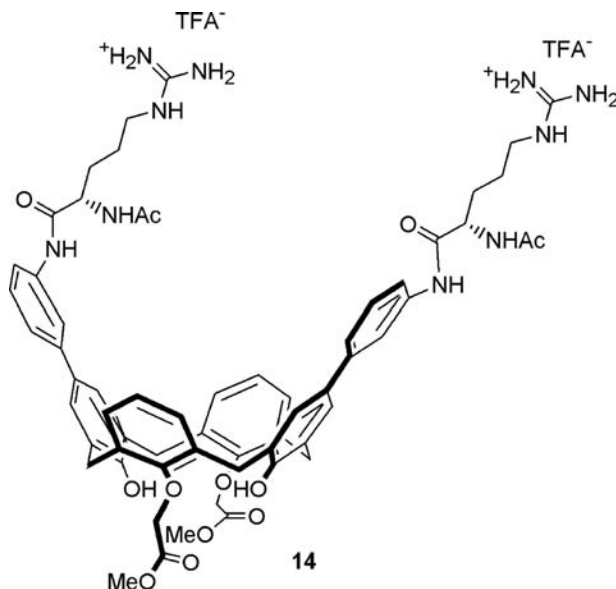


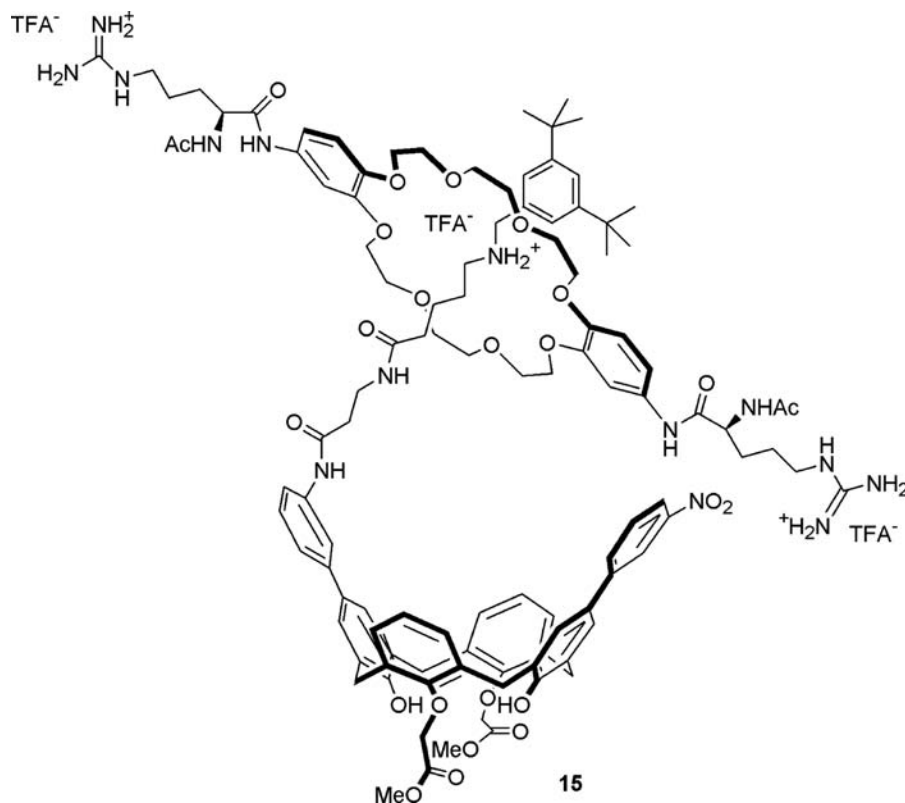
A closely related receptor proposed by Schmidtchen<sup>[32]</sup> and having a hydrophobic silyl ether is also able to efficiently transfer to  $\text{CH}_2\text{Cl}_2$  hydrophilic amino acids such as Ser and Gly, but not charged ones, although the enantioselectivity is lower. de Mendoza developed a receptor (**12**) where two deoxycholic acids are linked to a bicyclic guanidinium and which complex glucuronic and galacturonic acids with nearly the same strength in  $\text{CD}_3\text{CN}/\text{CDCl}_3$  (98/2). Steroid units only weakly influence the binding because of intramolecular hydrogen bonding observed in the free host.<sup>[33]</sup> Davis reported on the enantioselective extraction from  $\text{H}_2\text{O}$  to  $\text{CHCl}_3$  of *N*-Ac-amino



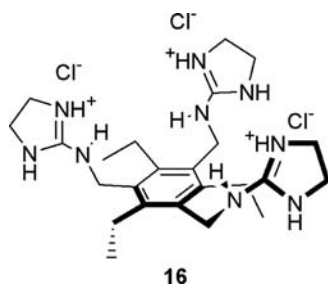
acids by using steroidal guanidines. The most selective receptor (**13**) is based on cholic acid and bears a monocyclic guanidinium side arm plus two carbamate functions whose H-bonding NH groups are activated through electron-withdrawing *p*-trifluoromethylbenzene units. Selectivity is in the order Phe > Trp > Met > Val > Ala with enantioselectivity (L/D) in the range 7/1–10/1.<sup>[34]</sup>

Smukste, House, and Smithrud<sup>[35]</sup> synthesized the [2]rotaxane host **15** having two guanidinium ions of arginine converging toward the calix[4]arene lipophilic cavity. The host **15** strongly binds *N*-Ac-L-Trp ( $10 \times 10^4 \text{ M}^{-1}$ ) and zwitterionic L-Trp ( $1 \times 10^4 \text{ M}^{-1}$ ) in DMSO via inclusion in the calixarene cavity of the Trp aromatic side chain and electrostatic interaction of the guanidinium with the carboxylate headgroup. The aromatic ring of the guest provides most of the binding free energy, as indole is also strongly bound in DMSO ( $4.2 \times 10^4 \text{ M}^{-1}$ ). However, the advantage of having convergent functional groups in rotaxane **15** was demonstrated by the low binding ( $9 \times 10^2 \text{ M}^{-1}$ ) of *N*-Ac-L-Trp with calixarene **14** having divergent guanidinium ions.<sup>[35]</sup>



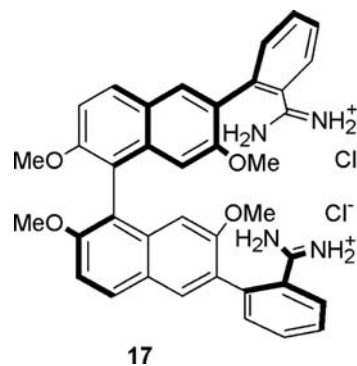


Anslyn introduced three monocyclic guanidinium side arms on the 1,3,5-triethylbenzene scaffold (**16**) and observed a strong binding of citrate anion ( $K_{\text{ass}} = 2.9 \times 10^5 \text{ M}^{-1}$ ) and good enantioselectivity.<sup>[36,37]</sup> Thanks to the steric barrier given by the three ethyl groups in **16**, guanidinium ions are preorganized on the same face of the benzene ring and can cooperate in the binding.



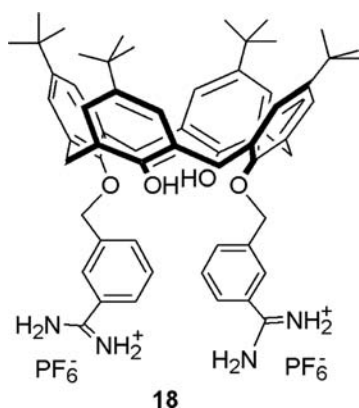
The amidinium cation, offering the possibility to coordinate carboxylate anions with a pair of hydrogen bonds strengthened by electrostatic interaction, shows a binding mode quite close to that of guanidinium cations. However, despite their stronger acidity they are much less used in anion binding. The bisamidinium receptors synthesized by Diederich using a 1,1'-binaphthalene scaffold (**17**) are efficient in the binding of dicarboxylates with selectivity for isophthalate and

glutarate anions. Calorimetric titration in MeOH evidenced that binding is mainly entropy driven because of the high solvent release from the charged species upon interaction.<sup>[38]</sup>



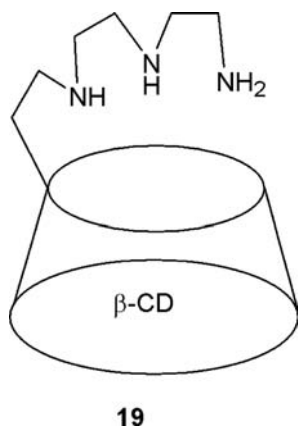
A tetramidinium resorcarenene receptor forms a 1:2 complex with an isophthalate and, in water solution, one of the aromatic rings of the guest is included in the lipophilic cavity of the host.<sup>[39]</sup> Calix[4]arenes functionalized at the lower rim with amidinium units (e.g., **18**) complex malonate and isophthalate anions in DMSO solution, where multiple host-guest stoichiometries are observed. In the X-ray crystal structure of the **18** × malonate 1:1 complex several different amidinium-carboxylate interactions are present, which

show the ability of these hosts to form an interesting hydrogen-bonding network.<sup>[40]</sup>

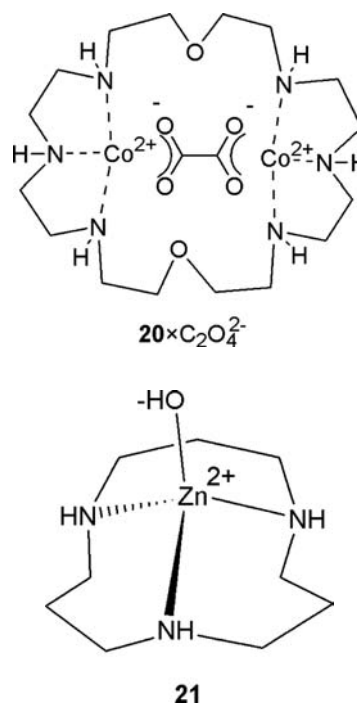


### CARBOXYLATE COORDINATION TO METAL CENTERS

Macrocyclic or cleftlike multidentate compounds having oxygen or nitrogen donor centers are able to bind metal ions in their cavity. In some cases, the complexed metal center is able to further interact with anionic species, giving rise to anion receptors. Most of the studies have been performed within the context of biomimetic catalysis of amide and ester bond cleavage because the transition state for these reactions have an anionic character and therefore the enzyme activity is also related to its ability to bind anions. One of the earliest examples of carboxylate anion recognition by metal-containing receptors was reported by Tabushi and coworkers.<sup>[41]</sup> The  $\beta$ -cyclodextrin ( $\beta$ -CD)-based receptor **19**, having a triazaalkane arm that binds zinc(II), forms stable complexes with adamantane-1-carboxylates ( $10^3 < K_{\text{ass}} < 10^5 \text{ M}^{-1}$ ) in  $\text{H}_2\text{O}$  at pH 10. Particularly interesting in this context are the transition metal complexes of polyazamacrocycles.



An early example of carboxylate anion binding was reported by Martell and Motekaitis.<sup>[42]</sup> The hexaaza-24-crown-8 (**20**) binds two  $\text{Co(II)}$  ions, and an oxalate dianion can bridge between the two metal centers. If two nitrogen atoms are protonated, the macrocycle binds to a single metal ion. However, the oxalate anion is bound to the  $\text{Co(II)}$  on one end of the macrocycle and to the protonated amine of the other end. In his extensive model studies for molecular recognition of carbonic anhydrases and carboxypeptidases, Kimura<sup>[43]</sup> produced several macrocyclic polyamines, which recognize anionic species when bound to  $\text{Zn(II)}$  ions. Although  $\text{Zn(II)}$ -1,5,9-triazacyclododecane<sup>[44]</sup> binds very strongly hydroxide anion (**21**) ( $\log K_{\text{ass}} = 6.4$ ) it also interacts with acetate anion ( $\log K_{\text{ass}} = 2.6$ ), which is an inhibitor of carbonic anhydrase.<sup>[45]</sup>



An interesting example of carboxylate anion recognition by a  $\text{Zn(II)}$  complex of a cyclen macrocycle having an acridine-pendant arm was reported by the same Japanese group.<sup>[46]</sup> Compound **22** is able to form a strong complex with benzoate anion in aqueous solution ( $\log K_{\text{ass}} = 2.25$ ).

Even more interesting is the observation that the terephthalate dianion forms an insoluble complex with this last host. The X-ray crystal structure of the complex shows that the terephthalate anion acts as a bridge between two macrocycles by interacting with two complexed  $\text{Zn(II)}$  ions (Fig. 1).

Inspection of the crystal lattice reveals that a well-organized chainlike self-assembled aggregate forms through the action of several supramolecular interactions such as metal coordination,  $\pi$ - $\pi$  stacking, and

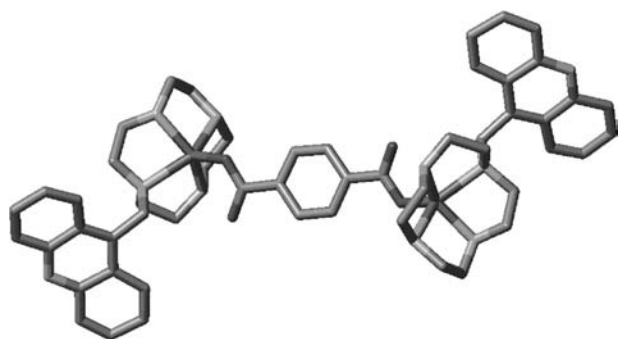
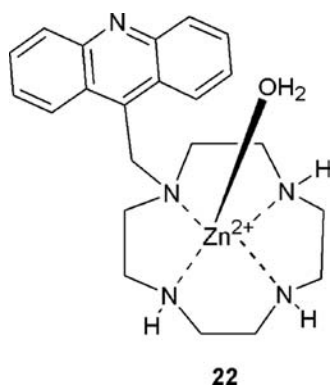
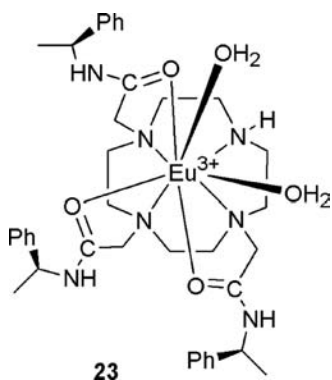


**Fig. 1** X-ray crystal structure of complex **22** and terephthalate anion.

solvent stabilization. The phthalate and isophthalate anion form similar 2:1 host/guest complexes, which, however, are water soluble. This circumstance allowed an easy separation of the phthalate *para* isomer with respect to the *ortho* and *meta* by crystallization.

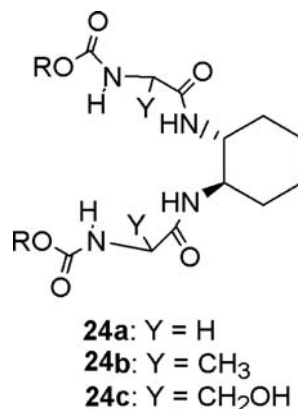
Lanthanide complexes have also been used as receptors for anions in general, and for carboxylates in particular. Parker and coworkers have used the 1,4,6,10-tetraazacyclododecane derivative with chiral side chains, which binds  $\text{Eu}^{3+}$  and  $\text{Tb}^{3+}$  through the four nitrogen atoms of the macrocycle and by the three amide oxygen atoms of the side arms. Two water molecules are also bound to complete the coordination sphere of the metal ion (**23**).<sup>[47,48]</sup>



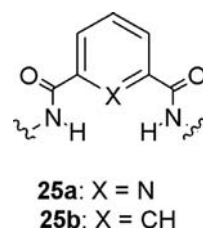
Carboxylate anions can displace these bound water molecules giving complexes characterized by binding constants that can reach a value of  $K_{\text{ass}} > 40000 \text{ M}^{-1}$  for citrate and malonate anions.

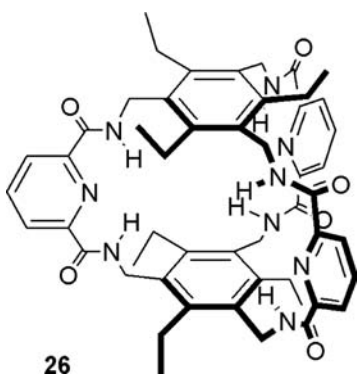
## NEUTRAL, HYDROGEN BONDING RECEPTORS

Many proteins and natural polypeptides are known to bind anions via hydrogen bonding involving the NH amide groups. Therefore, the incorporation of these groups into cleftlike or macrocyclic compounds has been considered as the most promising biomimetic approach in designing new receptors for carboxylate anion recognition.<sup>[49,50]</sup> Ten years ago, Hamilton and coworkers<sup>[51]</sup> reported the first example of a multiple-hydrogen-bonding receptor family **24**. The investigation of the molecular recognition properties of **24** actually revealed that urethane NHs, and serine OHs in the case of **24c**, rather than amide NHs are involved in the carboxylate anion complexation, suggesting other possibilities for the binding of this species. The association constant between **24c** and acetate anion was  $2.7 \times 10^5 \text{ M}^{-1}$  in  $\text{CD}_3\text{CN}$ , three orders of magnitude higher than that of **24a** and **24b**.

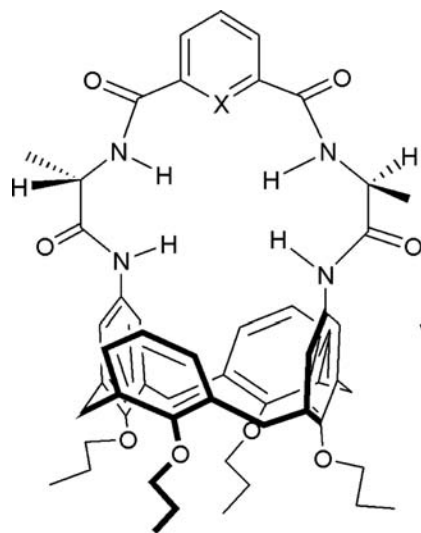
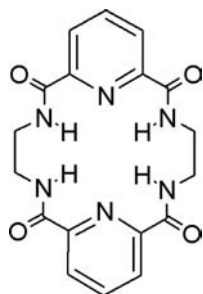


A common amide-containing molecular motif is the pyridine derivative **25a** and its benzene analogue **25b**. In the bicyclic cyclophane **26** reported by Bisson et al.<sup>[52]</sup> six NH protons converge toward the center of the binding pocket, as evidenced also in the X-ray crystal structure of the receptor. The structure of the 1:1 complex in the solid state with acetate ( $K_{\text{ass}} = 770 \text{ M}^{-1}$ ) shows the involvement of four of the six available NHs in the binding process.

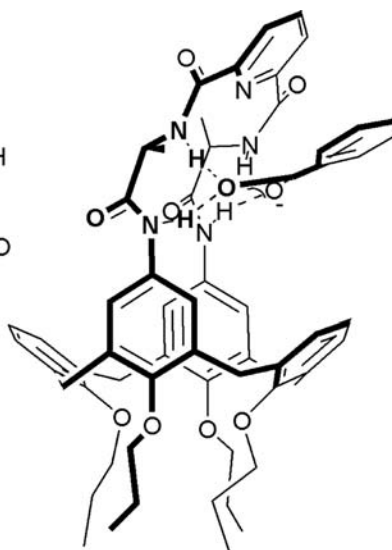




The identical pyridine moiety is found in the macrocyclic tetralactam **27**, which shows in DMSO a moderate selectivity for the acetate anion ( $K_{\text{ass}} = 2640 \text{ M}^{-1}$ ) over inorganic anions such as  $\text{F}^-$  ( $K_{\text{ass}} = 830 \text{ M}^{-1}$ ),  $\text{Cl}^-$  ( $K_{\text{ass}} = 65 \text{ M}^{-1}$ ), and  $\text{H}_2\text{PO}_4^-$  ( $K_{\text{ass}} = 1680 \text{ M}^{-1}$ ).<sup>[53]</sup> In solution the complex shows a 1:1 stoichiometry, whereas a 2:1 host:guest ratio is observed in the solid state. Note that only one oxygen atom of the carboxylate anion is interacting with each receptor molecule.



28b: X = CH



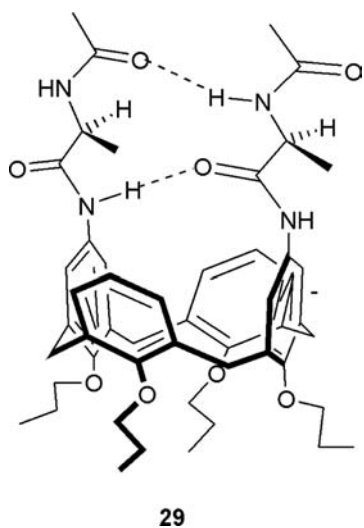
We exploited the dicarboxypyridine and the isophthalate units as rigid spacers bridging two alanine residues linked at the upper rim of a calix[4]arene.<sup>[54]</sup> The two peptidocalix[4]arenes **28a,b** present other two amide NH groups directly attached to the aromatic nuclei of the macrocyclic scaffold. The two macrobicyclic receptors show an interesting selectivity for the carboxylate over inorganic anions. The significant downfield shifts observed in  $\text{CDCl}_3$  for the signal relative to all NH protons by addition of substrates suggest their involvement in the binding.

The X-ray crystal structure of the free ligand **28a** shows the pyridine nucleus in the bridge to be tilted and almost parallel to one calix[4]arene aromatic nucleus. In this way a cleft is created and the host-guest interactions are maximized. This structure explains the great efficiency of these receptors toward the benzoate anion because the aromatic nucleus of the guest can interact with those of the host (**28a** × **benzoate**).

The preorganization of the two peptidocalixarenes plays an important role in determining the efficiency of their anion binding. In fact, the cleft-like analogue **29** shows the tendency to form intramolecular hydrogen bonds in  $\text{CDCl}_3$  and, as a consequence, it is a very poor anion receptor.<sup>[55]</sup>

One general way to increase the anion binding properties of amide receptors is to “activate” their hydrogen bonding donor ability through electron-withdrawing groups. Stibor and coworkers<sup>[56]</sup> introduced two pentafluorophenyl amide units at the upper rim of a calix[4]arene (**30**) and were able to observe in  $\text{CDCl}_3$  the complexation of dicarboxylate anions such as adipate ( $K_{\text{ass}} = 280 \text{ M}^{-1}$ ) and terephthalate





( $K_{\text{ass}} = 370 \text{ M}^{-1}$ ). Two pentafluorophenyl amides are also present in the calix[4]arene heteroditopic receptor **31** reported by our group.<sup>[57]</sup> The X-ray crystal structure of the complex obtained on addition of 1 equivalent of potassium acetate to a chloroform

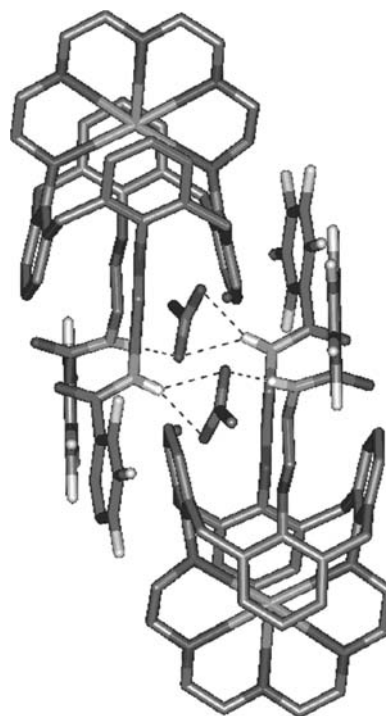
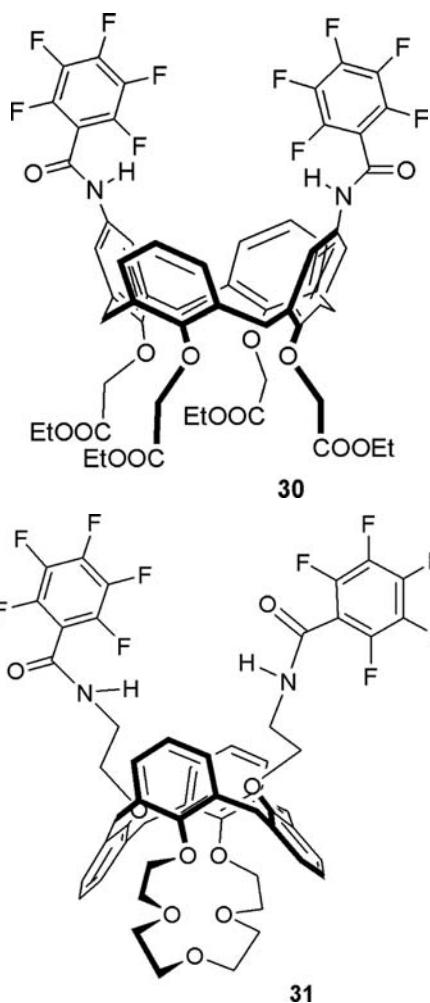
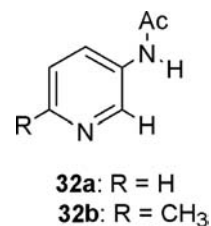


**Fig. 2** X-ray crystal structure of the complex between **31** and  $\text{CH}_3\text{COO}^- \text{K}^+$ .

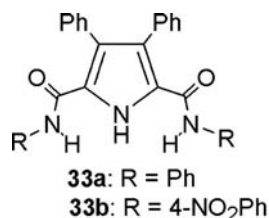
solution of the host shows an interesting 2:2:2 ligand:cation:anion stoichiometry (Fig. 2). This supramolecular structure is assembled by the simultaneous action of several non-covalent interactions, with each acetate ion bridging two host molecules through hydrogen bonding with their amide NHs.

In the simple 3-acetylaminopyridine **32a**, which interacts in  $\text{DMSO-}d_6$  with benzoate anion also through the more acidic protons in *ortho* and *para* position, the methylation of the pyridine nitrogen and the consequent introduction of a positive charge close to the hydrogen bonding donor groups enhances the affinity for the substrate.<sup>[58]</sup> Linking two **32b** units with a suitable spacer leads to interesting receptors able to complex adipate in 10%  $\text{D}_2\text{O}/\text{DMSO-}d_6$  with  $K_{\text{ass}} > 10^3 \text{ M}^{-1}$ .



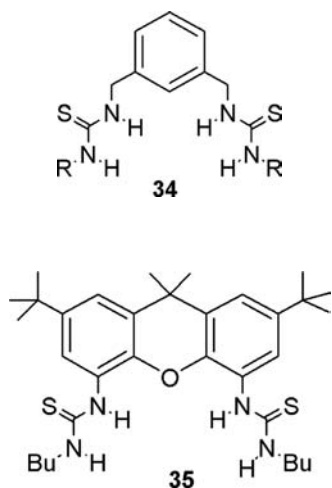
A series of diamidopyrrole-based compounds (**33**) containing amide groups has been prepared and studied by Gale and coworkers.<sup>[59]</sup> The benzoate complex in the solid state shows the cleft mode of binding with

all the three NH groups donating hydrogen bonds.<sup>[60]</sup> The presence of strong electron-withdrawing groups in **33b** increases the association for this anion ( $K_{\text{ass}} = 4150 \text{ M}^{-1}$ )<sup>[61]</sup> with respect to **33a** ( $K_{\text{ass}} = 560 \text{ M}^{-1}$ ) in 0.5%  $\text{D}_2\text{O}/\text{DMSO}$ .<sup>[59]</sup>



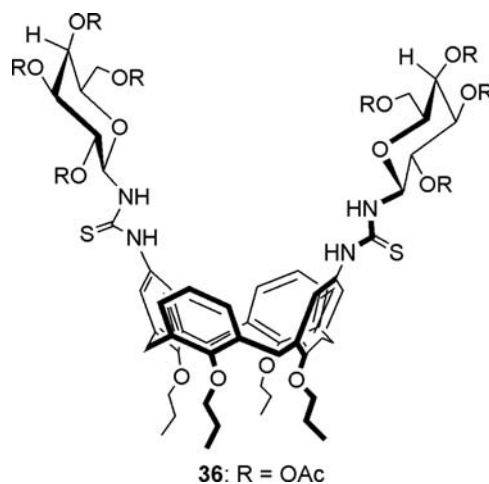
Since 1992,<sup>[62]</sup> urea and thiourea groups have been extensively used as neutral binding groups for anions.

An impressive series of cleftlike receptors containing two of these units have been reported. In general, a strong competition by the dihydrogen phosphate anion  $\text{H}_2\text{PO}_4^-$  is observed and often this substrate turned out to be the most efficiently bound. Buhlmann et al.<sup>[63]</sup> synthesized bithiourea receptors with a different degree of conformational freedom, observing an interesting positive effect of the host preorganization on its recognition properties. An increase of the association constant with acetate from  $470 \text{ M}^{-1}$  for compound **34** to  $38,000 \text{ M}^{-1}$  for **35** underlines the importance of this factor, also with regard to the absolute values of  $K_{\text{ass}}$ , considering that the solvent used is DMSO.

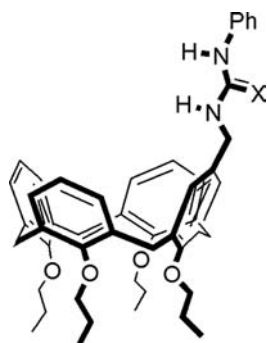


We have used glycosyl thioureido groups to functionalize the upper rim of calix[4]arenes.<sup>[64]</sup> Di- (e.g., **36**) and tetraglycosylated derivatives have been obtained with the goal of developing novel molecular delivery systems that exploit the anion recognition properties of the urea groups and the specific recognition ability of the glycoside units toward biological targets. Besides carboxylates, phosphate-containing substrates are complexed to the same extent and the binding in

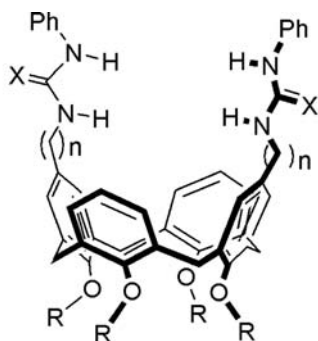
DMSO-*d*<sub>6</sub> is weaker than that found with simpler monothiourea receptors,<sup>[65]</sup> probably because of the steric crowding around the binding region. On the other hand, an interesting increase of the association constant is observed moving from acetate ( $K_{\text{ass}} = 17 \text{ M}^{-1}$ ) to benzoate ( $K_{\text{ass}} = 103 \text{ M}^{-1}$ ), suggesting a possible secondary interaction between the aromatic tail of the guest and the carbohydrate units. Furthermore, a specific interaction with selective carbohydrate-binding proteins discloses the possibility of vehiculate biologically active carboxylates toward relevant biomacromolecules. We have also explored the complexation properties of other calixarenes functionalized with urea and thiourea groups. The monothiourea **37** showed the best affinity with carboxylates ( $K_{\text{ass}} = 60\text{--}340 \text{ M}^{-1}$ ), over  $\text{H}_2\text{PO}_4^-$  and spherical anions ( $K_{\text{ass}} < 10 \text{ M}^{-1}$ ).<sup>[66]</sup> The higher values of association observed with benzoate, butyrate, and phenylacetate, compared with acetate, have been explained by the presence of additional weak interactions between the guest side groups and the cavity of the macrocycle. On the contrary, for acetate, an external binding mode was proposed. The opposite is observed with the bisurea receptor **38**, for which a significant preference for acetate ( $K_{\text{ass}} = 2200 \text{ M}^{-1}$ ) is evidenced because of urea-anion and  $\text{CH}_3\text{-}\pi$  interactions. The monourea **39** shows a behavior comparable with that of the thiourea analogue **37**, without a relevant decrease in efficiency despite the lower acidity of its NH protons. More efficient and with a remarkable selectivity for benzoate ( $K_{\text{ass}} = 1.61 \times 10^5 \text{ M}^{-1}$  in  $\text{CDCl}_3/\text{CD}_3\text{CN}$  4/1) is the bisurea **40** reported by Budka et al.<sup>[67]</sup> where the phenylthiourea groups are directly linked to the aromatic rings.



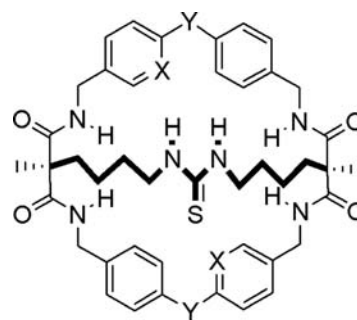
The insertion of the same binding group at the upper rim of a calix[4]arene tetramide gives rise to the ditopic receptors **41** and **42**.<sup>[68]</sup> When the thiourea NH is directly linked to the aromatic ring of the calixarene platform (**42**), the complexation of sodium ion at



37: X = S  
39: X = O

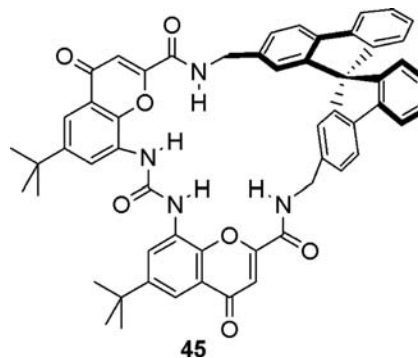


38: R = CH<sub>2</sub>CH<sub>2</sub>CH<sub>3</sub>; X = O; n = 1  
40: R = CH<sub>2</sub>CH<sub>2</sub>CH<sub>3</sub>; X = O; n = 0  
41: R = CH<sub>2</sub>C(O)NEt<sub>2</sub>; X = S; n = 1  
42: R = CH<sub>2</sub>C(O)NEt<sub>2</sub>; X = S; n = 0



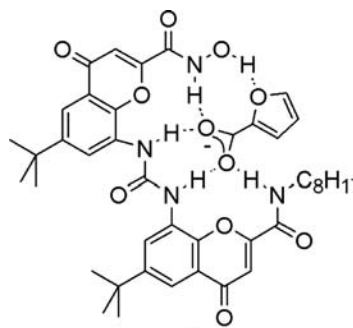
43: Y = CH<sub>2</sub>; X = CH  
44: Y = O; X = N

Another important class of receptors, with similar structural motifs, is that reported by de la Torre et al. and based on chromenones.<sup>[71]</sup> The central urea unit of **45** and **46** interacts with the carboxylate anion whereas the NH amide protons strengthen the complexation by coordinating the *anti* lone pair of the carboxylate oxygen atoms. A spirobifluorene moiety attached to the amide groups confers to macrocycle **45** an interesting enantioselectivity in recognizing the tetrabutylammonium salts of (*S*) and (*R*) lactic acid with  $K_{\text{ass}}$  of  $3.5 \times 10^3$  and  $3.5 \times 10^4 \text{ M}^{-1}$ , respectively.<sup>[72]</sup>



45

Substrates having more hydrogen bonding acceptor groups, such as carboxylates of  $\alpha$ -heterocyclic and  $\alpha$ -keto acids, get benefit by the presence of additional hydrogen bonding donor groups (e.g., **46**) in comparison with simple carboxylate anions.<sup>[71]</sup>



46

the lower rim determines a positive cooperative effect since the acidity of the NH groups increases.

In some receptors, a single thiourea unit is present in the structure accompanied by carboxamide groups, which actively cooperate in the complexation process. Important examples of these host molecules are the macrobicycles **43** designed by Kilburn.<sup>[69,70]</sup> The complexation studies toward a series of simple carboxylates and anions of *N*-acetyl *L*- and *D*-amino acids evidence the predominance of thiourea in the interaction with the substrates. In the case of the *D*-enantiomers, the data are quite consistent with an external 1:1 complex involving only the thiourea unit, but with the *L*-amino acids the complexation takes place within the cavity of the receptor involving also the amide groups, and this results in a higher association constant ( $1.3 \times 10^5 \text{ M}^{-1}$  in CDCl<sub>3</sub>) with the *N*<sup>ε</sup>-Ac-*L*-lysine. The presence of a pyridine unit in the bisaryl linkers (**44**) provides an additional hydrogen-bonding functionality that, in fact, seems to determine the mode of binding of *N*-Ac-*L*-asparagine, which interacts with its CONH<sub>2</sub> side chain ( $K_{\text{ass}} = 5.5 \times 10^4 \text{ M}^{-1}$  in CH<sub>2</sub>Cl<sub>2</sub>).

## CONCLUSION

Historically, the first supramolecular interactions to be exploited in synthetic receptors for anion recognition, and for carboxylate as well, were electrostatic or hydrogen bonds strengthened by positive charges as, e.g., in protonated macrocyclic amines. During the years, because of a growing interest in the biomimetic approach for the design of anion receptors, metal-containing macrocycles or hosts having only neutral, hydrogen bonding donor groups have been used more extensively, indicating a tendency that will probably continue in the near future. Besides representing interesting models for biological recognition involving carboxylates, these synthetic receptors constituted the active core of sensors and other supramolecular devices. Once the rules that control the specific molecular recognition of carboxylate anions are completely mastered, one can easily forecast that specially designed multivalent supramolecular systems will be synthesized and used, inter alia, to produce nanoscale, supramolecular functional devices based on carboxylate–receptor interaction.

## ACKNOWLEDGMENTS

We thank the Ministero dell'Istruzione, dell'Università e della Ricerca (M.I.U.R., "Supramolecular Devices" Project) and FIRB (Project RBNE019H9K Manipolazione molecolare per macchine nanometriche) for financial support of this research.

## REFERENCES

- Williams, D.H.; Bardsley, B. The vancomycin group of antibiotics and the fight against resistant bacteria. *Angew. Chem., Int. Ed. Engl.* **1999**, *38* (9), 1173–1193.
- Abeles, R.H.; Frey, P.A.; Jencks, W.P. Glycolysis and the Tricarboxylic Acid Cycle. In *Biochemistry*; Jones and Bartlett Publishers: Boston, 1992; 567–602.
- Hofmann, B.; Tolzer, S.; Pelletier, I.; Altenbuchner, J.; van Pee, K.H.; Hecht, H.J. Structural investigation of the cofactor-free chloroperoxidases. *J. Mol. Biol.* **1998**, *279* (4), 889–900.
- Morrow, J.D.; Jackson Roberts, L., II. Analgesic–antipyretic and antiinflammatory agents and drugs employed in the treatment of gout. In *Goodman & Gilman's: The Pharmacological Basis of Therapeutics*; Limbird, L.E., Hardman, J.G., Gilman, A.G., Eds.; McGraw-Hill Professional: New York, 2001; 687–732.
- Gale, P.A. Anion coordination and anion-directed assembly: Highlights from 1997 and 1998. *Coord. Chem. Rev.* **2000**, *199*, 181–233.
- Seel, C.; Galan, A.; de Mendoza, J. Molecular recognition of organic-acids and anions—Receptor models

- for carboxylates, amino-acids, and nucleotides. *Top. Curr. Chem.* **1995**, *175*, 101–132.
- Beer, P.D.; Gale, P.A. Anion recognition and sensing: The state of the art and future perspectives. *Angew. Chem., Int. Ed. Engl.* **2001**, *40* (3), 487–516.
  - Fitzmaurice, R.J.; Kyne, G.M.; Douheret, D.; Kilburn, J.D. Synthetic receptors for carboxylic acids and carboxylates. *J. Chem. Soc., Perkin Trans.* **2002**, *1* (7), 841–864.
  - Llinares, J.M.; Powell, D.; Bowman-James, K. Ammonium based anion receptors. *Coord. Chem. Rev.* **2003**, *240* (1–2), 57–75.
  - Kimura, E.; Sakonaka, A.; Yatsunami, T.; Kodama, M. Macromonocyclic polyamines as specific receptors for tricarboxylate-cycle anions. *J. Am. Chem. Soc.* **1981**, *103* (11), 3041–3045.
  - Dietrich, B.; Hosseini, M.W.; Lehn, J.M.; Sessions, R.B. Anion receptor molecules. Synthesis and anion-binding properties of polyammonium macrocycles. *J. Am. Chem. Soc.* **1981**, *103* (5), 1282–1283.
  - Daniele, P.G.; De Stefano, C.; Giuffrè, O.; Prenesti, E.; Sammartano, S. Interaction of L-malic acid with alkaline metals and open chain polyammonium cations in aqueous solution. *Talanta* **2001**, *54* (1), 25–36.
  - De Robertis, A.; De Stefano, C.; Foti, C.; Giuffrè, O.; Sammartano, S. Thermodynamic parameters for the binding of inorganic and organic anions by biogenic polyammonium cations. *Talanta* **2001**, *54* (6), 1135–1152.
  - Alfonso, I.; Rebolledo, F.; Gotor, V. Optically active dioxatetraazamacrocycles: Chemoenzymatic syntheses and applications in chiral anion recognition. *Chem. Eur. J.* **2000**, *6* (18), 3331–3388.
  - Alfonso, I.; Dietrich, B.; Rebolledo, F.; Gotor, V.; Lehn, J.M. Optically active hexaazamacrocycles: Protonation behavior and chiral-anion recognition. *Helv. Chim. Acta* **2001**, *84* (2), 280–295.
  - Pant, N.; Hamilton, A.D. Carboxylic acid complexation by a synthetic analog of the "carboxylate-binding pocket" of vancomycin. *J. Am. Chem. Soc.* **1988**, *110* (6), 2002–2003.
  - Pieters, R.J. Synthesis and binding studies of carboxylate binding pocket analogs of vancomycin. *Tetrahedron Lett.* **2000**, *41* (39), 7541–7545.
  - Casnati, A.; Sansone, F.; Ungaro, R. Peptido- and glycolixarenes: Playing with hydrogen bonds around hydrophobic cavities. *Acc. Chem. Res.* **2003**, *36* (4), 246–254.
  - Casnati, A.; Fabbi, M.; Pelizzi, N.; Pochini, A.; Sansone, F.; Ungaro, R.; Di Modugno, E.; Tarzia, G. Synthesis, antimicrobial activity and binding properties of calix[4]arene based vancomycin mimics. *Bioorg. Med. Chem. Lett.* **1996**, *6* (22), 2699–2704.
  - Frish, L.; Sansone, F.; Casnati, A.; Ungaro, R.; Cohen, Y. Complexation of a peptidocalix[4]arene, a vancomycin mimic, with alanine-containing guests by NMR diffusion measurements. *J. Org. Chem.* **2000**, *65* (16), 5026–5030.
  - Hinzen, B.; Seiler, P.; Diederich, F. Mimicking the vancomycin carboxylate binding site: Synthetic receptors for sulfonates, carboxylates, and N-protected

- alpha-amino acids in water. *Helv. Chim. Acta* **1996**, *79* (4), 942–960.
22. Hossain, M.A.; Schneider, H.J. Supramolecular chemistry, part 85. Flexibility, association constants, and salt effects in organic ion pairs: How single bonds affect molecular recognition. *Chem. Eur. J.* **1999**, *5* (4), 1284–1290.
  23. Best, M.D.; Tobey, S.L.; Anslyn, E.V. Abiotic guanidinium containing receptors for anionic species. *Coord. Chem. Rev.* **2003**, *240* (1–2), 3–15.
  24. Linton, B.; Hamilton, A.D. Calorimetric investigation of guanidinium–carboxylate interactions. *Tetrahedron* **1999**, *55* (19), 6027–6038.
  25. Schmuck, C. Carboxylate binding by 2-(guanidiniocarbonyl)pyrrole receptors in aqueous solvents: Improving the binding properties of guanidinium cations through additional hydrogen bonds. *Chem. Eur. J.* **2000**, *6* (4), 709–718.
  26. Schmuck, C. Carboxylate binding by 2-(guanidiniocarbonyl)pyrrole receptors in aqueous solvents: Improving the binding properties of guanidinium cations through additional hydrogen bonds (Vol. 6, p. 709, 2000). *Chem. Eur. J.* **2000**, *6* (8), 1279.
  27. Davies, M.; Bonnat, M.; Guillier, F.; Kilburn, J.D.; Bradley, M. Screening an inverted peptide library in water with a guanidinium-based tweezer receptor. *J. Org. Chem.* **1998**, *63* (24), 8696–8703.
  28. Gleich, A.; Schmidtchen, F.P.; Mikulcic, P.; Mueller, G. Enantiodifferentiation of carboxylates by chiral building blocks for abiotic anion receptors. *J. Chem. Soc., Chem. Commun* **1990**, (1), 55–57.
  29. Echavarren, A.; Galan, A.; de Mendoza, J.; Salmeron, A.; Lehn, J.M. Anion–receptor molecules: Synthesis of a chiral and functionalized binding subunit, a bicyclic guanidinium group derived from L- or D-asparagine. *Helv. Chim. Acta* **1988**, *71* (4), 685–693.
  30. Boyle, P.H.; Davis, A.P.; Dempsey, K.J.; Hosken, G.D. (4*S*,8*S*)-4,8-Bis(diphenylmethyl)-1,5,7-triazabicyclo[4.4.0]dec-5-ene a hindered, chiral, bicyclic guanidine base with effective C2-symmetry. *J. Chem. Soc., Chem. Commun* **1994**, (16), 1875–1876.
  31. Galan, A.; Andreu, D.; Echavarren, A.M.; Prados, P.; de Mendoza, J. A receptor for the enantioselective recognition of phenylalanine and tryptophan under neutral conditions. *J. Am. Chem. Soc.* **1992**, *114* (4), 1511–1512.
  32. Metzger, A.; Gloe, K.; Stephan, H.; Schmidtchen, F.P. Molecular recognition and phase transfer of underivatized amino acids by a foldable artificial host. *J. Org. Chem.* **1996**, *61* (6), 2051–2055.
  33. Segura, M.; Alcazar, V.; Prados, P.; de Mendoza, J. Synthetic receptors for uronic acid salts based on bicyclic guanidinium and deoxycholic acid subunits. *Tetrahedron* **1997**, *53* (38), 13119–13128.
  34. Lawless, L.J.; Blackburn, A.G.; Ayling, A.J.; Perez-Payan, M.N.; Davis, A.P. Steroidal guanidines as enantioselective receptors for *N*-acyl alpha-amino acids. Part 1. 3 alpha-Guanylated carbamates derived from cholic acid. *J. Chem. Soc., Perkin Trans.* **2001**, *1* (11), 1329–1341.
  35. Smukste, I.; House, B.E.; Smithrud, D.B. Host-[2]-rotaxane: Advantage of converging functional groups for guest recognition. *J. Org. Chem.* **2003**, *68* (7), 2559–2571.
  36. Metzger, A.; Anslyn, E.V. A chemosensor for citrate in beverages. *Angew. Chem., Int. Ed. Engl.* **1998**, *37* (5), 649–652.
  37. Metzger, A.; Lynch, V.M.; Anslyn, E.V. A synthetic receptor selective for citrate. *Angew. Chem., Int. Ed. Engl.* **1997**, *36* (8), 862–865.
  38. Sebo, L.; Schweizer, B.; Diederich, F. Cleft-type diamidinium receptors for dicarboxylate binding in protic solvents. *Helv. Chim. Acta* **2000**, *83* (1), 80–92.
  39. Sebo, L.; Diederich, F.; Gramlich, V. Tetrakis(phenylamidinium)-substituted resorcin[4]arene receptors for the complexation of dicarboxylates and phosphates in protic solvents. *Helv. Chim. Acta* **2000**, *83* (1), 93–113.
  40. Camiolo, S.; Gale, P.A.; Ogden, M.I.; Skelton, B.W.; White, A.H. Solid-state and solution studies of bis-carboxylate binding by bis-amidinium calix[4]arenes. *J. Chem. Soc., Perkin Trans.* **2001**, *2* (8), 1294–1298.
  41. Tabushi, I.; Shimizu, N.; Sugimoto, T.; Shiozuka, M.; Yamamura, K. Cyclodextrin flexibly capped with metal ion. *J. Am. Chem. Soc.* **1977**, *99* (21), 7100–7102.
  42. Martell, A.E.; Motekaitis, R.J. Formation and degradation of an oxalato- and peroxo-bridged dicobalt BISDIEN dioxygen complex: Binuclear complexes as hosts for the activation of two coordinated guests. *J. Am. Chem. Soc.* **1988**, *110* (24), 8059–8064.
  43. Kimura, E. Model studies for molecular recognition of carbonic anhydrase and carboxypeptidase. *Acc. Chem. Res.* **2001**, *34* (2), 171–179.
  44. Reichenbach-Klinke, R.; Konig, B. Metal complexes of azacrown ethers in molecular recognition and catalysis. *J. Chem. Soc., Dalton Trans.* **2002**, (2), 121–130.
  45. Bertini, I.; Luchinat, C. Cobalt(II) as a probe of the structure and function of carbonic anhydrase. *Acc. Chem. Res.* **1983**, *16* (8), 272–279.
  46. Kimura, E.; Ikeda, T.; Shionoya, M.; Shiro, M. Molecular recognition of terephthalic acid by supramolecular self-assembly of an acridine-pendant cyclen–Zn-II complex. *Angew. Chem., Int. Ed. Engl.* **1995**, *34* (6), 663–664.
  47. Dickins, R.S.; Gunlaugsson, T.; Parker, D.; Peacock, R.D. Reversible anion binding in aqueous solution at a cationic heptacoordinate lanthanide centre: Selective bicarbonate sensing by time-delayed luminescence. *Chem. Commun.* **1998**, (16), 1643–1644.
  48. Bruce, J.I.; Dickins, R.S.; Govenlock, L.J.; Gunlaugsson, T.; Lopinski, S.; Lowe, M.P.; Parker, D.; Peacock, R.D.; Perry, J.J.B.; Aime, S.; Botta, M. The selectivity of reversible oxy-anion binding in aqueous solution at a chiral europium and terbium center: Signaling of carbonate chelation by changes in the form and circular polarization of luminescence emission. *J. Am. Chem. Soc.* **2000**, *122* (40), 9674–9684.
  49. Choi, K.H.; Hamilton, A.D. Macrocyclic anion receptors based on directed hydrogen bonding interactions. *Coord. Chem. Rev.* **2003**, *240* (1–2), 101–110.
  50. Bondy, C.R.; Loeb, S.J. Amide based receptors for anions. *Coord. Chem. Rev.* **2003**, *240* (1–2), 77–99.

51. Albert, J.S.; Hamilton, A.D. Synthetic analogs of the ristocetin binding-site: Neutral, multidentate receptors for carboxylate recognition. *Tetrahedron Lett.* **1993**, *34* (46), 7363–7366.
52. Bisson, A.P.; Lynch, V.M.; Monahan, M.K.C.; Anslyn, E.V. Recognition of anions through NH- $\pi$  hydrogen bonds in a bicyclic cyclophane-selectivity for nitrate. *Angew. Chem., Int. Ed. Engl.* **1997**, *36* (21), 2340–2342.
53. Szumna, A.; Jurczak, J. A new macrocyclic polylactam-type neutral receptor for anions—Structural aspects of anion recognition. *Eur. J. Org. Chem.* **2001**, (21), 4031–4039.
54. Sansone, F.; Baldini, L.; Casnati, A.; Lazzarotto, M.; Ugozzoli, F.; Ungaro, R. Biomimetic macrocyclic receptors for carboxylate anion recognition based on C-linked peptidocalix[4]arenes. *Proc. Natl. Acad. Sci. U. S. A.* **2002**, *99* (8), 4842–4847.
55. Lazzarotto, M.; Sansone, F.; Baldini, L.; Casnati, A.; Cozzini, P.; Ungaro, R. Synthesis and properties of upper rim C-linked peptidocalix[4]arenes. *Eur. J. Org. Chem.* **2001**, (3), 595–602.
56. Stibor, I.; Hafeed, D.S.M.; Lhotak, P.; Hodacova, J.; Koca, J.; Cajan, M. From the amide bond activation to simultaneous recognition of anion–cation couple. *Gazz. Chim. Ital.* **1997**, *127* (11), 673–685.
57. Casnati, A.; Massera, C.; Pelizzi, N.; Stibor, I.; Pinkassik, E.; Ugozzoli, F.; Ungaro, R. A novel self-assembled supramolecular architecture involving cation, anion and a calix[4]arene heteroditopic receptor. *Tetrahedron Lett.* **2002**, *43* (41), 7311–7314.
58. Jeong, K.S.; Cho, Y.L. Highly strong complexation of carboxylates with 1-alkylpyridinium receptors in polar solvents. *Tetrahedron Lett.* **1997**, *38* (18), 3279–3282.
59. Gale, P.A.; Camiolo, S.; Chapman, C.P.; Light, M.E.; Hursthouse, M.B. Hydrogen-bonding pyrrolic amide cleft anion receptors. *Tetrahedron Lett.* **2001**, *42* (30), 5095–5097.
60. Camiolo, S.; Gale, P.A.; Hursthouse, M.B.; Light, M.E. Confirmation of a “cleft-mode” of binding in a 2,5-diamidopyrrole anion receptor in the solid state. *Tetrahedron Lett.* **2002**, *43* (39), 6995–6996.
61. Camiolo, S.; Gale, P.A.; Hursthouse, M.B.; Light, M.E. Nitrophenyl derivatives of pyrrole 2,5-diamides: Structural behaviour, anion binding and colour change signalled deprotonation. *Org. Biomol. Chem.* **2003**, *1* (4), 741–744.
62. Smith, P.J.; Reddington, M.V.; Wilcox, C.S. Ion-pair binding by a urea in chloroform solution. *Tetrahedron Lett.* **1992**, *33* (41), 6085–6088.
63. Buhlmann, P.; Nishizawa, S.; Xiao, K.P.; Umezawa, Y. Strong hydrogen bond-mediated complexation of  $\text{H}_2\text{PO}_4^-$  by neutral bis-thiourea hosts. *Tetrahedron* **1997**, *53* (5), 1647–1654.
64. Sansone, F.; Chierici, E.; Casnati, A.; Ungaro, R. Thiourea-linked upper rim calix[4]arene neoglycoconjugates: Synthesis, conformations and binding properties. *Org. Biomol. Chem.* **2003**, *1* (10), 1802–1809.
65. Fan, E.; Van Arman, S.A.; Kincaid, S.; Hamilton, A.D. Molecular recognition: Hydrogen-bonding receptors that function in highly competitive solvents. *J. Am. Chem. Soc.* **1993**, *115* (1), 369–370.
66. Casnati, A.; Fochi, M.; Minari, P.; Pochini, A.; Reggiani, M.; Ungaro, R.; Reinhoudt, D.N. Upper-rim urea-derivatized calix[4]arenes as neutral receptors for monocarboxylate anions. *Gazz. Chim. Ital.* **1996**, *126* (2), 99–106.
67. Budka, J.; Lhotak, P.; Michlova, V.; Stibor, I. Urea derivatives of calix[4]arene 1,3-alternate: An anion receptor with profound negative allosteric effect. *Tetrahedron Lett.* **2001**, *42* (8), 1583–1586.
68. Pelizzi, N.; Casnati, A.; Friggeri, A.; Ungaro, R. Synthesis and properties of new calixarene-based ditopic receptors for the simultaneous complexation of cations and carboxylate anions. *J. Chem. Soc., Perkin Trans.* **1998**, *2* (6), 1307–1311.
69. Pernia, G.J.; Kilburn, J.D.; Essex, J.W.; Mortishire-Smith, R.J.; Rowley, M. Stabilization of a cis amide bond in a host–guest complex. *J. Am. Chem. Soc.* **1996**, *118* (42), 10220–10227.
70. Jullian, V.; Shepherd, E.; Gelbrich, T.; Hursthouse, M.B.; Kilburn, J.D. New macrobicyclic receptors for amino acids. *Tetrahedron Lett.* **2000**, *41* (20), 3963–3966.
71. de la Torre, M.F.; Campos, E.G.; Gonzalez, S.; Moran, J.R.; Caballero, M.C. Binding properties of an abiotic receptor for complexing carboxylates of  $\alpha$ -heterocyclic and  $\alpha$ -keto acids. *Tetrahedron* **2001**, *57* (18), 3945–3950.
72. Tejada, A.; Oliva, A.I.; Simon, L.; Grande, M.; Caballero, M.C.; Moran, J.R. A macrocyclic receptor for the chiral recognition of hydroxycarboxylates. *Tetrahedron Lett.* **2000**, *41* (23), 4563–4566.



# Bionanoparticles

**Krishnaswami S. Raja**

*Department of Chemistry, Scripps Research Institute, La Jolla, California, U.S.A.*

**Sukanta Dolai**

**Wei Shi**

*City University of New York, New York, New York, U.S.A.*

**Qian Wang**

*Department of Chemistry and Biochemistry, University of Southern Carolina, Columbia, South Carolina, U.S.A.*

## INTRODUCTION

Bionanoparticles are naturally produced entities that are of nanometer dimension. For aeons, nature has been an avid and extremely sophisticated exponent of nanoscience. Viruses and other protein assemblies such as the iron storage protein ferritin are examples of naturally occurring nanoparticles.<sup>[1]</sup> The branch of bionanotechnology in which naturally occurring nanoparticles are modified and manipulated for various applications is a rich and newly emerging field of research. The current research in this area can be broadly classified as host-guest chemistry (including biomineralization) and the bioconjugate chemistry of bionanoparticles.<sup>[2–7]</sup> Bionanoparticles have marvelous and complex structures. Understanding their basic structural arrangement is essential to appreciate how they may be exploited for chemical applications. A separate section is devoted in this review for each nanoparticle.

The host-guest chemistry based on bionanoparticles is discussed. Three systems—ferritin, cowpea chlorotic mottle virus (CCMV), and tobacco mosaic virus (TMV)—have recently been used to package hard and conducting inorganic materials. Hybrid conducting quantum nanodots can be selectively patterned on two-dimensional substrates by engineering recognition elements on the biomaterial component to recognize specific sites on the two-dimensional substrate. This is one of the most promising approaches for developing nanoelectronic devices. Some recent work using Filamentous Bacteriophage M13 to bind and align nanocrystals in an ordered array is described in the following section. In another section of the review, the bioconjugate chemistry of bionanoparticles, especially of the Cowpea Mosaic Virus (CPMV) system, the MS2 Bacteriophage, Tobacco Mosaic Virus, and the Hepatitis B Surface Antigen (HBsAg)

is covered. These have potential applications in both the areas of materials science and biomedical research. Several decades ago, Paul Ehrlich<sup>[8]</sup> pioneered the “magic bullet concept,” where he proposed that a drug could be targeted with the help of ligands having defined affinity for specific cells. His predictions are close to practical realization, an example of such a construct is a ligand-decorated bionanoparticle,<sup>[9]</sup> which can selectively target the receptors present on specific cell types, to package and deliver therapeutic genes/drugs to target cells. The last section of this review covers the recent development of using bionanoparticles, especially adenoviruses, for gene delivery.

The practical examples discussed in this entry serve as a tribute to the accuracy of many of Richard Feynman’s predictions in his classic talk titled “There is plenty of room at the bottom” on December 29, 1959, at the annual meeting of the American Physical Society at Caltech.<sup>[10]</sup>

## FERRITINS

Ferritins are iron storage protein cages belonging to the Class II diiron-carboxylate proteins.<sup>[11]</sup> All ferritins have the capacity to remove  $\text{Fe}^{2+}$  ions from solution in the presence of oxygen, and to deposit iron into the protein interior in a mineral form. Iron is stored as iron(III) oxy-hydroxide, mainly ferrihydrite ( $5\text{Fe}_2\text{O}_3 \cdot 9\text{H}_2\text{O}$ ). The tertiary and quaternary structure of ferritins is highly conserved. All ferritins are composed of 24 subunits arranged in 432 symmetry, which self-assemble to form a 12 nm diameter cage with a 7.5–8 nm diameter cavity. About 4000 iron atoms can be stored in the central core. The crystal structure of Bullfrog M Ferritin at 2.8 Å resolution is shown in Fig. 1.<sup>[12]</sup> The protein has both hydrophilic and hydrophobic channels. Most ferritins are very stable particles, which can withstand 65°C and

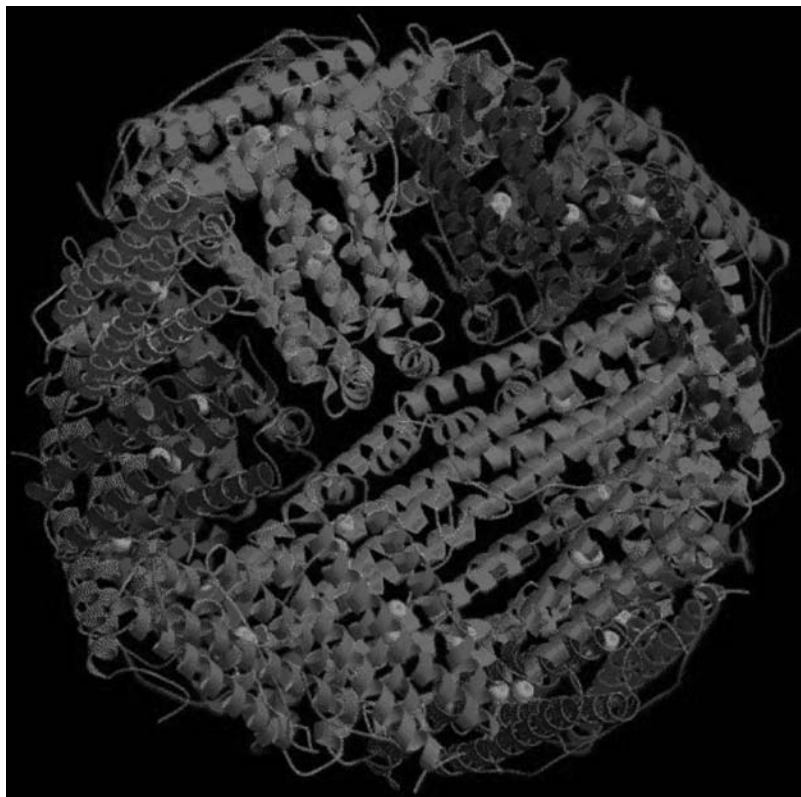


**Fig. 1** Crystal structure of Bullfrog M Ferritin. *Source:* From Protein Data Bank.

tolerate a pH range between 4 and 9 (<http://metallo.scripps.edu/PROMISE/FERRITIN.html>).

Douglas, Clark, and Rothschild<sup>[1]</sup> have used the crystalline proteinaceous surface layers of some bacteria as biologically produced nanoscale templates for lithography. Individual protein complexes of ferritin have been selectively self-assembled onto the metal-coated template. Yamashita<sup>[13]</sup> produced a two-dimensional array of ferritin by self-assembly at the air–water interface, which was then transferred onto a silicon surface. The protein coat of the ferritin molecules was then eliminated by heating at 500°C. Scanning electron microscopy (SEM) of the surface showed a well-ordered array of iron nanocrystals on the silicon surface. Atomic force microscopy (AFM), Fourier-transform infrared spectroscopy (FTIR), and weight measurement studies confirmed that the protein shell was indeed eliminated by the thermal treatment, leaving only the iron cores on the silicon substrate. The size and repeat distance of the iron cores was 6 and 12 nm, respectively. The arrays of nanocrystals produced by this process could be used for the fabrication of quantum electronic devices.

Ferritin has also been used as a catalyst for the selective hydroxylation of phenol using hydrogen peroxide as the oxidant.<sup>[14]</sup> Douglas and Stark<sup>[15]</sup> have used horse spleen ferritin as a constrained nanoreactor for the oxidative hydrolysis of Co(II) to achieve site-specific mineralization within the protein cage. The

catalytic effect promoting the mineralization process is driven by complementary electrostatic interactions between the protein interface and the incipient mineral. Wong et al.<sup>[16]</sup> have coupled long-chain primary amines to the surface carboxylic acid residues of ferritin, and the resulting alkylated nanoparticles were soluble and stable in methylene chloride. Transmission electron microscopy (TEM) and analytical ultracentrifugation analysis confirmed that the protein cages were indeed intact after derivatization and that they possess a significantly modified surface charge. However, the degree of derivatization of the ferritin molecules varied considerably; both high-performance liquid chromatography (HPLC) and mass spectroscopy (MS) studies confirmed the polydisperse nature of the samples.

### COWPEA CHLOROTIC MOTTLE VIRUS (CCMV)

Viruses are both important biological entities and chemical assemblies of fascinating structures and diversities. The structures of many viruses have been solved to near-atomic resolution. From a materials science viewpoint, these programmable nanoblocks have many advantages: 1) many viruses can be isolated in gram quantities; 2) most plant viruses cannot infect human beings and are biocompatible; 3) viruses display reactive functional groups on both the inside and outside surfaces of their coat protein, and by

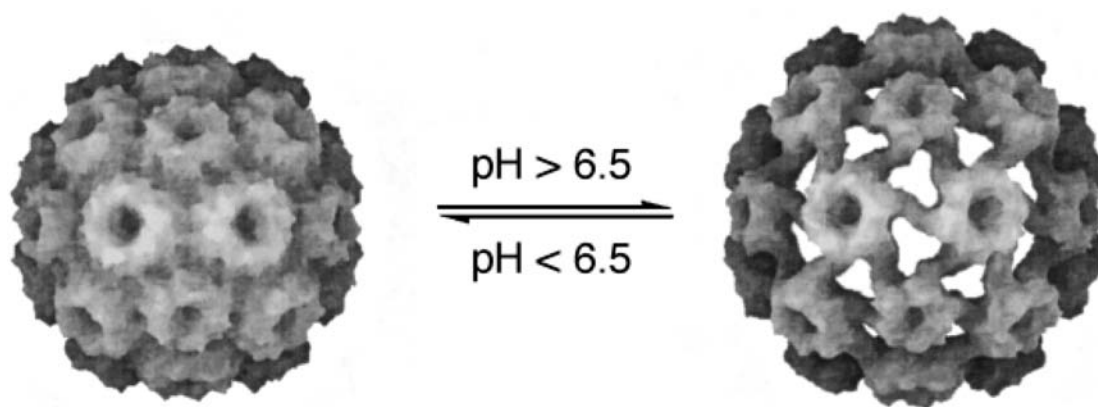


**Fig. 2** The collapsed (left) and swollen (right) forms of the cowpea chlorotic mottle virus (<http://mmtsb.scripps.edu/iper/iper.html>). Source: From Ref.<sup>[63]</sup>.

genetic manipulation, one can introduce amino acid residues with unique reactivity or even peptides with therapeutic properties in designated positions of the capsid protein. Biom mineralization studies based on viral scaffolds such as CCMV (in this section) is a mimicry of ferritin-based chemistry that nature has employed for aeons.

Douglas and Young used CCMV (Fig. 2) as a component to develop hybrid inorganic materials.<sup>[2,3]</sup> CCMV is an icosahedral virus composed of 180 identical 20 kDa protein subunits, which self-assemble around the viral nucleic acid to generate an intact icosahedral cage. The most important structural feature of CCMV is that it can undergo a reversible pH-dependent swelling, resulting in a 10% increase in virus size.<sup>[17,18]</sup> This transition is the result of an expansion at the pseudo threefold of the virus particle, which causes the formation of 60 separate openings, each ~20 Å in diameter, in the coat protein. The swollen virus allows free exchange between the virus cavity and the medium. In the non-swollen form, the pores are closed and no exchange of molecules takes place between the interior of the virus cavity and the bulk medium.

The inner surface of each protein subunit of CCMV presents nine basic residues (arginine and lysine) and this creates a highly positively charged interior, which presumably stabilizes the negatively charged nucleic acid. A wide variety of negatively charged poly-oxometallate species (vanadate, molybdate, and tungstate) were selectively mineralized within empty CCMV particles devoid of the nucleic acid; the size of the capsid cavity defines the size of mineralized particles.<sup>[2]</sup> The electrostatically driven mineralization was carried out at pH 5, at which the inorganic species underwent oligomerization and the viral pores closed. The mineralized viral particles were purified by sucrose gradient ultracentrifugation. Transmission electron microscopy images showed electron dense metal cores. Negative

staining was performed to confirm that the viral capsid protein was indeed intact.

Other negatively charged species that serve as a surrogate nucleic acid, such as the anionic polymer polyanetholesulfonic acid, have been encapsulated in CCMV; the virus gating mechanism coupled with an electrostatically driven internalization of the polymer was exploited to produce organic polymer–CCMV hybrid materials.<sup>[3]</sup> The polymer–virus hybrid materials were purified by sucrose gradient ultracentrifugation. The presence of the polymer was confirmed by ultraviolet (UV) spectroscopy and the intact nature of the particles was confirmed by TEM.

A genetically engineered mutant CCMV particle with a negatively charged interior (the nine basic residues at the N-terminus of CCMV were replaced with glutamic acid) was used to sequester nanoparticles of iron-oxide through spatially constrained oxidative hydrolysis of Fe(II); this serves as a ferritin mimic.<sup>[19]</sup> These semiconductor/metallic hybrid materials have potential applications in nanoelectronics and bionanotechnology.

### COWPEA MOSAIC VIRUS (CPMV)

Cowpea Mosaic Virus is a non-enveloped icosahedral plant virus, approximately 30 nm in diameter, which can be isolated from infected black eye pea plant in yields of 1–2 g per kg of leaves by using a simple and convenient procedure.<sup>[20]</sup> The physical, biological, and genetic properties of CPMV have been well characterized.<sup>[21,22]</sup> It is non-infectious toward other organisms and presents no biological hazard. Its structure has been determined to a resolution of 2.8 Å,<sup>[23]</sup> showing a picorna-like ( $T = 1$ ,  $P = 3$ ) protein shell (termed as “capsid”) composed of 60 copies of the asymmetric units. Each asymmetric unit contains three jellyroll  $\beta$ -sandwich folds formed by two polypeptides

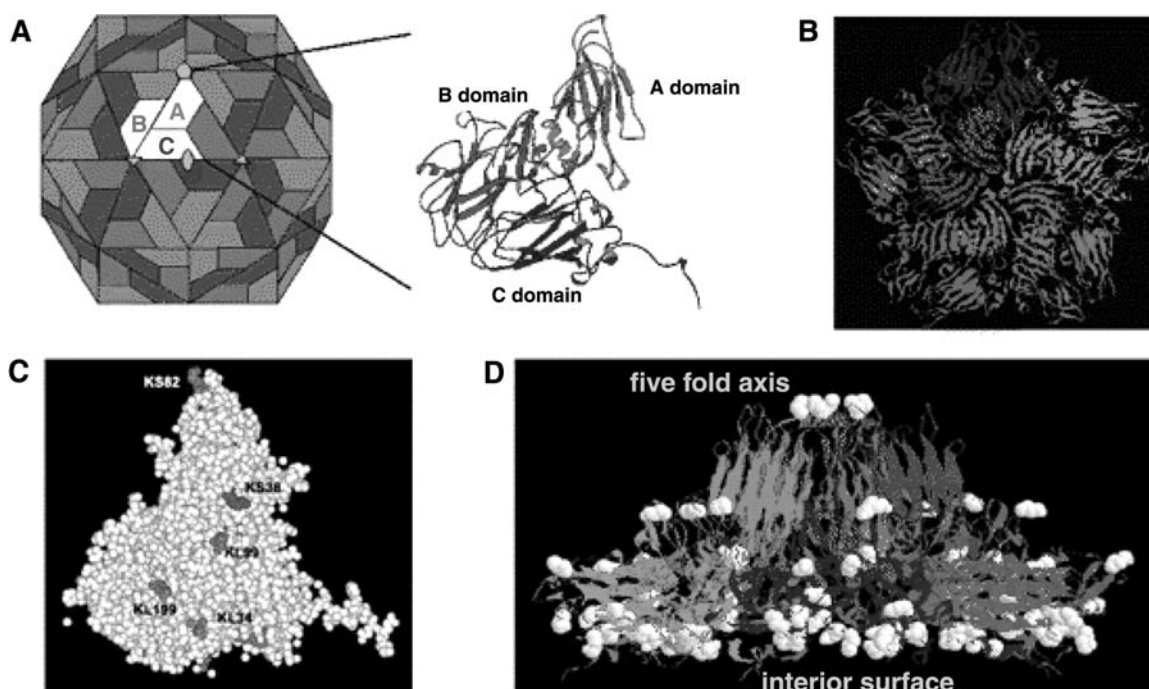


**Fig. 3** CPMV structure. (A) Left: A representation of CPMV showing the distribution of the two subunits comprising the “asymmetric unit,” 60 copies of which form the icosahedral particle. The trapezoids in red and green represent the two domains of the large subunit clustered around the threefold symmetry axes and the blue trapezoid represents the small subunit clustered about the fivefold symmetry axes. Right: Ribbon diagram of the two subunits. (B) Organization of five asymmetric units into the “pentamer” centered around a small hole at each fivefold axis. (C) Space filling model of the asymmetric units of coat protein showing the surface exposed lysines. (D) Side view of the ribbon diagram of the “pentamer” with all lysines highlighted. Most of the lysines are located at the interior surface of the protein cell to bind to the RNA inside.

termed as a “small” subunit, the A-domain; and a “large” subunit, the B + C-domains in Fig. 3. The CPMV particles are remarkably stable, maintaining their integrity at 60°C for at least 1 hr at pH range from 3.5 to 9. CPMV was the first virus to be treated as a natural analog of very large dendrimer<sup>[24,25]</sup> for organic reactions. It is also a powerful platform for bioconjugation and has been extensively studied as a model system.

Cowpea mosaic virus has five solvent exposed lysine residues per asymmetric subunit or 300 solvent exposed lysines per particle. Low molecular weight *N*-hydroxysuccinimide ester and isothiocyanate reagents have been employed to test the reactivity of the lysine residues of wild-type CPMV.<sup>[26]</sup> The pH of the reaction, the specific reagent employed, and the reagent/virus ratio used determine the number of dyes/reagent molecules attached per virion, at neutral pH the loading numbers reported are lower than that at higher pH. Loading numbers between 60 and 240 have been reported in literature depending on the ratio of reagent/virus and the pH of the buffer employed for bioconjugation.<sup>[26]</sup> The integrity of the reagent labeled virions was confirmed by sucrose gradient sedimentation and size exclusion fast performance liquid chromatography (FPLC).

The crystal structure of wild-type CPMV displays no free cysteine residue exposed on the exterior surface of the capsid. Chemically addressable cysteine residues have been introduced genetically at two solvent exposed sites on the exterior surface of CPMV.<sup>[27]</sup> Each of the virus mutants displays 60 of such insertions, arrayed in icosahedral symmetry on the 30 nm diameter capsid. The cysteine mutant viruses have been chemically labeled successfully with small molecule maleimide reagents and 1.4 nm monomaleimido-Nanogold<sup>®</sup>.<sup>[4]</sup>

The lysine residues of CPMV have been reacted with *N*-hydroxysuccinimide esters of poly(ethylene glycol) (5 kDa and 2 kDa) to give well-defined loadings of polymer on the outer surface of the virus. The intact nature of the polymer protein hybrids was confirmed by FPLC and TEM. The resulting conjugates have altered densities and reduced immunogenicity in the mouse model. These stealth viruses serve as a model system to further develop a tailored vehicle for drug delivery.<sup>[5]</sup> The attachment of biologically relevant ligands on CPMV was demonstrated by decorating the virus with lysine reactive phenylisothiocyanate derivatives of mannose, glucose, and galactose. These polyvalent constructs, which display carbohydrates at

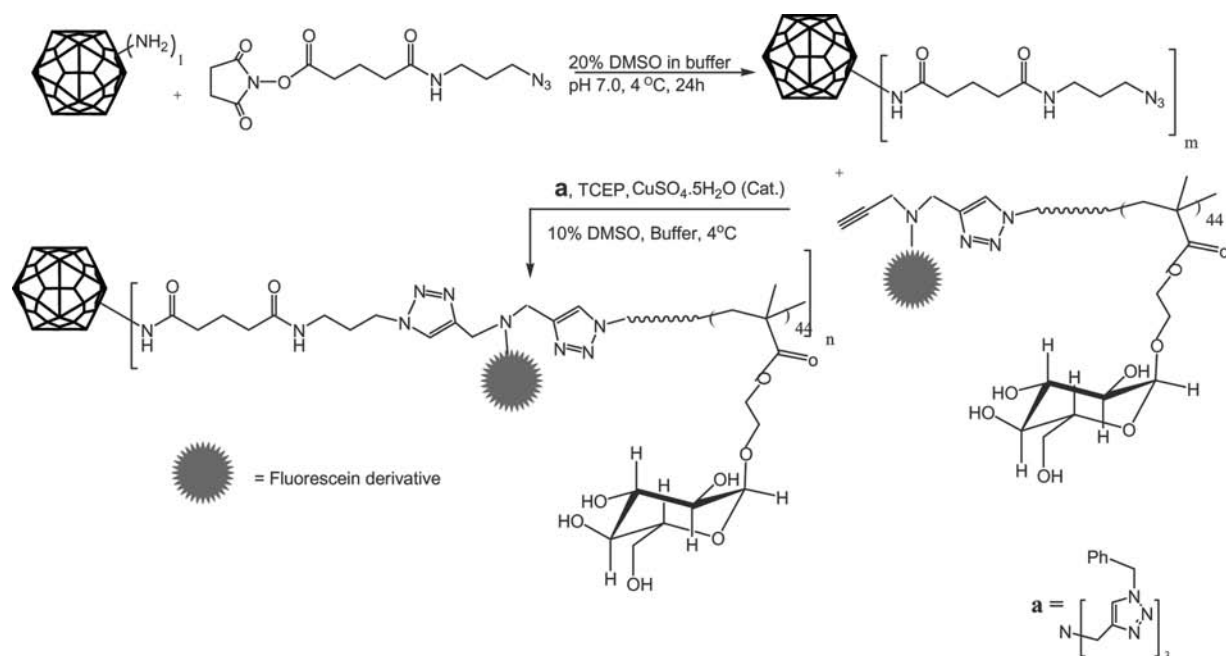


**Fig. 4** Synthesis of "clicked" CPMV neoglycopolymer conjugate.

well-defined distances, were shown to bind strongly to complementary lectins such as concanavalin A.<sup>[28]</sup> Similar carbohydrate–virus conjugates can be used to develop vaccines.

To achieve both reduced immunogenicity and targeting, one needs a polymer that possesses ligands and simultaneously the ability to shield the virus from the immune system. Such a system was developed: a dense array of carbohydrates was generated by attaching glycopolymer chains to CPMV using two highly efficient chemical steps. Atom transfer radical polymerization of glucosyl acrylate using an azide-containing ATRP initiator provided a well-defined end-functionalized neoglycopolymer. Derivatization and attachment of this material to the virus scaffold was further accomplished by the copper-catalyzed azide–alkyne "click" cycloaddition (Fig. 4).<sup>[29]</sup> By employing a calibrated dye absorbance, the number of polymer chains attached to CPMV was determined to be 77 and 140 per particle, respectively, depending on the reaction conditions; this represents the addition of approximately 1.0 and 1.9 million daltons of mass to the 5.6 mDa virion. The resulting hybrid particles show unprecedented levels of polyvalent affinity for concanavalin A, which is a complementary lectin.

Transmission electron microscopy shows the virus conjugates to be more rounded in shape, to take on uranyl acetate stain differently, and to be distinctly larger in size than the wild-type CPMV (Fig. 5). The neoglycopolymers completely shield the protein assembly from the immune system; in the mouse model, this system was less immunogenic than the

PEG-CPMV hybrid. This is the first example in which a neoglycopolymer has been attached to either a protein or a bionanoparticle in a biorthogonal fashion. CPMV-MRI agent conjugates<sup>[30]</sup> and CPMV-DNA hybrids<sup>[31]</sup> have also been reported recently. CPMV assembles at the perfluorodecaline–water interface. Rhodamine and biotin labeled CPMV assembled at such interfaces have been cross-linked either using glutaraldehyde or by the biotin–avidin interactions to produce stable and ultrathin membranes consisting of assembled viruses.<sup>[32]</sup> CPMV has thus served as a workhorse for the development of new bioconjugation reactions, analytical methods, and applications. Also, many of these chemistries and techniques have been

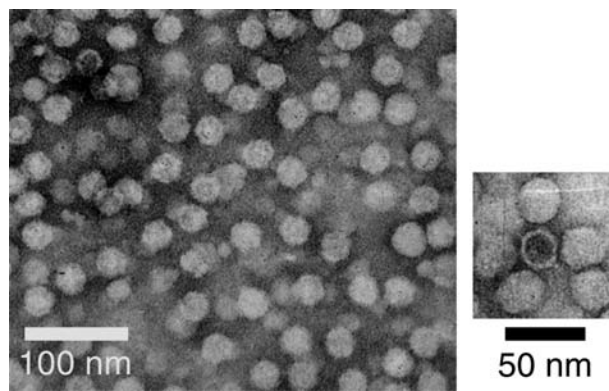


**Fig. 5** (Left) Negative-stained TEM of polymer-CPMV conjugate. (Right) TEM image of a WTCPMV particle surrounded by particles of polymer-CPMV conjugate.

translated to other bionanoparticles such as the MS2 bacteriophage and the tobacco mosaic virus (TMV).

### M13 BACTERIOPHAGE

The M13 bacteriophage is  $\sim 880$  nm long and 6.6 nm in diameter. The high aspect ratio of the phage predisposes it to form lyotropic liquid crystalline phases. Long-range ordered films can be fabricated by using M13 phages.<sup>[33]</sup> Lee et al.<sup>[34]</sup> used genetic engineering to generate a large library ( $10^9$  peptide inserts) of phages displaying random peptides at one end of the M13 virus. The library was then screened to select the phage that selectively binds zinc sulfide crystal surfaces. The bacteriophage displaying the zinc sulfide binding peptide motif (Sel\*Phage) was then isolated, cloned, and multiplied to liquid crystalline concentrations. The Sel\*Phage was suspended in a ZnS solution to form a Sel\*Phage–ZnS nanocrystal liquid crystalline suspension. The Sel\*Phage–ZnS nanocrystal solution formed a self-supporting nanoscale and micrometer-scale ordered hybrid film, which was continuous over a centimeter length scale. This approach of exploiting evolution for selecting bacteriophages, which bind to inorganic materials (along with the advantage that phages form liquid crystalline systems), is a powerful technology for ordering quantum dots or other functional motifs on a large scale.

### TOBACCO MOSAIC VIRUS (TMV)

Tobacco mosaic virus, which is the first isolated virus, has been studied for a long time. As a rod-like virus, TMV is a fascinating supramolecular assembly.<sup>[35]</sup> Wild-type TMV is composed of a spiral of 2130 wedge-shaped protein (CP) subunits. The TMV RNA contains about 6400 nucleotides. The assembly of the TMV particle involves the interaction between the CP subunits and the RNA, resulting in a rigid helical rod of ca.  $300 \times 18 \text{ nm}^2$  with an interior channel having a diameter of 4 nm (Fig. 6).<sup>[36,37]</sup>

Tobacco mosaic virus forms ordered aggregates in the presence of divalent metal cations such as  $\text{Cd}^{2+}$ ,  $\text{Zn}^{2+}$ ,  $\text{Pb}^{2+}$ ,  $\text{Cu}^{2+}$ , and  $\text{Ni}^{2+}$ . These divalent metal cations promote the precipitation of TMV from solution at a critical concentration, and the precipitate behaves as a nematic lyotropic liquid crystalline phase.<sup>[38,39]</sup> Metal binding sites present on the surface of TMV form metal bridges, which serve as cross-linking points. Drying on a glass slide produces highly ordered, optically birefringent films.<sup>[40]</sup> The highly polar exterior surface of TMV has been used for surface mineralization of iron-oxyhydroxides, CdS, PbS, and silica.<sup>[3]</sup> These materials form a thin coating over

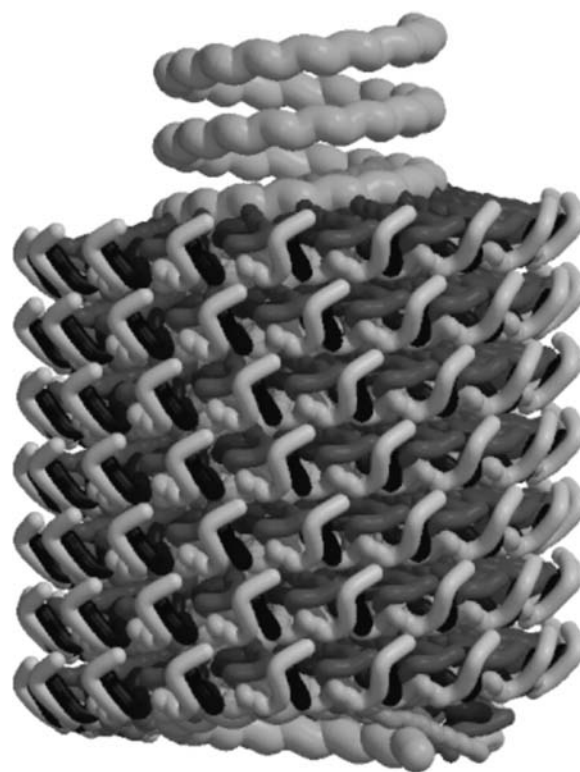


**Fig. 6** Structural representation of Tobacco Mosaic Virus.

the virus nanorod and result in inorganic nanofibrils of 20–30 nm diameter range, which are as long as 1  $\mu\text{m}$ . This is a result of the end-to-end assembly of TMV fibrils. These materials were characterized by energy-dispersive X-ray and transmission electron microscopy.<sup>[41]</sup>

Dujardin et al.<sup>[42]</sup> recently used TMV as a template for the alignment and controlled deposition of Pt, Au, and Ag nanoparticles. By varying the conditions of the deposition, they demonstrated that one can either specifically decorate the external surface with metallic nanoparticles via the chemical reduction of  $[\text{PtCl}_6]^{2-}$  or  $[\text{AuCl}_4]^{2-}$  or achieve constrained growth of Ag nanoparticles within the 4 nm internal channel present in the virus via the photochemical reduction of Ag-salts. In principle, one can thus prepare one-dimensional arrays of a wide range of quantum dots via molecular engineering of the internal or external surface of TMV.

At high concentrations, TMV particles form a nematic liquid crystal, which was employed as template to prepare mesostructured and mesoporous silica with periodicities of about 20 nm.<sup>[43]</sup> Silica nanoparticles consisting of a dense core surrounded by a radial array of mineralized TMV fragment has been synthesized. Chemical degradation of TMV yielded a stable fragment of about 50 nm in length, which was similar in size to those encapsulated in the silica shell of the nanoparticles. The general stability of TMV liquid crystals indicated that it should be possible to use a



similar approach to prepare a wide range of inorganic oxides, semiconductors, and metal-based mesophases and nanoparticles with mesostructured interiors. The exterior surface of TMV has been chemically modified by labeling tyrosine 139 and the interior has been modified by addressing glutamic acid residues 97 and 106.<sup>[44]</sup> Biotin, chromophores, crown ethers, and polyethylene glycol are some of the molecules successfully conjugated to TMV. TMV, thus, serves as a convenient bio-nanoscaffold for both biomineralization and bioconjugation.

## ADENOVIRUSES AND GENE DELIVERY

All adenovirus particles are similar: non-enveloped and 60–90 nm in diameter. They have icosahedral symmetry and are composed of 252 capsomers: 240 “hexons” + 12 “pentons” at vertices of the icosahedron (2–3–5 symmetry), which packages a DNA genome of approximately 36 kDa (Fig. 7).<sup>[45,46]</sup> Attachment to target cells is mediated by the binding of the fiber knob to its complementary receptor protein present on the cell. The viral penton base then interacts with cellular  $\alpha_v$  integrins to allow virus internalization.

Recombinant adenoviruses have been widely used as gene transfer vehicles.<sup>[47]</sup> Adenoviruses have been retargeted to specific cell types by displaying ligands (which are complementary to the receptors present on the cell type) on the surface of the virus. This has been achieved genetically and by other means. For instance, genetic modification of the fiber protein via the incorporation of small targeting peptide sequences, such as a polylysine sequence, has been developed to enhance muscle cell transduction.<sup>[48]</sup> Biospecific adaptor molecules consisting of cross-linked monoclonal antibodies have been used to bridge adenoviral vector protein to cell surface receptor molecules.<sup>[49]</sup>

An antibody/immunoglobulin (IgG) binding protein sequence (Z33) has been expressed on adenovirus fibers. The Z33-modified adenovirus particles were used to form antibody–virus complexes (the binding constant between the antibodies and the virus is

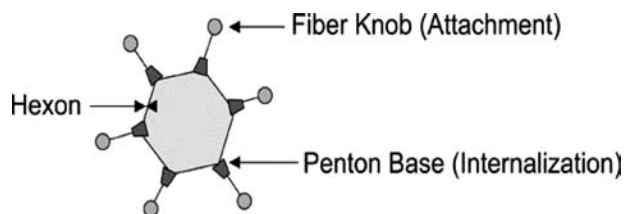


**Fig. 7** Cartoon representation of the structural features of adenovirus.

extremely high;  $K_D = 2.4$  nM) by preincubating them with monoclonal antibodies directed against neuronal cell-adhesion molecules or integrin  $\alpha_7$ . In targeting experiments with human muscle cells, up to a 77-fold increase in reporter gene transfer was achieved by this novel strategy. The approach is quite general and, by varying the cell-type-specific antibody one incubated with the Z33-adenovirus, a wide variety of cells can be targeted.<sup>[50]</sup> Adenoviruses have also been coated with polyethylene glycol (PEG) to avoid antibody-mediated neutralization of the virus in vivo.<sup>[51–53]</sup>

Retroviral vectors have also been used for targeted gene therapy. A targeting peptide along with trimerization domain has been linked on the N-terminus of the viral envelope glycoprotein using a linker, which is further cleaved by an enzyme (matrix metallo protease). These attachments shield the native receptor binding because of steric hindrance; the targeting peptide, which is on the exterior, mediates attachment to tumor cells displaying complementary receptors. After attachment to the tumor cells, the metalloprotease produced by the tumor cells cleaved the linker, thereby exposing the native viral envelope protein, which mediates cell entry into the tumor cells.<sup>[54–56]</sup>

## MS2 BACTERIOPHAGE

The MS2 coat protein consists of 180 copies of subunits, which self-assemble to form a 27.4 nm icosahedral capsid. The X-ray crystal structure of MS2 has

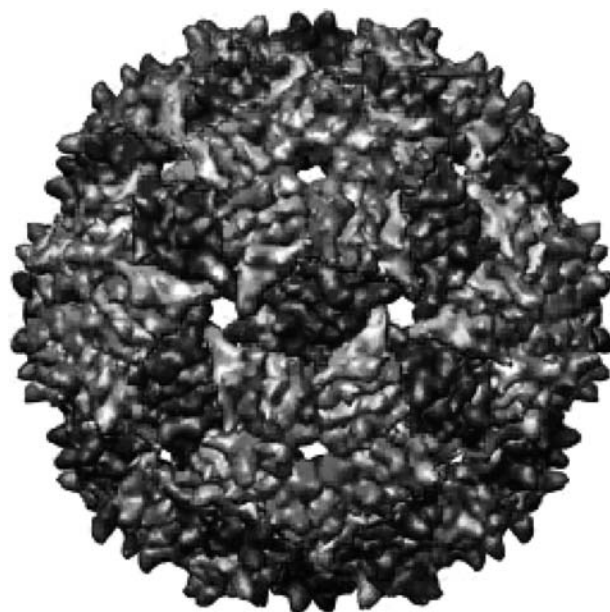


**Fig. 8** Refined structure of Bacteriophage MS2 at 2.8 Å resolution (picture courtesy Virus particle explorer). *Source:* From Ref.<sup>[63]</sup>.

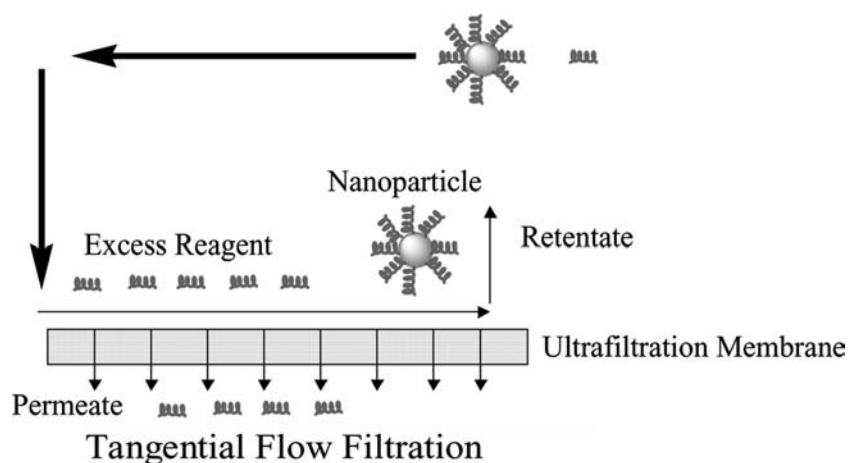


**Fig. 9** Tangential flow filtration method for separation of bionanoparticles from excess conjugation reagents.

been solved to Ångstrom level resolution (see Fig. 8). Each particle has 1080 covalently addressable lysine residues.<sup>[57]</sup> Around 500 lysine residues of MS2 capsid have been covalently modified with gadolinium diethylenetriaminopentaacetic acid (MRI contrast agent) to produce a bionanoparticles contrast agent, which polyvalently displays MRI agents. The  $T_1$  bionanoparticle contrast agent gives reflexivities over three orders of magnitude greater than a single low molecular weight Gd-DTPA moiety.<sup>[58]</sup> MS2 has recently been double labeled with fluorescein (drug mimic) and polyethyleneglycol (shields the particle from the immune system) to develop a model drug delivery vehicle.<sup>[59]</sup>

### HEPATITIS-B SURFACE ANTIGEN (HBsAg)

Clinical grade HBsAg is composed of a mixture of bionanoparticles and small aggregates of particles formed by the self-assembly of 100–150 copies of 25.4 kDa protein subunits.<sup>[60]</sup> HBsAg is a therapeutically relevant protein, and has covalently accessible lysine residues that can be modified with lysine-specific reagents. The current commercial hepatitis B virus (HBV) vaccine consists of HBsAg adsorbed to alum, which acts as an adjuvant. The synthesis and characterization of a novel Hepatitis B Virus vaccine (HBsIC-ISS) composed of Hepatitis B surface antigen (HBsAg) bionanoparticles conjugated to multiple copies of immunostimulatory sequence oligodeoxynucleotides has been recently reported.<sup>[61]</sup> This HBsIC-ISS conjugate, which polyvalently displays multiple copies of ISS-DNA, shows promise as a therapeutic vaccine against hepatitis B virus. The current methods of separation of bionanoparticles from small molecule/polymer and conjugation reagents, like ultracentrifugation

over sucrose gradients, pelletizing and resuspension of the conjugates are multi-step two-day processes and requires expensive equipment. A faster and efficient method for purification of bionanoparticles conjugates is necessary for scale up and commercial exploitation of these constructs. A novel rapid tangential flow filtration (TFF) method was developed to synthesize, purify, and formulate the HBsIC-ISS vaccine (Fig. 9). A 300 kDa molecular weight cut-off cellulose ultrafiltration membrane was employed to retain the large nanoparticles; removal of DMSO, NEM, and Sulfo-SMCC (small molecules), and polymeric ISS (7500 MW) was demonstrated via TFF, with excellent recoveries and short run times of under 1 hr. This TFF technique could serve as a general method for the separation of excess small molecule/polymeric conjugation reagents from virus like particles, viruses, and nanoparticles.

### CONCLUSION

As discussed here, many inroads have been made into harnessing bionanoparticles for nanoscience applications. A vast number of programmable nanoblocks have not yet been explored in this rich, new, and exciting field at the confluence of nanotechnology, biology, chemistry, and materials science. Biology provides a vast resource of nanoparticles and exquisite control of the recognition motifs displayed on the surface of these particles. Organic/bioconjugate chemistry immensely expands the scope of useful functional units such as dyes, sugars, and polymers, which one can use to decorate bionanoparticles for a wide range of applications. Inorganic chemistry/biomineralization affords a convenient route to preparing hard-soft bio-hybrid starting materials for nanoelectronic applications and materials science,

which is the last component in developing this kind of technology. Technological breakthroughs occurring in this field are in two broad directions: nanoelectronics and biomedical applications of nanotechnology. The former has more of a materials science component to it, and the latter has more of a molecular biology component with chemistry contributing richly in both directions. Both directions hold great promise in bringing about an electronic and biomedical revolution. The number of components that go into nanotechnology is almost as complex as the primordial soup<sup>[62]</sup> and what emerges from it promises to be as complex, rich, and unpredictable as life on our planet.

## ACKNOWLEDGMENTS

We thank all the authors whose names are given in the references list. In particular, we sincerely thank Dr. M. G. Finn for many invaluable discussions, and Dr. John E. Johnson for organizing the Mondiego Symposium, which has been the platform for exchanging the latest breakthrough among all the groups pursuing research in the area of virus chemistry. K. S. Raja thanks the College of Staten Island/CUNY for a start-up package and the PSC CUNY grant for partly funding this work. We thank Dr. Vijay Reddy for making Fig. 9.

## REFERENCES

- Douglas, K.; Clark, N.A.; Rothschild, K.J. Biomolecular solid-state nanoheterostructures. *Appl. Phys. Lett.* **1990**, *56*, 692–694.
- Douglas, T.; Young, M. Host–guest encapsulation of materials by assembled virus protein cages. *Nature* **1998**, *393*, 152–155.
- Douglas, T.; Young, M. Virus particles as templates for materials synthesis. *Adv. Mater.* **1999**, *11*, 679–681.
- Wang, Q.; Lin, T.; Tang, L.; Johnson, J.E.; Finn, M.G. Icosahedral virus particles as addressable nanoscale building blocks. *Angew. Chem., Int. Ed.* **2002**, *41*, 459–462.
- Raja, K.S.; Wang, Q.; Gonzalez, M.; Manchester, M.; Johnson, J.E.; Finn, M.G. Hybrid virus–polymer materials. 1. Synthesis and properties of peg-decorated cowpea mosaic virus. *Biomacromolecules* **2003**, *4*, 472–476.
- Vriezema, D.M.; Aragones, M.C.; Elemans, J.A.A.W.; Cornelissen, J.J.L.M.; Rowan, A.E.; Nolte, R.J.M. Self-assembled nanoreactors. *Chem. Rev.* **2005**, *105* (4), 1445–1489.
- Douglas, T.; Young, M. Viruses: making friends with old foes. *Science* **2006**, *312*, 873–875.
- Ehrlich, P.A. *Immunology and Cancer Research*; Pergamon Press: London, 1956; Vol. 2, 456–461.
- Wickham, T.J. Ligand-directed targeting of genes to the site of disease. *Nat. Med.* **2003**, *9*, 135–139.
- Feynman, R. There is plenty of room at the bottom. *Caltech's Eng. Sci.* **1960**, February Issue.
- Aisen, P.; Listowsky, I. Iron transport and storage proteins. *Annu. Rev. Biochem.* **1980**, *49*, 357–393.
- Ha, Y.; Shi, D.; Small, G.W.; Theil, E.C.; Allewell, N.M. Crystal structure of bullfrog M ferritin at 2.8 ang. Resolution: analysis of subunit interactions and the binuclear metal center. *J. Biol. Inorg. Chem.* **1999**, *4*, 243–256.
- Yamashita, I. Fabrication of a two-dimensional array of nano-particles using ferritin molecule. *Thin Solid Films* **2001**, *393*, 12–18.
- Zhang, N.; Li, F.; Fu, Q.J.; Tsang, S.C. *React. Kinet. Catal. Lett.* **2000**, *71*, 393–404.
- Douglas, T.; Stark, V.T. Nanophase cobalt oxyhydroxide mineral synthesized within the protein cage of ferritin. *Inorg. Chem.* **2000**, *39*, 1828–1830.
- Wong, K.K.W.; Whilton, N.T.; Douglas, T.; Mann, S.; Colfen, H. Hydrophobic proteins: synthesis and characterization of organic–soluble alkylated ferritins. *Chem. Commun.* **1998**, *16*, 1621–1622.
- Speir, J.A.; Munshi, S.; Wang, G.; Baker, T.S.; Johnson, J.E. Structures of the native and swollen forms of cowpea chlorotic mottle virus determined by X-ray crystallography and cryo-electron microscopy. *Structure* **1995**, *3*, 63–78.
- Liu, H.; Qu, C.; Johnson, J.E.; Case, D.A. Pseudoatomic models of swollen CCMV from cryo electron microscopy. *Abstr. Pap. Am. Chem. Soc.* **2001**, *221*, 183.
- Douglas, T.; Strable, E.; Willits, D.; Aitouchen, A.; Libera, M.; Young, M. Protein engineering of a viral cage for constrained nanomaterials synthesis. *Adv. Mater.* **2002**, *14*, 405–418.
- Siler, D.J.; Babcock, J.; Bruening, G. Electrophoretic mobility and enhanced infectivity of a mutant of cowpea mosaic virus. *Virology* **1976**, *71*, 560–567.
- Lomonosoff, G.P.; Shanks, M.; Holness, C.L.; Maule, A.J.; Evans, D.; Chen, Z.; Stauffacher, C.V.; Johnson, J.E. Comovirus capsid proteins: synthesis, structure, and evolutionary implications. *Proc. Phytochem. Soc. Eur.* **1991**, *32*, 76–91.
- Lomonosoff, G.P.; Johnson, J.E. The synthesis and structure of comovirus capsids. *Prog. Biophys. Mol. Biol.* **1991**, *55*, 107–137.
- Lin, T.; Chen, Z.; Usha, R.; Stauffacher, C.V.; Dai, J.B.; Schmidt, T.; Johnson, J.E. The refined crystal structure of cowpea mosaic virus at 2.8 ang. resolution. *Virology* **1999**, *265*, 20–34.
- Fisher, M.; Volgtle, F. Dendrimer: from design to application—a progress report. *Angew. Chem., Int. Ed.* **1999**, *38*, 884–905.
- Hecht, S.; Frechet, J.M.J. Dendritic encapsulation of function: applying nature's site isolation principle from biomimetics to materials science. *Angew. Chem., Int. Ed.* **2001**, *40*, 74–91.

26. Wang, Q.; Kaltgrad, E.; Lin, T.; Johnson, J.E.; Finn, M.G. Natural supramolecular building blocks: wild-type cowpea mosaic virus. *Chem. Biol.* **2002**, *9*, 805–812.
27. Wang, Q.; Lin, T.; Johnson, J.E.; Finn, M.G. Natural supramolecular building blocks: cysteine added mutants of cowpea mosaic virus. *Chem. Biol.* **2002**, *9*, 813–819.
28. Raja, K.S.; Wang, Q.; Finn, M.G. Icosahedral virus particles as polyvalent carbohydrate display platforms. *Chem. Biochem.* **2003**, *4*, 1348–1351.
29. Raja, K.S.; SenGupta, S.; Kaltgrad, E.; Strable, E.; Finn, M.G. Virus-glycopolymer conjugates by copper (I) catalysis of atom transfer radical polymerization and azide-alkyne cycloaddition. *Chem. Commun.* **2005**, 4315–4317.
30. Prasuhn, D.E., Jr.; Yeh, R.M.; Obenaus, A.; Manchester, M.; Finn, M.G. Viral MRI contrast agents: coordination of Gd by native virions and attachment of Gd complexes by azide-alkyne cycloaddition. *Chem. Commun.* **2007**, “in press”.
31. Strable, E.; Johnson, J.E.; Finn, M.G. Natural nanosynthetic building blocks: icosahedral virus particles organized by attached oligonucleotides. *Nano Lett.* **2004**, *4*, 1385–1389.
32. Russell, J.T.; Lin, Y.; Dker, A.B.; Su, L.; Carl, P.; Zettl, H.; He, J.; Still, K.; Tangirala, R.; Emrick, T.; Littrell, K.; Thiyagarajan, P.; Cookson, D.; Frey, A.; Wang, Q.; Russell, T.P. Self-assembly and cross-linking of bionanoparticles at liquid-liquid interfaces. *Angew. Chem.* **2005**, *117*, 2472–2478.
33. Lee, S.W.; Wood, B.M.; Belcher, A.M. Chiral smectic c structures of virus-based films. *Langmuir* **2003**, *19*, 1592–1598.
34. Lee, S.W.; Mao, C.B.; Flynn, C.E.; Belcher, A.M. Ordering of quantum dots using genetically engineered viruses. *Science* **2002**, *296*, 892–895.
35. Crick, F.H.C.; Watson, J.D. Structure of small viruses. *Nature* **1956**, *177*, 473–475.
36. Namba, K.; Pattanayek, R.; Stubbs, G. Visualization of protein–nucleic acid interactions in a virus. Refined structure of intact tobacco mosaic virus at 2.9 ang. resolution by X-ray fiber diffraction. *J. Mol. Biol.* **1989**, *208*, 307–325.
37. Namba, K.; Stubbs, G. Structure of tobacco mosaic virus at 3.6 ang. Resolution: implications for assembly. *Science* **1986**, *231*, 1401–1406.
38. Caspar, D.L.D. Structure of bushy stunt virus. *Nature* **1956**, *177*, 475–476.
39. Loring, H.S.; Fujimoto, Y.; Tu, A.T. Tobacco mosaic virus a calcium-magnesium coordination complex. *Virology* **1962**, *16*, 30–40.
40. Nedoluzhko, A.; Douglas, T. Ordered association of tobacco mosaic virus in the presence of divalent metal ions. *J. Inorg. Biochem.* **2001**, *84*, 233–240.
41. Shenton, W.; Douglas, T.; Young, M.; Stubbs, G.; Mann, S. Inorganic–organic nanotube composites from template mineralization of tobacco mosaic virus. *Adv. Mater.* **1999**, *11*, 253–256.
42. Dujardin, E.; Peet, C.; Stubbs, G.; Culver, J.N.; Mann, S. Organization of metallic nanoparticles using tobacco mosaic virus templates. *Nano Lett.* **2003**, *3*, 413–417.
43. Fowler, C.E.; Shenton, W.; Stubbs, G.; Mann, S. Tobacco mosaic virus liquid crystals as templates for the interior design of silica mesophases and nanoparticles. *Adv. Mater.* **2001**, *13*, 1266–1269.
44. Schlick, T.L.; Zhebo, D.; Kovacs, E.W.; Francis, M.B. Dual-surface modification of the tobacco mosaic virus. *J. Am. Chem. Soc.* **2005**, *127*, 3718–3723.
45. Stewart, P.L.; Burnett, R.M.; Cyrklaff, M.; Fuller, S.D. Image reconstruction reveals the complex molecular organization of adenovirus. *Cell* **1991**, *67*, 145–154.
46. Stewart, P.L.; Fuller, S.D.; Burnett, R.M. Difference imaging of adenovirus: bridging the resolution gap between X-ray crystallography and electron microscopy. *EMBO J.* **1993**, *12*, 2589–2599.
47. Ferber, D. Gene therapy. Safer and virus-free? *Science* **2001**, *294*, 1638–1642.
48. Bouri, K.; Feero, W.G.; Myerburg, M.M.; Wickham, T.J.; Kovesdi, I.; Hoffman, E.P.; Clemens, P.R. Polylysine modification of adenoviral fiber protein enhances muscle cell transduction. *Hum. Gene Ther.* **1999**, *10*, 1633–1640.
49. Wickham, T.J.; Segal, D.M.; Roelvink, P.W.; Carrion, M.E.; Lizonova, A.; Lee, G.M.; Kovesdi, I. Targeted adenovirus gene transfer to endothelial and smooth muscle cells by using bispecific antibodies. *J. Virol.* **1996**, *70*, 6831–6838.
50. Volpers, C.; Thirion, C.; Biermann, V.; Hussmann, S.; Kewes, H.; Dunant, P.; Von der Mark, H.; Herrmann, A.; Kochanek, S.; Lochmuller, H. Antibody mediated targeting of an adenovirus vector modified to contain a synthetic immunoglobulin  $\beta$ -binding domain in the capsid. *J. Virol.* **2003**, *77*, 2093–2104.
51. Chillon, M.; Lee, J.H.; Fasbender, A.; Welsh, M.J. Adenovirus complexed with polyethylene glycol and cationic lipid is shielded from neutralizing antibodies in vitro. *Gene Ther.* **1998**, *5*, 995–1002.
52. Croyle, M.A.; Yu, Q.C.; Wilson, J.M. Development of a rapid method for the pegylation of adenoviruses with enhanced transduction and improved stability under harsh storage conditions. *Hum. Gene Ther.* **2000**, *11*, 1713–1722.
53. O’Riordan, C.R.; Lachapelle, A.; Delgado, C.; Parkes, V.; Wadsworth, S.C.; Smith, A.E.; Francis, G.E. Pegylation of adenovirus with retention of infectivity and protection from neutralizing antibody in vitro and in vivo. *Hum. Gene Ther.* **1999**, *10*, 1349–1358.
54. Morling, F.J.; Peng, K.W.; Cosset, F.L.; Russell, S.J. Masking of retroviral envelope functions by oligomerizing polypeptide adaptors. *Virology* **1997**, *234*, 51–61.
55. Peng, K.W.; Morling, F.J.; Cosset, F.L.; Murphy, G.; Russell, S.J. A gene delivery system activatable by disease-associated matrix metalloproteinases. *Hum. Gene Ther.* **1997**, *8*, 729–738.
56. Peng, K.W.; Vile, R.; Cosset, F.L.; Russell, S. Selective transduction of protease-rich tumors by matrix metalloproteinase targeted retroviral vectors. *Gene Ther.* **1999**, *6*, 1552–1557.
57. van den Worm, S.H.; Stonehouse, N.J.; Valegard, K.; Murray, J.B.; Walton, C.; Fridborg, K.; Stockley, P.G.; Liljas, L. Crystal structures of MS2 coat protein mutants

- in complex with wild-type RNA operator fragments. *Nucleic Acids Res.* **1998**, *26*, 1345–1351.
58. Anderson, E.A.; Isaacman, S.; Peabody, D.S.; Wang, E.Y.; Canary, J.W.; Kirshenbaum, K. Viral nanoparticles donning a paramagnetic coat: conjugation of MRI contrast agents to the MS2 capsid. *Nano Lett.* **6**, 1160–1164.
  59. Kovacs, E.W.; Hooker, J.M.; Romanini, D.W.; Holder, P.G.; Berry, K.E.; Francis, M.B. Dual-surface-modified bacteriophage MS2 as an ideal scaffold for a viral capsid-based drug delivery system. *Bioconjugate Chem.* **2007**, in press.
  60. Schirmbeck, R.; Reimann, J. Revealing the potential of DNA-based vaccination: lessons learned from the hepatitis B virus surface antigen. *Biol. Chem.* **2001**, *382*, 543–552.
  61. Raja, K.S.; McDonald, R.; Tuck, S.; Rodriguez, R.; Milley, B.; Traquina, P. One-pot synthesis, purification, and formulation of bionanoparticle-CpG oligodeoxynucleotide hepatitis B surface antigen conjugate vaccine via tangential flow filtration. *Bioconjugate Chem.* **2007**, *18*, 285–288.
  62. Harris, D.A. The coupling ATPase complex: an evolutionary view. *BioSystems* **1981**, *14*, 113–121.
  63. Shepherd, C.M.; Borelli, I.A.; Lander, G.; Natarajan, P.; Siddavanahalli, V.; Bajaj, C.; Johnson, J.E.; Brooks, C.L.; Reddy, V.S. VIPERdb: a relational database for structural virology. *Nucleic Acids Res.* **2006**, *34*, 386–389.

# Bioremediation of Environmental Contaminants

**Xiomara C. Kretschmer**

*Department of Geological Sciences, University of Texas at El Paso,  
El Paso, Texas, U.S.A.*

**Russell R. Chianelli**

*Chemistry Department, University of Texas at El Paso,  
El Paso, Texas, U.S.A.*

## INTRODUCTION

The use of microbes, indigenous or foreign, in the cleanup of contaminated sites is termed bioremediation. Bioremediation has shown great promise in the removal of a wide variety of contaminants, especially at sites where the contaminant is widespread or is present at lower concentrations. Many larger contaminated sites have remained untreated because of high costs associated with traditional cleanup methods. Bioremediation is an attractive alternative to traditional clean up methods, because it may be performed on site, is less invasive, of lower overall costs than conventional methods, and can have higher public acceptance than harsher treatments. Bioremediation techniques are relatively inexpensive because capital and operating costs are generally much lower than, e.g., techniques such as soil removal and replacement. A study performed by Alper<sup>[1]</sup> states that bioremediation is six times lower in cost than incineration and three times cheaper than entombment. Lower cost is a result of the lower energy and time requirements during the application phase of nutrient enhancements and the low cost of the nutrients because of their large-scale use in agriculture.

Bioremediation techniques are also safe and consistent with the natural processes occurring in the contaminated areas. As described later in this entry, naturally occurring or indigenous organisms have been used exclusively up to the time of this writing. Indigenous organisms are present at the contaminated site and are therefore not added. Use of foreign or non-indigenous organisms remains a challenge for future research and development. Bioremediation can be applied to many situations including soil remediation, groundwater remediation, oil spills, and others as described below. Multiple contaminants can be attacked such as petroleum hydrocarbons, industrial solvents, organic wastes, and removal of metals.

The use of bioremediation does have its problems because it is a relatively immature technology where fundamental data still needs to be gathered. Information such as changes in the microbial community as biodegradation takes place is still lacking, due mainly to the fact that many of the microbes used in bioremediation cannot be successfully cultivated in a laboratory setting. For this reason, it is difficult to ascertain just how much removal of a contaminant observed in a study is directly a result of biological processes as opposed to other abiotic processes.<sup>[2]</sup> We also do not know how the ecosystem is affected following the use of bioremediation except in the special case of the Exxon Valdez oil spill that has been extensively studied from the point of view of ecological impact. Bioremediation is still considered to be a new technology and thus many opt for using the more traditional and expensive cleanup methods. The role of government regulators in generating a favorable environment for introducing novel and effective treatments needs to be reassessed. Finally, although bioengineered microbes offer great promise for the removal of contaminants, public and regulatory acceptance of their use remains lacking. This situation is similar to the controversy surrounding the use of genetically engineered foods. This entry will briefly discuss the current use of bioremediation for the removal of different types of contaminants, as well as the difficulties and benefits associated with the use of bioremediation in the removal of each contaminant.

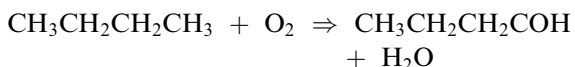
## POLLUTANTS IN THE ENVIRONMENT

### Hydrocarbons

Some microorganisms can completely degrade contaminants as exemplified by the bioremediation of hydrocarbons. Most commonly, *aerobic* organisms are found that add oxygen to the hydrocarbon, thus



starting the process of mineralization as indicated in the following example:



The process continues until the entire hydrocarbon is converted to carbon dioxide and the mineralization is complete, as exemplified in Fig. 1. In practice, only in simple hydrocarbons does complete mineralization occur rapidly. The process of bioremediation of higher hydrocarbons is more complex, as described later.

Hydrocarbon-degrading bacteria have been discovered in all marine environments and were originally discovered by Zobell.<sup>[3]</sup> Biodegradation, together with physical processes such as evaporation, is a major process by which petroleum is removed from the environment following an oil spill. The role of these processes for a large spill such as that of the Amoco Cadiz was described by Gundlach et al.<sup>[4]</sup> This study showed that biodegradation was acting as rapidly as evaporation even during the first days following the spill. It is thought that the high rate of biodegradation along the coast of Brittany was a result of the runoff of agricultural fertilizers from farms near the coast. The

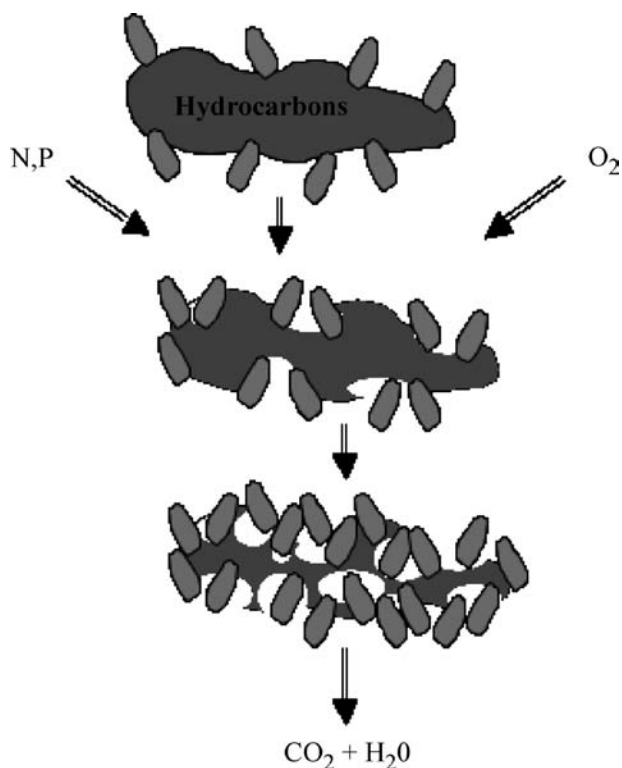


**Fig. 1** Schematic diagram illustrating the breakdown of hydrocarbons by hydrocarbon degrading bacteria. In the case of aerobic microbes, oxygen along with nitrogen and phosphorous are required for this mineralization to occur.

addition of nitrogen and phosphorous from this agricultural runoff enhanced the biodegradation on the beaches, presumably by removing the nitrogen and phosphorous limitation resulting from low naturally occurring levels of these elements in sea water (Atlas, R.M., personal communication, 1990).

The above process requires that hydrocarbon-degrading organisms are present and that there is sufficient oxygen. In some cases, *anaerobic* organisms, organisms that do not require oxygen, can be used to destroy the hydrocarbons by a different route. However, *anaerobic* processes are thought to be slow and are not yet widely used but promise to be a fruitful future research area. If sufficient organisms are present along with sufficient quantities of oxygen, the degradation of the hydrocarbons proceeds and the contaminant is destroyed. During this process, the microorganisms are also increasing in number. This increase in the microbial community requires nitrogen and phosphorous as well as carbon and oxygen for new biomass to be generated. Thus, in many cases, the remediation can be limited by the availability of nitrogen and phosphorous. This can be remedied by addition of nutrients; this commonly used process is called “nutrient enhanced bioremediation” or *biostimulation*. In some cases, the indigenous organisms are grown in a culture under ideal conditions until their numbers are very high and are then added back to the remediation site. This is known as *bioaugmentation* and can be used when a rapid “kick-start” is desired. If the oxygen supply is limited, as can be the case in groundwater remediation, it can be added by “bioventing.” Hydrocarbon degraders are thought to make up less than 1% of microbial communities, but may rapidly increase to more than 10% of the community following exposure to pollutants present in oil.<sup>[3]</sup> In the case of marine oil spills, the contaminants may be tackled via two different options. The first option involves the addition of fertilizers so that the performance of indigenous hydrocarbon degraders may be improved, while the second option involves seeding (*bioaugmentation*). Seeding simply refers to the rapid increase in the population of indigenous hydrocarbon-degrading microbes, which is accomplished by the addition of seed cultures. In the case of hydrocarbon-contaminated terrestrial sites, one may opt for using in situ bioremediation, enhanced land treatment, and slurry bioreactors. In situ bioremediation involves the addition of nutrients and oxygen to increase the activity of the hydrocarbon degrading community. The addition of substances such as nutrients, electron acceptors, and primary substrates presents the factor most likely to affect the rate of in situ bioremediation as these must all reach the microbial community for the technique to be successful.<sup>[5]</sup> In some cases, in situ bioremediation may be ruled out. One might then

choose a method where the contaminated soil is placed in a closed reactor in an aqueous slurry. Microbes are then added in order to treat the soil. Slurry bioreactors may be chosen for sites where mass transfer limitations may occur, field temperatures adversely affect the activity of the microbes, or where the soil is predominantly composed of clay.<sup>[6]</sup> Regardless of the mode of treatment used, one important consideration for bioremediation involves the concept of bioavailability. This simply refers to the portion of the contaminant that is available for microbial treatment. Factors such as oil-phase partitioning, adsorption, and rate-limiting diffusion are most likely to affect bioavailability because all these lead to a decrease in the amount of contaminant found in the aqueous phase, where transformation of the contaminant is most likely to occur.<sup>[7]</sup>

Fig. 2 is an optical micrograph of hydrocarbon degraders grown in laboratory cultures. In most cases, the identification of the specific organisms in the hydrocarbon degrading cultures has not been accomplished. In fact, it is generally considered that indigenous hydrocarbon degraders exist in complex *consortia* that contain many codependent species. The study of *consortia* is an important research area because their control and optimization is of major importance for the future of bioremediation.

### Polycyclic Aromatic Hydrocarbons (PAHs)

The previous section considered the remediation of various hydrocarbons. In this section, we discuss a special class of hydrocarbons, the polycyclic aromatic hydrocarbons (PAHs). These are very difficult to remediate and present particularly difficult and widespread environmental issues. Polycyclic aromatic hydrocarbons are often referred to as polynuclear

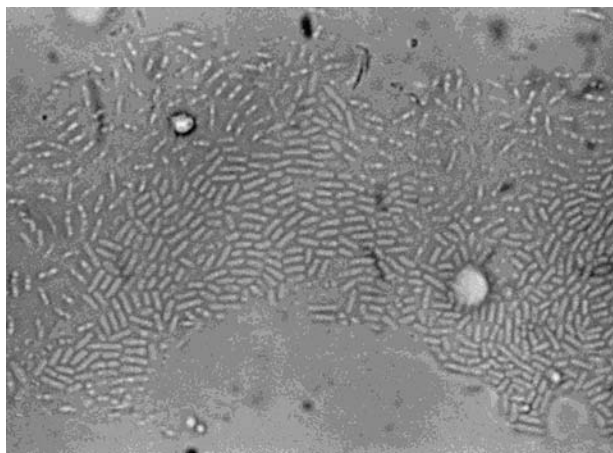


**Fig. 2** Optical micrograph of a marine hydrocarbon-degrading consortia cultured in the laboratory. Each rodlike bacterium is approximately 25  $\mu\text{m}$  in length.

aromatics (PNA). They are a class of very stable organic molecules made up of carbon and hydrogen. These molecules are flat, with each carbon having three neighboring atoms much like graphite. Polycyclic aromatic hydrocarbons (PAHs) are released into the atmosphere as gases or particles during the incomplete combustion of organic material. PAHs have a number of sources, including mobile cars, trucks, ships and aircraft, industrial-power generation, oil refining and waste incineration, and domestic—primarily combustion for heating and cooking, especially solid fuel heaters using wood and coal. The Department of Health and Human Services (DHHS) has determined that some PAHs may be reasonably expected to be carcinogens. Three- to five-ring PAHs occur as particles in air. PAHs with five or more rings tend to be solids, which attach themselves to the surface of other particulate matter in the atmosphere. PAHs are found in air, water, soils, marine organisms, and plants.

Because of their potential toxicity, bioremediation of these compounds has been under study for more than 30 years.<sup>[8]</sup> During this period, many naturally occurring or indigenous bacteria, fungi, and algae have been discovered that attack the lower-molecular-weight species of three rings or lower.<sup>[9,10]</sup> However, as the PAH becomes larger, it becomes more recalcitrant to attack by organisms, probably because of bioavailability considerations. Some fungi and algae have been discovered that attack higher-molecular-weight PAHs but their applicability has been limited by the slowness of their action. Organisms can cometabolize the larger PAHs if given a cometabolite such as phenanthrene (a three-ring PAH);<sup>[11]</sup> however, the success of this approach has been limited. The addition of surfactants to increase bioavailability has also produced limited enhancement of degradation rates.<sup>[12]</sup>

Part of the difficulty in producing better bioremediation processes is attributable to the lack of knowledge regarding the degradation pathways and therefore, their inherent limitations. It is thought that the initial addition of oxygen to the aromatic ring is the most difficult aspect of the degradation process. This occurs through the action of a dioxygenase in the organism. However, the biodegradation of PAHs, the inherent limitations and the subsequent metabolic pathways, is an area that requires a substantial research effort. In particular, bioavailability, adsorption, and mass transfer limitations must be improved in processes using naturally occurring organisms for bioremediation to be effective.

Recent results have indicated that new xenobiotic organisms have great potential for bioremediation of PAHs.<sup>[13]</sup> Genetically engineered organisms (GEMS) are showing progress in modifying metabolic pathways to enhance the effectiveness of organisms in degrading the PAHs. However, although the molecular biology

approach promises to further improve the ability of organisms to degrade PAHs, considerable work remains to be performed and further modification of the relevant DNA is required. Additionally, GEMS have been excluded from practical remediation projects and will likely be limited in the future until more knowledge on the effects of introducing genetically modified organisms into the environment is attained.

## Metals

Metals, particularly heavy metals such as chromium, lead, and copper, are also major pollutants in soil and water. Microorganisms possess the ability to catalyze the transformation of both organic and inorganic pollutants. In the case of organic compounds, the materials is destroyed. However, in the case of metals, the microorganisms are only able to stabilize or remove metal contamination from the treatment site, and one is still left with the problem of getting rid of the metal-containing biomass.<sup>[14]</sup> In his review on the use of microbes for environmental restoration, Francis<sup>[15]</sup> outlines several mechanisms used by microorganisms to accomplish this: oxidation/reduction reactions, changing pH, synthesis of sequestering agents, accumulation or adsorption of metals by functional groups present on bacterial cell walls, or the active uptake of metals into the intracellular space.

In the case of biosorption, the microbial biomass simply acts in the same manner as an ion exchange resin. Live bacteria as well as biopolymers have been successfully used as biosorbents.<sup>[16,17]</sup> Studies have illustrated that, in certain cases, the biomass may be regenerated after alkali treatment for use in additional sorption-desorption processes.<sup>[18]</sup> The main drawback to the implementation of biomaterials for the sorption of heavy metal ions can be attributed to the use of synthetic ion exchange resins, which are more established and therefore more widely used. Biosorbents offer two very important advantages. First, they are superior to synthetic ion exchange resins, in that they are able to remove metal ions present at dilute concentrations.<sup>[19]</sup> Furthermore, because of their specificity, biosorbents are also able to avoid the problem faced by the synthetic ion exchange resins, whose binding sites tend to saturate when alkaline-earth metals are present.

Bacteria may also be used to transform a metal to a lower redox state, as seen with the conversion of the toxic and mutagenic hexavalent chromium to trivalent chromium and reduction/precipitation of Tc(VII), U(VI), and Mo(VI) by sulfate-reducing bacteria (SRB).<sup>[20-22]</sup> The main challenge facing the widespread use of sulfate-reducing bacteria is their susceptibility to low levels of Cd(II), Zn(II), or Ni(II), which are toxic to them at concentrations of 20–200  $\mu\text{M}$ .<sup>[23]</sup> Because

of this, current research is centering on the use of molecular biology techniques to transfer genes involved in the sulfate reduction pathway to more resistant bacterial strains, such as was carried out when the thio-sulfate reductase gene from *Salmonella enterica* was transferred to *Escherichia coli* strains. This led to the production of one recombinant strain with the ability to take out 98% of the available cadmium.<sup>[24]</sup>

In addition to the more traditional metal ions, bacteria have illustrated their ability to enzymatically transform metalloids such as arsenic to methylarsenic, its less toxic form by biomethylating the metalloid. Methylarsenicals are thought to be less toxic than inorganic arsenic because they tend to be more easily excreted and less likely to bind to biomolecules and cell walls.<sup>[25]</sup> An example of genetically engineered bioremediation of arsenic involves the use of bacterial genes, which are then introduced into the *Arabidopsis thaliana* plant.<sup>[26]</sup> These plants are now able to accumulate lethal levels of arsenic in their leaves. In this case, the oxy-anion, arsenate, is transported by the plant above-ground and then reduced to arsenite, which is then sequestered in thiol-peptide complexes. It is hoped by the authors that the same scheme can be applied to larger and faster growing plants for the bioremediation of arsenic.

## BIOREMEDIATION TECHNIQUES

### Groundwater Bioremediation

The quality of groundwater in industrialized and developing countries has been rapidly deteriorating in recent years. This deterioration is closely related to industrial growth and the associated disposal of all kinds of wastes, uncontrolled spills of fuels and lubricants in shops, service stations and industrial plants, and the disposal of industrial wastewaters into open sewers, particularly in countries that are rapidly developing. A large variety of technologies have been developed for remediation of contaminated soils and aquifers including physical, chemical, thermal, and biological procedures. In the remediation of groundwater, the most widely used technology is the pump-and-treat technology. This consists of a pumping-treatment-recharging cycle that comprises extraction of the groundwater for treatment at the surface followed by reinjection into the aquifer. One study indicated that over 3000 “pump and treat” systems existed in the United States.<sup>[27]</sup> In spite of the widespread use of “pump and treat” technology, constraints exist that can limit the success of the process. For example, contaminants may be strongly adsorbed in certain soils making their removal difficult. Thus, when “pump and

“pump and treat” is used to successfully clean the water at the surface, reinjection of the treated water often leads to recontamination after a period of time as a result of contact with contaminants that are strongly adsorbed in the soil. In other situations, the soil may be of low permeability, inducing mass transfer constraints. Finally, the mechanical and energy requirements of “pump and treat” can become quite costly. Bioremediation techniques have recently shown promise in ameliorating groundwater contamination. Bioremediation is safe and economical compared with other technologies. If indigenous or naturally occurring organisms are used, reasonable public acceptance of such a “natural” process is achieved. Contaminants are transformed and degraded to carbon dioxide and water when the technology is properly applied by the mineralization process. The use of microorganisms in one site may not guarantee their success in a different site because microorganisms removed from their habitat and exported to a new environment with different characteristics are not likely to survive in this new environment. In situ bioremediation may be an option for the cleanup of aquifers contaminated with chlorinated solvents or metals. In both cases, nutrients would be pumped to the subsurface to stimulate the activity of organisms that biodegrade the contaminants, or in the case of metals, organisms that change the chemical forms of the metals. There is also promise for the use of sulfate-reducing bacteria (SRB) in the aboveground treatment of heavy metal contaminated groundwater.<sup>[28]</sup> Another variation of groundwater bioremediation is the passive barrier concept, in which contaminated groundwater passes through a permeable reactive zone where bioremediation takes place. Here the contaminants may be degraded or scavenged, thus resulting in the release of uncontaminated groundwater in the downgrade direction of the reactive zone. Advantages of the passive barrier option include the following factors: no aboveground facilities are required and no groundwater reinjection is needed.<sup>[29]</sup>

### Biofiltration

Biological treatment in air pollution control is a new and promising technique that is finding increasing use in many industries.<sup>[30]</sup> This use is fueled by an increasing concern regarding the release of volatile organic compounds (VOCs) into the atmosphere. Volatile organic compounds released in the atmosphere not only cause bad odors but can also have long-term toxic effects over extended periods of time.<sup>[31]</sup> VOCs such as acetone, methanol, toluene, methyl ethyl ketone, and other commonly used solvents are released during manufacturing processes. There is an increasing

move toward replacing these solvents with “environmentally” friendly processes such as “supercritical carbon dioxide” in the semiconductor industry. Nevertheless, processing release from industrial processes remains a major problem. Many food-processing industries also release VOCs into the atmosphere but these VOCs are primarily a concern because of the production of odors.

Recently, biological techniques for waste air treatment have gained interest.<sup>[32]</sup> There has been an increase in both research activity and in application of biofilters for the treatment of either odors or volatile organic compounds (VOCs) in process waste air. The two types of biofilters usually considered for air pollution control are biofilters and biotrickling filters. Both types use naturally occurring indigenous organisms converting the hydrocarbon pollutant to carbon dioxide and water. In a *biofilter*, a humid stream of contaminated air is passed through a damp packing material, usually compost mixed with wood chips or any other bulking agent, on which pollutant degrading bacteria are naturally immobilized. Biofilters are simple and cost-effective, requires low maintenance, and are particularly effective for the treatment of odor and volatile compounds that are easy to biodegrade. These factors have led to the increased use of *biofilters* in industrial applications. *Biotrickling filters* work in a similar manner to *biofilters*, except that an aqueous phase is trickled over the packed bed, and the packing usually consists of some synthetic or inert material (Fig. 3). Inorganic nutrients are added to the trickling solution, which is usually recycled. *Biotrickling*

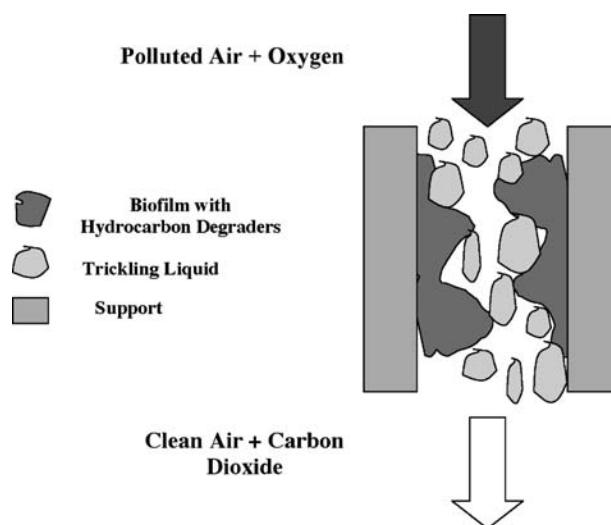


**Fig. 3** Schematic layout of a biotrickling filter. Top arrow indicates movement of contaminated air stream. Interaction of the pollutant with the biofilm leads to biological degradation of the pollutant; bottom arrow indicates the release of clean air.

filters are more complex than biofilters, yet are more effective, especially for the treatment of compounds that generate acidic by-products, such as  $H_2S$ . Because they are more complex and a more recent development, they have not been as widely commercialized. A review by Cox and Deshusses<sup>[33]</sup> provides more information on the potential of biotrickling filters, as well as areas where data remains lacking such as those of biofilm architecture, the population dynamics taking place within these filters, and the potential of using fungi instead of bacteria. The review also touches on the problems encountered with the use of these filters such as the clogging of filters that takes place when biomass accumulation is not controlled.

*Biofilters* and *biotrickling* filters are cost-effective and an environmentally friendly alternative to incineration, adsorption onto activated carbon, or chemical scrubbing. Potential applications include treatment of exhaust air processing industries, printing and painting shops, electronic and materials manufacturing, furniture and metal production, farming and food manufacturing, wastewater treatment operations, etc. They will become more effective as research leads to a better understanding of microbe/support interactions and other factors that determine the size and operating conditions of these filters. Companies such as Biorem, Haase, and Bohn are leaders in biofiltration.

## Phytoremediation

Although bioremediation is generally thought of as the use of microorganisms to remove chemical wastes, the use of plants to remove metal contaminants from soils or even from wetlands is a significant new application of bioremediation. The use of plants for this purpose is called *phytoremediation*. In this application, plants that naturally occur in the contaminated regions may sequester heavy metals such as chromium or lead, which are removed with great difficulty and expense by other methods. Plants that are effective in phytoremediation must take up substantial amounts of metals and are called *hyperaccumulators*. The removal of heavy metals by plants has been demonstrated. However, the contaminated biomass must then be disposed of in an alternate way. For example, the leaves roots and stems of a plant that is removing lead from a contaminated site must be disposed of in a landfill after being ashed to reduce volume. Fig. 4 illustrates a schematic layout of a plant taking up metal from contaminated soil. The first line of defense is to keep the metal out of the plant. The insert in Fig. 4 shows a lead carbonate deposit on the root of a mustard plant exposed to lead. If this first line of defense fails and the lead enters the plant, the metal may accumulate in vacuoles where it is stored or excreted in dead

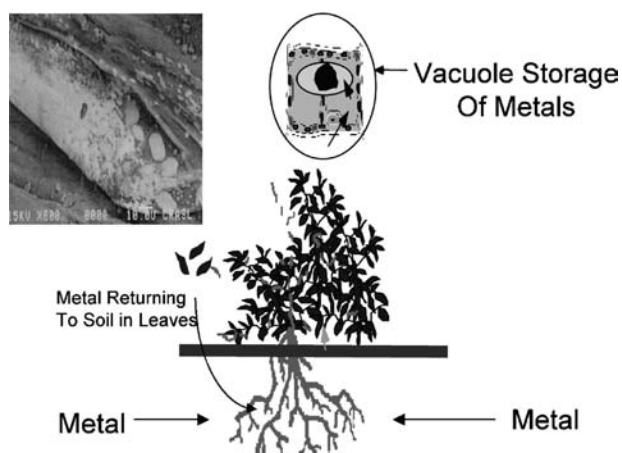


**Fig. 4** Schematic layout of metal uptake by plants. Arrows indicate movement of metals. Bioavailable metals are first excluded from the root. Insert shows scanning electron micrograph (SEM) of a *Brassica* (mustard plant) root following exposure to lead.

leaves or in dripping sap. In any case, the detritus must be removed with the plant for complete disposal of heavy metals. Phytoremediation using water lilies has been attempted to clear radioactive metals as a result of the Chernobyl disaster. In this case, the alternatives of removing hundreds of square miles of soil is not feasible.

## BIOREMEDIATION OF THE EXXON VALDEZ OIL SPILL: THE LARGEST SUCCESSFUL BIOREMEDIATION PROJECT

### Background

The Exxon Valdez spill of approximately 11 million gal of Alaskan North Slope crude oil in Prince William Sound, Alaska, in March 1989 resulted in the contamination of approximately 1300 miles of rocky intertidal shorelines within Prince William Sound and the Gulf of Alaska. Bioremediation was extensively used to accelerate the natural degradation of beached oil. This example is described in some detail because many aspects of instituting a successful project of large magnitude were encountered, including both technical and political obstacles. These obstacles were overcome, resulting in the largest bioremediation project ever attempted.<sup>[34]</sup>

Nitrogen-containing fertilizers were applied to stimulate the growth of indigenous hydrocarbon-degrading microorganisms within the intertidal zones. Shorelines were treated with Inipol EAP 22 (7.4% N, 0.7% P), an oleophilic liquid fertilizer, and Customblen (28% N, 3.5% P), a slow-release granulated fertilizer.

Approximately 50,000 kg of nitrogen and 5000 kg of phosphorus were applied to shorelines over the summers of 1989–1992.

In 1989, field tests on Exxon Valdez beached oil were carried out by the US Environmental Protection Agency (EPA) and Exxon. These tests provided evidence for the success of bioremediation in the cleanup of these beaches.<sup>[35]</sup> Treated areas were visibly cleaner than adjacent untreated areas within a few weeks of fertilizer application.<sup>[36,37]</sup> However, gravimetric analyses on heterogeneous sediments were statistically unconvincing. Laboratory testing confirmed that Inipol EAP 22 was not an effective agent for physically removing oil from sediments, and that oil removal occurred through biological activity.<sup>[38,39]</sup>

The Exxon Valdez bioremediation effort occurred in an extremely rapid crisis atmosphere. Controlled studies that were statistically valid were not performed in the initial year of the spill. However, in 1990, a statistically designed field test was conducted that included extensive chemical analyses of the oil. Results demonstrated that measured changes over time in the oil composition, relative to a stable, high-molecular-weight hydrocarbon present in the oil, allowed the quantification of the rate and extent of the oil biodegradation with high levels of statistical confidence. The authors found that hopane, a multiring saturated hydrocarbon, was not biodegraded and was thus a useful conserved standard. Monitoring hydrocarbon losses relative to hopane provided benchmark confirmation of oil biodegradation, and showed that adding fertilizers could accelerate the rate of oil removal by a factor of 5 or more. It was also found that the rate of oil biodegradation is a function of the nitrogen concentration maintained in the pore water of the intertidal sediments. These results suggested that bioremediation application could be further improved by monitoring nutrient level in real-time and maintaining the nutrient level at an optimum and safe level.<sup>[40]</sup> On-site monitoring of nutrients in sediment pore waters would provide practical, real-time guidance on amounts and frequency of fertilizer applications.

A concurrent monitoring program conducted in Alaska jointly by the EPA, Alaskan Department of Environmental Conservation (ADEC), and Exxon, incorporated comprehensive environmental monitoring, including tests for toxicity and potential stimulation of photosynthetic plankton.<sup>[41]</sup> No adverse effects were found, supporting the safety of bioremediation techniques and illustrating that more frequent fertilizer application would have been equally safe and even more effective. The ultimate rate of nutrient bioremediation will be limited by the amount of nutrients, which may be added without adversely affecting the indigenous biota.

## Lessons from the Exxon Valdez Oil Spill

Bioremediation has inherent limitations. Bioremediation is not likely to be effective on extensively degraded oil. Once the polar content of the oil residue reaches 60–70% of the total mass, nutrient availability will no longer be the limiting factor. This calls for a rapid response in case of an oil spill. Furthermore, adequate oxygen must be available; bioremediation within anaerobic fine sediments such as mud flats or marshes would probably be effective only at shallow depths, but oil penetration in such sediments is also restricted. Nevertheless, based on the statistically significant field tests along with a substantial body of laboratory testing, bioremediation is an important treatment for oil spills on rocky intertidal shorelines of the type found in Alaska.

The effectiveness of this approach was further confirmed and extended by the effectiveness of nutrient enhanced bioremediation on sandy beaches.<sup>[42]</sup> The study concluded that significant intrinsic biodegradation of petroleum hydrocarbons can take place naturally if sufficient nutrients already exist in the impacted area. The study also demonstrated that statistically significant rate enhancement occurs in the presence of an already high intrinsic rate by supplementing natural nutrient levels with inorganic mineral nutrients. It was also shown that bioaugmentation did not significantly contribute to the cleanup of an oil spill. The study developed first-order biodegradation rate constants for the resolvable normal and branched alkanes and two- and three-ring aromatic hydrocarbons present in light crude oil. This study also connected relative biodegradation rates in the field to those measured in the laboratory. The literature, which connects laboratory studies to field studies, is sparse, and considerably more work needs to be carried out. The difference between closed vessel studies, which are usually performed in the laboratory, and open systems, which occur in the field, has been discussed by Oudot.<sup>[43]</sup>

Of primary concern here is the fact that, in laboratory experiments, the products of biodegradation often inhibit microbial activity and retard degradation, whereas these products can be removed by tidal action or large volume dispersion in field environments.

The Exxon Valdez project and the Delaware project cited above demonstrated that bioremediation is an effective and safe technology for beached petroleum hydrocarbons in appropriate areas. Areas appropriate for this technology include those areas in which it can be demonstrated that hydrocarbon degraders are present and active. It is also necessary to demonstrate that the selected area is nutrient-limited. This is not always the case, as demonstrated by the “Amoco Cadiz” spill, in which fertilizer runoff from nearby



farms enhanced nutrition on oil-covered beaches. This also appears to be the case at the head of the Persian Gulf, where the Tigris and Euphrates rivers enter the Gulf, delivering nutrients washed from farmlands in Iraq. If the oil spill affected area receives a large input of nutrients, further addition maybe counterproductive.

Experience in the “Exxon Valdez” spill also indicated that bioremediation was perceived as a “natural technology,” yielding higher public acceptance. Adding nutrients, especially familiar agricultural products, gave the appearance of “helping nature.” Thus, higher public acceptance resulted in more rapid attainment of required approvals from public regulatory agencies for the application of bioremediation. Addition of non-indigenous organisms is ineffective and receives negative public scrutiny. Genetically modified organisms have not been demonstrated to yield any advantage at this point, and are often viewed with alarm by segments of the public. One great advantage in the “Exxon Valdez” project was the use of “town hall meetings” to respond to public concerns regarding bioremediation. These meetings were used to describe the bioremediation process and to answer any questions from those in the community. A frequently asked question was “what happens to the bacteria after they consume the oil”? The answer to this question is that the bacteria are consumed by higher organisms and safely converted to biomass, thus increasing “food” available to local species. This question is illustrative of the concerns expressed by the public. Bioremediation is a relatively inexpensive technology using available nutrient additives. Application involves low-impact application techniques and a low degree of labor intensity. Low-impact application techniques are an advantage in addressing the problem of beached hydrocarbon remediation with minimal disturbance of the beaches themselves. Nutrient enhancement bioremediation techniques are not only applicable to oil spills but also to soil remediation of weathered hydrocarbons, which widely occur in refineries and transportation terminals, although the case studies are not common in the open literature and mostly occur within the affected companies.

## FUTURE OF BIOREMEDIATION

Bioremediation is inexpensive, safe, and effective. However, many obstacles exist that prevent its wider use. Two of these obstacles are the lack of information on the application of bioremediation techniques, and research and policy issues that need to be addressed both in the short term and in the longer term. A major obstacle to the application of bioremediation techniques during an oil spill has been a lack of agreement

among all appropriate international, national, and local regulating agencies regarding the use of bioremediation techniques after the occurrence of an oil spill. This delays or, in some recent cases, eliminates the applicability of bioremediation as a tool for oil spill clean up. Because of the lack of agreement regarding the application of nutrient-enhanced bioremediation techniques, there has not been a general effort or plan in place for dealing with oil spills. Agreement followed by preparedness could greatly mitigate the effect of oil spills that will inevitably occur, especially in high-traffic areas. The same limitations apply as we go from the international to the national and regional level. Often, local environmental agencies are not prepared to allow for the use of novel bioremediation techniques because field demonstrations are required and the time and funding to perform them are not available. There is an urgent need for federally funded field demonstration of novel bioremediation technologies.

Application of nutrient-enhanced bioremediation techniques to problems of soils contaminated with weathered hydrocarbons has been hampered by the existence of published examples demonstrating success. This makes it difficult for regulators to approve the process for cleanup without extensive demonstration projects. The connection between published bioremediation projects that have been accomplished on “freshly spilled oil” and bioremediation of “weathered oil” has not been demonstrated. A particularly difficult point is the determination of an acceptable endpoint for the application. It is clear that bioremediation never fully mineralizes the oil leaving a residue. Therefore what is an acceptable endpoint for bioremediation? One answer appears to be that after limitations such as nutrients and oxygen are removed, the bacteria will proceed until no more hydrocarbons are “available.” By definition, if the hydrocarbons are not available to the bacteria, they are probably now in “safe” condition, and this may be an acceptable endpoint.

More research and field demonstrations need to be performed to overcome technological limitations. Foremost among these limitations is analytical determination of the agreed endpoint of bioremediation. Currently, established techniques such as the determination of “biomarker” molecules (e.g., hopanes that occur in small quantities) require costly mass spectrometry/gas chromatography. These techniques are very expensive and time-consuming. It is estimated that, in the case of the “Exxon Valdez,” the cost of application of these analytical techniques required to demonstrate effectiveness was of the same order as the nutrient-enhanced application itself. This fact is probably a major factor in preventing the occurrence of more bioremediation projects and the concurrent publication of scientifically sound results. Additionally,

the application of these techniques requires removal of the samples to remote facilities, elaborate chemical separation, and ensuing time delays. It would seem the development of a rapid technique based on molecular genetics that could be applied in the field would represent a major advance. Many questions exist, which are not only scientifically important but, if answered, will greatly advance the usefulness and applicability of bioremediation.

Insight into fundamental processes of bioremediation will be gained by pursuing the objectives described below:

1. *Development of strong laboratory/field connections:* Fundamental understanding of microbial transformations, which can be studied in the laboratory, are often difficult to connect to field bioremediation studies. In addition, expensive and time-consuming field experiments are required. When laboratory, macrocosm, and field experiments are strongly connected via proper statistical design of each, the time and cost required to demonstrate field effectiveness is greatly reduced. The utilization of controlled laboratory experiments having direct meaning to real environmental field situations would lead to advances in the use of bioremediation techniques.
2. *Development of strong connection between biological growth rates and rates of molecular transformation:* The work of microbiologists studying hydrocarbon degrading organisms and bioremediation scientists studying the rates of molecular destruction are often only weakly connected. Development of rates of transformation, which are strongly connected to biological dynamics, would greatly assist scientists and engineers to design, accelerate, and control bioremediation processes. For example, hydrocarbon destruction is most rapid when microbes are in the growth phase. Developing rate models, which directly relate the number of microbes in the growth phase with the rate of destruction of hydrocarbons, would greatly enhance our understanding of the process and ways to accelerate and control it. Greater control could be provided by biological assays (perhaps based on RNA/DNA), which would more easily and rapidly indicate the state of the bioremediating population, allowing for quicker intervention for the adjustment of unfavorable conditions.
3. *Development of an understanding of the microbial ecology of soil microorganisms:* Bioremediation experiments often slow down or accelerate in the field for reasons that are not well understood and are not related to the chemical composition of the substrate. Understanding of the relationship of the degrading organisms and their relation to physical surroundings is an important next step in controlling the delivery of nutrients and the removal of products. Such an understanding can lead to new treatments, which could greatly accelerate the rate of destruction and the completeness of remediation.
4. *Understanding predator/prey relations in bioremediation experiments:* As biomass accumulates during hydrocarbon destruction, higher organisms begin to feed on the microbes. If this occurs too rapidly, bioremediation may be slow. If it occurs too slowly, bioremediation may also slow because the microbes may fill available niches and stop growing. Understanding and control of predation could lead to new ways of accelerating bioremediation by removing biomass from the available niches, allowing more organisms to grow.
5. *Understanding of chemical endpoints of bioremediation processes:* In the destruction of spilled and/or aged hydrocarbons by microbial degradation, not all hydrocarbons are mineralized. The reason for this is not completely understood, although it is usually attributed to "bioavailability." However, there is evidence that microbes may participate in cross-linking heavier fractions of hydrocarbons via oxygen addition. This process has been termed "bioasphalting" by analogy to chemical asphaltting. If this can be demonstrated, it is good news for the bioremediation community because this could lead to the determination of a natural endpoint for the process. Bioasphalting renders that fraction which is not mineralized safe and inert.

Progress is being made in the areas described above. Longer-term research progress that will assure future improvements in the success of bioremediation will depend, to a large degree, in understanding how consortia survive and thrive in their natural environments. Furthermore, introduction of foreign organisms into the environment requires an understanding of the genetics that allow an organism to fit into its "niche" successfully. This understanding is not trivial and most introductions of foreign organisms into the environment fail because the introduced organisms are simply outcompeted by the indigenous organisms. This knowledge is essential whether the habitat is lakes, rivers, or soils; or whether we are asking the organisms to thrive in a bioreactor.

Bioremediation by anaerobic organisms continues to be of major interest especially in destroying

molecules that are recalcitrant to oxidative methods. Recently, it has been shown that anaerobic communities can destroy chlorinated benzoates, phenols, benzenes, and some pesticides. This includes PCBs, one of the most recalcitrant and ubiquitous pollutants. Ye et al.<sup>[44]</sup> reported that the dechlorination reaction is carried out by a previously unknown anaerobe that grows best in a consortium with other organisms; together, they create a food chain yielding methane and chloride. This finding emphasizes the importance of understanding the consortia and underscores the complexity contained therein. The reductive dechlorination reactions are among the very few ways that the chlorinated hydrocarbons can be destroyed. There is considerable interest in developing an anaerobic process based on this discovery. However, many hurdles need to be overcome for practical application.

Acceptance of introducing foreign organisms or genetically modified organisms into the environment requires more knowledge in understanding how genetic material is exchanged between organisms. DNA probe techniques are being developed for use in soil to detect specific gene sequences in the total soil population.<sup>[45]</sup> This allows for the study of naturally occurring gene exchange, rearrangement, and regulation. This approach will require years of research before we are able to say with certainty that we understand the processes, and that genetically modified organisms can be introduced into the environment with confidence.

## REFERENCES

- Alper, J. Biotreatment firms rush to the marketplace. *Bio/Technology* **1993**, *11*, 973–975.
- Iwamoto, T.; Nasu, M. Current bioremediation practice and perspective. *J. Biosci. Bioeng.* **2001**, *92* (1), 1–8.
- Zobell, C.E. Bacterial degradation of mineral oils at low temperatures. In *The Microbial Degradation of Oil Pollutants*; Publication No. LSU-SG-73-01; Ahearn, D.G., Meyers, S.P., Eds.; Center for Wetland Resources: Louisiana State University: Baton Rouge, 1973; 153–161.
- Gundlach, E.R.; Boehm, P.D.; Marchand, M.; Atlas, R.M.; Ward, D.M.; Wolfe, D.A. The fate of Amoco Cadiz oil. *Science* **1983**, *221* (4606), 122–129.
- Lee, M.D.; Thomas, M.J.; Borden, R.C.; Bedient, P.B.; Ward, C.H.; Wilson, J.T. Bioremediation of aquifers contaminated with organic compounds. *CRC Crit. Rev. Environ. Control* **1988**, *18* (1), 29–84.
- Pollard, S.J.T.; Hrukey, S.E.; Fedorak, P.M. Bioremediation of petroleum and creosote-contaminated soils: a review of constraints. *Waste Manage. Res.* **1994**, *12* (2), 173–194.
- Smith, J.R.; Nakles, D.V.; Sherman, D.F.; Neuhauser, E.F.; Loehr, R.C. *Environmental Fate Mechanisms Influencing Biological Degradation of Coal-Tar Derived Polynuclear Aromatic Hydrocarbons in Soil Systems*, Proceedings of the 3rd International Conference on New Frontiers in Hazardous Waste Management, 1989, 397–405. US, EPA/600/9-89-072.
- Juhász, A.L.; Naidu, R. Bioremediation of high molecular weight polycyclic aromatic hydrocarbons: a review of the microbial degradation of benzo[a]pyrene. *Int. Biodeterior. Biodegrad.* **2000**, *45* (1–2), 57–88.
- Cerniglia, C.E.; Heitkamp, M.A. Microbial degradation of polycyclic aromatic hydrocarbons in the aquatic environment. In *Metabolism of Polycyclic Aromatic Hydrocarbons in the Aquatic Environment*; Varanasi, U., Ed.; CRC Press: Boca Raton, FL, 1989; 41–68.
- Cerniglia, C.E. Biodegradation of polycyclic aromatic hydrocarbons. *Biodegradation* **1992**, *3* (2–3), 351–368.
- Kim, I.S.; Park, J.S.; Kim, K.W. Enhanced biodegradation of polycyclic aromatic hydrocarbons using non-ionic surfactants in soil slurry. *Appl. Geochem.* **2001**, *16* (11–12), 1419–1428.
- Tiehm, A.; Stieber, M.; Werner, P.; Frimmel, F.H. Surfactant-enhanced mobilization and biodegradation of polycyclic aromatic hydrocarbons in manufactured gas plant soil. *Environ. Sci. Technol.* **1997**, *31* (9), 2570–2576.
- Samanta, S.K.; Singh, O.V.; Jain, R.K. Polycyclic aromatic hydrocarbon: environmental pollution and bioremediation. *Trends Biotechnol.* **2002**, *20* (6), 243–248.
- Chang, J.S.; Huang, J.C. Selective adsorption/recovery of Pb, Cu, and Cd with multiple fixed beds containing immobilized bacterial biomass. *Biotechnol. Prog.* **1998**, *14* (5), 735–741.
- Francis, A.J. Microbial transformations of radioactive wastes and environmental restoration through bioremediation. *J. Alloy. Compd.* **1994**, *213–214*, 226–231.
- Gadd, G.M. Bioremediation potential of microbial mechanisms of metal mobilization and immobilization. *Curr. Opin. Biotechnol.* **2000**, *11* (3), 271–279.
- Gutnick, D.L.; Bach, H. Engineering bacterial biopolymers for the biosorption of heavy metals: new products and novel formulations. *Appl. Microbiol. Biotechnol.* **2000**, *54* (4), 451–460.
- Costley, S.C.; Wallis, F.M. Bioremediation of heavy metals in a synthetic wastewater using a rotating biological contractor. *Water Res.* **2001**, *35* (15), 3715–3723.
- Bunke, G.; Gotz, P.; Buchholz, R. Metal removal by biomass: physico-chemical elimination methods. In *Environmental Processes I*; Winter, J., Ed.; Wiley-VCH Verlag: Weinheim, 1999; 431–452.
- Wang, P.; Mori, T.; Komori, K.; Sasatsu, M.; Toda, K.; Ohtake, H. Isolation of an *Enterobacter cloacae* strain that reduces hexavalent chromium under anaerobic conditions. *Appl. Environ. Microbiol.* **1989**, *55* (7), 1665–1669.
- Lloyd, J.R.; Ridley, J.; Khizniak, T.; Lyalikova, N.N.; Macaskie, L.E. Reduction of technetium by *Desulfovibrio desulfuricans*: biocatalyst characterization and use in a flow-through bioreactor. *Appl. Environ. Microbiol.* **1999**, *65* (6), 2691–2696.
- Tucker, M.D.; Barton, L.L.; Thompson, B.M. Removal of U and Mo from water by immobilized *Desulfovibrio desulfuricans* in column reactors. *Biotechnol. Bioeng.* **1998**, *60* (1), 90–96.

23. White, C.; Gadd, G.M. Accumulation and effects of cadmium on sulphate-reducing bacterial biofilms. *Microbiology* **1998**, *144* (5), 1407–1415.
24. Bang, S.W.; Clark, D.S.; Keasling, J.D. Engineering hydrogen sulfide production and cadmium removal by expression of the thiosulfate reductase gene (phsABC) from *Salmonella enterica* serovar typhimurium in *Escherichia coli*. *Appl. Environ. Microbiol.* **2000**, *66* (9), 3939–3944.
25. Thayer, J.S. *Organometallic Compounds and Living Organisms*; Academic Press: New York, NY, 1984.
26. Dhankher, O.P.; Li, Y.; Rosen, B.P.; Shi, J.; Salt, D.; Senecoff, J.F.; Sashti, N.A.; Meagher, R.B. Engineering tolerance and hyperaccumulation of arsenic in plants by combining arsenate reductase and  $\gamma$ -glutamylcysteine synthetase expression. *Nat. Biotechnol.* **2002**, *20*, 1140–1145.
27. Kavanaugh, M.C. *Remediation of Contaminated Ground Water: A Technical and Public Policy Dilemma*, Proceedings of Forum in Mexico on Ground Water Remediation, 5–6 December; Mexico City, Mexico, 1995.
28. Diels, L.; Van der Lelie, N.; Bastiaens, L. New developments in treatment of heavy metal contaminated soils. *Rev. Environ. Sci. Technol.* **2002**, *1* (1), 75–82.
29. Kao, C.M.; Chen, S.C.; Wang, J.Y.; Chen, Y.L.; Lee, S.Z. Remediation of PCE-contaminated aquifer by an in situ two-layer biobarrier: laboratory batch and column studies. *Water Res.* **2003**, *37* (1), 27–38.
30. Leson, G.; Winer, A.M. Biofiltration—an innovative air pollution control technology for VOC emissions. *J. Air Waste Manage. Assoc.* **1991**, *41* (8), 1045–1054.
31. Cape, J.N. Effects of airborne volatile organic compounds on plants. *Environ. Pollut.* **2003**, *122* (1), 145–157.
32. Deviny, J.S.; Deshusses, M.A.; Webster, T.S. *Biological treatment*. In *Biofiltration for Air Pollution Control*; Lewis Publishers: Boca Raton, FL, 1999; 5–8.
33. Cox, H.H.J.; Deshusses, M.A. Biological waste air treatment in biotrickling filters. *Curr. Opin. Biotechnol.* **1998**, *9* (3), 256–262.
34. Chianelli, R.R. Bioremediation: helping nature's microbial scavengers. *Proc. R. Inst.* **1994**, *65*, 105–126.
35. Pritchard, P.H.; Costa, C.F. EPA's Alaska oil spill bioremediation report. *Environ. Sci. Technol.* **1991**, *25* (3), 372–379.
36. Pritchard, P.H.; Costa, C.P.; Suit, L. *Alaska Oil Spill Bioremediation Project, Report No. EPA/600/9.91/0.46a, b*; US Environmental Protection Agency: Gulf Breeze, FL, 1991.
37. Stone, R. Oil clean-up method questioned. *Science* **1992**, *257* (5068), 320–321.
38. Chianelli, R.R.; Aczel, T.; Bare, R.E.; George, G.N.; Genowitz, M.W.; Grossman, M.J.; Haith, C.E.; Kaiser, F.J.; Lessard, R.R.; Liotta, R.; Mastracchio, R.L.; Minak-Bernero, V.; Prince, R.C.; Robbins, W.K.; Stiefel, E.I.; Wilkinson, J.B.; Hinton, S.M.; Bragg, J.R.; McMillen, S.J.; Atlas, R.M. *Bioremediation Technology Development and Application to The Alaskan Spill*. In *Proc. Int. Oil Spill Conf.*; API: Washington, DC, 1991; 549–558.
39. Prince, R.C.; Hinton, S.M.; Bragg, J.R.; Elmendorf, D.E.; Lute, J.R.; Grossman, M.J.; Robbins, W.K.; Hsu, C.S.; Douglas, G.S.; Bare, R.E.; Haith, C.E.; Senius, J.D.; Minak-Bernero, V.; McMillen, S.J.; Rofall, J.C.; Chianelli, R.R. Laboratory studies of oil spill bioremediation toward understanding field behavior. In *Preprints of the Division of Petroleum Chemistry*; American Chemical Society: Washington, DC, 1993; 38, 240–244.
40. Bragg, J.R.; Prince, R.C.; Harner, E.J.; Atlas, R.M. Effectiveness of bioremediation for the Exxon Valdez oil spill. *Nature* **1994**, *368* (6470), 413–418.
41. Prince, R.C.; Clark, J.R.; Lindstrom, J.E. *Bioremediation Monitoring Program, Report to US Coast Guard, Exxon Co. USA, US EPA*; Alaska Dept. of Environmental Conservation: Anchorage, 1990.
42. Venosa, A.D.; Suidan, M.T.; Wrenn, B.A.; Srohmeier, K.L.; Haines, J.R.; Eberhart, D.; King Holder, E. Bioremediation of an experimental oil spill on the shoreline of Delaware Bay. *Environ. Sci. Technol.* **1996**, *30* (5), 1764–1775.
43. Oudot, J. Rates of microbial degradation of petroleum components as determined by the computerized gas chromatography and computerized mass spectrometry. *Mar. Environ. Res.* **1984**, *13* (4), 277–302.
44. Ye, D.; Quensen, J.F.; Tiedje, J.M.; Boyd, S.A. 2-Bromoethanesulfonate, sulfate, molybdate, and ethanesulfonate inhibit anaerobic dechlorination of polychlorobiphenyls by pasteurized microorganisms. *Appl. Environ. Microbiol.* **1999**, *65* (1), 327–329.
45. McGowan, C.; Fulthorpe, R.; Wright, A.; Tiedje, J.M. Evidence for interspecies gene transfer in the evolution of 2,4-dichlorophenoxyacetic acid degraders. *Appl. Environ. Microbiol.* **1998**, *64* (10), 4089–4092.

# Biosensor Applications: Porous Silicon Microcavities

**Benjamin L. Miller**

*Department of Dermatology, University of Rochester, Rochester, New York, U.S.A.*

**Philippe M. Fauchet**

*Department of Electrical and Computer Engineering, University of Rochester, Rochester, New York, U.S.A.*

**Scott R. Horner**

*Department of Biochemistry and Biophysics, University of Rochester, Rochester, New York, U.S.A.*

**Selena Chan**

*The Center for Future Health, University of Rochester, Rochester, New York, U.S.A.*

## INTRODUCTION

The development of rapid, label-free methods for detecting pathogenic organisms is of intense interest, both because of the scientific challenge it represents and because of its potential importance to society. Recently, several groups have begun examining the suitability of nanocrystalline silicon (or, simply, “porous silicon”) as a substrate material for the construction of such sensors. Our own efforts have focused on the photoluminescence of porous silicon microcavities, appropriately derivatized with probe molecules for a variety of model biopolymers, viruses, and bacteria.

## BACKGROUND

Optical biosensing has traditionally required labeling a probe molecule with a soluble reporter group, typically a dye or fluorescent molecule. In microbiology, one of the most venerable techniques uses just such a scheme. In 1860, Hans Christian Joachim Gram, a Danish physician, observed that certain bacteria turned purple when exposed to crystal violet, a common dye. This observation turned out to have medical significance (for underlying molecular reasons we will discuss later),<sup>[1]</sup> and the Gram stain became a key component of microbial analysis.<sup>[2]</sup> The Gram stain is illustrative of the difficulties inherent in any label-based analytical scheme: Correct preparation of the smear, involving an initial thin film deposition of the bacteria on a glass slide followed by a heat fixing step, is crucial for an accurate reading. Failure to precisely follow the steps leads to staining artifacts or the

complete washing away of the bacteria. Furthermore, although this procedure can be rapidly carried out by those “skilled in the art,” it is not suitable for broad deployment (i.e., to be carried out by those lacking extensive training), nor is it readily generalizable to a broad range of targets.

Likewise, many solid-supported assays (i.e., sensors) rely on a labeling step to produce a signal in the presence of a target. For example, microarray systems such as those developed by the Affymetrix group<sup>[3,4]</sup> and Iyer et al.<sup>[5]</sup> rely on fluorescence tagging of oligonucleotide sequences during a polymerase chain reaction (PCR) amplification step. In this example, and in many analogous systems, the substrate material serves only a passive role. An attractive alternative is for the substrate onto which the probe is attached to play an active role in sensing, transducing a signal generated by the binding event. The construction and testing of such devices is currently an area of intense research, and has produced some notable successes (for a review, see Ref.<sup>[6]</sup>).

## RECENT DEVELOPMENTS

Over the past several years, nanoporous silicon has generated considerable interest as a substrate material for the production of active biosensors. Produced via an electrochemical etching procedure, four primary advantages make porous silicon an attractive material for biosensing applications. First, its enormous surface area ranges from 90 to 783 m<sup>2</sup>/cm<sup>3</sup>.<sup>[7]</sup> Second, its photophysical properties are responsive to environmental changes, e.g., the presence of gases. Third, a rich body of chemistry exists for the attachment of a

wide range of probe molecules. Finally, the biocompatibility of porous silicon has been demonstrated, suggesting that the production of biosensors for continuous *in vivo* monitoring is a possibility.

In general, porous silicon optical biosensors may be divided into two broad classes: those that make use of changes in reflectance and those that rely on changes in luminescence. Reflectance-based examples include the detection of organic phosphines,<sup>[8]</sup> ethanol,<sup>[9]</sup> and streptavidin–biotin interactions.<sup>[10]</sup> In the remainder of this article, we will discuss our efforts to produce porous silicon biosensors capable of specifically detecting (or, sensitively differentiating) pathogenic viruses and bacteria.

In particular, our efforts have focused on the use of microcavity structures. Porous silicon microcavity resonators possess the unique characteristics of line narrowing and luminescence enhancement. The emission peak position is completely tunable by changing the properties of the central layer. Increasing the thickness of the central active layer introduces multiple narrow peaks in the luminescence spectrum.<sup>[11]</sup> The microcavity structure is highly sensitive and any slight change in the effective optical thickness modifies the reflectivity spectra, causing a spectral shift in the interference peaks. The characteristic luminescence spectrum of a single porous silicon layer has a full width at half maximum (FWHM) value of approximately 150 nm centered at a wavelength of 750 nm. This relatively broad band emission can be narrowed by confining the luminescence between two distributed Bragg reflectors.<sup>[12–14]</sup> This microcavity-resonating structure narrows the luminescence in the forward direction to a single peak with a FWHM value of 10 nm.<sup>[15]</sup> When the cavity thickness increases, the number of luminescence peaks also increases. The porosity of the cavity is kept relatively low (<70%), which allows the formation of thick films without stress-related instabilities. For a microcavity resonator, the FWHM values for each of the photoluminescence peaks can be as narrow as 3 nm and any slight shift in the peak positions is readily observable.

## DNA DETECTION

As an initial demonstration of the utility of porous silicon microcavities as biosensors, we decided to examine the ability of appropriately functionalized devices to detect DNA. (Portions of this section are adapted from Ref.<sup>[16]</sup>). Microcavities were prepared using a highly boron-doped substrate ( $p^+$ , 0.008–0.01  $\Omega$  cm), chosen because of the wide range of porosities that can be prepared using this substrate. A programmed etching sequence was used to produce alternating layers of low (43%) and high (62%) porosity flanking a thick

“active layer” of high porosity (Fig. 1). Construction of such three-dimensional structures is possible because etching only occurs at the interface between unetched silicon and the HF bath. As visualized by electron microscopy, pore diameters in these structures are in the range of 50–75 nm. This dimension is critical in that it must be well above the predicted size of the target analytes. As the diameter of double-stranded DNA is approximately 1.8 nm, this falls well within the needed range. Following the etching process, microcavities were subjected to thermal oxidation in ambient oxygen at 900°C for 10 min. In addition to stabilizing the optical properties of the microcavity,<sup>[17]</sup> this provides a surface layer of silicon oxides (Si-O-Si and Si-OH) ideal for attachment of probe molecules.

Several different chemistries have been employed for the attachment of probe molecules to glass, ranging from simple non-specific adhesion of polyanionic oligonucleotides to a polycation such as polylysine,<sup>[18,19]</sup> to significantly more complex schemes.<sup>[20,21]</sup> We chose to first silanize the oxidized porous silicon microcavity with 3-glycidoxypropyltrimethoxy silane, providing the surface with an electrophilic site in the form of an epoxide (Fig. 2). We next treated the sample with a DNA sequence (5'-TAG CTA TGG AAT TCC TCG TAG GCA-3') bearing a 3'-amino group. This acts as a nucleophile, opening the epoxide and providing a covalent attachment between the silicon surface and the DNA probe. After allowing the epoxide-functionalized microcavity to incubate with a solution of the amino-terminated DNA for 12 hr, it was washed with glass-distilled water and dried under a stream of nitrogen. Fourier-transform infrared (FT-IR) analysis, as well as parallel experiments with radiolabeled [<sup>32</sup>P]DNA, provided evidence that this procedure yielded a microcavity with the probe DNA sequence covalently immobilized.

Fig. 3 shows the photoluminescence spectrum of the resulting DNA-functionalized chip. When the chip is incubated with a 1- $\mu$ M buffered solution of the complementary DNA strand (5'-G CCT ACG AGG AAT TCC ATA GCT-3') for 1 hr, followed by a rinsing step, the luminescence spectrum red shifts (Fig. 3, middle). This 7-nm shift is particularly observable in the difference spectrum (Fig. 3, bottom). We attribute the red

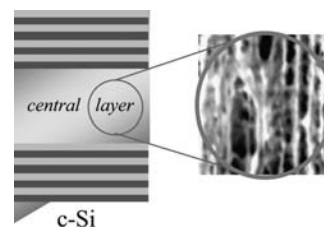


Fig. 1 Porous silicon microcavity.



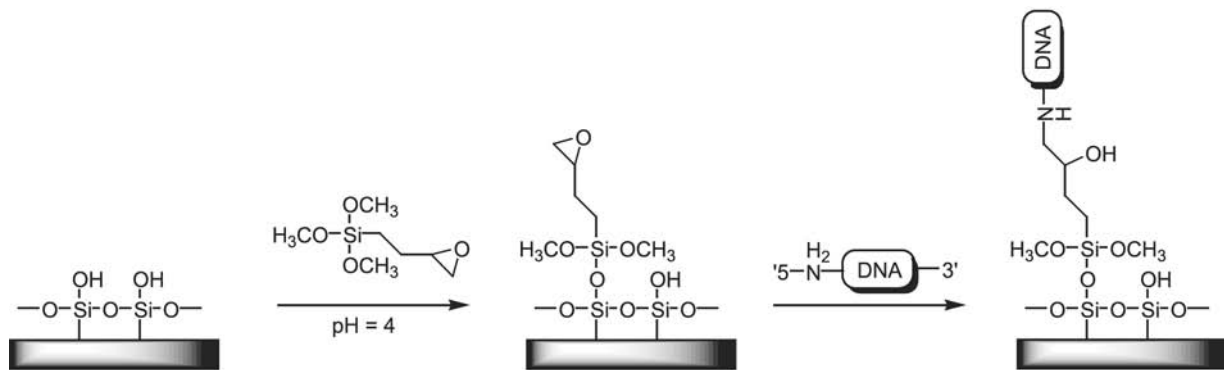


Fig. 2 Attachment chemistry of DNA to epoxide-derivatized silicon.

shift, which can be interpreted as a slight change in the optical thickness of the device, to binding of the solution-phase complementary DNA strand to the surface-immobilized sequence. Control experiments, including simple treatment of the chip with buffer, and incubation of the chip with a random DNA sequence, produced no change in the photoluminescence spectrum. Together, these results provided initial support for the idea that microcavity structures fabricated in porous silicon could have utility for detecting biological molecules.

## VIRUS DETECTION

For the detection of a more complex organism such as a virus, we next decided to examine the ability of the microcavity biosensor to detect  $\lambda$ -bacteriophage. Lambda is a double-stranded DNA bacteriophage that infects *Escherichia coli* (*E. coli*).<sup>[22,23]</sup> From the 48,502-base-pair genome of  $\lambda$ -bacteriophage, we selected the 30-base sequence 5'-TCG GAG AGC CTT CCT GTT CAA TAT CAT CAT-3'. This sequence, once again bearing a 3'-amino group, was obtained from a commercial vendor and covalently attached to the silicon surface as described above. The high base-pairing specificity of DNA is an advantage here with regard to specific identification of an organism; for example, a 16- to 18-base oligonucleotide is sufficient to uniquely define a sequence within the human genome. Likewise, we anticipated that this 30-base sequence would prove capable of uniquely identifying  $\lambda$ -bacteriophage. However, potentially more troublesome was the fact that  $\lambda$ -bacteriophage, such as all double-stranded DNA, exists in solution in a highly supercoiled (folded) conformation. In addition to potentially blocking access to the base sequence of interest, we were concerned that this large particle of DNA might not be capable of penetrating into the porous structure of the microcavity. To ameliorate both of these problems, the chip was heated to 89°C in a water bath, then exposed to a 194 fM solution of  $\lambda$ -bacteriophage (obtained from New England Biolabs, Inc.). At this temperature, the DNA uncoils, and the two strands of the double helix separate. Incubation was continued at this temperature for 1 hr. In addition to keeping the DNA uncoiled and separated into complementary strands, this also presumably provides thermodynamic assistance in the penetration of the target into the pores. The temperature was then reduced to 37°C, allowing hybridization of complementary DNA strands to occur.

Fig. 4 shows the results of this experiment. As with detection of the synthetic DNA oligomer, exposure of

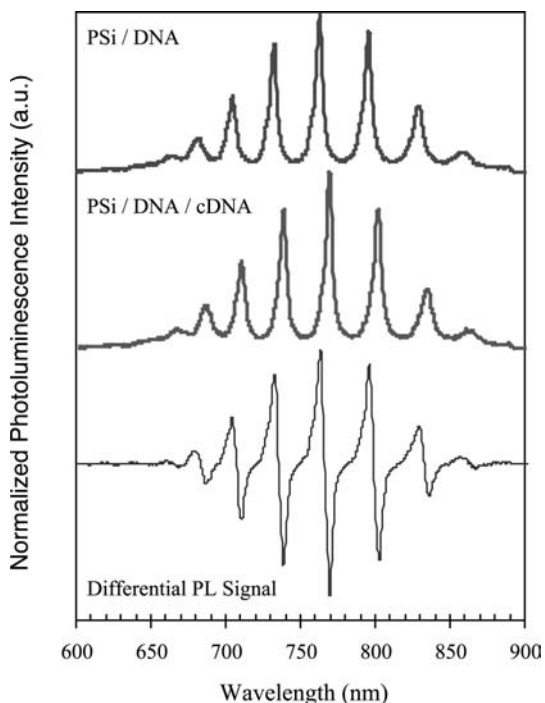
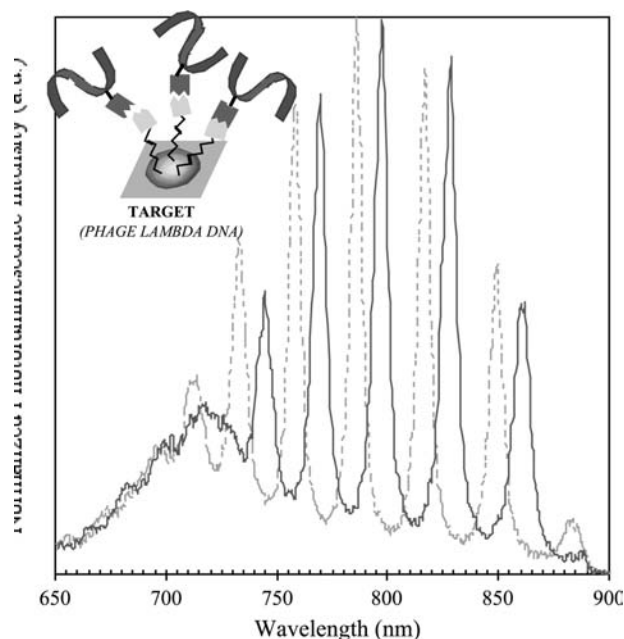


Fig. 3 Top: 50  $\mu$ M of DNA attached to a porous silicon microcavity structure. Middle: 1  $\mu$ M of complementary DNA is exposed to the DNA-attached porous silicon. A 7-nm red shift is observed, consistent with DNA binding. The difference spectrum is shown at the bottom.



**Fig. 4** Room temperature photoluminescence spectra taken before (dotted line) and after (solid line) recognition and binding of bacteriophage lambda to a 30-nucleotide complementary DNA sequence immobilized in a porous silicon microcavity structure. A 12-nm red shift is observed for a sensing bacteriophage lambda concentration of 194.2 fM.

the probe-functionalized chip to  $\lambda$ -phage causes a red shift in the photoluminescence spectrum, presumably because of the binding of the probe sequence to the complementary  $\lambda$ -DNA. In this case, a 12-nm shift was observed. While it is tempting to relate the magnitude of the red shift to the size and concentration of the DNA sequence detected (consistent with prediction and essential to establishing the porous silicon microcavity as both a *quantitative* as well as a *qualitative* sensor), significant additional experimentation will be necessary before making such a claim.

## BACTERIUM DETECTION

Following the successful demonstration of purified DNA oligonucleotides and  $\lambda$ -phage, we were next ready to examine the suitability of the porous silicon microcavity sensor as a detector for a bacterium. (Portions of this section are adapted from Ref.<sup>[24]</sup>). One could envision functionalizing the porous silicon structures with oligonucleotides unique to the genomic sequence of the target bacterium by direct analogy to the work described above. However, although targeting genomic DNA provides inherent advantages of *specificity*, and the molecular recognition entailed is relatively straightforward, it has inherent disadvantages

of *sensitivity*. Given that each bacterium has only a single copy of its genomic DNA sequence, unless the sensor is sensitive enough to detect single-copy-number targets, it is necessary to introduce an intermediate amplification (or bacterial culture) step. An alternative strategy is to target higher-abundance molecules. In essence, this is what the Gram stain does (Fig. 5). Gram (+) bacteria are so designated because their cell walls are largely made up of peptidoglycan, a polymeric molecule to which crystal violet adheres. In contrast, the cell wall of Gram (-) bacteria is more complex, including little peptidoglycan but an outer leaflet of lipopolysaccharide (LPS, Fig. 6). Lipopolysaccharide is a primary constituent of the outer cellular membrane of Gram (-) bacteria,<sup>[25]</sup> and is commonly known as bacterial endotoxin, the causative agent of sepsis.<sup>[26]</sup> The precise structure of LPS varies among bacterial species, but is overall composed of three parts: a variable polysaccharide chain, a core sugar, and lipid A.<sup>[27]</sup> As lipid A is highly conserved among LPS subtypes, this seemed a natural target. While molecules such as LPS and peptidoglycan do not provide species-level differentiation of bacteria, but rather separate bacteria into one of two broad classes, their inherent advantage is their extraordinarily high copy number per cell. Thus we have chosen to pursue a strategy of building bacterial biosensors in stages, constructing devices capable of detecting the highest-abundance (but, perhaps, lower specificity) molecules

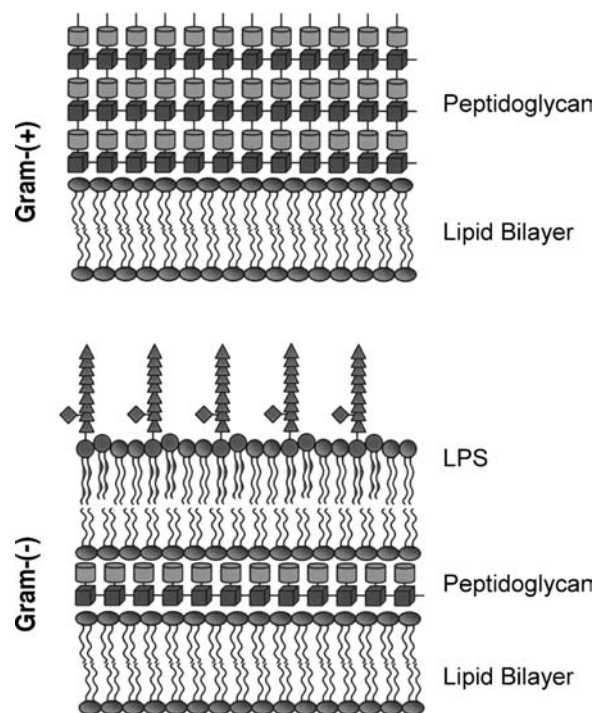


**Fig. 5** The molecular makeup of Gram (+) and Gram (-) bacterial cell walls.

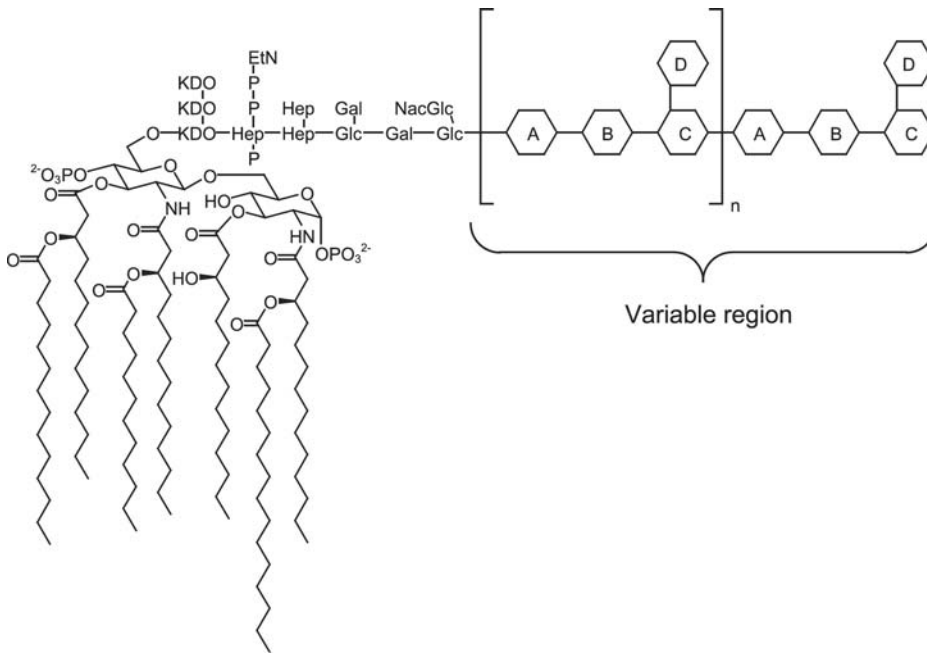


**Fig. 6** Structure of lipopolysaccharide (LPS). *Source:* From Ref.<sup>[27]</sup>.

first, and then progressing to lower-copy-number/higher-specificity targets. Fig. 7 schematically shows how this might be carried out: First, a sensor capable of detecting LPS and/or peptidoglycan would provide an initial indication that bacteria were present, and differentiate them based on their Gram category. Subsequent sensors would “hone in” on the species-level identification of the bacterium present, by differentiating Gram (-) bacteria (for example) based on differences among LPS subtypes, or based on the presence of species-specific, cell-surface proteins.

We designed and synthesized an organic receptor, tetratryptophan *ter*-cyclopentane, designated TWTCP, which binds to diphosphoryl lipid A in water with a dissociation constant of  $0.6 \mu\text{M}$ ,<sup>[28]</sup> as measured by UV-Vis spectrometric titration. Confirmation of

binding was provided by NMR and fluorescence titration experiments. While one could envision employing an antibody to LPS or lipid A as the probe molecule, several potential advantages attracted us to the use of an organic compound. First, although antibodies typically have exquisite binding selectivity and affinity, as proteins they are subject to a variety of environmental factors (e.g., thermal degradation and proteolysis) that might degrade the long-term stability of the device.<sup>[29]</sup> Second, because TWTCP can be produced via a relatively short synthetic sequence, it is potentially available in very large quantities. Third, it was anticipated that covalent attachment of TWTCP to the porous silicon matrix would be more straightforward than the analogous attachment of a complex antibody. However, it should be noted that

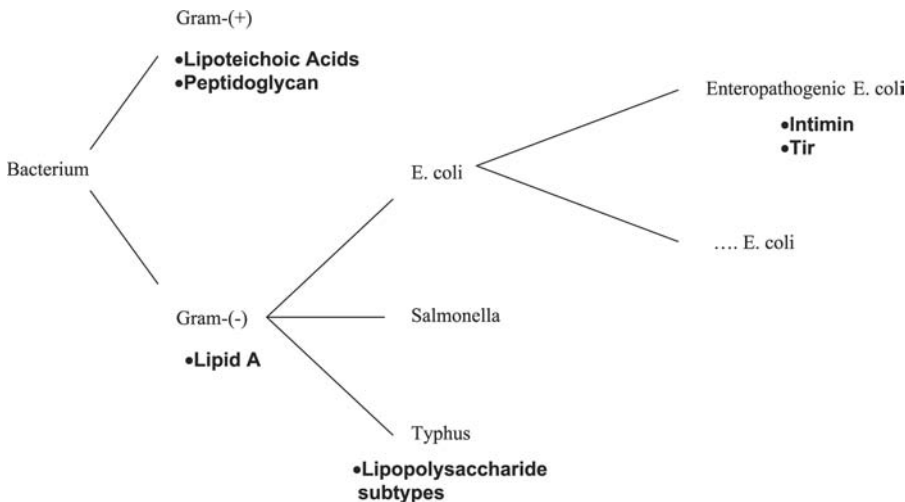


**Fig. 7** Schematic depiction of targets for bacterial biosensor development.

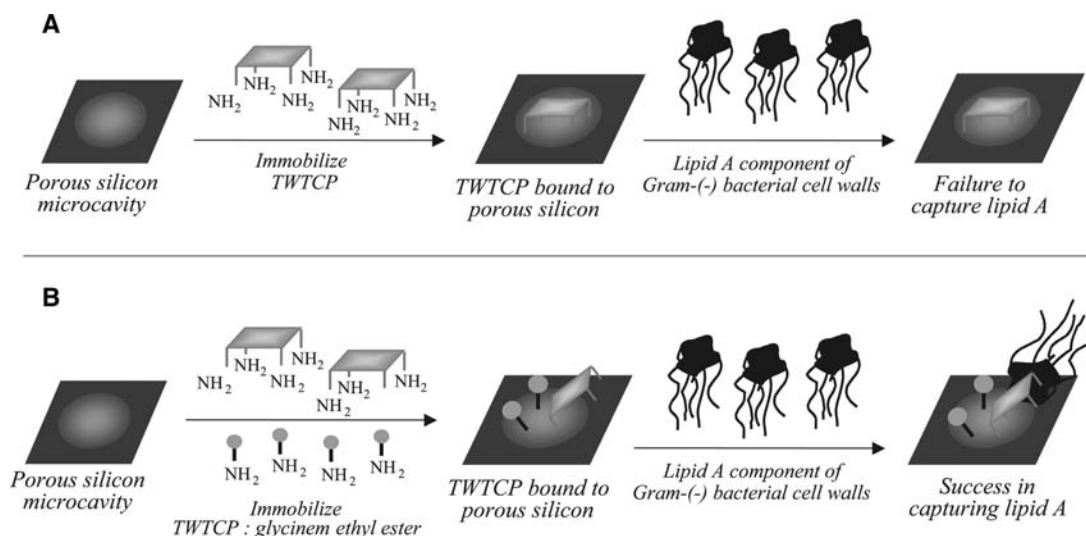


**Fig. 8** Functionalization of porous silicon microcavities with TWTCP and glycine methyl ester.

antibody-based porous silicon sensors also have considerable promise, and are an object of active research in our laboratories.

Detailed fabrication steps for the porous silicon microcavity resonator, including the electrochemical preparation and postthermal oxidation treatment, were as described above. As before, to provide functionality capable of forming a stable bond between the organic probe molecule and the inorganic silicon surface, the porous silicon microcavity resonator was treated with an aqueous solution of 3-glycidoxypropyltrimethoxy silane. Subsequent exposure of this epoxide-terminated surface to an aqueous solution of TWTCP in 6% dimethyl sulfoxide (DMSO), provided a surface functionalized with the lipid-A-binding receptor. To our surprise, we found that exposure of this device to purified diphosphoryl lipid A did not produce a shift in the photoluminescence spectrum of the chip. A consideration of our working model for the interaction of TWTCP with lipid A suggested that this could be due to a reaction of all four amino groups of the receptor reacting with the porous silicon surface, thus blocking access to the binding face of the receptor molecule, as shown in Fig. 8A. A second possibility is that binding of lipid A to the sensor is precluded if sufficient interstitial space between receptor molecules is not present, a problem that has been observed in some surface-immobilized DNA binding assays.<sup>[30]</sup> If either of these were indeed the case, we hypothesized that exposure of the epoxide-terminated surface to a mixture of TWTCP and a “blocking” amine would allow for the generation of a functional sensor (Fig. 8B).

Using glycine methyl ester as the blocking amine and examining the response of the sensor to purified lipid A, we found that the optimal ratio of receptor to blocker molecules was 1 : 10 TWTCP/glycine methyl

ester (Fig. 9). In this case, incubation of the sensor with a solution of lipid A produces an 8-nm red shift in the photoluminescence peak wavelength. When a 100% solution of TWTCP, or a 100% solution of glycine methyl ester, was immobilized in the porous matrix, no shifting of the luminescence peaks was detected after exposure to lipid A. To determine the ability of this sensor to differentiate between two classes of bacteria, independent overnight cultures of Gram (–) bacteria (*E. coli*) and Gram (+) bacteria (*Bacillus*

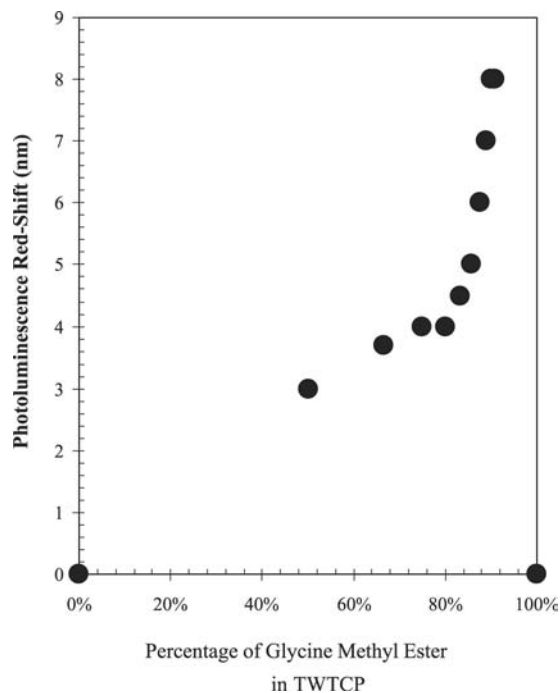


**Fig. 9** Dependence of lipid A recognition on the use of glycine methyl ester as a blocking group.

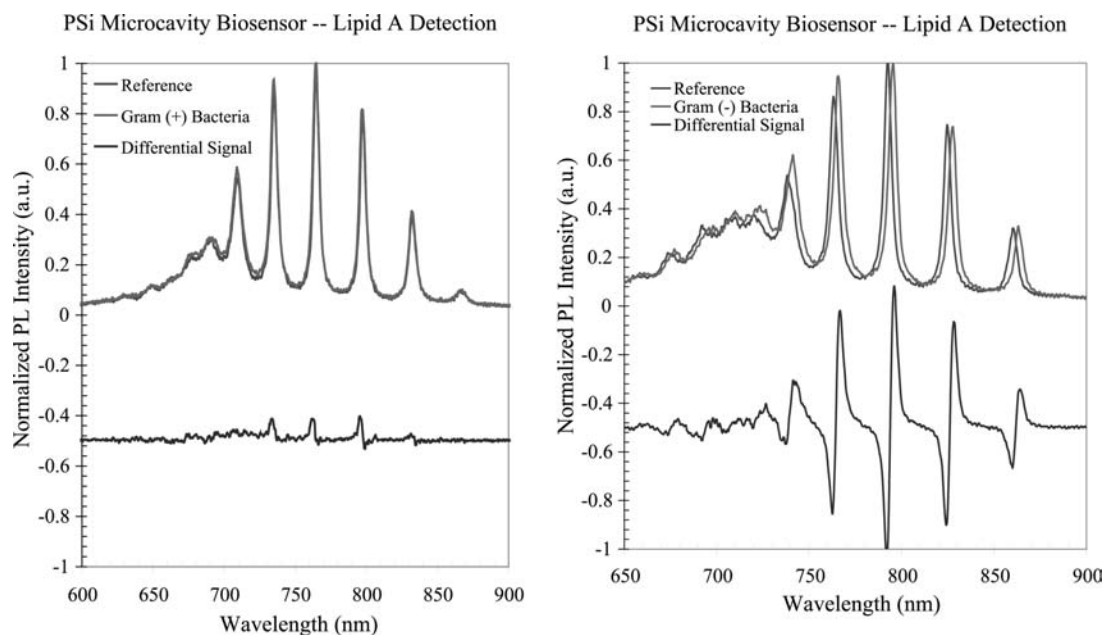


**Fig. 10** Response of TWTCP-functionalized porous silicon microcavities to Gram (+) bacteria (*B. subtilis*, left) and Gram (–) bacteria (*E. coli*, right).

*subtilis*) were grown up, centrifuged, and then individually lysed following resuspension in phosphate buffer solution. Upon exposure of the lysed Gram (–) cells to the immobilized TWTCP biochip, a 4-nm photoluminescence red shift is detected, (Fig. 10). The equilibrium recognition and binding time of TWTCP to lysed Gram (–) bacterial cells is an important variable to determine. It dictates the time it takes for the cells containing lipid A to diffuse into the pores to seek and bind to the receptors. Experimental results reveal that the minimum time it takes to red shift the photoluminescence peaks by 4 nm is 1 hr. Prolonged time exposures of up to 5 hr show no additional shifting.

However, when the microcavity sensor is exposed to a solution of lysed Gram (+) bacteria, no shifting of the luminescence peaks is observed, depicted by the left spectra of Fig. 10. While we attribute the large shift to the recognition and binding of the TWTCP receptor with the lipid A present in the bacterial cell wall, it is also conceivable that some other factor is responsible for the differential signal. Nonetheless, these results demonstrate the ability of a porous silicon biosensor to distinguish Gram (–) from Gram (+) bacteria through changes in the refractive index of the microcavity layers. Similarly, lysed solutions of *Salmonella minnesota* and *Pseudomonas aeruginosa*, both Gram (–) organisms, produced red shifts in the photoluminescence spectra of TWTCP-functionalized porous silicon microcavities. In contrast, lysed solutions of *Lactobacillus acidophilus*, a Gram (+) organism, did

not cause any detectable change in the photoluminescence spectrum.

## CONCLUSION

We have constructed a series of porous silicon microcavity devices functionalized with probes for synthetic oligonucleotides, viral genomic DNA, and bacterial lipopolysaccharides. In each case, exposure of the microcavity to a solution of the target molecule produces a specific change (a red shift) in the photoluminescence spectrum of the device. These early results are encouraging, given the potential advantages of porous silicon as a biosensing platform. Current efforts in our laboratories are focused on optimizing sensitivity and detection speed by modifying the geometry of the microcavity.

## REFERENCES

1. Dolley, C.S. *The Technology of Bacteria Investigation*; S.E. Cassino and Company: Boston, 1885.
2. Friedly, G. Importance of bacterial stains in the diagnosis of infectious disease. *J. Med. Technol.* **1985**, *1*, 823–833.
3. Fodor, S.P.; Read, J.L.; Pirrung, M.C.; Stryer, L.; Lu, A.T.; Solas, D. Light-directed, spatially addressable parallel chemical synthesis. *Science* **1991**, *251*, 767–773.

4. Wodicka, L.; Dong, H.; Mittmann, M.; Ho, M.-H.; Lockhart, D.J. Genome-wide expression monitoring in *Saccharomyces cerevisiae*. *Nat. Biotechnol.* **1997**, *15*, 1359–1367.
5. Iyer, V.R.; Eisen, M.B.; Ross, D.T.; Schuler, G.; Moore, T.; Lee, J.C.F.; Trent, J.M.; Staudt, L.M.; Hudson, J., Jr.; Boguski, M.S.; Lashkari, D.; Shalon, D.; Botstein, D.; Brown, P.O. The transcriptional program in the response of human fibroblasts to serum. *Science* **1999**, *283*, 83–87.
6. Cooper, M.A. Optical biosensors in drug discovery. *Nat. Rev., Drug Discov.* **2002**, *1*, 515–528.
7. Herino, R. *Properties of Porous Silicon*; Canham, L.T., Ed.; INSPEC, The Institution of Electrical Engineers: London, UK, 1997; 89 pp.
8. Sohn, H.; Letant, S.; Sailor, M.J.; Trogler, W.C. Detection of fluorophosphonate chemical warfare agents by catalytic hydrolysis with a porous silicon interferometer. *J. Am. Chem. Soc.* **2000**, *122*, 5340–5399.
9. Gao, J.; Gao, T.; Li, Y.Y.; Sailor, M.J. Vapor sensors based on optical interferometry from oxidized microporous silicon films. *Langmuir* **2002**, *18*, 2229–2233.
10. Janshoff, A.; Dancil, K.-P.S.; Steinem, C.; Greiner, D.P.; Lin, V.S.-Y.; Gurtner, C.; Motesharei, K.; Sailor, M.J.; Ghadiri, M.R. Macroporous p-type silicon Fabry–Perot layers. Fabrication, characterization, and applications in biosensing. *J. Am. Chem. Soc.* **1998**, *120*, 12,108–12,116.
11. Chan, S.; Fauchet, P.M.; Li, Y.; Rothberg, L.J.; Miller, B.L. Porous silicon microcavities for biosensing applications. *Phys. Status Solidi, A* **2000**, *182*, 541.
12. Berger, M.G.; Thönissen, M.; Arens-Fischer, R.; Münder, H.; Lüth, H.; Arntzen, M.; Theiß, W. Investigation and design of optical properties of porosity superlattices. *Thin Solid Films* **1995**, *255*, 313.
13. Berger, M.G.; Dieker, C.; Thönissen, M.; Vescan, L.; Lüth, H.; Münder, H.; Wernke, M.; Grosse, P. Porosity superlattices: a new class of Si heterostructures. *J. Phys., D. Appl. Phys.* **1994**, *27*, 1333–1336.
14. Frohnhoff, S.; Berger, M.G. Porous silicon superlattices. *Adv. Mater.* **1994**, *6*, 963–965.
15. Chan, S.; Fauchet, P.M. Tunable, narrow, and directional luminescence from porous silicon light emitting devices. *Appl. Phys. Lett.* **1999**, *75*, 274.
16. Chan, S.; Fauchet, P.M.; Li, Y.; Rothberg, L.J.; Miller, B.L. Porous silicon microcavities for biosensing applications. *Phys. Status Solidi, A* **2000**, *182*, 541–546.
17. Gao, T.; Gao, J.; Sailor, M.J. Tuning the response and stability of thin film mesoporous silicon vapor sensors by surface modification. *Langmuir* **2002**, *18*, 9953–9957.
18. Schena, S.; Shalon, D.; Davis, R.W.; Brown, P.O. Quantitative monitoring of gene expression patterns with a complementary DNA microarray. *Science* **1995**, *270*, 467–470.
19. Diehl, F.; Grahlmann, S.; Beier, M.; Hoheisel, J.D. Manufacturing DNA microarrays of high spot homogeneity and reduced background signal. *Nucleic Acids Res.* **2001**, *29*, e38.
20. Falsey, J.R.; Renil, M.; Park, S.; Li, S.; Lam, K.S. Peptide and small molecule microarray for high throughput cell adhesion and functional assays. *Bioconjug. Chem.* **2001**, *12*, 346–353.
21. MacBeath, G.; Koehler, A.N.; Schreiber, S.L. Printing small molecules as microarrays and detecting protein–ligand interactions en masse. *J. Am. Chem. Soc.* **1999**, *121*, 7967–7968.
22. Herskowitz, I. Control of gene expression in bacteriophage lambda. *Annu. Rev. Genet.* **1973**, *7*, 289.
23. Christensen, A.C. Bacteriophage lambda-based expression vectors. *Mol. Biotechnol.* **2001**, *17*, 219–224.
24. Chan, S.; Horner, S.R.; Miller, B.L.; Fauchet, P.M. Identification of gram negative bacteria using nanoscale silicon microcavities. *J. Am. Chem. Soc.* **2001**, *123*, 11,797–11,798.
25. Young, L.S.; Martin, W.J.; Meyer, R.D.; Weinstein, R.J.; Anderson, E.T. Gram-negative rod bacteremia: Microbiologic, immunologic, and therapeutic considerations. *Ann. Intern. Med.* **1977**, *86*, 456.
26. Raetz, C.R.H. Biochemistry of endotoxins. *Ann. Rev. Biochem.* **1990**, *59*, 129–170.
27. Strauss, E. Are drugs for sepsis the “impossible dream?” *Mod. Drug Discov.* **2000**, *3*, 37–43.
28. Hubbard, R.D.; Horner, S.R.; Miller, B.L. Highly substituted *ter*-cyclopentanes as receptors for lipid A. *J. Am. Chem. Soc.* **2001**, *123*, 5811–5812.
29. Ron, E.; Freeman, A.; Solomon, B. Stabilization and surface modification of monoclonal antibodies by “bi-layer engagement”. *J. Immunol. Methods* **1995**, *180*, 237–245.
30. Lin, Z.; Strother, T.; Cai, W.; Cao, X.; Smith, L.M.; Hamers, R.J. DNA attachment and hybridization at the silicon (100) surface. *Langmuir* **2002**, *18*, 788–796.



# Biosensor Applications: Surface Engineering

**Genady Zhavnerko**

*Institute of Chemistry of New Materials, National Academy of Sciences of Belarus,  
Minsk, Belarus*

**Kwon-Soo Ha**

*Department of Molecular and Cellular Biochemistry, Kangwon National University School of  
Medicine, Chuncheon, South Korea*

## Abstract

The aim of this review is to give an overview of the trends in surface modification for biosensor applications. We focused this review on developments in the past decade, describing the progress both in analytical techniques for detection of biomolecules and in the methods of receptor molecule immobilization on the surface of a transducer. The review is divided into several parts that characterize different approaches of surface modification, including local surface patterning, immobilization on self-assembled monolayers, and hybrid nanostructures bioengineering.

## INTRODUCTION

There has been a recent trend toward device miniaturization and functionalization for simultaneous analysis of multiple samples in the field of biotechnology. This trend can offer various advantages to the researchers because the devices are able to provide tools to handle ultra-small sample volumes and improve detection limit of nano-biosensors and -biochips by increasing the density of receptor elements. It is also possible to control the reactivity of the receptors by engineering them with molecular precision. In this entry, we will briefly characterize methods for biomolecular recognition on the surface and surface modification methods, such as Langmuir–Blodgett (LB), Layer-by-Layer (LbL), and Self-Assembly Monolayer (SAM) approaches. The most important step for successful surface engineering for biomolecules, which demands proper orientation, is also reviewed in details. The main goal of this entry is to show the trends in local surface patterning and subsequent receptor design on the solid surface for biosensor applications.

## OUTLINES

Biosensors are perspective tools in various fields such as medical diagnosis, drug screening, environmental monitoring, and defense applications.<sup>[1–4]</sup> Bioengineering on solid surface is essential for the surface development of biosensors and is a multi-disciplinary research field including biotechnology, chemistry, physics, microelectronics, material science, etc. The technologies for the production of protein microarrays are still

under development.<sup>[5–7]</sup> For application of biosensors, it is essential to immobilize receptors on sensor surfaces, which are directly attached to solid substrates and used to detect specific target molecules. Various biomolecules, such as antibodies, nucleic acids, proteins, or catalytic ones like enzymes, microorganisms, and biomimetic catalysts have been used as receptors.<sup>[6,7]</sup>

Biosensor devices have advantages over the enzyme-linked immunosorbent assay since molecular interactions can be monitored in real time by the biosensors without labeling. There has been a strong demand for miniaturization of the biosensors, since recently it has been more important to analyze hundreds to thousands of samples in parallel.<sup>[8]</sup> Scanning Probe Microscopy (SPM) has been widely used in life science for the researches of deoxyribonucleic acid (DNA) and protein structures with the molecular resolution.<sup>[9]</sup> It is now possible to handle molecular assemblies and to pattern monolayer films because of the constant progress of SPM technologies.<sup>[10]</sup> Scanning probe microscopy methods allow to pattern sensor surfaces in a molecular level with the precise control of structure and location. The resulting nanostructures will provide promising applications in the development of biochips in the nanometer scale.

## Analytical Techniques for Detection of Biomolecules

Instrumentation for bioanalytical purposes is now well elaborated and includes various techniques,<sup>[11]</sup> such as mass spectrometry, X-ray photoelectron spectroscopy, imaging ellipsometry, infrared reflection–absorption,

fluorescence spectroscopy, and SPM methods (atomic force microscopy (AFM), scanning tunneling microscopy (STM), near-field scanning optical microscopy (NSOM), etc.). These methods can provide the essential tools to analyze the presence of proteins on solid surface, to register the morphology changes, and to measure the biospecific interactions at the molecular level. Detection of molecular interactions by biosensors is mainly based on the optical and electrochemical techniques, such as surface plasmon resonance (SPR), total internal reflection fluorescence, time-resolved fluoroimmunoassay, the displacement flow immunoassay, and electrochemical impedance spectroscopy.<sup>[12–18]</sup>

Surface plasmon resonance is one of the prevalent methods for analysis of biomolecular interactions<sup>[12,13]</sup> because of its direct detection of analytes in real time. Surface plasmon resonance biosensors have been widely used for the analysis of antigen–antibody interactions,<sup>[17,19]</sup> and also used to characterize the conformational changes of protein molecules.<sup>[12]</sup> Recently, there has been an intensive investigation on the imaging of protein arrays by spectral SPR biosensors based on wavelength-interrogation (Fig. 1). One

drawback of SPR biosensors is the detection limit of low concentration or low molecular weight analytes, but the detection limit has been improved by oriented immobilization of proteins, enhancing the response signal by streptavidin-biotinylated protein complex,<sup>[13]</sup> or using modified colloidal gold particles.<sup>[14,20]</sup>

Quartz crystal microbalance,<sup>[15]</sup> electrochemical,<sup>[16]</sup> capacitive,<sup>[17]</sup> and microcantilever biosensors<sup>[21–23]</sup> can be also widely used by the integration with microelectronic chip technology. For example, the microcantilever-based sensors are suitable for “label-free” detection of biomolecules<sup>[21]</sup> and can be operated either as microbalances (using dynamic mode of AFM) or as surface stress sensors (static bending cantilever). This cantilever vibration or bending is caused by the forces involved in the adsorption process at the cantilever surface. A femtogram mass sensing biosensor can be designed using the resonance frequency shifts of cantilevers.<sup>[22]</sup> The cantilevers produced in silicon technology can also be scalable into arrays for the differentiation of the biochemical interactions.<sup>[23]</sup> Undoubtedly, these methods will play an important role in future, specially, in the microcircuit development.

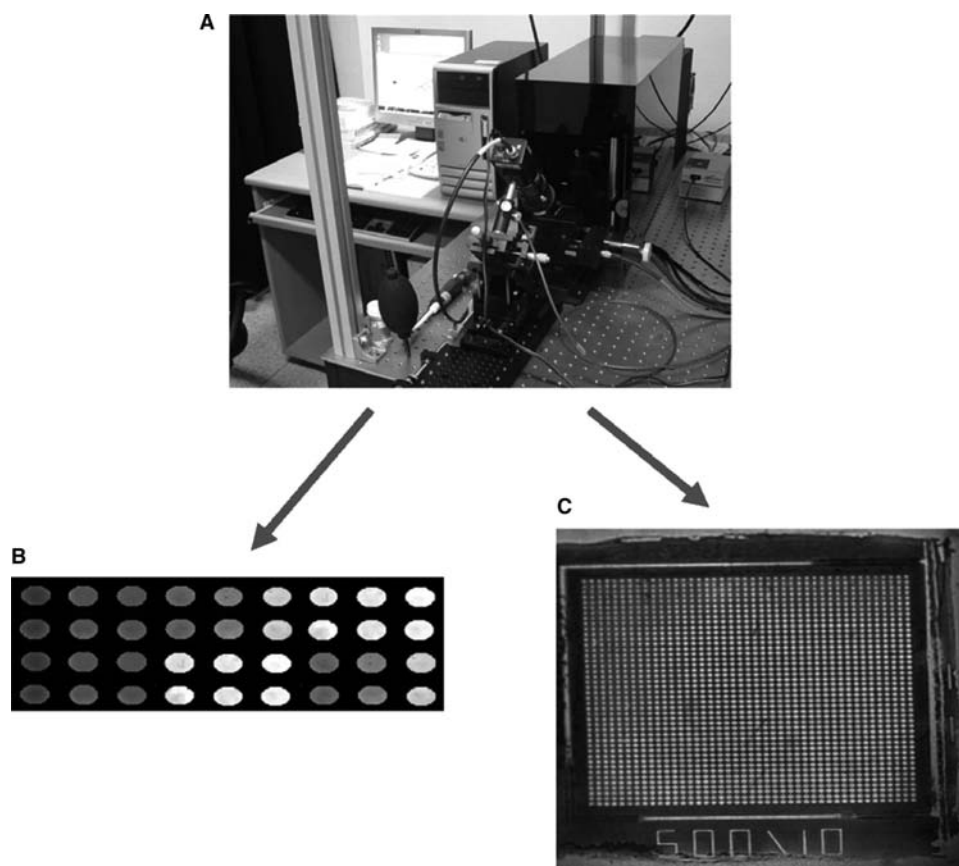


**Fig. 1** Analysis of protein arrays with a dual function spectral SPR biosensor. (A) A dual function spectral SPR biosensor. (B) Analysis of protein arrays by SPR imaging. (C) Analysis of protein arrays by surface plasmon microscopy.

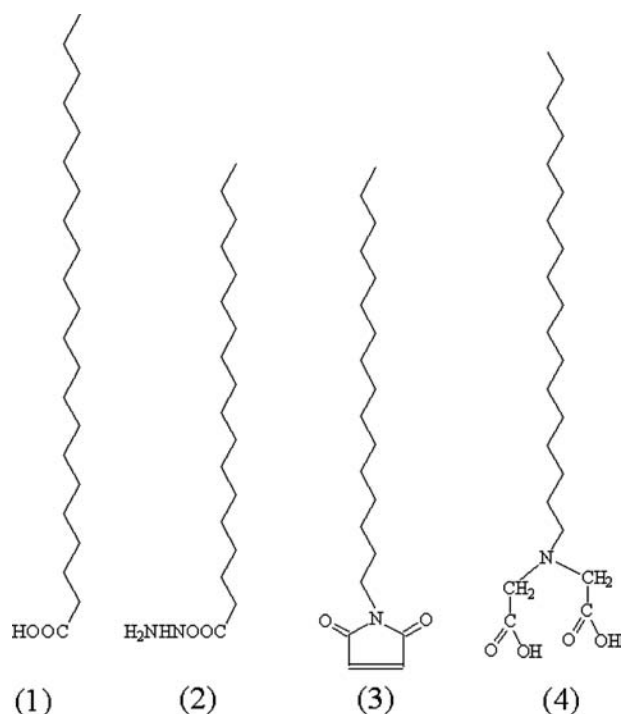


**Fig. 2** Examples of surface-active molecules for monolayer film formation by LB method. (1) Behenic acid, (2) octadecanoic acid hydrazide, (3) *N*-hexadecylmaleimide, (4) *N*-carboxymethyl-*N*-octadecylglycine.

### Methods of Surface Modification: LB, LbL, and SAM Approaches

These methods produce uniform and well-organized thin films with monomolecular thickness, which may be followed by a big variety of post-patterning modification. Appropriate molecules should be used for each method.

LB method is operated with amphiphilic molecules (Fig. 2) on the water interface and used for transferring monolayer films onto solid substrates.<sup>[24]</sup> Monolayer films are typically transferred onto substrates by dipping vertically the substrates through the interface. Some proteins form well-ordered monolayers at the water phase and can be transferred onto solid surfaces using the LB technique.<sup>[25]</sup> This technique can be used to design biosensor surfaces<sup>[26]</sup> because the orientation and surface density of biomolecules can be controlled.<sup>[27,28]</sup> Indeed, the LB method gives an opportunity to design functional biological systems with appropriate orientation in lipid monolayers.<sup>[29]</sup> Such an approach has been applied to the binding of histidine-containing peptides<sup>[30]</sup> and proteins<sup>[31]</sup> to chelator-lipid monolayers at the air-water interface. As a result, using determined receptor units inside the monolayer, e.g. calix[4]arene derivatives,<sup>[32]</sup> nanomolar concentrations of the proteins can be selectively detected. Various functionalized biomimetic

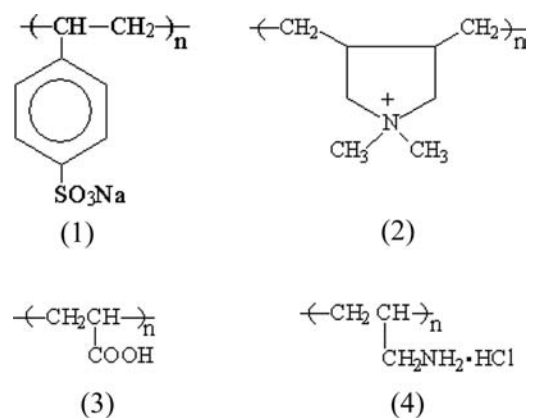


**Fig. 3** Typical polyelectrolyte molecules for LbL method. (1) Poly(diallyldimethylammonium) chloride (PDDA), (2) poly(sodium 4-styrenesulfonate) (PSS), (3) polyacrylic acid (PAA), (4) polyallylamine hydrochloride (PAH).

nanostructures oriented recognition site can be constructed<sup>[33]</sup> to study artificial cell membranes in an effort, for example, to speed up the discovery of new drugs for a variety of diseases.

LbL method consists of the step-by-step electrostatic adsorption of anionic and cationic polyelectrolytes (Fig. 3) on a charged surface in solution, which has been introduced by Decher,<sup>[34]</sup> and it provides a way to fabricate ultrathin functional films on solid surfaces with nanometer resolution. By the LbL method, it is possible to change the property of inorganic surfaces and create “friendly” monolayer environments (hydrocarbon, charged, etc.) for non-specific protein binding. The method has been extended and successfully applied to the surface formation with various biomolecules such as globular proteins,<sup>[35]</sup> enzymes,<sup>[36]</sup> and even viruses.<sup>[37]</sup>

Self-assembly monolayers provide an alternative means by which molecules are self-organized into densely packed structures on a surface.<sup>[38,39]</sup> This method was pioneered by Sagiv,<sup>[40]</sup> who has introduced the hydrophobization of silicon surface with octadecyltrichlorosilane molecules. A similar approach was successfully developed especially for organic thiolate molecules (Fig. 4) on gold surface.<sup>[41]</sup> The gold-thiol reaction may be regarded as an oxidative reaction of the S-H bond with gold surface followed by a reductive elimination of hydrogen.<sup>[41]</sup> The sulfur-to-gold bond is strong and the bond strength has been reported as 40 kcal/mol. Now, SAMs of organothiols on gold have been used as a spacer layer for biomolecule attachment to the gold surface.<sup>[38]</sup> In addition, SAMs can be further modified by subsequent treatments, for example, the photochemical addition of H<sub>2</sub>S to the terminal double bond of vinyl-terminated 18-nonadecyltrichlorosilane film and attachment of new molecular layers.<sup>[42]</sup>

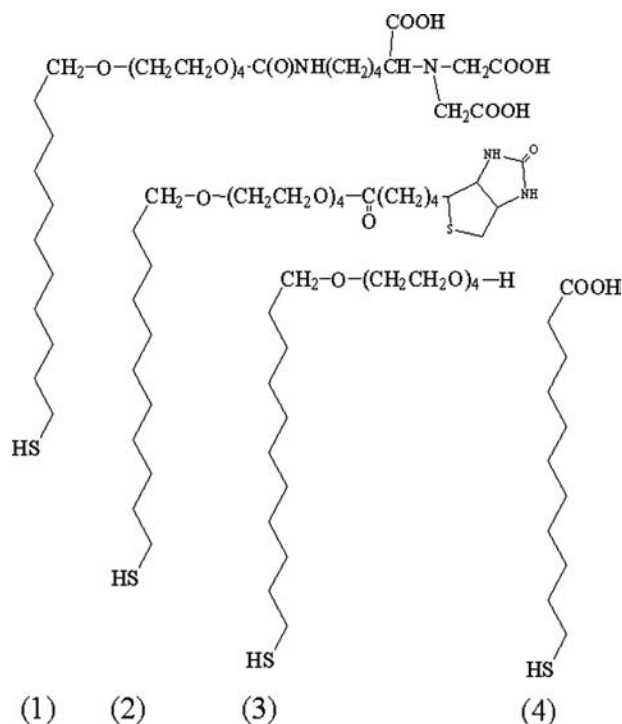


**Fig. 4** Organothiols for SAM film formation. (1) NTA-terminated tetra(ethylene glycol) undecylthiol, (2) biotin-capped tetra(ethylene glycol) undecanoat, (3) 1-mercapto-11-undecyl tetra(ethylene glycol), (4) 11-mercaptoundecanoic acid.

## PROTEIN IMMOBILIZATION

### Protein–Surface Interaction

Surface modification is a key technique for biosensor elaboration. However, protein–substrate and protein–protein interactions are quite complex. Protein

properties, especially, their conformation, can be changed by the contact with sensor surface, since proteins are affected at the sensor surface by van-der-Waals hydrophobic and electrostatic interactions, interfacial perturbations by multipoint attachments to the surface, pH environment, surface charge, co-adsorption of low molecular weight ions, and isoelectric points of proteins.<sup>[43]</sup> Bound proteins may lose their activity resulting from the immobilization chemistry or inappropriate orientation. Hence, the biological activity of biomolecules on immobilization on the chip surface should be preserved. Immobilized molecules must retain their native conformation to ensure proper function at the surface without denaturation. That is why, during the last few years, special interest has been paid to the studies on the nature of the protein–surface interaction to control the biomolecule adsorption process.<sup>[44]</sup> Biomolecules can be immobilized on the surfaces by other methods, for example, physisorption or chemisorption, copolymerization, covalent chemical coupling, and supramolecular interactions.<sup>[45,46]</sup> Immobilization of antibody molecules from immunoliposomes has been also used in several biotechnological applications.<sup>[47]</sup> In addition, protein solutions can be applied to the surfaces by inkjet printing or electrospray.<sup>[48]</sup> However, the deposition of liquid samples followed by drying can result in protein aggregation and loss of biological activity.

Simplest approach includes incorporation of antibodies<sup>[49]</sup> or enzymes<sup>[50]</sup> into thin films. This approach is quite promising because repeated assays by regeneration is possible. A whole range of antibodies with different specificities can be bound to and dissociated from the surfaces simply by lowering the pH of the solutions.<sup>[51]</sup> It has been reported<sup>[52]</sup> that the structure and orientation of adsorbed proteins is dependent on the charge of the film. For example,

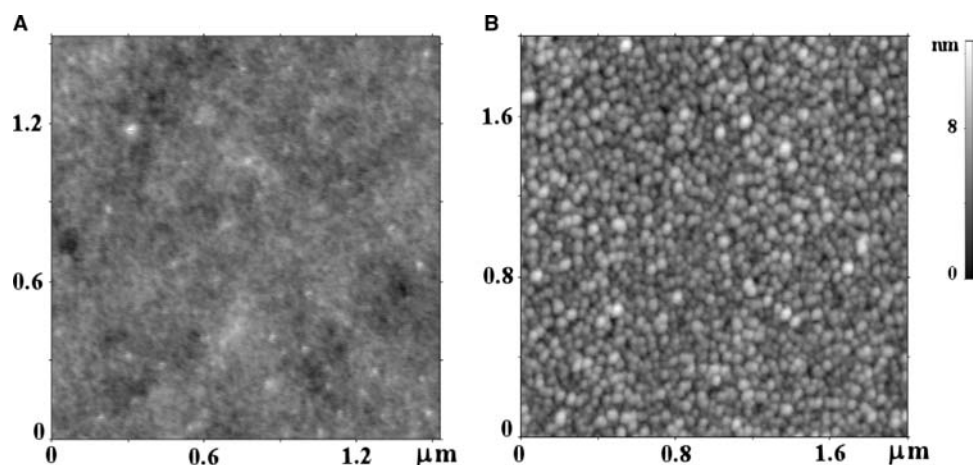


**Fig. 5** AFM-images of transferrin molecules (1 mg/ml) immobilized on (A) PDDA/PSS/PDDA and (B) (PDDA/PSS)<sub>2</sub> on mica surface.

transferrin bound to the negative charged surface displayed normal morphology and behavior, whereas the protein unfolded on the strongly positive-charged surface did not (Fig. 5).

The advantage of protein immobilization by physico-sorption method on film surfaces is reversible reaction. Indeed, protein interactions on surfaces have physical nature and the interactions are easily disturbed by salt concentration (phosphate buffered saline (PBS) solution, for example), pH environment, and competitive reactions in the solution. However, the immobilized biomolecules can be susceptible to the reduction of biological activities by inappropriate orientation of the biomolecules caused by physical adsorption.

### Covalent Immobilization

Covalent coupling of molecules, on the other hand, is irreversible and thus stable. Glass, quartz, or silicon surface can be modified with aminopropyltriethoxysilane or mercaptopropyltrimethoxysilane for biomolecule coupling. In particular, siloxy linkage can be applied for the activation of glass or silicon surface by aminopropyltriethoxysilane in dry toluene, resulted in the formation of covalently bound siloxane film.<sup>[53]</sup> However, majority of works have been focused on the gold surface immobilization due to its better-elaborated chemistry based on thiols.<sup>[54]</sup> The antibodies are usually linked to gold substrates using bifunctional reagents with a thiol group on one side.<sup>[55]</sup> Representative bifunctional molecules are shown in Fig. 6.

*N*-hydroxysuccinimide/ethylcarbodiimide cross-linking is one of the most popular methods for immobilization of proteins and nucleic acids on sensor surfaces.<sup>[56,57]</sup> The NHS/EDC covalent coupling results in the formation of mainly amide bonds between enzymes and SAM molecules.<sup>[58]</sup> However, immobilization by the covalent coupling may result in the random orientation of biomolecules because the functional groups used for the attachment can be found in more than one location of the biomolecule surfaces. So, the biomolecules may lose their biological activities by the random orientation on their support surfaces.<sup>[59]</sup>

The best approach to control the orientation of immobilized biomolecules is to selectively attach a pre-determined site of the protein on the sensor surface. There have been reports on the methods to control the orientation of immobilized proteins on the surface,<sup>[60–63]</sup> such as i) site-specific oriented attachment of biomolecules to gold surfaces through thiol- or cysteine-containing enzyme, ii) orientation with hetero-bifunctional photoactivatable cross-linking agents, and iii) oriented immobilization of antibodies by the use of immobilized protein A or G, or biotin–streptavidin interaction. Indeed, it is possible to genetically

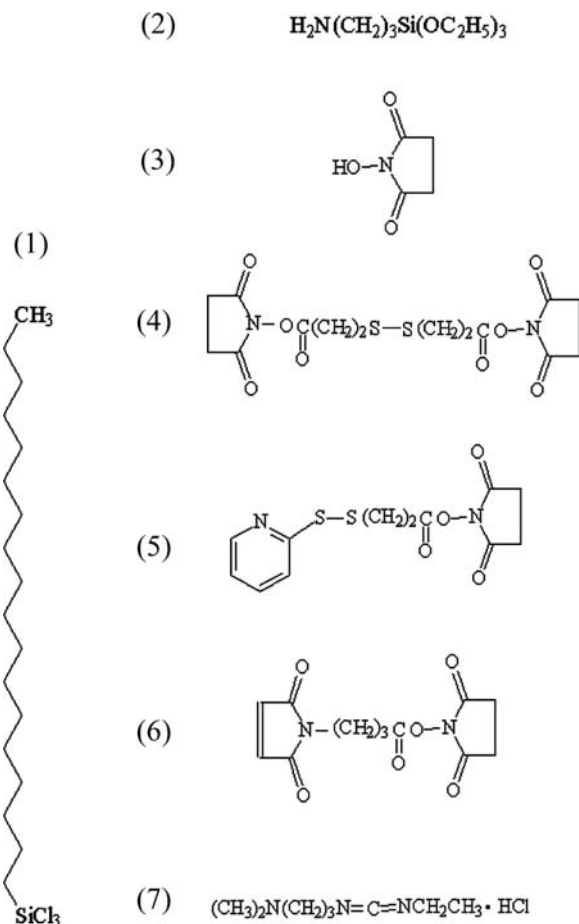


**Fig. 6** Chemicals commonly used for silicon (1,2) and gold surface modification (3–7). (1) Octadecyltrichlorosilane (OTS), (2) aminopropyltriethoxysilane (APTES), (3) *N*-hydroxysuccinimide (NHS), (4) di(*N*-succinimidyl)-3,3'-dithiodipropionate (DTSP), (5) 3-(2-pyridyldithio)propionic acid *N*-hydroxysuccinimide ester (SPDP), (6) 4-maleidobutyric acid *N*-hydroxysuccinimide ester, (7) *N*-(3-dimethylaminopropyl)-*N'*-ethylcarbodiimide (EDC).

incorporate functional coupling site(s) into the protein structure<sup>[60,61]</sup> or to implement reductive splitting of antibodies by 2-mercaptoethylamine<sup>[62]</sup> with subsequent immobilization to solid surfaces. Specific binding of antibodies against antigens was successfully observed by using splitted immunoglobulins<sup>[62]</sup> or cysteine-modified antibodies.<sup>[60]</sup>

The universal tools to properly orient antibody molecules are protein A and G from *Staphylococcus*, which specifically bind to the Fc regions of antibodies. After immobilizing protein A or G to the surface by NHS/EDS or SPDP/EDS cross-linking reaction, it is possible to attach antibodies with the desired orientation for the antigen binding. In addition, avidin and biotin can be used as a cross-linking bridge between proteins and surfaces. Indeed, avidin and streptavidin are tetrameric proteins and their binding

sites are located in pairs on either side of the protein molecule. Thus, when avidin or streptavidin is attached to gold surface via one or two binding sites, the other binding sites are exposed to the solution.<sup>[64]</sup> Hence, the appropriate binding of streptavidin or avidin to the solid surface<sup>[65]</sup> can produce an oriented protein film.

At last, there have been reports on heterobifunctional, photoactivatable cross-linking agents for protein conjugation,<sup>[66]</sup> which are commercially available. Most of these compounds contain aryl azides as the photophore. The major problem for patterning the substrates with photolithography is the chemicals involved in the process, which may denature the immobilized proteins and then reduce their activity.

### Immobilization on SAMs

Self-assembly monolayers prepared by bifunctional compounds (Fig. 4) are extremely important and promising for bioengineering of sensor surfaces. SAMs can be used for both adsorption of biomolecules and appropriate orientation of macromolecules. Covalent coupling of proteins and peptides is achieved by the conjugation of COOH-terminated SAMs with NHS esters. Such cross-linkers can be used to covalently attach biomolecules to the surfaces that are coated with thin films of hydrophilic polymers, e.g., poly(ethylene glycol) (PEG) or pluronic triblock copolymers.<sup>[67]</sup> Polynucleotides are also anchored to preformed alkanethiol SAMs via NHS/EDC cross-linking reaction.<sup>[68]</sup>

Quite perspective is the use of mixed SAMs for biomolecules. The mixture of two molecules allowed the creation of a range of surfaces with varying hydrophilicity and different functions.<sup>[39,69]</sup> In this approach, mixed monolayers, consisting of biotinylated alkanethiols and an ethylene glycol-terminated alkanethiol, were used. The latter helps to optimize the density of binding sites and to reduce non-specific binding to the surface.<sup>[69]</sup> Indeed, long-chain alkylthiols, terminated by PEG (Fig. 4), effectively prevent non-specific binding of proteins.<sup>[70]</sup> Minimization of non-specific interactions can also be obtained by covering gold- or glass-surfaces with thin layers of dextrans.<sup>[71]</sup>

In addition, protein immobilization on SAM can be achieved through chelating interactions. Indeed, gold surface can be modified by SAMs with metal-chelating alkanethiols<sup>[72]</sup> as well as oxide surfaces with metal-chelating silanes.<sup>[73]</sup> The free coordination sites of the chelator-metal complex subsequently react with histidine residues of proteins. The binding of proteins to the NTA derivative (Fig. 4) is highly specific and fully reversible on addition of a competitive ligand (histidine or imidazole), reprotonation of the histidine residues, or removal of the metal ion via EDTA.

### Hybrid Nanostructures for Bioengineering

Nanocrystals derivatized with biological molecules have been applied in biological research in recent years.<sup>[74,75]</sup>

There is a possibility that the conjugation of nanoparticles (NP) to different biomolecules such as DNA,<sup>[76]</sup> proteins,<sup>[77]</sup> antibodies,<sup>[78]</sup> short peptides<sup>[79]</sup> with subsequent conjugate targeting to receptor sites of analyte.

Self-assembly of chemically constructed hybrid metal-organic nanostructures from solution onto solid surface with molecular precision may be extremely useful for the fabrication of nanodimensional biosensors in future as an alternative to the conventional microfabrication techniques. Recent advances in this area are based on the use of ligand stabilized gold nanoparticles.<sup>[80,81]</sup> It has been reported that the conjugation of DNA oligomer-Au nanoparticle conjugates with complementary sequences are selective and reversible.<sup>[82]</sup> And there have been reports on a variety of Au nanoparticle-based DNA assays. Other standard system for the preparation of DNA-gold conjugates has used the biotin-streptavidin coupling method, in which biotinylated DNA binds to streptavidin-coated gold colloids.<sup>[83]</sup> In addition, DNA hybridization has been used to assemble Au nanoparticles onto patterned substrates prepared by the lithographic approach.<sup>[84]</sup> Gold nanoparticles emit light, so intense that it is easily possible to observe a single nanoparticle at laser sub-100 fs pulses of 790 nm light.<sup>[85]</sup> Hence, the NP conjugates are a viable alternative to fluorophores for biological labeling and imaging.

The biomolecule-nanoparticle hybrid systems can be also used for bioelectronic applications provides a high surface area matrix with excellent charge transport properties for the electrical contacting of enzymes with the electrode.<sup>[86]</sup> The fluorescent conjugates NPs with antibodies yields biomarkers, which can compete and even replace the traditional organic fluorescent tags in terms of biocompatibility, excitation, and photostability.<sup>[74,75]</sup> Nanoparticles have a broad excitation spectrum, but emit only at a characteristic emission wavelength. Some of them were bright enough to visualize even a single dot, and their subsequent conjugation with proteins do not affect the yields much. Various organic and inorganic materials have been utilized as capping materials on the surface of nanoparticles through covalent or ionic interactions.<sup>[38,87]</sup> These capping agents stabilize nanocrystals in solution. For example, CdSe NPs are often overcoated with ZnS layer; these improve the fluorescence quantum yield and decrease NC toxicity.<sup>[87]</sup> Cadmium selenide nanoparticles coated with zinc sulfide can then be functionalized with a bifunctional SAM either directly or via ligand exchange to tune a surface charge of the nanocrystals and incorporate any of the most relevant biological functional groups



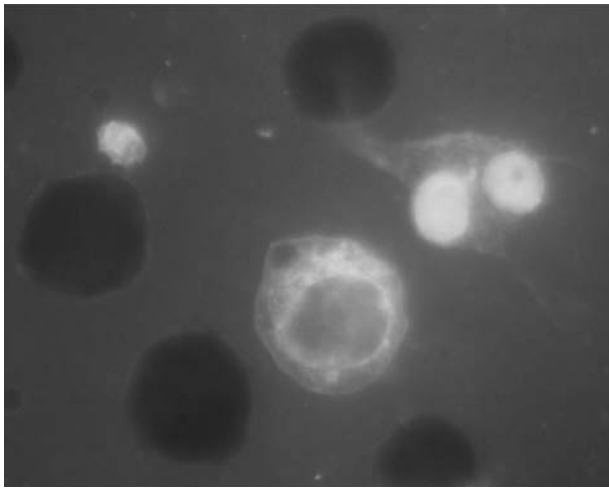


**Fig. 7** Fluorescence image of a cell culture decorated with “CdSe/ZnS/ligand” nanoparticles.

(-COOH, -NH<sub>2</sub>, -OH) for the generation of shells with biocompatible surfaces. Fluorescence image of cancer and living cells after treatment with the NPs shows selective NP penetration through outer membrane of living cells only (Fig. 7). Obviously, capping

molecules play a determined role as the connecting media of the NPs to the biological probe. As an ideal case, immobilization strategy should be based on specific interactions between the biological target molecule and tailored modifications of the NP surface.

## SURFACE PATTERNING

In biosensor technology, surface patterning has been increasingly perspective for the elaboration of high-density multianalyte chips. Surfaces can be chemically patterned using a number of techniques, such as photolithography,<sup>[88]</sup> microcontact printing ( $\mu$ CP),<sup>[89]</sup> and microfluidic patterning.<sup>[90]</sup> These techniques can also be sorted into two categories: i) indirect methods and ii) direct active placement. The active methods include inkjet and pipette deposition.<sup>[91]</sup> It is also possible to directly pattern biomolecules on a solid substrate by  $\mu$ CP without loss of biological activity.<sup>[89]</sup>

Photolithography creates protein patterns on the substrates by using chemical linkers to conjugate proteins.<sup>[66]</sup> Photochemical patterning uses chemically labile species, which can be activated on irradiation to target proteins for binding.<sup>[92]</sup>

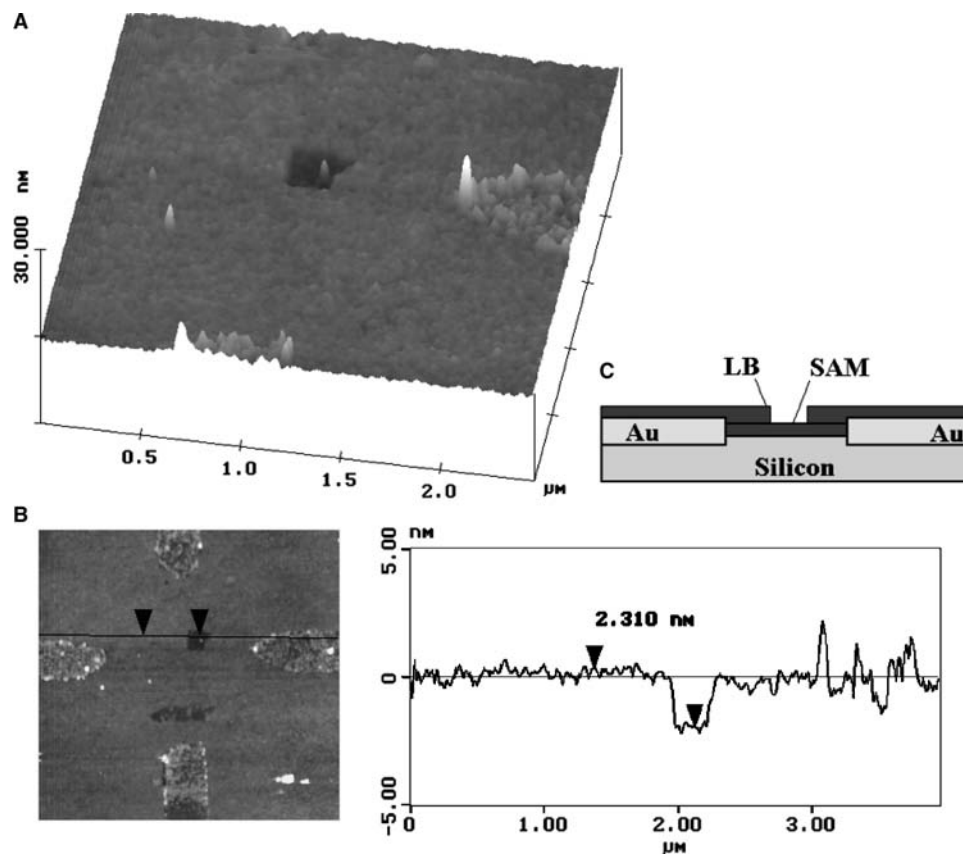


**Fig. 8** Result of mechanical scratching of topmost LB monolayer on SAM sub-layer. (A) 3D view, (B) cross-sectional analysis, and (C) schematic diagram of the sample.

Templates with variable surface chemical properties can be patterned on SAMs.<sup>[93]</sup> A patterned SAM can be fabricated by decomposition of UV light or an electron beam,<sup>[94]</sup> or etching the SAM by a SPM tip.<sup>[95]</sup> Argon ion or electron beam lithography can produce smaller patterns (down to tens of nanometers), but requires a high-vacuum environment. In addition, surface properties can be worse by photoresistance used. On the contrary,  $\mu\text{CP}$ <sup>[96]</sup> is a simple, flexible, and efficient patterning technique, which was introduced by Whitesides and coworkers in 1993 for patterning SAMs of alkanethiols onto gold substrates.  $\mu\text{CP}$  makes molecule-based patterns with sub-100-nm resolution and is well combined with the formation of microfluidic networks.  $\mu\text{CP}$  can transfer proteins onto a variety of substrates (hydrophilic or hydrophobic) including glass, gold, silicon, polymer surfaces, and monolayers on gold.

Microcontact printing of a pattern of hydrophobic alkanethiols can generate sites where proteins will deposit from solution after blocking the unprinted parts of the gold substrate with thiolated PEG.<sup>[56]</sup> In the process of surface patterning, proteins should selectively bind to the active surface and have strong repulsion from other regions of the substrate. This method provides a possibility to deposit proteins from solution into patterns.<sup>[97]</sup>

Recently, a new strategy to fabricate the SAM nanopattern by “dip-pen” nanolithography (DPN) has been reported.<sup>[98]</sup> Tips of microscope may have an influence on samples and commonly modify the sample surface on the molecular level. Because of this reason, SPM methods have been evolved into so-called Scanning Probe Lithographic (SPL) methods, which may be applied to the protein surface patterning. By SPL methods, it is possible to scratch SAM, LbL, or LB films mechanically (Fig. 8), and to derivatize electrode surfaces by STM.<sup>[99]</sup> It is also possible to transport organic molecules from the AFM tips to the surface in the area specifically defined by the tip/surface interaction by DPN,<sup>[98]</sup> and to incorporate reactive sites into SAMs by “nanoshaving”.<sup>[100]</sup>

In particular, DPN is a technique to fabricate patterns of chemical functionality like organothiols on gold,<sup>[101]</sup> and even gold particles on silicon.<sup>[102]</sup> It is shown that the molecular transport from the AFM tip with adsorbed molecules to substrates is determined by the probe geometry, water meniscus properties, and the chemical nature of the “ink”.<sup>[98]</sup> However, the mechanism of the DPN process is more complex. In particular, it was proved with octadecanethiol as an example that the water meniscus is not universally responsible for DPN molecular transport between the AFM tips and substrates.<sup>[103]</sup>

Reversible translocation has been observed in the hybrid CdTe/behenic acid composites, which is dependent on the applied force to the AFM tip.<sup>[104]</sup> Since monolayer films are easily self-reorganized on the surface,<sup>[105]</sup> it is reasonable to consider the DPN transfer as the local self-organization process, pushing molecules into energetically more favorable state on the surface. Hence, DPN process can be expanded on a big variety of surface-active molecules and considered as an extremely perspective technique for surface modification.

In addition, electrooxidation of terminal groups of alkylsilane SAMs seems quite promising, since only a few nanometer lines could be drawn by conducting AFM tip in inert matrix.<sup>[106]</sup> Subsequent self-assembly of organic and inorganic building blocks can be developed on the activated part of the SAM surfaces by surface chemistry.<sup>[42]</sup>

## CONCLUSION

It is clear that miniaturization and simultaneous analysis of multiple samples are the general tendency in the development of biosensors. Progress in nanotechnology will require approaches from various research fields of science and engineering. Indeed, SPM methods can not only visualize the surface of protein layers, but also recognize biomolecules. For example, by the methods, it is possible to quantify immunological reactions and to probe the adhesive forces of antigen–antibody interactions. In the near future, high-speed AFM imaging in solution may provide a tool to analyze biomolecule interactions on the sensor surface in real time.

Well-defined immobilization schemes and technological approaches have already been elaborated. Their combination will allow the construction of desired functions on the determined area of sensor surfaces. Indeed, it is possible to directly replace SAM molecules onto the sensor surface because the SAM molecules under AFM tip can be removed and replaced by the new adsorbate molecules into solution. This method can provide a new approach for site-directed attachment of functional molecules to the sensor surface. In addition, hybrid multi-structures can be constructed by the combination of patterning techniques with LB method on LbL or SAM films.

Thus, there has been a constant progress for nanotechnological development of biosensors, and continuous development will provide promising and powerful tools for the analysis of biomolecules in the near future. Nanoarrays are the next stage in the evolution of the miniaturization of microarrays.

## ACKNOWLEDGMENTS

We thank Dr. Thierry Ondarcuhu and EM team from CEMES, CNRS for the mutual work in the framework of Nanomol project. We also thank Drs. Jong Seol Yuk and Sun-Ju Yi for their works on the construction of SPR biosensor and protein microarray analysis. This work was supported in part by research grants from the Vascular System Research Center of KOSEF and the Advanced Backbone IT Technology Development Project from the Ministry of Information and Communication.

## REFERENCES

- Spangler, B.D.; Wilkinson, E.A.; Murphy, J.T.; Tyler, B.J. Comparison of the Spreeta® surface plasmon resonance sensor and a quartz crystal microbalance for detection of *Escherichia coli* heat-labile enterotoxin. *Anal. Chim. Acta.* **2001**, *444*, 149–161.
- Suzuki, M.; Ozawa, F.; Sugimoto, W.; Aso, S. Miniature surface-plasmon resonance immunosensors—rapid and repetitive procedure. *Anal. Bioanal. Chem.* **2002**, *372*, 301–304.
- Narang, U.; Gauger, P.R.; Ligler, F.S. A displacement flow immunosensor for explosive detection using microcapillaries. *Anal. Chem.* **1997**, *69*, 2779–2785.
- Narang, U.; Anderson, G.P.; Ligler, F.S.; Burans, J. Fiber optic-based biosensor for ricin. *Biosens. Bioelectron.* **1997**, *12*, 937–945.
- Wilson, G.S.; Hu, Y. Enzyme-based biosensors for in vivo measurements. *Chem. Rev.* **2000**, *100*, 2693–2704.
- Bilitewski, U. Protein-sensing assay formats and devices. *Anal. Chim. Acta* **2006**, *568*, 232–247.
- Madou, M.; Florkey, J. From batch to continuous manufacturing of microbiomedical devices. *Chem. Rev.* **2000**, *100*, 2679–2692.
- Chris, A.R.; Leonard, M.T.; Mark, J.F.; Joel, P.G.; Stephanie, B.S.; Brian, D.M.; John, J.C.; Frances, S.L. Array biosensor for simultaneous identification of bacterial, viral, and protein analytes. *Anal. Chem.* **1999**, *71*, 3846–3852.
- Hansma, H.G.; Hoh, J.H. Biomolecular imaging with the atomic force microscope. *Annu. Rev. Biophys. Biomol. Struct.* **1994**, *29*, 115–139.
- Nyffenegger, R.M.; Penner, R.M. Nanometer-scale surface modification using the scanning probe microscope: progress since 1991. *Chem. Rev.* **1997**, *97*, 1195–1230.
- Weimar, T. Recent trends in the application of evanescent wave biosensors. *Angew. Chem. Int. Ed. Engl.* **2000**, *39*, 1219–1221.
- Hiroyuki, S.; Yukio, H.; Masahiro, I. Detection of conformational changes in an immobilized protein using surface plasmon resonance. *Anal. Chem.* **1998**, *70*, 2019–2024.
- Yang, P.R.; Wang, E. Enhanced surface plasmon resonance immunosensing using a streptavidin-biotinylated protein complex. *Analyst.* **2001**, *126*, 4–6.
- Lyon, L.A.; Musick, M.D.; Natan, M.J. Colloidal Au-enhanced surface plasmon resonance immunosensing. *Anal. Chem.* **1998**, *70*, 5177–5183.
- Rickert, J.; Brecht, A.; Gopel, W. Quartz crystal microbalances for quantitative biosensing and characterizing protein multilayers. *Biosens. Bioelectron.* **1997**, *12*, 567–575.
- Ahuja, T.; Mir, I.A.; Kumar, D.; Rajesh. Biomolecular immobilization on conducting polymers for biosensing applications. *Biomaterials* **2007**, *28*, 791–805.
- Berggren, C.; Johansson, G. Capacitance measurements of antibody-antigen interactions in a flow system. *Anal. Chem.* **1997**, *69*, 3651–3657.
- Varshney, M.; Li, Ya. Interdigitated array microelectrode based impedance biosensor coupled with magnetic nanoparticle-antibody conjugates for detection of *Escherichia coli* O157:H7 in food samples. *Biosens. Bioelectron.* **2007**, *22*, 2408–2414.
- Yuk, J.S.; Jung, S.-H.; Jung, J.-W.; Hong, D.-G.; Han, J.A.; Kim, Y.-M.; Ha, K.-S. Analysis of protein interactions on protein arrays by a wavelength interrogation-based surface plasmon resonance biosensor. *Proteomics.* **2004**, *4*, 3468–3476.
- Endo, T.; Yamamura, Sh.; Nagatani, N.; Morita, Ya.; Takamura, Yu.; Tamiya, E. Localized surface plasmon resonance based optical biosensor using surface modified nanoparticle layer for label-free monitoring of antigen-antibody reaction. *Sci. Technol. Adv. Mater.* **2005**, *6*, 491–500.
- Hansen, K.M.; Thundat, T. Microcantilever biosensors. *Methods* **2005**, *37*, 57–64.
- Hosaka, S.; Chiyoma, T.; Ikeuchi, A.; Okano, H.; Sone, H.; Izumi, T. Possibility of using a self-sensing cantilever. *Curr. Appl. Phys.* **2006**, *6*, 384–388.
- Lechuga, L.M.; Tamayo, J.; Alvarez, M.; Carrascosa, L.G.; Yufera, A.; Doldan, R.; Peralias, E.; Rueda, A.; Plaza, J.A.; Zinoviev, K.; Dominguez, C.; Zaballos, A.; Moreno, M.; Martinez, C.; Wenn, D.; Harris, N.; Bringer, C.; Bardinal, V.; Camps, T.; Vergnenegre, C.; Fontaine, C.; Diaz, V.; Bernad, A. A highly sensitive microsystem based on nanomechanical biosensors for genomics applications. *Sensors Actuators* **2006**, *B 118*, 2–10.
- Kuzmenko, I.; Rapaport, H.; Kjaer, K.; Als-Nielsen, J.; Weissbuch, I.; Lahav, M.; Leiserowitz, L. Design and characterization of crystalline thin film architectures at the air-liquid interface: simplicity to complexity. *Chem. Rev.* **2001**, *101*, 1659–1696.
- Boussaad, S.; Dziri, L.; Arechabaleta, R.; Tao, N.J.; Leblanc, R.M. Electron-transfer properties of cytochrome c Langmuir-Blodgett films and interactions of cytochrome C with lipids. *Langmuir* **1998**, *14*, 6215–6219.
- Yin, F.; Shin, H.-K.; Kwon, Y.-S. A hydrogen peroxide biosensor based on Langmuir-Blodgett technique: direct electron transfer of hemoglobin in octadecylamine layer. *Talanta* **2005**, *67*, 221–226.

27. Girard-Egrot, A.P.; Godoy, S.; Blum, L.J. Enzyme association with lipidic Langmuir–Blodgett films: interests and applications in nanobioscience. *Adv. Colloid Interface Sci.* **2005**, *116*, 205–225.
28. Wang, H.; Brennan, J.D.; Gene, A.; Krull, U.J. Assembly of antibodies in lipid membranes for biosensor development. *Appl. Biochem. Biotechnol.* **1995**, *53*, 163–181.
29. Vikholm, I.; Albers, W.M. Oriented immobilization of antibodies for immunosensing. *Langmuir* **1998**, *14*, 3865–1872.
30. Gritsch, S.; Neumaier, K.; Schmitt, L.; Tampe, R. Engineered fusion molecules at chelator lipid interfaces imaged by reflection interference contrast microscopy (RICM). *Biosens. Bioelectron.* **1995**, *10*, 805–812.
31. Dietrich, C.; Boscheinen, O.; Scharf, K.D.; Schmitt, L.; Tampe, R. Functional immobilization of a DNA-binding protein at a membrane interface via histidine tag and synthetic chelator lipids. *Biochem.* **1996**, *35*, 1100–1105.
32. Zadmard, R.; Schrader, T. Nanomolar protein sensing with embedded receptor molecules. *J. Am. Chem. Soc.* **2005**, *127*, 904–915.
33. Girard-Egrot, A.P.; Godoy, S.; Blum, L.J. Enzyme association with lipidic Langmuir–Blodgett films: interests and applications in nanobioscience. *Adv. Colloid Interface Sci.* **2005**, *116*, 205–225.
34. Decher, G.F. Nanoassemblies: toward layered polymeric multicomposites. *Science* **1997**, *277*, 1232–1237.
35. Caruso, F.; Niikura, K.; Furlong, D.N.; Okahata, Y. Assembly of alternating polyelectrolyte and protein multilayer films for immunosensing. *Langmuir* **1997**, *13*, 3427–3433.
36. Onda, M.; Lvov, Y.; Ariga, K.; Kunitake, T. Sequential actions of glucose oxidase and peroxidase in molecular films assembled by layer-by-layer alternate adsorption. *Biotech. Bioeng.* **1996**, *51*, 163–167.
37. Kim, H.-S.; Jung, S.-H.; Kim, S.-H.; Suh, I.-B.; Kim, W.-J.; Jung, J.-W.; Yuk, J.S.; Kim, Y.-M.; Ha, K.-S. High-throughput analysis of mumps virus and the virus-specific monoclonal antibody on the arrays of a cationic polyelectrolyte with a spectral SPR biosensor. *Proteomics* **2006**, *6*, 6426–6432.
38. Love, J.Ch.; Estroff, L.A.; Kriebel, J.K.; Nuzzo, R.G.; Whitesides, G.M. Self-assembled monolayers of thiolates on metals as a form of nanotechnology. *Chem. Rev.* **2005**, *105*, 1103–1169.
39. Ulman, A.; Evans, S.D.; Shnidman, Y.; Sharma, R.; Eilers, J.E.; Chang, J.C. Concentration-driven surface transition in the wetting of mixed alkanethiol monolayers on gold. *J. Am. Chem. Soc.* **1991**, *113* (5), 1499–1506.
40. Sagiv, J. Organized monolayers by adsorption. I. Formation and structure of oleophobic mixed monolayers on solid surfaces. *J. Am. Chem. Soc.* **1980**, *102*, 92–98.
41. Ulman, A. Formation and structure of self-assembled monolayers. *Chem. Rev.* **1996**, *96*, 1533–1554.
42. Maoz, R.; Frydman, E.; Cohen, S.R.; Sagiv, J. Constructive nanolithography: site-defined silver self-assembly on nanoelectrochemically patterned monolayer templates. *Adv. Mater.* **2000**, *12*, 424–429.
43. Moulin, A.M.; O’Shea, S.J.; Badley, R.A.; Doyle, P.; Welland, M.E. Measuring surface-induced conformational changes in proteins. *Langmuir* **1999**, *15*, 8776–8779.
44. Ostuni, E.; Chapman, R.G.; Holmlin, R.E.; Takayama, S.; Whitesides, G.M. A survey of structure and property relationships of surfaces that resist the adsorption of protein. *Langmuir* **2001**, *17*, 5605–5620.
45. Chan, V.; Graves, D.J.; Fortina, P.; McKenzie, S.E. Adsorption and surface diffusion of DNA oligonucleotides at liquid/solid interfaces. *Langmuir* **1997**, *13*, 320–329.
46. Yang, M.; Yau, H.C.M.; Chan, H.L. Adsorption kinetics and ligand-binding properties of thiol-modified double-stranded DNA on a gold surface. *Langmuir* **1998**, *14*, 6120–6129.
47. Zhdanov, V.P.; Kasemo, B. Van der Waals interaction during protein adsorption on a solid covered by a thin film. *Langmuir* **2001**, *17*, 5407–5409.
48. Morozov, V.N.; Morozova, T.Y. Electrospray deposition as a method for mass fabrication of mono- and multicomponent microarrays of biological and biologically active substances. *Anal. Chem.* **1999**, *71*, 3110.
49. Seeger, S.; Bierbaum, K.; Dahint, R.; Feng, C.L.; Mantar, M.; Grunze, M. *Synthetic Microstructures in Biological Research*; Schnur, M., Ed.; Plenum Press: New York, 1992; 53–65.
50. Nassar, A.E.; Russling, J.F.; Nakashima, N. Electron transfer between electrodes and heme proteins in protein-DNA films. *J. Am. Chem. Soc.* **1996**, *118* (12), 3043–3044.
51. Palmer, D.A.; French, M.T.; Miller, J.N. Use of protein A as an immunological reagent and its application using flow injection, a review. *Analyst* **1994**, *119*, 2769–2776.
52. Zhavnerko, G.K.; Ha, K.-S.; Yi, S.-J.; Kweon, S.-M. Layer-by-layer method for immobilization of protein molecules on biochip surfaces. In *Frontiers of Multifunctional Nanosystems*; NATO Book Series; Buzaneva, E., Scharff, P., Eds.; Kluwer Academic Publishers, 2002; 79–90.
53. Abruna, H.D. Coordination chemistry in two dimensions: chemically modified electrodes. *Coord. Chem. Rev.* **1998**, *86*, 135–189.
54. Lang, H.; Duschl, C.; Vogel, H. A new class of thiolipids for the attachment of lipid bilayers on gold surfaces. *Langmuir* **1994**, *10*, 197–210.
55. Mirsky, V.M.; Riepl, M.; Wolfbeis, O.S. Capacitive monitoring of protein immobilization and antigen-antibody reactions on monomolecular alkylthiol films on gold electrodes. *Biosens. Bioelectron.* **1997**, *12*, 977–989.
56. Prime, K.; Whitesides, G.M. Self-assembled organic monolayers: model systems for studying adsorption of proteins at surfaces. *Science* **1991**, *252*, 1164–1167.
57. Jung, S.-H.; Jung, J.-W.; Suh, I.-B.; Yuk, J.S.; Kim, W.-J.; Choi, E.Y.; Kim, Y.-M.; Ha, K.-S. Analysis of C-reactive protein on amide-linked NHS-dextran

- arrays with a spectral SPR biosensor for serodiagnosis. *Anal. Chem.* **2007**, *79*, 5703–5710.
58. Sehgal, D.; Vijay, I.K. A method for the high efficiency of water-soluble carbodiimide-mediated amidation. *Anal. Biochem.* **1994**, *218*, 87–91.
  59. Lu, B.; Smyth, M.R.; O'Kennedy, R. Oriented immobilization of antibodies and its applications in immunoassays and immunosensors. *Analyst* **1996**, *121*, 29R–32R.
  60. Kanno, S.; Yanagida, Y.; Haruyama, T.; Kobatake, E.; Aizawa, M. Assembling of engineered IgG-binding protein on gold surface for highly oriented antibody immobilization. *J. Biotechnol.* **2000**, *76*, 207–214.
  61. Ng, K.; Pack, D.W.; Sasaki, D.Y.; Arnold, F.M. Engineering protein-lipid interactions: targeting of histidine-tagged proteins to metal-chelating lipid monolayers. *Langmuir* **1995**, *11*, 4048–4055.
  62. Karyakin, A.A.; Presnova, G.V.; Rubtsova, M.Y.; Egorov, A.M. Oriented immobilization of antibodies onto the gold surfaces via their native thiol groups. *Anal. Chem.* **2000**, *72*, 3805–3811.
  63. Turkova, J. Oriented immobilization of biologically active proteins as a tool for revealing protein interactions and function. *J. Chromatogr. B* **1999**, *722* (1–2), 11–31.
  64. Darst, S.A.; Ahlers, M.; Meller, P.H.; Kubalek, E.W.; Blankenburg, R.; Ribi, H.O.; Ringsdorf, H.; Kornberg, R.D. Two-dimensional crystals of streptavidin on biotinylated lipid layers and their interactions with biotinylated macromolecules. *Biophys. J.* **1991**, *59*, 387–396.
  65. Jung, S.H.; Son, H.Y.; Yuk, J.S.; Jung, J.W.; Kim, K.H.; Lee, Ch.H.; Hwang, H.; Ha, K.S. Oriented immobilization of antibodies by a self-assembled monolayer of 2-(biotinamido)ethanethiol for immunarray preparation. *Colloids Surfaces B: Biointerfaces* **2006**, *47*, 107–111.
  66. Dorman, G.; Prestwich, G.D. Using photolabile ligands in drug discovery and development. *Trends Biotech.* **2000**, *18*, 64–77.
  67. Nakamura, T.; Nagasaki, Y.; Kataoka, K. Synthesis of heterobifunctional poly(ethylene glycol) with a reducing monosaccharide residue at one end. *Bioconjugate Chem.* **1998**, *9*, 300–303.
  68. Swingle, D.M.; Staros, J.V.; Wright, R.W. Enhancement by N-hydroxysulfosuccinimide of water-soluble carbodiimide-mediated coupling reactions. *Anal. Biochem.* **1986**, *156*, 220–222.
  69. Prime, K.L.; Whitesides, G.M. Adsorption of proteins onto surfaces containing end-attached oligo(ethylene oxide): a model system using self-assembled monolayers. *J. Am. Chem. Soc.* **1993**, *115*, 10,714–10,721.
  70. Metzger, S.W.; Natesan, M.; Yanavich, C.; Schneider, J.; Lee, G.U. Development and characterization of surface chemistries for microfabricated biosensors. *J. Vacuum Sci. Technol. A* **1999**, *17*, 2623–2628.
  71. Lofas, S.; Johnsson, B. A novel hydrogel matrix on gold surfaces in surface plasmon resonance sensors for fast and efficient immobilization of ligands. *J. Chem. Soc. Commun.* **1990**, *21*, 1526–1528.
  72. Sigal, B.G.; Bamdad, C.; Barberis, A.; Strominger, J.; Whitesides, G.M. A self-assembled monolayer for the binding and study of histidine-tagged proteins by surface plasmon resonance. *Anal. Chem.* **1996**, *68*, 490–497.
  73. Schmid, E.L.; Keller, T.A.; Dienes, Z.; Vogel, H. Reversible oriented surface immobilization of functional proteins on oxide surfaces. *Anal. Chem.* **1997**, *69*, 1979–1985.
  74. Burda, C.; Chen, X.; Narayanan, R.; El-Sayed, M.A. Chemistry and properties of nanocrystals of different shapes. *Chem. Rev.* **2005**, *105*, 1025–1102.
  75. Sapsford, K.E.; Pons, T.; Medintz, I.L.; Mattoussi, H. Biosensing with luminescent semiconductor quantum dots. *Sensors* **2006**, *6*, 925–953.
  76. Parak, W.J.; Gerion, D.; Zanchet, D.; Woerz, A.S.; Pellegrino, T.; Micheel, C.; Williams, Sh.C.; Seitz, M.; Bruehl, R.E.; Bryant, Z.; Bustamante, C.; Bertozzi, C.R.; Alivisatos, A.P. Conjugation of DNA to silanized colloidal semiconductor nanocrystalline quantum dots. *Chem. Mater.* **2002**, *14*, 2113–2119.
  77. Goldman, E.R.; Balighian, E.D.; Mattoussi, H.; Kuno, M.K.; Mauro, J.M.; Tran, P.T.; Anderson, G.P. Avidin: a natural bridge for quantum dot-antibody conjugates. *J. Am. Chem. Soc.* **2002**, *124*, 6378–6382.
  78. Jaiswal, J.K.; Mattoussi, H.; Mauro, J.M.; Simon, S.M. Long-term multiple color imaging of live cells using quantum dot bioconjugates. *Nat. Biotechnol.* **2003**, *21*, 47–51.
  79. Qi, Ya.; Chen, J.; Wang, L.; Yang, B.; Li, W. Synthesis of quantum dots labeled short peptides and imaging the T cell surface receptors with QDs-labeled peptides. *Int. J. Peptide Res. Therapeutics* **2007**, *13*, 399–404.
  80. Schena, M.; Shalon, D.; Davis, R.W.; Brown, P.O. Quantitative monitoring of gene expression patterns with a complementary DNA microarray. *Science* **1995**, *270*, 467–470.
  81. Rosi, N.L.; Mirkin, Ch.A. Nanostructures in bionanotechnology. *Chem. Rev.* **2005**, *105*, 1547–1562.
  82. Taton, T.A.; Lu, G.; Mirkin, C.A. Two-color labeling of oligonucleotide arrays via size-selective scattering of nanoparticle probes. *J. Am. Chem. Soc.* **2001**, *123*, 5164–5165.
  83. Niemeyer, C.M.; Ceyhan, B.; Gao, S.; Chi, L.; Peschel, S.; Simon, U. Site-selective immobilization of gold nanoparticles functionalized with DNA oligomers. *Colloid Polym. Sci.* **2001**, *279*, 68–72.
  84. Moller, R.; Csaki, A.; Kohler, J.M.; Fritzsche, W. DNA probes on chip surfaces studied by scanning force microscopy using specific binding of colloidal gold. *Nucleic Acids Res.* **2000**, *28* (e91), 1–5.
  85. Farrer, R.A.; Butterfield, F.L.; Chen, V.W.; Fourkas, J.T. Highly efficient multiphoton-absorption-induced luminescence from gold nanoparticles. *Nano Lett.* **2005**, *5*, 1139–1142.
  86. Willner, I.; Willner, B.; Katz, E. Biomolecule-nanoparticle hybrid systems for bioelectronic applications. *Bioelectrochemistry* **2007**, *70*, 2–11.
  87. Kane, R.S.; Stroock, A.D. Nanobiotechnology: protein-nanomaterial interactions. *Biotechnol. Prog.* **2007**, *23*, 316–319.
  88. McFarland, C.D.; Thomas, C.H.; DeFilippis, C.; Steele, J.G.; Healy, K.E. Protein adsorption and cell

- attachment to patterned surfaces. *J. Biomed. Mater. Res.* **2000**, *49*, 200–210.
89. Bernard, A.; Delamarche, E.; Schmid, H.; Michel, B.; Bosshard, H.R.; Biebuyck, H. Printing patterns of proteins. *Langmuir* **1998**, *14*, 2225–2229.
90. Delamarche, E.; Bernard, A.; Schmid, H.; Michel, B.; Biebuyck, H. Patterned delivery of immunoglobulins to surfaces using microfluidic networks. *Science* **1997**, *276*, 779–781.
91. MacBeath, G.; Schreiber, S.L. Printing proteins as microarrays for high-throughput function determination. *Science* **2000**, *289*, 1760–1763.
92. Flounders, A.W.; Brandon, D.L.; Bates, A.H. Patterning of immobilized antibody layers via photolithography and oxygen plasma exposure. *Biosens. Bioelectron.* **1997**, *12*, 447–456.
93. Duschl, C.; Liley, M.; Corradin, G.; Vogel, H. Biologically addressable monolayer structures formed by templates of sulfur-bearing molecules. *Biophys. J.* **1994**, *67*, 1229–1237.
94. Huang, J.Y.; Dahlgren, D.A.; Hemminger, J.C. Photopatterning of self-assembled alkanethiolate monolayers on gold: a simple monolayer photoresist utilizing aqueous chemistry. *Langmuir* **1994**, *10*, 626–628.
95. Kim, Y.T.; Bard, A.J. Imaging and etching of self-assembled n-octadecanethiol layers on gold with the scanning tunneling microscope. *Langmuir* **1992**, *8*, 1096–1102.
96. Xia, Y.; Rogers, J.A.; Paul, K.E.; Whitesides, G.M. Unconventional methods for fabricating and patterning nanostructures. *Chem. Rev.* **1999**, *99*, 1823–1843.
97. Bieri, C.; Ernst, O.P.; Heyse, S.; Hofmann, K.P.; Vogel, H. Micropatterned immobilization of a G protein-coupled receptor and direct detection of G protein activation. *Nature Biotech.* **1999**, *17*, 1105–1108.
98. Piner, R.D.; Zhu, J.; Xu, F.; Hong, S.; Mirkin, C.A. “Dip-Pen” nanolithography. *Science* **1999**, *283*, 661–663.
99. Nowall, W.B.; Wipf, D.O.; Kuhr, W.G. Localized avidin/biotin derivatization of glassy carbon electrodes using SECM. *Anal. Chem.* **1998**, *70*, 2601–2606.
100. Wadu-Mesthrige, K.; Xu, S.; Amro, N.A.; Liu, G.Y. Fabrication and imaging of nanometer-sized protein patterns. *Langmuir* **1999**, *15*, 8580–8583.
101. Hong, S.H.; Zhu, J.; Mirkin, C.A. Multiple ink nanolithography: toward a multiple-pen nano-plotter. *Science* **1999**, *286*, 523–525.
102. Maynor, B.W.; Li, Y.; Liu, J. Au “Ink” for AFM “Dip-Pen” nanolithography. *Langmuir* **2001**, *17*, 2575–2578.
103. Schwartz, P.V. Molecular transport from an atomic force microscope tip: A comparative study of dip-pen nanolithography. *Langmuir* **2002**, *18*, 4041–4046.
104. Zhavnerko, G.K.; Agabekov, V.E.; Gallyamov, M.O.; Yaminsky, I.V.; Rogach, A.L. Composite Langmuir–Blodgett films of behenic acid and CdTe nanoparticles: the structure and reorganization on solid surfaces. *Colloids Surfaces A. Physicochem. Eng. Aspects* **2002**, *202*, 233–241.
105. Zhavnerko, G.K.; Zhavnerko, K.A.; Agabekov, V.E.; Gallyamov, M.O.; Yaminsky, I.V.; Rogach, A.L. Reorganization of Langmuir monolayers on solid surfaces. *Colloids Surfaces A. Physicochem. Eng. Aspects* **2002**, *198–200*, 231–238.
106. Maoz, R.; Cohen, S.R.; Sagiv, J. Nanoelectrochemical patterning of monolayer surfaces: toward spatially defined self-assembly of nanostructures. *Adv. Mater.* **1999**, *11*, 55–61.



# Biosensors Based on Carbon Nanotubes

Yuehe Lin

Wassana Yantasee

Fang Lu

*Pacific Northwest National Laboratory, Richland, Washington, U.S.A.*

Joseph Wang

Mustafa Musameh

*Department of Chemistry and Biochemistry, New Mexico State University,  
Las Cruces, New Mexico, U.S.A.*

Yi Tu

Zhifeng Ren

*Boston College, Chestnut Hill, Massachusetts, U.S.A.*

## INTRODUCTION

Carbon nanotube (CNT) is an attractive material for the development of biosensors because of its capability to provide strong electrocatalytic activity and minimize surface fouling of the sensors. This entry reviews the recent successful development of biosensors based on CNT materials. Specifically, biosensors from two fabrication regimes have been investigated: 1) the coimmobilization of CNTs and enzymes on electrode surfaces and 2) the growth of controlled-density aligned CNTs for the fabrication of nanoelectrode arrays. In the first regime, the CNTs are either dispersed in solvents [e.g., sulfuric acid, dimethylformamide (DMF)], dissolved in Nafion solution for electrode coating, or mixed with Teflon as an electrode material for reagentless biosensors. In the second regime, the nanoelectrode arrays consisting of millions of vertically aligned CNTs, each acting as an individual electrode, have been fabricated through a non-lithographic method. We also demonstrate the capability of CNTs to promote the oxidation/reduction (redox) reactions of hydrogen peroxide and nicotinamide adenine dinucleotide (NADH), which are involved in a wide range of amperometric biosensors associated with oxidase and dehydrogenase enzymes, respectively. With these electrocatalytic properties of CNTs, the applications of CNT-based biosensors examined in our laboratories include the low-potential detections of glucoses, organophosphorous compounds, and alcohol.

## BACKGROUND

There has been enormous interest in exploiting CNTs in electrochemical and biological sensors<sup>[1–21]</sup> since they were first introduced in 1991.<sup>[22]</sup> CNTs are distinguished according to their structural properties.<sup>[23]</sup> A single-wall CNT (SWCNT) consists of a single graphitic sheet rolled into a cylinder (with 1 to 2 nm o.d. and several microns in length), and multiwall CNT (MWCNT) consists of graphitic sheets rolled into closed concentric tubes (with 50 nm o.d. and microns in length), each separated by van der Waals forces to have a gap of 3.4 Å. Carbon nanotubes have been known to promote electron-transfer reactions of cytochrome *c*,<sup>[2]</sup> NADH,<sup>[1,6]</sup> catecholamine neurotransmitters,<sup>[3]</sup> and ascorbic acid.<sup>[4]</sup> This is attributed to their electronic structure, high electrical conductivity, and redox active sites. Carbon is also a versatile electrode material that can undergo various chemical and electrochemical modifications to produce suitable surfaces for high electrode responses. Carbon electrodes have a wide useful potential range, especially in the positive direction, because of the slow kinetics of carbon oxidation. These excellent properties of CNTs have been successfully exploited in our laboratories to develop either amperometric biosensors based on the immobilization of CNTs,<sup>[1,5]</sup> coimmobilization of CNTs and enzymes,<sup>[6,8]</sup> or the growth of controlled-density aligned CNTs into the nanoelectrode arrays<sup>[7,9,10]</sup> for the detection of glucoses,<sup>[5,6,10]</sup> organophosphorous compounds,<sup>[8]</sup> and alcohol,<sup>[6]</sup> as summarized in the following sections.

## BIOSENSORS BASED ON IMMOBILIZATION OF CNTS

### Solubilization and Immobilization of CNTs

CNTs have shown potential for applications in chemical/biological sensors and nanoscale electronic devices. A major barrier for developing such CNT-based devices is the insolubility of CNTs in most solvents. This challenge has been addressed through covalent modification<sup>[24,25]</sup> or non-covalent functionalization<sup>[26,27]</sup> of the CNTs. A “wrapping” of CNT in polymeric chains (i.e., poly(*p*-phenyl-enevinylene)<sup>[26]</sup> or poly{(*m*-phenylenevinylene)-*co*-[2,5-dioctyloxy-(*p*-phenylene)-vinylene]})<sup>[27]</sup> has improved the solubility of CNTs without impairing their physical properties.<sup>[28]</sup> In our work,<sup>[5]</sup> a well-known perfluorosulfonated polymer, Nafion, has been used to solubilize single-wall and multiwall CNTs. Because of their unique ion-exchange, discriminative, and biocompatibility properties, Nafion films have been used extensively to modify electrode surfaces and to construct amperometric biosensors.<sup>[29,30]</sup> Similar to other polymers used to wrap and solubilize CNTs, Nafion bears a polar side chain. We have found that CNTs can be suspended in solutions of Nafion in phosphate buffer or alcohol. Increasing the Nafion content from 0.1 to 5 weight percent (wt.%) results in a dramatic enhancement of the solubility of both single-wall and multiwall CNTs, which can be observed by the naked eye. A homogeneous solution of the Nafion/CNT complex is observed in Nafion solution, but no such solubilization is observed in ethanol or phosphate-buffer solutions containing no Nafion. The CNT/Nafion association does not impair the electrocatalytic properties of CNTs with respect to the redox reaction of hydrogen peroxide. The Nafion-induced solubilization of CNT thus permits a variety of applications, including the modification of electrode surfaces for preparing amperometric biosensors.

Because CNTs are insoluble in most solvents, previously reported CNT-modified electrodes have relied on casting a CNT/sulfuric acid solution onto a surface of electrodes,<sup>[1,31]</sup> a procedure that is not compatible with the immobilization of biocomponents. Therefore we have developed a new and simple method for preparing effective CNT-based biosensors from CNT/Teflon composite material.<sup>[6]</sup> Carbon composites, based on the dispersion of graphite powder within an insulator, offer convenient bulk modification for the preparation of reagentless and renewable biosensors. Teflon has been used as a binder for graphite particles for various electrochemical-sensing applications.<sup>[32,33]</sup> Our approach relies on CNTs as the sole conductive component rather than as the modifier cast on other electrode surfaces. The bulk of CNT/Teflon composites hence serve as a reservoir for the enzymes, in

the same manner as their graphite-based counterparts. The preparation is very simple: a certain amount of CNTs is hand-mixed in the dry-state with granular Teflon to obtain a desired composition of CNT/Teflon. The CNT content of the new composites has a large effect upon their electrochemical behavior. Fig. 1A compares the calibration plots for potassium ferricyanide obtained at electrodes containing different MWCNT loadings. All electrode compositions yield highly linear calibration plots over the entire concentration range. The sensitivity increases with the CNT loading between 10 and 60 wt.% and decreases thereafter. The influence of the CNT content was also examined using cyclic voltammetry (CV) experiments. The CV ferricyanide cathodic and anodic currents increased linearly with the CNT content between 30 and 70 wt.% (Fig. 1B). Composites containing more than 70 wt.% CNTs are too dry and porous and have

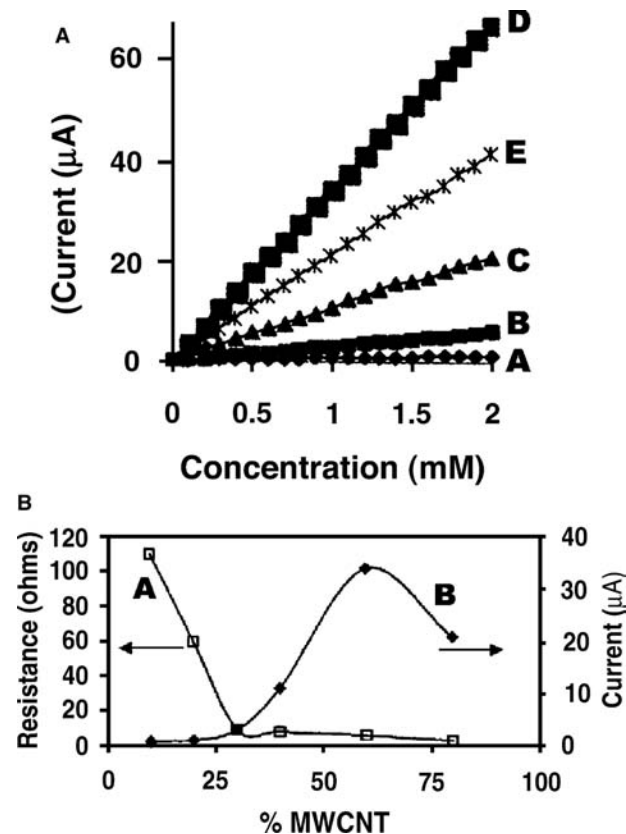


**Fig. 1** (A) Calibration plots for potassium ferricyanide using electrodes with varying MWCNT/Teflon ratio (by weight) of 10:90 (A), 30:70 (B), 40:60 (C), 60:40 (D), and 80:20 (E). Operating conditions: potential, +0.1 V; supporting electrolyte, phosphate buffer (0.05 M, pH 7.4); stirring rate, 400 rpm. (B) Influence of the CNT loading upon the electrode resistance (A) and amperometric response to 1 mM ferricyanide (B) measured with the 60:40 wt.% MWCNT/Teflon electrode. Other conditions are as in (a). Source: From Ref.<sup>[6]</sup>.

poor mechanical stability. Electrode resistance leading to a poorly defined and negligible CV is observed at the electrodes containing low CNT content. Fig. 1B shows the sensitivity-loading (B) and resistance-loading (A) profiles. Too high Teflon (<30 wt.% CNTs) leads to high resistance to a nearly insulating matrix and low sensitivity, while too high CNT (>75 wt.% CNT) leads to an operation beyond the mass-limiting plateau associated with the shift of the voltammetric signal. Therefore a CNT content of 40 to 60 wt.% is suggested.

The CNT/Teflon composites have the combined advantages of CNTs and bulk composite electrodes that permit a wide range of applications without the need for a graphite surface. Certain amounts of enzymes [e.g., glucose oxidase ( $\text{GO}_x$ ) and alcohol dehydrogenase (ADH)] and cofactor (e.g.,  $\text{NAD}^+$ ) can be mixed with the CNT/Teflon composite and used as electrode materials, depending upon specific needs. The CNT/Teflon coating was later investigated in our laboratory and displayed a marked electrocatalytic action toward hydrogen peroxide and NADH and hence is promising for the development of biosensors for glucose (in connection with oxidase enzymes) and ethanol (in connection with dehydrogenase enzymes), respectively.

### Electrocatalytic Activity of CNTs to Redox Reactions of Hydrogen Peroxide

Hydrogen peroxide is involved in a wide range of biosensing applications associated with oxidase enzymes. In our laboratories, the enhancement of the redox activity of hydrogen peroxide by CNTs is investigated using the previously described CNT/Nafion<sup>[5]</sup> and CNT/Teflon<sup>[6]</sup> electrode materials.

To study the electrocatalytic activity of CNTs for hydrogen peroxide oxidation/reduction, the CNT/Nafion (from a 0.5 wt.% Nafion solution containing 2 mg/mL of CNTs) is coated on a glassy carbon (GC) electrode surface. Fig. 2 displays the cyclic voltammograms for  $5 \times 10^{-3}$  M hydrogen peroxide recorded at a bare GC electrode (A) and the CNT/Nafion-modified GC electrode (B). Significant oxidation and reduction currents starting around +0.20 V are observed on the CNT/Nafion-coated electrode, while none is observed at the bare GC electrode. The CNT/Nafion-coated electrode offers a marked decrease in the overvoltage for hydrogen peroxide reaction and hence allows low-potential amperometric detection. The inset of Fig. 2 shows the amperometric response at 0.0 V to successive additions of hydrogen peroxide. While the modified electrode (B) responds very rapidly and favorably to the changes in hydrogen peroxide concentration, no response is observed at the bare GC electrode (A). A similar decrease in hydrogen

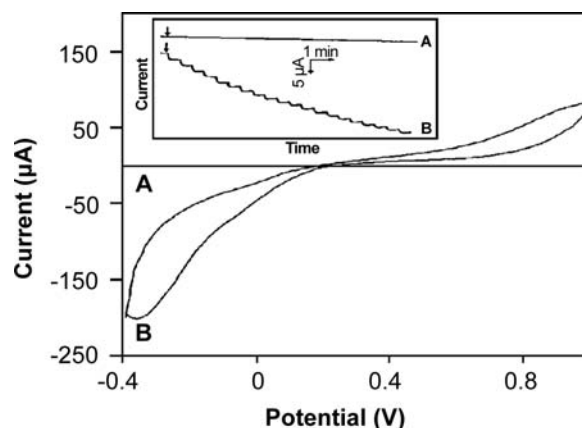


**Fig. 2** Cyclic voltammograms of  $5 \times 10^{-3}$  M hydrogen peroxide at unmodified (A) and MWCNT/Nafion-modified (B) GC electrodes. Operating conditions: scan rate, 50 mV/sec; electrolyte, phosphate buffer (0.05 M, pH 7.4). Upper inset shows the amperometric response after increasing hydrogen peroxide concentration for  $1 \times 10^{-3}$  M incrementally while potential is held at 0.0 V. Source: From Ref.<sup>[5]</sup>.

peroxide overvoltage is observed at other CNT-modified electrodes (not shown), indicating that Nafion does not impair the electrocatalytic properties of CNT. The CNT/Nafion-coated electrode is reliable and not affected by regenerating the surface; six successive measurements of hydrogen peroxide, each recorded on a freshly polished surface, show reproducible results with % RSD of less than 4.

Similar substantial lowering of the detection potential and significantly improved current signals for hydrogen peroxide by CNTs have also been found at CNT/Teflon electrodes, obtained by packing

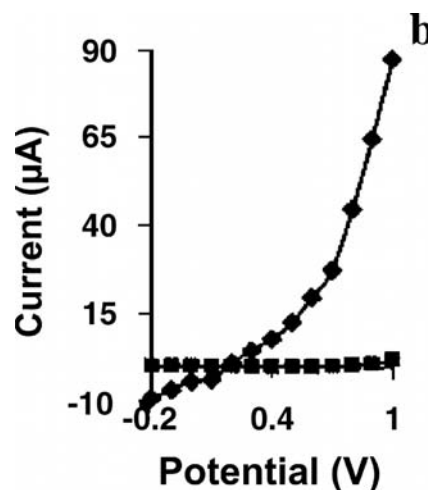


**Fig. 3** Hydrodynamic voltammograms for 1 mM hydrogen peroxide at the 60:40 wt.% graphite/Teflon electrode (A) and the 60:40 wt.% MWCNT/Teflon electrode (B). Other conditions are as in Fig. 1A. Source: From Ref.<sup>[6]</sup>.

60/40 wt.% of CNT/Teflon into the electrode cavity of a glass sleeve with a copper wire as the electrical contact. Control experiments, using graphite-based Teflon composites, were performed in parallel. Fig. 3 compares the hydrodynamic voltammograms (HDVs) for 1 mM hydrogen peroxide at the graphite/Teflon (a) and CNT/Teflon (b) electrodes. Compared to the graphite/Teflon electrode, the CNT/Teflon electrode responds more favorably to hydrogen peroxide over the entire potential range (0.0 to 1.0 V) with significant response starting at +0.20 V. The Teflon binder is proven to not impair the electrocatalytic properties of CNTs.

### Electrocatalytic Activity of CNTs to Redox Reactions of NADH

$\beta$ -Nicotinamide adenine dinucleotide (NADH) is a cofactor in several hundred enzymatic reactions of  $\text{NAD}^+$ /NADH-dependent dehydrogenases. The electrochemical oxidation of NADH has thus been the subject of numerous studies related to the development of amperometric biosensors.<sup>[34]</sup> Problems inherent to such anodic detection are the large overvoltage encountered for NADH oxidation at ordinary electrodes<sup>[35]</sup> and surface fouling associated with the accumulation of reaction products.<sup>[36]</sup> CNTs have thus been used in our recent work<sup>[1,6]</sup> as the new electrode material to reduce the overpotential for NADH oxidation and to alleviate surface fouling problems.

In the previous study,<sup>[1]</sup> single-wall and multiwall CNTs were dispersed in concentrated sulfuric acid, and each was subsequently cast on a glassy carbon electrode. Fig. 4A shows the cyclic voltammograms of NADH measured at unmodified (A), MWCNT-modified (B), and SWCNT-modified (C) glassy carbon electrodes. Both modified electrodes yield an approximately twofold larger NADH peak, compared to the unmodified electrode. The oxygen-rich groups on the CNT surface, introduced during the acid dispersion, are perhaps responsible for such electrocatalytic behavior for the oxidation of NADH. Fig. 4B shows a HDV of  $1 \times 10^{-4}$  M NADH, which reflects the electrocatalytic behavior of the CNT coating with varying potentials. The MWCNT-coated electrode (B) responds to NADH over the entire 0.0- to 1.0-V range, while the bare electrode (A) responds only at potentials higher than +0.6 V. Fig. 4C shows that successive additions of  $1 \times 10^{-4}$  M NADH result in increasing response detected at the CNT-modified electrode (B) but no response at the unmodified electrode (A) when the detection potential was kept low (i.e., 0.3 V). Evidently, the electrocatalytic action of CNT enables the fast response (i.e., 10 sec to reach the steady state) to the change of NADH concentrations at the

low-detection potential. The amperometric response of  $5 \times 10^{-3}$  M NADH appears to be very stable; the decay of the signal is less than 10% and 25% after a 60-min period at the MWCNT-modified and SWCNT-modified electrodes, compared with 75% and 53% at the graphite-coated and acid-treated electrodes, respectively. This shows the capability of CNTs in resisting the fouling effects and in preventing the diminishing of signals in successive cyclic voltammetric detections. The resistance to fouling of CNT-based electrodes has yet to be understood.

In our more recent study,<sup>[6]</sup> the electrocatalytic effect of CNTs to facilitate low-potential amperometric measurements of NADH has been investigated using CNT/Teflon electrodes. Fig. 5 compares the amperometric response (at +0.40 V) of the graphite/Teflon (a) and CNT/Teflon (b) electrodes to successive additions of 0.1 mM NADH. Only the CNT/Teflon electrode responds very rapidly to the changes in the level of NADH, producing steady-state signals within 8 to 10 sec. The favorable signals are accompanied by a low noise level.

The CNT coating offers remarkably decreased overvoltage for the NADH oxidation as well as reduced surface fouling effects of the electrodes. These characteristics indicate the great promise of CNTs for developing highly sensitive, low-potential, and stable amperometric biosensors based on dehydrogenase enzymes.

### Applications of CNT-Immobilized Biosensors

Our laboratories have exploited the capability of CNTs to promote redox activity of hydrogen peroxide to develop oxidase-based amperometric biosensors, including those for detecting glucose<sup>[5,6,10]</sup> and organophosphorous compounds.<sup>[8]</sup> Similarly, the electrocatalytic properties of CNTs in reducing the overpotential for the redox reaction of NADH suggest their potential use in dehydrogenase-based amperometric biosensors such as those for alcohol detection.<sup>[6]</sup> These applications of CNT-based biosensors are summarized as follows.

#### Glucose detection

The CNT/Nafion/ $\text{GO}_x$ -modified GC electrode was used in a flow-injection system to measure glucoses.<sup>[5]</sup> Fig. 6 compares the amperometric responses for relevant physiological levels of glucose, ascorbic acid, acetaminophen, and uric acid at the CNT/Nafion/ $\text{GO}_x$ -modified GC electrode (B) and Nafion/ $\text{GO}_x$ -modified GC electrode (A). In Fig. 6, the accelerated electron-transfer reaction of hydrogen peroxide at the CNT/Nafion/ $\text{GO}_x$ -modified GC electrode allows for

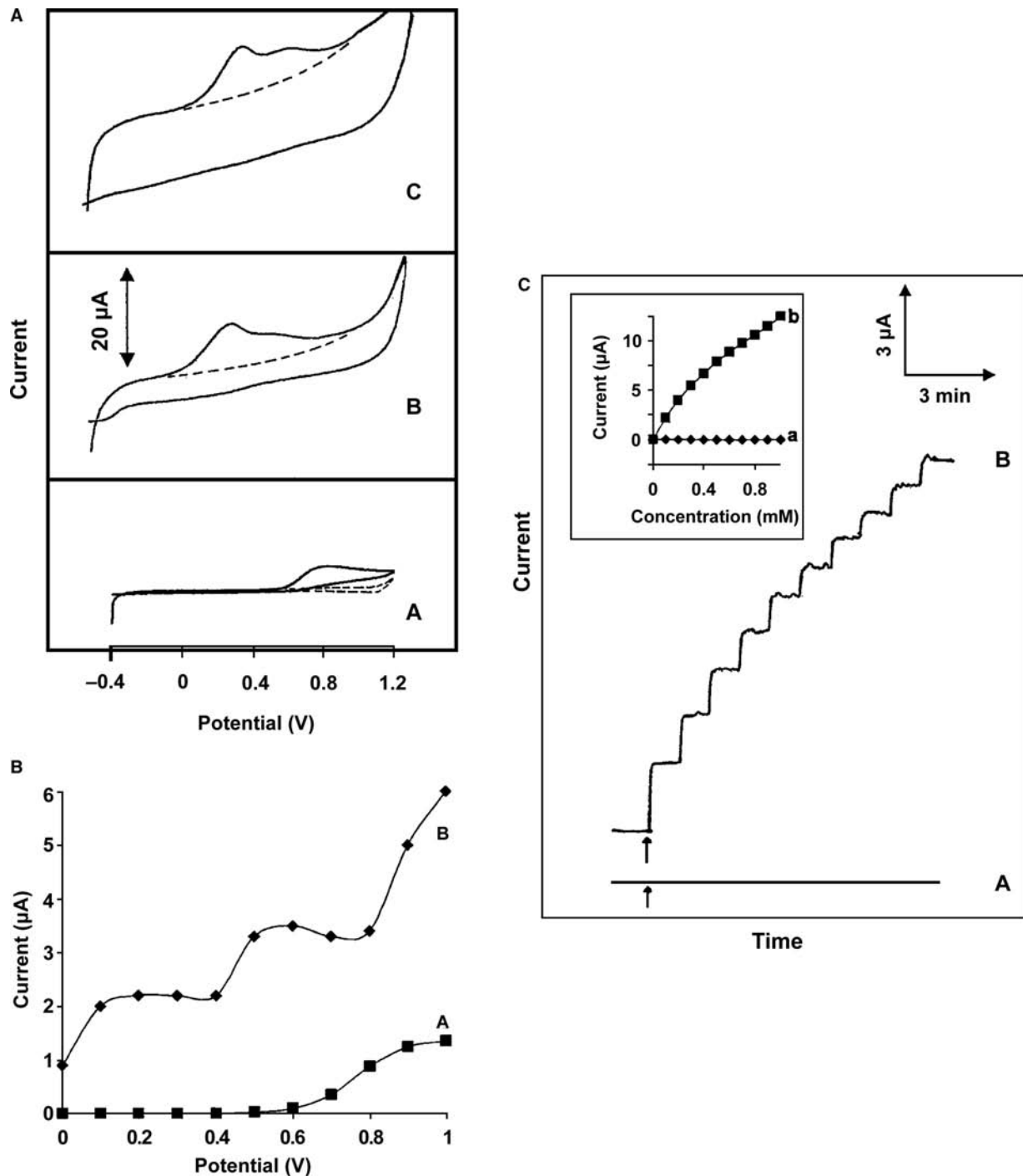


**Fig. 4** (A) Cyclic voltammograms for  $5 \times 10^{-3}$  M NADH at unmodified (A), MWCNT-modified (B), and SWCNT-modified (C) GC electrodes. Operating conditions: scan rate, 50 mV/sec; electrolyte, phosphate buffer (0.05 M, pH 7.4). Dotted lines represent the background response. (B) Hydrodynamic voltammograms for  $1 \times 10^{-4}$  M NADH at the unmodified (A) and the MWCNT-modified (B) GC electrodes. Operating conditions: stirring rate, 500 rpm; electrolyte, phosphate buffer (0.05 M, pH 7.4). (C) Current–time recordings obtained after increasing the NADH concentration of  $1 \times 10^{-4}$  M (each step) at unmodified (A) and MWCNT-modified (B) GC electrodes. Inset shows the corresponding calibration curve. Operating conditions: potential, + 0.3 V; others as in (B). *Source:* From Ref.<sup>[1]</sup>.

glucose measurements at very low potentials (i.e.,  $-0.05$  V) where interfering reactions are minimized. As a result, a well-defined glucose signal (d) is observed, while the signals of acetaminophen (a), uric

acid (b), and ascorbic acid (c) are negligible. No such discrimination is obtained at the Nafion/ $\text{GO}_x$  biosensor (without the CNT) (A) held at +0.80 V, where large oxidation peaks are observed for all interferences,

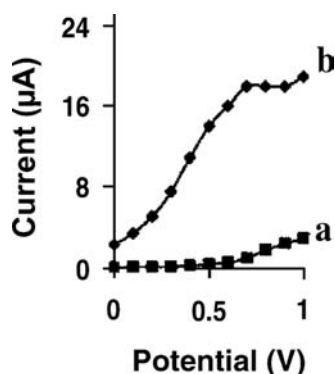


**Fig. 5** Hydrodynamic voltammograms for 1 mM NADH at the 60:40 wt.% graphite/Teflon electrode (A) and the 60:40 wt.% MWCNT/Teflon electrode (B). Other conditions are as in Fig. 1A. Source: From Ref.<sup>[6]</sup>.

indicating that the permselective (charge-exclusion) properties of Nafion are not adequate to fully eliminate anionic interferences. In short, the coupling of the permselective properties of Nafion with the electrocatalytic action of CNT allows for glucose detection with effective discrimination against both neutral and anionic redox constituents. Similarly, the CNT/Nafion-coated electrodes have also been demonstrated to dramatically improve the signal of dopamine in the presence of the common ascorbic acid interference.

The detection of glucose has also been performed on CNT/Teflon-based electrodes, which are immobilized

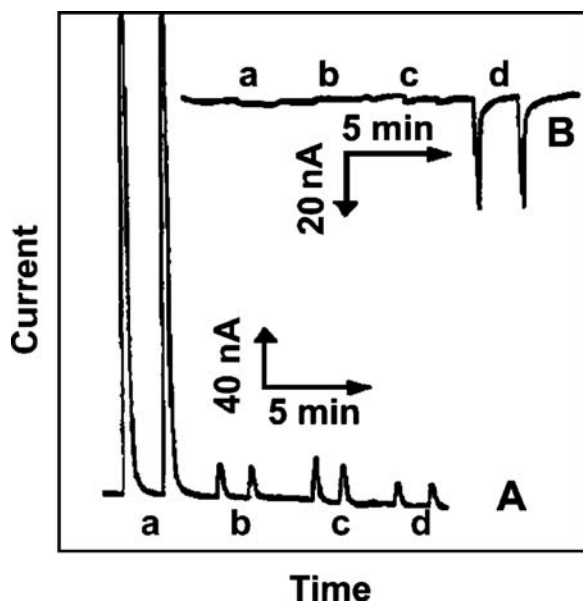


**Fig. 6** Flow-injection signals for  $2 \times 10^{-4}$  M acetaminophen (A),  $2 \times 10^{-4}$  M ascorbic acid (B),  $2 \times 10^{-4}$  M uric acid (C), and  $1 \times 10^{-2}$  M glucose (D), at the Nafion/ $\text{GO}_x$ -modified GC electrode (A) at +0.8 V, and the MWCNT/Nafion/ $\text{GO}_x$ -modified GC electrode (B) at -0.05 V, and flow rate of 1.25 mL/min. Source: From Ref.<sup>[5]</sup>.

with  $\text{GO}_x$  enzyme.<sup>[6]</sup> Fig. 7 compares the amperometric response to successive additions of 2 mM glucose at the graphite/Teflon/ $\text{GO}_x$  (a) and the MWCNT/Teflon/ $\text{GO}_x$  (b) electrodes using operating potentials of +0.6 V (A) and +0.1 V (B). The CNT-based bioelectrode offers substantially larger signals, especially at low potential, reflecting the electrocatalytic activity of CNT. Such low-potential operation of the CNT-based biosensor results in a highly linear response (over the entire 2- to 20-mM range) and a slower response time (~1 min vs. 25 sec at +0.6 V). The glucose biocomposite based on single-wall CNTs results in a more sensitive but slower response than that based on multiwall CNTs. The low-potential detection also leads to high selectivity (i.e., effective discrimination against coexisting electroactive species). Despite the absence of external (permselective) coating, the glucose response at +0.1 V was not affected by adding the common

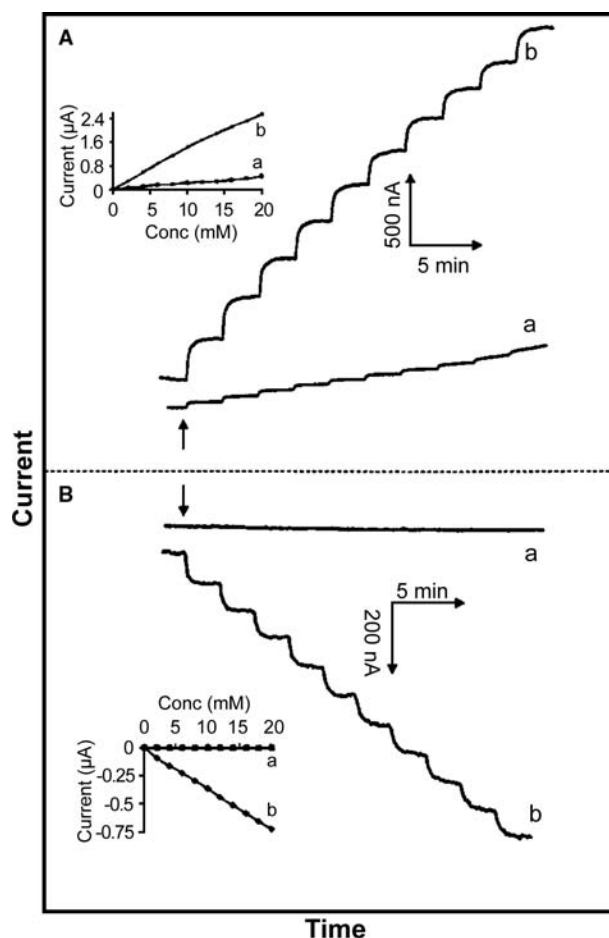


**Fig. 7** Current-time recordings for successive 2-mM additions of glucose at the graphite/Teflon/ $\text{GO}_x$  (A) and the MWCNT/Teflon/ $\text{GO}_x$  (B) electrodes measured at +0.6 (A) and +0.1 V (B). Electrode composition, 30:69:1 wt.% carbon/Teflon/ $\text{GO}_x$ . Other conditions are as in Fig. 1A. Source: From Ref.<sup>[1]</sup>.



acetaminophen and uric acid interferences at 0.2 mM. A similar addition of ascorbic acid resulted in a large interference, reflecting the accelerated oxidation of this compound at the CNT surface.<sup>[4]</sup> Reproducible activity was observed after 2 weeks of dry storage at 4°C, which is in good agreement with the high stability of enzymes in Teflon-based carbon composites.<sup>[33]</sup>

### Organophosphorus compound detection

Organophosphorous (OP) compounds are very toxic and are thus widely used as pesticides and chemical-warfare agents (CWAs). Recently, we have successfully used MWCNTs in developing an amperometric biosensor for OP compounds.<sup>[8]</sup> Specifically, the MWCNT is used to modify screen-printed carbon electrodes, which are subsequently coimmobilized with acetylcholinesterase (ACHE) and choline oxidase (CHO) enzymes. The MWCNT-modified electrode has demonstrated a significant catalytic effect for the redox reaction of hydrogen peroxide, leading to the development of a novel biosensor for the assay of OP compounds with enhanced sensitivity.

The ACHE enzyme is known to play an important role in cholinergic transmission as a catalyst for the rapid hydrolysis of the neurotransmitter acetylcholine to acetate and choline as follows:



However, in the presence of OP compounds, the rate of choline production is reduced. The capability of OP compounds to inhibit ACHE activity is well known<sup>[37–41]</sup> and thus is being exploited in developing biosensors for OP compound detection. In our work, the amperometric biosensor for OP compounds is based on coimmobilization of ACHE and CHO on a printed CNT electrode. In the biosensor based on ACHE/CHO enzymes, choline that is produced in reaction (1) serves as a substrate for the CHO enzyme in the presence of oxygen to produce hydrogen peroxide as follows:



The hydrogen peroxide that is produced in reaction (2) can be detected amperometrically, and the amperometric response is negatively proportional to the amount of an OP compound that is introduced into the system.

The inhibition of ACHE activity by OP compounds is an irreversible process; once exposed to the OP compounds, the enzyme is inactivated, and the sensor can be reused only after an appropriate enzyme reactivation.<sup>[42]</sup> Therefore we have attempted to develop

biosensors that are low-cost and disposable using screen-printed carbon electrodes.<sup>[8]</sup> To make the sensor, the suspension of MWCNTs in *N,N*-DMF was cast on the surface of screen-printed carbon electrodes to form a thin-film of CNTs. The screen-printed carbon only serves as a conducting base for the CNT electrode. The electrochemical method was used to oxidize CNTs to create a carboxylic acid group. Both enzymes, ACHE and CHO, were then coimmobilized on the CNTs via carbodiimide chemistry by forming amide linkages between their amine residues and carboxylic acid groups on the CNT surface.<sup>[10,43]</sup> The optimum biosensor was found to contain a loading of 0.8 mU ACHE and 1.5 U CHO on the electrode, with a 2-mM ACH as the substrate.

An amperometric method was employed to study the sensor response time of the ACHE inhibition after the spike of methyl parathion, as a representative OP compound. In Fig. 8, the amperometric response was rapid (i.e., within 30 sec) after the ACH addition, reflecting the fast diffusion of enzyme substrates and the products (as the CNTs are membrane-free porous). When methyl parathion was successively added to the test area of the biosensor, the response decreased significantly and rapidly in the first 10 min and more slowly thereafter. The significant inhibition effect of methyl parathion to the catalytic activity of ACHE reduces the production of hydrogen peroxide, leading to low signals.

In addition to methyl parathion, the inhibition effects of the other two OP compounds were investigated using the CNT-modified, ACHE/CHO-immobilized electrode. Fig. 8B compares the enzyme activities with a function of time after the spike of each OP compound, including (A) chlorpyrifos, (B) fenitrothion, and (C) methyl parathion.

The enzyme activity is the ratio of  $I_i$  (a steady-state current obtained in the presence of a given OP compound) to  $I_o$  (that obtained in the absence of the OP compound). After spiking with OP compounds, the enzyme activity decreases with time. The high inhibition effect of OP compounds can be correlated to low enzyme activity of ACHE. Their inhibition effects are in the following ascending order: methyl parathion > fenitrothion > chlorpyrifos.

The relative inhibition of methyl parathion at the CNT-modified, ACHE/CHO-immobilized biosensor as a function of methyl parathion concentration was investigated using a preincubation method in which the biosensor was exposed to the incubation solution containing methyl parathion for 10 min before the change in enzyme activity was measured. Successive incubation measurements were performed with varied methyl parathion concentrations. The CNT/ACHE/CHO biosensor has good analytical characteristics for methyl parathion, including a broad dynamic linear

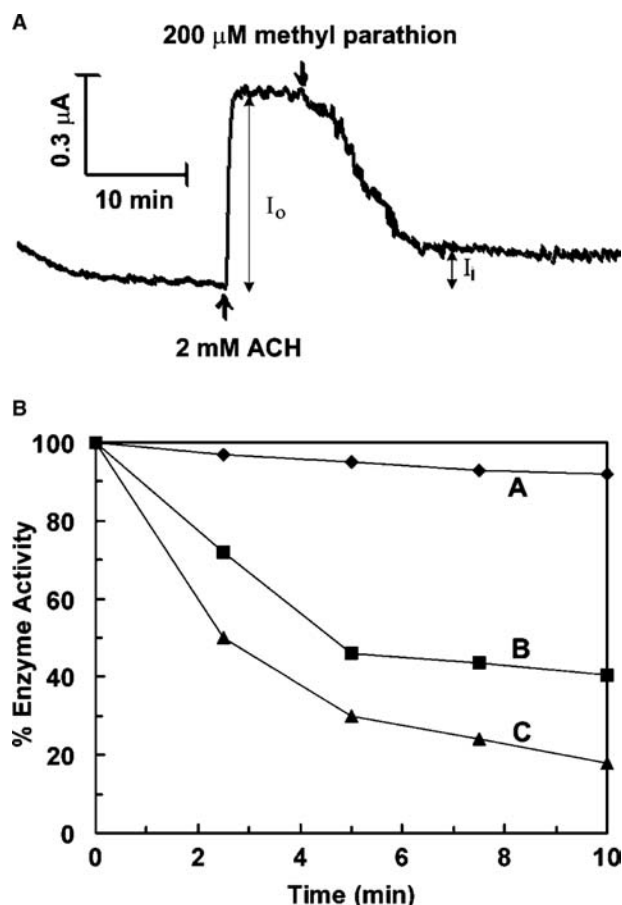


**Fig. 8** (A) Amperometric response of methyl parathion at the CNT/ACHE/CHO-immobilized screen-printed biosensor. Operating conditions: 0.1 M phosphate buffer/0.1 M NaCl (pH 7.4), potential of +0.50 V. (B) Inhibition effects by three organophosphates, chlorpyrifos (A), fenitrothion (B), and methyl parathion (C) on the enzyme activity, measured with the CNT/ACHE/CHO-immobilized screen-printed biosensor. Other conditions are as in (A). *Source:* From Ref.<sup>[8]</sup>.

range (up to 200  $\mu\text{M}$ ,  $r^2 = 0.96$ ), high sensitivity (0.48% inhibition/ $\mu\text{M}$ ), and low detection limit (LDL = 0.05  $\mu\text{M}$ ). These improved characteristics reflect the catalytic activity of CNTs that promotes the redox reaction of hydrogen peroxide produced during ACHE/CHO enzymatic reactions with their substrate, as well as the large surface area of CNT materials. The hand-held electrochemical detector (i.e., CHI1232 from CHI Instrument, Inc.) coupled with the disposable biosensor developed in this work will potentially facilitate the field screening of OP pesticides and nerve agents with fast speed, high efficiency, low cost, and small sample size needed.

#### Alcohol detection

The attractive low-potential detection of NADH, along with minimal surface fouling, makes CNT

extremely attractive for amperometric biosensors of ethanol through the incorporation of ADH/NAD<sup>+</sup> within the three-dimensional electrode matrix. Specifically, the reagentless biocomposite was prepared by mixing the desired amounts of the ADH enzyme and the NAD<sup>+</sup> cofactor with the CNT/Teflon composite to obtain the final composition of 28.5:65:1.5:5 wt.% CNT/Teflon/ADH/NAD<sup>+</sup>. The mixture was then packed firmly into the electrode cavity of a glass sleeve with a copper wire as the electrical contact. Fig. 9 compares the performance at a low detection potential (i.e., +0.20 V) of the CNT/Teflon-based electrode (b) to that of graphite/Teflon-based electrode (a). Only the CNT/Teflon-based electrode (b) responds favorably to successive additions of 1 mM ethanol. The response is relatively fast ( $\sim 60$  sec to reach steady state) and non-linear. The greatly enhanced biosensing of ethanol at the CNT-based electrode suggests the accelerated oxidation of NADH at low-potential detection. In addition to being reagentless, the biosensor does not require a redox mediator (to shuttle the electrons from the NADH product to the surface), which is commonly used for such low-potential detection of ethanol.

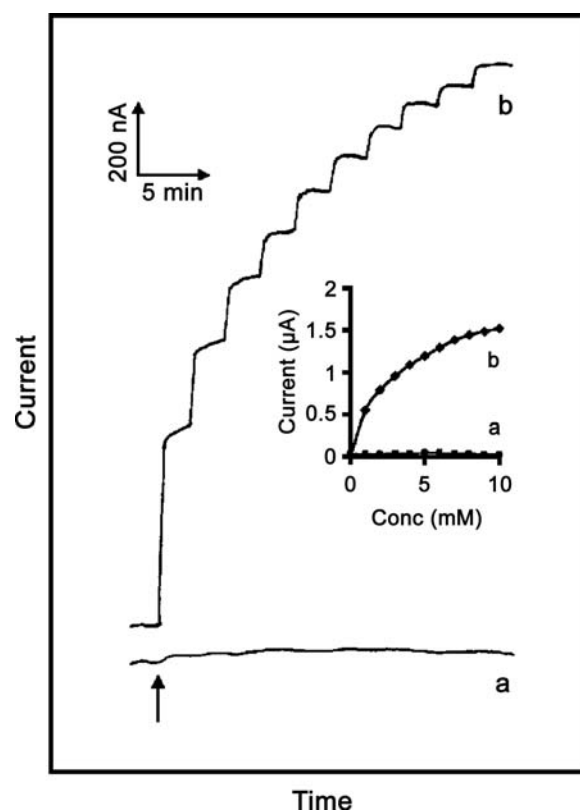


**Fig. 9** Current-time recordings for successive 1-mM additions of ethanol at the graphite/Teflon/ADH/NAD<sup>+</sup> (A) and the MWCNT/Teflon/ADH/NAD<sup>+</sup> (B). Operating potential, +0.2 V; electrode composition, 28.5:65:1.5:5 wt.% carbon/Teflon/ADH/NAD<sup>+</sup>. Other conditions are as in Fig. 1A. *Source:* From Ref.<sup>[6]</sup>.

## BIOSENSORS BASED ON CONTROLLED-DENSITY ALIGNED CNTs

### Fabrication

Although vertically aligned CNTs have good material properties<sup>[44]</sup> (e.g., good electrical conductivity, ability to promote electron transfer reactions) and are of the right size (20 to 200 nm) for nanoelectrode arrays (NEAs), they lack the right spacing. To make each nanotube work as an individual nanoelectrode, the spacing needs to be sufficiently larger than the diameter of the nanotubes to prevent the diffusion layer overlap from the neighboring electrodes.<sup>[45]</sup>

Recently, a nonlithography method that allows the fabrication of low-site-density aligned CNT arrays with an interspacing of more than several micrometers has been developed.<sup>[46]</sup> From these low site density CNTs, the NEAs consisting of millions of nanoelectrodes with each electrode being less than 100 nm in diameter were successfully fabricated.<sup>[7,9,10]</sup> As the total current of the loosely packed electrode arrays is proportional to the total number of individual electrodes, having the number of the electrodes up to millions is highly desirable. The size reduction of each individual electrode and the increased total number of the electrodes result in improved signal-to-noise ratio ( $S/N$ ) and detection limits.<sup>[47,48]</sup>

In growing the low-site-density aligned CNT arrays, Ni nanoparticles were randomly deposited on a 1-cm<sup>2</sup> Cr-coated silicon substrate (Fig. 10A) by applying a pulse current to the substrate in NiSO<sub>4</sub> electrolyte solution. The size and the site density of the Ni nanoparticles were controlled by the amplitude and the duration of the pulse current. On these Ni particles, the CNTs were grown [Fig. 10B] in the plasma-enhanced chemical vapor deposition (PECVD) system at 650°C for 8 min with 160 sccm NH<sub>3</sub> and 40 sccm C<sub>2</sub>H<sub>2</sub> gases with a total pressure of 15 Torr and a plasma intensity of 170 W. The aligned CNT arrays had a site density of  $1 \times 10^6$ – $3 \times 10^6$ /cm<sup>2</sup>, a length of 10 to 12 μm, and a diameter of 50 to 80 nm. In the early days of fabricating the electrode arrays,<sup>[7,46]</sup> a thin layer of SiO<sub>2</sub> was coated on the surface by magnetron sputtering to insulate the Cr layer. This was followed by applying M-Bond 610 coating (epoxy-phenolic adhesive from Vishay Intertechnology, Inc., Shelton, CT) to further insulate the Cr and provide mechanical support to the CNTs. This insulation is sometimes not sufficient to prevent current leakage, which results in the distortion of the cyclic voltammetry curve. Recently,<sup>[9,10]</sup> we improved the fabrication method using better insulating materials and packing procedures that solve the leakage problem, coupled with a pretreatment of the electrode to reduce the peak separation. We replaced the SiO<sub>2</sub> and M-bond coatings used as the passivation

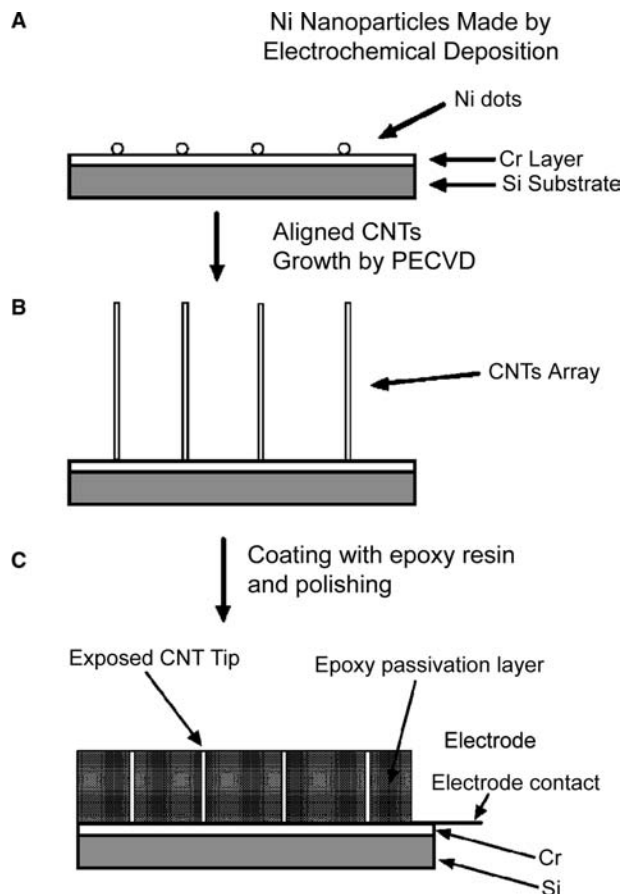


**Fig. 10** Fabrication scheme of a low-site-density aligned CNT nanoelectrode array. *Source:* From Ref.<sup>[7]</sup>.

layer in our previous attempts with Epon epoxy resin 828 (Miller-Stephenson Chemical Co., Inc., Sylmar, CA) and *m*-phenylenediamine (MPDA) as a hardener. After these steps, the CNTs were half-embedded in the polymer resin, and the protruding part of the CNTs beyond the polymer resin was mechanically removed by polishing with a lens, followed by ultrasonication in water. Then the electronic connection was made on the CNT-Si substrate to make the CNT nanoelectrode arrays (Fig. 10C). Finally, the electrode arrays were pretreated by electrochemical etching in 1.0 M NaOH at 1.5 V for 90 sec prior to the electrochemical characterizations. The lifetime of the NEAs employing new epoxy is significantly improved: there is no degradation for several weeks because of the excellent stability of the epoxy layer.

### Applications of Controlled-Density Aligned CNT Electrodes

The nanoelectrode array, consisting of millions of CNT electrodes, yields an excellent sigmoidal voltammogram for K<sub>3</sub>Fe(CN)<sub>6</sub> and a low  $S/N$ .<sup>[9]</sup>

The sigmoidal voltammogram is a characteristic of microelectrodes having radial diffusion. The steady-state current arises because the rate of electrolysis approximates the rate of diffusion of an analyte to the electrode surface.<sup>[49]</sup> The scan-rate-independent limiting current behavior was observed up to 500 mV/sec at the nanoelectrode array. This indicates that there is no diffusion layer overlapping between the electrodes because most of the CNTs are separated from their nearest neighbors by at least 5  $\mu\text{m}$ , much larger than the diameter of each nanotube (50 to 80 nm).

The CNT-NEAs have a wide range of applications. They have been investigated in our laboratory as electrochemical sensors without further modification for the detection of drugs, such as 4-acetamidophenol, and metal ions, such as lead.<sup>[9]</sup>

For use as a glucose biosensor,<sup>[10]</sup> the  $\text{GO}_x$  enzyme molecules were attached to the broken tips of the CNTs via carbodiimide chemistry by forming amide linkages between their amine residues and carboxylic

acid groups on the CNT tips. Fig. 11A and B compares the amperometric responses for 5 mM glucose (G), 0.5 mM ascorbic acid (AA), 0.5 mM acetaminophen (AC), and 0.5 mM uric acid (UA) at the  $\text{GO}_x$ -modified NEA and the potentials of +0.4 V (a) and -0.2 V (b). Well-defined cathodic and anodic glucose responses are obtained at the CNT/ $\text{GO}_x$ -based biosensor at both potentials. However, the glucose detection at lower operating potential (-0.2 V) is significantly less influenced by interferences, indicating high selectivity toward the glucose substrate. Such a highly selective response to glucose is obtained at the CNT/ $\text{GO}_x$ -based biosensor without the use of mediators and permselective membranes. The amperometric response at the CNT/ $\text{GO}_x$ -based biosensor for each successive addition of  $2 \times 10^{-3}$  M glucose is presented in Fig. 11C with the corresponding calibration curve in the inset. The linear response to glucose is up to 30 mM, and the steady state is reached within 20 to 30 sec.

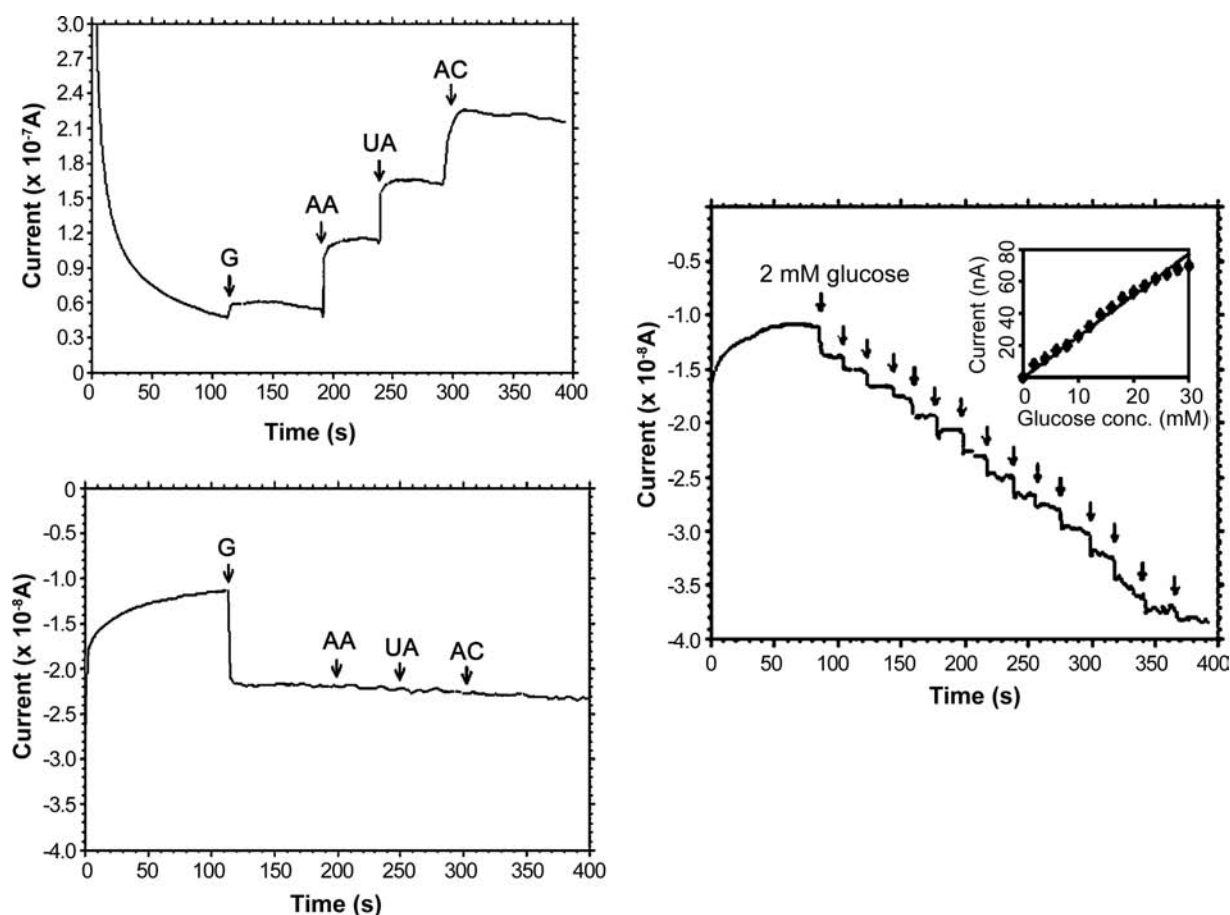


**Fig. 11** (A–B) Amperometric responses for 5 mM glucose (G), 0.5 mM ascorbic acid (AA), 0.5 mM acetaminophen (AC), and 0.5 mM uric acid (UA) at the  $\text{GO}_x$ -modified, CNT-nanoelectrode array and the potentials of +0.4V (A) and -0.2V (B). Electrolyte: 0.1 M phosphate buffer/0.1 M NaCl (pH 7.4). (C) Amperometric response at the  $\text{GO}_x$ -modified, CNT-nanoelectrode array for each successive addition of  $2 \times 10^{-3}$  M glucose. Inset shows the corresponding calibration curve. Potential: -0.2 V, other conditions are as in (A–B). Source: From Ref.<sup>[10]</sup>.

For many years, numerous researches have emphasized the use of anti-interference layers or artificial electron mediators for improving the selectivity of amperometric biosensors. CNTs eliminate potential interferences through the preferential detection of hydrogen peroxide at the CNT-based electrodes. Such development of interference-free transducers will significantly simplify the design and fabrication of biosensors. The biosensors based on low-site-density aligned CNTs are also suitable for the highly selective detection of glucose in a variety of biological fluids (e.g., saliva, sweat, urine, and serum).

## CONCLUSION

The electrocatalytic properties of CNTs in promoting the redox reaction of hydrogen peroxide and NADH are being exploited in our work in developing biosensors based on oxidase and dehydrogenase enzymes, respectively. With our CNT-based biosensors, low-potential detections of alcohol, organophosphorous compounds, and glucose are possible with many advantages over conventional devices. The capability of CNTs to reduce the overvoltage for the oxidation of hydrogen peroxide and NADH allows the detection of these species at low potential. At such low potential, most interfering species in the test samples do not undergo oxidation, thus eliminating potential interference. CNTs also minimize the surface fouling of biosensors, thus imparting higher stability onto these devices. While the CNT/Nafion-based biosensors use the electrocatalytic activity of CNTs and the permselectivity of Nafion to detect glucose with effective discrimination against most neutral and anionic redox constituents, the CNT/Teflon composite allows the reagentless approach to fabricate biosensors with flexible coimmobilization of enzymes and cofactors for specific biosensing needs. Owing to the CNTs' capability to promote electron-transfer activity, the artificial mediators that shuttle electrons between the enzymes and the electrodes are not required at the CNT-based biosensors, thereby eliminating the dependence upon the electroactive species and enhancing the reproducibility.

For future work, we will investigate the capability of CNTs to promote electron-transfer reactions of other biologically and environmentally important compounds. The biosensor fabrication technology demonstrated in this work holds a great future for developing routine, onsite amperometric biosensors based on both oxidase and dehydrogenase enzymes, such as those for cholesterol, alcohol, lactate, acetylcholine, choline, hypoxanthine, and xanthine. Although this entry focuses on biosensors based on CNTs, other oriented conducting nanowires, e.g., oriented conducting

polymer nanowires recently synthesized in our laboratory,<sup>[50,51]</sup> should also provide an alternative ideal platform for biosensing applications.

## ACKNOWLEDGMENTS

The work performed at Pacific Northwest National Laboratory (PNNL) was supported by the Laboratory Directed Research and Development program. The work performed at Boston College was supported by the U.S. Department of Energy (DOE) (DE-FG02-00ER45805) and by the National Science Foundation (NSF) (CMS-0219836). Work performed at New Mexico State University was supported by NSF. The research described in this entry was performed in part at the Environmental Molecular Sciences Laboratory, a national scientific user facility sponsored by the DOE's Office of Biological and Environmental Research and located at PNNL. PNNL is operated for DOE by Battelle under Contract DE-AC06-76RL01830.

## REFERENCES

1. Musameh, M.; Wang, J.; Merkoci, A.; Lin, Y. Low-potential stable NADH detection at carbon-nanotube-modified glassy carbon electrodes. *Electrochem. Commun.* **2002**, *4*, 743–746.
2. Wang, J.; Li, M.; Shi, Z.; Li, N.; Gu, Z. Direct electrochemistry of cytochrome *c* at a glassy carbon electrode modified with single-wall carbon nanotubes. *Anal. Chem.* **2002**, *74* (9), 1993–1997.
3. Wang, J.; Li, M.; Shi, Z.; Li, N.; Gu, Z. Electrocatalytic oxidation of norepinephrine at a glassy carbon electrode modified with single wall carbon nanotubes. *Electroanalysis* **2002**, *14* (3), 225–230.
4. Wang, Z.; Liu, J.; Liang, Q.; Wang, Y.; Luo, G. Carbon nanotube-modified electrodes for the simultaneous determination of dopamine and ascorbic acid. *Analyst* **2002**, *127* (5), 653–658.
5. Wang, J.; Musameh, M.; Lin, Y. Solubilization of carbon nanotubes by Nafion toward the preparation of amperometric biosensors. *J. Am. Chem. Soc.* **2003**, *125* (9), 2408–2409.
6. Wang, J.; Musameh, M. Carbon nanotube/teflon composite electrochemical sensors and biosensors. *Anal. Chem.* **2003**, *75*, 2075–2079.
7. Tu, Y.; Lin, Y.; Ren, Z.F. Nanoelectrode arrays based on low site density aligned carbon nanotubes. *Nano Lett.* **2003**, *3* (1), 107–109.
8. Lin, Y.; Lu, F.; Wang, J. Disposable carbon nanotube modified screen-printed biosensor for amperometric detection of organophosphorus pesticides and nerve agents. *Electroanalysis*, *in press*.
9. Tu, Y.; Lin, Y.; Yantasee, W.; Huang, Z.P.; Carnahan, D.L.; Ren, Z.F. Carbon nanotubes based nanoelectrode

- array: Fabrication, evaluation and the application in voltammetric detection. *Analyst*, submitted.
10. Lin, Y.; Lu, F.; Tu, Y.; Ren, Z.F. Glucose biosensor based on low site density aligned carbon nanotubes. *Nano Lett.*, submitted.
  11. Britto, P.J.; Santhanam, K.S.V.; Ajayan, P.M. Carbon nanotube electrode for oxidation of dopamine. *Bioelectrochem. Bioenerg.* **1996**, *41*, 121–125.
  12. Britto, P.J.; Santhanam, K.S.V.; Rubio, A.; Alonso, A.J.; Ajayan, P.M. Improved charge transfer at carbon nanotube electrodes. *Adv. Mater.* **1999**, *11*, 154–157.
  13. Campbell, J.K.; Sun, L.; Crooks, R.M. Electrochemistry using single carbon nanotubes. *J. Am. Chem. Soc.* **1999**, *121*, 3779–3780.
  14. Azamian, B.R.; Davis, J.J.; Coleman, K.S.; Bagshaw, C.B.; Green, M.L.H. Bioelectrochemical single-walled carbon nanotubes. *J. Am. Chem. Soc.* **2002**, *124*, 12664–12665.
  15. Nguyen, C.V.; Delzeit, L.; Cassell, A.M.; Li, J.; Han, J.; Meyyappan, M. Preparation of nucleic acid functionalized carbon nanotube arrays. *Nano Lett.* **2002**, *2*, 1079–1081.
  16. Li, J.; Ng, H.T.; Cassell, A.; Fan, W.; Chen, H.; Ye, Q.; Koehne, J.; Han, J.; Meyyappan, M. Carbon nanotube nanoelectrode array for ultrasensitive DNA detection. *Nano Lett.* **2003**, *3*, 597–602.
  17. Xu, J.Z.; Zhu, J.J.; Wu, Q.; Hu, Z.; Chen, H.Y. An amperometric biosensor based on the coimmobilization of horseradish peroxidase and methylene blue on a carbon nanotubes modified electrode. *Electroanalysis* **2003**, *15*, 219–224.
  18. Zhao, Q.; Gan, Z.H.; Zhuang, Q.K. Electrochemical sensors based on carbon nanotubes. *Electroanalysis* **2002**, *14*, 1609–1613.
  19. Yu, X.; Chattopadhyay, D.; Galeska, I.; Papadimitrakopoulos, F.; Rusling, J.F. Peroxidase activity of enzymes bound to the ends of single-wall carbon nanotube forest electrodes. *Electrochem. Commun.* **2003**, *5*, 408–411.
  20. Sotiropoulou, S.; Chaniotakis, N.A. Carbon nanotube array-based biosensor. *Anal. Bioanal. Chem.* **2003**, *375*, 103–105.
  21. Shim, M.; Kam, N.W.S.; Chen, R.J.; Li, Y.M.; Dai, H.J. Functionalization of carbon nanotubes for biocompatibility and biomolecular recognition. *Nano Lett.* **2002**, *2*, 285–288.
  22. Iijima, S. Helical microtubules of graphitic carbon. *Nature* **1991**, *354* (6348), 56–58.
  23. Saito, R.; Dresselhaus, G.; Dresselhaus, M.S. *Physical Properties of Carbon Nanotubes*; Imperial College Press: London, 1998.
  24. Chen, J.; Hamon, M.A.; Hu, H.; Chen, Y.S.; Rao, A.M.; Eklund, P.C.; Haddon, R.C. Solution properties of single-walled carbon nanotubes. *Science* **1998**, *282* (5386), 95–98.
  25. Boul, P.J.; Liu, J.; Mickelson, E.T.; Huffman, C.B.; Ericson, L.M.; Chiang, I.W.; Smith, K.A.; Colbert, D.T.; Hauge, R.H.; Margrave, J.L.; Smalley, R.E. Reversible sidewall functionalization of buckytubes. *Chem. Phys. Lett.* **1999**, *310* (3–4), 367–372.
  26. Star, A.; Stoddart, J.F.; Steuerman, D.; Diehl, M.; Boukai, A.; Wong, E.W.; Yang, X.; Chung, S.W.; Choi, H.; Heath, J.R. Preparation and properties of polymer-wrapped single-walled carbon nanotubes. *Angew. Chem., Int. Ed.* **2001**, *40* (9), 1721–1725.
  27. Riggs, J.E.; Guo, Z.X.; Carroll, D.L.; Sun, Y.P. Strong luminescence of solubilized carbon nanotubes. *J. Am. Chem. Soc.* **2000**, *122* (24), 5879–5880.
  28. O'Connell, M.J.; Boul, P.; Ericson, L.M.; Huffman, C.; Wang, Y.H.; Haroz, E.; Kuper, C.; Tour, J.; Ausman, K.D.; Smalley, R.E. Reversible water-solubilization of single-walled carbon nanotubes by polymer wrapping. *Chem. Phys. Lett.* **2001**, *342* (3–4), 265–271.
  29. Fan, Z.H.; Harrison, D.J. Permeability of glucose and other neutral species through recast perfluorosulfonated ionomer films. *Anal. Chem.* **1992**, *64* (11), 1304–1311.
  30. Fortier, G.; Vaillancourt, M.; Belanger, D. Evaluation of Nafion as media for glucose-oxidase immobilization for the development of an amperometric glucose biosensor. *Electroanalysis* **1992**, *4* (3), 275–283.
  31. Zhao, Q.; Gan, Z.H.; Zhuang, Q.K. Electrochemical sensors based on carbon nanotubes. *Electroanalysis* **2002**, *14* (23), 1609–1613.
  32. Wang, J.; Reviejo, A.J.; Angnes, L. Graphite–teflon enzyme electrode. *Electroanalysis* **1993**, *5* (7), 575–579.
  33. Del Cerro, M.A.; Cayuela, G.; Reviejo, A.J.; Pingarron, J.M.; Wang, J. Graphite–teflon–peroxidase composite electrodes. Application to the direct determination of glucose in musts and wines. *Electroanalysis* **1997**, *9* (14), 1113–1119.
  34. Lobo, M.J.; Miranda, A.J.; Tunon, P. Amperometric biosensors based on NAD(P)-dependent dehydrogenase enzymes. *Electroanalysis* **1997**, *9* (3), 191–202.
  35. Blaedel, W.J.; Jenkins, R.A. Study of the electrochemical oxidation of NADH. *Anal. Chem.* **1975**, *47* (8), 1337–1343.
  36. Wang, J.; Angnes, L.; Martinez, T. Scanning tunneling microscopic probing of surface fouling during the oxidation of nicotinamide coenzymes. *Bioelectrochem. Bioenerg.* **1992**, *29* (2), 215–221.
  37. Rosenberry, T.L. *Advances in Enzymology and Related Areas of Molecular Biology*; John Wiley & Sons, Inc.: New York, 1975; 43, 103.
  38. Zhang, S.; Zhao, H.; John, R. Development of a quantitative relationship between inhibition percentage and both incubation time and inhibitor concentration for inhibition biosensors—Theoretical and practical considerations. *Biosens. Bioelectron.* **2001**, *16* (9–12), 1119–1126.
  39. Fennouh, S.; Casimiri, V.; Burstein, C. Increased paraoxon detection with solvents using acetylcholinesterase inactivation measured with a choline oxidase biosensor. *Biosens. Bioelectron.* **1997**, *12* (2), 97–104.
  40. Cremisini, C.; Disario, S.; Mela, J.; Pilloton, R.; Palleschi, G. Evaluation of the use of free and immobilized acetylcholinesterase for paraoxon detection with an amperometric chlorine oxidase based biosensors. *Anal. Chim. Acta* **1995**, *311* (3), 273–280.
  41. Guerrieri, A.; Monaci, L.; Quinto, M.; Palmisano, F. A disposable amperometric biosensor for rapid screening



- of anticholinesterase activity in soil extracts. *Analyst* **2002**, *127* (1), 5–7.
42. Dzydevich, S.V.; Shul'ga, A.A.; Soldatkin, A.P.; Hendji, A.M.N.; Jaffrezic-Renault, N.; Martelet, C. Conductometric biosensors based on cholinesterases for sensitive detection of pesticides. *Electroanalysis* **1994**, *6*, 752–758.
  43. Edwards, R. *Immunodiagnosics—A Practical Approach*; Oxford University Press: Oxford, 1999; 67 pp.
  44. Ren, Z.F.; Huang, Z.P.; Xu, J.W.; Wang, J.H.; Bush, P.; Siegal, M.P.; Provencio, P.N. Synthesis of large arrays of well-aligned carbon nanotubes on glass. *Science* **1998**, *282* (5391), 1105–1107.
  45. Morf, W.E.; De Rooij, N.F. Performance of amperometric sensors based on multiple microelectrode arrays. *Sens. Actuators. B, Chem.* **1997**, *44* (1–3), 538–541.
  46. Tu, Y.; Huang, Z.P.; Wang, D.Z.; Wen, J.G.; Ren, Z.F. Growth of aligned carbon nanotubes with controlled site density. *Appl. Phys. Lett.* **2002**, *80* (21), 4018–4020.
  47. Menon, V.P.; Martin, C.R. Fabrication and evaluation of nanoelectrode ensembles. *Anal. Chem.* **1995**, *67* (13), 1920–1928.
  48. Weber, S.G. Single-to-noise ratio in microelectrode-array-based electrochemical detectors. *Anal. Chem.* **1989**, *61* (4), 295–302.
  49. Wehmeyer, K.R.; Wightman, R.M. Scan rate dependence of the apparent capacitance at microvoltammetric electrodes. *J. Electroanal. Chem.* **1985**, *196* (2), 417–421.
  50. Liang, L.; Liu, J.; Windisch, C.F.; Exarhos, G.J.; Lin, Y. Direct assembly of large arrays of oriented conducting polymer nanowires. *Angew. Chem. Int. Ed.* **2002**, *41* (19), 3665–3668.
  51. Liu, J.; Lin, Y.; Liang, L.; Voigt, J.A.; Huber, D.L.; Tian, Z.; Coker, E.; McKenzie, B.; McDermott, M.J. Templateless assembly of molecularly aligned conductive polymers nanowires: A new approach for oriented nanostructures. *Chem. Eur. J.* **2003**, *9* (3), 604–611.

# Biosensors: Fractal Analysis of Binding Kinetics

Harshala Butala

Ajit Sadana

*Department of Chemical Engineering, University of Mississippi,  
University, Mississippi, U.S.A.*

## INTRODUCTION

Biosensors find increasing applications in different areas such as the detection of biological agents, chemicals, explosives, food safety, environmental, and energy applications. The main reasons for the growing popularity of the biosensor-based applications are the simplicity of use, monitoring of the reactions in real time and radiolabel free detection of the binding or breakdown of complexes. There is a continual need to enhance the sensitivity, selectivity, stability, regenerability, and decrease the response time of the biosensor. Also, it is significant to obtain kinetic and dissociation rate coefficients for analyte–receptor interactions in order to obtain better physical insights into functionally dissimilar processes they are involved in. An analysis of the interaction wherein the receptor is immobilized on the sensor chip of a surface plasmon resonance (SPR) biosensor and the corresponding analyte is in solution is an initial step in this direction. This is an *in vitro* application. However, one recognizes that the receptor may not be immobilized in real-life application in the human body (for e.g., cellular interactions).

## Surface Plasmon Resonance Biosensor

The SPR biosensor protocol requires one of the components (receptor) to be detected to be immobilized on the biosensor-chip surface and the other component (analyte) to be in solution. The protocol analyzes the analyte–receptor interaction kinetic curves using classical saturation models under diffusion-free conditions. The analysis also assumes that the receptors are homogeneously distributed over the sensor surface. Computer programs and software that come with the equipment provide values of the rate coefficients (for e.g., Biacore 2002<sup>[1]</sup>). Although a careful analysis and experimental protocol may eliminate or minimize the

influence of diffusional limitations, realistically speaking, it is more appropriate to include a heterogeneous distribution of receptors on the sensing surface.

The immobilized receptor–analyte in solution system by its design is heterogeneous. Elimination of this heterogeneity may result in incorrect interpretation of the kinetics of the interactions. One possible way of accounting for the presence of heterogeneity that exists on the surface is by using fractals.<sup>[2]</sup> A characteristic feature of fractals is the self-similarity at different levels of scale and dilatational symmetry. Fractals are particularly useful for this type of analysis because they help characterize the heterogeneity on the biosensor surface and other factors such as mass-transport limitations. The heterogeneity on the surface can be described by a lumped parameter; the fractal dimension.

An alternate analysis is used in this manuscript to reanalyze the data obtained from literature that incorporates theoretically in the kinetic model the heterogeneous distribution of receptors on the sensing surface. This is a more realistic approach to the real-life situation. This would become more significant if the degree of heterogeneity of the receptors on the surface affects the binding and the dissociation rate coefficients to a large degree.

Osmond et al.<sup>[3]</sup> investigated protein–heparin interactions using BIAcore 2000. Protein interactions with heparin are widespread and mediate many biologically important processes. An understanding of the affinity and kinetics of these interactions is of considerable importance. Biotinylated heparin derivatives were immobilized on streptavidin sensor chips and several heparin-binding proteins were examined. In this entry we discuss the binding and dissociation interaction of lactoferrin (protein) binding to three biotinylated heparins, namely, EP–heparin, NH<sub>2</sub>–heparin and CO<sub>2</sub>H–heparin.

Along with the above example, drug–liposome interactions are analyzed using the fractal approach.

Baird, Courtenay, and Myszka<sup>[4]</sup> used both BIAcore 2000 and 3000 to study drug interactions with liposome surfaces. They used this study for predicting intestinal permeability of a drug. Liposomes captured on the biosensor chip surface create a lipid barrier representative of the membrane of an intestinal epithelial cell. As the drug flows over the chip surface, lipid interactions can be monitored in real time without any labeling.

## THEORY

Havlin<sup>[5]</sup> reviewed and analyzed the diffusion of reactants toward fractal surfaces. The details of the theory and the equations involved for the binding and the dissociation phases for analyte–receptor binding are available.<sup>[6]</sup> The details are not repeated here. A brief outline of the equations is given to permit an easier reading.

### Single-Fractal Analysis

#### Binding rate coefficient

Havlin<sup>[5]</sup> considered the diffusion of a particle (analyte) from a homogeneous solution to a solid surface (e.g., receptor-coated surface) on which it reacts to form a product (analyte–receptor complex). The concentration of the product [analyte–receptor] increases with time as follows:

$$\begin{aligned} & \text{(Analyte} \cdot \text{receptor)} \\ & \sim \begin{cases} t^{(3-D_{f,\text{bind}})/2} = t^p & (t < t_c) \\ t^{1/2} & (t > t_c) \end{cases} \quad (1a) \end{aligned}$$

Here  $D_{f,\text{bind}}$  is the fractal dimension of the surface during the binding step;  $t_c$  is the cross-over value. The cross-over value may be determined by the relationship  $t_c^2 \sim r_c^2$ . Above the characteristic length,  $r_c$ , the self-similarity is lost. Hence, above  $t_c$ , the surface may be considered homogeneous and “regular” diffusion is now present. For the present analysis,  $t_c$  is chosen arbitrarily and we assume that the value of the  $t_c$  is not reached.

In Eq. (1a) the concentration of the (analyte–receptor) complex on a solid fractal surface scales at two different scales with time: 1) with the coefficient,  $p = (3 - D_{f,\text{bind}})/2$ , at short timescales and 2)  $p = 1/2$  at intermediate timescales.<sup>[5]</sup> Note that the value of the coefficient,  $p$ , is different from the “normal” case,  $p = 0$ , which is the consequence of two different phenomena, the fractality (heterogeneity) and

the imperfect mixing (diffusion-limited) condition. For a homogeneous surface,  $D_{f,\text{bind}}$  is equal to 2.<sup>[5]</sup> When only diffusional limitations are present,  $p = 1/2$  as it should be. Another way of looking at the  $p = 1/2$  case is that the analyte in solution views the fractal object, in our case the receptor-coated biosensor surface, from a “large distance.” In essence, in the binding process, the diffusion of the analyte from the solution to the receptor surface creates a depletion layer of width  $(Dt)^{1/2}$ , where  $D$  is the diffusion constant. This gives rise to the fractal power law, [analyte–receptor]  $\sim t^{(3-D_{f,\text{bind}})/2}$ .

It is worthwhile commenting on the units of the binding and the dissociation rate coefficient(s) obtained for the fractal analysis. In general, for SPR biosensor analysis, the unit for the [analyte–receptor] complex on the biosensor surface is RU (resonance unit). One thousand resonance units is generally 1 ng/mm<sup>2</sup> of surface, or one resonance unit is 1 pg/mm<sup>2</sup>. Then, the unit for the binding rate coefficient,  $k_{\text{bind}}$ , from Eq. (1a) is pg mm<sup>-2</sup> sec<sup>( $D_{f,\text{bind}}-3$ )/2</sup>. Note that the unit of dependence in time exhibited by  $k_{\text{bind}}$  changes slightly depending on the corresponding fractal dimension obtained in the binding phase,  $D_{f,\text{bind}}$ . The fractal dimension value is less than or equal to three. Three is the highest value of the fractal dimension because the system is embedded in a three-dimensional system. Note that  $k_{\text{bind}}$  and  $k_{\text{diss}}$  are interchangeably used as  $k$  and  $k_d$ , respectively.

It would be useful to specify what the carrier of fractal properties is. It could be either the analyte surface, the receptor surface, or the immobilizing (in our case, the biosensor) surface. There is a considerable body of work on fractal surface properties of proteins.<sup>[7–10]</sup> Daily et al.<sup>[11]</sup> indicate that the active sites (in our case the receptors on the biosensor surface) may themselves form a fractal surface. Furthermore, the inclusion of non-specific binding sites on the surface would increase the fractal dimension of the surface. At present, we are unable to specify what the carrier of the fractal properties is. This is exacerbated by our reanalysis of kinetic data available in the literature. Presumably, it is because of a composite of some or all of the factors mentioned above.

#### Dissociation rate coefficient

The diffusion of the dissociated particle (receptor or analyte) from the solid surface (e.g., analyte–receptor complex coated surface) into solution may be given, as a first approximation by:

$$\begin{aligned} & \text{(Analyte} \cdot \text{receptor)} \sim -t^{(3-D_{f,\text{diss}})/2} \quad (t > t_{\text{diss}}) \\ & = -k_{\text{diss}} t^{(3-D_{f,\text{diss}})/2} \quad (1b) \end{aligned}$$

Here  $D_{f,diss}$  is the fractal dimension of the surface for the dissociation step;  $t_{diss}$  represents the start of the dissociation step. This corresponds to the highest concentration of the analyte–receptor complex on the surface. Henceforth, its concentration only decreases.  $D_{f,bind}$  may or may not be equal to  $D_{f,diss}$ .

The units for the dissociation rate coefficient,  $k_{diss}$ , are obtained in a similar manner as done for the binding rate coefficient. The unit for the  $k_{diss}$  is  $\text{pg mm}^{-2} \text{sec}^{(D_{f,diss}-3)/2}$ . Again, note that the unit dependence on time exhibited by  $k_{diss}$  changes slightly because of the dependence on  $D_{f,diss}$ .

## Dual-Fractal Analysis

### Binding rate coefficient

The single-fractal analysis has been extended to include two fractal dimensions. The concentration of the analyte–receptor complex is given by:

$$\begin{aligned} & (\text{Analyte} \cdot \text{receptor}) \\ & \sim \begin{cases} t^{(3-D_{f1,bind})/2} = t^{p1} & (t < t_1) \\ t^{(3-D_{f2,bind})/2} = t^{p2} & (t_1 < t < t_2 = t_c) \\ t^{1/2} & (t > t_c) \end{cases} \quad (1c) \end{aligned}$$

The time ( $t = t_1$ ) at which the first fractal dimension “changes” to the second fractal dimension is assumed to be arbitrary and empirical. One of the reasons for the “change” in fractal dimension is the fact that the analyte–receptor binding is different from catalytic reactions. In catalytic reactions, the catalytic surface exhibits an unchanging fractal surface to the reactant in the absence of fouling and other complications, whereas for analyte–receptor binding the biosensor surface exhibits a changing fractal surface to the analyte in solution. This occurs because as each binding reaction takes place, smaller and smaller amounts of “binding” sites or receptors are available on the biosensor surface to which the analyte may bind. Furthermore, as the reaction proceeds, there is an increasing degree of heterogeneity on the biosensor surface for some reaction systems. This is manifested by two degrees of heterogeneity, or two fractal dimensions on the biosensor surface.<sup>[12]</sup> In the theoretical limit one might envisage a temporal fractal dimension wherein there is a continuous change in the degree of heterogeneity on the surface, although of course, such situations would be rare.

At present, the dual-fractal analysis does not have a basis at the molecular level. This represents two different levels of heterogeneity on the biosensor surface. For the most part the use of dual fractal analysis is dictated by the data analyzed and the experience gained

by handling a single-fractal analysis. The  $r^2$  (regression coefficient) value obtained is also used to determine if a single-fractal analysis is sufficient to provide an adequate fit. Only if the  $r^2$  value is less than 0.97 for a single-fractal analysis do we use a dual-fractal model.

The binding rate coefficients,  $k_1$  and  $k_2$ , in the dual-fractal analysis have the same units,  $\text{pg mm}^{-2} \text{sec}^{(D_{f1,bind}-3)/2}$  and  $\text{pg mm}^{-2} \text{sec}^{(D_{f2,bind}-3)/2}$ , respectively, as the binding rate coefficient,  $k$ , in the single-fractal analysis.

### Dissociation rate coefficient

In this case the dissociation rate coefficient is given by:

$$\begin{aligned} & (\text{Analyte} \cdot \text{receptor}) \\ & \sim \begin{cases} -t^{(3-D_{f1,diss})/2} & (t_{diss} < t < t_{d1}) \\ -t^{(3-D_{f2,diss})/2} & (t_{d1} < t < t_{d2}) \end{cases} \quad (1d) \end{aligned}$$

Here  $D_{f,diss}$  is the fractal dimension of the surface for the dissociation step;  $t_{diss}$  represents the start of the dissociation step. This corresponds to the highest concentration of the [analyte–receptor] on the surface.  $D_{f,bind}$  may or may not be equal to  $D_{f,diss}$ . The dissociation rate coefficients,  $k_{d1}$  and  $k_{d2}$ , in the dual-fractal analysis have the same units,  $\text{pg mm}^{-2} \text{sec}^{(D_{f1,diss}-3)/2}$  and  $\text{pg mm}^{-2} \text{sec}^{(D_{f2,diss}-3)/2}$ , respectively, as the dissociation rate coefficient,  $k_d$ , in the single-fractal analysis.

The affinity,  $K = k_{diss}/k_{bind}$ , can be calculated using the above models. The  $K$  value is frequently used in analyte–receptor reactions occurring on biosensor surfaces. This ratio, besides providing physical insights into the analyte–receptor system, is of practical importance because it may be used to help determine (and possibly enhance) the regenerability, reusability, stability, and other biosensor performance parameters. The affinity  $K$  has the unit  $\text{sec}^{(D_{f,diss}-D_{f,bind})/2}$ . This applies to both the single- as well as the dual-fractal analysis. Note the difference in the units of affinity obtained for the classical as well as the fractal-type kinetics. Although the definition of affinity is the same in both types of kinetics, the difference(s) in the units of the different rate coefficients eventually leads to a different unit for the affinity in the two types of kinetics. This is not entirely unexpected because the classical kinetic analysis does not include the characteristics of the surface in the definition of the affinity  $K$ , whereas the present fractal analysis does. Thus, one may not be able to actually compare the affinities in these two types of systems. This is a significant difference in the kinetic analysis of binding and dissociation reactions on biosensor surfaces from what is available in the literature.

## RESULTS

A fractal analysis is applied to the data obtained for protein–heparin<sup>[3]</sup> and drug–liposome interactions<sup>[4]</sup> taken from the literature. Alternate expressions for fitting the data are available. These include saturation, first-order reaction, and no diffusion limitation cases, but these expressions are apparently deficient in describing the heterogeneity that inherently exists on the surface. The method widely used for modeling data is the Langmuirian approach. This approach may be used to model the data presented if one assumes the presence of discrete classes of sites (e.g., double-exponential analysis as compared with a single-exponential analysis).

Lee and Lee<sup>[13]</sup> indicate that the fractal approach has been applied to surface science, e.g., adsorption and reaction processes. These authors emphasize that

the fractal approach provides a convenient means to represent the different structures and morphology at the reaction surface. They also emphasize using the fractal approach to develop optimal structures and as a predictive approach. Another advantage of the fractal technique is that the analyte–receptor binding (as well as the dissociation reaction) is a complex reaction, and the fractal analysis via the fractal dimension and the rate coefficient provides a useful lumped parameter(s) analysis of the diffusion-limited reaction occurring on a heterogeneous surface. The parameters obtained by this analysis of the diffusion-limited binding kinetics occurring on heterogeneous surfaces provide a useful comparison of different receptor–analyte biosensor systems.

In the classical situation, to demonstrate fractality, one should make a log–log plot, and one should have a large amount of data. It may also be useful to

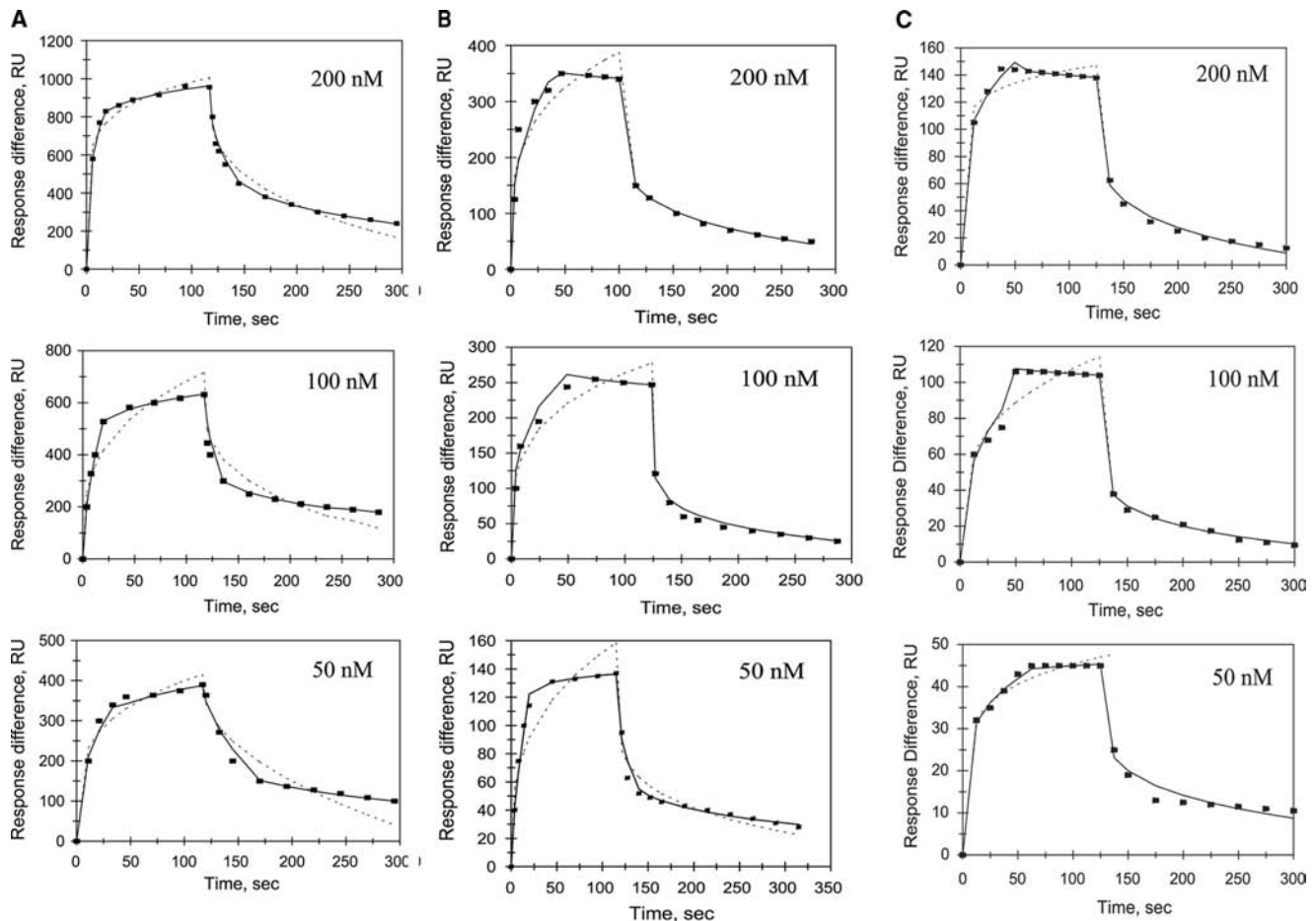


**Fig. 1** Binding curves of lactoferrin at various concentrations to immobilized heparin. (A) Lactoferrin binding to EP–heparin. (B) Lactoferrin binding to NH<sub>2</sub>–heparin. (C) Lactoferrin binding to CO<sub>2</sub>H–heparin. Legend: When only a solid line (—) is used then a single fractal analysis applies. When both a dotted (---) and a solid (—) line are used, then the dotted line (---) represents a single-fractal analysis, and the solid line (—) represents a dual-fractal analysis. The data points are represented by (■). Source: From Ref.<sup>[3]</sup>.

**Table 1** Fractal dimensions and binding and dissociation rate coefficients for different concentrations of lactoferrin in solution to three different ligands immobilized on a sensor chip surface

Lactoferrin binding to	$k_1$	$k_2$	$k$	$D_{f,1}$	$D_{f,2}$	$D_f$	$k_{d1}$	$k_{d2}$	$k_d$	$D_{fd,1}$	$D_{fd,2}$	$D_{fd}$	$K_1 = k_d/k_1$	$K_2 = k_{d2}/k_2$
Lactoferrin concentration: 200 nM														
CO <sub>2</sub> H-heparin	326.48 ± 13.32	651.73 ± 6.219	499.64 ± 35.34	2.3462 ± 0.098	2.8362 ± 0.012	2.706 ± 0.049	119.21 ± 19.31	282.46 ± 1.491	150.41 ± 22.94	2.1442 ± 0.128	2.6404 ± 0.010	2.359 ± 0.063	0.460	0.231
NH <sub>2</sub> -heparin	98.871 ± 21.18	402.46 ± 1.986	120.59 ± 23.51	2.311 ± 0.176	3.0	2.493 ± 0.11	n/a	n/a	118.31 ± 1.27	n/a	n/a	2.6482 ± 0.009	1.19	0.294
EP-heparin	57.626 ± 2.326	173.06 ± 0.40	90.734 ± 6.322	2.5132 ± 0.076	3.0	2.7948 ± 0.061	n/a	n/a	49.657 ± 1.665	n/a	n/a	2.63 ± 0.0268	0.862	0.287
Lactoferrin concentration: 100 nM														
CO <sub>2</sub> H-heparin	189.66 ± 4.06	393.49 ± 2.91	167.20 ± 29.52	1.800 ± 0.075	2.8 ± 0.010	2.3888 ± 0.099	48.27 ± 22.78	222.12 ± 1.60	93.34 ± 26.40	1.598 ± 0.594	2.720 ± 0.007	2.328 ± 0.1224	0.491	0.237
NH <sub>2</sub> -heparin	83.224 ± 10.94	332.88 ± 1.50	83.224 ± 10.94	2.398 ± 0.092	3.0	2.500 ± 0.076	n/a	n/a	114.77 ± 04.22	n/a	n/a	2.7422 ± 0.019	1.38	0.345
EP-heparin	22.49 ± 2.35	124.53 ± 0.09	30.283 ± 3.107	2.27 ± 0.131	3.0	2.449 ± 0.088	n/a	n/a	47.719 ± 0.795	n/a	n/a	2.736 ± 0.0134	2.12	0.386
Lactoferrin concentration: 50 nM														
CO <sub>2</sub> H-heparin	78.336 ± 6.722	204.21 ± 1.979	128.79 ± 14.59	2.175 ± 0.152	2.7304 ± 0.054	2.507 ± 0.103	19.943 ± 3.43	122.32 ± 0.87	27.455 ± 6.232	1.7548 ± 0.124	2.669 ± 0.021	2.018 ± 0.108	0.350	0.134
NH <sub>2</sub> -heparin	17.344 ± 1.933	109.55 ± 0.44	35.764 ± 7.968	1.6958 ± 0.174	2.907 ± 0.011	2.3708 ± 0.124	22.66 ± 3.987	55.835 ± 0.691	37.212 ± 4.85	2.20 ± 0.236	2.754 ± 0.015	2.576 ± 0.068	2.15	0.340
EP-heparin	18.533 ± 0.660	38.062 ± 0.522	21.616 ± 0.909	2.5834 ± 0.067	2.9224 ± 0.033	2.6754 ± 0.037	n/a	n/a	13.505 ± 0.982	n/a	n/a	2.6158 ± 0.057	0.728	0.354

n/a: not applicable.  
 Source: From Ref.<sup>[2]</sup>.



compare the fit to some other forms, such as exponential, or one involving saturation, etc. At present, we do not present any independent proof or physical evidence of fractals in the examples presented. It is a convenient means (because it provides a lumped parameter) of making the degree of heterogeneity that exists on the surface more quantitative. Thus, there is some arbitrariness in the fractal model to be presented.

Our analysis at present does not include the non-selective adsorption of the analyte. We do recognize that in some cases this may not be a significant component of the adsorbed material and that this rate of association, which is of a temporal nature, would depend on surface availability. If we were to accommodate the non-selective adsorption into the model, there would be an increase in the heterogeneity on the surface because by its very nature non-specific adsorption is more heterogeneous than specific adsorption. This would lead to higher fractal dimension values because the fractal dimension is a direct measure of the degree of heterogeneity that exists on the surface.<sup>[14]</sup>

For a first-order reaction, as expected, an increase in the degree of heterogeneity on the surface because of non-specific binding would lead to lower values of the (specific) binding rate coefficient. The deletion of this non-specific binding in the analysis would lead to (artificially) higher values of the binding rate coefficient for first-order reactions. Our reactions are, in general, higher than first order. Sadana and Chen<sup>[14]</sup> showed that for reaction orders higher than one a certain amount of heterogeneity is beneficial for the binding rate coefficient. There is apparently an optimum range because of steric factors. Thus, depending on whether one is inside or out of this optimum range, the deletion of non-specific binding in the analysis would lead to either an increase or a decrease in the binding rate coefficient. In other words, if one is in the optimum range for a particular reaction order, then the presence of non-specific binding would lead to higher values of the (specific) binding rate coefficient. In this case, the deletion of the non-specific binding leads to lower than real-life values of the binding rate coefficient.

The previous analyses used the software provided by the SPR biosensor manufacturer (Biacore 2002) to obtain the values of the rate coefficients and the affinities. The model did not take into account the heterogeneity present on the sensor chip surface. Here we present the reanalysis of these interactions using the above equations.

Osmond et al.<sup>[3]</sup> have analyzed binding and the dissociation of protein-heparin interactions. These authors have used SPR biosensor for the analysis of the kinetics. Biotinylated heparin derivatives were immobilized on streptavidin sensor chips and their effect was analyzed. Fig. 1A, B, and C shows the

binding curves of lactoferrin at various concentrations (200, 100, and 50 nM) to CO<sub>2</sub>H-heparin, NH<sub>2</sub>-heparin, and EP-heparin, respectively, immobilized on the sensor chip surface.

For EP-heparin, a dual-fractal analysis is adequate to describe the binding as well as the dissociation kinetics for all of the concentrations analyzed. A dual-fractal analysis was adequate to describe binding kinetics for NH<sub>2</sub>-heparin and CO<sub>2</sub>H-heparin complex immobilized on sensor-chip surface. However, a single-fractal analysis was sufficient to describe the dissociation of these reactions with an exception for 50 nM lactoferrin concentration binding to NH<sub>2</sub>-heparin; a dual fractal analysis was required for this case. The values of the binding and the dissociation rate coefficients are given in Table 1. These values were obtained from a regression analysis using Corel Quattro Pro 8.0<sup>[15]</sup> to model the data using Eqs. (1c) and (1d).

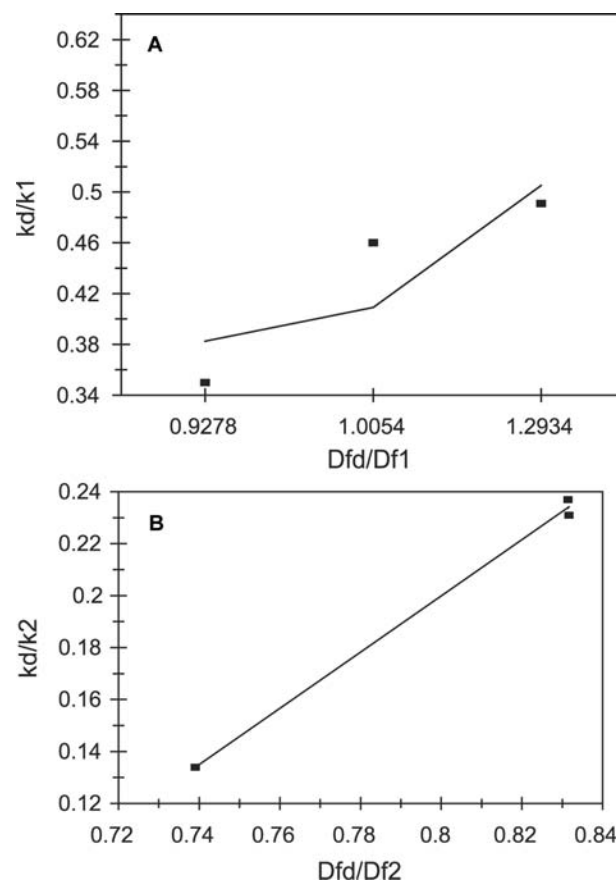


**Fig. 2** Relationship between the affinities and the ratio of fractal dimension for dissociation to that of binding for lactoferrin binding to EP-heparin. (A) Increase in the affinity,  $K_1$ , with an increase in the fractal dimension ratio,  $D_{fd}/D_{f1}$ . (B) Increase in the affinity,  $K_2$ , with an increase in the fractal dimension ratio,  $D_{fd}/D_{f2}$ . Legend: as in Fig. 1 legend.

As the concentration of lactoferrin binding to all three different ligands increases, there is an increase in the binding fractal dimension ( $D_f$ ) and in the dissociation fractal dimension ( $D_{fd}$ ). This leads to an increase in the binding rate coefficient,  $k$ , and the dissociation rate coefficient,  $k_d$ . The higher receptor concentration (200 nM) on the SPR surface leads to a higher degree of heterogeneity on the surface because of the saturation of the active sites on the surface. This leads to a higher binding rate coefficient for EP-heparin and CO<sub>2</sub>H-heparin immobilized on the biosensor surface. However, for the NH<sub>2</sub>-heparin ligand this surface saturation not only leads to increase in rate coefficients but also to a change in mechanism of dissociation, which can be seen by the use of a dual-fractal analysis to describe the process.

The affinity  $K_1$  ( $k_d/k$ ) values are also calculated. There is no trend in these values with respect to different ligands. However, if we compare the affinity values of different concentrations of lactoferrin binding to a particular ligand with the ratio of the fractal dimension for dissociation to the fractal dimension for binding ( $D_{fd}/D_{f1}$ ), we note an increasing trend. Fig. 2A shows that the affinity  $K_1$  ( $k_d/k_1$ ) increases, for the binding of lactoferrin to the CO<sub>2</sub>-heparin immobilized on the sensor surface, as the ratio  $D_{fd}/D_{f1}$  increases. For the data analyzed and presented in Table 1, the affinity  $K_1$  ( $k_d/k_1$ ) is given by:

$$K_1 = (0.6650 \pm 0.0179)(D_{fd}/D_{f1})^{6.196 \pm 0.2025} \quad (2a)$$

The affinity,  $K_1$ , is very sensitive to the degree of heterogeneity that exists on the surface as noted by

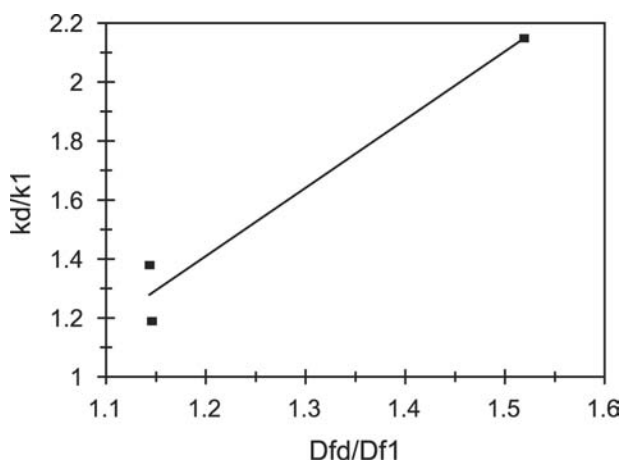


**Fig. 3** Relationship between the affinities and the ratio of fractal dimension for dissociation to that of binding for lactoferrin binding to NH<sub>2</sub>-heparin. Increase in the affinity,  $K_1$ , with an increase in the fractal dimension ratio,  $D_{fd}/D_{f1}$ .

the high value of the order of dependence of  $K_1$  on  $D_{fd}/D_f$ .

Fig. 2B relates the affinity  $K_2$  ( $k_d/k_2$ ) to ( $D_{fd}/D_{f2}$ ). The affinity can be given by

$$K_2 = (0.7544 \pm 0.0457)(D_{fd}/D_{f2})^{7.110 \pm 2.065} \quad (2b)$$

A similar analysis is done for binding of lactoferrin on NH<sub>2</sub>-heparin and CO<sub>2</sub>H-heparin ligands. The dependence of affinities on the ratio of fractal dimension is shown in Figs. 3 and 4, respectively. For the data analyzed of different concentrations of lactoferrin binding to NH<sub>2</sub>-heparin, the affinity,  $k_d/k_1$  is given by:

$$K_1 = (1.0158 \pm 0.1074)(D_{fd}/D_{f1})^{1.8256 \pm 0.4650} \quad (3a)$$

For the data analyzed of different concentrations of lactoferrin binding to CO<sub>2</sub>H-heparin, the affinities,

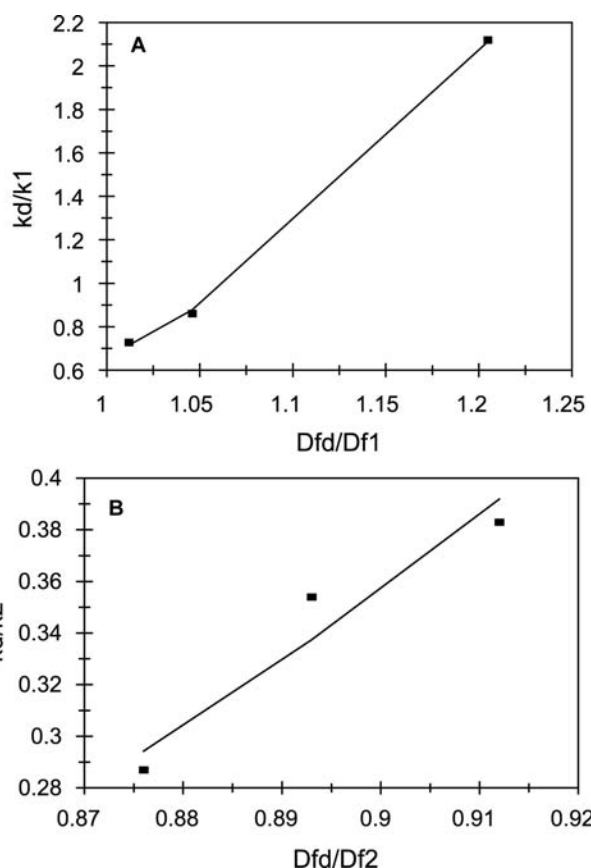


**Fig. 4** Relationship between the affinities and the ratio of fractal dimension for dissociation to that of binding for lactoferrin binding to CO<sub>2</sub>H-heparin. (A) Increase in the affinity,  $K_1$ , with an increase in the fractal dimension ratio,  $D_{fd}/D_{f1}$ . (B) Increase in the affinity,  $K_2$ , with an increase in the fractal dimension ratio,  $D_{fd}/D_{f2}$ . Legend: as in Fig. 1 legend.

Bionanoparticles - Block

$K_1$  and  $K_2$ , are given by:

$$(k_d/k_1) = (0.7042 \pm 0.1497) \times (D_{fd}/D_{f1})^{0.8367 \pm 0.6110} \quad (4a)$$

$$(k_d/k_2) = (0.5597 \pm 0.0193) \times (D_{fd}/D_{f2})^{4.728 \pm 2009} \quad (4b)$$

These results suggest heparin attached through the reducing terminus (EP-heparin) had the highest binding capacity followed by heparin immobilized via

intrachain bare amines ( $\text{NH}_2$ -heparin). Heparin immobilized through the carboxylate groups of uronic acids ( $\text{CO}_2\text{H}$ -heparin) had lowest binding capacity. This is in accordance with the results suggested by the authors.

To examine how drug-binding responses were affected by liposome capacity, Baird, Courtenay, and Myszka<sup>[4]</sup> used different amounts of lipids captured on a sensor chip surface by varying the concentration of liposome injected. Fig. 5 shows the binding and dissociation curves obtained for liposome concentrations from 0.25 to 4 mM. For all of the concentrations of

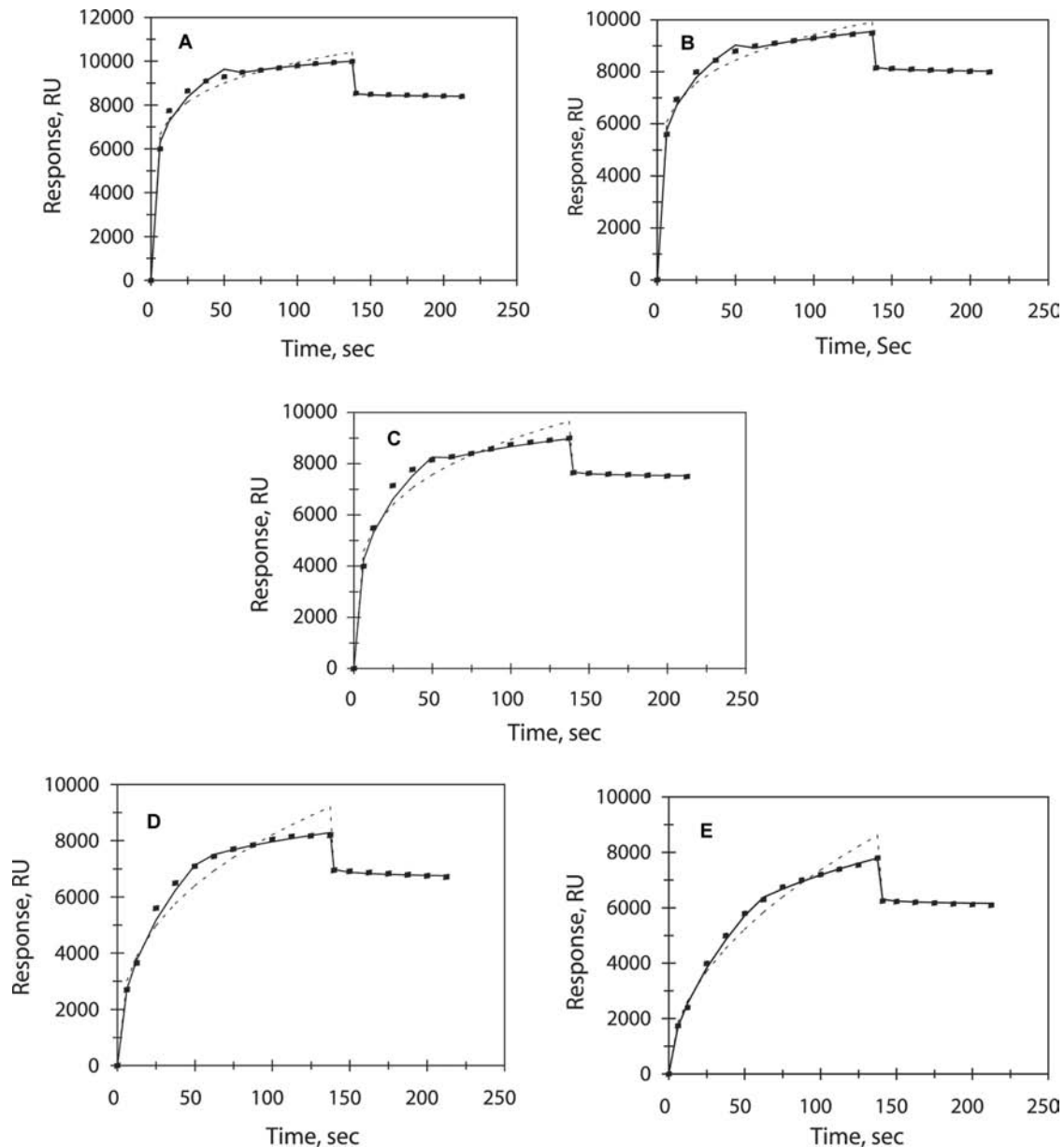


**Fig. 5** Binding and dissociation curves for different amounts of liposome captured for drug-binding response. (A) 4 mM liposome suspension. (B) 2 mM liposome suspension. (C) 1 mM liposome suspension. (D) 0.5 mM liposome suspension. (E) 0.25 mM liposome suspension. Legend: as in Fig. 1 legend. Source: From Ref.<sup>[4]</sup>.

**Table 2** Fractal dimensions and binding and dissociation rate coefficients for different concentrations of liposome suspension captured on a sensor chip surface

Liposome concentration (nM)	$k_1$	$k_2$	$k$	$D_{f,1}$	$D_{f,2}$	$D_f$	$k_d$	$D_{fd}$	$K_1 = k_d/k_1$	$K_2 = k_d/k_2$
4	4339.4 ± 244.4	7176.5 ± 10.08	5123.2 ± 262.93	2.590 ± 0.064	2.866 ± 0.004	2.711 ± 0.031	1454.81 ± 17.39	2.957 ± 0.008	0.335	0.203
2	3903.4 ± 139.8	6252.5 ± 38.54	4562.38 ± 200.96	2.571 ± 0.041	2.827 ± 0.009	2.684 ± 0.026	1294.76 ± 21.00	2.941 ± 0.011	0.331	0.207
1	2369.4 ± 159.3	5221.8 ± 16.78	2956.10 ± 232.70	2.361 ± 0.066	2.778 ± 0.009	2.519 ± 0.047	1294.76 ± 21.00	2.941 ± 0.011	0.546	0.248
0.5	1178.9 ± 67.08	4475.3 ± 67.08	1569.81 ± 152.31	2.078 ± 0.056	2.749 ± 0.024	2.282 ± 0.057	1166.22 ± 30.97	2.901 ± 0.018	0.989	0.260
0.25	589.44 ± 28.40	2222.9 ± 19.35	756.90 ± 65.45	1.836 ± 0.047	2.490 ± 0.025	2.012 ± 0.051	1477.05 ± 18.48	2.942 ± 0.009	2.506	0.664

Source: From Ref.<sup>[3]</sup>.

liposome suspension analyzed, a dual-fractal analysis is required to adequately describe the drug–liposome binding kinetics. The dissociation phase is well described by a single-fractal analysis. The values of the binding and the dissociation rate coefficients are given in Table 2. According to the authors there are two types of drugs. Type I drugs dissociate rapidly from the lipid surface and Type II drugs display at least two distinct kinetic phases during the binding and the dissociation. This suggests diffusion of the drug into the phospholipid bilayer. This can be one of the reasons for the need of a dual-fractal analysis (instead of single-fractal analysis) to adequately describe the association (binding) of the drug–liposome interaction. The second reason can be the sigmoidal shape of the binding curve. A sigmoidal curve is usually observed when there is a change in the binding mechanism. For the dissociation case, there is a sharp decrease in the response, suggesting a single mechanism at work, justifying the use of single fractal analysis.

As in the protein–heparin example,<sup>[3]</sup> as the liposome suspension concentration increases, the binding as well as the dissociation rate coefficient increases.

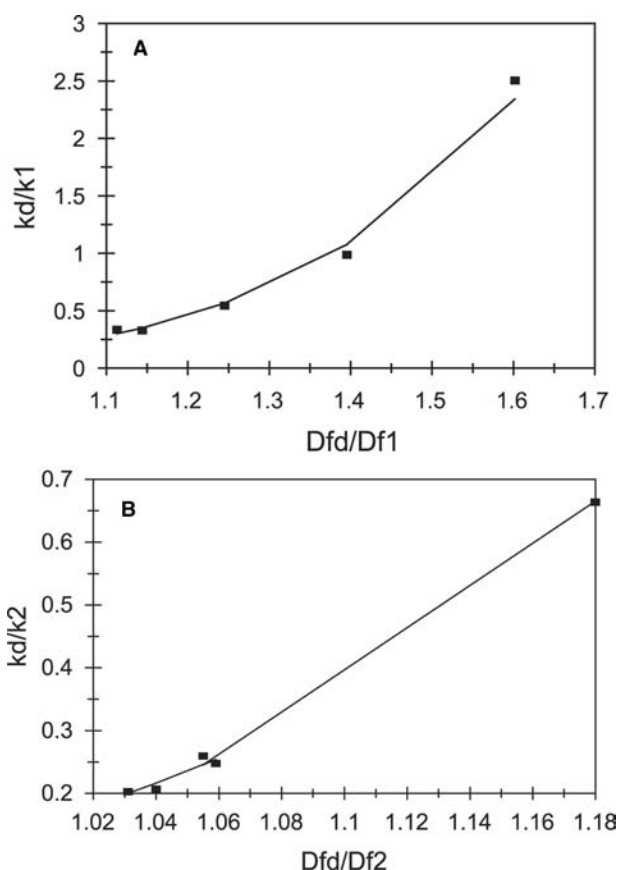


**Fig. 6** (A) Increase in the affinity,  $K_1$ , with an increase in the fractal dimension ratio,  $D_{fd}/D_{f1}$ . (B) Increase in the affinity,  $K_2$ , with an increase in the fractal dimension ratio,  $D_{fd}/D_{f2}$ . Legend: as in Fig. 1 legend.

This leads to an increase in the fractal dimension for binding and dissociation. The reason for this increase in the rate coefficients is the increase in heterogeneity on the sensor chip surface because of increase in density of liposome in solution. An increase in density gives rise to multiple collisions. This in turn increases the effective reaction order, which leads to an increase in the fractal dimension.<sup>[16]</sup>

The affinity values ( $k_d/k$ ) are also calculated and presented in Table 2. Both the affinity values,  $K_1$  ( $k_d/k_1$ ) and  $K_2$  ( $k_d/k_2$ ), exhibit decrease with increase in the concentration of the liposome.

Fig. 6A shows the plot of  $K_1$  vs. the ratio  $D_{fd}/D_{f1}$ . For the data analyzed of different concentrations of liposome, the affinity,  $K_1$ , is given by:

$$(k_d/k_1) = (0.1643 \pm 0.0166) \times (D_{fd}/D_{f1})^{5.638 \pm 0.320} \quad (5a)$$

Note that as indicated earlier, the units of  $k_d$  and  $k_1$  are slightly different.

Fig. 6B shows the plot of  $K_2$  versus the ratio  $D_{fd}/D_{f2}$ . For different concentrations of liposome analyzed, the affinity,  $K_2$ , is given by:

$$(k_d/k_2) = (0.1526 \pm 0.0069) \times (D_{fd}/D_{f2})^{8.896 \pm 0.4046} \quad (5b)$$

Both Eqs. (5a) and (5b) suggest a strong dependence of the affinities on the ratio of fractal dimensions. For correct cell signaling, lower values of  $K$  are beneficial, whereas for incorrect cell signaling higher  $K$  values are beneficial. Knowing the relation of affinity with the fractal dimension (degree of heterogeneity) may suggest useful means by which appropriate interactions (to promote correct cell signaling) and inappropriate interactions (deleterious to health signaling) may be better controlled.

## CONCLUSIONS

A fractal analysis of the binding and dissociation of protein–heparin and drug–liposome interactions along with the influence of different ligands on these interactions occurring on SPR biosensor applications is studied. This analysis provides a quantitative indication of the state of disorder or roughness in terms of fractal dimension on the biosensor chip surface and its effect on the binding and the dissociation rate coefficients and affinity values. This analysis can be considered as an alternate way to understand the kinetics on the heterogeneous surface with diffusion-limited reactions occurring toward structured surfaces.

For example, data taken from the literature<sup>[3,4]</sup> is reanalyzed to include the degree of heterogeneity present on the surface and its influence on the binding and the dissociation kinetics. The analysis of both the binding and the dissociation steps provide a more complete picture of the reaction occurring on the sensor chip surface. The fractal analysis also provides a value of the affinity,  $K$  (the ratio of the dissociation rate coefficient,  $k_d$ , and the binding rate coefficient,  $k$ ). The  $K$  values obtained may give us an idea or provide a basis for *selective modulation* of the surface, thereby changing the binding as well as the dissociation reactions in desired directions. This has biomedical as well as environmental implications.

The degree of heterogeneity can be quantitatively measured in terms of the fractal dimension. The degree of heterogeneity is affected by the presence of ligands on the sensor chip surface. In general, the degree of heterogeneity for the binding and the dissociation phases is different. Both types of examples are presented wherein either a single- or a dual-fractal analysis is required to adequately describe the binding and/or the dissociation kinetics. The dual-fractal analysis is used only when the single fractal analysis did not provide an adequate fit (sum of least squares less than 0.97). This was done by regression analysis provided by Quattro Pro.

Predictive expressions are developed for the affinities,  $K_1$  ( $k_d/k_1$ ) and  $K_2$  ( $k_d/k_2$ ), as a function of the ratio,  $D_{fd}/D_{f1}$  and  $D_{fd}/D_{f2}$ , respectively. The fractal dimension for the binding or the dissociation phase is not a typical independent variable and cannot be directly manipulated. The predictive relationships provide a means by which these binding or the dissociation rate coefficients may be manipulated by changing either the analyte concentration in solution or the degree of heterogeneity that exists on the surface. Note that a change in the degree of heterogeneity on the surface would, in general, lead to changes in both the binding as well as the dissociation rate coefficient. Thus, a careful consideration is required to get the desired result.

It is interesting to note that the fractal surface leads to turbulence, which enhances mixing, decreases diffusional limitations, and leads to an increase in the binding rate coefficient.<sup>[17]</sup> This also applies to the dissociation rate coefficient. For this to occur, the characteristic length of this turbulent boundary layer may have to extend a few monolayers above the sensor surface to affect bulk diffusion to and from the surface. However, given the extremely laminar flow regimes in most biosensors this may not actually take place. A fractal surface is characterized by grooves and ridges, and this surface morphology may lead to eddy diffusion. This eddy diffusion can then help to enhance

the mixing and extend the characteristic length of the boundary layer to affect the bulk diffusion to and from the surface.

In both of the examples discussed above, as the concentration of ligand on the sensor chip surface (for the protein–heparin case) or in solution (for the drug–liposome case) increases, there is an increase in the binding as well as in the dissociation rate coefficient.

Even though the analysis is presented for these interactions occurring on biosensor surfaces, they do provide insights into these reactions occurring on cellular surfaces. More such studies are required to determine if the binding and dissociation rate coefficients are sensitive to the degree of heterogeneity that exists on the biosensor or cellular surfaces. The analysis should encourage cellular experimentalists, particularly people dealing with analyte–nuclear receptor reactions, to pay increasing attention to the nature of the surface and how it may be modulated to control cellular analyte–nuclear receptor reactions in desired directions.

## REFERENCES

1. Biacore, AB. *BIAevaluation, 3.2 Software*; Uppsala, Sweden, 2002.
2. Kopleman, R. Fractal reaction kinetics. *Science* **1988**, *241*, 1620.
3. Osmond, R.I.W.; Kett, W.C.; Skett, S.E.; Coombe, D.R. Protein–heparin interactions measured by BIAcore 2000 are affected by the method of heparin immobilization. *Anal. Biochem.* **2002**, *310*, 199–207.
4. Baird, C.L.; Courtenay, E.S.; Myszkka, D.G. Surface plasmon resonance characterization of drug/liposome interactions. *Anal. Biochem.* **2002**, *310*, 93–99.
5. Havlin, S. Molecular diffusion and reaction. In *The Fractal Approach to Heterogeneous Chemistry: Surface, Colloids, Polymers*; Avnir, D., Ed.; Wiley: New York, 1989; 251 pp.
6. Sadana, A. A kinetic study of analyte–receptor binding and dissociation. *Anal. Biochem.* **2001**, *291* (1), 34.
7. Lewis, M.; Rees, D. Fractal structures of proteins. *Science* **1985**, *230*, 1163–1165.
8. Pfeifer, P.; Wu, Y.J.; Cole, M.W.; Krim, J. Multilayer adsorption on a fractally rough surface. *Phys. Rev. Lett.* **1989**, *62*, 1997–2000.
9. Fedorov, B.A.; Fedorov, B.B.; Schmidt, P.W. An analysis of the fractal properties of the surfaces of globular proteins. *J. Chem. Phys.* **1993**, *99*, 4076–4083.
10. Dewey, T.G. Algorithmic complexity and thermodynamics of sequence: Structure relationships in proteins. *Phys. Rev., E* **1997**, *56*, 4545–4552.
11. Daily, W.; Ramirez, A.; Labrecque, D.; Nitao, J. Electrical resistivity tomography of vadose water movement. *Water Resour. Res.* **1992**, *28*, 1429–1442.



12. Sadana, A.; Vo-Dinh, T. Biomedical implications of protein folding and misfolding. *Biotechnol. Appl. Biochem.* **2001**, *33*, 17–31.
13. Lee, C.K.; Lee, S.L. Multi-fractal scaling analysis of reactions over fractal surfaces. *Surf. Sci.* **1995**, *325*, 294–310.
14. Sadana, A.; Chen, Z. Influence of non-specific binding on antigen–antibody binding kinetics for biosensor applications. *Biosens. Bioelectron.* **1996**, *11* (8), 769–782.
15. *Corel Quattro Pro*; Corel Corporation Limited: Ottawa, Canada, 1997.
16. Anacker, L.W.; Parson, R.P.; Kopelman, R. Diffusion-controlled reaction kinetics on fractal and Euclidean lattices: Transient and steady-state annihilation. *J. Phys. Chem.* **1985**, *89*, 4758–4761.
17. Martin, J.S.; Frye, G.C.; Ricco, A.J.; Senturia, A.D. Effect of surface roughness on the response of thickness-shear mode resonators in liquids. *Anal. Chem.* **1993**, *65* (20), 2910–2922.

# Biosurfaces: Water Structure at Interfaces

**Yan-Yeung Luk**

*Department of Chemical Engineering, University of Wisconsin–Madison,  
Madison, Wisconsin, U.S.A.*

## INTRODUCTION

Science at surfaces and interfaces is central to many phenomena in the life sciences.<sup>[1]</sup> For instance, the topography of the surface of a properly folded protein is almost always more important than its hydrophobic core for functions, such as catalysis, dimerization, or assembly.<sup>[2]</sup> On a higher architectural hierarchy at cellular or tissue level, protein binding at the surface of cell membrane determines the cell physiology including proliferation, differentiation, and viability. This set of biosurfaces bears characteristics that are different from any other man-made surface in both complexity and scale. The surface of a protein contains a wide variety of functional groups, and the surface of cell membrane contains dynamic lipid bilayers imbedded with proteins, which is hardly resembled by any man-made surface such as palladium catalyst. Furthermore, most of the events occurring on these biosurfaces are at nanometer scale. For example, the functional assembly of ribosome executing protein synthesis and the focal adhesion mediating cell adhesion are both on the scale of 40–80 nm. For single protein catalysis, the active side is usually of a dimension larger than 1 nm. In contrast, most man-made surfaces function either at molecular level (catalysis) or at micrometer scale (lithography).<sup>[3]</sup>

The importance of biosurfaces is both highlighted and revealed by the rapid development of biotechnology in recent years.<sup>[4]</sup> In particular, a well-defined problem—bioinertness—first appears as a technological problem, and soon evolves into an intricate puzzle of fundamental science. In this entry, the origin of this unique problem, the development of its solutions and the evolution of theories over a relative short span of time—less than 10 years—will be reviewed. Furthermore, the significance and implication of this problem and its solution will be discussed in the context of life sciences.

## BIOINERTNESS—DEFINING THE PROBLEM

Translating solution assays into arrays on a chip provides an opportunity to accelerate the rate (high

throughput) and scope discovery of biological events and design of drugs. These chip-based, high-content and high-throughput assays are a central theme of contemporary biotechnology. The success of the DNA chip marked one of such example.<sup>[5,6]</sup> However, protein chip technology aimed to decipher the protein–protein binding events in the cell signaling pathways and protein–drug interactions, so called proteomics, faces several challenges that are absent for DNA chips. The key to these challenges lies in the fact that protein's function depends on a folded three-dimensional structure that can easily denature. Hence when immobilizing proteins onto a surface, a number of criteria must be fulfilled to maintain an optimal activity for biological assays.<sup>[7]</sup> The surface should immobilize only desired protein with control of native folding, density, and orientation so that optimal activity or function of immobilized protein is rendered on surface. Among these requirements, the most basic one is the prevention of non-specific protein adsorption, coined by the term bioinertness of the surface. Although the physio-adsorbed protein assays such as enzyme-linked immunosorbent assay (ELISA) has long existed, multiarray chip assays limits the amount of protein immobilized on surface. Thus searching for a bioinert surface that can render the activity of every immobilized protein becomes paramount to the success of proteomics. Bioinertness is defined at two levels. First, resisting protein adsorption; second, resisting cell adhesion.

## RESISTING PROTEIN ADSORPTION

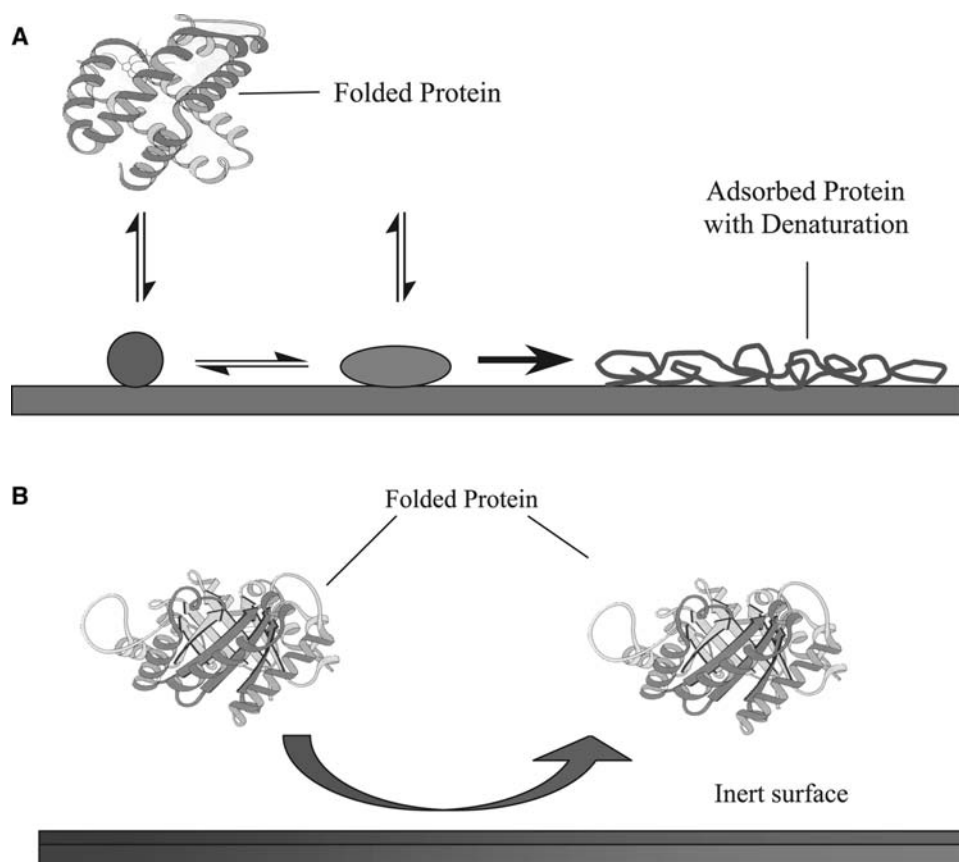
Proteins have a ubiquitous tendency to physically adsorb onto almost all kind of surfaces.<sup>[8]</sup> Biologically active proteins are always folded into three-dimensional structures, burying most of the hydrophobic residues and exposing most of the hydrophilic residues. In vitro, this folded structure is very sensitive to its micro-environment. When the microenvironment such as solvation denies the stabilization of the folded structure, the protein has a high propensity to denature to expose its hydrophobic core that allows interaction with its environment. Hence proteins, by nature, have the

tendency to function as glue to any surface *in vitro*. However, almost all proteins in biological systems depend on properly folded structures. For instance, the protein binding events in the cell signaling processes, cells adhesion, and migration are precisely orchestrated by the activities of proteins through processes such as focal adhesion, fibril formation, and protein binding at the interfaces of cell and extracellular matrix (ECM).

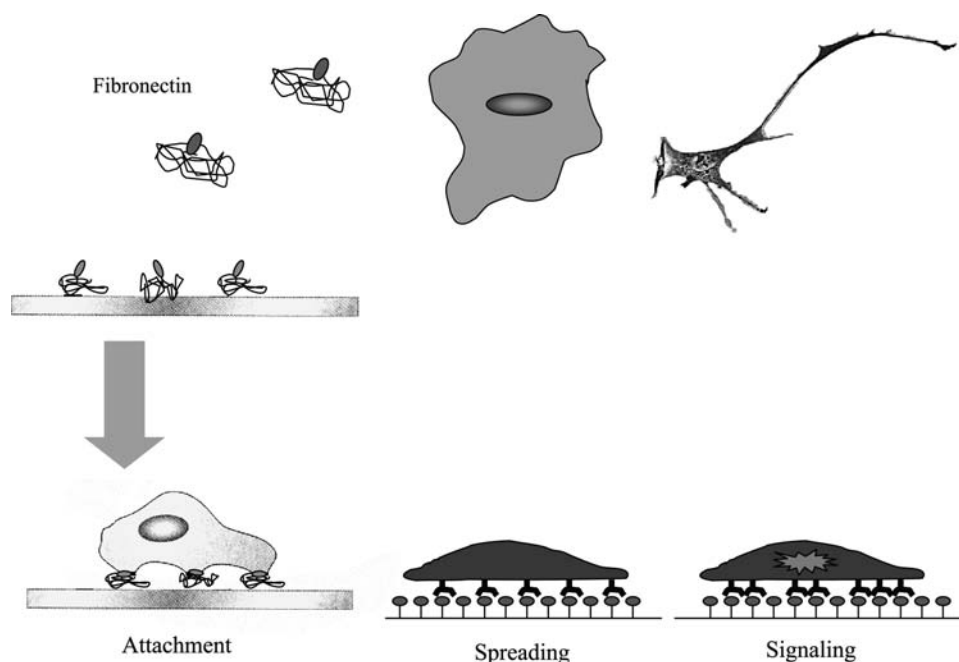
The adsorption of protein under conditions *in vitro* is complicated by various multistage processes (Scheme 1A).<sup>[8]</sup> Depending on the nature of the surface, protein adsorption involves a combination of some of the following processes: 1) dissociation from the surface back to the bulk solution; 2) orientation change; 3) conformation change with retention of activity; 4) denaturation and activity loss; and, 5) exchange with other proteins in the solution. These processes are further complicated by lateral protein-protein interaction on the surface and interactions between the proteins from the bulk and the adsorbed proteins on the surface. An ideal bioinert surface should prevent all of these adsorption processes (Scheme 1B).

## RESISTING CELL ADHESION

For almost all the mammalian cells, their viability depends critically on anchoring and spreading onto a surface, including other cells and the extracellular matrix (ECM). When removed from their animal host, most cells must adhere onto a surface for initiating proliferation. Such anchorage and adhesion is mediated by specific protein binding between various membrane proteins on the cells and external proteins that are produced and secreted by the cells themselves. A membrane protein of cells called integrin specific for fibronectin is responsible for mediating cell adhesion on ECM, as well as on surfaces *in vitro*. The principal recognition sequence in fibronectin for  $\alpha\beta$  receptors in the integrin is just a tripeptide ligand Arg-Gly-Asp (RGD) (Scheme 2). Cell adhesion onto substrate *in vitro* is a complex multistage process including cell attachment, spreading, focal adhesion formation, extracellular matrix deposition, and rearrangement.<sup>[9,10]</sup> When cells are completely denied attachment onto a surface, a suicidal program—apoptosis—is carried out which results in cell death, dissimulation, and release of all its cellular components involving cytolitic



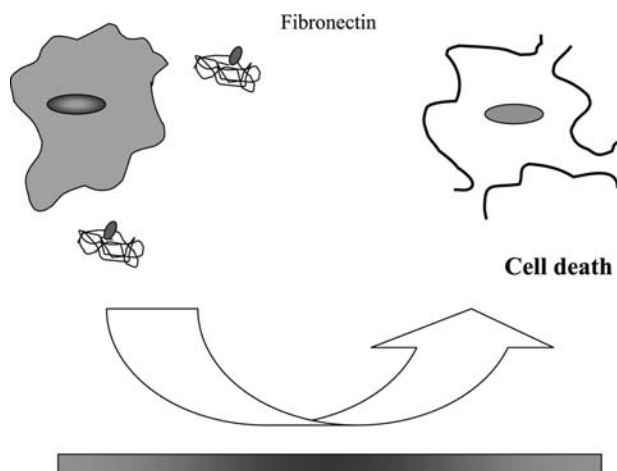
Scheme 1 Resisting protein adsorption.



Scheme 2 Cell adhesion.

and membrane proteins into the medium (Scheme 3). Hence on almost all surfaces, the fibronectin secreted by cells will physically adsorb to surfaces and facilitate cell attachment, adhesion, proliferation, and other cell activities.

Because cell culture in medium lasts weeks or longer, an ideal bioinert surface should resist protein adsorption and subsequent cell adhesion over long periods of time. Therefore resisting long-term cell adhesion is a more stringent requirement than resisting protein adsorption alone. This requirement also sets the standard to differentiate the strength of the bioinertness between surfaces that appear to be equally competent at resisting protein adsorption alone.



Scheme 3 Resisting cell adhesion.

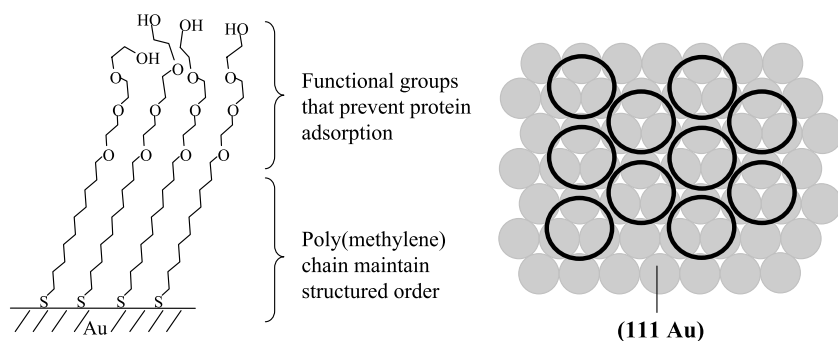
### KNOWLEDGE FROM POLYMER-COLLOIDAL SCIENCE

Efforts using different means have been devoted to identify bioinert surfaces. An early strategy involves grafting a surface with polymers—poly(ethylene glycol)—to resist protein adsorption.<sup>[11]</sup> These polymer-grafted surfaces suffer from the inability to present ligands at the surface with known density, orientation, and degree of exposure. Another widely adopted strategy uses preadsorption of a protein—usually bovine serum albumin (BSA)—that resists the adsorption of other proteins.<sup>[12]</sup> This pretreatment of surfaces with BSA suffers from problems associated with denaturation of blocking protein over time, and exchange with other proteins in solution. In short, both strategies present an undefined microenvironment on surfaces that cannot be controlled with molecular resolution, which is of paramount importance for chip-based protein assays.

For controlling the chemistry of the surface on which protein is to be immobilized, self-assembled monolayers (SAMs) of alkanethiols on gold provides an ideal system to allow for molecular-level control of surface properties.<sup>[13]</sup>



This particular class of SAMs differs from others in that they form a well-packed monolayer, presenting almost a two-dimensional crystalline structure on surface. Furthermore, because organic synthesis provides



**Scheme 4** Self-assembled monolayer of alkanethiols on gold.

a powerful means to tether almost any functional groups (R) to the alkanethiol, this class of monolayer provides a versatile range of functional groups on surfaces, thus the surface chemistry and interfacial properties is rationally controlled.

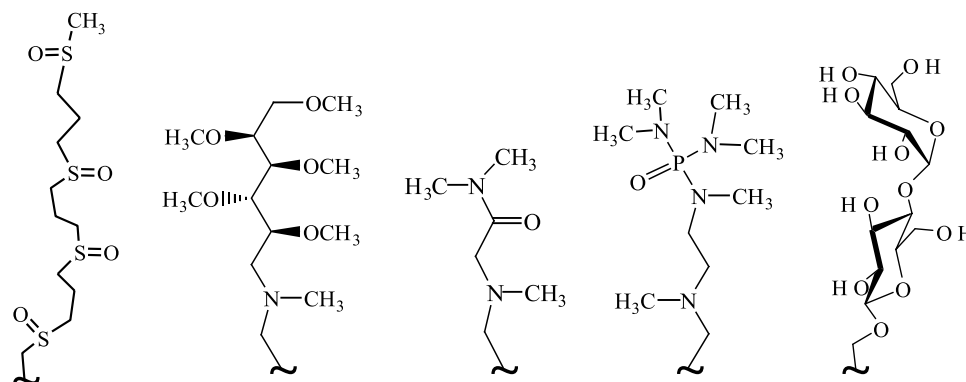
In an early effort of designing the terminal functional groups of alkanethiols that assemble into a bioinert monolayer, knowledge was brought from polymer/colloidal science. It turns out that poly(ethylene glycol) is known to prevent colloid coagulation, and shows signs of resisting adsorption of proteins. Prime and Whitesides<sup>[14]</sup> synthesized oligo(ethylene glycol)-terminated SAMs and tested their resistance to protein adsorption. This class of SAMs turns out to resist, to a great extent, both non-specific protein adsorption and cell adhesion, and become the current standard for bioinert surfaces (Scheme 4).<sup>[15]</sup>

The mechanistic origin of the bioinertness of this class of surface is not clear. One possible mechanism is the theory of steric repulsion for poly(ethylene glycol) developed by Jeon and coworkers.<sup>[11]</sup> The theory consists of two thermodynamic considerations. First, adsorption of protein to PEG results in a compression of the glycol chains, causing an entropic penalty because of the restriction in conformational dynamics of the polymer chains. Second, this compression also results in desolvation of polymers, thus

transferring solvated water into the bulk, which incurs an enthalpic penalty. However, the validity of translating this theory from polymer science to surface is in question. Feldman and coworkers<sup>[16]</sup> demonstrated some experimental evidence that disputed the relevance of this theory to the bioinertness of an oligo(ethylene glycol)-terminated SAMs.

### SOME EDISONIAN ATTEMPTS

Apart from the ambiguity in the science of how a bioinert surface resists the non-specific adsorption of proteins, it is of both fundamental and practical interest to develop other bioinert surfaces other than oligo(ethylene glycol)-terminated SAMs. Several Edisonian attempts have been carried out to search for a second bioinert SAM that is at least as good as oligo(ethylene glycol)-terminated SAMs (Scheme 5). For instance, Whitesides noted some scattered observation that hydrogen bond acceptors seem to be important for inertness, whereas hydrogen bond donors promote protein adsorption.<sup>[17]</sup> Another consideration is the effect of surface charges by a Zwitterion-terminated SAM, which essentially resembles the "skin" of a protein.<sup>[18]</sup> While all these surfaces resist protein adsorption to some extent, they all



**Scheme 5** Examples of other attempts by an Edisonian approach.

fall short when compared with oligo(ethylene glycol)-terminated SAMs at resisting long-term cell adhesion.

## WONDERS OF AN ANCIENT SCIENCE

When examining all these examples of different bioinert SAMs, more puzzling is the fact that there is no sufficient correlation between the bioinertness and any surface properties such as hydrophobicity, hydrogen bond donors/acceptors, or surface charges. With this seemingly insurmountable puzzle, the hope for finding another bioinert surface that is at least as good as oligo(ethylene glycol)-terminated SAMs seems hopeless. However, a rare phenomenon in the history of protein science leads to a new way of looking at this problem of bioinertness. This rarity centered at an ancient empirical discovery, which is not well understood but still widely used in protein chemistry today.

In 1888 A.D., Frank Hofmeister discovered some stabilizing and destabilizing effects of a series of cations and anions on protein structure, which have been used and unchallenged for the last 115 years in handling protein samples (Scheme 6).<sup>[19]</sup> The observation indicated that the same charge on different metal species bears significant different, sometime opposite, effect on the stability of folded protein structure. The mechanistic origin of this observation is not well understood, and thus the ions are empirically classified into two categories. Chaotropic ions destabilizing protein folding are thought to be, loosely speaking, disruptive to water structure, whereas kosmotropic ions stabilizing protein structure are regarded as enhancing water structure. It is generally believed, without rigorous evidence, that shells of water are induced by the solvated ions.<sup>[20]</sup> Depending on the identity of the ions, the structure of these water layers either disrupts (chaotropic) or enhances (kosmotropic) the stability of the folded structures of protein.

## CUES FROM CONTEMPORARY SCIENCE

An interesting theoretical work by Sharp in 1998 further shed light on the significance and subtlety of these water structures.<sup>[21,22]</sup> Sharp demonstrated by computer simulation that while both amino and hydroxyl groups are hydrophilic, each induced a

Anions:  $\text{SCN}^- > \text{NO}_3^- > \text{Cl}^- > \text{citrate}^- > \text{acetate}^- > \text{phosphate}^- > \text{SO}_4^{2-}$   
 Cations:  $\text{Ca}^{2+} > \text{Mg}^{2+} > \text{Na}^+ = \text{K}^+ > \text{NH}_4^+ > \text{N}(\text{CH}_3)_4^+$

Chaotropic (structure breaker)  $\longleftrightarrow$  Kosmotropic (structure maker)

**Scheme 6** Hofmeister series.

drastically different water structure that can be distinguished by properties such as density and heat capacity. Surprisingly, amino groups behave similarly to that of a hydrophobic methyl group in this regard of inducing water structure in the shells of solvation. From an experimentalist point of view, this theoretical prediction is astonishing, and perhaps bears a profoundness much overlooked. This is because while the hydrophobicity is completely opposite to each other, both amine- and methyl-terminated surfaces are highly “sticky” for protein adsorption.

## WORKING HYPOTHESIS BASED ON WATER STRUCTURE

Lessons from this century-old science and contemporary theoretical work lead me to a perhaps silly question that humanizes protein: “What if proteins are presented to a surface that they cannot ‘see’?” Furthering this concept, if the protein cannot “feel” the presence of any surface, then there is nothing for them to adsorb to.<sup>[23]</sup> With all the past failures providing me the notion that “what else could be worse?,” I translated this idea into a workable system by covalently “fusing” water molecules into the terminal groups of a surface (Fig. 1). Returning to the terminology in chemical science, this system provides a chemically chiral surface presenting self-assembled monolayer of polyol-terminated alkanethiols. The chirality comes from the fact that substitution of each hydroxyl group, except the very last one, causes a chiral tetrahedron carbon center. Natural isomeric forms of sugars—alditols—provide a convenient building block for synthesizing polyol-terminated alkanethiols. D-Mannitol was chosen from 16 possible stereoisomers of alditols primarily for the synthetic feasibility.

## ANALYTICAL TOOLS FOR MEASURING THE BIOINERTNESS

Surface plasmon resonance (SPR) spectroscopy is used to measure the amount of protein adsorbed on a surface.<sup>[24]</sup> SPR is an optical technique that measures the changes in the attenuated total reflection of a thin layer of metal film as a result of the changes in refractive index at the interface of the metal and bulk solution. With a thin layer of metal film, the resonance between the electron oscillation in the metal film and the light at a certain incident angle causes absorption of light and attenuation of the total reflection (ATR). The ATR is extremely sensitive to small changes of the refractive index at the interface of the gold film and the bulk solution, and hence provides a means to accurately measure the adsorption phenomena in the



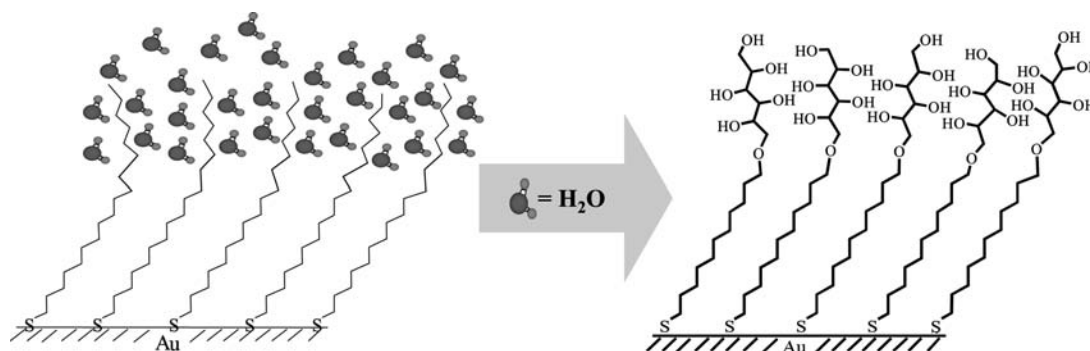


**Fig. 1** The rationale of creating an analog of water layer at the interface. To mimic a layer of solvated water at the surface (A), water molecules are covalently “fused” into the terminal region of alkanethiols in the form of polyols (B).

medium near (within  $\sim 200$  nm) the metal surface, which causes increase in the refractive index. Fig. 2A shows a schematic representation of the measurement by SPR. Monochromatic, p-polarized light is reflected from the backside of the glass–gold interface. The changes in the refractive index of a solution near the interface with a gold film are measured by changes in the angle ( $\Delta\theta_m$ ) at which p-polarized light reflected from the glass/gold interface has a minimum intensity (Fig. 2B). When the refractive index increases at the interface, the angle of ATR increases.

Fig. 3 shows a hypothetical plot to illustrate an SPR experiment for the irreversible adsorption of a protein to the sensing surface. SAMs were mounted against a flow cell and experiments were performed by first flowing a phosphate-buffered saline (PBS) buffer through the cell for 5 min, then a solution of protein in the same buffer (0.5 mg/mL) for 5 min, and finally the original PBS buffer for 5 min.<sup>[25]</sup> The increase in  $\Delta\theta_m$  upon introduction of the protein solution has

two contributions. The first is a result of the increase in refractive index of the solution caused by the dissolved protein—the “bulk effect”—and does not represent protein adsorption.<sup>[25]</sup> The second contribution is a result of the adsorption of protein to the SAM. The amount of protein that adsorbs irreversibly to the SAM is determined by comparing the shift in  $\theta_m$  before and after the SAM is exposed to protein. An increase in  $\theta_m$  of  $0.1^\circ$  corresponds to an increase in density of adsorbed protein of  $1 \text{ ng/mm}^2$ .

Microcontact printing of monolayers of alkanethiols is used to create spatially resolved islands that are sticky to protein adsorption surrounded by the SAMs, on which the resistance against cell adhesion is to be tested. The procedures for creating microcontact printed patterns are simple and easy to perform (Scheme 7).<sup>[26]</sup> Starting with a commercially purchased (or custom-made) cast, an elastic stamp is molded out of cross-linked polymer polydimethylsiloxane (PDMS) elastomer. The stamp is first inked with a 2-mM

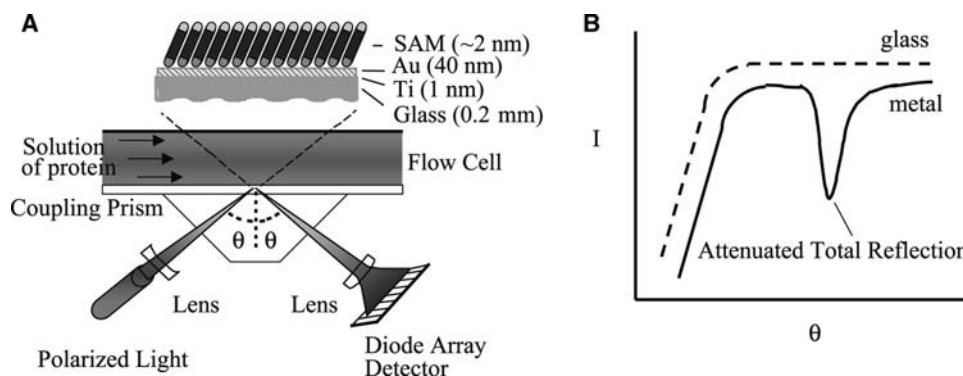


**Fig. 2** A general scheme on the operation of surface plasmon resonance spectroscopy to measure the adsorption of protein to a self-assembled monolayer (SAM) in situ and in real-time (A). The attenuated total reflection by electron oscillation in thin metal film (B). As the incident angle ( $\theta$ ) increases, the intensity of reflected light ( $I$ ) increases until a maximum equal to the intensity of the incident light is reached (total reflection). With a thin layer of metal film, a sharp decrease of the reflected light occurs in the region of total reflection due to the resonance between the light at a certain incident angle and the electron oscillation. This resonance causes absorption of light and attenuation of the total reflection (ATR) at a specific incident angle.

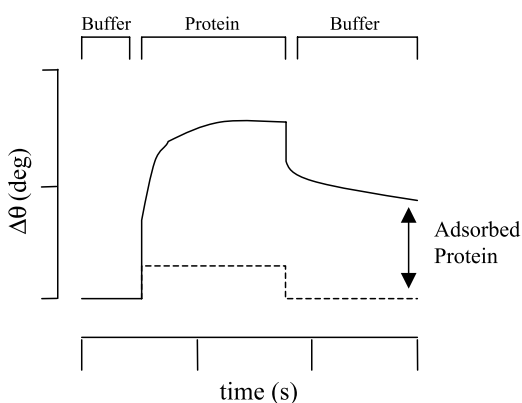
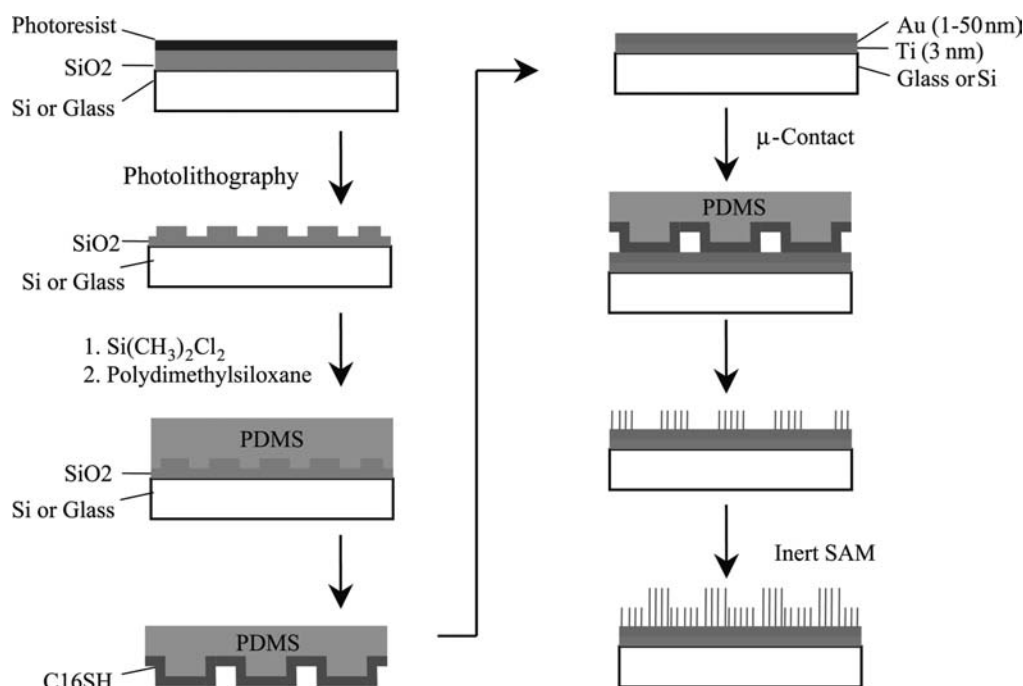


**Fig. 3** A hypothetical plot to illustrate an SPR experiment for irreversible adsorption of a protein to the sensing surface. SPR records the angle of minimum reflectivity of incident light versus time. A buffer flows through the channel, replaced by the same buffer but containing the protein, and then returns to the buffer without the protein.  $\theta_m$  increases when the protein is passed through the cell, as a result of both the increase of bulk refractive index and the irreversible adsorption of protein on the surface, and then decreases to another plateau as the blank buffer is introduced again. The buffer passes through the channel removing all the protein in the bulk but leaving the irreversibly adsorbed protein on the surface. The dashed curve represents the contribution to  $\Delta\theta_m$  of dissolved protein (bulk effect) that increases the refractive index of the buffer. The difference between the two curves at the end of the experiments measures the amount of protein adsorbed to SAM. *Source:* From Refs.<sup>[24]</sup> and <sup>[25]</sup>. American Chemical Society.

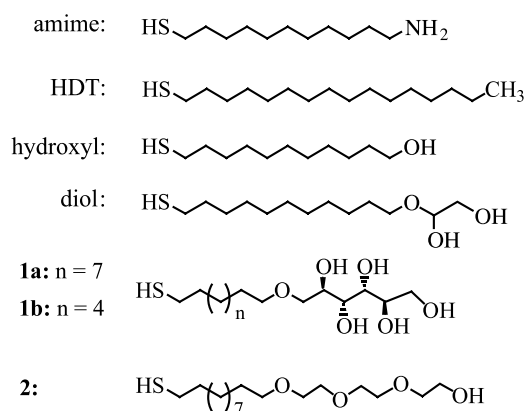
ethanolic solution of methyl-terminated alkanethiol. Then, a very brief contact (stamping) of 15–20 sec on the gold film results in a patterned self-assembled monolayer. Followed by soaking in ethanolic solution of a second alkanethiol, the naked gold films surrounding the patterned SAMs are filled with monolayers of the second alkanethiols. The patterned SAMs are placed into a culture medium, in which cells adhered and proliferated on the surface of the SAMs. The inertness of the SAMs (both the microcontact printed and back filled regions) is then monitored by observing the cell adhesion through a light microscope at desired time points over long-term (weeks) cell culture.

### THE BIOINERTNESS OF POLYOL-TERMINATED SAMs—RESISTING PROTEIN ADSORPTION

With the working hypothesis of an invisible wall to the proteins, we compared protein adsorption and cell attachment on seven different SAMs (Scheme 8).<sup>[23,27]</sup> SAMs presenting methyl groups [hexadecanethiol (HDT)] and tri(ethylene glycol) group were again used as standards for sticky and inert surfaces, respectively. The two monolayers presenting the mannitol groups differed in the length of the alkyl chain to which the mannitol group was appended. Alkanethiol **1a** has an alkyl chain of 11 methylene units, which is the standard length in SAMs that are used in biointerfacial science.



**Scheme 7** Microcontact printing.



**Scheme 8** Alkanethiols for bio-inert and sticky surfaces.

Alkanethiol **1b** has three fewer methylene units in the alkyl chain, and was investigated with the goal of finding inert monolayers that are overall thinner. The amine-, hydroxyl-, and diol-terminated SAMs served for evaluating the bioinertness/stickiness by different properties of the surface due to the organized functional groups at the terminus.

Fig. 4 shows data for investigating the adsorption of protein fibrinogen onto the four SAMs by SPR. A complete monolayer of protein, which corresponds to a protein density of  $3500 \text{ pg/mm}^2$ , adsorbs to the SAM of hexadecanethiol. The two monolayers presenting mannitol groups, by contrast, show essentially

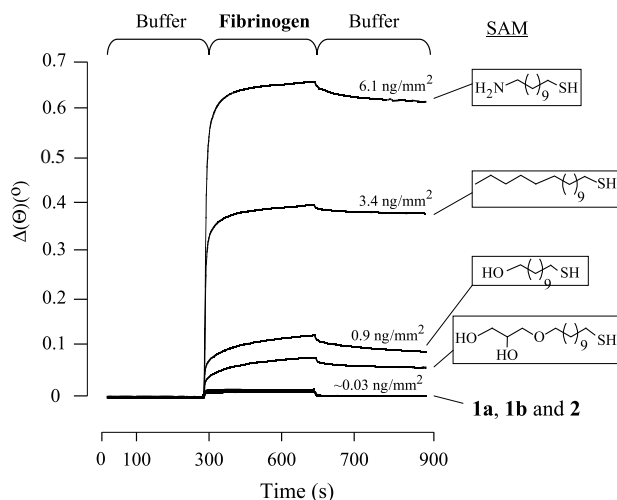


**Fig. 4** Data from surface plasmon resonance spectroscopy for the adsorption of fibrinogen ( $0.5 \text{ mg/mL}$  protein in  $10 \text{ mM}$  phosphate,  $150 \text{ mM}$  sodium chloride,  $\text{pH} = 7.6$ ) to each of the seven SAMs (Scheme 8). The monolayer is indicated to the right of each plot. The relative change in angle of minimum reflectivity ( $\Delta\theta_m$ ) is plotted as solutions are flowed over the SAM. Source: From Ref.<sup>[27]</sup>. American Chemical Society.

no adsorption of fibrinogen. This lack of adsorption is indistinguishable from that of monolayers presenting tri(ethylene glycol) groups. Experiments with the four other proteins yielded similar results, and demonstrated that the mannitol group is broadly effective at preventing protein adsorption (Table 1). For all five proteins, the amount of irreversible adsorption on D-mannitol-terminated SAMs was less than 2% of the total amount that adsorbed on the methyl-terminated SAMs (HDT). Fibrinogen, being a tetrameric protein complex, is the most sticky protein known and is used as the most stringent test for bioinertness of a surface toward protein adsorption. This set of results indicates that mannitol-terminated SAMs are highly inert against protein adsorption, and its bioinertness toward protein adsorption is indistinguishable from the current standard—oligo(ethylene glycol)-terminated SAMs. The amount of protein adsorption on other SAMs, amine-, hydroxyl-, and diol-terminated monolayers, is consistent with the working hypothesis of an invisible wall to the proteins. The amine-terminate SAM, a surface thought to disrupt the water structure at interface, bears the greatest amount of adsorbed fibrinogen. The diol-terminated SAMs bear the amount of adsorbed fibrinogen in between hydroxyl- and mannitol-terminated SAMs.

## THE BIOINERTNESS OF POLYOL-TERMINATED SAMs—TWO-DIMENSIONAL JAIL FOR ADHERENT CELLS

The bioinertness of mannitol-terminated monolayers against adhesion and growth of living cells 3T3 fibroblasts are evaluated on patterned SAMs.<sup>[27]</sup> Scheme 9 shows a schematic representation of the patterned SAMs on gold films by microcontact printing. Sets of circular regions of hexadecanethiol of different diameters were surrounded by inert SAMs of **1a**, **1b**, or **2**. The cross section of the mannitol head group occupies a larger area than that of the methyl group of the HDT region. The thiol-gold coordination of D-mannitol-terminated alkanethiols on gold surface is not known, but a close-packed monolayer is expected. The methyl-terminated SAM created by microcontact printing is known to adopt the close hexagonal packing of alkanethiol on gold just as those assembled from free molecules in solution.

Cells are known to adhere to methyl-terminated monolayers, but regions of D-mannitol are hypothesized to be inert. Four different sizes of circular HDT pattern were used on the same gold substrate, as indicated beneath the schematic representation of the pattern. When a suspension of cells is introduced to the patterned SAMs, cells should initially only attach,

**Table 1** Adsorption of protein on D-mannitol-terminated SAMs

SAM	Thickness (Å) <sup>a</sup>	Fibrinogen <sup>b</sup> 340 kDa, <sup>c</sup> 5.5 <sup>d</sup>	Pepsin 35 kDa, <1	Lysozyme 14 kDa, 11.4	Insulin 5.4 kD, 5.4	Trypsin 24 kDa, 0.5
<b>1a</b>	18.0	27 <sup>e</sup>	<10	19	15	<10
<b>1b</b>	15.7	45	12	10	25	16
<b>2</b>	19.5	29	<10	<10	<10	<10
HDT	20.0	3432	1337	1023	688	661

<sup>a</sup>Thickness of the SAM measured by ellipsometry.

<sup>b</sup>All protein solutions were 0.5 mg/ml in PBS (10 mM phosphate, 150 mM sodium chloride, pH = 7.6).

<sup>c</sup>Molecular weight of the protein.

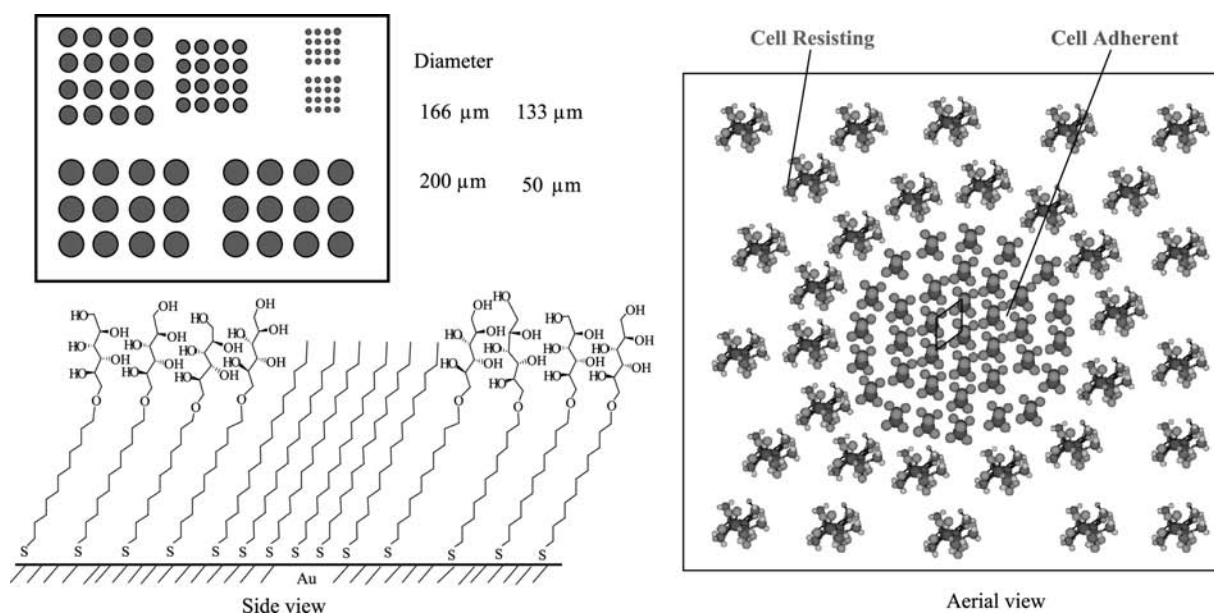
<sup>d</sup>pI of the protein.

<sup>e</sup>The density of irreversibly adsorbed protein in units of pg/mm<sup>2</sup> as determined by SPR.

spread, and proliferate on the methyl-terminated regions, but over time, may invade the surrounding inert regions. The time period that cells remain confined to the hydrophobic region is a quantitative measure of the bioinertness of the surface.

Patterned cell adhesion of albino 3T3-Swiss fibroblasts was maintained at 37°C in serum-containing media for 4 weeks. Media was exchanged every 5 days, and cells were photographed daily. Fig. 5 shows the cell adhesion confinement in the methyl-terminated region surrounded by inert alkanethiols, **1a** and **1b**, in comparison with surfaces presenting alkanethiol **2**. On all three surfaces, cells remained patterned to the circular regions of hexadecanethiol for at least 6 days in culture. The tri(ethylene glycol)-terminated monolayers began to fail after 7 days, with cells spreading onto the inert regions. After 12 days, cells had migrated from the circular regions and divided to give

a confluent monolayer of cells, with a complete loss of pattern. Monolayers terminated in the mannitol group (**1a**) were substantially more effective at confining cells for longer periods. Even after 21 days, cells remained completely confined to the patterns. After 25 days in culture, the physiology of the adherent cells may have changed extensively, and thus preventing cell adhesion may no longer be relevant. Monolayers presenting the mannitol group on the shorter alkyl chain (prepared from alkanethiol **1b**) were also more effective than monolayers presenting tri(ethylene glycol) group, but were not as effective as monolayers of **1a**. Monolayers of **1b** generally failed at 2 weeks in culture. We have repeated these long-term patterning experiments on three separate occasions with consistent results: monolayers of **2** fail at approximately 1 week, monolayers of **1b** fail at approximately 2 weeks, and monolayers of **1a** are effective for at least 3 weeks.

**Scheme 9** Representation of patterned SAMs by microcontact printing.

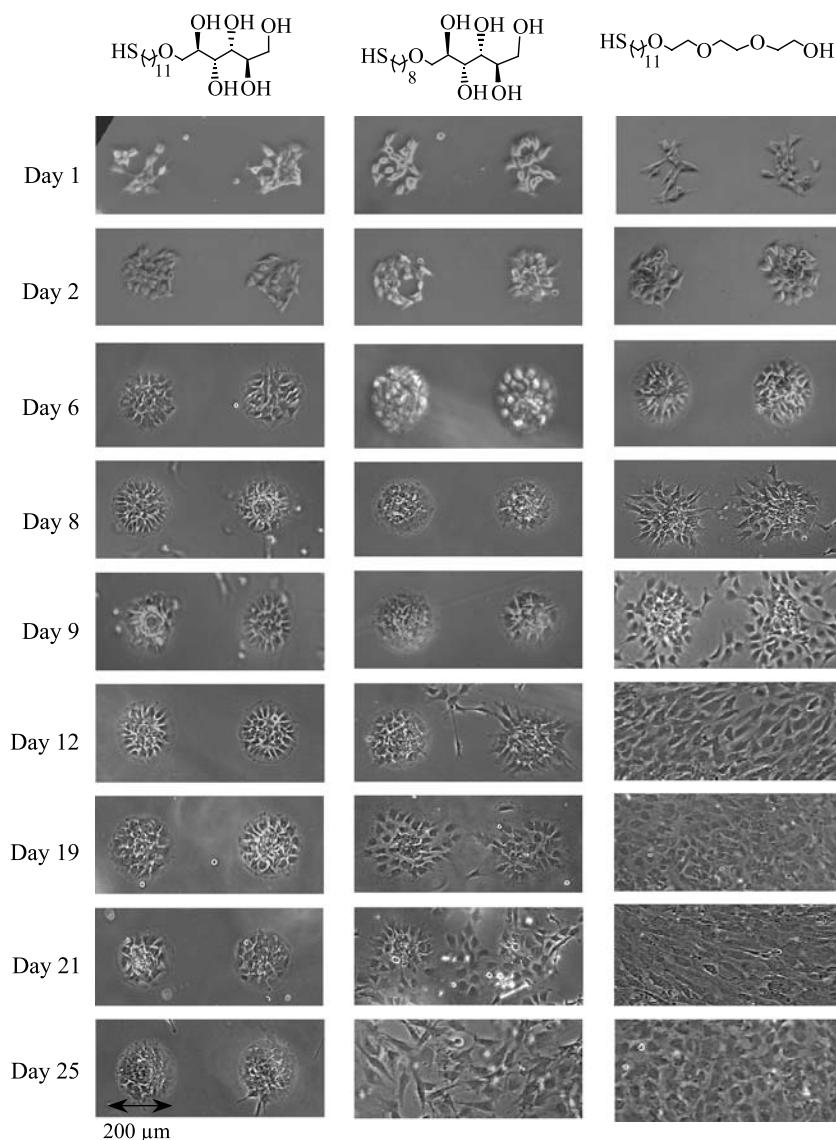


**Fig. 5** Comparison of the bioinertness against cell adhesion by D-mannitol-terminated SAMs vs. tri(ethylene glycol)-terminated SAM. 3T3 fibroblast cells were confined to SAMs patterned into circular regions (200  $\mu\text{m}$  in diameter) of hexadecanethiol (HDT) with intervening regions of **1a**, **1b**, or **2**. Optical micrographs are shown for cells attached to each of three patterned monolayers over a period of 25 days. The structures of the alkanethiols comprising the inert regions of the patterned monolayers are indicated above each column of photographs. The number of days that substrates were in culture is indicated to the left. *Source:* From Ref.<sup>[27]</sup>. American Chemical Society.

## THEORETICAL CONSIDERATIONS AND PERSPECTIVES

Other approaches using polymer grafted surfaces has also been explored. However, in those cases, the surface chemistry cannot be well defined at molecular level.<sup>[28,29]</sup> For example, the grafted polymer was fabricated into three-dimensional “corrals” having walls of  $\sim 5.2 \mu\text{m}$  in height and lateral dimensions on the order of  $60 \mu\text{m}$ .<sup>[29]</sup> Considering that adherent cells are only  $1\text{--}2 \mu\text{m}$  in thickness, it is difficult to determine whether the resistance of cell adhesion in the later period of cell culture is attributable to geometric confinement or the bioinertness of the surface.

The success in mannitol-terminated SAMs echoes the initial rationale of creating a water layer that the protein cannot “see.” However, extreme caution and rigor must be exercised when correlating bioinertness

and protein stability to water structure. The following mechanism for bioinertness is nevertheless proposed. At the interface of bulk water and any surface, a layer of water templated from the surface possesses a certain organization of hydrogen bonding network that is, in general, different from the hydrogen bond network in the bulk. When a protein is present, this templated water layer at the interface influence the stability of the folded protein structure leading to either adsorption (destabilize protein structure) or solvation (stabilize protein structure). Adopting an artwork by M. C. Escher, **Fig. 6** shows a schematic illustration of this proposed mechanism for bioinertness. The value of  $30 \text{ nm}$  of templated water structure shown in the scheme is adopted based on a force measurement (atomic force microscopy) of protein-coated tip approaching to the tri(ethylene glycol)-terminated monolayers by Feldman and coworkers.<sup>[16]</sup>



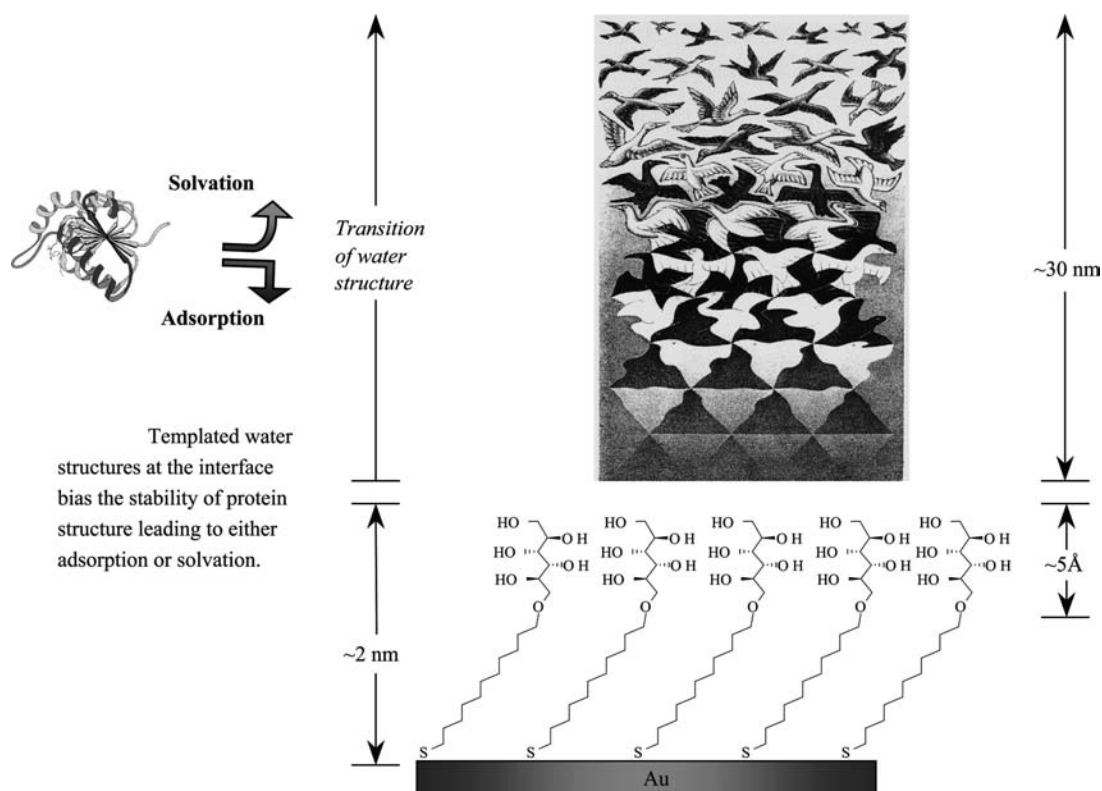


**Fig. 6** Schematic illustration of the proposed mechanism for bioinertness. The terminal functionality at the surface of the SAM templates particular water structure at the interface that is different from the bulk water. Such transition of water structure is represented by an artwork by M.C. Escher entitled “Liberation.”

It is very important to note that the study of water structure has been both difficult and controversial.<sup>[30–32]</sup> Notable examples of pathological science related to water structures include the “water memory,”<sup>[33]</sup> and “cold fusion.”<sup>[34]</sup> Both of these two examples have stirred considerable attention and enjoyed a very brief pyrotechnic fame in the scientific community, but were eventually determined as perhaps unintentional, fakery, or misinterpretation of results. Yet a range of discoveries—as early as Hofmeister effect.<sup>[19,20]</sup>—continue to suggest that water structure is at the heart of a range of observations in the life sciences.<sup>[35–38]</sup> In a recent report regarding bioinertness, Kane and coworkers<sup>[39]</sup> updated the surface properties of SAM that gave rise to bioinertness, and summarized that kosmotropes may form the basis of protein-resistant surface. Throughout their article, the authors have entirely avoided using ambiguous terms such as “water structure” or even “hydrogen bonding network.” This rigor is perhaps rightfully justified. However, it is equally important to point out that it is conceivable that certain stereochemical arrangement of hydroxyl group—a kosmotrope—can template a certain water structure at the interface that bias the resistance to protein adsorption and cell adhesion. Some early

experimental results have been obtained with respect to this hypothesis.<sup>[23]</sup>

## CONCLUSION

Biosurfaces is central to many phenomena in the life sciences at the scale ranging from nanometer (protein binding) to micrometers (cell adhesion and behavior). The first and foremost requirement for working with biosurfaces is the control of non-specific adsorption of protein and adhesion of cells. While the empirical chemistry providing a bioinert surface is largely established, the exact mechanism (science) of bioinertness remains to be investigated. These mechanistic studies bear much intricate and valuable science that will have great impact on areas such as drug design, medical implants, as well as scaffold for tissue engineering.

## EXPERIMENTALS

All experimental procedures presented in this entry are well documented in the published journal articles, except the organic synthesis of mannitol-terminated



alkanethiols. Organic synthesis essentially represents a molecular carpentry that allows never-existed molecules to be made. The craftsmanship is then both the design of reactions leading to the final desired product, as well as the technical skill for executing each reaction.

The synthesis of mannitol-terminated alkanethiol is documented below. The synthesis consists of six steps of published discovery that spans across the long history of organic synthesis (Scheme 10). A brief summary of the synthesis consists of bromine oxidation of a mannose to afford mannonic 1,5-lactone, followed by acetone protection of the adjacent diols. Open 1,2:3,4-di-*o*-isopropylidene-alditol was obtained by reducing the protected lactone with lithium aluminum hydride to expose a primary hydroxyl group (and a secondary hydroxyl group in the middle). Alkylation with the alkenylic bromide affords alkyl ether tethering protected polyols. Deprotection by acid hydrolysis of the ether affords the final product of mannitol-terminated alkanethiols. Two-dimensional nuclear magnetic resonance (NMR) experiments were used to establish atomic confirmation of the regioselectivity for the primary hydroxyl group. Each of the protons was assigned by a combination of homonuclear decoupling and correlated spectroscopy (COSY) NMR experiments. Nuclear Overhauser enhancement spectroscopy (NOESY) experiment was also used to confirm the spatial connectivity.

### D-Mannonic- $\gamma$ -1,5-Lactone

To a solution of D-mannose (2 g, 11.1 mmol) in deionized water (30 mL) was added bromine (31 g, 10.5 mL, 194.25 mmol). The solution was sealed by a balloon filled with N<sub>2</sub>, and was stirred for 20 hr at

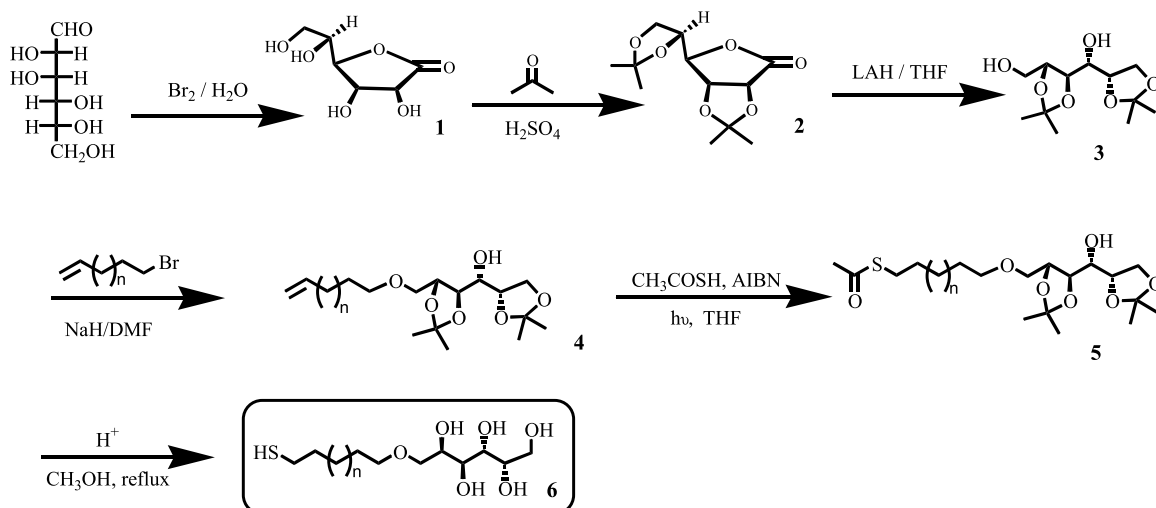
room temperature. Then the bromine was removed through vacuum until the reddish solution turned colorless. Silver (I) carbonate was added with stirring until the solution turned neutral. The solution was then filtered to remove AgBr and excess Ag<sub>2</sub>CO<sub>3</sub>, and dried by lyophilization to give 1.4 g (7.86 mmol, 71%) of D-Mannonic- $\gamma$ -lactone as a white solid: <sup>1</sup>H NMR (400 MHz, CD<sub>3</sub>OD)  $\delta$  4.60 (d, *J* = 5.54, 1H), 4.43 (dd, 2H), 3.83–3.80 (q, 2H), 3.637 (d, 2H).

### Protected D-Mannonic 1,5-Lactone, 2

To a solution of D-Mannonic 1,5-lactone **1**, (1.62 mmol) in acetone was added 0.04 mL of 12 N H<sub>2</sub>SO<sub>4</sub> and anhydrous CuSO<sub>4</sub> (200 mg). The solution was stirred for 7 hr and dried in vacuo. Purification by flash chromatography (silica gel, 2% methanol/methylene chloride) gave milligrams of desired **2** (1.31 mmol, 80%): <sup>1</sup>H NMR (400 MHz, CDCl<sub>3</sub>):  $\delta$  4.58–4.65 (dd, 1H), 4.40–4.47 (q, 1H), 4.38 (s, 1H), 4.16–4.13 (t, 1H) 3.99–3.95 (dd, 1H), 1.44 (s, 3H), 1.43 (s, 3H), 1.40 (s, 3H), 1.37 (s, 3H).

### 1,2:3,4-di-*o*-Isopropylidene-D-Mannitol, 3

To a solution of protected D-Mannonic 1,5-lactone **2** (1.66 mmol) in THF was added 3.32 mL of LiAlH<sub>4</sub> (1 M in ether). The solution was stirred under nitrogen for 7 hr and dried in vacuo. Purification by flash chromatography (silica gel, 10% methanol/methylene chloride) gave mg (1.25 mmol, 75%) of desired **2**: <sup>1</sup>H NMR (400 MHz, CD<sub>3</sub>OD):  $\delta$  4.38–4.35 (dd, 1H), 4.32–4.27 (m, 1H), 4.14–4.08 (m, 2H), 3.99–3.93 (td, 1H), 3.87–3.75 (m, 2H), 3.62–3.60 (m, 1H), 1.55 (s, 3H), 1.40 (s, 3H), 1.37 (s, 3H), 1.35 (s, 3H).



Scheme 10 Synthesis of mannitol-terminated alkanethiols.

### Undecenyl 1,2:3,4-di-*o*-Isopropylidene-*D*-Mannon Ether, 4

To a solution of 1,2:3,4-di-*o*-isopropylidene-*D*-mannitol **3**, (316 mg, 1.20 mmol) in *N,N*-Dimethyl Formamide (DMF) (10 mL) was added sodium hydride (30 mg, 60% dispersion in oil, 1.20 mmol). The solution was stirred for 10 min at room temperature and then 8-bromo-1-octene (220 mg, 1.20 mmol) was added over a period of 5 min. The solution was stirred for 12 hr and then concentrated in vacuo. The residue was purified by flash chromatography (1.5% CH<sub>3</sub>OH/CH<sub>2</sub>Cl<sub>2</sub>) to give 330 mg (0.883 mmol, 73%) of **4** as a colorless oil: <sup>1</sup>H NMR (400 MHz, CDCl<sub>3</sub>) δ 5.82–5.72 (m, 1H), 4.92 (q, *J* = 10.2, 2H), 4.41–4.30 (m, 2H), 4.12–3.95 (m, 3H), 3.77–3.65 (m, 2H), 3.13 (d, *J* = 6.16, 1H), 2.00 (q, *J* = 7.1, 2H), 1.53 (s, 3H), 1.42 (s, 3H), 1.40 (s, 3H), 1.37 (s, 3H), 1.18 (m, 6H).

### Thioester *S*-(11-Undecenyl 1,2:3,4-di-*o*-Isopropylidene-*D*-Mannon Ether, 5

A solution of **4** (151 mg, 0.41 mmol), thiol acetic acid (91 mg, 1.2 mmol), and 2,2'-azobisisobutyronitrile (AIBN) (80 mg, 0.487 mmol) in tetrahydrofuran (THF) (15 mL) was irradiated with UV light (Rayonet Photochemical Reactor Lamp) in a photochemical reactor for 5 hr with stirring. The solution was concentrated in vacuo and the residue was purified by flash chromatography (1% CH<sub>3</sub>OH/CH<sub>2</sub>Cl<sub>2</sub>) to give 147 mg of **4** (0.328 mmol, 82%) as a colorless oil: <sup>1</sup>H NMR (400 MHz, CDCl<sub>3</sub>) δ 4.41–4.30 (m, 2H), 4.12–3.95 (m, 3H), 3.77–3.65 (m, 2H), 3.57–3.47 (m, 3H), 3.14–3.12 (d, *J* = 6.16, 1H), 2.90–2.85 (t, *J* = 7.38, 2H), 2.33 (s, 3H), 1.64–1.55 (m, 4H), 1.53 (s, 3H), 1.42 (s, 3H), 1.40 (s, 3H), 1.37 (s, 3H), 1.41 (m, 6H).

### 6-(11-Mercapto-Undecyloxy)-*D*-Mannitol, 6

(Mannitol-terminated alkanethiol, **1b**) To a solution of **5** (147 mg, 0.328 mmol) in methanol (15 mL) was added 5 drops of 12 N HCl. The solution was refluxed for 8 hr, cooled to room temperature, and concentrated in vacuo. The residue was purified by recrystallization from methanol to give 61 mg of **1b** (0.187 mmol, 57%) as a white solid: <sup>1</sup>H NMR (400 MHz, CD<sub>3</sub>OD) δ 3.85–3.59 (m, 6H), 3.58–3.46 (m, 4H), 2.52–2.45 (t, 2H), 1.64–1.55 (m, 4H), 1.45–1.28 (m, 8H).

### A POSTLUDE

A little later (on the time scale of scientific publication) after the establishment of the bioinertness of mannitol-terminated SAM, Tan and coworkers<sup>[40]</sup> discovered an

interesting, even anomalous, property of oligo(ethylene glycol)-terminated SAMs with respect to resisting protein adsorption. Using microcontact printing, Tan and coworkers immobilized protein onto a number of SAMs under “dry” condition. That is, the protein are inked on an elastomeric stamp, and then transferred onto SAMs in the absence of any water or solvent. Surprisingly, SAMs presenting oligo(ethylene glycol)s were loaded with more protein than other hydrophobic SAMs under this “dry” condition. This result suggests that protein adsorption on surface is not merely determined by the properties of protein and the chemistry of the surface alone, but the solvent effect, microenvironment of the protein (i.e., solvation), and the interface of the surface must also be taken into account. This microenvironment surrounding the proteins and in the interface above a surface inevitably points to the intricate realm of different water structures.

### ACKNOWLEDGMENT

I would like to thank my advisor, professor Milan Mrksich, for the opportunity of completing this work. He introduced me to the fascinating world of the life sciences, and taught me the use of a valuable tool—bioorganic chemistry—to work in such interdisciplinary areas. I also appreciate his support and encouragement throughout graduate school, and his tolerance of my sometimes excessive free spirit.

### REFERENCES

1. Kasemo, B. Biological surface science. *Surf. Sci.* **2002**, *500* (1–3), 656–677.
2. Oscarsson, S. Factors affecting protein interaction at sorbent interfaces. *J. Chromatogr., B* **1997**, *699* (1–2), 117–131.
3. Xia, Y.N.; Whitesides, G.M. Soft lithography. *Angew. Chem., Int. Ed.* **1998**, *37* (5), 551–575.
4. Tiefenauer, L.; Ros, R. Biointerface analysis on a molecular level—New tools for biosensor research. *Colloids Surf., B Biointerfaces* **2002**, *23* (2–3), 95–114.
5. Mirmohammadsadegh, A.; Baer, A.; Schulte, K.W.; Bardenheuer, W.; Hengge, U.R. DNA chip technology and proteomics in melanoma: Identification of new targets for gene therapy. *Mol. Ther.* **2003**, *7* (5), S415.
6. Schena, M.; Shalon, D.; Heller, R.; Chai, A.; Brown, P.O.; Davis, R.W. Parallel human genome analysis: Microarray-based expression monitoring of 1000 genes. *Proc. Natl. Acad. Sci. U. S. A.* **1996**, *93* (20), 10614–10619.
7. Lee, Y.S.; Mrksich, M. Protein chips: From concept to practice. *Trends Biotechnol.* **2002**, *20* (12), S14–S18.

8. Mrksich, M.; Whitesides, G.M. Using self-assembled monolayers to understand the interactions of man-made surfaces with proteins and cells. *Annu. Rev. Biophys. Biomol. Struct.* **1996**, *25*, 55–78.
9. Ingber, D.E. The origin of cellular life. *Bioessays* **2000**, *22* (12), 1160–1170.
10. Ingber, D.E. The architecture of life. *Sci. Am.* **1998**, *278* (1), 48–57.
11. Jeon, S.I.; Lee, J.H.; Andrade, J.D.; Degennes, P.G. Protein surface interactions in the presence of polyethylene oxide. I. Simplified theory. *J. Colloid Interface Sci.* **1991**, *142* (1), 149–158.
12. Kim, S.R.; Abbott, N.L. Rubbed films of functionalized bovine serum albumin as substrates for the imaging of protein–receptor interactions using liquid crystals. *Adv. Mater.* **2001**, *13* (19), 1445–1449.
13. Mrksich, M. Using self-assembled monolayers to understand the biomaterials interface. *Curr. Opin. Colloid Interface Sci.* **1997**, *2* (1), 83–88.
14. Prime, K.L.; Whitesides, G.M. Self-assembled organic monolayers—Model systems for studying adsorption of proteins at surfaces. *Science* **1991**, *252* (5009), 1164–1167.
15. Chen, C.S.; Mrksich, M.; Huang, S.; Whitesides, G.M.; Ingber, D.E. Geometric control of cell life and death. *Science* **1997**, *276* (5317), 1425–1428.
16. Feldman, K.; Hahner, G.; Spencer, N.D.; Harder, P.; Grunze, M. Probing resistance to protein adsorption of oligo(ethylene glycol)-terminated self-assembled monolayers by scanning force microscopy. *J. Am. Chem. Soc.* **1999**, *121* (43), 10134–10141.
17. Ostuni, E.; Chapman, R.G.; Holmlin, R.E.; Takayama, S.; Whitesides, G.M. A survey of structure–property relationships of surfaces that resist the adsorption of protein. *Langmuir* **2001**, *17* (18), 5605–5620.
18. Holmlin, R.E.; Chen, X.X.; Chapman, R.G.; Takayama, S.; Whitesides, G.M. Zwitterionic SAMs that resist nonspecific adsorption of protein from aqueous buffer. *Langmuir* **2001**, *17* (9), 2841–2850.
19. Hofmeister, F. *Arch. ExPathol. Pharmakol.* **1888**, *24*, 247–260.
20. Cacace, M.G.; Landau, E.M.; Ramsden, J.J. The Hofmeister series: Salt and solvent effects on interfacial phenomena. *Q. Rev. Biophys.* **1997**, *30* (3), 241–277.
21. Gallagher, K.R.; Sharp, K.A. A new angle on heat capacity changes in hydrophobic solvation. *J. Am. Chem. Soc.* **2003**, *125* (32), 9853–9860.
22. Vanzi, F.; Madan, B.; Sharp, K. Effect of the protein denaturants urea and guanidinium on water structure: A structural and thermodynamic study. *J. Am. Chem. Soc.* **1998**, *120* (41), 10748–10753.
23. Luk, Y.-Y.I. Bio-inertness and Stereochemical Control of Cell Adhesion on Chiral Surfaces. II. Surface Chemistry of Self-Assembled Monolayers and Nano-Colloids. In *Ph.D. thesis*; 2001.
24. Sigal, G.B.; Mrksich, M.; Whitesides, G.M. Using surface plasmon resonance spectroscopy to measure the association of detergents with self-assembled monolayers of hexadecanethiolate on gold. *Langmuir* **1997**, *13* (10), 2749–2755.
25. Mrksich, M.; Sigal, G.B.; Whitesides, G.M. Surface-plasmon resonance permits in-situ measurement of protein adsorption on self-assembled monolayers of alkanethiolates on gold. *Langmuir* **1995**, *11* (11), 4383–4385.
26. Mrksich, M.; Dike, L.E.; Tien, J.; Ingber, D.E.; Whitesides, G.M. Using microcontact printing to pattern the attachment of mammalian cells to self-assembled monolayers of alkanethiolates on transparent films of gold and silver. *ExCell. Res.* **1997**, *235* (2), 305–313.
27. Luk, Y.Y.; Kato, M.; Mrksich, M. Self-assembled monolayers of alkanethiolates presenting mannitol groups are inert to protein adsorption and cell attachment. *Langmuir* **2000**, *16* (24), 9604–9608.
28. Lahann, J.; Balcells, M.; Rodon, T.; Lee, J.; Choi, I.S.; Jensen, K.F.; Langer, R. Reactive polymer coatings: A platform for patterning proteins and mammalian cells onto a broad range of materials. *Langmuir* **2002**, *18* (9), 3632–3638.
29. Amirpour, M.L.; Ghosh, P.; Lackowski, W.M.; Crooks, R.M.; Pishko, M.V. Mammalian cell cultures on micro-patterned surfaces of weak-acid, polyelectrolyte hyper-branched thin films on gold. *Anal. Chem.* **2001**, *73* (7), 1560–1566.
30. Wiggins, P.M. Role of water in some biological processes. *Microbiol. Rev.* **1990**, *54* (4), 432–449.
31. Israelachvili, J.; Wennerstrom, H. Role of hydration and water structure in biological and colloidal interactions. *Nature* **1996**, *379* (6562), 219–225.
32. Wiggins, P.M. Hydrophobic hydration, hydrophobic forces and protein folding. *Physica A* **1997**, *238* (1–4), 113–128.
33. Dagani, R. Nature paper rebuts water memory claim. *Chem. Eng. News* **1993**, *71* (50), 8–9.
34. Ritter, S.K. Science, religion, and the art of cold fusion. *Chem. Eng. News* **2003**, *81* (34), 33.
35. Plumridge, T.H.; Waigh, R.D. Water structure theory and some implications for drug design. *J. Pharm. Pharmacol.* **2002**, *54* (9), 1155–1179.
36. Singer, P.T.; Smalas, A.; Carty, R.P.; Mangel, W.F.; Sweet, R.M. The hydrolytic water molecule in trypsin. Revealed by time-resolved Laue crystallography. *Science* **1993**, *259* (5095), 669–673.
37. Somero, G.N., Osmond, C.B., Bolis, C.L., Eds.; *Water and Life—Comparative Analysis of Water Relationships at the Organismic, Cellular, and Molecular Level*; Springer-Verlag Inc.: New York, 1992.
38. Wiggins, P.M. Water in complex environments such as living systems. *Physica A* **2002**, *314* (1–4), 485–491.
39. Kane, R.S.; Deschatelets, P.; Whitesides, G.M. Kosmotropes form the basis of protein-resistant surfaces. *Langmuir* **2003**, *19* (6), 2388–2391.
40. Tan, J.L.; Tien, J.; Chen, C.S. Microcontact printing of proteins on mixed self-assembled monolayers. *Langmuir* **2002**, *18* (2), 519–523.

# Block Copolymer Nanoparticles

Sandrine Pensec  
Daniel Portinha  
Laurent Bouteiller

*Laboratoire de Chimie Macromoléculaire, Université Pierre et Marie Curie,  
Paris, France*

Christophe Chassenieux

*Laboratoire de Physico-Chimie Macromoléculaire, Université Pierre et Marie Curie,  
Paris, France*

## INTRODUCTION

The use of nanoscale objects is a way to enhance properties of materials in a wide range of fields because the small dimensions of the objects can be responsible for high specific surface or for quantum effects. Nanotechnology is consequently of great interest in electronic materials or biomedical applications. The challenge is to realize nanoscale systems with size and morphology control. In this context, our aim is to study the self-assembly of AB block copolymers containing two incompatible polymers to form nanoparticles in solution.

It has been known for many years that when AB block copolymers are dissolved in a solvent that is selective for one of the blocks, colloidal aggregates such as micelles can form as a result of the association of the insoluble blocks. When the insoluble A block is flexible, spherical micelles with an amorphous core are obtained, whereas if the A block is rigid, micelles with anisotropic shapes can result.

In this entry, we study the formation of nanoparticles obtained in solution by cocrystallization of AB and A'B diblock copolymers, where the A and A' blocks can cocrystallize. In a selective solvent (good for B and bad for A and A'), the mixture is expected to self-assemble in particles with a crystalline core (AA') surrounded by a shell (B) swollen with the solvent.

This type of complex can be obtained by mixing optically active polymers with identical chemical structures but opposite optical configurations. Poly(L-lactide) (PLLA) and poly(D-lactide) (PDLA) are semicrystalline polymers that form a racemic crystal called stereocomplex. We have thus synthesized poly(L-lactide)-poly( $\epsilon$ -caprolactone) (PCL) and poly(D-lactide)-poly( $\epsilon$ -caprolactone) diblock copolymers and have studied

their association in a good solvent for the poly( $\epsilon$ -caprolactone) block.

## NANOPARTICLES OF BLOCK COPOLYMERS IN DILUTE SOLUTION

### Organization of Diblock Copolymers in a Selective Solvent

In the case of a diblock copolymer AB dissolved in a solvent selective for one of the two blocks (B in the following), the copolymer spontaneously self-organizes, forming particles of varied sizes and shapes. For coil-coil systems, spherical micelles are commonly obtained.<sup>[1-4]</sup> The resulting structure consists of a core region made up of insoluble A blocks surrounded by a shell region made up of B blocks swollen by the solvent. Non-spherical aggregates of block copolymers in solution such as cylindrical micelles<sup>[5]</sup> or giant wormlike micelles<sup>[6]</sup> have been only rarely observed. Multiple morphologies (spheres, rods, and vesicles) of aggregates prepared from a given diblock copolymer in solution have been reported by Eisenberg et al.<sup>[7,8]</sup> Factors such as the water content in the solvent mixture, the solvent nature and composition, the presence of additives, and the polymer concentration were successfully employed to control the aggregate shape and size.

In the case of rod-coil systems or when the insoluble block is able to crystallize, various morphologies such as spherical micelles,<sup>[9]</sup> vesicles,<sup>[10]</sup> or lamellar platelets<sup>[11]</sup> can be encountered. Besides the nature of the insoluble block, various parameters can influence the size or shape of the nanoparticles. The preparation technique of the solutions, the nature of the solvent, the molecular weight, and the composition of each block in the copolymer<sup>[12,13]</sup> were more specifically studied.

## Complexation of Block Copolymers by Supramolecular Interactions

Complexation by supramolecular interactions of two block copolymers is another way used to develop nanoparticles. An intermacromolecular complex can self-assemble if the two copolymer chains involved in the complexation have specific and complementary sites of interaction. If we consider a mixture of two copolymers A-b-B and C-b-D where the blocks B and D can interact, then nanoparticles can be obtained. The aggregate formed is often a spherical micelle, with the insoluble complex in the core, stabilized in solution by a crown of the other soluble blocks (A and C) swollen by the solvent. Non-covalent specific interactions liable to form a complex can potentially be of a different nature:<sup>[14,15]</sup> van der Waals interactions, hydrogen bonding, metal–ligand bonds, ionic interactions, hydrophobic interactions, aromatic  $\pi$  stacking, and charge-transfer interactions. As studied in the literature, stable and monodisperse polyion complex micelles were thus prepared in an aqueous medium through electrostatic interactions between a poly(ethylene glycol)–polycation block copolymer and a poly(ethylene glycol)–polyanion block copolymer.<sup>[16]</sup> In such systems, molecular recognition based on associative block lengths occurred.<sup>[17]</sup> Furthermore, nanoparticles have been obtained in a non-selective solvent for a block copolymer by hydrogen-bonding complexation of one of the blocks and a complementary polymer. The micellelike structures are very stable because dilution has no effect on their size and molecular weight. Besides, these characteristics are dependent on the initial polymer concentration, indicating that the complexation is a diffusion-controlled process.<sup>[18]</sup>

### Stereocomplexation between Polymers of Opposite Configuration: Case of Poly(lactide)

Besides complexes formed by polymers with different chemical structures and complementary sites of interaction, intermacromolecular complexes can be formed between polymers with identical chemical compositions and different stereochemical structures. This type of interaction is called “stereocomplexation.” The association is a result of weak van der Waals interactions. Stereoassociation of poly(methyl methacrylate) of different tacticity is the most well known. Mixing of solutions of isotactic and syndiotactic poly(methyl methacrylate) in suitable solvents leads to the formation of a stereocomplex by the association between isotactic and syndiotactic sequences. The structure of this complex has long been investigated.<sup>[19]</sup> Another type of stereocomplex can also be formed by mixing optically active polymers with identical chemical

structures but with opposite configurations. Examples of optically active polymers that form stereocomplexes are numerous in the literature.<sup>[20–22]</sup> Polylactide, because of its biodegradability and biocompatibility, was extensively investigated. Equimolar mixtures of isotactic polylactides PLLA and PDLA have been first studied in the solid state.<sup>[23,24]</sup> Results have shown that the stereocomplex obtained with the mixture has a melting point about 50°C higher than the melting points of both polyenantiomers. The influence of various parameters on the formation of stereocomplexes has been investigated. Thus, stereocomplexes without formation of homocrystallites are exclusively obtained with an equimolar mixture of D-lactide and L-lactide,<sup>[25]</sup> with a molecular weight ranging from 500 to 10<sup>5</sup> g mol<sup>-1</sup><sup>[26]</sup> and with optically pure monomers.<sup>[27]</sup> To understand the mechanism of formation of the polylactide stereocomplex, the crystallization behavior of polylactides was studied. It has been reported that the crystals in the homopolymers of PLLA (or PDLA) have a 10<sub>3</sub> helix structure, whereas the stereocomplex forms a more compact 3<sub>1</sub> helix and is more stable.<sup>[28,29]</sup> Several approaches were investigated to design new poly(lactide)-based polymers. Thus, stereocomplexes were observed by differential scanning calorimetry (DSC) for stereodiblocks PLLA-b-PDLA<sup>[30]</sup> and for some copolymers where the poly(lactide) was associated with another polymer sequence. Few studies deal with the behavior of copolymers with a poly( $\epsilon$ -caprolactone) sequence. Stereocomplexation was observed with statistical copolymers,<sup>[31]</sup> with mixtures of triblock polyenantiomers PLA-b-PCL-b-PLA,<sup>[32]</sup> and with diblock copolymers PCL-b-PLA.<sup>[33]</sup> This last study indicates that the melting temperature of the crystalline PCL and PLA phases strongly depends on the composition of the block copolymer. Accordingly, stereocomplexes are observed for copolymers where the poly(lactide) sequence has at least 40 lactyl units.

New properties and applications of the stereocomplexation of enantiomeric poly(lactide) copolymers were investigated. Thus, it was recently reported that the stereocomplex of the two enantiomeric triblock copolymers poly(lactide)-b-poly(ethyleneglycol)-b-poly(lactide) were used to make microspheres for protein release.<sup>[34]</sup> Few studies, however, were carried out on stereocomplexation in solution. In concentrated solutions, an irreversible gel was formed through stereocomplexation of poly(D-lactide) and poly(L-lactide). The PLA complex gel is thermoirreversible and insensitive to dilution.<sup>[31]</sup> In dilute solutions, with a good solvent for the polylactide sequence, stereocomplexation was not observed, but in hot acetonitrile, the turbid solution first obtained precipitated rapidly.<sup>[25]</sup>

We report in this entry on the stereocomplexation of diblock enantiomeric copolymers poly(lactide)-b-poly

( $\epsilon$ -caprolactone) (PLA-*b*-PCL) in solution. The influence of different parameters (concentration, length of the blocks) on the stereocomplexation are discussed.

## FORMATION OF NANOPARTICLES OF BLOCK COPOLYMERS CONTAINING ENANTIOMERIC LACTIDE SEQUENCES IN SOLUTION

### Synthesis and Characterization of Block Copolymers PCL-*b*-PLA

Block copolymer PCL-*b*-PLLA (PCL-*b*-PDLA) was synthesized by addition of L-lactide (D-lactide) to a living poly( $\epsilon$ -caprolactone) (PCL), which was prepared with an yttrium alkoxide initiator [Y(OCH<sub>2</sub>-CH<sub>2</sub>OCH(CH<sub>3</sub>)<sub>2</sub>)<sub>3</sub>] as previously described.<sup>[35]</sup> The structure was confirmed by size exclusion chromatography (SEC) with tetrahydrofuran (THF) as eluent, <sup>1</sup>H and <sup>13</sup>C NMR in CDCl<sub>3</sub>, and MALDI-TOF mass spectrometry and polarimetry in THF. The degrees of polymerization (DP) were determined by combination of SEC of the PCL precursors and the integration of PLA (5.28 ppm) and PCL (4.14 ppm) signals on the <sup>1</sup>H NMR spectra of the copolymers. The use of the yttrium alkoxide initiator allowed us to prepare block copolymers under satisfactorily controlled conditions. Thus we have obtained copolymers with variable compositions in PCL (DP = 60–120) and PLA (DP = 40–120) blocks. The molecular characteristics of PCL-*b*-PLA diblock copolymers are given in Table 1. For the PLA sequences, degrees of polymerization are given in lactyl units.

### Association of PCL-*b*-PLA Block Copolymers and Nature of the Interactions

The nature of the association was first studied for one system where the two blocks PCL and PLA had roughly the same molecular weight (L1 and D1). The formation of the stereocomplex was first checked in the solid state. The mixture of the two enantiomeric copolymers L1 and D1 has a melting point of 207°C, as determined by DSC, against 157°C for both polyenantiomers (Table 2). This indicates the presence of strong interactions between the two enantiomers. Their association in solution in THF was then studied. THF is a poor solvent for the semicrystalline PLA, but a good one for the PCL sequence. It is then possible to solubilize the copolymers PCL-*b*-PLA in a wide range of concentrations. Samples were prepared by dissolving separately the same weight of each copolymer (L1 and D1) in THF at room temperature. After a few minutes, the two solutions were mixed to obtain a 10 g/L S1 solution. To ensure that the association is the result of interactions between the two enantiomeric PLA sequences, the behavior of the mixture was compared to the behavior of the pure copolymer (L1 or D1), called the reference. Study of the reference L1 by light scattering indicated the presence of two species in solution: free chains and aggregates.<sup>[36]</sup> The aggregates involve only a small fraction of the copolymers and the kinetics of their formation is very slow. A two-step mechanism is proposed: first, copolymers self-assemble to form micellelike aggregates, then the aggregates form larger and larger agglomerates.<sup>[37]</sup> In the case of the mixture S1, the formation of the aggregates is much faster and involves a larger fraction of chains than in the case of the reference. Nanoparticles with a radius

**Table 1** Molecular characteristics of the copolymers PCL-*b*-PLA

PCL- <i>b</i> -PLLA						
Samples	L1 70- <i>b</i> -120	L2 60- <i>b</i> -40	L3 70- <i>b</i> -60	L4 105- <i>b</i> -80	L5 120- <i>b</i> -120	L8 70- <i>b</i> -80
DP <sub>PCL</sub> <sup>a</sup>	72	59	69	105	117	66
DP <sub>PLA</sub> <sup>b</sup>	112	36	62	84	100	70
<i>I</i> <sub>p</sub> <sup>a</sup>	1.19	1.17	1.16	1.11	1.12	1.16
PCL- <i>b</i> -PDLA						
Samples	D1 70- <i>b</i> -120	D2 60- <i>b</i> -40	D3 70- <i>b</i> -60	D4 105- <i>b</i> -80	D5 120- <i>b</i> -120	D8 70- <i>b</i> -80
DP <sub>PCL</sub> <sup>a</sup>	77	69	77	112	123	68
DP <sub>PLA</sub> <sup>b</sup>	124	42	76	80	106	80
<i>I</i> <sub>p</sub> <sup>a</sup>	1.16	1.14	1.18	1.12	1.14	1.14

<sup>a</sup>Determined by SEC in THF. Molecular weight was measured by comparison to polystyrene standards and converted according to Ref.<sup>[38]</sup>.

<sup>b</sup>Determined by <sup>1</sup>H NMR.



**Table 2** Thermal properties of the references L (pure copolymers PCL-b-PLLA) and the mixtures S (PCL-b-PLLA + PCL-b-PDLA) (DSC, 10°C/min)

	References					
	L1	L2	L3	L4	L5	L8
$T_{mPCL}$ (°C)	52.9	54.3	51.9	53.2	52.7	52.6
$\Delta H_{PCL}$ (J/g)	62.5	68.6	54.9	59.1	64.5	63.3
$T_{mPLA}$ (°C)	156.9	131.7	149.1	146.6	154.0	149.5
$\Delta H_{PLA}$ (J/g)	54.9	46.8	52.3	64.0	74.4	57.5

	Mixtures					
	S1	S2	S3	S4	S5	S8
$T_{mPCL}$ (°C)	49.5	53	49.2	50.8	50.6	47.2
$\Delta H_{PCL}$ (J/g)	66.3	69.5	67.2	58.7	64.0	66.1
$T_{mPLA}$ (°C)	205.3	191.6	198.4	194.3	202.8	194.6
$\Delta H_{PLA}$ (J/g)	63.3	48.8	63.2	59.9	64.3	66.8

of 300 nm were obtained after 10 days and then precipitated after a few weeks. This results from specific interactions between the PLA enantiomeric sequences. The formation of the stereocomplex was proved by the appearance of a new carbonyl vibration ( $1747\text{ cm}^{-1}$ ) on the Fourier transform infrared spectroscopy (FTIR) spectra of the mixture.

### Influence of Different Parameters on the Stereocomplexation of Enantiomeric Block Copolymers

Complexation characteristics, such as association kinetics, conversion of associated sequences, or size of the aggregates, can be potentially tuned by changing the length of each block, the solvent, the concentration, or the temperature. We synthesized various copolymers with relatively good control of the PCL and PLA block lengths (Table 1). Thus, considering systems S1 (70-b-120), S2 (70-b-60), and S3 (60-b-40), which have comparable PCL block lengths, we can evaluate the influence of the complexing block (PLA) length on stereocomplexation. In the same way, to determine the influence of the solubilizing block length on the association, systems where PLA sequences have comparable degrees of polymerization (S1 and S5, S4 and S8) have been studied. For each case, the evolution of the size and stability of the aggregates with time have been determined in solution. Equimolar mixtures of isotactic block copolymers PCL-b-PLLA and PCL-b-PDLA for each system have been first studied in the solid state. Results indicate that the stereocomplex obtained with the mixture has a melting point about 50°C higher than both polyenantiomers. In addition, the melting points are much higher for longer PLA sequences (Table 2).

### Influence of PLA sequence length on stereocomplexation

Equimolar mixtures of each enantiomeric copolymer for the systems S1, S2, and S3 were prepared by dissolving separately the same weight of each copolymer (L1 and D1, L2 and D2, L3 and D3) in THF at room temperature to obtain solutions with a concentration of 10 g/L. For all the systems, the behavior of the mixture in solution was compared to the reference solution. This solution was used to prepare the mixture and contained the single enantiomeric copolymer. The behavior of the reference solutions L1, L2, and L3 was observed by static and dynamic light scattering (DLS). Measurements were performed on filtered solutions (Whatman Anotop filters, porosity 0.2  $\mu\text{m}$ ) with an experimental setup previously described,<sup>[39]</sup> at a wavelength ( $\lambda$ ) of 514.5 nm. Results of the characterization by static light scattering (SLS) for the reference solutions L1, L2, and L3 are represented by the variation of the Rayleigh ratio as a function of time and are reported in Fig. 1. At a given observation angle ( $\theta$ ), the intensity scattered by the solution ( $I_{\theta,\text{solution}}$ ) is proportional to the molecular weight of the particles and is a function of their sizes and the interactions. The Rayleigh ratio ( $\Delta R_{\theta}$ ) using toluene as a reference is defined as:

$$\Delta R_{\theta} = \frac{I_{\theta,\text{solution}} - I_{\theta,\text{solvent}}}{I_{\theta,\text{reference}}} \times R_{\theta,\text{reference}}$$

where  $I_{\theta,\text{solvent}}$  and  $I_{\theta,\text{reference}}$  are the intensity scattered by the solvent and the toluene, respectively. Over the range of time investigated, the Rayleigh ratio of the L1 and L3 solutions increases whereas the Rayleigh ratio of the L2 solution remains constant. Thus, for

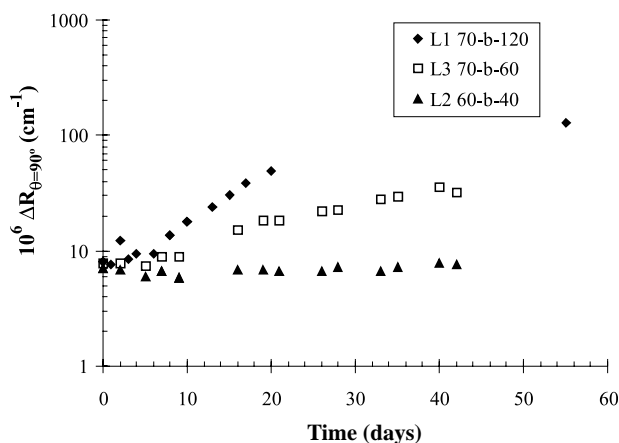


**Fig. 1** Semilogarithmic time dependence of the Rayleigh ratio measured at  $\theta = 90^\circ$  for the solutions L1, L2, and L3 ( $C_T = 10 \text{ g/L}$ ,  $T = 25^\circ\text{C}$ ).

L1 and L3 solutions some aggregation occurs, whereas for solutions containing one enantiomeric copolymer with a small PLA block ( $\text{DP}_{\text{lactyl units}} = 40$ ), no association is observed. The distributions of relaxation times obtained from DLS at different observation times for the L1 and L3 solutions are bimodal, with a fast component corresponding to the individual diblock copolymer chains (unimers) and a slow component corresponding to some aggregates. To characterize these two species in the L1 and L3 solutions, the apparent hydrodynamic radius  $R_{h,\text{app}}^i$  was estimated from the analysis of the normalized autocorrelation function  $g_2(t, q)$  (Fig. 2A and B). For a solution containing two species, the function  $g_2(t, q)$  can be written as:

$$g_2(t, q) = A_{\text{uni}}(q) \exp(-t/\tau_{\text{uni}}) + A_{\text{agg}}(q) \exp(-t/\tau_{\text{agg}})$$

with  $A_i \propto w_i M_i$

where  $w_i$  is the weight fraction of the species  $i$ ;  $A_{\text{uni}}(q)$  and  $A_{\text{agg}}(q)$  are the contributions of the unimers (fast mode) and of the aggregates (slow mode), respectively. The relaxation times  $\tau_{\text{uni}}$  and  $\tau_{\text{agg}}$  are  $q^2$  dependent and are used to calculate an apparent diffusion coefficient  $D_{i,\text{app}} = (\tau_i q^2)^{-1}$ , where  $q$  is the scattering wave vector defined as  $q = 4\pi n/\lambda \sin(\theta/2)$ , with  $n$  the refractive index of the solvent. Finally, an apparent hydrodynamic radius has been estimated using the Stokes–Einstein relation:  $R_{h,\text{app}}^i = kT/6\pi\eta_0 D_{i,\text{app}}$ , where  $k$  is the Boltzmann constant,  $T$  the absolute temperature, and  $\eta_0$  the viscosity of the solvent. The apparent hydrodynamic radius of the unimers remains constant with time ( $R_{h,\text{app}}^{\text{uni}} = 3 \pm 0.5 \text{ nm}$  for L1 and  $2.5 \pm 0.5 \text{ nm}$  for L3). The fraction of aggregates increases slowly with time for L1 and an equilibrium seems to be reached after 2 months with an  $R_{h,\text{app}}^{\text{agg}}$  of 80 nm. For the L3 solution, the same behavior is observed with a weaker

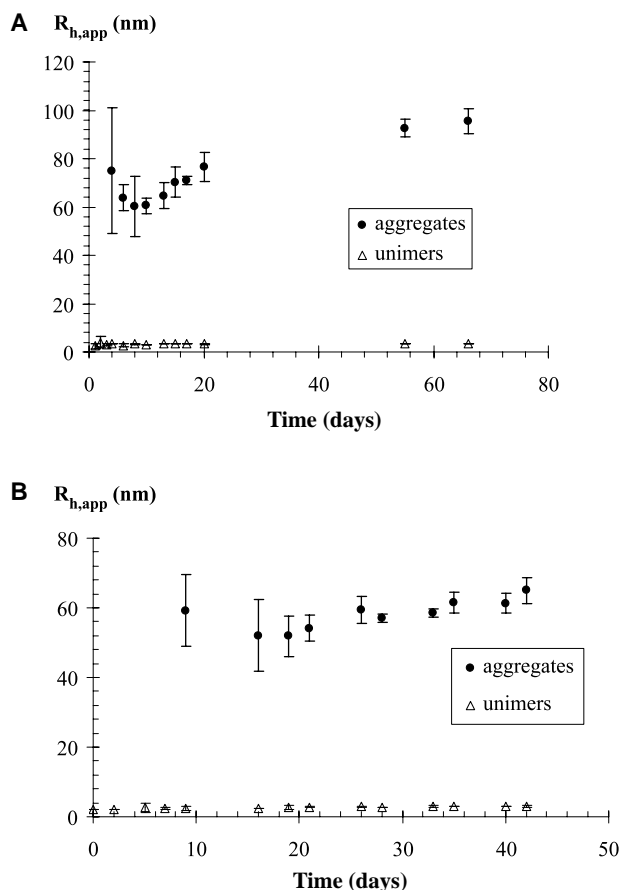


**Fig. 2** Apparent hydrodynamic radius ( $R_{h,\text{app}}$ ) of aggregates and unimers vs. time ( $C_T = 10 \text{ g/L}$ ,  $T = 25^\circ\text{C}$ ) for the solutions (A) L1 (70-b-120) and (B) L3 (70-b-60).

$R_{h,\text{app}}^{\text{agg}}$  (60 nm after 40 days). To estimate the contribution of aggregates to the overall scattered intensity, a suitable method consists in using the variation of the ratio  $A_{\text{agg}}/A_{\text{uni}}$  vs.  $q^2$ .<sup>[40]</sup> Neglecting interactions between unimers and aggregates and taking for the molecular weight of the unimers the apparent one measured before the formation of aggregates, one gets the concentrations of unimers and aggregates:

$$C_{\text{uni}} = \frac{(I_{\theta,\text{solution}} - I_{\theta,\text{solvent}})_{\theta \rightarrow 0} [A_{\text{u}}]_{q \rightarrow 0}}{KM_{\text{uni}}} \quad \text{and}$$

$$C_{\text{agg}} = C_T - C_{\text{uni}}$$

where  $K$  is an optical constant.<sup>[40]</sup> The weight average and the aggregation number ( $N_{\text{agg,app}}$ ) were also deduced:

$$N_{\text{agg,app}} = \frac{M_{\text{agg,app}}}{M_{\text{uni,app}}} = \left[ \frac{A_{\text{agg}}}{A_{\text{uni}}} \right]_{q \rightarrow 0} \frac{C_{\text{uni}}}{C_{\text{agg}}}$$

Results are presented in Figs. 3 and 4. A qualitative analysis of the solutions L1 and L3 indicates a similar

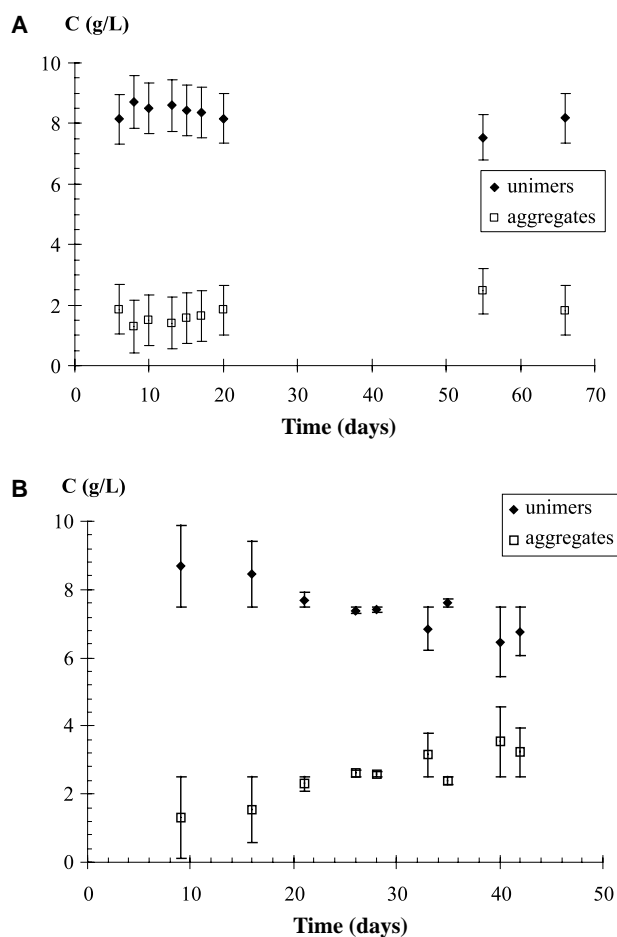


**Fig. 3** Concentration of unimers and aggregates vs. time ( $C_T = 10$  g/L,  $T = 25^\circ\text{C}$ ) for the solutions (A) L1 and (B) L3.

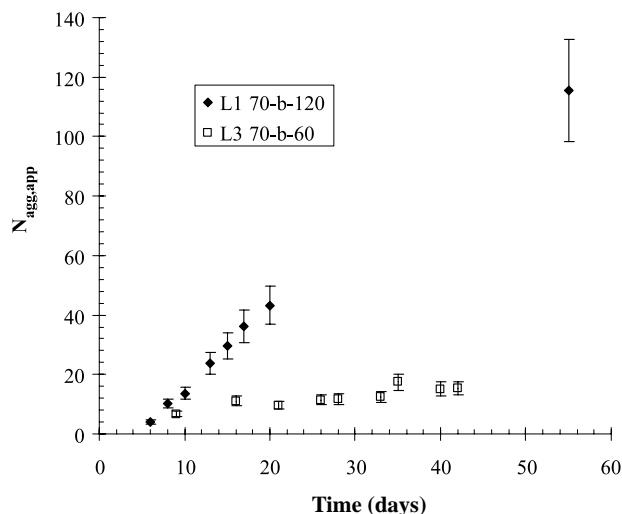


**Fig. 4** Aggregation number of the aggregates vs. time for the solutions L1 and L3 ( $C_T = 10$  g/L,  $T = 25^\circ\text{C}$ ).

behavior: aggregates self-assemble in solution and are detected rapidly. Quantitatively, the concentration of aggregates after 20 days is slightly higher for L3 (2.5 to 3 g/L) (Fig. 3B) than for L1 (2 g/L) (Fig. 3A). Thus, the aggregation number (Fig. 4) in L3 is lower than for L1. In contrast to L1 aggregates, which have an aggregation number increasing rapidly with time, the aggregation number of L3 increases slowly over the range of time investigated. The two-step association mechanism proposed for the L1 solution is no more valid for L3. In the latter case, the second step (agglomeration) is not observed.

The length of the PLA block also has a strong influence on the organization of a single enantiomeric copolymer PCL-b-PLA. For a PCL sequence with a degree of polymerization of 70 and at a concentration of 10 g/L, the size of the aggregates increases with the size of the PLA block. With a short PLA block (case of L2 solution) no aggregate is detected by light scattering, whereas for copolymers with sufficient PLA length, aggregates are observed. Complexation kinetics as well as its mechanism depends strongly on the PLA block. Thus, the degree of polymerization of the PLA block is a critical factor that directly influences the organization of the single enantiomeric copolymer in THF.

After studying the behavior of reference solutions L1, L2, and L3, equimolar mixtures of each enantiomeric copolymer were prepared at the same concentration. Systems S1, S2, and S3 were studied by static and dynamic light scattering and by FTIR. Light scattering results for solutions S1, S2, and S3 are very different from those of their respective reference solutions. Rayleigh ratios are much higher, indicating that enantiomeric PLA sequences interact in solution. For solutions S2 and S3, the distributions of relaxation times determined from DLS show the same profile as those of S1 solution: a monomodal distribution with high relaxation time is obtained, indicating the presence of large diffusing objects. The apparent hydrodynamic radius  $R_{h,app}$  relative to the mixtures S1, S2, and S3 and prepared in THF at 10 g/L are presented in Fig. 5. Accordingly, results indicate that the behavior of an equimolar mixture of enantiomeric PCL-b-PLA is strongly dependent on the PLA block length. Qualitatively, after 7 days at room temperature, the S3 and S1 solutions become cloudy whereas the S2 solution remains perfectly clear over many months. Quantitatively, a very strong increase of the apparent hydrodynamic radius is observed for S3 and S1 solutions, followed by stabilization beyond 10 days. However, if the global behavior is similar, the dimensions of the aggregates are strongly affected by the PLA block length. Hydrodynamic radii obtained by DLS are much larger for larger PLA sequences. Thus, the size of aggregates is directly dependent on the degree of polymerization of the complexing block (PLA).

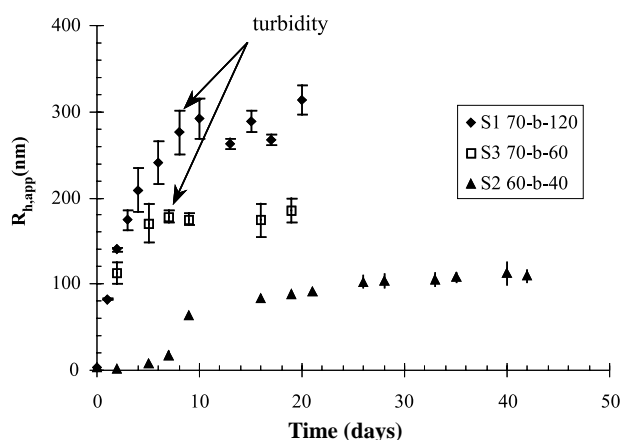


**Fig. 5** Apparent hydrodynamic radius ( $R_{h,app}$ ) of mixtures S1, S2, and S3 vs. time ( $C_T = 10 \text{ g/L}$ ,  $T = 25^\circ\text{C}$ ).

This confirms that the association by stereocomplexation of PLA sequences is the driving force of the copolymer association in solution. To estimate the conversion to stereocomplex, solutions of S1, S2, and S3 were analyzed by FTIR. IR spectra of the mixtures presented three distinctive peaks between 1700 and  $1800 \text{ cm}^{-1}$ : at  $1737 \text{ cm}^{-1}$ , the carbonyl vibration corresponding to PCL sequences; at  $1763 \text{ cm}^{-1}$ , the carbonyl vibration corresponding to the nonassociated PLA sequences; and at  $1747 \text{ cm}^{-1}$ , a vibration assigned to the stereocomplex.<sup>[41]</sup> The signal was deconvoluted into Lorentzian curves. The characteristic parameters of the peaks at  $1737 \text{ cm}^{-1}$  (PCL sequences) and at  $1763 \text{ cm}^{-1}$  (non-associated PLA sequences) were first estimated from values determined for the reference solutions L1, L2, and L3. The conversion was estimated by considering the diminution of the “free” PLA signal ( $1763 \text{ cm}^{-1}$ ).  $R_t$  is defined as the ratio of intensities of signals of non-associated PLA and PCL sequences, respectively [ $R_t = I(\text{PLA})_t / I(\text{PCL})_t$ ]. The conversion is then defined as follows: conversion ( $t$ ) =  $(R_0 - R_t) / R_0$ , where  $R_0$  is taken just after mixing the solutions of enantiomeric copolymers. Variation of the conversion vs. time for the three mixtures is reported in Fig. 6. Again, significant differences between S2 on one hand and S1 and S3 on the other hand are observed. For the solution S2, the proportion of stereocomplex increases weakly before reaching 10% at 60 days. The length of the PLA sequences of this system corresponds to the minimum value reported in the literature that is able to form a stereocomplex.<sup>[32]</sup> In this case, the kinetics of stereocomplexation is slow. For mixtures S1 and S3, the evolution is faster and reaches a value of 30% after 20 days. The difference between S1 and S3 is very small, and the apparently higher conversion for S3 is presently not understood. The solutions S1 and S3 were also studied by LS at a smaller concentration ( $C_T = 1 \text{ g/L}$ ). For solutions S1

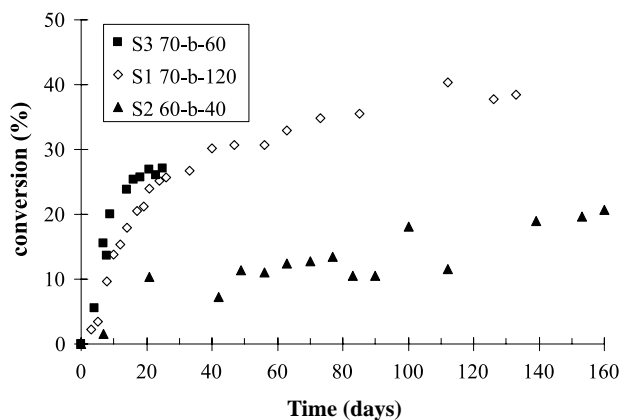


**Fig. 6** Conversion in stereocomplex vs. time for the mixtures S1, S2, and S3 (FTIR,  $C_T = 10 \text{ g/L}$ ,  $T = 25^\circ\text{C}$ ).

and S3, aggregates are more stable; no precipitation was observed even after several months. However, the association is very slow and the size of the aggregates is smaller than at the concentration of  $10 \text{ g/L}$ . Once again, if the systems S1 and S3 are compared, apparent hydrodynamic radii are smaller in the case of the copolymer with a shorter PLA block (Fig. 7).

In conclusion, the comparative study of S1 and S3 solutions indicates that the degree of polymerization of PLA sequences strongly affects the size of the aggregates, not only for the single copolymers but also for the enantiomeric equimolar mixtures. For very short sequences (S2) the association of enantiomeric copolymers is relatively slow and leads to the formation of stable particles in solution.

#### Influence of PCL block length on nanoparticle formation

To determine the influence of the solubilizing block lengths on the association, two pairs of systems where PLA sequences have comparable degrees of

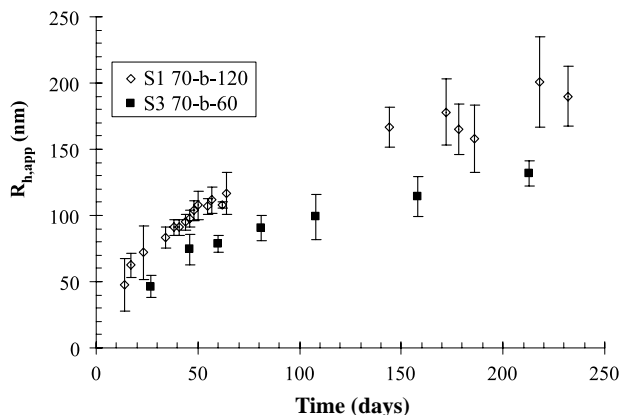


**Fig. 7** Apparent hydrodynamic radius ( $R_{h,app}$ ) of mixtures S1 and S3 ( $C_T = 1 \text{ g/L}$ ,  $T = 25^\circ\text{C}$ ).

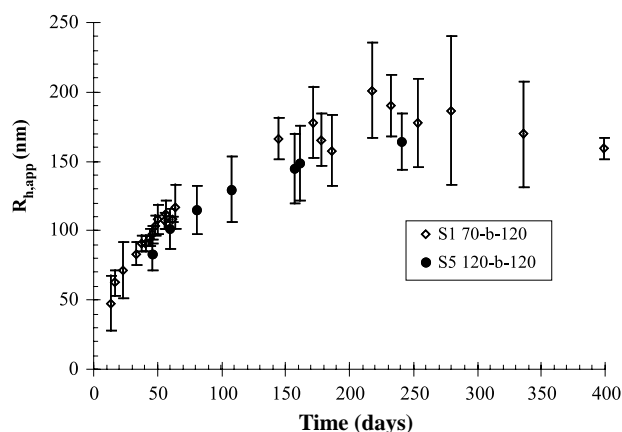


**Fig. 8** Apparent hydrodynamic radius ( $R_{h,app}$ ) of mixtures S1 and S5 ( $C_T = 1$  g/L,  $T = 25^\circ\text{C}$ ).

polymerization (S1 and S5, S4 and S8) were studied. S1 and S5 mixtures of copolymers, which have each a PLA block of 120 lactyl units, were prepared as previously described at a concentration of 1 g/L in THF. Measurements carried out by DLS on the reference solutions (L1 and L5) indicated (as for all references at this concentration) that there is no association. The association of the equimolar mixtures S1 and S5 at 1 g/L was observed and no precipitation appeared, even after 1 year. The formation of large aggregates as a function of time was confirmed by DLS. The variation of the apparent hydrodynamic radius for the solutions S1 and S5 is represented in Fig. 8. A similar behavior is observed for the two solutions. Nevertheless, for the system S5, the radius of the aggregates seems to be slightly smaller than for the S1 solution. In the same way, the solutions S4 and S8 containing copolymers with a PLA block of 80 lactyl units were characterized at 1 g/L in THF. Results obtained by light scattering for the reference solutions (L4 and L8) indicated that the solutions did not show any association at this concentration, whereas the association of equimolar enantiomeric copolymer mixtures was clearly observed: scattered intensity (SLS) increased and aggregates (DLS) appeared. Furthermore, the solutions were very stable for at least several months. The evolution of the apparent hydrodynamic radius of formed aggregates for systems S4 and S8 vs. time are represented in Fig. 9. The curves obtained for the two solutions S4 and S8 are similar, but the values for the system S8 are slightly higher. The lengthening of the PCL solubilizing block seems to hinder the association but this effect is limited.

## CONCLUSION

We have studied the association of various block copolymers poly(lactide)-b-poly( $\epsilon$ -caprolactone) in THF, a

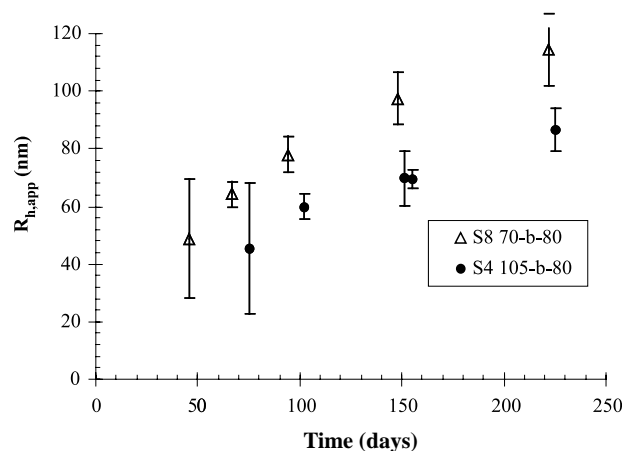


**Fig. 9** Apparent hydrodynamic radius ( $R_{h,app}$ ) of mixtures S8 and S4 ( $C_T = 1$  g/L,  $T = 25^\circ\text{C}$ ).

selective solvent of the poly(caprolactone) block. Light scattering measurements on solutions of the single PCL-b-PLLA copolymers indicate, in some cases, the formation of aggregates. Complexation kinetics as well as its mechanism depends strongly on the size of the PLA block in the copolymer. With a short PLA sequence, no aggregate was detected, whereas with some large PLA blocks, aggregates were formed. Their size increases with the degree of polymerization of the PLA sequence.

In the case of the mixtures of enantiomeric block copolymers, the association appears more rapidly. Nanoparticles are formed as a result of specific interactions between the PLA enantiomeric sequences. This stereocomplexation is not quantitative because a high fraction of the sequences remains free without being involved in the complex. The degree of polymerization of PLA sequences strongly affects the size of the aggregates (80 to 200 nm), whereas the PCL block length has a limited influence on the stereocomplexation. The concentration is also a parameter that affects the size and the stability of the particles. Optimal conditions to form stable nanoparticles in solution (short PLA block or low concentration) have been identified.

## ACKNOWLEDGMENTS

Alexandre Richez is acknowledged for performing some FTIR measurements. We thank PURAC Biochem for providing the lactide monomers used in this work.

## REFERENCES

1. Mandema, W.; Zeldenrust, H.; Emeis, C.A. Association of blocks copolymers in selective solvents. 1. Measurements on hydrogenated poly(styrene-isoprene) in

- decane and in *trans*-decalin. *Makromol. Chem.* **1979**, *180*, 1521–1538.
- Xu, R.; Winnik, M.A.; Hallett, F.R.; Riess, G.; Croucher, M.D. Light-scattering study of the association behavior of styrene–ethylene oxide block copolymers in aqueous solution. *Macromolecules* **1991**, *24*, 87–93.
  - Nagarajan, R.; Ganesh, K. Block copolymer self-assembly in selective solvents: spherical micelles with segregated cores. *J. Chem. Phys.* **1989**, *90* (10), 5843–5856.
  - Förster, S.; Zisenis, M.; Wenz, E.; Antonietti, M. Micellization of strongly segregated block copolymers. *J. Chem. Phys.* **1996**, *104* (24), 9956–9970.
  - Antonietti, M.; Heinz, S.; Schmidt, M.; Rosenauer, C. Determination of the micelle architecture of polystyrene/poly(4-vinylpyridine) block copolymers in dilute solution. *Macromolecules* **1994**, *27*, 3276–3281.
  - Won, Y.-Y.; Davis, H.T.; Bates, F.S. Giant wormlike rubber micelles. *Science* **1999**, *283*, 960–963.
  - Choucair, A.; Eisenberg, A. Control of amphiphilic block copolymer morphologies using solution conditions. *Eur. Phys. J., E* **2003**, *10*, 37–44.
  - Zhang, L.; Eisenberg, A. Multiple morphologies and characteristics of crew-cut micelle-like aggregates of polystyrene-*b*-poly(acrylic acid) diblock copolymers in aqueous solution. *J. Am. Chem. Soc.* **1996**, *118*, 3168–3181.
  - François, B.; Pitois, O.; François, J. Polymer films with a self-organized honeycomb morphology. *Adv. Mater.* **1995**, *7* (12), 1041–1044.
  - Sommerdijk, N.A.J.M.; Holder, S.J.; Hiorns, R.C.; Jones, R.G.; Nolte, R.J.M. Self-assembled structures from an amphiphilic multiblock copolymer containing rigid semiconductor segments. *Macromolecules* **2000**, *33*, 8289–8294.
  - Gast, A.P.; Vinson, P.K.; Cogan-Farinas, K.A. An intriguing morphology in crystallizable block copolymers. *Macromolecules* **1993**, *26*, 1774–1776.
  - Massey, J.A.; Temple, K.; Cao, L.; Rharbi, Y.; Raez, J.; Winnik, M.A.; Manners, I. Self-assembly of organometallic block copolymers: the role of crystallinity of the core-forming polyferrocene block in the micellar morphologies formed by poly(ferrocenylsilane-*b*-dimethylsiloxane) in *n*-alkane solvents. *J. Am. Chem. Soc.* **2000**, *122*, 11,577–11,584.
  - Richter, D.; Schneiders, D.; Monkenbusch, M.; Willner, L.; Fetters, L.J.; Huang, J.S.; Lin, M.; Mortensen, K.; Farago, B. Polymer aggregates with crystalline cores: the system polyethylene–poly(ethylenepropylene). *Macromolecules* **1997**, *30*, 1053–1068.
  - Whitesides, G.M.; Mathias, J.P.; Seto, C.T. Molecular self-assembly and nanochemistry: a chemical strategy for the synthesis of nanostructures. *Science* **1991**, *254*, 1312–1319.
  - Tsuchida, E.; Abe, K. Interactions between macromolecules in solution and intermacromolecular complexes. *Adv. Polym. Sci.* **1982**, *45*, 2–118.
  - Harada, A.; Kataoka, K. Formation of polyion complex in an aqueous milieu from a pair of oppositely-charged block copolymers with poly(ethylene glycol) segments. *Macromolecules* **1995**, *28*, 5294–5299.
  - Harada, A.; Kataoka, K. Chain length recognition: core–shell supramolecular assembly from oppositely charged block copolymers. *Science* **1999**, *283*, 65–67.
  - Liu, S.; Zhu, H.; Zhao, H.; Jiang, M.; Wu, C. Interpolymer hydrogen-bonding complexation induced micellization from polystyrene-*b*-poly(methyl methacrylate) and PS(OH) in toluene. *Langmuir* **2000**, *16*, 3712–3717.
  - Katime, I.A.; Quintana, J.R. Stereoassociation of poly(-methyl methacrylate): study on the complexation stoichiometry and structural characteristics of the aggregates. *Makromol. Chem.* **1988**, *189*, 1373–1385.
  - Dumas, Ph.; Spassky, N.; Sigwalt, P. Preparation and polymerization of racemic and optically active *tert*-butyl thiirane. *Makromol. Chem.* **1972**, *156*, 55–64.
  - Spassky, N.; Dumas, Ph.; Sepulchre, M.; Sigwalt, P. Properties and methods of synthesis of several optically active polyoxiranes and polythiiranes. *J. Polym. Sci., Polym. Symp.* **1975**, *52*, 327–349.
  - Grenier, D.; Prud'homme, R.E. Complex formation between enantiomeric polyesters. *J. Polym. Sci., Polym. Phys. Ed.* **1984**, *22*, 577–587.
  - Ikada, Y.; Jamshidi, K.; Tsuji, H.; Hyon, S.-H. Stereo-complex formation between enantiomeric poly(lactides). *Macromolecules* **1987**, *20*, 904–906.
  - Murdoch, J.R.; Loomis, G.L. Polylactide Compositions. US Patent 4,800,219, Jan. 24, 1989.
  - Tsuji, H.; Hyon, S.-H.; Ikada, Y. Stereocomplex formation between enantiomeric poly(lactic acid)s. 5. Calorimetric and morphological studies on the stereocomplex formed in acetonitrile solution. *Macromolecules* **1992**, *25*, 2940–2946.
  - de Jong, S.J.; van Dijk-Wolthuis, W.N.E.; Kettenes-van den Bosch, J.J.; Schuyf, P.J.W.; Hennink, W.E. Monodisperse enantiomeric lactic acid oligomers: preparation, characterization, and stereocomplex formation. *Macromolecules* **1998**, *31* (19), 6397–6402.
  - Tsuji, H.; Ikada, Y. Crystallization from the melt of poly(lactide)s with different optical purities and their blends. *Makromol. Chem. Phys.* **1996**, *197*, 3483–3499.
  - De Santis, P.; Kovacs, A.J. Molecular conformation of poly(S-lactic acid). *Biopolymers* **1968**, *6* (3), 299–306.
  - Okihara, T.; Tsuji, M.; Kawaguchi, A.; Katayama, K.-I.; Tsuji, H.; Hyon, S.-H.; Ikada, Y. Crystal structure of stereocomplex of poly(L-lactide) and poly(D-lactide). *J. Macromol. Sci., Phys.* **1991**, *B30* (1 and 2), 119–140.
  - Yui, N.; Dijkstra, P.J.; Feijen, J. Stereo block copolymers of L- and D-lactides. *Makromol. Chem.* **1990**, *191*, 481–488.
  - Loomis, G.L.; Murdoch, J.R.; Gardner, K.H. Polylactide stereocomplexes. *Polym. Prepr. (Am. Chem. Soc., Div. Polym. Chem.)* **1990**, *31* (2), 55.
  - Pensec, S.; Leroy, M.; Akkouche, H.; Spassky, N. Stereocomplex formation in enantiomeric diblock and triblock copolymers of poly( $\epsilon$ -caprolactone) and polylactide. *Polym. Bull.* **2000**, *45*, 373–380.
  - Stevens, W.M.; Ankoné, M.J.K.; Dijkstra, P.J.; Feijen, J. Stereocomplex formation in AB di-block copolymers of poly( $\epsilon$ -caprolactone) (A) and poly(lactide) (B). *Macromol. Symp.* **1996**, *102*, 107–113.
  - Lim, D.W.; Park, T.G. Stereocomplex formation between enantiomeric PLA–PEG–PLA triblock



- copolymers: Characterization and use as protein-delivery microparticulate carriers. *J. Appl. Polym. Sci.* **2000**, *75* (9), 1615–1623.
35. Simic, V.; Pensec, S.; Spassky, N. Synthesis and characterization of some block copolymers of lactides with cyclic monomers using yttrium alkoxide as initiator. *Macromol. Symp.* **2000**, *153*, 109–121.
  36. Portinha, D.; Belleney, J.; Bouteiller, L.; Pensec, S.; Spassky, N.; Chassenieux, C. Formation of nanoparticles of polylactide-containing diblock copolymers: is stereocomplexation the driving force? *Macromolecules* **2002**, *35*, 1484–1486.
  37. Portinha, D.; Bouteiller, L.; Pensec, S.; Richez, A. Influence of preparation conditions on the self-assembly by stereocomplexation of polylactide containing diblock copolymers. *Submitted*.
  38. Dubois, P.; Barakat, I.; Jerome, R.; Teysié, P. Macromolecular engineering of polyactones and polyactides. 12. Study of the depolymerization reactions of poly( $\epsilon$ -caprolactone) with functional aluminum alkoxide end groups. *Macromolecules* **1993**, *26* (17), 4407–4412.
  39. Chassenieux, C.; Nicolai, T.; Durand, D. Association of hydrophobically end-capped poly(ethylene oxide). *Macromolecules* **1997**, *30* (17), 4952–4958.
  40. Raspaud, E.; Lairez, D.; Adam, M.; Carton, J.-P. Triblock copolymers in a selective solvent. 1. Aggregation process in dilute solution. *Macromolecules* **1994**, *27*, 2956–2964.
  41. Kister, G.; Cassanas, G.; Vert, M. Structure and morphology of solid lactide–glycolide copolymers from  $^{13}\text{C}$  NMR, infra-red and Raman spectroscopy. *Polymer* **1998**, *39* (15), 3335–3340.

# Cadmium Selenide Quantum Dots

**Kenzo Maehashi**

**Hisao Nakashima**

*Institute of Scientific and Industrial Research, Osaka University,  
Osaka, Japan*

## INTRODUCTION

II–VI semiconductors such as ZnSe, ZnS, and CdSe have wider band gap and larger exciton binding energies as compared with III–V semiconductors. Excitons of II–VI semiconductors still exist at room temperature. Therefore II–VI semiconductor devices indicate a possibility of new devices using excitons, such as optical modulators and self-electro-optic effect devices.<sup>[1–5]</sup> Furthermore, in the field of optical data transmission, green laser is suitable for short- and medium-range communication purposes using plastic optical fibers with polymethyl methacrylate cores, which have an advantage of lower costs than silica fibers. Therefore II–VI semiconductors are also optimum candidates for light source of optical data transmission through plastic optical fibers.

Semiconductor quantum structures have been intensively investigated since Esaki and Tsu<sup>[6]</sup> proposed novel artificial superlattice structures. Recently, quantum dots (QDs) have attracted much attention for the optoelectronic device applications and fundamental physics because they provide zero-dimensional structures with  $\delta$ -function density of states, which dramatically improve performances of optoelectronic devices such as semiconductor lasers. To fabricate lower-dimensional structures, great efforts have been made using various methods, such as selective epitaxial growth, lithography, etching, etc.<sup>[7–12]</sup> However, these techniques give film damages, such as defects and contamination. On the other hand, self-organized QDs have an advantage of fabrication of high-density and high-quality QDs. Especially, InAs QDs of III–V materials have been known to be formed on GaAs surfaces, which are followed by the two-dimensional growth of InAs wetting layer, because InAs has a larger lattice constant by 7% than GaAs.<sup>[13–18]</sup>

CdSe/ZnSe system is expected to naturally form QDs because of large lattice mismatch of about 7% between ZnSe and CdSe. In this session, we have investigated the formation and optical properties of

self-organized CdSe QDs on ZnSe (001) surfaces with the use of photoluminescence (PL) and transmission electron microscopy (TEM) measurements. Moreover, applying the QD system to optoelectronic devices to understand carrier dynamics and energy structures of QDs is very important. For example, relaxation mechanism of InAs QDs has been reported by PL excitation measurements.<sup>[19,20]</sup> As compared with InAs QDs, CdSe QDs have stronger electron–phonon interactions and much larger band-gap energy. Then, the carrier relaxation mechanisms in self-organized CdSe QDs are more interesting subjects. In this study, we have also investigated optical properties of self-organized CdSe QDs by selectively excited PL measurements.

## GROWTH OF CdSe/ZnSe STRUCTURES

ZnSe/CdSe/ZnSe structures were fabricated by molecular beam epitaxy (MBE) on GaAs (001) substrates after GaAs buffer layer growth. Compound sources of ZnSe and CdSe, whose purities are 6N, were used for ZnSe and CdSe growth, respectively.<sup>[21]</sup> In the case of compound materials, the temperatures necessary to obtain beam enough flux intensity for MBE growth are much higher as compared with the temperatures needed in the conventional case for columns II and VI elemental sources. As a result, it is convenient to control the beam flux and to precisely control the composition beam flux ratio. In addition, because only molecules of Se<sub>2</sub> are generated, the sticking coefficient of molecules is enhanced as compared with elemental sources. Therefore high-quality films are expected to be obtained.

The polished GaAs (001) substrates were etched in a 4:1:1 solution of H<sub>2</sub>SO<sub>4</sub>:H<sub>2</sub>O:H<sub>2</sub>O<sub>2</sub> before placing them in the MBE loading chamber with In backing on Mo blocks. The substrates were annealed at 580°C with As irradiation to remove native oxide. First, the 200-nm-thick GaAs buffer layer was grown at 580°C in the MBE system. Next, ZnSe layer

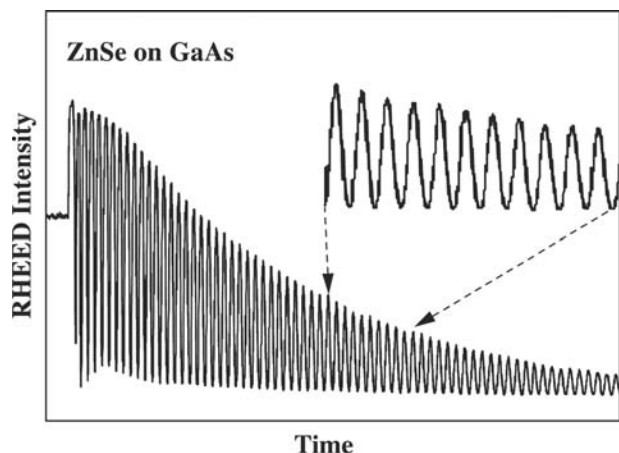


**Fig. 1** RHEED intensity oscillation of ZnSe growth on GaAs (001) surfaces.

(100 nm) was grown on the GaAs surfaces at 290°C. When ZnSe growth starts on the GaAs surfaces, the GaAs ( $2 \times 4$ ) reconstruction pattern disappeared immediately and the reflection high-energy electron diffraction (RHEED) intensity oscillation starts, as shown in Fig. 1. The RHEED intensity oscillation during ZnSe growth on GaAs surfaces continued until more than 100-nm thickness of ZnSe film. This indicates that ZnSe proceeds in layer-by-layer mood on GaAs surfaces and that flat interfaces are formed between ZnSe films and GaAs surfaces. The RHEED patterns during ZnSe growth showed both ( $2 \times 1$ ) and  $c(2 \times 2)$  reconstruction patterns. Therefore ZnSe films with high quality were obtained.<sup>[22]</sup>

Then, a few monolayers (MLs) of CdSe were grown on the ZnSe surfaces at 290°C. The growth rate of CdSe was 1.1 ML/min, which was measured by RHEED intensity oscillation. To confirm the formation of self-organized CdSe QDs, the bulk spot intensity of RHEED was monitored during the growth of CdSe with the use of both a combination of a charge-coupled device (CCD) camera and a photodiode.<sup>[23]</sup> Finally, ZnSe layer was grown after the CdSe growth without growth interruption.

## FORMATION OF CdSe QUANTUM DOTS

Fig. 2 shows PL spectra measured for the samples with various CdSe coverages.<sup>[24]</sup> Photoluminescence measurement was carried out at liquid He temperature using a 32-cm grating monochromator with a cooled CCD camera. A He–Cd laser line of 325 nm was used as an excitation light. With increasing the CdSe thickness from 1.3-ML coverages, the PL peaks shift to lower energy, which is a result of the quantum size effect. The small jump in peak position between 2.2

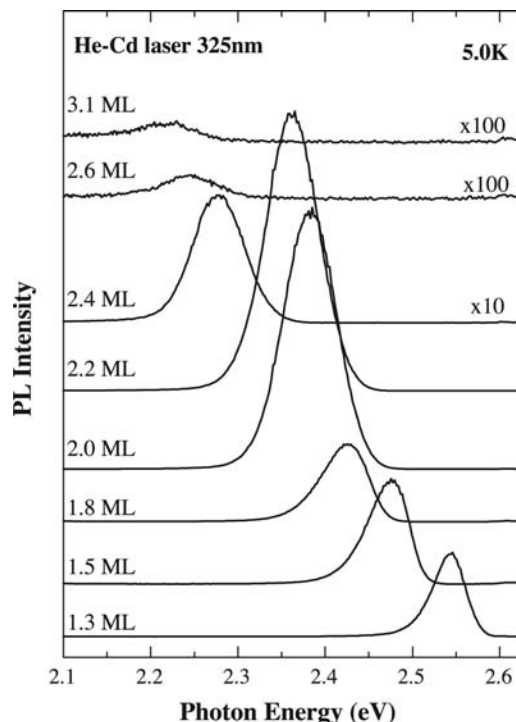


**Fig. 2** Photoluminescence spectra as a function of CdSe thickness. Source: From Ref.<sup>[24]</sup>.

and 2.4 ML CdSe coverages is also observed. Photoluminescence intensity and full widths at half maximum (FWHMs) gradually increase with increasing the CdSe thickness from 1.3-ML coverages. The maximum PL intensity is obtained at about 2.2 ML CdSe coverages. However, at more than 2.4 ML CdSe coverages, PL intensities dramatically decrease, as shown in Fig. 2. The emission is hardly observed at 2.6 and 3.1 ML CdSe coverages.

Next, cross-sectional TEM images are observed for the samples with various CdSe coverages. The cross-sectional TEM specimens were prepared by mechanical polish and dimpling followed by ion etching. The TEM images were observed by JEOL JEM-3000F electron microscope at 300 kV. Fig. 3A shows a cross-sectional TEM image of CdSe 1.6-ML coverages taken along the [011] direction. The dark region shows the CdSe layer. A lot of CdSe QDs are clearly observed, indicating that CdSe QDs are naturally formed on ZnSe surfaces. Any defects are not found in this image. Fig. 3b shows a cross-sectional high-resolution TEM image of single CdSe QD. Single CdSe QD with several nanometers size is observed. Kirmse et al.<sup>[25]</sup> have reported with plan-view TEM images that two classes of CdSe QDs coexist with an average lateral size of <math><10\text{ nm}</math> (area density of  $100\ \mu\text{m}^{-2}$ ) and  $10\text{--}50\text{ nm}$  ( $20\ \mu\text{m}^{-2}$ ), respectively. However, we did not observe such large CdSe QDs. As compared with the atomic force microscopy image in Ref.<sup>[26]</sup>, the diameter of

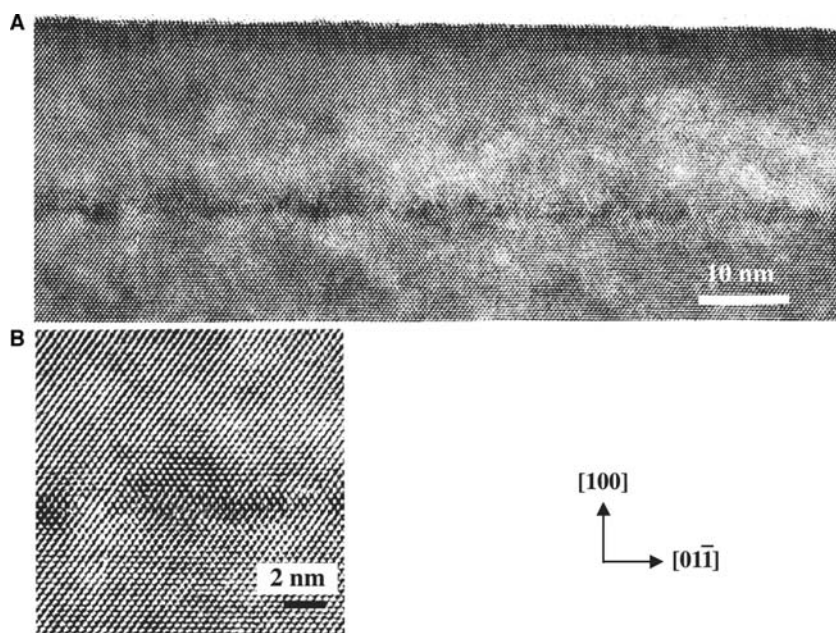


**Fig. 3** (A) Cross-sectional TEM image of CdSe 1.6-ML coverage taken along the  $[011]$  direction and (B) cross-sectional high-resolution TEM images of single CdSe QD.

CdSe QDs in Fig. 3 is smaller and the density is much higher. Fig. 4A shows a cross-sectional TEM image of 2.6-ML coverages taken along the  $[0\bar{1}1]$  direction. This reveals that much stacking faults are observed in the ZnSe capping layer. It is found that these stacking faults have an origin at around CdSe/ZnSe interfaces. Fig. 4B shows a cross-sectional high-resolution TEM image at the interface between CdSe/ZnSe. The stacking faults start from the interface between ZnSe capping layer and CdSe QDs. Therefore stacking faults are considered to be induced by large stress after ZnSe cap layer growth.

Photoluminescence and TEM results indicate that the PL intensity at less than 2.2 ML CdSe coverages shown in Fig. 2 comes from CdSe QDs. This is consistent with the result that the defects in the samples reduce dramatically the luminescence intensity of thick samples, as shown in Figs. 2 and 4. Furthermore, CdSe

QDs showed a strong green emission even at room temperature.<sup>[27]</sup> These results indicate that CdSe QDs with high quality are formed on ZnSe surfaces.

To investigate the optical properties for the effect of the QD shape, polarization dependence of PL from CdSe QDs is measured.<sup>[28]</sup> Fig. 5 shows PL spectra of 2.0 ML CdSe coverages at 5 K. The solid curve and the dashed curve are spectra of polarization components, which are parallel to the  $[1\bar{1}0]$  direction and to the  $[110]$  direction, respectively, as shown in Fig. 5. A peak at 2.38 eV comes from the CdSe QDs, and no peak from wetting layers is observed. The intensity for the polarization parallel to the  $[1\bar{1}0]$  direction ( $I[1\bar{1}0]$ ) is larger than that to the  $[110]$  direction ( $I[110]$ ), as shown in Fig. 5. No polarization anisotropy was observed between the  $[100]$  and  $[010]$  directions. Therefore the PL spectra are strongly polarized parallel to the  $[1\bar{1}0]$  direction. The PL peaks shown in Fig. 5

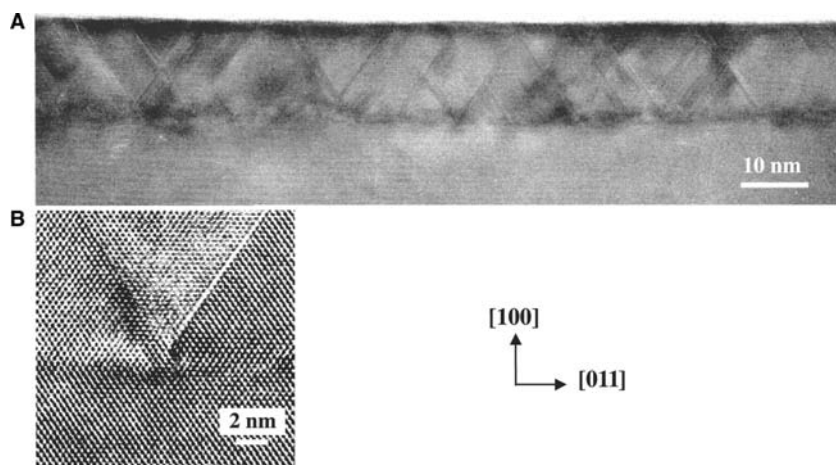


**Fig. 4** (A) Cross-sectional TEM image of CdSe 2.6-ML coverage taken along the  $[0\bar{1}1]$  direction and (B) cross-sectional high-resolution TEM image at the interface between CdSe/ZnSe.

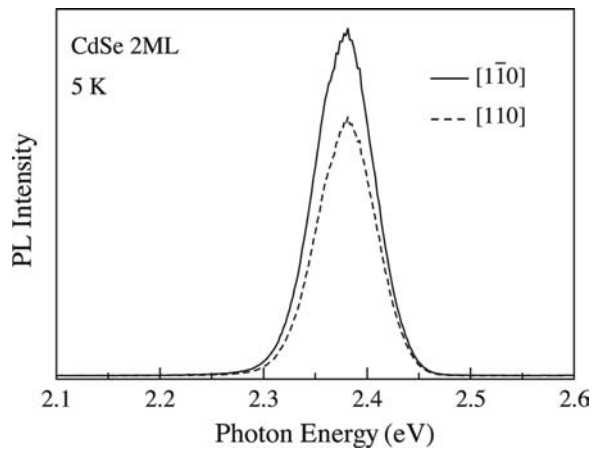


**Fig. 5** Photoluminescence polarization dependence of CdSe QDs at 5 K. *Source:* From Ref.<sup>[28]</sup>.

come from the heavy-hole transition, and the strong polarization is considered to be a result of the heavy-hole confinement in CdSe QDs, indicating that lateral confinement along the  $[1\bar{1}0]$  direction is weaker than that along the  $[110]$  direction. Consequently, CdSe QDs are considered to have the longer axis along the  $[1\bar{1}0]$  direction than the  $[110]$  direction.

From Fig. 5, a PL polarization degree of CdSe QDs was estimated to be 14.6%, which is defined by  $(I[1\bar{1}0] - I[110]) / (I[1\bar{1}0] + I[110])$ . We also discuss about the CdSe coverage dependence of polarization PL spectra. Fig. 6 shows the PL polarization degrees as a function of CdSe coverage from 1.5 to 2.4 ML at 5 K. The PL spectrum for each CdSe coverage was clearly polarized parallel to the  $[1\bar{1}0]$  direction, indicating that the shape of QDs for each CdSe coverage has the long axis along the  $[1\bar{1}0]$  direction. The PL polarization degrees increase with increasing CdSe coverage, as shown in Fig. 6. The result reveals that the PL

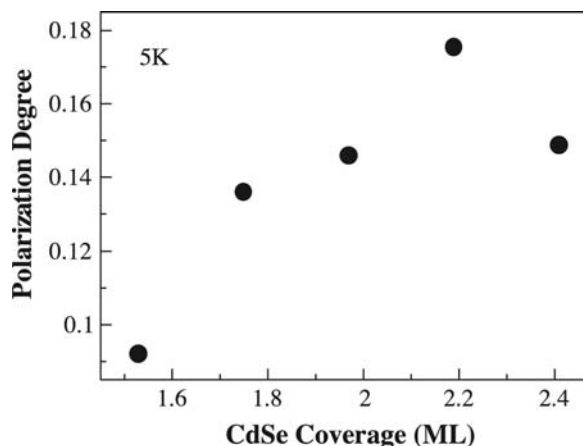


**Fig. 6** CdSe coverage dependence of PL polarization degree at 5 K. *Source:* From Ref.<sup>[28]</sup>.

polarization degrees increase with QD formation, suggesting that the ratio of length along the  $[110]$  direction to that along the  $[1\bar{1}0]$  direction increases with CdSe coverage. At 2.2-ML coverages, PL spectrum has maximum polarization degree. At 2.4 ML CdSe coverages, defects were induced and, simultaneously, polarization degree decreases as shown in Fig. 6, which is considered to be a result of the release from the stress in CdSe QDs.

## OPTICAL PROPERTIES OF CdSe QUANTUM DOTS

### Microphotoluminescence

The FWHM of CdSe QDs is about several tens of microelectron volts, which is much broader than that of ZnCdSe quantum well.<sup>[29]</sup> The broad spectral width is considered to be a result of the nonuniformity of CdSe QD structures. The fluctuation in dot size causes the fluctuation in strain, resulting in more nonuniform dot structures and the broad spectral width. So it is impossible to clarify the optical properties of the single CdSe QD by macro-PL. To reduce the number of observed QDs, we put Al masks with submicron size apertures on the sample surfaces.<sup>[30]</sup> The 100-nm-thick Al masks were made by electron-beam lithography and liftoff techniques. The diameters of the apertures were varied from 0.6 to 1  $\mu\text{m}$ . Microphotoluminescence measurements were performed as follows. The sample fixed on a cold finger in a cryostat was cooled down using helium gas. The 458-nm line of Ar-ion laser was used to excite the QDs. The excitation laser was focused to about 0.8- $\mu\text{m}$  spot size through a microscope objective. The CCD camera cooled by liquid nitrogen detected the luminescence through a monochromator. The spectral resolution is  $\sim 500 \mu\text{eV}$ . The micro-PL experiments were performed in the temperature range of 4 to 60 K.

Fig. 7 shows micro-PL spectra of CdSe QDs, which are measured through several different size apertures at 4 K. The excitation power of each spectrum was 100  $\mu\text{W}$ . Fig. 7A shows a spectrum of micro-PL with focusing the excitation laser on the sample surface without Al masks. The wide FWHM of the broad peak is a result of the size distribution of the QDs. With decreasing the size of the aperture from 1 to 0.6  $\mu\text{m}$ , as shown in Fig. 7B and C, respectively, the broad peaks observed through the apertures split into a number of anomalously very sharp lines having linewidths of  $\sim 500 \mu\text{eV}$ . These sharp lines in Fig. 7C indicate zero-dimensional density of states of the QDs. The characteristic features of the spectrum in Fig. 7C are as follows. In lower-energy region ranged from 2.28 to 2.34 eV, the sharp lines are clustered close together



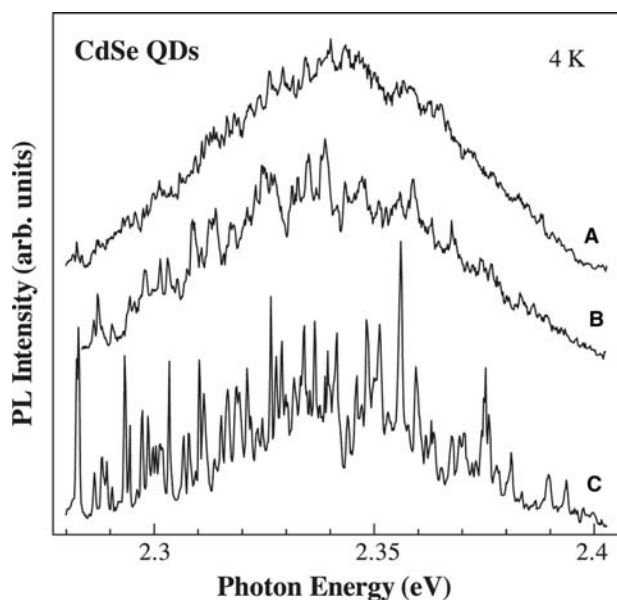


**Fig. 7** Microphotoluminescence spectra of CdSe QDs at 4 K: (A) without Al mask, (B) 1  $\mu\text{m}$ , and (C) 0.6- $\mu\text{m}$  size aperture. *Source:* From Ref.<sup>[24]</sup>.

in comparison with those in the higher-energy region ranged from 2.34 to 2.40 eV. The integrated intensities of the lower-energy lines are larger than those of the higher-energy lines. The linewidths of the lower-energy lines are narrower than those of the higher-energy lines. These phenomena are similar to the result in the report of CdSe QDs by Kim et al.<sup>[31]</sup> They also found that the micro-PL spectra resulted from two different kinds of states. The micro-PL spectrum in Fig. 7c seems to have the broad band under the sharp lines. However, this is not clear at the present stage.

Fig. 8 shows the temperature dependence of micro-PL spectra measured through the 0.6- $\mu\text{m}$  aperture. The temperature was ranged from 4 to 60 K. The excitation power is 100  $\mu\text{W}$ . Fig. 8A and b is obtained from lower- and higher-energy regions, respectively. These spectra reveal that the peaks have Lorentzian line shapes. The linewidths shown in Fig. 8A, which come from larger QDs, are almost constant until 20 K and increase rapidly above 30 K. At 60 K, they are  $\sim 3.5$  meV, which are about six times larger than that at 4 K. The behavior shown in Fig. 8A is similar to the result in the report of InAs QDs.<sup>[32]</sup> With increasing the temperature, excitons in the ground state are gradually scattered into higher states by the absorption of acoustic phonons. The increase in the FWHMs with temperature shown in Fig. 8A is a result of the increase of the scattering rate. On the other hand, the linewidths shown in Fig. 8B, which come from smaller QDs, hardly increase with the temperature. These results reveal that the degree of the linewidth broadening depends on the peak energy position, corresponding

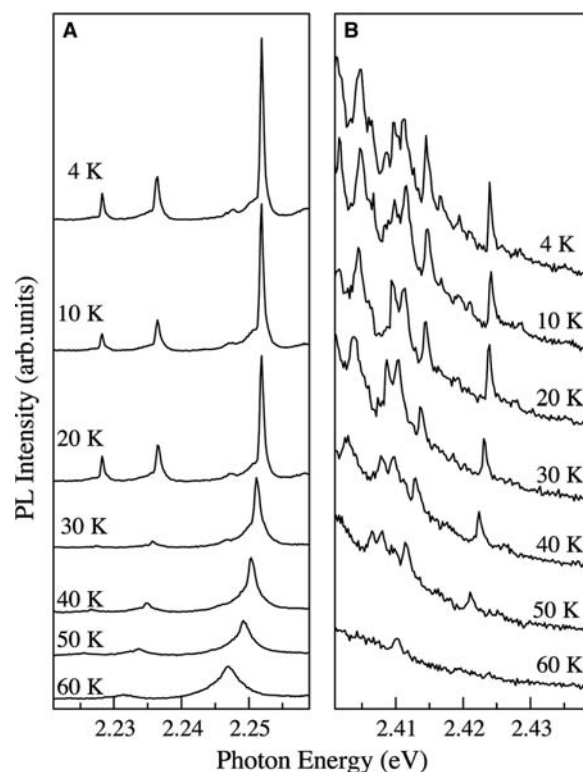


**Fig. 8** Temperature dependence of micro-PL spectra of CdSe QDs taken through the 0.6- $\mu\text{m}$  aperture. *Source:* From Ref.<sup>[24]</sup>.

to the QD size, and that the linewidths of the smaller QDs are less temperature-dependent than those of the larger QDs. The difference shown in Fig. 8A and b might be able to be explained with the use of the energy level spacing of CdSe QDs. The smaller QDs have larger energy level spacing than the larger QDs because the smaller QDs have larger confinement energy, resulting in the reduction in the scattering rate of excitons from the ground state to higher states. As a result, the linewidths of smaller QDs are considered to be less temperature-dependent, as shown in Fig. 8B.

### Selectively Excited Photoluminescence

A 500-W Xe lamplight dispersed with a 0.3-m monochromator served as a tunable light source for selectively excited PL measurements. The light was focused on the sample with rectangle shape using a microscope objective. The spectral width of the dispersed light was about 0.3 nm at 500 nm. The sample was mounted on a cold finger in vacuum in a small, continuous gas flow cryostat. The luminescence was collected using optical glass fibers, dispersed with a 0.5-m single-grating monochromator, and detected with a CCD camera cooled by liquid nitrogen. Fig. 9 shows the PL spectra of CdSe QDs at different



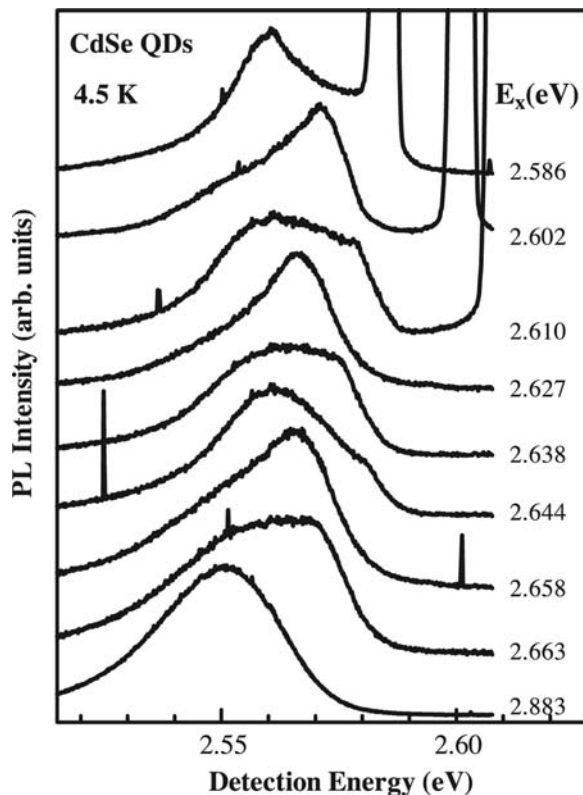


**Fig. 9** Photoluminescence spectra of 1.6 ML CdSe coverage sample at different excitation energies at 4.5 K.

excitation energy at 4.5 K. The spectrum at the bottom of Fig. 9 is measured for excitation above the band-gap energy of the ZnSe barrier layers. In this spectrum, there is a peak at 2.551 eV with a FWHM of 30 meV, which originates from CdSe QDs.<sup>[27]</sup> The shape of this spectrum is almost the same as that excited by a He–Cd laser. The broad spectral width is a result of the inhomogeneous size of CdSe QDs.<sup>[24,28]</sup> When the excitation energy decreases, the PL intensities are dramatically reduced. In addition, the spectra have a number of shape features at higher detection energies, as shown in Fig. 9. These peak positions depend upon the excitation energy. However, the features of the PL spectra in Fig. 9 do not seem to change regularly with decreasing excitation energy. These results are considered to be due to the selective excitation of QDs with different sizes in their ground states or in their excited states.

To clarify the origin of the spectra in Fig. 9, the PL spectra of CdSe QDs are measured successively in the excitation energy range from 2.82 to 2.55 eV at 4.5 K. Fig. 10 shows a contour map of the PL intensity of CdSe QDs as a function of the detection energy and the excitation energy. Energy scale of the abscissa is expanded as compared with that of the ordinate. Horizontal sections at several excitation energies correspond to the PL spectra in Fig. 9. The abrupt and

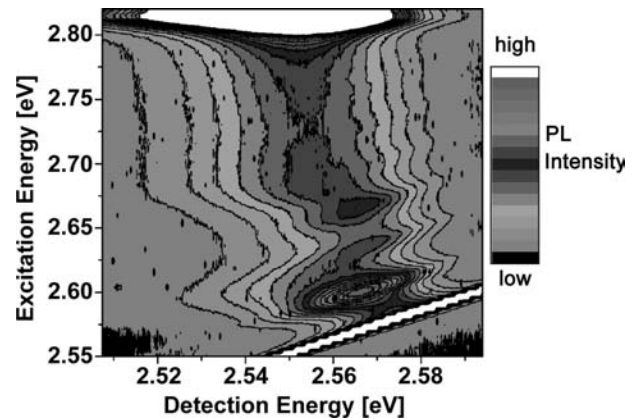


**Fig. 10** Contour map of PL intensity of CdSe QDs at 4.5 K as a function of detection energy and excitation energy.

quite strong absorption edge is clearly observed at 2.81-eV excitation energy for whole detection energy, which corresponds to the band-gap energy of the ZnSe barrier layer. This reveals that carriers generated in the ZnSe barrier layers diffuse in the sample efficiently into CdSe QDs and then emit luminescence there. This result indicates that CdSe QDs with high quality are formed on ZnSe surfaces.

At lower PL detection energy below approximately 2.54 eV in Fig. 10, a quite weak absorption band is observed at about 2.60-eV excitation energy, which is independent of detection energy, and a step-like broad absorption band above 2.675-eV excitation energy is also found, which continues up to ZnSe barrier absorption edge at 2.81-eV excitation energy. Moreover, several sharp absorption structures appear at higher PL detection energy, as shown in Fig. 10. The energy differences of these peaks are found to be roughly independent of the detection energy. These energy separations are estimated to be about 30 meV, which corresponds to the longitudinal-optical (LO) phonon energy in CdSe/ZnSe systems. Particularly, multiple LO-phonon structures up to the 6th order are clearly observed at around 2.58-eV detection energy. These phonon structures are terminated at the band-gap energy of ZnSe barrier layer. As compared with the PL excitation spectra of ZnCdSe reference quantum wells, absorption peaks from heavy- and light-hole excitons are not observed in that of CdSe QDs. These results indicate that the excitons in CdSe QDs are relaxed by multiple LO-phonon processes, resulting from strong confinement of excitons in zero-dimensional structures. Above the ZnSe band-gap energy, phonon structures in PL spectra are not observed, as shown in the PL spectrum at the bottom of Fig. 9, which is a result of the continuum states in the ZnSe layers.

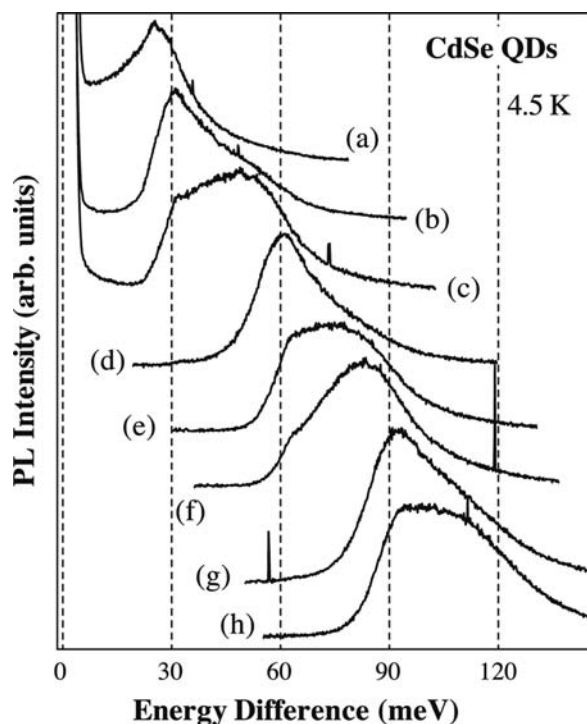


**Fig. 11** Photoluminescence spectra of CdSe QDs at 4.5 K as a function of the energy difference between the excitation and detection energies. These PL spectra are the same as those in Fig. 9. Photoluminescence spectrum at the bottom in Fig. 9 is not used in this figure.

To investigate the details of the relaxation process, we rearrange the PL spectra of CdSe QDs at 4.5 K as a function of the energy differences between the excitation and detection energies, as shown in Fig. 11. These spectra are obtained by horizontally shifting the PL spectra in Fig. 9 by the amount corresponding to the excitation energies. Although, as mentioned above, the spectra have the peaks at around 30, 60, and 90 meV, the peak positions are slightly dependent on excitation energies, as shown in Fig. 11. A peak is found at 25 meV in spectrum (a) in Fig. 11. This energy agrees with the 1-LO-phonon energy of CdSe bulk. This indicates that pure CdSe region exists in QDs, which seems to be inconsistent with the results of TEM measurements.<sup>[33–35]</sup> The spectra (b), (c), and (d) in Fig. 11 have peaks at 31 meV, and the spectra (e), (f), and (g) in Fig. 11 have peaks at 62 meV, corresponding to the 1-LO- and 2-LO-phonon energies of ZnSe bulk, respectively.

The relationship between phonon energy and detection energy of phonon structures can be obtained from Figs. 9 and 11. Fig. 12 shows the 1-LO- and 2-LO-phonon energies as functions of the detection energy of the phonon structures in PL spectra, which are obtained from Fig. 10. For detection at lower-energy side, the observed 1-LO- and 2-LO-phonon energies

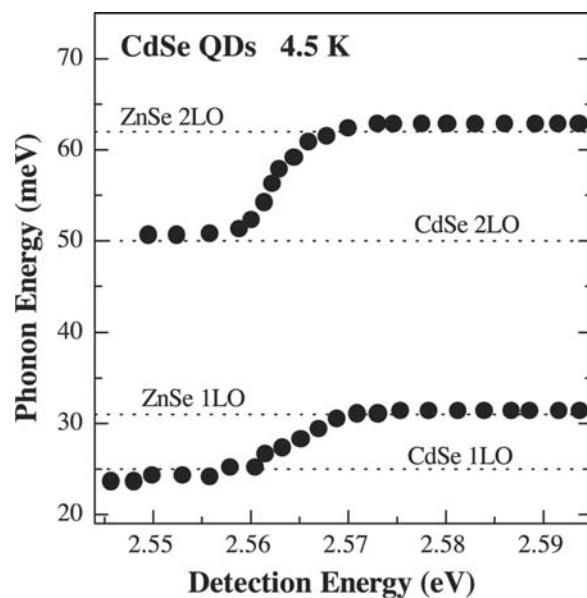


**Fig. 12** 1-LO- and 2-LO-phonon energies as functions of the detection energy of the phonon structures in PL spectra, which are based on the results shown in Fig. 10.

are estimated to be 25 and 50 meV, respectively, which agree with the LO-phonon energies of CdSe bulk. For higher detection energy side, phonon replicas can be resolved with energies of 31 and 62 meV, which correspond to the LO-phonon energies of ZnSe bulk. The size of CdSe QDs at higher detection energy is smaller than that at lower detection energy. This means that the wave functions of excitons at lower detection energy are confined better inside CdSe QDs than those at higher detection energy. Therefore for detection at lower-energy side (larger QDs), excitons are more interacted with the LO phonons of CdSe QDs, resulting in relaxation by using CdSe LO phonons, as shown in Fig. 12. On the other hand, the excitons at higher detection energies (smaller QDs) are weakly localized and their wave functions extend to the surrounding ZnSe barrier layers. Therefore excitons are more interacted with LO phonons of ZnSe barrier layer. As a result, excitons are relaxed by using ZnSe LO phonons, as shown in Fig. 12. At middle detection energy region (from 2.56 to 2.67 eV), phonon energies gradually change from 25 to 31 meV. These phonon energies might be a result of the contributions of both ZnSe and CdSe phonons or of ZnCdSe mixed crystals. The investigations of the Raman spectra of ZnCdSe bulk mixed crystal have shown that the LO-phonon spectra vs. crystal composition are the one-mode type,<sup>[36]</sup> indicating that the LO-phonon energy has changed monotonically with composition. It is difficult to clarify that excitons are relaxed by using both CdSe and ZnSe LO phonons or ZnCdSe LO phonons at middle detection energy region.

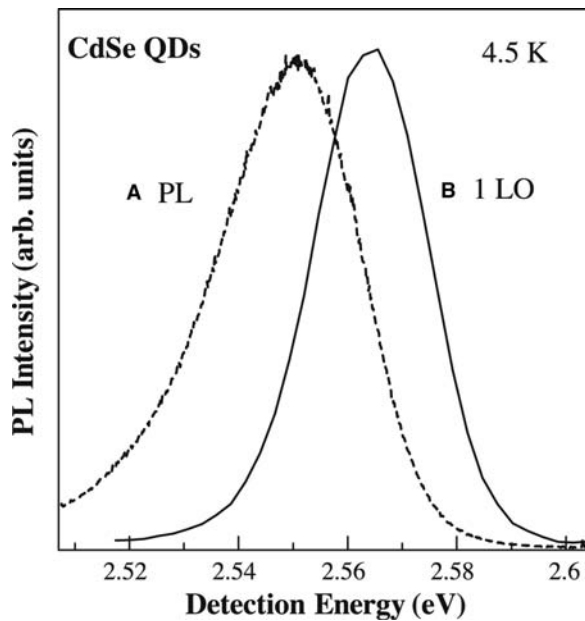


**Fig. 13** (A) Photoluminescence spectrum excited at 2.833 eV above the ZnSe band-gap energy at 4.5 K and (B) a distribution curve of PL intensity related with the 1-LO-phonon structure obtained from Fig. 10.

Next, the effect of interactions between CdSe QDs will be discussed. Fig. 13A shows a PL spectrum excited at 2.833 eV for above ZnSe band-gap energy at 4.5 K, which has a peak at 2.551 eV. A distribution curve of PL intensity related with the 1-LO-phonon structure is also shown in Fig. 13b, which is obtained from Fig. 10. This curve has a peak at 2.565 eV. The distribution curve (b) in Fig. 13 shifts to higher detection energy by about 14 meV than the PL spectrum (a) in Fig. 13. In the case of InAs QDs on GaAs substrates, the intensity curves of LO phonons were identical to PL spectra for the above GaAs band-gap excitation.<sup>[30]</sup> This difference in the peak positions in Fig. 13a and b is considered to be a result of the interaction between CdSe QDs.

Because wave functions at higher excited states of CdSe QDs are more extended than those at the ground states, the interactions between the wave function of QDs become stronger. Then, when CdSe QDs are excited at higher excitation energy, carriers can easily move from smaller QDs to larger QDs. As a result, lower detection energy side in PL intensity is enhanced, as shown in the spectrum in Fig. 13A. The broad absorption band at 2.675-eV excitation shown in Fig. 10 is considered to result from the strong interactions between the wave functions of QDs. This broad absorption band is continuous with the ZnSe barrier absorption edge.

On the other hand, because wave functions are confined better at the ground states in CdSe QDs, the interactions between the wave function of QDs are

quite weak. Then, when CdSe QDs are excited at lower excitation energy, PL is obtained from the same CdSe QDs. Consequently, the distribution curve in Fig. 13B is considered to represent real size distribution curve of CdSe QDs. However, the weak absorption, which is independent of detection energy, is obtained at 2.60-eV excitation energy in Fig. 10. This might result from the weak interaction between wave functions of QDs at the ground states.

Recently, carrier relaxation dynamics of CdSe QDs have been investigated by time-resolved PL measurements,<sup>[37]</sup> revealing that the decay time at higher-energy side is decreased with increasing detection energy. This result is considered to be due to the interactions between CdSe QDs, which is consistent with that of the selectively excited PL measurements.

## CONCLUSION

We have investigated the formation and optical properties of self-organized CdSe QDs on ZnSe (001) surfaces with the use of TEM and PL measurements. CdSe QDs with high quality are naturally formed on ZnSe surfaces by MBE when the thickness of CdSe layers is less than about 2 ML. CdSe QDs show a strong green emission even at room temperature. The polarization dependences of PL from CdSe QDs exhibit that the PL spectra are strongly polarized parallel to the  $[1\bar{1}0]$  direction. The CdSe coverage dependence of polarization PL spectra indicates that PL polarization degrees increase with QD formation.

Using micro-PL, single CdSe QD has high-resolved sharp lines, indicating zero-dimensional density of states of the QDs. It is found that the linewidths of the larger-size QDs are more temperature-dependent than those of smaller ones, suggesting to be a result of the difference in the energy level spacing of CdSe QDs.

The carrier relaxation mechanisms in self-organized CdSe QDs have been also investigated by selectively excited PL measurements. The contour map of PL intensity of CdSe QDs reveals that the strong and abrupt absorption edge of the ZnSe barrier layer is clearly observed for whole detection energy. In addition, photoexcited carriers that form excitons are relaxed by emitting multiple LO phonons in CdSe QDs, resulting from the strong confinement of excitons in zero-dimensional structures. At low and high detection energy, LO phonons of CdSe and ZnSe are dominated for relaxation process, respectively. The weak absorption and broad absorption bands observed at lower PL detection energy in the contour map can be interpreted by the interactions between wave functions of CdSe QDs. Stronger interactions between wave functions of CdSe QDs at higher excitation energy induce the difference in the peak positions between

PL spectrum in Fig. 13A and the distribution curve in Fig. 13B. Therefore the distribution curve in Fig. 13B is considered to represent the real size distribution curve of CdSe QDs.

## ACKNOWLEDGMENTS

The authors would like to thank Prof. Koichi Inoue, Dr. Takeshi Ota, Dr. Yasuhiro Murase, and Mr. Nobuhiro Yasui of Osaka University for experimental supports and useful discussions. The authors are also grateful to Prof. Yoshihiko Hirotsu, Dr. Takeshi Hanada, and Mr. Takeshi Ishibashi of Osaka University for TEM operations and Prof. Kazuo Murase and Dr. Kenichi Oto of Osaka University for electron-beam lithography and liftoff techniques.

## REFERENCES

- Freeman, M.R.; Awschalom, D.D. Femtosecond probes of magnetic phenomena: Spin-polarization spectroscopy in dilute-magnetic-semiconductor quantum wells. *J. Appl. Phys.* **1990**, *67*, 5102–5107.
- Haase, M.; Qiu, J.; DePuydt, J.; Cheng, H. Blue-green laser diodes. *Appl. Phys. Lett.* **1991**, *59*, 1272–1274.
- Ema, K.; Kuwata-Gonokami, M.; Shimizu, F. All-optical sub-Tbits/s serial-to-parallel conversion using excitonic giant nonlinearity. *Appl. Phys. Lett.* **1991**, *59*, 2799–2801.
- Ding, J.; Jeon, H.; Ishihara, T.; Hagerott, M.; Nurmikko, A.V.; Luo, H.; Samarth, N.; Furdyna, J. Excitonic gain and laser emission in ZnSe-based quantum wells. *Phys. Rev. Lett.* **1992**, *69*, 1707–1710.
- Bagnall, D.M.; Chen, Y.F.; Zhu, Z.; Yao, T.; Koyama, S.; Shen, M.Y.; Goto, T. Optically pumped lasing of ZnO at room temperature. *Appl. Phys. Lett.* **1997**, *70*, 2230–2232.
- Esaki, L.; Tsu, R. Superlattice and negative differential conductivity in semiconductor. *IBM J. Res. Develop.* **1970**, *14*, 61–65.
- Gershoni, D.; Temkin, H.; Dolan, G.J.; Dunsmuir, J.; Chu, S.N.G.; Panish, M.B. Effects of two-dimensional confinement on the optical properties of InGaAs/InP quantum wire structures. *Appl. Phys. Lett.* **1988**, *53*, 995–997.
- Kapon, E.; Simhony, S.; Bhat, R.; Hwang, D.M. Single quantum wire semiconductor lasers. *Appl. Phys. Lett.* **1989**, *55*, 2715–2717.
- Tsuchiya, M.; Gaines, J.M.; Yan, R.H.; Simes, R.J.; Holtz, P.O.; Coldren, L.A.; Petroff, P.M. Optical anisotropy in a quantum-well-wire array with two-dimensional quantum confinement. *Phys. Rev. Lett.* **1989**, *62*, 466–469.
- Goni, A.R.; Pfeiffer, L.N.; West, K.W.; Pinczuk, A.; Baranger, H.U.; Stormer, H.L. Observation of quantum wire formation at intersecting quantum wells. *Appl. Phys. Lett.* **1992**, *61*, 1956–1958.
- Nagamune, Y.; Tsukamoto, S.; Nishioka, M.; Arakawa, Y. Growth process and mechanism of nanometer-scale GaAs dot-structures using MOCVD selective growth. *J. Cryst. Growth* **1993**, *126*, 707–717.
- Tsutui, K.; Hu, E.; Wilkinson, W. Reactive ion etched II–VI quantum dots: Dependence of etched profile on pattern geometry. *Jpn. J. Appl. Phys.* **1993**, *32*, 6233–6236.
- Goldstein, L.; Glas, F.; Marzin, J.; Charasse, M.; LeRoux, G. Growth by molecular beam epitaxy and characterization of InAs/GaAs strained-layer superlattices. *Appl. Phys. Lett.* **1985**, *47*, 1099–1101.
- Leonard, D.; Krishnamurthy, M.; Reaves, C.; DenBaars, S.; Petroff, P. Direct formation of quantum-sized dots from uniform coherent islands of InGaAs on GaAs surfaces. *Appl. Phys. Lett.* **1993**, *63*, 3203–3205.
- Fafard, S.; Leonard, D.; Merz, J.L.; Petroff, P.M. Selective excitation of the photoluminescence and the energy levels of ultrasmall InGaAs/GaAs quantum dots. *Appl. Phys. Lett.* **1994**, *65*, 1388–1390.
- Marzin, J.-Y.; Gerard, J.-M.; Izrael, A.; Barrier, D.; Bastard, G. Photoluminescence of single InAs quantum dots obtained by self-organized growth on GaAs. *Phys. Rev. Lett.* **1994**, *73*, 716–719.
- Oshinowo, J.; Nishioka, M.; Ishida, S.; Arakawa, Y. Highly uniform InGaAs/GaAs quantum dots (~15 nm) by metalorganic chemical vapor deposition. *Appl. Phys. Lett.* **1994**, *65*, 1421–1423.
- Grundmann, M.; Christen, J.; Ledentsov, N.; Böhrer, J.; Bimberg, D.; Ruvimov, S.; Werner, P.; Richter, U.; Gösele, U.; Heydenreich, J.; Usti-nov, V.; Egorov, A.; Zhukov, A.; Kop'ev, P.; Alferov, Zh. Ultrannarrow luminescence lines from single quantum dots. *Phys. Rev. Lett.* **1995**, *74*, 4043–4046.
- Steer, M.J.; Mowbray, D.J.; Tribe, W.R.; Skolnick, M.S.; Sturge, M.D.; Hopkinson, M.; Cullis, A.G.; Whitehouse, C.R. Electronic energy levels and energy relaxation mechanisms in self-organized InAs/GaAs quantum dots. *Phys. Rev., B* **1996**, *54*, 17738–17744.
- Heitz, R.; Veit, M.; Ledentsov, N.N.; Hoffmann, A.; Bimberg, D.; Ustinov, V.M.; Kop'ev, P.S.; Alferov, Zh.I. Energy relaxation by multiphonon processes in InAs/GaAs quantum dots. *Phys. Rev., B* **1997**, *56*, 10435–10445.
- Maehashi, K.; Morota, N.; Murase, Y.; Nakashima, H. Molecular beam epitaxial growth of ZnSe films on vicinal GaAs(110) substrates. *Jpn. J. Appl. Phys.* **1999**, *38*, 1339–1342.
- Maehashi, K.; Morota, N.; Murase, Y.; Yasui, N.; Shikimi, A.; Nakashima, H. Formation of the charge balanced ZnSe/GaAs(110) interfaces by molecular beam epitaxy. *J. Cryst. Growth* **1999**, *201/202*, 486–489.
- Murase, Y.; Noma, T.; Maehashi, K.; Nakashima, H. Formation and photoluminescence of stacked CdSe quantum dots grown by molecular beam epitaxy. *J. Vac. Sci. Technol., B* **2001**, *19*, 1459–1462.
- Maehashi, K.; Yasui, N.; Murase, Y.; Ota, T.; Noma, T.; Nakashima, H. Formation and characterization of self-organized CdSe quantum dots. *J. Electron. Mater.* **2000**, *29*, 542–548.

25. Kirmse, H.; Schneider, R.; Rabe, M.; Neumann, W.; Henneberger, F. Transmission electron microscopy investigation of structural properties of self-assembled CdSe/ZnSe quantum dots. *Appl. Phys. Lett.* **1998**, *72*, 1329–1331.
26. Xin, S.; Wang, P.; Yin, A.; Yin, C.; Dobrowolska, M.; Merz, J.; Furdya, J. Formation of self-assembling CdSe quantum dots on ZnSe by molecular beam epitaxy. *Appl. Phys. Lett.* **1996**, *69*, 3884–3886.
27. Maehashi, K.; Yasui, N.; Murase, Y.; Shikimi, A.; Nakashima, H. Formation of self-organized CdSe quantum dots on ZnSe(100) surfaces by molecular beam epitaxy. *Appl. Surf. Sci.* **2000**, *166*, 322–325.
28. Maehashi, K.; Yasui, N.; Ota, T.; Noma, T.; Murase, Y.; Nakashima, H. Structural and optical properties of CdSe/ZnSe self-organized quantum dots. *J. Cryst. Growth* **2001**, *227–228*, 1116–1120.
29. Murase, Y.; Ota, T.; Yasui, N.; Shikimi, A.; Noma, T.; Maehashi, K.; Nakashima, H. Temperature dependence of photoluminescence spectra of self-organized CdSe quantum dots. *J. Cryst. Growth* **2000**, *214/215*, 770–773.
30. Ota, T.; Murase, Y.; Noma, T.; Maehashi, K.; Nakashima, H.; Oto, K.; Murase, K. Micro-photoluminescence from CdSe quantum dots. *J. Cryst. Growth* **2000**, *214/215*, 778–781.
31. Kim, J.C.; Rho, H.; Smith, L.; Jackson, H.E.; Lee, S.; Dobrowolska, M.; Furdyna, J.K. Temperature-dependent micro-photoluminescence of individual CdSe self-assembled quantum dots. *Appl. Phys. Lett.* **1999**, *75*, 214–216.
32. Ota, K.; Usami, N.; Shiraki, Y. Temperature dependence of microscopic photoluminescence spectra of quantum dots and quantum wells. *Physica, E* **1998**, *2*, 573–577.
33. Strassburg, M.; Kutzer, V.; Pohl, U.W.; Hoffmann, A.; Broser, I.; Ledentsov, N.N.; Bimberg, D.; Rosenauer, A.; Fischer, U.; Gerthsen, D.; Krestnikov, I.L.; Maximov, M.V.; Kop'ev, P.S.; Alferov, Zh.I. Gain studies of (Cd, Zn)Se quantum islands in a ZnSe matrix. *Appl. Phys. Lett.* **1998**, *73*, 942–944.
34. Kümmell, T.; Weigand, R.; Bacher, G.; Forchel, A.; Leonardi, K.; Hommel, D.; Selke, H. Single zero-dimensional excitons in CdSe/ZnSe nanostructures. *Appl. Phys. Lett.* **1998**, *73*, 3105–3107.
35. Litvinov, D.; Rosenauer, A.; Gerthsen, D.; Ledentsov, N.N. Character of the Cd distribution in ultrathin CdSe layers in a ZnSe matrix. *Phys. Rev., B* **2000**, *61*, 16819–16826.
36. Lozykowski, H.J.; Shastri, V.K. Excitonic and Raman properties of ZnSe/Zn<sub>1-x</sub>Cd<sub>x</sub>Se strained-layer quantum wells. *J. Appl. Phys.* **1991**, *69*, 3235–3242.
37. Ota, T.; Murase, Y.; Maehashi, K.; Nakashima, H.; Watatani, C.; Edamatsu, K.; Itoh, T.; Oto, K.; Murase, K. Investigation of carrier relaxation dynamics in single CdSe/ZnSe self-organized quantum dot by time-resolved micro-photoluminescence. *J. Electron. Mater.* **2001**, *30*, 448–452.

# Cadmium Selenide Quantum Rods: Anisotropy

Liang-shi Li

A. Paul Alivisatos

*Department of Chemistry, University of California–Berkeley,  
Berkeley, California, U.S.A.*

## INTRODUCTION

Semiconductor nanocrystals, also known as “quantum dots,” have been intensively studied because of their novel properties caused by quantum confinement and their potential to be used in making electro-optical devices.<sup>[1,2]</sup> The colloidal nanocrystals synthesized by wet chemistry methods have in particular drawn much attention because of their chemical processibility<sup>[3,4]</sup> and their capability to be incorporated into various matrices such as conducting polymer<sup>[5–8]</sup> and biological systems.<sup>[9–12]</sup> Studies of CdSe nanocrystals with the wurtzite lattice structure have played an important role in our understanding of quantum confinement<sup>[13,14]</sup> and of the growth mechanism of nanocrystals.<sup>[15]</sup> The recent advances in synthesizing rodlike,<sup>[16–18]</sup> disc-like,<sup>[19,20]</sup> and more exotically shaped<sup>[21,22]</sup> nanocrystals have opened a new field to study the shape dependence of their properties. In this article, we review some of the work on CdSe nanorods (or “quantum rods”) that has been done recently in our group. First, we talk about the synthesis of CdSe quantum rods with tightly controlled variable lengths and diameters and second, their optical and dielectric properties. Because the alignment of the quantum rods is desirable for both fundamental studies and applications, we will also cover our work on the formation of the lyotropic nematic phase of these geometrically anisotropic objects in solution, and the large-scale alignment of the quantum rods by taking advantage of the liquid crystalline phase. Then we will finish by briefly discussing some of their potential applications.

## GROWTH OF CdSe QUANTUM RODS

Generally, CdSe nanocrystals are made by injecting the mixture of precursors (dimethyl cadmium and Se powder dissolved in tributylphosphine) into a hot surfactant protected in inert gases.<sup>[15]</sup> The thermal decomposition of the precursors results in the nucleation of the CdSe particles and the subsequent

crystal growth. Typically, the precursors are injected at 360°C and then the temperature is lowered to 250°C for crystal growth. When trioctylphosphine oxide (TOPO) is used as the surfactant, the CdSe nanocrystals have nearly spherical shape (aspect ratio <1.2). These nanocrystals are coated by organic molecules so that they do not aggregate easily and can be dispersed in organic solvents. These nanocrystals have wurtzite lattice structure, like CdSe bulk crystals. Recently, Peng et al. found that when a mixture of TOPO and hexylphosphonic acid (HPA) is used as the surfactant, rodlike CdSe nanocrystals can be made.<sup>[17]</sup> The CdSe nanorods also have a wurtzite crystalline lattice, and are elongated in the *c*-crystallographic axis. However, the surfactant mixture of TOPO and HPA does not give us the capability to control the monodispersity or to tune the length and width of the quantum rods. This is because the growth of the nanorods is so fast that the growth of the nanocrystals is very sensitive to subtle changes in the reaction conditions such as speed of precursor injection. Consequently, nanocrystals with broad size distribution and even with different shapes are made.<sup>[21]</sup> On the other hand, it was observed that when HPA is replaced with a phosphonic acid with a longer alkyl chain, tetradecylphosphonic acid (TDPA), the speed of the growth of the nanocrystals is dramatically reduced,<sup>[23]</sup> so much so that only nanorods with very small aspect ratio are made without further addition of the precursors during the growth process. To tune the growth rate of the nanorods, we use a mixture of HPA and TDPA with TOPO, and we found that the controllability of the synthesis is greatly improved.<sup>[24,25]</sup> By changing the molar ratio of HPA and TDPA, the speed of growth of the nanorods in both transverse and longitudinal directions can be tuned, so that the nanorods with tightly controlled dimensions can be made reproducibly.<sup>[24,25]</sup> Extraction of part of the reaction solution and subsequent quenching with a large excess of toluene at different time in the early stage of the reaction results in nanorods with different lengths but almost the same diameter. In our study, the HPA/TDPA ratio is



systematically changed and the products examined by transmission electron microscopy (TEM). A HPA/TDPA ratio of 1:3 results in nanorods with large diameter (>4 nm) but small aspect ratio (1–10), whereas increasing the amount of HPA in the mixture but with fixed total molar ratio of the phosphonic acids and TOPO produces nanorods with smaller diameter but large aspect ratio. When the HPA/TDPA ratio is higher than 3:1, the reaction loses control and nanoparticles with broad size and shape distribution are produced. Fig. 1 shows the electron transmission micrographs (TEM) of CdSe quantum rods made with this method. No size selection was performed on the samples after syntheses.

Despite the success in controlling the length and width of CdSe quantum rods, little is known about their microscopic growth mechanism, mainly because of the lack of suitable experimental techniques. However, based on the analysis of the products made by varying the growth conditions, a few observations have been made.<sup>[21,23]</sup> First, rod growth is possible only when the monomer concentration is high enough. The monomers are believed to be some complexes of cadmium that formed at high temperature and may be very different from the species stable at room temperature, and their nature is not yet known. To maintain the monomer concentration for the quantum rods to steadily grow along the *c* axis, the presence of phosphonic acids is required. Second, when the monomers

are depleted, unless more Cd and Se precursors are added the quantum rods will grow fatter and shorter so that eventually nearly spherical nanocrystals are formed. This suggests that the formation of elongated CdSe nanocrystals would be kinetically favored whereas that of nearly spherical ones thermodynamically favored. Third, the growth of the CdSe quantum rods is unidirectional. This is based on the observation that when the amount of HPA in the surfactant mixture is higher than needed for quantum rod growth, nanocrystals with unidirectional shapes such as pencil-, arrow-, or treelike shapes are made.<sup>[21]</sup>

Based on the observations described above, so far two mechanisms have been proposed: selective adsorption<sup>[21]</sup> and diffusion-controlled growth mechanisms.<sup>[23]</sup> The selective adsorption mechanism is based on the different chemical affinity of phosphonic acids to the different faces on the nanocrystals, and thus the different energy of crystal faces in the presence of phosphonic acid molecules. According to this model, all crystal faces except (001) is coated by the phosphonic acid molecules, and therefore the nanocrystals grow unidirectionally to form rods. The diffusion-controlled growth mechanism assumes the mass transport of the monomers to be the determining step of the nanocrystal growth, so that the concentration gradient of the monomers in the bulk solution and the stagnant solution around the quantum rods determines the shape evolution of the CdSe nanocrystals.

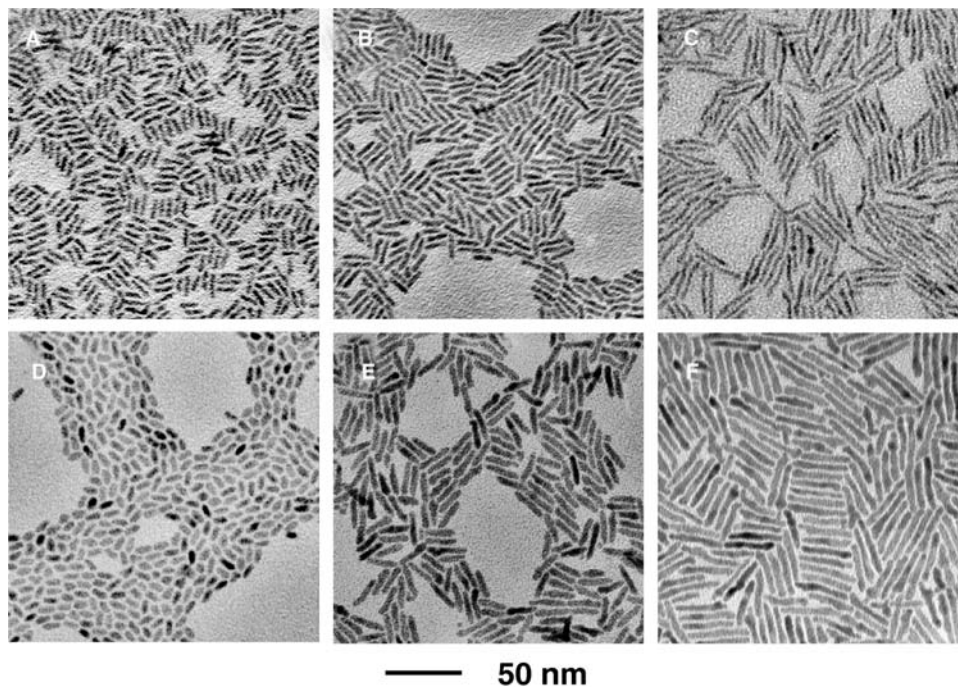


**Fig. 1** TEM images of CdSe quantum rods made by using a mixture of HPA, TDPA, and TOPO as the surfactant. By changing the molar ratio of HPA and TDPA, the length and width of the nanocrystals can be systematically controlled. *Source:* Reproduced with permission from Ref.<sup>[53]</sup>. © 2002 American Chemical Society.

## OPTICAL PROPERTIES

As is well known for (nearly) spherical semiconductor nanocrystals, the absorption and photoluminescence spectra of rodlike nanocrystals are also dependent on their sizes, i.e., both lengths and widths.<sup>[25]</sup> Fig. 2 shows the length and width dependence of the photoluminescence energy of CdSe quantum rods with various lengths and width. The overall tendency is that with increasing length or width, the luminescence shifts to lower energy, which is the same as that of spherical nanocrystals. These figures also show that the width dependence is stronger than the length dependence in the size range we have studied. This is because the confinement of the photo-excited carriers is mainly imposed in the lateral directions.

It has been well known that elongation in the shape of nanocrystals results in anisotropy in their optical properties.<sup>[26,27]</sup> Even in the spherical CdSe nanocrystals, polarization of the photoluminescence in the *a*-*b* crystal plane has been theoretically predicted<sup>[28,29]</sup> and experimentally verified,<sup>[30]</sup> because of crystal field splitting in the hexagonal wurtzite crystal structure. The perturbation treatment of the nearly spherical CdSe nanocrystals<sup>[31]</sup> suggested that the ellipticity compensated for the crystal field splitting and even changed the order of the lowest electronic states and thus the polarization of the fluorescence. To study the polarization of the photoluminescence emitted from CdSe quantum rods, single-molecule fluorescence spectroscopy was performed on CdSe quantum rods with variable aspect ratio at room temperature.<sup>[24]</sup> CdSe quantum rods are sparsely deposited on a glass substrate and are excited by a circularly polarized CW Ar<sup>+</sup> laser (480 nm). A beam displacement crystal is used to spatially split the photoluminescence from individual quantum rods into two beams with

perpendicular polarizations and subsequently imaged on a CCD camera at the same time. The rotation of the crystal and therefore the rotation of the polarization directions of the two split beams show the oscillating intensity. Images of luminescence from a single quantum rod with 10:1 aspect ratio (Fig. 3A) demonstrate the change of the fluorescence intensity with detection angle along the two perpendicular polarization directions. The polarization factor *r* for this rod sample is determined to be 86% by fitting the intensity ratio  $r = (I_{\parallel} - I_{\perp}) / (I_{\parallel} + I_{\perp})$  vs. detection angle with a sinusoidal function (filled circle in Fig. 3B). In comparison, the polarization factor of spherical dots is usually less than 10% (filled triangles in Fig. 3B). We have measured samples with aspect ratios from 1:1 to 30:1 at room temperature. The polarization factor changes rapidly from nearly zero to ~70% (e.g.,  $I_{\parallel}:I_{\perp} \cong 5.5:1$ ) when aspect ratio increases from 1:1 to 2:1, then remains almost constant afterward (Fig. 3C).

Semiempirical pseudopotential calculation performed on the CdSe quantum rods<sup>[24,32]</sup> has shown that the linearly polarized photoluminescence from the CdSe quantum rods is indeed a result of the energy level crossing in the highest occupied electronic states. Qualitatively, the lowest excited electronic state of the bulk CdSe semiconductor arises when an electron is excited from an occupied Se 4*p* atomic orbital to an empty Cd 5*s* orbital. This excitation is distributed throughout many unit cells of the solid, and there is a pronounced dependence of the bandgap on the size of the crystals. Because the *p* atomic orbitals are degenerate, the interaction between Se 4*p* orbitals in the crystal field and the effect of spin-orbit coupling play important roles in the electronic structure of CdSe nanocrystals. The empirical pseudopotential calculation was performed to study the evolution of the electronic structure when CdSe nanocrystals evolve

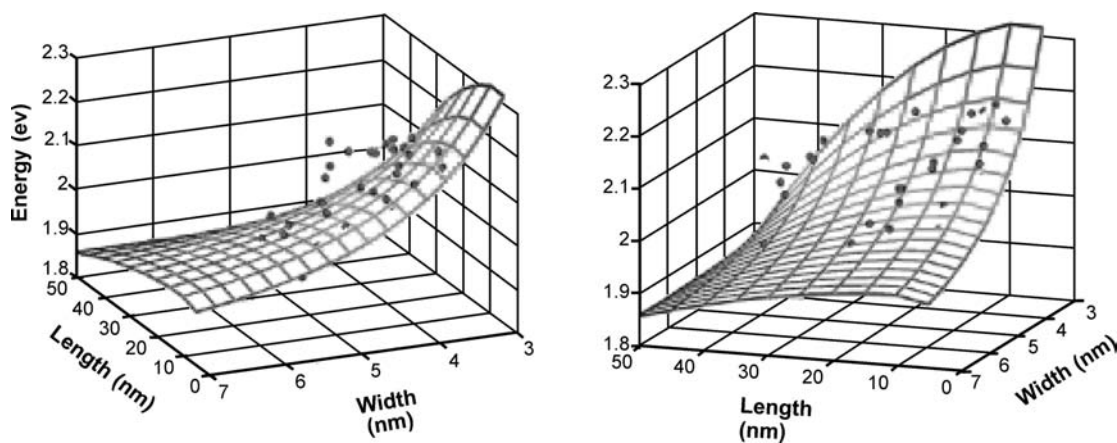


**Fig. 2** The photoluminescence energy of CdSe quantum rods as a function of their length and width. It is more sensitive to width than to length. The meshes drawn are the best polynomial fit. *Source:* Reproduced with permission from Ref.<sup>[25]</sup>. © 2001 American Chemical Society.

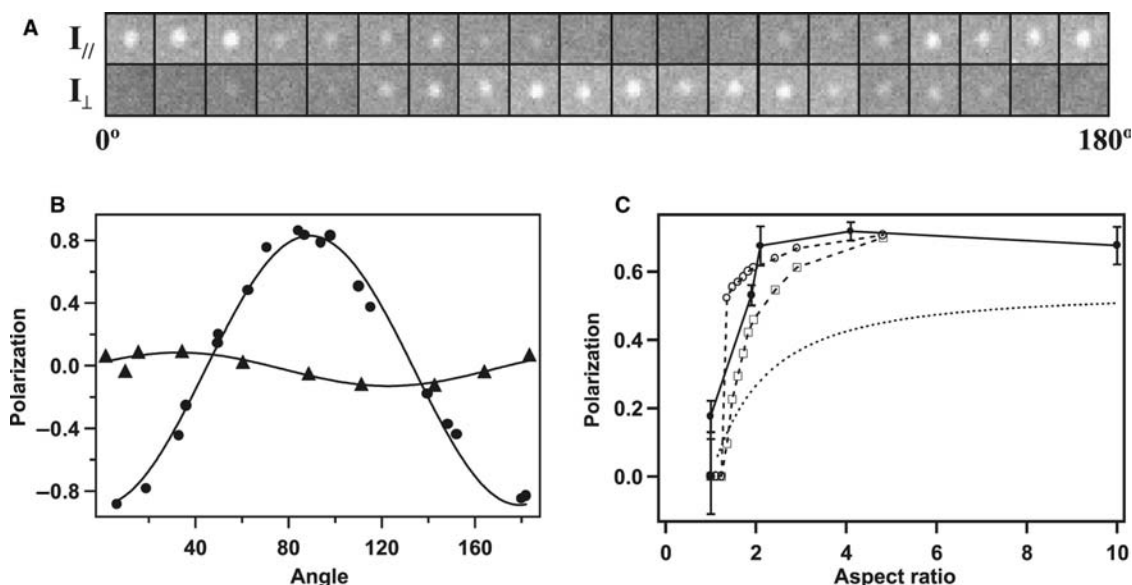


**Fig. 3** Luminescence polarization measurements from individual quantum rods at room temperature. (A) Luminescence images of a single rod simultaneously recorded in two perpendicular polarization directions at detection angles changing from  $0^\circ$  to  $180^\circ$ . The rods have an aspect ratio of 10:1. (B) The intensity ratio  $r = (I_{\parallel} - I_{\perp}) / (I_{\parallel} + I_{\perp})$  calculated from the luminescence images in A (filled circles) and fitted with sinusoidal function (solid line) to give a polarization factor of 0.86. The data from spherical dots (filled triangles) show much smaller polarization factors. (C) Polarization factor vs. aspect ratio. The filled circles with error bars are from experiments, unfilled circles from empirical pseudopotential calculations for 0 K, and squares from empirical pseudopotential calculations for room temperature. Each experimental data point was obtained by measuring more than 40 individual rods. The lines simply connect data points, and the dotted line is from the fitting based on the dielectric model proposed in Ref.<sup>[27]</sup> to the data points. *Source:* Reproduced with permission from Ref.<sup>[24]</sup>. © 2001 AAAS.

from a spherical to a rodlike shape. We started from a spherical dot with a diameter of 3.0 nm and increased the aspect ratio by inserting a cylindrical segment along the  $c$  axis. The four lowest unoccupied and four highest occupied electronic states were calculated for quantum rods with aspect ratios ranging from 1:1 to 5:1. As the aspect ratio increases from unity, a crossover of the two highest occupied electronic states occurs at an aspect ratio of 1.25 (Fig. 4). Before this point, the electronic states with predominantly Se  $4p_x$ ,  $4p_y$  components have higher energy than that of states that are mainly  $4p_z$ . The electronic energy levels of these states all increase with increasing size. The  $4p_z$  orbital has greater momentum projected onto the  $c$  axis of the crystal compared to  $4p_x$  and  $4p_y$ , so the energy levels with greater  $4p_z$  component are more sensitive to the rod length. These states exchange position relative to each other at an aspect ratio greater than 1.25. Calculations for the cases of 2.1- and 3.8-nm-wide rods show similar results and the crossing point is 1.25 and 1.36 respectively.

## DIELECTRIC PROPERTIES

In contrast to their well-studied optical and electronic properties, the dielectric properties of CdSe nanocrystals

have been seldom investigated, especially their permanent dipole moment. On one hand, theoretical analyses have suggested the presence of a permanent dipole moment along the  $c$  crystallographic axis because of the lack of inversion symmetry of the wurtzite structure,<sup>[33–35]</sup> on the other hand, dielectric dispersion measurements performed on concentrated solutions of the spherical CdSe<sup>[36,37]</sup> nanocrystals have revealed a permanent dipole moment as a result of surface trapped charges, while the contribution of the noncentrosymmetric lattice is negligible in the size range studied.

However, the surface charge model does not address the direction of the permanent dipole moment, nor does the dielectric dispersion measurement itself because it does not distinguish the uniaxial nature of the spherical nanocrystals. The elongated shape of the CdSe nanorods gives us an opportunity to answer this question.

Transient electric birefringence (TEB) is a method that has been widely used to study the rotational diffusion, size, shape, and polarization properties of objects with anisotropic geometry, especially macromolecules and biological systems such as DNA, viruses, and proteins.<sup>[38,39]</sup> The transient behavior of the birefringence reflects the alignment mechanism of these molecules in response to a pulsed electric field. In particular, for a suspension of elongated objects

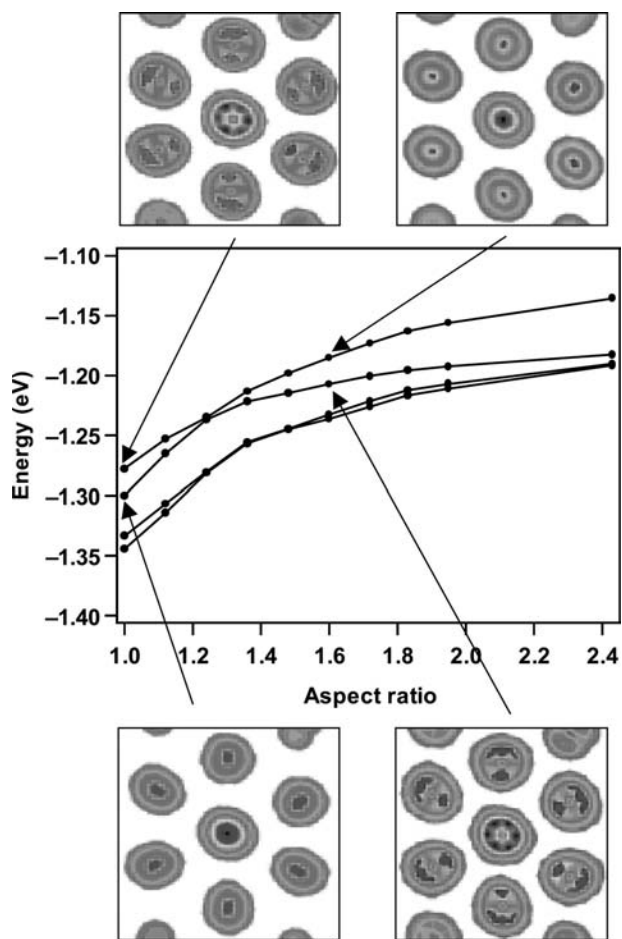


**Fig. 4** The four highest occupied electronic states of 3.0-nm-diameter CdSe quantum rods calculated with an empirical pseudopotential method with different aspect ratios. The two highest energy levels have a crossing at an aspect ratio around 1.25. Insets: Contour plots of the two highest occupied states for rods with an aspect ratio of 1.00 and 1.60, respectively. They show the projection of electron density around some Se atoms in a plane, with density increasing from red to blue. This plane intersects the rod in the middle, perpendicular to the long axis ( $c$  axis). The crossing over of the predominantly  $p_{x,y}$  and predominantly  $p_z$  levels vs. aspect ratio can be seen. *Source:* Reproduced with permission from Ref.<sup>[24]</sup>. © 2001 AAAS.

with axial symmetry and a large aspect ratio ( $\geq 5$ ), the rising ( $\Delta n_r$ ) and falling ( $\Delta n_f$ ) edges of the birefringence (difference between the refractive indices of the sample along and perpendicular to the applied electric field) on application and removal of an external electric field are given, respectively, by<sup>[40]</sup>

$$\begin{aligned} \Delta n_r(t) &= \Delta n_s \left( 1 + \frac{\gamma - 2}{2(\gamma + 1)} \exp(-6D_R t) \right. \\ &\quad \left. - \frac{3\gamma}{2(\gamma + 1)} \exp(-2D_R t) \right) \\ \Delta n_f(t) &= \Delta n_s \exp(-6D_R t) \end{aligned} \quad (1)$$

where  $\Delta n_s = \Delta n_r(t \rightarrow \infty)$ ,  $\gamma = \mu_z^2 / [k_b T (\alpha_{\parallel} - \alpha_{\perp})]$ ,  $\mu_z$  is the screened value of the electric dipole moment along the long axis of the rods,  $\alpha_{\parallel}$  and  $\alpha_{\perp}$  the static electric polarizability along and perpendicular to the long axis, respectively, and  $D_R$  the rotational diffusion constant around an axis normal to the long axis of the rods. According to Eq. 1, the rise time of the birefringence will be slower than the fall time only when there is a permanent dipole moment along the long axes of the nanorods. Benoit<sup>[40]</sup> used this method to study tobacco mosaic virus (TMV), and from the symmetric falling and rising edges he concluded that TMVs do not have permanent dipole moment in aqueous solution.

To measure the electric birefringence we use the procedure of O'Konski and Zimm,<sup>[41,42]</sup> as described in detail in Ref.<sup>[43]</sup>. The quantum rods under electric field have birefringence of the same sign as nitrobenzene, indicating that the nanorods align along (rather than perpendicular to) the electric field. Fig. 5A shows a typical transient electric birefringence curve measured for CdSe nanorods.<sup>[43]</sup> As suggested by Eq. 1, the asymmetric falling and rising edges indicate the existence of a permanent electric dipole moment along the long axis. The hexagonal symmetry of CdSe nanorods allows us to approximately treat them as being axially symmetric, thus we can fit the TEB curves with Eq. 1 to obtain the rotational diffusion constants and the ratio of permanent dipole moment to the polarizability anisotropy ( $\gamma$ ).

To get the permanent dipole moment from  $\gamma$ , we calculate the electric polarizability of CdSe nanorods by assuming a revolute prolate shape for the nanorods, so that the principle axes of polarizability coincide with the geometrical axes. The polarizabilities are calculated by<sup>[44]</sup>

$$\alpha_{\parallel(\perp)} = \varepsilon_0 v (\varepsilon_{\parallel(\perp)} - 1) / [1 + A_{\parallel(\perp)} (\varepsilon_{\parallel(\perp)} - 1)]$$

where  $v$  is the volume of individual nanorod,  $\varepsilon$ 's the relative dielectric constants between nanorods and the solvent along ( $\parallel$ ) or perpendicular ( $\perp$ ) to the long axis of the nanorods, and  $A$ 's the geometrical factors that can be calculated from the dimension of the nanorods.<sup>[45]</sup> The dielectric constants of CdSe nanorods are taken as bulk material values ( $\varepsilon_{\parallel} = 10.2$ ,  $\varepsilon_{\perp} = 9.33$ ), and that of cyclohexane is taken as 2.02.

The unscreened permanent dipole moments  $\mu_z$  of five nanorod samples are plotted in Fig. 5B vs. their volume. Considering the ensemble nature of the measurement, these are the root mean square dipole moment of the samples. It is an average not only over the finite size distribution, but also over the possible structural distribution. An empirical pseudopotential

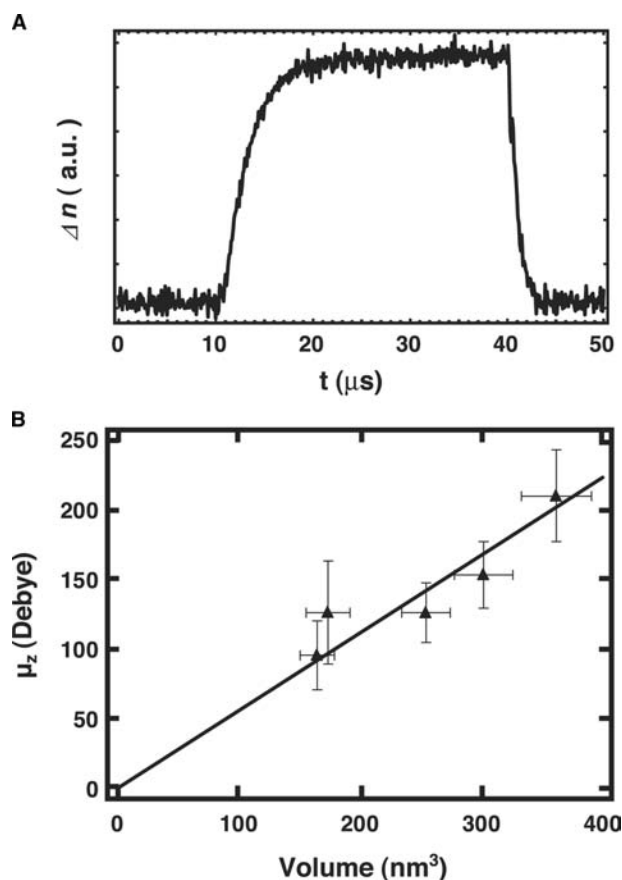


**Fig. 5** (A) A typical TEB curve (in linear scale) on the application and subsequent removal of the electric field. The asymmetric rising and falling edges indicate the existence of a permanent dipole moment along the long axis of the quantum rods. In this particular case, the CdSe quantum rods are 4.8 nm wide and 30 nm long. (B) The unscreened dipole moment of CdSe quantum rods with different sizes. The solid triangles are the values measured with the TEB method, and the straight line is the best fit, with a slope of  $0.19 \mu\text{C}/\text{cm}^2$ . Source: Modified with permission from Ref.<sup>[43]</sup>. © 2003 American Physical Society.

calculation showed that the dipole moment strongly depends on the detailed structure of the nanocrystals and can vary significantly on small structural changes.<sup>[35]</sup> Within the experimental error, however, a linear dependence of  $\mu_z$  vs. volume is obtained, and no correlation between rod length or width and  $\mu_z$  can be realized. This is consistent with theoretical analyses that the polarity is intrinsic to the crystallographic lattice of CdSe because of the lack of inversion symmetry. Our results are not consistent with a random dipole moment resulting from trapped surface charges, as proposed for spherical CdSe nanocrystals. From the slope, we get the polarization of CdSe nanorods to be  $0.19 \mu\text{C}/\text{cm}^2$  along the  $c$  crystallographic axis, which is in good agreement with the value of  $0.6 \mu\text{C}/\text{cm}^2$  as estimated<sup>[34]</sup> from a phenomenological

rule that was proved experimentally only for ferroelectric materials.

### LYOTROPIC LIQUID CRYSTALLINE PHASE OF CdSe QUANTUM ROD DISPERSION

The anisotropic properties of the quantum rods may find applications in devices such as solar cells, polarizing light-emitting diodes, and electro-optical switches. However, to achieve this, it is important to align the quantum rods on a large scale. Recently, enormous effort has been devoted to aligning the geometrically anisotropic nanoscale objects such as nanowires, nanotubes, and nanorods.<sup>[16,46]</sup> On the other hand, it has been well known that rodlike or disclike objects, when dispersed in a solvent to a high enough concentration, will spontaneously form lyotropic liquid crystalline phases in which the geometrically anisotropic objects are orientationally ordered. This is clearly illustrated by the rigid rod model proposed by Onsager in 1949.<sup>[47]</sup> In this model, the free energy of a dispersion of long, thin spherocylinders (aspect ratio  $>100$ ) in a solvent can be obtained by a virial expansion,<sup>[48]</sup>

$$\frac{\Delta F}{NkT} = \frac{\mu^0}{kT} + \ln(\Lambda^3 \rho) - 1 + \left\{ \int f(\Omega) \ln[4\pi f(\Omega)] d\Omega + \frac{1}{2} \rho \iint v_{\text{exclusive}}(\Omega, \Omega') f(\Omega) f(\Omega') d\Omega d\Omega' + \dots \right\}$$

where  $f(\Omega)$  is the orientational distribution function of the rodlike objects, and  $\rho$  the number density of the spherocylinders. The first term in the curved bracket is called orientational entropy, which favors a random orientational distribution; while the second term is called packing entropy, which favors an orientationally ordered phase. The packing entropy term dominates only when the density of the rods is high enough so that a nematic lyotropic phase can spontaneously form. Famous examples include rodlike organic macromolecules such as poly( $\gamma$ -benzyl  $\alpha$ ,L-glutamate) (PBLG)<sup>[49]</sup> rodlike tobacco mosaic virus,<sup>[50]</sup> etc. Lyotropic liquid crystalline mesophases based on all-inorganic minerals have also been known for quite a long time, and have been reviewed by several authors;<sup>[48,51,52]</sup> however, this area has rarely been explored because of the lack of the interest other than purely academic purposes, in contrast with their thermotropic counterpart. The recent success in the synthesis of the highly soluble and processible metallic semiconductors and magnetic nanocrystals with anisotropic geometries<sup>[16–20]</sup> and the need for aligning them in order to use their anisotropic properties have provided us a new opportunity to study these liquid crystalline phases.



The most important requirement for the formation of lyotropic liquid crystalline phases is the high dispersion concentration, which is not trivial for most of the inorganic nanocrystals. Recently, we have succeeded in making the nematic phase of solution of CdSe quantum rods in organic solvent.<sup>[53]</sup> The solvent we use is anhydrous cyclohexane or anhydrous hexanes, which can dissolve CdSe quantum rods to a volume percentage up to 60%. Dilute solutions of quantum rods in a vial are concentrated by blowing with dry nitrogen, and a birefringent phase starts to appear at a certain concentration as observed under an optical polarizing microscope. The solutions are then transferred to NMR tubes or capillary tubes for further study. Special care has to be taken during the process to avoid the exposure of the solution to the air, because the inclusion of even trace amount of water would result in thermoreversible gelation,<sup>[54–56]</sup> which is also often seen in suspensions of organic rodlike polymers and has been attributed to the degradation of the solvent. Fig. 6A shows isotropic-liquid crystalline phase separation in a 300- $\mu\text{m}$ -diameter capillary tube, and the characteristic disclinations for a nematic phase observed in a thin layer of the solution of CdSe  $3.8 \times 40\text{-nm}$  quantum rods. The red color is due to the absorption of this quantum rod sample.

The formation of the liquid crystalline phase allows us to align the quantum rods by taking advantage of the collective behavior in a liquid crystalline solution.<sup>[57]</sup> Various methods have been applied to align the liquid crystalline materials such as electric and magnetic fields as well as curved surfaces. Fig. 7 shows the X-ray diffraction patterns of a liquid crystalline solution of CdSe quantum rods in a 300  $\mu\text{m}$  capillary tube.<sup>[58]</sup> These rods have a length of  $\sim 60$  nm and width of 3.0 nm. In both figures, the capillary tube remains vertical. In Fig. 7A, the sharp arcs in the vertical position are due to (002) planes of the CdSe crystalline lattice within individual quantum rods. The high intensity and sharpness of the arcs are determined by the elongated shape of the CdSe quantum rods. The anisotropy of the pattern demonstrates macroscopic alignment of the long axis of the rods. Consistently, in Fig. 7B the diffuse arcs in the equator direction correspond to the lateral distance of the quantum rods, suggesting the short axis is aligned as well. Together, the patterns demonstrate the preferential alignment of the CdSe quantum rods along the capillary tube axis direction, which is attributed to the curved surface of the capillary tube. It can be estimated that about 70% of the quantum rods are oriented within  $20^\circ$  from the axis of the capillary tube.

Alignment of lyotropic liquid crystalline solution with magnetic fields has been reported.<sup>[59]</sup> Even when none of the components is ferromagnetic, the anisotropy of the magnetic susceptibility of individual

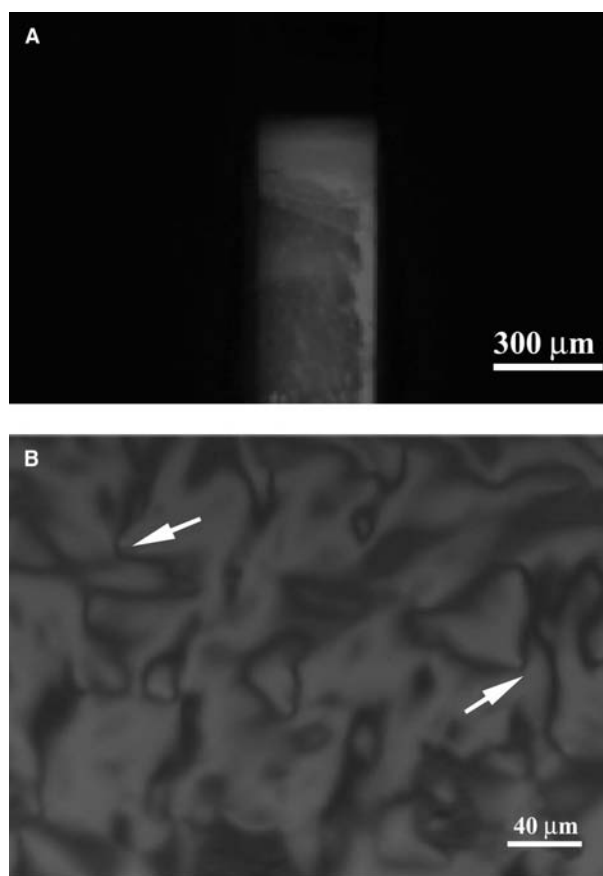


**Fig. 6** (A) Isotropic-liquid crystalline phase separation observed between crossed polarizers. The birefringent liquid crystalline phase is on the bottom due to the high density, while the isotropic phase on the top is not visible because of the complete extinction of the transmitted light. (B) The typical defect structures observed in a thin film of liquid crystalline solution of CdSe nanorod solution. The arrows point to the disclinations. The red color is due to the absorption of the CdSe nanocrystals. *Source:* Modified with permission from Ref.<sup>[53]</sup>. © 2002 American Chemical Society.

constituent molecules adds up because the long-range orientational correlation in the liquid crystalline phases, and therefore the energy gain because of the alignment can easily exceed the thermal fluctuation  $kT$ . The alignment of CdSe quantum rods in a liquid crystalline solution under a magnetic field is observed with NMR. A few drops of deuterated chloroform are added into a solution of CdSe quantum rods in cyclohexane, which has a high enough concentration to have both isotropic and liquid crystalline phases present. Fig. 8 shows our preliminary result of DNMR spectrum observed in a 500-MHz spectrometer at  $30^\circ\text{C}$ . The central peak is confirmed to be due to the isotropic part of the solution, while the other two peaks are due to the quadruple splitting of the deuterium nuclei in the anisotropic liquid crystalline



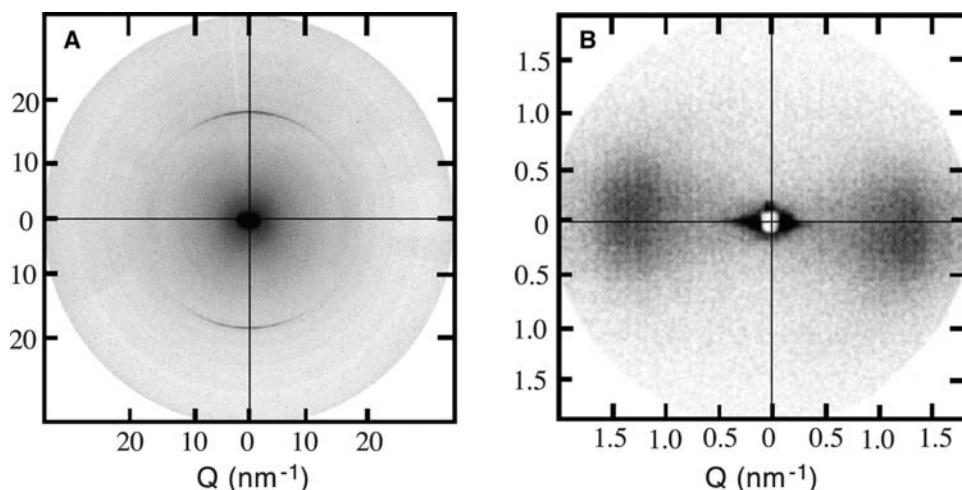


**Fig. 7** Wide-angle X-ray diffraction and small-angle X-ray scattering of the same nematic solution of CdSe quantum rods in a 300- $\mu\text{m}$ -thick capillary tube show the preferential alignment of these quantum rods along the axis of the capillary tube. In both measurements, the capillary tube is held vertically. (A) Wide-angle X-ray diffraction pattern. The vertical sharp, intense arcs correspond to the (002) planes of wurtzite CdSe lattice. At about the same radius, weak arcs corresponding to the (100) and (101) planes can also be seen, but they are much more diffuse. (B) Small-angle X-ray scattering pattern. The two diffuse arcs at  $Q \sim 1.5 \text{ nm}^{-1}$  on the equator corresponds to the lateral spacing between the rods in the nematic phase. The arcs corresponding to the longitudinal spacing are not resolved. *Source:* Reproduced with permission from Ref.<sup>[58]</sup>. © 2003 Wiley-VCH.

medium. The comparison of the spectrum with a typical Pake powder pattern<sup>[60,61]</sup> indicates the alignment of the C–D bond in  $\text{CDCl}_3$ , presumably as a result of both the alignment of the quantum rods by the magnetic field and the interaction between the nanorods and  $\text{CDCl}_3$  molecules. The exact mechanism is still under investigation.

In spite of the formation of the liquid crystalline phase of the CdSe quantum rod solution, tremendous challenges exist in the alignment of the CdSe quantum rods, especially on a substrate. It is not straightforward to apply the techniques used in liquid crystal display industry such as rubbed surfaces.<sup>[62]</sup> Furthermore, the volatile nature of the solvent in the CdSe liquid crystalline solution and the propensity of the solution to gel on the exposure to the air or water make the solution difficult to handle.

## POTENTIAL APPLICATIONS

Even though the development of the devices with semiconductor quantum rods is still in the early stage, the recent success in using CdSe quantum rods–conjugated polymer composite to make solar cell with high power conversion efficiency<sup>[63]</sup> has demonstrated the huge potential of the nanocrystals as an active component in electro-optical devices. The solar cells made with inorganic–organic composite take advantage of both the high carrier mobility in inorganic semiconductors and the easy processibility of organic polymers. Furthermore, the presence of the interface between two

materials with very different electron affinities enhances the charge separation of the photo-excited carriers. The high extinction coefficient of CdSe nanocrystals makes a very thin film ( $\sim 100 \text{ nm}$ ) of the composite adequate to absorb all of the solar radiation. The application of CdSe quantum rods in the

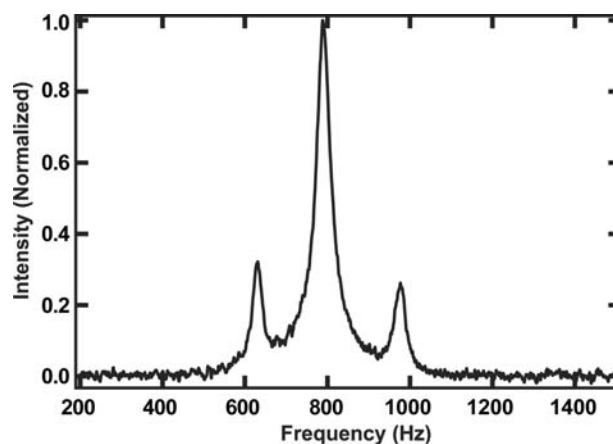


**Fig. 8** The deuterium NMR spectrum of a solution of CdSe quantum rods at 30°C in which isotropic phase and liquid crystalline phase coexist. The solution is doped with  $\text{CDCl}_3$ . The central peak is caused by the isotropic part of the solution, which significantly broadens because of the high viscosity of the solution, while the two side peaks are caused by quadruple splitting of the deuterium nuclei in the liquid crystalline phase. The comparison with a powder pattern indicates the alignment of the quantum rods in the liquid crystalline solution.

composite, as compared to the nearly spherical nanocrystals, provides a natural path for electrical transport after the charge separation, so that the probability of recombination of photocarriers is reduced. Recently, a power conversion efficiency of 1.7% has been achieved by mixing  $7 \times 60$ -nm CdSe quantum rods with poly(3-hexylthiophene) (P3HT). The rod length dependence study shows that the charge transport improves substantially when the aspect ratio of the quantum rods increases from 1 to 10. Further improvement to the power conversion efficiency is still on the way, which includes the alignment of the quantum rods perpendicular to the film, the improvement to the interface between the nanocrystals and the polymer, and using nanocrystals of other materials such as CdTe. Other possible applications include polarizing light-emitting diodes and electro-optical switches by taking advantage of the anisotropic linear and non-linear optical properties of these quantum rods.

## CONCLUSIONS

In summary, we have discussed the recent development in the study of CdSe quantum rods. It is just the beginning of the investigation of the shape-dependent properties of semiconductor nanocrystals, and we believe the advent of the new methods to make nanocrystals with more complicated shapes, such as tetrapods and even dendritic inorganic nanocrystals,<sup>[21,22]</sup> will further advance this kind of study. In addition, the success in the macroscopic alignment of the nanorods provides us unique opportunities to investigate some anisotropic ensemble properties such as optical or X-ray absorption, surface selectivity of ligands, interaction between nanorods and solvent, etc. However, much work still needs to be done to make the nanorods applicable for devices. Currently work is under way in our laboratory to make the liquid crystalline solutions more robust so that they can survive various processing procedures. Furthermore, methods to align the nanorods on substrates have to be developed.

## REFERENCES

1. Alivisatos, A.P. Semiconductor clusters, nanocrystals, and quantum dots. *Science* **1996**, *271* (5251), 933–937.
2. Brus, L. Quantum crystallites and nonlinear optics. *Appl. Phys., A* **1991**, *53* (6), 465–474.
3. Steigerwald, M.L.; Alivisatos, A.P.; Gibson, J.M.; Harris, T.D.; Kortan, R.; Muller, A.J.; Thayer, A.M.; Duncan, T.M.; Douglass, D.C.; Brus, L.E. Surface derivatization and isolation of semiconductor cluster molecules. *J. Am. Chem. Soc.* **1988**, *110* (10), 3046–3050.
4. Schmid, G. Large clusters and colloids—metals in the embryonic state. *Chem. Rev.* **1992**, *92* (8), 1709–1727.
5. Colvin, V.L.; Schlamp, M.C.; Alivisatos, A.P. Light-emitting-diodes made from cadmium selenide nanocrystals and a semiconducting polymer. *Nature* **1994**, *370* (6488), 354–357.
6. Dabbousi, B.O.; Bawendi, M.G.; Onotsuka, O.; Rubner, M.F. Electroluminescence from CdSe quantum-dot polymer composites. *Appl. Phys. Lett.* **1995**, *66* (11), 1316–1318.
7. Huynh, W.U.; Peng, X.; Alivisatos, A.P. CdSe nanocrystal rods/poly(3-hexylthiophene) composite photovoltaic devices. *Adv. Mater.* **1999**, *11* (11), 923–927.
8. Tessler, N.; Medvedev, V.; Kazes, M.; Kan, S.H.; Banin, U. Efficient near-infrared polymer nanocrystal light-emitting diodes. *Science* **2002**, *295* (5559), 1506–1509.
9. Bruchez, M.; Moronne, M.; Gin, P.; Weiss, S.; Alivisatos, A.P. Semiconductor nanocrystals as fluorescent biological labels. *Science* **1998**, *281* (5385), 2013–2016.
10. Chan, W.C.W.; Nie, S.M. Quantum dot bioconjugates for ultrasensitive nonisotopic detection. *Science* **1998**, *281* (5385), 2016–2019.
11. Parak, W.J.; Boudreau, R.; Le Gros, M.; Gerion, D.; Zanchet, D.; Micheel, C.M.; Williams, S.C.; Alivisatos, A.P. Cell motility and metastatic potential studies based on quantum dot imaging of phagokinetic tracks. *Adv. Mater.* **2002**, *14* (12), 882–885.
12. Loweth, C.J.; Caldwell, W.B.; Peng, X.; Alivisatos, A.P.; Schultz, P.G. DNA-based assembly of gold nanocrystals. *Angew. Chem., Int. Ed. Engl.* **1999**, *38* (12), 1808–1812.
13. Efros, A.L.; Rosen, M. The electronic structure of semiconductor nanocrystals. *Annu. Rev. Mater. Sci.* **2000**, *30*, 475–521.
14. Nirmal, M.; Norris, D.J.; Bawendi, M.G.; Efros, A.L.; Rosen, M. Observation of the dark exciton in CdSe quantum dots. *Phys. Rev. Lett.* **1995**, *75* (20), 3728–3781.
15. Peng, X.; Wickham, J.; Alivisatos, A.P. Kinetics of II–VI and III–V colloidal semiconductor nanocrystal growth: “Focusing” of size distributions. *J. Am. Chem. Soc.* **1998**, *120* (21), 5343–5344.
16. Li, M.; Schnablegger, H.; Mann, S. Coupled synthesis and self-assembly of nanoparticles to give structures with controlled organization. *Nature* **1999**, *402* (6760), 393–395.
17. Peng, X.; Manna, L.; Yang, W.; Wickham, J.; Scher, E.; Kadavanich, A.; Alivisatos, A.P. Shape control of CdSe nanocrystals. *Nature* **2000**, *404* (6773), 59–61.
18. Chang, S.; Shih, C.; Chen, C.; Lai, W.; Wang, C.R.C. The shape transition of gold nanorods. *Langmuir* **1999**, *15* (3), 701–709.
19. Puntès, V.F.; Zanchet, D.; Erdonmez, C.K.; Alivisatos, A.P. Synthesis of hcp-Co nanodisks. *J. Am. Chem. Soc.* **2002**, *124* (43), 12874–12880.
20. Jin, R.C.; Cao, Y.W.; Mirkin, C.A.; Kelly, K.L.; Schatz, G.C.; Zheng, J.G. Photoinduced conversion of silver nanospheres to nanoprisms. *Science* **2001**, *294* (5548), 1901–1904.
21. Manna, L.; Scher, E.C.; Alivisatos, A.P. Synthesis of soluble and processable rod-, arrow-, teardrop-, and

- tetrapod-shaped CdSe nanocrystals. *J. Am. Chem. Soc.* **2000**, *122* (51), 12700–12706.
22. Jun, Y.; Lee, S.; Kang, N.; Cheon, J. Controlled synthesis of multi-armed CdS nanorod architectures using monosurfactant system. *J. Am. Chem. Soc.* **2001**, *123* (21), 5150–5151.
  23. Peng, Z.A.; Peng, X. Mechanisms of the shape evolution of CdSe nanocrystals. *J. Am. Chem. Soc.* **2001**, *123* (7), 1389–1395.
  24. Hu, J.; Li, L.-S.; Yang, W.; Manna, L.; Wang, L.-W.; Alivisatos, A.P. Linearly polarized emission from colloidal semiconductor quantum rods. *Science* **2001**, *292* (5524), 2060–2063.
  25. Li, L.-S.; Hu, J.; Yang, W.; Alivisatos, A.P. Band gap variation of size- and shape-controlled colloidal CdSe quantum rods. *Nano Lett.* **2001**, *1* (7), 349–351.
  26. El-Sayed, M.A. Some interesting properties of metals confined in time and nanometer space of different shapes. *Acc. Chem. Res.* **2001**, *34* (4), 257–264.
  27. Kovalev, D.; Benchorin, M.; Diener, J.; Koch, F.; Efros, A.L.; Rosen, M.; Gippius, N.A.; Tikhodeev, S.G. Porous Si anisotropy from photoluminescence polarization. *Appl. Phys. Lett.* **1995**, *67* (11), 1585–1587.
  28. Efros, A.L. Luminescence polarization of CdSe microcrystals. *Phys. Rev., B* **1992**, *46* (12), 7448–7458.
  29. Efros, A.L.; Rosen, M.; Kuno, M.; Nirmal, M.; Norris, D.J.; Bawendi, M. Band-edge exciton in quantum dots of semiconductors with a degenerate valence band: Dark and bright exciton states. *Phys. Rev., B* **1996**, *54* (7), 4843–4856.
  30. Empedocles, S.A.; Neuhauser, R.; Bawendi, M.G. Three-dimensional orientation measurements of symmetric single chromophores using polarization microscopy. *Nature* **1999**, *399* (6732), 126–130.
  31. Efros, A.L.; Rodina, A.V. Band-edge absorption and luminescence of nonspherical nanometer-size crystals. *Phys. Rev., B* **1993**, *47* (15), 10005–10007.
  32. Hu, J.; Wang, L.-W.; Li, L.-S.; Yang, W.; Alivisatos, A.P. Semiempirical pseudopotential calculation of electronic states of CdSe quantum rods. *J. Phys. Chem.* **2002**, *106* (10), 2447–2452.
  33. Huang, N.Q.; Birman, J.L. Origin of polarization in polar nanocrystals. *J. Chem. Phys.* **1998**, *108* (5), 1769–1772.
  34. Schmidt, M.E.; Blanton, S.A.; Hines, M.A.; Guyot-Sionnest, P. Polar CdSe nanocrystals: Implications for electronic structure. *J. Chem. Phys.* **1997**, *106* (12), 5254–5259.
  35. Rabani, E.; Hetényi, B.; Berne, B.J.; Brus, L.E. Electronic properties of CdSe nanocrystals in the absence and presence of a dielectric medium. *J. Chem. Phys.* **1999**, *110* (11), 5355–5369.
  36. Blanton, S.A.; Leheny, R.L.; Hines, M.A.; Guyot-Sionnest, P. Dielectric dispersion measurements of CdSe nanocrystal colloids: Observation of a permanent dipole moment. *Phys. Rev. Lett.* **1997**, *79* (5), 865–868.
  37. Shim, M.; Guyot-Sionnest, P. Permanent dipole moment and charges in colloidal semiconductor quantum dots. *J. Chem. Phys.* **1999**, *111* (15), 6955–6964.
  38. O'Konski, C.T. Kerr Effect. In *Encyclopedia of Polymer Science and Technology*; Interscience: New York, 1968; Vol. 9, 551–590.
  39. Yoshioka, K.; Watanabe, H. Dielectric Properties of Proteins II. Electric Birefringence and Dichroism. In *Physical Principles and Techniques of Protein Chemistry*; Leach, S.J., Ed.; Academic Press: New York, 1969; 335–367. Pt. A.
  40. Benoit, H. Contribution a L'Étude de L'Effet Kerr Présenté par Les Solutions Diluées de Macromolécules Rigides. *Ann. Phys. (Paris)* **1951**, *6*, 561–608.
  41. O'Konski, C.T.; Zimm, B.H. New method for studying electrical orientation and relaxation effects in aqueous colloids: Preliminary results with tobacco mosaic virus. *Science* **1950**, *111* (2875), 113–116.
  42. Newman, J.; Swinney, H.L. Length and dipole moment of TMV by laser signal-averaging transient electric birefringence. *Biopolymers* **1976**, *15*, 301–315.
  43. Li, L.-S.; Alivisatos, A.P. Origin and scaling of the permanent dipole moment in CdSe nanorods. *Phys. Rev. Lett.* **2003**, *90* (9), 097402.
  44. Böttcher, C.J.F. *Theory of Electric Polarization*; Elsevier Scientific: New York, 1973.
  45. Osborn, J.A. Demagnetizing factors of the general ellipsoid. *Phys. Rev.* **1945**, *67* (11), 351–357.
  46. Kim, F.; Kwan, S.; Akana, J.; Yang, P.D. Langmuir-Blodgett nanorod assembly. *J. Am. Chem. Soc.* **2001**, *123* (18), 4360–4361.
  47. Onsager, I. The effect of shape on the interaction of colloidal particles. *Ann. N. Y. Acad. Sci.* **1949**, *51* (4), 627–659.
  48. Vroege, G.J.; Lekkerkerker, H.N.W. Phase transitions in lyotropic colloidal and polymer liquid crystals. *Rep. Prog. Phys.* **1992**, *55* (8), 1241–1309.
  49. Robinson, C.; Ward, J.C. Liquid-crystalline structures in polypeptides. *Nature* **1957**, *180* (4596), 1183–1184.
  50. Bawden, F.C.; Pirie, N.W.; Bernal, J.D.; Fankuchen, I. Liquid crystalline substances from virus-infected plants. *Nature* **1936**, *138*, 1051–1052.
  51. Gabriel, J.-C.P.; Davidson, P. New trends in colloidal liquid crystals based on mineral moieties. *Adv. Mater.* **2000**, *12* (1), 9–20.
  52. Sonin, A.S. Inorganic lyotropic liquid crystals. *J. Mater. Chem.* **1998**, *8* (12), 2557–2574.
  53. Li, L.-S.; Walda, J.; Manna, L.; Alivisatos, A.P. Semiconductor nanorod liquid crystals. *Nano Lett.* **2002**, *2* (6), 557–560.
  54. Gunton, J.D.; San Miguel, M.; Sahni, P.S. The Dynamics of First Order Phase Transition. In *Phase Transitions and Critical Phenomena*; Domb, C., Lebowitz, J.L., Eds.; Academic Press: New York, 1983; Vol. 8, 269–482.
  55. Tohyama, K.; Miller, W.G. Network structure in gels of rod-like polypeptides. *Nature* **1981**, *289* (5800), 813–816.
  56. Frey, M.W.; Cuculo, J.A.; Ciferri, A.; Theil, M.H. A review of lattice theory for lyotropic liquid crystalline polymers, spinodal decomposition, and gel formation.

- J. M. S. Rev. Macromol. Chem. Phys., C **1995**, 35, 287–325.
57. Chandrasekhar, S. *Liquid Crystals*; University Press: Cambridge, 1992.
58. Li, L.-S.; Alivisatos, A.P. Semiconductor nanorod liquid crystals and their assembly on a substrate. *Adv. Mater.* **2003**, 15 (5), 408–411.
59. Firouzi, A.; Schaefer, D.J.; Tolbert, S.H.; Stucky, G.D.; Chmelka, B.F. Magnetic-field-induced orientational ordering of alkaline lyotropic silicate-surfactant liquid crystals. *J. Am. Chem. Soc.* **1997**, 119 (40), 9466–9477.
60. Forrest, B.J.; Reeves, L.W. New lyotropic liquid crystals composed of finite nonspherical micelles. *Chem. Rev.* **1981**, 81 (1), 1–14.
61. Seelig, J. Deuterium magnetic resonance: Theory and application to lipid membranes. *Q. Rev. Biophys.* **1977**, 10 (3), 353–418.
62. Jerome, B. Surface effects and anchoring in liquid crystals. *Rep. Prog. Phys.* **1991**, 54 (3), 391–451.
63. Huynh, W.U.; Dittmer, J.J.; Alivisatos, A.P. Hybrid nanorod–polymer solar cells. *Science* **2002**, 295 (5564), 2425–2427.

# Cadmium Sulfate Nanocrystals: Computational Analysis

**Stacie Nunes**

*Department of Physics, State University of New York, New Paltz, New York, U.S.A.*

**Zhigang Zhou**

**Jeffrey D. Evanseck**

*Center for Computational Sciences and Department of Chemistry and Biochemistry, Duquesne University, Pittsburgh, Pennsylvania, U.S.A.*

**Jeffrey D. Madura**

*Department of Chemistry and Biochemistry, Duquesne University, Pittsburgh, Pennsylvania, U.S.A.*

## INTRODUCTION

The challenge of creating functionalized, robust quantum confined group II–VI semiconductor nanoclusters (NCs) involves the ability to realize size-controlled and size-stable nanocrystallites. The size and stability issues are non-trivial problems that are at the forefront of nanotechnology research.<sup>[1–3]</sup> Several recent and key spectroscopic,<sup>[4–9]</sup> synthetic,<sup>[10,11]</sup> and engineering results have set the stage for timely computational studies that will make significant advances in the atomistic-level and fundamental understanding of the structure, stability, and aqueous assembly of CdS NCs and of higher-order NC architectures with unique physical properties. Building upon previous experimental and computational work, our research objective is to provide both fundamental insights into the aqueous assembly of CdS nanoclusters (our model is shown in Fig. 1), as well as practical knowledge used for the construction of higher-order nanocluster architectures with unique physical properties.

The first four sections of this work briefly review the experimental and theoretical knowledge about semiconductor nanocrystals. A more detailed coverage of experimental and theoretical work in semiconductor nanotechnology has been reported.<sup>[12]</sup> The last three sections cover the application of quantum mechanical (ab initio, DFT, and semiempirical) as well as hybrid quantum/molecular mechanical methods to characterize organic and peptide capped nanocrystals.

## SEMICONDUCTOR NANOCRYSTALS

In general, the chemical and physical properties of a substance do not depend on the amount of the sample.

However, when the size of a material fragment becomes sufficiently small this may no longer be true. It has been demonstrated in a wide range of semiconductors that many properties become dependent on cluster size once the cluster diameter is below some threshold value unique to the material being examined. The size dependency is observed in semiconductor fragments on the order of nanometers in diameter and referred to as nanoclusters. The changes occur as the cluster is transformed from a fragment of bulk material to a “molecule-like” cluster. There are two aspects of the transformation that play a role in this effect. First, as the cluster size decreases, the proportion of surface atoms to interior atoms increases substantially. Consequently, surface effects such as relaxation, rearrangement, dangling bonds, and other defects become more significant as the size of the nanocrystal decreases. Second, the density of states of a nanocrystal is altered as a result of the quantum size effect.<sup>[3,13–15]</sup> The alteration occurs as the cluster size is decreased because excitons that are delocalized over large distances in the bulk are increasingly confined. The electronic and optical properties of the clusters are particularly sensitive to changes in the density of states. These quantum dots with size-dependent electronic and optical properties have important potential applications as LEDs,<sup>[16]</sup> in solar cells<sup>[17]</sup> and for photoswitches. The quantum size effect and surface characteristics have also been shown<sup>[18,19]</sup> to be an important factor in the efficiency of photocatalysis of organic reactions by semiconductor nanocrystals.

The II–VI semiconductors are of interest for a variety of reasons. These materials are direct gap semiconductors with band gap energies in the visible spectrum. In addition, their chemical properties make them good candidates for the preparation of colloidal

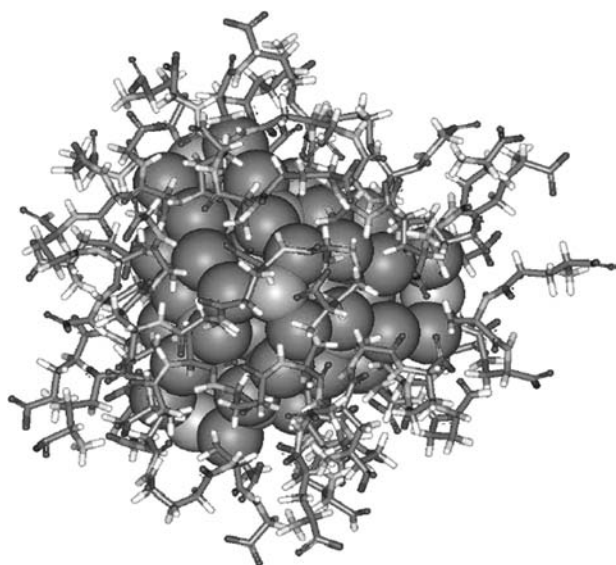


**Fig. 1** Structure of  $\text{Cd}_{32}\text{S}_{14}$  coated with 13  $(\gamma\text{-Glu-Cys})_3\text{-Gly}$  units (1066 atoms total) peptides. The yellow-colored spheres represent the sulfur and cadmium, respectively.

dispersions and organically capped clusters. In this entry we focus on the study of the electronic and optical properties of CdS nanoclusters.

### WELL-CHARACTERIZED CLUSTERS OF CdS AVAILABLE FOR STUDY

Over the last three decades experimental studies have demonstrated the effects of varying the size of semiconductor nanoclusters both qualitatively and quantitatively. For the most part, early work<sup>[20–23]</sup> was performed using samples that contained a distribution of cluster sizes. This work clearly demonstrated trends in the values of various properties with cluster size and established similarities between these trends in various materials. However, in order to study systematically the effect of changing cluster size both experimentally and theoretically it is desirable to have well-defined clusters of fixed and known composition. Semiconductor nanocrystals are prepared in different ways<sup>[3,15]</sup> but only one method has led to the preparation of well-characterized clusters of known composition and structure. Chemical synthesis of larger clusters from smaller precursor species has resulted in clusters in the size range of interest that have a core of bulk-like material. The cluster surface is passivated by saturating the dangling bonds with organic ligands. In addition to passivating the surface, the ligands improve the solubility of the clusters and function to maintain their integrity in solution. We describe below several ligand-capped clusters that are available for study.

One of the early significant developments in the synthesis of organically capped nanoclusters of CdS was the synthesis and subsequent characterization of  $[\text{Cd}_{17}\text{S}_4(\text{SPh})_{28}]^{2-}$  by X-ray crystallography,<sup>[24]</sup> where SPh is thiophenolate ( $\text{SC}_6\text{H}_5^-$ ) (Fig. 2). The inner core of this cluster  $\text{Cd}^{\text{I}}(\mu_4\text{-S})_4(\text{Cd}^{\text{c}})_{12}$  consists of CdS in the sphalerite (zincblende) form. This core is capped by four cages  $\{\text{S}(\text{Cd}^{\text{c}})_3(\mu\text{-SPh})_3\text{Cd}\}$  with structure similar to the wurtzite (hexagonal) lattice. Although the size of this cluster is not in the range of interest it was recognized that this species had the potential to serve as a precursor to larger clusters in the same family.

The first CdS cluster with a diameter in the range of interest to be synthesized and characterized<sup>[25]</sup> was  $\text{Cd}_{32}\text{S}_{14}(\text{SPh})_{36}\cdot\text{DMF}_4$ , a homolog of the  $[\text{Cd}_{17}\text{S}_4(\text{SPh})_{28}]^{2-}$  cluster described above. This larger cluster has an 82-atom bulk core similar in structure to that of its smaller homolog and is similarly capped by wurtzite-like (hexagonal) CdS units at four tetrahedral corners. The four solvent molecules are bound at these corners. Excitation, luminescence, and absorption spectra are available<sup>[25]</sup> for the crystallized molecular solid and for clusters dissolved in tetrahydrofuran (THF), *N,N*-dimethylformamide (DMF), and acetonitrile.

Synthesis and characterization of a superlattice structure from units consisting of two  $\text{Cd}_{17}\text{S}_4(\text{SCH}_2\text{CH}_2\text{OH})_{26}$  clusters covalently bound by a  $\mu\text{-SR}$  bridge has also been accomplished<sup>[26]</sup> (Fig. 3). These clusters are identical in structure to the  $[\text{Cd}_{17}\text{S}_4(\text{SPh})_{28}]^{2-}$  clusters described earlier<sup>[24]</sup> with  $-\text{CH}_2\text{CH}_2\text{OH}$  replacing the

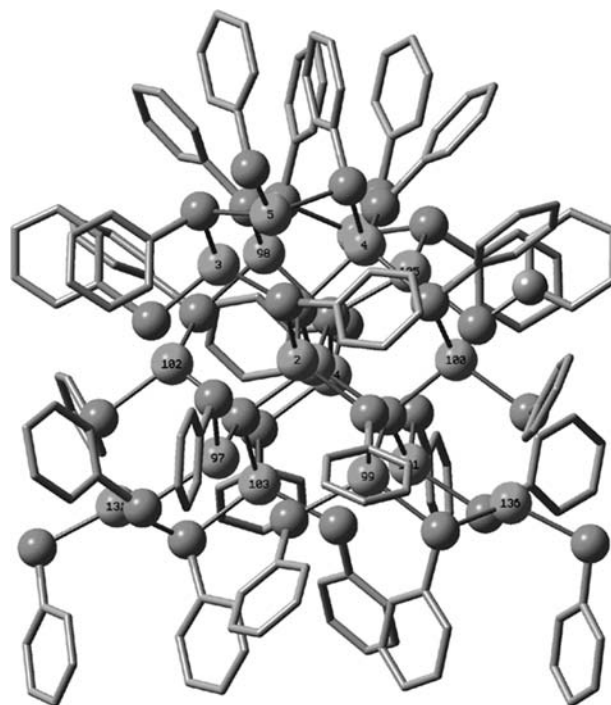


**Fig. 2** The structure of  $[\text{Cd}_{17}\text{S}_4(\text{SPh})_{28}]^{2-}$ . Source: From Ref.<sup>[24]</sup>.



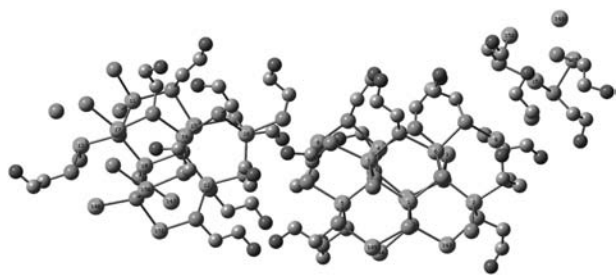


**Fig. 3** Basic unit of the superlattice described in Vossmeier et al.<sup>[26]</sup> Each unit consists of two covalently bound  $\text{Cd}_{17}\text{S}_4(\text{SCH}_2\text{CH}_2\text{OH})_{26}$  clusters.

phenyl groups and two vertices of the cluster left uncapped. In the superlattice solid, covalent  $\mu$ -SR bridges connect each  $\text{Cd}_{17}\text{S}_4(\text{SCH}_2\text{CH}_2\text{OH})_{26}$  cluster to four others, one at each of its four vertices. In solution the clusters have been shown to be capped by two thiolate ligands with two vertices remaining unsaturated.<sup>[26]</sup> Photoluminescence and absorption spectra are available for the superlattice solid and solutions of the cluster in water, dimethyl sulfoxide (DMSO), and DMF.<sup>[26]</sup>

Further work by the same investigators resulted in the synthesis and crystallization of the  $\text{Cd}_{32}\text{S}_{14}(\text{SCH}_2\text{CH}(\text{OH})\text{CH}_3)_{36}\cdot 4\text{H}_2\text{O}$  cluster.<sup>[27]</sup> This larger cluster is a structural homolog of the  $\text{Cd}_{17}\text{S}_4(\text{SCH}_2\text{CH}_2\text{OH})_{26}$  cluster and has a diameter in the range of interest. The core structure is the same as that of the  $\text{Cd}_{32}\text{S}_{14}(\text{SC}_6\text{H}_5)_{36}\cdot \text{DMF}_4$  cluster described earlier.<sup>[25]</sup> A superlattice structure is formed in the molecular crystal that is not of the same structure as that formed by the smaller homolog. Absorption spectra are available for the superlattice in thin film form and for the nanocrystals dissolved in DMF.<sup>[27]</sup>

## EXPERIMENTAL OPTICAL AND ELECTRONIC PROPERTIES

In all semiconductor nanocrystals studied, regardless of the method of preparation, as cluster size is decreased the onset of the lowest energy transition is blue shifted. This corresponds to an increase in the band gap energy with decreasing cluster size. In CdS nanoclusters, this effect is observed for clusters with diameters in the range of approximately 1 to 10 nm.<sup>[13]</sup> The actual value of the observed band gap energy varies depending upon the semiconductor, how the clusters have been prepared, and the characteristics of the cluster surfaces. In CdS, the band gap energy varies from the bulk value of 2.5 eV to about 4.5 eV.

Specific data on the electronic and optical properties of the well-defined crystals described above are available as mentioned earlier. The lowest energy absorption band observed in the optical spectra of solid-state crystals of  $\text{Cd}_{32}\text{S}_{14}(\text{SC}_6\text{H}_5)_{36}\cdot \text{DMF}_4$

occurs at 325 nm, whereas in the spectrum of the dissolved clusters it occurs at 358 nm.<sup>[25]</sup> In the  $\text{Cd}_{32}\text{S}_{14}(\text{SCH}_2\text{CH}(\text{OH})\text{CH}_3)_{36}\cdot 4\text{H}_2\text{O}$  cluster of similar structure, the corresponding band gap energy occurs at about 325 nm in both the thin film and in solution.<sup>[27]</sup> In the spectra of the smaller  $\text{Cd}_{17}\text{S}_4(\text{SCH}_2\text{CH}_2\text{OH})_{26}$  clusters in solution the band occurs at 290 nm.<sup>[26]</sup> In all cases this is a blue shift from the bulk value as expected (Fig. 4). These results suggest that the type of capping ligand is of importance in determining the actual values of the electronic and optical properties of the clusters.

The lowest energy absorption band in all three clusters studied is characterized by a large extinction coefficient (on the order of 84,500, 138,000, and 84,000  $\text{M}^{-1}\text{cm}^{-1}$ , respectively). Whenever absorption spectra were obtained for the same cluster in different solvents, the band was found to vary little as the polarity of the solvent varied.<sup>[25,26]</sup>

The results of photoluminescence studies were also reported for  $\text{Cd}_{32}\text{S}_{14}(\text{SC}_6\text{H}_5)_{36}\cdot \text{DMF}_4$ <sup>[25]</sup> and  $\text{Cd}_{17}\text{S}_4(\text{SCH}_2\text{CH}_2\text{OH})_{26}$ .<sup>[26]</sup> The solid-state crystals of the former structure emit green light at approximately 520 nm, whereas in THF solution the band is

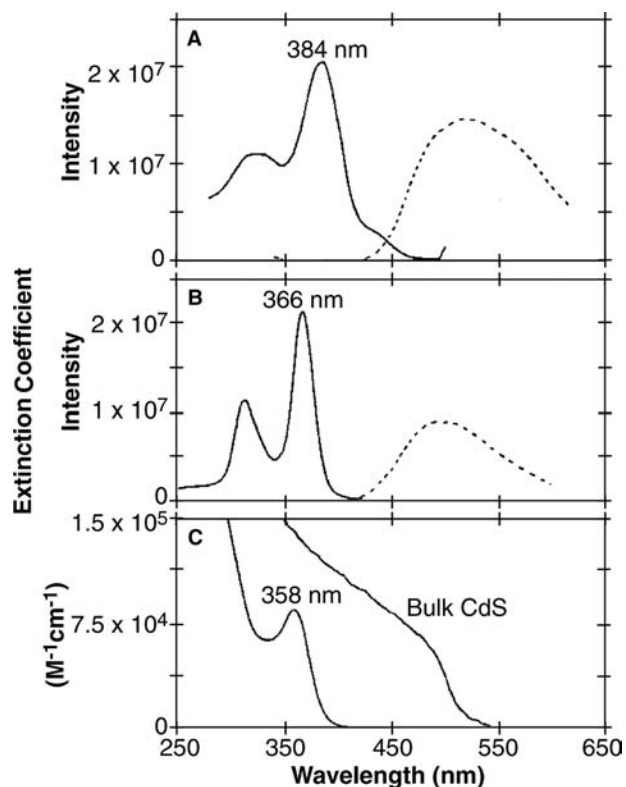


**Fig. 4** Excitation (solid) and luminescence (dotted) spectra of polycrystalline (A)  $\text{Cd}_{32}\text{S}_{14}(\text{SC}_6\text{H}_5)_{36}\cdot \text{DMF}_4$  clusters and the same dissolved in THF (B) and absorption spectrum (C) of the dissolved clusters. *Source:* From Ref.<sup>[25]</sup>. Reprinted with permission from Herron et al., *Science* 254: 1426–1428 (1993). © 1993 AAAS.

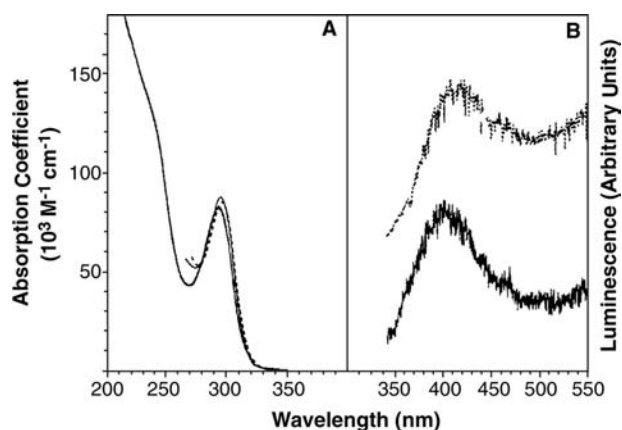


**Fig. 5** Absorption spectra (A) of  $\text{Cd}_{17}\text{S}_4(\text{SCH}_2\text{CH}_2\text{OH})_{26}$  clusters dissolved in water, DMSO, and DMF. Luminescence spectra (B) of the same crystals in solid form (upper) and aqueous solution (lower). *Source:* From Ref.<sup>[26]</sup>. Reprinted with permission from Vossmeier et al., *Science* 267: 1476–1479 (1995). © 1995 AAAS.

slightly blue-shifted. Luminescence spectra of the superlattice structure based on the latter structure shows a band at 400 nm. When the clusters are dissolved in water the band is blue shifted approximately 5 nm. In none of these spectra is there a peak present that corresponds to the strong band that is observed in the absorption spectra (Fig. 5).

### THEORETICAL STUDY OF QUANTUM SIZE EFFECTS ON ELECTRONIC AND OPTICAL PROPERTIES OF NANOCCLUSERS

It is incumbent upon any theoretical study of the quantum size effect in semiconductor nanocrystals to explain both qualitatively and quantitatively the observed shifts in electronic and optical properties with decreasing cluster size. The earliest theoretical approaches<sup>[28–31]</sup> to describe quantum size effects on the CdS system were variations on a very simple theory. The effective mass approximation to account for the “lattice-like” effects has been used together with a particle-in-the-box treatment to incorporate the quantum confinement. These models readily demonstrated an increase in the lowest energy transition as the cluster size was decreased within the range of interest. However, it has been only possible to achieve quantitative agreement with experiment for large clusters. In part this is because surface effects become increasingly important relative to “bulk-like” effects as the cluster size decreases. These models could not treat the surface in any realistic way.

There are significant challenges in treating these nanosystems with accuracy particularly when the optical and electronic properties are the main interest.

With surface effects clearly playing an important role it is highly desirable to use a method that takes into account individual atoms. As the cluster sizes in the range of interest contain up to several thousand Cd and S atoms, computations can be extremely intensive. When organic ligands are included, as in the ligand-capped clusters, the number of atoms increases even further. In addition, predicting transition energies and probabilities requires a method that has a demonstrated ability to treat excited states with accuracy. These methods add substantially to the computational time.

Several different techniques have been used in succession in an attempt to improve upon the effective mass description. These included the use of empirical pseudopotentials,<sup>[32]</sup> and several techniques based upon tight-binding theory.<sup>[33,34]</sup> In most cases, surface effects have not been incorporated into the method. Further, the majority of the work, including one study in which surface considerations were included,<sup>[34]</sup> focused on bare semiconductor clusters. Working with bare clusters has the advantage of avoiding the additional computation time required to incorporate the ligand atoms and determine the structure of surface ligands. However, samples of bare clusters cannot be prepared that are uniform in composition nor can the surface composition and characteristics be precisely controlled. This complicates the comparison between the theoretical studies using a cluster of fixed composition and the results of experiments performed with a distribution of clusters. Nevertheless, these works did, for the most part, succeed in extending the good agreement between the predicted energy of the band gap and the experimental values for different size clusters to somewhat smaller clusters.

The first theoretical work that used *ab initio* methods to model ligand-capped clusters of CdS for which experimental data were available involved the use of a semiempirical method (complete neglect of differential overlap, CNDO).<sup>[35]</sup> The computationally intensive configuration interaction with single excitations (CIS) method was employed to improve the description of the excited states. Because of the time intensive computational technique employed, the clusters studied had to be very small, in particular the computed systems were  $[\text{Cd}(\text{SPh})_4]^{2-}$ ,  $[\text{Cd}_2(\text{SPh})_6]^{2-}$ , and  $[\text{Cd}_4(\text{SPh})_{10}]^{2-}$ . Agreement between the theoretical and experimental results was good; however, these clusters are substantially smaller than the size regime of interest.

Techniques based on density functional theory (DFT) hold promise for more accurate treatment of larger clusters. DFT has been shown to be capable of giving a good description of the ground state in transition metal systems. Early applications of DFT in the local density approximation to both CdSe and CdS clusters to the determination of transition energies significantly underestimated band gap energies. Recent

**Table 1** Summary of CdS monomer bond lengths and HOMO/LUMO energies at different levels of theory and basis sets

	Cd/S	SVWN	B3LYP	HF	MP2	MP3	MP4	PM3
	Lanl2dz/6-31G*	2.267	2.319	2.290	2.258	2.298	2.278	
	Sadlej/6-31G*	2.243	2.300	2.311	2.265	2.298	2.274	
	PM3							2.312
HOMO	Lanl2dz/6-31G*	-0.2105	-0.2184	-0.3178	-0.3177	-0.3179	-0.3178	
LUMO		-0.1985	-0.1597	-0.0595	-0.0588	-0.0596	-0.0592	
		0.32	1.60	7.03	7.05	7.03	7.04	eV
HOMO	Sadlej/6-31G*	-0.1943	-0.2163	-0.3019	-0.3023	-0.3020	-0.3022	
LUMO		-0.1812	-0.1578	-0.0570	-0.0561	-0.057	-0.0563	
		0.35	1.59	6.66	6.70	6.67	6.69	eV

Band lengths are reported in Angstroms and HOMO/LUMO energies in atomic units.

advances in methodology indicate that DFT will be capable of describing excited states and predicting band gap energies as well as the currently accepted methods while requiring less computer time.<sup>[36]</sup> Application of a time-dependent density functional theory in the local density approximation (TDLDA) has been used with some success to predict the absorption spectra of bare CdSe clusters with sizes in the regime of interest.<sup>[37]</sup>

It seems clear that any theoretical technique that is to describe accurately the optical and electronic properties of CdS nanoclusters over the full range of sizes in which the quantum size effect is evident must explicitly treat the cluster surface. In order to be able to compare the results of the calculations with experimental values, it is highly desirable to model the well-defined organically capped clusters that have been prepared. Optical properties have been shown to be dependant on the ligand structure<sup>[25-27]</sup> and so a method that models the capping-ligands as well as the core structure is needed.

## QUANTUM CALCULATIONS ON CdS

We are undertaking a systematic study of basis sets and computational methods on CdS as well as CdS dimers. The goal of the study is to find the best level of theory that will yield the most accurate results for the least amount of computational effort. Table 1 summarizes our results to date.

One observes from Table 1 that the CdS bond length is much shorter than the bulk CdS bond length of 2.519 Å. The bond length at the highest level of theory (MP4) and the largest all electron basis set sadlej/6-31G\* is 2.274 Å. The DFT functional SVWN using the LANL2DZ on cadmium and 6-31G\* on sulfur appears to be very close to the 2.274 Å value from the “best” level of theory and all electron basis set. The computational time saving is approximately a factor of 100. The semiempirical PM3 bond length is 0.038 Å too large when compared to the MP4/(Sadlej/

6-31G\*) value. The sign of the HOMO/LUMO gaps is reversed to what is typically expected between ab initio and DFT results. The ab initio HOMO/LUMO gaps for this system should be smaller, whereas the DFT numbers should be larger. The experimental band gap for the Cd<sub>32</sub> monocluster is approximately 4 eV. The PM3 HOMO/LUMO gap is 6.76 eV.

We calculated the geometry for the CdS dimer using the LANL2DZ/6-31G\* basis set at different levels of theory (Table 2). Again we see that the DFT functional SVWN performs as well as MP3 using the same basis set. Our conclusion at this point is that we can use the SVWN method and LANL2DZ/6-31G\* basis set on the cadmium and sulfur atoms in our electronic structure calculations. This conclusion is also based on the results from additional calculations using other larger basis sets and higher level of theory.

## SEMIEMPIRICAL CALCULATIONS ON ENCAPSULATED CdS CLUSTERS

Recent advances in computer hardware and semiempirical quantum mechanical codes permit the calculation of large (~2000 atom) systems in a reasonable amount of CPU (2 hr) time. Timings are based on a PM3 single-point calculation using MOPAC2002 on a 2.0-GHz Pentium IV. In order to test how well a semiempirical method will work on CdS nanocrystals we optimized two bare CdS nanocrystals and four

**Table 2** Summary of bond lengths for a CdS dimer at different levels of theory

Lanl2dz/ 6-31G*	SVWN	B3LYP	HF	MP2	MP3	PM3
Cd-S	2.472	2.514	2.453	2.460	2.460	2.411
Cd-Cd	2.821	2.910	2.850	2.786	2.799	2.883
S-S	4.059	4.100	3.992	4.054	4.046	3.865

Bond lengths are reported in Angstroms.

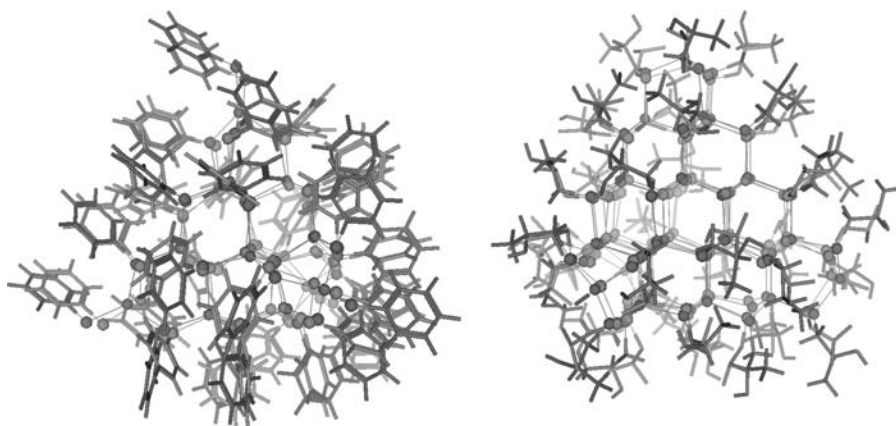


**Fig. 6** PM3 optimized (green) vs. X-ray (red) structures for the  $[\text{Cd}_{17}\text{S}_4(\text{SPh})_{28}]^{2-}$  (left) and  $\text{Cd}_{32}\text{S}_{14}(\text{S-iPrOH})_{26}$  (right) organic capped cadmium sulfide clusters. The RMSD (without hydrogens) for the  $\text{Cd}_{17}$  cluster is 1.65 Å and for the  $\text{Cd}_{32}$  cluster it is 2.0 Å. The average CdS bond length is approximately 2.55 Å for both PM3-optimized structures.

different organic capped CdS nanocrystals. The X-ray structures for two of the organic capped systems have been published and the coordinates were available. We used MOPAC2002 on a 677-MHz alpha processor to perform the calculations. The results from these calculations are summarized in Figs. 6–9.

Fig. 6 shows a remarkable agreement between the PM3-optimized structure and X-ray structure. The CdS nanocrystal core essentially remains unchanged,

whereas the organic ligands have moved slightly. Figs. 7 and 8 are plots of the highest occupied molecular orbital (HOMO) and the lowest unoccupied molecular orbital (LUMO), respectively. For the  $\text{Cd}_{17}$  nanocluster, one observes the HOMO to be the capped ligand, whereas on the  $\text{Cd}_{32}$  nanocluster the HOMO electron density resides on the CdS core (Fig. 8). Comparing these results with bare nanocrystal HOMOs (Fig. 9), we see that the larger  $\text{Cd}_{32}$  nanocrystal

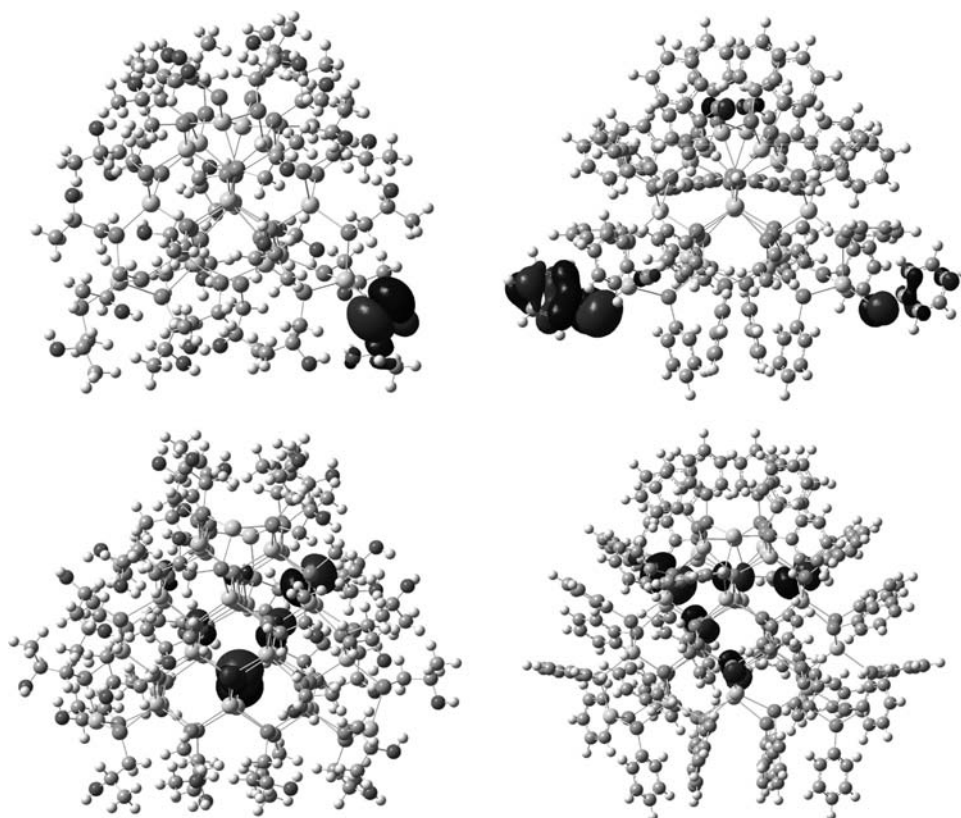


**Fig. 7** The highest occupied molecular orbital (HOMO) for the four organic capped cadmium sulfide clusters. The upper left is the  $\text{Cd}_{17}$  cluster with the isopropyl ligands, whereas the upper right is the  $\text{Cd}_{17}$  with the thiophenyl ligands. The lower left is the  $\text{Cd}_{32}$  cluster with the isopropyl ligands, whereas the lower right is the  $\text{Cd}_{32}$  cluster with the thiophenyl ligands. These orbitals were obtained from optimized capped clusters using the semiempirical PM3 method.

systems are similar (a capped vs. bare), whereas in the Cd<sub>17</sub> case the HOMO has moved to capping ligands.

### QUANTUM MECHANICS/MOLECULAR MECHANICS CALCULATIONS ON ENCAPSULATED CdS CLUSTERS

The encapsulation of the nanocluster CdS atoms by 10–30 phytochelatin-like peptides or peptidomimetic ligands (an additional 200–600 non-hydrogen atoms) represents a major obstacle in modeling functionalized nanoelectronic assemblies. Fortunately, classical computations that use molecular mechanics (MM) force fields have been extremely successful in providing valuable and meaningful insights about intermolecular interactions for biomolecules in solution.<sup>[38]</sup> The two independent computational methods, QM and MM, have been combined (known as QM/MM methods) over the last decade to formulate an alternative approach to the ubiquitous size and timescale problem in computational chemistry. Excellent reviews are available.<sup>[39–43]</sup> QM/MM methods have been widely used to study the chemical reactivity in large molecular systems. One of the main areas of concentration has

been in the study of solvation and reactivity of small molecules in the condensed phase,<sup>[44]</sup> but other recent applications include studies of surface reactivity,<sup>[45]</sup> zeolites,<sup>[46]</sup> and crystal formation.<sup>[47]</sup>

The overall scheme of QM/MM methods is to treat the reactive or electronically sensitive portions with quantum mechanics, whereas the stable or unreactive portions are treated with molecular mechanics. Most of the QM/MM methods share a common methodological approach. The system of interest is typically partitioned into two or more subsystems. The nanocluster system will be used to explain the basic ideas. The QM region contains the electronically sensitive portion of the molecular assembly, the CdS core. The MM region contains the solvent and phytochelatin molecules. The Hamiltonian for the entire molecular system is written as.

$$H = H_{QM} + H_{MM} + H_{QM/MM}$$

where  $H_{QM}$  is the QM Hamiltonian,  $H_{MM}$  is the empirical force field, and  $H_{QM/MM}$  is the Hamiltonian that describes the interactions between the QM and MM regions. Consequently, the total energy of

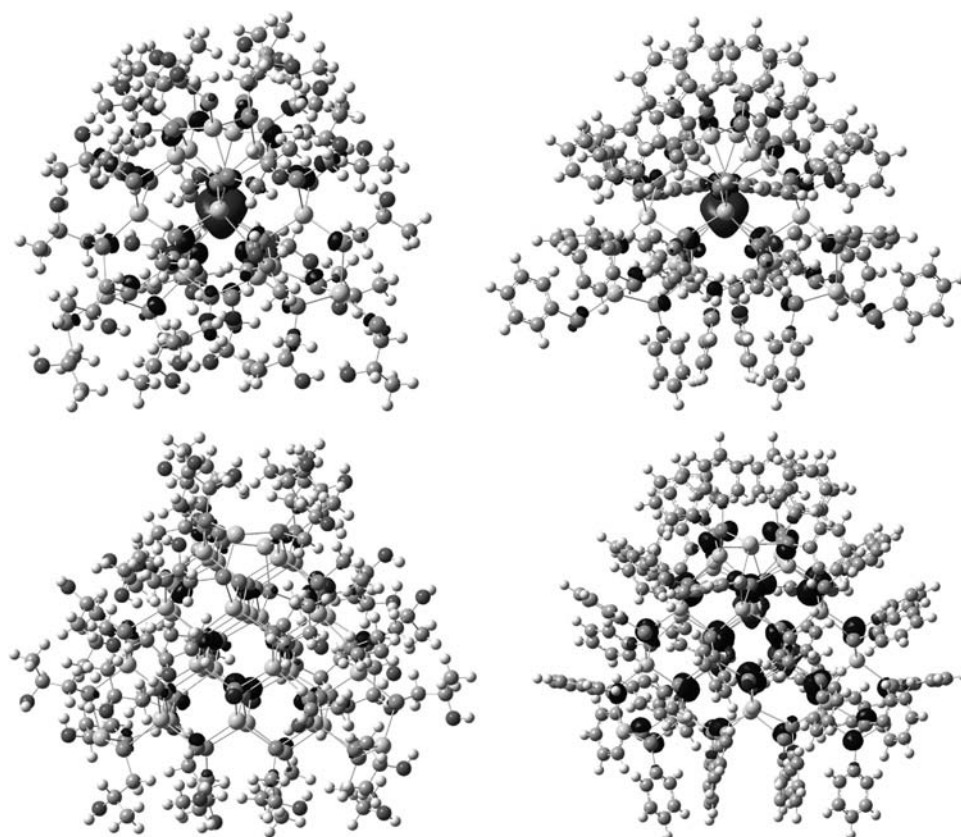


**Fig. 8** The lowest unoccupied molecular orbital (LUMO) for the four organic capped cadmium sulfide clusters. The upper left is the Cd<sub>17</sub> with isopropyl ligands, whereas the upper right is the Cd<sub>17</sub> with the thiophenyl ligands. The bottom left is the Cd<sub>32</sub> with isopropyl ligands, whereas the lower right is the Cd<sub>32</sub> with the thiophenyl ligands. These orbitals were obtained from optimized capped clusters using the semiempirical PM3 method.

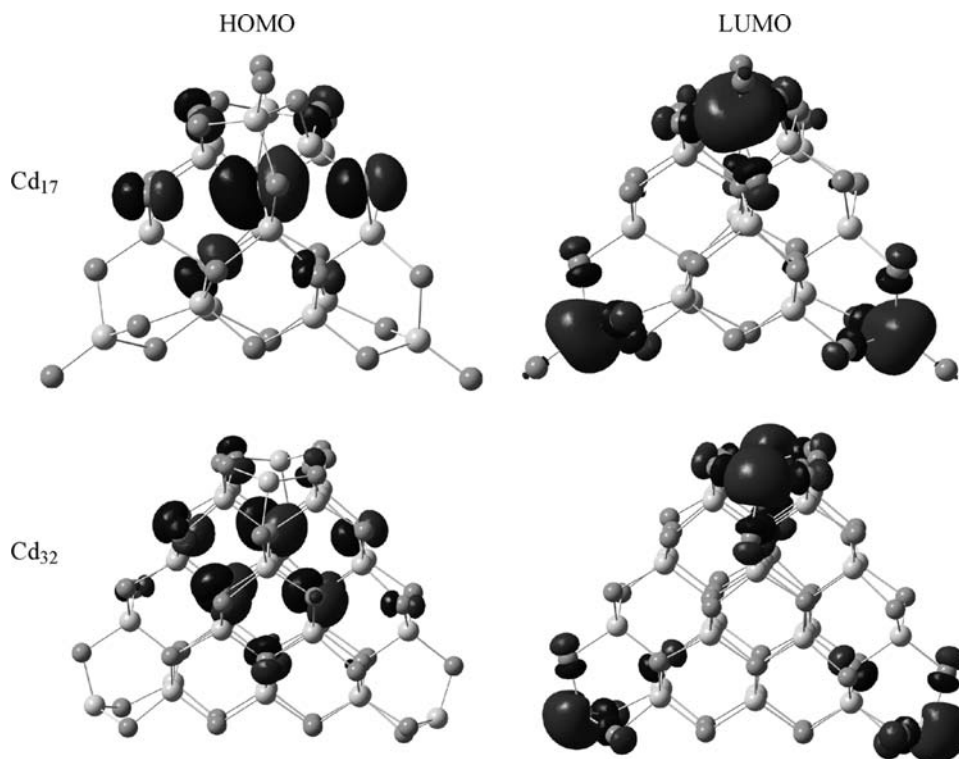


**Fig. 9** The highest occupied molecular orbital (left) and lowest unoccupied molecular orbital (right) for the  $\text{Cd}_{17}\text{S}_{32}^{-30}$  and  $\text{Cd}_{32}\text{S}_{50}^{-36}$  nanoclusters. The structures were optimized using the PM3 semiempirical method.

the system is written as a sum of the individual components.

$$E = E_{\text{QM}} + E_{\text{MM}} + E_{\text{QM/MM}}$$

One of the key aspects of the QM/MM method resides in the interactions between the QM and MM regions. Considerable debate has arisen when the partitioning between the two regions cuts across covalent bonds.<sup>[42,48,49]</sup> The most common method in modeling this middle-space is to use the “link atom” method. It consists of adding QM hydrogen atoms in order to fill the free valencies of the QM atoms that are connected to the atoms described by MM. These dummy atoms are treated explicitly during the QM calculations but do not interact with the MM atoms. Whether or not these link atoms should interact by means of Coulombic interactions is still open to debate. This approach is not ideal but in this respect, the problem of describing the phytochelatin coat by molecular mechanics and the CdS nanocluster core by the modified DFT method is well suited for the QM/MM method, as the partition is across intermolecular bonds only. It is typically agreed upon that this type of QM/MM implementation lends itself to greater accuracy and reliability.

Based upon what we have learned from the previous two sections we have begun testing the hybrid QM/MM ONIOM method on the organic capped CdS nanocrystals. In the ONIOM method various QM and MM methods are assigned to different layers.

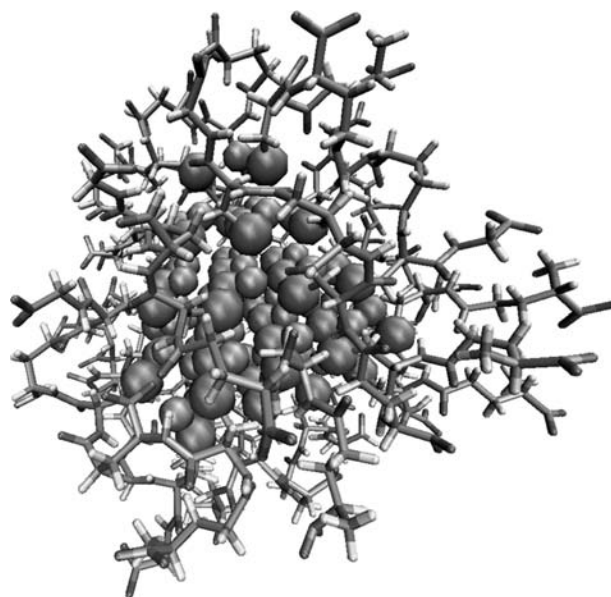


**Fig. 10** Model peptide encapsulated CdS nanocrystals. The model contains eight  $(\gamma\text{-glucys})_3\text{gly}$  peptides.



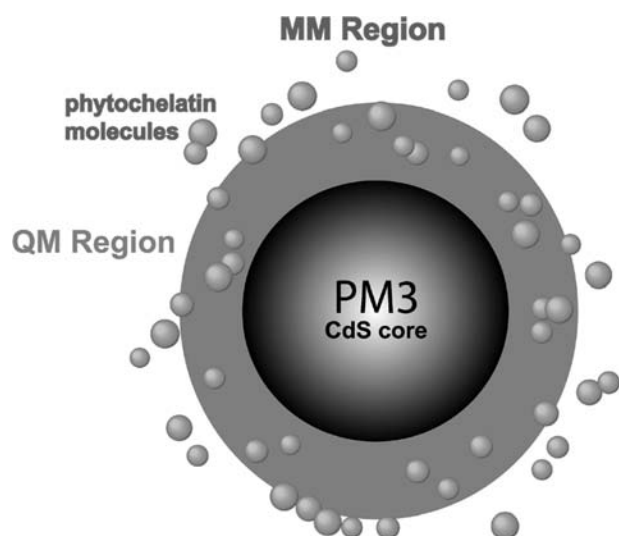


**Fig. 11** An illustration of the different regions to be used in an ONIOM calculation on a large peptide encapsulated cadmium sulfide nanocrystal.

Our model peptide encapsulated CdS nanocrystal contains a  $\text{Cd}_{17}\text{S}_{30}$  core with eight  $(\gamma\text{-glucy})_3\text{gly}$  peptides (Fig. 10). The system contains 1078 atoms. In this system the ONIOM inner layer (i.e., the core) will consist of LanL2dz on cadmium and 6-31G(d) on sulfur. A lower-level basis set is placed on the peptides. Based upon this description, the system contains  $\sim 900$  basis functions and requires 1 hr of CPU time on the marvel processors at the Pittsburgh Supercomputing Center. In a “real” peptide encapsulated CdS nanocrystal, we approximate the CdS core to be composed of 693 atoms. In this situation, the plan is to use PM3 on the inner CdS atoms with LanL2dz on the surface cadmium and 6-31G(d) on the surface sulfurs. Again lower-level basis sets will be used on the peptides. Fig. 11 is an illustration of the ONIOM method applied to a “real” peptide encapsulated CdS nanocrystal.

## CONCLUSION

Our goal is to understand the electronic structure properties of large peptide encapsulated cadmium sulfide nanocrystals as a function of molecular size. We have performed a systematic study on different levels of theory on sample CdS monomers and dimers. From these calculations, we have identified the DFT functional SVWN along with the LanL2dz/6-31G\* basis set to give satisfactory results. Using experimentally observed organic capped CdS nanocrystals, we have shown that the semiempirical PM3 method gives reasonable results. Based on these calculations, we propose that a combination of PM3, DFT, and molecular mechanics methods can be used to study

accurately and effectively “real” peptide encapsulated nanocrystals.

## REFERENCES

1. Remacle, F.; Levine, R.D. Quantum dots as chemical building blocks: elementary theoretical considerations. *ChemPhysChem* **2001**, *2*, 20–36.
2. Eychemüller, A. Structure and photophysics of semiconductor nanocrystals. *J. Phys. Chem., B* **2000**, *104*, 6514–6528.
3. Alivisatos, A.P. Semiconductor clusters, nanocrystals, and quantum dots. *Science* **1996**, *271*, 933–937.
4. Kagan, C.R.; Murray, C.B.; Bawendi, M.G. Synthesis, structural characterization, and optical spectroscopy of close packed CdSe nanocrystallites. *MRS Symp. Proc.* **1995**, *358*, 219–224.
5. Shiang, J.J. et al. Symmetry of annealed wurtzite CdSe nanocrystals: assignment to the  $C_{3v}$  point group. *J. Phys. Chem.* **1995**, *99*, 17,417–17,422.
6. Kagan, C.R.; Murray, C.B.; Bawendi, M.G. Long-range resonance transfer of electronic excitations in close-packed CdSe quantum-dot solids. *Phys. Rev., B* **1996**, *54*, 8633–8643.
7. Korgel, B.A.; Fitzmaurice, D. Condensation of ordered nanocrystal thin films. *Phys. Rev. Lett.* **1998**, *80*, 3531–3534.
8. Korgel, B.A.; Fitzmaurice, D. Small-angle X-ray-scattering study of silver-nanocrystal disorder–order phase transitions. *Phys. Rev., B* **1999**, *59*, 14,191–14,221.
9. Sun, S.; Murray, C.B. Synthesis of monodisperse cobalt nanocrystals and their assembly into magnetic superlattices. *J. Appl. Phys.* **1999**, *85*, 4325–4330.
10. Murray, C.B.; Norris, D.J.; Bawendi, M.G. Synthesis and characterization of nearly monodisperse CdE ( $E = \text{S}, \text{Se}, \text{Te}$ ) semiconductor nanocrystallites. *J. Am. Chem. Soc.* **1993**, *115*, 8706–8715.
11. Vossmeier, T. et al. CdS nanoclusters: synthesis, characterization, size dependent oscillator strength, temperature shift of the excitonic transition energy, and reversible absorbance shift. *J. Phys. Chem.* **1994**, *98*, 7665.
12. Charles, P.; Poole, J. *Introduction to Nanotechnology*; John Wiley & Sons: New York, 2003.
13. Wang, H.; Herron, N. Nanometer-sized semiconductor clusters: materials synthesis, quantum size effects, and photophysical properties. *J. Phys. Chem.* **1991**, *95*, 525–532.
14. Yoffe, A.D. Low dimensional systems: quantum size effects and electronic properties of semiconductor microcrystallites (zero-dimensional systems and some quasi two-dimensional systems). *Adv. Phys.* **1993**, *42* (2), 173–266.
15. Alivisatos, A.P. Perspectives on the physical chemistry of semiconductor nanocrystals. *J. Phys. Chem.* **1996**, *100*, 13,226–13,239.
16. Colvin, V.L.; Schlamp, M.C.; Alivisatos, A.P. Light-emitting diodes made from cadmium selenide

- nanocrystals and a semiconducting polymer. *Nature* **1994**, *370*, 354–357.
17. Gal, D. et al. Size-quantized CdS films in thin film CuInS<sub>2</sub> solar cells. *Appl. Phys. Lett.* **1998**, *73* (21), 3135–3137.
  18. Yanagida, S. et al. Semiconductor photocatalysis quantum photoreduction of aliphatic ketones to alcohols using defect free ZnS quantum crystallites. *J. Phys. Chem.* **1990**, *94*, 3104–3111.
  19. Kuczynski, J.; Thomas, J.K. Photochemistry at the surface of colloidal cadmium sulfide. *Chem. Phys. Lett.* **1982**, *88*, 445.
  20. Henglein, A.; Bunsenges, B. Dynamics of interfacial electron-transfer processes in colloidal semiconductor systems. *Phys. Chem.* **1982**, *86*, 301.
  21. Duonghong, D.; Ramsden, J.; Gratzel, M. Dynamics of interfacial electron-transfer processes in colloidal semiconductor systems. *J. Am. Chem. Soc.* **1982**, *104*, 2977–2985.
  22. Rossetti, R.; Beck, S.M.; Brus, L.E. Transient Raman scattering observation of surface reactions in aqueous TiO<sub>2</sub> colloids. *J. Am. Chem. Soc.* **1982**, *104*, 7322.
  23. Rossetti, R.; Nakahara, S.; Bru, L.E. Quantum size effects in the redox potentials, resonance Raman spectra, and electronic spectra of CdS crystallites in aqueous solution. *J. Chem. Phys.* **1983**, *79* (2), 1086–1088.
  24. Lee, G.S.H. et al. [S<sub>4</sub>Cd<sub>17</sub>(SPh)<sub>28</sub>]<sup>2-</sup>, the first member of a third series of tetrahedral [SWMX (SR)<sub>y</sub>]<sub>z</sub> clusters. *J. Am. Chem. Soc.* **1988**, *110*, 4863–4864.
  25. Herron, N. et al. Crystal structure and optical properties of Cd<sub>32</sub>S<sub>14</sub>(SC<sub>6</sub>H<sub>5</sub>)<sub>36</sub>•DMF<sub>4</sub>, a cluster with a 15 angstrom cadmium sulfide core. *Science* **1993**, *259*, 1426–1428.
  26. Vossmeier, T. et al. A “double-diamond superlattice” built up of Cd<sub>17</sub>S<sub>4</sub>(SCH<sub>2</sub>CH<sub>2</sub>OH)<sub>26</sub> clusters. *Science* **1995**, *267*, 1476–1479.
  27. Vossemeier, T. et al. Double-layer superlattice structure built up of Cd<sub>32</sub>S<sub>14</sub>(SCH<sub>2</sub>CH(OH)CH<sub>3</sub>)<sub>36</sub>•4H<sub>2</sub>O clusters. *J. Am. Chem. Soc.* **1995**, *117*, 12,881–12,882.
  28. Brus, L.E. A simple model for the ionization potential, electron affinity, and aqueous redox potentials of small semiconductor crystallites. *J. Phys. Chem.* **1983**, *79* (11), 5566–5571.
  29. Brus, L.E. Electron–electron and electron–hole interactions in small semiconductor crystallites: the size-dependence of the lowest excited electronic state. *J. Phys. Chem.* **1984**, *80* (9), 4403–4409.
  30. Weller, H. et al. Photochemistry of colloidal semiconductors. Onset of light absorption as a function of size of extremely small cadmium sulfide particles. *Chem. Phys. Lett.* **1986**, *124* (6), 557–560.
  31. Kayanuma, Y. Quantum-size effects of interacting electrons and holes in semiconductor microcrystals with spherical shape. *Phys. Rev., B* **1988**, *38*, 9797–9805.
  32. Krishna, R.; Friesner, R.A. Quantum confinement effects in semiconductor clusters. *J. Phys. Chem.* **1991**, *95* (11), 8309–8322.
  33. Lippens, P.E.; Lannoo, M. Comparison between calculated and experimental values of the lowest excited electronic state of small CdSe crystallites. *Phys. Rev., B* **1990**, *41*, 6079.
  34. Hill, N.A.; Whaley, K.B. Electronic structure of semiconductor nanoclusters: a time-dependent theoretical approach. *J. Chem. Phys.* **1993**, *99* (5), 3707–3715.
  35. Liu, H.; Hupp, J.T.; Ratner, M.A. Electronic structure and spectroscopy of cadmium thiolate clusters. *J. Phys. Chem.* **1996**, *100*, 12,203–12,213.
  36. Muscat, J.; Wander, A.; Harrison, N.M. On the prediction of band gaps from hybrid functional theory. *Chem. Phys. Lett.* **2001**, *342* (3–4), 397–401.
  37. Troparevsky, M.C.; Kronik, L.; Chelikowsky, J.R. Optical properties of CdSe quantum dots. *J. Chem. Phys.* **2003**, *119* (4), 2284–2287.
  38. MacKerell, A.D.J.E.A. All-atom empirical potential for molecular modeling and dynamics studies of proteins. *J. Phys. Chem.* **1998**, *102*, 3586.
  39. Dapprich, S. et al. A new ONIOM implementation in Gaussian98: part I. The calculation of energies, gradients, vibrational frequencies and electric field derivatives. *J. Mol. Struct., Theochem* **1999**, *461–462*, 1–21.
  40. Hillier, I.A. Chemical reactivity studied by hybrid QM/MM methods. *J. Mol. Struct., Theochem* **1999**, *463*, 45.
  41. Monard, G.; Mertz, K.M.J. Combined quantum mechanical/molecular mechanical methodologies applied to biomolecular systems. *Acc. Chem. Res.* **1999**, *32*, 904.
  42. Gordon, M.S. et al. The effective fragment potential method: a QM-based MM approach to modeling environmental effects in chemistry. *J. Phys. Chem., A* **2001**, *105*, 293–307.
  43. Mulholland, A.J. The QM/MM approach to enzymatic reactions. *Theor. Comput. Chem.* **2001**, *9*, 597–653.
  44. Gao, J. *Reviews in Computational Chemistry*; Lipkowitz, K.B., Boyd, D.B., Eds.; VCH: New York, 1996; 119–185.
  45. Carmer, C.S.; Weiner, B.E.A. Molecular dynamics with combined quantum and empirical potentials: acetylene adsorption on silicon(100). *J. Chem. Phys.* **1993**, *99*, 1356.
  46. Sherwood, P. et al. Computer simulation of zeolite structure and reactivity using embedded cluster methods. *Faraday Discuss.* **1997**, *106*, 79–92.
  47. Eichler, U.E.A. Combining ab initio techniques with potential functions for structure predictions of large systems: method and application to crystalline silica polymorphs. *J. Comput. Chem.* **1997**, *18*, 463.
  48. Naray-Szabo, G. Chemical fragmentation in quantum mechanical methods. *Comput. Chem.* **2000**, *24*, 287.
  49. Sauer, J.; Sierka, M. Combining quantum mechanics and interatomic. *J. Comput. Chem.* **2000**, *21*, 1470–1493.

# Capsules: Polymer Microcapsules

Gleb B. Sukhorukov

Max Planck Institute of Colloids and Interfaces,  
Potsdam/Golm, Germany

## INTRODUCTION

The nanoengineering of colloidal surfaces and the design of functional colloid particles are currently interesting topics of applied chemistry and biochemistry in the field engaged in developing new materials with tailored properties. Research on composite colloidal particles (core-shell structures with size ranging from 1 to 1000 nm) has created interest because of various applications expected in the areas of coatings, electronics, photonics, catalysis, biotechnology, sensorics, medicine, ecology, and others. In general, the research on core-shell structure and encapsulation implies the formation of a colloidal core of defined content and size, and the preparation of a shell providing the required stability, permeability, compatibility, release of core material, and catalytic or affinity properties. Tailoring the different components of one particle becomes important to develop these functionalized colloids (i.e., to combine several properties in one core-shell structure). The desired properties may be adjusted to facilitate the interaction of the core with different solvents or cell membranes. The shell may also have magnetic, optical, conductive, or targeting properties for directing and manipulating the core containing bioactive materials.

A major task in the development of advanced drug formulations deals with the elaboration of delivery systems for providing the sustained release of bioactive materials. Mostly, these systems comprise polymer particles in the size range of 50–100  $\mu\text{m}$ . Drug molecules are embedded in polymer matrices, or in core-shell structures. In the latter case, the shell permeability or degradation rate determines the release rate of the bioactive core material. The composition of the shell may additionally provide certain functionalities.

This review is devoted to the literature on recently introduced novel pathways to fabricate nanoengineered core-shell structures, which can employ a great variety of substances as shell constituents and can be incorporated into hollow spheres. The way the shells are assembled on colloids resembles the formation of ultrathin polymer films by layer-by-layer (LbL)

adsorption on macroscopic flat support, an idea proposed by Iler<sup>[1]</sup> in 1966 and later developed by Lee et al.<sup>[2]</sup> In 1991, Decher and Hong<sup>[3]</sup> proposed a method of forming polyelectrolyte films by using the alternate adsorption of polycations and polyanions. A crucial factor for polyionic LbL assembly is the change of the sign of the surface charge on polyelectrolyte adsorption. Beginning in 1998, this strategy of LbL assembly of charged species was transferred to coat micron-sized and submicron-sized colloidal particles (Fig. 1).<sup>[4]</sup> The idea emerged to employ the nanoengineered properties of multilayers as shell structures formed on colloidal particles.

## MULTILAYER ASSEMBLY ON COLLOIDAL PARTICLES

The main problem in applying the LbL technology to coat surfaces of colloidal particles is how to separate the remaining free polyelectrolytes from the particles prior to the next deposition cycle. Today, there are several approaches for that difficulty, including centrifugation, filtration protocols for washing particles with adsorbed polyelectrolytes, and the so-called sequential adding of polyelectrolytes at matched concentrations. For details of these approaches, their advantages, and their drawbacks, refer to Sukhorukov et al.<sup>[4]</sup> Donath et al.<sup>[5]</sup> and Voigt et al.<sup>[6]</sup> It should be mentioned that the filtration method<sup>[6]</sup> is the only method applicable for scaling up the coating of different colloidal particles in large volumes. The monitoring of the process of film formation (i.e., charge reversal and continuous layer growth) was followed at each step by electrophoresis, dynamic light scattering, single particle light scattering (SPLS), and fluorescent intensity measurements.<sup>[4,7]</sup> Fig. 2 illustrates the typical particle charge ( $\zeta$ -potential) changes recorded on layer deposition for polycation/polyanion pairs. The  $\zeta$ -potential alternates between positive and negative values, indicating the successful recharging of the particle coated with the adsorbed polyelectrolyte multilayer on each layer deposition. The evidence for sequential layer growth has been obtained by means

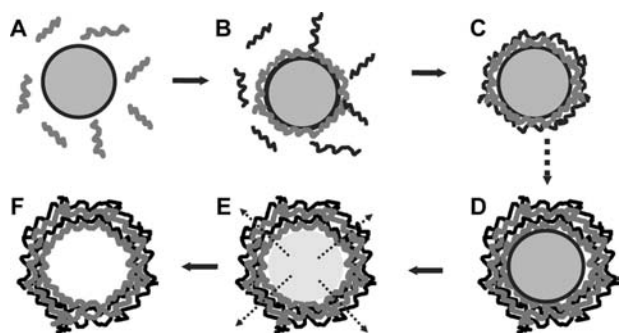


**Fig. 1** Consecutive adsorption of positively (gray) and negatively (black) charged polyelectrolytes onto negatively charged colloidal particles (A–E). After dissolution of colloidal core (E), a suspension of polyelectrolyte capsules is obtained (F).

of SPLS.<sup>[4,6]</sup> In Fig. 3, the intensity distribution of the control naked particles is compared with particles coated with eight layers assembled by filtration technique. From the shift of the peak of the intensity distribution, the adsorbed mass can be derived. These data can be converted into a layer thickness of the adsorbed polyelectrolyte multilayers, assuming a given refractive index.<sup>[4]</sup> The increase of polyelectrolyte film thickness is proportional to the layer number (Fig. 3, bottom). Mean polyelectrolyte layer thickness was found to be 1.5 nm for the case of polystyrene sulfonate (PSS) and polyallylamine (PAH) alternatively assembled from 0.5 M NaCl. It should be noted that the average layer thickness of polyelectrolyte multilayers strongly

depends on the kind of polyelectrolytes and the salt concentration used at polyelectrolyte assembly. More rigid polymers and an increased salt concentration lead to a thicker adsorption layer.<sup>[8]</sup>

Multilayer assembly can be performed not only on solid particles such as silica, PS latex particles, or organic crystals, but also on “soft” particles formed just before multilayer buildup, such as protein aggregates and the compact form of DNA. The micron-sized aggregates of proteins (lactate dehydrogenase<sup>[9]</sup> and chemotrypsin<sup>[10]</sup>) were applied as templates for polyelectrolyte multilayer assembly. The polyelectrolyte multilayer coating of these aggregates captures the proteins inside the capsules and, at the same time, provides a selective barrier for the diffusion of different species (substrates, inhibitors) from the exterior. The concept of polyelectrolyte multilayer assembly on aggregates is similar to that on the surface of colloidal particles.<sup>[4]</sup> Here, instead of solid colloidal particles, the preformed protein aggregates have been used as templates for polyelectrolyte multilayer assembly. As shown in Ref.<sup>[10]</sup>, the chemotrypsin aggregates in high-salt solution form particles of 100–300 nm. After these particles are covered with a polyelectrolyte layer, the capsule can be transferred to a low-salt solution, where chemotrypsin is captured by a polyelectrolyte shell. The method of LbL shell formation on protein aggregates provides encapsulation efficiency close to 100%. Indeed, one can always find a condition for protein aggregation (for instance, it usually happens at the isoelectric point). The subsequent release of proteins from the shell can be controlled by certain

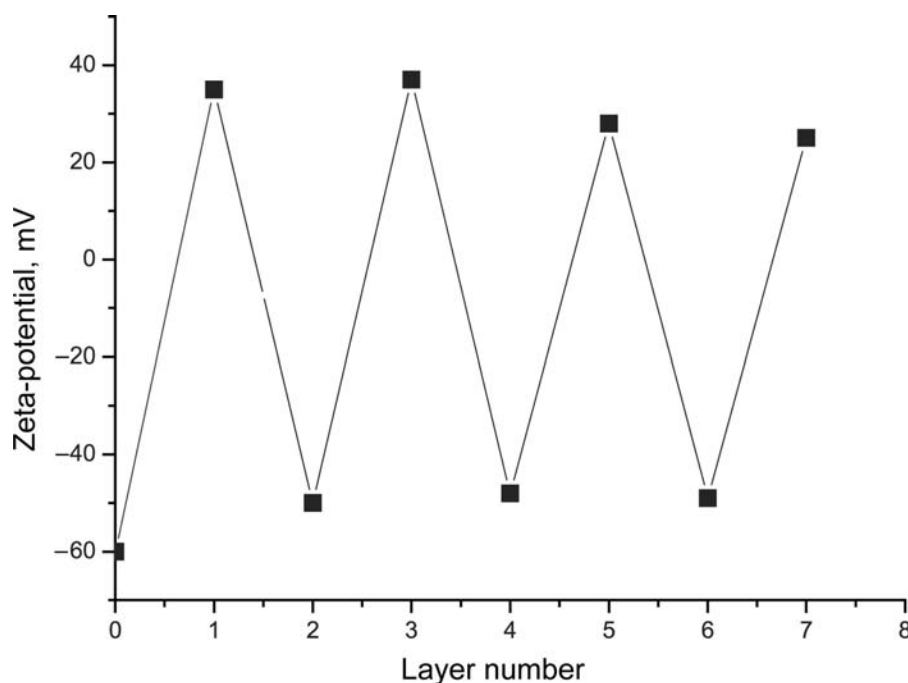


**Fig. 2**  $\zeta$ -Potential as a function of layer number for PSS/PAH alternatively coated polystyrene latex particles. Particle diameter = 640 nm.

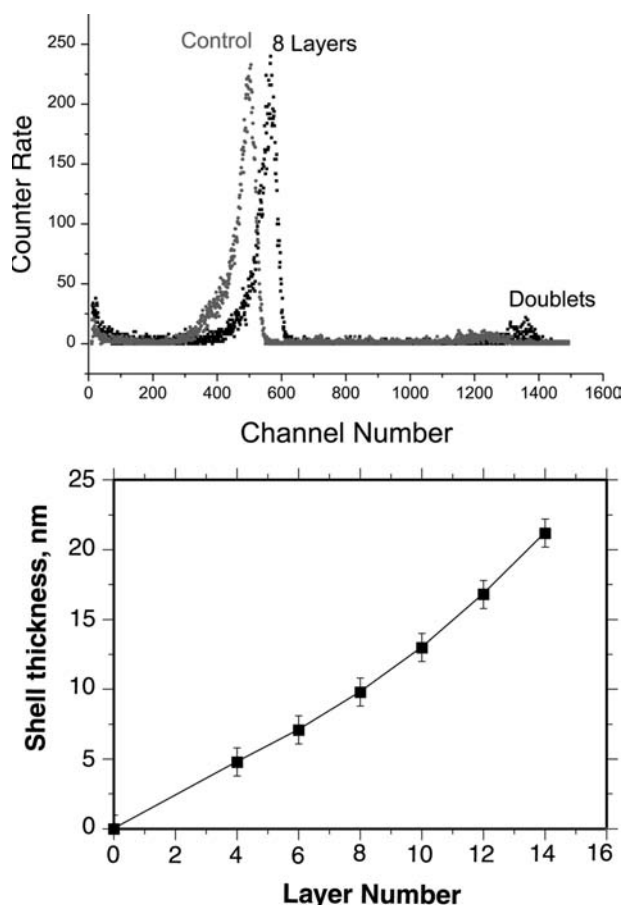


**Fig. 3** Top: Normalized light scattering intensity distributions (SPLS) of PAH/PSS-coated polystyrene sulfate latex particles ( $\text{\O} = 640 \text{ nm}$ ). Particles with eight layers are compared with uncoated ones. Bottom: Shell thickness as a function of layer number.

polyelectrolyte compositions. It makes such systems very suitable as drug delivery systems with controlled-release properties.

The assembly of three polyelectrolyte layers was performed also on condensed DNA particles with size of about 50–100 nm. A certain polymer composition used for coating DNA particles provides stable suspension<sup>[11,12]</sup> and facilitates the uptake of these particles by biological cells, with the outermost layer bearing certain receptors. Sequential gene expression of cells after the uptake of such particles has been illustrated.<sup>[12,13]</sup>

The method of LbL adsorption of oppositely charged macromolecules onto colloidal particles has been applied already for different templates with sizes ranging from 50 nm to tens of microns, such as organic and inorganic colloid particles, protein aggregates, emulsion droplets, biological cells, and drug nanocrystals. Various materials (e.g., synthetic polyelectrolytes, chitosan and its derivatives, proteins, DNA, lipids, multivalent dyes, and magnetic nanoparticles) have

been used as layer constituents to fabricate the shell. The possibility of using different materials allows the shell to adjust its design based on the required stability biocompatibility and affinity properties of the capsules. The most commonly used methods to monitor LbL deposition on monodisperse PS latex particles for various substances are the SPLS method and microelectrophoresis. Inorganic [magnetite, silica, titania, and fluorescent quantum (Q) dots] nanoparticles,<sup>[14–16]</sup> lipids,<sup>[17–19]</sup> and proteins (albumin, immunoglobulin, and others)<sup>[7,20,21]</sup> were incorporated as building blocks for shell formation on colloidal particles. In Schuler and Caruso,<sup>[21]</sup> the construction of enzyme multilayer films on colloidal particles for biocatalysis was demonstrated. The enzyme multilayers were assembled on submicrometer-sized polystyrene spheres via the alternate adsorption of poly(ethyleneimine) and glucose oxidase. The high surface area of particles coated with biomultilayers was subsequently utilized in enzymatic catalysis. The step-by-step coating of different lipids alternated with polyelectrolytes was performed by the adsorption of preformed vesicles onto the capsule surface. As was shown by Moya et al.<sup>[18]</sup> the lipids form a bilayer structure on the surface of polyelectrolyte multilayers. The fabrication of inorganic shells on colloidal particles envisages the application of such core-shell structures in catalysis and colloidal band gap crystals.<sup>[14,16]</sup> Introducing magnetic particles into the shell composition opens the possibility of manipulating them by applying external field.<sup>[15,17]</sup>

## COLLOIDAL CORE DECOMPOSITION AND FORMATION OF HOLLOW CAPSULE

Different colloidal cores can be decomposed after multilayers are assembled on their surface. If the products of core decomposition are small enough to be expelled out of polyelectrolyte multilayers, the process of core dissolution leads to the formation of hollow polyelectrolyte shells (Fig. 1D–F). Up to now, various colloidal templates, such as organic templates [melamine formaldehyde (MF) particles, poly-D,L-lactic acid (PLA), or poly-D,L-lactic-co-glycolic acid (PDLA) microparticle and nanoparticle organic crystals], and inorganic cores, such as carbonate or silica oxide microparticles and biological cells, have all been used as templates for hollow capsule fabrication. Decomposition can be performed by different means, such as low pH for MF and carbonate particles;<sup>[22]</sup> organic water-miscible solvents for PLA, PDLA, or organic crystals;<sup>[23]</sup> and HF treatment for silica oxide microparticles, and strong oxidizing agents (NaOCl) for biological cells with same the MF particles.<sup>[24,25]</sup>



The formation of hollow capsules was more intensively studied on MF particles.<sup>[5,26]</sup> These particles dissolve onto oligomers at 0.1 M NaCl and in some water-miscible solvents such as DMF or DMSO. Subjecting the coated eight PSS/PAH layers of MF particles to low pH results in solubilization of the core. The MF oligomers, which have a characteristic cross-sectional extension of about 2–3 nm, are expelled from the core and permeate through the polyelectrolyte layers, forming the shells. This observation is consistent with the finding that polyelectrolyte-coated MF particles are readily permeable to molecules of a few nanometers in size.<sup>[4]</sup> The MF oligomers are finally separated from the hollow shells by centrifugation or filtration protocols.

The fabricated hollow polyelectrolyte capsules were characterized using scanning electron microscopy (SEM), transmission electron microscopy (TEM), atomic force microscopy (AFM), and confocal fluorescent microscopy techniques.<sup>[5–7,17,24,27]</sup> An AFM image of hollow polyelectrolyte capsules is shown in Fig. 4. The numerous folds and creases observed are attributed to the collapse of the hollow capsules under drying. The shells are flattened and some spreading is noticed. The diameter of the capsules shown in Fig. 4 is larger than the diameter of the templated MF particle (5  $\mu\text{m}$ ). This increase in diameter is ascribed to collapsing and adhesive forces attracting the polyelectrolyte shell to the surface. From the AFM image, it was also deduced<sup>[27]</sup> that the thickness of the polyelectrolyte film is on the order of 20 nm for the

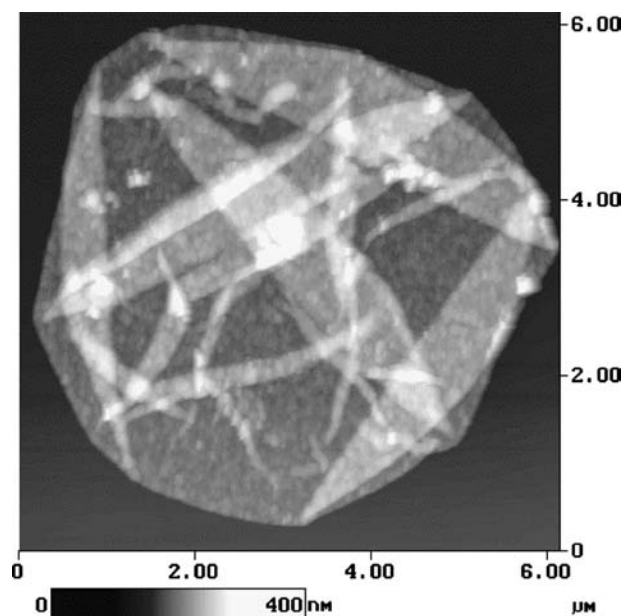


**Fig. 4** Atomic force microscopy image of the capsules composed of eight PSS/PAH layers templated on MF particles.

eight-layer polyelectrolyte film. This value is consistent with SPLS data on layer thickness obtained for polyelectrolyte-coated polystyrene particles (Fig. 3). Nevertheless, Gao et al.<sup>[26]</sup> reported on the rest of the core materials found in polyelectrolyte shells after MF particles decomposition.

The nature of the colloid does not significantly affect the thickness of the polyelectrolyte layers. It should be noted that the polyelectrolyte capsules completely repeat the shape of the templating colloids, as was shown by the example of echinocyte cells, which have starlike shape.<sup>[24]</sup> The choice of the core is determined by concrete tasks. For instance, carbonate cores are decomposable at  $\text{pH} < 4$ ; they are convenient to fabricate into hollow capsules composed of biological polymers. Calcium and manganese carbonate crystals were used as core materials for the fabrication of hollow polyelectrolyte capsules by means of LbL assembly in Ref.<sup>[28]</sup> The use of inorganic templates is a significant step toward the biocompatibility of polyelectrolyte multilayer capsules. Scanning electron microscopy and energy-dispersive X-ray (EDX) measurements proved the purity of the capsules from the core materials.

Another study proposed the use of decomposable biocompatible templates composed of PLA and PDLA.<sup>[23]</sup> These particles were used to build a shell composed of biocompatible polyelectrolytes. Uniform, complete coating with oppositely charged polyelectrolyte pairs was achieved for different combinations investigated. After core dissolution in water-miscible organic solvents such as acetone, stable hollow capsules with tailored properties were obtained. The results reported in Ref.<sup>[23]</sup> demonstrate that polyester microparticles could serve as viable alternative components to conventionally employed templates to derive hollow capsules with shape and shell thickness exploring a “biofriendly” process. The only drawback of such particles is some polydispersity in the size, but for many uses, this parameter is not important.

At present, hollow polyelectrolyte capsules with diameters varying from 0.2 to 10  $\mu\text{m}$  and with wall thicknesses from a few to tens of nanometers were obtained. Many compounds, such as synthetic and natural polyelectrolytes, dyes, and inorganic nanoparticles, were used as layer constituents to build the hollow capsules. Uniform inorganic and hybrid inorganic–organic hollow microspheres have been produced by coating colloidal core templates with alternating layers of oppositely charged nanoparticles and polymers, and thereafter removing the core by heating to 500°C.<sup>[14,29]</sup> Hollow rigid silica spheres were obtained by calcination of polymer latex spheres coated with multilayers of silica nanoparticles ( $\text{SiO}_2$ ) bridged by polycations.



## Permeability and Release Properties

The potential use of polyelectrolyte coating on colloidal particles as depot systems for controllable release requires data on the permeation of small molecules (molecular weights up to 500) through polyelectrolyte walls. To achieve sustained-release properties for shells, it would be advantageous to be able to decrease the layer permeability for small polar molecules once they are encapsulated. The small polar fluorescent markers, such as fluorescein, are reasonable models for permeability study. The formation of thicker capsule walls composed of polyelectrolyte multilayers with increasing layer number might be a way to decrease permeation. Verification of this approach was performed in Ref.<sup>[30]</sup>. Microparticles of fluorescein of about 5  $\mu\text{m}$  in size were covered with a different number of PSS/PAH polyelectrolyte layers in conditions where fluorescein is not soluble, pH = 2. It should be noted here that when pH = 2, both polyelectrolytes are strongly charged, and hence the resulting multilayer films possess the same amount of amino and sulfur groups. After multilayer formation, core dissolution was initiated by a pH change and monitored by increasing fluorescence in the bulk. The scheme on Fig. 5 illustrates coating fluorescein particles and subsequent fluorescein release when the particles become soluble. After LbL adsorption (Fig. 5A–C), core dissolution is initiated by changing the pH from 2 to 8 (Fig. 5D) and is completed after a certain period of time (Fig. 5E).

Fluorescein particles rapidly dissolve at pH 8. Thus the idea was to slow down the rate of core dissolving by covering the particles with polyelectrolyte multilayers. Shell walls consisting of a different number of layers were fabricated and examined with regard to their fluorescein permeability behavior. Fluorescence

spectroscopy is a convenient tool for the determination of the core dissolving rate because the fluorescence of the core is completely suppressed as a consequence of the self-quenching of the dye. On releasing the dye into the bulk, fluorescence intensity increases. Thus the rate of dissolving can be directly followed by measuring the fluorescence increase in the sample.

Fig. 6 shows typical time-dependent fluorescence curves obtained by switching the pH to 8. Fluorescein particles covered by layers of different thickness (9, 13, 15, and 18 layers) are compared with controls demonstrating the dissolving of naked fluorescein particles. As shown on release profiles after a comparatively short induction period, the rate of dissolving becomes constant before the fluorescence in the bulk finally levels off. The initially slowly increasing fluorescence is related to the start of core dissolving. At this stage of the process, the structure of the polyelectrolyte multilayer may change because of the nascent osmotic pressure coming from dissolved fluorescein molecules. Shortly after the beginning of core dissolution, the concentration of fluorescein inside the capsules becomes constant and almost saturated because a steady-state situation between progressing core dissolution and permeation is established. One may further assume a constant concentration gradient between the shell interior and the bulk because the bulk solution can be assumed as being infinitely diluted. Therefore the rate of fluorescein penetration through the polyelectrolyte layers to the bulk becomes constant. Indeed, a linear increase of the fluorescence is observed. This state corresponds to the stage of dissolution depicted in Fig. 5. The slope of the linear region decreases with the number of polyelectrolyte layers. Obviously, an increasing number of adsorbed layers reduce the fluorescein penetration. After the core is completely dissolved, the fluorescein concentration inside the shell equilibrates

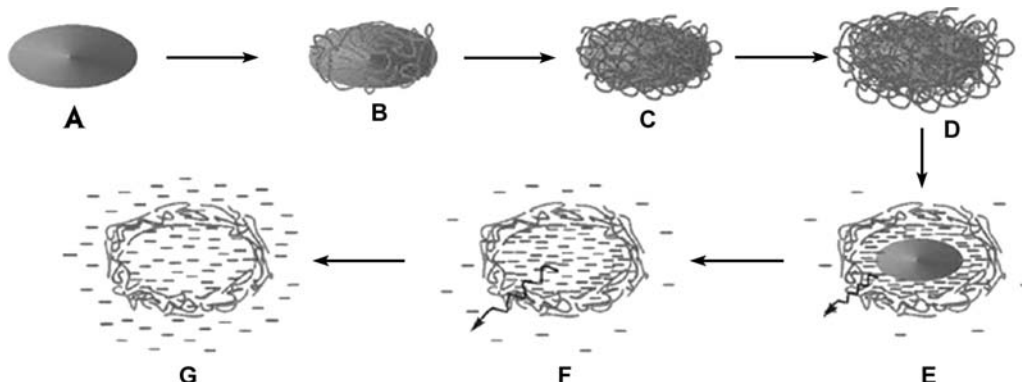


**Fig. 5** Scheme of the polyelectrolyte multilayer deposition process and of the subsequent core dissolution. The initial steps (A, B) involve stepwise shell formation on a fluorescein core. After the desired number of polyelectrolyte layers is deposited, the coated particles are exposed to pH = 8 (C) and core dissolution with fluorescein penetration into the bulk is initiated, resulting finally in fully dissolved cores and remaining empty capsules (D).

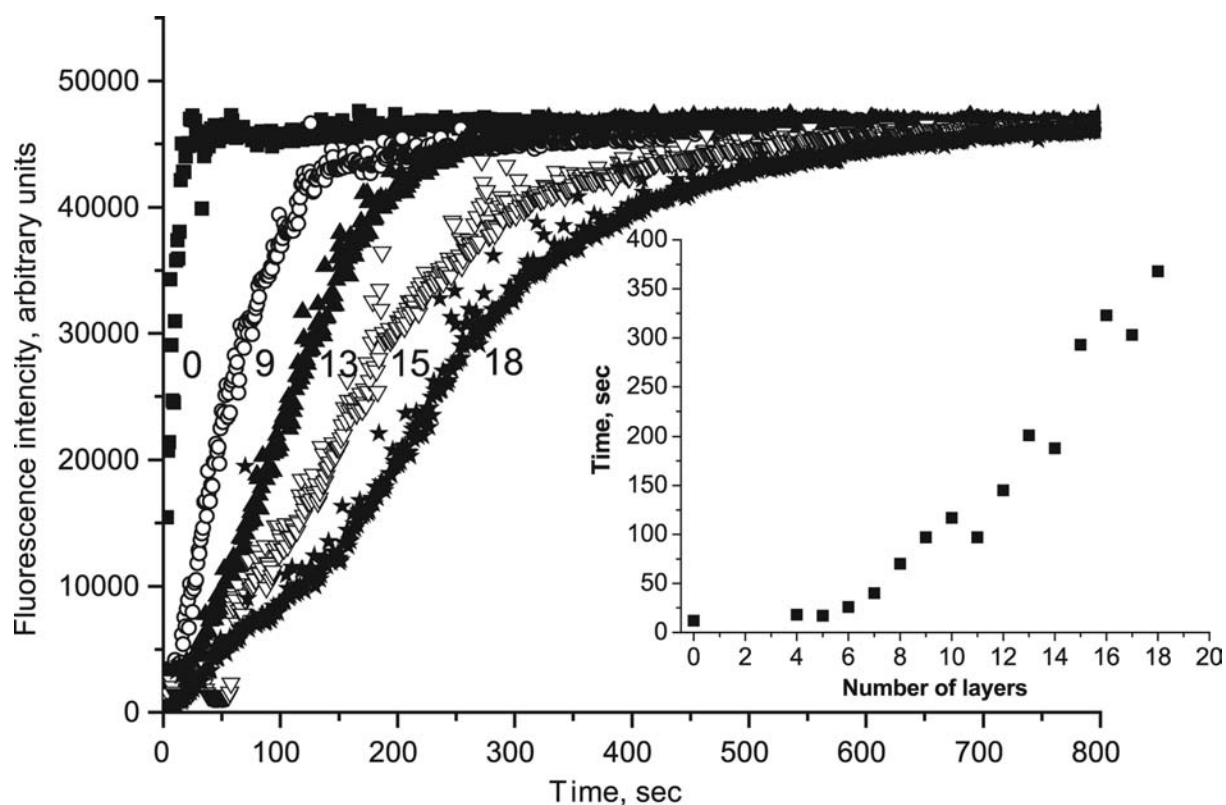


**Fig. 6** Fluorescence increase on time, obtained by dissolving fluorescein particles covered with shells of different thickness (9, 13, 15, and 18 layers), compared with naked (0) fluorescein particles. Inset: Time dependence of core decomposition time on the number of layers in the shells.

with the bulk. The driving force for diffusion decreases and the release levels off.

In Antipov et al.<sup>[30]</sup> the permeability value was found to be on the order of  $10^{-8}$  m/sec. Assuming a single polyelectrolyte layer thickness of 2 nm, the permeability can be converted into a diffusion coefficient ( $D$ ) by multiplying the permeability with the shell wall thickness. The calculated diffusion coefficients are on the order of  $10^{-15}$  m<sup>2</sup>/sec.

If the permeability of the polyelectrolyte multilayer is provided by diffusion through the entangled polymer network, it should scale with the inverse of the layer thickness. The behavior of the time of complete release as a function of the number of layers is shown in Fig. 6 (inset). As can be seen in Fig. 6, the increasing layer number sustains the fluorescein release. This effect becomes remarkable when the layer number exceeds eight, which corresponds to 15- to 20-nm-thick shell. This finding is consistent with observations<sup>[13]</sup> where it was shown that the conformation of the first eight layers differs from that of further assembled layers. These deeper layers are more dense and result in a five-fold reduction of the estimated diffusion coefficient. Naturally, these data are only particular to the case of PSS/PAH layers, and the permeation might be

different if the capsules are made of other polyelectrolytes. Nevertheless, the tendency to sustain the penetration of small molecules with layer number is demonstrated.

Polyelectrolyte complexes are known to be very sensitive to the presence of salt.<sup>[31]</sup> Therefore the permeability coefficient of polyelectrolyte multilayers is influenced by ionic strength. In the presence of small ions, ionic couples in multilayers are partially dissolved, which makes the polyelectrolyte film more penetrable for solutes.<sup>[32]</sup> Permeability coefficient data derived from release curves show a dramatic change of an increase of one order of magnitude in NaCl concentration change from 1 to 500 mM.<sup>[33]</sup>

Thus the polyelectrolyte multilayer shells with enough number of layers assembled around cores consisting of low-molecular-weight compounds provide barrier properties for release under conditions where the core is dissolved. Increasing the shell thickness to more than 20 nm might cause barrier difficulties for low-molecular-weight compounds passing through the capsule wall. Multilayer coating on microparticles and nanoparticles is a promising approach for the fabrication of systems with prolonged-release and controlled-release properties. The release can be

adjusted with the number of assembled polyelectrolyte layers. A large variety of synthetic polyelectrolytes with different properties, polysaccharides, and other biopolymers used for multilayer assembly may provide many possibilities to fine-tune the release properties of shells with biocompatibility and possibility of using various cores. The assembly of shells by LbL technique opens new pathways for biotechnological applications, where controlled release and sustained release of a substance are required. Many problems connected with drug formulation, release, and delivery; controlling concentrations in the organism; and the periodicity of its reception might be solved by the formation of shells on precipitates and nanocrystals. This approach has been already explored for drug formulations with controlled-release properties of biocompatible shells.<sup>[34,35]</sup> It seems to be not difficult to add targeting properties to the polyelectrolyte layer. This way, the affinity of polyelectrolyte multilayer-coated drugs to specific or injured tissues can be increased.

Thermal treatment of polyelectrolyte capsules results in the reduction of permeability coefficients. As investigated in Ref.<sup>[36]</sup>, the permeability coefficient of hollow capsules templated on MF cores can be decreased by two orders of magnitude. Thermal annealing of the capsules causes polyelectrolyte rearrangements, which leads to a more compact structure. Some defects in polyelectrolyte shells because of core dissolution processes can be repaired.

### Macromolecules Encapsulation

Basically, the multilayer polyelectrolyte capsules have semipermeable properties. If the film thickness is about

10–20 nm, small molecules can penetrate whereas high-molecular-weight compounds are excluded. However, there are several approaches to introduce macromolecules inside hollow polyelectrolyte capsules, when the core is decomposed. The first approach is opening and closing the pores in capsule walls in a controllable way. One can cause segregation in polyelectrolyte multilayers either by pH or solvent change. Indeed, polyelectrolyte multilayers undergo transition at a certain pH at about the  $pK$  of charged groups. This transition works on segregation because of the accumulation of charges by a network of entangled polyelectrolytes. As a result, such segregation leads to the formation of pores large enough for macromolecules to penetrate the capsule wall.<sup>[22,37]</sup> This process is completely reversible. Changing the pH back, the capsules become non-permeable for polymers again (Fig. 7). Thus the captured polymers stay inside. Several macromolecules, such as albumin, chymotrypsin, and dextran, have been encapsulated by this protocol.<sup>[37,38]</sup> The reversed segregation in polyelectrolyte multilayers can be introduced also by solvent mixtures such as water–ethanol, as was demonstrated by Lvov et al.<sup>[39]</sup> for encapsulation of proteins.

Another approach for encapsulation consists of the precipitation of polymers onto surfaces of colloid particles before the main multilayer buildup. The precipitated materials are harvested on the surface of particles. The proper choice of the concentration of particles, polymers, and the speed of heterocoagulation allows a smooth coverage of colloidal particles to form by precipitating polymers. A polyelectrolyte LbL shell is formed on particles already covered by precipitated polymers. After formation of the stable outer shell, the colloidal template could be decomposed. The

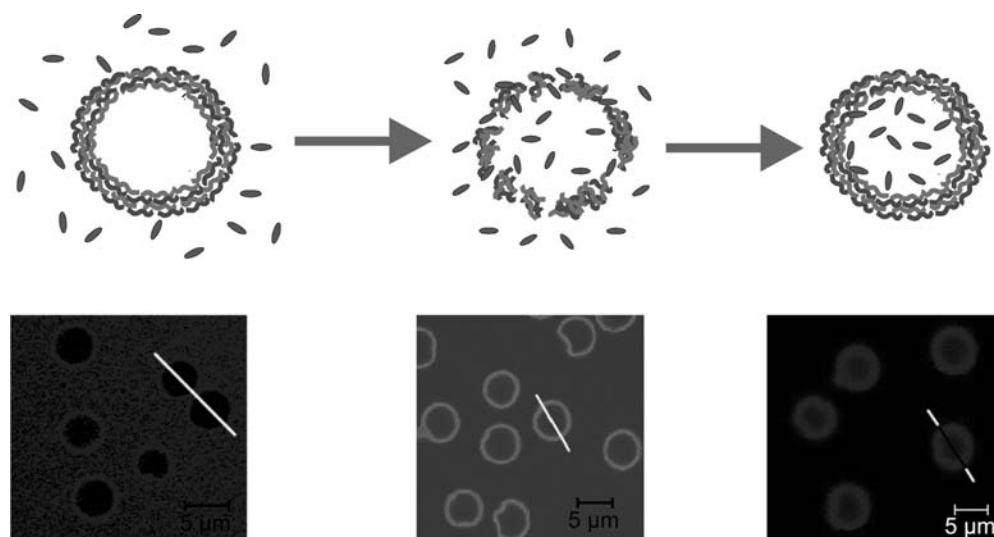


**Fig. 7** Permeation and encapsulation of dextran FITC into polyion multilayer capsules. Left,  $pH > 7$ ; middle,  $pH < 6$ ; and right, the capsule with encapsulated dextran FITC again at  $pH > 7$ .

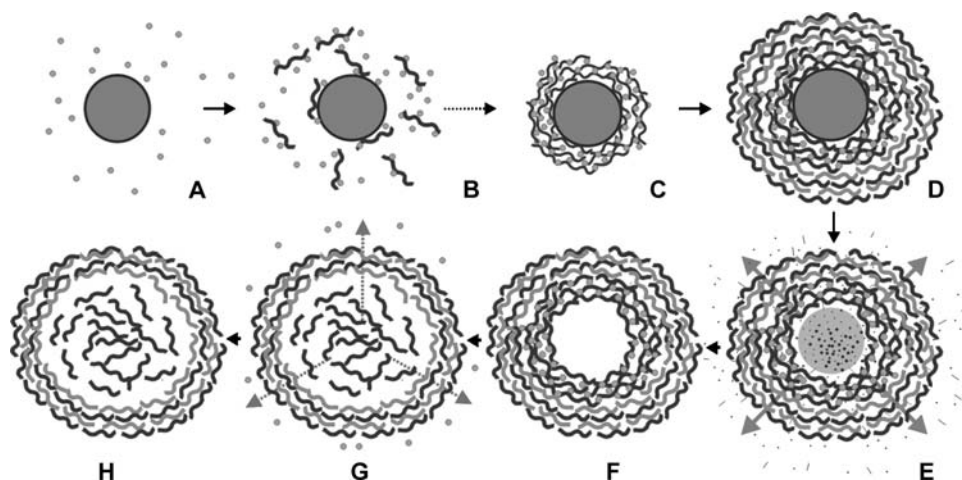


**Fig. 8** A schematic illustration of the preparation of a capsule loaded with polyelectrolytes.

polymer molecules underneath the stable shell can be dissolved in the shell interior. In fact, this approach comprises of three stages (Fig. 8): 1) precipitation of polymers on a colloidal surface (Fig. 8A–C); 2) capture of precipitated polymers on colloidal particles by stable shell formation (Fig. 8D); and 3) decomposition of the core; the products of decomposition are expelled through capsule wall, whereas the polymers dissolve and float in the capsule interior (Fig. 8E–H). This approach has been tested for encapsulation of non-charged polysaccharides (i.e., dextran and polyelectrolyte as PSS and PAH).<sup>[40]</sup> Dextran was precipitated by adding ethanol drop by drop whereas polyelectrolytes formed an insoluble complex with multivalent ions such as  $\text{Me}^{3+}$  and  $\text{CO}_3^{2-}$  for PSS and PAH, respectively. Some swelling of the capsule after polymer dissolution into the interior was observed because of osmotic pressure. Naturally, the amount of loaded polymers per capsule is the amount of all added polymers divided by the number of colloidal particles harvesting precipitating polymers. The possible loss of used polymers because of breakage of capsules did not exceed 10–15%. The described procedure allows the dosage of macromolecular contents in the capsule in tiny (less than nanograms) amounts.

To summarize the approaches on how to encapsulate the macromolecules by precipitation and then to capture by LbL shell fabrication, the positive and negative features should be stressed. In fact, encapsulation via precipitation could reach encapsulation efficiency close to 100%. Indeed, for encapsulation via harvesting of polymers on colloidal particles as described above, we have achieved about 80–90% encapsulation efficiency.<sup>[40]</sup> The more important peculiarities of using initial colloidal templates as polymer collectors are as follows: 1) the size distribution is

determined by original templates; 2) the amount of loaded polymers can be dosed and homogeneously distributed in each capsule; and 3) there are possibilities to load the capsule with several different substances. The last point has not yet been demonstrated, but one expects no significant difficulties in composing a multicomponent shell, and precipitating on the surface of colloidal particles several macromolecules, sequentially or at the same time, if they could be precipitated at the same condition. One has to consider only the compatibility of conditions for each precipitation step and further LbL fabrication of stable polyelectrolyte shells. The captured macromolecules are kept in the capsule interior until it is non-permeable for macromolecules. This might be utilized for fabricating enzyme microreactors when the substrates and reaction products diffuse through the capsule wall freely. The loaded macromolecules might be released after a certain pH or salt treatment.

## PHYSICOCHEMICAL REACTIONS INSIDE POLYELECTROLYTE CAPSULES

### Caused by pH Gradient

The capsule wall has semipermeable properties that allow for different physicochemical properties of the capsule interior compared to the exterior. Incorporation of polymers into the capsule allows the use of such capsules with modified inner volume for providing chemical reactions only in the capsule interior. Here we describe two possible ways for the precipitation of dyes as drug model substances within capsule interiors loaded with polymers. Precipitation occurs, then solubility dramatically decreases.

One can establish polarity or pH gradient through the capsule wall when the capsules are filled with certain polymers. Indeed, the presence of a polyelectrolyte on only one side of the membrane might significantly change such properties as pH value. For instance, if a polyanion is placed inside capsule, the pH value inside has to be acidic due to electroneutrality because  $H^+$  ions compensate for negative charges of polyanions. The resulting pH has to be closer to the  $pK$  value of charged groups of polyelectrolytes. This situation on pH gradient is considered in more details in Refs.<sup>[41,42]</sup> Here we give an illustration for the precipitation of carboxytetramethylrhodamines (CRs) inside the capsule. Carboxytetramethylrhodamine has pH-dependent solubility and becomes non-soluble at pH lower than 3.5. In the presence of capsules filled with PSS maintaining a pH value near 2.5, the CR molecules penetrate the capsule wall and, when facing lower pH, begin to precipitate. Here we provide typical SEM images of CR precipitates formed in the capsules (Fig. 9). The capsules look filled with solid materials.

As was shown previously, the encapsulated polyelectrolytes can establish pH gradient through the capsule wall. In particular, the capsules containing PAH have more basic pH than that in the outer solution. This method has been utilized for the selective synthesis of magnetic, 20-nm  $Fe_3O_4$  nanoparticles<sup>[43]</sup> and non-magnetic, elongated, 250-nm hematite  $Fe_2O_3$ <sup>[42]</sup> particles inside the polyelectrolyte capsules filled with polycations. The iron oxide particles were visualized by TEM (Fig. 10). The structure of the particles

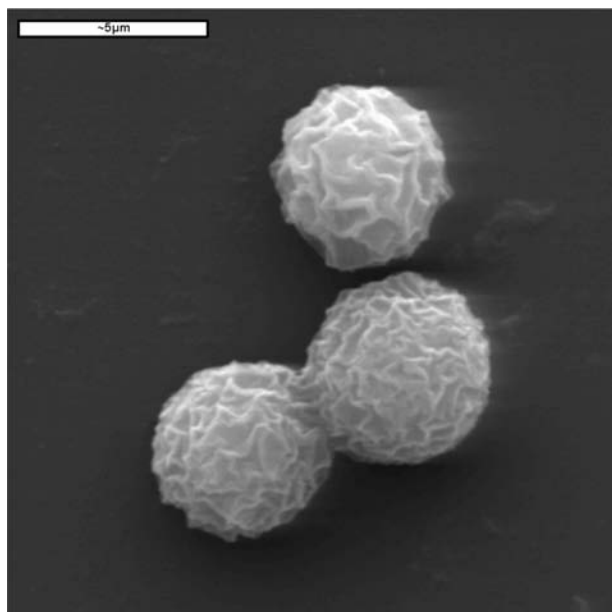


**Fig. 9** Scanning electron microscopy image of CR precipitates formed in capsules loaded with PSS.

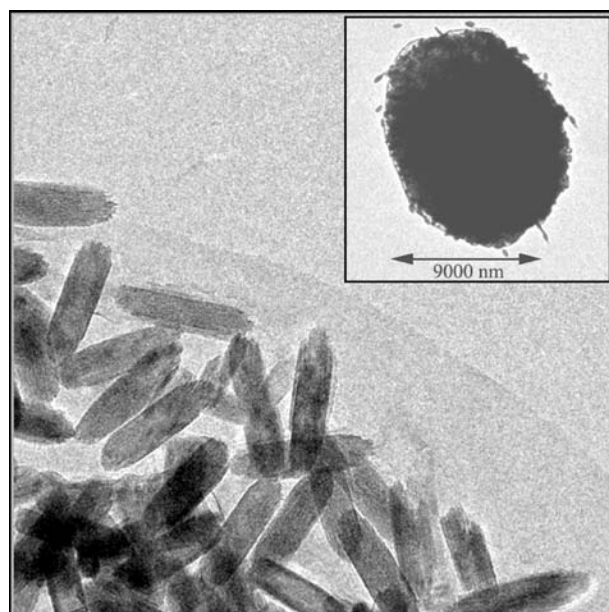


**Fig. 10** Transmission electron microscopy image of Fe-based precipitates (240-nm elongated iron oxide particles) in capsules filled with PAH.

depends on the given  $Fe^{2+}/Fe^{3+}$  ratio in the outer solution as was proven by wide-angle X-ray scattering (WAXS) measurements. These revealed diffraction peaks corresponding to  $Fe_2O_3$  and  $Fe_3O_4$  lattices. Besides magnetite, different ferrites ( $CoFe_2O_4$ ,  $ZnFe_2O_4$ , and  $MnFe_2O_4$ ) were synthesized from corresponding salts exclusively inside polyelectrolyte capsules of 6  $\mu m$  diameter.<sup>[43]</sup> Polyelectrolyte capsules with synthesized ferrite (magnetite) particles possess enough magnetic activity to be easily manipulated in water solution by an external magnetic field. The SEM images demonstrate that capsules with synthesized nanoparticles keep a bulky shape on drying, which is apparently because of the formation of rigid walls presenting inorganic nanoparticles glued to organic polymers.

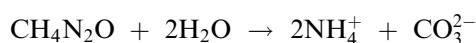
### Caused by Polarity Gradient

Another way to fill the capsule with small molecules is by establishing a polarity gradient of hydrophilic polymers. These capsules were suspended in a water/organic solvent mixture to keep a higher water content in the interior because of the hydrophilicity of encapsulated polyelectrolytes.<sup>[44]</sup> With the preparation of a water/acetone or water/acetone mixture with an overall high ratio of organic solvents, one can dissolve many poor water-soluble (PWS) molecules. However, inside the capsule, we have media with low solubility and PWS molecules should precipitate there. At slow

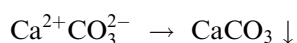
evaporation of organic solvents, the PWS molecules are collected in the capsule interior because of lower solubility there. Finally, one has an aqueous suspension of capsules containing precipitates of organic molecules.<sup>[44]</sup> Scanning electron microscopy images of capsules filled with PWS are similar to the image shown in Fig. 9. Incidentally, we found that the precipitates formed inside the capsules did not show any X-ray diffraction signals unless later annealed. Hence they are either amorphous or exist as nanocrystallites. This is a highly desirable feature for many drug applications because it facilitates dissolution and hence release.

## ENZYMATIC REACTIONS

In Lvov et al.<sup>[39]</sup> and Antipov et al.<sup>[45]</sup> the encapsulation of urease by solvent variation and its enzymatic activity were demonstrated. Urease catalyzes the reaction:



In the presence of  $\text{Ca}^{2+}$  ions, calcium carbonate is formed:



Carbonate ions generated by urease in the capsule interior immediately react with calcium ions and freely

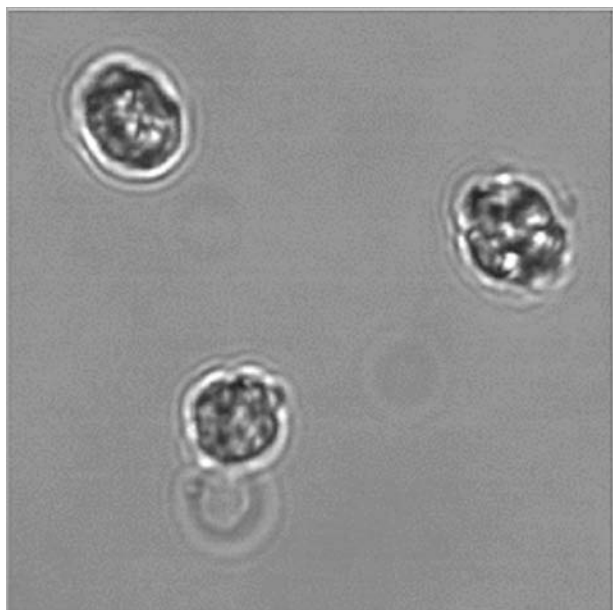


**Fig. 11** Optical microscopy image of urease-catalyzed  $\text{CaCO}_3$  crystal growth inside 5- $\mu\text{m}$  polyelectrolyte capsules.

diffuse through the capsule wall. As shown by Antipov et al.<sup>[45]</sup> calcium carbonate crystals presumably grow within the capsule interior until they occupy the whole capsule lumen (Fig. 11). The formation of calcium carbonate particles might also occur outside of the capsule because of the diffusion of carbonates, but in certain conditions, calcium carbonate particles might be found almost only inside the capsule. As investigated by electron diffraction, the lattices of calcium carbonate grown within the capsule interior exhibit vaterite structure. Remarkably, there was no growth of calcium carbonates over the capsule wall. Thus the microcapsules with an imported enzyme can be a suitable model to mimic inorganic processes in biological cells.

Another illustration of enzymatic reactions inside capsules has been reported in Ref.<sup>[38]</sup>. A proteolytic enzyme,  $\alpha$ -chemotrypsin, was homogeneously distributed in the capsule interior with a concentration of 50 g/L. Encapsulated chemotrypsin was found to retain a high physiological activity of about 70%, as shown with fluorescent products.

## CONCLUSION

The uniformity, simplicity, and versatility of possible applications are significant points of the abovescribed technology. The particular aspects coming from the basic concept of the technology are outlined in Fig. 12. As an initial matrix, we have a colloidal template. Organic and inorganic particles, drug nanocrystals, biological cells, protein aggregates, emulsion droplets, and, in fact, any colloidal particles ranging in size from 50 nm to tens of microns are possible templates to fabricate shells. The shell can be composed of a variety of materials. The choice of polymers to build the shell is determined by application to reach the desired stability and comparability. Actually, one could choose the proper line to pursue certain tasks using the scheme in Fig. 12 to achieve the desired characteristics of core-shell structures or capsules.

Selective shell permeability makes it possible to keep macromolecules in the capsules. Macromolecules can be incorporated into the inner volume of the capsule by different means, either through their aggregation in the solution or precipitation onto the surface of collecting colloidal particles, followed by their capture through the formation of stable polyelectrolyte shells afterward, or the opening and closing of pores in the capsule wall by pH, salt, and solvent. These approaches to load macromolecules into the capsules differ by the size of capsules, their monodispersity, low or high macromolecule concentrations in the capsules, encapsulation efficiency, and possibilities



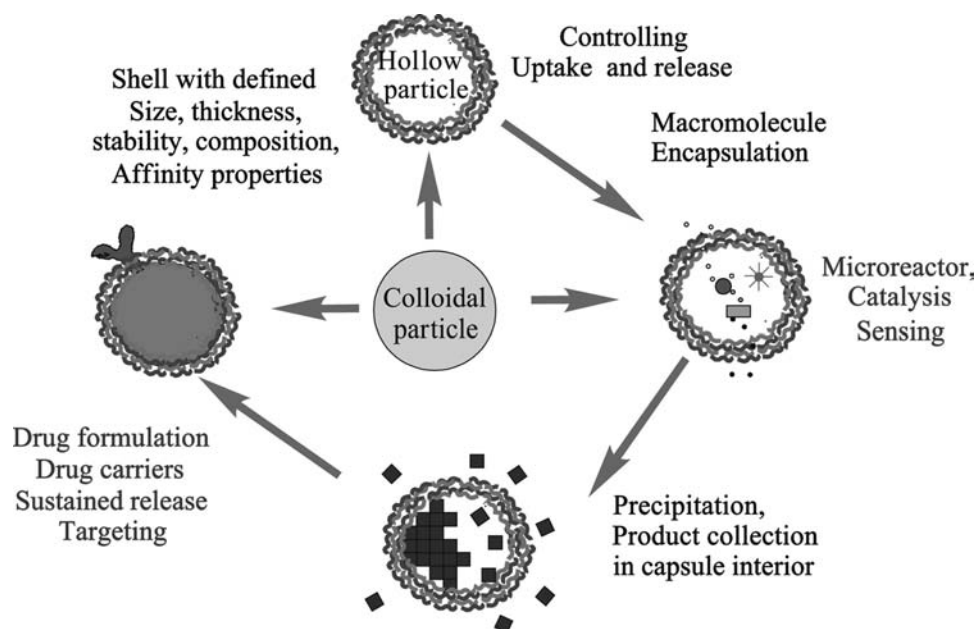


Fig. 12 Comprehensive illustration of applications of stepwise shell formation on colloidal particles.

to incorporate several substances in one capsule. Of course, the macromolecules can be incorporated as layer constituents during shell buildup. Layer-by-layer deposition on colloidal particles at fabrication could supply the LbL degradation of components afterward. One could find the optimum time scale for this process as well. Generally speaking, one also has to choose the most profitable way according to the aims these capsule are supposed to serve. Talking about encapsulation of enzymes, it should be stressed that selective permeability provides the elaboration of enzymatic microreactors where the proteins are placed into the capsule interior, whereas substrates and products of the one-step or multistep enzymatic reactions in the capsules can readily penetrate the capsule wall. In addition, the encapsulated enzymes have higher stability and are protected by the outer shell against high-molecular-weight inhibitors and proteolytic agents. The capsules themselves can be easily withdrawn from one solution, washed, and placed in another by filtration or centrifugation, or they can be driven by applying magnetic fields if the magnetite particles were used as layer constituents. We did not mention here any chemical treatment of the capsules after they have been assembled. Obviously, further modifications, such as cross-linking, can significantly change the properties of the capsules, such as permeability or stability.

The capsules might be used as combinatorial libraries. For instance, Gaponik et al.<sup>[46]</sup> modified the polyelectrolyte capsules with different semiconductor

luminescent nanoparticles (Q-dots). A variety of possibilities to impart fluorescent fingerprint characteristics (labelling with defined mixtures of different Q-dots) open an avenue to make many experiments with capsules in one pot. Indeed, the capsules of each functionality, size, or composition discriminated by unique fluorescent characteristics can be followed at the same time in *in vitro* or *in vivo* testing.

Fundamental research on these capsules should be mentioned. They represent a unique system to study the chemical and physical phenomena in micron-sized and submicron-sized volumes. In comparison with liposomes, the polyelectrolyte capsules, besides their higher stability, give the possibility of varying the content of the inner volume in a controllable way. Defined inner composition allows chemical reactions in restricted volumes, which has been demonstrated up to now only as precipitation reactions for small organic molecules and inorganic salts in the capsule interior. There are no doubts that such a philosophy might be expanded further. Selective permeability and related solubility, pH, and temperature are background parameters to modify the capsule interior. The complexity provides more possibilities. For example, if one establishes a different pH in the capsules loaded with different enzymes to achieve the optimal conditions for catalytic reactions in each capsule, these capsules might either exchange intermediate products or selectively collect them in each tape of capsules. These capsules might be a device to study single-molecule effects. Indeed, the concentration of substances

$10^{-7}$  M means about one molecule of this substance in capsules of 300 nm diameter. Defined inputs into the interior could register discrete chemical reactions occurring in the capsule interior.

The polyelectrolyte capsules could serve also as support for lipid bilayers. As shown in Refs.<sup>[19]</sup> and <sup>[47]</sup>, lipid bilayers assembled on polyelectrolyte capsules reduce the permeation for small ions. Thus there are perspectives to reconstitute channel formers into the lipid bilayer supported by polymeric shells and to use this as a stable model. Such research might aim to construct artificial cells, cell compartments, or artificial organs because of the emerging possibilities to introduce different substances into the capsule and build the shell (i.e., “membrane”) using a variety of compatible materials. The hollow and loaded capsules are novel types of cages for compartmentalization of materials, and are good models for research on biomineralization.

Mimicking the processes in biological cells and cell compartments foresees the involvement of a number of enzymes, which work together at the same time. The method of controllable opening and closing pores provides also a possibility to encapsulate several proteins at the same time and at certain concentrations in the capsules to catalyze sequential enzymatic reactions (for instance, glucose oxidation by glucose oxidase followed by utilization of hydrogen peroxide by peroxidase). The loaded enzyme, as we showed, might be released out of the capsule after a certain pH treatment, which could find some applications for systems with controlled release.

A wide range of possible uses, interplays of several approaches, the solving of different problems, and the focus on fundamental and application aspects in diverse areas of life and material sciences attract interest and stimulate further research on the development of approaches for nanoengineering surfaces of colloidal particles and polymeric capsules.

## ACKNOWLEDGMENT

The author expresses his gratitude to Prof. Dr. H. Möhwald (MPI Colloids and Interfaces, Potsdam) for continuous support of the work on this topic and stimulating discussions. Dr. E. Donath is acknowledged for fruitful collaboration over the years. Members of the group at MPI—Dr. A. Voigt, Dr. D. Shchukin, Dr. K. Glinel, Dr. D. Shenoy, Dr. O. Tiourina, I.L. Radtchenko, and A.A. Antipov—are thanked for providing a creative atmosphere, collaboration, and help in the research on nanoengineered polymeric microcapsules.

## REFERENCES

1. Iler, R.K. Multilayers of colloidal particles. *J. Colloid Interface Sci.* **1966**, *21*, 569–572.
2. Lee, H.; Kepley, L.J.; Hong, H.G.; Akhter, S.; Mallouk, T.E. Adsorption of ordered zirconium phosphonate multilayer films on silicon and gold surfaces. *J. Phys. Chem.* **1988**, *92*, 2597–2601.
3. Decher, G.; Hong, J.-D. Build up of ultrathin multilayer films by a self-assembly process: I. Consecutive adsorption of anionic and cationic bipolar amphiphiles. *Macromol. Chem., Macromol. Symp.* **1991**, *46*, 321–327.
4. Sukhorukov, G.B.; Donath, E.; Lichtenfeld, H.; Knippel, E.; Knippel, M.; Budde, A.; Möhwald, H. Layer-by-layer self-assembly of polyelectrolytes onto colloidal particles. *Colloids Surf., A* **1998**, *137*, 253–266.
5. Donath, E.; Sukhorukov, G.B.; Caruso, F.; Davis, S.; Möhwald, H. Novel hollow polymer shells: Fabrication, characterization and potential applications. *Angew. Chem., Int. Ed. Engl.* **1998**, *37*, 2201–2205.
6. Voigt, A.; Lichtenfeld, H.; Zastrow, H.; Sukhorukov, G.B.; Donath, E.; Möhwald, H. Membrane filtration for microencapsulation and microcapsules fabrication by layer-by-layer polyelectrolyte adsorption. *Ind. Eng. Chem. Res.* **1999**, *38*, 4037–4043.
7. Sukhorukov, G.B.; Donath, E.; Davis, S.A.; Lichtenfeld, H.; Caruso, F.; Popov, V.I.; Möhwald, H. Step-wise polyelectrolyte assembly on particle surfaces—A novel approach to colloid design. *Polym. Adv. Technol.* **1998**, *9*, 759–767.
8. Lvov, Y.M.; Decher, G.; Möhwald, H. Assembly, structural characterization, and thermal behaviour of layer-by-layer deposited ultrathin films of poly(vinyl sulfate) and poly(allylamine). *Langmuir* **1993**, *9*, 481–486.
9. Bobreshova, M.E.; Sukhorukov, G.B.; Saburova, E.A.; Elfimova, L.I.; Sukhorukov, B.I.; Sharabchina, L.I. Lactate dehydrogenase in interpolyelectrolyte complex. Function and stability. *Biophysics* **1999**, *44*, 813–820.
10. Balabushevitch, N.G.; Sukhorukov, G.B.; Moroz, N.A.; Larionova, N.I.; Donath, E.; Möhwald, H. Encapsulation of proteins by layer-by-layer adsorption of polyelectrolytes onto protein aggregates: Factors regulating the protein release. *Biotechnol. Bioeng.* **2001**, *76*, 207–213.
11. Trubetskoy, V.S.; Loomis, A.; Hagstrom, J.E.; Budker, V.G.; Wolff, J.A. Layer-by-layer deposition of oppositely charged polyelectrolytes on the surface of condensed DNA particles. *Nucleic Acids Res.* **1999**, *27*, 3090–3095.
12. Finsinger, D.; Remy, J.S.; Erbacher, P.; Koch, C.; Plank, C. Protective copolymers for nonviral gene vectors: Synthesis, vector characterization and application in gene delivery. *Gene Ther.* **2000**, *7*, 1183–1192.
13. Dallüge, R.; Haberland, A.; Zaitsev, S.; Schneider, M.; Zastrow, H.; Sukhorukov, G.; Böttger, M.

- Characterization of structure and mechanism of transfection-active peptide-DNA complexes. *Biochim. Biophys. Acta* **2002**, *1576*, 45–52.
14. Caruso, F. Hollow capsule processing through colloidal templating and self-assembly. *Chem. Eur. J.* **2000**, *6*, 413–419.
  15. Caruso, F.; Susha, A.S.; Giersig, M.; Mohwald, H. Magnetic core-shell particles: Preparation of magnetite multilayers on polymer latex microspheres. *Adv. Mater.* **1999**, *11*, 950–953.
  16. Rogach, A.; Sucha, A.; Caruso, F.; Sukhorukov, G.; Kornovski, A.; Kershaw, S.; Möhwald, H.; Eychmüller, A.; Weller, H. Nano- and microengineering: 3D colloidal photonic crystals prepared from submicron sized polystyrene latex spheres pre-coated with luminescent polyelectrolyte/nanocrystal shells. *Adv. Mater.* **2000**, *12*, 333–336.
  17. Sukhorukov, G.B.; Donath, E.; Moya, S.; Susha, A.S.; Voigt, A.; Hartmann, J.; Möhwald, H. Microencapsulation by means of step-wise adsorption of polyelectrolytes. *J. Microencapsul.* **2000**, *17*, 177–185.
  18. Moya, S.; Donath, E.; Sukhorukov, G.B.; Auch, M.; Bäuml, H.; Lichtenfeld, H.; Möhwald, H. Lipid coating on polyelectrolyte surface modified colloidal particles and polyelectrolyte capsules. *Macromolecules* **2000**, *33*, 4538–4544.
  19. Georgieva, R.; Moya, S.; Loporatti, S.; Neu, B.; Bäuml, H.; Reichle, C.; Donath, E.; Mohwald, H. Conductance and capacitance of polyelectrolyte and lipid-polyelectrolyte composite capsules as measured by electrorotation. *Langmuir* **2000**, *16*, 7075–7081.
  20. Caruso, F.; Fiedler, H.; Haage, K. Assembly of beta-glucosidase multilayers on spherical colloidal particles and their use as active catalysts. *Colloids Surf., A* **2000**, *169*, 287–293.
  21. Schuler, C.; Caruso, F. Preparation of enzyme multilayers on colloids for biocatalysis. *Macromol. Rapid Commun.* **2000**, *21*, 750–753.
  22. Antipov, A.A.; Sukhorukov, G.B.; Loporatti, S.; Radtchenko, I.L.; Donath, E.; Möhwald, H. Polyelectrolyte multilayer capsule permeability control. *Colloids Surf., A* **2002**, *198–200*, 535–541.
  23. Shenoy, D.; Antipov, A.A.; Sukhorukov, G.B.; Möhwald, H. Layer-by-layer engineering of biocompatible, decomposable core-shell structures. *Biomacromolecules* **2003**, *4*, 265–272.
  24. Neu, B.; Voigt, A.; Mitlohner, R.; Loporatti, S.; Donath, E.; Gao, C.Y.; Kiesewetter, H.; Möhwald, H.; Meiselman, H.J.; Bäuml, H. Biological cells, as templates for hollow microcapsules. *J. Microencapsul.* **2001**, *18*, 385–395.
  25. Georgieva, R.; Moya, S.; Hin, M.; Mitlohner, R.; Donath, E.; Kiesewetter, H.; Mohwald, H.; Bäuml, H. Permeation of macromolecules into polyelectrolyte microcapsules. *Biomacromolecules* **2002**, *3*, 517–524.
  26. Gao, C.; Moya, S.; Lichtenfeld, H.; Casoli, A.; Fiedler, H.; Donath, E.; Möhwald, H. The decomposition process of melamine formaldehyde cores: The key step in the fabrication of ultrathin polyelectrolyte multilayer capsules. *Macromol. Mater. Eng.* **2001**, *286*, 355–361.
  27. Loporatti, S.; Voigt, A.; Mithöhner, R.; Sukhorukov, G.B.; Donath, E.; Möhwald, H. Scanning force microscopy investigation of polyelectrolyte nano- and microcapsule wall texture. *Langmuir* **2000**, *16*, 4059–4063.
  28. Antipov, A.A.; Shchukin, D.; Fedutik, Y.A.; Petrov, A.I.; Sukhorukov, G.B.; Möhwald, H. Carbonate microparticles for hollow polyelectrolyte capsules fabrication. *Colloids Surf., A*, in press.
  29. Caruso, F.; Caruso, R.A.; Mohwald, H. Nanoengineering of inorganic and hybrid hollow spheres by colloidal templating. *Science* **1998**, *282*, 1111–1114.
  30. Antipov, A.A.; Sukhorukov, G.B.; Donath, E.; Möhwald, H. Sustained release properties of polyelectrolyte multilayer capsules. *J. Phys. Chem., B* **2001**, *105*, 2281–2286.
  31. Klitzing, R.V.; Mohwald, H. A realistic diffusion model for ultrathin polyelectrolyte films. *Macromolecules* **1996**, *29*, 6901–6907.
  32. Kabanov, V.; Zezin, A. Soluble interpolyelectrolyte complexes as a new class of synthetic polyelectrolytes. *Pure Appl. Chem.* **1984**, *56*, 343–350.
  33. Qiu, X.P.; Donath, E.; Mohwald, H. Permeability of ibuprofen in various polyelectrolyte multilayers. *Macromol. Mater. Eng.* **2001**, *286*, 591–597.
  34. Ai, H.; Jones, S.A.; de Villiers, M.M.; Lvov, Y. Nano-encapsulation of furosemide microcrystals for controlled drug release. *J. Control. Release* **2003**, *86*, 59–68.
  35. Antipov, A.A.; Sukhorukov, G.B.; Möhwald, H. Influence of the ionic strength on the polyelectrolyte multilayers permeability. *Langmuir* **2003**, *19*, 2444–2448.
  36. Ibarz, G.; Dahne, L.; Donath, E.; Mohwald, H. Controlled permeability of polyelectrolyte capsules via defined annealing. *Chem. Mater.* **2002**, *14*, 4059–4062.
  37. Sukhorukov, G.B.; Antipov, A.A.; Voigt, A.; Donath, E.; Möhwald, H. Incorporation of macromolecules into polyelectrolyte micro- and nanocapsules via surface controlled precipitation on colloidal particles. *Macromol. Rapid Commun.* **2001**, *22*, 44–46.
  38. Tiourina, O.P.; Sukhorukov, G.B. Multilayer alginate/protamine microcapsules: Encapsulation of alpha-chymotrypsin and controlled release study. *Int. J. Pharm.* **2002**, *242*, 155–161.
  39. Lvov, Y.; Antipov, A.A.; Mamedov, A.; Mohwald, H.; Sukhorukov, G.B. Urease encapsulation in nanoorganised microshells. *Nano Lett.* **2001**, *1*, 125–128.
  40. Radtchenko, I.L.; Sukhorukov, G.B.; Mohwald, H. Incorporation of macromolecules into polyelectrolyte micro- and nanocapsules via surface controlled precipitation on colloidal particles. *Colloids Surf., A* **2002**, *202*, 127–133.
  41. Sukhorukov, G.B.; Donath, E.; Brumen, M.; Mohwald, H. Hollow polyelectrolyte shells: Exclusion of polymers and Donnan equilibrium. *J. Phys. Chem., B* **1999**, *103*, 6434–6440.

42. Radtchenko, I.L.; Gierzig, M.; Sukhorukov, G.B. Inorganic particle synthesis in confined micron-sized polyelectrolyte capsules. *Langmuir* **2002**, *18*, 8204–8208.
43. Shchukin, D.; Radtchenko, I.L.; Sukhorukov, G.B. Synthesis of nanosized magnetic ferrite particles inside hollow polyelectrolyte capsules. *J. Phys. Chem., B* **2003**, *107*, 86–90.
44. Radtchenko, I.L.; Sukhorukov, G.B.; Mohwald, H. A novel method for encapsulation of poorly water-soluble drugs: Precipitation in polyelectrolyte multilayer shells. *Int. J. Pharm.* **2002**, *242*, 219–223.
45. Antipov, A.A.; Shchukin, D.; Fedutik, Y.; Zaneskina, I.; Klechkovskaya, V.; Sukhorukov, G.B.; Möhwald, H. Urease-catalyzed carbonate precipitation inside restricted volume of polyelectrolyte capsules. *Macromol. Rapid Commun.* **2003**, *24*, 274–277.
46. Gaponik, N.; Radtchenko, I.L.; Sukhorukov, G.B.; Weller, H.; Rogach, A.L. Toward encoding combinatorial libraries: Charge-driven microencapsulation of semiconductor nanocrystals luminescing in the visible and near IR. *Adv. Mater.* **2002**, *14*, 879–882.
47. Tiourina, O.P.; Radtchenko, I.L.; Sukhorukov, G.B.; Möhwald, H. Artificial cell based on lipid hollow polyelectrolyte microcapsules: Channel reconstruction and membrane potential measurement. *J. Membr. Biol.* **2002**, *190*, 9–16.

# Capsules: Specific Layer Structures

Lars Dähne

*Capsulation Nanoscience AG, Berlin, Germany*

Claire S. Peyratout

*Max Planck Institute of Colloids and Interfaces, Potsdam, Germany*

## INTRODUCTION

Encapsulation techniques gained great importance during the last decades to protect, store or release materials in well-defined ways. As in other technical fields, the miniaturization of capsules progressed parallel to the development of new materials and techniques. At the present time, microcapsules are already used in many technical applications in the pharmaceutical, cosmetic, food, textile, adhesive, printing, and agricultural industries.<sup>[1–5]</sup>

Several approaches are used to fabricate nanocapsules:<sup>[6]</sup> first, one can use aggregates of lipid molecules in spherically closed bilayer structures, the so-called vesicles or liposomes.<sup>[7,8]</sup> These relatively unstable structures can be stabilized by cross-linking. In a similar fashion, amphiphilic block copolymers in aqueous solution can also aggregate to vesicular structures.<sup>[9]</sup>

Other approaches to prepare capsules concern suspension and emulsion polymerization techniques around latex particles,<sup>[10,11]</sup> dendrimers or hyperbranched polymers.<sup>[12,13]</sup> Finally, one can cover a sacrificial template core with a membrane permeable for the products of core dissolution. Based on this approach, a new type of microcapsule prepared from polyelectrolytes (PE) was developed 5 years ago using the layer-by-layer (LbL) technology for encapsulating dissolvable templates in the micrometer and nanometer range (see Fig. 1).<sup>[14]</sup> The LbL technology enables the nanometer-precise assembling of multilayers. A wide variety of materials can be combined yielding capsules, which can have simultaneously several functions in the capsule wall as well as an adjustable semipermeability. Furthermore, the inner and outer capsule surface can be easily functionalized by biological or chemical binding sites, and the interior can be filled with macromolecules or with precipitates of low molecular weight agents. Monodispersity of the capsules can be achieved by using monodisperse templates.

## PREPARATION OF POLYELECTROLYTE CAPSULES

### LbL Method on Planar Substrates

In polymer thin films research, the most influential domain in the use of non-covalent interactions is the electrostatic layer-by-layer assembly.<sup>[15–18]</sup> This 11-year-old technique<sup>[8]</sup> is based on the alternating adsorption of multiply charged cationic and anionic species driven by electrostatic interactions (Fig. 1). During the self-assembly process of a polyion to an oppositely charged surface, the polymer adsorption proceeds until the surface charge is reversed. This allows in a next step the adsorption of a counterpolyion. The alternating adsorption of polycations and polyanions can be repeated at will. Because of the self-limitation of the process, the amount of polymer adsorbed in one step is constant and yields for usual polyelectrolytes a layer thickness of 1.5 to 3 nm.<sup>[19–21]</sup>

Diverse charged functional polymers have been successfully assembled into thin films by LbL (see reviews<sup>[19–21]</sup> and references therein) and comprise conducting and light-emitting polymers, non-conjugated redox-active polymers, reactive polymers, polymers bearing non-linear optically active dyes, liquid crystalline polyelectrolytes, temperature-sensitive and switchable polymers, and dendrimers. A variety of colloidal objects have also been placed in multilayer films, such as stable colloidal dispersions of charged silica, metal oxides, polyoxometalates, semiconductors, and fullerenes, as well as metal colloids, metallosupramolecular complexes, charged latex spheres, microcrystallites, clay platelets, or charged inorganic sheets. In addition, natural polyelectrolytes such as nucleic acids, proteins, polysaccharides, as well as certain charged supramolecular biological assemblies have been used for LbL.

In principle, all of these materials can also be combined for the preparation of polyelectrolyte capsules. However, some restrictions exist. First, assembling of

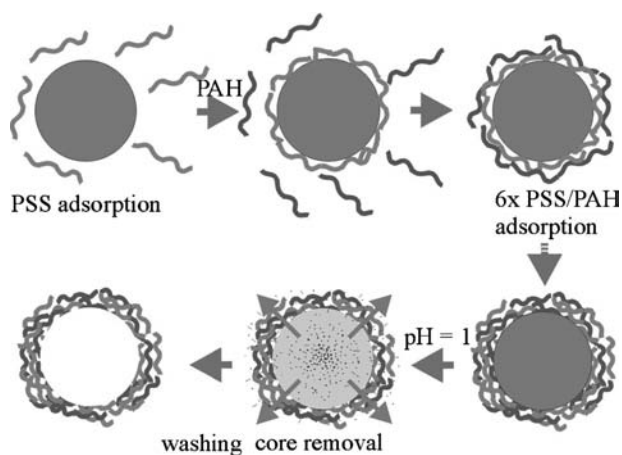


**Fig. 1** Preparation of hollow polyelectrolyte capsules: scheme of the polyelectrolyte deposition process and of subsequent MF-core decomposition.

polyelectrolytes on colloids does not allow a drying step after each layer, as it is often described with planar films. Second, colloidal suspensions in the nanometer- and micrometer-size range have to be stabilized against coagulation, which requires charged and hydrophilic surfaces. Third, the dissolution process of the templating core requires special conditions such as low pH, organic solvents, or oxidative environment. Fourth, the permeability of the LbL wall has to be tuned to allow the permeation (evacuation) of core dissolution products.

### LbL Technology on Colloidal Particles

As mentioned above, the initial colloidal substrate as well as each of the PE species have to be sufficiently charged to ensure adsorption and to prevent flocculation.<sup>[22–26]</sup> Moreover, it has to be ensured that the concentration of the adsorbing polyelectrolyte is large enough to provide saturation conditions. Incomplete covering yields charge differences within one colloidal batch, followed by coagulation. Excess polyelectrolyte molecules must be removed before adding the next PE to avoid formation of complexes in solution (Fig. 1). This separation can be achieved either by centrifugation or filtration.<sup>[27]</sup> Centrifugation yields often problems with resuspension, difficulties for smaller particles of low density to settle, loss of materials, and a lengthy process. The filtration method yields problems in filling the filters, in turn producing low yields. However, this method can be practically scaled-up and automated.<sup>[27]</sup> In particular, cross-flow filtration can solve the problems of small-scale batches.

### Removal of the Templates

The decomposition of the encapsulated template is a key step for the capsule fabrication (Fig. 1). Several

templates have been used for the capsule preparation such as weakly cross-linked melamine-formaldehyde lattice,<sup>[14]</sup> organic<sup>[28–30]</sup> and inorganic crystals,<sup>[31,32]</sup> silica particles, polystyrene lattice,<sup>[33]</sup> metal nanoparticles and nanorods,<sup>[34–36]</sup> and biological templates.<sup>[37–39]</sup> None of them has all qualities required for a “perfect” core, i.e., stability toward the LbL process, insensitivity of the multilayers structure at template dissolution conditions, and residues-free dissolution.

The majority of capsules have been prepared up to now with weakly polymerized, monodisperse melamine formaldehyde (MF) templates, produced in the size range from 300 to 10000 nm (Microparticle GmbH, Germany). The template can be dissolved in 0.1 M HCl within seconds into MF oligomers.<sup>[40]</sup> During the decomposition of the MF core, the capsules swell as demonstrated on a sample made with 6 layers of poly(allylamine) (PAH) and 6 layers of poly(styrene-sulfonate) (PSS) (Fig. 2). This swelling is caused by an elevation of the internal osmotic pressure induced by dissolved MF oligomers inside the capsules.<sup>[40]</sup> The capsules show a higher permeability as expected from planar and unstressed polyelectrolyte films of the same material and thickness. Presumably, the high mechanical pressure during the dissolution process induces pores in the capsule wall that determine the permeability more than the intrinsic diffusion properties of the polyelectrolyte films do.<sup>[41]</sup>

To reduce the permeability of MF capsules, further polyelectrolyte layers can be assembled after the dissolution of the core, resulting in a closing of the pores and a decrease of the permeability.<sup>[42]</sup> Another disadvantage of MF capsules is given by cytotoxic MF residues. Otherwise, the presence of MF residues was exploited for trapping water-soluble substances.<sup>[43–45]</sup> However, this encapsulation method is not controlled enough for viable applications.

Colloidal polystyrene (PS) latices have been used as core, which can be dissolved in tetrahydrofuran

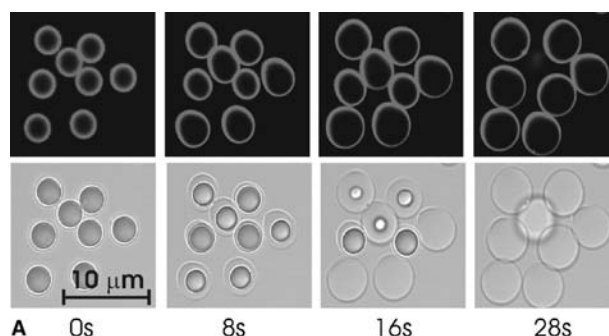


**Fig. 2** Swelling of capsules during the dissolution of MF templates encapsulated in 6 PAH/PSS bilayers in 0.1 M HCl (top confocal micrograph: fluorescence of the labelled wall, bottom: transmission micrograph).



(THF).<sup>[46]</sup> The swelling of PS in THF leads to a large volume increase that is directly often responsible for a high percentage of capsule fractures.

Red blood cells present an alternative to MF particles: they are available in nonspherical shapes, are quasi-monodisperse, and are inexpensive.<sup>[37]</sup> Moreover, the encapsulation of cells and cellular materials may have important applications in biotechnology and medicine. The decomposition of the biological templates is achieved by using a pH 12 sodium hypochlorite solution. However, under these harsh conditions, the polyelectrolyte wall is partly oxidized.<sup>[43]</sup>

A current development is the use of inorganic crystals such as  $\text{CdCO}_3$ ,  $\text{CaCO}_3$ , or  $\text{MnCO}_3$  as templates, which can be prepared in the range between 3 and 8  $\mu\text{m}$ . The dissolution is performed under mild conditions, and the products leave the capsule interior without problem.

Silicon dioxide particles have been used recently as templates and subsequently dissolved in hydrofluoric acid.  $\text{SiO}_2$  particles are available over a broad size range and high monodispersity. The core is decomposed in 1 M HF within few seconds into  $\text{SiF}_6^{2-}$  ions, which leave the capsule wall without problems. Confocal imaging of this dissolution process does not show any swelling of the capsule wall. Hence the mechanical stress applied onto the wall during the dissolution is negligibly small, and the polyelectrolyte layer structure is kept almost unchanged. Indeed, such capsules exhibit a lower permeability than capsules based on MF templates.

## PROPERTIES OF SIMPLE HOLLOW POLYELECTROLYTE CAPSULES

### Diameter

In general, the capsules size matches the template diameter. The size of hollow capsules ranges generally

between 500 nm and 5  $\mu\text{m}$ , but it can be extended below 100 nm and up to 15  $\mu\text{m}$ . However, for too thin walls or too large diameters, deviations from the spherical shape are reported.

### Wall Thickness

The wall thickness depends on the layer number and the material. The mostly used combination of PAH/PSS yields a thickness of around 4 nm per layer pair. These values have been measured by scanning force microscopy (SFM) on hollow capsules, dried on a mica substrate. During the drying process, the capsules collapse like an inflatable plastic ball after complete loss of the air. The thickness of the dry double wall can be taken directly from the profile of the atomic force microscopy (AFM) image (Fig. 3).

### Surface Charge

The outer surface charge of the capsules is simply determined by the last layer. The charge of the inner layer is assumed to correspond to the first layer on the former template. For example, in case of MF-templated capsules, the first layer PSS should result in a negative inner-layer surface. However, it is not quite clear how far adsorbed residues of positively charged MF oligomers influence the inner surface.

### Capsule Permeability

Capsule permeability has been tackled by two approaches. One approach consists in encapsulating soluble materials and in measuring their release from the capsule interior. Another approach consists in adding a fluorescence-labeled substance to the outer solution of a hollow capsules suspension and in monitoring the penetration into the capsules by means of confocal laser scanning microscopy (CLSM). Using

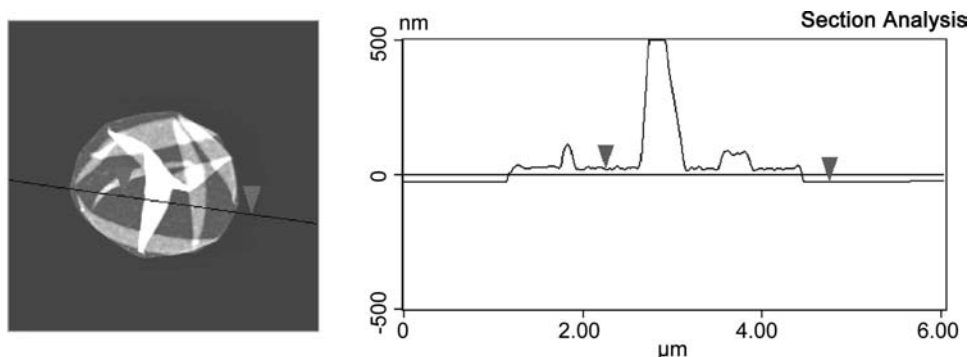


**Fig. 3** Scanning force microscopy image of a  $(\text{PAH}/\text{PSS})_4$  capsule, dried on mica and the corresponding height profile.

fluorescence-labeled PAH molecules, first rough estimations gave a cutoff of 5000 g/mol for capsules prepared from (PSS/PAH)<sub>4</sub> on MF cores.<sup>[14]</sup> In case of fast permeating smaller molecules, fluorescence recovery after photobleaching (FRAP) experiments have been performed. The dyes in the interior were bleached and the fluorescence recovery has been measured which is connected with the diffusion of fluorescence molecules from the outside to the interior.<sup>[42]</sup>

For the first approach, several fluorescent dyes were used as model and coated with various numbers of PSS/PAH multilayers under conditions of low solubility of the materials.<sup>[29,32,47]</sup> Results on PSS/PAH-encapsulated fluorescein reveal an increase of the release rate with pH and ionic strength and a decrease with the layer number (Fig. 4).<sup>[47]</sup> The diffusion coefficient per layer was determined to be approximately  $10^{-16}$  m<sup>2</sup>/sec in the presence of salt.

Similar results obtained with ibuprofen release studies support a model of two release channels, one by diffusion and one by pressure through pore-like structures presumably formed during the dissolution process.<sup>[48–52]</sup> Further studies showed that the permeability depends strongly on the polyelectrolyte material as known from planar films.<sup>[51]</sup> PAH/PSS MF capsules are less permeable than poly(diallyldimethylamine)/PSS capsules.<sup>[49]</sup>

The permeability depends furthermore on the environment such as ionic strength, pH and temperature.<sup>[55–62]</sup> It was reported that the permeability of PSS/PAH capsule could be controlled by pH<sup>[53]</sup> and ionic strength.<sup>[14,63]</sup> Capsules could be switched between an open (low pH or high ionic strength) and a closed state (high pH or low ionic strength). This was exploited for the encapsulation of macromolecules under mild conditions.

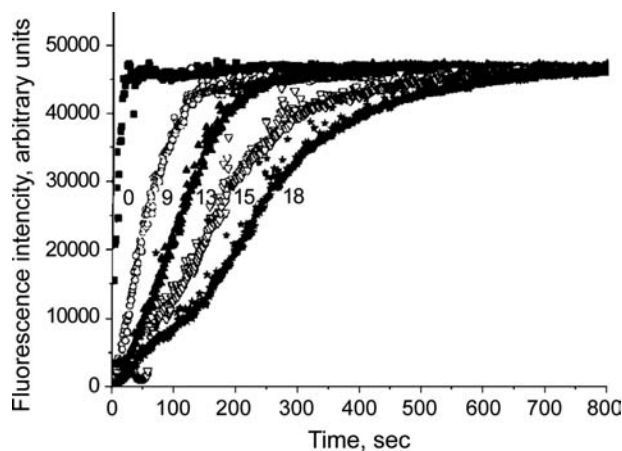


**Fig. 4** Release of fluorescein from encapsulated fluorescein crystals into a buffer solution as a function of the layer number. *Source:* From Ref.<sup>[29]</sup>.

## Mechanical Stability

Hollow capsules maintain a spherical shape up to a diameter of 15  $\mu$ m although the wall thickness is only 30 nm. The resistance against pressure was quantified by addition of polyelectrolytes to a capsule suspension. Because of the impermeability of the capsules for these molecules, high osmotic pressure from the outside modifies the capsules shape. Above a specific concentration of outside polymer or a critical pressure  $P_c$ , a shape transition from a spherical to a sickle shape was observed (Fig. 5). From this observation, an elasticity modulus between 500 and 700 Mpa was calculated. This value is comparable to macroscopic plastic materials, and reflect a high degree of local interactions between the polyanion and the polycation.<sup>[64,65]</sup>

The elasticity of capsules was investigated by loading microcapsules with 1 M PSS solution and decreasing the polyelectrolyte concentration outside. This leads to a swelling of the capsules proportional to the concentration difference.<sup>[72]</sup> Higher pressure caused the capsules to break. In contrast, at smaller swelling, a partly reversible elastic behavior was reported.<sup>[66]</sup> The investigation of the MF core dissolution, where a reversible swelling of the capsule was observed, also points to an elastic behavior (see Fig. 2).<sup>[40,67]</sup>

The deformability and osmotic properties of hollow PSS/PAH microcapsules assembled on the decomposable template MF were studied by means of the micropipette video microscopic technique.<sup>[68]</sup> The microcapsules reacted to micropipette suction with plastic deformation. The upper limit value of the plastic modulus  $D_p$  was evaluated at roughly 5 kPa. Addition of lipids yields a high degree of plasticity, at least in the range of the applied mechanical forces.<sup>[68]</sup>

## Physicochemical Stability

Standard PAH/PSS capsules are stable in aqueous solution between pH 0 and 13 and at high ionic strength. PAH/PSS capsules were also suspended in various organic media by a gradual solvent exchange with a preservation of shell stability and integrity.<sup>[53,69]</sup> The stability in organic solvents renders possible the preparation of oil-in-water or water-in-oil emulsions without employing any surfactants. The obtained microdrops are highly stable and have a high degree of monodispersity.<sup>[69]</sup>

Combinations of weak polyelectrolytes or of materials with only small amount of charges are more sensitive against pH and ion strength, which lead to strong enhancement of the permeability up to the dissolution of the LbL capsules.

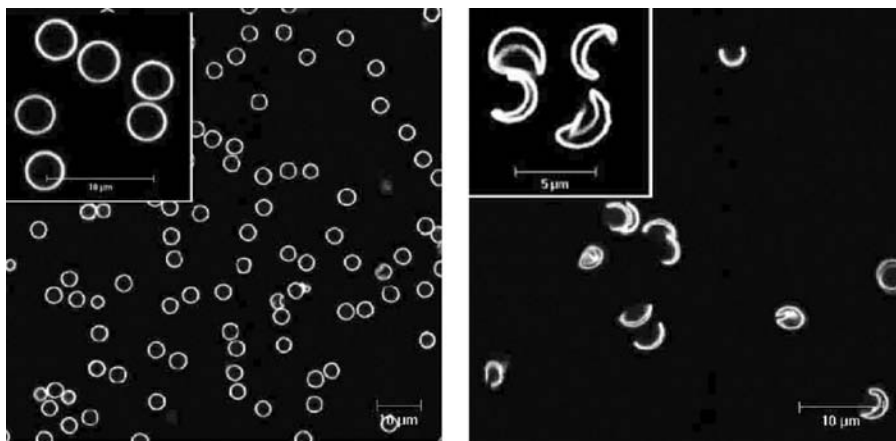


**Fig. 5** Transformation of the spherical capsules to a sickle shape under the osmotic pressure of an outer PSS solution. *Source:* From Refs.<sup>[64]</sup> and <sup>[65]</sup>.

## MODIFICATION OF THE POLYELECTROLYTE CAPSULES

Because of the variable applicability of the LbL process, the capsules can be widely modified. This concerns the interior, the wall, and the inner and outer surface of the capsule wall.

### Permanent Filling of the Interior with Functional Macromolecules

In most cases, precipitation of low molecular weight materials in presence of hollow capsules happens on the wall surface or in the bulk solution but not as desired in the interior of capsules.<sup>[70,71]</sup> A solution to tackle this problem is offered by immobilization of functional macromolecules in the capsule interior. They result in different physical properties of capsule interior and bulk solution and induce preferably precipitation inside the capsules. Three approaches have been followed to immobilize macromolecules permanently in the capsule interior (Fig. 6).

In the ship-in-bottle approach, monomers are incubated together with empty preformed shells (Fig. 6A).<sup>[72]</sup> After diffusion of monomers and initiator inside the shell, the polymerization is started inside and outside the capsule. The resulting polymers are trapped, and after washing, capsules filled with high polymer concentrations are isolated. This is demonstrated in Fig. 7A, where PSS copolymerized with acrylrhodamine is shown. The polymer concentration in the interior can be up to 1 monomolar, although the high osmotic pressure attained induce a remarkable capsule swelling. A drawback of this efficient method is the limitation to synthetic polymers.

For the encapsulation of preformed polymers or biomacromolecules, two other approaches have been developed. In one method, polymers are precipitated with complex-forming auxiliaries or alone under

specific conditions onto the melamine core (Fig. 6C).<sup>[66]</sup> Onto this initial layer, stable classical LbL polyelectrolyte multilayers are assembled. The core is removed, the initial layers are dissolved under specific conditions, and the auxiliaries are washed away. Then the inside of the capsules is filled with the polymer.<sup>[73]</sup> This approach requires for each application specific conditions under which the desired polymer can be precipitated and is difficult to implement practically.

Another approach for encapsulation consists in loading preformed capsules by switching the shell wall

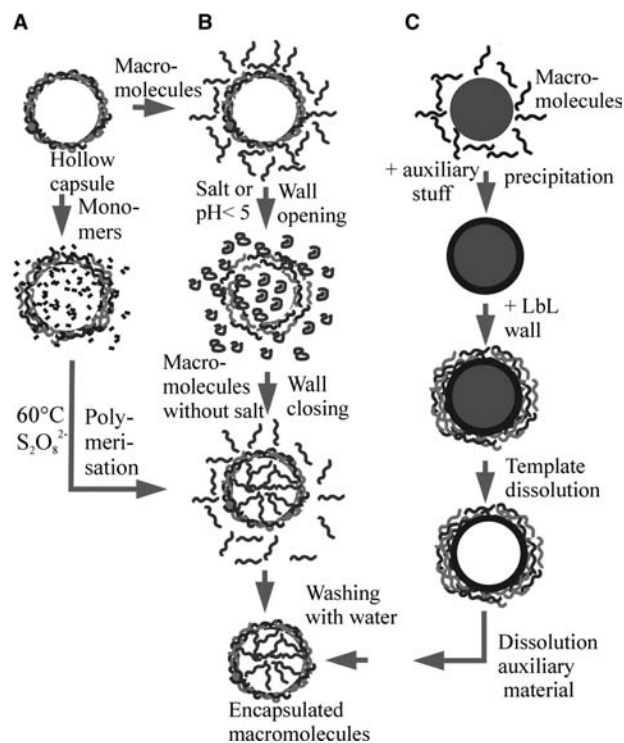


**Fig. 6** Methods to immobilize macromolecules in the capsule interior: (A) ship in bottle synthesis, (B) loading by switching the permeability, (C) loading by controlled precipitation.

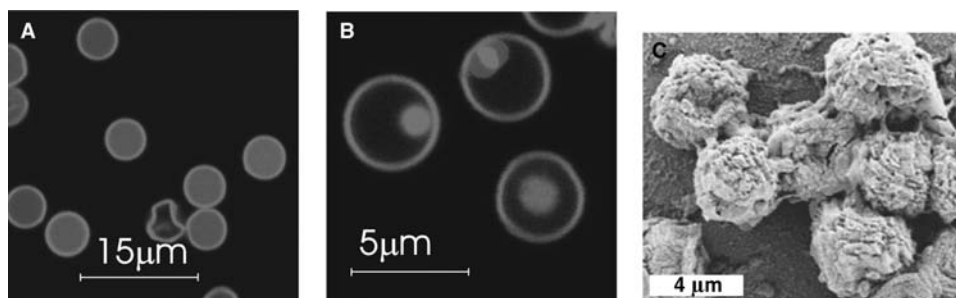


**Fig. 7** Confocal laser scanning images of capsules: (A) filled with PSS-rhodamine copolymer 0.5 M;<sup>[72]</sup> (B) capsules after complexation of PSS in the interior with fluorescent pseudoisocyanine J-aggregates;<sup>[54]</sup> (C) scanning electron microscopy image of CaCO<sub>3</sub> crystals grown in the capsule interior by enzymatic reaction. *Source:* From Ref.<sup>[72,54,83]</sup>

permeability through variation in environmental conditions, such as pH<sup>[41,74,75]</sup> or ionic strength (Fig. 6B).<sup>[76]</sup> In the capsule open state, surrounding macromolecules can diffuse into the interior. Switching the pH or ion strength back, the capsule wall closes and the macromolecules in the interior are captured. This method can only be performed with specifically designed capsules of suitable permeability. Furthermore, only low polymer concentrations can be achieved.

Capsules filled with functional polymers or with biomolecules can fulfill many tasks:

1. A gradient of the physicochemical properties between the outer and inner solution such as pH, ion strengths, polarity, charge distribution (Donnan potential), etc. can be used for the accumulation or selective precipitation of low molecular weight substances in the capsules. For example, if PSS-filled capsules (Fig. 7B) are placed in a mixture of water and non-polar solvents, the water content in the vicinity of the entrapped polyelectrolytes increases. This effect has been used for encapsulation of poorly water-soluble drugs.<sup>[77]</sup> Several dyes and inorganic salts, such as fluorescein, rhodamine, calcium carbonate, and barium carbonate, were precipitated inside PE capsules by using such gradients.<sup>[70,71]</sup> Electrostatic adsorption in polymer-filled shells has been used to trap semiconductor nanocrystals, iron oxide, or nanosized magnetic ferrite particles.<sup>[78–80]</sup>
2. The incorporation of polymer-bound catalysts or biocatalysts results in microreaction containers. Small molecular weight educts can diffuse into the capsules and react with the catalyst, and the products are released.
3. The capsule wall can prevent poisoning or destruction of biocatalysts because large molecules such as polymers, enzymes, and bacteria cannot enter the capsules. The concept of

macromolecule encapsulation in MF microshells by opening and closing pores was applied to enzymes. For instance,  $\alpha$ -chymotrypsin was encapsulated in hollow PSS/PAH shells by method 3. The protein in the capsules retained a high activity (50–60%) and long storage stability.<sup>[81]</sup>

Urease was also encapsulated into PSS/PAH shell using a similar approach: the pore-controlling factor was, in this case, the solvent choice.<sup>[82]</sup> Ethanol was added to a urease/microshells suspension and opened the pores.<sup>[44,45]</sup> Using these urease-loaded PAH/PSS capsules, calcium carbonate was synthesized exclusively inside of the capsules (Fig. 7C). The carbonate anions were generated inside of the capsules by a urease-catalyzed urea decomposition. Addition of calcium ions produced precipitation of calcium carbonate, which completely filled the capsule volume. Because of the easiness in varying experimental parameters, such as the wall thickness, internal composition, and influx, these PE capsule-based systems can be used to study fundamental aspects of biomineralization processes.<sup>[83]</sup>

Encapsulation of enzyme crystals or aggregates with the LbL technique<sup>[84,85]</sup> has been performed for chymotrypsin<sup>[86]</sup> and lactate dehydrogenase. The encapsulated lactate dehydrogenase exhibits increased lifetimes due to higher stability to denaturation and is not substrate-inhibited.<sup>[87]</sup>

### Modification of the Wall

So far, the most and best-studied polyelectrolyte association on surfaces, core shells, and capsules has been poly(allylamine)/poly(styrenesulfonate). Nevertheless, shells based on other synthetic polyelectrolytes such as poly(diallyldimethylamine), poly(ethyleneimine), or Nafion have recently been synthesized.<sup>[49,88]</sup> Because of the potential applications in the pharmaceutical industry, there are increasing activities in the

area of naturally occurring polyelectrolytes: recently, LbL capsules containing carrageenan,<sup>[89]</sup> dextran sulfate,<sup>[63]</sup> chitosan/chitosan sulfate,<sup>[90]</sup> sodium alginate, carboxymethyl cellulose,<sup>[48]</sup> or protamine<sup>[91]</sup> were reported. In contrast to planar films from biomolecules, the preparation of polyelectrolyte capsules is limited because of the harsh conditions used for the dissolution of the core. However, the development of new templates such as CaCO<sub>3</sub> particles extends the preparation possibilities. Decomposable hollow capsules based on deoxyribonucleic acid (DNA) and spermidine (SP) were already prepared.<sup>[33]</sup>

Several functionalities can be easily introduced in the capsule wall using polymers which were labeled before the assembly process. Capsules with increased stability have been prepared by cross-linking of water-soluble ionene precursor polymers yielding luminescent conjugated oligofluorenes.<sup>[46]</sup> A copolymer of poly(aniline) and PSS was introduced to obtain walls with reducing properties.<sup>[92]</sup> By using polymers presenting photoreactive diazo groups, the ionic bonds between the negative PSS and the positive diazoresin are converted to covalent cross-links. Cross-linked hollow capsules are mechanically more stable in various chemical environments than their ionically linked counterparts.<sup>[93]</sup> Photochromic hollow shells using an azobenzene-containing polymer were produced.<sup>[89]</sup>

The use of hollow or filled capsules for combinatorial purposes requires a tagging of the capsule wall. Polymers with covalently bound fluorescent dyes have been incorporated in the capsule walls. A luminescent library of (PAH/PSS)<sub>5</sub> capsules were prepared by

assembling four different dyes, each covalently attached in several PAH layers. Different layer combinations yielded 16 tagged capsules (Fig. 8). The intermediate layers minimize perturbing interactions between the layers. Although all capsules have the same size and properties, they can easily be distinguished by multichannel confocal fluorescence microscopy or by flow cytometry.<sup>[94]</sup>

Water-insoluble organic dyes were incorporated in capsule walls by depositing them in nonaqueous solution alternatively with polyelectrolytes in aqueous solution.<sup>[95]</sup> Using different fluorescent dyes, a two-step energy transfer cascade in the wall of hollow microcapsules was constructed.<sup>[96,97]</sup> The dyes were assembled in such a way that fluorescence resonance energy transfer through the capsule wall from outside to inside happened. Nanoporous capsule walls or shell-in-shell structures have been constructed by consecutive alternating adsorption of polyelectrolytes and SiO<sub>2</sub> on melamine formaldehyde particles, followed by removal of MF cores with HCl acid and of the sandwiched SiO<sub>2</sub> particle layers between indestructible PAH/PSS walls with HF. The inner and outer shell could be distinguished by labeling the inner shell with fluorescein and the outer shell with rhodamine B. Although the distance between the two shells is only 50 nm, confocal microscopy could resolve this difference (Fig. 9).<sup>[98]</sup> The two shell walls are separated by an intermediate PAH solution which acts as an osmotic pressure buffer and yields higher mechanical stability against outside pressure.<sup>[98]</sup>

Several inorganic materials can be prepared as charged nanoparticles. SiO<sub>2</sub>, TiO<sub>2</sub>, laponite,<sup>[99]</sup> and

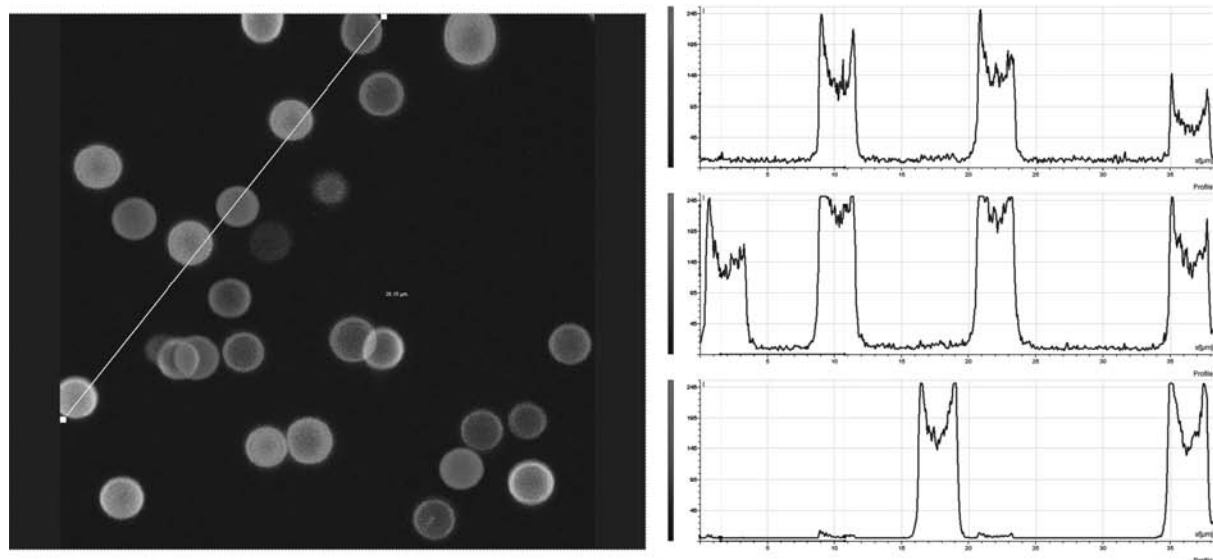


**Fig. 8** Combinatorial library of (PAH/PSS)<sub>5</sub> capsules with different combinations of dye molecules (fluorescein, rhodamine, Cy5, and pyrene) covalently linked to the PAH layers in the capsule wall; the right image shows the fluorescence intensity along a line through the dye tagged capsules. One can clearly differentiate the dye constituents and their amount.

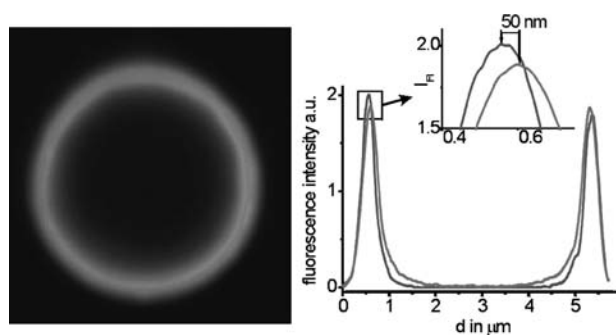


**Fig. 9** Confocal image of a shell in shell structure. The outer shell is labeled by fluorescein and the inner shell is labeled by rhodamine; the right image shows the distance between both shells, analyzed by two-color imaging. *Source:* From Ref.<sup>[98]</sup>.

CdTe nanoparticles have been used for the preparation of capsules.<sup>[100–102]</sup> Incorporation of colloidal dispersion of charged silica nanobeads as one of the wall components led to composite organic/inorganic colloidal materials.<sup>[103–105]</sup> Depending on the method chosen to remove the core, one obtains either a hollow inorganic/organic hybrid wall by dissolution of the MF core in HCl or a hollow silica sphere by thermal decomposition of the organic compounds.<sup>[106,107]</sup> Calcination of a composite between core-shell silica and gold nanoparticles (Au@SiO<sub>2</sub>)/PDADMAC deposited onto polymer spheres gave rise to hollow spheres of Au@SiO<sub>2</sub>.<sup>[110]</sup> Noble metals, such as silver, were incorporated either inside the capsule or in the capsule wall.<sup>[92]</sup>

Functional nanoparticles were incorporated into capsules to introduce magnetic, fluorescent, or catalytic properties. Superparamagnetic magnetite (Fe<sub>3</sub>O<sub>4</sub>) was mounted as a component of the shell wall<sup>[108–111]</sup> or as a part of the capsule interior.<sup>[79]</sup>

The combination of lipids and PE capsules creates an artificial system, mimicking biological membranes. Confocal microscopy images of capsules coated with fluorescent lipids demonstrated, within the resolution of the instrument, a homogeneous coverage of the capsule surface by lipid bilayers or multilayers.<sup>[112]</sup> The permeability for polar substances decreased remarkably after deposition of the lipid bilayer onto the hollow PE capsules. However, studies on electrical properties showed an increase in conductivity with the bulk electrolyte concentration, which was attributed to the presence of pores or defects in the lipid film.<sup>[113]</sup>

### Modification of the Surface

The outer surface of polyelectrolyte capsules can be functionalized using in the last assembling step a polyelectrolyte which contains the desired function. The

simplest example to tune the surface charge is the choice of a cationic or anionic polyelectrolyte. A more sophisticated application is the introduction of a high density of coupling sites, where subsequent functionalization can be performed. The commonly used chemical surface groups such as carboxyl or amino functions can be easily introduced by using poly(acrylic acid) or poly(allylamine). The disadvantage of the last layer is its stability in solution. While the inner layers of LbL films are fully immobilized, the outermost layer equilibrates in a solution because of the high charge density. Hence some of the polymer chains containing functional groups get lost under extreme conditions such as high or low pH, high ionic strength, etc. This problem can be solved by cross-linking the last layer.

### CONCLUSION

One important milestone in the fast development of the LbL polyelectrolyte films<sup>[14,115]</sup> was their use in 1998 for the preparation of hollow capsules. These closed LbL films extended remarkably the application fields of the method. The large versatility and modularity of the LbL capsules led to a fast development in the last 5 years as demonstrated on the selected examples in this review.

The LbL capsules will not substitute all other encapsulation technologies, but due to their specific properties, they can contribute to new applications especially in high technology fields. These properties are summarized in the following paragraph, together with the actual drawbacks and problems:

- The capsule preparation is simple and does not need expensive equipment, but the procedures are rather time-consuming. In addition, an upscaling of the process is under way, but not solved yet.
- The selection of arbitrary templates allows the preparation of capsules in a wide size range, with a well-defined shape and a high monodispersity, but the ideal template has not been found yet. Therefore, the LbL film is stressed during the core dissolution, leading to changes in permeability, size and internal structure as well as to remaining residues of the templates.
- The capsules exhibit semipermeable properties, which can be tuned in a broad region by the layer number, the material, or subsequent crosslinking. However, the permeability could not be lowered enough for the encapsulation of small water-soluble molecules.
- PSS/PAH capsules possess an extremely high physicochemical stability against aggressive media,



like acids, bases, high salt contents and organic solvents. But also instable capsules can be designed, which decompose under defined circumstances and release their interior.

- Interior, wall and outer surface of LbL capsules can be more easily modified than in other capsule systems. The nanometer precise deposition of functionalized layers and intermediate layers allows the combination of many different functions in one capsule without cross-reactions.

Due to the short time of the capsule development and the almost infinite possibilities to vary parameters in the preparation process, there are still many open questions, but also a very high potential for further important developments in this field. Especially in the bio-sciences, many surprises can be expected due to the potential of the capsules to serve as model systems for cells, viruses etc. The use of PE shells as biomimetic systems is under research as for example combinations of capsules and lipid bilayers equipped with ion channels. Research on modifications of the capsule surface in order to recognize specific biological materials or interfaces is started. The use of the capsules as micro-vessels for DNA amplification (PCR) or as non-viral gene transfection systems is planned. One important step is the further miniaturization down to 30 nm which has been recently achieved without aggregation.<sup>[118]</sup>

## REFERENCES

1. Brannonpeppas, L. Controlled-release in the food and cosmetics industries. *ACS Symp. Ser.* **1993**, *520*, 42–52.
2. Jung, J.; Perrut, M. Particle design using supercritical fluids: literature and patent survey. *J. Supercrit. Fluids* **2001**, *20* (3), 179–219.
3. Rafler, G. Mikropartikel in Forst und Landwirtschaft. *Spektrum Wiss.* **1994**, 122–124.
4. Schleicher, L.; Green, B.K. Manifold Record Material. US Patent US2,730,456, January 10, 1956.
5. Wasan, K.M. Formulation and physiological and biopharmaceutical issues in the development of oral lipid-based drug delivery systems. *Drug Dev. Ind. Pharm.* **2001**, *27* (4), 267–276.
6. Meier, W. Polymer nanocapsules. *Chem. Soc. Rev.* **2000**, *29* (5), 295–303.
7. Lutz, S.; Essler, F.; Panzner, S. Serum stable nanocapsules from liposomal templates. In *Controlled Release Society 29th Annual Meeting*; 2002.
8. Decher, G.; Hong, J.D.; Schmitt, J. Buildup of ultrathin multilayer films by a self-assembly process 3. In *Consecutively Alternating Adsorption of Anionic and Cationic Polyelectrolytes on Charged Surfaces*; Thin Solid Films; 1992; *210* (1–2), 831–835.
9. Forster, S.; Plantenberg, T. From self-organizing polymers to nanohybrid and biomaterials. *Angew. Chem., Int. Ed.* **2002**, *41* (5), 689–714.
10. Renken, A.; Hunkeler, D. Microencapsulation: a review of polymers and technologies with a focus on bioartificial organs. *Polimery* **1998**, *43* (9), 530–539.
11. Hunkeler, D. Polymers for bioartificial organs. *Trends Polym. Sci.* **1997**, *5* (9), 286–293.
12. Manna, A.; Imae, T.; Aoi, K.; Okada, M.; Yogo, T. Synthesis of dendrimer-passivated noble metal nanoparticles in a polar medium: comparison of size between silver and gold particles. *Chem. Mater.* **2001**, *13*, 1674–1681.
13. Sunder, A.; Kramer, M.; Hanselmann, R.; Muhaupt, R.; Frey, H. Molecular nanocapsules based on amphiphilic hyperbranched polyglycerols. *Angew. Chem., Int. Ed. Engl.* **1999**, *38*, 3552–3555.
14. Donath, E.; Sukhorukov, G.B.; Caruso, F.; Davis, S.A.; Moehwald, H. Novel hollow polymer shells by colloid-templated assembly of polyelectrolytes. *Angew. Chem., Int. Ed.* **1998**, *37* (16), 2202–2205.
15. Decher, G. Layered nanoarchitectures via directed assembly of anionic and cationic molecules. In *Comprehensive Supramolecular Chemistry*; Sauvage, J.-P., Ed.; Pergamon Press: Oxford, 1996; 507–552.
16. Decher, G. Fuzzy nanoassemblies: toward layered polymeric multicomposites. *Science* **1997**, *277* (5330), 1232–1237.
17. Decher, G.; Eckle, M.; Schmitt, J.; Struth, B. Layer-by-layer assembled multicomposite films. *Curr. Opin. Colloid Interface Sci.* **1998**, *3* (1), 32–39.
18. Knoll, W. Self-assembled microstructures at interfaces. *Curr. Opin. Colloid Interface Sci.* **1996**, *1* (1), 137–143.
19. Bertrand, P.; Jonas, A.; Laschewsky, A.; Legras, R. Ultrathin polymer coatings by complexation of polyelectrolytes at interfaces: suitable materials, structure and properties. *Macromol. Rapid Commun.* **2000**, *21*, 319–348.
20. Arys, X.; Jonas, A.; Laschewsky, A.; Legras, R. *Supramolecular Polymers*; Marcel Dekker: New York, 2000; 505–563.
21. Decher, G. Polyelectrolyte multilayers, an overview. In *Multilayer Thin Films*; Decher, G., Schlenoff, J.B., Eds.; Wiley VCH: New York/Bassel, 2003; 1–46.
22. Moehwald, H.; Lichtenfeld, H.; Moya, S.; Voigt, A.; Baumler, H.; Sukhorukov, G.; Caruso, F.; Donath, E. From polymeric films to nanoreactors. *Macromol. Symp.* **1999**, *145*, 75–81.
23. Moehwald, H. From Langmuir monolayers to nanocapsules. *Colloids Surf., A Physicochem. Eng. Asp.* **2000**, *171* (1–3), 25–31.
24. Moehwald, H.; Donath, E.; Sukhorukov, G.B. Smart capsules. In *Multilayer Thin Films*; Wiley VCH: New York, 2003; 363–392.
25. Sukhorukov, G.B. Designed nano-engineered polymer films on colloidal particles and capsules. In *Novel Methods to Study Interfacial Layers*; Miller, M.R., Ed.; Elsevier Science, 2001; 384–414.
26. Sukhorukov, G.B. Multilayer Hollow Microspheres. In *MML Series*; Citus Books, 2002; 111–147.

27. Voigt, A.; Lichtenfeld, H.; Sukhorukov, G.B.; Zastrow, H.; Donath, E.; Baumler, H.; Moehwald, H. Membrane filtration for microencapsulation and microcapsules fabrication by layer-by-layer polyelectrolyte adsorption. *Ind. Eng. Chem. Res.* **1999**, *38* (10), 4037–4043.
28. Caruso, F.; Yang, W.J.; Trau, D.; Renneberg, R. Microencapsulation of uncharged low molecular weight organic materials by polyelectrolyte multilayer self-assembly. *Langmuir* **2000**, *16* (23), 8932–8936.
29. Antipov, A.A.; Sukhorukov, G.B.; Donath, E.; Moehwald, H. Sustained release properties of polyelectrolyte multilayer capsules. *J. Phys. Chem., B* **2001**, *105* (12), 2281–2284.
30. Trau, D.; Yang, W.J.; Seydack, M.; Caruso, F.; Yu, N.T.; Renneberg, R. Nanoencapsulated microcrystalline particles for superamplified biochemical assays. *Anal. Chem.* **2002**, *74* (21), 5480–5486.
31. Dai, Z.F.; Voigt, A.; Donath, E.; Moehwald, H. Novel encapsulated functional dye particles based on alternately adsorbed multilayers of active oppositely charged macromolecular species. *Macromol. Rapid Commun.* **2001**, *22* (10), 756–762.
32. Petrov, A.I.; Gavryushkin, A.V.; Sukhorukov, G.B. Effect of temperature, pH and shell thickness on the rate of Mg<sup>2+</sup> and Ox(2<sup>-</sup>) release from multilayered polyelectrolyte shells deposited onto microcrystals of magnesium oxalate. *J. Phys. Chem., B* **2003**, *107* (3), 868–875.
33. Schuler, C.; Caruso, F. Decomposable hollow biopolymer-based capsules. *Biomacromolecules* **2001**, *2* (3), 921–926.
34. Gittins, D.I.; Caruso, F. Multilayered polymer nanocapsules derived from gold nanoparticle templates. *Adv. Mater.* **2000**, *12* (24), 1947–1948.
35. Gittins, D.I.; Caruso, F. Tailoring the polyelectrolyte coating of metal nanoparticles. *J. Phys. Chem., B* **2001**, *105* (29), 6846–6852.
36. Mayya, K.S.; Gittins, D.I.; Dibaj, A.M.; Caruso, F. Nanotubules prepared by templating sacrificial nickel nanorods. *Nano Lett.* **2001**, *1* (12), 727–730.
37. Neu, B.; Voigt, A.; Mitlohner, R.; Leporatti, S.; Gao, C.Y.; Donath, E.; Kiesewetter, H.; Moehwald, H.; Meiselman, H.J.; Baumler, H. Biological cells as templates for hollow microcapsules. *J. Microencapsul.* **2001**, *18* (3), 385–395.
38. Diaspro, A.; Silvano, D.; Krol, S.; Cavalleri, O.; Gliozzi, A. Single living cell encapsulation in nano-organized polyelectrolyte shells. *Langmuir* **2002**, *18* (13), 5047–5050.
39. Donath, E.; Moya, S.; Neu, B.; Sukhorukov, G.B.; Georgieva, R.; Voigt, A.; Baumler, H.; Kiesewetter, H.; Moehwald, H. Hollow polymer shells from biological templates: fabrication and potential applications. *Chem. Eur. J.* **2002**, *8* (23), 5481–5485.
40. Gao, C.Y.; Moya, S.; Lichtenfeld, H.; Casoli, A.; Fiedler, H.; Donath, E.; Moehwald, H. The decomposition process of melamine formaldehyde cores: The key step in the fabrication of ultrathin polyelectrolyte multilayer capsules. *Macromol. Mater. Eng.* **2001**, *286* (6), 355–361.
41. Sukhorukov, G.B.; Antipov, A.A.; Voigt, A.; Donath, E.; Moehwald, H. pH-Controlled macromolecule encapsulation in and release from polyelectrolyte multilayer nanocapsules. *Macromol. Rapid Commun.* **2001**, *22* (1), 44–46.
42. Ibarz, G.; Daehne, L.; Donath, E.; Moehwald, H. Resealing of polyelectrolyte capsules after core removal. *Macromol. Rapid Commun.* **2002**, *23* (8), 474–478.
43. Moya, S.; Daehne, L.; Voigt, A.; Leporatti, S.; Donath, E.; Moehwald, H. Polyelectrolyte multilayer capsules templated on biological cells: core oxidation influences layer chemistry. *Colloids Surf., A Physicochem. Eng. Asp.* **2001**, *183*, 27–40.
44. Gao, C.Y.; Liu, X.G.; Shen, J.C.; Moehwald, H. Spontaneous deposition of horseradish peroxidase into polyelectrolyte multilayer capsules to improve its activity and stability. *Chem. Commun.* **2002**, (17), 1928–1929.
45. Gao, C.Y.; Donath, E.; Moehwald, H.; Shen, J.C. Spontaneous deposition of water-soluble substances into macrocapsules: Phenomenon, mechanism and application. *Angew. Chem., Int. Ed. Engl.* **2002**, *41* (20), 3789–3793.
46. Park, M.K.; Xia, C.J.; Advincula, R.C.; Schutz, P.; Caruso, F. Cross-linked, luminescent spherical colloidal and hollow-shell particles. *Langmuir* **2001**, *17* (24), 7670–7674.
47. Shi, X.Y.; Caruso, F. Release behavior of thin-walled microcapsules composed of polyelectrolyte multilayers. *Langmuir* **2001**, *17* (6), 2036–2042.
48. Qiu, X.P.; Leporatti, S.; Donath, E.; Moehwald, H. Studies on the drug release properties of polysaccharide multilayers encapsulated ibuprofen microparticles. *Langmuir* **2001**, *17* (17), 5375–5380.
49. Qiu, X.P.; Donath, E.; Moehwald, H. Permeability of ibuprofen in various polyelectrolyte multilayers. *Macromol. Mater. Eng.* **2001**, *286* (10), 591–597.
50. Mendelsohn, J.D.; Barrett, C.J.; Chan, V.V.; Pal, A.J.; Mayes, A.M.; Rubner, M.F. Fabrication of microporous thin films from polyelectrolyte multilayers. *Langmuir* **2000**, *16* (11), 5017–5023.
51. Shiratori, S.S.; Rubner, M.F. pH-Dependent thickness behavior of sequentially adsorbed layers of weak polyelectrolytes. *Macromolecules* **2000**, *33* (11), 4213–4219.
52. Hiller, J.; Mendelsohn, J.D.; Rubner, M.F. Reversibly erasable nanoporous anti-reflection coatings from polyelectrolyte multilayers. *Nat. Mater.* **2002**, *1*, 59–63.
53. Antipov, A.A.; Sukhorukov, G.B.; Leporatti, S.; Radtchenko, I.L.; Donath, E.; Moehwald, H. Polyelectrolyte multilayer capsule permeability control. *Colloids Surf., A Physicochem. Eng. Asp.* **2002**, *198*, 535–541.
54. Peyratout, C.S.; Daehne, L. Preparation of photosensitive dye aggregates and fluorescent dye nanocrystals in

- microreaction containers. *Adv. Mater.* **2003**, *15* (20), 1722–1726.
55. Harris, J.J.; Stair, J.L.; Bruening, M.L. Layered polyelectrolyte films as selective, ultrathin barriers for anion transport. *Chem. Mater.* **2000**, *12*, 1941–1946.
  56. Harris, J.J.; Bruening, M.L. Electrochemical and in situ ellipsometric investigation of the permeability and stability of layered polyelectrolyte films. *Langmuir* **2000**, *16* (4), 2006–2013.
  57. Steitz, R.; Leiner, V.; Siebrecht, R.; v. Klitzing, R. Influence of the ionic strength on the structure of polyelectrolyte films at the solid/liquid interface. *Colloids Surf., A Physicochem. Eng. Asp.* **2000**, *163*, 63–70.
  58. Lvov, Y.; Decher, G.; Moehwald, H. Assembly, structural characterization, and thermal behavior of layer-by-layer deposited ultrathin films of poly(vinylsulfite) and poly(allylamine). *Langmuir* **1993**, *9* (2), 481–486.
  59. Dubas, S.T.; Schlenoff, J.B. Polyelectrolyte multilayers containing a weak polyacid: construction and deconstruction. *Macromolecules* **2001**, *34* (11), 3736–3740.
  60. Fery, A.; Schoeler, B.; Cassagneau, T.; Caruso, F. Nanoporous thin films formed by salt-induced structural changes in multilayers of poly(acrylic acid) and poly(allylamine). *Langmuir* **2001**, *17* (13), 3779–3783.
  61. Farhat, T.R.; Schlenoff, J.B. Ion transport and equilibria in polyelectrolyte multilayers. *Langmuir* **2001**, *17*, 1184–1192.
  62. Antipov, A.A.; Sukhorukov, G.B.; Moehwald, H. Influence of the ionic strength on the polyelectrolyte multilayers permeability. *Langmuir* **2003**, *19*, 2444–2448.
  63. Georgieva, R.; Moya, S.; Hin, M.; Mitlohner, R.; Donath, E.; Kiesewetter, H.; Moehwald, H.; Baumler, H. Permeation of macromolecules into polyelectrolyte microcapsules. *Biomacromolecules* **2002**, *3* (3), 517–524.
  64. Gao, C.; Donath, E.; Moya, S.; Dudnik, V.; Moehwald, H. Elasticity of hollow polyelectrolyte capsules prepared by the layer-by-layer technique. *Eur. Phys. J., E* **2001**, *5*, 21–27.
  65. Gao, C.Y.; Leporatti, S.; Moya, S.; Donath, E.; Moehwald, H. Stability and mechanical properties of polyelectrolyte capsules obtained by stepwise assembly of poly(styrenesulfonate sodium salt) and poly(diallyldimethyl ammonium) chloride onto melamine resin particles. *Langmuir* **2001**, *17* (11), 3491–3495.
  66. Radtchenko, I.L.; Sukhorukov, G.B.; Leporatti, S.; Khomutov, G.B.; Donath, E.; Moehwald, H. Assembly of alternated multivalent ion/polyelectrolyte layers on colloidal particles. Stability of the multilayers and encapsulation of macromolecules into polyelectrolyte capsules. *J. Colloid Interface Sci.* **2000**, *230* (2), 272–280.
  67. Gao, C.Y.; Moya, S.; Donath, E.; Moehwald, H. Melamine formaldehyde core decomposition as the key step controlling capsule integrity: Optimizing the polyelectrolyte capsule fabrication. *Macromol. Chem. Phys.* **2002**, *203* (7), 953–960.
  68. Baumler, H.; Artmann, G.; Voigt, A.; Mitlohner, R.; Neu, B.; Kiesewetter, H. Plastic behaviour of polyelectrolyte microcapsules derived from colloid templates. *J. Microencapsul.* **2000**, *17* (5), 651–655.
  69. Moya, S.; Sukhorukov, G.B.; Auch, M.; Donath, E.; Moehwald, H. Microencapsulation of organic solvents in polyelectrolyte multilayer micrometer-sized shells. *J. Colloid Interface Sci.* **1999**, *216* (2), 297–302.
  70. Sukhorukov, G.; Daehne, L.; Hartmann, J.; Donath, E.; Moehwald, H. Controlled precipitation of dyes into hollow polyelectrolyte capsules based on colloids and biocolloids. *Adv. Mater.* **2000**, *12* (2), 112–115.
  71. Sukhorukov, G.B.; Susha, A.S.; Davis, S.; Leporatti, S.; Donath, E.; Hartmann, J.; Moehwald, H. Precipitation of inorganic salts inside hollow micrometer-sized polyelectrolyte shells. *J. Colloid Interface Sci.* **2002**, *247* (1), 251–254.
  72. Daehne, L.; Leporatti, S.; Donath, E.; Moehwald, H. Fabrication of micro reaction cages with tailored properties. *J. Am. Chem. Soc.* **2001**, *123* (23), 5431–5436.
  73. Radtchenko, I.L.; Sukhorukov, G.B.; Moehwald, H. Incorporation of macromolecules into polyelectrolyte micro- and nanocapsules via surface controlled precipitation on colloidal particles. *Colloids Surf., A Physicochem. Eng. Asp.* **2002**, *202* (2–3), 127–133.
  74. Sukhorukov, G.B.; Brumen, M.; Donath, E.; Moehwald, H. Hollow polyelectrolyte shells: exclusion of polymers and donnan equilibrium. *J. Phys. Chem., B* **1999**, *103* (31), 6434–6440.
  75. Khopade, A.J.; Caruso, F. Stepwise self-assembled poly(amidoamine) dendrimer and poly(styrenesulfonate) microcapsules as sustained delivery vehicles. *Biomacromolecules* **2002**, *3* (6), 1154–1162.
  76. Ibarz, G.; Daehne, L.; Donath, E.; Moehwald, H. Smart micro- and nanocontainers for storage, transport, and release. *Adv. Mater.* **2001**, *13* (17), 1324–1327.
  77. Radtchenko, I.L.; Sukhorukov, G.B.; Moehwald, H. A novel method for encapsulation of poorly water-soluble drugs: Precipitation in polyelectrolyte multilayer shells. *Int. J. Pharm.* **2002**, *242* (1–2), 219–223.
  78. Gaponik, N.; Radtchenko, I.L.; Sukhorukov, G.B.; Weller, H.; Rogach, A.L. Toward encoding combinatorial libraries: charge-driven microencapsulation of semiconductor nanocrystals luminescing in the visible and near IR. *Adv. Mater.* **2002**, *14* (12), 879–882.
  79. Shchukin, D.G.; Radtchenko, I.L.; Sukhorukov, G.B. Synthesis of nanosized magnetic ferrite particles inside hollow polyelectrolyte capsules. *J. Phys. Chem., B* **2003**, *107* (1), 86–90.
  80. Radchenko, I.L.; Giersig, M.; Sukhorukov, G.B. Inorganic particle synthesis in confined micron-sized polyelectrolyte capsules. *Langmuir* **2002**, *18*, 8204–8208.
  81. Tiourina, O.P.; Antipov, A.A.; Sukhorukov, G.B.; Larionova, N.L.; Lvov, Y.; Moehwald, H. Entrapment of alpha-chymotrypsin into hollow polyelectrolyte microcapsules. *Macromol. Biosci.* **2001**, *1* (5), 209–214.
  82. Lvov, Y.; Antipov, A.A.; Mamedov, A.; Moehwald, H.; Sukhorukov, G.B. Urease encapsulation in nanoorganized microshells. *Nano Lett.* **2001**, *1* (3), 125–128.

83. Antipov, A.A.; Shchukin, D.G.; Fedutik, Y.A.; Zhanaveskina, I.; Klechkovskaya, V.; Sukhorukov, G.B.; Moehwald, H. Urease-catalyzed carbonate precipitation inside the restricted volume of polyelectrolyte capsules. *Macromol. Rapid Commun.* **2003**, *24* (3), 274–277.
84. Caruso, F.; Trau, D.; Moehwald, H.; Renneberg, R. Enzyme encapsulation in layer-by-layer engineered polymer multilayer capsules. *Langmuir* **2000**, *16* (4), 1485–1488.
85. Jin, W.; Shi, X.Y.; Caruso, F. High activity enzyme microcrystal multilayer films. *J. Am. Chem. Soc.* **2001**, *123* (33), 8121–8122.
86. Balabushevitch, N.G.; Sukhorukov, G.B.; Moroz, N.A.; Volodkin, D.V.; Larionova, N.I.; Donath, E.; Moehwald, H. Encapsulation of proteins by layer-by-layer adsorption of polyelectrolytes onto protein aggregates: factors regulating the protein release. *Biotechnol. Bioeng.* **2001**, *76* (3), 207–213.
87. Bobreshova, M.E.; Sukhorukov, G.B.; Saburova, E.A.; Elfimova, L.I.; Shabarchina, L.I.; Sukhorukov, B.I. Lactate dehydrogenase in interpolyelectrolyte complex. Function and stability. *Biofizika* **1999**, *44* (5), 813–820.
88. Dai, Z.F.; Moehwald, H. Highly stable and biocompatible Nafion-based capsules with controlled permeability for low-molecular-weight species. *Chem. Eur. J.* **2002**, *8* (20), 4751–4755.
89. Jung, B.D.; Hong, J.D.; Voigt, A.; Leporatti, S.; Daehne, L.; Donath, E.; Moehwald, H. Photochromic hollow shells: Photoisomerization of azobenzene polyionene in solution, in multilayer assemblies on planar and spherical surfaces. *Colloids Surf., A Physicochem. Eng. Asp.* **2002**, *198*, 483–489.
90. Berth, G.; Voigt, A.; Dautzenberg, H.; Donath, E.; Moehwald, H. Polyelectrolyte complexes and layer-by-layer capsules from chitosan/chitosan sulfate. *Biomacromolecules* **2002**, *3* (3), 579–590.
91. Tiourina, O.P.; Sukhorukov, G.B. Multilayer alginate/protamine microsized capsules: encapsulation of alpha-chymotrypsin and controlled release study. *Int. J. Pharm.* **2002**, *242* (1–2), 155–161.
92. Antipov, A.A.; Sukhorukov, G.B.; Fedutik, Y.A.; Hartmann, J.; Giersig, M.; Moehwald, H. Fabrication of a novel type of metallized colloids and hollow capsules. *Langmuir* **2002**, *18* (17), 6687–6693.
93. Pastoriza-Santos, I.; Scholer, B.; Caruso, F. Core-shell colloids and hollow polyelectrolyte capsules based on diazoresins. *Adv. Funct. Mater.* **2001**, *11* (2), 122–128.
94. Härmä, H. Particle technologies in diagnostics. *Technol. Rev.* **2002**, *126*, 1–30.
95. Dai, Z.F.; Voigt, A.; Leporatti, S.; Donath, E.; Daehne, L.; Moehwald, H. Layer-by-layer self-assembly of polyelectrolyte and low molecular weight species into capsules. *Adv. Mater.* **2001**, *13* (17), 1339–1342.
96. Dai, Z.F.; Daehne, L.; Donath, E.; Moehwald, H. Mimicking photosynthetic two-step energy transfer in cyanine triads assembled into capsules. *Langmuir* **2002**, *18* (12), 4553–4555.
97. Dai, Z.F.; Daehne, L.; Donath, E.; Moehwald, H. Downhill energy transfer via ordered multichromophores in light-harvesting capsules. *J. Phys. Chem., B* **2002**, *106* (44), 11501–11508.
98. Dai, Z.F.; Daehne, L.; Moehwald, H.; Tiersch, B. Novel capsules with high stability and controlled permeability by hierarchic templating. *Angew. Chem., Int. Ed.* **2002**, *41* (21), 4019–4022.
99. Caruso, R.A.; Susha, A.; Caruso, F. Multilayered titania, silica, and laponite nanoparticle coatings on polystyrene colloidal templates and resulting inorganic hollow spheres. *Chem. Mater.* **2001**, *13* (2), 400–409.
100. Caruso, F. Nanoengineering of particle surfaces. *Adv. Mater.* **2001**, *13* (1), 11–22.
101. Caruso, F. Generation of complex colloids by polyelectrolyte-assisted electrostatic self-assembly. *Aust. J. Chem.* **2001**, *54* (6), 349–353.
102. Caruso, F. Engineering of core-shell particles and hollow capsules. In *Nano-Surface Chemistry*; Rosoff, M., Ed.; Marcel Dekker: New York, 2002; 505–526.
103. Caruso, F.; Lichtenfeld, H.; Giersig, M.; Moehwald, H. Electrostatic self-assembly of silica nanoparticle—polyelectrolyte multilayers on polystyrene latex particles. *J. Am. Chem. Soc.* **1998**, *120* (33), 8523–8524.
104. Caruso, F.; Moehwald, H. Preparation and characterization of ordered nanoparticle and polymer composite multilayers on colloids. *Langmuir* **1999**, *15* (23), 8276–8281.
105. Caruso, F. Hollow capsule processing through colloidal templating and self-assembly. *Chem. Eur. J.* **2000**, *6* (3), 413–419.
106. Caruso, F.; Caruso, R.A.; Moehwald, H. Nanoengineering of inorganic and hybrid hollow spheres by colloidal templating. *Science* **1998**, *282* (5391), 1111–1114.
107. Caruso, F.; Caruso, R.A.; Moehwald, H. Production of hollow microspheres from nanostructured composite particles. *Chem. Mater.* **1999**, *11* (11), 3309–3314.
108. Sukhorukov, G.B.; Donath, E.; Moya, S.; Susha, A.S.; Voigt, A.; Hartmann, J.; Moehwald, H. Microencapsulation by means of step-wise adsorption of polyelectrolytes. *J. Microencapsul.* **2000**, *17* (2), 177–185.
109. Voigt, A.; Buske, N.; Sukhorukov, G.B.; Antipov, A.A.; Leporatti, S.; Lichtenfeld, H.; Baumler, H.; Donath, E.; Moehwald, H. Novel polyelectrolyte multilayer micro- and nanocapsules as magnetic carriers. *J. Magn. Magn. Mater.* **2001**, *225* (1–2), 59–66.
110. Caruso, F.; Spasova, M.; Susha, A.; Giersig, M.; Caruso, R.A. Magnetic nanocomposite particles and hollow spheres constructed by a sequential layering approach. *Chem. Mater.* **2001**, *13* (1), 109–116.
111. Caruso, F.; Susha, A.S.; Giersig, M.; Moehwald, H. Magnetic core-shell particles: preparation of magnetite multilayers on polymer latex microspheres. *Adv. Mater.* **1999**, *11* (11), 950–953.
112. Moya, S.; Donath, E.; Sukhorukov, G.B.; Auch, M.; Baumler, H.; Lichtenfeld, H.; Moehwald, H. Lipid

- coating on polyelectrolyte surface modified colloidal particles and polyelectrolyte capsules. *Macromolecules* **2000**, *33* (12), 4538–4544.
113. Georgieva, R.; Moya, S.; Leporatti, S.; Neu, B.; Baumler, H.; Reichle, C.; Donath, E.; Moehwald, H. Conductance and capacitance of polyelectrolyte and lipid–polyelectrolyte composite capsules as measured by electrorotation. *Langmuir* **2000**, *16* (17), 7075–7081.
  114. The principle of electrostatic multilayer deposition was first described in Iler, R.K. Multilayers of colloidal particles. *J. Colloid Interface Sci.* **1966**, *21*, 569–594.
  115. Decher, G. Polyelectrolyte multilayers, an overview. In *Multilayer Thin Films*; Decher, G., Schlenoff, J.B., Eds.; Wiley VCH: New York, 2003; 1–46.
  116. Shenoy, D.B.; Sukhorukov, G.B.; Moehwald, H. Layer-by-layer engineering of biocompatible. Decomposable core-shell structures. *Biomacromolecules* **2003**, *4* (2), 265–272.
  117. Tiourina, O.P.; Radtchenko, I.; Sukhorukov, G.B.; Moehwald, H. Artificial cell based on lipid hollow polyelectrolyte microcapsules: Channel reconstruction and membrane potential measurement. *J. Membr. Biol.* **2002**, *190* (1), 9–16.
  118. Daehne, L.; Moehwald, H.; Decher, G.; Sukhorukov, G.; Lvov, Y. Private communication.

# Carbon-Based Nanostructures: Hydrogen Storage

Xianxian Wu

Nidia C. Gallego

*Carbon Materials Technology Group, Materials Science and Technology Division,  
Oak Ridge National Laboratory, Oak Ridge, Tennessee, U.S.A.*

## Abstract

The reported hydrogen storage capacities of carbon nanotubes, nanofibers, nanostructured graphite, activated carbons, activated carbon fibers, graphite, and metal-doped carbon nanostructures are widely spread. While some unusually high values were claimed for carbon nanotubes and nanofibers in earlier years, most studies in recent years suggest that the hydrogen storage capacity in carbon materials, including nanotubes and nanofibers, increases with hydrogen pressure, but is less than 1 wt% at room temperature. A capacity of a few percents is only possible at low temperatures, such as 77 K, and high pressures. There is increasing evidence from both experimental and theoretical reports that carbon nanotubes, including high-purity single-wall carbon nanotubes, do not have hydrogen storage characteristics superior to the conventional high-surface area graphite powder and activated carbons. Dispersing small amounts of metals, especially transition metals, in carbons appears to be a promising approach to increase the hydrogen storage capacity at room temperature. However, more efforts are needed in understanding the fundamentals of the storage process, such as what is the exact chemical state of the hydrogen stored in carbon materials. This chapter presents a comprehensive review on the experimentally measured and theoretically predicted hydrogen storage capacities of different nanostructured carbon materials.

## BACKGROUND

There are four technologies available today to store hydrogen for on-board vehicular applications:<sup>[1]</sup> (1) physical storage via compression or liquefaction, (2) chemical storage in irreversible hydrogen carriers (e.g. methanol, ammonia), (3) reversible metal and chemical hydrides, and (4) gas-on-solid adsorption. Although each method possesses desirable characteristics, no one approach satisfies all efficiencies, size, weight, cost, and safety requirements for transportation or utility use. The main drawbacks for physical storage are the need for high-pressure tanks or low-temperature systems for liquefaction and handling of liquefied hydrogen (21 K) as well as the high cost. Chemical storage generally needs a conversion process, which makes the system more complex. Storage by metallic hydrides has the advantage of the low pressure but the storage system is heavy and additional heating is needed for hydrogen release. The last possibility, hydrogen adsorption in porous solids, has been studied since the 1960s,<sup>[2]</sup> and is still being considered as an attractive technology. Carbon materials as adsorbents offer additional advantage because of their low mass density. Hydrogen storage in carbon materials has attracted much attention in recent years owing to the development of novel nanomaterials such as carbon nanotubes and nanofibers and the claims of some unusual high storage capacities.

Several comprehensive reviews on hydrogen storage in carbon nanotubes are available.<sup>[3–6]</sup> However, in

view of the fact that very large differences in hydrogen storage capacities were historically reported for not so much dissimilar materials, this entry is focused on the variation of storage capacities measured for a wide variety of carbon materials and identification of those microstructural parameters that appear to affect the materials' hydrogen uptake. Special attention is given to activated carbons and metal-containing carbon materials, which are receiving increasing attention nowadays. In addition, a review of theoretical predictions and a discussion on issues still not fully clarified, especially related to the fundamentals in hydrogen adsorption, are included. Since reliable measurement methods are always crucial for the experimental evaluation of materials, a brief review on the techniques used for measuring hydrogen storage capacity is presented first.

## TECHNIQUES FOR MEASURING HYDROGEN STORAGE CAPACITY

Hydrogen adsorption measurements on small samples, on the order of several milligrams, need very sophisticated experimental conditions and measurement procedures to carefully eliminate all parasitic effects that may contribute to erroneous hydrogen uptake.<sup>[7]</sup> The evaluation of the reliability of the experimental techniques and data interpretation procedures, therefore, need to be very cautious. The hydrogen storage capacity of an adsorbent is generally expressed as a



percentage of the weight of the materials and can be determined by different techniques.

The *volumetric* method, also known as Sievert's method, measures pressure changes in a calibrated volume caused by hydrogen adsorption or desorption in the presence of the solid specimen. This method typically requires a relatively large amount of sample (>500 mg)<sup>[8]</sup> and highly sensitive pressure sensors to achieve a good accuracy. Possible errors may come from gas leakage or temperature instability of the apparatus, and other sources.<sup>[9]</sup> The majority of the reports that claim high storage capacities at room temperature used this experimental method. The results of measurements using the volumetric method are usually expressed in the form of adsorption isotherms (usually up to 0.1 MPa) or pressure-composition isotherms (PCI).

The *gravimetric* method measures the weight changes of the specimen due to adsorption or desorption of hydrogen. A small amount of sample (in the range of ca. 10 mg) may be enough to achieve good accuracy. Since this technique is based only on the measured weight changes, it is less selective to hydrogen and the presence of other adsorbing impurities in the gas phase may cause errors in the results. Therefore, to achieve reliable results by this method, very high purity hydrogen needs to be used.<sup>[10,11]</sup>

Hydrogen storage capacity can also be measured by *thermal desorption spectroscopy* (TDS) or more often called *temperature programmed desorption* (TPD) technique. The capacity is calculated from the amount of desorbed hydrogen, which is generally monitored by mass spectrometry. This method can be selective and highly sensitive, but a careful calibration using a well-known standard specimen is necessary.<sup>[12]</sup>

Carbon materials can also store hydrogen electrochemically. A capacity of 0.39 wt% at room temperature has been reported for samples containing only a small amount of nanotubes,<sup>[13]</sup> and a capacity of 2.9 wt% has been reported for samples containing 80% of single-wall carbon nanotubes (SWNTs).<sup>[14]</sup> In electrochemical measurements, carbon materials are formed as an electrode by mixing them with a conductive powder (e.g. copper, gold),<sup>[13,14]</sup> and a nickel counter-electrode is generally used. Both electrodes are placed in a KOH electrolyte. The amount of hydrogen stored can then be calculated from the measured discharge capacities. Experiments have shown that the measured hydrogen storage capacities by electrochemical method are comparable with those measured by gas adsorption techniques.<sup>[15,16]</sup>

Hydrogen storage capacity of porous carbons at high pressure and ambient temperatures may also be quantitatively predicted from H<sub>2</sub> adsorption measurements at cryogenic temperature below 0.1 MPa by using a model based on the non-local density functional theory

(NLDFT).<sup>[17,18]</sup> This approach is significant from a practical point of view, in that, if reliable theoretical models can be developed, standard adsorption measurements will be sufficient for predicting hydrogen storage capacity at high pressure.

## EXPERIMENTALLY MEASURED HYDROGEN STORAGE CAPACITY

A large number of carbon materials have been studied for hydrogen storage. Because of the large volume of literature, this section is subdivided into a review of the storage capacities of: (i) single-wall carbon nanotubes (SWNTs); (ii) multi-wall carbon nanotubes (MWNTs) and other nanostructured carbon materials such as graphite nanofibers (GNF), nanostructured graphite (NSG), and carbon nanofibers (CNF) mostly grown from chemical vapor deposition (CVD); (iii) "conventional" carbons including activated carbons (AC), activated carbon fibers (ACF), and graphite; and (iv) metal-doped carbon nanostructures.

### Single-Wall Carbon Nanotubes

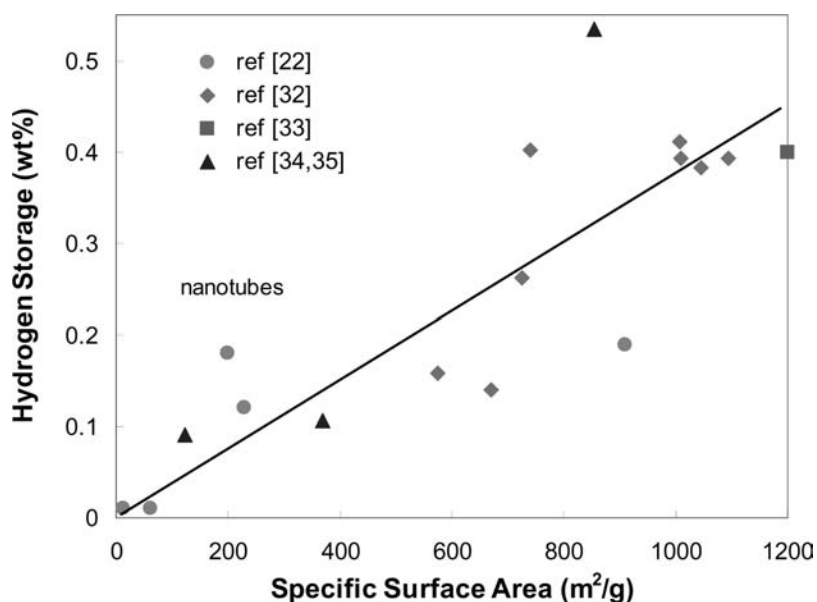
Dillon et al.<sup>[19]</sup> first reported the hydrogen adsorption capacity in carbon nanotubes. The experimental results on soot containing about 0.1–0.2 wt% SWNTs were used to extrapolate the hydrogen storage capacity of pure SWNTs. They predicted that SWNTs with diameters of 16.3 Å and 20 Å would meet the Department of Energy's (DOE) H<sub>2</sub> uptake target (6.5 wt%) at near room temperatures if modest H<sub>2</sub> over-pressures compensated for the lower heats of adsorption expected in the larger cavities.<sup>[19]</sup> This estimate, however, was not validated by the experimental observations of Ye et al.<sup>[20]</sup> who reported a capacity of 8.0 wt% at 80 K and 11 MPa in their purified SWNTs and stated that such capacities are not attainable at 300 K and pressures below 0.1 MPa. In addition, a capacity of 4.2 wt% was reported at room temperature ( $T = 293$  K) under high pressure (12 MPa).<sup>[21]</sup> Following these early reports, more controversial results have been reported on carbon nanotubes; however, none of the high capacities reported has been independently confirmed by others.

Table 1 summarizes the reported hydrogen storage capacities of SWNTs synthesized by different methods. It is observed that there exist large discrepancies in these results, which could be attributed to variations of a multitude of factors between various research groups, such as: (i) the structure of the materials used, (e.g., diameter, length, opened or partially opened nanotubes), (ii) sample weight (generally very small samples were used, on the order of micrograms),

**Table 1** Reported hydrogen storage capacity of SWNTs

Authors, year	Methods of SWNTs synthesis	Techniques for measurement	Temperature (K)	Pressure (MPa)	H <sub>2</sub> uptake (wt%)
Dillon et al., <sup>[19]</sup> 1997	Electric arc co-evaporation	TPD	273	0.04	5.0
Ye et al., <sup>[20]</sup> 1999	Laser vaporation	Volumetric	80	11.1	8.0
Liu et al., <sup>[21]</sup> 1999	Arc discharge	Volumetric	298	12	4.2
Tibbetts, Meisner, and Olk, <sup>[9]</sup> 2001	Laser vaporation (Tubes@Rice)	PCI	296	3.58	0.05
Fazle Kibria et al., <sup>[23]</sup> 2001	Laser ablation (Li-doped)	Electrochemical	293	n/a	2.3
Fazle Kibria et al., <sup>[23]</sup> 2001	Laser ablation	Electrochemical	293	n/a	1.6
Nishimiya et al., <sup>[24]</sup> 2002	Torch arc	Adsorption isotherm	295	0.1	0.932
			77	0.1	2.37
Züttel et al., <sup>[25]</sup> 2002	SWNT soot (MER)	TDS	78	2	0.6
Hirscher et al., <sup>[8]</sup> 2002	Arc discharge	TDS	293	0.08	1.0
Wang et al., <sup>[26]</sup> 2002	Arc discharge	Volumetric	293	0.05	0.21
Pradhan et al., <sup>[27]</sup> 2002	Arc discharge (CarboLex)	High-pressure TGA	77	0.2	~6
Züttel et al., <sup>[28]</sup> 2002	>10 samples, mostly from arc discharge	Electrochemical	298	n/a	0.04–2.0
Kajiura et al., <sup>[29]</sup> 2003	Purified HiPco <sup>TM</sup>	Volumetric	293	8	0.43
Li et al., <sup>[30]</sup> 2003	Arc discharge	High-pressure microbalance	295	1	0.1
Tarasov et al., <sup>[31]</sup> 2003	Arc evaporation	Volumetric + TDS	123	2.5	2.4
Gundiah et al., <sup>[15]</sup> 2003	Arc-discharge (acid treated)	Volumetric	300	14	0.4
Ansón et al., <sup>[16]</sup> 2004	Electric arc	Volumetric and gravimetric	298	2	0.1
Lan and Mukasyan, <sup>[22]</sup> 2005	HiPCO CVD	Gravimetric	293	11.5	0.19
Hass et al., <sup>[32]</sup> 2005	CVD, purified	Volumetric	298	10.7	~0.47
Yang, Lachawiec, and Yang, <sup>[33]</sup> 2006	CVD, purified	Volumetric	298	10	~0.4

n/a—data not available.



**Fig. 1** Hydrogen storage capacity at room temperature and 10 MPa as a function of the surface area of SWNTs. *Source:* Data extracted from Refs.<sup>[22,32–35]</sup>.

(iii) degree of purity (most samples were not completely purified SWNTs, and contained amorphous carbon and metal impurities, generally catalytic residues resulting from their synthesis), and (iv) measurement techniques and measuring conditions. Purification of SWNTs, for example by treatment with acids, removes the catalyst particles left from arc-discharge synthesis. Such a treatment increases the storage capacity of SWNTs slightly,<sup>[15]</sup> but negative effects have also been reported.<sup>[22]</sup>

Several research groups<sup>[22,25,28,32,34,35]</sup> have tried to correlate the hydrogen storage capacity of SWNTs with their effective surface area (calculated by the BET method from nitrogen adsorption data at  $T = 77$  K). A fairly linear relationship has been reported for measurements performed both at liquid nitrogen temperature (77 K) and at room temperature. Figure 1 summarizes the data reported for SWNTs at room temperature and 10 MPa. The slope of the straight line that best fits the data in these conditions is about 0.4 wt% per 1000 m<sup>2</sup>/g. Up to a pressure of 6.6 MPa, a slope of 0.23 wt% and 1.91 wt% per 1000 m<sup>2</sup>/g was reported for room temperature and 77 K, respectively, based on an investigation using different carbon materials including SWNTs.<sup>[35]</sup>

With the exception of the high H<sub>2</sub> uptake values reported by several early works,<sup>[19–21]</sup> most recent results seem to support one main point—the storage capacity of SWNTs cannot meet the DOE targets at room temperature; even though SWNTs can store significant amounts of H<sub>2</sub> at cryogenic conditions (close to the temperature of liquid N<sub>2</sub>). The results also indicate that the SWNTs studied so far do not show improved hydrogen storage characteristics over conventional high surface area graphite powder and

activated carbons.<sup>[28,32]</sup> All claims of high storage capacities (larger than ~1 wt%) at room temperature are doubtful, possibly attributable to experimental errors.<sup>[22]</sup>

### Multi-Wall Carbon Nanotubes and Other Nanostructured Carbons

Multi-wall carbon nanotubes (MWNTs) consist of multiple concentric graphitic layers. The typical diameters of MWNTs vary from 15 to 50 nm. Table 2 lists the hydrogen storage capacities of MWNTs and other carbon nanostructures. An uptake of over 3 wt% of hydrogen was claimed for well-aligned carbon nanotube bundles at room temperature and under moderate pressure (~10 MPa).<sup>[36]</sup> Values as high as 6.3 wt% of hydrogen storage capacities (31.6 kg/m<sup>3</sup> of volumetric capacity) have been reported for bulk MWNT samples at room temperature under an equilibrium pressure of 14.8 MPa.<sup>[37]</sup> The high capacity was attributed to the opening of tubes, large micropore structure, and purification of MWNTs. There are, however, several works where very low hydrogen storage capacities for MWNTs were reported. Values lower than 0.04 wt%,<sup>[29]</sup> and a capacity of around 0.1 wt% have also been measured electrochemically for MWNTs.<sup>[23,28]</sup>

Carbon nanotubes used in most studies were produced by catalytic decomposition of light hydrocarbons at high temperature in the presence of a catalyst. The as-prepared materials contained impurities and other forms of carbon (amorphous carbon). The experimental results showed that the MWNTs purified by water washing and acid treatment had a much higher hydrogen storage capacity than the

**Table 2** Reported hydrogen storage capacity in MWNTs and carbon nanofibers

Authors, year	Materials	Techniques for Measurement	Temperature (K)	Pressure (MPa)	H <sub>2</sub> uptake (wt%)
Zhu et al., <sup>[36]</sup> 2001	MWNTs	Volumetric	290	~10	>3.0
Fazle Kibria et al., <sup>[23]</sup> 2001	MWNTs	Electrochemical	293	n/a	0.1
Hou et al., <sup>[37]</sup> 2002	MWNTs	Volumetric	296	14.1	2.0
	MWNTs, Purified		296	14.5	6.5
Züttel et al., <sup>[28]</sup> 2002	MWNTs	Electrochemical	298	n/a	0.13
Johansson et al., <sup>[38]</sup> 2002	MWNTs	Volumetric	300	10	2.6
			77	10	4.1
Gundiah et al., <sup>[15]</sup> 2003	MWNTs, acid treated	Volumetric + electrochemical	300	14	3.3
Kajiura et al., <sup>[29]</sup> 2003	MWNTs	Volumetric	293	8	<0.04
Ci et al., <sup>[39]</sup> 2003	Annealed MWNTs	Volumetric	298	10	3.98
Chambers et al., <sup>[40]</sup> 1998	GNF, CVD	Volumetric	298	11.3	11.26–67.55
Ahn et al., <sup>[41]</sup> 1998	GNF, CVD	Volumetric	300	16	0.24
Tibbetts, Meisner, and Olk, <sup>[9]</sup> 2001	CNF, CVD	PCI	296	3.6	0.04
Poirier, Chahine, and Bose, <sup>[42]</sup> 2001	CNF, CVD	Volumetric	295	10.5	0.7
Hirscher et al., <sup>[8]</sup> 2002	GNF, CVD	TDS	293	0.08	0.5
Browning et al., <sup>[43]</sup> 2002	CNF, CVD	Volumetric	293	12	4.18
Zhu et al., <sup>[44]</sup> 2002	Platelet-vapor grown CNF	Volumetric	298	~9	~4.0
Kajiura et al., <sup>[45]</sup> 2003	NSG	Volumetric	293	6	~0.25
Zhu et al., <sup>[46]</sup> 2003	CNF, CVD	Volumetric	298	10	1.29
Rzepka et al., <sup>[47]</sup> 2005	CNF, CVD	Volumetric	298	14	<0.4
Lueking et al., <sup>[48]</sup> 2005	GNF	Gravimetric	300	2	0.02
	GNF, exfoliated		300	2	0.29
Blackman, Patrick, and Snape, <sup>[49]</sup> 2006	CNF, CVD, 270 m <sup>2</sup> /g	Volumetric	303	10	0.25

n/a—data not available.

as-prepared MWNT products.<sup>[37]</sup> It was also reported that annealing carbon nanotubes at temperatures in the range of 1700–2200°C can remarkably improve the storage capacity.<sup>[39,50]</sup> The as-grown nanotubes only showed a capacity of 1.29 wt% at room temperature and 10 MPa, while the samples annealed at 2200°C showed a capacity of 3.98 wt% at the same conditions.

Besides single- and multi-walled nanotubes, other nanostructured carbons that have been studied for hydrogen storage include graphite nanofibers, nanostructured graphite, and carbon nanofibers. The reported hydrogen storage capacities in these materials are summarized in the lower half of Table 2. A capacity of as high as 67.55 wt% was reported for GNF by the group of Baker and Rodriguez.<sup>[40,51]</sup> The same group claimed that careful pretreatment of GNF samples is a critical procedure to remove chemisorbed gases from edge and step regions of the structures. Failure to achieve this condition results in a dramatic decline in the performance of the materials to subsequently

adsorb hydrogen.<sup>[52]</sup> The reported high capacities were questioned by other researches on both theoretical and experimental grounds. Based on the use of a hypothetical potential, which implied a strong interaction between atomic hydrogen and a graphitic surface and negligible desorption at ambient pressure, Monte Carlo simulation of hydrogen adsorption in graphitic pores<sup>[53]</sup> showed that adsorption values greater than 17 wt% are unreasonable. Several recent independent experiments<sup>[8,20,41,47]</sup> suggested that a high hydrogen storage capacity (e.g., 6.0 wt%) in pure carbon nanostructures can only be achieved at, or near liquid nitrogen temperatures, but not at near room temperatures.

Orimo et al.<sup>[54]</sup> prepared nanostructured graphite (NSG) by mechanically milling graphite powder under hydrogen atmosphere at a pressure of 1 MPa and room temperature. The milling process leads to nanocrystallization, first along the directions perpendicular to the basal plane of graphite (cuttingly milling), and second parallel to the basal plane (cleavingly milling).<sup>[55]</sup> After

the expansion of the graphite interlayer, the long-range ordering of the interlayer disappears gradually with increasing milling time. After milling for 80 h, the crystallite size was estimated to have dropped to only 4 nm and the hydrogen concentration reached up to 7.4 wt% ( $\text{CH}_{0.95}$ ). It was suggested that mechanically prepared nanostructured graphite exhibits a specific interaction with hydrogen, probably due to the partial formation of the defect mediated hydrogen sorption.<sup>[56]</sup> Mechanical milling results in the formation of dangling carbon bonds in graphite, and thus the relative ratio of the  $\text{CH}_x$  covalent bonds increases if milling is performed under hydrogen atmosphere. Using the same mechanical milling process at a pressure of  $2.0 \times 10^{-4}$  Pa, Kajiuira et al.<sup>[45]</sup> also prepared the nanostructured graphite from graphite powder. They found that the untreated graphite adsorbed 0.02 wt% of hydrogen, while the nanostructured graphite was able to repeatedly adsorb 0.20–0.25 wt% hydrogen.

Filamentous carbon materials produced by chemical vapor deposition (CVD) are usually called carbon nanofibers; they may contain a mixture of amorphous carbon, carbon filaments, and carbon nanotubes. As listed in Table 2, the reported hydrogen storage capacities for this type of materials are also diverse. Since this type of materials generally has low porosity and surface area ( $<270 \text{ m}^2/\text{g}$ ), a recent study investigated the effect of activation on the hydrogen storage capacities of carbon nanofibers. The results showed that the increased surface area did not correspond directly to a proportional increase in hydrogen storage capacity.<sup>[57]</sup>

### Activated Carbons and Graphite

“Classical” forms of carbons, such as activated carbons, are relatively inexpensive and readily available. There has been some renewed interest in considering activated carbons as candidate materials for hydrogen storage media because of the controversial reports on the behavior of carbon nanotubes. The hydrogen storage capacities of classical forms of carbon materials (including activated carbon fibers) are summarized in Table 3. At low temperature (78 K), a capacity of 6.8 wt% was reported for activated carbons at 4.2 MPa,<sup>[58]</sup> and the amount of hydrogen adsorbed was found to increase with increasing surface area.<sup>[59]</sup> Under a pressure up to 6.6 MPa, an almost linear relation between the storage capacity and the specific surface area of activated carbon was reported,<sup>[35,60]</sup> and a similar relationship was also reported between the capacity and the micropore volume.<sup>[35,60,61]</sup> It was also found that the presence and nature of surface functional groups may affect the amount of hydrogen adsorbed on the surface, but no correlation has been

found between the amount of oxygen present on the surface and the amount of hydrogen stored per unit area of the carbon sample.<sup>[59]</sup> The amount of hydrogen adsorbed, however, increases as the number of surface acidic groups increases.

As listed in Table 3, the hydrogen storage capacities at room temperature of activated carbons, especially those reported recently, are less than 1.0 wt% even at high hydrogen pressure. Based on these data, a correlation between the BET effective surface area and the hydrogen sorption capacity at 298 K and 10 MPa is presented in Fig. 2. It is seen that the hydrogen uptake of activated carbons, in general, increases with surface area and a linear relation seems to be able to describe such dependence. Actually, such a linear relation was also predicted by a theoretical study based on graphite slit-like pores.<sup>[62]</sup> A capacity of  $\sim 1.4$  wt% at 303 K and 10 MPa was predicted for carbon materials with surface area of about  $2000 \text{ m}^2/\text{g}$ .

Theoretical studies suggested that there exists an optimum pore geometry and pore size for hydrogen adsorption;<sup>[65,70]</sup> however, discrepancies exist regarding the value of this optimum pore size. In general, hydrogen storage is favored in small micropores and it has been suggested that the optimum pore size should be able to accommodate two layers of adsorbed  $\text{H}_2$ .<sup>[71]</sup> Therefore, the micropore ( $<2 \text{ nm}$ ) volume of activated carbons has been correlated to their hydrogen storage capacity at both at 77 and 293 K (Fig. 3). Similar linear relationship has also been reported by Panella et al. at 298 K and 6.6 MPa.<sup>[35]</sup> Such a direct correlation suggests that high microporosity in carbon materials should benefit hydrogen storage at both liquid nitrogen and room temperature. For activated carbon fibers, an experimental study also showed that the storage capacity increased with the degree of activation and that is closely linked to the micropores.<sup>[69]</sup> These authors suggested that micropores of about 0.6 nm are responsible for the greater increase in storage capacity.

Graphite, often used as the reference sample, has also been tested for the hydrogen storage capacity. The results are also presented in Table 3. It is evident that the values are much lower when compared with those of activated carbon.

### Heteroatom-Incorporated Carbon Materials

The two possible storage models considered up to this point include adsorption of hydrogen as a monolayer at the surface of nanostructured carbon materials and condensation in the narrow cavities of carbon nanotubes or in the micropores of activated carbon, at densities comparable with the density of liquid hydrogen. Another possible mechanism to enhance

**Table 3** Reported H<sub>2</sub> storage capacity in activated carbons (AC) and graphite

Authors, year	Materials, BET (m <sup>2</sup> /g)	Techniques for Measurement	Temperature (K)	Pressure (MPa)	H <sub>2</sub> uptake (wt%)
Carpetis and Peschka, <sup>[58]</sup> 1980	AC, 1250	Adsorption isotherm	78	4.2	~6.8
Agarwal et al., <sup>[59]</sup> 1987	AC, 1500	Gravimetric	78	2.53	~3.3
Chahine and Bose, <sup>[63]</sup> 1994	AC, 3000	Volumetric	298	6	0.5
			77	1	5.0
Zhou and Zhou, <sup>[64]</sup> 1996	AC, 3000	Volumetric	77	6	0.5
			298	6	0.04
Chambers et al., <sup>[40]</sup> 1998	AC, n/a	Volumetric	298	11.3	1.63
Rzepka, Lamp, and de la Casa-Lillo, <sup>[65]</sup> 1998	AC, 2290	Volumetric	300	6	0.6
Ströbel et al., <sup>[66]</sup> 1999	AC, ~1500	Gravimetric	296	12.5	1.5
Poirier, Chahine, and Bose, <sup>[42]</sup> 2001	AC, 3000	Volumetric	295	10.5	0.7
Tibbetts, Meisner, and Olk, <sup>[9]</sup> 2001	AC, 700	PCI	296	3.6	0.041 ± 0.014
Kiyobayashi et al., <sup>[67]</sup> 2002	AC, 3000	Volumetric	308	6	0.45
Zielinski et al., <sup>[68]</sup> 2005	AC, 1073	Volumetric	293	2	0.1
Hass et al., <sup>[32]</sup> 2005	AC, 2478	Volumetric	298	10.7	0.61
Panella, Hirscher, and Roth, <sup>[35]</sup> 2005	AC, 2564	Volumetric	77	6.6	4.5
			298	6.6	0.54
Blackman, Patrick, and Snape, <sup>[49]</sup> 2006	AC, 3201	Volumetric	303	10	0.60
Salvador-Palacios et al., <sup>[69]</sup> 2006	AC, 1326	Adsorption isotherms	273	0.1	0.037
Jagiello, Anson, and Martinez, <sup>[18]</sup> 2006	AC, 1120	Gravimetric	298	8.4	0.5
Kajiura et al., <sup>[29]</sup> 2003	ACF, n/a	Volumetric	293	8	0.35–0.41
Salvador-Palacios et al., <sup>[69]</sup> 2006	ACF, 1804	Adsorption isotherms	273	0.1	0.054
Chambers et al., <sup>[40]</sup> 1998	Graphite	Volumetric	298	11.3	4.52
Tibbetts, Meisner, and Olk, <sup>[9]</sup> 2001	Graphite flakes	PCI	296	3.6	0.018 ± 0.011
Kajiura et al., <sup>[29]</sup> 2002	Graphite powder	Volumetric	293	8	<0.04
Züttel et al., <sup>[28]</sup> 2002	Graphite, 297	Electrochemical	298	n/a	0.25
Hirscher et al., <sup>[8]</sup> 2002	Graphite powder	TDS	293	0.08	0.3
Kajiura et al., <sup>[29]</sup> 2003	Vitreous carbon	Volumetric	293	8	<0.04

n/a—data not available.

the adsorption capacity is by dissociation of hydrogen molecules followed by chemisorption of atoms in a tight-binding (covalent) state, or by transfer of an electron to the host material as in metal hydrides,<sup>[25]</sup> or recombination of H atoms to form physisorbed H<sub>2</sub>. These processes could possibly be enhanced by incorporating heteroatoms into carbon structures.

Intercalation of alkalis (Li, K, etc.) into purified carbon nanotubes resulted in absorption of up to 20 wt% hydrogen at room temperature and ambient pressure,

according to Chen et al.<sup>[72]</sup> Such large weight gains, however, were proved in a subsequent experiment to be the result of alkali hydroxide formation from a H<sub>2</sub> stream that was contaminated with water.<sup>[11]</sup> Experiments with ultra-pure dry H<sub>2</sub> indicated that lithium-doped SWNTs were capable of adsorbing about 2.5 wt% and potassium-doped nanotubes of about 1.8 wt%. In addition, a capacity of 0.59 wt% was electrochemically measured at room temperature for Li-doped CNTs, higher than the capacity of the



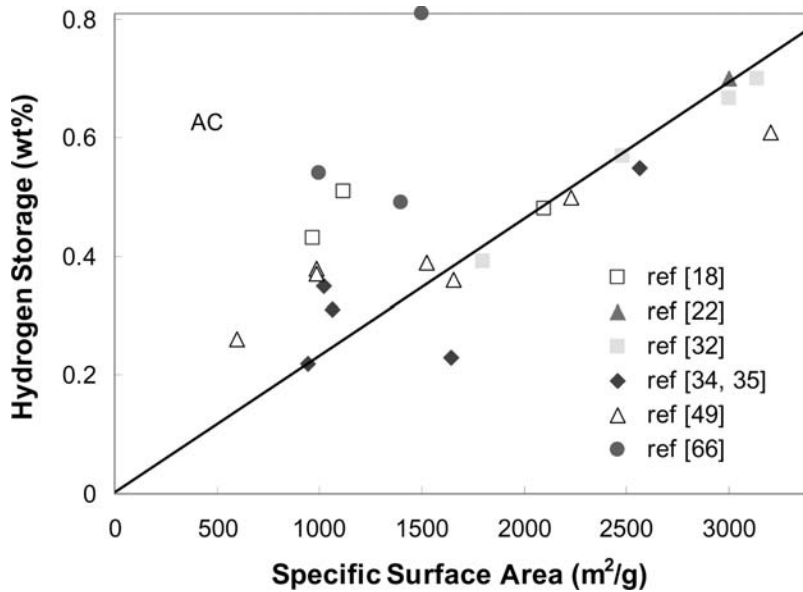


**Fig. 2** Hydrogen storage capacity at 298 K and 10 MPa as a function of the surface area of activated carbons. *Source:* Data extracted from Ref.<sup>[18,22,32,34,35,49,66]</sup>

corresponding undoped CNTs of only 0.1 wt%.<sup>[23]</sup> While such observations were very encouraging, thermogravimetric measurement of hydrogen adsorption in alkali-modified carbon materials showed no evidence of significant improvement.<sup>[10]</sup>

The possible effect of nitrogen atoms incorporated into carbon on the hydrogen storage capacity of carbon materials synthesized from a CVD process has been tested by adding N<sub>2</sub> gas during synthesis.<sup>[73]</sup> A capacity of 0.7–0.8 wt% at room temperature and under hydrogen pressure of 7 MPa was measured by a thermogravimetric method for materials grown in a gas composition containing a carbon source, H<sub>2</sub>, and N<sub>2</sub>.

Recent works have been focused on dispersing a small amount of transition metals (e.g. Pd, Pt, or Ni) in carbon to aid the adsorption of hydrogen. It is

believed that the hydrogen storage capacity of carbon could be increased by the presence of such metal particles.<sup>[74,75]</sup> Enhanced hydrogen uptakes have been observed when transition metals were added to graphite,<sup>[76]</sup> SWNTs or MWNTs,<sup>[77–84]</sup> carbon nanofibers,<sup>[43,85,86]</sup> and activated carbons.<sup>[68,83]</sup> The results are summarized in Table 4; the hydrogen uptakes listed are, in general, the maximum values of reported overall hydrogen storage capacities. It is, in general, agreed that the improvement of hydrogen storage by adding metal particles is attributed to a well-documented hydrogen spillover mechanism.<sup>[87,88]</sup> The presence of metal particles helps the initial hydrogen adsorption and the dissociation of hydrogen molecules into hydrogen atoms, which then spill onto nearby available carbon sites through the interface between

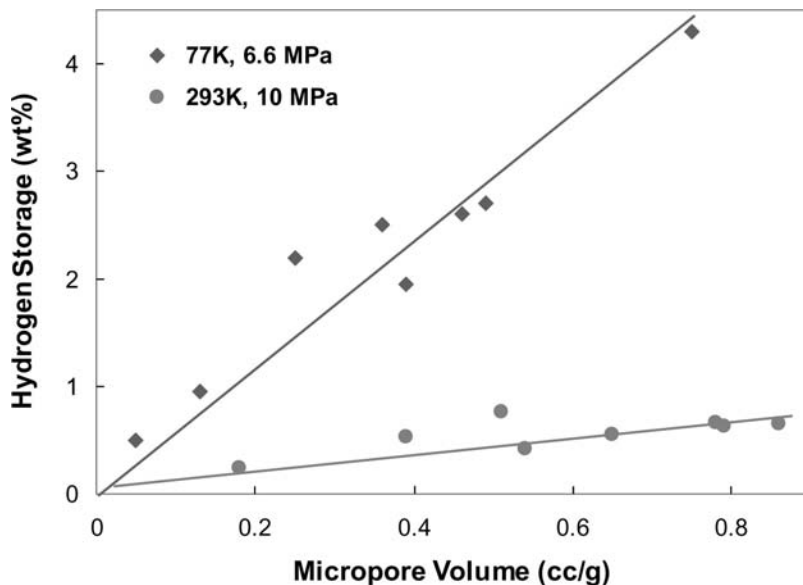


**Fig. 3** Hydrogen storage capacity as a function of micropore volume of activated carbons. *Source:* Data extracted from Ref.<sup>[35,71]</sup>

**Table 4** Reported enhancement of H<sub>2</sub> storage capacity of carbon by adding metals

Author, year	Materials, Metal content	Measurement method	Temperature (K)	Pressure (MPa)	H <sub>2</sub> uptake (wt%)
Chen et al., <sup>[72]</sup> 1999	Li-/K-MWNTs, 6.25 atom%	Gravimetric	293	0.1	~20
Yang, <sup>[11]</sup> 2000	Alkali-MWNTs	Gravimetric	293	0.1	~2.0
Fazle Kibria et al., <sup>[23]</sup> 2001	Li/MWNTs, n/a	Electrochemical	293	n/a	0.59
Hirscher et al., <sup>[82]</sup> 2001	Ti/SWNTs, 59.6 wt%	TDS	293	0.1	1.5
Zhong et al., <sup>[76]</sup> 2002	Ni (Co)/graphite, 20 wt%	TPD	773	3–5	2.8
Lueking and Yang, <sup>[85]</sup> 2003	MWNTs/NiMgO, n/a	Volumetric	293	6.9	3.6
Yoo et al., <sup>[81]</sup> 2004	Pd/ CNT, n/a	TPD	573	0.1	1.0
Callejas et al., <sup>[78]</sup> 2004	Ni/Y/SWNTs, 15.5 wt% Ni, 2.1 wt% Y	Volumetric	77	0.04	~3.0
Zacharia et al., <sup>[77]</sup> 2005	Pd/CNT, 2.5 wt%	Volumetric	293	2	0.66
Zacharia et al., <sup>[77]</sup> 2005	V/CNT, 1.5 wt%	Volumetric	293	2	0.69
Kim et al., <sup>[80]</sup> 2005	Ni/MWNTs, 6 wt%	TDS	300	4	~2.8
Costa, Coleman, and Green, <sup>[79]</sup> 2005	Ni/Y/SWNTs, 25.35 wt% Ni, 1.65 wt% Y	Volumetric	293	6	0.115
Zieliński et al., <sup>[68]</sup> 2005	Ni/AC, 1 wt%	Volumetric	293	3	0.53
Ansón et al., <sup>[83]</sup> 2006	Pd/SWNTs, 31.5 wt%	Gravimetric	293	2	~0.45
Ansón et al., <sup>[83]</sup> 2006	Pd/AC, 49.1 wt%	Gravimetric	293	2	~0.52
Mu et al., <sup>[84]</sup> 2006	Pd/MWNTs, ~20 wt% Pd	Volumetric	293	10.7	4.5

n/a—not available.

the metal and carbon. Such a spillover is also believed to exist from metal oxide catalysts to MWNTs and is responsible for the increased hydrogen storage capacity of a MWNT/NiMgO system.<sup>[85,89,90]</sup> In addition, experiments showed that initial hydrogen adsorption kinetics for metal-added-CNTs was nearly two times faster than that of pristine samples.<sup>[77]</sup>

While this approach for increasing the hydrogen storage capacity of carbon materials is perhaps promising, a better understanding of the mechanism is still needed. Hydrogen spillover is an accepted mechanism, but other critical issues, such as the effect of metal particle size and dispersion, the nature of the interfacial contact between carbon and metal atoms or nanoparticles, and how to achieve a better dispersion and interfacial contact, are still not well understood. It is also not known what the optimal metal content in a particular system is, which would result in the best improvement of capacity by doping the least amount of metal. In general, carbon-supported metal nanoparticles are better dispersed at relatively low metal content and show improved kinetics of sorption and desorption of hydrogen when compared with their counterparts with larger particle sizes.<sup>[91]</sup> This implies that the reduction in metal particle sizes and the increase in dispersion, in a sense, are more important than to increase metal loading in sample preparation. In addition, loading a large amount of metal usually

results in a tremendous decrease in the effective surface area of carbon materials.

The accessibility of metal particles for hydrogen molecules in various carbon materials, especially carbon nanotubes, is also critical for metal-assisted hydrogen adsorption. The presence of residual metal catalyst particles has been assumed not to influence the values of adsorbed hydrogen in SWNTs since they were encapsulated in graphitic shells, which would prevent any contact between the gas and the metals.<sup>[19]</sup> But the observed sorption of hydrogen in SWNT samples synthesized by the arc-discharge method was found to be highly dependent on the presence of Ni.<sup>[79]</sup>

## THEORETICALLY PREDICTED HYDROGEN STORAGE CAPACITY

All theoretical estimations of the hydrogen uptake by carbon adsorbents must be based on the knowledge of the exact state of H<sub>2</sub> in adsorbed state, but up to now there is no agreement on this point. Currently, most of the calculations are based on either physisorption of hydrogen molecules or chemisorption of hydrogen atoms. The physisorption models generally use grand canonical Monte Carlo simulations to determine the adsorption isotherms, and have the

advantage that the temperature dependence of adsorption can also be predicted. The two basic assumptions of this approach are: (1) there is no chemical transformation taking place during hydrogen adsorption; (2) the interaction between carbon materials and hydrogen molecules can be described via a classical empirical potential. The chemisorption models consider that a chemical process takes place during H<sub>2</sub> adsorption, and simulates the electronic states by employing classical or quantum molecular simulations and the density functional theory; this approach has the advantage of showing the nature of the interaction between atoms.

Hydrogen storage capacities of carbon adsorbents predicted by Monte Carlo simulations are summarized in Table 5. The targeted carbon forms include SWNTs, graphitic nanofibers, activated carbons, and even metal-doped carbon bundles, but most of the calculations were based on SWNTs. In the simulations, SWNTs were mostly considered as open, well-structured tubes, without amorphous carbon and

impurities, having well-determined and chosen diameters and geometrical location in the bundles, while slit pores were used to approximate the structure of nanofibers and activated carbons. The geometry assumed for the adsorbent (the tube diameter and van der Waals gap in the case of tubes, or the pore width and interplanar distance in the case of slit pores) is a critical factor for estimating storage capacities and comparing the results from different investigators; this is only more complicated by the use of different potentials and the consideration of quantum effects by various authors.<sup>[92]</sup> Basically, the numbers listed in Table 5 are the maximal capacities predicted for the optimized adsorbent structures. It is seen that none of the adsorbate configurations studied are able to approach the DOE storage goals at ambient temperatures, with the exception of the unusually high capacity predicted by Yin et al. for triangular arrays of SWNTs.<sup>[93]</sup> Some of the recent theoretical studies are seen to be in good agreement with some experimental data acquired for SWNTs.<sup>[94]</sup>

**Table 5** Predicted hydrogen uptakes by Monte Carlo simulations

Authors, year	Modeled materials	Temperature (K)	Pressure (MPa)	H <sub>2</sub> uptake (wt%)
Darkrim and Levesque, <sup>[95]</sup> 2000	Opened SWNT	77	15	11.24
Rzepka, Lamp, and de la Casa-Lillo, <sup>[65]</sup> 1998	SWNTs	77	Low	2.0
Williams and Eklund, <sup>[96]</sup> 2000	Isolated (10,10) SWNTs	77	10	9.6
		300	10	1.4
Wang and Johnson, <sup>[97]</sup> 1999	(9,9) SWNT arrays	77	5	~6.5
Yin, Mays, and McEnaney, <sup>[93]</sup> 2000	Triangular SWNT arrays	77	7	33.0
		298	10	4.7
Gu et al., <sup>[98]</sup> 2001	SWNTs	293	10	1.1
Levesque et al., <sup>[99]</sup> 2002	SWNTs	77	10	5.0
		293	10	1.0
Simonyan and Johnson, <sup>[100]</sup> 2002	SWNT bundles	298	12	1.2
Zhang, Cao, and Chen, <sup>[94]</sup> 2003	SWNT arrays ( $D = 2.719$ nm)	77	4	7.1
		300	18	0.7
Guay, Stansfield, and Rochefort, <sup>[101]</sup> 2004	SWNTs	293	10	0.6
Rzepka, Lamp, and de la Casa-Lillo, <sup>[65]</sup> 1998	An ideal slit pore carbon ( $S = 2600$ m <sup>2</sup> /g)	300	6	0.7
		300	10	1.3
Yin, Mays, and McEnaney, <sup>[93]</sup> 2000	Slit pores (modeling AC)	77	7	4.2–15.3
		298	7	0.5–1.9
Wang and Johnson, <sup>[70]</sup> 1999	Idealized slit pores	77	5	~6.5
Cracknell, <sup>[53]</sup> 2001	Slit pores	298	12	1.5
Simonyan and Johnson, <sup>[100]</sup> 2002	Alkali-metal intercalated SWNT bundles	298	12	1.9
Kowalczyk et al., <sup>[62]</sup> 2005	Graphite slitlike pores	303	10	1.4
Cao, Feng, and Wu, <sup>[102]</sup> 2004	Graphitic carbon inverse opal	298	30.4	5.9

Graphitic slit pores are used as a first approximation to the structure of graphitic nanofibers.<sup>[70,103]</sup> Modeling showed that the idealized slit pores give significantly better performance for hydrogen storage than SWNT arrays.<sup>[65,70]</sup> Similar results were also reached by Cracknell.<sup>[53,104]</sup> It is believed that most of the differences can be attributed to the curvature of the pores. In addition, the simulation results also indicated that hydrogen adsorption in carbon nanostructures is strongly influenced by the structure of the porosity.<sup>[101]</sup> When ideal slit pores were used to approximate activated carbon, the amount of absorbed hydrogen depends on the surface area of the sample and the maximum is 0.6 wt% ( $T = 300\text{ K}$ ;  $P = 6\text{ MPa}$ ),<sup>[65]</sup> which was verified experimentally with an excellent agreement.

Grand canonical Monte Carlo computer simulation also predicted that the doping of carbon nanotubes with electron donor and electron acceptor heteroatoms increases the hydrogen storage capacity of SWNTs.<sup>[105]</sup> The total adsorption of hydrogen predicted for metal-doped SWNT bundles, however, is still around 2.0 wt%, which is significantly smaller than the DOE target.<sup>[100]</sup> Calculated isotherms indicate that charged nanotube arrays (by doping) cannot meet the target for hydrogen storage at normal temperatures, unless the charges on the nanotubes are unrealistically large.

Quantum chemistry calculations have shed light into the interaction of hydrogen with carbon sites. One can search for hydrogen chemisorption sites, investigate activation barrier for  $\text{H}_2$  dissociation, study the stability of chemisorbed hydrogen, and predict the (maximum) storage capacity by performing geometry optimization and calculating potential energy surfaces for the dissociative adsorption of  $\text{H}_2$  on carbon sites of graphene or carbon nanotubes. First principles studies suggested that for the case of  $\text{H}_2$  interaction with graphene structures, the adsorption energies of H atoms are sensitive to the carbon sites;<sup>[106]</sup> the activation barriers for  $\text{H}_2$  dissociation on an unrelaxed graphene layer is considerably higher than that on a relaxed structure.<sup>[107]</sup>

Such theoretical calculations on carbon nanotubes have been the subject of several reviews.<sup>[3,5,92,108]</sup> Chemisorption starting from the physisorbed  $\text{H}_2$  molecule is difficult because of the existence of a substantial activation barrier,<sup>[108–110]</sup> however, while hydrogen chemisorption on some sites is energetically more favorable,<sup>[111]</sup> the kinetic energy of hydrogen atoms may affect where hydrogen is adsorbed.<sup>[112]</sup> Chemisorbed hydrogen induces strong deformation in nanotubes and weakens the C–C bond.<sup>[109,113]</sup> In a recent study, Yang, Lachawiec, and Yang<sup>[33]</sup> suggested that the energy of chemisorption decreases with hydrogen coverage. They also predicted that the activation energy of desorption for some adsorbed hydrogen may be below 10–15 kcal/mol, which allows desorption to take place readily at room temperature. Another

study also showed that the interaction of hydrogen with SWNTs is very weak and that a slight increase in temperature may cause hydrogen diffusion from the tube walls.<sup>[110]</sup>

A hydrogen storage capacity of more than 14 wt% was predicted for (10, 10) nanotubes by Lee et al. based on density functional theory.<sup>[113]</sup> This value is much higher than the estimated value of 3.3 wt% from the geometrical model,<sup>[114]</sup> and it is believed to be unrealistic.<sup>[100,112]</sup> A more recent theoretical evaluation by Li et al.<sup>[115]</sup> suggested that contribution from chemisorption has a theoretical upper limit of 7.7 wt% for hydrogen sorption in carbon nanotubes, but this upper limit would be very difficult to achieve in practice. Another theoretical calculation also suggested that maximum hydrogen storage capacity is limited by the repulsive energies between  $\text{H}_2$  molecules inside nanotubes and those between  $\text{H}_2$  molecules and the tube wall.<sup>[112]</sup> The highest volumetric density calculated for hydrogen stored in SWNTs is as high as  $132.4\text{ kg/m}^3$ , which corresponds to about 15 wt%. At this value, the pressure estimated to be imposed on the inner wall of the SWNT capsule is about 40 GPa at room temperature.<sup>[112]</sup> In addition, a theoretical study also suggested that there is no rational reason for carbon nanotubes to have superior hydrogen uptake capacity than other graphitic structures in terms of either binding energies or kinetics.<sup>[115]</sup>

## UNANSWERED QUESTIONS RELATED TO HYDROGEN STORAGE IN CARBON MATERIALS

Although a large volume of experimental and theoretical research has been done on adsorption of hydrogen in carbon nanotubes and other forms of nanostructured carbons, several key issues, especially those related to the fundamental understanding of hydrogen adsorption in nanostructured carbon materials, are still open to discussion.

A basic issue is, what is the exact chemical state of hydrogen when it is adsorbed in carbon materials, or in other words, what is the precise nature of the interaction between hydrogen and a given carbon surface?<sup>[1]</sup> It is generally accepted that hydrogen adsorption at liquid nitrogen temperature (77 K) is a physisorption process, but the extent of physisorption contribution in adsorption at room temperature is still an arguable issue. Hirscher et al.<sup>[34,35]</sup> suggested that room temperature adsorption is a typical physisorption process because both fast kinetics and high reversibility were observed for hydrogen adsorption in different carbon nanostructures, including SWNTs, AC, MWNTs, and a mixture of nanotubes. Additionally, the amount of hydrogen adsorbed depends almost

linearly on the specific surface area of the carbon materials, both at low temperature and at room temperature, and is independent from the type of carbon nanostructure.<sup>[35]</sup> Rzepka et al.<sup>[47]</sup> studied several types of nanofibers and claimed that all experimental results at room temperature can be adequately explained by pure physical adsorption on carbon surfaces. A recent investigation using Raman spectroscopy found that no charge transfer phenomena were involved in the interaction between hydrogen and activated carbons in the range of 40 K to room temperature and at a pressure of up to 10 MPa.<sup>[116]</sup> It was suggested that physisorption is the mechanism of hydrogen adsorption, while chemisorption, if any, should be negligible, because no C–H stretching signals in the region of 2800–3300 cm<sup>-1</sup> were detected.

If the H<sub>2</sub> uptake at room temperature is caused by physisorption, this process alone cannot explain the relatively high hydrogen uptakes measured at room temperature in well-controlled conditions. Thermal desorption studies revealed that weakly bonded physisorbed hydrogen accounts for ca. 90% and chemically bonded hydrogen for ca. 10%. The latter was released at temperatures above 450°C as a result of breaking of the covalent C–H bonds.<sup>[31]</sup> Experiments also showed that 78.3% of the adsorbed hydrogen could be released under ambient pressure at room temperature, while the release of the residual stored hydrogen required some heating of the sample.<sup>[21]</sup> TPD studies<sup>[25]</sup> of hydrogen loaded SWNT with high pressure (2 MPa) hydrogen gas at room temperature showed that there are at least two different sites for hydrogen in the SWNT samples. The physisorbed molecular hydrogen at the surface of the carbon desorbs around 105 K, while tightly bound hydrogen desorbs at temperatures above 500 K. Even though the tightly bound hydrogen was suggested to be incorporated during the synthesis of the nanotubes, the possibility of forming chemisorbed hydrogen during adsorption still cannot be ruled out. It has also been suggested<sup>[56]</sup> that an intermediate state between physisorption and chemisorption may be possible, i.e. “defect-mediated hydrogen sorption,” and this state would possibly participate in hydrogen storage on carbon nanostructures. A better understanding of the role that these possible states play during adsorption is necessary for finding answers to other issues. It would also provide the fundamental support to all other approaches for increasing the gas uptake, such as purification, annealing, increasing specific area of the materials, opening of the tubes, or intercalation of heteroatoms.

Another important parameter is the heat of adsorption of hydrogen. This energetic parameter varies with surface coverage and is very sensitive to any surface irregularities, distribution of pore size, and presence of various chemical groups on the surface. This parameter

may provide quantitative information about the nature of the interaction between hydrogen and the adsorbent. Experiments at 77 K showed that the heat of adsorption of hydrogen on activated carbons is about 4 kJ/mol.<sup>[63]</sup> The values obtained from the van't Hoff isochore at various surface coverages were in the range of 3.9–5.2 kJ/mol.<sup>[117]</sup> These numbers are well supported by theoretical predictions.<sup>[118]</sup> At room temperature, a wide range of values (e.g. between 31.4 kJ/mol<sup>[111]</sup> and 7.54 kJ/mol)<sup>[115]</sup> have been theoretically predicted for the adsorption energies of H atom to graphitic surfaces (nanotubes and graphene), but systematic experimental studies are still missing. In addition, a thermodynamic study suggested that a suitable adsorbent capable of storing hydrogen at ambient temperature should have a heat of adsorption of hydrogen of about 15.1 kJ/mol. This value corresponds to the optimum affinity of hydrogen: strong enough to store a large amount of hydrogen gas at the charging pressure (about 3 MPa) but weak enough to release most of that hydrogen at the discharge pressure (about 0.15 MPa).<sup>[119]</sup>

One question derived from the basic issue is the following: if hydrogen adsorption at low temperature is a physisorption process, is it possible for hydrogen to access and condense inside carbon nanotubes? Or, “is adsorption in nanotubes a reliable mode of hydrogen storage?”<sup>[6]</sup> The main difference between CNTs and high surface area graphite is the curvature of the graphene sheets and the cavity inside the tube. In microporous solids with capillaries that have a width not exceeding a few molecular diameters, the potential fields from opposite walls will overlap, so that the attractive force acting on adsorbate molecules will be larger than that of an open surface. The condensation of hydrogen by such “capillary effect” then allows nanotubes, especially SWNTs, to store more hydrogen than the amount potentially adsorbed only by surface adsorption. But the assumption that hydrogen condenses inside the nanotubes is questionable because the critical temperature of hydrogen is 32.98 K and therefore it would only condense below a temperature of 33 K. In addition, the adsorption isotherms of nanotubes are of type II and no differences in the shape of the isotherm from nanotubes and high surface area graphite were found.<sup>[25]</sup> The specific surface areas calculated from the BET method (using N<sub>2</sub> adsorption at 77 K) on various nanostructured carbon samples range from 73 to 377 m<sup>2</sup>/g. No indication for the condensation of nitrogen inside the tubes was found. It was argued that the inner surface of the tubes was inaccessible because the tubes were possibly capped. This stimulated efforts for opening of the tubes. It is essential to ensure that hydrogen molecules can enter the tube because these molecules cannot penetrate through the carbon atom hexagons.

Other debatable issues are: What is the capacity of carbon surface for chemisorbing hydrogen? Does

chemisorption play a significant role in the hydrogen adsorption or storage process? If hydrogen is able to form a covalent bond with carbon, what are the possible sites for the interaction? Are both edge sites and in-plane sites of graphene sheets the possible sites for chemisorption? The contribution of simulations in answering these questions should guide any practical approach of improving the hydrogen storage capacity in carbons by chemical modification such as heteroatom incorporation. If the answer is positive, introducing metals that can help the dissociative adsorption of hydrogen and “transfer” hydrogen to carbon sites (“spillover” mechanism) in/into carbon adsorbents would certainly be beneficial. In addition, it is suggested that most of the hydrogen species should be adsorbed on carbon, not on metals such as Ni (or Co),<sup>[76]</sup> while metals serve mainly as an active center to assist the dissociative adsorption of hydrogen molecules. A following question, then, is what types of carbon sites are the receivers of hydrogen transferred from metal sites? It was argued that hydrogen molecules adsorbed by metal nanoparticles was subsequently dissociated and spilled over to carbon nanotubes to those defect sites.<sup>[81]</sup> Then, could any carbon site be the receiver for such spillover?

For carbon nanotubes, there are two more arguable issues. One is what are the optimum sizes of nanotubes and their spatial arrangement for reaching high storage capacity. Another one is whether or not nanotubes have better adsorption capacity than “classical” carbon materials such as activated carbons. Related to the former issue, if there is an optimal geometry, then, is it possible to control these structural parameters in practice? Modeling calculations<sup>[25]</sup> showed that the bulk absorption in the cavity of nanotubes is proportional to the diameter of the tubes and is highest for SWNT. Based on the assumption that hydrogen would condense in the nanotube cavity, calculations showed that the mass percentage of adsorbed hydrogen increases with the tube diameter. Monte Carlo simulations have shown that hydrogen adsorption can be optimized by suitable sizes of nanotube diameters and of space between nanotubes in the bundles.<sup>[95,96,100,120]</sup> A definitive answer from experimentation is still not available.

For the question regarding the superiority of carbon nanotubes over “classical” carbon materials, both positive (e.g. Ref.<sup>[93]</sup>) and negative (e.g. Ref.<sup>[115]</sup>) answers have been derived from theoretical studies. On experimental grounds, and disregarding the high but unverified capacities claimed by early studies,<sup>[19,40]</sup> nanotubes did not always show higher capacities than activated carbons. Actually, from the data listed in “Theoretically Predicted Hydrogen Storage Capacity”, almost all results reported recently showed that nanotubes (and nanofibers) have much less

storage capacity than high-surface activated carbons.<sup>[25,28,29,32,67]</sup> In addition, Züttel et al.<sup>[25,28]</sup> studied a large number of different carbon samples and showed that the adsorption of hydrogen on nanotubes is a surface phenomenon, which is similar to the adsorption of hydrogen on high-surface area graphite.

For the experimental study of hydrogen storage in carbon materials, there are three aspects that need attention. First, there is insufficient understanding of the adsorption and desorption kinetics of hydrogen on carbons. Up to now, most studies have been performed at equilibrium conditions. Measurements of the hydrogen adsorption rate at constant pressure and pore-size distribution suggest that the hydrogen molecules are adsorbed through a diffusion process into pores with a diameter less than 1 nm.<sup>[45]</sup> The diffusion process has still not been kinetically defined. Second, systematic experiments are necessary using reliable measurement techniques and sufficient quantities, of high-purity, and well-characterized carbon samples with structures including numerous openings for hydrogen accessibility. Third, more studies on the performance of metal-added carbon materials after the first adsorption/desorption cycle are necessary. A repeatable hydrogen uptake is expected for storage materials used in practice. The reproducibility of hydrogen uptake in repeated cycles then should be another important parameter for evaluating storage materials, especially in the cases where chemisorption is involved. It was observed that<sup>[76]</sup> the high-temperature H<sub>2</sub> uptake and release could be repeated for many cycles in Ni (Co) added graphite composites, with a slight decrease in the H<sub>2</sub> storage capacity after the first cycle. Probably, some of the transition metal particles migrated out from the carbon matrix and agglomerated after the H<sub>2</sub> adsorption/desorption cycles, which may reduce the synergism between the transition metal and carbon, and thus the H<sub>2</sub> storage capacity.<sup>[76]</sup> In the case of CNTs, the amount of hydrogen storage decreased from an initial 1.0 wt% to 0.2 wt% in the second H<sub>2</sub> uptake-release cycle.<sup>[81]</sup> The reason might involve the recrystallization of the defective CNTs on releasing hydrogen by heating to 1100 K,<sup>[81]</sup> because the amount of hydrogen stored in CNTs decreased with increasing annealing temperature.

Besides the large variation of reported storage capacity of carbon adsorbents, and the lack of basic modeling research on the proper conditions, physical and chemical, for optimum hydrogen storage, other challenges still exist for application of carbon materials, especially nanostructural materials, in hydrogen storage. For carbon nanotubes, the main challenges are the high cost and the difficulty of large-scale production. As analyzed by Bunger and Zittel,<sup>[7]</sup> a storage cost of about \$3 million per vehicle is projected if single-wall nanotubes were used at the commercial



price available today. Based on a technical and economic analysis, they concluded “hydrogen storage in carbon nanostructures is still at a research level and not yet mature for industrial application. From today’s point of view, at least for the first generation of direct hydrogen applications (such as fuel cell vehicles, battery replacement), other alternatives such as compressed or liquid storage are required.”<sup>[7]</sup>

## CONCLUSION

The reported hydrogen storage capacities in carbon adsorbents do not converge into a certain narrow range. Most recent experimental observations seem to support the conclusion that carbon nanotubes are not likely to store the amount of hydrogen required for automotive applications at moderate pressures and close to room temperature, and those results are supported by some theoretical studies reported recently. Experimental results reported in the past couple of years implied that different carbon materials, except metal-doped materials, in general only have less than 1.0 wt% hydrogen storage capacities at room temperature (even at high pressure). At both liquid nitrogen temperature and room temperature, the storage capacities of activated carbons increase with the increase in effective surface area and micropore volume, and a broadly linear relationship can describe such dependences. A promising approach to enhance the hydrogen storage capacities of carbon materials may be metal doping, but more systematic studies are necessary. Some key issues related to the fundamentals of hydrogen storage in nanostructured carbon materials are still open to discussion. More fundamental studies using both theoretical and experimental approaches are still needed.

## ACKNOWLEDGMENTS

The authors acknowledge support from the Division of Materials Science and Engineering, Office of Basic Energy Sciences, U.S. Department of Energy under contract DE-AC05-00OR-22725 with UT-Battelle, LLC. The work was supported in part by an appointment to the ORNL Postdoctoral Research Associates Program administered jointly by ORISE and ORNL.

## REFERENCES

1. Dillon, A.C.; Heben, M.J. Hydrogen storage using carbon adsorbents: past, present and future. *Appl. Phys. A* **2001**, *72* (2), 133–142.

2. Kidnay, A.; Hiza, M. High pressure adsorption isotherm of neon, hydrogen and helium at 76 K. *Adv. Cryogenic Eng.* **1967**, *12*, 730.
3. Ding, R.G.; Lu, G.Q.; Yan, Z.F.; Wilson, M.A. Recent advances in the preparation and utilization of carbon nanotubes for hydrogen storage. *J. Nanosci. Nanotechnol.* **2001**, *1* (1), 7–29.
4. Cheng, H.M.; Yang, Q.H.; Liu, C. Hydrogen storage in carbon nanotubes. *Carbon* **2001**, *39* (10), 1447–1454.
5. Hirscher, M.; Becher, M. Hydrogen storage in carbon nanotubes. *J. Nanosci. Nanotechnol.* **2003**, *3* (1–2), 3–17.
6. Darkrim, F.L.; Malbrunot, P.; Tartaglia, G.P. Review of hydrogen storage by adsorption in carbon nanotubes. *Int. J. Hydrogen Energy* **2002**, *27* (2), 193–202.
7. Bünger, U.; Zittel, W. Hydrogen storage in carbon nanostructures – still a long road from science to commerce? *Appl. Phys. A* **2001**, *72* (2), 147–151.
8. Hirscher, M.; Becher, M.; Haluska, M.; Quintel, A.; Skakalova, V.; Choi, Y.M.; Dettlaff-Weglikowska, U.; Roth, S.; Stepanek, I.; Bernier, P.; Leonhardt, A.; Fink, J. Hydrogen storage in carbon nanostructures. *J. Alloys Comp.* **2002**, *330–332*, 654–658.
9. Tibbetts, G.G.; Meisner, G.P.; Olk, C.H. Hydrogen storage capacity of carbon nanotubes, filaments, and vapor-grown fibers. *Carbon* **2001**, *39* (15), 2291–2301.
10. Pinkerton, F.E.; Wicke, B.G.; Olk, C.H.; Tibbetts, G.G.; Meisner, G.P.; Meyer, M.S.; Herbst, J.F. Thermogravimetric measurement of hydrogen absorption in alkali-modified carbon materials. *J. Phys. Chem. B* **2000**, *104* (40), 9460–9467.
11. Yang, R.T. Hydrogen storage by alkali-doped carbon nanotubes-revisited. *Carbon* **2000**, *38* (4), 623–626.
12. Hirscher, M.; Becher, M.; Haluska, M.; von Zeppelin, F.; Chen, X.H.; Dettlaff-Weglikowska, U.; Roth, S. Are carbon nanostructures an efficient hydrogen storage medium? *J. Alloys Comp.* **2003**, *356–357*, 433–437.
13. Nützenadel, C.; Züttel, A.; Chartouni, D.; Schlapbach, L. Electrochemical storage of hydrogen in nanotube materials. *Electrochem. Solid-State Lett.* **1999**, *2* (1), 30–32.
14. Rajalakshmi, N.; Dhathathreyan, K.S.; Govindaraj, A.; Satishkumar, B.C. Electrochemical investigation of single-walled carbon nanotubes for hydrogen storage. *Electrochim. Acta* **2000**, *45* (27), 4511–4515.
15. Gundiah, G.; Govindaraj, A.; Rajalakshmi, N.; Dhathathreyan, K.S.; Rao, C.N.R. Hydrogen storage in carbon nanotubes and related materials. *J. Mater. Chem.* **2003**, *13* (2), 209–213.
16. Ansón, A.; Benham, M.; Jagiello, J.; Callejas, M.A.; Benito, A.M.; Maser, W.K.; Züttel, A.; Sudan, P.; Martinez, M.T. Hydrogen adsorption on a single-walled carbon nanotube material: A comparative study of three different adsorption techniques. *Nanotechnology* **2004**, *15* (11), 1503–1508.
17. Jagiello, J.; Thommes, M. Comparison of DFT characterization methods based on N<sub>2</sub>, Ar, CO<sub>2</sub>, and H<sub>2</sub> adsorption applied to carbons with various pore size distributions. *Carbon* **2004**, *42* (7), 1227–1232.
18. Jagiello, J.; Anson, A.; Martinez, M.T. DFT-based prediction of high-pressure H<sub>2</sub> adsorption on porous

- carbons at ambient temperatures from low-pressure adsorption data measured at 77 K. *J. Phys. Chem. B* **2006**, *110* (10), 4531–4534.
19. Dillon, A.C.; Jones, K.M.; Bekkedahl, T.A.; Kiang, C.H.; Bethune, D.S.; Heben, M.J. Storage of hydrogen in single-walled carbon nanotubes. *Nature* **1997**, *386* (6623), 377–379.
  20. Ye, Y.; Ahn, C.C.; Witham, C.; Fultz, B.; Liu, J.; Rinzler, A.G.; Colbert, D.; Smith, K.A.; Smalley, R.E. Hydrogen adsorption and cohesive energy of single-walled carbon nanotubes. *Appl. Phys. Lett.* **1999**, *74* (16), 2307–2309.
  21. Liu, C.; Fan, Y.Y.; Liu, M.; Cong, H.T.; Cheng, H.M.; Dresselhaus, M.S. Hydrogen storage in single-walled carbon nanotubes at room temperature. *Science* **1999**, *286* (5442), 1127–1129.
  22. Lan, A.D.; Mukasyan, A. Hydrogen storage capacity characterization of carbon nanotubes by a microgravimetric approach. *J. Phys. Chem. B* **2005**, *109* (33), 16,011–16,016.
  23. Fazle Kibria, A.K.M.; Mo, Y.H.; Park, K.S.; Nahm, K.S.; Yun, M.H. Electrochemical hydrogen storage behaviors of CVD, AD and LA grown carbon nanotubes in KOH medium. *Int. J. Hydrogen Energy* **2001**, *26* (8), 823–829.
  24. Nishimiya, N.; Ishigaki, K.; Takikawa, H.; Ikeda, M.; Hibi, Y.; Sakakibara, T.; Matsumoto, A.; Tsutsumi, K. Hydrogen sorption by single-walled carbon nanotubes prepared by a torch arc method. *J. Alloys Comp.* **2002**, *339* (1–2), 275–282.
  25. Züttel, A.; Sudan, P.; Mauron, P.; Kiyobayashi, T.; Emmenegger, C.; Schlapbach, L. Hydrogen storage in carbon nanostructures. *Int. J. Hydrogen Energy* **2002**, *27* (2), 203–212.
  26. Wang, Q.K.; Zhu, C.C.; Liu, W.H.; Wu, T. Hydrogen storage by carbon nanotube and their films under ambient pressure. *Int. J. Hydrogen Energy* **2002**, *27* (5), 497–500.
  27. Pradhan, B.K.; Harutyunyan, A.R.; Stojkovic, D.; Grossman, J.C.; Zhang, P.; Cole, M.W.; Crespi, V.; Goto, H.; Fujiwara, J.; Eklund, P.C. Large cryogenic storage of hydrogen in carbon nanotubes at low pressures. *J. Mater. Res.* **2002**, *17* (9), 2209–2216.
  28. Züttel, A.; Nützenadel, C.; Sudan, P.; Mauron, P.; Emmenegger, C.; Rentsch, S.; Schlapbach, L.; Weidenkaff, A.; Kiyobayashi, T. Hydrogen sorption by carbon nanotubes and other carbon nanostructures. *J. Alloys Comp.* **2002**, *330*, 676–682.
  29. Kajiura, H.; Tsutsui, S.; Kadono, K.; Kakuta, M.; Ata, M.; Murakami, Y. Hydrogen storage capacity of commercially available carbon materials at room temperature. *Appl. Phys. Lett.* **2003**, *82* (7), 1105–1107.
  30. Li, X.S.; Zhu, H.W.; Xu, C.L.; Mao, Z.Q.; Wu, D.H. Measuring hydrogen storage capacity of carbon nanotubes by tangent-mass method. *Int. J. Hydrogen Energy* **2003**, *28* (11), 1251–1253.
  31. Tarasov, B.P.; Maehlen, J.P.; Lototsky, M.V.; Muradyan, V.E.; Yartys, V.A. Hydrogen sorption properties of arc generated single-wall carbon nanotubes. *J. Alloys Comp.* **2003**, *356–357*, 510–514.
  32. Haas, M.K.; Zielinski, J.M.; Dantsin, G.; Coe, C.G.; Pez, G.P.; Cooper, A.C. Tailoring singlewalled carbon nanotubes for hydrogen storage. *J. Mater. Res.* **2005**, *20* (12), 3214–3223.
  33. Yang, F.H.; Lachawiec, A.J., Jr.; Yang, R.T. Adsorption of spillover hydrogen atoms on single-wall carbon nanotubes. *J. Phys. Chem. B* **2006**, *110* (12), 6236–6244.
  34. Hirscher, M.; Panella, B. Nanostructures with high surface area for hydrogen storage. *J. Alloys Comp.* **2005**, *404*, 399–401.
  35. Panella, B.; Hirscher, M.; Roth, S. Hydrogen adsorption in different carbon nanostructures. *Carbon* **2005**, *43* (10), 2209–2214.
  36. Zhu, H.W.; Cao, A.Y.; Li, X.S.; Xu, C.L.; Mao, Z.Q.; Ruan, D.B.; Liang, J.; Wu, D.H. Hydrogen adsorption in bundles of well-aligned carbon nano tubes at room temperature. *Appl. Surf. Sci.* **2001**, *178* (1–4), 50–55.
  37. Hou, P.X.; Yang, Q.H.; Bai, S.; Xu, S.T.; Liu, M.; Cheng, H.M. Bulk storage capacity of hydrogen in purified multiwalled carbon nanotubes. *J. Phys. Chem. B* **2002**, *106* (5), 963–966.
  38. Johansson, E.; Hjörvarsson, B.; Ekström, T.; Jacob, M. Hydrogen in carbon nanostructures. *J. Alloys Comp.* **2002**, *330*, 670–675.
  39. Ci, L.J.; Zhu, H.W.; Wei, B.Q.; Xu, C.L.; Wu, D.H. Annealing amorphous carbon nanotubes for their application in hydrogen storage. *Appl. Surf. Sci.* **2003**, *205* (1–4), 39–43.
  40. Chambers, A.; Park, C.; Baker, R.T.K.; Rodriguez, N.M. Hydrogen storage in graphite nanofibers. *J. Phys. Chem. B* **1998**, *102* (22), 4253–4256.
  41. Ahn, C.C.; Ye, Y.; Ratnakumar, B.V.; Witham, C.; Bowman, R.C.; Fultz, B. Hydrogen desorption and adsorption measurements on graphite nanofibers. *Appl. Phys. Lett.* **1998**, *73* (23), 3378–3380.
  42. Poirier, E.; Chahine, R.; Bose, T.K. Hydrogen adsorption in carbon nanostructures. *Int. J. Hydrogen Energy* **2001**, *26* (8), 831–835.
  43. Browning, D.J.; Gerrard, M.L.; Lakeman, J.B.; Mellor, I.M.; Mortimer, R.J.; Turpin, M.C. Studies into the storage of hydrogen in carbon nanofibers: Proposal of a possible reaction mechanism. *Nano Lett.* **2002**, *2* (3), 201–205.
  44. Zhu, H.W.; Li, C.H.; Li, X.S.; Xu, C.L.; Mao, Z.Q.; Liang, J.; Wu, D.H. Hydrogen storage by platelet-carbon fibers at room temperature. *Mater. Lett.* **2002**, *57* (1), 32–35.
  45. Kajiura, H.; Kadono, K.; Tsutsui, S.; Murakami, Y. Repeatable hydrogen adsorption using nanostructured graphite at room temperature. *Appl. Phys. Lett.* **2003**, *82* (12), 1929–1931.
  46. Zhu, H.W.; Li, X.S.; Ci, L.J.; Xu, C.L.; Wu, D.H.; Mao, Z.Q. Hydrogen storage in heat-treated carbon nanofibers prepared by the vertical floating catalyst method. *Mater. Chem. Phys.* **2003**, *78* (3), 670–675.
  47. Rzepka, M.; Bauer, E.; Reichenauer, G.; Schliermann, T.; Bernhardt, B.; Bohmhammel, K.; Henneberg, E.; Knoll, U.; Maneck, H.E.; Braue, W. Hydrogen storage capacity of catalytically grown carbon nanofibers. *J. Phys. Chem. B* **2005**, *109* (31), 14,979–14,989.

48. Lueking, A.D.; Pan, L.; Narayanan, D.L.; Clifford, C.E.B. Effect of expanded graphite lattice in exfoliated graphite nanofibers on hydrogen storage. *J. Phys. Chem. B* **2005**, *109* (26), 12,710–12,717.
49. Blackman, J.M.; Patrick, J.W.; Snape, C.E. An accurate volumetric differential pressure method for the determination of hydrogen storage capacity at high pressures in carbon materials. *Carbon* **2006**, *44* (5), 918–927.
50. Li, X.S.; Zhu, H.W.; Ci, L.J.; Xu, C.L.; Mao, Z.Q.; Wei, B.Q.; Liang, J.; Wu, D.H. Hydrogen uptake by graphitized multi-walled carbon nanotubes under moderate pressure and at room temperature. *Carbon* **2001**, *39* (13), 2077–2079.
51. Rodriguez, N.M.; Baker, R.T.K. Storage of hydrogen in layered nanostructures. US Patent 5,653,951, August 5, 1997.
52. Park, C.; Anderson, P.E.; Chambers, A.; Tan, C.D.; Hidalgo, R.; Rodriguez, N.M. Further studies of the interaction of hydrogen with graphite nanofibers. *J. Phys. Chem. B* **1999**, *103* (48), 10,572–10,581.
53. Cracknell, R.F. Molecular simulation of hydrogen adsorption in graphitic nanofibers. *Phys. Chem. Chem. Phys.* **2001**, *3* (11), 2091–2097.
54. Orimo, S.; Majer, G.; Fukunaga, T.; Zuttel, A.; Schlapbach, L.; Fujii, H. Hydrogen in the mechanically prepared nanostructured graphite. *Appl. Phys. Lett.* **1999**, *75* (20), 3093–3095.
55. Orimo, S.; Matsushima, T.; Fujii, H.; Fukunaga, T.; Majer, G. Hydrogen desorption property of mechanically prepared nanostructured graphite. *J. Appl. Phys.* **2001**, *90* (3), 1545–1549.
56. Orimo, S.; Zuttel, A.; Schlapbach, L.; Majer, G.; Fukunaga, T.; Fujii, H. Hydrogen interaction with carbon nanostructures: Current situation and future prospects. *J. Alloys Comp.* **2003**, *356*, 716–719.
57. Blackman, J.M.; Patrick, J.W.; Arenillas, A.; Shi, W.; Snape, C.E. Activation of carbon nanofibers for hydrogen storage. *Carbon* **2006**, *44* (8), 1376–1385.
58. Carpetis, C.; Peschka, W. A study on hydrogen storage by use of cryoadsorbents. *Int. J. Hydrogen Energy* **1980**, *5*, 539–554.
59. Agarwal, R.K.; Noh, J.S.; Schwarz, J.A.; Davini, P. Effect of surface acidity of activated carbon on hydrogen storage. *Carbon* **1987**, *25* (2), 219–226.
60. Nijkamp, M.G.; Raaymakers, J.E.M.J.; van Dillen, A.J.; de Jong, K.P. Hydrogen storage using physisorption – Materials demands. *Appl. Phys. A* **2001**, *72* (5), 619–623.
61. Gadiou, R.; Texier-Mandoki, N.; Piquero, T.; Saadallah, S.E.; Parmentier, J.; Patarin, J.; David, P.; Vix-Guterl, C. The influence of microporosity on the hydrogen storage capacity of ordered mesoporous carbons. *Adsorption–J. Int. Adsorption Soc.* **2005**, *11*, 823–827.
62. Kowalczyk, P.; Tanaka, H.; Holyst, R.; Kaneko, K.; Ohmori, T.; Miyamoto, J. Storage of hydrogen at 303 K in graphite slitlike pores from grand canonical Monte Carlo simulation. *J. Phys. Chem. B* **2005**, *109* (36), 17,174–17,183.
63. Chahine, R.; Bose, T.K. Low-pressure adsorption storage of hydrogen. *Int. J. Hydrogen Energy* **1994**, *19* (2), 161–164.
64. Zhou, L.; Zhou, Y. A comprehensive model for the adsorption of supercritical hydrogen on activated carbon. *Ind. Eng. Chem. Res.* **1996**, *35* (11), 4166–4168.
65. Rzepka, M.; Lamp, P.; de la Casa-Lillo, M.A. Physisorption of hydrogen on microporous carbon and carbon nanotubes. *J. Phys. Chem. B* **1998**, *102* (52), 10,894–10,898.
66. Ströbel, R.; Jörissen, L.; Schliermann, T.; Trapp, V.; Schütz, W.; Bohmhammel, K.; Wolf, G.; Garcke, J. Hydrogen adsorption on carbon materials. *J. Power Sources* **1999**, *84* (2), 221–224.
67. Kiyobayashi, T.; Takeshita, H.T.; Tanaka, H.; Takeichi, N.; Zuttel, A.; Schlapbach, L.; Kuriyama, N. Hydrogen adsorption in carbonaceous materials—How to determine the storage capacity accurately. *J. Alloys Comp.* **2002**, *330*, 666–669.
68. Zielinski, M.; Wojcieszak, R.; Monteverdi, S.; Mercy, M.; Bettahar, M.M. Hydrogen storage on nickel catalysts supported on amorphous activated carbon. *Catal. Commun.* **2005**, *6* (12), 777–783.
69. Salvador-Palacios, F.; Sanchez-Montero, M.J.; Sanguesa-Dominguez, I.; Izquierdo-Misiego, C. Importance of textural characteristics in the adsorption of hydrogen onto activated carbon and activated carbon fibers. *Mater. Sci. Forum* **2006**, *514–516*, 427–431.
70. Wang, Q.Y.; Johnson, J.K. Molecular simulation of hydrogen adsorption in single-walled carbon nanotubes and idealized carbon slit pores. *J. Chem. Phys.* **1999**, *110* (1), 577–586.
71. de la Casa-Lillo, M.A.; Lamari-Darkrim, F.; Cazorla-Amoros, D.; Linares-Solano, A. Hydrogen storage in activated carbons and activated carbon fibers. *J. Phys. Chem. B* **2002**, *106* (42), 10,930–10,934.
72. Chen, P.; Wu, X.; Lin, J.; Tan, K.L. High H<sub>2</sub> uptake by alkali-doped carbon nanotubes under ambient pressure and moderate temperatures. *Science* **1999**, *285* (5424), 91–93.
73. Badzian, A.; Badzian, T.; Breval, E.; Piotrowski, A. Nanostructured, nitrogen-doped carbon materials for hydrogen storage. *Thin Solid Films* **2001**, *398*, 170–174.
74. Schwarz, J.A. Metal assisted carbon cold storage of hydrogen. US Patent 4,716,736, January 5, 1988.
75. Ozaki, J.; Ohizumi, W.; Oya, A.; Illan-Gomez, M.J.; Roman-Martinez, M.C.; Linares-Solano, A. Comparison of hydrogen adsorption abilities of platinum-loaded carbon fibers prepared using two different methods. *Carbon* **2000**, *38* (5), 778–780.
76. Zhong, Z.Y.; Xiong, Z.T.; Sun, L.F.; Luo, J.Z.; Chen, P.; Wu, X.; Lin, J.; Tan, K.L. Nanosized nickel (or cobalt)/graphite composites for hydrogen storage. *J. Phys. Chem. B* **2002**, *106* (37), 9507–9513.
77. Zacharia, R.; Kim, K.Y.; Kibria, A.; Nahm, K.S. Enhancement of hydrogen storage capacity of carbon nanotubes via spill-over from vanadium and palladium nanoparticles. *Chem. Phys. Lett.* **2005**, *412* (4–6), 369–375.
78. Callejas, M.A.; Anson, A.; Benito, A.M.; Maser, W.; Fierro, J.L.G.; Sanjuan, M.L.; Martinez, M.T. Enhanced hydrogen adsorption on single-wall carbon nanotubes by sample reduction. *Mater. Sci. Eng.*

- B-Solid State Mater. Adv. Technol. **2004**, *108* (1–2), 120–123.
79. Costa, P.M.F.J.; Coleman, K.S.; Green, M.L.H. Influence of catalyst metal particles on the hydrogen sorption of single-walled carbon nanotube materials. *Nanotechnology* **2005**, *16* (4), 512–517.
80. Kim, H.S.; Lee, H.; Han, K.S.; Kim, J.H.; Song, M.S.; Park, M.S.; Lee, J.Y.; Kang, J.K. Hydrogen storage in Ni nanoparticle-dispersed multiwalled carbon nanotubes. *J. Phys. Chem. B* **2005**, *109* (18), 8983–8986.
81. Yoo, E.; Gao, L.; Komatsu, T.; Yagai, N.; Arai, K.; Yamazaki, T.; Matsuishi, K.; Matsumoto, T.; Nakamura, J. Atomic hydrogen storage in carbon nanotubes promoted by metal catalysts. *J. Phys. Chem. B* **2004**, *108* (49), 18,903–18,907.
82. Hirscher, M.; Becher, M.; Haluska, M.; Dettlaff-Weglikowska, U.; Quintel, A.; Duesberg, G.S.; Choi, Y.-M.; Downes, P.; Hulman, M.; Roth, S.; Stepanek, I.; Bernier, P. Hydrogen storage in sonicated carbon materials. *Appl. Phys. A: Mater. Sci. Process.* **2001**, *72* (2), 129–132.
83. Ansón, A.; Lafuente, E.; Urriolabeitia, E.; Navarro, R.; Benito, A.M.; Maser, W.K.; Martínez, M.T. Hydrogen capacity of palladium-loaded carbon materials. *J. Phys. Chem. B* **2006**, *110* (13), 6643–6648.
84. Mu, S.C.; Tang, H.L.; Qian, S.H.; Pan, M.; Yuan, R.Z. Hydrogen storage in carbon nanotubes modified by microwave plasma etching and Pd decoration. *Carbon* **2006**, *44* (4), 762–767.
85. Lueking, A.; Yang, R.T. Hydrogen storage in carbon nanotubes: Residual metal content and pretreatment temperature. *AIChE J.* **2003**, *49* (6), 1556–1568.
86. Lupu, D.; Radu Biris, A.; Misan, I.; Jianu, A.; Holzhuter, G.; Burkel, E. Hydrogen uptake by carbon nanofibers catalyzed by palladium. *Int. J. Hydrogen Energy* **2004**, *29* (1), 97–102.
87. Robell, A.J.; Ballou, E.V.; Boudart, M. Surface diffusion of hydrogen on carbon. *J. Phys. Chem.* **1964**, *68* (10), 2748–2753.
88. Boudart, M.; Aldag, A.W.; Vannice, M.A. On the slow uptake of hydrogen by platinized carbon. *J. Catal.* **1970**, *18* (1), 46–51.
89. Lueking, A.; Yang, R.T. Hydrogen spillover from a metal oxide catalyst onto carbon nanotubes—implications for hydrogen storage. *J. Catal.* **2002**, *206*, 165–168.
90. Lueking, A.D.; Yang, R.T. Hydrogen spillover to enhance hydrogen storage—study of the effect of carbon physicochemical properties. *Appl. Catal. A: General* **2004**, *265* (2), 259–268.
91. Zaluska, A.; Zaluski, L.; Ström-Olsen, J.O. Sodium alanates for reversible hydrogen storage. *J. Alloys Comp.* **2000**, *298* (1–2), 125–134.
92. Meregalli, V.; Parrinello, M. Review of theoretical calculations of hydrogen storage in carbon-based materials. *Appl. Phys. A: Mater. Sci. Process.* **2001**, *72* (2), 143–146.
93. Yin, Y.F.; Mays, T.; McEnaney, B. Molecular simulations of hydrogen storage in carbon nanotube arrays. *Langmuir* **2000**, *16* (26), 10,521–10,527.
94. Zhang, X.R.; Cao, D.P.; Chen, J.F. Hydrogen adsorption storage on single-walled carbon nanotube arrays by a combination of classical potential and density functional theory. *J. Phys. Chem. B* **2003**, *107* (21), 4942–4950.
95. Darkrim, F.; Levesque, D. High adsorptive property of opened carbon nanotubes at 77 K. *J. Phys. Chem. B* **2000**, *104* (29), 6773–6776.
96. Williams, K.A.; Eklund, P.C. Monte Carlo simulations of H<sub>2</sub> physisorption in finite-diameter carbon nanotube ropes. *Chem. Phys. Lett.* **2000**, *320* (3–4), 352–358.
97. Wang, Q.Y.; Johnson, J.K. Optimization of carbon nanotube arrays for hydrogen adsorption. *J. Phys. Chem. B* **1999**, *103* (23), 4809–4813.
98. Gu, C.; Gao, G.H.; Yu, Y.X.; Mao, Z.Q. Simulation study of hydrogen storage in single walled carbon nanotubes. *Int. J. Hydrogen Energy* **2001**, *26* (7), 691–696.
99. Levesque, D.; Gicquel, A.; Darkrim, F.L.; Kayiran, S.B. Monte Carlo simulations of hydrogen storage in carbon nanotubes. *J. Phys.: Cond. Matter* **2002**, *14* (40), 9285–9293.
100. Simonyan, V.V.; Johnson, J.K. Hydrogen storage in carbon nanotubes and graphitic nanofibers. *J. Alloys Comp.* **2002**, *330–332*, 659–665.
101. Guay, P.; Stansfield, B.L.; Rochefort, A. On the control of carbon nanostructures for hydrogen storage applications. *Carbon* **2004**, *42* (11), 2187–2193.
102. Cao, D.P.; Feng, P.Y.; Wu, J.Z. Molecular simulation of novel carbonaceous materials for hydrogen storage. *Nano Lett.* **2004**, *4* (8), 1489–1492.
103. Wang, Q.Y.; Johnson, J.K. Computer simulations of hydrogen adsorption on graphite nanofibers. *J. Phys. Chem. B* **1999**, *103* (2), 277–281.
104. Cracknell, R.F. Simulation of hydrogen adsorption in carbon nanotubes. *Mol. Phys.* **2002**, *100* (13), 2079–2086.
105. Simonyan, V.V.; Diep, P.; Johnson, J.K. Molecular simulation of hydrogen adsorption in charged single-walled carbon nanotubes. *J. Chem. Phys.* **1999**, *111* (21), 9778–9783.
106. Yang, F.H.; Yang, R.T. Ab initio molecular orbital study of adsorption of atomic hydrogen on graphite: insight into hydrogen storage in carbon nanotubes. *Carbon* **2002**, *40* (3), 437–444.
107. Miura, Y.; Kasai, H.; Dino, W.; Nakanishi, H.; Sugimoto, T. First principles studies for the dissociative adsorption of H<sub>2</sub> on graphene. *J. Appl. Phys.* **2003**, *93* (6), 3395–3400.
108. Froudakis, G.E. Hydrogen interaction with carbon nanotubes: a review of ab initio studies. *J. Phys.—Cond. Matter* **2002**, *14* (17), R453–R465.
109. Arellano, J.S.; Molina, L.M.; Rubio, A.; López, M.J.; Alonso, J.A. Interaction of molecular and atomic hydrogen with (5,5) and (6,6) single-wall carbon nanotubes. *J. Chem. Phys.* **2002**, *117* (5), 2281–2288.
110. Mpourmpakis, G.; Tylianakis, E.; Froudakis, G. Hydrogen storage in carbon nanotubes: A multi-scale theoretical study. *J. Nanosci. Nanotechnol.* **2006**, *6* (1), 87–90.

111. Cheng, H.; Pez, G.P.; Cooper, A.C. Mechanism of hydrogen sorption in single-walled carbon nanotubes. *J. Am. Chem. Soc.* **2001**, *123* (24), 5845–5846.
112. Ma, Y.C.; Xia, Y.Y.; Zhao, M.W.; Wang, R.J.; Mei, L.M. Effective hydrogen storage in single-wall carbon nanotubes. *Phys. Rev. B* **2001**, *63* (11), 115–422.
113. Lee, S.M.; Lee, Y.H. Hydrogen storage in single-walled carbon nanotubes. *Appl. Phys. Lett.* **2000**, *76* (20), 2877–2879.
114. Dresselhaus, M.S.; Williams, K.A.; Eklund, P.C. Hydrogen adsorption in carbon materials. *MRS Bull.* **1999**, *24* (11), 45–50.
115. Li, J.; Furuta, T.; Goto, H.; Ohashi, T.; Fujiwara, Y.; Yip, S. Theoretical evaluation of hydrogen storage capacity in pure carbon nanostructures. *J. Chem. Phys.* **2003**, *119* (4), 2376–2385.
116. Centrone, A.; Brambilla, L.; Zerbi, G. Adsorption of H<sub>2</sub> on carbon-based materials: A Raman spectroscopy study. *Phys. Rev. B* **2005**, *71*, 245–406.
117. Zhao, X.B.; Xiao, B.; Fletcher, A.J.; Thomas, K.M. Hydrogen adsorption on functionalized nanoporous activated carbons. *J. Phys. Chem. B* **2005**, *109* (18), 8880–8888.
118. Heine, T.; Zhechkov, L.; Seifert, G. Hydrogen storage by physisorption on nanostructured graphite platelets. *Phys. Chem. Chem. Phys.* **2004**, *6* (5), 980–984.
119. Bhatia, S.K.; Myers, A.L. Optimum conditions for adsorptive storage. *Langmuir* **2006**, *22* (4), 1688–1700.
120. Darkrim, F.; Levesque, D. Monte Carlo simulations of hydrogen adsorption in single-walled carbon nanotubes. *J. Chem. Phys.* **1998**, *109* (12), 4981–4984.

# Carbon Forms Structured by Energetic Species

Yeshayahu Lifshitz

Center of Super-Diamond and Advanced Films, City University of Hong Kong, Hong Kong, China, and Soreq Nuclear Research Center, Yavne, Israel

## INTRODUCTION

Modern materials science aims at the development of controlled ways of structuring novel materials. High-pressure, high-temperature (HPHT) methods (initiated by the legendary pioneering work of Bridgman<sup>[1]</sup>) indeed provide numerous exotic phases for thousands of materials. Among the most important ones that find a billion-size market are diamond and cubic boron nitride. The massive nature of HPHT systems inhibits their use for modern (thin film) technology. An alternative emerging technique (in the past 30 years) for the structuring of materials is the application of energetic species for deposition and surface and bulk modification. It is now very well established that the use of energetic species either by direct ion beam deposition or by bombardment of materials (ion beam-assisted methods) provides a way to structure materials (metals, semiconductors, ceramic, and polymers) controlling a variety of physical properties (including hardness, density, wear resistance, resistivity, optical transparency, surface morphology, and oriented/epitaxial growth).<sup>[2]</sup> Surprisingly, utilization of energetic species sometimes produced metastable phases previously reported only from HPHT experiments. It is most important to note that ion beam techniques currently provide the most controlled technique known to the semiconductor industry for material modification (e.g., doping) and is extensively used.

In the last decade many efforts were dedicated to the emerging field of nanostructuring of materials, which is the topic of this encyclopedia. Top-down and bottom-up techniques have been developed to structure nanosized materials. A crucial issue in most of the approaches utilized, which have successfully produced a host of novel nanosized materials, is the controlled growth, i.e., processes that yield materials with a narrow distribution of size, structure, and composition thus possessing well-defined properties.

The purpose of this entry is to describe how ion beams can be used in a controlled way to nanostructure a wide spectrum of materials: amorphous, medium-range (multiwall tubes and fullerene-like),

and crystalline. Ion beams use the idea of HPHT in a very localized region (nano-HPHT) taking advantage of the control offered by ion beam techniques. Carbon, with its wealth of configurations that will be highlighted in the next section, offers the best study case to demonstrate the idea of ion beam structuring of materials. This entry shortly discusses the experimental systems used for ion beam structuring of carbon and for characterization of the products. It presents the basic physical processes leading to the formation of the nanostructured materials and then describes how amorphous, medium-range, and crystalline forms can be structured and their properties can be tuned accordingly. For additional reading the reader is referred to recent reviews<sup>[2-9]</sup> covering structuring of carbon forms by energetic species, structuring by energetic species in general, and superhard materials in general.

## CARBON—AN IDEAL MODEL SYSTEM TO STUDY STRUCTURING BY ENERGETIC SPECIES

Carbon is unique in the variety of configurations it makes within itself and with other elements.<sup>[3-6,10]</sup> A carbon atom can be involved in three different local configurations ( $sp^1$ ,  $sp^2$ ,  $sp^3$ ). A carbon matrix can be amorphous or have medium and long-range order. It forms large molecules (e.g., fullerenes), one-dimensional structures (e.g., nanotubes), and fibers (exploited for making composite materials). Carbon also has a variety of crystalline forms among which graphite (the  $sp^2$  form) and cubic diamond (the  $sp^3$  structure) are the most known. The richness of carbon forms makes it one of the most important materials, both scientifically and technologically. This is why carbon forms have been applied or are being considered for a large number of mechanical, tribological, optical, and electrical applications. As far as structuring by energetic species, the richness of carbon forms enables to follow the possibilities offered by energetic species in one single system.



## EXPERIMENTAL TECHNIQUES USED FOR GROWTH AND CHARACTERIZATION OF ION BEAM STRUCTURED CARBON

Structuring of materials using ion beams can be performed in two basic ways:<sup>[2-6]</sup> 1) use of ion beams (or energetic species) in the growth process itself (ion impact effects occur simultaneously with the material growth); 2) modifications by ion beams (energetic species) of target materials (i.e., no growth occurs, just modifications because of ion impact). For the first case the minimal species energy required is small (a few tenths of eV). For the second the size of the modified layer is determined by the range of the ions in the target material, i.e., keV ions are required to modify a layer which is, say, several nanometers thick. The variety of systems that use energetic species for nanostructuring of materials during the growth process include: 1) techniques in which energetic species are created first and then bombard the substrate so that most of the energetic species are growth species incorporated in the material (direct ion beams, arc discharge systems, laser ablation systems, sputtering systems); 2) techniques in which the energetic species (e.g., noble gas species) transfer momentum to the evolving material and are not necessarily incorporated (ion-assisted systems). In the latter most of the growth species are not energetic and the modifications are only due to the assisting energetic species. Plasma deposition systems make a special case in which both non-energetic and more energetic species exist and the balance between them is determined by the applied bias. Most systems applying energetic species are characterized by a complex nature in terms of a composition of a variety of different particles with a large distribution of energies. This makes the controlled growth and study very difficult. Mass selected ion beam deposition (MSIBD) systems offer excellent control of all relevant parameters (filtered isotopically pure species, defined energy, and impinging angle). Second best in control are filtered arc systems, which are much cheaper and available than MSIBD systems. Modifications of existing material by energetic species require ion beam systems with energies of several kilo electron volts at least as previously stated.

A variety of characterization methods are applied to study ion beam nanostructured carbon.<sup>[3-6]</sup> The composite nature and the intrinsic non-homogeneity of the carbon nanostructured materials require the use of characterization methods with a very high resolution. The best characterization tool thus available is transmission electron microscopy (TEM), preferably high-resolution TEM (HRTEM) and its derivatives [transmission electron diffraction (TED) and transmission electron energy loss spectroscopy (EELS)]. These methods offer determination of the local configuration ( $sp^3$  fraction), information on  $sp^2$  structures

(carbon nanotubes, nanoions, graphitic domains) and their orientation, and identification of crystalline forms (graphite, diamond). Of special interest also are composite forms (crystalline/amorphous, amorphous  $sp^2$ /amorphous  $sp^3$ , layered structures, etc.). The morphology of the carbon nanostructured materials can be detected by both atomic force and scanning tunneling microscopies (AFM/STM)<sup>[11]</sup> and also by scanning electron microscopy (SEM), preferably high-resolution SEM (HRSEM).

Raman spectroscopy is the most common technique applied for the characterization of nanostructured carbon, very often in an erroneous way.<sup>[3-6,12]</sup> Raman in the visible light is very sensitive to  $sp^2$  carbon forms and insensitive to  $sp^3$  forms, which can be detected only with UV Raman when mixed in amorphous  $sp^2$  forms.<sup>[3-6,13]</sup> The correct identification of  $sp^2$  forms requires expertise and is aided by looking at the dispersion behavior of the spectra at different excitation wavelengths.

Nanostructured carbon characterization including Raman, surface analysis, and other properties characterization (optical, electrical, mechanical) is very useful. Its correct interpretation, however, requires an understanding of the complex nature of the nanostructured material in terms of inhomogeneity, layered structure, and orientation for which the high-resolution methods are essential as a first step.<sup>[14]</sup>

## BASIC PROCESSES INVOLVED IN ION BEAM STRUCTURING

It is now very well established that the deposition process from energetic ( $\sim 10$  eV–1 keV) species is a shallow implantation (“subplantation”) process<sup>[3-6,11,15-17]</sup> and not a surface process. For each deposition scheme the following quantities very well known from ion implantation studies should be considered:

1. The range ( $R$ ) and the distribution ( $\Delta R$ , straggling) of the subplanted species;
2. The trapping efficiency;
3. The sputtering of target material atoms; and
4. The damage created by the bombarding species (no. of atomic displacements or no. of remaining vacancies).

It should also be noted that three different time scales are involved<sup>[4,15-17]</sup> in the actual stopping and trapping of the bombarding species and the resulting material modifications and film growth:

1. Stopping via (atomic) collisions, ionization, and phonon excitations (the “collisional stage,”  $\sim 10^{-13}$  sec);
2. Dissipation of the excess energy in the target (the “thermalization stage,”  $\sim 10^{-12}$  sec); and

3. The long-term relaxation stage ( $\sim 10^{-10}$  sec up to seconds) where diffusion, chemical reactions, and phase transformations take place.

It is currently widely accepted that the subplantation process advances through the following stages:<sup>[3-6,15-17]</sup>

1. Penetration (of carbon species) to subsurface layers;
2. Incorporation (of carbon atoms) inducing local stresses;
3. Sputtering and dilution of the target atoms until a pure carbon layer evolves; and
4. Growth of the pure carbon layer upon successive bombardment.

The C species need a critical energy to penetrate to subsurface layers of the pure C layer in which they are now stopped. The final site, which the C projectile occupies, determines the structure and properties of the evolving carbon film. Trapping of C species in subsurface sites leads to elastic expansion, which is associated with compressive stress. The incorporation of these trapped C species leads to increased density (stress). The increased density (which occurs because of the combined effect of the incorporation of C projectiles and forward displacements of C atoms along the trajectories of the impinging C projectiles) induces an increase of the  $sp^3$  fraction of the amorphous matrix that evolves. When a maximal density (stress) is reached, plastic deformation may occur which sets the density and  $sp^3$  fraction to a constant maximal value upon further incorporation of C species. Local relaxations (e.g., the “thermal spike”<sup>[3-6,17]</sup> relaxation) permit local modifications of the highly dense (stressed) amorphous region in which the C atom is embedded. These modifications may either initiate or suppress  $sp^3$  bonds. Contrary to the previous explanation of density (stress)-driven  $sp^3$  formation, some researchers believe that it is the rapid relaxation (quenching) of the “thermal spike” region that drives the carbon atom to a metastable  $sp^3$  state (claiming that the  $sp^3$  bonding is the thermodynamic stable configuration for the local high-pressure, high-temperature region induced by the “thermal spike”<sup>[3-6,17]</sup>). Relaxation and detrapping processes (thermal migration, radiation damage) may remove some of the densification (stress). The  $sp^3$  fraction is thus determined by the equilibrium between the densification and detrapping processes.

## STRUCTURING OF AMORPHOUS CARBON FORMS

The understanding of the basic processes involved in subplantation enables the further discussion of how

amorphous carbon (a-C) films can be nanostructured. Three important parameters govern the phase evolution and can be used for nanostructuring carbon films:<sup>[3-6]</sup>

1. The ion energy ( $E$ );
2. The substrate temperature ( $T_s$ ); and
3. The deposition rate.

The C ion energy is a key factor in the determination of the  $sp^3$  fraction and the nature of carbon films.<sup>[3-6]</sup> This subsection discusses the role of  $E$  under conditions where the substrate temperature is low enough so that thermal migration of the trapped carbon species is not significant. Four different energy regions were identified<sup>[3-6]</sup> for carbon deposition from energetic species going from low to high  $E$  (Fig. 1):

1. Surface deposition;
2. Tetrahedral amorphous carbon (ta-C) ( $sp^3 > 70\%$ ) deposition;
3. Amorphous carbon with a significant  $sp^3$  fraction decreasing with  $E$ ; and
4. Graphitic films.

Below a certain critical energy  $E_p$  needed to penetrate to subsurface layers amorphous  $sp^2$  films are deposited ( $sp^2$  is the stable C configuration under normal temperature and pressure conditions) via surface growth processes [region (1)]. The surface nature of the deposition in this region is manifested by the rough surface morphology that develops<sup>[4,11]</sup> (as shown in Figs. 1 and 2), which is also affected by an increased adatom surface mobility (compared to thermal deposition) due to the C ion energy. In region (2) the C species penetrate to subsurface layers where they are subplanted. The densification (and stress formation<sup>[3-6]</sup>) due to incorporation of C species leads to the formation of carbon films with a predominant  $sp^3$  fraction ( $>70\%$ ). Such films have a tetrahedral local configuration with a nearest neighbor distance of 1.54 Å and a bond angle of  $\sim 110^\circ$ , which is why they are denoted ta-C. They are the analogue of amorphous silicon and should be distinguished from diamondlike carbon (DLC), a broader family of films for which the  $sp^3$  fraction ranges between  $>0\%$  and 85%. The detrapping and relaxations induced by  $E$  in region (2) are insufficient to decrease the  $sp^3$  fraction below this high value of 70%. This is the optimal  $E$  region for ta-C formation. The internal growth nature of the DLC films leads to a surface morphology identical to the initial morphology of the substrate, so that atomically smooth films can be deposited on atomically smooth Si (100) substrates<sup>[4,11]</sup> (Figs. 1 and 2). In region (3) both the total energy dissipated along the ion trajectory (via phonon excitations and ionizations) and the

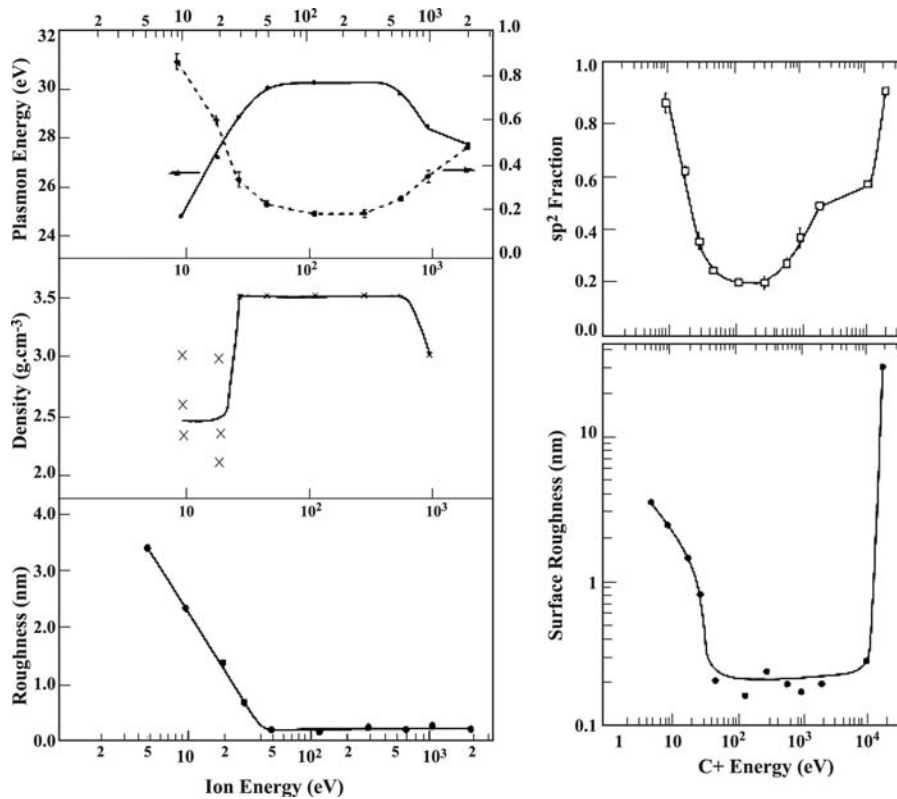


**Fig. 1** Properties of carbon films deposited using C ions with different energies onto Si (100) held at room temperature: roughness (AFM), density,  $sp^2$  fraction, and plasmon energy. Left— $5 \text{ eV} \leq E \leq 2 \text{ keV}$ , right— $5 \text{ eV} \leq E \leq 20 \text{ keV}$ . Note: 1) wide energy region for ta-C formation ( $30 \text{ eV} \leq E \leq 600 \text{ eV}$ ) associated with atomically smooth surface (sub-surface growth); 2) for  $E \leq 30 \text{ eV}$  surface roughening occurs associated with  $sp^2$  formation (surface growth); 3) for  $600 \text{ eV} < E \leq 10 \text{ keV}$  radiation damage partially suppresses  $sp^3$  bonding; 4) for  $20 \text{ keV} \leq E$  radiation damage completely suppresses  $sp^3$  bonding and surface roughening occurs.

radiation damage (e.g., displaced atoms and “vacancies”) increase with  $E$ , gradually suppressing the  $sp^3$  fraction of the DLC films.<sup>[3–6]</sup> The films are characterized by a defective layer which is  $sp^2$  rich,<sup>[3–6]</sup> the thickness of which scales with the ion range  $R_p$ . The  $sp^3$ -rich

layer is internally growing below the defective layer, at a depth  $R_p \pm \Delta R_p$  below the surface, in which the C species are incorporated. The size of the excited region around the final sites of the stopped C species, as well as the radiation damage (e.g., density of displaced

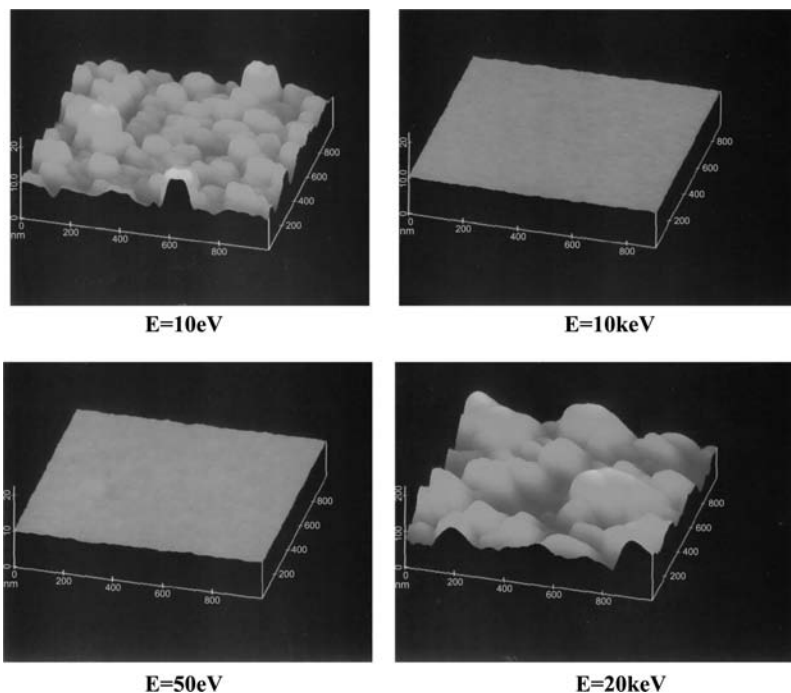


**Fig. 2** AFM images of 100-nm C films deposited using C ions with different energies onto Si (100) held at room temperature. Scale:  $1 \mu\text{m} \times 1 \mu\text{m}$ .  $Z = 20 \text{ nm}$  for  $10 \text{ eV}–10 \text{ keV}$ ,  $Z = 200 \text{ nm}$  for  $E = 20 \text{ keV}$ . Note: atomically smooth films for  $E = 50 \text{ eV}–10 \text{ keV}$ , rough films for  $E < 30 \text{ eV}$ ,  $E = 20 \text{ keV}$ .

atoms and vacancies) in this region, increases with energy.<sup>[17,18]</sup> This gradual increase of the damage with  $E$  (in the region where the C is incorporated and densification occurs) leads to a gradual suppression of the  $sp^3$  bonding, but even for  $E = 10$  keV the films still have a significant  $sp^3$  component ( $\sim 40\%$ ).<sup>[4,18]</sup> In region (3) the relaxation processes occur below the surface, the film growth is still internal and the atomically smooth nature of the initial substrate is still retained (Figs. 1 and 2). It is only in region (4) ( $E > 20$  keV) that the damage sufficiently enhances the mobility of the C species (to the surface) to eliminate the densification and completely suppress the  $sp^3$  fraction. Films with  $\sim 100\%$   $sp^2$  and very rough surfaces are formed, indicating the dominant role of surface processes in this  $E$  region.<sup>[4,17,18]</sup> The high mobility also initiates  $sp^2$  clustering to form nanocrystalline graphite, which does not occur at room temperature for  $E < 20$  keV. Fig. 1 shows that all properties of the films ( $sp^3$  fraction, density, surface roughness) vary systematically according to the above discussion, as well as other properties shown in Fig. 3.

The previous discussion assumed that the substrate temperature is low so that the (thermal) mobility of the C species is low as well, and once  $E > E_p$  they are trapped in subsurface positions leading to densification, stress, and the formation of atomically smooth  $sp^3$ -rich films via internal growth. The trapping sites used for DLC deposition are, however, very shallow ( $R_p$  equals  $\sim 5$  and  $\sim 25$  Å for 100 and 1000 eV, respectively<sup>[16,18]</sup>) so that thermal migration to the surface would eliminate the incorporation of C interstitials and the associated stress and densification. It is expected that  $sp^2$ -rich films will be formed via surface processes under such conditions. This was indeed verified by experiments<sup>[4]</sup> showing a sharp transition from  $sp^3$ -rich films to  $sp^2$ -rich films when  $T_s$  exceeds

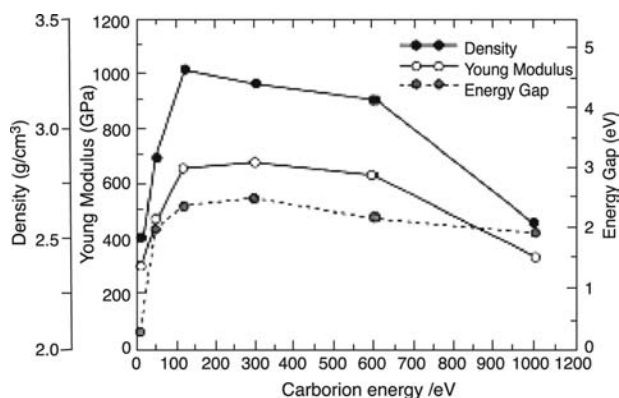


**Fig. 3** Density, Young's modulus, and optical energy gap of carbon films deposited using C ions with different energies onto Si (100) held at room temperature. *Note:* properties follow the  $sp^2$  fraction (Fig. 1).

a critical temperature  $T_c = 150^\circ\text{C}$  for 120-eV deposition<sup>[4]</sup> (Fig. 4). Atomic force microscopy studies<sup>[4,11]</sup> (Fig. 5) indicate surface roughening of 100-nm-thick C films with increasing  $T_s$  (a transition from subsurface to surface processes), while all other properties (density,  $sp^3$  fraction, Raman, optical properties, elastic modulus) indicate (Fig. 4) an associate formation of nanocrystalline graphitic films.<sup>[4]</sup>  $T_c$  may be dependent on  $E$  and on the rate of bombardment by energetic species. This is because the amount of densification is determined by the equilibrium between the incoming flux of subplanted atoms (bombardment rate) and the outgoing flux of atoms thermally migrating to the surface (from a distance which increases with increasing  $E$ ) to reduce the density gradient formed by subplantation. Films with a significant  $sp^3$  fraction ( $>70\%$ ) have been deposited

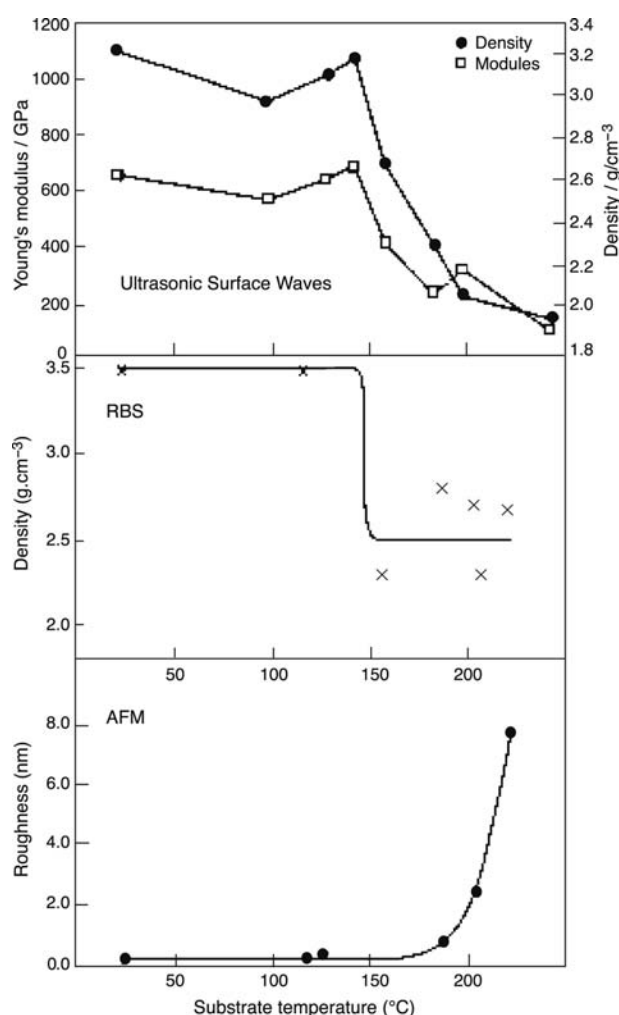


**Fig. 4** Density [by Rutherford backscattering (RBS) or ultrasonic surface waves], Young's modulus (ultrasonic surface waves), and roughness (AFM) of 100-nm C films deposited using 120-eV C ions onto Si (100) held at different temperatures.

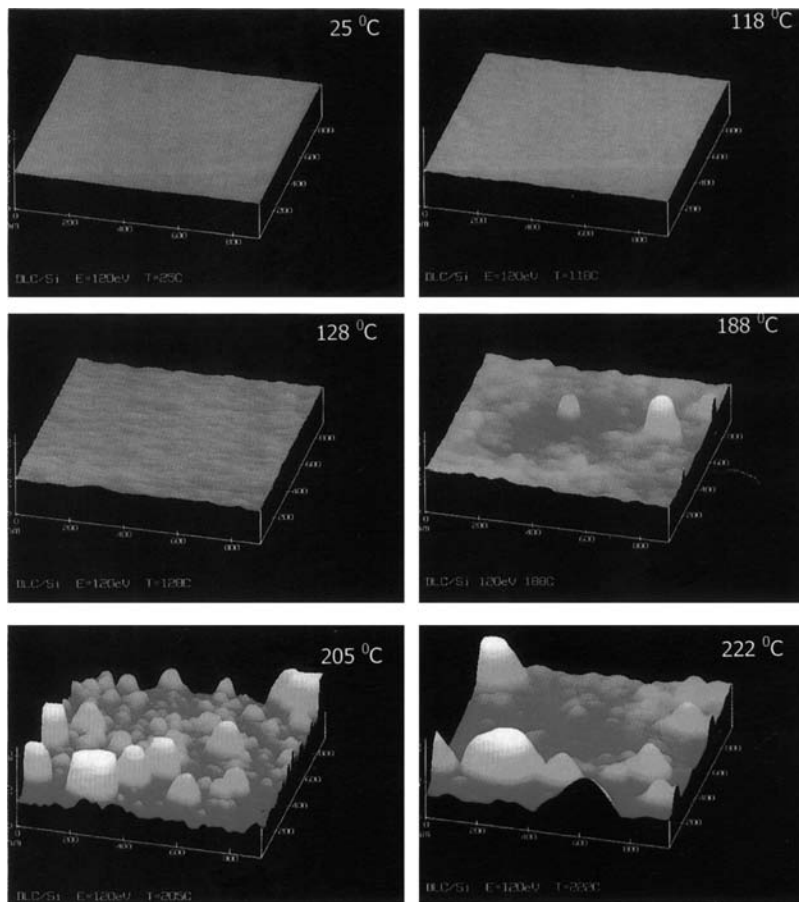


**Fig. 5** AFM images of 100-nm C films deposited using 120-eV C ions onto Si (100) held at different temperatures. Scale:  $1\ \mu\text{m} \times 1\ \mu\text{m}$ .  $Z = 20\ \text{nm}$ . Note: atomically smooth films for  $T < 150^\circ\text{C}$ , rough films for  $T > 150^\circ\text{C}$ .

using very low energy deposition ( $\sim 10\text{--}20\ \text{eV}$ ) on different substrates held at 77 K, showing a significant increase in the  $\text{sp}^3$  fraction compared to 300-K deposition.<sup>[4,19]</sup> This implies the possible existence of very shallow  $\text{sp}^3$  configurations that are frozen at very low  $T_s$  and are stabilized by coverage of the bombarding C species.

## STRUCTURING OF ORDERED $\text{SP}^2$ FORMS

The previous section details how the  $\text{sp}^3$  fraction of carbon films deposited at room temperature can be tuned between 0% and 85% (the  $\text{sp}^2$  fraction between 100% and 15%). Such films are essentially amorphous and the  $\text{sp}^2$ -bonded carbon can form clusters of different sizes. In ta-C films most of the carbons are  $\text{sp}^3$  bonded so that the few  $\text{sp}^2$ -bonded carbons form pairs and their chances of forming larger  $\text{sp}^2$  clusters are slim.<sup>[3,4]</sup> As the  $\text{sp}^3$  fraction decreases and the  $\text{sp}^2$  fraction increases larger clusters of  $\text{sp}^2$ -bonded carbons may form as chains or as rings. Carbon films with the same  $\text{sp}^3$  fraction may possess different distributions of  $\text{sp}^2$  clusters. Annealing of the DLC films increases the average size of the clusters of  $\text{sp}^2$ -bonded carbons

without necessarily affecting the  $\text{sp}^3$  fraction.<sup>[20,21]</sup> This annealing process in which the size of the  $\text{sp}^2$  clusters increases relieves the stress incorporated in the DLCs during their formation at room temperature.<sup>[12]</sup> Transformation of  $\text{sp}^3$  to  $\text{sp}^2$ -bonded carbon upon annealing is occurring only when the  $\text{sp}^2$  cluster size is large enough to enable graphitization, i.e., the formation of nanometer-sized crystallites of graphite.<sup>[21]</sup> The volume available for  $\text{sp}^2$  clustering increases with decreasing  $\text{sp}^3$  fraction, which is why the graphitization temperature of DLC films decreases with increasing  $\text{sp}^2$  fraction.<sup>[21]</sup> The thermal stability of ta-C films is very high and they can be annealed to  $1000^\circ\text{C}$  without graphitization or a change in their  $\text{sp}^3$  fraction.<sup>[21]</sup> The only effect would be an increase in the size of the  $\text{sp}^2$  clusters embedded in the predominantly  $\text{sp}^3$  skeleton.<sup>[21]</sup> The study of the structural changes occurring in annealed carbon films indicates that different clustering and layering phenomena occur, but it should be noted that this study is just in its initial stage.

Clustering of  $\text{sp}^2$  forms occur not only upon postdeposition annealing of DLC films, but also upon deposition at elevated temperatures, exceeding a critical temperature  $T_c$  as described in a previous section. It was previously explained that in such a deposition

the thermal migration to the surface eliminates the subplantation-induced densification leading to 100%  $sp^2$  films. Structural analysis of the films deposited under carbon ion bombardment at elevated temperatures reveals the formation of graphitic planes that are perpendicular to the substrate.<sup>[22]</sup> These graphitic planes may expand in different directions (i.e., the normal to the graphitic plane may have different directions in a plane parallel to the substrate). Some graphitic planes close to form carbon multiwall tubes, embedded in the graphitic matrix<sup>[23]</sup> (Fig. 6). This is a random process so that some innermost tubes possess the smallest diameter of carbon nanotubes possible, which is 4 Å.<sup>[23]</sup> The relative fraction of multiwall tubes embedded in the graphitic matrix may be controlled by the proper selection of the carbon ion energy and the deposition temperature.

Two possible mechanisms were suggested for the formation of the oriented graphitic planes in carbon ion deposition at elevated temperatures. The first one is a stress-induced mechanism according to which the ion bombardment introduces compressive stress forcing the films to align themselves in the most compressible way, i.e., with graphitic planes perpendicular to the stress vector.<sup>[17,22–24]</sup> Indeed, the graphitic planes in films deposited at 200°C and 120 eV are compressed by 5% with respect to the basal planes of hexagonal graphite.<sup>[22]</sup> The alternative mechanism explaining the oriented formation of graphitic planes perpendicular to the surface involves preferential displacements.<sup>[15–17]</sup> The energy required to displace graphitic atoms in the basal planes (C–C bond energy 7.4 eV) is larger than that required to displace C perpendicular to the basal plane (C–C bond energy 0.86 eV). Under ion bombardment the carbons of those graphitic planes formed in a direction parallel to the surface

(perpendicular to the ion beam) will be easily displaced and these planes will be damaged and their growth suppressed. The graphitic planes aligned perpendicular to the surface (parallel to the beam) will be damaged to a much lesser extent, explaining the preferred orientation. It should be noted that the temperatures involved in the formation of these structured graphitic films are moderate ( $\sim 200$ – $300^\circ\text{C}$ ), and much lower than those necessary for the graphitization of DLC films by postdeposition annealing (ta-C is stable up to  $1000^\circ\text{C}$ ,<sup>[21]</sup> see previous discussion). The effects of deposition at elevated temperatures should be thus distinguished from those due to postdeposition annealing.

Another channel of the formation and clustering of  $sp^2$ -bonded carbon is through energetic ion impact, even at room temperature.<sup>[7,17,18,24]</sup> Carbon ion deposition using very high energies ( $\sim 20$  keV and up) induces complete suppression of the  $sp^3$  fraction and initiates graphitization, i.e., the formation of nanosized graphitic domains. For annealing of DLC films clustering occurs via thermal migration of  $sp^2$ -bonded carbon. Energetic ions bombarding a target are stopped through atomic displacements, ionization, and phonon excitations along their track. Apart from direct removal of atoms from their original positions, ion bombardment induces enhanced diffusion because of the excess energy dissipated along the ion track coupled with the formation of radiation defects. These bombardment effects cause graphitization at low temperatures in which carbon does not regularly graphitize but remains amorphous. For small doses the modified material is arranged in isolated tracks with a width of several nanometers and a length that scales with the ion range, while the surrounding matrix is much less affected. For higher doses all tracks coalesce and the material becomes more homogenous. The graphitic

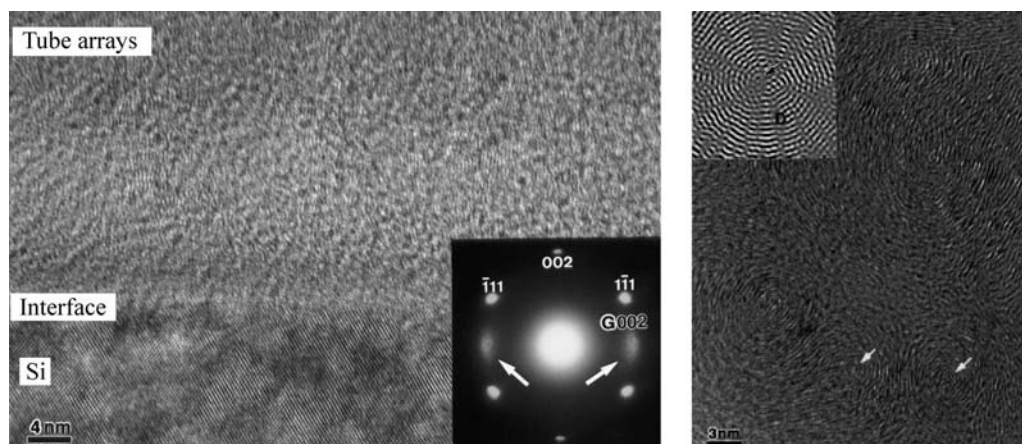


**Fig. 6** Cross-sectional (left) and plan view (right) HRTEM images of a 100-nm thick C film deposited using 120-eV C ions onto Si (100) at  $300^\circ\text{C}$ . *Note:* left image—graphitic planes perpendicular to substrate (directly seen in image and enlarged graphitic spots aligned with respect to Si substrate spots in SAED pattern in inset); right image—multiwall carbon nanotubes with innermost tube of 4 Å in diameter indicated by arrows. Inset—Fourier-transformed filtered image of one multiwall tube.



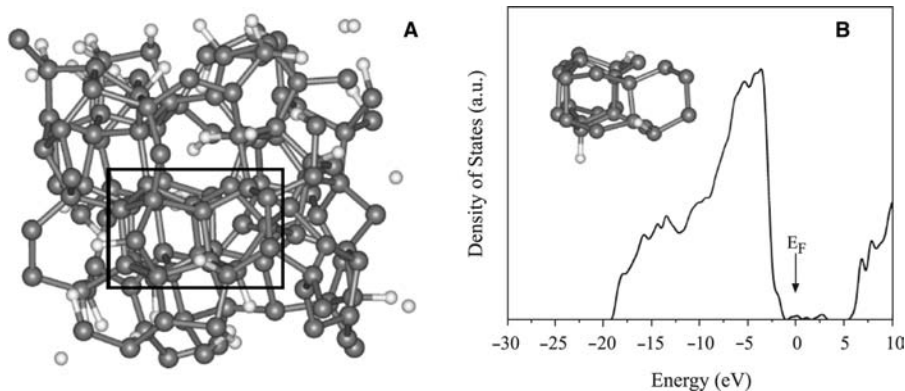


**Fig. 7** Molecular dynamic simulation of dense hydrogenated amorphous carbon matrix indicates precipitation of a 100%  $sp^3$  cluster of C atoms (dark spheres) which is decorated by hydrogen atoms (light spheres). Cluster indicated by square and its electronic density of states shows the wide energy gap of diamond.

carbon formed by ion impact is oriented with the basal plane along the ion beam. The graphitic layers formed by tens of kilo-electron-volt impact are characterized by spacings larger than for hexagonal graphite,<sup>[24]</sup> so that no compressive stress is associated with their formation. This is in contrast with the oriented graphitic layers formed at energies lower than 1 keV, which are compressed.<sup>[22]</sup> It means that the stress-induced graphitic orientation can be excluded and the graphitic orientation induced by ion beam impact is due to preferential displacement.

### STRUCTURING CRYSTALLINE CARBON FORMS

The last issue considered in this entry is the formation of  $sp^3$ -bonded crystallites by ion impact. It is very well known<sup>[10,25,26]</sup> that it is graphite, the  $sp^2$ -bonded carbon crystalline form, that is stable at ambient temperature and pressure conditions. The  $sp^3$  forms (cubic diamond and hexagonal diamond) are more stable than graphite only at high-temperature, high-pressure conditions occurring on Earth at depths of hundreds of kilometers. Indeed, diamond was first made artificially in GE applying the necessary high-pressure, high-temperature conditions. Later, it was found that diamond can be grown at subatmospheric pressure and medium temperatures by chemical vapor deposition (CVD), applying an excited plasma of ~1%  $CH_4$  and 99%  $H_2$  onto diamond held at ~700–800°C. The only way to nucleate diamond on non-diamond substrates, found by trial-and-error methods, is to apply bias to the above plasma and nucleate diamond through bombardment with energetic species [a process denoted “bias enhanced nucleation” (BEN)].<sup>[25,26]</sup>

The diamond nucleation mechanism, which is an extension of the subplantation process to form metastable crystalline phases, was very recently elucidated.<sup>[25]</sup> The first step of BEN is the formation

of a dense amorphous carbon hydrogenated matrix in a regular subplantation process. This matrix has a density of ~3 g/cm<sup>3</sup> and a hydrogen content of ~20%. The second step of the diamond nucleation is the precipitation of 100%  $sp^3$  C clusters (Fig. 7), most of which are amorphous, but a very small fraction (~10<sup>-5</sup>–10<sup>-6</sup>) are perfect diamond clusters of tens of atoms. These clusters are stabilized by hydrogen

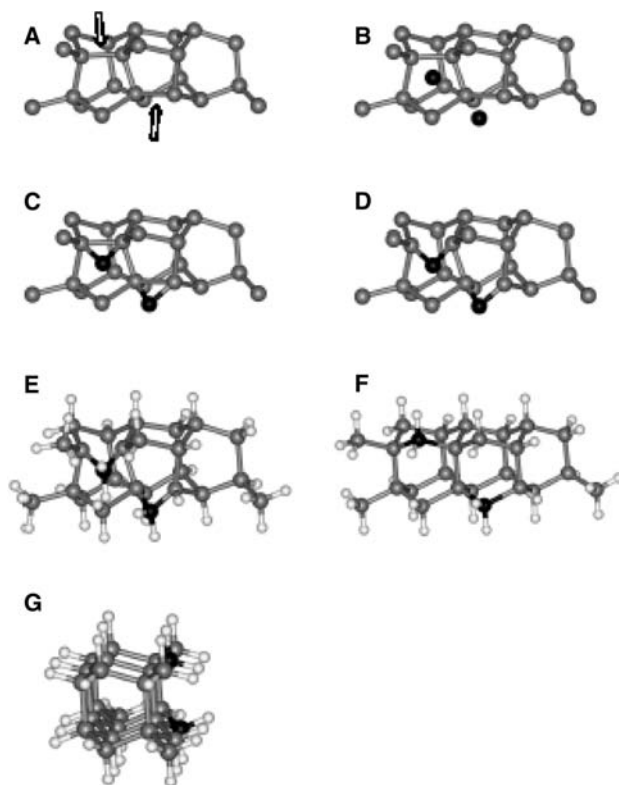


**Fig. 8** Annealing of the faulty cluster to form a perfect diamond: (A) original cluster with its reactive sites into which two carbon interstitials are added (B) and form bonds [(C) and (D)] Decoration by hydrogen (E) relaxes the cluster to perfect diamond as shown in (F) and in a projection (G) rotated by 90° with respect to the cluster in (F).

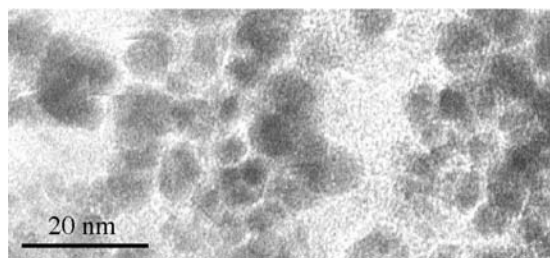


**Fig. 9** Cross-sectional TEM image of diamond crystallites embedded in an amorphous carbon matrix.

termination and by appropriate nucleation sites. The diamond crystallites are continuously bombarded by energetic ions, which preferentially displace amorphous carbon atoms leaving the more rigid diamond atoms intact. The displaced amorphous carbons at the a-C/diamond interface can occupy diamond positions leading to the growth of the diamond crystallite consuming C atoms from the a-C surrounding matrix. Faults in the diamond crystallites can be annealed by carbon interstitials and hydrogen decoration (Fig. 8). Finally, several nanometer-sized diamond crystallites containing tens of thousands of carbon atoms form (as observed in HRTEM (Fig. 9)). The BEN-treated material can now be exposed to a regular CVD environment in which the diamond crystallites grow to micron sizes and up, and the a-C component is etched away by the atomic hydrogen component of the CVD plasma.

It is interesting to note that ion beam impact induces epitaxial growth of diamond, say, on a step on Si<sup>[26]</sup> (Fig. 10). The Si step serves as a mold to the evolving diamond crystallite (the ratio between the lattice parameters of diamond and silicon is 2:3 and their structure is identical). The two Si surfaces on which the diamond nucleates restrict it to grow in perfect epitaxial relations, i.e., diamond (111)/Si (111). It should also be noted<sup>[27]</sup> that not only cubic diamond [with a stacking 3C of its (111) planes, i.e., ABCABCABC] can be grown by ion beam impact, but also other

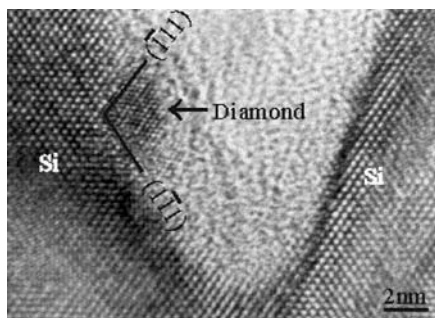


**Fig. 10** A HRTEM image of a diamond crystallite (~2 nm) grown directly on a Si step with an epitaxial alignment.

diamond polytypes with a different stacking sequence: hexagonal diamond (2H, stacking sequence ABABAB) and 9R diamond (stacking sequence ABCBCACAB).

## CONCLUSION

Ion beam structuring was shown to be able to grow carbon in a variety of carbon forms: amorphous, ordered sp<sup>2</sup> (including carbon multiwall tubes), and ordered sp<sup>3</sup> (crystalline diamond). The basic mechanisms involved in ion beam structuring were underlined. The capability to tune amorphous carbon to have a specific sp<sup>3</sup> fraction ranging from 0% to 85% by varying the ion energy and the substrate temperature was shown. Formation of different ordered sp<sup>2</sup> structures through ion beam deposition at elevated temperatures and energetic ion beam impact was described and the mechanisms involved (stress induced and preferential displacement) explained. Finally, the nucleation of metastable phases by ion impact was highlighted. The methodology described is not unique for carbon and can be applied to a variety of other materials.

## REFERENCES

1. Bridgman, P.W. *Collected Experimental Papers*; Harvard University Press: Cambridge, 1964.
2. Monteiro, O.R. Thin film synthesis by energetic condensation. *Annu. Rev. Mater. Res.* **2001**, *31*, 111.
3. Robertson, J. Diamond-like amorphous carbon. *Mater. Sci. Eng., R Rep.* **2002**, *271*, 1.
4. Lifshitz, Y. Diamond-like carbon-present status. *Diamond Relat. Mater.* **1999**, *8*, 1659.
5. Silva, S.R.P.; Carey, J.D.; Khan, R.U.A.; Gerstner, E.G.; Anguita, J.V. Amorphous Carbon Thin Films. In *Handbook of Thin Film Materials: Vol. 4. Semiconductor and Superconductor Thin Films*; Nalva, H.S., Ed.; Academic Press, 2002, Chapter 9. ISBN 0-12-512912-2/\$35.00.
6. Silva, S.R.P., Ed. *Properties of Amorphous Carbon*; IEE INSPEC Series; INSPEC IEE, 2002.
7. Banhart, F. Irradiation effects in carbon nanostructures. *Rep. Prog. Phys.* **1999**, *62*, 1181.
8. Anders, A. Energetic deposition using filtered cathodic arc plasmas. *Vacuum* **2002**, *67*, 673.
9. Haines, J.; Leger, J.M.; Bocquillon, G. Synthesis and design of superhard materials. *Annu. Rev. Mater. Res.* **2001**, *31*, 1.
10. Dresselhaus, M.S.; Dresselhaus, C.; Ecklund, P.C. *Science of Fullerenes and Carbon Nanotubes*; Acad. Press: New York, 1996.
11. Lifshitz, Y.; Lempert, G.D.; Grossman, E. Substantiation of subplantation model for diamondlike film growth from by atomic force microscopy. *Phys. Rev. Lett.* **1994**, *72*, 2753.

12. Prawer, S.; Nugent, K.W.; Lifshitz, Y.; Lempert, G.D.; Grossman, E.; Kalish, R.; Avigal, Y. Systematic variation of the Raman spectra of DLC films as a function of  $sp^2:sp^3$  composition. *Diamond Relat. Mater.* **1996**, *5* (3-5), 433.
13. Gilkes, K.W.R.; Prawer, S.; Nugent, K.W.; Robertson, J.; Sands, H.S.; Lifshitz, Y.; Xu, S. Direct quantitative detection of the  $sp^3$  bonding in diamond-like carbon films using UV and visible Raman spectroscopy. *J. Appl. Phys.* **2000**, *87* (10), 7283.
14. Lifshitz, Y. Pitfalls in amorphous carbon studies. *Diamond Relat. Mater.* **2003**, *12*, 130.
15. Lifshitz, Y.; Kasi, S.R.; Rabalais, J.W. Subplantation model for film growth from hyperthermal species: Application to diamond. *Phys. Rev. Lett.* **1989**, *62*, 1290.
16. Lifshitz, Y.; Kasi, S.R.; Rabalais, J.W.; Eckstein, W. Subplantation model for film growth from hyperthermal species. *Phys. Rev., B* **1990**, *41*, 10468.
17. Lifshitz, Y. Growth of Amorphous Carbon Films Using Energetic Species. In *Properties of Amorphous Carbon*; Silva, S.R.P., Ed.; IEE INSPEC Series, 2002.
18. Grossman, E.; Lempert, G.D.; Kulik, J.; Marton, D.; Rabalais, J.W.; Lifshitz, Y. Role of ion energy in determination of the  $sp^3$  fraction of ion beam deposited carbon films. *Appl. Phys. Lett.* **1996**, *68* (9), 1214.
19. Lossy, R.; Pappas, D.L.; Roy, R.A.; Doyle, J.P.; Cuomo, J.J.; Bruely, J. Properties of amorphous diamond films prepared by a filtered cathodic arc. *J. Appl. Phys.* **1995**, *77* (9), 4750.
20. Friedmann, T.A.; Sullivan, J.P.; Knapp, J.A.; Tallant, D.R.; Follstaedt, D.R.; Meldin, D.L.; Mirkarimi, P.B. Thick stress-free amorphous-tetrahedral carbon films with hardness near that of diamond. *Appl. Phys. Lett.* **1997**, *71*, 3820.
21. Kalish, R.; Lifshitz, Y.; Nugent, K.; Prawer, S. Thermal stability and relaxation in DLC; A Raman study of films with different  $sp^3$  fractions (ta-C to a-C). *Appl. Phys. Lett.* **1999**, *74* (20), 2936.
22. Kulik, J.; Lempert, G.; Grossman, E.; Lifshitz, Y. Oriented graphitic carbon film grown mass-selected ion beam deposition at elevated temperatures. *MRS Proc.* **2000**, *593*, 305.
23. Peng, H.Y.; Wang, N.; Zheng, Y.F.; Lifshitz, Y.; Kulik, J.; Zhang, C.S.; Lee, S.T. Smallest diameter carbon nanotubes. *Appl. Phys. Lett.* **2000**, *77* (18), 2831.
24. McCulloch, D.G.; McKenzie, D.R.; Prawer, S. Compressive stress-induced formation of preferred orientation in glassy-carbon following high-dose  $C^+$  implantation. *Philos. Mag., A* **1995**, *72*, 1031.
25. Lee, S.T.; Peng, H.Y.; Zhou, X.T.; Wang, N.; Lee, C.S.; Bello, I.; Lifshitz, Y. A nucleation site and mechanism leading to epitaxial growth of diamond films. *Science* **2000**, *287*, 104.
26. Lifshitz, Y.; Köhler, Th.; Frauenheim, Th.; Guzmán, I.; Hoffman, A.; Zhang, R.Q.; Zhou, X.T.; Lee, S.T. The mechanism of diamond nucleation from energetic species. *Science* **2002**, *297*, 1531.
27. Lifshitz, Y.; Duan, X.F.; Shang, N.G.; Li, Q.; Wan, L.; Bello, I.; Lee, S.T. Epitaxial diamond polytypes on silicon. *Nature* **2001**, *412*, 404.

# Carbon Nanotransistors

Po-Wen Chiu

Siegmar Roth

Max Planck Institut für Festkörperforschung, Stuttgart, Germany

## INTRODUCTION

A great deal of attention has been given to carbon nanotube (CNT)-based electronics. The unique electronic properties of CNTs<sup>[1]</sup> pave the way to future applications in electronics, with a further reduction of weight, size, and power consumption, and a faster switching time. Carbon nanotubes present a paradigm for potential building blocks in nanoscale electronics. This is not only simply because of their small dimensions, but also because of their many superior electronic properties compared with silicon. For example, electrons propagating in a nanotube experience much less scattering;<sup>[2,3]</sup> hence there is a reduction of power consumption and heat dissipation. An individual CNT can sustain a remarkably high current density of more than  $10^9$  A/cm<sup>2</sup>.<sup>[4]</sup> The trans-conductance of a CNT field-effect transistor (CNTFET), which represents how fast the on/off states can be switched, is about one order of magnitude higher than that of a silicon metal-oxide semiconductor FET (MOSFET).<sup>[5]</sup> These unique electrical properties of CNTs stem from the seamlessly curved conjugated structure and drive many researchers to quest for practical nanodevices. In the following sections, we review a broad range of studies on CNTs in transistor devices. The fundamental electronic structure of CNTs as well as different carbon nanotransistors will be discussed in detail.

## BACKGROUND

In 1956, the Nobel Prize was awarded to Shockley, Bardeen, and Brattain for their discovery of the transistor effect in 1947.<sup>[6]</sup> The transistor is one of the most important inventions of the past century and is often cited as an example of how scientific research can lead to useful commercial products. The integration of transistors in modern semiconductor electronics led to another revolution in human history, and the Nobel Prize was awarded for this great contribution in 2000. Half a century after the invention of the first

transistor, the dimensions of the modern transistor have shrunk by a factor of  $10^6$ , jumping from the millimeter scale to the nanometer scale. The number of transistors integrated in a current semiconductor microprocessor readily exceeds 45 million.<sup>[7]</sup> This staggering downsizing rate is based on the continuous improvement of the semiconductor manufacture processing, including precise lithography and reliable lift-off techniques.

The basic function of a transistor is as an electrical switch through which one can define the “0” (off) and “1” (on) states in a logic operation. It was predicted by Gordon Moore<sup>[8]</sup> that for silicon-based integrated circuits, the number of transistors per square centimeter doubles every 12 months. The productivity and improvement of silicon-based electronics have generally followed Moore’s law for the past 40 years. This trend of rapid increase of device density in an integrated circuit will, however, soon reach its “ceiling” owing to the inherent limitations of materials and present technologies. In this respect, many novel nanosystems have been explored intensively over the last few years as potential building blocks for the next generation of electronics. Among them, the CNT serves as a kind of parade horse. It has been demonstrated that semiconducting CNTs, which are only few nanometers in diameter, also exhibit transistor-like behavior. Fifty years after Shockley came up with the first idea of an electrical switch in the Bell labs, the transistor size has been approaching the atomic scale.

## FUNDAMENTAL LIMITATION OF MINIATURIZATION

### Heat Dissipation

Scaling down the dimensions of transistor devices, as well as the integrated circuits into which they are incorporated, causes an abundance of problems. The most intuitive problem is how to reduce the heat generated by charge carriers traveling inside the smaller and more

complicated circuits. The amount of heat given off by many chips can far exceed that of most cooking surfaces, and the situation is progressively worsening owing to the continuous decrease of the device feature size. In addition to seeking more effective coolants to prevent the chips from melting, researchers search for alternative materials such as CNTs and various nanowires, as candidates to be adopted in modern semiconductor processing technology.

### High-Field Effect

Disregarding the aforementioned heat dissipation, the background thermal voltage in an integrated circuit is approximately 25 mV at room-temperature operation. To discernibly recognize a desired signal in a circuit, the operating voltage needs to be several times higher than the thermal noise. In other words, this thermal voltage sets a fundamental constraint upon the lowest operating voltage of a transistor. As the dimensions of a transistor become smaller, the same operating voltage between the drain and source is now applied over a shorter distance. It leads to an increase of electric field between the two contacts. As a consequence, the charge carriers move faster and gain more energy. Once these charge carriers reach a critical energy within the transistor channel, they will cause impact ionization and subsequently launch an avalanche,<sup>[9]</sup> an uncontrollable surge of current that disables the switching function. Therefore, the avalanche breakdown sets a maximum electric field that can be applied in a transistor and is one of the limiting factors to device scaling.

### Gate-Oxide Tunneling

All the transistors integrated in a circuit are separated from each other by an insulator so as not to couple the operation of one transistor to the others. From the perspective of classical physics, if the total energy of an electron in a transistor is less than the height of the potential barrier, the electron is unable to penetrate through the barrier to reach the neighboring transistors. In accordance with quantum mechanics, however, as long as the barrier is thin enough, there is a certain probability for an electron to pass through the barrier even if its energy is less than the barrier height. This process is called “tunneling,” and its probability increases exponentially with the decreasing width of the energy barrier, and thus imposes a limit on the packing density of transistors in a circuit. For a MOSFET with channel length of 100 nm or less, an oxide thickness of greater than 3 nm is needed to prevent tunneling.<sup>[10]</sup> This thickness comprises only a few

layers of atoms and gives rise to a nonnegligible off-state leakage current owing to direct tunneling.

### SHORT-CHANNEL EFFECT

Another severe challenge for future MOSFET device designs is maintaining a required off-state leakage specification while maximizing the device drive current. For conventional MOSFETs, the dominant leakage mechanism is owing to the short-channel effect by which the drain potential lowers the source–junction barrier for charge carrier tunneling.<sup>[9]</sup> The origin of the short-channel effect can be understood by considering the potential barrier at the surface between the drain and the source. In the long-channel case, the potential barrier is flat, except at the very end of the channel that is in contact with the drain and the source. In the “off” state, the potential barrier (p-type region), which is only governed by the gate voltage, prevents electrons from flowing into the drain. As the channel length is shortened, the source–drain field penetrates deeply into the middle of the channel and lowers the potential barrier, so that the electrons can directly tunnel through the channel. This results in a substantial increase of the subthreshold current.

## CNTS AS ELECTRONIC DEVICES

### Electronic Structure of CNTs

An individual single-walled CNT can be thought of as a seamless cylindrical form of a graphene sheet rolled up in a specific orientation. To understand the electronic properties of nanotubes, we begin with the band structure of the graphene, which frames the one-dimensional (1-D) energy dispersion of nanotubes.<sup>[11]</sup> Carbon atoms in a graphene have four valence electrons, three of which form  $sp^2$  bonds with neighboring atoms in  $\sigma$  orbitals. They lie far below the Fermi level and do not contribute to the electrical conduction. The fourth electron occupies a  $\pi$  orbital resulting from a  $2p_z$  bond, through which the transport takes place. In a tight binding approximation,<sup>[12–14]</sup> the energy dispersion for the  $\pi$  electrons in a graphene is shown in Fig. 1. Imposing the boundary condition along the circumferential direction of a rolled-up graphene, we can readily deduce the band structure of nanotubes by slicing the energy dispersion of a graphene sheet. The electron energy is thus quantized in the circumferential direction and the electrons are only free to move in the axial direction. The energy quantization gives rise to discrete numbers of parallel equidistant lines, representing the allowed  $k$  modes in the reciprocal space of the graphene. Each line corresponds to a 1-D

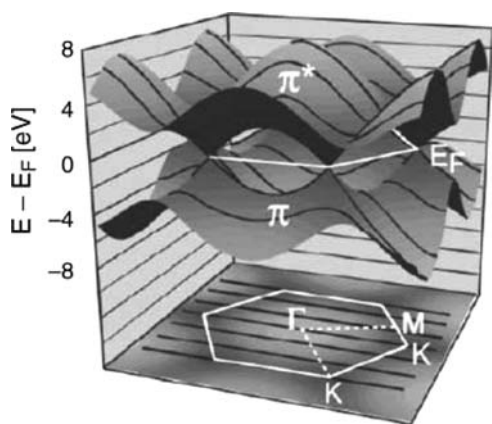


**Fig. 1** Band structure of a 2-D graphene sheet. The bottom hexagon defines the first Brillouin zone and the solid lines present the allowed states in a nanotube, which are obtained by imposing the boundary condition along the circumference of the tube. *Source:* From Ref.<sup>[14]</sup>.

channel for conduction along the nanotube. The distance between adjacent lines,  $2/d_t$ , is inversely proportional to the nanotube diameter  $d_t$ , and the orientation of the lines are given by the chiral angle  $\theta$ . The projection of Fig. 1 shows the energy contours for the bonding band in the first Brillouin zone, which is outlined by the hexagon. The parallel lines through the first Brillouin zone are examples of allowed  $k$  modes in an armchair nanotube. The Fermi energy at the vertices of the Brillouin zone is sitting exactly on the allowed  $k$  modes, giving the metallic nature. In case no cuts pass through the vortices of the Brillouin zone, the tubes are semiconductors. In other words, an  $(n, m)$  tube is metallic when  $n = m$ , or when  $n - m$  is a

multiple of 3, while CNTs with  $n - m$  not a multiple of 3 are semiconducting. This energy gap of semiconducting tubes is inversely proportional to the nanotube diameter and typically ranges from 0.2 eV to 0.6 eV. The spatial resolved atomic structure of CNTs and the corresponding electronic density of states have been confirmed by means of scanning tunneling microscope.<sup>[15–17]</sup>

## FETs

In 1997, the research group in Delft first showed that the tiny nanotubes also exhibited transistor-like behavior.<sup>[18]</sup> The current flowing through the nanotube can be turned on or off by applying a gate voltage, bearing an analogy to the conventional MOSFETs.<sup>[19–21]</sup> The prototype of a CNTFET is shown in Fig. 2A. It is a three-terminal device with the terminals designated as “gate,” “source,” and “drain.” The nanotube spanning the source and the drain contacts is the active “channel” [section B in the cross-sectional view of Fig. 2A] and is critical for current conduction. The substrate, which is usually made of heavily doped polysilicon, acts as a global back gate, with a thin layer of thermally oxidized silicon on top. The gate is used for varying the electrostatic potential of the channel and controls the charge carriers flowing through the channel. Figure 2B depicts the  $I$ - $V_{ds}$  characteristics obtained from a semiconducting nanotube at different gate voltages. Applying a negative gate voltage causes an increase of current, whereas a positive gate voltage suppresses current and forms a current gap at large positive gate values. The semiconducting nanotube behaves as a hole conductor. In the inset of Fig. 2B,

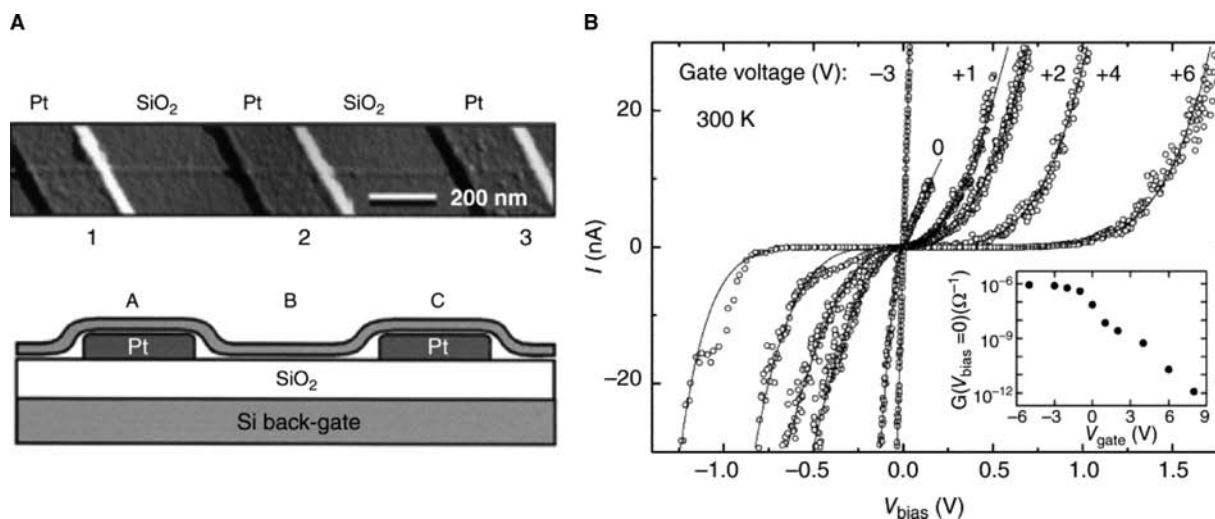


**Fig. 2** (A) Device layout of the prototype of a CNTFET. The tube is lying on a Si/SiO<sub>2</sub> substrate with predefined Pt electrodes. (B) The output characteristics of the transistor at room temperature. The inset shows the gate-dependent conductance changes. *Source:* From Ref.<sup>[18]</sup>.



the zero-bias conductance is plotted against gate voltage. The change of gate voltage, spanning over 10 V, produces a conductance modulation by six orders of magnitude, as pronounced as that produced in a Si-based MOSFET.

In the subsequent studies,<sup>[22–24]</sup> the p-type conducting mechanism of semiconducting nanotubes was attributed to the oxygen adsorption on the tube wall. The oxygen molecules on the wall function as electron acceptors and turn the nanotube that should be intrinsic in nature into p-type. More recently, this argument has been further polished by the IBM group, as will be discussed below. Irrespective of the detailed influence of oxygen molecules on the conduction of semiconducting nanotubes, one can achieve different types of conduction by varying the coverage of oxygen molecules on the tube wall or by applying an appropriate passivation on the tube. On-tube junctions or even logic gates can be hence designed and demonstrated.<sup>[25]</sup>

### Switching Mechanism of CNT Transistors

Although both the output and the transfer characteristics of semiconducting nanotubes much resemble the p-channel MOSFETs, the dominating switching mechanism in nanotubes is, however, distinct. A conventional MOSFET can be thought of as two back-to-back p–n junction diodes with fairly low leakage current present. For a p-channel MOSFET, the channel region is made of n-type silicon. When a sufficiently large negative voltage is applied to the gate, the silicon surface is inverted to p-type. It forms a 2D hole gas at the interface between the gate dielectric and silicon as well as ohmic contacts between the conducting channel and the p + source/drain. The switching in a MOSFET is consequently determined solely by the channel conduction, which is a function of carrier concentration and modulated by the gate voltage. For CNTs, it was shown that Schottky barriers are formed at the contact with electrodes.<sup>[20,26]</sup> With an

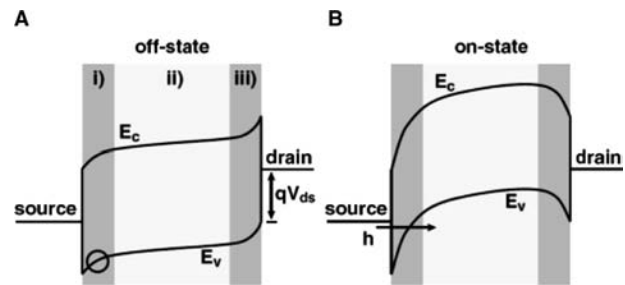


**Fig. 3** Band bending at a fixed source–drain voltage. (A) For a gate voltage below threshold voltage, the transistor stays in the “off” state. (B) For a gate voltage above threshold voltage, the transistor is turned on by holes tunneling through the Schottky barriers. *Source:* From Ref.<sup>[26]</sup>.

applied negative gate voltage, holes accumulate in the valance band. Even though there is substantial carrier density in the channel, current will still be blocked by the Schottky barriers. Increasing the voltage difference between the gate and the source electrodes results in the reduction of Schottky barrier width and allow holes to conduct via thermally assisted tunneling. The band structure is suggested in Fig. 3. The current flow in such a device is not limited by the channel as it is in conventional MOSFETs, but instead by the geometry of the contact at which the Schottky barrier forms. In addition to this difference, CNTFETs are sensitive to the gas molecules adsorbed onto the walls of the nanotubes. By annealing a nanotube in vacuum, one can remove the adsorbed oxygen molecules and transform the tube from p-type to n-type. At an intermediate stage of gas desorption, it is turned into an ambipolar transistor where the electrons conduct at a positive gate voltage and holes conduct at a negative gate voltage. The band structures near the metal contact at different oxygen contents are schematically illustrated in Fig. 4. These distinct working mechanisms have important implications for a potential CNTFET-based technology in that CNTFETs obey different scaling rules and are capable of novel designs and functionalities.

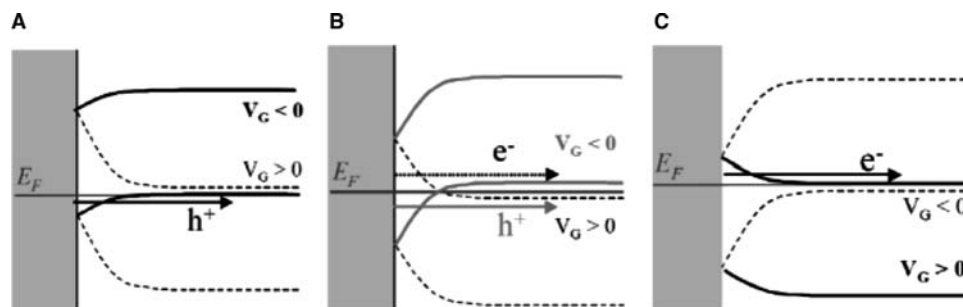


**Fig. 4** Schematic drawing of band structures near the contact for p-type (A), ambipolar; (B), and n-type; (C) CNTFETs. The change from (A) to (C) corresponds to the high-to-low oxygen adsorption on the tube. *Source:* From Ref.<sup>[10]</sup>.

## Ballistic Nanotube Transistors

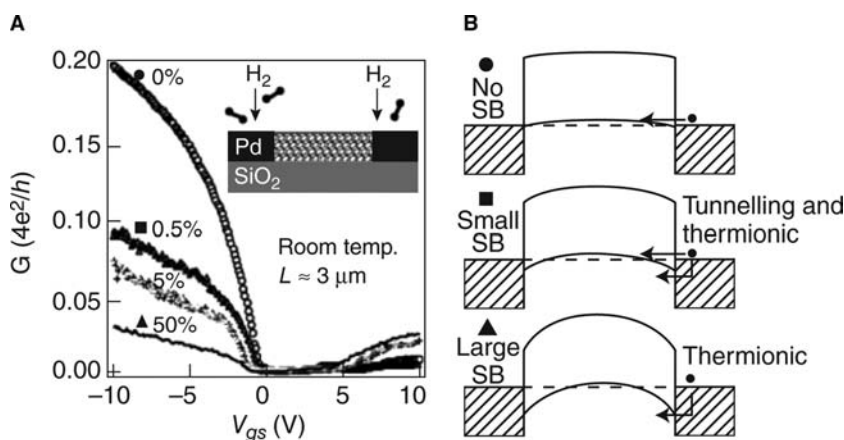
Searching for an ohmic electrical contact for CNTs is one of the goals in realizing high-performance CNTFETs. As aforementioned, the device properties of early prototypes were mainly dominated by the contacts. Some inherent properties like ballistic transport as well as the ability to carry high current density are suppressed owing to the presence of Schottky barriers. Some high work-function metals such as platinum ( $\phi = 5.7$  eV) and Au ( $\phi = 5.2$  eV) were initially anticipated to show ohmic contact to semiconducting tubes. Experimental results, however, indicate that these metals cause high-energy barriers at the contacts. This could be owing to poor sticking or wetting interaction between the metal and the nanotube. Recently, it has been shown that palladium with  $\phi = 5.1$  eV can effectively enhance the nanocontacts and give rise to electrical conductance of semiconducting tubes approaching quantum limit,  $4e^2/h$ , in the charge accumulation regime.<sup>[27]</sup> This fundamental limit in conductance is owing to the mismatch of conducting channels in a nanotube ( $N = 2$ ) and a metal lead. Interestingly, a Schottky barrier-free semiconducting nanotube also behaves like a metallic tube in which the temperature-dependent conductance first increases as temperature is lowered and then turns down below  $\sim 200$  K. This is in contrast to the monotonic decrease of conductance as a function of temperature, which occurs for semiconducting nanotubes with Schottky barriers at the contacts. These properties unambiguously demonstrate that the Schottky barriers are eliminated or minimized by contacting the nanotubes with palladium.

Fig. 5 shows the transfer characteristics of a 3- $\mu\text{m}$ -long semiconducting nanotube at different contact conditions. For a pure palladium contact, the conductance approaches  $0.2(4e^2/h)$  at large negative gate voltages. Exposing the device to hydrogen results in the formation of palladium hydride, which reduces the work function of the electrode. At small

concentrations of hydrogen, small Schottky barriers build up at the contacts, as schematically shown in the middle panel of Fig. 5B, and the conductance drops by a factor of two. Increasing the content of hydrogen up to 50% in the electrodes further enlarges the barriers and hence continues to lower the conductance. It should be noted that scattering in semiconducting nanotubes is more effective than in metallic tubes because the initial and final states are not orthogonal in semiconducting tubes. To reduce the scattering events in semiconducting tubes, one can simply shorten the channel length. It was found that for a 0.3- $\mu\text{m}$ -long semiconducting tube the conductance can be as high as  $0.4(4e^2/h)$ . It is clear that the transistor is now operating in the channel-limiting regime, instead of being blocked by Schottky barriers. In the channel-limiting mode, the transistor is turned on as long as charge carriers populate the two sub-bands responsible for charge propagation, whereas, in the Schottky barrier mode, the transistor is turned on only when the applied gate voltage has lowered the width of barriers sufficiently so that the populated charge carriers can tunnel through the barrier. In the former case, the tube is capable of carrying a higher current density and dissipates much less heat.

## Nanotube Single-Electron Transistors

So far we have only addressed the issue of using semiconducting nanotubes as a switching element. In fact, metallic nanotubes also exhibit interesting transistor-like behavior. If we replace the semiconducting tubes with metallic tubes in the same FET configuration, we are able to see the transistor behavior resulting from the single-electron charging phenomena. There are two fundamental prerequisites to observe single-electron tunneling behavior. The first condition is based on the Heisenberg uncertainty relation: The quantum fluctuation in the particle numbers must be



**Fig. 5** (A) Transfer characteristics of a ballistic CNTFET with channel length of 3  $\mu\text{m}$ . The inset is the schematic representation of the device layout. (B) Band diagrams illustrating the underlying principle of p-channel ballistic FETs at different concentrations of hydrogen. Increasing the content of hydrogen in the palladium contacts causes the formation of Schottky barriers at the contacts and lowers the conductance accordingly. *Source:* From Ref.<sup>[27]</sup>.

sufficiently small so that the charge is well localized in the nanotube. This requires the minimum tunneling resistance to be  $R_{s,d} \gg h/e^2 = 25.8 \text{ k}\Omega$ . Another condition is that the energy required to add one electron to the nanotube,  $e^2/C$ , must exceed the thermal energy.

To construct such a single-electron transistor, the nanotube which acts as a quantum island is contacted by a drain and a source electrode, and then coupled to a gate electrode capacitively, as shown in Fig. 6A and B.

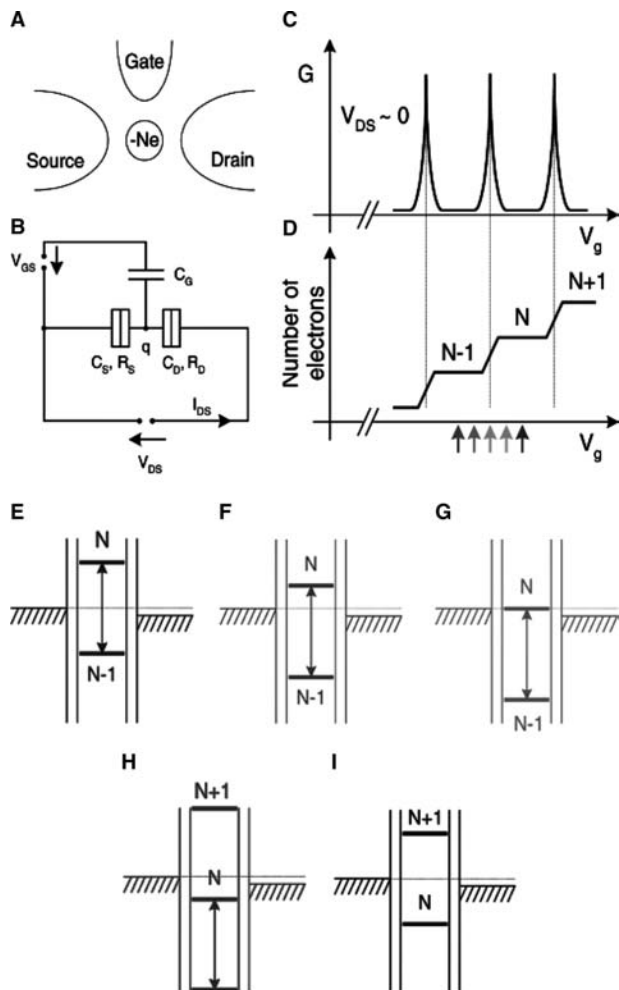


**Fig. 6** (A) The three-terminal geometry of a single-electron transistor. (B) Equivalent circuit for a single-electron transistor. The tunnel junction is represented by a parallel combination of the tunneling resistance  $R_{s,d}$  and the capacitance  $C_{s,d}$ . (C) Conductance vs. gate voltage in the linear response regime of a single-electron transistor. The conductance of the device oscillates as a function of gate voltage with a period that corresponds to the addition of a single electron to the island. (D) The number of electrons on the island. The number stays constant in the Coulomb blockade regime and jumps one charge quantum in single-electron tunneling regime. (E)–(i) Band diagrams of the single-electron transistor under different gate voltages indicated in (D).

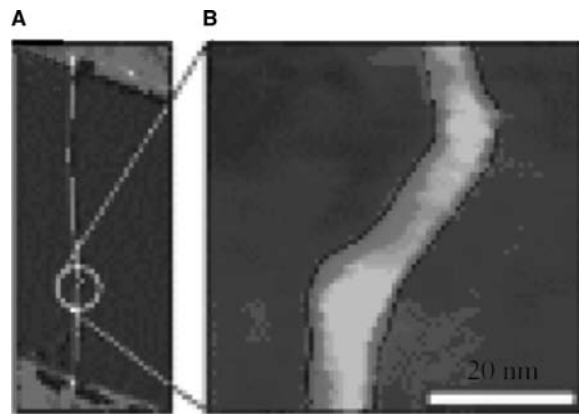


**Fig. 7** (A) An Atomic force microscope (AFM) image of a metallic nanotube lying on top of two electrodes. In the marked region, two kinks were made by AFM manipulations. The highly doped Si substrate is used as a gate electrode to modulate the electrostatic potential of the island sandwiched by the two kinks for single-electron tunneling at room temperature. (B) Enlargement of the double-junction structure. *Source:* From Ref.<sup>[28]</sup>.

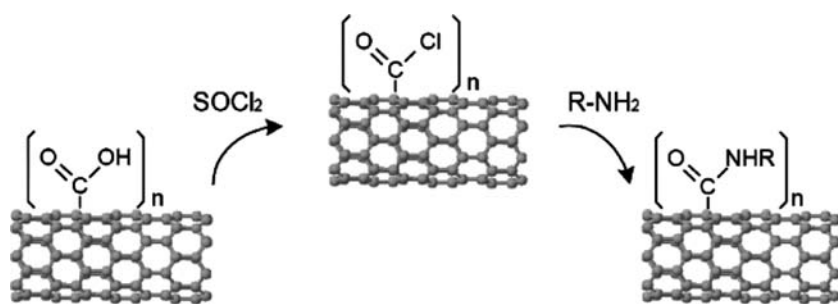
The mesoscopic size of nanotubes significantly reduces the total capacitance of a nanotube required to transport one electron into or out of the island. In combination with high contact resistance, one can readily observe the single-electron effect at a cryogenic temperature.

Recently, room-temperature single-electron transistors were realized within an individual metallic nanotube.<sup>[28]</sup> The devices were constructed “on a tube” within which two tunnel barriers were created by the AFM manipulation technique. A short nanotube section (between 20 and 50 nm) is defined by the two kinks and acts as a “quantum island” in a single-electron transistor configuration. The AFM images of the structure are shown in Fig. 7.

The device is assembled on a highly doped Si substrate that allows one to change the electrostatic potential of the island and to control the transistor in the single-electron tunneling state (on) or in the Coulomb-blockade state (off). A charging energy of about 120 meV has been recorded for such a device, capable of performing single-electron switching at room temperature.

### All-Carbon Transistors

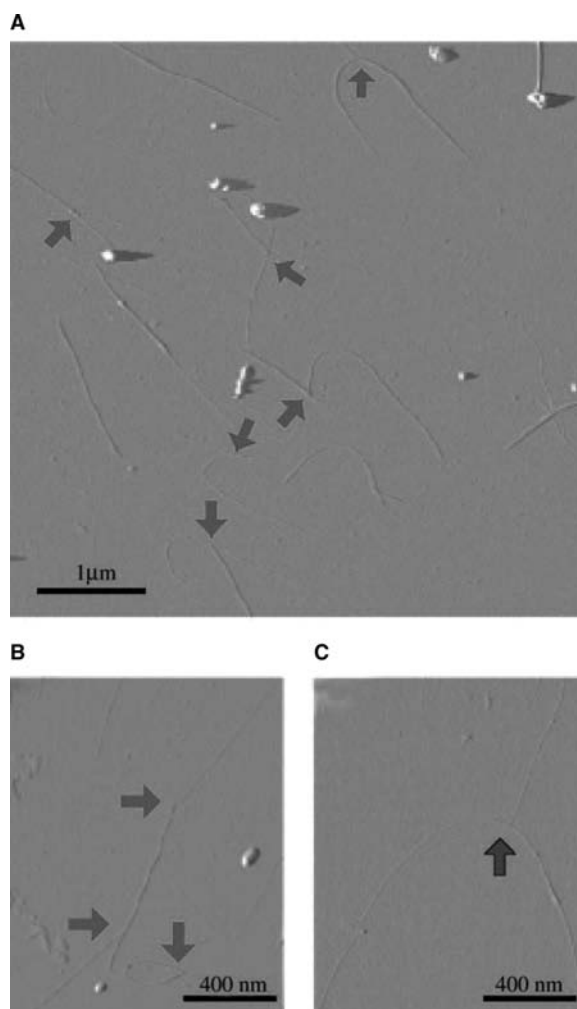
The first generation of the CNTFETs consisted of nanotubes placed over metal leads on a silicon chip.<sup>[18]</sup> The leads served as source and drain and the doped silicon substrate acted as a gate. The on/off ratio of these transistors was about  $\sim 10^5$ – $10^6$ , but the gain



**Fig. 8** Sequence of chemical functionalization in CNTs. First, the chloride acid groups are attached to the ends or sidewalls of the nanotubes. Then diamino groups are incorporated into the nanotubes by replacing the chloride acid. The diamino groups can link two nanotubes to form T junctions.

(defined as the change in output voltage divided by the change in gate voltage) was very low ( $\ll 1$ ), owing to the fairly thick oxide layer needed to prevent leakage currents. This would lead to a problem with implementation when they are integrated into a circuit, because the output of one gate cannot drive the next properly. To solve this problem, Bachtold et al. presented a novel electrode configuration where the gate is an aluminum strip and the native aluminum oxide allows the gate electrode to be so close to the nanotube that the transistor reaches a gain of about 10.<sup>[29]</sup> Later, the IBM group reported on a complementary CNTFET as a logic gate with a gain of 1.6<sup>[25]</sup> and Dai and coworkers have presented an array of some 100 nanotube transistors assembled on a silicon chip.<sup>[30]</sup> The nanotube transistors reported so far are not really “nanoscale” devices. The conducting channel consists of a single nanotube and this is, of course, nanoscale. The source and drain, however, are made by electron beam lithography, and are about 100 nm wide and several micrometers long. In the first generation nanotube transistors, the gate is even macroscopic. The aluminum gate of the second generation transistors is lithographic like the source and drain and still not nanoscale. To take the dimensional advantage of CNTs and to shrink the active channel to few nanometers in all three dimensions, one possibility is to use a nanotube that is located close to the nanotube channel as a local gate, resembling the local gating by an AFM tip. This nanotube gate can be attached to the nanotube channel by chemical functionalization. Taking an insulating chemical linker, one can assemble T-shape interjunctions and construct the device in such a way that the active part of the device is truly confined to the vicinity of the nanotube gate. This device is all-carbon, except for few nitrogen and oxygen atoms in the molecular linkers! To assemble nanotube T junctions, we start with chemical functionalization (Fig. 8). It is well known that graphite is chemically inert. When a graphite layer is rolled up to form a cylindrical structure, its chemical reactivity is modified. This stems from the curvature-induced pyramidalization and misalignment of the  $\pi$ -orbitals of the carbon atoms, giving rise to a local strain in CNTs.<sup>[31–33]</sup> The relief of these

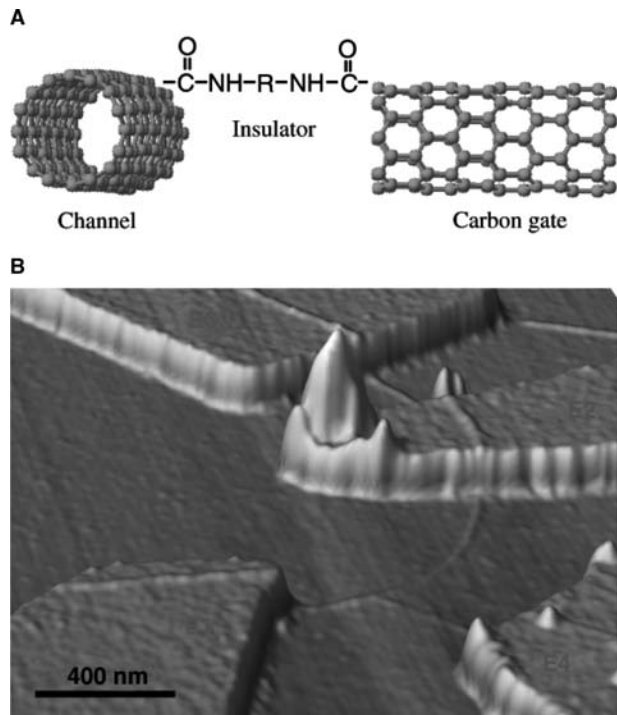
strains accompanies addition reactions in the caps and sidewall of nanotubes. By treating nanotubes with aggressive reagents like nitric acid, phenolic and carboxylic acid groups can be readily derivatized on the end caps or sidewall of nanotubes.<sup>[34–37]</sup> The



**Fig. 9** (A) AFM images of CNT interjunctions. The junctions are indicated by arrows. A more complicated junction structure is shown in (B). Both end-to-side and end-to-end attachments are observable on a tube. In (C) an individual Y junction is clearly discernible. *Source:* From Ref.<sup>[41]</sup>.

carboxylic acid groups can be converted into acylchloride groups by treating with thionylchloride.<sup>[36,38]</sup> The acid chloride-functionalized CNTs are then susceptible to react with amines. The resulting chemically functionalized nanotubes are shown to be able to form a closed ring shape,<sup>[39]</sup> or be attached to a normal Si AFM tip used for a single-molecular sensor or probe.<sup>[40]</sup>

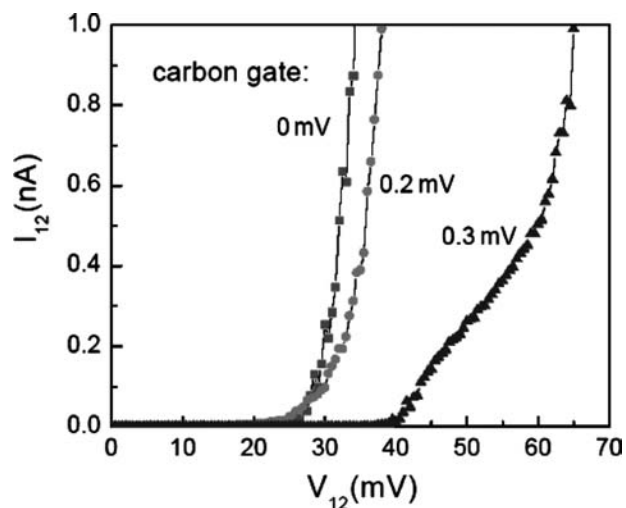
After chemical functionalization, most of the nanotubes form a network and connect side by side.<sup>[41]</sup> To untangle the network, appropriate ultrasonic agitation is applied to the nanotube suspension. Figure 9 shows AFM images of CNTs after functionalization with tripropylentetramin. In most cases, the nanotubes form end-to-side junctions. End-to-end junctions are rarely found. Under an appropriate functionalization process, around one-third of the nanotubes form end-to-side junctions, whereas less than 2% of the pristine nanotubes show similar junctions. The junctions observed in the pristine nanotube samples were mainly the result of the splitting of bundles. The attachment of different chemical groups was identified by x-ray photoelectron spectroscopy, and the induced changes in electronic structure by the functional groups were also studied by Raman and theoretical modeling.<sup>[42]</sup>



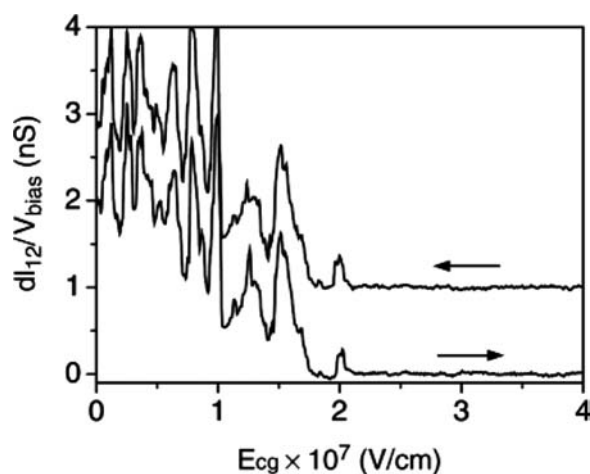
**Fig. 10** (A) A schematic representation of an all-carbon transistor where the channel and the gate are both constituted by nanotubes and the gate dielectric is played by an insulating molecule. (B) A 3-D AFM image of the transistor with gold electrodes applied on top. *Source:* From Ref.<sup>[43]</sup>.

Fig. 10A illustrates the device layout of an all-carbon transistor, and B shows a 3-D AFM image of such a device, which consists of two individual nanotubes glued by a bifunctional amine linker. The bar of the “T” is the tube between the leads E1 and E2, and acts as a conducting channel, and the stem connected to E4 is the “nanotube gate.” The resolution of the AFM is not sufficient to exhibit the diamino linker molecule at the junction. The leads E1, E2, and E4 connect to source, drain, and nanotube gate, respectively. As a further diagnostic tool, we can use the (degenerately doped) silicon substrate as a global “back gate” to characterize the electric properties of the various sections of the tubes.

As is well known, there are semiconducting and metallic CNTs, and it is not yet possible to synthesize only one type or to separate the types after synthesis. In an ideal case for an all-carbon FET, the channel and the gate will be composed of an individual semiconducting and metallic tube, respectively. In between the two nanotubes, the long molecular chain and the perpendicular linkage keep the nanotubes in proximity without allowing contact. Figure 11 shows the output characteristics of such a device (channel current vs. voltage across channel for several voltages at the nanotube gate). At a bias of 35 mV between source and drain we can pass a current of 1 nA through the channel tube (An upper limit for a possible leakage current through the linker molecule has experimentally been found to be by two orders of magnitude smaller). If we apply a nanotube gate voltage of 0.3 mV, we can effectively suppress this current. Thus, we see that a



**Fig. 11** Current vs. voltage characteristics of an all-carbon transistor with the semiconducting nanotube as channel, with different voltages at the nanotube in-plane gate. The back gate is kept at 0 V throughout the measurements, and the data were recorded at 4 K.



**Fig. 12** Conductance vs. electric field at the nanotube gate. The channel is composed of a metallic nanotube. Two curves are shown: one ascending sweep and another descending. The latter case is offset by 1 nS for clarity. The sufficiently high electric field applied through the nanotube gate can reversibly switch on or off the metallic nanotube. (From Ref.<sup>[43]</sup>.)

gain of about 100 can be obtained easily in all-carbon transistors.

Because the T junctions are formed nonselectively in the process of chemical reactions, in many cases the bar tubes are metallic. An interesting question that is raised is whether the metallic tubes can also act as “field-effect” channels. Intuitively, this would not work, for a metallic nanotube has a considerably higher electron density than a semiconducting one and, therefore, cannot be modulated by a gate before it runs into dielectric breakdown. To address this question, we constructed the device in a similar way, except that the linker molecule between the bar and the stem was intentionally destroyed by burning it at 150°C. We now have a metallic bar as the conducting channel and a nanotube gate approximately 1.5 nm away from the bar. The conductance vs. the electric field applied through the nanotube gate at liquid helium temperature is shown in Fig. 12. The channel conductance first oscillates as a function of the nanotube gate electric

field, then drops to zero at field strengths higher than 20 MV/cm. The metallic nanotube behaves like a FET when it is subjected to a high electric field. This is owing to the fact that high field causes the redistribution of charge density in the highest occupied molecular orbital and the lowest unoccupied molecular orbital, and eventually results in a gap opening in the metallic tube. Now one can switch off the conductance of a metallic channel by applying a sufficiently high electric field that is normally not accessible with a back gate. The critical field needed to turn the metallic state into an insulating state resembles the threshold voltage in a FET structure.

### Transparent Nanotube Network Transistors

Another novel application of nanotube-based transistors is the network FET, which is transparent and flexible.<sup>[44]</sup> The devices were prepared on a sheet of polyester, as illustrated in Fig. 13A. The nanotubes used for this purpose were first homogeneously dispersed in a 1 wt% sodium dodecyl sulfate solution. A dense nanotube network was subsequently sprayed on the polyester substrate as a gate electrode. A thin layer of parylene N is then evaporated on top of the dense network for gate dielectrics. To form active channels, a diluted nanotube suspension was used for adsorbing a sparse network. The nanotube network transistors exhibit several advantages beyond the conventional transparent transistors, which have been fabricated using polymers<sup>[45–47]</sup> or inorganic oxides.<sup>[48,49]</sup> They have a lighter weight, a higher carrier mobility, and a superior flexibility for bending, and are easy to process at room temperature. One shortcoming of the nanotube network transistor is the low on/off ratio, which is only  $10^2$  for the prototype device. This is owing to the mixture of metallic and semiconducting nanotubes in the network channel and less effective gating. Nevertheless, it opens up a new opportunity for potential applications in the so-called “plastic electronics,” such as paper displays and wearable computers.

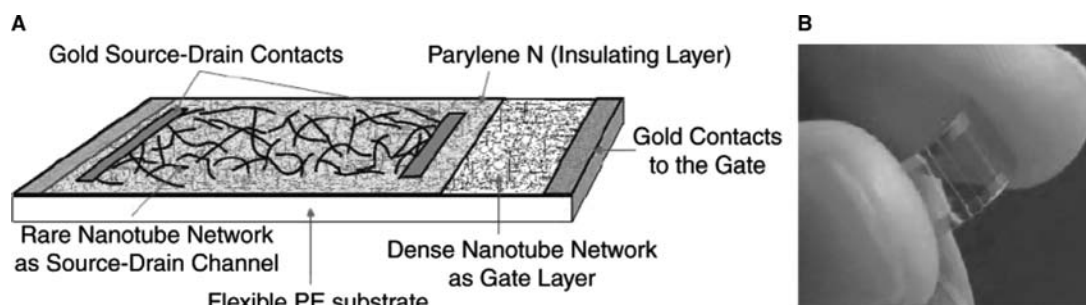


**Fig. 13** (A) Schematic representation of nanotube transparent network transistor. (B) The picture shows the prototype of network transistor. *Source:* From Ref.<sup>[44]</sup>.



## CONCLUSIONS

It is clear that plenty of challenges lie ahead before CNT devices could work their way into any practical electronic devices. Two key questions remain unsolved and need to be addressed for implementation into manufacturable nanoscale devices: 1) easy separation of metallic and semiconducting nanotubes or even controllable chirality-dependent growth and 2) integration of nanotubes either by nondirected growth method with subsequent manipulation or directed growth at desired locations. However, on the way to nanotube-based electronic devices, a great deal of new physics that underlies the behavior of nanostructures has been learned, including the distinct device properties of CNTs to Si-based devices, rich quantum transport behavior in confined structures, and the intriguing electronic properties of sophisticated hybrid nanostructures. This demonstrates that the quest for functional nanostructures also greatly contributes to the understanding and the development of the basic science.

## REFERENCES

- Charlier, J.C.; Iijima, S. Electronic properties, junctions, and defects of carbon nanotubes. In *Growth Mechanisms of Carbon Nanotubes*, Topics in Applied Physics; Dresselhaus, M.S., Dresselhaus, G., Avouris, Ph., Eds.; Springer-Verlag: Heidelberg, 2001; Vol. 80.
- McEuen, P.L.; Bockrath, M.; Cobden, D.H.; Yoon, Y.G.; Louie, S.G. Disorder, pseudospins, and backscattering in carbon nanotubes. *Phys. Rev. Lett.* **1999**, *83*, 5098–5101.
- McEuen, P.L. Single-wall carbon nanotubes. *Phys. World* **2000**, *13*, 31–36.
- Yao, Z.; Kane, C.L.; Dekker, C. High-field electrical transport in single-wall carbon nanotubes. *Phys. Rev. Lett.* **2000**, *84*, 2941–2944.
- Martel, R.; Derycke, V.; Appenzeller, J.; Wind, S.; Avouris, Ph. Carbon nanotube field-effect transistors and logic circuits, 39th Design Automation Conference Proceeding, New Orleans, Louisiana, June, 10–14, 2002.
- Riordan, M.; Hoddeson, L.; Herring, C. The invention of the transistor. *Rev. Mod. Phys.* **1999**, *71*, S336–S345.
- Intel press release. Available on the web; <http://www.intel.com/research/silicon/mooreslaw.htm>.
- Moore, G.E. Cramping more components onto integrated circuits. *Electronics* **1965**, *38*. Available on the web <ftp://download.intel.com/research/silicon/moorespaper.pdf>.
- Taur, Y.; Ning, T.H. *Fundamentals of Modern VLSI Devices*; Cambridge University Press: Cambridge, 1998; 90 pp.
- Taur, Y. CMOS design near the limit of scaling. *IBM J. Res. Dev.* **2002**, *46*, 213–222.
- White, C.T.; Robertson, D.H.; Mintmire, J.W. Helical and rotational symmetry of nanoscale graphitic tubules. *Phys. Rev. B* **1993**, *47*, 5485–5488.
- Odom, T.W.; Huang, J.-L.; Kim, P.; Lieber, C.M. Structure and electronic properties of carbon nanotubes. *J. Phys. Chem. B* **2000**, *104*, 2794–2809.
- Saito, R.; Fujita, M.; Dresselhaus, G.; Dresselhaus, M.S. Electronic structure of graphene tubules based on C<sub>60</sub>. *Phys. Rev. B* **1992**, *46*, 1804–1811.
- Avouris, Ph. Carbon nanotube electronics. *Chem. Phys.* **2002**, *281*, 429–445.
- Odom, T.W.; Huang, J.-L.; Kim, P.; Lieber, C.M. Atomic structure and electronic properties of single-walled carbon nanotubes. *Nature* **1998**, *391*, 62–64.
- Ouyang, M.; Huang, J.-L.; Cheung, C.L.; Lieber, C.M. Energy gaps in “metallic” single-walled carbon nanotubes. *Science* **2001**, *292*, 702–705.
- Wildoer, J.W.G.; Venema, L.C.; Rinzler, A.G.; Smalley, R.E.; Dekker, C. Electronic structure of atomically resolved carbon nanotubes. *Nature* **1998**, *391*, 59–62.
- Tans, S.J.; Verschueren, A.R.M.; Dekker, C. Room-temperature transistor based on a single carbon nanotube. *Nature* **1998**, *393*, 49–52.
- Martel, R.; Schmidt, T.; Shea, H.R.; Hertel, T.; Avouris, Ph. Single- and multi-wall carbon nanotube field-effect transistors. *Appl. Phys. Lett.* **1998**, *73*, 2447–2449.
- Martel, R.; Derycke, V.; Lavoie, C.; Appenzeller, J.; Chan, K.K.; Tersoff, J.; Avouris, Ph. Ambipolar electrical transport in semiconducting single-wall carbon nanotubes. *Phys. Rev. Lett.* **2001**, *87*, 256805–256808.
- Zhou, C.; Kong, J.; Yenilmez, E.; Dai, H. Modulated chemical doping of individual carbon nanotubes. *Science* **2000**, *290*, 1552–1555.
- Collins, P.G.; Bradley, K.; Ishigami, M.; Zettle, A. Extreme oxygen sensitivity of electronic properties of carbon nanotubes. *Science* **2000**, *287*, 1801–1804.
- Sumanasekera, G.U.; Adu, C.K.W.; Fang, S.; Eklund, P.C. Effects of gas adsorption and collisions on electrical transport in single-walled carbon nanotubes. *Phys. Rev. Lett.* **2000**, *85*, 1096–1099.
- Bradley, K.; Jhi, S.-H.; Collins, P.G.; Hone, J.; Cohen, M.L.; Louie, S.G.; Zettl, A. Is the intrinsic thermoelectric power of carbon nanotube positive? *Phys. Rev. Lett.* **2000**, *85*, 4361–4364.
- Derycke, V.; Martel, R.; Appenzeller, J.; Avouris, Ph. Carbon nanotube inter- and intramolecular logic gates. *Nano Lett.* **2001**, *1*, 453–456.
- Heinze, S.; Tersoff, J.; Martel, R.; Derycke, V.; Appenzeller, J.; Avouris, Ph. Carbon nanotubes as Schottky barrier transistors. *Phys. Rev. Lett.* **2002**, *89*, 106801-1–106801-4.
- Javey, A.; Guo, J.; Wang, Q.; Lundstrom, M.; Dai, H. Ballistic carbon nanotube field-effect transistors. *Nature* **2003**, *424*, 654–657.
- Postma, H.W.C.; Teepen, T.; Yao, Z.; Grifoni, M.; Dekker, C. Carbon nanotube single-electron transistors at room temperature. *Science* **2001**, *293*, 76–79.
- Bachtold, A.; Hadley, P.; Nakanishi, T.; Dekker, C. Logic circuits with carbon nanotube transistors. *Science* **2001**, *294*, 1317–1320.
- Javey, A.; Wang, Q.; Ural, A.; Li, Y.M.; Dai, H.J. Carbon nanotube transistor arrays for multistage complementary logic and ring oscillators. *Nano Lett.* **2002**, *2*, 929–932.

31. Haddon, R.C. Chemistry of the fullerenes: the manifestation of strain in a class of continuous aromatic molecules. *Science* **1993**, *261*, 1545–1550.
32. Srivastava, D.; Brenner, D.W.; Schall, J.D.; Ausman, K.D.; Yu, M.; Ruoff, R.S. Prediction of enhanced chemical reactivity to regions of local conformational strain on carbon nanotubes: kinky chemistry. *J. Phys. Chem. B* **1999**, *103*, 4330–4337.
33. Weedon, B.R.; Haddon, R.C.; Spielmann, H.P.; Meier, M.S. Fulleroid addition regiochemistry is driven by pi-orbital misalignment. *J. Am. Chem. Soc.* **1999**, *121*, 335–340.
34. Chiang, I.W.; Brinson, B.E.; Smalley, R.E.; Margrave, J.L.; Hauge, R.H. Purification and characterization of single-wall carbon nanotubes. *J. Phys. Chem. B* **2001**, *105*, 1157–1161.
35. Hamon, M.A.; Hu, H.; Bhowmik, P.; Niyogi, S.; Zhao, B.; Itkis, M.E.; Haddon, R.C. End-group and defect analysis of soluble single-walled carbon nanotubes. *Chem. Phys. Lett.* **2001**, *347*, 8–12.
36. Liu, J.; Rinzler, A.G.; Dai, H.; Hafner, J.H.; Bradley, R.K.; Boul, P.J.; Lu, A.; Iverson, T.; Shelimov, K.; Huffman, C.B.; Rodriguez-Macias, F.; Shon, Y.-S.; Lee, T.R.; Colbert, D.T.; Smalley, R.E. Fullerene pipes. *Science* **1998**, *280*, 1253–1256.
37. Mawhinney, D.B.; Naumenko, V.; Kuznetsova, A.; Yates, J.T., Jr.; Liu, J.; Smalley, R.E. Surface defect site density on single walled carbon nanotubes by titration. *Chem. Phys. Lett.* **2000**, *324*, 213–216.
38. Chen, J.; Hamon, M.A.; Hu, H.; Chen, Y.; Rao, A.M.; Eklund, P.C.; Haddon, R.C. Solution properties of single-walled carbon nanotubes. *Science* **1998**, *282*, 95–98.
39. Sano, M.; Kamino, A.; Okamura, J.; Shinkai, J. Ring closure of carbon nanotubes. *Science* **2001**, *293*, 1299–1301.
40. Wong, S.S.; Joselevich, E.; Woolley, A.T.; Cheung, C.L.; Lieber, C.M. Covalently functionalized nanotubes as nanometer-sized probes in chemistry and biology. *Nature* **1998**, *394*, 52–55.
41. Chiu, P.W.; Duesberg, G.S.; Dettlaff-Weglikowska, U.; Roth, S. Interconnection of carbon nanotubes by chemical functionalization. *Appl. Phys. Lett.* **2002**, *80*, 3811–3813.
42. Dettlaff-Weglikowska, U.; Skakalova, V.; Graupner, R.; Jhang, S.H.; Kim, B.H.; Lee, H.J.; Ley, L.; Park, Y.W.; Berber, S.; Tomanek, D.; Roth, S. Effect of SOCl<sub>2</sub> treatment on electrical and mechanical properties of single-wall carbon nanotube networks. *J. Am. Chem. Soc.* **2005**, *127*, 5125–5131.
43. Chiu, P.W.; Kaempgen, M.; Roth, S. Band-structure modulation in carbon nanotube T junctions. *Phys. Rev. Lett.* **2004**, *92*, 246802-1–246802-4.
44. Artukovic, E.; Kaempgen, M.; Hecht, D.S.; Roth, S.; Gruner, G. Transparent and flexible carbon nanotube transistors. *Nano Lett.* **2005**, *5*, 757–760.
45. Stutzman, N.; Friend, R.H.; Sirringhaus, H. Self-aligned, vertical-channel, polymer field-effect transistors. *Science* **2003**, *299*, 1881–1884.
46. Dimitrakopoulos, C.D.; Purushothaman, S.; Kymissis, J.; Callegari, A.; Shaw, J.M. Low-voltage organic transistors on plastic comprising high-dielectric constant gate insulators. *Science* **1999**, *283*, 822–824.
47. Dimitrakopoulos, C.D.; Malenfant, P.R.L. Organic thin film transistors for large area electronics. *Adv. Mater.* **2002**, *14*, 99–117.
48. Nomura, K.; Ohta, H.; Takagi, A.; Kamiya, T.; Hirano, M.; Hosona, H. Room-temperature fabrication of transparent flexible thin-film transistors using amorphous oxide semiconductors. *Nature* **2003**, *432*, 488–492.
49. Nomura, K.; Ohta, H.; Ueda, K.; Kamiya, T.; Hirano, M.; Hosona, H. Thin-film transistor fabricated in single-crystalline transparent oxide semiconductor. *Science* **2003**, *300*, 1269–1272.

# Carbon Nanotube–Conducting Polymer Composites in Supercapacitors

Mark Hughes

Department of Materials Science and Metallurgy,  
University of Cambridge, Cambridge, U.K.

## INTRODUCTION

Supercapacitors, also referred to as electrochemical capacitors or ultracapacitors, are devices used to store and deliver electrical energy in high-power pulses.<sup>[1,2]</sup> With the advent of electric vehicles, digital communication, and other electronic devices that require significant bursts of electrical energy, the need for supercapacitors has expanded rapidly. At present, the most promising materials on which supercapacitors are based can be divided into two categories—those that make use of a double-layer charge storage mechanism (e.g., carbon nanotubes, carbon aerogels, and activated carbon black) and those employing a redox pseudo-capacitive charge storage mechanism (e.g., conducting polymers and transition metal oxides).<sup>[3,4]</sup> Already, the electrical charge that can be stored in each of these materials is typically several orders of magnitude larger than that of most commercially available conventional capacitors. However, it has been shown in recent times that even greater charge storage capacitances can be achieved in composites made by combining carbon nanotubes (a double-layer capacitive material) with a conducting polymer (a redox pseudo-capacitive material). The superior charge storage performance of carbon nanotube-conducting polymer composite supercapacitors arises from their ability to merge the properties that separately make carbon nanotubes and conducting polymers so suited to their respective charge storage mechanisms. That is to say, the composites are able to combine the high surface area and electrical conductivity of carbon nanotubes with the redox electrochemistry of conducting polymers.<sup>[5]</sup>

## CARBON NANOTUBE-CONDUCTING POLYMER COMPOSITES

### Structure and Fabrication

Most carbon nanotube-conducting polymer composites used in supercapacitor devices display a nanoporous network structure in which each nanotube is

coated by a thin layer of conducting polymer. This structure maximizes the exposed surface area of the conducting polymer while retaining the conductive network of the carbon nanotubes.

The nanoporous structures possible for carbon nanotube-conducting polymer composites are generally not observed when making conducting polymer composites with other high surface area forms of carbon such as activated carbon black and carbon aerogels.<sup>[6,7]</sup> In these cases the conducting polymer generally blocks the electrolyte pores. The other carbon structures are also unable to achieve the exceptionally low percolation thresholds possible with carbon nanotubes.<sup>[8]</sup>

Electron microscopy, elemental analysis, X-ray diffraction, nuclear magnetic resonance, and Raman spectroscopy studies indicate that there is good physical interaction between the carbon nanotubes and the conducting polymer (Fig. 1). In general, these techniques give no indication that there is a chemical reaction between the two components.<sup>[9–11]</sup> However, it has been reported that Raman spectroscopy on composites of arc-grown multiwalled carbon nanotubes and polyaniline indicates a site-selective interaction between the quinoid ring of the doped polymer and the carbon nanotubes.<sup>[12]</sup>

Recent reports have shown that composites of carbon nanotubes and conducting polymers such as polypyrrole, polyaniline, poly(3-methylthiophene), poly(3-hexylthiophene), poly(3-octylthiophene), and poly(*p*-phenylene vinylene) can be prepared using a variety of chemical<sup>[9,11,12]</sup> and electrochemical<sup>[13–17]</sup> polymerization techniques or by simply mixing the polymer and nanotubes.<sup>[18–20]</sup> To date, most carbon nanotube-conducting polymer composites have been made using multiwalled carbon nanotubes (MWNTs) as they generally offer uniform conductivity combined with a greater susceptibility to chemical oxidation and a lower cost relative to single-walled carbon nanotubes (SWNTs). The uniformity and thickness of the conducting polymer coating on each nanotube, in addition to the degree of porosity, are crucial in determining the composite's properties and are largely dependent on the fabrication technique employed.

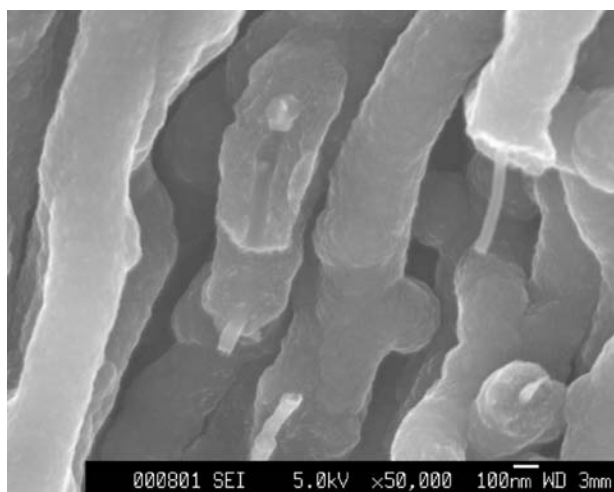


**Fig. 1** Scanning electron microscopy image of the fractured cross section of multiwalled carbon nanotubes coated with polypyrrole. The tubes cleaved during fracture give an indication of the close interaction between the nanotubes and conducting polymer. *Source:* From M. Hughes.

Routes for producing carbon nanotube–conducting polymer composites based on chemical polymerization generally require a solution containing the desired monomer (typically pyrrole or phenylacetylene) and carbon nanotubes in suspension.<sup>[9,11,21]</sup> Polymerization is then initiated by the addition of a dopant such as  $(\text{NH}_4)_2\text{S}_2\text{O}_8$ . While the conducting polymer is observed to coat each individual nanotube using this technique, there have been some reports that the deposit tends to be inhomogeneous with some aggregation of the deposited polymer.<sup>[22]</sup> This in situ method of polymerization offers excellent processing flexibility in that the coated nanotubes can be deposited as a uniform composite film during polymerization or maintained as distinct coated nanotubes in suspension.<sup>[9]</sup> If the coated carbon nanotubes are maintained in suspension, they can subsequently be formed into a film or pellet using techniques such as spin-coating or vacuum drying.

Electrochemical composite growth techniques can be further divided into those that polymerize the conducting polymer onto a carbon nanotube preform<sup>[14–17,23]</sup> and those in which the nanotubes and conducting polymer are simultaneously deposited from the electrolyte<sup>[5,13]</sup> during polymerization. When using an aligned MWNT preform, the conducting polymer (usually polypyrrole<sup>[14,16]</sup> or polyaniline<sup>[24]</sup>) tends to form a continuous, uniform coating over each individual carbon nanotube (Fig. 2). In this way, the basic structure of the carbon nanotube preform is retained, making it possible to produce composites with a very high surface area. While conducting polymers can also be deposited electrochemically on unaligned carbon nanotube preforms, there is a tendency in this case

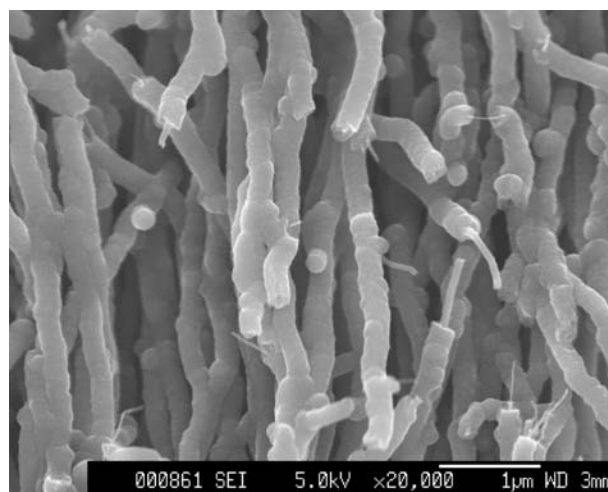


**Fig. 2** Scanning electron microscopy image of the fractured cross section of an aligned array of MWNTs in which each MWNT has been coated with polypyrrole. *Source:* From M. Hughes.

for the deposited conducting polymer to block electrolyte channels into the preform, preventing uniform coating of each carbon nanotube.<sup>[17]</sup>

For electrochemical synthesis routes in which the carbon nanotubes and conducting polymer are simultaneously deposited, the electrolyte used contains suspended carbon nanotubes in addition to the desired monomer (such as pyrrole or 3-methylthiophene) and any supporting electrolyte required.<sup>[5,25]</sup> Polymerization is then initiated via the application of an applied potential, resulting in the deposition of a nanoporous composite film in which each MWNT is uniformly coated by the conducting polymer (Fig. 3). If the suspended carbon nanotubes used in this technique are functionalized via an appropriate acid treatment step before they are added to the polymerization electrolyte, it is possible for the nanotubes to dope the deposited conducting polymer.<sup>[27,28]</sup> This eliminates the need for a supporting electrolyte during film growth and establishes several other advantages for supercapacitor applications that will be discussed later.

Composites formed by simply mixing the carbon nanotubes and conducting polymer generally make use of a suspension containing carbon nanotubes and a presynthesized conducting polymer such as poly(*p*-phenylene vinylene), poly(3-hexylthiophene), or poly(3-octylthiophene).<sup>[18,20,29]</sup> The suspension is ultrasonicated to mix the two constituents and is then spin-cast to form a carbon nanotube–conducting polymer composite film. The resulting composite structure is quite dense with conducting polymer enveloping the carbon nanotubes and the spaces between them.<sup>[19]</sup> It is worth noting that carbon nanotube–conducting polymer composites have also been produced by

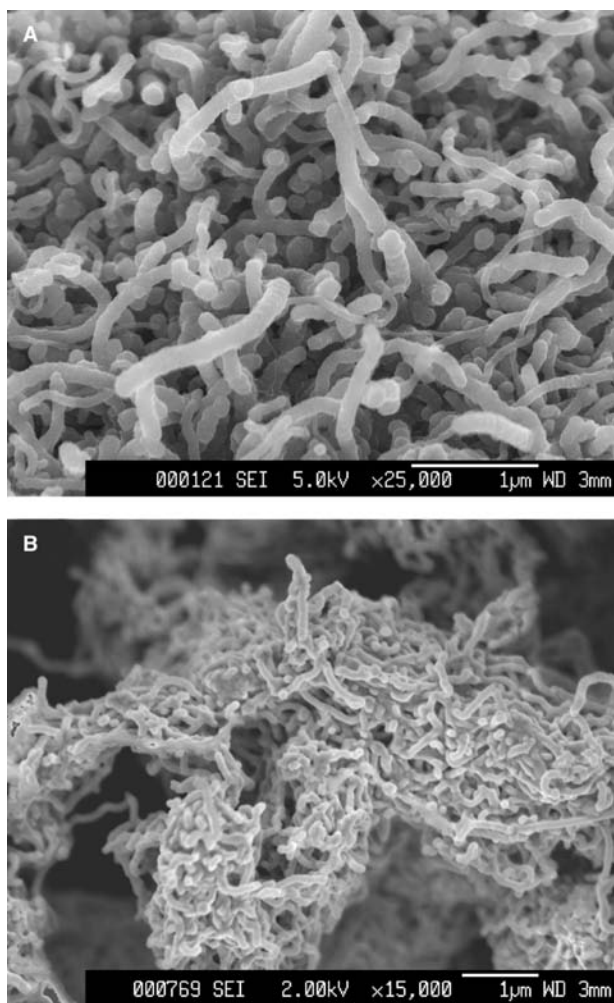


**Fig. 3** Scanning electron microscopy images of nanoporous composite films formed by the simultaneous electrochemical deposition of MWNTs with (A) polypyrrole and (B) poly(3-methylthiophene). *Source:* From Ref.<sup>[26]</sup>.

simply spin coating the conducting polymer directly onto a MWNT preform.<sup>[30,31]</sup>

### Properties and Applications

The responsiveness of conducting polymer films to their external environment makes them very attractive materials for a variety of applications including photovoltaics,<sup>[32]</sup> sensors,<sup>[33,34]</sup> light emitting devices,<sup>[35,36]</sup> actuators,<sup>[37,38]</sup> and supercapacitors.<sup>[4]</sup> However, the response times of these devices are generally restricted by limited electrical conductivity and rates of ionic diffusion in the conducting polymer. The general improvement in electrical conductivity (up to 10 orders of magnitude) observed when carbon nanotubes are introduced into conducting polymers offers some alleviation of this problem.<sup>[18,19,29,39]</sup> Perhaps even more important for electrochemical applications is

the increase in the amount of conducting polymer surface exposed to the electrolyte and the reduced diffusion distances in nanoporous carbon nanotube-conducting polymer composites.<sup>[13]</sup>

Carbon nanotube additions have been observed to increase the strength,<sup>[40]</sup> thermal conductivity,<sup>[41]</sup> stability in air,<sup>[19]</sup> and photodegradation resistance<sup>[11]</sup> of polymers. These properties combine well with the excellent photovoltaic efficiency<sup>[30]</sup> and strong photosensitivity<sup>[20]</sup> exhibited by composites of carbon nanotubes with conducting polymers such as poly(3-hexylthiophene), poly(3-octylthiophene), and poly(*p*-phenylene vinylene), making them suitable for photovoltaic<sup>[31]</sup> and light-sensing<sup>[42]</sup> applications. For light-emitting applications, increasing the electrical conductivity of conducting polymers via the addition of untreated nanotubes is particularly advantageous as this does not introduce states within the polymer bandgap that quench luminescence, as is generally the case when conductivity is increased by doping the polymer.<sup>[19,43]</sup>

Electrochemical devices, such as actuators and supercapacitors, made from carbon nanotube-conducting polymer composites have been shown to display the electrochemical redox behavior of conducting polymers while retaining the conductive network of the carbon nanotubes.<sup>[13,25,44]</sup> This combination of desirable properties is associated with an increase in the storage capacity of the composite supercapacitors relative to the component materials and will be discussed in detail in the following section.<sup>[5]</sup> Unfortunately, reports to date on the actuation of carbon nanotube-conducting polymer films appear to indicate that strain is limited by the nanotubes,<sup>[44]</sup> which are much stiffer than the conducting polymer.

## SUPERCAPACITORS

Capacitors are devices used to accumulate and deliver electrical charge. Capacitors can be divided into conventional capacitors, generally based on a ceramic<sup>[45]</sup> or polymer<sup>[46]</sup> film dielectric, and supercapacitors, which make use of an electrolyte. The most promising supercapacitors at present make use of materials such as high surface area carbons,<sup>[47]</sup> conducting polymers,<sup>[4]</sup> and transition metal oxides<sup>[48]</sup> that are combined with an aqueous or organic electrolyte.

Traditional ceramic and polymer capacitors consist of two parallel conductive plates separated by a ceramic or polymeric dielectric, respectively. When a voltage is applied across the plates one of them adopts a positive charge and the other a negative charge. Conventional ceramic and polymer capacitors are frequently used in lighting, televisions, stereos, induction heaters, computers, and other electronic devices.<sup>[49]</sup> Like their more conventional counterparts, supercapacitors

consist of two opposing electrodes; however, the electrodes are separated by an electrolyte instead of a polymer or ceramic dielectric. While supercapacitors are limited to operating at a few volts, their capacitance far exceeds that of conventional capacitors resulting in significantly higher energy densities.<sup>[50]</sup>

The large capacitance exhibited by supercapacitor systems is related to two main charge storage mechanisms, either double-layer capacitance or redox pseudo-capacitance. Double-layer capacitance involves storing charge in the electrical double-layer formed at the electrode–electrolyte interface. Ions within the electrolyte accumulate at the electrode surfaces, compensating for the electronic charge injected into the electrodes. Depending on the electrolyte used, an electrical double-layer can typically store about 10–40  $\mu\text{F cm}^{-2}$  of interface; hence the surface area of the electrode material is critical.<sup>[51–53]</sup> Supercapacitors based on high surface area carbon electrodes, such as carbon nanotube mats, are of this type.

Redox pseudo-capacitance, on the other hand, involves the storage of charge via the reversible oxidation and reduction of an electrode material. Redox switching is accompanied by the transfer of charge-balancing counterions between the electrolyte and the solid electrode. In this case, charge is stored within the bulk of each redox-active electrode, not just at the interface with the electrolyte.<sup>[54]</sup> Conducting polymer and transition metal oxide-based supercapacitors employ this charge storage mechanism. The comparative performance of supercapacitors based on high surface area carbons, conducting polymers, and transition metal oxides is shown in Table 1.

### Carbon Nanotube Supercapacitors

High surface area carbon electrochemical double-layer capacitors generally exhibit an excellent response time, cycle life, specific power, and stability. Because the capacitance of these devices is related to the amount of available electrode surface area, there has been extensive research aimed at increasing the surface area of carbon electrodes for double-layer capacitors. From this work, several techniques have been reported on the use of additives such as metals and metal oxides,<sup>[50]</sup> the

pyrolysis of carbon-based polymers,<sup>[58]</sup> and the production of carbon foam, paste, and nanotube electrodes.<sup>[74,75]</sup> The molecular dimensions and high aspect ratio of carbon nanotubes in particular enable them to form exceptionally high surface area structures.<sup>[76]</sup>

It has been widely observed that carbon micropores less than 2 nm in size have detrimental effects on the kinetics and amount of charge stored by carbon-based capacitors.<sup>[77]</sup> This limitation arises because the pore dimensions approach that of the double-layer thereby inhibiting double-layer formation.<sup>[74]</sup> In addition to their extremely high surface areas, carbon nanotube electrodes typically exhibit an open structure with pore sizes in excess of 2 nm.<sup>[77]</sup> This is particularly advantageous for the electrolyte accessibility of carbon nanotubes relative to other high surface area carbon electrode materials, such as activated carbon black, which generally possess a significant portion of pores smaller than 2 nm. As a result, carbon nanotube supercapacitors are frequently capable of a greater capacitance, specific energy, specific power, and response time relative to other carbon structures used in double-layer supercapacitors.<sup>[56]</sup>

### Conducting Polymer Supercapacitors

Conducting polymer supercapacitors utilize their reversible redox states to store and deliver charge. While other redox pseudo-capacitors, such as those based on transition metal oxides such as ruthenium oxide, may have higher specific capacitances by mass, conducting polymer supercapacitors generally have comparatively superior rates of response, specific power capabilities, and operating voltages.<sup>[50,78–82]</sup> Conducting polymers are also more amenable to use in complex shapes and lower in cost relative to ruthenium oxide-based supercapacitors.<sup>[83]</sup>

The majority of the promising conducting polymer supercapacitors currently being investigated are based on polypyrrole,<sup>[84]</sup> polyaniline,<sup>[85]</sup> poly(3-phenylthiophene),<sup>[86–88]</sup> and poly(3-methylthiophene).<sup>[61]</sup> While these conducting polymers are generally used in liquid electrolytes, it is possible to employ polymer and gel electrolytes to create solid-state capacitors. It should be noted, however, that the response time

**Table 1** Relative performance of modern supercapacitor materials

Material	Maximum capacitance ( $\text{F g}^{-1}$ )	Maximum capacitance ( $\text{mF cm}^{-2}$ )	Power ( $\text{kW kg}^{-1}$ )	Energy ( $\text{Wh kg}^{-1}$ )	Max voltage (V)
High area carbons <sup>[50–60]</sup>	180	173	20	7	3
Conducting polymers <sup>[17,61–68]</sup>	268	600	11	42	3
Ruthenium oxides <sup>[48,69–73]</sup>	840	500	0.5	27	1



and specific capacitance of solid-state supercapacitors are generally inferior to those obtained when using a liquid electrolyte.<sup>[89]</sup>

## CARBON NANOTUBE-CONDUCTING POLYMER COMPOSITE SUPERCAPACITORS

### Fundamental Findings

While the capacitance and specific energy of supercapacitors far exceed that of conventional capacitors, the charge storage mechanisms of supercapacitors generally result in a rate of charge and discharge that is several orders of magnitude slower than many commercially available conventional capacitors. For example, it can take redox supercapacitors tens of seconds to accumulate and deliver charge, whereas many commercial ceramic and polymer dielectric capacitors can charge and discharge in a matter of nanoseconds. To improve supercapacitor kinetics and specific power, it is essential that the combined resistivity of the matrix and electrolyte be minimized. In the case of redox supercapacitors, it is also important to select a redox reaction that has a large exchange current density.<sup>[1]</sup>

Double-layer capacitors have a natural advantage in terms of capacitance kinetics as their charge storage mechanism does not involve the slower ion intercalation and deintercalation processes observed in redox pseudo-capacitors. In fact, carbon-based double-layer capacitors have been produced that can accept and deliver charge in a period of microseconds.<sup>[57]</sup> In addition, modern double-layer capacitors generally exhibit cycle lives in excess of  $10^5$  cycles and good stability,<sup>[74]</sup> typically surpassing that of redox pseudo-capacitive systems. On the other hand, the three-dimensional adsorption process found in redox pseudo-capacitors enables much higher values of specific energy storage and greater voltage consistency during delivery than is found in processes that are limited to the electrode surface such as double-layer capacitance.<sup>[1]</sup> Supercapacitors based on composites of high surface area carbon nanotubes (a double-layer capacitive material) and a conducting polymer (a redox pseudo-capacitive material) can, to a large extent, bridge the gap between fast capacitor kinetics and substantial energy storage.

To date, investigations into the supercapacitive properties of carbon nanotube-conducting polymer composites have been based on samples made by chemically or electrochemically polymerizing either polypyrrole,<sup>[5,14,22,90]</sup> polyaniline,<sup>[17,91]</sup> or poly(3-methylthiophene)<sup>[26,92]</sup> in the presence of SWNTs or MWNTs. These first studies already indicate that carbon nanotube-conducting polymer composites are capable of specific capacitances per mass and

geometric electrode area as high as  $265 \text{ F g}^{-1}$ <sup>[90]</sup> and  $2.6 \text{ F cm}^{-2}$ ,<sup>[14]</sup> respectively. These reported values are already significantly higher than that of the pure polymer or carbon nanotubes used in each case. It has also been shown that carbon nanotube-conducting polymer composite films are capable of charge and discharge rates that are approximately an order of magnitude faster than similarly prepared and tested samples of the relevant conducting polymer.<sup>[5]</sup>

As the available reports on carbon nanotube-conducting polymer composite supercapacitors were compiled by various researchers, using a range of sample conformations and an assortment of test conditions, it is difficult to compare the relative merits of each composite system. Indeed, even the process of measuring capacitance can be accomplished using a range of techniques including cyclic voltammetry, electrochemical impedance spectroscopy, and charge-discharge analysis—each of which has its own merits, which are too exhaustive to discuss here. However, the collective data available for carbon nanotube-conducting polymer composite supercapacitors do indicate some fundamental deductions that can be applied generally across the range of composite systems studied.

The first of these deductions is the importance of using nanotubes that are able to form a connected three-dimensional network that promotes efficient charge transfer within the composite without inhibiting electrolyte access (i.e., avoids pore sizes  $< 2 \text{ nm}$ <sup>[77]</sup>). It is also advantageous to maximize the surface area of conducting polymer exposed to the electrolyte, thereby optimizing the redox-pseudocapacitive contribution of the conducting polymer. For this reason, it is desirable to obtain a thin, uniform, and continuous coating of conducting polymer over each of the carbon nanotubes. Composite growth techniques in which the carbon nanotubes and conducting polymer are deposited simultaneously have an advantage in this respect relative to techniques that make use of a carbon nanotube preform; polymer deposition onto carbon nanotube preforms, particularly those in which the nanotubes are randomly oriented, can be limited by pore blocking and uneven distribution of the conducting polymer. It has also been reported that electrochemical growth techniques are able to produce a more homogeneous polymer coating with less aggregation than observed for composite synthesis routes that make use of chemical polymerization.<sup>[22]</sup>

Recent work has shown that if MWNTs are acid treated (resulting in the attachment of hydroxyl, carbonyl, and carboxylic functional groups to the tube surface) prior to electrochemical synthesis of MWNT–polypyrrole composite films, the MWNTs are able to partially dope the conducting polymer.<sup>[93]</sup> As mentioned earlier, this eliminates the need for a supporting

electrolyte during film growth. However, the use of functionalized carbon nanotubes also benefits the supercapacitive behavior of the composites produced as will be discussed in the following section.

### Carbon Nanotube Doping of the Conducting Polymer

Fig. 4 shows scanning electron microscopy images of MWNT–polypyrrole composite films made using different concentrations of functionalized MWNTs.<sup>[28]</sup>

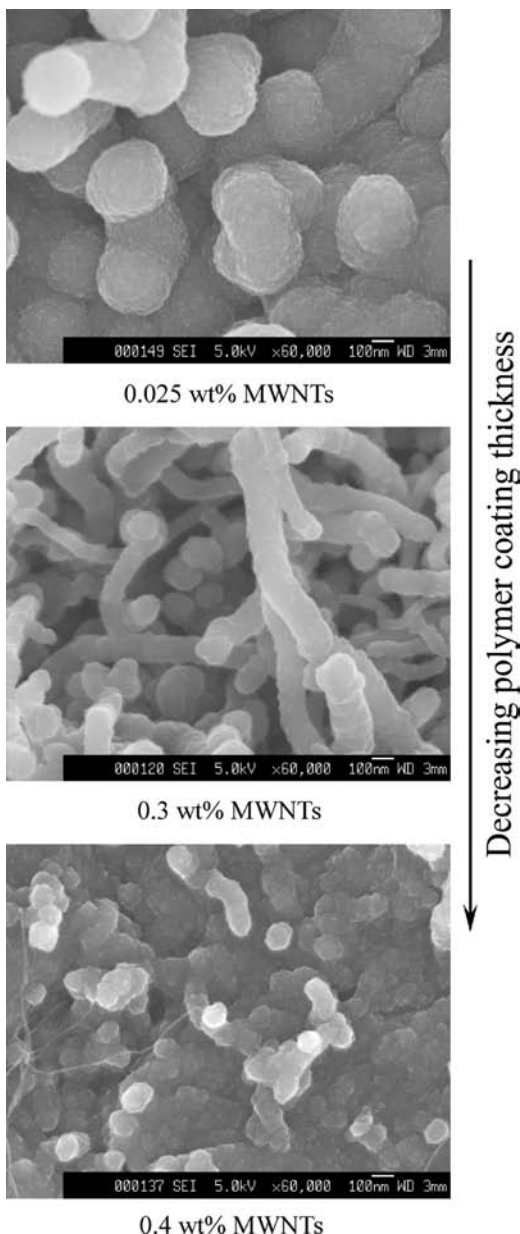


**Fig. 4** Scanning electron microscopy images of MWNT–polypyrrole composite films made using polymerization electrolytes containing the indicated concentrations of functionalized MWNTs. *Source:* From Ref.<sup>[28]</sup>.

It can be seen that as the concentration of functionalized MWNTs in the polymerization electrolyte is increased from 0.025 to 0.4 wt.%, the polypyrrole coating thickness on each MWNT decreases, thereby increasing the loading fraction of MWNTs in the composite. For comparison, it is also possible to electrochemically grow MWNT–polypyrrole composite films using pristine (not functionalized) aligned arrays of MWNTs. In this case, the loading fraction of aligned MWNTs can be raised by simply using longer MWNTs with the same amount of deposited conducting polymer.<sup>[14]</sup> The length of the aligned MWNT array can be varied, while keeping the nanotube diameter and packing density approximately constant, via manipulation of the reaction parameters used to synthesize the MWNTs.<sup>[94]</sup>

Fig. 5 shows the specific capacitance vs. film-formation charge (a measure of the amount of polymer deposited) for MWNT–polypyrrole composite films made using functionalized MWNTs and aligned MWNT arrays that were not functionalized. In both cases, the capacitance of similarly prepared pure polypyrrole films (chloride ion doped) is shown for comparison. For the pure polypyrrole samples, it can be seen that as the amount of polymer deposited increased (as indicated by the film-formation charge), the proportion of total polymer that contributed to the measured capacitance decreased. This restriction arises from the limited electronic and ionic conductivity in the conducting polymer. Such limitations are alleviated in the composite films by the high surface area conductive MWNT network that gives rise to reduced diffusion distances, improved electrolyte access, and superior electronic conductivity. As a result, it is possible to deposit significantly more conducting polymer in the composite films without a marked deterioration in the proportion of polymer contributing to the measured capacitance.

It can be seen in Fig. 5A that as the loading fraction of functionalized MWNTs is increased, via an increase in the concentration of MWNTs in the polymerization electrolyte, the specific capacitance also increases for a given film-formation charge. On the contrary, as the loading fraction of aligned MWNTs (not functionalized) is increased by using longer MWNTs, the specific capacitance is not significantly effected for a given film-formation charge (Fig. 5B). Although there are factors to be considered such as the difference in diameter, length, conductivity, and distribution of the functionalized MWNTs relative to the pristine aligned MWNTs, it would appear that such primarily kinetic influences are insufficient to fully account for this difference in behavior. Instead, the increased level of doping provided by the functionalized MWNTs with increasing loading fraction is thought to be linked with the increase in capacitance for a given film-formation

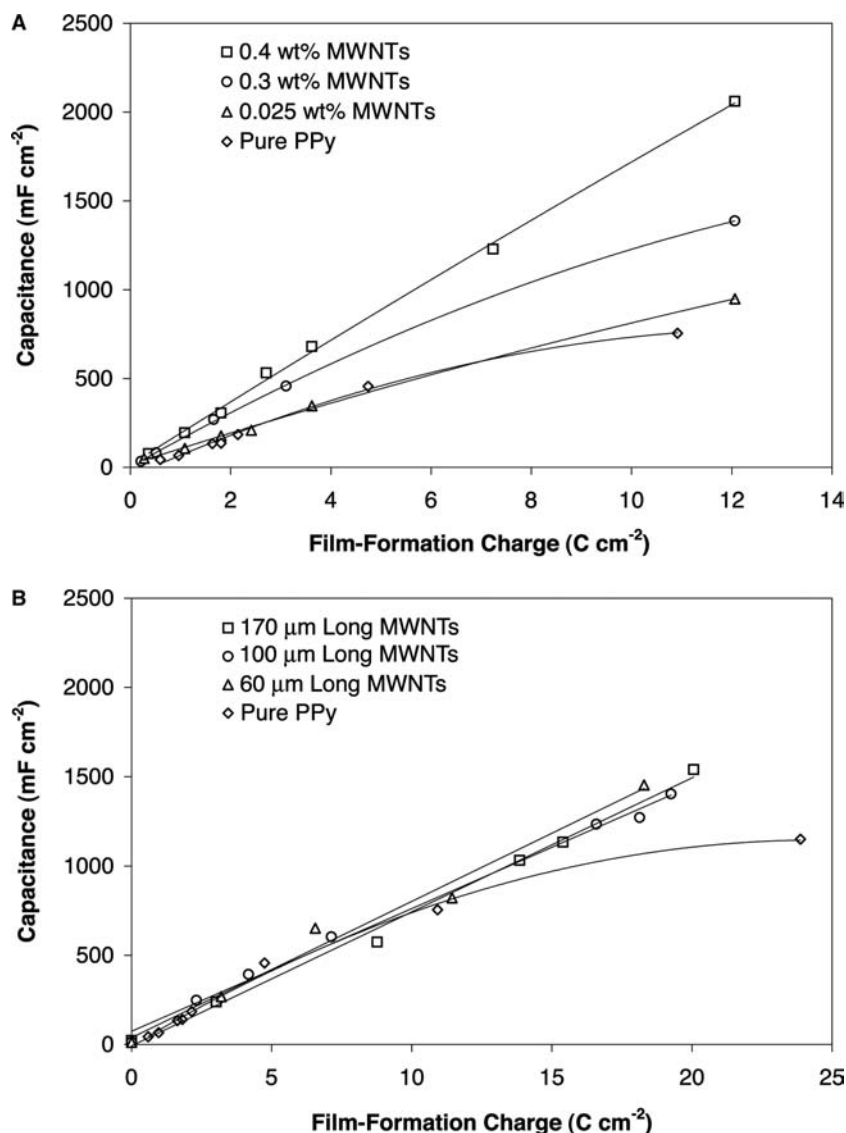


**Fig. 5** The specific capacitance vs. film-formation charge (a measure of the amount of polymer deposited) for MWNT-polypyrrole composite films made using (A) functionalized MWNTs of various concentrations and (B) pristine (not functionalized) aligned MWNT arrays of various lengths. Source: From Ref.<sup>[28]</sup>.

charge. This is an important finding because it indicates that the role of carbon nanotubes can be extended beyond that of a high surface area conductive substrate in carbon nanotube-conducting polymer films. By adopting the additional role of macromolecular dopant, carbon nanotubes can facilitate even greater performance benefits in carbon nanotube-conducting polymer composite supercapacitors.

The doping of conducting polymers with functionalized MWNTs is still under investigation, although there does appear to be some similarities with doping using anions that are relatively immobile within the conducting polymer, such as dodecyl sulphate ions.<sup>[93]</sup> However, large anions such as dodecyl sulphate do not contribute to the formation of a high surface area conductive network as functionalized MWNTs can. Accordingly, dodecyl sulphate-doped polypyrrole does not offer the large capacitances of MWNT-polypyrrole composite films. For the samples shown in Fig. 4, it is

possible to calculate the theoretical maximum thickness of polypyrrole that could be doped by the negatively charged surface groups along the MWNT surface (2.4 meg g<sup>-1</sup>).<sup>[95]</sup> Such calculation yields a polypyrrole coating thickness of approximately 8 nm (assuming there are four pyrrole units per negative surface charge<sup>[96,97]</sup>). This result implies that only a fraction of the deposited polypyrrole is actually in the oxidized state during film-growth when functionalized MWNTs are the only source of dopant anions added to the polymerization electrolyte. Therefore the functionalized MWNTs allow the continuous electrochemical growth of polypyrrole, as does a more conventional anionic dopant, which would otherwise cease due to the insulating nature of unoxidized polypyrrole. However, the mechanism by which this occurs seems to be the formation of a conductive network comprising the MWNTs and adjacent layer of doped polypyrrole, rather than the incorporation of sufficient anionic

dopant to ensure comprehensive oxidation of the polypyrrole.

It is interesting to note the effect of competing dopant anions when growing carbon nanotube-conducting polymer composites using functionalized MWNTs. Adding additional sources of dopant anions to the polymerization electrolyte, such as dodecyl sulphate ions, makes it possible for polypyrrole to grow in areas further displaced from the functionalized MWNT surfaces. Consequently, the porosity of the composite structures produced is significantly reduced.<sup>[28]</sup> In the case of dodecyl sulphate ions, the reduction in film porosity was sufficient to produce a surface morphology quite similar to that observed for pure polypyrrole (Fig. 6). The reduced porosity of composite films grown with dodecyl sulphate additions

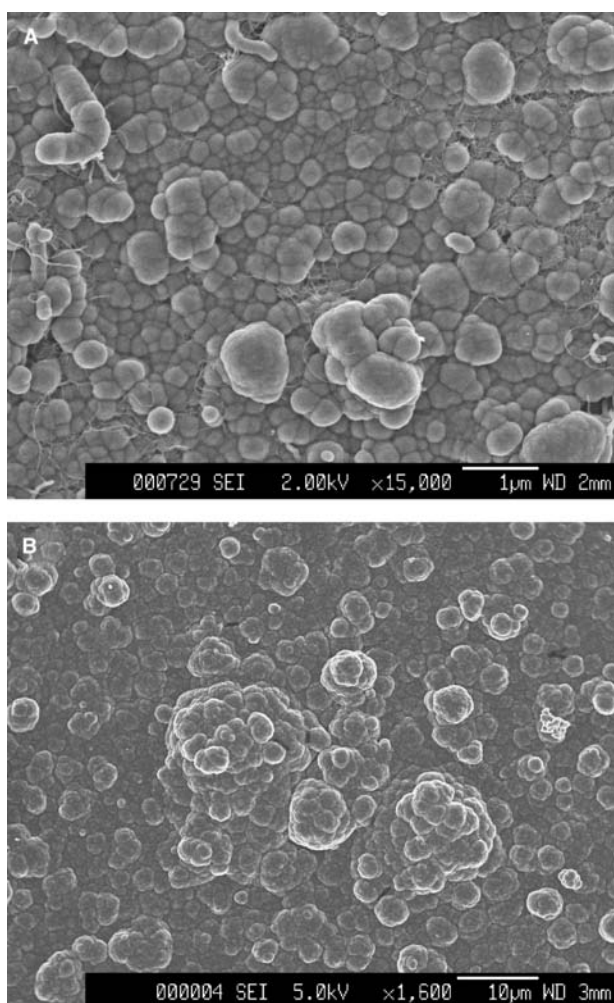


**Fig. 6** Scanning electron microscopy images of (A) a MWNT–polypyrrole composite film made using a polymerization electrolyte containing 0.4 wt.% functionalized MWNTs, 0.01 M sodium dodecyl sulphate, and 0.5 M pyrrole; and (B) a pure polypyrrole film made using a polymerization electrolyte containing 0.5 M KCl and 0.5 M pyrrole. Source: From Ref.<sup>[28]</sup>.

is likely to be associated with a decrease in the loading fraction of functionalized MWNTs. These structural changes were accompanied by a sizable decline in capacitance and rate of response relative to composite films grown without competing dopant anions. This finding provides further indication of the importance of the three-dimensional network of nanopores and loading fraction of functionalized MWNTs in carbon nanotube-conducting polymer composites for supercapacitors.

### Prototype Devices

The work described above has primarily aimed at characterizing the charge storage properties of carbon nanotube-conducting polymer composites. Of the carbon nanotube-conducting polymer composite systems investigated to date, those based on polypyrrole have received the widest attention because of the charge storage capabilities, ease of polymerization, relative stability, and processing flexibility of this particular conducting polymer system. While polypyrrole is capable of existing in an oxidized (p-doped) and neutral state, displaying excellent redox properties between these two states, it is unable to redox cycle beyond the neutral state into a truly reduced form (n-doped). While this limitation does not prevent the characterization of charge storage in polypyrrole-based composites, it does inhibit the use of such composites in real supercapacitor devices where it is desirable for one of the two electrodes in the capacitor to be oxidized while the other is reduced during charging. In this case, polypyrrole-based films are ideally only suited to use in the oxidized electrode of supercapacitors.

Several other conducting polymers, such as poly(3-methylthiophene), are capable of being oxidized (p-doped) or reduced (n-doped) from the neutral state and have also been shown to possess excellent charge storage properties.<sup>[6,7,83,98,99]</sup> Carbon nanotube-conducting polymer composites based on such polymers can be used effectively in both electrodes of a supercapacitor. For this reason, current work aimed at developing prototype carbon nanotube-conducting polymer composite supercapacitors is looking closely at the choice of conducting polymer for each of the electrodes within the supercapacitor device. For example, it is possible to produce symmetric supercapacitors based entirely on, say, carbon nanotube-poly(3-methylthiophene) composites, or unsymmetric supercapacitors with, say, a carbon nanotube-poly(3-methylthiophene) composite as the reduced electrode and a carbon nanotube-polypyrrole composite as the oxidized electrode. It is also possible to produce hybrid supercapacitors that combine a carbon nanotube-conducting polymer composite electrode with a simple

carbon nanotube electrode. However, recent work indicates that such hybrid supercapacitors are outperformed by those based on a suitable combination of carbon nanotube-conducting polymer composites.<sup>[92]</sup>

It is recognized that the properties of conducting polymers can deteriorate significantly with prolonged potential cycling, which is of concern for many supercapacitor applications. The cycle life limitations of conducting polymers are often attributed to progressive assimilation of free space by the polymer chains.<sup>[96,100]</sup> This free space is required by the counterions that diffuse in and out of the polymer during potential cycling, hence its assimilation by the polymer chains limits the degree of doping possible for each successive cycle. Cycle life testing on prototype MWNT-polypyrrole composite films indicates that, for as many as 10,000 cycles, the capacitance dropped by less than 36%.<sup>[25,101]</sup> This is a substantial improvement relative to similarly prepared pure polypyrrole films in which capacitance dropped by 95% over 10,000 cycles. It is thought that the rigid nanotubes in carbon nanotube-conducting polymer composites inhibit the expansion and contraction of the composite, thereby limiting progressive compaction with potential cycling. In this way, the deleterious effect of potential cycling on the incorporation of counterions is reduced. The network of nanopores maintained in carbon nanotube-conducting polymer composites also helps to ensure effective electrolyte access over the full potential cycle.

## CONCLUSION

Nanoporous carbon nanotube-conducting polymer composites are able to effectively combine the high surface area electrically conductive network of carbon nanotubes with the three-dimensional charge storage capabilities of redox-active conducting polymers. This combination of properties is particularly advantageous for supercapacitors, which need to be able to store and deliver relatively large amounts of electrical energy in high power pulses. Recent work has shown carbon nanotube-conducting polymer composites to exhibit specific capacitances per mass and geometric electrode area as high as  $265 \text{ F g}^{-1}$ <sup>[90]</sup> and  $2.6 \text{ F cm}^{-2}$ ,<sup>[14]</sup> respectively. These values are already significantly higher than that of the pure polymer or carbon nanotubes used in each case and there is still much room for further optimization. Manipulation of the various composite synthesis techniques available—particularly those producing films in which the nanotubes are able to dope the conducting polymer—is expected to provide many opportunities to build on the exceptional findings discussed in this entry.

## REFERENCES

- Huggins, R.A. Supercapacitors. *Philos. Trans. R. Soc. Lond. Ser. A: Math. Phys. Eng. Sci.* **1996**, *354* (1712), 1555.
- Faggioli, E.; Rena, P.; Danel, V.; Andrieu, X.; Mallant, R.; Kahlen, H. Supercapacitors for the energy management of electric vehicles. *J. Power Sources* **1999**, *84* (2), 261.
- Liu, C.Y.; Bard, A.J.; Wudl, F.; Weitz, I.; Heath, J.R. Electrochemical characterization of films of single-walled carbon nanotubes and their possible application in supercapacitors. *Electrochem. Solid-State Lett.* **1999**, *2* (11), 577.
- Kalaji, M.; Murphy, P.J.; Williams, G.O. The study of conducting polymers for use as redox supercapacitors. *Synth. Met.* **1999**, *102* (1–3), 1360.
- Hughes, M.; Chen, G.Z.; Shaffer, M.S.P.; Fray, D.J.; Windle, A.H. Electrochemical capacitance of a nanoporous composite of carbon nanotubes and polypyrrole. *Chem. Mater.* **2002**, *14* (4), 1610.
- Mastragostino, M.; Paraventi, R.; Zanelli, A. Supercapacitors based on composite polymer electrodes. *J. Electrochem. Soc.* **2000**, *147* (9), 3167.
- Di Fabio, A.; Giorgi, A.; Mastragostino, M.; Soavi, F. Carbon-poly(3-methylthiophene) hybrid supercapacitors. *J. Electrochem. Soc.* **2001**, *148* (8), A845.
- Sandler, J.K.W.; Kirk, J.E.; Kinloch, I.A.; Shaffer, M.S.P.; Windle, A.H. Ultra-low electrical percolation threshold in carbon-nanotube-epoxy composites. *Polymer* **2003**, *44* (19), 5893.
- Fan, J.H.; Wan, M.X.; Zhu, D.B.; Chang, B.H.; Pan, Z.W.; Xe, S.S. Synthesis, characterizations, and physical properties of carbon nanotubes coated by conducting polypyrrole. *J. Appl. Polym. Sci.* **1999**, *74* (11), 2605.
- Chang, B.H.; Liu, Z.Q.; Sun, L.F.; Tang, D.S.; Zhou, W.Y.; Wang, G.; Qian, L.X.; Xie, S.S.; Fen, J.H.; Wan, M.X. Conductivity and magnetic susceptibility of nanotube/polypyrrole nanocomposites. *J. Low Temp. Phys.* **2000**, *119* (1–2), 41.
- Tang, B.Z.; Xu, H.Y. Preparation, alignment, and optical properties of soluble poly(phenylacetylene)-wrapped carbon nanotubes. *Macromolecules* **1999**, *32* (8), 2569.
- Cochet, M.; Maser, W.K.; Benito, A.M.; Callejas, M.A.; Martinez, M.T.; Benoit, J.M.; Schreiber, J.; Chauvet, O. Synthesis of a new polyaniline/nanotube composite: “In-situ” polymerisation and charge transfer through site-selective interaction. *Chem. Commun.* **2001**, (16), 1450.
- Chen, G.Z.; Shaffer, M.S.P.; Coleby, D.; Dixon, G.; Zhou, W.Z.; Fray, D.J.; Windle, A.H. Carbon nanotube and polypyrrole composites: Coating and doping. *Adv. Mater.* **2000**, *12* (7), 522.
- Hughes, M.; Shaffer, M.S.P.; Renouf, A.C.; Singh, C.; Chen, G.Z.; Fray, J.; Windle, A.H. Electrochemical capacitance of nanocomposite films formed by coating aligned arrays of carbon nanotubes with polypyrrole. *Adv. Mater.* **2002**, *14* (5), 382.

15. Gao, M.; Huang, S.M.; Dai, L.M.; Wallace, G.; Gao, R.P.; Wang, Z.L. Aligned coaxial nanowires of carbon nanotubes sheathed with conducting polymers. *Angew. Chem., Int. Ed.* **2000**, *39* (20), 3664.
16. Chen, J.H.; Huang, Z.P.; Wang, D.Z.; Yang, S.X.; Wen, J.G.; Ren, Z.R. Electrochemical synthesis of polypyrrole/carbon nanotube nanoscale composites using well-aligned carbon nanotube arrays. *Appl. Phys., A Mater. Sci. Process.* **2001**, *73* (2), 129.
17. Downs, C.; Nugent, J.; Ajayan, P.M.; Duquette, D.J.; Santhanam, S.V. Efficient polymerization of aniline at carbon nanotube electrodes. *Adv. Mater.* **1999**, *11* (12), 1028.
18. Coleman, J.N.; Curran, S.; Dalton, A.B.; Davey, A.P.; McCarthy, B.; Blau, W.; Barklie, R.C. Percolation-dominated conductivity in a conjugated-polymer-carbon-nanotube composite. *Phys. Rev., B Condens. Matter* **1998**, *58* (12), R7492.
19. Curran, S.A.; Ajayan, P.M.; Blau, W.J.; Carroll, D.L.; Coleman, J.N.; Dalton, A.B.; Davey, A.P.; Drury, A.; McCarthy, B.; Maier, S.; Strevens, A. A composite from poly(*m*-phenylenevinylene-co-2,5-dioctoxy-*p*-phenylenevinylene) and carbon nanotubes: A novel material for molecular optoelectronics. *Adv. Mater.* **1998**, *10* (14), 1091.
20. Yoshino, K.; Kajii, H.; Araki, H.; Sonoda, T.; Take, H.; Lee, S. Electrical and optical properties of conducting polymer–fullerene and conducting polymer–carbon nanotube composites. *Fuller. Sci. Technol.* **1999**, *7* (4), 695.
21. Fan, J.H.; Wan, M.X.; Zhu, D.B.; Chang, B.H.; Pan, Z.W.; Xie, S.S. Synthesis and properties of carbon nanotube–polypyrrole composites. *Synth. Met.* **1999**, *102* (1–3), 1266.
22. Jurewicz, K.; Delpeux, S.; Bertagna, V.; Beguin, F.; Frackowiak, E. Supercapacitors from nanotubes/polypyrrole composites. *Chem. Phys. Lett.* **2001**, *347*, 36.
23. Chen, J.H.; Huang, Z.P.; Wang, D.Z.; Yang, S.X.; Li, W.Z.; Wen, J.G.; Ren, Z.F. Electrochemical synthesis of polypyrrole films over each of well-aligned carbon nanotubes. *Synth. Met.* **2001**, *125* (3), 289.
24. Hassanien, A.; Gao, M.; Tokumoto, M.; Dai, L. Scanning tunneling microscopy of aligned coaxial nanowires of polyaniline passivated carbon nanotubes. *Chem. Phys. Lett.* **2001**, *342* (5–6), 479.
25. Hughes, M. *Composites of Carbon Nanotubes and Conducting Polymers*; University of Cambridge: Cambridge, UK, 2002.
26. Hughes, M.; Chen, G.Z.; Shaffer, M.S.P.; Fray, D.J.; Windle, A.H. The Effect of Nanotube Loading and Dispersion on the Three-Dimensional Nanostructure of Carbon Nanotube–Conducting Polymer Composite Films. In *Proceedings of the MRS Fall Meeting*; MRS: Boston, MA, USA, 2002; Vol. 739, H5.3.1–H5.3.6.
27. Snook, A.G.; Chen, G.Z.; Fray, D.J.; Hughes, M.; Shaffer, M.S.P. Studies of deposition of and charge storage in polypyrrole–chloride and polypyrrole–carbon nanotube composites by electrochemical quartz crystal microbalance measurements. *J. Electroanal. Chem.*, submitted.
28. Hughes, M.; Chen, G.Z.; Shaffer, M.S.P.; Fray, D.J.; Windle, A.H. Doping and Electrochemical Capacitance of Carbon Nanotube–Polypyrrole Composite Films. In *Proceedings of the MRS Fall Meeting*; MRS: Boston, MA, USA, 2001; Vol. 703, 553–558.
29. Musa, I.; Baxendale, M.; Amaratunga, G.A.J.; Eccleston, W. Properties of regioregular poly(3-octylthiophene)/multi-wall carbon nanotube composites. *Synth. Met.* **1999**, *102* (1–3), 1250.
30. Ago, H.; Petritsch, K.; Shaffer, M.S.P.; Windle, A.H.; Friend, R.H. Composites of carbon nanotubes and conjugated polymers for photovoltaic devices. *Adv. Mater.* **1999**, *11* (15), 1281.
31. Ago, H.; Shaffer, M.S.P.; Ginger, D.S.; Windle, A.H.; Friend, R.H. Electronic interaction between photoexcited poly(*p*-phenylene vinylene) and carbon nanotubes. *Phys. Rev., B* **2000**, *61* (3), 2286.
32. Sene, C.; Cong, H.N.; Chartier, P. Effect of the structural and electronic changes induced in poly(3-methylthiophene), PMeT, by the monomer concentration on the characteristics of sprayed CdS(Al)-PMeT based photovoltaic junctions. *J. Mater. Sci., Mater. Electron.* **1997**, *8* (2), 85.
33. Zotti, G. Electrochemical sensors based on poly-conjugated conducting polymers. *Synth. Met.* **1992**, *51* (1–3), 373.
34. Nguyen, T.A.; Kokot, S.; Ongarato, D.M.; Wallace, G.G. The use of cyclic voltammetry and principal component analysis for the rapid evaluation of selectivity of conductive polymer sensors. *Electroanalysis* **2000**, *12* (2), 89.
35. Granstrom, M.; Berggren, M.; Inganas, O. Micrometer-sized and nanometer-sized polymeric light-emitting-diodes. *Science* **1995**, *267* (5203), 1479.
36. Dai, L.M.; Winkler, B.; Dong, L.M.; Tong, L.; Mau, A.W.H. Conjugated polymers for light-emitting applications. *Adv. Mater.* **2001**, *13* (12–13), 915.
37. Baughman, R.H. Conducting polymer artificial muscles. *Synth. Met.* **1996**, *78* (3), 339.
38. Pei, Q.B.; Inganas, O. Conjugated polymers and the bending cantilever method—Electrical muscles and smart devices. *Adv. Mater.* **1992**, *4* (4), 277.
39. Coleman, J.N.; Curran, S.; Dalton, A.B.; Davey, A.P.; McCarthy, B.; Blau, W.; Barklie, R.C. Physical doping of a conjugated polymer with carbon nanotubes. *Synth. Met.* **1999**, *102* (1–3), 1174.
40. Wagner, H.D.; Lourie, O.; Feldman, Y.; Tenne, R. Stress-induced fragmentation of multiwall carbon nanotubes in a polymer matrix. *Appl. Phys. Lett.* **1998**, *72* (2), 188.
41. Biercuk, M.J.; Llaguno, M.C.; Radosavljevic, M.; Hyun, J.K.; Johnson, A.T.; Fischer, J.E. Carbon nanotube composites for thermal management. *Appl. Phys. Lett.* **2002**, *80* (15), 2767.
42. Romero, D.B.; Carrard, M.; DeHeer, W.; Zuppiroli, L. A carbon nanotube organic semiconducting polymer heterojunction. *Adv. Mater.* **1996**, *8* (11), 899.
43. Dalton, A.B.; Byrne, H.J.; Coleman, J.N.; Curran, S.; Davey, A.P.; McCarthy, B.; Blau, W. Optical absorption and fluorescence of a multi-walled nanotube–polymer composite. *Synth. Met.* **1999**, *102* (1–3), 1176.



44. Spinks, G.; Wallace, G.; Carter, C.; Zhou, D.; Fifield, L.; Kincaid, C.; Baughman, R. Conducting Polymer, Carbon Nanotube and Hybrid Actuator Materials. In *Proceedings of the International Society for Optical Engineering*; SPIE: Newport Beach, CA, USA, 2001; Vol. 4329, 199–208.
45. Kumar, K. Ceramic capacitors: An overview. *Electron. Inf. Plann.* **1998**, *25* (11), 559.
46. Kumar, K. Plastic film capacitors (PFCs): A status report. *Electron. Inf. Plann.* **1996**, *23* (10), 545.
47. Fricke, J.; Emmerling, A. Aerogels—Recent progress in production techniques and novel applications. *J. Sol-Gel Sci. Technol.* **1998**, *13* (1–3), 299.
48. Long, J.W.; Swider, K.E.; Merzbacher, C.I.; Rolison, D.R. Voltammetric characterization of ruthenium oxide-based aerogels and other RuO<sub>2</sub> solids: The nature of capacitance in nanostructured materials. *Langmuir* **1999**, *15* (3), 780.
49. Jones, R.E.; Maniar, P.D.; Moazzami, R.; Zurcher, P.; Witowski, J.Z.; Lii, Y.T.; Chu, P.; Gillespie, S.J. Ferroelectric non-volatile memories for low-voltage, low-power applications. *Thin Solid Films* **1995**, *270* (1–2), 584.
50. Sarangapani, S.; Tilak, B.V.; Chen, C.P. Materials for electrochemical capacitors—Theoretical and experimental constraints. *J. Electrochem. Soc.* **1996**, *143* (11), 3791.
51. Kotz, R.; Carlen, M. Principles and applications of electrochemical capacitors. *Electrochim. Acta* **2000**, *45* (15–16), 2483.
52. Conway, B. Origin and Significance of ‘Redox Supercapacitance’ and Its Manifestation at Various Inorganic Materials. In *Proceedings of the Symposium on New Sealed Rechargeable Batteries and Supercapacitors*; The Electrochemical Society: Honolulu, HI, USA, 1993; Vol. 15.
53. Conway, B.E. Transition from supercapacitor to battery behavior in electrochemical energy-storage. *J. Electrochem. Soc.* **1991**, *138* (6), 1539.
54. Laforgue, A.; Simon, P.; Fauvarque, J.F.; Sarrau, J.F.; Lailier, P. Hybrid supercapacitors based on activated carbons and conducting polymers. *J. Electrochem. Soc.* **2001**, *148* (10), A1130.
55. Sawai, K.; Ohzuku, T. A method of impedance spectroscopy for predicting the dynamic behavior of electrochemical system and its application to a high-area carbon electrode. *J. Electrochem. Soc.* **1997**, *144* (3), 988.
56. Niu, C.M.; Sichel, E.K.; Hoch, R.; Moy, D.; Tennent, H. High power electrochemical capacitors based on carbon nanotube electrodes. *Appl. Phys. Lett.* **1997**, *70* (11), 1480.
57. Mund, K.; Richter, G.; Weidlich, E.; Fahlstrom, U. Electrochemical properties of platinum, glassy-carbon, and pyrographite as stimulating electrodes. *Pace-Pacing Clin. Electrophysiol.* **1986**, *9* (6), 1225.
58. Rossier, J.S.; Girault, H.H. Nanocrystalline carbon film electrodes generated and patterned by UV-laser ablation of polystyrene. *Phys. Chem., Chem. Phys.* **1999**, *1* (15), 3647.
59. An, K.H.; Kim, W.S.; Park, Y.S.; Choi, Y.C.; Lee, S.M.; Chung, D.C.; Bae, D.J.; Lim, S.C.; Lee, Y.H. Supercapacitors using single-walled carbon nanotube electrodes. *Adv. Mater.* **2001**, *13* (7), 497.
60. An, K.H.; Kim, W.S.; Park, Y.S.; Moon, J.M.; Bae, D.J.; Lim, S.C.; Lee, Y.S.; Lee, Y.H. Electrochemical properties of high-power supercapacitors using single-walled carbon nanotube electrodes. *Adv. Funct. Mater.* **2001**, *11* (5), 387.
61. Mastragostino, M.; Arbizzani, C.; Paraventi, R.; Zanelli, A. Polymer selection and cell design for electric-vehicle supercapacitors. *J. Electrochem. Soc.* **2000**, *147* (2), 407.
62. Fusalba, F.; Belanger, D. Electropolymerization of polypyrrole and polyaniline–polypyrrole from organic acidic medium. *J. Phys. Chem., B* **1999**, *103* (42), 9044.
63. Carlberg, J.C.; Inganas, O. Poly(3,4-ethylenedioxythiophene) as electrode material in electrochemical capacitors. *J. Electrochem. Soc.* **1997**, *144* (4), L61.
64. Ghosh, S.; Inganas, O. Conducting polymer hydrogels as 3D electrodes: Applications for supercapacitors. *Adv. Mater.* **1999**, *11* (14), 1214.
65. Gurunathan, K.; Murugan, A.V.; Marimuthu, R.; Mulik, U.P.; Amalnerkar, D.P. Electrochemically synthesised conducting polymeric materials for applications towards technology in electronics, optoelectronics and energy storage devices. *Mater. Chem. Phys.* **1999**, *61* (3), 173.
66. Fusalba, F.; Elmehdi, N.; Breau, L.; Belanger, D. Physicochemical and electrochemical characterization of polycyclopenta[2,1-b;3,4-b']dithiophen-4-one as an active electrode for electrochemical supercapacitors. *Chem. Mater.* **1999**, *11* (10), 2743.
67. Soudan, P.; Ho, H.A.; Breau, L.; Belanger, D. Chemical synthesis and electrochemical properties of poly(cyano-substituted-diheteroareneethylene) as conducting polymers for electrochemical supercapacitors. *J. Electrochem. Soc.* **2001**, *148* (7), A775.
68. Hu, C.C.; Lin, X.X. Ideally capacitive behavior and X-ray photoelectron spectroscopy characterization of polypyrrole—Effects of polymerization temperatures and thickness/coverage. *J. Electrochem. Soc.* **2002**, *149* (8), A1049.
69. Zheng, J.P.; Jow, T.R. A new charge storage mechanism for electrochemical capacitors. *J. Electrochem. Soc.* **1995**, *142* (1), L6.
70. Cimino, A.; Carra, S. *Electrodes of Conductive Metallic Oxides—Part A*; Trasatti, S., Ed.; Elsevier: New York, NY, USA, 1980; 97 pp.
71. Zheng, J.P.; Cygan, P.J.; Jow, T.R. Hydrous ruthenium oxide as an electrode material for electrochemical capacitors. *J. Electrochem. Soc.* **1995**, *142* (8), 2699.
72. Jeong, Y.U.; Manthiram, A. Amorphous ruthenium–chromium oxides for electrochemical capacitors. *Electrochem. Solid-State Lett.* **2000**, *3* (5), 205.
73. Miousse, D.; Lasia, A. Hydrogen evolution reaction on RuO<sub>2</sub> electrodes in alkaline solutions. *J. New Mater. Electrochem. Syst.* **1999**, *2* (1), 71.
74. Mayer, S.T.; Pekala, R.W.; Kaschmitter, J.L. The aerocapacitor—An electrochemical double-layer energy-storage device. *J. Electrochem. Soc.* **1993**, *140* (2), 446.

75. Ma, R.Z.; Liang, J.; Wei, B.Q.; Zhang, B.; Xu, C.L.; Wu, D.H. Processing and performance of electric double-layer capacitors with block-type carbon nanotube electrodes. *Bull. Chem. Soc. Jpn.* **1999**, *72* (11), 2563.
76. Britto, P.J.; Santhanam, K.S.V.; Rubio, A.; Alonso, J.A.; Ajayan, P.M. Improved charge transfer at carbon nanotube electrodes. *Adv. Mater.* **1999**, *11* (2), 154.
77. Diederich, L.; Barborini, E.; Piseri, P.; Podesta, A.; Milani, P.; Schneuwly, A.; Gallay, R. Supercapacitors based on nanostructured carbon electrodes grown by cluster-beam deposition. *Appl. Phys. Lett.* **1999**, *75* (17), 2662.
78. Killian, J.G.; Gofer, Y.; Sarker, H.; Poehler, T.O.; Searson, P.C. Electrochemical synthesis and characterization of a series of fluoro-substituted phenylene-2-thienyl polymers. *Chem. Mater.* **1999**, *11* (4), 1075.
79. Miller, J.M.; Dunn, B. Morphology and electrochemistry of ruthenium/carbon aerogel nanostructures. *Langmuir* **1999**, *15* (3), 799.
80. Zheng, J.P. Ruthenium oxide-carbon composite electrodes for electrochemical capacitors. *Electrochem. Solid-State Lett.* **1999**, *2* (8), 359.
81. Lin, C.; Ritter, J.A.; Popov, B.N. Development of carbon–metal oxide supercapacitors from sol–gel derived carbon–ruthenium xerogels. *J. Electrochem. Soc.* **1999**, *146* (9), 3155.
82. Ma, R.Z.; Wei, B.Q.; Xu, C.L.; Liang, J.; Wu, D.H. The development of carbon nanotubes/RuO<sub>2</sub>·xH<sub>2</sub>O electrodes for electrochemical capacitors. *Bull. Chem. Soc. Jpn.* **2000**, *73* (8), 1813.
83. Arbizzani, C.; Mastragostino, M.; Meneghello, L. Polymer-based redox supercapacitors: A comparative study. *Electrochim. Acta* **1996**, *41* (1), 21.
84. Otero, T.F.; Cantero, I. Statistical design to optimize specific charges in polypyrrole by electrosynthesis. *J. Electrochem. Soc.* **1999**, *146* (11), 4118.
85. Barsukov, V.; Chivikov, S. The “capacitor” concept of the current-producing process mechanism in polyaniline-type conducting polymers. *Electrochim. Acta* **1996**, *41* (11–12), 1773.
86. Ferraris, J.P.; Eissa, M.M.; Brotherston, I.D.; Loveday, D.C.; Moxey, A.A. Preparation and electrochemical evaluation of poly(3-phenylthiophene) derivatives: Potential materials for electrochemical capacitors. *J. Electroanal. Chem.* **1998**, *459* (1), 57.
87. Laforgue, A.; Simon, P.; Sarrazin, C.; Fauvarque, J.F. Polythiophene-based supercapacitors. *J. Power Sources* **1999**, *80* (1–2), 142.
88. Laforgue, A.; Simon, P.; Fauvarque, J.F. Chemical synthesis and characterization of fluorinated polyphenylthiophenes: Application to energy storage. *Synth. Met.* **2001**, *123* (2), 311.
89. Hashmi, S.A.; Latham, R.J.; Linford, R.G.; Schlindwein, W.S. Conducting polymer-based electrochemical redox supercapacitors using proton and lithium ion conducting polymer electrolytes. *Polym. Int.* **1998**, *47* (1), 28.
90. An, K.H.; Jeon, K.K.; Heo, J.K.; Lim, S.C.; Bae, D.J.; Lee, Y.H. High-capacitance supercapacitor using a nanocomposite electrode of single-walled carbon nanotube and polypyrrole. *J. Electrochem. Soc.* **2002**, *149* (8), A1058.
91. Frackowiak, E.; Beguin, F. Carbon materials for the electrochemical storage of energy in capacitors. *Carbon* **2001**, *39* (6), 937.
92. Xiao, Q.F.; Zhou, X. The study of multiwalled carbon nanotube deposited with conducting polymer for supercapacitor. *Electrochim. Acta* **2003**, *48* (5), 575.
93. Hughes, M.; Chen, G.Z.; Shaffer, M.S.P.; Fray, D.J.; Windle, A.H. Tailoring the Electrochemical Properties of Carbon Nanotube–Polypyrrole Composite Films for Electrochemical Capacitor Applications. In *Proceedings of the 202nd ECS Meeting*; The Electrochemical Society: Salt Lake City, UT, USA, 2002; Vol. 25, 68–77.
94. Singh, C.; Shaffer, M.; Kinloch, I.; Windle, A. Production of aligned carbon nanotubes by the CVD injection method. *Phys., B Condens. Matter* **2002**, *323* (1–4), 339.
95. Shaffer, M.S.P. *Carbon Nanotubes: Dispersions, Assemblies, and Composites*; University of Cambridge: Cambridge, UK, 1999.
96. Pei, Q.B.; Inganäs, O. Electrochemical applications of the bending beam method: 2. Electroshrinking and slow relaxation in polypyrrole. *J. Phys. Chem.* **1993**, *97* (22), 6034.
97. Vork, F.T.A.; Schuermans, B.; Barendrecht, E. Influence of inserted anions on the properties of polypyrrole. *Electrochim. Acta* **1990**, *35* (2), 567.
98. Mastragostino, M.; Arbizzani, C.; Soavi, F. Polymer-based supercapacitors. *J. Power Sources* **2001**, *97*–8, 812.
99. Mastragostino, M.; Arbizzani, C.; Soavi, F. Conducting polymers as electrode materials in supercapacitors. *Solid State Ionics* **2002**, *148* (3–4), 493.
100. Pei, Q.B.; Inganäs, O. Electrochemical applications of the bending beam method: 1. Mass-transport and volume changes in polypyrrole during redox. *J. Phys. Chem.* **1992**, *96* (25), 10507.
101. Frackowiak, E.; Jurewicz, K.; Szostak, K.; Delpoux, S.; Beguin, F. Nanotubular materials as electrodes for supercapacitors. *Fuel Process. Technol.* **2002**, *77*, 213.

# Carbon Nanotube Electrodes

Valentina Lazarescu

I.G. Murgulescu Institute of Physical Chemistry, Bucharest, Romania

## INTRODUCTION

Carbon nanotubes discovered by Iijima<sup>[1]</sup> in 1991 as a by-product of fullerene synthesis by an arc plasma method have entailed extensive theoretical and experimental work, opening a new and rapidly expanding research field on nanoscale materials. Large-scale production of these particularly interesting materials has become, in the meantime, available in gas phase, either by evaporation of pure carbon using high-power energy sources (e.g., electric arc,<sup>[2]</sup> laser ablation,<sup>[3]</sup> and sunlight<sup>[4]</sup>), or by chemical vapor deposition (CVD) techniques (reviewed in Ref.<sup>[5]</sup>), as well as in molten salts via electrolysis.<sup>[6,7]</sup>

Consisting of one or a few graphite (graphene) sheets rolled up into single-walled or multiwalled cylinder-like structures with lengths in the micrometer scale, carbon nanotubes considerably enlarged the family of carbon nanostructures. Single-wall nanotubes (SWNTs) may self-organize into long crystalline “ropes”<sup>[3]</sup> with diameters of 10–50 nm corresponding to 30–600 tubes per rope. Multiwall nanotubes (MWNTs) consisting of manifold wrapping of a single graphitic sheet (Scroll model), or closed concentric cylinders (Russian doll model) have external diameters of up to 50 nm. However, SWNTs arising from the folding of a single graphene sheet have diameters ( $d$ ) of only 1–2 nm, strictly depending on the way the graphene sheet is wrapped up, which is defined by the chiral vector  $C_h = na_1 + ma_2 \equiv (n,m)$ .<sup>[8]</sup>

$$d = \frac{\sqrt{n^2 + m^2 + nm}}{\pi} a \quad (1)$$

where  $a = \sqrt{3}a_{C-C} = 2.46 \text{ \AA}$  is the length of the unit vector. A large number of *chiral* carbon nanotubes can be formed for arbitrary values of  $n$  and  $m$ . The limit cases are the so-called *armchair* tubes (when  $n = m$ ) and *zigzag* tubes (when  $n = 0$ ), taking into account the atomic configuration along the circumference. These remarkable structural features of carbon nanotubes that were thoroughly investigated by local and global probes (reviewed in Ref.<sup>[9]</sup>) were found to be intimately related with most of their unusual properties: electronic,<sup>[10,11]</sup> electrical,<sup>[12,13]</sup> optical,<sup>[14,15]</sup> and

mechanical properties,<sup>[16,17]</sup> as a direct consequence of their 1-D quantum behavior.<sup>[8,12]</sup>

In terms of electronic properties, it has been initially theoretically predicted<sup>[18–20]</sup> and, subsequently, experimentally proven<sup>[21–24]</sup> that  $(n,m)$  nanotubes have either a small band gap and metallic behavior if they satisfy the  $(n - m) = 3l$  ( $l = 0,1,2,\dots$ ) condition, or a moderate band gap if they do not. Thus carbon nanotubes have the unique property to exhibit conductivity, which can be either metallic or semiconducting depending on  $(n,m)$ . Furthermore, Kociak et al.<sup>[13]</sup> have reported that some ropes of SWNTs prepared by an electrical arc method, with a mixture of nickel and yttrium a catalyst, exhibit even superconducting behavior. The peculiar electronic and electrical properties of these novel molecular scale wires not only make them ideal model systems for 1-D solids physics studies, but have also considerable potential for tailoring new field emission and nanoelectronics devices.<sup>[25–28]</sup> Having high surface area, good chemical stability, and significant mechanical strength, SWNTs and MWNTs proved also to be excellent new electrode materials for a wide range of electrochemical applications (such as: energy, lithium ion and hydrogen storage, sensors, and actuators) reviewed in this paper along with their electrochemical properties.

## ELECTRODES IN ELECTROCHEMICAL CAPACITORS

Carbon nanotube electrodes exhibit usually a featureless cyclic voltammogram (CV) over a rather large potential range in aqueous<sup>[29]</sup> and non-aqueous solutions,<sup>[30–32]</sup> showing a typical double-layer behavior that recommends them from the start as excellent candidates for electrochemical capacitors. The featureless aspect of CV was explained as an overlapping of many closely spaced peaks representing electron transfer into each nanotube,<sup>[29,30]</sup> or as double-layer capacitor bulk carbon-like behavior.<sup>[29]</sup> Although the nanotubes' diameter and chirality distribution are expected to be quite large and to involve consequently a fairly large spectrum of electronic properties,<sup>[10,11]</sup> the hypothesis of the averaged multiple peaks is not consistent with the similar curves observed whatever SWNTs or

MWNTs are involved. The second explanation seems more plausible because the double-layer charging current may exceed, by far, the faradaic current<sup>[29]</sup> as a result of high specific surface area, with the total inside and outside specific surface areas of carbon nanotubes being theoretically estimated at 2630 m<sup>2</sup>/g.<sup>[33]</sup> The latter assumption is also in good agreement with the observation that the increase in the total amount of SWNTs deposited on the Pt electrode produced only higher currents keeping strictly the same shape.<sup>[30]</sup> Broad redox responses shifting positively with increasing pH have been sometimes observed,<sup>[34,35]</sup> and were associated with oxygen-containing functional groups attached to the nanotube surface and/or carbonaceous impurities in the sample.<sup>[32,34,35]</sup>

The current potential profiles of SWNTs were found to be practically insensitive to anion or cation molar mass, ion charge, or ion hydrophobicity<sup>[32,34]</sup> displaying the same capacitive dominating behavior. However, the electrochemical quartz crystal microbalance studies revealed<sup>[31,32]</sup> that the applied potential results in sizeable (on average around 1% of the sample weight) electrode mass changes. Because no relation could be established with cation mass, the mass change at negative potentials has been ascribed to changes in relative anion and cation concentrations caused by double-layer charging.<sup>[31]</sup> The mass increase observed at positive potentials in sulfuric acid has been assigned<sup>[31]</sup> to the electrochemical doping of bisulfate ions into SWNTs revealed by the Raman-active tangential mode frequency upshift.<sup>[36]</sup> By analogy with graphite intercalation compounds, SWNT bundles were supposed to be oxidatively (reductively) intercalated, with the guest ions occupying sites in the interstitial channels of the rope lattice.<sup>[36]</sup> Further in situ Raman<sup>[35,37–39]</sup> and Vis-NIR<sup>[37,40]</sup> studies brought conclusive evidence in this respect, proving that the population of the SWNT valence band electronic states is electrochemically tunable. It has been found that changes in the intensity and frequency of both the main Raman-active tangential displacement mode (TDM) and the radial breathing mode (RBM) are dependent on the applied potential and reversible to a great extent.<sup>[35,37,38]</sup> Such effects have been explained by the resonance enhancement of electronic transitions between the first singularities in the 1-D electronic density of states<sup>[39]</sup> and interpreted as depletion/filling of their valence and conduction bands.<sup>[35,37–39]</sup> Electrochemical charging of SWNTs causes also reversible bleaching of the electronic transitions between Van Hove singularities in the Vis-NIR region,<sup>[37,40]</sup> resulting in filling (electroreduction) and depletion (electrooxidation) of electrons in the corresponding occupied bands. The conduction electron spin resonance measurements on K-doped SWNTs in 1 M KCN in (C<sub>2</sub>H<sub>5</sub>)<sub>3</sub>B/THF electrolyte showed

also a continuous and reversible valence electron transfer from K to SWNT, proving once more that electrochemical doping is a powerful and precise technique to control the electronic properties of carbon nanotubes.<sup>[41]</sup> The possibility of alkali ion (Li<sup>+</sup> particularly) insertion into carbon nanotubes has attracted considerable attention from material scientists for its potential use in lithium secondary batteries as discussed in detail below.

The high ability of carbon nanotubes for accumulation of charges makes them one of the most attractive electrode materials for building capacitors. The values of specific capacitance reported in the literature vary over a wide range from 4<sup>[42]</sup> to 180 F/g,<sup>[43,44]</sup> depending on the type of nanotubes or/and their posttreatments. Niu et al.<sup>[45]</sup> have reported that *free-standing mats* of entangled catalytically grown MWNTs with an open porous structure exhibit a specific capacitance of 104 F/g and a power density of 8 kW/kg in a solution of 38 wt.% H<sub>2</sub>SO<sub>4</sub>. By using binding materials, Ma et al.<sup>[46]</sup> prepared *block-type* carbon nanotube electrodes with a specific capacitance of 90 F/g from similarly produced MWNTs and the same electrolyte. With highly pure SWNTs prepared by the HiPco process (thermocatalytic decomposition of CO under high pressure), Shiraishi et al.<sup>[33]</sup> found a rather low value of specific capacitance (per surface area unit) of only 10 μF/cm<sup>2</sup> in a 1-M LiClO<sub>4</sub>/propylene carbonate solution. However, An et al.<sup>[43,44]</sup> obtained a maximum specific capacitance of 180 F/g and measured a power density of 20 kW/kg with bundles of SWNTs produced by arc discharge after a careful optimization of the key factors controlling functional performance, such as annealing temperature, charging time, and discharging current density. As seen in Fig. 1A, specific capacitance increases with heat treatment temperature, reaching the highest saturated value (180 F/g) and the smallest drop (about 10%) even for large discharging current density (Fig. 1B) at 1000°C. The CV (Fig. 1C) is close to the ideal rectangular shape, and the complex plane impedance plot (Fig. 1D) indicates the lowest electrode resistance (equal to the semicircle diameter) and an almost ideal diffusive line (representing the resistivity of the electrolyte within the electrode pores) for such a high-temperature treated sample. The remarkable effect of high-temperature annealing on electrical capacitance has been attributed to specific surface area increase and enhancement of lower pore size (30–50 Å).<sup>[43,44]</sup> The amount of electrical charge accumulated by pure electrostatic forces depends indeed on the electrode/electrolyte interface dimension and the easy access of charge carriers to it,<sup>[47,48]</sup> both of them being adjustable by proper heating procedures. But the effects of thermal treatment are not always beneficial: SWNTs (Tubes@Rice) were found to decrease

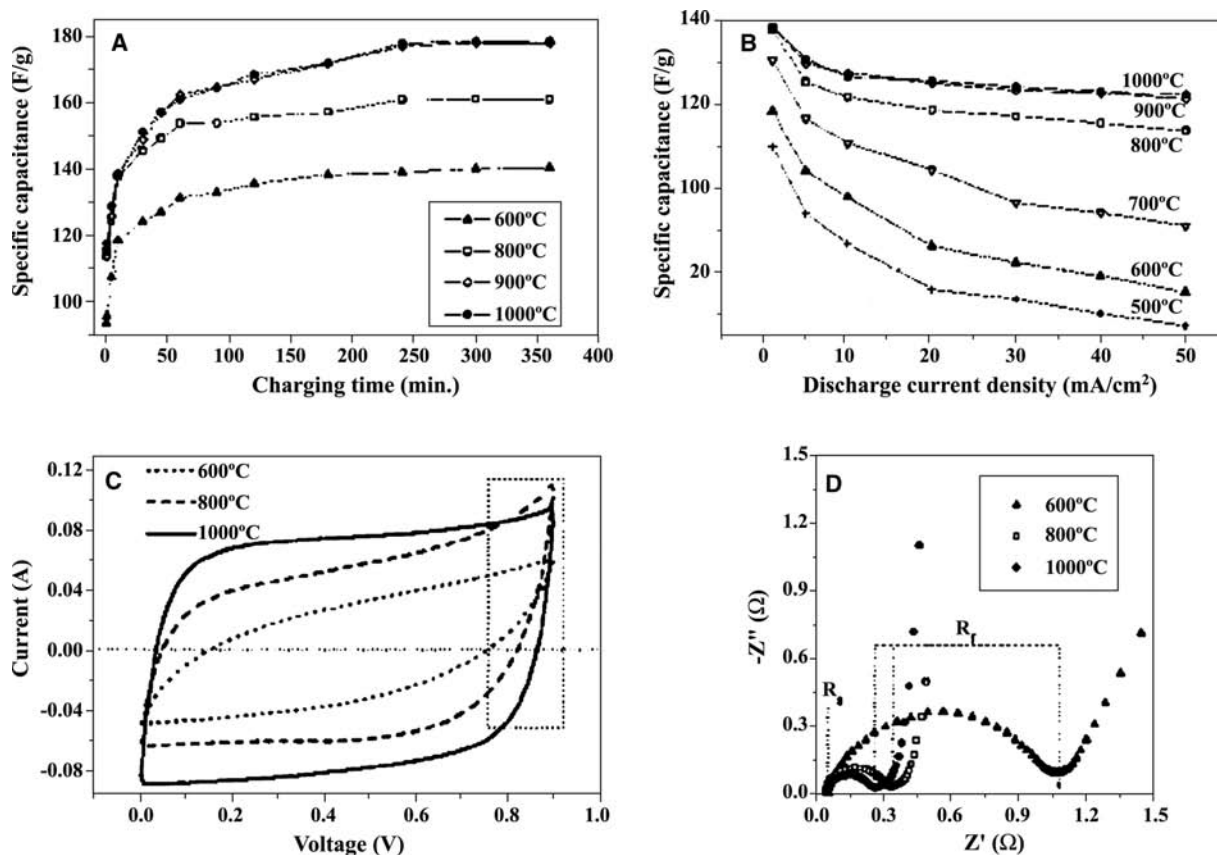


**Fig. 1** Electrochemical properties of a supercapacitor built with SWNT bundles produced by arc discharge. Specific capacitance of electrodes heated at various temperatures as a function of charging time at 0.9 V (A); discharging current density at 0.9 V for 10 min (B); CV taken at 100 mV/sec (C); and complex plane impedance plots taken from 7.5 M KOH at an a.c. voltage amplitude of 5 mV for samples annealed at various temperatures (D) ( $Z''$  = imaginary impedance;  $Z'$  = real impedance). *Source:* From Ref.<sup>[43]</sup>.

their capacitance from 40 to 18 F/g after annealing at 1650°C because of a better arrangement of the tubes in the bundles, hindering ion diffusion toward the active surface.<sup>[48]</sup> However, heating is not the only way to increase capacitance. Electrochemical capacitors known as supercapacitors or ultra-capacitors combine actually two kinds of energy storage: the pure electrostatic attraction of ions in the electrical double layer and pseudo-capacitance faradaic surface reactions.<sup>[47–49]</sup> Therefore a distinct manner to increase capacitance values is the enhancement of pseudo-capacitance effects resulting in fast faradaic charge reactions (e.g., H and metal atoms electrosorption, redox reactions of electroactive species).<sup>[47]</sup> This desiderate has been achieved by various chemical and electrochemical modifications. *Chemical oxidation* has been successfully used (e.g., with 69% HNO<sub>3</sub><sup>[42]</sup> when the specific capacitance increased from 80 to 137 F/g) for opening the nanotubes and expanding surface functionality<sup>[48]</sup> and pore size.<sup>[50]</sup> The *chemical insertion of electroactive particles of transition metal oxides* such as RuO<sub>2</sub> raised the specific capacitance up to 560 F/g.<sup>[51]</sup> The *chemical insertion*

of  *$\pi$ -conjugated conducting polymers* (such as polyaniline<sup>[52]</sup> or polypyrrole<sup>[53–56]</sup>) resulted in specific capacitances as high as 163<sup>[53]</sup> and 192 F/g<sup>[55]</sup> because they can be subsequently further charged by ion insertion.<sup>[53]</sup> Pseudo-capacitance effects were also observed after additional *functionalization* of carbon nanotubes<sup>[54]</sup> that could be electrochemically achieved (e.g., via electrochemical reduction of a variety of aryl diazonium salts).<sup>[57]</sup>

## ANODES IN SECONDARY LITHIUM ION BATTERIES

The electrochemical insertion of alkali ions into carbon nanotubes has attracted much attention not only for the basic interest to control their electronic properties as discussed above, but also for their very promising potential use as anodes in lithium ion rechargeable batteries.

Electrochemical doping with lithium of carbon nanotubes has been largely investigated by galvanostatic

charge–discharge experiments<sup>[58–64]</sup> on Li/carbon nanotube half-cells using organic electrolytes consisting of  $\text{LiClO}_4/\text{LiPF}_6$  dissolved in a mixture of dimethyl carbonate/diethyl carbonate/ethylene carbonate/propylene carbonate. Typically, a large capacity is observed during the first discharge (lithium intercalation) cycle, which considerably decreases in the following ones, as seen in Fig. 2A. The significant hysteresis observed during the extraction of lithium (discharge cycle) is associated with electrolyte decomposition and the formation of a passivate film or solid electrolyte interphase on the carbon surface<sup>[58,61,64]</sup> evidenced by long plateau at about 0.9 V in the first discharge step. Usually, the capacitance of the first<sup>[58,62]</sup> or the second charge<sup>[60]</sup> cycle defines *reversible capacity* (i.e., the amount of intercalated Li that can be deintercalated), whereas the difference between the first discharge and the first charge<sup>[60]</sup> or between the first discharge and the second discharge<sup>[63,65]</sup> denotes *irreversible capacity*. Large irreversible capacity and large voltage hysteresis are limiting factors for using carbon nanotubes for  $\text{Li}^+$  battery applications. Therefore much effort has been invested for understanding the mechanism and for identifying the factors controlling process reversibility to lower these drawbacks.

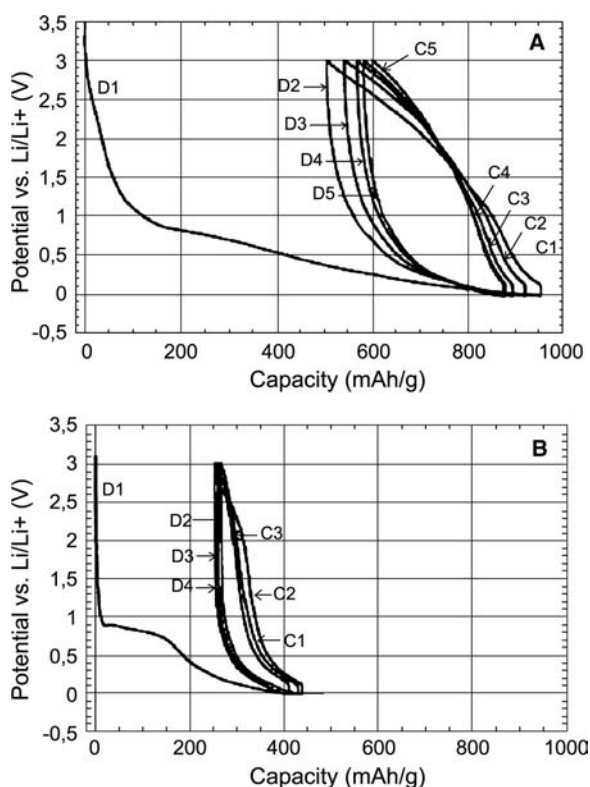


**Fig. 2** Charge–discharge characteristics of lithium insertion into MWNT before (A) and after heat treatment at  $2000^\circ\text{C}$  (B) at a current of  $17\text{ mA/g}$  in  $1\text{ M LiPF}_6$  in ethylene carbonate/diethyl carbonate (1:1) mixture. *Source:* From Ref.<sup>[58]</sup>.

Galvanostatic charge–discharge and cyclic voltameter indicated that there is no well-defined redox potential for lithium insertion or removal in the nanotube lattice, ruling out the hypothesis of a staging mechanism via interstitial sites,<sup>[64]</sup> in good agreement with information inferred from Raman spectra.<sup>[66]</sup> The spectral changes of the Raman  $\text{E}_{2g}$  band centered around  $1580\text{ cm}^{-1}$ , which corresponds to the vibrations of graphene layers adjacent to intercalates, showed that lithium is intercalated between graphene layers of the MWNTs, bringing about an increase in electron density and hence electrical conductivity.<sup>[66]</sup>  $^7\text{Li}$  nuclear magnetic resonance (NMR) spectroscopy<sup>[65]</sup> has also evidenced intercalated Li species residing between graphene shells, whereas in situ resistance measurements showed a 20-fold decrease upon doping, consistent with charge transfer between lithium and carbon.<sup>[64]</sup> The decrease in the electric resistivity of the electrode upon doping has been confirmed by the lowering of charge transfer resistance in electrochemical impedance spectra (EIS), too.<sup>[64,67]</sup> Electrochemical impedance spectra investigations have identified three distinct steps in Li insertion in SWNT: charge transfer across the electrode/electrolyte interface, mesoscale diffusion through the porous structure of SWNTs, and nanoscale diffusion in individual SWNT ropes, suggesting that Li intercalates in the channels between nanotubes, decorating internal and external rope surfaces.<sup>[67]</sup> This is in a good agreement with the in situ X-ray diffraction proof that Li doping induces irreversible structural disorder inside the rope lattice.<sup>[64]</sup>

However, the origin of the high reversible capacity of SWNTs is not clear yet. As long as the inner core space of the SWNTs is not accessible for intercalation because of the closed structure and because  $\text{Li}^+$  is expected to decorate only the outer surface of the nanotubes (analogous to occupying one side of isolated graphene sheets), the saturation capacity should be close to  $\text{LiC}_6$ . However, the purified SWNTs synthesized by laser ablation exhibited reversible capacities of  $460$ <sup>[64]</sup> and  $600\text{ mA hr/g}$ <sup>[63]</sup> corresponding to a saturation composition of  $\text{Li}_{1.2}\text{C}_6$  and  $\text{Li}_{1.6}\text{C}_6$ , respectively, much higher than the ideal value of  $\text{LiC}_6$  ( $372\text{ mA hr/g}$ ) for graphite. Moreover, after processing the nanotubes by mechanical ball milling, the reversible saturation composition became even higher,  $\text{Li}_{2.7}\text{C}_6$  ( $1000\text{ mA hr/g}$ ).<sup>[63]</sup> The latter data point to structural defects (notably increased during mechanical ball milling processing) as key factors in the mechanism of Li reversible insertion, facilitating  $\text{Li}^+$  diffusion into the nanotube.<sup>[63]</sup> A similar conclusion has been drawn from important morphology modifications induced by Li insertion in MWNTs revealed by X-ray diffraction and transmission electron microscopy (TEM).<sup>[65]</sup>

However, there are many other different opinions with respect to the role played by structural defects



in Li insertion. Yang and Wu<sup>[60]</sup> consider that lithium inserted into the inner core of the nanotubes cannot be deintercalated because of capillary force. By performing charge–discharge measurements on closed and opened MWNTs, they found significant differences in irreversible Li capacity and cycling performances (the first one being much higher and the latter being poorer for the opened nanotubes) but the same reversible capacity (125 mA hr/g),<sup>[60,68]</sup> which led them to the conclusion that lithium is reversibly doped only on the outer surfaces of MWNTs. Such a mechanism might be plausible in the case of their low reversible capacity (corresponding to only  $\text{Li}_{0.33}\text{C}_6$ ), but it is quite improbable for the much higher values reported by other groups (e.g. 700<sup>[69]</sup> and 447 mA hr/g<sup>[58]</sup> corresponding to stoichiometries of  $\text{Li}_{1.87}\text{C}_6$  and  $\text{Li}_{1.19}\text{C}_6$ , respectively). Besides, according to data reported by Ishihara et al.<sup>[70]</sup> the reversible Li capacity decreases when the graphitic nanotube surface area increases.

Gao et al.<sup>[63]</sup> found a diminished irreversible Li capacity on increasing structural defects density, but there are many experimental data proving the opposite. High-temperature heating up to 2800°C (Fig. 2B), which certainly improves structural and microtextural organization, considerably reduces the large hysteresis observed during the extraction of lithium from MWNTs, as seen in Fig. 2B.<sup>[58]</sup> Accordingly, Frackowiak et al.<sup>[58]</sup> and Leroux et al.<sup>[59]</sup> considered microstructural irregularities in the tube walls<sup>[58,59]</sup> along with surface-oxygenated groups generated by the oxidative chemical treatment fully responsible for the irreversible Li sorption phenomena. The substantial increase of the irreversible Li storage in the acid-oxidized MWNTs drove Yang, Wu, and Simard<sup>[62]</sup> to presume also that residual acid traces create defects and pores that contribute to a stronger Li bonding.

Li binding near H atoms present in MWNTs prepared by catalytic decomposition of hydrocarbons is an alternative explanation for their large irreversible Li capacities.<sup>[69]</sup> This assumption is based on the <sup>1</sup>H NMR data reported by Ivanov et al.<sup>[71]</sup> which showed that the total H amount (around 2 wt.%) in such samples saturating all free carbon vacancies in  $\text{sp}^3$  defects of the graphitic structure strongly decreases with an increase in reaction temperature. Other authors correlate the irreversible Li intercalation with the large amorphous carbon content identified by TEM investigations<sup>[72]</sup> and in Raman spectra,<sup>[73]</sup> dependent on MWNT synthesis conditions. The strong tendency of MWNTs for charges cumulating as condensers has been also proposed as an explanation for the large irreversible Li capacity<sup>[58]</sup> because the electrostatic attraction of lithium ions and other charged species during Li insertion at negative polarization may hinder the reverse process and involve higher voltage.

## ELECTRODES IN SECONDARY HYDROGEN BATTERY AND FUEL CELLS

The reversible hydrogen capacity of soot containing 0.1–0.2 wt.% SWNTs reported by Dillon et al.<sup>[74]</sup> draws attention to the possibility of hydrogen storage into the large empty space inside carbon nanotubes. They estimated a maximum hydrogen storage capacity of pure SWNTs of 5–10 wt.%, which was subsequently confirmed by experimental data (4.2<sup>[75]</sup> and 8 wt.%<sup>[76]</sup>) obtained at room temperature and modestly high pressure. Such values suggest carbon nanotubes as attractive candidates for secondary hydrogen battery and fuel cells electrodes. Nützenadel et al.<sup>[77]</sup> were the first to investigate the electrochemical hydrogen storage capacity of SWNTs, which are more practical for such applications. They showed that 20% SWNT-containing electrodes can electrochemically store relatively large amounts (110 mA hr/g corresponding to 0.39 wt.%) of hydrogen in half-cells with 6 M KOH electrolyte and Ni as counterelectrode. The electrodes for these electrochemical measurements were usually produced by mixing the nanotube sample with Ni,<sup>[78–80]</sup> but also with Cu,<sup>[77,81]</sup> Au, and Pd<sup>[77]</sup> as compacting powder for their stabilization. However, higher storage capacities have been obtained, such as 316 mA hr/g (1.2 wt.%) with purified and thermally treated SWNTs of large mean diameter (1.85 nm)<sup>[79]</sup> and 800 mA hr/g (2.9 wt.%)<sup>[81]</sup> by increasing the SWNT weight to 80%, respectively.

The experimental and theoretical studies reported by Lee et al.<sup>[78]</sup> brought valuable information on the electrochemical hydrogen storage of carbon nanotubes.<sup>[78]</sup> They found several steps in the hydrogen discharge cycles (Fig. 3A) suggesting the existence of different adsorption sites in good agreement with complex-shaped CV peaks (Fig. 3B). The peak height proportionality (1:1) to the sweep rate<sup>[80]</sup> proves that hydrogen adsorption/desorption controls the whole process. By using a self-consistent charge density functional-based tight-binding calculation formalism, Lee et al.<sup>[78]</sup> identified possible adsorption sites as top sites at the exterior and the interior of the tube wall for *atomic H*, and in the empty spaces inside the SWNTs for *molecular hydrogen*. The Raman spectra taken for hydrogen-charged samples annealed at high temperatures evidenced the existence of H<sub>2</sub> inside the carbon nanotubes and revealed the enlargement of tube diameters because of hydrogen storage.<sup>[78]</sup> Lee et al.<sup>[78]</sup> concluded that SWNTs are better than MWNTs for hydrogen storage because the hydrogen capacity increases linearly with tube diameters only in the first case, and predicted a maximum value of 14.3 wt.%.

Further theoretical calculations<sup>[82]</sup> have shown that C–H bonding changes the electronic properties of

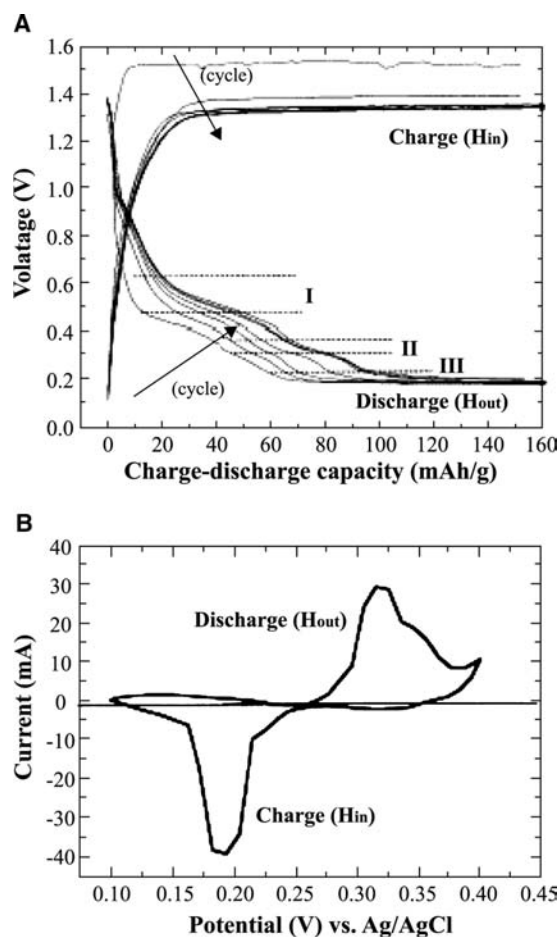


**Fig. 3** Hydrogen charge–discharge curves of SWNT-based electrodes at a constant current of 0.4 mA for the first seven cycles (A) and typical cyclic voltammetric profile measured at 10 mV/sec in 6 M KOH (B). *Source:* From. Ref.<sup>[78]</sup>.

metallic carbon nanotubes to semiconductors, and have suggested that doping or addition of conductive materials may compensate for such undesirable effects. Qin et al.<sup>[80]</sup> found indeed that Ni used not only as compacting powder but also as porous substrate for preparing a 0.15% MWNT electrode exhibited a high discharge capacity (200 mA hr/g) as well as long charge–discharge cycle life. However, the chemical decoration of the carbon nanotubes with metallic Ni particles turned out to be more effective in improving the discharge capacity, to the prejudice of the cycle life, owing to a dramatic increase of the surface reaction resistance.<sup>[83]</sup>

Carbon nanotube electrodes also revealed interesting electrocatalytic properties in the reduction of dissolved oxygen as well as in methanol oxidation, which are important fuel cell reactions.<sup>[84]</sup> Chemical deposition<sup>[84]</sup> or inclusion of Pd, Ag,<sup>[84]</sup> Pt, and Ru<sup>[85,86]</sup> on/into carbon nanotubes has considerably improved such an electrocatalytic activity. As regards

electrochemical metal deposition on carbon nanotubes, it is surprising that only one report<sup>[87]</sup> exists so far despite the fact that a large number of metals and metal compounds have been inserted/deposited into/on carbon nanotubes (Refs.<sup>[88]</sup> and <sup>[89]</sup> and references therein).

## ELECTRODES IN ELECTROCHEMICAL SENSORS AND ACTUATORS

The electrocatalytic properties mentioned above recommend them as possible competitors for promoting electron transfer reactions in other electrochemical systems, too. Therefore it is not surprising that they have been already found active in the electrooxidation of some important biological molecules, proving their potential for biosensing devices. Britto, Santhanam, and Ajayan<sup>[90]</sup> reported the achievement of a high degree of reversibility in the oxidation of dopamine (an important neurotransmitter) on MWNT electrodes without any pretreatment to induce surface activation. The glassy carbon electrode modified with SWNTs manifested a very stable electrochemical behavior in catalyzing the oxidation of 3,4-dihydroxyphenylacetic acid (the metabolite of neurotransmitter dopamine)<sup>[91]</sup> up to a detection limit of  $4 \times 10^{-7}$  M. Considering their nanometer dimensions, such results may be useful for in vivo studies of neurotransmitters. The films of SWNTs functionalized with carboxylic acid groups showed also very stable cyclic voltammetric profiles in buffer solutions and promising electrocatalytic activity in the oxidation of biomolecules such as dopamine, epinephrine, and ascorbic acid.<sup>[92]</sup> The redox proteins cytochrome *c* and azurin, immobilized on/within open<sup>[93]</sup> and oxidized<sup>[94]</sup> MWNTs or DNA-modified MWNTs,<sup>[95]</sup> were found to give reproducible and well-behaved voltammetric responses, too.

Among the exceptional properties of carbon nanotubes, one counts their electrochemical actuator behavior, allowing for the direct conversion of electrical energy to mechanical energy. Discovered by Baughman et al.<sup>[96]</sup> the property of SWNTs of acting like artificial muscles was shown to generate higher stress than natural muscles and higher strains than ferroelectric actuators under physiological environment (e.g., in salt water) and low voltage.<sup>[97]</sup> Consisting of quantum chemical-based expansion because of electrochemical double-layer charging (Fig. 4), the actuation mechanism of SWNT electrodes was also found superior to that of conducting polymer actuators because it does not involve ion intercalation, which limits rate, cycle life, and energy conversion efficiencies.<sup>[96]</sup> Therefore single-walled carbon nanotubes offer interesting perspectives for

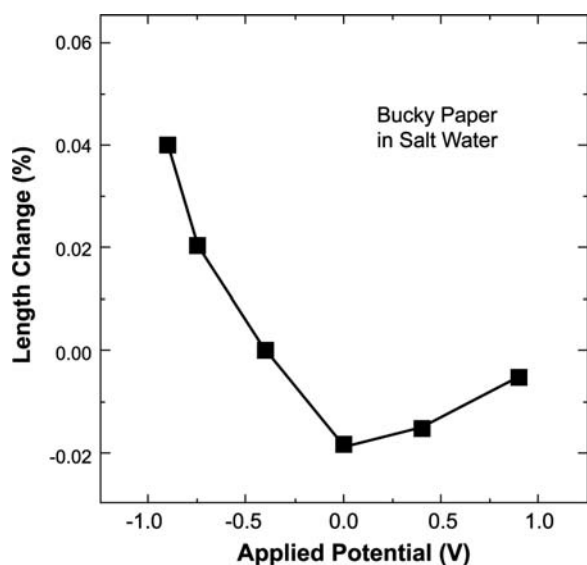


**Fig. 4** Variation of the strain of SWNT (bucky paper) strip vs. applied potential. *Source:* From Ref.<sup>[97]</sup>.

developing high-performance electromechanical transducers required for such diverse needs as robotics, optical fiber switches, or medical prosthetic devices.<sup>[97]</sup>

## CONCLUSION

Discovered in 1991,<sup>[1]</sup> carbon nanotubes unveiled remarkable properties that opened a broad field of possible applications. The electrochemical applications reviewed here propose attractive electrode materials for supercapacitors, secondary lithium and hydrogen batteries, fuel cells, biosensors, and actuators. There are also reports mentioning the possibility of using SWNTs as tips in scanning probe microscopy<sup>[98,99]</sup> and electrochemical NO sensing.<sup>[100]</sup> Many of them require, of course, further research effort to improve performance or to overcome setbacks, but they obviously offer valuable alternative solutions in various technological fields. Therefore carbon nanotube electrodes are expected to remain an inviting subject of study in nanoscience and nanotechnology for many years to come.

## REFERENCES

1. Iijima, S. Helical microtubules of graphitic carbon. *Nature* **1991**, *354*, 56–58.
2. Yumura, M.; Ohshima, S.; Uchida, K.; Tasaka, Y.; Kuriki, Y.; Ikazaki, F.; Saito, Y.; Uemura, S. Synthesis and purification of multi-walled nanotubes for field emitter applications. *Diam. Relat. Mater.* **1999**, *8*, 785–791.

3. Thess, A.; Lee, R.; Nikolaev, P.; Dai, H.J.; Petit, P.; Robert, J.; Xu, C.H.; Lee, Y.H.; Kim, S.G.; Rinzler, A.G.; Colbert, D.T.; Scuseria, G.E.; Tomanek, D.; Fischer, J.E.; Smalley, R.E. Crystalline ropes of metallic carbon nanotubes. *Science* **1996**, *273*, 483–487.
4. Heben, M.J.; Bekkedahl, T.A.; Schulz, D.L.; Jones, K.M.; Dillon, A.C.; Curtis, C.J.; Bingham, C.; Pitts, J.R.; Lewandowski, A.; Fields, C.L. *Production of Single-Wall Carbon Nanotubes Using Concentrated Sunlight*; Electrochemical Society Series; Kadish, K.M., Ed.; Electrochemical Society Inc.: Pennington, 1996; 96 (10), 803–811.
5. Dai, H. Carbon nanotubes: opportunities and challenges. *Surf. Sci.* **2002**, *500*, 218–241.
6. Hsu, W.K.; Terrones, M.; Hare, J.P.; Kroto, H.W.; Walton, D.R.M. Electrolytic formation of carbon nanostructures. *Chem. Phys. Lett.* **1996**, *262*, 161–166.
7. Dimitrov, A.T.; Chen, G.Z.; Kinloch, I.A.; Fray, D.J. A feasibility of scaling-up the electrolytic production of carbon nanotubes in molten salts. *Electrochim. Acta* **2002**, *48*, 91–102.
8. Dresselhaus, M.S.; Dresselhaus, G.; Saito, R. Physics of carbon nanotubes. *Carbon* **1995**, *33*, 883–891.
9. Lambin, Ph.; Loiseau, A.; Culot, C.; Biró, L.P. Structure of carbon nanotubes probed by local and global probes. *Carbon* **2002**, *40*, 1635–1648.
10. Mintmire, J.W.; White, C.T. Electronic and structural properties of carbon nanotubes. *Carbon* **1995**, *33*, 893–902.
11. Knupfer, M. Electronic properties of carbon nanostructures. *Surf. Sci. Rep.* **2001**, *42*, 1–74.
12. Bezryadin, A.; Verschueren, A.R.M.; Tans, S.J.; Dekker, C. Multiprobe transport experiments on individual single-wall carbon nanotubes. *Phys. Rev. Lett.* **1998**, *80* (18), 4036–4039.
13. Kociak, M.; Kasumov, A.Yu.; Guéron, S.; Reulet, B.; Khodos, I.I.; Gorbatov, Yu.B.; Volkov, V.T.; Vaccarini, L.; Bouchiat, H. Superconductivity in ropes of single-walled carbon nanotubes. *Phys. Rev. Lett.* **2001**, *86* (11), 2416–2419.
14. Eklund, P.C.; Holden, J.M.; Jishi, R.A. Vibrational modes of carbon nanotubes—spectroscopy and theory. *Carbon* **1995**, *33*, 959–972.
15. Tasaki, S.; Maekawa, K.; Yamabe, T.  $\pi$ -Band contribution to the optical properties of carbon nanotubes: effects of chirality. *Phys. Rev., B* **1998**, *57* (15), 9301–9318.
16. Hernández, E.; Goze, C.; Bernier, P.; Rubio, A. Elastic properties of C and  $B_xC_yN_z$  composite nanotubes. *Phys. Rev. Lett.* **1998**, *80* (20), 4502–4505.
17. Avouris, Ph.; Hertel, T.; Martel, R.; Schmidt, T.; Shea, H.R.; Walkup, R.E. Carbon nanotubes: nanomechanics, manipulation, and electronic devices. *Appl. Surf. Sci.* **1999**, *141*, 201–209.
18. Mintmire, J.W.; Dunlap, B.I.; White, C.T. Are fullerene tubules metallic? *Phys. Rev. Lett.* **1992**, *68* (5), 631–634.
19. Hamada, N.; Sawada, S.I.; Oshiyama, A. New one-dimensional conductors: graphitic microtubules. *Phys. Rev. Lett.* **1992**, *68* (10), 1579–1581.

20. Saito, R.; Fujita, M.; Dresselhaus, G.; Dresselhaus, M.S. Electronic structure of chiral graphene tubules. *Appl. Phys. Lett.* **1992**, *60* (18), 2204–2206.
21. Issi, J.P.; Langer, L.; Heremans, J.; Olk, C.H. Electronic properties of carbon nanotubes: experimental results. *Carbon* **1995**, *33*, 941–948.
22. Wildoer, J.W.G.; Venema, L.C.; Rinzler, A.G.; Smalley, R.E.; Dekker, C. Electronic structure of atomically resolved carbon nanotubes. *Nature* **1998**, *391*, 59–62.
23. Odom, T.W.; Huang, J.L.; Kim, P.; Lieber, C.M. Structure and electronic properties of carbon nanotubes. *J. Phys. Chem., B* **2000**, *104* (13), 2794–2809.
24. Ouyang, M.; Huang, J.L.; Cheung, C.L.; Lieber, C.M. Energy gaps in metallic single walled carbon nanotubes. *Science* **2001**, *292*, 702–705.
25. De Heer, W.A.; Chatelain, A.; Ugarte, D. A carbon nanotube field-emission electron source. *Science* **1995**, *270*, 1179–1180.
26. Nakayama, Y.; Akita, S. Field-emission device with carbon nanotubes for a flat panel display. *Synth. Met.* **2001**, *117*, 207–210.
27. Tans, S.J.; Verschueren, A.R.M.; Dekker, C. Room-temperature transistor based on a single carbon nanotube. *Nature* **1998**, *393*, 49–52.
28. Rueckes, T.; Kim, K.; Joselevich, E.; Tseng, G.Y.; Cheung, C.L.; Lieber, C.M. Carbon nanotube based nonvolatile random access memory for molecular computing. *Science* **2000**, *289*, 94–97.
29. Chen, J.H.; Li, W.Z.; Wang, D.Z.; Yang, S.X.; Wen, J.G.; Ren, Z.F. Electrochemical characterization of carbon nanotubes as electrode in electrochemical double layer capacitors. *Carbon* **2002**, *40*, 1193–1197.
30. Liu, C.Y.; Bard, A.J.; Wudl, F.; Weitz, I.; Heath, J.R. Electrochemical characterization of films of single-walled carbon nanotubes and their possible application in supercapacitors. *Electrochem. Solid-State Lett.* **1999**, *2* (11), 577–578.
31. Barisci, J.N.; Wallace, G.G.; Baughman, R.H. Electrochemical quartz crystal microbalance studies of single-wall carbon nanotubes in aqueous and non-aqueous solutions. *Electrochim. Acta* **2000**, *46*, 509–517.
32. Barisci, J.N.; Wallace, G.G.; Baughman, R.H. Electrochemical characterization of single-walled carbon nanotube electrodes. *J. Electrochem. Soc.* **2000**, *147* (12), 4580–4583.
33. Shiraishi, S.; Kurihara, H.; Okabe, K.; Hulicova, D.; Oya, A. Electric double layer capacitance of highly pure single-walled carbon nanotubes (HiPco<sup>TM</sup>Buckytubes<sup>TM</sup>) in propylene carbonate electrolytes. *Electrochem. Commun.* **2002**, *4*, 593–598.
34. Barisci, J.N.; Wallace, G.G.; Baughman, R.H. Electrochemical studies of single-wall carbon nanotubes in aqueous solutions. *J. Electroanal. Chem.* **2000**, *488*, 92–98.
35. Kavan, L.; Rapta, P.; Dunsch, L. In situ Raman and Vis–NIR spectroelectrochemistry at single-walled carbon nanotubes. *Chem. Phys. Lett.* **2000**, *328*, 363–368.
36. Sumanasekera, G.U.; Allen, J.L.; Fang, S.L.; Loper, A.L.; Rao, A.M.; Eklund, P.C. Electrochemical oxidation of single wall carbon nanotube bundles in sulfuric acid. *J. Phys. Chem.* **1999**, *103*, 4292–4297.
37. Kavan, L.; Rapta, P.; Dunsch, L.; Bronikowski, M.J.; Willis, P.; Smalley, R.E. Electrochemical tuning of electronic structure of single-walled carbon nanotubes: in-situ Raman and Vis–NIR study. *J. Phys. Chem., B* **2001**, *105*, 10,764–10,771.
38. An, C.P.; Vardeny, Z.V.; Iqbal, Z.; Spinks, G.; Baughman, R.H.; Zakhidov, A. Raman scattering study of electrochemically doped single wall nanotubes. *Synth. Met.* **2001**, *116*, 411–414.
39. Pimenta, M.A.; Marucci, A.; Empedocles, S.A.; Bawendi, M.G.; Hanlon, E.B.; Rao, A.M.; Eklund, R.E.; Smalley, R.E.; Dresselhaus, G.; Dresselhaus, M.S. Raman modes of metallic carbon nanotubes. *Phys. Rev., B* **1998**, *58* (24), R16016–R160119.
40. Kazaoui, S.; Minami, N.; Kataura, H.; Achiba, Y. Absorption spectroscopy of single-wall carbon nanotubes—effects of chemical and electrochemical doping. *Synth. Met.* **2001**, *121*, 1201–1202.
41. Claye, A.S.; Nemes, N.M.; Janossy, A.; Fischer, J.E. Structure and electronic properties of potassium-doped single-wall carbon nanotubes. *Phys. Rev., B* **2000**, *62* (8), R4845–R4848.
42. Frackowiak, E.; Metenier, K.; Bertagna, V.; Beguin, F. Supercapacitor electrodes from multiwalled carbon nanotubes. *Appl. Phys. Lett.* **2000**, *77* (15), 2421–2423.
43. An, K.H.; Kim, W.S.; Park, Y.S.; Choi, Y.C.; Lee, S.M.; Chung, D.C.; Bae, D.J.; Lim, S.C.; Lee, Y.H. Supercapacitors using single-walled carbon nanotube electrodes. *Adv. Mater.* **2001**, *13* (7), 497–500.
44. An, K.H.; Kim, W.S.; Park, Y.S.; Moon, J.M.; Bae, D.J.; Lim, S.C.; Lee, Y.S.; Lee, Y.H. Electrochemical properties of high-power supercapacitors using single-walled carbon nanotube electrodes. *Adv. Funct. Mater.* **2001**, *11* (5), 387–392.
45. Niu, C.M.; Sichel, E.K.; Hoch, R.; Moy, D.; Tennent, H. High power electrochemical capacitors based on carbon nanotube electrodes. *Appl. Phys. Lett.* **1997**, *70* (11), 1480–1482.
46. Ma, R.; Liang, J.; Wei, B.; Zhang, B.; Xu, C.; Wu, D. Processing and performance of electric double-layer capacitors with block-type carbon nanotube electrodes. *Bull. Chem. Soc. Jpn.* **1999**, *72*, 2563–2566.
47. Frackowiak, E.; Beguin, F. Carbon materials for the electrochemical storage of energy in capacitors. *Carbon* **2001**, *39*, 937–950.
48. Frackowiak, E.; Beguin, F. Electrochemical storage of energy in carbon nanotubes and nanostructured carbons. *Carbon* **2002**, *40*, 1775–1787.
49. Conway, B.E. *Electrochemical Supercapacitors—Scientific Fundamentals and Technological Applications*; Kluwer Academic/Plenum: New York, 1999.
50. Ma, R.Z.; Liang, J.; Wei, B.Q.; Zhang, B.; Xu, C.L.; Wu, D.H. Study of electrochemical capacitors utilizing carbon nanotube electrodes. *J. Power Sources* **1999**, *84*, 126–129.
51. Ma, R.Z.; Wei, B.Q.; Xu, C.L.; Liang, J.; Wu, D.H. The development of carbon nanotubes/RuO<sub>2</sub>·xH<sub>2</sub>O

- electrodes for electrochemical capacitors. *Bull. Chem. Soc. Jpn.* **2000**, *73*, 1813–1816.
52. Downs, C.; Nugent, J.; Ajayan, P.M.; Duquette, D.J.; Santhanam, K.S.V. Efficient polymerization of aniline at carbon nanotube electrodes. *Adv. Mater.* **1999**, *11* (12), 1028–1031.
  53. Jurewicz, S.; Delpeux, V.; Bertagna, F.; Béguin, F.; Frackowiak, E. Supercapacitors from nanotubes/polypyrrole composites. *Chem. Phys. Lett.* **2001**, *347*, 36–40.
  54. Frackowiak, E.; Jurewicz, K.; Delpeux, S.; Béguin, F. Nanotubular materials for supercapacitors. *J. Power Sources* **2001**, *97–98*, 822–825.
  55. Hughes, M.; Chen, G.Z.; Shaffer, M.S.P.; Fray, D.J.; Windle, A.H. Electrochemical capacitance of a nanoporous composite of carbon nanotubes and polypyrrole. *Chem. Mater.* **2002**, *14*, 1610–1613.
  56. Chen, J.H.; Huang, Z.P.; Wang, D.Z.; Yang, S.X.; Li, W.Z.; Wen, J.G.; Ren, Z.F. Electrochemical synthesis of polypyrrole films over each of well-aligned carbon nanotubes. *Synth. Met.* **2002**, *125*, 289–294.
  57. Bahr, J.L.; Yang, J.P.; Kosynkin, D.V.; Bronikowski, M.J.; Smalley, R.E.; Tour, J.M. Functionalization of carbon nanotubes by electrochemical reduction of aryl diazonium salts—a bucky paper electrode. *J. Am. Chem. Soc.* **2001**, *123*, 6536–6542.
  58. Frackowiak, E.; Gautier, S.; Gaucher, H.; Bonnamy, S.; Béguin, F. Electrochemical storage of lithium multi-walled carbon nanotubes. *Carbon* **1999**, *37*, 61–69.
  59. Leroux, F.; Méténier, K.; Gautier, S.; Frackowiak, E.; Bonnamy, S.; Béguin, F. Electrochemical insertion of lithium in catalytic multi-walled carbon nanotubes. *J. Power Sources* **1999**, *81–82*, 317–322.
  60. Yang, Z.H.; Wu, H.Q. Electrochemical intercalation of lithium into carbon nanotubes. *Solid State Ionics* **2001**, *143*, 173–180.
  61. Yang, Z.H.; Wu, H.Q. Electrochemical intercalation of lithium into raw carbon nanotubes. *Mater. Chem. Phys.* **2001**, *71*, 7–11.
  62. Yang, Z.H.; Wu, H.Q.; Simard, B. Charge–discharge characteristics of raw acid-oxidized carbon nanotubes. *Electrochem. Commun.* **2002**, *4*, 574–578.
  63. Gao, B.; Kleinhammes, A.; Tang, X.P.; Bower, C.; Fleming, L.; Wu, Y.; Zhou, O. Electrochemical intercalation of single-walled carbon nanotubes with lithium. *Chem. Phys. Lett.* **1999**, *307*, 153–157.
  64. Claye, A.S.; Fischer, J.E.; Huffman, C.B.; Rinzler, A.G.; Smalley, R.E. Solid-state electrochemistry of the Li single wall carbon nanotube system. *J. Electrochem. Soc.* **2000**, *147* (8), 2845–2852.
  65. Maurin, G.; Bousquet, Ch.; Henn, F.; Bernier, P.; Almairac, R.; Simon, B. Electrochemical intercalation of lithium into multiwall carbon nanotubes. *Chem. Phys. Lett.* **1999**, *312*, 14–18.
  66. Maurin, G.; Bousquet, Ch.; Henn, F.; Bernier, P.; Almairac, R.; Simon, B. Electrochemical lithium intercalation into multiwall carbon nanotubes: a micro-Raman study. *Solid State Ionics* **2000**, *136–137*, 1295–1299.
  67. Claye, A.; Fischer, J.E.; Métrot, A. Kinetics of alkali insertion in single wall carbon nanotubes: an electrochemical impedance spectroscopy study. *Chem. Phys. Lett.* **2000**, *330*, 61–67.
  68. Yang, Z.H.; Wu, H.Q. The electrochemical impedance measurements of carbon nanotubes. *Chem. Phys. Lett.* **2001**, *343*, 235–240.
  69. Wu, G.T.; Wang, C.S.; Zhang, X.B.; Yang, H.S.; Qi, Z.F.; Li, W.Z. Lithium insertion into CuO/carbon nanotubes. *J. Power Sources* **1998**, *75*, 175–179.
  70. Ishihara, T.; Fukunaga, A.; Akiyoshi, R.; Yoshio, M.; Takita, Y. Graphitic carbon tube obtained by catalytic decomposition of CH<sub>4</sub> for anode of Li ion rechargeable battery. *Electrochemistry* **2000**, *68*, 38–41.
  71. Ivanov, V.; Fonseca, A.; Nagy, J.B.; Lucas, A.; Lambin, P.; Bernaerts, D.; Zhang, X.B. Catalytic production and purification of nanotubules having fullerene-scale diameters. *Carbon* **1995**, *33*, 873–883.
  72. Sharon, M.; Hsu, W.K.; Kroto, H.W.; Walton, D.R.M.; Kawahara, A.; Ishihara, T.; Takita, Y. Camphor-based carbon nanotubes as an anode in lithium secondary batteries. *J. Power Sources* **2002**, *104*, 148–153.
  73. Ishihara, T.; Kawahara, A.; Nishiguchi, H.; Yoshio, M.; Takita, Y. Effects of synthesis condition of graphitic nanocarbon tube on anodic property of Li-ion rechargeable battery. *J. Power Sources* **2001**, *97–98*, 129–132.
  74. Dillon, A.C.; Jones, K.M.; Bekkedahl, T.A.; Kiang, C.H.; Bethune, D.S.; Heben, M.J. Storage of hydrogen in single-walled carbon nanotubes. *Nature* **1997**, *386*, 377–379.
  75. Liu, C.; Fan, Y.Y.; Liu, M.; Cong, H.T.; Cheng, H.M.; Dresselhaus, M.S. Hydrogen storage in single-walled carbon nanotubes at room temperature. *Science* **1999**, *286*, 1127–1129.
  76. Ye, Y.; Ahn, C.C.; Witham, C.; Fultz, B.; Liu, J.; Rinzler, A.G.; Colbert, D.; Smith, K.A.; Smalley, R.E. Hydrogen adsorption and cohesive energy of single-walled carbon nanotubes. *Appl. Phys. Lett.* **1999**, *74*, 2307–2309.
  77. Nützenadel, C.; Zuttel, A.; Chartouni, D.; Schlapbach, L. Electrochemical storage of hydrogen in nanotube materials. *Electrochem. Solid-State Lett.* **1999**, *2* (1), 30–32.
  78. Lee, S.M.; Park, K.S.; Choi, Y.C.; Park, Y.S.; Bok, J.M.; Bae, D.J.; Nahm, K.S.; Choi, Y.G.; Yu, S.C.; Kim, N.; Fraunheim, T.; Lee, Y.H. Hydrogen adsorption and storage in carbon nanotubes. *Synth. Met.* **2000**, *113*, 209–216.
  79. Dai, G.P.; Liu, M.; Chen, D.M.; Hou, P.X.; Tong, Y.; Cheng, H.M. Electrochemical charge–discharge capacity of purified single-walled carbon nanotubes. *Electrochem. Solid-State Lett.* **2002**, *5* (4), E13–E15.
  80. Qin, X.; Gao, X.P.; Liu, H.; Yuan, H.T.; Yan, D.Y.; Gong, W.L.; Song, D.Y. Electrochemical hydrogen storage of multiwalled carbon nanotubes. *State Lett.* **2000**, *3* (12), 532–535.
  81. Rajalakshmi, N.; Dhathathreyan, K.S.; Govindaraj, A.; Satishkumar, B.C. Electrochemical investigation of single-walled carbon nanotubes for hydrogen storage. *Electrochim. Acta* **2000**, *45*, 4511–4515.

82. Lee, S.M.; An, K.H.; Kim, W.S.; Lee, Y.H.; Park, Y.S.; Seifert, G.; Frauenheim, T. Hydrogen storage in carbon nanotubes. *Synth. Met.* **2001**, *121*, 1189–1190.
83. Gao, X.P.; Lan, Y.; Pan, G.L.; Wu, F.; Qu, J.Q.; Song, D.Y.; Shen, P.W. Electrochemical hydrogen storage by carbon nanotubes decorated with metallic nickel. *Electrochem. Solid-State Lett.* **2001**, *4* (10), A173–A175.
84. Britto, P.J.; Santhanam, K.S.V.; Rubio, A.; Alonso, J.A.; Ajayan, P.M. Improved charge transfer at carbon nanotube electrodes. *Adv. Mater.* **1999**, *11* (2), 54–157.
85. Che, G.; Lakshmi, B.B.; Fisher, E.R.; Martin, C.R. Carbon nanotube membranes for electrochemical energy storage and production. *Nature* **1998**, *393*, 346–349.
86. Che, G.; Lakshmi, B.B.; Martin, C.R.; Fisher, E.R. Metal-nanocluster-filled carbon nanotubes: catalytic properties and possible applications in electrochemical energy storage and production. *Langmuir* **1999**, *15*, 750–758.
87. Dunsch, L.; Janda, P.; Mukhopadhyay, K.; Shinohara, H. Electrochemical metal deposition on carbon nanotubes. *New Diam. Front. Carbon Technol.* **2001**, *11* (6), 427–435.
88. Monthieux, M. Filling single-wall carbon nanotubes. *Carbon* **2002**, *40*, 1809–1823.
89. Duclaux, L. Review of the doping of carbon nanotubes (multiwalled and single-walled). *Carbon* **2002**, *40*, 1751–1764.
90. Britto, P.J.; Santhanam, K.S.V.; Ajayan, P.M. Carbon nanotube electrode for oxidation of dopamine. *Bioelectrochem. Bioenerg.* **1996**, *41*, 121–125.
91. Wang, J.; Li, M.; Shi, Z.; Li, N.; Gu, Z. Electrocatalytic oxidation of 3,4-dihydroxyphenylacetic acid at a glassy carbon electrode modified with single-wall carbon nanotubes. *Electrochim. Acta* **2001**, *47*, 651–657.
92. Luo, H.; Shi, Z.; Li, N.; Gu, Z.; Zhuang, Q. Investigation of the electrochemical and electrocatalytic behavior of single-wall carbon nanotube film on a glassy carbon electrode. *Anal. Chem.* **2001**, *73*, 915–920.
93. Davis, J.J.; Coles, R.J.; Hill, H.A.O. Protein electrochemistry at carbon nanotube electrodes. *J. Electroanal. Chem.* **1997**, *440*, 279–282.
94. Wang, J.X.; Li, M.X.; Shi, Z.J.; Li, N.Q.; Gu, Z.N. Direct electrochemistry of cytochrome-*c* at a glassy-carbon electrode modified with single-wall carbon nanotubes. *Anal. Chem.* **2002**, *74*, 1993–1997.
95. Wang, G.; Xu, J.J.; Chen, H.Y. Interfacing cytochrome *c* to electrodes with a DNA-carbon nanotube composite film. *Electrochem. Commun.* **2002**, *4*, 506–509.
96. Baughman, R.H.; Cui, C.X.; Zakhidov, A.A.; Iqbal, Z.; Barisci, J.N.; Spinks, G.M.; Wallace, G.G.; Mazzoldi, A.; De Rossi, D.; Rinzler, A.G.; Jaschinski, O.; Roth, S.; Kertesz, M. Carbon nanotube actuators. *Science* **1999**, *284*, 1340–1344.
97. Fraysse, J.; Minett, A.I.; Jaschinski, O.; Duesberg, G.S.; Roth, S. Carbon nanotubes acting like actuators. *Carbon* **2002**, *40*, 1735–1739.
98. Dai, H.J.; Hafner, J.H.; Rinzler, A.G.; Colbert, D.T.; Smalley, R.E. Nanotubes as nanoprobe in scanning probe microscopy. *Nature* **1996**, *384*, 147–150.
99. Campbell, J.K.; Sun, L.; Crooks, R.M. Electrochemistry using single carbon nanotubes. *J. Am. Chem. Soc.* **1999**, *121*, 3779–3780.
100. Zhao, G.C.; Wu, F.H.; Wei, X.W. Catalytic activity of multiwalled carbon nanotubes for the oxidation of nitric oxide. *Chem. Lett.* **2002**, 520–521.



# Carbon Nanotube Interconnects

Alain E. Kaloyeros

Kathleen A. Dunn

Autumn T. Carlsen

*College of Nanoscale Science and Engineering, State University of New York at Albany,  
Albany, New York, U.S.A.*

Anna W. Topol

*IBM T.J. Watson Research Center, Yorktown Heights, New York, U.S.A.*

## Abstract

Carbon nanotubes (CNTs) have generated a high level of enthusiasm and interest in the nanoelectronics research community due primarily to their promising electrical conductivity and mechanical performance. In particular, theoretical and modeling studies have indicated that CNTs exhibit ballistic (scatter-less) electron transport properties, with minimal heat generation, along the axis of the tube. These projections have led to a wide range of explorative studies to determine the viability and applicability of CNTs as building blocks of nanoscale devices and signal interconnects in emerging integrated circuitry nodes. Accordingly, the current report is designed to provide a comprehensive review of pertinent features and characteristics of CNT technologies, including a description of synthesis, separation, and alignment techniques, a summary of potential inter-nanotube contacts, junctions, and connections, and an overview of possible pathways for nanotube integration in interconnect architectures for computer chips.

## INTRODUCTION

The historical drive toward higher speed and increased density in emerging generations of integrated circuitry (IC) has caused significant interest in innovative interconnect solutions that exploit the electrical properties of carbon nanotubes (CNTs). This interest is driven primarily by the projected property of “ideal” CNTs to sustain ballistic (scatter-free) electron transport, with little energy dissipation along the tube. Accordingly, nanotubes could provide critical performance enhancements in gigascale interconnect architectures, when compared with traditional electrical wires, thus potentially ensuring the continuation of Moore’s law well into the nanoscale regime.

In this respect, significant progress has been reported over the last few years in the development of CNT networks that display promising properties and performance in nanometer-scale devices and wiring schemes.<sup>[1,2]</sup> However, the potential gains presented by CNT-based wiring schemes have been hindered by practical considerations pertaining to challenges with current CNT fabrication and integration protocols.

Strategies to surmount this challenge can be divided into two broad categories, namely, non-directed and directed. The former involves precise postgrowth manipulation into desired positions, whereas the latter consists of directed assembly at desired locations through controlled synthesis. Both strategies share common issues and challenges. Common challenges include tailoring the electrical properties (metallic vs. semiconductor) of the nanotubes, establishing reliable ohmic contacts between nanotubes and metallic leads, and forming tightly controlled internanotube connections in complex wiring architectures. In addition, directed self-assembly still necessitates a high thermal budget that is prohibitive to integration with Si complementary metal oxide semiconductor (CMOS) technologies.

Accordingly, this entry summarizes achievements to-date, highlights ongoing roadblocks in CNT-based interconnect design and assembly, and presents potential prospects for future innovative solutions. It is divided into the following sections: “Synthesis, Separation, and Alignment” deals with CNT synthesis and alignment challenges, and “Internanotube Contacts, Junctions, and Connections” addresses CNT integration into predesigned and useful architectural schemes.

## BACKGROUND

One primary challenge in the implementation of CNTs into interconnect technologies is the ability to position the nanotubes controllably and reproducibly at pre-specified locations with nanometer-scale precision.

## SYNTHESIS, SEPARATION, AND ALIGNMENT

This section is intended as a brief overview of CNT fabrication techniques because the topic has already been discussed in detail elsewhere.<sup>[1]</sup> As indicated

above, CNT synthesis can be divided into non-directed and directed. The first case requires postgrowth positioning, a method that is time-consuming, highly inefficient, not amenable to scale-up procedures for manufacturing, and inconsistent with prevailing silicon fabrication protocols.

In contrast, directed synthesis of tubes at predetermined locations, basically through direct patterning of the substrate or through predeposition patterning of a solid catalyst on the substrate, offers a significantly higher throughput option. However, these approaches are subject to the same lithographic limitations in shrinking design rules as those faced by conventional interconnects. In addition, because directed synthesis is highly surface-sensitive, nanotube orientation is determined, at least in part, by substrate-controlled growth. Alternatively, postsynthesis manipulation offers user-defined orientation, an advantage that may prove to be useful in advanced device architectures.

### Non-directed Synthesis

Various methods for synthesizing tubes in large quantities have been reported, including arc discharge,<sup>[2–4]</sup> laser ablation,<sup>[5]</sup> and chemical vapor deposition (CVD).<sup>[6–9]</sup> All these approaches require a two-step fabrication process, wherein the nanotubes are grown first, then individually transported to the substrate and manipulated into the desired location. This method is sometimes referred to as “Grow-then-Place” technique. In these methods, undesirable materials such as amorphous carbons, residual catalyst particles, partially formed nanotubes, and even fullerenes are present in the resulting product, which typically consists of graphite-like soot that contains embedded nanotubes. Therefore, fully formed nanotubes must be separated prior to use (Fig. 1). In this respect, synthesis-produced impurities, as well as any carbon overcoat on the tubes, can be removed by oxidation purification, either in an oxygen environment at elevated temperatures,<sup>[2]</sup> or by refluxing nanotubes in a nitric acid solution to oxidize amorphous carbon and metal catalyst particles.<sup>[10]</sup> Unfortunately, these treatments require a high thermal budget (exceeding 3000°C), and are time-consuming and inefficient.

As-grown tubes generally stack into a hexagonal lattice with parallel alignment of individual tube axes. In this form, the bundled tubes, sometimes referred to as a rope, resemble a log pile (Fig. 2). Although these as-grown tube bundles may contain impurities, recent work suggests that the ropes could “clean” themselves as they dry up from the solution, forcing previously enmeshed carbon spherules into an outer shell surrounding an inner core of predominantly

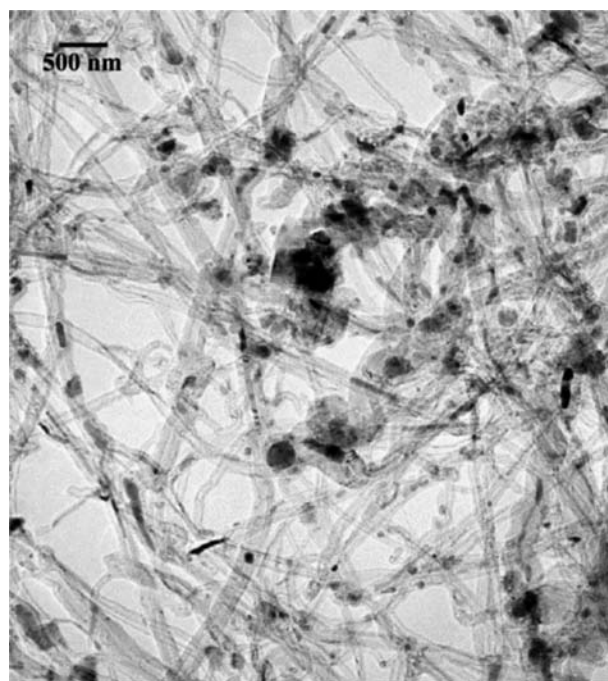


**Fig. 1** Bright field TEM image of CNTs grown by non-directed synthesis. The resulting products of non-directed synthesis techniques typically contain residual catalyst particles, partially formed nanotubes, and undesired carbon-based compounds from which fully formed tubes must be separated prior to utilization.

aligned nanotubes.<sup>[11]</sup> Additional solution chemistry-based techniques have been used to grow ropes that self-assemble into periodic cross-bar structures.<sup>[12]</sup>

CVD growth of nanotubes requires a catalyst in the form of solid particles (primarily transition metals such as Fe or Ni) or gaseous compounds (typically ferrocene), which are introduced into the reactor with the precursor hydrocarbon gas. The possibility of patterning either the solid catalyst or the substrate in the case of gaseous precursor will be discussed “Directed Synthesis.”

Once purified (if necessary), tube bundles may need to be separated to use individual tubes.<sup>[13]</sup> This separation is often accomplished through sonication in a surfactant, such as sodium dodecyl sulfate. The surfactant overcomes the van der Waals attraction between the tubes, allowing dispersion on a surface.<sup>[14]</sup> Alternatively, the intertube attractive force can be overcome through the application of a lateral separation force via use of an atomic force microscope tip.<sup>[15]</sup> Still another route under exploration is chemical derivatization. When attached to nanotube sidewalls, large organic groups block bundle formation by intervening between tubes to overcome van der Waals forces.<sup>[16]</sup> This functionalization process may also prove useful at rendering specific types of tubes more soluble than

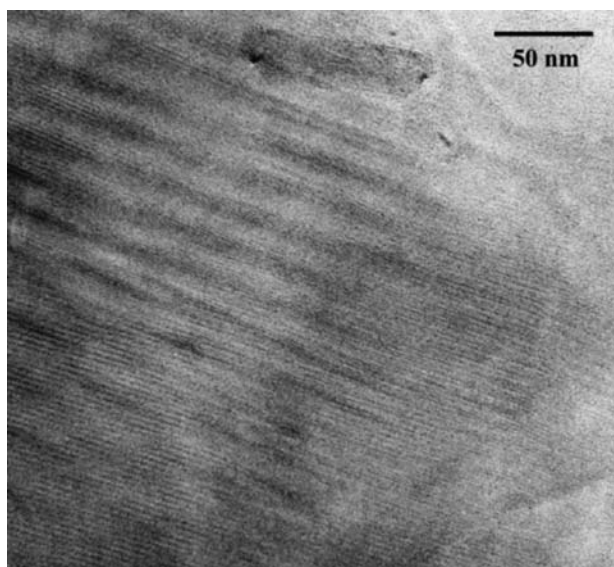


**Fig. 2** Bright field TEM image showing multiple single-walled CNTs aligned in bundles.

others. For example, in a population of nanotubes with varying diameters, certain metal complexes seem to preferentially solubilize smaller-diameter tubes.<sup>[17,18]</sup>

After separation, individual tubes are dispersed on a substrate and then manipulated into place to form the desired circuit elements. A number of techniques have been used to achieve the desired placement of tubes, including mechanical forces, external electric fields, liquid and gas flows, Langmuir–Blodgett films, and self-assembly. Of these, the first three are the most common and most promising methods, and will be discussed in more detail.

The most common method of manipulation is to physically drive a tube across a surface using the tip of a scanning probe microscope (Fig. 3).<sup>[19,20]</sup> Any desired wiring scheme could be formed in this manner. However, controllability of this mechanical process is achieved in this process at the expense of scalability, and it is highly unlikely that this approach will ever

be considered for applications in nanoscale interconnect fabrication schemes.

More recent demonstrations of tube-positioning methods have involved nanotube functionalization, including connecting biological molecules, such as deoxyribonucleic acid (DNA), to the tubes to form more easily manipulated colloidal suspensions.<sup>[21]</sup> The exploitation of DNA recognition properties provides an elegant pathway to control interactions between nanotubes, and to customize engagements with substrate features, such as DNA-labeled electrodes.<sup>[22]</sup> Similar biological molecules offer a variety of chemical handles to enable both selective surface attachment and electrical/optical behavior modification.<sup>[23]</sup>

More importantly, this functionalization approach offers the potential to utilize the ability of DNA to self-assemble into well-organized molecular helical chains from building blocks called peptides. Peptide self-assembly can occur in various forms, including the well-known DNA helix, and flat, laminar arrays called  $\beta$ -sheets. The latter can self-align to form mesoscopic layered structures called lamellae, a process that is controllable, reproducible, and amenable to scaleup on large area substrates.<sup>[24,25]</sup> Thus, the identification of reliable protocols for integration of nanotubes with DNA molecules could eliminate a key obstacle to their incorporation into mainstream Si electronics by exploiting manufacturable DNA self-assembly techniques that are compatible with prevailing silicon fabrication processes.

Another method used in nanotube processing is often referred to as a field-driven method. In the past, dielectrophoresis has been used for manipulating, trapping and separating micro- and nanoparticles. For example, researchers from Rice University used dielectrophoresis to separate SNW tubes according to their size.<sup>[26]</sup> More recently, this technique has been successfully extended to placement of carbon nanotubes.<sup>[27]</sup> More specifically, when a polarizable object is placed in a non-uniform electric field, due to its interaction with the field, it exhibits a translation motion, which

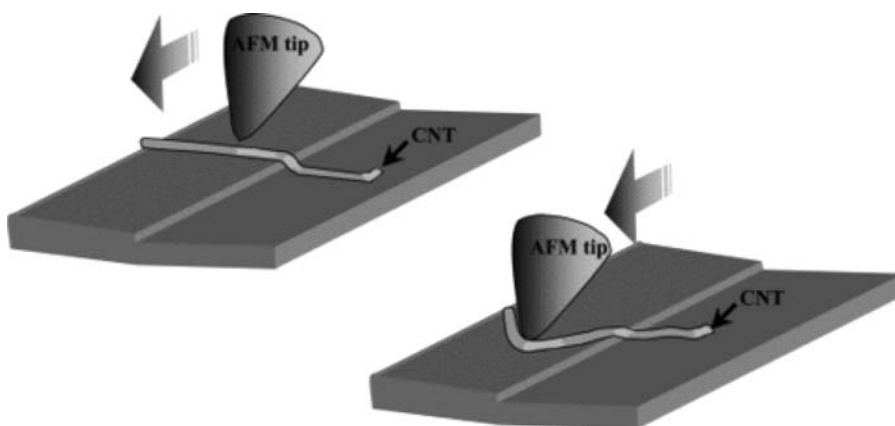


**Fig. 3** Schematic diagram depicting the manipulation of a single CNT by the tip of an atomic force microscope. Although this method allows for precise control of tube placement, it is inherently slow, inefficient, and not amenable to large-volume manufacturing.

forms the basis of dielectrophoretic assembly. In the presence of the field, nanomaterials are attracted in gaps where the gradient of the electric field is maximum or minimum.<sup>[28]</sup>

Assembly of carbon nanotubes has also been achieved recently in what is referred to as a “flow-directed” process, using either a liquid<sup>[29]</sup> or a gas<sup>[30]</sup> to provide the microfluidic force. Such methods rely on the shape anisotropy of the nanotubes in a droplet of solution to enact the alignment. Tubes that are not parallel to the flow will experience a force in proportion to the projected cross-section they present to the direction of flow, and will thus rotate to align with that flow, much the same as logs being transported down a river align with its flow. The degree of alignment, in other words, the distribution of angular orientations can be controlled by a number of experimental parameters such as flow rate and substrate choice. Use of this technique can result in highly aligned collections of nanotubes, although the ability to place of individual tubes, for example between two electrical contacts, is limited. The combination of a flow-based system in a microfluidic channel may be able to overcome this issue, although the fabrication of the channel system would be subject to the same lithography challenges facing conventional interconnects.

## Directed Synthesis

In contrast to non-directed synthesis, directed synthesis could result in the controlled and selective growth of CNTs in a one-step process on predetermined locations on a substrate. This method is often referred to as “Grow-in-Place” technology. Three principal methods have been employed: 1) template-directed synthesis, in which nanopores constrain tube growth locations; 2) solid catalyst-controlled synthesis, in which tube growth occurs exclusively in catalyst-rich locations; and 3) patterned substrate-driven synthesis, in the case of a gaseous catalyst, in which selective growth occurs only on specific surfaces (e.g., on SiO<sub>2</sub>) but not on Si or native oxide. Relevant details of each method are described below, along with respective advantages and disadvantages as pertaining to interconnect applications.

### Template-directed synthesis

Template-directed synthesis uses preexisting nanopores to constrain the growth of nanotubes. The template material (e.g., aluminum oxide) is anodized to form nanopores.<sup>[31,32]</sup> Individual pore diameter and length are controlled by anodization processing parameters, in particular the applied voltage, duration, and chemistry of the solution to which the aluminum oxide is

exposed.<sup>[33,34]</sup> Carbon nanotubes are then synthesized within the pores. In addition to the physical constraint imposed by pore size, tube thickness is controlled by the concentration of reaction gases.<sup>[34]</sup> Because tubes grow in accordance with the structure of the nanopores, variations in template profiles generate associated changes in nanotube shapes, for example, a template consisting of Y-shaped nanoholes to the growth of similarly branched nanotubes, thus resolving a significant issue for nanotubes, namely, the formation of nanotube junctions. However, it should be noted that the resulting resistance of a branched tube is increased—an effect that is attributed to the formation of a heterojunction with local variations in tube diameter.

### Catalyst-controlled synthesis

In systems employing solid catalysts, the directed growth of nanotubes can be controlled through the predeposition patterning of catalyst particles. This approach has been successful in producing aligned CNT structures,<sup>[35–39]</sup> although growth is generally constrained to one dimension (Fig. 4). In a recent demonstration of this concept, a methodology was developed to grow nanotubes in a direction perpendicular to the surface of a patterned catalyst, and then fill the gaps between tubes with silicon dioxide.<sup>[40]</sup> A subsequent chemical-mechanical polishing step removed the surface of the silicon dioxide to expose the tips of the nanotubes. Electrical contacts could then be patterned to engage individual tubes or rows of tubes, depending on the spacing between the tubes as determined by the spacing within the patterned catalyst matrix.

Another recent method places the catalyst in patterned vias and contact holes.<sup>[41]</sup> This approach eliminates the need for added architectural or processing manipulation, as the wiring scheme used in this approach requires minimal modification from current metallization schemes for electrical interconnects. Because the catalyst is metallic, it can act as one of the electrical contacts to the underlying device layers, although the upper electrode must still be deposited by other means—in this case, focused ion beam (FIB). Using a similar approach, the entire nanotube networks have been synthesized using prepatterned metallic contacts that act as “catalytic anchors.”<sup>[6]</sup> In this case, ropes of single-walled nanotubes (SWNT) self-align in a cross-bar pattern on the surface.<sup>[42]</sup>

### Patterned substrate-driven synthesis

In this case, the catalyst is introduced as a gaseous precursor, such as ferrocene, into the CVD reactant mixture.<sup>[43]</sup> Such a growth often leads to encapsulated



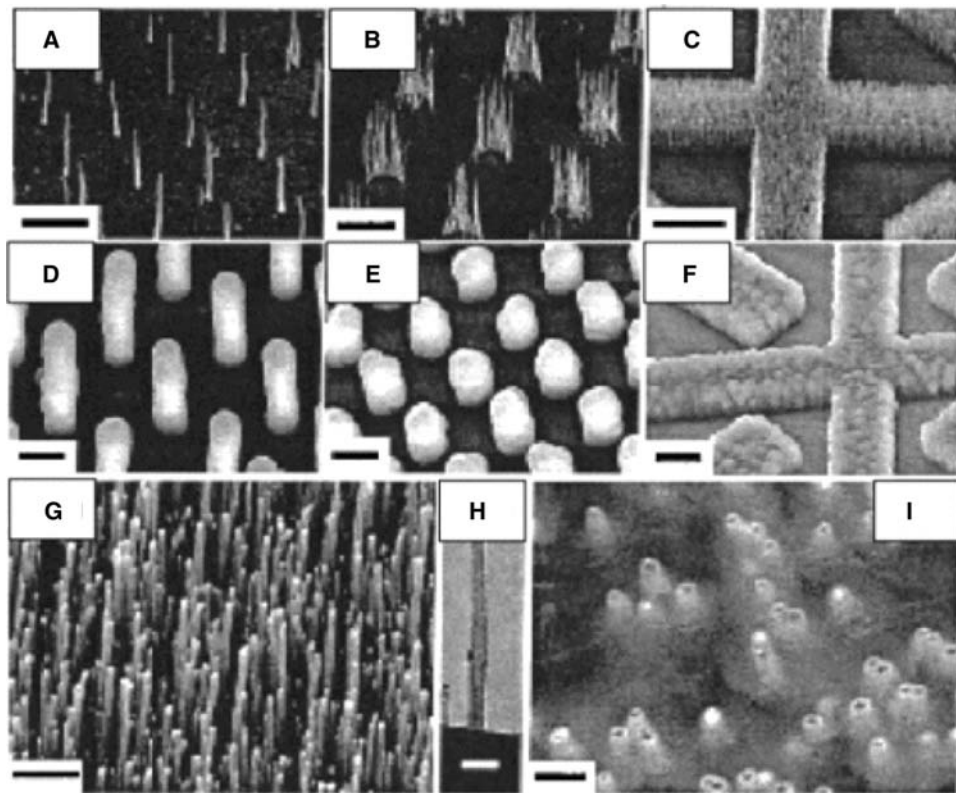


**Fig. 4** Scanning electron microscopy (SEM) images of as-grown MWNTs on (A) 100-nm-diameter catalyst spots; (B) 2- $\mu\text{m}$ -diameter catalyst spots; (C) a catalyst film deposited at aligned markers over 10  $\mu\text{m}$  in size; (D–F) images corresponding to those in (A–C), respectively, after being encapsulated in  $\text{SiO}_2$ ; (G) high-magnification SEM image of an MWNT array; (H) TEM image of the single MWNT from the array; (I) SEM image of the top surface of the embedded CNT array after CMP. The perspective of all the SEM images is  $45^\circ$ . The scale bars are 5, 3, 10, 2, 5, 10, 1, 0.2, and 0.2  $\mu\text{m}$ , respectively. *Source:* From Ref.<sup>[37]</sup>.

catalyst material within the core of the nanotube. Selective nanotube growth is driven primarily by the identity of the substrate surface. For example, in the case of a patterned surface consisting of Si and  $\text{SiO}_2$ , the fabrication process can be customized to grow nanotubes perpendicular to any exposed  $\text{SiO}_2$  surfaces, but not on the native oxide or Si.<sup>[43,44]</sup> Nanotube growth can occur not only perpendicularly to the wafer surface, but also in arbitrary directions, simply by customizing the orientation of the  $\text{SiO}_2$  surfaces prior to nanotube growth<sup>[41]</sup> (Fig. 5). Clever choices in the geometry of the  $\text{SiO}_2$  allow three-dimensional (3D) architectures such as networks.

In one embodiment of this technique, growth was initiated from the facets of magnesium oxide (MgO) crystallites, which also resulted in the encapsulation of Fe particles within the core of nanotubes (Fig. 6). Although the nanotube diameter and shape are unaffected by the crystal orientation of MgO, the nucleation density of tubes is much larger along the (111) plane than the (100) plane.<sup>[43]</sup>

In another embodiment of this technique, vertically aligned nanotube structures were grown under

patterned Ni films, actually lifting the Ni off the underlying Si substrate.<sup>[45]</sup> The concentrations of Ni catalyst and vapor reactants determined the nature of tube growth, which occurs either in oriented bundles or in a “furlike” manner. A key advantage of this method is that patterning of the metallic film prior to nanotube growth not only controls the location of nanotube growth, but also provides metallic (ohmic) contact to the nanotube. The disadvantage is that this approach is restricted by the limitations of current lithography techniques because the latter are applied to pattern the catalyst layer.

In summary, the directed synthesis methodology offers distinct advantages over its non-directed synthesis counterpart for interconnect applications. These advantages include controlled growth of nanotube structures selectively and reproducibly, directly over large-area substrates in a one-step process, and demonstrate customization of nanotube shape, direction, and intertube junction formation. In addition, directed synthesis offers the promise of scalability, and thus the potential for incorporation in nanoscale interconnect fabrication schemes. However, its disadvantages

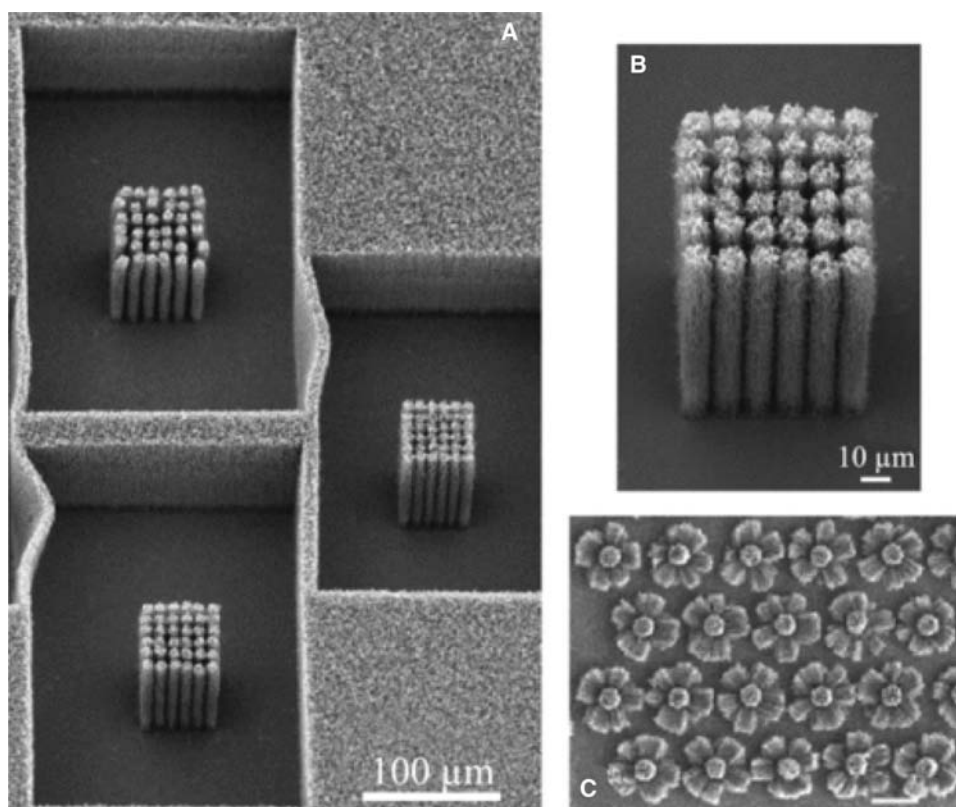


**Fig. 5** SEM images of nanotube arrays grown on patterned substrates using gaseous catalyst. (A) Columns consisting of tens of nanotubes grown vertically on patterned SiO<sub>2</sub> substrates. No growth occurs on exposed Si surfaces. (B) Higher-magnification image of one set of columns. (C) Repeating patterns of nanotubes demonstrating growth perpendicular to orthogonal silica surfaces. Vertical growth occurs on the top surface of the SiO<sub>2</sub>, whereas horizontal growth emanates from the sidewalls of the patterned SiO<sub>2</sub>. *Source:* From Ref.<sup>[41]</sup>.

include the need for high processing temperatures that are prohibitive to integration with Si CMOS technologies. In addition, it lacks flexibility in the formation of complex wiring schemes given that nanotubes typically grow in one specific direction relative to the surface.

### INTERNANOTUBE CONTACTS, JUNCTIONS, AND CONNECTIONS

“Synthesis, Separation, and Alignment” highlighted opportunities and challenges in the fabrication of CNT interconnects for incorporation in complex metallization schemes. This section presents progress to-date and associated challenges in the formation of actual intertube contacts, junctions, and connections. Although still in its very early stages of feasibility, the successful demonstration of reliable intertube connections is an essential prerequisite to the successful development of nanotube interconnect schemes.

As described earlier, intertube connections can be formed during growth. For example, Y-shaped tubes

can be made using Y-shaped nanopores during template-based synthesis. Similarly, nanotubes grown on metallic catalysts or patterned metal sites are already coupled to a metallic contact that could be used to input or extract signal from the nanotube. However, postgrowth tube–tube connection methods are also of considerable technological interest. Accordingly, the most promising methods will be described in this section. Tube–tube junctions fall into two categories: crossed-tube junctions, wherein physical contact between two tubes forms the basis of a connection, and on-tube junctions, wherein chemical bonding provides the basis of the connection, with interfacial chemical bonds within individual tubes being rearranged to join the constituent tubes.

### Crossed-tube Junctions

Crossed-tube junction behavior is closely related to that of structures containing multiple tubes, such as multiwalled nanotubes (MWNTs) and SWNT ropes. Although in close physical proximity, the tubes within



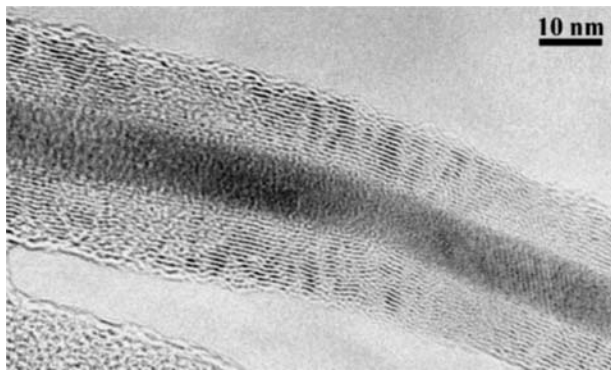


**Fig. 6** High-resolution TEM image of a multiwall CNT with an iron-filled core. Because this image is a projection of the structure, the concentric walls of a CNT can be seen as nearly parallel lines in the outer regions of the tube. The core is filled with iron, which was used as a catalyst in the growth of this tube. In the lower right portion of the image, a regular array of dots can be seen, corresponding to individual columns of iron atoms.

such structures are not chemically bonded to one another (Fig. 7).<sup>[46]</sup> Therefore, the conduction mechanism through such assemblages is more complex than the simple ballistic transport expected for a perfect SWNT, and is significantly impacted by intratube and intertube structural deformations.

In the case of crossed tubes, intertube distances can be controlled through the application of pressure, via an AFM tip for example.<sup>[18]</sup> The pressure generates an overlap of the electronic wave functions across the junction, thus favoring intertube tunneling. In the case of small structural deformations that induce only a smooth bending of the tubes, minimal scattering is expected to occur.<sup>[47]</sup> Theoretical calculations also suggest that, at least for these moderate contact forces, electron backscattering is also suppressed.<sup>[48]</sup> However, significant structural deformations may produce appreciable scattering, thus causing resistive losses. In the extreme case that one tube is actually kinked around another, local  $\sigma$ - $\pi$  bond mixing may be induced, which results in electron backscattering similar to that caused by impurities.

In the case of SWNT ropes, recent calculations suggest that intertube couplings within ropes do significantly affect fundamental SWNT rope properties. In simulations of a large, perfectly ordered rope composed of (10,10) tubes, broken symmetry because of intertube interactions resulted in band repulsion and formation of a pseudo-gap in the density of states of approximately 0.1 eV. Because of the presence of this pseudo-gap, electronic transport properties were predicted to be altered.<sup>[49]</sup> Furthermore, recent experimental studies examined the coupling between individual tubes in a rope of SWNTs.<sup>[50]</sup> In this case, the top

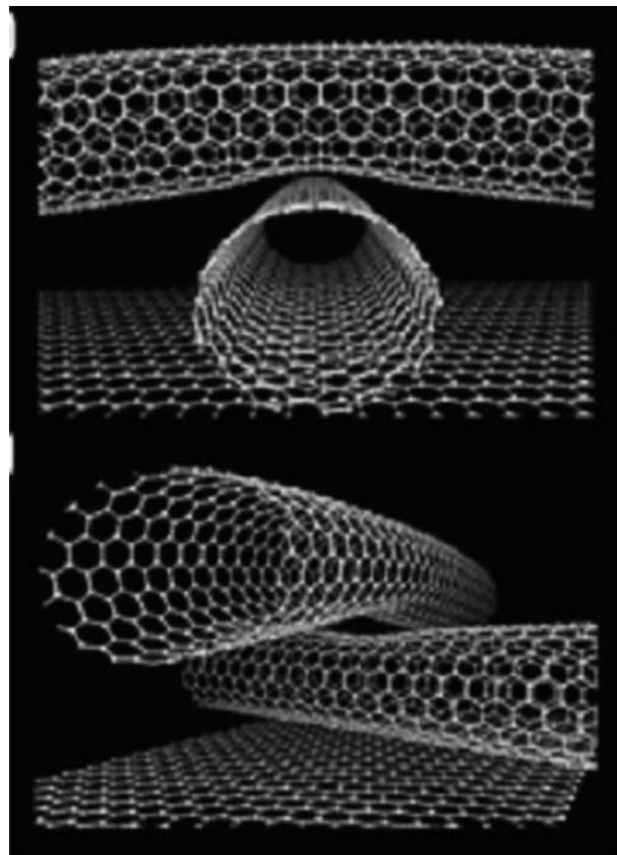


**Fig. 7** Schematic representation of crossed nanotube junctions. The contact between tubes can be enhanced by the application of pressure (e.g., by pressing on the junction with an AFM tip). Source: From Ref.<sup>[46]</sup>.

tubes in a rope were deliberately damaged by ion sputtering prior to electrode deposition, which introduced strong scattering centers in the current-carrying tubes at the rope surface. Under low-temperature conditions, the charge tunneled into an undamaged, metallic tube in the bulk of the rope, leading to a dramatic decrease in resistance. Measured intertube resistance indicated direct tunneling transport between tubes with a penetration depth of approximately 1.25 nm.<sup>[50]</sup>

One novel methodology for joining tubes using a “bandage” of double-walled CNTs to bind other strands together has been used to form structures of arbitrary length.<sup>[51]</sup> A wet “bandage” is wrapped around the end of two strands and allowed to dry, during which process it shrinks and binds the other strands together. Electrical testing showed that the joined section had a lower resistivity than the unwrapped segments, and burnout failures occurred away from the joint. These joined strands were capable of carrying current densities as high as  $10^7$  A/cm<sup>2</sup>, although the contact areas between the tubes within the strand still limited the overall performance of the structure.

In the case of MWNTs, the interplanar stacking disorder of adjacent layers decreases the electronic coupling between such layers when compared with graphite.<sup>[52]</sup> Because there is only weak coupling between MWNT shells at low bias or low temperature,<sup>[53,54]</sup> the current applied to the system under these conditions is essentially transported through the outermost layer of the tube—the only shell in contact with electrodes.

One study took advantage of this characteristic by exposing MWNTs to high current densities, exceeding  $10^9$  A/cm<sup>2</sup>, to execute a controlled breakdown of successive outer shells. This allowed a systematic study of the electronic properties of each concentric constituent shell of the MWNT.<sup>[13]</sup> It was determined that leakage current through inner metallic shells contributes to electron transport at room temperature and low bias, whereas all shells in the MWNT contribute to electronic transport under high-bias conditions. In either case, charge transport in the innermost MWNT shells is tunneling barrier-dominated, as these tubes are separated from electrical contacts by a barrier composed of a series of intervening graphitic shells.<sup>[13]</sup>

Accordingly, the theoretical models and experimental findings are in agreement that in their current form, crossed-tube junctions of SWNT ropes and MWNTs might not be appropriate vehicles for nanoscale interconnect applications, primarily because of the inability to control intratube and intertube electron transport mechanisms, leading to adverse and undesirable conductivity characteristics.

### On-tube junctions

On-tube junctions, although more difficult to fabricate than their crossed-tube junction counterparts, are more desirable because of their potential to provide innovative, diverse, and flexible approaches to the formation of nanotube interconnects with the desired conductivity behavior. The simplest form of an “on-tube junction” can result from bending a straight tube sufficiently to introduce a pentagon–heptagon structural pair into the graphitic matrix.<sup>[55]</sup> This action results in a permanent bend in the tube, which could be considered a junction between two tubes meeting at a small angle, thus resulting in some quite interesting electron transport characteristics.

For instance, a symmetric pentagon–heptagon junction tends to resist the flow of electrons, whereas its asymmetrical analog allows electronic flow. In this respect, topology alone cannot determine the electrical behavior of a junction because a bent junction may provide a better electrical path than a straight one. In theory, it is possible to connect two metallic nanotubes using pentagon–heptagon pairs by choosing appropriate tube diameters. Theory further predicts

that “X,” “Y,” and “T” SWNT junctions are stable and could be used as multiterminal electronic devices or joined wiring structures (Fig. 8).<sup>[45,56–58]</sup> However, theoretical predictions indicate the possible existence of localized interference states at these junctions, depending on tube diameter and chirality. The effect of such states on the stability and use of these junctions is still not clear.<sup>[57,58]</sup>

Although several such junctions have been observed experimentally,<sup>[13,17]</sup> the controlled synthesis of these structures remains challenging. As was previously described, it is possible to form “Y”-shaped nanotubes during growth by using a template with suitably shaped nanopores.<sup>[33]</sup> Other growth processes and nanofabrication manipulations have been used to make one-dimensional (1D) and two-dimensional (2D) connections with such nanotubes.<sup>[34,59,60]</sup> However, a majority of current methods for creating such junctions focus on postgrowth formation by connecting tubes that were not initially joined during synthesis. These methods also require a high thermal budget and necessitate additional processing steps, such as concurrent electron irradiation.

For example, SWNT “X” junctions were fabricated by irradiation of crossed nanotubes at 800°C in a 1.25-MeV, 10-A/cm<sup>2</sup>, 100-nm-diameter beam in a transmission electron microscope “X.”<sup>[48]</sup> By adjusting the irradiation conditions, one of the “arms” was removed to create stable Y or T junctions. Thus, junction geometry can be tailored as needed, albeit slowly because of the serial nature of the process. In this respect, heat-assisted irradiation is necessary to avoid significant sputtering effects that would have taken

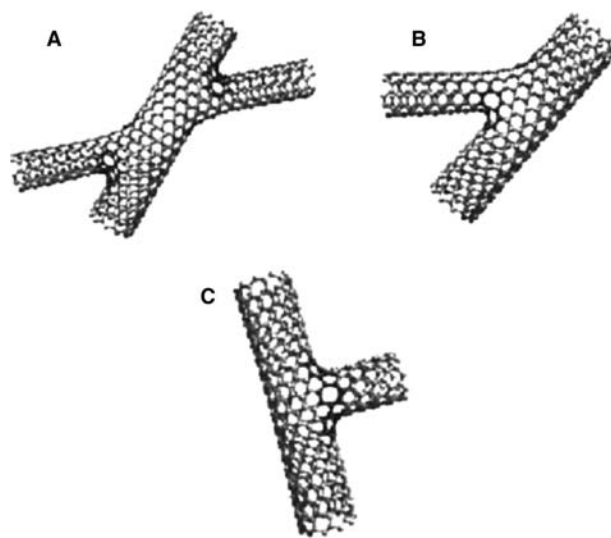


**Fig. 8** Atomic model of the CNT “on-tube” junctions: (A) “X”-like, (B) “Y”-like, and (C) “T”-like junction, respectively. Source: From Refs.<sup>[45,48]</sup>

place at room temperature irradiation, leading to undesirable dimensional changes and surface reconstructions.<sup>[61,62]</sup> The application of elevated temperature allows recombination of vacancy-interstitial pairs prior to the formation of interstitial agglomerates.<sup>[56,63–65]</sup> Although the topology of the resulting junctions matched those predicted from idealized molecular modeling, the latter structures could not be confirmed. Furthermore, theoretical calculations of local density of states for “treated” and perfect junctions suggest that the latter do not alter the metallic or semiconducting behavior of the tubes, although no experimental confirmation has been provided yet.<sup>[48]</sup>

Unfortunately, on-tube junction fabrication processes continue to be a challenge in terms of complexity, scalability, and adaptability to prevailing large-volume semiconductor manufacturing protocols.

## NANOTUBE INTEGRATION IN INTERCONNECT ARCHITECTURES

### Densification

Carbon nanotubes are promising candidates for IC interconnect because in addition to their ability to carry a very high current density ( $\sim 10^9$  A/cm<sup>2</sup>) exhibit a ballistic transport along the tube, and resist against electromigration,<sup>[66–68]</sup> they can potentially have higher conductivity than copper. However, a high nanotube site density (i.e., tubes per unit growth area) and closely packed structures are required for interconnect applications since the more the conduction channels are available, the less is the resistance expected.<sup>[68]</sup> Unfortunately, the reported CNT site densities<sup>[69–71]</sup> are still one or two orders of magnitude below the ideal one. Therefore, densification techniques have been investigated targeting growth of CNTs to prove their potential benefits over traditional copper interconnect technology.

The first method is based on CNT densification after their growth process. It has been noted that after immersing CNTs into a liquid and drying, CNTs can aggregate into “hut”-like structures<sup>[72–74]</sup> or cellular patterns<sup>[74,75]</sup> due to capillary coalescence. Liu et al. immersed the as-grown CNT bundles in the organic solvent isopropyl alcohol and then dried out the samples by evaporation in atmosphere at room temperature. Isopropyl alcohol (IPA) evaporation lowers the liquid level pulling CNTs toward each other by the capillary forces, bringing them close enough for the van de Waals force to dominate and result in sticking of the tubes to each other. It was observed that for optimized length of the CNTs (in the range of 30–65  $\mu$ m), good densification was obtained, and bundle

diameter reduced from the original 20  $\mu$ m to 8.3  $\mu$ m, increasing site density 5.8 times.<sup>[76]</sup> The site density value was still  $\sim 20$  times less than the theoretical value for tube with these dimensions, but since it was noted that densification is affected by the bundle height, diameter, pitch, and the CNT properties (e.g., diameter, shell number, density, alignment, and uniformity), the assumption is that densification method could be further improved by process optimization.

The second approach to densification of aligned carbon nanotubes (ACNTs) focuses on filling the interstitial space between nanotubes with solid materials.<sup>[77–79]</sup> One of the methods employed uses chemical vapor infiltration (CVI), which extends the commonly used chemical vapor deposition (CVD) process by altering the deposition kinetics toward a mass-transfer limited process.<sup>[80,81]</sup> Two approaches have been taken, one in which infiltration of ACNT films were conducted in a separate CVD/CVI process,<sup>[77,78]</sup> and second in which a simultaneous growth of nanotubes and their densification by carbon infiltration was performed in one process step.<sup>[82]</sup> Measurements of CNTs grown using the simultaneous CVD/CVI densification method showed increased by an order of magnitude in both diameters and bulk density (defined as the mass of the film divided by its volume) of the ACNT films. This simplified densification method resulted in conformal coating of ACNTs by partially graphitized pyrolytic carbon and when optimized (longer growth times  $>1$  hr) showed more than five times increased total film conductivity.<sup>[82]</sup>

### Contacts

Clearly, the successful development of nanotube interconnect architectures requires nanotube integration with more traditional metal and semiconductor leads and contact pads. However, the significantly different physical, chemical, and electrical properties of nanotubes, when compared with conventional metals and semiconductors, add another level of complexity to the challenges facing their potential use. Material compatibility issues are further compounded by the adverse effects that current metal, lead, and contact deposition processes could exert on the structure and chemistry of the nanotubes, and on the stability of the nanotube–metal interface.

A novel approach to studying this nanotube–metal interface was recently reported by Avouris et al. Inhomogeneities, such as defect sites or the Schottky barriers found at metal–nanotube interfaces, produce resistance and can thus generate local electric fields capable of accelerating carriers and generating electron–hole pairs “through an intra-nanotube impact-excitation process.”<sup>[83]</sup> A fraction of this energy can

then be emitted in the form of photons, much as in the widely known electroluminescence process currently employed in devices such as light-emitting diodes (LEDs). Further study of this radiative emission and of the reverse process, photoconductivity, could provide useful insight into the nature and effects of CNT contacts on electrical properties.<sup>[84]</sup> Such information is vital to successful integration of nanotubes into traditional material sets.

First integration attempts involved nanotube dispersal on lithographically defined contact pads on an insulating surface. However, it was later shown that a tunneling barrier formed at the metal/CNT interface, which hampered transport studies.<sup>[60,85]</sup> More recent approaches involved the deposition of electrodes, typically by electron- or ion-beam induced deposition (EBID or IBID, respectively) in an FIB, directly onto the CNTs (Fig. 9).<sup>[41,86–90]</sup> The IBID approach produced partial collapse at the edges of the tube,<sup>[91]</sup> thus resulting in improved physical and electrical contact, although the potential exists for significant ion-implantation damage to the CNT, which can be avoided through the use of EBID.

The charged-particle beam methods can provide an elegant approach to nanomodulate the interfacial structure and electrical characteristics of a nanotube through location-specific doping of a narrow transition region between a nanotube and a metal or semiconductor. One key advantage of this methodology is the successful integration of nanotubes within a metal or a semiconductor matrix through the formation of a

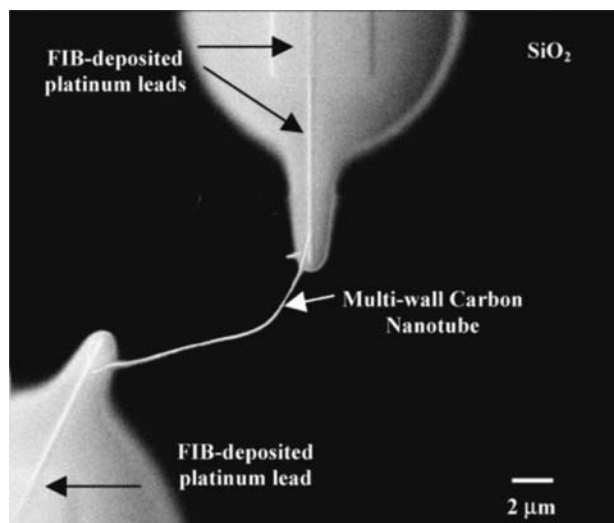


**Fig. 9** FIB image of CNT-Pt contacts. The Pt leads were fabricated directly on the multiwall CNT by IBID in an FIB microscope. The contacts were connected by intermediate leads (one of which is visible at the top of the image) to large ( $150 \times 150 \mu\text{m}^2$ ) probe pads patterned by conventional lithography on a  $\text{SiO}_2$  substrate. Source: From Ref.<sup>[87]</sup>.

gradual transition region between these two dissimilar material systems. Another advantage is the ability to use a dual-beam FIB/SEM system as an in situ alternative to ex situ electron beam (e-beam) lithography for the fabrication of ultrathin metal lines for the formation of reliable CNT-metal contacts.

These advantages are exemplified in Fig. 10, which displays an IBID-grown MWNT-Pt pad.<sup>[85,87]</sup> In particular, the transmission electron microscopy (TEM) image of the MWNT-Pt contact (Fig. 10B) highlights the buildup of Pt along the sides of the MWNT, whereas the associated high-resolution TEM image of the Pt/MWNT interface demonstrates the presence of Pt nanocrystals only on the outermost wall of the nanotube, with the overall integrity of the MWNT preserved.

Alternatively, tube nanocontacts can be fabricated by e-beam lithography and subsequent liftoff of metal electrodes, such as Ti or Au.<sup>[92]</sup> As in the case of IBID, these techniques require further investigation to document the effects of the metal deposition process on nanotube structure and chemistry, and stability of the CNT/metal interface. In some cases, these effects can be minimized by post-treating the samples by rapid thermal annealing (RTA) to form an ohmic contact at the metal-nanotube junction,<sup>[33]</sup> or through the use of an Au coating on the electrodes to reduce contact resistance to the nanotube.<sup>[93]</sup>

One recent publication offers yet another alternative for creating well-bonded contacts to CNTs using an ultrasonic wire bonder.<sup>[94]</sup> A droplet of solution containing nanotubes was allowed to dry on top of the electrodes, then fortuitously positioned CNTs were chosen for bonding using a clamping force of 78.4 mN with an ultrasonic vibration of 60 kHz applied through a transducer. This combined action of the vibrations and normal clamping force embedded the ends of the CNTs into the Ti electrodes. Subsequent electrical testing deduced an effective barrier height of  $\sim 6.6$  meV, less than half of what has been reported for the high-temperature annealing method ( $\sim 15$  meV). The Schottky barrier width was estimated at  $\sim 0.9$  nm at  $V = 0$ , two orders of magnitude lower than has been previously reported in the literature. The feasibility of implementing a technique over large areas has yet to be studied, but the results are quite encouraging.

On the other hand, Kumar et al. used a more traditional packaging-like approach in which the as-grown CNTs were transferred onto the contact pads using low temperature solder alloys such as eutectic AuSn and SnAg.<sup>[95]</sup> This process involved the annealing of solder substrate in tight contact with carbon nanotube substrate. The carbon nanotube bundles penetrated into the molten solder surface and were entrapped during solidification of the solder pads.

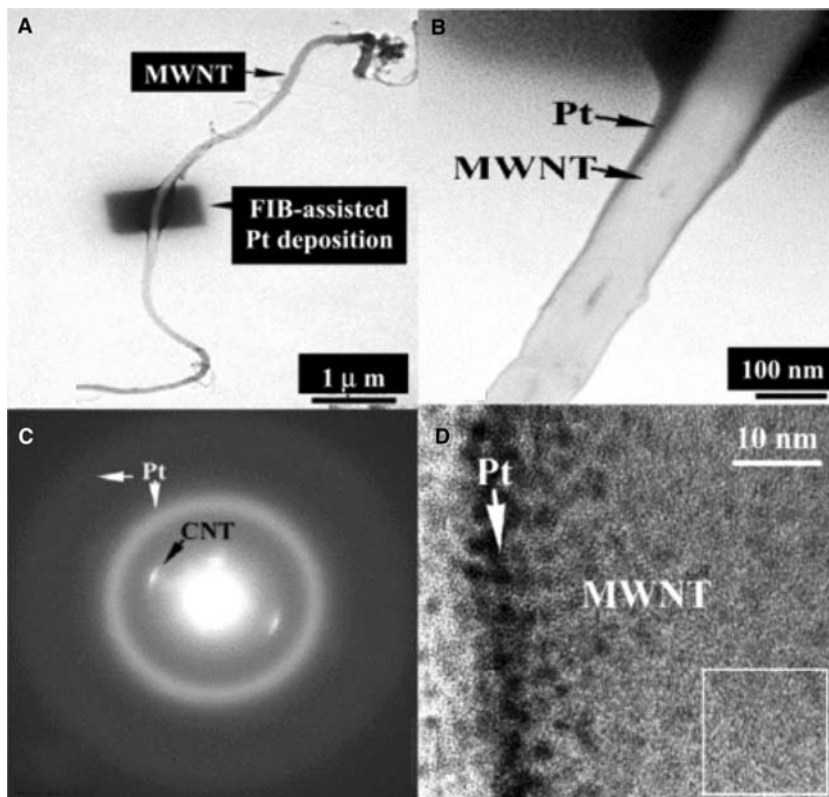


**Fig. 10** (A) Low-magnification TEM image of a Pt pad deposited on top of an MWNT using an 11-pA ion beam current and a  $\text{Ga}^+$  dose of  $10^{16}$  ions/ $\text{cm}^2$ . (B) A higher-magnification section of the MWNT-Pt contact highlights the buildup of Pt along the sides of the MWNT. (C) Associated selected area diffraction pattern shows both a diffused ring pattern attributed to amorphous Pt, and an arc pattern ascribed to the 0.34-nm interwall distance of the MWNT. (D) High-resolution TEM image of the Pt/MWNT interface demonstrates the presence of Pt nanocrystals on the outermost wall of the nanotube. *Source:* From Ref.<sup>[87]</sup>.

In this method, the final nanotube structure is defined simply by the solder pattern predefined on the substrate. The electrical and field emission measurements show that good contacts of CNTs can be made with the conducting substrates after solder-based transfer. Similar observations were made by the Zhu et al. study in which the CNTs were transferred using PbSn solder.<sup>[96]</sup>

## CONCLUSIONS

The knowledge base in materials, processing, and integration necessary for the design and fabrication of specific nanotube structures continues to grow steadily, but has not yet matured to the level necessary for implementation into manufacturable nanoscale interconnect schemes.<sup>[97]</sup> Researchers today are faced with some of the same fundamental challenges faced in early investigations of these materials, including the lack of reliability and reproducibility in the large-scale, high-volume fabrication of nanotubes with predefined diameter and chirality, and therefore controlled electronic properties.

Beyond the issue of nanotube synthesis lie serious engineering challenges in the application of nanotubes as interconnects. Ongoing research has focused on two main pathways for integration: 1) non-directed growth

approach with subsequent manipulation of tubes to desired locations, and 2) directed growth at desired locations through exploitation of surface selectivity of prepatterned substrates or catalysts. Several recent reports have demonstrated organized assemblies of CNTs in architectures analogous to conventional interconnect topographies, such as vias and contact holes; however their use is limited at the moment by non-sufficient site density (i.e., tubes per unit growth area).

A corollary to the integration issue is the need for better control of nanotube–nanotube and nanotube–contact-joining methods. In particular, current assumptions suggest that perfectly straight tubes may be required to achieve ballistic transport in interconnects.<sup>[54]</sup> Therefore, to minimize losses at junctions, it is crucial to develop and optimize reliable methods, such as electron irradiation, template-mediated growth, and nanotube manipulation. Similarly, advances have been made regarding the quality and integrity of metal/tube interfaces, a key prerequisite that will ultimately determine whether the promising electrical and optical properties of CNTs will ever be realized.

## ACKNOWLEDGMENTS

A portion of the results presented was supported by the Microelectronics Advanced Research Corporation

(MARCO) and the Defense Advanced Research Programs Agency (DARPA), through their cosponsored Interconnect Focus Center for Hyperintegration, and the New York State Office of Science, Technology, and Academic Research (NYSTAR). This support is gratefully acknowledged.

## REFERENCES

- Charlier, J.-C.; Iijima, S. Electronic properties, junctions, and defects of carbon nanotubes. In *Growth Mechanisms of Carbon Nanotubes*; Topics in Applied Physics; Dresselhaus, M.S., Dresselhaus, G., Avouris, Ph., Eds.; Springer-Verlag: Heidelberg, 2001; Vol. 80, 55 pp.
- Ebbesen, T.W.; Ajayan, P.M. Large-scale synthesis of carbon nanotubes. *Nature* **1992**, *358*, 220.
- Bethune, D.S.; Kiang, C.H.; DeVries, M.; Gorman, G.; Savoy, R.; Vazquez, J.; Beyers, R. Cobalt-catalyzed growth of carbon nanotubes with single-atomic-layer walls. *Nature* **1993**, *363*, 605.
- Journet, C.; Maser, W.K.; Bernier, P.; Loiseau, A.; Delachapelle, M.L.; Lefrant, S.; Deniard, P.; Lee, R.; Fisher, J.E. Large-scale production of single-walled carbon nanotubes by the electric-arc technique. *Nature* **1997**, *388*, 756.
- Thess, A.; Lee, R.; Nikolaev, P.; Dair, H.J.; Petit, P.; Robert, J.; Xu, C.H.; Lee, Y.H.; Kim, S.G.; Rinzler, A.G.; Colbert, D.T.; Scuseria, G.E.; Tomanek, D.; Fischer, J.E.; Smalley, R.E. Crystalline ropes of metallic carbon nanotubes. *Science* **1996**, *273*, 483.
- Dai, H.; Kong, J.; Zhou, C.; Franklin, N.; Tomblor, T.; Cassell, A.; Fan, S.; Chapline, M. Controlled chemical routes to nanotube architectures, physics, and devices. *J. Phys. Chem., B* **1999**, *103* (51), 11,246.
- Hafner, J.; Bronikowski, M.; Azamian, B.; Nikolaev, P.; Colbert, D.; Smalley, R. Catalytic growth of single wall carbon nanotubes from metal particles. *Chem. Phys. Lett.* **1998**, *296* (1–2), 195.
- Tibbetts, G.G.; Devour, M.G.; Rodda, E.J. An adsorption-diffusion isotherm and its application to the growth of carbon filaments on iron catalyst particles. *Carbon* **1987**, *25* (3), 367.
- Amelinckx, S.; Zhang, X.B.; Bernaerts, D.; Zhang, X.F.; Ivanov, V.; Nagy, J.B. A formation mechanism for catalytically grown helix-shaped graphite nanotubes. *Science* **1994**, *265*, 635.
- Liu, J.; Rinzler, A.G.; Dai, H.; Hafner, J.H.; Bradley, R.K.; Boul, P.J.; Lu, A.; Iverson, T.; Shelimov, K.; Huffman, C.B.; Rodriguez-Macias, F.; Shon, Y.-S.; Lee, T.R.; Colbert, D.T.; Smalley, R.E. Fullerene pipes. *Science* **1998**, *280*, 1253.
- Vigolo, B.; Penicaud, A.; Coulon, C.; Sauder, C.; Pailler, R.; Journet, C.; Bernier, P.; Poulin, P. Macroscopic fibers and ribbons of oriented carbon nanotubes. *Science* **2000**, *290*, 1331.
- Diehl, M.R.; Yaliraki, S.N.; Beckman, R.A.; Barahona, M.; Heath, J.R. Self-assembled, deterministic carbon nanotubes wiring networks. *Angew. Chem., Int. Ed. Engl.* **2002**, *41* (2), 353.
- Collins, P.G.; Arnold, M.S.; Avouris, Ph. Engineering carbon nanotubes and nanotube circuits using electrical breakdown. *Science* **2001**, *292* (5517), 706.
- Hunter, R.J. *Foundations of Colloid Science*; Oxford University Press: Oxford, 1989; Vol. 1.
- Shen, Z.; Liu, S.; Hou, S.; Gu, Z.; Xue, Z. In situ splitting of carbon nanotube bundles with atomic force microscopy. *J. Phys., D. Appl. Phys.* **2003**, *36*, 2050.
- Banerjee, S.; Kahn, M.G.C.; Wong, S.S. Rational chemical strategies for carbon nanotube functionalization. *Chem. Eur. J.* **2003**, *9*, 1898.
- Yao, Z.; Postma, H.W.Ch.; Balents, L.; Dekker, C. Carbon nanotube intermolecular junctions. *Nature (London)* **1999**, *402*, 273.
- Fuhrer, M.S.; Nygård, J.; Shih, L.; Ferero, M.; Yoon, Y.-G.; Mazzone, M.S.C.; Choi, H.J.; Ihm, J.; Louie, S.G.; Zettl, A.; McEuen, P.L. Crossed nanotube junctions. *Science* **2000**, *288* (5465), 494.
- <http://www.research.ibm.com/nanoscience/manipulation.html>
- Postma, H.W.Ch.; Teepen, T.; Yao, X.; Grifoni, M.; Dekker, C. Carbon nanotube single-electron transistors at room temperature. *Science* **2001**, *293*, 76.
- Zheng, M. Keynote lecture: Manipulating carbon nanotubes using biological molecules. AICHE Symposium: Issues in Carbon Nanotubes I New York, NY, 2004, 220 pp.
- Williams, K.A.; Veenhuizen, P.T.M.; de la Torre, B.G.; Eritja, R.; Dekker, C. Towards DNA-mediated self assembly of carbon nanotube. In *Molecular devices*; AIP Conference Proceedings Tirol, Austria; Kuzmany, H., Fink, J., Mehring, M., Roth, S., Eds.; Springer-Verlag: Heidelberg, 2002; Vol. 633, i1.
- Wang, S.; Humphreys, E.S.; Chung, S.-Y.; Delduco, D.F.; Lustig, S.R.; Wang, H.; Parker, K.N.; Rizzo, N.W.; Subramoney, S.; Chiang, Y.-M.; Jagota, A. Peptides with selective affinity for carbon nanotubes. *Nat. Mater.* **2003**, *2* (3), 196.
- Dawson, S.L.; Tirrell, D.A. Peptide-derived self-assembled monolayers: Absorption of N-stearoyl l-cysteine methyl ester on gold. *J. Mol. Recognit.* **1997**, *10*, 18.
- Kaloyeros, A.E.; Eisenbraun, E.T.; Welch, J.; Geer, R.E. Molecular interconnects: Exploiting nanotechnology for terahertz interconnects. *Semicond. Int.* **2003**, *1*, 56–59.
- Peng, H.; Alvarez, N.T.; Kittrell, C.; Hauge, R.H.; Schmidt, H.K. Dielectrophoresis field flow fractionation of single-walled carbon nanotubes. *J. Am. Chem. Soc.* **2006**, *128*, 8396.
- Chen, X.Q.; Saito, T.; Yamada, H.; Matsushige, K. Aligning single-wall carbon nanotubes with an alternating-current electric field. *Appl. Phys. Lett.* **2001**, *78*, 3714.
- Pohl, H.A. *Dielectrophoresis*; Cambridge University Press: NY, USA, 1978.
- Lay, M.D.; Novak, J.P.; Snow, E.S. Simple route to large-scale ordered arrays of liquid-deposited carbon nanotubes. *Nano Lett.* **2004**, *4* (4), 603.



30. Xin, H.; Woolley, A.T. Directional orientation of carbon nanotubes on surfaces using a gas flow cell. *Nano Lett.* **2004**, *4* (8), 1481.
31. Wind, S.J.; Appenzeller, J.; Martel, R.; Derycke, V.; Avouris, Ph. Vertical scaling of carbon nanotube field effect transistors using top gate electrodes. *Appl. Phys. Lett.* **2002**, *80* (20), 3817.
32. Bae, E.J.; Jeong, K.S.; Chu, J.U.; Yoo, I.K.; Choi, W.B.; Pak, G.-S.; Song, S. Selective growth of carbon nanotubes on pre-patterned porous anodic aluminum oxide. *Adv. Mater.* **2002**, *14* (4), 277.
33. Choi, W.B.; Lee, Y.H. Carbon nanotube and its application to nanoelectronics. In *Industrial Applications of Electron Microscopy*; Li, Z., Ed.; Marcel Dekker: New York, 2002; Chap. 14.
34. Li, C.; Papadopoulos, C.; Xu, J. Nanoelectronics: growing Y-junction carbon nanotubes. *Nature (London)* **1999**, *402*, 253.
35. Li, W.Z.; Xie, S.S.; Qian, L.X.; Chang, B.H.; Zou, B.S.; Zhou, W.Y.; Zhao, A.; Wang, G. Large-scale synthesis of aligned carbon nanotubes. *Science* **1996**, *274*, 1701.
36. Terrones, M.; Grobert, N.; Olivares, J.; Zhang, J.P.; Terrones, H.; Kordatos, K.; Hsu, W.K.; Hare, J.P.; Townsend, P.D.; Prassides, K.; Cheetham, A.K.; Kroto, H.W.; Walton, D.R.M. Controlled production of aligned-nanotube bundles. *Nature* **1997**, *388*, 52.
37. Fan, S.S.; Chapline, M.G.; Franklin, N.R.; Tomblor, T.W.; Cassell, A.M.; Dai, H.J. Self oriented regular arrays of carbon nanotubes and their field emission properties. *Science* **1999**, *283* (5401), 512.
38. Franklin, N.R.; Wang, Q.; Tomblor, T.W.; Javey, A.; Shim, M.; Dai, H. Integration of arrays of suspended carbon nanotubes into electronic devices and electromechanical systems. *Appl. Phys. Lett.* **2002**, *81*, 913.
39. Tseng, Y.C.; Xuan, P.; Javey, A.; Malloy, R.; Wang, Q.; Bokor, J.; Dai, H. Monolithic integration of carbon nanotube devices with silicon MOSTechnology. *Nano Lett.* **2004**, *4* (1), 123.
40. Li, J.; Ye, Q.; Cassell, A.; Ng, H.T.; Stevens, R.; Han, J.; Meyyappan, M. Bottom-up approach for carbon nanotube interconnects. *Appl. Phys. Lett.* **2003**, *82*, 2491.
41. Kreupl, F.; Graham, A.P.; Duesberg, G.S.; Steinhogel, W.; Liebau, M.; Unger, E.; Honlein, W. Carbon nanotubes in interconnect applications. *Microelectron. Eng.* **2002**, *64*, 399.
42. Marty, L.; Bouchiat, V.; Bonnot, A.M.; Chaumont, M.; Fournier, T.; Decossas, S.; Roche, S. Batch processing of nanometer-scale electrical circuitry based on in-situ grown single-walled carbon nanotubes. *Microelectron. Eng.* **2002**, *61–62*, 485.
43. Wei, B.Q.; Vajtai, R.; Jung, Y.; Ward, J.; Zhang, R.; Ramanath, G.; Ajayan, P.M. Organized assembly of carbon nanotubes. *Nature* **2002**, *416*, 495.
44. Zhang, Z.J.; Wei, B.Q.; Ramanath, G.; Ajayan, P.M. Substrate site selective growth of aligned carbon nanotubes. *Appl. Phys. Lett.* **2000**, *77* (23), 3764.
45. Vajtai, R.; Wei, B.Q.; Zhang, Z.J.; Jung, Y.; Ramanath, G.; Ajayan, P.M. Building carbon nanotubes and their smart architecture. *Smart Mater. Struct.* **2002**, *11*, 691.
46. Hertel, T.; Walkup, R.E.; Avpuris, P. Deformation of carbon nanotubes by surface van der Waals forces. *Phys. Rev. B* **1998**, *58* (20), 13,870.
47. Kane, C.L.; Mele, E.J. Size, shape, and low energy electronic structure of carbon nanotubes. *Phys. Rev. Lett.* **1997**, *78*, 1932.
48. Terrones, M.; Banhart, F.; Grobert, N.; Charlier, J.-C.; Terrones, H.; Ajayan, P.M. Molecular junctions by joining single-walled carbon nanotubes. *Phys. Rev. Lett.* **2002**, *89*, 75505-1.
49. Louie, S.G. Electronic properties, junctions, and defects of carbon nanotubes. In *Carbon Nanotubes: Synthesis, Structure, Properties and Applications*; Topics in Applied Physics; Dresselhaus, M.S., Dresselhaus, G., Avouris, Ph., Eds.; Springer-Verlag: Heidelberg, 2001; Vol. 80, 113 pp.
50. Stahl, H.; Appenzeller, J.; Martel, R.; Avouris, Ph. Intertube coupling in ropes of single-wall carbon nanotubes. *Phys. Rev. Lett.* **2000**, *85* (24), 5186.
51. Gong, T.; Zhang, Y.; Liu, W.; Wei, J.; Li, C.; Wang, K.; Wu, D.; Zhong, M. Connection of macro-sized double-walled carbon nanotube strands by bandaging with double-walled carbon nanotube films. *Carbon* **2007**, *45*, 2235.
52. Farró, L.; Schöenberger, C. Physical properties of multi-wall nanotubes. In *Carbon Nanotubes: Synthesis, Structure, Properties and Applications*; Topics in Applied Physics; Dresselhaus, M.S., Dresselhaus, G., Avouris, Ph., Eds.; Springer-Verlag: Heidelberg, 2001; Vol. 80, 329 pp.
53. Strunk, B.A.; Salvetat, C.; Bonard, J.P.; Forro, J.M.; Nussbaumer, L.; Schonenberger, T.; Aharonov, C. Bohm oscillations in carbon nanotubes. *Nature (London)* **1999**, *397*, 673.
54. Frank, S.; Poncharal, P.; Wang, Z.L.; de Heer, W.A. Carbon nanotube quantum resistors. *Science* **1998**, *280*, 1744.
55. Nardelli, M.B.; Yakobson, B.I.; Bernhole, J. Brittle and ductile behavior in carbon nanotubes. *Phys. Rev. Lett.* **1998**, *81* (21), 4656.
56. Scuseria, G.E. The equilibrium structures of giant fullerenes: faceted or spherical shape? An ab initio Hartree-Fock study. *Chem. Phys. Lett.* **1992**, *195*, 534.
57. Chico, L.; Crespi, V.H.; Benedict, L.X.; Louie, S.G.; Cohen, M.L. Pure carbon nanoscale devices: Nanotube heterojunctions. *Phys. Rev. Lett.* **1996**, *76* (6–7), 971.
58. Menon, M.; Srivastava, D. Carbon nanotube t junctions: nanoscale metal semiconductor metal contact devices. *Phys. Rev. Lett.* **1997**, *79* (22), 4453.
59. Kong, J.; Soh, H.T.; Cassell, A.M.; Quate, C.F.; Dai, H.J. Synthesis of individual single-walled carbon nanotubes on patterned silicon wafers. *Nature* **1998**, *395*, 878.
60. Tans, T.J.; Verschuere, R.M.; Dekker, C. Room-temperature transistor based on a single carbon nanotube. *Nature* **1998**, *393*, 49.
61. Ajayan, P.M.; Ravikumar, V.; Charlier, J.-C. Surface reconstructions and dimensional changes in single walled carbon nanotubes. *Phys. Rev. Lett.* **1998**, *81* (7), 1437.

62. Banhart, F. Irradiation effects in carbon nanostructures. *Rep. Prog. Phys.* **1999**, *62*, 1181.
63. Andriotis, A.N.; Menon, M.; Srivastava, D.; Chernozatonskii, L.A. Rectification properties of carbon nanotube Y junctions. *Phys. Rev. Lett.* **2001**, *87* (6), 66,802.
64. Mackay, A.L.; Terrones, H. Diamond from graphite. *Nature* **1991**, *352*, 762.
65. Treboux, G.; Lapstun, P.; Silverbrook, K. Conductance in nanotube Y junctions. *Chem. Phys. Lett.* **1999**, *306* (5–6), 402.
66. Wei, B.Q.; Vajtai, R.; Ajayan, P.M. Reliability and current carrying capacity of carbon nanotubes. *Appl. Phys. Lett.* **2001**, *79* (8), 1172.
67. Frank, S.; Poncharal, P.; Wang, Z.L.; de Heer, W.A. Carbon nanotube quantum resistors. *Science* **1998**, *280* (5370), 1744.
68. Naemi, A.; Sarvari, R.; Meindl, J.D. On-chip interconnect networks at the end of the roadmap, limits and opportunities. IITC, Session 12.1 Novel IT, 2006, 221 pp.
69. Horibe, M.; Nihei, M.; Kondo, D.; Kawabata, A.; Awano, Y. Carbon nanotube growth technologies using tantalum barrier layer for future ULSIs with Cu/Low-k interconnect processes. *Jap. J. Appl. Phys.* **2005**, *44* (7A), 5309.
70. Sato, S.; Nihei, M.; Mimura, A.; Kawabata, A.; Kondo, D.; Shioya, H.; Iwai, T.; Mishima, M.; Ohfuti, M.; Awano, Y. Novel approach to fabricating carbon nanotube via interconnects using size-controlled catalyst nanoparticles. IITC Session 12.4 Novel IT, 230 pp.
71. Futaba, D.N.; Hata, K.; Namai, T.; Yamada, T.; Mizuno, K.; Hayamizu, Y.; Yumura, M.; Iijima, S. Catalyst activity of water-assisted growth of single walled carbon nanotube forest characterization by a statistical and macroscopic approach. *J. Phys. Chem. B* **2006**, *110* (15), 8035.
72. Fan, J.-G.; Dyer, D.; Zhang, G.; Zhao, Y.-P. Nanocarpet effect: pattern formation during the wetting of vertically aligned nanorod arrays. *Nano Lett.* **2004**, *4* (11), 2133.
73. Lau, K.K.S.; Bico, J.; Teo, K.B.K.; Chhowalla, M.; Amaratunga, G.A.J.; Milne, W.I.; McKinley, G.H.; Gleason, K.K. Superhydrophobic carbon nanotube forests. *Nano Lett.* **2003**, *3* (12), 1701.
74. Correa-Duarte, M.A.; Wagner, N.; Rojas-Chapana, J.; Morszeck, C.; Thie, M.; Giersig, M. Fabrication and biocompatibility of carbon nanotube-based 3D networks as scaffolds for cell seeding and growth. *Nano Lett.* **2004**, *4* (11), 2233.
75. Chakrapani, N.; Wei, B.; Carrilo, A.; Ajayan, P.M.; Kane, R.S. Capillarity-driven assembly of two-dimensional cellular carbon nanotube foams. *PNAS* **2004**, *101* (12), 4009.
76. Liu, Z.; Bajwa, N.; Ci, L.; Lee, S.H.; Kar, S.; Ajayan, P.; Lu, J.-Q. Densification of carbon nanotube bundles for interconnect application. International Interconnect Technology Conference, IEEE Session 11.1. 2007; 201 pp.
77. Yurdumakan, B.; Raravikar, N.R.; Ajayan, P.M.; Dhinojwala, A. Synthetic gecko foot-hairs from multiwalled carbon nanotubes. *Chem. Commun.* **2005**, *30*, 3799.
78. Gong, Q.M.; Li, Z.; Li, D.; Bai, X.D.; Liang, J. Fabrication and structure: a study of aligned carbon nanotube/carbon nanocomposites. *Solid State Commun.* **2004**, *131*, 399.
79. Gong, Q.M.; Li, Z.; Bai, X.D.; Li, D.; Zhao, Y.; Liang, J. Thermal properties of aligned carbon nanotube/carbon nanocomposites. *Mater. Sci. Eng. A* **2004**, *384*, 209.
80. Naslain, R.; Hagenmuller, P.; Christin, F.; Heraud, L.; Choury, J.J. The carbon fiber – Carbon and silicon carbide binary matrix composites: a new class of materials for high temperature applications. In *Advances in Composite Materials*; Bunsell, A.R., Bathias, C., Martrenchar, A., Menkes, D., Verchery, G., Eds.; Pergamon: Oxford, 1980; Vol. 2, 1084.
81. Naslain, R. Design, preparation and properties of non-oxide CMCs for application in engines and nuclear reactors: an overview. *Compos Sci. Technol.* **2004**, *64*, 155.
82. Li, X.; Ci, L.; Kar, S.; Soldano, C.; Kilpatrick, S.J.; Ajayan, P.M. Densified aligned carbon nanotube films via vapor phase infiltration of carbon. *Carbon* **2006**, *45* (4), 847.
83. Martel, R.; Schmidt, T.; Shea, H.R.; Hertel, T.; Avouris, P. Single and multi wall nanotube field effect transistors. *Appl. Phys. Lett.* **1998**, *73* (17), 2447.
84. Avouris, P.; Chen, Z.; Perebeinos, V. Carbon-based electronics. *Nat. Nanotechnol.* **2007**, *2*, 605.
85. Freitag, M.; Tsang, J.C.; Bol, A.; Yuan, D.; Liu, J.; Avouris, P. Imaging of the Schottky barriers and charge depletion in carbon nanotube transistors. *Nano Lett.* **2007**, *7* (7), 2037.
86. Bachtold, A.; Henny, M.; Terrier, C.; Strunk, C.; Shonenberger, C.; Salvetat, J.-P.; Bonard, J.-M.; Forró, L. Contacting carbon nanotubes selectively with low-ohmic contacts for four-probe electric measurements. *Appl. Phys. Lett.* **1998**, *73* (2), 274.
87. Kaloyeros, A.E.; Welch, J.; Castracane, J.; Oktyabrsky, S.; Geer, R.; Dovidenko, K. Interconnect nanotechnology. Overarching concepts and demonstration vehicles. Annual Review of the Interconnect Focus Center, 2002, Atlanta, GA.
88. Dovidenko, K.; Rullan, J.; Moore, R.; Dunn, K.; Geer, E.E.; Heuchling, F. FIB-assisted Pt deposition for carbon nanotube integration and 3-D nanoengineering. *Mater. Res. Soc.* **2002**, *716*, 557.
89. Vajtai, R.; Wei, B.-Q.; Shusterman, Y.V.; Dunn, K.; Dovidenko, K.; Schowalter, L.J.; Ajayan, P.M. Nanotubes: science and applications topical conference. In *15th International Vacuum Congress of the American Vacuum Society, AVS 48th International Symposium and 11th International Conference on Solid Surfaces*, San Francisco, CA.
90. Soh, H.T.; Quate, C.F.; Morpurgo, A.F.; Marcus, C.M.; Kong, J.; Dai, H. Integrated nanotube circuits: controlled growth and ohmic contacting of single walled carbon nanotubes. *Appl. Phys. Lett.* **1999**, *75* (5), 627.

91. Wei, B.-Q.; Kohler-Redlich, P.; Bader, U.; Heiland, B.; Spolenak, R.; Arzt, E.; Ruhle, M. Selective specimen preparation for TEM observation of the cross section of individual carbon nanotube/metal junctions. *Ultra-microscopy* **2000**, *85* (2), 93.
92. Sagnes, M.; Broto, J.-M.; Raquet, B.; Ondarçuhu, T.; Laurent, Ch.; Flahaut, E.; Vieu, Ch.; Carcenac, F. Alignment and nano-connections of isolated carbon nanotubes. *Microelectron. Eng.* **2003**, *67–68*, 683.
93. Austin, D.W.; Puretzky, A.A.; Geohegan, D.B.; Britt, P.F.; Guillorn, M.A.; Simpson, M.L. The electrodeposition of metal at metal/carbon nanotube junctions. *Chem. Phys. Lett.* **2002**, *361*, 525.
94. Chen, C.; Liu, L.; Lu, Y.; Kong, E.S.-W.; Zhang, Y.; Sheng, X.; Ding, H. A method for creating reliable and low-resistance contacts between carbon nanotubes and microelectrodes. *Carbon* **2007**, *45*, 436.
95. Kumar, A.; Pushparaj, V.I.; Kar, S.; Nalamasu, O.; Ajayan, P.M.; Baskaran, R. Contact transfer of aligned carbon nanotube arrays onto conducting substrates. *Appl. Phys. Lett.* **2006**, *89* (16), id. 163120.
96. Zhu, L.; Sun, Y.; Hess, D.W.; Wong, C.-P. Well-aligned open-ended carbon nanotube architectures: an approach for device assembly. *Nano Lett.* **2006**, *6* (2), 243.
97. <http://public.itrs.net>

# Carbon Nanotube–Metal Matrix Composites

Efraín Carreño-Morelli

Design and Materials Unit, University of Applied Sciences of Western Switzerland, Sion, Switzerland

## INTRODUCTION

Metal matrix composites (MMCs) are currently employed in high-performance applications in the transportation, aerospace, defense, and electronic industries. They combine the most attractive properties of their constituents such as the formability and toughness of the metal matrix and the high strength and stiffness of the ceramic reinforcement, or the high thermal conductivity of the matrix and the low thermal expansion of the reinforcement. In particular, aluminum- or magnesium-based MMCs offer a unique combination of lightweight, high specific stiffness, good fatigue properties, and good electrical and thermal conductivity. Titanium-based MMCs exhibit high strength and stiffness and elevated temperature performance. Copper matrices are of interest when high thermal conductivity and temperature resistance are required, for example, in electronic packaging applications.

Most MMC fabrication is carried out by melt infiltration of ceramic preforms, slurry casting, powder compaction, and spray deposition methods. By an appropriate selection of matrix, reinforcement, processing route, and postprocessing thermomechanical treatment, the final material properties can be designed for specific applications. In structural applications, a good *interfacial strength* ensuring effective *load transfer* between matrix and reinforcement under an external applied stress is essential for the overall mechanical performance.<sup>[1–5]</sup>

The discovery of carbon nanotubes (CNTs) by Iijima<sup>[6]</sup> opened new perspectives for the development of composite materials, because of their remarkable mechanical, electrical, and thermal properties. As a matter of fact, high Young's modulus up to 1.3 TPa makes CNT the ultimate high strength fibers to be used as reinforcements in composite materials.<sup>[7,8]</sup> Moreover, CNTs have very high thermal conductivity and excellent electrical conductivity. In recent years, the research has been focused in the development of nanotube reinforced polymers and ceramics.<sup>[9–11]</sup> In addition, several papers deal with nanotube coated with metals and nanotube decorated or filled with metal particles.<sup>[12–14]</sup> On the other hand, only few

works have been concerned with the manufacturing and properties of bulk metal–nanotube composites, which remain almost a virgin field. This entry presents both original results and a literature review of the recent advances in the field.

## HISTORICAL BACKGROUND

The literature on bulk CNT–MMCs is limited to about 20 papers.<sup>[15–32]</sup> A pioneering work on processing CNT reinforced aluminum was published by Kuzumaki et al. in 1998.<sup>[15]</sup> They produced composite wires by hot extrusion of CNT–Al powder blends, which were previously mounted on a silver sheath. The resulting wire microstructure consisted of partially aligned nanotubes on a metal matrix. Transmission electron microscopy (TEM) observations showed that the nanotubes were not damaged by the processing method, and that no reaction at the nanotube/aluminum interface was visible after annealing for 24 hr at 983 K. The tensile strength of the composite wires was similar to that of pure aluminum produced in similar powder metallurgy process, but the wires retained the strength by annealing at 873 K, while the strength of aluminum wires significantly decreased with time. The same authors published a further work on CNT reinforced titanium<sup>[16]</sup> that was prepared by hot compaction at 1208 K for 2 hr, at 30 MPa, in vacuum. TEM observations revealed that the nanotubes did not react with the Ti matrix. A significant increase in microhardness and elastic modulus (evaluated by ultrasonic spectrum microscopy) was measured and compared with pure titanium obtained by the same processing route.

In 1999, Xu et al. published a work on the electrical properties of Al–CNT composites.<sup>[17]</sup> The manufacturing method was hot pressing of hand-blended CNTs and Al powders. A slight increase in resistivity was observed, which was attributed to scattering of charge carriers by nanotube agglomerates at grain boundaries, porosity, and to the presence of carbide phases. The most interesting result of this work was a kind of “superconducting” transition at low temperatures: an abrupt resistivity drop of more than 90% measured

at about 80 K. These results remain unexplained, and no additional experimental evidence has been reported.

Zhong, Cong, and Hou<sup>[18]</sup> and Tang et al.<sup>[19]</sup> processed Al–CNT composites by using Al nanopowders of mean size 50 nm and single-wall arc-discharged nanotubes, which were soaked in alcohol and stirred ultrasonically in different volume fractions. The blends were compacted at 1.5 GPa at room temperature, followed by compaction at 1.0 GPa at 380°C in vacuum. The hardness of the composites was up to twice the hardness of unreinforced Al processed from nanopowders at the same conditions. In addition, the coefficient of thermal expansion of Al–15 vol.% CNTs was reduced by 65% when compared with unreinforced aluminum.

The powder metallurgy processing of both Mg–CNT and Al–CNT composites by Carreño-Morelli et al.<sup>[20–22]</sup> will be presented in the next section. In addition, these authors have suggested the use of metal-coated nanotubes to improve the matrix–reinforcement bonding strength. For instance, a coating method of nanotubes with magnesium has been described,<sup>[20,33]</sup> which would be promising to improve the Mg–CNT interface bonding strength.

The liquid metal infiltration route was explored by Yang and Schaller.<sup>[23]</sup> The authors processed a hybrid ceramic preform by growing nanotubes on a short Al<sub>2</sub>O<sub>3</sub> SAFFIL fiber preform. The hybrid preform was infiltrated with magnesium in a gas pressure infiltration device. The nanotubes, which act as interface modifiers, are responsible for a slight decrease in the transient damping during thermal cycling. In addition, an increase of 20% in the elastic shear modulus of Mg–25 vol.% SAFFIL–CNTs was reported when compared with Mg–25 vol.% SAFFIL.

Several techniques of mixing and consolidation have been used to prepare CNT–copper composites. Dong, Tu, and Zhang,<sup>[24]</sup> Tu et al.,<sup>[25]</sup> and Chen et al.<sup>[26]</sup> used catalytic chemical vapor deposition (CCVD) nanotubes, which were nickel coated by electroless plating to improve adherence with the copper matrix. After wet ball milling, Cu–CNT blends were isostatically pressed at 350 MPa, followed by sintering at 850°C for 2 hr in vacuum, rolling, and annealing at 600°C for 3 hr<sup>[24]</sup> or isostatically pressed at 600 MPa and 100°C, followed by sintering at 800°C for 2 hr in vacuum.<sup>[25,26]</sup> Both hardness and tribological tests were performed. The coefficient of friction and weight loss were measured on a block-on-ring apparatus. Compared with carbon fiber reinforced copper, nanotube–copper composites had a lower coefficient of friction and wear rate. The optimum nanotube content for hardness and tribological behavior was about 12%. In addition, Ni–P–CNT coatings were applied by electroless plating on carbon steel.<sup>[26]</sup> Compared with

Ni–P–SiC and Ni–P–graphite coatings, Ni–P–CNT exhibited higher wear resistance and lower friction coefficient.

Ahn et al.<sup>[27]</sup> processed Cu–CNT composites by different methods. Ball milling followed by sintering–rolling–sintering consolidation was found to give the best results concerning density, uniform distribution of nanotubes, and low resistivity. The consolidation was achieved by spark-plasma sintering at 350 MPa and 900°C for 2 hr, followed by cold rolling and a second sintering at 900°C for 1 hr. The authors also found that high-energy ball milling resulted in nanotube degradation to amorphous carbon, a problem which has been also found after attrition milling of Al–CNT mixtures.<sup>[28]</sup> Kim et al.<sup>[29]</sup> processed Cu–CNT composites by ball milling of nanosized Cu powders ( $D_{50} \sim 40$  nm) and multiwall CNTs blends, followed by spark-plasma sintering at 700°C for 1 min, at a pressure of 40 MPa. The hardness of the composites increases as the volume fraction of CNTs increases from 0% to 10%. In addition, the hardness of composites processed from Cu nanopowders was about 2.2 times the hardness of composites processed from coarse Cu powders.

Recently, some novel manufacturing routes have been explored. Laha et al.<sup>[30]</sup> processed nanotube reinforced Al–Si parts by plasma spray forming. Al–Si powders and CCVD CNTs were mixed by ball milling. The blended composite powder was plasma sprayed on a cryogenically cooled, rotating, smooth, tapered 6061 Al mandrel. Near-net shape cone-shaped parts were manufactured. Density measurements, X-ray diffraction, and energy dispersive spectroscopy microanalysis showed the presence of graphite and aluminum oxide that is formed during the deposition process. The formation of other carbon allotropes from CNTs was also probable. No aluminum carbide, Al<sub>4</sub>C<sub>3</sub>, was detected by TEM observations. Despite the high temperatures involved in the process, which can melt or sublime the nanotubes, a fraction of them was retained as revealed by scanning electron microscopy (SEM) observation of fracture surfaces. This is because big Al–Si/CNT agglomerates were only partially molten during the spray deposition process. An increase in microhardness was measured, but it is still not clear if this is because of the presence of nanotubes or other phases developed during spray forming.

Noguchi et al.<sup>[31]</sup> have developed a new method to obtain a uniform dispersion of nanotubes in aluminum matrix. It consists of two steps: first, elaboration of a “precursor” consisting of nanotubes dispersed in an elastomer matrix; and second, displacement of the elastomer by aluminum. The precursor was prepared by mixing in a two-roll mill multiwall CNTs, Al powder, Mg powder, natural rubber, and a free-radical initiator. Precursor sheets of 2-mm thickness were

placed in molds and formed by compression molding at 80°C. In the second step, the precursor was placed between Al plates and heated up to 800°C under nitrogen. The rubber is decomposed and gasified while molten Al fills the pores. After cooling, the resulting material shows a rather uniform microstructure without nanotube agglomerates. A significant improvement in the compression resistance, strain, and elastic limits was measured in Al/1.6%CNT and Al/0.8%CNT specimens when compared with pure Al specimens prepared by the same method. To explain these results, the authors consider the radicals resulting from the decomposition of elastomer molecules as responsible

for two key features: 1) the reduction of the Al<sub>2</sub>O<sub>3</sub> layer covering the Al powders and 2) a reaction that activates the surfaces of multiwall nanotubes and improves the wettability by molten Al.

Finally, an interesting concept for creating ultralow resistivity composites has been suggested by Hjortstam et al.<sup>[32]</sup> The authors show that a room-temperature resistivity 50% lower than copper is achievable. This would be possible because of ballistic conduction in single-wall nanotubes, which can have an electron mean free path of several orders of magnitude more than metal conductors such as Al, Cu, and Ag. Among the problems to solve for the development of such ultralow resistivity composites, one can notably cite the need for a processing method that guarantees good contact and alignment of nanotubes on a metal matrix, and the production of bulk quantities of ballistically conducting CNTs.

### CNTs FOR MMCs

The current processing routes of CNTs are electric arc discharge, CCVD, and laser ablation, which have been extensively described in the literature.<sup>[34]</sup> These processes differ in nanotube structure and quality, price, and scaling-up capability. Laser ablation produces high quality and almost free-of-defect CNTs, but the cost of producing large amounts of nanotubes by this technique would be prohibitive. On the other hand, CCVD offers a great potential for scaling-up. Fig. 1 shows multiwall CNTs processed and purified at the Swiss Federal Institute of Technology, Lausanne. Long nanotubes are entangled, and some remaining

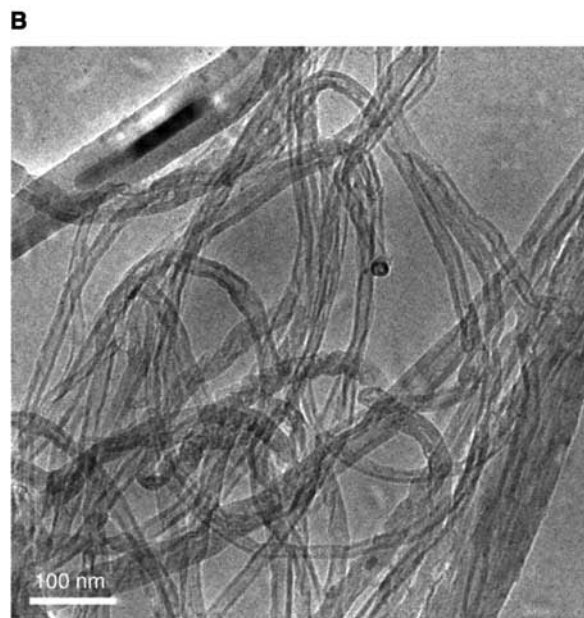
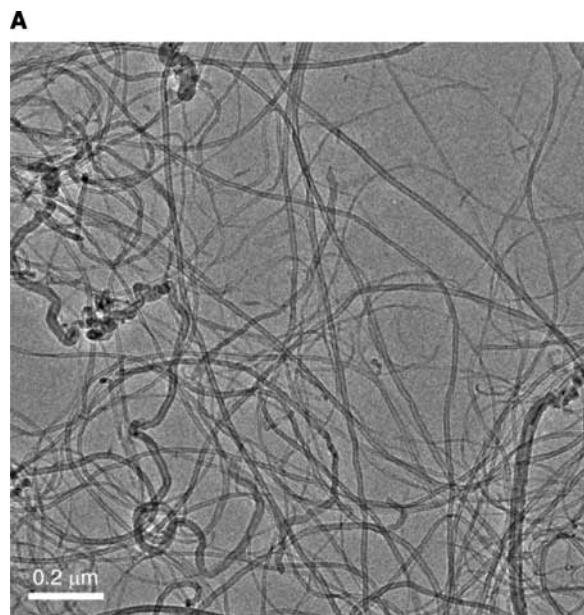


**Fig. 1** TEM images of CCVD-processed multiwall nanotubes. *Source:* A. Magrez.

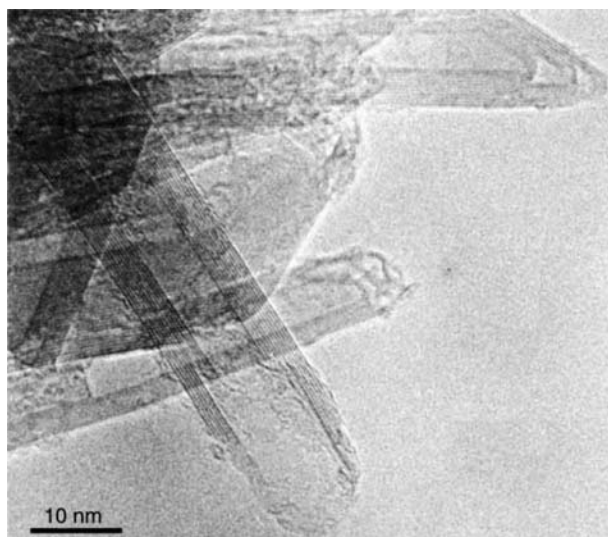


**Fig. 2** TEM image of arc-discharged multiwall nanotubes. *Source:* V.A. Ryzhkov.



catalyst particles are visible. The processing technique is the catalytic decomposition of acetylene in a fixed-bed flow reactor at 720°C over  $\text{Fe}_{1-x}\text{Co}_x$  catalyst supported by  $\text{CaCO}_3$ . The concentration of metal catalyst is about 5% relative to calcium carbonate. A further purification step by sonication in a nitric acid solution is necessary to remove catalyst particles, support the material, and amorphous carbon. For continuous production, a method based on a rotary tube furnace has been developed. It provides high-purity CNTs, less damage to graphitic walls, and high yield up to 500 g/day.<sup>[35]</sup>

Arc-discharge processed multiwall CNTs have a much better purity, because no magnetic materials are used in their production. Nevertheless, they have to be separated from carbonaceous by-products as amorphous carbon, polyhedral particles, and fullerenes. A rather low yield and high specific energy consumption have been common issues in this

processing technique. However, recent developments allow production with a mean average yield up to 1–3 g/min with low specific consumption of electricity. Fig. 2 shows multiwall CNTs processed at Rosseter Holdings Ltd. by cracking of liquid hydrocarbons, driven by a self-regulated, low-voltage contact arc discharge.<sup>[36]</sup>

The mechanical properties of CNTs strongly depend on their structure that is determined by the fabrication process. Both theoretical and experimental studies have shown that arc-discharged and laser ablation single-wall CNTs exhibit Young's modulus up to 1.3 TPa.<sup>[7,8,37]</sup> Arc-discharged multiwall CNTs contain very few defects and have modulus comparable to single-wall nanotubes. On the other hand, catalytic CNTs can be one to two orders of magnitude less stiff; their Young's modulus decreases as the number of defects and disorder within the graphene walls increases.<sup>[38]</sup>

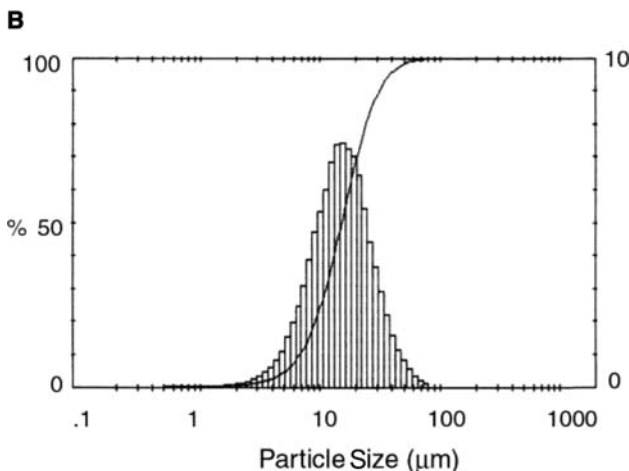
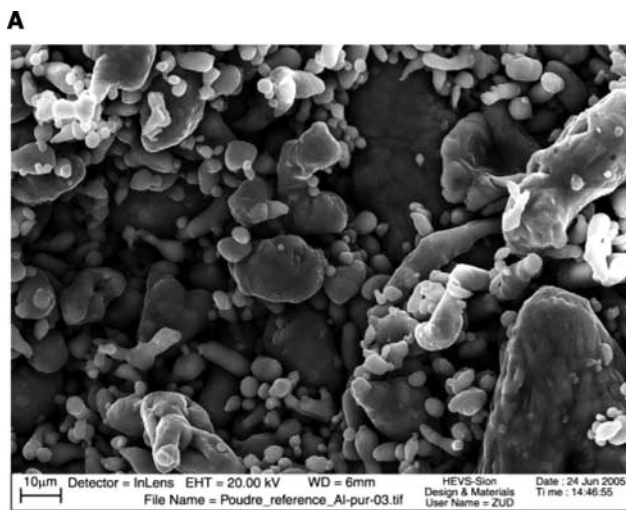


**Fig. 3** Al powder, 99.5% purity: (A) scanning electron micrograph and (B) size distribution.

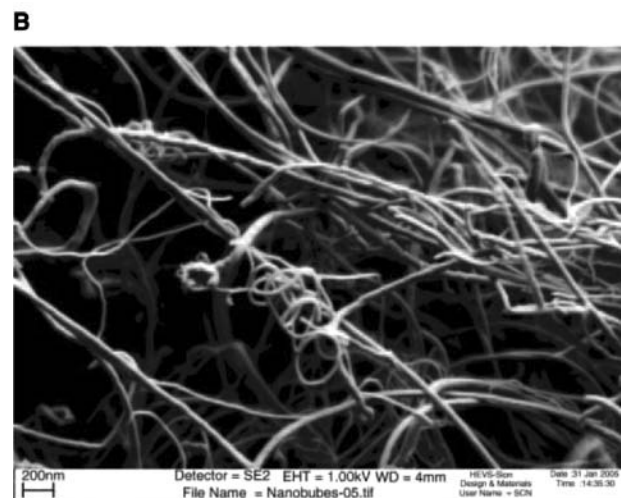
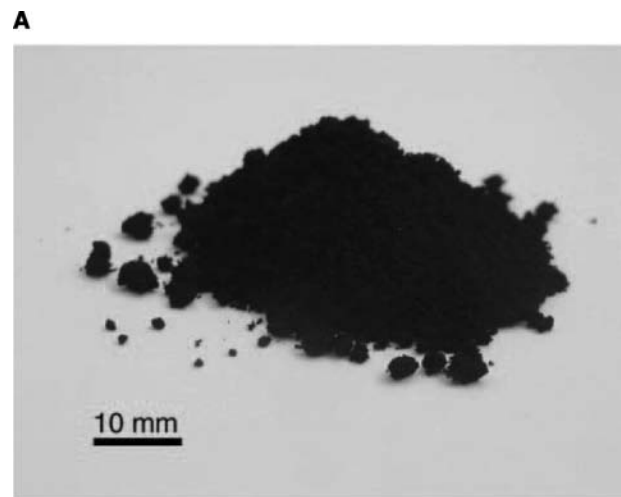


**Fig. 4** Scanning electron micrograph of CCVD nanotube agglomerates.

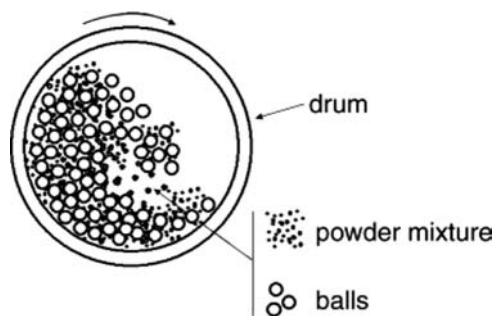


Fig. 5 Schematics of ball milling.

## POWDER METALLURGY PROCESSING OF CNT–METAL COMPOSITES

Among the current methods for processing MMCs, liquid metal infiltration can be ruled out because of the poor wettability of nanotubes by molten metals,

the difficulty of manufacturing CNT preforms, the difficulty in infiltrating loose CNT beds, and the easy formation of nanotube agglomerates.

Uniform dispersion of reinforcement in the metal matrix is of prime importance in the manufacturing of MMCs with controlled properties. Powder metallurgy seems to be the most promising route to accomplish this goal, provided that uniform mixing of matrix powder and CNTs is performed before compaction and sintering. Fig. 3 shows typical aluminum powder morphology and size distribution measured by laser diffractometry. Fig. 4 shows agglomerates of CCVD grown nanotubes. Nanotube agglomeration occurs because of entanglement, high specific surface area, and the action of van der Waals attraction and electrostatic forces. In general, agglomeration makes packing, flow, mixing, compaction, and sintering more difficult.<sup>[39]</sup> De-agglomeration can be achieved by ball milling, i.e., rolling a jar partially filled with powder and balls, and allowing the balls to fall and impact

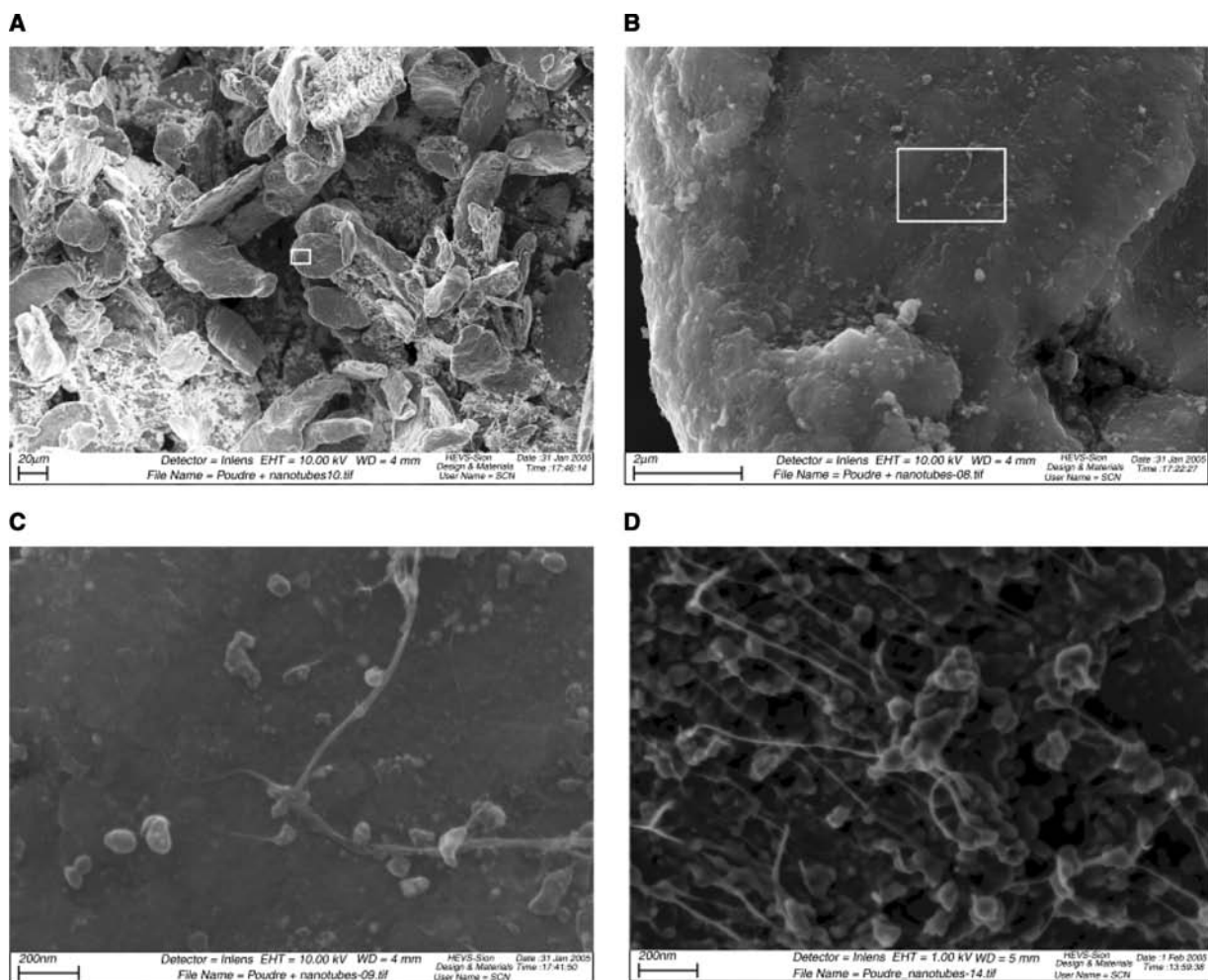


Fig. 6 Scanning electron micrographs of Mg–CNT ball-milled powders, CCVD grown nanotubes: (A) composite powder; (B) details of a particle surface; and (C, D) nanotubes partially embedded in the surface of metal particles.

on the powder (Fig. 5). Different types of mills can be used, e.g., drum mills, planetary mills, and shaker mills. The efficiency of ball milling depends on the ball-to-powder mass ratio and on the energy of individual ball–powder–ball collisions.<sup>[40,41]</sup> Depending on the powder properties, ceramic or metallic balls can be used. Because CCVD multiwall nanotubes contain remaining catalyst particles that are magnetic, Al<sub>2</sub>O<sub>3</sub> balls have to be used for de-agglomeration and mixing. On the other hand, for arc-discharged multiwall nanotubes steel balls can be used, which allows one to increase the ball-to-powder mass ratio and achieve a better mixing.

Fig. 6 and 7 show composite powders obtained after ball milling in a Turbula type shaker mill. Multiwall CCVD CNTs and Mg powders were milled with ceramic balls for 5 hr, with a ball-to-powder mass ratio of 3. In addition, multiwall arc-discharged CNTs and Al powders were milled with steel balls for 12 hr, with a ball-to-powder mass ratio of 5. Fig. 6C and D show

nanotubes partially embedded in the surface of metal particles. Fig. 7A and B show composite particles in which nanotubes are uniformly dispersed. In addition, emerging nanotubes are visible in some small composite particles (Fig. 7C). These results demonstrate the potential of ball milling to disperse nanotube agglomerates and produce a new composite powder for better sintering.

An effective method of sintering metal–nanotube powders is hot compaction. The blends are placed in a double-action graphite tooling consisting of a die and two cylindrical pistons. Heating to sintering temperature is achieved by direct resistive heating while applying compaction pressure. An optional further consolidation step by hot isostatic pressing can be performed to improve sintering and ductility. In this way, disk-shaped compacts (Ø53 mm × 5 mm) are obtained by hot pressing at 600°C in vacuum under a pressure of 50 MPa for 30 min, followed by hot isostatic pressing at 600°C for 60 min under an argon

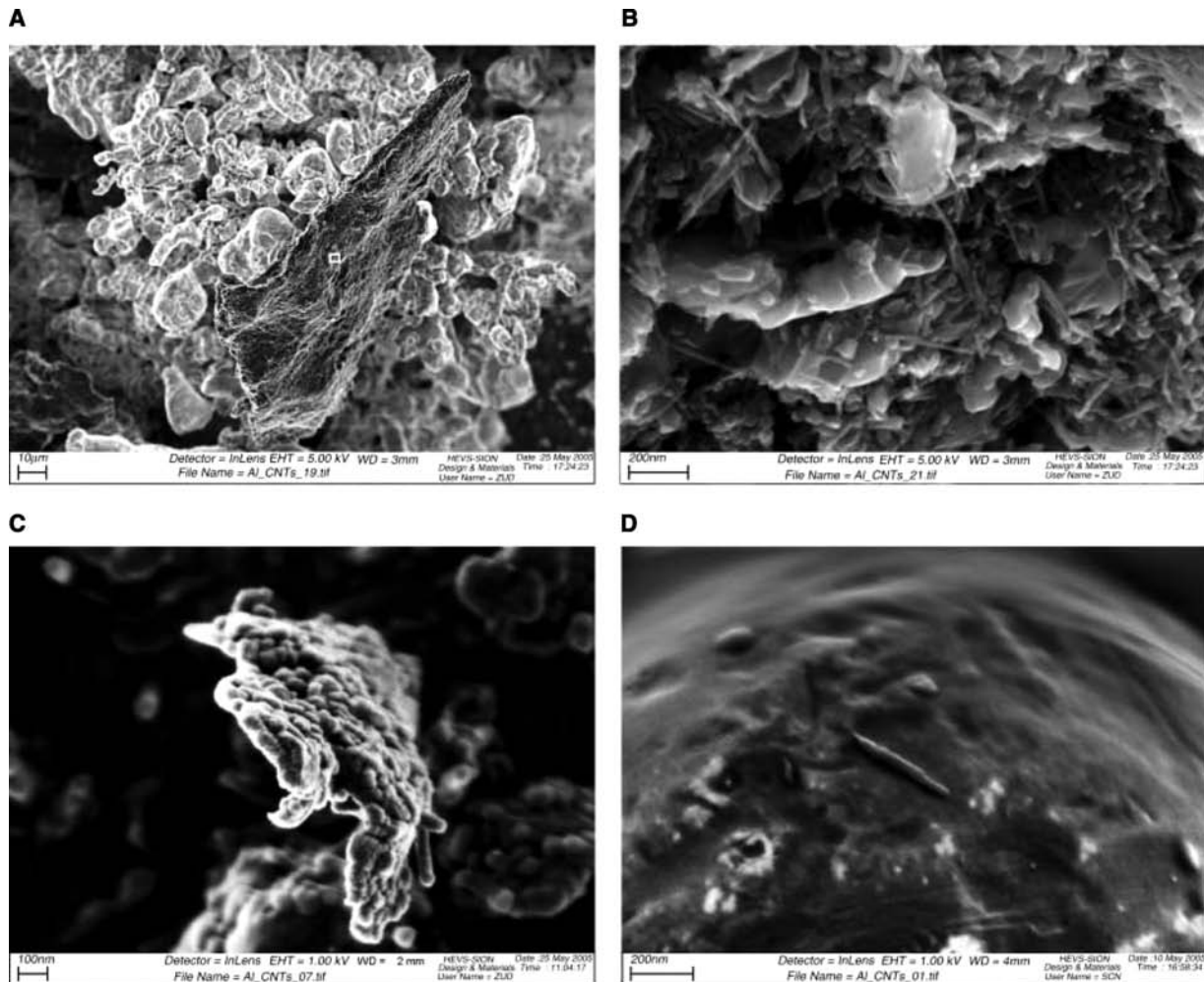


**Fig. 7** Scanning electron micrographs of Al–CNT ball-milled powders, arc-discharge grown nanotubes: (A) composite powder; (B) details of a broken composite particle showing uniform dispersion of CNTs; (C) composite particle showing emerging nanotubes; and (D) nanotube on the surface of a metal particle.



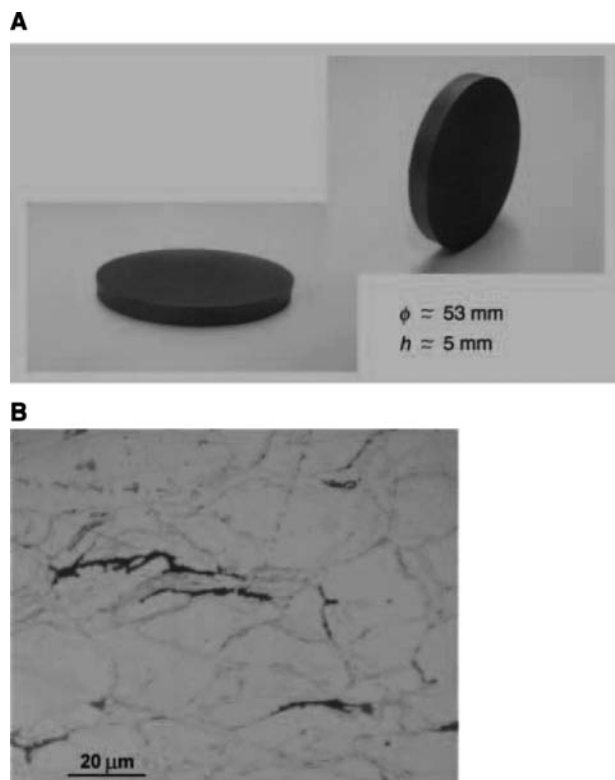


**Fig. 8** Hot pressed Mg–2%CNT compacts (A) and metallographic observation (B).

pressure of 1800 bar (Fig. 8A).<sup>[20]</sup> The density of Mg–2%CNT compacts (CCVD nanotubes) is about 98% of the theoretical density calculated from a mixture law (values of about 96% are measured for Al–2%CNT). Metallographic observations reveal a microstructure consisting of Mg grains with nanotubes along grain boundaries and nanotube clusters (Fig. 8B). It is a goal to reduce the number of such clusters that are detrimental for mechanical properties. These results show that both mixing and sintering conditions need to be improved.

Mg–CNT composites exhibit a ductile behavior, which suggests good bonding between nanotubes and the metal matrix. Yield strength (89 MPa), ultimate strength (140 MPa), and strain after fracture (~3%) are similar to the values measured for sintered magnesium under similar conditions. Resonant measurements of the Young modulus show an improvement of about 9% for Mg–2%CNT ( $38.6 \pm 0.7$  GPa) when compared with unreinforced sintered Mg ( $35.3 \pm 0.8$  GPa). SEM observations of fracture surfaces reveal a rather uniform distribution of nanotubes and nanotube pull-out from the metal matrix (Fig. 9).<sup>[20–22]</sup>

Sintering of Al–CNT composites is difficult, because of the aluminum oxide layer at the powder surface, which acts as a diffusion barrier. Despite good density after hot compaction, the result is usually a brittle

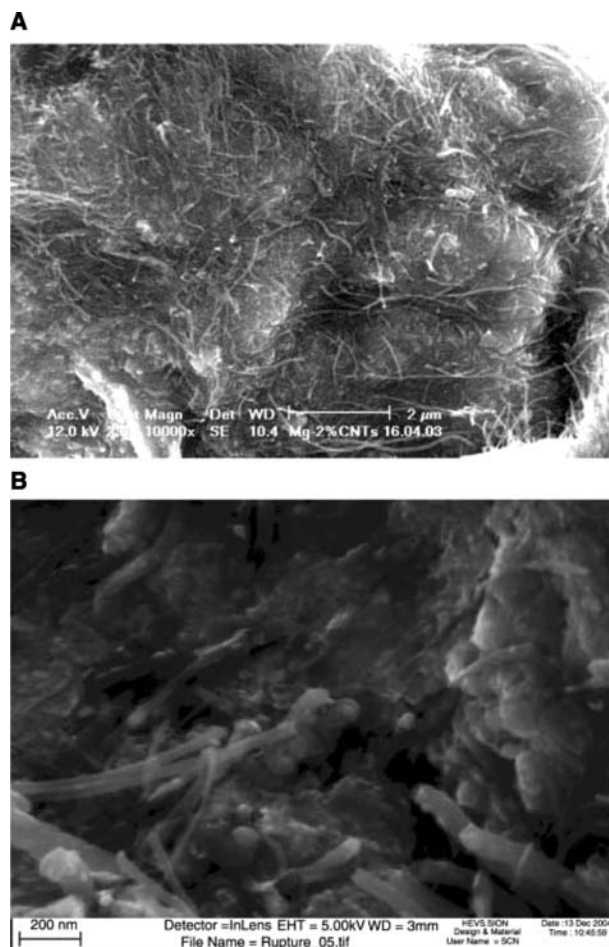


**Fig. 9** Rupture surface of Mg–2%CNT (CCVD nanotubes) after tensile tests.

material. The material properties should be improved by sintering blends of prealloyed aluminum powders and arc-discharged CNTs. The research is in progress, and the results will be published elsewhere.<sup>[42]</sup>

## CONCLUSIONS

CNTs offer a great potential for the development of a new generation of MMCs. Until now, few works on the subject have been published, and only slight enhancement of mechanical, tribological, or electrical properties has been obtained. However, there is a trend toward an increase of the research effort to develop reliable processing methods to manage main issues such as nanotube dispersion in the metal matrix and matrix–nanotube interfacial strength. The cost effective processing of high quality CNTs combined with appropriate powder metallurgy techniques would offer a suitable route for the development of high-performance affordable composites. The major challenge for the future is to make this happen.

## ACKNOWLEDGMENTS

The author wishes to thank Dr. R. Schaller (EPFL Lausanne) and Dr. D. Tománek (Michigan State University) for fruitful discussions. The technical support of N. Schmidt, D. Zufferey, and S. Héritier is gratefully acknowledged. This work was supported by the Swiss Innovation Promotion Agency under CTI Contract No. 5990.3 TNS and by the University of Applied Sciences of Western Switzerland under HEVs Grant.

## REFERENCES

1. Taya, M.; Arsenault, R.J. *Metal Matrix Composites*; Pergamon Press: Oxford, 1989.
2. Suresh, S.; Mortensen, A.; Needleman, A.; Eds. *Fundamentals of Metal Matrix Composites*; Butterworth-Heinemann: Boston, 1993.
3. Clyne, T.W. *Comprehensive Composite Materials. Vol. 3: Metal Matrix Composites*; Elsevier: Amsterdam, 2000.
4. Miracle, D.B.; Donaldson, S.L.; Eds. *ASM Handbook. Vol. 21: Composites*; ASM International: Materials Park, OH, 2001.
5. Chawla, K.K.; Chawla, N. *Metal Matrix Composites*; Springer: New York, 2005.
6. Iijima, S. Helical microtubules of graphitic carbon. *Nature* **1991**, *354*, 56–58.
7. Wong, E.W.; Sheehan, P.E.; Lieber, C.M. Nanobeam mechanics: elasticity, strength, and toughness of nanorods and nanotubes. *Science* **1997**, *277*, 1971–1975.
8. Salvetat, J.-P.; Briggs, G.A.D.; Bonard, J.-M.; Bacsá, R.R.; Kulik, A.J.; Stöckli, T.; Burnham, N.A.; Forró, L. Elastic and shear moduli of single-walled carbon nanotube ropes. *Phys. Rev. Lett.* **1999**, *82*, 944–947.
9. Thostenson, E.T.; Ren, Z.; Chow, T.-W. Advances in the science and technology of carbon nanotubes and their composites: a review. *Comp. Sci. Tech.* **2001**, *61*, 1899–1911.
10. Harris, P.J.F. Carbon nanotube composites. *Int. Mater. Rev.* **2004**, *49*, 31–43.
11. Curtin, W.A.; Sheldon, B.W. CNT-reinforced ceramics and metals. *Mater. Today* **2004**, *11*, 44–49.
12. Hernadi, K.; Ljubovic, E.; Seo, J.W.; Forró, L. Synthesis of MWNT-based composite materials with inorganic coating. *Acta Mater.* **2003**, *51*, 1447–1452.
13. Weidenkaff, A.; Ebbinghaus, S.G.; Mauron, Ph.; Reller, A.; Zhang, Y.; Zuttel, A. Metal nanoparticles for the production of carbon nanotube composite materials by decomposition of different carbon sources. *Mater. Sci. Eng. C* **2002**, *19*, 119–123.
14. Wang, F.; Arai, S.; Endo, M. Metallization of multi-walled carbon nanotubes with copper by an electroless deposition process. *Electrochem. Commun.* **2004**, *6*, 1042–1044.
15. Kuzumaki, T.; Miyazawa, K.; Ichinose, H.; Ito, K.J. Processing of carbon nanotube reinforced aluminum composite. *Mater. Res.* **1998**, *13*, 2445–2449.
16. Kuzumaki, T.; Ujiie, O.; Ichinose, H.; Ito, K. Mechanical characteristics and preparation of carbon nanotube fiber-reinforced Ti composite. *Adv. Eng. Mater.* **2000**, *2*, 416–418.
17. Xu, C.L.; Wei, B.Q.; Ma, R.Z.; Liang, J.; Ma, X.K.; Wu, D.H. Fabrication of aluminum–carbon nanotube composites and their electrical properties. *Carbon* **1999**, *37*, 855–888.
18. Zhong, R.; Cong, H.; Hou, P. Fabrication of nano-Al based composites reinforced by single-walled carbon nanotubes. *Carbon* **2003**, *41*, 848–851.
19. Tang, Y.; Cong, H.; Zhong, R.; Cheng, H.-M. Thermal expansion of a composite of single-walled carbon nanotubes and nanocrystalline aluminum. *Carbon* **2004**, *42*, 3251–3272.
20. Carreño-Morelli, E.E.; Yang, J.; Schaller, R.; Bonjour, C. Tiny tubes boost for metal matrix composites. *Metal Powder Rep.* **2004**, *7*, 40–43, reprinted from Proceedings of European Conference on Powder Metallurgy 2003, Valencia, Spain, Oct 20–22, 2003; European Powder Metallurgy Association: Shrewsbury, UK, 2003; Vol. 2, 59–62.
21. Carreño-Morelli, E.; Yang, J.; Couteau, E.; Hernadi, K.; Seo, J.W.; Bonjour, C.; Forró, L.; Schaller, R. Carbon nanotube/magnesium composites. *Phys. Stat. Sol. (a)* **2004**, *201*, R53–R55.
22. Carreño-Morelli, E.; Schmidt, N.; Schaller, R.; Forró, L. Carbon nanotube/light-metal composites. *TMS Lett.* **2005**, *2*, 119–120.
23. Yang, J.; Schaller, R. Mechanical spectroscopy of Mg reinforced with Al<sub>2</sub>O<sub>3</sub> short fibers and C nanotubes. *Mater. Sci. Eng. A* **2004**, *370*, 512–515.
24. Dong, S.R.; Tu, J.P.; Zhang, X.B. An investigation of the sliding wear behavior of Cu-matrix composite reinforced by carbon nanotubes. *Mater. Sci. Eng. A* **2001**, *313*, 83–87.
25. Tu, J.P.; Yang, Y.Z.; Wang, L.Y.; Ma, X.C.; Zhang, X.B. Tribological properties of carbon-nanotube-reinforced copper composites. *Tribol. Lett.* **2001**, *10*, 225–228.
26. Chen, W.X.; Tu, J.P.; Wang, L.Y.; Gan, H.Y.; Xu, Z.D.; Zhang, X.B. Tribological application of carbon nanotubes in a metal-based composite coating and composites. *Carbon* **2003**, *41*, 215–222.
27. Ahn, J.H.; Shin, H.S.; Kim, Y.J.; Chung, H. Properties of multiwall carbon nanotube-reinforced Cu matrix composites, Proceedings of Powder Metallurgy World Congress PM2004, Vienna, Austria, Oct 17–21, 2004; Danninger, H., Ratzi, R., Eds.; European Powder Metallurgy Association: Shrewsbury, UK, 2004; Vol. 4, 335–342.
28. Edtmaier, C.; Wallnoefer, E.; Koeck, A. Aluminium based carbon nanotube composites by mechanical alloying, Proceedings of Powder Metallurgy World Congress PM2004, Vienna, Austria, Oct 17–21, 2004; Danninger, H., Ratzi, R., Eds.; European Powder Metallurgy Association: Shrewsbury, UK, 2004; Vol. 1, 413–418.
29. Kim, K.T.; Lee, K.H.; Cha, S.I.; Mo, C.B.; Hong, S.H. Fabrication of carbon nanotube/Cu nanocomposites by spark plasma sintering process, Proceedings of Powder

- Metallurgy World Congress PM2004, Vienna, Austria, Oct 17–21, 2004; Danninger, H., Rätzl, R., Eds.; European Powder Metallurgy Association: Shrewsbury, UK, 2004; Vol. 1, 337–342.
30. Laha, T.; Agarwal, A.; McKechnie, T.; Seal, S. Synthesis and characterization of plasma spray formed carbon nanotube reinforced aluminum composite. *Mater. Sci. Eng. A* **2004**, *381*, 249–258.
  31. Noguchi, T.; Margario, A.; Fukazawa, S.; Shimizu, S.; Beppu, J.; Seki, M. Carbon nanotube/aluminum composites with uniform dispersion. *Mater. Trans.* **2004**, *45*, 602–604.
  32. Hjortstam, O.; Isberg, P.; Söderholm, S.; Dai, H. Can we achieve ultra-low resistivity in carbon nanotube-based metal composites. *Appl. Phys. A* **2004**, *78*, 1175–1179.
  33. Seo, J.W.; Couteau, E.; Umek, P.; Hernadi, K.; Marcoux, P.; Lukić, B.; Mikó, Cs.; Milas, M.; Gáal, R.; Forró, L. Synthesis and manipulation of carbon nanotubes. *New J. Phys.* **2003**, *5*, 120.1–120.22.
  34. Popov, V.N. Carbon nanotubes: properties and application. *Mater. Sci. Eng. R* **2004**, *43*, 61–102.
  35. Magrez, A.; Seo, J.-W.; Mikó, C.; Hernádi, K.; Forró, L. Growth of carbon nanotubes with alkaline earth carbonate as support. *J. Phys. Chem. B* **2005**, *109*, 10,087–10,091.
  36. Ryzhkov, V.A. Carbon nanotube production by a cracking of liquid hydrocarbons. *Physica B* **2002**, *323*, 324–326.
  37. Srivastava, D.; Wei, C.; Cho, K. Nanomechanics of carbon nanotubes and composites. *Appl. Mech. Rev.* **2003**, *56*, 215–230.
  38. Salvétat, J.-P.; Kulik, A.J.; Bonard, J.-M.; Briggs, G.A.D.; Stöckli, T.; Méténier, K.; Bonnamy, S.; Béguin, F.; Burnham, N.A.; Forró, L. Elastic modulus of ordered and disordered multiwalled carbon nanotubes. *Adv. Mater.* **1999**, *11*, 161–165.
  39. German, R.M. *Powder Metallurgy Science*, 2nd Ed.; MPIF: Princeton, NJ, 1994.
  40. Eisen, W.B.; Ferguson, B.L.; German, R.M.; Iacocca, R.; Lee, P.W.; Madan, D.; Moyer, K.; Sanderow, H.; Trudel, Y.; Eds. *ASM Handbook. Vol. 7, Powder Metal Technologies and Applications*; ASM International: Materials Park, OH, 1998.
  41. Suryanarayana, C. *Mechanical Alloying and Milling*; Marcel Dekker: New York, 2004.
  42. Carreño-Morelli, E.; Tománek, D.; Ryzhkov, V. *In press*.



# Carbon Nanotubes: Electrochemical Modification

Kannan Balasubramanian

Marko Burghard

Klaus Kern

Max Planck Institut für Festkörperforschung, Stuttgart, Germany

## INTRODUCTION

Carbon nanotubes (CNTs) are important because of their outstanding structural, mechanical, and electronic properties,<sup>[1]</sup> and are finding applications in molecular electronics,<sup>[2]</sup> chemical sensors,<sup>[3,4]</sup> scanning probes,<sup>[5]</sup> special capillaries,<sup>[6]</sup> supercapacitors,<sup>[7]</sup> energy storage devices,<sup>[8]</sup> and electromechanical actuators.<sup>[9]</sup> CNTs are expected to exhibit superior electrochemical properties in comparison with other carbon materials that are widely used in electrochemical applications.<sup>[10]</sup> Because CNTs have length scales similar to those of biological molecules such as enzymes and proteins, they can act as effective biosensing electrodes.<sup>[11]</sup> Furthermore, potential applications such as Coulter counters,<sup>[12]</sup> bio-electrochemical sensors,<sup>[13]</sup> as well as electrochemical hydrogen<sup>[14]</sup> and lithium<sup>[8]</sup> storage have stimulated an increasing amount of research into the electrochemical properties of CNTs.

Chemical functionalization is developing to be an effective tool to broaden the application spectrum of CNTs.<sup>[15]</sup> Until now, functionalization of CNTs has been accomplished by three different approaches, namely, thermally activated chemistry, photochemical functionalization, and electrochemical modification (ECM). Among these, ECM offers the specific advantage that the energy level of a chosen nanotube can be selectively tuned, allowing one to functionalize the tubes in a controlled manner.

To devise novel ECM schemes, it is essential to investigate the electrochemical properties of CNTs, such as their charging and discharging behaviors in various media, electron transfer (ET) rates for different redox couples, etc. In the following entry, the electrochemical characteristics of various types of nanotube electrodes are first presented. Then various ECM methods reported until now are reviewed. The modification of bulk CNTs is detailed first, followed by the modification of individual nanotubes. Finally, various (electro)chemical applications of pristine and electrochemically modified CNTs are discussed.

## NANOTUBE ELECTRODES

### Bulk Electrodes

Bulk nanotube electrodes have been realized from single-walled nanotubes (SWNTs) and multiwalled nanotubes (MWNTs). The most common types of bulk CNT electrodes are:

- *Powder microelectrodes.* These are fabricated by filling CNT powder into a microcavity, which is in contact with a metal wire.<sup>[16]</sup>
- *Paste electrodes.* Here, SWNTs<sup>[17]</sup> or MWNTs<sup>[18]</sup> are dispersed in an organic liquid containing an appropriate binder. The first CNT paste electrodes were made by packing a composite mixture of MWNTs, mineral oil, water, and bromoform into a capillary.<sup>[13]</sup> Alternatively, the CNTs can be mixed with polymers such as Teflon<sup>[19]</sup> or Nafion<sup>[20]</sup> as binders to form composite electrodes.
- *Film electrodes.* Films of SWNTs and MWNTs have been deposited on glassy carbon (GC) or metal supports. Typically, the CNTs are cast from an aqueous dispersion with or without a surfactant,<sup>[21]</sup> or from a dispersion in *N,N*-dimethylformamide (DMF).<sup>[22]</sup>
- *Arrays of vertically aligned CNTs.* This type of electrode has been obtained via chemical coupling of end-functionalized SWNTs onto surface-modified gold electrodes.<sup>[23]</sup> Additionally, electrodes composed of closely spaced MWNTs, forming so-called multiwalled nanotube towers (MWNTTs),<sup>[24]</sup> have been synthesized by thermal chemical vapor deposition (CVD), with the thickness of the grown films reaching up to 100  $\mu\text{m}$ .
- *Paper electrodes.* The SWNT “bucky” paper (SWNTP) is prepared by vacuum filtration of a SWNT suspension through a membrane filter.<sup>[25]</sup> The electrode is composed of sheets of entangled SWNT bundles held together by van der Waals interaction and probably some adhesive impurities.
- *Microbundle electrodes.* These are made by attaching a single MWNT<sup>[26]</sup> bundle to the end of a metal wire.<sup>[26]</sup>

In general, the aforementioned CNT electrodes show a featureless cyclic voltammogram (CV), as distinguished from  $C_{60}$  films, which exhibit several pairs of discrete redox waves characteristic of individual redox molecules. The broad CV signal mainly results from the fact that the CNT electrodes comprise a mixture of semiconducting and metallic tubes, both existing in a distribution of diameters and chiralities. As a consequence, bulk CNT electrodes behave similarly to other carbon-related electrodes such as gas chromatographs (GCs) or highly oriented pyrolytic graphites (HOPGs), and are well suited to probe the redox behavior of small inorganic redox couples as well as organic compounds including larger biomolecules.

CNT bulk electrodes are characterized by a large capacitance, reflecting the high effective surface area of the nanotube material. In many cases, the electrolyte is capable of (partially) penetrating through the electrode because of the porosity of the latter. For example, the surface-specific capacitance of SWNTP electrodes has been found to be  $125 \mu\text{F}/\text{mm}^2$ , three to four orders of magnitude higher than that of conventional carbon electrodes.<sup>[24]</sup> MWNTs also exhibit a large capacitance<sup>[27]</sup> similar to their single-walled counterparts.

Electrodes made from as-prepared or purified CNTs often show faradaic peaks superimposed on the predominant capacitive charging background.<sup>[28]</sup> This behavior has been ascribed to redox reactions associated with functional groups (e.g., quinone or carboxylic functions) introduced by the purification process, or adsorbates.<sup>[22,29]</sup> The faradaic responses can be removed by annealing the CNTs at  $\sim 1000^\circ\text{C}$ , which eliminates impurities.<sup>[30]</sup> It is noteworthy that removal of surface-bonded oxides reduces, at the same time, the wetting capability of the electrodes toward aqueous solutions.

Electrodes composed of SWNTs or MWNTs have remarkably fast ET rates for various redox reactions. The ET kinetics of SWNTP electrodes has been studied by using the  $\text{Fe}(\text{CN})_6^{3-}/\text{Fe}(\text{CN})_6^{4-}$  couple,<sup>[24]</sup> which is a standard benchmark<sup>[10]</sup> for comparing the ET rates at different carbon electrodes. The corresponding CV of the SWNTP electrode exhibits forward and backward redox waves with a separation of 96 mV (Fig. 1), comparable with that obtained with other carbon electrodes. Faster kinetics has been observed for the same redox couple with the MWNT microbundle electrode.<sup>[26]</sup> In this case, the peak-to-peak separation of the redox waves has been found to be only 59 mV, indicative of an ideal, reversible, one-electron transfer that is purely Nernstian in nature.<sup>[31]</sup> This ET rate is higher than that obtained using any other carbon electrode, and is most likely related to the fact that in the bundle electrode, the nanotube ends represent a significant fraction of the CNT surface exposed to the

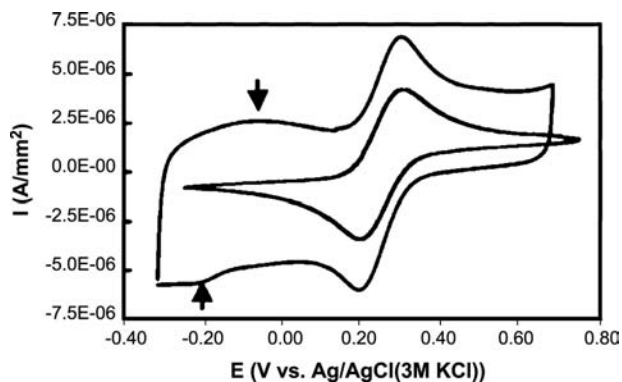


**Fig. 1** CV curves obtained with a SWNTP electrode (outer line) and a carbon paste electrode (inner line) in an aqueous solution of 5 mM  $\text{K}_4\text{Fe}(\text{CN})_6$  with 0.1 M KCl. The well-separated anodic and cathodic currents indicate a larger capacitance for the SWNTP. Arrows indicate pseudo-capacitive current arising probably because of oxides. *Source:* From Ref.<sup>[24]</sup>.

electrolyte. The tube ends can give fast charge transfer, similar to graphite edge planes. CNT electrodes show fast ET kinetics also with organic molecules. In an early study, it has been demonstrated that the oxidation/reduction of dopamine is more facile at MWNT electrodes compared with other carbon surfaces.<sup>[13]</sup> Based on this, facile ET was later also observed for other organic compounds, including ascorbic acid, uric acid, and the biologically relevant  $\beta$ -nicotinamide adenine dinucleotide (NADH; reduced form).<sup>[17–19]</sup>

A comparative study of the ET rates obtained with SWNTs (paper electrodes) and MWNTs (MWNTTs) has revealed an increasing separation between the redox peaks when moving from SWNTPs, through as-produced MWNTTs, to the heat-treated MWNTTs, signifying that the ET rate is maximum for the SWNTPs. Fig. 2 shows a schematic representation of these three types of CNT electrodes. The faster ET rate of the SWNTPs can be explained as resulting from the oxidative purification process, which introduces a large number of edge-plane-like defect sites in the sidewalls. A possible reason for the relatively fast electron transfer kinetics with the as-produced MWNTTs may be the presence of an amorphous coating on the sidewall of tubes, such that the electrochemically active surface consists mainly of tube ends.

### Single-Nanotube Electrode

Electrodes have been constructed also with single CNTs. An electrode consisting of a single MWNT attached to a sharpened platinum wire is shown in Fig. 3. The corresponding CVs of  $\text{Ru}(\text{NH}_3)_6^{3+}$  in aqueous solution show a sigmoidal response characteristic

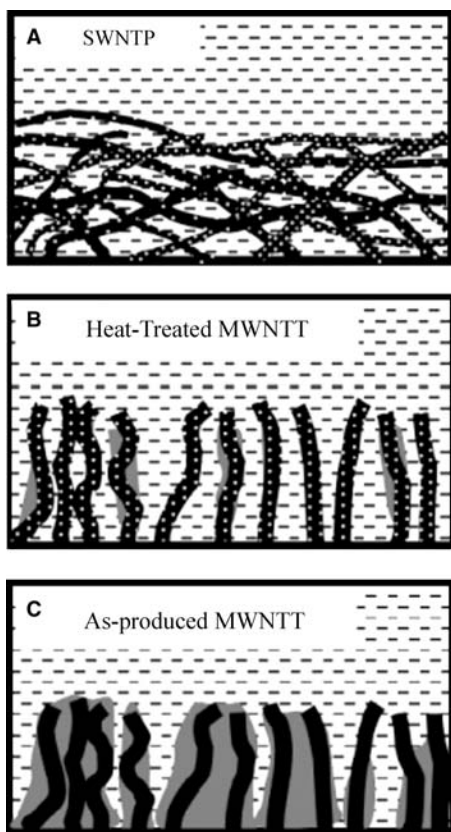


**Fig. 2** Schematic representation of the various types of CNT electrodes in increasing order of effective capacitance. The dots represent defects on the CNT surface and the shaded areas covering the CNTs indicate amorphous carbon. *Source:* From Ref.<sup>[24]</sup>.

of steady-state radial diffusion.<sup>[32]</sup> Furthermore, the limiting current varies linearly with the depth of immersion. When the sidewalls of the nanoelectrode are insulated with a polymer layer, a constant limiting current originating exclusively from the unexposed bottom surface of the bundle is observed.

## ECM OF NANOTUBES

Electrochemistry is a versatile tool for modification of CNTs in a controlled and selective manner. ECM is normally performed potentiostatically or galvanostatically in a solution containing a molecular agent as precursor for an active species (e.g., a radical or radical ion) that will be formed through ET with the CNT electrode. Many organic radical species have a tendency to react with the precursor or to self-polymerize, resulting in a polymer coating on the tubes. Such a polymer deposition may or may not be accompanied by the formation of covalent bonds to the carbon framework of the nanotubes. In general, electrochemical deposition procedures, in addition to being simple,

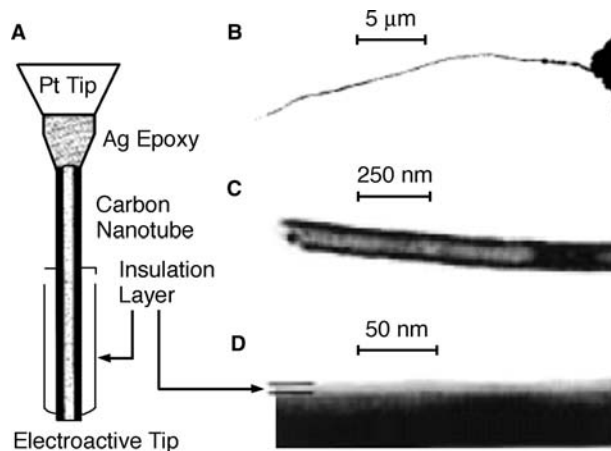


**Fig. 3** Single-carbon nanotube electrode. (A) Schematic showing a partially insulated single MWNT electrode attached to a Pt tip through silver epoxy. TEM images of nanotubular electrodes showing (B) a 30- $\mu\text{m}$ -long electrode, (C) the tip of a  $\sim 100\text{-nm}$ -diameter uninsulated electrode, and (D) the tip of a  $\sim 22\text{-nm}$  electrode coated with a  $\sim 10\text{-nm}$ -thick insulation layer of polyphenol. The uninsulated electrodes show a limiting current proportional to their length of immersion in the solution, whereas the insulated electrodes display a constant limiting current arising from the bottommost uninsulated electroactive part. *Source:* From Ref.<sup>[32]</sup>.

clean, and efficient, also allow good control over the rate and extent of film deposition by the application of appropriate electrochemical conditions. Adjusting these conditions further enables one to tailor the chemical and physical properties of the resulting film. In the following, the covalent and non-covalent ECM of bulk CNT electrodes will be discussed first, followed by a description of ECM applied to single CNTs.

## Covalent Modification of CNTs in Bulk

Until now, covalent modification of CNTs has been successfully employed to attach organic (aromatic) residues, as well as oxygen (oxidation) and halogen atoms (halogenation). In these cases, the formation of covalent bonds has been concluded from changes in the optical absorption or Raman spectra of the tubes. As the chemical reactivity of CNTs increases with increasing curvature of their sidewalls,<sup>[15]</sup> small-diameter tubes have often been used for covalent functionalization. Especially the HiPco SWNT material was frequently chosen because it has a minimum diameter of 0.6 nm.<sup>[33]</sup> However, it should be noted that the chemical reactivity of CNTs is not fully explored, and there is some evidence that also larger-diameter tubes are sufficiently reactive, at least toward highly active species.<sup>[34]</sup>

Aromatic groups can be covalently linked to CNTs via reductive coupling of diazonium salts. The diazonium-based attachment of (substituted) phenyl rings to SWNT electrodes represents the first example of covalent ECM of CNTs.<sup>[35]</sup> Pronounced changes have been observed in the Raman spectra after modification, specifically an increase in the relative intensity of the disorder mode peak at ca.  $1290\text{ cm}^{-1}$  (also called the D-line), and a lowering of the intensity of the radial breathing mode. While the former change directly indicates an increased amount of  $\text{sp}^3$ -hybridized carbons, the latter signifies the disturbance in the carbon framework of the sidewalls. Chemical analysis of the modified products revealed that the extent of modification depends on the type of aryl diazonium salt. Functionalization degrees of up to 0.05 have been found, which corresponds to 1 in 20 carbon atoms bearing an aromatic residue. In the simplest scenario, the diazonium salt is reduced by accepting an electron from the CNT, followed by loss of nitrogen to form an aryl radical and covalent binding of this radical to the intact sidewall via addition to the partial double bonds. However, there are experimental indications that the preferred attachment sites are defects.<sup>[36]</sup> Once started at such an initiation site, the locally enhanced curvature would enhance the attachment of further radicals, thus enabling the reaction to spread along the tube. The aryl diazonium coupling is compatible with a range of different substituents on the aromatic ring. Hence, a proper choice of the substituent allows to control the surface properties of the modified tubes (e.g., to produce a polar, acidic surface with the aid of diazonium salts containing a carboxylic acid function).

Electrochemistry offers a viable route to CNT oxidation. The electrochemical oxidation of SWNT bundles has been investigated by *in situ* Raman spectroscopy under constant current flow.<sup>[37]</sup> In the initial stage, the Raman spectra reveal a continuing shift in the G-line frequency (Fig. 4) resulting from spontaneous and electrochemical charge transfer. On exceeding a critical doping level, irreversible formation of C–O bonds takes place, which is manifested in a decrease in the rate of the G-line frequency change.

Covalent attachment of chlorine or bromine atoms to CNTs has been achieved through anodic oxidation of the corresponding halide ions in an aqueous solution. In particular, bulk MWNT electrodes have been functionalized in this manner.<sup>[38]</sup> Every 1 in 23 carbon atoms has been found to be functionalized, which is relatively high considering the ratio of carbon atoms in the outermost shell to the inner ones. The modified MWNTs were found to be soluble in water or alcohol without adding a surfactant. This property points toward the simultaneous introduction of oxygen-containing functionalities such as hydroxyl or carboxylic groups.

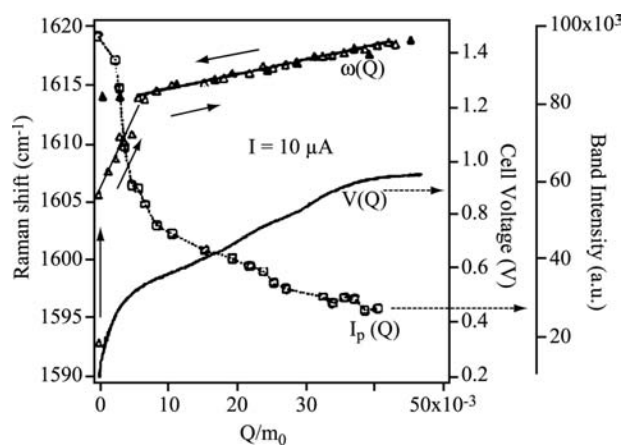


**Fig. 4** Evolution of the SWNT G-line frequency  $\omega$ , its intensity  $I_p$ , and the cell potential  $V$  as a function of the electrochemical charge per unit (initial) electrode mass. The cell current was kept constant at  $10\ \mu\text{A}$ . The open triangles are measured during charging when  $V_{\text{SWNT vs. Pt}} < 0$  and the closed triangles during discharging when  $V_{\text{SWNT vs. Pt}} > 0$ . The irrecoverable change in the G-line frequency signified by the kink is interpreted as being caused by the irreversible formation of C–O bonds. *Source:* From Ref.<sup>[37]</sup>.

### Non-covalent Modification of CNTs in Bulk

The attachment of molecules onto the CNTs in a non-covalent manner is of interest for some applications because the carbon framework of the tubes remains intact; therefore their electronic properties are largely preserved. Non-covalent ECM has been utilized to coat CNTs with a polymer consisting of polypyrrole or polyaniline, which allows to combine the specific properties of CNTs and electrically conducting polymers (ECPs) in a novel composite material. Electropolymerization of monomers has been performed under various conditions. For instance, pyrrole was polymerized in an aqueous solution containing chemically oxidized CNTs at a potential between 0.7 and 1 V vs. saturated calomel electrode (SCE).<sup>[39]</sup> High-resolution scanning electron microscopy (SEM) images revealed the presence of CNTs incorporated within the polypyrrole matrix, and the formation of dense, high-quality composite films. Here, the CNTs with their negatively charged surface groups act as a conductive dopant. Careful inspections have suggested that there must be a polymer coating around the surface of most of the nanotubes, as is shown in Fig. 5. It is possible to control the thickness of the polymer coating on the tubes through the magnitude of the applied potential and the duration of electropolymerization. Formation of polyaniline layers on MWNTs has been accomplished via oxidative polymerization of aniline using a potential of  $\sim 0.8\text{ V}$  vs. SCE in dilute sulfuric acid.<sup>[40]</sup> The thickness of polyaniline films can be up to 10 times

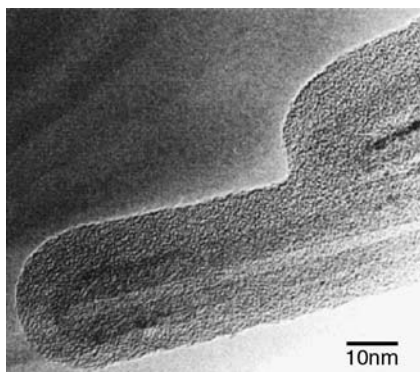


**Fig. 5** High-resolution TEM image of two nanotubes coated with polypyrrole, showing the inner CNT framework and the outer amorphous polymer layer. The coating was performed by applying a potential of 0.8 V for 2 min onto a bare copper grid on a Pt wire in a degassed solution containing 0.2% CNTs and 0.5 M pyrrole. *Source:* From Ref.<sup>[39]</sup>.

higher than that formed on a Pt electrode after passing the same amount of charge, which can be traced back to the relatively large surface area of the CNT electrode.

An inorganic variant of non-covalent ECM is the electrodeposition of metals onto CNTs. Although metal-carbon bonds may be formed on evaporation of certain metals onto CNTs under ultrahigh vacuum (UHV) conditions,<sup>[41]</sup> the reduction of metal ions at the surface of adsorbate-covered tubes more likely results in physisorbed metal particles. Electrodeposition has been used to decorate purified MWNTs deposited onto HOPGs with metallic clusters of copper.<sup>[42]</sup> The clusters start forming at sites where the MWNT is in contact with the HOPG and continue to grow over time. Moreover, magnetic nanoparticles consisting of Ni, Fe, and Co have been electrodeposited from aqueous solutions onto carbon nanowalls as templates.<sup>[43]</sup> Carbon nanowalls are two-dimensional carbon nanosheets grown on Cu substrates using microwave plasma-enhanced CVD.<sup>[44]</sup> The shape and size of the deposited metal particles can be tailored by the detailed characteristics of the applied bipolar current density profile, which induces cycles of nanoparticle deposition and partial etching. A representative example of the deposited nanoparticles is shown in Fig. 6. On closer inspection, it was concluded that the clusters were deposited on the corners and edges of the nanowalls, as can be expected from the current intensity being higher at these positions.

### ECM of Single Nanotubes

Electrochemistry is particularly attractive for the chemical alteration of single molecular objects because

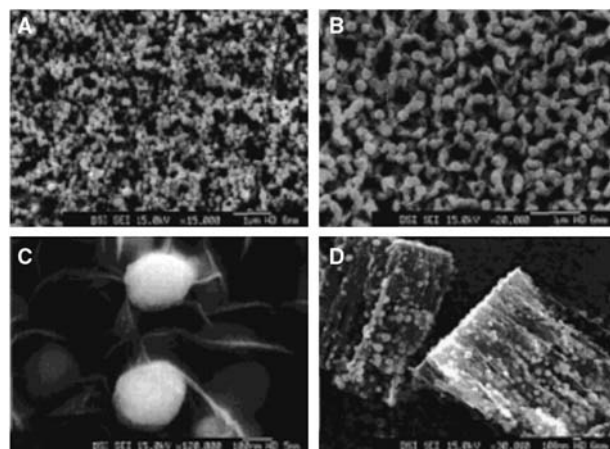


**Fig. 6** SEM images of magnetic nanoparticles electrodeposited onto carbon nanowalls. The scale bars are 1  $\mu\text{m}$  in (A) and (B), and 100 nm in (C) and (D). This sample was fabricated by applying a current density of 75  $\text{mA}/\text{cm}^2$  for 15 sec followed by a subsequent etch time of 3 sec at a current density of  $-25 \text{ mA}/\text{cm}^2$ . *Source:* From Ref.<sup>[43]</sup>.

the extent of modification can be controlled by the electrochemical potential.<sup>[45]</sup> This has been demonstrated by the attachment of substituted phenyl groups to appropriately contacted SWNTs, resulting in homogeneous coatings on the individual tubes.<sup>[36]</sup> For that purpose, single SWNTs/bundles are deposited on a Si/SiO<sub>2</sub> substrate and contacted with electrode lines on top. Both a covalent and a non-covalent coupling scheme have been developed for ECM at the single-tube level. The covalent modification scheme is based on reductive coupling of an aromatic diazonium salt (Fig. 7B), analogous to the modification of CNTs in the bulk,<sup>[35]</sup> whereas the noncovalent scheme involves oxidation of a substituted aromatic amine at anodic

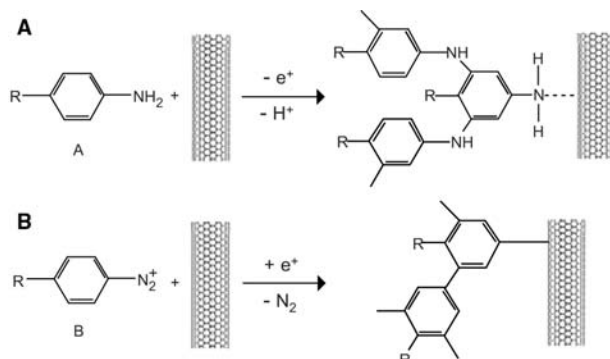


**Fig. 7** Reaction schemes for (A) oxidative ECM with 4-aminobenzylamine and (B) reductive ECM with an aryl diazonium salt. In the former case, the modified SWNT is covered by a polymeric layer of aminobenzyl groups without the formation of a chemical bond, whereas in the latter case, polyphenyl groups that are covalently attached to the nanotube are formed. *Source:* From Ref.<sup>[34]</sup>.



potentials (Fig. 7A). After both types of couplings, one observes a homogeneous coating on the nanotube originating from polymerization among the created radicals (or by reaction between the radicals and the attached molecules). The formation of electrodeposited layers is apparent from atomic force microscopy (AFM) images, as exemplified in Fig. 8A and B for an individual SWNT before and after ECM with 4-aminobenzylamine. This specific tube reveals a height increase of  $\sim 4$  nm, as seen from the line profiles in Fig. 8C. The thickness of such layers is found to increase with the time of ECM, the magnitude of the applied potential, as well as the concentration of the diazonium salt or amine. In practice, the thickness of the coated layers can be adjusted between  $\sim 2$  and  $\sim 15$  nm.

The respective covalent and non-covalent characters of the two coupling schemes have been concluded from a combined electrical transport and confocal Raman spectroscopic study of the coated SWNTs.<sup>[34]</sup> This study was performed separately with metallic and semiconducting pristine tubes. The diazonium coupling to

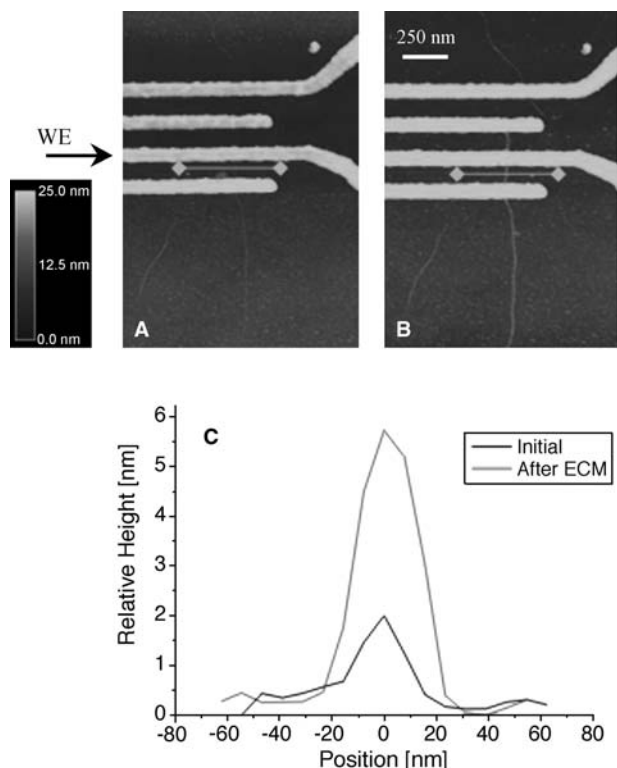


**Fig. 8** Oxidative electrochemical modification of individual SWNTs using 4-aminobenzylamine. (A) AFM image of a single SWNT/bundle contacted by four electrodes on top. (B) AFM image of the same sample after performing ECM on the electrode marked WE. (C) Topological line profiles along the lines marked in the AFM images. The modified SWNTs show a clear increase in height, which appears to be relatively homogeneous.

the metallic and semiconducting SWNTs resulted in an increase of both the resistance and the relative D-line intensity after ECM, which signifies the formation of chemical bonds between the polymer layer and the carbon framework of the nanotube. By contrast, only minor changes in the confocal Raman spectra were detected after oxidative amine coupling on metallic and semiconducting SWNTs. For this type of coupling, the electrical resistance of the metallic SWNTs remained unchanged, whereas that of the semiconducting SWNTs showed a moderate increase in resistance. This increase in resistance can be understood by the decreased p-doping level of the semiconducting tubes as a result of the electrons accepted during oxidation of the amine.

Until now, only one report on ECM of individual MWNTs has appeared, which involves their strong electrochemical oxidation. Single MWNTs coated with an amorphous carbon layer have been electrochemically etched in an aqueous electrolyte solution.<sup>[46]</sup> The onset potential for the anodic current was found to be 1.3 V vs. Ag/AgCl. At potentials higher than 1.7 V, MWNTs and the surrounding amorphous carbon layer begin to etch. Chronoamperometric measurements have revealed that the etching follows a kinetically controlled mechanism. Three different models have been proposed for the etching mechanism, as shown in Fig. 9. In the first model, etching starts from the amorphous carbon layer at the distal end (probably because of the creation of a high field) and proceeds to the proximal end. In a second scenario, the MWNT is

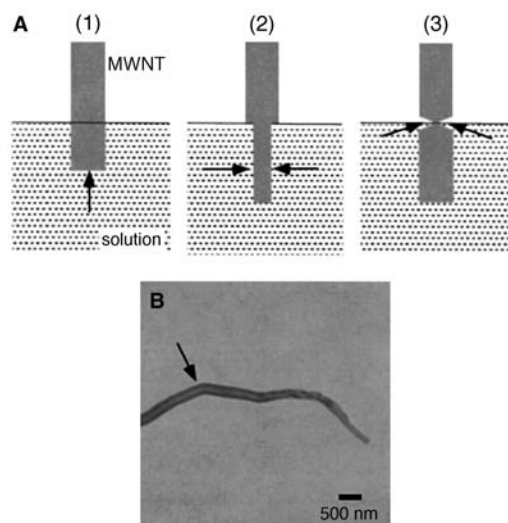


**Fig. 9** (A) Possible mechanisms for the electrochemical etching of MWNTs: (1) longitudinal etching from the distal end to the proximal end; (2) uniform etching in a radial direction; and (3) preferential etching at the air/electrolyte interface. (B) TEM image of the distal end of a partially etched MWNT. The arrow indicates the level of the electrolyte solution. *Source:* From Ref.<sup>[46]</sup>.



etched uniformly from the periphery toward the inner graphitic core. A third model involves the selective etching at the air/electrolyte solution interface, possibly because of the less probable occurrence of a defect at this interface. It was concluded from transmission electron microscopy (TEM) images of the etched MWNTs that the former two models are the predominant mechanisms that operate simultaneously, with the amorphous layer being etched more quickly than the graphitic core.

## ELECTROCHEMICAL APPLICATIONS OF CNTs

### (Bio)Electrochemical Sensors

CNT-based electrodes are very useful in the electrochemical study of biomolecules because of their electrocatalytic property, which is well documented for nicotinamide adenine dinucleotide (NADH) and biological amines.<sup>[17,19]</sup> Moreover, amperometric biosensors have been fabricated by incorporating enzymes such as glucose oxidase or alcohol dehydrogenase into a CNT matrix.<sup>[18–20]</sup> An illustrative example is provided by Fig. 10, where a glucose sensor is obtained by immobilizing glucose oxidase onto SWNTs deposited on a GC surface.<sup>[47]</sup>

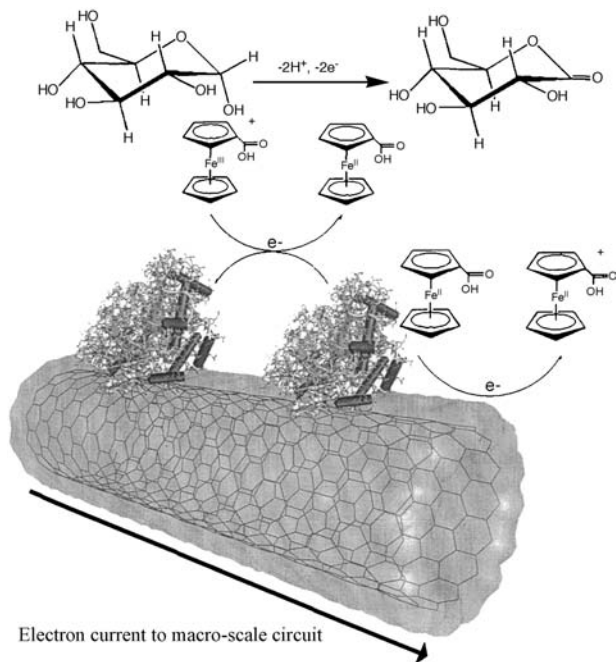


**Fig. 10** Schematic showing the functioning of the SWNT-based glucose sensor. Glucose oxidase enzymes immobilized on the SWNT electrode turn over the solution-phase D-glucopyranose, and this redox signal is communicated to the underlying nanotube through ferrocene monocarboxylic acid acting as a diffusive mediator. *Source:* From Ref.<sup>[47]</sup>.

Their high aspect ratio and diameter in the nanometer range make CNTs particularly well suited for direct electrochemical communication with the redox site of a protein, without requiring any mediator. When properly arranged, a nanotube should have the capability to act as one-dimensional channel guiding electrons into the redox center. Direct ET has been achieved with various types of CNT electrodes for cytochrome *c*,<sup>[48]</sup> horseradish peroxidase,<sup>[16]</sup> glucose oxidase,<sup>[11]</sup> as well as myoglobin.<sup>[49]</sup> In some cases, an oxidative pretreatment introducing negatively charged surface groups on the CNTs was necessary to achieve the high ET rates. In a strategy to optimize the accessibility of the redox center, aligned CNT arrays have been fabricated using self-assembly techniques, followed by covalent attachment of microperoxidase to the tube ends.<sup>[50]</sup> For obtaining the best signal-to-background ratio, the CNT electrodes must be grown with a low density such that the intertube distance is in the same order of magnitude as the diffusion layer thickness.<sup>[24]</sup> Along this direction, a high-sensitivity neurotransmitter sensor,<sup>[51]</sup> where the reduced density has been achieved by a soft lithographic method, has recently been demonstrated.

ECM of CNT electrodes can be employed within the fabrication scheme of (bio)electrochemical sensors for various purposes. One example is the electrodeposition of polypyrrole onto vertically aligned MWNTs,<sup>[52]</sup> yielding a versatile composite system that allows one to exploit the sensing capabilities of inherently conductive polymers.<sup>[53]</sup>

### Batteries and Fuel Cells

CNTs have strong applicability in energy storage because of their excellent chemical stability, light mass, and large surface area. Electrochemical lithium insertion has been studied for both SWNT bundles<sup>[54]</sup> and MWNTs,<sup>[55]</sup> with respect to their application as anodes in rechargeable batteries. SWNTs whose ends were opened by chemical etching show storage capacity comparable with that of  $LiC_3$ , which is twice the value observed in intercalated graphite.<sup>[56]</sup> A major problem is the decrease in storage capacity with increasing number of cycles, caused by, for example, the formation of insoluble salt layers that block the CNT surface.<sup>[8]</sup>

Bulk CNT electrodes are also promising for applications in fuel cells. For example, electrocatalytic reduction of oxygen has been observed in MWNT electrodes,<sup>[57]</sup> and MWNTs covered with platinum particles proved useful as cathodes in direct methanol cells.<sup>[58]</sup> In the latter work, the particles were formed via thermal decomposition of a platinum salt. For this purpose, platinum electrodeposition could be an alternative option.

## Hydrogen Storage

Recent years have witnessed a strong interest in CNTs as high-performance hydrogen storage material. As the maximum values obtained for the storage capacity of molecular hydrogen showed low reproducibility,<sup>[59]</sup> research activities were partially shifted toward reversible electrochemical storage of hydrogen. In a pioneering experiment, electrodes made of pressed pellets containing SWNTs were studied.<sup>[14]</sup> Remarkably, the electrodes were able to deliver still 70% of the initial capacity after 100 charge/discharge cycles. The mechanism of electrochemical hydrogen storage is still under debate.<sup>[60]</sup> Several possibilities have been suggested, including covalent bonding<sup>[61]</sup> and physisorption of molecular hydrogen.<sup>[62]</sup>

ECM has proven to be a useful tool to open the ends of CNTs, which can be exploited to improve the hydrogen storage capacity. It has been observed that electrochemical oxidation at high anodic potentials occurs preferentially at the end regions of MWNTs.<sup>[63]</sup> The open ends created in such a manner allow hydrogen to invade the hollow spaces of the MWNTs during the cathodic reduction.

## Actuators

Various applications in robotics, optical fiber switches, prosthetic devices, sonar projectors, and microscopic pumps rely on the direct conversion of electrical to mechanical energy through a material response. Recently, a bimorph cantilever actuator has been constructed by attaching two sheets of SWNT to the two sides of a Scotch double-stick tape.<sup>[9]</sup> On application of a potential across the two strips of the actuator immersed in an electrolyte, the tape showed deflection because of double-layer charging and change in the carbon/carbon bond length within the rolled graphene sheets.

## CONCLUSION

Because of their good electrical conductivity, nanoscopic size, and high aspect ratio, CNTs have turned out to be excellent candidates for electrochemical applications. CNT electrodes have been found to display significantly superior characteristics in comparison with other carbon materials. Further improvements in the fabrication of single-nanotube electrodes would represent an important step toward the development of nanoscale probes useful in biophysics and neurochemistry. The ECM methods developed to date for bulk CNT electrodes and individual CNTs have broadened the application spectrum of CNTs.

Covalent functionalization of bulk and individual CNTs has been successfully utilized to produce soluble nanotubes, and is also promising for the creation of molecular-scale electronic devices such as diodes or single-electron transistors by the local attachment of appropriate functional groups. However, non-covalent ECM allows researchers to tailor the surface properties of the tubes without disturbing their electrical properties. Both approaches will be of importance in the future for the controlled design and fabrication of novel (bio)electrochemical sensors, composite materials, actuators, batteries, and fuel cells.

## REFERENCES

1. Saito, R.; Dresselhaus, G.; Dresselhaus, M. *Physical Properties of Carbon Nanotubes*; Imperial College Press: London, 1998.
2. Reed, M.A. *Molecular Electronics*; Academic Press: London, 2000.
3. Kong, J.; Franklin, N.R.; Zhou, C.; Chapline, G.M.; Peng, S.; Kyeongjae, D.; Dai, H.J. Nanotube molecular wires as chemical sensors. *Science* **2000**, *287* (5453), 622–625.
4. Collins, P.G.; Bradley, K.; Ishigami, M.; Zettle, A. Extreme oxygen sensitivity of electronic properties of carbon nanotubes. *Science* **2000**, *287* (5459), 1801–1804.
5. Wong, S.S.; Woolley, A.T.; Joselevich, E.; Cheung, C.L.; Lieber, C.M. Covalently-functionalized single-walled carbon nanotube probe tips for chemical force microscopy. *J. Am. Chem. Soc.* **1998**, *120* (33), 8557–8558.
6. Ajayan, P.M.; Iijima, S. Capillarity-induced filling of carbon nanotubes. *Nature* **1993**, *361* (6410), 333–334.
7. Niu, C.; Sichel, E.K.; Hoch, R.; Moy, D.; Tennent, H. High power electrochemical capacitors based on carbon nanotube electrodes. *Appl. Phys. Lett.* **1997**, *70* (11), 1480–1482.
8. Frackowiak, E.; Gautier, S.; Gaucher, H.; Bonnamy, S.; Beguin, F. Electrochemical storage of lithium multi-walled carbon nanotube. *Carbon* **1999**, *37* (1), 61–69.
9. Baughman, R.H.; Cui, C.; Zakhidov, A.A.; Iqbal, Z.; Barisci, J.N.; Spinks, G.M.; Wallace, G.G.; Mazzoldi, A.; De Rossi, D.; Rinzler, A.G.; Jaschinski, O.; Roth, S.; Kertesz, M. Carbon nanotube actuators. *Science* **1999**, *284* (5418), 1340–1344.
10. McCreery, R.L. *Electroanalytical Chemistry*; Bard, A.J., Ed.; Marcel Dekker, Inc.: New York, 1991; Vol. 17, 221–374.
11. Guiseppi-Elie, A.; Lei, C.; Baughman, R.H. Direct electron transfer of glucose oxidase on carbon nanotubes. *Nanotechnology* **2002**, *13* (5), 559–564.
12. Sun, L.; Crooks, R.M. Single carbon nanotube membranes: A well-defined model for studying mass transport through nanoporous materials. *J. Am. Chem. Soc.* **2000**, *122* (49), 12340–12345.
13. Britto, P.J.; Santhanam, K.S.V.; Ajayan, P.M. Carbon nanotube electrode for oxidation of dopamine. *Bioelectrochem. Bioenerg.* **1996**, *41* (1), 121–125.

14. Nuetzenadel, C.; Zuetzel, A.; Emmenegger, C.; Sudan, P.; Schlapbach, L. *Science and Application of Nanotubes*; Tomanek, D., Enbody, R.J., Eds.; Kluwer Academic/Plenum: New York, 2000.
15. Bahr, J.L.; Tour, J.M. Covalent chemistry of single-wall carbon nanotubes. *J. Mater. Chem.* **2002**, *12* (7), 1952–1958.
16. Zhao, Y.; Zhang, W.; Chen, H.; Luo, Q.; Li, S.F.Y. Direct electrochemistry of horseradish peroxidase at carbon nanotube powder microelectrode. *Sens. Actuators, B* **2002**, *87* (1), 168–172.
17. Valentini, F.; Amine, A.; Orlanducci, S.; Terranova, M.L.; Palleschi, G. Carbon nanotube purification: Preparation and characterization of carbon nanotube paste electrodes. *Anal. Chem.* **2003**, *75* (20), 5413–5421.
18. Rubianes, M.D.; Rivas, G.A. Carbon nanotubes paste electrode. *Electrochem. Commun.* **2003**, *5* (8), 689–694.
19. Wang, J.; Musameh, M. Carbon nanotube/Teflon composite electrochemical sensors and biosensors. *Anal. Chem.* **2003**, *75* (9), 2075–2079.
20. Wang, J.; Musameh, M.; Lin, Y. Solubilization of carbon nanotubes by Nafion toward the preparation of amperometric biosensors. *J. Am. Chem. Soc.* **2003**, *125* (9), 2408–2409.
21. Liu, C.-Y.; Bard, A.J.; Wudl, F.; Weitz, I.; Heath, J.R. Electrochemical characterization of films of single-walled carbon nanotubes and their possible application in supercapacitors. *Solid-State Lett.* **1999**, *2* (11), 577–578.
22. Luo, H.; Shi, Z.; Li, N.; Gu, Z.; Zhuang, Q. Investigation of the electrochemical and electrocatalytic behavior of single-wall carbon nanotube film on a glassy carbon electrode. *Anal. Chem.* **2001**, *73* (5), 915–920.
23. Diao, P.; Liu, Z.; Wu, B.; Nan, X.; Zhang, J.; Wei, Z. Chemically assembled single-wall carbon nanotubes and their electrochemistry. *ChemPhysChem* **2002**, *3* (10), 898–901.
24. Li, J.; Cassell, A.; Delzeit, L.; Han, J.; Meyyappan, M. Novel three-dimensional electrodes: Electrochemical properties of carbon nanotube ensembles. *J. Phys. Chem., B* **2002**, *106* (36), 9299–9305.
25. Rinzler, A.G.; Liu, J.; Dai, H.; Nikolaev, P.; Huffman, C.B.; Rodriguesmacias, F.J.; Boul, P.J.; Lu, A.H.; Heymann, D.; Colbert, D.T.; Lee, R.S.; Fisher, J.E.; Rao, A.M.; Eklund, P.C.; Smalley, R.E. Large-scale purification of single-wall carbon nanotubes: Process, product, and characterization. *Appl. Phys., A* **1998**, *67* (1), 29–37.
26. Nugent, J.M.; Santhanam, K.S.V.; Rubio, A.; Ajayan, P.M. Fast electron transfer kinetics on multiwalled carbon nanotube microbundle electrodes. *Nano Lett.* **2001**, *1* (2), 87–91.
27. Chen, J.; Li, W.; Huang, Z.; Wang, D.; Yang, S.; Wen, J.; Ren, Z. Electrochemistry of Carbon Nanotubes and Their Potential Application in Supercapacitors, Proceedings of the 197th Meeting of the Electrochemical Society, Toronto, Canada, May, 14–18, 2000; Electrochemical Society: Pennington, NJ, 2000.
28. Barisci, J.N.; Wallace, G.G.; Baughman, R.H. Electrochemical studies of single-wall carbon nanotubes in aqueous solutions. *J. Electroanal. Chem.* **2000**, *488* (2), 92–98.
29. Kavan, L.; Raptap, P.; Dunsch, L.; Bronikowski, M.J.; Willis, P.; Smalley, R.E. Electrochemical tuning of electronic structure of single-walled carbon nanotubes: In-situ Raman and vis-NIR study. *J. Phys. Chem., B* **2001**, *105* (44), 10764–10771.
30. Barisci, J.N.; Wallace, G.G.; Chattopadhyay, D.; Papadimitrakopoulos, F.; Baughman, R.H. Electrochemical properties of single-wall carbon nanotube electrodes. *J. Electrochem. Soc.* **2003**, *150* (9), E409–E415.
31. Bard, A.J.; Faulkner, L.R. *Electrochemical Methods*; Wiley: New York, 1980.
32. Campbell, J.K.; Sun, L.; Crooks, R.M. Electrochemistry using single carbon nanotubes. *J. Am. Chem. Soc.* **1999**, *121* (15), 3779–3780.
33. Nikolaev, P.; Bronikowski, M.J.; Bradley, R.K.; Rohmund, F.; Colbert, D.T.; Smith, K.A.; Smalley, R.E. Gas-phase catalytic growth of single-walled carbon nanotubes from carbon monoxide. *Chem. Phys. Lett.* **1999**, *313* (1–2), 91–97.
34. Balasubramanian, K.; Friedrich, M.; Jiang, C.; Fan, Y.; Mews, A.; Burghard, M.; Kern, K. Electrical transport and confocal Raman studies of electrochemically modified individual carbon nanotubes. *Adv. Mater.* **2003**, *15* (18), 1515–1518.
35. Bahr, J.L.; Yang, J.; Kosynkin, D.V.; Bronikowski, M.J.; Smalley, R.E.; Tour, J.M. Functionalization of carbon nanotubes by electrochemical reduction of aryl diazonium salts: A bucky paper electrode. *J. Am. Chem. Soc.* **2001**, *123* (27), 6536–6542.
36. Kooi, S.E.; Schlecht, U.; Burghard, M.; Kern, K. Electrochemical modification of single carbon nanotubes. *Angew. Chem. Int. Ed.* **2002**, *41* (8), 1353–1355.
37. Sumanasekera, G.U.; Allen, J.L.; Fang, S.L.; Loper, A.L.; Rao, A.M.; Eklund, P.C. Electrochemical oxidation of single wall carbon nanotube bundles in sulfuric acid. *J. Phys. Chem., B* **1999**, *103* (21), 4292–4297.
38. Unger, E.; Graham, A.; Kreupl, F.; Liebau, M.; Hoenlein, W. Electrochemical functionalization of multi-walled carbon nanotubes for solvation and purification. *Appl. Phys.* **2002**, *2* (2), 107–111.
39. Chen, G.Z.; Shaffer, M.S.P.; Coleby, D.; Dixon, G.; Zhou, W.; Fray, D.J.; Windle, A.H. Carbon nanotube and polypyrrole composites: Coating and doping. *Adv. Mater.* **2000**, *12* (7), 522–527.
40. Downs, C.; Nugent, J.; Ajayan, P.M.; Duquette, D.J.; Santhanam, K.S.V. Efficient polymerization of aniline at carbon nanotube electrodes. *Adv. Mater.* **1999**, *11* (12), 1028–1031.
41. Menon, M.; Andriotis, A.N.; Froudakis, G.E. Curvature dependence of the metal catalyst atom interaction with carbon nanotubes walls. *Chem. Phys. Lett.* **2000**, *320* (5–6), 425–434.
42. Dunsch, L.; Janda, P.; Mukhopadhyay, K.; Shinohara, H. Electrochemical metal deposition on carbon nanotubes. *New Diam. Front. Carbon Technol.* **2001**, *11* (6), 427–435.
43. Yang, B.; Wu, Y.; Zong, B.; Shen, Z. Electrochemical synthesis and characterization of magnetic nanoparticles

- on carbon nanowall templates. *Nano Lett.* **2002**, *2* (7), 751–754.
44. Wu, Y.H.; Yang, B.J. Effects of localized electric field on the growth of carbon nanowall. *Nano Lett.* **2002**, *2* (4), 355–359.
  45. Knez, M.; Sumser, M.; Bittner, A.M.; Wege, C.; Jeske, H.; Kooi, S.; Burghard, M.; Kern, K. Electrochemical modification of individual nano-objects. *J. Electroanal. Chem.* **2002**, *522* (1), 70–74.
  46. Ito, T.; Sun, L.; Crooks, R.M. Electrochemical etching of individual multiwall carbon nanotubes. *Solid-State Lett.* **2003**, *6* (1), C4–C7.
  47. Davis, J.J.; Coleman, K.S.; Azamian, B.R.; Bagshaw, C.B.; Green, M.L.H. Chemical and biochemical sensing with modified single walled carbon nanotubes. *Chem. Eur. J.* **2003**, *9* (16), 3732–3739.
  48. Wang, J.; Li, M.; Shi, Z.; Li, N.; Gu, Z. Direct electrochemistry of cytochrome *c* at a glassy carbon electrode modified with single-wall carbon nanotubes. *Anal. Chem.* **2002**, *74* (9), 1993–1997.
  49. Zhao, G.-C.; Zhang, L.; Wei, X.-W.; Yang, Z.S. Myoglobin on multi-walled carbon nanotubes modified electrode: Direct electrochemistry and electrocatalysis. *Electrochem. Commun.* **2003**, *5* (9), 825–829.
  50. Gooding, J.J.; Wibowo, R.; Liu, J.; Yang, W.; Losic, D.; Orbons, S.; Mearns, F.J.; Shapter, J.G.; Hibbert, D.B. Protein electrochemistry using aligned carbon nanotube arrays. *J. Am. Chem. Soc.* **2003**, *125* (30), 9006–9007.
  51. Ng, H.T.; Fang, A.P.; Li, J.; Li, S.F.Y. Flexible carbon nanotube membrane sensory system: A generic platform. *J. Nanosci. Nanotechnol.* **2001**, *1* (4), 375–379.
  52. Gao, M.; Dai, L.; Wallace, G.G. Biosensors based on aligned carbon nanotubes coated with inherently conducting polymers. *Electroanalysis* **2003**, *15* (13), 1089–1094.
  53. McQuade, D.T.; Pullen, A.E.; Swager, T.M. Conjugated polymer-based chemical sensors. *Chem. Rev.* **2000**, *100* (7), 2537–2574.
  54. Claye, A.; Fischer, J.E. Electrochemical doping of single wall carbon nanotubes with lithium. *Mol. Cryst. Liq. Cryst.* **2000**, *340*, 743–748.
  55. Che, G.; Lakshmi, B.B.; Fisher, E.R.; Martin, C.R. Carbon nanotubule membranes for electrochemical energy storage and production. *Nature* **1998**, *393* (6683), 346–349.
  56. Shimoda, H.; Gao, B.; Tang, X.P.; Kleinhammes, A.; Fleming, L.; Wu, Y.; Zhou, O. Lithium intercalation into opened single-wall carbon nanotubes: Storage capacity and electronic properties. *Phys. Rev. Lett.* **2002**, *88* (1), 1–4. 015502.
  57. Britto, P.J.; Santhanam, K.S.V.; Rubio, A.; Alonso, J.A.; Ajayan, P.M. Improved charge transfer at carbon nanotube electrodes. *Adv. Mater.* **1999**, *11* (2), 154–157.
  58. Li, W.; Liang, C.; Qiu, J.; Zhou, W.; Han, H.; Wei, Z.; Sun, G.; Xin, Q. Carbon nanotubes as support for cathode catalyst of a direct methanol fuel cell. *Carbon* **2002**, *40* (5), 791–794.
  59. Hirscher, M.; Becher, M.; Haluska, M.; von Zeppelin, F.; Chen, X.H.; Dettlaff-Weglikowska, U.; Roth, S. Are carbon nanostructures an efficient hydrogen storage medium? *J. Alloys Compd.* **2003**, *356*, 433–437.
  60. Watanabe, M.; Tachikawa, M.; Osaka, T. On the possibility of hydrogen intercalation of graphite-like carbon materials—Electrochemical and molecular orbital studies. *Electrochim. Acta* **1997**, *42* (17), 2707–2717.
  61. Orimo, S.; Majer, G.; Fukunaga, T.; Züttel, A.; Schlapbach, L.; Fujii, H. Hydrogen in the mechanically prepared nanostructured graphite. *Appl. Phys. Lett.* **1999**, *75* (20), 3093–3095.
  62. Dai, G.P.; Zhao, Z.G.; Liu, M.; Hou, P.X.; Wang, M.Z.; Cheng, H.M. Electrochemical study of hydrogen storage mechanism of carbon nanotubes. *New Carbon Mater.* **2002**, *17* (4), 49–52.
  63. Skowronski, J.M.; Scharff, P.; Pfaender, N.; Cui, S. Room temperature electrochemical opening of carbon nanotubes followed by hydrogen storage. *Adv. Mater.* **2003**, *15* (1), 55–57.

# Carbon Nanotubes: Flow Control in Membranes

Scott A. Miller  
Charles R. Martin

*Department of Chemistry, University of Florida, Gainesville, Florida, U.S.A.*

## INTRODUCTION

Carbon nanotubes are currently of great interest in both fundamental and applied sciences.<sup>[1–10]</sup> Potential applications for these tubular nanostructures include use in nanoelectronics,<sup>[1–4]</sup> hydrogen storage,<sup>[5,6]</sup> and battery<sup>[7,8]</sup> and field-emitting display<sup>[9,10]</sup> technologies. We and others have shown that carbon nanotubes can be prepared via the template method<sup>[11–13]</sup> by chemical vapor deposition (CVD) of carbon along the pore walls of nanoporous alumina membranes.<sup>[8,14–17]</sup> These membranes have cylindrical pores with monodisperse diameters, and a corresponding cylindrical nanotube is deposited within each pore. Carbon nanotubes with outside diameters as small as 20 nm have been prepared via this method.<sup>[14]</sup> Using an alternative template material and method, Joo et al.<sup>[7]</sup> have prepared carbon nanotubes with outside diameters of 9 nm.

At a recent workshop, it was suggested that carbon nanotubes might be used as chemically selective filters.<sup>[18]</sup> This membrane separations application requires alignment of the tubes<sup>[10,19–21]</sup> into a defect-free, mechanically strong membrane, where each tube spans the complete thickness of the membrane and the tube mouths are open at the faces of the membrane. Although Sun and Crooks<sup>[22]</sup> have recently developed an elegant procedure for doing this with a single carbon nanotube, template synthesis inherently provides nanotube-containing membranes of this type, with up to  $10^{11}$  nanotubes  $\text{cm}^{-2}$  of membrane surface area.<sup>[13]</sup> Having large numbers of nanotubes per square centimeter of membrane area is essential to enhancing flux across the membrane—a critical issue in membrane separation processes. These highly porous carbon nanotube membranes (CNMs) have monodisperse pore dimensions, which can be controlled by template synthesis. Template-prepared CNMs have a number of advantageous properties such as versatile surface chemistry and good electrochemical properties, which make them an interesting membrane material.

Flux can also be enhanced by augmenting diffusive transport across the membrane with electrophoresis, or pressure-driven or electroosmotic flow (EOF). Sun and Crooks<sup>[22]</sup> demonstrated diffusive, pressure-driven, and electrophoretic transport of colloidal particles across their single CNMs. To our knowledge, we have performed the only investigation of EOF in CNMs.<sup>[15,23]</sup> Electroosmotic flow was driven across template-prepared CNMs by allowing the membrane to separate two electrolyte solutions and by using an electrode in each solution to pass a constant ionic current through the nanotubes. According to Bath et al.<sup>[24,25]</sup> EOF was investigated by measuring the flux of a probe molecule across the membrane. The as-synthesized CNMs have anionic surface charge and, as a result, EOF is in the direction of cation migration across the membrane. Electroosmotic flow in the direction of diffusion enhances permeant flux, whereas EOF in the opposite direction of diffusion lowers flux. Measurements of the rate of EOF as a function of applied transmembrane current provided the zeta ( $\zeta$ ) potential. The effect of pH on  $\zeta$  provided the  $\text{p}K_a$  for the surface acidic sites responsible for this anionic charge; the acidic site density was also determined. An electrochemical derivatization method was used to attach carboxylate groups to the nanotube walls;<sup>[26–28]</sup> this enhances the anionic surface charge density, resulting in a corresponding increase in the EOF rate. Electrochemical derivatization was also used to attach cationic ammonium sites to the nanotube walls to yield CNMs that show EOF in the opposite direction of the as-synthesized or carboxylated membranes.

## PREPARATION OF CARBON NANOTUBE MEMBRANES

Anodic alumina template membranes with different pore diameters are available commercially, or can be prepared in the laboratory.<sup>[8,15,29–31]</sup> The outside diameters of template-prepared carbon nanotubes

are defined by the pore diameter of the template membrane, whereas the length is determined by the template thickness. The CVD template method has been described previously.<sup>[8,15–17]</sup> Briefly, a heat-treated alumina template membrane was placed vertically in the CVD reactor and heated to the desired temperature, 650–950°C, under argon flow. When the temperature stabilized, the Ar flow was terminated and, simultaneously, a 20-sccm flow of ethylene gas mixture was initiated. Under these conditions, ethylene pyrolyzes to yield carbon nanotubes on the pore walls, as well as thin carbon films on both faces of the membrane. After deposition was completed, the Ar flow was resumed, the ethylene flow was terminated, the furnace was turned off, and the CNM was allowed to cool to room temperature.

Scanning electron microscopy (SEM) and transmission electron microscopy (TEM) were used to image the carbon nanotubes prepared within the pores of the alumina template membrane. This was accomplished by first dissolving away the alumina by immersion (for 12 hr) in 49% hydrofluoric acid. Hydrofluoric acid was removed by pipette, leaving the liberated nanotubes (connected together by the carbon surface films; Fig. 1), which were rinsed with methanol and then sonicated in methanol for 20 min. For imaging, the resulting suspension was pipetted onto the appropriate sample holder and the methanol was allowed

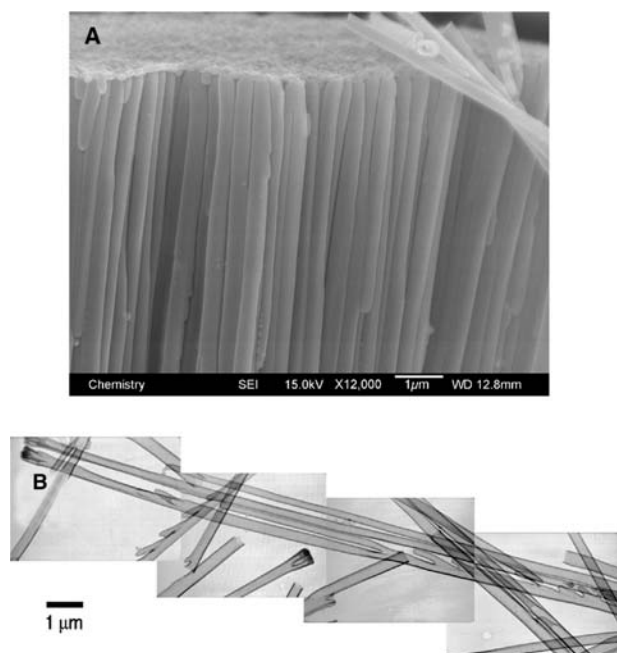


**Fig. 1** A CNM synthesized within a 200-nm Anodisc template at 670°C for 5.5 hr. (A) A SEM image of a CNM cross section at the unbranched face after removal of the alumina template. (B) A TEM image montage of individual carbon nanotubes removed from a CNM.

to evaporate. For SEM imaging, gold was sputtered onto the sample to improve electrical conductivity.

Figs. 1–3 show SEM and TEM images of nanotubes from three different CNMs after dissolution of the alumina template. The CNMs were prepared using templates with differing pore morphologies and at different CVD conditions. Fig. 1A shows a SEM image of a CNM, such as those used in the EOF studies.<sup>[15,23]</sup> This membrane was synthesized in a commercially available Whatman Anodisc 200-nm filtration membrane. Carbon was deposited at 670°C for 5.5 hr. At these conditions, carbon deposition was very slow and resulted in nanotube walls of highly uniform 40 nm thickness (Fig. 1B). Although it is not evident from these images, this carbon surface film does not block the mouths of the nanotubes. The outside diameter of the nanotubes (~300 nm) is larger than the 200-nm nominal pore diameter of the template. Our SEM and TEM images indicate that this is because the pores are, in fact, larger than the nominal diameter for most of the thickness of the membrane, but branch at one face of the membrane into smaller (diameter ~200 nm) pores. This branching can be seen in the TEM image shown in Fig. 1B. Branching undoubtedly results from the voltage reduction technique used during the final step of the electrochemical process used to prepare these alumina membranes.<sup>[29]</sup>

Fig. 2 shows images of a CNM synthesized within a Whatman Anodisc 20-nm filtration membrane.<sup>[16]</sup> Like the 200-nm Anodisc, this template has large pores (diameters of ~300 nm) along ~99% of their length, but branch into many much smaller nanotubes (diameter ~20 nm) at the branched face of the membrane. Chemical vapor deposition was performed at 900°C for 0.5 hr, which resulted in a much more rapid rate of carbon deposition. At this higher temperature, deposition tends to be a diffusion-controlled process and occurs more rapidly at the face of the template as opposed to the interior of the small pores. The substantial surface film on the branched-face is seen in Fig. 2A. This results in a CNM that acts as an electrochemical actuator when  $\text{Li}^+$  is intercalated into and deintercalated out of the carbon nanostructures.<sup>[16]</sup>

Carbon nanotubes have also been prepared in laboratory-grown anodic aluminum oxide membranes for a variety of purposes.<sup>[31–35]</sup> The CNM shown in Fig. 3A was grown in a highly ordered template of 30  $\mu\text{m}$  thickness and an 80-nm pore diameter. These pores are extremely straight and do not branch at either face of the membrane. Chemical vapor deposition was performed for 2 hr at 670°C, resulting in nanotubes with highly monodisperse dimensions. From TEM images of individual nanotubes (Fig. 3B), the CNM was determined to have a 60-nm pore diameter with nanotube walls of very uniform thickness. Carbon nanotube membranes such as these can be



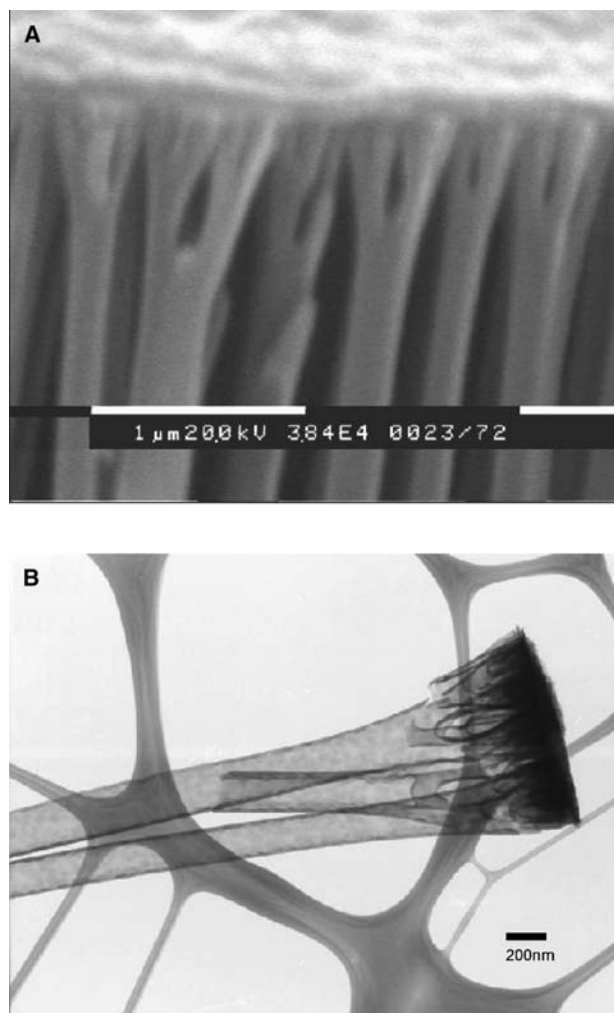


**Fig. 2** A CNM synthesized within a 20-nm Anodisc template at 900°C for 0.5 hr. (A) A SEM image of a CNM cross section at the branched face after removal of the alumina template. (B) A TEM image of individual branched carbon nanotubes removed from a CNM.

prepared with larger or smaller pore dimensions and could be utilized for size-based separations.

### TRANSPORT PROPERTIES OF CARBON NANOTUBE MEMBRANES

After synthesis, CNMs to be used in transport studies were stored in air for at least 24 hr prior to use. This results in oxidation of the carbon surfaces to yield acidic surface sites on the nanotube walls.<sup>[36–38]</sup> Carbon nanotube membranes treated in this way are referred to as “as-synthesized” membranes. The CNMs were mounted in a supporting assembly<sup>[15]</sup> and placed in a simple U-tube permeation cell.<sup>[39]</sup> The permeation half-cells were filled with 25 ml of pH = 7.2

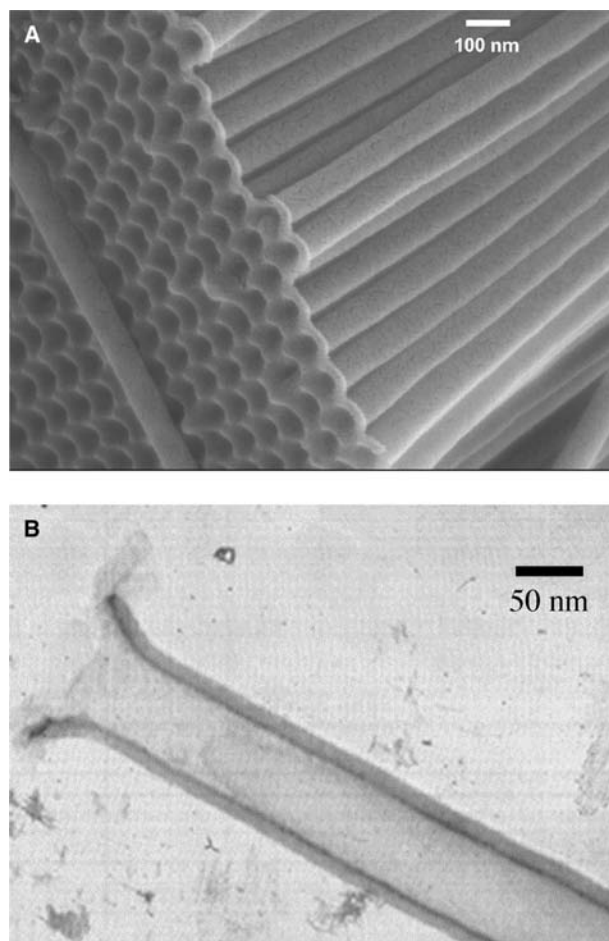


**Fig. 3** A CNM synthesized within a highly ordered, anodic alumina template at 670°C for 2 hr. (A) A SEM image of a CNM cross section after removal of the alumina template. (B) A TEM image of an individual carbon nanotube removed from a CNM.

phosphate buffer of 0.01 M ionic strength. The feed half-cell was 4.82 mM in the small, electrically neutral, chromophoric probe phenol.

According to Bath et al.<sup>[24,25]</sup> the rate of EOF was determined by monitoring the transport of the probe molecule across the membrane and into the permeate half-cell. A constant current, passed through the CNM, was responsible for the EOF in the membrane. The following sign convention was employed: For a positive applied current, the anode was in the feed half-cell and the cathode was in the permeate half-cell. In this case, cations migrated from feed to permeate, and anions migrated from permeate to feed. A negative applied current had the opposite configuration (i.e., cathode in the feed half-cell and anode in the permeate half-cell). The current values are reported here as the current density, defined as the applied current divided by the total pore area of the membrane.

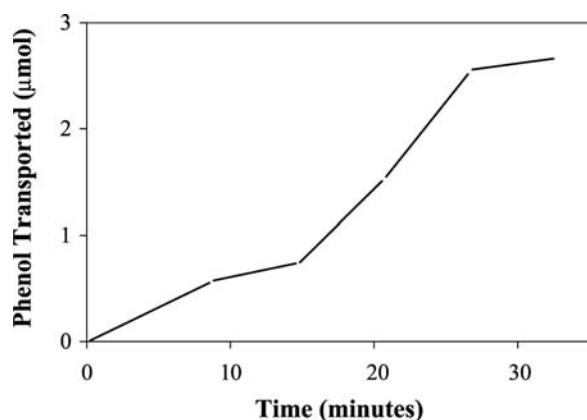


**Fig. 4** Micromoles of phenol transported vs. time at various values of applied current density (see text for current density values).

Fig. 4 shows a plot of micromoles of phenol transported across the CNM at various values of applied current density. This plot consists of five linear segments, and the slope of each segment is the flux of phenol ( $N_J$ ) at that applied current density (Table 1). The first linear segment in Fig. 4 (0–8.5 min) was obtained with no applied current, and the flux in this case is simply the diffusive flux of phenol  $N_{diff}$  from the feed across the membrane and into the permeate. The second linear segment (9–14.5 min) was obtained with an applied current density  $J_{app} = -7.2 \text{ mA cm}^{-2}$ . The flux of phenol across the membrane was observed to decrease, indicating EOF in the opposite direction of the diffusive flux (EOF from permeate solution to feed solution). This is confirmed by data in the third linear segment (15–20.5 min), which were obtained with  $J_{app} = +7.2 \text{ mA cm}^{-2}$ ; now the net flux is higher than the diffusive flux (Table 1), indicating EOF in the direction of diffusive transport. The final two linear segments were obtained at higher positive and negative applied current densities, and further enhancement and diminution, respectively, in the flux is observed.

**Table 1** Effect of applied current density on the flux, enhancement factor, and electroosmotic velocity in the carbon nanotube membrane

$J_{app}$ [mA cm <sup>-2</sup> ]	Flux [nmol (min cm <sup>2</sup> ) <sup>-1</sup> ] <sup>a</sup>	$E$	$v_{eo}$ [μm sec <sup>-1</sup> ]
-10.1	25.8	0.280	-35.0
-7.2	39.3	0.426	-24.5
0.0	92.1	1.000	0.0
+7.2	187.1	2.030	26.3
+10.1	237.9	2.581	37.6

<sup>a</sup>The geometric area of the membrane (0.713 cm<sup>2</sup>) was used.

## CALCULATION OF THE ELECTROOSMOTIC FLOW VELOCITY

In the presence of the applied transmembrane current, the steady-state flux of permeant across a membrane is described by the Nernst–Planck equation:<sup>[40]</sup>

$$N_J = -D[\partial C(x)/\partial x] - zF(RT)^{-1}DC[\partial\phi(x)/\partial x] \pm Cv_{eo} \quad (1)$$

where  $D$ ,  $C$ , and  $z$  are the diffusion coefficient, concentration, and charge of the permeate molecule, respectively;  $\partial C(x)/\partial x$  is the concentration gradient in the  $x$  direction across the membrane;  $\partial\phi(x)/\partial x$  is the potential gradient in the electrolyte within the nanotubes; and  $v_{eo}$  is the electroosmotic velocity. The three terms in Eq. (1) describe the diffusive, migrational, and EOF convective transport processes, respectively. Because phenol is a neutral molecule at the pH used here, Eq. (1) simplifies to:

$$N_J = -D[\partial C(x)/\partial x] + Cv_{eo} \quad (2)$$

When  $J_{app} = 0$ , only the first term in Eq. (2) is operative and the flux is the diffusive flux  $N_{diff}$ .

The experimental flux data in Table 1 can be used to calculate a parameter called the enhancement factor  $E$ , which can then be used to calculate the electroosmotic velocity.<sup>[40]</sup>  $E$  is given by:

$$E = N_J/N_{diff} \quad (3)$$

(i.e., the ratio of the flux in the presence of an applied current to the flux at  $J_{app} = 0$ ).  $E$  values for the data in Fig. 4 are presented in Table 1. When a positive current is applied,  $E$  is greater than unity, indicating, again, EOF in the direction of the diffusional flux. Analogous results were obtained by Bath et al.<sup>[24]</sup> for Nafion membranes, where EOF is because of the polymer's fixed sulfonate sites. This indicates that as would be expected for air-treated carbon, the pore walls on the carbon nanotubes have fixed negatively charged sites.<sup>[36–38]</sup>

Following Srinivasan and Higuchi,<sup>[40]</sup> the Peclet number ( $Pe$ ) can be calculated from  $E$  via:

$$E = Pe/(1 - (\exp(-Pe))) \quad (4)$$

$Pe$  can then be used to calculate  $v_{eo}$  using:<sup>[40]</sup>

$$v_{eo} = PeD/l \quad (5)$$

where  $l$  is the thickness of the membrane. Because the inside diameter of the carbon nanotubes (~120 nm) is ~500 times larger than the diameter of phenol, hindered diffusion<sup>[41]</sup> does not occur in these tubes, and

the bulk solution diffusion coefficient can be used in Eq. (5). This and the membrane thickness (0.006 cm) give the  $v_{eo}$  data shown in the last column of Table 1. As would be expected, current densities of the same magnitude but opposite sign give  $v_{eo}$  values of approximately the same magnitude but opposite sign.

### EFFECT OF APPLIED CURRENT DENSITY ON ELECTROOSMOTIC FLOW

Phenol transport data such as those shown in Fig. 4 were obtained for 16 different  $J_{app}$  values between +19.3 and  $-19.3 \text{ mA cm}^{-2}$ . Fig. 5A shows the corresponding flux vs.  $J_{app}$  data. As would be expected from the above results, the flux increases with  $J_{app}$  for positive currents, indicating the increasing importance of EOF to the transport of permeate across the membrane. At sufficiently negative  $J_{app}$  values, the net flux asymptotically approaches zero. In this case, EOF from the permeate half-cell to the feed half-cell negates the diffusive flux from feed to permeate.<sup>[24]</sup>

The Helmholtz–Smoluchowski equation<sup>[42]</sup> describes the relationship between electroosmotic velocity and

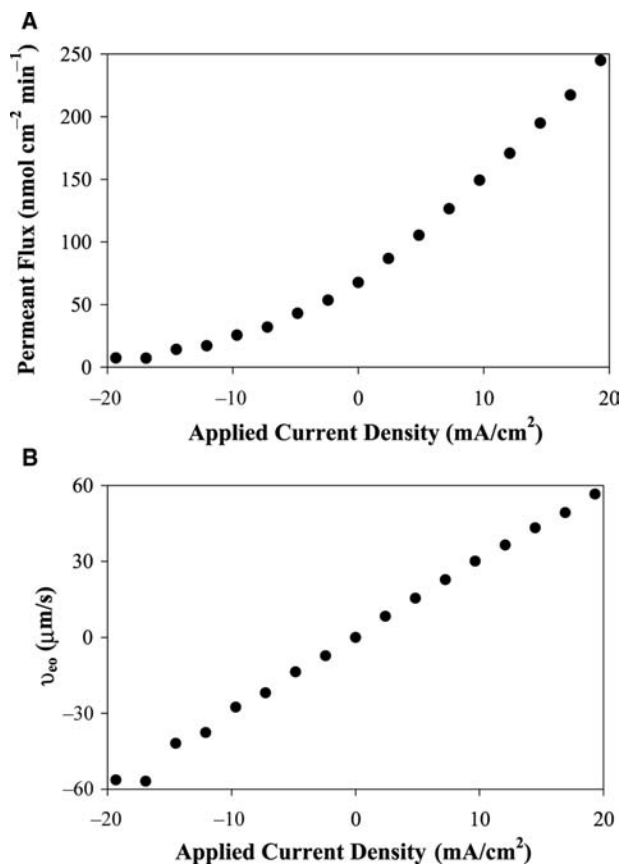


Fig. 5 (A) Plot of phenol flux vs. applied current density. (B) Plot of EOF vs. applied current density.

linear electric field gradient ( $E(x)$ ) [ $\text{V cm}^{-1}$ ] across the membrane:

$$v_{eo} = -\varepsilon\zeta E(x)/\eta \quad (6)$$

where  $\varepsilon$  and  $\eta$  are the permittivity and viscosity of the solution within the nanotubes, respectively; and  $\zeta$  is the zeta potential of the tube walls. Substituting the product of the applied current density and the resistivity of the electrolyte within the nanotubes  $\rho$ , the  $E(x)$  in Eq. (6) gives:

$$v_{eo} = -\varepsilon\zeta J_{app}\rho/\eta \quad (7)$$

which shows that  $v_{eo}$  is linearly related to the applied current density. Eqs. (4) and (5) were used to calculate  $v_{eo}$  from the flux data in Fig. 5A. Fig. 5B shows a plot of  $v_{eo}$  vs. current density; in agreement with Eq. (7), a linear relationship is obtained. (Some deviation is observed at the highest negative  $J_{app}$  values. This is because the flux is nearly zero at such large negative  $J_{app}$  values, making the error in the measurement large.)

According to Eq. (7), the slope of the  $v_{eo}$  vs.  $J_{app}$  plot in Fig. 5B is  $-\varepsilon\zeta\rho/\eta$ . Using the known values for the permittivity and viscosity of water ( $6.95 \times 10^{-10} \text{ C}^2 \text{ J}^{-1} \text{ m}^{-1}$  and 0.890 cP, respectively)<sup>[43]</sup> and the measured resistivity of the electrolyte (2.23 kΩ cm), the slope can be used to calculate the zeta potential for the CNM. A value of  $\zeta = -17.3 \text{ mV}$  was obtained from these data. Bismarck and Springer<sup>[37]</sup> obtained similar zeta potential values for carbon fibers, and Garcia et al.<sup>[38]</sup> obtained somewhat larger zeta potential values ( $\sim -45 \text{ mV}$ ) after grinding such carbon fibers.

It should be noted that Eqs. (6) and (7) are based on the assumption that the thickness of the double layer at the pore wall is much smaller than the pore radius. Because the double layer at this electrolyte concentration is less than 3 nm in thickness,<sup>[42]</sup> this is clearly a valid assumption. Finally, for this reason and because the measured zeta potential is relatively low, deviations because of surface conductance, or changes in permittivity and viscosity within the nanotubes are negligible.<sup>[44,45]</sup> Thus it is reasonable to use the resistivity, permittivity, and viscosity of the bulk solution in the zeta potential calculation.

### EFFECT OF IONIC STRENGTH ON ELECTROOSMOTIC FLOW

Phenol transport data were obtained at applied current densities of +19.7 and  $-19.7 \text{ mA cm}^{-2}$  in solutions with ionic strength varying from 0.01 to 0.50 M (Fig. 6). The pH of the electrolyte was maintained at 7.2. Transport data for the case  $J_{app} = 0$  were also

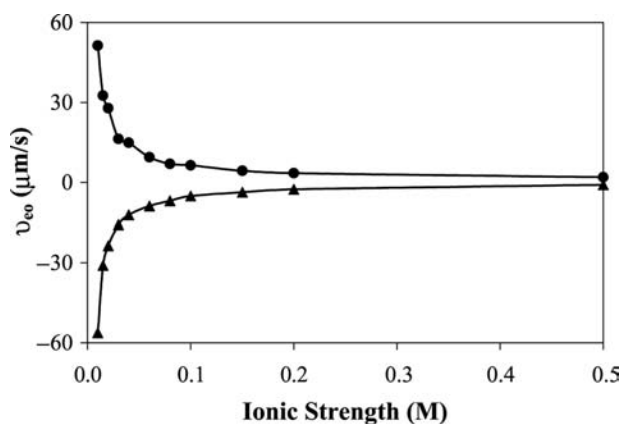


**Fig. 6** Plots of EOF vs. the ionic strength of the permeate and feed solutions. Applied current densities were ( $\blacktriangle$ )  $-19.7 \text{ mA cm}^{-2}$  and ( $\bullet$ )  $+19.7 \text{ mA cm}^{-2}$ .

obtained over this electrolyte concentration range. No change in the diffusional flux was observed ( $< 3\%$  relative standard deviation), indicating that the diffusion coefficient for phenol does not vary with electrolyte concentration over this concentration range. Fig. 6 shows plots of  $v_{eo}$  vs. ionic strength obtained from the transport data. The general trend—that the absolute value of  $v_{eo}$  decreases with increasing ionic strength—is expected.

Returning to Eq. (7), we see that  $v_{eo}$  is directly proportional to the zeta potential, which is related to the Debye length  $\kappa^{-1}$  (the effective thickness of the electrical double layer) by:<sup>[46]</sup>

$$\zeta = 2kT/ze \sinh^{-1}(\sigma\kappa^{-1}ze/(2\epsilon kT)) \quad (8)$$

where  $k$  is the Boltzmann constant,  $T$  is the temperature,  $e$  is the elementary charge, and  $\sigma$  is the surface charge density at the plane of shear between the nanotube wall and the electrolyte. For the zeta potential and Debye length ranges investigated here, Eq. (8) simplifies to:

$$\zeta = \sigma\kappa^{-1}/\epsilon \quad (9)$$

For a symmetrical electrolyte,  $\kappa^{-1}$  is related to the concentration of the electrolyte via:<sup>[42]</sup>

$$\kappa^{-1} = 9.61 \times 10^{-9}(z^2c)^{-1/2} \quad (10)$$

Eq. (10) shows that the double-layer thickness decreases with increasing ionic strength of the electrolyte, which means that the zeta potential decreases with increasing ionic strength [Eq. (9)]. This, in turn, causes  $|v_{eo}|$  to decrease with increasing ionic strength [Eq. (7)], which is the experimentally observed trend in Fig. 6.

A second factor contributes to the observed decrease in  $|v_{eo}|$  with increasing ionic strength. Eq. (7)

shows that  $v_{eo}$  is also proportional to the resistivity of the electrolyte  $\rho$ , which, of course, is inversely proportional to the number of charge-carrying ions in the solution. Hence  $\rho$  decreases with increasing ionic strength of the electrolyte, and Eq. (7) predicts that this would also contribute to the observed decrease in  $v_{eo}$  with increasing ionic strength (Fig. (6)).

If it is assumed that  $\kappa^{-1}$  decreases with ionic strength ( $\mu$ ) as  $\kappa^{-1} \propto \mu^{-1/2}$  [Eq. (10)] and that  $\rho$  decreases with  $\mu$  as  $\rho \propto \mu^{-1}$ , we would predict that  $v_{eo}$  would decrease with  $\mu$  via  $v_{eo} \propto \mu^{-3/2}$ . The experimental data (Fig. 6) were fitted to the relationships  $v_{eo} \propto \mu^{-0.9}$  ( $R^2 = 0.993$ ) for the positive current density and  $v_{eo} \propto -\mu^{-1.0}$  ( $R^2 = 0.997$ ) for the negative current density. Hence the experimental fall-off of  $v_{eo}$  with increasing  $\mu$  is less than the predicted value.

Another factor needs to be considered. As shown in Eq. (9), the zeta potential is also directly proportional to the charge density. The charge density can be divided into two general categories: covalently bound charge and adsorbed charge. We discuss the effect of the quantity of covalently bound charge on  $v_{eo}$  in “Effect of Solution pH on Electroosmotic Flow.” It is possible that over the very large ionic strength range investigated in Fig. 6, there is a significant change in the quantity of adsorbed charge from the electrolyte. Adsorbed charge would primarily come from the anions of the electrolyte, and this adsorbed negative charge would increase with increasing  $\mu$ . This would cause both the zeta potential and  $v_{eo}$  to increase with increasing  $\mu$ . Because this is the trend opposite to the  $\kappa^{-1} \propto \mu^{-1/2}$  and  $\rho \propto \mu^{-1}$  dependencies discussed above, this would make the net decrease in  $v_{eo}$  with increasing  $\mu$  less extreme than the predicted  $\mu^{-3/2}$  dependence, and this is what is observed experimentally.

Finally, at the highest ionic strength used in Fig. 6, both the negative and positive electroosmotic velocities decrease nearly to zero. This shows that the effect of double-layer compression on the zeta potential (which causes  $v_{eo}$  to decrease with increasing ionic strength) dominates any effect of increasing adsorbed negative charge at high ionic strengths.

## EFFECT OF SOLUTION pH ON ELECTROOSMOTIC FLOW

Phenol transport data were obtained at applied current densities of positive and negative  $24.9 \text{ mA cm}^{-2}$  from solutions that were  $10 \text{ mM}$  in NaCl and  $0.5 \text{ mM}$  in phosphate, with the pH adjusted to values between 3 and 8. The NaCl served to maintain the ionic strength at a constant value. The  $v_{eo}$  vs. solution pH data are shown in Fig. 7A. In general, the expected trend for surface acidic sites is observed (i.e.,  $v_{eo}$  is high at high pH values, where the sites are deprotonated, and goes

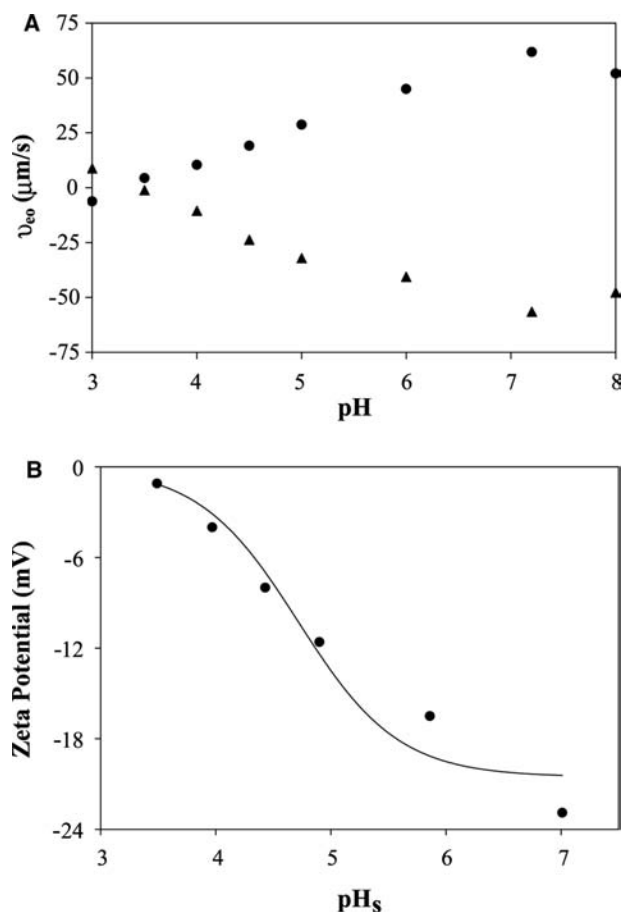


**Fig. 7** (A) Plots of EOF vs. pH. Applied current densities were ( $\blacktriangle$ )  $-24.9 \text{ mA cm}^{-2}$  and ( $\bullet$ )  $+24.9 \text{ mA cm}^{-2}$ . (B) Plot of zeta potential of the CNM vs. surface pH [Eq. (11)]. The points are the experimental data and the curve is the best fit to Eq. (13).

to zero at lower pH values, where the sites are protonated). However, there are two features of the data in Fig. 7A that are unexpected.

First, although  $v_{eo}$  goes to zero at  $\text{pH} \sim 3.5$ , at lower pH, the flow resumes again, but in the opposite direction. This indicates that positive sites are introduced by protonation of some very weakly basic surface functional groups. Such protonatable carbon sites have been known for some time and have been attributed to two chemical features of the carbon:<sup>[47]</sup> pyrone-like structures and basal plane sites that act as Lewis bases. These protonatable carbon sites have also been observed in zeta potential measurements of carbon fibers.<sup>[37,38]</sup> The presence of these sites makes the EOF characteristics of the carbon nanotubes quite interesting because the direction of EOF can be switched by controlling the pH of the contacting solution phase.

The second unexpected feature of the data in Fig. 7A is that  $|v_{eo}|$  at  $\text{pH} = 8.0$  is lower than at  $\text{pH} = 7.2$ .

Although it is tempting to attribute this to experimental error, it was observed at all current densities studied and with both positive and negative currents. This is unexpected because the fraction of the deprotonated form of a monoprotic weak acid ( $\alpha_1$ ) goes to a maximum ( $\alpha_1 = 1$ ) at some high pH and does not change at higher pH values. Hence the plots of  $v_{eo}$  vs. pH would be expected to become flat at high pH. The unexpected decrease in  $|v_{eo}|$  suggests that anionic surface charge density decreases from  $\text{pH} = 7.2$  to  $\text{pH} = 8.0$ . As discussed above, it is possible that adsorbed phosphate contributes to the surface charge on the carbon nanotubes. Perhaps at  $\text{pH} = 8.0$ , adsorbed  $\text{HPO}_4^{2-}$  is displaced by  $\text{OH}^-$ , resulting in a net decrease in the negative surface charge density.

The data in Fig. 7A can be used to determine both the number density and  $\text{pK}_a$  of the surface acidic sites on the CNMs.<sup>[46]</sup> The Boltzmann equation is first used to calculate the surface hydronium ion concentration ( $[\text{H}^+]_s$ ) from the bulk solution hydronium ion concentration ( $[\text{H}^+]_o$ ):

$$[\text{H}^+]_s = [\text{H}^+]_o \exp(-e\zeta/2kT) \quad (11)$$

The requisite zeta potential values at each pH are obtained as before from the  $v_{eo}$  data (Fig. 7A). Following Jimbo, Tanioka, and Minoura<sup>[46]</sup> the surface charge density is related to the number density of acidic sites ( $N_a$ ) and the surface  $\text{pK}_a$  via:

$$\sigma = -[(eN_a)/(1 + 10^{\text{pK}_a - \text{pH}_s})] \quad (12)$$

Eq. (9) can be solved for  $\sigma$  and set equal to Eq. (12). Solving for the zeta potential gives:

$$\zeta = -[(eN_a)/(1 + 10^{\text{pK}_a - \text{pH}_s})](\kappa^{-1}/\epsilon) \quad (13)$$

Fig. 7B shows a plot of  $\zeta$  vs.  $\text{pH}_s$  obtained from the data in Fig. 7A, omitting the highest and lowest pH values where unusual effects (vide supra) were observed. The points are the experimental data, and the curve is the result of a nonlinear least squares regression fit of Eq. (13) to the experimental data using the surface  $\text{pK}_a$  and  $N_a$  as adjustable parameters. The best fit ( $R^2 = 0.95$ ) was obtained for  $\text{pK}_a = 4.7$  and  $N_a = 0.03$  acidic sites  $\text{nm}^{-2}$ .

The surface  $\text{pK}_a$  value obtained is typical of that for an alkyl carboxylic acid (e.g., acetic acid) dissolved in aqueous solution. However, it is often the case that  $\text{pK}_a$  values for surface-bound species differ from those obtained when the corresponding molecule is dissolved in an aqueous solution. For example, the  $\text{pK}_a$  values for *p*-aminobenzoic acid (PABA)<sup>[28]</sup> and 4-carboxyphenyl<sup>[48]</sup> immobilized on glassy carbon electrode surfaces were measured to be 3.0 and 2.8, respectively. These values are significantly different

from the  $pK_a$  values for the same molecules dissolved in aqueous solution (PABA = 4.6 and benzoic acid = 4.2). For this reason, although the most likely assignment for the surface acidic sites is carboxylic acid, we cannot unambiguously make this assignment at this time. A less likely alternative would be to posit a surface phenolic site whose surface  $pK_a$  has been dramatically shifted from the typical solution value. One potential source for discrepancies between surface and free solution  $pK_a$  values is electrostatic interactions between the surface-bound sites. The site density of  $0.03 \text{ nm}^{-2}$  indicates that the sites are, on average, 3 nm apart.<sup>[49]</sup> This is comparable to the double-layer thickness at the ionic strength used to obtain the data in Fig. 7. Hence electrostatic interactions between surface acidic sites should not be significant.

### EFFECT OF ELECTROCHEMICAL DERIVATIZATION ON ELECTROOSMOTIC FLOW

An interesting advantage of the CNMs is that they are electronically conductive and thus can be used as electrodes in electrochemical experiments.<sup>[8,16,17]</sup> This has allowed us to electrochemically derivatize the carbon nanotube walls to augment or change the fixed surface charge.<sup>[15,23]</sup> The derivatization method entails the electrooxidation of a primary amine to a cation radical at the carbon nanotube walls. This results in the formation of a C–N bond, thus covalently attaching the amine to the tube walls.

Fig. 8 shows a plot of  $v_{eo}$  vs. applied current density for an as-synthesized CNM and for membranes that had been electrochemically derivatized with either 2-(4-aminophenyl)ethylamine (APEA) or PABA.<sup>[28]</sup> The pH = 7.2 buffer used was such that the

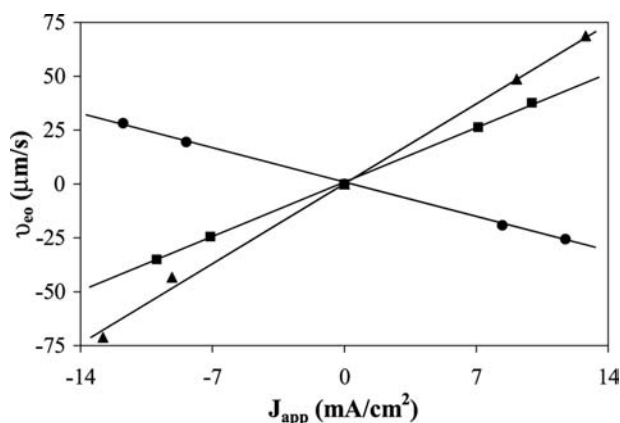


**Fig. 8** Plots of electroosmotic velocity vs. applied current density for (▲) PABA-derivatized membrane, (■) as-synthesized membrane, and (●) APEA-derivatized membrane.

carboxylic acid was deprotonated and the amine was protonated. Considering the as-synthesized membrane first, we see the expected (Table 1) change from positive EOF at the positive applied current, to zero flow at no applied current, to negative EOF at negative applied current. The measured slope of the line corresponds to  $\zeta = -20.8 \text{ mV}$ . The same trend is observed for the PABA-derivatized membrane, but the slope of the  $v_{eo}$  vs. applied current density line is steeper and corresponds to  $\zeta = -30.6 \text{ mV}$ . This indicates that there is greater negative surface charge density after the attachment of PABA, which was the anticipated result.

For the APEA-derivatized membrane, positive EOF is observed at negative applied currents and negative EOF is observed at positive applied currents (Fig. 8). This indicates that the zeta potential, and thus surface charge, are now positive, again the anticipated result. The zeta potential for the APEA-derivatized membrane was determined to be  $+13.2 \text{ mV}$ . However, note that the magnitude of the zeta potential for the APEA-derivatized membrane is not as great as for either the underivatized or PABA-derivatized membranes. Although this might be because of a lower surface charge density for the APEA-derivatized membrane, other factors contributing to zeta potential [Eq. (8)] must also be considered. For the as-synthesized and PABA-derivatized membranes, the solution side of the double layer contains monovalent  $\text{Na}^+$  ions. In contrast, for the APEA-derivatized membrane, the double layer contains a mixture of monovalent  $\text{H}_2\text{PO}_4^-$  and divalent  $\text{HPO}_4^{2-}$  ions. The presence of the divalent ions (which are electrostatically preferred over the monovalent) will compress the double layer relative to the case where only monovalent ions are present.<sup>[50]</sup> As a result, at any surface charge density value, the double layer will be thinner when divalent ions are present. This will cause the zeta potential to be lower and  $v_{eo}$  to be smaller than in the monovalent case. This factor undoubtedly contributes to the smaller slope for the APEA-derivatized membrane (Fig. 8).

### CONCLUSION

Template synthesis is a highly flexible method for preparation of CNMs that can be used for a variety of purposes. For instance, EOF can be driven across template-prepared CNMs, and the rate and direction of flow can be controlled by changing the magnitude and the sign of the transmembrane current. The direction of EOF can also be switched by varying the pH of the contacting solution phase, and all of the pH-induced changes in EOF are reversible. This means, for example, that returning a membrane that had been exposed to pH = 3.5 buffer, where no EOF is



observed (Fig. 7A), to pH = 7.2 buffer restored the flow. Electrochemical derivatization methods can be used to attach specific surface functional groups to the carbon nanotubes and this provides another route for adjusting the rate and direction of EOF.

There is a third possible way to affect the rate and direction of EOF in such membranes. We have shown with gold nanotube membranes that the sign and magnitude of the excess surface charge can be controlled potentiostatically by simply applying a potential to the membrane in an electrolyte solution.<sup>[51]</sup> When negative potentials are applied, the nanotubes have excess negative (electron) surface charge, and when positive potentials are applied, the nanotubes have excess positive surface charge. This ability to control excess surface charge potentiostatically is unique to membranes that are electronically conductive, as are Au and CNMs. We are currently investigating whether this simple potentiostatic charging method can be used to control EOF in the CNMs.

## ACKNOWLEDGMENTS

Aspects of this work were supported by the National Science Foundation and the Office of Naval Research. The authors acknowledge valuable discussions with Prof. Henry White and Prof. Richard McCreery. Thanks are offered to Dr. David Mitchell for SEM analysis and Lacramioara Trofin for preparation of anodic alumina templates.

## REFERENCES

1. McEuen, P.L. Nanotechnology—Carbon-based electronics. *Nature* **1998**, *393* (6680), 15–17.
2. Tans, S.J.; Verschueren, A.R.M.; Dekker, C. Room-temperature transistor based on a single carbon nanotube. *Nature* **1998**, *393* (6680), 49–52.
3. Ouyang, M.; Huang, J.-L.; Lieber, C.M. Energy gaps in “metallic” single-walled carbon nanotubes. *Science* **2001**, *292* (5517), 702–705.
4. Rueckes, T.; Kim, K.; Joselevich, E.; Tseng, G.Y.; Cheung, C.-L.; Lieber, C.M. Carbon nanotube-based nonvolatile random access memory for molecular computing. *Science* **2000**, *289* (5476), 94–97.
5. Liu, C.; Fan, Y.Y.; Cong, H.T.; Cheng, H.M.; Dresselhaus, M.S. Hydrogen storage in single-walled carbon nanotubes at room temperature. *Science* **1999**, *286* (5442), 1127–1129.
6. Chen, P.; Wu, X.; Lin, J.; Tan, K.L. High H<sub>2</sub> uptake by alkali-doped carbon nanotubes under ambient pressure and moderate temperatures. *Science* **1999**, *285* (5424), 91–93.
7. Joo, S.H.; Choi, S.J.; Oh, I.; Kwak, J.; Liu, Z.; Terasaki, O.; Ryoo, R. Ordered nanoporous arrays of carbon

supporting high dispersions of platinum nanoparticles. *Nature* **2001**, *412* (6843), 169–172.

8. Che, G.; Lakshmi, B.B.; Fisher, E.R.; Martin, C.R. Carbon nanotubule membranes for electrochemical energy storage and production. *Nature* **1998**, *393* (6683), 346–349.
9. de Heer, W.A.; Châtelain, A.; Ugarte, D. A carbon nanotube field-emission electron source. *Science* **1995**, *270* (5239), 1178–1180.
10. Fan, S.; Chapline, M.G.; Franklin, N.R.; Tomblor, T.W.; Cassell, A.M.; Dai, H. Self-oriented regular arrays of carbon nanotubes and their field emission properties. *Science* **1999**, *283* (5401), 512–515.
11. Martin, C.R.; Mitchell, D.T. Nanomaterials in analytical chemistry. *Anal. Chem.* **1998**, *70* (09), 322A–327A.
12. Hulteen, J.C.; Martin, C.R. A general template-based method for the preparation of nanomaterials. *J. Mater. Chem.* **1997**, *7* (7), 1075–1087.
13. Martin, C.R. Nanomaterials: A membrane-based synthetic approach. *Science* **1994**, *266* (5193), 1961–1966.
14. Kyotani, T.; Tsai, L.F.; Tomita, A. Formation of platinum nanorods and nanoparticles in uniform carbon nanotubes prepared by a template carbonization method. *Chem. Commun.* **1997**, *7*, 701–702.
15. Miller, S.A.; Young, V.Y.; Martin, C.R. Electroosmotic flow in template-prepared carbon nanotube membranes. *J. Am. Chem. Soc.* **2001**, *123* (49), 12335–12342.
16. Che, G.; Miller, S.A.; Fisher, E.R.; Martin, C.R. An electrochemically driven actuator based on a nanostructured carbon material. *Anal. Chem.* **1999**, *71* (15), 3187–3191.
17. Che, G.; Lakshmi, B.B.; Martin, C.R.; Fisher, E.R. Metal-nanocluster-filled carbon nanotubes: Catalytic properties and possible applications in electrochemical energy storage and production. *Langmuir* **1999**, *15* (3), 750–758.
18. Baum, R.M. Nurturing nanotubes. *Chem. Eng. News* **1997**, *75* (26), 39–41.
19. Schlittler, R.R.; Seo, J.W.; Gimzewski, J.K.; Durkan, C.; Saifullah, M.S.M.; Welland, M.E. Single crystals of single-walled carbon nanotubes formed by self-assembly. *Science* **2001**, *292* (5519), 1136–1139.
20. Li, W.Z.; Xie, S.S.; Qian, L.X.; Chang, B.H.; Zou, B.S.; Zhou, W.Y.; Zhao, R.A.; Wang, G. Large-scale synthesis of aligned carbon nanotubes. *Science* **1996**, *274* (5293), 1701–1703.
21. Ren, Z.F.; Huang, Z.P.; Xu, J.W.; Wang, J.H.; Bush, P.; Siegal, M.P.; Provencio, P.N. Synthesis of large arrays of well-aligned carbon nanotubes on glass. *Science* **1998**, *282* (5391), 1105–1107.
22. Sun, L.; Crooks, R.M. Single carbon nanotube membranes: A well-defined model for studying mass transport through nanoporous materials. *J. Am. Chem. Soc.* **2000**, *122* (49), 12340–12345.
23. Miller, S.A.; Martin, C.R. Controlling the rate and direction of electroosmotic flow in template-prepared carbon nanotube membranes. *J. Electroanal. Chem.* **2002**, *522* (1), 66–69.
24. Bath, B.D.; Lee, R.D.; White, H.S.; Scott, E.R. Imaging molecular transport in porous membranes. Observation and analysis of electroosmotic flow in individual pores

- using the scanning electrochemical microscope. *Anal. Chem.* **1998**, *70* (6), 1047–1058.
25. Bath, B.D.; White, H.S.; Scott, E.R. Electrically facilitated molecular transport. Analysis of the relative contributions of diffusion, migration, and electroosmosis to solute transport in an ion-exchange membrane. *Anal. Chem.* **2000**, *72* (3), 433–442.
  26. Barbier, B.; Pinson, J.; Desarmot, G.; Sanchez, M. Electrochemical bonding of amines to carbon-fiber surfaces toward improved carbon–epoxy composites. *J. Electrochem. Soc.* **1990**, *137* (6), 1757–1764.
  27. Deinhammer, R.S.; Ho, M.; Anderegg, J.W.; Porter, M.D. Electrochemical oxidation of amine-containing compounds: A route to the surface modification of glassy carbon electrodes. *Langmuir* **1994**, *10* (4), 1306–1313.
  28. Liu, J.; Cheng, L.; Liu, B.; Dong, S. Covalent modification of a glassy carbon surface by 4-aminobenzoic acid and its application in fabrication of a polyoxometalates-consisting monolayer and multilayer films. *Langmuir* **2000**, *16* (19), 7471–7476.
  29. Hornyak, G.L.; Patrissi, C.J.; Martin, C.R. Fabrication, characterization, and optical properties of gold nanoparticle/porous alumina composites: The nonscattering Maxwell–Garnett limit. *J. Phys. Chem.* **1997**, *101* (9), 1548–1555.
  30. Masuda, H.F.K. Ordered metal nanohole arrays made by a two-step replication of honeycomb structures of anodic alumina. *Science* **1995**, *268* (5216), 1466–1468.
  31. Li, J.; Papadopoulos, C.; Xu, J. Growing Y-junction carbon nanotubes. *Nature* **1999**, *402* (6759), 253–254.
  32. Li, J.; Papadopoulos, C.; Xu, J.M. Highly-ordered carbon nanotube arrays for electronics applications. *Appl. Phys. Lett.* **1999**, *75* (3), 367–369.
  33. Kyotani, T.; Tsai, L.; Tomita, A. Formation of ultrafine carbon tubes by using an anodic aluminum oxide film as a template. *Chem. Mater.* **1995**, *7* (8), 1427–1428.
  34. Kyotani, T.; Tsai, L.; Tomita, A. Preparation of ultrafine carbon tubes in nanochannels of an anodic aluminum oxide film. *Chem. Mater.* **1996**, *8* (8), 2109–2113.
  35. Rouhi, A.M. From membranes to nanotubules. *Chem. Eng. News* **2001**, *79* (24), 29–33.
  36. Panzer, R.E.; Elving, P.J. Nature of the surface compounds and reactions observed on graphite electrodes. *Electrochim. Acta* **1975**, *20* (9), 635–647.
  37. Bismarck, A.; Springer, J. Characterization of fluorinated pan-based carbon fibers by zeta potential measurements. *Colloids Surf., A Physicochem. Eng. Asp.* **1999**, *159* (2–3), 331–339.
  38. Garcia, A.B.; Cuesta, A.; Montes-Moran, M.A.; Martinez-Alonso, A.; Tascon, J.M.D. Zeta potential as a tool to characterize plasma oxidation of carbon fibers. *J. Colloid Interface Sci.* **1997**, *192* (2), 363–367.
  39. Jirage, K.B.; Hulteen, J.C.; Martin, C.R. Effect of thiol chemisorption on the transport properties of gold nanotubule membranes. *Anal. Chem.* **1999**, *71* (21), 4913–4918.
  40. Srinivasan, V.; Higuchi, W.I. A model for iontophoresis incorporating the effect of convective solvent flow. *Int. J. Pharm.* **1990**, *60* (2), 133–138.
  41. Renkin, E.M. Filtration, diffusion, and molecular sieving through porous cellulose membranes. *J. Gen. Physiol.* **1954**, *38* (2), 225–243.
  42. Probstein, R.F. *Physicochemical Hydrodynamics*; Butterworth: Stoneham, MA, 1989; 185–198.
  43. Weast, R.C.; Astle, M.J.; Beyer, W.H., Eds.; *CRC Handbook of Chemistry and Physics* 66th Ed., CRC Press, Inc.: Boca Raton, FL, 1985.
  44. Rice, C.L.; Whitehead, R. Electrokinetic flow in a narrow cylindrical capillary. *J. Phys. Chem.* **1965**, *69* (11), 4017–4024.
  45. Levine, S.; Marriott, J.R.; Neale, G.; Epstein, N. Theory of electrokinetic flow in fine cylindrical capillaries at high zeta-potentials. *J. Colloid Interface Sci.* **1975**, *52* (1), 136–149.
  46. Jimbo, T.; Tanioka, A.; Minoura, N. Characterization of an amphoteric-charged layer grafted to the pore surface of a porous membrane. *Langmuir* **1998**, *14* (25), 7112–7118.
  47. Leon y Leon, C.A.; Solar, J.M.; Calemma, V.; Radovic, L.R. Evidence for the protonation of basal-plane sites on carbon. *Carbon* **1992**, *30* (5), 797–811.
  48. Saby, C.; Ortiz, B.; Champagne, G.Y.; Belanger, D. Electrochemical modification of glassy carbon electrode using aromatic diazonium salts: 1. Blocking effect of 4-nitrophenyl and 4-carboxyphenyl groups. *Langmuir* **1997**, *13* (25), 6805–6813.
  49. Cheng, I.F.; Whiteley, L.D.; Martin, C.R. Ultramicroelectrode ensembles. Comparison of experimental and theoretical responses and evaluation of electroanalytical detection limits. *Anal. Chem.* **1989**, *61* (7), 762–766.
  50. Burns, D.B.; Zydny, A.L. Buffer effects on the zeta potential of ultrafiltration membranes. *J. Membr. Sci.* **2000**, *172* (1–2), 39–48.
  51. Nishizawa, M.; Menon, V.P.; Martin, C.R. Metal nanotubule membranes with electrochemically switchable ion-transport selectivity. *Science* **1995**, *268* (5311), 700–702.

# Carbon Nanotubes: Functionalization

**Bin Zhao**

*Departments of Chemistry and Chemical and Environmental Engineering,  
University of California–Riverside, Riverside, California, U.S.A.*

**Hui Hu**

**Elena Bekyarova**

**Mikhail E. Itkis**

**Sandip Niyogi**

*University of California–Riverside, Riverside, California, U.S.A.*

**Robert C. Haddon**

*Center for Nanoscale Science and Engineering, University of California–Riverside,  
Riverside, California, U.S.A.*

## INTRODUCTION

The discovery of carbon nanotubes (CNTs) in the early 1990s has stimulated intensive research to characterize their structure and properties. The outstanding electronic and mechanical properties suggest that CNTs may find application in electronic devices, composite materials, energy storage, field emission, biology, medicine, and chemical sensors. Most of these applications take advantage of the structure and physical properties of CNTs, such as high mechanical strength, excellent thermal and electric conductivity, high aspect ratio, and the hollow cavity. Chemical functionalization has been employed to tailor the properties of CNTs and to enhance the ability to manipulate CNTs.

CNTs contain only conjugated carbon atoms and therefore they are chemically inert, and this is reflected by their properties such as insolubility in all solvents and low chemical reactivity. The inert nature of CNTs limits the available identification and characterization tools, and hinders the manipulation and application of carbon nanotubes. Chemical functionalization of CNTs is a useful tool for addressing these problems, and functionalized CNTs have found broad application, including composite materials, sensors, and biomaterials. In the present entry we review the structure and properties of CNTs, but in the main we focus on the chemistry of carbon nanotubes including previous work and recent development.

## STRUCTURE AND PROPERTIES OF CARBON NANOTUBES

CNTs can be classified as single-walled carbon nanotubes (SWNTs) and multiwalled carbon nanotubes

(MWNTs). The structure of an individual SWNT can be regarded as a two-dimensional (2-D) graphene sheet cut at various angles with respect to the hexagonal lattice that has been wrapped up into a seamless cylinder, which is capped by fullerene hemispheres at both ends (Fig. 1). MWNTs are composed of concentric cylinders placed around a common central hollow, with spacing between the layers close to that of the interlayer distance in graphite ( $\sim 0.34$  nm).

CNTs can be metallic or semiconducting, depending on their diameter and chirality. “Armchair” tubes have energy bands that cross the Fermi level and are therefore metallic. “Chiral” and “zigzag” nanotubes are expected to be metallic when  $n - m = 3l$  (where  $l$  is an integer) or semiconducting with an energy gap of order  $\sim 1$  eV when  $n - m \neq 3l$ .  $n$  and  $m$  are integers of the vector equation  $\mathbf{R} = n\mathbf{a}_1 + m\mathbf{a}_2$ , where  $\mathbf{a}_1$  and  $\mathbf{a}_2$  are the unit cell vectors of a graphene sheet. Fig. 2 shows the electronic density of states (DOS) of a metallic and a semiconducting SWNT close to Fermi level. For the metallic SWNT, there is a finite value of the DOS at the Fermi level. On the other hand, a complete gap between the spikes close to Fermi level can be found in the semiconducting SWNT. The energy separation between each pair of peaks represents the band gap of SWNTs. By using simple tight-binding (STB) theory, in which the electronic band structure is assumed to arise from a pure p-orbital at each conjugated carbon atom, the low-energy band gap transitions take a simple analytical form:  $S_{11} = 2a\beta/d$ ,  $S_{22} = 4a\beta/d$ ,  $M_{11} = 6a\beta/d$ , where  $a$  is the carbon-carbon bond length (0.142 nm),  $\beta$  is the transfer or resonance integral between the p- and  $\pi$ -orbitals ( $\beta = 2.9$  eV), and  $d$  is the diameter (nm) of the particular semiconducting or metallic SWNT.  $S_{11}$  and  $S_{22}$  are the first and second pairs of singularities in the

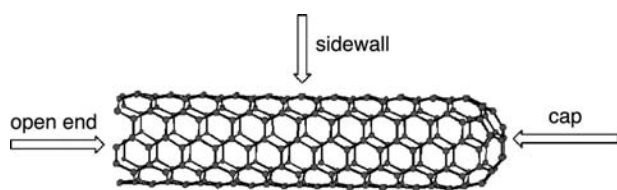


Fig. 1 Structure of the single-walled carbon nanotube.

DOS of semiconducting SWNTs, respectively.  $M_{11}$  corresponds to the transition between the first pair of singularities in the DOS of metallic SWNTs.<sup>[1-3]</sup> The characteristic interband electronic transitions provide the spectroscopic signature of the SWNTs in the near-IR (NIR)/VIS spectral region (Fig. 2). As most SWNT preparations are a mixture of metallic and semiconducting SWNTs, the interband transitions arising from both species are visible.

Besides these unique electronic properties, CNTs exhibit excellent mechanical and thermal properties. CNTs exhibit the highest Young's modulus and tensile strength of all known materials. The Young's modulus for an individual (10, 10) SWNT is  $\sim 0.64$  TPa<sup>[4]</sup> and up to 1.47 TPa for a 15-SWNT rope,<sup>[5]</sup> which is much higher than that of conventional carbon fibers which have values in the range of 200–800 GPa.<sup>[6]</sup> Young's modulus of MWNTs was reported to be 1–2 TPa,<sup>[7]</sup> and the bending strength of individual MWNTs reaches 28.5 GPa.<sup>[8]</sup> The measured thermal conductivity of an individual MWNT ( $\sim 3000$  W/m<sup>2</sup>K) is larger than that of natural diamond and the basal plane of graphite (both 2000 W/m<sup>2</sup>K).

## CHEMISTRY OF CARBON NANOTUBES

The covalent chemistry of CNTs may be classified into two categories.<sup>[9]</sup> The first involves functionalization at

the ends or at defect sites of the CNTs, where there exists the possibility to add to the carbon nanotube at a  $\sigma$ -bonded site, without attacking the  $\pi$ -system; this type of chemistry usually involves reaction at a previously introduced carboxylic acid group. These carboxylic acid groups are usually generated by nitric acid treatment and can be used as precursors in functionalizations such as amidation and esterification.<sup>[10,11]</sup> The second type of covalent chemistry involves sidewall functionalization in which the carbon-carbon double bonds on the sidewall of CNTs react. Such reactions include fluorination,<sup>[12]</sup> carbene<sup>[9,11,13,14]</sup> or nitrene addition, Birch reduction,<sup>[9,15]</sup> 1,3-dipolar addition,<sup>[16]</sup> and reactions with radicals.<sup>[17-19]</sup>

## Purity Evaluation of SWNTs

In current preparations, a large amount of impurities, such as metal catalysts, amorphous carbon, and carbon nanoparticles, are generated during SWNT production. In order to develop a rigorous macromolecular science of CNTs it is necessary to work with materials of the same high level of purity that is found in the pharmaceutical, electronics, and polymer industries. An obvious first step is the development of quality control and quality assurance criteria for the bulk purity of CNTs. Recently, a method was reported to quantitatively evaluate the carbonaceous purity of electric arc produced as-prepared SWNT soot by using solution-phase near-IR spectroscopy (NIR), in which the purity of a SWNT sample (X-SWNT) was evaluated against a reference sample (R-SWNT) by using the region of the second interband transition ( $S_{22}$ ) for semiconducting SWNTs;<sup>[20-22]</sup> whereas the metal content is obtained by thermogravimetric analysis.<sup>[22]</sup> As illustrated in Fig. 3, AA(T, R-SWNT) and AA(T, S-SWNT) (areal absorbance) are obtained by integration

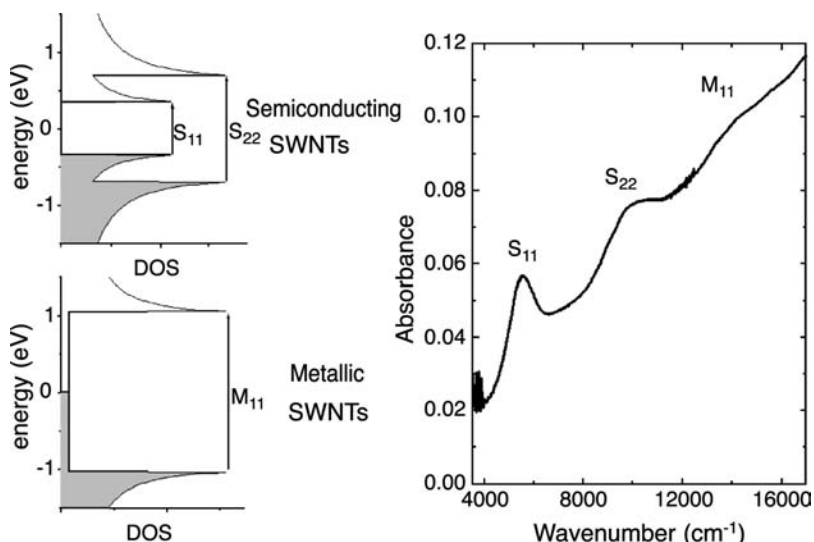


Fig. 2 Interband transition of arc-produced SWNTs near Fermi level.

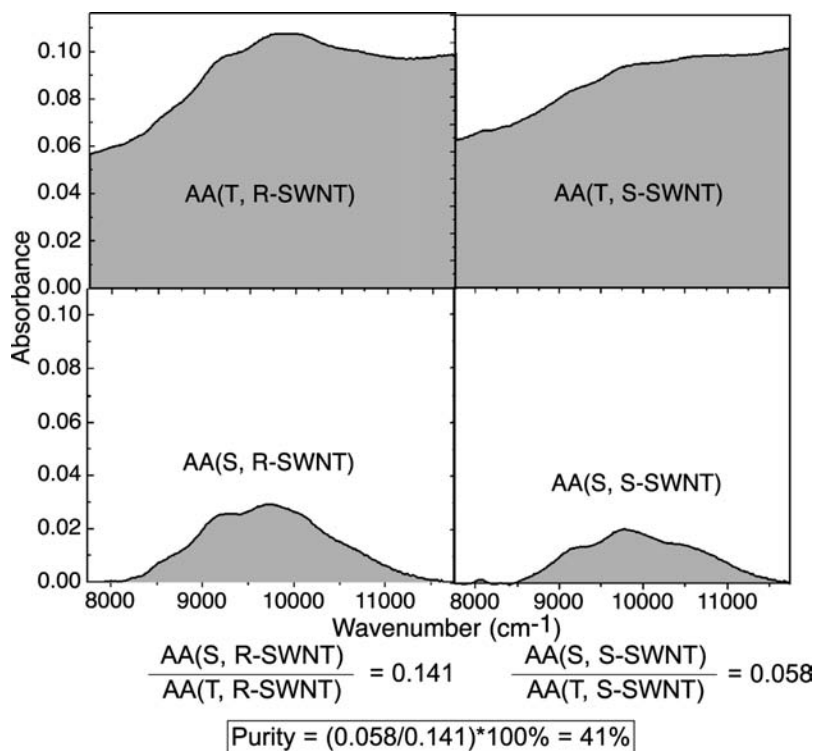


Fig. 3 Purity evaluation of SWNTs.

of the NIR spectra between the spectral cutoffs of  $SCL = 7750$  and  $SCH = 11,750 \text{ cm}^{-1}$ , whereas  $AA(S, R-SWNT)$  and  $AA(S, S-SWNT)$  represent the area under the  $S_{22}$  absorption after baseline correction. In the example shown in Fig. 3, the carbonaceous relative purity of X-SWNT is then obtained as:

$$\begin{aligned} \text{Purity} &= [AA(S, S-SWNT) \div AA(T, S-SWNT)] \\ &\div [AA(S, R-SWNT) \div AA(T, R-SWNT)] \\ &= 0.058 \div 0.141 = 41\% \end{aligned}$$

This method is also applicable to the evaluation and optimization of SWNT purification procedures, and makes it possible to investigate the effects of purification treatment on SWNTs in a quantitative manner.<sup>[21,22]</sup>

### Reactivity of SWNTs

The strain in non-planar-conjugated organic molecules arises from two principal sources: pyramidalization of the conjugated carbon atoms, and  $\pi$ -orbital misalignment between adjacent pairs of conjugated atoms.<sup>[23–25]</sup> It is well known that the chemistry of the fullerenes is characterized by addition reactions.<sup>[26–29]</sup> The relatively high reactivity of  $C_{60}$  results from the conversion of trigonal carbon atoms ( $sp^2$ -hybridized) to tetrahedral carbon atoms ( $sp^3$ -hybridized). This serves to release the tremendous strain present in the spheroidal geometry, because the pyramidalization angle  $\theta_p$ , which is related

to the curvature at a conjugated carbon atom, of  $C_{60}$  ( $\theta_p = 11.64^\circ$ ) is actually closer to the ideal tetrahedral angle ( $\theta_p = 19.47^\circ$ ) than to the planar geometry required for trigonal hybridization ( $\theta_p = 0$ ).<sup>[25,30]</sup> Fig. 4 shows the pyramidalization angle of  $sp^2$ - and  $sp^3$ -hybridized carbon atoms. As a result of the spheroidal geometry there is no  $\pi$ -orbital misalignment in  $C_{60}$ .

From the standpoint of chemistry, carbon nanotubes can be divided into two regions: the end caps and the sidewall. The origins of the strain in the end caps and the sidewall of CNTs are somewhat different. The end cap of a CNT can be regarded as a hemispherical fullerene, and the carbon-carbon bonds in this region of the carbon nanotube therefore experience

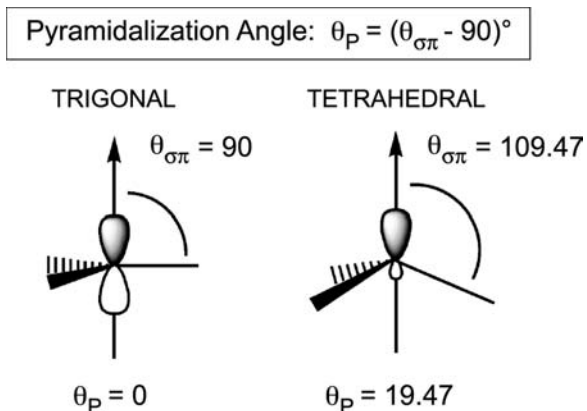
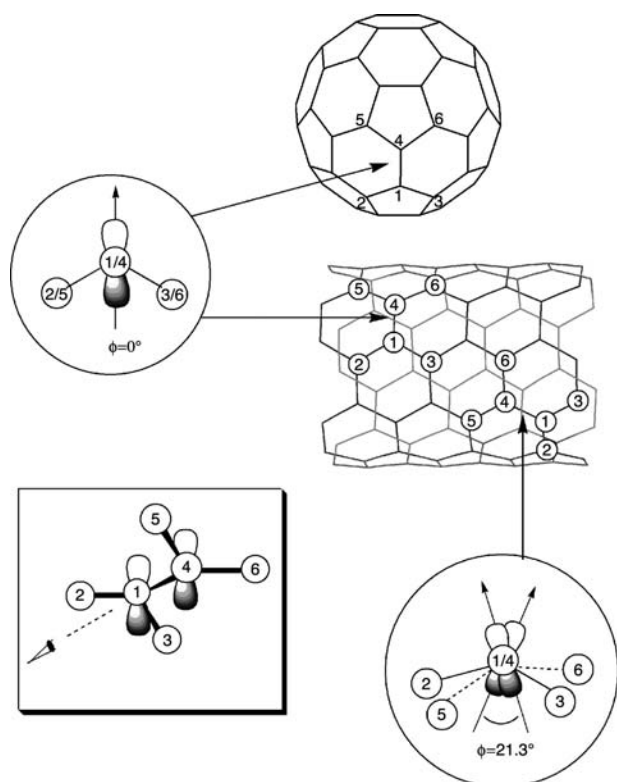


Fig. 4 Pyramidalization angle ( $\theta_p$ ) of  $sp^2$  (left)- and  $sp^3$  (right)-hybridized carbon.



**Fig. 5** The  $\pi$ -orbital misalignment angles ( $\phi$ ) along the C1–C4 in the (5, 5) SWNT and fullerene.

a similar degree of strain due to pyramidalization to that of the equivalent fullerene. However, as the curvature in the sidewall of a CNT is much less than that in a fullerene of equivalent diameter, the carbon–carbon bonds in the sidewall of a carbon nanotube are much less reactive than those in the end cap.<sup>[9,31]</sup> In the fullerenes, pyramidalization is essentially the only source of strain because the  $\pi$ -orbital alignment is almost perfect because of the quasi-spheroidal geometry.<sup>[30,31]</sup>

In the case of the armchair CNT shown in Fig. 5, there are two types of carbon–carbon bonds in the sidewall: one is parallel to the circumference plane (which is perpendicular to the axis of the CNT), whereas the other lies at an angle to the circumference plane. As may be seen in Fig. 5, the first bond is reminiscent of the situation in the fullerenes with perfect alignment of the lobes of the  $\pi$ -orbitals, whereas the second bonding geometry requires a twist of the  $\pi$ -bond.<sup>[9,31]</sup> In the latter case, the angle between the lobes of the  $\pi$ -orbitals of the adjacent carbon atoms [ $\pi$ -orbital misalignment angle ( $\phi$ )] will differ from zero and this is a source of strain in the carbon nanotubes that is almost totally absent in the fullerenes. This strain due to orbital misalignment leads to a differentiation between the bonds in the CNTs that may be reflected in their relative reactivity.

In the foregoing discussion we have adopted the  $\pi$ -orbital axis vector (POAV) analysis, which was successful in the analysis of the electronic structure and chemistry of the fullerenes,<sup>[25]</sup> and applied it to the CNTs. This analysis relies on the local geometry of the structures; however, the CNTs possess an extended electronic structure and this leads to the development of energy bands, which in the case of the metallic SWNTs produces a finite DOS at the Fermi level;<sup>[13,32]</sup> the semiconducting SWNTs, of course, have an energy gap at the Fermi level. Thus there should be a marked difference in the reactivity of metallic and semiconducting SWNTs in chemical reactions that are initiated by electron donation or electron transfer processes.<sup>[9,19]</sup>

## Covalent Functionalization

### Oxidation of Carbon nanotubes

Oxidative processes were among the first chemical reactions to be applied to CNTs,<sup>[33]</sup> mainly for the purposes of purification and catalyst removal. Heating of CNTs in air at 700°C for 10 min leads to the opening of the hemispherical end caps of CNTs and demonstrated the different reactivities of the bonds in CNTs (end cap vs. sidewall). The controlled annealing of SWNTs in O<sub>2</sub> is an effective method of purification.<sup>[21]</sup> Other gas-phase oxidation methods including the use of H<sub>2</sub>S + O<sub>2</sub><sup>[34]</sup> and O<sub>3</sub><sup>[35]</sup> have also been reported. Liquid-phase oxidation processes, such as treatment with HNO<sub>3</sub>,<sup>[22,36–40]</sup> HNO<sub>3</sub> + H<sub>2</sub>SO<sub>4</sub>,<sup>[10,40]</sup> H<sub>2</sub>SO<sub>4</sub> + KMnO<sub>4</sub>,<sup>[41]</sup> and KMnO<sub>4</sub>,<sup>[40]</sup> have been widely used in the processing of CNTs. These oxidants can remove the end caps of CNTs and introduce functional groups, such as –COOH, –OH, –C–O, at the dangling bonds.<sup>[40,42]</sup> Among these functionalities, the carboxylic acid group is of great importance as it has been employed in a large number of CNT functionalization reactions. After nitric acid treatment of SWNTs, the concentration of carboxylic acid groups is about 1–3 at.% based on acid–base titration.<sup>[43]</sup>

### End functionalization

As the carbon atoms at the ends have larger curvature than carbon atoms in the sidewall, they can be oxidized more easily than the other carbon atoms. The end (and defect) functionalization of the CNTs has important ramifications:

1. End functionalization does not destroy the extended  $\pi$ -network, thereby retaining the unaltered electronic and mechanical properties of the CNTs.



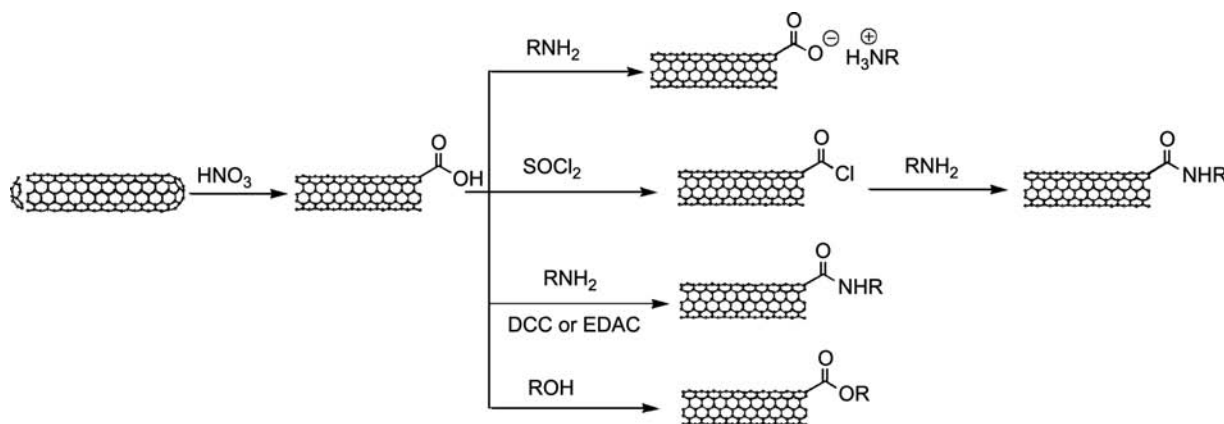


Fig. 6 Schematic representation of end functionalization of SWNTs.

- End functionalization can dramatically change the chemical and physical properties of CNTs, enhance their solubility, and facilitate the manipulation of CNTs.

The carboxylic acid groups that terminate the ends and defect sites of SWNTs act as chemical precursors for the functionalization chemistry (Fig. 6). The first chemical synthesis of soluble SWNTs was reported in 1998.<sup>[11]</sup> The functionalization methodology was based on the amidation of SWNTs with a long-chain amine [octadecylamine (ODA)]. Acid-treated SWNTs were first reacted with thionyl chloride to form an acyl chloride intermediate.<sup>[10]</sup> Then the acyl chloride intermediate was heated with ODA at 90°C to 100°C for 96 hr. The resulting amide form of SWNTs was soluble in many common organic solvents, including chloroform, dichloromethane, aromatic solvents (benzene, toluene, chlorobenzene), and CS<sub>2</sub>. The solubility of the s-SWNTs in 1,2-dichlorobenzene and CS<sub>2</sub> is higher than 1 mg/mL. This important finding not only provides a new method for obtaining well-characterized highly purified SWNT materials by separating soluble SWNTs from insoluble impurities,<sup>[44,45]</sup> but also opened the door for the study of SWNT chemistry in the organic solution phase. Various solution spectroscopy can be applied to characterize the dissolved SWNTs.<sup>[11,46,47]</sup>

Based on the same method, other amines, such as 4-dodecyl-aniline,<sup>[46]</sup> glucosamine<sup>[48]</sup> and amine-rich polymers, dendra, and proteins,<sup>[49–52]</sup> have been used to functionalize SWNTs. The methodology of these reactions is based on amidation via acyl chloride intermediate or the 1-ethyl-3-(3-dimethylaminopropyl)carbodiimide (EDAC)- or 1,3-dicyclohexylcarbodiimide (DCC)-activated reaction. The poly(propionylethylenimine-co-ethylenimine (PPEI-EI)-<sup>[51]</sup> and bovine serum albumin (BSA)-functionalized SWNTs<sup>[52]</sup> were quite soluble in water as well as organic solvents. Sonication during the

reaction can promote EDAC-activated amidation.<sup>[51]</sup> The ring closure of SWNTs by reaction between the –COOH and –OH at their ends has also been reported.<sup>[53]</sup>

Solution-phase mid-IR spectroscopy had been used to estimate the ratio of the carbon atoms in the SWNT backbone to the carbon atoms in the end-groups and at defect sites of the ODA-functionalized soluble SWNTs.<sup>[47]</sup> By measuring the intensity of  $\nu_{(C-H)}$  stretching vibrations that originate from the ODA alkyl chains and comparing with an external standard, the fractional amount of the alkyl chains in the soluble SWNTs samples can be determined. A quantitative C<sup>13</sup> NMR study of ODA functionalized MWNTs has also been used to discuss the relationship between the content of ODA and the solubility of the CNTs.<sup>[54]</sup>

### Sidewall functionalization

As the carbon–carbon bonds in the sidewall of the CNTs are of lower reactivity than the bonds in fullerenes, reagents with high chemical reactivity have been involved in the sidewall functionalization of CNTs (Fig. 7). Such reagents include carbenes,<sup>[9,11,13]</sup> fluorine,<sup>[12]</sup> aryl radicals,<sup>[17,18,55]</sup> and azomethine ylides.<sup>[16]</sup> Several methods for the metal reduction of SWNTs have also been reported,<sup>[9,15]</sup> and SWNTs with alkyl substituents were obtained by treating the fluorinated SWNTs with nucleophilic reagents such as alkyllithium and alkyl magnesium bromides.<sup>[56,57]</sup>

Once the sidewall functionalization of SWNTs had been accomplished, the properties of the SWNTs change dramatically. The carbon atoms on the sidewalls of SWNTs that react with functional groups are converted from sp<sup>2</sup> into sp<sup>3</sup> hybridization. The saturation of the  $\pi$ -network leads to a significant change in the electronic band structure of SWNTs that can be monitored by optical spectroscopy.<sup>[11,13,14,17,18,55]</sup> The presence of sp<sup>3</sup>-hybridized carbon atoms in the SWNT framework can be detected by Raman spectroscopy<sup>[12,14,17,18,55,58,59]</sup>

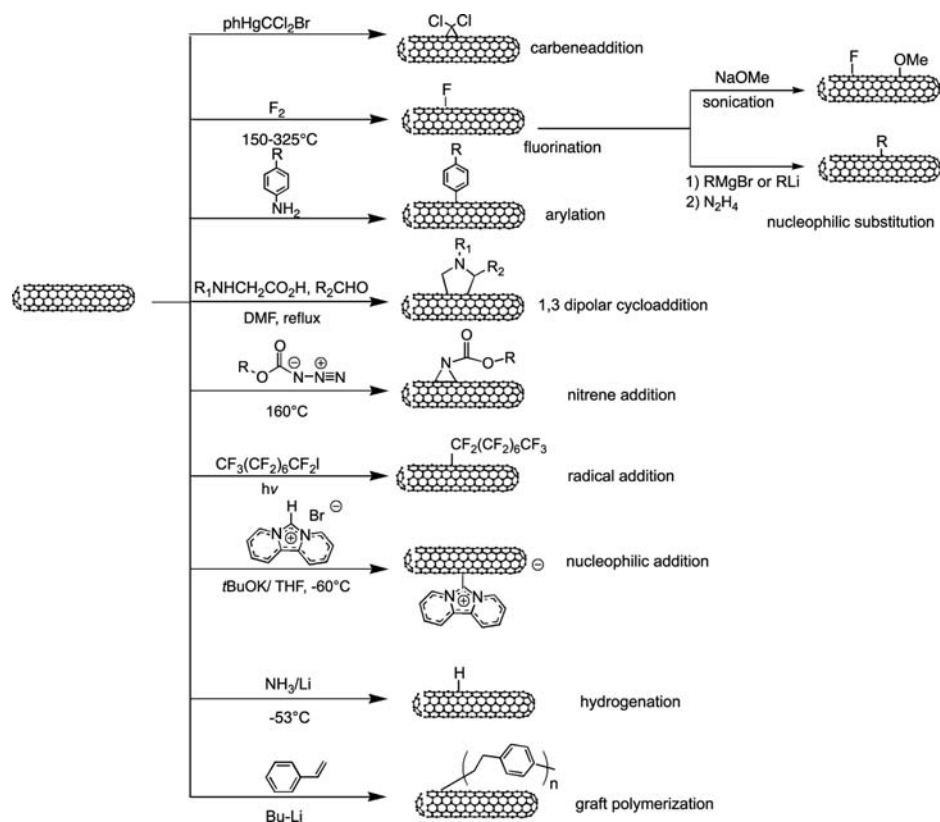


**Fig. 7** Schematic representation of sidewall functionalization of SWNTs.

and is reflected by an increase in the relative intensity of the disorder mode of the SWNTs after sidewall functionalization. The solubility of sidewall-functionalized SWNTs in organic solvents or water is usually improved by the addition of different functional groups.

Phenyl(bromodichloromethyl)-mercury has been used to add dichlorocarbene to both soluble and insoluble SWNTs (Fig. 8).<sup>[9,11,13,14]</sup> The degree of dichlorocarbene functionalization of soluble HiPco SWNTs can be as high as 23%, which is sufficient to almost completely eliminate all vestiges of the interband transitions in the SWNTs. The transitions at the Fermi level in the metallic SWNTs that appear in the far-infrared (FIR) region of the spectrum (Fig. 9) show a dramatic decrease of intensity on dichlorocarbene functionalization, which indicates that the dichlorocarbene addition significantly perturbs the conjugated  $\pi$ -network and

converts a metal into semiconductor. On the other hand, the reaction of the SWNTs with oxidants causes an increase in the intensity of absorption at the Fermi level that was observable in the FIR due to hole doping of the semiconducting SWNTs.<sup>[13,32]</sup> Therefore the FIR region of the spectrum allows a clear differentiation between covalent and the ionic chemistry of SWNTs.<sup>[14]</sup>

The fluorination of SWNTs can produce a high degree of functionalization (up to the composition  $C_2F$ ) by using elemental fluorine at temperatures from 150°C to 600°C.<sup>[12]</sup> FT-IR spectra confirmed that the fluorine was covalently bonded to the carbon on the sidewall ( $\nu_{C-F}$  at 1220–1250  $\text{cm}^{-1}$ ). TEM images of these highly functionalized SWNTs showed that the nanotubes were significantly degraded. The electrical conductivity of the functionalized SWNTs (resistance

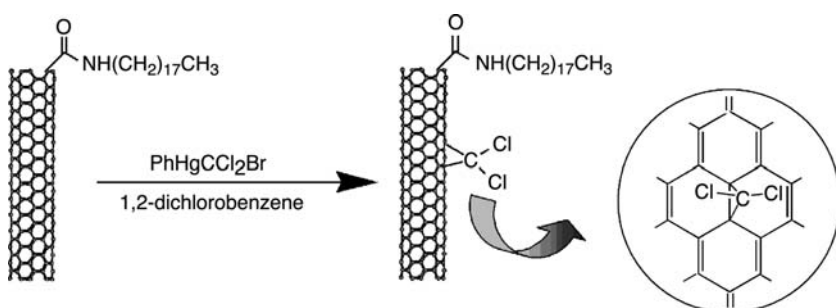


**Fig. 8** Schematic representation of dichlorocarbene addition to soluble SWNTs.

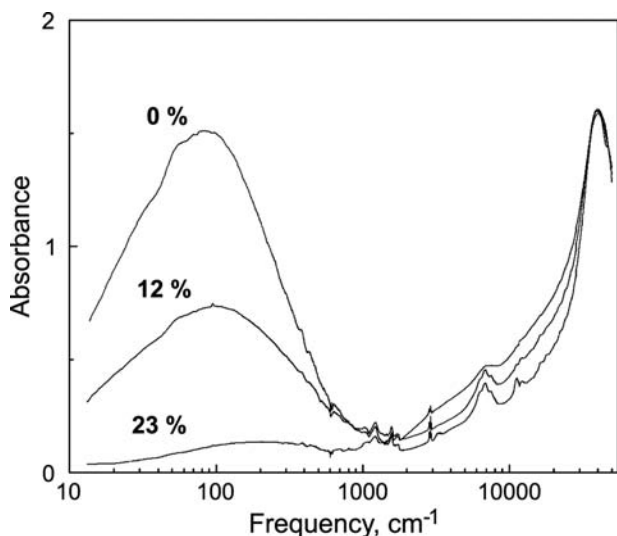
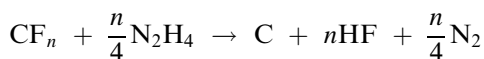


**Fig. 9** Absorption spectra of films of soluble SWNTs functionalized with dichlorocarbene (right). The curves are labeled with the degree of functionality. Spectra are normalized to the value of the absorption at the  $\pi$ -plasmon peak at  $37,000\text{ cm}^{-1}$ .

$>20\text{ M}\Omega$ ) is greatly decreased in comparison with the pristine SWNTs (resistance  $10\text{--}15\text{ }\Omega$ ), which indicates a disruption of the conjugated  $\pi$  network. Hydrazine was used to defluorinate the SWNTs.



When the temperature of fluorination was  $400^\circ\text{C}$  or higher, most of the SWNT structure was destroyed. This was confirmed by Raman spectroscopy that showed that the radial ( $186\text{ cm}^{-1}$ ) and tangential ( $1580\text{ cm}^{-1}$ ) modes decreased, whereas the disorder mode ( $1340\text{ cm}^{-1}$ ) increased.

The fluorinated SWNTs are soluble in alcohols after ultrasonication.<sup>[58]</sup> Nucleophilic reagents such as alkyl-lithium and alkyl magnesium bromides have been used to convert fluorinated SWNTs to alkylated SWNTs.<sup>[56]</sup> The alkylated SWNTs, such as hexyl-SWNTs, were soluble in THF and methylene chloride. Pristine SWNTs could be recovered from hexyl-SWNTs by heating in air at  $250^\circ\text{C}$  for 1 hr. The weight loss of these derivatized tubes was about 35%, corresponding to the attachment of a hexyl group to 1 in every 10 sidewall carbon atoms.

Aryl diazonium salts are known to react with olefins<sup>[60]</sup> and have been used for the sidewall functionalization of SWNTs.<sup>[17,18]</sup> A series of aryl radicals have been generated by electrochemical reduction of aryl diazonium salts to derivatize SWNTs. The estimated degree of aryl radical functionalization was as high as 1 out of every 20 carbons in the SWNTs. Such

high functionalization significantly improved the solubility of the SWNTs in organic solvents (THF, DMF, chloroform). The Raman spectra showed a significant increase in the disorder mode of the SWNTs at  $1290\text{ cm}^{-1}$ , and a complete loss of structure in the solution-phase absorption spectra was observed. The functional groups can be removed by heating at  $500^\circ\text{C}$  in argon, restoring the pristine SWNTs. In a solvent-free sidewall functionalization of SWNTs, the SWNTs were mixed with 4-substituted aniline and vigorously stirred at  $60^\circ\text{C}$  in the presence of isoamyl nitrite or sodium nitrite.<sup>[55]</sup> The isoamyl nitrite or sodium nitrite converted the aniline into diazonium salts which then reacted with SWNTs. The products showed a significant loss of the fine structure of interband transitions in the NIR-VIS region of the spectrum and a strong increase in the disorder mode in the Raman spectra. The aryldiazonium salts have also been used to react with individual SDS-coated SWNTs in aqueous solution to form aryl functionalized SWNTs.<sup>[61]</sup> 4-(10-hydroxydecyl)benzoate-SWNTs have been produced by the same method and used to make composite materials with polystyrene.<sup>[59]</sup>

Sidewall functionalization of SWNTs by using aryldiazonium salts shows high chemoselectivity with metallic SWNTs vs. the semiconducting SWNTs.<sup>[19]</sup> The high selectivity is reflected in the optical spectra of the SWNTs that show a different degree of functionalization in the metallic and semiconducting SWNTs. The absorption intensity of the electronic interband transitions of the metallic SWNTs decreased with increasing degree of functionalization, whereas the absorption intensity of semiconducting SWNTs was unaffected. The result was confirmed by Raman spectroscopy on a sample with 22.4 groups attached per 1000 carbon atoms, in which all of the metallic modes had disappeared but the semiconductor modes remained. The reaction was explained in terms of the formation of a charge-transfer salt involving the aryldiazonium salt at the SWNT surface. Because the metallic SWNTs are superior electron donors they react preferentially with the diazonium salts.

The 1,3-dipolar cycloaddition reaction of azomethine ylides is another important method used in sidewall functionalization of SWNTs.<sup>[16]</sup> This 1,3-dipolar cycloaddition has been widely applied to the organic modification of fullerenes.<sup>[62,63]</sup> The 1,3-dipolar cycloaddition of azomethine ylides to SWNTs has been accomplished by using aldehyde and a N-substituted glycine derivative. The glycine derivative has a long ether chain to enhance the solubility of SWNTs in organic solvents such as chloroform, methylenechloride, acetone, alcohol, and even water. The degree of functionalization was estimated to be 1 in 95 SWNT carbon atoms. The NIR spectra of these pyrrolidine

functionalized SWNTs showed some loss of the electronic properties of the parent SWNTs. The pyrrolidine-functionalized SWNTs associated in bundles with diameters of 100 nm. The authors found that the pyrene-modified tubes formed more compact bundles than other functionalized SWNTs.

Recently, SWNTs were functionalized with polystyrene via an in situ polymerization.<sup>[64]</sup> First, the SWNTs were treated with *sec*-butyllithium to form carbanions. When styrene monomer was added, both free *sec*-butyllithium and the SWNT carbanions initiated polymerization, resulting in an intimately mixed composite system. The loading of SWNTs in the graft polymer was about 0.05 wt.%. The composite was soluble in organic solvents such as dimethylformamide, chloroform, and tetrahydrofuran.

### Noncovalent Functionalization

The advantage of noncovalent functionalization is that it does not destroy the conjugation in the CNTs. One strategy for non-covalent functionalization is based on the usage of an amphiphilic molecule or polymer to interact with CNTs via its hydrophobic part, whereas the hydrophilic part of this molecule can enhance the solubility of CNTs or react with other molecules. Another method is the ionic interaction of SWNTs, which leads to the formation of acid–base salts or charge-transfer complexes. For example, the acid form of SWNTs was heated with melted octadecylamine to form an SWNT-carboxylate zwitterion.<sup>[65]</sup> Such a form of SWNTs is soluble (>0.5 mg/mL) in tetrahydrofuran and 1,2-dichlorobenzene. Generally, a 0.1 mg/mL solution is stable for more than 10 days and is visually non-scattering. The majority of the SWNT ropes were exfoliated into small ropes (2–5 nm in diameter) and individual SWNTs with length of several micrometers during the dissolution process.

Non-covalent functionalization of SWNTs has been achieved by using small molecules such as 1-pyrenebutanoic acid succinimidyl ester.<sup>[65]</sup> This amphiphilic molecule can attach to the surface of SWNTs by  $\pi$ – $\pi$  interaction with the pyrene moiety, while the hydrophilic ester of this molecule enhances the solubility of SWNTs, and this approach has been used in protein immobilization, including the study of ferritin, streptavidin, and biotin–PEO–amine. These bioactive molecules have been attached to the surface of SWNTs via a nucleophilic substitution of *N*-hydroxysuccinimide by using the amine group on the proteins to form an amide.

Molecules of high molecular weight can wrap themselves around the surfaces of SWNTs. Polymers, including polyvinyl pyrrolidone (PVP) and polystyrene sulfonate (PSS),<sup>[66]</sup> poly(phenylacetylene) (PPA),<sup>[67]</sup>

poly(metaphenylenevinylene) (PmPV),<sup>[68]</sup> poly(aryleneethynylene)s (PPE),<sup>[69]</sup> poly-anisidine (POAS),<sup>[70]</sup> amylose,<sup>[71]</sup> amphiphilic copolymer poly(styrene)-block-poly(acrylic acid),<sup>[72]</sup> and natural polymer,<sup>[73]</sup> have been used to wrap or encapsulate CNTs.

The interaction between the CNTs and the polymer hosts usually originates from the van der Waals interaction between the surface of the CNTs and the hydrophobic part of the host polymer. The mechanism of these polymer-wrapping methods depends on both the interaction between SWNTs and polymers, and the structure of the polymers. A thermodynamically driven model for wrapping SWNTs has been suggested, wherein the polymer disrupted both the hydrophobic interface with water and nanotube–nanotube interactions in the CNT aggregates.<sup>[66]</sup> AFM investigation revealed that the individual PVP–SWNT displayed a uniform diameter along its length, which indicates that the polymers were uniformly wrapped along the surface of the SWNTs rather than being randomly attached. A helical wrapping model was used to explain the solubilization of SWNTs at the molecular level. In another case, a straight, rigid polymer, poly(aryleneethynylene)s (PPE), has been used to interact with SWNTs.<sup>[69]</sup> Because the polymer is short and rigid, it attached to the surface of SWNTs in a non-wrapping form parallel to the nanotube axis.

### APPLICATIONS OF CHEMICALLY FUNCTIONALIZED CARBON NANOTUBES

The functionalized CNTs can have higher solubility or differing molecular affinity or electronic response and this allows for more effective use of their outstanding electronic and mechanical properties. It is already clear that the CNTs will find applications in electronics, sensors, composite materials, biology, and medicine.

The strength and high aspect ratio of CNTs are particularly valuable in the design of probe tips for scanning probe microscopy,<sup>[74–76]</sup> electrochemistry,<sup>[77]</sup> and biological analysis.<sup>[78,79]</sup> In 1998, a nanometer-size probe was made with covalently modified MWNTs.<sup>[75]</sup> Using carbodiimide chemistry, carboxyl groups at the tip ends coupled with different amines to form amide-linked groups. By employing the characteristic properties of these amide groups, this chemically modified MWNT probe could be used for titrating acid and base groups, to image patterned samples based on molecular interactions, and for measuring the binding force between single protein–ligand pairs. Individual semiconducting SWNT-based chemical sensors are reliable for the detection of small amounts of gases such as NH<sub>3</sub> and NO<sub>2</sub>.<sup>[80]</sup> The mechanism of this sensor action is based on charge transfer between the

SWNTs and NO<sub>2</sub> or NH<sub>3</sub>. Exposure to the gases affected the electronic properties of the SWNTs and led to a change in the conductivity. It was observed that the conductance of the SWNT sample dramatically increased in NO<sub>2</sub> and decreased in NH<sub>3</sub>.

Because of their 1-D structure and excellent mechanical properties, CNTs are the ideal reinforcing fibers for composite materials. By the addition of CNTs, the strength, elasticity, toughness, durability, and conductivity of the composite material can be improved. The major challenge in using CNTs for composite materials lies in achieving a homogeneous dispersion of CNTs throughout the matrix without destroying their integrity, and an enhanced interfacial bonding with the matrix. Functionalized CNTs show great potentials in this field and CNT composite materials are under active investigation. Conducting polymers such as polypyrrole (PPy) has been used to grow composite films with MWNTs by electrochemistry,<sup>[81]</sup> a SWNT/PmPV composite has been used in making organic light-emitting diodes,<sup>[82]</sup> poly(*p*-phenylene benzobisoxazole) (PBO) has been applied to produce PBO/SWNT fibers.<sup>[83]</sup>

Recently, there has been intense interest in exploring the novel properties of CNTs and especially SWNTs for biological applications. The 1-D structure of SWNTs makes them an ideal candidate for the development of a new generation of biodevices. Because SWNTs are molecular wires with every carbon atom exposed on the surface, SWNTs are promising candidate for the development of extremely sensitive biosensors. Because of their small dimensions SWNTs can be easily introduced into cells with little or no disturbance of the cell function. Additionally, the outstanding electronic properties of SWNTs will allow biological events to be addressed electronically. The progress in understanding the interactions between CNTs and biomolecules has stimulated extensive research on the fabrication of bio-nanodevices and especially biosensors. SWNT devices have shown high sensitivity in the detection of redox enzymes,<sup>[84–86]</sup> DNA,<sup>[87]</sup> and proteins.<sup>[88]</sup>

Yet the interactions of biomolecules with SWNTs are poorly understood. Early studies have focused on the non-specific interactions between proteins and CNTs arising from the hydrophobic nature of the nanotube walls. It has been demonstrated that streptavidin and HupR form highly ordered helical structures upon adsorption on MWNTs.<sup>[89]</sup> Non-specific binding on SWNTs has been shown to be a general phenomenon with a wide range of proteins, including streptavidin, avidin, bovine serum albumin, glucosidase, staphylococcal protein A, and human IgG.<sup>[65,84,89–91]</sup> These non-specific interactions could be explored for the controlled organization of SWNTS into useful architectures. It has been shown that specifically designed amphiphilic  $\alpha$ -helical peptides wrap and solubilize nanotubes, enabling controlled assembly of peptide-wrapped

nanotubes into macromolecular structures.<sup>[92]</sup> The importance of the non-specific interactions between SWNTs and biomolecules has been recently demonstrated in a study on the separation of metallic from semiconducting nanotubes by DNA-assisted dispersion in aqueous solution.<sup>[93]</sup> It has been suggested that the highly efficient mechanism for dispersion of individual SWNTs in solution involves  $\pi$ -stacking interactions between the nanotube walls and the DNA-bases, resulting in helical wrapping of the nanotubes, complemented by hydrophilic interactions between the sugar-phosphate groups in the backbone of DNA and water molecules, rendering the hybrid structure soluble in water. Strategies to prevent the nonspecific binding of proteins to SWNTs by immobilization of PEG in the presence of surfactant have also been developed.<sup>[90]</sup>

As the biocompatibility and biorecognition properties are key issues regarding biological applications of SWNTs, recent research focuses on the functionalization of SWNTs. Both covalent and noncovalent functionalization with proteins, enzymes, and DNA has been explored. The non-covalent approach involves  $\pi$ -stacking of 1-pyrenebutanoic acid succinimidyl ester onto the sidewalls of SWNTs.<sup>[65]</sup> This technique has enabled the immobilization of a wide range of biomolecules on the sidewalls of SWNTs including ferritin, streptavidin, and biotin-PEO-amine.<sup>[65]</sup> The immobilization is robust and its application has been demonstrated in biosensors based on glucose oxidase-functionalized SWNTs.<sup>[91]</sup>

An alternative approach to tethering biological molecules to SWNTs in a controlled manner is covalent functionalization. Covalent functionalization provides better integrity, stability, and reproducibility of the fabricated devices. Typically, covalent binding of proteins and enzymes utilizes the diimide-activated amidation of carboxylic acid-functionalized carbon nanotubes as schematically illustrated in Fig. 10 (paths a and b).<sup>[52,94–96]</sup> For covalent attachment of DNA, amine-terminated SWNTs are cross-linked with succinimidyl 4-(*N*-maleimidomethyl)cyclohexane-1-carboxylate (SMCC) to produce maleimide groups further reacted with thiol-terminated DNA (path c).<sup>[97]</sup>

A method for functionalization of SWNTs with *N*-protected amino acids based on the 1,3-dipolar cycloaddition reaction to the external walls of SWNTs has also been reported.<sup>[98]</sup>

While in most cases the functionalization is essential to impart biorecognition properties to SWNTs, it should be noted that antifullerene IgG monoclonal antibody<sup>[99]</sup> and several peptides have been shown to bind specifically to SWNTs.<sup>[100]</sup>

The ultimate goal of this work is the utilization of the CNTs in medicine leading to the development of a broad-based effort in nanomedicine which offers the promise of conquering disease at the level at which

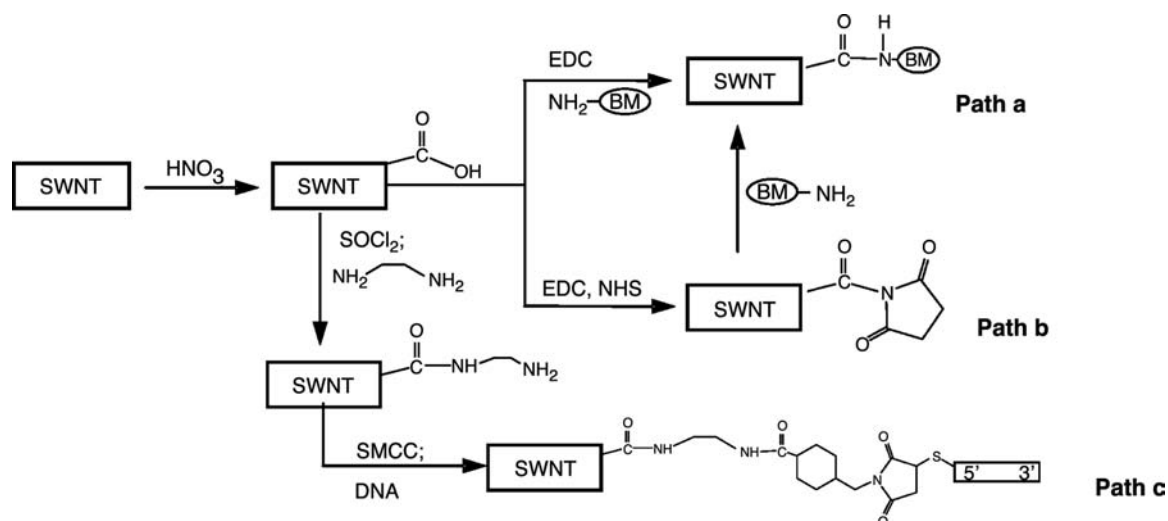


Fig. 10 Schematic representation of functionalized SWNTs in biological application.

it occurs—the molecular level. Thus it is important to begin to investigate the interaction of CNTs with live cells. The first efforts in this direction explored the use of CNTs as the substratum for neuron growth.<sup>[101]</sup>

## CONCLUSION

The chemistry of CNTs has made enormous strides, and it is clear that this subject will drive the applications of carbon nanotubes. In order to further refine the chemically functionalized CNTs, it is important to begin the chemistry with high quality materials. Functionalization of individual CNT, and particularly CNTs of defined length, diameter, and chirality, is the next step that will lead to the control of CNT-based materials and devices at the molecular level.

## ACKNOWLEDGMENTS

This work was supported by the MRSEC Program of the National Science Foundation under Award No. DMR-9809686 and by DOD/DARPA/DMEA under Award No. DMEA90-02-2-0216.

## REFERENCES

1. Wildoer, J.W.G.; Venema, L.C.; Rinzler, A.G.; Smalley, R.E.; Dekker, C. Electronic structure of atomically resolved carbon nanotubes. *Nature (Lond.)* **1998**, *391*, 59–61.
2. Odom, T.W.; Huang, J.-L.; Kim, P.; Lieber, C.M. Atomic structure and electronic properties of single-walled carbon nanotubes. *Nature (Lond.)* **1998**, *391*, 62–64.
3. Hamon, M.A.; Itkis, M.E.; Niyogi, S.; Alvaraez, T.; Kuper, C.; Menon, M.; Haddon, R.C. Effect of rehybridization on the electronic structure of single-walled carbon nanotubes. *J. Am. Chem. Soc.* **2001**, *123*, 11292–11293.
4. Gao, G.; Cagin, T.; Goddard, W.A., III. Energetics, structure, mechanical and vibrational properties of single-walled carbon nanotubes. *Nanotechnology* **1998**, *9*, 184–191.
5. Yu, M.F.; Files, B.S.; Arepalli, S.; Ruoff, R.S. Tensile loading of ropes of single wall carbon nanotubes and their mechanical properties. *Phys. Rev. Lett.* **2000**, *84*, 5552–5555.
6. Peebles, L.H. *Carbon Fibers: Formation, Structure, and Properties*; CRC Press: Boca Raton, 1995.
7. Treacy, M.M.J.; Ebbesen, T.W.; Gibson, J.M. Exceptionally high Young's modulus observed for individual carbon nanotubes. *Nature* **1996**, *381*, 678–680.
8. Wong, E.W.; Sheehan, P.E.; Lieber, C.M. Nanobeam mechanics: elasticity, strength, and toughness of nanorods and nanotubes. *Science* **1997**, *277*, 1971–1975.
9. Chen, Y.; Haddon, R.C.; Fang, S.; Rao, A.M.; Eklund, P.C.; Lee, W.H.; Dickey, E.C.; Grulke, E.A.; Pendergrass, J.C.; Chavan, A.; Haley, B.E.; Smalley, R.E. Chemical attachment of organic functional groups to single-walled carbon nanotube material. *J. Mater. Res.* **1998**, *13*, 2423–2431.
10. Liu, J.; Rinzler, A.G.; Dai, H.; Hafner, J.H.; Bradley, R.K.; Boul, P.J.; Lu, A.; Iverson, T.; Shelimov, K.; Huffman, C.B.; Rodriguez-Macias, F.; Shon, Y.-S.; Lee, T.R.; Colbert, D.T.; Smalley, R.E. Fullerene pipes. *Science* **1998**, *280*, 1253–1255.
11. Chen, J.; Hamon, M.A.; Hu, H.; Chen, Y.; Rao, A.M.; Eklund, P.C.; Haddon, R.C. Solution properties of single-walled carbon nanotubes. *Science* **1998**, *282*, 95–98.
12. Mickelson, E.T.; Huffman, C.B.; Rinzler, A.G.; Smalley, R.E.; Hauge, R.H.; Margrave, J.L. Fluorination of single-wall carbon nanotubes. *Chem. Phys. Lett.* **1998**, *296*, 188–194.



13. Kamaras, K.; Itkis, M.E.; Hu, H.; Zhao, B.; Haddon, R.C. Covalent bond formation to a carbon nanotube metal. *Science* **2003**, *301*, 1501.
14. Hu, H.; Zhao, B.; Hamon, M.A.; Kamaras, K.; Itkis, M.E.; Haddon, R.C. Sidewall functionalization of single-walled carbon nanotubes by addition of dichlorocarbene. *J. Am. Chem. Soc.* **2003**, *125*, 14,893–14,900.
15. Pekker, S.; Salvétat, J.-P.; Jakab, E.; Bonard, J.-M.; Forro, L. Hydrogenation of carbon nanotubes and graphite in liquid ammonia. *J. Phys. Chem., B* **2001**, *105*, 7938–7943.
16. Georgakilas, V.; Kordatos, K.; Prato, M.; Guldi, D.M.; Holzinger, M.; Hirsch, A. Organic functionalization of carbon nanotubes. *J. Am. Chem. Soc.* **2002**, *124*, 760–761.
17. Bahr, J.L.; Yang, J.; Kosynkin, D.V.; Bronikowski, M.J.; Smalley, R.E.; Tour, J.M. Functionalization of carbon nanotubes by electrochemical reduction of aryl diazonium salts: a bucky paper electrode. *J. Am. Chem. Soc.* **2001**, *123*, 6536–6542.
18. Bahr, J.L.; Tour, J.L. Highly functionalized carbon nanotubes using in situ generated diazonium compounds. *Chem. Mater.* **2001**, *13*, 3823–3824.
19. Strano, M.S.; Dyke, C.A.; Usrey, M.L.; Barone, P.W.; Allen, M.J.; Shan, H.; Kittrell, C.; Hauge, R.H.; Tour, J.M.; Smalley, R.E. Electronic structure control of single-walled carbon nanotube functionalization. *Science* **2003**, *301*, 1519–1522.
20. Itkis, M.E.; Perea, D.; Niyogi, S.; Rickard, S.; Hamon, M.; Hu, H.; Zhao, B.; Haddon, R.C. Purity evaluation of as-prepared single-walled carbon nanotube soot by use of solution phase near-IR spectroscopy. *Nano Lett.* **2003**, *3*, 309–314.
21. Sen, R.; Rickard, S.M.; Itkis, M.E.; Haddon, R.C. Controlled purification of single-walled carbon nanotube films by use of selective oxidation and near-IR spectroscopy. *Chem. Mater.* **2003**, *15*, 4273–4279.
22. Hu, H.; Zhao, B.; Itkis, M.E.; Haddon, R.C. Nitric acid purification of single-walled carbon nanotubes. *J. Phys. Chem. B* **2003**, *107*, 13838–13842.
23. Haddon, R.C. pi-Electrons in three-dimensions. *Acc. Chem. Res.* **1988**, *21*, 243–249.
24. Haddon, R.C. Measure of nonplanarity in conjugated organic molecules: which structurally characterized molecule displays the highest degree of pyramidalization?. *J. Am. Chem. Soc.* **1990**, *112*, 3385–3389.
25. Haddon, R.C. Chemistry of the fullerenes: the manifestation of strain in a class of continuous aromatic molecules. *Science* **1993**, *261*, 1545–1550.
26. Wudl, F. Chemical properties of buckminsterfullerenes (C<sub>60</sub>) and the birth and infancy fullerenes. *Acc. Chem. Res.* **1992**, *25*, 157–161.
27. Taylor, R.; Walton, D.M.R. The chemistry of the fullerenes. *Nature* **1993**, *363*, 685.
28. Diederich, F.; Thilgen, C. Covalent fullerene chemistry. *Science* **1996**, *271*, 317–324.
29. Meier, M.S.; Wang, G.-W.; Haddon, R.C.; Brock, C.P.; Lloyd, M.L.; Selegue, J.P. Benzene adds across a closed 5–6 ring fusion in C<sub>70</sub>: evidence for bond delocalization in fullerenes. *J. Am. Chem. Soc.* **1998**, *120*, 2337–2342.
30. Haddon, R.C. C<sub>60</sub>—sphere or polyhedron? *J. Am. Chem. Soc.* **1997**, *119*, 1797–1798.
31. Niyogi, S.; Hamon, M.A.; Hu, H.; Zhao, B.; Bhowmik, P.; Sen, R.; Itkis, M.E.; Haddon, R.C. Chemistry of single-walled carbon nanotubes. *Acc. Chem. Res.* **2002**, *35*, 1105–1113.
32. Itkis, M.E.; Niyogi, S.; Meng, M.; Hamon, M.; Hu, H.; Haddon, R.C. Spectroscopic study of the Fermi level electronic structure of single walled carbon nanotubes. *Nano Lett.* **2002**, *2*, 155–159.
33. Ajayan, P.M.; Ebbesen, T.W.; Ichihashi, T.; Iijima, S.; Tanigaki, K.; Hiura, H. Opening carbon nanotubes with oxygen and implications for filling. *Nature* **1993**, *362*, 522–524.
34. Jeong, T.; Kim, W.-Y.; Hahn, Y.-B. A new purification method of single-wall carbon nanotubes using H<sub>2</sub>S and O<sub>2</sub> mixture gas. *Chem. Phys. Lett.* **2001**, *344*, 18–22.
35. Mawhinney, D.B.; Naumenko, V.; Kuznetsova, A.; Yates, J.T.J.; Liu, J.; Smalley, R.E. Infrared spectral evidence for the etching of carbon nanotubes: ozone oxidation at 298 K. *J. Am. Chem. Soc.* **2000**, *122*, 2382.
36. Tsang, S.C.; Chen, Y.K.; Harris, P.J.F.; Green, M.L.H. A simple chemical method of opening and filling carbon nanotubes. *Nature* **1994**, *372*, 159–162.
37. Dillon, A.C.; Gennett, T.; Jones, K.M.; Alleman, J.L.; Parilla, P.A.; Heben, M.J. A simple and complete purification of single-walled carbon nanotube materials. *Adv. Mater.* **1999**, *11*, 1354–1358.
38. Dujardin, E.; Ebbesen, T.W.; Krishnan, A.; Treacy, M.M.J. Purification of single-shell nanotubes. *Adv. Mater.* **1998**, *10*, 611–613.
39. Nagasawa, S.; Yudasaka, M.; Hirahara, K.; Ichihashi, T.; Iijima, S. Effect of oxidation on single-walled carbon nanotubes. *Chem. Phys. Lett.* **2000**, *328*, 374–380.
40. Zhang, J.; Zou, H.; Qing, Q.; Yang, Y.; Li, Q.; Liu, Z.; Guo, X.; Du, Z. Effect of chemical oxidation on the structure of single-walled carbon nanotubes. *J. Phys. Chem., B* **2003**, *107*, 3712–3718.
41. Hiura, H.; Ebbesen, T.W.; Tanigaki, K. Opening and purification of carbon nanotubes in high yields. *Adv. Mater.* **1995**, *7*, 275–276.
42. Kuznetsova, A.; Popova, I.; Yates, J.T.; Bronikowski, M.J.; Huffman, C.B.; Liu, J.; Smalley, R.E.; Hwu, H.H.; Chen, J.G. Oxygen-containing functional groups on single walled carbon nanotubes: NEXAFS and vibrational spectroscopic studies. *J. Am. Chem. Soc.* **2001**, *123*, 10699–10704.
43. Hu, H.; Bhowmik, P.; Zhao, B.; Hamon, M.A.; Itkis, M.E.; Haddon, R.C. Determination of the acidic sites of purified single-walled carbon nanotubes by acid–base titration. *Chem. Phys. Lett.* **2001**, *345*, 25–28.
44. Niyogi, S.; Hu, H.; Hamon, M.A.; Bhowmik, P.; Zhao, B.; Rozentzhak, S.M.; Chen, J.; Itkis, M.E.; Meier, M.S.; Haddon, R.C. Chromatographic purification of soluble single-walled carbon nanotubes (s-SWNTs). *J. Am. Chem. Soc.* **2001**, *123*, 733–734.
45. Zhao, B.; Hu, H.; Niyogi, S.; Itkis, M.E.; Hamon, M.; Bhowmik, P.; Meier, M.S.; Haddon, R.C. Chromatographic purification and properties of soluble single

- walled carbon nanotubes. *J. Am. Chem. Soc.* **2001**, *123*, 11,673–11,677.
46. Hamon, M.A.; Chen, J.; Hu, H.; Chen, Y.; Rao, A.M.; Eklund, P.C.; Haddon, R.C. Dissolution of single-walled carbon nanotubes. *Adv. Mater.* **1999**, *11*, 834–840.
  47. Hamon, M.A.; Hu, H.; Bhowmik, P.; Niyogi, S.; Zhao, B.; Itkis, M.E.; Haddon, R.C. End-group and defect analysis of soluble single-walled carbon nanotubes. *Chem. Phys. Lett.* **2001**, *347*, 8–12.
  48. Pompeo, F.; Resasco, D.E. Water solubilization of single-walled carbon nanotubes by functionalization with glucosamine. *Nano Lett.* **2002**, *2*, 369–373.
  49. Czerw, R.; Guo, Z.; Ajayan, P.M.; Sun, Y.P.; Carroll, D.L. Organization of polymers onto carbon nanotubes: a route to nanoscale assembly. *Nano Lett.* **2001**, *1*, 423–427.
  50. Fu, K.; Huang, W.; Lin, Y.; Riddle, L.A.; Carroll, D.L.; Sun, Y.-P. Defunctionalization of functionalized carbon nanotubes. *Nano Lett.* **2001**, *1*, 439–441.
  51. Huang, W.; Lin, Y.; Taylor, S.; Gaillard, J.; Rao, A.M.; Sun, Y.-P. Sonication-assisted functionalization and solubilization of carbon nanotubes. *Nano Lett.* **2002**, *2*, 231–234.
  52. Huang, W.; Taylor, S.; Fu, K.; Lin, Y.; Zhang, D.; Hanks, T.W.; Rao, A.M.; Sun, Y.-P. Attaching proteins to carbon nanotubes via diimide-activated amidation. *Nano Lett.* **2002**, *2*, 311–314.
  53. Sano, M.; Kamino, A.; Okamura, J.; Shinkai, S. Ring closure of carbon nanotubes. *Science* **2001**, *293*, 1299–1301.
  54. Xu, M.; Huang, Q.; Chen, Q.; Guo, P.; Sun, Z. Synthesis and characterization of octadecylamine grafted multi-walled carbon nanotubes. *Chem. Phys. Lett.* **2003**, *375*, 598–604.
  55. Dyke, C.A.; Tour, J.M. Solvent-free functionalization of carbon nanotubes. *J. Am. Chem. Soc.* **2003**, *125*, 1156–1157.
  56. Boul, P.J.; Liu, J.; Mickelson, E.T.; Huffman, C.B.; Ericson, L.M.; Chiang, I.W.; Smith, K.A.; Colbert, D.T.; Hauge, R.H.; Margrave, J.L.; Smalley, R.E. Reversible sidewall functionalization of buckytubes. *Chem. Phys. Lett.* **1999**, *310*, 367–372.
  57. Saini, R.K.; Chiang, I.W.; Peng, H.; Smalley, R.E.; Billups, W.E.; Hauge, R.H.; Margrave, J.L. Covalent sidewall functionalization of single wall carbon nanotubes. *J. Am. Chem. Soc.* **2003**, *125*, 3617–3621.
  58. Mickelson, E.T.; Chiang, I.W.; Zimmerman, J.L.; Boul, P.J.; Lozano, J.; Liu, J.; Smalley, R.E.; Hauge, R.H.; Margrave, J.L. Solvation of fluorinated single-wall carbon nanotubes in alcohol solvents. *J. Phys. Chem. B* **1999**, *103*, 4318–4322.
  59. Mitchell, C.A.; Bahr, J.L.; Arepalli, S.; Tour, J.M.; Krishnamoorti, R. Dispersion of functionalized carbon nanotubes in polystyrene. *Macromolecules* **2002**, *35*, 8825–8830.
  60. Obushak, M.D.; Lyakhovych, M.B.; Ganushchak, M.I. Arenediazonium tetrachlorocuprates(II). Modification of the Meerwein and Sandmeyer reactions. *Tetra Lett.* **1998**, *39*, 9567–9570.
  61. Dyke, C.A.; Tour, J.M. Unbundled and highly functionalized carbon nanotubes from aqueous reactions. *Nano Lett.* **2003**, *3*, 1215–1218.
  62. Maggini, M.; Scorrano, G. Addition of azomethine ylides to C60: synthesis, characterization, and functionalization of fullerene pyrrolidines. *J. Am. Chem. Soc.* **1993**, *115*, 9798–9799.
  63. Prato, M.; Maggini, M. Fulleropyrrolidines: a family of full-fledged fullerene derivatives. *Acc. Chem. Res.* **1998**, *31*, 519–526.
  64. Viswanathan, G.; Chakrapani, N.; Yang, H.; Wei, B.; Chung, H.; Cho, K.; Ryu, C.Y.; Ajayan, P.M. Single-step in situ synthesis of polymer-grafted single-wall nanotube composites. *J. Am. Chem. Soc.* **2003**, *125*, 9258–9259.
  65. Chen, R.J.; Zhang, Y.; Wang, D.; Dai, H. Noncovalent sidewall functionalization of single-walled carbon nanotubes for protein immobilization. *J. Am. Chem. Soc.* **2001**, *123*, 3838–3839.
  66. O'Connell, M.J.; Boul, P.; Ericson, L.M.; Huffman, C.; Wang, Y.; Haroz, E.; Kuper, C.; Tour, J.; Ausman, K.D.; Smalley, R.E. Reversible water-solubilization of single-walled carbon nanotubes by polymer wrapping. *Chem. Phys. Lett.* **2001**, *342*, 265–271.
  67. Tang, B.Z.; Xu, H. Preparation, alignment and optical properties of soluble poly(phenylacetylene)-wrapped carbon nanotubes. *Macromolecules* **1999**, *32*, 2569–2576.
  68. Star, A.; Stoddart, J.F.; Steuerman, D.; Diehl, M.; Boukai, A.; Wong, E.W.; Yang, X.; Chung, S.-W.; Choi, H.; Heath, J.R. Preparation and properties of polymer-wrapped single-walled carbon nanotubes. *Angew. Chem. Int. Ed.* **2001**, *40*, 1721–1725.
  69. Chen, J.; Liu, H.; Weimer, W.A.; Halls, M.D.; Waldeck, D.H.; Walker, G.C. Noncovalent engineering of carbon nanotube surfaces by rigid, functional conjugated polymers. *J. Am. Chem. Soc.* **2002**, *124*, 9034–9035.
  70. Valter, B.; Ram, M.K.; Nicolini, C. Synthesis of multi-walled carbon nanotubes and poly(*o*-anisidine) nanocomposite material: fabrication and characterization of its Langmuir–Schaefer films. *Langmuir* **2002**, *18*, 1535–1541.
  71. Kim, O.-K.; Je, J.; Baldwin, J.W.; Kooi, S.; Pehrsson, P.E.; Buckley, L.J. Solubilization of single-wall carbon nanotubes by supramolecular encapsulation of helical amylose. *J. Am. Chem. Soc.* **2003**, *125*, 4426–4427.
  72. Kang, Y.; Taton, T.A. Micelle-encapsulated carbon nanotubes: a route to nanotube composites. *J. Am. Chem. Soc.* **2003**, *125*, 5650–5651.
  73. Bandyopadhyaya, R.; Nativ-Roth, E.; Regev, O.; Yerushalmi-Rozen, R. Stabilization of individual carbon nanotubes in aqueous solutions. *Nano Lett.* **2002**, *2*, 25–28.
  74. Dai, H.J.; Hafner, J.H.; Rinzler, A.G.; Colbert, D.T.; Smalley, R.E. Nanotubes as nanoprobe in scanning probe microscopy. *Nature* **1996**, *384*, 147–151.
  75. Wong, S.S.; Joselevich, E.; Woolley, A.T.; Cheung, C.L.; Lieber, C.M. Covalently functionalized

- nanotubes as nanometresized probes in chemistry and biology. *Nature* **1998**, *394*, 52.
76. Bard, A.J.; Fan, F.F.; Pierce, D.T.; Unwin, P.R.; Wipf, D.O.; Zhou, F. Chemical imaging of surfaces with the scanning electrochemical microscope. *Science* **1991**, *254*, 68–74.
  77. Campbell, J.K.; Sun, L.; Crooks, R.M. Electrochemistry using single carbon nanotubes. *J. Am. Chem. Soc.* **1999**, *121*, 3779–3780.
  78. Strein, T.G.; Ewing, A.G. Characterization of submicron-sized carbon electrodes insulated with a phenol-allylphenol copolymer. *Anal. Chem.* **1992**, *64*, 1368–1373.
  79. Uchida, I.; Abe, T.; Itabashi, T.; Matsue, T. Intracellular voltammetry in single protoplast with an ultramicroelectrode. *Chem. Lett.* **1990**, 1227–1230.
  80. Kong, J.; Franklin, N.R.; Zhou, C.; Chapline, M.G.; Peng, S.; Cho, K.; Dai, H. Nanotube molecular wires as chemical sensors. *Science* **2000**, *287*, 622–625.
  81. Hughes, M.; Chen, G.Z.; Shaffer, M.S.P.; Fray, D.J.; Windle, A.H. Electrochemical capacitance of a nanoporous composite of carbon nanotubes and polypyrrole. *Chem. Mater.* **2002**, *14*, 1610–1613.
  82. Woo, H.S.; Czerw, R.; Webster, S.; Carroll, D.L.; Ballato, J.; Strevens, A.E.; O'Brien, D.; Blau, W.J. Hole blocking in carbon nanotube-polymer composite organic light-emitting diodes based on poly-*m*-phenylene vinylene-co-2, 5-dioctoxy-*p*-phenylene vinylene. *Appl. Phys. Lett.* **2000**, *77*, 1393–1395.
  83. Kumar, S.; Dang, T.D.; Arnold, F.E.; Bhattacharyya, A.R.; Min, B.G.; Zhang, X.; Vaia, R.A.; Park, C.; Adams, W.W.; Hauge, R.H.; Smalley, R.E.; Ramesh, S.; Willis, P.A. Synthesis, structure, and properties of PBO/SWNT composites. *Macromolecules* **2002**, *35*, 9039–9043.
  84. Boussaad, S.; Tao, N.J.; Zhang, R.; Hopson, T.; Nagahara, L.A. In situ detection of cytochrome C adsorption with single walled carbon nanotube device. *Chem. Commun.* **2003**, 1502–1503.
  85. Besteman, K.; Lee, J.O.; Wiertz, F.G.; Heering, H.A.; Dekker, C. Enzyme-coated carbon nanotubes as single-molecule biosensors. *Nano Lett.* **2003**, *3*, 727–730.
  86. Gooding, J.J.; Wibowo, R.; Liu, J.; Yang, W.; Losic, D.; Orbons, S.; Merarns, F.J.; Shapter, J.G.; Hoibbert, D.B. Protein electrochemistry using aligned carbon nanotube arrays. *J. Am. Chem. Soc.* **2003**, *125*, 9006–9007.
  87. Li, J.; Ng, H.T.; Cassell, A.; Fan, W.; Chen, H.Y.; Ye, Q.; Koehne, J.; Han, J.; Meyyappan, M. Carbon nanotube nanoelectrode array for ultrasensitive DNA detection. *Nano Lett.* **2003**, *3*, 597–602.
  88. Star, A.; Gabriel, J.-C.P.; Bradley, K.; Gruner, G. Electronic detection of specific protein binding using nanotube FET devices. *Nano Lett.* **2003**, *3*, 459–463.
  89. Balavoine, F.; Schultz, P.; Richard, C.; Mallouh, V.; Ebbesen, T.W.; Mioskowski, C. Helical crystallization of proteins on carbon nanotubes: a first step towards the development of new biosensors. *Angew. Chem. Int. Ed.* **1999**, *38*, 1912–1917.
  90. Shim, M.; Kam, N.W.S.; Chen, R.J.; Li, Y.; Dai, H. Functionalization of carbon nanotubes for biocompatibility and biomolecular recognition. *Nano Lett.* **2002**, *2*, 285–288.
  91. Besteman, K.; Lee, J.O.; Wiertz, F.G.; Heering, H.A.; Dekker, C. Enzyme-coated carbon nanotubes as single-molecule biosensors. *Nano Lett.* **2003**, *3*, 727–730.
  92. Dieckmann, G.R.; Dalton, A.B.; Johnson, P.A.; Razal, J.; Chen, J.; Giordano, G.M.; Munoz, E.; Musselman, I.H.; Baughman, R.H.; Draper, R.K. Controlled assembly of carbon nanotubes by designed amphiphilic peptide helices. *J. Am. Chem. Soc.* **2003**, *125*, 1770–1777.
  93. Zheng, M.; Jagota, A.; Semke, E.D.; Diner, B.A.; McLean, R.S.; Lustig, S.R.; Richardson, R.E.; Tassi, N.G. DNA-assisted dispersion and separation of carbon nanotubes. *Nat. Mater.* **2003**, *2*, 338–342.
  94. Dwyer, C.; Guthold, M.; Falvo, M.; Washburn, S.; Superfine, R.; Erie, D. DNA-functionalized single-walled carbon nanotubes. *Nanotechnology* **2002**, *13*, 601–604.
  95. Williams, K.A.; Veenhuizen, P.T.M.; de la Torre, B.G.; Eritja, R.; Dekker, C. Carbon nanotubes with DNA recognition. *Nature* **2002**, *420*, 761.
  96. Azamian, B.R.; Davis, J.J.; Coleman, K.S.; Bagshaw, C.B.; Green, M.L.H. Bioelectrochemical single-walled carbon nanotubes. *J. Am. Chem. Soc.* **2002**, *124*, 12,664–12,665.
  97. Baker, S.E.; Cai, W.; Lasseter, T.L.; Weidkamp, K.P.; Hamers, R.J. Covalently bonded adducts of deoxyribonucleic acid (DNA) oligonucleotides with single-walled carbon nanotubes: synthesis and hybridization. *Nano Lett.* **2002**, *2*, 1413–1417.
  98. Georgakilas, V.; Tagmatarchis, N.; Pantarotto, D.; Bianco, A.; Briand, J.P.; Prato, M. Amino acid functionalization of water soluble carbon nanotubes. *Chem. Commun.* **2002**, 3050–3051.
  99. Erlanger, B.F.; Chen, B.X.; Zhu, M.; Brus, L. Binding of an anti-fullerene IgG monoclonal antibody to single wall carbon nanotubes. *Nano Lett.* **2001**, *1*, 465–467.
  100. Wang, S.; Humphreys, E.S.; Chung, S.Y.; Delduco, D.F.; Lusting, S.R.; Wang, H.; Parker, K.N.; Rizzo, N.W.; Subramoney, S.; Chiang, Y.M.; Jagota, A. Peptides with selective affinity for carbon nanotubes. *Nat. Mater.* **2003**, *2*, 196–200.
  101. Mattson, M.P.; Haddon, R.C.; Rao, A.M. Molecular functionalization of carbon nanotubes and use as substrates for neuronal growth. *J. Mol. Neurosci.* **2000**, *14*, 175–182.

# Carbon Nanotubes: Gas Adsorption Properties

**Juan Manuel Diez Tascón**

*Instituto Nacional del Carbón, CSIC, Oviedo, Spain*

**Eduardo J. Bottani**

*Instituto de Investigaciones Fisicoquímicas Teóricas y Aplicadas,  
La Plata, Argentina*

## INTRODUCTION

Carbon nanotubes, single or multiwalled, have been the object of a large amount of studies since their discovery in the last decade of the 20th century. Those studies revealed the nature of this material, its chemical structure, and many of its physical and chemical properties. Almost immediately after its discovery, a major technological application was envisioned as potential medium to store hydrogen, and other gases employed as fuel. Despite the large amount of work performed in this area, there is no agreement in many basic questions concerning the gas storage capacity of this material. Here we review the work performed in the area of gas adsorption on carbon nanotubes. Those studies aimed to determine the adsorption capacity of different gases, to characterize the structure of the material through the adsorption of nitrogen, to explore the molecular sieving properties of nanotubes, and to test models involving matter in quasi one-dimension or in confined spaces.

## GAS PHYSISORPTION

Gas physisorption is mostly employed to characterize the surface structure of carbon nanotubes.<sup>[1–11]</sup> Stan et al.<sup>[12]</sup> analyzed the conditions required for a given gas to be adsorbed in carbon nanotubes or their bundles; their results confirm the intuitive expectation that small molecules can be adsorbed within both the interstitial channels and the tubes. It has been demonstrated<sup>[13]</sup> that the entry ports of single-walled carbon nanotubes (SWNT) are blocked with functional groups (quinone, carboxylic, etc.) that can be eliminated through a thermal activation at moderate temperatures; Fig. 1 is a schematic representation of an open-ended SWNT containing carboxylic acid groups at the entry ports of the nanotube. Heating in vacuum above 600 K removes these blocking groups.<sup>[13]</sup>

Other researchers claimed that certain adsorbates can penetrate the tubes producing a radial deformation.<sup>[14,15]</sup>

In opposition to those results, Froudakis<sup>[16]</sup> performed theoretical calculations that showed that no chemisorption and no penetration can occur, and that radial deformation is found upon adsorption of certain adsorbates. Other authors<sup>[17]</sup> claimed to have demonstrated that chemisorption can occur on the outer wall when the energy of the incident H atom is between 96 and 289 kJ/mol. They estimated that the energy required to penetrate through a hexagon of the wall is 1350 kJ/mol. Another conclusion is that the hole on the wall, produced by the atom passing through it, can be healed after relaxation.

Eswaramoorthy, Sen and Rao<sup>[18]</sup> detected a marked hysteresis in N<sub>2</sub> adsorption isotherms on SWNT that the authors assigned to capillary condensation in the intertubular space. In the same study, benzene cross-sectional area was estimated to be between 0.3 and 0.4 nm<sup>2</sup>.

Migone et al.<sup>[19,20]</sup> reported experimental results on adsorption of Xe, methane, and Ne on samples of closed-ended SWNT. Using classical techniques, the authors calculated the adsorption energies of those gases. The obtained values are 21.4 kJ/mol for CH<sub>4</sub>, 27.2 kJ/mol for Xe, and 5 kJ/mol for Ne. All these values are ca. 70% larger than the corresponding values obtained for adsorption on the basal plane of graphite. These authors also indicated that, if physisorption is the prevailing adsorption mechanism for H<sub>2</sub>, and, if geometric factors are determinant, this gas cannot occupy the interstitial channels of SWNT bundles as its dynamic molecular diameter is 0.29 nm. Xe adsorption has also been studied using computer simulations,<sup>[21]</sup> and the main conclusion is that the interaction potential between a Xe atom and the SWNT walls can be well represented by the same potential for a flat graphite surface. Some controversy exists with respect to the possibility of Xe to be adsorbed in the interstitial sites of a bundle of nanotubes. According to Muris et al.<sup>[22]</sup> Xe, as well as CF<sub>4</sub> and SF<sub>6</sub>, can only be adsorbed on the outer part of the bundle. Xe binding energy has been also estimated using thermal desorption spectroscopy<sup>[23]</sup> and

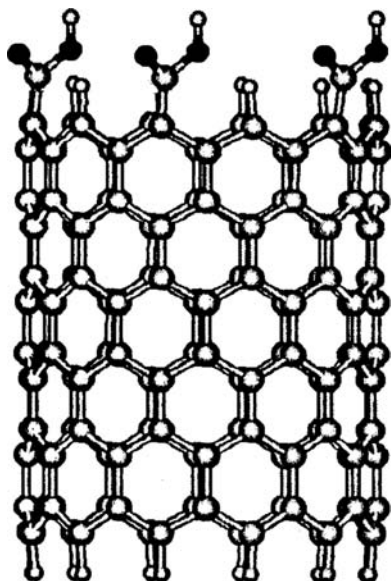


**Fig. 1** Schematic representation of an open-ended SWNT containing carboxylic acid groups at the entry ports of the nanotube.

the obtained value is 27% higher than the corresponding value for highly oriented pyrolytic graphite (HOPG) in agreement with other experimental techniques. If the same comparison is made for oxygen,<sup>[24]</sup> the value obtained for SWNT (18.5 kJ/mol) is ca. 55% larger than the corresponding one for HOPG (12 kJ/mol).

N<sub>2</sub>, Ar, H<sub>2</sub>, and D<sub>2</sub> isosteric heats of adsorption experimentally determined have been recently reported.<sup>[25]</sup> The heat profiles correspond to a heterogeneous surface, and the obtained values were 15 kJ/mol for nitrogen and argon, 9 kJ/mol for deuterium, and 7 kJ/mol for hydrogen. N<sub>2</sub> value is somehow low compared to other reported experimental and theoretical values that put it closer to 17–18 kJ/mol.<sup>[26,27]</sup>

Carbon nonohorns are another form of nanotubes that are capped with a cone instead of half fullerene molecule. The adsorption potential on these tubes has been analyzed in detail by Murata et al.<sup>[28]</sup> Xe adsorbed on single-walled carbon nanohorns (SWNH) in a “dahlia flower” arrangement<sup>[29]</sup> has a smaller (20%) binding energy compared to the value obtained for SWNT.

Nitrogen physisorption in carbon nanotubes has been studied mainly to characterize the porous texture of the samples.<sup>[30]</sup> Grand Canonical Monte Carlo (GCMC) computer simulations have been employed in a pioneering paper dealing with nitrogen and argon adsorption on carbon nanotubes.<sup>[31]</sup> The authors found that both gases were strongly adsorbed in a 1.02-nm SWNT at 77 K. They also showed that the adsorption isotherms were of Type I in IUPAC

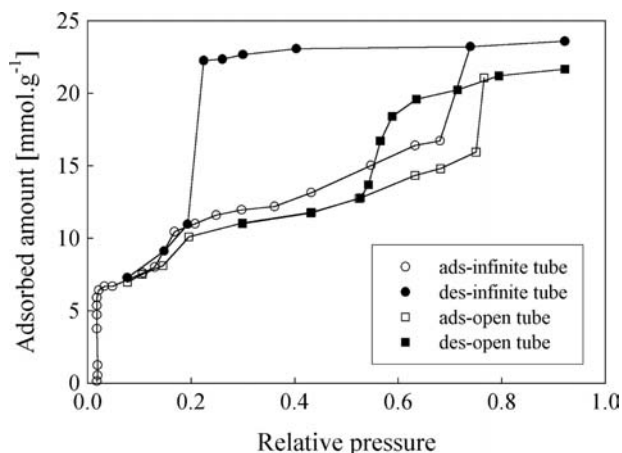


**Fig. 2** Ar adsorption isotherms in a semiinfinite carbon nanotube at 77 K. Source: Adapted from Ref.<sup>[31]</sup>.

classification system. In the cases where hysteresis was found, the isotherms were of Type IV in IUPAC classification. Thus Fig. 2 shows simulated adsorption–desorption isotherms for argon at 77 K on a 4.78-nm double buckytube, either semiinfinite, or open. The hysteresis loop covers a broader pressure range for the semiinfinite model.

Other computer simulations performed on bundles of SWNT in a square array<sup>[32,33]</sup> showed some qualitative agreement between experiments and simulations. Other conclusions derived from the simulations are that adsorption is dominated by geometric factors, and that the interstitial spaces make a significant contribution to the total adsorption capacity. Other authors<sup>[34]</sup> found that the quadrupole moment of nitrogen has a little effect on the adsorption in SWNT; nevertheless, it has been proved that the opposite is true.<sup>[35,36]</sup>

First-principles calculations of the adsorption of NO<sub>2</sub>, O<sub>2</sub>, NH<sub>3</sub>, N<sub>2</sub>, CO<sub>2</sub>, CH<sub>4</sub>, H<sub>2</sub>O, H<sub>2</sub>, and Ar have been reported,<sup>[37]</sup> nevertheless, a poor agreement between the calculations and other theoretical estimates and experiments (see, e.g., the Ar case<sup>[38]</sup> and previously cited data on methane adsorption) is obtained for the adsorption energies. In the case of oxygen, the disagreement between theoretical calculations is more pronounced (compare the two previous cited papers with Ref.<sup>[39]</sup>). Oxygen adsorption on carbon nanotubes and graphite has been studied using density functional theory (DFT) calculations by Giannozzi, Car, and Scoles.<sup>[40]</sup> These authors report the formation of a weak bond between oxygen and the wall of a nanotube or a graphene layer of graphite, which is characteristic of physisorption. This bond does not involve any charge transfer between the molecule and the solid. The authors also point out the inability of current approximation functionals to correctly deal with dispersion forces. Nevertheless,

other studies<sup>[41]</sup> indicate that the curvature of the walls of SWNT exerts a large influence on the adsorption potential.<sup>[21,40]</sup>

Methane adsorption on carbon nanotubes has been studied in detail by Migone et al.<sup>[42–44]</sup> Along these studies, the authors found that hysteresis in the adsorption isotherms is present only when the tubes are open-ended and that the filling of nanotubes is controlled by the wetting characteristics of the adsorbate–nanotube system. Liquid methane completely wets the tubes whereas an incomplete wetting is found for solid methane. The isosteric heat of adsorption was determined (21.4 kJ/mol), which is 76% larger than the corresponding value for graphite. This increment in the adsorption energy with respect to graphite agrees with what was found for other gases. Other authors<sup>[45]</sup> studied methane adsorption, and they concluded that density functional theory (DFT) is a good method, provided that the interaction potential is described by a well-defined analytical function; otherwise, GCMC is a better method. They also showed that adsorption in the interstices formed by the tubes in the bundle is significant.

Using DFT, Tanaka et al.<sup>[46]</sup> showed that methane adsorption is enhanced through CH<sub>4</sub>–CH<sub>4</sub> interactions between molecules inside and outside the tube. As an illustration, Fig. 3 shows excess methane adsorption isotherms on the internal and external surfaces of an isolated tube of reduced diameter (= 4.2 at 303 K). Both endohedral and exohedral adsorptions are enhanced by fluid–fluid interactions across the carbon wall. Butane physisorption on multiwalled carbon nanotubes (MWNT) has been studied at room temperature,<sup>[47]</sup> and it was found that most of the butane is adsorbed on the external surface of the tubes.

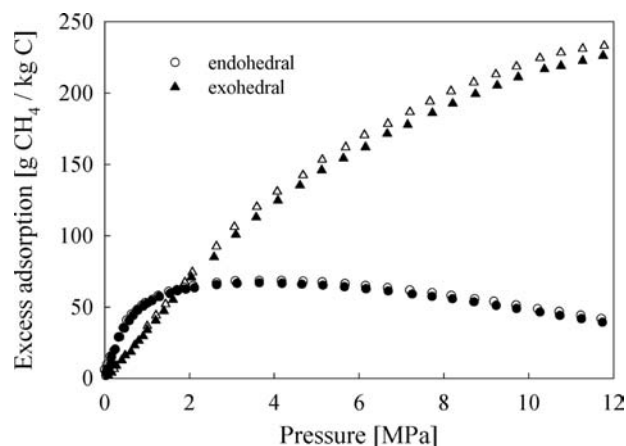


**Fig. 3** Excess adsorption isotherms of methane at 303 K on carbon nanotubes. Open symbols indicate that the gas–gas interactions across carbon walls are not taken into account, while filled symbols include these interactions. *Source:* Adapted from Ref.<sup>[46]</sup>.

Moreover, no hysteresis was observed between adsorption and desorption experiments.

Ethane adsorption on SWNT bundles forming a square array has been investigated using GCMC computer simulations.<sup>[48]</sup> The authors found that the adsorbed phase inside the tubes is quite disordered. Nevertheless, their conclusions should be revised in view of certain assumptions done in the simulation model.

The adsorption of several types of alkylamine on SWNT induced large changes in the electrical conductance of semiconducting nanotubes.<sup>[49]</sup> The phenomenon is reversible, and it took, according to the authors, 12 hr to restore the initial characteristics of the studied samples. Decane adsorbed in SWNT has been shown<sup>[50]</sup> to be in a fluid state that is highly inhomogeneous and anisotropic. Molecular dynamics computer simulations have been performed to explore the behavior of SWNT toward the adsorption of gaseous mixtures.<sup>[51]</sup> The main and obvious conclusion is that the efficiency in the separation of molecules decreases as the tube diameter increases.

## GAS STORAGE CAPACITY OF CARBON NANOTUBES

Before a massive use of hydrogen in fuel cells is achieved, it is necessary to be able to store it safely and efficiently.<sup>[52]</sup> The U.S. Department of Energy (DOE) has elaborated an energy plan that includes hydrogen as a potential source provided a weight efficiency of 6.5 weight percentage (wt.%) and volumetric density of 62 kg H<sub>2</sub>/m<sup>3</sup> are achieved at ambient temperature. Carbon nanotubes are fascinating objects that could be employed for gas storage, particularly hydrogen.<sup>[53,54]</sup> Hirscher et al.<sup>[55]</sup> summarized the available experimental data on hydrogen sorption capacity in carbon nanotubes. They conclude that none of the promising experiments on H<sub>2</sub> uptake could be repeated by an independent group. The authors also provided evidence for a small reversible hydrogen uptake for SWNT and for the need of opening or cutting of the tubes as a prerequisite for high storage capacity. Fig. 4 compares thermal desorption spectra of deuterium in high vacuum for SWNT, graphite nanofibers, and graphite ball-milled under D<sub>2</sub> atmosphere. However, the D<sub>2</sub> release from SWNT not submitted to ball milling was practically negligible.

Several authors have studied the influence of synthesis and purification methods of carbon nanotubes upon H<sub>2</sub> sorption capacity.<sup>[56–64]</sup> The influence of the structure (packing) of the bundles has also been investigated.<sup>[65,66]</sup>

Wang and Johnson<sup>[67]</sup> performed computer simulations, classical and quantum path integral, of hydrogen



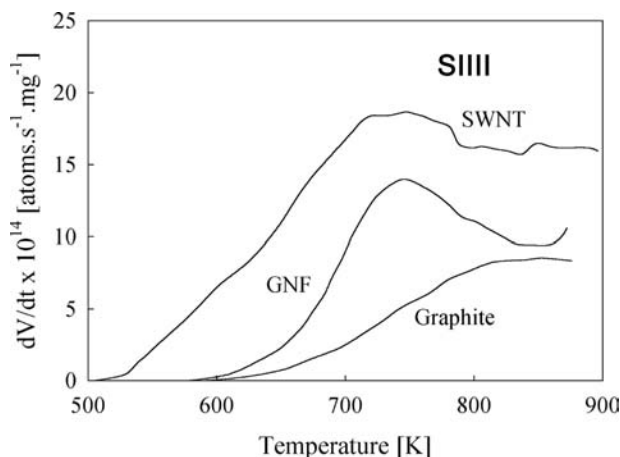


**Fig. 4** Thermal desorption rate of  $D_2$  from SWNT, graphite nanofibers (GNF), and ball-milled-graphite (graphite). *Source:* Adapted from Ref.<sup>[55]</sup>.

adsorption in SWNT and carbon slit pores. Among their conclusions, the most relevant are: quantum effects are important in hydrogen adsorption in the interstices even at room temperature; a reasonable agreement exists between their simulations and experimental data; and the adsorption capacity of carbon slit pores is larger than that of the SWNT bundles. They also concluded that none of the materials studied in their work were able to approach DOE's target for hydrogen storage capacity. Gu and Gao<sup>[68]</sup> arrived to almost the same conclusions using the same computational methods; they also found that DOE's requirements could be achieved at ca. 18 K. Nevertheless, Darkrim and Levesque<sup>[69]</sup> found using computer simulations a gravimetric density storage equal to ca. 11 wt.% at 77 K. This value leads the authors to conjecture that SWNT could be employed for hydrogen storage systems. Recently, Hou et al.<sup>[70]</sup> reported a storage capacity of 6.3 wt.% and 31.6 kg/m<sup>3</sup> at room temperature. This unconfirmed result shows an acceptable gravimetric hydrogen uptake but the volumetric efficiency is still 50% of DOE's target.

Hydrogen adsorption has also been studied using Raman spectroscopy,<sup>[71]</sup> which showed no indication of chemisorption but physisorption on multiple sites of the SWNT ropes at 85 K and up to 8 atm. Hydrogen adsorption produces the separation of the individual SWNT at ca. 40 bar and 80 K because of a small cohesive energy between the tubes, 0.48 kJ/mol.<sup>[72]</sup> Single-walled carbon nanohorns have also been investigated to determine their hydrogen uptake capacity at supercritical conditions.<sup>[73]</sup>

From the experimental point of view, the studies on hydrogen storage in carbon nanotubes indicate that this material is not suitable from DOE's criteria, at least for the structures already known. Nevertheless,

there is a controversy when the problem is analyzed with theoretical tools. There are several computer simulation studies predicting a good sorption capacity;<sup>[74–76]</sup> moreover, other studies claim to have partially accomplished with DOE's requirements.<sup>[77]</sup> On the other side, there are several studies indicating that carbon nanotubes are not suitable according to DOE's criteria.<sup>[78–81]</sup>

## MATTER IN CONFINED SPACES

Stan and Cole<sup>[82]</sup> published one of the pioneering works on the theory of adsorption in carbon nanotubes. In that paper, the authors found that carbon nanotubes provide a physical realization of a quasi 1-D system for both classical and quantum gases. This subject is reprised in more detail by Calbi et al.<sup>[83–86]</sup> where the authors analyzed a very rich collection of phases found for the adsorbate. Grand Canonical Monte Carlo simulation results have been reported for the adsorption of Ar and Kr on SWNT bundles.<sup>[87]</sup> The calculated isotherms revealed phase transitions associated with the formation of quasi 1-D lines of atoms on the grooves between two nanotubes; as an illustration, Fig. 5 shows calculated adsorption isotherms of Ar at several temperatures. The quasi 1-D character of <sup>4</sup>He adsorbed inside carbon nanotubes has been explored by several authors.<sup>[88,89]</sup> Equations of state have been derived for H<sub>2</sub> and D<sub>2</sub> in pure 1-D geometry.<sup>[90,91]</sup> The obtained equation of state predicts a liquid H<sub>2</sub> phase inside a (5,5) carbon nanotube. To study transport properties of fluids in confined spaces, carbon nanotubes can be employed as they constitute a model system with real existence.<sup>[92]</sup>

Quantum molecular sieving effects have been studied<sup>[93,94]</sup> by comparing computer simulations with the

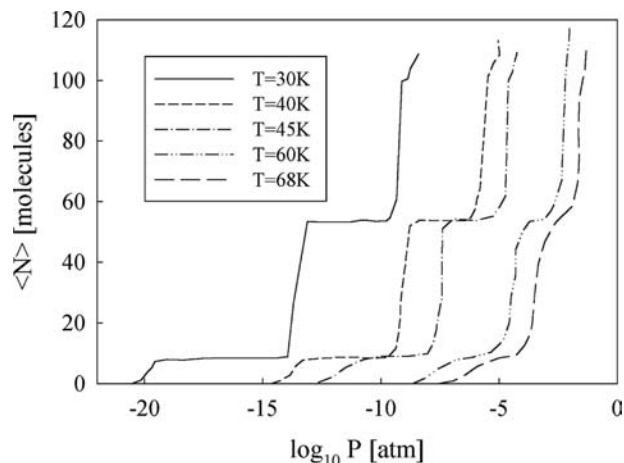


**Fig. 5** Simulated Ar adsorption isotherms over a wide temperature range. *Source:* Adapted from Ref.<sup>[87]</sup>.

predictions of a simple model. The studied systems included  $H_2-T_2$ ;  $^3He-^4He$ ;  $CH_4-CD_4$ ; and  $H_2-HD$ .

Ayappa<sup>[95,96]</sup> reported a quite complete study on binary mixtures adsorbed in carbon nanotubes. The author studied equimolar binary Lennard–Jones gas mixtures using Grand Canonical Monte Carlo simulations. He found that for mixtures of species with different sizes, the energetically favored species is adsorbed at high temperatures. However, at moderate and lower temperatures and intermediate nanotube diameter, a complete exclusion of the larger species is observed. If both species are of similar size, the most favored energetically is adsorbed at all temperatures. Hydrogen and CO mixtures have been studied by Gu et al.<sup>[97]</sup> The authors showed that CO is adsorbed inside the tubes and  $H_2$  is kept outside the tubes. At higher pressure, the situation is reversed because  $H_2$ , being smaller than CO, can be easily packed inside the tube.

Transport and diffusion of gases in carbon nanotubes have been studied by several authors.<sup>[98–100]</sup>

## GAS CHEMISORPTION ON CARBON NANOTUBES

The work carried out in this area mainly concerns the behavior of carbon nanotubes as field emitters and the mechanism of field emission.<sup>[101]</sup> The first paper<sup>[102]</sup> to be commented on reported an increment in the field emission current as a result of the presence of unknown chemisorbed species on the surface of carbon nanotubes. A recent study<sup>[103]</sup> using density functional calculation concluded that all the molecules studied, except nitrogen, dissociate and then chemisorb. The Fermi levels are moved toward the valence bands for the adsorption of oxygen, hydrogen, and water. Nitrogen does not change the Fermi level position. Their main conclusion was that water enhances the field emission current whereas oxygen adsorption decreases it. The increasing field emission properties of carbon nanotubes as a result of oxygen adsorption have also been investigated.<sup>[104]</sup> Using first-principles calculations, the authors found that all the analyzed configurations produce an enhancement of the emission current. Similar results have been reported by Grujicic, Cao, and Gersten<sup>[105]</sup> including that the effect increases with the magnitude of the dipole moment of linear adsorbates. This phenomenon is illustrated in Fig. 6, where the decrease in ionization potential (and concomitant increase in field emission) shows a complex relationship with the dipolar moment, which suggests the additional contribution of other factors.

According to density functional calculations,<sup>[106]</sup> carbon nanotubes can survive adsorption and desorption

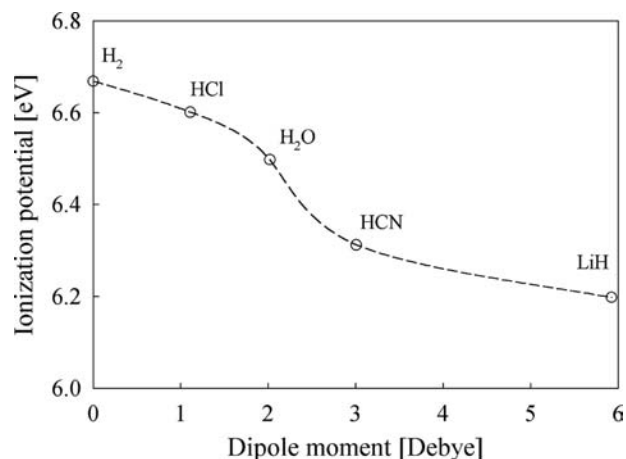


**Fig. 6** Nanotube ionization potential as a function of the magnitude of the dipole moment of linear-single-molecule adsorbates. *Source:* Adapted from Ref.<sup>[105]</sup>.

of chemisorbed oxygen provided a precise control on the annealing temperature is exerted.

Hydrogen dissociation and chemisorption on carbon nanotubes has been investigated using different approaches and theoretical tools. The obtained results predict dissociation and then chemisorption of the H atoms.<sup>[107–109]</sup> There are several studies that confirm the dissociative adsorption of hydrogen on SWNT and that the energy barrier is very high, even when the nanotubes are doped with Li.<sup>[110]</sup> The DFT theory was employed to study  $H_2$  interaction with SWNT and the calculations indicate that when the molecule has enough kinetic energy, it can be dissociated on the surface and the resulting atoms chemisorbed to two nearest-neighbor carbon atoms.<sup>[111]</sup> Finally, another reported DFT study concluded that  $H_2$  cannot be adsorbed on the inner wall of any nanotube included in the study.<sup>[112]</sup>

## CONCLUSION

Carbon nanotubes and other tubular forms of carbon are investigated since their discovery a decade ago. Although the structures of these new forms of carbon are well known, their properties are not fully disclosed. One of the most important aspects of carbon nanotubes is related to its potential use as hydrogen storage devices. Unfortunately, there is no agreement between experiments and theory. Several factors contribute to this disagreement. From the experimental point of view, there are still problems in the postproduction purification of nanotubes. Depending on the method employed, different adsorption capacities are obtained and the final materials are still quite irreproducible.

From the theoretical point of view, two main research lines can be found: computer simulations

using Monte Carlo or Molecular Dynamics method, and quantum mechanics calculations. The most reliable computer simulations predict that DOE's requirements could not be achieved by carbon nanotubes. On the other hand, other theoretical calculations are in disagreement between themselves. Several authors predict high adsorption capacities using methods that are questioned in their ability to model dispersion forces, while other authors predict no adsorption at all. There is no agreement in several theoretical aspects such as the effect of wall curvature on the adsorption potential.

There is agreement in several aspects. Hydrogen dissociation on the wall of carbon nanotubes has a large activation energy. When dealing with gas mixtures, carbon nanotubes exhibit molecular sieving properties. The dependence of selectivity on temperature is well known. The radial deformation of carbon nanotubes upon adsorption of certain molecules has been predicted by several authors using different methods. Carbon nanotubes can resist mild oxidation processes provided the annealing temperature is carefully controlled. The penetration of hydrogen atoms in the tubes is possible if the atoms have enough kinetic energy. The hole produced can be healed by relaxation.

It is accepted, from the theoretical point of view, that SWNT can be considered as a physical realization of many model systems.

## ACKNOWLEDGMENTS

EJB is researcher of the Comisión de Investigaciones Científicas de la Provincia de Buenos Aires, and Professor at the Universidad Nacional del Litoral, Argentina. Financial support from Consejo Nacional de Investigaciones Científicas y Técnicas (CONICET), Universidad Nacional de La Plata (UNLP), and CIC, is acknowledged. JMDT acknowledges financial support from the Spanish MCYT/FEDER (project MAT2002-00341).

## REFERENCES

- Breton, J.; González-Platas, J.; Girardet, C. Endohedral adsorption in graphitic nanotubes. *J. Chem. Phys.* **1994**, *101* (4), 3334–3340.
- Masenelli-Varlot, K.; McRae, E.; Dupont-Pavlovsky, N. Comparative adsorption of simple molecules on carbon nanotubes. Dependence of the adsorption properties on the nanotube morphology. *Appl. Surf. Sci.* **2002**, *196*, 209–215.
- Bougrine, A.; Dupont-Pavlovsky, N.; Ghanbaja, J.; Billaud, D.; Béguin, F. Adsorption studies of a krypton film adsorbed on catalytically synthesized multiwalled carbon nanotubes. Dependence on the nanotube morphology. *Surf. Sci.* **2002**, *506*, 137–144.
- Yang, Q.H.; Hou, P.X.; Bai, S.; Wang, M.Z.; Cheng, H.M. Adsorption and capillarity of nitrogen in aggregated multi-walled carbon nanotubes. *Chem. Phys. Lett.* **2001**, *345*, 18–24.
- Fujiwara, A.; Ishii, K.; Suematsu, H.; Kataura, H.; Maniwa, Y.; Suzuki, S.; Achiba, Y. Gas adsorption in the inside and outside of single-walled carbon nanotubes. *Chem. Phys. Lett.* **2001**, *336*, 205–211.
- Stepanek, I.; Maurin, G.; Bernier, P.; Gavillet, J.; Loiseau, A.; Edwards, R.; Jaschinski, O. Nano-mechanical cutting and opening of single wall carbon nanotubes. *Chem. Phys. Lett.* **2000**, *337*, 125–131.
- Bekyarova, E.; Kaneko, K.; Kasuya, D.; Takahashi, K.; Kokai, F.; Yudasaka, M.; Iijima, S. Pore structure and adsorption properties of single-walled carbon nanohorn bud-like aggregates treated in different atmospheres. *Physica, B* **2002**, *323*, 143–145.
- Cinke, M.; Li, J.; Chen, B.; Cassell, A.; Delzeit, L.; Han, J.; Meyyappan, M. Pore structure of raw and purified HiPco single-walled carbon nanotubes. *Chem. Phys. Lett.* **2002**, *365*, 69–74.
- Bittner, E.W.; Smith, M.R.; Bockrath, B.C. Characterization of the surfaces of single-walled carbon nanotubes using alcohols and hydrocarbons: A pulse adsorption technique. *Carbon* **2003**, *41*, 1231–1239.
- Kuznetsova, A.; Yates, J.T., Jr.; Liu, J.; Smalley, R.E. Physical adsorption of xenon in open single walled carbon nanotubes: Observation of a quasi-one-dimensional Xe phase. *J. Chem. Phys.* **2000**, *112* (21), 9590–9598.
- Kuznetsova, A.; Yates, J.T., Jr.; Simonyan, V.V.; Johnson, J.K.; Huffman, C.B.; Smalley, R.E. Optimization of Xe adsorption kinetics in single walled carbon nanotubes. *J. Chem. Phys.* **2001**, *115* (14), 6691–6698.
- Stan, G.; Bojan, M.J.; Curtarolo, S.; Gatica, S.M.; Cole, M.W. Uptake of gases in bundles of carbon nanotubes. *Phys. Rev., B* **2000**, *62* (3), 2173–2180.
- Kuznetsova, A.; Mawhinney, D.B.; Naumenko, V.; Yates, J.T., Jr.; Liu, J.; Smalley, R.E. Enhancement of adsorption inside of single-walled nanotubes: Opening the entry ports. *Chem. Phys. Lett.* **2000**, *321*, 292–296.
- Takaba, H.; Katagiri, M.; Kubo, M.; Vetrivel, R.; Miyamoto, A. Molecular design of carbon nanotubes for the separation of molecules. *Microporous Mater.* **1995**, *3*, 449–455.
- Barajas-Barraza, R.E.; Guirado-López, R.A. Clustering of H<sub>2</sub> molecules encapsulated in fullerene structures. *Phys. Rev., B* **2002**, *66*, 155426-1–155426-12.
- Froudakis, G.E. Hydrogen interaction with single-walled carbon nanotubes: A combined quantum-mechanics/molecular-mechanics study. *Nano Lett.* **2001**, *1* (4), 179–182.
- Ma, Y.; Xia, Y.; Zhao, M.; Ying, M.; Liu, X.; Liu, P. Collision of hydrogen atom with single-walled carbon nanotube: Adsorption, insertion, and healing. *J. Chem. Phys.* **2001**, *115* (17), 8152–8156.
- Eswaramoorthy, M.; Sen, R.; Rao, C.N.R. A study of micropores in single-walled carbon nanotubes by the

- adsorption of gases and vapors. *Chem. Phys. Lett.* **1999**, *304*, 207–210.
19. Talapatra, S.; Zambano, A.Z.; Weber, S.E.; Migone, A.D. Gases do not adsorb on the interstitial channels of closed-ended single-walled carbon nanotube bundles. *Phys. Rev. Lett.* **2000**, *85* (1), 138–141.
  20. Talapatra, S.; Krungleviciute, V.; Migone, A.D. Higher coverage gas adsorption on the surface of carbon nanotubes: Evidence for a possible new phase in the second layer. *Phys. Rev. Lett.* **2002**, *89* (24), 246106-1–246106-4.
  21. Simonyan, V.V.; Johnson, J.K.; Kusnetsova, A.; Yates, J.T., Jr. Molecular simulation of xenon adsorption on single-walled carbon nanotubes. *J. Chem. Phys.* **2001**, *114* (9), 4180–4185.
  22. Muris, M.; Dupont-Pavlovsky, N.; Bienfait, M.; Zeppenfeld, P. Where are the molecules adsorbed on single-walled nanotubes?. *Surf. Sci.* **2001**, *492*, 67–74.
  23. Ulbricht, H.; Kriebel, J.; Moos, G.; Hertel, T. Desorption kinetics and interaction of Xe with single-walled carbon nanotube bundles. *Chem. Phys. Lett.* **2002**, *363*, 252–260.
  24. Ulbricht, H.; Moos, G.; Hertel, T. Physisorption of molecular oxygen on single-wall carbon nanotube bundles and graphite. *Phys. Rev., B* **2002**, *66*, 075404-1–075404-7.
  25. Wilson, T.; Tyburski, A.; DePies, M.R.; Vilches, O.E.; Becquet, D.; Bienfait, M. Adsorption of H<sub>2</sub> and D<sub>2</sub> on carbon nanotube bundles. *J. Low Temp. Phys.* **2002**, *126* (1/2), 403–408.
  26. Yoo, D.H.; Rue, G.H.; Chan, M.H.W.; Hwang, Y.H.; Kim, H.K. Study of nitrogen adsorbed on open-ended nanotube bundles. *J. Phys. Chem., B* **2003**, *107*, 1540–1542.
  27. Paredes, J.I.; Suárez-García, F.; Villar-Rodil, S.; Martínez-Alonso, A.; Tascón, J.M.D.; Bottani, E.J. N<sub>2</sub> physisorption on carbon nanotubes: Computer simulation and experimental results. *J. Phys. Chem., B* **2003**, *107*, 8905–8916.
  28. Murata, K.; Kaneko, K.; Steele, W.A.; Kokai, F.; Takahashi, K.; Kasuya, D.; Hirahara, K.; Yudasaka, M.; Iijima, S. Molecular potential structures of heat-treated single-wall carbon nanohorn assemblies. *J. Phys. Chem., B* **2001**, *105*, 10210–10216.
  29. Zambano, A.J.; Talapatra, S.; Lafdi, K.; Aziz, M.T.; McMillin, W.; Shaughnessy, G.; Migone, A.D.; Yudasaka, M.; Iijima, S.; Kokai, F.; Takahashi, K. Adsorbate binding energy and adsorption capacity of xenon on carbon nanohorns. *Nanotechnology* **2002**, *13*, 201–204.
  30. Ohba, T.; Kaneko, K. Internal surface area evaluation of carbon nanotube with GCMC simulation-assisted N<sub>2</sub> adsorption. *J. Phys. Chem., B* **2002**, *106*, 7171–7176.
  31. Maddox, M.W.; Gubbins, K.E. Molecular simulation of fluid adsorption in Buckytubes. *Langmuir* **1995**, *11*, 3988–3996.
  32. Yin, Y.F.; Mays, T.; McEnaney, B. Adsorption of nitrogen in carbon nanotube arrays. *Langmuir* **1999**, *15*, 8714–8718.
  33. Alain, E.; Yin, Y.F.; McEnaney, B. *Molecular Simulation and Measurement of Adsorption in Porous Carbon Nanotubes*; Stud. Surf. Sci. Catal.; Unger, K.K. et al., Eds.; Elsevier: Amsterdam, 2000; 128, 313–322.
  34. Khan, I.A.; Ayappa, K.G. Density distributions of diatoms in carbon nanotubes: A grand canonical Monte Carlo study. *J. Chem. Phys.* **1998**, *109* (11), 4576–4586.
  35. Bottani, E.J.; Bakaev, V.A. The Grand Canonical ensemble Monte Carlo simulation of nitrogen on graphite. *Langmuir* **1994**, *10*, 1550.
  36. Bottani, E.J. Nitrogen physisorption on a columnar carbonaceous solid. *Langmuir* **2001**, *17*, 2733–2738.
  37. Zhao, J.; Buldum, A.; Han, J.; Lu, J.P. Gas molecule adsorption in carbon nanotubes and nanotube bundles. *Nanotechnology* **2002**, *13*, 195–200.
  38. Yoo, D.H.; Rue, G.H.; Seo, J.Y.; Hwang, Y.H.; Chan, M.H.W.; Kim, H.K. Study of argon adsorbed on open-ended carbon nanotube bundles. *J. Phys. Chem., B* **2002**, *106*, 9000–9003.
  39. Sorescu, D.C.; Jordan, K.D.; Avouris, P. Theoretical study of oxygen adsorption on graphite and the (8,0) single-walled carbon nanotube. *J. Phys. Chem., B* **2001**, *105*, 11227–11232.
  40. Giannozzi, P.; Car, R.; Scoles, G. Oxygen adsorption on graphite and nanotubes. *J. Chem. Phys.* **2003**, *118* (3), 1003–1006.
  41. Shu, D.J.; Gong, X.G. Curvature effect on surface diffusion: The nanotube. *J. Chem. Phys.* **2001**, *114* (24), 10922–10926.
  42. Mackie, E.B.; Wolfson, R.A.; Arnold, L.M.; Lafdi, K.; Migone, A.D. Adsorption studies of methane films on catalytic carbon nanotubes and on carbon filaments. *Langmuir* **1997**, *13*, 7197–7201.
  43. Weber, S.E.; Talapatra, S.; Journet, C.; Zambano, A.; Migone, A.D. Determination of the binding energy of methane on single-walled carbon nanotube bundles. *Phys. Rev., B* **2000**, *61* (19), 13150–13154.
  44. Talapatra, S.; Migone, A.D. Adsorption of methane on bundles of closed-ended single-wall carbon nanotubes. *Phys. Rev., B* **2002**, *65*, 45416-1–45416-6.
  45. Zhang, X.; Wang, W. Methane adsorption in single-walled carbon nanotubes arrays by molecular simulation and density functional theory. *Fluid Phase Equilib.* **2002**, *194–197*, 289–295.
  46. Tanaka, H.; El-Merraoui, M.; Steele, W.A.; Kaneko, K. Methane adsorption on single-walled carbon nanotube: A density functional theory model. *Chem. Phys. Lett.* **2002**, *352*, 334–341.
  47. Hilding, J.; Grulke, E.A.; Sinnott, S.B.; Qian, D.; Andrews, R.; Jagtoyen, M. Sorption of butane on carbon multiwall nanotubes at room temperature. *Langmuir* **2001**, *17*, 7540–7544.
  48. Zhang, X.; Wang, W. Adsorption of linear ethane molecules in single walled carbon nanotube arrays by molecular simulation. *Phys. Chem., Chem. Phys.* **2002**, *4*, 3048–3054.
  49. Kong, J.; Dai, H. Full and modulated chemical gating of individual carbon nanotubes by organic amine compounds. *J. Phys. Chem., B* **2001**, *105*, 2890–2893.

50. Zhang, F. Molecular dynamics studies of chainlike molecules confined in a carbon nanotube. *J. Chem. Phys.* **1999**, *111* (19), 9082–9085.
51. Mao, Z.; Sinnott, S.B. Separation of organic molecular mixtures in carbon nanotubes and bundles: Molecular dynamics simulations. *J. Phys. Chem., B* **2001**, *105*, 6916–6924.
52. Cheng, H.M.; Yang, Q.H.; Liu, C. Hydrogen storage in carbon nanotubes. *Carbon* **2001**, *39*, 1447–1454.
53. Liu, C.; Fan, Y.Y.; Liu, M.; Cong, H.T.; Cheng, H.M.; Dresselhaus, M.S. Hydrogen storage in single-walled carbon nanotubes at room temperature. *Science* **1999**, *286*, 1127–1129.
54. Fischer, J.E. Storing energy in carbon nanotubes. *Chem. Innov.* **2000**, 21–27, October.
55. Hirscher, M.; Becher, M.; Haluska, M.; Quintel, A.; Skakalova, V.; Choi, Y.M.; Dettlaff-Weglikowska, U.; Roth, S.; Stepanek, I.; Bernier, P.; Leonhardt, A.; Fink, J. Hydrogen storage in carbon nanostructures. *J. Alloys Compd.* **2002**, *330–332*, 654–658.
56. Lueking, A.; Yang, R.T. Hydrogen spillover from a metal oxide catalyst onto carbon nanotubes—Implications for hydrogen storage. *J. Catal.* **2002**, *206*, 165–168.
57. Pradhan, B.K.; Sumanasekera, G.U.; Adu, K.W.; Romero, H.E.; Williams, K.A.; Eklund, P.C. Experimental probes of the molecular hydrogen–carbon nanotube interaction. *Physica, B* **2002**, *323*, 115–121.
58. Li, X.; Zhu, H.; Ci, L.; Xu, C.; Mao, Z.; Wei, B.; Liang, J.; Wu, D. Hydrogen uptake by graphitized multi-walled carbon nanotubes under moderate pressure and at room temperature. *Carbon* **2001**, *39*, 2077–2088.
59. Gundiah, G.; Govindaraj, A.; Rajalakshmi, N.; Dhathathreyan, K.S.; Rao, C.N.R. Hydrogen storage in carbon nanotubes and related materials. *J. Mater. Chem.* **2003**, *13*, 209–213.
60. Simonyan, V.V.; Diep, P.; Johnson, J.K. Molecular simulation of hydrogen adsorption in charged single-walled carbon nanotubes. *J. Chem. Phys.* **1999**, *111* (21), 9778–9783.
61. Shiraiishi, M.; Takenobu, T.; Ata, M. Gas–solid interactions in the hydrogen/single-walled carbon nanotube system. *Chem. Phys. Lett.* **2003**, *367*, 633–636.
62. Huang, W.Z.; Zhang, X.B.; Tu, J.P.; Kong, F.Z.; Ma, J.X.; Liu, F.; Lu, H.M.; Chen, C.P. The effect of pre-treatments on hydrogen adsorption of multi-walled carbon nanotubes. *Mater. Chem. Phys.* **2002**, *78*, 144–148.
63. Pradhan, B.K.; Harutyunyan, A.R.; Stojkovic, D.; Grossman, J.C.; Zhang, P.; Cole, M.W.; Crespi, V.; Goto, H.; Fujiwara, J.; Eklund, P.C. Large cryogenic storage of hydrogen in carbon nanotubes at low pressures. *J. Mater. Res.* **2002**, *17* (9), 2209–2216.
64. Chen, Y.; Shaw, D.T.; Bai, X.D.; Wang, E.G.; Lund, C.; Lu, W.M.; Chung, D.D.L. Hydrogen storage in aligned carbon nanotubes. *Appl. Phys. Lett.* **2001**, *78* (15), 2128–2130.
65. Williams, K.A.; Eklund, P.C. Monte Carlo simulations of H<sub>2</sub> physisorption in finite-diameter carbon nanotube ropes. *Chem. Phys. Lett.* **2000**, *320*, 352–358.
66. Gu, C.; Gao, G.H.; Yu, Y.X.; Mao, Z.Q. Simulation study of hydrogen storage in single walled carbon nanotubes. *Int. J. Hydrogen Energy* **2001**, *26*, 691–696.
67. Wang, Q.; Johnson, J.K. Molecular simulation of hydrogen adsorption in single-walled carbon nanotubes and idealized carbon slit pores. *J. Chem. Phys.* **1999**, *110* (1), 577–586.
68. Gu, C.; Gao, G.H. Path integral simulation of hydrogen adsorption in single-walled carbon nanotubes at low temperatures. *Phys. Chem., Chem. Phys.* **2002**, *4*, 4700–4708.
69. Darkrim, F.; Levesque, D. High adsorptive property of opened carbon nanotubes at 77 K. *J. Phys. Chem., B* **2000**, *104*, 6773–6776.
70. Hou, P.; Yang, Q.; Bai, S.; Xu, S.; Liu, M.; Cheng, H. Bulk storage capacity of hydrogen in purified multi-walled carbon nanotubes. *J. Phys. Chem., B* **2002**, *106*, 963–966.
71. Williams, K.A.; Pradhan, B.K.; Eklund, P.C.; Kostov, M.K.; Cole, M.W. Raman spectroscopic investigation of H<sub>2</sub>, HD, and D<sub>2</sub> physisorption on ropes of single-walled carbon nanotubes. *Phys. Rev. Lett.* **2002**, *88* (16), 165502-1–165502-4.
72. Ye, Y.; Ahn, C.C.; Witham, C.; Fultz, B.; Liu, J.; Rinzler, A.G.; Colbert, D.; Smith, K.A.; Smalley, R.E. Hydrogen adsorption and cohesive energy of single-walled carbon nanotubes. *Appl. Phys. Lett.* **1999**, *74* (16), 2307–2309.
73. Murata, K.; Kaneko, K.; Kanoh, H.; Kasuya, D.; Takahashi, K.; Kokai, F.; Yudasaka, M.; Iijima, S. Adsorption mechanism of supercritical hydrogen in internal and interstitial nanospaces of single-wall carbon nanohorn assembly. *J. Phys. Chem., B* **2002**, *106*, 11132–11138.
74. Darkrim, F.; Levesque, D. Monte Carlo simulations of hydrogen adsorption in single-walled carbon nanotubes. *J. Chem. Phys.* **1998**, *109* (12), 4981–4984.
75. Lee, S.M.; Park, K.S.; Choi, Y.C.; Park, Y.S.; Bok, J.M.; Bae, D.J.; Nahm, K.S.; Choi, Y.G.; Yu, S.C.; Kim, N.; Frauenheim, T.; Lee, Y.H. Hydrogen adsorption and storage in carbon nanotubes. *Synth. Met.* **2000**, *113*, 209–216.
76. Ma, Y.; Xia, Y.; Zhao, M.; Wang, R.; Mei, L. Effective hydrogen storage in single-wall carbon nanotubes. *Phys. Rev., B* **2001**, *63*, 115422-1–115422-6.
77. Yin, Y.F.; Mays, T.; McEnaney, B. Molecular simulations of hydrogen storage in carbon nanotube arrays. *Langmuir* **2000**, *16*, 10521–10527.
78. Dodziuk, H.; Dolgonos, G. Molecular modeling study of hydrogen storage in carbon nanotubes. *Chem. Phys. Lett.* **2002**, *356*, 79–83.
79. Züttel, A.; Nützenadel, Ch.; Sudan, P.; Mauron, Ph.; Emmenegger, Ch.; Rentsch, S.; Schlapbach, L.; Weidenkaff, A.; Kiyobayashi, T. Hydrogen sorption by carbon nanotubes and other carbon nanostructures. *J. Alloys Compd.* **2002**, *330–332*, 676–682.
80. Cracknell, R.F. Simulation of hydrogen adsorption in carbon nanotubes. *Mol. Phys.* **2002**, *100* (13), 2079–2086.
81. Gordon, P.A.; Saeger, R.B. Molecular modeling of adsorptive energy storage: Hydrogen storage in

- single-walled carbon nanotubes. *Ind. Eng. Chem. Res.* **1999**, *38*, 4647–4655.
82. Stan, G.; Cole, M.W. Low coverage adsorption in cylindrical pores. *Surf. Sci.* **1998**, *395*, 280–291.
83. Calbi, M.M.; Cole, M.W.; Gatica, S.M.; Bojan, M.J.; Stan, G. Condensed phases of gases inside nanotube bundles. *Rev. Mod. Phys.* **2001**, *73* (4), 857–865.
84. Calbi, M.M.; Gatica, S.M.; Bojan, M.J.; Cole, M.W. Phases of neon, xenon, and methane adsorbed on nanotube bundles. *J. Chem. Phys.* **2001**, *115* (21), 9975–9981.
85. Trasca, R.A.; Calbi, M.M.; Cole, M.W. Lattice model of gas condensation within nanopores. *Phys. Rev., E* **2002**, *65*, 61607-1–61607-9.
86. Calbi, M.M.; Gatica, S.M.; Bojan, M.J.; Cole, M.W. Ground state and thermal properties of a lattice gas on a cylindrical surface. *Phys. Rev., E* **2002**, *66*, 61107-1–61107-7.
87. Gatica, S.M.; Bojan, M.J.; Stan, G.; Cole, M.W. Quasi-one- and two-dimensional transitions of gases adsorbed on nanotube bundles. *J. Chem. Phys.* **2001**, *114* (8), 3765–3769.
88. Teizer, W.; Hallock, R.B.; Dujardin, E.; Ebbesen, T.W. <sup>4</sup>He desorption from single wall carbon nanotube bundles: A one-dimensional adsorbate. *Phys. Rev. Lett.* **1999**, *82* (26), 5305–5308.
89. Gordillo, M.C.; Boronat, J.; Casulleras, J. Quasi-one-dimensional <sup>4</sup>He inside carbon nanotubes. *Phys. Rev., B* **2000**, *61* (2), R878–R881.
90. Gordillo, M.C.; Boronat, J.; Casulleras, J. Zero temperature equation of state of quasi-one-dimensional H<sub>2</sub>. *Phys. Rev. Lett.* **2000**, *85* (11), 2348–2351.
91. Gordillo, M.C.; Boronat, J.; Casulleras, J. Isotopic effects of hydrogen adsorption in carbon nanotubes. *Phys. Rev., B* **2001**, *65*, 14503-1–14503-8.
92. Düren, T.; Keil, F.J.; Seaton, N.A. Molecular simulation of adsorption and transport diffusion of model fluids in carbon nanotubes. *Mol. Phys.* **2002**, *100* (23), 3741–3751.
93. Wang, Q.; Challa, S.R.; Sholl, D.S.; Johnson, J.K. Quantum sieving in carbon nanotubes and zeolites. *Phys. Rev. Lett.* **1999**, *82* (5), 956–959.
94. Challa, S.R.; Sholl, D.S.; Johnson, J.K. Light isotope separation in carbon nanotubes through quantum molecular sieving. *Phys. Rev., B* **2001**, *63*, 245419-1–245419-9.
95. Ayappa, K.G. Simulations of binary mixture adsorption in carbon nanotubes: Transitions in adsorbed fluid composition. *Langmuir* **1998**, *14*, 880–890.
96. Ayappa, K.G. Influence of temperature on mixture adsorption in carbon nanotubes: A grand canonical Monte Carlo study. *Chem. Phys. Lett.* **1998**, *282*, 59–63.
97. Gu, C.; Gao, G.H.; Yu, Y.X.; Nitta, T. Simulation for separation of hydrogen and carbon monoxide by adsorption on single-walled carbon nanotubes. *Fluid Phase Equilib.* **2002**, *194–197*, 297–307.
98. Ramírez-Pastor, A.J.; Eggarter, T.P.; Pereyra, V.D.; Riccardo, J.L. Statistical thermodynamics and transport of linear adsorbates. *Phys. Rev., B* **1999**, *59* (16), 11027–11036.
99. Mao, Z.; Sinnott, S.B. A computational study of molecular diffusion and dynamic flow through carbon nanotubes. *J. Phys. Chem., B* **2000**, *104*, 4618–4624.
100. Skoulidas, A.I.; Ackerman, D.M.; Johnson, J.K.; Sholl, D.S. Rapid transport of gases in carbon nanotubes. *Phys. Rev. Lett.* **2002**, *89* (18), 185901-1–185901-4.
101. Hata, K.; Takakura, A.; Saito, Y. Field emission from multiwall carbon nanotubes in controlled ambient gases, H<sub>2</sub>, CO, N<sub>2</sub> and O<sub>2</sub>. *Ultramicroscopy* **2003**, *95*, 107–112.
102. Hata, K.; Takakura, A.; Saito, Y. Field emission microscopy of adsorption and desorption of residual gas molecules on a carbon nanotube tip. *Surf. Sci.* **2001**, *490*, 296–300.
103. Kim, C.; Choi, Y.S.; Lee, S.M.; Park, J.T.; Kim, B.; Lee, Y.H. The effect of gas adsorption on the field emission mechanism of carbon nanotubes. *J. Am. Chem. Soc.* **2002**, *124*, 9906–9911.
104. Park, N.; Han, S.; Ihm, J. Effects of oxygen adsorption on carbon nanotube field emitters. *Phys. Rev., B* **2001**, *64*, 125401-1–125401-4.
105. Grujicic, M.; Cao, G.; Gersten, B. Enhancement of field emission in carbon nanotubes through adsorption of polar molecules. *Appl. Surf. Sci.* **2003**, *206*, 167–177.
106. Zhu, X.Y.; Lee, S.M.; Lee, Y.H.; Frauenheim, T. Adsorption and desorption of an O<sub>2</sub> molecule on carbon nanotubes. *Phys. Rev. Lett.* **2000**, *85* (13), 2757–2760.
107. Lee, S.M.; An, K.H.; Lee, Y.H.; Seifert, G.; Frauenheim, T. A hydrogen storage mechanism in single-walled carbon nanotubes. *J. Am. Chem. Soc.* **2001**, *123*, 5059–5063.
108. Cheng, H.; Pez, G.P.; Cooper, A.C. Mechanism of hydrogen sorption in single-walled carbon nanotubes. *J. Am. Chem. Soc.* **2001**, *123*, 5845–5846.
109. Chan, S.P.; Chen, G.; Gong, X.G.; Liu, Z.F. Chemisorption of hydrogen molecules on carbon nanotubes under high pressure. *Phys. Rev. Lett.* **2001**, *87* (20), 205502-1–205502-4.
110. Lee, E.C.; Kim, Y.S.; Jin, Y.G.; Chang, K.J. First-principles study of hydrogen adsorption on carbon nanotube surfaces. *Phys. Rev., B* **2002**, *66*, 073415-1–073415-4.
111. Arellano, J.S.; Molina, L.M.; Rubio, A.; López, M.J.; Alonso, J.A. Interaction of molecular and atomic hydrogen with (5,5) and (6,6) single-wall carbon nanotubes. *J. Chem. Phys.* **2002**, *117* (5), 2281–2282.
112. Tada, K.; Furuya, S.; Watanabe, K. Ab initio study of hydrogen adsorption to single-walled carbon nanotubes. *Phys. Rev., B* **2001**, *63*, 155405-1–155405-4.



# Carbon Nanotubes: Hydrogen Storage

**Masashi Shiraishi**

*Pi-electron Materials Research Lab, Sony Corporation, Yokohama, Japan*

**Taishi Takenobu**

*Institute of Materials Research, Sony Corporation, Yokohama, Japan*

**Hikomichi Kataura**

*Department of Physics, Tokyo Metropolitan University, Tokyo, Japan*

**Masafumi Ata**

*Materials Laboratories, Sony Corporation, Yokohama, Japan*

## INTRODUCTION

This entry shows the mechanisms of hydrogen sorption in carbon nanotubes. The research topic was inconclusive and controversial, but fabrication of precise measuring system and high-purity single-walled carbon nanotubes made it possible to obtain fully reproducible results of hydrogen physisorption.

## OVERVIEW

Since its discovery in 1991,<sup>[1]</sup> carbon nanotubes have attracted much expectation to store hydrogen because they have cylindrical structures and hollow spaces inside of their sidewalls. Novel carbonaceous materials for hydrogen storage are strongly needed for fuel cell (FC) devices because conventional hydrogen storage materials are too heavy for compact FC devices and, on the other hand, carbon is light, stable, and abundant. Fig. 1 shows the comparison of hydrogen amount in various adsorbent. One can see that when 5 wt.% of hydrogen storage in nanotubes can be realized the Department of Energy (DOE) target is almost achieved. Compared with the other adsorbent, such as alloys, carbon can store much hydrogen in the energy density per weight.

The pioneering work by Dillon et al.<sup>[2]</sup> on the possibility of 5–10 wt.% storage in single-walled carbon nanotubes (SWNTs)<sup>[3]</sup> at room temperature aroused interest toward SWNTs and other carbonaceous materials in this research field.<sup>[4–7]</sup> However, it was very difficult to fabricate apparatus for precise measurements because the leakage problem of high-pressure hydrogen was serious, and much attention should have been paid for the measurement of the change of introduced hydrogen pressure because in some cases temperature

dependence of hydrogen pressure (before equilibrium) was believed to be the evidence of hydrogen sorption. In addition, the lack of understanding in sorption prevented to obtain reliable results (for instance, the origin of abnormally high value of sorption cannot be fully explained). Thus further efforts were awaited for the establishment of fully reproducible and convincing data.<sup>[8–13]</sup> In particular, a question remained as to whether the adsorption site for hydrogen existed in carbon at moderate temperature. At present, about 7 wt.% of hydrogen desorption from nanographite at high temperature ( $\sim 700$  K)<sup>[14]</sup> and the storage of 8 wt.% of hydrogen in SWNTs at low temperature (80 K)<sup>[15]</sup> have so far been believed to be reliable.

This report is focusing on detailed analyses of hydrogen adsorption in carbon nanotube systems and its mechanisms. Hydrogen physisorption at room temperature was characterized by using SWNTs and C<sub>60</sub> encapsulated SWNTs (peapods), and the physisorption was achieved by fabricating and activating subnanometer-scale pores. Adsorption potential of the pores was estimated to be about  $-0.21$  eV and this large potential induced the physisorption.<sup>[16,17]</sup> Molecular dynamics of hydrogen adsorbed in the pores was also characterized by nuclear magnetic resonance (NMR) and the result suggested the hydrogen strongly interacts with the sidewalls of the SWNTs.<sup>[18]</sup> Future prospects and a guideline of material designing are summarized in the end of the report.

## EXPERIMENTS

Single-walled carbon nanotubes were synthesized by Nd:YAG laser ablation using Ni/Co catalysts. The metal/carbon target was heated to 1200°C in a furnace. The diameter of the SWNTs is typically 1.4 nm. For purification, carbon soot containing the SWNTs

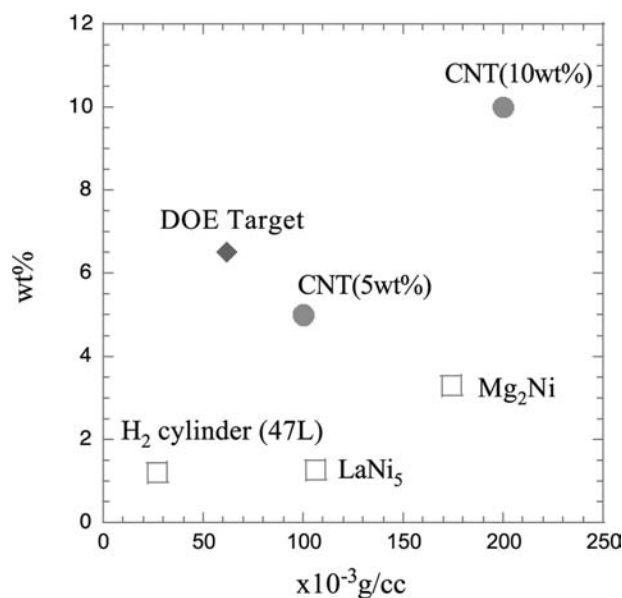


**Fig. 1** Comparison of hydrogen adsorbent. DOE target means the target of the Department of Energy.

was refluxed in an aqueous solution of  $\text{H}_2\text{O}_2$  for 3 hr. After the removal of any amorphous carbon, the sample was treated with HCl overnight to eliminate the remaining catalytic metals. Thermogravimetric analysis of this product showed that the metal contents were decreased less than 3 wt.%. For further purification, the purified SWNTs were treated with aqueous NaOH.<sup>[16,19,20]</sup> Small particles of by-products in the  $\text{H}_2\text{O}_2$  purification, amorphous carbon, which covered a surface of the SWNTs and occupied intertube pores, were removed in this process by ultrasonication in the NaOH (pH = 10–11) for 2 hr. The effect of the NaOH treatment was checked by the change in Raman spectra. The intensity ratio of the G- to the D-band (G/D) changed from 50 to 90 after this treatment; this observation indicates that the amorphous carbon particles were removed and the SWNTs were cleaned. Transmission electron microscopy (TEM) measurements also verified the cleaning of the SWNTs. Fig. 2 shows that amorphous carbon particles coated the surface of the SWNTs before treatment, whereas they were removed and the sidewalls of the SWNTs were clearly seen after the treatment. It is concluded from these characterizations that NaOH treatment is effective for cleaning of the sidewalls and that the resulting SWNT bundles have minute intertube pores suitable for hydrogen adsorption.

A peapod is a new form of a SWNT-based material which has unique physical properties.<sup>[21–28]</sup> The inside of peapods is filled with  $\text{C}_{60}$  molecules (or other fullerenes and metallofullerenes) and peapods differ from SWNTs only in this structural point. This structural difference is suitable to examine the gas adsorption sites in SWNT-based materials. In this work peapods ( $\text{C}_{60}$ @SWNTs)

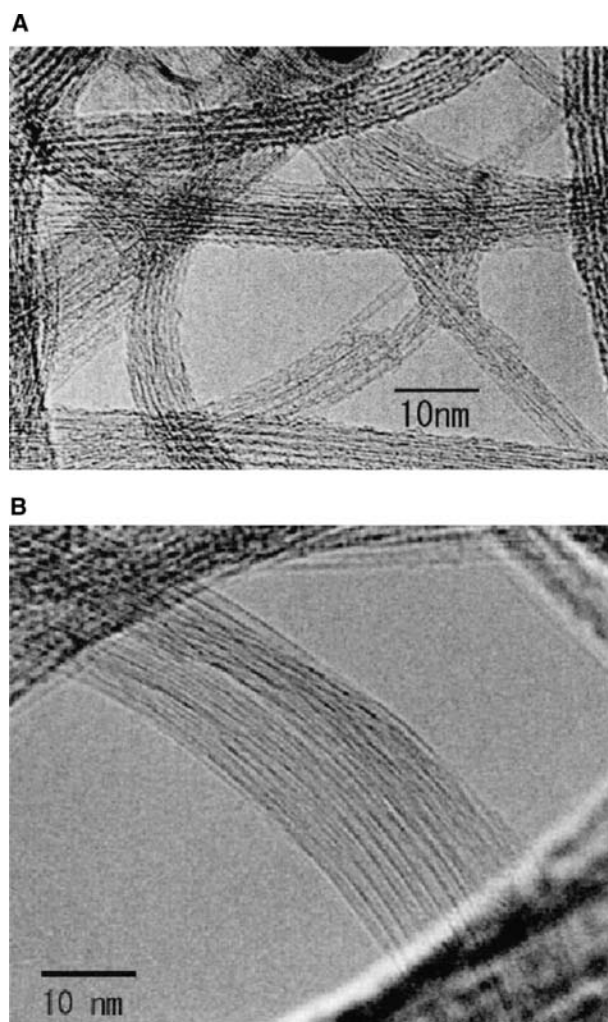


**Fig. 2** TEM photographs of purified SWNTs. (A) Before NaOH treatment, in which case many tube sidewalls were covered with amorphous carbon clusters. (B) After NaOH treatment, by which carbon clusters were removed and sidewalls were clearly seen.

were synthesized<sup>[23]</sup> from the same batch of SWNTs after NaOH treatment. The filling rate of  $\text{C}_{60}$ s in the SWNTs was estimated to be about 85%.<sup>[24]</sup> After washing the sample by toluene to remove unreacted  $\text{C}_{60}$  on the sidewalls,<sup>[23]</sup> the sample was heated in a vacuum for complete elimination of the toluene. The whole procedures for sample preparations are summarized in Fig. 3.

Hydrogen desorption was studied by a custom-made temperature-programmed-desorption (TPD) system, by which desorption of the gaseous species was measured as a function of temperature under about  $10^{-5}$  Pa.<sup>[2]</sup> A pretreatment condition of the samples was  $T = 873$  K,  $P = 10^{-4}$  Pa for 1 hr. The pretreatment of the sample is a critical procedure for the adsorption and desorption of hydrogen. The purity of hydrogen was 99.99999%. The applied pressure was 6 MPa and ca. 0.1 MPa at room temperature,

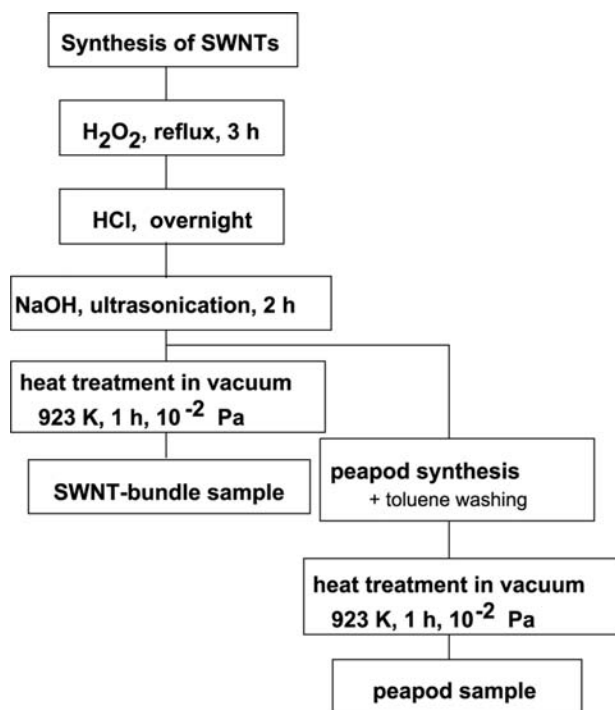


Fig. 3 Detailed procedures for a sample preparation.

and the pressure dependence of hydrogen desorption can be of help to distinguish whether hydrogen was extrinsically introduced or not.

Hydrogen adsorption capability was measured up to 9 MPa, and care was taken to eliminate the leakage of the system for precise measurements. The amount of the SWNTs was increased to about 1 g to suppress the error bar, and the volume of the applied hydrogen was evaluated with allowance for the temperature effect and by taking sufficient time to let hydrogen reach equilibrium.

A NMR study was carried out to obtain information about the molecular dynamics of the hydrogen trapped in the intertube pores, as in the case of  $H_2$  in a  $C_{60}$  solid.<sup>[29]</sup> We performed solid-state  $^1H$  magic angle spinning (MAS) NMR observation of the hydrogen at 293 K with a CMX-300 Infinity (Chemagnetics Co.; 298.99 MHz) after introducing hydrogen at 9 MPa for 5 days. The MAS was adopted at 3000 rpm because of the low intensity of the spectral pattern of the powder. The inversion recovery method was used for the determination of the spin-lattice relaxation time,  $T_1$ , with the application of a  $\pi/\tau/\pi/2$  pulse sequence. Therefore the  $T_1$  thus obtained under rotation is  $T_{1\rho}$ .

## RESULTS AND DISCUSSION

### Sorption Mechanisms

Before showing the experimental results, we discuss the mechanisms of adsorption. Physisorption and

chemisorption are possible mechanisms of hydrogen adsorption. In chemisorption, hydrogen is covalently bonded with host materials and desorption temperature is too high ( $>500$  K) for commercial use. In physisorption, the van der Waals force between hydrogen molecules and the host materials is a main force to stabilize hydrogen on the surface. The desorption temperature is generally near room temperature, and so physisorption is much more preferable for industrial applications. Thus we focus only on the physisorption of hydrogen in SWNTs.

Physisorption is controlled by a relation between chemical potential of gases,  $\mu$ , and adsorption potential of solids,  $\varepsilon$ . Coverage of adsorption sites,  $f$ , is determined by the Langmuir adsorption isotherm, typically

$$f = \frac{1}{1 + \exp\left(\frac{\varepsilon - \mu}{kT}\right)} \quad (1)$$

When  $\varepsilon = \mu$ , the coverage is equal to 0.5 and this means about 4 wt.% of hydrogen adsorption. The temperature and pressure dependence of the chemical potential of hydrogen gas,  $\mu$ , shown in Fig. 4, was calculated by the use of experimental values of enthalpy,  $H$ , entropy,  $S$ , taken from Ref.<sup>[30]</sup> and Eq. (2),

$$G = H - TS$$

$$\mu = \frac{\partial G}{\partial n} \quad (2)$$

where  $G$  is Gibbs free energy and  $n$  is the number of molecules. The adsorption potential of the inside and

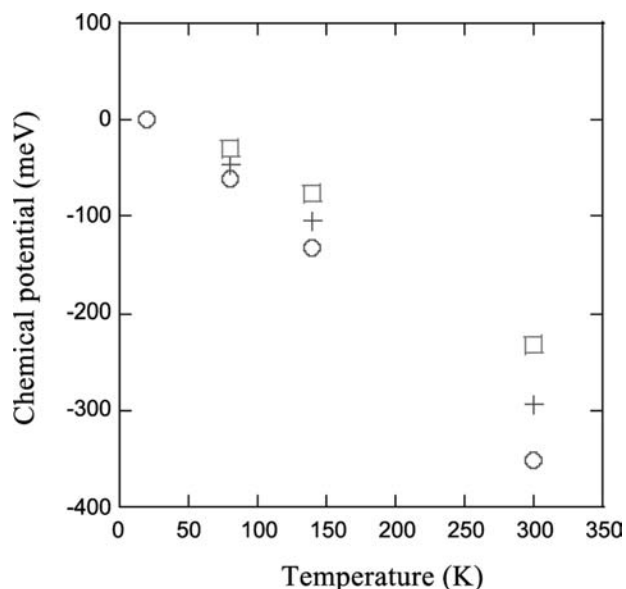


Fig. 4 Temperature dependence of the chemical potential of hydrogen,  $\mu$ . Open circles, crosses, and open squares represent  $\varepsilon$  at 0.1, 1, and 10 MPa, respectively.

outside of an individual SWNT has been estimated to be at most  $-0.09$  eV.<sup>[31]</sup> Thus one can see that hydrogen adsorption on the outer surface and the intratube pores can occur only at low temperature. According to Ye et al.,<sup>[15]</sup> hydrogen adsorption amount at 80 K is about 8 wt.%, the coverage  $f$  being nearly equal to 1. This value seems to be a reasonable estimate, because the chemical potential of hydrogen is small enough at such low temperature. On the contrary, one cannot expect hydrogen physisorption at room temperature unless the adsorption potential is significantly enhanced by the modification of adsorption pore structures. In our material systems, the intertube pores are small enough and one can expect that they have large adsorption potential, as mentioned in the following subsections.

### Experimental Evidence for Hydrogen Physisorption at Room Temperature

Results of temperature-programmed-desorption analyses

Fig. 5A–D shows TPD profiles of gas desorption from the SWNTs and the peapods after application of

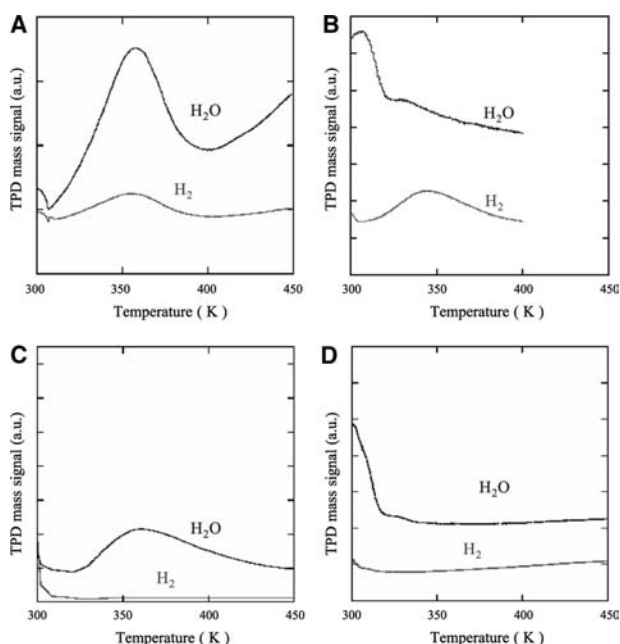


**Fig. 5** TPD observations for hydrogen and water. (A) Desorption from the SWNTs after application of 6-MPa hydrogen. Both hydrogen and water were desorbed. (B) Desorption from the peapods after application of 6-MPa hydrogen. Only hydrogen was desorbed. (C) Desorption from the SWNTs after application of 0.1-MPa hydrogen. (D) Desorption from the peapods after application of 0.1-MPa hydrogen.

6 MPa and ca. 0.1 MPa of hydrogen. Hydrogen desorption was observed around 350 K from the SWNTs and the peapods which experienced only the application of high-pressure hydrogen. This fact suggests that hydrogen was introduced extrinsically and adsorbed at room temperature. Water desorption was observed only from the SWNTs, and the appearance of the peak was independent of the hydrogen pressure. These facts suggest that all sites in the peapods for water adsorption were fully occupied by  $C_{60}$  molecules so that no more spaces were available.

The similarity of the hydrogen desorption profiles obtained from the SWNTs to that from the peapods suggests that the hydrogen adsorption sites in these samples are essentially the same. Because  $C_{60}$ s are embedded inside the tubes, the inside of the tubes cannot contribute to hydrogen adsorption. Moreover, desorption temperature of about 350 K excludes the possibility of surface adsorption. Therefore the possible sites for hydrogen adsorption are the intertube sites in the bundles.

Fig. 6 shows a size comparison of the inter- and intratube pores in SWNT bundles. SWNTs form a triangular lattice, and the pore size can be estimated by taking the van der Waals radii of carbon atoms into account. Because the diameter of the SWNTs is 1.4 nm, the size of the intertube pores is about 0.2–0.3 nm, while the size of the intratube pores is about 1 nm. On the other hand, the size of water and hydrogen molecules is 0.39 and 0.24 nm, respectively. This comparison indicates that the intertube pores can adsorb hydrogen only when high-pressure hydrogen is applied, whereas they cannot store the water molecule because it is too large to penetrate into the intertube pore. Here the size and the adsorption potential of the intratube pore are 1 nm and  $-0.09$  eV, respectively. Because the size of the intertube pore is 0.2–0.3 nm, one can expect that the pores have larger adsorption potential, which allows hydrogen physisorption. In the next subsection, we discuss the mechanism of hydrogen adsorption.

### Adsorption mechanisms

To determine the adsorption mechanism, desorption energy analysis is a commonly used procedure. The relationship of the desorption energy,  $E_d$ , the heating rate,  $\beta$ , and the temperature at the desorption peak maximum,  $T_m$ , is represented as<sup>[32]</sup>

$$\frac{T_m^2}{\beta} = \frac{R}{E_d} \tau_0 \exp\left(\frac{E_d}{RT_m}\right) \quad (3)$$

where  $R$  is the gas constant and  $\tau_0$  can be interpreted as the mean lifetime of the gas molecules adsorbed



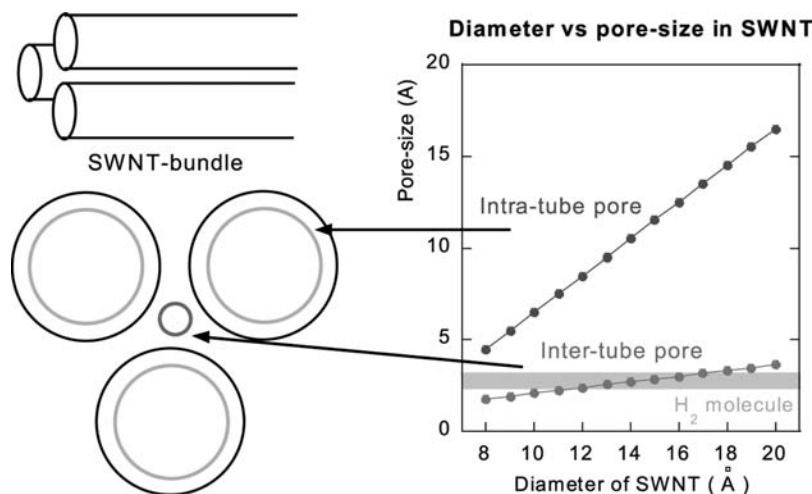


Fig. 6 Size comparison between the intra- and the intertube pores and hydrogen.

on a surface. The desorption energy is evaluated by changing the heating rate, as shown in Fig. 7. The estimated energy, 0.21 eV, clearly indicates that the adsorption mechanism is physisorption; if hydrogen were chemisorbed, the value should be about 10 times larger. In addition, when deuterium instead of hydrogen was introduced in the SWNTs, a similar desorption peak at 350 K was observed and the desorption energy was estimated to be about  $-0.20$  eV. From these experimental results, we can conclude that hydrogen (and deuterium) is *physisorbed at room temperature*. This is the first reliable report on hydrogen physisorption at room temperature by using well-purified SWNTs.

The estimated desorption energy can be regarded as the adsorption potential of the intertube pores when the surface of the pores is clean enough.<sup>[32]</sup> Eq. (4) shows the relation between the desorption energy,  $E_d$ ,

the activation energy for adsorption,  $E_a$ , and the heat of adsorption,  $q$ ,

$$E_d = E_a + q \quad (4)$$

When the surface is clean,  $E_a$  is nearly equal to zero and  $q$  is equal to the desorption energy. In this work, the surface of the SWNTs was rinsed by NaOH and it was clean enough. Thus the measure  $E_d$  can be regarded as the adsorption potential of the hydrogen adsorption sites,  $\epsilon$ . As a result, the adsorption potential of the intertube pores is about  $-0.21$  eV. This value is about 2.3 times larger than the calculated value of the intratube pores ( $-0.09$  eV), and the minute intertube pores (0.2–0.3 nm) surely have larger adsorption potential. Murata et al. calculated the adsorption potential of pores in nitrogen/single-walled carbon nanohorns (SWNHs) system.<sup>[33]</sup> Although the size of SWNH is 2 nm and the interaction between  $N_2$  and SWNHs was focused, the ratio between the adsorption potential of the inter- and intrananohorn is 1.8, and this has good accordance with our experimental result.

Hydrogen adsorption capability and validity of our model

Fig. 8 shows the hydrogen adsorption capability of the SWNTs. The amount of adsorbed hydrogen depends on the applied hydrogen pressure, and the storage of hydrogen at 9 MPa is about 0.3 wt.%. In this experimental scheme, hydrogen is adsorbed only in the intertube pores. The maximum amount of adsorbed hydrogen in the intertube pores is limited and estimated to be about 0.8 wt.%.<sup>[34]</sup> This means that the coverage of the pore is about 0.38 in our experiments. Fig. 9 shows a comparison of the adsorption potential of the intertube pores and the chemical potential of hydrogen. The coverage of the intertube pores at

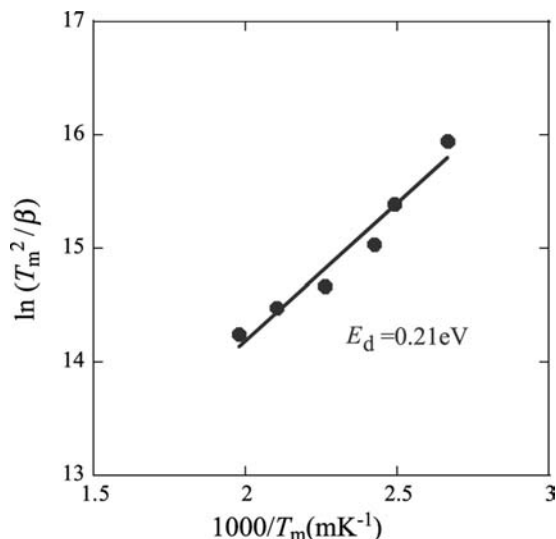
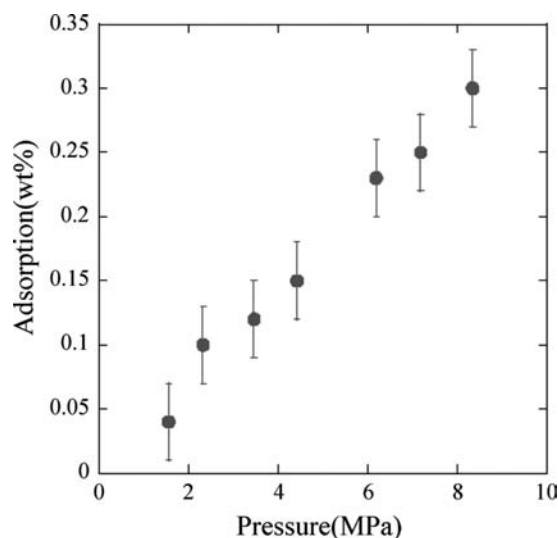
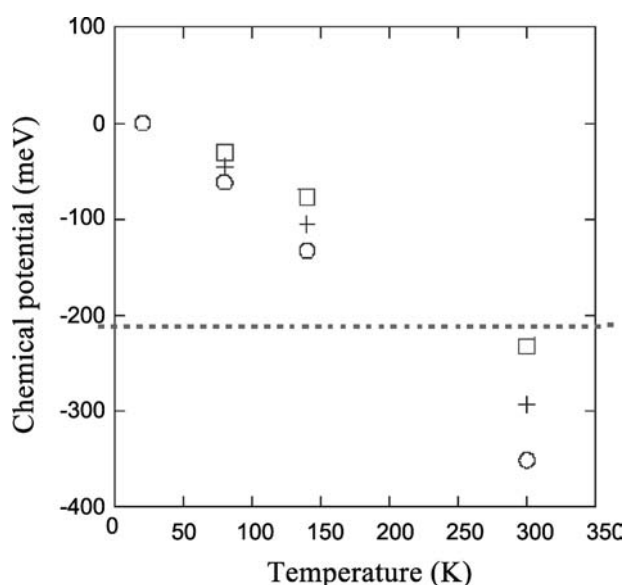


Fig. 7 Kissinger's plot of  $\ln(T_m^2/\beta)$  against  $1/T_m$  with  $\beta$  varying from 0.017 to 0.17 K/sec.



**Fig. 8** Amount of adsorbed hydrogen (wt.%) against applied hydrogen pressure,  $P$ . The error bar is estimated to be 0.03% from the precision of the pressure gauge.

300 K and 10 MPa,  $f = 0.31$ , as estimated from the  $\mu$  value in Fig. 9 and the experimental  $\varepsilon$  value, is comparable with the measured value, 0.38. This similarity corroborates our experimental results and the Langmuir model used in this study. The corresponding coverage for the intratube pores,  $f = 0.0044$ , is smaller by two orders of magnitude, although the adsorption potential of the intertube pores is at most 2–3 times as large as that of the intratube pores. In other words, only a small difference in  $\varepsilon$  induces a major difference in  $f$ . Therefore fabrication of minute pores, with 0.2–0.3 nm in size and with large  $\varepsilon$ , is indeed a crucial



**Fig. 9** Comparison of the adsorption potential of the intertube pores and the chemical potential of hydrogen.

factor to achieve hydrogen physisorption at room temperature. This indicates the importance of fabricating “subnanometer-ordered” spaces.

#### A NMR study on hydrogen trapped in SWNT bundles

In the previous subsections, physisorption of hydrogen in SWNTs was analyzed in detail. The next concern is the condition under which hydrogen exists in the pores. In this subsection, a NMR characterization of the adsorbed hydrogen in the intertube pores is discussed. A NMR study can give information about the molecular dynamics of hydrogen trapped in hollow spaces, for instance, an interstitial site in solid  $C_{60}$ .<sup>[29]</sup>

Fig. 10A and B shows the  $^1H$  MAS NMR spectra observed for the no- $H_2$ -adsorbed sample (sample A) and the  $H_2$ -adsorbed sample (sample B). A clear peak at 5.1 ppm was observed in sample B, although no peak was able to be seen in sample A. It is notable that the peak position is close to that for water molecules.<sup>[35]</sup> Actually, liquid water has a peak at 4.96 ppm at 296.3 K. To confirm whether the peak is attributable to hydrogen or water, sample B was exposed to  $SO_2$  gas mixed with the same volume of dry  $N_2$  gas for 3.5 hr. If the peak is attributed to the remaining water molecules in the sample, the water would easily interact with the  $SO_2$  gas and the peak would change or disappear. After 3.5 hr of exposure, no change in the peak position or shape was observed [Fig. 10C]. From this result and the fact that no peak was observed in sample A, it is concluded that the peak at 5.1 ppm is attributable to hydrogen molecules in the intertube pores. The value, 5.1 ppm, is comparable with the previously reported value of hydrogen molecules loaded in silica,  $4.8 \pm 0.2$  ppm.<sup>[36,37]</sup> In that work, hydrogen was loaded in the non-heat-treated silica at 1.09 MPa for 70 days. As discussed later, the relaxation time  $T_1$  in both cases is also very similar. The similarity also supports the validity of our experimental results.

Hydrogen is trapped in the intertube pores, as mentioned above. Judging from the size of the pores, hydrogen is trapped in the minute pores and it can interact strongly with the sidewalls of the SWNTs. The spin-lattice relaxation time,  $T_1$ , can be a good index of the strength of interaction in this case. Fig. 11A shows the inverse recovery of the NMR signals, and the time dependence of the normalized peak intensity is shown in Fig. 11B. In Fig. 11B, the difference between the initial and the final intensity is regarded to be  $M_0$ , and the difference between the initial and the time-dependent intensity at each measuring time is normalized by  $M_0$ . From this result,  $T_1$  is estimated to be about 0.1–0.2 sec.  $T_1$  of hydrogen molecules in a-Si and silica is about 0.45<sup>[38]</sup> and 1 sec,<sup>[36]</sup> respectively. In both cases, hydrogen



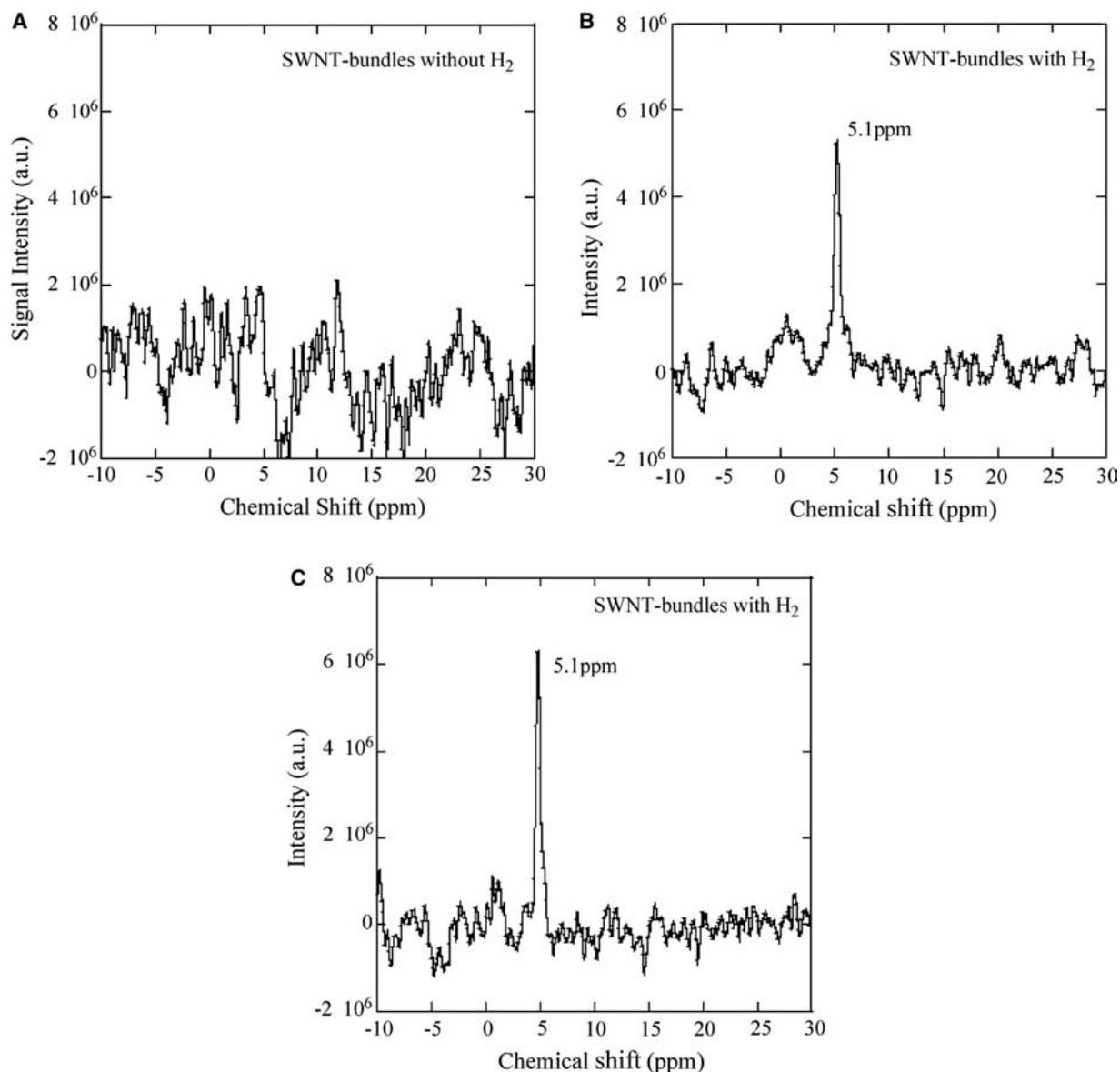


**Fig. 10** NMR signals of hydrogen in SWNTs bundles. (A) Sample A (non-adsorbed). (B) Sample B (adsorbed). (C) NMR signal from sample B after exposure to  $\text{SO}_2$  and  $\text{N}_2$  mixture for 3.5 hr.

molecules exist in the minute space, for instance, interstitial sites. In our case also, hydrogen is trapped tightly in the minute spaces. Therefore the similarity of  $T_1$  in each case can be explained by the similarity of circumstances where hydrogen molecules exist.

## CONCLUSION

In this report the adsorption of hydrogen in SWNTs and its mechanisms were studied, and the first hydrogen physisorption at room temperature in the well-purified SWNTs and peapods was achieved by using NaOH-rinsed SWNTs. Hydrogen was adsorbed in the intertube pores of the SWNT bundles, because

the pores are 0.2–0.3 nm in size and therefore they have sufficiently large adsorption potential ( $-0.21$  eV) for the achievement of physisorption. This suggests the importance of subnanometer-ordered spaces. By  $^1\text{H}$  MAS NMR measurements, it was clarified that the adsorbed hydrogen strongly interacts with the side-walls of the SWNTs as the hydrogen does in silica and a-Si. Until this work, the research topic of hydrogen storage in SWNTs was not conclusive, but we believe that this work can be of help in understanding the fundamental mechanisms.

The most important point of hydrogen physisorption in SWNT systems is to fabricate and activate minute pores. At present, intratubes cannot be available because they are too large for hydrogen. However,

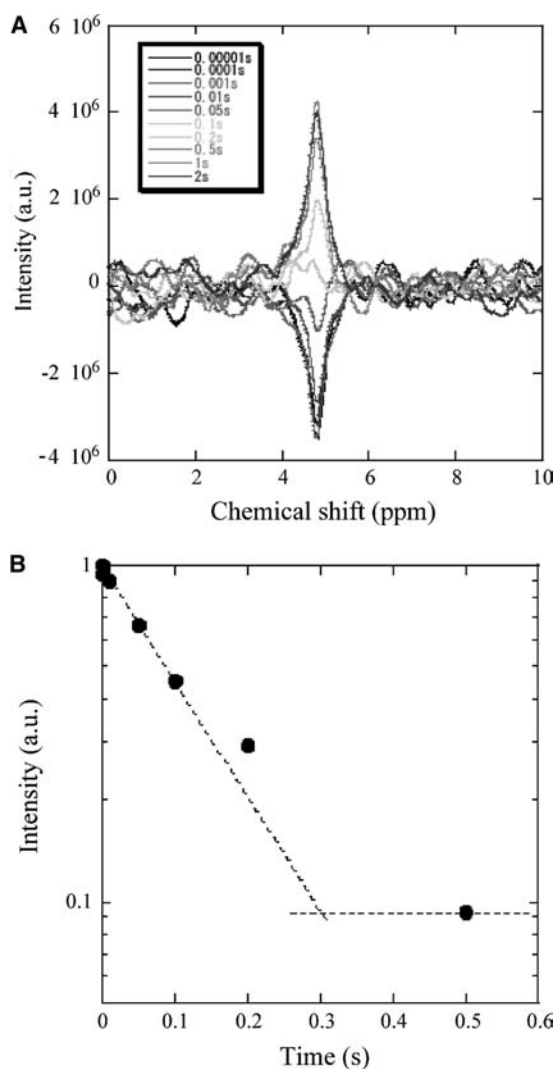


**Fig. 11** (A) The inverse recovery of the NMR signals in sample B. (B) The time dependence of the normalized peak intensity.

if one can succeed in synthesizing small-sized-materials encapsulated SWNTs, the intratube pores also become suitable spaces. Similarly, double-walled carbon nanotubes (DWNTs), SWNTs with very small diameter, seem to be promising candidates. “Nanotechnology” is becoming a key term in science now, but we would like to emphasize that “subnanotechnology” is also important in this field.

## ACKNOWLEDGMENT

The authors (M.S., M.A.) thank Mr. Y. Murakami for his TEM observation and Dr. Kajiura for providing Fig. 1.

## REFERENCES

- Iijima, S. Helical microtubules of graphitic carbon. *Nature* **1991**, *354*, 56–58.
- Dillon, A.C.; Jones, K.M.; Bekkedahl, T.A.; Kiang, C.H.; Bethune, D.S.; Heben, M.J. Storage of hydrogen in single-walled carbon nanotubes. *Nature* **1997**, *386*, 377–379.
- Iijima, S.; Ichihashi, T. Single-shell carbon nanotubes of 1-nm diameter. *Nature* **1993**, *363*, 603–605.
- Dillon, A.C.; Gennet, T.; Alleman, J.L.; Jones, K.M.; Parilla, P.A.; Heben, M.J. In *Carbon Nanotube Materials for Hydrogen Storage*, Proceedings of the 2000 Hydrogen Program Review, May, 8–10, 2000; NREL/CP-570-28890.
- Chen, P.; Wu, X.; Lin, J.; Tan, K.L. High H<sub>2</sub> uptake by alkali-doped carbon nanotubes under ambient pressure and moderate temperatures. *Science* **1999**, *285*, 91–93.
- Chambers, A.; Park, C.; Terry, R.; Baker, K.; Rodriguez, N.M. Hydrogen storage in graphite nanofiber. *J. Phys. Chem., B* **1998**, *102*, L4253–L4256.
- Liu, C.; Fan, Y.Y.; Liu, M.; Cong, H.T.; Cheng, H.M.; Dresselhaus, M.S. Hydrogen storage in single-walled carbon nanotubes at room temperature. *Science* **1999**, *286*, 1127–1129.
- Hirscher, M.; Becher, M.; Haluska, M.; Detlaff-Weklikowska, U.; Quintel, A.; Duesberg, G.S.; Choi, Y.-M.; Downes, P.; Hulman, M.; Roth, S.; Stepanek, I.; Bernier, P. Hydrogen storage in sonicated carbon materials. *Appl. Phys., A* **2001**, *72*, 129–132.
- Ahn, C.C.; Ye, Y.; Ratnakumar, B.V.; Witham, C.; Bowman, R.C.; Fultz, B. Hydrogen desorption and adsorption measurements on graphite nanofibers. *Appl. Phys. Lett.* **1998**, *73* (23), 3378–3380.
- Tang, R.T. Hydrogen storage by alkali-doped carbon nanotubes—revisited. *Carbon* **2000**, *38*, 623–641.
- Zandonella, C. Is it all just a pipe dream? *Nature* **2001**, *410*, 734–735.
- Tibbetts, G.G.; Meisner, G.P.; Olk, C.H. Hydrogen storage capacity of carbon nanotubes, filaments, and vapor-grown fibers. *Carbon* **2001**, *39*, 2291–2301.
- Cheng, H.; Pez, G.P.; Cooper, A.C. Mechanism of hydrogen sorption in single-walled carbon nanotubes. *J. Am. Chem. Soc.* **2001**, *123*, 5845–5846.
- Orimo, S.; Matsunaga, T.; Fujii, H.; Fukunaga, T.; Majer, G. Hydrogen desorption property of mechanically prepared nanostructured graphite. *Appl. Phys. Lett.* **2001**, *90* (4), 1545–1549.
- Ye, Y.; Ahn, C.C.; Witham, C.; Fultz, B.; Liu, J.; Rinzler, A.G.; Colbert, D.; Smith, K.A.; Smalley, R.E. Hydrogen adsorption and cohesive energy of single-walled carbon nanotubes. *Appl. Phys. Lett.* **1999**, *74* (16), 2307–2309.
- Shiraishi, M.; Takenobu, T.; Yamada, A.; Ata, M.; Kataura, H. Hydrogen storage in single-walled carbon nanotubes and peapods. *Chem. Phys. Lett.* **2002**, *358*, 213–218.
- Shiraishi, M.; Takenobu, T.; Ata, M. Gas-solid interactions in the hydrogen/single-walled carbon nanotube system. *Chem. Phys. Lett.* **2003**, *367*, 633–636.
- Shiraishi, M.; Ata, M. Nuclear magnetic resonance of molecular hydrogen in single-walled carbon nanotube bundles. *J. Nanosci. Nanotechnol.* **2002**, *2*, 463–465.
- Rinzler, A.G.; Liu, J.; Dai, H.; Nikolaev, P.; Hufmann, C.B.; Rodriguez-Macias, F.J.; Boul, P.J.; Lu, A.H.; Heymann, D.; Colbert, D.T.; Lee, R.S.; Fischer, J.E.;

- Rao, A.M.; Eklund, P.C.; Smalley, R.E. Large-scale purification of single-walled carbon nanotubes: process, product, and characterization. *Appl. Phys., A* **1998**, *67*, 29–37.
20. Vaccarini, L.; Goze, C.; Aznar, R.; Micholet, V.; Journet, C.; Bernier, P. Purification procedure of carbon nanotubes. *Synth. Met.* **1999**, *103*, 2492–2493.
  21. Smith, B.W.; Monthieux, M.; Luzzi, D.E. Encapsulated C<sub>60</sub> in carbon nanotubes. *Nature* **1998**, *296*, 323–325.
  22. Kataura, H.; Maniwa, Y.; Kodama, T.; Kikuchi, K.; Hirahara, K.; Suenaga, K.; Iijima, S.; Suzuki, S.; Achiba, Y.; Kraeschmer, W. High-yield fullerene encapsulation in single-walled carbon nanotubes. *Synth. Met.* **2001**, *121*, 1195–1196.
  23. Kataura, H.; Maniwa, Y.; Abe, M.; Fujiwara, A.; Kodama, T.; Kikuchi, K.; Imahori, H.; Misaki, Y.; Suzuki, S.; Achiba, Y. Optical properties of fullerene and non-fullerene peapods. *Appl. Phys., A* **2002**, *74*, 349–354.
  24. Hirahara, K.; Suenaga, K.; Bandow, S.; Kato, H.; Okazaki, T.; Shinohara, H.; Iijima, S. One-dimensional metallofullerene crystal generated inside single-walled carbon nanotubes. *Phys. Rev. Lett.* **2000**, *85* (25), 5384–5387.
  25. Okada, S.; Saito, S.; Ishiyama, A. Energetics and electronic structure of encapsulated C<sub>60</sub> in a carbon nanotube. *Phys. Rev. Lett.* **2001**, *86* (17), 3835–3838.
  26. Pichler, T.; Kuzmany, H.; Kataura, H.; Achiba, Y. Metallic polymer of C<sub>60</sub> inside single-walled carbon nanotubes. *Phys. Rev. Lett.* **2001**, *87* (26), 26,7401–26,7404.
  27. Chiu, P.W.; Gu, G.; Kim, G.T.; Philipp, G.; Roth, S.; Yang, S.F.; Yang, S. Temperature-induced change from p to n conduction in metallofullerene nanotubes peapods. *Appl. Phys. Lett.* **2001**, *79* (23), 3845–3847.
  28. Lee, J.; Kim, H.; Kahng, S.-J.; Kim, G.; Son, Y.-W.; Ihm, J.; Kato, H.; Wang, Z.W.; Okazaki, T.; Shinohara, H.; Kuk, Y. Bandgap modulation of carbon nanotubes by encapsulated metallofullerenes. *Nature* **2002**, *415*, 1005–1008.
  29. Tomaselli, M.; Meier, B.H. Rotational selective nuclear magnetic resonance spectra of hydrogen in a molecular trap. *J. Chem. Phys.* **2001**, *115* (24), 11,017–11,020.
  30. McCarty, R.D.; Hord, J.; Roder, H.M. Selected Properties of Hydrogen, U.S. Department of Commerce, Malcolm Baldrige; U.S. Government Printing Office: Washington DC, 1981.
  31. Stan, G.; Cole, M.W. Hydrogen adsorption in nanotubes. *J. Low Temp. Phys.* **1998**, *110*, 539–541.
  32. Madix, R.J. The application of flash desorption spectroscopy to chemical reactions on surfaces: temperature programmed reaction spectroscopy. In *Chemistry and Physics of Solid Surface*; CRC: Boca Raton, 1979; 63–72.
  33. Murata, K.; Kaneko, K.; Steele, W.A.; Kokai, F.; Takahashi, K.; Kasuya, D.; Hirahara, K.; Yudasaka, M.; Iijima, S. Molecular potential structures of heat-treated single-walled carbon nanohorn assemblies. *J. Phys. Chem., B* **2001**, *105*, 10,210–10,216.
  34. Fujiwara, A.; Ishii, K.; Suematsu, H.; Kataura, H.; Maniwa, Y.; Suzuki, S.; Achiba, Y. Gas adsorption in the inside and outside of single-walled carbon nanotubes. *Chem. Phys. Lett.* **2001**, *336*, 205–211.
  35. Bastow, T.J.; Hodge, R.M.; Hill, A.J. *J. Membr. Sci.* **1997**, *131*, 207.
  36. Zeng, Q.; Stebbins, J.F.; Heaney, A.D.; Erdogan, T. Hydrogen speciation in hydrogen-loaded, germania-doped silica glass: a combined NMR and FTIR study of the effects of UV irradiation and heat treatment. *J. Non-Cryst. Solids* **1999**, *258*, 78–91.
  37. Hartwig, C.M.; Vitko, J., Jr. Raman spectroscopy of molecular hydrogen and deuterium dissolved in vitreous silica. *Phys. Rev., B* **1978**, *18* (7), 3006–3014.
  38. Baugh, J.; Han, D.; Kleinhammes, A.; Liu, C.; Wu, Y.; Wang, Q. Microstructure and dynamics of hydrogen in a-Si:H detected by nuclear magnetic resonance. *J. Non-Cryst. Solids* **2000**, *266–269*, 185–189.

# Carbon Nanotubes: Modeling of Hydrogen Chemisorption

Ronald C. Brown

Department of Chemistry, Mercyhurst College, Erie, Pennsylvania, U.S.A.

## INTRODUCTION

Among the potential storage materials for use in portable hydrogen-containing devices, carbon nanotubes have received a relatively large amount of attention. Their adsorptive properties and relatively light weight make carbon nanotubes ideal candidates for the development of efficient H<sub>2</sub>-powered vehicular fuel cells. Evidence for hydrogen adsorption levels large enough to be used in such devices was first reported by Dillon et al. in 1997.<sup>[1]</sup> Since that time, experiments attempting to reproduce these results and to optimize the levels of hydrogen adsorption<sup>[2–8]</sup> have been inconclusive as to the applicability of carbon nanotubes toward this technology. The difficulty in reproducing high adsorption levels has led to a number of computational studies concerning hydrogen interactions with carbon nanotubes. Many computational studies have attempted to model the process of hydrogen adsorption to nanotubes to quantify the relationship between environmental parameters and hydrogen uptake amounts. In an attempt to clarify the experimental results, adsorption models have been designed and simulations based on these models<sup>[9–19]</sup> have been performed. Yet the results of many of these simulations have not corresponded with the observed experimental levels of hydrogen adsorption. This has led to questions concerning both the validity of the experimental results and the physical reality of the models. A central uncertainty is the nature of the molecular-level mechanism through which adsorption occurs. To resolve this critical uncertainty, researchers turned to atomistic investigations of interactions between hydrogen and nanotube surfaces. Molecular dynamics simulations,<sup>[20]</sup> kinetic studies,<sup>[21]</sup> and first principles calculations<sup>[22–33]</sup> have all been performed recently in an attempt to elucidate more clearly the adsorption mechanism. Among the significant conclusions derived from the results of the atomistic studies are that the deformation of the carbon nanotubes should be considered during the adsorption process<sup>[20]</sup> and that localized, chemical bonds must be formed between adsorbed hydrogen and the nanotube walls<sup>[21,25]</sup> to explain the experimental findings. In

addition, the atomistic studies make it clear that the energetics of potential adsorption mechanisms strongly depend on the nanotube geometry. The purpose of this article is to review the current understanding of the adsorption process and to establish the necessity for a further understanding of the adsorption mechanism. The dependence of hydrogen adsorption on the geometry of the nanotubes will be demonstrated. Because of the atomistic nature of the adsorption process, first principles calculations should play a vital role in resolving uncertainties regarding the applicability of carbon nanotubes to hydrogen storage.

## BACKGROUND

### Nanotube Structure and Hydrogen Adsorption Results

An atomistic description of hydrogen adsorption mechanisms to carbon nanotubes requires a clear understanding of tube geometry. Although the synthesis of both multiwalled and single-walled nanotubes (MWNTs and SWNTs, respectively) has been achieved, the high levels of hydrogen adsorption have been primarily observed with SWNTs. The structure of an SWNT can be described as a graphene sheet cylindrically wrapped about an axis. The cylindrical tubes that result are of varying radii and lengths, and are typically enclosed at both ends by fullerene-like structures.<sup>[34]</sup> Similar to the structure of a graphene sheet, the surface of a nanotube is composed of interlocking sp<sup>2</sup> carbon atoms. The central feature that geometrically distinguishes the type of SWNT is the location of the tube axis in relation to the original graphene sheet. The orientations of a perpendicular pair of tube axes relative to a graphene sheet are shown in Fig. 1. The tubes resulting from these axis orientations, termed zigzag and armchair nanotubes, are geometrical extremes and have been the subjects of most computational studies. The accepted convention for the geometrical classification of SWNTs is an indexing system composed of two integers,  $(n_1, n_2)$ , derived from the coefficients of the Bravais lattice

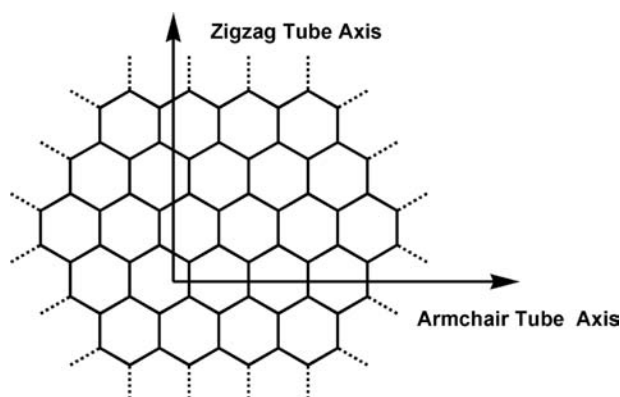


Fig. 1 Zigzag and armchair tube axis orientations.

vectors.<sup>[34]</sup> The geometries of zigzag tubes yield  $n_2 = 0$ , whereas armchair tube geometries yield  $n_1 = n_2$ . As a result, zigzag tubes have indices in the form  $(n,0)$  and armchair tubes have indices of  $(n,n)$ . Examples of several cross-sectional models for zigzag and armchair nanotubes are shown in Figs. 2 and 3, respectively. It is significant to note that the bulk properties of the tubes are strongly dependent on tube geometry. However, for most of the adsorption investigations described in this article, the primary differences between armchair and zigzag tubes are attributed to variations in the local geometry at the adsorption site. In addition to the axis orientation, the radii of the tubes influence the local environment of the carbon atoms. The radii of the tubes increase with increasing  $n$  values—a trend clearly seen in Figs. 2 and 3. If the C–C bond length is represented by  $d$ , the radii of curvatures for zigzag and armchair tubes can be determined by using  $r = (\sqrt{3}dn/2\pi)$ , and  $r = (3dn/2\pi)$ , respectively.

The potential use of carbon nanotubes in hydrogen storage devices has been the subject of a number of recent reviews.<sup>[35–38]</sup> The Department of Energy (DOE) has determined that, in order for nanotubes to be considered as a material for use in such devices, they must have the ability to adsorb a minimum of 6.5 wt.% hydrogen.<sup>[35]</sup> In 1997, Dillon et al.<sup>[1]</sup> reported results suggesting a range of hydrogen adsorption by carbon nanotubes between 5.0 and 10.0 wt.%. Subsequent investigations have sought to confirm these

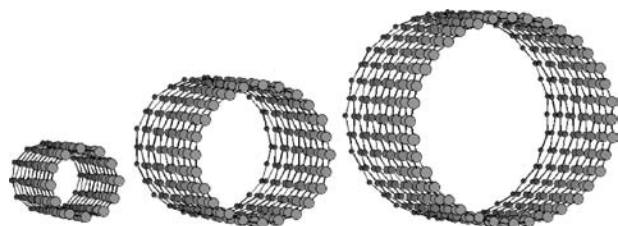


Fig. 2 Cross-sectional models of zigzag nanotubes.

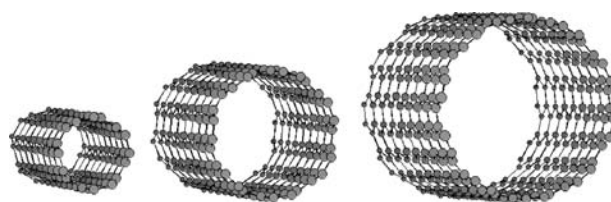


Fig. 3 Cross-sectional models of armchair nanotubes.

findings and to optimize the environmental parameters leading to hydrogen adsorption. Since the study by Dillon et al., other researchers<sup>[2–7]</sup> have reported adsorption levels near or above the DOE minimum under a variety of conditions. However, the positive results have been controversial because experiments at room temperature<sup>[8]</sup> have not produced adsorption levels as high as those initially reported by Dillon et al. Because of the disparate results, the validity of the positive findings was questioned. Proponents of nanotube utilization countered with the argument that the high sensitivity of adsorption levels to experimental conditions make reproducibility difficult. The controversy has led to the design of computational models, in which parameters can easily be varied to determine both the optimal conditions for adsorption and the viability of the process.

### Models for Hydrogen Adsorption

In addition to the goals stated above, simulation models could presumably be used to determine the optimal nanotube geometries for hydrogen adsorption. Both the nanotube geometries described in the previous section and the arrangement of the tubes can be easily varied in adsorption models. Indeed, the determination of hydrogen storage feasibility and the optimization of geometrical variables are codependent goals. A simulation model producing hydrogen adsorption levels at or above the DOE threshold would strongly support the use of nanotubes in hydrogen fuel cells. Thus far, however, many of the simulation models have not reproduced the required DOE levels of adsorption.<sup>[9–14]</sup> Other models have given hydrogen adsorption amounts at or above the DOE levels at low temperatures or high pressures.<sup>[16–19]</sup> This discord with experimental observations has led to suggestions that the hydrogen adsorption mechanisms considered are insufficient. Most of the initial simulation models considered the adsorption of hydrogen through the process of physical adsorption—or physisorption. Physisorption describes the adhesion of an adsorbate  $H_2$  molecule via dispersion forces to the nanotubes. Adsorption models have used a variety of potentials to describe these van der Waals interactions between the carbon atoms and hydrogen. Researchers who

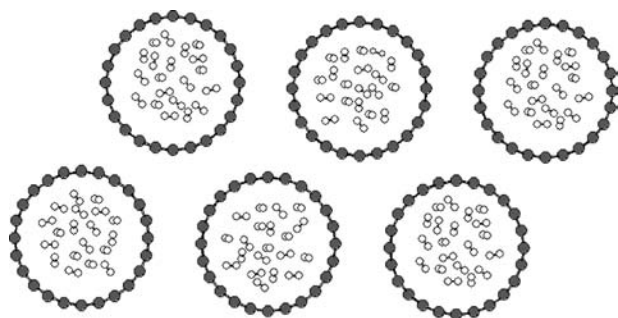


Fig. 4 Endohedral hydrogen physisorption.

believe that physisorption is insufficient have pointed to chemical adsorption—or chemisorption—as another possible mechanism to consider.<sup>[9,20,35]</sup> Chemisorption involves the formation of a direct chemical bond between a hydrogen atom and a carbon atom on the nanotube surface. An additional complicating issue that simulation models must address is whether the hydrogen storage process is most efficient inside the tubes or in the interstitial spaces between tubes. Hypothetical examples of these two possibilities, termed endohedral and exohedral adsorption, are shown in Figs. 4 and 5, respectively. If a significant amount of endohedral adsorption is necessary to realize the DOE levels, mechanisms must exist both for inserting and extracting hydrogen from the interior of the tubes.

In a series of grand canonical Monte Carlo simulations, Johnson and coworkers<sup>[12–14]</sup> modeled the exohedral and endohedral physisorption of hydrogen molecules in arrays of carbon nanotubes. They found that the DOE target could be approached only at a temperature that is too low for use in vehicular fuel cells.<sup>[13]</sup> Similar results were found with other models that use physisorption mechanisms to simulate adsorption of hydrogen to arrays of nanotubes<sup>[10,11]</sup> The DOE levels of adsorption were met or exceeded in several Monte Carlo physisorption simulations, yet these occurred only at low temperatures or at high pressures.<sup>[16,18,19]</sup> Taken together, the results of the modeling studies

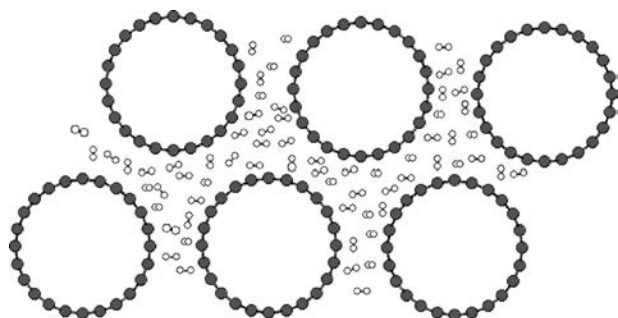


Fig. 5 Exohedral hydrogen physisorption.

support the assertion that the uptake of hydrogen by nanotubes through physisorption alone is insufficient to account for the experimental observations. A Monte Carlo simulation by Cracknell<sup>[9]</sup> used, in addition to a physisorption mechanism, a hypothetical chemisorption mechanism. It was found that chemisorption was necessary if the experimental results of Dillon et al. were to be approached. In addition to the need to address a chemisorption mechanism, Cheng and coworkers<sup>[20]</sup> have suggested that the lower levels of adsorption observed in models could also be attributable to the neglect of nanotube deformation. They found evidence for partial reconstruction of the nanotubes on adsorption of hydrogen and have suggested that this may increase the favorability of the interaction between the tubes and hydrogen. It is evident that the phenomena that may facilitate a more realistic modeling of hydrogen adsorption, chemisorption, and nanotube deformation are processes occurring locally at an adsorption site. The study of localized processes at the nanotube surface can be undertaken by using first principles calculations. For this reason, atomistic investigations that use first principles calculations to more clearly understand the hydrogen adsorption are of primary importance.

## FIRST PRINCIPLES INVESTIGATIONS OF HYDROGEN ADSORPTION

### Computational Strategies

First principles calculations are ideal for studying localized events such as hydrogen chemisorption to a nanotube or the deformation of a nanotube surface site. A critical step in the implementation of any such study is the design of the nanotube model. Ideally, cross-sectional models such as those in Figs. 1 and 2 could be used to study local phenomena occurring either exo- or endohedrally. Unfortunately, levels of ab initio theory such as configuration interaction (CI) calculations, which provide a rigorously defined degree of accuracy, are intractable with all but the smallest nanotube models. This problem has been circumvented in studies using density functional theory (DFT) calculations. Because DFT is an efficient and generally reliable means of calculating energies for relatively large systems, it has been extensively used with nanotubes. Researchers have used DFT in conjunction with classical potentials,<sup>[31]</sup> with plane-wave pseudopotentials<sup>[22,23,29,30]</sup> and with a tight-binding method.<sup>[24–26]</sup> If relatively small clusters of atoms are used to model nanotubes, CI calculations give a more rigorously reliable energy for local phenomena. However, the accuracy of the results may be compromised because of errors associated with the cluster size. The size of



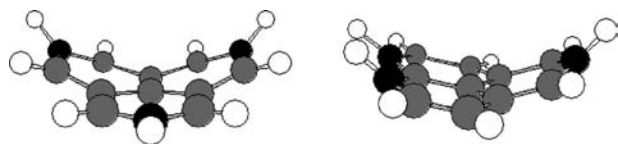


Fig. 6 Small cluster models for nanotubes.

cluster models that can be used with these methods do not allow for a complete cross section for most nanotubes (Fig. 6). Studies have been performed<sup>[27,39]</sup> using small clusters and terminating the boundary carbons with hydrogen. Because the terminating hydrogen atoms do not allow for the continuation of the  $sp^2$  network, significant errors may be introduced if the boundaries are in close proximity to the adsorption site. Care must be taken to either minimize or to account for these errors. Bauschlicher<sup>[27,28]</sup> and Froudakis<sup>[32]</sup> have used a mix quantum mechanics and molecular mechanics (QM/MM) method. Specifically, they used an ONIOM approach, which treats a relatively large nanotube model with molecular mechanics and an embedded smaller model with more accurate *ab initio* calculations. Another study of small clusters using CI calculations is an energetic comparison, as opposed to an absolute determination, of adsorption energies.<sup>[39]</sup> In this study, it was assumed that the errors introduced by cluster size were equally present in all models and would effectively cancel for the comparison. The computational strategy used for extended systems such as nanotubes largely depends on the goals of the study and the process under investigation.

### Physisorption Studies

Many of the simulation models discussed in the “Background” section use potentials to describe the physisorption of  $H_2$  molecules to carbon nanotubes.<sup>[9–18]</sup> In large part, the parameters for these potentials have been developed using hydrogen–carbon interactions in systems other than nanotubes. A potentially more accurate description of hydrogen–nanotube interactions could be developed. However, as dispersion interactions are relatively weak and are highly delocalized compared to a chemical bond, accurate physisorption binding energies are difficult to determine using first principles calculations. A few successful studies have been performed. Using DFT, Arellano and coworkers<sup>[29]</sup> studied the binding energy of a physisorbed hydrogen molecule to (5,5) and (6,6) armchair tubes. They were able to detect loosely bound endo- and exohedral configurations. Despite the presence of these loosely bound states, they found that if enough energy were present to allow for an  $H_2$  to approach the nanotube, the hydrogen molecule would

dissociate and chemisorb to the wall, possibly leading to the decomposition of the nanotube structure.

Cheng and coworkers<sup>[20]</sup> suggested that the neglect of nanotube deformation in simulation models could explain the discrepancies between models and experimental results. Li and coworkers<sup>[30]</sup> studied the degree to which tube deformation plays a role in the physisorption of  $H_2$  to a (7,7) nanotube. Using a DFT plane wave pseudopotential approach, they calculated physisorption energies with allowance for the full relaxation of both the hydrogen molecule and all nanotube carbon atoms. They found that the allowance for tube deformation does not significantly increase the physisorption binding energy at room temperature. In addition, no evidence for an increased stability of physisorbed  $H_2$  on nanotubes as compared to a graphene sheet was found. Even with an allowance for tube deformation, this study suggests that physisorption alone is too weak to explain the observed experimental levels of hydrogen adsorption. For this reason, mechanisms of hydrogen adsorption that involve chemisorption are now the principal focus. Because chemisorption is a highly localized process, first principles calculations constitute a critical method in these investigations.

### Chemisorption Studies

Results from both first principles calculations and modeling studies suggest that room temperature hydrogen adsorption at or above the DOE limit can only be accounted for by a mechanism that includes chemisorption to some degree. Early adsorption models did not consider chemisorption for several reasons. The complexity of a chemisorption model is greater as a result of the number of steps that are necessarily involved. The energy of chemisorption, or binding energy, for atomic hydrogen exhibits a significant dependence on the local geometry of the adsorption site. Thus if chemisorption is to be modeled, an accounting of individual chemisorption site geometries must be established. If endohedral adsorption processes are to be considered, a mechanism for incorporating chemisorbed hydrogen into the interior of the tube must be determined. Because of the variation of local chemisorption geometries that warrant consideration, a detailed chemisorption model would need to address the local environment of adsorption—in other words, the model must be atomistic in nature. This dependence on local environment necessitates the use of first principles calculations in which local model geometries can be easily controlled.

The most direct approach in a chemisorption study is the computation of the binding energy for a single hydrogen atom chemisorbed to a nanotube model.

Such an approach is identical to the calculation of the C–H bond energy on the surface of a nanotube. A typical strategy is to compute the energies of a nanotube cluster model with and without a single chemisorbed hydrogen atom. If  $E(\text{cluster-H})$  represents the energy of the cluster model with a chemisorbed hydrogen,  $E(\text{cluster})$  is the energy of the “clean” cluster, and  $E(\text{H})$  is the energy of a lone hydrogen atom, then the binding energy,  $E_b$ , can be determined using the formula below.

$$E_b = [E(\text{cluster}) + E(\text{H})] - E(\text{cluster-H})$$

Several recent investigations have used first principles calculations to determine hydrogen chemisorption energies. In Bauschlicher’s ONIOM study,<sup>[27]</sup> the innermost layer was treated at the B3LYP/4-31G level of theory. The binding energy of hydrogen to a (10,0) tube was found to be 20.9 kcal mol<sup>-1</sup>. In addition, the barrier to hydrogen migration on the tube was found to be larger than the binding energy itself. Using a DFT plane wave pseudopotential method, Gülseren and coworkers<sup>[22]</sup> investigated the binding energy of hydrogen to a series of zigzag(*n*,0) tubes. Allowing full relaxation, they found that the binding energies on zigzag tubes decrease with increasing radius. They attributed this difference to the increased sp<sup>3</sup> character of a C–H bond formed at a “sharp site” of a nanotube. Smaller tubes, because of the larger degree of curvature, will have sites that more readily fit this description. Another recent study<sup>[39]</sup> determined chemisorption energies to smaller clusters by using CI calculations at the QCISD(T)/6-31G(d,p) level. The QCISD(T) method uses quadratic configuration interaction calculations including single and double substitutions with a triples correction. This study modeled both zigzag and armchair nanotubes to compare the adsorption energies as a function of tube geometry. A trend with respect to tube radius similar to that reported by Gülseren and coworkers was found. The higher degree of curvature, and hence sp<sup>3</sup> character, present in the models for smaller tubes (Fig. 7) offers an explanation for this trend. Yet it was also found that, for a single adsorption event, hydrogen chemisorption to an armchair site is slightly more favorable than chemisorption to a zigzag site of similar radius. It is precisely these dependencies of chemisorption

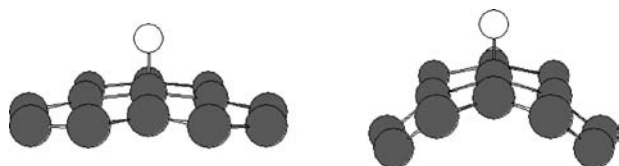


Fig. 7 Curvature of possible hydrogen chemisorption sites.

energetics on localized site geometry that must be considered in an atomistic chemisorption model.

However, in order for any model to accurately consider the necessary levels of adsorption, the dependency of the chemisorption process on hydrogen coverage must also be determined. The degree of coverage is significant because, if the DOE limit were to be achieved through chemisorption of hydrogen alone, 83% of the carbon atoms in a nanotube must have a chemisorbed hydrogen. Furthermore, because of the changes in localized geometries upon adsorption, it is expected that the hydrogen chemisorption energy will depend on surface coverage. The different chemisorption environments are evident in Fig. 8, which shows two cross sections of a (8,0) nanotube; one with a single hydrogen atom chemisorbed and one at full hydrogen coverage. Froudakis<sup>[32]</sup> has shown, using QM/MM calculations on a (4,4) armchair tube, that there is a significant increase in tube volume upon hydrogen chemisorption. The evidence for tube deformation upon adsorption coupled with the observed variance in chemisorption energy with tube geometry suggests that a dependence of chemisorption energy with hydrogen coverage exists. This dependence was studied by Bauschlicher<sup>[28]</sup> using the ONIOM approach. It was found that binding energies increase for the first several chemisorbed hydrogen atoms on a (10,0) zigzag tube, but decrease from 57.3 to 38.6 kcal mol<sup>-1</sup> as hydrogen coverage increases from 50% to 100%. Similar results were found by Li et al.,<sup>[30]</sup> who studied the fully relaxed (7,7) armchair tube with DFT. In addition, they found strong evidence for tube reconstruction at full hydrogen coverage. At full hydrogen coverage on a (7,7) nanotube, the most stable structure was a reconstructed tube with 50% of the hydrogen chemisorbed endohedrally and 50% of the hydrogen chemisorbed exohedrally. Compared to the separated nanotube and hydrogen molecules, the structure was found to be stable by 8.3 kcal mol<sup>-1</sup> per H atom. A range of armchair and zigzag nanotube models at full hydrogen coverage were also studied

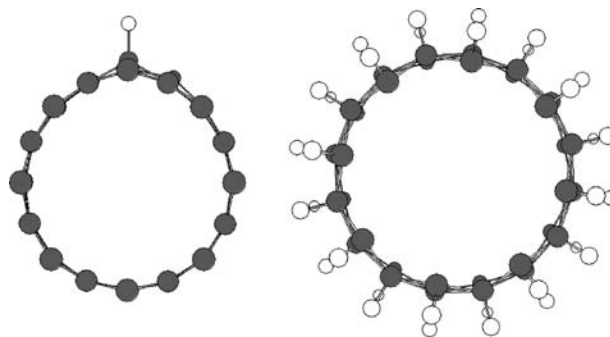
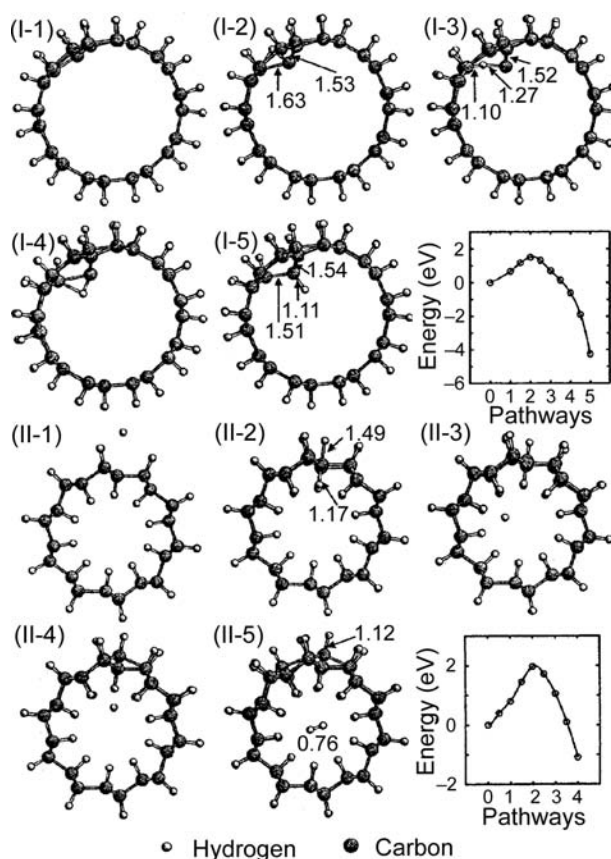


Fig. 8 Single H-atom chemisorption and full hydrogen coverage.

by Yildirim, Gülseren, and Ciraci.<sup>[23]</sup> using the DFT plane wave pseudopotential method. Binding energies as a function of nanotube geometry were determined. Interestingly, at full coverage, the binding energy of chemisorbed H atoms to zigzag tubes was found to be lower by  $0.69 \text{ kcal mol}^{-1}$ . This effect is in sharp contrast to the one found in the single-hydrogen-atom chemisorption study previously described. This suggests that, as the hydrogen coverage on armchair tubes increases, the binding energy declines in relation to zigzag tubes.

### From Hydrogen Adsorption to Hydrogen Storage

The apparent decline of hydrogen binding energies above 50% coverage<sup>[28]</sup> suggests that additional mechanisms may be necessary to account for the achievement of the DOE minimum. It is possible that a combination of chemisorption and physisorption mechanisms must be considered to achieve the required levels. Lee and coworkers<sup>[24–26]</sup> proposed a mechanism that converts exohedrally chemisorbed hydrogen on a tube into endohedrally physisorbed hydrogen molecules. They used a tight-binding DFT approach to initially investigate a process for converting a full exohedral covered (10,10) tube into a stable structure similar to that found by Li et al.<sup>[30]</sup> This structure has 50% of the hydrogen chemisorbed exohedrally and 50% chemisorbed endohedrally. Lee and coworkers<sup>[25]</sup> have termed the conversion process the “flip-in” mechanism and found an activation barrier of  $34.8 \text{ kcal mol}^{-1}$ . Following the flip-in mechanism, they propose a “kick-in” mechanism that provides a pathway for endohedrally chemisorbed hydrogens to recombine as hydrogen molecules in the interior of the tube. The kick-in mechanism was found to have an activation barrier of  $45.5 \text{ kcal mol}^{-1}$ . Their flip-in and kick-in mechanisms are shown in Fig. 9. With these mechanisms, Lee and coworkers have shown that a maximum hydrogen storage capability of 14 wt.% is possible with the (10,10) tube. In addition to suggesting a pathway for exceeding the DOE thresholds, such mechanisms also provide a viable description of a hydrogen insertion process. Further study on these and similar mechanisms is necessary to determine their dependencies on the geometries, sizes, and spatial arrangements of carbon nanotubes. If a complete mechanistic picture is established, atomistic models for the hydrogen adsorption process can be developed. From such models, the dependencies of nanotube adsorptive properties on geometry and arrangement can be determined, and a better understanding of the experimental parameters necessary to optimize the process could ultimately be gained.



**Fig. 9** Proposed mechanisms of Lee and coworkers. *Source:* Reprinted with permission from reference<sup>[25]</sup>. © 2001 American Chemical Society.

Even if a mechanism for hydrogen adsorption and storage can be established, a concomitant mechanism for hydrogen abstraction from the tube must also be developed. It was estimated by Li et al.<sup>[30]</sup> that to achieve hydrogen desorption from their fully hydrogenated structure, temperatures above 600 K would be required. Such temperatures would be prohibitive for use in vehicular fuel cells. In addition, any storage mechanisms involving hydrogen chemisorption will require an efficient means of dissociating molecular hydrogen ( $\text{H}_2$ ) into atomic hydrogen. Despite such barriers, it is clear that first principles calculations constitute a flexible and reliable method for examining adsorption and storage mechanisms that occur at localized nanotube sites. There are several significant issues that must be addressed by future computational studies. If the levels of hydrogen adsorption observed by Dillon et al. are to be accurately modeled, some degree of chemisorption must be considered. The dependence of this chemisorption process on the local geometry of the adsorption site could be further developed. For example, the finding that hydrogen chemisorption occurs most favorably to nanotube surfaces with high degrees of curvature<sup>[22]</sup> suggests that chemisorption

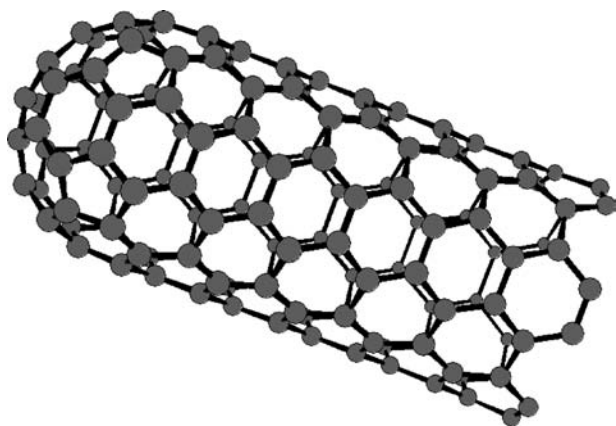


Fig. 10 The cap at the end of a nanotube.

of hydrogen on the capped end of a nanotube (Fig. 10) may occur more readily. Combined with mechanisms similar to those developed by Lee and coworkers,<sup>[25]</sup> the chemisorption to a tube end or reconstructed nanotube site may lead to more favorable storage pathways. In addition, the deformation of the nanotubes should be considered in any study or model that is developed. To achieve these goals, models with increased atomistic design that consider variable environments for each carbon atom need to be developed.

## CONCLUSION

If an adsorption model is to be developed that matches experimental findings, several critical aspects of hydrogen adsorption to carbon nanotubes must be considered. First, mechanisms involving some degree of chemisorption are necessary to explain the high levels of hydrogen adsorption observed experimentally. While some degree of chemisorption is necessary, the lower binding energies at high hydrogen coverages suggest that it is unlikely that chemisorption is the exclusive mechanism for achieving the necessary levels outlined by the DOE. Secondly, the role that nanotube deformation may play in the hydrogen adsorption process is not clear. Models that do not include any tube deformation do not achieve the levels of adsorption that have been observed experimentally. To address localized chemisorption and tube deformation, future studies must involve a deeper understanding of mechanisms that occur at the nanotube surface. First principles calculations can play a key role in clarifying the energetics of the mechanistic steps. As soon as mechanisms for adsorption and storage can be established, models that are atomistic in approach can be used to help predict the dependency of adsorption levels upon nanotube geometry and spatial arrangement. Such atomistic models could potentially

determine the ultimate applicability of carbon nanotubes toward hydrogen storage and serve to optimize any such utilization.

## ACKNOWLEDGMENT

Acknowledgment is made to the Donors of the American Chemical Society Petroleum Research Fund for support of this research.

## REFERENCES

1. Dillon, A.C.; Jones, K.M.; Bekkedahl, T.A.; Kiang, C.H.; Bethune, D.S.; Heben, M.J. Storage of hydrogen in single-walled carbon nanotubes. *Nature* **1997**, *386* (6623), 377–379.
2. Chen, P.; Wu, X.; Lin, J.; Tan, K.L. High H<sub>2</sub> uptake by alkali-doped carbon nanotubes under ambient pressure and moderate temperatures. *Science* **1999**, *285* (5424), 91–93.
3. Chen, Y.; Shaw, D.T.; Bai, X.D.; Wang, E.G.; Lund, C.; Lu, W.M.; Chung, D.D.L. Hydrogen storage in aligned carbon nanotubes. *Appl. Phys. Lett.* **2001**, *78* (15), 2128–2130.
4. Liu, C.; Fan, Y.Y.; Liu, M.; Cong, H.T.; Cheng, H.M.; Dresselhaus, M.S. Hydrogen storage in single-walled carbon nanotubes at room temperature. *Science* **1999**, *286* (5442), 1127–1129.
5. Pradham, B.K.; Harutyunyan, A.R.; Stojkovic, D.; Grossman, J.C.; Zhang, P.; Cole, M.W.; Crespi, V.; Goto, H.; Fujiwara, J.; Eklund, P.C. Large cryogenic storage of hydrogen in carbon nanotubes at low pressures. *J. Mater. Res.* **2002**, *17* (9), 2209–2216.
6. Ye, Y.; Ahn, C.C.; Witham, C.; Fultz, B.; Liu, J.; Rinzler, A.G.; Colbert, D.; Smith, K.A.; Smalley, R.E. Hydrogen adsorption and cohesive energy of single-walled carbon nanotubes. *Appl. Phys. Lett.* **1999**, *74* (16), 2307–2309.
7. Liu, C.; Yang, Q.H.; Tong, Y.; Cong, H.T.; Cheng, H.M. Volumetric hydrogen storage in single-walled carbon nanotubes. *Appl. Phys. Lett.* **2002**, *80* (13), 2389–2391.
8. Ritschel, M.; Uhlemann, M.; Gutfleisch, O.; Leonhardt, A.; Graff, A.; Täschner, C.; Fink, J. Hydrogen storage in different carbon nanostructures. *Appl. Phys. Lett.* **2002**, *80* (16), 2985–2987.
9. Cracknell, R.F. Simulation of hydrogen adsorption in carbon nanotubes. *Mol. Phys.* **2002**, *100* (13), 2079–2086.
10. Gordon, P.A.; Saeger, R.B. Molecular modeling of adsorptive energy storage: Hydrogen storage in single-walled carbon nanotubes. *Ind. Eng. Chem. Res.* **1999**, *38* (12), 4647–4655.
11. Rzepka, M.; Lamp, P.; de la Casa-Lillo, M.A. Physisorption of hydrogen on microporous carbon and carbon nanotubes. *J. Phys. Chem., B* **1998**, *102* (52), 10894–10898.
12. Wang, Q.; Johnson, J.K. Molecular simulation of hydrogen adsorption in single-walled carbon nanotubes

- and idealized carbon slit pores. *J. Chem. Phys.* **1999**, *110* (1), 577–586.
13. Wang, Q.; Johnson, J.K. Optimization of carbon nanotube arrays for hydrogen adsorption. *J. Phys. Chem., B* **1999**, *103* (23), 4809–4813.
  14. Simonyan, V.V.; Diep, P.; Johnson, J.K. Molecular simulation of hydrogen adsorption in charged single-walled carbon nanotubes. *J. Chem. Phys.* **1999**, *111* (21), 9778–9783.
  15. Smith, M.R., Jr.; Bittner, E.W.; Shi, W.; Johnson, J.K.; Bockrath, B.C. Chemical activation of single-walled carbon nanotubes for hydrogen adsorption. *J. Phys. Chem., B* **2003**, *107* (16), 3752–3760.
  16. Yin, Y.F.; Mays, T.; McEnaney, B. Molecular simulations of hydrogen storage in carbon nanotube arrays. *Langmuir* **2000**, *16* (26), 10521–10527.
  17. Darkrim, F.; Levesque, D. Monte Carlo simulations of hydrogen adsorption in single-walled carbon nanotubes. *J. Chem. Phys.* **1998**, *109* (12), 4981–4984.
  18. Darkrim, F.; Levesque, D. High adsorptive property of opened carbon nanotubes at 77 K. *J. Phys. Chem., B* **2000**, *104* (29), 6773–6776.
  19. Williams, K.A.; Eklund, P.C. Monte Carlo simulations of H<sub>2</sub> physisorption in finite-diameter carbon nanotube ropes. *Chem. Phys. Lett.* **2000**, *320* (3–4), 352–358.
  20. Cheng, H.; Pez, G.P.; Cooper, A.C. Mechanism of hydrogen sorption in single-walled carbon nanotubes. *J. Am. Chem. Soc.* **2001**, *123* (24), 5845–5846.
  21. Browning, D.J.; Gerrard, M.L.; Lakeman, B.; Mellor, I.M.; Mortimer, R.J.; Turpin, M.C. Studies into the storage of hydrogen in carbon nanofibers: Proposal of a possible reaction mechanism. *Nano Lett.* **2002**, *2* (3), 201–205.
  22. Gülseren, O.; Yildirim, T.; Ciraci, S. Tunable adsorption on carbon nanotubes. *Phys. Rev. Lett.* **2001**, *87* (11), 116802.
  23. Yildirim, T.; Gülseren, O.; Ciraci, S. Exohydrogenated single-wall carbon nanotubes. *Phys. Rev., B* **2001**, *64* (7), 75404.
  24. Lee, S.M.; Lee, Y.H. Hydrogen storage in single-walled carbon nanotubes. *Appl. Phys. Lett.* **2000**, *76* (20), 2877–2879.
  25. Lee, S.M.; An, K.H.; Lee, Y.H.; Seifert, G.; Frauenheim, T. A hydrogen storage mechanism in single-walled carbon nanotubes. *J. Am. Chem. Soc.* **2001**, *123* (21), 5059–5063.
  26. Lee, S.M.; Lee, Y.H.; Seifert, G.; Frauenheim, T. Hydrogen insertion and extraction mechanism in single-walled carbon nanotubes. *AIP Conf. Proc.* **2001**, *590* (1), 117–120.
  27. Bauschlicher, C.W., Jr. Hydrogen and fluorine binding to the sidewalls of a (10,0) carbon nanotube. *Chem. Phys. Lett.* **2000**, *322* (3–4), 237–241.
  28. Bauschlicher, C.W., Jr. High coverages of hydrogen on a (10,0) carbon nanotube. *Nano Lett.* **2001**, *1* (5), 223–226.
  29. Arellano, J.S.; Molina, L.M.; Rubio, A.; Lopez, M.J.; Alonso, J.A. Interaction of molecular and atomic hydrogen with (5,5) and (6,6) single-wall carbon nanotubes. *J. Chem. Phys.* **2002**, *117* (5), 2281–2288.
  30. Li, J.; Furuta, T.; Goto, H.; Ohashi, T.; Fujiwara, Y.; Yip, S. Theoretical Evaluation of hydrogen storage capacity in pure carbon nanostructures. *J. Chem. Phys.* **2003**, *119* (4), 2376–2385.
  31. Zhang, X.; Cao, D.; Chen, J. Hydrogen adsorption storage on single-walled carbon nanotube arrays by a combination of classical potential and density functional theory. *J. Phys. Chem., B* **2003**, *107* (21), 4942–4950.
  32. Froudakis, G.E. Hydrogen interaction with single-walled carbon nanotubes: A combined quantum mechanics: Molecular mechanics study. *Nano Lett.* **2001**, *1* (4), 179–182.
  33. Miura, Y.; Kasai, H.; Dino, W.; Nakanishi, H.; Sugimoto, T. First principles studies for the dissociative adsorption of H<sub>2</sub> on graphene. *J. Appl. Phys.* **2003**, *93* (6), 3395–3400.
  34. Ajayan, P.M. Nanotubes from carbon. *Chem. Rev.* **1999**, *99* (7), 1787–1799.
  35. Dillon, A.C.; Heben, M.J. Hydrogen storage using carbon adsorbents: Past, present and future. *Appl. Phys., A* **2001**, *72* (2), 133–142.
  36. Meregalli, V.; Parrinello, M. Review of theoretical calculations of hydrogen storage in carbon-based materials. *Appl. Phys., A* **2001**, *72* (2), 143–146.
  37. Zandonella, C. Is it all just a pipe dream?. *Nature* **2001**, *410* (6830), 734–735.
  38. Ward, M.D. Molecular fuel tanks. *Science* **2003**, *300* (5622), 1104–1105.
  39. Brown, R.C. *In preparation*.

# Carbon Nanotubes: Optical Properties

## R. Saito

*Department of Electronic Engineering, University of Electro-Communications, Tokyo, Japan*

## Mildred S. Dresselhaus

*Department of Electrical Engineering and Computer Science, Massachusetts Institute of Technology, Cambridge, Massachusetts, U.S.A.*

## G. Dresselhaus

*Francis Bitter Magnet Laboratory, Massachusetts Institute of Technology, Cambridge, Massachusetts, U.S.A.*

## A. Jorio

*Departamento de Física, Universidade Federal de Minas Gerais, Belo Horizonte, Brazil*

## A. G. Souza Filho

*Universidade Federal do Ceará, Fortaleza, Brazil*

## M. A. Pimenta

*Departamento de Física, Universidade Federal de Minas Gerais, Belo Horizonte, Brazil*

## INTRODUCTION

The interaction between light and solids gives rise to many optical properties in solid-state systems that can be observed by a variety of experimental techniques such as photo absorption and emission, infrared absorption, Raman scattering, photoelectron and Auger spectroscopy, and ultraviolet and X-ray photoelectron spectroscopy. Especially in one-dimensional (1-D) solids, such as carbon nanotubes,<sup>[1–3]</sup> much useful information on the optical properties can be obtained by exploiting low-dimensional effects, such as the direction of the polarization of the light relative to the nanotube axis, the resonance between the laser excitation energy and a singularity in the joint density of states, and the variety of crystal structures of nanotubes stemming from their chirality. Thus, by rotating the orientation angle of the nanotube relative to the incident and scattered light polarization directions, by changing the laser excitation energies, or by selecting different geometries for the nanotubes, we can systematically investigate the optical properties for many different types of carbon nanotubes in a consistent way. Especially fruitful has been the study of the resonance Raman spectra from only one nanotube by using micro-Raman measurements of a nanotube on a Si/SiO<sub>2</sub> substrate. Because of the large amount of detailed information

that can be obtained from this technique, micro-Raman spectroscopy is considered to be a standard nanotechnique for probing the optical properties of a nanotube in a quick, nondestructive way at room temperature and atmospheric pressure.

Since the reported observation of carbon nanotubes in 1991, high-resolution transmission electron microscopy (HRTEM) and scanning probe microscopy [SPM, such as scanning tunneling microscopy/spectroscopy (STM/STS), atomic force microscopy (AFM), Kelvin force microscopy (KFM), magnetic force microscopy (MFM), and so on] have provided definitive tools for observing tiny samples on nanometer length scales. However, for single-wall carbon nanotubes (SWNTs), the high quality required of the measurement instruments and of the personnel to observe structure at the atomic level restricts the number of instruments and researchers who can make such measurements.

The finding of so many new phenomena and concepts in the nanotube field in the past decade reminds us of the good old times of the adventurers on sailing ships who ventured out to find the new world. In the next decade, nanotube research will enter a new period in which nanotube samples are easily obtained, in which many nanotube-based industrial technologies and applications will be developed, and in which fundamental physics and chemistry discoveries will



continue to be made, but more and more the research will be stimulated by the needs of the applications and by the availability of new measurement tools. In this sense, a standard technique to characterize nanotubes is highly desirable. Here it is proposed that resonance Raman spectroscopy should fill this role.

## OVERVIEW

One unique feature of a SWNT is the fact that the electronic structure is either metallic or semiconducting, depending only on the chirality of the nanotube and not on the impurities that it contains.<sup>[1]</sup> Here the chirality of a SWNT denotes the spiral geometries of a nanotube structure, which is specified by two integers ( $n$ ,  $m$ ) as discussed below. Thus, the interaction of the conduction electrons in the metallic nanotube with light can be investigated, e.g., by comparing the Raman spectra of metallic nanotubes with that of semiconducting nanotubes that have no doping with noncarbon atoms. Thus, carbon nanotubes provide an ideal material for understanding the physical properties of a low-dimensional solid. Another important fact about nanotubes is that the diameter of a nanotube is much smaller than the wavelength of light, but the length of the nanotube is usually comparable to or greater than the optical wavelength. Thus microscopic and macroscopic views of nanotubes can coexist within a single nanotube, and it is expected that these unique properties will lead to new optical applications in the future.

Among the various optical techniques, resonance Raman spectroscopy of nanotubes has been investigated in depth during the last few years. The resonance Raman effect is a strong enhancement ( $\sim 10^3$ ) of the Raman intensity when a real optical absorption takes place in the excitation process. The resonance condition for each nanotube is very sharp in energy, known as van Hove singularities, with a width of less than 10 meV. Because the resonant energies of each ( $n$ ,  $m$ ) nanotube are different from one another, the energies of the van Hove singularities can be used for identification (something like a fingerprint) of the nanotube atomic structure. Thus, van Hove singularity is a key word to understand optical properties of nanotubes. We can select a particular ( $n$ ,  $m$ ) SWNT for investigation by selecting the appropriate laser energy  $E_{\text{laser}}$ , or we can investigate metallic or semiconducting nanotubes separately by selecting  $E_{\text{laser}}$ , even for samples consisting of SWNT bundles containing a mixture of metallic and semiconducting SWNTs. Recently, using a chemical vapor deposition (CVD) growth technique for preparing isolated SWNTs on a Si/SiO<sub>2</sub> substrate, we have observed resonance Raman spectroscopy from one nanotube. Compared with the

spectra from SWNT bundle samples, single nanotube spectroscopy gives much more definitive information on the electronic and phonon properties of SWNTs.

In this entry, we first discuss the singular nature of the electronic energy states and then discuss optical absorption and the resonance Raman spectra. Finally, we present the double resonance theory of Raman nanotubes, which is necessary for describing the experimentally observed dispersive phonon modes in SWNTs.

## VAN HOVE SINGULARITIES

A single-wall carbon nanotube is a graphene (honeycomb) sheet rolled up into a cylinder. In Fig. 1, we show the cylindrical structures of SWNTs. Each end of the nanotube is terminated by a hemisphere of fullerene containing six pentagonal carbon rings. Because it is considered that nanotubes grow with a cap, the cap structure is essential for generating different kinds of geometries for nanotubes. The relative positions of the pentagonal rings with respect to one another is almost arbitrary except for the requirement that two pentagonal rings do not touch each other (isolated pentagon rule), thus giving rise to many possible geometries for generating nanotube structures. Among the various nanotube structures, there are only two kinds of nanotubes that have mirror symmetry along the nanotube axis, namely, the armchair and zigzag nanotubes, as shown in Fig. 1A and B, respectively. The names armchair and zigzag are taken from the shape of the edge cuts shown on the right side of

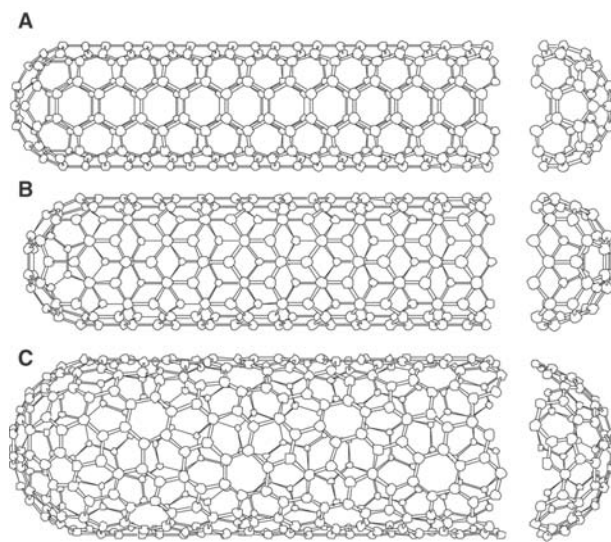


**Fig. 1** Single-wall carbon nanotubes. The ends of nanotubes are capped by fullerene hemispheres. (A) Armchair nanotube, (B) zigzag nanotube, and (C) chiral nanotube.

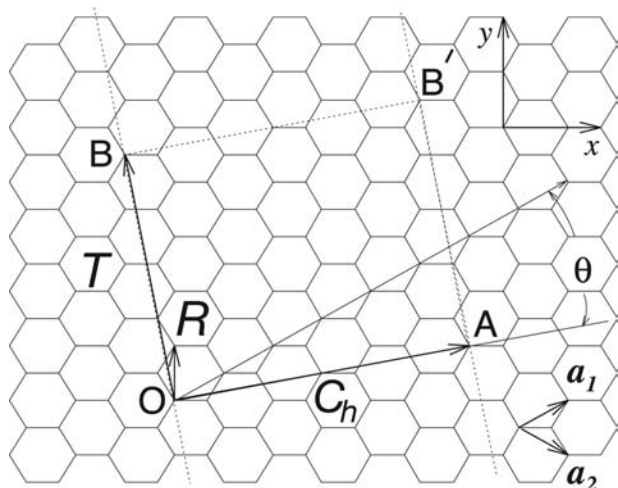


**Fig. 2** The unrolled honeycomb lattice of a nanotube. OA is the equator of the nanotube and OB corresponds to the translation vector of this 1-D material. By connecting OB to AB', we can make a seamless cylindrical shape. OAB'B is a unit cell of the nanotube. The figure corresponds to the (4,2) chiral nanotube and there are  $N = 28$  hexagons in the unit cell.

**Fig. 1.** All other nanotubes (Fig. 1C) exhibit axial chirality and are called chiral nanotubes.

The geometry of a nanotube is uniquely expressed by two integers,  $(n, m)$ . In Fig. 2, the rectangle OAB'B is shown, and by connecting OB to AB', we can make the cylindrical shape of the nanotube. In this case, the vector OA (hereafter we call OA the chiral vector) corresponds to the equator of the nanotube. OA can be expressed by a linear combination of the two unit vectors,  $\mathbf{a}_1$  and  $\mathbf{a}_2$ , of the honeycomb lattice, so that

$$OA = n\mathbf{a}_1 + m\mathbf{a}_2 \equiv (n, m) \quad (1)$$

The length of OA divided by  $\pi$  gives the diameter of the nanotube,  $d_t$ . Two lattice vectors OB and AB', which are perpendicular to OA, correspond to the translational vector  $\mathbf{T}$  in the 1-D lattice of the nanotube, and  $\mathbf{T}$  is a function of  $n$  and  $m$ , as shown in Table 1. The rectangle OAB'B denotes the unit cell of the nanotube containing  $N$  hexagons and  $2N$  carbon atoms, where  $N$  is expressed by

$$N = \frac{2(n^2 + m^2 + nm)}{d_R} \quad (2)$$

The integer  $d_R$  is the common multiple divisor of  $(2n+m)$  and  $(2m+n)$ . Further details of the mathematics describing these variables are given in Table 1 and are further explained in Ref.<sup>[1]</sup>. (This introductory textbook of nanotube can be cited for the "Introduction" and "van Hove Singularity" sections.)

The valence electrons of  $sp^2$  carbons, such as graphite and nanotubes, consist of  $\pi$  ( $2p$ ) electrons. Because a carbon atom in a nanotube has one  $\pi$  electron (and because there are  $2N$  carbon atoms in the nanotube unit cell),  $2N$  1-D electronic  $\pi$  bands are obtained for a SWNT by applying periodic boundary conditions around the circumferential direction OA. Such a treatment for the electronic structure is called "zone folding." Along the direction OA, the wave vectors ( $2\pi/\text{wavelength}$ ), which are perpendicular to the nanotube axis direction  $\mathbf{k}_\perp$ , are discrete and are given by the condition:

$$\mathbf{C}_h \cdot \mathbf{k}_\perp^p = 2\pi p, \quad (p = 1, \dots, N) \quad (3)$$

Thus, one obtains  $N$  inequivalent  $\mathbf{k}_\perp^p = 2\pi p/|\mathbf{C}_h| = 2p/d_t$  discrete wave vectors for bonding and antibonding  $\pi$  bands and the 1-D wave vectors  $\mathbf{k}_\parallel$ , parallel to the nanotube axis, are continuous ( $-\pi/T \leq \mathbf{k}_\parallel \leq \pi/T$ ) for an infinitely long SWNT.

One-dimensional energy dispersion relations for a nanotube  $E_{1-D}(p, \mathbf{k}_\parallel)$  are obtained by cutting the 2-D energy dispersion relations of graphite  $E_{2-D}(k)$  along the  $\mathbf{k}_\parallel$  direction with wave vectors  $\mathbf{k}_\perp^p$  placed at equal distances of  $2/d_t$  with a length of  $2\pi/T$ ,

$$E_{1-D}(p, \mathbf{k}_\parallel) = E_{2-D}(\mathbf{k}_\perp^p + \mathbf{k}_\parallel) \quad (4)$$

where, by a tight binding calculation,  $E_{2-D}(k)$  is given by:

$$E_{g2-D}(k_x, k_y) = \pm\gamma_0 \left\{ 1 + 4 \cos\left(\frac{\sqrt{3}k_x a}{2}\right) \cos\left(\frac{k_y a}{2}\right) + 4 \cos^2\left(\frac{k_y a}{2}\right) \right\}^{1/2} \quad (5)$$

in which the coordinates of  $k_x$  and  $k_y$  are given in Table 1. The plus and minus signs in Eq. (5) correspond to unoccupied (antibonding) and occupied (bonding)  $\pi$  energy bands, respectively.  $\gamma_0 > 0$  is the tight-binding nearest-neighbor overlap energy parameter. When we plot the  $E_{g2-D}$  in the hexagonal 2-D Brillouin zone (BZ) (Fig. 3), the bonding and antibonding energy dispersion relations touch each other at the hexagonal corners, the  $K$  and  $K'$  points of the 2-D Brillouin zone. Because of the periodicity of  $E_{g2-D}(k_x, k_y)$  in  $k$  space, the  $K$  and  $K'$  points are inequivalent to each other. The asymmetry between the shapes of the bonding and antibonding  $\pi$  bands comes not directly from Eq. (5) but from the higher-order correction to the tight-binding parameters known as the overlap parameter  $s$ . In the following discussion, however, for simplicity, we use  $s = 0$ .

**Table 1** Parameters for carbon nanotubes

Symbol	Name	Formula	Value
$a$	Length of unit vector	$a = \sqrt{3}a_{C-C} = 2.49\text{\AA}$	$a_{C-C} = 1.44\text{\AA}$
$\mathbf{a}_1, \mathbf{a}_2$	Unit vectors	$\left(\frac{\sqrt{3}}{2}, \frac{1}{2}\right)a, \left(\frac{\sqrt{3}}{2}, -\frac{1}{2}\right)a$	$x, y$ coordinates
$\mathbf{b}_1, \mathbf{b}_2$	Reciprocal lattice vectors	$\left(\frac{1}{\sqrt{3}}, 1\right)\frac{2\pi}{a}, \left(\frac{1}{\sqrt{3}}, -1\right)\frac{2\pi}{a}$	$k_x, k_y$ coordinates
$\mathbf{C}_h$	Chiral vector	$\mathbf{C}_h = n\mathbf{a}_1 + m\mathbf{a}_2 \equiv (n, m)$	$(0 \leq  m  \leq n)$
$L$	Length of $\mathbf{C}_h$	$L =  \mathbf{C}_h  = a\sqrt{n^2 + m^2 + nm}$	
$d_t$	Diameter	$d_t = L/\pi$	
$\theta$	Chiral angle	$\sin \theta = \frac{\sqrt{3}m}{2\sqrt{n^2 + m^2 + nm}}$ $\cos \theta = \frac{2n + m}{2\sqrt{n^2 + m^2 + nm}}$	$0 \leq  \theta  \leq \pi/6$ $\tan \theta = \frac{\sqrt{3}m}{2n + m}$
$d$	$\text{gcd}(n, m)^a$		
$d_R$	$\text{gcd}(2n + m, 2m + n)^a$	$d_R = \begin{cases} d & \text{if } (n - m) \text{ is not multiple of } 3d \\ 3d & \text{if } (n - m) \text{ is multiple of } 3d \end{cases}$	
$\mathbf{T}$	Translation vector	$\mathbf{T} = t_1\mathbf{a}_1 + t_2\mathbf{a}_2 \equiv (t_1, t_2)$	$\text{gcd}(t_1, t_2) = 1^a$
		$t_1 = \frac{2m + n}{d_R}, t_2 = -\frac{2n + m}{d_R}$	
$T$	Length of $\mathbf{T}$	$T =  \mathbf{T}  = \frac{\sqrt{3}L}{d_R}$	
$N$	Number of hexagons in the nanotube unit cell	$N = \frac{2(n^2 + m^2 + nm)}{d_R}$	

$n, m, t_1, t_2, p,$  and  $q$  are integers and  $d, d_R, N,$  and  $M$  are integer functions of these integers.

<sup>a</sup> $\text{gcd}(n, m)$  denotes the greatest common divisor of the two integers  $n$  and  $m$ .

Cutting these 2-D energy dispersion relations by equidistant lines parallel to the nanotube axis (hereafter we call these lines ‘‘cutting lines’’) corresponds to obtaining the 1-D energy dispersion of nanotubes,

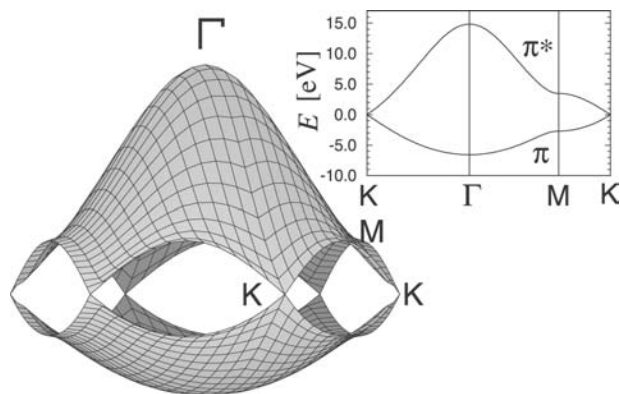


**Fig. 3** The energy dispersion relations for 2-D graphite are shown throughout the whole region of the Brillouin zone. The inset shows the energy dispersion along the high symmetry lines.

as shown in Fig. 4. In this formulation the Fermi energy is located at  $E(\mathbf{k})/t =$ , and thus depending on whether there are energy bands that cross the Fermi energy or not, the nanotube is either metallic or semiconducting, respectively. The condition to get either metallic or semiconducting nanotubes is whether the cutting lines cross the  $K$  or  $K'$  points where the bonding and antibonding  $\pi$  bands of 2-D graphite touch each other (Fig. 3).

In Fig. 5, we show by solid lines the electronic density of states (DOS) for (A) (10,0) and (B) (9,0) zigzag nanotubes. Dotted lines denote the DOS for 2-D graphite for comparison. For metallic nanotubes, the density of states at the Fermi energy is constant as a function of energy, while there is an energy gap for semiconducting nanotubes. The value of the density of states for metallic SWNTs at the Fermi energy,  $D(E_F)$  is  $8/\sqrt{3}\pi a \gamma_0$  in units of states per unit length along the nanotube axis per electron volt, which is independent of diameter. If  $D(E_F)$  is given by per gram per electron volt, the  $D(E_F)$  is relatively large for small-diameter nanotubes. The many spikes in the DOS for

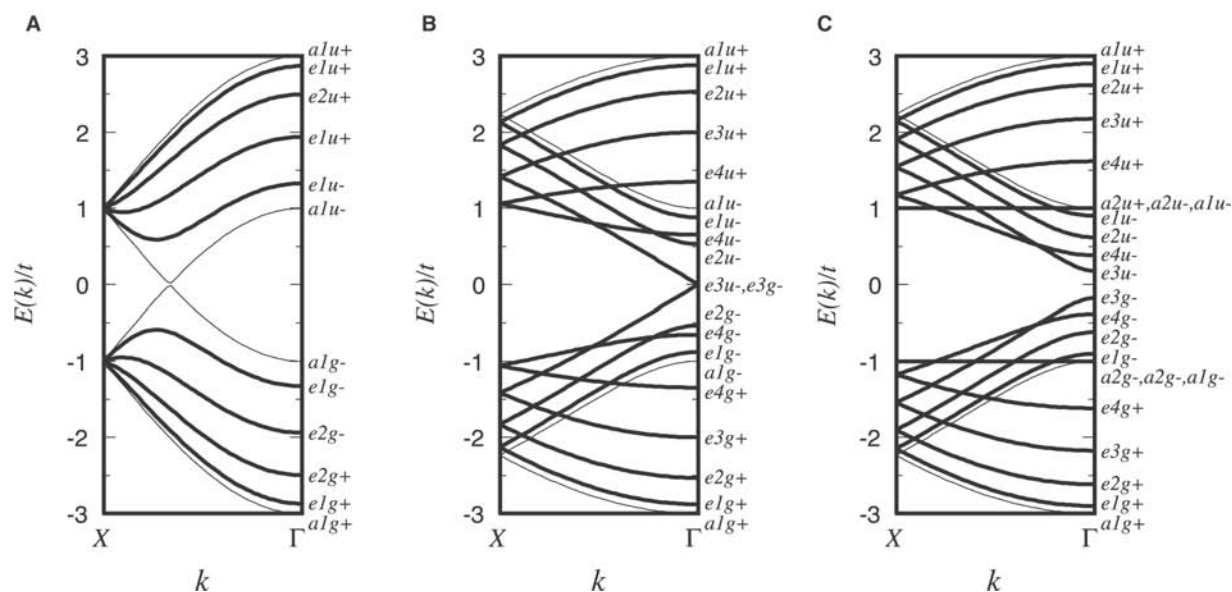


**Fig. 4** The energy dispersion relations for carbon nanotubes. (A) (5,5) Armchair, (B) (9,0) zigzag, (C) (10,0) zigzag nanotubes. Bold and thin lines are doubly or singly degenerate energy bands, respectively. The Fermi energy is located at  $E(k)/t = 0$ . (5,5) and (9,0) are metallic nanotubes while (10,0) is semiconducting.

nanotubes correspond to the energy positions of the minima (or maxima) of the energy dispersion curves of Fig. 4. Each spike exhibits a singularity of  $1/\sqrt{E - E_0}$  (where  $E_0$  is the energy extremum) that is characteristic of 1-D materials and is known as a van Hove singularity.

The energy position of the van Hove singularity near the Fermi energy is determined by how the cutting lines are oriented near the  $K$  point of the 2-D BZ. In Fig. 6, we show the cutting lines around the  $K$  point for (A) metallic and (B) semiconducting nanotubes. In the case of metallic nanotubes, the central cutting line just goes through the  $K$  point, and the two nearest cutting lines are located at the same distance of  $\mathbf{K}_2$  from the  $K$  point. The corresponding energy dispersions for the central line and for the two neighboring lines are, respectively, metallic linear energy dispersions, and are the first subbands (Fig. 4A), which give the van Hove singularities nearest to the Fermi energy. An important fact about the energy dispersion of 2-D graphite around the  $K$  point is that the energy dispersion of Eq. (4) is linear in  $k$ , when we measure  $k$  from the  $K$  point, i.e.,

$$E(k) = \pm \frac{\sqrt{3}\gamma_0}{2} |k| \quad (6)$$

Within the linear approximation of the energy dispersion, the equienergy contour of 2-D graphite is a circle around the  $K$  point (Fig. 7). Thus, only the distance of the two neighboring cutting lines from the  $K$  point is

essential for determining the energy position of a van Hove singularity. Because the separation between two cutting lines,  $\mathbf{K}_2$ , is inversely proportional to the diameter of the nanotube,  $d_t$ , the van Hove singular energies relative to the Fermi energy are inversely proportional to  $d_t$ , too.

In the case of a semiconducting nanotube, on the other hand, the  $K$  point is always located at a position one-third of the distance between the two lines as shown in Fig. 6B. Thus, the first and the second van Hove singular energies from the Fermi energy correspond to the 1-D energy dispersion for the nearest and the second nearest cutting lines, respectively, whose energies are one-third and two-thirds of the smallest energy separation of the van Hove singularity of metallic nanotubes with a similar diameter.

The linear energy approximation, however, does not work well for  $k$  points far from the  $K$  point. In this case, the equienergy contours deform with a deformation that increases with increasing  $k$ , and eventually become a triangle that connects three  $M$  points around the  $K$  point (Fig. 7) when we consider the periodicity of the electron dispersion relations in  $k$  space. This effect is known as the trigonal warping effect of the energy dispersion. When the trigonal warping effect is included, the direction of the cutting lines, which depends on the chiral angle of the nanotube (or simply on its chirality), is essential to determine the precise positions of the van Hove energies. For example, the two neighboring cutting lines in the metallic nanotube in Fig. 6A are not equivalent to each other, which gives

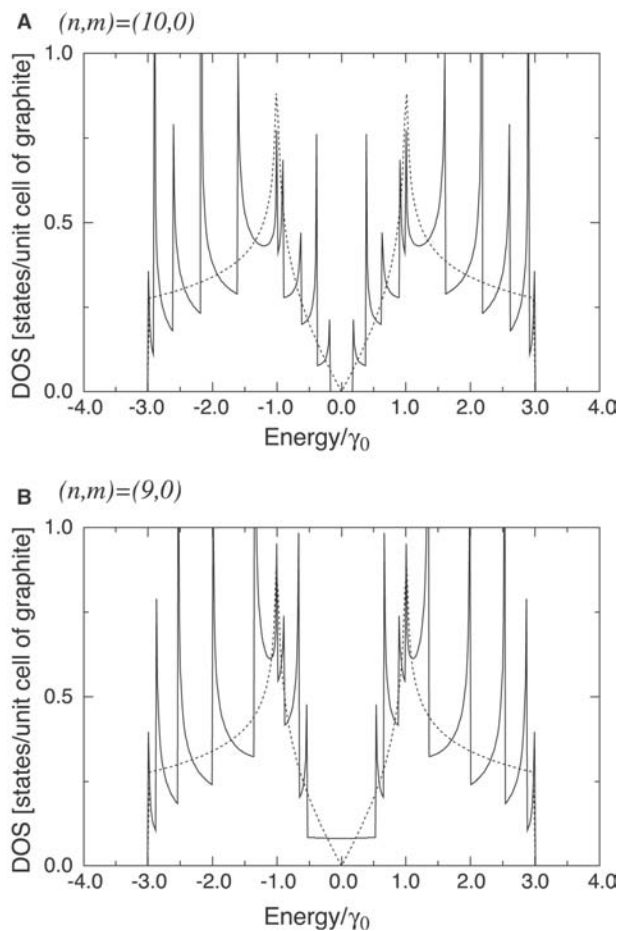


**Fig. 5** Electronic density of states for the (A) (10,0) semiconducting zigzag nanotube, (B) (9,0) metallic zigzag nanotube. Dotted lines denote the density of states for 2-D graphite.

rise to a splitting of the van Hove peaks in the DOS. This splitting of van Hove peaks is a maximum for zigzag nanotubes and monotonically decreases to zero for armchair nanotubes for which the two neighboring cutting lines are equivalent to each other. For both metallic and semiconducting nanotubes, the trigonal warping effect appears as a modification of the energy position of the van Hove singularities that depends on chirality. This value of the splitting of the van Hove singularities (0.1 eV at most) is large enough to be easily detected by the energy accuracy of resonance Raman spectroscopy (10 meV). It is therefore possible to specify the  $(n, m)$  values for SWNTs from a detailed analysis of the resonance Raman spectra of each SWNT using a tunable laser.

**OPTICAL ABSORPTION**

Optical absorption of an electron occurs “vertically” at a  $k$  point of the Brillouin zone from an occupied

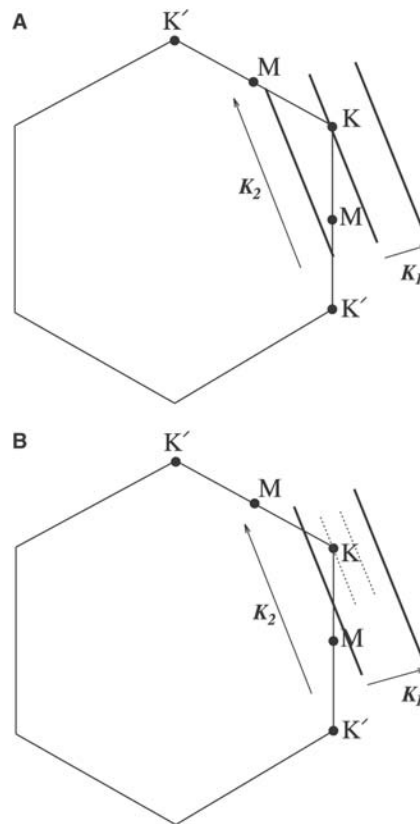


**Fig. 6** Cutting lines around the  $K$  point in the Brillouin zone for (A) metallic and (B) semiconducting nanotubes.

to an unoccupied energy band. An optical transition from an occupied 2p to an unoccupied 2p atomic orbital in the same carbon atom is forbidden. However, the transition from the 2p orbital of one atom to the 2p orbital of another atom (mainly a nearest

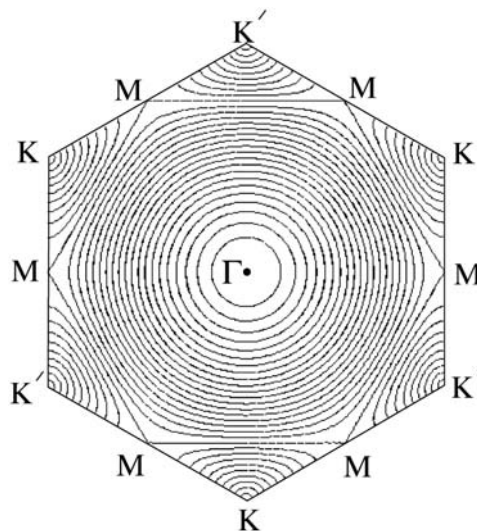


**Fig. 7** Equienergy contours for the electronic  $\pi$  bands of 2-D graphite.



neighbor atom) is possible, which makes  $\pi$  to  $\pi^*$  transitions possible in graphite and carbon nanotubes.

First-order time-dependent perturbation theory gives the following formula for the absorption probability per unit time  $W(\mathbf{k})$  for an electron with wave vector  $\mathbf{k}$ ,

$$W(\mathbf{k}) = \frac{4e^2\hbar^4 I}{\tau\epsilon m^2 c^3 E_{\text{laser}}^2} |\mathbf{P} \cdot \langle \Psi^c(\mathbf{k}) | \nabla | \Psi^v(\mathbf{k}) \rangle|^2 \times \frac{\sin^2[E_c(\mathbf{k}) - E_v(\mathbf{k}) - E_{\text{laser}}](\tau/2\hbar)}{[E_c(\mathbf{k}) - E_v(\mathbf{k}) - E_{\text{laser}}]^2} \quad (7)$$

where  $\Psi^c$  and  $\Psi^v$  ( $E_c$  and  $E_v$ ) are the wave functions (energies) of the valence and conduction bands, respectively,  $\mathbf{P}$  is the polarization vector of light, and  $E_{\text{laser}}$ ,  $I$ ,  $\epsilon$ ,  $m$ , and  $\tau$  are the incident laser energy and intensity, dielectric constant, mass of the electron, and the time used for taking the average, respectively. The value of  $\tau = \Delta x/c = 2\pi/\Delta\omega$  is determined by the uncertainty relation and the width of the incident laser frequency  $\Delta\omega$ . Typical values of  $\tau$  for  $\Delta\omega = 10\text{ cm}^{-1}$  correspond to 0.5 psec. If we take a sufficiently large value for  $\tau$ , the function  $\sin^2 X/X^2$   $\{X = [E_c(\mathbf{k}) - E_v(\mathbf{k}) - E_{\text{laser}}]\tau/2\hbar\}$  appearing in the second line of Eq. (7), becomes the delta function  $\delta[E_c(\mathbf{k}) - E_v(\mathbf{k}) - E_{\text{laser}}]$ , and Eq. (7) is known as Fermi's golden rule.  $\Psi_c$  and  $\Psi_v$  can be written as a sum of the two Bloch functions consisting of the two carbon atoms, A and B in the graphite unit cell,  $\Phi_j(\mathbf{k}, \mathbf{r})$ , ( $j = A, B$ )

$$\Psi^i(\mathbf{k}, \mathbf{r}) = \sum_{j=A,B} C_j^i(\mathbf{k}) \Phi_j(\mathbf{k}, \mathbf{r}), \quad (i = c, v) \quad (8)$$

where  $C_j^i(\mathbf{k})$  is the coefficient of the Bloch functions that is obtained by solving the 2-D Hamiltonian and overlap matrices ( $H$  and  $S$ ) for 2-D graphite.

In the case of graphite, simple zone folding of the energy bands gives the wavefunction of the nanotube in which  $\Psi^i(\mathbf{k}, \mathbf{r})$  of graphite is changed to  $\Psi_p^i(\mathbf{k}_{\parallel}, \mathbf{r})$  for the nanotubes, where the subband index  $p$  and the 1-D wave vectors  $\mathbf{k}_{\perp}$  and  $\mathbf{k}_{\parallel}$  are given by Eqs. (3) and (4).

The dipole selection rule is given by group theory applied to the  $\Gamma$  point (zone center) of the Brillouin zone, because each eigenfunction belongs to an irreducible representation of the space group. This rule can be extended smoothly to lower symmetry  $k$  points, even though there is no longer strict selection rule for the lower symmetry  $k$  points. The optical intensity can be directly obtained by calculating the dipole matrix element, as shown in Eq. (7). When the light polarization is parallel to the nanotube axis, the optical transition occurs between valence and conduction subbands that come from the same cutting line. When the

light polarization is perpendicular to the nanotube axis, the optical transition occurs between the two subbands that belong to nearest neighbor cutting lines in the 2-D Brillouin zone.

Hereafter we mainly consider the case of light polarization parallel to the nanotube axis, because the optical absorption for perpendicular polarization is relatively much weaker. The reason why the perpendicular polarization is weak is that 1) the nanotubes have a high aspect ratio of nanotube diameter to length, 2) the van Hove singular  $k$  points are not the same for the valence and conduction energy subbands for different cutting lines, and 3) there is a strong screening effect of the electric field perpendicular to the nanotube axis [depolarization effect, see H. Ajiki and T. Ando, Physica 201 (1994) 349]. Especially for isolated single nanotube spectroscopy, no Raman signals are observed for light polarization perpendicular to the nanotube axis.

In Fig. 8A the energy separations  $E_{ii}$  between the  $i$ th valence and the  $i$ th conduction band van Hove singular energies, which are dipole allowed for parallel light polarization, are plotted as a function of the nanotube diameter,  $d_t$ . Here the subband label  $i$  is counted from the subband closest to the Fermi energy. Each point of this figure corresponds to van Hove singularities for a different  $(n, m)$  nanotube. For a given tube diameter, we can obtain optical transitions for the first and the second van Hove singularities in the joint density of states (JDOS) for semiconducting nanotubes,  $E_{11}^S$ ,  $E_{22}^S$  when we increase the laser energy. The next band in Fig. 8A is for metallic nanotubes  $E_{11}^M$ , followed by  $E_{33}^S$  for semiconducting nanotubes. For a given laser energy, we can find possible diameter regions of nanotubes that have an optical transition between two van Hove singularities. In this sense, the excitation laser light selects the diameter of a nanotube within a mixed sample containing nanotubes with a diameter distribution.

In Fig. 8B, typical Raman signals at the single nanotube level are shown for 3 different  $(n, m)$  SWNTs at three different locations on the sample obtained by illuminating an individual SWNT with a 1- $\mu\text{m}$ -diameter laser light spot on a Si/SiO<sub>2</sub> substrate. The Raman feature at around 300 and 225  $\text{cm}^{-1}$  come from the nonresonant Si substrate. Although the number of carbon atoms is much smaller than the number of Si atoms (Si/C  $\sim 10^6$ ), the Raman signal of one nanotube is comparable to that of Si. This is because the Raman signal in the nanotube comes from a resonance effect in which the resonant signal is enhanced by more than  $10^3$  times relative to the nonresonant signal. This enhancement factor can be observed by changing the laser excitation energy on the same light spot. Because a SWNT is too small to see with an optical microscope, the signal from a resonant SWNT is obtained by



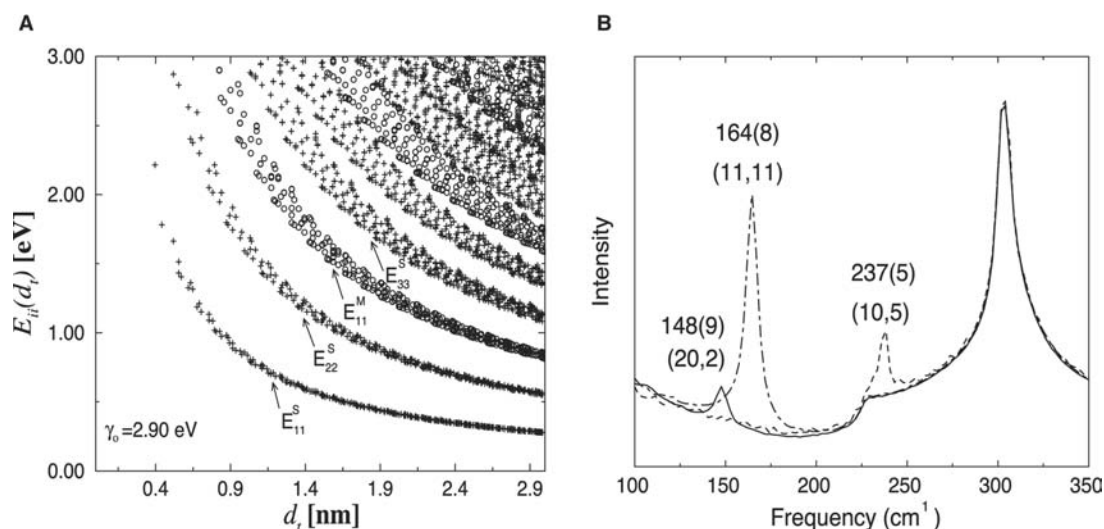


**Fig. 8** (A) Energy separations  $E_{ii}$  between valence and conduction band van Hove singularities are plotted as a function of nanotube diameter. (B) Raman spectra (radial breathing mode) from three different  $(n, m)$  isolated single-wall nanotubes.

putting many light spots on the Si/SiO<sub>2</sub> substrate that has previously been scanned by an AFM probe to determine the location of the SWNTs in the sample.

The three spectra correspond to the radial breathing mode (RBM) of a SWNT in which the carbon atoms of the nanotube are vibrating in the radial direction. The RBM frequency  $\omega_{\text{RBM}}$  for an isolated SWNT is inversely proportional to the tube diameter and is independent of chirality:

$$\omega_{\text{RBM}} = \alpha/d_t \quad (9)$$

The  $(n, m)$  assignment is done by fitting two empirical theoretical parameters,  $\gamma_0$  in Eq. (5) and  $\alpha$  in Eq. (9), to reproduce many RBM frequencies observed in the experiment. The values of the parameters that were obtained for isolated SWNT sample on a Si/SiO<sub>2</sub> substrate are  $\gamma_0 = 2.89 \text{ eV}$  and  $\alpha = 248 \text{ cm}^{-1} \text{ nm}$ . These parameters work well to three effective digits for a laser excitation energy  $E_{\text{laser}} = 1.58 \text{ eV}$  and in the nanotube diameter range  $1 < d_t < 2 \text{ nm}$  for isolated SWNTs on a Si/SiO<sub>2</sub> substrate. In other cases, a few possible  $(n, m)$  identifications are possible. Then, using the same two parameters, more accurate Raman techniques, such as the Stokes/anti-Stokes intensity ratio or a tunable laser approach, are necessary (see Ref.<sup>[4]</sup> for details. This is a review entry on Raman spectroscopy in single-carbon nanotubes and “Resonant Raman Process” and is relevant to this entry). However, the accuracy of the  $(n, m)$  assignments might decrease in the following situations: 1) for SWNT diameters smaller than 1 nm, where we expect departures to occur from the calculation of  $E_{ii}$  described above, 2) for thick SWNT bundles in which we expect nanotube–nanotube interactions, and 3) for higher

excitation energies ( $E_{\text{laser}} > 3 \text{ eV}$ ) where  $\sigma$ -band contributions become more important.

In Fig. 9, we show the optical absorption spectra of SWNT bundles synthesized using the laser ablation method and four different catalysts. In the laser ablation method, the pulsed YAG laser hits a graphite rod containing the indicated catalysts in a furnace kept at about 1200°C with an Ar gas flow, and the smoke emerging from the rod and containing the SWNT bundles is transported by Ar gas flow out of the furnace. By controlling the temperature of the furnace and the selection of catalysts, a narrow diameter distribution of nanotubes is obtained. Although there are SWNTs with many different chiralities mixed in the SWNT bundle sample, we can see three peaks in the optical absorption in Fig. 9, where each peak corresponds to either  $E_{11}^S$ ,  $E_{22}^S$ , or  $E_{11}^M$ . By comparing the energies where the peaks in Fig. 9 occur with the results of Fig. 8A, we can estimate the diameter distribution produced by each catalyst and these estimates are confirmed by the RBM spectra shown in the inset of Fig. 9.

When such a bundle of SWNTs is doped with an alkali metal, a charge transfer of electrons occurs from the alkali metal donor ions to the nanotube or from the nanotube to acceptor ions. In the case of donor ions, the unoccupied states of the pristine sample become occupied with electrons starting from the lowest available conduction band energies. This causes a disappearance of the optical absorption peaks starting from the lower-energy side as the doping concentration increases, because of a lack of unoccupied excited states to allow optical transitions to occur. An electrochemical doping or a field effect transistor (FET) type doping method would be good for observing this

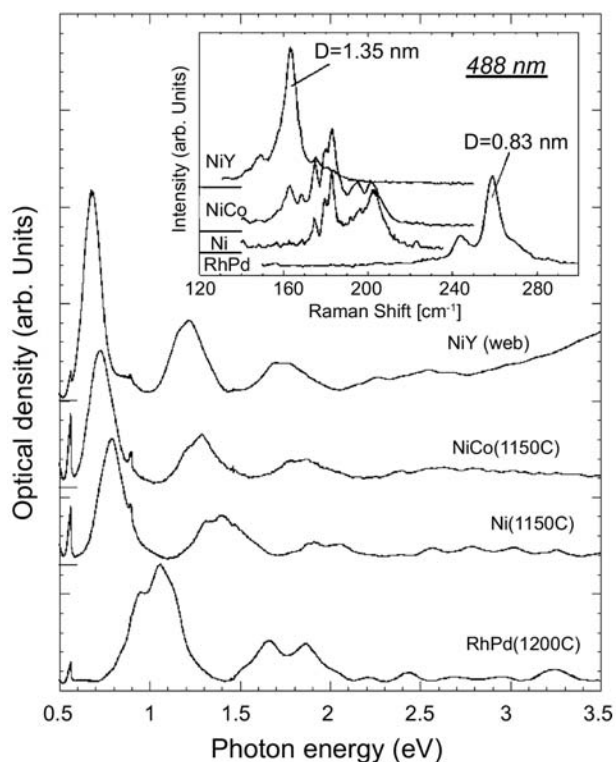


**Fig. 9** Optical absorption spectra are taken for single-wall nanotubes synthesized using four different catalysts, each yielding a different diameter distribution, namely, NiY (1.24–1.58 nm), NiCo (1.06–1.45 nm), Ni (1.06–1.45 nm), and RhPd (0.68–1.00 nm). Peaks at 0.55 and 0.9 eV are due to absorption by the quartz substrate. The inset shows the corresponding RBM modes of Raman spectroscopy obtained using 488-nm laser excitation with the same four catalysts, and the tube diameters corresponding to RBM peaks are given for two catalysts. *Source:* From H. Kataura et al. *Synthetic Metals* 103 (1999) 2555.

phenomenon since the Fermi energy can be modified by changing the gate voltage. Although direct optical absorption measurements of one nanotube will be very difficult because there is no special enhancement mechanism available such as resonance Raman spectroscopy, a combination of optical absorption with resonance Raman spectroscopy should make it possible to observe the Fermi energy shift associated with donor or acceptor doping.

Optical emission or fluorescence signals from a nanotube are not easy to observe, because most SWNT samples contain bundles of nanotubes in which one of three nanotubes are metallic. In a metallic nanotube, the electron–hole recombination occurs non-radiatively along the metallic energy dispersion. Furthermore, optical or direct coupling between nanotubes in the bundle suppresses fluorescence in semiconducting nanotubes, but if a semiconducting nanotube is isolated from other nanotubes, it is then possible to

measure the fluorescence. Such spectra have been obtained for nanotubes separated from one another in a zeolite or when covered by a micelle (soap) structure [see Z. M. Li et al. *Phys. Rev. Lett.* 87 (2001) 127401 and M. J. O’Connell et al. *Science* 297 (2002) 593]. The fluorescence of nanotubes occurs at the real energy gap  $E_{11}^S$  of semiconducting nanotubes and provides a good probe of excitonic effects in SWNTs. If high spatial resolution greater than the average distance between two nanotubes is available, we can assign  $(n, m)$  values from the fluorescence measurement.

## Resonance Raman Process

One of the most powerful optical measurements for carbon nanotubes is resonance Raman spectroscopy. The resonance enhancement effect which is caused by a real optical absorption or emission process makes it possible to observe a signal from even one nanotube, as shown in Fig. 8B. Recently much progress in Raman spectroscopy has been made, and therefore it is not possible to explain the many important advances in detail (see Ref.<sup>[4]</sup>) within the available space of this review. The present summary therefore only provides an overview of Raman spectroscopy of carbon nanotubes, and only a few essential points that are important for analyzing the many features of the observed resonance Raman spectra of SWNTs are discussed (Fig. 10).

In carbon nanotubes, the Raman spectra show a variety of features associated with first-order processes, as well as combination or overtone modes up to  $3200\text{ cm}^{-1}$ . The characteristic mode that is not observed in other  $\text{sp}^2$  carbons, but is observed only in nanotube samples, is the radial breathing mode (RBM). The RBM frequency appears from  $100$  to  $550\text{ cm}^{-1}$ , depending on the SWNT diameter, ranging from  $2.5$  to  $0.4\text{ nm}$ , respectively. To check if a sample contains any nanotubes, the RBM spectra provides an easy way to do just that. It is further noted that if no RBM spectra are observed, this does not always mean that there are no SWNTs in the sample, because we can imagine the case that the resonance condition for a given diameter distribution of SWNTs might be far from the available laser excitation energy. In some cases, because of the large noise signal from the Rayleigh (elastically) scattered light, the RBM signal cannot be resolved in the noisy Rayleigh background signal. Use of a notch filter is a simple way to avoid this problem, but use of a notch filter in practice limits observations to  $\omega_{\text{RBM}} > 100\text{ cm}^{-1}$ .

In Fig. 11B we plot  $E_{ii}$  as a function of inverse tube diameter  $1/d_t$ . Circles and crosses correspond, respectively, to metallic and semiconducting  $(n, m)$  tubes. For a laser energy of  $1.579\text{ eV}$ , only a few metallic

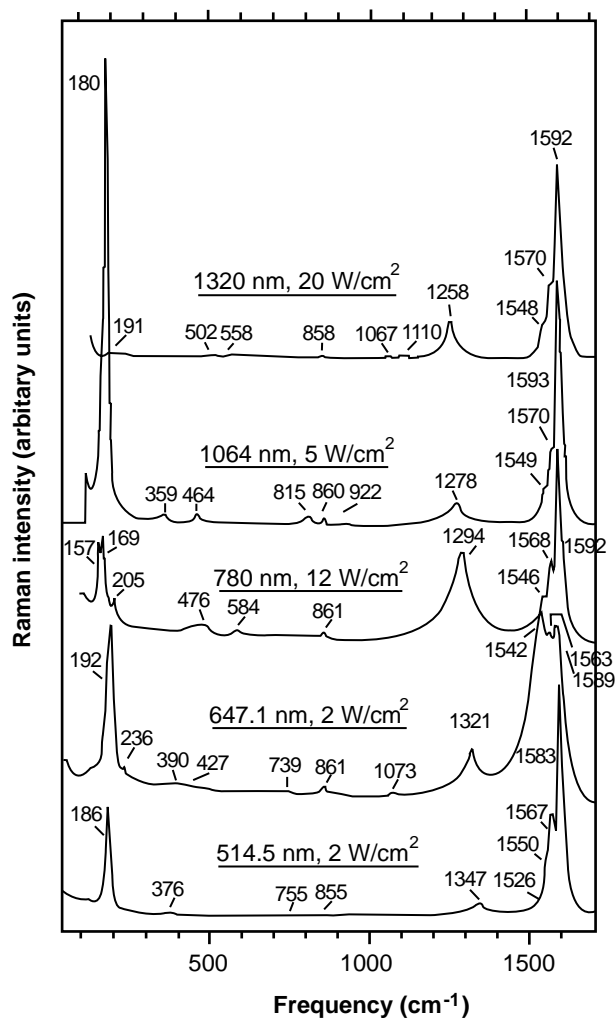


**Fig. 10** Room-temperature Raman spectra for purified single-wall carbon nanotube bundles excited at five different laser frequencies, showing RBM modes around  $200\text{ cm}^{-1}$ ,  $G$  band ( $\sim 1590\text{ cm}^{-1}$ ), and  $D$  band ( $1250\text{--}1350\text{ cm}^{-1}$ ). We can also see some weak features in the intermediate frequency region around  $800\text{ cm}^{-1}$ . *Source:* From A. M. Rao et al. *Science* 275 (1997) 187.

and semiconducting  $(n, m)$  tubes with  $E_{11}^M$  and  $E_{22}^S$  van Hove singularities satisfy the resonance condition, as seen in Fig. 11A. Since the RBM frequency can be measured to the accuracy of  $1\text{ cm}^{-1}$  out of  $100\text{--}200\text{ cm}^{-1}$ , the difference between the peak frequencies of different  $(n, m)$  tubes are easily distinguished.

The second important Raman feature is the  $G$ -band mode that appears near  $1590\text{ cm}^{-1}$  in SWNTs. This mode is the Raman-active mode of  $sp^2$  carbons (graphite), and thus many graphitic materials show this spectral feature. What is special in nanotubes is that the  $G$  band mainly splits into two peaks, denoted by  $G^+$  and  $G^-$ , and this is because of the properties of the six (or three) phonon modes that are active for chiral (or achiral) nanotubes around this phonon

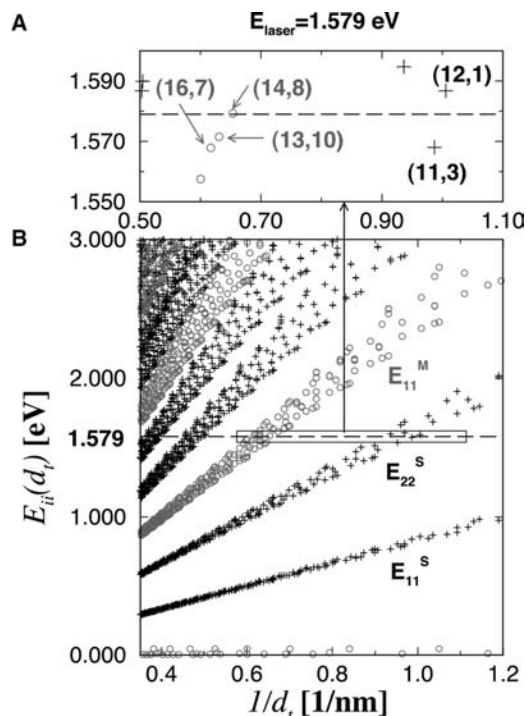


**Fig. 11** Van Hove singular energies in the JDOS,  $E_{ii}$  as a function of  $1/d_t$  are shown in (B) where circles and crosses correspond, respectively, to metallic and semiconducting  $(n, m)$  chirality tubes. For  $1.579\text{-eV}$  laser excitation, expansion of the rectangular section in (B) is shown in (A). The resonance condition satisfies only a limited number of  $(n, m)$  tubes whose RBM frequencies can almost always be distinguished from one another.

frequency region. Among Raman-active modes, two  $A$  (or  $A_{1g}$ ) modes are considered to be the strongest and account for the two peaks,  $G^+$  and  $G^-$ . Regarding the other four Raman-active modes, two have  $E_1$  and two have  $E_2$  symmetries (or two Raman-active modes  $E_{1g}$  or  $E_{2g}$  for achiral tubes), and the  $E_1$  and  $E_2$  modes are relatively weak. The presence of the  $E_1$  and  $E_2$  modes are mainly seen from the Lorentzian decompositions of the line shape of the observed spectra using polarized light when carrying out polarization studies. The frequency difference between the two  $G$  band spectral features,  $G^+ - G^-$ , is inversely proportional to  $d_t^2$ , which comes from the curvature effect that is responsible for the splitting of the degenerate in-plane optic phonon modes,  $E_{2g}$ , of 2-D graphite at the  $\Gamma$  point.

Around  $1250\text{--}1350\text{ cm}^{-1}$ , defect-induced Raman modes, called the  $D$  band, appear only for defect-rich  $sp^2$  carbons. The appearance of a  $D$  band in nanotubes means that a nanotube (or a non-SWNT carbon impurity in the sample) has many defects. The nanotubes synthesized by CVD are known to be defective relative to other nanotubes. The  $D$ -band mode is

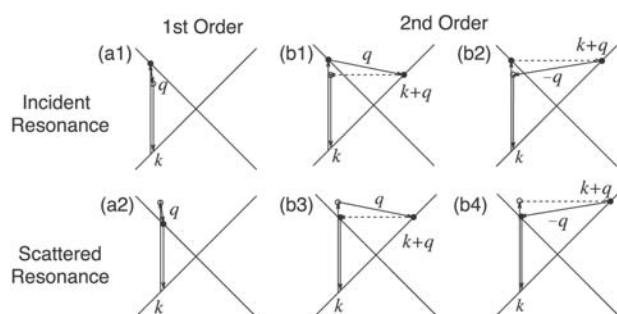


**Fig. 12** (A) First-order Raman processes that are resonant with (a1) the incident and (a2) the scattered laser light. Solid and open dots denote resonance and nonresonance scattering processes, respectively. Crossed lines show the linear energy dispersion of 2-D graphite around the  $K$  point. (B) Second-order Raman processes that are resonant with (b1, b2) the incident laser light, and with (b3, b4) the scattered laser light. The solid scattered vectors and dashed scattered vectors with wave vector  $\mathbf{q}$ , respectively, denote inelastic and elastic scattering processes.

known as a dispersive phonon mode in which the D-band frequency increases by  $53\text{ cm}^{-1}$  with a  $1\text{ eV}$  increase in the laser excitation energy. The physical origin of this very large dispersiveness has been recently explained by double resonance Raman theory<sup>[5]</sup> in which the photon-absorbed electron is scattered twice before final recombination. Although this process is a second-order light-scattering process, the intensity is comparable to that of the first-order resonance process when two of the three intermediate states are in resonance with the real electronic states.

In Fig. 12, inequivalent (A) first-order and (B) second-order Raman processes are shown. The crossed lines for each figure denote the electronic energy states of graphite around the  $K$  points in the Brillouin zone about which the optical transition occurs. The upper figures are for the incident resonance condition for laser light in which the laser excitation is at almost the same energy as the energy required for optical absorption. The lower figures are for the scattered resonance condition, in which the scattered electron energy,  $(E_{\text{laser}} - E_{\text{phonon}})$ , is almost the same as the optical emission energy. Both resonance conditions give a similar Raman intensity, but the resonance laser energy differs in the two cases by the phonon energy. More precisely, the laser energy for the scattered resonance energy is higher by  $E_{\text{phonon}}$  than that for the incident resonance energy in a Stokes scattering process, which creates a phonon. Note that for all Raman-active phonon modes, the incident resonance condition gives the same resonance laser energy, whereas the scattered resonance condition gives different laser energies, depending on the energy of phonons. Thus,

by observing more than one Raman spectral feature for the same tube or not, respectively, we know whether the observed resonance Raman process is with an incident photon or with a scattered photon.

In the first-order process, in order to recombine an electron and a hole at the original  $k$  point, the phonon wave vector  $\mathbf{q}$  should be sufficiently small. This is why we see in most solid-state textbooks that the Raman spectra of solids can be observed only for zone-center ( $\mathbf{q} = 0$ ) Raman-active phonon modes. In the second-order double resonance process, it is clear from Fig. 12 that the phonon wave vector  $\mathbf{q}$  is not zero. Furthermore, when the laser energy increases, the electron  $k$  vector moves further from the  $K$  point to satisfy the requirements for optical absorption, and thus the corresponding  $\mathbf{q}$  vectors become longer. Here we use the requirement of the double resonance process that the intermediate  $k + q$  states should be unoccupied electronic states, too. This is the reason why the dispersive phonon modes change their Raman frequencies when the laser excitation energy is changed, since the phonon wave vector  $\mathbf{q}$  that satisfies the double resonance Raman condition changes when the excitation laser energy changes.

In 2-D graphite, there are two inequivalent corners of the Brillouin zone,  $K$  and  $K'$ , as shown in Fig. 7. In the electron scattering by phonons or impurities (elastic scattering), there are two possibilities. One is an intravalley scattering process in which an electron scatters within the same region of the  $K$  (or  $K'$ ) point. The other is intervalley scattering in which an electron is scattered from the  $K$  to the  $K'$  region (or  $K'$  to  $K$ ). The corresponding phonon  $\mathbf{q}$  vectors for intravalley and intervalley scattering are phonons around the  $\Gamma$  and  $K$  points, respectively. Thus, we try to find the phonon dispersion point around either the  $\Gamma$  or  $K$  points that satisfies the double resonance condition.

In Fig. 13A the phonon  $\mathbf{q}$  vectors for the double resonance condition are shown as a function of  $E_{\text{laser}}$  (bottom axis) and of the  $\mathbf{q}$  vector along  $\Gamma-K$  (top axis). Solid and open circles correspond to phonon modes around the  $K$  and  $\Gamma$  points, respectively. In Fig. 13B are collected the many experimental Raman signals that have been observed in many disordered graphitic materials for many years, and these are here plotted in the Brillouin zone of 2-D graphite. By specifying either  $\Gamma$  or  $K$  point phonons, all of the experimental points could be assigned to one of the phonon energy dispersion relations (six solid lines), thus providing clear evidence that double resonance theory can work well for the dispersive phonon modes of 2-D graphite. The resulting dispersion relations show how resonance Raman scattering can be used to obtain phonon dispersion relations experimentally based on double resonance theory.



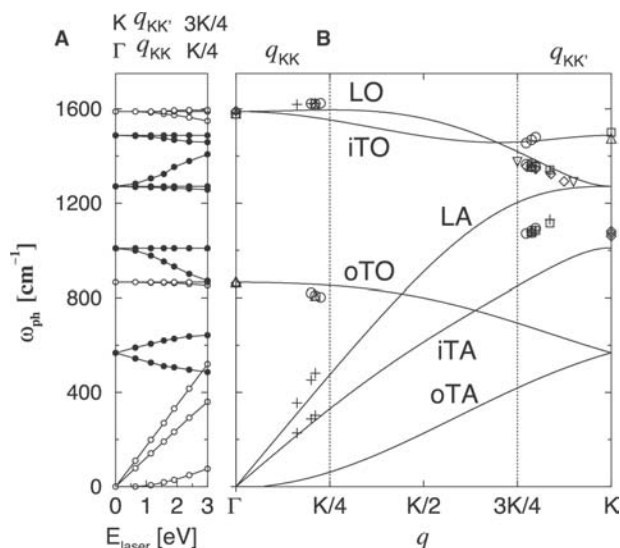


**Fig. 13** (A) Calculated Raman frequencies for the double resonance condition as a function of  $E_{\text{laser}}$  (bottom axis) and  $q$  vector along  $\Gamma$ -K (top axis). Solid and open circles correspond to phonon modes around the K and  $\Gamma$  points, respectively. (B) The six graphite phonon dispersion curves (lines) and experimental Raman observations (symbols) are placed according to double resonance theory.

All second-order phonon processes shown here are one-phonon emission processes. Thus, one of the two scattering processes shown in Fig. 12B should not be a phonon-scattering process. We consider that the nonphonon scattering process is an elastic electron scattering caused by an impurity or a defect in which electronic states with momentum  $k$  are mixed with each other. This is the reason why the dispersive phonon modes appear in a frequency region lower than  $1600\text{ cm}^{-1}$  only for defective carbon materials. If the two scattering processes are both phonon-scattering processes, we do not need the defect scattering process, and thus strong dispersive overtone phonon modes appear. An example of a two-phonon process is the  $G'$  band appearing around  $2700\text{ cm}^{-1}$  with its large dispersion of  $106\text{ cm}^{-1}/\text{eV}$ .

## CONCLUSION

In summary, the optical properties of carbon nanotubes shows rich spectra because of low-dimensional physics phenomena, such as van Hove singularities in the density of states. The resonance Raman spectra, in particular, provide a powerful tool for observing individual nanotubes in the sample, and especially for specifying  $(n, m)$  values of individual nanotubes. Double resonance theory explains the dispersive Raman phonon modes, and can be used to provide information about the dispersion relations for submicron-sized samples, too small for study by neutron scattering techniques.

## ACKNOWLEDGMENTS

R. S. acknowledges a grant-in-aid (No. 13440091) from the Ministry of Education, Japan. A.J./A.G.S.F. acknowledge support from the Brazilian agency CNPq. The MIT authors acknowledge support under NSF grants DMR 01-16042 and INT 00-00408.

## REFERENCES

1. Saito, R.; Dresselhaus, G.; Dresselhaus, M.S. *Physical Properties of Carbon Nanotubes*; Imperial College Press: London, 1998.
2. Dresselhaus, M.S.; Dresselhaus, G.; Eklund, P.C. *Science of Fullerenes and Carbon Nanotubes*; Academic Press: New York, NY, 1996. This textbook covers a large area of fullerenes and nanotubes for "Introduction" sections.
3. Topics in Applied Physics; Dresselhaus, M.S., Dresselhaus, G., Avouris, Ph., Eds.; Carbon Nanotubes: Synthesis, Structure, Properties, and Applications; Springer-Verlag: Berlin, 2001. This covers recent progress of nanotubes by many authors. "Optical absorption" section is related to this book.
4. Dresselhaus, M.S.; Dresselhaus, G.; Jorio, A.; Souza Filho, A.G.; Saito, R. *Carbon* **2002**, *40*, 2043.
5. Thomsen, C.; Reich, S. Double resonant Raman scattering in graphite. *Phys. Rev. Lett.* **2000**, *85*, 5214.

# Carbon Nanotubes and Other Carbon Materials

**Morinobu Endo**  
**Yoong Ahm Kim**  
**Takuya Hayashi**

*Shinshu University, Nagano, Japan*

**Mauricio Terrones**

*Department of Advanced Materials, Institute Potosino of Scientific and Technological Research (IPICYT), San Luis Potosí, Mexico*

**Mildred S. Dresselhaus**

*Department of Electrical Engineering and Computer Science, Massachusetts Institute of Technology, Cambridge, Massachusetts, U.S.A.*

## INTRODUCTION

Graphite exhibits a three-dimensional (3-D) stacking ordering of large graphene layers (where an individual carbon layer in the honeycomb graphite lattice is called a graphene layer) of planar hexagonal networks of carbon atoms based on  $sp^2$  bonding. In contrast, carbons consist of *randomly stacked* defective and relatively small graphene sheets, which are termed turbostratic carbons (T-carbons). Furthermore, carbon nanotubes are seamless cylindrical forms of such graphene layers of nanometer-size diameter, consisting of single- or concentric multilayers.<sup>[1–3]</sup> The diameter of the central hollow core is basically of fullerene size (around 1 nm), and the minimum size diameter that has been observed is 0.4 nm.<sup>[4]</sup> These carbon nanotubes are strongly related to 3-D-graphite or T-carbon when considering their large curvature (see Fig. 1). The nanotube curvature introduces some  $sp^3$  bonding into the  $sp^2$  planar bonding of the graphene sheet. Numerous unusual properties of carbon nanotubes arise from the  $sp^2$  graphene layers by imposing additional quantum confinement and topological constraints in the circumferential direction of the nanotubes. In this entry, carbon nanotubes are first reviewed in terms of their relevance to typical carbon and graphite materials and then are connected with other fibrous forms of carbon and graphite.

## BASIC CONCEPTS FROM FIBERS TO NANOTUBES

As carbon nanotubes might be the ultimate 1D form of carbon, their structure and properties are

closely related to those of other forms of carbon, especially to crystalline 3-D-graphite, T-carbons, and to their constituent 2D layers. Therefore several forms of conventional carbon materials should be mentioned in terms of their similarities and differences relative to a carbon nanotube. Especially, a direct comparison should be made between typical 1D materials of carbon and graphite (carbon fibers), because the carbon fiber acts as a bridge between carbon nanotubes and conventional bulky carbon materials.

Carbon fibers were developed in the early 1960s and have given many breakthroughs to carbon science because of their unique fibrous morphology.<sup>[5,6]</sup> Therefore it is necessary to compare the structure and properties of carbon nanotubes with conventional carbon fibers exhibiting diameters around 10  $\mu\text{m}$ . Furthermore, there are also very important materials that can be related to both carbon nanotubes and carbon fibers. These are called the vapor-grown carbon fibers (VGCFs) synthesized directly by the catalytically assisted pyrolysis of hydrocarbons.<sup>[7–10]</sup> Vapor-grown carbon fibers have diameters ranging from 1 nm to 10  $\mu\text{m}$ , the thinner ones corresponding to carbon nanotubes and the thicker ones are similar to carbon fibers. It has been reported that the central core of a VGCF consists of a carbon nanotube.<sup>[11]</sup> Through precise control of the synthesis conditions, it is possible to produce carbon nanotubes and carbon fibers on a large scale. Both materials have been industrialized for different practical applications.<sup>[12]</sup> Therefore the structures of carbon nanotubes and carbon fibers as well as VGCFs, in which the latter connects both typical materials, are strongly emphasized in this account.



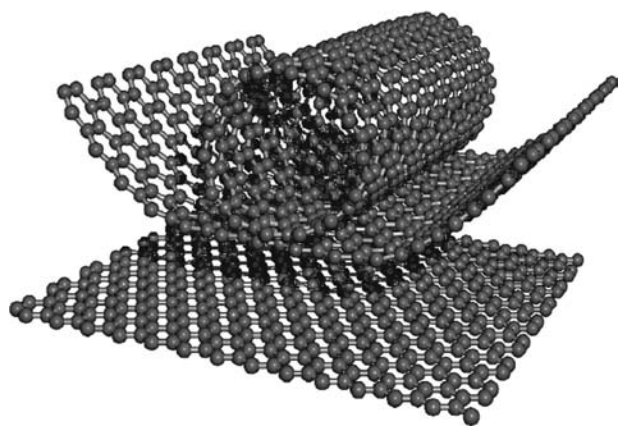


**Fig. 1** Schematic diagram of an individual carbon layer in the honeycomb graphite lattice called a graphene layer, and how it can be rolled to form a carbon nanotube.

We will also show the similarities and differences of these 1D carbon materials.

## BONDING NATURE OF CARBON ATOMS

Carbon is the sixth element in the periodic table and has the lowest atomic number of any of the elements in column IV. Each carbon atom has six electrons which occupy  $1s^2$ ,  $2s^2$ , and  $2p^2$  atomic orbitals. The  $1s^2$  orbital contains two strongly bound core electrons. Four more weakly bound electrons occupy the  $2s^2 2p^2$  valence orbitals. In the crystalline phase, the valence electrons give rise to  $2s$ ,  $2p_x$ ,  $2p_y$ , and  $2p_z$  orbitals, which are important in forming covalent bonds within carbon materials. Because the energy difference between the upper  $2p$  energy levels and the lower  $2s$  level in carbon is small compared to the binding energy of the chemical bonds, the electronic wave functions for these four electrons can readily mix with each other, thereby changing the occupation of the  $2s$  and three  $2p$  atomic orbitals, so as to enhance the binding energy of a C atom with its neighboring atoms. The general mixing of  $2s$  and  $2p$  atomic orbitals is called hybridization, whereas the mixing of a single  $2s$  electron with one, two, or three  $2p$  electrons is called  $sp^n$  hybridization with  $n = 1, 2, 3$ .<sup>[13,14]</sup>

Thus three possible hybridizations occur in carbon:  $sp$ ,  $sp^2$ , and  $sp^3$ , while other group IV elements, such as Si and Ge, exhibit primarily  $sp^3$  hybridization. Carbon differs from Si and Ge because carbon has no inner atomic orbitals, except for the spherical  $1s$  orbitals, and the absence of nearby inner orbitals facilitates hybridizations involving only valence  $s$  and  $p$  orbitals for carbon. The various bonding states are connected with certain structural arrangements, so that  $sp$  bonding gives rise to a chain structure such as carbynes,  $sp^2$

bonding to planar structures such as graphene, and  $sp^3$  bonding to a tetrahedral structure such as diamond.

The carbon phase diagram (see Fig. 2) guided the historical synthesis of diamond in 1960 and has continued to inspire interest in novel forms of carbon, as they are discovered.<sup>[15,16]</sup> While  $sp^2$  bonded graphite is the ground-state phase of carbon under ambient conditions, at higher temperatures and pressures,  $sp^3$  bonded cubic diamond is stable. Other regions of the phase diagram show stability ranges for hexagonal diamond, hexagonal carbynes,<sup>[17,18]</sup> and liquid carbon.<sup>[19]</sup> The triple point of the graphite–diamond–liquid phase is located at 123 kbar and 4100 K. It is expected that a variety of novel  $\pi$ -electron carbon bulk phases still remain to be discovered and explored.

A carbon nanotube is a graphene sheet appropriately rolled into a cylinder of nanometer-size diameter.<sup>[2,3,20–23]</sup> The curvature of the nanotubes admixes a small amount of  $sp^3$  bonding so that the force constant (bonding) in the circumferential

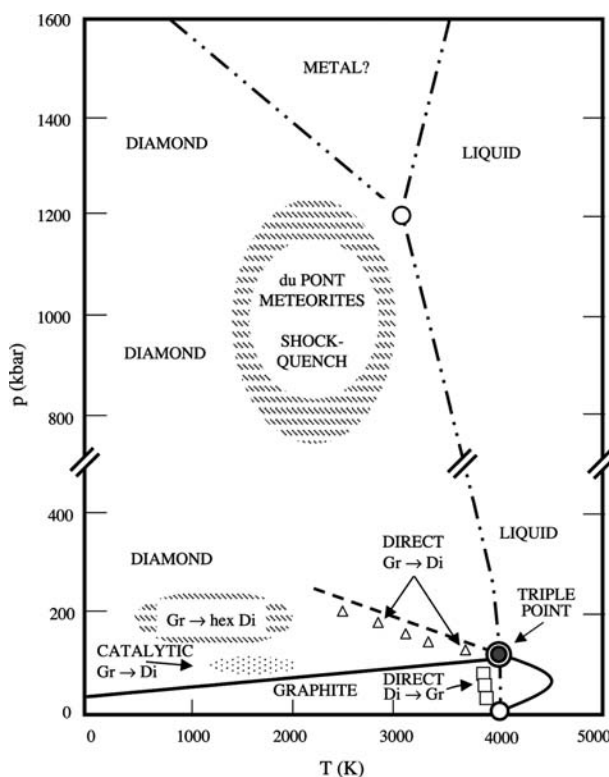


**Fig. 2** The phase diagram of carbon.<sup>[15]</sup> The diamond (Di) and graphite (Gr) phases are emphasized in this figure. Other phases shown in the diagram include hexagonal diamond and a high-temperature–high-pressure phase, denoted in the diagram by du Pont, meteorites, and shock-quench, which has not been studied in much detail and may be related to carbynes. Liquid carbon, which has been studied at low pressures and high temperatures, and an unexplored high-pressure phase, which may be metallic, are also indicated on the figure.

direction is slightly weaker than along the nanotube axis. Because the single-wall carbon nanotube (SWNT) is only one atom thick and has a small number of atoms around its circumference, only a few wave vectors are needed to describe the periodicity of the nanotubes. These constraints lead to quantum confinement of the wavefunctions in the radial and circumferential directions, with plane wave motion occurring only along the nanotube axis, corresponding to a large number or closely spaced allowed wave vectors. Thus although carbon nanotubes are related to a 2D graphene sheet, the tube curvature and the quantum confinement in the circumferential direction lead to a host of 1D properties that are different from those of a graphene sheet. As nanotubes can be rolled from a graphene sheet in many ways, there are numerous possible orientations of the hexagons on the nanotubes, although the basic shape of the carbon nanotube wall is a cylinder, where the two indices ( $n$ ,  $m$ ) that fully identify each carbon nanotube are specified.<sup>[2,3,23]</sup> The rolling of a single graphene layer, which is a honeycomb network of carbon atoms, to form a carbon nanotube is well reviewed in many review papers and books.<sup>[2,3,20–23]</sup> Carbon nanotubes ( $n$ ,  $m$ ) can be either metallic ( $n-m = 3q$ ,  $q = 0, 1, 2, \dots$ ) or semiconducting ( $n-m = 3q \pm 1$ ,  $q = 0, 1, 2, \dots$ ), and likewise the individual constituents of multiwall nanotubes or single-wall nanotube bundles can be metallic or

semiconducting.<sup>[2,3,21]</sup> These remarkable electronic properties follow from the electronic structure of 2D graphite under the constraints of quantum confinement in the circumferential direction.<sup>[2]</sup>

## GRAPHITES AND DISORDERED CARBONS

The ideal crystal structure of graphite (Fig. 3A) consists of layers in which the carbon atoms are arranged in an open honeycomb network, such that the A and B atoms on consecutive layers are on top of one another, but the A' atoms in one plane are over the hexagon centers of the adjacent layers, and similarly for the B' atoms.<sup>[24]</sup> This gives rise to an ABAB planar stacking arrangement (called Bernal stacking) shown in Fig. 3A, with an in-plane nearest neighbor distance  $a_{C-C}$  of 1.421 Å, an in-plane lattice constant  $a_o$  of 2.456 Å, a  $c$ -axis lattice constant  $c_o$  of 6.708 Å, and an interplanar distance of 3.354 Å. This structure is consistent with the  $D_{6h}^4$  ( $P6^3/mmc$ ) space group and has four atoms per unit cell.

Another ordered graphite phase is rhombohedral graphite with ABC stacking of the graphene sheets; it has  $a_o = 2.456$  Å (same as for Bernal-stacked hexagonal graphite),  $c_o = 3(3.438) = 10.044$  Å, and space group  $D_3^7$  ( $R32$ ).<sup>[24]</sup> When describing the ABC stacking of graphene sheets in the hexagonal structure, it is

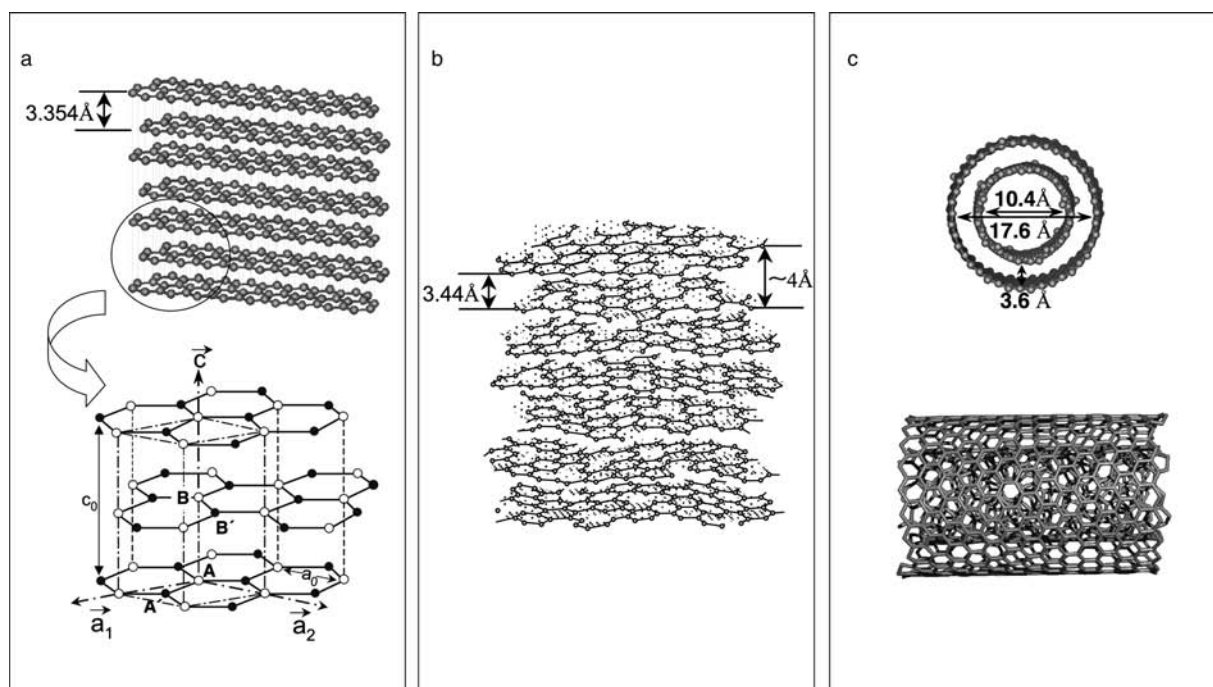


**Fig. 3** Schematic diagrams exhibiting (a) a 3-D graphite lattice (b) a turbostratic structure,<sup>[24]</sup> and (c) a schematic structural model of the outer two layers for a multiwall carbon nanotube.<sup>[33]</sup> The inset in (a) depicts the A and B carbon sites denoted by open circles and the A' and B' sites by black circles. The in-plane lattice constant is denoted by  $a_o$ , and the vectors of the unit cell in the direction  $a_1$ ,  $a_2$ , and  $c$  are indicated. The nearest-neighbor carbon distance  $a_{C-C}$  in graphite is 1.421 Å.

**Table 1** Cohesive energy per carbon atom for various carbon-related structures

Structure	Cohesive energy (meV/atom)	Ref.
3-D graphite	20.0	[25–27]
Rhombohedral graphite	19.9	[27]
2D graphene sheet	10.3	[25–27]
Carbon nanotube (based on C <sub>60</sub> )	9.76	[25]

necessary to consider six atoms per unit cell, but if the rhombohedral description is used, only two atoms per unit cell are needed. Because the total energy for rhombohedral graphite differs only slightly from that of the more stable Bernal ABAB stacking (Table 1), graphite crystals tend to have stacking faults where ABC rhombohedral stacking is found admixed with the AB Bernal stacking for the ideal graphite crystal. Most of graphite crystals and natural graphite follow the hexagonal system, but, sometimes, natural graphite and artificial graphite heat-treated at high temperatures have been observed to include several percent of the rhombohedral system. Also, mechanical grinding and ball milling increase the rhombohedral component.

Stacking disorder tends to have little effect on the in-plane lattice constant largely because the in-plane C–C bond is very strong and the nearest-neighbor C–C spacing is very small. As has already been mentioned elsewhere, the C–C spacing in fullerenes and carbon nanotubes is very close to  $a_{C-C}$ . Disorder does, however, have a significant effect on the interplanar spacing, because of the weak interplanar bonding based on the van der Waals force. One consequence of the small value of  $a_{C-C}$  and the large value of the interplanar  $c$ -axis separation is that impurity species are unlikely to enter the in-plane lattice sites substitutionally, but rather impurities tend to occupy some interstitial positions between the layer planes as to form intercalation compounds.

Weak disorder results in stacking faults (meaning departure from the ABAB stacking order) and gives rise to a small increase in the interlayer distance. This increase is modest when ABC stacking faults are occasionally introduced. Greater disorder is introduced when the stacking become random or uncorrelated and departs from AB or ABC stacking. The greater the stacking disorder the greater the interlayer distance, until random stacking occurs. When the interlayer spacing reaches a value of about 3.44 Å, the stacking of the individual graphene layers becomes uncorrelated. The resulting 2D honeycomb structure of uncorrelated graphene layers is called turbostratic carbon (see Fig. 3b).<sup>[24]</sup>

In both structures, the bonding force between adjacent carbon hexagonal networks is the van der Waals force. The degree of 3-D ordering or the stacking fidelity is defined in terms of the degree of graphitization ( $g$ ) as a function of the interlayer spacing ( $d_{002}$ ), by the following equation,<sup>[28]</sup> where  $g$  is the probability to preserve 3-D stacking.

$$d_{002} = 3.354g + 3.44(1 - g) \quad (1)$$

For interlayer spacings larger than 3.44 Å, the probability of 3-D stacking is 0, and  $d_{002} = 3.354$  Å gives perfect 3-D graphite ordering with  $g = 1$ . Between  $g = 0 - 1$ , various forms of carbon materials exist as a function of heat treatment temperatures. For carbonaceous materials exhibiting a  $g$  value in the range between 0.5 and 1 when heat-treated up to 3000°C, these pristine carbons are called graphitizing or soft carbons.<sup>[29,30]</sup> In contrast, carbonaceous materials with lower  $g$  values, exhibiting a high resistance for graphitization, are so-called nongraphitizing or hard carbons.<sup>[29,30]</sup> These graphitization behaviors are strongly dependent on the microstructure of carbonaceous materials, where highly oriented small carbon networks (the smallest called a basic structural unit) generally determine the graphitizability. The chemical and physical properties, such as the electrical resistivity and mechanical strength, are largely affected by the graphitizing nature of a carbon. Therefore structural control of the pristine material, namely, the starting organic material, is very important for designing the desired performance of carbons and graphite.<sup>[31,32]</sup>

The electronic structure of turbostratic graphite, a zero-gap semiconductor, is qualitatively different from that of ideal graphite, a semimetal with a small band overlap (0.04 eV). As the crystalline disorder is further increased and the in-plane ordering in the graphene sheets is reduced, the interlayer spacing also continues to increase. Such disorder further modifies the electronic properties of the ideal 2D graphite and introduces an effective energy gap.

Multiwall carbon nanotubes (MWNTs) relate closely to the layer stacking of graphite, insofar as the interlayer spacing is found to vary from 3.4 to 3.6 Å between adjacent cylinders, possibly due to glide defects (see Fig. 3c).<sup>[33]</sup> Magnetoresistance measurements provide a highly sensitive measure of the degree of 3-D crystalline order using the following equation.

$$\Delta\rho/\rho_0 = [\rho(B) - \rho(0)]/\rho(0) \quad (2)$$

where  $\rho(B)$  and  $\rho(0)$  are the electrical resistivity with and without a magnetic field  $B$ , respectively. As shown in Fig. 4,<sup>[12,34–36]</sup> highly oriented pyrolytic graphite with the highest degree of structural perfection shows

large positive transverse magnetoresistance, with smaller values of positive  $\Delta\rho/\rho_0$  [mesophase-pitch-based carbon fibers (MPCFs) at 3000°C] corresponding to more disordered graphite. As more disorder is introduced, the 3-D ordering disappears and the fibers assume 2D or turbostratic ordering, where there is no interlayer site correlation between adjacent graphene planes. The magnetoresistance for the turbostratic carbon is characteristically negative, with the magnitude of the negative magnetoresistance decreasing as the disorder increases. For the case of VGCFs heat treated at 2000°C<sup>[35]</sup> and multiwall carbon nanotubes,<sup>[36]</sup> the negative magnetoresistance strongly suggests that the stacking infidelity of the shells is quite similar to that of turbostratic graphite regarding their electronic properties along the tube axis (see the dotted curve in Fig. 4). The curvature of the coaxial layers, however, excludes the possibility of the AB or ABC stacking of the graphene layers, and in this sense, the stacking of layers in a MWNT is equivalent to turbostratic stacking (see Fig. 3c). As some interlayer site correlation between carbon atoms exists in nanotubes, especially regarding the direction of the nanotube axis, the interlayer stacking is not completely turbostratic. Also, for small-diameter carbon nanotubes, there is

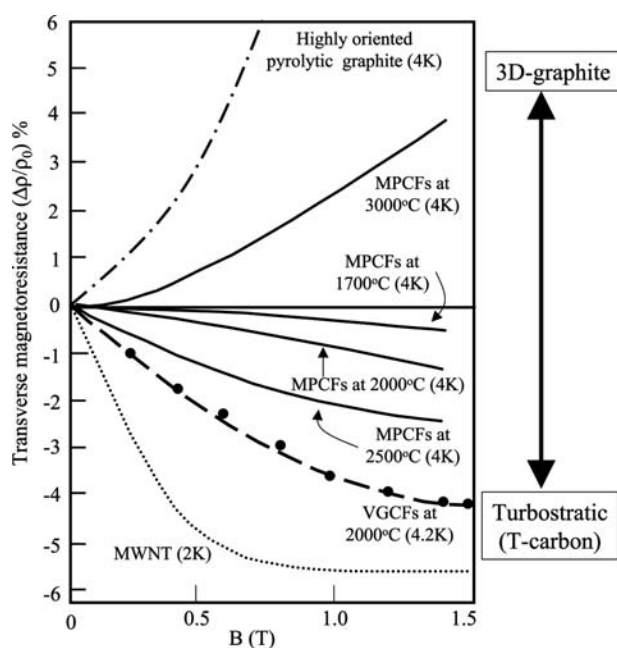


**Fig. 4** Comparative study of transverse magnetoresistance at low temperature (as indicated in parenthesis) for highly oriented pyrolytic graphite (the dot-dashed curve),<sup>[34]</sup> typical mesophase-pitch-based carbon fibers heat treated at different temperatures (the solid curves),<sup>[13]</sup> vapor-grown carbon fibers (the dashed curve),<sup>[35]</sup> and multiwall carbon nanotubes (the dotted curve).<sup>[36]</sup> Vapor-grown carbon fibers exhibit a similar magnetoresistance behavior to that of multiwall carbon nanotubes.

a limited number of possible nanotube diameters, and these depend also on the nanotube chirality, so that it is not in general possible to find a nested set of nanotubes which all have the same chirality and also show a close packing of cylindrical shells. Thus the electronic properties of multiwall carbon nanotubes have some differences and some similarities when compared with T-carbons.

In order to describe the electronic and phonon dispersion relations of 3-D graphite, the Brillouin zone (see Fig. 5) is used.<sup>[3,13]</sup> As the in-plane nearest-neighbor distance in real space is much smaller than the interplanar separation, the Brillouin zone for graphite has a small length in reciprocal space along  $k_z$ . As the interplanar correlation becomes less and less important, as in the case of turbostratic 2D graphene layers, the Brillouin zone is reduced to a sheet. The special point *K* at the Brillouin zone corner in 2D graphite is the location of the Fermi level, and of the symmetry-imposed degeneracy of the conduction and valence bands,<sup>[37]</sup> making 2D graphite a zero band gap semiconductor. The band structure model for graphite near the Fermi energy ( $E_F$ ) focuses on the electronic dispersion relations in the vicinity of the *HKH* and *H'K'H'* edges of the Brillouin zone.

## MULTI- AND SINGLE-WALL CARBON NANOTUBES

Carbon nanotubes can be visualized as rolled sheets of graphene that are sometimes capped (by a fullerene-like hemisphere) on each end. They can be single-walled with diameters as small as about 0.4 nm, or multiwalled (2 to 30 concentric tubes positioned within one another) with outer diameters ranging from 5 to 100 nm. The constituent shells of MWNTs can possess many different helical structures, and variations in the radii and helical structures have been predicted to affect the nanotube's electronic transport, which can vary from metallic to semiconducting.<sup>[2,3]</sup> As shown

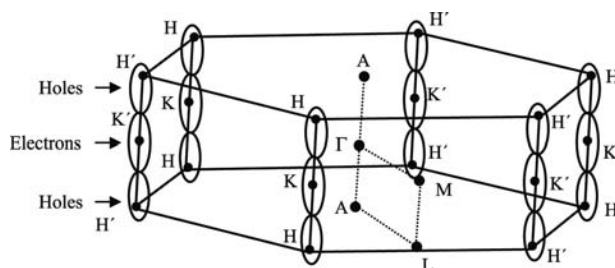


**Fig. 5** Graphite Brillouin zone showing several high-symmetry points and a schematic version of the graphite electron and hole Fermi surfaces located along the *HKH* and *H'K'H'* axes. Source: From Refs.<sup>[3,13]</sup>

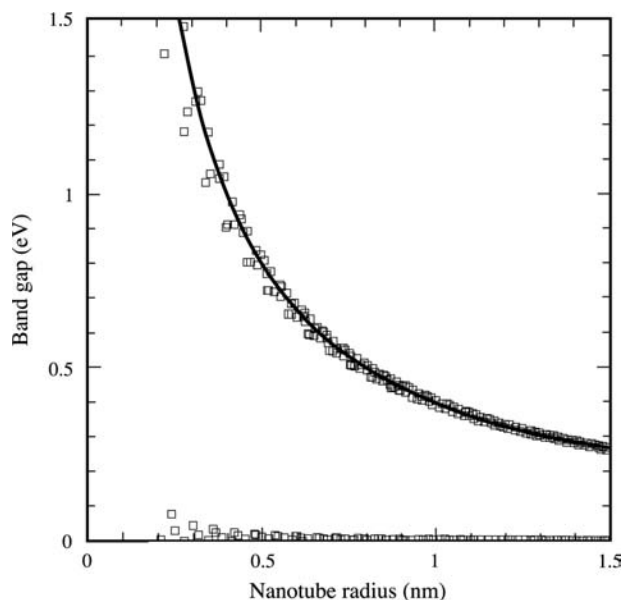


**Fig. 6** Band gap as a function of nanotube radius calculated using an empirical tight-binding Hamiltonian. *Source:* From Ref.<sup>[38]</sup>.

in Fig. 6, the band gap estimated by an empirical tight-binding method as a function of nanotube radius suggests that as the nanotube's diameter gets larger, thus decreasing the pronounced curvature of a graphene layer, the value of the band gap corresponds to that of graphene sheet.<sup>[38]</sup> Three typical structures of SWNT have been proposed (Fig. 7), and their structures have been confirmed by scanning tunneling microscopy (STM) and electron diffraction

studies.<sup>[3,39,40]</sup> If the  $C_{60}$  molecule is bisected normal to a fivefold axis, the cap for an "armchair" nanotube is formed, and if the  $C_{60}$  molecule is bisected normal to a threefold axis, the cap for a "zigzag" nanotube is formed. In addition to the armchair and zigzag nanotubes, a large number of chiral carbon nanotubes can be formed with a screw axis along the axis of the nanotube, which is terminated by a variety of "hemispherical"-like caps.

On the other hand, in MWNTs, no graphitic 3-D stacking is established, although an individual shell of the multilayers consists of perfect graphene sheets. Also, each tube has different and independent chirality, which might contribute to a larger inter-shell spacing than is found in graphite. These characteristic structures of SWNTs and MWNTs indicate that they are unique 1D materials with fascinating electronic and mechanical properties.

## FIBROUS FORMS OF CARBON AND GRAPHITE

Carbon fibers represent an important class of graphite-related materials that are closely related to carbon nanotubes, with regard to structure and properties. Carbon fibers have been studied scientifically since the late 1950s and fabricated industrially since 1963. They are now becoming a technologically and commercially important material in the aerospace, construction, sports, electronic device, and automobile industries. The global carbon fiber

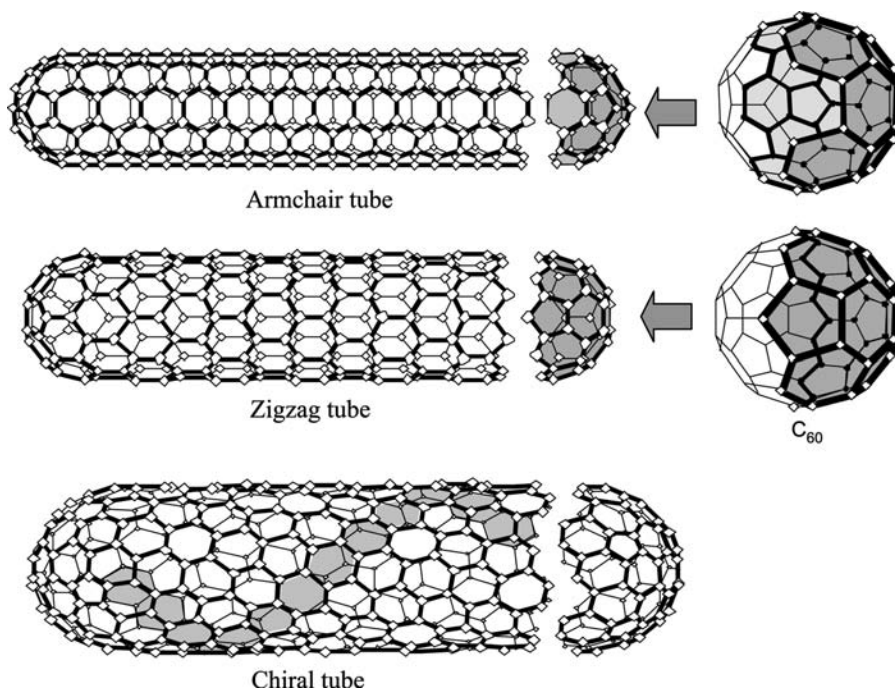


**Fig. 7** Three typical structural models for SWNTs, where the nanotubes are related to rolling a graphene sheet into a cylinder.<sup>[2,3]</sup> Fullerene caps for the armchair and zigzag tubes are also indicated.



market has now grown to about 12,500 tons/year of product, after 40 years of continuous R&D work.<sup>[41]</sup> Carbon fibers are defined as a filamentary form of carbon with an aspect ratio (length/diameter) greater than 100. Probably, the earliest documented carbon fibers are the bamboo-char filaments made by Edison for use in the first incandescent light bulb in 1880. With time, carbon fibers were replaced by the more robust tungsten filaments in light bulb applications, and, consequently, carbon fiber R&D vanished at that early time. But in the late 1950s, carbon fibers once again became important because of the aggressive demand from aerospace technology for the fabrication of lightweight, strong composite materials, in which carbon fibers are used as a reinforcement agent in conjunction with plastics, metals, ceramics, and bulk carbons. The specific strength (strength/weight) and specific modulus (stiffness/weight) of carbon fiber-reinforced composites demonstrate their importance

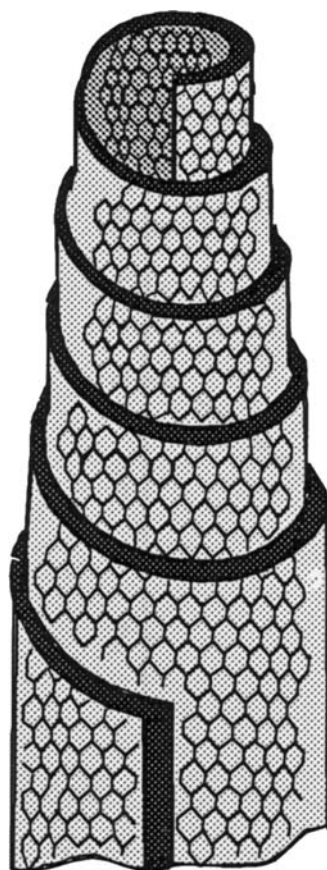


**Fig. 8** Model for graphite whiskers grown by the DC arc-discharge of graphite electrodes.<sup>[42]</sup> Whiskers were reported to have the carpet-rolling structure of graphite sheets and to have high mechanical strength and modulus along the fiber axis, similar to the ideal values of a graphene sheet.

as engineering materials, because of the high performance of their carbon fiber constituents.

Because the temperature and pressure necessary to prepare a carbon fiber from the liquid phase is at the triple point ( $T = 4100\text{ K}$ ,  $p = 123\text{ kbar}$ , see Fig. 2), it would be almost impossible to prepare carbon fibers from the melt under industrial processing conditions. Carbon fibers are therefore prepared from organic precursors. This preparation is generally done in three steps, including stabilization of a precursor fiber in air (at  $\sim 300^\circ\text{C}$ ), carbonization at  $\sim 1100^\circ\text{C}$ ,

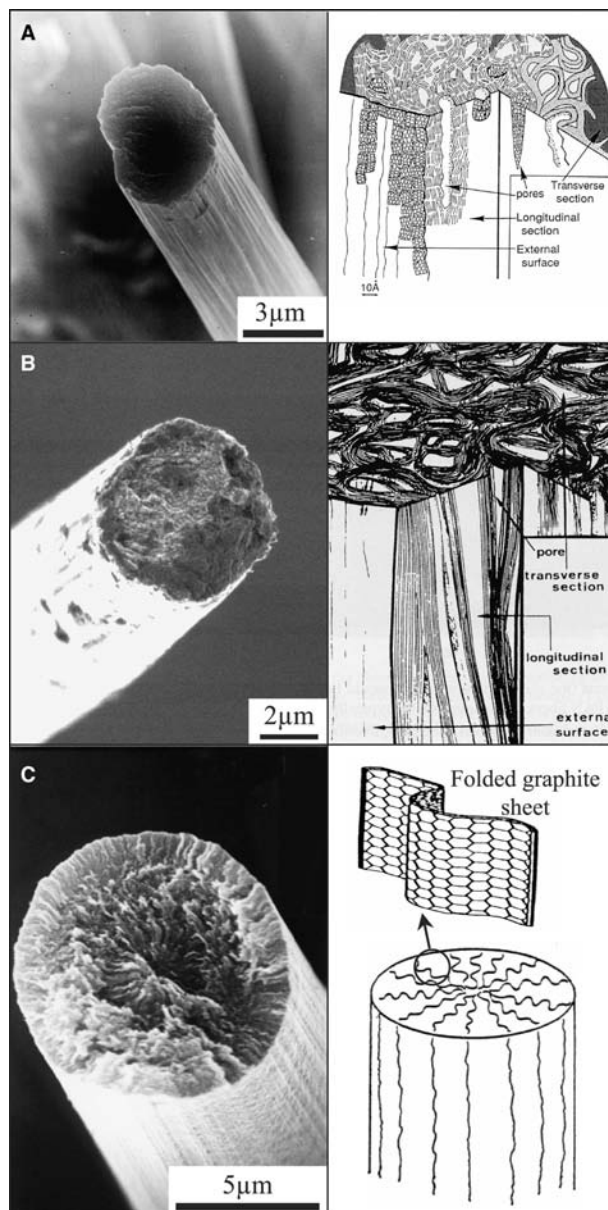


**Fig. 9** SEM micrographs of three types of carbon fibers and their corresponding structural models: (A) a high-strength PAN-based fiber, (B) a high-modulus PAN-based fiber, and (C) MPCF.<sup>[43,44]</sup> On the right-hand side of each fiber type, a schematic diagram of the fiber structure is shown.



and subsequent graphitization (above 2500°C). Fibers undergoing only the first two steps are commonly called “carbon fibers,” while fibers undergoing all three steps are called “graphite fibers.” Carbon fibers are generally used for their high strength, while graphite fibers are used for their high modulus.

Historically, Bacon’s graphite whisker (see Fig. 8) has demonstrated the highest mechanical properties of a carbon fiber (with regard to both strength and modulus), comparable to the ideal value for a graphite network.<sup>[42]</sup> Graphitic whiskers were grown under conditions near the triple point of graphite. Then, the structural model was proposed, in which the layers consisting of graphene sheets are wound around the axis as in rolling up a carpet. These whiskers were used as the performance target in the early stages of

carbon fiber technology, although they have never been produced on a large scale.

### Synthesis and Properties of Carbon Fibers

SEM photographs together with schematic structural models are shown in Fig. 9 for typical carbon fibers: a high-strength polyacrylonitrile (PAN)-based fiber (Fig. 9A), a high-modulus PAN-based fiber (Fig. 9B), and a MPCF (Fig. 9C).<sup>[43,44]</sup> The PAN-based fibers consist of small  $sp^2$ -carbon structural units preferentially aligned with the carbon hexagonal segments parallel to the fiber axis. This orientation is responsible for the high tensile strength of PAN-based carbon fibers.<sup>[45]</sup> By varying the processing conditions (e.g., oxidation conditions, choice of precursor material,

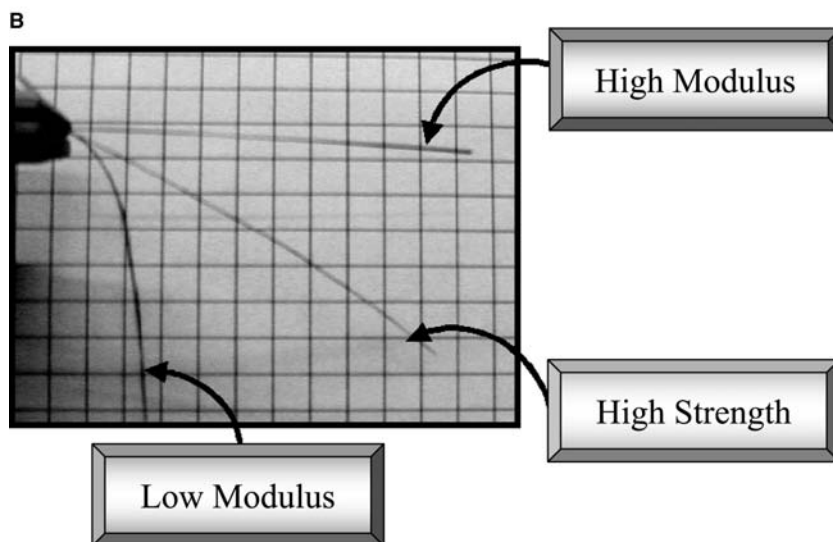
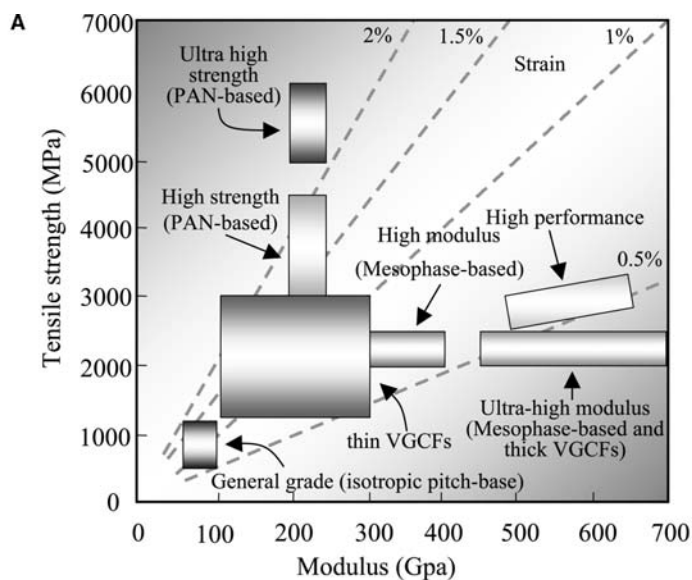


**Fig. 10** (A) The mechanical properties of various kinds of carbon and graphite fibers<sup>[13,32]</sup> and (B) a direct comparison of the mechanical properties for high strength and high modulus fibers, where low modulus fiber droops under its own weight, but the high modulus fibers do not.

and especially by increasing the heat treatment temperature) of PAN fibers, a better alignment of the graphene layers can be achieved (see the structural model of Fig. 9B), thus leading to stiffer, higher-modulus PAN fibers, but with lower strength.<sup>[44]</sup> Polyacrylonitrile-based fibers are one of the typical hard carbons. MPCFs consist of well-aligned graphitic layers arranged nearly parallel to the fiber axis, and this high degree of preferred orientation is responsible for their high modulus or stiffness as well as their relatively high graphitizability. The structures described above give rise to different physical properties, although each type of fiber features carbon hexagonal networks, possessing the strongest covalent bonds in nature (C–C bonds). These strong interatomic bonds lie in sheets essentially parallel to the fiber axis and are responsible for the high mechanical performance of these carbon fibers.

Referring to Fig. 10A we see that PAN-based fibers have high strength and MPCFs have high modulus, while VGCFs provide mainly ultra-high modulus materials.<sup>[13,32]</sup> In this figure we also observe isotropic pitch-based (general grade) fibers, exhibiting much lower modulus and strength, but widely used in composites with cement matrix for construction because of their low cost and chemical stability. Fig. 10B demonstrates a direct indication of the differences in the mechanical properties of various carbon fibers, from low modulus-high strength to high modulus-low

strength fibers from the lower left to the upper right in the photograph, where a yarn containing 500 fibers was initially placed in a horizontal position. These fibers are combined with other materials in order to design suitable mechanical properties and the fibers are used as a filler for various advanced composite materials. In order to get high performance in carbon and graphite fibers, it is very important to control the microstructure by selecting the appropriate organic precursor as well as the processing conditions.

### Vapor-Grown Carbon Fibers

Vapor-grown carbon fibers have a very special structure such as annular-rings (see Fig. 11A) and are synthesized by a somewhat different formation process than that used to produce PAN-based and MPCFs. In particular, VGCFs are not prepared from a fibrous precursor, but rather from hydrocarbon gas, using a catalytic growth process outlined in Fig. 11B.<sup>[7–10,43,46]</sup> Ultra-fine transition metal particles, such as iron particles with a diameter of less than 10 nm, are dispersed on a ceramic substrate, and a hydrocarbon, such as benzene diluted with hydrogen gas, is introduced at temperatures of about 1100°C. Hydrocarbon decomposition takes place on the catalytic particle, leading to a continuous carbon uptake by the catalytic particle and a continuous output by the particle of well-organized tubular filaments of

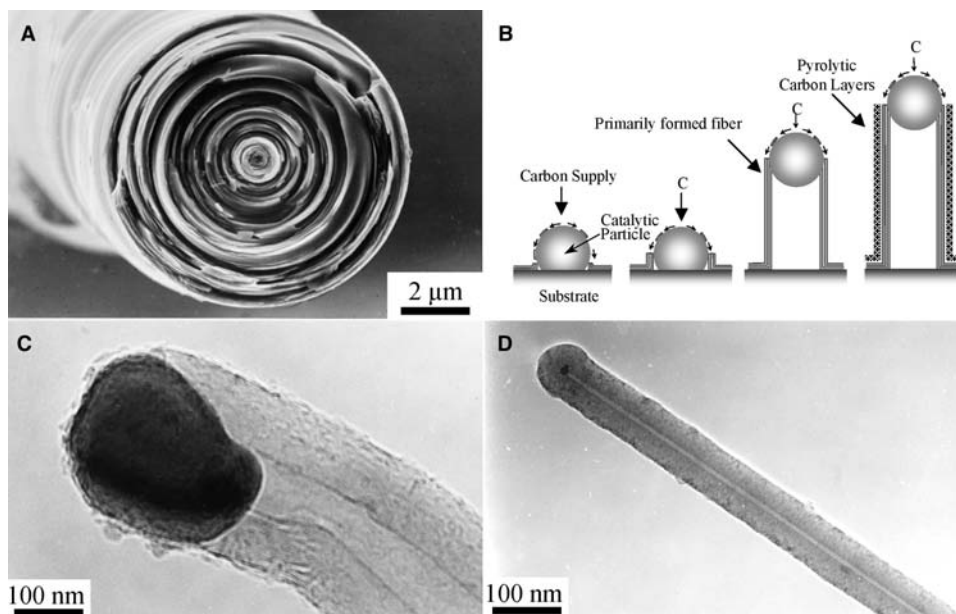


**Fig. 11** (A) SEM image of vapor-grown carbon fibers (VGCFs),<sup>[43]</sup> (B) suggested growth mechanism of VGCFs using ultra-fine catalytic metal particles,<sup>[7]</sup> (C) very early stage of fiber growth in which the catalytic-particle is still active for promoting elongation growth. The primary fiber thus formed acts as a core for vapor-grown fibers.<sup>[43]</sup> (D) The fiber is obtained through a thickening process, such as the pyrolytic deposition of carbon layers on the primary thin fibers.<sup>[43]</sup> The encapsulated catalytic particle can be seen at the tip of the hollow core.

hexagonal  $sp^2$ -carbon. The rapid growth rate of several tens of  $\mu\text{m}/\text{min}$ , which is  $10^6$  times faster than that observed for the growth of common metal whiskers,<sup>[42]</sup> allows the production of commercially viable quantities of VGCFs. Evidence in support of this growth model is the presence of catalytic particles at the tips of the resulting VGCFs (Fig. 11C).<sup>[43]</sup> The primary thin hollow fiber is first formed by the catalytic process (with a diameter of less than several nanometers), and the fiber is then thickened by a successive chemical vapor deposition (CVD) process, corresponding to the deposition

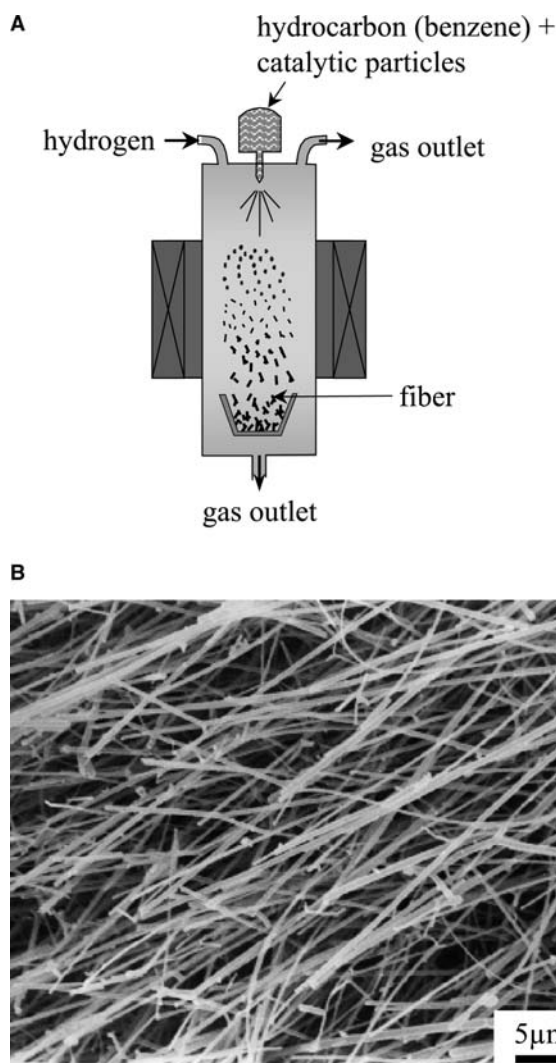


**Fig. 12** (A) A vertical-type fiber synthesis system for the floating reactant method in which benzene vapor containing an organic-metallic compound such as ferrocene is introduced into a vertical-type reactor by hydrogen gas. The fibers grow while the catalytic particles are floating in the growth region of the reactor<sup>[13,43]</sup> and (B) VGCFs, obtained under controlled growth conditions, exhibit relatively homogeneous diameter along the fiber length and also high purity.

of pyrolytic carbon layers on the primary tubular core (Fig. 11D).

Such a high growth rate of the primary core fiber provides the possibility of employing a 3-D growth process involving a floating catalyst in a reaction chamber without the presence of a solid substrate (see Fig. 12A). In this process, the nanometer-sized catalytic particles of metal can float (or be suspended) for a specified time in the hot zone of the reaction chamber in order to produce thin (100 nm homogeneous diameter) VGCFs of several hundred microns in length.<sup>[13,43]</sup> The resulting VGCFs sample shown in Fig. 12B consists of straight fibers with high purity, implying that the individual fibers experienced uniform reaction conditions as they passed through the reactor.<sup>[43]</sup> By proper choice of growth conditions, large quantities of high purity VGCFs can be obtained continuously. Furthermore, the fiber diameter can be varied through control of the residence time of

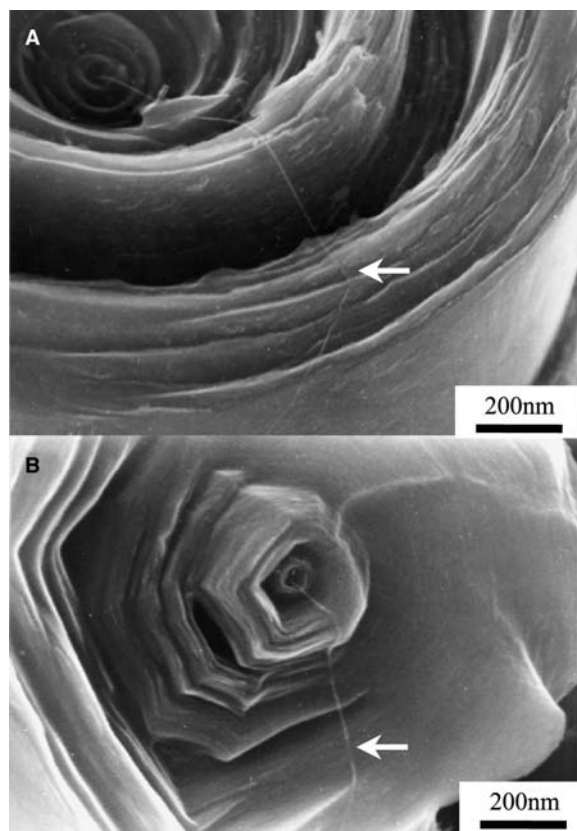


**Fig. 13** (A) Carbon nanotube exposed at the breakage edge of a vapor-grown carbon fiber as grown (A) and heat-treated at  $3000^\circ\text{C}$  (B). The sample is fractured by pulverization and the core diameter is  $\sim 50 \text{ \AA}$ . (B) These photos suggest a structural discontinuity between the nanotube core of the fiber and the CVD-deposited carbon layers. The images show the strong mechanical properties of the nanotube core, which maintains its form after breakage of the periphery. Source: From Ref.<sup>[11]</sup>.



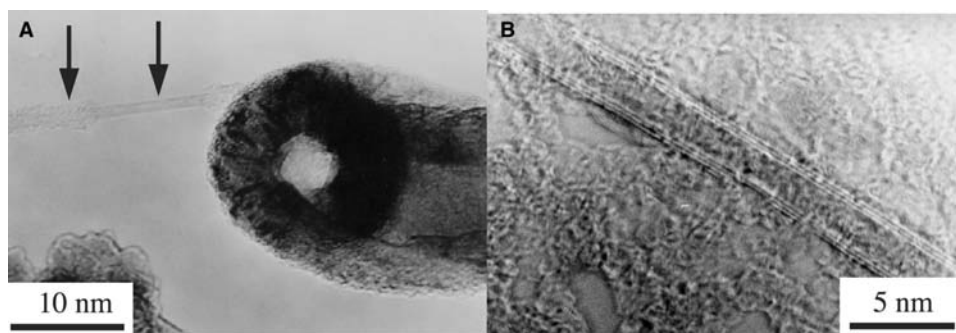


**Fig. 14** (A) Co-existence of a VGCF and a single-wall carbon nanotube (with a diameter of about 20 nm) obtained by the pyrolysis of benzene.<sup>[50]</sup> The deposition of a partial carbon layer on a carbon nanotube during the thickening process is observed. (B) Carbon nanotube (obtained by benzene decomposition) and subsequently heat treated at 2800°C, yielding the same structure as nanotubes prepared by the arc method. *Source:* From Ref.<sup>[50]</sup>.

the fiber in the reaction zone and of the pressure of the hydrocarbon feed stock. This basic process could be used for the large-scale production of carbon nanotubes by a CVD process based on the catalytic growth.<sup>[10,13,43,47–49]</sup>

In Fig. 13A, we observe the broken edge of a thick VGCF. At the center of the annular ring structure, we can clearly observe an extruded carbon nanotube (with a diameter of ~5 nm), which serves as a template for growing the thicker carbon fiber.<sup>[11]</sup> This tubular core implies a discontinuity in the structure between the core and the thickened periphery of the carbon fiber. Such a discontinuity in structure is retained even after heat treatment at temperatures as high as 3000°C. This graphitization process introduces a fully developed graphite structure in the peripheral region of a VGCF exhibiting a polygonal shape (see Fig. 13B). Fig. 14A shows the early stage of fiber growth of a thin tubule corresponding to a SWNT, which has both a bare region and a region partially coated with pyrolytically deposited carbon.<sup>[50]</sup> Sometimes it is possible to observe an isolated carbon nanotube without a pyrolytic carbon coat at the early stage of formation (Fig. 14B). This type of nanotube can be produced

by the same process as VGCFs by carefully controlling the vapor pressure of the hydrocarbon and using a much smaller size of catalytic particle.<sup>[50]</sup>

The CVD synthesis method has been considered as a promising method for the large-scale production of SWNTs and also MWNTs, especially using a floating reactant technique.<sup>[10,13,43,47–49]</sup> In terms of the manufacturing process, this process has been shown to be more controllable and cost efficient as compared with the arc discharge or laser vaporization methods. Fig. 15A and B exhibits a double-wall carbon nanotube and a four-wall carbon nanotube produced by a catalytic CVD method.<sup>[12,49,51]</sup> For the fabrication of a carbon nanotube transistor,<sup>[52]</sup> this synthesis technique appears to be highly efficient because of the reproducibility and low cost when compared to other routes.<sup>[53,54]</sup>

Exceptional mechanical properties of carbon nanotubes are expected, when few structural defects are present. The TEM image (Fig. 16A) and a theoretical simulated image (Fig. 16B) demonstrate that carbon nanotubes have nearly ideal mechanical properties because nanotubes do not break even after twisting, bending, or flattening. This particular behavior does

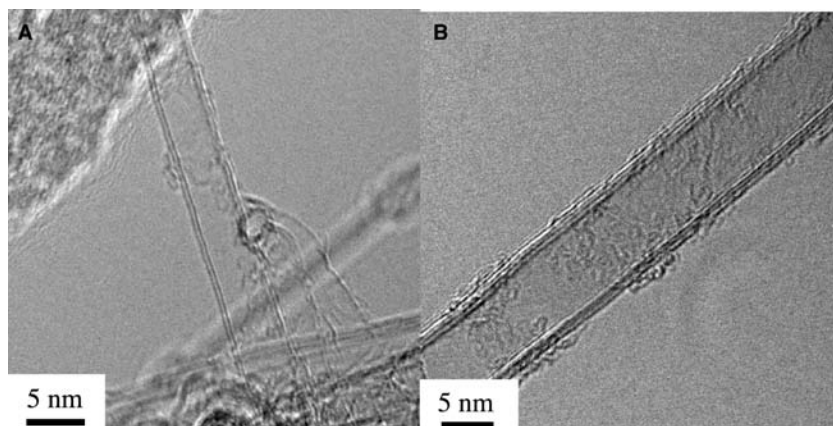


**Fig. 15** (A) Double-wall carbon nanotube and (B) a four-wall carbon nanotube produced by a catalytic CVD method.

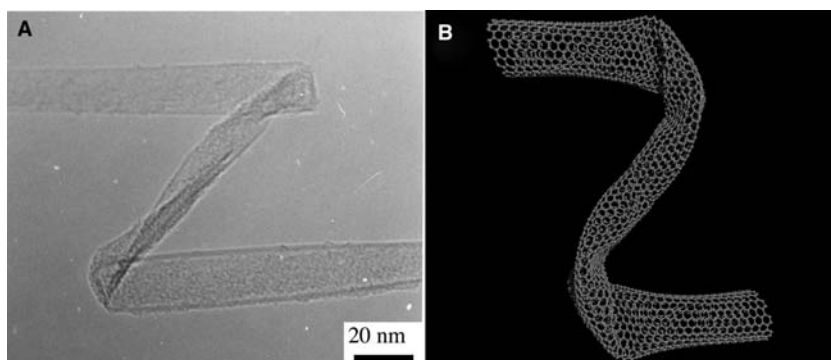


**Fig. 16** (A) HRTEM image of a distorted single-wall carbon nanotube and (B) a computer-simulated model. *Source:* From Ref.<sup>[50]</sup>.

not occur in carbon fibers, because they are brittle and more fragile.<sup>[50]</sup>

### INTERCALATION AND DOPING BY FOREIGN MOLECULES OR ATOMS

Because of the weak van der Waals interlayer forces associated with the  $sp^2$  bonding in graphite, graphite intercalation compounds (GICs) may be formed by the insertion of layers of guest species between the layers of a graphite host material,<sup>[55,56]</sup> as shown in Fig. 17A and B. The guest species may be either atomic or molecular. In the so-called donor GICs, electrons are transferred from the donor intercalate species (such as a layer of the alkali metal potassium) into the

graphite layers, thereby raising the Fermi level in the graphitic electronic states, and increasing the mobile electron concentration by two or three orders of magnitude, while leaving the intercalate layers positively charged. Conversely, for acceptor GICs, electrons are transferred to the intercalate species (which is usually molecular, such as  $Br_2$ ) from the graphite layers, thereby lowering the Fermi level in the graphitic electronic states and creating an equal number of positively charged hole states in the graphitic  $\pi$ -band. The enhanced electrical conduction in GICs (whether they are donors or acceptors) occurs predominantly in the graphene layers and as a result of the charge transfer between the intercalate and host layers. The electrical conductivity between adjacent graphene layers is very poor. It is noteworthy that among the GICs, Li-based

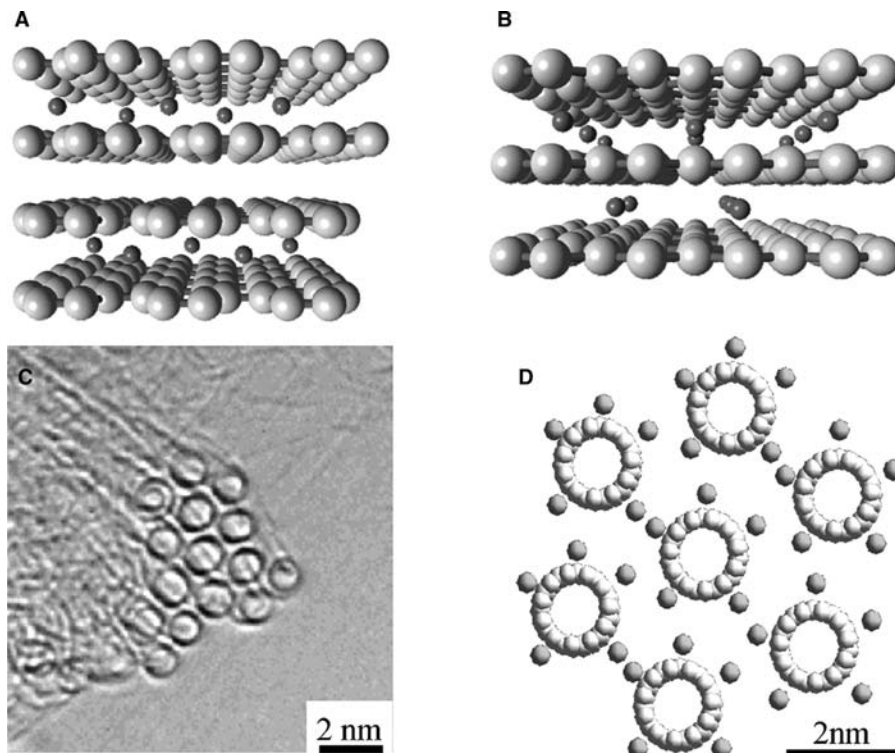


**Fig. 17** (A,B) Schematic model for a Li graphite intercalation compound showing the stacking of graphite layers (networks of hexagons on a sheet) and of intercalate (e.g., lithium) layers, (C) TEM image of an individual rope consisting of single-walled nanotubes aligned along the axis,<sup>[57]</sup> (D) a simulated image of a potassium-intercalated single-walled carbon nanotube rope superlattice. *Source:* From Ref.<sup>[58]</sup>.

GICs are widely used as anode materials in commercialized Li-ion secondary batteries for cell phones, personal computers, and electric vehicle batteries.<sup>[31]</sup>

Basic concepts similar to those occurring in GICs have been applied to carbon nanotubes in terms of the variation in structures, modification of electronic properties, and functionalities through the intercalation process. Namely, the bonding force between SWNT bundles or ropes (see Fig. 17C) is governed by the weak van der Waals force,<sup>[57]</sup> so that foreign species, such as atoms or molecules, can be intercalated in the van der Waals gaps, similar to graphite. Donor species, such as alkali metal atoms, can be easily intercalated into the trigonal lattice of nanotube ropes (see Fig. 17D),<sup>[58]</sup> while acceptor intercalation has proved more difficult. This result indicates the lack of 3-D structural fidelity within these nanotube ropes as it is found in 3-D bulk graphite.

Not only interstitial but also substitutional doping of foreign atoms into the carbon network of graphene sheets has also been studied widely for altering their electronic and structural properties for potential applications, such as high-temperature oxidation protection for carbon/carbon composites and as an anode material for Li-ion batteries, because, for instance, boron-doping introduces an electron acceptor level.<sup>[59]</sup> Fig. 18A shows an STM image of a 3-D surface plot and a sectional analysis of highly oriented pyrolytic graphite doped with boron.<sup>[60]</sup> Each bright area consists of boron atoms, with the highest electron density located at the center of six surrounding sites, and with medium electron density corresponding to carbon atoms. Also, the electron density distribution of a substitutional boron atom and of the surrounding six carbon atoms clearly appears in the 3-D surface plot (Fig. 18A inset). The substitutional boron atom

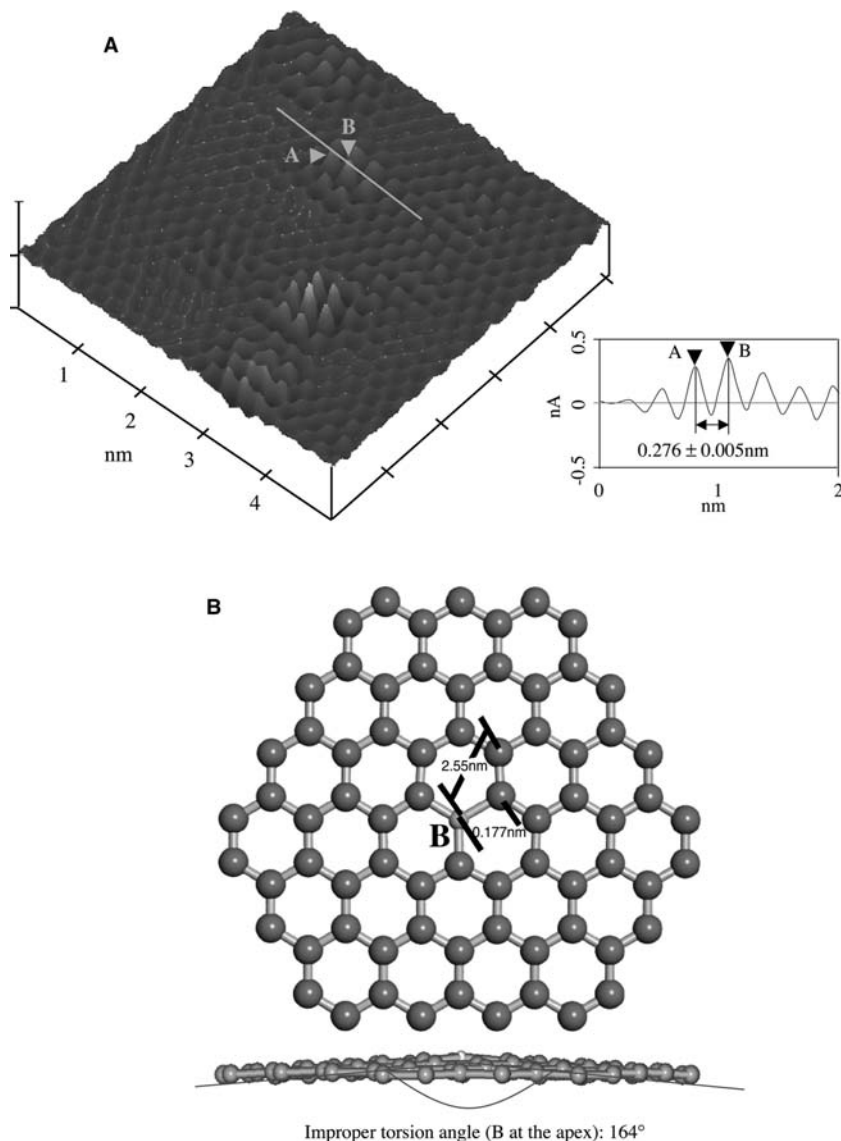


**Fig. 18** (A) STM image of a three-dimensional surface plot and a section analysis for boron-doped highly oriented pyrolytic graphite<sup>[60]</sup> and (B) schematic model of the top view and the side view of a boron-doped graphene sheet based on the measured dimensions of B-C<sub>1</sub> and C<sub>1</sub>-C<sub>1</sub>. *Source:* From Ref.<sup>[60]</sup>.



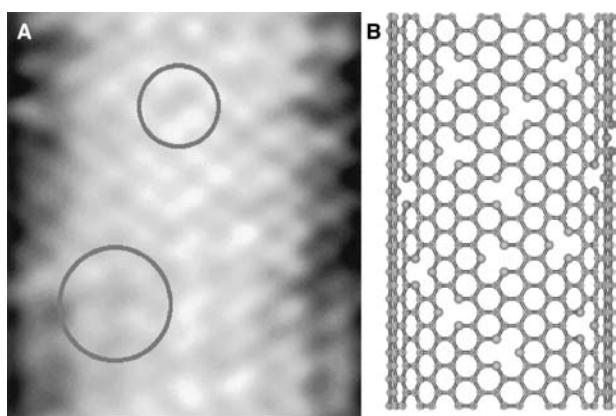


**Fig. 19** (A) STM image of the surface of a 20-nm  $CN_x$  nanotube and (B) suggested structural model for a  $CN_x$  tube. Source: From Ref.<sup>[61]</sup>.

exhibits the highest electron density in the center. Also, the substitution of boron should slightly deform the flatness of the basal plane (Fig. 18B). By restricting the measured bond length between the B–C atoms obtained from Fig. 18A, the optimized structure of a graphene sheet has been simulated. An improper torsion angle (B at the apex) is calculated to be  $164^\circ$  as shown in Fig. 18B, while the original plane is almost flat with an angle of  $179^\circ$ . For the case of multiwall carbon nanotubes, a comprehensive study of the effect of nitrogen doping was carried out using STM.<sup>[61]</sup> Fig. 19A shows an STM image of a nitrogen-doped carbon nanotube, exhibiting both distortion and holes. The suggested structure of a  $CN_x$  nanotube is shown in Fig. 19B. This type of hole might be due to pyridine-like and highly coordinated nitrogen atoms replacing carbon atoms. Substitutional doping into carbon nanotubes thus provides a useful method to modify the electronic and mechanical properties and enlarge the functionality of carbon nanotubes even further.

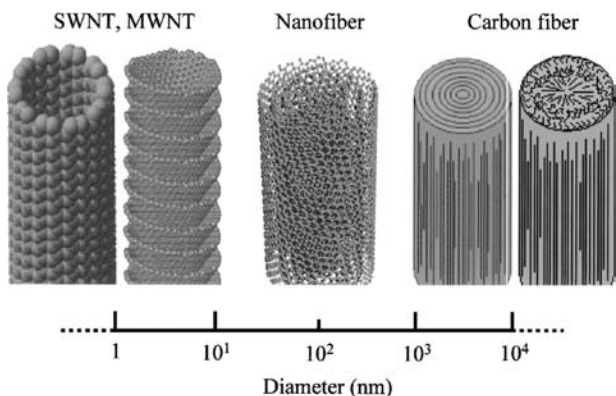


**Fig. 20** Schematic comparisons of the diameter dimensions for various types of fibrous carbons. Source: From Ref.<sup>[62]</sup>.

## CONCLUSION

It has been demonstrated that carbon nanotubes, consisting of graphene tubes of nanometer-size diameter, are different from conventional carbon and graphite materials, even from carbon fibers consisting of oriented planar graphene sheets. The structure of VGCFs exhibiting a carbon nanotube core can relate to both carbon nanotubes and fibers (Fig. 20).<sup>[62]</sup> The diameters range from 1 nm for nanotubes to  $10^4$  nm for carbon fibers, and VGCFs are located between the two. Bulk effects that are based on the Bernal stacking of planar graphene sheets disappear with decreasing diameter, and new quantum effects based on the thin nanotube morphology appear in the range of nanotube diameters corresponding to those of single- and multiwall carbon nanotubes. The special characteristics of carbon nanotubes in this diameter range can expand carbon science and provide new opportunities for developing innovative and exciting applications in the nanotechnology field.

## REFERENCES

1. Iijima, S. Helical microtubules of graphitic carbon. *Nature* **1991**, *354* (7), 56–58.
2. Saito, R.; Dresselhaus, M.S.; Dresselhaus, G. *Physical properties of carbon nanotubes*; Imperial College Press: London, 1998.
3. Dresselhaus, M.S.; Dresselhaus, G.; Eklund, P.C. *Science of Fullerenes and Carbon Nanotubes*; Academic Press: San Diego, 1996.
4. Qin, L.C.; Zhao, X.; Hirahara, K.; Miyamoto, Y.; Ando, Y.; Iijima, S. The smallest carbon nanotube. *Nature* **2000**, *408* (2), 50.
5. Bahl, O.P.; Shen, Z.; Lavin, J.G.; Ross, R.A. *Manufacture of Carbon Fibers*. In *Carbon Fibers*, Third Ed.; Donnet, J.B., Wang, T.K., Peng, J.C.M., Rebouillat, S., Eds.; Marcel Dekker: New York, 1998; 1–83.
6. Donnet, J.B.; Bansal, R.C. *Carbon Fibers*; Marcel Dekker Inc.: New York, 1984.
7. Oberlin, A.; Endo, M.; Koyama, T. Filamentous growth of carbon through benzene decomposition. *J. Cryst. Growth* **1976**, *32*, 335–349.
8. Baker, R.T.K. Catalytic growth of carbon filaments. *Carbon* **1989**, *27* (3), 315–323.
9. Tibbetts, G.G. Why are carbon filaments tubular? *J. Cryst. Growth* **1984**, *66*, 632–637.
10. Endo, M. Grow carbon fibers in the vapor phase. *Chem. Tech.* **1988**, *18*, 568–576.
11. Endo, M.; Takeuchi, K.; Kobori, K.; Takahashi, K.; Kroto, H.W.; Sarkar, A. Pyrolytic carbon nanotubes from vapor-grown carbon fibers. *Carbon* **1995**, *33* (7), 873–881.
12. <http://www.sdk.co.jp/enews/news01/01-06.htm> (accessed August 2002) (for mass production of nanofiber and nanotube); .

13. Dresselhaus, M.S.; Dresselhaus, G.; Sugihara, K.; Spain, I.L.; Goldberg, H.A. Graphite Fibers and Filaments; Springer Series in Materials Science; Springer-Verlag: Berlin, 1988; 5.
14. Kelly, B.T. Physics of Graphite; Applied Science: London, 1981.
15. Bundy, F.P.; Bassett, W.A.; Weathers, M.S.; Hemley, R.J.; Mao, H.K.; Goncharov, A.F. The pressure-temperature phase and transformation diagram for carbon. *Carbon* **1996**, *34* (2), 141–153.
16. Grumbach, M.P.; Martin, R.M. Phase diagram of carbon at high pressures and temperatures. *Phys. Rev., B* **1996**, *54* (22), 15730–15741.
17. Whittaker, A.G.; Watts, E.J.; Lewis, R.S.; Anders, E. Carbynes: Carriers of primordial noble gases in meteorites. *Science* **1980**, *209*, 1512.
18. Li, S.Y.; Zhou, H.H.; Gu, J.L.; Zhu, J. Does carbyne really exist?—Carbynes in expanded graphite. *Carbon* **2000**, *38* (6), 935–937.
19. Dresselhaus, M.S.; Steinbeck, J. Liquid carbon. *Tanso* **1988**, *132*, 44–56.
20. Dresselhaus, M.S.; Dresselhaus, G.; Avouris, Ph. Introduction to carbon material research. In *Carbon Nanotubes Topics in Applied Physics 80*; Dresselhaus, M.S., Dresselhaus, G., Avouris, Ph., Eds.; Springer-Verlag: Heidelberg, 2001; 1–9 Chapter 1.
21. Louie, S.G. Electronic Properties, junctions and defects of carbon nanotubes. In *Carbon Nanotubes Topics in Applied Physics 80*; Dresselhaus, M.S., Dresselhaus, G., Avouris, Ph., Eds.; Springer-Verlag: Heidelberg, 2001; 113–145 Chapter 6.
22. Saito, R.; Kataura, H. Optical properties and raman spectroscopy of carbon nanotubes. In *Carbon Nanotubes Topics in Applied Physics 80*; Dresselhaus, M.S., Dresselhaus, G., Avouris, Ph., Eds.; Springer-Verlag: Heidelberg, 2001; 213–247 Chapter 9.
23. Dresselhaus, M.S.; Dresselhaus, M.; Eklund, P.C.; Saito, R.; Endo, M. Introduction to carbon materials. In *Carbon Nanotubes*; Ebbesen, T.W., Ed.; CRC: New York, 1997; 1–34 Chapter 1.
24. Bokros, J.C. Deposition, structure and properties of pyrolytic carbon. In *Chemistry and Physics of Carbon*; Walker, P.L., Jr., Ed.; Marcel Dekker: New York, 1969; Vol. 5, 1–110.
25. Charlier, J.C. Carbon nanotubes and fullerenes. In *Ph.D. Thesis; Department of Physics*; Catholic University of Louvain, May, 1994.
26. Charlier, J.C.; Gonze, X.; Michenaud, J.P. First principles study of carbon nanotube solid-state packings. *Europhys. Lett.* **1995**, *29*, 43.
27. Charlier, J.C.; Gonze, X.; Michenaud, J.P. First principles study of the stacking effect on the electronic properties of graphite. *Carbon* **1994**, *32*, 289–299.
28. Maire, J.; Méring, J. Graphitization of soft carbons. In *Chemistry and Physics of Carbon*; Walker, P.L., Jr., Ed.; Marcel Dekker: New York, 1970; Vol. 6, 125.
29. Fischbach, D.B. The Kinetics and Mechanism of Graphitization; *Chemistry and Physics of Carbon*; Walker, P.L., Jr., Ed.; Marcel Dekker: New York, 1969; Vol. 7, 1–97.
30. Pacault, A. The kinetics of graphitization; *Chemistry and Physics of Carbon*; Walker, P.L., Jr., Ed.; Marcel Dekker: New York, 1969; Vol. 7, 107–153.
31. Endo, M.; Kim, C.; Nishimura, K.; Fujino, T.; Miyashita, K. Recent development of carbon materials for Li ion batteries. *Carbon* **2000**, *38* (2), 183–197.
32. Endo, M.; Kim, Y.A.; Hayashi, T.; Nishimura, K.; Matushita, T.; Miyashita, K.; Dresselhaus, M.S. Vapor-grown carbon fibers (VGCs) basic properties and battery application. *Carbon* **2001**, *39* (9), 1287–1297.
33. Sun, X.; Kiang, C.H.; Endo, M.; Takeuchi, K.; Furuta, T.; Dresselhaus, M.S. Stacking characteristics of graphene shells in carbon nanotubes. *Phys. Rev., B* **1996**, *54* (18), 1–4.
34. Inagaki, M. New carbons: control of structure and functions; Elsevier: New York, 2000.
35. Endo, M.; Hishiyama, Y.; Koyama, T. Magnetoresistance effect in graphitizing carbon fibres prepared by benzene decomposition. *J. Phys., D. Appl. Phys.* **1982**, *15*, 353–363.
36. Issi, J.P.; Charlier, J.C. Electrical Transport Properties in Carbon Nanotubes. In *The Science and Technology of Carbon Nanotubes*; Tanaka, K., Yamabe, T., Fukui, K., Eds.; Elsevier: New York, 1999; 107–127. Chapter 10.
37. Wallace, P.R. The band theory of graphite. *Phys. Rev.* **1947**, *71*, 622–634.
38. Mintmire, J.W.; White, C.T. Electronic and structural properties of carbon nanotubes. *Carbon* **1995**, *33* (7), 893–902.
39. Ge, M.; Sattler, K. Vapor-condensation generation and STM analysis of fullerene tubes. *Science* **1993**, *260*, 515–518.
40. Wildöer, J.W.G.; Venema, L.C.; Rinzler, A.G.; Smalley, R.E.; Dekker, C. Electronic structure of atomically resolved carbon nanotubes. *Nature* **1998**, *391*, 59–62.
41. Donnet, J.B. Preface. In *Carbon Fibers*, Third Ed.; Donnet, J.B., Wang, T.K., Peng, J.C.M., Rebouillat, S., Eds.; Marcel Dekker: New York, 1998; iii.
42. Bacon, R. Production of graphite whiskers. *J. Appl. Phys.* **1960**, *31*, 283–290.
43. Endo, M.; Saito, R.; Dresselhaus, M.S.; Dresselhaus, G. From Carbon Fibers to Carbon Nanotubes. In *Carbon Nanotubes*; Ebbesen, T.W., Ed.; CRC: New York, 1997; 35–105.
44. Oberlin, A. High-Resolution TEM studies of carbonization and graphitization. In *Chemistry and Physics of Carbon*; Thrower, P.A., Ed.; Marcel Dekker: New York, 1989; Vol. 22, 1–135.
45. Peebles, L.H.; Yanovsky, Y.G.; Sirota, A.G.; Bogdanov, V.V.; Levit, P.M. Mechanical properties of carbon fibers. In *Carbon Fibers*, Third Ed.; Donnet, J.B., Wang, T.K., Peng, J.C.M., Rebouillat, S., Eds.; Marcel Dekker: New York, 1998; 311–370.
46. Oberlin, A.; Endo, M.; Koyama, T. High resolution electron microscope observations of graphitized carbon fibers. *Carbon* **1976**, *14*, 133–135.
47. Endo, M.; Kim, Y.A.; Fukai, Y.; Hayashi, T.; Terrones, M.; Terrones, H.; Dresselhaus, M.S. Comparison study of semi-crystalline and highly crystalline multiwalled carbon nanotubes. *Appl. Phys. Lett.* **2001**, *79* (10), 1531–1533.

48. Endo, M.; Kim, Y.A.; Hayashi, T.; Fukai, Y.; Oshida, K.; Terrones, M.; Yanagisawa, T.; Higaki, S.; Dresselhaus, M.S. Structural characterization of cup-stacked carbon nanofibers with an entirely hollow core. *Appl. Phys. Lett.* **2002**, *80* (7), 1267–1269.
49. Tanaka, K.; Endo, M.; Takeuchi, K.; Hsu, W.K.; Kroto, H.W.; Terrones, M.; Walton, D.R.M. Large-scale synthesis of carbon nanotubes by Pyrolysis. In *The Science and Technology of Carbon Nanotubes*; Tanaka, K., Yamabe, T., Fukui, K., Eds.; Elsevier: New York, 1999; 143–152. Chapter 12.
50. Endo, M.; Takeuchi, K.; Igarshi, S.; Kobori, K.; Shiraishi, M.; Kroto, H.W. The production and structure of pyrolytic carbon nanotubes (PCNTs). *J. Phys. Chem. Solids* **1994**, *54* (12), 1841–1848.
51. Endo, M.; Hayashi, T.; Kasai, T.; Kim, Y.A.; Fukai, F.; Matoba, T. Mass production and application of carbon nanotube and nanofiber. *M&E* **2001**, *8*, 164–172. (in Japanese).
52. Tans, S.J.; Verschueren, A.R.M.; Dekker, C. Room-temperature transistor based on a single carbon nanotube. *Nature* **1998**, *393*, 49–52.
53. Homma, Y.; Kobayashi, Y.; Ogino, T.; Yamashita, T. Growth of suspended carbon nanotube networks on 100-nm-scale silicon pillars. *Appl. Phys. Lett.* **2002**, *81* (12), 1–3.
54. Homma, Y.; Yamashita, T.; Finnie, P.; Tomita, M.; Ogino, T. Single-walled carbon nanotube growth on silicon substrate using nanoparticle catalysts. *Jpn. J. Appl. Phys.* **2002**, *41*, L89–L91.
55. Dresselhaus, M.S.; Dresselhaus, G. Intercalation compounds of graphite. *Adv. Phys.* **1981**, *30* (2), 139–326.
56. Zabel, H.; Solin, S.A. Graphite intercalation compounds: I structure and dynamics; Springer-Verlag: Berlin, 1990; Vol. 14.
57. Terrones, M.; Terrones, H.; Banhart, F.; Charlier, J.C.; Ajayan, P.M. Coalescence of single-wall carbon nanotubes. *Science* **2000**, *288*, 1226–1229.
58. Endo, M.; Nishimura, K.; Hakamada, K.; Minoura, F.; Hara, H. Giant fullerene “carbon nanotubes”—preparation and structure. *Ceramics* **1998**, *33*, 424–427. (In Japanese).
59. Marchand, A. *Electronic Properties of Doped Carbon; Chemistry and Physics of Carbon*; Walker, P.L., Jr., Ed.; Marcel Dekker: New York, 1969; Vol. 7, 155–188.
60. Endo, M.; Hayashi, T.; Hong, S.H.; Enoki, T.; Dresselhaus, M.S. Scanning tunneling microscope study of boron-doped highly oriented pyrolytic graphite. *J. Appl. Phys.* **2001**, *90* (11), 5670–5674.
61. Czerw, R.; Terrones, M.; Charlier, J.-C.; Blase, X.; Foley, B.; Kamalakaran, R.; Grobert, N.; Terrones, H.; Tekleab, D.; Ajayan, P.M.; Blau, W.; Ruhle, M.; Carroll, D.L. Identification of electron donor states in N-doped carbon nanotubes. *Nano Lett.* **2001**, *1* (9), 457–460.
62. Endo, M.; Kim, Y.A.; Matusita, M.; Hayashi, T. From vapor-grown carbon fibers (VGCFs) to carbon Nanotubes. In *Carbon Filaments and Nanotubes: Common Origins, Differing Applications?* Nato Science Series; Biro, L.P., Bernardo, C.A., Tibbetts, G.G., Lambin, Ph., Eds.; Kluwer Academic Publishers: London, 2001; Vol. 372, 51–61.

# Carbon Nanotubes for Storage of Energy: Supercapacitors

**Elzbieta Frackowiak**

*Institute of Chemistry and Technical Electrochemistry,  
Poznan University of Technology, Poznan, Poland*

## **Abstract**

Carbon nanotubes (CNTs) due to their excellent conducting and mechanical properties play a useful role of electrode material in supercapacitors. Pure nanotubes (multi-walled as well as single-walled) supply moderate capacitance values because of their well developed mesoporosity but very limited microporosity. Microporosity of CNTs, hence, capacitance can be enhanced by functionalization and activation of CNTs (KOH treatment at high temperatures). On the other hand, CNTs are a perfect component of composites with electrically conducting polymers (ECP) and transition metal oxides, e.g.  $\text{MnO}_2$ . The three-dimensional network of the nanotubular composite enables an easy penetration of ions, in turn, a good performance of capacitor. Another interesting capacitor material could be obtained by carbonization of various carbon precursors, e.g. polymers, in the presence of nanotubes. In this case, attractive C/C composites have been prepared. Especially, peculiar properties have been found if the carbon precursor was rich in nitrogen (polyacrylonitrile, melamine). The presence of nitrogen in the capacitor material was responsible for pseudocapacitance effects. Nanotubular composites with pseudocapacitive materials offer a great progress in supercapacitor development.

## **INTRODUCTION**

Carbon nanotubes (CNTs), because of their exceptional physicochemical properties, have been used for energy storage devices such as supercapacitors. Especially, conducting and microtextural properties of CNTs are noteworthy for this electrochemical application. The presence of more or less continuous graphitic layers, cylindrically rolled, together with a tight entanglement of nanotubes supply a conducting and well-accessible carbon network with a moderate surface area (ca.  $100\text{--}400\text{ m}^2/\text{g}$ ). Because the performance of electrochemical capacitors is connected with the accumulation of charges in the electrode/electrolyte interface, such a material in the form of an easily available web is of great interest. However, for supercapacitor application, apart from small mesopores, which are perfect for ion transportation, easily accessible micropores are required for the accumulation of ions in the electrical double layer (EDL). Ultramicropores with diameter below 1 nm are especially adapted for efficient charging of EDL because they well match with dimensions of ions. Generally, as a capacitor electrode material, a highly developed specific surface area carbons are used. Carbon nanotubes can be used as electrode material but the capacitance values will be very moderate because CNTs are mesoporous with negligible microporosity. The values of capacitance strictly depend on nanotube microtexture. The more defected the outer walls of CNTs, the higher the capacitance values. The presence of a thin amorphous carbon layer on the CNT walls can supply better conditions for charge accumulation. Additionally, catalytic

impurities of nanotubes remaining from the production process could be a source of redox reactions giving pseudocapacitance effects. Hence, CNTs directly used as the electrode material has a limited interest; on the other hand, they can serve as a perfect additive or support of active material in composite electrodes.

Generally, from the literature data, a high discrepancy of capacitance for pure CNTs is found because the values strongly depend on CNTs' preparation method, purification, or modification process. Some research has been devoted to elucidate the effect of microtexture on capacitance properties. Enhancement of CNTs' capacitance has been achieved by an increase in their surface area. A few fold increase of capacitance has been obtained by KOH activation at  $800^\circ\text{C}$  because of the development of microporosity while preserving the mesoporous character. This interesting phenomenon can be explained by the insertion or intercalation of potassium in the walls of nanotubes at  $800^\circ\text{C}$  and the subsequent formation of micropores. Consequently, the opening of nanotube tips was also observed that could be profitable for charge accumulation. Higher values of capacitance can also be obtained if CNTs are used as a conducting component or support in the composite electrode. In this case, conducting polymers or redox species are mainly responsible for the capacitance values (giving the so-called pseudocapacitance). Generally, a synergy effect is obtained between the components of the supercapacitor electrode. A nanocomposite gives better results than its components alone.

Carbon nanotubes can also be used as a frame for carbon obtained from different polymeric precursors.

In this case, the nanotube skeleton is very profitable to prevent shrinkage during the carbonization process and to allow a simultaneous autoactivation of carbon by the evolving gases and consequently an interesting CNT/carbon composite is obtained for supercapacitor application.

## UNIQUE CHARACTERISTICS OF CNTs

The discovery of CNTs by Iijima in 1991<sup>[1]</sup> has generated great interest in carbon materials and nanotechnology. Carbon nanotubes have exceptional electrical, mechanical, thermal, optical, and textural properties, which are attractive for various potential applications ranging from nanoelectronics to biomedical devices.<sup>[2]</sup> Their unique characteristics result from the helical or fishbone arrangement of the graphitic layers, the presence of a central canal, as well as entanglement or bundle formation. The areas of nanotube interest include composites, field emitters, electronic devices (nanotransistor, one-dimensional quantum wire), gas adsorption, catalyst support, templating, sensors, and others. However, the scope for using CNTs in practical applications has been limited by a moderate-scale production and their high cost. One of the most promising uses of CNTs seems to be energy storage device, i.e., supercapacitor, where CNTs could be used as an electrode component, which allows a nanoscale dispersion of active material on such three-dimensional well-conducting skeleton.

## SUPERCAPACITOR PERFORMANCE

An electrochemical capacitor (supercapacitor) is a very attractive energy source due to its high power, i.e., fast delivery of energy and long-term durability.<sup>[3–8]</sup> It is

built from a positive electrode with electron deficiency, whereas the second one is negative with electron excess (Fig. 1). In such a simple model, capacitor consists of two polarizable electrodes, a separator and the electrolytic solution. A pure electrostatic attraction between ions and the charged surface of an electrode takes place. Figure 1 shows a reversible charging/discharging of supercapacitor. The amount of electrical energy  $W$  accumulated in such a capacitor is proportional to capacitance  $C$  and voltage  $U$ .

$$W = 1/2CU^2 \quad (1)$$

The operating voltage of the capacitor is determined by the decomposition potential of electrolyte. The electrical energy of the capacitor can be significantly enhanced by the selection of an aprotic electrolytic solution where the decomposition potential of the electrolyte varies from 3 to 5 V. The performance of an electrochemical capacitor is based on the charge accumulation in the EDL, without the Faradaic reactions that take part in typical accumulators. The stored energy is based on the separation of charged species across the electrode/solution interface. As far as a pure electrostatic attraction of ions is involved, the electrode capacitance  $C$  is proportional to the electrode/electrolyte interface (to the electrode surface) according to the following equation.

$$C = S\epsilon/d \quad (2)$$

The capacitance is also proportional to the relative permittivity of the solution  $\epsilon$ , and reciprocally dependent on the thickness  $d$  of the EDL. It is noteworthy that the overall capacitance  $C$  is determined by the series connection of two electrodes  $C_1$  and  $C_2$ ; hence, in the case of a capacitor built from two electrodes with different surfaces, the component of smaller capacitance will contribute more to the total value

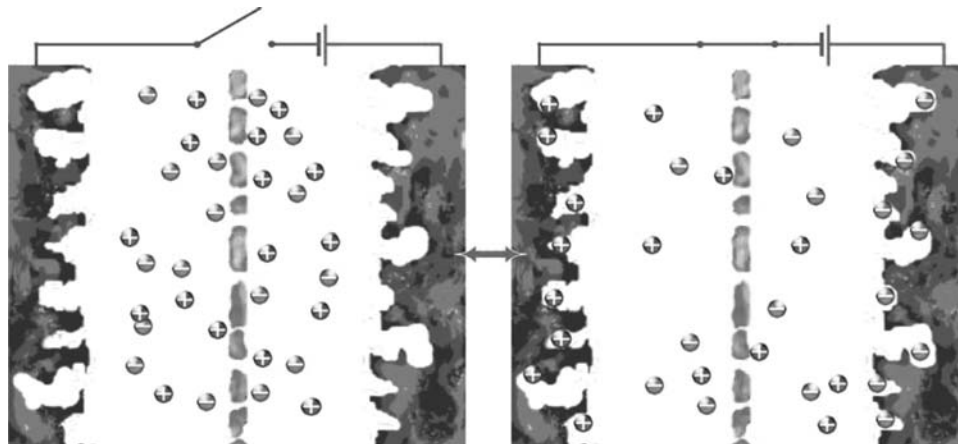


Fig. 1 Charging/discharging of electrochemical capacitor.

due to reciprocal dependence.

$$1/C = 1/C_1 + 1/C_2 \quad (3)$$

The capacitance unit is a farad (F), which is the charge accumulated in the defined range of voltage (coulomb per volt). The specific capacitance can be related to the electrode mass (F/g), to the electrode volume (F/cm<sup>3</sup>), or the electrode surface (F/cm<sup>2</sup>).

Values of capacitance are strictly determined by the porosity of electrode material. It is well known that micropores (with a diameter less than 2 nm) play an essential adsorption role in the formation of the EDL, whereas mesopores (diameter from 2 to 50 nm) are responsible for the adsorption of ions and for their quick transportation to the bulk of the electrode material. Obviously, taking into account size of ions, only the smallest mesopores could play some useful role.

The enhancement of capacitance values can be realized through a redox pseudocapacitive mechanism by the simultaneous combination of two kinds of energy storage, i.e., an electrostatic attraction of ions together with Faradaic reactions. Large charge-storage capabilities obtained through this process have been observed in the case of conducting polymers and transition metal oxides. The transfer of counter ions between the electrolyte and the bulk of the electrode material proceeds as a response to the electron transfer processes associated with oxidation and reduction of the material. In this case, the capacitor is named ultra- or supercapacitor.

## NANOTUBES AS SUPERCAPACITOR ELECTRODES

Carbon nanotubes, either aligned or randomly entangled, present interesting capacitance properties and have been widely used for supercapacitor application.<sup>[7–29]</sup> Both arrangements supply an open network of mesopores due to the entanglement, presence of central canal, or mutual interconnections. Even if the capacitance values are very moderate, such a good accessibility of the electrode/electrolyte interface of the nanotubular material facilitates the charging of the EDL and allows very high dynamics of charge propagation, typical for good performance of a supercapacitor. Both types of CNTs, i.e., single and multi-walled, will be considered for this application.

### Single-Walled Nanotubes as Electrode Materials

Single-walled nanotubes (SWNTs) have been tested as electrode materials for electrochemical

capacitors.<sup>[8,13–16]</sup> The bucky paper from nanotubes (Rice University, USA) allowed one to get self-standing electrodes that can be directly used for the capacitor assembly. They supply a value of 40 F/g in the alkaline 6 M KOH solution.<sup>[13]</sup> After their annealing at 1650°C, the capacitance diminishes to 18 F/g because of a better arrangement of the tubes in the bundles that decreases microporosity.

Raw materials containing 30% of SWNTs have also been used for the preparation of supercapacitor electrodes after mixing with poly(vinylidene chloride) (PVDC) and pyrolysis of the mixture at 1000°C. The authors attribute the high capacitance value of 180 F/g measured in 7.5 M KOH to the SWNT material.<sup>[14]</sup> However, in reality the carbonization of PVDC at 1000°C produces microporous carbon, and as a consequence the high capacitance values are due to the carbon obtained from the polymeric binder but not to SWNTs.

The electric double layer capacitance of highly pure SWNTs (HiPco™) was carefully studied in organic medium, i.e., 1 M LiClO<sub>4</sub> in propylene carbonate.<sup>[15]</sup> The gravimetric capacitance of SWNTs is around 45 F/g and does not diminish with the increase in current density from 10 to 160 mA/g. The specific capacitance per unit surface area was compared for SWNTs and for activated carbon fibers (ACFs). The authors found higher values of 10 μF/cm<sup>2</sup> for SWNTs and only 5.5 μF/cm<sup>2</sup> for ACFs due to ion sieving in the case of highly microporous ACFs. The open mesoporous network of SWNTs is profitable for a quick charge propagation, especially when an organic medium is used as electrolytic solution.

Some research was devoted to modification of SWNTs by chromium oxide.<sup>[16]</sup> The capacitance values increased two times and the electrode material was characterized by very good charge propagation.

After careful analysis of literature data, it is clear that pure single-walled nanotubes without catalyst impurities and without any modification cannot supply higher values than ca. 45 F/g due to their limited surface area and negligible microporosity. Similar moderate capacitance values (20–40 F/g) for SWNTs have been found as well in aqueous and non-aqueous solutions by electrochemical investigation.<sup>[30]</sup>

### Multi-Walled Nanotubes for Capacitor Application

Multi-walled carbon nanotubes (MWNTs) as a typical mesoporous material were carefully investigated for supercapacitor applications in the form of electrodes or electrode component.<sup>[7–13,17–24]</sup> The specific surface area of different nanotubes varied from 120 to 450 m<sup>2</sup>/g. Generally, the values of capacitance for



nanotubes widely range from 5 to 80 F/g. Higher values of 110 F/g have been also found<sup>[9]</sup> when the catalytically grown nanotubes were chemically modified by nitric acid treatment (10% of the carbon atoms on the surface were bound to oxygen). Such functionalized MWNTs were self-adhesive and could easily form very thin freestanding mat. A good frequency response is mentioned by the authors for this material (100 F/g was withdrawn at 1 Hz). However, the stability of supercapacitor performance during subsequent cycles was not investigated. On the other hand, values of 15–25 F/cm<sup>3</sup> that give ca. 20 F/g have been measured for MWNTs in the same solution, i.e., 38% H<sub>2</sub>SO<sub>4</sub>.<sup>[10]</sup>

The high discrepancy in the capacitance values of various MWNTs can be easily explained by their different microtextures and composition. Typically, the smaller capacitance values were observed with CNTs of low surface area. For example, purified nanotubes obtained by the decomposition of acetylene at 600°C using the in situ catalyst formed from the solid solution Co<sub>x</sub>Mg<sub>(1-x)</sub>O,<sup>[31]</sup> with a specific surface area of 220 m<sup>2</sup>/g, supplied only 15 F/g. Figure 2 shows an entangled network of these nanotubes and Fig. 3 presents a detailed transmission electron microscopy (TEM) image of a few representatives. The high purity of these nanotubes, quite regular walls, and a lack of any disordered carbon are responsible for limited capacitance properties. A completely different nanotubular product is obtained from the decomposition of acetylene at 700°C using a silica support for the cobalt catalyst.<sup>[7]</sup> It is striking that a value of 80 F/g could be reached for such catalytic nanotubes, which possess a moderate surface area of only 430 m<sup>2</sup>/g. In this case, a thin layer of pyrolytic carbon on the nanotubes with a number of surface defects gives the high values of capacitance. Generally, the more defective the walls and the better developed the surface area of the nanotubes, the higher

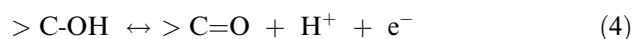
the values of capacitance. On the other hand, nanotubes with perfect walls and a high degree of graphitization provided limited capacitance values from 5 to 20 F/g.<sup>[8,17]</sup> From a careful analysis of the results, it seems that the values of capacitance and amount of micropores, even if quite limited, are well correlated.

For the pure nanotubular materials, it is clear that capacitance can be improved in two ways: development of microporosity and surface functionality by chemical activation.

### Modification of MWNTs by Functionalization and Chemical Activation

Carbon nanotubes can be easily modified by hot nitric acid treatment, which introduces oxygenated surface groups. Voltammetry characteristic of capacitor built from oxidized nanotubes is shown in Fig. 4. Capacitance increased up to 135 F/g through functionalization of CNTs by concentrated nitric acid at 80°C for 1 hr.<sup>[7,8,11]</sup> However, owing to the irreversible character of redox reactions of some surface groups, e.g. carboxylic, the pseudocapacitance effect can diminish with cycling. On the other hand, the redox couple of quinone–hydroquinone is reversible and stable.

The great increase in capacitance visible as a well-defined hump at ca. 0.2 V has been attributed to the following quinone–hydroquinone redox reactions<sup>[7,8,11]</sup>



In the case of CNTs directly grown on a graphite foil,<sup>[9]</sup> to improve the electrical contact between the substrate and nanotubes, the authors introduced functional groups on the nanotube surface by a special exposure of the material to air. Finally, capacitance

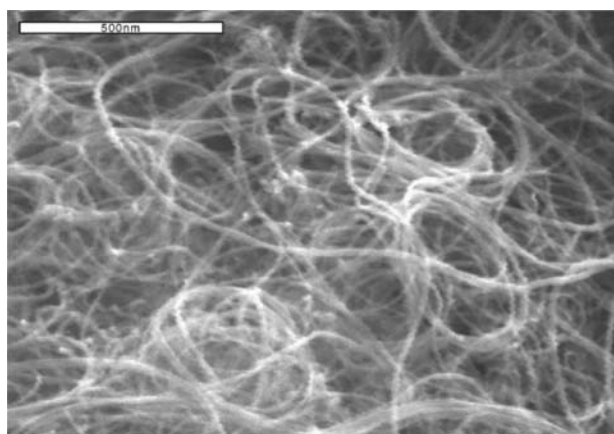


**Fig. 2** SEM image of nanotubes obtained by the decomposition of acetylene at 600°C using the in situ formed catalyst from a Co<sub>x</sub>Mg<sub>(1-x)</sub>O solid solution.

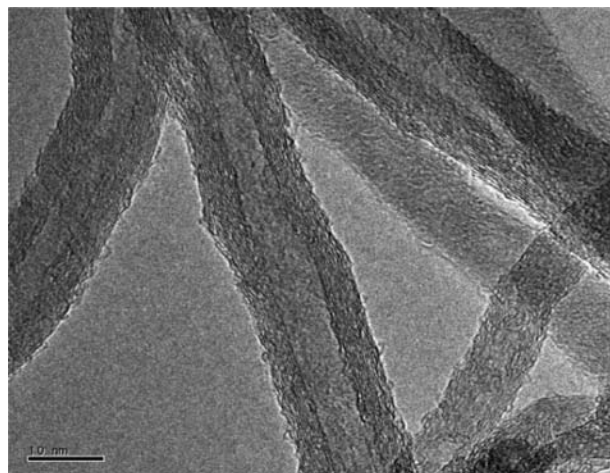


**Fig. 3** TEM image of nanotubes prepared using the Co<sub>x</sub>Mg<sub>(1-x)</sub>O solid solution.

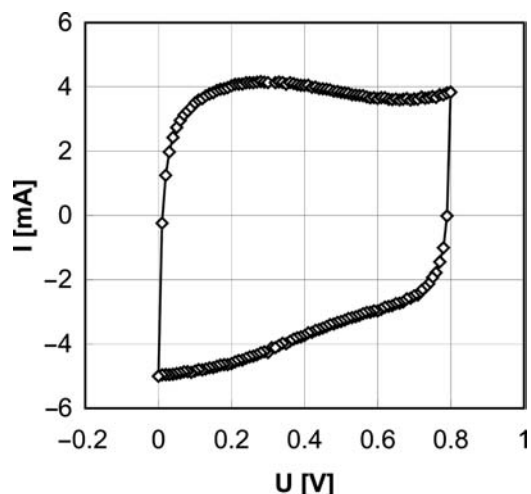


**Fig. 4** Voltammetry characteristics (10 mV/s) of a supercapacitor built from multiwalled CNTs modified by hot nitric acid. Electrolyte: 6 M KOH. *Source:* Reprinted with permission from Ref.<sup>[11]</sup>.

results reached values of 115 F/g due to the presence of oxygen in nanotubular material. Stability of pseudocapacitance during cycling has not been investigated by authors.

Chemical KOH activation is another very attractive method to develop microporosity of nanotubes.<sup>[17,19,20,32]</sup> In some cases, the specific surface area increases four times and the values of capacitance increase from 15 to 90 F/g.<sup>[17,19]</sup> The nanotubes are opened and micropores are formed because of the various possible reactions. The insertion or intercalation of free potassium between

the graphitic-type layers of nanotubes plays an extremely important role in the formation of microporosity. The process starts preferentially from the tips, the separation of the graphene layers is also observed on the walls of nanotubes. KOH attack can also proceed in the central canal of nanotubes. The final effect of activation can be easily demonstrated by the increase in nitrogen adsorbed in the first part of the adsorption/desorption isotherm at 77 K.<sup>[19]</sup> The IV type isotherm with a hysteresis loop presented in Fig. 5 confirms a wide distribution of pores due to highly defected walls, cracks, and surface irregularities, but a still preserved mesoporous character for the activated nanotubes. Because of activation, the micropore volume increases from ca. 0.1 to 0.4 cm<sup>3</sup>/g. The specific surface area of these nanotubes increased from 220 to 880 m<sup>2</sup>/g giving a significant enhancement in capacitance values from 15 to 90 F/g in 6 M KOH, whereas reaching 85 F/g in 1 M H<sub>2</sub>SO<sub>4</sub> and 65 F/g in organic medium.<sup>[17,19]</sup> Voltammetry characteristics for a supercapacitor built from activated nanotubes present a regular square shape that proves high dynamics of charge propagation for such an activated nanotubular material with developed microporosity. The values of time constant ( $RC$ ), where  $R$  is the resistance and  $C$  is the capacitance, estimated from impedance measurements vary from 0.1 to 1 s. The smaller the values of time constant, the quicker the charge propagation in the capacitor.

It has been found that the optimal KOH/C ratio for the activation process is 4:1, whereas the higher ratio 5:1 gives total destruction of the nanotubes into a microporous carbon.<sup>[32]</sup>

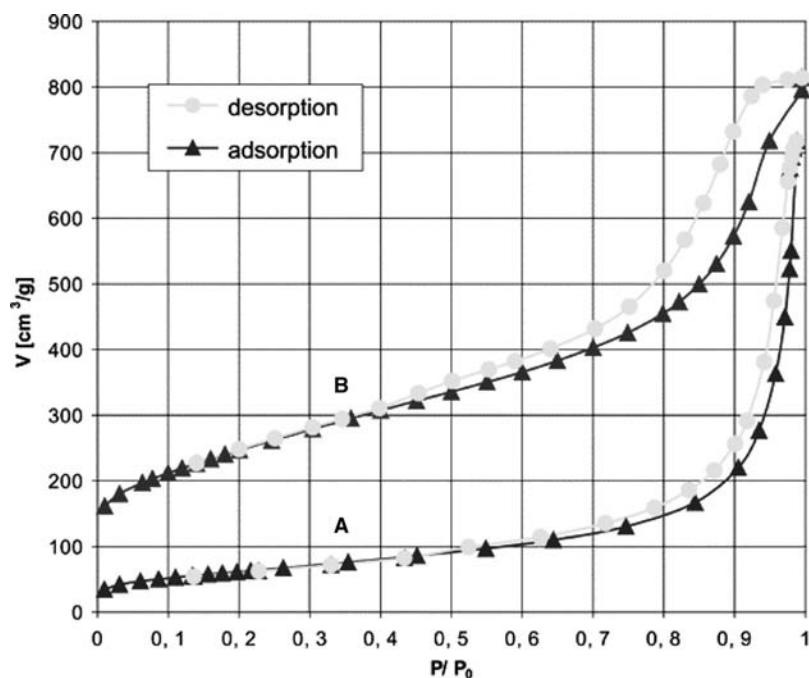


**Fig. 5** Nitrogen adsorption/desorption at 77 K for nanotubes prepared using the  $\text{Co}_x\text{Mg}_{(1-x)}\text{O}$  solid solution: (A) before KOH activation, (B) after KOH activation. *Source:* Reprinted from Ref.<sup>[19]</sup>.

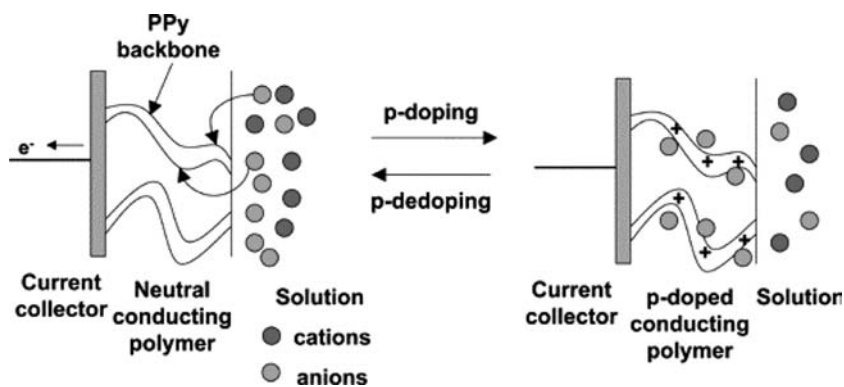


Fig. 6 Doping/dedoping process of polypyrrole.

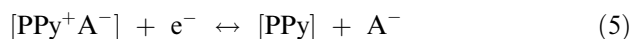
Development of microporosity has been also realized by activation and ammoxidation process. In this case, apart from microporosity, nanotubular material was enriched in heteroatoms such as oxygen and nitrogen.<sup>[33]</sup> Some research was also devoted to modification of nanotubes by air oxidation and various chemical oxidations<sup>[34]</sup> as well as electrochemical treatment.<sup>[35]</sup>

As a conclusion, a well-performed KOH activation, controlled oxidation, or ammoxidation seems to be an attractive method for the development of nanotube microporosity, compared with CO<sub>2</sub> activation, which removes the outer graphitic layers by a gasification process without penetrating into the walls. The oxidative treatment also affects hydrophilicity and conductivity of nanotubes.<sup>[36]</sup>

## NANOTUBES AND CONDUCTING POLYMERS COMPOSITES

The specific capacitance of nanotubular carbon materials can be increased by pseudocapacitance effects. It can be realized through the preparation of novel CNT-conducting polymer composites.<sup>[8,13,21–25,37–50]</sup> Such a modification supplies, apart from the electrostatic attraction of ions, also stable Faradaic reactions (pseudocapacitance).

One of the most interesting aspects of conducting polymers is the coupling of an electron transfer reaction and of the counterion exchange during the electrochemical oxidation and reduction of the polymer. In the case of polypyrrole (PPy), this is schematically represented in Fig. 6 and described by the following reaction:



Polypyrrole has been especially selected for its high conductivity, stability in the oxidized form, and ability to be electrochemically switched between the conducting and isolating states. Polypyrrole supplies a high specific capacitance because of its high doping level;

however, it is valid only for thin films that have limited practical application. Generally, the thicker layers of PPy undergo shrinkage and swelling that is the cause of film degradation and conductivity loss. Such aggravation with cycling is also observed with other electrically conducting polymers (ECPs).

The combination of the two components, i.e., nanotubes and ECP, allows one to overcome this problem and to efficiently use the mesoporous nanotubular network as a perfect support for the highly conducting polymer. It is the most effective solution, which has been proposed to improve the mechanical and electrochemical properties of electrodes based on ECPs.<sup>[8,13,21–25,40–50]</sup> Swelling and shrinkage of ECPs does not occur during doping/dedoping of ECP material with nanotubes, because they adapt to volumetric changes and protect electrode from mechanical degradation. Hence, fading of the electrochemical performance is not observed during cycling if the suitable operating voltage range of capacitor is selected.

For the preparation of CNT composites with ECPs, the chemical or electrochemical polymerization of the monomer, e.g., pyrrole, aniline, 3,4-ethylenedioxythiophene on the nanotubular materials

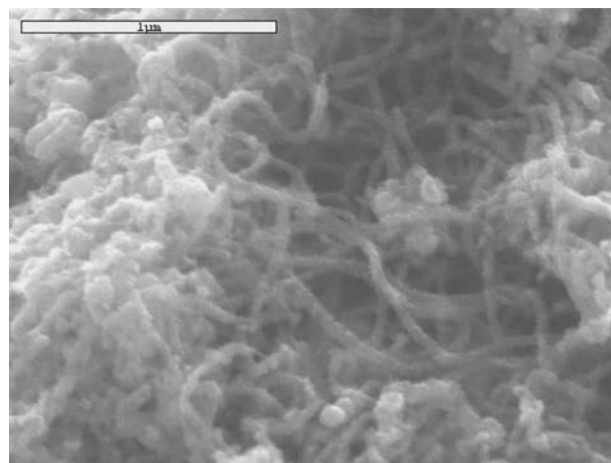
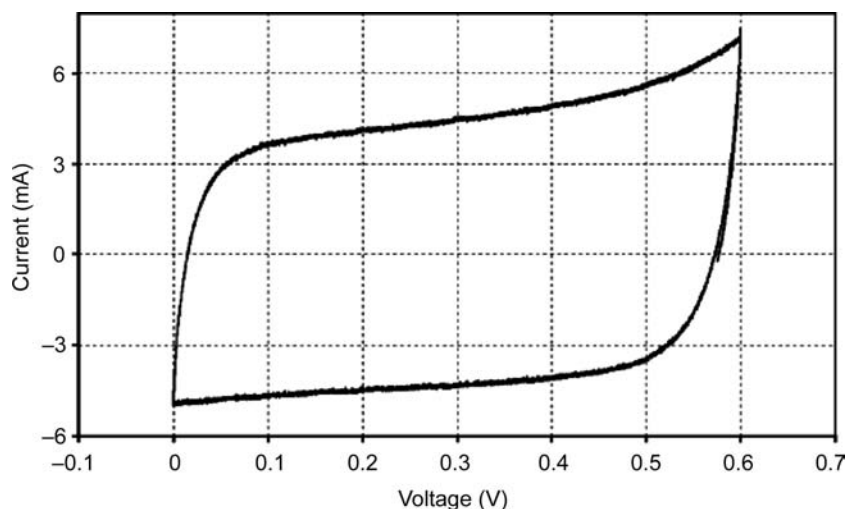


Fig. 7 SEM image of a MWNT (15%)/PEDOT (85%) composite.



**Fig. 8** Voltammetry charge/discharge of a supercapacitor built from the MWNT/PPy composite at 5 mV/s scan rate. Mass of each electrode: 8.6 mg. *Source:* Reprinted from Ref.<sup>[45]</sup>.

was applied.<sup>[21–25,37–50]</sup> The SEM micrograph (Fig. 7) shows a quite uniform polymer coating of a nanotube material by PEDOT chemically deposited. Such composite was characterized by a good performance and cyclability with a wider voltage range than other ECP.<sup>[41,43]</sup>

A lot of research was devoted especially to PPy nanocomposites. Coating with a thin layer of polypyrrole has been achieved on MWNTs,<sup>[21,44]</sup> well-aligned MWNTs,<sup>[38,39]</sup> and SWNTs.<sup>[25]</sup> When MWNTs are oxidized, their surface is covered with oxygen-containing groups, which can be used as anionic dopants of a PPy film electrodeposited on the MWNTs.<sup>[22]</sup> These films are notably less brittle and more adhesive to the electrode than those formed using an aqueous electrolyte as a source of counter ion.

The electrochemical behavior of ECP/CNT composites has been studied either in two- or three-electrode cells. A comparison of the redox performance of PPy films on aligned MWNTs and on flat Ti and Pt

surfaces shows a noticeable improvement for the case of the composites with MWNTs owing to the high accessible surface area of the CNTs in the aligned arrays.<sup>[39]</sup> The authors present only the values of capacitance per surface that give limited information about the possibility of practical application of this material in a real capacitor. In contrast, the results found with SWNT/PPy nanocomposites<sup>[25]</sup> are probably of limited application because: 1) the nickel foam used as current collector supplies an additional capacity in the alkaline solution used for the study; 2) PPy degrades quickly in alkaline solution. For the electrochemically obtained MWNTs/PPy composite where the layer of PPy was about 5 nm, the values of capacitance in acidic medium reach ca. 170 F/g with a good cyclic performance (over 2000 cycles) at current load of 350 mA/g.<sup>[21]</sup>

From a careful analysis of results, it seems that a non-homogeneous layer of ECP deposited chemically can supply even higher values of capacitance.

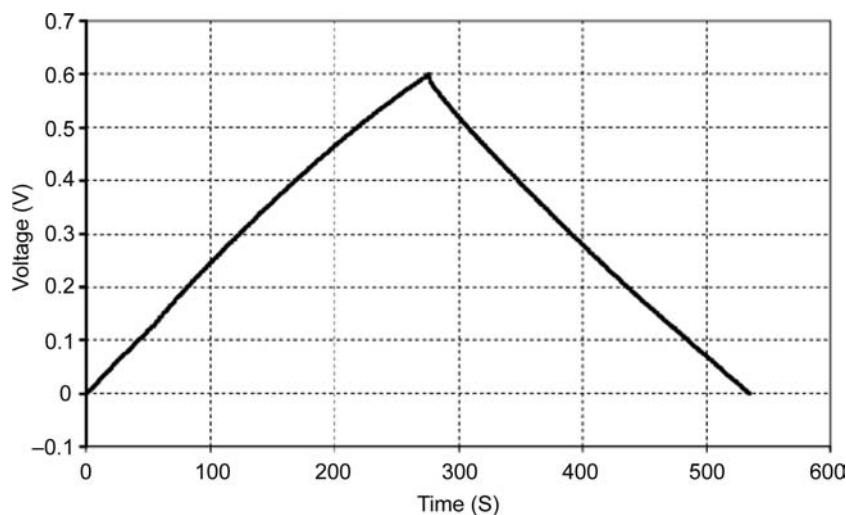


**Fig. 9** Galvanostatic charge/discharge of a supercapacitor built from the MWNT/PPy composite. Current:  $I = 2$  mA. Mass of each electrode: 8.6 mg. *Source:* Reprinted from Ref.<sup>[45]</sup>.

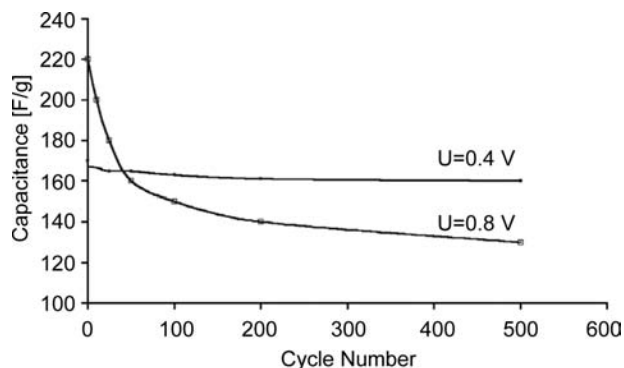


**Fig. 10** Specific capacitance of electrode based on PPy/MWNT composite vs cycle number during galvanostatic charge–discharge of supercapacitor using 1 M  $\text{H}_2\text{SO}_4$  as electrolyte.

Polypyrrole obtained by a chemical method<sup>[37,40,45]</sup> was more porous and less compact; hence, the diffusion of ions could proceed more easily. For a composite containing only 20 wt.% of MWNTs (prepared by decomposition of acetylene on the solid solution  $\text{Co}_x\text{Mg}_{(1-x)}\text{O}$ ), a good distribution of PPy was obtained and high energy could be extracted from the conducting PPy. In this case, the values of capacitance reach 200 F/g with long-term durability if a limited range of capacitor voltage (0.6 V) is selected.<sup>[45]</sup> It is noteworthy that both components alone, i.e., bulk PPy and pure nanotubes, supply at the same current load (200–400 mA/g) very low capacitance values (below 20 F/g). Figure 8 shows the charge/discharge characteristics of such a supercapacitor built from the nanotube/PPy nanocomposite in 1 M  $\text{H}_2\text{SO}_4$  using voltammetry technique at 5 mV/s scan rate. Figure 9 presents a galvanostatic cycling of the same capacitor with 2 mA current load (the mass of each electrode is 8.6 mg).

It has been shown that the values of capacitance for the composites with polyaniline (PANI) and PPy strongly depend on the cell construction.<sup>[45]</sup> With chemically deposited ECPs, extremely high values of specific capacitance can be found—from 250 to 1100 F/g—using a three-electrode cell, whereas smaller values of 190 F/g for MWNTs/PPy and 360 F/g for MWNTs/PANI have been measured in a two-electrode cell. It highlights the fact that only two-electrode cells allow the materials performance to be well estimated in electrochemical capacitors. The applied voltage was found to be the key factor influencing the specific capacitance of ECPs-based nanocomposites. Generally, it cannot exceed 0.6–0.8 V due to oxygen evolution in the positive range of potentials and switching to an insulating state in the negative values.<sup>[45]</sup> The effect of selection of appropriate voltage range is shown in Fig. 10 for MWNT/PPy composite and in Fig. 11 for PANI/MWNT composite. Good capacitor cyclability was reached only with a narrow operating voltage range.

It is observed (Fig. 11) that capacitance values only slightly diminish after cycling but charge propagation is well preserved. At a frequency of 1 Hz, composites still supplied 100 F/g in both cases.

An interesting strategy was recently selected for the elaboration of nanotube/conducting polymer composites, using the electrochemical synthesis of PPy on well-aligned CNT electrodes.<sup>[38,39]</sup> The nanotubular material instead of a flat metallic surface accelerates the redox processes proceeding in PPy, demonstrating the high profitability of using this composite.

A careful analysis of the above-presented results shows that both types of nanotubes (MWNTs and SWNTs) are attractive components of composite electrodes with ECP. Such novel nanocomposite electrodes for supercapacitors combine the complementary

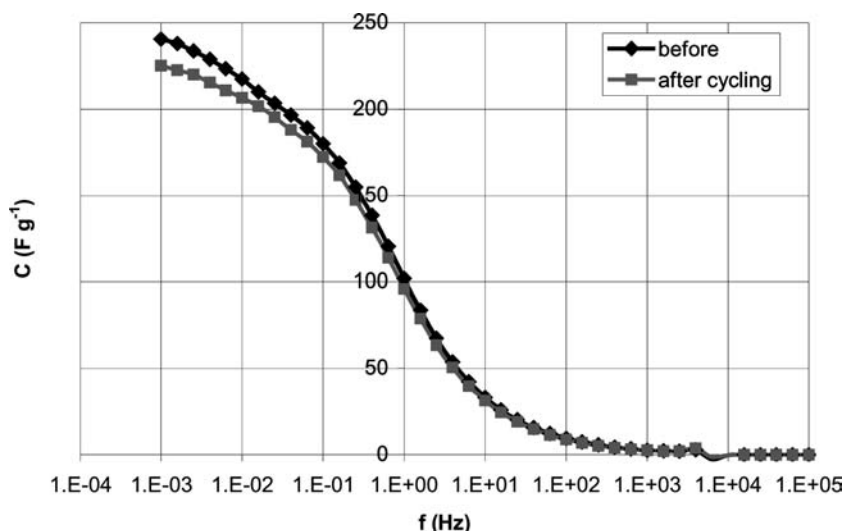


**Fig. 11** Dependence of capacitance vs. frequency for PANI/MWNT composite before and after 3000 cycles at current load of 300 mA/g. Voltage range of capacitor 0.6 V. Source: Reprinted from Ref.<sup>[40]</sup>.



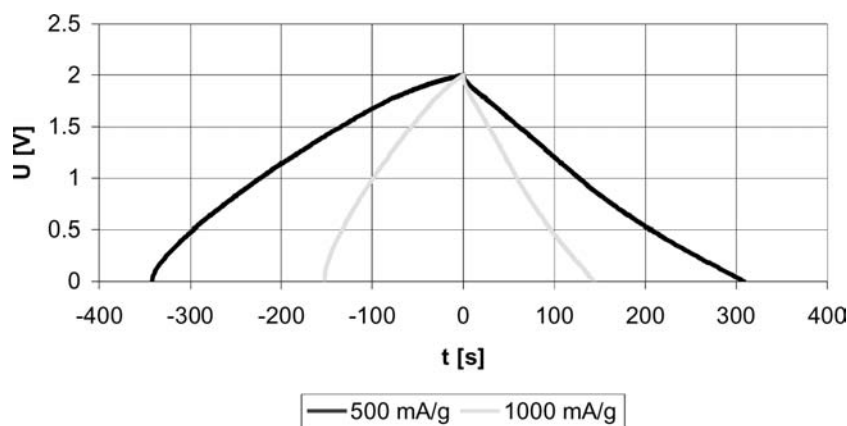


**Fig. 12** Galvanostatic charge/discharge of capacitor built from  $\text{MnO}_2$  (30%)/MWNT (70%) composite. Electrolyte: 1 M  $\text{Na}_2\text{SO}_4$ .

unique properties of CNTs and conducting polymers owing to an efficient three-dimensional charge distribution and easily accessible electrode/electrolyte interface.

Comparing the results of the two coating techniques, the non-homogeneous PPy layer deposited chemically is more porous and less compact than that electrochemically deposited. Consequently, the diffusion of ions proceeds more easily, giving a better efficiency for charge storage.<sup>[45]</sup> It is noteworthy that ECP nanocomposites due to their limited operating voltage range are perfect material for hybrid application with two different electrodes.<sup>[40,43]</sup>

### NANOTUBES/METAL OXIDES COMPOSITES

Carbon nanotubes can also be a perfect support for cheap transition metal oxides of poor electrical conductivity, such as amorphous manganese oxide ( $\alpha\text{-MnO}_2 \cdot n\text{H}_2\text{O}$ ).<sup>[51–56]</sup> The  $\alpha\text{-MnO}_2$ /MWNT composite can be prepared by precipitation of  $\alpha\text{-MnO}_2$  from a  $\text{KMnO}_4 + \text{Mn}(\text{OAc})_2 \cdot 4\text{H}_2\text{O}$  mixture, which contains a predetermined amount of CNTs. Such composites can also be obtained by galvanostatic deposition of  $\text{MnO}_2$  on nanotubes by galvanostatic or potentiodynamic method. In both cases, a remarkable template effect of the entangled nanotubes framework is observed. Consequently, the composite electrodes have a good resiliency, and their porosity is high enough to favor the access of ions to the bulk of the active material. The  $\text{MnO}_2$ /MWNT composite has a capacitance of 140–160 F/g and can operate with good cyclability and high dynamic of charge propagation but in the narrow voltage range. The voltage window of  $\text{MnO}_2$ -based capacitors is limited to 0.6 V, because of the irreversible conversion of Mn(IV) to Mn(II) at the negative electrode and Mn(IV) to Mn(VII) at the positive one.<sup>[52,53]</sup> To circumvent this drawback, an asymmetric configuration has been proposed, where the positive electrode consists of  $\text{MnO}_2$  and the

negative is built from activated carbon.<sup>[43,51–53]</sup> When the  $\text{MnO}_2$ /MWNT composite is used as the positive electrode, the supercapacitor can be operated up to 2 V in aqueous medium with an extremely good cyclability.<sup>[51–53,56]</sup> Figure 12 presents galvanostatic characteristics of capacitor built from activated carbon as negative electrode and  $\text{MnO}_2$ /MWNTs nanocomposite as positive electrode. In this case, electrochemical method (galvanostatic) was used for  $\text{MnO}_2$  deposition. Composites contain 70% of nanotubes and 30% of manganese oxide (by weight). At current of 500 mA/g, the capacitance of 158 F/g was reached whereas for 1000 mA/g, it was 144 F/g.

Instead of  $\text{MnO}_2$ , different oxides have also been used for preparation of nanocomposites with nanotubes.<sup>[57–62]</sup> Some research was devoted to hydrous ruthenium oxide composite.<sup>[57–59]</sup> However, taking into account a high cost of Ru, the composite with manganese oxide seems to be more interesting.

An asymmetric or hybrid configuration, with two electrodes of different nature, e.g., conducting

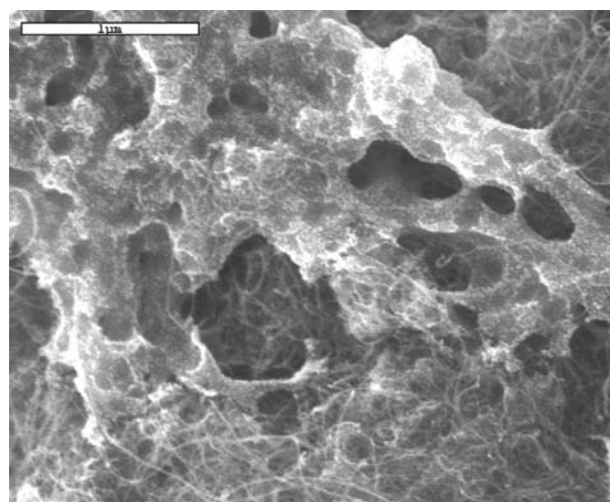


**Fig. 13** Texture of C/C composite from PAN (70%)/MWNT (30%) blend.



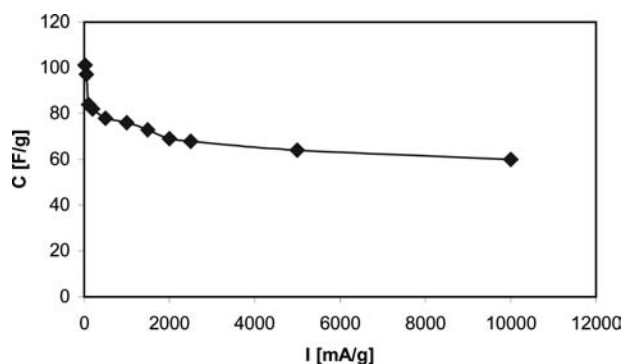


**Fig. 14** Capacitance of C/C composite obtained by carbonization of PAN (70%)/MWNT (30%) blend.

polymer, transition metal oxide, and activated carbon<sup>[43,53,56,60]</sup> taking into account the optimal potential range of each electrode, is an excellent way to reach a wide operating voltage. The most promising material for use as a negative electrode is activated

carbon, whereas conducting polymers composites, e.g. PEDOT, PPy can easily operate as positive or negative electrode. The advantage of the asymmetric combination over the symmetric one is clearly proved. A significant increase in energy and power can easily be obtained especially owing to the extension of the supercapacitor voltage.

### CARBON/CARBON COMPOSITES BASED ON NANOTUBES

Nanotubes have also been extensively used for preparation of composites based on different polymers, such as polyacrylonitrile (PAN), polymerized blend of melamine with formaldehyde and others.<sup>[10,63–66]</sup> For example, a cheap C/C composite electrode for supercapacitor was prepared by pressing a CNTs/polyacrylonitrile blend, followed by one-step pyrolysis of the pellet under neutral atmosphere

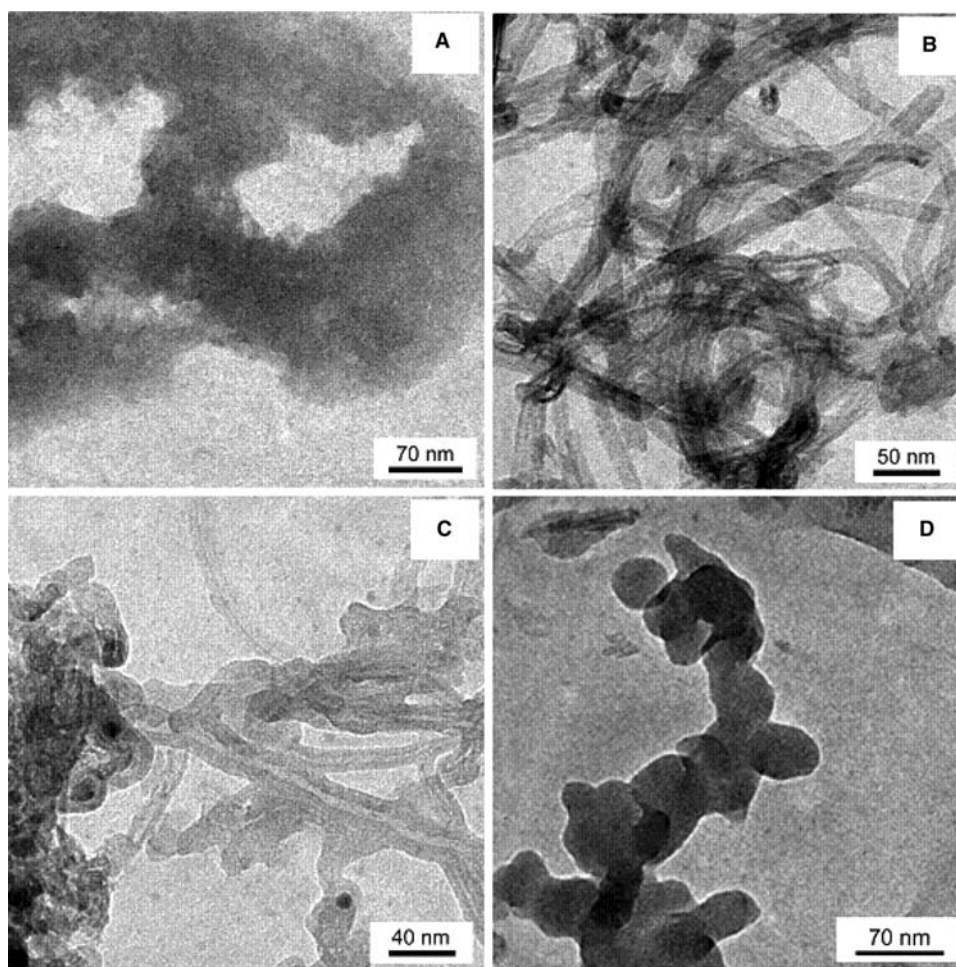


**Fig. 15** TEM images of composites with a variable N content (A–D). Sample (A) stands for M + F, (B) for Nt + M + F, (C) for (Nt + 2M + F), (D) for Nt + 3M + F. *Source:* Reprinted from Ref.<sup>[64]</sup>.

**Table 1** Physicochemical and electrochemical characteristics of Nt composites rich in nitrogen. Capacitance was estimated at 5 A/g current load

Sample	N [wt.%]	$S_{\text{BET}}$ [ $\text{m}^2/\text{g}$ ]	$V_{\text{total}}$ [ $\text{cm}^3/\text{g}$ ]	$V_{\text{micro}}$ [ $\text{cm}^3/\text{g}$ ]	C [F/g]	C [ $\mu\text{F}/\text{cm}^2$ ]
M + F	21.7	329	0.162	0.152	4	1.2
Nt + 3M + F	14.0	403	0.291	0.174	100	24.8
Nt + 2M + F	11.7	393	0.321	0.167	126	32.1
Nt + M + F	7.4	381	0.424	0.156	83	21.8

Source: Reprinted from Ref.<sup>[64]</sup>, with permission from Elsevier.

(850°C). MWNTs used as a 30 wt% component improved the electrical conductivity and mechanical properties of electrode,<sup>[63]</sup> offering additional porosity of the composite. Polyacrylonitrile (PAN) was selected for obtaining an electrochemically active carbon matrix containing in-frame incorporated nitrogen, because of its high carbonization yield and high residual nitrogen content in the char. Although specific surface area of C/C composite was very low, e.g., 200  $\text{m}^2/\text{g}$ , it demonstrated high values of capacitance, up to 100 F/g. These remarkable values are due to the nanotexture of the composite (Fig. 13) and the pseudo-Faradaic properties of the in-frame incorporated nitrogen functionality.

Nanotubes not only play an essential role from the mechanical point of view, but also are very profitable for a good electronic conductivity of the electrodes. Such C/C composites prepared without any activation treatment are very promising for high volumetric energy density capacitors, where high apparent density carbon materials are requested. A good performance of composite in acidic medium at high current loads until 10 A/g is shown in Fig. 14.

A series of nitrogen-rich composites with a wide range of nitrogen content from 7.4 to 21.7 wt.% has been synthesized by carbonization of melamine (M)/formaldehyde (F) polymer blends in the presence

of carbon nanotubes (Nt) without any activation.<sup>[64]</sup> Carbonization was performed at 750°C for 1 hr under nitrogen flow. Texture of C/C composites enriched in nitrogen is shown in Fig. 15A–D. Sample M + F (Fig. 15A) does not contain nanotubes, whereas the proportion of melamine in polymer blend gradually increases being the highest for Nt + 3M + F. Good conducting and mechanical properties of MWNTs used for carbonization of a polymer blend allowed to prepare unique composites with a comparable texture (surface area of ca. 400  $\text{m}^2/\text{g}$ ) but variable nitrogen content. Pseudocapacitance effects related to the nitrogen presence in carbon composite, where nanotubes played the role of a three-dimensional conducting support, have been efficiently used in electrodes of supercapacitor. Useful effect of nitrogen has been already proved for different carbon materials rich in nitrogen.<sup>[67,68]</sup>

In the case of nanotubular composites from ex-melamine, the exceptionally good dynamic of charge was obtained especially for composite with ca. 12 wt% of N, i.e., Nt + 2M + F sample. The capacitance values of 160 F/g at 1 mHz frequency diminish only to 120 F/g at 1 Hz and remain equal to 55 F/g at 10 Hz that proves a good charge propagation.

Table 1 shows a detailed physicochemical data together with capacitance values taken at high current load of 5 A/g in 1 M sulfuric acid.

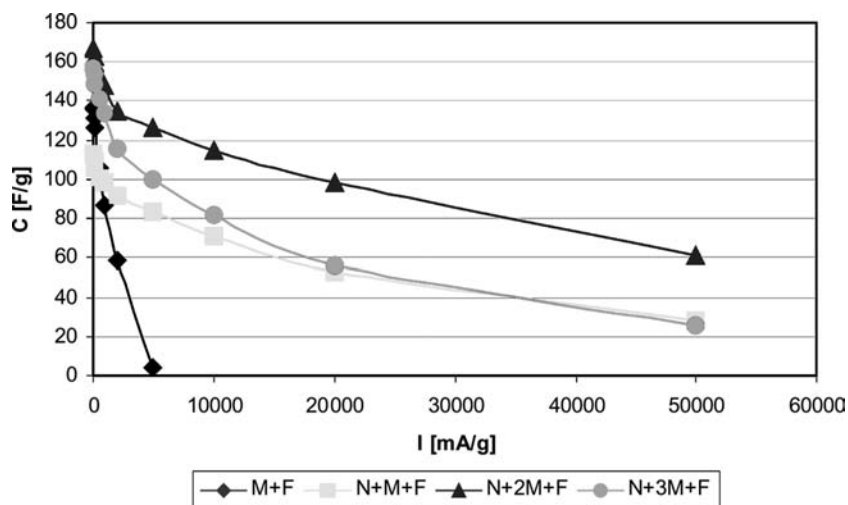


**Fig. 16** Capacitance values vs. current load for composites obtained by carbonization of melamine/formaldehyde polymer blend. Electrolyte: 1 M sulfuric acid.

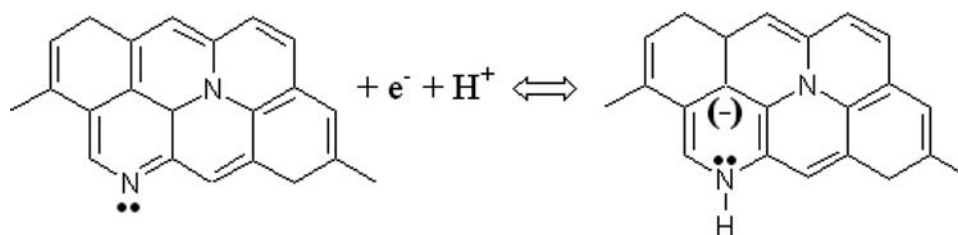


Fig. 17 Scheme of possible redox reactions with pyridinic groups.

Nt + 2M + F composite could be loaded at extremely high current density of 50 A/g because mesoporous network allowed a pseudocapacitance effect of nitrogen to be efficiently used (Fig. 16).

The positive effect of nitrogen is connected with Faradaic reactions not only because of the presence of pyridinic groups (Fig. 17) but also because of the presence of quaternary nitrogen, which could be responsible for significant modification of the electronic states density. Obviously, effect of pyridinic groups will take part only in aqueous medium.

Exceptional capacitor behavior of composites can be explained by synergy effect of both components, i.e. nanotubes and carbon from melamine. During carbonization process, nanotubes play a perfect template role; they allow to evolve gases with a simultaneous slight autoactivation. Substitutional heteroatoms in the carbon network are a promising way to improve capacitor performance. Suitable amount of nitrogen without conductivity aggravation is able to not only enhance capacitance but also improve electrode wettability in aqueous medium. The beneficial effect on overall capacitance induced by nitrogen groups has also been proved by cycling. Obviously, only stable pseudocapacitance effects are demanded and they seem to be the future for the development of high-performance supercapacitors.

The role of nanotubes is effective for decreasing the resistance because they enhance both ionic and electronic conductivity in the electrode network. Because of their higher electronic conductivity than activated carbons, one interesting approach is to use them as a conductivity additive for activated carbons. For the CNTs themselves, the conductivity varies from a few S/cm up to 1000 S/cm, depending on the CNT types (single-walled, double-walled, multi-walled, ...).<sup>[69]</sup> Intensive research has been devoted to study effect of nanotubes as an electrode component with activated carbon.<sup>[70–74]</sup> The evolution of the equivalent series resistance was studied for a supercapacitor constructed using electrodes obtained by adding CNTs to a commercial activated carbon. A nanotube content of 15 wt% seems to be the percolation threshold of such a system.<sup>[70]</sup> A significant improvement of power and charge propagation was observed in all cases.

## CONCLUSION

Carbon nanotubes, because of their highly accessible surface area, low resistivity, and good stability in electrolytic solutions, offer potential possibilities as electrode components for supercapacitors. A high discrepancy of capacitance values for nanotubes, from 10 to 80 F/g, has been found because of their various microtextures. Both types of nanotubes (SWNTs as well as MWNTs) in the purified state, without amorphous carbon film on the walls and catalyst residues, supply rather moderate capacitance values below 40 F/g independent of the electrolytic solution. Even if the capacitance values are low, they could have some potential application when extremely high charge propagation is demanded, taking into account that they can be charged/discharged even at 1 V/s with a good performance.<sup>[75]</sup>

Surface modification of nanotubes by nitric acid or chemical KOH activation at 800°C enhance the capacitance values up to 135 F/g because of the introduction of functional groups on the surface and increase in microporosity, respectively.

On the other hand, CNTs, owing to their unique morphology, exceptional conducting, and mechanical properties, can be used directly as three-dimensional supports for active materials because the percolation with CNTs is very efficient. The open mesoporous network formed by the entanglement of nanotubes allows the ions to diffuse easily to the active surface of the composite components. The two latter properties are essential to lower the equivalent series resistance (ESR) and consequently increase the power of the device. Finally, since the nanotubular materials are characterized by a high resiliency, the composite electrodes can easily adapt to the volumetric changes during charge and discharge, which improves drastically the cycling performance. Hence, CNTs regardless of the type (MWNTs and SWNTs) are a perfect support for conducting polymers, redox species, microporous carbon, in various composites, giving excellent enhancement of capacitance values for the final product. Especially, high improvement of supercapacitor performance can be reached by coating of nanotubes with conducting polymers. The mesoporous

network of well-conducting nanotubes forms a frame for the polymer, which explains the synergy effect between the two components of the CNT/ECP composite electrodes, because of good access of ions from the electrolyte. Such composites seem to be especially adapted for operating in organic electrolytic solutions. However, operating voltage of ECP/CNT as well as oxide/CNT composites should be carefully selected. Hybrid configuration with two different electrode material is preferred.

It has been demonstrated that nanotubes also play a perfect role in carbon/carbon composite obtained by carbonization of polymeric blend. In this case, pseudocapacitance effects of nitrogen or oxygen present in the carbon network can be efficiently used.

In conclusion, composites incorporating a nanotubular backbone coated by an active phase with pseudo-capacitive properties represent an important breakthrough for developing a new generation of supercapacitors.

## REFERENCES

- Iijima, S. Helical microtubules of graphitic carbon. *Nature* **1991**, *354*, 56–58.
- Dresselhaus, M.S.; Dresselhaus, G.; Eklund, P.C. *Science of Fullerenes and Carbon Nanotubes*; Academic Press: San Diego, 1996; 756–917.
- Conway, B.E. *Electrochemical Supercapacitors—Scientific Fundamentals and Technological Applications*; Kluwer Academic/Plenum: New York, 1999.
- Qu, D.; Shi, H. Studies of activated carbons used in double-layer capacitors. *J. Power Sources* **1998**, *74*, 99–107.
- Burke, A. Ultracapacitors: why, how, and where is the technology. *J. Power Sourc.* **2000**, *91*, 37–50.
- Kotz, R.; Carlen, M. Principles and applications of electrochemical capacitors. *Electrochim. Acta* **2000**, *45*, 2483–2498.
- Frackowiak, E.; Béguin, F. Carbon materials for the electrochemical storage of energy in capacitors. *Carbon* **2001**, *39*, 937–950.
- Frackowiak, E.; Béguin, F. Electrochemical storage of energy in carbon nanotubes and nanostructured carbons. *Carbon* **2002**, *40*, 1775–1787.
- Niu, C.; Sichel, E.K.; Hoch, R.; Moy, D.; Tennet, H. High power electrochemical capacitors based on carbon nanotube electrodes. *Appl. Phys. Lett.* **1997**, *70*, 1480–1482.
- Ma, R.Z.; Liang, J.; Wei, B.Q.; Zhang, B.; Xu, C.L.; Wu, D.H. Study of electrochemical capacitors utilizing carbon nanotube electrodes. *J. Power Sourc.* **1999**, *84*, 126–129.
- Frackowiak, E.; Méténier, K.; Bertagna, V.; Béguin, F. Supercapacitor electrodes from multiwalled carbon nanotubes. *Appl. Phys. Lett.* **2000**, *77*, 2421–2423.
- Zhang, B.; Liang, J.; Xu, C.L.; Wei, B.Q.; Ruan, D.B.; Wu, D.H. Electric double-layer capacitors using carbon nanotube electrodes and organic electrolyte. *Mater. Lett.* **2001**, *51* (60), 539–542.
- Frackowiak, E.; Jurewicz, K.; Delpeux, S.; Béguin, F. Nanotubular materials for supercapacitors. *J. Power Sourc.* **2001**, *97–98*, 822–825.
- An, K.H.; Kim, W.S.; Park, Y.S.; Hoi, Y.C.; Lee, S.M.; Chung, D.C.; Bae, D.J.; Lim, S.C.; Lee, Y.H. Super capacitors using single-walled carbon nanotube electrodes. *Adv. Mater.* **2001**, *13* (7), 497–500.
- Shiraishi, S.; Kurihara, H.; Okabe, K.; Hulicova, D.; Oya, A. Electric double layer capacitance of highly pure single-walled carbon nanotubes (HiPco™ Buckytubes™) in propylene carbonate electrolytes. *Electrochem. Commun.* **2002**, *4*, 593–598.
- Lota, G.; Frackowiak, E.; Mittal, J.; Monthieux, M. High performance supercapacitor from chromium oxide-nanotubes based electrodes. *Chem. Phys. Lett.* **2007**, *434* (1–3), 73–77.
- Frackowiak, E.; Jurewicz, K.; Szostak, K.; Delpeux, S.; Béguin, F. Nanotubular materials as electrodes for supercapacitors. *Fuel Process. Technol.* **2002**, *77–78*, 213–219.
- Chen, J.H.; Li, W.Z.; Wang, D.Z.; Yang, S.X.; Wen, J.G.; Ren, Z.F. Electrochemical characterization of carbon nanotubes as electrode in electrochemical double-layer capacitors. *Carbon* **2002**, *40* (8), 1193–1197.
- Frackowiak, E.; Delpeux, S.; Jurewicz, K.; Szostak, K.; Cazorla-Amoros, D.; Béguin, F. Enhanced capacitance of carbon nanotubes through chemical activation. *Chem. Phys. Lett.* **2002**, *361*, 35–41.
- Jiang, Q.; Qu, M.Z.; Zhou, G.M.; Zhang, B.L.; Yu, Z.L. A study of activated carbon nanotubes as electrochemical supercapacitors electrode materials. *Mater. Lett.* **2002**, *57*, 988–991.
- Jurewicz, K.; Delpeux, S.; Bertagna, V.; Béguin, F.; Frackowiak, E. Supercapacitors from nanotubes/polypyrrole composites. *Chem. Phys. Lett.* **2001**, *347*, 36–40.
- Hughes, M.; Shaffer, M.S.P.; Renouf, A.C.; Singh, C.; Chen, G.Z.; Fray, D.J.; Windle, A.H. Electrochemical capacitance of nanocomposite films formed by coating aligned arrays of carbon nanotubes with polypyrrole. *Adv. Mater.* **2002**, *14* (5), 382–385.
- Hughes, M.; Chen, G.Z.; Shaffer, M.S.P.; Fray, D.J.; Windle, A.H. Electrochemical capacitance of a nanoporous composite of carbon nanotubes and polypyrrole. *Chem. Mater.* **2002**, *14* (4), 1610–1613.
- Lee, Y.H.; An, K.H. European Patent EP 1 146 527 A2 (KR 2000 01 9232), October 17, 2001.
- An, K.H.; Jeon, K.K.; Heo, J.K.; Lim, S.C.; Bae, D.J.; Lee, Y.H. High-capacitance supercapacitor using a nanocomposite electrode of single-walled carbon nanotube and polypyrrole. *J. Electrochem. Soc.* **2002**, *149* (8), A1058–A1062.
- Portet, C.; Yushin, G.; Gogotsi, Y. Electrochemical performance of carbon onions, nanodiamonds, carbon black and multiwalled nanotubes in electrical double layer capacitors. *Carbon* **2007**, *45*, 2511–2518.
- Zhang, H.; Cao, G.; Yang, Y. Electrochemical properties of ultra-long, aligned, carbon nanotube array electrode in organic electrolyte. *J. Power Sourc.* **2007**, *172*, 476–480.

28. Tashima, D.; Kurosawatsu, K.; Uota, M.; Karashima, T.; Otsubo, M.; Honda, C.; Sung, Y.M. Space charge distributions of an electric double layer capacitor with carbon nanotubes electrode. *Thin Solid Films* **2007**, *515*, 4234–4239.
29. Zhang, H.; Cao, G.; Yang, Y.; Gu, Z. Capacitive performance of an ultralong aligned carbon nanotube electrode in an ionic liquid at 60°C. *Carbon* **2008**, *46*, 30–34.
30. Barisci, J.N.; Wallace, G.G.; Baughman, R.H. Electrochemical quartz crystal microbalance studies of single-wall carbon nanotubes in aqueous and non-aqueous solutions. *Electrochim. Acta* **2000**, *46*, 509–517.
31. Delpeux, S.; Szostak, K.; Frackowiak, E.; Bonnamy, S.; Béguin, F. High yield of pure multiwalled carbon nanotubes from the catalytic decomposition of acetylene on in-situ formed cobalt nanoparticles. *J. Nanosci. Nanotech.* **2002**, *2* (5), 481–484.
32. Raymundo-Pinero, E.; Cazorla-Amoros, D.; Linares-Solano, A.; Delpeux, S.; Frackowiak, E.; Szostak, K.; Béguin, F. High surface area carbon nanotubes prepared by chemical activation. *Carbon* **2002**, *40*, 1614–1617.
33. Jurewicz, K.; Babel, K.; Pietrzak, R.; Delpeux, S.; Wachowska, H. Capacitance properties of multi-walled carbon nanotubes modified by activation and ammoxidation. *Carbon* **2006**, *44*, 2368–2375.
34. Hu, C.; Su, J.H.; Wen, T.C. Modification of multi-walled carbon nanotubes for electric double-layer capacitors: tube opening and surface functionalization. *J. Phys. Chem. Solids* **2007**, *68*, 2353–2362.
35. Liu, C.G.; Fang, H.T.; Li, F.; Liu, M.; Cheng, H.M. Single-walled carbon nanotubes modified by electrochemical treatment for application in electrochemical capacitors. *J. Power Sourc.* **2006**, *160*, 758–761.
36. Kim, Y.T.; Mitani, T. Competitive effect of carbon nanotubes oxidation on aqueous EDLC performance: balancing hydrophilicity and conductivity. *J. Power Sourc.* **2006**, *158*, 1517–1522.
37. Fan, J.; Wan, M.; Zhu, D.; Chang, B.; Pan, Z.; Xie, S. Synthesis, characterizations, and physical properties of carbon nanotubes coated by conducting polypyrrole. *J. Appl. Polym. Sci.* **1999**, *74*, 2605–2610.
38. Chen, J.H.; Huang, Z.P.; Wang, D.Z.; Yang, S.X.; Wen, J.G.; Ren, Z.F. Electrochemical synthesis of polypyrrole/carbon nanotube nanoscale composites using well-aligned carbon nanotube arrays. *Appl. Phys. A: Mater. Sci. Process.* **2001**, *73* (2), 129–131.
39. Chen, J.H.; Huang, Z.P.; Wang, D.Z.; Yang, S.X.; Li, W.Z.; Wen, J.G.; Ren, Z.F. Electrochemical synthesis of polypyrrole films over each of well-aligned carbon nanotubes. *Synth. Met.* **2002**, *125*, 289–294.
40. Frackowiak, E.; Khomenko, V.; Jurewicz, K.; Lota, K.; Béguin, F. Supercapacitors based on conducting polymers/nanotubes composites. *J. Power Sourc.* **2006**, *153*, 413–418.
41. Lota, K.; Khomenko, V.; Frackowiak, E. Capacitance properties of poly(3,4-ethylenedioxythiophene)/carbon nanotubes composites. *J. Phys. Chem. Solids* **2004**, *65* (2–3), 295–301.
42. Frackowiak, E. Carbon materials for supercapacitor application. *Phys. Chem. Chem. Phys.* **2007**, *9*, 1774–1785.
43. Khomenko, V.; Raymundo-Pinero, E.; Frackowiak, E.; Béguin, F. High-voltage asymmetric supercapacitors operating in aqueous electrolyte. *Appl. Phys. A* **2006**, *82*, 567–573.
44. Béguin, F.; Frackowiak, E. Nanotextured carbons for electrochemical energy storage. In *Handbook of Nanomaterials*; Gogotsi, Y., Ed.; CRC Press, Taylor & Francis, 2006; Chap. 26, 713–737.
45. Khomenko, V.; Frackowiak, E.; Béguin, F. Determination of the specific capacitance of conducting polymer/nanotubes composite electrodes using different cell configuration. *Electrochim. Acta* **2005**, *50*, 2499–2506.
46. Xiao, Q.; Zhou, X. The study of multiwalled carbon nanotube deposited with conducting polymer for supercapacitor. *Electrochim. Acta* **2003**, *48*, 575–580.
47. Zhou, Y.; He, B.; Zhou, W.; Huang, J.; Li, X.; Wu, B.; Li, H. Electrochemical capacitance of well-coated single-walled carbon nanotube with polyaniline composites. *Electrochim. Acta* **2004**, *49*, 257–262.
48. Peng, C.; Jin, J.; Chen, G.Z. A comparative study on electrochemical co-deposition and capacitance of composite films of conducting polymers and carbon nanotubes. *Electrochim. Acta* **2007**, *53*, 525–537.
49. Sivakkumar, S.R.; Kim, W.J.; Choi, J.A.; MacFarlane, D.R.; Forsyth, M.; Kim, D.W. Electrochemical performance of polyaniline nanofibres and polyaniline/multi-walled carbon nanotube composite as an electrode material for aqueous redox supercapacitors. *J. Power Sourc.* **2007**, *171*, 1062–1068.
50. Dong, B.; He, B.L.; Xu, C.L.; Li, H.L. Preparation and electrochemical characterization of polyaniline/multi-walled carbon nanotubes composites for supercapacitor. *Mater. Sci. Engineer. B* **2007**, *143*, 7–13.
51. Frackowiak, E.; Béguin, F. Application of nanoporous carbons and nanotube composites for supercapacitors. In *Recent Advances in Supercapacitors*; Gupta, V., Ed.; Transworld Research Network: Kerala, India, 2006; Chap. 5, 79–114.
52. Raymundo-Pinero, E.; Khomenko, V.; Frackowiak, E.; Béguin, F. Performance of manganese oxide/CNTs composites as electrode materials for electrochemical capacitors. *J. Electrochem. Soc.* **2005**, *152* (1), A229–A235.
53. Khomenko, V.; Raymundo-Piñero, E.; Béguin, F. Optimisation of an asymmetric manganese oxide/activated carbon capacitor working at 2 V in aqueous medium. *J. Power Sourc.* **2005**, *153*, 183–190.
54. Wang, G.X.; Zhang, B.L.; Yu, Z.L.; Qu, M.Z. Manganese oxide/MWNTs composite electrodes for supercapacitors. *Solid State Ionics* **2005**, *176*, 1169–1174.
55. Chen, Y.; Liu, C.G.; Liu, C.; Lu, G.Q.; Cheng, H.M. Growth of single-crystal  $\alpha$ -MnO<sub>2</sub> nanorods on multi-walled carbon nanotubes. *Mater. Res. Bull.* **2007**, *42*, 1935–1941.
56. Ma, S.B.; Nam, K.W.; Yoon, W.S.; Yang, X.Q.; Ahn, K.Y.; Oh, K.H.; Kim, K.B. A novel concept of hybrid capacitor based on manganese oxide materials. *Electrochem. Commun.* **2007**, *9*, 2807–2811.
57. Park, J.H.; Ko, J.M.; Park, O.O. Carbon nanotube/RuO<sub>2</sub> nanocomposite electrodes for supercapacitors. *J. Electrochem. Soc.* **2003**, *150* (7), A864–A867.

58. Arabale, G.; Wagh, D.; Kulkarni, M.; Mulla, I.S.; Vernekar, S.P.; Vijayamohan Rao, A.M. Enhanced supercapacitance of multiwalled carbon nanotubes functionalised with ruthenium oxide. *Chem. Phys. Lett.* **2003**, *376*, 207–213.
59. Deng, G.H.; Xiao, X.; Chen, J.H.; Zeng, X.B.; He, D.L.; Kuang, Y.F. A new method to prepare RuO<sub>2</sub> xH<sub>2</sub>O/carbon nanotube composite for electrochemical capacitors. *Carbon* **2005**, *43*, 1566–1569.
60. Wang, X.; Ruan, D.; You, Z. Application of spherical Ni(OH)<sub>2</sub>/CNTs composite electrode in asymmetric supercapacitors. *Trans. Nonferrous Met. Soc. China* **2006**, *16*, 1129–1134.
61. Shan, Y.; Gao, L. Formation and characterization of multi-walled carbon nanotubes/Co<sub>3</sub>O<sub>4</sub> nanocomposites for supercapacitors. *Mater. Chem. Phys.* **2007**, *103*, 206–210.
62. Wang, G.; Qu, M.; Yu, Z.; Yuan, R. LiNi<sub>0.8</sub>Co<sub>0.2</sub>O<sub>2</sub>/MWCNT composite electrodes for supercapacitors. *Mater. Chem. Phys.* **2007**, *105*, 169–174.
63. Béguin, F.; Szostak, K.; Lota, G.; Frackowiak, E. A self-supporting electrode for supercapacitors prepared by one-step pyrolysis of carbon nanotubes/polyacrylonitrile blends. *Adv. Mater.* **2005**, *17*, 2380–2384.
64. Lota, G.; Lota, K.; Frackowiak, E. Nanotubes based composites rich in nitrogen for supercapacitor application. *Electrochem. Commun.* **2007**, *9* (7), 1828–1832.
65. Zhou, C.; Liu, T.; Wang, T.; Kumar, S. PAN/SAN/SWNT ternary composite: Pore size control and electrochemical supercapacitor behavior. *Polymer* **2006**, *47* (16), 5831–5837.
66. Liu, T.; Sreekumar, T.V.; Kumar, S.; Hauge, R.H.; Smalley, R.E. SWNT/PAN composite film-based supercapacitors. *Carbon* **2003**, *41*, 2440–2442.
67. Lota, G.; Grzyb, B.; Machnikowska, H.; Machnikowski, J.; Frackowiak, E. Effect of nitrogen in carbon electrode on the supercapacitor performance. *Chem. Phys. Lett.* **2005**, *404*, 53–58.
68. Frackowiak, E.; Lota, G.; Machnikowski, J.; Vix-Guterl, C.; Béguin, F. Optimization of supercapacitors using carbons with controlled nanotexture and nitrogen content. *Electrochim. Acta* **2006**, *51*, 2209–2214.
69. Wei, J.; Zhu, H.; Jiang, B.; Ci, L.; Wu, D. Electronic properties of double-walled carbon nanotube films. *Carbon* **2003**, *41*, 2495–2500.
70. Emmenegger, Ch.; Mauron, Ph.; Sudan, P.; Wenger, P.; Hermann, V.; Gally, R.; Züttel, A. Investigation of electrochemical double-layer (ECDL) capacitors electrodes based on carbon nanotubes and activated carbon materials. *J. Power Sourc.* **2003**, *124*, 321–329.
71. Portet, C.; Taberna, P.L.; Simon, P.; Flahaut, E.; Laberty-Robert, C. High power density electrodes for carbon supercapacitor applications. *Electrochim. Acta* **2005**, *50*, 4174–4181.
72. Albina, A.; Taberna, P.L.; Cambronne, J.P.; Simon, P.; Flahaut, E.; Lebey, T. Influence of carbonaceous electrodes on capacitance and breakdown voltage for hybrid capacitor. *Microelectron. J.* **2007**, *38*, 642–648.
73. Show, Y.; Imaizumi, K. Electric double layer capacitor with low series resistance fabricated by carbon nanotube addition. *Diamond Relat. Mater.* **2007**, *16*, 1154–1158.
74. Bordjiba, T.; Mohamedi, M.; Dao, L.H. Synthesis and electrochemical capacitance of binderless nanocomposite electrodes formed by dispersion of carbon nanotubes and carbon aerogels. *J. Power Sourc.* **2007**, *172*, 991–998.
75. Du, C.; Yeh, J.; Pan, N. High power density supercapacitors using locally aligned carbon nanotube electrodes. *Nanotechnology* **2005**, *16*, 350–353.



# Carbon Nanotubes: Supramolecular Mechanics

**Boris I. Yakobson**

*Department of Mechanical Engineering and Materials Science, Rice University,  
Houston, Texas, U.S.A.*

**Luise S. Couchman**

*Naval Research Laboratory, Washington, District of Columbia, U.S.A.*

## INTRODUCTION

Supramolecular interactions are usually short-range (near contact) forces between the molecules, too weak to cause the intermolecular changes or bond formation between the particles. At the same time, their strength and range are sufficient to cause self-assembly of the molecular units or certain elastic deformations of these building blocks. Because of the weakness of supramolecular interactions, the resulting organization is sensitive to external conditions and ensures certain ease of transformations in response to external fields. Well known is a fascinating class of liquid crystals, whose “liquid” aspect is exactly a result of relatively small energy of intermolecular forces. Nanoparticles and especially nanotubes offer a kind of building blocks that can be efficiently glued by weak supramolecular forces in a self-assembly process. In case of nanotubes, because of their hollow structure and large aspect ratio, same forces or interaction between them can cause deformations of bending, torsion, flattening polygonization, etc. In turn, the degree of such deformation can enhance (like in case of partial polygonization of nanotubes in the array bundles) supramolecular attraction or decrease it under other circumstances. Supramolecular behavior of nanotubes is therefore intrinsically coupled with their own mechanical properties which we will discuss in some detail.

Unique mechanical properties of carbon nanotubes indirectly lead to unusual role of the forces *between* them. These *supramolecular* interactions are normally weak and, for most molecular species, are easily overcome by thermal agitation. However, they turn out to be significant in case of nanotubes, building up very strong attractive potentials over the extensive aligned contacts ( $\sim 0.5$  eV/nm). The general aspects and issues of supramolecular mechanics are discussed, including an overview of the mechanical properties of nanotubes, especially linear elastic parameters and their relation with persistence length, non-linear elastic instabilities, and buckling. Furthermore, inelastic relaxation, yield strength, and fracture mechanisms, including their

kinetic theory, are also discussed. A discussion of theoretical and computational studies is supplemented by brief summaries of experimental results for the entire range of the deformation amplitudes. Atomistic scenarios of “strong” supramolecular interactions, when polymerization and coalescence welding occur, are also discussed because of their significance in potential applications.

## OVERVIEW

Nanomechanics is generally distinguished from the well-established dynamics of molecules in that it relies on the heuristics and methods of mechanical engineering and structural mechanics. It deals with objects of distinct shape and function: rods, beams, shells, plates, membranes, etc. At the same time, because of the small length scale, nanomechanics also relies on physics of interatomic and molecular forces, quantum chemistry, solid state theory, and statistical thermodynamics. With these come a variety of numerical and computational methods (molecular dynamics, Monte Carlo simulations, classical empirical interatomic potentials, tight-binding approximation, density functional theory, etc.). This cross-disciplinary aspect makes this area both complex and exciting for research and education.

Among the numerous subjects of nanomechanics research (tips, contact junctions, pores, whiskers, etc.), carbon nanotubes (CNTs)<sup>[1]</sup> have earned a spotlight (see Ref.<sup>[2]</sup> for a popular review). Their atomically precise structure, elongated and hollow, an effective absence of a surface (which is no different than the bulk, at least for the single-walled cylinders, SWNTs), and superlative covalent bond strength are among the traits that put CNTs in the focus of nanomechanics. Discussion of numerous other objects as well as details of the multiscale methods involved in nanomechanics (for example, see recent monograph)<sup>[3]</sup> is far beyond the scope of this article.

It is noteworthy that the term *resilient* has been first applied not to nanotubes, but to smaller fullerene

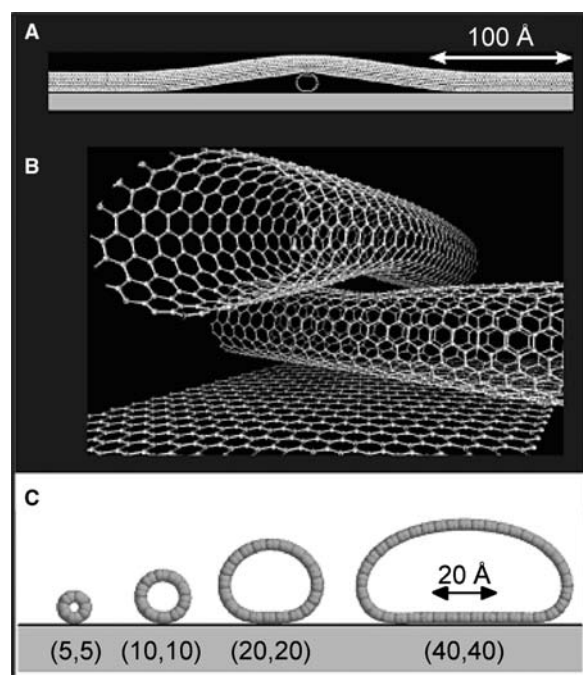


**Fig. 1** Simulations of the axial and radial deformation of nanotubes. (A) Axial deformation resulting from the crossing of two (10,10) nanotubes. (B) Perspective close-up of the same crossing showing that both tubes are deformed near the contact region. (C) Computed radial deformations of single-wall nanotubes adsorbed on graphite. *Source:* From Ref.<sup>[4]</sup>.

cages, in the study of high-energy collisions of  $C_{60}$ ,  $C_{70}$ , and  $C_{84}$  bouncing from a solid wall of H-terminated diamond. The absence of any fragmentation or other irreversible atomic rearrangement in the rebounding cages was somewhat surprising and indicated the ability of fullerenes to sustain great elastic distortion. The very same property of resilience becomes more significant in case of carbon nanotubes because their elongated shape, with the aspect ratio close to a thousand, makes the mechanical properties especially interesting and important because of potential structural applications. An accurate simulation (with realistic interatomic and van der Waals forces) in Fig. 1<sup>[4]</sup> vividly illustrates the appeal of CNTs as a nanomechanical object: well-defined cylindrical shape, compliance to external forces, and an expected type of response qualitatively analogous to a common macroscopic behavior places these objects between molecular chemical physics, elasticity theory, and mechanical engineering.

The utility of nanotubes as elements in nanoscale devices or composite materials remains a powerful motivation for the research in this area. While the feasibility of the practical realization of these applications is currently unknown, another incentive comes from the fundamental materials physics. There is an interesting duality in the nanotubes. Carbon nanotubes

possess simultaneously molecular size and morphology as well as sufficient translational symmetry to perform as very small (nano-) crystals with well-defined primitive cell, surface, possibility of transport, etc. Moreover, in many respects, they can be studied as well defined as engineering structures and many properties can be discussed in traditional terms of moduli, stiffness or compliance, or geometric size and shape. The mesoscopic dimensions (a nanometer diameter) combined with the regular, almost translation-invariant morphology along the micrometer lengths (unlike other polymers, usually coiled) make nanotubes a unique and attractive object of study.

In the following, “Linear Elastic Properties” discusses theoretical *linear elasticity* and results for the elastic moduli, compared wherever possible with the experimental data. In “Van der Waals Interactions,” the weak supramolecular interactions are quantified in the form of *van der Waals* force potential, and the large-scale mechanical deformations of nanotubes caused by their attraction to each other are outlined. The *non-linear elastic* behavior, buckling instabilities, and shell model are presented in “Supramolecular Morphology Changes Within Elastic Shell Model,” with mentioning of experimental evidence parallel to theoretical results. *Yield and failure* mechanisms in tensile load are presented in “Failure and Relaxation Mechanisms,” with the emphasis on the combined dislocation theory and computational approach. More recent results of *kinetic theory* of fracture and strength evaluation in application to CNTs are briefly presented in “Kinetic Approach to Strength-Failure Evaluation”; fast molecular tension tests are recalled in the context of kinetic theory. “Coalescence of Nanotubes as a Reversed Failure” presents some of the more recent result on CNT *coalescence welding*, a process essentially reverse to fracture. In “Tensegrity at Supramolecular Scale,” we also briefly discuss the concept of *tensegrity* and how it might be implemented in nanoscale by combining mechanically stiff and flexible supramolecular units. Throughout the discussions, we do not attempt to provide a comprehensive review of broad activities in the field. Broader or a more comprehensive discussion can be found in other relatively recent reviews by the author.<sup>[2,5]</sup>

## LINEAR ELASTIC PROPERTIES

Numerous theoretical calculations are dedicated to linear elastic properties when displacements (strain) are proportional to forces (stress). We recently revisited<sup>[6]</sup> this issue to compare within the same method the elasticity of three different materials: pure carbon (C), boron nitride (BN), and fluorinated carbon ( $C_2F$ ). Because of obvious uncertainty in definition of

a nanotube “cross section,” the results should be represented by the values of in-plane stiffness,  $C$  ( $\text{J}/\text{m}^2$ ). The values computed with Gaussian-based density functional theory are  $C = 345, 271,$  and  $328 \text{ N}/\text{m}$  for C, BN, and  $\text{C}_2\text{F}$ , respectively. These values in ab initio calculations are almost independent of nanotube diameter and chirality [consistent with the isotropic elasticity of a hexagonal two-dimensional (2-D) lattice], somewhat in contrast to previous reports based on tight binding or classical empirical approximations. Notably, substantial fluorination causes almost no change in the in-plane stiffness because the bonding involves mainly  $\pi$ -system while the stiffness is largely a result of in-plane  $\sigma$ -system. For “material” property assessments, the values of bulk moduli (based on a graphite-type 0.34-nm spacing of layers) yield 1029, 810, and 979 GPa—all very high. Knowing the elastic shell parameter  $C$  immediately leads to accurate calculation of a nanotube beam-bending stiffness  $K$  (proportional to the cube of diameter,  $\sim d^3$ ) as discussed later in “Van der Waals Interactions” and “Coalescence of Nanotubes as a Reversed Failure.” It also allowed us to compute vibration frequencies of the tubules, e.g., symmetric breathing mode frequency,  $f \sim 1/d$ ,<sup>[6]</sup> detectable in Raman spectroscopy.

An unexpected feature discovered in the course of that study<sup>[6]</sup> is the localized strain induced by the attachment of fluorine. This shifts the energy minimum of the  $\text{C}_2\text{F}$  shell lattice from an “unstrained” sheet toward the highly curved polygonal cylinders (for  $\text{C}_2\text{F}$  composition of a near square shape, Fig. 2). Equilibrium free angle is  $\sim 72^\circ$ .

Theoretical values agree reasonably well with experimental values of the Young’s modulus. It was first estimated<sup>[7]</sup> by measuring freestanding room-temperature vibrations in a transmission electron microscope (TEM). The motion of a vibrating cantilever is governed by the known fourth-order wave equation,  $y_{\text{tttt}} = -(YI/\rho A)y_{\text{xxxx}}$ , where  $A$  is the cross-sectional area and  $\rho$  is the density of the rod material. For a clamped rod, the boundary conditions are such that

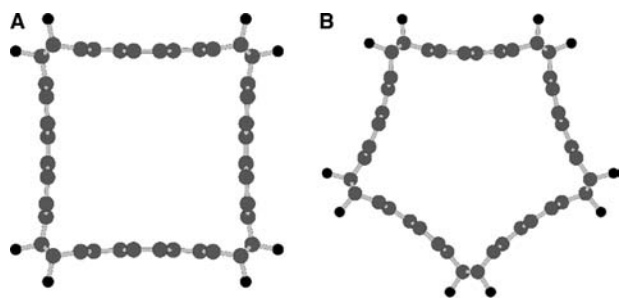


**Fig. 2** Geometries of the polygonal fluorinated carbon tubes: (A) square  $\text{F}_4$ -(10,10) and (B) pentagonal  $\text{F}_5$ -(10,10). Source: From Ref.<sup>[6]</sup>.

the function and its first derivative are zero at the origin and the second and third derivative are zero at the end of the rod. Thermal nanotube vibrations are essentially elastic, relaxed phonons in equilibrium with the environment; therefore the amplitude of vibration changes stochastically with time. The amplitude of those oscillations was defined by means of careful TEM observations of a number of CNTs and yields the values of moduli within a range near 1 TPa.

Another way to probe the mechanical properties of nanotubes is to use the tip of an atomic force microscope (AFM) to bend an anchored CNT while simultaneously recording the force exerted by the tube as a function of the displacement from its equilibrium position.<sup>[8]</sup> Obtained values also vary from sample to sample but generally are close to  $Y = 1 \text{ TPa}$ . Similar values have been obtained in Ref.<sup>[9]</sup> with yet another accurate technique based on a resonant electrostatic deflection of a multiwall carbon nanotube under an external a.c. field. The detected decrease in stiffness must be related to the emergence of a different bending mode for the nanotube. In fact, this corresponds to a wavelike distortion buckling of the inner side of the CNT. Non-linear behavior is discussed in more detail in the next section. Although experimental data on elastic modulus are not very uniform, it corresponds to the values of in-plane rigidity  $C = 340\text{--}440 \text{ N}/\text{m}$  to the values  $Y = 1.0\text{--}1.3 \text{ GPa}$  for multiwall tubules and to  $Y = 4C/d = (1.36\text{--}1.76) \text{ TPa nm}/d$  for SWNTs of diameter  $d$ .

## VAN DER WAALS INTERACTIONS

Supramolecular interactions between the SWNTs are mainly because of van der Waals forces (VdW), except special situations when local charge or covalently bonded functional group introduce additional electrostatic fields. van der Waals forces play also an important role in the interaction of the nanotubes with the substrata. The different shells of a MWNT (multiwall nanotube) interact primarily by van der Waals forces; single-wall tubes form ropes for the same reason.

An interesting manifestation of van der Waals interactions involves the self-interaction between two segments of the same single-wall CNT to produce a closed ring (loop).<sup>[10]</sup> Single-walled nanotube rings were first observed in trace amounts in the products of laser ablation of graphite and assigned a toroidal structure. More recently, rings of SWNTs were synthesized with large yields ( $\sim 50\%$ ) from straight nanotube segments. These rings were shown to be loops and not tori.<sup>[10]</sup> The synthesis involves the irradiation of raw SWNTs in a sulfuric acid–hydrogen peroxide solution by ultrasound. This treatment both etches the CNTs,

shortening their length to about 3–4  $\mu\text{m}$ , and induces ring formation.

Fundamentally, van der Waals attraction between the CNT is a result of dispersion forces, i.e., electrostatic dipole-to-dipole interaction (which gives  $V \sim 1/r^3$  dependence of potential energy), and because the dipoles are mutually induced excited states, this actually yields nonzero effect only in the second-order perturbation theory, an always negative shift in potential energy  $U^{(2)} \sim -V^2 \sim -1/r^6$ .

For nanotubes and other carbon-cage structures, the van der Waals energy can be obtained from a universal graphitic potential<sup>[11]</sup> and for (10,10) tubes is

$$U(s) = -0.9516 \text{ eV/nm} (5/3)[(1 + 0.291s)^{-4} - (2/5)(1 + 0.291s)^{-10}] \quad (1)$$

Equilibrium point  $s = 0$  corresponds to intercenter distance 1.67 nm that is wall-to-wall distance 0.315 nm, with the potential well depth about 0.95 eV/nm. This value is equivalent to energy of 0.04 eV per each pair of C-atoms facing across the van der Waals spacing, or near 0.9 kcal/mol (e.g., of inserted spacer group that would push the nanotubes off the energy-minimum position). Although significant, this attraction energy decays fast with the nanotube separation: to the half of the value at only 1 Å from equilibrium and almost vanishes at 3–5 Å, as Fig. 3 shows.

The formation of coils by CNTs is particularly intriguing. While coils of biomolecules and polymers are well-known structures, they are stabilized by a number of interactions that include hydrogen bonds and ionic interactions. On the other hand, the formation of nanotube coils is surprising given the high flexural rigidity ( $K = \text{Young's modulus times areal moment}$

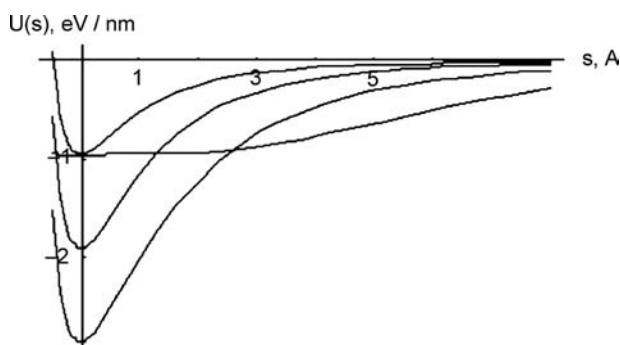


**Fig. 3** van der Waals energy per unit length is shown as function of displacement from equilibrium. From top down, three lines correspond to the tube deflecting from a contact with one, a pair, or a triplet of others; shallow plot corresponds to deflection in tangential direction *Source*: From Ref.<sup>[12]</sup>.

of inertia) of CNTs and the fact that CNT coils can only be stabilized by van der Waals forces. However, estimates based on continuum mechanics show that, in fact, it is easy to compensate for the strain energy induced by the coiling process through the strong adhesion between tube segments in the coil. Details of this analysis can be found in the original reports<sup>[10]</sup> or in our recent review.<sup>[5]</sup> Here we will outline briefly a different and more common situation where the competition of elastic energy and the intertubular linkage is important. Following our recent work,<sup>[12]</sup> we will discuss the connection between the nanomechanics of CNTs and their *random* curling in a suspension or a raw synthesized material of bucky paper.

Single-walled nanotubes are often compared with polymer chains as having very high rigidity and therefore large persistence length. To quantify this argument, we note that a defectless CNT has almost no static flexing, although 5/7 defects, for example, introduce small kink angle 5–15° and could cause some static curvature, but their energies are high and concentration is usually negligible. Only dynamic elastic flexibility should be considered. If  $\mathbf{u}(s)$  is a unit direction vector tangent to the CNT at contour length point  $s$ , and the bending stiffness is  $K$ , then statistical probability of certain shape  $\mathbf{u}(s)$  is

$$P[\mathbf{u}(s)] = \exp[-1/2(K/k_bT) \int (\partial\mathbf{u}/\partial s)^2 ds] = \exp[-(1/2)L \int (\partial\mathbf{u}/\partial s)^2 ds] \quad (2)$$

Here persistence length is  $L = (K/k_bT)$ . For a (10,10) SWNT of radius  $R = 0.7 \text{ nm}$  and the effective wall thickness  $h = 0.09 \text{ nm}$  (see “[Linear Elastic Properties](#)” and “[van Der Waals Interactions](#)”), the bending stiffness is very close to  $K = \pi CR^3$  ( $C = 345 \text{ N/m}$  is the in-plane stiffness, based on ab initio calculations). Persistence length at room temperature therefore is  $L_1[(10,10), 293 \text{ K}] \sim 0.1 \text{ mm}$ , in the macroscopic range much greater than for most polymer molecules. The result can be generalized for a single SWNT of radius  $R$ ,

$$L_1 = (30K/T)(R/0.7 \text{ nm})^3 \text{ mm} \quad (3)$$

or  $N$  times more for a bundle of  $N$  tubes (assuming additive stiffness for the case of weak lateral cohesion of the constituent SWNTs). For example, for a smallest close packed bundle of seven (one surrounded by six neighbors), this yields  $L_7 = 1 \text{ mm}$ . Such incoherent bundle and a solid-coherent bundle with perfect lateral adhesion provide the lower and upper limits for the persistence length,  $NL_1 < L_N < N^2L_1$ . Remarkably, these calculations show that the true thermodynamic persistence length of small CNT bundles or even an individual

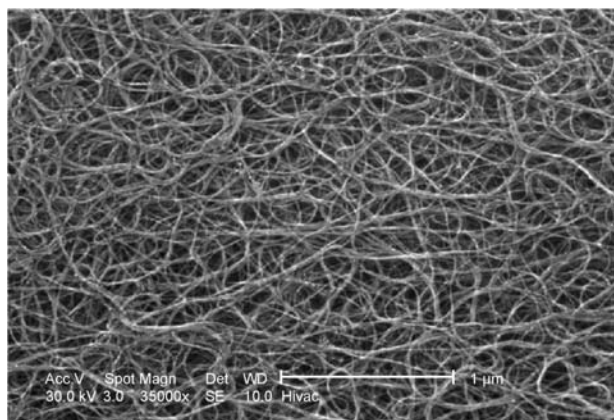


**Fig. 4** Raw-produced SWNTs often form ropes–bundles entangled bent into a rubbery structure called “bucky paper.” The length scale of bends is much smaller than the persistence length for the constituent filaments. Shown here is such material produced by HiPco (high pressure CO) synthesis method *Source:* From O’Connell et al., *Chem. Phys. Lett.*, 342, 265, 2001.

SWNT is in the macroscopic range from a fraction of a millimeter and greater. This means that highly curved structures often observed in bucky-paper mats (Fig. 4) are attributed not to thermodynamic fluctuations, but rather to residual mechanical forces preventing these coils from unfolding. Elastic energy of a typical micron size ( $r \sim 1 \mu\text{m}$ ) curl-arc is much greater than thermal,  $U_{\text{curl}} \sim k_b T(L/r)^2 \gg k_b T$ .<sup>[12]</sup> At the same time, a force required to maintain this shape  $F_{\text{curl}} \sim K/r^2 = N \text{ pN}$ , several piconewtons, where  $N$  is the number of SWNTs in each bundle. This is much less than a force per single chemical bond ( $\sim 1 \text{ nN}$ ), and therefore any occasional lateral bonding between the tubules can be sufficient to prevent them from disentanglement.

### SUPRAMOLECULAR MORPHOLOGY CHANGES WITHIN ELASTIC SHELL MODEL

Almost any molecular structure can sustain very large deformations, compared with the range common in macroscopic mechanics. A less obvious property of CNTs is that the specific features of large non-linear strain can be understood and predicted in terms of continuum theories. One of the outstanding features of nanotubes is their hollow structure, built of atoms densely packed along a closed surface that defines the overall shape. This also manifests itself in dynamic properties of molecules, resembling so much the macroscopic objects of continuum elasticity known as *shells*. Macroscopic shells and rods have long been of interest: the first study dates back to Euler, who discovered the elastic instability. A rod subject to longitudinal compression remains straight but shortens

by some fraction  $\varepsilon$ , proportional to the force, until a critical value (the Euler force) is reached. It then becomes unstable and buckles sideways at  $\varepsilon > \varepsilon_{\text{cr}}$ , while the force almost does not vary. For hollow tubules, there is also a possibility of local buckling in addition to buckling as a whole. Therefore more than one bifurcation can be observed, thus causing an overall non-linear response to the large deforming forces (note that local mechanics of the constituent shells may well still remain within the elastic domain).

In nanomechanics, the theory of shells was first applied in our early analysis of buckling and since then serves a useful guide.<sup>[13–16]</sup> Its relevance for a covalent-bonded system of only a few atoms in diameter was far from being obvious. Molecular dynamics simulations seem better suited for objects that are small.

Fig. 5 shows a simulated nanotube exposed to *axial compression*. The atomic interaction was modeled by the Tersoff–Brenner potential, which reproduces the

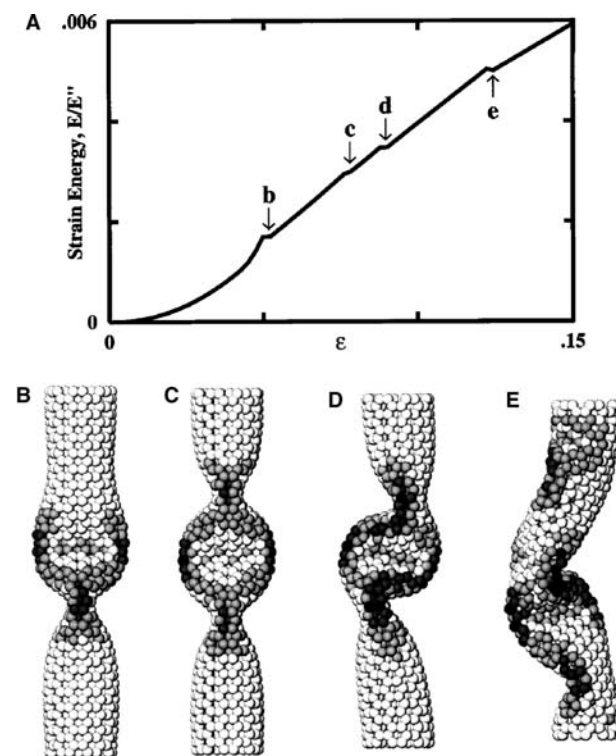


**Fig. 5** Simulation of a (7,7) nanotube exposed to axial compression,  $L = 6 \text{ nm}$ . The strain energy (A) displays four singularities corresponding to shape changes. At  $\varepsilon_c = 0.05$ , the cylinder buckles into the pattern (B), displaying two identical flattenings—“fins” perpendicular to each other. Further increase of  $\varepsilon$  enhances this pattern gradually until at  $\varepsilon_2 = 0.076$ , the tube switches to a three-fin pattern (C), which still possesses a straight axis. In a buckling sideways at  $\varepsilon_3 = 0.09$ , the flattenings serve as hinges, and only a plane of symmetry is preserved (D). At  $\varepsilon_4 = 0.13$ , an entirely squashed asymmetric configuration forms (E). *Source:* From Ref.<sup>[13]</sup>.

lattice constants and binding energies of graphite and diamond. The end atoms were shifted along the axis by small steps and the whole tube was relaxed by conjugate-gradient method while keeping the ends constrained. At small strains, the total energy (Fig. 5A) grows as  $E(\varepsilon) = (1/2)E''\varepsilon^2$ . The presence of four singularities at higher strains was quite a striking feature and the patterns (b)–(e) illustrate the corresponding morphological changes. The shading indicates strain energy per atom, equally spaced from below 0.5 eV (brightest) to above 1.5 eV (darkest). The sequence of singularities in  $E(\varepsilon)$  corresponds to a loss of molecular symmetry from  $D_{\infty h}$  to  $S_4$ ,  $D_{2h}$ ,  $C_{2h}$ , and  $C_1$ . This evolution of the molecular structure can be put in the framework of continuum elasticity.

The intrinsic symmetry of a graphite sheet is hexagonal, and the elastic properties of 2-D hexagonal structure are isotropic. A curved sheet can also be approximated by a uniform shell with only two elastic parameters: flexural rigidity  $D$  and its in-plane stiffness  $C$ . The energy of a shell is given by a surface integral of the quadratic form of local deformation,

$$E = \frac{1}{2} \int \int \{ D[(\kappa_x + \kappa_y)^2 - 2(1 - \nu)(\kappa_x\kappa_y - \kappa_{xy}^2)] + \frac{C}{(1 - \nu^2)} [(\varepsilon_x + \varepsilon_y)^2 - 2(1 - \nu)(\varepsilon_x\varepsilon_y - \varepsilon_{xy}^2)] \} dS \quad (4)$$

where  $\kappa$  is the curvature variation,  $\varepsilon$  is the in-plane strain, and  $x$  and  $y$  are local coordinates. To adapt this formalism to a graphitic tubule, the values of  $D$  and  $C$  can be identified by comparison with the detailed ab initio and semiempirical studies of nanotube energetics at small strains. Indeed, the second derivative of total energy with respect to axial strain corresponds to the in-plane rigidity  $C$  (cf. “Linear Elastic Properties”). Similarly, the strain energy as a function of tube diameter  $d$  corresponds to  $2D/d^2$  in Eq. (4). Using recent ab initio calculations,<sup>[6]</sup> one obtains  $C = 56 \text{ eV/atom} = 340 \text{ J/m}^2$  and  $D = 1.46 \text{ eV}$ . The Poisson ratio  $\nu = 0.15$  was extracted from a reduction of the diameter of a tube stretched in simulations. A similar value is obtained from experimental elastic constants of single crystal graphite. One can make a further step toward a more tangible picture of a tube as having wall thickness  $h$  and Young modulus  $Y_s$ . Using the standard relations  $D = Yh^3/12(1 - \nu^2)$  and  $C = Y_s h$ , one finds  $Y_s = 3.9 \text{ TPa}$  and  $h = 0.089 \text{ nm}$ . With these parameters, linear stability analysis allows one to assess the nanotube behavior under strain.

To illustrate the efficiency of the shell model, consider briefly the case of imposed axial compression. A trial perturbation of a cylinder has a form of Fourier harmonics, with  $M$  azimuthal lobes and  $N$  halfwaves

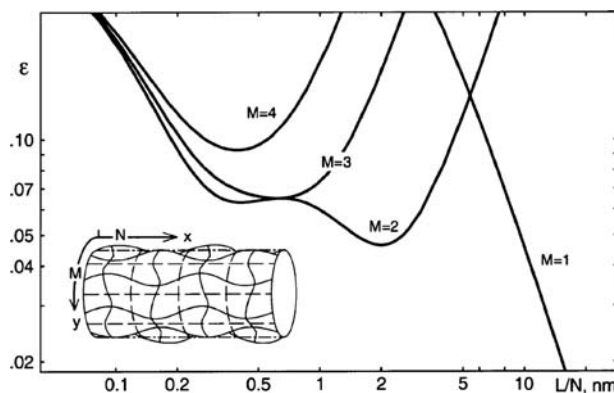


**Fig. 6** The critical strain levels for a continuous, 1-nm-wide shell tube as a function of its scaled length  $L/N$ . A buckling pattern  $(M, N)$  is defined by the number of halfwaves  $2M$  and  $N$  in  $y$  and  $x$  directions, respectively, e.g., a  $(4, 4)$ -pattern is shown in the inset. The effective moduli and thickness are fit to graphene. Source: From Ref.<sup>[13]</sup>.

along the tube (Fig. 6 inset), i.e., sines and cosines of arguments  $2My/d$  and  $N\pi x/L$ . At a critical level of the imposed strain,  $\varepsilon_c(M, N)$ , the energy variation (4.1) vanishes for this shape disturbance. The cylinder becomes unstable and lowers its energy by assuming an  $(M, N)$  pattern. For tubes of  $d = 1 \text{ nm}$  with the shell parameters identified above, the critical strain is shown in Fig. 6. According to these plots, for a tube with  $L > 10 \text{ nm}$ , the bifurcation is first attained for  $M = 1, N = 1$ . The tube preserves its circular cross section and buckles sideways as a whole; the critical strain is close to that for a simple rod,

$$\varepsilon_c = 1/2(\pi d/L)^2 \quad (5)$$

or four times less for a tube with hinged (unclamped) ends. For a shorter tube, the situation is different. The lowest critical strain occurs for  $M = 2$  (and  $N \geq 1$ , see Fig. 6), with a few separated flattenings in directions perpendicular to each other, while the axis remains straight. For such a local buckling, in contrast to (4.2), the critical strain depends little on length and estimates to  $\varepsilon_c = 4\sqrt{D/C}d^{-1} = (2/\sqrt{3})(1 - \nu^2)^{-1/2}hd^{-1}$  in the so-called Lorenz limit. For a nanotube, one finds

$$\varepsilon_c = 0.1 \text{ nm}/d \quad (6)$$

Specifically, for the 1-nm-wide tube of length  $L = 6 \text{ nm}$ , the lowest critical strains occur for  $M = 2$  and  $N = 2$  or  $3$  (Fig. 6). This is in accord with the two- and three-fin patterns seen in Fig. 5B and C. Higher singularities cannot be quantified by the linear analysis, but they look like a sideways beam buckling, which at this stage becomes a non-uniform object.

Axially compressed tubes of greater length and/or tubes simulated with hinged ends (equivalent to a



doubled length) first buckle sideways as a whole at a strain consistent with (5). After that, the compression at the ends results in bending and a local buckling inward. This illustrates the importance of the “beam-bending” mode, the softest for a long molecule and most likely to attain significant amplitudes because of either thermal vibrations or environmental forces. In simulations of *bending*, a torque rather than force is applied at the ends and the bending angle  $\theta$  increases stepwise. While a notch in the energy plot can be mistaken for numerical noise, its derivative  $dE/d\theta$  drops significantly. This unambiguously shows an increase in tube compliance—a signature of a buckling event. In bending, only one side of a tube is compressed and thus can buckle. Assuming that it buckles when its local strain,  $\varepsilon = \kappa d/2$ , where  $\kappa$  is the local curvature, is close to that in axial compression, Eq. (6), we estimate the critical curvature as

$$\kappa_c = 0.2 \text{ nm}/d^2 \quad (7)$$

In simulation of *torsion*, the increase of azimuthal angle  $\phi$  between the tube ends results in abrupt changes of energy and morphology.<sup>[13,14,17]</sup> In continuum model, the analysis based on Eq. 4 is similar to that outlined above, except that it involves skew harmonics of arguments such as  $N\pi x/L \pm 2My/d$ . For overall beam buckling ( $M = 1$ ),

$$\phi_c = 2(1 + \nu)\pi \quad (8)$$

and for the cylinder-helix flattening ( $M = 2$ ),

$$\phi_c = 0.06 \text{ nm}^{3/2}L/d^{5/2} \quad (9)$$

The latter should occur first for  $L < 140d^{5/2}$  nm, which is true for all tubes we simulated. However, in simulations, it occurs later than predicted by Eq. (9). The ends, kept circular in simulation, which is physically justifiable, by a presence of rigid caps on normally closed ends of a molecule, deter the thorough flattening necessary for the helix to form (unlike the local flattening in the case of an axial load).

Experimental evidence provides sufficient support to the notion of high resilience of SWNT. An early observation of noticeable flattening of the walls in a close contact of two MWNT has been attributed to van der Waals forces pressing the cylinders to each other.<sup>[18]</sup> Collapsed forms of the nanotube (“nanoribbons”), also caused by van der Waals attraction, have been observed in experiment, and their stability can be explained by the competition between the van der Waals and elastic energies.<sup>[19]</sup> Any additional torsional strain imposed on a tube in experimental environment also favors flattening<sup>[13,14]</sup> and facilitates the collapse. Graphically more striking evidence of resilience is

provided by bent structures,<sup>[20]</sup> as well as the more detailed observations that actually stimulated our research in nanomechanics.<sup>[21]</sup> An accurate measurement with the atomic force microscope (AFM) tip detects the “failure” of a multiwall tubule in bending,<sup>[8]</sup> which essentially represents non-linear buckling on the compressive side of the bent tube. The estimated measured local stress is 15–28 GPa, very close to the calculated value.<sup>[22,23]</sup> Buckling and ripple of the outermost layers in a dynamic resonant bending has been directly observed and is responsible for the apparent softening of MWNT of larger diameters.<sup>[5,24]</sup>

## FAILURE AND RELAXATION MECHANISMS

The important issue of ultimate tensile strength of CNTs is inherently related with the atomic relaxation in the lattice under high strain. This thermally activated process was first predicted to consist of a sequence of individual bond rotations in the approach based on dislocation theory.<sup>[22,25,26]</sup> Careful computer simulations demonstrate feasibility of this mechanism and allowed us to quantify important energy aspects.<sup>[27,28]</sup> It has been shown that in a crystal lattice such as the wall of a CNT, a yield to deformation must begin with a homogeneous nucleation of a slip by the shear stress present. The non-basal edge dislocations emerging in such slip have a well-defined core, a pentagon–heptagon pair, 5/7. Therefore the prime dipole is equivalent to the Stone–Wales (SW) defect. The nucleation of this prime dislocation dipole “unlocks” the nanotube for further relaxation: either brittle cleavage or a plastic flow. Remarkably, the latter corresponds to a motion of dislocations along the helical paths (glide “planes”) within the nanotube wall. This causes a stepwise (quantized) necking, when the domains of different chiral symmetry and therefore different electronic structure are formed, thus coupling the mechanical and electrical properties.<sup>[22,25,26]</sup> It has further been shown<sup>[22,23,25,28–30]</sup> that the energy of such nucleation explicitly depends on CNT helicity (chirality).

Below, we deduce starting with dislocation theory the atomistics of mechanical relaxation under extreme tension. Locally, the wall of a nanotube differs little from a single graphene sheet, a 2-D crystal of carbon. When a uniaxial tension  $\sigma$  (N/m—for the 2-D wall, it is convenient to use force per unit length of its circumference) is applied, it can be represented as a sum of expansion (locally isotropic within the wall) and a shear of a magnitude  $\sigma/2$  (directed at  $\pm 45^\circ$  with respect to tension). Generally, in a macroscopic crystal, the shear stress relaxes by a movement of *dislocations*, the edges of the atomic extraplanes. Burgers vector  $\mathbf{b}$  quantifies the mismatch in the lattice as a result of a

dislocation. Its glide requires only local atomic rearrangements and presents the easiest way for strain release, provided sufficient thermal agitation. In an initially *perfect* lattice such as the wall of a nanotube, a yield to a great axial tension begins with a homogeneous *nucleation* of a slip, when a dipole of dislocations [a tiny loop in three-dimensional (3-D) case] first has to form. The formation and further glide are driven by the reduction of the applied-stress energy, as characterized by the elastic Peach–Koehler force on a dislocation. The force component along  $\mathbf{b}$  is proportional to the shear in this direction and thus depends on the angle between the Burgers vector and the circumference of the tube,

$$f_b = -(1/2)\sigma|b|\sin 2\theta \quad (10)$$

The max  $|f_b|$  is attained on two  $\pm 45^\circ$  lines, which mark the directions of a slip in an isotropic material under tension.

The graphene wall of the nanotube is not isotropic; its hexagonal symmetry governs the three glide planes—the three lines of closest zigzag atomic packing, oriented at  $120^\circ$  to each other (corresponding to the  $\{10\bar{1}l\}$  set of planes in 3-D graphite). At non-zero shear, these directions are prone to slip. The corresponding *c*-axis edge dislocations involved in such slip are indeed known in graphite. The six possible Burgers vectors  $1/3a\langle 2\bar{1}10 \rangle$  have a magnitude  $b = a = 0.246$  nm (lattice constant), and the dislocation core is identified as a  $5/7$  pentagon–heptagon pair in the honeycomb lattice of hexagons. Therefore the primary nucleated dipole must have a  $5/7/7/5$  configuration (a  $5/7$  attached to an inverted  $7/5$  core). This configuration is obtained in the perfect lattice (or a nanotube wall) by a  $90^\circ$  rotation of a single C–C bond, well known in fullerene science as a Stone–Wales diatomic interchange. One is led to conclude that the SW transformation is equivalent to the smallest slip in a hexagonal lattice and must play a key role in the nanotube relaxation under external force.

The preferred glide is the closest to the maximum shear  $\pm 45^\circ$  lines and depends on how the graphene strip is rolled up into a cylinder. This depends on nanotube helicity specified by the chiral indices ( $c_1, c_2$ ) or a chiral angle  $\theta$  indicating how far the circumference departs from the leading zigzag motif  $\mathbf{a}_1$ . The max  $|f_b|$  is attained for the dislocations with  $\mathbf{b} = \pm(0,1)$  and their glide reduces the strain energy

$$E_g = -|f_b a| = -Ca^2/2 \sin(2\theta + 60)\varepsilon \quad (11)$$

per one displacement,  $a$ . Here  $\varepsilon$  is the applied strain and  $C = Yh = 342$  N/m can be derived from the Young's modulus of  $Y = 1020$  GPa and the interlayer spacing  $h = 0.335$  nm in graphite; one then obtains

$Ca^2/2 = 64.5$  eV. Eq. (11) allows one to compare different CNTs (assuming similar amount of preexisting dislocations): the more energetically favorable is the glide in a tube, the earlier it must yield to applied strain.

In a pristine nanotube molecule, the  $5/7$  dislocations have to first emerge as a dipole by a prime SW transformation. Topologically, the SW defect is equivalent to either one of the two dipoles, each formed by an  $\sim a/2$  slip. Applying Eq. 11 to each of the slips, one finds

$$E_{SW} = E_O - A\varepsilon - B\sin(2\theta + 30)\varepsilon \quad (12)$$

The first two terms, the zero-strain formation energy and possible isotropic dilation, do not depend on chiral symmetry. The symmetry-dependent third term, which can also be derived as a leading term in the Fourier series, describes the fact that SW rotation gains more energy in an armchair ( $\theta = 30^\circ$ ) CNT, making it thermodynamically the weakest and most inclined to SW nucleation of the dislocations, in contrast to the zigzag ( $\theta = 0$ ) where the nucleation is least favorable.

Consider for example a (*c,c*) armchair CNT as a typical representative (we will also see below that this armchair type can undergo a more general scenario of relaxation). The initial stress-induced SW rotation creates a geometry that can be viewed as either a dislocation dipole or a tiny crack along the equator. Once “unlocked,” the SW defect can ease further relaxation. At this stage, both brittle (dislocation pileup and crack extension) and plastic (separation of dislocations and their glide away from each other) routes are possible, the former usually at larger stress and the latter at higher temperatures.

Formally, both routes correspond to a further sequence of SW switches. The  $90^\circ$  rotation of the bonds at the “crack tip” (Fig. 7, left column) will result in a  $7/8/7$  flaw and then  $7/8/8/7$ , etc. This further strains the bonds—partitions between the larger polygons, leading eventually to their breakage, with the formation of greater openings such as  $7/14/7$ , etc. If the crack, represented by this sequence, surpasses the critical Griffith size, it cleaves the tubule.

In a more interesting distinct alternative, the SW rotation of another bond (Fig. 7, top row) divides the  $5/7$  and  $7/5$ , as they become two dislocation cores separated by a single row of hexagons. A next similar SW switch results in a double-row separated pair of the  $5/7$ 's and so on. This corresponds, at very high temperatures, to a plastic flow *inside* the nanotube molecule, when the  $5/7$  and  $7/5$  twins glide away from each other driven by the elastic forces, thus reducing the total strain energy [cf. Eq. (11)]. One remarkable feature of such glide is a result of mere cylindrical geometry: the glide

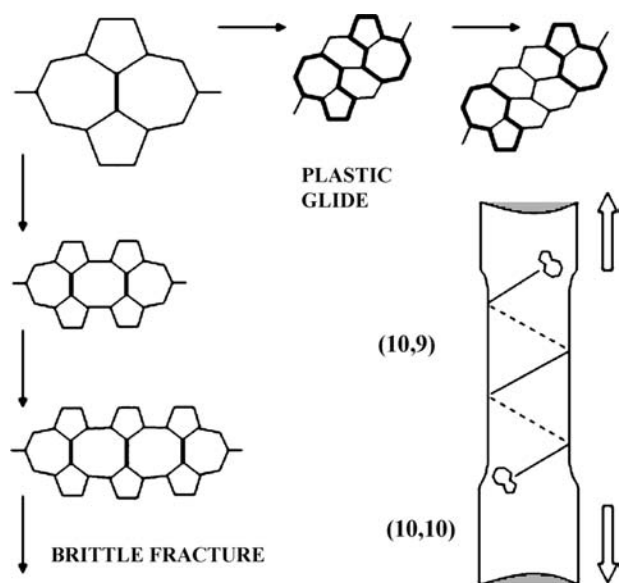


**Fig. 7** SW transformations of an equatorially oriented bond into a vertical position create a nucleus of relaxation (top left corner). It evolves further as either a crack—brittle fracture route, left column—or as a couple of dislocations gliding away along the spiral slip “plane” (plastic yield, top row). In both cases, only SW rotations are required as elementary steps. The stepwise change of the nanotube diameter reflects the change of chirality, bottom right image, causing the corresponding variations of electrical properties *Source*: From Ref.<sup>[25]</sup>.

“planes” in case of nanotubes are actually spirals, and the slow thermally activated Brownian walk of the dislocations proceeds along these well-defined trajectories. Similarly, their extraplanes are just the rows of atoms also curved into the helices.

A nanotube with a 5/7 defect in its wall loses axial symmetry and has a bent equilibrium shape; the calculations show<sup>[31]</sup> the junction angles  $<15^\circ$ . Interestingly then, an exposure of an even achiral nanotube to the axially symmetric tension generates two 5/7 dislocations, and when the tension is removed, the tube “freezes” in an asymmetric configuration, S-shaped or C-shaped, depending on the distance of glide, i.e., time of exposure. This seemingly “symmetry-violating” mechanical test is a truly nanoscale phenomenon. Of course, the symmetry is conserved statistically because many different shapes form under identical conditions.

When the dislocations sweep a noticeable distance, they leave behind a tube segment changed strictly following the topological rules of dislocation theory. By considering a planar development of the tube segment containing a 5/7, for the new chirality vector  $\mathbf{c}'$ , one finds

$$(\mathbf{c}'_1, \mathbf{c}'_2) = (\mathbf{c}_1, \mathbf{c}_2) - (\mathbf{b}_1, \mathbf{b}_2) \quad (13)$$

with the corresponding reduction of diameter,  $d$ . While the dislocations of the first dipole glide away, a generation of another dipole results, in further narrowing and proportional elongation under stress, thus forming a neck as shown above. The orientation of a generated dislocation dipole is determined every time by the Burgers vector closest to the lines of maximum shear ( $\pm 45^\circ$  cross at the endpoint of the current circumference vector  $\mathbf{c}$ ). The evolution of a  $(c,c)$  tube will be:  $(c,c) \rightarrow (c,c-1) \rightarrow (c,c-2) \rightarrow \dots (c,0) \rightarrow [(c-1,1)$  or  $(c,-1)] \rightarrow (c-1,0) \rightarrow [(c-2,1)$  or  $(c-1,-1)] \rightarrow (c-2,0) \rightarrow [(c-3,1)$  or  $(c-2,-1)] \rightarrow (c-3,0)$ , etc. It abandons the armchair  $(c,c)$  type entirely, but then oscillates in the vicinity of zigzag  $(c,0)$  kind, which appears a peculiar attractor. Correspondingly, the diameter for a (10,10) tube changes stepwise,  $d = 1.36, 1.29, 1.22, 1.16$  nm, etc., the local stress grows in proportion, and this quantized necking can be terminated by a cleave at late stages. Interestingly, such plastic flow is accompanied by the change of electronic structure of the emerging domains, governed by the vector  $(c_1, c_2)$ . The armchair tubes are metallic, and others are semiconducting with the different band gap values. The 5/7 pair separating two domains of different chirality has been discussed as a pure-carbon heterojunction, is argued to cause the current rectification detected in a nanotube nanodevice,<sup>[32]</sup> and can be used to modify, in a controlled way, the electronic structure of the tube. Here we see how this electronic heterogeneity can arise from a mechanical relaxation at high temperature: if the initial tube was armchair-metallic, the plastic dilation transforms it into a semiconducting type irreversibly.<sup>[25,26,33]</sup>

While the above analysis is based on atomic picture (structure and interactions), recent developments<sup>[34]</sup> offer an approach where the fracture nucleation can be described rather elegantly within non-linear continuum mechanics (based on classical interatomic forces for carbon). Whether this approach can describe change in chirality, temperature dependence, or temporal aspects of relaxation should yet be explored.

The dislocation theory allows one to expand the approach to other materials, and we have recently applied it to boron nitride (BN) nanotubes.<sup>[35,36]</sup> While the binding energy in BN is lower than in CNT, the formation of 5/7/7/5 defect can be more costly because of Coulomb repulsion between emerging BB and NN pairs (Fig. 8A) (bonding in BN is partially ionic with strong preference to chemical neighbor alternation in the lattice). Another dislocation pair 4/8/8/4 that preserves the alternation must be considered (Fig. 8B). It turns out that the quantitative results are sensitive to the level of theory accuracy. Tight binding approximation<sup>[37]</sup> underestimates the repulsion by almost 3 eV.<sup>[35,36]</sup> Ab initio DFT calculations show that 5/7/7/5 is metastable lowest energy

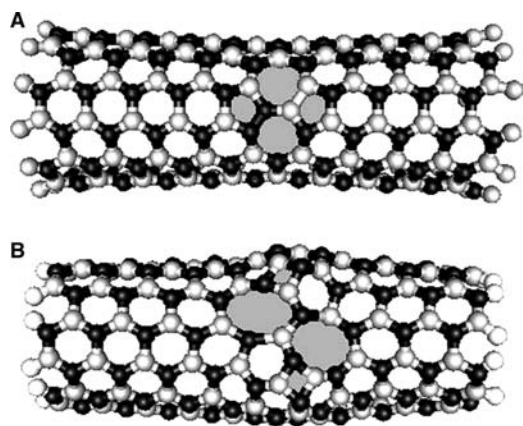


**Fig. 8** The geometries of (5,5) BN tubule with (A) 5/7/7/5 defect emerging at high tension and temperature and (B) 4/8/8/4 dislocation dipole. *Source:* From Ref.<sup>[35]</sup>.

defect in BN, and its formation energy 5.5 eV is higher than 3.0 eV in carbon,<sup>[35,36]</sup> thus suggesting higher thermodynamic stability of BN under tensile load. Relaxation under compression is different as it involves skin-type buckling also investigated recently.<sup>[38]</sup>

### KINETIC APPROACH TO STRENGTH-FAILURE EVALUATION

Computer simulations have provided a compelling evidence of the mechanisms discussed above. By carefully tuning a *quasi-static* tension in the tubule and gradually elevating its temperature, with extensive periods of MD annealing, the first stages of the mechanical yield of CNT have been observed (Fig. 9).<sup>[27,28]</sup> In simulation of tensile load, the novel patterns in plasticity and breakage, just as described above, clearly emerge. At very *high strain* rate, the details of primary defects cannot be seen and they only begin to emerge at higher strain level, giving impression of exceedingly high breaking strain.<sup>[17]</sup>

Fracture, of course, is a *kinetic* process where time is an important parameter. Even a small tension, as any non-hydrostatic stress, makes material thermodynamically metastable and a generation of defects energetically favorable. Thus the important issue of strength remains beyond the defect formation energy and its reduction with the applied tension. Recently, we developed kinetic theory in application to CNT.<sup>[30,39]</sup> In this approach, we evaluate conditions (strain  $\varepsilon$ , temperature  $T$ ) when the probability  $P$  of defect formation becomes significant within laboratory test time  $\Delta t$ ,

$$P = \nu \Delta t N_B / 3 \sum_m \exp[-E_m(\varepsilon, \chi) / k_b T] \sim 1 \quad (14)$$

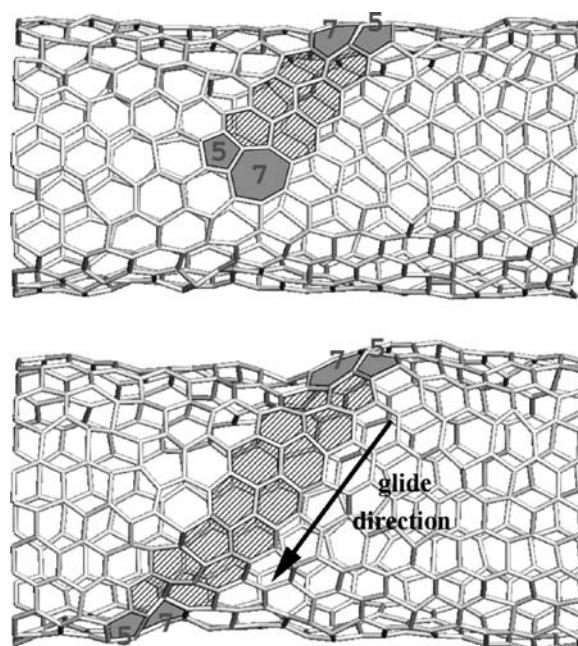


**Fig. 9**  $T = 3000$  K, strain 3%, plastic flow behavior (about 2.5 nsec). The shaded area indicates the migration path of the 5/7 edge dislocation. *Source:* From Ref.<sup>[28]</sup>.

Here  $\nu = k_b T / h$  is the usual attempt frequency and  $N_B$  is the number of bonds in the sample. Activation barrier  $E_m(\varepsilon, \chi)$  must be computed as a function of strain and chirality  $\chi$  of the tubule, and then the solution of this equation with respect to  $\varepsilon$  gives the breaking strain values. This approach involved substantial computational work in finding the saddle points and energies (Fig. 10A) for a variety of conditions and for several transition state modes (index  $m$  in the summation above). Obtained yield strain near 17% (Fig. 10B),<sup>[30,39]</sup> is in reasonable agreement with the series of experimental reports. We currently are implementing similar approach with ab initio level of saddle point barrier calculations.<sup>[40]</sup> Preliminary data show higher 8–9 eV barriers, but their reduction with tension is also faster.

Previously performed high strain rate simulations have shown temperature dependence of breaking strain,<sup>[14,17]</sup> consistent with the kinetic theory.<sup>[30]</sup> In a constant strain rate arrangement (when the ends of the sample are pulled from the equilibrium with certain rate), the rate equation is slightly modified to its integral form. However, the main contribution comes from the vicinity of the upper limit,

$$P = \nu N_B / 3 \int \sum_m \exp\{-E_m[\varepsilon(t), \chi] / k_b T\} dt \sim 1 \quad (15)$$

Simple analysis reveals certain invariant  $T \times \log(\nu \Delta t)$  of the time of failure and temperature (provided the constant strain). Detailed simulations could shed



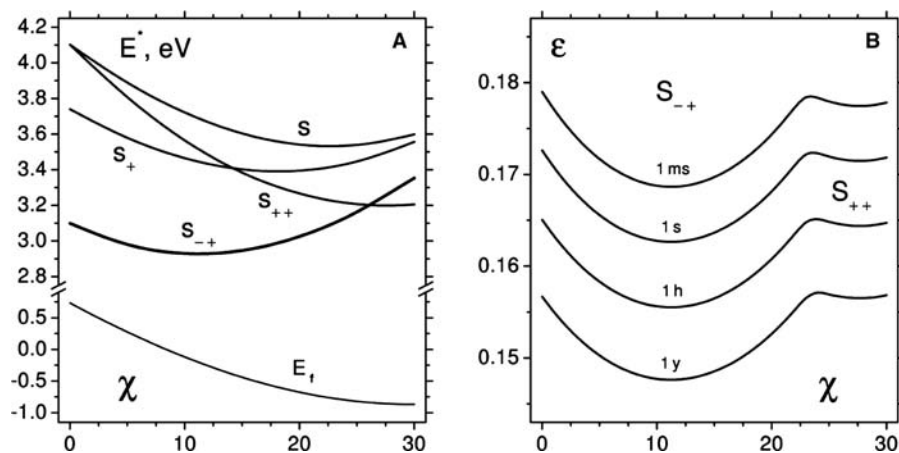


**Fig. 10** Activation barrier values (here computed within classical multibody potential, (A) serve as input to the rate equation (14) and the calculation of the yield strain as a function of time (here from 1 msec to 1 year, (B), temperature (here 300 K), and chiral symmetry ( $\chi$ ). Source: From Ref.<sup>[30]</sup>.

additional light on this aspect (Cho et al., private communication, 2002). More significant finding reported recently<sup>[41]</sup> is that kinetic probability of SW bond rotation at room temperatures can be rather small and the actual mechanism of failure is a brittle cleave, through a sequence of “lattice-trapped” states corresponding to individual broken bonds, from one to two, three, etc.<sup>[41]</sup>

### COALESCENCE OF NANOTUBES AS A REVERSED FAILURE

Understanding the details of failure mechanism has led us recently<sup>[42–44]</sup> to investigate an opposite process, a coalescence of nanoscale clusters analogous to macroscopic sintering or welding. Fusion of smaller components into a larger whole is a ubiquitous process in condensed matter. In molecular scale, it corresponds to chemical synthesis, where exact rearrangement of atoms can be recognized. Coalescence or sintering of macroscopic parts is usually driven by the well-defined thermodynamic forces (frequently, surface energy reduction), but the atomic evolution path is redundant and its exact identification is irrelevant. Exploring a possibility of the two particles merging with atomic precision becomes compelling in nanometer scale, where one aspires to “arrange the atoms one by one.” Are the initial and final states connected by a feasible path of atomic movements, or separated by insurmountable barriers? Direct molecular dynamics (MD) investigation is usually hampered by energy landscape traps and beyond very few atomic steps needs to be augmented with additional analysis.

An example of very small particles is offered by fullerene cages and CNTs. Fusion of fullerenes has been previously reported and the lateral merging (diameter-doubling) of CNT has been observed and simulated.<sup>[45,46]</sup> In contrast, head-to-head coalescence of CNT segments remained unexplored and of

particular theoretical and practical interest: Is it permitted by rigorous topology rules to eliminate all the pentagons always present in the CNT ends and thus dissolve the caps completely? Can this occur through a series of well-defined elementary steps and what is overall energy change if the system evolves through the intermediate disordered states to the final purely hexagonal lattice of continuous tubule? If feasible, such “welding” can lead to increase of connectivity in CNT arrays in bundles/ropes and crystals and thus significantly improve the mechanical, thermal, and electrical properties of material. In addition, determining the atomistic steps of small-diameter tube coalescence (with the end caps identical to half-buckyball) can shed light on the underlying mechanism of condensed phase conversion or CNT synthesis from  $C_{60}$  components.

In Ref.<sup>[42]</sup> we have reported for the first time atomically precise routes for complete coalescence of generic fullerene cages: cap-to-cap CNT and  $C_{60}$  merging together to form defectless final structure. The entire process is reduced to sequence of Stone–Wales bond switches and therefore is likely the lowest energy path of transformation. Several other examples of merging follow immediately as special cases: coalescence of buckyballs in peapod, joining of the two (5,5) tubes as in Fig. 11, “welding” the (10,10) to (10,10) following Fig. 12, etc. The approach remains valid for arbitrary tubes with the important constraint of unavoidable grain boundary for the tubes of different chirality. The junction of  $(n,m)$  and  $(n',m')$  must contain  $5/7$  dislocations or their equivalent of  $(n - n', m - m')$  total Burgers vector.<sup>[25]</sup> The proposed mechanism<sup>[42–44]</sup> has important implications for nanotube material (crystals, ropes) processing and property enhancement, engineering of nanoscale junctions of various types, possible growth mechanisms with the  $C_{60}$  and other nanoparticles as feedstock. In the context of nanomechanics, an interesting feature of the late stages of coalescence is the annealing and annihilation of  $5/7$  pairs in a process

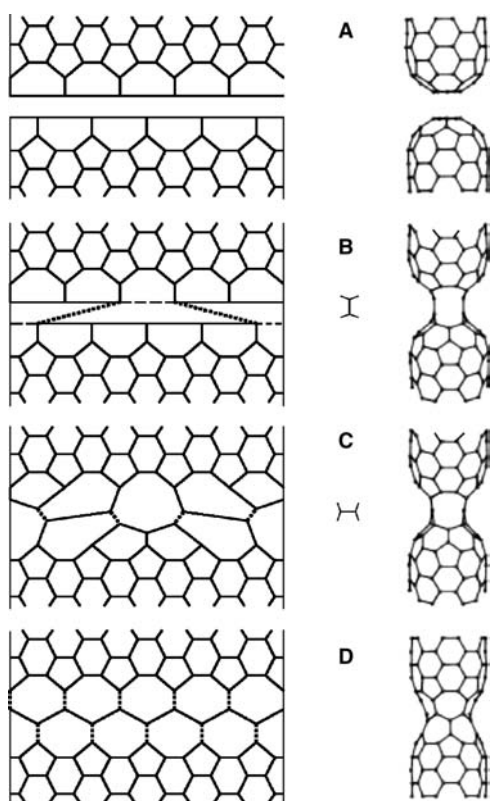


**Fig. 11** 2-D geodesic projection (left) and the actual 3-D structures (right) show the transformations from a pair of separate (5,5) tubes (A) to a single defect-free nanotube. Primary “polymerization” links form as two other bonds break (B, dashed lines). The  $\pi/2$  rotations of the links (the bonds subject to such SW flip are dotted) and the SW flips of the four other bonds in (C) produce a (5,0) neck (D). It widens by means of another 10 SW rotations, forming a perfect single (5,5) tubule (not shown). *Source:* From Ref.<sup>[42]</sup>.

exactly reverse to the formation and glide of these dislocation cores in the course of yield and failure under tension. On the other hand, although covalent bond flip represents intramolecular process, it is remarkable how it can lead to possibility of global supramolecular shape changes and reactions, from merging coalescence to interpenetration and encapsulation.

### TENSEGRITY AT SUPRAMOLECULAR SCALE

Usual supramolecular interactions possess the same generic properties as any other interatomic forces: weak but always present attraction at large distances (from tens of nanometers) results in a relatively shallow potential minimum at intermolecular vicinity of 0.2–0.5 nm spacing. Closer, it turns into a steep repulsive potential which, upon sufficient compression, can yield to a covalent bonding. Therefore supramolecular forces by themselves are unlikely to be able to support

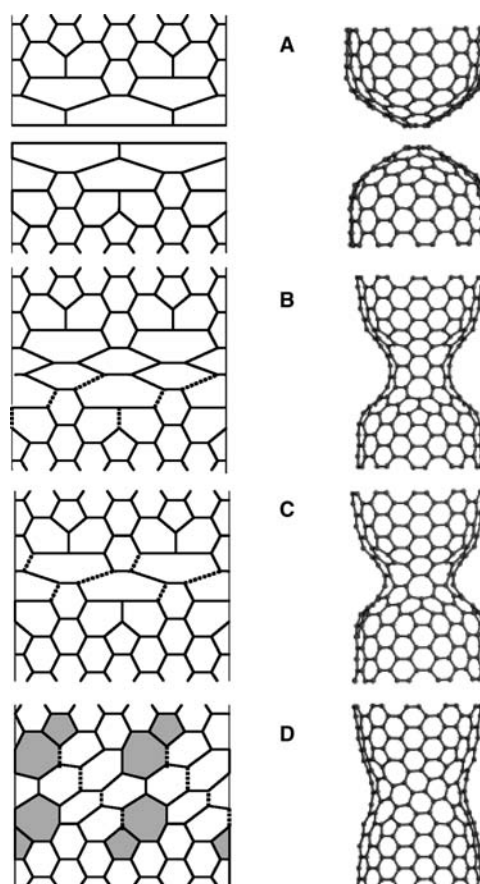


**Fig. 12** 2-D projections (left) and the computed 3-D intermediate structures (right) in the coalescence of the two (10,10) nanotubes: separate caps (A) in a sequence similar to Fig. 8 develop a (5,5) junction (B), which then shortens (C) and widens into a (10,5) neck (D). Glide of the shaded 5/7 dislocations completes the annealing into a perfect (10,10) CNT (not shown). Due to the fifth-fold symmetry, only two cells are displayed. *Source:* From Ref.<sup>[42]</sup>.

low-density assembly of molecules and nanotubes in particular: they would form aligned bundles or at least relatively dense random mats. In this context, it became of interest recently to explore transferability of certain ideas of macroengineering and to connect rigid nanotubes by chemically attached polymer segments to keep them apart. This seems at a first glance counterintuitive—how adding *flexible* links can prevent rigid beams from lumping together? However, at the macroscopic scale, the idea goes back to Fuller,<sup>[47]</sup> who has proposed and patented *tensile-integrity structures*, hence the terms *tensegrity* in the literature. Tensegrity is a design principle that describes how network structures achieve shape stability. The main point is that a disconnected set of rigid beams can be tethered by sparse series of tensile threads (each perfectly bendable and unresponsive to any compression) in such a way that global structure



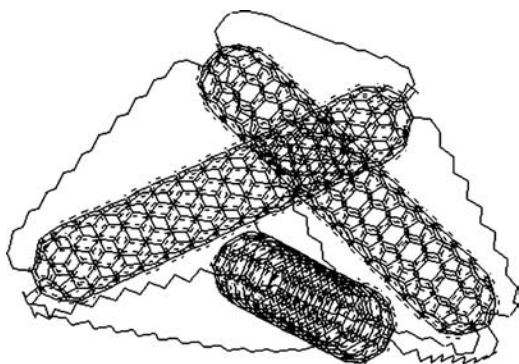


**Fig. 13** Molecular mechanics (relaxed with realistic interatomic force-field and weak van der Waals interaction) simulation of the simplest tensegrity structure c3t9 of carbon nanotube beams connected by covalently attached to the cap pentagons polyethylene chains *Source: From Ref.*<sup>[49]</sup>.

can become rigid, sustain compressive global load, and possess all-finite vibration eigenfrequencies. Such engineered structures can be found in architecture, furniture, entertainment, and aerospace applications (because of lightweight and “foldability”). In cell biology, cytoskeleton is also suggested to possess tensegrity properties.<sup>[48]</sup> Fig. 13 shows simplest simulated tensegrity unit (3 beams compression members connected by 9 chains tension members, c3t9 per Skelton’s nomenclature) composed of rigid carbon nanotubes tethered by polymer chains.<sup>[49]</sup> We have analyzed stability changes in such and several similar structures upon removal of one chain or adding a few extras.

## CONCLUSION

Mechanics of nanotubes has attracted keen interest since their discovery and over the past decade. Above, we have described several established facts and properties together with other, yet speculative aspects and possibilities. It may be useful to reiterate in conclusion some observations and notions of the field as discussed in this entry.

Because of qualitative differences, nanotube mechanics can be subdivided into *intramolecular*, involving bond rearrangements and atomic removal or insertion within the carbon lattice of the tube wall, and *supramolecular* mechanics of interactions *between* the tube molecules. As illustrated above, the latter can be a result of weak distant interactions via dispersion van der Waals forces, stronger direct electrostatic potentials, or by means of much stronger covalent linkage-tethering of nanotubes through intermediate functional groups or elongated chains (as in the example of tensegrity designs). While supramolecular interactions play central role in colloid chemistry, in

numerous biochemical processes, and have been broadly studied, in case of nanotubes, certain special aspects stand out. Great strength of carbon lattice makes it qualitatively different from most other molecules often involved in supramolecular processes: lowest activation barrier for intratube bond rearrangements is 7–9 eV high, which makes even covalent bonding with some other species or between the tubes relatively small supramolecular perturbation.

In contrast, the very same stiffness and “surface” smoothness of the tubes results in dramatic amplification or the traditionally weak dispersion forces. van der Waals interactions add up along the tube–tube contact and yield typically ~1 eV per each nanometer of length, i.e., many electron volts for a typical lateral contact. In turn, this makes solubility or even mechanical separation of nanotube bundles a very challenging task. These distinct features of supramolecular mechanics of nanotubes play critical role in their assembly in arrays-bundles of ropes, nematic crystals, or in their distribution in and coupling with solvents or matrix substances in composite materials.

## ACKNOWLEDGMENTS

This entry is supported by the Office of Naval Research, Air Force Research Laboratory, and the Nanoscale Science and Engineering Initiative of the National Science Foundation, award number EEC-0118007 (BIY).

## REFERENCES

1. Iijima, S. Helical microtubules of graphitic carbon. *Nature* **1991**, *354*, 56–58.
2. Yakobson, B.I.; Smalley, R.E. Fullerene nanotubes: C<sub>1,000,000</sub> and beyond. *Am. Sci.* **1997**, *85* (4), 324–337.
3. Phillips, R.B. *Crystals, Defects and Microstructures*; Cambridge University Press: Cambridge, 2001; 780 pp.
4. Hertel, T.; Walkup, R.E.; Avouris, P. Deformation of carbon nanotubes by surface van der Waals forces. *Phys. Rev., B* **1998**, *58* (20), 13,870–13,873.
5. Yakobson, B.I.; Avouris, P. Mechanical Properties of Carbon Nanotubes. In *Carbon Nanotubes*; Dresselhaus, M.S., Dresselhaus, G., Avouris, P., Eds.; Springer: Berlin, 2001; 287–327.
6. Kudin, K.N.; Scuseria, G.E.; Yakobson, B.I. C<sub>2</sub>F, BN and C nano-shell elasticity by ab initio computations. *Phys. Rev., B* **2001**, *64*, 235406.
7. Treacy, M.M.J.; Ebbesen, T.W.; Gibson, J.M. Exceptionally high Young’s modulus observed for individual carbon nanotubes. *Nature* **1996**, *381*, 678–680.
8. Wong, E.W.; Sheehan, P.E.; Lieber, C.M. Nanobeam mechanics: elasticity, strength and toughness of nanorods and nanotubes. *Science* **1997**, *277*, 1971–1975.

9. Poncharal, P.; Wang, Z.L.; Ugarte, D.; Heer, W.A. Electrostatic deflections and electromechanical resonances of carbon nanotubes. *Science* **1999**, *283* (5407), 1513–1516.
10. Martel, R.; Shea, H.R.; Avouris, P. Rings of single-wall carbon nanotubes. *Nature* **1999**, *398*, 582.
11. Girifalco, L.A.; Hodak, M.; Lee, R.S. Carbon nanotubes, buckyballs, ropes, and a universal graphitic potential. *Phys. Rev., B* **2000**, *62* (19), 13,104–13,110.
12. Yakobson, B.I.; Couchman, L.S. Persistence length and nanomechanics of random bundles of nanotubes. **2003**.
13. Yakobson, B.I.; Brabec, C.J.; Bernholc, J. Nanomechanics of carbon tubes: instabilities beyond the linear response. *Phys. Rev. Lett.* **1996**, *76* (14), 2511–2514.
14. Yakobson, B.I.; Brabec, C.J.; Bernholc, J. Structural mechanics of carbon nanotubes: from continuum elasticity to atomistic fracture. *J. Comput.-Aided Mater. Des.* **1996**, *3*, 173–182.
15. Garg, A.; Han, J.; Sinnott, S.B. Interactions of carbon-nanotubule proximal probe tips with diamond and graphite. *Phys. Rev. Lett.* **1998**, *81* (11), 2260–2263.
16. Srivastava, D.; Menon, M.; Cho, K. Nanoplasticity of single-wall carbon nanotubes under uniaxial compression. *Phys. Rev. Lett.* **1999**, *83* (15), 2973–2976.
17. Yakobson, B.I.; Campbell, M.P.; Brabec, C.J.; Bernholc, J. High strain rate fracture and C-chain unraveling in carbon nanotubes. *Comput. Mater. Sci.* **1997**, *8*, 341–348.
18. Ruoff, R.S.; Tersoff, J.; Lorents, D.C.; Subramoney, S.; Chan, B. Radial deformation of carbon nanotubes by van der Waals forces. *Nature* **1993**, *364*, 514–516.
19. Chopra, N.G.; Benedict, X.; Crespi, V.H.; Cohen, M.L.; Louie, S.G.; Zettl, A. Fully collapsed carbon nanotubes. *Nature* **1995**, *377*, 135–138.
20. Despres, J.F.; Daguerre, E.; Lafdi, K. Flexibility of graphene layers in carbon nanotubes. *Carbon* **1995**, *33* (1), 87–92.
21. Iijima, S.; Brabec, C.J.; Maiti, A.; Bernholc, J. Structural flexibility of carbon nanotubes. *J. Chem. Phys.* **1996**, *104* (5), 2089–2092.
22. Yakobson, B.I. Dynamic topology and yield strength of carbon nanotubes. In *Fullerenes, Electrochemical Society*; ECS, Pennington: Paris, 1997.
23. Smalley, R.E.; Yakobson, B.I. The future of the fullerenes. *Solid State Commun.* **1998**, *107* (11), 597–606.
24. Liu, J.Z.; Zheng, Q.; Jiang, Q. Effect of a rippling mode on resonances of carbon nanotubes. *Phys. Rev. Lett.* **2001**, *86*, 4843–4846.
25. Yakobson, B.I. Mechanical relaxation and ‘intramolecular plasticity’ in carbon nanotubes. *Appl. Phys. Lett.* **1998**, *72* (8), 918–920.
26. Yakobson, B.I. Physical Property Modification of Nanotubes. United States Patent. US 6,280,677 B1, 2001.
27. Nardelli, M.B.; Yakobson, B.I.; Bernholc, J. Mechanism of strain release in carbon nanotubes. *Phys. Rev.* **1998**, *B57*, R4277.
28. Nardelli, M.B.; Yakobson, B.I.; Bernholc, J. Brittle and ductile behavior in carbon nanotubes. *Phys. Rev. Lett.* **1998**, *81* (21), 4656–4659.
29. Yakobson, B.I.; Samsonidze, G.; Samsonidze, G.G. Atomistic theory of mechanical relaxation in fullerene nanotubes. *Carbon* **2000**, *38*, 1675.
30. Samsonidze, G.G.; Samsonidze, G.G.; Yakobson, B.I. Kinetic theory of symmetry-dependent strength in carbon nanotubes. *Phys. Rev. Lett.* **2002**, *88*, 065501.
31. Chico, L.; Crespi, V.H.; Benedict, L.X.; Loui, S.G.; Cohen, M.L. Pure carbon nanoscale devices: nanotube heterojunctions. *Phys. Rev. Lett.* **1996**, *76* (6), 971–974.
32. Collins, P.G.; Zettl, A.; Bando, H.; Thess, A.; Smalley, R.E. Nanotube nanodevice. *Science* **1997**, *278*, 100–103.
33. Tekleab, D.; Carroll, D.L.; Samsonidze, G.G.; Yakobson, B.I. Strain-induced electronic property heterogeneity of a carbon nanotube. *Phys. Rev., B* **2001**, *64*, 035419/5.
34. Zhang, P.; Huang, Y.; Gao, H.; Hwang, K.C. Fracture nucleation in SWNT under tension: a continuum analysis incorporating interatomic potential. *ASME Trans. J. Appl. Mech.* **2002**, *69*, 454–458.
35. Bettinger, H.; Dumitrica, T.; Scuseria, G.E.; Yakobson, B.I. Mechanically induced defects and strength of BN nanotubes. *Phys. Rev., B Rapid Commun.* **2002**, *65*, 041406.
36. Dumitrica, T.; Bettinger, H.F.; Scuseria, G.E.; Yakobson, B.I. Thermodynamics of yield in boron nitride nanotubes. *Phys. Rev., B* **2003**, *68*, 085412.
37. Zhang, P.; Crespi, V.H. Plastic deformations of boron-nitride nanotubes: an unexpected weakness. *Phys. Rev., B* **2000**, *62*, 11,050.
38. Srivastava, D.; Menon, M.; Cho, K.J. Anisotropic nanomechanics of boron nitride nanotubes: nanostructured “skin” effect. *Phys. Rev., B* **2001**, *63*, 195413.
39. Samsonidze, G.G.; Samsonidze, G.G.; Yakobson, B.I. Energetics of Stone–Wales defects in deformations of monoatomic hexagonal layers. *Compos. Mater. Sci.* **2002**, *23*, 62–72.
40. Dumitrica, T.; Hua, M.; Bettinger, H.; Yakobson, B.I. Stone–Wales barriers and kinetic theory of strength for nanotubes. **2003**, in progress.
41. Dumitrica, T.; Belytschko, T.; Yakobson, B.I. Bond-breaking bifurcation states in carbon nanotube fracture. *J. Chem. Phys.* **2003**, *118* (21), 9485–9488.
42. Zhao, Y.; Yakobson, B.I.; Smalley, R.E. Dynamic topology of fullerene coalescence. *Phys. Rev. Lett.* **2002**, *88* (18), 185501.
43. Zhao, Y.; Smalley, R.E.; Yakobson, B.I. Coalescence of fullerene cages: topology, energetics, and molecular dynamics simulation. *Phys. Rev., B* **2002**, *66* (195409).
44. Zhao, Y.; Lin, Y.; Yakobson, B.I. Fullerene shape transformations via Stone–Wales bond rotations. *Phys. Rev., B* **2003**, *68*, 233403.
45. Nikolaev, P.; Thess, A.; Rinzler, A.G.; Colbert, D.T.; Smalley, R.E. Diameter doubling of single-wall nanotubes. *Chem. Phys. Lett.* **1997**, *266*, 422.
46. Terrones, M.; Terrones, H.; Banhart, F.; Charlier, J.-C.; Ajayan, P.M. Coalescence of single-walled carbon nanotubes. *Science* **2000**, *288*, 1226–1229.
47. Fuller, R.B. Tensile-integrity structures. US Patent 3,063,521/1962.
48. Wang, N.; Butler, J.P.; Ingber, D.E. Mechanotransduction across the cell surface and through the cytoskeleton. *Science* **1993**, *260*, 1124–1127.
49. Needham, J.; Wilson, S.; Yakobson, B.I. Possibility of nanotube-based tensegrity structures. **2003**, (in progress).

# Carbon Nanotubes: Thermal Properties

J. Hone

Department of Mechanical Engineering, Columbia University, New York, New York, U.S.A.

## INTRODUCTION

As nanoscale graphitic structures, carbon nanotubes are of great interest not only for their electronic and mechanical properties, but also for their thermal properties. Because of their small size, quantum effects are important, and the low-temperature specific heat and thermal conductivity show direct evidence of 1-D quantization of the phonon bandstructure. Modeling of the low-temperature specific heat allows for determination of the on-tube phonon velocity, the splitting of phonon subbands on a single tube, and the interaction between neighboring tubes in a bundle. The thermal conductivity of nanotubes has been examined both theoretically and experimentally. Theoretical work predicts a room-temperature thermal conductivity that is larger than graphite or diamond. Measurements show a room-temperature thermal conductivity over 200 W/m K for bulk samples of single-walled nanotubes (SWNTs), and over 3000 W/m K for individual multi-walled nanotubes (MWNTs). Addition of nanotubes to epoxy resin can double the thermal conductivity for a loading of only 1%, showing that nanotube composite materials may be useful for thermal management applications.

The first part of this manuscript discusses theoretical and experimental work on the specific heat of nanotubes. The section “Specific Heat” provides an introduction to specific heat. In the section “Phonon Density of States,” the theoretically derived phonon density of states of nanotubes and nanotube bundles is compared to that of 2-D graphene and 3-D graphite. In “Theoretically Derived Specific Heat,” the measured specific heat of nanotubes is compared to theoretical models.

The second part of this manuscript reviews the thermal conductivity of nanotubes. The first section provides an introduction to thermal conductivity. The section “Thermal Conductivity: Theory” discusses theoretical treatments of the thermal conductivity. “Measured  $K(T)$  of SWNTs” reviews measurements of the thermal conductivity of single-walled nanotubes, and “Measured  $K(T)$  of MWNTs” reviews measurements of the thermal conductivity of multiwalled nanotubes. Finally, “Applications” describes thermal conductivity measurements of nanotube-based composites.

## Specific Heat

The specific heat  $C(T)$  of a material is a sensitive probe of the low-energy excitations. In 3-D graphite, 2-D graphene, and nanotubes, phonons are the dominant excitations, and the phonon specific heat  $C_{\text{ph}}$  dominates  $C(T)$  at most temperatures.  $C_{\text{ph}}$  depends on the phonon density of states  $\rho(\omega)$ , and can be obtained by integrating  $\rho(\omega)$  together with a temperature-dependent convolution factor accounting for the temperature-dependent occupation of each phonon state<sup>[1]</sup>

$$C_{\text{ph}} = \int k_{\text{B}} \left( \frac{\hbar\omega}{k_{\text{B}}T} \right)^2 \frac{e^{\left(\frac{\hbar\omega}{k_{\text{B}}T}\right)} \rho(\omega) d\omega}{\left( e^{\frac{\hbar\omega}{k_{\text{B}}T}} - 1 \right)^2} \quad (1)$$

At a given temperature  $T$ , the convolution factor decreases from a value of 1 at  $\omega = 0$  to a value of  $\sim 0.1$  at  $\hbar\omega = k_{\text{B}}T/6$ , so that phonons above this energy do not appreciably contribute to the specific heat. In general, Eq. (1) must be evaluated numerically.

At low temperatures,  $C_{\text{ph}}$  probes only the lowest energy phonons. These are the acoustic modes, whose dispersion can often be expressed as a power law,  $\rho(\omega) \propto \omega^{\alpha}$ . For a single such mode, Eq. (1) simplifies to

$$C_{\text{ph}} \propto T^{(d/\alpha)} \quad (2)$$

where  $d$  is the dimensionality of the system. For a linearly dispersing mode ( $\alpha = 1$ ), the specific heat is linear in  $T$  for a 1-D system, and shows the familiar Debye  $T^3$  behavior for a 3-D system.

## Phonon Density of States

The phonon bandstructure of isolated nanotubes has been calculated by Saito et al.<sup>[2,3]</sup> and by Sanchez-Portal et al.<sup>[4]</sup> From the bandstructure, it is straightforward to calculate the phonon density of states. Fig. 1 shows the phonon density of states of a (10,10) nanotube, compared to the density of states of a single 2-D sheet of graphene. When a graphene sheet is “rolled” into a nanotube, the 2-D

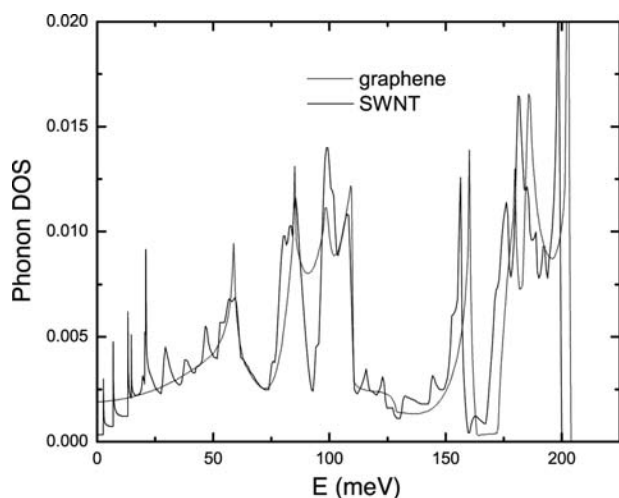


**Fig. 1** Phonon density of states of an isolated SWNT (solid line), compared to a 2-D graphene sheet. *Source:* From Ref.<sup>[2]</sup>.

bandstructure folds into a large number of 1-D subbands. For a (10,10) tube, for instance, the six phonon bands (three acoustic and three optical) of the graphene sheet become 66 separate 1-D subbands. A direct result of this folding is that the nanotube density of states has a number of sharp peaks as a result of 1-D van Hove singularities, which are absent in graphene and graphite. In spite of the presence of these singularities, the overall density of states is similar at high energies, so that the high-temperature specific heat should be roughly equal as well. This is to be expected: the high-energy phonons are more reflective of carbon-carbon bonding than the geometry of the graphene sheet.

At low energies, the geometry of the nanotube causes the phonon structure to substantially differ from that of the parent graphene sheet. Fig. 2 shows the theoretically derived low-energy phonon bandstructure of an isolated (10,10) nanotube. There are four acoustic modes (those with  $\omega \rightarrow 0$  as  $k \rightarrow 0$ ). All four have a linear dispersion,  $\omega = \nu k$ , near the zone center. The longitudinal (LA) mode has  $\nu = 24$  km/sec, the (doubly degenerate) transverse (TA) mode has  $\nu = 9$  km/sec, and the “twist” mode has  $\nu = 15$  km/sec. The first (doubly degenerate) optical mode enters at 2.7 meV.

The inset to Fig. 2 shows the nanotube phonon density of states (solid line) derived from the bandstructure shown. Only the four acoustic modes are present below 2.7 meV, producing a constant density of states. At the band edge of each optical mode, the density of states displays a van Hove singularity characteristic of 1-D dispersion, and increases stepwise. By comparison, 2-D graphene and 3-D graphite have very different low-energy phonon structure. The dot-dashed line shows the phonon density of states for an isolated

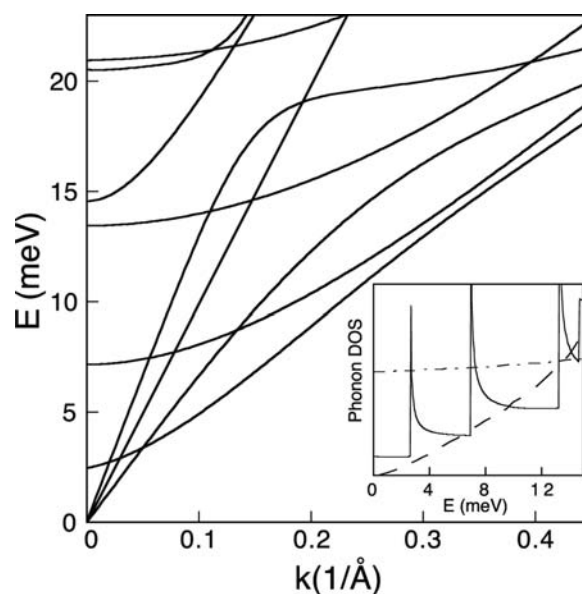


**Fig. 2** Low-energy phonon bandstructure of an isolated (10,10) SWNT. The inset shows the low-energy phonon density of states, compared to that of 2-D graphene and 3-D graphite.

graphene sheet.<sup>[3]</sup>  $\rho(\omega)$  is large and roughly constant at low energy, and does not extrapolate to zero at zero energy. This is because a graphene sheet has an out-of-plane acoustic mode (corresponding to a sheet-rolling motion) that is quadratic in energy. For a 2-D system, this corresponds to a constant  $\rho(\omega)$ . The phonon density of states for 3-D graphite, shown as the dashed line in the inset to Fig. 2, is significantly smaller than that of 2-D graphene, and approaches zero at  $k = 0$ . This is because interlayer coupling introduces dispersion in the  $z$  direction, and moves low-energy states upward in energy. The characteristic energy scale for this process is the Debye energy  $E_D^{\perp}$  of the interlayer modes, which is roughly 10 meV.

By analogy to the case of graphite, intertube interaction in bundles should depress the low-energy density of states in SWNT bundles. The characteristic energy for this process is the Debye energy of intertube modes. Because of the heterogeneous nature of nanotube bundles, it is difficult to calculate these modes theoretically. Mizel et al.<sup>[5]</sup> considered the case in which the coupling is graphite-like. By adjusting standard coupling constants for graphite for the case of tubular structures, they derived a bandstructure that has  $E_D^{\perp} \sim 5$  meV. However, because of issues of incommensurability between neighboring nanotubes, the true intertube coupling is likely to be weaker than this. Fig. 3 shows the 3-D dispersion of the nanotube acoustic modes calculated by Mizel et al.

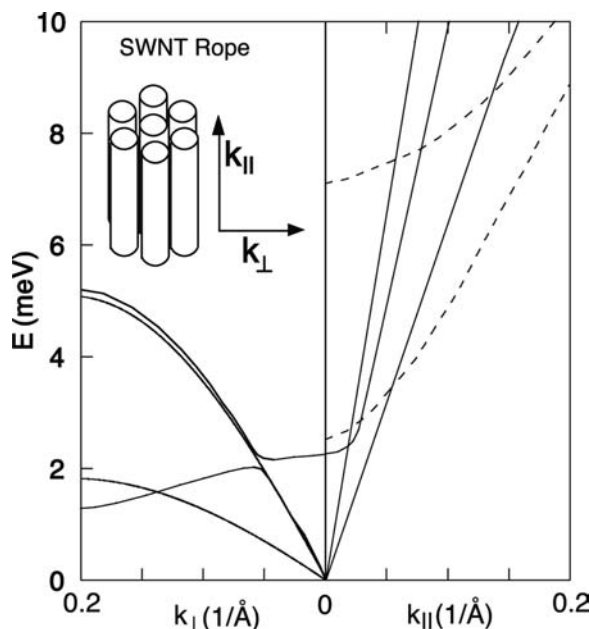


**Fig. 3** Calculated low-energy phonon bandstructure of a SWNT bundle, for the case of graphite-like (“strong”) coupling. Source: From Ref.<sup>[5]</sup>.

### Theoretically Derived Specific Heat

For a given  $\rho(\omega)$ , it is straightforward to calculate  $C(T)$  using Eq. (1). The lines in Fig. 4 show the specific heat calculated from the known phonon bandstructure of graphene and graphite, from the predicted bandstructure of an isolated SWNT, and from the predicted

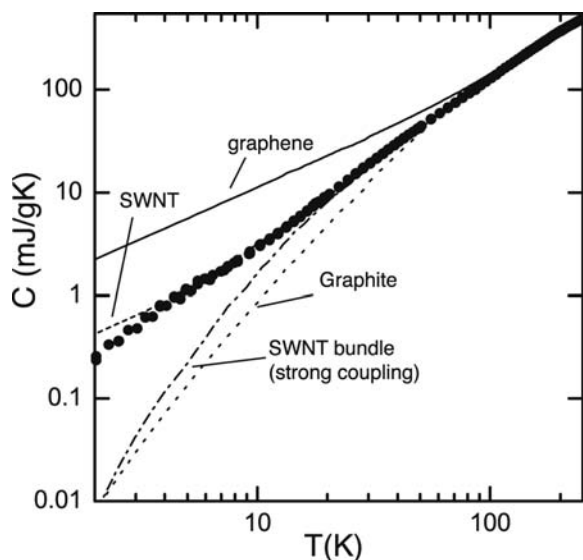


**Fig. 4** Calculated specific heat (lines) of graphene, isolated SWNTs, graphite, and strongly coupled SWNT bundles. The solid points represent the measured specific heat of a bulk sample of SWNTs. Source: From Ref.<sup>[7]</sup>.

bandstructure of a SWNT bundle in the case of graphite-like (“strong”) coupling. At temperatures above  $\sim 100$  K, the specific heat of all four materials is quite similar. However, at lower temperatures, the specific heats diverge substantially. The isolated graphene sheet displays the largest specific heat, which is roughly linear in  $T$  because of the 2-D quadratic sheet-rolling mode. The isolated nanotube specific heat is smaller, as a result of the absence of the rolling mode. At the lowest temperatures, the isolated nanotube  $C(T)$  is linear in  $T$ . The contribution of each acoustic mode to  $C(T)$  can be analytically expressed:<sup>[6]</sup>

$$C_{\text{ph}} = \frac{\pi k_{\text{B}}^2 T}{\hbar \nu \rho_{\text{m}}} \quad (3)$$

where  $\rho_{\text{m}}$  is the linear mass density. Above  $\sim 8$  K, the slope of  $C(T)$  increases, as the optical subbands begin to contribute. The linear behavior at low  $T$  is a direct signature of the 1-D quantized nature of the nanotube phonon bandstructure. Interlayer coupling (in graphite) and intertube coupling (in strongly coupled bundles) depresses the  $C(T)$  at low  $T$ . In real samples, the temperature at which the measured  $C(T)$  diverges from the single-tube curve provides measure of the actual intertube coupling.

### Electronic Specific Heat

A metallic SWNT is a one-dimensional metal with a constant density of states near the Fermi level. At low temperatures, it will have an electronic heat capacity that is linear in temperature, with a magnitude given by:<sup>[6]</sup>

$$C_{\text{el}} = \frac{4\pi k_{\text{B}}^2 T}{3\hbar \nu_{\text{F}} \rho_{\text{m}}} \quad (4)$$

where  $\nu_{\text{F}}$  is the Fermi velocity. Because there are four acoustic phonon modes, the ratio between the phonon and electron specific heat is

$$\frac{C_{\text{ph}}}{C_{\text{el}}} \approx \frac{\nu_{\text{F}}}{\nu_{\text{ph}}} \approx 100 \quad (5)$$

so that, as expected, the phonon contribution will dominate the electron contribution.

### Measured Specific Heat of SWNTs

The solid circles in Fig. 4 represent the measured specific heat of a bulk sample of highly purified single-walled nanotubes over the range 2–300 K.<sup>[7]</sup> The measured  $C(T)$  data agree with all of the theoretical curves

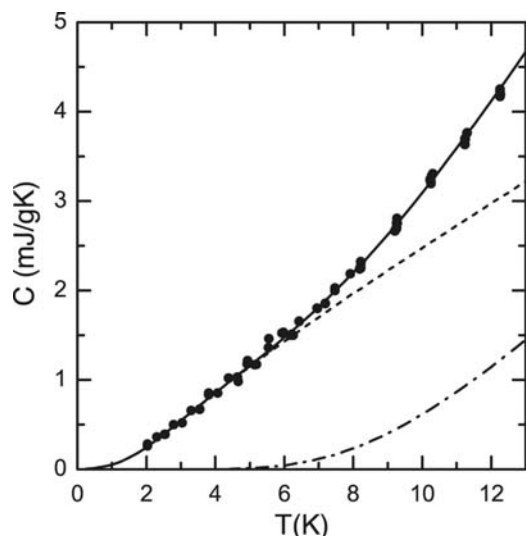


**Fig. 5** Measured specific heat of SWNTs at low temperature, fit with a simplified model. The fitting parameters are given in the text. *Source:* From Ref.<sup>[7]</sup>.

at high  $T$ , as is to be expected; this is a good confirmation that experimental errors such as sample contamination were not significant. At low  $T$ , the measured  $C(T)$  follows the predicted curve for isolated SWNTs over almost the entire temperature range, diverging below the single-tube curve only below  $\sim 5$  K. This surprising result indicates that the tube-tube coupling in real samples is substantially weaker than would be expected from a straightforward analogy to graphite.

Fig. 5 highlights the specific heat data at low temperature. The measured  $C(T)$  shows a linear temperature dependence from 2 to 8 K, with an upturn above 8 K. This behavior is a direct signature of the 1-D quantized nature of the SWNT phonon bandstructure, as discussed above. The lines in Fig. 5 represent the results of fitting the measured data to a simplified theory that takes into account intertube coupling. The low-energy phonon structure is simplified to include two phonon modes: a fourfold-degenerate acoustic mode with (high) on-tube Debye energy  $E_D$  and (low) transverse Debye energy  $E_D^\perp$ ; and a doubly degenerate optical subband with a band minimum at  $E_{\text{sub}}$ . The lines shown are obtained after varying all three parameters to obtain the best fit to the data. The dot-dashed line represents the contribution from the acoustic modes, with  $E_D = 92$  meV and  $E_D^\perp = 1.2$  meV. Its contribution is roughly cubic at low temperatures, then roughly linear above  $\sim 2$  K, corresponding to the saturation of the intertube modes. The dashed line represents the contribution from the optical mode, with  $E_{\text{sub}} = 4.1$  meV. This mode begins to contribute at  $\sim 7$  K, and the sum of the two contributions (solid line) fits the data well over

the entire range from 2–12 K, above which it can be expected that other optical subbands will begin to contribute.

The values for the fitting parameters in this model are directly related to the mechanical properties of nanotube bundles. The measured value of  $E_D$  (92 meV) agrees well with the value of 103 meV that can be derived from theory, confirming the high phonon velocity in the tubes, which is a direct result of their high Young's modulus and low density. On the other hand, the value of  $E_D^\perp$  is much weaker than would be expected from a simple analogy to graphite. This indicates that coupling between the tubes in bundles is very weak, an issue that will need to be carefully considered for applications such as high-strength composites. The measured value of  $E_{\text{sub}}$  (4.1 meV) is slightly larger than the theoretically derived value of 2.7 meV, which may be a result of mode stiffening due to radial tube-tube interaction. In fact, the measured value is in good agreement with theoretical calculations for nanotube bundles.<sup>[8]</sup> An unresolved issue is the seeming contradiction between the weak tube-tube coupling implied by the low transverse Debye energy, and the stiffening of the first optical mode. It may be that bundles are relatively well coupled radially, but are weak in shear. Detailed theoretical investigation of this matter is still needed.

## THERMAL CONDUCTIVITY

Because of the high thermal conductivity of diamond and graphite, it is interesting to examine whether nanotubes exhibit high thermal conductivity, a property that might complement their extraordinary electrical and mechanical properties. This property has been addressed theoretically for single tubes, experimentally for bulk samples of SWNTs, and experimentally for individual multiwalled nanotubes

In general, the thermal conductivity  $K$  is a tensor quality, but for this discussion, it is only important to consider the diagonal elements:

$$K_{zz} = \sum C \nu_z^2 \tau \quad (6)$$

where  $C$  is the specific heat, and  $\nu_z$  and  $\tau$  are the group velocity ( $\nu = d\omega/dk$ ) and relaxation time of a given phonon state. At low temperatures ( $T \ll \Theta_D$ ), the relaxation time is determined by scattering off of fixed impurities, defects, sample boundaries, etc. and is roughly constant. Therefore in ordinary materials, the low-temperature thermal conductivity has the same temperature dependence as the specific heat. However, in anisotropic materials, this relationship does not strictly hold. Because the contribution of each state is



weighted by the scattering time and the square of the velocity, the thermal conductivity preferentially samples states with high  $v$  and  $\tau$ . For instance, in graphite, the thermal conductivity parallel to the basal planes is only weakly dependent on the interlayer phonons. In SWNT bundles, it is likely that  $K(T)$  depends only on the on-tube phonons, rather than the intertube modes.

Thermal conductivity is of particular interest in low-dimensional systems. For a 1-D ballistic electronic channel, the electronic conductance is quantized, with a universal value of

$$G_0 = \frac{2e^2}{h} \quad (7)$$

Similarly, for a single ballistic 1-D channel, the thermal conductance is independent of materials parameters, and there exists a quantum of thermal conductance, which is linear in temperature.

$$G_{\text{th}} = \frac{\pi^2 k_B^2 T}{3h} \quad (8)$$

Conditions for observation of this quantum were first examined in detail by Rego and Kirczenow.<sup>[9]</sup> Using lithographically defined nanostructures, Schwab et al.<sup>[10]</sup> confirmed this value experimentally.

At high temperatures, three-phonon Umklapp scattering begins to limit the phonon relaxation time. Therefore the phonon thermal conductivity displays a peak and decreases with increasing temperature. Umklapp scattering requires production of a phonon beyond the Brillouin zone boundary; because of the high Debye temperature of diamond and graphite, the peak in the thermal conductivity of these materials is near 100 K, significantly higher than for most other materials. In less crystalline forms of graphite, such as carbon fibers, the peak in  $K(T)$  occurs at higher temperatures, because defect scattering remains dominant over Umklapp scattering to higher temperature.<sup>[11]</sup> In low-dimensional systems, it is difficult to conserve both energy and momentum for Umklapp processes,<sup>[12]</sup> and so it may be possible that Umklapp scattering is suppressed in nanotubes relative to 2-D or 3-D forms of carbon.

A measurement of  $K(T)$  yields the combined contribution of the electrons and phonons. However, a simultaneous measurement of the electrical conductivity  $\sigma$  provides a measure of the electron thermal conductivity  $K_e$  from the Wiedemann–Franz law<sup>[1]</sup>

$$\frac{K_e}{\sigma T} \approx L_0 = 2.45 \times 10^{-8} \text{ (V/K)}^2 \quad (9)$$

In this way, the phonon contribution can be deduced by subtracting the electronic contribution from the total measured thermal conductivity.

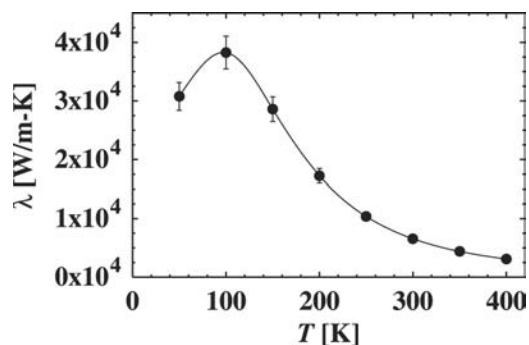


Fig. 6 Calculated thermal conductivity of an isolated SWNT, as a function of temperature. Source: From Ref.<sup>[13]</sup>.

### Thermal Conductivity: Theory

Berber et al.<sup>[13]</sup> have calculated the phonon thermal conductivity of isolated nanotubes. Fig. 6 shows the results of theoretical calculations of the phonon thermal conductivity of an isolated SWNT.  $K(T)$  peaks near 100 K, and then decreases with increasing temperature. The value of  $K$  at the peak (37,000 W/m K) is comparable to the highest thermal conductivity ever measured (41,000 W/m K for an isotopically pure diamond sample at 104 K). Even at room temperature, the thermal conductivity is quite high (6600 W/m K), exceeding the reported room-temperature thermal conductivity of isotopically pure diamond by almost a factor of 2.

Fig. 7 shows the calculated nanotube thermal conductivity compared to the calculated thermal conductivity of a single plane of graphene and that of 3-D graphite. In graphite, the interlayer interactions quench the thermal conductivity by nearly 1 order of magnitude. It is likely that the same process occurs in nanotube bundles. Thus it is significant that the

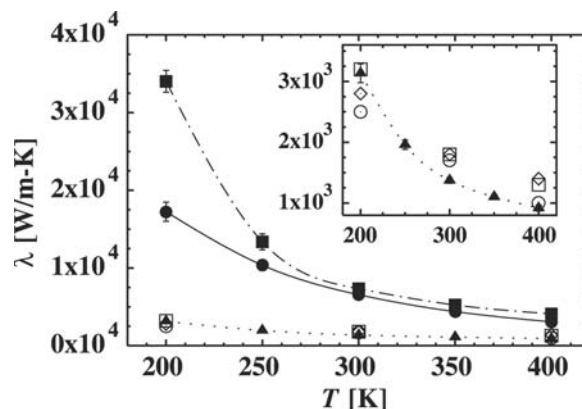


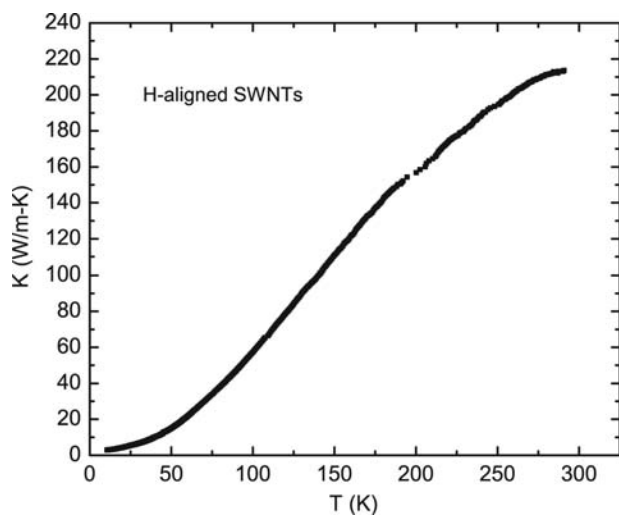
Fig. 7 Calculated nanotube thermal conductivity (solid line) compared to the thermal conductivity of a 2-D graphene sheet (dot-dashed line) and 3-D graphite (dotted line). Source: From Ref.<sup>[13]</sup>.

coupling between tubes in bundles is weaker than expected. It may be that this weak coupling, which is problematic for mechanical applications of nanotubes, is an advantage for thermal applications.

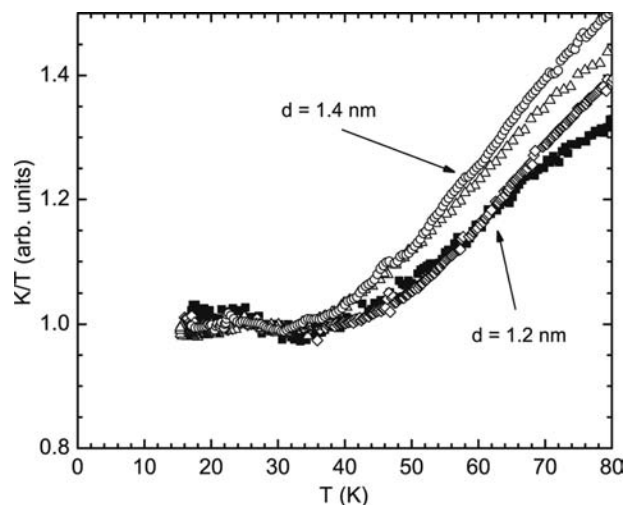
### Measured $K(T)$ of SWNTs

Fig. 8 shows the measured  $K(T)$  of a bulk sample of SWNTs.<sup>[14–16]</sup>  $K(T)$  increases with increasing temperature to 300 K; the decreasing slope at high temperature may indicate the onset of Umklapp scattering. It is difficult to ascertain the intrinsic thermal conductivity of an individual tube from these measurements, although they point strongly to a very high value. In disordered “mat” samples, the room-temperature thermal conductivity is  $\sim 35$  W/m K.<sup>[15]</sup> However, the nanotubes in such a sample are highly tangled, and the thermal path is considerably longer than the direct distance between points. This effect can be reduced by aligning the nanotubes; in samples where the nanotubes have been aligned by filtration in a magnetic field, the thermal conductivity is significantly higher, above 200 W/m K,<sup>[14]</sup> which is comparable to that of a good metal. Even in these samples, the thermal conductivity is likely to be limited by tube–tube junctions, so that the intrinsic single-tube thermal conductivity is certainly higher. Significantly, the temperature dependence of the thermal conductivity is roughly the same for both types of samples, suggesting that the measured  $K(T)$  reflects the intrinsic temperature dependence of the single-tube  $K(T)$ .

Using Eq. (7), it is possible to calculate the electronic contribution to the thermal conductivity. In all



**Fig. 8** Temperature-dependent thermal conductivity of a bulk sample of SWNTs which have been aligned by filtration in a high magnetic field. *Source:* From Ref.<sup>[14]</sup>.



**Fig. 9** Thermal conductivity divided by temperature for SWNT samples with different average diameters. The smaller-diameter tubes exhibit linear  $K(T)$  up to higher temperature, consistent with quantization effects. *Source:* From Ref.<sup>[16]</sup>.

samples, simultaneous measurement of the electrical and thermal conductivity shows that the electronic contribution to the thermal conductivity is only  $\sim 1\%$  of the total, so that phonons dominate  $K(T)$  at all temperatures.

At low temperature, SWNT samples exhibit a linear  $K(T)$ , strongly suggesting quantum effects. Because of the large number of nanotubes in a bulk sample, it is not possible to directly observe the thermal conductivity quantum measured by Schwab et al.<sup>[10]</sup> However, it is possible to measure the  $K(T)$  of SWNT samples with varying diameters: the phonon subband splitting is higher in smaller-diameter tubes, so that the linear  $K(T)$  behavior should extend to higher temperature. Fig. 9 shows the thermal conductivity divided by temperature,  $K/T$ , of two nanotube samples, one with average diameter 1.2 nm and the other with average diameter 1.4 nm.<sup>[16]</sup> In both samples,  $K/T$  approaches a constant value at low  $T$ , just as is expected for 1-D channels. At higher temperatures,  $K/T$  increases as more phonon modes contribute. In the 1.2-nm diameter sample, the upturn in  $K/T$  occurs  $\sim 5$  K higher than in the 1.4-nm diameter sample. This shift provides additional evidence that the low- $T$  linear behavior is true 1-D thermal conductivity. However, one unresolved issue is the different temperature ranges of the 1-D regime in heat capacity vs. thermal conductivity. For constant scattering time, the temperature ranges should be approximately identical. One possible explanation is that the phonons in the optical bands are much more strongly scattered, and so do not begin to contribute to the thermal conductivity until higher temperatures.

### Measured $K(T)$ of MWNTs

Because of the large diameter of MWNTs, the temperature scale for quantum effects should be quite small, and their thermal conductivity should be that of a 2-D system with linear acoustic phonons. The  $K(T)$  of such a 2-D sheet should follow a  $T^2$  temperature dependence. Graphite shows a temperature dependence closer to  $T^{2.3}$ , because of the effect of the quadratically dispersing out-of-plane mode.<sup>[17]</sup> As was discussed above, interlayer effects can be ignored when considering the thermal conductivity.

Yi et al.<sup>[18]</sup> have measured  $K(T)$  for bulk samples of MWNTs. They found a roughly  $T^2$  temperature dependence up to 100 K, as expected. The room-temperature thermal conductivity of these samples is only  $\sim 25$  W/m K, possibly as a result of the effects of tube-tube contacts, or also of the incomplete graphitization in their samples.

Recently, Kim et al.<sup>[19]</sup> have used a microfabricated structure (inset to Fig. 10) to directly measure the thermal conductivity of individual MWNTs. The data in Fig. 10 show the measured thermal conductivity of

one MWNT.  $K(T)$  increases as  $T^2$  up to  $\sim 100$  K, peaks near 300 K, and decreases above this temperature. Again, the quadratic temperature dependence is exactly what would be expected for large-diameter nanotubes that essentially act as 2-D sheets. The room-temperature value of  $K(T)$  is over 3000 W/m K.

### Applications

The high thermal conductivity of nanotubes may be useful for a number of thermal management applications, such as heat sinking of silicon processors, or to increase the thermal conductivity of plastics in such areas as housing for electric motors. Although many groups have studied nanotube-epoxy composite materials for their mechanical properties, their possible thermal properties have only recently attracted attention.

Biercuk et al.<sup>[20]</sup> have measured the thermal conductivity of epoxy resin loaded with SWNTs. Fig. 11 shows the enhancement in the thermal conductivity for loadings up to 1% SWNTs, and the enhancement

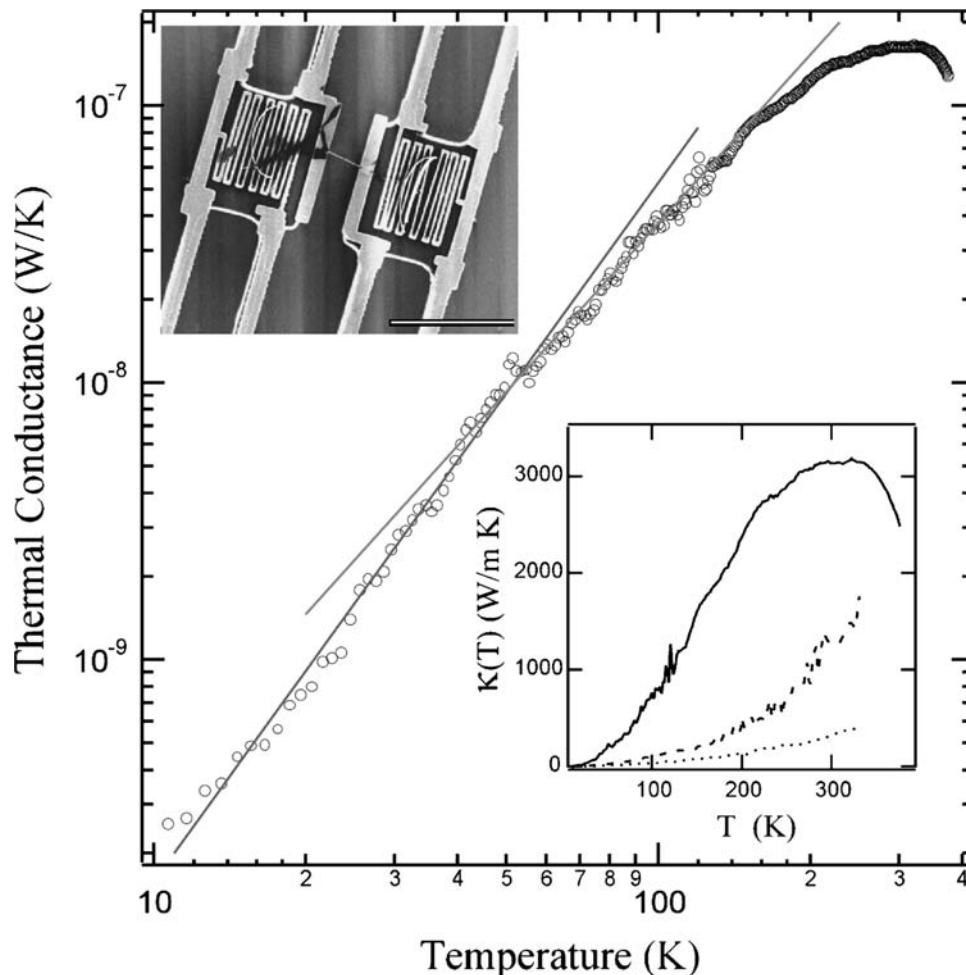
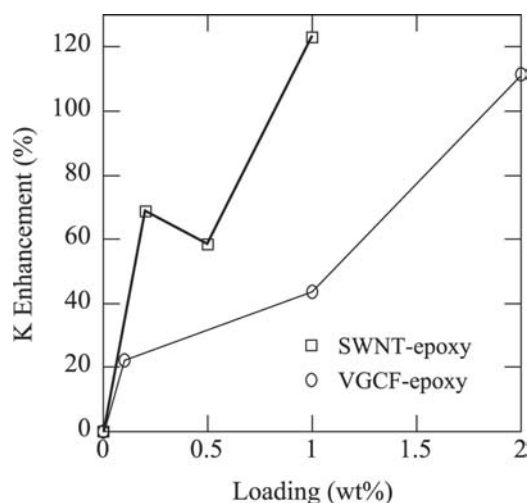


Fig. 10 Measured thermal conductivity of a single MWNT. Source: From Ref.<sup>[19]</sup>.



**Fig. 11** Enhancement of the thermal conductivity of epoxy resin as a function of loading by SWNTs and by carbon fibers. Source: From Ref.<sup>[20]</sup>.

for identical loadings of graphitic carbon fibers. Addition of 1% SWNTs doubles the thermal conductivity of the epoxy, while the same loading of carbon fibers provides only a  $\sim 40\%$  increase. This initial result is quite promising for the development of composites for thermal management.

## CONCLUSION

The thermal properties of carbon nanotubes are dominated by phonons. The measured specific heat of SWNTs closely matches calculations based on the phonon bandstructure of isolated nanotubes, and shows direct evidence of 1-D quantization of the phonon bandstructure. This shows that coupling between nanotubes in a bundle is relatively weak; detailed modeling permits direct measurement of the tube-tube coupling strength, as well as the low-energy phonon structure. Theoretical work predicts a room-temperature thermal conductivity of 6600 W/m K for individual nanotubes. Measurements show a room-temperature thermal conductivity over 200 W/m K for bulk samples of single-walled nanotubes, and over 3000 W/m K for individual multiwalled nanotubes. Addition of nanotubes to epoxy resin can double the thermal conductivity for a loading of only 1%, showing that nanotube composite materials may be useful for thermal management applications.

## REFERENCES

1. Ashcroft, N.W.; Mermin, N.D. *Solid State Physics*; Harcourt Brace: New York, 1976.
2. Saito, R.; Takeya, T.; Kimura, T.; Dresselhaus, G.; Dresselhaus, M.S. Raman intensity of single-wall carbon nanotubes. *Phys. Rev., B* **1998**, *57*, 4145–4153.
3. Saito, R.; Dresselhaus, G.; Dresselhaus, M.S. *Physical Properties of Carbon Nanotubes*; Imperial College Press: London, 1998.
4. Sanchez-Portal, D.; Artacho, E.; Solar, J.M.; Rubio, A.; Ordejon, P. Ab initio structural, elastic, and vibrational properties of carbon nanotubes. *Phys. Rev., B* **1999**, *59*, 12678–12688.
5. Mizel, A.; Benedict, L.X.; Cohen, M.L.; Louie, S.G.; Zettl, A.; Budraa, N.K.; Beyermann, W.P. Analysis of the low-temperature specific heat of multiwalled carbon nanotubes and carbon nanotube ropes. *Phys. Rev., B* **1999**, *60*, 3264–3270.
6. Benedict, L.X.; Louie, S.G.; Cohen, M.L. Heat capacity of carbon nanotubes. *Solid State Commun.* **1996**, *100*, 177–180.
7. Hone, J.; Batlogg, B.; Benes, Z.; Johnson, A.T.; Fischer, J.E. Quantized phonon spectrum of single-wall carbon nanotubes. *Science* **2000**, *289*, 1730–1733.
8. Kahn, D.; Lu, J.P. Vibrational modes of carbon nanotubes and nanoropes. *Phys. Rev., B* **1999**, *60*, 6535–6540.
9. Rego, L.G.C.; Kirczenow, G. Quantized thermal conductance of dielectric quantum wires. *Phys. Rev. Lett.* **1998**, *81*, 232–235.
10. Schwab, K.; Henriksen, E.A.; Worlock, J.M.; Roukes, M.L. Measurement of the quantum of thermal conductance. *Nature* **2000**, *404*, 974–977.
11. Heremans, J.; Beetz, C.P. Thermal-conductivity and thermopower of vapor-grown graphite fibers. *Phys. Rev., B* **1985**, *32*, 1981–1986.
12. Peierls, R.E. *Quantum Theory of Solids*; Oxford University Press: London, 1955.
13. Berber, S.; Kwon, Y.K.; Tomanek, D. Unusually high thermal conductivity of carbon nanotubes. *Phys. Rev. Lett.* **2000**, *84*, 4613–4616.
14. Hone, J.; Llaguno, M.C.; Nemes, N.M.; Johnson, A.T.; Fischer, J.E.; Walters, D.A.; Casavant, M.J.; Schmidt, J.; Smalley, R.E. Electrical and thermal transport properties of magnetically aligned single wall carbon nanotube films. *Appl. Phys. Lett.* **2000**, *77*, 666–668.
15. Hone, J.; Whitney, M.; Piskoti, C.; Zettl, A. Thermal conductivity of single-walled carbon nanotubes. *Phys. Rev., B* **1999**, *59*, R2514–R2516.
16. Hone, J.; Llaguno, M.C.; Biercuk, M.J.; Johnson, A.T.; Batlogg, B.; Benes, Z.; Fischer, J.E. Thermal properties of carbon nanotubes and nanotube-based materials. *Appl. Phys., A Mater.* **2002**, *74*, 339–343.
17. Kelly, B.T. *Physics of Graphite*; Applied Science: London, 1981.
18. Yi, W.; Lu, L.; Zhang, D.L.; Pan, Z.W.; Xie, S.S. Linear specific heat of carbon nanotubes. *Phys. Rev., B* **1999**, *59*, R9015–R9018.
19. Kim, P.; Shi, L.; Majumdar, A.; McEuen, P.L. Thermal transport measurements of individual multiwalled nanotubes. *Phys. Rev. Lett.* **2001**, *8721*, art. no. 215502.
20. Biercuk, M.J.; Llaguno, M.C.; Radosavljevic, M.; Hyun, J.K.; Johnson, A.T.; Fischer, J.E. Carbon nanotube composites for thermal management. *Appl. Phys. Lett.* **2002**, *80*, 2767–2769.

# Catalysis by Supported Gold Nanoclusters

D. Wayne Goodman

Department of Chemistry, Texas A&M University, College Station, Texas, U.S.A.

## INTRODUCTION

The physical and chemical properties of supported Au clusters are markedly sensitive to cluster size and morphology. To investigate the origin of the unique properties of nanosized Au clusters, model catalysts consisting of Au clusters of varying sizes have been prepared on single crystal TiO<sub>2</sub>(110) and ultrathin films of single crystalline TiO<sub>2</sub>, SiO<sub>2</sub>, and Al<sub>2</sub>O<sub>3</sub>. The morphology, electronic structure, and catalytic properties of these supported Au clusters have been investigated using an array of surface analytical techniques with particular emphasis to the unique properties of clusters <5.0 nm in size. These studies illustrate the novel and unique physical and chemical properties of nanosized supported metal clusters.

## BACKGROUND

Unique electronic and chemical properties are known to develop in solids when the dimensions of the solid reach the nanoscale.<sup>[1–3]</sup> These changes, which include discrete electronic structures, modified physical structures, and altered chemical reactivities, manifest themselves as new physical and chemical properties not observed in the “bulk” form of the material. Developing an understanding and ability to control the key features of nanoscale catalysts are daunting scientific challenges, yet could lead to the long-sought goals of optimum catalytic activities combined with highly specific selectivities.

It is well established that ultrasmall metal clusters on supports have catalytic properties distinct from those properties of large bulk-like particles, as illustrated by the selective oxidation of propylene to propylene oxide by gold,<sup>[4]</sup> alkene and arene hydrogenation catalysis,<sup>[5]</sup> and CO oxidation.<sup>[6–8]</sup> In these examples, the catalytic properties improve as the clusters become smaller. On the other hand, a reduction in size of the metal cluster can lead to less desirable catalytic properties as seen for ammonia synthesis on iron.<sup>[9]</sup> Various explanations have been offered to account for the unique properties of nanoscaled metal catalysts,<sup>[6–8]</sup> however, much remains to be understood. Clearly, experimental and theoretical studies will be

required to develop an in-depth understanding of the unique catalytic properties of limited dimensional solids.

The complexity of high surface area technical catalysts makes developing an atomic-level understanding an extremely challenging problem. Surface science studies offer atomic-level information regarding the details of catalytically relevant surfaces, but have traditionally focused on well-defined, single-crystal metal surfaces to address the relationship between reactivity and surface morphology. Single crystal studies, however, obviously do not address the size-dependent structural and electronic properties that are unique to metal nanoparticles. Toward the goal of understanding the properties of supported metal clusters, several groups have begun investigations of metal clusters supported on planar oxide surfaces.<sup>[10–14]</sup> Our group, in particular, has focused extensively on the unique properties of supported gold clusters for selective oxidation reactions.<sup>[15]</sup>

Our approach to studying supported metal clusters has been to combine ultrahigh vacuum (UHV) surface analytical methods with an elevated pressure reactor system shown schematically in Fig. 1. The design has been described in detail.<sup>[14,16]</sup> This arrangement allows pressures to 1 bar in the high-pressure cell without significantly altering the vacuum integrity of the UHV chamber. This arrangement facilitates the acquisition of kinetic data at elevated pressures using a conventional gas chromatograph. Polarization modulation infrared reflection absorption spectroscopy (PM-IRAS) is available as a probe of surface species present under reaction conditions.<sup>[13]</sup>

The oxide surfaces used as supports in these studies were either a TiO<sub>2</sub>(110) single crystal (Commercial Crystal Laboratories) or single crystalline TiO<sub>2</sub>, Al<sub>2</sub>O<sub>3</sub>, or SiO<sub>2</sub> thin films synthesized on a refractory metal substrate. Thin film TiO<sub>2</sub> was deposited onto a Mo(110) single crystal.<sup>[17]</sup> Similarly, the SiO<sub>2</sub> and Al<sub>2</sub>O<sub>3</sub> supports were epitaxially grown as thin films deposited onto Mo(110)<sup>[18–20]</sup> and Re(0001)<sup>[21–23]</sup> substrates, respectively. Details of the sample mounting, cleaning, etc. can be found elsewhere.<sup>[14]</sup>

The Au doser was constructed by wrapping high-purity Au wire (99.99%) around 0.010-diameter tungsten filaments (H&R Cross), which were then

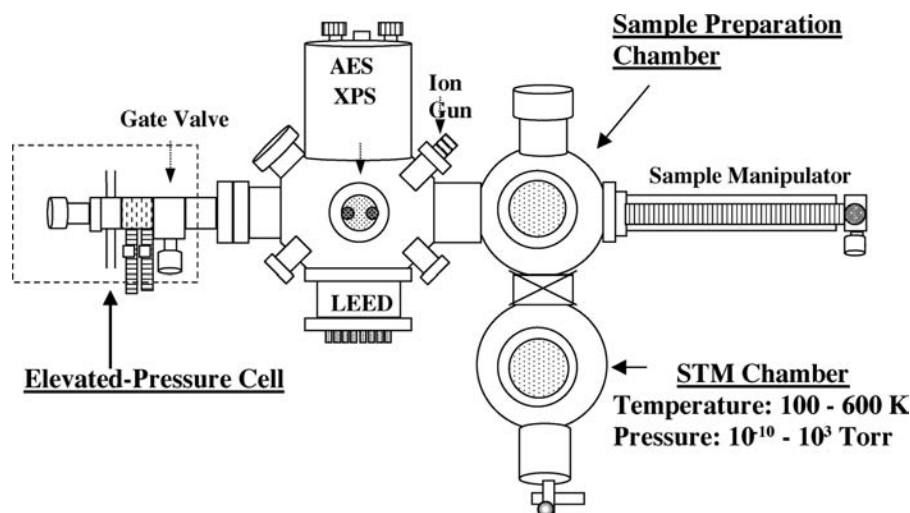


Fig. 1 Schematic of the combined surface analytical chamber with an elevated pressure reactor.

resistively heated in vacuum by passing current through the filament wires. The Au wire wrapping was melted and thoroughly outgassed to remove impurities prior to use. The Au flux was calibrated via integrating the Au temperature-programmed desorption peak area from a Re(0001) substrate<sup>[15]</sup> and also using the metal-to-substrate Auger intensity “break” to denote the first monolayer equivalent (ML).<sup>[24]</sup>

This entry focuses on our recent studies on these model catalysts to understand the special properties that nanosized clusters exhibit with respect to a variety of catalytic reactions.

## MODEL CATALYSTS: RESULTS AND DISCUSSION

### Synthesis

The synthesis of a typical model catalyst used in these studies is shown schematically in Fig. 2. The procedure

begins with a refractory metal substrate, such as Mo, Ta, or Re, that has been cleaned by standard procedures and verified clean with surface analytical techniques. The structure of the substrate is chosen specifically to match the particular oxide film to be grown since crystal orientation and the nature of the interface or critical parameters in obtaining a high-quality film. A thin metal oxide film, typically 1–10 nm thick, is then deposited onto the metal substrate by vapor deposition of the parent metal in an O<sub>2</sub> environment. Thin films of SiO<sub>2</sub>,<sup>[18–20]</sup> Al<sub>2</sub>O<sub>3</sub>,<sup>[21–23]</sup> Ti<sub>x</sub>O<sub>y</sub>,<sup>[17,25]</sup> MgO,<sup>[26–29]</sup> NiO,<sup>[30–33]</sup> and Fe<sub>x</sub>O<sub>y</sub>,<sup>[34]</sup> have been prepared using this methodology. Finally, metal clusters are formed on the oxide thin film by vapor depositing the metal of choice. By the judicious control of the metal deposition parameters, metal clusters of varying size can be routinely achieved.<sup>[14]</sup> A variety of oxide/metal systems have been synthesized in our laboratories including Cu/SiO<sub>2</sub>,<sup>[35,36]</sup> Pd/SiO<sub>2</sub>,<sup>[37]</sup> Ni/SiO<sub>2</sub>,<sup>[38]</sup> Pd/Al<sub>2</sub>O<sub>3</sub>,<sup>[39–41]</sup> Cu/Al<sub>2</sub>O<sub>3</sub>,<sup>[23,39]</sup> Au/Al<sub>2</sub>O<sub>3</sub>,<sup>[39]</sup> Ni/Al<sub>2</sub>O<sub>3</sub>,<sup>[42]</sup> Au/TiO<sub>2</sub>,<sup>[43]</sup> and Pd/MgO.<sup>[43]</sup>

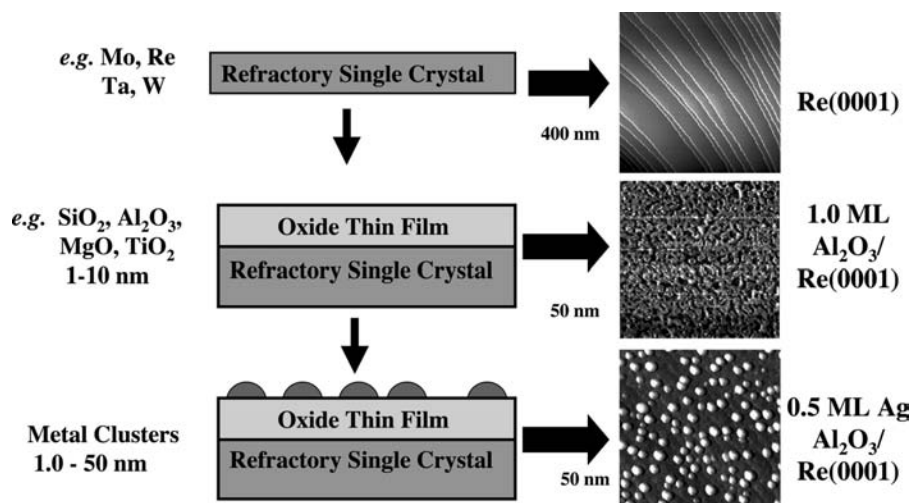


Fig. 2 Schematic of the preparation method for the synthesis of supported metal clusters on thin film oxide surfaces.



## Characterization

Scanning tunneling microscopy (STM) is an indispensable technique for characterizing planar surfaces with sufficient conductivity. Fig. 3A shows a CCT-STM micrograph of 0.25 ML Au deposited onto a single crystal  $\text{TiO}_2(110)$ .<sup>[8,15]</sup> The deposition was performed at 300 K followed by an anneal of the  $\text{TiO}_2$  surface to 850 K. Three-dimensional (3-D) Au clusters have average diameters of  $\sim 2.6$  and  $\sim 0.7$  nm height (corresponding to 2–3 atoms thick) and preferentially nucleate on step edges. Quasi-two-dimensional (2-D) clusters are characterized by heights of 1–2 atomic layers.<sup>[44]</sup> An enlarged STM micrograph ( $150 \times 150 \text{ nm}^2$ ) of a Au-covered (1.0 ML)  $\text{TiO}_2(110)$  surface is shown in Fig. 3B. Hemispherical clusters with a narrow size distribution grow preferentially along the step edges with clusters on the flat terraces evident as well. At a Au coverage of 1.0 ML, more than 60% of the substrate is still metal-free and separated by mono-atomic steps, consistent with 3-D clustering or a Volmer–Weber (VW) growth mode.

Cluster size and density were studied as a function of metal coverage. With increasing Au coverage, the average cluster size (diameter) increases from 2.0 nm for 0.10 ML Au to 5.4 nm for 4.0 ML Au. However, the cluster density rapidly increases upon deposition of 0.10 ML Au, while the cluster density remains essentially constant at higher Au coverages ( $>1.0$  ML). With an increase in the Au coverage from 0.10 to 0.25 ML, the cluster density increases by  $\sim 30\%$ , with a further increase of  $\sim 50\%$  from 0.25 to 1.0 ML Au. The cluster density reaches a maximum at  $\sim 2.0$  ML where  $\sim 70\%$  of the substrate surface is covered by Au clusters. At higher Au coverages, the cluster density declines because of cluster coalescence and agglomeration. Approximately 60% of the nucleating sites are populated at a coverage of 0.25 ML.<sup>[45]</sup>

The cluster size, in contrast to cluster density, increases continuously with Au coverage. Increasing the Au deposition from 0.10 to 2.0 ML increases the cluster size from 2.0 to 4.5 nm. A rapid increase in Au cluster size occurs for very low Au coverages (below 0.10 ML). Higher Au coverages correlate with a limited cluster growth. It is noteworthy that the increase in cluster volume is not proportional to the increase in cluster size. For example, a 22% increase in the average cluster diameter, from 3.7 (1.0) to 4.5 nm (2.0 ML), corresponds to an 80% increase in the average cluster volume. This correlation between Au coverage and Au cluster diameter demonstrates that vacuum deposition can produce a specific size range and shape of Au clusters for model catalyst studies.<sup>[45]</sup>

## Catalytic Properties

A correlation has been observed between the Au cluster size and the catalytic activity for the partial oxidation of CO on  $\text{Au}/\text{TiO}_2(110)-(1 \times 1)$ . Fig. 4A shows a plot of the activity for CO oxidation [expressed as (product molecules)  $\times$  (total Au atoms on surface sites) $^{-1} \text{sec}^{-1}$  or turnover frequency (TOF)] at 350 K as a function of the size of Au clusters supported on a  $\text{TiO}_2(110)-(1 \times 1)$  substrate.<sup>[8,46]</sup> The CO and  $\text{O}_2$  (1:5 mixture of  $\text{CO}:\text{O}_2$ ) reaction was carried out over  $\text{Au}/\text{TiO}_2$  catalysts at 40-Torr total pressure.<sup>[8,46,47]</sup> A thin film of  $\text{TiO}_2$  epitaxially grown on a  $\text{Mo}(100)$  substrate<sup>[17]</sup> onto which Au clusters were deposited was used for the reaction kinetics measurements carried out in the reactor portion of Fig. 1. Scanning tunneling microscopy measurements of Au deposited onto a  $\text{TiO}_2(110)-(1 \times 1)$  single crystal were carried out in parallel with the kinetic measurements. The product ( $\text{CO}_2$ ) was extracted from the reactor with a vacuum syringe, compressed and analyzed with a

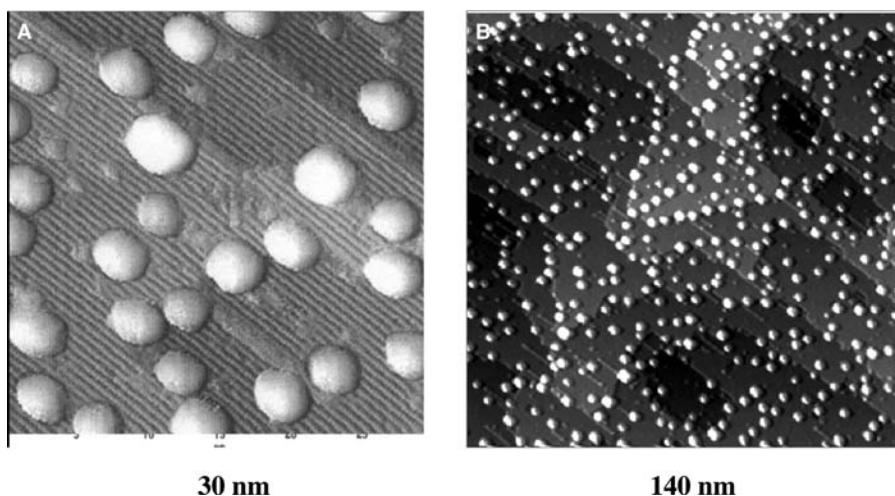


**Fig. 3** (A) A CCT-STM image of a 0.25 ML Au deposited onto  $\text{TiO}_2(110)-(1 \times 1)$  prepared just prior to a  $\text{CO}:\text{O}_2$  reaction. The sample had been annealed to 850 K for 2 min. (B) General morphology of Au clusters on the  $\text{TiO}_2(110)$  surface (2.0 V, 2.0 nA). The evaporation rate was  $0.083 \text{ ML min}^{-1}$  and the Au coverage was 1.0 ML.

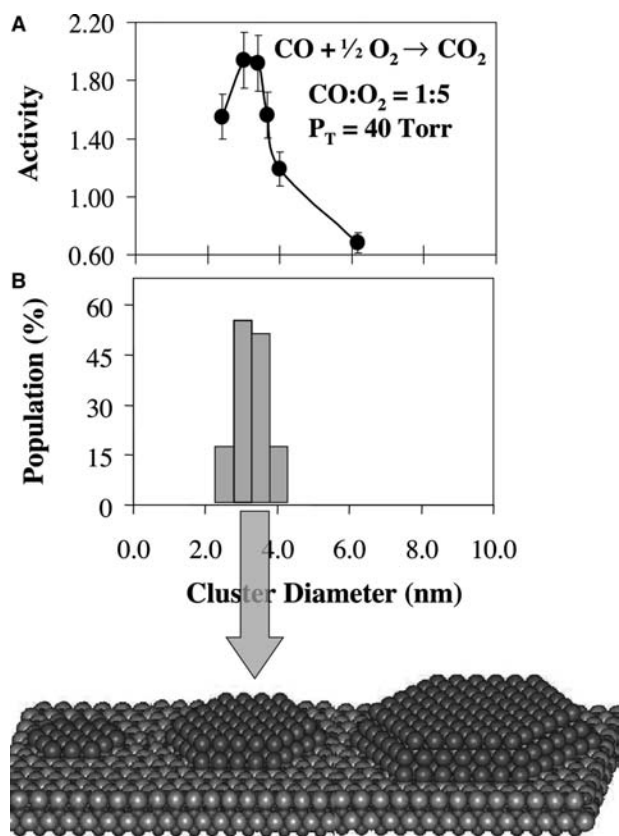


**Fig. 4** (A) The activity for CO oxidation at 350 K as a function of Au cluster size supported on  $\text{TiO}_2(110)-(1 \times 1)$ . A 1:5  $\text{CO}:\text{O}_2$  mixture was used at a total pressure of 40 Torr. Activity is expressed as  $(\text{product molecules}) \times (\text{total Au atoms})^{-1} \text{sec}^{-1}$ . (B) Histogram of the distribution of cluster sizes and morphologies.

GC. For each point in Fig. 4A, a particular Au cluster size was prepared then subjected to the  $\text{CO}_2:\text{O}_2$  reaction. The cluster sizes of the Au particles and coverage of the surface sites obtained from parallel STM imaging experiments were used to calculate the TOF. The activity of the  $\text{Au}/\text{TiO}_2$  catalysts exhibits a maximum TOF at an average Au cluster diameter of  $\sim 3.5$  nm and decreases with an increase in diameter.

Fig. 4B is a histogram that shows the distribution of Au clusters with sizes ranging from 2.0 to 4.0 nm that are specifically two atoms thick (with diameters between 2.5 and 3.0 nm). The close correspondence between the maximum in the histogram and the maximum in the reactivity data is strongly suggestive that 2-atom-thick Au structures are optimally active for CO oxidation.<sup>[8]</sup>

Fig. 5 shows a plot of the scanning tunneling spectroscopy (STS) band gaps measured over the cluster size regime used for the  $\text{CO}:\text{O}_2$  reactions of Fig. 4A. There is a clear correlation between the onset of

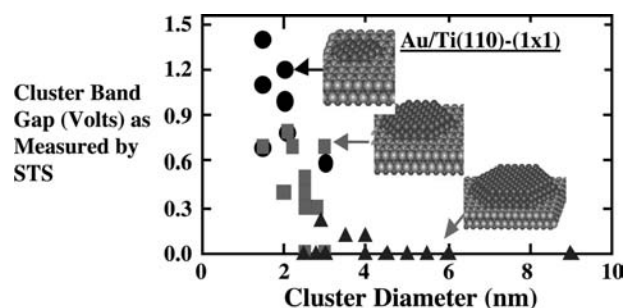


**Fig. 5** Cluster band gaps measured by STS as a function of Au cluster size supported on  $\text{TiO}_2(110)-(1 \times 1)$ . The band gaps were obtained while the corresponding topographic scan was acquired on various Au coverages ranging from 0.2 to 4.0 ML. ●: Two-dimensional (2-D) clusters; ◆: 3-D clusters, 2-atom layers in height; ▲: 3-D clusters, 3-atom layers or greater in height.

catalytic activity and the observed metal-to-non-metal transition in the supported Au clusters. The average Au cluster size where non-metallic properties become apparent is 3.5 nm in diameter and 1.0 nm in height, corresponding to approximately 300 atoms per cluster. The square data in Fig. 5 are for those clusters two layers thick ranging in size from 2.0 to 4.0 nm in diameter and are those clusters which exhibit optimum catalytic activity for the CO oxidation reaction. The STS-measured band gaps of this group of clusters range from 0.2 to 0.6 V. These results demonstrate that electronic properties as a function of cluster size play a crucial role in defining the catalytic reactivity of small clusters.<sup>[8,46]</sup>

### Adsorbate Binding Energies

Thermodynamic data regarding the adsorption of CO on  $\text{Au}/\text{TiO}_2$  catalysts with varying Au cluster sizes have been acquired with TPD using the well-known Redhead method<sup>[48]</sup> and with IRAS using the Clausius–Clapeyron relationship.<sup>[49,50]</sup> Results for these measurements are displayed in Fig. 6. CO adsorption on Au clusters larger than  $\sim 4.0$  nm behaves as bulk Au. However, as the clusters become smaller, the heat of CO adsorption increases from  $12 \text{ kcal mol}^{-1}$  to a maximum of  $19 \text{ kcal mol}^{-1}$  for clusters  $\sim 3.0$  nm in diameter.<sup>[51]</sup> Both sets of data in Fig. 6 suggest a marked increase in the adsorption energy with a decrease in cluster size; however, the results derived using the Clausius–Clapeyron relationship show a maximum that correlates remarkably close to the maximum observed in the reactivity measurements of Fig. 4A. A similar increase in the binding energy of  $\text{O}_2$  with a decrease in the Au cluster size on  $\text{TiO}_2$  has been observed recently.<sup>[52]</sup> In any case, clearly, the

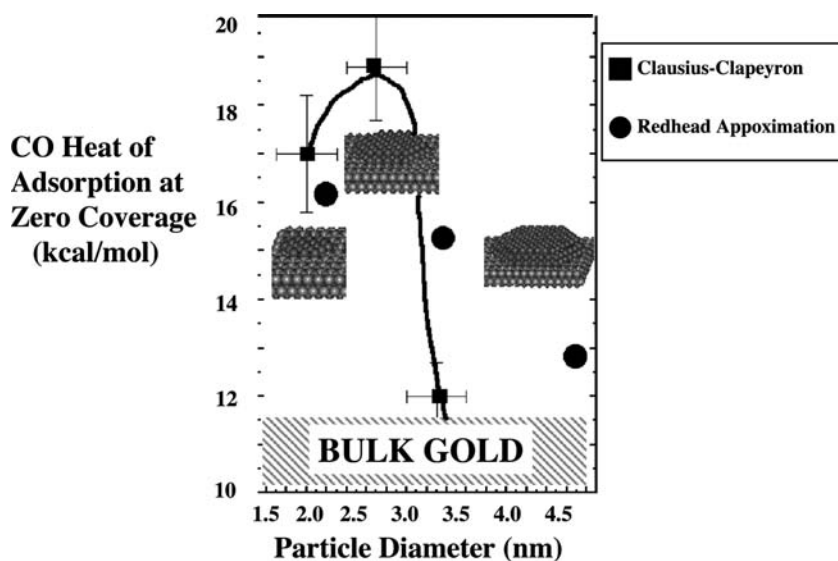


Fig. 6 CO heats of adsorption as a function of Au cluster size on a  $\text{TiO}_2(110)$  support.

effects of cluster size on the adsorption properties of Au clusters are significant and likely a key to the altered catalytic properties displayed by ultrasmall Au clusters.

### Electronic Properties

Fig. 7A shows the core level binding energies (BE) for the Au  $4f_{7/2}$  core level as a function of Au cluster coverage on a  $\text{TiO}_2(110)$  surface.<sup>[15]</sup> A +0.8-eV BE shift is evident for small clusters (0.02 ML, ~2-nm diameter) with a gradual shift to the bulk value of Au  $4f_{7/2} = 84.0 \text{ eV}$ <sup>[53]</sup> with increasing cluster size (6 ML Au coverage, ~5-nm diameter). This increase in the BE with a decrease in cluster size is consistent with an earlier XPS study by Mason<sup>[54]</sup> where the relative BE shifts of Au clusters (of varying sizes) supported on  $\text{SiO}_2$  and  $\text{Al}_2\text{O}_3$  were shown to depend upon the relative abilities of the substrate to screen

the outgoing photoelectrons (final state effects). However, a comparison of the relative core level BE shifts of the Au/ $\text{TiO}_2$  with the Au/ $\text{SiO}_2$  shows that the BE shift for Au/ $\text{SiO}_2$  is significantly larger (+1.6 eV) than that for Au/ $\text{TiO}_2$  (+0.8 eV) in the transition from large to small cluster sizes. Differences in the magnitudes of these Au cluster core level BE shifts are believed to result from the relative strengths of the interaction of Au with the two metal oxide supports. Recent theoretical calculations<sup>[55]</sup> predict an initial state *reduction* in the BE of 1.1–1.5 eV for the  $4f_{7/2}$  core levels of Au on  $\text{TiO}_2$ . As shown in Fig. 7B, this relatively large initial state contribution to the core level shift of Au/ $\text{TiO}_2$  relative to Au/ $\text{SiO}_2$  is sufficient to account for the 0.8-eV difference observed for the total BE shifts measured for these two oxide supports. Fig. 8 shows the total density of states (TDOS) calculated for bulk Au compared with Au adsorbed on  $\text{TiO}_2$ .<sup>[55]</sup> For adsorbed Au, the Au  $d$  bands are much closer to  $E_f$  because of the charge polarization in the

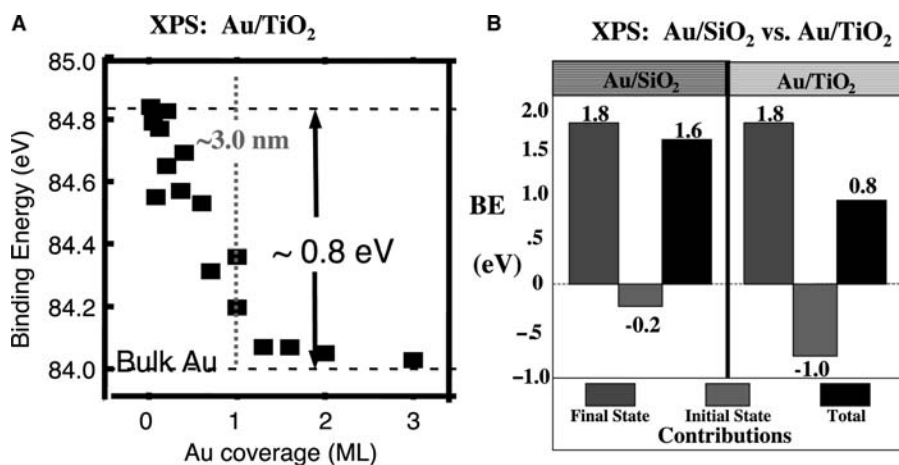
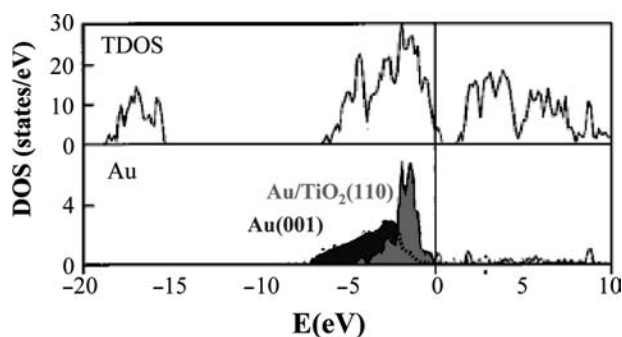


Fig. 7 (A) XPS binding energies of the Au  $4f_{7/2}$  core level as a function of Au cluster coverage (ranging from 0.02 ML—bulk) on  $\text{TiO}_2(110)$ . (B) XPS binding energies for Au clusters on  $\text{TiO}_2$  compared with Au clusters on  $\text{SiO}_2$ . The histogram takes into account the initial and final contributions to the observed overall BE shifts for Au on the two supports.



**Fig. 8** The total density of states (TDOS) of Au/TiO<sub>2</sub>(110) in the top panel and the local density of states for Au on TiO<sub>2</sub>(110) compared with Au in bulk Au(001).

interfacial region and a subsequent increase of the potential in the adlayer. Such a large energy shift of the Au 5*d* band toward the  $E_f$ , as discussed by Hammer and Norskov,<sup>[56]</sup> should strongly alter the surface chemical properties of Au/TiO<sub>2</sub> from those of a clean bulk Au surface.

### Cluster Sublimation Energies

Temperature-programmed desorption (TPD) is a useful tool for obtaining detailed information on adsorbate-surface bonding and on adsorbate-adsorbate interactions, desorption kinetics, and determining binding energies of metals adsorbed onto surfaces. Temperature-programmed desorption binding energy determinations also allow for comparative estimations of admetal cluster size on different oxide supports. In a

series of TPD spectra acquired for Au on SiO<sub>2</sub>, a marked decrease in the Au cluster binding energies, denoted by the peak temperature maximum ( $T_m$ ) in the TPD of the clusters, is observed.<sup>[15]</sup> Fig. 9A shows a family of TPD spectra taken of the Au clusters deposited onto a SiO<sub>2</sub> thin film. The leading edge of the TPD peak maxima shifts to higher temperatures as the Au coverage increases. The inset shows a plot of the sublimation energy ( $E_{\text{sub}}$ ) as a function of Au coverage, determined using the leading edge analysis.<sup>[57]</sup> At 0.2 ML, the  $E_{\text{sub}}$  at  $\sim 50$  kcal mol<sup>-1</sup> increases rapidly (with increasing Au coverage) to the bulk value at  $\sim 90$  kcal mol<sup>-1</sup> at 5.0 ML. The decrease in  $E_{\text{sub}}$  can be explained by the fact that an atom at the edge of a small cluster has fewer nearest neighbors than larger ones and hence desorbs more easily because of decreased surface tension.

The interaction of Au with TiO<sub>2</sub>(001) has also been determined using the same approach. The results are shown in Fig. 9B. In this case, however, only a single desorption feature is observed with a common leading edge for all Au coverages. Using the leading edge analysis, the Au binding energy on TiO<sub>2</sub>(001) is found to be 50 kcal mol<sup>-1</sup>, considerably smaller than the Au bulk sublimation energy of 90 kcal mol<sup>-1</sup>. This dramatic decrease of the sublimation energies *at all cluster sizes*, from the smallest to the largest, is clearly related to the strong interaction between the Au clusters and the TiO<sub>2</sub> support. This strong interaction leads to a greater degree of wetting of the TiO<sub>2</sub> by Au compared with Au/SiO<sub>2</sub>, and thus the lower sublimation energies found for the clusters may arise because of the preferential evaporation of Au at the

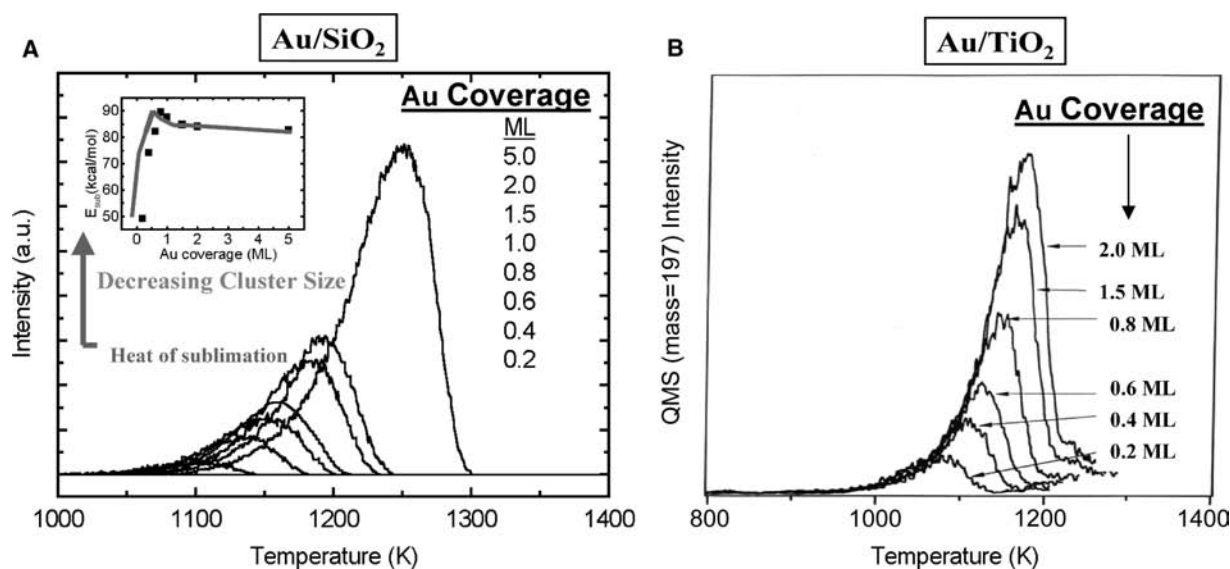


**Fig. 9** A set of TPD spectra of Au ( $m/e = 197$ ) on a 2.5-nm-thick SiO<sub>2</sub> thin film on Mo(110) at Au cluster coverages ranging from 0.2 to 5.0 ML. The inset shows a plot of  $E_{\text{sub}}$  determined from leading edge analysis.

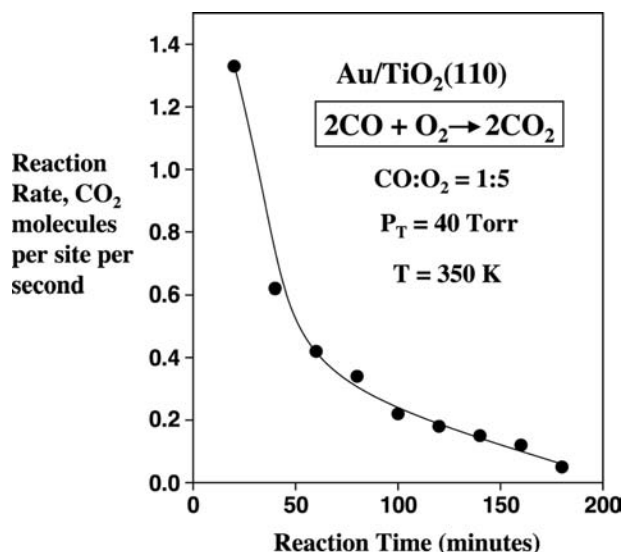


**Fig. 10** The activity for CO conversion as a function of reaction time at 300 K on a model Au/TiO<sub>2</sub>(001) catalyst. The initial average Au cluster size was 2.4 nm.

periphery of the clusters. In any case, this contrast of behavior regarding the sublimation of Au from SiO<sub>2</sub> and TiO<sub>2</sub> highlights the role of the support in altering the properties of ultrasmall clusters of Au.

### Catalyst Deactivation and Cluster Sintering

The presence of reactant gases at realistic conditions can affect the admetal's ability to wet the surface and

thereby alter particle size and distribution. For example, although the TiO<sub>2</sub>-supported Au catalysts exhibit a high activity for the low-temperature CO oxidation, the catalysts are often rapidly deactivated.<sup>[46]</sup> This is illustrated by Fig. 10, where the CO conversion is plotted as a function of reaction time for CO oxidation at 300 K on a catalyst prepared by depositing 0.25 ML Au on TiO<sub>2</sub>. The model Au/TiO<sub>2</sub> catalyst, which exhibits a high initial activity, deactivates after a CO:O<sub>2</sub> (1:5) reaction of ~120 min at 40 Torr. The deactivation is a result of the agglomeration of the Au clusters induced by interaction of O<sub>2</sub> with the Au clusters.<sup>[58,59]</sup>

In Fig. 11, a selected area is shown in (A) for UHV conditions and in (B) for 665 Pa of a CO:O<sub>2</sub> (1:5) reaction mixture.<sup>[59]</sup> There are noteworthy parallels between the instability of the small Au clusters, their catalytic activity, and the change in their catalytic activity with time. Au clusters of approximately 3 nm are optimum as CO oxidation catalysts. Clearly, reaction-induced sintering of these small clusters is a mechanism for the loss of activity with time.

### CONCLUSION

Model catalyst systems combined with surface-sensitive methods constitute a valuable methodology for probing the electronic and morphological structure of supported metal clusters. From detailed STM/STS studies combined with other surface analytical techniques, a physical basis for understanding the enhanced

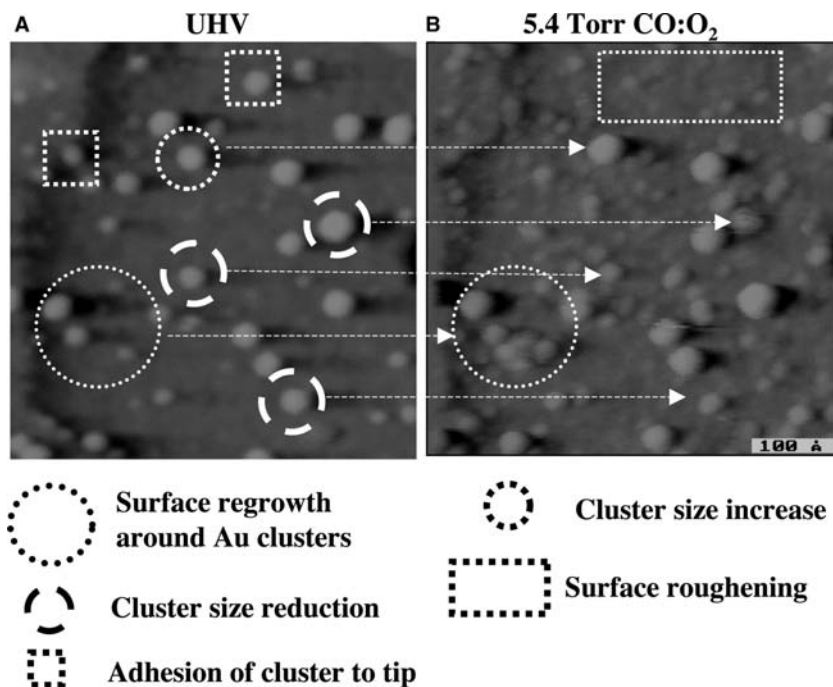


**Fig. 11** A 50 × 50 nm<sup>2</sup> image of the same area taken at 450 K: (A) under ultrahigh vacuum conditions; (B) during exposure to a reaction mixture consisting of a 665 Pa CO:O<sub>2</sub> mixture.



catalytic activities of nanosized, dispersed metal clusters is developing. The results summarized in this entry show a close correlation among cluster size, morphology, electronic properties, and catalytic activity. The use of model catalysts prepared with metal clusters supported on thin oxide films has been essential for the development of these new insights into the special electronic and chemical properties that govern the unique catalytic chemistry of nanosized metal clusters. Future studies toward a more in-depth understanding of nanostructured supported clusters will undoubtedly lead to the design and the development of practical catalysts.

## ACKNOWLEDGMENTS

Support by the Department of Energy, Office of Basic Energy Sciences, Division of Chemical Sciences; the Robert A. Welch Foundation and the Texas Advanced Technology Program under Grant No. 010366-0022-2001 are gratefully acknowledged.

## REFERENCES

- Fendler, J.H. Self-assembled nanostructured materials. *Chem. Mater.* **1996**, *8*, 1616.
- Henglein, A. Small-particle research - physicochemical properties of extremely small colloidal metal and semiconductor particles. *Chem. Rev.* **1989**, *89*, 1861.
- Mohamed, M.B.; Burda, C.; El Sayed, M.A. Shape dependent ultrafast relaxation dynamics of CdSe nanocrystals: Nanorods vs. nanodots. *Nano Lett.* **2001**, *1*, 589.
- Haruta, M. Size-and support-dependency in the catalysis of gold. *Catal. Today* **1997**, *36*, 153.
- Xu, Z.; Xiao, F.S.; Purnell, S.K.; Alexeev, O.; Kawi, S.; Deutsch, S.E.; Gates, B.C. Size-dependent catalytic activity of supported metal-clusters. *Nature* **1994**, *372*, 346.
- Haruta, M.; Date, M. Advances in the catalysis of Au nanoparticles. *Appl. Catal., A Gen.* **2001**, *222*, 427.
- Sanchez, A.; Abbet, S.; Heiz, U.; Schneider, W.D.; Hakkinen, H.; Barnett, R.N.; Landman, U. When gold is not noble: Nanoscale gold catalysts. *J. Phys. Chem., A* **1999**, *103*, 9573.
- Valden, M.; Lai, X.; Goodman, D.W. Onset of catalytic activity of gold clusters on titania with the appearance of nonmetallic properties. *Science* **1998**, *281*, 1647.
- Topsoe, H.; Topsoe, N.; Bohlbro, H.; Dumesic, J.A. *Proc. 7th Intl. Congress Catalysis*; Seiyama, T., Tamabe, K., Eds.; Kodansha: Tokyo, 1981.
- Freund, H.J.; Baumer, M.; Kuhlenbeck, H. Catalysis and surface science: What do we learn from studies of oxide-supported cluster model systems? *Adv. Catal.* **2000**, *45*, 333.
- Gunter, P.L.J.; Niemantsverdriet, J.W.; Ribeiro, F.H.; Somorjai, G.A. Surface science approach to modeling supported catalysts. *Catal. Rev., Sci. Eng.* **1997**, *39*, 77.
- Heiz, U.; Schneider, W.D. Nanoassembled model catalysts. *J. Phys., D, Appl. Phys.* **2000**, *33*, R85.
- Goodman, D.W. Model catalysts: From imagining to imaging a working surface. *J. Catal.* **2002**, *216*, 213.
- Rainer, D.R.; Goodman, D.W. Metal clusters on ultrathin oxide films: Model catalysts for surface science studies. *J. Mol. Catal., A Chem.* **1998**, *131*, 259.
- Chusuei, C.C.; Lai, X.; Luo, K.; Goodman, D.W. Modeling heterogeneous catalysts: Metal clusters on planar oxide supports. *Top. Catal.* **2001**, *14*, 71.
- Goodman, D.W. Model studies in catalysis using surface science probes. *Chem. Rev.* **1995**, *95*, 523.
- Oh, W.S.; Xu, C.; Kim, D.Y.; Goodman, D.W. Preparation and characterization of epitaxial titanium oxide films on a Mo(100). *J. Vac. Sci. Technol., A* **1997**, *15*, 1710.
- He, J.W.; Xu, X.; Corneille, J.S.; Goodman, D.W. X-ray photoelectron spectroscopic characterization of ultrathin silicon oxide films on a Mo(100) surface. *Surf. Sci.* **1992**, *279*, 119.
- Xu, X.P.; Goodman, D.W. New approach to the preparation of ultrathin silicon dioxide films at low temperatures. *Appl. Phys. Lett.* **1992**, *61*, 774.
- Xu, X.P.; Goodman, D.W. The preparation and characterization of ultra-thin silicon dioxide films on a Mo(110) surface. *Surf. Sci.* **1993**, *282*, 323.
- Chen, P.J.; Goodman, D.W. Epitaxial growth of ultrathin Al<sub>2</sub>O<sub>3</sub> films on Ta(110). *Surf. Sci.* **1994**, *312*, L767.
- Goodman, D.W. Chemical and spectroscopic studies of metal oxide surfaces. *J. Vac. Sci. Technol., A* **1996**, *14*, 1526.
- Wu, M.C.; Goodman, D.W. Particulate Cu on ordered Al<sub>2</sub>O<sub>3</sub>: Reactions with nitric oxide and carbon monoxide. *J. Phys. Chem.* **1994**, *98*, 9874.
- Feldman, L.C.; Mayer, J.W. *Fundamentals of Surface and Thin Film Analysis*; North-Holland: New York, 2002.
- Guo, Q.; Oh, W.S.; Goodman, D.W. Titanium oxide films grown on Mo(110). *Surf. Sci.* **1999**, *437*, 49.
- Corneille, J.S.; He, J.W.; Goodman, D.W. XPS characterization of ultra-thin MgO films on a Mo(100) surface. *Surf. Sci.* **1994**, *306*, 269.
- Wu, M.C.; Corneille, J.S.; Estrada, C.A.; He, J.W.; Goodman, D.W. Synthesis and characterization of ultra-thin MgO films on Mo(100). *Chem. Phys. Lett.* **1991**, *182*, 472.
- Wu, M.C.; Corneille, J.S.; He, J.W.; Estrada, C.A.; Goodman, D.W. Preparation, characterization and chemical properties of ultrathin MgO films on Mo(100). *J. Vac. Sci. Technol., A* **1992**, *10*, 1467.
- Wu, M.C.; Estrada, C.A.; Corneille, J.S.; Goodman, D.W. Model surface studies of metal oxides: Adsorption of water and methanol on ultrathin MgO films on Mo(100). *J. Chem. Phys.* **1992**, *96*, 3892.
- Truong, C.M.; Wu, M.C.; Goodman, D.W. Adsorption and reaction of formic acid on NiO(100) films on Mo(100): TPD and HREELS studies. *J. Chem. Phys.* **1992**, *97*, 9447.



31. Truong, C.M.; Wu, M.C.; Goodman, D.W. Adsorption of formaldehyde on nickel oxide studied by thermal programmed desorption and high-resolution electron energy loss spectroscopy. *J. Am. Chem. Soc.* **1993**, *115*, 3647.
32. Wu, M.C.; Truong, C.M.; Goodman, D.W. Interactions of ammonia with a NiO(100) surface studied by high resolution electron energy loss spectroscopy and temperature programmed desorption spectroscopy. *J. Phys. Chem.* **1993**, *97*, 4182.
33. Wu, M.C.; Truong, C.M.; Goodman, D.W. Interactions of alcohols with a NiO(100) surface studied by high-resolution electron energy loss spectroscopy and temperature-programmed desorption spectroscopy. *J. Phys. Chem.* **1993**, *97*, 9425.
34. Corneille, J.S.; He, J.W.; Goodman, D.W. Preparation and characterization of ultra-thin iron oxide films on a Mo(100) surface. *Surf. Sci.* **1995**, *338*, 211.
35. Xu, X.P.; Vesecky, S.M.; Goodman, D.W. Infrared reflection-adsorption spectroscopy and STM studies of model silica-supported copper catalysts. *Science* **1992**, *258*, 788.
36. Xu, X.P.; Goodman, D.W. Structural and chemisorptive properties of model catalysts: Copper supported on SiO<sub>2</sub> thin films. *J. Phys. Chem.* **1993**, *97*, 683.
37. Berlowitz, P.J.; Goodman, D.W. Chemisorption on ultra-thin Pd layers on W(110) and W(100): Adsorption of H<sub>2</sub> and CO. *Langmuir* **1988**, *4*, 1091.
38. Coulter, K.; Xu, X.P.; Goodman, D.W. Structural and catalytic properties of model supported nickel catalysts. *J. Phys. Chem.* **1994**, *98*, 1245.
39. Rainer, D.R.; Xu, C.; Holmblad, P.M.; Goodman, D.W. Pd, Cu, and Au particles on Al<sub>2</sub>O<sub>3</sub> thin films: An IRAS study of monometallic and bimetallic planar model supported catalysts. *J. Vac. Sci. Technol., A* **1997**, *15*, 1653.
40. Rainer, D.R.; Koranne, M.; Vesecky, S.M.; Goodman, D.W. The CO + O<sub>2</sub> and CO + NO reactions over Pd/Al<sub>2</sub>O<sub>3</sub> catalysts. *J. Phys. Chem., B* **1997**, *101*, 10769.
41. Rainer, D.R.; Vesecky, S.M.; Koranne, M.; Oh, W.S.; Goodman, D.W. The CO + NO reaction over Pd: A combined study using single crystal, planar model supported, and high surface area Pd/Al<sub>2</sub>O<sub>3</sub> catalysts. *J. Catal.* **1997**, *167*, 234.
42. Xu, C.; Lai, X.F.; Goodman, D.W. Local electronic structure of metal particles on metal oxide surfaces: Ni on alumina. *Faraday Discuss.* **1996**, *105*, 247.
43. Xu, C.; Oh, W.S.; Liu, G.; Kim, D.Y.; Goodman, D.W. Characterization of metal clusters (Pd and Au) supported on various metal oxide surfaces (MgO and TiO<sub>2</sub>). *J. Vac. Sci. Technol., A* **1997**, *15*, 1261.
44. Lai, X.; St. Clair, T.P.; Valden, M.; Goodman, D.W. Scanning tunneling microscopy studies of metal clusters supported on TiO<sub>2</sub>(110): Morphology and electronic structure. *Prog. Surf. Sci.* **1998**, *59*, 25.
45. Lai, X.F.; Goodman, D.W. Structure-reactivity correlations for oxide-supported metal catalysts: New perspectives from STM. *J. Mol. Catal., A Chem.* **2000**, *162*, 33.
46. Valden, M.; Pak, S.; Lai, X.; Goodman, D.W. Structure sensitivity of CO oxidation over model Au/TiO<sub>2</sub> catalysts. *Catal. Lett.* **1998**, *56*, 7.
47. Valden, M.; Goodman, D.W. Structure-activity correlations for Au nanoclusters supported on TiO<sub>2</sub>. *Isr. J. Chem.* **1998**, *38*, 285.
48. Redhead, P.A. Thermal desorption of gases. *Vacuum* **1962**, *12*, 203.
49. Szanyi, J.; Kuhn, W.K.; Goodman, D.W. CO adsorption on Pd(111) and Pd(100): Low and high pressure correlations. *J. Vac. Sci. Technol., A* **1993**, *11*, 1969.
50. Truong, C.M.; Rodriguez, J.A.; Goodman, D.W. CO adsorption isotherms on Cu(100) at elevated pressures and temperatures using IRAS. *Surf. Sci.* **1992**, *271*, L385.
51. Meier, D.; Goodman, D.W. The influence of metal cluster size on adsorption energies: CO adsorbed on Au clusters supported on TiO<sub>2</sub>. *J. Am. Chem. Soc.* submitted.
52. Bondzie, V.A.; Parker, S.C.; Campbell, C.T. Oxygen adsorption on well-defined gold particles on TiO<sub>2</sub>(110). *J. Vac. Sci. Technol., A* **1999**, *17*, 1717.
53. Seah, M.P. Post-1989 calibration energies for x-ray photoelectron spectrometers and the 1990 Josephson constant. *Surf. Interface Anal.* **1989**, *14*, 488.
54. Mason, M.G. Electronic-structure of supported small metal-clusters. *Phys. Rev., B* **1983**, *27*, 748.
55. Yang, Z.X.; Wu, R.Q.; Goodman, D.W. Structural and electronic properties of Au on TiO<sub>2</sub>(110). *Phys. Rev., B* **2000**, *61*, 14066.
56. Hammer, B.; Norskov, J.K. Electronic factors determining the reactivity of metal surfaces. *Surf. Sci.* **1995**, *343*, 211.
57. Habenschaden, E.; Kupperts, J. Evaluation of flash desorption spectra. *Surf. Sci.* **1984**, *138*, L147.
58. Lai, X.F.; St. Clair, T.P.; Goodman, D.W. Oxygen-induced morphological changes of Ag nanoclusters supported on TiO<sub>2</sub>(110). *Faraday Discuss.* **1999**, *114*, 279.
59. Kolmakov, A.; Goodman, D.W. Imaging gold clusters on TiO<sub>2</sub>(110) at elevated pressures and temperatures. *Catal. Lett.* **2000**, *70*, 93.

*Encyclopedia of*

# Nanoscience and Nanotechnology

*Second Edition*

## Volume II

*Pages 753 through 1490*

*Catalyst – Halide*

Catalyst – Charge

Chemical –  
Computational

Conducting  
– Cyclic

Dendritic – DNA

Dynamic –  
Electronic

Enantioselectivity  
– Fluorofullerenes

Fullerenes –  
Functionalization

Gecko – Halide

# Catalyst Nanostructures: X-Ray Absorption

**Jeffrey T. Miller**

*British Petroleum (BP), Naperville, Illinois, U.S.A.*

**M. K. Neylon**

*Chemical Technology Division, Argonne National Laboratory, Argonne, Illinois, U.S.A.*

**C. L. Marshall**

**Arthur Jerome Kropf**

*Argonne National Laboratory, Argonne, Illinois, U.S.A.*

## INTRODUCTION

In recent years, X-ray absorption fine structure (XAFS) spectroscopy has become a routine method for determining the coordination environment and local structure of metallic nanoparticles. Because of the penetrating power of high-energy X-rays, XAFS data may be obtained under realistic operating conditions. In this entry, we provide a short overview of XAFS spectroscopy and some features that make it attractive for characterization of nanoparticles. We also give several examples of how XAFS has been applied to problems in catalysis. Special emphasis will be given to highlighting XAFS data taken on supported catalytic nanoparticles under realistic preparation, pretreatment, reaction, and deactivation conditions.

## INTRODUCTION TO EXTENDED X-RAY ABSORPTION FINE-STRUCTURE SPECTROSCOPY—THEORY AND TECHNIQUE

The interaction of X-rays with matter can be described by the attenuation of an X-ray beam as it penetrates through a sample. The absorption coefficient,  $\mu$ , is defined by

$$\frac{dI(x)}{dx} = -\mu I \quad (1)$$

where  $I$  is the incident X-ray intensity in some homogeneous region and  $x$  is a position in the region. The solution of Eq. (1) is the familiar exponential relation

$$I = I_0 e^{-\mu(E)x} \quad (2)$$

where  $I_0$  is the incident intensity and  $\mu(E)$  is written as a function of the incident photon energy,  $E$ , as the absorption coefficient is energy-dependent.

While there are multiple processes that contribute to the attenuation of photons, in the X-ray energy range up to 40 keV, the dominant process is photoelectric absorption; the other processes are scattering by electrons and nuclei and, at much higher energies, pair production. At X-ray energies, as the energy of the incident photons is increased through an atomic energy level, a new excitation channel becomes available and there is an increase in the absorption of photons. This increase is not a sharp-step increase, but has a structure that can be interpreted.

The region from slightly below the absorption-edge energy,  $E_0$ , up to as much as 2000 eV higher is the X-ray absorption fine-structure region (Fig. 1). The edge energy,  $E_0$ , primarily depends on the atomic species and the electron shell that is excited, but also, to a small degree, on the chemical environment. Absorption by a particular element may be measured by scanning an appropriate energy range. Using this feature of the absorption of X-rays, we can probe individual elements in a sample to the exclusion of all others. The X-ray absorption near-edge structure (XANES) region can provide information on the chemical and electronic states of the absorbing atoms.<sup>[1]</sup> Edge shifts of a couple electron volts reflect changes in the oxidation state of the absorbing element; an increasing edge energy typically corresponds to a higher oxidation state.

To describe the extended X-ray absorption fine-structure (EXAFS) region, we consider that the absorption of an X-ray photon excites a photoelectron wave, which propagates from the excited atom and scatters off of the surrounding atoms. It is the interference of the backscattered photoelectron wave function with the initial outgoing wave function at the site of the absorbing atom that modulates the absorption coefficient and produces the EXAFS. Thus the fine-structure oscillations can provide information about the number, type, and distance of neighboring atoms

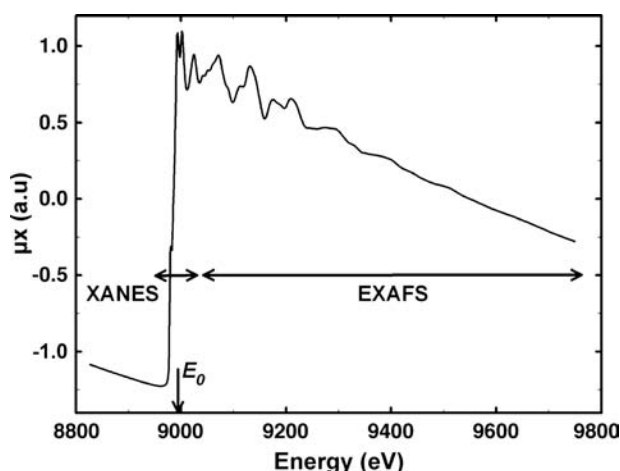


**Fig. 1** Plot of the absorption coefficient,  $\mu x = \ln(I_0/I)$ , vs. incident X-ray energy for the Cu K-edge of a Cu foil sample. The edge energy,  $E_0$ , as well as the XANES and EXAFS regions are denoted on the plot.

to the absorbing atom. These oscillations have a relatively high frequency in  $E$  while the other attenuation modes are relatively slowly varying over the energy range. Only the oscillatory part of the absorption coefficient is of interest as a structural probe. The EXAFS is then defined as

$$\chi(E) = \frac{\mu(E) - \mu_0(E)}{\mu_0(E)} \quad (3)$$

where  $\mu_0(E)$  is the slowly varying background absorption (or attenuation) from an isolated absorbing atom and other processes. It can be shown that the EXAFS oscillations are periodic in terms of  $k$  (the electron wave number) and the equation is frequently written as

$$\chi(k) = \frac{\mu(k) - \mu_0(k)}{\mu_0(k)} \quad (4)$$

where  $E$  has been transformed to  $k$  as

$$k = \left( \frac{2m_e}{\hbar^2} (E - E_0) \right)^{\frac{1}{2}} \quad (5)$$

The equation describing EXAFS can be written as

$$\chi(k) = \sum_i \frac{N_i S_0^2}{2kR_i^2} |f_i(k, \pi)| \times \sin[2kR_i + \delta_i(k) - \pi] e^{-2k^2\sigma_i^2} \quad (6)$$

where  $N_i$  is the number of  $i$ -type atoms at a distance  $R_i$ ,  $S_0^2$  is the amplitude reduction factor,  $f_i(k, \pi)$  is the back-scattering amplitude function,  $\delta_i(k)$  is the phase shift, and  $\sigma_i^2$  is the EXAFS Debye–Waller factor. Because  $f_i$

is unique to a particular atom, one is able to distinguish different types of neighboring atoms based on the shape of  $\chi(k)$ . Many good books and articles that explain EXAFS in much greater detail have been written.<sup>[2–7]</sup>

The Debye–Waller factor introduced in the exponential at the end of the equation deals with the fact that the X-ray absorption event takes a snapshot of the local environment and the thermal motion of the atoms will cause them to be separated by different distances at different times. Because of the  $kR_i$  term in the sine function, the signal will get smeared out at higher  $k$  because of the relative motion of the atoms. This term is a first approximation and can also include static structural disorder. Thermal vibration and static structural disorder become very important, especially in the case of small particles having a large fraction of surface atoms.

Because all atoms of a particular element will exhibit increased absorption at the absorption-edge energy, EXAFS is typically a bulk measurement technique. However, in the case of very small particles, such as in most active catalysts, the surface atoms contribute a significant fraction to the overall signal. In these cases, EXAFS can be used to probe surface interactions. Also, as a result of the bulk averaging intrinsic in an EXAFS measurement, it is difficult to interpret the data in an individual measurement if there are even two phases present that contain significant quantities of the probed element. Obtaining useful information when three phases are present is nearly impossible because all scattering paths interfere. However, if many measurements are made as the sample is changing in some way (e.g., temperature-programmed reduction), it may become possible to identify the unique contribution of individual phases in a mixed-phase system using factor analysis.<sup>[8]</sup>

## Synchrotrons and Capabilities

The proliferation of synchrotron X-ray sources means that it is easier than ever to find a facility to do high-quality X-ray absorption spectroscopy research. In the last decade, three large new sources have been built for generating high-energy X-rays: the European Synchrotron Radiation Facility (ESRF, Grenoble, France), the Advanced Photon Source (APS, Argonne, Illinois, USA), and the Super Photon Ring (SPring-8, Hyogo, Japan). Several other smaller facilities with more modest, but nonetheless comparable, capabilities have also been built.<sup>[9]</sup> These newer, third-generation sources have been specifically optimized for insertion device beamlines. Other older synchrotron facilities, such as the Stanford Synchrotron Radiation Laboratory (SSRL, Stanford, California, USA) are upgrading their storage rings to take advantage of insertion devices and other advances in accelerator technology.

Insertion devices, which are large arrays of magnets, generate a high-brightness beam with a typical size of about  $1 \times 2$  mm (unfocused) at 60-m distance from the source at a third-generation source, compared to a large fan of radiation, 2 mm by several centimeters (more accurately, several milliradians), generated by bending magnet sources. The multiple magnets of an insertion device, first of all, increase the source power proportional to the number of magnets. Also, when the magnets are arranged in a periodic array, they can concentrate the emitted power into intense spikes in the energy spectrum.<sup>[10]</sup> Because the electron-beam deflection is much smaller in an insertion device compared to a bending magnet, the beam has very low divergence, rather than that of a broad fan. An undulator (a type of insertion device) beamline at the APS with a Si(111) double-crystal monochromator can generate  $\sim 10^{13}$  photons/sec in a  $1 \times 2$ -mm beam at 10 keV. With a second-generation bending magnet source, a typical intensity would be  $\sim 10^{11}$  photons/sec in an unfocused  $1 \times 10$ -mm beam.

### New Source Capabilities

The availability of higher-power X-ray sources means that experiments can be performed in much less time, opening up new classes of experiments. A simple transmission EXAFS measurement made on a second-generation bending magnet beamline may take up to an hour. A similar measurement on an undulator beamline at the APS can be made as fast as several seconds. At these rates, it becomes practical to monitor reactions in situ, as the measurement time is comparable to the timescale of the bulk properties of catalytic reactions. In situ measurements are strongly preferred for studying catalytic systems in many cases because there can be large differences between the state of the sample under reaction conditions and the state at room temperature or atmospheric pressure.

Instead of using the higher flux for faster measurements, one may attempt previously impractical measurements, such as measuring the XAFS of lower active catalyst concentrations or dilute alloying elements. More exotic experiments may also be considered, such as combining fluorescence spectrometry with XAFS, which may provide even higher site specificity.<sup>[11–15]</sup>

### INTRODUCTION TO HETEROGENEOUS CATALYSTS

Much of the productivity improvements in the chemical industry within the last century could not have occurred without the help of catalysts. Catalytic materials provide improvements in reaction rate and

product selectivity by lowering the activation energy by which chemical reactions occur. A wide variety of chemical substances show catalytic activity, but most industrial processes employ heterogeneous catalysts that are comprised of metal, metal oxide, or metal sulfide nanosize particles on porous, high-surface-area supports.

Heterogeneous catalysts are typically prepared by impregnating a support with a solution containing a metal compound, followed by thermal treatment or calcination to remove water and convert the metal salt to a supported phase that is readily transformed into the active phase under reaction conditions. Alternatively, metals can be added to the support by deposition of volatile species from the gas phase, addition of organometallic species, mixing of solid phases, ionic exchange, or numerous other methods. In some cases, pretreatment of the catalyst with reactive gases is performed to achieve the desired formation and dispersion of an active phase that cannot be obtained directly by impregnation and calcination. For example, pretreatment of supported metal oxides by  $H_2$  or  $H_2S$  gives reduced metal or metal sulfide particles.

While catalytic materials are theoretically not altered or consumed during the course of reaction, both reversible and irreversible changes inevitably occur. These can include the adsorption and desorption of reactant and product species, the transformation of the catalyst species to a new phase, the poisoning of the catalyst surface by trace contaminants in the reaction mixture, sintering and agglomeration of the dispersed active phase into large particles, and the blocking of active sites by the formation of carbonaceous deposits, called coke. Understanding the deactivation mechanisms can be used to design more rugged and stable catalysts. Alternatively, the catalysts may be regenerated, typically by oxidizing and rereducing the catalyst to restore the active phase.

Of interest to most catalyst researchers is the structure of the active site, especially under reaction conditions. While there are a number of instrumental methods used to characterize the active site in nanoparticles, many of these methods require idealized materials or conditions such as thin films, ultrahigh vacuum, low temperature, etc. This is in contrast with typical operating conditions requiring reaction pressures from atmospheric up to several hundred atmospheres and temperatures up to 700°C. Data obtained under ambient conditions may significantly differ from those obtained under realistic operating conditions. However, XAFS can be used to determine the average local electronic and structural environment of a catalytic metal site under realistic conditions, thus overcoming both the pressure and materials gap. As a result, the use of XAFS as a key method for nanoparticle characterization of heterogeneous catalysts has

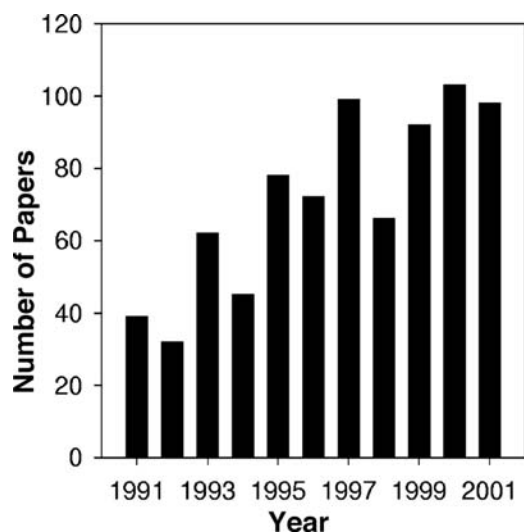


**Fig. 2** Publication rate from 1991 to 2001 that includes characterization of heterogeneous catalytic nanoparticles by XANES and EXAFS spectroscopy.

considerably grown in the last decade (Fig. 2). Several excellent reviews describe EXAFS in the context of catalyst characterization.<sup>[1,16–25]</sup> The increase in the use of XAFS in catalysis is in part also a result of the increased availability of synchrotrons, improved data quality, and improvements in both hardware and software for data analysis.

While more catalysis researchers are using XAFS characterization, there is still a push for the development of in situ data collection methods to observe catalysts under reaction conditions. As one must allow X-ray access to the sample and detect X-rays from inside the sample chamber, reactor design can be quite involved. Any material that intercepts the X-ray beam, including the sample in transmission XAFS, must be somewhat transparent at the X-ray energy being used. There are a limited number of materials that are nearly transparent to X-rays, are non-reactive, and have high mechanical strength. Transmission measurements are relatively simple because only a small window is needed for X-ray entrance and exit. Catalyst samples are typically mounted as self-supporting wafers to reduce the detrimental absorption from a support. Several of these specially designed reactors are described in the open literature.<sup>[26–36]</sup>

## CATALYST PREPARATION

Although there are many methods for the preparation of supported catalysts, catalytic nanoparticles are most often prepared by dissolution of metal compounds in a suitable solvent and contacting with a high-surface-area support. Subsequently, the solvent is dried and the metal salts may be thermally treated,

reduced, oxidized, or sulfided. There are numerous examples in the catalytic literature where the choice of metal compound and methods of deposition and pretreatment greatly affect the final-phase composition or particle size and, thus, the catalytic performance. The reasons for these differences for compositionally equivalent materials are often unclear. In addition, many catalysts include metallic and nonmetallic promoters, which significantly alter their activity, selectivity, or stability. The degree of interaction of the promoter with the active component is often determined by the choice of metal compounds and pretreatment steps during the synthesis. Extended X-ray absorption fine-structure (EXAFS) spectroscopy has been increasingly applied to the study of catalyst preparations, providing structural details and insights often not readily available from other spectroscopic techniques.

## Addition of Metals to the Support

For economic reasons, most commercial heterogeneous catalysts are prepared from readily available inorganic metal salts soluble in water. The steps of catalyst impregnation can be explained by the speciation of the metal salts in aqueous solution and by the electric double-layer theory of solid oxides.<sup>[37–39]</sup> For example, with the increased sensitivity of the new generation of synchrotrons, the speciation of  $\text{H}_2\text{PtCl}_6$  (chloroplatinic acid, or CPA) in water, which is used to prepare very small metallic Pt particles on alumina, has been investigated by EXAFS.<sup>[37]</sup> Determination of the number of chloride and oxygen ligands of dilute CPA solutions at pHs typically used to prepare highly dispersed catalysts indicates that the solution chemistry is more complex than generally assumed. At a pH of about 2.5, there is rapid exchange of approximately three chloride ligands by water. For solutions at a higher pH, the number of Cl ligands decreases, while addition of HCl decreases the pH and increases the Cl concentration, leading to an increase in Cl coordination, reversibly giving  $\text{PtCl}_6^{2-}$ . Therefore specific Pt species depends on the pH as well as the CPA and  $\text{Cl}^-$  concentrations.

Catalyst supports significantly alter the pH of the impregnating solution because of the buffering effect of the oxide, determined by its point of zero charge (PZC). The effect of the support on the Coulombic interaction between the oxide surface and the aqueous metal species is twofold. First, there is a shift in the solution pH, which may alter the solution metal species, and, second, the adsorbed species appears to behave as if it is in the liquid phase at the pH of the adsorption plane.<sup>[38]</sup> The aqueous speciation of  $\text{AuCl}_4^-$  is strongly dependent on the solution pH, as shown in Fig. 3.



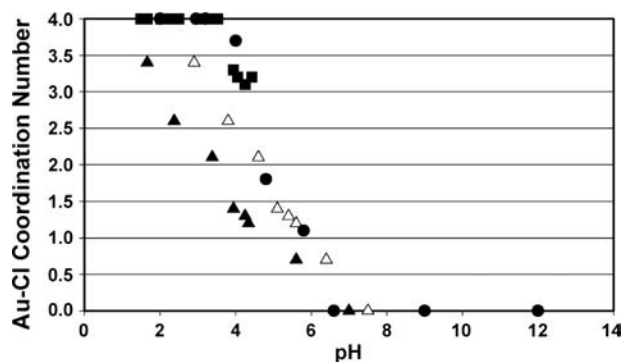


**Fig. 3** Effect of pH on the Au–Cl coordination number for  $\text{NaAuCl}_4$  in aqueous solution and adsorbed on alumina. Solid square: 200-ppm  $\text{AuCl}_4^-$ ; open square: 200-ppm  $\text{AuCl}_4^-$  plus 50 times molar excess of  $\text{Cl}^-$ ; solid circle: 500-ppm  $\text{AuCl}_4^-$ ; solid triangle: 200-ppm  $\text{AuCl}_4^-$  adsorbed on alumina at the solution pH; open triangle: 200-ppm  $\text{AuCl}_4^-$  adsorbed on alumina at the calculated pH of the alumina surface. The sum of the Au–Cl and Au–O coordination numbers is 4. Source: From Ref.<sup>[39]</sup>.

Below about a pH of 4, the solution species have four Cl ligands at a distance of 0.280 nm. As the pH increases to about 7, the average number of Cl ligands linearly decreases, being replaced by hydroxyl ligands at a distance of 0.203 nm. At pHs above about 7, all Au–Cl ligands are replaced by hydroxyl ligands, giving  $\text{Au}(\text{OH})_4^-$  in aqueous solution. Adsorption of Au onto alumina (PZC = 8.0) (solid triangles in Fig. 3) results in a decrease in the number of Cl ligands compared to aqueous solutions at the same pH. The Au–Cl coordination of adsorbed Au species follows the trend for the pH calculated at the surface of the support rather than the pH in the bulk solution (open triangles in Fig. 3). These results suggest that the composition of the adsorbed species is determined by the oxide properties of the support and that alumina is more basic than the aqueous solutions used to prepare the catalysts. Similar results have been obtained for  $\text{Na}_2\text{PtCl}_4$  and  $\text{Na}_2\text{PdCl}_4$  on alumina, CPA on carbons with different PZC, and  $\text{Pt}(\text{NH}_3)_4(\text{NO}_3)$  on silica.<sup>[39]</sup>

When the metals are added to supports that do not favor a strong Coulombic attraction, the subsequent treatments often lead to much larger particles. The effect of the method of metals addition on the size of the nanoparticles is demonstrated for Ni on silica.<sup>[40]</sup> Silica has a PZC of about 3; thus it is strongly deprotonated at pHs greater than about 8. Under these conditions, cationic metal salts are strongly adsorbed. Incipient wetness impregnation of an aqueous solution at nickel nitrate (pH of 4–5) leads to a weak interaction with the support and the formation of large NiO particles. The Ni–O and Ni–Ni coordination numbers (CNs) and bond distances are similar to those for bulk NiO after calcination in air at 500°C. By contrast, the

Ni–O and Ni–Ni CNs for impregnation of cationic ethylenediamine Ni(II) complexes at a pH of 12, i.e., a deprotonated silica surface, indicate surface-stabilized Ni that gives significantly smaller nickel oxide particles upon calcination.

The effect of metal loading and support composition on the adsorbed and reduced species has been investigated for chromium on silica, alumina, and silica–alumina with various alumina contents.<sup>[41]</sup> The hydrated adsorbed species differ on the different supports. For example, with incipient wetness impregnation of  $\text{CrO}_3$  at a 4% Cr loading on silica, the first shell Cr–O CN is near 4 at a distance of 0.158 nm, while on alumina and silica–alumina, the CN is near 6 at a distance of 0.165 nm. Calcination lowers the Cr–O CNs with little change in the bond distances. The lower the isoelectric point of the support and the higher the chromium loading, the greater the fraction of surface polychromates. In addition, upon reduction, the XANES spectra indicate that all catalysts contain both Cr(II) and Cr(III). However, the fraction of Cr(II) increases in the order silica > silica–alumina > alumina. Furthermore, at low loading, the Cr(II) species on silica are highly coordinatively unsaturated and correlate with high catalytic activity for ethylene polymerization. This example demonstrates that both the support and the metal loading can affect the phase composition and particle size, giving widely varying activities for catalysts of similar metal composition.

Three-way catalysts (TWC) are widely used to treat gasoline vehicle emissions (hydrocarbon, CO, and  $\text{NO}_x$ ). The method of Pt and Rh addition onto cerium-oxide-promoted alumina greatly affects the performance.<sup>[42]</sup> Coimpregnation of Pt and Rh displays low activity for propane oxidation (due principally to Pt) after calcination at 900°C. The Pt EXAFS spectrum indicates the formation of large metallic particles (bond distance 0.277 nm) with total CN (Pt–Pt and Pt–Rh) near 12. In addition, by comparison of the Pt–Rh EXAFS coordination number (CN) to the bulk composition, it is concluded that the particles are a PtRh alloy with high surface Rh content. Sequential deposition and reduction of Pt gives metallic Pt and reduced Ce. Subsequent Rh addition selectively deposited on the partially reduced Ce gives a catalyst with much higher activity. After calcination at 900°C, the large metallic particles are again formed; however, there is little alloy formation. Extended X-ray absorption fine structure spectroscopy is one of the few techniques whereby alloy formation, phase segregation, composition, and structure can be determined in bimetallic nanoparticles.

Catalytic nanoparticles can also be prepared from organometallic and metal carbonyl compounds dissolved in organic solvent.<sup>[43]</sup> Generally, with organometallic compounds, some of the ligands react with the support

hydroxyl groups to give attached metal species. Supported nanoparticles have been prepared from  $\pi$ -allyl compounds of Rh, Ni, Pd, and Pt. Reaction of the support hydroxyl groups leads to the loss of 1–2 ligands and the formation of a M–O coordination. The degree of reaction can often be determined by EXAFS. Reduction in hydrogen of the adsorbed Rh allyl species on silica leads to formation of 1.3-nm Rh particles; the Rh–Rh CN was 5.0 at a distance of 0.264 nm. From the EXAFS of the adsorbed species, the Rh–Rh CN (3.0) and bond distance (0.270 nm), and Rh–C (0.184 nm) and Rh–O (oxygen atom from the CO ligand) bond distances (0.293 nm) could be determined. Multimetallic carbonyl clusters have also been used to prepare nanoclusters having narrow particle size distributions. For example, EXAFS analysis of the Ir–Ir CN and bond distance of  $\text{Ir}_4(\text{CO})_{12}$  adsorbed onto  $\text{MgO}^{[44]}$  and  $\text{TiO}_2^{[45]}$  from pentane is consistent with formation of an  $[\text{H}(\text{Ir}_4(\text{CO})_{11})]^-$  complex. When the adsorbed complex is thermally decarbonylated at 300°C in He, an Ir–Ir coordination is found at a distance of 0.267 nm with a CN of 3.0, suggesting the formation of four-atom Ir nanoparticles. In addition, with these very small particles, two distances from the metal atom to the oxygen ions of support were resolved in the EXAFS spectrum at 0.219 and 0.268 nm. When the adsorbed Ir complex was decomposed in  $\text{H}_2$  at the same temperature, larger particles were formed (CN = 6.7). For Ir nanoparticles, the  $\text{H}_2$  and CO chemisorption capacities sharply decreased as the particle size decreased. As a result, accurate information on the particle size could only be determined from the EXAFS Rh–Rh coordination numbers. Similar catalysts with narrow particle size distributions have been prepared and characterized by EXAFS for  $\text{Rh}_6(\text{CO})_{16}$  on  $\text{TiO}_2^{[46]}$  and  $[\text{HOS}_3(\text{CO})_{11}]^-$  on NaY zeolite.<sup>[47]</sup>

The choice of metal salt and pretreatment conditions often affect the nanoparticle composition, and thus the catalytic performance. Alumina-supported Mo and W sulfide catalysts are widely used in petroleum refining for removing S and N heteroatoms. However, to meet future more stringent emissions regulations, more active and selective catalysts must be developed. Vapor deposition of  $\text{Mo}(\text{CO})_6$  into NaY zeolite followed by sulfidation at 400°C leads to very small or highly disordered, fully sulfided Mo particles, which possess high catalytic activity.<sup>[48]</sup> The Mo–S and Mo–Mo bond distances are consistent with that of  $\text{MoS}_2$ , and from the Mo–Mo coordination number of about 1, these are proposed to be dimeric Mo species. Oxidation of  $\text{Mo}(\text{CO})_6$  at 100°C produced Mo-oxide dimers with a Mo–Mo coordination number of 0.8, which upon sulfiding also gave  $\text{MoS}_2$  dimers. Catalysts with a similar Mo content but are prepared by aqueous impregnation of ammonium heptamolybdate formed tetrahedrally coordinated Mo–O species in the calcined catalysts, as determined from the

XANES spectra; however, these particles could not be fully sulfided at 400°C. These materials displayed much lower activity than those prepared from  $\text{Mo}(\text{CO})_6$ , which was ascribed to the incomplete formation of a sulfided Mo phase and lower dispersion.

### Catalyst Pretreatment

Once the metals are deposited on the support, the catalyst is usually treated prior to reaction, to produce the active state of the catalyst or, at least, to produce a phase that readily transforms into the active catalyst under reaction conditions. Typical pretreatment conditions are to increase the temperature in air (or inert gas) followed by reduction of the metals in hydrogen, oxidation in air, or sulfiding with  $\text{H}_2\text{S}$ . The catalyst's activity is often greatly affected by the pretreatment conditions. For many catalysts, the changes that occur during pretreatment and the reasons for the dramatic changes in activity are not well understood. The EXAFS technique is being increasingly applied to this phase in the development of catalyst preparations.

Reduction of noble metal catalysts, e.g., Pt, Rh, Ir, etc., by hydrogen gives metallic nanoparticles. For particles less than about 2.0 nm, a large fraction of the atoms are in contact with the support and the structure of the metal–support interface can be resolved in the EXAFS spectrum of the metal.<sup>[49]</sup> Because the energy dependence of the backscattering amplitudes of M–O<sub>support</sub> and M–M paths are different, the two overlapping contributions can be resolved. Deconvolution of the two EXAFS contributions is accomplished by fitting the M–M shell with a high-*k* weighting of the data. This contribution can be then subtracted from the data and the difference spectrum is fit with a low-*k* weighting, allowing determination of the M–O shell.<sup>[50,51]</sup> Analysis of the EXAFS spectra indicates that the distance of the metal atoms in small particles to the support oxide surface is dependent on the reduction temperature. For example, for Pt on  $\text{Al}_2\text{O}_3$  catalysts reduced at high temperature, i.e., ca. 450°C, the distance of the Pt atoms to the support is about 0.220 nm, which is approximately the sum of the covalent radii of metallic Pt and oxide ions.<sup>[52]</sup> However, low-temperature reduction, e.g., 300°C, gives a Pt-support distance of 0.270 nm. This long distance has been interpreted as resulting from atomic hydrogen being inserted between the metal particles and the support. The hydrogen atoms are not observed in the normal EXAFS spectrum because the hydrogen backscattering amplitude is small. Similar M–O<sub>support</sub> distances have been reported for several other supported noble metal catalysts.<sup>[49,53,54]</sup>

The effect of reduction temperature on particle morphology for Pt supported on  $\alpha$ -alumina single

crystals has been studied by polarized total reflection fluorescence spectroscopy.<sup>[55]</sup> By analysis of the EXAFS spectra at different angles to the incident beam, it is possible to obtain three-dimensional structural information. For Pt reduced at low temperature (110°C), the ratio of the Pt–Pt coordination numbers with the sample placed parallel and perpendicular to the beam is 0.5. Model calculations indicate that under these conditions, a single layer of Pt atoms is in contact with the support. Upon high-temperature (400°C) reduction, spherical Pt particles are formed. The application of angle-dependent EXAFS to nanoparticles supported on single crystals provides structural information on particle morphology not generally available by standard EXAFS analysis with nanoparticles on amorphous supports.

### Temperature-Programmed Pretreatments

For many years, thermal and mass-spectroscopic, temperature-programmed pretreatment methods have been used to characterize catalytic nanoparticles. In the last few years, two methods for rapid data acquisition have made it possible to collect high-quality, time-resolved EXAFS spectra for determination of the structural transformations that accompany these changes. Dispersive EXAFS uses a bent crystal monochromator to simultaneously expose the sample to all X-ray energies. The trajectory of the X-rays depends on the energy, and the transmitted flux is detected with a multielement photodiode detector. Depending on the sample concentration, a spectrum can be obtained from a fraction of a second to minutes.<sup>[56,57]</sup> Alternatively, by continuously scanning the monochromator, one can collect a quick EXAFS spectrum within a

few seconds to minutes. This latter technique can be used with a more conventional beamline design and detectors. For both techniques, kinetic EXAFS data can be collected for processes such as reduction, poisoning, phase change, sintering, etc. that occur on the timescale of minutes to hours.<sup>[58]</sup>

Copper-exchanged ZSM-5 zeolite is catalytically active for the reduction and disproportionation of nitrogen oxides (NO<sub>x</sub>) to N<sub>2</sub>. In addition, there are several possible oxidation states [Cu(0), Cu(I), and Cu(II)] that could be catalytically active. Analysis of the Cu XANES spectra can be used to determine the amounts of each oxidation state, as a result of the significant differences between the XANES features of each state, particularly the pre-edge peak of Cu(I). High-resolution *in situ* XANES and EXAFS were used to follow the temperature-programmed reduction of Cu-ZSM-5 in hydrogen (Fig. 4).<sup>[59]</sup> Using principal component analysis, the stepwise transformation of Cu(II) to Cu(I) to Cu(0) was apparent from the XANES spectra. In addition, as a result of the highly resolved Cu(I) pre-edge feature, two Cu(I) species were detected, differing in their coordination geometry. The reduction steps were also observable in the EXAFS spectra. At high temperature, the formation of Cu–Cu metallic bonds indicates that reduced Cu particles are formed, which are undesirable for good catalytic activity.

Cu/ZnO catalysts are commercially used for synthesis of methanol at high pressure from CO plus H<sub>2</sub>. At low pressure, Cu also decomposes methanol and is being investigated for production of hydrogen for automotive fuel cell applications. The active catalyst is synthesized by precipitation of a mixed CuO/ZnO phase followed by reduction and reaction. The evolution of the catalytic precursors was followed during temperature-programmed reduction by XANES and

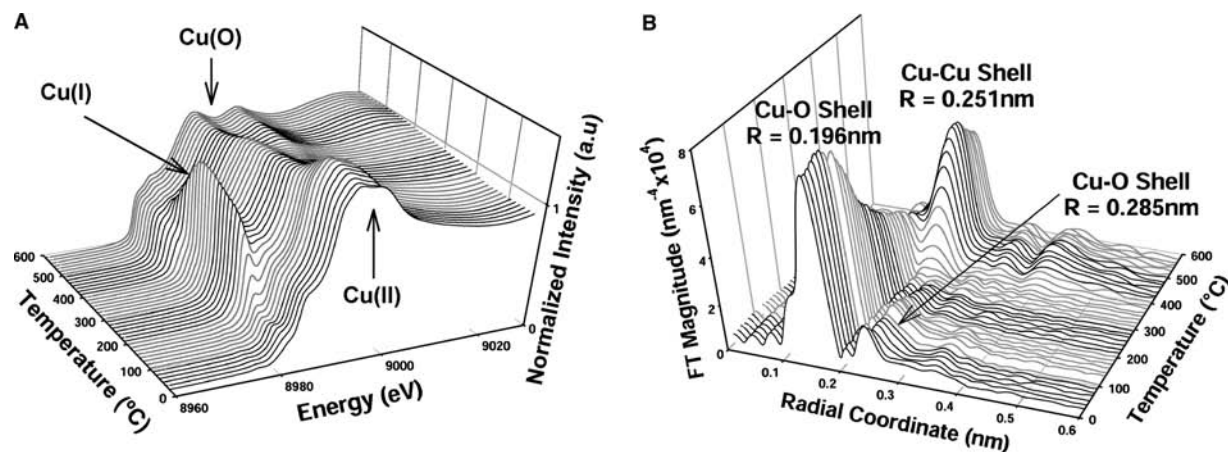


**Fig. 4** Changes in Cu K-edge XANES and EXAFS spectra of Cu-ZSM-5 during temperature-programmed reduction in hydrogen. (A) Plot of XANES edges during the reduction process, showing the strong Cu(I) pre-edge feature ca. 8980 eV that was observed due to a high energy-resolution beamline. (B) The Fourier transform of the EXAFS spectra during the reduction process, along with some of the major features fitted during analysis. *Source:* From Ref.<sup>[59]</sup>.

EXAFS spectroscopy.<sup>[60]</sup> With decreasing amounts of CuO, the onset of reduction decreased from 200°C to 170°C and the Cu (metallic) crystallite size decreased from 21.0 to 4.0 nm. From the XANES spectra, the reduction was observed to proceed from Cu(II) to Cu(I) to Cu(0). Addition of O<sub>2</sub> during reforming led to a mixture of Cu(II) and Cu(I) and loss of catalytic activity. The catalyst compositions and methods of preparation and pretreatment that led to small metallic Cu nanoparticles gave high catalytic activity.

The effect of pretreatment conditions on the nanoparticle size has also been studied by temperature-programmed reduction of Pt(NH<sub>3</sub>)<sub>4</sub><sup>2+</sup> supported on silica.<sup>[61]</sup> Direct reduction in H<sub>2</sub> rapidly occurs at 150–200°C with the formation of moderately small Pt particles, based on a Pt–Pt CN of 8.0 and a hydrogen chemisorption (H/Pt) ratio of 0.89. During H<sub>2</sub> reduction, there is a sharp decrease in the white-line intensity, loss of Pt–N bonds, and the formation of Pt–Pt bonds. H<sub>2</sub> reduction at 400°C leads to larger Pt particles with a CN of 9.5. Thermal treatment in inert gas leads to autoreduction of the Pt(NH<sub>3</sub>)<sub>4</sub><sup>2+</sup> in multiple steps. At about 200°C, there is a loss of Pt–N ligands and a small decrease in the white-line intensity. The white-line intensity continues to decrease until about 300°C, after which the reduction is complete, with a final Pt–Pt CN of 7.8 and H/Pt ratio of 1.09. Thermal treatment at higher temperature did not lead to further growth of the nanoparticles. Calcination of Pt(NH<sub>3</sub>)<sub>4</sub><sup>2+</sup> leads to a gradual change in the white-line intensity over a temperature range from about 150°C to 325°C and a decrease in the Pt–N CN from 5.3 to 4.0. No Pt–Pt bonds are formed in the presence of O<sub>2</sub>. It was concluded that the key to making small metallic particles with uniform particle size distributions involves stable immobile surface species. Clearly, both the phase and particle size of the Pt nanoparticles are influenced by the gas composition and temperature of the pretreatment.

Molybdenum oxide is a key component in many selective oxidation catalysts and is known to form a number of well-defined suboxides whose average valence is between +6 and +4. A combination of the XANES spectra and X-ray diffraction (XRD) analysis was used to study the isothermal and temperature-programmed reduction kinetics of MoO<sub>3</sub>.<sup>[62]</sup> Below 425°C, MoO<sub>3</sub> is reduced to MoO<sub>2</sub> in a single step without the formation of intermediates. At higher temperatures, Mo metal and Mo<sub>4</sub>O<sub>11</sub> were formed in parallel. The average oxidation state was determined from the XANES spectra, while the crystallite size was determined from the XRD. Under the reaction conditions for propene oxidation, Mo<sub>4</sub>O<sub>11</sub> is not formed; thus it is not the catalytic species. In addition, because no other molybdenum oxide phases were observed, it was proposed that oxygen deficiencies on MoO<sub>2</sub> are the catalytic centers.

During pretreatment of NiMo hydrotreating catalysts, it is essential to fully sulfide the metals, produce small particles, and maximize the interaction between Ni and Mo. Temperature-programmed sulfidation of Mo indicates that sulfide formation is a complex series of steps.<sup>[63,64]</sup> Below about 100°C, Mo remains fully oxidized with a Mo–Mo bond and several Mo–O distances. From 100°C to 225°C, there is a loss of the Mo–Mo bond and the longest Mo–O distance, accompanied by the formation of Mo–S bonds. The Mo–Mo distance of 0.28 nm in the initial sulfided species is similar in structure to MoS<sub>3</sub>. In this temperature range, it is likely that Mo=O bonds are unreactive. The transformation of the remaining Mo–O bonds continues up to about 350°C, when the formation of MoS<sub>2</sub> is complete. Because EXAFS is element-specific, the sulfiding of Ni and Mo can be independently studied. For Ni, little sulfiding occurs below about 50°C, but is complete by 140°C. Addition of chelating ligands during preparation retards the onset of Ni sulfidation, but has little effect on Mo. Therefore chelating ligands were added during catalyst synthesis to retard the sulfiding of Ni, which maximizes the interaction of Ni with Mo, leading to higher activity.

## STRUCTURAL CHARACTERIZATION DURING REACTION

While EXAFS has become a standard technique for structural characterization of catalytic nanoparticles, the increased sensitivity of modern synchrotrons and improved analysis methods (software and theoretical standards) has provided an ever-increasing level of detail and understanding of the reactivity of the active site and catalyst promoters. To maximize the data quality and reduce the structural and thermal disorder, EXAFS analysis is often conducted on samples directly after pretreatment or reaction at low temperature. Generally, it is assumed that the structure of the active phase at low temperature is equivalent to that under reaction conditions. For many analytical methods, characterization is not generally possible under realistic reaction conditions, i.e., high temperature, pressure, and flow of reactants. However, with high-energy X-rays, it is possible to conduct EXAFS experiments under these conditions. In several instances, the results of structural analysis under reaction conditions significantly differ from that obtained at lower temperature and pressure and in the absence of a reactant.

### Characterization of the Catalytically Active Site

The structure of CoMoS<sub>2</sub> on alumina hydrotreating catalysts has been extensively studied, and there is

general agreement that the active phase consists of small MoS<sub>2</sub> particles promoted by isolated Co atoms bridge-bonded at the edges of the particles. However, EXAFS analysis of these catalysts under reaction conditions has recently provided further insight about the site of catalytic activity.<sup>[65]</sup> For example, during the reaction with organo-Se compounds at low temperature, ca. 200°C, Se exclusively replaces the terminal Co–S bond. This study is particularly interesting because the EXAFS spectra of the reactant molecule (Se) as well as the catalyst (Co and Mo) were obtained to determine the location of the Se in the catalyst during catalytic conversion. At higher reaction temperatures, e.g., 400°C, Se also replaces the bridging S between Co and Mo. Therefore the active site consists of two types of S sites, which differ in structure and activity.

Similar conclusions about the identity of the reactive Co–S bonds were suggested from a study of the adsorption of O<sub>2</sub> at room temperature and 100°C on CoMoS<sub>2</sub> supported on alumina.<sup>[66]</sup> Adsorption of O<sub>2</sub> leads to the selective replacement of the terminal Co–S bonds. Inspection of the spectra indicates a small change; however, direct analysis of the contribution due to the Co–O bond was not possible as it overlapped with the very large Co–S peak in the EXAFS spectrum (Fig. 5A). However, by analysis of the difference spectrum, i.e., the difference of the EXAFS spectrum of CoMoS<sub>2</sub> before and after O<sub>2</sub> chemisorption, it was possible to fit the peak due to Co–O at about 0.14 nm (Fig. 5B, not phase shift corrected). In addition, in the fit of the difference spectrum, there was a peak due to the loss of one Co–S at a distance of 0.225 nm. This reactive terminal Co–S has a slightly longer distance than the less-reactive, bridge-bonded Co–S (0.218 nm).

Pt, Pd, and Rh are used as catalysts for a large number of industrially important reduction and oxidation reactions. It is well known that when supported on certain materials, reduction of these metals at high temperature leads to a suppression of the H<sub>2</sub> and CO chemisorption capacities. This strong metal-support-interaction (SMSI) effect occurs most often for titania, ceria, and other partially reducible oxide supports. The nature of the SMSI effect has been investigated by EXAFS for Pt on cerium oxide.<sup>[67]</sup> While there was no evidence for the formation of a PtCe alloy, sintering, or decoration of the Pt particles by cerium oxide at any reduction temperature, there were significant differences in both of the Pt L<sub>III</sub> and L<sub>II</sub> edges in the presence and absence of hydrogen. There were additional changes for the catalyst reduced at low (200°C) and high temperature (500°C). Several factors contribute to the difference in the adsorption edges in the presence and absence of hydrogen. At the L<sub>II</sub> edge, the difference is primarily because of the scattering of chemisorbed hydrogen. The scattering from hydrogen occurs only at low photoionization energy; thus it is not observed in the normal EXAFS region. Differences in the Pt–H EXAFS for high- and low-temperature reduction indicate that there is a change in the mode of hydrogen chemisorption as evidenced by changes in the Pt–H bond distances. The changes in chemisorption capacity were thought to be due to electronic changes in the nanoparticles resulting from an interaction with the oxidized and partially reduced support at low and high temperature, respectively.

The effect of chemisorbed hydrogen on the L<sub>II</sub> and L<sub>III</sub> adsorption edges of Pt has been investigated in more detail for Pt on alumina.<sup>[68]</sup> Standard volumetric hydrogen chemisorption experiments indicate that

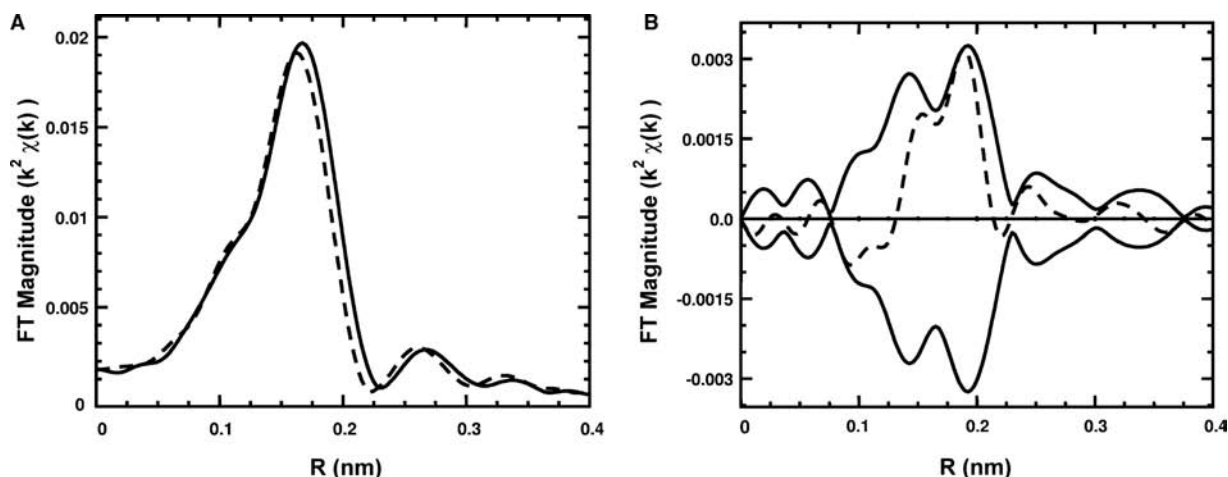


**Fig. 5** Room temperature Co-edge EXAFS of CoMoS<sub>2</sub> on alumina catalyst. (A) Magnitude of the Fourier transform ( $k^2$ -weighted,  $\Delta r = 2.8$ – $11.0$ ). Solid line: catalyst sulfided at 400°C; dotted line: adsorption of O<sub>2</sub> at room temperature on freshly sulfided catalyst. (B) Fourier transform (FT) of the difference spectrum between the CoMo sulfide catalyst with adsorbed O<sub>2</sub> and freshly sulfided catalyst. Solid line: magnitude of FT; dotted line: imaginary part of FT. *Source:* From Ref.<sup>[66]</sup>.

there are two types of adsorbed hydrogen that differ by their desorption temperature. Weakly chemisorbed hydrogen can be desorbed under vacuum at room temperature, while strongly chemisorbed hydrogen is desorbed at about 100°C. The Pt–H bond distances, fit using theoretical references, were 0.189 and 0.194 nm for strongly and weakly chemisorbed hydrogen, respectively. The Pt–H EXAFS spectra indicate that both weakly and strongly adsorbed hydrogen are dissociatively adsorbed.

It is well known that the interaction of a second metal with a metallic supported catalyst results in important changes in the adsorptive properties and catalytic performance. EXAFS spectroscopy is one of the most effective characterization techniques for establishing the formation of bimetallic particles. Addition of Sn as a promoter to Pt/alumina naphtha reforming catalysts significantly reduces the amount of carbon deposits, extending the time between regenerations. Analysis of the EXAFS spectrum for the reduced, bimetallic PtSn catalysts is complex because of an unusual interference between PtSn and Pt particles that coexist on the catalyst.<sup>[69]</sup> In the Fourier transform, two peaks are observed at about 0.215 and 0.275 nm. The shorter distance has previously been proposed to be due to oxidized or chlorided Pt. However, from the XANES spectrum, the white-line intensity precludes the possibility of oxidized Pt. The spectrum was successfully modeled by assuming that there were two types of nanoparticles, Pt and a PtSn alloy. The fraction of metal Pt in each particle was also determined from the experimental coordination numbers. From a multiple shell model fit, the Pt–Pt bond distance in the pure Pt fraction was 0.274 nm, which is similar to the bond distance in other Pt nanoparticles. However, the Pt–Pt distance in the PtSn alloy was significantly shorter (0.263 nm). The Pt–Sn distance was also 0.265 nm.

Bimetallic catalysts are also commonly used to minimize the effects of poisoning; however, the added complexity often makes identification of the active site more difficult.<sup>[70,71]</sup> For example, EXAFS analysis of bimetallic Pt and Pd indicates that alloys are formed.<sup>[72]</sup> As the ratio of Pd increases, the Pt–Pt bond distance in the bimetallic particle decreases from 0.274 nm in pure Pt particles to 0.270 nm in particles with a 3:1 Pd-to-Pt ratio. At the same time, there is little change in the Pd–Pd bond distance at about 0.275 nm. However, for pure Pd catalysts, the Pd–Pd bond distance is increased (0.281 nm), likely because of the formation of Pd hydride. Furthermore, modeling the metal coordination numbers indicates that the nanoparticles are surface-enriched in Pd with a core of Pt. Although much detail about the nanostructure can be obtained by EXAFS, it is unclear whether the enhanced catalytic activity and sulfur tolerance of

the catalysts are because of the stabilization of a metallic surface layer that does not form hydrides, because of a change in the Pd–Pd or Pt–Pd bond distance, or because of a fundamental change in the reactivity of the metals in the bimetallic particles.

### X-Ray Absorption Fine-Structure Spectroscopy under Reaction Conditions (High Temperature and Pressure)

Pd is known to readily form stable palladium hydrides and carbides. While metallic Pd is a highly active hydrogenation catalyst, palladium hydride is inactive. Similarly, palladium carbide leads to a loss in H<sub>2</sub> adsorption capacity and a loss of catalytic activity compared to metallic Pd. The EXAFS spectra obtained for reduced Pd on carbon or alumina exposed to H<sub>2</sub> at 100°C show an increase in the Pd–Pd distance of 2.5%, from 0.275 to 0.282 nm, indicating the formation of palladium hydride.<sup>[73]</sup> The amount of hydrogen dissolved in the Pd metal was approximately half of that in bulk palladium hydride. In 3.5% H<sub>2</sub> and above about 150°C, the palladium hydride decomposed to metallic Pd. Treatment of the Pd nanoparticles in 1% ethylene at 150°C lead to an expansion of the Pd–Pd distance of about 1.2%, which is consistent with the formation of palladium carbide. This study demonstrates that characterization of the catalyst at low temperature may not be equivalent to that of the catalyst under reaction conditions. At reaction conditions, metallic Pd or palladium hydride may be present, depending on the temperature and hydrogen partial pressure. In addition, palladium carbides may be formed quickly or after longer reaction times. It is likely that the structure of the catalyst at steady state is different from that after pretreatment.

For many catalysts, there is an initial period just after the catalyst is brought on-line where the activity rapidly changes. During this period, the pretreated catalyst is converted to its steady state activity and structure. Recently, a new catalyst containing both Mo and acidic zeolites such as H-ZSM-5 has been reported for the non-oxidative conversion of methane to benzene.<sup>[74,75]</sup> Mo is added as ammonium heptamolybdate, followed by calcination or thermal activation at temperatures up to 700°C. Heating the ammonium heptamolybdate indicates a spreading of the Mo oxide species, likely into the pores of the zeolite. Structural characterization suggests that the oxidized Mo species are similar to Mo<sub>2</sub>O<sub>7</sub><sup>2-</sup>, with a Mo–O coordination number of 4 at distances from 0.169 to 0.184 nm and a Mo–Mo coordination number of 1 at a distance of 0.370 nm. However, under reaction conditions (e.g., conversion of methane to benzene at 700°C), the molybdenum oxide is converted to isolated molybdenum



carbide particles within the zeolite pores. The Mo–Mo and Mo–C coordination numbers were 0.1 and 3.2, respectively. The Mo–C bond distance of 0.209 nm is consistent with molybdenum carbides, and is significantly longer than that for molybdenum oxides. The EXAFS and XANES spectra clearly indicate that the active catalytic phase is formed by reaction of methane at high temperature.

Rh supported on alumina, vanadia, and other supports is highly active for conversion of synthesis gas (CO plus H<sub>2</sub>) to methanol. Addition of RhCl<sub>3</sub>·xH<sub>2</sub>O to Al<sub>2</sub>O<sub>3</sub> followed by reduction at 400°C gives 1.0-nm metallic nanoparticles, or particles with about 10 Rh atoms per particle.<sup>[76]</sup> These catalysts produce methanol, higher alcohols, and hydrocarbons at pressures from 5 to 30 bar using a 1:1 H<sub>2</sub>-to-CO syngas ratio at 250°C. Analysis by EXAFS of the Rh particles exposed to CO at room temperature indicates that the small metallic particles are converted to Rh(CO)<sub>2</sub>Cl<sub>2</sub>. By contrast, at 250°C and 1 bar of syngas, the Rh particles are present as small metallic particles, and thus are responsible for the catalytic activity.

The low-temperature dissociation of small Rh particles in the presence of CO also appears to require the presence of Cl.<sup>[77]</sup> When similar Rh nanoparticles were prepared from rhodium nitrate, the metal particles were stable in CO. Thus not only can the reaction conditions, gases, temperature, pressure, etc. influence the phase present on the catalyst, but the presence of other trace elements, such as Cl, can also have a dramatic effect on the structure. Even in the absence of Cl, EXAFS has shown that small metallic Ru<sup>[78]</sup> and Pt<sup>[79]</sup> particles may be converted into metal carbonyl clusters at low temperature, while large metallic particles only chemisorb CO.

Catalytic-transition metal nanoparticles with multiple stable oxidations are among the most structurally complex materials; they are difficult to characterize. The factors affecting catalytic activity and selectivity are often poorly understood. In addition, the number of active sites often changes depending on the reaction temperature and gas composition. Under realistic reaction conditions, EXAFS and XANES spectra often provide the most reliable insight into the active state of the working catalyst. Propane can be partially oxidized over Ag, Cd, and Fe molybdenum phosphates to propylene and acrolein.<sup>[80]</sup> Analysis of the XANES spectra of AgMo<sub>3</sub>P<sub>2</sub>O<sub>14</sub>, at reaction temperatures between 300°C and 460°C (propane/O<sub>2</sub>/N<sub>2</sub> of 60:20:20), indicate that the average oxidation state of Mo decreases from 5.66 in the pretreated catalyst to 5.25. For CdMo<sub>3</sub>P<sub>2</sub>O<sub>14</sub>, the Mo oxidation state increases under reaction conditions; however, the average oxidation state is very similar to that in silver molybdenum phosphate, i.e., 5.25. Although the

reaction environment results in a change in the average oxidation state, there is little change in the Mo–O and Mo–Mo coordination numbers or bond distances. Incorporation of Fe, even in small amounts, leads to a loss of catalytic activity. In all Fe-containing cadmium molybdenum phosphate catalysts, only Mo(V) ions are present. It is concluded that selective partial oxidation catalysts require both Mo(V) and Mo(VI) ions in about a 2:1 ratio. Propane is thought to be activated on the Mo(V) ion and then react with the oxygen ion located on the Mo(VI) site, which is regenerated by oxygen.

An EXAFS study of a rhodium-on-alumina catalyst for partial oxidation of methane to produce syngas demonstrates that the structure of the catalyst under reaction conditions can be very different from that of the used catalyst at low temperature.<sup>[81]</sup> Reduction of Rh<sub>4</sub>(CO)<sub>12</sub> on alumina at 500°C leads to 6.0-nm Rh particles, as indicated by a Rh–Rh CN of 10.3 at 0.269 nm. At temperatures below the ignition temperature of about 330°C, the large metallic particles are oxidized. The resulting structure is similar to that of the metal particles in O<sub>2</sub> at the same temperature. Above 330°C in 6%CH<sub>4</sub>/3%O<sub>2</sub>/He, the partial oxidation of methane was accompanied by reduction of oxidized Rh particles with the formation of smaller metallic particles. Upon cooling to room temperature in the reaction mixture, large metallic Rh particles are again formed. In this study, the reaction products were simultaneously monitored with the EXAFS data collection; thus the state of the active surface could be clearly identified and was only present under the reaction conditions.

Pt and Rh three-way autoexhaust catalysts also undergo changes in structure with the composition of the reaction gases.<sup>[82,83]</sup> During the catalytic cycle, the gas composition alternates between reducing and oxidizing. Exposure of the pretreated catalyst, which contained fully oxidized Pt and Rh, to a reducing gas mixture at 250°C led to the partial reduction of Pt (6.8 Pt–Pt at 0.272 nm and 1.3 Pt–O at 0.199 nm), but Rh remained fully oxidized (6.5 Rh–O at 0.203 nm). At 350°C, Pt was fully reduced (11.0 Pt–Pt and 1.0 Pt–Rh at 0.265 nm), while Rh was partially reduced (6.5 Rh–Rh at 0.270 nm, Rh–Pt at 0.266 nm, 2.7 Rh–O at 0.199 nm, and 1.1 Rh–O at 0.219 nm). Analysis of both the Pt and Rh edges indicates the partial formation of bimetallic particles at 350°C. Under oxidizing conditions, Pt is difficult to oxidize and remains largely reduced, while Rh is readily oxidized. However, oxidation of Rh did not affect the oxidation activity of Pt.

Ion-exchange of H-ZSM-5 with an aqueous-ammonia solution of Cu(NH<sub>3</sub>)<sub>4</sub><sup>2+</sup> leads to incorporation of an amount of Cu in excess of the ion-exchange capacity, which is active for the decomposition of NO into

$N_2+O_2$ .<sup>[84,85]</sup> After calcination at 500°C, the XANES spectrum indicates that Cu(II) is present with a Cu–O coordination number of 3.7. By contrast, pretreatment in He at 500°C leads to the autoreduction of about 70% of the Cu(II) to Cu(I). In the presence of  $O_2$ , Cu(I) is readily oxidized to Cu(II). Under steady state reaction conditions of NO decomposition, the XANES spectra indicate that about 25% of the Cu/ZSM-5 is reduced to Cu(I). The catalytic activity is strongly influenced by the temperature and correlated with the amount of Cu(I) present in the catalyst. Thus the number of catalytic sites depends on the reaction temperature and  $O_2$  concentration, which is dependent on the NO conversion.

Cu(I) was also identified as the active species in Cu/ZSM-5 during reduction of  $NO_x$  by CO.<sup>[86]</sup> As previously observed,<sup>[84,85]</sup> pretreatment of the catalyst in He leads to the autoreduction of about 70% of the divalent Cu to Cu(I). Under the reducing reaction conditions, one CO molecule chemisorbs on each Cu(I) site at a Cu–C bond distance of 0.189 nm. However, with increasing temperature, the surface CO coverage decreases. Therefore two factors determine the catalytic activity. The rate increases with increasing temperature because of the activation energy, but decreases at higher temperature because of the lower CO surface coverage. Therefore the number of catalytic sites and activities are a strong function of the reaction temperature and CO concentration.

A catalytically active copper species that is selective for partial oxidation of methanol to formaldehyde has been determined by a new surface-sensitive, in situ X-ray absorption technique. In situ, time-resolved EXAFS analysis at the Cu K-edge of polycrystalline and reduced supported Cu catalysts indicates that at temperatures from 300°C to 400°C and in a flow of air–methanol (1:2 ratio), the metal phase does not change, i.e., no copper oxides were detected.<sup>[87]</sup> By contrast, exposure of the catalysts to air results in the loss of the Cu–Cu peak at about 0.22 nm (not phase-corrected) and the simultaneous formation of the Cu–O peak at 0.19 nm due to bulk  $Cu_2O$ . The transformation of metallic copper to  $Cu_2O$  occurs in about 5 min at 400°C.  $Cu_2O$  is further converted to CuO after an additional 10 min in air at 400°C. X-ray absorption near-edge spectroscopy analysis of these catalysts at the O K-edge or Cu  $L_{III,II}$  edge are normally performed in ultrahigh vacuum.<sup>[36,88]</sup> However, under vacuum, metallic copper is primarily converted to  $Cu_2O$ , which is active for total oxidation of methanol to  $CO_2$ . On the other hand, XANES analysis of the Cu  $L_{III,II}$  edges at 400°C and 0.1 mbar of methanol–air indicates no oxidation of the metallic Cu, results that are in agreement with that obtained in situ at the Cu K edge. However, at the O K-edge, the XANES spectrum is different from those of bulk copper oxides, suggesting that the catalytically active site corresponds to metallic

Cu with a surface film of atomic oxygen. This copper suboxide phase could only be observed at the reaction temperature and under pressure. The XANES spectra obtained after cooling to room temperature were characteristic of that for  $Cu_2O$ . Similar evidence for a catalytic silver suboxide phase has also been reported from the surface-sensitive in situ XANES spectra.<sup>[88]</sup>

While the nature of the nanoparticle surface in oxidation catalysts is often strongly influenced by the reaction conditions, structural changes in metallic nanoparticles may also occur under reducing conditions. In small metal particles, the motion of the surface atoms is more anharmonic than that of the bulk atoms. Therefore as the size of the particles gets smaller, the fraction of surface atoms increases and the EXAFS pair distribution function gets increasingly asymmetric.<sup>[89]</sup> For a Cu/ZnO/ $Al_2O_3$  methanol synthesis catalyst, as the reacting gas composition ( $CO$ ,  $CO_2$ ,  $H_2$ , and  $H_2O$ ) changes, the catalytic activity also changes. In addition, under similar reaction conditions, there are changes in the Cu–Cu coordination number from about 6.8 to 9.5. By analysis of the non-Gaussian pair distribution function, it was concluded that the metallic Cu particles are spherical in the presence of water, while the particles are disk-like under dry conditions. Because of the differences in particle morphology, the number of active sites is not the same under the different gas compositions. Correcting the kinetic rates by the number of surface atoms gave nearly identical turnover rates. Failure to account for the non-Gaussian pair distribution in the EXAFS analysis of small metal particles leads to an underestimation of the particle size from the coordination numbers.<sup>[90]</sup>

## CATALYST DEACTIVATION AND REGENERATION

Ideally, catalysts do not change or participate in the reactions they catalyze. However, nearly every catalyst suffers some form of deactivation that must be accounted for in the design of a commercial process. For metallic nanoparticles, sintering and poisoning of the surface are the primary modes of deactivation. In addition, for many catalysts, carbon deposition, or coking, of the surface blocks active sites and lowers the activity. For some catalysts, deactivation may be reversible and the active state may be regenerated by additional treatment, typically through high-temperature oxidation and rereduction. However, for other catalysts, deactivation may be irreversible, motivating researchers to modify the catalyst composition to minimize these deleterious effects. Analysis by the EXAFS and XANES methods are often informative in understanding the structural changes

that accompany deactivation and have led to development of improved regeneration procedures or deactivation-resistant catalysts.

### Deactivation by Poisoning

Trace levels of sulfur in the reaction stream can easily and irreversibly poison the activity of metallic platinum catalysts. After an initial reduction, Pt supported on  $\text{Al}_2\text{O}_3$  was found to exist mostly as metallic nanosize Pt particles.<sup>[91,92]</sup> Upon exposure to  $\text{H}_2\text{S}$  at  $450^\circ\text{C}$ , the platinum particles were disrupted, and only Pt–S coordination (CN = 2.8) was observed. Although some metallic character was present after high-temperature reduction in  $\text{H}_2$ , the Pt–S coordination remained largely unchanged, indicating the irreversibility of the sulfur poisoning. However, when Pt was alloyed with Re, the Pt–S CN was 2.0 after  $\text{H}_2\text{S}$  treatment, and further decreased to 1.0 after rereduction. In addition, there was only minimal change in the metallic coordinations of Pt–Pt and Pt–Re. Alloy formation with Re and other metals helps to stabilize the metallic Pt phase and minimizes the amount of surface-adsorbed S.

Sulfur poisoning of Pt can also accelerate the formation of coke on the metallic particles. Pt nanoparticles on both alkaline and acidic LTL (Linde Type L) zeolite are active for the hydrogenolysis and isomerization of neopentane. Sulfur poisoning blocks active sites and leads to a loss of about 90–95% of the S-free activity.<sup>[93]</sup> With poisoned catalysts, Pt–S bonds are formed on the surface of each particle. While the sulfur coverage was found to be only slightly higher on alkaline-supported Pt nanoparticles, coke deactivation was very rapid, whereas on acidic supports deactivation was low. It is suggested the higher S surface coverage of Pt in alkaline LTL leads to nearly isolated sites, which rapidly deposit coke.

Platinum is also the active component in many fuel cells, and is easily poisoned by trace quantities of CO in the  $\text{H}_2$  fuel. Cyclic voltammetry studies of a Pt/C electrode exposed to  $\text{CO}$ <sup>[94]</sup> were carried out using in situ EXAFS analysis. CO readily adsorbed on the small metallic Pt particles with nearly full surface coverage blocking the adsorption of  $\text{H}_2$ , thus altering the effectiveness of the electrode. CO can be oxidized at higher oxidation potential and before the irreversible oxidation of Pt. The addition of a second electro-negative metal can beneficially alter the absorption properties of CO on Pt and minimize the effect of CO poisoning. The effect of CO poisoning on the performance of two Pt–Ru/C fuel cell electrodes was dependent on the composition of the nanoparticles.<sup>[95]</sup> For one electrode wherein the Pt and Ru were present as separate phases, as elucidated by EXAFS, there was

no significant advantage of the second metal. However, for the electrode with small Pt–Ru alloy clusters, there was a significant improvement in the electrochemical performance in the presence of low concentrations of CO, emphasizing the importance of nanostructure on catalytic performance.

### Deactivation by Sintering

Many metals are prone to sintering at high reaction temperatures. Several previous examples showed the sintering of metal particles under calcination or other pretreatment steps, but very few studies have actually looked at the sintering of a catalyst during the course of reaction. The deactivation of Cu/ZnO during the reaction of NO and CO was monitored with EXAFS and XANES analysis with time on stream.<sup>[96]</sup> Initially, the activity of the catalyst at  $250^\circ\text{C}$  quickly dropped, but continued to slowly decline after about 2 hr. The analysis showed that the surface initially consists of a highly dispersed Cu(II) phase interacting with the support. After an hour, the Cu was still highly dispersed, but had been reduced to a Cu(I), based on the change in pre-edge XANES features and Cu–O coordination distance. After 5 hr, the Cu–O coordination had changed, and new Cu–Cu coordination was observed that was consistent with the formation of small Cu particles. These particles continued to grow slightly with additional time on stream, which was indicative of sintering. However, upon high-temperature treatment in  $\text{O}_2$  or NO, the catalyst was regenerated to the original Cu(II) structure. The reversible reduction and sintering of the isolated copper species was determined to be the primary cause of deactivation.

### Deactivation by Coking

Platinum catalysts used for a variety of hydrocarbon conversions are easily coked. As with poisoning, alloy formation can improve coke resistance. In situ EXAFS data were collected for Pt/ $\text{Al}_2\text{O}_3$ , Pt–Re/ $\text{Al}_2\text{O}_3$ , and Pt–Sn/ $\text{Al}_2\text{O}_3$  during hydrogen reduction and heptane conversion.<sup>[97]</sup> For Pt/ $\text{Al}_2\text{O}_3$ , the reduced Pt existed primarily as small metallic clusters with Pt–Pt coordination of 5.0. During heptane conversion at  $500^\circ\text{C}$ , the Pt–Pt coordination dropped to 4.4 and a significant Pt–C contribution was observed, which was attributed to the formation of coke. On the other hand, the reduced Pt–Re/ $\text{Al}_2\text{O}_3$  system was primarily composed of small Pt–Re alloy particles. Under identical reaction conditions, these nanoparticles did not undergo any structural changes nor indicate the formation of Pt–C bonds. Similar observations were made with the Pt–Sn catalysts. The addition of Re or Sn to Pt appears to lower the adsorption strength of the hydrocarbon

species that eventually leads to coke formation. A similar analysis was also made for Ni/C and Au–Ni/C catalysts used for steam reforming.<sup>[98]</sup> While Ni alone is quickly deactivated as a result of graphite formation, addition of Au and formation of an alloy showed no appreciable deactivation due to the formation of graphite. For Ni, the formation of graphite is thought to require several adjacent Ni atoms. In the alloy, inactive Au atoms isolate surface Ni atoms.

### Regeneration and Deactivation/Regeneration Cycles

While long-term investigations of the effects of regeneration and cyclic operations with EXAFS are impractical, the state of the catalytic metals under similar conditions can be simulated. For example, Pt/Al<sub>2</sub>O<sub>3</sub> and Pt–Sn/Al<sub>2</sub>O<sub>3</sub> catalysts were treated to several redox cycles while being monitored by in situ EXAFS.<sup>[97]</sup> The fresh Pt/Al<sub>2</sub>O<sub>3</sub> prior to any reduction shows a Pt–O coordination of 6.0, indicating isolated Pt species on the support. After two and four redox cycles, the Pt–O coordination dropped to 4.0 and 3.0, respectively. Moreover, increasing Pt–Pt coordination (after rereduction) was observed, suggesting that repeated cycling caused the Pt particles to sinter. Alternatively, Pt–Sn showed no change in the Pt–O coordination of 6.0 after four cycles, suggesting that Sn was stabilizing the isolated Pt species during regeneration treatment and would help to maintain the catalyst's activity for many more regeneration cycles.

### FUTURE PROSPECTS

In addition to the standard structural and electronic information currently extracted from the EXAFS and XANES spectra, it is likely that future developments will provide more detailed structural information including three-dimensional geometric data on nanoparticle morphology and how the morphology changes upon chemisorption of reactants. In general, the large single-scattering contributions in the EXAFS spectra are used for determination of local structure. However, multiple scattering contributions can provide information about the bond angle of the scattering pair. Small changes in the multiple scattering contributions to the Fourier transform were shown to correlate with changes in the tetrahedral geometry of the zincate ion, i.e., Zn(OH)<sub>4</sub><sup>1-</sup>, in an alkaline battery as a result of hydrogen bonding with the cation.<sup>[99]</sup> While, currently, multiple scattering peaks are seldom analyzed, development of reliable methods for interpreting these peaks could provide crucial information about small

changes in the geometry of the active site and the resulting changes upon interaction with adsorbates.

Good progress has also already been made with respect to the geometry of nanoparticles supported on single crystals.<sup>[55,100–106]</sup> For example, analysis of the fluorescence spectra at different orientations of the X-ray beam relative to the support surface has shown that when Mo(CO)<sub>6</sub> on TiO<sub>2</sub> is reduced, the orientation of the metallic Mo–Mo bonds is parallel to the (001) direction.<sup>[106]</sup> On the other hand, calcination of ammonium heptamolybdate on TiO<sub>2</sub> gives molybdenum oxide dimers with Mo–Mo bonds perpendicular to the (001) direction. The effect of the support on the orientation of the nanoparticles to the surface and its effect on catalytic activity are poorly understood, and detailed characterization of particle morphology may provide new insights into the influence of the support on the function of catalysts.

Because chemical transformations occur at the surface of nanoparticles and small changes in the energy of the valence orbitals of these reaction centers can have a significant effect on the catalytic performance, techniques that can provide a better understanding of these properties are also likely to be developed in the coming years. Recently, two new XAFS techniques, which demonstrate that electronic changes parallel changes in catalytic performance, have been applied to metallic Pt nanoparticles on heterogeneous catalysts. Adsorption of hydrogen leads to the formation of a Pt–H bond and an empty antibonding orbital near the Fermi level. Taking the double difference in the Pt L<sub>III</sub> and L<sub>II</sub> edges in the presence and absence of chemisorbed hydrogen can isolate this shape resonance in the near-edge region of the spectrum.<sup>[107–115]</sup> Fitting the shape resonance with a Fano line shape indicates that the energy of the Pt–H antibonding orbital shifts to lower ionization potential as the alkalinity of the support increases, which is consistent with data obtained from more established techniques, like X-ray photoelectron spectroscopy and infrared spectroscopy of adsorbed CO.<sup>[110,111,113]</sup> Shape resonance analysis has also been applied to the Pt electrodes for fuel cell applications in H<sub>2</sub>SO<sub>4</sub> and HClO<sub>4</sub> to determine the surface species with different applied voltage. From 0 to 0.54 V, Pt–H bonds dominate the surface, while at higher voltages, Pt–O species are present.<sup>[114,115]</sup>

A second XAFS technique provides information on important electronic changes in metallic particles resulting from alloy formation, the metal–support interaction, or changes in applied voltage on electrodes. This atomic XAFS, or AXAFS, can be obtained from scattered photoelectrons involving the electrons at the periphery of the absorbing atom<sup>[116–121]</sup> and can be observed in the low R peaks (<0.15 nm) in the Fourier transform. Changes in the Pt potential experienced by the charge on the oxygen ions from

the support result in a shift in the intensity and position of the XAFS peak.<sup>[108,120,121]</sup> It is expected that further development of these latter two techniques will be applied to other elements and used in a number of other applications related to properties of nanoparticles in catalysis and electrocatalysis.

## CONCLUSION

The rapid increase in the number of XAFS papers applied to the characterization of heterogeneous supported catalytic nanoparticles is a testament to the increasing availability of synchrotrons, improved data quality, and user-friendly software. The number and availability of new synchrotrons is expected to continue to increase within the next 10 years. In addition, data quality continues to improve and data acquisition time continues to decrease. Spectra that once took several hours to collect can now be obtained within a few minutes. At the same time, commercial software is now readily available for data analysis and calculation of theoretical standards.

In some cases, XAFS may be the only technique available to obtain structural information on heterogeneous catalyst systems, while the newer in situ techniques have proven to be extremely useful at examining catalysts under typical working conditions (T, P, SV, etc.) and are providing unprecedented looks at the mechanisms of catalytic reactions. These tools will provide stronger links between catalyst testing at pilot plant stage and the fundamental of the catalysts. This should lead to a much greater fundamental understanding of nanophase catalysts as well as improved catalyst activity and selectivity.

## REFERENCES

1. Fernández-García, M. XANES analysis of catalytic systems under reaction conditions. *Catal. Rev.* **2002**, *44* (1), 59.
2. Koningsberger, D.C.; Prins, R. *Chemical Analysis, Vol. 91: X-Ray Absorption: Principles, Applications, Techniques of EXAFS SEXAFS, and XANES*; John Wiley & Sons: New York, 1988.
3. Teo, B.K.; Joy, D.C. *EXAFS [Extended X-Ray Absorption Fine Structure] Spectroscopy: Techniques and Applications*; Plenum Press: New York, 1981.
4. Lee, P.A.; Citrin, P.H.; Eisenberger, P.; Kincaid, B.M. Extended X-ray absorption fine structure—its strengths and limitations as a structural tool. *Rev. Mod. Phys.* **1981**, *53* (4 Pt. 1), 769.
5. Fay, M.J.; Proctor, A.; Hoffmann, D.P.; Hercules, D.M. Unraveling EXAFS spectroscopy. *Anal. Chem.* **1988**, *60* (21), 1225.

6. Fornasini, P. EXAFS: A powerful probe of local structure in disordered materials. *Chim. Ind. (Milan)* **2000**, *82* (2), 177.
7. Moraweck, B. *X-Ray Absorption Spectroscopy: EXAFS and XANES*; Catal. Charact.; Imelik, B., Vedrine, J.C., Eds.; Plenum Press: New York, 1994; 377 pp.
8. Malinowski, E.R. *Factor Analysis in Chemistry*, 2nd Ed.; John Wiley & Sons: New York, 1991.
9. <http://www.esrf.fr/navigate/synchrotrons.htm> (accessed June 2002).
10. Vaughan, D. *X-Ray Data Booklet*, 2nd Ed.; Lawrence Berkeley Laboratory: Berkeley, CA, 1986.
11. Koster, A.S.; Mendel, H. X-Ray K $\beta$  emission spectra and energy levels of compounds of 3d-transition metals—I: oxides. *J. Phys. Chem. Solids* **1970**, *31*, 2511.
12. Koster, A.S.; Mendel, H. X-Ray K $\beta$  emission spectra and energy levels of compounds of 3d-transition metals—II: non-oxide compounds. *J. Phys. Chem. Solids* **1970**, *31*, 2523.
13. Butorin, S.M.; Gue, J.-H.; Magnuson, M.; Kuiper, P.; Nordgren, J. Low-energy *d-d* excitations in MnO studied by resonant fluorescence spectroscopy. *Phys. Rev., B* **1996**, *54*, 4405.
14. Wang, X.; Grush, M.M.; Froeschner, A.G.; Cramer, S.P. High-resolution X-ray fluorescence and excitation spectroscopy of metalloproteins. *J. Synchrotron Radiat.* **1997**, *4*, 236.
15. Peng, G.; Wang, X.; Randall, C.R.; Moore, J.A.; Cramer, S.P. Spin-selective X-ray absorption spectroscopy: demonstration using high-resolution Fe K $\beta$  fluorescence. *Appl. Phys. Lett.* **1994**, *65*, 2527.
16. Iwasawa, Y. *X-Ray Absorption Fine Structure for Catalysis and Surfaces*; World Scientific: Singapore, 1996.
17. Vlaic, G.; Andreatta, D.; Colavita, P.E. Characterization of heterogeneous catalysts by EXAFS. *Catal. Today* **1998**, *41* (1–3), 261.
18. Conesa, J.C.; Esteban, P.; Dexpert, H.; Bazin, D. Characterization of catalyst structures by extended X-ray absorption spectroscopy. *Stud. Surf. Sci. Catal.* **1990**, *57*, A225 (Spectrosc. Charact. Heterog. Catal., Pt. A).
19. Iwasawa, Y. Applications of X-ray absorption fine structure to catalysts and model surfaces. *J. Phys., IV* **1997**, *7*, 67 (C2, X-Ray Absorption Fine Structure, Vol. 1).
20. Koningsberger, D.C.; Mojet, B.L. XAFS spectroscopy: fundamental principles and data analysis. *Top. Catal.* **2000**, *10*, 143.
21. Chao, K.J.; Wei, A.C. Characterization of heterogeneous catalysts by X-ray absorption spectroscopy. *J. Electron Spectrosc. Relat. Phenom.* **2001**, *119* (2–3), 175.
22. Meitzner, G. Experimental aspects of X-ray absorption spectroscopy. *Catal. Today* **1998**, *39* (4), 281.
23. Johnston, P.; Wells, P.B. EXAFS Spectroscopy of supported metal catalysts. *Radiat. Phys. Chem.* **1995**, *45* (3), 393.
24. Izumi, Y. X-ray absorption fine structure spectroscopy as a probe of chemical state of catalysts. *Trends Inorg. Chem.* **1998**, *5*, 43.

25. Bertagnolli, H.; Ertel, T.S. X-ray absorption spectroscopy of amorphous solids, liquids, and catalytic and biochemical systems: capabilities and limitations. *Angew. Chem.* **1994**, *106* (1), 15.
26. Bazin, D.; Dexpert, H.; Lynch, J. In situ XAFS measurement of catalysts. *Ser. Synchrotron Radiat. Tech. Appl.* **1996**, *2*, 113(X-Ray Absorption Fine Structure for Catalysts and Surfaces).
27. Odzak, J.F.; Argo, A.M.; Lai, F.S.; Gates, B.C.; Pandya, K.; Feraria, L. A flow-through X-ray absorption spectroscopy cell for characterization of powder catalysts in the working state. *Rev. Sci. Instrum.* **2001**, *72* (10), 3943.
28. Schneider, S.; Bazin, D.; Dubuisson, J.M.; Ribbens, M.; Sonnevile, H.; Meunier, G.; Garin, F.; Maire, G.; Dexpert, H. Development of a reactive cell for EXAFS in situ studies of automotive postcombustion catalytic converters. *J. X-Ray Sci. Technol.* **2000**, *8* (4), 221.
29. Shannon, I.J.; Maschmeyer, T.; Sankar, G.; Thomas, J.M.; Oldroyd, R.D.; Sheehy, M.; Madill, D.; Waller, A.M.; Townsend, R.P. A new cell for the collection of combined EXAFS/XRD data in situ during solid/liquid catalytic reactions. *Catal. Lett.* **1997**, *44* (1,2), 23.
30. Pinxt, H.H.C.M.; Kuster, B.F.M.; Koningsberger, D.C.; Marin, G.B. Online characterization by EXAFS of tin promoted platinum graphite catalysts in the aqueous phase. *Catal. Today* **1998**, *39* (4), 351.
31. Pettiti, I.; Gazzoli, D.; Inversi, M.; Valigi, M.; De Rossi, S.; Ferraris, G.; Porta, P.; Colonna, S. Cell for the in situ study of heterogeneous catalysts by transmission and fluorescence XAS spectroscopy. *J. Synchrotron Radiat.* **1999**, *6* (6), 1120.
32. Kampers, F.W.H.; Maas, T.M.J.; van Grondelle, J.; Brinkgreve, P.; Koningsberger, D.C. An in-situ cell for transmission EXAFS measurements on catalytic samples. *Rev. Sci. Instrum.* **1989**, *60* (8), 2635.
33. Neils, T.L.; Burlitch, J.M. High-pressure reaction chamber for in situ EXAFS spectroscopy of catalysts. *J. Catal.* **1989**, *118* (1), 79.
34. van Bokhoven, J.A.; van Der Eerden, A.M.J.; Smith, A.D.; Koningsberger, D.C. Design and construction on an in situ cell for catalytic studies on elements with  $12 < Z < 20$ . *J. Synchrotron Radiat.* **1999**, *6* (3), 201.
35. van der Eerden, A.M.J.; van Bokhoven, J.A.; Smith, A.D.; Koningsberger, D.C. Apparatus for in situ X-ray absorption fine structure studies on catalytic systems in the energy range  $1000 \text{ eV} < E < 3500 \text{ eV}$ . *Rev. Sci. Instrum.* **2000**, *71* (9), 3260.
36. Havecker, M.; Knop-Gericke, A.; Schedel-Niedrig, T. High-pressure soft X-ray absorption spectroscopy: application of a new in situ spectroscopic method in catalysis research. *Appl. Surf. Sci.* **1999**, *142*, 438.
37. Spieker, W.A.; Liu, J.; Miller, J.T.; Kropf, A.J.; Regalbuto, J.R. An EXAFS study of the coordination chemistry of hydrogen hexachloroplatinate(IV): Speciation in aqueous solution. *Appl. Catal. A: Gen.* **2002**, *232*, 219.
38. Spieker, W.A.; Liu, J.; Hao, X.; Miller, J.T.; Kropf, A.J.; Regalbuto, J.R. An EXAFS study of the coordination chemistry of hydrogen hexachloroplatinate(IV) 2. Speciation of complexes adsorbed onto alumina. *Applied Catalysis, A: General* **2003**, *243* (1), 53–66.
39. Regalbuto, J.R.; Schrier, M.; Hao, X.; Spieker, W.A.; Kim, J.G.; Miller, J.T.; Kropf, A.J. Toward a molecular understanding of noble metal catalyst impregnation. *Studies in Surface Science and Catalysis (Scientific Bases for the Preparation of Heterogenous Catalysts VIII)* **2002**, *143*, 45–53.
40. Yang, J.C.; Shul, Y.G.; Loius, C.; Che, M. In situ EXAFS study of the nucleation and crystal growth of Ni particles on  $\text{SiO}_2$  support. *Catal. Today* **1998**, *44*, 315.
41. Weckhuysen, B.M.; Schoonheydt, R.A.; Jehng, J.-M.; Wachs, I.E.; Cho, S.J.; Ryoo, R.; Kijlstra, S.; Poels, E. Combined DRS–RS–EXAFS–XANES–TPR study of supported chromium catalysts. *J. Chem. Soc., Faraday Trans.* **1995**, *91* (8), 3245.
42. Pirault, L.; Guerin, M.; Maire, F.; Marecot, P.; Barbier, J. Catalytic activity and EXAFS characterization of three-way automotive Pt–Rh/alumina–ceria catalysts from different preparations. *Appl. Catal. A: Gen.* **1998**, *172*, 249.
43. Asakura, K.; Iwasawa, Y. Supported multimetal sites. *Ser. Synchrotron Radiat. Tech. Appl.* **1996**, *2*, (X-ray Absorption Fine Structure for Catalysts and Surfaces), 216.
44. Alexeev, O.S.; Kim, D.-O.; Gates, B.C. Partially decarbonylated tetrairidium clusters on MgO: structural characterization and catalysis of toluene hydrogenation. *J. Mol. Catal. A: Chem.* **2000**, *162*, 67.
45. Goellner, J.F.; Guzman, J.; Gates, B.C. Synthesis and structure of tetrairidium clusters on  $\text{TiO}_2$  powder: characterization by infrared and extended x-ray absorption fine structure spectroscopies. *J. Phys. Chem., B* **2002**, *106*, 1229.
46. Goellner, J.F.; Gates, B.C. Synthesis and characterization of site-isolated hexarhodium clusters on titania powder. *J. Phys. Chem., B* **2001**, *105*, 3269.
47. Enderle, B.; Labouriau, A.; Ott, K.C.; Gates, B.C. Osmium carbonyls in zeolite NaX: Characterization by  $^{129}\text{Xe}$  NMR and extended x-ray absorption fine structure spectroscopies. *J. Phys. Chem., B* **2002**, *106*, 2109.
48. Yamamoto, Y.; Matsuzaki, T.; Ohdan, K.; Okamoto, Y. Structure and electronic state of  $\text{PdCl}_2\text{–CuCl}_2$  catalysts supported on activated carbon. *J. Catal.* **1996**, *161*, 577.
49. Koningsberger, D.C.; Gates, B.C. Nature of the metal–support interface in supported metal catalysts: results from X-ray absorption spectroscopy. *Catal. Lett.* **1992**, *14*, 271.
50. van Zon, F.B.M.; Visser, G.; Koningsberger, D.C. *Study of the Metal-Support Interface in a  $\gamma\text{-Al}_2\text{O}_3$  Supported Reduced  $\text{Ir}_4(\text{CO})_{12}$  Catalytic System by Extended X-Ray Absorption Fine Structure (EXAFS)*, Proceedings of the 9th International Congress on Catalysis, Calgary, Canada, June, 1988; Phillips, M.J., Ternan, M., Eds.; Chemical Institute of Canada: Ottawa, 1988, 1386.
51. van Zon, F.B.M.; Maloney, S.D.; Gates, B.C.; Koningsberger, D.C. Structure and nature of the metal-support interface: Characterization of iridium



- clusters on magnesium oxide by extended x-ray absorption fine structure spectroscopy. *J. Am. Chem. Soc.* **1993**, *115*, 1993.
52. Vaarkamp, M.; Miller, J.T.; Modica, F.S.; Koningsberger, D.C. On the relation between particle morphology, structure of the metal-support interface and catalytic properties of Pt/ $\gamma$ -Al<sub>2</sub>O<sub>3</sub>. *J. Catal.* **1996**, *163*, 294.
53. Miller, J.T.; Meyes, B.L.; Modica, F.S.; Lane, G.S.; Vaarkamp, M.; Koningsberger, D.C. Hydrogen temperature programmed desorption (H<sub>2</sub> TPD) of supported platinum catalysts. *J. Catal.* **1993**, *143*, 395.
54. Triantafyllou, N.D.; Miller, J.T.; Gates, B.C. Iridium clusters in KLTL-zeolite: Structure and catalytic selectivity for n-butane aromatization. *J. Catal.* **1995**, *155*, 131.
55. Shirai, M.; Chun, W.-J.; Tomishige, K.; Asakura, K.; Iwasawa, Y. Anisotropic structures and oriented bonds of active surface sites by in situ polarized total-reflection fluorescence X-ray absorption fine structure. *Stud. Surf. Sci. Catal.* **1995**, *92*, 263.
56. Dent, A.; Evans, J.; Newton, M.; Corker, J.; Russel, A.; Rahman, A.M.B.; Fiddy, S.; Mathew, R.; Farrow, R.; Salvini, G.; Atkinson, P. High-quality energy-dispersive XAFS on the 1 second timescale applied to electrochemical and catalyst systems. *J. Synchrotron Radiat.* **1999**, *6*, 381.
57. Fiddy, S.G.; Newton, M.A.; Dent, A.J.; Salvini, G.; Corker, J.M.; Turnin, S.; Campbell, T.; Evans, J. In situ dispersive EXAFS (EDE) of low loaded Pt(AcAc)<sub>2</sub>H<sub>1</sub> SiO<sub>2</sub> catalyst precursors on a timescale of seconds or below. *Chem. Commun.* **1999**, *1999* (9), 851.
58. Thomas, J.M.; Greaves, G.N. Combined EXAFS and XRD for the in situ structural elucidation of solid catalysts under operating conditions. *Catal. Lett.* **1993**, *20*, 337.
59. Neylon, M.K.; Marshall, C.L.; Kropf, A.J. In situ XAFS analysis of the temperature programmed reduction of Cu-ZSM-5. *J. Am. Chem. Soc.* **2002**, *124* (9), 5457.
60. Gunter, M.M.; Ressler, T.; Jentoft, R.E.; Bems, B. Redox behavior of copper oxide/zinc oxide in steam reforming of methanol studies by in situ X-ray diffraction and absorption spectroscopy. *J. Catal.* **2001**, *203*, 133.
61. Oudenhuijzen, M.K.; Kooyman, P.J.; Tappel, B.; van Bokhoven, J.A.; Koningsberger, D.C. Understanding the influence of the pre-treatment procedure on platinum particle size and particle size distribution of SiO<sub>2</sub> impregnation with Pt(NH<sub>3</sub>)(NO<sub>3</sub>)<sub>2</sub>: a combination of HRTEM, mass spectroscopy and quick EXAFS. *J. Catal.* **2002**, *205*, 135.
62. Ressler, T.; Jentoft, R.E.; Wienold, J.; Gunter, M.M.; Timpe, O. In situ XAS and XRD studies on the formation of Mo suboxides during reduction of MoO<sub>3</sub>. *J. Phys. Chem., B* **2000**, *104*, 6360.
63. Cattaneo, R.; Weber, T.; Shido, T.; Prins, R. A quick EXAFS study of the sulfidation of NiMo/SiO<sub>2</sub> hydrotreating catalysts prepared with chelating ligands. *J. Catal.* **2000**, *191*, 225.
64. Cattaneo, R.; Shido, T.; Prins, R. QEXAFS study of the sulfidation of NiMo/alumina hydrotreating catalysts. *J. Synchrotron Radiat.* **2001**, *8*, 156.
65. Leliveld, R.G.; van Dillen, A.J.; Gues, J.W.; Koningsberger, D.C.; de Boer, M. Structure and nature of the active sites in CoMo hydrotreating catalysts. An EXAFS study of the reaction with selenophene. *J. Phys. Chem., B* **1997**, *101*, 11,160.
66. Miller, J.T.; Marshall, C.L.; Kropf, A.J. (Co)MoS<sub>2</sub>/alumina hydrotreating catalysts: An EXAFS study of the chemisorption and partial oxidation with O<sub>2</sub>. *J. Catal.* **2001**, *202*, 89.
67. Bitter, J.H.; Cauqui, M.A.; Gatica, J.M.; Barnal, S.; Ramaker, D.E.; Koningsberger, D.C. Changes in the electronic structure of Pt/CeO<sub>2</sub> based DENOX catalysts as a function of the reduction treatment. Detection of a Pt-H anti-bonding shape resonance and Pt-H EXAFS. *Stud. Surf. Sci. Catal.* **2000**, *130*, 3183.
68. Oudenhuijzen, M.K.; Bitter, J.H.; Koningsberger, D.C. The nature of the Pt-H bonding for strongly and weakly bonded hydrogen on platinum: an XAFS spectroscopy study of the Pt-H antibonding shape resonance and Pt-H EXAFS. *J. Phys. Chem. B* **2001**, *105*, 4616.
69. Borgna, A.; Stagg, S.M.; Resasco, D.E. Interference phenomena in the EXAFS spectra of Pt-Sn bimetallic catalysts. *J. Phys. Chem. B* **1998**, *102*, 5077.
70. van den Burg, J.P.; Lucien, J.P.; Germaine, G.; Theilemans, G.L.B. Deep desulfurization and aromatics saturation for automotive gas-oil manufacturing. *Fuel Process. Technol.* **1993**, *35*, 119.
71. Fujikawa, T.; Idei, K.; Ohki, K.; Mizuguchi, J.; Usui, K. Kinetic behavior of hydrogenation of aromatics in diesel fuel over silica-alumina supported bimetallic Pt-Pd catalyst. *Appl. Catal. A: Gen.* **2001**, *205*, 71.
72. Hansen, P.L.; Molenbroek, A.M.; Ruban, A.V. Alloy formation and surface segregation in zeolite-supported Pt-Pd bimetallic catalysts. *J. Phys. Chem. B* **1997**, *101*, 1861.
73. McCalley, J.A. In situ X-ray absorption spectroscopy studies of hydride and carbide formation in supported palladium catalysts. *J. Phys. Chem.* **1993**, *97*, 10,372.
74. Renteria, M.; Traverse, A.; Anuiziatea, O.A.; Ledo, E.J.; Pierella, L.; Requejo, F.G. In situ and ex situ XANES study of the nanodispersed Mo species in zeolites used in fine chemistry catalysis. *J. Synchrotron Radiat.* **2001**, *8*, 631.
75. Li, W.; Meitzner, G.D.; Borry, R.W.; Iglesia, E. Raman and X-ray absorption studies of Mo species in Mo/H-ZSM-5 catalysts for non-oxidative CH<sub>4</sub> reactions. *J. Catal.* **2000**, *191*, 373.
76. Johnston, P.; Joyner, R.W.; Pudney, D.A.; Shpiro, E.S.; Williams, B.P. In situ studies of supported rhodium catalysts. *Faraday Discuss. Chem. Soc.* **1990**, *89*, 91.
77. Johnston, P.; Joyner, R.W. Influence of chlorine on the lability of small rhodium particles in carbon monoxide. *J. Chem. Soc., Faraday Trans.* **1993**, *89* (5), 863.
78. Mizushima, T.; Tohji, K.; Udagawas, Y.; Ueno, A. EXAFS study of the CO-adsorption-induced morphology change in ruthenium clusters supported on alumina. *J. Phys. Chem.* **1990**, *94*, 4980.
79. Mojet, B.L.; Miller, J.T.; Koningsberger, D.C. The effect of CO adsorption at room temperature on the structure of supported Pt particles. *J. Phys. Chem. B* **1999**, *103*, 2724.

80. Costentin, G.; Lavalley, J.C.; Studer, F. Mo Oxidation state of Cd, Fe and Ag catalysis under propane mild oxidation conditions. *J. Catal.* **2001**, *200*, 360.
81. Grunwaldt, J.-D.; Basini, L.; Clausen, B.S. In situ EXAFS study of Rh/alumina catalysts for catalytic partial oxidation of methane. *J. Catal.* **2001**, *200*, 321.
82. Pitchon, V.; Howitt, C.; Maire, F.; Bazin, D.; Berhardt, P.; Maire, G. An in situ study of a Pt–Rh/alumina three-way catalyst operating under controlled gas mixtures (CO, NO, C<sub>3</sub>H<sub>8</sub>, O<sub>2</sub>). *Nucl. Instrum. Methods Phys. Res., B* **1995**, *97*, 33.
83. Pitchon, V.; F., G.; Maire, O. Influence of the surrounding atmosphere upon the catalytic performance of three-way catalysts. *Appl. Catal. A: Gen.* **1997**, *149*, 245.
84. Liu, D.-J.; Robota, H.J. In situ EXAFS and XANES characterization of Cu in Cu-ZSM-5 during NO decomposition catalysis. *Am. Chem. Soc., Div. Pet. Chem.* **1994**, *39* (1), 175.
85. Yamashita, H.; Matsuoka, M.; Tsuji, K.; Shioya, Y.; Giamello, E.; Che, M.; Anpo, M. In situ investigation of the interaction of NO and CO with Cu<sup>+</sup>/ZSM-5 catalyst. *Stud. Surf. Sci. Catal.* **1995**, *92*, 227 (Science and Technology in Catalysis 1994).
86. Kumashiro, R.; Kuroda, Y.; Nagao, M. New analysis of oxidation state and coordination environment of copper ion-exchanged in ZSM-5 zeolite. *J. Phys. Chem., B* **1999**, *103*, 89.
87. Bottger, I.; Schedel-Niedrig, T.; Timpe, O.; Gottschall, R.; Havecker, M.; Ressler, T.; Schlögl, R. Catalytic methanol oxidation over copper: observation of reaction-induced nanoscale restructuring by means of in situ time-resolved X-ray absorption spectroscopy. *Chem. Eur. J.* **2000**, *6* (10), 1870.
88. Havecker, M.; Knop-Gericke, A.; Schedel-Niedrig, T.; Schlögl, R. High-pressure soft X-ray absorption spectroscopy: a contribution to overcoming the pressure gap in the study of heterogeneous catalytic processes. *Angw. Chem. Int. Ed.* **1998**, *37* (13/14), 1939.
89. Clausen, B.S.; Schiøtz, J.; Grabaek, L.; Ovesen, C.V.; Jacobsen, K.W. Wetting/non-wetting phenomena during catalysis: Evidence from in situ on-line EXAFS studies of Cu-based catalysis. *Top. Catal.* **1994**, *1*, 367.
90. Ovesen, C.V.; Clausen, B.S.; Schiøtz, J.; Topsøe, H. Kinetic implications of dynamical changes in morphology during methanol synthesis over Cu/ZnO catalysts. *J. Catal.* **1997**, *168*, 133.
91. Bensaddik, A.; Dexpert, H.; Bazin, D.; Caballero, A.; Villain, F.; Didillon, B.; Lynch, J. In situ study by XAS of the sulfidation of the Pt and PtRe/alumina systems. *Physica B* **1995**, *208&209*, 677.
92. Bensaddik, A.; Caballero, A.; Bazin, D.; Dexpert, H.; Didillon, B.; Lynch, J. In situ study by XAS of the sulfidation of industrial catalysts: The Pt and PtRe/alumina systems. *Appl. Catal. A: Gen.* **1997**, *162*, 171.
93. Miller, J.T.; Koningsberger, D.C. The origin of sulfur tolerance in supported platinum catalysts: the relationship between structural and catalytic properties in acidic and alkaline Pt/LTL. *J. Catal.* **1996**, *162*, 209.
94. Maniguet, S.; Mathew, R.J.; Russell, A.E. EXAFS of carbon monoxide oxidation on supported Pt fuel cell electrocatalysts. *J. Phys. Chem., B* **2000**, *104*, 1998.
95. Lin, S.D.; Hsiao, T.-C.; Change, J.-R.; Lin, A.S. Morphology of carbon supported Pt–Ru electrocatalyst and the CO tolerance of anodes for PEM fuel cells. *J. Phys. Chem., B* **1999**, *103*, 97.
96. Okamoto, Y.; Kubota, T.; Gotoh, H.; Ohto, Y.; Aritani, H.; Tanaka, T.; Yoshida, S. XAFS Study of zirconia-supported copper catalysts for the NO–CO reaction: deactivation, rejuvenation and stabilization of Cu species. *J. Chem. Soc., Faraday Trans.* **1998**, *94* (24), 3743.
97. Caballero, A.; Villain, F.; Dexpert, H.; Lepeltier, F.; Didillon, B.; Lynch, J. In situ EXAFS studies of modifications to supported metallic catalysts under reactive atmospheres. *Catal. Lett.* **1993**, *20*, 1.
98. Besenbacher, F.; Chorkendorff, I.; Clausen, B.S.; Hammer, B.; Molenbroek, A.M.; Nørskov, J.K.; Stensgaard, I. Design of a surface alloy catalyst for steam reforming. *Science* **1998**, *279*, 1913.
99. Ramaker, D.E.; Sambe, H.; Qian, X.; O'Grady, W.E. Application of a novel differential XAFS approach for determination of coordination geometries. *J. Phys., IV Coll.* **1997**, *C2*, C2.
100. Shirai, M.; Asakura, K.; Iwasawa, Y. Anisotropic structure analysis for cobalt oxides on  $\alpha$ -alumina (0001) by polarized total-reflection fluorescence extended x-ray absorption fine structure. *Catal. Lett.* **1992**, *15*, 247.
101. Asakura, K.; Shirai, M.; Iwasawa, Y. Asymmetric structure analysis of active surface sites by in situ polarized total-reflection fluorescence EXAFS. *Catal. Lett.* **1993**, *20*, 117.
102. Iwasawa, Y. The Effects of Coadsorbates on the Behavior of Surface Species and Sites in Catalysis by Means of EXAFS and FTIR. In *Elementary Reaction Steps in Heterogeneous Catalysis*; Joyner, R.W., Santen, R.A.v., Eds.; Kluwer Academic Publishers: Dordrecht, 1993; 287.
103. Shirai, M.; Inoue, T.; Onishi, H.; Asakura, K.; Iwasawa, Y. Polarized total-reflection fluorescence EXAFS study of anisotropic structure analysis of Co oxides on  $\alpha$ -alumina (0001) as model surfaces for active oxidation catalysts. *J. Catal.* **1994**, *145*, 159.
104. Chun, W.-J.; Asakura, K.; Iwasawa, Y. Surface structure analysis of dispersed metal sites on single crystal metal oxides by means of polarized-dependent total-reflection fluorescent EXAFS. *Appl. Surf. Sci.* **1996**, *100/101*, 143.
105. Asakura, K.; Chun, W.-J.; Iwasawa, Y. Polarization-dependent total-reflection fluorescence EXAFS study about active structures on single crystal oxides as model catalyst surfaces. *Top. Catal.* **2000**, *10*, 209.
106. Chun, W.-J.; Asakura, K.; Iwasawa, Y. Anisotropic ordering of Mo species deposited on TiO<sub>2</sub> (110) characterized by polarization-dependent total-reflection fluorescence EXAFS (PTRF-EXAFS). *Catal. Today* **2001**, *66*, 97.
107. Mojet, B.L.; Ramaker, D.E.; Miller, J.T.; Koningsberger, D.C. Observation of a hydrogen-induced shape resonance on Pt/LTL catalysts and its relation with support acidity/alkalinity. *Catal. Lett.* **1999**, *62*, 15.

108. Koningsberger, D.C.; Mojet, B.L.; Miller, J.T.; Ramaker, D.E. XAFS spectroscopy in catalysis research: AXAFS and shape resonances. *J. Synchrotron Radiat.* **1999**, *6*, 135.
109. Ramaker, D.E.; Mojet, B.L.; Oostenbrink, M.T.G.; Miller, J.T.; Koningsberger, D.C. Contribution of shape resonance and Pt–H EXAFS in the Pt  $L_{2,3}$  x-ray absorption edges of supported Pt particles: application and consequences for catalyst characterization. *Phys. Chem. Chem. Phys.* **1999**, *1*, 2293.
110. Koningsberger, D.C.; Oudenhuijzen, M.K.; Bitter, J.H.; Ramaker, D.E. Study of geometrical and electronic effects induced by hydrogen chemisorption on supported Pt particles: Analysis of Pt–H EXAFS and Pt–H anti-bonding state shape resonances. *Top. Catal.* **2000**, *10*, 167.
111. Mojet, B.L.; Miller, J.T.; Ramaker, D.E.; Koningsberger, D.C. A new model describing the metal-support interaction on noble catalysts. *J. Catal.* **1999**, *186*, 373.
112. Koningsberger, D.C.; Ramaker, D.E.; Miller, J.T.; de Graaf, J.; Mojet, B.L. The direct influence of the support on the electronic structure of the active sites in supported metal catalysts: evidence from the anti-bonding shape resonance and Pt–CO FTIR data. *Top. Catal.* **2001**, *15* (1), 35.
113. Miller, J.T.; Mojet, B.L.; Ramaker, D.E.; Koningsberger, D.C. A new model for the metal-support interaction: evidence for a shift in the energy of the valence orbitals. *Catal. Today* **2000**, *62*, 101.
114. O'Grady, W.E.; Ramaker, D.E. Shape resonances and EXAFS scattering in the Pt  $L_{2,3}$  XANES from a Pt electrode. *J. Synchrotron Radiat.* **1999**, *6*, 599.
115. Ramaker, D.E.; O'Grady, W.E. Electrocatalysis at a Pt electrode surface in fuel cell as observed in situ from Pt–H and Pt–O shape resonance and EXAFS scatters in Pt  $L_{2,3}$  XANES. *Stud. Surf. Sci. Catal.* **2000**, *130*, 419.
116. O'Grady, W.E.; Qian, X.; Ramaker, D.E. Systematic chemical effects observed in atomic x-ray absorption fine structure. *J. Phys. Chem., B* **1997**, *101*, 5624.
117. O'Grady, W.E.; Ramaker, D.E. Atomic X-ray absorption fine structure: a new tool for examining electrochemical interfaces. *Electrochem. Acta* **1998**, *44*, 1998.
118. Ramaker, D.E.; Mojet, B.L.; Koningsberger, D.C.; O'Grady, W.E. Understanding atomic X-ray absorption spectra. *J. Phys., Condens. Matter* **1998**, *10*, 8753.
119. Ramaker, D.E.; Qian, X.; O'Grady, W.E. Atomic X-ray absorption structure: a new tool for examining electronic and ionic polarization effects. *Chem. Phys. Lett.* **1999**, *299*, 221.
120. Ramaker, D.E.; van Dorssen, G.E.; Mojet, B.L.; Koningsberger, D.C. An atomic X-ray absorption fine structure study of the influence of hydrogen chemisorption and support on the electronic structure of supported Pt particles. *Top. Catal.* **2000**, *10*, 157.
121. Ramaker, D.E.; de Graaf, J.; van Veen, J.A.R.; Koningsberger, D.C. Nature of the metal-support interaction in supported Pt catalysts: shift in Pt valence orbital energy and charger rearrangement. *J. Catal.* **2001**, *203*, 7.

# Catalysts by Nanoscale Design

Chaitanya Kumar Narula

*Physical Chemistry of Materials, Materials Science and Technology Division,  
Oak Ridge National Laboratory, Oak Ridge, Tennessee, U.S.A.*

## Abstract

The development of new catalytic materials is still dominated by trial-and-error methods. Although it has been successful, the empirical development of catalytic materials is time-consuming and expensive with no guarantee of success. In our laboratories, we are developing a comprehensive “catalysts by design” approach which involves state-of-the-art first principle density functional theory calculations, experimental design of catalyst sites, and sub-Ångström resolution imaging with an aberration-corrected electron microscope to characterize the microstructure. In this entry, we focus on supported platinum cluster catalyst systems, which are one of the most important industrial catalysts and attempt to demonstrate the feasibility of the “catalyst by design” concept.

## INTRODUCTION

Supported metal clusters have been synthesized and extensively studied over the last several decades, and their best-known application is in emission treatment system for transportation vehicles.<sup>[1–3]</sup> Other nanotechnology applications include fuel cells, sensors, and catalysts for chemical processes.<sup>[4–7]</sup> Generally, metal clusters are deposited on a high surface area substrate employing metal salts solution and subsequent decomposition at a slow rate to obtain a relatively uniform distribution of particles. The control on the particle size and distribution is necessary to obtain an efficient catalyst, since smaller particle size translates into a larger number of catalyst sites for the desired catalyst loading. Unfortunately, despite extensive efforts to define relationships between surface morphology, particle size and shape, and catalytic activity, the understanding of catalytic mechanisms is often lacking. The nature of bonding between support and metal clusters has been indirectly inferred but is approximate. It is in part due to the difficulty in preparing supported monodispersed catalyst particles of small size. The small size is highly desirable to increase the catalyst surface because the active part of a catalyst is its surface where low-coordinated atoms reside.<sup>[8]</sup> Thus, increasing the centers that are responsible for catalysis can lead to a decreased use of precious metals that are generally the catalysts of choice for heterogeneous catalysis. New synthetic approaches have made it possible to synthesize small clusters from a variety of techniques allowing supported clusters of Re, Os, Rh, Ir, Pt, and Au to be synthesized.<sup>[9–18]</sup> Under operating conditions, the particles start to grow in size resulting in a reduced number of catalyst sites.<sup>[19–23]</sup> Thus, the catalysts are designed to function over a desired period of time.

The development of new catalytic materials is still dominated by trial-and-error methods. Although it has been successful, the empirical development of catalytic materials is time-consuming and expensive with no guarantee of success. Theoretical studies have generally been carried out on gas-phase isolated atoms and have not provided insights into practical catalyst systems. Now, the advances in computation methods make it possible to model and understand experimentally simple but theoretically complex systems, thereby bridging the gap between theory and experiments. Thus, it is now possible to establish a “catalysts by design” protocol that combines the power of theoretical modeling and experiments (see Fig. 1). The essential component of this approach is that the catalysts are iteratively examined by both theoretical and experimental methods. This approach involves state-of-the-art first principle density functional theory calculations, experimental design of catalyst sites, and sub-Ångström resolution imaging with an aberration-corrected electron microscope to characterize the microstructure. A comprehensive approach, employing this protocol, is being developed in our laboratories; components of this approach are beginning to appear in the literature. For examples, theoretical models of supported gold catalyst have been studied to understand the factors that are important in catalysis such as the roles of undercoordinated sites, particle-support interface, altered oxidation state, and quantum size effects.<sup>[24–27]</sup>

In this entry, we will focus on supported platinum cluster catalyst systems that have been examined by both theory and experiments and we will attempt to demonstrate the feasibility of the “catalyst by design” concept. We selected alumina-supported platinum catalyst because it is one of the most important industrial catalysts and is utilized in a large variety of processes.<sup>[28–36]</sup>

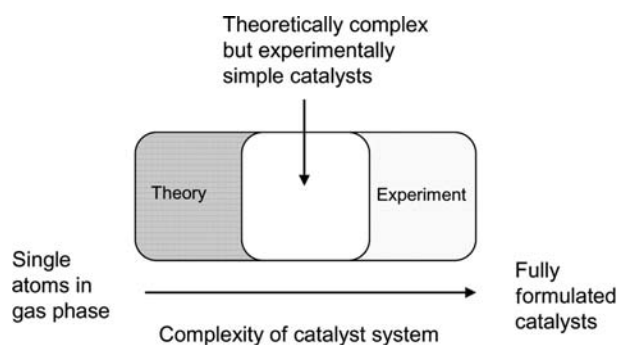


Fig. 1 “Catalyst by design” concept.

## STRUCTURE OF SUPPORTED PLATINUM NANOCLUSTERS

The first automotive catalyst was platinum supported on  $\gamma$ -alumina and designed to oxidize CO and hydrocarbons in the emission stream.<sup>[1]</sup> Since then, several advanced versions of automotive catalysts have been deployed but supported Pt clusters remain an integral component of the catalysts. The synthetic approach is quite simple and involves coating  $\gamma$ -alumina with platinum salts dissolved in water using incipient wetness or suspension methods. Subsequent pyrolysis leads to Pt/ $\gamma$ -Al<sub>2</sub>O<sub>3</sub> powders that are generally degreened under reducing environment.

The nanostructure of freshly prepared catalyst has been a subject of speculation. In fact, nanoparticles of platinum were invisible when examined by X-ray techniques or high-resolution electron microscopes. Chemical activity and X-ray absorption studies had suggested the presence of isolated atoms, which was confirmed in 1996 by the first direct imaging of the atomic configuration of ultradispersed Pt particles.<sup>[37]</sup> Individual atoms, two atoms, triangular trimers, and

larger clusters of Pt atoms were observed in this entry. Since such electron microscopes are available only at a handful of laboratories even today, most of the characterization of supported Pt clusters is still carried out employing dark field images obtained from a variety of electron microscopes that can provide Å-resolution images. A typical high-angle annular dark-field image of 2% Pt/ $\gamma$ -alumina, recorded in our laboratory, by scanning transmission electron microscopy showed an average diameter of 0.9 nm and a size range from 0.6 to 1.4 nm for Pt particles (Fig. 2). A similar result was reported in the literature previously by Kang et al.<sup>[38]</sup> where a distribution of Pt centered at 0.9 nm was observed. The clusters were determined to be hemispherical in shape with  $\sim 90\%$  containing  $12 \pm 5$  atoms and the rest containing  $35 \pm 7$  atoms. The small clusters (individual atoms, 2-atom, or 3-atom) were not observed in this study. The EXAFS study of this sample showed average first shell coordination number to be  $5.5 \pm 0.2$ , which is consistent with a 15-atom hemispherical Pt cluster. Authors also noted an unexpected  $\sim 3\%$  Pt–Pt bond distance contraction from the bulk value in these hydrogen-treated catalysts, which was dependent on temperature.<sup>[38]</sup>

Previous experimentally observed Pt–Pt bond distances for a Pt trimer by electron microscopy are  $2.7 \pm 0.2$ ,  $3.2 \pm 0.2$ , and  $3.4 \pm 0.2$  Å.<sup>[37]</sup> Density functional theoretical calculation of a model with five layers of  $\gamma$ -alumina exposing the 110C face and a Pt-trimer occupying two oxygen and one aluminum vacancies show Pt–Pt bond distances to be 2.59, 2.65, and 2.73 Å.<sup>[39]</sup> The calculated distances are typical of Pt–Pt bond distances but do not agree with observed values. The calculated bond distances of Pt atom clusters on oxygen-terminated  $\gamma$ -alumina were found to be 2.6, 2.6, and 3.6 Å, which are also outside the error limits of observed distances. The authors conclude that if a Pt-trimer structure is capped with –OH, the computed

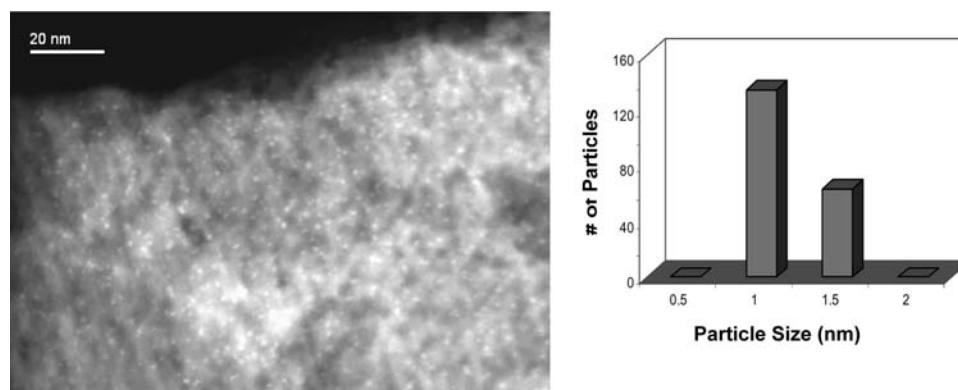
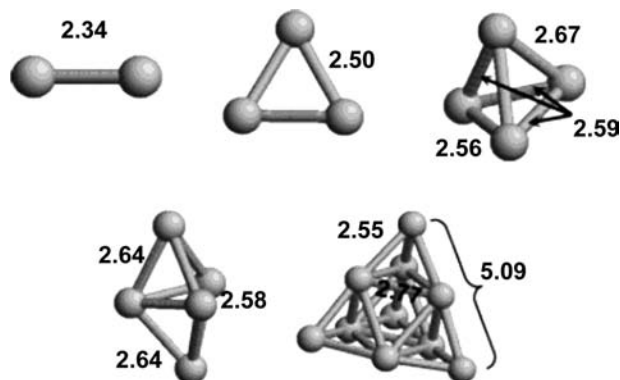


Fig. 2 High-angle annular dark-field image of 2% Pt/ $\gamma$ -alumina (left) and Pt particles size distribution (right). Source: From Ref.<sup>[50]</sup>; Reprinted with permission from SAE paper #2007-01-1018 © 2007 SAE International.

distances are 2.6, 3.1, and 3.6 Å, which are in good agreement with their experimentally observed values.

One needs to be careful about these models because they employ an overly simplified version of  $\gamma$ -alumina models. There is still disagreement on the structure of  $\gamma$ -alumina. Traditionally,  $\gamma$ -alumina is described as having a defective spinel structure derived from  $\text{MgAl}_2\text{O}_4$ .<sup>[40–42]</sup> The cubic unit cell of the structure is an fcc sublattice of oxygen with 96 (64 tetrahedral and 32 octahedral) interstices between oxygen ions and cation vacancies at tetrahedral 8a positions. Literature reports differ on the distribution of cation vacancies.<sup>[42–45]</sup> Experimental studies have also not been able to resolve this issue, but a recent density functional theoretical (DFT) study favors cation vacancies in energetically preferred octahedral sites.<sup>[42]</sup> The presence of hydroxyl groups further complicates the structure of  $\gamma$ -alumina. Although it is generally accepted that hydroxyl groups are present on the surface, there is disagreement on the presence of hydrogen in the bulk structure. There is some experimental evidence for the presence of hydrogen in the bulk structure, but theoretical models suggest that hydrogen spinel is thermodynamically unstable<sup>[42]</sup> and will decompose into anhydrous defect spinel and boehmite. A recent DFT study combined with Rietveld refinement analysis on different spinel and non-spinel structures show that spinel-based models represent structural features of  $\gamma$ -alumina better than non-spinel models and are able to reproduce synchrotron X-ray powder diffraction patterns.<sup>[46]</sup>

Density functional theoretical studies of gas-phase Pt clusters and Pt supported on  $\alpha$ -alumina provide useful information that is helpful in explaining the experimental observations. Gas-phase studies show that 2-, 3-atom Pt clusters are two-dimensional while 4-atom and larger Pt clusters have three-dimensional shape.<sup>[47,48]</sup> The calculated bond distances of small



**Fig. 3** Platinum clusters containing 2, 3, 4, 5, and 10 atoms. Selected bond lengths are also shown. *Source:* From Ref.<sup>[47]</sup>; Reprinted with permission from *J. Phys. Chem. B*, **2006**, *110*, 5839–5846 © 2006 American Chemical Society.

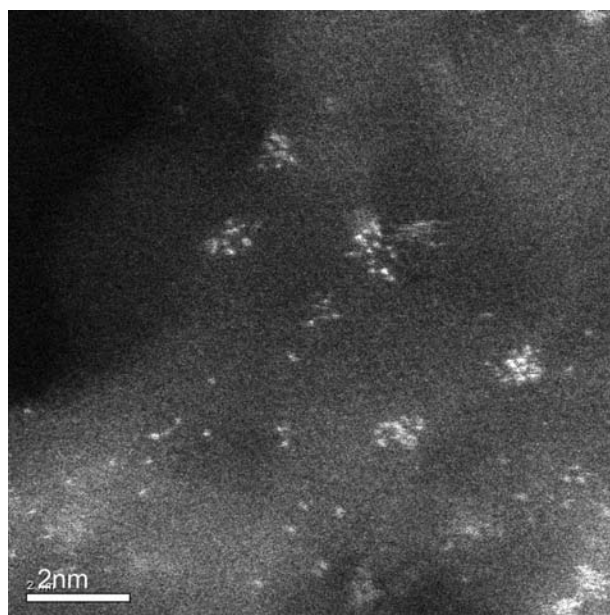


**Fig. 4** ACEM HA-ADF STEM images of 2% Pt/ $\gamma$ -alumina. *Source:* From Ref.<sup>[50]</sup>; Reprinted with permission from SAE paper #2007-01-1018 © 2007 SAE International.

clusters are shown in Fig. 3. The atomization energy of these clusters increases with cluster size, i.e. atoms are held together more strongly as the cluster size increases. Clusters with 13-atoms are generally considered important because 13-atom clusters form high symmetry icosahedral and cuboctahedral structures according to geometric shell models. Density functional theoretical calculations of 13-atom Pt clusters show that a stacked triangular structure and a square structure combined with a tetrahedron have the lowest energy.<sup>[49]</sup>

The sample, 2% Pt/ $\gamma$ -alumina, shown in Fig. 2, was also examined via aberration-corrected electron microscope (ACEM) in scanning transmission electron microscopy (STEM) in scanning transmission electron microscopy (STEM) mode. The high-angle annular dark-field (HA-ADF) images of this catalyst obtained on an ACEM in STEM mode show that there are isolated atoms, 2–3 atom clusters, and several 10–20 atom clusters of Pt (Fig. 4).<sup>[50]</sup> The directly measured Pt–Pt bond distances are 2.35, 2.54, 2.7, and 3.2 Å for 2-atom clusters. Theoretical bond distance for Pt–Pt dimer in the gas phase is 2.34 Å. While it appears that one of the observed bond distance matches closely with the calculated one for gas-phase Pt–Pt dimers, it is not a good comparison because gas-phase dimers do not include substrate interactions. Theoretical models of oxides of Pt nanoclusters suggest them to be two-dimensional in the gas phase (Fig. 5). The calculated Pt–Pt bond distance for a  $\text{Pt}_2\text{O}_4$  cluster is 2.77 Å and although it matches the observed value, we are reluctant to assign  $\text{Pt}_2\text{O}_4$  structure to Pt-dimers primarily



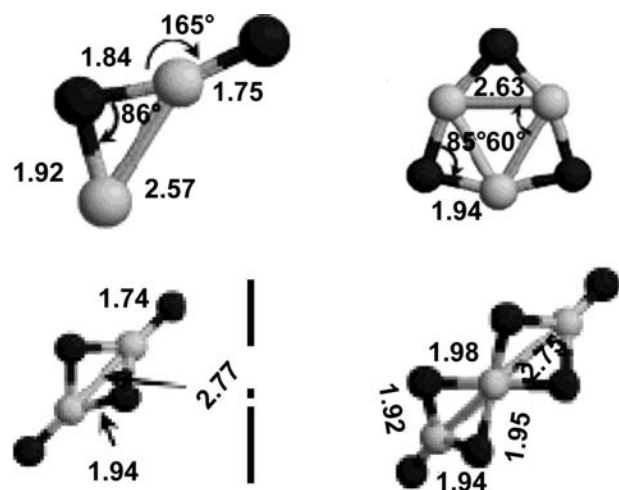


**Fig. 5** Gas-phase Pt and  $\text{Pt}_x\text{O}_{2x}$  dimers and trimers. *Source:* From Ref.<sup>[47]</sup>; Reprinted with permission from *J. Phys. Chem. B*, **2006**, *110*, 5839–5846 © 2006 American Chemical Society.

due to the two-dimensionality of the calculated structure. None of the large clusters exhibit two-dimensional structures. A better comparison is with Pt dimers supported on  $\alpha$ -alumina where they occupy two adjacent  $\text{Al}_T\text{-Al}_T$  sites and exhibit bond distance of 2.723 Å.<sup>[51]</sup> This study also suggests that a Pt–Pt dimer undergoes dissociative adsorption on two adjacent  $\text{O}_{3h}$  sites with each Pt atom occupying an  $\text{O}_{3h}$  site. This would probably explain the larger bond distance of 3.2 Å observed for Pt dimers.

The calculated Pt–Pt bond distances for gas-phase Pt trimers are 2.5 Å and do not match with observed bond distances of 2.3 and 2.8 Å perhaps owing to substrate interactions. These observed values are also different from previously reported values of  $2.7 \pm 0.2$  Å,  $3.2 \pm 0.2$  Å, and  $3.4 \pm 0.2$  Å. This calculated value for a gas-phase trimer is also different from the calculated value described previously for  $\gamma$ -alumina supported Pt trimers. Interestingly, the calculated Pt–Pt bond distances of  $\text{Pt}_3\text{O}_6$  clusters are 2.75 Å, which is close to our observed value, but the observed structure of Pt trimers is different from the two-dimensional gas-phase structure of  $\text{Pt}_3\text{O}_6$ . The calculated Pt–Pt distances of Pt trimer supported on  $\alpha$ -alumina are a better match with our observed values. In the theoretical model, Pt-trimer orients itself parallel to the (0001) surface forming an equilateral triangle with each Pt atom occupying an  $\text{O}_{3h}$  site. In this model, the Pt–Pt bond distance is 2.696 Å (see Fig. 6).

Thus, there is still a need for theoretical study of Pt supported on  $\gamma$ -alumina since simplified models do not adequately explain the observed structures of Pt nanoclusters.

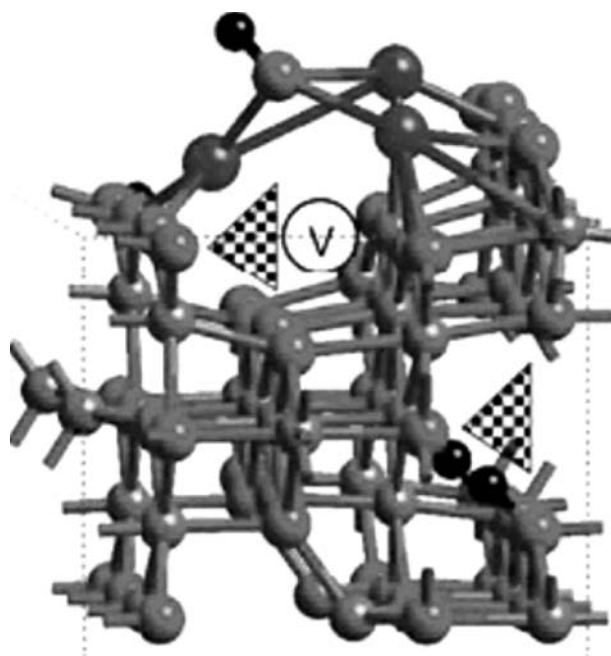


**Fig. 6** Platinum trimer capped by  $-\text{OH}$  group on oxygen-terminated alumina slab. *Source:* From Ref.<sup>[39]</sup>; Reprinted from *ChemPhysChem* **2004**, *5*, 1893 © Wiley-VCH Verlag GmbH & Co. KGaA. Reproduced with permission.

### OXIDATION OF CARBON MONOXIDE ON SUPPORTED PLATINUM NANOCLUSTERS ( $\text{Pt}/\gamma\text{-Al}_2\text{O}_3$ )

Oxidation of carbon monoxide (CO) on 2%  $\text{Pt}/\gamma\text{-Al}_2\text{O}_3$  with 10–20 atom clusters of Pt initiates at 180°C and completes at 210°C (Fig. 7).<sup>[52]</sup> After two cycles of testing and cooling the catalyst to 25°C and retesting, no change in the quantitative conversion temperatures is observed in the third cycle. The nanostructural analysis of the recovered sample suggested some growth in particle size but we could not rule out sample-to-sample variation. It is important to note that change in CO-oxidation activity between fresh and successive cycles of supported Pt catalyst has been observed previously.<sup>[53]</sup> A study of 19 catalyst samples showed “light-off,” on average, at 207°C, just below isokinetic temperature of  $216 \pm 15.3^\circ\text{C}$ . The mean activation energy was  $85.7 \pm 16.9 \text{ kJ mol}^{-1}$ .

The particle size effect on CO oxidation has been observed previously too. The reaction rates for unit amounts of catalyst with platinum dispersions of 0.63, 0.29, and 0.2 were similar but turnover frequency (Fig. 8) increased with increasing particle size.<sup>[53]</sup> Thus, the catalytic activity per surface platinum atom increased with increasing particle size. Zafirris and Gorte<sup>[54]</sup> reported that the turnover frequency of a catalyst with a particle size of 14 nm was 10-fold greater than that of a catalyst with a particle size of

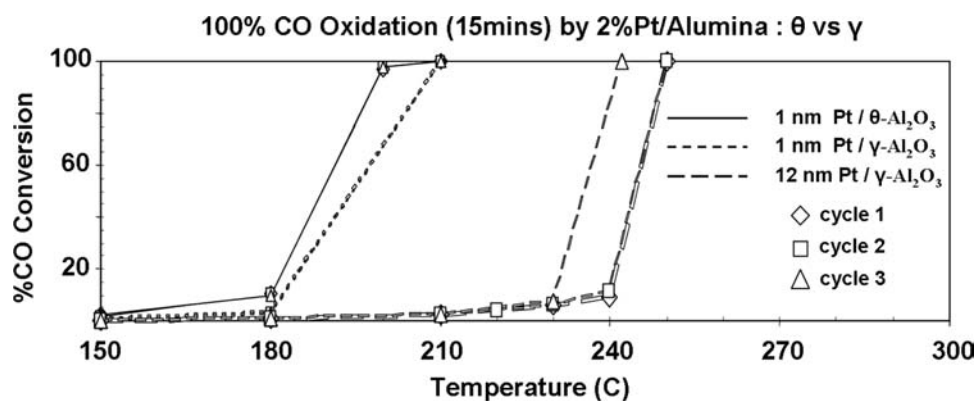


**Fig. 7** Complete conversion of CO to CO<sub>2</sub> as a function of temperature with sampling after 15 min at the given temperature. The dotted lines are results for 2% Pt/ $\gamma$ -Al<sub>2</sub>O<sub>3</sub> (ca. 1 nm Pt), the solid lines are results of 2% Pt/ $\theta$ -Al<sub>2</sub>O<sub>3</sub> (ca. 1 nm Pt), and the dashed lines are results for the 2% Pt/ $\gamma$ -Al<sub>2</sub>O<sub>3</sub> annealed at 650°C (ca. 12 nm Pt). *Source:* From Ref.<sup>[52]</sup>.

1.7 nm. This probably is due to increased fraction of planar sites when compared with low-coordination sites such as edges and corners.<sup>[55]</sup> Interestingly, the temperature required to achieve 50% CO conversion increased with a decrease in dispersion, i.e. a catalyst with a dispersion of 0.83 showed  $T_{50}$  of 217°C while the catalyst with a dispersion of 0.03 showed  $T_{50}$  of 299°C.

Theoretical studies on the adsorption of O, O<sub>2</sub>, CO, CO<sub>2</sub>, NO, and NO<sub>2</sub> on Pt nanoclusters show that the adsorption of these species is highly size-dependent and substantially stronger than that on the bulk Pt surface (Fig. 9).<sup>[50]</sup> As a result, the energy profiles of CO and NO oxidation on Pt<sub>x</sub> nanoclusters also differ from that on Pt bulk-surface.

Carbon monoxide oxidation on the bulk Pt surface is exothermic along the reaction path. But, the enhanced adsorption of CO leads to a minimum in

energy when CO adsorbs on the clusters (Fig. 10). Theoretical studies also show that NO adsorbs strongly on clusters indicating that the ability of the Pt nanoclusters to catalyze CO and NO oxidation may be inhibited by the strongly adsorbed CO and NO. Furthermore, strongly adsorbed O atom diminishes the energetic driving force for Pt<sub>x</sub>-O + NO(g) → NO<sub>2</sub>(g) due to smaller enthalpy of the overall reaction NO(g) + 1/2O<sub>2</sub>(g) → NO<sub>2</sub>(g) and makes the Pt<sub>x</sub> clusters inefficient oxidizers for NO oxidation. On the other hand, the adsorption of O, CO, and NO on the Pt<sub>x</sub>O<sub>x</sub> and Pt<sub>x</sub>O<sub>2x</sub> clusters is weaker when compared with Pt clusters. This suggests that CO and NO oxidation may be more favorable on the small oxidized Pt clusters than on the metallic clusters. Thus, theoretical models of CO interaction with gas phase Pt nanoclusters provide a rationale

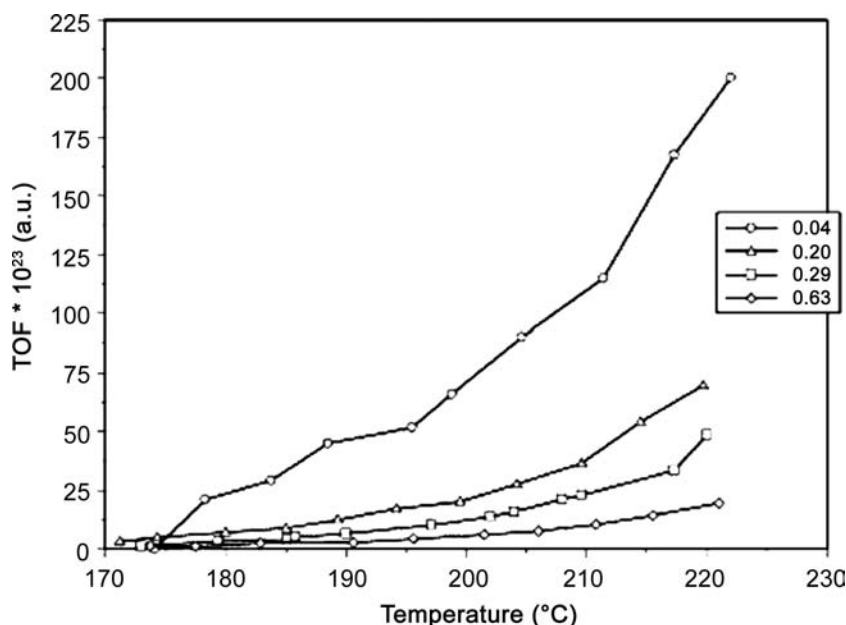


**Fig. 8** The effect of particle size on the turnover frequency of CO oxidation reaction. *Source:* From Ref.<sup>[35]</sup>; Reprinted from *J. Catal.*, **2006**, *241*, 268–275 with permission from Elsevier.

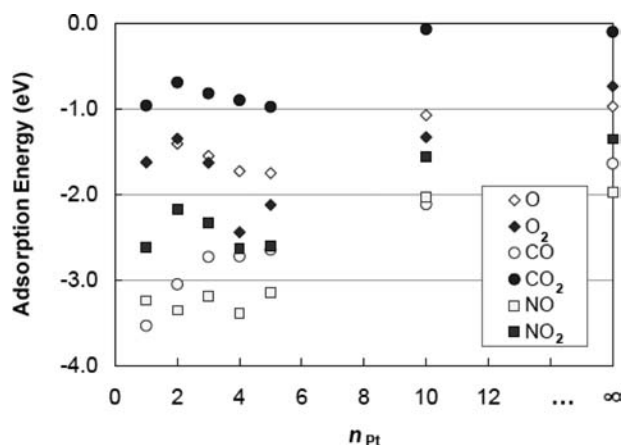


**Fig. 9** The adsorption energies of O, O<sub>2</sub>, CO, CO<sub>2</sub>, NO, and NO<sub>2</sub> on Pt<sub>x</sub> nanoclusters plotted against the number of Pt atoms in the Pt<sub>x</sub> clusters. *Source:* From Ref.<sup>[50]</sup>; Reprinted with permission from SAE paper #2007-01-1018 © 2007 SAE International.

for explaining the experimentally observed CO oxidation behavior on supported Pt clusters.

### NANOSTRUCTURAL CHANGES IN SUPPORTED PLATINUM NANOCLUSTERS

The nanostructural analysis of the recovered sample suggested some growth in particle size. To determine if the particle size growth indeed occurs and is not due to sample-to-sample variation, we carried out CO-oxidation studies employing the ex situ reactor available at Oak Ridge National Laboratory. The ex situ reactor is specially designed to expose catalyst samples on a TEM grid to various operating conditions. This enables monitoring of structural changes in selected areas by electron microscopy after every

experiment. For CO oxidation experiments, the fresh sample was exposed to the following conditions: (1) quantitative CO oxidation conditions at 210°C, (2) quantitative CO oxidation at 210°C and then temperature raised to 450°C for two cycles, and (3) quantitative CO oxidation at 210°C and then temperature raised to 450°C for three cycles. As expected, the fresh sample showed isolated Pt atoms and 10–20 atom Pt clusters (Fig. 11A). Atomic resolution imaging of the sample after two cycles of quantitative CO oxidation at 210°C and then raising the temperature to 450°C shows that the Pt cluster/particles have sintered significantly, although a few clusters of ~1 nm size could still be seen (Fig. 11C). After three cycles of quantitative CO conversion and then raising temperature to 450°C, the number of larger Pt clusters/particles increased and the larger Pt particles exhibited well-ordered structures. For example, a bcc Pt<sub>3</sub>O<sub>4</sub> particle looking down the (120) lattice plane can be seen in Fig. 11D. It is important to note that isolated Pt atoms, dimers, trimers, and 10–20 atom clusters were still present in samples; they do not appear in the micrograph shown in Fig. 11D since they are out of focus at this resolution.

Recent studies on platinum nanoclusters of 7–10 atoms, supported on Al<sub>2</sub>O<sub>3</sub>/SiO<sub>2</sub>/Si(100), have been carried out employing grazing incidence small-angle X-ray scattering technique.<sup>[56]</sup> The results show that these clusters are unusually stable at 400°C under vacuum or hydrogen. Our results, on the other hand, clearly showed instability of Pt nanoclusters under CO oxidation conditions. Thus, a study of stability under hydrogen or vacuum is not a good indicator of catalyst stability under operating conditions.

Theoretical studies point to three pathways for nanocluster growth—triangular packing of subnanoclusters is energetically favored and as Pt cluster size

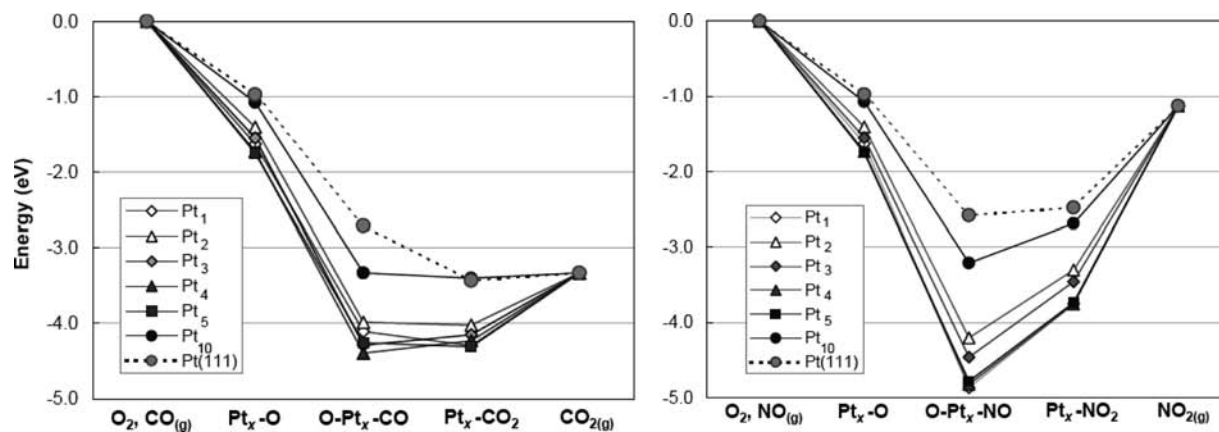


**Fig. 10** The reaction energy profiles for CO +  $\frac{1}{2}$ O<sub>2</sub> → CO<sub>2</sub> and NO +  $\frac{1}{2}$ O<sub>2</sub> → NO<sub>2</sub> on Pt<sub>x</sub> ( $x = 1-5$  and 10). The profiles on the bulk Pt surface (represented by the Pt(111) surface) are included. *Source:* From Ref.<sup>[50]</sup>; Reprinted with permission from SAE paper #2007-01-1018 © 2007 SAE International.

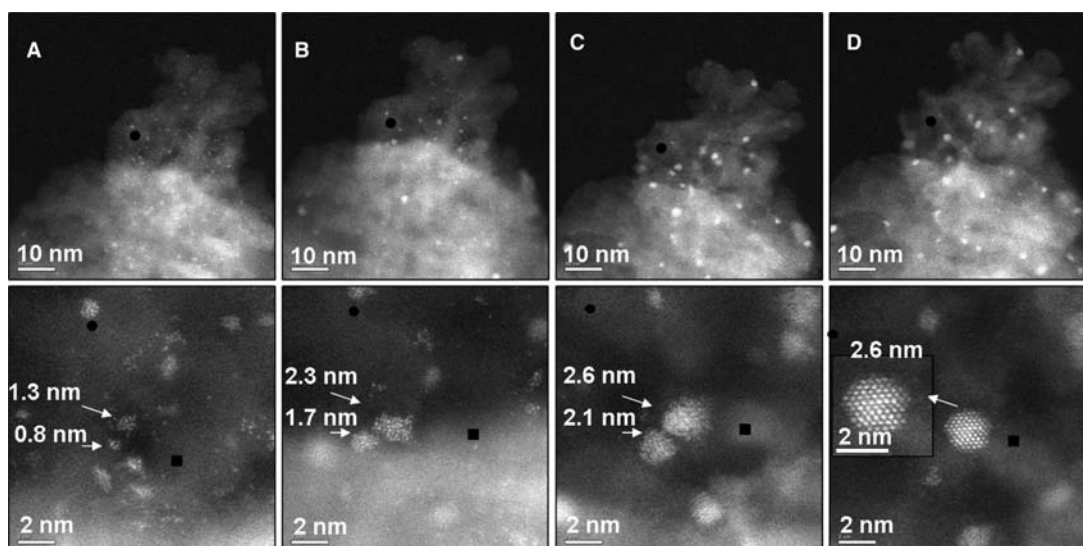


**Fig. 11** ACEM HAADF-STEM images of the exact same sample area of fresh 2% Pt/ $\gamma$ -Al<sub>2</sub>O<sub>3</sub> (A), after quantitative CO oxidation at 210°C (B), after 2- (C), and 3-cycles of quantitative CO-conversion at 450°C (D). The second row shows the area at higher magnification for each stage, respectively. Circles and squares are located at the same place on each image to allow monitoring of Pt growth at each stage of testing. *Source:* From Ref.<sup>[52]</sup>.

approaches 19-atoms, triangular clusters transform to icosahedral clusters. Further increase in Pt cluster to 38-atoms results in transition of fcc-like clusters.<sup>[48]</sup> A recent combined EXAFS and DFT study of platinum supported on carbon suggests that a 37-atom Pt cluster already has a bulk like average Pt–Pt bond and fcc (111)-stacked cuboctahedral geometry.<sup>[57]</sup> Thus, theoretical models and experimental evidence suggests that platinum clusters, after agglomerating to 38 atoms, attain the structure of bulk metal.

### IMPACT OF Pt PARTICLE SIZE—Pt/ $\gamma$ -Al<sub>2</sub>O<sub>3</sub> PARTICLES

Previous studies have demonstrated the impact of Pt particles size on CO oxidation activity<sup>[16–18]</sup> and the Pt particles of less than 5 nm have been shown to either

exhibit decreased activity or no strong size dependence. We sintered 2% Pt/ $\gamma$ -Al<sub>2</sub>O<sub>3</sub> sample at 650°C for 5 hr to obtain Pt particles size distribution of more than 5 nm. Electron microscopy studies of our thermally treated sample showed  $\sim$ 12 nm Pt particles. The CO-oxidation on this catalyst starts at  $\sim$ 240°C and becomes quantitative at  $\sim$ 250°C in the first two cycles. Third cycle of CO oxidation starts at  $\sim$ 230°C (Fig. 8). Transmission electron Microscopy analysis of fresh samples, samples after exposure to CO-oxidation initiation conditions, and after three cycles of quantitative CO-conversion showed a slight particle size growth and could be attributed to sample-to-sample variation based on a subsequent ex situ reactor study, which clearly ruled out particle size growth under these reaction conditions (Fig. 12).

Thus, the behavior of large particles is quite different from nanoparticles where 1, 2, 3, 10–20 atom clusters in fresh samples rapidly sintered under our

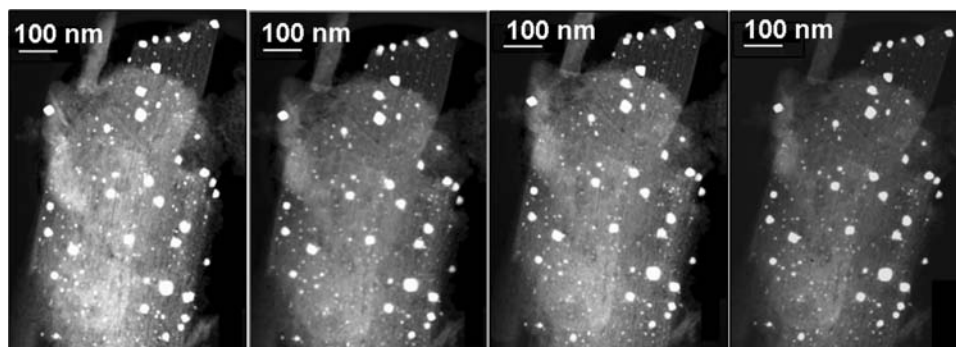


**Fig. 12** HAADF-STEM images of the exact same sample area: Fresh 2% Pt/ $\gamma$ -Al<sub>2</sub>O<sub>3</sub> and after Initiation testing, two-cycles and three-cycles of quantitative CO oxidation (left to right, respectively). *Source:* From Ref.<sup>[52]</sup>.



experimental conditions. Our study suggests that catalyst particles become stable as they increase in size. The TEM analysis suggests that these crystalline Pt particles are most probably oxidized on the surface. The structure of surface oxide is under determination.

### IMPACT OF SUBSTRATE MORPHOLOGY—Pt/ $\theta$ -Al<sub>2</sub>O<sub>3</sub> NANOCCLUSERS

In principle, any experimentally observed difference in the catalytic activity of Pt/ $\theta$ -Al<sub>2</sub>O<sub>3</sub> when compared with Pt/ $\gamma$ -Al<sub>2</sub>O<sub>3</sub> can be attributed to substrate morphology change and changes in Pt nanoclusters—substrate interaction provided Pt nanocluster distribution is identical for both catalysts. In practice, it is difficult to obtain and stabilize identical Pt nanocluster distribution on two different substrates. We followed an experimental protocol identical to that previously used to impregnate  $\gamma$ -Al<sub>2</sub>O<sub>3</sub> in an attempt to obtain almost identical Pt nanocluster distribution on  $\theta$ -Al<sub>2</sub>O<sub>3</sub>. The average Pt particle size was 0.9 nm (range 0.6–1.3 nm) as observed in STEM images of fresh 2% Pt/ $\theta$ -Al<sub>2</sub>O<sub>3</sub> catalyst. This particle size distribution is almost identical to that seen for a fresh catalyst sample of Pt supported on  $\gamma$ -Al<sub>2</sub>O<sub>3</sub>. Interestingly, the CO oxidation reaction on 2% Pt/ $\theta$ -Al<sub>2</sub>O<sub>3</sub> catalyst also initiates around 170–180°C with ~5% conversion (Fig. 8). The catalyst sample, collected after stopping the reaction at this stage, also exhibits Pt particle size growth. Scanning transmission electron microscopy analysis shows that the average Pt size is 1.8 nm with the clusters/particles ranging in size from 0.6 to 4.0 nm. Thus, platinum nanoclusters dispersed on  $\gamma$ -Al<sub>2</sub>O<sub>3</sub> and  $\theta$ -Al<sub>2</sub>O<sub>3</sub> exhibit almost identical nanostructural changes under CO oxidation initiation conditions.

In another experiment, the CO oxidation reaction was allowed to attain quantitative conversion over 2% Pt/ $\theta$ -Al<sub>2</sub>O<sub>3</sub> catalyst and then the reaction was stopped and reactor was cooled. A catalyst sample was collected after three cycles of quantitative CO conversion and cooling. An average Pt size of 2.0 nm that ranges from 0.7 to 5.1 nm was observed in STEM images of multiple areas of catalyst sample. This nanostructural observation is also comparable with that observed for 2% Pt/ $\gamma$ -Al<sub>2</sub>O<sub>3</sub> under CO oxidation conditions. There is no difference in CO oxidation activity of both catalysts under our experimental conditions.

While there is still disagreement on the structure of  $\gamma$ -Al<sub>2</sub>O<sub>3</sub>,  $\theta$ -Al<sub>2</sub>O<sub>3</sub> has a well-ordered crystal lattice making it possible to examine it by theoretical models. We have initiated theoretical studies of Pt/ $\theta$ -Al<sub>2</sub>O<sub>3</sub> catalyst and its CO oxidation behavior to explain the nanostructural differences from Pt/ $\gamma$ -Al<sub>2</sub>O<sub>3</sub> system. Experimentally observed similarities in Pt/ $\theta$ -Al<sub>2</sub>O<sub>3</sub> and

Pt/ $\gamma$ -Al<sub>2</sub>O<sub>3</sub> suggest that the local environment of Pt clusters must be identical in both catalysts. It is important to point out that Pt–Pt bond strengthening has been suggested to govern the reaction behavior of co-adsorbed species on Pt/TiO<sub>2</sub> nanoclusters caused by strong adsorption of O<sub>2</sub> at low-coordination sites of Pt.<sup>[58]</sup> Assuming that this model also applies to Pt/Al<sub>2</sub>O<sub>3</sub> systems, the degree of Pt–Pt bond strengthening must be very similar in Pt/ $\theta$ -Al<sub>2</sub>O<sub>3</sub> and Pt/ $\gamma$ -Al<sub>2</sub>O<sub>3</sub> catalysts.

### CONCLUSIONS

Advances in computation methods, experimental techniques, and instrumentation make it possible to model and understand experimentally simple but theoretically complex systems. The platinum–alumina system described in this entry clearly shows that it is possible to synthesize subnanoclusters of platinum supported on alumina. It is also possible to directly observe the clusters and monitor changes that occur under operating conditions. Density functional theoretical models suggest structures and reactivity of clusters that match the experimental observations.

Even for an experimentally simple system such as platinum–alumina, extensive theoretical modeling was found to be necessary to provide insights into the nanostructures. It is still necessary to use experimental observations as inputs to carry out theoretical models of this system to better understand substrate interactions.

In our studies, theoretical modeling of CO oxidation reaction was able to forecast that platinum nanoclusters in gas phase were less catalytically active for CO oxidation than oxidized Pt nanoclusters. Theoretical studies on various supported clusters also point to stable structures for Pt dimers and trimers. This is the first step towards “catalyst by design” approach. The ability to examine a complex system will indeed make this approach highly valuable in the design of catalysts.

### ACKNOWLEDGMENTS

This research is sponsored by the U.S. Department of Energy, Assistant Secretary for Energy Efficiency and Renewable Energy, Office of Vehicle Technologies, as part of the Propulsion Materials Program, under contract DE-AC05-00OR22725 with UT-Battelle, LLC.

### REFERENCES

1. Heck, R.F.; Farrauto, R.J. *Catalytic Air Pollution Control, Commercial Technology*; Van Nostrand Reinhold: New York, 2002.

2. Narula, C.K.; Allison, J.E.; Bauer, D.; Gandhi, H.S. Materials chemistry issues related to automotive applications of advanced materials. *Chem. Mater.* **1996**, *8*, 984–1003.
3. Narula, C.K.; Daw, C.S.; Hoard, J.W.; Hammer, T. Materials issues related to catalysts for treatment of diesel exhaust. *Int. J. Appl. Ceram. Tech.* **2005**, *2*, 452–455.
4. Lambert, R.M.; Paccionni, G.; Eds. *Chemisorption and Reactivity of Supported Clusters and Thin Films*; NATO ASI Series E; Kluwer: Dordrecht, 1997; 331pp.
5. Campbell, C.T. Ultrathin metal films and particles on oxide surfaces: structural, electronic and chemisorptive properties. *Surf. Sci. Rep.* **1997**, *27*, 1–111.
6. Schmid, G.; Baumle, M.; Geerkens, M.; Heim, I.; Osemann, C.; Sawitowski, T. Current and future applications of nanoclusters. *Chem. Soc. Rev.* **1999**, *28*, 179–185.
7. Freund, H.J. Clusters and islands on oxides: from catalysis via electronics and magnetism to optics. *Surf. Sci.* **2002**, *500*, 271–299.
8. Knickerbein, M.B. Reactions of transition metal clusters with small molecules. *Ann. Rev. Phys. Chem.* **1999**, *50*, 79–115.
9. Parks, E.K.; Weiller, B.H.; Bechthold, P.S.; Hoffman, W.F.; Nieman, G.C.; Pobo, L.G.; Riley, S.J. Chemical probes of metal cluster structure: reactions of iron clusters with hydrogen, ammonia, and water. *J. Chem. Phys.* **1987**, *88*, 1622–1626.
10. Xu, Z.T.; Rheingold, A.L.; Gates, B.C.  $[\text{Pt}_6(\text{CO})_{12}]^{2-}$  and  $[\text{Pt}_9(\text{CO})_{18}]^{2-}$  supported on magnesia: synthesis and spectroscopic characterization. *J. Phys. Chem.* **1993**, *97*, 9465–9469.
11. Gates, B.C. Supported metal clusters: synthesis, structure, and catalysis. *Chem. Rev.* **1995**, *95*, 511–522.
12. Enderle, B.; Gates, B.C. Alkene hydrogenation catalyzed by rhenium carbonyls bonded to highly dealuminated Y zeolite: spectroscopic characterization of the working catalyst. *J. Mol. Catal. A: Chem.* **2003**, *204*, 473–481.
13. Lamb, H.H.; Wolfer, M.; Gates, B.C. A structurally simple supported metal catalyst prepared from decaosmium carbonyl clusters on magnesium oxide. *J. Chem. Soc., Chem. Commun.* **1990**, 1296–1298.
14. Bhirud, V.; Goellner, J.F.; Argo, A.M.; Gates, B.C. Hexarhodium clusters on lanthana: synthesis, characterization, and catalysis of ethene hydrogenation. *J. Phys. Chem. B* **2004**, *108*, 9752–9763.
15. Argo, A.M.O.; Gates, B.C. Role of cluster size in catalysis: spectroscopic investigation of  $-\text{Al}_2\text{O}_3$ -supported Ir4 and Ir6 during ethene hydrogenation. *J. Am. Chem. Soc.* **2003**, *125*, 7107–7115.
16. Larsen, G.; Haller, G.L. Metal-support effects in Pt/I-zeolite catalysts. *Catal. Lett.*, **1989**, *3*, 103–110.
17. Davis, R.J. Aromatization on zeolite L-supported Pt clusters. *Heterog. Chem. Rev.* **1994**, *1*, 41–53.
18. Fierro-Gonzalez, J.C.; Gates, B.C. Mononuclear Au(III) and Au(I) complexes bonded to zeolite NaY: catalysts for CO oxidation at 298 K. *J. Phys. Chem. B* **2004**, *108*, 16,999–17,002.
19. Min, B.K.; Santra, A.K.; Goodman, D.W. Understanding silica-supported metal catalysts: Pd/silica as a case study. *Catal. Today* **2003**, *85*, 113–124.
20. Hayashi, K.; Horiuchi, T.; Suzuki, K.; Mori, T. Sintering behavior of Pt metal particles supported on silica-coated alumina surface. *Catal. Lett.* **2002**, *78*, 43–47.
21. Chen, Z.X.; Smith, G.C.; Putman, C.A.J.; ter Voert, E.J.M. The preparation and characterization of nanometer platinum colloids on silicon wafers as model catalysts. *Catal. Lett.* **1998**, *50*, 49–57.
22. Rothschild, W.G.; Yao, H.C.; Plummer, H.K. Surface interaction in the Pt/ $\gamma$ - $\text{Al}_2\text{O}_3$  system. 5. Effects of atmosphere and fractal topology on the sintering of Pt. *Langmuir* **1986**, *2*, 588–593.
23. Chu, Y.F.; Ruckenstein, E. On the sintering of platinum on alumina model catalyst. *J. Catal.* **1978**, *55*, 281–298.
24. Lopez, N.; Janessens, T.V.W.; Clausen, B.S.; Xu, Y.; Mavrikakis, M.; Bligaard, T.; Norskov, J.K. On the origin of the catalytic activity of gold nanoparticles for low-temperature CO oxidation. *J. Catal.* **2004**, *223*, 232–235.
25. Molina, L.M.; Hammer, B. Active role of oxide support during CO oxidation at Au/MgO. *Phys. Rev. Lett.* **2003**, *90*, 206102.
26. Liu, Z.P.; Jenkins, S.J.; King, D.A. Origin and activity of oxidized gold in water-gas-shift catalysis. *Phys. Rev. Lett.* **2005**, *94*, 196102.
27. Boyen, H.G.; Kastle, G.; Weigl, F.; Koslowski, B.; Dietrich, C.; Ziemann, P.; Spartz, J.P.; Riethmuller, S.; Hartmann, C.; Moller, M.; Schmid, G.; Oelhafen, P. Oxidation-resistant Gold-55 clusters. *Science* **2002**, *297*, 1533.
28. Palazov, A.; Bonev, C.; Shopov, D.; Lietz, G.; Sarkany, A.; Voelter, J. Adsorption and hydrogenation of ethylene, 1-hexene, and benzene and CO adsorption on Pt/ $\text{Al}_2\text{O}_3$  and Pt-Sn/ $\text{Al}_2\text{O}_3$  catalysts. *J. Catal.* **1987**, *103*, 249–260.
29. Altman, E.I.; Gorte, R.J. Temperature-programmed desorption study of nitric oxide on platinum particles supported on  $\alpha$ -alumina {0001}. *J. Phys. Chem.* **1989**, *93*, 1993–1997.
30. Hensley, D.A.; Kesmodel, L.L. Application of HREELS to model catalysts: Carbon monoxide and ethene adsorption on platinum/alumina. *J. Phys. Chem.* **1991**, *95*, 1368–1373.
31. DeJong, V.; Cieplik, M.K.; Louw, R. Formation of dioxins in the catalytic combustion of chlorobenzene and a micropollutant-like mixture on Pt/ $-\text{Al}_2\text{O}_3$ . *Environ. Sci. Technol.* **2004**, *38*, 5217.
32. Gonzalez-Marcos, M.P.; Innara, B.; Guil, J.M.; Gutierrez-Ortiz, M.A. Use of test reactions for the characterization of bimetallic Pt-Sn/ $\text{Al}_2\text{O}_3$  catalysts. *Appl. Catal. A* **2004**, *273*, 259–268.
33. Alexeev, O.S.; Li, F.; Amiridis, M.D.; Gates, B.C. Effects of adsorbates on supported platinum and iridium clusters: characterization in reactive atmospheres and during alkene hydrogenation catalysis by X-ray absorption spectroscopy. *J. Phys. Chem. B* **2005**, *109*, 2338–2349.
34. Cooper, V.R.; Kolpak, A.M.; Yourdshahyam, Y.; Rappe, A.M. Supported metal electronic structure: implications for molecular adsorption. *Phys. Rev. B* **2005**, *72*, 081409-1–081409-4.



35. Atalik, B.; Uner, D. Structure sensitivity of selective CO oxidation over Pt/ $\gamma$ -Al<sub>2</sub>O<sub>3</sub>. *J. Catal.* **2006**, *241*, 268–275.
36. Minemura, Y.; Kuriyama, M.; Ito, S.; Tomishige, K.; Kunimori, K. Additive effect of alkali metal ions on preferential CO oxidation over Pt/Al<sub>2</sub>O<sub>3</sub>. *Catal. Commun.* **2006**, *7*, 623–626.
37. Nellist, P.D.; Pennycook, S.J. Direct imaging of the atomic configuration of ultradispersed catalysts. *Science* **1996**, *274*, 413.
38. Kang, J.H.; Menard, L.D.; Nuzzo, R.G.; Frenke, A.I. Unusual non-bulk properties of nanoscale materials: thermal metal-metal bond contraction of  $\gamma$ -alumina. *J. Am. Chem. Soc.* **2006**, *128*, 12,068.
39. Sohlberg, K.; Rashkeev, S.; Borisevich, A.Y.; Pennycook, S.J.; Patelides, S.T. Origin of anomalous Pt-Pt distances in the Pt/alumina catalytic system. *Chem. Phys. Chem.* **2004**, *5*, 1893.
40. Chou, T.C.; Nieh, T.G. Nucleation and concurrent anomalous grain growth of  $\alpha$ -Al<sub>2</sub>O<sub>3</sub> during  $\gamma$ - $\alpha$  phase transformation. *J. Am. Ceram. Soc.* **1991**, *74*, 2270–2279.
41. Sickafus, K.E.; Willis, J.M.; Grimes, N.W. Structure of spinel. *J. Am. Ceram. Soc.* **1999**, *82*, 3279–3292.
42. Wolverton, C.; Haas, K.C. Phase stability and structure of spinel-based transition aluminas. *Phys. Rev. B* **2000**, *63*, 24,102–24,116.
43. Lee, M.-H.; Cheng, C.-F.; Heine, V.; Klinowski. Distribution of tetrahedral and octahedral Al sites in gamma alumina. *J. Chem. Phys. Lett.* **1997**, *265*, 673–679.
44. Wang, J.A.; Bokhimi, X.; Morales, A.; Novaro, O.; Lopez, T.; Gomez, R. Aluminum local environment and defects in the crystalline structure of sol-gel alumina catalyst. *J. Phys. Chem. B* **1999**, *103*, 299.
45. Pecharroman, C.; Sobrados, I.; Iglesias, J.E.; Gonzalez-Carreno, T.; Sanz, J. Thermal evolution of transitional aluminas followed by NMR and IR spectroscopies. *J. Phys. Chem. B* **1999**, *103*, 6160–6170.
46. Sun, M.; Nelson, A.E.; Adjaye, J. Examination of spinel and nonspinel structural models for  $\gamma$ -alumina by DFT and Rietveld refinement simulations. *J. Phys. Chem. B* **2006**, *110*, 2310–2317.
47. Xu, Y.; Shelton, W.A.; Schneider, W.F. Effect of particle size on the oxidizability of platinum clusters. *J. Phys. Chem. B* **2006**, *110*, 5839–5846.
48. Nie, A.; Wu, J.; Zhou, C.; Yao, S.; Luo, C.; Forrey, R.C.; Cheng, H. Structural evolution of subnano platinum clusters. *Int. J. Quantum Chem.* **2007**, *107*, 219–224.
49. Wang, L.-L.; Johnson, D.D. Density functional study of structural trends for late-transition-metal 13-atom clusters. *Phys. Rev. B* **2007**, *75*, 235405.
50. Narula, C.K.; Moses, M.J.; Xu, Y.; Bom, D.A.; Allard, L.F.; Shelton, W.A.; Schneider, W.F. Catalysis by design – Theoretical and experimental studies of model catalysts. *SAE Technical Paper Series* **2007**, 2007-01-1018.
51. Zhou, C.; Wu, J.; Dhilip Kumar, T.J.; Balakrishnan, N.; Forrey, R.C.; Cheng, H. Growth pathway for Pt clusters on  $\alpha$ -alumina(0001) surface. *J. Phys. Chem. C* **2007**, *111*, 13,786–13,793.
52. Narula, C.K.; Allard, L.F.; Blom, D.A.; Moses-DeBusk, M.M. Bridging the gap between theory and experiments - Nanostructural changes in supported catalysts under operating conditions. *SAE Technical Paper Series* **2008**, 2008-01-0416.
53. Galwey, A.K.; Bettany, D.G.; Mortimer, M. Kinetic compensation effects observed during oxidation of carbon monoxide on  $\gamma$ -alumina supported palladium, platinum, and rhodium metal catalysts: towards a mechanistic explanation. *Int. J. Chem. Kinetics* **2006**, *38*, 689–702.
54. Zafiris, G.S.; Gorte, R.J. CO oxidation on Pt/ $\alpha$ -Al<sub>2</sub>O<sub>3</sub>(0001): evidence for structure sensitivity. *J. Catal.* **1993**, *140*, 418–423.
55. Schimpf, S.; Lucas, M.; Mohr, C.; Rodemerk, U.; Bruckner, A.; Radnik, J.; Hofmeister, H.; Claus, P. Supported gold nanoparticles: In-depth catalyst characterization and application in hydrogenation and oxidation reactions. *Catal. Today* **2002**, *72*, 63–78.
56. Winans, R.E.; Vajda, S.; Ballentine, G.E.; Elam, J.W.; Lee, B.; Pellin, M.J.; Seifert, S.; Tikhonov, G.Y.; Tomczyk, N.A. Reactivity of supported platinum nanoclusters studied by in situ GISAXS: clusters stability under hydrogen. *Topics Catal.* **2006**, *39*, 145–149.
57. Wang, L.-L.; Khare, S.V.; Chirita, V.; Johnson, D.D.; Rockett, A.A.; Frenkel, A.I.; Mack, N.H.; Nuzzo, R.G. Origin of bulklike structure and bond length disorder of Pt<sub>37</sub> and Pt<sub>6</sub>Ru<sub>31</sub> clusters on carbon: comparison of theory and experiment. *J. Am. Chem. Soc.* **2006**, *128*, 131–142.
58. Rashkeev, S.N.; Lupini, A.R.; Overbury, S.H.; Pennycook, S.J.; Pantelides, S.T. Role of nanoscale in catalytic CO oxidation by supported Au and Pt nanostructures. *Phys. Rev. B* **2007**, *76*, 035438.

# Catalytic Processes: Nanoscale Simulations

Vladimir I. Elokhin

*Boreskov Institute of Catalysis, Novosibirsk, Russia*

Aleksandr V. Myshlyavtsev

*Omsk State Technical University, Omsk, Russia*

## INTRODUCTION

In heterogeneous catalysis, adsorption and reaction processes usually occur on supported metal nanoparticles. To study such processes experimentally, a variety of surface science techniques came into use in the last decades of the 20th century. Along with the appearance of high-precision techniques for surface characterization, considerable progress in the manufacturing of model catalysts with well-defined properties such as particle size, shape, and separation has been achieved. For example, modern electron beam lithography makes it possible to fabricate equidistant particles on the scale down to  $\sim 10$  nm. Despite this progress, the cognitive potential of the experimental studies in this field is still limited because the measurements are usually indirect and the information derived demands quantitative processing and interpretation. This can be done only with the use of mathematical models. Successful interpretation of the results requires constructing mathematical models providing accurate descriptions of the systems under consideration. Application of conventional mean-field models is often limited here because of the peculiarities of the reaction performance on the nanometer scale, including the inherent heterogeneity of metal crystallites as well as spontaneous and adsorbate-induced changes of the shape and degree of dispersion of supported catalysts. Under such circumstances, the use of stochastic simulations based, e.g., on the Monte Carlo (MC) technique, is almost inevitable. This entry focuses on theoretical studies (simulations) of catalytic reaction kinetics on active supported nanoparticles. Our goal is to describe the main achievements of the corresponding theoretical works.

## SPECIFICS OF CATALYTIC REACTIONS ON NANOMETER-SIZED PARTICLES

It is well known that the overwhelming majority of real commercial catalysts consists of particles of nanometer

size (1–100 nm) deposited on a porous support with a high surface area. Recently, the synthesis of such systems made great strides toward manufacturing of well-characterized particles with regular structure on the nanometer scale.<sup>[1,2]</sup> Use of these model catalysts provides a bridge between fundamental studies of single-crystal reactivities and applied studies of high-surface-area catalyst activities. These objects attract attention from both applied and theoretical points of view because their properties differ significantly from those of similar systems with large dimensions. Particularly, the surface morphology of supported nanoparticles is not fixed and can appreciably change during reaction. This phenomenon of “building of the catalytic surface to the reaction condition” confirms G. K. Boreskov’s thesis about the mutual interaction between the catalyst and the surrounding reaction medium. At the same time, the specific catalytic activity (the rate per surface metal atom or per adsorption site) can substantially depend on the size of the active particle.<sup>[3]</sup>

The turnover rate of catalytic reactions often depends on the diameter of the particle,  $d$ , indicating that the relationship between the reaction kinetics on nanoparticles and those measured on single-crystal surfaces is not straightforward. This structure gap between the kinetics may have different origins, as indicated schematically in Fig. 1. The geometric shape, exposed crystal planes, etc. of nanometer-size crystallites depend in general on their size, properties of the support (including the metal–support interaction), temperature, and the method of fabrication. For clusters or very small metal particles with  $d < 4$  nm the electron structure is significantly different from that of bulk metals and their catalytic activities are also different. This factor may be crucial to understanding the catalytic activity of such small particles. The metal–support interaction may modify the catalytic properties, and this effect may be important for particles up to  $d \sim 4$  nm. For crystallites with  $4 < d < 10$  nm, the role of edges is usually believed to be appreciable. For  $d > 10$  nm, the particles are electronically

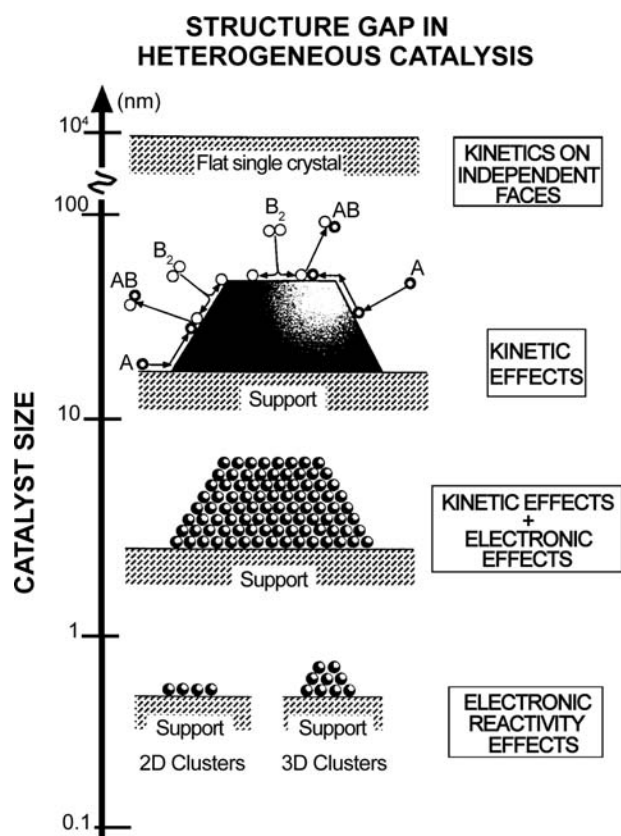


**Fig. 1** Electronic and kinetic effects as ingredients of the structure gap in heterogeneous catalysis. *Source:* From Ref.<sup>[4]</sup> with permission from Elsevier.

identical to bulk metal but may still exhibit remarkably different kinetics compared to single crystals. In this case, reactions may occur primarily on facets although the edges may of course be important as well. From the theoretical point of view, the latter size range is especially interesting because on this scale there is hope of understanding the special features of the size-dependent reaction kinetics based on kinetic data obtained for single-crystal surfaces. In particular, the kinetics on facets are expected to be the same (for a given coverage) as for the corresponding single-crystal faces, and the influence of facet boundaries may be inferred from those steps on single crystals.

The main reasons why kinetic phenomena do not occur on single crystals as opposed to supported catalysts are as follows:<sup>[5]</sup> 1) the different catalytic activities on different facets of a small supported crystalline particle become coupled in a strongly nonlinear (synergistic) fashion because of diffusion occurring over facet boundaries; 2) equilibrium-shape changes of small particles, caused by adsorbates, induce changes in catalytic behavior; 3) different kinetic rate constants at the facet boundaries of a supported particle compared to those for the perfect facets give rise to new kinetics; and 4) spillover by diffusion of reactants between the particle

and its support also create new kinetics. These peculiarities of the supported nanosystems dictate the special requirements to theoretical models aimed at the simulation of catalytic properties of nanometer-scale particles.

Factors (1)–(4) mentioned above are expected to be especially important for *rapid bistable* reactions (“rapid” means that the surface reaction steps between intermediates are fast compared to adsorption) because in this case the reaction regimes on different facets of a catalyst may be very different and the adsorbed overlayer is often far from adsorption–desorption equilibrium. The most interesting feature of rapid reactions is the existence of kinetic phase transitions (for a review, see Ref.<sup>[6]</sup>). An analysis of rapid reactions on the nanometer scale almost inevitably requires the use of MC simulations.

### POSSIBLE APPROACHES TO SIMULATIONS

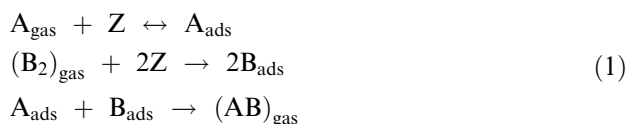
In modeling catalytic supported systems, two lines of investigation should be conventionally marked out: modeling of the fabrication process of the supported system itself (e.g., Refs.<sup>[7,8]</sup>) and modeling of physico-chemical processes in particular supported systems. Both these directions are now rapidly progressing. We shall pay our attention to the latter and will not consider modeling the processes of nanoparticle manufacturing. The theoretical study of supported catalysts is a rather complicated problem, and an analysis of reaction performance on the small particles almost inevitably requires use of atomic-scale computer simulations taking into account the intrinsic heterogeneity of nanoparticles.

There are three main classes of atomic-scale computer techniques: molecular dynamics, Monte Carlo algorithms based on Metropolis-like procedures, and the so-called kinetic (or dynamic) Monte Carlo. Despite the potential power of molecular dynamics, the use of this technique for analysis of physico-chemical processes over supported particles is rather limited because of the short length and time scales typical for this approach<sup>[9]</sup> The most effective tool for simulation of the spatiotemporal dynamics of adsorbed species on real catalytic surfaces, whose structure and properties can change under the influence of the reaction, are now the stochastic methods based on the Monte Carlo technique permitting one to obtain qualitatively new results. The Monte Carlo method<sup>[10,11]</sup> considers the dynamics of the processes occurring on the catalytic surface as a random Markovian chain of elementary events (adsorption, reaction, diffusion, local surface reconstruction, etc.) on the active sites of the catalysts, represented as the cells of a lattice with predetermined rigid or dynamically

changed structure. An obvious disadvantage of stochastic methods is the large body of calculations involved, whereas their main advantage is the possibility of precise control over the local environment and state of each active site on the surface of the catalyst. Another attractive advantage of the Monte Carlo technique is the possibility of including in the simulation all relevant physical and chemical processes (specifically those that can hardly be described analytically) with the corresponding characteristic rate constants obtained from experimental data or from molecular dynamics simulations. Active use of the Monte Carlo technique for simulation of heterogeneous catalytic reaction kinetics (see, e.g., Refs.<sup>[6,12]</sup>) started after the pioneering and nowadays classical paper.<sup>[13]</sup>

At present, the theoretical study of adsorption and reaction processes over supported catalysts is at its very beginning. A comprehensive and careful review of simulations of the reaction kinetics on supported nanoparticles has been published recently by Zhdanov and Kasemo.<sup>[5]</sup> Adapting the key points of that review, we also discuss the results of more recent studies.

Details of simulations of reaction kinetics on supported nanometer catalyst particles depend on the particle structure, reaction mechanism, and ratio between the rates of elementary reaction steps (such as adsorption, desorption, reaction steps, and surface diffusion). Thereupon, one more shortcoming of the kinetic Monte Carlo algorithms should be mentioned—it is difficult to take into account real ratios between the rates of adsorption, reaction, and diffusion. Let us consider the  $2A + B_2 = 2AB$  reaction mimicking CO oxidation on such catalysts as Pt, Rh, and Pd (this reaction is often used in simulations to compare reaction performance on the flat homogeneous surfaces of single crystals and small supported particles). It occurs via the standard Langmuir–Hinshelwood (LH) mechanism,



As stated in Refs.<sup>[5,14]</sup>, the following relationships should be fulfilled between the rate constants for diffusion jumps of A and B particles to nearest-neighbor vacant sites and for the reaction between two nearest-neighbor reactants: the rate of A diffusion is usually *rapid* compared to the LH step, whereas the rate constant for the LH step might be higher, close to, or lower than that for B diffusion.

In some Monte Carlo simulations presented below,<sup>[4–6,14,20–22,24–28]</sup> adsorbed A particle diffusion is always considered to be fast compared to the LH step; the latter is in turn much faster than adsorption

(a special MC algorithm had been designed especially for this case). On the other hand, B particles are assumed to be immobile. This practically important limit ( $k_{\text{dif}}^B \ll k_r \ll k_{\text{dif}}^A$ ) is far from the mean-field (MF) approximation and from the case when the LH step is considered to be instantaneous<sup>[13]</sup> (the latter assumption is widely used in MC simulations of reaction kinetics on single-crystal surfaces, but often does not correspond to reality).

## REACTANT SUPPLY VIA THE SUPPORT (SPILLOVER)

A factor of both fundamental and practical importance in catalysis, which might change the reaction kinetics on supported systems,<sup>[5]</sup> is the possibility of adsorption of reactants on the support followed by diffusion to the catalyst and vice versa. The early models<sup>[15,16]</sup> focused primarily on reactant adsorption, desorption, and diffusion along the support toward catalytic particles, which were assumed to be widely separated (no interference of the diffusion zones)<sup>[15]</sup> or regularly distributed with overlapping diffusion zones.<sup>[16]</sup> The reaction kinetics on the catalyst in those studies has, however, not been analyzed explicitly. CO oxidation reaction on metal particles has been simulated<sup>[17]</sup> by combining CO adsorption, desorption, and diffusion on the support with the reaction steps on the catalyst. Diffusion jumps from the support to the metal were considered rapid and irreversible.

In Ref.<sup>[14]</sup> this effect was analyzed on the example of CO oxidation reaction occurring via LH mechanism (1) by solving the MF equations for the reaction kinetics on the catalyst particle self-consistently with the diffusion equation describing the net flux of A particles from the support to the catalysts. (We do not consider hereinafter the detailed formulation of the problems under consideration and the peculiarities of used algorithms; these can be found in cited papers.) The model used includes circularly shaped catalyst particles regularly distributed on the support. Typical results obtained in the limit when the A diffusion zones around different catalytic particles are not overlapping (i.e., the particles are sufficiently far apart) are shown in Fig. 2 together with the results corresponding to the case when there is no A supply via the support. Because of the A supply from the support, the position of the maximum reaction rate shifted to a lower value of the  $P_A/(P_A + P_{B_2})$  ratio. This intuitively expected result could be expressed in terms of an increased “effective pressure” of the reactant(s) supplied to the catalyst via adsorption on the support and diffusion to the catalyst. Note also that with the action of the support to trap reactant particles, a much higher (by a factor of two) maximum rate becomes possible,

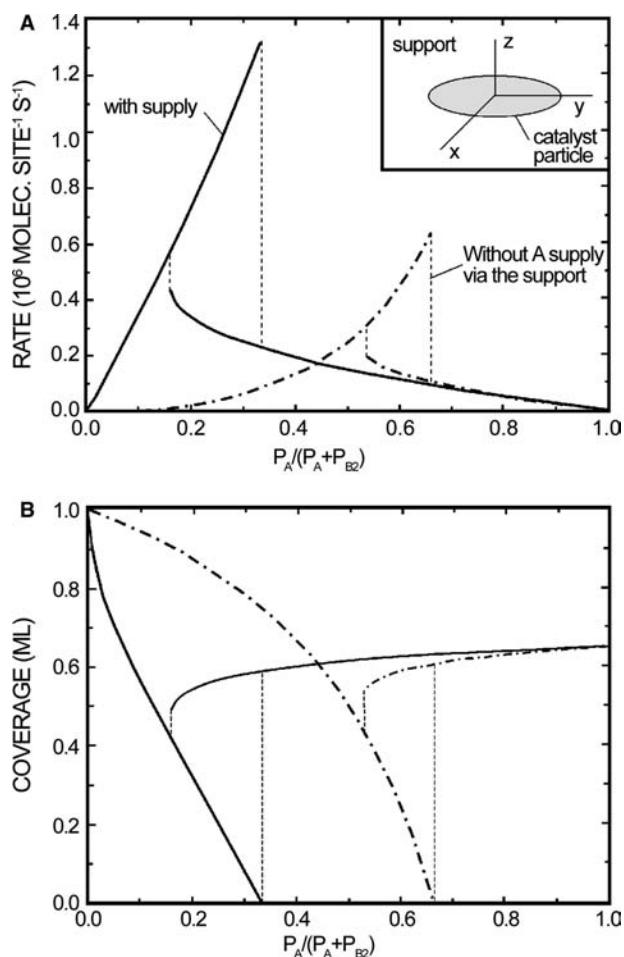


**Fig. 2** (A) Reaction rate and (B) reactant coverages for the rapid  $2A + B_2 \rightarrow 2AB$  reaction under steady-state conditions. The solid and dashed lines show, respectively, the kinetics with and without A supply via the support. The inset on panel (A) exhibits the model used in calculations. *Source:* From Ref.<sup>[21]</sup> with permission from Elsevier.

compared with an inert support. Similar effects were revealed by MC simulation<sup>[18]</sup> considering the same LH reaction mechanism, but with irreversible A adsorption. Another aspect of the spillover phenomena

has been studied by scanning tunneling microscopy (STM) and the corresponding Monte Carlo simulation.<sup>[19]</sup> It has been shown that Pd nanoparticles enhance the rate of reoxidation of a substoichiometric  $TiO_2(110)$  surface. The authors propose that  $O_2$  dissociatively adsorbs on Pd and then spills over onto the support, where  $Ti^{n+}$  interstitial ions in the bulk crystal lattice react with the spillover oxygen at the surface, preferentially growing  $TiO_2$  around and over the particles. The kinetic Monte Carlo model used, in which mobile species spills over from the metal particle and performs a random walk until it reaches a step edge where it may react to form  $TiO_2$ , is in good agreement with STM images.

### INTERPLAY OF KINETICS ON DIFFERENT ADJACENT FACETS

During catalytic reactions on nanometer-size crystallites, adjacent crystal facets can communicate with each other by reactant diffusion. The effect of this factor on the reaction kinetics has been simulated<sup>[5,20]</sup> by using the same  $2A + B_2 \rightarrow 2AB$  catalytic reaction (steps 1–3 with irreversible A adsorption) on the catalyst particle shaped into a truncated pyramid (Fig. 3), with top and bottom (100) faces and (111) side faces, with the largest (100) facet attached to the substrate. In kinetic simulations<sup>[20]</sup> the pyramidal particle was represented by a  $100 \times 100$  square lattice, where the central  $50 \times 50$  array of sites mimics the top (100)-(1  $\times$  1) facet, and the periphery corresponds to the side (111) facets. In the framework of this model, one can use different values of the  $B_2$  (and/or A) sticking coefficient for adsorption on the top (central) and side (peripheral) facets. The A and/or B binding energies and the LH reaction rate constants for the different facets may be different as well. Many other effects can also be easily incorporated into the model, but even the simplest case, when the central part and the periphery of the lattice differ only in the sticking

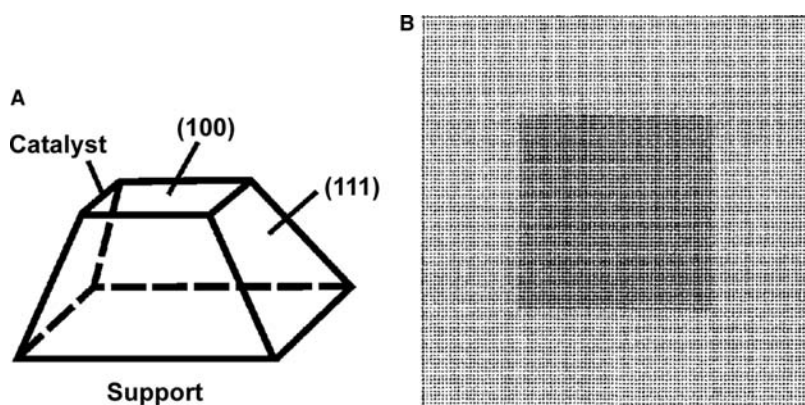


**Fig. 3** (A) Typical shape of the supported metal particle. (B) 2-D  $100 \times 100$  lattice mimicking a particle. The central  $50 \times 50$  part of the lattice represents the top (100) facet. The periphery models the side (111) facet. *Source:* From Ref.<sup>[20]</sup> with permission from Elsevier.

coefficients for  $B_2$  adsorption (differing by a factor 10), can provide the unexpected results. Usually, it is assumed that the geometry of the nanoparticle surface area introduces no additional complications. Small particles exposing different crystal faces are then simply regarded as presenting a superposition of the contributions from different structural elements. This statement is illustrated in Fig. 4A where the total reaction rate for a finite catalyst particle is given simply by a superposition of the rates corresponding to two infinite faces (without communication between the facets). However, if there is diffusion-mediated coupling of the reaction on the different crystal planes, distinctly new kinetics appear (Fig. 4B), compared to those for the infinite surfaces, and completely different compared to that predicted by using the conventional superposition prescription. Specifically, a single new reaction window appears, which is very different from those on either facet. Compared to the isolated facets, the communicating facets provide new channels for A particles. The central facet, which in isolation can resist self-poisoning by A particles up to high values of  $p$  (here  $p$  is the governing parameter defined as the ratio

of the A impingement rate to the total impingement rate), will in a communicating system receive an additional supply of A particles from the adjacent peripheral area, which is less resistant to A poisoning because the  $B_2$  sticking coefficient is 10 times smaller there. This latter net flow of A particles from the peripheral to the central area facilitates A poisoning of the central facet at high values of  $p$  and simultaneously prevents A poisoning from occurring on the peripheral area at relatively low values of  $p$ . Addition to the considered model of the effect of the edge sites (i.e., the sites located on the boundaries between the central and peripheral facets) on the reaction rate makes the resulting global kinetics even more complicated.<sup>[21]</sup> The contribution of the edge sites to the reaction rate is significant if the  $B_2$  sticking coefficient for adsorption on these sites is much higher compared to that on the facet sites. The most important result of these studies is that it has been explicitly shown that the kinetics on nanometer-sized particles exposing different crystalline facets can be dramatically different from the mere superposition of the kinetics on the individual facets because of the combined effect of the difference in the sticking coefficients and the diffusion transport of reactants over the facet boundaries.

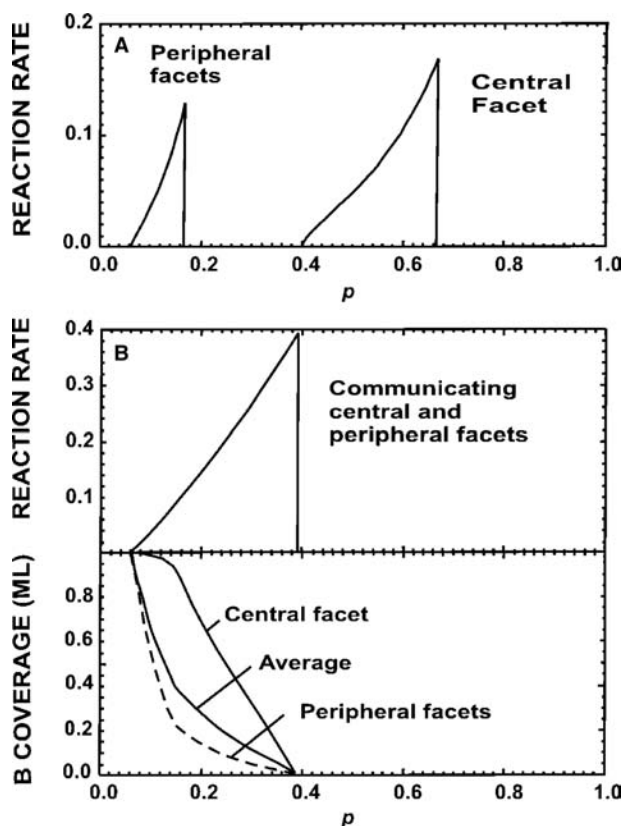


**Fig. 4** Modeling the influence of adsorbate diffusion on the overall kinetics of reaction on a nanoparticle exposing two different kinds of planes (Fig. 3): (A) without diffusion; (B) with rapid diffusion across the facet boundaries. Source: From Ref.<sup>[20]</sup> with permission from Elsevier.

## ADSORBATE-INDUCED RESHAPING OF CRYSTALLITES

Crystallite shape transformations, due to adsorbed reactants, may affect the steady-state kinetics of catalytic reactions. In particular, adsorbates can change the surface energy situation of a crystallite participating in a catalytic reaction, so that it transforms into a new shape with new kinetic conditions. To study such transformations, MC simulations of the  $A + B_2 = 2AB$  reaction kinetics combined with the use of the Wulff rule has been used.<sup>[22]</sup>

The equilibrium geometric shape of small, clean particles is determined by the Wulff rule, stating that the shape is a consequence of minimizing the total surface free energy. Specifically, the rule states that the geometric distance from a common center to a particular facet is proportional to its surface tension. In the case of adsorption, the standard derivations of the Wulff rule holds as well if there is an adsorption-desorption equilibrium. The only difference is that the properly defined surface tension becomes dependent on adsorbate coverages. In this case, the clean surface shape may no longer minimize the surface energy. A shape transformation then occurs (unless it is kinetically hindered), including changes in the relative areas of exposed facets, or even removal and/or creation of new facets. In open, chemically reactive systems, application of the Wulff rule with



coverage-dependent surface tension can also often be justified, but not always. Anyway, this rule is a reasonable starting point for the analysis even far from equilibrium. The conventional Wulff rule is strictly applicable for rather large particles because it neglects, e.g., edge and corner energies, which may be important at smaller sizes. Despite this shortcoming, the Wulff rule is usually robust at least for  $d > 10$  nm. Often the Wulff rule works reasonably well even for smaller particles.<sup>[5]</sup>

In simulations,<sup>[22]</sup> in the absence of adsorbates, the equilibrium shape was assumed to be a truncated pyramid with the (111) and (100) faces, similar to Fig. 3. During the reaction, the particle shape and reaction kinetics were calculated self-consistently by assuming a linear dependence of the surface tension of the (100) facet on B coverage (shape transformations were considered to occur instantaneously when they were energetically favorable). If this dependence is sufficiently strong, the pyramid-shaped catalyst particles become unstable with respect to reconfiguration to the parallelepiped shape with (100) facets. Such reconfiguration results in shifting the reaction window to higher values of  $p$  (Fig. 5). If the adsorbate-induced transition from one shape to another is energetically impossible, the adsorbate-induced changes in the relative areas of different facets may still take place and influence the reaction kinetics. An interesting example illustrating this case has recently been given in Ref.<sup>[23]</sup>. The kinetics of methanol synthesis on nanometer-size Cu particles supported by ZnO has been analyzed. The generalized surface tension for the substrate-particle interface was assumed to be dependent on the reduction potential of the gas phase. The latter resulted in the dependence of the areas of the (111), (100), and (110) facets on the gas-phase concentrations [such changes were observed by using extended X-ray absorption fine structure (EXAFS)]. This dynamic microkinetic model is able to describe the change in particle morphology (i.e., the number of active sites and the exposed facets) with change in feed gas composition as well as the reaction rate over the three basal Cu surface planes. The total reaction rate, represented as a sum of the reaction rates on different facets, was strongly affected by the changes in particle morphology.

Thus, it has been shown that adsorbate-induced reshaping of nanometer-sized catalyst particles may result in dramatic changes in the steady-state reaction kinetics. Experimental search for such changes is of course not always easy, because the transitions from one catalyst structure to another might be slow especially at mild conditions, e.g., at  $T \sim 500$  K. Physically, it is clear that the transition time strongly depends on the crystallite size, temperature, and reaction conditions.

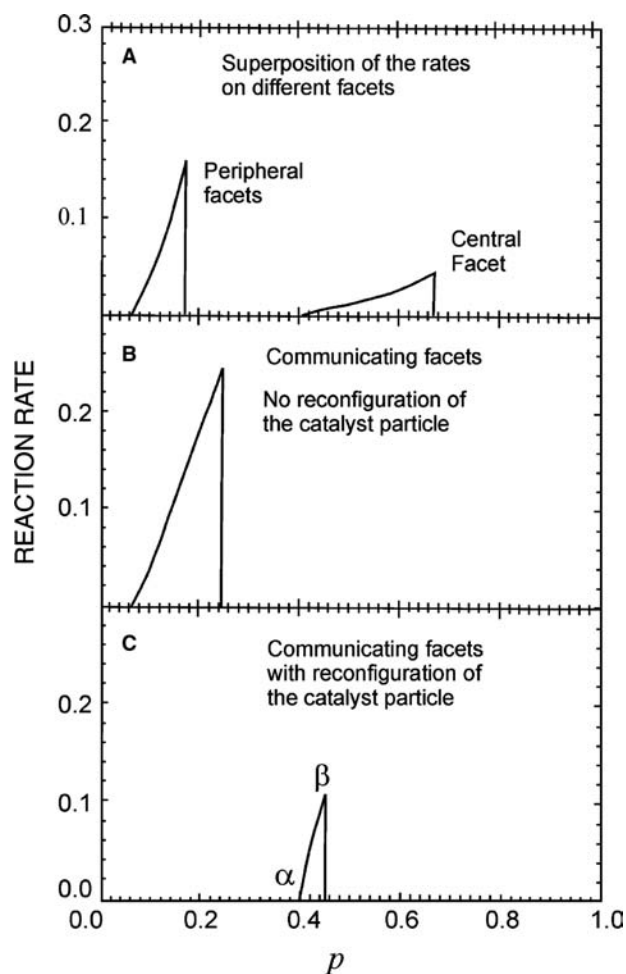


**Fig. 5** Reaction rate as a function of the ratio of the A impingement rate to the total impingement rate  $p$ : (A) superposition of the reaction rates corresponding to two infinite facets; (B) kinetics for the crystallite with communicating facets and fixed facet areas; (C) kinetics obtained by taking into account B-induced changes in the shape of the crystal particle. Along the line  $\alpha\beta$ , the catalyst is shaped as a parallelepiped (the point  $\beta$  corresponds to reconfiguration of the catalyst shape from a parallelepiped to a pyramid). Source: From Ref.<sup>[21]</sup> with permission from Elsevier.

## OSCILLATIONS AND CHAOS

In the previous section the effect of adsorbate-induced 3-D reshaping of catalyst crystallites on the reaction kinetics was considered. In this section, the opposite case—when there are no changes in the global shape of a crystallite but there is adsorbate-induced surface restructuring of one of the crystallite facets—will be treated.<sup>[5,24–26]</sup> This restructuring in interplay with purely chemical reaction steps may cause kinetic oscillations in catalytic reactions. Classic examples are CO oxidation reactions over Pt(100) and Pt(110) single crystals. For example, Pt(100) undergoes the reversible adsorbate-induced surface structure reconstruction

[Pt(100): hex  $\leftrightarrow$   $1 \times 1$ ] depending on adsorbate coverage. The lifting of the hex  $\leftrightarrow$   $1 \times 1$  reconstruction is accompanied by an increase in the oxygen sticking coefficient from  $\approx 0.001$  (hex) to  $\approx 0.3$  ( $1 \times 1$ ) thus inducing a transition from a catalytic inactive state into an active state with high sticking coefficient for oxygen. The competition of the O<sub>2</sub> and CO adsorption in combination with the processes of the surface structure transition hex  $\leftrightarrow$   $1 \times 1$  is a driving force for self-oscillations. It has been shown<sup>[21,24–26]</sup> that such oscillations (and chaotic behavior) are distinctly different on the supported nanometer-sized catalyst particles, compared with extended crystals, mainly because of diffusion communication between facets.

In the models constructed for CO oxidation reaction over Pt(100),<sup>[21,24–27]</sup> adsorbate-induced surface restructuring, treated as a first-order phase transition, occurs only on the central (100) facet. That means that the active centers of the central facet could exist in two different states: active  $Z_{1 \times 1}$  and inactive  $Z_{\text{hex}}$ . The reaction under consideration is run via the conventional LH mechanism (CO = A, O<sub>2</sub> = B<sub>2</sub>). The peripheral (111) facets are considered to be stable (no adsorbate-induced restructuring, i.e., no oscillations). Physically, it is clear that here the interplay of the reaction kinetics on different facets may weaken or even suppress oscillations on the central facet. The simulations show, however, that the amplitude of oscillations may still be large and, in addition, may exhibit qualitatively new features.<sup>[5,24]</sup>

For example, one of the conceptually simplest cases had been considered<sup>[5,24]</sup> when 1) A adsorption, desorption, and diffusion are realized on the peripheral facets with the same MC rules as on the perfect central facet and 2) B<sub>2</sub> adsorption on the peripheral facets is negligible (because of low sticking probability). In this case, the main role of the peripheral facets is to provide an additional supply of A particles to the central face via adsorption and surface diffusion. This supply shifts the oscillation window to lower  $p_A$  values and results in a strongly nonuniform phase distribution on the central facet. In particular, the facet is restructured primarily near the boundaries. In this case, the conditions for oscillations on different regions of the central facet are quite different. This results in a wide distribution of oscillation frequencies. In addition, the kinetics becomes very sensitive with respect to small fluctuations in adsorbate coverages. These special features taken as a whole result in chaotic oscillations. Such chaos, connected with the interplay of the reaction kinetics on adjacent (100) and (111) facets, seems to be inherent for reactions on nanometer-size particles and can hardly be observed in reactions on single-crystal surfaces.

The role of edges mimicked as the rows of sites located on the boundaries between the central (100)

and peripheral (111) facets was considered in Ref.<sup>[21]</sup>. It was shown that for rapid oscillating catalytic reactions the effect of edge sites on the reaction rate can be considerable if the B<sub>2</sub> sticking coefficient for these sites is much higher than for facets. With regard to the diffusion and reaction steps, they have to be slowed down toward that of the rate-limiting adsorption step to cause significant effect in the global kinetics. The influence of other factors (e.g., of higher A-binding energy on edge sites or higher reactivity of edge sites) on the reaction kinetics was demonstrated to be minor.<sup>[5,21]</sup>

The algorithm constructed on the rules of statistical physics<sup>[21,24–27]</sup> makes it possible to take into account substrate–substrate, substrate–adsorbate, and adsorbate–adsorbate lateral interactions. The MC algorithm combines kinetic Monte Carlo procedures for the calculation of probabilities of elementary steps (1)–(3) of the LH mechanism, and Metropolis rules for attempts of surface restructuring and A<sub>ads</sub> particle diffusion; that is, the latter events, as well as A<sub>ads</sub> desorption, depend on local environment of the lattice sites and their respective states. It has been shown,<sup>[27]</sup> using the restricted set of lateral interactions (e.g., the nn A–A and A–B interactions have not been used), that the model predicts the formation of well-developed restructured islands with a size of 5–10 nm (phase separation), in agreement with experimental data.

The dependence of oscillation features on the size of nanoparticles was studied in Ref.<sup>[26]</sup>. The facet size was varied from  $50 \times 50$  to  $5 \times 5$ . With decreasing size, oscillations become less regular. More or less regular oscillations accompanied by formation of CO islands are found for sizes down to  $15 \times 15$ . This means that for observation of such oscillations the particle diameter should be above  $\sim 4$  nm. These findings are in agreement with available experimental data.

An alternative version for the oscillatory behavior of catalytic reaction, such as the formation of subsurface oxygen, has been considered in Ref.<sup>[28]</sup>. The model includes the conventional LH mechanism (1) and the stages of subsurface oxygen formation and removal. The analysis focused on such aspects as CO supply via the support, the role of this supply in synchronization of oscillations on adjacent catalyst particles, and cooperative effects in the subsurface oxygen formation. It was shown<sup>[28]</sup> that 1) CO supply via the support shifts the oscillatory windows to lower CO pressures, as was shown above,<sup>[14]</sup> and may also result in nonuniform oxide distribution on the catalyst particle; 2) with physically reasonable model parameters, synchronization of oscillations on the adjacent catalyst particles due to the CO supply via the support seems to be unlikely; 3) heterogeneous nucleation and cooperative effects in the subsurface oxygen formation may worsen oscillations. In combination with CO adsorption via

precursor states, oscillations may, however, be well developed.<sup>[28]</sup>

The results presented in this section illustrate that catalytic reactions occurring on a single nanometer-size particle may exhibit oscillatory regimes.<sup>[5]</sup> Oscillations may be more or less regular or chaotic. On the macroscopic scale, observation of such oscillations may be hampered if synchronization of oscillations on different particles is not effective. Practically, synchronization is expected to occur via the gas phase (see, e.g., Ref.<sup>[29]</sup>.) or, in exothermic reactions, due to thermal conductivity via the support. Simulations describing the latter aspect of the reaction kinetics on nanometer-size particles are just beginning and not numerous. One of the first studies in this field<sup>[30]</sup> uses the Monte Carlo method for simulation of CO oxidation over nonisothermal supported catalysts. The reaction proceeded via LH mechanism (1) on square  $L \times L$  crystallites ( $L = 5\text{--}100$ ); the total number of islands ( $n = 1\text{--}20$ ) was distributed on the grid mimicking the support. The reaction kinetics on the crystallites were simulated by using the MC technique in combination with the conventional partial differential energy balance to describe the heat transfer over the support. Two general conclusions drawn in Ref.<sup>[30]</sup> are of interest: 1) Oscillatory behavior of reaction (1) was not observed even in the case of nonisothermal surfaces. 2) To reproduce oscillations, the LH mechanism was complemented by subsurface oxygen formation and removal, as in Ref.<sup>[29]</sup>. The latter made it possible to obtain oscillations and changes in oscillatory behavior with temperature and the  $O_2/CO$  ratio. The simulations also show that thermal communications among active particles affect the shape of global oscillations: regular, irregular, and chaotic oscillations were observed depending on crystallite size, activity, and distribution of the particles on the support.

## REACTION SELECTIVITY AND PARTICLE SIZE

The relatively simple model reaction occurring via the LH mechanism (steps 1–3) represents a wide class of important real catalytic reactions occurring via a few elementary steps and resulting in the formation of a single product. Simulations have in fact been very much focused on catalytic reactions belonging to this class.<sup>[5]</sup> The world of real catalytic reactions is, of course, much wider and richer. Very often, real catalytic reactions involve complex polyatomic molecules, occur via a large number of steps, and result in the (parallel) formation of several products. Increasing the selectivity of catalytic reactions toward desirable products is often the main goal of applied catalytic chemistry. For this reason, understanding the factors influencing selectivity of catalytic reactions is an

important and challenging problem. The following reaction, mimicking hydrocarbon hydrogenation, has been considered<sup>[31]</sup> to occur on 2-D islands located on a  $128 \times 128$  square lattice with periodic boundary conditions:

- 1)  $(A_n)_{\text{gas}} \rightarrow (A_n)_{\text{ads}}$
- 2)  $B_{\text{gas}} \rightarrow B_{\text{ads}}$
- 3)  $2(A_n)_{\text{ads}} \rightarrow C_{\text{gas}}$
- 4)  $(A_n)_{\text{ads}} + B_{\text{ads}} \rightarrow D_{\text{gas}}$
- 5)  $2B_{\text{ads}} \rightarrow E_{\text{gas}}$

Both regular islands, consisting of a simple rectangular pattern, and irregular islands, generated by a Voronoi tessellation of the lattice, have been used to represent the catalyst surface. In the latter case, the lattice is divided into a set of polygons constructed by using randomly distributed Poisson points as the polygon centroids. Each polygon is then randomly given an identity, either as an active catalytic region or as an inactive region of the support material. By assigning a greater number fraction of the polygons as active regions, the average size of such regions increases because of coalescence of the individual polygons into larger single islands and vice versa. The goal of the simulations<sup>[31]</sup> was to determine the extent to which simple geometrical parameters, such as the average size of catalyst particles and the spatial distribution of active sites, determine the selectivity of complex catalytic reactions. The simulations<sup>[31]</sup> showed that the total reaction rate  $W_{\text{tot}} = \sum W_i$  and selectivity  $S_i = W_i/W_{\text{tot}}$  toward different products for regular islands are nearly the same as those for irregular islands; that is, the reaction under consideration is insensitive with respect to the island structure. In contrast, the dependence of the reaction rate and selectivity on the average island size is rather strong. On the nanometer scale, the total reaction rate decreases with the decline of the average island size. The C and D selectivities decrease as well. On the other hand, the E selectivity increases with decreasing average island size. All these findings are rationalized by noting that small islands inhibit adsorption of larger molecules and so favor reactions in which smaller molecules are reactants.

If reactant diffusion is incorporated in simulations, the results become quantitatively, but not qualitatively, different (this has actually been demonstrated in Ref.<sup>[32]</sup>). In particular, the influence of hydrogen spillover on the rate of hydrogenation reaction was shown to be negligible. The main qualitative conclusion in Refs.<sup>[31,32]</sup> that the influence of the catalyst particle size on the reaction activity and selectivity becomes significant below a particle size of approximately 10–20 nm is

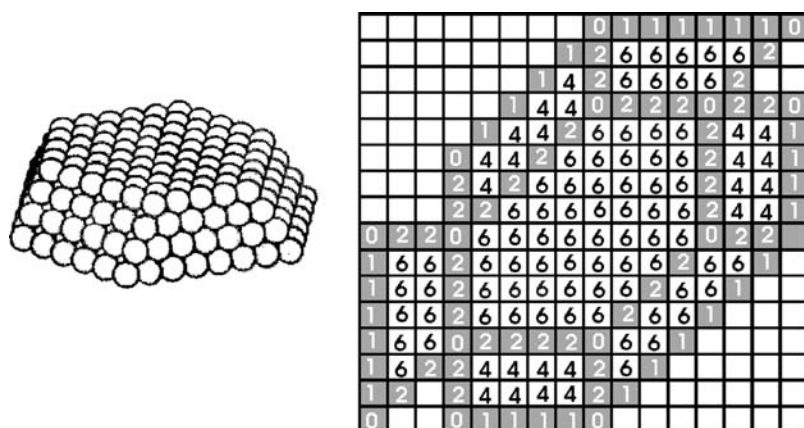


**Fig. 6** Crystallite size model and lattice representation. 0: corner site; 1: base site; 2: edge site; 4: site on (100) plane with four nearest neighbors (NN); 6: site on (111) plane with six NN. *Source:* From Ref.<sup>[35]</sup> with permission from Elsevier.

expected to be robust.<sup>[5]</sup> This conclusion is in agreement with experimental observations for a range of hydrocarbon reactions over supported catalysts.<sup>[3]</sup>

## REACTION KINETICS AND PARTICLE SURFACE MORPHOLOGY

As inferred from the experimental data, the influence of the various surface defects appearing under the action of the reaction media, as well as the change of the shape and size of deposited particles, can significantly determine the catalyst performance. For example, it was shown recently that in some cases, nanoparticles undergo reversible adsorbate-induced shape changes ( $\text{H}_2 + \text{H}_2\text{O}$  and  $\text{CO} + \text{H}_2$  over Cu/ZnO system studied by in situ transmission electron microscopy,<sup>[33]</sup>) and even disintegrate into atoms (effects of CO and NO adsorption on the morphological changes of Rh/TiO<sub>2</sub> studied by scanning tunneling microscopy<sup>[34]</sup>). For better understanding of the reaction kinetics, one should take into account these processes and the inherent heterogeneity of supported particles.

In the bulk of the theoretical studies cited above (except Refs.<sup>[22,23]</sup>), the change of surface morphology

was not taken into account; that is, the specificity of active centers, their state, and coordination (configuration) are defined by introducing the proper lateral interactions. The attempt to distinguish the active centers according to their coordination on the surface was undertaken in Ref.<sup>[35]</sup> where the influence of crystallite size on the activity of a supported catalyst for the LH reaction mechanism (steps 1–3) has been investigated. The active surface was modeled (following the model proposed in Ref.<sup>[36]</sup>) as a set of particles, each one represented as the top projection of a truncated hexagonal pyramid on a flat support surface (Fig. 6). Catalytic centers with different configuration (edges, corners, etc.) have differing activity with respect to the elementary reaction steps. These activities were calculated as a product of specific process rates for adsorption, desorption, and reaction and of some additional weight coefficients, which account for enhancement or reduction of these rates on each type of center. The ratio between the number of different active centers depends, of course, on the size of the crystallites (the relative concentration of surface defects increase with decreasing particle size). The important result of simulations<sup>[35]</sup> is that the structural features affect the production rate in ways that depend

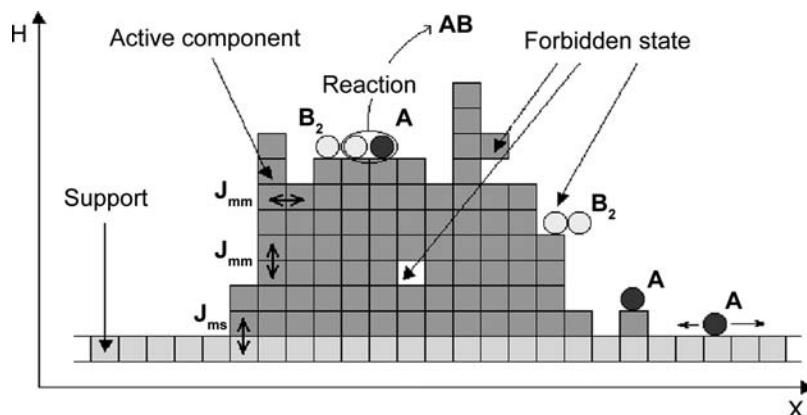


**Fig. 7** Scheme of the supported catalytic particle model: cross cut of the Kossel crystal. *Source:* From Ref.<sup>[18]</sup> by permission of The Royal Society of Chemistry on behalf of the PCCP Owner Societies.

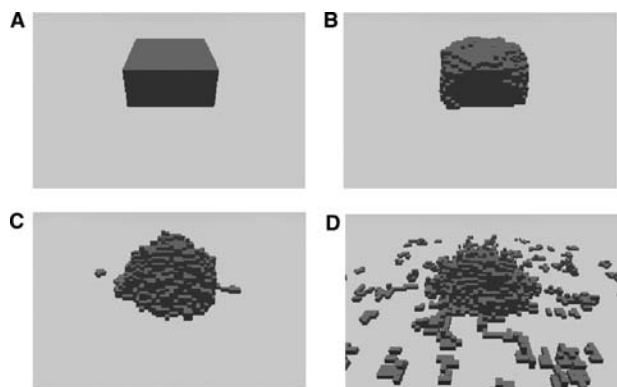


**Fig. 8** The initial (A) and equilibrium (b–d) shapes of the metal particles simulated at different temperatures: (B) –500 K, (C) –900 K, (D) –1100 K. The size of the initial particle is  $21 \times 21 \times 10$  atoms.  $J_{mm} = -10$  kJ/mol,  $J_{ms} = -2.5$  kJ/mol. Source: From Ref.<sup>[18]</sup> by permission of The Royal Society of Chemistry on behalf of the PCCP Owner Societies.

on which of the elementary steps in the reaction mechanism is altered by the presence of different types of sites. In other words, there is no universal trend on the effect of particle size, but rather it is an integral effect that depends on the importance of the interaction of these structural features and the reactants.<sup>[35]</sup>

Recently,<sup>[18,37]</sup> a statistical lattice model has been proposed that imitates the physicochemical processes that proceed on the supported particle. To simulate the active metal particle, the finite Kossel crystal<sup>[38]</sup> located on the inert support was chosen (Fig. 7). The surface morphology of the particle is defined by distribution of heights of the metal atom columns. The metal atoms attract the nearest neighbors and the atoms of the support. The change of morphology is caused by thermal diffusion of the surface atoms. To model diffusion of metal atoms on the metal and support surfaces, the Metropolis algorithm has been used. (Similar algorithm was used in Ref.<sup>[39]</sup> for the modeling of catalyst sintering behavior.) As a result, the equilibrium shapes of the particle were observed depending on the temperature and the relative ratio of metal–metal and metal–support interaction energies  $J_{mm}$  and  $J_{ms}$  (Fig. 8). Although this model is two-dimensional, it allows one to model adsorption, diffusion, and reaction events on the dynamically changed surface of the particle to take into account various lateral metal–adsorbate and adsorbate–adsorbate interactions. It was shown<sup>[18]</sup> that the reaction kinetics on such particles can be qualitatively and quantitatively different from those corresponding to the flat surface only because of the change of the shape and surface morphology of nanoparticles and spillover phenomena. The simulations show that if the adsorbate–metal

interaction energies become comparable with the metal–metal ones the nanoparticle undergoes reversible adsorbate-induced reshaping,<sup>[37]</sup> and that the particle size determines the degree of reshaping as in experiments.<sup>[33]</sup> The proposed approach offers new routes to model catalytic reactions closer to reality (see also 3-D models of supported nanoparticles published recently<sup>[40]</sup>).

## CONCLUSION

The most important message from the simulations reviewed is that *the kinetics of catalytic reactions occurring on nanometer-sized metal particles, exposing different crystalline facets, can be dramatically different from the mere superposition of the kinetics of the individual facets.*<sup>[5]</sup> This finding has far-reaching consequences both for the interpretation of kinetic data from supported and nanofabricated catalysts and for the design of catalysts. In particular, one should, in analysis of experimental data, consider the special kinetics *inherently* associated with nanoparticles before more complex explanations are tried, such as size-related electron-structure effects, support-related effects, special active sites, etc. With respect to catalyst design, the kinetics on supported catalysts may be manipulated by influencing the relative amounts of different facets, the size of the nanoparticles, and the adsorption properties of the support. Modeling of heterogeneous catalytic processes over supported nanoparticles demands the construction of new statistical lattice models describing in detail the fcc or bcc nanometer-sized metal crystallites and kinetic MC models for elementary steps of particular catalytic reactions. The mutual influence of the reaction media on the particles shape and surface structure, and vice versa, of nanoparticle characteristics on the reaction kinetics is one of the fundamental problems in heterogeneous catalysis. The simulations are expected to be strengthened by using the parameters provided by ab initio quantum mechanical calculations. Such a combined approach will be a powerful complementary tool to high-resolution kinetic experiments.<sup>[41]</sup>

## ACKNOWLEDGMENTS

We thank Prof. V. P. Zhdanov for useful discussions and gratefully acknowledge him for illustrations of his works included in this entry.

## REFERENCES

1. Henry, C.R. Surface studies of supported model catalysts. *Surf. Sci. Rep.* **1998**, *31*, 231–325.

2. Gunter, P.L.J.; Niemantsverdriet, J.W.; Ribeiro, F.H.; Somorjai, G.A. Surface science approach to modeling supported catalysts. *Catal. Rev., Sci. Eng.* **1997**, *39* (1 and 2), 77–168.
3. Che, M.; Bennett, C.O. The influence of particle size on the catalytic properties of supported metals. *Adv. Catal.* **1989**, *36*, 55–160.
4. Zhdanov, V.P. Impact of surface science on the understanding of kinetics of heterogeneous catalytic reactions. *Surf. Sci.* **2002**, *500*, 966–985.
5. Zhdanov, V.P.; Kasemo, B. Simulations of the reaction kinetics on nanometer supported catalyst particles. *Surf. Sci. Rep.* **2000**, *39* (2–4), 25–104.
6. Zhdanov, V.P.; Kasemo, B. Kinetic phase transitions in simple reactions on solid surfaces. *Surf. Sci. Rep.* **1994**, *20* (3), 111–189.
7. Jensen, P. Growth of nanostructures by cluster deposition: Experiments and simple models. *Rev. Mod. Phys.* **1999**, *71* (5), 1695–1735.
8. Fang, T.-H.; Weng, C.-I.; Chang, J.-G. Molecular dynamic simulation of nano-lithography process using atomic force microscopy. *Surf. Sci.* **2002**, *501* (1), 138–147.
9. Wang, L.; Clancy, P. Kinetic Monte Carlo simulation of the growth of polycrystalline Cu films. *Surf. Sci.* **2001**, *473* (1), 25–38.
10. Binder, K.; Heermann, D.W. *Monte-Carlo Simulation in Statistical Physics*, 2nd Ed.; Springer Verlag: Berlin, 1992.
11. Landau, D.P.; Binder, K. *A Guide to Monte-Carlo Simulation in Statistical Physics*; Cambridge University Press: Cambridge, 2000.
12. Albano, E.V. The Monte Carlo simulation method: A powerful tool for the study of reaction processes. *Heterog. Chem. Rev.* **1996**, *3*, 389–418.
13. Ziff, R.M.; Gulari, E.; Barshad, Y. Kinetic phase transitions in an irreversible surface-reaction model. *Phys. Rev. Lett.* **1986**, *56* (13), 2553–2556.
14. Zhdanov, V.P.; Kasemo, B. Kinetics of rapid heterogeneous reactions on the nanometer scale. *J. Catal.* **1997**, *170* (2), 377–389.
15. Aris, R. Surface diffusion and reaction at widely separated sites. *J. Catal.* **1971**, *22* (2), 282–284.
16. Kuan, D.-J.; Davis, H.T.; Aris, R. Effectiveness of catalytic archipelagos. I. Regular arrays of regular islands. *Chem. Eng. Sci.* **1983**, *38* (5), 719–732.
17. Henry, C.R. The effect of the diffusion of carbon monoxide on the substrate during CO oxidation on supported palladium clusters. *Surf. Sci.* **1989**, *223* (2), 519–526.
18. Kovalyov, E.V.; Resnyanskii, E.D.; Elokhin, V.I.; Bal'zhinimaev, B.S.; Myshlyavtsev, A.V. Novel statistical lattice model for the supported nanoparticle. Features of the reaction performance influenced by the dynamically changed shape and surface morphology of the supported particle. *Phys. Chem. Chem. Phys.* **2003**, *5*, 784–790.
19. Ramires-Cuesta, A.J.; Bennet, R.A.; Stone, P.; Mitchell, P.C.H.; Bowker, M. STM investigation and Monte-Carlo modelling of spillover in a supported metal catalyst. *J. Mol. Catal., A: Chem.* **2001**, *167* (1), 171–179.
20. Zhdanov, V.P.; Kasemo, B. Monte Carlo simulation of the kinetics of rapid reactions on nanometer catalyst particles. *Surf. Sci.* **1998**, *405* (1), 27–37.
21. Persson, H.; Thormählen, P.; Zhdanov, V.P.; Kasemo, B. Simulation of the kinetics of rapid reactions on supported catalyst particle. *Catal. Today* **1999**, *53* (2), 273–288.
22. Zhdanov, V.P.; Kasemo, B. Kinetics of rapid heterogeneous reactions accompanied by the reshaping of supported catalyst crystallites. *Phys. Rev. Lett.* **1998**, *81* (12), 2482–2485.
23. Ovesen, C.V.; Clausen, B.S.; Schiøtz, J.; Stoltze, P.; Topsøe, H.; Nørskov, J.K. Kinetic implications of dynamic changes in catalysts morphology during methanol synthesis over Cu/ZnO catalysts. *J. Catal.* **1997**, *168* (2), 133–142.
24. Zhdanov, V.P.; Kasemo, B. Oscillations and chaos in catalytic reactions on the nm scale. *Phys. Rev., E* **2000**, *61*, R2184–R2188.
25. Zhdanov, V.P.; Kasemo, B. Surface restructuring, kinetic oscillations, and chaos in heterogeneous catalytic reactions. *J. Stat. Phys.* **2000**, *101* (1/2), 631–647.
26. Zhdanov, V.P.; Kasemo, B. Kinetic oscillations on nm-sized catalyst particles: Surface restructuring. *Surf. Sci.* **2002**, *513*, L385–L390.
27. Zhdanov, V.P. Simulation of kinetic oscillations in catalytic reactions accompanied by adsorbate-induced surface restructuring. *Surf. Sci.* **1999**, *426* (2), 345–357.
28. Zhdanov, V.P.; Kasemo, B. Kinetic oscillations on nm-sized catalyst particles: Oxide model. *Surf. Sci.* **2002**, *511* (1), 23–33.
29. Slinko, M.M.; Ukharskii, A.A.; Jaeger, N.I. Global and non-local coupling in oscillating heterogeneous reactions: The oxidation of CO on zeolite supported palladium. *Phys. Chem. Chem. Phys.* **2001**, *3*, 1015–1021.
30. Qin, F.; Tagliabue, L.; Piovesan, L.; Wolf, E.E. Monte Carlo simulations of self-sustained oscillations of CO oxidation over non-isothermal supported catalysts. *Chem. Eng. Sci.* **1998**, *53* (5), 911–931.
31. McLeod, A.S.; Gladden, L.F. Relating metal particle geometry to the selectivity and activity of supported-metal catalysts: A Monte Carlo study. *J. Catal.* **1998**, *173* (1), 43–52.
32. McLeod, A.S. Monte Carlo simulations of heterogeneous catalytic reactions on highly dispersed supported metal catalysts. *Catal. Today* **1999**, *53* (2), 289–302.
33. Hansen, P.L.; Wagner, J.B.; Helveg, S.; Rostrup-Nielsen, J.R.; Clausen, B.S.; Topsøe, H. Atomic resolved imaging of dynamic shape changes in supported copper nanocrystals. *Science* **2002**, *295* (5562), 2053–2055.



34. Berko, A.; Solymosi, F. Adsorption-induced structural changes of Rh supported by  $\text{TiO}_2(110)-1 \times 2$ : An STM study. *J. Catal.* **1999**, *183* (1), 91–101.
35. Gracia, F.; Wolf, E.E. Monte Carlo simulations of the effect of crystallite size on the activity of a supported catalyst. *Chem. Eng. J.* **2001**, *82* (1–3), 291–301.
36. Mavrikakis, M.; Stoltze, P.; Nørskov, J.K. Making gold less noble. *Catal. Lett.* **2000**, *64* (1), 101–106.
37. Kovalyov, E.V.; Elokhin, V.I.; Myshlyavtsev, A.V.; Bal'zhinimaev, B.S. New statistical lattice model of a supported nanoparticle: Influence of dissociative adsorption on the equilibrium shape and surface morphology of a particle. *Dokl. Phys. Chem.* **2001**, *381* (4–6), 309–313.
38. Lapujoulade, J. The roughening of metal surfaces. *Surf. Sci. Rep.* **1994**, *20*, 191–294.
39. Sault, A.G.; Tikare, V. A new Monte Carlo model for supported-catalyst sintering. *J. Catal.* **2002**, *211* (1), 19–32.
40. Sayle, D.C.; Watson, G.W. Atomistic structure of 25000-atom oxide nanoparticles supported on an oxide substrate. *J. Phys. Chem., B* **2002**, *106* (42), 10793–10807.
41. Libuda, J.; Freund, H.-J. Reaction kinetics on complex model catalysts under single scattering conditions. *J. Phys. Chem., B* **2002**, *106* (19), 4901–4915.

# Ceramic Nanocomposites: Self-Diagnostic Ability of Catastrophic Damage

Pavol Šajgalík  
Zoltán Lenčič

*Institute of Inorganic Chemistry, Slovak Academy of Sciences,  
Bratislava, Slovakia*

## INTRODUCTION

Ceramic nanocomposites are widely used as engineering materials owing to their excellent mechanical properties. In the last decade ceramic nanocomposites found new uses as a different kind of sensor. In this entry, examples of the preparation of electroconductive ceramic nanocomposites are shown together with their utilization as self-monitoring sensors for crack initiation and propagation. Four different methods for synthesis of nanocomposite ceramics are presented, and their effects on the structure of nanocomposites are compared. The self-diagnostic ability of graded and layered ceramic nanocomposites was not accompanied by any sizable deterioration of mechanical properties.

## BACKGROUND

In modern material science there is a trend toward more flexibility and an increased interest in “smart” and “adaptive” materials. These are generally structural composite materials with constituents, which include functions, such as conductivity, sensing/activating properties, health monitoring abilities, thermal-load dissipation, tailorable thermal expansion, environmental protection, etc., as an inherent part of their design and application. This multifunctionality applies to the new scientific and engineering approaches required for the development of these new ceramic materials. The latest achievements in ceramic nanotechnology offer solutions for these market demands. On the other hand, ceramic materials generally exhibit brittleness with relatively low reliability. A fundamental approach to improve reliability is the design of ceramic materials with high fracture toughness and strength. Promising results have been achieved for ceramic nanocomposites exhibiting such properties.<sup>[1,2]</sup> Unfortunately, brittleness remains an intrinsic character of ceramic materials, and it is difficult to overcome this problem completely in ceramics for practical use. Accordingly, the development of

screening techniques and methods for damage detection and fracture forecasting are important to ensure the reliability of structural ceramics.<sup>[3]</sup> Incorporation of real-time damage sensors into ceramic materials can assist in lifetime predictions of complex structures. Until now, the most common applied sensor for detection of defect initializing strain was a gauge method. However, this is not practical for the determination of maximum strain applied after the load has been removed. The other nondestructive methods using x-ray, ultrasonic, and acoustic emission demand large-scale equipment and their applications in the practical use of ceramic parts are limited.

In the beginning of the 1990s, Yanagida proposed a new method of fracture forecasting by electrical measurements.<sup>[4]</sup> This self-diagnosis mechanism as an intelligent function in ceramic materials is based on the observation that there is a correlation between the increase of electrical resistivity and crack propagation. The majority of works are focused on forecasting the fatal fracture in carbon- or SiC-fiber reinforced plastics and ceramic composites by measuring electrical resistance.<sup>[3,5,6]</sup> The change in electrical resistance occurs with a change in connectivity of C or SiC fibers/whiskers in the composites. A similar approach can be applied also for ceramic composites with spherical micro-/nanoelectroconductive particles.

Although it is promising to fabricate ceramic composites with such a self-diagnosis mechanism, available conductive ceramic systems are limited and it seems difficult to maintain the mechanical properties at a level equivalent to those of the structural ceramics already used. In addition, because engineering ceramics usually show a small strain prior to fracturing, it is necessary that the electrical resistance change induced by the strain be large. Such behavior is observed near the percolation threshold of conductive phase, when the resistivity can vary by several orders of magnitude. Depending on the size and distribution of electroconductive ceramic particles, the percolation threshold varies from 8 to 30 vol%.

There are several processing routes for the introduction of electroconductive phase. Conductive ceramic

nanostructures are produced using molecular beam epitaxy, organometallic vapor phase epitaxy, top-down lithography, etc. These composites include, among others, sensors, actuators, or even miniaturized systems comprising sensing, processing, and/or actuating functions. These systems can sense, control, and activate on the micro-/nanoscale and function individually or in arrays to generate effects on the macroscale.<sup>[7]</sup> However, all the above-mentioned processing routes of nanoceramics are rather expensive and the size of the products is limited. The market demands multifunctional materials with acceptable production costs and shape flexibility. Examples of relatively low-cost processing of structural ceramics with  $\text{Si}_3\text{N}_4$  or  $\text{Al}_2\text{O}_3$  matrix and electroconductive carbon, SiC, or TiN are shown in this work. Four different methods have been used for in situ preparation of nanosized electroconductive phases: 1) addition of an organometallic precursor to commercial  $\text{Si}_3\text{N}_4$  powder as a source of nanoinclusions; 2) carbothermal reduction of ultrafine  $\text{SiO}_2$  with carbon black to SiC and C; 3) pyrolysis of organometallic Si/N/C precursors with SiC,  $\text{Si}_3\text{N}_4$ , and C products; and 4) preparation of conductive TiN by exchange reaction between titanium butoxide or fine  $\text{TiO}_2$  and AlN.

The structure of shown nanocomposites varies from homogenous bulk  $\text{Si}_3\text{N}_4/\text{SiC}$  or  $\text{Al}_2\text{O}_3/\text{SiC}$  ceramics, through organometallic polymer-derived functionally graded materials (FGM) on the base of  $\text{Si}_3\text{N}_4/\text{SiC}$  with controlled electroconductive C content to layered  $\text{Si}_3\text{N}_4/\text{TiN}$  composites prepared by tape casting. The two later ceramic nanocomposites showed self-diagnostic ability without sizeable degradation of mechanical properties.

### $\text{Si}_3\text{N}_4/\text{SiC}$ NANO-/MICROCOMPOSITES

Silicon nitride-based ceramics is a promising material for a wide variety of applications. The diapason of applications is very broad, from cast industry—where these materials are used as a new generation of refractories—to the high-tech applications in the automotive and space industry. The main requirement for application of this ceramics is an increased reliability at room temperature as well as at high temperature. An example of a material that fulfills such requirements is the  $\text{Si}_3\text{N}_4/\text{SiC}$  nanocomposite (SNC).

Samples were prepared by mixing  $\text{Si}_3\text{N}_4$  matrix powder (Ube E-10, Japan) with 5 wt%  $\text{Y}_2\text{O}_3$  (H.C. Starck, Germany) sintering additive and 20 wt% pyrolyzed polysilazane-based precursor (NCP 200, Japan) in isopropanol. The detailed processing route of the reference materials is already described elsewhere.<sup>[8]</sup>

Samples were hot-pressed under nitrogen atmosphere and mechanical pressure of 30 MPa at 1750°C

for 2 hr. The hot-pressed samples were cut to bars of  $3 \times 4 \times 45$  mm and polished to 1  $\mu\text{m}$  final finish. The creep tests in bending (20/40 inner/outer span) were performed in air from 1200°C to 1400°C, with the step of 50°C. The stepwise-loading regime was applied at each temperature. The creep experiment started with a load of 50 MPa for 24 hr, then 100 MPa for the next 24 hr, and 150 MPa for the last 24 hr to speed up the collection of data.

These nano-/microcomposites consist of the major crystalline silicon nitride phase and the minor silicon carbide phase. The larger matrix  $\text{Si}_3\text{N}_4$  grains have an elongated shape with a mean diameter below 1  $\mu\text{m}$  and lengths up to 15  $\mu\text{m}$ . SiC nano-/microparticles are randomly distributed along the grain boundaries (inter-SiC grains; diameter 300–600 nm) as well as within the  $\text{Si}_3\text{N}_4$  micrograins (intra-SiC grains, diameter 5–100 nm) as shown in Fig. 1.

The distribution of inter- and intra-SiC grains within the  $\text{Si}_3\text{N}_4$  matrix is shown in Fig. 2. The larger grains were found at the grain boundaries (inter-SiC grains), while the finer SiC were determined within the  $\text{Si}_3\text{N}_4$  host grains (intra-SiC grains). The number of intra- vs. inter-SiC grains was estimated from transmission electron microscopy micrographs and a ratio of 80 vs. 20 was determined.

### Room Temperature Properties

The room temperature properties of the  $\text{Si}_3\text{N}_4/\text{SiC}$  composite (sample SNC) and of the reference  $\text{Si}_3\text{N}_4$  materials (sample SN) are listed in Table 1.

The distinctly higher Weibull modulus of SNC confirms the homogeneity of this composite. The homogeneity of the SNC microstructure is reached by the pinning effect of randomly distributed SiC nanograins, which hinder the abnormal grain growth of  $\text{Si}_3\text{N}_4$ . The length of  $\beta\text{-Si}_3\text{N}_4$  grains was below 15  $\mu\text{m}$ . This effect has already been presented elsewhere, and it is a general feature of SNCs.<sup>[9]</sup>

The fracture toughness of SN sample (7.4  $\text{MPa m}^{1/2}$ ) is slightly higher compared to SNC (6.9  $\text{MPa m}^{1/2}$ ). Lower fracture toughness of nano-/microcomposite material compared to the relative monolithic material is attributed to the more equiaxed microstructure of  $\text{Si}_3\text{N}_4$  matrix and the low number of intra-SiC grains, only 20% (see Fig. 2). However, the intrainclusions of the second phase with a similar (but not the same) ratio of thermal expansion coefficients as in the present case should have a positive effect on the fracture toughness of the two-phase composite.<sup>[10]</sup>

The amount of SiC phase within the microstructure also plays an important role because of SiC influence on the grain growth and simultaneously on residual internal stresses. The optimum amount of SiC

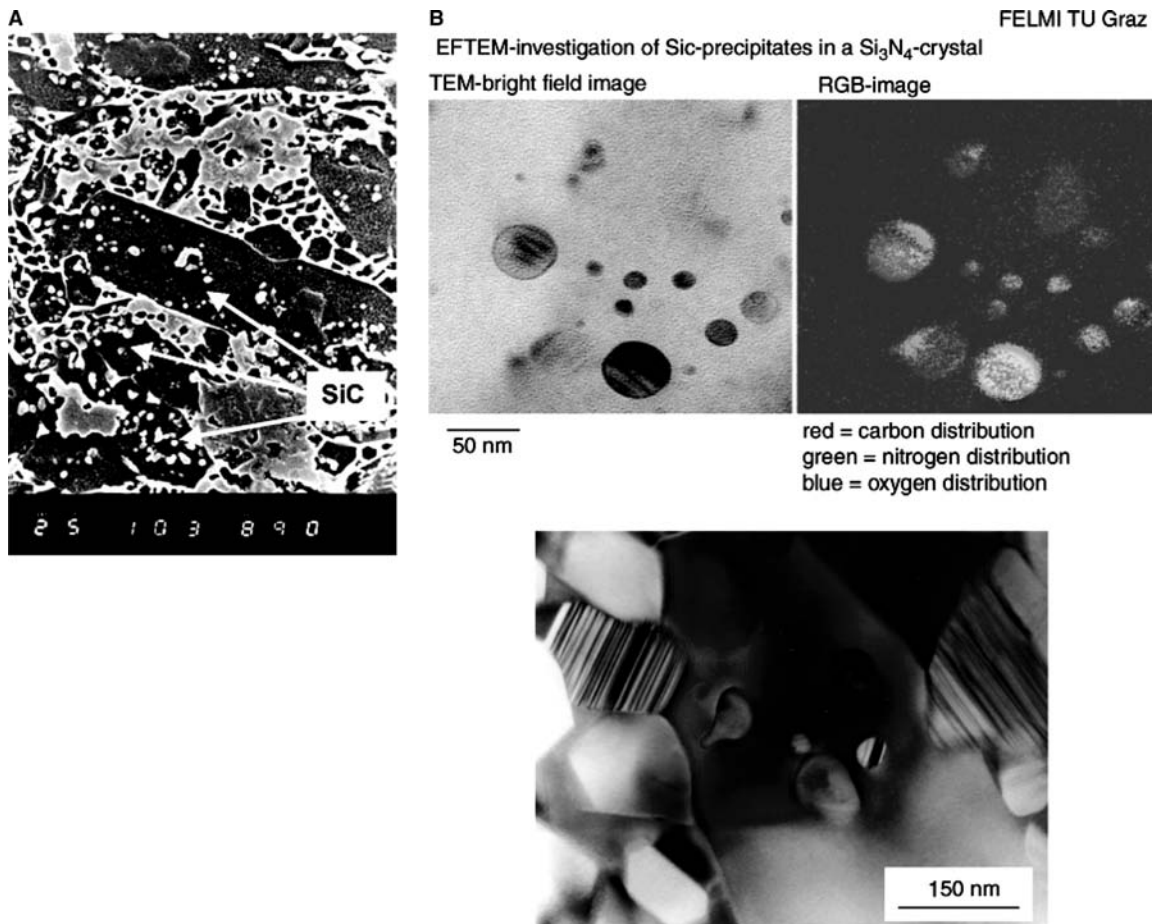


**Fig. 1** (A) SEM image of the Si<sub>3</sub>N<sub>4</sub>/SiC micro-/nanocomposite; white dots are SiC inclusions. (B) TEM image of the SiC nanoinclusions within the Si<sub>3</sub>N<sub>4</sub> grains. *Source:* From Ref.<sup>[29]</sup>.

nanograins for room temperature properties is in the range of 5–10 wt%.<sup>[11]</sup> The amount of SiC nanograins present in the SNC nano-/microcomposite is only 2.7 wt%, i.e., much lower than the indicated optimum

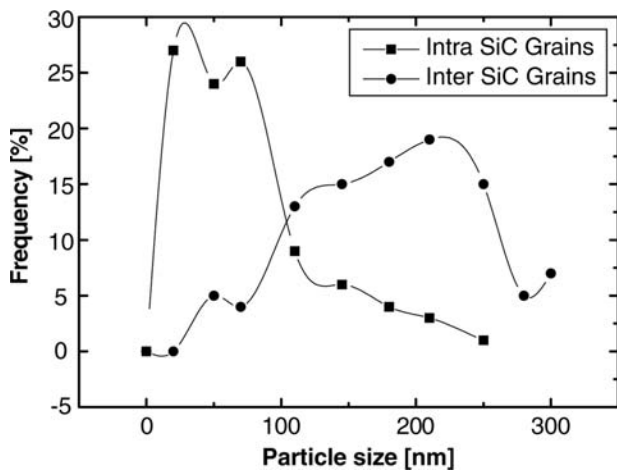


**Fig. 2** SiC particle size distribution within the Si<sub>3</sub>N<sub>4</sub> matrix. *Source:* From Ref.<sup>[14]</sup>.

of 5–10 wt%. The fact that the present composite has excellent room temperature properties at such low levels of SiC phase indicates the potential for further increase in the fraction of SiC. Moreover, depending on the content of SiC and the remaining free-carbon content, the electrical conductivity of the nanocomposite can be varied.

### High-Temperature Properties

The SNC has almost one order of magnitude higher creep resistance compared to the reference SN material (Fig. 3). The difference is smaller at higher temperatures. The apparent activation energy of SNC at stress load 100 MPa is 566 kJ/mol; for the reference material SN it is only 289 kJ/mol. A more detailed analysis showed that cavitation was the controlling mechanism at lower temperatures, while at higher temperatures diffusion creep dominated. Frequent cavitation was observed in sample SN after creep test; on the other hand, sample SNC was almost free of cavities.

**Table 1** Room temperature mechanical properties of  $\text{Si}_3\text{N}_4$ -based materials

Sample	$K_{IC}$ ( $\text{MPa m}^{1/2}$ )	Strength (MPa)	Weibull modulus
SN	7.4	990	7
SNC	6.9	1203	19

Abbreviations: SN, reference  $\text{Si}_3\text{N}_4$  material; SNC,  $\text{Si}_3\text{N}_4/\text{SiC}$  micro/nanocomposite.

The improvement of the creep resistance is usually attributed to the distribution of the fine SiC nanograins along the grain boundaries.<sup>[12]</sup> A recent publication of Rendtel et al. shows that there exists an optimum of SiC nanograins content, which lies within the range of 10–15 wt%.<sup>[13]</sup> The amorphous SiCN powder added in the amount of 20 wt% to the starting mixture yields only 5.5 wt% of SiC present in the SNC nano-/microcomposite. The reason for the improved creep resistance is an excess of the carbon in SiCN amorphous powder, which reduces the residual glassy phase on the grain boundaries and/or changes its chemistry and increases the viscosity of the glassy phase.<sup>[14,15]</sup>

### $\text{Al}_2\text{O}_3/\text{SiC}$ Nanocomposites

A similar approach has been used for the preparation of alumina-based nanocomposites.<sup>[16]</sup> Nanosized alumina powder (Taimicron TM DAR, particle size 150 nm) was used as a matrix with 5 wt%  $\text{CaO} \cdot 5\text{SiO}_2$  sintering additive. An organic granulation additive (Dolapix ET85) was used as a source of carbon. The SiC inclusions were prepared by in situ reactions between  $\text{SiO}_2$  sintering additive and carbon. Samples

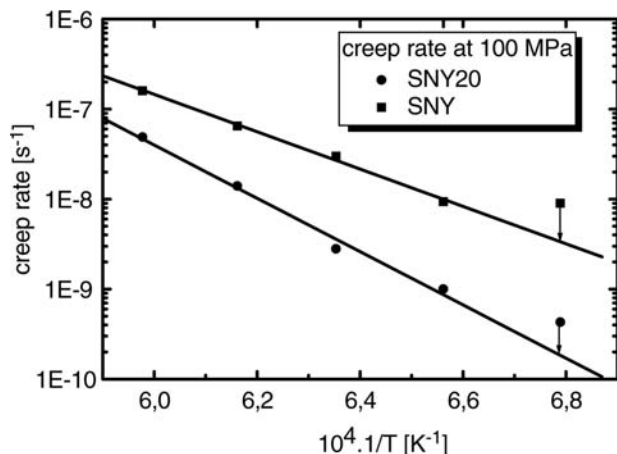


**Fig. 3** Comparison of the creep resistance of  $\text{Si}_3\text{N}_4$  material (SNY) and  $\text{Si}_3\text{N}_4/\text{SiC}$  nanocomposite prepared from  $\text{Si}_3\text{N}_4$  and pyrolyzed polysilazane mixture (SNY20). Source: From Ref.<sup>[8]</sup>.

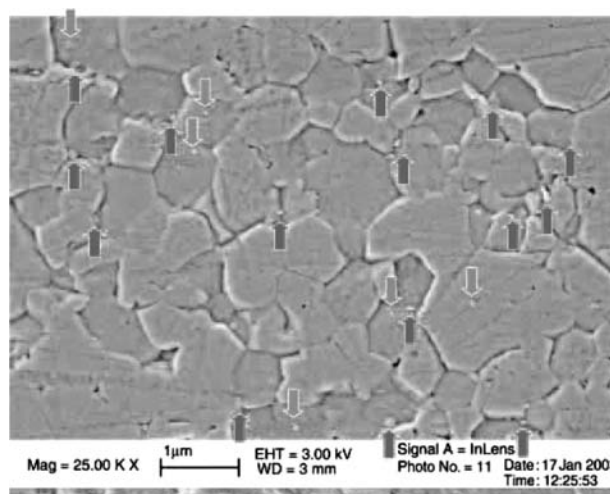


**Fig. 4** SEM of  $\text{Al}_2\text{O}_3/\text{SiC}$  nanocomposite; upside arrows indicate intergranular SiC inclusions and downside arrows indicate intra-SiC inclusions.

were densified by hot-pressing at 1450°C in argon and 30 MPa mechanical load.

The results showed that  $\text{Al}_2\text{O}_3/\text{SiC}/\text{C}$  nanocomposites could be prepared by in situ pyrolysis of organic additives. The mean grain size of the alumina matrix was finer compared with the carbon-free reference samples (Fig. 4). The remaining free carbon did not impair the mechanical properties. The hardness of densified materials increased from 20.3 to 23.2 GPa because of the presence of in situ formed SiC nanoinclusions and reduction of grain boundary glassy phase. This is a promising method for nonexpensive in situ preparation of  $\text{Al}_2\text{O}_3\text{-SiC}$  nanocomposites.

### Low-Cost SNCs

Silicon nitride–silicon carbide nanocomposite has been prepared by an in situ method that utilizes the formation of SiC nanograins by carbothermal reduction of  $\text{SiO}_2$  in the temperature range 1450–1630°C, prior to the final sintering process.<sup>[17,18]</sup> The developed  $\text{SiO}_2 + \text{C}$ -derived nanocomposite consists of a silicon nitride matrix with an average  $\text{Si}_3\text{N}_4$  matrix grain diameter of approximately 200 nm with inter- and intragranular SiC inclusions with sizes of approximately 150 and 40 nm, respectively. No pores, clusters of grains/phases were identified in the microstructure of the nanocomposite. However, there were small areas of free carbon with the maximum size of several micrometers. The mean value of room temperature four-point bending strength is 670 MPa with a Weibull modulus of 7.5 and indentation fracture toughness of  $7.4 \text{ MPa m}^{1/2}$ . The Vickers hardness was  $\text{HV1} = 28.1 \text{ GPa}$ . The creep behavior was investigated in bending at temperatures

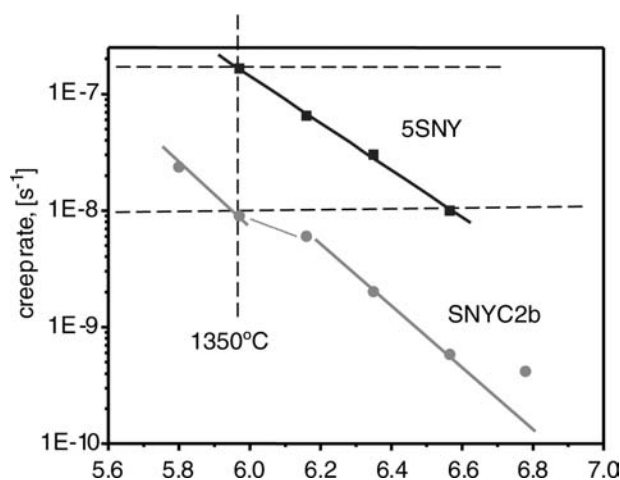


**Fig. 5** Comparison of the creep rate of  $\text{Si}_3\text{N}_4$  material (5SNY) and  $\text{Si}_3\text{N}_4/\text{SiC}$  nanocomposite prepared from  $\text{Si}_3\text{N}_4$  and  $\text{SiO}_2 + \text{C}$  mixture (SNYC2b). Source: From Ref.<sup>[19]</sup>.

from 1200°C to 1450°C under stresses ranking from 50 to 150 MPa in air. The creep resistance of the nanocomposite was significantly higher compared to the creep resistance of the monolithic  $\text{Si}_3\text{N}_4$  (Fig. 5). This improvement was achieved by the incorporation of intergranular SiC nanoparticles into the  $\text{Si}_3\text{N}_4$  matrix.

The cutting performance of the ceramic cutting inserts prepared from this low-cost SNC shows a three times longer lifetime compared to the commercially available  $\text{Si}_3\text{N}_4$ -based cutting inserts.<sup>[19]</sup>

### MULTIFUNCTIONAL Si-C-N BULK CERAMIC NANOCOMPOSITES PREPARED BY PYROLYTIC CONVERSION OF POLYHYDRIDOMETHYLSILAZANE

Formation of ceramics from polymer precursors is desirable because the processing is done at lower temperatures and with simpler procedures than conventional processes of sintering ceramic powders. Although the preceramic polymers offer many advantages over conventional coating techniques, the large shrinkage that occurs on conversion from polymer to ceramic remains a processing problem. This shrinkage can exceed 50% and causes warping or cracking in a coating or bulk material. The two main methods for elimination of this effect are employing compatible fillers (either active or passive) into the polymer, or using a preceramic precursor with high ceramic yield. On pyrolysis, the active filler reacts with the surrounding matrix or a reactive atmosphere and expands, thereby compensating for the shrinkage of the polymer. Concerning the latter method, preceramic precursors with ceramic yield higher than 85% became recently available. In both methods two steps are applied,

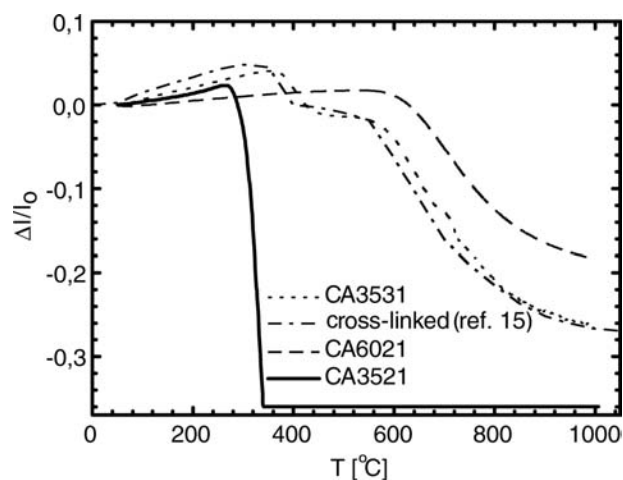


**Fig. 6** The results of thermal mechanical analysis characteristic for different states of cross-linking of polysilazane NCP200. Sample CA3531 is optimally cross-linked. Source: From Ref.<sup>[24]</sup>.

cross-linking of a liquid precursor into a rigid polymer followed by pyrolysis of the polymer into a monolithic SiCN ceramic. These steps must be optimized for each precursor. An example of optimal cross-linking conditions of NCP200 polyhydridomethylsilazane is shown in Fig. 6.<sup>[20]</sup>

The composition of polyorganosilazane precursor and, consequently, the final ratio of  $\text{Si}_3\text{N}_4/\text{SiC}$  can be modified. Pyrolysis in argon results in an amorphous product with composition  $\text{Si}_1\text{C}_{0.58}\text{N}_{0.90}$ , while carbon-free specimens with compositions close to that of stoichiometric  $\text{Si}_3\text{N}_4$  were prepared by heat treatment in ammonia ( $\text{NH}_3$ ) atmosphere.<sup>[21–23]</sup> In our earlier work it was shown that by heat treatment of polysilazane in mixed Ar/ $\text{NH}_3$  atmosphere with different volume ratio or ammonia, the carbon content could be adjusted in a wide range.<sup>[24]</sup> The optimal annealing temperature for adjustment of carbon content in amorphous Si-C-N ceramics was found between 500°C and 550°C. Higher annealing temperatures within this interval and longer dwell periods at the respective temperatures resulted in lower carbon content in the product of pyrolysis. The increase of the volume ratio of  $\text{NH}_3$  in reactive atmosphere from 10 to 50 vol% resulted in faster carbon removal from the specimens. Dwell periods at intermediate temperature in argon promoted the formation of Si-C bonds, and produced specimens with higher carbon content. Optimization of the pyrolysis conditions up to 1100°C yielded crack-free amorphous bulk specimens with carbon contents in the range of 0.3–16.2 wt%. After crystallization of such stoichiometric tough amorphous intermediates,  $\text{Si}_3\text{N}_4$ -SiC micro-nanocomposites with different volume fractions of SiC nanoparticles could be obtained.



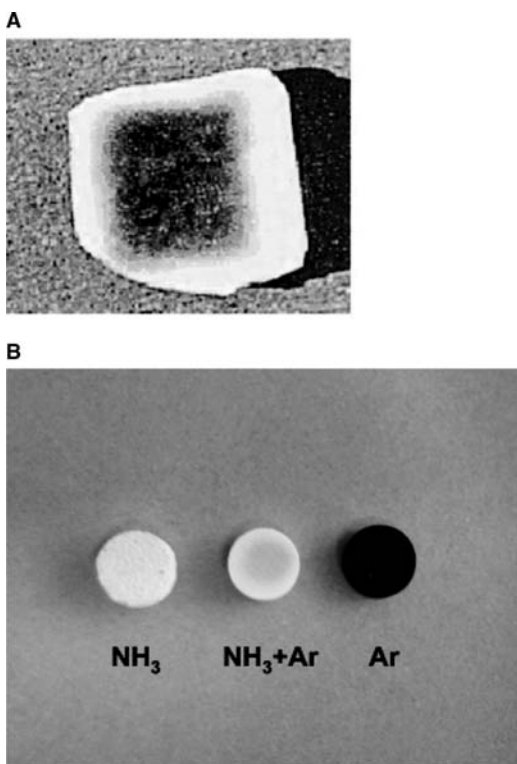


**Fig. 7** Optical micrograph of polymer-derived nanocomposite annealed in (A) combined Ar and Ar + NH<sub>3</sub> atmosphere; (B) NH<sub>3</sub>; (C) Ar + 10% NH<sub>3</sub>; and (D) Ar.

In addition, the Si–C–N stoichiometry can also be tailored in the cross section of amorphous ceramics.<sup>[25]</sup> Graded carbon content was achieved by changing the conditions of reactive heat treatment (temperature, holding time, Ar/NH<sub>3</sub> ratio, and gas flow rate) of polycarbosilazane polymer during processing (Fig. 7). Topochemical carbon analysis of a reference sample with homogenous carbon distribution and of samples heat-treated for 5, 7, 9, and 12 hr in the reactive atmosphere (Ar + 10 vol% NH<sub>3</sub>) at 525°C are shown in Fig. 8A. A core-shell carbon distribution is evident. The time dependence of the carbon content in the core of a specimen under the same conditions is shown in Fig. 8B. Depending on the carbon content, the electrical conductivity of Si–N–C materials also varies. Fig. 9 illustrates the differences in DC-conductivity of two amorphous Si/C/N ceramics with approximately 0.5 and 13.53 wt% C-content.<sup>[26]</sup> Lowering the C-content from 13.5 to 0.5 wt% by ammonia treatment decreases the DC-conductivity over the whole measured temperature range by approximately four orders of magnitude.

The relative simplicity of preparation of specimens with different concentrations of carbon in the surface layer and in the core opens the possibility for easy preparation of FGM with respect to their electrical properties.<sup>[27]</sup> Fig. 10 highlights the range of DC-conductivity

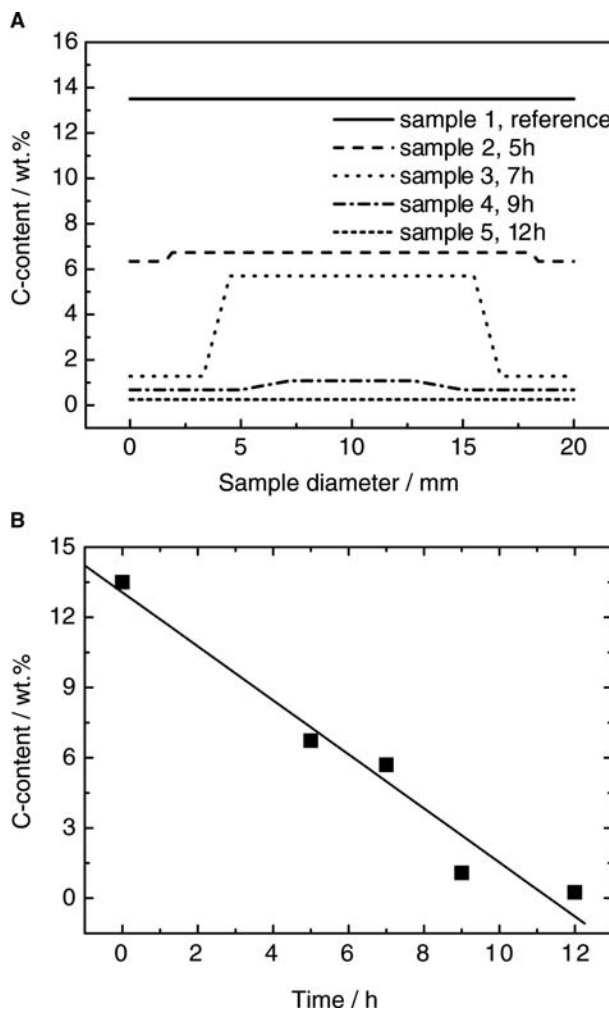


**Fig. 8** (A) Topochemical analysis of a reference sample and samples heat-treated 5, 7, 9, and 12 hr in the reactive atmosphere (Ar + 10 vol% NH<sub>3</sub>) at 525°C. (B) Time dependence of the carbon content in the core of a specimen pyrolyzed at 525°C. Source: From Ref.<sup>[25]</sup>.

that can be covered by polysilazane-derived samples through reactive ammonia treatment, nonreactively pyrolyzed samples in argon, and also subsequent aging at elevated temperatures (between 1100°C and 1450°C). This opens the opportunity for the preparation of novel high-temperature resistant electrical conductors mechanically reinforced by insulator the Si<sub>3</sub>N<sub>4</sub> surface layer.

#### LAYERED CERAMIC NANOCOMPOSITES WITH SELF-DIAGNOSTIC ABILITY

Designing ceramic composites with laminated structure has gained increasing attention, because these materials show improved mechanical properties (due to decreased sensitivity to defects) and display a

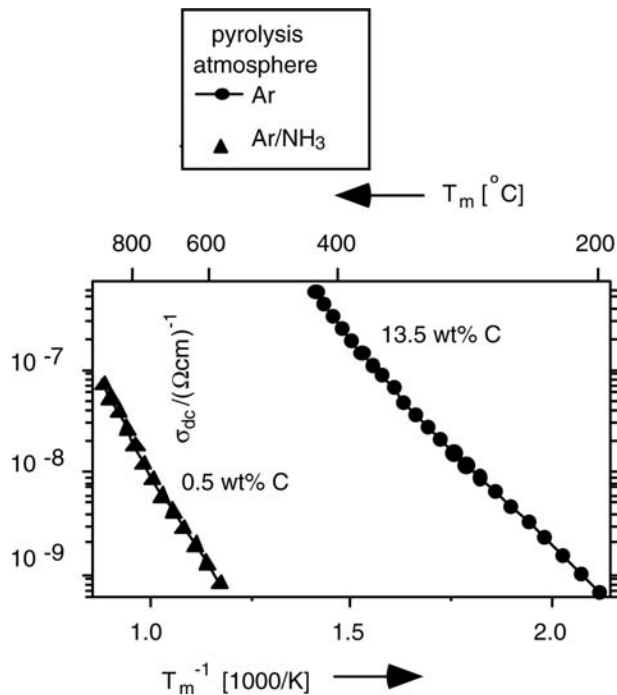


**Fig. 9** Variation of DC-conductivity of amorphous Si/C/N ceramic body with temperature and carbon content. Source: From Ref.<sup>[25]</sup>.

balanced combination of other engineering properties (like thermal and electrical conductivity, oxidation and wear resistance, etc.). Nature has many objects with laminated or graded structures. An example is the nacre of abalone shell: a natural multifunctional

nanolaminated ceramic-polymer composite material with good mechanical properties and the ability to repair itself.<sup>[28]</sup>

Inspired by the nature, a similar design of layered materials was used for the preparation of composites with multifunctional properties. Ceramic laminates based on  $\text{Si}_3\text{N}_4$  with different TiN content (from 0 to 33 vol%) were prepared by tape casting and hot-pressing.<sup>[29,30]</sup> TiN was prepared by in situ reaction of titanium butoxide or fine grade rutile ( $\text{TiO}_2$ ) with AlN according to the following reaction:



TiN derived from titanium butoxide had an average diameter of 100 nm, while the size of particles obtained from rutile was several micrometers (Fig. 11).

During the design of the layer sequence special attention was paid to the minimization of residual stresses in the layered composite, and the TiN content was gradually increased from 0 to 3, 8, 10, 15, 20, 25, and 33 vol%.<sup>[31]</sup> The bending strength normal to the layers and the fracture toughness of materials are shown in Figs. 12A and 12B. Both properties are markedly higher for the layered L4-10 material in comparison to the monolithic M-10 sample ( $\text{Si}_3\text{N}_4$  with 10 vol% TiN). The high increase of fracture toughness can be explained by the laminated structure, by strong alignment of elongated  $\beta\text{-Si}_3\text{N}_4$  particles, and by reasonable thermal expansion mismatch between  $\text{Si}_3\text{N}_4$  and  $\text{Si}_3\text{N}_4 + \text{TiN}$  layers.

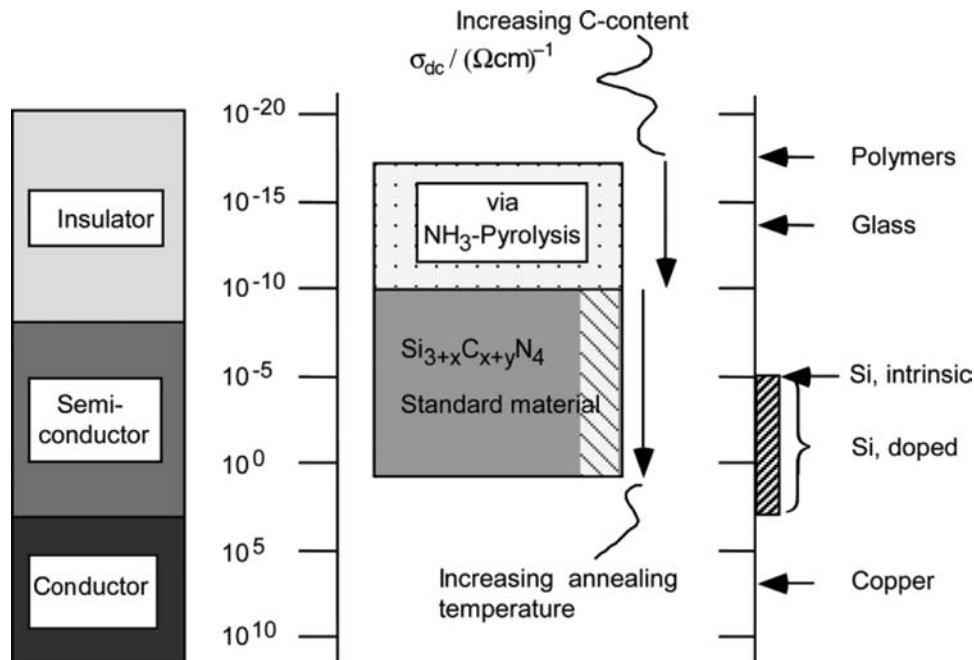


**Fig. 10** DC-conductivities [ $\sigma_{\text{dc}}, (\Omega\text{cm})^{-1}$ ] of various materials at 20°C.

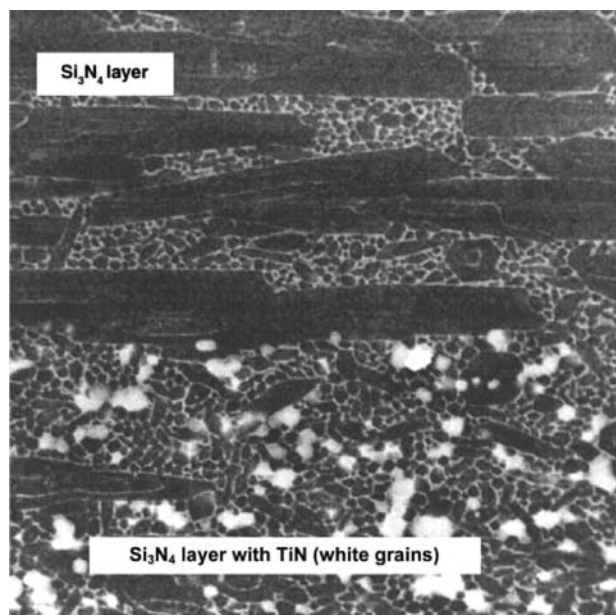


**Fig. 11** Scanning electron micrograph of the interface between seeded  $\text{Si}_3\text{N}_4$  layer and  $\text{Si}_3\text{N}_4 + 10 \text{ vol}\% \text{ TiN}$  layer. Source: From Ref.<sup>[29]</sup>.

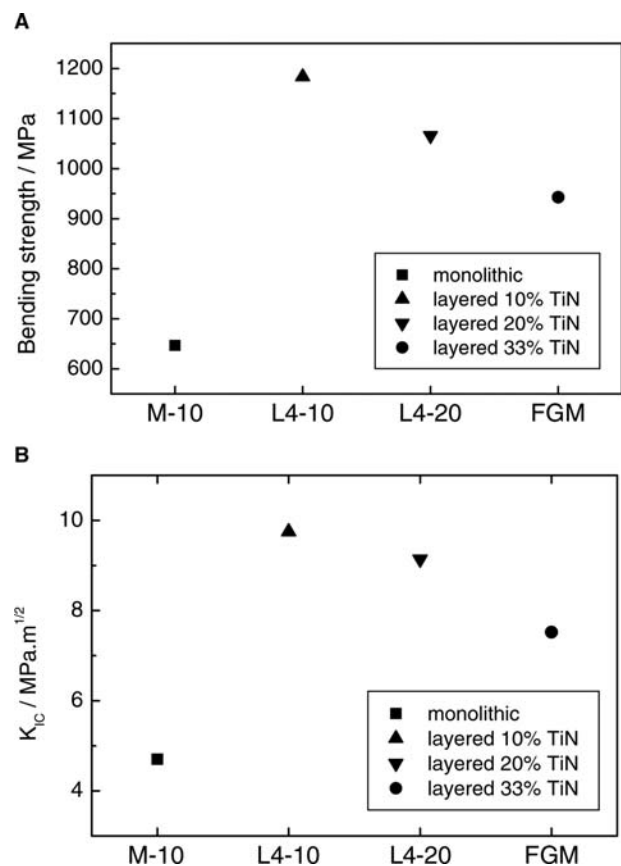


**Fig. 12** (A) Three-point bending strength of the monolithic and layered samples. (B) Fracture toughness (SEVNB) of monolithic and layered samples. Source: From Ref.<sup>[29]</sup>.

**Table 2** Electrical resistivity  $\rho$  of monolithic (M-10) and layered samples

Sample	TiN (vol%)	$\rho_x$ ( $\Omega \text{ cm}$ )	$\rho_y$ ( $\Omega \text{ cm}$ )
M-10	10	$5.10^6$	$5 \times 10^6$
L4-10	10	$8.10^7$	$2 \times 10^{12}$
L4-20	20	$6.10^{-2}$	$5 \times 10^{11}$
FGM	33	$4.10^{-4}$	$8 \times 10^{10}$

The higher strength of the layered composites compared to the monolithic M-10 sample is caused by the presence of strong  $\text{Si}_3\text{N}_4$  layers. However, on increasing the TiN content to 33 vol%, the strength of the layered samples decreases because of higher residual stresses.

The anisotropic electrical conductivity was measured for the layered L4-20 and FGM samples in parallel ( $x$ ) and perpendicular ( $y$ ) direction to the layers (Table 2). In the parallel direction, the presence of electroconductive TiN caused an increase in conductivity. On the other hand, the electrical conductivity decreased in the direction perpendicular to the layer alignment because of the presence of insulating  $\text{Si}_3\text{N}_4$  layers. Very good conductivity was obtained for the layered material with 33 vol% TiN.

The listed results show that a remarkable improvement in strength and fracture toughness was achieved for the layered ceramic materials. Nevertheless, the possibility for catastrophic failure of ceramic components hinders their wider application in the industry. Fracture prediction in engineering ceramics is a promising method to increase the reliability and practical application of ceramic materials. One of the possible methods for forecasting the fracture is the measurement of electrical resistivity of the conductive layer based on the fact that, generally, the resistivity increases with cracks generation.

For this reason, electroconductive self-monitoring layer was joined to the layered composite (Fig. 13). The monitoring layer contained a threshold volume fraction of conductive phase, 19 vol% TiN.<sup>[32]</sup> The testing bars were positioned on the four-point bend test holder and the piezo-electric displacement transducer stepwise increased the programmed load. The load was released at a certain level, and the bar reloaded again. The results of electrical resistivity measurements under tensile load are shown in Fig. 14. The increase in electrical resistivity can be explained by the formation of microcracks in the conductive layer, which were also observed by SEM. The change of electrical resistance was of the order of  $0.1 \Omega \text{ cm}$  and can be recorded with the available measuring devices. The output of the measuring device can be simply recorded, and if the derivative of the electrical resistance by load is equal to zero ( $d\rho/dF = 0$ ), it means that the probability of

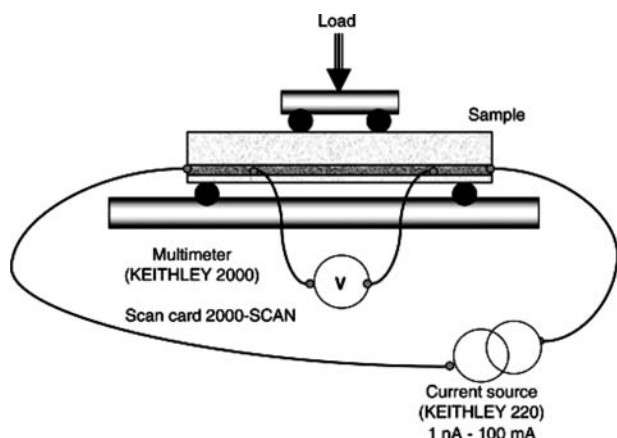


Fig. 13 Schematic of the electrical conductivity measurement on the self-diagnostic layered material.

crack formation increased to a serious level. In practical use, it indicates that the ceramic component should be replaced.

The above results demonstrate that the ceramic materials with electroconductive nano-inclusions can be used as a simple and useful tool for the crack formation and failure of brittle ceramic materials.

## CONCLUSIONS

Silicon nitride or alumina-based ceramic nanocomposites with electroconductive carbon, SiC, or TiN inclusions can be used for the preparation of self-monitoring sensors with an ability to detect crack initiation and crack propagation. Four different methods of nanocomposite synthesis have been compared:

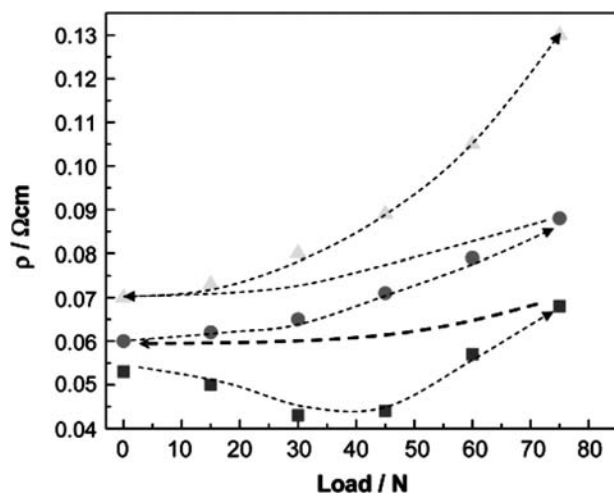


Fig. 14 Change of electrical resistivity after cyclic loading/unloading of self-diagnostic layered sample. Increasing resistivity indicates crack formation.

1) adding an organometallic precursor to commercial  $\text{Si}_3\text{N}_4$  powder as a source of nano-inclusions; 2) carbothermal reduction of ultrafine  $\text{SiO}_2$  with carbon black to SiC and C nano-inclusions; 3) pyrolysis of organometallic Si/N/C precursors with fine SiC,  $\text{Si}_3\text{N}_4$ , and C products; and 4) preparing conductive TiN by exchange reaction between titanium butoxide or fine  $\text{TiO}_2$  and AlN.

Depending on the preparation method, the structure of nanocomposites varies from homogenous bulk  $\text{Si}_3\text{N}_4/\text{SiC}$  or  $\text{Al}_2\text{O}_3/\text{SiC}$  ceramics, through organometallic polymer-derived functionally graded  $\text{Si}_3\text{N}_4/\text{SiC}$ -based materials to layered  $\text{Si}_3\text{N}_4/\text{TiN}$  composites prepared by tape casting. The graded and layered ceramic nanocomposites showed self-diagnostic ability without a sizeable degradation of mechanical properties.

## ACKNOWLEDGMENTS

This work was supported by the Slovak Grant Agency, project No. VEGA 2/4072/24, VEGA 2/3101/23, grant ŠO 51/03R80600/03R0603, APVT-51-049702, and Centrum of Excellence NANOSMART. Both the authors acknowledge the financial support by the Alexander von Humboldt Foundation, Germany.

## REFERENCES

1. Niihara, K. New design concept of structural ceramic—ceramic nanocomposites. *J. Ceram. Soc. Jpn.* **1991**, *99* (10), 974–982.
2. Wakai, F.; Kodama, Y.; Sakaguchi, S.; Murayama, N.; Izaki, K.; Niihara, K. A superplastic covalent crystal composite. *Nature* **1990**, *344* (6265), 421–423.
3. Hirano, S.; Kishimoto, A.; Miyayama, M. Conductive coating on structural ceramics for strain detection utilizing electrical measurements. *J. Eur. Ceram. Soc.* **1999**, *19*, 2087–2095.
4. Yanagida, H. Intelligent ceramics. *Ferroelectrics* **1990**, *102*, 251–257.
5. Ishida, A.; Miyayama, M.; Yanagida, H. Prediction of fracture and detection of fatigue in ceramic composites from electrical resistivity measurements. *J. Am. Ceram. Soc.* **1994**, *77* (4), 1057–1061.
6. Ishida, A.; Miyayama, M.; Kishimoto, A.; Yanagida, H. Change of electrical resistance in electrically conductive ceramic composites under tension and compression load. *J. Ceram. Soc. Jpn.* **1995**, *103* (6), 576–581.
7. Bhushan, B. *Springer Handbook of Nanotechnology*; Springer-Verlag: Berlin, Germany, 2004; V–IX, 1–4.
8. Šajgalík, P.; Hnatko, M.; Lenčič, Z. Silicon nitride/ceramic nano/micro composites for room as well as high temperature applications. *Key Eng. Mater.* **2000**, *175–176*, 289–300.
9. Šajgalík, P.; Dusza, J.; Hofer, F.; Warbichler, P.; Reece, M.; Boden, G.; Kozánková, J. Structural development

- and properties of SiC–Si<sub>3</sub>N<sub>4</sub> nano/micro-composites. *J. Mater. Sci. Lett.* **1993**, *15*, 72–76.
10. Nandy, M.-O.; Schmauder, S.; Kim, B.-N.; Watanabe, M.; Kishi, T. Simulation of crack propagation in alumina particle-dispersed SiC composites. *J. Eur. Ceram. Soc.* **1999**, *19*, 329–334.
  11. Sasaki, G.; Sukanuma, K.; Fujita, T.; Hiraga, K.; Niihara, K. Interface structure of Si<sub>3</sub>N<sub>4</sub> matrix composite with nano-meter scale SiC particles. *Mater. Res. Symp. Proc.* **1993**, *287*, 335–340.
  12. Niihara, K.; Hirano, T.; Izaki, K.; Wakai, F. High temperature creep deformation of Si<sub>3</sub>N<sub>4</sub>/SiC nanocomposites. In *Silicon-Based Structural Ceramics*; Sheldon, B.W., Danforth, S.C., Eds.; Ceramic Transactions, The American Ceramic Society: Ohio, 1994; *42*, 208–219.
  13. Rendtel, P.; Rendtel, A.; Hübner, H.; Klemm, H.; Herrmann, M. Effect of long term oxidation on creep and failure of Si<sub>3</sub>N<sub>4</sub> and Si<sub>3</sub>N<sub>4</sub>/SiC nanocomposites. *J. Eur. Ceram. Soc.* **1999**, *19* (2), 217–226.
  14. Šajgalík, P.; Hnatko, M.; Lofaj, F.; Hvizdoš, P.; Dusza, J.; Warbichler, P.; Hofer, F.; Riedel, R.; Lecomte, E.; Hoffmann, M.J. SiC/Si<sub>3</sub>N<sub>4</sub> nano/microcomposites—processing, RT, and HT mechanical properties. *J. Eur. Ceram. Soc.* **2000**, *20* (4), 453–462.
  15. Šajgalík, P.; Hnatko, M.; Lenčič, Z. Properties of silicon nitride/carbide nano/micro composites—role of SiC nano-inclusions and grain boundary chemistry. In *Ceramic Materials and Components for Engines*; Heinrich, G., Aldinger, F., Eds.; Wiley-VCH: Weinheim, 2001; 559–564.
  16. Sedláček, J.; Galusek, D.; Švančárek, P.; Brown, A.; Brydson, R. Alumina–carbon composites with high hardness. *Key Eng. Mater.* **2004**, *264*, 841–844.
  17. Hnatko, M.; Šajgalík, P.; Lenčič, Z.; Monteverde, F.; Dusza, J.; Warbichler, P.; Hofer, F. Low cost SiC/Si<sub>3</sub>N<sub>4</sub> nanocomposites. *Key Eng. Mater.* **2002**, *206–213*, 1061–1064.
  18. Šajgalík, P.; Hnatko, M.; Lenčič, Z.; Warbichler, P.; Hofer, F. C-derived SiC–Si<sub>3</sub>N<sub>4</sub> nanocomposite. *Z. Metall.* **2001**, *92*, 937–941.
  19. Šajgalík, P.; Hnatko, M.; Lenčič, Z.; Dusza, J.; Kašiarová, M.; Kovalčík, J.; Šída, V. Low cost Si<sub>3</sub>N<sub>4</sub>/SiC nanocomposites, processing, RT, and HT properties. *Key. Eng. Mater. in press*.
  20. Riedel, R.; Seher, M.; Mayer, J.; Vinga Szabó, D. Polymer derived Si-based bulk ceramics, part I: preparation, processing, and properties. *J. Eur. Ceram. Soc.* **1995**, *15*, 703–715.
  21. Riedel, R.; Friess, M. *Organometallic Precursor for the Preparation of High Performance Non-Oxide Ceramics and Ceramic Matrix Composites*; Final Technical Report; BRITE/EURAM Project No BREU-0106-C(JR), Darmstadt, 1993.
  22. Riedel, R.; Seher, M. Crystallization behavior of amorphous silicon nitride. *J. Eur. Ceram. Soc.* **1991**, *7*, 21–25.
  23. Burns, G.T.; Chandra, G. Pyrolysis of preceramic polymers in ammonia: preparation of silicon nitride powders. *J. Am. Ceram. Soc.* **1989**, *72*, 333–337.
  24. Galusek, D.; Reschke, S.; Lenčič, Z.; Dressler, W.; Riedel, R.; Šajgalík, P.; Majling, J. In-situ carbon content adjustment in Si–C–N bulk ceramics prepared by pyrolytic conversion of polyhydridomethylsilazane. *J. Eur. Ceram. Soc.* **1999**, *19*, 1911–1921.
  25. Reschke, S.; Haluschka, C.; Lenčič, Z.; Galusek, D.; Riedel, R. In-situ generated homogeneous and functionally graded ceramic materials derived from polysilazane. *J. Eur. Ceram. Soc.* **2003**, *23* (11), 1963–1970.
  26. Haluschka, C.; Engel, C.; Riedel, R. Silicon carbonitride ceramics derived from polysilazanes part II. Investigation of electrical properties. *J. Eur. Ceram. Soc.* **2000**, *20*, 1365–1374.
  27. Riedel, R. Advanced ceramics from inorganic polymers. In *Materials Science and Technology*; Cahn, R.W., Haasen, P., Kramer, E.J., Brook, R.J., Eds.; VCH Verlagsgesellschaft: Weinheim, 1996; *17B*, 2–50.
  28. Sarikaya, M.; Aksay, I.A. Nacre of abalone shell: a natural multifunctional nanolaminated ceramic-polymer composite material. *Results Probl. Cell Differ.* **1992**, *19*.
  29. Lenčič, Z.; Šajgalík, P.; Roncari, E.; Hirao, K. Design of Si<sub>3</sub>N<sub>4</sub> based layered composites for multifunctional application. *Key Eng. Mater.* **2000**, *175–176*, 173–182.
  30. Lenčič, Z.; Šajgalík, P.; Toriyama, M.; Brito, M.E.; Kanzaki, S. Multifunctional Si<sub>3</sub>N<sub>4</sub>/(β-SiAlON + TiN) based layered composites. *J. Eur. Ceram. Soc.* **2000**, *20*, 347–355.
  31. Šajgalík, P.; Lenčič, Z. Silicon nitride layered composites—relationship between residual stresses and fracture behaviour. 6th International Symposium on Ceramic Materials and Components for Engines. Niihara, K., Hirano, S., Kanzaki, S., Komeya, K., Morinaga, K., Eds.; Technoplasza Co.: Japan, 1997; 675–678.
  32. Lenčič, Z.; Šajgalík, P.; Balog, M.; Fröhlich, K.; Roncari, E. Layered Si<sub>3</sub>N<sub>4</sub>/(SiAlON + TiN) composites with self-diagnostic ability. In *Ceramic Materials and Components for Engines*; Heinrich, G., Aldinger, F., Eds.; Wiley-VCH: Weinheim, 2001; 559–564.



# Charge Carrier Dynamics of Nanoparticles

Fanxin Wu  
Jin Z. Zhang

*Department of Chemistry and Biochemistry, University of California–Santa Cruz,  
Santa Cruz, California, U.S.A.*

## INTRODUCTION

Nanomaterials, studied extensively during the past two decades, represent a class of materials with at least one relevant dimension on the length scale of a few to a few hundred nanometers.<sup>[1–17]</sup> In this size regime, properties of nanomaterials become strongly dependent on factors such as surface characteristics, shape, and size due to the quantum confinement effect.<sup>[1,6,7,18]</sup> It is, in principle, possible to adjust the properties such as the color and redox potentials of nanomaterials by changing the particle size or shape, without any change of chemical composition. Nanomaterials become increasingly important in applications such as transistors,<sup>[19]</sup> light emitting diodes,<sup>[20,21]</sup> sensors,<sup>[22]</sup> solar cells,<sup>[23]</sup> and lasers.<sup>[24]</sup>

Compared with the static properties such as optical absorption and emission, dynamic properties of charge carrier in nanomaterials are relatively less understood. Considerable progress has been made in the study and understanding of charge carrier dynamics recently.<sup>[3–5,11,13–17,24–31]</sup> Most studies have focused on issues such as charge carriers trapping, carrier interaction, recombination, and their dependence on particle size, shape, surface characteristics. Studies of dynamic properties provide complementary information to static studies and help to gain a better fundamental understanding of the charge carrier behavior in nanomaterials.

Several powerful time-resolved laser techniques have been employed to investigate charge carrier dynamics, including transient absorption, transient bleach, and time-resolved fluorescence. In a transient absorption measurement, samples are first excited with an ultrafast laser pulse. A second laser pulse, delayed with respect to the first (excitation) pulse, is used to detect the population of charge carriers in excited states.<sup>[32]</sup> Transient bleach has been used to monitor the population of ground states in a similar pump–probe setup.<sup>[33,34]</sup> The excited-state population has also been monitored by time-resolved fluorescence combined with a fluorescence up-conversion method<sup>[35]</sup> or stimulated emission.<sup>[36]</sup>

This entry reviews the recent advances in the studies of charge carrier dynamics and optical properties of

semiconductor and metal nanoparticles (NPs). It starts with a general picture of photoexcited electron relaxation in semiconductor NPs. Specific nanoparticle systems are then discussed in some detail, including CdS, CdSe, CdTe, PbS, Cu<sub>2</sub>S, Ag<sub>2</sub>S, GaAs, InP, Mn<sup>2+</sup>-doped ZnS, Mn<sup>2+</sup>-doped ZnSe, TiO<sub>2</sub>, Fe<sub>2</sub>O<sub>3</sub>, AgI, AgBr, MoS<sub>2</sub>, PbI<sub>2</sub>, BiI<sub>3</sub>, and Si. The dynamic properties of metal NPs are then illustrated with examples such as Ag and Au NPs. Possible dependence of charge carrier dynamics on parameters such as size, shape, and surface characteristics is discussed with appropriate examples. A summary is given at the end of the entry.

## CHARGE CARRIER DYNAMICS IN SEMICONDUCTOR NANOPARTICLES

### General Picture of Charge Carrier Dynamics in Semiconductor Nanoparticles

A general scheme of charge carrier relaxation in semiconductor NPs can be illustrated in Fig. 1. Upon photoexcitation, an electron is generated in the conduction band (CB) and a hole in the valence band (VB). The hot electron then relaxes to the bottom of the CB and hole to the top of the VB. Because of Coulombic attraction, an exciton is formed from the electron and hole. The exciton can decay radiatively or non-radiatively through electron–hole recombination. If there are no states within the bandgap, as in single crystal semiconductors, the recombination will be mainly radiative, producing bandedge emission, and the lifetime should be on the order of nanoseconds for direct bandgap semiconductors. However, if states exist within the bandgap because of defects or surface dangling bonds, as in semiconductor NPs, photoexcited charge carriers can be trapped in these states on time scales faster than radiative recombination.

Trapping time constants have been reported for different semiconductor NPs. For example, a trapping time of about 100 fsec has been suggested for CdS NPs.<sup>[32,37]</sup> For CdSe NPs, a trapping time of 0.5–8 psec has been reported.<sup>[38]</sup> A much longer trapping time of



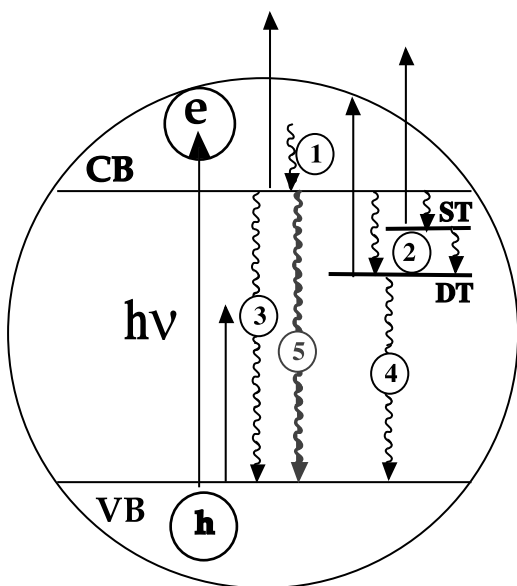


**Fig. 1** Schematic illustration of charge carrier relaxation in semiconductor NPs and the pump–probe scheme for monitoring the carrier dynamics. The long solid line with upward arrow indicates excitation and the short solid lines with upward arrows indicate the probe of the conduction band, shallow and deep trap states, and valence band, respectively. The curved lines with downward arrows indicate different relaxation processes: (1) electronic relaxation within the conduction band, (2) trapping into shallow trap (ST) and deep trap (DT) states and further trapping from ST to DP, (3) bandedge electron–hole recombination, (4) trapped electron–hole recombination, and (5) exciton–exciton annihilation. *Source:* From Fig. 4 of Ref. [11].

30 psec has been suggested for CdS NPs based on measurements of trap state emission<sup>[39,40]</sup> and the study of electron acceptor such as viologen derivatives on particle surface.<sup>[41]</sup> The variation of trapping time may be due to the difference in samples, experimental conditions, and/or different data interpretations. However, it is reasonable to conclude that the time constants for trapping in semiconductor NPs are on the order of a few hundred femtoseconds to a few tens of picoseconds, depending on the nature of the NPs or quality of sample.

The trapped carriers can further recombine radiatively or non-radiatively. The radiative decay will produce trap state emission that is red shifted with respect to bandedge emission. Trap states in NPs have lifetimes from a few tens of picoseconds to nanoseconds or longer, depending on the nature of trap states.

At high excitation intensities, nonlinear processes come into play. For example, exciton–exciton annihilation could take place when there is a high density of excitons within a small volume of sample at a given time. This can happen for both bulk and nanoparticle semiconductors. For nanoparticles, interestingly, this

has been observed only when trap states are saturated and accumulation of excitons becomes possible. Exciton–exciton annihilation is a non-radiative process and occurs on the time scale of a few picoseconds or longer depending on the exciton concentration. Auger recombination, another non-radiative, non-linear decay pathway, becomes significant at very high excitation intensity as well and ionization is involved in this process. Experimentally, it is often difficult to distinguish between exciton–exciton annihilation and Auger recombination.

The general picture described above will be illustrated next with specific nanoparticle systems.

### Metal Chalcogenide Semiconductor Nanoparticles

Metal chalcogenide semiconductor NPs such as CdS and CdSe have been the most extensively studied systems. Earlier picosecond studies on charge carrier dynamics observed a strong transient bleach feature near the excitonic absorption region.<sup>[42–48]</sup> The peak of the bleach was found to shift with time and attributed to increased screening by charge carriers for the particles.<sup>[49]</sup> Also, a red shift of the transient absorption features was observed in CdSe, which was explained as a result of the formation of biexciton.<sup>[50,51]</sup> Later, femtosecond studies found that the transient bleach decay follows a double exponential decay with the fast component increasing with excitation intensity faster than the slower component.<sup>[33]</sup>

A similar excitation intensity dependence of the transient absorption signals was observed for CdS NPs.<sup>[32,52]</sup> The decay profiles feature a fast 2–3-psec and a slow 50-psec decay component. As shown in Fig. 2, the amplitude of the fast component increases faster than the slower component with increasing excitation intensity. The fast decay component was initially assigned to nongeminate electron–hole recombination at high excitation intensities.<sup>[32]</sup> More detailed investigations on both CdS and CdTe NPs were subsequently carried out using both transient absorption and time-resolved fluorescence.<sup>[53]</sup> The bandedge fluorescence was found to be power dependent as well. The power-dependent fast component was then assigned to exciton–exciton annihilation, as suggested previously.<sup>[54]</sup> The slower decays were attributed to trapping and the recombination of trapped carriers. It was concluded that the transient absorption signals observed have contributions from both bandedge electrons (excitons) and trapped electrons. At early times, the excitons have significant contributions, especially at high excitation intensities. The contribution from trapped electrons becomes more important and eventually the signal is basically all from trapped

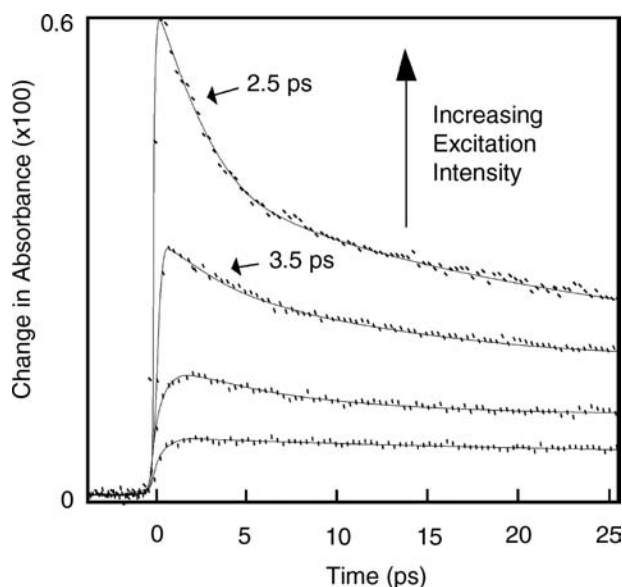


**Fig. 2** Excitation intensity-dependent photoinduced electron relaxation dynamics of CdS NPs probed at 780 nm, following excitation at 390 nm. The fast decay component increases nonlinearly with excitation intensity and is absent at low intensity. *Source:* From Fig. 5 of Ref.<sup>[11]</sup>.

charge carriers on long time scales. This is believed to be true for many other colloidal semiconductor nanoparticles.<sup>[28,55–58]</sup>

Recently, femtosecond fluorescence up-conversion spectroscopy has been used to study the charge carrier dynamics in CdSe nanocrystals.<sup>[59]</sup> Both the rise time and decay of bandedge emission show a direct correlation to the size of nanocrystal and the rise time is dependent on excitation intensity. The long-lived bandedge emission was assigned to the slow relaxation of “dark exciton” from triplet states to ground state, which is consistent with other studies.<sup>[60,61]</sup> The deep trap emission was attributed to ultrafast relaxation of a surface selenium dangling bond electron to the valence band where it recombines radiatively with the initially photogenerated hole; and this process attenuates the bandedge emission within 2–6 psec.

A recent study of the emission lifetimes on nanosecond time scale of surface passivated and unpassivated CdS nanoparticles showed that the passivated samples have a lower excitation threshold for observing exciton–exciton annihilation.<sup>[62]</sup> In surface passivated samples, the density of trap states is expected to be lower due to more effective capping. It is therefore easier to observe the saturation of trap states. The observation supports the model of exciton–exciton annihilation upon trap state saturation at high excitation intensities. Excitation intensity dependence has also been observed in the ultrafast transient absorption signals of CdTe NPs.<sup>[63]</sup> In addition, the fluorescence of thiol-capped CdTe NPs has been measured using

nanosecond laser spectroscopy.<sup>[64]</sup> The amplitude of fluorescence signal has been found to decrease unexpectedly with increasing excitation intensity at high excitation intensities. This unusual excitation intensity dependence was explained by nonlinear exciton–exciton annihilation or Auger photoionization. The results indicate that CdTe NPs show strong nonlinear optical properties due to strong quantum confinement effect than other II–VI semiconductor NPs.

It is interesting to note that very different time constants have been reported for the fast excitation-intensity-dependent component. Zhang et al. have observed 1–4 psec in both CdS colloid and glass, Zn<sub>0.5</sub>Cd<sub>0.5</sub>S colloids, and trioctylphosphine oxide (TOPO)-capped CdS colloids in toluene. The time constant for the fast excitation-intensity-dependent component of the bleach has been found to decrease from 1.3 to 0.8 psec with increasing power.<sup>[33]</sup> Using time-resolved photoluminescence, exciton recombination times in CdS<sub>0.081</sub>Se<sub>0.919</sub> glass decrease from 4 nsec to hundreds of picoseconds with increasing laser intensity.<sup>[54]</sup> A power-dependent decay on the time scale of 1–3 nsec has been observed in the measurements of emission lifetimes for surface passivated CdS NPs.<sup>[62]</sup> For the 2.3-nm CdSe colloids, time constant decreases from 510 to 10 psec for decays from one to four electron–hole pair.<sup>[12]</sup> The different time constants are possibly due to the difference in excitation intensities. Under low excitation intensities when there is on average one or less electron–hole pair (exciton) created per particle, linear processes such as trapping and subsequent recombination from the trapped states dominate the relaxation process of charge carrier in nanoparticles. With increasing excitation intensity, more excitons can be generated in one particle, higher-order processes such as exciton–exciton annihilation and Auger recombination become more important. It can be envisioned that the higher-order process becomes more significant at higher excitation intensities and the decay time constant would vary accordingly. Therefore the different nonlinear decay constants reported could be a reflection of the different excitation intensities used.

The variation of time constants can also be due to differences in particle size, embedding environment (solvent or glass), and experimental techniques used. It was found that the fast decay time constant changes from 363 to 6 psec when the radius of CdSe NPs was reduced from 4.1 to 1.2 nm.<sup>[12]</sup> Compared with colloidal solutions, semiconductor NPs embedded in glass usually have reduced lifetimes because of photoionization and greatly enhanced Auger interaction in ionized particles.<sup>[65–67]</sup> Time-resolved fluorescence measurements are often more sensitive than transient absorption, as fluorescence is a zero-background measurement and absorption is not. This leads to lower *S/N* ratio for

transient absorption data and thereby larger uncertainties in the time constant measured. Also, as the non-linear component decreases in amplitude quickly with decreasing excitation intensities, the uncertainty becomes larger in the time constant from data fitting.

Effects of shape on charge carrier dynamics have also been investigated by several groups. Earlier attempt showed that ultrafast dynamic profiles of PbS nanoparticles were not dependent on the shape of particles.<sup>[58]</sup> This shape independence has been attributed to the dominance of surface properties on the electronic relaxation. If density of surface trap states is high and dynamics are dominated by the surface trap states, the effect of shape may not be observed. Other attempts to study the shape effect compared nanorods with nanoparticles. For example, CdSe nanorods of different aspect ratios have been synthesized.<sup>[68,69]</sup> Nanorods exhibit linearly polarized emission along long axis.<sup>[70]</sup> Static absorption and emission spectra showed that the bandgap of nanorods depends mainly on the width and only slightly affected by the length.<sup>[71]</sup> Femtosecond transient bleach spectroscopy was used to compare the dynamics of CdSe nanorods with that of nanodots.<sup>[72]</sup> It was found that higher energy excitons relax faster in nanorods than in nanodots, but lower energy excitons decay slower in nanorods than in nanodots. It was suggested that the faster decay of higher energy excitons is due to the higher density of exciton states at higher energy in the nanorods caused by the decrease in symmetry and the splitting of degeneracy. However, no detailed explanation has been offered for the slower decay in nanorods for lower energy excitons.

In another comparison of nanorods vs. quantum dots, elongated NPs were found to have increased optical gain lifetime and lower gain threshold.<sup>[73]</sup> The improved optical gain performances of nanorods have been attributed to increased absorption cross sections, stronger quantum confinement, and weaker interference from excited state absorption. Very recently, comparison of CdS nanorods and nanoparticles has been performed in our lab using ultrafast transient absorption.<sup>[74]</sup> A fast decay component appears to be faster in nanorods than spherical particles. The slow decay components remain unaffected by the shape of particle.

It is clear from the above studies that there is no consensus on the dependence of dynamic properties on particle shape. This could be because there are competitive factors that influence the shape dependence. On one hand, nanorods have larger volume per rod/particle if the diameter of the cross section of the nanorods is the same or similar to that of spherical nanoparticles. In the meantime, nanorods have enhanced local field factor.<sup>[75]</sup> As the absorption cross section is linearly proportional to the volume and local

field factor,<sup>[75]</sup> the increased volume and local field factor should lead to a larger absorption cross section and thereby shorter radiative exciton lifetime for nanorods.

On the other hand, quantum confinement effect is weaker in nanorods,<sup>[76,77]</sup> because the three-dimensional confinement in quantum dots becomes two-dimensional in nanorods. One may expect that lifetimes in nanorods to be longer than that in NPs given the reduced quantum confinement. Also, for the same number of excitons per nanoparticle or nanorod, the effective exciton (charge carrier) density is lower for nanorods because of their larger volume. The exciton lifetimes in nanorods should be longer than in NPs as the reduced effective carrier density decreases the probability of fast nonlinear processes such as exciton–exciton annihilation.

However, because nanorods have larger volume than NPs with the same diameter/width, the number of particles/rods per volume would be smaller for nanorods than in NPs if the samples have the same optical density. Given the same excitation intensity, rod samples will have more excitons per rod and thereby shorter lifetimes, as nonlinear processes such as Auger recombination or exciton–exciton annihilation have relatively short lifetimes that are inversely proportional to exciton population.

Density of states (DOS) is another factor to consider. Theoretical studies show that elongation of particles to rods can cause the splitting of degenerated states and change the distribution of the electronic states. This could increase or decrease the exciton lifetime, depending on the state distribution. On average, a higher DOS is expected for nanorods than for nanoparticles if the nanorods have a larger volume. This should generally lead to a shorter exciton lifetime in nanorods due to better exciton and phonon spectral overlap. In the meantime, elongation can also introduce new surface states that could shorten the exciton lifetime in nanorods.<sup>[70,78,79]</sup> Overall, all the factors, including quantum confinement effect, local field factor, charge carrier density, distribution of states, and DOS, are dependent on the aspect ratio of the nanorod. The exciton lifetime in nanorods could be longer or shorter than that in spherical particles, depending on the aspect ratio and how the various factors change with the aspect ratio.

Other metal chalcogenide semiconductor NPs include  $\text{Cu}_x\text{S}$  and  $\text{Ag}_2\text{S}$ . Copper sulfides can have various stoichiometries between  $\text{Cu}_2\text{S}$  and  $\text{CuS}$ , and the variations in structure and valence result in some unique properties.<sup>[80–90]</sup> In a study of  $\text{CuS}$  NPs, an IR band was found to disappear after the reduction of  $\text{CuS}$  to  $\text{Cu}_2\text{S}$  and was attributed to the presence of  $\text{Cu(II)}$ .<sup>[80,81]</sup> The IR band was attributed to a middle-gap, electron donor state but the model appears to have some inconsistencies.<sup>[91]</sup> Both  $\text{Cu}_2\text{S}$  and  $\text{CuS}$

NPs have been studied using femtosecond transient absorption spectroscopy.<sup>[91]</sup> They were found to exhibit different dynamic behavior with competing transient absorption and bleach features as well as power dependence attributed to trap state saturation. Based on a simple kinetic model developed, an alternative explanation for the middle-gap state has been proposed. The state was suggested to be electron-acceptor state or unoccupied and the IR band corresponds to a transition from the valence band to this state.<sup>[91]</sup> Similarly, in the dynamics study of cystine and glutathione capped Ag<sub>2</sub>S NPs, it was found that the signal has contributions from both transient absorption and transient bleach and the transient absorption becomes more dominant over bleach with increasing excitation intensity.<sup>[92]</sup> The observed excitation intensity dependence was attributed to saturation of shallow trap states at high excitation intensities.

### III–V Semiconductor Nanoparticles

Most dynamic studies of III–VI semiconductor NPs have focused on charge carrier cooling in the CB or VB. Carrier cooling is extremely important for many device applications such as transistors, lasers, and photocathodes.<sup>[14]</sup> A fundamental question is how electron cooling may be different in NPs from that in bulk materials. Electron cooling time has been found to be slower in NPs than in bulk for a series of self-assembled III–V semiconductor nanoparticles. Mukai et al. reported the electron cooling time in self-assembled InGaAs NPs ranging from 10 psec to 1 nsec using time-resolved photoluminescence measurements.<sup>[93–95]</sup> Slow cooling (~1 nsec) was found for strain-induced GaAs NPs.<sup>[96]</sup> In another study under condition of high injection, a lifetime of 500 psec for excited electronic states was observed for self-assembled InAs/GaAs NPs.<sup>[97]</sup> The hole cooling time was reported to be 400 psec for InAs/GaAs NPs.<sup>[98,99]</sup> Heitz et al. also reported a 40-psec hole relaxation time for stacked layer of InAs NPs deposited on GaAs.<sup>[100]</sup>

The above slow relaxation times for electron and hole cooling were all reported for self-assembled NPs. The studies for carrier cooling in colloidal III–V semiconductor NPs are rare because of the difficulties in synthesis. The best results to date have been obtained for InP NPs.<sup>[101–103]</sup> The charge carrier relaxations in colloidal InP quantum dots have been found to be dependent on excitation intensity,<sup>[104]</sup> particle size, and surface chemistry.<sup>[105]</sup> With increasing excitation intensity, efficiency of charge carrier relaxation to bandedge states is reduced. It was also found that the 1P to 1S relaxation rate increases with decreasing size of quantum dots.<sup>[105]</sup> The relaxation rate of chemically injected electrons was found out to be

slower than that of photoexcited excitons by approximately an order of magnitude.

### Doped II–VI Semiconductor Nanoparticles

Among all the doped II–VI semiconductor NPs, Mn<sup>2+</sup>-doped ZnS has been the most extensively studied because of its interesting magnetic<sup>[106–110]</sup> and electron-optical properties.<sup>[111–115]</sup> In 1994, Bhargava et al. reported for the first time that Mn<sup>2+</sup>-doped ZnS has high luminescence efficiency accompanied by significantly shortened lifetime (~20 nsec).<sup>[111]</sup> The spin-forbidden transition of Mn<sup>2+</sup> <sup>4</sup>T<sub>1</sub> to <sup>6</sup>A<sub>1</sub> in bulk ZnS has a lifetime of about 1.8 msec. The shortened lifetime was explained by the strong interaction of Mn<sup>2+</sup> d electronic states with the sp electronic states of ZnS. However, a subsequent study found that the Mn<sup>2+</sup> emission in Mn<sup>2+</sup>-doped ZnS NPs is the same as that in bulk.<sup>[116]</sup> This has been confirmed by other studies recently.<sup>[117–119]</sup> The fast nanosecond decay observed was apparently due to trap state emission from the ZnS NPs.

Mn<sup>2+</sup>-doped ZnSe is another interesting doped semiconductor NPs system. Photoluminescence measurements of Mn<sup>2+</sup>-doped ZnSe showed distinct ZnSe bandedge emission at 440 nm and Mn<sup>2+</sup> emission at 560 nm.<sup>[120]</sup> The lifetime of Mn<sup>2+</sup> emission (in hundreds of microseconds) was reported to be an order of magnitude smaller than that of the bulk (msec). The shortened lifetime has been attributed to stronger spin-orbit coupling between Mn<sup>2+</sup> and Se<sup>2-</sup> than Mn<sup>2+</sup> and S<sup>2-</sup>. It was also found that Mn<sup>2+</sup> emission decreases from 290 to 190 μsec when the concentration of Mn<sup>2+</sup> increases from 0.2% to 0.9% because of the exchange interaction between Mn<sup>2+</sup> pairs. However, the presence of Mn<sup>2+</sup> defect sites and their effect on the luminescence were not fully addressed.

The optical and surface structure properties of Mn<sup>2+</sup>-doped ZnSe NPs have recently been investigated using UV–visible absorption, fluorescence, electron spin resonance (ESR), and X-ray absorption fine structure (XAFS) techniques.<sup>[121]</sup> It was found that the amount of ZnS bandedge, trap states, and Mn<sup>2+</sup> <sup>4</sup>T<sub>1</sub> to <sup>6</sup>A<sub>1</sub> emission was dependent on the amount of Mn<sup>2+</sup> present. The ESR and EXAFS data indicated the presence of two different Mn<sup>2+</sup> sites. One is the Mn<sup>2+</sup>-substituted Zn<sup>2+</sup> lattice site and the other is the surface Mn<sup>2+</sup> site. EXAFS data suggested that the core of NPs resembles that of bulk ZnSe, and the surface of the particle has a higher concentration of metal atoms. It was then proposed that surface Mn<sup>2+</sup> possessed an octahedral geometry due to significant OH<sup>-</sup>/O<sup>2-</sup> coordination and the interior Mn<sup>2+</sup> occupied the Zn<sup>2+</sup> tetrahedral site. It was also suggested that surface Mn<sup>2+</sup> quenched the ZnSe bandedge

emission and promoted the ZnSe trap state emission but gave no  $\text{Mn}^{2+}$  emission.  $\text{Mn}^{2+}$   ${}^4\text{T}_1$  to  ${}^6\text{A}_1$  emission increased with  $\text{Mn}^{2+}$  present in the reaction solution because of the interior  $\text{Mn}^{2+}$  that occupied the  $\text{Zn}^{2+}$  lattice site, but the overall fluorescence quantum yield went down.

## Metal Oxide Nanoparticles

Metal oxide NPs such as  $\text{TiO}_2$ ,  $\text{ZnO}$ , and  $\text{Fe}_2\text{O}_3$  have found applications in various fields such as catalysis, paint pigment, and solar cells. Among them,  $\text{TiO}_2$  NPs received the most attention because of its stability, availability, and its application in solar energy conversion.<sup>[122]</sup> Charge carrier dynamics have been studied for  $\text{TiO}_2$  NPs alone and in conjunction with dye sensitization. For  $\text{TiO}_2$  NPs alone, the electrons excited by a 310 nm light were found to decay following second-order kinetics with a recombination rate of  $1.8 \times 10^{-10} \text{ cm}^3/\text{sec}$ .<sup>[123]</sup> Trapping of electrons was suggested to occur on the time scale of 180 fsec.<sup>[37]</sup>

Dye sensitization of  $\text{TiO}_2$  has been extensively studied as  $\text{TiO}_2$  alone does not absorb visible light. Dye sensitization helps to extend the absorption into the visible region. In dye sensitization, visible light is absorbed and creates electrons in the excited states of dye molecules. Electrons are then injected from the excited states of dye molecules to the conduction band of  $\text{TiO}_2$  NPs. A Ru dye with the best performance showed light-to-electricity conversion efficiency as high as 10%.<sup>[122,124]</sup> This high efficiency has stimulated considerable interest in the study of charge carrier injection and relaxation processes in dye-sensitized NPs. It has been found that the forward electron transfer rate is generally very fast. For example, electron injection rate was found to be around 200 fsec for coumarin dye on  $\text{TiO}_2$ <sup>[125]</sup> and less than 50 fsec for the Ru ( $\text{N}_3$ ) dye on  $\text{TiO}_2$ .<sup>[126,127]</sup> However, there are some questions about the possible degradation of the dye used.<sup>[126,128]</sup> A slower electron injection time (20 psec) was reported based on a picosecond infrared study.<sup>[129]</sup> Cherepy et al. have studied the charge carrier dynamics of anthocyanin dye on  $\text{TiO}_2$  NPs and an electron injection rate of  $\sim 100$  fsec has been determined.<sup>[130]</sup> Compared with forward electron injection, the rate of back electron injection has been found to be much slower, on the time scales from 10 psec to  $\mu\text{sec}$ , depending on the nature of dyes<sup>[130,131]</sup> and the methods used to synthesize  $\text{TiO}_2$  NPs.<sup>[131]</sup>

In a recent review of electron injection dynamics from a ruthenium dye to  $\text{TiO}_2$  nanocrystalline thin films, the effects of parameters such as absorbate redox potential, pH of solution, solvent, and excitation wavelength have been studied using a tunable femtosecond infrared spectrometer.<sup>[16]</sup> The injection kinetics

typically features an ultrafast ( $< 100$  fsec) component and a slower component. The fast component showed no noticeable variation within the 200-fsec time resolution of the measurements. For the slow component, the amplitude increased and the relaxation rate decreased with increasing pH of the solution. A two-state injection model was developed, with the fast decay component attributed to injection from a non-thermalized excited state and the slow component attributed to injection from the thermalized excited state.

Iron oxide ( $\text{Fe}_2\text{O}_3$ ) NPs have been used as pigments, photocatalysts, electrodes, and high-density recording media.<sup>[132–135]</sup> Photoexcited electron dynamics of  $\gamma$ - and  $\alpha$ - $\text{Fe}_2\text{O}_3$  have been performed using femtosecond laser spectroscopy.<sup>[55]</sup> It has been determined that  $\gamma$ - $\text{Fe}_2\text{O}_3$  NPs are spherical and paramagnetic and  $\alpha$ - $\text{Fe}_2\text{O}_3$  NPs are spindle-shape and diamagnetic. Despite the significant differences in shape and magnetic properties, both  $\gamma$ - and  $\alpha$ - $\text{Fe}_2\text{O}_3$  NPs show similar ultrafast electronic relaxation that seems to be dominated by non-radiative processes, possibly because of the high density of trap states or simply strong coupling between trap states. The ultrafast relaxation is consistent with weak luminescence of the NPs and low photocurrent efficiency of typical  $\text{Fe}_2\text{O}_3$  electrodes, as the rapid electron–hole recombination is unfavorable for charge transport in photocurrent generation.

## Silicon Nanoparticles

Bulk silicon (Si) is an indirect band gap semiconductor with a band gap of 1.1 eV and a very weak luminescence. The discovery of visible luminescence from porous silicon<sup>[136]</sup> has stimulated great interest in Si NPs because luminescence silicon is highly desirable for optoelectronics applications. Various techniques have been used to produce luminescent Si NPs, including electrochemical etching,<sup>[136]</sup> sputtering,<sup>[137–139]</sup> ion implantation,<sup>[140–142]</sup> and plasma-enhanced chemical vapor deposition.<sup>[143,144]</sup> The mechanism of the luminescence from Si NPs has been extensively studied but remains somewhat controversial. One explanation for the observed luminescence is quantum confinement.<sup>[136,145]</sup> Another explanation is surface effect<sup>[146]</sup> that attributes the luminescence to localized states on the Si surface<sup>[147,148]</sup> or at the Si/ $\text{SiO}_2$  interface.<sup>[149–152]</sup>

A few studies have been reported on the dynamics of Si NPs. In a transient absorption study, ion-implanted Si NPs showed two photoinduced absorption features.<sup>[153]</sup> One is the short-lived high-energy band and it was attributed to quantized states in Si NPs. The other one is the low-energy band due to Si/ $\text{SiO}_2$  interfaces states. In another recent study of porous silicon using infrared photoinduced absorption spectroscopy, intraband transitions between

sublevels in the conduction and valence bands were observed, which supports the model of quantum confinement.<sup>[154]</sup> Also, additional features in the photoinduced absorption spectrum were found and correlated with the Si=O vibrational modes, indicating a strong coupling between bulk excitonic states and surface states in Si NPs. These studies seem to suggest that both quantum confinement and surface effect contribute to the emission process in Si nanoparticles.

### Layered Semiconductor Nanoparticles

Layered semiconductors have unique crystal structures composed of extended, thin layers with weak van der Waals interaction in between layers. There are only a few studies on the dynamic properties of layered semiconductor NPs. Using picosecond transient absorption spectroscopy, it was found that charge carrier relaxation in MoS<sub>2</sub> NPs was dominated by trap states.<sup>[155]</sup> Femtosecond transient absorption spectroscopy has been used to study the dynamics in PbI<sub>2</sub><sup>[56]</sup> and BiI<sub>3</sub><sup>[156]</sup> NPs. The electronic relaxation dynamics in PbI<sub>2</sub> and BiI<sub>3</sub> are both found to be sensitive to solvent and insensitive to particle size. Interestingly, oscillations at early times with a period changing with solvent but not with particle size have been observed. The strong surface (solvent) dependence and size independence indicate that either the relaxation is dominated by surface characteristics that do not change significantly with size or quantum confinement is not significant in the size regime studied.<sup>[157,158]</sup>

### Silver Halide Nanoparticles

Interest in the dynamics of silver halide NPs has been partly due to their application in photography. The ultrafast charge carrier dynamics in AgI and proposed “core/shell” structures of AgI/Ag<sub>2</sub>S and AgBr/Ag<sub>2</sub>S have been studied.<sup>[57]</sup> Dynamic profiles of AgI NPs showed a fast 2.5-psec decay component and a slow component (>0.5 nsec). The fast decay was attributed to trapping and nonradiative electron–hole recombination dominated by a high density of trap states. The slow decay was assigned to the reaction of deep-trapped electrons with silver cations to form silver atom, which is the basis for latent image formation in photography. The slow decay is consistent with early nanosecond study.<sup>[159]</sup> Comparison between two “core/shell” systems, AgI/Ag<sub>2</sub>S and AgBr/Ag<sub>2</sub>S, revealed a new 4-psec rise component with AgBr/Ag<sub>2</sub>S. It was taken as an indication of electron transfer from Ag<sub>2</sub>S to AgBr initially. However, a similar dynamics was observed later in pure Ag<sub>2</sub>S NPs. The rise is more likely due to transient bleach as there is

noticeably ground-state absorption at the probe wavelength.<sup>[92]</sup>

## CHARGE CARRIER DYNAMICS OF METAL NANOPARTICLES

Metal NPs have long been of interest because of their applications in areas such as optical waveguides,<sup>[160]</sup> catalysis,<sup>[161]</sup> sensors,<sup>[162]</sup> and in surface-enhanced Raman scattering (SERS).<sup>[163,164]</sup> Metal NPs such as silver and gold have some unique optical properties, typified by a strong absorption band in the visible, termed as surface plasmon absorption. Mie theory,<sup>[165–168]</sup> which is essentially the solution of Maxwell’s equation for the scattering of light off a small charged sphere in a dielectric medium, can be used to quite accurately describe the surface plasmon absorption of most metal NPs.

Charge carrier dynamics of metal NPs has received considerable attention recently. Hot electron relaxation in metals occurs on ultrafast timescales because of strong electron–phonon interaction. One of the important issues in the dynamics of metal NPs is whether the relaxation is dependent on the particle size or not. Theoretically, electron and phonon spectral overlap is expected to decrease with decreasing size, leading to weaker electron–phonon interaction. Early electronic relaxation measurements by Smith et al. suggested a possible size dependence of the electronic relaxation in the 1–40-nm range.<sup>[169]</sup> However, Hodak et al. and El-Sayed et al. found no size dependence of the relaxation down to the size of 2.5 nm recently.<sup>[29,170,171]</sup> The relaxation time in Au NPs was reported to be the same as that of bulk gold (~1 psec). Excitation intensity dependence of the relaxation time could be the reason for the discrepancy. It is likely that the excitation intensities used in earlier work are much higher than those used in later measurements. Another possible explanation for the difference is surface and/or solvent environment, which was found to affect electronic relaxation of Au NPs.<sup>[172–174]</sup> It seems consistent that electron–phonon coupling constant is the same for Au NPs as for bulk, at least for particles down to 2 nm in diameter.<sup>[175]</sup>

However, when the particle size is smaller than 1 nm, the electronic relaxation time seems to become significantly longer than that of bulk. An earlier study of Au<sub>13</sub> and Au<sub>55</sub> found that the electron lifetime becomes significantly longer for Au<sub>13</sub> nanoclusters than for Au<sub>55</sub> or larger nanoparticles, indicating bulk to molecule transitions in the size regimes of 55 and 13 Au atoms.<sup>[169]</sup> A recent study of Au<sub>28</sub> clusters found biexponential decays with a subpicosecond and a nanosecond component.<sup>[176]</sup> The fast component was attributed to relaxation from a higher lying excited state



to lower electronic states, and the longer nanosecond component was assigned to the radiative lifetime of the Au<sub>28</sub> clusters.<sup>[177]</sup> More recently, studies of electronic relaxation in Au<sub>11</sub> clusters revealed a similar long-lived component (~1 nsec).<sup>[178]</sup> The longer lifetime again suggests that for very small metal clusters, particles are becoming molecule-like in nature and the electron–phonon interaction becomes weaker, similar to that found for Au<sub>13</sub>.<sup>[169]</sup>

Another interesting issue concerning metal NPs is the oscillations recently observed in the electronic relaxation dynamics of Au and bimetallic core/shell particles.<sup>[175,179–182]</sup> As shown in Fig. 3A, femtosecond transient absorption data for Au particles probed at 550 nm following 400-nm pulse excitation show clearly

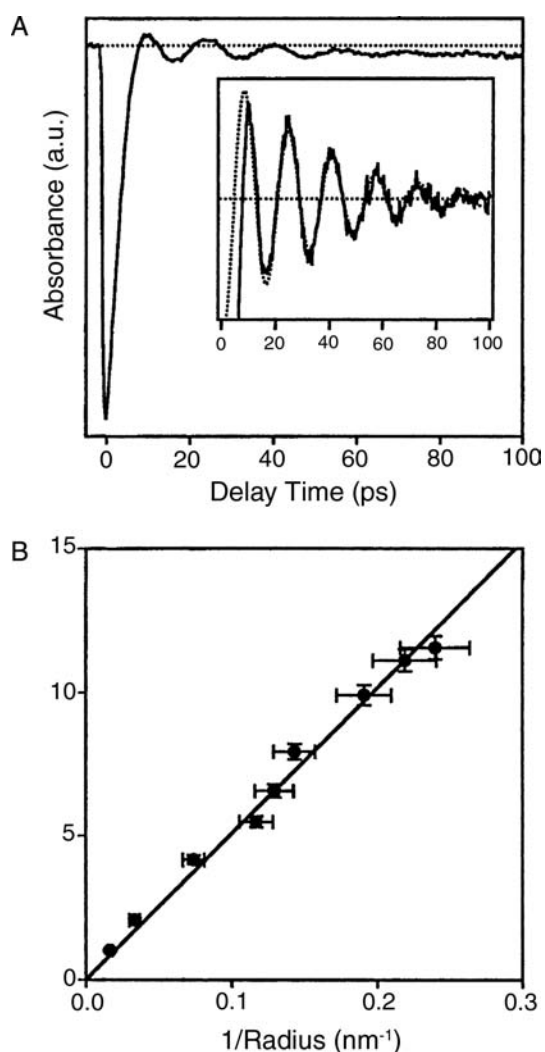


**Fig. 3** (A) Transient absorption data for 60-nm-diameter Au particles recorded with 400-nm pump and 550-nm probe pulses. Modulations due to the coherently excited breathing motion can be clearly seen. (B) Plot of the measured frequencies vs.  $1/R$  for different Au samples. A straight line fit to the data is also shown. *Source:* From Fig. 6 of Ref.<sup>[175]</sup>.

modulations with a period of about 16 psec. The frequency of the oscillation was found to increase linearly with decreasing particle size [Fig. 3B]. The oscillations have been attributed to a coherent excitation of the radial breathing vibrational modes of the particles. Photoexcited electrons can transfer their energy into the lattice, heating up the particle and causing a rapid expansion. The expansion and distraction of particle volume over time cause the electron density of particle to change and periodic shift of the surface plasmon absorption band, manifesting itself as a modulation in the transient absorption signal.

Similar oscillation has been observed more recently in silver ellipsoids,<sup>[183]</sup> Au nanorods,<sup>[184]</sup> and strongly coupled Au aggregates.<sup>[185]</sup> Time-resolved laser spectroscopy has been used to investigate Au nanorods with aspect ratio from 2 to 5.<sup>[184]</sup> Coherent excitation of the acoustic vibrational modes in Au nanorods results in the oscillation of transient absorption signals. The period of the oscillation has been found to be  $2L/c_t$ , where  $L$  is the length of the rod and  $c_t$  is the transverse speed of sound in bulk gold. This is different from the results of silver ellipsoids, where the period is determined to be  $2d/c_l$ , where  $d$  is the length or width of the ellipsoid, and  $c_l$  is the longitudinal speed of sound in silver.<sup>[183]</sup> The discrepancy has been explained by the different natures of the vibrational motion and elastic properties.<sup>[184]</sup>

Aggregates of metal NPs are fundamentally interesting as they can be used to study interparticle interactions. The interaction between particles can be roughly divided into three regimes: weak, moderate, and strong. In weakly or moderately interacting systems such as DNA-linked Au NPs<sup>[186,187]</sup> and superlattice structures of Au NPs,<sup>[188]</sup> the transverse plasmon band shift noticeably to the red. In strongly interacting systems such as Au nanoparticle aggregates, a whole new absorption band, termed extended plasmon band (EPB), appears near 700–950 nm in addition to the transverse surface plasmon band (~520 nm).<sup>[189,190]</sup> The EPB is similar to the longitudinal plasmon absorption in nanorods and its appearance is a signature of strong interaction between nanoparticles. In a recent dynamic study of strongly interacting Au aggregates, the electronic relaxation time appeared to be similar to those of isolated particles and bulk.<sup>[185]</sup> Surprisingly, periodic oscillations and probe wavelength dependence of the oscillation period were observed in the dynamic profiles of Au nanoparticle aggregates. The oscillations have been attributed to the coherent excitation of vibration of the aggregates. The dependence of oscillation period on probe wavelength indicates that the broad EPB in static absorption spectrum is inhomogeneously broadened because of different aggregate sizes, supported by a spectral hole burning experiment. Interestingly, the

observed oscillation period is longer than that predicted based on an elastic sphere model. A possible explanation is that the vibrational motion in aggregates is “softer” than that of isolated hard spherical particles. This study shows that transient absorption measurements can provide information on size distribution and vibrational frequencies of metal nanoparticle aggregates or similar systems.

## CONCLUSION

In summary, charge carrier dynamics of nanomaterials have been studied with powerful time-resolved laser techniques to provide important information complementary to static or equilibrium studies. The recent progress in synthesizing high-quality nanomaterials samples has made it possible to start to explore some of the most fundamental issues concerning the effects of size, shape, structure, and surface on charge carrier dynamics. Further research is clearly needed to better control these parameters in order to achieve a more complete understanding of the dynamic properties of charge carriers in nanomaterials.

## ACKNOWLEDGMENTS

We are grateful for the financial support from The Petroleum Research Fund administered by the American Chemical Society, UCSC Faculty Research Fund, the Materials Research Institute of LLNL, the Collaborative UC/Lab (LANL) Research Program, and the Campus (UC)/Lab (LLNL) Exchange (CLE) Program.

## REFERENCES

1. Brus, L. Electronic wave functions in semiconductor clusters: experiment and theory. *J. Phys. Chem.* **1986**, *90* (12), 2555–2560.
2. Gratzel, M. *Heterogeneous Photochemical Electron Transfer*; CRC Press: Boca Raton, 1989.
3. Steigerwald, M.L.; Brus, L.E. Semiconductor crystallites—a class of large molecules. *Acc. Chem. Res.* **1990**, *23* (6), 183–188.
4. Bawendi, M.G.; Steigerwald, M.L.; Brus, L.E. The quantum mechanics of larger semiconductor clusters (quantum dots). *Annu. Rev. Phys. Chem.* **1990**, *41*, 477–496.
5. Wang, Y.; Herron, N. Nanometer-sized semiconductor clusters—materials synthesis, quantum size effects, and photophysical properties. *J. Phys. Chem.* **1991**, *95* (2), 525–532.
6. Heath, J.R. The chemistry of size and order on the nanometer scale. *Science* **1995**, *270* (5240), 1315–1316.

7. Murray, C.B.; Kagan, C.R.; Bawendi, M.G. Self-organization of CdSe nanocrystallites into three-dimensional quantum dot superlattices. *Science* **1995**, *270* (5240), 1335–1338.
8. Alivisatos, A.P. Perspectives on the physical chemistry of semiconductor nanocrystals. *J. Phys. Chem.* **1996**, *100* (31), 13226–13239.
9. Weller, H. Self-organized superlattices of nanoparticles. *Angew. Chem., Int. Ed. Engl.* **1996**, *35* (10), 1079–1081.
10. Kamat, P.V. Native and surface modified semiconductor nanoclusters. *Prog. Inorg. Chem.* **1997**, *44*, 273–343.
11. Zhang, J.Z. Interfacial charge carrier dynamics of colloidal semiconductor nanoparticles. *J. Phys. Chem., B* **2000**, *104* (31), 7239–7253.
12. Klimov, V.I.; Mikhailovsky, A.A.; McBranch, D.W.; Leatherdale, C.A.; Bawendi, M.G. Quantization of multiparticle Auger rates in semiconductor quantum dots. *Science* **2000**, *287* (5455), 1011–1013.
13. El-Sayed, M.A. Some interesting properties of metals confined in time and nanometer space of different shapes. *Acc. Chem. Res.* **2001**, *34* (4), 257–264.
14. Nozik, A.J. Spectroscopy and hot electron relaxation dynamics in semiconductor quantum wells and quantum dots. *Annu. Rev. Phys. Chem.* **2001**, *52*, 193–231.
15. Varnavski, O.P.; Mohamed, M.B.; El-Sayed, M.A.; Goodson, T. Relative enhancement of ultrafast emission in gold nanorods. *J. Phys. Chem., B* **2003**, *107* (14), 3101–3104.
16. Asbury, J.B.; Anderson, N.A.; Hao, E.C.; Ai, X.; Lian, T.Q. Parameters affecting electron injection dynamics from ruthenium dyes to titanium dioxide nanocrystalline thin film [review]. *J. Phys. Chem., B* **2003**, *107* (30), 7376–7386.
17. Hu, M.; Hartland, G.V. Heat dissipation for Au particles in aqueous solution: Relaxation time versus size. *J. Phys. Chem., B* **2003**, *107* (5), 1284.
18. Alivisatos, A.P. Semiconductor clusters, nanocrystals, and quantum dots. *Science* **1996**, *271* (5251), 933–937.
19. Feldheim, D.L.; Keating, C.D. Self-assembly of single electron transistors and related devices. *Chem. Soc. Rev.* **1998**, *27*, 1.
20. Schlamp, M.C.; Peng, X.G.; Alivisatos, A.P. Improved efficiencies in light emitting diodes made with CdSe(CdS) core/shell type nanocrystals and a semiconducting polymer. *J. Appl. Phys.* **1997**, *82* (11), 5837–5842.
21. Coe, S.; Woo, W.K.; Bawendi, M.; Bulovic, V. Electroluminescence from single monolayers of nanocrystals in molecular organic devices. *Nature* **2002**, *420* (6917), 800–803.
22. Nayral, C.; Ould-Ely, T.; Maisonnat, A.; Chaudret, B.; Fau, P.; Lescouzeres, L.; Peyre-Lavigne, A. A novel mechanism for the synthesis of tin oxide nanoparticles of low size dispersion and of nanostructured SnO<sub>2</sub> for the sensitive layers of gas sensors. *Adv. Mater.* **1999**, *11* (1), 61–63.
23. O'Regan, B.; Schwartz, D.T.; Zakeeruddin, S.M.; Gratzel, M. Electrodeposited nanocomposite n-p heterojunctions for solid-state dye-sensitized photovoltaics. *Adv. Mater.* **2000**, *12* (17), 1263–1267.

24. Klimov, V.I.; Mikhailovsky, A.A.; Xu, S.; Malko, A.; Hollingsworth, J.A.; Leatherdale, C.A.; Eisler, H.J.; Bawendi, M.G. Optical gain and stimulated emission in nanocrystal quantum dots. *Science* **2000**, *290* (5490), 314–317.
25. Kamat, P.V. Interfacial charge transfer processes in colloidal semiconductor systems. *Prog. React. Kinet.* **1994**, *19* (3), 277–316.
26. Efros, A.L.; Rosen, M.; Kuno, M.; Nirmal, M.; Norris, D.J.; Bawendi, M. Band-edge exciton in quantum dots of semiconductors with a degenerate valence band-dark and bright exciton states. *Phys. Rev., B, Condens. Matter* **1996**, *54* (7), 4843–4856.
27. Mews, A.; Kadavanich, A.V.; Banin, U.; Alivisatos, A.P. Structural and spectroscopic investigations of CdS/HgS/CdS quantum-dot quantum wells. *Phys. Rev., B, Condens. Matter* **1996**, *53* (20), 13,242–13,245.
28. Zhang, J.Z. Ultrafast studies of electron dynamics in semiconductor and metal colloidal nanoparticles: effects of size and surface. *Acc. Chem. Res.* **1997**, *30* (10), 423–429.
29. Link, S.; El-Sayed, M.A. Spectral properties and relaxation dynamics of surface plasmon electronic oscillations in gold and silver nanodots and nanorods. *J. Phys. Chem., B* **1999**, *103* (40), 8410–8426.
30. Rogach, A.L.; Kornowski, A.; Gao, M.Y.; Eychmuller, A.; Weller, H. Synthesis and characterization of a size series of extremely small thiol-stabilized CdSe nanocrystals. *J. Phys. Chem., B* **1999**, *103* (16), 3065–3069.
31. Murray, C.B.; Kagan, C.R.; Bawendi, M.G. Synthesis and characterization of monodisperse nanocrystals and close-packed nanocrystal assemblies. *Annu. Rev. Mater. Sci.* **2000**, *30*, 545–610.
32. Zhang, J.Z.; O’Neil, R.H.; Roberti, T.W. Femtosecond studies of photoinduced electron dynamics at the liquid–solid interface of aqueous CdS colloids. *J. Phys. Chem.* **1994**, *98* (14), 3859–3864.
33. Ernsting, N.P.; Kaschke, M.; Weller, H.; Katsikas, L. Colloidal  $Zn_{1-x}Cd_xS$ -optical saturation of the exciton band and primary photochemistry studied by subpicosecond laser flash photolysis. *J. Opt. Soc. Am., B, Opt. Phys.* **1990**, *7* (8), 1630–1637.
34. Kamalov, V.F.; Little, R.; Logunov, S.L.; El-Sayed, M.A. Picosecond electronic relaxation in CdS/HgS/CdS quantum dot quantum well semiconductor nanoparticles. *J. Phys. Chem.* **1996**, *100* (16), 6381–6384.
35. Iwai, S.; Murata, S.; Tachiya, M. Ultrafast fluorescence quenching by electron transfer and fluorescence from the second excited state of a charge transfer complex as studied by femtosecond up-conversion spectroscopy. *J. Chem. Phys.* **1998**, *109* (14), 5963–5970.
36. Dneprovskii, V.S.; Klimov, V.I.; Okorokov, D.K.; Vandyshev, Y.V. Strong optical nonlinearities and laser emission of semiconductor microcrystals. *Solid State Commun.* **1992**, *81* (3), 227–230.
37. Skinner, D.E.; Colombo, D.P.; Cavaleri, J.J.; Bowman, R.M. Femtosecond investigation of electron trapping in semiconductor nanoclusters. *J. Phys. Chem.* **1995**, *99* (20), 7853–7856.
38. Mittleman, D.M.; Schoenlein, R.W.; Shiang, J.J.; Colvin, V.L.; Alivisatos, A.P.; Shank, C.V. Quantum size dependence of femtosecond electronic dephasing and vibrational dynamics in CdSe nanocrystals. *Phys. Rev., B, Condens. Matter* **1994**, *49* (20), 14,435–14,447.
39. O’Neil, M.; Marohn, J.; McLendon, G. Picosecond measurements of exciton trapping in semiconductor clusters. *Chem. Phys. Lett.* **1990**, *168* (2), 208–210.
40. Klimov, V.; Bolivar, P.H.; Kurz, H. Ultrafast carrier dynamics in semiconductor quantum dots. *Phys. Rev., B, Condens. Matter* **1996**, *53* (3), 1463–1467.
41. Logunov, S.; Green, T.; Marguet, S.; El-Sayed, M.A. Interfacial carriers dynamics of CdS nanoparticles. *J. Phys. Chem., A* **1998**, *102* (28), 5652–5658.
42. Dimitrijevic, N.M.; Kamat, P.V. Transient photo-bleaching of small CdSe colloids in acetonitrile. Anodic decomposition. *J. Phys. Chem.* **1987**, *91*, 2096–2099.
43. Haase, M.; Weller, H.; Henglein, A. Photochemistry of colloidal semiconductors: 26. Photoelectron emission from CdS particles and related chemical effects. *J. Phys. Chem.* **1988**, *92*, 4706–4712.
44. Hilinski, E.F.; Lucas, P.A.; Ying, W. A picosecond bleaching study of quantum-confined cadmium sulfide microcrystallites in a polymer film. *J. Chem. Phys.* **1988**, *89* (6), 3534–3541.
45. Kamat, P.V.; Dimitrijevic, N.M.; Nozik, A.J. Dynamic Burstein–Moss shift in semiconductor colloids. *J. Phys. Chem.* **1989**, *93*, 2873–2875.
46. Kamat, P.V.; Dimitrijevic, N.M. Photochemistry in semiconductor particulate systems: 13. Surface modification of CdS semiconductor colloids with diethyldithiocarbamate. *J. Phys. Chem.* **1989**, *93*, 4259–4263.
47. Wang, Y.; Suna, A.; McHugh, J.; Hilinski, E.F.; Lucas, P.A.; Johnson, R.D. Optical transient bleaching of quantum-confined CdS clusters—the effects of surface-trapped electron hole pairs. *J. Chem. Phys.* **1990**, *92* (11), 6927–6939.
48. Vossmeier, T.; Katsikas, L.; Giersig, M.; Popovic, I.G.; Diesner, K.; Chemseddine, A.; Eychmuller, A.; Weller, H. CdS nanoclusters—synthesis, characterization, size dependent oscillator strength, temperature shift of the excitonic transition energy, and reversible absorbance shift. *J. Phys. Chem.* **1994**, *98* (31), 7665–7673.
49. Henglein, A.; Kumar, A.; Janata, E.; Weller, H. Photochemistry and radiation chemistry of semiconductor colloids: reaction of the hydrated electron with CdS and non-linear optical effects. *Chem. Phys. Lett.* **1986**, *132* (2), 133–136.
50. Kang, K.I.; Kepner, A.D.; Gaponenko, S.V.; Koch, S.W.; Hu, Y.Z.; Peyghambarian, N. Confinement-enhanced biexciton binding energy in semiconductor quantum dots. *Phys. Rev., B, Condens. Matter* **1993**, *48* (20), 15,449–15,452.
51. Klimov, V.; Hunsche, S.; Kurz, H. Biexciton effects in femtosecond nonlinear transmission of semiconductor quantum dots. *Phys. Rev., B, Condens. Matter* **1994**, *50* (11), 8110–8113.
52. Zhang, J.Z.; O’Neil, R.H.; Roberti, T.W.; McGowen, J.L.; Evans, J.E. Femtosecond studies of trapped electrons at the liquid–solid interface of aqueous CdS colloids. *Chem. Phys. Lett.* **1994**, *218* (5-6), 479–484.

53. Roberti, T.W.; Cherepy, N.J.; Zhang, J.Z. Nature of the power-dependent ultrafast relaxation process of photoexcited charge carriers in II–VI semiconductor quantum dots: effects of particle size, surface, and electronic structure. *J. Chem. Phys.* **1998**, *108* (5), 2143–2151.
54. Zheng, J.P.; Kwok, H.S. Exciton and biexciton recombination in semiconductor nanocrystals. *Appl. Phys. Lett.* **1994**, *65* (9), 1151–1153.
55. Cherepy, N.J.; Liston, D.B.; Lovejoy, J.A.; Deng, H.M.; Zhang, J.Z. Ultrafast studies of photoexcited electron dynamics in gamma- and alpha-Fe<sub>2</sub>O<sub>3</sub> semiconductor nanoparticles. *J. Phys. Chem., B* **1998**, *102* (5), 770–776.
56. Sengupta, A.; Jiang, B.; Mandal, K.C.; Zhang, J.Z. Ultrafast electronic relaxation dynamics in PbI<sub>2</sub> semiconductor colloidal nanoparticles: a femtosecond transient absorption study. *J. Phys. Chem., B* **1999**, *103*, 3128–3137.
57. Brelle, M.C.; Zhang, J.Z. Femtosecond study of photo-induced electron dynamics in AgI and core/shell structured AgI/Ag<sub>2</sub>S and AgBr/Ag<sub>2</sub>S colloidal nanoparticles. *J. Chem. Phys.* **1998**, *108* (8), 3119–3126.
58. Patel, A.A.; Wu, F.X.; Zhang, J.Z.; Torres-Martinez, C.L.; Mehra, R.K.; Yang, Y.; Risbud, S.H. Synthesis, optical spectroscopy and ultrafast electron dynamics of PbS nanoparticles with different surface capping. *J. Phys. Chem., B* **2000**, *104* (49), 11,598–11,605.
59. Underwood, D.F.; Kippeny, T.; Rosenthal, S.J. Ultrafast carrier dynamics in CdSe nanocrystals determined by femtosecond fluorescence upconversion spectroscopy. *J. Phys. Chem., B* **2001**, *105* (2), 436–443.
60. Burda, C.; Link, S.; Mohamed, M.; El-Sayed, M. The relaxation pathways of CdSe nanoparticles monitored with femtosecond time-resolution from the visible to the IR: assignment of the transient features by carrier quenching. *J. Phys. Chem., B* **2001**, *105* (49), 12,286–12,292.
61. Burda, C.; Link, S.; Mohamed, M.B.; El-Sayed, M. The pump power dependence of the femtosecond relaxation of CdSe nanoparticles observed in the spectral range from visible to infrared. *J. Chem. Phys.* **2002**, *116* (9), 3828–3833.
62. Wu, F.; Zhang, J.Z.; Kho, R.; Mehra, R.K. Radiative and nonradiative lifetimes of band edge states and deep trap states of CdS nanoparticles determined by time-correlated single photon counting. *Chem. Phys. Lett.* **2000**, *330* (3–4), 237–242.
63. Wu, F.; Zhang, J. Ultrafast studies of photoexcited electronic dynamics in thiol-capped CdTe semiconductor nanoparticles. *Proc. SPIE* **2002**, *4807*, 189.
64. Wu, F.X.; Lewis, J.W.; Klinger, D.S.; Zhang, J.Z. Unusual excitation intensity dependence of fluorescence of CdTe nanoparticles. *J. Chem. Phys.* **2003**, *118* (1), 12–16.
65. Chepic, D.I.; Efros, A.L.; Ekimov, A.I.; Ivanov, M.G.; Kharchenko, V.A.; Kudriavtsev, I.A.; Yazeva, T.V. Auger ionization of semiconductor quantum drops in a glass matrix. *J. Lumin.* **1990**, *47*, 113–127.
66. Flytzanis, C.; Ricard, D.; Schanneklein, M.C. The role of photodarkening and Auger recombination in the dynamics of the optical response for Cd(S, Se) nanoparticles. *J. Lumin.* **1996**, *70*, 212–221.
67. Ghanassi, M.; Schanneklein, M.C.; Hache, F.; Ekimov, A.I.; Ricard, D.; Flytzanis, C. Time-resolved measurements of carrier recombination in experimental semiconductor-doped glasses—confirmation of the role of Auger recombination. *Appl. Phys. Lett.* **1993**, *62* (1), 78–80.
68. Peng, X.G.; Manna, L.; Yang, W.D.; Wickham, J.; Scher, E.; Kadavanich, A.; Alivisatos, A.P. Shape control of CdSe nanocrystals. *Nature* **2000**, *404* (6773), 59–61.
69. Manna, L.; Scher, E.C.; Alivisatos, A.P. Synthesis of soluble and processable rod-, arrow-, teardrop-, and tetrapod-shaped CdSe nanocrystals. *J. Am. Chem. Soc.* **2000**, *122* (51), 12,700–12,706.
70. Hu, J.T.; Li, L.S.; Yang, W.D.; Manna, L.; Wang, L.W.; Alivisatos, A.P. Linearly polarized emission from colloidal semiconductor quantum rods. *Science* **2001**, *292* (5524), 2060–2063.
71. Li, L.S.; Hu, J.T.; Yang, W.D.; Alivisatos, A.P. Band gap variation of size- and shape-controlled colloidal CdSe quantum rods. *Nano Lett.* **2001**, *1* (7), 349–351.
72. Mohamed, M.B.; Burda, C.; El-Sayed, M.A. Shape dependent ultrafast relaxation dynamics of CdSe nanocrystals: nanorods vs. nanodots. *Nano Lett.* **2001**, *1* (11), 589–593.
73. Htoon, H.; Hollingworth, J.A.; Malko, A.V.; Dickerson, R.; Klimov, V.I. Light amplification in semiconductor nanocrystals: quantum rods versus quantum dots. *Appl. Phys. Lett.* **2003**, *82* (26), 4776–4778.
74. Wu, F.; Yu, J.H.; Joo, J.; Hyeon, T.; Zhang, J. Ultrafast electronic dynamics of monodisperse PbS and CdS nanoparticles/nanorods: Effects of size on optical nonlinearity. **2003**, to be submitted.
75. Klimov, V.I. Optical nonlinearities and ultrafast carrier dynamics in semiconductor nanocrystals. *J. Phys. Chem., B* **2000**, *104* (26), 6112–6123.
76. Kayanuma, Y. Wannier excitons in low-dimensional microstructures: shape dependence of the quantum size effect. *Phys. Rev., B* **1991**, *44* (23), 13,085–13,088.
77. Goff, S.L.; Stébé, B. Influence of longitudinal and lateral confinements on excitons in cylindrical quantum dots of semiconductors. *Phys. Rev., B* **1993**, *47* (3), 1383–1391.
78. Efros, A.L.; Rodina, A.V. Band-edge absorption and luminescence of nonspherical nanometer-size crystals. *Phys. Rev., B* **1993**, *47* (15), 10,005–10,007.
79. Cantele, G.; Ninno, D.; Iadonisi, G. Confined states in ellipsoidal quantum dots. *J. Phys. Condens. Matter* **2000**, *12* (42), 9019–9036.
80. Silvester, E.J.; Grieser, F.; Sexton, B.A.; Healy, T.W. Spectroscopic studies on copper sulfide sols. *Langmuir* **1991**, *7* (12), 2917–2922.
81. Drummond, K.M.; Grieser, F.; Healy, T.W.; Silvester, E.J.; Giersig, M. Steady-state radiolysis study of the reductive dissolution of ultrasmall colloidal CuS. *Langmuir* **1999**, *15* (20), 6637–6642.
82. Gotsis, H.J.; Barnes, A.C.; Strange, P. Experimental and theoretical investigation of the crystal structure

- of CuS. *J. Phys. Condens. Matter* **1992**, *4* (50), 10,461–10,468.
83. Grijalva, H.; Inoue, M.; Boggavarapu, S.; Calvert, P. Amorphous and crystalline copper sulfides, CuS. *J. Mater. Chem.* **1996**, *6* (7), 1157–1160.
84. Nozaki, H.; Shibata, K.; Ohhashi, N. Metallic hole conduction in CuS. *J. Solid State Chem.* **1991**, *91* (2), 306–311.
85. Saito, S.; Kishi, H.; Nie, K.; Nakamaru, H.; Wagatsuma, F.; Shinohara, T. Cu-63 NMR studies of copper sulfide. *Phys. Rev., B, Condens. Matter* **1997**, *55* (21), 14,527–14,535.
86. Sugiura, C.; Yamasaki, H.; Shoji, T. X-ray spectra and electronic structures of CuS and Cu<sub>2</sub>S. *J. Phys. Soc. Jpn.* **1994**, *63* (3), 1172–1178.
87. Yumashev, K.V.; Prokoshin, P.V.; Malyarevich, A.M.; Mikhailov, V.P.; Artemyev, M.V.; Gurin, V.S. Optical transient bleaching and induced absorption of surface-modified copper sulfide nanocrystals. *Appl. Phys., B* **1997**, *64* (1), 73–78.
88. Klimov, V.; Bolivar, P.H.; Kurz, H.; Karavanskii, V.; Krasovskii, V.; Korkishko, Y. Linear and nonlinear transmission of Cu<sub>x</sub>S quantum dots. *Appl. Phys. Lett.* **1995**, *67* (5), 653–655.
89. Grozdanov, I.; Najdoski, M. Optical and electrical properties of copper sulfide films of variable composition. *J. Solid State Chem.* **1995**, *114* (2), 469–475.
90. Artemyev, M.V.; Gurin, V.S.; Yumashev, K.V.; Prokoshin, P.V.; Maljarevich, A.M. Picosecond absorption spectroscopy of surface modified copper sulfide nanocrystals in polymeric film. *J. Appl. Phys.* **1996**, *80* (12), 7028–7035.
91. Brelle, M.C.; Torres-Martinez, C.L.; McNulty, J.C.; Mehra, R.K.; Zhang, J.Z. Synthesis and characterization of Cu<sub>x</sub>S nanoparticles: nature of infrared band and charge carrier dynamics. *Pure Appl. Chem.* **2000**, *72*, 101.
92. Brelle, M.C.; Zhang, J.Z.; Nguyen, L.; Mehra, R.K. Synthesis and ultrafast study of cysteine- and glutathione-capped Ag<sub>2</sub>S semiconductor colloidal nanoparticles. *J. Phys. Chem., A* **1999**, *103*, 10,194–10,201.
93. Mukai, K.; Sugawara, M. Slow carrier relaxation among sublevels in annealed self-formed InGaAs/GaAs quantum dots. *Jpn. J. Appl. Phys.* **1998**, *37* (10), 5451–5456.
94. Mukai, K.; Ohtsuka, N.; Shoji, H.; Sugawara, M. Emission from discrete levels in self-formed InGaAs/GaAs quantum dots by electric carrier injection— influence of phonon bottleneck. *Appl. Phys. Lett.* **1996**, *68* (21), 3013–3015.
95. Sugawara, M.; Mukai, K.; Shoji, H. Effect of phonon bottleneck on quantum-dot laser performance. *Appl. Phys. Lett.* **1997**, *71* (19), 2791–2793.
96. Gfroerer, T.H.; Sturge, M.D.; Kash, K.; Yater, J.A.; Plaut, A.S.; Lin, P.S.D.; Florez, L.T.; Harbison, J.P.; Das, S.R.; Lebrun, L. Slow relaxation of excited states in strain-induced quantum dots. *Phys. Rev., B, Condens. Matter* **1996**, *53* (24), 16,474–16,480.
97. Yu, H.P.; Lycett, S.; Roberts, C.; Murray, R. Time resolved study of self-assembled InAs quantum dots. *Appl. Phys. Lett.* **1996**, *69* (26), 4087–4089.
98. Adler, F.; Geiger, M.; Bauknecht, A.; Scholz, F.; Schweizer, H.; Pilkuhn, M.H.; Ohnesorge, B.; Forchel, A. Optical transitions and carrier relaxation in self assembled InAs/GaAs quantum dots. *J. Appl. Phys.* **1996**, *80* (7), 4019–4026.
99. Adler, F.; Geiger, M.; Bauknecht, A.; Haase, D.; Ernst, P.; Dornen, A.; Scholz, F.; Schweizer, H. Self-assembled InAs/GaAs quantum dots under resonant excitation. *J. Appl. Phys.* **1998**, *83* (3), 1631–1636.
100. Heitz, R.; Veit, M.; Ledentsov, N.N.; Hoffmann, A.; Bimberg, D.; Ustinov, V.M.; Kopev, P.S.; Alferov, Z.I. Energy relaxation by multiphonon processes in InAs/GaAs quantum dots. *Phys. Rev., B, Condens. Matter* **1997**, *56* (16), 10,435–10,445.
101. Banin, U.; Cerullo, G.; Guzelian, A.A.; Alivisatos, A.P.; Shank, C.V. Quantum confinement and ultrafast dephasing dynamics in InP nanocrystals. *Phys. Rev., B, Condens. Matter* **1997**, *55* (11), 7059–7067.
102. Mičić, O.I.; Cheong, H.M.; Fu, H.; Zunger, A.; Sprague, J.R.; Mascarenhas, A.; Nozik, A.J. Size-dependent spectroscopy of InP quantum dots. *J. Phys. Chem., B* **1997**, *101* (25), 4904–4912.
103. Ahrenkiel, S.P.; Mičić, O.I.; Miedaner, A.; Curtis, C.J.; Nedeljkovic, J.M.; Nozik, A.J. Synthesis and characterization of colloidal InP quantum rods. *Nano Lett.* **2003**, *3* (6), 833–837.
104. Ellingson, R.J.; Blackburn, J.L.; Yu, P.R.; Rumbles, G.; Mičić, O.I.; Nozik, A.J. Excitation energy dependent efficiency of charge carrier relaxation and photoluminescence in colloidal InP quantum dots. *J. Phys. Chem., B* **2002**, *106* (32), 7758–7765.
105. Blackburn, J.L.; Ellingson, R.J.; Mičić, O.I.; Nozik, A.J. Electron relaxation in colloidal InP quantum dots with photogenerated excitons or chemically injected electrons. *J. Phys. Chem., B* **2003**, *107* (1), 102–109.
106. Kennedy, T.A.; Glaser, E.R.; Klein, P.B.; Bhargava, R.N. Symmetry and electronic structure of the Mn impurity in ZnS nanocrystals. *Phys. Rev., B, Condens. Matter* **1995**, *52* (20), 14,356–14,359.
107. Igarashi, T.; Isobe, T.; Senna, M. EPR study of Mn<sup>2+</sup> electronic states for the nanosized ZnS:Mn powder modified by acrylic acid. *Phys. Rev., B, Condens. Matter* **1997**, *56* (11), 6444–6445.
108. Feltin, N.; Levy, L.; Ingert, D.; Pileni, M.P. Magnetic properties of 4-nm Cd<sub>1-y</sub>Mn<sub>y</sub>S nanoparticles differing by their compositions. *J. Phys. Chem., B* **1999**, *103* (1), 4–10.
109. Counio, G.; Esnouf, S.; Gacoin, T.; Boilot, J.P. CdS:Mn Nanocrystals in transparent xerogel matrices: synthesis and luminescence properties. *J. Phys. Chem.* **1996**, *100* (51), 20,021–20,026.
110. Wang, Z.J.; Zhang, H.M.; Zhang, L.G.; Yuan, J.S.; Yan, S.G.; Wang, C.Y. Synthesis and size control of monodisperse manganese-doped ZnS nanoparticles by methacrylate polymer. *Colloid Polym. Sci.* **2003**, *281* (2), 178–181.
111. Bhargava, R.N.; Gallagher, D.; Hong, X.; Nurmikko, A. Optical properties of manganese-doped nanocrystals of ZnS. *Phys. Rev. Lett.* **1994**, *72* (3), 416–419.
112. Bhargava, R.N. Doped nanocrystalline materials— physics and applications. *J. Lumin.* **1996**, *70*, 85–94.

113. Yu, J.Q.; Liu, H.M.; Wang, Y.Y.; Jia, W.Y. Hot luminescence of  $Mn^{2+}$  in ZnS nanocrystals. *J. Lumin.* **1998**, *79* (3), 191–199.
114. Pohl, U.W.; Gumlich, H.E. Optical transitions of different Mn-ion pairs in ZnS. *Phys. Rev., B, Condens. Matter* **1989**, *40* (2), 1194–1201.
115. Devisschere, P.; Neyts, K.; Corlatan, D.; Vandenbossche, J.; Barthou, C.; Benalloul, P.; Benoit, J. Analysis of the luminescent decay of ZnS–Mn electroluminescent thin films. *J. Lumin.* **1995**, *65* (4), 211–219.
116. Bol, A.A.; Meijerink, A. Doped semiconductor nanoparticles—a new class of luminescent materials?. *J. Lumin.* **2000**, *87-89*, 315–318.
117. Smith, B.A.; Zhang, J.Z.; Joly, A.; Liu, J. Luminescence decay kinetics of  $Mn^{2+}$ -doped ZnS nanoclusters grown in reverse micelles. *Phys. Rev., B* **2000**, *62* (3), 2021–2028.
118. Murase, N.; Jagannathan, R.; Kanematsu, Y.; Watanabe, M.; Kurita, A.; Hirata, K.; Yazawa, T.; Kushida, T. Fluorescence and EPR characteristics of  $Mn^{2+}$ -doped ZnS nanocrystals prepared by aqueous colloidal method. *J. Phys. Chem., B* **1999**, *103* (5), 754–760.
119. Chung, J.H.; Ah, C.S.; Jang, D.-J. Formation and distinctive times of surface- and lattice-bound  $Mn^{2+}$  impurity luminescence in ZnS nanoparticles. *J. Phys. Chem., B* **2001**, *105*, 4128–4132.
120. Suyver, J.F.; Wuister, S.F.; Kelly, J.J.; Meijerink, A. Luminescence of nanocrystalline ZnSe: $Mn^{2+}$ . *Phys. Chem. Chem. Phys.* **2000**, *2* (23), 5445–5448.
121. Norman, T.J.; Magana, D.; Wilson, T.; Burns, C.; Cao, D.; Bridges, F.; Zhang, J.Z. Optical and surface structural properties of  $Mn^{2+}$ -doped ZnSe nanoparticles. *J. Phys. Chem., B* **2003**, *107*, 6309–6317.
122. O'Regan, B.; Gratzel, M. A low-cost, high-efficiency solar cell based on dye-sensitized colloidal  $TiO_2$  films. *Nature* **1991**, *353* (6346), 737–740.
123. Colombo, D.P.; Roussel, K.A.; Saeh, J.; Skinner, D.E.; Cavaleri, J.J.; Bowman, R.M. Femtosecond study of the intensity dependence of electron hole dynamics in  $TiO_2$  nanoclusters. *Chem. Phys. Lett.* **1995**, *232* (3), 207–214.
124. Nazeeruddin, M.K.; Kay, A.; Rodicio, I.; Humphrybaker, R.; Muller, E.; Liska, P.; Vlachopoulos, N.; Gratzel, M. Conversion of light to electricity by *cis*-X2bis(2,2'-bipyridyl-4,4'-dicarboxylate)ruthenium(II) charge-transfer sensitizers ( $X = Cl^-$ ,  $Br^-$ ,  $I^-$ ,  $CN^-$ , and  $SCN^-$ ) on nanocrystalline  $TiO_2$  electrodes. *J. Am. Chem. Soc.* **1993**, *115* (14), 6382–6390.
125. Rehm, J.M.; McLendon, G.L.; Nagasawa, Y.; Yoshihara, K.; Moser, J.; Grätzel, M. Femtosecond electron-transfer dynamics at a sensitizing dye-semiconductor ( $TiO_2$ ) interface. *J. Phys. Chem.* **1996**, *100*, 9577.
126. Hannappel, T.; Burfeindt, B.; Storck, W.; Willig, F. Measurement of ultrafast photoinduced electron transfer from chemically anchored Ru-dye molecules into empty electronic states in a colloidal anatase  $TiO_2$  film. *J. Phys. Chem., B* **1997**, *101* (35), 6799–6802.
127. Ellingson, R.J.; Asbury, J.B.; Ferrere, S.; Ghosh, H.N.; Sprague, J.R.; Lian, T.Q.; Nozik, A.J. Dynamics of electron injection in nanocrystalline titanium dioxide films sensitized with [Ru(4,4'-dicarboxy-2,2'-bipyridine)(2)(NCS)(2)] by infrared transient absorption. *J. Phys. Chem., B* **1998**, *102* (34), 6455–6458.
128. Moser, J.E.; Noukakis, D.; Bach, U.; Tachibana, Y.; Klug, D.R.; Durrant, J.R.; HumphryBaker, R.; Gratzel, M. Comment on “measurement of ultrafast photoinduced electron transfer from chemically anchored Ru-dye molecules into empty electronic states in a colloidal anatase  $TiO_2$  film”. *J. Phys. Chem., B* **1998**, *102* (18), 3649–3650.
129. Heimer, T.A.; Heilweil, E.J. Direct time-resolved infrared measurement of electron injection in dye-sensitized titanium dioxide films. *J. Phys. Chem., B* **1997**, *101* (51), 10,990–10,993.
130. Cherepy, N.J.; Smestad, G.P.; Gratzel, M.; Zhang, J.Z. Ultrafast electron injection: Implications for a photoelectrochemical cell utilizing an anthocyanin dye-sensitized  $TiO_2$  nanocrystalline electrode. *J. Phys. Chem., B* **1997**, *101* (45), 9342–9351.
131. Martini, I.; Hodak, J.H.; Hartland, G.V. Effect of structure on electron transfer reactions between anthracene dyes and  $TiO_2$  nanoparticles. *J. Phys. Chem., B* **1998**, *102* (47), 9508–9517.
132. Cornell, R.M.; Schwertmann, U. *The Iron Oxides*; VCH: New York, 1996.
133. Faust, B.C.; Hoffmann, M.R.; Bahnemann, D.W. Photocatalytic oxidation of sulfur dioxide in aqueous suspensions of  $\alpha$ - $Fe_2O_3$ . *J. Phys. Chem.* **1989**, *93*, 6371–6381.
134. Pulgarin, C.; Kiwi, J. Iron oxide-mediated degradation, photodegradation, and biodegradation of aminophenols. *Langmuir* **1995**, *11* (2), 519–526.
135. Vassiliou, J.K.; Mehrotra, V.; Russell, M.W.; Giannelis, E.P.; McMichael, R.D.; Shull, R.D.; Ziolo, R.F. Magnetic and optical properties of  $\gamma$ - $Fe_2O_3$  nanocrystals. *J. Appl. Phys.* **1993**, *73* (10), 5109–5116.
136. Canham, L.T. Silicon quantum wire array fabrication by electrochemical and chemical dissolution of wafers. *Appl. Phys. Lett.* **1990**, *57* (10), 1046–1048.
137. Kanzawa, Y.; Kageyama, T.; Takeoka, S.; Fujii, M.; Hayashi, S.; Yamamoto, K. Size-dependent near-infrared photoluminescence spectra of Si nanocrystals embedded in  $SiO_2$  matrices. *Solid State Commun.* **1997**, *102* (7), 533–537.
138. Tsybeskov, L.; Hirschman, K.D.; Duttagupta, S.P.; Zacharias, M.; Fauchet, P.M.; McCaffrey, J.P.; Lockwood, D.J. Nanocrystalline-silicon superlattice produced by controlled recrystallization. *Appl. Phys. Lett.* **1998**, *72* (1), 43–45.
139. Charvet, S.; Madelon, R.; Rizk, R. Structural, ellipsometry and photoluminescence spectroscopy studies of silicon nanograins embedded in a silica matrix. *Solid-State Electron.* **2001**, *45* (8), 1505–1511.
140. Garrido, B.; Lopez, M.; Ferre, S.; Romanorodriguez, A.; Perezrodriguez, A.; Ruterana, P.; Morante, J.R. Visible photoluminescence of  $SiO_2$  implanted with carbon and silicon. *Nucl. Instrum. Methods Phys. Res.,*



- B Beam Interact. Mater. Atoms **1996**, *120* (1-4), 101–105.
141. Song, H.Z.; Bao, X.M. Visible photoluminescence from silicon-ion-implanted SiO<sub>2</sub> film and its multiple mechanisms. *Phys. Rev., B, Condens. Matter* **1997**, *55* (11), 6988–6993.
142. Cheylan, S.; Elliman, R.G. Effect of particle size on the photoluminescence from hydrogen passivated Si nanocrystals in SiO<sub>2</sub>. *Appl. Phys. Lett.* **2001**, *78* (13), 1912–1914.
143. Prakash, G.V.; Cazzanelli, M.; Gaburro, Z.; Pavesi, L.; Iacona, F.; Franzo, G.; Priolo, F. Nonlinear optical properties of silicon nanocrystals grown by plasma-enhanced chemical vapor deposition. *J. Appl. Phys.* **2002**, *91* (7), 4607–4610.
144. Inokuma, T.; Wakayama, Y.; Muramoto, T.; Aoki, R.; Kurata, Y.; Hasegawa, S. Optical properties of Si clusters and Si nanocrystallites in high-temperature annealed SiO<sub>x</sub> films. *J. Appl. Phys.* **1998**, *83* (4), 2228–2234.
145. Calcott, P.D.J.; Nash, K.J.; Canham, L.T.; Kane, M.J.; Brumhead, D. Spectroscopic identification of the luminescence mechanism of highly porous silicon. *J. Lumin.* **1993**, *57* (1-6), 257–269.
146. Koch, F.; Petrovskoch, V.; Muschik, T. The luminescence of porous Si—the case for the surface state mechanism. *J. Lumin.* **1993**, *57* (1-6), 271–281.
147. Prokes, S.M.; Carlos, W.E. Oxygen defect center red room temperature photoluminescence from freshly etched and oxidized porous silicon. *J. Appl. Phys.* **1995**, *78* (4), 2671–2674.
148. Torchynska, T.V.; Korsunskaya, N.E.; Dzhusmaev, B.R.; Khomenkova, L.Y. Three approaches to surface substance role investigation in porous silicon photoluminescence and its excitation. *J. Phys. Chem. Solids* **2000**, *61* (6), 937–941.
149. Kanemitsu, Y. Light-emitting silicon materials. *J. Lumin.* **1996**, *70*, 333–342.
150. Torchynska, T.V.; Rodriguez, M.M.; Espinoza, F.G.B.; Khomenkova, L.Y.; Korsunskaya, N.E.; Scherbina, L.V. Ballistic effect in red photoluminescence of Si wires—Art. no. 115313. *Phys. Rev., B* **2002**, *6511* (11), 5313.
151. Becerril-Espinoza, F.G.; Torchynska, T.V.; Rodriguez, M.M.; Khomenkova, L.; Scherbina, L.V. Formation of Si/SiO<sub>x</sub> interface and its influence on photoluminescence of Si nano-crystallites. *Microelectron. J.* **2003**, *34* (5-8), 759–761.
152. Zhang, L.B.; Coffey, J.L.; Xu, W.; Zerda, T.W. Luminescent Si nanoparticles in sol-gel matrices stabilized by amino acids. *Chem. Mater.* **1997**, *9* (11), 2249–2251.
153. Klimov, V.I.; Schwarz, C.J.; McBranch, D.W.; White, C.W. Initial carrier relaxation dynamics in ion-implanted Si nanocrystals: femtosecond transient absorption study. *Appl. Phys. Lett.* **1998**, *73* (18), 2603–2605.
154. Krapf, D.; Davidi, A.; Shappir, J.; Sa'ar, A. Infrared photo-induced absorption spectroscopy of porous silicon. *Phys. Status Solidi, A, Appl. Res.* **2003**, *197* (2), 566–571.
155. Doolen, R.; Laitinen, R.; Parsapour, F.; Kelley, D.F. Trap state dynamics in MoS<sub>2</sub> nanoclusters. *J. Phys. Chem., B* **1998**, *102* (20), 3906–3911.
156. Sengupta, A.; Mandal, K.C.; Zhang, J.Z. Ultrafast electronic relaxation dynamics in layered iodide semiconductors: a comparative study of colloidal BiI<sub>3</sub> and PbI<sub>2</sub> nanoparticles. *J. Phys. Chem., B* **2000**, *104* (40), 9396–9403.
157. Lifshitz, E.; Yassen, M.; Bykov, L.; Dag, I.; Chaim, R. Nanometer-sized particles of PbI<sub>2</sub> embedded in SiO<sub>2</sub> films. *J. Phys. Chem.* **1994**, *98* (5), 1459–1463.
158. Tang, Z.K.; Nozue, Y.; Goto, T. Quantum size effect on the excited state of HgI<sub>2</sub>, PbI<sub>2</sub> and BiI<sub>3</sub> clusters and molecules in zeolite LTA. *J. Phys. Soc. Jpn.* **1992**, *61*, 2943–2950.
159. Micic, O.I.; Meglic, M.; Lawless, D.; Sharma, D.K.; Serpone, N. Semiconductor photophysics: 5. Charge carrier trapping in ultrasmall silver iodide particles and kinetics of formation of silver atom clusters. *Langmuir* **1990**, *6* (2), 487–492.
160. Oldenburg, S.J.; Hale, G.D.; Jackson, J.B.; Halas, N.J. Light scattering from dipole and quadrupole nanoshell antennas. *Appl. Phys. Lett.* **1999**, *75* (8), 1063–1065.
161. Henglein, A. Colloidal palladium nanoparticles: reduction of Pd(II) by H<sub>2</sub>; Pd<sub>core</sub>Au<sub>shell</sub>Ag<sub>shell</sub> particles. *J. Phys. Chem., B* **2000**, *104* (29), 6683–6685.
162. Meriaudeau, F.; Downey, T.; Wig, A.; Passian, A.; Buncick, M.; Ferrell, T.L. Fiber optic sensor based on gold island plasmon resonance. *Sens. Actuators, B, Chem.* **1999**, *54* (1–2), 106–117.
163. Michaels, A.M.; Jiang, J.; Brus, L. Ag Nanocrystal junctions as the site for surface-enhanced Raman scattering of single Rhodamine 6G molecules. *J. Phys. Chem., B* **2000**, *104* (50), 11,965–11,971.
164. Nikoobakht, B.; El-Sayed, M.A. Surface-enhanced Raman scattering studies on aggregated gold nanorods. *J. Phys. Chem.* **2003**, *107* (18), 3372–3378.
165. Mie, G. Contribution to optical properties of turbulent media, specifically colloidal metal dispersions. *Ann. Phys.* **1908**, *25* (3), 377–445.
166. Kreibig, U.; Vollmer, M. *Optical Properties of Metal Clusters*; Springer: Berlin, 1995.
167. Creighton, J.A.; Eadon, D.G. Ultraviolet visible absorption spectra of the colloidal metallic elements. *J. Chem. Soc., Faraday Trans.* **1991**, *87* (24), 3881–3891.
168. Quinten, M. The color of finely dispersed nanoparticles. *Appl. Phys., B, Lasers Opt.* **2001**, *73* (4), 317–326.
169. Smith, B.A.; Zhang, J.Z.; Giebel, U.; Schmid, G. Direct probe of size-dependent electronic relaxation in single-sized Au and nearly monodisperse Pt colloidal nanoparticles. *Chem. Phys. Lett.* **1997**, *270* (1–2), 139–144.
170. Logunov, S.L.; Ahmadi, T.S.; El-Sayed, M.A.; Khoury, J.T.; Whetten, R.L. Electron dynamics of passivated gold nanocrystals probed by subpicosecond transient absorption spectroscopy. *J. Phys. Chem., B* **1997**, *101* (19), 3713–3719.
171. Hodak, J.; Martini, I.; Hartland, G.V. Ultrafast study of electron-phonon coupling in colloidal gold particles. *Chem. Phys. Lett.* **1998**, *284* (1–2), 135–141.

172. Faulhaber, A.E.; Smith, B.A.; Andersen, J.K.; Zhang, J.Z. Femtosecond electronic relaxation dynamics in metal nano-particles—effects of surface and size confinement. *Mol. Cryst. Liq. Cryst. Sci. Technol., Sect. A Mol. Cryst. Liq. Cryst.* **1996**, *283*, 25–30.
173. Darugar, Q.; Landes, C.; Link, S.; Schill, A.; El-Sayed, M.A. Why is the thermalization of excited electrons in semiconductor nanoparticles so rapid? Studies on CdSe nanoparticles. *Chem. Phys. Lett.* **2003**, *373* (3-4), 284–291.
174. Link, S.; Hathcock, D.J.; Nikoobakht, B.; El-Sayed, M.A. Medium effect on the electron cooling dynamics in gold nanorods and truncated tetrahedra. *Adv. Mater.* **2003**, *15* (5), 393.
175. Hodak, J.H.; Henglein, A.; Hartland, G.V. Photo-physics of nanometer sized metal particles: Electron-phonon coupling and coherent excitation of breathing vibrational modes. *J. Phys. Chem., B* **2000**, *104* (43), 9954–9965.
176. Link, S.; El-Sayed, M.A.; Schaaff, T.G.; Whetten, R.L. Transition from nanoparticle to molecular behavior: a femtosecond transient absorption study of a size-selected 28 atom gold cluster. *Chem. Phys. Lett.* **2002**, *356* (3-4), 240–246.
177. Link, S.; Beeby, A.; FitzGerald, S.; El-Sayed, M.A.; Schaaff, T.G.; Whetten, R.L. Visible to infrared luminescence from a 28-atom gold cluster. *J. Phys. Chem., B* **2002**, *106* (13), 3410–3415.
178. Grant, C.D.; Schwartzberg, A.M.; Yang, Y.; Chen, S.; Zhang, J.Z. Ultrafast study of electronic relaxation dynamics in Au<sub>11</sub> nanoclusters. *Chem. Phys. Lett.* **2003**, *in press*.
179. Nisoli, M.; DeSilvestri, S.; Cavalleri, A.; Malvezzi, A.M.; Stella, A.; Lanzani, G.; Cheyssac, P.; Kofman, R. Coherent acoustic oscillations in metallic nanoparticles generated with femtosecond optical pulses. *Phys. Rev., B, Condens. Matter* **1997**, *55* (20), 13,424–13,427.
180. Hodak, J.H.; Martini, I.; Hartland, G.V. Observation of acoustic quantum beats in nanometer sized Au particles. *J. Chem. Phys.* **1998**, *108* (22), 9210–9213.
181. Voisin, C.; Del Fatti, N.; Christofilos, D.; Vallee, F. Ultrafast electron dynamics and optical nonlinearities in metal nanoparticles. *J. Phys. Chem., B* **2001**, *105* (12), 2264–2280.
182. Voisin, C.; Christofilos, D.; Del Fatti, N.; Vallee, F. Environment effect on the acoustic vibration of metal nanoparticles. *Physica B* **2002**, *316*, 89–94.
183. Perner, M.; Gresillon, S.; Marz, J.; von Plessen, G.; Feldmann, J.; Porstendorfer, J.; Berg, K.J.; Berg, G. Observation of hot-electron pressure in the vibration dynamics of metal nanoparticles. *Phys. Rev. Lett.* **2000**, *85* (4), 792–795.
184. Hartland, G.V.; Hu, M.; Wilson, O.; Mulvaney, P.; Sader, J.E. Coherent excitation of vibrational modes in gold nanorods. *J. Phys. Chem., B* **2002**, *106* (4), 743–747.
185. Grant, C.D.; Schwartzberg, A.M.; Norman, T.J.; Zhang, J.Z. Ultrafast electronic relaxation and coherent vibrational oscillation of strongly coupled gold nanoparticle aggregates. *J. Am. Chem. Soc.* **2003**, *125* (2), 549–553.
186. Lazarides, A.A.; Schatz, G.C. DNA-linked metal nanosphere materials: Fourier-transform solutions for the optical response. *J. Chem. Phys.* **2000**, *112* (6), 2987–2993.
187. Storhoff, J.J.; Lazarides, A.A.; Mucic, R.C.; Mirkin, C.A.; Letsinger, R.L.; Schatz, G.C. What controls the optical properties of DNA-linked gold nanoparticle assemblies? *J. Am. Chem. Soc.* **2000**, *122* (19), 4640–4650.
188. Heath, J.R.; Knobler, C.M.; Leff, D.V. Pressure/temperature phase diagrams and superlattices of organically functionalized metal nanocrystal monolayers: the influence of particle size, size distribution, and surface passivant. *J. Phys. Chem., B* **1997**, *101* (2), 189–197.
189. Shipway, A.N.; Lahav, M.; Gabai, R.; Willner, I. Investigations into the electrostatically induced aggregation of Au nanoparticles. *Langmuir* **2000**, *16* (23), 8789–8795.
190. Norman, T.J.; Grant, C.D.; Magana, D.; Zhang, J.Z.; Liu, J.; Cao, D.L.; Bridges, F.; Van Buuren, A. Near infrared optical absorption of gold nanoparticle aggregates. *J. Phys. Chem., B* **2002**, *106* (28), 7005–7012.

# Charge Transfer in Metal–Molecule Heterostructures

**Debasish Kuila**

*Department of Chemistry, Louisiana Tech University, Ruston, Louisiana, U.S.A.*

**David B. Janes**

*School of Electrical and Computer Engineering, Purdue University, West Lafayette, Indiana, U.S.A.*

**Clifford P. Kubiak**

*Department of Chemistry, University of California–San Diego, La Jolla, California, U.S.A.*

## INTRODUCTION

What is nanoscale? Albert Einstein's doctoral research, using experimental data on the diffusion of sugar in water, showed that each single sugar molecule measures about a nanometer in diameter, a billionth of a meter. One nanometer is the approximate width of 10 hydrogen atoms laid side by side. It is one thousandth the length of a typical bacterium ( $\sim 1\ \mu\text{m}$ ,  $10^{-6}\ \text{m}$ ), one millionth the size of a pin head, one billionth the length of Michael Jordan's well-muscled legs ( $\sim 1\ \text{m}$ ). While the exact definition of "nanotechnology" is somewhat imprecise, the term generally implies devices or structures with at least two characteristic dimensions in the range of 1–100 nm. Along with biomedical research and defense—fighting cancer and building missile shields—nanotechnology has become a visible and energized discipline in science and technology. It spans fields from condensed matter physics, engineering, molecular biology to large swath of chemistry<sup>[1,2]</sup> (Fig. 1). Key themes within this area include 1) the ability to understand, and ultimately to control, important properties of materials and structures at the nanometer scale; and 2) improved understanding of how nanostructured elements interact with the external environment.

In contrast to the relatively recent recognition of nanotechnology as a field, charge transfer has been known for decades.<sup>[3,4]</sup> It is a very important process in chemistry, biology, and physics in semiconductor devices and in electronics. Our respiration, photosynthesis, many biological processes, and thin films of tunnel-diode involve electron or charge transfer, in some cases even at a large distance.<sup>[5]</sup> In both respiration and photosynthesis, the primary action of the energy source (combustion of substrate by oxygen in respiration and absorption of light by chlorophyll or bacteriochlorophyll in photosynthesis) is to move charges or

electrons, a long distance, in an electron-transport chain.<sup>[6,7]</sup> Charge transfer in photosynthetic reaction centers<sup>[8]</sup> and in protein–protein electron-transfer complexes such as hemoglobin<sup>[9]</sup> can even occur at liquid helium temperature. The measurement of electrical currents,  $I$ , tunneling through insulating layers, as in the invention of Esaki tunnel-diode, is a classic example of charge transfer in semiconductor devices.<sup>[10]</sup> In this entry, results about charge transfer at the nanoscale from the electrostatic surface potential (ESP) measurements of self-assembled monolayers (SAMs) are presented. A brief overview of current theoretical understanding including our ongoing calculations is included.

## AN OVERVIEW OF MOLECULAR ELECTRONICS

The quest for miniaturization of semiconductor devices has created a tremendous interest in nanomaterials in recent years.<sup>[11,12]</sup> Nanoscale structures have now become essential parts of integrated circuit (IC) technologies for providing faster computer chips. Decades before computers pervaded our workplaces and homes, Gordon Moore, cofounder of Intel Corporation, observed that the number of transistors per unit area in an IC chip was doubling approximately every 18 months. This relationship, widely known as Moore's Law,<sup>[13]</sup> has held for over 30 years. It drives much of the technology development and is responsible for the continuous increase in computer speeds, memory capacities, and capabilities of components based on ICs. In the first international conference on nanomanufacturing at MIT in April 2003, Intel showed their progress toward 100-nm computer chips. However, there is a limit to the top-down approach, a concern shared by the researchers in semiconductor industry.<sup>[14]</sup>

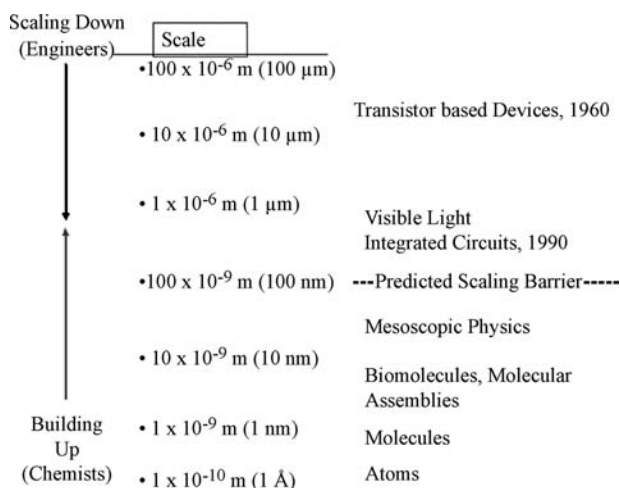


**Fig. 1** An overview of micro- and nanoscale.

The gap between the top-down approach and the size of an individual molecule (Fig. 1) may be best realized using a bottom-up approach. Nanotechnology with direct impact on commercial application of nanoscale systems will depend on their assembly with predefined geometry either in solution or on a solid support. Interesting new phenomena such as single-electron charging effects<sup>[15]</sup> and conductance quantization<sup>[16]</sup> have already been discovered. As decreasing the size of microfabricated components becomes increasingly difficult, it is possible that molecular electronic approaches can play a significant role in electronics. As molecules with sizes in the range of 1–3 nm have been shown to have interesting functionality when integrated into device structures, this approach should provide inherent scalability to the nanoscale (Fig. 2).

Aviram and Ratner originally proposed in 1974 that molecules could replace computer-chip components and a single molecule with a donor-spacer-acceptor would behave as a diode when placed between two

electrodes.<sup>[17]</sup> This has now been extended to electronics using hybrid molecular and monomolecular devices and has been reviewed recently by Aviram and his colleagues at IBM.<sup>[18]</sup> More significantly in the past 5 years, nanoscale devices ranging from simple switches and wires to more complex transistors and circuits have been unveiled. Let us review briefly what is inside an IC and a few major accomplishments in the past 5 years.

An IC chip, the heart of a computer, is made of silicon, a semiconductor material. A stamp-size chip can hold billions of components, primarily the transistors that allow a computer to process instructions, perform calculations, and manage data flow. The transistor is a switch that controls and generates electrical signals using three terminals: the source, gate, and drain. More sophisticated functions can be performed using multiple transistors.<sup>[19]</sup> In computational circuits such as microprocessors, the transistors are typically interconnected to form logic gates, which represent and manipulate data using a binary system often designated as “1” and “0.” The binary system, or rather the patterns and sequences of 1 (“on”) or 0 (“off”) can be interpreted as numbers. Generally, the state (“1” or “0”) of a given logic gate is determined by the voltage state at the output of that gate. The state of a logic gate switches in a specified response to its inputs, based on the configuration of wires that interconnect the gates within the IC. The switching signals consist of voltages, and associated electronic charge/current, flowing through the wires leading into the logic gate. Within an IC, bits of information can also be stored in memory cells, where a bit is typically represented by a quantity of electronic charge or a voltage state.<sup>[19]</sup>

Typically, the wires in ICs are made from metals, which are good electrical conductors. In the past decade, individual molecules have been shown to conduct electricity; the Aviram-Ratner mechanism, slightly

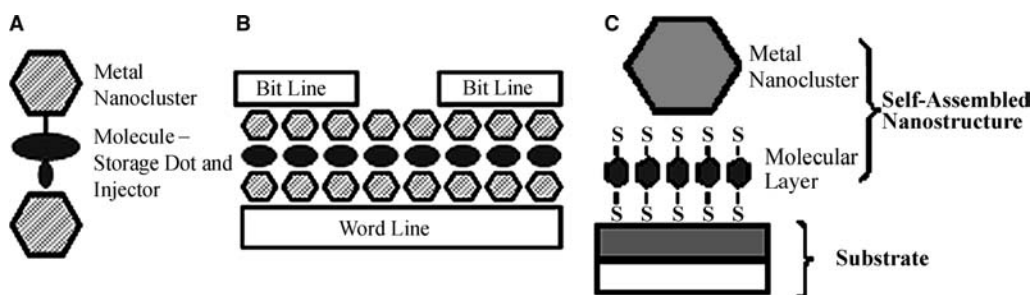


**Fig. 2** (A) A schematic representation of a unit cell of metal/molecule/metal device structure. (B) Potential scalable logic/memory circuit using unit cell devices. (C) Characterization of self-assembled metal/molecule/substrate structure with well-controlled interfaces. Using a flat Au substrate, this structure provided the first report of the resistance of organic molecules and the first room-temperature Coulomb staircase in a controlled nanostructure. (Source: Andres, R. P.; Bein, T.; Dorogi, M.; Feng, S.; Henderson, J. I.; Kubiak, C. P.; Mahoney, W.; Osifchin, R. G.; Reifenberger, R. “Coulomb staircase” at room temperature in a self-assembled molecular nanostructure. *Science*, **1996**, 272 (5266), 1323–1325.

modified, has been confirmed both in macroscopic and nanoscopic conductivity measurements.<sup>[20]</sup> Simulations have shown that gold nanowires can be stretched to one-atom thickness. Phaedon Avouris at IBM designed a “NOT” gate (similar to the part of a computer’s logic circuitry) with nanotubes.<sup>[21,22]</sup> A nanotube covering gold electrodes formed two p-type transistors: one covered with an insulator and the other was exposed to chemical processes, converting it to n-type.

As with a typical transistor in IC, containing three terminals: the source, gate, and drain, conductive tripod-shaped molecules have been attached to three terminals to form a transistor. Charles Lieber and his group at Harvard University have designed a nanoscale memory device using crisscrossed nanotubes as both wires and, at their junctions, switches.<sup>[23,24]</sup> The tubes that touch are “on” and that do not are “off” and they can hold that state indefinitely. Cees Dekker, of Delft University, unveiled a transistor that worked at room temperature using a semiconductor carbon nanotube, an electrode, and a substrate.<sup>[25]</sup> In contrast, Mark Reed at Yale and James Tour at Rice have designed organic molecules that serve as conductors. When a voltage is applied and varied to the molecule containing a para-nitro aniline moiety (aromatic species), it functions as a switch.<sup>[26]</sup>

The Yale–Rice team followed the bottom-up approach to assemble the system on a gold surface using chemical self-assembly which relies on ordered and functional structure formed by dipping a Au-substrate into a solution containing the aromatic thiol. This is the basis of a common bottom-up approach for making nanoscale devices based on self-assembled monolayers (SAMs). The SAMs of organic thiols have been widely studied and they have been reviewed in recent literature.<sup>[27,28]</sup>

The current–voltage measurement of SAMs is one of the most active area of research because of its role in molecular electronics and other sensing applications.

The resistance or conductance of molecules bonded to an Au electrode has been measured using scanning probe techniques by different groups.<sup>[29–34]</sup> For example, in the case of insulating SAMs of dodecanethiol (DDT), octadecylthiol (ODT), and resorcinarene C10 tetrasulfide (RC10TS) on Au(111), the electrical conductivity of the monolayers, measured using scanning tunneling microscopy (STM), is observed to depend both on the monolayer thickness and on the nature of the Au/S bond. Leakage current densities across 1.4-nm DDT and 2.0-nm RC10TS on Au indicate superior insulating properties of the latter at high voltages. The SiO<sub>2</sub> layers with comparable leakage current densities were calculated to have a thickness of 1.0 and 1.5 nm, respectively. These data strongly suggest that organic SAMs are capable of providing necessary insulation for the efficient operation of molecular or nanoscale electronic circuits.<sup>[35]</sup>

A close coupling between theoretical modeling<sup>[36]</sup> and experimental measurements is necessary to provide useful insights into the conductance spectra of organic molecules interfaced with semiconductor and metal surfaces. This can be exemplified by the work of the teams led by Datta and Reifenger of Purdue University.<sup>[34,37,38]</sup> The basic picture for molecular conduction is fairly straightforward in principle. Consider a molecule of phenyl dithiol sandwiched between two gold electrodes as shown in Fig. 3. The molecular energy levels consist of a set of occupied levels separated by a gap from a set of unoccupied levels (Fig. 3B). At equilibrium, the Fermi energy ( $E_f$ ) is typically located somewhere in the gap between the highest occupied molecular orbital (HOMO) and the lowest unoccupied molecular orbital (LUMO). When a bias is applied, the Fermi energy in the right contact ( $\mu_2$ ) floats up by  $eV_d$  relative to the left contact ( $\mu_1$ ), i.e.,  $\mu_2 - \mu_1 = eV_d$ . The low bias conductance is determined by tunneling near the Fermi energy. The conductance of the molecule increases dramatically when the bias is large enough that one or more of the molecular energy

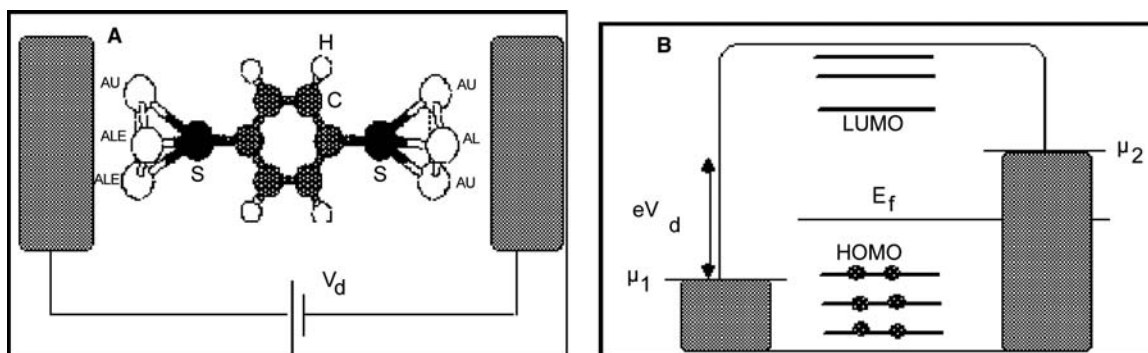


**Fig. 3** (A) Phenyl dithiol (1,4-benzenedithiol) sandwiched between two gold electrodes. (B) Schematic diagram showing molecular energy levels and electrochemical potentials of the contacts.

levels lie between  $\mu_1$  and  $\mu_2$ . This basic picture has been extended into a quantitative model using the standard methods of quantum chemistry.<sup>[38]</sup>

## ELECTROSTATIC SURFACE POTENTIAL

Although significant progress has been made in different areas of nanotechnology, a proper understanding of charge transfer at the metal–molecule interface is still lacking. In contrast to  $I$ – $V$  studies, the electrostatic surface potential of SAMs—due to the presence of dipoles on a surface—has not been explored that much. As shown in Fig. 4, ESP arises from the dipoles created by the chemisorbed aromatic thiol on Au (Fig. 4). Now the question arises, why is this important? First of all, the measurement of ESP

gives an insight into the electronic properties of SAMs. Secondly, such measurements provide a diagnostic feature for the molecule and better models for  $I$ – $V$  measurements. Furthermore, a knowledge of ESP can help build a potential chemical field-effect transistor (FET) for nanoelectronic devices. The origin of the measured potential is intimately related to orientation and bonding as well as the molecule itself. Thus ESP measurement is of fundamental interest and has potential applications for chemical and biochemical sensors (Fig. 4 bottom).

What follows next is a description of ESP measurements and experimental results derived from our collaborative efforts as well as that of other groups. A brief overview of current theoretical understanding of ESP measurements including our ongoing calculations is included.

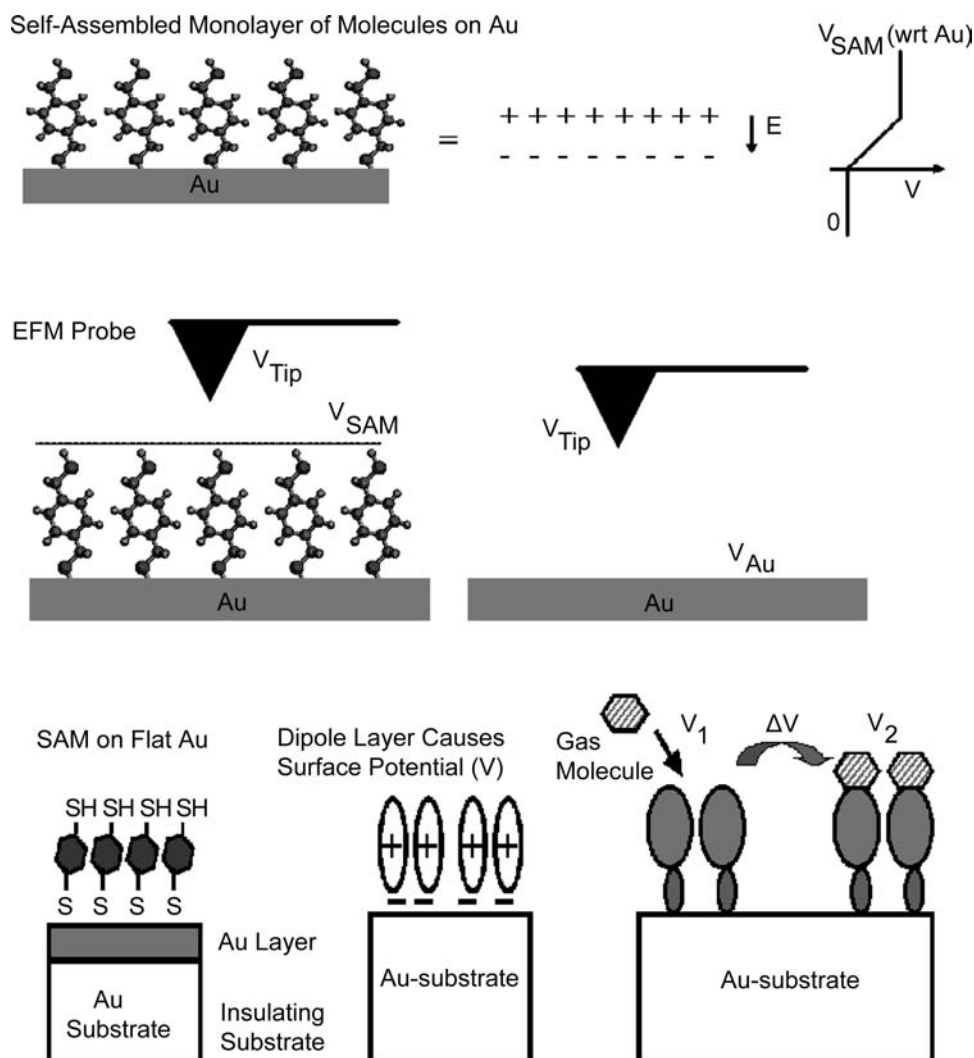


**Fig. 4** Top: Self-assembled monolayers of xylyldithiol chemisorbed on gold; the opposite charge dipoles produce electrostatic surface potential (ESP). Middle: The ESP measured with or without the molecule chemisorbed on the surface using electrostatic force microscopy (EFM). Bottom: A schematic view of potential chemical sensors based on electrostatic surface potential measurements of a SAM of an organometallic compound before and after it is exposed to a gas.



## ESP Measurements

Although several techniques exist for measuring the surface potential of monolayers, the most widely used method is the vibrating Kelvin probe developed initially to measure the contact-potential differences (CPDs) between two conducting materials.<sup>[39,40]</sup> When two metals are electrically connected, electrons flow immediately from one metal to the other until an equilibrium is established, i.e., when both metals reach the same electrochemical potential. The potentials outside the metals are no longer strictly constant due to these slight surface charges, creating a potential drop from one metal to another, which is described as the local CPD between these two metals (Fig. 5). The CPD for clean metal surfaces is the difference in work functions (defined by removal of an electron from the surface to vacuum) of the two materials. The work function is modified as the surface is coated with SAMs of different dipole moments (Fig. 5). However, as the work function of the tip is the same for both measurements, the surface potential of the SAM-coated Au can be referenced to the bare Au substrate (Fig. 4).

A commercial AFM can be modified as the Kelvin probe to enable surface potential measurements (Fig. 6). Two conductors are arranged as a parallel plate capacitor with a small spacing (nanometer scale), and the resultant CPD (as shown above in Fig. 5), in a simple sense, can be defined as  $V_{\text{CPD}} = -(\phi_1 - \phi_2)/e$ , where  $\phi_1$  and  $\phi_2$  are the work functions of the conductors that include the adsorbed layers. A periodic vibration between the two plates at a frequency  $\omega$  gives an alternating current (a.c.) with the same frequency  $\omega$

when the two plates have different work functions.<sup>[39]</sup>

$$I(t) = (V_{\text{bias}} + V_{\text{CPD}})\omega\Delta C \cos \omega t$$

The zero point of a.c. can be detected when the additional bias voltage is applied between the two plates until the electric field between them disappears, i.e.,  $V_{\text{CPD}} = -V_{\text{bias}}$ . The spatial resolution of CPD in electrostatic force microscopy (EFM) can be improved using a Kelvin probe tip and has been called Kelvin probe force microscope (KFM) by Wickramasinghe and coworkers.<sup>[40]</sup>

The electrostatic surface potential ( $V_s$ ) measurement is based on the standard noncontact force detection technique described elsewhere.<sup>[41,42]</sup> In short, the tip is held at a fixed distance of approximately 100 nm above the sample using a noncontact topographic feedback system as shown in Fig. 6. This system controls the separation by monitoring and maintaining a specific mechanical vibration of the cantilever ( $\omega_r$ ) near its resonance frequency.

The electrostatic force on a conducting tip held close to a conducting surface is given by  $F = -(1/2)V_s^2 (dc/dZ)$ ; where  $V_s$  or  $V_{\text{SAM}}$  is ESP.

The ESP for a SAM, relative to that of a bare metal surface, is defined as:

$$V_{\text{SAM}} = \frac{N_{\text{mol}}}{2K\epsilon_0} \vec{p}\hat{n} \quad (1)$$

where  $N_{\text{mol}}$  is the local density of molecules in the SAM (assuming uniform coverage),  $\vec{p}$  is the dipole moment of the adsorbed molecule,  $\hat{n}$  is a unit vector normal to the

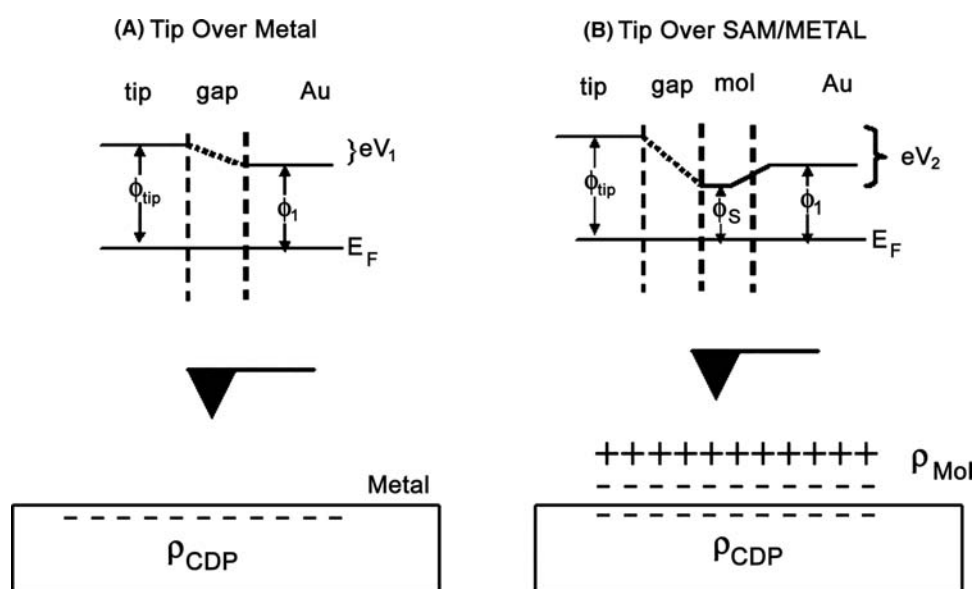


**Fig. 5** The contact potential difference (CPD) due to difference in work functions resulting from the AFM tip over metal and the metal coated with the self-assembled monolayer of a molecule.



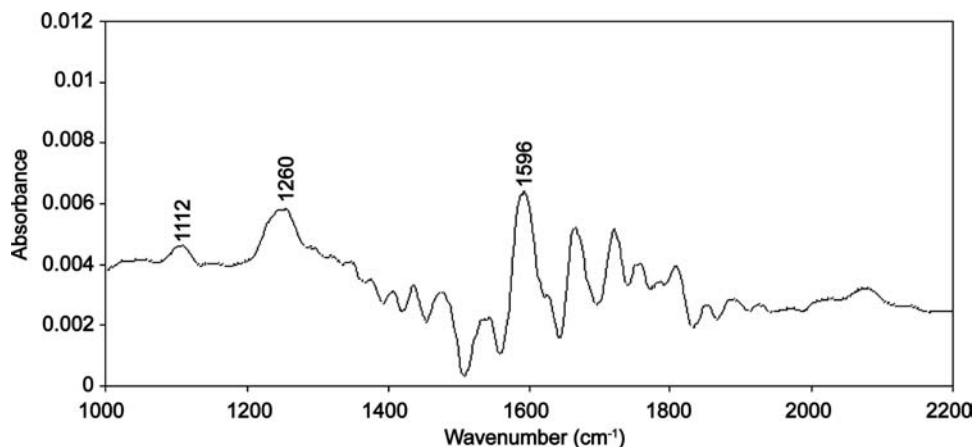


Fig. 8 A reflectance absorption infrared spectrum of tetramethylxylyldithiol chemisorbed on Au.

A typical RAIR spectrum of an aromatic thiol, with thickness of 0.8 nm, used to form a charge-transfer (CT) complex (see “[Surface Potential Measurements of a CT Complex](#)”) is shown in Fig. 8 (see Ref.<sup>[42]</sup>).

### Electrostatic Surface Potential Results

Evans and Ulman first studied the ESPs of SAMs of alkanethiols on gold surfaces using a macroscopic Kelvin probe.<sup>[43]</sup> As the probe diameter was on the order of a few millimeters, the surface potential produced by a large number of molecules ( $\sim 10^{13}$ ) was measured. These measurements indicated a dependence of the ESP on the number of  $\text{CH}_2$  groups that formed the backbone of the alkanethiols. A change of  $\sim 10$  mV per  $\text{CH}_2$  group was observed. Thus while the ESP of dodecanethiol (DDT) was  $\sim 520$  mV, that of octadecylthiol (ODT) was measured to be  $\sim 580$  mV.

In these studies, Evans and Ulman modeled SAMs as a two-dimensional ensemble of dipoles with length  $l$ , where  $l$  is approximately the length of the molecule (Fig. 7). A layer of negative charge resides very close to the Au substrate, while the positive charge is thought to lie at the tail of the molecule, approximately a distance  $l$  above the gold surface. The orientation of the dipole moment is inferred from the positive slope in the surface potential as the chain length is increased. This suggests that increase in ESP is directly related to the change in distance between the two charged sheets. In molecular terms, this implies that the effective  $\text{R}^+-\text{S}^-$  dipole (where  $\text{R} = \text{C}_n\text{H}_{2n+1}$ ) must be larger than the  $\text{Au}^+-\text{S}^-$  dipole and this is reasonable as the  $\text{Au}^+$  can be screened within a very short distance by the electrons within the metal, whereas this cannot be applicable for the monolayer (see “[Negative Surface Potential](#)”).

Recently, Lü et al. used a KFM to measure the surface potential of alkanethiol SAMs transferred to a gold substrate using microcontact printing techniques.<sup>[44]</sup> The lateral resolution in this case was  $\sim 50$  nm. As in the case of Evans and Ulman, a dependence of surface potential on the chain length is observed ( $\sim 14$  mV per  $\text{CH}_2$  unit). These measurements were made with respect to a  $-\text{COOH}$ -terminated thiol SAM, making it difficult to estimate the absolute value of the potential produced by the molecules themselves. However, these studies clearly established a strong dependence in the polarity and magnitude of the ESP on the number of  $\text{CH}_2$  groups present in an alkanethiol molecule.

The ESP measurements of alkanethiols using a modified AFM or EFM at Purdue have yielded much lower values than that reported by Evans and Ulman. An average surface potential of  $100 \pm 20$  mV for DDT SAMs and  $230 \pm 30$  mV for ODT SAMs (Fig. 9) are observed. Although the ESP measurements of alkanethiols by Evans and Ulman, Lü et al., and that measured by the Purdue group are somewhat different from each other, they may still be compared on a qualitative sense as shown in Fig. 10.

The large difference between the surface potential measured by the Purdue group and those reported by Evans and Ulman may arise due to different standards. As the electrostatic force is a long-range interaction, the cantilever as well as the tip contributes to the electrostatic force. It is estimated that SAM interrogated by the EFM technique is roughly given by a circular region with a diameter of  $\sim 40$   $\mu\text{m}$ , a dimension determined roughly by the triangular region of the cantilever supporting the tip. Thus due to the uncertainties of the absolute values of the surface potential, it is more relevant to discuss only the relative changes between alkanethiols with different chain

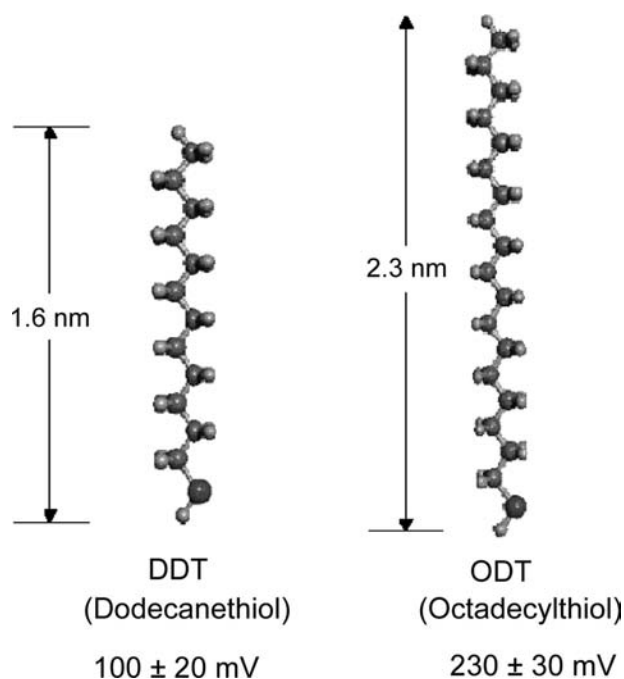


**Fig. 9** The electrostatic surface potentials of dodecanethiol (DDT) and octadecylthiol (ODT) chemisorbed on Au.

lengths. The relative dependence of ESP on chain length is in agreement with that reported by Lü et al.<sup>[44]</sup>

There are other factors that may explain the observed difference in ESP values. Evans and Ulman did reference their measurements to polycrystalline Au.<sup>[43]</sup> If the S–Au bonding is affected by the orientation of the surface Au atoms, then it is possible that the charge associated with S–Au bond also depends on the orientation of the surface Au atoms. Thus the charge associated with the S–Au bond can cause an offset in the magnitude of the surface potential. Further investigation is necessary to know the effect of the orientation of the Au atoms on surface potential.

The ESP measurements are further complicated by contamination of the surface. The preparation of the Au surface can affect the packing density as well as the orientation of the molecule. A “bare” Au substrate has been considered as a control sample in our measurements. Zehner et al. have shown in their studies that the ESP value varies with time using hexadecanethiol (HDT) SAM as a reference.<sup>[45]</sup> In our studies also, we have observed the ESPs of DDT and ODT SAMs decrease slightly with time.<sup>[41]</sup> This may indicate that SAM organizes further with time and this is consistent with structural changes observed over time by Barrena et al.<sup>[46]</sup> Similarly, Saito et al. have used a monolayer of octadecyltrimethoxysilane (ODS) and have shown how the electrostatic potential depends on the surface coverage of the monolayer.<sup>[47]</sup> Thus how exactly different factors such as the substrate and packing of SAMs affect surface potential may need to be addressed further.

#### Effect of Solvent on ESP Measurements

To our knowledge, this aspect has not been reported in the literature. We have examined the surface potential of SAMs of ODT prepared from different solvents such as ethanol, dichloromethane, and acetonitrile. The solvents used for SAM formation do not form a chemical bond with Au as they are removed by evaporation. Thus it is unlikely that the solvents themselves can form a close-packed monolayer. This is corroborated by IR spectroscopic investigations of Gericke, Simon-Kutscher, and Huehnerfuss<sup>[48]</sup> which provide no evidence of solvent molecules embedded in the monolayer. Our ESP measurements yield an average surface potential of  $200 \pm 50$  mV for ODT SAMs (prepared from different solvents) with respect to bare Au(111), thus showing no significant effect of solvent on surface potential measurements.

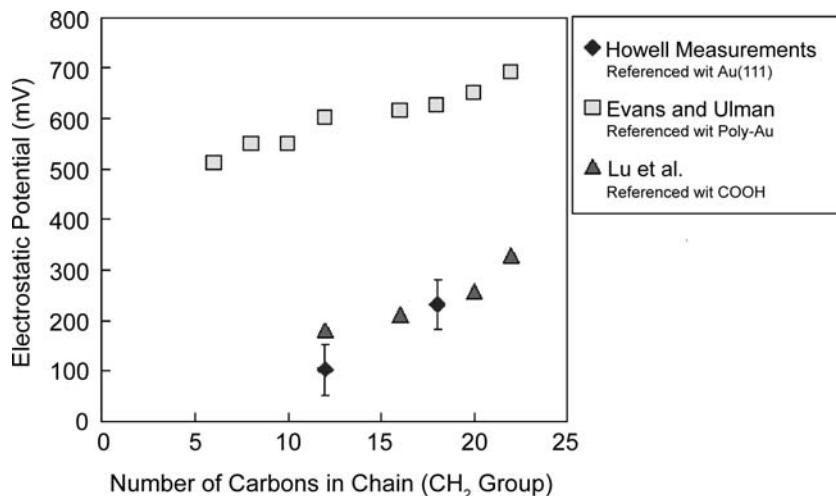


**Fig. 10** The electrostatic surface potentials of alkanethiols measured at Purdue and elsewhere. Source: From Ref.<sup>[41]</sup>.

## ESP Measurements of Symmetric and Nonsymmetric Aromatic Thiols

The structure of the molecule may play a significant role and we investigated this by ESP studies of symmetric and nonsymmetric aromatic molecules shown in Fig. 11. The SAMs of these molecules were characterized using RAIR and ellipsometry<sup>[41,42]</sup> and the RAIR spectrum of a typical sample such as tetramethyl-xylyldithiol (TMXYL) is shown in Fig. 8 (above). The molecules with a symmetric structure, xylyldithiol (XYL) and TMXYL, show a small surface potential with respect to Au ( $\sim +50$  and  $\sim +16$  mV). The non-symmetric molecules show significantly higher potential: benzyl mercaptan, which is equivalent to replacing one of the  $\text{CH}_2\text{SH}$  groups of XYL with a hydrogen atom yields an average surface potential that is  $> +200$  mV with respect to gold. Similarly, the replacement of one  $\text{CH}_2\text{SH}$  group with  $-\text{CH}_3$  in PMBM results in a large surface potential with respect to bare Au(111) (Fig. 11) substrate.

The difference in surface potential (Fig. 11) may be explained on the basis of the structures considering the absence of symmetry or lower symmetry in benzyl mercaptan (BM) and pentamethylbenzyl mercaptan (PMBM). In both XYL and TMXYL, there is a symmetry present in the structures. So the expected dipole moment of these systems before attachment to the Au surface will be low or negligible. However, it is not obvious what happens to the dipole moment of the system when the hydrogen is replaced by gold and attached to only one side of the molecule. Experimental results seem to suggest that the Au–S and H–S dipoles, in some sense, cancel each other; but preliminary theoretical calculations suggest that this may not be the case; attachment of three, six, and seven

Au clusters does produce significant dipole moments for the symmetric molecule (see “[Theoretical Modeling of the Surface Potential of SAMs](#)”). Overall, these measurements suggest that the molecular structure plays a significant role in the charge transfer between S and Au.

## Negative Surface Potential

The molecular structure and attachment of  $\text{sp}^2$ -hybridized carbon to sulfur bound to Au can have a profound effect on the charge transfer or on the ESP measurements of the SAMs of phenyl, biphenyl, and triphenyl thiols (Fig. 12). The ESP of mono-phenyl thiol becomes negative with respect to bare Au ( $-0.38$  V) and increases further for biphenyl,  $-0.76$ , and levels off for the triphenyl species at  $-0.72$  V (Table 1). The surface potential produced by these thiols can be estimated using the formula described in Eq. (1) (Fig. 7). The angle of inclination can be estimated using the RAIRS data and with respect to normal they are  $0^\circ$ ,  $31.79^\circ$ , and  $36.13^\circ$ , respectively. Both the calculations from isolated molecule (unpublished) and ESP data show a significant shift in ESP when an additional phenyl ring is attached to phenyl thiol and it levels off with three phenyl rings.<sup>[49]</sup>

It is interesting to compare the observed ESP results of phenylthiols with other aromatic thiols and alkanethiols. From a chemical standpoint, the bonding of sulfur to gold produces polarization:  $[\text{Au}]^+-\text{SR}$ . SR. In contrast to the situation in aliphatic thiols or benzyl mercaptan with a  $\text{CH}_2$  group attached to S that is bonded to Au, the negative charge on the sulfur of phenyl thiols becomes relatively large as it can be delocalized through several conjugated structures.

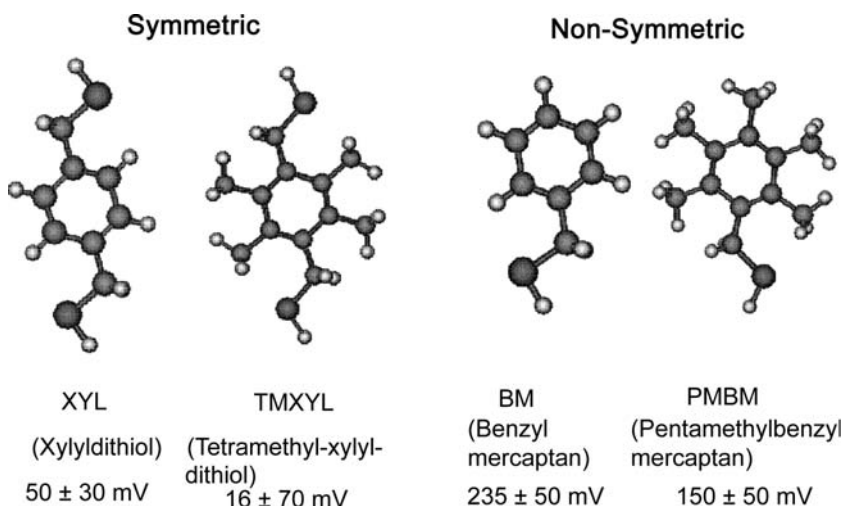
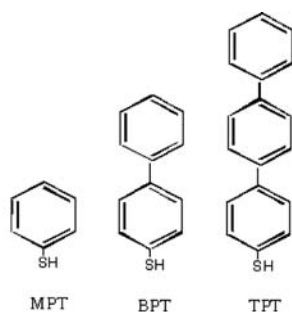


**Fig. 11** The electrostatic surface potentials of symmetric and nonsymmetric aromatic thiols chemisorbed on Au.





MPT, monophenylthiol; BPT, bi-phenylthiol; TPT, tri-phenylthiol

**Fig. 12** The electrostatic surface potentials of mono-, di-, and tri-phenyl thiols.

Hence a negative surface potential is observed (see below).

Negative surface potential has also been measured for SAMs of helix peptides. Miura et al.<sup>[50]</sup> have prepared SAMs of two peptides with different molecular length, LipoA16B and LipoA24B (Fig. 13; notice that LipoA24B, figure on the right, is much longer), and observed a few hundred millivolts negative surface potential. These peptide SAMs with N-terminal attached to sulfur, that is connected to gold, show tilt angles of the helix axis from the surface normal to be 36° and 30°, respectively, by FTIR-RAIR spectroscopy. The large dipole moment of the helices directs toward the surface, with a negatively charged surface of the SAM exposed outside (Fig. 13). The molecular arrangement is important for the evaluation of the effect of the large dipole moment of the helices because the alkyl-thiol SAMs, described above, produce a positive surface potential. Clearly, the large dipole moment of the helices exceeds over the effect of Au<sup>+</sup>–S<sup>–</sup> to yield the observed negative surface potential of the peptides. Further, the surface potential of LipoA24B (tetracosapeptide) is much larger than LipoA16B (hexadecapeptide) and is consistent with the view that it originates from the dipoles aligned toward the surface. The calculated dipole moments, using MOPAC, are 55 D for the hexadecapeptide and 83 D for the tetracosapeptide and consistent with the observed experimental results. These results further emphasize that in contrast to physically adsorbed species, where the effect of individual dipoles on the

**Table 1** The electrostatic surface potentials of mono-, di-, and tri-phenyl thiols (Fig. 12)

Phenylthiols	ESP, V
Monophenyl thiol	$-0.38 \pm 0.04$
Biphenylthiol	$-0.76 \pm 0.04$
Triphenylthiol	$-0.72 \pm 0.02$

surface potential is approximately evaluated only by considering the mutual depolarization of a set of dipoles, the dipole moment or ESP of a chemisorbed adsorbance cannot be predicted easily.<sup>[51]</sup>

### Surface Potential Measurements of a Charge Transfer (CT) Complex

The interplay between positive and negative ESP can be controlled by chemistry alone. A CT complex SAM can be formed by reacting a strong electron acceptor such as tetracyanoethylene (TCNE) with a SAM of TMXYL which is an electron donor<sup>[42]</sup> (Fig. 14). It has been shown previously that molecular conduction is greatly influenced by the location of the equilibrium Fermi level within the HOMO–LUMO gap (Fig. 15).<sup>[34,37,38]</sup> Thus mixing of the orbitals or rather the energy levels can produce a significant surface potential of the SAM. As shown in Table 2, the surface potential of TMXYL is close to that of bare Au(111) because of the molecule's symmetric structure. However, complexation to yield a CT complex of TMXYL–TCNE produces a negative surface potential which is due to the accumulation of negative charge on the surface of the complex as observed for the peptides above. As TCNE is a strong  $\pi$ -electron acceptor, a significant amount of electron density is withdrawn from TMXYL, the donor molecule, and is redistributed over the complex. This can be confirmed by the removal of TCNE using tetrathifulvelene (a strong donor), which returns the surface potential to the value before the reaction of TMXYL with TCNE.

### Theoretical Modeling of the Surface Potential of SAMs

Although we have measured the surface potential of several SAMs, there is no quantitative understanding of these measurements at present. As a first step for the SAMs on gold, we have used a quantum chemistry software, Hyperchem Pro 6 software<sup>[41]</sup> (parameters for the ab initio calculations; basis set STO-3G, Fletcher–Reeves geometry optimization). These initial calculations determine the dipole moment of alkanethiol molecules without their attachment to the Au(111) atoms. The dipole moments from these calculations for DDT, HDT (hexadecanethiol, CH<sub>3</sub>(CH<sub>2</sub>)<sub>15</sub>SH), and ODT are 0.67, 0.72, and 0.74 D, respectively (1 D = 3.336 × 10<sup>–30</sup> C m).

Now using the Eq. (1) above and typical parameters such as a packing density of 4.46 × 10<sup>18</sup> molecules/m<sup>2</sup>,<sup>[52]</sup> and a molecular tilt of 30°,<sup>[53]</sup> and a dielectric constant of ~2.5,<sup>[43]</sup> the model potentials for DDT, HDT, and ODT are calculated to be +450, +480, and +500 mV, respectively (Fig. 10). The magnitude of the calculated potentials is close to the data



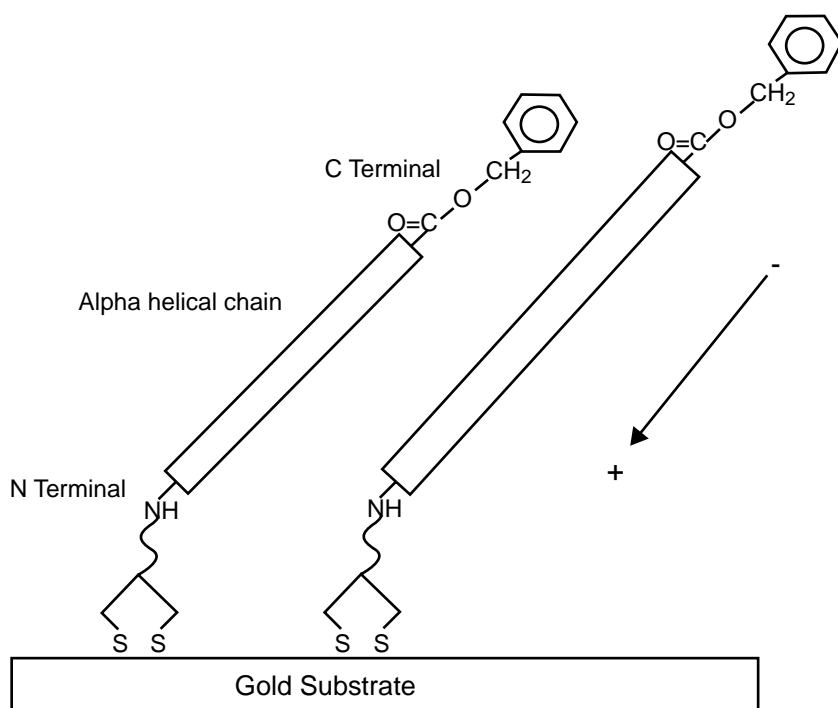


**Fig. 13** The electrostatic surface potentials of N-terminal peptides with different lengths chemisorbed on Au; the one on the right is longer than that of the left peptide. *Source:* Adapted from Ref.<sup>[50]</sup>.

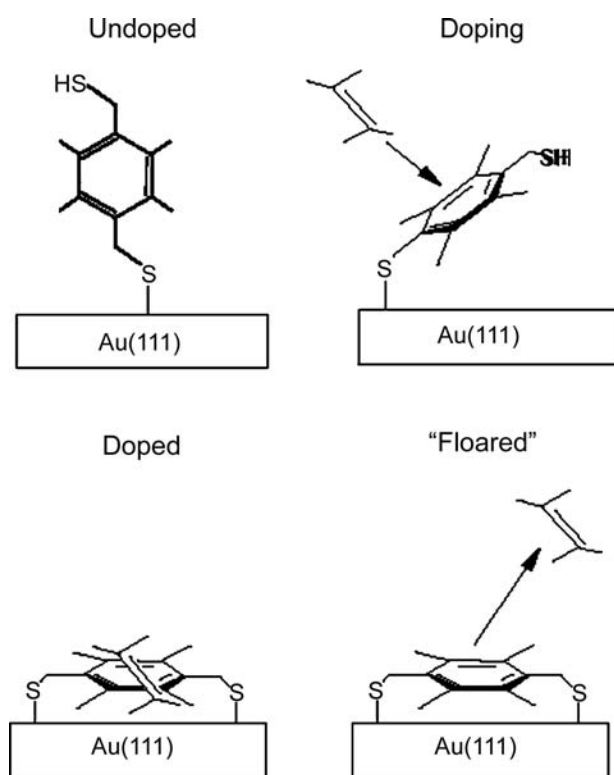


**Fig. 14** A molecular doping experiment to produce a charge-transfer (CT) complex of tetramethyl-xylyldithiol (TMXYL) and tetracyanoethylene (TCNE); orientation of TMXYL changes before and after its reaction with TCNE and after removal of TCNE from the complex. *Source:* From Ref.<sup>[42]</sup>.

published by Evans and Ulman,<sup>[43]</sup> which may suggest that EFM measurement is probably an indicator of how well the SAM is organized when it is bound to a metallic surface.

It is possible to calculate the dipole moments of DDT and ODT from the surface potentials measured by the Purdue group. Using the same parameters, the dipole moments are estimated to be 0.17 and 0.39 D, respectively. These are smaller than the calculated values. Furthermore, the dependence of the dipole moments on the number of CH<sub>2</sub> groups present in the molecule is different by a factor of three between the calculated and measured values.

Similar difference between experimental and theoretical results has been observed by Taylor for the surface potential of monolayers both at the air–water interface and deposited onto solid supports.<sup>[51]</sup> The ESP calculated for an un-ionized stearic acid monolayer,  $\Delta V_{\text{Head}} + \Delta V_{\text{Tail}} = 727 \text{ mV}$ , is almost twice the experimental value of  $390 \pm 10 \text{ mV}$ . Such a discrepancy, however, is not surprising as the model ignored 1) possible hydration effects on the head group; 2) imaging effects in the subphase; and 3) reorientation of water molecules. A significant negative contribution from these sources would reduce the discrepancy between the experimental and theoretical results.

In order to establish the measured surface potential on a firm ground and especially those of the aromatic systems adsorbed on gold, we have done quantum chemistry calculations using the supercomputer

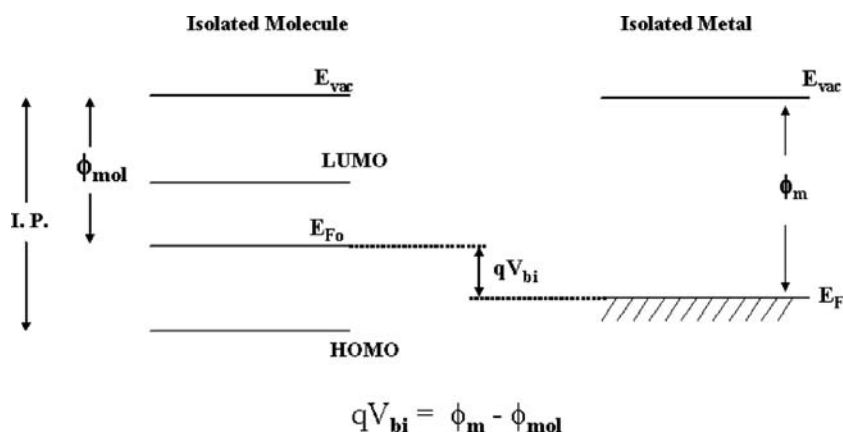


**Fig. 15** The HOMO–LUMO diagram of an isolated metal and an isolated molecule.

facilities at La Tech. As a starting point, we have considered benzenethiol and benzenedithiol molecules adsorbed on Au surfaces.<sup>a</sup>

Quantum chemistry can provide orientation and dipole moment, two important factors, which can be used to determine the ESP described in Eq. (1). First, it is necessary to optimize the geometry of the molecule adsorbed on the metal surface of interest to a reasonable approximation, and then calculate its dipole moment in that configuration. The orientation of the molecule can be experimentally verified using RAIR spectroscopy.

The gold surfaces are modeled by a single layer of 3 and 6 gold atoms and clusters of 4, 7, 10, and 13 gold atoms, all of which have (111) lattice. Figure 16 shows the structure of the benzenedithiol molecule adsorbed on a typical cluster of gold atoms using a mixed basis set.<sup>[54]</sup> The smallest unit of the gold surface (111) consists of a cluster of three gold atoms, which can be denoted as Au<sub>3</sub> hereafter. The preferred bonding site of the S atom in the interaction of thiols with (111) gold surfaces<sup>[55]</sup> is a hexagonal close-packing (hcp) hollow site; however, it cannot be adequately represented by the Au<sub>3</sub> unit. It requires the presence of a fourth gold atom below the plane of the triangle, denoted as

Au<sub>4</sub> in Fig. 16. Larger gold clusters consisting of 6, 7, 10, and 13 gold atoms, denoted as Au<sub>6</sub>, Au<sub>7</sub>, Au<sub>10</sub>, and Au<sub>13</sub>, respectively, were also considered to determine the influence of additional layers of metal atoms. The Au<sub>13</sub> cluster has been designated as a “magic number” cluster by Larsson et al., where an octahedral cluster has been shown to have the lowest energy from Density Functional Theory (DFT) calculations.<sup>[56]</sup> It should be mentioned, in this context, that recently a 20-atom cluster, Au<sub>20</sub>, has been found to have exceptional stability and a large band gap,<sup>[57]</sup> but this cluster lacks the symmetry of the clusters studied here.

The results of our ongoing calculations show that both symmetric and nonsymmetric molecules bonded to Au<sub>n</sub> clusters have significant dipole moments.<sup>[54]</sup> In general, the symmetric molecules tend to have smaller dipole moments, which is qualitatively consistent with experimental observations. However, the calculations indicate that the origins of these dipole moments may have less to do with the Au–S bonds rather than the charge distribution in the rest of the molecule. A careful analysis of the charges is currently underway. These comments further underscore the fact that a fundamental theoretical understanding of the mechanisms by which SAMs develop ESPs on gold is still lacking.

### Organosilane SAMs

In contrast to the SAMs on Au, the experimental surface potentials of organosilane SAMs agree very well with the calculated values acquired by KFM. In the ab initio molecular calculations of surface

**Table 2** The electrostatic surface potentials ( $V_{SAM}$ ) of TMXYL and the charge-transfer complex TMXYL–TCNE on Au(111) (Fig. 14)

Species	ESP, mV
TMXYL (upright)	20 ± 70
TMXYL–TCNE	–140 ± 25
TMXYL (flat)	30 ± 60

<sup>a</sup>The quantum chemistry calculations for this work are all done with the Gaussian98 package of programs, using density functional theory and the details will be published elsewhere (Ref.<sup>[54]</sup>). The popular B3LYP functional is used for all calculations. Different basis sets are used for different atoms: the LanL2DZ basis set, which consists of a double zeta basis along with the Los Alamos relativistic effective core potential, is used for the gold atoms, the 6–31G(*d*) basis for the carbon and sulfur, and the 4–31G(*d*) for the H atoms. Most of the previous studies have used basis sets such as the LanL2DZ for all the atoms in the system. The use of the *n*–31G(*d*) family of basis sets on the nonmetal atoms yields a much lower variational energy compared to a calculation in which LanL2DZ is used for all the atoms. The additional flexibility of the basis set and the presence of the extra *d*-functions to describe polarization effects allow for a more accurate description of the molecular structure, charge density distribution, and, therefore, of the dipole moment. Our objective has been to use the largest basis set possible while keeping the calculations to a manageable size.

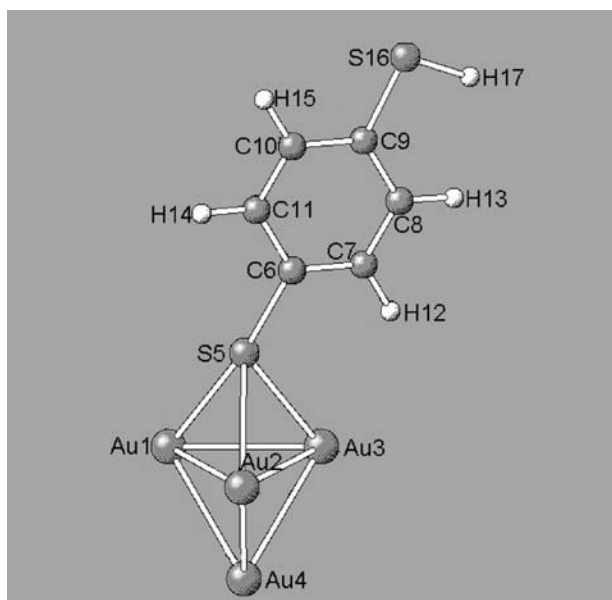


**Fig. 16** The optimized geometry of a phenyldithiol molecule attached to four-atom gold cluster.

potentials of organosilane SAMs, Saito et al. used  $\text{H}_3\text{C}(\text{CH}_2)_{15}\text{CH}_3$  for *n*-octadecyltrimethoxysilane (ODS),  $\text{F}_3\text{C}(\text{CF}_2)_7\text{CH}_2\text{CH}_3$  for heptadecafluoro-1,1,2,2-tetrahydro-decyl-1-trimethoxysilane (FAS), and  $\text{H}_2\text{N}(\text{CH}_2)_6\text{NH}(\text{CH}_2)_2\text{CH}_3$  for *n*-(6-aminoethyl)aminopropyltrimethoxysilane (AHAPS) as models.<sup>[47]</sup> The structures of ODS-, FAS-, and AHAPS molecules were gauche and antiforms, respectively. The ODS, FAS, and AHAPS molecules have net dipole moments of 0.03, 2.38, and 0.57 D, respectively. If these alkyls stand normal to the substrate, the dipole moment would be zero according to Eq. (1). In reality, these molecules are tilted on the surface and the calculated ESP values match well with the values acquired by KFM. These results perhaps indicate that molecule–semiconductor interface behaves differently from that of metal–molecule heterostructure.

## CONCLUSION

Nanoscale charge transfer studies at the interface of metal–molecule heterostructures are very important to provide a better understanding of useful nanostructures. Research from different laboratories suggests that building SAMs on a surface can bridge the gap between the top-down approach and the size of individual molecules. The electrostatic surface potential studies of SAMs are limited in contrast to their *I–V* measurements. The Kelvin probe measurements using a modified AFM can produce reliable ESP results. Although the absolute values of ESP may differ

because of substrate preparation, contamination, etc., the qualitative values of the alkanethiols compare well among different groups; the ESP values increase with the increase in chain length. The solvents used to prepare the SAMs do not appear to have any major effect on the measured values. However, the structure, especially symmetry, plays a significant role on the ESP values of aromatic thiols; while the ESP of xylyldithiol and tetramethyl–xylyldithiol are quite low, their non-symmetric counterparts such as benzyl mercaptan and pentamethylbenzylthiol produce a significant positive surface potential. The molecular structure and the attachment of  $\text{sp}^2$ -hybridized carbon of phenyl thiol to Au(111) can have a profound effect on ESP as its sign is reversed and becomes more negative with the addition of the second aromatic ring. This, however, levels off for triphenyl thiols.

A negative surface potential, i.e., nanoscale charge transfer in the opposite direction, has also been observed in helical peptides. Furthermore, chemistry alone through the formation of a CT complex of tetramethyl–xylylthiol (TMXYL) with tetracyano-ethylene (TCNE) can reverse the sign and magnitude of ESP.

Theoretical calculations, to understand charge transfer in Au/S heterostructures using Hyperchem Pro 6 and Gaussian 98, seem to predict the trend, but not the magnitudes of dipole moments or ESP of the molecules. Further, in contrast to the observed experimental results, our initial calculations show that both symmetric and non-symmetric molecules bonded to Au clusters have significant dipole moments. Thus the use of 4, 6, or 13 gold atoms to represent the gold surface may not be adequate to compare the calculated ESPs with the experimental results. Although the ab initio calculations of organosilane SAMs by Saito et al. match quite well with the experimental results, extensive theoretical studies will be necessary to have a better understanding of the ESP measurements of organothiol SAMs on gold.

## ACKNOWLEDGMENTS

We thank Professors Ron Reifenberger and Supriyo Datta, and Drs. Steve Howell, Bala Kasibhatla and Helen McNally for experimental results and some of the theoretical discussions presented here. We are very grateful to Professor Bala Ramachandran and Mr. Devendra Patel for the quantum chemistry calculations done using the supercomputing facilities at La tech. We also thank Professor Purna Das, Dr. Avik Ghosh, Dr. Prashant Damle, and Mr. Titas Rakshit for useful discussions. D.K. would like to thank Dr. S. Howell for some of the Figures and Mr. D. Patel and Mr. R. Aithal for their help with the manuscript and Louisiana Tech for its support to write this entry.

## REFERENCES

- Havancsak, K. Nanotechnology at present and its promise for the future. *Mat. Sci. Forum* **2003**, 414–415, 85–93. (3rd Hungarian Conference on Materials Science, Testing and Informatics, 2001).
- Tolles, W.M. Nanoscience and nanotechnology Europe. *Nanotechnology* **1996**, 7 (2), 59–105.
- Fenby, D.V. Hexafluorobenzene–benzene and related systems. *Rev. Pure Appl. Chem.* June **1972**, 22, 55–65.
- Rampi, M.A.; Whitesides, G.M. A versatile experimental approach for understanding electron transport through organic materials. *Chem. Phys.* **2002**, 281 (2–3), 373–391.
- DeVault, D. *Quantum-Mechanical Tunnelling in Biological Systems*; Cambridge University Press: New York, 1984.
- Beratan, D.N. Molecular control of electron transfer events within and between biomolecules. *NATO Sci. Ser., II: Math. Phys. Chem.* **2003**, 96, 227–236. (Molecular Electronics: Bio-Sensors and Bio-Computers).
- Heath, J.R.; Ratner, M.A. Molecular electronics. *Phys. Today* **2003**, 56 (5), 43–49.
- Fukuzumi, S. New perspective of electron transfer chemistry. *Org. Biomol. Chem.* **2003**, 1 (4), 609–620.
- Dick, L.A.; Malfant, I.; Kuila, D.; Nebolsky, S.; Nocek, J.M.; Hoffman, B.M.; Ratner, M.A. Cryogenic electron tunneling within mixed-metal hemoglobin hybrids: protein glassing and electron-transfer energetics. *J. Am. Chem. Soc.* **1998**, 120, 11,401–11,407.
- Esaki, L. Innovation and evolution: Reflections on a life in science—from the Esaki tunnel diode to semiconductor superlattices and quantum wells. *Tsinghua Sci. Technol.* **1998**, 3 (1), 936–938.
- Boilot, J.-P.; Besson, S.; Buissette, V.; Gacoin, T.; Huignard, A.; Ricolleau, C. Active hybrid materials by nanoscale chemistry. *Mater. Res. Soc. Symp. Proc.* **2002**, 726, 331–342 (Organic/Inorganic Hybrid Materials—2002).
- Andrievski, R.A. State-of-the-art and perspectives in particulate nanostructured materials. *Mat. Sci. Forum* **1998**, 282–283, 1–9 (Advanced Materials and Processes).
- Moore, G.E. Cramming more components onto integrated circuits. *Electronics* **1965**, 38 (8), 114–117.
- 1st International Conference on Nano-manufacturing at MIT, Boston, MA, April 2003.
- Averin, D.V.; Likharev, K.K. *Mesoscopic Phenomena in Solids*; Altshuler, B.L., Lee, P.A., Webb, R.A., Eds.; Elsevier: Amsterdam, 1991.
- Petty, M.C.; Bryce, M.R.; Bloor, D., Eds. *Introduction to Molecular Electronics*; Oxford University Press: New York, 1995.
- Aviram, A.; Ratner, M. Molecular rectifiers. *Chem. Phys. Lett.* **1974**, 29, 277–283.
- Joachim, C.; Gimzewski, J.K.; Aviram, A. Electronics using hybrid-molecular and mono-molecular devices. *Nature* **2000**, 408, 541–548.
- Raymo, F.M. Digital processing and communication with molecular switches. *Adv. Mater. (Weinheim, Germany)* **2002**, 14 (6), 401–414.
- Metzger, R.M. Electrical rectification by a molecule: the advent of unimolecular devices. *Acc. Chem. Res.* **1999**, 32, 950–957, and the references cited therein.
- Collins, P.G.; Avouris, P. Nanotubes for electronics. *Sci. Am. Dec.* **2000**, 283 (6), 62–69.
- Collins, P.G.; Arnold, M.S.; Avouris, P. Engineering carbon nanotubes and nanotube circuits using electrical breakdown. *Science* **2001**, 292, 706–709, and the references cited therein.
- Lieber, C.M. The incredible shrinking circuit. *Sci. Am.* **2001**, 285 (3), 59–64.
- Ouyang, M.; Huang, J.-L.; Lieber, C.M. Fundamental electronic properties and applications of single-walled carbon nanotubes. *Acc. Chem. Res.* **2002**, 35 (12), 1018–1025.
- Bachtold, A.; Hadley, P.; Nakanishi, T.; Dekker, C. Logic circuits with carbon nanotube transistors. *Science* **2001**, 294 (5545), 1317–1320.
- Chen, J.; Reed, M.A.; Rawlett, A.M.; Tour, J.M. Large on–off ratios and negative differential resistance in a molecular electronic device. *Science* **1999**, 286, 1550–1552.
- Chabinc, M.L.; Holmlin, R.E.; Haag, R.; Chen, X.; Ismagilov, R.F.; Rampi, M.A.; Whitesides, G.M. Molecular electronics with a metal-insulator-metal junction based on self-assembled monolayers. *ACS Symp. Ser.* **2003**, 844, 16–35. (Molecules as Components of Electronic Devices).
- Ishida, T. Self-assembled monolayers for molecular nanoelectronics. *Springer Ser. Chem. Phys.* **2003**, 70, 91–106. (Chemistry of Nanomolecular Systems).
- Wold, D.J.; Frisbie, C.D. Fabrication and characterization of metal-molecule-metal junctions by conducting probe atomic force microscopy. *J. Am. Chem. Soc.* **2001**, 123, 5549–5556.
- Wold, D.J.; Haag, R.; Rampi, M.A.; Frisbie, C.D. Distance dependence of electron tunneling through self-assembled monolayers measured by conducting probe atomic force microscopy: Unsaturated versus saturated molecular junctions. *J. Phys. Chem.* **2002**, 106 (11), 2813–2816.
- Cui, X.D.; Primak, A.; Zarate, X.; Tomfohr, J.; Sankey, O.F.; Moore, A.L.; Moore, T.A.; Gust, D.; Harris, G.; Lindsay, S.M. Reproducible measurement of single-molecule conductivity. *Science* **2001**, 294 (5542), 571–574.
- Reichert, J.; Ochs, R.; Beckmann, D.; Weber, H.B.; Mayor, M.; Lohneysen, H.v. Driving current through single organic molecules. *Phys. Rev. Lett.* **2002**, 88 (17), 6804.
- Reichert, J.; Weber, H.B.; Mayor, M.; Lohneysen, H.v. Low temperature conductance measurements on single molecules. *Appl. Phys. Lett.* **2003**, 82 (23), 4137–4139.
- Andres, R.P.; Datta, S.; Janes, D.B.; Kubiak, C.P.; Reifenberger, R. The design, fabrication, and electronic properties of self-assembled molecular nanostructures. *Handb. Nanostruct. Mater. Nanotechnol.* **2000**, 3, 179–231.
- Labonte, A.P.; Tripp, S.L.; Reifenberger, R.; Wei, A. Scanning tunneling spectroscopy of insulating self-assembled monolayers on Au(111). *J. Phys. Chem., B* **2002**, 106, 8721–8725.

36. Nitzan, A.; Ratner, M. Electron transport in molecular wire junctions. *Science* **2003**, *300*, 1384–1389, and the references cited therein.
37. Paulsson, M.; Zahid, F.; Datta, S. Resistance of a molecule. Los Alamos Natl. Lab., Prepr. Arch. Condens. Matter **2002**, *1*, 1–32. arXiv:cond-mat/0208183. CODEN: LNCMFR <http://www.lanl.gov/pdf/cond-mat/0208183>.
38. Damle, P.; Ghosh, A.W.; Datta, S. First-principles analysis of molecular conduction using quantum chemistry software. *Chem. Phys.* **2002**, *281* (2–3), 171–187.
39. Fujihira, M. Kelvin probe force microscopy of molecular surfaces. *Annu. Rev. Mater. Sci.* **1999**, *29*, 353–380.
40. Nonnenmacher, M.; O’Boyle, M.; Wickramasinghe, H.K. Kelvin probe force microscopy. *Appl. Phys. Lett.* **1991**, *58*, 2921–2923.
41. Howell, S. Electrostatic Force Microscopy Studies of Nanoscale Systems. In *Ph.D. Thesis*; Purdue University, 2001.
42. Howell, S.; Kuila, D.; Kasibhatla, B.; Kubiak, C.P.; Janes, D.; Reifenberger, R. Molecular electrostatics of conjugated self-assembled monolayers on Au(111) using electrostatic force microscopy. *Langmuir* **2002**, *8*, 5120–5125.
43. Evans, S.D.; Ulman, A. Surface potential studies of alkyl-thiol monolayers adsorbed on gold. *Chem. Phys. Lett.* **1990**, *170* (5,6), 462–466.
44. Lü, J.; Delamar, E.; Eng, L.; Bennewitz, R.; Meyer, E.; Guntherodt, H.-J. Kelvin probe force microscopy on surfaces: Investigation of the surface potential of self-assembled monolayers on gold. *Langmuir* **1999**, *15*, 8184–8188.
45. Zehner, R.W.; Parsons, B.F.; Hsung, R.P.; Sita, L.R. Tuning the work function of gold with self-assembled monolayers derived from X-[C<sub>6</sub>H<sub>4</sub>-C=C-]nC<sub>6</sub>H<sub>4</sub>-SH (*n* = 0, 1, 2; X = H, F, CH<sub>3</sub>, CF<sub>3</sub>, and OCH<sub>3</sub>). *Langmuir* **1999**, *15*, 1121–1127.
46. Barrena, E.; Ocal, C.; Samuelson, M. Evolution of the structure and mechanical stability of self-assembled alkanethiol islands on Au(111) due to diffusion and ripening. *J. Chem. Phys.* **1999**, *111*, 9797–9802.
47. Saito, N.; Hayashi, K.; Sugimura, H.; Takai, O.; Nakagiri, N. Surface potentials of patterned organosilane self-assembled monolayers acquired by Kelvin probe force microscopy and ab initio molecular calculations. *Chem. Phys. Lett.* **2001**, *349*, 172–177.
48. Gericke, A.; Simon-Kutscher, J.; Huehnerfuss, H. Influence of the spreading solvent on the properties of monolayers at the air/water interface. *Langmuir* **1993**, *9* (8), 2119–2127.
49. McNally, H.; Janes, D.B.; Kasibhatla, B.; Kubiak, C.P. Electrostatic investigation into the bonding of poly(phenylene)thiols to gold. *Superlattices Microstruct.* **2002**, *31* (5), 239–245.
50. Miura, Y.; Kimura, S.; Kobayashi, S.; Iwamoto, M.; Imanishi, Y.; Umemura, J. Negative surface potential produced by self-assembled monolayers of helix peptides oriented vertically to a surface. *Chem. Phys. Lett.* **1999**, *315*, 1–6.
51. Taylor, D.M. Developments in the theoretical modeling and experimental measurement of the surface potential of condensed monolayers. *Adv. Colloid Interface Sci.* **2000**, *87*, 183–203.
52. Alves, C.A.; Smith, E.L.; Porter, M.D. Atomic scale imaging of alkanethiolate monolayers at gold surfaces with atomic force microscopy. *J. Am. Chem. Soc.* **1992**, *114* (4), 1222–1227.
53. Porter, M.D.; Bright, T.B.; Allara, D.L.; Chidsey, C.E.D. Spontaneously organized molecular assemblies: 4. Structural characterization of *n*-alkyl thiol monolayers on gold by optical ellipsometry, infrared spectroscopy, and electrochemistry. *J. Am. Chem. Soc.* **1987**, *109* (12), 3559–3568.
54. Patel, D.S.; Ramachandran, B.; Kuila, D.; Das, P.; Datta, S.; Janes, D.; Truhlar, D.G. Structure and properties of benzenethiol and benzenedithiol adsorbed on Au(111) surfaces: A density functional theory study. *J. Phys. Chem.* (submitted).
55. Yaliraki, S.N.; Roitberg, A.E.; Gonzalez, C.; Mujica, V.; Ratner, M.A. The injecting energy at molecule/metal interfaces: implications for conductance of molecular junctions from an ab initio molecular description. *J. Chem. Phys.* **1999**, *111* (15), 6997–7002.
56. Larsson, J.A.; Nolan, M.; Greer, J.C. Interactions between thiol molecular linkers and the Au<sub>13</sub> nanoparticle. *J. Phys. Chem., B* **2002**, *106* (23), 5931–5937.
57. Li, J.; Li, X.; Zhai, H.-J.; Wang, L.-S. Au<sub>20</sub>: a tetrahedral cluster. *Science* **2003**, *293*, 864–867.

# Charge Transport in Multilayer Nanostructures

Daniel M. Schaadt

*Department of Electrical and Computer Engineering, University of California–San Diego,  
La Jolla, California, U.S.A.*

## INTRODUCTION

The demand to increase device speeds and to obtain higher data storage densities leads to decreased device sizes and new device design proposals, of which some were based on multilayer or granular metal/insulator structures, which consist of metallic nanoclusters embedded within an insulating matrix. The design and optimization of devices incorporating these materials require a detailed understanding of the relevant nanoscale electrical transport properties, which can be investigated by scanning probe techniques. This entry reviews recent studies of the nanoscale charge transport properties of multilayer or granular metal/insulator structures, and the application of the results of these studies in a novel magnetic field sensor design based on the combination of charge storage and tunnel-magnetoresistance in magnetic discontinuous magnetic multilayer structures is discussed briefly. In particular, charge deposition into Co nanoclusters embedded in a SiO<sub>2</sub> matrix and the decay of the charge as a function of time are discussed. Local charge deposition into and removal from Co nanoclusters was achieved by applying a voltage pulse to a conductive probe tip in a scanning probe microscope. Electrostatic force microscopy (EFM) was used to image charged areas, to determine quantitatively the amount of stored charge, and to characterize charge transport within the Co layer and into the Si substrate. Measurements of decay times for positive and negative charge as a function of nominal Co layer film thickness are presented, and the dynamics of the charge decay for positively and negatively charged nanoclusters is analyzed as a consequence of Coulomb-blockade effects at room temperature considering a detailed model for charge transport within the Co layer as well as from charge Co nanoclusters into the Si substrate.

## BACKGROUND

### Nanoscale Multilayer Structures

Structures consisting of metallic nanoparticles embedded in an insulating matrix have attracted increasing attention over the past decade because of their new

or unusual physical properties and the resulting possible use in various fields and applications such as non-volatile high density data storage. For instance, the possibility to store electrical charge with long retention times<sup>[1,2]</sup> in these materials might be used to build non-volatile floating gate memory devices,<sup>[3]</sup> or spin-polarized tunneling between ferromagnetic metal nanoparticles embedded in a non-magnetic insulator<sup>[4–8]</sup> can be used in magnetic sensors such as read head for hard disks.<sup>[9]</sup> These materials are generally easy to fabricate by co-sputtering of the metal and the oxide and they are very stable both chemically and electrically.<sup>[10]</sup>

### Investigations of nanoscale charge transport properties

The use of granular or discontinuous metal/insulator materials in non-volatile memory applications or in magnetic field sensors requires a detailed understanding of the charge transport between the metal nanoclusters, which can be measured on a large scale using standard electrodes.<sup>[11]</sup> However, the reduction of device sizes due to the requirements of increased speed and higher data storage density increases the need to complement large area measurements with investigations of the charge transport properties on the nanoscale, especially in the case of memory applications where charge retention times and decay mechanism are of importance. In recent years, scanning probe microscopes<sup>[12]</sup> (SPM) have been employed to characterize the properties of locally deposited charge and its decay over time. It was demonstrated that electrical charges can be stored locally in nitride-oxide-semiconductor structures,<sup>[13,14]</sup> insulator films,<sup>[15,16]</sup> nanocrystals,<sup>[2,17–20]</sup> or quantum dots.<sup>[21,22]</sup> Charge storage in these studies was achieved by applying a bias voltage pulse between the SPM probe tip and the sample. The deposited charge was typically characterized by EFM. Further, studies to investigate charge retention times and decay mechanisms were conducted.<sup>[2,23–25]</sup> These studies have led to improvements in and better understanding of the measurement techniques,<sup>[26,27]</sup> have helped to illuminate the charge decay mechanisms in discontinuous Co/SiO<sub>2</sub> multilayer structures,<sup>[23]</sup> and have resulted in a novel magnetic



field sensor design based on the combination of charge storage and tunnel-magnetoresistance in magnetic discontinuous multilayer structures.<sup>[28,29]</sup>

Combination of charge storage and tunnel-magnetoresistance in multilayer structures: a new magnetic field sensor

The possibility to store electrical charges with long retention times in a tunnel-magnetoresistive film allows the design of a novel magnetic field sensor design. In this device design, a granular tunnel-magnetoresistive (TMR)  $\text{Co}_x(\text{SiO}_2)_{1-x}$  thin film is placed between two oxide layers within the gate of a p-channel Si metal-oxide-semiconductor-field-effect transistor (MOSFET). Two contacts are placed on the TMR film outside the gate structure. The basic concept is, however, applicable to any field-effect transistor as well as other granular TMR materials, which show the possibility of charge storage in the metal clusters. If fixed voltage  $V_{\text{MR}}$  is applied across the contacts to TMR film, a current  $I_{\text{MR}}$  flows through the TMR film and leads to charge  $Q$  build-up within the Co nanoclusters. This charge in turn yields a shift in the threshold voltage of the transistor.  $I_{\text{MR}}$  changes with changing externally applied magnetic field due to spin-dependent tunneling of charge between the Co nanoclusters. Therefore the total charge  $Q$  within the gate and thus the transistor threshold voltage  $V_{\text{T}}$  are magnetic field dependent. In the prototype device described in Refs.<sup>[28]</sup> and <sup>[29]</sup>, a maximum threshold voltage shift of approximately 50 mV is reached when the external magnetic field was changed from 0 Oe to the saturation field of about 6 kOe. This results in an absolute change in the transistor saturation current of approximately 30  $\mu\text{A}$ , a factor of 500 larger than the corresponding change in  $I_{\text{MR}}$ , which is about 60 nA. The absolute change in transistor subthreshold current is about 200 nA, corresponding to a relative change of about 20%. Compared to the relative change in  $I_{\text{MR}}$  of about 5%, this is an amplification in sensitivity of a factor of four. This demonstrates that the nanoscale charge transport properties of multilayer structures consisting of (magnetic) metal nanoclusters embedded in an insulating matrix can be used in sensor devices with increased performance and are therefore worth investigating in detail.

## NANOSCALE CHARGE TRANSPORT EXPERIMENTS

### Experimental Procedure

#### Sample structure and preparation

Samples were prepared by alternating sputtering from two separate targets onto a heavily doped n-type Si

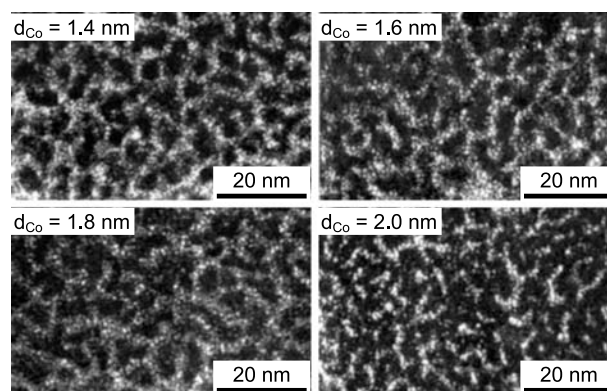


**Fig. 1** Plan-view transmission electron micrographs of Co/SiO<sub>2</sub> with varying nominal Co film thickness  $d_{\text{Co}}$  ranging from 1.4 to 2.0 nm. The light speckled contrast corresponds to amorphous SiO<sub>2</sub> and the dark contrast to crystalline Co. As  $d_{\text{Co}}$  increases, the Co particles become more connected.

(100) substrate covered with a native oxide layer of about  $\sim 2.5$  nm thickness. The Co was d.c. sputtered and the SiO<sub>2</sub> was rf sputtered. Deposition was performed at room temperature with 2 mTorr Ar pressure. The base pressure in the sputtering system was  $\sim 10^{-7}$  Torr. The nominal deposited film structures were SiO<sub>2</sub>(3 nm)/Co(1.0–2.0 nm)/SiO<sub>2</sub>(3 nm) as determined from the deposition times and rates (0.9–1.3 nm/min for the Co and 2.0–3.0 nm/min for the SiO<sub>2</sub>), which were calibrated by low-angle X-ray reflection. Transmission electron microscopy (TEM) studies<sup>[7,10,30]</sup> have shown that, when deposited on SiO<sub>2</sub>, the Co layer is discontinuous with formation of Co nanoclusters, as shown in Fig. 1. The nanoscale structure of the Co layer depends sensitively on the nominal Co film thickness and consists of isolated spherical Co nanoclusters for films with a nominal thickness of approximately less than 1.4 nm and of a chain-like arrangement of spherical Co nanoclusters to tubes of Co for nominal thicker films.<sup>[7,10,30]</sup>

#### Charge deposition and imaging of deposited charge

Scanning probe studies were performed at room temperature under ambient conditions using a Digital Instruments MultiMode<sup>™</sup> Scanning Probe Microscope<sup>a</sup> with a heavily doped p<sup>+</sup>-Si tip. Sample charging was achieved during TappingMode<sup>™</sup> operation<sup>[9]</sup> by holding the tip at the center of the scan area for 10 sec with a bias voltage  $V_{\text{ch}}$  applied to the tip and the sample grounded, as shown in Fig. 2.

EFM was used to image charged regions and to estimate the total stored charge. EFM images were

<sup>a</sup>MultiMode, TappingMode and LiftMode are trademarks of Digital Instruments, Santa Barbara, CA.

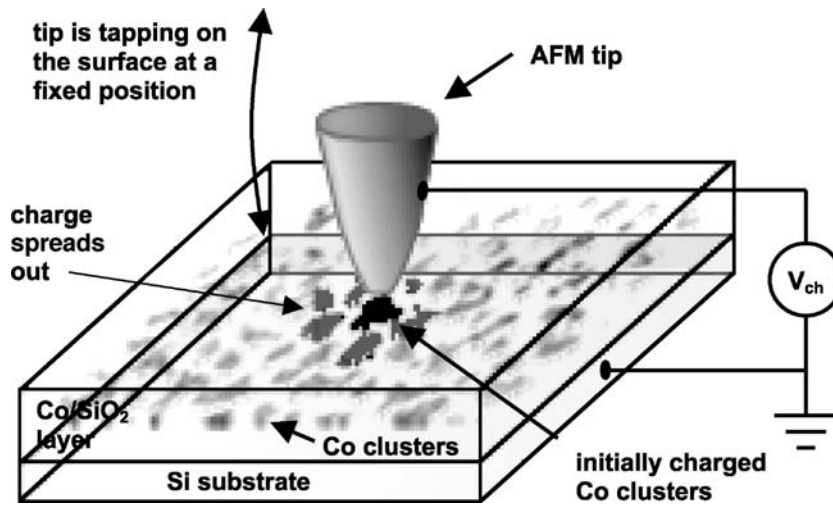


**Fig. 2** Schematic diagram showing the charging of Co clusters embedded in the Co/SiO<sub>2</sub> layer. The Si substrate is grounded and a bias voltage  $V_{ch}$  is applied to the probe tip, which is tapping on the surface. This causes current to flow from the tip into the Co clusters and from the Co clusters into the Si substrate as well as into neighboring clusters. Charge is initially deposited directly under the tip and spreads out to neighboring clusters.

obtained using LiftMode.<sup>a</sup> First, a scan line of the topography is recorded using TappingMode. Then the probe tip is lifted about 20 nm above the surface and an imaging bias  $V_{EFM}$  is applied. Finally, the probe tip is scanned at the fixed tip-sample distance with VEFM applied by retracing the previously recorded topography scan. During this second scan, the probe tip reacts to long-range forces such as electrostatic interactions between the deposited charge in the sample and its image charge in the probe tip.

The contrast observed in the EFM image may be used to calculate the total stored charge  $Q$ . An exact calculation of the deposited charge can be complicated because of the complex arrangement of image charges in the probe tip and the sample.<sup>[27]</sup> Possible artifacts in the topography scan due to electrostatic forces between the image and these charges can lead to an incorrectly measured topography and can cause difficulties separating EFM contrast from topography. However, if the deposited charge is small, its influence on the topography scan is minimal and might not lead to these artifacts. Further, if the tip-sample separation is large enough and the deposited charge small, the EFM response becomes symmetric with respect to imaging bias  $V_{EFM}$ .<sup>[27]</sup> It is easy to check if these conditions are met by imaging the topography after charge has been deposited and by recording the EFM signal for opposite imaging voltages. Assuming that no artifacts are visible before and after charging in the topography and the EFM signal is symmetric with respect to  $V_{EFM}$ , a simple approach can be used to estimate the deposited charge. Specifically, the shift  $\Delta f$  in the resonant frequency of the cantilever is related to the force gradient  $F' \equiv dF/dz$  by the expression.<sup>[31]</sup>

$$\Delta f = -f_0 F'(z_0)/(2k) \quad (1)$$

where  $z_0 = 20$  nm is the lift height during EFM imaging,  $f_0 = 232$  kHz the cantilever resonant frequency, and  $k$  the cantilever spring constant, which was calculated from the lever geometry to be  $90 \pm 10$  N/m. The force  $F(z)$  arises from Coulomb interactions of the stored charge, its image charges in the tip and Si substrate, and the induced charges due to the voltage  $V_{EFM}$  applied during imaging. From an electrostatic analysis of the tip-sample system modeled using a simple parallel-plate geometry, the force is found to be given by<sup>[21]</sup>

$$F(z) = \frac{1}{(z + (d_1 + d_2)/\epsilon_{SiO_2})^2} \times \left( -\frac{d_1^2 Q^2}{\epsilon_{SiO_2}^2 \epsilon_0 A} + \frac{2d_2 Q V_{EFM}}{\epsilon_{SiO_2}} + \frac{\epsilon_0 A V_{EFM}^2}{2} \right) \quad (2)$$

where  $d_1$  and  $d_2$  are the thicknesses of the top and bottom oxide layer, respectively,  $\epsilon_{SiO_2}$  the relative dielectric constant of SiO<sub>2</sub>,  $z$  the tip-sample separation, and  $A$  the area of the charged region. If the deposited charge  $Q$  is small, the first term in the bracket in Eq. (2) is small. The third term in the bracket is independent of the stored charge and yields a constant background frequency shift at all points in the EFM image. Thus the final contrast observed is proportional to the stored charge  $Q$  and to  $V_{EFM}$ . Using the values for  $f_0$ ,  $k$ ,  $z$ ,  $d_1$ , and  $d_2$  given above, the total charge  $Q$  is then given by

$$Q = 18 \pm 2e/V \cdot \text{Hz} V_{EFM} \Delta f \quad (3)$$

As mentioned above and provided that  $Q$  is small, the EFM response  $\Delta f$  is symmetric with respect to  $V_{EFM}$ , which can be readily checked in control experiments.

## Results and Discussion

### Nanoscale charge storage

A series of topography and EFM images obtained with  $V_{\text{EFM}} = 1\text{ V}$  and  $V_{\text{EFM}} = -1\text{ V}$  before and after charging of a nominally 1.4-nm-thick Co layer with  $V_{\text{ch}} = -12\text{ V}$  for 10 sec are shown in Fig. 3. No image-charge artifacts are observed in the topography and EFM images before charging. After charging, charged areas are observed in the EFM images as peaks or dips with a symmetric resonant frequency shift of about 1 and  $-1\text{ Hz}$ , depending on the relative sign of the imaging voltages. No charge-induced artifacts are observed in the topography images after charge has been deposited, and measurements with  $V_{\text{EFM}} = 0\text{ V}$  are showing no contrast difference between charged and uncharged regions. Such a contrast difference would be expected if the amount of deposited charge is large enough to cause an attractive force between the deposited charge and its image charge in the tip.<sup>[27]</sup> The above observations suggest, however, that the amount of deposited charge  $Q$  is small and therefore the simplified approach to estimate  $Q$  from the EFM contrast, as described above, can be used.

No charging was observed in a control sample in which no Co layer was present, and it is therefore concluded that the deposited charge is stored in the Co layer. Little variation in sample charging was observed for charging times longer than 5 sec. Deposited charge can be erased by applying a voltage pulse of opposite sign.<sup>[23]</sup>

The charging of the Co/SiO<sub>2</sub> film is believed to occur in the following way: when the tip approaches the sample surface, charges tunnel from the tip through the top oxide layer into the Co clusters. At the same time, charges tunnel to neighboring uncharged Co clusters and through the thicker bottom oxide layer into the Si substrate. The currents that charge and discharge clusters are initially different because of the different oxide thicknesses of the top oxide layer and

the oxide layer between the Co clusters and the Si substrate. These currents equilibrate over time as a consequence of the adjustments in the electric fields across the oxide layers due to the charge build-up in the Co layer, in a manner analogous to the charging process in a floating-gate MOS structure. Once equilibrium is reached, the charge in the Co layer does not increase any further and its value is determined by the tip-sample capacitance.

### Nanoscale charge transport

Previous measurements have shown that the deposited charge decays over time, with most of the stored charge tunneling into the Si substrate and some carrier transport also occurring between Co nanoclusters.<sup>[23]</sup> Decay times for positive and negative charges were measured and a strong dependence on the nanoscale Co film structure was observed. However, because of the difficulties in extracting the exact amount of charge as a function of time after charging, large error bars were observed in the decay times. To overcome the uncertainties and to confirm these measurements, additional measurements and analysis were performed. Fig. 4 shows the decay in charge for regions charged at 12 V and  $-12\text{ V}$  for various nominal Co layer film thicknesses. The charge decay appears exponential in all cases, but with different decay times  $\tau_+$  and  $\tau_-$  for positive and negative stored charge, respectively.

The difference in the decay times for positive and negative charging can be interpreted as a consequence of the Coulomb blockade energy  $E_0 = q^2/(2C_{\text{Co}})$  of a single Co cluster with capacitance  $C_{\text{Co}}$ . Assuming in a first approximation that charge decay occurs only between Co clusters and the Si substrate, this leads to a difference in barrier heights for escape of positive and negative charge, given, respectively, by  $\phi_+ = \phi_0 + E_0$  and  $\phi_- = \phi_0 - E_0$ , where  $\phi_0 = (\phi_{\text{Co}} + \chi_{\text{Si}} - 2\chi_{\text{SiO}_2})/2$  is the barrier height of the Co–SiO<sub>2</sub>–Si tunnel barrier,  $\phi_{\text{Co}}$  the Co workfunction,  $\chi_{\text{Si}}$  the Si electron affinity,  $\chi_{\text{SiO}_2}$  the SiO<sub>2</sub> electron

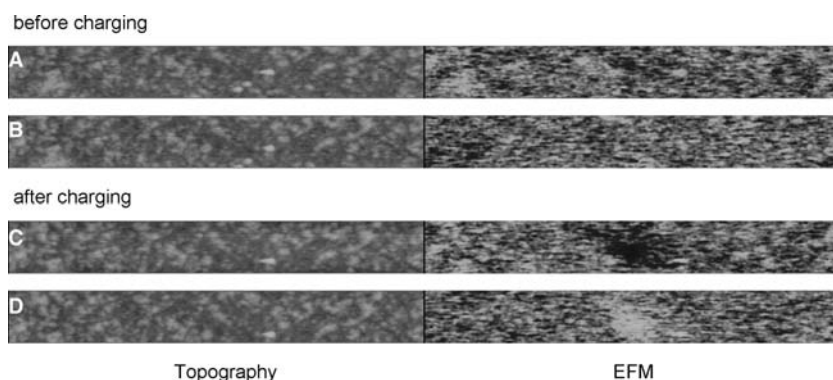


**Fig. 3** Topography (left) and EFM images (right) before charging using (A)  $V_{\text{EFM}} = 1\text{ V}$  and (B)  $V_{\text{EFM}} = -1\text{ V}$ , and after charging using (C)  $V_{\text{EFM}} = 1\text{ V}$  and (D)  $V_{\text{EFM}} = -1\text{ V}$ . Charge was deposited with  $V_{\text{ch}} = -12\text{ V}$  for 10 sec. The image sizes are 500 nm by 2  $\mu\text{m}$ . There are no image-charge-induced artifacts visible in the topography and EFM images before charging. After charging, the topography images show no artifacts due to the deposited charge, while the EFM images show a peak and dip with a height of about 1 and  $-1\text{ Hz}$ , respectively.

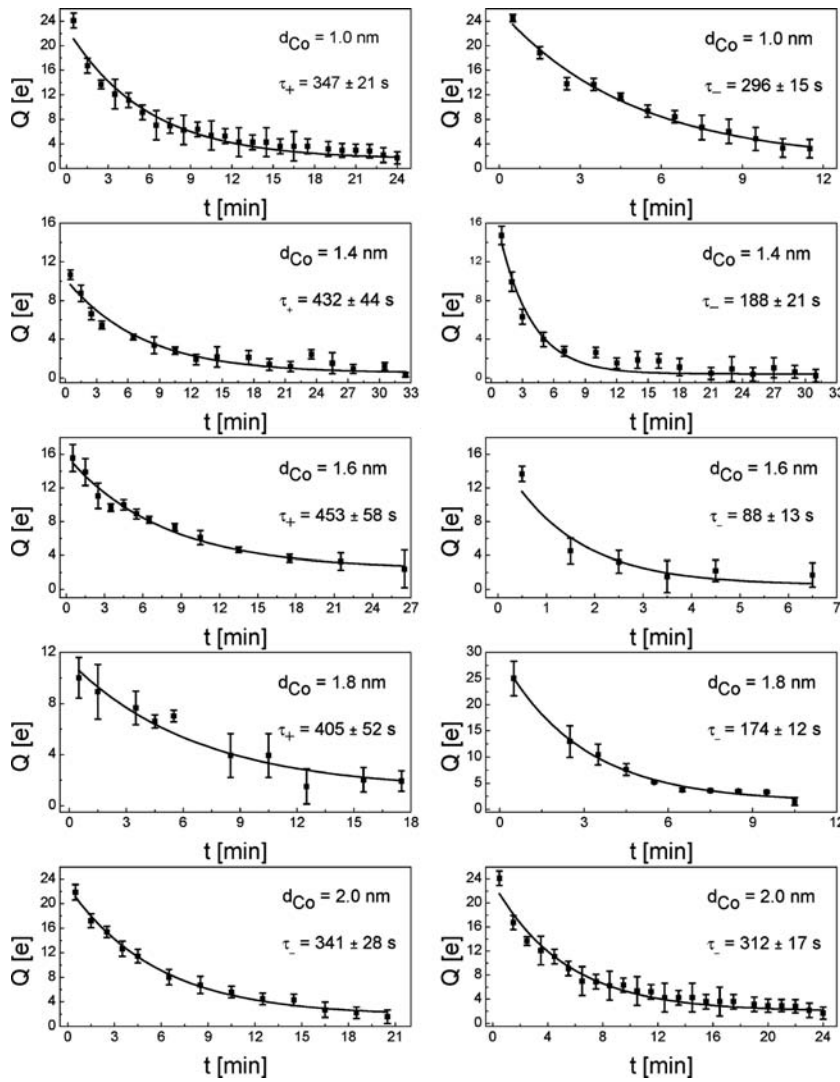


**Fig. 4** Decay of positive charge (left column) and negative charge (right column) for Co/SiO<sub>2</sub> films with nominal Co film thickness ranging from 1.0 to 2.0 nm. The retention times  $\tau_+$  and  $\tau_-$ , obtained by first-order exponential fits to the peak height for positive charge and the valley depth for negative charge in the EFM images, respectively, depend strongly on the nominal Co film thickness. The retention time  $\tau_+$  for positive charge is for all film thicknesses larger than the retention time  $\tau_-$  for negative charge.

affinity, and  $q$  the electron charge. As the dependence of the tunneling probability  $T$  on barrier height  $\phi$  and barrier thickness  $d$  is given approximately by  $T \propto \exp(-2d\sqrt{2mq\phi}/\hbar)$  and the retention is inversely proportional to  $T$ ,<sup>[2]</sup> the relation between the decay times is given approximately by

$$\frac{\tau_+}{\tau_-} \approx e^{\frac{2\sqrt{2m}}{\hbar}d_{SiO_2}(\sqrt{q\phi_0 + E_0} - \sqrt{q\phi_0 - E_0})} \approx 1 + \frac{2\sqrt{2m}}{\hbar} \frac{d_{SiO_2}}{\sqrt{q\phi_0}} E_0 \text{ for } E_0 \ll q\phi_0 \quad (4)$$

Solving Eq. (4) for the charging energy and using the measured values for  $\tau_+$  and  $\tau_-$  of the nominally 1.4-nm-thick Co layer, we obtain  $E_0 = 33 \pm 6$  meV. As seen in the TEM image shown in Fig. 1, the Co particles are roughly spherical with a radius of  $\sim 1.5$  nm and are roughly arranged in chains with typical lengths of 3–6 particles for a nominally 1.4-nm-thick Co film.

The charging energy of such nanoclusters is approximately  $31 \pm 10$  meV, which is in very good agreement with the value estimated from measured decay times. The Coulomb-blockade energy  $E_0$  depends strongly on the size and shape of the Co cluster, and it is observed that the retention times depend strongly on the nanoscale structure of the Co layer. Fig. 5 shows the retention times  $\tau_+$  for positive charge and  $\tau_-$  for negative charge as functions of the nominal Co film thickness. The results are comparable to the previously measured retention times but show smaller errors in the values.  $\tau_+$  first increases with increasing  $d_{Co}$ , reaching a maximum for  $d_{Co} = 1.6$  nm, and then decreases and approaches  $\tau_-$ . In contrast, the negative charge retention time  $\tau_-$  shows the opposite behavior, first decreasing with increasing  $d_{Co}$ , reaching a minimum for  $d_{Co} = 1.6$  nm, and then increasing with increasing  $d_{Co}$ . As expected from the above simplified model, the retention time for positive charge is larger than that for negative charge over the entire range of values of  $d_{Co}$ .

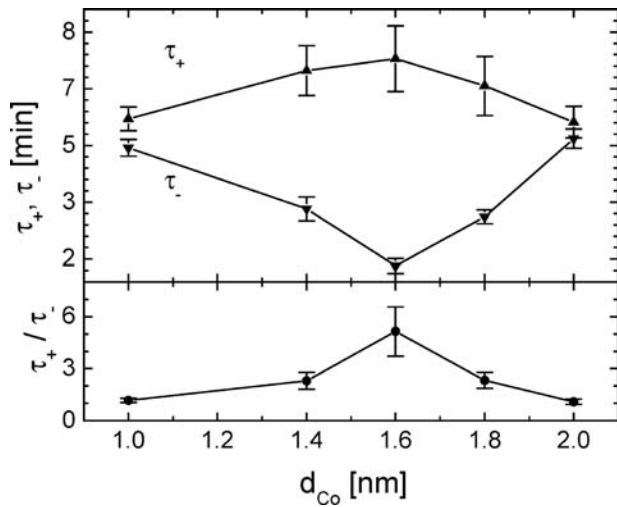


**Fig. 5** Retention times for  $\tau_+$  positive charge and  $\tau_-$  for negative charge and the ratio  $\tau_+/\tau_-$  plotted as functions of nominal Co film thickness  $d_{Co}$ .  $\tau_+$  first increases with increasing  $d_{Co}$ , reaching a maximum for  $d_{Co} = 1.6$  nm, and then decreases and approaches  $\tau_-$ . In contrast, the negative charge retention time  $\tau_-$  shows the opposite behavior, first decreasing with increasing  $d_{Co}$ , reaching a minimum for  $d_{Co} = 1.6$  nm, and then increasing with increasing  $d_{Co}$ .

and for  $d_{Co}$  larger than 1.6 nm the difference in retention times becomes smaller as  $d_{Co}$  increases, i.e., as the Coulomb blockade energy decreases. However, the decreasing difference in retention times with decreasing  $d_{Co}$  below 1.4 nm is not expected from the simplified model. This behavior of the retention times can be explained by a model including discharging from the Co nanoclusters into the Si substrate and charge decay within the Co layer. The total retention times  $\tau_+$  and  $\tau_-$  will then be given by

$$\frac{1}{\tau_{+,-}} = \frac{1}{\tau_{+,-}^{\text{in}}} + \frac{1}{\tau_{+,-}^{\text{out}}} \quad (5)$$

where  $\tau_+^{\text{in}}$  and  $\tau_-^{\text{in}}$  are the characteristic retention times for charge transport within the Co layer and  $\tau_+^{\text{out}}$  and  $\tau_-^{\text{out}}$  pertain to charge transport from the Co layer into the Si substrate. As the retention times depend strongly on the barrier width as well as the Coulomb-blockade energy, it is necessary to account for the nanoscale structure of the Co layer. It is known from TEM micrographs that the Co layer consists of isolated spherical clusters for a nominal layer thickness of about 1.4 nm and below, and of chainlike or tubelike arrangements of connected spherical particles for nominally thicker films.<sup>[7,10,30]</sup> As the Co clusters increase in size with increasing nominal thickness above 1.4 nm, the capacitance of these clusters increases and thus the Coulomb-blockade energy decreases. As the nominal film thickness decreases below about 1.4 nm, the

Co particles remain spherical and the spacing between the particles increases.<sup>[7,10,30]</sup> Thus the Coulomb-blockade energy remains fairly constant below nominal thicknesses of about 1.4 nm.

For discharging within the Co layer, the retention times are given by<sup>[23]</sup>

$$\tau_{+,-}^{\text{in}} \propto e^{\frac{2\sqrt{2m_{\text{SiO}_2}^{\text{h,e}}}}{h} d_{\text{sp}} \sqrt{q\phi_{\text{Co}} - q\chi_{\text{SiO}_2} \pm E_0}} \quad (6)$$

where  $d_{\text{sp}}$  is the spacing between the Co clusters, and  $m_{\text{SiO}_2}^{\text{h}}$  and  $m_{\text{SiO}_2}^{\text{e}}$  are the effective mass of holes and electrons in  $\text{SiO}_2$ , respectively.  $\tau_+^{\text{in}}$  and  $\tau_-^{\text{in}}$  increase exponentially with increasing  $d_{\text{sp}}$  as the nominal Co film thickness decreases below 1.4 nm, and approach each other as  $E_0$  decreases for Co films with nominal thickness above 1.4 nm. For small Coulomb-blockade energies  $E_0 \leq kT$ , where  $k$  is the Boltzmann constant, a hole will tunnel from the Co cluster into the conduction band of the Si substrate, and  $\tau_+^{\text{out}}$  is given by<sup>[23]</sup>

$$\tau_+^{\text{out}} \propto e^{\frac{2\sqrt{2q}}{h} \int_0^{d_{\text{SiO}_2}+W} \sqrt{m^{\text{h}} \phi(x)} dx} \approx e^{\frac{2\sqrt{2}}{h} \left( d_{\text{SiO}_2} \sqrt{m_{\text{SiO}_2}^{\text{h}} (q\phi_0 + E_0)} + \frac{\pi}{2} W \sqrt{qm_{\text{Si}}^{\text{h}} V_{\text{bi}}} \left( 1 + \frac{E_0}{qV_{\text{bi}}} \right) - W \sqrt{2m_{\text{Si}}^{\text{h}} E_0} \right)} \quad (7)$$

where the barrier height is given by  $\phi(x) = \phi_{\text{Co}} - \chi_{\text{SiO}_2} + E_0/q + (\chi_{\text{Si}} - \phi_{\text{Co}})x/d_{\text{SiO}_2}$  for  $0 \leq x \leq d_{\text{SiO}_2}$  and  $\phi(x) = V_{\text{bi}} + E_0/q - V_{\text{bi}}(x - d_{\text{SiO}_2})^2/W^2$  for  $d_{\text{SiO}_2} < x < d_{\text{SiO}_2} + W$ ,  $m_{\text{Si}}^{\text{h}}$  is the effective hole mass in Si,  $W = \sqrt{2\varepsilon_{\text{Si}} V_{\text{bi}} / (qN_{\text{C}})}$  is the depletion width,  $\varepsilon_{\text{Si}}$  is the Si permittivity,  $N_{\text{C}}$  the effective density of states in the Si conduction band, and  $V_{\text{bi}}$  the built-in potential. As the Coulomb-blockade energy increases with decreasing  $d_{\text{Co}}$ ,  $\tau_+^{\text{out}}$  increases.

For Coulomb-energies in the range  $kT < E_0 < E_{\text{g}} - qV_{\text{bi}} - kT$ , where  $E_{\text{g}}$  is the Si bandgap, no hole states exist on the semiconductor side. The tunneling probability becomes very small and thus the retention time  $\tau_+^{\text{out}}$  reaches a maximum value. According to Eq. (5), the total retention time  $\tau_+$  for positive charge will be limited by  $\tau_+^{\text{in}}$  in this regime.

Finally, for Coulomb energies  $E_0 \geq E_{\text{g}} - qV_{\text{bi}} - kT$ , tunneling of holes into the valence band is possible, and  $\tau_+^{\text{out}}$  is given by<sup>[23]</sup>

$$\tau_+^{\text{out}} \propto e^{\frac{2\sqrt{2m_{\text{SiO}_2}^{\text{h}}}}{h} d_{\text{SiO}_2} \sqrt{q\phi_0 + E_0 + (E_{\text{g}} - qV_{\text{bi}})/2}} \quad (8)$$

For tunneling from a negatively charged Co cluster into the Si substrate, the tunneling barrier width depends on the Coulomb-blockade energy  $E_0$  due to



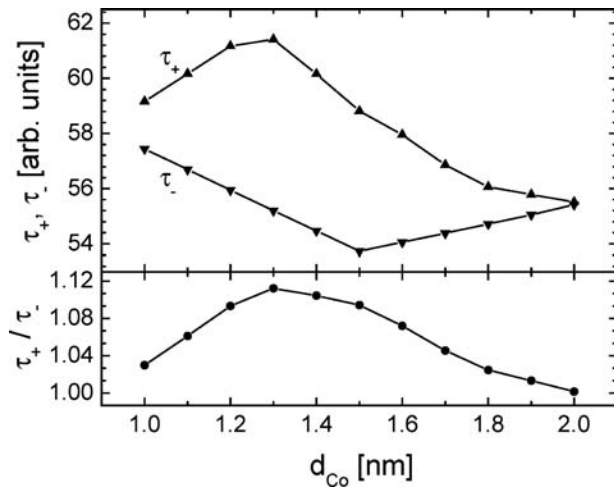


**Fig. 6** Calculated retention times as functions of nominal Co film thickness. The computed curves follow the measured curves qualitatively but cannot reproduce the exact behavior because of uncertainties in the Coulomb blockade energies of the Co clusters and the detail band structure.

the band bending within the Si substrate layer.  $\tau_{-}^{\text{out}}$  is then given, in a manner analogous to that used to obtain Eq. (7), by<sup>[23]</sup>

$$\tau_{-}^{\text{out}} \propto e^{\frac{2\sqrt{2}}{\hbar} \left( d_{\text{SiO}_2} \sqrt{m_{\text{SiO}_2}^c (q\phi_0 - E_0)} + \frac{\pi}{2} W \sqrt{q m_{\text{Si}}^c V_{\text{bi}}} \left( 1 - \frac{E_0}{qV_{\text{bi}}} \right) \right)} \quad (9)$$

where  $m_{\text{Si}}^c$  is the effective electron mass in Si.

The expressions for  $\tau_{+,-}^{\text{in}}$ ,  $\tau_{+,-}^{\text{out}}$ , and  $\tau_{+,-}$  derived in Eqs. [5–9] may be used to analyze the dependence of  $\tau_{+,-}$  on  $d_{Co}$ . As exact values for the Coulomb-blockade energies and the spacing between Co clusters are unknown or difficult to extract from TEM images, the following values are assumed, which are believed to be physically reasonable. A value of 2.05 nm was assumed for  $d_{sp}$  for  $d_{Co} = 1.0$  nm, decreasing linearly to 2 nm for  $d_{Co} = 1.4$  nm and then remaining constant for  $d_{Co} > 1.4$  nm.  $E_0$  is assumed to decrease linearly from 0.11 to 0.01 eV for  $d_{Co}$  increasing from 1.0 to 2.0 nm. The computed dependence of  $\tau_+$  and  $\tau_-$  on  $d_{Co}$ , as shown in Fig. 6, qualitatively reproduces the experimentally observed dependence quite closely. However, discrepancies exist between the measured and simulated values because of the uncertainties in the estimation of values such as the Coulomb energies, barrier thicknesses, and barrier heights.

## CONCLUSION

The use of granular or discontinuous metal/insulator materials in memory or sensor devices requires a detailed understanding of the nanoscale charge transport, which can be investigated by scanning probe

techniques. Electrostatic force microscopy was used to demonstrate and characterize local charge deposition and transport in Co nanoclusters embedded in an insulating  $\text{SiO}_2$  matrix. Positive and negative charge can be deposited controllably and reproducibly in such nanoclusters, typically in quantities of  $\sim 5$ – $20$  electrons within areas 30–50 nm in radius. The charge decays over several minutes with part of it spreading out in the discontinuous Co film and the rest tunneling into the Si substrate. The charge retention times  $\tau_+$  for positive charge and  $\tau_-$  for negative charge as well as their ratio depend strongly on the nanoscale structure of the discontinuous metal cluster film. These results were interpreted as a consequence of Coulomb-blockade effects, and a detailed model considering charge transport within the Co layer as well as from the Co cluster into the Si substrate was used to explain the dependence of the retention times on the nanoscale Co/ $\text{SiO}_2$  film structure qualitatively. These studies have led to a novel magnetic field sensor design based on the combination of charge storage and tunnel-magnetoresistance of the Co/ $\text{SiO}_2$  film, which shows a significant improvement in magnetic field sensitivity as compared to the tunnel-magnetoresistance of the Co/ $\text{SiO}_2$  film alone. Incorporation of a granular metal/insulator magnetoresistive film into the gate of a field-effect transistor structure allows the magnetoresistive response to be converted to a shift in the threshold voltage of the transistor, resulting in a large amplification in sensitivity to an external magnetic field. In a prototype device based on a p-channel MOSFET, a threshold voltage shift of 50 mV upon application of a 6-kOe magnetic field was obtained at room temperature. This resulted in a fourfold amplification in relative current response, and an increase in absolute current response by a factor of 500 in the saturation regime, as compared to the response attainable in the magnetoresistive film alone.

## ACKNOWLEDGMENTS

Part of this work was supported by NSF (Award No. ECS95-01469 and DMR 9400439) and ONR (Grant No. N00014-95-1-0996). I thank S. Sankar and A.E. Berkowitz for the preparation of the Co/ $\text{SiO}_2$  films and for providing me with TEM micrographs of these films. Special thank goes to E.T. Yu for support, guidance, and helpful discussions. I also acknowledge helpful comments from P.M. Asbeck and S.S. Lau.

## REFERENCES

1. Boer, E.A.; Brongersma, M.L.; Atwater, H.A.; Flagan, R.C.; Bell, L.D. Localized charge injection in  $\text{SiO}_2$  films



- containing silicon nanocrystals. *Appl. Phys. Lett.* **2001**, *79* (6), 791–793.
2. Schaadt, D.M.; Yu, E.T.; Sankar, S.; Berkowitz, A.E. Charge storage in Co nanoclusters embedded in SiO<sub>2</sub> by scanning force microscopy. *Appl. Phys. Lett.* **1999**, *74* (3), 472–474.
  3. Tiwari, S.; Rana, F.; Hanafi, H.; Hartstein, A.; Crabbé, E.F.; Chan, K. A silicon nanocrystals based memory. *Appl. Phys. Lett.* **1996**, *68* (10), 1377–1379.
  4. Gittleman, J.I.; Goldstein, Y.; Bozowski, S. Magnetic properties of granular nickel films. *Phys. Rev.*, **B 1972**, *5* (9), 3609–3621.
  5. Coffey, K.R.; Hylton, T.L.; Parker, M.A.; Howard, J.K. Thin film structures for low field granular giant magnetoresistance. *Scr. Metall. Mater.* **1995**, *33* (10–11), 1593–1602.
  6. Sankar, S.; Dieny, B.; Berkowitz, A.E. Spin-polarized tunneling in discontinuous CoFe/HfO<sub>2</sub> multilayers. *J. Appl. Phys.* **1997**, *81* (8), 5512–5514.
  7. Sankar, S.; Berkowitz, A.E.; Smith, D.J. Spin-dependent tunneling in discontinuous Co–SiO<sub>2</sub> magnetic tunnel junctions. *Appl. Phys. Lett.* **1998**, *73* (4), 535–537.
  8. Dinia, A.; Schmerber, G.; Ulhaq, C.; El Bahraoui, T. Magnetic and transport properties of discontinuous metal-oxides multilayers. *Mater. Sci. Eng.* **2003**, *B97*, 231–234.
  9. Parker, M.A.; Coffey, K.R.; Howard, J.K.; Tsang, C.H.; Fontana, R.E.; Hylton, T.L. Overview of progress in giant magnetoresistive sensors based on NiFe/Ag multilayers. *IEEE Trans. Magn.* **1996**, *32* (1), 142–148.
  10. Dieny, B.; Sankar, S.; McCartney, M.R.; Smith, D.J.; Bayle-Guillemaud, P.; Berkowitz, A.E. *J. Magn. Magn. Mater.* **1998**, *185* (3), 283–292.
  11. Kakazei, G.N.; Lopes, A.M.L.; Pogorelov, Y.G.; Santos, J.A.M.; Sousa, J.B.; Freitas, P.P.; Cardoso, S.; Snoeck, E. Time-dependent transport effects in CoFe/Al<sub>2</sub>O<sub>3</sub> discontinuous multilayers. *J. Appl. Phys.* **2000**, *87* (9), 6328–6330.
  12. Binnig, G.; Quate, C.F.; Gerber, C. Atomic force microscope. *Phys. Rev. Lett.* **1986**, *56* (9), 930–933.
  13. Barrett, R.C.; Quate, C.F. Charge storage in a nitride-oxide-silicon medium by scanning capacitance microscopy. *J. Appl. Phys.* **1991**, *70* (5), 2725–2733.
  14. Dreyer, M.; Wiesendanger, R. Scanning capacitance microscopy and spectroscopy applied to local charge modifications and characterization of nitride-oxide-silicon heterostructures. *Appl. Phys.* **1995**, *A61* (4), 357–362.
  15. Terris, B.D.; Stern, J.E.; Rugar, D.; Mamin, H.J. Contact electrification using force microscopy. *Phys. Rev. Lett.* **1989**, *63* (24), 2669–2772.
  16. Terris, B.D.; Stern, J.E.; Rugar, D.; Mamin, H.J. Localized charge force microscopy. *J. Vac. Sci. Technol.*, **A 1990**, *8* (1), 374–377.
  17. Jones, J.T.; Bridger, P.M.; Marsh, O.J.; McGill, T.C. Charge storage in CeO<sub>2</sub>/Si/CeO<sub>2</sub>/Si(111) structures by electrostatic force microscopy. *Appl. Phys. Lett.* **1999**, *75* (9), 1326–1328.
  18. Boer, E.A.; Bell, L.D.; Brongersma, M.L.; Atwater, H.A.; Ostraat, M.L.; Flagan, R.C. Charging of single Si nanocrystals by atomic force microscopy. *Appl. Phys. Lett.* **2001**, *78* (20), 3133–3135.
  19. Mélin, T.; Deresmes, D.; Stiévenard, D. Charge injection in individual silicon nanoparticles deposited on a conductive substrate. *Appl. Phys. Lett.* **2002**, *81* (26), 5054–5056.
  20. Decossas, S.; Mazen, F.; Baron, T.; Souifi, A.; Brémond, G. Electric measurements by AFM on silicon nanocrystals. *Physica E* **2003**, *17*, 543–545.
  21. Tevaarwerk, E.; Rugheimer, P.; Castellini, O.M.; Keppel, D.G.; Utley, S.T.; Savage, D.E.; Lagally, M.G.; Eriksson, M.A. Electrically isolated SiGe quantum dots. *Appl. Phys. Lett.* **2002**, *80* (24), 4626–4628.
  22. Guillemot, C.; Budau, P.; Chevrier, J.; Marchi, F.; Comin, F.; Alandi, C.; Bertin, F.; Buffet, N.; Wyon, Ch.; Mur, P. Imaging of stored charges in Si quantum dots by tapping and electrostatic force microscopy. *Eur. Phys. Lett.* **2002**, *59* (4), 566–571.
  23. Schaadt, D.M.; Yu, E.T.; Sankar, S.; Berkowitz, A.E. Proximal probe characterization of nanoscale charge transport properties in Co/SiO<sub>2</sub> multilayer structures. *J. Electron. Mater.* **2000**, *29* (11), 1299–1303.
  24. Felidj, N.; Lambert, J.; Guthmann, C.; Saint-Jean, M. Charge stability on thin insulators studied by atomic force microscopy. *Eur. Phys. J. AP* **2000**, *12*, 85–91.
  25. Buh, G.H.; Chung, H.J.; Kuk, Y. Real-time evolution of trapped charge in a SiO<sub>2</sub> layer: an electrostatic force microscopy study. *Appl. Phys. Lett.* **2001**, *79* (13), 2010–2012.
  26. Boer, E.A.; Bell, L.D.; Brongersma, M.L.; Atwater, H.A. Models for quantitative charge imaging by atomic force microscopy. *J. Appl. Phys.* **2001**, *90* (6), 2764–2772.
  27. Lambert, J.; Guthmann, C.; Saint-Jean, M. Relation between charge distribution and its image by electrostatic force microscopy. *J. Appl. Phys.* **2003**, *93* (9), 5369–5376.
  28. Schaadt, D.M.; Yu, E.T.; Sankar, S.; Berkowitz, A.E. A monolithic field-effect-transistor-amplified magnetic field sensor. *Appl. Phys. Lett.* **1999**, *75* (5), 731–733.
  29. Schaadt, D.M.; Yu, E.T.; Sankar, S.; Berkowitz, A.E. Characterization and analysis of a novel hybrid magnetoelectronic device for magnetic field sensing. *J. Vac. Sci. Technol.*, **A 2000**, *18* (4), 1834–1837.
  30. Sankar, S. *Correlation of Microstructural, Magnetic, and Transport Properties of Composite Metal-Insulator Films, UMI Microform 9963657*; Bell & Howell Information and Learning Company: Ann Arbor, MI, 2000; 50 pp.
  31. Martin, Y.; Williams, C.C.; Wickramasinghe, H.K. Atomic force microscope-force mapping and profiling on a sub 100-Å scale. *J. Appl. Phys.* **1987**, *61* (10), 4723–4729.

# Chemical Warfare Agents: Biosensors for Detection

## Elias Greenbaum

*Chemical Sciences Division, Oak Ridge National Laboratory, Oak Ridge, Tennessee, U.S.A., and Center for Environmental Biotechnology, Graduate School of Genome Science and Technology, University of Tennessee, Knoxville, Tennessee, U.S.A.*

## Miguel Rodriguez, Jr.

*Life Sciences Division, Oak Ridge National Laboratory, Oak Ridge, Tennessee, U.S.A.*

## Charlene A. Sanders

*Chemical Sciences Division, Oak Ridge National Laboratory, Oak Ridge, Tennessee, U.S.A.*

## INTRODUCTION

### Detection of Chemical Warfare Agents in Water

Working with primary-source freshwater drinking samples from the Clinch and Tennessee Rivers, we have developed a tissue-based biosensor detection system that uses naturally occurring aquatic photosynthetic tissue as the sensing material for the detection of chemical antagonists in the water. Sensor readout is based on well-known principles of fluorescence induction by living photosynthetic tissue. The Clinch River is the main source of drinking water for Oak Ridge, TN, while the Tennessee River is a major source for the city of Knoxville. We have successfully detected algae in every sample that we examined and readily monitored changes in the characteristic fluorescence induction curves when the samples were exposed to potassium cyanide (KCN), methyl parathion (MPt), *N*(3,4-dichlorophenyl)-*N*,*N*-dimethylurea (DCMU), and paraquat. The percentage decreases in photochemical yields observed in Tennessee River samples after a 25-min exposure to KCN, MPt, and DCMU were  $21.89 \pm 0.76$ ,  $3.28 \pm 0.18$ , and  $14.77 \pm 1.81$ , respectively. For a site at the Clinch River, the percentage decreases were  $22.78 \pm 1.63$ ,  $8.32 \pm 0.21$ , and  $17.71 \pm 1.32$  (Table 1). For each percentage decrease, the probable error is the computed error based on standard error analysis.<sup>[44]</sup> The unique aspect of this approach to real-time water-quality monitoring is that unlike conventional sensing devices, this sensor material is external to the detecting instrument and is continuously refreshed. These biosensors may be used as continuous rapid-warning sentinels for the detection of chemical warfare (CW) agents in sunlight-exposed drinking water supplies.

### Detection of Chemical Warfare Agents in Air

Tissue biosensors based on immobilized whole cell photosynthetic microorganisms have been developed

for the detection of airborne CW agents and simulants. The sensor read-out is based on well-known principles of fluorescence induction by living photosynthetic tissue. Like the cyanobacteria and algae from which they were constructed, the sensors are reasonably robust and mobile. Commercially available handheld fluorometric detector systems were used to measure Photosystem II (PSII) photochemical efficiency of green algae and cyanobacteria entrapped on filter paper disks. Toxic agents flowing in the gas stream through the sensors can alter the characteristic fluorescence induction curves with resultant changes in photochemical yields. Tabun (GA), sarin (GB), mustard agent, tributylamine (TBA; a sarin stabilizer), and dibutylsulfide (DBS; a mustard agent analog) were tested. Upper threshold limits of detectability for GA, TBA, and DBS are reported. With additional research and development, these biosensors may find application in stand-off detection of chemical and perhaps biological warfare agents under real-world conditions.

## BACKGROUND

### Detection of Chemical Warfare Agents in Water

Algae and cyanobacteria are present in all surface waters that are exposed to sunlight. The unattached microscopic organisms that are found individually or in small clumps floating in rivers and lakes are composed of phytoplankton and zooplankton. Most of the phytoplankton is composed of algae.<sup>[1]</sup> Based on cell count, biomass, and photosynthetic carbon fixation, green microalgae are a major component of the phytoplankton population. Microalgae are ubiquitous and can grow year-round. Their small size and efficient uptake mechanisms enable them to utilize nutrients in low concentrations or in forms that are unsuitable for larger cells.<sup>[2]</sup>

**Table 1** Decrease in photochemical yields of naturally occurring algae in primary-source drinking waters from the Clinch and Tennessee rivers following exposure to toxic agents

	Sample site	Toxic agent [ $\Delta \pm$ probable error (%)] <sup>a</sup>		
		KCN	MPt	DCMU
1	Clark Center Recreation Park	22.78 $\pm$ 1.63	8.32 $\pm$ 0.21	17.71 $\pm$ 1.32
2	Melton Hill Hydroelectric Dam	29.85 $\pm$ 4.17	7.66 $\pm$ 0.90	23.45 $\pm$ 4.77
3	Oak Ridge Marina	25.88 $\pm$ 0.90	8.58 $\pm$ 0.27	12.81 $\pm$ 0.81
4	Tennessee River	21.89 $\pm$ 0.76	3.28 $\pm$ 0.18	14.77 $\pm$ 1.81

<sup>a</sup>For each agent,  $\Delta$  is defined as the decrease in photochemical yield following a 25-min exposure. It was computed by subtracting the value obtained for each toxic agent from its corresponding control. The entries for rows 1 and 4 correspond to the 25-min data points shown in Figs. 6 and 7. Similar plots (not shown) were obtained for the data in rows 2 and 3. The probable error is the computed error (the square root of the sum of the squares of the sample standard deviations of the toxin and control data) based on standard error analysis. Source: From Ref.<sup>[44]</sup>.

Source: From Ref.<sup>[3]</sup>.

The focus of the first part of this entry is the detection of toxic agents in sunlight-exposed primary-source drinking waters.<sup>[3]</sup> The agents used in this study were methyl parathion (MPt), potassium cyanide (KCN), Diuron (DCMU), and paraquat. MPt is an organophosphorus insecticide used to control soil-dwelling pests and a wide range of insects and mites that infest agricultural crops. It is a cholinesterase inhibitor that is structurally and functionally similar to the CW agents classified as nerve agents (including VX and GA). Severe exposure in humans and animals can lead to convulsions, unconsciousness, cardiac arrest, and death. Hydrogen cyanide has an odor characteristic of bitter almonds and is completely miscible in water. For these experiments, the water-soluble salt KCN was used. The cyanide ion is an extremely toxic and fast-acting poison. Food and drinking water are the main sources of cyanide exposure for individuals not subjected to occupational exposures.<sup>[4]</sup> Typical symptoms of cyanide poisoning are headache, nausea, weakness, palpitations, tremors, and breathlessness. In cases of severe poisoning, the nervous and respiratory systems are the first to fail. With high levels of exposure, death results from respiratory arrest. The U.S. Army has proposed field drinking water standards for cyanide of 2 and 6 mg/L, assuming a water consumption of 15 and 5 L/day, respectively.<sup>[5]</sup> Paraquat is a herbicide that is usually sold as paraquat dichloride. It is used as an inhibitor of weeds infesting seed crops and orchards, as a crop defoliant on cotton and potato vines, and as a harvest aid for soybeans. Because it possesses high solubility, paraquat may remain in water for several days following its use in aquatic weed control. Acute poisoning may cause respiratory distress and effects on the nervous system and kidneys. Death is usually due to progressive pulmonary fibrosis and epithelial proliferation in the lungs. DCMU (Diuron) is a substituted urea-based herbicide employed principally for the control of vegetation in noncrop areas, including irrigation and

drainage ditches. Diuron is a non-ionic compound with moderate water solubility. The U.S. Environmental Protection Agency has ranked Diuron fairly high (i.e., as a Priority B Chemical) with respect to potential for groundwater contamination. Diuron is of low acute toxicity.<sup>[4]</sup>

There is increased interest in the development of biosensors for the detection of pesticides in drinking water supplies. Merz and colleagues<sup>[6]</sup> isolated plant chloroplasts (pea seedlings or lettuce) and exposed them to herbicides of the triazine/phenylurea group, which accelerate an increase in PSII fluorescence induction. Frende and coinvestigators<sup>[7]</sup> reported the use of an optical biosensor that incorporated the green alga *Scenedesmus subspicatus* for the detection of herbicides in wastewater. The filter paper-immobilized algae covered with alginate did not lose significant fluorescence properties after 6 months of storage at 4°C. Rizzuto and colleagues<sup>[8]</sup> tested a biosensor consisting of PSII particles of the cyanobacterium *Synechococcus elongatus* for the detection of herbicides in three rivers in the Lazio region in Italy. By washing the sensor, they were able to reuse it for several assays after the removal of the toxic agent. Koblizek and associated researchers<sup>[9]</sup> used this type of biosensor and reported a detection limit of  $5 \times 10^{-10}$  M for Diuron, a lower limit that is comparable to that of the most sensitive enzyme-linked immunosorbent assay (ELISA). Pogacnik and Franko<sup>[10]</sup> used a photothermal sensor to determine organophosphate and carbamate pesticides in spiked drinking water and fruit juices. Pesticide detection in a single sample by the biosensor consisting of the enzyme acetylcholinesterase was performed within 15 min. Another approach for the determination of herbicides in river water samples is the application of immunosensors. Mallat and colleagues<sup>[11]</sup> reported the use of an optical immunosensor with fluorescently labeled antiparaquat antibodies. The fluorescence signal was indirectly related to the paraquat concentration in the sample.

Mallat et al. then used capillary zone electrophoresis with ultraviolet detection to validate the paraquat immunosensor response. Although the immunosensor achieved a lower paraquat detection limit of 0.06 µg/L in river water, the procedure was quite elaborate, requiring labeling of antiparaquat antibodies. Recently, fiberoptic biosensors with entrapped algae in membranes have been developed to monitor the effects of herbicides. Fiber optics provide a fast method to transmit a reproducible signal. The membranes are inexpensive to prepare and easy to handle. Campanella and associated researchers<sup>[12]</sup> reported the effect of triazinic herbicides on a biosensor containing the cyanobacterium *Spirulina subsalsa*. Naessens and colleagues<sup>[13]</sup> detected a response to atrazine, simazine, and Diuron using a *Chlorella vulgaris* biosensor.

There is an increased awareness of the possibility of attacks on metropolitan areas using chemical and biological warfare agents. Depending on the specific agent used, the low water solubilities of these agents may allow contaminants to persist for a long period of time, constituting in effect a time-release system that moves from insoluble agent to the aqueous environment. A large volume of the released agent may stay effective for years if the water is still or moving slowly. Factors that can accelerate hydrolysis of nerve agents are dilution, turbulence, high pH, and heat. Higher temperatures can enhance degradation of nerve agents by increasing their solubility in water. Also, the presence of certain ions in the salt content of seawater significantly increases the hydrolysis of specific nerve agents when compared with those in freshwater.<sup>[14]</sup> Application of entrapped cyanobacteria and algae for the detection of airborne CW agents has been reported.<sup>[15]</sup>

Degenhardt-Langelaan and Kientz<sup>[16]</sup> used a large-volume injection (200 µL) to detect the nerve agents sarin, tabun, soman, DFP, and VX at levels as low as parts per trillion in freshly prepared water samples. They used a gas chromatographic procedure in which intact nerve agents were isolated from water by solid-phase extraction with Amberlite resin (XAD-4) followed by extraction with ethyl acetate. Jones and Hoegh-Guldberg<sup>[17]</sup> studied the effects of cyanide on the photosynthesis of symbiotic algae in hard coral from Australia. As in our study, they used pulse-amplitude-modulated (PAM) chlorophyll fluorescence techniques to measure the maximum potential quantum yield of PSII in dark-adapted samples. Examining photochemical and nonphotochemical quenching, they observed that cyanide inhibited the Calvin cycle and damaged the PSII reaction center. Singh and colleagues<sup>[18]</sup> reported the use of activated carbon for the removal of dichloroethyl ether, the oxygen analog of sulfur mustard agent, and phenol from water. This analog possesses higher stability in water than sulfur mustard, which has a hydrolysis half-life of 3 min.

However, this procedure has disadvantages. Activated carbon must be dried at 120°C for 6 h prior to the experiment. Also, a period of 4 h is required for the adsorbed material to reach steady state in solution before analysis.

Wang and associated researchers<sup>[19]</sup> utilized a miniaturized analytical system with combined on-chip micellar electrokinetic chromatographic separation for amperometric detection of organophosphate nerve agents. They reported a lower detection limit of  $2.4 \times 10^{-6}$  M for MPt in spiked samples from the Rio Grande River at Las Cruces, NM. Their microsystem was composed of microphotolithographically fabricated capillary electrophoresis glass chips with planar thick-film electrodes on ceramic wafers.<sup>[20]</sup> Finally, solid-phase microextraction is a new technique that has been developed in the last decade for the determination of CW agents<sup>[21]</sup> and organophosphorus pesticides<sup>[22]</sup> in freshwater samples. It enables detection of toxic agents at very low levels. However, the analytes may require a period of at least 30 min to reach equilibrium.

### Detection of Chemical Warfare Agents in Air

Photosynthetic conversion of electromagnetic energy into stored chemical energy is triggered by the absorption of light by chlorophyll pigment molecules. Visible photons energize the electron transport chain of the photosynthetic apparatus via the photoreaction centers, PSI and PSII, that do the work of photosynthesis. Some of the absorbed energy is dissipated as heat or emitted as fluorescence at a wavelength that is typically longer than the initial excitation energy. Only a small portion (~3% of absorbed light) is released from PSII as fluorescence.<sup>[23]</sup> Photosynthetic prokaryotes and eukaryotes fluoresce when illuminated by light following a period of darkness. However, structural differences between the two types of organisms affect the fluorescence signal produced and their sensitivity to perturbing factors, such as toxic agents, which alter the characteristic fluorescence pattern of healthy photosynthetic tissue. The kinetic time profile and interpretation of the fluorescence induction curve and the overall fluorescence yield are dependent upon the structure of the photosynthetic apparatus, the proximity of antennae to reaction centers, and the composition and concentration of photosynthetic pigments.<sup>[24]</sup> The time course of fluorescence is an indication of the organism's ability to perform photosynthesis and is directly related to its physical well being. One of the most useful parameters in fluorescence analysis from photosynthetic tissue is the efficiency of PSII photochemistry. It may be calculated from a measurement of the ambient and maximum values of

fluorescence from photosynthetic tissue that is subjected to a saturating flash of light.<sup>[25,26]</sup>

These principles have been applied to the detection of fluorescence emitted by *C. vulgaris*, a unicellular green alga, and *Nostoc commune*, a cyanobacterium. Whole cell microorganisms were immobilized onto glass fiber filter disks. The sensor fluorescence detection system compared fluorescence emissions from algae and cyanobacteria exposed to a benign stream of air with air carrying a toxic chemical agent and used this information to calculate the efficiency of PSII photochemistry. The development of a field-deployable biosensor requires that the immobilized biological tissue comprising the sensor retains viable fluorescence and PSII efficiency after it has been stored as inventory prior to field applications and then transported overland or by air to a remote location. *N. commune* was chosen for study as a biosensor because it has been extensively characterized by Potts and his research group as being inherently resistant to dehydration stress for long periods of time.<sup>[27–30]</sup> Also, the well-studied alga of photosynthesis research, *C. vulgaris*, was chosen because it, like *Nostoc*, can grow using atmospheric CO<sub>2</sub> as the sole carbon source, thereby eliminating the need for complicated media formulations. Systematic control experiments of fluorescence emissions from these organisms measured before and after storage give a clear indication of the storage conditions most favorable for preserving their long-term stability for use as biosensors. Generally speaking, this includes storage in 0.5 mL growth medium in darkness. After 40 days, a normal fluorescence signature was restored within 1 hr.

The CW agents and CW simulants used in this study were airborne when they contacted the biosensors. Live CW agents pose a credible threat to military personnel and large population centers. The agents were developed specifically to be highly toxic to humans at low concentrations. They are easily produced from inexpensive raw materials and can be readily released into the environment. Fig. 1 displays

the agents and simulants tested in this study and their chemical structures. The nerve agents tabun (GA) and sarin (GB) are organophosphorus anticholinesterase compounds. GA is more volatile than GB, but both are lethal, resulting ultimately in death from respiratory failure.<sup>[31]</sup> Bis(2-chloroethyl)sulphide, better known as distilled sulfur mustard agent (HD), is a vesicant (blister agent) which affects eyes, lungs, and the skin. Dibutylsulfide (DBS) is a simulant of mustard gas. It is structurally similar to mustard agent, but not as lethal. Tributylamine (TBA) is a nerve agent (GB) stabilizer<sup>[32]</sup> with 2% of the toxicity of GB.

There are several instruments currently in use for measuring airborne CW agents. The SAW MINICAD is a surface-acoustic-wave gas microsensors.<sup>[33]</sup> Chemical vapors alter the resonant frequency of the chemical coating on the SAW sensor surface. The Improved Chemical Agent Monitor (ICAM)<sup>[34]</sup> and Bruker IMS<sup>[35]</sup> detect CW agent vapors by ion mobility spectrometry. These are all handheld instruments to be operated by personnel in protective clothing in the field. The M21 Remote Sensing Chemical Agent Alarm is a stand-off detector (remotely operated) which senses agents by infrared spectroscopy but is not mobile or launchable. Tissue biosensors made from immobilized bacteria are being developed to detect levels of gas-phase solvents such as benzene.<sup>[36]</sup> Using a Clark electrode, Naessens and Tran-Minh<sup>[37,38]</sup> monitored oxygen evolution from algal films to study the antagonistic effect of methanol and volatile organic compounds on the algae. Lee and Karube<sup>[39]</sup> also used a Clark electrode to measure dissolved oxygen to study the inhibitory effect of potassium cyanide. Recently, Naessens and colleagues<sup>[13]</sup> developed a fluorometric fiberoptic biosensor using *C. vulgaris* for the determination of herbicides in water. To this point, however, photosynthetic tissue-based biosensors have not been tested for the detection of CW agents. It is well known that toxic compounds can affect fluorescence induction in algae.<sup>[7,13]</sup> CW agents and simulants are known for their detrimental effects on mammalian tissue.

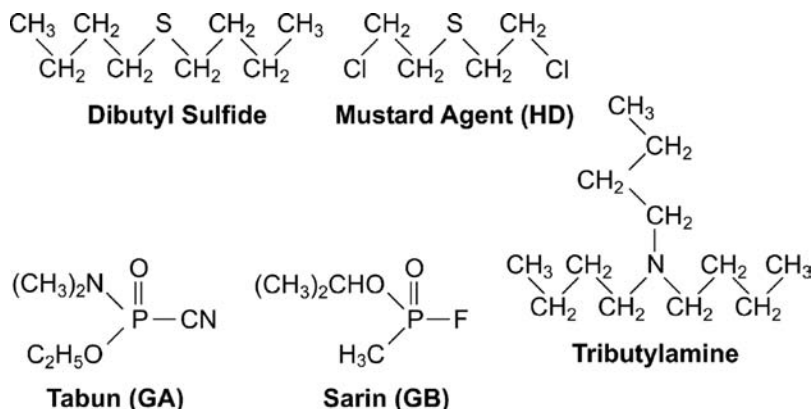


Fig. 1 Structures of selected chemical warfare agents and simulants. Source: From Ref.<sup>[15]</sup>.

The objective of the present work is to test whether they can affect electron transport and/or excitonic energy transfer mechanisms in photosynthetic organisms at concentrations that may be useful for possible field applications.

## METHODOLOGY

### Detection of Chemical Warfare Agents in Water

Prior to the experiments with river water samples, preliminary studies used axenic cultures of *C. vulgaris* that were grown on rotary shakers in liquid culture in minimal medium for 2 weeks under a bank of fluorescent lamps at an intensity of  $50 \mu\text{E m}^{-2} \text{sec}^{-1}$ . Total chlorophyll ( $a + b$ ) was determined in warm methanol ( $60\text{--}70^\circ\text{C}$ ) extracts in dim light according to the method of Wellburn and Lichtenthaler.<sup>[40]</sup> Field studies were performed using “as-is” freshwater samples and their naturally occurring populations of phytoplankton.

### Cell Chamber, Fluorescence Measurements, and Toxic Agents

Two classes of experiments are reported: batch and continuous. In the batch experiments, chemical agents were added directly to a fluorescence cuvette that contained the water sample and the progressive effect of the agent was monitored as a function of time. The second class of experiments, illustrated in Fig. 2, was designed to mimic the flow of river or lake water

through the fluorescence detection system. The cell chamber/optical unit (Fig. 2) is a flow system containing the fluorescence cell. Continuous experiments were performed using a flow-through cell (Hellma Cells, Inc., Model QS-131, Plainview, NY). Fluorescence induction curves were measured before and during exposure to toxic agents using a Walz XE-PAM fluorometer (Walz, Effeltrich, Germany). Fluorescence excitation and emission wavelengths were 660 and 685 nm, respectively. A halogen lamp actinic light source illuminated the cuvette at an intensity of  $500 \mu\text{E m}^{-2} \text{sec}^{-1}$  via a fiberoptic cable through direct connection to the cell chamber. Fluorescence induction curves were recorded every 5 min, and data collection for each curve was completed within 10 sec. Data extracted from the fluorescence induction curves were used to calculate  $F_s$ ,  $F_{\text{max}}$ ,  $F_v$  (variable fluorescence,  $=F_{\text{max}} - F_s$ ), and the efficiency of PSII photochemistry ( $F_v/F_{\text{max}}$ ). A 200-mL water sample was placed in a jacketed reservoir. The sample was continuously stirred and maintained in darkness with a black cloth. The reservoir was connected to the flow-through fluorescence cell with flexible tubing. To obtain a homogeneous sample before each recording, the volume in the fluorescence cell was replaced three times. After control data were collected, the volume in the reservoir was adjusted to 100 mL and the toxic agent was added. The toxic agents (Fig. 3) were prepared as stock solutions prior to addition to the reservoir and were injected directly into the top of the vessel and immediately mixed with the sample. Spent samples were drained into a waste bottle (Fig. 2). Upon arrival in the laboratory from collection sites at the rivers, the

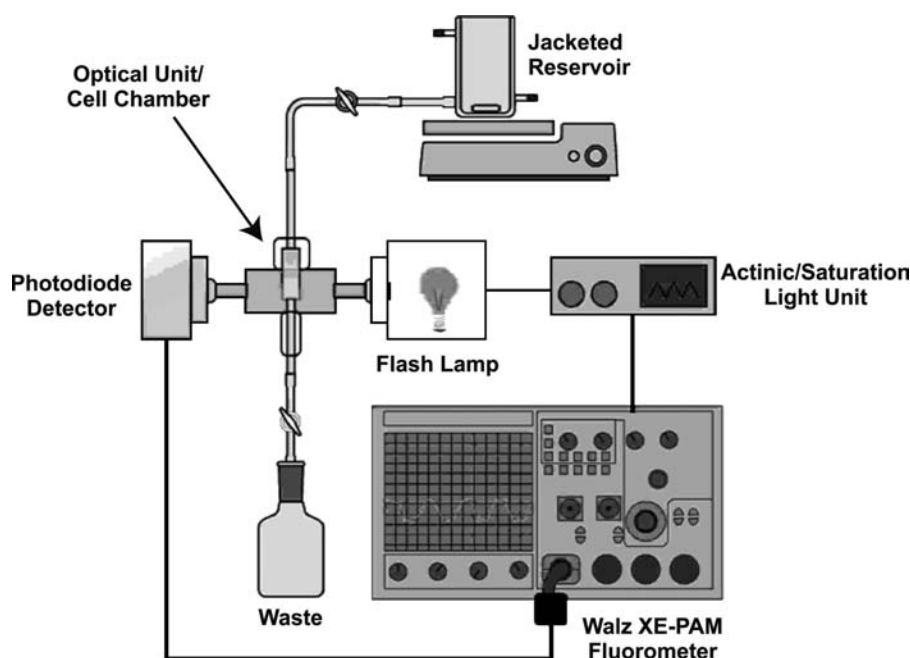


**Fig. 2** Experimental apparatus for continuous water quality monitoring. Batch experiments used a static fluorescence cuvette. Continuous experiments used a flow-through cuvette. Source: From Ref.<sup>[3]</sup>.



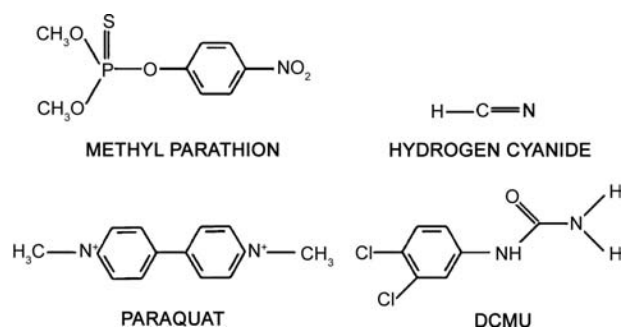


**Fig. 3** Chemical structures of selected toxic agents used for water quality monitoring. (From Ref.<sup>[3]</sup>)

water samples were kept under a fluorescent lamp at an illumination of  $50 \mu\text{E m}^{-2} \text{sec}^{-1}$  until use.

## Detection of Chemical Warfare Agents in Air

### Microorganisms and biosensor preparation

Axenic cultures of *N. commune* (UTEX 584) were grown on rotary shakers in BG-11 medium for 2 weeks under a 400-W high-pressure sodium lamp with an illumination intensity of  $1000 \mu\text{E m}^{-2} \text{sec}^{-1}$ . *Chlorella vulgaris* was grown on rotary shakers in liquid culture in minimal medium for 2 weeks under a fluorescent lamp light bank at  $50 \mu\text{E m}^{-2} \text{sec}^{-1}$ . *Nostoc* was harvested, homogenized to break up large colonies, and

resuspended in BG-11. *Chlorella* is unicellular; it does not require further processing before biosensor preparation. Total chlorophyll (*a* + *b*) in *Chlorella* and chlorophyll *a* in *Nostoc* were determined in warm ( $60\text{--}70^\circ\text{C}$ ) methanol extracts by the method of Wellburn and Lichtenthaler.<sup>[40]</sup> To make the sensors, 0.2–0.6 mL of the whole-cell suspensions containing 1.2–6  $\mu\text{g}$  chlorophyll were immobilized onto Millipore APFD fiber glass filter disks (Bedford, MA.) using a Millipore filtration apparatus and bench vacuum.

### Cell chamber and fluorescence measurements

The cell chamber (Fig. 4) is a closed system aeration apparatus designed to infuse bench air through the fiber glass entrapped biosensor at a constant rate of 200 mL/min. The sensor is housed in the top of the cell chamber on a glass frit. The humidifiers contain water for regulation of the relative humidity in the gas stream. Flow rates were adjusted with needle valves in the rotameters illustrated in Fig. 4, allowing alterations in the flow of air through the toxic agent while maintaining a total flow rate of 200 mL/min and relative humidity of 85%. The absolute flow rate was measured with a soap film flow meter connected to the cell chamber vent. The toxic agent in the U tube was isolated from the clean air flow path by a three-way valve while control fluorescence measurements were made. When the valve was switched, air flowed through the toxic agent tube carrying vapors directly to the sensor.

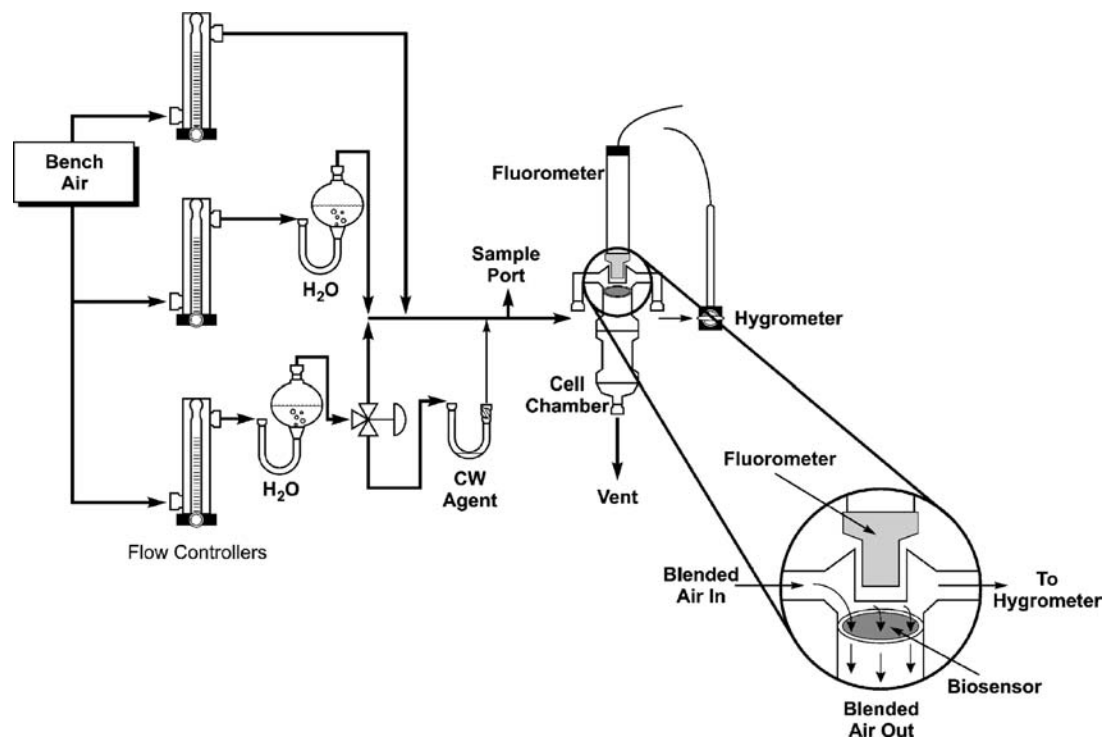


**Fig. 4** Experimental apparatus for exposing algal and cyanobacterial biosensors to airborne CW vapors. Source: From Ref.<sup>[15]</sup>.

Fluorescence induction curves were measured before and during exposure to toxic agents using Opti-Sciences OS1-FL and OS5-FL modulated fluorometers (Tyngsboro, MA). The OS1-FL is a handheld fluorometer with a pulse modulated detection system. The modulation was adjusted so that the minimal fluorescence signal in low background laboratory light ( $F_s$ ) was in the range of 90–150 relative fluorescence units (RFU). A halogen lamp from the actinic light source of a Walz XE-PAM fluorometer illuminated the sensor at an intensity of  $1500 \mu\text{E m}^{-2} \text{sec}^{-1}$  via the OS1-FL fiberoptic cable through a window over the sensor in the top of the cell apparatus. Fluorescence induction curves were recorded every 5 min and data collection for each curve were completed within 10 sec. The OS5-FL fluorometer was fitted with an avalanche photodiode to improve signal-to-noise ratio. The minimal fluorescence signal was set to 130–150 RFU in low laboratory light. Fluorescence induction curves were recorded when the sensors were illuminated from the OS5-FL fiberoptic cable at 5-min intervals (3-sec duration) at an intensity of  $1570 \mu\text{E m}^{-2} \text{sec}^{-1}$ . Data extracted from the fluorescence induction curves were used to calculate  $F_s$ ,  $F_{\text{max}}$  (maximum fluorescence),  $F_v$  (variable fluorescence,  $=F_{\text{max}} - F_s$ ), and the efficiency of Photosystem II photochemistry ( $F_v/F_{\text{max}}$ ).

### Chemical warfare agents and simulants

The mustard agent simulant DBS (300  $\mu\text{L}$ ) and the nerve agent stabilizer TBA (300  $\mu\text{L}$ ) were injected in the bubbler U tube in the cell chamber, and the output vapors were contacted with the algal biosensors. Initial control fluorescence curves were taken without the agents in an air-only gas stream. The airflow through the tube was altered to vary the concentration of the simulant vapor reaching the sensor per unit time. Sensor fluorescence was measured at 5-min intervals during exposure to the toxic agents. Control chlorophyll fluorescence signals emitted from a sensor were compared with signals from the same sensor measured during DBS or TBA exposure. The concentration of the agents in the gas stream was measured on an Alltech  $30 \text{ m} \times 0.25 \text{ mm}$  I.D. capillary column in a Hewlett-Packard 5890 Gas Chromatograph (GC). The detector was a Hewlett-Packard 5971 Series Mass Selective Detector. Standard curves were constructed from solutions of known concentration solubilized in acetone. The initial temperature of the GC temperature ramp program was  $50^\circ\text{C}$ , rising to a temperature of  $150^\circ\text{C}$  ( $10^\circ\text{C}/\text{min}$ ), then  $20^\circ\text{C}/\text{min}$  to a final temperature of  $280^\circ\text{C}$ . In the Applied Chemistry Laboratory, Edgewood Laboratories, Aberdeen Proving Ground, MD, the same cell apparatus was used on experiments with GA, GB, and HD on *Nostoc* and *Chlorella* biosensors.

## RESULTS

### Detection of Chemical Warfare Agents in Water

#### *Chlorella* batch experiments

Fig. 5 illustrates typical raw fluorescence data obtained with healthy naturally occurring algae from the Clinch River and associated parameters that are used to analyze these data. The parameters  $F_{\text{max}}$ ,  $F_s$ , and  $F_v$  ( $=F_{\text{max}} - F_s$ ), as well as their interpretation, are well known in the literature of photosynthesis.<sup>[25]</sup> We were able to detect changes in the photochemical yield of *Chlorella*, defined as  $F_v/F_{\text{max}}$ , at the relatively low chlorophyll concentration of  $0.063 \mu\text{g}/\text{mL}$  (Figs. 6 and 7). Fig. 6 shows the percentage decrease in photochemical yield for DCMU exposure over time. Fig. 7 presents similar data for MPT. After testing and optimizing the experimental setup with laboratory-cultured *Chlorella*, we proceeded to experiment with samples drawn directly from the Clinch and Tennessee Rivers.

#### Freshwater batch experiments

Field samples were drawn from selected locations of the Clinch River, Oak Ridge, TN, and the Tennessee River, Knoxville, TN. Fig. 8 presents the decrease in photochemical yield of toxic agent-exposed water samples from the Clark Center Recreation Park. Fig. 9 presents the decrease in photochemical yield for samples drawn from the Tennessee River. Fig. 10 contains

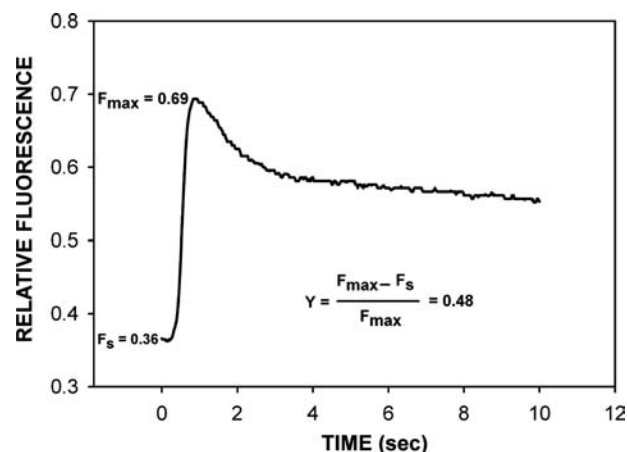


**Fig. 5** A typical fluorescence induction curve recorded from naturally occurring algae in untreated Clinch River (Clark Center Recreation Park) water, illustrating the basic data output from the Walz XE-PAM fluorometer. Data extracted from fluorescence induction curves provided the values of  $F_s$  and  $F_{\text{max}}$  that were used to calculate the variable fluorescence,  $F_v = F_{\text{max}} - F_s$ , and the photochemical yield ( $Y$ ),  $F_v/F_{\text{max}}$ . Source: From Ref.<sup>[3]</sup>.

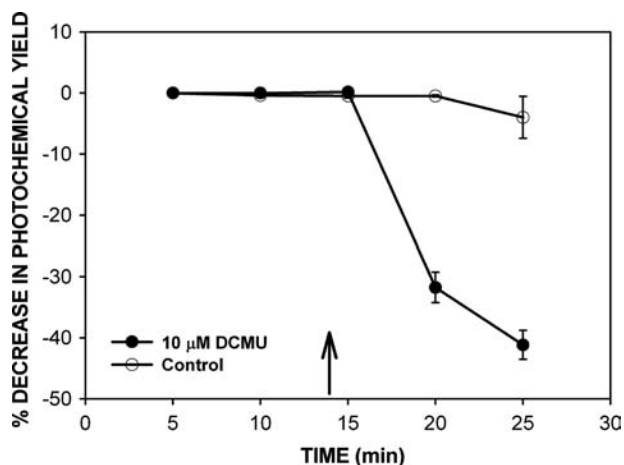


**Fig. 6** Decrease in photochemical yield in laboratory-grown *Chlorella vulgaris*. The first data point was taken after 5 min of dark adaptation. DCMU was added to the sample at 14 min, and fluorescence yields were measured at 15, 20, and 25 min. Yields were computed from two runs and are expressed as means  $\pm$  1 S.D. *Source:* From Ref.<sup>[3]</sup>.

paraquat data for Tennessee River water samples. Following injection of paraquat into the cuvette, the sample was exposed to a light intensity of  $50 \mu\text{E m}^{-2} \text{sec}^{-1}$  for 10 min. Unlike the herbicide DCMU, which binds directly to the reducing site of the PSII reaction center (in the presence or absence of light), the destructive action of paraquat (methyl viologen) results from its reduction by PSI. Reduced paraquat reacts with dissolved molecular oxygen, which leads to the formation of superoxide anions and hydrogen peroxide, both of which are toxic to the cell.

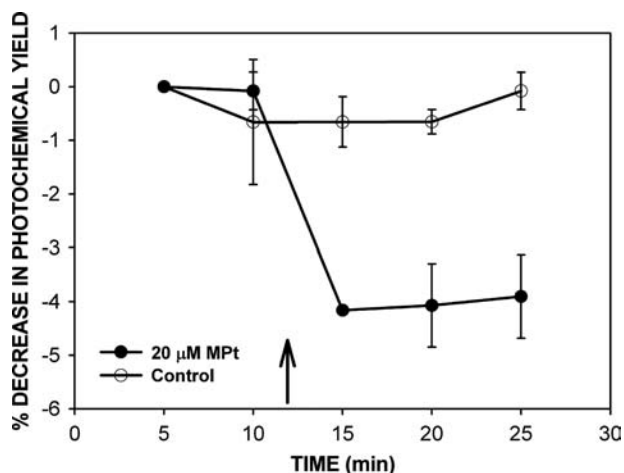


**Fig. 7** Time-dependent values of the PSII photochemical yield of *Chlorella vulgaris* in the presence of MPt (plus accompanying control). The first data points were taken after 5 min of dark adaptation. As indicated by the vertical arrow, MPt was added to the sample at 12 min, and fluorescence was measured at 15, 20, and 25 min. Yields were computed from two runs and are expressed as means  $\pm$  1 S.D. *Source:* From Ref.<sup>[3]</sup>.

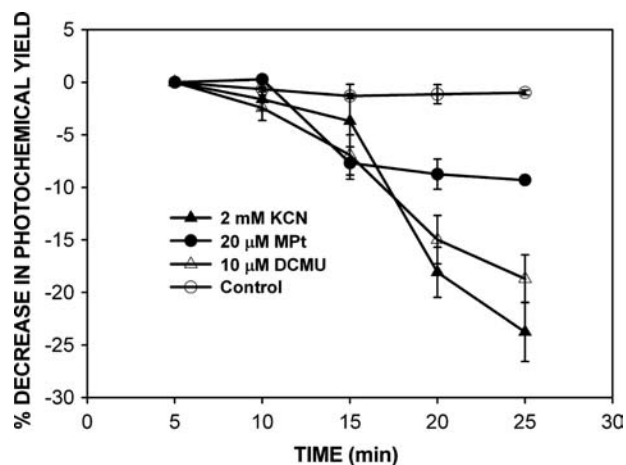


**Fig. 8** Decrease in photochemical yield of naturally occurring algae in Clinch River (Clark Center Recreation Park) water. The first data points were taken after 5 min of dark adaptation. MPt was added at 12 min, and KCN and DCMU were added to the sample at 14 min. Fluorescence was measured at 15, 20, and 25 min. These are three separate experiments (plus control), with the data values normalized to their respective values at 5 min. Yields were computed from three experimental runs and two control runs. Results are expressed as means  $\pm$  1 S.D. *Source:* From Ref.<sup>[3]</sup>.

### Continuous experiments

Following the batch experiments, the standard fluorescence cuvette in the Walz fluorometer was replaced with the flow-through model. The cuvette inlet was connected to a glass-bottle reservoir that contained the water samples, and the outlet drained to waste.

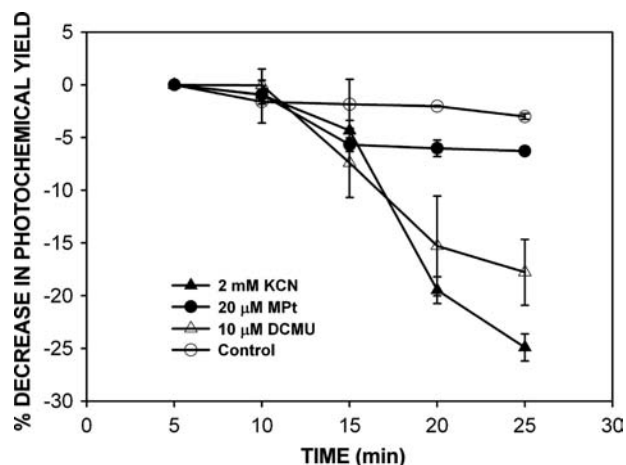


**Fig. 9** Decrease in the photochemical yield of naturally occurring algae in Tennessee River water. The first data point was recorded after 5 min of dark adaptation. MPt was added at 12 min, and KCN and DCMU were added to the sample at 14 min. Fluorescence was measured at 15, 20, and 25 min. Yields were computed from three experimental runs and two control runs. Results are expressed as means  $\pm$  1 S.D. *Source:* From Ref.<sup>[3]</sup>.

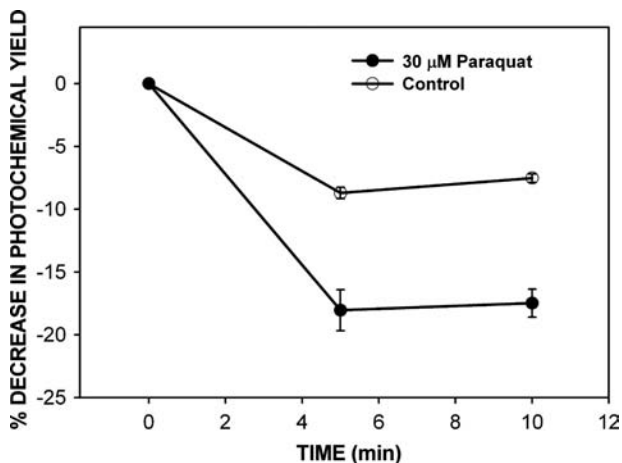


**Fig. 10** Decrease in photochemical yield in the Tennessee River biosensor. Paraquat was added to the sample cuvette at 10 min, and fluorescence was measured at 5 and 10 min after an illumination period of 10 min at 50  $\mu$ E. Control runs were performed in a similar manner with the addition of deionized water. Yields were computed from four experimental runs and two control runs. Results are expressed as means  $\pm$  1 S.D. *Source:* From Ref.<sup>[3]</sup>.

This experimental arrangement allowed continuous monitoring and replacement of water samples in a manner similar to that for the contemplated operation of a real-world biosensor system. Continuous experiments were performed with samples drawn from the Clark Center Recreation Park (Fig. 11).

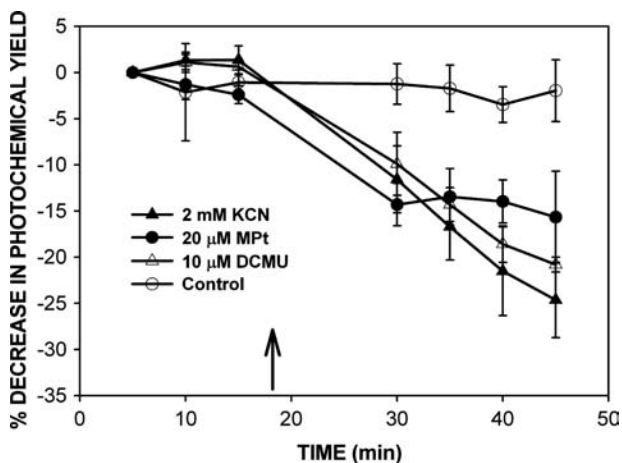


**Fig. 11** Decrease in photochemical yield of naturally occurring algae in Clinch River (Clark Center Recreation Park) water. The first data points were recorded after 5 min of dark adaptation. MPT, KCN, and DCMU were added at 18 min (indicated by arrow), and fluorescence data were recorded at 30, 35, 40, and 45 min. All yields were computed from three runs, except for MPT yields, which were computed from data collected from two runs. Results are expressed as means  $\pm$  1 S.D. *Source:* From Ref.<sup>[3]</sup>.

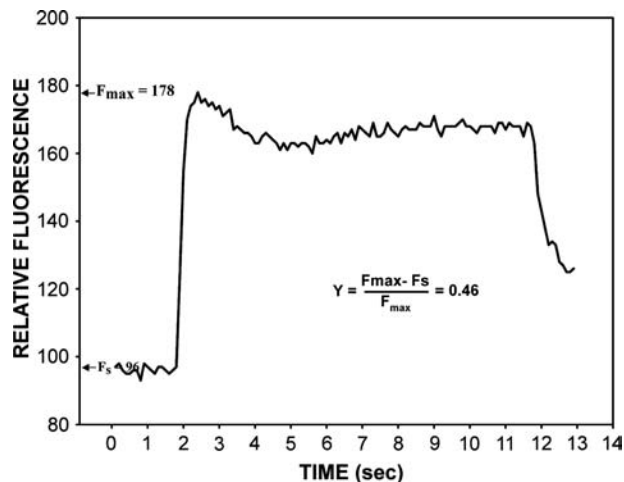


**Fig. 12** Typical fluorescence induction curve recorded from the cyanobacterial sensor *Nostoc commune*. *Source:* From Ref.<sup>[15]</sup>.

## Detection of Chemical Warfare Agents in Air

### Sensor response to dBS

A typical fluorescence induction curve of the biosensor *N. commune* (6  $\mu$ g chlorophyll *a*) is shown in Fig. 12. The parameters indicated on the curve are used to evaluate the photosynthetic capacity of the algae or cyanobacteria. The fluorescence yield ( $Y = 0.46$  for the data of Fig. 12) represents the total PSII photochemical efficiency of the sensor under control conditions with no toxic agent present.

In Fig. 13, *Nostoc* sensors were placed in the cell chamber in an air stream flowing at 200 mL/min. At

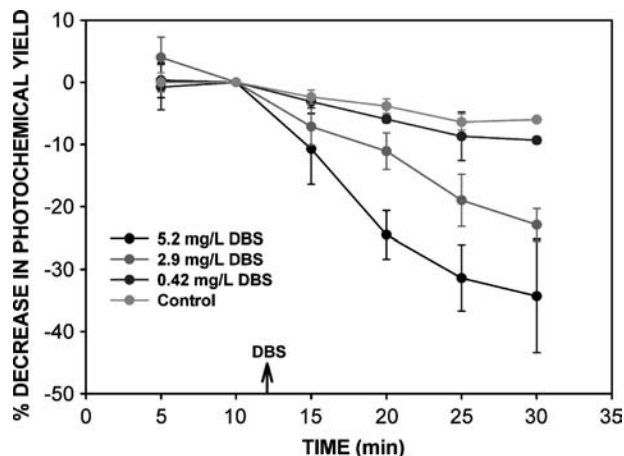


**Fig. 13** *Nostoc* sensor. DBS concentration-dependent change in photochemical yield. DBS was injected into the carrier gas stream at 12 min and was measured at 15, 20, 25, and 30 min. Yields were computed from data collected from three runs and are expressed as means  $\pm$  1 S.D. *Source:* From Ref.<sup>[15]</sup>.

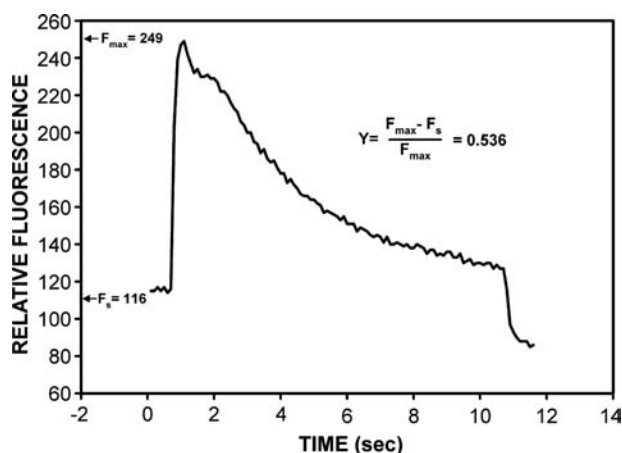


Fig. 14 Typical fluorescence induction curve from the algal biosensor *Chlorella vulgaris*. Source: From Ref.<sup>[15]</sup>.

5-min intervals, light from the OS1-FL fluorometer illuminated the sensors for 10 sec and fluorescence induction curves were recorded. Flow rates through the DBS U tube were adjusted to obtain 0.42, 2.9, and 5.2 mg/L DBS in a constant-flow air stream of 200 mL/min. Fig. 13 presents the change in yield of PSII photochemistry with DBS in the air stream. Fig. 14 shows a typical fluorescence induction curve for the *C. vulgaris* (1.2 µg total chlorophyll) sensor. *Chlorella* fluorescence, following exposure to DBS (5.2 mg/L) under the same conditions as the *Nostoc* sensor, is presented in Fig. 15.

#### Biosensor response to TBA

The response of the *Nostoc* (6 µg chlorophyll *a*) sensor to TBA was tested in the cell chamber by recording fluorescence induction curves every 5 min during

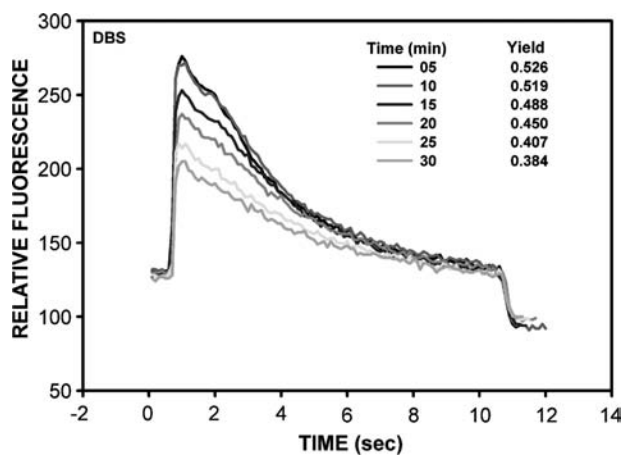


Fig. 15 Time-dependent fluorescence induction curves from the *Chlorella* sensor during exposure to DBS. DBS entered the air stream at 12 min. Source: From Ref.<sup>[15]</sup>.

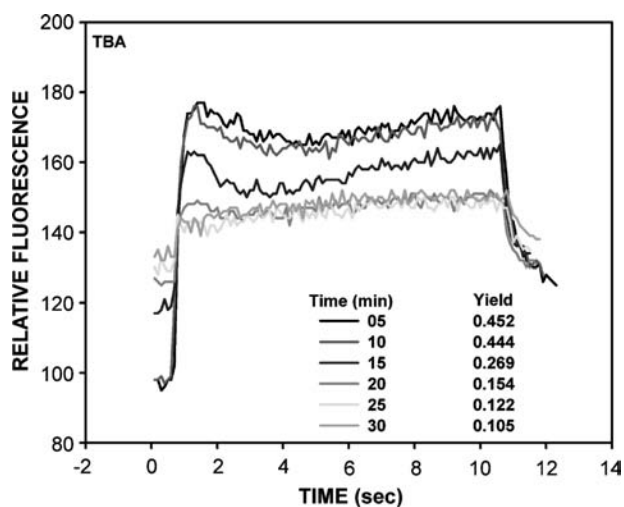


Fig. 16 Fluorescence induction curves from the *Nostoc* sensor during exposure to TBA. TBA exposure began 12 min into the run. Source: From Ref.<sup>[15]</sup>.

contact of the sensor with TBA (Fig. 16). Dose-response curves (Fig. 17) for 7.4, 248, and 642 µg/L TBA showed a good correlation between TBA concentration and change in yield.

#### Sensor response to live chemical warfare agents

In the Applied Chemistry Laboratory, Edgewood Laboratories, Aberdeen Proving Ground, MD, *Nostoc* and *Chlorella* sensors were contacted with GA (9, 10, and 11 µg/L), GB (6, 7, and 21 µg/L), and HD (7, 8,

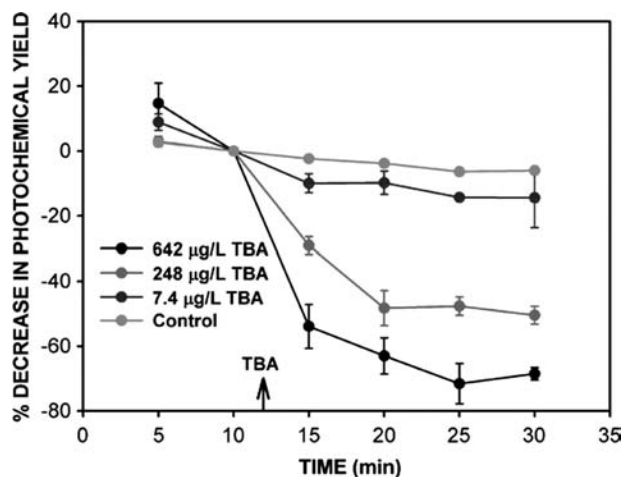
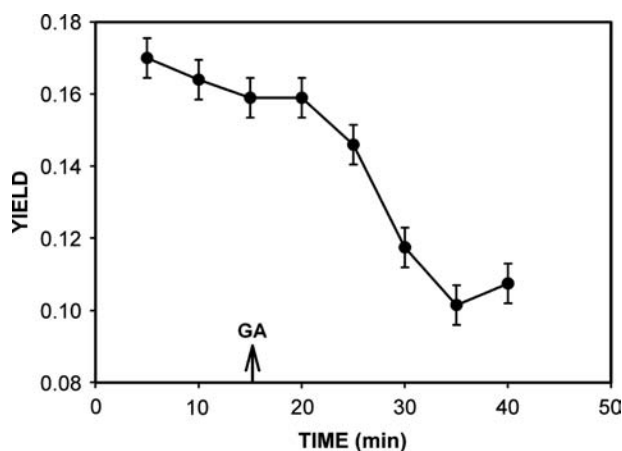


Fig. 17 TBA concentration-dependent decreases in photochemical yields of the *Nostoc* sensor with time of exposure. TBA was injected in the gas stream at 12 min and fluorescence was measured at 15, 20, 25, and 30 min. Yields were computed from data collected from three runs of 642 and 7.4 µg/L TBA and two runs of 248 µg/L. Results are expressed as means  $\pm$  1 S.D. Source: From Ref.<sup>[15]</sup>.



**Fig. 18** Fluorescence yields vs. time from the *Nostoc* sensor, recorded before (control) and after exposure to 9 µg/L GA. Source: From Ref.<sup>[15]</sup>.

17, and 23 µg/L). Fig. 18, shows the average of two runs using GA (9 µg/L) on the *Nostoc* sensor. Changes in the PSII photochemical efficiency of the *Chlorella* sensor were apparently not affected by exposure to GA at the stated levels, but preliminary data do suggest differences in the overall kinetic time profile, especially near the end of the respective traces between sample and control (fluorescence induction curves not shown). No changes in the fluorescence induction curves of either sensor were observed with GB or HD at the stated concentrations.

## DISCUSSION

### Detection of Chemical Warfare Agents in Water

Fluorescence induction curves can be used as real-time diagnostic assays for exposure of photosynthetic microorganisms to environmental stress. The availability of portable commercial fluorimeters has simplified the use of chlorophyll fluorescence measurements under field conditions to study the effects of toxic agents on photosynthetic organisms. Fluorescence techniques have been refined over recent years, and dark-adapted measurements made in combination with those in the light now allow extremely detailed analyses of photosynthetic performance in situ.<sup>[41]</sup> Because of their sensitivity and reliability for measurement of in vivo biological activity, these techniques have led to the development and refinement of environmental biosensors. Our results demonstrate that naturally occurring freshwater algae can be used as biosensor material for the detection of toxic agents in sunlight-exposed primary drinking water supplies. These agents block electron transport, impair light energy transfer, or generate toxic secondary photoproducts,

all of which provide signals that can trigger an alarm. Our results showed that the tissue-based biosensors experienced a decrease in photochemical yield when exposed to MPt, KCN, paraquat, and DCMU. A detectable effect was observed in every freshwater sample tested.

### Detection of Chemical Warfare Agents in Air

Fluorescence induction curves from photosynthetic organisms are good indicators of the presence of environmental stresses surrounding the organisms and the effects those stresses have on the photosynthetic apparatus.<sup>[41]</sup> In this respect, fluorometric assays form a potentially attractive approach to the development of environmental biosensors because they are rapid, sensitive, non-invasive, and non-destructive monitors of in vivo biological activity. The sensors are relatively rugged and mobile, and may be stored and transported for use in the field. Exposing the algal and cyanobacterial sensors to CW agents and simulants can impair energy migration in the chlorophyll antenna lattice and electron transport reactions within the photosynthetic membrane, thereby altering the normal fluorescence induction curve in measurable and predictable ways. Sensors in a gas stream containing DBS and TBA showed concentration-dependent decreases in the efficiency of PSII photochemistry. Yields measured during DBS contact decreased in both sensors. The yield reduction in the *Nostoc* sensor was due solely to an increase in minimal fluorescence,  $F_s$ , whereas that of the *Chlorella* sensor was due to a decrease in  $F_{max}$ . In both sensors the loss of fluorescence was dependent on the concentration of the toxic agent contacting the sensors. The different responses of the two sensors are related to differences in the structure of their photosynthetic apparatus. Minimal fluorescence in algae arises only from antennae pigments. Cyanobacterial minimal fluorescence, however, is emitted not only from antennae but also from PSII and possibly PSI reaction centers and photosynthetic pigments other than chlorophyll.<sup>[24]</sup> Ögren and Sjöström<sup>[42]</sup> credited the increase in minimal fluorescence observed following photoinhibition of willow leaves to a decrease in the efficiency of PSII photochemistry. A decrease in minimal fluorescence would indicate enhanced non-light-induced quenching in the antennae of PSII, but an increase is directly related to the photochemical state of the reaction center itself. The decrease in maximal fluorescence seen in the algal sensor reflects an increased quenching of fluorescence by non-photochemical quenching. Genty and colleagues<sup>[43]</sup> have determined that the quantum yield of fluorescence can be calculated from measured parameters of the induction curve and, as noted above, is a measure of both PSII reaction center efficiency and total



availability of reaction center sites for electron transport. Rizzuto and associated researchers<sup>[8]</sup> showed that the activity of their PSII particle sensor was reduced when herbicides contacted it in aqueous solution. Merz and coinvestigators<sup>[6]</sup> analyzed the effect of triazine and phenylurea herbicides on the kinetics of chlorophyll fluorescence induction curves from isolated plant chloroplast biosensors in water. DBS and TBA vapors may damage sensor PSII reaction sites and induce non-photochemical fluorescence quenching. Reaction centers that remain partially closed or are no longer functional will report higher minimal fluorescence compared to non-treated controls.

Contacting the algal and cyanobacterial biosensors with the real CW agents HD, GA, and GB can produce results analogous to the simulants; however, changes in total fluorescence yields were evident only with GA at the concentrations used. The concentrations of the CW agents were lower than the simulants, indicating that sensor sensitivity is a factor for HD and GB. This, however, is not true for GA, because it showed alterations in the fluorescence induction curves with both sensors as well as characteristic decreases in fluorescence quantum yield. The sensor responses show that they are particularly sensitive to GA and not to nerve agents in general. Previous experiments in our laboratory with these sensors have shown a good response to cyanide, a key component in the structure of GA (Sanders and Greenbaum, unpublished data). Jones and Hoegh-Guldberg<sup>[17]</sup> examined the effect of cyanide on the photosynthesis of algae using chlorophyll fluorescence techniques. Cyanide reduced the maximum quantum yield of PSII. The effect was light-dependent, indicative of photoreactions mediated by cyanide inhibition of NADP<sup>+</sup> and ATP production and light-driven over stimulation of the electron transport chain. Photoinhibition may also contribute to damage to the PSII reaction centers when biosensors are exposed to GA.

## CONCLUSION

### Detection of Chemical Warfare Agents in Water

The data presented in this entry indicate that biosensors based on fluorescence induction curves of naturally occurring freshwater algae can be used to detect methyl parathion, cyanide, paraquat, and DCMU in primary water supplies under appropriate experimental conditions. In the context of current state-of-the-art biosensor research, they are unique: in the case of sunlight-exposed drinking water, the biosensors occur naturally in the medium to be protected. When combined with encrypted telecommunication data and a database-lookup library containing

pertinent data for healthy algae, this approach to protection of sunlight-exposed primary drinking water supplies may be of practical value under real-world conditions.

### Detection of Chemical Warfare Agents in Air

The data presented in this entry indicate that biosensors based on fluorescence induction curves of the cyanobacterium *N. commune* and the green alga, *C. vulgaris*, can be used to detect GA and CW simulants under appropriate experimental conditions. In the context of current biosensor state-of-the-art research they are relatively inexpensive to prepare and reasonably rugged. Moreover, they can be integrated into commercially available handheld fluorescence instrumentation for field applications. However, in our hands at least, they should not be thought of as ultrasensitive, early warning sensors. Their presently contemplated utility lies in the fact that they can be constructed to withstand inertial forces of launching or dropping into suspected danger zones and, with encrypted telecommunication data transmission, provide a survey of potential hazards in remote locations at levels that are expected to be encountered under real-world combat conditions.

## ACKNOWLEDGMENTS

“Detection of Chemical Warfare Agents in Water” (from Ref.<sup>[3]</sup>).

The authors thank Drs. John W. Barton and Brian H. Davison for their assistance with the methyl parathion experiments. We also thank Dr. K. Thomas Klasson for designing spreadsheets for data analysis, Ms. Angela R. Jones and Ms. Patricia A. Wilson for secretarial support, and Drs. Barton and Marsha K. Savage for reviewing the manuscript. This research was supported by the Tissue-Based Biosensors Program, Defense Advanced Research Projects Agency, under MIPR No. 99-H250 with Oak Ridge National Laboratory. It was also supported by the U.S. Department of Energy Office of Basic Energy Sciences. Oak Ridge National Laboratory is managed by UT-Battelle, LLC, for the U.S. Department of Energy under contract DE-AC05-00OR22725.

“Detection of Chemical Warfare Agents in Air” (from Ref.<sup>[15]</sup>).

The authors thank the staff of the Edgewood Applied Chemistry Laboratory, Aberdeen Proving Ground, MD, K. Ong, T. Longworth, J. Barnhouse, and J. Baranoski for their help in working with CW agents. We also thank A. Jones for secretarial support. This research was supported by the Tissue-Based

Biosensors Program, Defense Advanced Research Projects Agency (DARPA) under MIPR No. 99-H250 with Oak Ridge National Laboratory. It was also supported by the U.S. Department of Energy Office of Basic Energy Sciences. Oak Ridge National Laboratory is managed by UT-Battelle, LLC for the Department of Energy under contract DE-AC05-00OR22725.

## ABBREVIATIONS

DCMU	<i>N</i> '-(3,4-dichlorophenyl)- <i>N,N</i> -dimethylurea
KCN	Potassium cyanide
MPt	Methyl parathion
$F_o$	Steady-state fluorescence in ambient or dim light
$F_{max}$	Maximum fluorescence following a saturating pulse of light
$F_v$	Variable fluorescence
PSII	Photosystem II reaction center
DIMP	Diisopropyl methylphosphonate
CW	Chemical warfare
DBS	Dibutylsulfide
GA	Tabun
GB	Sarin
HD	Distilled sulfur mustard agent
TBA	Tributylamine
ELISA	Enzyme-linked immunosorbent assay
PAM	Pulse amplitude modulated fluorometry
RFU	Relative fluorescence units

## REFERENCES

- Palmer, C.M. *Algae in Water Supplies*; Public Health Service Publication No. 657; U.S. Department of Health, Education, and Welfare: Cincinnati, OH, 1959.
- Happey-Wood, C.M. Ecology of freshwater planktonic green algae. In *Growth and Reproductive Strategies of Freshwater Phytoplankton*; Sandgren, C.D., Ed.; Cambridge University Press: New York, 1988; 175–226.
- Rodriguez, M., Jr.; Sanders, C.A.; Greenbaum, G. Biosensors for rapid monitoring of primary-source drinking water using naturally-occurring photosynthesis. *Biosens. Bioelectron.* **2002**, *17* (10), 843–849.
- Guidelines for Canadian Drinking Water Quality. Ministry of Supply and Services. Ottawa, Canada, 1996.
- Guidelines for Chemical Warfare Agents in Military Field Drinking Water. National Research Council, National Academy Press: Washington, DC, 1995.
- Merz, D.; Geyer, M.; Moss, D.A.; Ache, H.J. Chlorophyll fluorescence biosensor for the detection of herbicides. *Fresenius' J. Anal. Chem.* **1996**, *354* (3), 299–305.
- Frense, D.; Muller, A.; Beckmann, D. Detection of environmental pollutants using optical biosensor with immobilized algae cells. *Sens. Actuators, B* **1998**, *51* (1–3), 256–260.
- Rizzuto, M.; Polcaro, C.; Desiderio, C.; Koblizek, M.; Pilloton, R.; Giardi, M.T. In *Herbicide Monitoring in Surface Water Samples with a Photosystem-II Based Biosensor*, Proceedings of the 2nd Workshop on Chemical Sensors and Biosensors; Mazzei, F., Pilloton, R., Eds.; E.N.E.A.: Rome, 2000; 346–357.
- Koblizek, M.; Masojidek, J.; Komenda, J.; Kucera, J.; Pilloton, R.; Mattoo, A.K.; Giardi, M.T. A sensitive photosystem II-based biosensor for detection of a class of herbicides. *Biotechnol. Bioeng.* **1998**, *60* (6), 664–669.
- Pogacnik, L.; Franko, M. Determination of organophosphate and carbamate pesticides in spiked samples of tap water and fruit juices by a biosensor with photo-thermal detection. *Biosens. Bioelectron.* **1999**, *14* (6), 569–578.
- Mallat, E.; Barzen, C.; Abuknesha, R.; Gauglitz, G.; Barcelo, D. Fast determination of paraquat residues in water by an optical immunosensor and validation using capillary electrophoresis-ultraviolet detection. *Anal. Chim. Acta* **2001**, *427* (2), 165–171.
- Campanella, L.; Cubadda, F.; Sammartino, M.P.; Saoncella, A. An algal biosensor for the monitoring of water toxicity in estuarine environments. *Water Res.* **2001**, *35* (1), 69–76.
- Naessens, M.; Leclerc, J.C.; Tran-Minh, C. Fiber optic biosensor using *Chlorella vulgaris* for determination of toxic compounds. *Ecotoxicol. Environ. Saf.* **2000**, *46* (2), 181–185.
- Khordagui, H.K. Fate and control of nerve chemical warfare agents in the desalination industry of the Arabian–Persian Gulf. *Environ. Int.* **1995**, *21* (4), 363–379.
- Sanders, C.A.; Rodriguez, M., Jr.; Greenbaum, E. Stand-off tissue-based biosensors for the detection of chemical warfare agents using photosynthetic fluorescence induction. *Biosens. Bioelectron.* **2001**, *16* (7–8), 439–446.
- Degenhardt-Langelaan, C.E.A.M.; Kientz, Ch.E. Capillary gas chromatography analysis of nerve agents using large volume injections. *J. Chromatogr., A* **1996**, *723* (1), 210–214.
- Jones, R.J.; Hoegh-Guldberg, O. Effects of cyanide on coral photosynthesis: Implications for identifying the cause of coral bleaching and for assessing the environmental effects of cyanide fishing. *Mar. Ecol., Prog. Ser.* **1999**, *177*, 83–91.
- Singh, B.; Madhusudhanan, S.; Dubey, V.; Nath, R.; Rao, N.B.S.N. Active carbon for removal of toxic chemicals from contaminated water. *Carbon* **1996**, *34* (3), 327–330.
- Wang, J.; Chatrathi, M.P.; Mulchandani, A.; Chen, W. Capillary electrophoresis microchips for separation and detection of organophosphate nerve agents. *Anal. Chem.* **2001**, *73* (8), 1804–1808.
- Wang, J.; Tian, B.; Sahlin, E. Micromachined electrophoresis chips with thick-film electrochemical detectors. *Anal. Chem.* **1999**, *71* (23), 5436–5440.
- Lakso, H.A.; Ng, W.F. Determination of chemical warfare agents in natural water samples by solid-phase microextraction. *Anal. Chem.* **1997**, *69* (10), 1866–1872.

22. Su, P.-G.; Huang, S.-D. Determination of organophosphorus pesticides in water by solid-phase micro-extraction. *Talanta* **1999**, *49* (2), 393–402.
23. Krause, G.H.; Weis, E. Chlorophyll fluorescence and photosynthesis: the basics. *Annu. Rev. Plant Physiol.* **1991**, *42*, 313–349.
24. Campbell, D.; Hurry, V.; Clarke, A.K. Chlorophyll fluorescence analysis of cyanobacterial photosynthesis and acclimation. *Microbiol. Mol. Biol. Rev.* **1998**, *62* (3), 667–683.
25. Schreiber, U.; Bilger, W.; Neubauer, C. Chlorophyll Fluorescence as a Noninvasive Indicator for Rapid Assessment of *in vivo* Photosynthesis. In *Ecophysiology of Photosynthesis*; Schulze, E.D., Caldwell, M.M., Eds.; Springer-Verlag: Heidelberg, 1994; 49–70.
26. Falkowski, P.G.; Raven, J.A. *Aquatic Photosynthesis*; Blackwell Science: Malden, MA, 1997.
27. Potts, M.; Friedmann, E.I. Effects of water stress on cryptoendolithic cyanobacteria from hot desert rocks. *Arch. Microbiol.* **1981**, *130* (4), 267–271.
28. Potts, M. Desiccation tolerance of prokaryotes. *Microbiol. Rev.* **1994**, *58* (4), 755–805.
29. Potts, M.; Bowman, M.A. Sensitivity of *Nostoc commune* UTEX 584 (Cyanobacteria) to water stress. *Arch. Microbiol.* **1985**, *141* (1), 51–56.
30. Potts, M. The anhydrobiotic cyanobacterial cell. *Physiol. Plant.* **1996**, *97*, 788–794.
31. Munro, N.B.; Ambrose, K.R.; Watson, A.P. Toxicity of the organophosphate chemical warfare agents GA, GB, and VX: implications for public protection. *Environ. Health Perspect.* **1994**, *102* (1), 18–38.
32. Klein, A.K.; Nasr, M.L.; Goldman, M. The effects of *in vitro* exposure to the neurotoxins sarin (GB) and soman (GD) on unscheduled DNA synthesis by rat hepatocytes. *Toxicol. Lett.* **1987**, *38* (3), 239–249.
33. Rebiere, D.; Bordieu, C.; Pistre, J. Improvement of surface acoustic wave gas sensor response time using neural network pattern recognition. *Sens. Actuators, B* **1995**, *25* (1–3), 777–780.
34. Dworzanski, J.P.; Kim, M.G.; Snyder, A.P.; Arnold, N.S.; Henk, L.C. Performance advances in ion mobility spectrometry through combination with high speed vapor sampling, preconcentration and separation techniques. *Anal. Chim. Acta* **1994**, *293* (3), 219–235.
35. Kientz, C.E. Chromatography and mass spectrometry of chemical warfare agents, toxins and related compounds: state of the art and future prospects. *J. Chromatogr.* **1998**, *814* (1–2), 1–23.
36. Gil, G.C.; Mitchell, R.J.; Chang, S.T.; Gu, M.B. A biosensor for the detection of gas toxicity using a recombinant bioluminescent bacterium. *Biosens. Bioelectron.* **2000**, *15* (1–2), 23–30.
37. Naessens, M.; Tran-Minh, C. Whole-cell biosensor for direct determination of solvent vapours. *Biosens. Bioelectron.* **1998**, *13* (3–4), 341–346.
38. Naessens, M.; Tran-Minh, C. Biosensor using immobilized *Chlorella* microalgae for determination of volatile organic compounds. *Sens. Actuators, B* **1999**, *59* (2–3), 100–102.
39. Lee, J.I.; Karube, I. Development of a biosensor for gaseous cyanide in solution. *Biosens. Bioelectron.* **1996**, *11* (11), 1147–1154.
40. Wellburn, A.R.; Lichtenthaler, H. Formulae and program to determine total carotenoids and chlorophylls *a* and *b* of leaf extracts in different solvents. In *Advances in Photosynthesis Research*; Sybesma, C., Ed.; Martinus Nijhoff: Dordrecht, 1984; Vol. II, 9–12.
41. Maxwell, K.; Johnson, G.N. Chlorophyll fluorescence—a practical guide. *J. Exp. Bot.* **2000**, *51* (345), 659–668.
42. Ögren, E.; Sjöström, M. Estimation of the effect of photoinhibition on the carbon gain in leaves of a willow canopy. *Planta* **1990**, *181* (4), 560–567.
43. Genty, B.; Briantais, J.M.; Baker, N.R. The relationship between the quantum yield of photosynthetic electron transport and quenching of chlorophyll fluorescence. *Biochim. Biophys. Acta* **1989**, *990* (1), 87–92. Elsevier.
44. Sime, R.J. *Physical Chemistry: Methods, Techniques, and Experiments*; Saunders College Publishing: Philadelphia, 1990; 136–146.

# Colloid Systems: Micelles and Nanocrystals

**B.L.V. Prasad**

*Materials Chemistry Division, National Chemical Laboratory, Pune, India*

**Savka I. Stoeva**

*Department of Chemistry, Kansas State University, Manhattan, Kansas, U.S.A.*

## INTRODUCTION

Colloids, which are basically a dispersion of one of the states of matter, i.e., gas, liquid or solid, in the other, are important for a variety of reasons. From natural colloids such as milk, blood, and egg white, etc. to synthetic ones such as paints, inks, creams, sprays, and fire extinguishers, we encounter colloidal systems daily in one way or the other. Generally, the usage of the term colloids would refer to the dispersion of particles (usually polydisperse) in the size range  $1\ \mu\text{m}$ – $1\ \text{nm}$  in another medium without any order. The class of colloids called micelles are formed when molecules consisting of long hydrocarbon tails and polar head groups self-assemble into an ordered structure beyond a critical concentration. Another class of colloid systems, where the particles are highly monodisperse in nature especially in the size range of few nanometer ( $1\ \text{nm} = 10^{-9}\ \text{m}$  or  $10^{-7}\ \text{cm}$ ), have recently attracted renewed interest because of the enormous promise these materials hold for future technologies. These materials—generally called nanoparticles or, if they consist single crystalline phase, nanocrystals—are envisioned to be the building blocks of every new technology from here onward. The control of size and shape of these particles with a penchant to form long-range ordered structures is expected to be very crucial for the fields of electronics, optoelectronics, and smart chips for future devices. Unlike the traditional atomic or molecular crystal lattices, these superlattices consist of a two-tier structure. Here each nanocrystal results from the regular arrangement of the atoms or molecules of the constituent material, in which the crystal sizes are restricted to a few nanometers only. These nanocrystals then become the building blocks of the superlattices. The properties of the resulting superlattices are controlled both by the constituent materials and their structural order.

The purpose of this entry is to introduce the reader to the field of colloids, focusing on two subclasses of these systems—micelles and nanocrystals and the

superlattices of nanocrystals. Among these, micelles have been studied for a long period of time and there are excellent reviews and books that are dedicated to these systems.<sup>[1]</sup> Hence only a brief introduction to these systems is given here. The reader is encouraged to refer to more elaborate treatises on this subject for further details. On the other hand, nanocrystals and their superlattices are relatively new entries to this field, and a great deal of attention is being given to them recently because of their applications to various fields, either already established or envisioned. Here we present the recent advances in the synthesis of monodisperse nanocrystals and their arrangement into 2-D or 3-D superlattices. Factors governing their arrangement into different types of superlattices are presented and discussed.

## COLLOIDS

We start this entry by giving a brief introduction to colloids. Usage of colloids by mankind dates back to the earliest traces of civilization.<sup>[1]</sup> Evidences of colloidal pigments were found in the stone-age paintings in the Lascaux caves of France and the written records of Egyptian Pharaohs. Many of the initial technological processes such as paper making, pottery making, and the making of soap and cosmetics, involved the manipulation of colloidal systems. However, the establishment of colloid science as a scientific discipline can be traced back only to the mid-nineteenth century. Initially, Francesco Selmi called these processes “Pseudo Solutions” while he was studying the clear or slightly turbid solutions of silver chloride, sulfur, and Prussian Blue in water. Faraday’s extensive studies on gold sols in water are another classical example of colloidal systems, although he never used the term “colloid.” He observed that the dispersion of the solid gold particles in water is kinetically stabilized, and that once they are coagulated, the process cannot be reversed. On the other hand, if properly prepared,

these colloidal systems are stable for years, and some of the colloidal systems that Faraday himself has prepared are, in fact, still on display in the British Museum in London.

The word “colloid” was first introduced by Thomas Graham in 1860s,<sup>[2]</sup> while he was studying diffusion. He classified materials as crystalloids—substances which, in water solution, would easily diffuse through a membrane, and colloids (after a Greek word for glue)—substances which have very slow diffusion rates through the membranes. From the slow diffusion rates of these materials, he deduced that the particles of these materials must be very large, at least on the order of  $10^{-7}$  cm (1 nm in modern terms). On the other hand, the failure for sedimentation implied a minimum size limit of  $10^{-4}$  cm (1  $\mu$ m). In fact, his size range for colloidal domain is still valid today.

Apart from their size, which prevents individual colloidal particles from sedimentation, there are several other parameters that stabilize these from the close approach of two colloidal particles and consequent collapse into a single particle, called coagulation. For example, there might be a protective film that stabilizes the interface and that cannot be penetrated when the two particles touch each other. Another major source of kinetic stability is the existence of an electric charge on the particle surfaces. Because of this, particles having similar charges oppose each other, thereby preventing coagulation. The charges are usually a result of adsorption of ions from the solution due to the defect sites on the surfaces of the particles. Surface charges on the particle are usually compensated by an array of ions of opposite charge from solution, forming an electric double layer.<sup>[3,4]</sup>

The principal character of colloids is the greater surface area they possess compared to their bulk material counterparts. For example, a material is in the form of a sphere with a radius of 1 cm. It has a surface area of  $4\pi\text{cm}^2$ , whereas a 1-nm radius sphere of the same material has a surface area of  $4\pi \times 10^{-14}\text{cm}^2$ . Therefore if the 1-cm sphere is cut and redispersed as 1021 spheres with a radius of 1 nm, the total surface area would increase from  $4\pi\text{cm}^2$  to  $4\pi \times 10^7\text{cm}^2$ . Another important feature is the significant increase in the surface-to-volume ratio. The surface to volume ratio of a sphere is equivalent to  $3/r(\frac{4\pi r^2}{4/3\pi r^3})$ . For a 1-cm radius sphere, the ratio is  $3\text{cm}^{-1}$ , whereas for a 1-nm sphere the ratio is  $3 \times 10^{-7}\text{cm}^{-1}$ , indicating the importance of surface species in the colloidal particles.

The different classes of colloids that we encounter are sols (dispersion of solid in liquid), emulsion (liquid in liquid), aerosols (liquids or solids in gases), and foams (gases in liquids or solids). In general, sols are further classified as lyophilic (solvent liking) and lyophobic (solvent disliking).

A number of techniques can be used to study the colloidal systems. Because colloidal particles are substantially smaller than the wavelength of light, these could be studied by scattering techniques. In 1924, Svedberg invented the ultracentrifuge, which can cause sedimentation in colloidal sols at observable rates. From these rates, the particle sizes and masses could be accurately determined. The electron microscope is another valuable tool in viewing the colloidal particles.

## MICELLES

One of the most extensively studied colloidal systems is micelles.<sup>[5]</sup> Micelles result from the self-assembly of surfactants in a dispersion medium. As the name implies, surfactants are species accumulating at the interface of two fluids. A typical surfactant consists of a long hydrocarbon tail and a polar head group. The long hydrocarbon tail favors hydrocarbon or other non-polar solvents, while the polar head group preferentially dissolves in a polar solvent. The best examples of such compounds are the sodium salts of the long alkylchain fatty acids, which are extensively used in soaps. In aqueous solutions, the solubility of the surfactants is conferred by their polar head groups, usually either cationic or anionic. As the surfactant concentration increases, these molecules try to cluster together in aggregates called micelles. The concentration above which they are formed is called as critical micelle concentration (CMC). The size of the micelle formed as such mainly depends on the size of the surfactant molecules, but is typically in the range of colloidal domain. The shape of individual micelles varies with concentration. Close to critical micelle concentration, they are spherical and, at higher concentration, they assume lamellar or rodlike structures (Fig. 1). Micelles are very important in industry and biology because of their solubilizing properties. They are extensively used as detergents and soaps, and as drug carriers. They are also increasingly used in natural synthesis and petroleum recovery.

There are several methods that give us vital insights on the structure and properties of micelles. Many physical properties of surfactants undergo an abrupt change at the CMC. Surface tension and conductance are two simple and widely used methods for measuring the CMC. For example, at concentrations below CMC, adding sodium dodecylsulphate (SDS) to water decreases the surface tension with increase in SDS concentration. An abrupt decrease in surface tension is observed as the concentration reaches the CMC. It then slowly decreases and reaches a plateau as more SDS is added to the water. In the initial stages, as the hydrocarbon chain of SDS is not soluble in water, the molecules are concentrated at the air–water

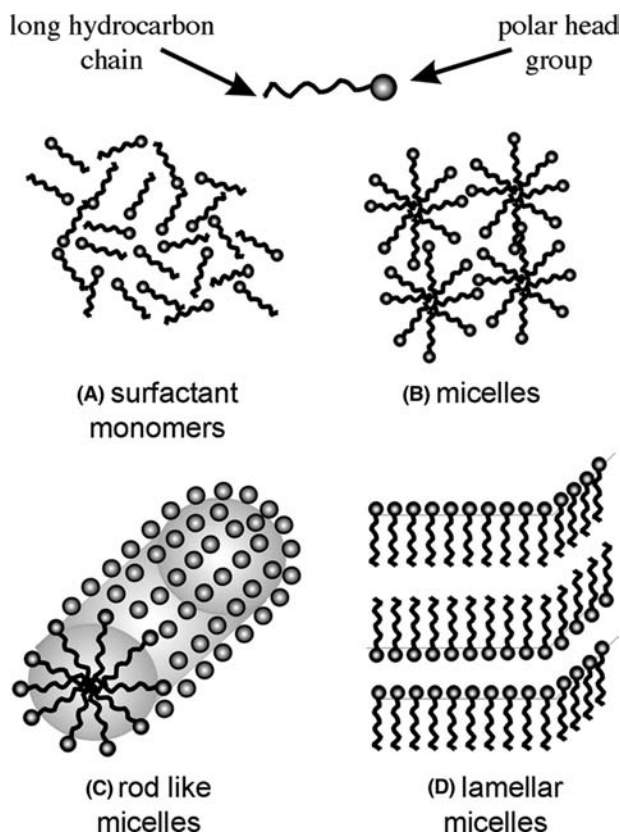


**Fig. 1** Structural transitions associated with the ordering of surfactant molecules as the concentration is increased.

interface with the hydrocarbon chain oriented toward the vapor phase. Because the surface tension of water is higher than that of the hydrocarbons, adding more surfactant results in a decrease in surface tension. However, above the CMC, the surfactant molecules self-assemble to form micelles, in which the hydrocarbon chains orient themselves inside the aggregate and the polar head groups orient toward the aqueous phase. Above the CMC, adding more surfactants simply produces more micelles, keeping the surface tension almost constant. Similarly, the conductivity of many surfactants display (especially anionic or cationic surfactants) a slow decline in conductance at concentrations below the CMC. Above CMC, the conductance shows a sharp break as a result of the micellization.

## NANOCRYSTALS AND THEIR SUPERLATTICES

Although nanocrystals are nothing but crystalline colloidal particles, they were not specifically targeted for systematic studies until recently.<sup>[7]a</sup> The main interest in this area stems from the unique physical properties

of these nanoscale materials, such as quantum confinement. Quantum confinement results from the size of the particle where the electron trapped in the nanoparticle cannot jump to other particles because of the potential barrier between them, which arises as a result of the insulating, protective ligand shell on each particle and the distance between the particles. However, if the particles are brought sufficiently closer, the electrons can tunnel between the particles and the tunneling strength decreases exponentially with distance. Thus the quantum confinement properties of the nanoscale particles crucially depend on the choice of the material, the size of each particle, the temperature, and the surrounding environment. Apart from this, ordered arrays of these nanoscale particles are expected to manifest novel electronic, magnetic, and optical properties because of the cooperative interactions between the particles.

There are two interesting directions in the study of nanoparticles and their ordered arrays. The first one is the packing of individual atoms inside a nanoparticle. The other one is the packing of these nanoparticles into ordered 2-D or 3-D arrays. It is often observed that in the nanoscale regime, atoms aggregate into many interesting crystal motifs quite different from their bulk crystal structures. For example, X-ray diffraction pattern of cobalt nanoparticles prepared by reduction of hot cobalt chloride solution revealed a complex cubic structure related to the  $\beta$ -phase of elemental manganese ( $\epsilon$ -Co).<sup>[8,9]</sup> On the other hand, bulk cobalt adopts a hexagonally close packed structure. Sometimes the stabilization of different crystal motifs in the nanoscale regime is attributable to kinetic considerations, where the particles are arrested in a metastable state. In other cases, the different motif is actually found to be energetically favorable for that particular size due to surface considerations.

The second direction, formation of ordered arrays of nanoparticles in 2-D and 3-D, is one of the major areas of research attracting the attention of innumerable research groups in the world today.<sup>[10]</sup> The main requirement for the formation/self-assembly of the nanoparticle arrays (superlattices) is the synthesis of monodisperse colloids. Strictly speaking, a monodisperse colloid means particles with sizes indistinguishable from each other. However, in the field of nanocrystal superlattices (NCs), a standard deviation of ( $\sigma$ )  $\leq 5\%$  in the size is accepted as monodisperse. Apart from the size, the crystallinity of the core and the shape of surfaces play an important role in controlling the formation of superlattices.

There are several techniques generally employed to synthesize monodisperse nanoparticles, which differ slightly from each other depending on the type of material to be synthesized. Some of the important synthetic methods are detailed below. For synthesizing

<sup>a</sup>See the articles in the special Issue of *Sci. Am.* Ref.<sup>[6]</sup>.



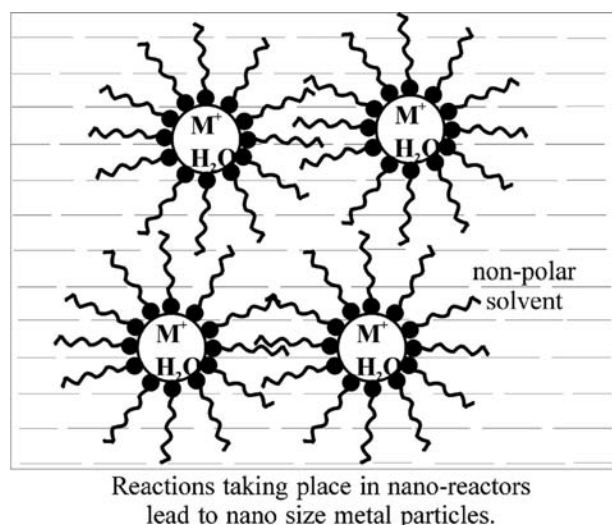


**Fig. 2** Schematic of the nano-reactors in which the formation of nanoparticles takes place.

noble metal nanoparticles (Ag, Au, Pt, etc.), the most popular synthetic procedure is to reduce the metal salt in the presence of surfactant and stabilizing agent.<sup>[11]</sup> In a typical procedure, aqueous solution of the metal salts are mixed with a toluene solution containing surfactants such as long-chain alkylammonium salts. The metal ion is then transferred to the organic phase by vigorous stirring. A capping agent (usually alkane-thiols) is subsequently added to this solution. The metal salt is then reduced by a reducing agent ( $\text{NaBH}_4$  or hydrazine) to nucleate the metal nanoparticles. Here the size of the nanoparticle is restricted in the nanometer scale, because the reaction itself takes place in the nano-reactor formed by the long-chain-length alkylammonium ions. These ions self-assemble into a micellar structure, where the polar head groups trap the metal ions in the aqueous phase (Fig. 2). The size of the nanoparticles can also be controlled by the reaction rate, by temperature, and by adjusting the ratio of capping agents to the initial metal salt concentration. The size distribution is further narrowed by size-selective precipitation. A similar procedure based on inverse micelles, where the metal salt is dissolved in a solution of surfactant in a hydrocarbon solvent and subsequently reduced by the addition of an aqueous solution of the reducing agent, is found to be equally effective.<sup>[12,13]</sup>

Transition metal nanoparticles are usually prepared by a very similar technique but at slightly higher temperatures.<sup>[8–10]</sup> Here the metal salts and the capping agents are dissolved in very high boiling solvents such as dioctylether or phenyl ether. After heating the mixture to  $\sim 200\text{--}250^\circ\text{C}$ , a hot reducing agent is added, leading to the nucleation and growth of metal nanoparticles stabilized by the capping agents. In the

semiconductor nanoparticle synthesis, the solvents usually employed are mixtures of long-chain alkyl phosphines, phosphine oxides, alkyl amines, etc. Generally, a metathesis ( $\text{AB} + \text{CD} \rightarrow \text{AC} + \text{BD}$ ) reaction of metal alkyls (dimethyl cadmium, diethyl zinc, dibenzyl mercury) and organophosphine or silylchalcogenides ( $\text{R}_3\text{PE}$  or  $\text{TMS}_2\text{E}$ , where TMS = trimethylsilyl and E = S, Se, or Te) is carried out to prepare semiconductor nanoparticles.<sup>[10]</sup> However, all these procedures require a size-selective precipitation step to achieve the narrow size distribution mandatory for the formation of the ordered arrays of the respective nanoparticles. Other drawbacks of the above chemical synthetic procedures are the usage of highly toxic chemicals and difficulty in scaling up the yields.

Alternative procedures, such as aerosol and solvated cluster dispersion techniques, have been reported which alleviate some of the problems associated with the above chemical routes. In these methods, the required material is directly evaporated (Au, Ag, Pt, or CdS, ZnS, etc.) and captured in a solvent or inert gas stream.<sup>[14,15]</sup> The solvent or inert gas employed works as a stabilizing agent or diluent, respectively. The matrix is then allowed to mix with the capping ligand, which preserves the size of the clusters in the nanoscale region. Although large quantities of the required nanomaterials could be prepared via these routes, they also usually result in broad size distributions of the nanoparticles. In a significant development, Klabunde et al.<sup>[16–18]</sup> proposed a digestive ripening technique which allows researchers to convert a broad size distributed colloid to a nearly monodisperse one. In this technique, a broad size distributed colloid in a solvent is refluxed in the presence of a surface active agent. This simple procedure significantly narrows down the size distribution and allows the synthesis of large quantities of monodisperse particles.

An important point to remember in the synthesis of monodisperse nanoparticles is the choice of capping agent. The selection of capping agent is usually determined by the material to be synthesized. The popular capping agents for several materials synthesized are provided in Table 1. The list is not very exhaustive

**Table 1** Popular ligand groups used to stabilize different materials in the nanoscale regime

Material	Ligand groups
Noble metals (Au, Ag, Pt, etc.)	RSH, $\text{RNH}_2$ , $\text{R}_3\text{P}$ , and $\text{RSiH}_3$
Transition metals and magnetic compounds	$\text{RCOOH}$
Semiconductors	RSH, $\text{R}_3\text{P}$ , and $\text{R}_3\text{PO}$

The most popular “R” groups employed are  $\text{C}_8\text{H}_{17}$ – (for RSH,  $\text{R}_3\text{P}$ , and  $\text{R}_3\text{PO}$ ),  $\text{C}_{12}\text{H}_{25}$ – (for RSH and  $\text{RNH}_2$ ), and  $\text{C}_{18}\text{H}_{37}$ – (for  $\text{RSiH}_3$ ).

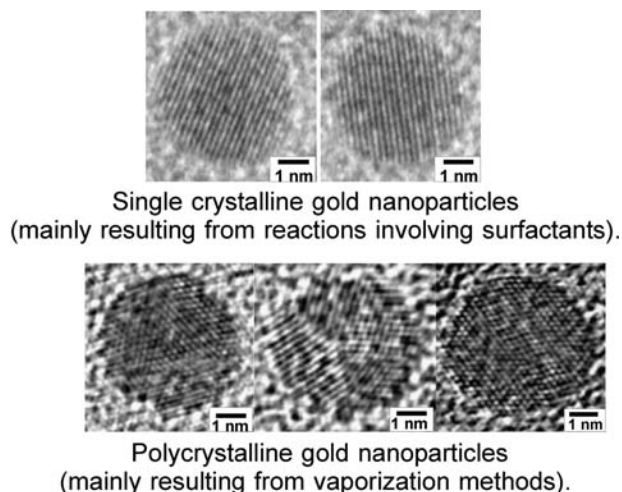


**Fig. 3** Single crystalline and polycrystalline gold nanoparticles resulting from different procedures.

but should provide a guideline in finding the popular ligands generally used.

Thus there are several methods now available to prepare monodisperse nanoparticles of different materials protected by several capping agents. However, the size, shape, and morphologies of these nanoparticles are crucially dependent on their synthetic routes. These differences not only determine their different physical properties but also control the way the 2-D and 3-D superlattices are formed from these nanoparticles. For example, the two-phase procedure for noble metal nanoparticles generally results in the formation of 2–3 nm particles.<sup>[11]</sup> The routes involving inverse micelles and the subsequent digestive ripening lead to the formation of 5–6 nm particles.<sup>[16–18]</sup> As mentioned above, the individual morphology of each particle also is critically determined by the procedure used. While methods involving surfactants routinely lead to single crystalline gold nanoparticles with truncated

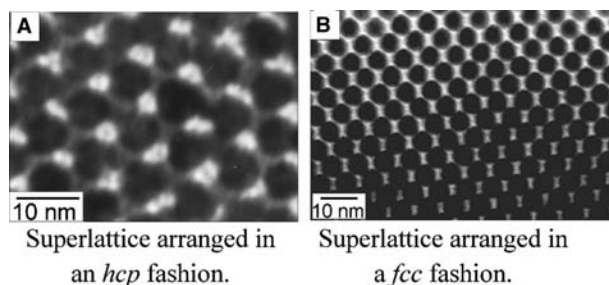


**Fig. 4** Self-assembled superlattices of the monodisperse gold nanoparticles prepared by two different methods: (A) solvated metal atom dispersion method, (B) inverse micelle method.

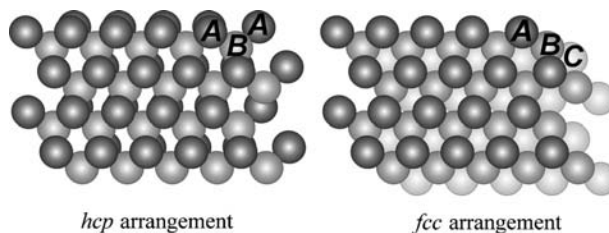
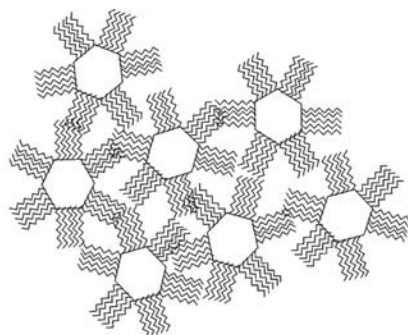


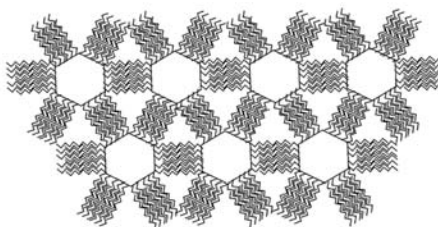
**Fig. 5** Schematic of the two different superlattice formations.

octahedral shapes, solvated dispersion and aerosol techniques result in polycrystalline particles with many defects (Fig. 3).<sup>[15,19]</sup> This difference in morphology is known to critically determine the final ordering of the superlattices, either in face centered cubic (*fcc*) type or hexagonally close packed (*hcp*) type.

In this respect, it is generally observed that particles with multiple defects usually behave like hard spheres and arrange themselves into an *hcp* lattice.<sup>[15,19]</sup> A typical triangular-shaped contrast image observed by electron microscopy of the superlattices formed by



Individual nanocrystals in a colloidal solution. Notice the ligands form self assembled layers on the surface.



Superlattices of nanoparticles. Notice the interdigitation of ligands on adjacent particles.

**Fig. 6** Schematic of the self-assembled monolayers of ligand molecules on the nanoparticle surfaces and the formation of the superlattices with interdigitation of ligand molecules on adjacent particles.

the polycrystalline particles is presented in Fig. 4A. This image results from the organization of roughly 5-nm Au nanoparticles oriented along the [0001] direction in an *hcp* arrangement. In an *hcp* arrangement, the hexagonally packed particles of adjacent layers are arranged in an *ABAB...* fashion. In contrast, the superlattice resulting from the *fcc* arrangement of a similarly sized, perfect single crystalline nanoparticles is shown in Fig. 4B.<sup>[19]</sup> This specific arrangement results from the [110] projection of *fcc* lattice. Here the particles from the adjacent layers are arranged in an *ABCABC...* type fashion.<sup>[19,20]</sup> A pictorial difference of the *hcp*- and *fcc*-type arrangements is presented in Fig. 5.

It is also generally observed that the 3-D superlattice formation is encouraged by interdigitation (bundling) of the capping agents on adjacent particles. It is well known that ligands such as thiols form self-assembled monolayers on flat bulk Au (111) surfaces. They form similar self-assembled monolayers on the 3-D nanoparticles as well, fixing the alkyl chain length of the thiol molecule preferentially in an all *trans* arrangement.<sup>[21]</sup> Then, the alkyl chains of the adjacent particles can penetrate into each other leading to the phenomenon called interdigitation (Fig. 6). Particle-to-particle distance obtained by electron microscopy pictures and diffraction patterns reveal that the distance between the adjacent particles in a superlattice is generally equivalent to one ligand chain length supporting this phenomenon.<sup>[22]</sup>

Until now, superlattices of several materials (most of the noble metals, numerous semiconductor and transition metal nanoparticles, and numerous magnetic compounds) have been prepared and well characterized. However, most of these superlattices are grown on some substrates. Isolation of a big “supercrystal” formed by the nanoparticles still remains elusive at this point. Nevertheless, with the amount of activity currently going on in this field, it appears that this goal might be achieved soon. This might open the hitherto unknown new avenues for the scientific community in the nanotechnology field.

## ACKNOWLEDGMENTS

The authors wish to sincerely thank Prof. Kenneth J. Klabunde and Prof. Christopher M. Sorensen for many enlightening discussions. We also thank Dr. Vladimir Zaikovski of Boreskov Institute of Catalysis, Novosibirsk, Russia, for the high-resolution TEM pictures.

## REFERENCES

1. Evans, D.F.; Wennerstrom, H. Why colloidal systems are important. In *The Colloidal Domain*; VCH: Weinheim, 1994; xxv–xxxii.
2. Graham, T. On the properties of silicic acid and other analogous colloidal substances. *J. Chem. Soc., Lond.* **1864**, *17*, 318–323.
3. Israelachvili, J.N. Electrostatic forces between surfaces in liquids. In *Intermolecular and Surface Forces*; Academic Press: New York, 1992.
4. Hirtzel, C.S.; Rajagopalan, R. Colloidal stability. In *Colloidal Phenomena*; Noyes Publications: Park Ridge, 1985; 73–116.
5. Hirtzel, C.S.; Rajagopalan, R. Colloids and Colloidal Phenomena. In *Colloidal Phenomena*; Noyes Publications: Park Ridge, 1985; 15–26.
6. *Sci. Am.* **2001**, 285.
7. Kralchevsky, P.; Nagayama, K. Two dimensional crystallization of particulates and proteins. In *Particles at Fluid Interfaces and Membranes*; Elsevier: Amsterdam, 2001; 517–590.
8. Dinega, D.P.; Bawendi, M.G. A solution-phase chemical approach to a new crystal structure of cobalt. *Angew. Chem., Int. Ed.* **1999**, *38*, 1788.
9. Sun, S.; Murray, C.B. Synthesis of monodisperse cobalt nanocrystals their assembly into magnetic superlattices. *J. Appl. Phys.* **1999**, *85*, 4325.
10. Murray, C.B.; Kagan, C.R.; Bawendi, M.G. Synthesis and characterization of monodisperse nanocrystals and close-packed nanocrystal assemblies. *Annu. Rev. Mater. Sci.* **2000**, *30*, 545–610.
11. Brust, M.; Walker, M.; Bethell, D.; Schiffrin, D.J.; Whyman, R. Synthesis of thiol derivatised gold nanoparticles in a two phase liquid/liquid system. *J. Chem. Soc., Chem. Commun.* **1994**, 801–802.
12. Pileni, M.P. Water in oil colloidal droplets used as microreactors. *Adv. Colloid Interface Sci.* **1993**, *46*, 139–163.
13. Lin, X.M.; Sorensen, C.M.; Klabunde, K.J. Ligand-induced gold nanocrystal superlattice formation in colloidal solution. *Chem. Mater.* **1999**, *11*, 198–202.
14. Stoeva, S.; Klabunde, K.J.; Sorensen, C.M.; Dragieva, I. Gram-scale synthesis of monodisperse gold colloids by the solvated metal atom dispersion method and digestive ripening and their organization into two- and three-dimensional structures. *J. Am. Chem. Soc.* **2002**, *124*, 2305–2311.
15. Harfenist, S.A.; Wang, Z.L.; Whetten, R.L.; Vezmar, I.; Alvarez, M.M. Three-dimensional hexagonal close-packed superlattice of passivated Ag nanocrystals. *Adv. Mater.* **1997**, *9*, 817–822.
16. Lin, X.M.; Sorensen, C.M.; Klabunde, K.J. Digestive ripening, nanophase segregation and superlattice formation in gold nanocrystal colloids. *J. Nanopart. Res.* **2000**, *2*, 157–164.
17. Prasad, B.L.V.; Stoeva, S.I.; Sorensen, C.M.; Klabunde, K.J. Digestive ripening of thiolated gold

- nanoparticles: the effect of alkyl chain length. *Langmuir* **2002**, *18*, 7515–7520.
18. Prasad, B.L.V.; Stoeva, S.I.; Sorensen, C.M.; Klabunde, K.J. Digestive ripening agents for gold nanoparticles: alternatives to thiols. *Chem. Mater.* **2003**, *15*, 935–942.
  19. Stoeva, S.I.; Prasad, B.L.V.; Uma, S.; Stoimenov, P.K.; Zaikovski, V.; Sorensen, C.M.; Klabunde, K.J. Face-centered cubic and hexagonal closed-packed nanocrystal superlattices of gold nanoparticles prepared by different methods. *J. Phys. Chem., B* **2003**, *107*, 7441.
  20. Harfenist, S.A.; Wang, Z.L.; Alvarez, M.M.; Vezmar, I.; Whetten, R.L. Highly oriented molecular Ag nanocrystal arrays. *J. Phys. Chem.* **1996**, *100*, 13,904–13,910.
  21. Badia, A.; Lennox, R.B.; Reven, L. A dynamic view of self assembled monolayers. *Acc. Chem. Res.* **2000**, *33*, 475–481.
  22. Wang, Z.L.; Harfenist, S.A.; Whetten, R.L.; Bentley, J.; Evans, N.D. Bundling and interdigitation of adsorbed thiolate groups in self-assembled nanocrystal superlattices. *J. Phys. Chem., B* **1998**, *102*, 3068–3072.

# Colloidal Nanometals as Fuel Cell Catalyst Precursors

Helmut Bönnemann

K. S. Nagabhushana

*Department of Heterogeneous Catalysis, Max Planck Institut für Kohlenforschung,  
Mülheim an der Ruhr, Germany*

## INTRODUCTION

The goal of this entry is to highlight the incentives and methods that are typically used for using nanomaterials as precursors of fuel cell catalysts. Our “precursor” concept for the manufacturing of heterogeneous metal colloid catalysts was developed in the last decade.<sup>[1–8]</sup> This method facilitates ready accessibility to homogeneous alloys, segregated alloys, layered bimetallics, or “decorated” metal particles and because of which it is now possible to tailor the precursor metallic colloids with controlled structures and metal interfaces. The advantage here is one can preprepare and thoroughly characterize active components of the electrocatalysts using modern analytical tools.

Nanostructured metal particles were considered potential catalysts essentially because of their unique electronic structures combined with extremely large surface areas. In general, isolable particles between 1 and 50 nm that are prevented from agglomeration by protective shells are termed “nanostructured metal colloids.” These colloids can be redispersed in both water (“hydrosols”) and organic solvents (“organosols”) depending on the nature of the protecting shell used. A wealth of knowledge has been acquired about these materials over the past decades.<sup>[1–3,9–18]</sup> Highly dispersed mono- and bimetallic colloids have been used as precursors for a variety of catalysts applicable in chemical catalysis.<sup>[4,19–27]</sup> This contribution, however, will deal only with those applications significant to fuel cell technology.

## BACKGROUND

Numerous methods have been explored to manipulate colloidal metal precursors. There are manifold advantages of using the precursor method over the conventional salt-impregnation method in that both size and composition of the colloidal metal precursors may be tailored independent of the support. Metal particle surfaces may be modified by different protective shells and coated by intermediate layers, e.g., by using metal oxides. A change in the precursor can be brought about

by SnO<sub>2</sub> and WO<sub>3</sub> dopants. Dipping the support in the appropriate solution of the preprepared particles results in the adsorption of the particles on to the support. The result of such an exercise is an eggshell catalyst, which contains a thin layer of the active metal particles on the surface of the support. It is important to note that no subsequent calcination is required. Supports such as charcoal, various oxidic support materials, and even low-surface materials such as quartz, sapphire, and highly oriented pyrolytic graphite (HOPG) have been used (Fig. 1).<sup>[1–8]</sup>

Interaction of platinum hydrosols with oxide (sapphire, quartz) and graphite single-crystal substrates have been monitored by the combination of X-ray and microscopic techniques<sup>[28,29]</sup> (Fig. 2). The protected Pt metal colloid is immediately adsorbed on to the surface of the dipped support, resulting in a carpetlike coat of the protected colloids. Upon annealing at 280°C and higher within an ultrahigh vacuum, the protecting shell decomposes. Thermal degradation studies monitored by X-ray photoelectron spectroscopy (XPS) and scanning tunneling microscopy (STM) revealed Pt particles virtually unchanged up to 800°C, above which sintering is observed.

## Fuel Cells and Catalysts

Fuel cells convert chemical energy into electrical energy and the catalyst system forms the most important component of this conversion.<sup>[30]</sup> The wide-ranging applications of fuel cells include low-emission transport systems, stationary power stations, and combined heat and power sources for small devices. Although metal Pt is adequate as a fuel cell catalyst for pure hydrogen feed, Pt alloy particles (e.g., Pt–Ru) of 1- to 3-nm size best serve as the active catalyst component for reformer gas or methanol into electricity. These systems offer improved efficiency and tolerance against contaminants, especially CO in the anode feed.<sup>[31–36]</sup> It is not clear what type of fuel will be the best to supply the cells in future vehicles. The options currently available include hydrogen, methanol, and synthetic fuel.<sup>[37]</sup> Whereas engineers and clean air experts favor pressurized hydrogen,

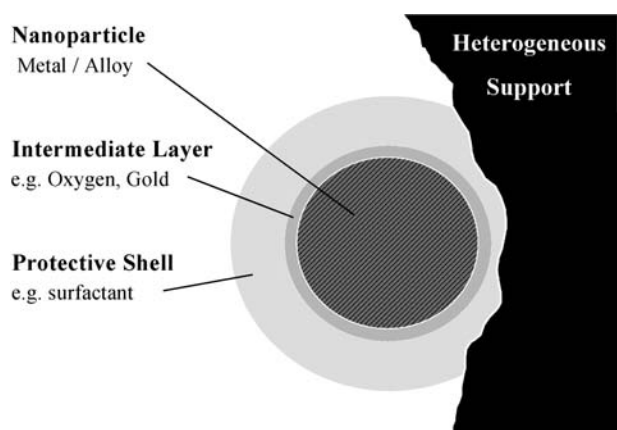


**Fig. 1** The precursor concept. *Source:* From Ref.<sup>[2]</sup>. Adapted with permission from Elsevier Science.

automakers are banking on methanol because of the ease of distribution.

In essence, bi- or multimetallic colloids are the need of the hour. Bimetallic colloids are readily accessible by the controlled coreduction or stepwise reduction of two different metal ions.<sup>[1,2,4,38–54]</sup> The catalytic aspects and structural characterization of some bimetallics have been reviewed.<sup>[15]</sup> Influences of each metal in a nanostructured bimetallic colloid catalyst combined with recent advances in the preparation of bimetallic colloids have provided catalysts of several compositions. Composition gradients from the core to the shell bimetallic particles have been prepared by successive reduction of mixed metal ions.<sup>[55–59]</sup> Truly, layered particles consisting of a gold core plated by palladium or vice versa have also been synthesized.<sup>[60]</sup> Electronegativity differences between two elements brings in a novel electronic structure and is seen in the case of Pd and Au as they contain partially filled and completely filled d bands, respectively.<sup>[61–69]</sup> Simon and coworkers have successfully prepared  $\text{Au}_{\text{core}}\text{Pd}_{\text{shell}}$ ,  $\text{Pd}_{\text{core}}\text{Au}_{\text{shell}}$  bimetallic colloids of 20–56 nm using classical seed growth method, which is complimented by sequential reduction of the metals followed by stabilization using trisulfonated triphenylphosphane and sodium sulfanilate, resulting in more than 90% metal to be isolated in the solid state and which is redispersible in water in high concentrations.<sup>[60]</sup>

Formic acid in the presence of different amounts of alkaloid (colloidal stabilizer) has given rise to platinum colloidal catalysts with varied particle sizes from platinum tetrachloride. The preparation of a fully alloyed Pd–Au colloid of 3.0-nm particle size, by the coreduction of Pd and Au salts with tetraalkylammonium triethylhydroborate<sup>[1]</sup> in a modified sol–gel procedure using tetrahydrofuran (THF) as the solvent, has been described.<sup>[70]</sup> The integrity of the incorporated Pd–Au alloy particles remained virtually untouched.

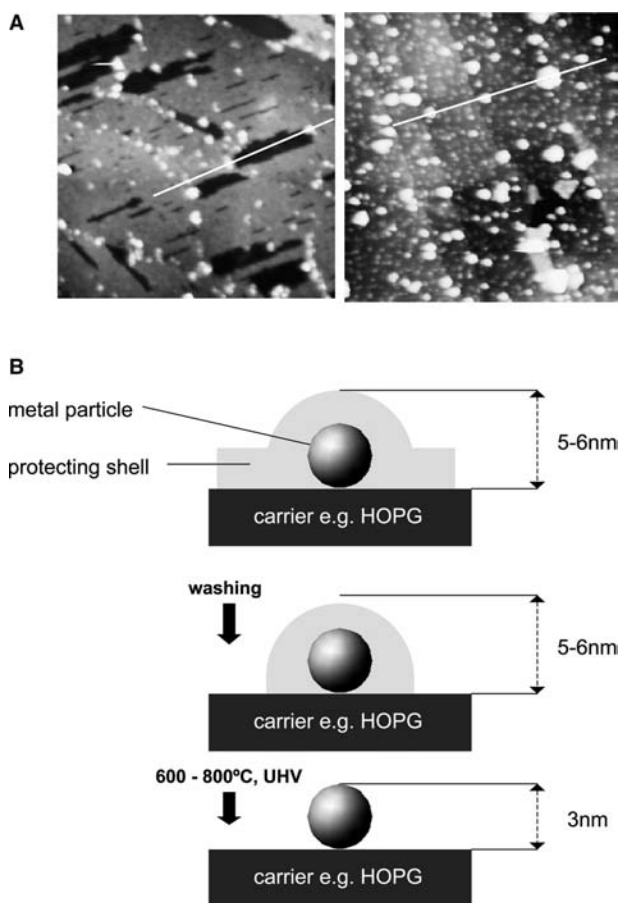


**Fig. 2** (A) AFM investigation of a sulfobetaine-12 stabilized Pt hydrosol (3 nm) absorbed on highly oriented pyrolytic graphite (HOPG) after dipping (left) and after additional washing (right). (B) Scheme of the Pt hydrosol adsorption on HOPG derived from a combined STM and XPS study. *Source:* From Ref.<sup>[29]</sup>. Adapted with permission from Elsevier Science.

A mesoporous texture with a comparatively narrow pore distribution remained after removing the protecting surfactant. According to physical characterization by a combination of techniques,  $\text{SiO}_2$  is seen to preserve the size and structural characteristics of the embedded Pd–Au colloidal metal precursor. The material exhibits excellent catalytic properties in selective hydrogenation test reactions. The following sections give various methods applied for the synthesis of colloidal nanoparticles.

## PREPARATION METHODS

The two principles of obtaining nanostructured metal colloids are “top-down” and “bottom-up” methods. The top-down method makes use of stabilizing the broken-down smaller structures from the bulk metal



using protecting agents.<sup>[71,72]</sup> An offshoot of this principle is the metal vapor technique,<sup>[73–78]</sup> a highly demanding proposition. On the other hand, the bottom-up method of wet chemical nanoparticle preparation relies on the chemical reduction of metal salts, electrochemical pathways, or the controlled decomposition of metastable organometallic compounds. The primarily formed nanoclusters are prevented from agglomeration using stabilizers, e.g., donor ligands, polymers, and surfactants.

## Modes of Stabilization

Protective agents are imperative for the stabilization of nanostructured metals and for prevention of their coagulation. Two basic modes of stabilization have been distinguished.<sup>[79]</sup>

Electrostatic stabilization is caused by the coulombic repulsion between the particles adsorbed at the particle surface (e.g., sodium citrate) and the corresponding counter ions. This causes an electrical double layer by ions. An example is gold sols prepared by the reduction of  $[\text{AuCl}_4^-]$  using sodium citrate.<sup>[9–11]</sup> A second mode is steric stabilization, achieved by the coordination of sterically bulky organic molecules that act as protective shields on the metallic surface. The nanometallic cores are thus separated from each other, preventing coagulation. The main classes of protective groups studied to date are the following: polymers<sup>[38–41]</sup> and block copolymers;<sup>[80–91]</sup> P, N, S donors (e.g., phosphines, amines, thioethers);<sup>[4,60,92–104]</sup> solvents such as THF;<sup>[4,105]</sup> THF/MeOH,<sup>[106]</sup> or propylene carbonate;<sup>[48]</sup> long-chain alcohols;<sup>[80–91]</sup> surfactants;<sup>[1–8,42–53]</sup> and organometallics.<sup>[107–111]</sup> Lipophilic protective agents yield metal colloids that are soluble in organic media (“organosols”); hydrophilic agents yield water-soluble colloids (“hydrosols”). A monolayer of the surfactant coat in the form of tetraalkylammonium halides is seen over the metal core in the case of Pd organosols.<sup>[109]</sup> Pt or Pt/Au particles have been hosted in the hydrophobic holes of nonionic surfactants, e.g., polyethylene monolaurate.<sup>[112,113]</sup>

## WET CHEMICAL REDUCTION

### Metal Salt Reduction Method

In 1857, Faraday was the first to report on the chemical reduction of transition metal salts in the presence of stabilizing agents to generate metal colloids.<sup>[114]</sup> This reliable approach has been extensively used.<sup>[15,16,79]</sup> Turkevich, nearly a century later,<sup>[9–11]</sup> gave the first reproducible standard recipe for the preparation of gold metal colloids by using sodium citrate for the

reduction of  $[\text{AuCl}_4^-]$ . He proposed a step-by-step formation of nanoclusters based on nucleation, growth, and agglomeration mechanisms. A refinement of this model was done (Fig. 3) based on the results from recent thermodynamic and kinetic results and modern analytical techniques.<sup>[115–124]</sup>

The general understanding is zerovalent metal atoms are generated in the embryonic stage of nucleation<sup>[115]</sup> by metal salt reduction. These atoms can collide in solution with other metal ions, metal atoms, or clusters to form an irreversible “seed” of stable metal nuclei. Depending on the strength of the metal–metal bonds, the difference in redox potentials of the metal salt, and the reducing agent used, the diameter of the “seed” nuclei can be well below 1 nm.

On the mechanism of colloidal particle formation, there have been some advances in the recent past.<sup>[119–123]</sup> Platinum colloid formation by using trialkylaluminum as both reducing agent and protecting group has been carefully studied with the formation of an intermediate, which decomposes in solution to result in nanoparticles having an average diameter of 1.2 nm. This sequence of reactions is shown in Fig. 4.

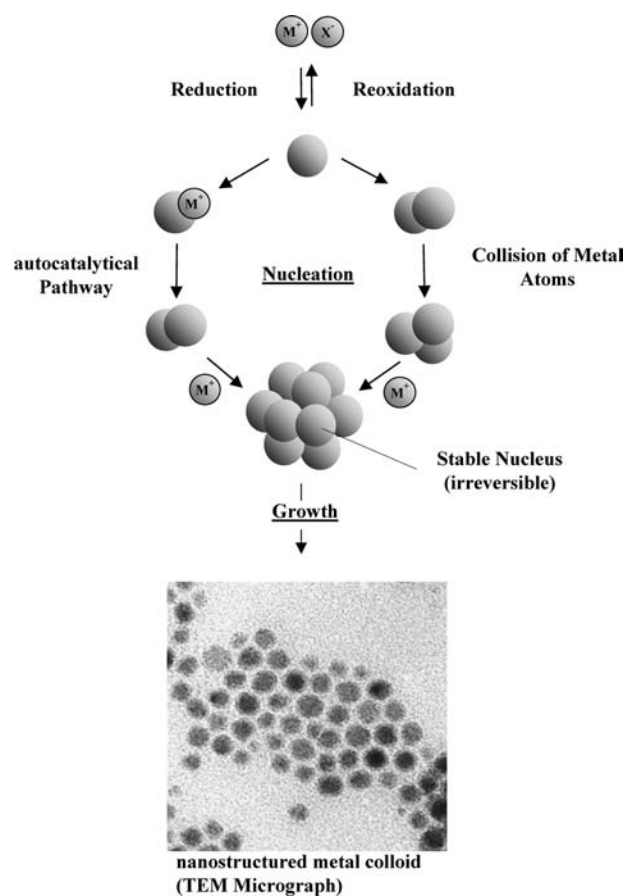


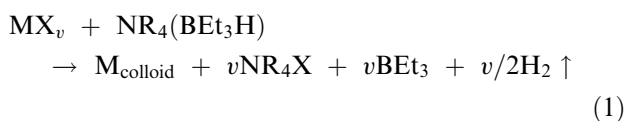
**Fig. 3** Formation of nanostructured metal colloids via the “salt reduction” method. *Source:* Adapted from Ref.<sup>[124]</sup>.



and Ir.<sup>[131–134]</sup> Colloidal Pt in water was obtained using CO, formic acid or sodium formate, formaldehyde, and benzaldehyde as reductants.<sup>[10,135,136]</sup> Silanes were found to be effective for the reductive preparation of Pt sols.<sup>[137,138]</sup> A reducing agent in tetrakis(hydroxymethyl) phosphonium chloride (THPC), which allows the size- and morphology-selective synthesis of Ag, Cu, Pt, and Au nanoparticles from the corresponding metal salts has been successfully introduced by Duff et al.<sup>[139,140]</sup> and Vogel, Duff, and Baiker<sup>[141]</sup> Furthermore, hydrazine,<sup>[142]</sup> hydroxylamine,<sup>[143]</sup> and electrons trapped in  $K^+ [(crown)_2K]^-$ <sup>[144]</sup> have been applied as reductants. In addition,  $BH_4^-$  is a powerful and valuable reagent for the salt reduction method. A disadvantage, however, is that transition metal borides are often found along with the nanometallic particles.<sup>[145,146]</sup> Very recently, solvent-stabilized platinum and its alloy with Ru, Mo, W, and Ni with an average diameter of 1.7 nm have been reported. In an attempt to produce direct methanol fuel cell (DMFC) catalysts, the reduction of a mixture of platinum and the second metal halides was performed using  $LiBH_4$  as a reducing agent. The resulting nanoparticles are stabilized by the solvent THF and later recovered by suitable treatment.<sup>[147]</sup>

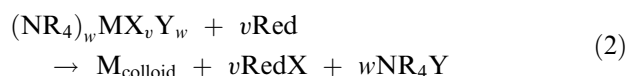
### Stabilized Metal Colloids

Tetraalkylammoniumhydrotriorganoborate<sup>[1–8]</sup> offers a wide range of application in the wet chemical reduction of transition metal salts. In this case, the reductant  $[BEt_3H^-]$  is combined with the stabilizing agent (e.g.,  $NR_4^+$ ). The surface-active  $NR_4^+$  salts are formed immediately at the reduction center in high local concentration that prevents particle aggregation. The advantage here is that trialkylboron can be recovered from the reaction and no borides contaminate the products.



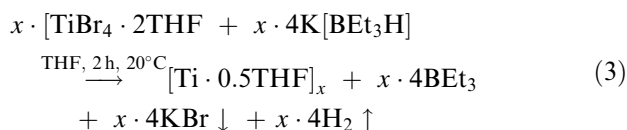
M = metals of the groups 6–11; X = Cl, Br;  $v = 1, 2, 3$ ; and R = alkyl,  $C_6-C_{20}$ .

As obtained, the  $NR_4^+$ -stabilized metal “raw” colloids typically contain 6–12 wt.% of metal. This, upon work up with ethanol or ether and subsequent reprecipitation by a solvent of different polarity (Table 9 in Ref.<sup>[1]</sup>), yields “purified” transition metal colloids containing ca. 70–85 wt.% of metal. When  $NR_4X$  is coupled to the metal salt before the reduction step, the preparation of  $[NR_4^+BEt_3H^-]$  can be avoided.  $NR_4^+$ -stabilized transition metal nanoparticles can also be obtained from  $NR_4X$ -transition metal double salts. Because the local concentration of the protecting group is sufficiently high, a number of conventional reducing agents may be applied (Eq. 2).<sup>[2,4]</sup>



M = metals; Red =  $H_2$ , HCOOH, K, Zn, LiH,  $LiBEt_3H$ ,  $KBEt_3H$ ; X, Y = Cl, Br;  $v, w = 1-3$ ; and R = alkyl,  $C_6-C_{12}$ .

In a recent review, the scope and limitations of this method have been evaluated.<sup>[16]</sup> Isolable metal colloids of the zerovalent early transition, which are stabilized only with THF, have been prepared via the  $[BEt_3H^-]$  reduction of the preformed THF adducts of  $TiBr_4$  (Eq. 3),  $ZrBr_4$ ,  $VBr_3$ ,  $NbCl_4$ , and  $MnBr_2$ . Table 1 summarizes the results.



Detailed studies of  $[Ti \cdot 0.5THF]^{[105]}$  show that it consists of  $Ti_{13}$  clusters in the zerovalent state, stabilized by six intact THF molecules (Fig. 5).

By analogy,  $[Mn \cdot 0.3THF]$  particles (1–2.5 nm) were prepared<sup>[148]</sup> and their physical properties studied.<sup>[149]</sup> The THF in Eq. 3 has been successfully replaced by tetrahydrothiophene (THT) for Mn, Pd, and Pt organosols; but attempts to stabilize Ti and V this way led to decomposition.<sup>[4]</sup>

Fig. 6 gives a survey of the  $[BEt_3H^-]$  method.

**Table 1** THF-stabilized organosols of early transition metals

Product	Starting material	Reducing agent	Temperature (°C)	Time (hr)	Metal content (%)	Size (nm)
[Ti·0.5THF]	$TiBr_4 \cdot 2THF$	$K[BEt_3H]$	RT	6	43.5	(<0.8)
[Zr·0.4THF]	$ZrBr_4 \cdot 2THF$	$K[BEt_3H]$	RT	6	42	–
[V·0.3THF]	$VBr_3 \cdot 3THF$	$K[BEt_3H]$	RT	2	51	–
[Nb·0.3THF]	$NbCl_4 \cdot 2THF$	$K[BEt_3H]$	RT	4	48	–
[Mn·0.3THF]	$MnBr_2 \cdot 2THF$	$K[BEt_3H]$	50	3	70	1–2.5

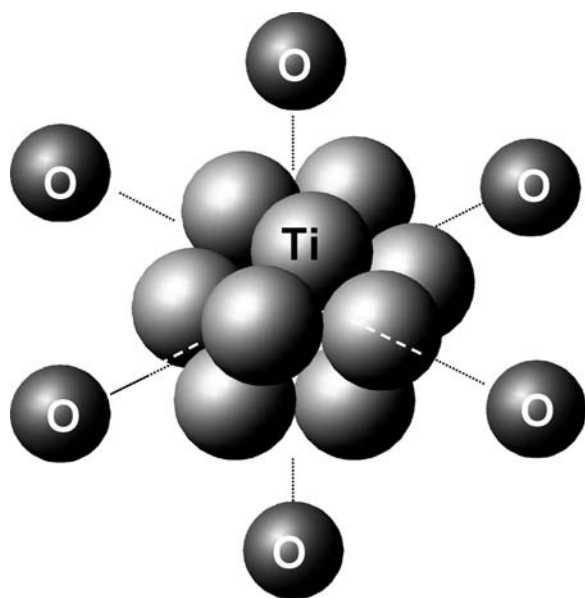
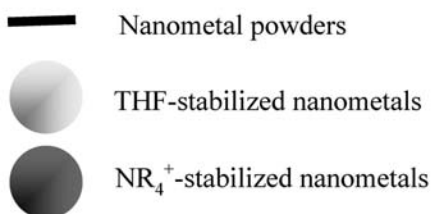


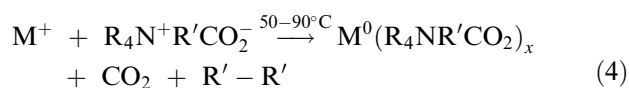
**Fig. 5**  $Ti_{13}$  cluster stabilized by the six THF-O atoms in an octahedral configuration. *Source:* From Ref.<sup>[2]</sup>. Adapted with permission from Elsevier Science.

The advantages of this method are as follows (Fig. 6): the method is generally applicable to salts of metals in groups 4–11 in the periodic table; it yields extraordinarily stable metal colloids that are easy to isolate as dry powders; the particle size distribution is nearly monodisperse; bimetallic colloids are easily accessible by coreduction of different metal salts; and the synthesis is suitable for multigram preparations and is easy to scale up. The only drawback to this method is that by altering the reaction conditions the particle size of the resulting sols cannot be varied.

<b>Ti</b> <0.8	<b>V</b>	<b>Cr</b> 3.0	<b>Mn</b> 1-2.5	<b>Fe</b> 3.0	<b>Co</b> 2.8	<b>Ni</b> 2.8	<b>Cu</b> 8.3
<b>Zr</b>	<b>Nb</b>	<b>Mo</b> 2-3		<b>Ru</b> 1.3	<b>Rh</b> 2.1	<b>Pd</b> 2.5	<b>Ag</b> 2-13
			<b>Re</b>	<b>Os</b>	<b>Ir</b> 1.5	<b>Pt</b> 2.8	<b>Au</b> 10



Protecting groups in betaines instead of  $NR_4^+$  salts [in Eq. (1)] can be conveniently used to generate zero-valent precious metal hydrosols. In Eq. 2, a broad variety of hydrophilic surfactants can be used.<sup>[2,4,6,7]</sup> Reetz and Maase<sup>[150–152]</sup> have reported a new method for the size- and morphology-selective preparation of metal colloids using tetraalkylammonium carboxylates of the type  $NR_4^+R'CO_2^-$  ( $R = \text{octyl}$ ,  $R' = \text{alkyl, aryl, H}$ ) [Eq. (4)]. The resulting particle sizes were found to depend on the electronic nature of the  $R'$  group in the carboxylate with electron donors producing small nanoclusters while electron-withdrawing substituent  $R'$ , in contrast, yielded larger particles. Pd particles of 2.2-nm size are found when  $Pd(NO_3)_2$  is treated with an excess of tetra(n-octyl)ammonium carboxylate bearing  $R' = (CH_3)_3CCO_2^-$  as the substituent, but the particle size was 5.4 nm when  $R' = Cl_2CHCO_2^-$  (an electron-withdrawing substituent) was used.



$R = \text{octyl}$  and  $R' = \text{alkyl, aryl, and H}$ .

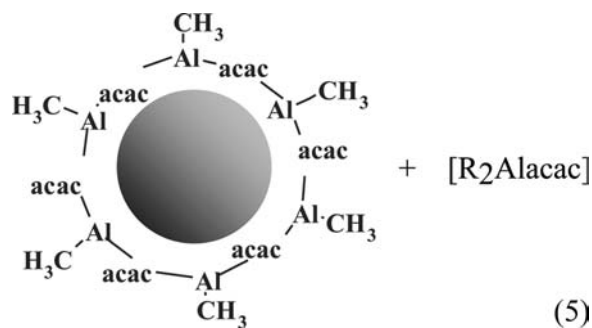
A number of bimetallic colloids were obtained with tetra(n-octyl) ammonium formate as the reductant: Pd/Pt (2.2 nm), Pd/Sn (4.4 nm), Pd/Au (3.3 nm), Pd/Rh (1.8 nm), Pt/Ru (1.7 nm), and Pd/Cu (2.2 nm). The shape of the particles was also found to depend on the reducing agent used, e.g., with tetra(n-octyl) ammonium glycolate  $Pd(NO_3)_2$  a significant amount of trigonal particles in the resulting Pd colloid was detected.

Mono and bimetallic nanoparticles have been prepared by “reductive stabilization” using organoaluminum compounds [Eq. (5) and Table 2].<sup>[107,110,149]</sup>

**Fig. 6** Nanopowders and nanostructured metal colloids accessible via the  $[Bet_3H^-]$ -reduction method (Eqs. 1 and 2) (including the mean particle sizes obtained). *Source:* From Ref.<sup>[2]</sup>. Adapted with permission from Elsevier Science.

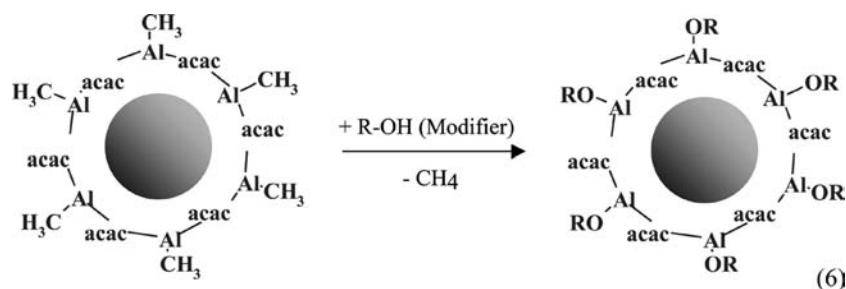
**Table 2** Mono- and bimetallic nanocolloids prepared via the organo-aluminum route

Metal salt	g/mmol	Reducing agent	g/mmol	Solvent, toluene (mL)	Conditions		Product m (g)	Metal content (wt.%)	Particle size $\Phi$ (nm)
					T (°C)	t (hr)			
Ni (acac) <sub>2</sub>	0.275/1	Al (I-but) <sub>3</sub>	0.594/3	100	20	10	0.85	Ni: 13.8	2–4
Fe (acac) <sub>2</sub>	2.54/10	Al (me) <sub>3</sub>	2.1/30	100	20	3	2.4	n.d.	
RhCl <sub>3</sub>	0.77/3./1	Al (oct) <sub>3</sub>	4.1/11.1	150	40	18	4.5	Rh: 8.5 Al: 6.7	2–3
Ag-neodecanoate	9.3/21.5	Al (oct) <sub>3</sub>	8.0/21.8	1000	20	36	17.1	Ag: 11.8 Al: 2.7	8–12
Pt (acac) <sub>2</sub>	1.15/3	Al (me) <sub>3</sub>	0.86/7.6	150	20	24	1.45	Pt: 35.8 Al: 15.4	2.5
PtCl <sub>2</sub>	0.27/1	Al (me) <sub>3</sub>	0.34/3	125	40	16	0.47	Pt: 41.1 Al: 15.2	2.0
Pd (acac) <sub>2</sub>	0.54/1.8	Al (et) <sub>3</sub>	0.46/4	500	20	2	0.85	Pd: 22 Al: 12.7	3.2
Pt (acac) <sub>2</sub>	0.09/0.24							Pt: 5.5 Al: 12.7	
Pt (acac) <sub>2</sub>	7.86/20	Al (me) <sub>3</sub>	8.64/120	400	60	21	17.1	Pt: 20.6 Ru: 10.5 Al: 19.6	1.3
Ru (acac) <sub>3</sub>	7.96/20								
Pt (acac) <sub>2</sub>	1.15/2.9	Al (me) <sub>3</sub>	0.86/12	100	60	2	1.1	Pt: 27.1 Sn: 5.2 Al: 14.4	n.d
SnCl <sub>2</sub>	0.19/1								



M = metals of groups 6–11 periodic system of elements (PSE); X = halogen, acetylacetonate;  $n = 2-4$ ; R = C<sub>1</sub>–C<sub>8</sub> alkyl, particle sizes 1–12 nm.

From Eq. (5), it is clear that colloids of zerovalent elements of groups 6–11 of the periodic table (and also of tin) can be prepared in the form of stable, isolable organosols. This method is now shown to be a reliable approach for the production of a wide range of small zerovalent transition metal particles. The key feature of this synthesis is the formation of an organometallic colloidal protecting shell (e.g., Al–C<sub>2</sub>H<sub>5</sub> or Al–CH<sub>3</sub>) around the particles. Formation of alkyl aluminum protecting shell over platinum nanocluster was confirmed by quantitative protonolysis experiments using modifiers (monofunctional) and spacer molecules (bifunctional) [Eq. (6)].

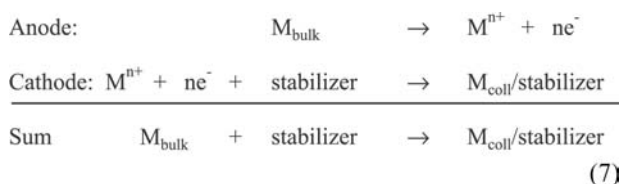


Modifiers are alcohols, carbonic acids, silanols, sugars, polyalcohols, PVP, surfactants, silica, alumina, etc.

By suitable “modification” [Eq. (6)] of the organoaluminum protecting shell it is possible to tailor the dispersion characteristics of the original organosols. A vast spectrum of dissolubilities of the colloidal metals in hydrophobic and hydrophilic media (including water) has been achieved in this manner.

### Electrochemical Synthesis

Mono- and bimetallic nanostructured colloids have been prepared by this versatile method by Reetz and his group since 1994.<sup>[14,42–44]</sup> The overall process of electrochemical synthesis can be divided into six steps. They are (1) oxidative dissolution of the sacrificial  $\text{Met}_{\text{bulk}}$  anode, (2) migration of  $\text{Met}^{n+}$  ions to the cathode, (3) reductive formation of zerovalent metal atoms at the cathode, (4) formation of metal particles by nucleation and growth, (5) arrest of the growth process and stabilization of the particles by colloidal protecting agents, e.g., tetraalkylammonium ions, and (6) precipitation of the nanostructured metal colloids [Eq. (7)].



The advantages of the electrochemical pathway include no contamination in by-products and easy isolation of product as precipitate. Reetz et al. have conducted several experiments using a commercially available Pd sheet as the sacrificial anode and the surfactant as the electrolyte and stabilizer. Parameters such as solvent polarity, current density, charge flow, distance between electrodes, and temperature are found to have an effect on the particle size of the  $(\text{C}_8\text{H}_{17})_4\text{N}^+\text{Br}^-$ -stabilized  $\text{Pd}^{(0)}$ . These manipulations are used carefully to control the size of Pd nanoparticles in the range of 1.2–5 nm.<sup>[42,53]</sup> In other words, it is possible to have size-selective particle formation by electrochemical preparation. With the electrochemical method, a number of monometallic organosols and hydrosols including Pd, Ni, Co, Fe, Ti, Ag, and Au have been successfully prepared on a scale of several hundred milligrams with yields >95%.<sup>[42–53]</sup> In addition, solvent-stabilized (propylene carbonate) palladium particles (8–10 nm) have also been obtained.<sup>[48]</sup> When two sacrificial  $\text{Met}_{\text{bulk}}$  anodes are used in a single electrolysis cell, bimetallic nanocolloids (Pd/Ni, Fe/Co, and Fe/Ni) are obtained.<sup>[49]</sup> Metals such as Pt, Rh, Ru, and Mo, which are anodically less readily soluble, have been prepared using the corresponding metal salts that were electrochemically reduced at the cathode (Table 3).

**Table 3** Electrochemical colloid synthesis

Metal salt	<i>d</i> (nm)	EA <sup>a</sup>
PtCl <sub>2</sub>	2.5 <sup>b</sup>	51.21% Pt
PtCl <sub>2</sub>	5.0 <sup>c</sup>	59.71% Pt
RhCl <sub>3</sub> ·xH <sub>2</sub> O	2.5	26.35% Rh
RuCl <sub>3</sub> ·xH <sub>2</sub> O	3.5	38.55% Ru
OsCl <sub>3</sub>	2.0	37.88% Os
Pd(OAc) <sub>2</sub>	2.5	54.40% Pd
Mo <sub>2</sub> (OAc) <sub>4</sub>	5.0	36.97% Mo
PtCl <sub>2</sub> + RuCl <sub>3</sub> ·xH <sub>2</sub> O	2.5	41.79% Pt + 23.63% Rh <sup>d</sup>

<sup>a</sup>Based on stabilizer-containing material.

<sup>b</sup>Current density: 5.00 mA cm<sup>-2</sup>.

<sup>c</sup>Current density: 0.05 mA cm<sup>-2</sup>.

<sup>d</sup>Pt–Ru dimetallic cluster.

Nanocolloids with layered bimetallics (e.g., Pt/Pd) have been synthesized by modifying the electrochemical method.<sup>[45,52]</sup> It has been recently reported that preparation of bimetallic colloids electrochemically uses a new strategy based on the use of a preformed colloid, e.g.,  $(\text{n-C}_8\text{H}_{17})_4\text{N}^+\text{Br}^-$  stabilized Pt particles and a sacrificial anode, e.g., Pd sheet<sup>[53]</sup> (Fig. 7).

The preformed Pt core may be regarded as a “living metal polymer” on which the Pd atoms are deposited to give “onion-type” bimetallic nanoparticles (5 nm) the structure of which has been characterized by a combination of analytical methods.

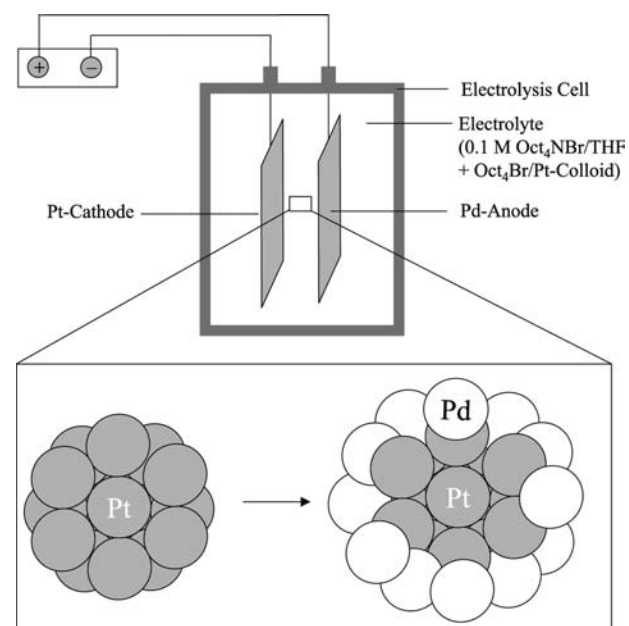


**Fig. 7** Modified electrolysis cell for the preparation of layered bimetallic Pt/Pd nanocolloids. *Source:* Adapted from Ref.<sup>[45]</sup>.



## Decomposition of Low-Valent Transition Metal Complexes

Decomposition of low-valent organometallic complexes and several organic derivatives of the transition metals generate short-lived nucleation particles of zerovalent metals. As an example, thermolysis<sup>[153–160]</sup> of cobalt carbonyl leads to rapid decomposition to give colloidal cobalt in organic solutions.<sup>[153,154]</sup> Colloidal Pd, Pt, and bimetallic Pd/Cu nanoparticles have been obtained by thermolysis of labile precious metal salts in the absence of stabilizers.<sup>[155]</sup> These results were improved when the thermolysis was performed in the presence of stabilizing polymers, such as PVP.<sup>[156]</sup>

Microwave heating in a simple household oven was recently used to prepare nanosized metal particles and colloids.<sup>[157–160]</sup> Recent work by Boxall et al. demonstrated the applicability of this technique to fuel cell catalyst preparation.<sup>[159,160]</sup> Through the use of microwave heating of an organometallic precursor, which contains both Pt and Ru, PtRu/Vulcan nanocomposites have been prepared, which consist of PtRu alloy nanoparticles highly dispersed on a powdered carbon support.<sup>[159]</sup> Two types of these nanocomposites containing 16 and 50 wt.% metal with alloy nanoparticles of 3.4 and 5.4 nm, respectively, are formed with only 100 or 300 sec of microwave heating time. The 50 wt.% supported nanocomposite has demonstrated fuel cell anode activity superior to that of a 60 wt.% commercial catalyst in preliminary measurements.

The energy induced in the sonochemical decomposition of metal salts and organometallic complexes<sup>[161–166]</sup> is produced by the formation, growth, and implosive collapse of bubbles in a liquid. Sonochemical preparations have been successfully developed by Suslick et al.<sup>[161]</sup> and Gedanken et al.<sup>[162–164]</sup> With this method Fe, Mo<sub>2</sub>C, Ni, Pd, and Ag nanoparticles in various stabilizing environments have been prepared, and size control has been observed in the case of Pd nanoparticles immobilized on alumina.<sup>[165]</sup>

The growth of very clean colloidal metals has been achieved by the photolysis of organometallics and metal salts.<sup>[112,167–171]</sup> Henglein et al.<sup>[172–180]</sup> and Belloni et al.<sup>[181]</sup> have studied the  $\gamma$ -radiolytic decomposition of metal ions to give nanostructured metal colloids. Although there are many studies aimed at synthesizing mono- and bimetallic systems,<sup>[173,176,179,182]</sup> there is serious drawback in that nanostructured colloids cannot be obtained on a preparative scale.

Upon the addition of CO or H<sub>2</sub> in the presence of appropriate stabilizers, multigram amounts of the isolable products can be obtained by controlled chemical decomposition of zerovalent transition metal complexes.<sup>[183–190]</sup> The growth of metallic Ru particles from Ru(COT)(COD) (COT = cyclooctatetraene,

COD = cycloocta-1,5-diene) with low-pressure dihydrogen was first reported by Ciardelli and Perticci.<sup>[183]</sup> Bradley et al. and Chaudret et al.<sup>[101–104,184–190]</sup> have demonstrated the use of low-valent transition metal olefin complexes as a very clean source for the preparation of nanostructured mono- and bimetallic colloids.

Organometallic complexes of the type [M(dba)<sub>2</sub>] (dba = dibenzylidene acetone, M = Pt, Pd) decompose under low carbon monoxide pressure in the presence of PVP to give nanosized colloidal Pt or Pd particles with a FCC structure. Remarkably, the surface of the resulting particles undergoes no measurable interaction with the stabilizing polymer or with the solvent. Nanoparticles of Ru, Au, and Cu were obtained analogously from Ru(COT)(COD), (THT)AuCl (THT = tetrahydrothiophene), and (C<sub>5</sub>H<sub>5</sub>)Cu(Bu<sup>4</sup>NC). Colloidal molybdenum, silver and bimetallic Cu/Pd colloids were also reported where a polymer matrix of PVP, dimethylphenylene oxide (PPO), or nitrocellulose (NC) was used as the stabilizing agent.<sup>[101,102,183,188–190]</sup> Chaudret and Bradley have described ligand-influenced platinum and palladium nanoparticles when stabilized by carbonyl and phosphines.<sup>[103,104]</sup> The hydrogenolysis of zerovalent organometallic olefin complexes has been established in the literature as a very clean and elegant method, e.g., for the manufacture of monometallic colloids via the decomposition of Fe(COT)<sub>2</sub>, Ru(COT)(COD), Co(C<sub>8</sub>H<sub>13</sub>)(COD) (C<sub>8</sub>H<sub>13</sub> =  $\eta^3$ -cyclooctenyl), and Ni(COD)<sub>2</sub> under H<sub>2</sub>. The hydrogenolysis method has been used to obtain a number of nanostructured Au, Pd, Pt colloids and of bimetallic systems (Pt/Ru, Pt/Co, and Cu/Pd) in a polymer matrix.<sup>[184–186]</sup> Ultrafine cobalt particles have been obtained by the hydrogenolytic decomposition of Co( $\eta^3$ -C<sub>8</sub>H<sub>13</sub>)( $\eta^4$ -C<sub>8</sub>H<sub>12</sub>) in the presence of polyphenylphenyleneoxide to give particles of 4.2-nm size. When the same procedure was performed with PVP, the size of the resulting particles was 1.4 nm. These results indicate that a close relationship exists between the synthesis conditions and the structure of the resulting particles.<sup>[187]</sup>

## APPLICATION IN FUEL CELL CATALYSIS

This section focuses on recent catalyst developments in phosphoric acid fuel cells (PAFCs), proton exchange membrane fuel cells (PEMFCs), and the previously mentioned DMFCs. A PAFC uses orthophosphoric acid as the electrolyte with the operating temperature between 160° and 220°C; the anode catalyst is Pt and the cathode can be, e.g., Pt/Cr/Co.<sup>[37,191–194]</sup> A trimetallic colloidal precursor of the composition Pt<sub>50</sub>Co<sub>30</sub>Cr<sub>20</sub> (size 3.8 nm) was prepared for this purpose by the coreduction of corresponding metal salts.<sup>[195–197]</sup>

From XRD measurements, an ordered FCT structure attributed to the alloyed trimetallic particle was evidenced. The electrocatalytic performance was compared with an industrial standard catalyst (trimetallic crystallites of 5.7-nm size) manufactured by coprecipitation and subsequent annealing to 900°C in a standard half cell. The advantage of the trimetallic colloid catalysts lies in their improved durability, which is essential for PAFC applications. After 22 hr, the potential had decayed by less than 10 mV.<sup>[198]</sup>

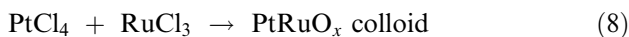
In a PEMFC, a solid proton-conducting polymer is used as the electrolyte and operated between 50° and 125°C. The cathode catalysts are based on Pt alone, but because of the required tolerance to CO, a combination of Pt and Ru is preferred for the anode.<sup>[31–36]</sup> Colloidal Pt/Ru catalysts are currently under broad investigation for low-temperature (80°C) polymer membrane fuel cells (PEMFCs). These have also been proposed for use in DMFCs or PEMFCs, where the feed is CO-contaminated hydrogen produced in on-board methanol reformers. The ultimate dispersion state of the metals is essential for CO-tolerant PEMFC, and alloyed Pt/Ru colloid particles of less than 2-nm size seem to fit these requirements.<sup>[22,23,25,31,33,199–202]</sup> Alternatively, bimetallic Pt/Ru PEM catalysts have been developed for the same purpose, where non-alloyed Pt nanoparticles <2 nm and Ru particles <1 nm are dispersed on the carbon support.<sup>[33]</sup> It can be concluded from the results that a Pt/Ru interface is essential for the CO tolerance of the catalyst regardless of their alloying. For the manufacture of DMFC catalysts, in contrast, Pt/Ru nanopowders of 3- to 5-nm size or thin films are used as precursors.<sup>[34–36]</sup> For the electrocatalytic methanol oxidation, a Pt metal or a Pt metal alloy catalyst has been developed where a Ru phthalocyanine complex is added as a dopant to reinforce the catalytic effect substantially.<sup>[197]</sup> The electrocatalytic activity of this was compared with that of a bimetallic Pt<sub>50</sub>/Ru<sub>50</sub>-N(Oct)<sub>4</sub>Cl colloid prepared by the salt coreduction method.<sup>[1,5–8]</sup> Alloyed state of the particles was verified by point-resolved energy dispersive X-ray (EDX) analysis, while from high-resolution transmission electron microscopy (HRTEM), the mean particle diameter was 1.7 nm.

A new method for the preparation and characterization of Pt–Ru alloy colloids, which are suitable as precursors for fuel cell catalysts, has been reported.<sup>[111]</sup> This method uses an organometallic compound both for reduction and as colloid stabilizer, leading to a Pt/Ru colloid with lipophilic surfactant stabilizers that can easily be modified to demonstrate hydrophilic properties. Reactive annealing in O<sub>2</sub> and H<sub>2</sub> ensures surfactant shell removal before electrochemical measurements. This colloid had nearly identical electrocatalytic activity to several other recently developed

Pt/Ru colloids as well as commercially available Pt/Ru catalysts. This demonstrates the potential for the development of colloid precursors for bimetallic catalysts especially when considering the ease of manipulating the alloy composition using these methods.

Recently, X-ray absorption near edge structure spectroscopy (XANES) has been used to examine Pt/Ru alloy catalysts.<sup>[111,203]</sup> An industrial (DMFC) alloy catalyst black and a carbon-supported Pt/Ru catalyst were both found to be predominantly in the form of Pt and Ru oxides. These catalysts were reduced to the metallic form upon introduction into an electrochemical cell and brought to the potential region where methanol oxidation occurs. Glassy carbon-supported Pt<sub>50</sub>/Ru<sub>50</sub>-N(Oct)<sub>4</sub>Cl colloids were examined by CO-stripping voltammetry and the data were essentially identical with those found in well-characterized bulk alloy electrodes. In a rotating disk electrode, the activity of the colloid toward the continuous oxidation of 2% CO in H<sub>2</sub> was determined at 25°C in 0.5 M H<sub>2</sub>SO<sub>4</sub>, and the results led to the conclusion that these Pt/Ru colloids are very suitable precursors for high-surface-area fuel cell catalysts.<sup>[25]</sup> In situ XRD via Debye function analysis helped in getting the structural information of the precursor. In addition, the XANES data support the bimetallic character of the particles. In situ XRD revealed the catalytic function of the alloyed Ru in the CO oxidation: surface oxide species, which slowly coalesce to RuO<sub>2</sub> particles, are formed on the Ru surface at 280°C. After re-reduction, the catalyst shows a pure hexagonal close packing (HCP) ruthenium phase and larger platinum-enriched alloy particles.<sup>[203]</sup> Scanning probe microscopy (SPM) has been applied to characterize the real-space morphology of the electrode surfaces of supported nanostructured metal colloids.<sup>[204]</sup> Colloidal Pt<sub>50</sub>/Ru<sub>50</sub> precursors (<2 nm) raise the tolerance to CO, allowing higher CO concentrations in the H<sub>2</sub> feed of a PEMFC without a significant drop in performance.<sup>[23,25]</sup> A selective Pt/Mo oxidation catalyst for the oxidation of H<sub>2</sub> in the presence of CO in fuel cells comprises Pt<sub>x</sub>Mo<sub>y</sub> particles where *x* is 0.5–0.9 and *y* is 0.1–0.5.<sup>[205]</sup> The colloid method was found to be a highly suitable exploratory approach to finding improved formulations for binary and ternary anode electrocatalysts. The metals used include Pt, Ru, W, Mo, and Sn.<sup>[24]</sup> Results of electrochemical measurements demonstrated that the introduction of a transition metal oxide (WO<sub>x</sub>, MoO<sub>x</sub>, VO<sub>x</sub>) leads to an improvement of catalytic activity toward methanol oxidation.<sup>[27]</sup> The combinatorial screening method has successfully been applied to electrocatalysts,<sup>[206]</sup> and it is an obvious step to include colloids in these experiments. As an alternative to the reductive metal colloid synthesis, the so-called “metal oxide concept” was developed, which allows the fabrication of binary and ternary colloidal metal oxides as

electrocatalyst precursors [Eq. (8)].<sup>[207–209]</sup>



Surfactant-stabilized colloidal Pt/RuO<sub>x</sub> (1.5 ± 0.4 nm) was prepared by cohydrolysis of PtCl<sub>4</sub> and RuCl<sub>3</sub> under basic conditions. By varying the stoichiometry of the transition metal salts, the Pt:Ru ratio in the colloids was between 1:4 and 4:1. The corresponding zerovalent metal colloids are obtained by the subsequent application of H<sub>2</sub> to the colloidal Pt/Ru oxides (optionally in the immobilized form). To prepare binary and ternary mixed metal oxides in the colloidal form, additional metals have been included in the “metal oxide concept” [Eq. (8)]. Pt/Ru/WO<sub>x</sub> is regarded as a good precatalyst especially for the application in DMFCs. Main group elements such as Al have been included in multimetallic alloy systems to improve the durability of fuel cell catalysts. Pt<sub>3</sub>AlC<sub>0.5</sub> alloyed with Cr, Mo, or W particles of 4- to 7-nm size has been prepared by sequential precipitation on conductive carbon supports such as highly disperse Vulcan XC72<sup>®</sup>.<sup>[210]</sup> Alternatively, colloidal precursors composed of Pt/Ru/Al allow the manufacture of multimetallic fuel cell catalysts (1–2 nm) having a metal loading of >20%. The three-step catalyst preparation is summarized in Fig. 8.

The organoaluminum route discussed earlier is used to prepare colloidal Pt/Ru/Al precursor. In the absence of stabilizers, the coreduction of organic Pt and Ru salts using Al(CH<sub>3</sub>)<sub>3</sub> gives halogen-free, multimetallic Pt colloids, e.g., Pt<sub>50</sub>Ru<sub>50</sub>/Al (size 1.2 ± 0.3 nm). When the stoichiometric ratio of the metal salts is changed, the ratio of Pt to the second metal in the

colloid can be adjusted. The addition of alcohols or suitable surfactants allows the dispersivity of the colloidal precursor in organic media or water to be tailored without affecting the particle size. In the second step, the Pt/Ru/Al colloid is adsorbed on high-surface-area carbon by treatment at 40°C for 24 hr. In the third step (conditioning) the dried Pt/Ru/Al Vulcan catalyst powders are exposed to O<sub>2</sub> and H<sub>2</sub> for 30 min each at 250–300°C to remove the surfactants completely. The particle size of the Pt/Ru/Al colloid adsorbed on the support was found to be virtually untouched (1.3 ± 0.4 nm), and after the thermal treatment only a moderate growth was determined (1.5 ± 0.4 nm). The aluminum was found to be present on the Pt/Ru surface in an oxidized form. This accounts for the size stabilization observed in the Pt/Ru particles and for the improved durability of the resulting electrocatalysts. Based on combustion method,<sup>[211]</sup> Colomer et al. have recently obtained Pt/Ru/Al and Pt/Ru/La precursors. The structure of these novel precursors has recently been analyzed by XAS and it showed that Pt(0) clusters are associated with Al oxide.<sup>[212]</sup> Recently, a fuel cell for generating electric power from a liquid organic fuel (“synfuel”) was described. It comprised a solid electrolyte membrane directly supporting the anode and cathode layers, containing 7–10% Pt and Ru, 70–80% of perfluorovinyl ether sulfonic acid, and 15–20% polytetrafluoroethylene.<sup>[202]</sup> Since 2000, there has been a tremendous input into the production of electrocatalysts with enhanced performance.<sup>[213–216]</sup> The goal here is to produce a better-performing catalyst in terms of their CO tolerance and its long-time durability under the fuel cell conditions. The creation of a potential

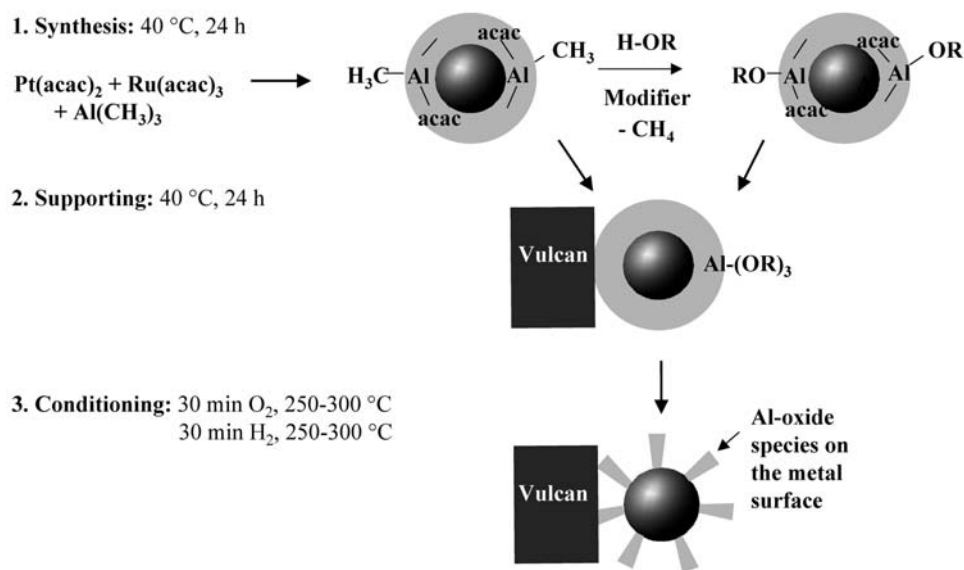


**Fig. 8** Scheme of the preparation of colloidal Pt/Ru/Al PEMFC anode catalyst (>20% metal on Vulcan XC72) via the “precursor concept.” Source: Adapted from Ref.<sup>[199]</sup>.

anode is quite advanced and there are a number of catalyst systems generated for this purpose. A concerted effort in generating an efficient cathode will continue, as there is still room for generating a better-efficiency cathode.

## CONCLUSION

Nanostructured metal colloids are promising precursors for manufacturing multimetallic fuel cell catalyst precursors that are truly nanosized. The advantages of using the "precursor concept" in generating colloidal metal catalysts has been highlighted. A survey of wet chemical preparation methods with emphasis on preparing fuel cell catalysts has been discussed. It remains to be seen how this research will meet the environmental and industrial requirements in the next few years.

## REFERENCES

- Bönnemann, H.; Brijoux, W.; Brinkmann, R.; Fretzen, R.; Jousen, T.; Köppler, R.; Neiteler, P.; Richter, J. Preparation, characterization, and application of fine metal particles and metal colloids using hydrotriorganoborates. *J. Mol. Catal.* **1994**, *86*, 129–177.
- Bönnemann, H.; Braun, G.; Brijoux, W.; Brinkmann, R.; Schulze Tilling, A.; Seevogel, K.; Siepen, K. Nano-scale colloidal metals and alloys stabilized by solvents and surfactants. Preparation and use as catalyst precursors. *J. Organomet. Chem.* **1996**, *520*, 143–162.
- Bönnemann, H.; Brijoux, W. Catalytically active metal powders and colloids. In *Active Metals*; Fürstner, A., Ed.; VCH: Weinheim, 1996; 339–379.
- Bönnemann, H.; Brijoux, W. Surfactant-stabilized nanosized colloidal metals and alloys as catalyst precursors. In *Advanced Catalysts and Nanostructured Materials, Chapter 7*; Moser, W., Ed.; Academic Press: San Diego, 1996; 165–196.
- Bönnemann, H.; Brijoux, W.; Jousen, T. (To Studiengesellschaft Kohle mbH), Microcrystalline-to-Amorphous Metal and/or Alloy Powders Dissolved Without Protective Colloid in Organic Solvents. U.S. Pat. 5,580,492, Aug. 26, 1993.
- Bönnemann, H.; Brijoux, W.; Brinkmann, R.; Dinjus, E.; Jousen, T.; Korall, B. Erzeugung von kolloiden Übergangsmetallen in organischer phase und ihre anwendung in der katalyse. *Angew. Chem.* **1991**, *103*, 1344–1346.
- Bönnemann, H.; Brijoux, W.; Brinkmann, R.; Dinjus, E.; Jousen, T.; Korall, B. Erzeugung von kolloiden Übergangsmetallen in organischer phase und ihre anwendung in der katalyse. *Angew. Chem. Int. Ed.* **1991**, *30*, 1312.
- Bönnemann, H.; Brijoux, W.; Brinkmann, R.; Richter, J. (To Studiengesellschaft Kohle mbH), Process for Producing Tenside-Stabilized Colloids of Mono- and Bimetals of the Group VIII and Ib of the Periodic System in the Form of Precursors for Catalysts Which are Isolable and Water Soluble at High Concentration. U.S. Pat. 849,482, Aug. 29, 1997.
- Turkevich, J.; Stevenson, P.C.; Hillier, J. Nucleation and growth process in the synthesis of colloidal gold. *J. Disc. Faraday Soc.* **1951**, *11*, 55–80.
- Turkevich, J.; Kim, G. Palladium-preparation and catalytic properties of particles of uniform size. *Science* **1970**, *169*, 873.
- Turkevich, J. Colloidal gold: Part I. Historical and preparative aspects, morphology and structure. *Gold Bull.* **1985**, *18*, 86–91.
- Schmid, G. Large Transition Metal Clusters-Bridges between Homogeneous and Heterogeneous Catalysts? In *Aspects of Homogeneous Catalysis, Vol. 7*; Ugo, R., Ed.; Kluwer: Dordrecht, 1990; 1–33.
- Schmid, G., Ed.; *Clusters and Colloids*; VCH: Weinheim, 1994.
- Reetz, M.T.; Helbig, W.; Quaiser, S.A. Electrochemical methods in the synthesis of nanostructured transition metal clusters. In *Active Metals*; Fürstner, A., Ed.; VCH: Weinheim, 1996; 279–297.
- Toshima, N.; Yonezawa, T. Bimetallic nanoparticles—novel materials for chemical and physical applications. *New J. Chem.* **1998**, *22* (11), 1179–1201.
- Aiken, J.D., III; Finke, R.G. A review of modern transition metal nanoclusters: their synthesis, characterization, and applications in catalysis. *J. Mol. Catal., A* **1999**, *145* (1–2), 1–44.
- Johnson, B.F.G. From clusters to nanoparticles and catalysis. *Coord. Chem. Rev.* **1999**, *190–192*, 1269–1285.
- Froba, M.; Reller, A. Synthesis and reactivity of functional metal oxides in nanoscopic systems. *Prog. Solid State Chem.* **1999**, *27*, 1–27.
- Schmid, G. Ligand-stabilized clusters and colloids. In *Applied Homogeneous Catalysis with Organometallic Compounds*; Cornils, B., Herrmann, W.A., Eds.; Wiley-VCH: Weinheim, 1996; Vol. 2, 636–644.
- Herrmann, W.A.; Cornils, B. Homogeneous Catalysis—Quo Vadis? In *Applied Homogeneous Catalysis with Organometallic Compounds, Vol. 2*; Cornils, B., Herrmann, W.A., Eds.; Wiley-VCH: Weinheim, 1996; 1171–1172.
- Bönnemann, H.; Brijoux, W. Catalysis and dynamics and physical properties of metal clusters. In *Potential Applications of Nanostructured Metal Colloids, Metal Clusters in Chemistry, Vol. 2*; Braunstein, P., Oro, L.A., Raithby, P.R., Eds.; Wiley-VCH: Weinheim, 1999; 913–931.
- Schmidt, T.J.; Noeske, M.; Gasteiger, H.A.; Behm, R.J.; Britz, P.; Brijoux, W.; Bönnemann, H. Electrocatalytic activity of PtRu alloy colloids for CO and CO/H<sub>2</sub> electrooxidation stripping voltammetry and rotating disk measurements. *Langmuir* **1997**, *13*, 2591–2595.
- Auer, E.; Behl, W.; Lehmann, T.; Stenke, U. (To Degussa AG), CO Tolerant Anode Catalyst for PEM Fuel Cells and Method for Its Production. EP 09 24 784 A1, June 23, 1999.

24. Götz, M.; Wendt, H. Binary and ternary anode catalyst formulations including the elements W, Sn and Mo for PEMFCs operated on methanol or reformate gas. *Electrochim. Acta* **1998**, *43* (24), 3637–3644.
25. Schmidt, T.J.; Noeske, M.; Gasteiger, H.A.; Behm, R.J.; Britz, P.; Bönnemann, H. PtRu alloy colloids as precursors for fuel cell catalysts. *J. Electrochem. Soc.* **1998**, *145*, 925–931.
26. O'Grady, W.E.; Hagans, P.L.; Pandya, K.I.; Maricle, D.L. The structure of Pt/Ru catalysts using x-ray absorption near edge structure studies, XANES. *Langmuir* **2001**, *17*, 3045–3050.
27. Lasch, K.; Jorissen, L.; Garche, J. The effect of metal oxides as co-catalysts for the electro-oxidation of methanol on platinum–ruthenium. *J. Power Sources* **1999**, *84*, 225–230.
28. Witek, G.; Noeske, M.; Mestl, G.; Shaikhutdinov, S.; Behm, R.J. Interaction of platinum colloids with single crystalline oxide and graphite substrates: a combined AFM, STM and XPS Study. *Catal. Letters* **1996**, *37*, 35–39.
29. Shaikhutdinov, S.K.; Möller, F.A.; Mestl, G.; Behm, R.J. Electrochemical deposition of platinum hydrosol on graphite observed by scanning tunneling microscopy. *J. Catal.* **1996**, *163*, 492–495.
30. Kordesch, K.; Simader, G. *Fuel Cells and Their Applications*; VCH: Weinheim, 1996.
31. Petrow, H.G.; Allen, R.J. (To Prototech Comp.), Finely Particulated Colloidal Platinum Compound and Sol for Producing the Same, and Method of Preparation of Fuel Cell Electrodes and the Like Employing the Same. US 4,044,193, August 23, 1977.
32. Burstein, G.T.; Barnett, C.J.; Kucernak, A.R.; Williams, K.R. Aspects of the anodic oxidation of methanol. *Catal. Today* **1997**, *38*, 425–437.
33. Auer, E.; Freund, A.; Lehmann, T.; Starz, K.-A.; Schwarz, R.; Stenke, U. (To Degussa AG), CO-Tolerant Anode Catalyst for PEM Fuel Cell and Its Method of Manufacturing. EP 0 880 188 A2, November 25, 1998.
34. Wilson, M.S.; Gottesfeld, S. Thin-film catalyst layers for polymer electrolyte fuel cell electrodes. *J. Appl. Electrochem.* **1992**, *22*, 1–7.
35. Wilson, M.S.; Ren, X.; Gottesfeld, S. High performance direct methanol polymer electrolyte fuel cells. *J. Electrochem. Soc.* **1996**, *143*, L 12.
36. Thomas, S.C.; Ren, X.; Gottesfeld, S. Influence of ionomer content in catalyst layers on direct methanol fuel cell performance. *J. Electrochem. Soc.* **1999**, *146* (12), 4354–4359.
37. Service, R.F. Bringing fuel cells down to earth. *Science* **1999**, *285*, 682–685.
38. Hirai, H.; Nakao, Y.; Toshima, N.; Adachi, K. Colloidal Rh in polyvinylalcohol as hydrogenation catalysts for olefins. *Chem. Lett.* **1976**, *5*, 905–910.
39. Hirai, H.; Nakao, Y.; Toshima, N. Colloidal Rh in poly(vinylpyrrolidone) as hydrogenation catalysts for internal olefins. *Chem. Lett.* **1978**, *7*, 545–548.
40. Hirai, H.; Nakao, Y.; Toshima, N. Preparation of colloidal rhodium in polyvinylalcohol by reduction with methanol. *J. Macromol. Sci., Chem.* **1978**, *A12*, 1117–1141.
41. Hirai, H.; Nakao, Y.; Toshima, N. Preparation of colloidal transition-metals in polymers by reduction with alcohols or ethers. *J. Macromol. Sci. Chem.* **1979**, *A13*, 727–750.
42. Reetz, M.T.; Helbig, W. Size-selective synthesis of nanostructured transition metal clusters. *J. Am. Chem. Soc.* **1994**, *116*, 7401–7402.
43. Reetz, M.T.; Helbig, W.; Quaiser, S. (To Studiengesellschaft Kohle), Electrochemical Reduction of Metal Salts as a Method of Preparing Highly Dispersed Metal Colloids and Substrate Fixed Clusters by Electrochemical Reduction of Metal Salts. U.S. Pat. 5,620,564, Apr. 15, 1997.
44. Reetz, M.T.; Helbig, W.; Quaiser, S. (To Studiengesellschaft Kohle), Electrochemical Reduction of Metal Salts as a Method of Preparing Highly Dispersed Metal Colloids and Substrate Fixed Clusters by Electrochemical Reduction of Metal Salts. U.S. Pat. 5,925,463, July 20, 1999.
45. Winter, M.A. Tensidstabilisierte Metallkolloide. Größenselektive Elektrochemische Synthese, Charakterisierung und neue Anwendungen. Ph.D. Thesis; Verlag Mainz: Aachen, 1998, ISBN 3-89653-355.
46. Becker, J.A.; Schäfer, R.; Festag, W.; Ruland, W.; Wendorf, J.H.; Pebler, J.; Quaiser, S.A.; Helbig, W.; Reetz, M.T. Electrochemical growth of superparamagnetic cobalt clusters. *J. Chem. Phys.* **1995**, *103*, 2520–2527.
47. Reetz, M.T.; Quaiser, S.A.; Merk, C. Electrochemical preparation of nanostructured titanium clusters: characterization and use in McMurry-type coupling reactions. *Chem. Ber.* **1996**, *129*, 741–743.
48. Reetz, M.T.; Lohmer, G. Propylene carbonate stabilized nanostructured palladium clusters as catalysts in Heck reaction. *Chem. Commun. (Cambridge)* **1996**, (16), 1921–1922.
49. Reetz, M.T.; Helbig, W.; Quaiser, S.A. Electrochemical preparation of nanostructural bimetallic clusters. *Chem. Mater.* **1995**, *7*, 2227–2228.
50. Reetz, M.T.; Quaiser, S.A. A new method for the preparation of nanostructured metal clusters. *Angew. Chem.* **1995**, *107*, 2461–2463.
51. Reetz, M.T.; Quaiser, S.A. A new method for the preparation of nanostructured metal clusters. *Angew. Chem., Int. Ed. Engl.* **1995**, *34*, 2240.
52. Kolb, U.; Quaiser, S.A.; Winter, M.; Reetz, M.T. Investigation of tetraalkylammonium bromide stabilized palladium/platinum bimetallic clusters using extended X-ray absorption fine structure spectroscopy. *Chem. Mater.* **1996**, *8*, 1889–1894.
53. Reetz, M.T.; Winter, M.; Breinbauer, R.; Thurn-Albrecht, T.; Vogel, W. Size-selective electrochemical preparation of surfactant-stabilized Pd-, Ni- and Pt/Pd colloids. *Chem. Eur. J.* **2001**, *7*, 1084–1094.
54. Schmid, G.; Lehnert, A.; Malm, J.-O.; Bovin, J.-O. Ligand stabilized bimetallic colloids identified by HREM and EDX. *Angew. Int. Ed. Engl.* **1991**, *30*, 874–876.

55. Toshima, N.; Yonezawa, T.; Kushihashi, K. Polymer protected Pd–Pt bimetallic clusters preparation, catalytic properties and structural considerations. *J. Chem. Soc., Faraday Trans.* **1993**, *89* (14), 2537–2543.
56. Bönemann, H.; Brijoux, W.; Richter, J.; Becker, R.; Hormes, J.; Rothe, J. The preparation of colloidal Pt/Rh alloys stabilized by NR<sub>4</sub><sup>+</sup>- and PR<sub>4</sub><sup>+</sup>-groups and their characterization by X-ray-absorption spectroscopy. *Z. Naturforsch.* **1995**, *50b*, 333–338.
57. Aleandri, L.E.; Bönemann, H.; Jones, D.J.; Richter, J.; Rozière, J. Structural investigation of bimetallic Rh–Pt nanoparticles through X-ray absorption spectroscopy. *J. Mater. Chem.* **1995**, *5*, 749–752.
58. Toshima, N. Colloidal dispersion of bimetallic nanoparticles. In *Fine Particles Science and Technology*; Pelizzetti, E., Ed.; Kluwer Academic Publishers, 1996; 371–383.
59. Harada, M.; Asakura, K.; Toshima, N. Structural analysis of polymer-protected platinum/rhodium bimetallic clusters using extended x-ray absorption fine structure spectroscopy. Importance of microclusters for the formation of bimetallic clusters. *J. Phys. Chem.* **1994**, *98*, 2653–2662.
60. Simon, U.; Flesch, R.; Wiggers, H.; Schön, G.; Schmid, G. Chemical tailoring of charging energy in metal cluster arrangements by use of bifunctional spacer molecules. *J. Mater. Chem.* **1998**, *8*, 517–518.
61. Joice, B.J.; Rooney, J.J.; Wells, P.B.; Wilson, G.R. Nature and reactivity of intermediates in hydrogenation of buta 1,3-diene catalyzed by cobalt and palladium–gold alloys. *Disc. Faraday Soc.* **1966**, *41*, 223–236.
62. Juszczak, W.; Karpinski, Z.; Lomot, D.; Pielaszek, J.; Sobczak, J.W. Pd–Au/SiO<sub>2</sub>: characterization and catalytic activity. *J. Catal.* **1995**, *151*, 67–76.
63. Cinneide, A.O.; Clarke, J.K.A. The exchange with deuterium and deuteration of benzene on evaporated palladium–gold alloy films. *J. Catal.* **1972**, *26*, 233–241.
64. Inami, S.H.; Wise, W. Olefin hydrogenation catalyzed by supported and unsupported mixed metals. *J. Catal.* **1972**, *26*, 92–96.
65. Visser, C.; Zuidwijk, I.G.P.; Ponc, V. Reaction of hydrocarbon on palladium–gold alloys. *J. Catal.* **1974**, *35*, 407–416.
66. Toshima, N. Polymer-protected bimetallic clusters. Preparation and application to catalysis. *J. Macromol. Sci., Part A* **1990**, *A 27*, 1225–1238.
67. Cinneide, A.O.; Gault, F.G. Reaction s of hexanes, unlabeled and labelled with <sup>13</sup>C, on alumina supported palladium–gold and platinum–gold alloy. *J. Catal.* **1975**, *37*, 311–323.
68. Toshima, N.; Harada, H.; Yamazaki, Y.; Asakura, K. Catalytic activity and structural analysis of polymer protected Au–Pd bimetallic clusters prepared by the simultaneous reduction of HAuCl<sub>4</sub> and PdCl<sub>2</sub>. *J. Phys. Chem.* **1992**, *96*, 9927–9931.
69. Liu, H.; Mao, C.; Meng, S. Preparation and characterization of the polymer-protected palladium–gold colloidal bimetallic catalysts. *J. Mol. Catal.* **1992**, *74*, 275–284.
70. Bönemann, H.; Endruschat, U.; Tesche, B.; Rufinska, A.; Lehmann, C.W.; Wagner, F.E.; Filoti, G.; Parvulescu, V.; Parvulescu, V.I. An SiO<sub>2</sub>-embedded nanoscopic Pd/Au alloy colloid. *Eur. J. Chem.* **2000**, (5), 819–822.
71. Gaffet, E.; Tachikart, M.; El Kedim, O.; Rahouadj, R. Nanostructural materials formation by mechanical alloying–morphologic analysis bases on transmission and scanning electron microscopic observations. *Mater. Charact.* **1996**, *36* (4–5), 185–190.
72. Amulyavichus, A.; Daugvila, A.; Davidonis, R.; Sipavichus, C. Chemical composition of nanostructured erosion products produced upon laser cutting of steel. *Fiz. Met. Metalloved.* **1998**, *85*, 111–117.
73. Schalnikoff, A.; Roginsky, R. Eine neue methode der Herstellung kolloider Lösungen. *Z. Kolloid* **1927**, *43*, 67–70.
74. Blackborrow, J.R.; Young, D. Metal Vapor in Organometallic Chemistry. In *Reactivity and Structural Concept in Organic Chemistry*; Springer Verlag: New York, 1979; Vol. 9.
75. Klabunde, K.J. *Chemistry of Free Atoms and Particles*; Academic Press: New York, 1980.
76. Klabunde, K.J.; Li, Y.-X.; Tan, B.-J. Solvated metal atom dispersed catalysts. *Chem. Mater.* **1991**, *3*, 30–39.
77. Bradley, J.S. Chemistry of Transition Metal Colloids. In *Clusters and Colloids*; Schmid, G., Ed.; VCH: Weinheim, 1994; 459–537.
78. Klabunde, K.J.; Cardenas-Trivino, G.C. Metal Atom/Vapor Approaches to Active Metal Clusters/Particles. In *Active Metals*; Fürstner, A., Ed.; VCH: Weinheim, 1996; 237–278.
79. Bradley, J.S. The Chemistry of Transition Metal Colloids. In *Clusters and Colloids*; Schmid, G., Ed.; VCH: Weinheim, 1994; 469–473.
80. Tanori, J.; Pileni, M.P. Control of the shape of copper metallic particles by using a colloidal system as template. *Langmuir* **1997**, *13*, 639–646.
81. Pileni, M.P. Nanosized particles made in colloidal assemblies. *Langmuir* **1997**, *13*, 3266–3276.
82. Antonietti, M.; Göltner, C. Superstructures of functional colloids—chemistry on the nanometer scale. *Angew. Chem., Int. Ed. Engl.* **1997**, *36*, 910–928.
83. Pileni, M.P. Colloidal self-assemblies used as templates to control size, shape and self-organization of nanoparticles. *Supramol. Sci.* **1998**, *5*, 321–329.
84. Petit, C.; Taleb, A.; Pileni, M.P. Self-organization of magnetic nanosized cobalt particles. *Adv. Mater.* **1998**, *10*, 259–261.
85. Storhoff, J.J.; Mucic, R.C.; Mirkin, C.A. Strategies for organizing nanoparticles into aggregate structures and functional materials. *J. Clust. Sci.* **1997**, *8*, 179–216.
86. Sergeev, G.B.; Petrukhina, M.A. Encapsulation of small metal particles in solid organic matrices. *Prog. Solid State Chem.* **1996**, *24*, 183–211.
87. Wilcoxon, J.P.; Provencio, P. Use of surfactant micelles to control the structural phase of nanosize iron clusters. *J. Phys. Chem., B* **1999**, *103*, 9809–9812.
88. Selvan, S.T.; Nogami, M.; Nakamura, A.; Hamanaka, Y. A facile sol–gel method for the encapsulation of gold nanoclusters in silica gels and their optical properties. *J. Non-Cryst. Solids* **1999**, *255*, 254–258.



89. Maye, M.M.; Theng, W.; Leibowitz, F.L.; Ly, N.K.; Zhong, C.J. Heating-induced evolution of thiolate-encapsulated gold nanoparticles: A strategy for size and shape manipulations. *Langmuir* **2000**, *16*, 490–497.
90. Konomi, I.; Hyodo, S.; Motohiro, T. Simulation of MEIS spectra for quantitative understanding of average size, composition, and size distribution of Pt–Rh alloy nanoparticles. *J. Catal.* **2000**, *192*, 11–17.
91. Wu, M.L.; Chen, D.H.; Huang, T.C. Preparation of Au/Pt bimetallic nanoparticles in water-in-oil micro-emulsions. *Chem. Mater.* **2001**, *13* (2), 599–606.
92. Schmid, G.; Pfeil, R.; Boese, R.; Bandermann, F.; Meyer, S.; Calis, G.H.M.; van der Velden, J.A.W. Au<sub>55</sub>(P(C<sub>6</sub>H<sub>5</sub>)<sub>3</sub>)<sub>12</sub>Cl<sub>6</sub>—Ein gold cluster ungewöhnlicher gröÙe. *Chem. Ber.* **1981**, *114*, 3634–3642.
93. Schmid, G. Metal clusters and cluster metals. *Polyhedron* **1988**, *7*, 2321–2329.
94. Tominaga, T.; Tenma, S.; Watanabe, H.; Giebel, U.; Schmid, G. Tracer diffusion of a ligand stabilized two shell gold cluster. *Chem. Lett.* **1996**, *25*, 1033–1034.
95. Schmid, G. Large clusters and colloids. Metals in the embryonic state. *Chem. Rev.* **1992**, *92*, 1709–1727.
96. Houbertz, R.; Feigenspan, T.; Mielke, F.; Memmert, U.; Hartmann, U.; Simon, U.; Schön, G.; Schmid, G. STM investigation of compact Au<sub>55</sub> cluster pallets. *Europhys. Lett.* **1994**, *28*, 641.
97. Schmid, G.; Mähack, V.; Lantermann, F.; Peschel, S. Ligand-stabilized metal clusters and colloids: Properties and applications. *J. Chem. Soc. Dalton Trans.* **1996**, (5), 589–596.
98. Schmid, G.; West, H.; Malm, J.-O.; Bovin, J.-O.; Grenthe, C. Catalytic properties of layered gold–palladium colloids. *Chem. Eur. J.* **1996**, *2*, 1099–1103.
99. Schmid, G.; Peschel, S. Preparation and scanning probe microscopic characterization of monolayers of ligand-stabilized transition metal clusters and colloids. *New J. Chem.* **1998**, *22*, 669–675.
100. Schmid, G.; Pugin, R.; Malm, J.-O.; Bovin, J.-O. Silsesquioxanes as ligands for gold clusters. *Eur. J. Inorg. Chem.* **1998**, (6), 813–817.
101. Dassenoy, F.; Philippot, K.; Ould Ely, T.; Amiens, C.; Lecante, P.; Snoeck, E.; Mosset, A.; Casanove, M.-J.; Chaudret, B. Platinum nanoparticles stabilized by CO and octanethiol ligands or polymers: FT-IR, NMR, HREM and WAXS studies. *New J. Chem.* **1998**, *22* (7), 703–711.
102. Amiens, C.; de Caro, D.; Chaudret, B.; Bradley, J.S. Selective synthesis, characterization, and spectroscopic studies on a novel class of reduced platinum and palladium particles stabilized by carbonyl and phosphine ligands. *J. Am. Chem. Soc.* **1993**, *115*, 11,638–11,939.
103. Rodriguez, A.; Amiens, C.; Chaudret, B.; Casanove, M.-J.; Lecante, P.; Bradley, J.S. Synthesis and isolation of cuboctahedral and icosahedral platinum nanoparticles. Ligand-dependent structures. *Chem. Mater.* **1996**, *8*, 1978–1986.
104. Bardaji, M.; Vidoni, O.; Rodriguez, A.; Amiens, C.; Chaudret, B.; Casanove, M.-J.; Lecante, P. Synthesis of platinum nanoparticles stabilized by CO and tetrahydrothiophene. Facile conversion to molecular species. *New J. Chem.* **1997**, *21*, 1243–1249.
105. Franke, R.; Rothe, J.; Pollmann, J.; Hormes, J.; Bönnemann, H.; Brijoux, W.; Hindenburg, Th. A study of the electronic and geometric structure of colloidal TiO<sub>2</sub>.5THF. *J. Am. Chem. Soc.* **1996**, *118*, 12,090–12,097.
106. Vidoni, O.; Philippot, K.; Amiens, C.; Chaudret, B.; Balmes, O.; Malm, J.-O.; Bovin, J.-O.; Senocq, F.; Casanove, M.-J. Novel spongelike ruthenium particles of controllable size stabilized only by organic solvents. *Angew. Chem., Int. Ed. Engl.* **1999**, *38*, 3736–3738.
107. Bönnemann, H.; Brijoux, W.; Brinkmann, R. (To Studiengesellschaft Kohle), Method for Modifying the Dispersion Characteristics of Metal–Organic–Prestabilized or Pre-treated Nanometal Colloids. WO 99/59713, Nov. 25, 1999.
108. Bradley, J.S.; Hill, E.W.; Leonowicz, M.E.; Witzke, H. Clusters, colloids and catalysis. *J. Mol. Catal.* **1987**, *41*, 59–74.
109. Reetz, M.T.; Helbig, W.; Quaiser, S.A.; Stimming, U.; Breuer, N.; Vogel, R. Visualization of surfactants on nanostructured Pd clusters by a combination of STM and high resolution TEM. *Science* **1995**, *267*, 367–369.
110. Bönnemann, H.; Brijoux, W.; Brinkmann, R.; Endruschat, U.; Hofstadt, W.; Angermund, K. The reductive stabilization of nanometal colloids by organo-aluminium compounds. *Rev. Roum. Chim.* **1999**, *44*, 1003–1010.
111. Paulus, U.A.; Endruschat, U.; Feldmeyer, G.J.; Schmidt, T.J.; Bönnemann, H.; Behm, R.J. New PtRu alloy colloids as precursors for fuel cell catalysts. *J. Catal.* **2000**, *195*, 383–393.
112. Toshima, N.; Takahashi, T.; Hirai, H. Colloidal platinum catalysts prepared by hydrogen and photoreduction in the presence of surfactants. *Chem. Lett.* **1985**, 1245–1248.
113. Yonezawa, T.; Toshima, N. Polymer- and micelle-protected gold/platinum bimetallic systems. Preparation, application to catalysis for visible-light-induced hydrogen evolution, and analysis of formation process with optical methods. *J. Mol. Catal.* **1993**, *83*, 67–181.
114. Faraday, M. Experimental relations of gold (and other metals) to light. *Philos. Trans. R. Soc. Lond.* **1857**, *147*, 145–153.
115. Leisner, T.; Rosche, C.; Wolf, S.; Granzer, F.; Wöste, L. The catalytic role of small coinage metal clusters in photography. *Surf. Rev. Lett.* **1996**, *3*, 1105–1108.
116. Michaelis, M.; Henglein, A. Reduction of palladium (II) in aqueous solution: stabilization and reactions of an intermediate cluster and palladium colloid formation. *J. Phys. Chem.* **1992**, *96*, 4719–4724.
117. Watzky, M.A.; Finke, R.G. Transition metal nanocluster formation kinetic and mechanistic studies. A new mechanism when hydrogen is the reductant: slow, continuous nucleation and fast autocatalytic surface growth. *J. Am. Chem. Soc.* **1997**, *119*, 10,382–10,400.
118. Rothe, J.; Hormes, J.; Bönnemann, H.; Brijoux, W.; Siepen, K. In situ x-ray absorption spectroscopy

- investigation during the formation of colloidal copper. *J. Am. Chem. Soc.* **1998**, *120*, 6019–6023.
119. Angermund, K.; Bühl, M.; Endruschat, U.; Mauschick, M.T.; Mörtel, R.; Mynott, R.; Tesche, B.; Waldöfner, N.; Bönnemann, H.; Köhl, G.; Modrow, H.; Hormes, J.; Dinjus, E.; Gassner, F.; Haubold, H.-G.; Vad, T. Nanoscopic Pt colloids in the “embryonic state”. *Angew. Chem., Int. Ed.* **2002**, *41* (21), 4041–4044.
  120. Jana, N.R.; Gearheart, L.; Murphy, C.J. Evidence for seed mediated nucleation in the chemical reduction of gold salts to gold nanoparticles. *Chem. Mater.* **2002**, *13* (7), 2313–2323.
  121. Brown, K.R.; Walter, D.G.; Natan, M.J. Seeding of colloidal Au nanoparticles solutions. 2. Improved control of particle size and shape. *Chem. Mater.* **2000**, *12*, 306–313.
  122. Heng, H.; Gibbons, P.C.; Kelton, K.F.; Buhro, W.E. Heterogeneous seeded growth: a potentially general synthesis of monodisperse metallic nanoparticles. *J. Am. Chem. Soc.* **2001**, *123*, 9198–9199.
  123. Jana, N.R.; Gearheart, L.; Murphy, C.J. Seeding growth for size control of 5–40 nm diameter gold nanoparticles. *Langmuir* **2001**, *17*, 6782–6786.
  124. Maase, M. Ph.D. Thesis: Neue Methoden zur größen- und formselektiven Darstellung von Metallkolloiden. Bochum, Germany, 1998. Verlag Mainz: Aachen, 1999, ISBN 3-89653-463-7.
  125. Tausch-Treml, R.; Henglein, A.; Lilie, J. Reactivity of silver atoms in aqueous solution: II. A pulse radiolysis study. *Ber. Bunsenges. Phys. Chem.* **1978**, *82*, 1335–1343.
  126. Henglein, A. Reduction of Ag(CN)<sub>2</sub>-on silver and platinum colloidal nanoparticles. *Langmuir* **2001**, *17* (8), 2329–2333.
  127. Santos, I.-P.; Liz-Marzan, L.M. Synthesis of silver nanoprisms in DMF. *Nano Lett.* **2002**, *2* (8), 903–905.
  128. Dalmia, A.; Lineken, C.L.; Savinell, R.F. Synthesis of ion conducting polymer protected nanometer size platinum colloids. *J. Colloid Interface Sci.* **1998**, *205* (2), 535.
  129. Fievet, F.; Lagier, J.P.; Figlarz, M. Preparing monodisperse metal powders in micrometer and submicrometer sizes by the polyol process. *MRS Bull.* **1989**, *14*, 29.
  130. Kang, S.; Harell, J.W.; Nikles, D.E. Reduction of the fcc to L10 ordering temperature for self-assembled FePt nanoparticles containing Ag. *Nano Lett.* **2002**, *2* (10), 1033.
  131. Rampino, L.D.; Nord, F.F. Preparation of palladium and platinum synthetic high polymer catalysts and the relationship between particle size and rate of hydrogenation. *J. Am. Chem. Soc.* **1941**, *63*, 2745–2749.
  132. Rampino, L.D.; Nord, F.F. Applicability of palladium synthetic high polymer catalysts. *J. Am. Chem. Soc.* **1941**, *63*, 3268.
  133. Rampino, L.D.; Nord, F.F. Systematic studies on palladium–synthetic high polymer catalysts. *J. Am. Chem. Soc.* **1941**, *65*, 2121–2125.
  134. Dunsworth, W.P.; Nord, F.F. Investigations on the mechanism of catalytic hydrogenations. XV. Studies with colloidal iridium. *J. Am. Chem. Soc.* **1950**, *72*, 4197–4198.
  135. Mucalo, M.R.; Cooney, R.P. F.T.I.R spectra of carbon monoxide adsorbed on platinum sols. *J. Chem. Soc., Chem. Commun.* **1989**, (2), 94–95.
  136. Meguro, K.; Torizuka, M.; Esumi, K. The preparation of organo colloidal precious metal particles. *Bull. Chem. Soc. Jpn.* **1988**, *61*, 341–345.
  137. Lewis, L.N.; Lewis, N. Platinum-catalyzed hydrosilylation–colloid formation as the essential step. *J. Am. Chem. Soc.* **1986**, *108*, 7228–7231.
  138. Lewis, L.N.; Lewis, N. Preparation and structure of platinum group metal colloids: Without solvent. *Chem. Mater.* **1989**, *1*, 106–114.
  139. Duff, D.G.; Curtis, A.C.; Edwards, P.P.; Jefferson, D.A.; Johnson, B.F.G.; Logan, D.E. The microstructure of colloidal silver: evidence for a polytetrahedral growth sequence. *J. Chem. Soc., Chem. Commun.* **1987**, (16), 1264–1266.
  140. Duff, D.G.; Baiker, A.; Edwards, P.P. A new hydrosol of gold clusters. I. Formation and particle size variation. *Langmuir* **1993**, *9*, 2301–2309.
  141. Vogel, W.; Duff, D.G.; Baiker, A. X-ray structure of a new hydrosol of gold clusters. *Langmuir* **1995**, *11*, 401–404.
  142. van Rheeunen, P.R.; McKelvey, M.J.; Glaunsinger, W.S. Synthesis and characterization of small platinum particles formed by the chemical reduction of chloroplatinic acid. *J. Solid State Chem.* **1987**, *67*, 151–169.
  143. Duff, D.G.; Baiker, A. Scientific basis for the preparation of heterogenous catalysis. In *Preparation of Catalysts VI*; Poncelet, G., Martens, J., Delmon, B., Jacobs, P.A., Eds.; Elsevier Science, 1995; 505–512.
  144. Tsai, K.-L.; Dye, J.L. Synthesis, properties, and characterization of nanometer-size metal particles by homogeneous reduction with alkalides and electrides in aprotic solvents. *Chem. Mater.* **1993**, *5*, 540–546.
  145. van Wonerghem, J.; Mørup, S.; Koch, C.J.W.; Charles, S.W.; Wells, S. Formation of ultrafine amorphous alloy particles by reducing in aqueous solutions. *Nature* **1986**, *322*, 622–623.
  146. Glavee, G.N.; Klabunde, K.J.; Sorensen, C.M.; Hadjipanayis, G.C. Sodium borohydride reduction of cobalt ions in nonaqueous media. Formation of ultrafine particles (nanoscale) of cobalt metal. *Inorg. Chem.* **1993**, *32*, 474–477.
  147. Lee, S.-A.; Park, K.-W.; Choi, J.-H.; Kwon, B.-K.; Sung, Y.-E. Nanoparticle synthesis and electrocatalytic activity of Pt alloys for direct methanol fuel cells. *J. Electrochem. Soc.* **2002**, *149* (10), A1299–A1304.
  148. Franke, R.; Rothe, J.; Becker, R.; Pollmann, J.; Hormes, J.; Bönnemann, H.; Brijoux, W.; Köppler, R. An X-ray photoelectron and X-ray absorption spectroscopic study of colloidal [Mn<sub>0.0.3</sub>THF]<sub>x</sub>. *Adv. Mater.* **1998**, *10*, 126–132.
  149. Sinzig, J.; de Jongh, L.J.; Bönnemann, H.; Brijoux, W.; Köppler, R. Antiferromagnetism of colloidal [Mn<sub>0.0.3</sub>THF]<sub>x</sub>. *Appl. Organomet. Chem.* **1998**, *12*, 387–391.
  150. Maase, M. Neue Methoden zur größen- und formselektiven Darstellung von Metallkolloiden. Ph.D. Thesis Bochum, 1998.

151. Reetz, M.T.; Maase, M. Redox-controlled size-selective fabrication of nanostructured transition metal colloids. *Adv. Mater.* **1999**, *11* (9), 773–779.
152. Bradley, J.S.; Tesche, B.; Busser, W.; Maase, M.; Reetz, M.T. Surface spectroscopic study of the stabilization mechanism for shape-selectively synthesized nanostructured transition metal colloids. *J. Am. Chem. Soc.* **2000**, *122*, 4631–4636.
153. Hess, P.H.; Parker, P.H. Polymers for stabilization of colloidal cobalt particles. *J. Appl. Polym. Sci.* **1966**, *10*, 1915–1927.
154. Thomas, J.R. Preparation and magnetic properties of colloidal cobalt particles. *J. Appl. Phys.* **1966**, *37*, 2914–2915.
155. Esumi, K.; Tano, T.; Torigue, K.; Meguro, K. Preparation and characterization of bimetallic palladium–copper colloids by thermal decomposition of their acetate compounds in organic solvents. *Chem. Mater.* **1990**, *2*, 564–567.
156. Bradley, J.S.; Hill, E.W.; Klein, C.; Chaudret, B.; Duteil, A. Synthesis of monodispersed bimetallic palladium–copper nanoscale colloids. *Chem. Mater.* **1993**, *5*, 254–256.
157. Wada, Y.; Kuramoto, H.; Sakata, T.; Mori, H.; Sumida, T.; Kitamura, T.; Yanagida, S. Preparation of nanosized nickel metal particles by microwave irradiation. *Chem. Lett.* **1999**, *28* (7), 607–608.
158. Yu, W.; Tu, W.; Liu, H. Synthesis of nanoscale platinum colloids by microwave dielectric heating. *Langmuir* **1999**, *15*, 6–9.
159. Boxall, D.L.; Deluga, G.A.; Kenik, E.A.; King, W.D.; Lukehart, C.M. Rapid synthesis of a PtRu/carbon nanocomposite using microwave irradiation: A DMFC anode catalyst of high relative performance. *Chem. Mater.* **2001**, *13*, 891–900.
160. Boxall, D.L.; Lukehart, C.M. Rapid synthesis of Pt or Pd/carbon nanocomposites using microwave irradiation. *Chem. Mater.* **2001**, *13*, 806–810.
161. Suslick, K.S.; Hyeon, T.; Fang, M.; Cichowlas, A. Sonochemical preparation of nanostructural catalysts. In *Advanced Catalysts and Nanostructured Materials, Chapter 8*; Moser, W., Ed.; Academic Press: San Diego, 1996; 197–212.
162. Dhas, A.; Gedanken, A. Sonochemical preparation and properties of nanostructured palladium metallic clusters. *J. Mater. Chem.* **1998**, *8*, 445–450.
163. Koltypin, Y.; Fernandez, A.; Rojas, C.; Campora, J.; Palma, P.; Prozorov, R.; Gedanken, A. Encapsulation of nickel nanoparticles in carbon obtained by the sonochemical decomposition of Ni(C<sub>8</sub>H<sub>12</sub>)<sub>2</sub>. *Chem. Mater.* **1999**, *11*, 1331–1335.
164. Salkar, R.A.; Jeevanandam, P.; Aruna, S.T.; Koltypin, Y.; Gedanken, A. The sonochemical preparation of amorphous silver nanoparticles. *J. Mater. Chem.* **1999**, *9*, 1333–1335.
165. Okitsu, K.; Nagaoka, S.; Tanabe, S.; Matsumoto, H.; Mizukoshi, Y.; Nagata, Y. Sonochemical preparation of size controlled palladium nanoparticle on alumina surface. *Chem. Lett.* **1999**, *28* (3), 271–272.
166. Rojas, T.C.; Sayagués, M.J.; Caballero, A.; Koltypin, Y.; Gedanken, A.; Posonnet, L.; Vacher, B.; Martin, J.M.; Fernández, A. TEM, EELS and EFTEM characterization of nickel nanoparticles encapsulated in carbon. *J. Mater. Chem.* **2000**, *10*, 715–721.
167. Yonezawa, Y.; Sato, T.; Ohno, M.; Hada, H. Photochemical formation of colloidal metals. *J. Chem. Soc., Faraday Trans.* **1987**, *83*, 1559–1567.
168. Yonezawa, Y.; Sato, T.; Kuroda, S.; Kuge, K. Photochemical formation of colloidal silver: Peptizing action of acetone ketyl radical. *J. Chem. Soc., Faraday Trans.* **1991**, *87*, 1905–1910.
169. Sato, T.; Kuroda, S.; Takami, A.; Yonezawa, Y.; Hada, H. Photochemical formation of silver–gold (Ag–Au) composite colloids in solutions containing sodium arginate. *Appl. Organomet. Chem.* **1991**, *5*, 261–268.
170. Torigue, K.; Tano, T.; Meguro, K. Preparation and characterization of bimetallic palladium–copper colloids by thermal decomposition of their acetate compounds in organic solvents. *Chem. Mater.* **1990**, *2*, 564–587.
171. Torigue, K.; Esumi, K. Preparation of bimetallic silver–palladium colloids from silver(I) bis(oxalato)-palladate(II). *Langmuir* **1993**, *9*, 1664–1667.
172. Henglein, A. Catalysis of chemical reactions by colloidal metals and semiconductors. In *Modern Trends in Colloid Science in Chemistry and Biology, International Symposium on Colloid and Surface Science*; Eicke, H.F., Ed.; Birkhauser Verlag: Basel, 1985; 126–147.
173. Ershov, B.G.; Janata, E.; Henglein, A.; Fojtik, A. Silver atoms and clusters in aqueous solution: absorption spectra and the particle growth in the absence of stabilizing Ag<sup>+</sup> ions. *J. Phys. Chem.* **1993**, *97*, 4589–4594.
174. Henglein, A. Physicochemical properties of small metal particles in solution: “Microelectrode” reactions, chemisorption, composite metal particles, and the atom-to-metal transition. *J. Phys. Chem.* **1993**, *97*, 5457–5471.
175. Ershov, B.G.; Janata, E.; Henglein, A. Growth of silver particles in aqueous solution: Long-lived “magic” clusters and ionic strength effects. *J. Phys. Chem.* **1993**, *97*, 339–343.
176. Henglein, A.; Giersig, M. Radiolytic formation of colloidal tin and tin–gold particles in aqueous solution. *J. Phys. Chem.* **1994**, *98*, 6931–6935.
177. Henglein, A.; Gutierrez, M.; Janata, E.; Ershov, B. Absorption spectrum and chemical reactions of colloidal cadmium in aqueous solution. *J. Phys. Chem.* **1992**, *96*, 4598–4602.
178. Mulveney, P.; Giersig, M.; Henglein, A. Surface chemistry of colloidal gold: deposition of lead and accompanying optical effects. *J. Phys. Chem.* **1992**, *96*, 10,419–10,424.
179. Henglein, A.; Meisel, D. Radiolytic control of the size of colloidal gold nanoparticles. *Langmuir* **1998**, *14*, 7392–7396.
180. Henglein, A. Preparation and optical absorption spectra of Au@Pt shell and Pt@Au shell colloidal nanoparticles in aqueous solution. *J. Phys. Chem., B.* **2000**, *104*, 2201–2203.
181. Belloni, J.; Mostafavi, M.; Remita, H.; Marignier, J.-L.; Delcourt, M.-O. Radiation-induced synthesis of

- mono- and multi-metallic clusters and nanocolloids. *New J. Chem.* **1998**, *22*, 1239–1255.
182. Belapurkar, A.D.; Kapoor, S.; Kuldreshtha, S.K.; Mittal, J.P. Radiolytic preparation and catalytic properties of nanophase nickel metal particles. *Mater. Res. Bull.* **2000**, *35*, 143.
  183. Ciardelli, F.; Pertici, P. Structure and reactivity of aromatic polymers/ruthenium catalysts. *Z. Naturforsch.* **1985**, *40b*, 133–140.
  184. Osuna, J.; deCaro, D.; Amiens, C.; Chaudret, B.; Snoeck, E.; Respaud, M.; Broto, J.-M.; Fert, A. Synthesis, characterization, and magnetic properties of cobalt nanoparticles from an organometallic precursor. *J. Phys. Chem.* **1996**, *100*, 14,571–14,574.
  185. Ould-Ely, T.; Amiens, C.; Chaudret, B.; Snoeck, E.; Verelst, M.; Respaud, M.; Broto, J.M. Synthesis of nickel nanoparticles. Influence of aggregation induced by modification of poly(vinylpyrrolidone) chain length on their magnetic properties. *Chem. Mater.* **1999**, *11*, 526–529.
  186. Bradley, J.S.; Hill, E.W.; Chaudret, B.; Duteil, A. Surface chemistry on colloidal metals. Reversible adsorbate-induced surface composition changes in colloidal palladium–copper alloys. *Langmuir* **1995**, *11*, 693–695.
  187. Dassenoy, F.; Casanove, M.-J.; Lecante, P.; Verelst, M.; Snoeck, E.; Mosset, A.; Ould Ely, T.; Amiens, C.; Chaudret, B. Experimental evidence of structural evolution in ultrafine cobalt particles stabilized in different polymers—from a polytetrahedral arrangement to the hexagonal structure. *J. Chem. Phys.* **2000**, *112*, 8137–8145.
  188. Bradley, J.S.; Hill, E.W.; Behal, S.; Klein, C.; Chaudret, B.; Duteil, A. Preparation and characterization of organosols of monodispersed nanoscale palladium. Particle size effects in the binding geometry of adsorbed carbon monoxide. *Chem. Mater.* **1992**, *4*, 1234–1239.
  189. Duteil, A.; Quéau, R.; Chaudret, B.; Mazel, R.; Roucau, C.; Bradley, J.S. Preparation of organic solutions or solid films of small particles of ruthenium, palladium, and platinum from organometallic precursors in the presence of cellulose derivatives. *Chem. Mater.* **1993**, *5*, 341–347.
  190. de Caro, D.; Agelou, V.; Duteil, A.; Chaudret, B.; Mazel, R.; Roucau, Ch.; Bradley, J.S. Activation of CH, CO, CC, C–Cl and CS bonds and some applications. *New J. Chem.* **1995**, *19*, 1265–1274.
  191. Acres, G.J.K.; Frost, J.C.; Hards, G.A.; Potter, R.J.; Ralph, T.R.; Thompsett, D.; Burstein, G.T.; Hutchings, G. Electrocatalysts for fuel cells. *J. Catal. Today* **1997**, *38*, 393–400.
  192. Cawthorn, R.G. The platinum and palladium resources of the Bushveld complex. *South Afr. J. Sci.* **1999**, *95*, 481–489.
  193. Information available from “World Fuel Cell Council” e.V., Kroegerstrasse 5, D-60313 Frankfurt. <http://www.fuelcellworld.org/>
  194. Cameron, D.S. The sixth grove fuel cell symposium. *Platin. Met. Rev.* **1999**, *43* (4), 149–154.
  195. Luczak, F.J.; Landsman, D.A. (To United Technologies Corp.), Method for Making Ternary Fuel Cell Catalysts Containing Platinum Cobalt and Chromium. U.S. Pat. 4,613,582, September 23, 1986.
  196. Wittholt, W. Mehrmetallische Pt–Kolloidkatalysatoren und ihre Anwendung in der Halonitroaromatenreduktion bzw. In *Phosphorsäure-Brennstoffzellen*; Ph.D. Thesis; RWTH Aachen, 1996.
  197. Wendt, H.; Götz, M. (To Degussa-Hüls AG), Fuel Cell Anode for the Oxidation of Methanol. EP 0951 084 A2, October 20, 1999.
  198. Freund, A.; Lang, J.; Lehmann, T.; Starz, K.A. Improved Pt alloy catalysts for fuel cells. *Catal. Today* **1996**, *27*, 279–283.
  199. Bönemann, H. Nanoscopic Pt-metal alloy collaids as catalyst precursors. In *Extended Abstracts of the 3rd International Symposium on New Materials for Electrochemical Systems*; Savadogo, O., Ed.; École Polytechnique de Montréal: Canada, 1999; 31–33, ISBN 21-553-00739-6.
  200. Bönemann, H.; Brinkmann, R.; Britz, P.; Endruschat, U.; Mörtel, R.; Paulus, U.A.; Feldmeyer, G.J.; Schmidt, T.J.; Gasteiger, H.A.; Behm, R.J. Nanoscopic Pt–bimetal colloids as precursors for PEM fuel cell catalysts. *J. New Mater. Electrochem. Syst.* **2000**, *3*, 199–206.
  201. Itoh, T.; Sato, J. (To N.E. Chemcat Corporation), Supported Pt–Ru Electrocatalyst, and Electrodes, Membrane–Electrode Assembly and Solid Polymer Electrolyte Fuel Cells, Using Said Electrocatalyst. EP 0 952 241, October 27, 1999.
  202. Narayanan, S.; Surampudi, S.; Halpert, G. (To California Institute of Technology), Direct Liquid-Feed Fuel Cell with Membrane Electrolyte and Manufacturing Thereof. U.S. Pat. 5,945,231, August 31, 1999.
  203. Vogel, W.; Britz, P.; Bönemann, H.; Rothe, J.; Hormes, J. Structure and chemical composition of surfactant-stabilized PtRu alloy colloids. *J. Phys. Chem., B* **1997**, *101*, 11,029–11,036.
  204. Stimming, U.; Vogel, R. Electrodes with defined mesoscopic structure. In *Electrochemical Nanotechnology*; Lorenz, W.J., Plieth, W., Eds.; Wiley-VCH: Weinheim, 1998; 73–86.
  205. Giallombardo, J.R.; De Castro, E.S. (To De Nora S.P.A.), Improved Composition of a Selective Oxidation Catalyst for Use in Fuel Cells. WO 99/53557, April 14, 1999.
  206. Reddington, E.; Sapienza, A.; Gurau, B.; Viswanathan, R.; Sarangapani, S.; Smotkin, E.S.; Mallouk, T.E. Combinatorial electrochemistry: a highly parallel, optical screening method for discovery of better electrocatalysts. *Science* **1998**, *280*, 1735–1737.
  207. Reetz, M.T.; Koch, M.G. (To Studiengesellschaft Kohle m.b.H), Water Soluble Nanostructured Metal-Oxide Colloids and Method for Preparing the Same. WO0029332, November 9, 1999.
  208. Reetz, M.T.; Koch, M. Water-soluble colloidal Adams catalyst: preparation and use in catalysis. *J. Am. Chem. Soc.* **1999**, *121*, 7933–7934.
  209. Koch, M.G. Wasserlösliche Metall- und Metalloxid-Kolloide: synthese, Charakterisierung und katalytische

- Anwendungen. Ph.D. Thesis. Aachen: Verlag Mainz, 1999, ISBN 3-89653-514-5.
210. Freund, A.; Lehmann, T.; Starz, K.-A.; Heinz, G.; Schwarz, R. (To Degussa AG), Platinum–Aluminium Alloy-Containing Catalysts for Fuel Cell and Process for Their Preparation. EP 0 743 092 A1, November 20, 1996.
  211. Colomer, M.T.; Fumo, D.A.; Jurado, J.R.; Segadaes, A.M. Non stoichiometric  $\text{La}_{(1-x)}\text{NiO}_{(3-\delta)}$  perovskites produced by combustion synthesis. *J. Mater. Chem.* **1999**, *9*, 2505–2510.
  212. Jurado, J.R.; Chinarro, E.; Berta, M.; Bönnemann, H.; Modrow, H. *University of Bonn*; (Manuscript under preparation).
  213. Mukerjee, S.; Urian, R.C. Bifunctionality in Pt alloy nanocluster electrocatalysts for enhanced methanol oxidation and CO tolerance in PEM fuel cells: electrochemical and in situ synchrotron spectroscopy. *Electrochim. Acta* **2002**, *47*, 3219–3231.
  214. Boxall, D.L.; Deluga, G.A.; Kenik, E.A.; King, W.D.; Lukehart, C.M. Rapid synthesis of PtRu/carbon nanocomposite using microwave irradiation: a DMFC anode catalyst of high relative performance. *Chem. Mater.* **2001**, *13*, 891–900.
  215. Tripkovic, A.V.; Popovic, K.D.; Grgur, B.N.; Blizanac, B.; Ross, P.N.; Markovic, N.M. Methanol electrooxidation on supported Pt and PtRu catalysts in acid and alkaline solutions. *Electrochim. Acta* **2002**, *47*, 3707–3714.
  216. Steigerwalt, E.S.; Deluga, G.A.; Lukehart, C.M. Pt–Ru/carbon fiber nanocomposites: Synthesis, characterization and performance as anode catalysts of direct methanol fuel cells. A search for exceptional performance. *J. Phys. Chem., B* **2002**, *106*, 760–766.

# Colloidal Nanoparticles: Aggregation Patterns at Surfaces

Hamidou Haidara

Karine Mougin

*Institut de Chimie des Surfaces et Interfaces-ICSI-CNRS, Mulhouse, France*

## INTRODUCTION

Apart from some specific applications related to microfluidics and targeted delivery where functionalized and freely moving nanocolloids are suited, nanoparticles mostly enter nanostructured materials as one-, two-, or three-dimensional networks, either grown (or embedded) at a solid–solid, solid–fluid, or fluid–fluid interface.<sup>[1–5]</sup> As in many natural and technological processes and phenomena, this brings the basic question on the role of the underlying substrate properties on the spatial organization and stability of the nanoparticle network. The answer to this question at least partly depends on the methodology used to create the nanoparticle patterns. The following discussion mainly deals with some of the basic features related to nanoparticle assemblies that may result from the adsorption and drying of nanocolloidal suspensions onto a substrate. In addition to the elaboration of well-ordered, two-dimensional nanoparticles arrays,<sup>[6]</sup> applications and phenomena related to nanocolloidal dispersions nearly concern all domains and materials, ranging from inorganic,<sup>[2–4,7]</sup> to polymers<sup>[1]</sup> and biological objects.<sup>[8]</sup> For these nanocolloidal suspensions, the evaporation of the solvent may either result in random and featureless aggregates<sup>[4]</sup> or lead to the formation of well-ordered complex fractal or dendrites structures<sup>[7,8]</sup> of nanosize particles on the substrate (Fig. 1A–B). For some of these drying patterns, the mechanisms and interface phenomena that drive the aggregation and ultimately determine their fascinating topological features (order, fractality, symmetry) still remain insufficiently understood. Comprehension of the underlying mechanisms and critical parameters governing the emergence and topological features of these nanocolloid drying patterns is thus fundamental for both biocolloid applications and the controlled elaboration of fractal surface networks that are increasingly used by engineers to model flow and percolation in complex media.<sup>[9]</sup>

Even on an ideal substrate, pattern formation in drying nanocolloids suspensions is a rather complex

process, involving the whole range of interface phenomena (wetting dynamics, adsorption, adhesion). This complexity essentially arises from the strong time dependence of both the internal flow (particle diffusion) and competing interparticle and particle–substrate interactions through the solvent, which govern the particle aggregation, especially in low-to-semidilute suspensions. This, of course, is less the case for highly concentrated suspensions that are already close to their gelation point at drop deposition. For these gel-like suspensions, it is the extraction kinetic of the residual (interstitial) solvent and the very short-range repulsive interactions, rather than the interparticle and particle–substrate interactions, that dominates the final morphology (porosity) and mechanical properties of the particle network, as observed for solvent-based synthesis of ceramic and zeolite films.<sup>[10–12]</sup> As opposed to these dense and relatively “thick” gel particle networks, the drying of low- to semiconcentrated nanocolloid dispersions rather form open aggregates of lower surface coverage  $\Gamma_s$  and fractal dimension  $D \leq d_{\text{space}}$ . It is these structures that are strongly sensitive and critically determined by the drying kinetics and the above-mentioned competitive interparticle and particle–substrate interactions that constitute the main focus of the following discussion. One can produce nanoparticle assemblies (well-ordered arrays, open aggregates, or thick deposits) from colloidal suspensions, either by deep coating or by drying deposited drops or films. In both cases, the final morphology of the assembly is strongly determined by the surface properties of the underlying substrate, which control the extent of the surface coverage, the particle–substrate adhesion, and henceforth, the whole late-stage drying events. These involve the contact line pinning vs. slip, the often-observed thick particle deposit at the drop edge,<sup>[13–16]</sup> the hydrodynamic flow and related shear at the substrate–suspension interface, and the possible formation and rupture of a residual film. A complete understanding of these structure formations thus requires both the use of model surfaces and the simultaneous investigations and correlation between the aggregation patterns forming in



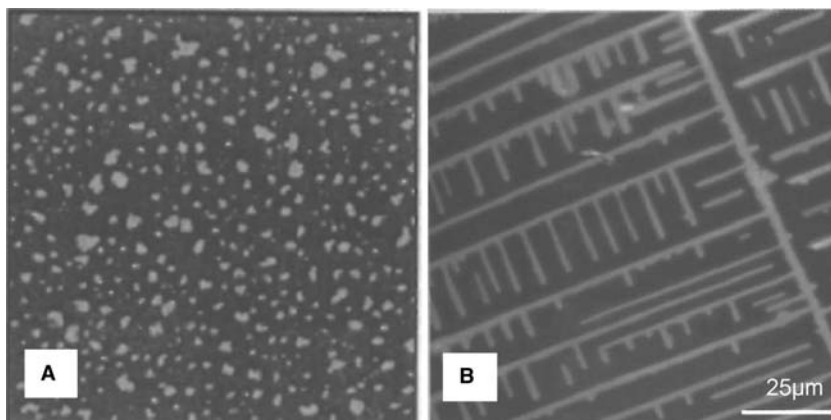


**Fig. 1** (A)  $15 \times 15 \mu\text{m}$  height scans of adsorbed  $\alpha\text{-Al}_2\text{O}_3$  colloids for contact time  $t_c$  of 600 sec. (B) Tapping mode AFM image of self-assembly from 0.15 mg/mL CPMV (*Cowpea Mosaic Virus*) solution dried on freshly cleaved mica, where CPMV particles self-assemble into parallel and orthogonal lines over a large area. *Source:* From Ref.<sup>[4]</sup>. © 2002 American Chemical Society. From Ref.<sup>[8]</sup>. © 2002 American Chemical Society.

deep-coating adsorption, and may also develop to some extent in evaporating drops, and serve as sub-layer to the arising patterns. Therefore, we will successively discuss and relate these *adsorption and drying nanocolloidal patterns*, highlighting the *critical role of the surface and the potential its functionalization offers toward the elaboration of nanocolloidal patterns of well-defined morphology*. But first, we will start with the section “Materials,” which briefly describes the elaboration and main characteristics of both the model molecular surfaces and nanocolloidal gold particles used herein.

## MATERIALS

An ensemble of three model homogeneous and two heterogeneous binary surfaces, consisting of self-assembled organosilane molecular films onto rigid silicon wafers, were used. The organosilane compounds composing the molecular films were 1) hexadecyltrichlorosilane (hydrophobic compound referred to as  $\text{CH}_3$ ), 2) amine terminated, 6-aminopropyltrimethoxysilane (hydrophilic electron acceptor compound referred to as  $\text{NH}_2$ ), and 3) nitrogen dioxide terminated 3-(2,4-dinitrophenylamino)propyltriethoxysilane (hydrophilic electron donor compound referred to as  $\phi\text{-NO}_2$ ). The homogeneous molecular films were obtained by vapor-phase adsorption<sup>[17]</sup> of the silanes onto clean silanol-enriched silicon wafers ( $\text{SiO}_x\text{H}$ ), in a dynamically evacuated chamber (40 min at  $5 \times 10^{-3}$  Torr). The binary heterogeneous surfaces were sequentially elaborated, based on the time control of the early-stage nucleation and domain growth mechanisms already known for solvent-coated organosilanes films.<sup>[18]</sup> The nanodomains were first realized by immersing the virgin silicon wafers in millimolar (1 mM) solutions of either the  $\text{CH}_3$  terminated compound in carbon-tetrachloride ( $20^\circ\text{C}$ , for 1 min), or  $\text{NH}_2$  terminated compound in ethanol ( $20^\circ\text{C}$ , for 6 min). The complete

heterogeneous binary molecular surfaces were obtained by assembling, in the remaining room of the silicon substrate, a continuous monolayer of the  $\text{NH}_2$  terminated compound around the  $\text{CH}_3$  nanodomains (and vice versa), via vapor-phase deposition technique.<sup>[17]</sup> The compositional (chemical) and topographical heterogeneities of the binary surfaces were characterized by X-ray photoelectron spectroscopy (XPS), contact angle, and atomic force microscopy (AFM) analyses. Typical structures of these nanoscale heterogeneous surfaces, as revealed by AFM in both height and phase contrast modes, are shown in panels

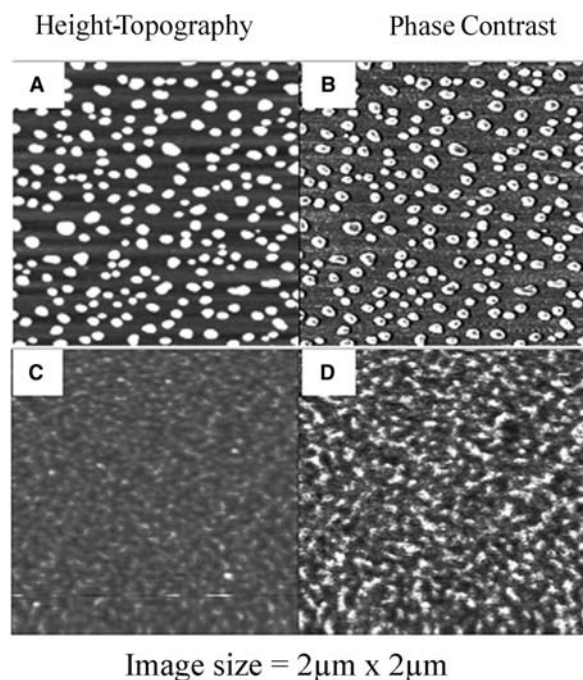


**Fig. 2** Height and phase AFM images of the binary heterogeneous molecular films: (A) and (B)  $\text{CH}_3\text{-NH}_2$  surfaces; (C) and (D),  $\text{NH}_2\text{-CH}_3$  surfaces. In both (A)–(B) and (C)–(D) panels, the lighter patches correspond to  $\text{CH}_3$  domains (in  $\text{NH}_2$  continuum) and  $\text{NH}_2$  domains (in  $\text{CH}_3$  continuum), respectively.

**Table 1** Wetting properties of the model molecular surfaces

Substrates	Contact angles $\theta$ of water drops ( $\pm 2^\circ$ )			
	Equilibrium $\theta_e$	Static advancing $\theta_a$	Static receding $\theta_r$	Hysteresis ( $\theta_a - \theta_r$ )
CH <sub>3</sub>	105	112	103	9
NH <sub>2</sub>	45	60	20	40
$\phi$ -NO <sub>2</sub>	50	64.5	25	39.5
CH <sub>3</sub> -NH <sub>2</sub>	66	85	59	26
NH <sub>2</sub> -CH <sub>3</sub>	67	86	51	35

(A)–(B) of Fig. 2 for the heterogeneous substrate composed of CH<sub>3</sub> domains in NH<sub>2</sub> continuum (referred to as CH<sub>3</sub>-NH<sub>2</sub>), and in panel (C)–(D) for NH<sub>2</sub> domains in CH<sub>3</sub> continuum (referred to as NH<sub>2</sub>-CH<sub>3</sub>). The wetting properties of the different substrates, including equilibrium, static advancing, and static receding contact angles against water drops are reported below in Table 1.

As in most of the current investigations dealing with the formation and functional properties of nanosize metal particles, this discussion is deliberately confined to aqueous nanocolloidal gold suspensions that are becoming a “standard,” both for their immense technological significance and their relatively easy synthesis. These colloidal suspensions are commonly synthesized using tetrachloroauric(III)-acid hydrate [HAuCl<sub>4</sub>] · H<sub>2</sub>O, a crystalline powder. Tetrachloroauric(III)-acid hydrate is dispersed by vigorous stirring in water, and stabilized by adding citric acid trisodium salt dihydrate C<sub>6</sub>H<sub>5</sub>Na<sub>3</sub>O<sub>7</sub> · 2H<sub>2</sub>O. The reduction of HAuCl<sub>4</sub> by trisodium citrates molecules in the aqueous phase leads to stabilized Au nanoparticles bearing the negative charge of the citrate ions.<sup>[2,19]</sup> Four nominal (here, meaning initial) concentrations of nanocolloidal suspensions of particle size  $d_p = 30 \pm 5$  nm, referred to as “30 nm susp,” were prepared in this manner.<sup>[17,20]</sup> A smaller particle size suspension,  $d_p = 10 \pm 3$  nm, referred to as “10 nm susp” was also prepared following the same general procedure, supplemented in this case by the addition, under stirring, of an aqueous solution of NaBH<sub>4</sub> to enhance the dispersion toward smaller particle size.<sup>[2,19,20]</sup> The nominal characteristics of these suspensions and their wetting parameters on

the model surfaces are reported in Tables 2 and 3, respectively.

## ADSORPTION PATTERNS

Here the main issue is addressed as follows. How the lateral ordering, topology, and characteristic length scales of a two- or three-dimensional assembly of nanoparticles are, or can be, controlled by the physical and chemical properties of the underlying substrate, when these particles are allowed to “freely” adsorb from a colloidal suspension onto these substrates? Are model hydrophobic and hydrophilic surfaces, such as electron donating-accepting surfaces, and their structuring in antagonistic binary hydrophobic/hydrophilic domains, capable of tuning the binding, coverage, and lateral organization of the Au nanoparticles during adsorption? To answer these questions, the model substrates were simply immersed for different times in the suspension bath, at 21°C. After this adsorption step, the samples were taken from the bath and washed off with pure water to remove the remaining thick dispersion film that is drawn from the bath. The thin water film, which may result from this washing step (depending on the substrate’s wetting property), is then allowed to dry in ambient conditions [21°C, 30% relative humidity (RH)], and the samples characterized for the lateral ordering of the adsorbed and self-organized nanoparticles arrays. The AFM pictures of Fig. 3A–E represent the typical adsorption patterns obtained on the different substrates, after 1 hr immersion in the reference “30 nm susp” of volume fraction  $\phi_{ref} = 1.5 \times 10^{-5}$ . For CH<sub>3</sub>,  $\phi$ -NO<sub>2</sub>, and NH<sub>2</sub>, the extent of the surface coverage during the deep coating is readily accounted for by classical surface thermodynamics, based on the balance of the intermolecular forces involved in these adsorption processes. Neglecting gravity-driven precipitation, the adsorption at the hydrophobic substrate solely arises from the low-magnitude CH<sub>3</sub>-particle interactions, which mainly involves the long-range London-van der Waals dispersion forces (vdW). Thus the very low coverage of CH<sub>3</sub> substrates (Fig. 3A) simply arises from the unfavorable competition between the higher

**Table 2** Nominal characteristics of the investigated nanocolloidal gold suspensions

	Particle size (nm)	Nominal concentration		Nominal pH
		Wt. %	Volume fraction $\phi$	
Reference <sup>a</sup> “30 nm susp”	30 ± 5	0.03	$1.5 \times 10^{-5}$	~6.5
“10 nm susp”	10 ± 3	0.01	$5 \times 10^{-6}$	~6.5

<sup>a</sup>“10 nm susp” refers to the smaller particle size suspension,  $d = 10$  nm.

<sup>a</sup>Reference “30 nm susp” refers to the suspension of particle size and volume fraction of  $d = 30 \pm 5$  nm and  $\phi_{ref} = 1.5 \times 10^{-5}$ , respectively. Three other concentrations, prepared from this reference “30 nm susp” were investigated: 1)  $\phi = 10^{-2}\phi_{ref}$ ; 2)  $\phi = 0.1 \times \phi_{ref}$ ; and 3)  $\phi = 5\phi_{ref}$ .

**Table 3** Equilibrium and receding wetting parameters of the reference “30 nm susp” drop on the different model substrates, measured at 20°C and 30% relative humidity (RH), using 8  $\mu\text{L}$  drops (the one hereafter used for drying experiments)

Model molecular surfaces	$\text{CH}_3$	$\text{NH}_2$	$\phi\text{-NO}_2$	$\text{CH}_3\text{-NH}_2$	$\text{NH}_2\text{-CH}_3$
Equilibrium contact angle ( $^\circ$ )	101	5	57	85	85
Contact diameter $2R$ (mm)	$\sim 2$	10	4	$\sim 3$	$\sim 3$
Receding contact angle ( $^\circ$ )	$\sim 90$	$\sim 0$	$\sim 15$	—	—

solvent retention (higher solvent–particle interaction) and the low-magnitude vdW particle–substrate ones. In addition, the washing step that follows the deep coating also contributes to draw away loosely attached particles. On the other hand, a highly packed and cohesive array, mainly composed of single Au nanoparticles, is formed onto the hydrophilic and electron-accepting amine terminated  $\text{NH}_2$  substrate (Fig. 3B). The formation of the dense particle arrays here is driven by the strong specific particle–surface interactions involved in this system. At  $\text{NH}_2$  terminated surfaces that can protonate ( $\text{NH}_3^+$ ) in the aqueous suspension during adsorption, the negatively charged gold particles  $[\text{Au}(\text{citrate})_{\text{ads}}^-]$  can either bind to the substrate via hydrogen bonds (H-b) or electrostatic interactions. At ambient temperature (298 K), the strength of these specific interactions lies between 10 kT per bond, for electron donor–acceptor and H-bonds such as in  $[\text{Au}(\text{citrate})_{\text{ads}}^- \text{H}_2\text{N}]$ , and 200 kT per bond for interactions, such as in the ionic structure  $[\text{Au}(\text{citrate})_{\text{ads}}^- \text{H}_3^+\text{N}]$ . These bonds are much stronger than  $\sim 1$  kT/bond of the vdW forces involved in  $\text{CH}_3$  substrate–particle interactions. As a result, one thus expects both the strength of the particle–substrate attachment as well as the rate and extent of the surface coverage to be of higher magnitude at  $\text{NH}_2$  substrates. This extent of surface coverage  $\Gamma$  is finally well

accounted for by the Gibbs equation  $\Gamma \sim sC_{\text{vi}} \exp(-\Delta F/kT)$ , where  $s$  and  $C_{\text{vi}}$  are the particle size and concentration at the interface and  $\Delta F$  is the free energy of adsorption. Assuming the entropy loss,  $-T\Delta S$ , for the adsorbed particles (clusters) to be comparable at both substrates, it is essentially the energy term,  $\Delta U = (U_{\text{ads}} - U_{\text{sol}})$ , that drives the adsorption amount at equilibrium, as discussed above. This naturally applies to the hydrophilic electron-donating  $\phi\text{-NO}_2$  substrate (Fig. 3C), where one may even expect  $\Delta U$  to be  $> 0$  (or, at least,  $\sim 0$ ), because of the repulsive electrostatic interactions between the identically charged gold particles and electron-donating  $\phi\text{-NO}_2$  surface groups. Of particular interest is the strong cohesion and stability of the nanogold particle assemblies formed at the amine terminated substrate that remains unchanged, at the same AFM observation scale, after  $\sim 30$  sec sonication in water. Although heterogeneous substrates present comparable surface fraction<sup>[21]</sup> of the two molecular phases and wetting properties (Tables 1 and 3), the adsorption structures formed at these substrates are significantly different in both their coverage and aggregation topology. As for homogenous substrates, the adsorption pattern at the binary  $\text{NH}_2\text{-CH}_3$  surface (Fig. 3D) is dominated by the intermolecular forces and related adsorption thermodynamics. This leads to an aggregation pattern

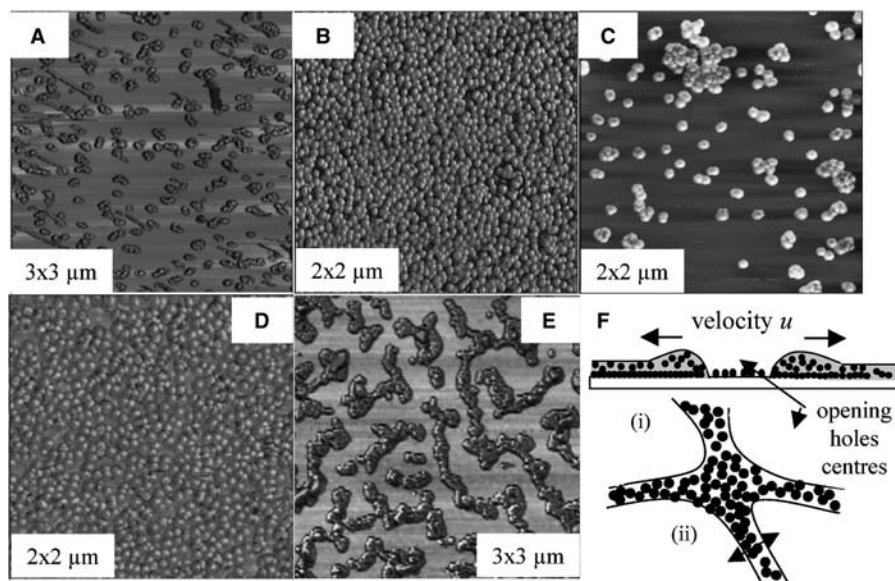


**Fig. 3** AFM images represent the adsorption patterns obtained after 1-hr immersion in the “30 nm susp” on the homogeneous (A)  $\text{CH}_3$ , (B)  $\text{NH}_2$ , (C)  $\phi\text{-NO}_2$  substrates, and binary heterogeneous (D)  $\text{NH}_2\text{-CH}_3$  and (E)  $\text{CH}_3\text{-NH}_2$  substrates. The growth mechanism of the interconnected network [panel (E)] is sketched out in (F). Here the reorganization of the particles arise from both the specific surface structure and the balance between shear and resisting adhesion forces,  $\tau a_c > \mu F_{\text{adh}}$ , that drive the collection of the particles ( $a_c$  and  $\mu$  being the particle/substrate contact area and friction coefficient, respectively).

similar (although less dense) to the one formed on  $\text{NH}_2$  substrates. On the other hand, a more complex pattern, not easily predictable from the above thermodynamic considerations, is observed at the heterogeneous  $\text{CH}_3\text{-NH}_2$  (Fig. 3E). Furthermore, there is no trivial length-scale correlation between the emerging adsorption patterns and the nanoscale organization of the antagonistic molecular domains at the underlying heterogeneous substrates, as one could expect, for instance, from simple size matching and selective adsorption at the  $\text{NH}_2\text{-CH}_3$  substrate. Thus it seems that neither the macroscopic surface properties, which are comparable for both  $\text{NH}_2\text{-CH}_3$  and  $\text{CH}_3\text{-NH}_2$  (Tables 1 and 3), nor the discrete organization of the domain phases can independently account for the emergence and topological features of nanocolloidal adsorption patterns at these nanoscale heterogeneous substrates. As sketched out in Fig. 3F, it is the late-stage drying of the residual film, either drawn from the immersion bath or left behind by the washing step, that definitely determines the topology of these adsorption patterns, especially the interconnected network observed at the heterogeneous  $\text{CH}_3\text{-NH}_2$  substrate. This is particularly the case when an adsorbed sublayer particle array exists, to which the drying of the residual film (dewetting, drainage) can be correlated to some extent. This was shown to be the case for the heterogeneous  $\text{CH}_3\text{-NH}_2$  by a closer (nanoscale) observation of the intersegments space,<sup>[17]</sup> contrary to the low coverage  $\text{CH}_3$ ,  $\phi\text{-NO}_2$ , and  $\text{NH}_2\text{-CH}_3$  substrates. Fig. 3F describes the three steps involved in this possible mechanism of formation of the segments network: the late-stage dewetting (rupture) of the drying film, the collection of loosely adsorbed particles in the moving rims around the opening holes, and the formation of the interconnected segments by conjoining rims that are stable against Rayleigh instabilities.<sup>[22]</sup> Finally, these results show that two parameters, both related to the surface properties of the substrate, can structure the aggregation pattern arising from the adsorption of nanosize particles from a colloidal suspension. On smooth and homogenous substrates, it is the macroscopic surface properties (surface energy, intermolecular forces, wetting) that predominate, at both length scales the final pattern. On the other hand, this pattern is determined on substrates which are heterogeneous at the nanoscale by the organization of the heterogeneities that strongly couple with the late-stage dewetting, thus causing redistribution and reorganization of particles at the substrate.

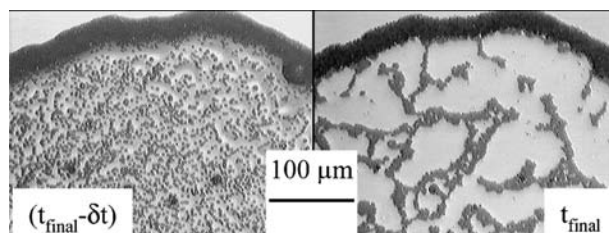
## DRYING PATTERNS

The drying of suspension drops, and in particular, the growth mechanisms of the often-observed thick

peripheral particle deposits (rings) have been extensively addressed in the literature.<sup>[13–16]</sup> Such particle rings were shown to arise as a result of the pinning of the contact line and the outward solvent (and particles) flow that is driven by the evaporation gradient along the drop radius, as illustrated in Fig. 4.<sup>[23]</sup> On the other hand, the dependence of these drying patterns on the structural properties of the underlying substrates, and more specifically, those involving nanosize colloidal particles have received considerably less attention. As shown in the central region of the drying drop in Fig. 4, micronsized particles can already form structures that are significantly different from the peripheral rings, even at non-attaching (adsorbing) substrates. In drying nanocolloidal suspensions, large-scale patterns of much higher complexity can form,<sup>[4,8,24]</sup> because of the stronger coupling between the late-stage dewetting and the time evolution of the suspension bulk properties,<sup>[24]</sup> which are here amplified by size effects: high number of particles in the drop for comparable volume fraction, low hydrodynamic radius and inertia, and high diffusion. The present section is focused on the discussion of large-scale complex patterns emerging in drying nano-colloidal suspensions, with a special emphasis on the underlying mechanisms and critical parameters governing both their formation and topological features.

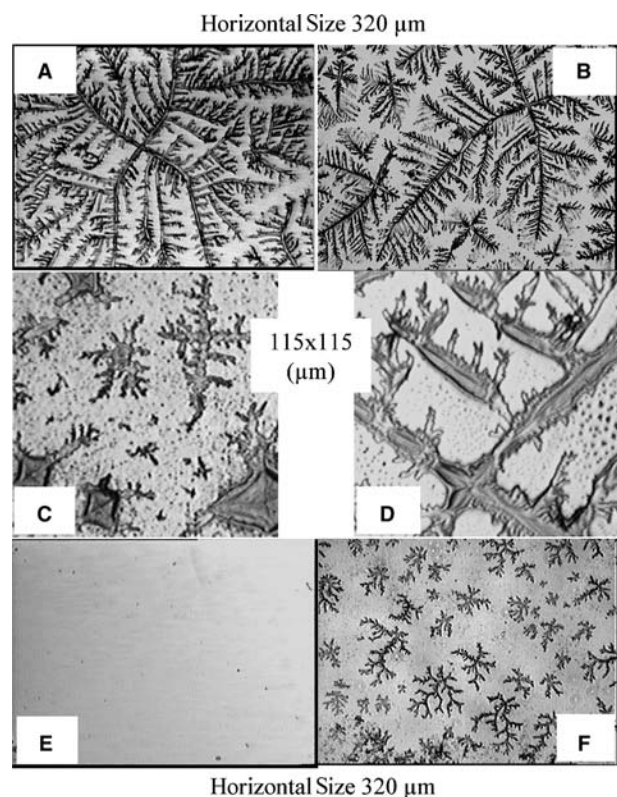
The experiments were generally performed (unless otherwise specified) by depositing 8  $\mu\text{L}$  drop of suspension on the substrates, and drying under ambient conditions (21°C, 33% RH). The drying kinetics was observed and recorded by using an optical microscope equipped with a video-camera device. Under these conditions, the evaporation rate  $v_e$  and time scale at complete evaporation  $t_e$  of the reference “30 nm susp” drop ( $d_p = 30 \text{ nm}$ ,  $\phi_{\text{ref}} = 1.5 \times 10^{-5}$ ), as measured by weighing its mass on a microbalance, were found to be  $\sim 3 \mu\text{g}/\text{sec}$  and  $\sim 30 \text{ min}$ , respectively, in  $\text{NH}_2$  and  $\phi\text{-NO}_2$  substrates.

Fig. 5 shows the most relevant results obtained for the three volume fractions of the “30 nm susp”



**Fig. 4** Evaporation of a micronsized (3  $\mu\text{m}$ ) polystyrene suspension drop on a nonwetting substrate, showing both the peripheral aggregation and the late-stage dewetting structure in the center of drying spot. *Source:* From Ref.<sup>[23]</sup>, unpublished result.





**Fig. 5** Drying patterns of “30 nm susp” drops formed at the virgin (A)  $\text{NH}_2$ , (B)  $\phi\text{-NO}_2$ , (C)  $\text{NH}_2\text{-CH}_3$ , and (D)  $\text{CH}_3\text{-NH}_2$  substrates using  $8\ \mu\text{L}$  of the reference volume fraction  $\phi_{\text{ref}} = 1.5 \times 10^{-5}$ , (E) at the virgin  $\text{NH}_2$  substrate using  $8\ \mu\text{L}$  of volume fractions  $\phi = 10^{-2}$  to  $0.1\phi_{\text{ref}}$ , and (f) using  $40\ \mu\text{L}$  of volume fraction  $\phi = 0.1\phi_{\text{ref}}$ .

(Table 2) at the virgin model substrates. At hydrophobic  $\text{CH}_3$  substrates (not represented here), only a thick and featureless particle deposit is obtained at the center of the drop at the end of the drying. The absence of structured pattern on this substrate was somehow predictable because of the high contact angle and the too-low contact area of the suspension drop. In this case, both the nonwetting solvent and nonattaching particles accumulating in the wedge are entrained by the retiring drop, up to the complete line pinning for some critical amount of the peripheral aggregate. This results in a residual gel-like droplet that dries and forms the observed single deposit. Panels (A) and (B), on the other hand, show large-scale and coarse multibranch aggregates, characterized by a main fourfold dendrite-like structure, along which  $\pi/2$ -oriented and bifurcating secondary branches are formed on the hydrophilic wetted  $\text{NH}_2$  and  $\phi\text{-NO}_2$  substrates. The early line pinning resulting from these wetting properties is further increased throughout the evaporation by the outward particles–solvent flow. Nevertheless, because of the low contact angles (reduced wedge volume) and large contact areas

(especially for  $\text{NH}_2$ ), which favor the confinement of the particles in the center of the drop and impede their convective migration, substantially less peripheral deposits are formed in these cases. It is this particular distribution of particles and clusters within a rather extended remaining suspension film (as opposed to non-wetting substrates) and the late-stage dewetting process of this film that give rise to the complex structure formation on  $\text{NH}_2$  and  $\phi\text{-NO}_2$ . At the heterogeneous and low wettability substrates (Tables 1 and 3), the aggregation patterns are of lower complexity (Fig. 5C,D) and are mostly composed of coarse fourfold dendrites and pyramidal (“degenerated” dendrites) aggregates. Although they strikingly demonstrate the non-random character and critical dependence of the observed patterns on the surface properties of the underlying substrate, the above results (Fig. 5A–D) involving unique “30 nm susp” drops of nominal volume fraction  $\phi_{\text{ref}} = 1.5 \times 10^{-5}$  cannot account for the influence of the bulk parameters (concentration) in this pattern formation. This influence is illustrated in Fig. 5E, using suspension drops of concentrations  $\phi = 0.1\phi_{\text{ref}}$  (or  $10^{-2}\phi_{\text{ref}}$ ), at the pattern-forming  $\text{NH}_2$  substrate (in the sense of its wetting properties). The absence of pattern in this dilute regime ( $\phi \leq 0.1\phi_{\text{ref}}$ ) and the densification of the emerging aggregates (not shown here, see Ref.<sup>[20]</sup>) at higher concentrations ( $\phi \geq 5\phi_{\text{ref}}$ ) clearly indicate that a nominal volume fraction range exists that allows, through its time evolution, a critical (threshold) volume fraction  $\phi^*$  to be reached, which is required for complex structures to form in the late stage of drying. To obtain further insights regarding the influence of these time-dependent bulk properties (namely the time increase of the volume fraction with the evaporation) on the emergence and morphology of the aggregates, the structural evolution within “30 nm susp” drops of nominal volume fractions  $\phi_{\text{ref}}$  and  $0.1\phi_{\text{ref}}$  was investigated at both pattern-forming  $\text{NH}_2$  and  $\phi\text{-NO}_2$  substrates. As shown in Fig. 6, large-size ( $\sim 50\ \mu\text{m}$ ), interconnected wormlike clusters<sup>[7,24]</sup> are formed in the late stage of the evaporation within the “30 nm susp” drop of volume fraction  $\phi_{\text{ref}}$ , at both pattern-forming substrates. In the low volume fraction drop ( $0.1\phi_{\text{ref}}$ ), only micronsize aggregates, comparable to those formed in the early drying stage of the “30 nm susp” drop of volume fraction  $\phi_{\text{ref}}$ , were observed in the late stage of the drying (Fig. 6C). Thus these results strongly suggest that the emergence of the complex drying patterns requires, in addition to the surface properties of the underlying substrate, that a threshold volume fraction  $\phi^*$ , at which interconnected bulk aggregates appear in the suspension, be reached during the evaporation. One now can reasonably think that these large-size, wormlike bulk clusters actually constitute the initial seeds for the formation of the complex

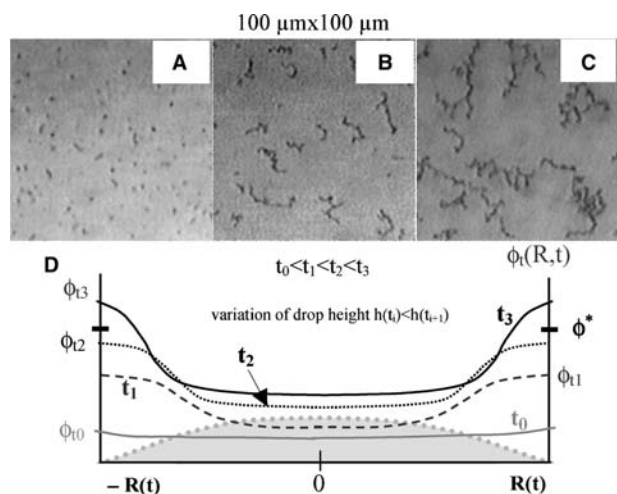


**Fig. 6** Structural evolution of the drying suspension in the (A) early, (B) medium, and (C) late stages of the evaporation where bulk clusters appear, and (D) phenomenological picture of this structural evolution in terms of the time and spatial variations of the suspension volume fraction  $\phi(R,t) = \phi_t$ , where  $R$  is the radius of the drying drop.

aggregations patterns that develop through the late-stage dewetting of the remaining film and related hydrodynamic effects (see below). We actually brought an indirect evidence of this conjuncture by depositing on the pattern-forming  $\text{NH}_2$  substrate a larger drop volume (40 vs.  $8\ \mu\text{L}$ ) of the “30 nm susp” suspension of concentration  $\phi = 0.1\phi_{\text{ref}}$ , which is subcritical as regards the pattern formation, when deposited at the standard volume of  $8\ \mu\text{L}$ . By doing this, one could restore both the formation of wormlike bulk clusters and complex aggregation patterns on the substrate (Fig. 5F). Basically, this experiment simply amounts to increasing the total number of particles  $n_0$  in the reservoir (drop). If  $v_p$  is the average nanoparticle volume, this total number of particles, which is conserved during the evaporation, is related to the nominal concentration  $\phi$  and initial drop volume  $v_0$  as  $n_0 \sim (\phi v_0 / v_p)$ , from which the time dependence of the evaporating drop volume fraction follows as  $\phi_t = (\phi v_0) v_t^{-1}$ , where  $v_t$  is the actual drop volume at time  $t$ . In the late stage of the drying,  $v_t \ll v_0$ , and the volume fraction  $\phi_t$  of the suspension that remains subcritical for smaller initial drop volumes is now shifted toward the threshold value  $\phi^*$ , where both interconnected bulk clusters and complex aggregation patterns appear on a pattern-forming substrate. And as long as the total number of particles in the drop is below a certain value, the interparticle separation during drying will always lie above length scales (hundreds nm to  $\mu\text{m}$ ), where long-range intermolecular and hydrodynamic forces usually develop and drive particle–particle aggregation. Using a simple scaling, the dependence of this interparticle separation  $d_{\text{pp}}$  on the residual

volume  $v_t$  can be roughly computed as  $d_{\text{pp}} \approx 6(v_t / \pi n_0)^{1/3}$ , assuming the whole residual volume to be virtually occupied by the nanoparticles,  $v_t \sim n_0 v_p = (\pi d_{\text{pp}}^3 / 6) n_0$ . As the evaporation proceeds and  $v_t$  decreases, the long range vdW and electrostatic forces, to which one should add diffusion and electrostatic forces, vary respectively, as  $(1/n_0)^{2/3}$  and  $\exp(-1/n_0^{1/3})$ , and control particle sticking and bulk cluster formation in the drying suspension. A simplified phenomenological picture of these structural changes within the drying suspension, as expressed by the time dependence and spatial variation of the volume fraction  $\phi_t$  with the drop radius, is sketched out in Fig. 6D. Actually, these concentration-dependent morphological transitions and the existence of critical volume fractions are well known from phase diagrams studies of colloidal suspensions.<sup>[25]</sup> Finally, whenever the bulk conditions (threshold  $\phi^*$  and related seeds formation) are satisfied in a drying drop, both the emergence and morphological features of the complex patterns exclusively depend on the late-stage dewetting and hydrodynamics, which are controlled by the underlying substrates properties, as further evidenced by the drying patterns shown in Fig. 7. These results are obtained for the same general drying conditions of “30 nm susp” drop of volume fraction  $\phi = \phi_{\text{ref}}$ , on *precoated*  $\text{NH}_2$ ,  $\text{CH}_3\text{-NH}_2$ , and  $\text{NH}_2\text{-CH}_3$  substrates (substrates bearing the adsorption layer formed by deep-coating). Once again, the change in the complex aggregate morphology is strongly determined by the wetting properties and specific topology of these precoated substrates. While the patterns (not shown here) obtained on the precoated  $\phi\text{-NO}_2$  substrate are all comparable to the ones already observed on the virgin one, more complex aggregates now appear at the *precoated*  $\text{CH}_3\text{-NH}_2$  (Fig. 7A) and the initial coarse dendrites, which were formed on the virgin substrate, are now much finer. On the other hand, more qualitative differences emerge on *precoated*  $\text{NH}_2$  (Fig. 7B) and  $\text{NH}_2\text{-CH}_3$  (Fig. 7C) substrates. Contrary to its virgin homologous, large-scale multibranching aggregates, quite similar to those observed on virgin  $\text{NH}_2$  and  $\text{NO}_2$ , now appear on *precoated*  $\text{CH}_3\text{-NH}_2$  substrates. The most significant change arising from precoating is observed at  $\text{NH}_2$  substrate (Fig. 3B) where much finer and highly ordered fractal aggregates are formed (Fig. 7B), whose symmetry depends on the location in which they are formed along the drop radius. Whereas symmetric aggregates appear in the late stage of the drying at the center of the drop, during the dewetting (rupture) of the residual suspension film, the asymmetrical ones are formed at the periphery of the receding drop. The determining fingerprint of the underlying surface properties (wetting, topology), which shows up in the aggregates morphology, thus



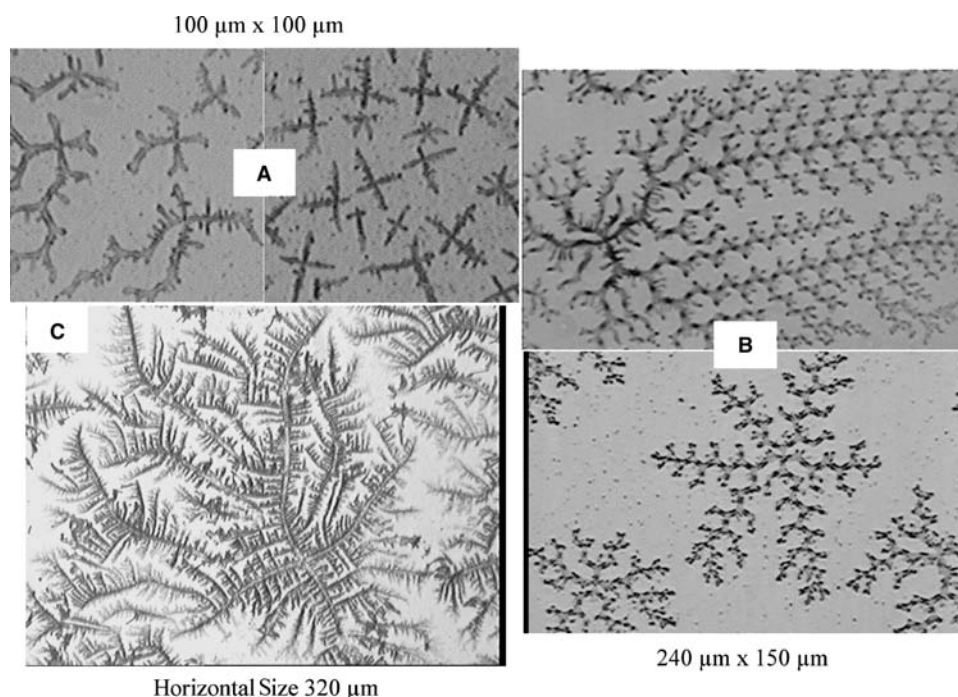


**Fig. 7** Drying patterns of the reference volume fraction “30 nm susp” drops at the precoated substrates, showing the two structural types of aggregates formed on (A)  $\text{CH}_3\text{-NH}_2$  and (B)  $\text{NH}_2$ , and (C) the representative aggregation pattern observed on  $\text{NH}_2\text{-CH}_3$ .

seems to arise through the late-stage hydrodynamic shear that develops during the dewetting, and structures both the confined seeds (bulk clusters) and free particles in the residual film. The parameters that control this shear structuring are 1) the receding contact angle  $\theta_r$  and 2) the surface topography (roughness, porosity) of the substrate, which determines the magnitude of the shear stress experienced by the seeds. Assuming interface tension gradients,  $\partial\gamma/\partial x$ , at the suspension–air interface to be negligible,<sup>[26]</sup> the structuring of the seeds is mainly provided by the viscous shear  $\tau$  at the solid–liquid interface, which is related to the velocity  $u$  in a unidirectional flow (along  $x$  axis  $\sim$  drop radius) through the phenomenological relation,<sup>[24]</sup>

$$\begin{aligned}\tau &= h(\partial p/\partial x) = -c^{te}\eta(u/h^*) \\ &\sim -\eta u(l\text{tg}\theta_r + b)^{-1}\end{aligned}\quad (1)$$

where  $(\partial p/\partial x)$  is the pressure gradient in the confined film (wedge),  $h^* = (h + b)$ , and  $h \sim l\text{tg}\theta_r$ .

Although both terms in Eq. (1) determine, to some extent, the magnitude of  $\tau$  (suspension viscosity  $\eta$ ,  $u$ ,  $\theta_r$ , and  $l$ , the lateral size of the wedge), the one that explicitly accounts for the particle attachment is  $h^* = (h + b)$ , the fluid thickness  $h$  in the receding wedge, augmented by the eventual slippage of the particles at the substrate, characterized by the length  $b$ .<sup>[27]</sup> Instead of the slippage length that is of general use

for liquid phases flowing past a wall, one may prefer for these nanoparticles the sticking coefficient  $\chi \sim (1 + b)^{-1}$  that rigorously accounts for the same boundary condition. Because of the complexity of the system, the direct determination of  $l$  and  $b$  that are necessary to a quantitative evaluation is rather difficult. On the other hand, the above relation provides a phenomenological basis for the qualitative discussion of the critical interplay between the surface properties, the late-stage dewetting and hydrodynamic shear, and the emergence and morphological feature of the complex nano-colloidal surface patterns. For instance, at nonwetted and nonparticle attaching  $\text{CH}_3$  substrates ( $\theta_r \gg 1$  rad, high  $b$  or equivalently low  $\chi$ ), one expects the magnitude of the shear  $\tau$  to be very low. Both free particles and seeds (if they exist) are simply collected within the rather large moving wedge, leading to the observed residual dense deposit in this case. On wetting and particle sticking substrates ( $\text{tg}\theta_r \sim \theta_r \ll 1$  rad, high  $\chi$ , or  $b \sim 0$ ), a higher magnitude shear stress  $\tau$  develops within the receding wedge. The confined seeds and free particles are further connected and stretched along the substrate, leading upon the retraction of the fluid to well-organized multibranching patterns.

As illustrated on *precoated*  $\text{NH}_2$  and heterogeneous substrates, these late-stage hydrodynamic effects can strongly couple with the topography of the underlying substrate to critically determine the specific topology and structural order of the aggregates. The most

illustrative demonstration of this is given by the *precoated* NH<sub>2</sub> substrate, which actually constitutes a 2-D nanoporous lattice that can drive both the flow and the alignment of the aggregates along preferential “streamlines” of the porous bed during the shear-ordering. Contrary to micronscale particles that can individually (as opposed to clusters) protrude out of the residual solvent, allowing both meniscus and capillary forces to develop, one does not expect such attractive capillary force to play a determining role for nanocolloids, as long as their size remains comparable or less than the thickness at which the residual film dewets. This may, of course, no longer be true when clusters having thickness large enough to form such “interclusters” meniscus are present in the drop. Yet, the net force resulting from the balance between the late-stage hydrodynamic shear and anchoring forces would have largely dominated these attractive capillary forces which are essentially significant on non-attaching surfaces, on the pattern-forming NH<sub>2</sub> substrate, for instance. The high structural order of the patterns at these *precoated* NH<sub>2</sub> substrates, characterized by the repetition of hexagonal units cells along the aggregate branches, thus seems to be strongly correlated to the topography of the underlying preadsorbed particles lattice. However, the explicit length scale and structural correlations between the morphological features of the patterns, on one hand, and the underlying surface topography (preadsorbed particles lattice) and hydrodynamic flow, on the other, remain essentially obscure, and would certainly deserve more systematic model investigations. On the other hand, these investigations clearly show that the symmetry of the aggregate, which depends on its location in the drying spot (periphery or center), is exclusively determined by the local dewetting–retiring mode of the residual fluid, as illustrated in Fig. 8. The aggregates forming at the drop periphery as the contact line recedes have the characteristic asymmetry of the flow

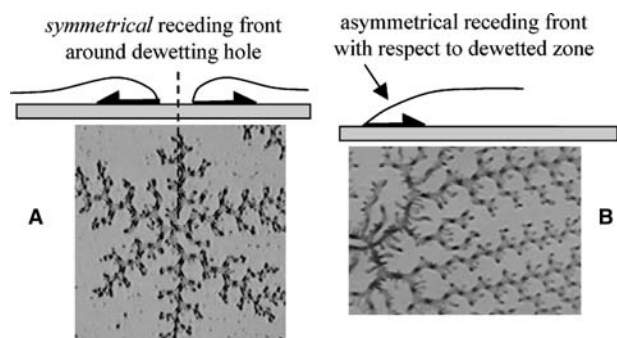


**Fig. 8** Late-stage dewetting events and mechanisms that determine the topological feature of the emerging aggregates, (A) symmetrical and (B) asymmetrical dewetting-flow and aggregate stretching modes.

and viscous shear (Fig. 8A–B) associated with the inward motion of the fluid that highly structures these aggregates along the flow (peripheral nucleation, inward stretching, and propagation of the branches). The aggregates appearing in the center of the drying spot, on the other hand, are formed during the rupture-dewetting of the residual suspension film. These aggregates have the axisymmetry of the flow (fluid rims) and viscous shear around the nucleation point of the growing dewetting holes (Fig. 8A–B), which coincides with the aggregate center. One noteworthy factor here is the strong similitude between these nanocolloids drying patterns and their formation process, and those usually produced via Saffman–Taylor instabilities in Hele–Shaw cells.<sup>[28]</sup> Also, for these Hele–Shaw structures, the configuration of the flow, axial or radial, determines the symmetry of the resulting complex patterns.<sup>[28]</sup> In most of these flow-induced structures, both the symmetric and asymmetrical aggregates formed on the *precoated* NH<sub>2</sub> substrates (Fig. 8) are fractal, with dimensions  $D$  of 2.03 and 1.61, respectively, as determined from the log–log plot of the number of particles  $N$  contained in concentric boxes of radius  $R$ , using the standard relation  $N \sim R^D$ . Interestingly, the asymmetrical peripheral aggregates are almost completely absent, or are of very low stretching magnitude on lower wettability substrates (NO<sub>2</sub>, heterogeneous and, of course, CH<sub>3</sub>) compared to NH<sub>2</sub>. Furthermore, it was shown that these asymmetrical aggregates may not necessarily form, even on substrates that are wetted by the suspension solvent (Ref.<sup>[20]</sup>, see also Fig. 9C). This seems to suggest that the condition of wetting required for the formation of a large residual thin film can be achieved, principally with respect to the solvent of the dispersion, for a negligible attachment (adhesion, anchoring) of the dispersed particles to the substrate. On these substrates, the peripheral retraction of the drop mainly involves the simple entrainment and accumulation of the loosely attached particles and clusters, which therefore experience a negligible shear-induced stretching. Therefore it seems that not only the condition of wetting, which may be achieved by the solvent independently of the particles, is required for the two aggregation symmetries to appear, but also that of particle anchoring, which is necessary for the shear-induced stretching to develop within the clusters (bulk seeds, especially) at the receding drop edge.

If the two critical parameters that determine both the emergence topology of the drying patterns are the actual volume fraction of the suspension in the late stage of the drying and the surface properties of the underlying substrates, the size of the nanoparticles also provides an additional parameter for the control of the aggregates morphology. Once the required bulk criterion is satisfied, one disposes of two key parameters that can

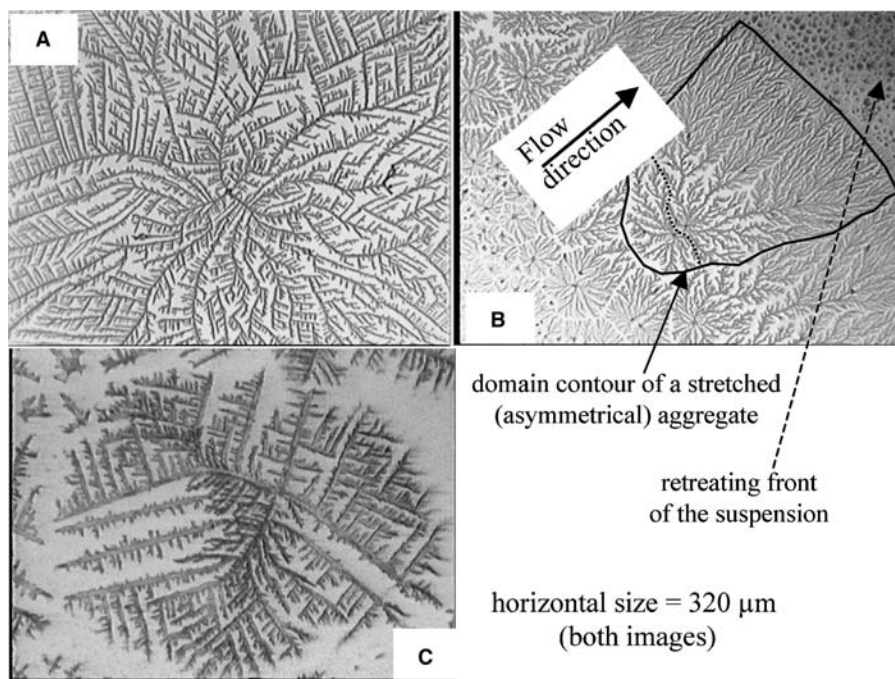


**Fig. 9** (A) and (B) Influence of particle size on the morphology of emerging patterns, as shown on the precoated  $\text{NH}_2$  substrate using “10 nm susp” drops ( $d_p = 10$  nm,  $\phi_{\text{ref}} = 5 \times 10^{-6}$ ); (B) further illustration of the predominating influence of the surface properties, provided here by the drying of the reference “30 nm susp” on the hydroxylated inorganic  $\text{SiO}_x\text{H}$  substrate, as opposed to the organic ones used throughout the entry.

be used to tune the late-stage drying events and produce nanocolloids aggregates of desired complexity and topological features (fractality, size, structural ordering). These are 1) *the critical surface parameters* (wetting, topography) and 2) *the size and distribution of the nanocolloids particles*. The potential effect of this particle size is demonstrated in Fig. 9A–B, which represents the drying pattern of “10 nm susp” drops on the *precoated*  $\text{NH}_2$  substrates. As for “30 nm susp” drops on the same substrates, both the symmetric aggregates appearing at the center of the drying spot and highly stretched peripheral (asymmetrical) ones are formed in these drying “10 nm susp” drops. However, at the difference of the “30 nm susp” that forms thicker and highly structured branches composed of hexagonal units cells on *precoated*  $\text{NH}_2$  substrates, the aggregates resulting from the “10 nm susp” drops are composed of much finer and higher number density branches that are essentially  $\pi/2$ -oriented with each other (dendrites). On the other hand, the presence in these drying “10 nm susp” drops of both symmetric and highly stretched (asymmetrical) aggregates (which are therefore independent on the particle size) well supports the existing conjuncture on the predominance of the substrate properties and related dewetting mode in the emergence of these two aggregation symmetries. The already demonstrated effect of the critical surface parameter is further highlighted in Fig. 9C, which shows one of the most representative aggregation topologies resulting from the drying of the reference “30 nm susp” drop ( $8 \mu\text{L}$ , nominal volume fraction  $\phi_{\text{ref}} = 1.5 \times 10^{-5}$ ), on a clean hydroxylated bare silicon wafer. On this

inorganic substrate, which is almost completely wetted by the suspension, one could reasonably expect from all the above results and discussion, the formation of large-scale complex aggregates, which are here composed of  $\pi/2$ -oriented secondary branches that emerge from the main fourfold dendrites.

## CONCLUSION

Based on the extended experimental results, we discussed the formation of both nanometer-scale and micronscale aggregation patterns that form during deep-coating adsorption and drying of nano-colloidal suspension drops (and films), respectively, at a representative ensemble of model substrates. Our results show that large-scale and well-organized dendrites and multibranch patterns can form during these processes, the emergence and topological feature of which were shown to be essentially controlled by two critical parameters. These are 1) the actual volume fraction of the drop in the late stage of the drying and, 2) the hydrodynamic shear involved in the dewetting and receding motion of either the macroscopic drop or the thin residual suspension film. The former determines a *threshold volume fraction* required for wormlike bulk clusters to form in the drying drop, and which lately serve as seeds for the formation of the complex surface patterns. The second parameter explicitly depends on the *surface properties* (wetting, particle adhesion, nanoscale topography), and determines the magnitude of the shear-induced structuring

(stretching) experienced by the confined particles and seeds within the receding wedge and residual suspension film. It was demonstrated that once the required bulk criterion was satisfied, both the particle size and their distribution provide additional parameters, which can be used with their critical surface counterpart (shown to be adjustable) to tune the morphological features of the networks. Simple phenomenological models were proposed, which account for some of the observed experimental results. However, some fundamental questions remain. In particular, the relationship between the *underlying surface structure and properties*, on one hand, and the *characteristic length scales* (short and long-range ones) and *structural order in the emerging patterns*, on the other, remain essentially obscure. Understanding of these correlations is not only of fundamental importance regarding self-organization phenomena at interfaces, but also provides the practical key parameter toward the controlled elaboration of well-ordered, large-scale patterns from drying nanocolloidal dispersions. This issue certainly constitutes a central task that would deserve both theoretical and model experimental investigations in the near future.

## REFERENCES

- Kunz, M.S.; Shull, K.R.; Kellock, A.J. Colloidal gold dispersion in polymeric matrices. *J. Colloid Interface Sci.* **1993**, *156*, 240–249.
- Li, W.; Huo, L.; Wang, D.; Zeng, G.; Xi, S.; Zhao, B.; Zhu, J.; Wang, J.; Shen, Y.; Lu, Z. Self-assembled multilayers of alternating gold nanoparticles and dithiols: approaching to superlattice. *Colloids Surf., A* **2000**, *175*, 217–223.
- Templeton, A.C.; Chen, S.; Gross, S.M.; Murray, R.W. Water soluble, isolable clusters protected by tiopronin and coenzyme a monolayers. *Langmuir* **1999**, *15*, 66–76.
- Thill, A.; Spalla, O. Capillary against adhesion forces during drying of particle submonolayers on a solid substrate. *Langmuir* **2002**, *18*, 4783–4789.
- Wickman, H.H.; Korley, J.N. Colloidal crystal self-organization and dynamics at air/water interface. *Nature* **1998**, *393* (4), 445–447.
- Li, Q.; Zheng, J.; Liu, Z. Site-selective assemblies of gold nanoparticles on an AFM tip-defined silicon template. *Langmuir* **2003**, *19*, 166–171.
- Leontidis, E.; Kleitou, K.; Kyprianidou-Leodidou, T.; Bekiari, V.; Lianos, P. Gold colloids from cationic surfactant solutions. I. Mechanisms that control particle morphology. *Langmuir* **2002**, *18*, 3659–3668.
- Fang, J.; Soto, C.M.; Lin, T.; Johnson, J.E.; Ratna, B. Complex pattern formation by cowpea mosaic virus nanoparticles. *Langmuir* **2002**, *18*, 308–310.
- Bunde, A.; Havlin, S. *Fractals in Science*; Springer: Berlin, 1994.
- Soler-Illia, G.J.de A.A.; Sanchez, C.; Lebeau, B.; Patarin, J. Chemical strategies to design textured materials: from microporous and mesoporous oxides to nanometer networks and hierarchical structures. *Chem. Rev. Am. Chem. Soc.* **2002**, *102*, 4093–4138.
- Sicard, L.; Lebeau, B.; Patarin, J.; Zana, R. Study of the mechanism of formation of a mesostructured hexagonal alumina by means of fluorescence probing techniques. *Langmuir* **2002**, *18*, 74–82.
- Scoeman, B.J.; Babouchkina, E.; Mintovas, S.; Valtchev, V.; Sterte, J. The synthesis of discrete colloidal crystals of zeolite beta and their application in the preparation of thin microporous films. *J. Porous Mater.* **2001**, *8*, 13–22.
- Maenosono, S.; Dushkin, C.D.; Saita, S.; Yamaguchi, Y. Growth of a semiconductor nanoparticle ring during the drying of a suspension droplet. *Langmuir* **1999**, *15*, 957–965.
- Deegan, R.D.; Bagajin, O.; Dupont, T.F.; Huber, G.; Nagel, S.R.; Witten, T.A. Capillary flow as the cause of ring stains from dried liquid drops. *Nature* **1997**, *389*, 827–829.
- Parisse, F.; Allain, C. Shape changes of colloidal suspension droplets during drying. *J. Phys., II France* **1996**, *6*, 1111–1119.
- Deegan, R.D. Pattern formation in drying drops. *Phys. Rev. Lett.* **2000**, *61*, 475–485.
- Mougin, K.; Haidara, H.; Castelein, G. Controlling the two-dimensional adhesion and organization of colloidal gold particles. *Colloids Surf., A* **2001**, *193*, 231–237.
- Schwartz, D.K.; Steinberg, S.; Israelachvili, J.; Zasadzinski, J.A.N. Self-assembled monolayer by fractal aggregation. *Phys. Rev. Lett.* **1992**, *69*, 3354–3357.
- Grabar, K.C.; Allison, K.J.; Baker, B.E.; Bright, R.M.; Brown, K.R.; Freeman, R.G.; Fox, A.P.; Keating, C.D.; Musick, M.D.; Natan, M.J. Two-dimensional arrays of colloidal gold particles: A flexible approach to macroscopic metal surfaces. *Langmuir* **1996**, *12*, 2353–2361.
- Mougin, K. Surfaces Moléculaires Binaires Nanostructurées: compréhension et Contrôle des Phénomènes D'interface. In *Ph.D. Thesis*; Université de Haute Alsace: Mulhouse, France, Décembre, 2001; Chap. 4.
- Mougin, K.; Haidara, H. Wetting of thin liquid films at nanoscale heterogeneous surfaces. *Europhys. Lett.* **2003**, *61* (5), 660–666.
- Srolovitz, D.J.; Safran, S.A. Capillary instabilities in thin films. I. Energetics. *J. Appl. Phys.* **1986**, *60*, 2472–2475.
- Vonna, L. Phénomènes D'interface en Milieu Tensioactif Hors-Équilibre. In *Ph.D. Thesis*; Université de Haute Alsace: Mulhouse, France, Novembre, 1999; 144 pp.
- Mougin, K.; Haidara, H. Complex pattern in drying dispersions. *Langmuir* **2002**, *18*, 9566–9569.
- Romer, S.; Scheffold, F.; Schurtenberger, P. Sol-gel transition of concentrated colloidal suspensions. *Phys. Rev. Lett.* **2000**, *85*, 4980–4983.
- Haidara, H.; Vonna, L.; Schultz, J. Surfactant induced Marangoni motion of a droplet into an external liquid medium. *J. Chem. Phys.* **1997**, *107*, 630–637.
- de Gennes, P.G. On fluid/wall slippage. *Langmuir* **2002**, *18*, 3413–3414.
- Van Damme, H. Flow and interfacial instabilities in newtonian and colloidal fluids. In *The Fractal Approach to Heterogeneous Chemistry*; Avnir, D., Ed.; John Wiley & Sons Ltd.: Chichester, 1989; 199–226.

# Colloidal Nanoparticles: Electrokinetic Characterization

**Kunio Furusawa**

*Department of Chemistry, University of Tsukuba, Ibaraki, Japan*

**Hideo Matsumura**

*National Institute of Advanced Industrial Science and Technology,  
Tsukuba, Japan*

## INTRODUCTION

A charged colloidal particle suspended in an electrolyte solution is surrounded by a cloud of counterions. The set of the surface charges and countercharges is called the electrical double layer. The electrical double layer plays an essential role in various interfacial electrical phenomena on the particle surface and in the particle–particle interaction of colloid suspension.

Generally, it is almost impossible to measure the surface potential on colloid particles. However, we can measure the potential near the particle surface. It is called the zeta ( $\zeta$ ) potential. The zeta potential is the potential at the hydrodynamic slipping plane in the electrical double layer, hence its value is not precisely the same as that of making a stable suspension because the total interaction potential between two particles a bit distant from their surface is essential for a stable dispersion. The  $\zeta$ -potential has been considered to provide useful information necessary for preparing stable colloidal suspensions in many application fields including food preparation, agriculture, pharmaceuticals, paper industry, ceramics, paints, coatings, photographic emulsions, etc. The concept of the zeta potential is also very important in such diverse processes as environmental transport of nutrients, sol–gel synthesis, mineral recovery, waste water treatment, corrosion, and many more.

## OVERVIEW

These are several origins from which solid surfaces are charged: dissociation of chemical groups on the surface, preferential adsorption of cation or anion onto the surface, etc. The distribution of each ionic compound between the surface and the solution bulk is determined by the differences in the electrochemical potential of each compound between two phases: the

solid (surface) phase and the solution phase. Therefore the composition of the solution is an important factor that determines surface potentials. When  $H^+$  is the potential-determining ion, we can change the amount of surface charge by changing the pH of the solution. It is important to know the position of the isoelectrical point (IEP) (i.e., the pH value at which the particles have zero  $\zeta$ -potential). At the IEP, there are no repulsive forces and the particles are strongly aggregated because of the attractive van der Waals forces. In many cases, the stable colloidal particle dispersion is desired, so the colloidal suspensions are designed such that the pH of the suspension is well away from the IEP. The IEP data for a number of colloids of various compositions have been reported.<sup>[1]</sup> [Table 1](#) lists the IEP for some typical dispersions.

If colloid particles are brought to a concentrated situation through some engineering processes, it is not certain if the surface charges, and hence surface potential, hold the same values as those in diluted dispersions. It must be measured experimentally, and several methods have been explored in recent years.

Here, we briefly describe experimental methods of the measurements of  $\zeta$ -potential for the diluted and the concentrated particle systems, and how the control of zeta potential is useful for preparing composite particle systems in the last part of this report. The fundamentals of electrokinetics in colloidal systems have been described in numerous books in recent years.<sup>[1–3]</sup>

## MEASUREMENTS OF $\zeta$ OF PARTICLES IN DILUTED SUSPENSION

### Regular Method by Electrophoresis

The historical prominence of  $\zeta$ -potential has been because of its experimental accessibility via measurement of the electrophoretic mobility  $\mu$ . Electrophoretic

**Table 1** Isoelectric points

Compound	IEP (pH)
$\alpha$ -AlOOH	9.4
$\gamma$ -AlOOH	5.5–7.5
$\alpha$ -Al(OH) <sub>3</sub>	5.0–5.2
$\gamma$ -Al(OH) <sub>3</sub>	9.3
CdO	10.4
Co <sub>3</sub> O <sub>4</sub>	5.5
Co(OH) <sub>2</sub>	10.5
$\alpha$ -Fe <sub>2</sub> O <sub>3</sub>	8.3
$\beta$ -Fe <sub>2</sub> O <sub>3</sub>	6.7–8.0
Mg(OH) <sub>2</sub>	12
MnO, MnO <sub>2</sub>	6
NiO	9.5
SiO <sub>2</sub>	1.8–2.5
SnO <sub>2</sub>	4.5
TiO <sub>2</sub>	6
ZrO <sub>2</sub>	4

mobility is the velocity of the colloid particle  $v$  per unit field strength  $E$ :

$$v = \mu E \quad (1)$$

where  $\zeta$  is related with mobility by the equation from von Smoluchowski:<sup>[4]</sup>

$$\mu = \varepsilon \zeta / \eta \quad (2)$$

where  $\varepsilon$  or  $\eta$  are the permittivity or viscosity of the medium, respectively. In regular electrophoretic apparatus, we utilize a narrow capillary cell of cylindrical or rectangular shape. The migration velocity of the particles is measured by optical microscopy for larger-sized particles, or by observation of Doppler shift of laser light scattering signal for smaller particles. However, the capillary cells walls also bear electrical charges and hence have electrical double layers. Therefore the application of electrical fields causes the movement of charged liquid medium in the double layer, which is called electroosmosis. The electrophoretic migration of colloid particles is always superimposed on the electroosmotic liquid flow from the cell wall. The closed sample cell causes a back liquid flow through the generation of hydrostatic pressure gradient. At equilibrium, there are two positions where the liquid flow has zero velocity. These are called the stationary levels. Thus we can observe the true electromigration velocity of colloid particles at the stationary levels. Von Smoluchowski<sup>[4]</sup> showed the profile of electroosmotic

flow velocity ( $U_{\text{osm}}$ ) for a cylindrical cell:

$$U_{\text{osm}} = U_0(h^2/b^2 - 1) \quad (3)$$

and for a flat cell, which has an infinitely long width:

$$U_{\text{osm}} = U_0/2(3h^2/b^2 - 1) \quad (4)$$

where  $h$  is the distance from the cell center in the direction of cell thickness,  $b$  is the half-thickness of the cell, and  $U_0$  is the electroosmotic flow at the cell wall ( $h = b$ ). The stationary levels are located at a distance from the cell center to each side by the quantity  $h = b/\sqrt{2}$  for the cylindrical cell, or  $h = b/\sqrt{3}$  for the flat cell. Komagata<sup>[5]</sup> showed a more practically useful equation for a rectangular cell, which has a thickness of  $2b$  and a width of  $2w$  ( $b < w$ ); the stationary level is located at a distance from the cell center to each side by the quantity  $h = b\sqrt{(1/3)(1 + 384b/\pi^5w)}$ . The traditional measurements of zeta potentials of particles are conducted at these stationary levels.

### Electrophoretic Measurements Using a Standard Sample

The profile of electroosmotic flow is parabolical. Thus the velocity gradient of the liquid at the stationary levels is usually large and the observed velocity of the particles changes rapidly with cell depth. It causes substantial errors in electrophoretic mobility measurements from the wrong setting of observing points. However, if the electrophoretic measurements can be carried out by using a reference sample as a standard, the electrophoretic mobility of the unknown sample can be determined at any cell depth by subtracting the mobility of the reference particles at the same level, because the velocity of electroosmotic liquid flow induced by the cell wall has the same value under the same experimental conditions. Therefore one can obtain real electrophoretic mobility rather accurately by measuring the velocity at the cell center, where the velocity gradient is zero.

The apparent electrophoretic mobility ( $U_{\text{app}}$ ) of an unknown colloid sample is always the sum of two contributions, one of which is the real electrophoretic mobility ( $U_{\text{el}}$ ) and the other is the liquid flow velocity induced by the electroosmotic effect ( $U_{\text{osm}}$ ) of the cell wall, which changes as a parabolical function of the cell depth:

$$U_{\text{app}} = U_{\text{el}} + U_{\text{osm}} \quad (5)$$

Similarly, the apparent velocity of the reference sample ( $U'_{\text{app}}$ ) was also indicated by the sum of the real



electrophoretic mobility ( $U'_{el}$ ) and the electroosmotic flow velocity ( $U'_{osm}$ ), that is,

$$U'_{app} = U'_{el} + U'_{osm} \quad (6)$$

Under the same experimental conditions, using a finite electrophoretic cell ( $U_{osm} = U'_{osm}$ ), the following relationship holds from Eqs. (5) and (6):

$$U_{el} - U'_{el} = U_{app} - U'_{app} \quad (7)$$

If  $U'_{el}$  is known exactly, the  $U_{el}$  value of the unknown sample can be determined from the difference between the two apparent mobilities at any cell depth. Thus if the particle mobilities of unknown samples and the reference sample are measured at the cell center where the migration velocity has a maximum, the real electrophoretic mobility of the unknown sample is given by:

$$U_{el} - U'_{el} = U_{app}(\text{maximum}) - U'_{app}(\text{maximum}) \quad (8)$$

Fig. 1 shows an example indicating the electrophoretic mobility profiles obtained experimentally for the reference sample (PSSNa lattices) and an unknown sample (SM lattices) along the cell depth in a  $1 \times 10^{-3}$  M KCl solution at 25°C. The SM lattices employed as an unknown sample were prepared by the copolymerization of styrene with 5% methacrylic acid (MA) at 70°C. It is apparent that both profiles indicate reasonable parabolical curves, and the curve for the reference

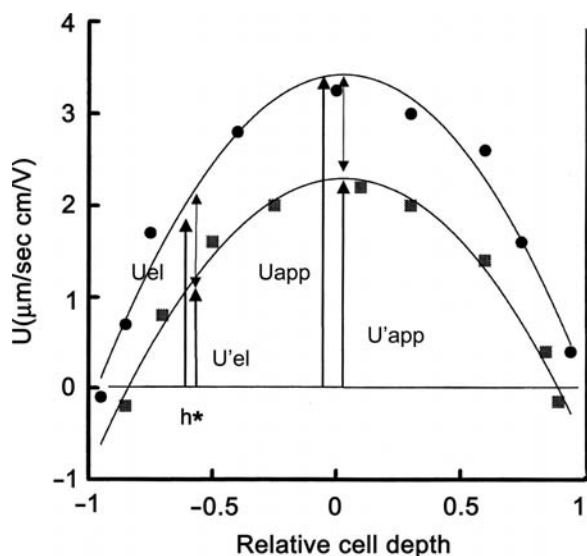
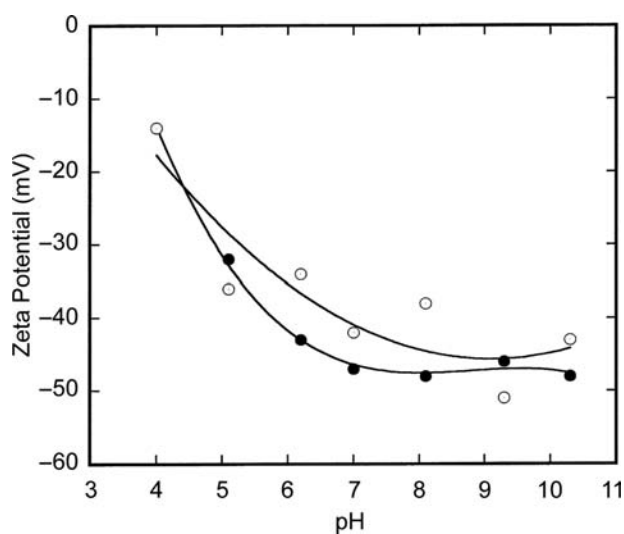


**Fig. 1** Examples of electrophoretic mobility profiles of PSSNa lattices ( $U'$ ) and SM lattices ( $U$ ). ( $h^*$ ) stationary level; (■) PSSNa lattices; (●) SM lattices ( $1 \times 10^{-3}$  M KCl, 25°C).

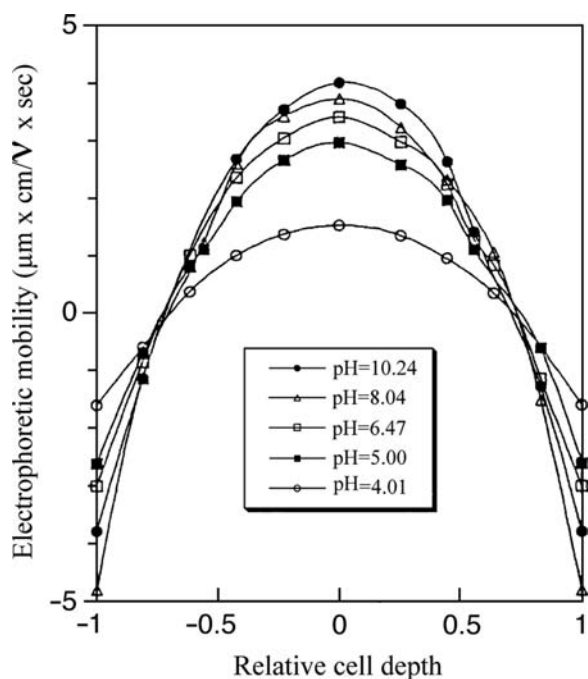
lattices shows a constant mobility at the two stationary levels. Furthermore, the difference between the two apparent mobilities at the cell center agrees well with the velocity of the SM lattices at the stationary level.

Fig. 2 shows the  $\zeta$ -potential vs. pH curves for the SM lattices, which have been determined from the maximum mobilities using the PSSNa lattices as a standard.<sup>[6]</sup> The same relation obtained from the velocity of the SM lattices at the stationary level is also indicated. As can be seen, both curves agree fairly well over the whole pH range. All of these results indicate that if we have a reliable colloid sample whose  $\zeta$ -potential is exactly determined, the  $\zeta$ -potential of the unknown sample can be determined precisely from the measurements of apparent electrophoretic mobility at the cell center. In that case, slight errors in focusing (i.e., errors because of the view field) are less important because the velocity gradient near the level of observation is very small.

According to Eqs. (3) and (4),  $U_0$  and hence the  $\zeta$ -potential of the cell wall are determined using a reference sample. The electroosmotic velocity ( $U_0$ ) obtained by the extrapolation of the velocity profile to the cell wall permits the determination of the  $\zeta$ -potential of the cell wall–solution interface, and the  $\zeta$ -potential measurement of various solid–solution interfaces,<sup>[7]</sup> including the dissimilar cell system,<sup>[8]</sup> has been determined. Here, we would like to emphasize again that the determination of the  $\zeta$ -potential of the cell wall is also possible from the maximum velocity of the reference sample, instead of the tedious plane interface procedure. According to Eq. (4), the apparent velocity of the reference sample at the cell center (at  $h = 0$ ) is  $U'_{app} = U'_{el} - U'_0/2$ . Therefore  $U'_0$  and hence the



**Fig. 2**  $\zeta$ -Potential vs. pH curves of unknown sample (SM lattices) determined by the maximum velocity of reference sample (●) and the usual method (○).



**Fig. 3** Apparent flow velocity profile of standard latex samples at various pH values ( $1 \times 10^{-3}$  M KCl,  $25^\circ\text{C}$ ).

$\zeta$ -potential of the cell wall can be quickly determined if the  $U_{cl}^0$  has been previously known.

Fig. 3 shows some examples of apparent flow velocity profiles of standard latex samples (PSSNa lattices) at various pH values in which both boundaries refer to the glass–solution interface. A symmetrical parabola was given at all pH conditions where the surface charge of glass is consistent with both sides.

## ELECTROKINETIC CHARACTERIZATIONS IN CONCENTRATED DISPERSIONS

In recent years, electroacoustics offered studies on surface characterization and the stability of suspended colloid particles. The term electroacoustics refer to two kinds of related phenomena: 1) colloid vibration potential (CVP), in which an electrical field arises in colloidal suspension when a sound wave passes through the dispersion (i.e., ultrasonic vibration causes the difference in movement between charged core particles and countercharges around them, which induces oscillating dipole moments and hence the potential drop in the sample cell),<sup>[9]</sup> and 2) electrokinetic sonic amplitude (ESA), the reciprocal effect of the above phenomena, in which an alternating electrical field is applied to a suspension and a sound wave arises as a result of the inertia of the particles, caused by their time-alternating electrophoresis (i.e., high-frequency electrical waves cause a difference in movement

between the core particles and the countercharges, which generates an ultrasonic waves in the sample cell).<sup>[10,11]</sup>

A very important advantage of these electroacoustical techniques is their ability to provide accurate measurements of the  $\zeta$ -potential in concentrated colloid systems. In this section, two of the typical data obtained by these methods are shown.

## Surface Characterization of Concentrated Latex Suspensions

In this section, the CVP technique is demonstrated for zeta potential measurements of concentrated suspensions of latex particles with different surface groups.<sup>[12]</sup> Three types of polystyrene lattices with different surface groups were synthesized in emulsifier-free systems. The usual polystyrene (PSt) lattices were prepared by the method of Kotera et al.,<sup>[13]</sup> and the two others (PStn and PStm) were synthesized by incorporating small amounts of ionic comonomer, methacrylic acid, and sodium polyvinylphenylsulfonate (NaSS) into a polystyrene chain, respectively, as in Juang and Krieger.<sup>[14]</sup> To increase the particle size, PStn was prepared in a system with  $1 \times 10^{-4}$  mol/dm<sup>3</sup> MgSO<sub>4</sub>. These latex samples were sufficiently dialyzed with distilled water and were then brought into contact with an ion exchange resin to remove ionic impurities. The samples were all composed of highly monodispersed spherical particles with  $D_w/D_n = 1.02$ , and the surface charge densities of the latex particles were measured by potentiometric and conductometric titration, as in Van den Hul and Vanderhoff.<sup>[15]</sup> The characterization data of all the samples are summarized in Table 2.

To compare the CVP with the conventional electrokinetic technique, first, the zeta potential of each sample in a dilute state was determined in a  $1 \times 10^{-3}$  mol/dm<sup>3</sup> KCl solution at different pH values using the microelectrophoretic technique. The resulting data for four samples are shown in Fig. 4. The  $\zeta$ -potential of the latex samples, especially the PStn sample, appears to be essentially independent of the medium pH. The zeta potential of PSt increases gradually from acidic to neutral pH. This behavior is probably dependent

**Table 2** Characterization of colloid particles

Sample	Diameter (nm)	Surface charge density ( $\mu\text{C}/\text{cm}^2$ )		
		Strong acid	Weak acid	Total
PSt	480	5.3	2.5	7.8
PStn	610	18	0	18
PStm	530	5	33	38

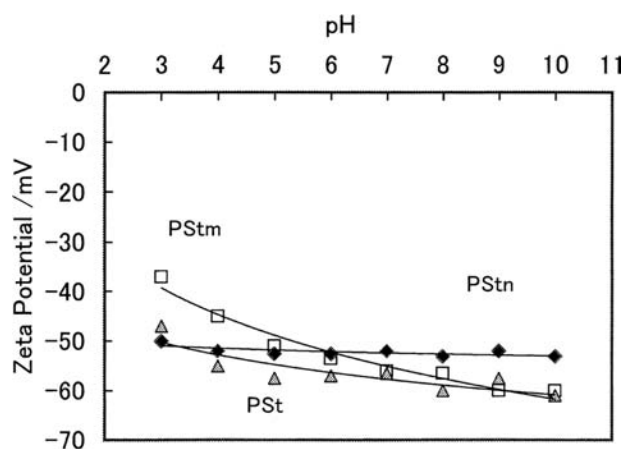


**Fig. 4** pH dependence of zeta potential in dilute state measured by the microelectrophoretic technique in  $1 \times 10^{-3}$  mol/dm<sup>3</sup> KCl at 25°C.

on the existence of carboxyl groups on the surface (with  $pK_a$  values between about 4 and 5), which are produced by the hydrolysis and subsequent oxidation of the  $OSO_3^-$  groups that come from the radical fragments used as an initiator ( $K_2S_2O_8$ ).<sup>[16–18]</sup>

The CVP measurements of polystyrene lattices give reliable data only in high-volume fraction ( $\phi$ ) systems above  $\phi = 0.1$  because the density of the latex particles is small ( $\rho_2 = 1.05$  g/cm<sup>3</sup>) and significant differences of CVP against the background signal can be detected only at high concentration ranges. Figs. 5 and 6 are graphs of the zeta potentials determined by CVP measurements for three kinds of polystyrene lattices at pH 5 and 9, as a function of the  $\phi$  value of each latex. It is apparent that the zeta potentials for

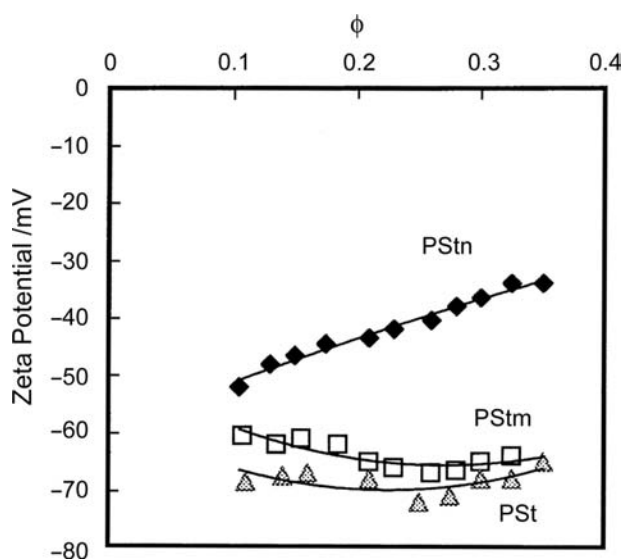


**Fig. 5** Concentration dependence of zeta potential for polystyrene latex suspensions in  $1 \times 10^{-3}$  mol/dm<sup>3</sup> KCl at 25°C and pH 5.

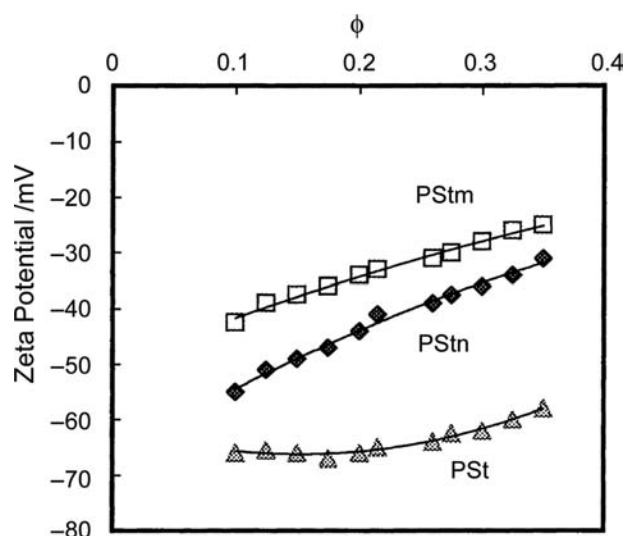


**Fig. 6** Concentration dependence of zeta potential for polystyrene latex suspensions in  $1 \times 10^{-3}$  mol/dm<sup>3</sup> KCl at 25°C and pH 9.

PSt and PStm at pH 5 and for PSt at pH 9 have nearly constant values over the entire concentration range of particles, and that the cell model theory is nearly valid for those systems. However, the zeta potentials for PStn at pH 5 and for PStn and PStm at both pH values decrease strongly as the particle concentrations increase. Furthermore, it was found that those of PStm at pH 9 are lower than those at pH 5, which is opposite in tendency to those in Fig. 4, determined directly in dilute states by the microelectrophoretic technique. It is thought, from a comparison with Table 2, that this abnormal behavior of the  $\zeta$ -potential is related to the high surface charge densities of the latex samples (i.e., PStn has many sulfonate groups on the surface brought about by the NaSS component), which dissociate completely under both pH conditions, and PStm becomes covered with thick carboxyl layers coming from the MA molecules, which gradually dissociate as the pH increases. These high surface charge densities bring about an expansion of the surface layer and may cause a double-layer overlapping at moderate particle concentrations, which results in restrictions for the prerequisite of the cell model of Levine, Neale, and Epstein<sup>[19]</sup>

To understand the abnormal behavior of the CVP and  $\zeta$ -potential that appeared in the latex suspensions, including the particles with high surface charge densities, the concentration dependence of conductivity was measured in the respective systems. The concentration dependence of the conductivity depends largely on the surface nature of the particles.<sup>[12]</sup> The conductivity of polystyrene latex systems increases as the particle concentration increases. This tendency is especially remarkable in the PStn systems at pH 5

and 9 and in the PStm system at pH 9. From a comparison with the results of the CVP, it was realized that this increasing tendency of the conductivity is closely related to the abnormal behavior of the CVP. This is explained as follows. On the highly charged surfaces of PStn or PStm at pH 9, a polyelectrolyte-like (“hairy”) layer is present. These layers overlap each other in this concentrated state, allowing electrical conduction through the hairy layer; thus the hairy layer results in interparticle surface conductance. The degree of interparticle surface conduction is affected by the particle concentration and the thickness of the hairy layer, which in turn depend on the surface charge density of the particle and the pH of the medium.

### Application of Electrokinetic Sonic Amplitude Technique in the Ceramic Industry

The concept of colloidal suspension processing has been successfully applied to the field of structural ceramic where inherent properties of dense suspension are used to transform a fluid suspension to a stiff gel. During colloidal processing, the state of dispersion has a significant influence on the casting behavior and the resulting green body properties. The good dispersion of particles gives optimum packing state (high green density), which influences the sinterability of the ceramic body and hence the physical and chemical properties of the final product. At present, fine-grained and uniform microstructures are desirable for most ceramic applications in producing strong and reliable structural parts.

Traditionally in the ceramic industry, polyelectrolytes have been utilized to prevent the flocculation of particles. Because of the charged nature of the polyelectrolyte, they impart stability to the particles via an electrosteric mechanism. Hence the adsorption of these charged molecules onto a particle surface will alter the surface charge and hence the zeta potential. Thus using electroacoustics, it is possible to follow the changes in the zeta potential with increasing amounts of polyelectrolyte. This is extremely useful in determining the optimum amount of polyelectrolyte required to stabilize the particles under different conditions.

Fig. 7 shows how the zeta potential of an alumina suspension (background electrolyte, 10 mM KCl) can be altered by the addition of three commercially available polyelectrolytes.<sup>[20]</sup> Initially, the zeta potential of the suspension is such that the suspension becomes more stable. The trend for all dispersants is very similar in that, initially, the zeta potential changes strongly with small amounts of dispersants and then after a certain concentration, the zeta potential begins to plateau out as no more dispersant is adsorbed on the

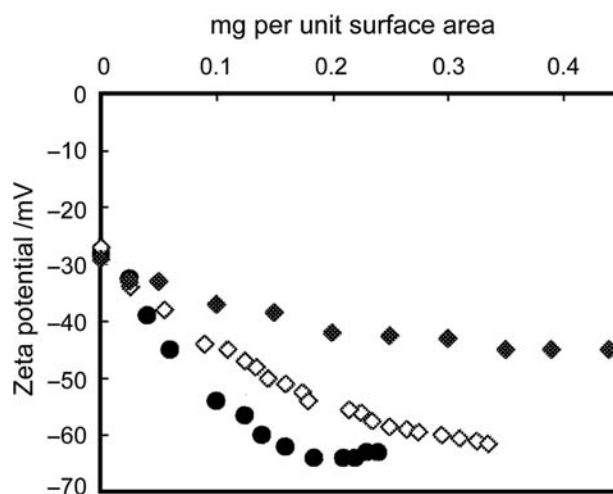


Fig. 7 Effect of three commercial dispersants on alumina suspension in  $1 \times 10^{-4}$  mol/dm<sup>3</sup> KCl: (●) Poly-CA; (◇) Poly-PC33; (◆) Poly-CE64.

surface. However, each dispersant imparts a different final zeta potential and requires a different amount of dispersants to cover the particles. Of these, Poly-CA imparts the greatest final zeta potential, so this would be an excellent dispersant for the alumina. However, it must be noted that the likely stabilization mechanism for polyelectrolyte dispersants is electrosteric stabilization. Therefore there may well be a steric contribution to the stabilization mechanism depending on how the dispersant adsorbs. Poly-CE64 imparts a final zeta potential of  $-45$  mV and requires approximately twice as much dispersant to do so, making it a poor candidate in comparison. The zeta potential from the suspension stabilized with Poly-PC 33 does not appear to level out, and further data points would be required to determine the optimum amount.

### ELECTROKINETIC MEASUREMENTS IN SYNTHESIS OF COMPOSITE PARTICLES

There is a variety of methods currently used to fabricate a wide range of stable, composite, and coating particles of various compositions. These include heterocoagulation,<sup>[21]</sup> seed polymerization,<sup>[22]</sup> emulsion/phase separation,<sup>[23]</sup> sacrificial core techniques,<sup>[24]</sup> and so on. The notion of adsorbing particles onto solid substrates in a layer-by-layer manner was introduced by Iier<sup>[25]</sup> in the mid-1960s. Decher and Hong<sup>[26]</sup> extended Iier's work to a combination of linear polycations and polyanions in the early 1990s. Decher<sup>[27]</sup> later adapted the layer-by-layer technique to include inorganic nanoparticles, biomolecules, clays, and dyes in polyelectrolyte multilayer assemblies. Very recently, Caruso and Mohwald<sup>[28]</sup> and Caruso, Caruso, and

Mohwald<sup>[29]</sup> reported very interesting results, which included a detailed investigation of the stepwise formation of the silica–nanoparticle/polymer multilayer templating of some latex particles. In this chapter, we demonstrate how we can utilize electrophoretic measurements in synthesis and coating processes of composite particles.

### Heterocoagulation Behavior of Polymer Lattices with Spherical Silica

Gherardi and Matijevic<sup>[30]</sup> have investigated various behaviors of mixed colloid particles obtained by mixing differently preformed particles. They showed that the nature of a mixing system depends on the conditions of preparations, and concluded that the most important parameter in controlling the morphology of composite particles is the surface charge of the component particles, especially the contrast between surface charges of the two component particles. A stable system consisting of a regular composite particle could be prepared only in a medium controlled at a definite pH, where the two components are charged with opposite signs. Typical results of the electrophoretic mobility for the single silica and the latex suspension are shown in Fig. 8.

The next important parameter to control morphology is the particle size ratio of the component particles when they are mixed in the vessel. Fig. 9 shows schematic pictures of the morphology of heterocoagulates of different silica particles and amphoteric

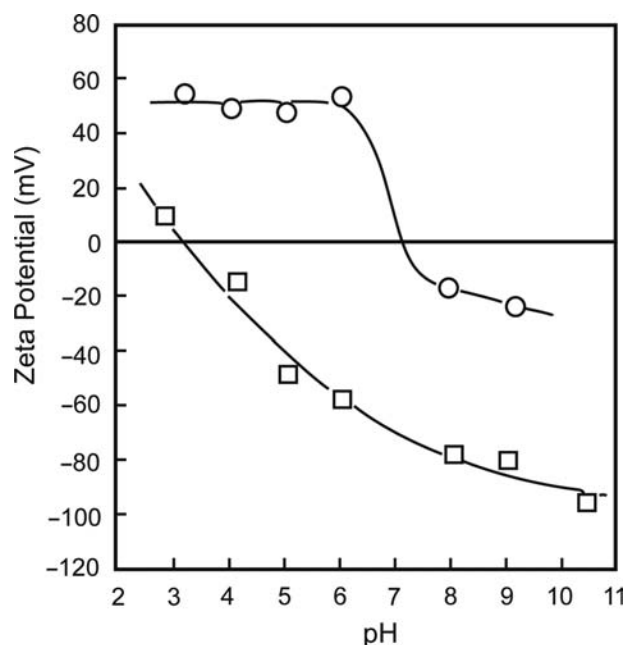


**Fig. 8**  $\zeta$ -Potentials of silica (□) and latex particles (○) as a function of pH at  $5 \times 10^{-3}$  mol/dm<sup>3</sup> KCl.

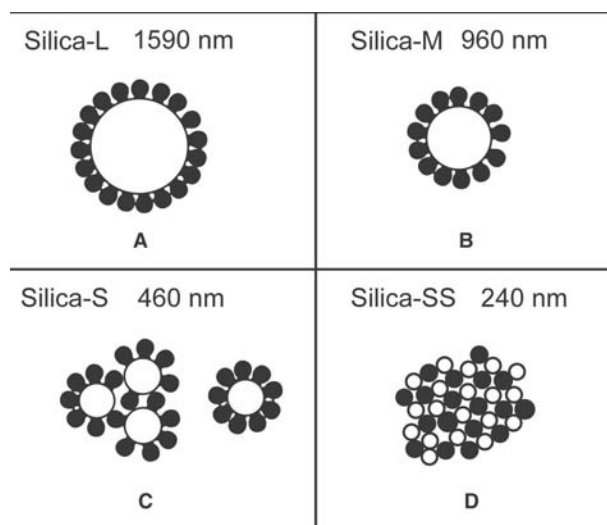


**Fig. 9** Schematic pictures showing the morphology of heterocoagulate particles formed from different silica samples.

lattices. Fig. 10 shows an optical micrograph of the real heterocoagulate generated from different silica samples and amphoteric latex systems, where the other conditions (e.g., the particle number ratio,  $N_{\text{silica}}/N_{\text{latex}} = 1/300$ ; medium pH 5.6) have been kept constant. The microscope used for observations was a lateral-type metallurgical microscope (Axio Mart, Carl Zeiss, Germany). It may be seen that at a particle size ratio ( $r = D_{\text{silica}}/D_{\text{latex}}$ ) higher than 3, the suspension is composed of uniform heterocoagulate particles and each heterocoagulate undergoes Brownian motion as

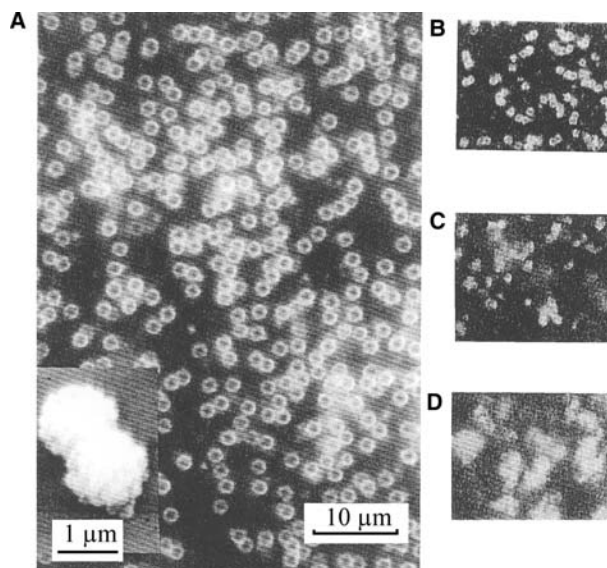


**Fig. 10** Optical micrograph showing the heterocoagulates prepared from different silica samples: (A) Silica-L; (B) Silica-M; (C) Silica-S; (D) Silica-SS.

an isolated unit. The insert of Fig. 10A shows a scanning electron micrograph of the heterocoagulate. It is apparent that the heterocoagulate takes a raspberry shape with one silica particle in the core. In contrast to this, the heterocoagulates generated at a particle size ratio lower than  $r = 3$  (Fig. 10C and D) are composed of large, irregular aggregates, and regular coagulates were hardly formed at any medium pH and particle number ratio investigated.<sup>[31,32]</sup>

It is interesting to analyze the different heterocoagulation behaviors from the concept of the adhesion isotherm for the amphoteric lattices on the silica particles. Fig. 11 shows some typical isotherms for the lattices on Silica-L at various  $K_2SO_4$  concentrations, where all the systems were controlled at pH 5.2. It is evident that the isotherms are all well defined and of very high affinity type, and the plateau value increases with increasing  $K_2SO_4$  concentration within the range from  $10^{-5}$  to  $10^{-2}$  mol/dm<sup>3</sup>. This means that in this concentration range, adhesion proceeds in a way characteristic of monolayer adhesion. This may be because of the strong blocking effect of adhering particles. However, in  $K_2SO_4$  aqueous solutions more concentrated than  $2 \times 10^{-2}$  mol/dm<sup>3</sup>, no reproducible isotherm could be obtained under any conditions tested, and only some irregular aggregates were generated in the course of the experiment.<sup>[31]</sup> In Fig. 12, the  $\zeta$ -potentials of the heterocoagulates prepared at different electrolyte concentrations, as well as the data on the amphoteric lattices, are presented as a function of the medium pH. As may be seen, a reversal of charge is observed in all samples, and the IEP in the heterocoagulated systems occurs at about pH 8, which is not so different from the IEP of the single lattices. Moreover, the fact that the limiting net positive  $\zeta$ -potential attained at  $3 < \text{pH} < 6$  increases with

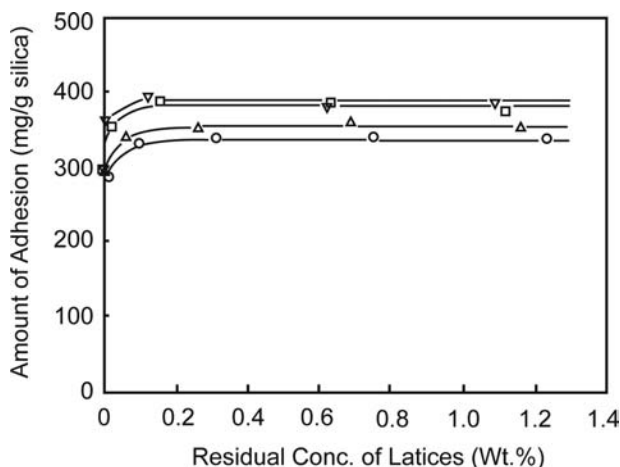


**Fig. 11** Adhesion isotherms of amphoteric lattices onto Silica-L at various  $K_2SO_4$  concentrations: ( $\nabla$ )  $1.46 \times 10^{-2}$  M; ( $\square$ )  $1.46 \times 10^{-3}$  M; ( $\triangle$ )  $1.46 \times 10^{-4}$  M; ( $\circ$ ) 0 M.

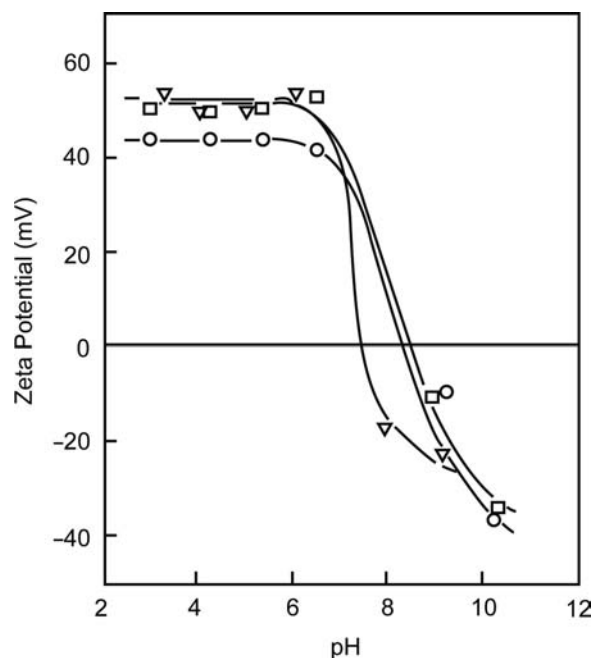


**Fig. 12**  $\zeta$ -Potentials vs. pH curves for heterocoagulate particles prepared at different electrolytes: ( $\nabla$ ) heterocoagulates prepared at  $2.48 \times 10^{-1}$  M  $MgCl_2$ ; ( $\circ$ ) heterocoagulates prepared at  $1 \times 10^{-5}$  M  $KCl$ ; ( $\square$ ) amphoteric lattices.

increasing electrolyte concentration is also in line with the increase in latex adhesion with increasing electrolyte concentration.

### Multilayer Composite Particles Comprising Silica/Vesicle/Silica Particles

Composite particles, including vesicle particles, are an important topic in application fields. Composite particles can be used frequently in the biomedical field for diagnostic purposes and for treatment medicine. Here, we describe one example of such systems,<sup>[33]</sup> that is, PC vesicles, which are typical biocolloid systems and are introduced into composites as a one-component particle.

The silica/PC vesicle/silica multilayer composite particles were prepared by the alternate adsorption of PC vesicles and small silica particles on the large silica particles with negative charges (Fig. 13). In this study, electrostatic attraction is taken into account as the driving force. It is important that the silica and the vesicle surfaces bear opposite charges to be effective. We can control the surface charges of the vesicle and silica particles by adjusting the concentration of  $LaCl_3$ . In Fig. 14, the  $\zeta$ -potentials of PC vesicles and silica particles are shown as a function of  $LaCl_3$  concentration. The  $\zeta$ -potential of PC vesicles decreases with increasing  $LaCl_3$  concentration, and becomes positive over a



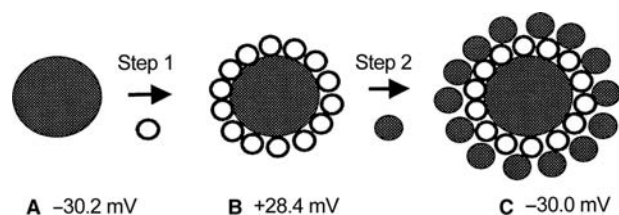


**Fig. 13** Schematic showing the process of synthesizing multilayer composite particles: (A) core silica; (B) PC vesicle/silica composite particle; (C) silica/PC vesicle/silica composite particle.

certain concentration of  $\text{LaCl}_3$ . This is because of the binding effect of  $\text{La}^{3+}$  ions to the phospholipids head group.<sup>[34]</sup> However, for silica dispersions, the  $\zeta$ -potential remained negative over the  $10^{-6}$ – $10^{-2}$  M concentration range of  $\text{LaCl}_3$ . Thus at  $10^{-4}$  M  $\text{LaCl}_3$ , the  $\zeta$ -potentials of the silica and PC vesicles were  $-30$  and  $+32$  mV, respectively. It is assumed that a strong electrostatic attraction will occur between the vesicles and the silica particles. Therefore we selected  $10^{-4}$  M  $\text{LaCl}_3$  as the heterocoagulation condition.

After mixing the PC vesicles with the core silica dispersion, the free vesicles were removed from the dispersion and the  $\zeta$ -potentials of the composite particles generated were measured. The value was determined to be  $+28$  mV. The positive  $\zeta$ -potential indicates that the PC vesicles are adsorbed on the silica surface because the surface of the PC vesicles binds with  $\text{La}^{3+}$  ions.

For the PC vesicle adsorption state on the silica surface, there are two possible states: 1) as a vesicle particle layer, or 2) as a lipid molecular bilayer. To

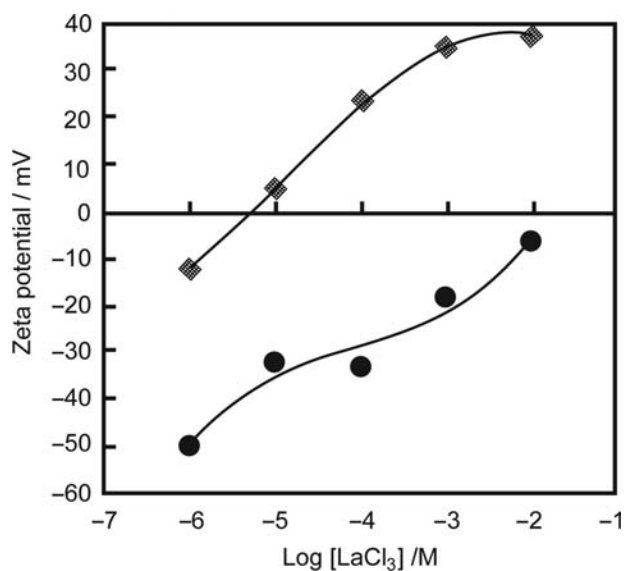


**Fig. 14**  $\zeta$ -Potentials vs. the concentration of  $\text{LaCl}_3$ : (◆) PC vesicles; (●) silica particles.

clarify the adsorption state of the vesicles, as the next stage, the adsorption amounts of PC on the silica surface have been measured. In Fig. 15, the results are shown as a function of the PC concentration. Adsorption amounts are expressed by the number of phospholipids molecules adsorbed per square meter of silica surface. The solid line represents a theoretical curve for the adsorption amount of the single bilayer model, assuming the area per PC molecule equals  $0.7 \text{ nm}^2$ . The dotted line shows a theoretical curve for the adsorption of a single vesicle layer model, assuming that the vesicles are of uniform size and have a unilamellar spherical shape. The saturated adsorption amounts in the experiments are located near the value for the latter, but over it. This is because of the existence of some multilamellar PC vesicles in the sample (i.e., the existence of multilamellar PC vesicles will induce a large number of PC molecules than the value of unilamellar vesicles). Thus we can expect that the PC vesicles will be adsorbed on the silica surface as a unilamellar vesicle layer (i.e., the composite particles have been generated as shown in Fig. 13B). Furthermore, we then separated the PC vesicle/silica composites from the free PC vesicles by the ultra-filtration method (with a polycarbonate membrane filter, pore size  $1.0 \mu\text{m}$ ), and determined the mean size of the composite particles by the dynamic light scattering (DLS) method. The diameter of the composite particles is  $1.93 \mu\text{m}$ , and this value is close to  $1.9 \mu\text{m}$ , which was calculated by the single particle layer model. This result means that the PV vesicles will be adsorbed on silica particles as the same spherical particle size.

In the second stage of composite formation, we mixed the PC vesicle/silica composite particles with a small silica ( $2a = 0.5 \mu\text{m}$ ) dispersion under the same  $10^{-4}$  M  $\text{LaCl}_3$  solution. The  $\zeta$ -potentials of the products reversed from positive ( $+28.4$  mV) to negative ( $-30$  mV) again, which indicates that the small silica particles (with negative charges) were adsorbed on the surface of the positively charged composite particles (Fig. 13C).

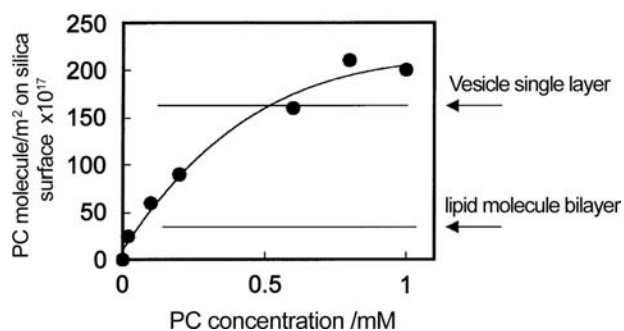


**Fig. 15** Adsorption amount for PC on core silica surface in  $10^{-4}$  M  $\text{LaCl}_3$  at  $25^\circ\text{C}$ .

The direct observation of the multilayer formation of composite particles is provided by a special optical microscopy technique. In Fig. 16, the composite particles of the silica/PC vesicle/core silica in the  $10^{-4}$  M  $\text{LaCl}_3$  solution are shown. We cannot clearly see the image of the PC vesicles on the silica because the PC vesicle has a large water core and a thin lipid bilayer (about 5 nm). Therefore the total refractive indices of the PC vesicle are close to those of water. However, the formation of the silica/PC vesicle/silica composite particles is indicated clearly in Fig. 16; the small silica particles are adsorbed on the spherical surface of the PC vesicle/core silica composite and are located on the outer layer of the composite particles.

### The Buildup of Polyelectrolyte and/or Colloid Particle Multilayer on Solid Surfaces

The multilayer formation of polyelectrolytes on colloid particles is usually characterized by a stepwise increase of the adsorbed amount and layer thickness, and by alternating highly positive and negative  $\zeta$ -potentials of the covered particles. Here, we describe two kinds of multicomponent layer systems using polyelectrolyte and colloid particles. One is the formation of polyelectrolyte multilayers on polymer colloids. Another is the formation of composite particles including organic and inorganic colloid particles using a layer-by-layer technique of polyelectrolytes.<sup>[35]</sup>

To emphasize the influence of the polarity of the substrate, three kinds of polystyrene lattices are employed. PS-740 lattices with large size ( $2a = 740$  nm) were prepared by the usual surfactant-free emulsion polymerization technique;<sup>[12]</sup> NaSS-190 lattices were made by incorporating a small amount of an ionic comonomer, sodium-*p*-vinylbenzyl-sulfate, into the polystyrene chain according to Kotera et al.<sup>[13]</sup> The charge density

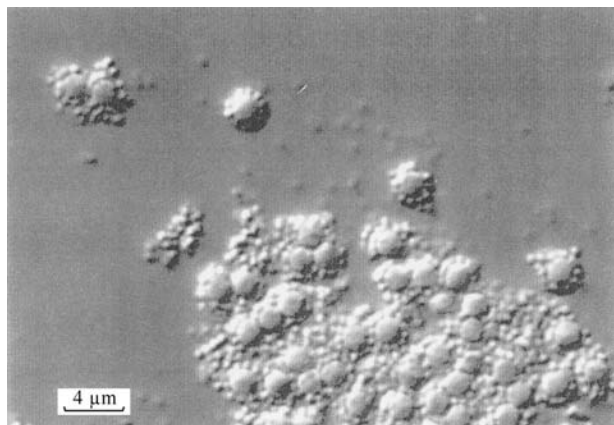


**Fig. 16** Optical micrograph of silica/PC vesicles/silica composite particles.

of NaSS-190 lattices is much higher than that of PS-740 latex. DEAM-250 lattices consist of amphoteric particles prepared by the method described by Homola and James.<sup>[36]</sup> Characteristic data for these samples are shown in Table 3. Silica samples with different particle sizes ( $2a = 500, 300,$  and  $20$  nm), which were obtained from Nippon Catalisitic Co. Ltd. and Nissan Chemical Co. Ltd., were used. All these single dispersions consisted of monodisperse spherical particles with  $D_w/D_n < 1.04$  always, and were used after extensive dialysis.

As the cationic polymer, poly-L-lysine (PLL-19) with a fixed molecular weight ( $M = 190,000$ ) was used, and as the anionic polymer, polystyrene sulfonate (PSSNa-50) with  $M = 500,000$  was used. PSSNa-50 carries a constant charge for pH 3–10. However, PLL-19 is pH-dependently charged and it is known that a fixed positive charge is carried only in the region of pH 3–7.

The adsorption of polyelectrolytes was allowed to take place for 1.5–2 hr at a 0.1–0.3 mg/mL PLL or PSSNa solution using a very dilute latex or silica suspension ( $\phi = 0.0001$ ) and a saturated concentration without any free polymer of each polyelectrolyte that was determined by mobility measurements of the core particles. During the adsorption process, suspensions of the core particles were mixed slowly by means of rotating end-over-end.

The DLS measurements were carried out to assess the development of hydrodynamic layer thickness on the addition of PLL or PSSNa molecules. The heterocoagulated state of composite particles was observed directly by the optical microscope and scanning electron microscope.

### Multilayer formation of polyelectrolytes on colloid particles

In Fig. 17, a typical cyclical curve of  $\zeta$ -potential on alternating additions of PLL-19 and PSSNa-50 on negatively charged NaSS-190 latex surfaces is shown. The switch to either of the new polyelectrolytes is

**Table 3** Particle diameters,  $\zeta$ -potentials, and functional groups of the colloids

Particle	Diameter (nm)	$\zeta$ -Potential (mV) in $10^{-3}$ M NaCl	Functional group
NaSS-190 latex	190	−50 (pH 4)	$\text{SO}_3^-$
DEAM-250 latex	252	+60 (pH 4)	$\text{NH}_3^+$
PS-740 latex	740	−30 (pH 4)	$\text{OSO}_3^-$
Silica-500	500	−30 (pH 6)	$\text{SiO}_2^-$
Silica-300	300	−30 (pH 6)	$\text{SiO}_2^-$
Silica-20	20	−30 (pH 6)	$\text{SiO}_2^-$

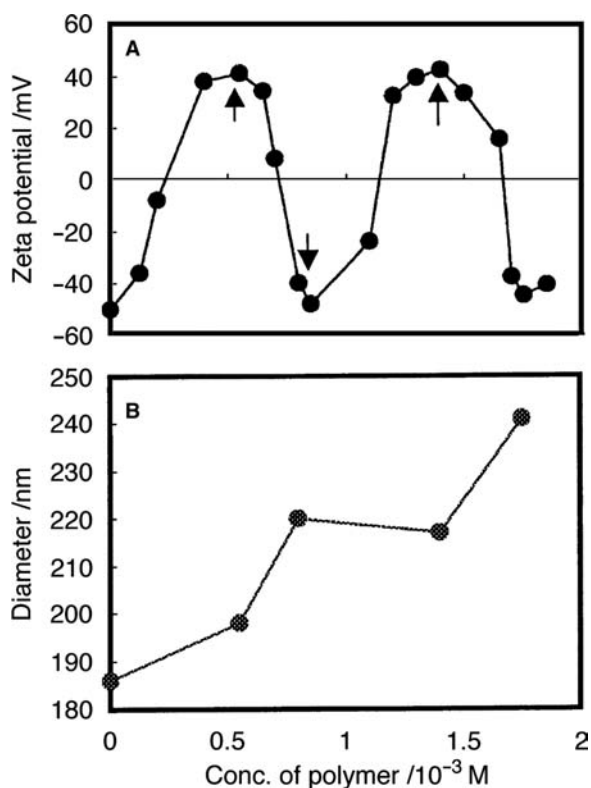


**Fig. 17**  $\zeta$ -Potential (A) and total particle size (B) of the composite system by multilayer deposition of PLL-19 and PSSNa-50 on NaSS-10 lattices against the concentrations of each polyelectrolyte solution ( $\phi = 7.5 \times 10^{-3}$  wt.%, pH 4,  $[\text{NaCl}] = 1 \times 10^{-3}$  M). The switch to a new polymer solution is indicated by the arrows.

indicated by the arrows. In the figure, the abscissa axis indicates the total number of repeating units of both polyelectrolyte molecules. The change of the  $\zeta$ -potential is substantial (i.e., the  $\zeta$ -potential is highly positive after the addition of PLL-19 and highly negative after the addition of PSSNa-50). This result indicates clearly that, on the adsorption of polyelectrolyte, the oppositely charged surface is not just compensated but strongly overcompensated. An overcompensation of polyelectrolyte adsorption is the main reason for progressing the multilayer formation. The buildup process was also confirmed from the stepwise increase of the layer thickness of the core latex particles. The stepwise increase of the layer thickness, especially after the adsorption of PSSNa-50 molecules on the core particle surfaces, is also shown in Fig. 17.

In the next stage, we tried to produce polyelectrolyte multilayers under different medium compositions. In Fig. 18, the results of multilayer formations of PSSNa-50 and PLL-19 in pure water at pH 4,  $10^{-2}$  M NaCl solution, and  $10^{-2}$  M BaCl<sub>2</sub> solution are indicated. In these experiments, the positively charged

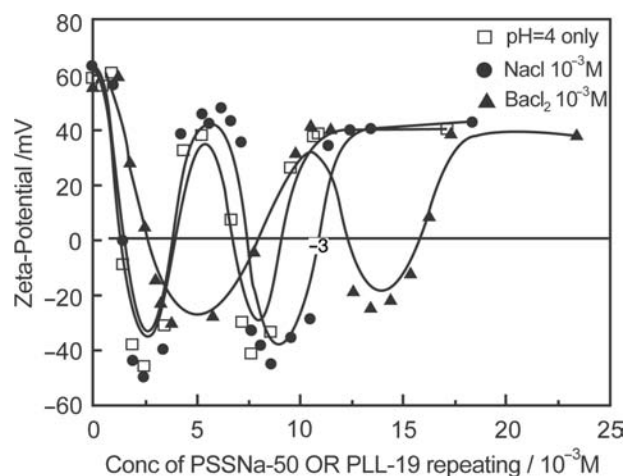


**Fig. 18**  $\zeta$ -Potential of multilayers of PSSNa-50 and PLL-19 on DEAM-250 lattices against the concentrations of each polyelectrolyte solution under different salt conditions ( $\phi = 7.5 \times 10^{-3}$  wt.%, pH 4).

DEAM-250 lattices were used as the core particles. In this figure, the locus of  $\zeta$ -potentials obtained under different salt conditions is plotted for the total amounts of repeating units of PLL-19 and PSSNa-50 molecules. As can be seen, the step in the  $\zeta$ -potential obtained in the BaCl<sub>2</sub> solution is delayed, indicating that the electrostatic attraction between PSSNa-50 and the charged surface of DEAM-250 lattices is weakened. This is caused by the strong affinity of Ba<sup>2+</sup> to SO<sub>3</sub><sup>-</sup> in PSSNa-50 molecules. The existence of such a specific effect has been reported in the literature.<sup>[37,38]</sup>

Fig. 19 indicates the stepwise increase of layer thickness on DEAM-250 latex particles under different salt

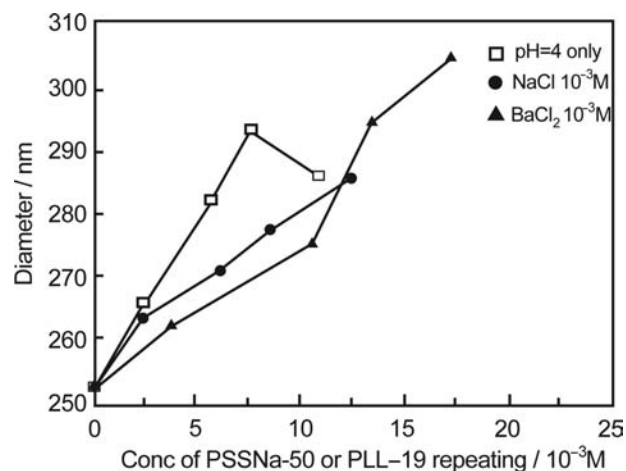


**Fig. 19** The total particle sizes in each step to stable multilayers of PSSNa-50 and PLL-19 on DEAM-250 lattices under different salt conditions ( $\phi = 7.5 \times 10^{-3}$  wt.%, pH 4).

conditions. Surprisingly, in the  $10^{-2}$  M  $\text{BaCl}_2$  solutions, the layer thickness of adsorbed polyelectrolytes increased steadily and the weak attraction effect coming from  $\text{Ba}^{2+}$  was not observed on the layer-by-layer formation. However, in distilled water, the layer thickness increased quickly at an early stage of deposition. However, in the final stage, the layer shrunk. The reason for this phenomenon cannot be explained, but this result indicates surely that strong electrostatic attraction is not always the sole factor necessary to form a stable multilayer.

#### Multilayer formation of colloid particles with polyelectrolytes

The layer-by-layer deposition technique of polyelectrolytes can be applied to the formation of composite particles comprising organic and inorganic colloid particles. Fig. 20 shows the buildup processes of colloid particles using PS-740 latex sample as the core. Here, PLL-19 was used as a binder polyelectrolyte. The abscissa axis in this figure indicates the total amounts of the binder polyelectrolyte + adhering particles. As can be seen from the figure, the  $\zeta$ -potential of the core particle has changed from a negative value to a positive value by adsorption of PLL-19 molecules, and changed again to negative values with an increasing number of adhering silica particles (Silica-300). These results suggest that the composite formation of colloid particles has progressed reasonably by the binder layer of

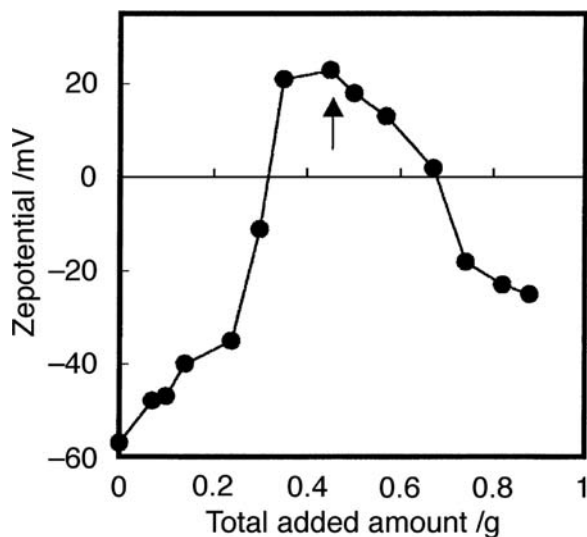


**Fig. 20**  $\zeta$ -Potential of composite particles by multilayer deposition of PLL-19 (concentration,  $2 \times 10^{-4}$  wt.%) and Silica-300 (concentration,  $1.0 \times 10^{-3}$  wt.%) on PS-740 lattices ( $\phi = 7.5 \times 10^{-4}$  wt.%, pH 6,  $[\text{NaCl}] = 1 \times 10^{-3}$  M). The switch to Silica-300 from PLL-19 is indicated by the arrow.

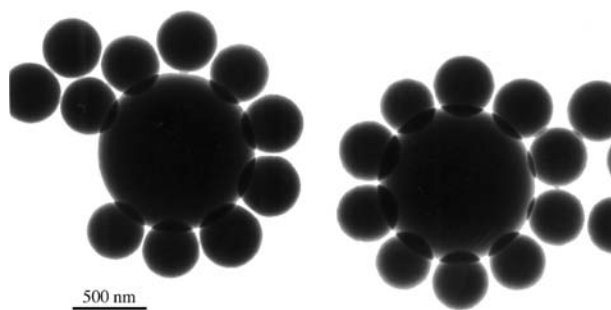


**Fig. 21** Electron micrograph showing hybrid particles of outer Silica-300 particles on core PS-740 lattices.

PLL-19 molecules. Fig. 21 is a photograph showing a typical example of hybrid particles consisting of outer Silica-300 particles on core PS-740 latex as prepared in this experiment. It is known that the composite consists of regular hybrid particles comprising organic and inorganic particles. However, the structure form is not so stable and sometimes the system includes free silica particles.

In the next stage, the synthetic process of hybrid particles with multilayers of silica particles on PS-740 was examined. As the binder polyelectrolyte, the PLL-19 molecule was also used under the same medium conditions. Fig. 22 shows the cyclical behavior of the  $\zeta$ -potential in the formation process of multilayers of Silica-20 and PLL-19 layers. As can be seen, the cycle of  $\zeta$ -potential after adhesion is systematical, indicating that the deposition of PLL and Silica-20 has progressed regularly. Fig. 23 is a photograph of

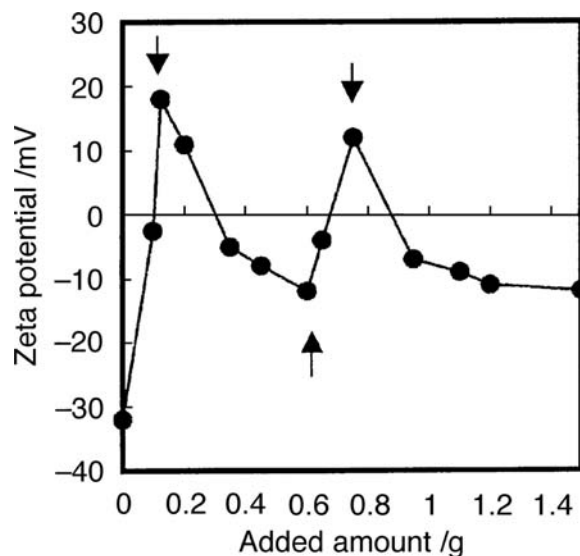


**Fig. 22**  $\zeta$ -Potential of composite particles by multilayer deposition of pair (PLL-19 + Silica-20) layers. The switch is indicated by the arrow.

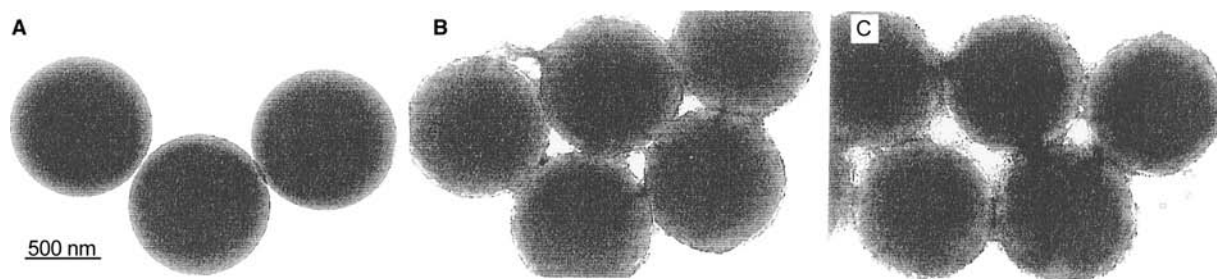


**Fig. 23** Electron micrograph showing hybrid particles of small Silica-20 particles on core PS-740 latex particles: (A) PS-740 lattices; (B) hybrid particles deposited by a single (PLL-19 + Silica-20) layer; (C) hybrid particles deposited by pair (PLL-19 + Silica-20) layers.

an original PS-740 latex and two kinds of composite particles covered with a single silica + polymer layer and two silica + polymer layers. Two kinds of composite particles can be distinguished based on the thickness of the adhering silica particle layer.

From these results, it is concluded that, by combining a multilayer formation of polyelectrolytes and charged colloid particles, we can prepare many new synthetic materials comprising different chemical species, different structures, and different shapes.

## CONCLUSION

Here, several preparation processes of composite particles relating to the electrical properties of particles are described: 1) the heterocoagulation process of amphoteric polymer lattices on spherical silica; 2) composite formation comprising silica/vesicle or silica/vesicle/silica particles; and 3) the buildup process of polyelectrolyte or colloid particle multilayers on latex or silica surfaces. All these results indicate that the electrokinetic measurement is an essential and powerful technique for monitoring the formation process of composite particles with different compositions. Finally, the present authors would like to stress that the formation processes described here were concerned with the semimicron-sized particles, but these techniques can be applied to systems, including nanosized particles with slight reversions.

## REFERENCES

- Matijevic, E. *Interfacial Electrokinetics and Electrophoresis*; Surfactant Science Series; Delgado, A.V., Ed.; Marcel Dekker, Inc.: New York, 2002; 106, 199–218.
- Ohshima, H., Furusawa, K., Eds. *Electrical Phenomena at Interfaces*; Surfactant Science Series; Marcel Dekker, Inc.: New York, 1998; 76.
- Lyklema, J. *Fundamentals of Interface and Colloid Science*; Academic Press, Inc.: London, 1995; vol. II.
- von Smoluchowski, M. *Handbuch der Electricitat und des Magnetismus*; Graetz, W., Ed.; Barth: Leipzig, 1914; vol. II, 366.
- Komagata, S. *Nihon Kagaku Kaishi* **1932**, 53, pp. 342, 969.
- Furusawa, K.; Uchiyama, K. *J. Colloid Interface Sci.* **1998**, *140*, 217.
- Sasaki, H.; Muramatsu, A.; Arakatsu, H.; Usui, S. *J. Colloid Interface Sci.* **1991**, *142*, 266.
- Usui, S.; Imamura, Y.; Sasaki, H. *J. Colloid Interface Sci.* **1987**, *118*, 335.
- Marlow, B.J.; Fairhurst, D.; Pendse, H.P. *Langmuir* **1988**, *4*, 611.
- O'Brien, R.W.; Midmore, B.R.; Lamb, A.; Hunter, R.J. *Faraday Discuss. Chem. Soc. (London)* **1990**, *90*, 301.
- Dukhin, A.S.; Shilov, V.N.; Oshima, H.; Goetz, P.J. *Langmuir* **1999**, *15*, pp. 6692, 3445.
- Hozumi, Y.; Furusawa, K. *Colloid Polym. Sci.* **1990**, *268*, 469.
- Kotera, A.; Furusawa, K.; Takeda, Y. *Kolloid-Z. Z. Polym.* **1970**, *239*, 677.
- Juang, M.S.; Krieger, I.M. *J. Polym. Sci.* **1976**, *14*, 2089.
- Van den Hul, H.J.; Vanderhoff, J.W. *Electroanal. Chem.* **1972**, *37*, 161.
- Kolthoff, I.M.; Miller, I.K. *J. Am. Chem. Soc.* **1951**, *73*, 3055.
- Ottewill, R.H.; Shaw, J.N. *Kolloid-Z. Z. Polym.* **1976**, *218*, 34.
- Hearn, J.; Ottewill, R.H.; Shaw, J.N. *Br. Polym. J.* **1972**, *2*, 116.
- Levine, S.; Neale, G.; Epstein, N. *J. Colloid Interface Sci.* **1976**, *57*, 427.
- Greenwood, R.; Bergstrom, L. *J. Eur. Ceram. Soc.* **1997**, *17*, 537.
- Furusawa, K.; Anzai, C. *Colloid Polym. Sci.* **1987**, *265*, 882.
- Furusawa, K.; Kimura, Y.; Tagawa, T. *J. Colloid Interface Sci.* **1986**, *109*, 69.
- Velev, O.D.; Furusawa, K.; Nagayama, K. *Langmuir* **1996**, *12*, pp. 2374, 2385.
- Wilcox, D.L.; Berg, M. *Hollow and Solid Spheres and Microspheres*. In *Science and Technology Associated*

- with Their Fabrication and Application*; Proceedings of the Materials Research Society, Pittsburgh; Wilcox, P.L. et al., Eds.; 1995; vol. 372, 3–13.
25. Iier, K.K. J. Colloid Interface Sci. **1966**, *21*, 569.
  26. Decher, G.; Hong, J.D. Ber. Bunsenges. Phys. Chem. **1991**, *95*, 1439.
  27. Decher, G. Science **1997**, *277*, 1232.
  28. Caruso, F.; Mohwald, H. Langmuir **1999**, *8276*, 15.
  29. Caruso, F.; Caruso, R.A.; Mohwald, H. Science **1988**, *1111*, 282.
  30. Gherardi, P.; Matijevic, E. Colloid Interface Sci. **1986**, *109*, 57.
  31. Furusawa, K.; Anzai, C. Colloids Surf. **1992**, *63*, 103.
  32. Furusawa, K.; Velev, O.D. Colloids Surf., A Physicochem. Eng. Asp. **1999**, *159*, 359.
  33. Yang, B.; Matsumura, H.; Katoh, K.; Kise, H.; Furusawa, K. Langmuir **2001**, *17*, 2283.
  34. Lehrmann, R.; Seeling, J. Biochim. Biophys. Acta **1994**, *1189*, 89.
  35. Furusawa, K.; Satou, S. Colloids Surf. **2001**, *195*, 143.
  36. Homola, A.; James, R.M. J. Colloid Interface Sci. **1977**, *59*, 123.
  37. van Duelm, P.; Norde, W.; Lyklema, J. J. Colloid Interface Sci. **1977**, *59*, 123.
  38. Furusawa, K.; Tomotsu, N. J. Colloid Interface Sci. **1983**, *93*, 504.



# Colloidal Structures on Patterned Surfaces

## Aránzazu del Campo

*Max-Planck-Institut für Metallforschung, Stuttgart, Germany, and Functional Surfaces, Leibniz-Institut für Neue Materialien (INM), Saarbrücken, Germany*

## Anne-Sophie Duwez

*Research Center in Micro and Nanoscopic Materials and Electronic Devices (CERMIN), Université catholique de Louvain, Louvain-la-Neuve, Belgium*

## Charles-André Fustin

### Ulrich Jonas

*Max Planck Institute for Polymer Research, Mainz, Germany*

## INTRODUCTION

Colloidal particles are liquid or solid objects with dimensions ranging from a few to several hundred nanometers (and, in a broader sense, up to many micrometers), that are suspended in a solid, liquid, or gas matrix.<sup>[1–3]</sup> These particles can show very distinct properties compared to small molecules and macroscopic systems, because of their mesoscopic size with the resulting large surface-to-volume ratio and intermediate dynamics. One of the most common forms of colloids are solid particles suspended in a liquid medium, such as paint and adhesives, and this format will be discussed here. Solid colloid particles are available from many different materials, such as organic compounds (drugs and pigments), polymers, and inorganic materials (ceramics and semiconductors). Depending on the interactions between the particles and of the particles with the suspending medium, the colloids can form aggregates and ordered structures in three dimensions, e.g., colloidal crystals (Fig. 1A). Such 3-D aggregates may serve as mesoporous materials for filter applications, or if the particle diameter is in the wavelength range of visible light, colloid crystals can diffract and filter light of specific wavelength (photonic bandgap structures).<sup>[4]</sup>

If the particles additionally interact with a surface, colloid adsorption can take place that leads to planar structures (Fig. 1B). For such structured surfaces, many current and potential applications exist, such as self-cleaning, superhydrophobic or antireflecting surfaces, adhesion control (like protein adsorption and antifouling), chemo- and biosensors, optical filters and switches, electromechanical devices, microfluidics, and surfaces for separation technology.<sup>[5]</sup> For such applications, lateral patterning of the colloid layer is

often required (Fig. 1C, which can be achieved via various methods, such as site-selective surface modification or templating with a 3-D mold).

This entry provides an overview on the methods and effects that lead to structured colloid assemblies at substrate surfaces. Besides the fundamental interactions in colloidal systems that lead to 3-D and 2-D assembly structures, several techniques are discussed which can be used to build highly ordered particle assemblies with complex lateral structure in a controlled way. The patterning is realized by the application of templates and directing methods during particle deposition, which will be presented in further detail.

## FUNDAMENTAL INTERACTIONS IN COLLOID SYSTEMS AND SURFACES

Interactions between colloidal particles and between surfaces and colloidal particles are primarily governed by three main force types: van der Waals, electrostatic, and capillary forces (listed by increasing strength).<sup>[1,2,6]</sup> We present an overview of these colloidal forces, which play a crucial role in determining the particle deposition efficiency and stability. Other types of interactions are briefly discussed, as they can be important in particular cases.

### van der Waals Interactions

The universal attractive forces between atoms and molecules, known as van der Waals forces, operate between all particles in any suspension medium and are responsible for particle flocculation.<sup>[7]</sup> When these forces occur between two atoms or molecules, their

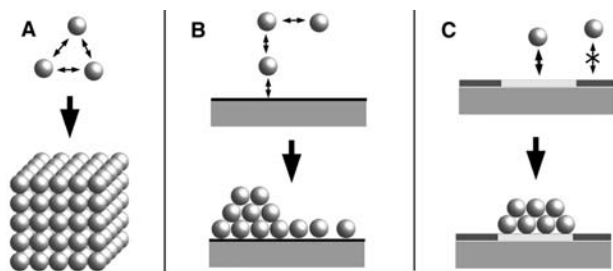


**Fig. 1** Progression of interactions in colloidal particle systems that lead to: (A) 3-D aggregates by particle-particle interactions; (B) particle layers on planar substrates by additional interaction with the substrate surface; (C) and structured colloid assemblies by lateral patterning of the substrate surface.

range is in the order of a nanometer or less (potential  $V$ -separation  $r$  dependence:  $V \sim 1/r^6$ ), but when colloidal particles are considered, these forces can act at a much longer distance. This is because the atoms of a particle mutually interact, to some extent, with all the atoms of other particles, and these effects are partially additive. The potential associated to such interactions is usually expressed as  $V = -A/12\pi r^2$ , where  $A$  is the Hamaker constant of the particular system and  $r$  is the distance between the particles.

### Electrostatic Interactions

These long-range forces are usually responsible for the stabilization of colloidal suspensions through repulsion between identically charged particles. The associated potential is expressed as  $V = C \exp(-\kappa r)$ , where  $1/\kappa$  is the Debye-Hückel length,  $r$  is the distance between the particles, and  $C$  is a term depending on  $\kappa$ , on temperature, on the surface potential of the particles, and on the electrolyte concentration. In an electrolyte solution, the distribution of ions in the vicinity of the solid surface (the diffusion layer) is determined by electrostatic interactions with the surface and the thermal motion of the diffusing ions. Solid surfaces of similar charge that approach each other repel when their diffusion layers overlap. On the other hand, solid surfaces with opposite charge experience an attraction when they come close to each other. This attraction is utilized in colloid self-assembly on charged surfaces and leads to irreversible adhesion.<sup>[8]</sup>

### Capillary Forces

Similar particles floating on a fluid attract each other by lateral capillary forces and can form clusters. These flotation capillary forces are caused by the

deformation of the interface due to the effect of gravity pulling the particles into the liquid and the surface tension that tends to minimize the liquid surface.<sup>[6]</sup> The energy of capillary interactions between floating particles becomes negligible, i.e., smaller than the thermal energy  $kT$ , for particles smaller than 5–10  $\mu\text{m}$ . Particles on a solid surface partially immersed in a liquid are also subject to similar attractive forces, called immersion capillary forces, which occur at the liquid–solid interface (e.g., during drying). Because of the confinement at a solid surface, the energy of immersion interactions is much larger, for the same particle size, than the energy of flotation interactions, and it can be substantially greater than  $kT$  even for particles of nanometer size. These very strong (about 3 orders of magnitude higher than the electrostatic forces) and long-range forces (up to macroscopic dimensions) pull the particles together and are responsible for their ordering, yielding 2-D or 3-D crystalline layers in certain cases.<sup>[6,9]</sup> The potential of immersion forces can be expressed as  $V \sim CR/(r-2R)$ , where  $R$  is the radius of the particle,  $r$  is the distance between the particles, and  $C$  is a factor depending on the surface tension, on the contact line at the surface of the particle, and on the mean slope angle of the meniscus at the contact line. These forces are attractive between objects of the same polarity (both wetting or non-wetting, same curvature of liquid meniscus at particle–liquid–air contact line), and repulsive between objects of different polarity (wetting in contact with nonwetting objects, opposite liquid meniscus at object–liquid–air contact line).

There are several other types of interactions which can be important in certain cases and may play a large role in determining whether or not particles will adhere to each other or to other surfaces. In aqueous systems, the effect of hydration can be important. This is often associated with hydration of ions at particle surfaces, and usually gives an extra repulsion. Hydrophobic effects, which are associated with the high internal structure in water, can also be relevant and may provide an extra interaction between particles or between particle and surfaces. Other significant effects arise from external forces, such as gravity and hydrodynamic drag. These external forces have a strong dependence on particle size. For instance, the gravity force is proportional to the mass of particle and hence, to the cube of the particle size. The hydrodynamic forces (particularly relevant in electrophoretic particle deposition), as a result of fluid flow, depend roughly on the square of particle size. This means that, for large particles, gravitational and drag forces will predominate over colloidal forces, while the latter may be much more significant for small colloidal particles.

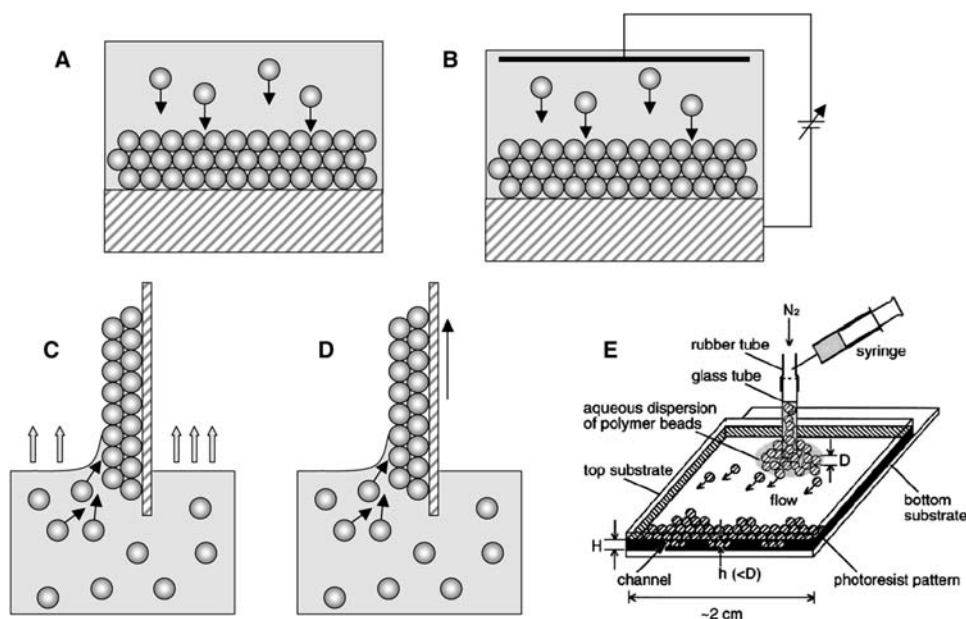


**Fig. 2** Schematic outlines of five common procedures to assemble colloids into 3-D crystalline structures: (A) sedimentation in a gravitational field; (B) electrophoretic method; (C) vertical deposition by evaporation; (D) deposition by vertically lifting of the substrate; (E) flow cell technique. *Source:* From Ref.<sup>[18]</sup>. © 1999 American Chemical Society.

## COLLOID ASSEMBLY IN 3-D

Three-dimensional closed pack structures of monodisperse microspheres, also called synthetic opals, present a spatial periodic variation of the dielectric constant. Thus they can influence the propagation of electromagnetic waves in a similar way as semiconductors do for electrons, i.e., there exists a bandgap that excludes the propagation of photons in a given range of frequencies. These so-called photonic crystals attract major interest because they represent promising candidates for the manipulation of the flow of light. Several methods to assemble colloidal crystals have been reported; the five most common procedures will be presented here, as schematically outlined in Fig. 2. Whatever method is applied, the utilization of monodisperse colloids, i.e., polydispersity below 5%, is a prerequisite to obtain ordered crystals with a low defect density. Usually, fcc structures with the (111) direction oriented perpendicular to the surface of the film are obtained.

### Sedimentation in a Gravitational Field

This is a simple technique requiring no special equipment (Fig. 2A), in which a particle suspension is standing undisturbed over a long period of time.<sup>[10,11]</sup> The colloids settle at the bottom of the container due to gravity and form dense 3-D crystalline structures. However, several parameters such as the size and density of colloids and the sedimentation rate, which has

to be slow enough to allow a disorder-to-order transition to occur, have to be carefully controlled to obtain a 3-D ordered lattice. Silica colloids are usually employed in sedimentation because of their high density ( $\sim 2.2 \text{ g cm}^{-3}$ ). The major drawbacks of this method are the long time needed to obtain colloidal crystals (days to months), the restricted control over the morphology of the top surface and over the number of layers, and the limited size range of colloidal spheres that can be used (300–550 nm).

### Electrophoretic Deposition

Several of the above-mentioned problems can be circumvented by the electrophoretic deposition method, which uses an electric field to control the sedimentation rate (Fig. 2B).<sup>[12,13]</sup> The particle suspension is held between two parallel electrodes and an applied voltage generates an electric field that drives the particles to the bottom electrode. With this technique, a broader range of particle sizes, with diameters up to 900 nm, can be used and the time needed to settle small spheres is substantially decreased.

### Vertical Deposition by Evaporation

A convenient and versatile way to obtain colloidal crystals is the vertical deposition technique, in which a hydrophilic substrate is vertically immersed into a colloidal suspension while the liquid medium is allowed to evaporate (Fig. 2C).<sup>[14,15]</sup> In this case, capillary forces are

responsible for the organization of the colloids (see the section “Colloid Assembly at Planar Surfaces” below). The thickness of the crystal can be precisely controlled by adjusting the concentration of the suspension and the sphere size. Ethanol is usually used as suspending medium because of its relatively fast evaporation rate at room temperature; however, water can also be used if the temperature is raised to about 50–60°C.<sup>[16]</sup>

### Vertical Lifting

A variant of the vertical evaporation method has been developed, where the substrate is withdrawn from an aqueous suspension at a controlled speed instead of letting the solvent evaporate (Fig. 2D).<sup>[17]</sup> The withdrawing speed provides an additional parameter to control the thickness of the deposited film and can substantially decrease the preparation time.

### Flow Cell

Colloids have also been assembled into ordered 3-D structures by using a flow cell (Fig. 2E).<sup>[18]</sup> An aqueous dispersion of particles is injected into a cell formed by two glass substrates and a square frame of photoresist that is patterned on the surface of one of the substrates. One side of the frame has channels on the upper rim that can retain the particles while letting the solvent flow through. External gas pressure generating a flow and agitation by sonication are the driving forces to assemble the particles into a close-packed structure. This method can be applied to a relatively broad range of particle sizes and the number of layers in the crystalline assemblies is controlled by the distance between the two opposing glass slides.

## COLLOID ASSEMBLY AT PLANAR SURFACES

Planar colloid layer systems consisting of particle monolayers and multilayers can be classified by their preparation method or by the interactions that control their formation. There are various techniques to deposit colloid particles at planar surfaces that allow the formation from disordered to highly crystalline particle mono- and multilayers, depending on the particular method and the intrinsic properties of the particles. Such methods are partially related to the techniques described above for 3-D colloid assemblies. Examples include spin coating of particle suspensions, centrifugation, evaporation of suspensions on surfaces, adsorption from solution/self-assembly, electrophoretic deposition from suspension, Langmuir–Blodgett (LB) deposition of colloidal monolayers from the air–water interface, or laminar flow methods.<sup>[19]</sup>

The various interactions that drive particle deposition and possibly ordering in the layer are van der Waals attraction between particles and the substrate surface, polar interactions and hydrogen bonding if polar groups and hydrogen donor–acceptor pairs are present, and strong Coulomb forces (electrostatic interactions) if charged surface functions are available. If the colloid particles are suspended in an aqueous medium and the thickness of the liquid film reaches the particle diameter, strong long-range capillary forces, in combination with convective flow, can cause high order in the colloid layers.

Three characteristic deposition methods and the involved interactions are described in more details below.

### Evaporation from Suspension on Planar Surfaces

The controlled evaporation of a latex suspension (concentration usually around 1 wt.%) in a very thin liquid film leads to the formation of densely packed colloid layers (Fig. 3A).<sup>[20]</sup> If the particles are monodisperse, highly ordered two-dimensional colloid crystals are formed. The ordering process occurs where the thickness of the liquid film reaches the particle diameter and a meniscus is formed between the colloids, pulling them tightly together by capillary forces. The driving force is the high surface tension of water that tends to minimize the free liquid surface between the particles. In addition, water evaporation in the dense particle layer generates a convective flow of the surrounding liquid with its suspended particles toward the colloid layer. It was found that high evaporation rates (controlled by ambient humidity) favor higher order in the colloid films and that smaller particles crystallize faster. The shape or slope of the drying meniscus controls the formation of multilayers, with a steeper meniscus producing thicker layers.

### Adsorption from Solution/Self-Assembly

By immersing a substrate into a colloid suspension, particles can adsorb onto the surface if sufficiently strong attractions between the substrate surface and the particles exist (Fig. 3B).<sup>[19]</sup> Very often, oppositely charged substrates and particles are used in which strong electrostatic attraction causes irreversible adsorption. In such cases, the substrate surface either carries an intrinsic charge (such as mica, a layered mineral), or the charge is introduced by surface modification with charged molecules. For this purpose, charged thiols can be adsorbed on gold, while oxidic surfaces such as glass are modified with charged silanes or polyelectrolytes. The complementary latex particles can be synthesized with charged surface groups by adding the corresponding monomer during

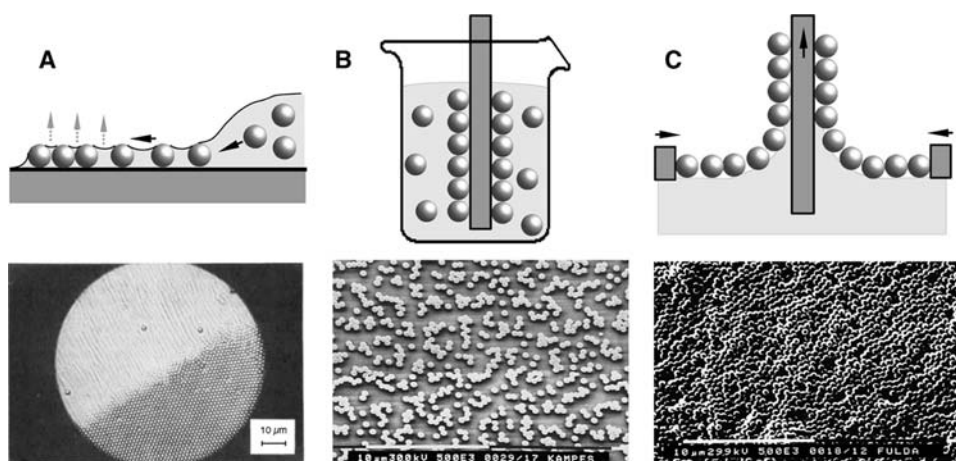


**Fig. 3** (A) Formation of ordered particle mono- and multilayers by capillary forces upon drying. (B) Self-assembly of colloid monolayers by adsorption from suspension. (C) Formation of a Langmuir–Blodgett particle film by transfer of a colloid monolayer from the air–water interface. *Source:* From Ref.<sup>[20]</sup>. © 1992 American Chemical Society. From Ref.<sup>[56]</sup>. © 1999 Elsevier. From Ref.<sup>[19]</sup>.

polymerization. Here often carboxylic acid functions (e.g., from acrylic acid) are used that are negatively charged at  $\text{pH} > 5$ . Because of the irreversible adsorption via electrostatic interactions in disordered particle layers, the maximum absolute surface coverage that can be practically achieved is about 56%, compared to a theoretical coverage of 91% in a dense hexagonal lattice. The process can be described by the theoretical model of “random sequential adsorption” (RSA), in which irreversibly and randomly adsorbed particles do not move laterally and prevent rearrangement into densely packed layers.<sup>[21]</sup> By alternately immersing the substrate in suspensions of oppositely charged colloids, highly disordered particle multilayers are obtained. If functional groups of the particles can react with groups on the substrate surface to form chemical bonds, very stable particle layers are obtained by chemisorption.<sup>[22]</sup>

### Langmuir–Blodgett (LB) Deposition of Colloid Monolayers from the Air–Water Interface

Polar colloid particles (e.g., sulfonated or carboxylated polystyrene latex) can be spread from an organic solvent (like ethanol) at the air–water interface, similar to low molar mass amphiphiles (Fig. 3C).<sup>[19]</sup> After solvent evaporation, the colloids float at the air–water interface, and by reduction of the free surface area with a moving barrier, the initially disperse particle layer is compressed up to the point where the colloids are tightly packed. The colloid monolayer formation is favored by low pH and high salt concentration, which drives the particles from the aqueous subphase to the surface as a result of the reduced polarity of the

screened charges. When a submerged substrate is vertically pulled up through the compressed colloid film, the particle monolayer can be transferred to the solid support. By annealing the transferred film close to the glass transition temperature of the latex material, the particles slightly deform and then adhere sufficiently to the substrate to allow an additional colloid layer transfer. Repeated transfer and annealing cycles allow the formation of particle multilayers. The colloid monolayers are usually disordered with many defects, and in particular, the multilayers possess a high surface roughness.

### STRUCTURED COLLOID ASSEMBLIES AT SURFACES

As discussed above, monodisperse colloidal particles can assemble into long-range ordered lattices under appropriate conditions, but self-assembly alone is restricted to the formation of 2-D or 3-D particle arrays and usually does not lead to more complex patterns. However, additional degrees of control over the colloidal structures can be achieved through the application of external electric, magnetic, or optical fields, by selective deposition onto previously patterned substrates, or by the use of templating structures (Fig. 4). These laterally structured surfaces can be fabricated by different techniques such as lithography with photons, particles, and scanning probes, replication against masters via physical contact (printing, molding, embossing), molecular self-assembly, or templated deposition.<sup>[23]</sup> Colloidal assembly onto such patterned surfaces, as outlined in Fig. 4, and the mechanisms governing the deposition will be discussed in the following sections.

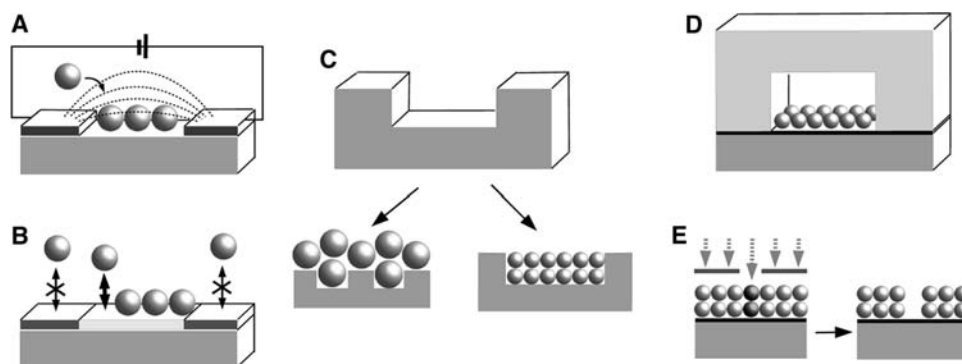


**Fig. 4** Various concepts for the generation of structured colloid assemblies in 2-D and 3-D on solid substrates: (A) external field templating (here, electrical field example); (B) chemically patterned surface; (C) topographic surface structure (with feature sizes in the colloid dimension lead to directed crystallization/epitaxy, left, while large feature sizes induce structuring of whole crystals, right); (D) 3-D template; (E) direct lithographic patterning of colloid layers.

## External Fields

### Electrical fields

As outlined before, colloidal particles can be manipulated with electric fields to form 2-D and 3-D ordered crystals. Two conceptual geometries can be distinguished by the orientation of the electric field with respect to the substrate surface: first, a parallel plate geometry, as presented in Fig. 2B, with the field vector perpendicular to the surface, and second, an in-plane electrode arrangement, as shown in Fig. 4A, with the principal field vector parallel to the substrate surface.

The *parallel plate geometry* has been used for the electrophoretic deposition of colloidal particle layers,<sup>[12,24,25]</sup> but this technique does not necessarily generate complex lateral structures by itself. Some basic in-plane structuring was observed during the different stages in the deposition process, such as initial random adsorption of isolated particles after short adsorption times, followed by the formation of 2-D clusters and islands of particles at longer times, and the coalescence of these individual domains up to complete coverage. The islands showed high order, but the crystallographic axes of neighboring islands were not correlated. Changes in the magnitude of the current did modulate the strength of the lateral attraction and allowed the formation of different 2-D “gas,” “liquid,” and crystalline colloidal arrays on the electrode. The ordering phenomena in electrophoretic deposition were explained with electrokinetics (charged particle acceleration in the electric field), electrohydrodynamics (flow of the liquid medium due to particle and ion migration), and Brownian diffusion (driven by thermal energy).<sup>[26,27]</sup>

More complex in-plane structures could be obtained by a combination of vertical confinement (which is controlled by the electrode separation) with variations

of the applied electric field.<sup>[28]</sup> A close electrode separation in the range of the colloid diameter strongly influences the electroosmotic (and hydrodynamic) fluid flow and switches it from an attractive into a repulsive character. By variation of the nature of the applied electric field and the degree of particle confinement, the relative strength of attraction and repulsion can be independently varied, providing a way to tune both the strength and range of the effective interaction potential. The technique allowed ordering and structure formation in the colloid layers from extended crystalline lattices with periodicities larger than the particle diameter over dense crystal patches to honeycomb and worm-like structures (Fig. 5).

A larger control over the lateral patterning of colloid layers with electric fields can be achieved by *in-plane structured electrodes*. It was shown that, on a planar patterned electrode in the parallel plate geometry (Fig. 2B), the colloid particles migrate laterally at the surface from the non-conducting to the conducting regions by electrohydrodynamic flow.<sup>[29]</sup> In the in-plane geometry of Fig. 4A, the electrode and counter electrode are on the same substrate surface and produce an in-plane field when a voltage is applied. Protein-covered latex microspheres were collected and coagulated onto the micrometer-sized gaps between two addressable electrodes under the action of a nonuniform electric field, an effect known as dielectrophoresis.<sup>[30]</sup> After particle fixation by induced coagulation, such colloid structures can be used in biosensor arrays with direct electric conductivity readout (after target molecule binding, tagging with colloidal gold and enhancement by silver nucleation).

Defined 2-D structuring in electrophoretic colloid deposition can also be obtained by a combination with lithographic illumination.<sup>[31]</sup> In this experiment, colloid particles were deposited in the parallel plate geometry onto an indium tin oxide (ITO) electrode that was



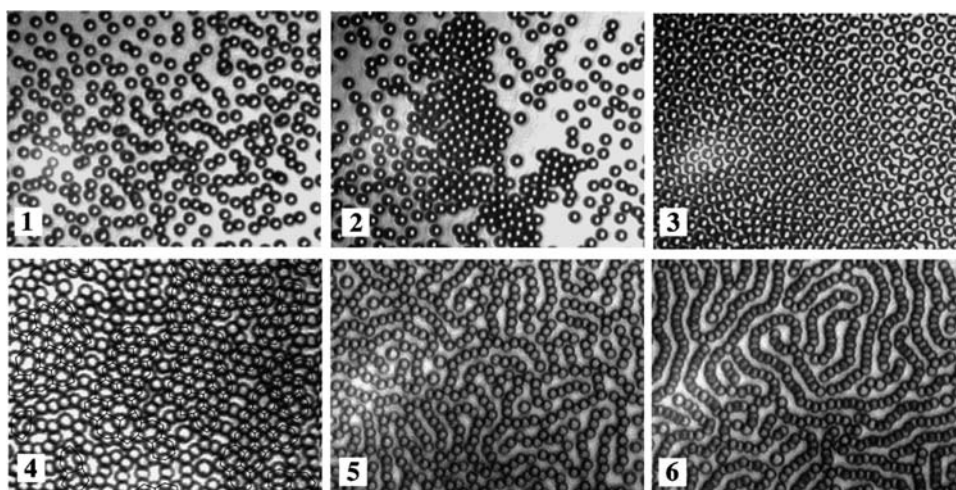


**Fig. 5** Colloid monolayer structures prepared by electrophoretic deposition in confined geometry (particle diameter, 4.2  $\mu\text{m}$ ). Source: From Ref.<sup>[28]</sup>. © 2002 American Chemical Society.

irradiated from the other side with ultraviolet (UV) light through a mask. The irradiated electrode regions showed a photochemically induced higher current density that, in turn, led to particle aggregation on these regions, while the non-irradiated areas were depleted of particles. By this method, crystalline particle monolayers with the shape of the mask geometry can be generated (Fig. 6).

### Optical fields

Individual colloid particles made of dielectric material can be optically trapped and manipulated in a strong electromagnetic field gradient of focused laser beams, a technique which is nowadays referred to as “optical tweezers.”<sup>[32]</sup> The dielectric particles are drawn into the region of highest light intensity and accelerated in the direction of the light propagation by the radiation pressure. If a laser beam hits a substrate surface in a perpendicular manner, the colloid particles become trapped at the intersection of the beam with the surface. An extension of this technique, called scanning laser optical trapping, was used to simultaneously trap multiple colloids in a designed pattern which was locked-in by photopolymerization of a monomer-containing solvent (Fig. 7).<sup>[33]</sup>

If three laser beams are brought to interference at a substrate surface, a standing wave 2-D pattern is generated, which allows entrapping of particles in the virtual lattice geometry of the interference pattern.<sup>[34]</sup> Such systems were used to create arrays of extended crystalline and noncrystalline colloid structures and to study the crystallization and melting of the 2-D colloid lattice by modulation of the light potential.<sup>[35]</sup> The use of optical fields to pattern surfaces with colloidal particles features the following advantages: 1) it does

not require contact with a probe, 2) it is not limited in particle number or morphology, and 3) it offers a very precise control over particle position.<sup>[36]</sup>

### Chemical Patterning

The combination of the modern patterning techniques with the ability of functionalized thiols or silanes to form self-assembled monolayers (SAM) onto specific surfaces (gold, silica) provides convenient methods to generate regions of modulated surface potentials on a substrate by differences in their chemical nature. The contrast between the opposite regions in the pattern is achieved by differences in wetting (hydrophobic against hydrophilic regions), charge (charged against opposite charged or neutral regions), or chemical affinity (covalent bonding) of the head groups located at the top of the SAM. Colloids with specific surface functions can

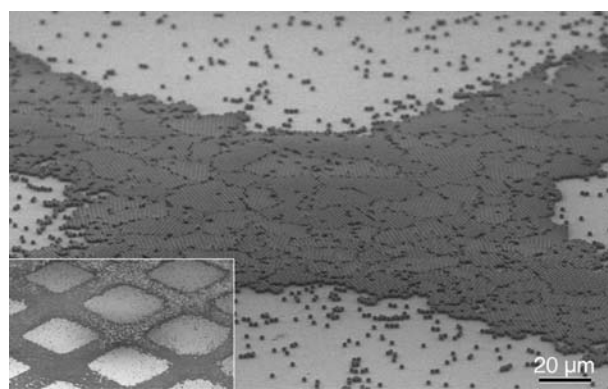


**Fig. 6** Photopatterned colloid assembly by electrophoretic deposition combined with illumination through a mask. Source: From Ref.<sup>[31]</sup>. © 2000 Nature.

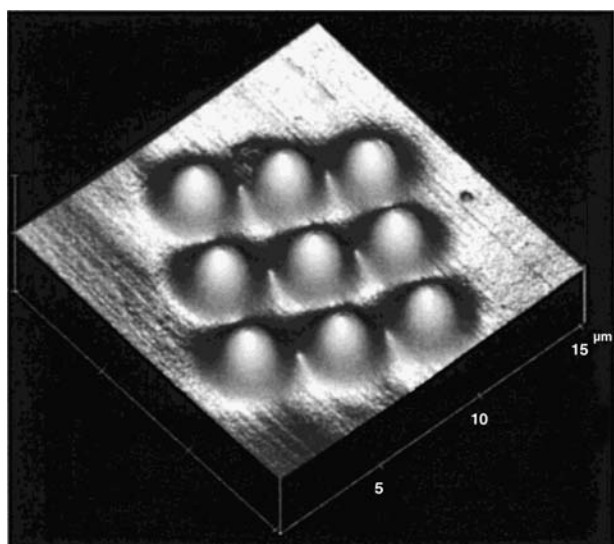


**Fig. 7** Ordered colloid cluster generated by scanning laser optical trapping. *Source:* From Ref.<sup>[33]</sup>. © 1999 American Chemical Society.

be assembled onto the substrates by a combination of attractive or repulsive interactions between the surface groups of the particles and the substrate, and the effect of the capillary forces upon drying.

Utilizing wetting, selective particle deposition could be obtained for magnetite colloids on thiol and silane pattern or for polystyrene particles on gold patterns on mica.<sup>[37]</sup> Upon drying of the latex suspension on the patterned surfaces, the liquid retracts onto the hydrophilic regions and selectively deposits the particles there.

A higher selectivity could be achieved with the assembly of charged spheres onto micropatterned substrates bearing cationic and anionic regions that were prepared by  $\mu$ CP of thiols on gold (Fig. 8).<sup>[9]</sup> Observation of the colloidal assembly in the wet state and during drying suggests two steps in the assembly mechanism. First, a selective attachment of colloids onto the substrate in a loose packing is driven by long-range attractive electrostatic forces between oppositely charged particles and the pattern. Second, rearrangement of the structure occurs upon drying through capillary forces that displace the particles toward the center of the pattern and induce the formation of dense clusters.

Patterned SAMs of charged thiols could be further modified by alternating polyelectrolyte adsorption from solution, which reverses the surface charge.<sup>[38]</sup> Colloid adsorption onto the polyelectrolyte multilayer patterns was controlled by three independent parameters: pH of the colloidal suspension (determines ionization of the surface), ionic strength of the suspension (charge screening by salt addition), and concentration of added surfactant (leads to charge screening

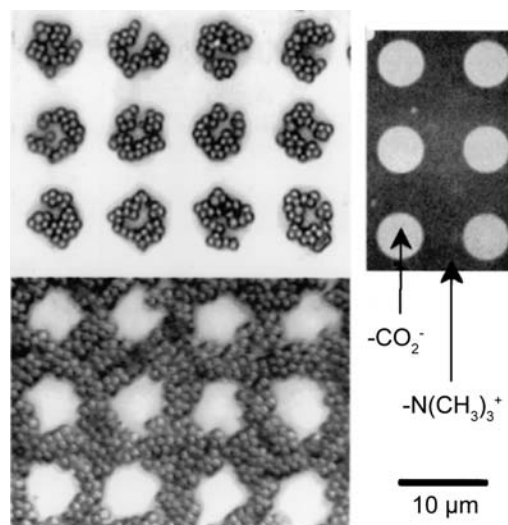


**Fig. 8** Localized adsorption of charged colloids onto oppositely charged thiol monolayers on gold. *Source:* From Ref.<sup>[9]</sup>. © 2000 American Physical Society.

and hydrophobic interactions). By reducing the size of the polyelectrolyte regions to less than three times the particle diameter, clusters of controlled size and packing geometry were obtained (Fig. 9).<sup>[57]</sup>

Colloid assembly experiments with negatively charged polymer spheres on photolithographically patterned alkylsilane SAMs on silica surfaces showed the competition of selective wetting and pH-dependent charge effects during the wet and dry states of the assembly process. By changing the pH from 1 to 9, the particle selectivity could be switched between adsorption onto the hydrophilic silica surface and deposition onto the hydrophobic alkylsilane patterns.<sup>[5]</sup>

The high selectivity of biological recognition can also be introduced into the colloid assembly process on chemically patterned surfaces by the utilization of short DNA strands. The complementary single strands of oligodeoxynucleotides are attached onto the colloids and specific regions on the substrate surface, respectively, and site-selective particle deposition is directed by hybridization of the complementary strands. Polystyrene beads as well as gold nanoparticles could be selectively deposited by this method.<sup>[39,40]</sup> The advantage of DNA to guide the assembly is the large number of recognition elements that can be encoded by the nucleotide sequence. Moreover, as the length of the sequence increases, the number of recognition elements increases dramatically, providing an almost limitless number of interaction pairs that can be designed to guide multicomponent assembly.

Photochemistry at the surface has been proven as an elegant way to directly obtain chemically patterned surfaces without the use of extra structuring tools.<sup>[41]</sup> Surface modification of a silicon substrate with a

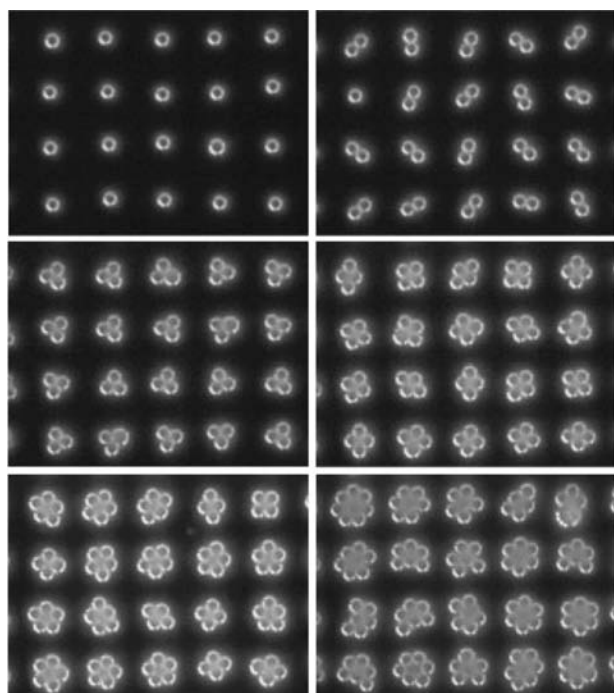


**Fig. 9** Selective clustering of charged colloid particles onto small polyelectrolyte regions with opposite charge (particle diameter,  $4.34\ \mu\text{m}$ ). *Source:* From Ref.<sup>[57]</sup>. © 2002 Wiley-VCH.

photosensitive silane and subsequent irradiation through a mask generates active surface groups at selected positions.<sup>[42]</sup> The chemical contrast between exposed and unexposed areas guides the posterior colloidal assembly, as was shown on a photoprotected aminosilane surface with carboxylated latex particles, which assembled specifically onto the free amino regions of the irradiated areas by Coulomb attraction (Fig. 10).

Radiation damage processes can be also used to selectively remove SAMs from a surface and generate alternating modified and unmodified regions on the substrate to guide the site-selective assembly of particles. By high-energy UV irradiation of a thiol monolayer through a mask and subsequent SAM formation with a charged thiol, a charge pattern was prepared and used for electrostatic colloid deposition.<sup>[43]</sup> Irradiation of a fluoroalkylsilane monolayer on a titanium dioxide surface resulted in the photochemical degradation of the silane and generation of very hydrophilic surface regions, which allowed selective colloid deposition by the vertical transfer method (as outlined in Fig. 2D).<sup>[44]</sup>

### Topographic Patterning

Several examples of colloids deposited onto topographically patterned surfaces are reported in the literature, which can be divided into three classes:

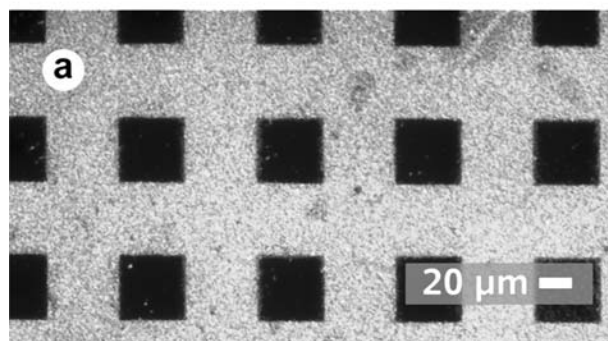
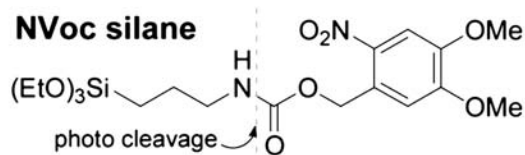


**Fig. 10** Photopatterning of a light-sensitive silane monolayer by irradiation through a mask led to selective particle adsorption onto the irradiated regions. *Source:* From Ref.<sup>[42]</sup>. © 2002 National Academy of Sciences USA.

1) the crystallization of colloids in 2-D confining media (Fig. 4C), 2) the crystallization of colloids in 3-D confining media (Fig. 4D), 3) the growth of colloidal crystals with an induced orientation, i.e., colloidal epitaxy (Fig. 4C, left).

### Colloid crystallization in lateral confinement (2-D)

Ribbons of colloid monolayers were obtained by electrophoretic deposition (Fig. 2B) of charged colloidal spheres onto stripe-patterned ITO electrodes with a groove depth exceeding half the particle diameter.<sup>[45]</sup> Variation of the conducting groove width had a substantial influence on the order in the particles bands, depending on the width being commensurate or incommensurate with the dimensions of a discrete number of colloidal spheres. For commensurate grooves smaller than eight times the particle diameter, ordered particle monolayers were obtained (Fig. 11).

Rectangular-shaped microchannels, prepared by etching (plasma, reactive ion etching (RIE)) of a silicon wafer or by micromolding, were used as template to generate stripes of colloidal crystals.<sup>[4,46]</sup> Colloids were deposited on such patterned surfaces, either by vertical evaporation (Fig. 2C) or vertical lifting (Fig. 2D). Colloids are deposited selectively in the microchannels because of the strong capillary-driven directional mass flow of colloids from the dispersion exclusively into the microchannels and not on the top of the unetched area (Fig. 12A–C).

If the feature size of the templating surface allows the accommodation of only a small number of particles, colloid clusters of well-defined size and

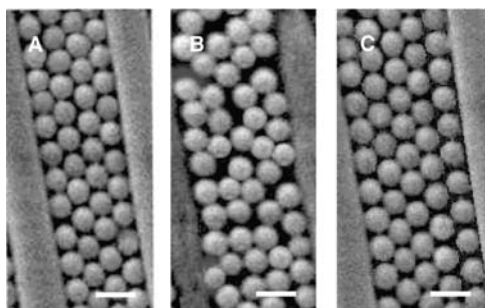


**Fig. 11** Electrophoretic deposition of colloids in grooves of a structured electrode (particle diameter,  $0.58\ \mu\text{m}$ ). For grooves which are commensurable with the particle packing, ordered layers are obtained (A,C), while incommensurable widths yield disordered layers (B). *Source:* From Ref.<sup>[45]</sup>. © 2002 Wiley-VCH.

geometry can be fabricated—triangular, squared, pentagonal, and hexagonal aggregates (Fig. 12D–I).<sup>[47]</sup>

### Colloid crystallization in spatial confinement (3-D)

Two related methods have been reported to grow colloidal crystals in 3-D confining templates. The first one,

called microfluidic colloidal self-assembly, utilizes a pattern of V-shaped grooves (made by anisotropic etching of a Si(100) wafer), which are covered with a polydimethylsiloxane (PDMS) block in conformal contact.<sup>[48]</sup> A drop of an aqueous colloid dispersion is then added at the interface between the patterned silicon wafer and the block. The spheres are driven into the V-shaped grooves by capillary forces and form a close-pack structure, with the (100) orientation perpendicular to the wafer surface, upon evaporation of the water. The shape (opening angle) of the grooves induces the (100) orientation and is therefore an example of colloidal epitaxy (see below and Fig. 14A,B). The second method, called micromolding in capillaries (MIMIC), consists of placing a microstructured PDMS mold onto a flat surface, then adding a drop of a colloidal suspension at the interface, which is drawn into the microchannels as described above.<sup>[49]</sup> When the water has evaporated, the PDMS mold is removed and close-packed colloidal structures with the (111) orientation perpendicular to the surface is obtained on the planar substrate (Fig. 13). In both of these techniques, the channels have to be open at both ends to allow the flow and evaporation of the aqueous colloid suspension.

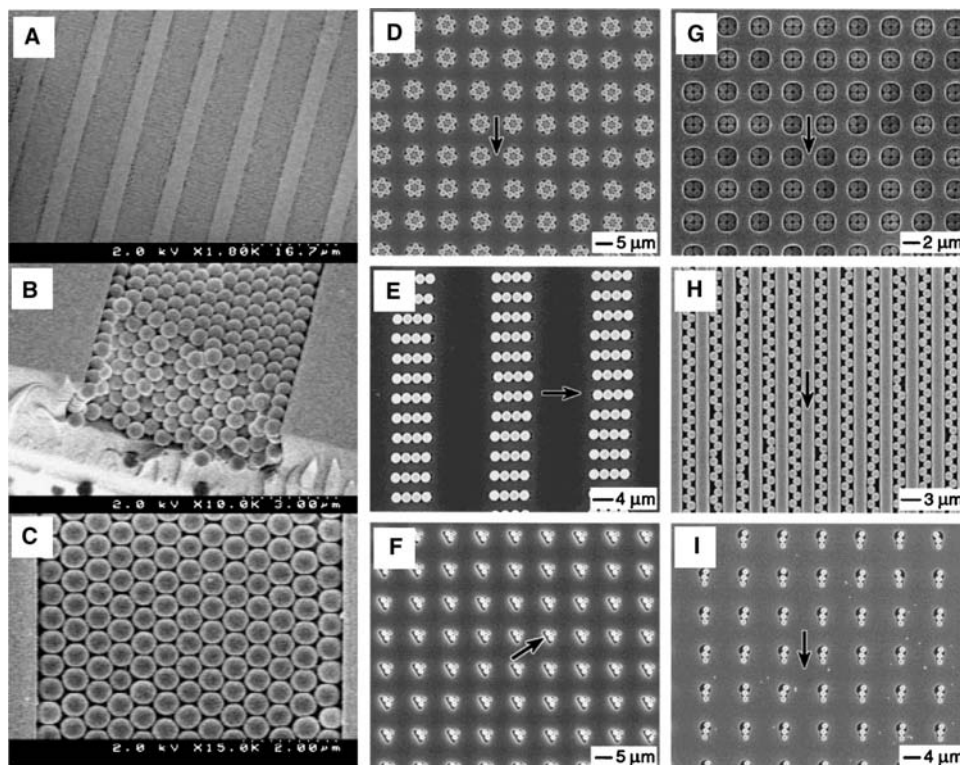


**Fig. 12** (A–C) Stripes of crystalline particle multilayers by vertical evaporation onto topographically structured substrates. (D–I) Cluster formation of particles in topographically structured substrates with defined feature sizes. *Source:* From Ref.<sup>[4]</sup>. © 2002 Wiley-VCH. From Ref.<sup>[47]</sup>. © 2001 American Chemical Society.

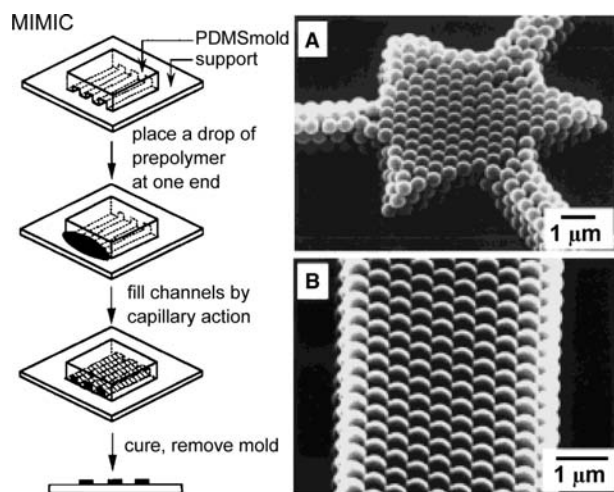


**Fig. 13** Micromolding in capillaries technique (MIMIC) and crystalline colloid structures obtained by MIMIC. Source: From Ref.<sup>[49]</sup>. © 1998 Wiley-VCH.

### Templated colloidal epitaxy

Colloidal epitaxy is the controlled crystallization of colloid particles on a structured surface with topographic periodicities commensurate to the colloid

crystal lattice dimensions, where the crystal orientation is induced by the surface structure. In early examples of colloidal epitaxy, silica spheres were sedimented onto a polymer film bearing holes (drilled by electron beam lithography).<sup>[50]</sup> When the pattern of holes is commensurate with the (100) or (110) plane of a fcc lattice, colloid crystal growth proceeds with the (100) or (110) plane parallel to the substrate surface. The major drawback of this technique is the small feature sizes of the template in dimensions of individual colloids, which requires advanced nanolithographic techniques for colloids smaller than 500 nm. To circumvent this problem, square or rectangular pyramidal pits much larger than the particles were anisotropically etched in a Si(100) wafer and used to grow small colloidal crystals within these pits by spin coating.<sup>[48]</sup> The apex angle of the pits determines the packing geometry, and if a square lattice is favored inside the pits, eventually the whole crystal on top of the substrate will grow with the (100) plane parallel to the surface (Fig. 14C,D).<sup>[51,52]</sup> With other apex angles, non-fcc packing geometries are obtained. Additional parameters that control bulk crystal growth are the lateral dimensions and the separation between the square pyramidal pits.

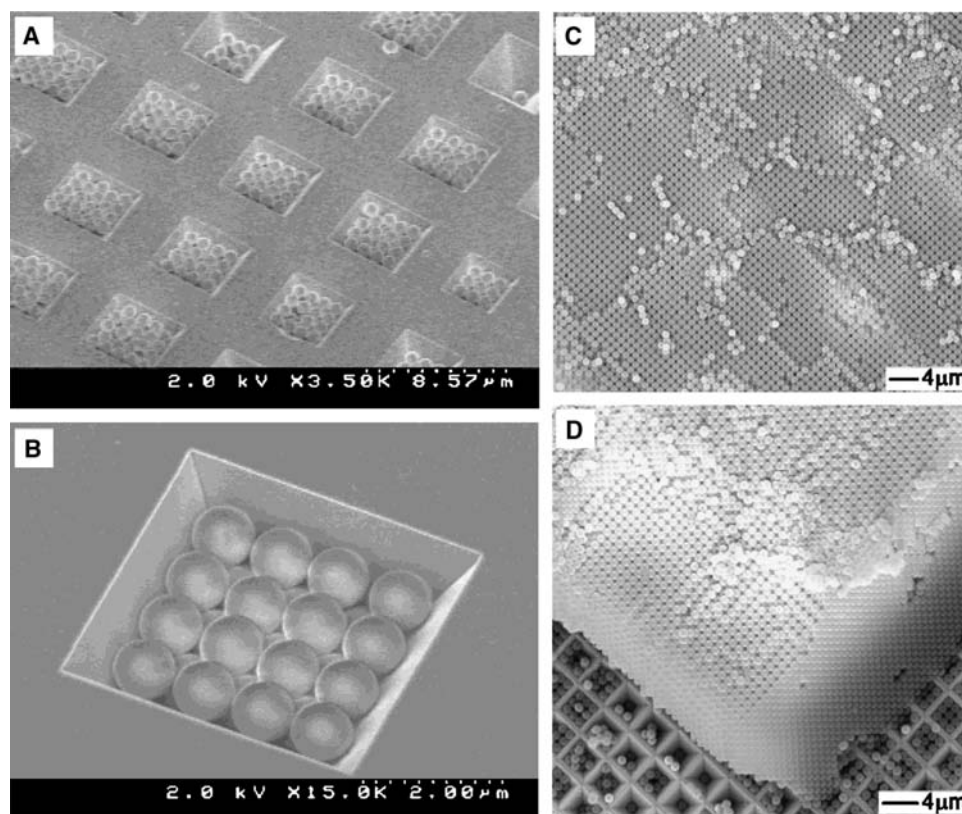


**Fig. 14** (A,B) Epitaxial growth of the (100) orientation of close-packed colloid crystals in pyramidal pits by spin coating self-assembly. (C,D) Bulk colloid crystallization of the (100) orientation by epitaxial growth on pyramidal pit template by flow cell deposition (see Fig. 2e). Source: From Ref.<sup>[48]</sup>. © 2001 Wiley-VCH. From Ref.<sup>[51]</sup>. © 2002 Wiley-VCH.

The stabilization of crystalline structures on patterned substrates can be considerably enhanced by entropic depletion or excluded-volume effects when smaller particles or nonadsorbing polymers are added to the colloidal suspension.<sup>[53]</sup> In suspensions of large and small particles or macromolecules, such forces push the large spheres together, toward flat walls, and toward inner corners on surfaces. This attraction is due to the extra volume that becomes available when the larger particles approach one another as a result of the overlap of the exclusion zones, with the consequent increase in the entropy of the system. These effects were exploited to confine large spheres from a binary mixture in the corners of a patterned surface and to sort particles according to size and shape without sensitivity to surface charge or surface chemistry. On patterned template surfaces with periodic 1-D and 2-D height profiles, the formation of 1-D, 2-D, and 3-D commensurate structures of polymethylmethacrylate (PMMA) spheres in the presence of dissolved, non-adsorbing polymers was investigated as a function of sphere size and grating periodicity.<sup>[54]</sup>

### Direct Lithographic Patterning of Colloidal Layers

The direct patterning of colloid layers can be achieved by selective irradiation of the particles with high energy radiation or particle bombardment (electrons, ions), which changes the material properties of the irradiated particles (Fig. 4e). Multilayers of polymethylmethacrylate particles could be patterned by e-beam lithography and selective dissolution of the irradiated colloids.<sup>[55]</sup>

### CONCLUSION

As reviewed by this entry, complex colloid particle structures can be prepared by applying the intrinsic interactions and self-organizing properties of colloids to deposition and lateral patterning methods on substrate surfaces. These colloid structures of particle mono- or multilayers can be obtained in disordered to highly ordered and crystalline states, depending primarily on the particle size distribution and the structure preparation method. Of particular interest for future applications are highly crystalline colloid assemblies with particle diameters in the wavelength of visible light, which can be fabricated by the described methods. Such particle structures show photonic properties (filtering and manipulation of specific wavelengths) and thus might be implemented in optical chips for information and data processing via light.<sup>[48]</sup>

### ACKNOWLEDGMENTS

Anne-Sophie Duwez is Chargé de Recherches of the Belgian National Fund for Scientific Research and would like to credit her permanent position at the Unité de Chimie et de Physique des Hauts Polymères and Research Center in Micro and Nanoscopic Materials and Electronic Devices (CERMIN), Université Catholique de Louvain, Louvain-la-Neuve, Belgium. The authors would like to thank Prof. Hans Wolfgang Spiess and Prof. Rudolf Zentel for their helpful discussion and continued support of this research. Financial support by the Max Planck Society, the Fonds der Chemischen Industrie, the European Commission, and the Gesellschaft Deutscher Chemiker/Dr. Hermann Schnell Stiftung is highly appreciated.

### REFERENCES

- Hiemenz, P.C. *Principles of Colloid and Surface Chemistry*, 2nd Ed.; Lagowski, J.J., Ed.; Marcel Dekker: New York, 1986.
- Hunter, R.J. *Introduction to Modern Colloid Science*; Oxford University Press: Oxford, 1993.
- Xia, Y.N.; Gates, B.; Yin, Y.D.; Lu, Y. Monodispersed colloidal spheres: old materials with new applications. *Adv. Mater.* **2000**, *12* (10), 693–713.
- Yang, S.M.; Miguez, H.; Ozin, G.A. Opal circuits of light-planarized microphotonic crystal chips. *Adv. Funct. Mater.* **2002**, *12* (6–7), 425–431.
- Kruger, C.; Jonas, U. Synthesis and pH-selective adsorption of latex particles onto photolithographically patterned silane layers. *J. Colloid Interface Sci.* **2002**, *252* (2), 331–338.
- Kralchevsky, P.A.; Nagayama, K. Capillary interactions between particles bound to interfaces, liquid films and biomembranes. *Adv. Colloid Interface Sci.* **2000**, *85* (2–3), 145–192.
- Israelachvili, J. *Intramolecular and Surface Forces*, 2nd Ed.; Academic Press Limited: London, 1995, Fifth Printing.
- Adamczyk, Z.; Weroni, P. Application of the DLVO theory for particle deposition problems. *Adv. Colloid Interface Sci.* **1999**, *83* (1–3), 137–226.
- Aizenberg, J.; Braun, P.V.; Wiltzius, P. Patterned colloidal deposition controlled by electrostatic and capillary forces. *Phys. Rev. Lett.* **2000**, *84* (13), 2997–3000.
- Davis, K.E.; Russel, W.B.; Glantschnig, W.J. Disorder-to-order transition in settling suspensions of colloidal silica-x-ray measurements. *Science* **1989**, *245* (4917), 507–510.
- Salvarezza, R.C.; Vazquez, L.; Miguez, H.; Mayoral, R.; Lopez, C.; Meseguer, F. Edward–Wilkinson behavior of crystal surfaces grown by sedimentation of SiO<sub>2</sub> nanospheres. *Phys. Rev. Lett.* **1996**, *77* (22), 4572–4575.
- Trau, M.; Saville, D.A.; Aksay, I.A. Field-induced layering of colloidal crystals. *Science* **1996**, *272* (5262), 706–709.



13. Holgado, M.; Garcia-Santamaria, F.; Blanco, A.; Ibisate, M.; Cintas, A.; Miguez, H.; Serna, C.J.; Molpeceres, C.; Requena, J.; Mifsud, A.; Meseguer, F.; Lopez, C. Electrophoretic deposition to control artificial opal growth. *Langmuir* **1999**, *15* (14), 4701–4704.
14. Jiang, P.; Bertone, J.F.; Hwang, K.S.; Colvin, V.L. Single-crystal colloidal multilayers of controlled thickness. *Chem. Mater.* **1999**, *11* (8), 2132–2140.
15. Vlasov, Y.A.; Bo, X.Z.; Sturm, J.C.; Norris, D.J. On-chip natural assembly of silicon photonic bandgap crystals. *Nature* **2001**, *414* (6861), 289–293.
16. Ye, Y.H.; LeBlanc, F.; Hache, A.; Truong, V.V. Self-assembling three-dimensional colloidal photonic crystal structure with high crystalline quality. *Appl. Phys. Lett.* **2001**, *78* (1), 52–54.
17. Gu, Z.Z.; Fujishima, A.; Sato, O. Fabrication of high-quality opal films with controllable thickness. *Chem. Mater.* **2002**, *14* (2), 760–765.
18. Park, S.H.; Xia, Y.N. Assembly of mesoscale particles over large areas and its application in fabricating tunable optical filters. *Langmuir* **1999**, *15* (1), 266–273.
19. Tieke, B.; Fulda, K.-F.; Kampes, A. *Nano-Surface Chemistry*; Rosoff, M., Ed.; Marcel-Dekker: New York, 2001; 213–242.
20. Denkov, N.D.; Velev, O.D.; Kralchevsky, P.A.; Ivanov, I.B.; Yoshimura, H.; Nagayama, K. Mechanism of formation of 2-dimensional crystals from latex-particles on substrates. *Langmuir* **1992**, *8* (12), 3183–3190.
21. Talbot, J.; Tarjus, G.; Tassel, P.R.V.; Viot, P. From car parking to protein adsorption: An overview of sequential adsorption processes. *Colloids Surf., A* **2000**, *165* (1–3), 287–324.
22. Taniguchi, T.; Ohashi, T.; Yamaguchi, K.; Nagai, K. Chemical immobilization of polymeric microspheres onto inorganic solid surfaces. *Macromol. Symp.* **2000**, *151* (1), 529–534.
23. Xia, Y.N.; Rogers, J.A.; Paul, K.E.; Whitesides, G.M. Unconventional methods for fabricating and patterning nanostructures. *Chem. Rev.* **1999**, *99* (7), 1823–1848.
24. Giersig, M.; Mulvaney, P. Preparation of ordered colloid monolayers by electrophoretic deposition. *Langmuir* **1993**, *9* (12), 3408–3413.
25. Bohmer, M. In situ observation of 2-dimensional clustering during electrophoretic deposition. *Langmuir* **1996**, *12* (24), 5747–5750.
26. Solomentsev, Y.; Guelcher, S.A.; Bevan, M.; Anderson, J.L. Aggregation dynamics for two particles during electrophoretic deposition under steady fields. *Langmuir* **2000**, *16* (24), 9208–9216.
27. Sides, P.J. Electrohydrodynamic particle aggregation on an electrode driven by an alternating electric field normal to it. *Langmuir* **2001**, *17* (19), 5791–5800.
28. Gong, T.Y.; Wu, D.T.; Marr, D.W.M. Two-dimensional electrohydrodynamically induced colloidal phases. *Langmuir* **2002**, *18* (26), 10,064–10,067.
29. Trau, M.; Saville, D.A.; Aksay, I.A. Assembly of colloidal crystals at electrode interfaces. *Langmuir* **1997**, *13* (24), 6375–6381.
30. Velev, O.D.; Kaler, E.W. In situ assembly of colloidal particles into miniaturized biosensors. *Langmuir* **1999**, *15* (11), 3693–3698.
31. Hayward, R.C.; Saville, D.A.; Aksay, I.A. Electrophoretic assembly of colloidal crystals with optically tunable micropatterns. *Nature* **2000**, *404* (6773), 56–59.
32. Ashkin, A. Acceleration and trapping of particles by radiation pressure. *Phys. Rev. Lett.* **1970**, *24* (4), 156–159.
33. Mio, C.; Marr, D.W.M. Tailored surfaces using optically manipulated colloidal particles. *Langmuir* **1999**, *15* (25), 8565–8568.
34. Burns, M.M.; Fournier, J.M.; Golovchenko, J.A. Optical matter—crystallization and binding in intense optical-fields. *Science* **1990**, *249* (4970), 749–754.
35. Wei, Q.H.; Bechinger, C.; Rudhardt, D.; Leiderer, P. Experimental study of laser-induced melting in two-dimensional colloids. *Phys. Rev. Lett.* **1998**, *81* (12), 2606–2609.
36. Hoogenboom, J.P.; Vossen, D.L.J.; Faivre-Moskalenko, C.; Dogterom, M.; van Blaaderen, A. Patterning surfaces with colloidal particles using optical tweezers. *Appl. Phys. Lett.* **2002**, *80* (25), 4828–4830.
37. Palacin, S.; Hidber, P.C.; Bourgoin, J.P.; Miramond, C.; Fermon, C.; Whitesides, G.M. Patterning with magnetic materials at the micron scale. *Chem. Mater.* **1996**, *8* (6), 1316–1325.
38. Chen, K.M.; Jiang, X.P.; Kimerling, L.C.; Hammond, P.T. Selective self-organization of colloids on patterned polyelectrolyte templates. *Langmuir* **2000**, *16* (20), 7825–7834.
39. Esener, S.; Hartmann, D.; Güncer, S.; Fan, C. DNA-assisted assembly of photonic devices and crystals. *OSA TOPS Spatial Light Modulators* **1997**, *14*, 65–68.
40. Demers, L.M.; Park, S.J.; Taton, T.A.; Li, Z.; Mirkin, C.A. Orthogonal assembly of nanoparticle building blocks on dip-pen nanolithographically generated templates of DNA. *Angew. Chem., Int. Ed.* **2001**, *40* (16), 3071–3073.
41. Vossmeier, T.; Jia, S.; Delonno, E.; Diehl, M.R.; Kim, S.H.; Peng, X.; Alivisatos, A.P.; Heath, J.R. Combinatorial approaches toward patterning nanocrystals. *J. Appl. Phys.* **1998**, *84* (7), 3664–3670.
42. Jonas, U.; del Campo, A.; Kruger, C.; Glasser, G.; Boos, D. Colloidal assemblies on patterned silane layers. *Proc. Natl. Acad. Sci. U.S.A.* **2002**, *99* (8), 5034–5039.
43. Friebel, S.; Aizenberg, J.; Abad, S.; Wiltzius, P. Ultraviolet lithography of self-assembled monolayers for submicron patterned deposition. *Appl. Phys. Lett.* **2000**, *77* (15), 2406–2408.
44. Gu, Z.Z.; Fujishima, A.; Sato, O. Patterning of a colloidal crystal film on a modified hydrophilic and hydrophobic surface. *Angew. Chem., Int. Ed.* **2002**, *41* (12), 2068–2070.
45. Kumacheva, E.; Golding, R.K.; Allard, M.; Sargent, E.H. Colloid crystal growth on mesoscopically patterned surfaces: Effect of confinement. *Adv. Mater.* **2002**, *14* (3), 221–224.
46. Ferrand, P.; Egen, M.; Griesebock, B.; Ahopelto, J.; Muller, M.; Zentel, R.; Romanov, S.G.; Torres, C.M.S. Self-assembly of three-dimensional photonic crystals on structured silicon wafers. *Appl. Phys. Lett.* **2002**, *81* (15), 2689–2691.
47. Yin, Y.D.; Lu, Y.; Gates, B.; Xia, Y.N. Template-assisted self-assembly: a practical route to complex

- aggregates of monodispersed colloids with well-defined sizes, shapes, and structures. *J. Am. Chem. Soc.* **2001**, *123* (36), 8718–8729.
48. Ozin, G.A.; Yang, S.M. The race for the photonic chip: colloidal crystal assembly in silicon wafers. *Adv. Funct. Mater.* **2001**, *11* (2), 95–104.
  49. Kim, E.; Xia, Y.N.; Whitesides, G.M. Two- and three-dimensional crystallization of polymeric microspheres by micromolding in capillaries. *Adv. Mater.* **1996**, *8* (3), 245–247.
  50. van Blaaderen, A.; Ruel, R.; Wiltzius, P. Template-directed colloidal crystallization. *Nature* **1997**, *385* (6614), 321–324.
  51. Yin, Y.D.; Xia, Y.N. Growth of large colloidal crystals with their (100) planes orientated parallel to the surfaces of supporting substrates. *Adv. Mater.* **2002**, *14* (8), 605–608.
  52. Yin, Y.; Li, Z.Y.; Xia, Y. Template-directed growth of (100)-oriented colloidal crystals. *Langmuir* **2003**, *19* (3), 622–631.
  53. Dinsmore, A.D.; Yodh, A.G.; Pine, D.J. Entropic control of particle motion using passive surface microstructures. *Nature* **1996**, *383* (6597), 239–242.
  54. Lin, K.H.; Crocker, J.C.; Prasad, V.; Schofield, A.; Weitz, D.A.; Lubensky, T.C.; Yodh, A.G. Entropically driven colloidal crystallization on patterned surfaces. *Phys. Rev. Lett.* **2000**, *85* (8), 1770–1773.
  55. Muller, M.; Zentel, R.; Maka, T.; Romanov, S.G.; Torres, C.M.S. Dye-containing polymer beads as photonic crystals. *Chem. Mater.* **2000**, *12* (8), 2508–2512.
  56. Kampes, A.; Tiede, B. Self-assembly of carboxylated latex particles at charged surfaces: influences of preparation conditions on the state of order of the monolayers. *Mater. Sci. Eng., C* **1999**, *8–9*, 195–204.
  57. Lee, I.; Zheng, H.P.; Rubner, M.F.; Hammond, P.T. Controlled cluster size in patterned particle arrays via directed adsorption on confined surfaces. *Adv. Mater.* **2002**, *14* (8), 572–577.

# Computational Analysis Using Normal and Multibody Modes

**Bryan C. Hathorn**

**Donald W. Noid**

**Bobby G. Sumpter**

*Division of Computer Science and Mathematics, Oak Ridge National Laboratory,  
Oak Ridge, Tennessee, U.S.A.*

**Chao Yang**

*National Energy Research Science Computer Center, Lawrence Berkeley National Laboratory,  
Berkeley, California, U.S.A.*

**William A. Goddard III**

*Department of Chemistry, California Institute of Technology, Pasadena, California, U.S.A.*

## INTRODUCTION

The complexity of real materials with their intriguing interplay between chemical composition, atomic arrangements, microstructures, and macroscopic behavior makes computational modeling and materials design extremely difficult. Even with the fundamental laws of quantum mechanics and statistical physics, the availability of high-performance computers, and with the growing range of sophisticated software systems accessible to an increasing number of scientists and engineers, the goal of designing novel materials from first principles continues to elude most attempts. On the other hand, computational experiments have led to increased understanding of atomistic origins of molecular structure and dynamics. In particular, the molecular dynamics and mechanics methods have yielded a wealth of knowledge on the structural and dynamical behavior of various polymeric materials as a function of temperature and pressure.

For a number of years, computational scientists have been able to perform first principles quantum mechanical calculations on small systems, typically tens to hundreds of atoms and molecular dynamics simulations on larger systems composed of thousands of atoms. Calculations on larger systems, however, remain at the edge of tractability, due to memory, storage, and computation limits. These systems include a wide range of important applications, from biological applications such as protein modeling, to materials applications such as bulk properties of ceramics, metals, and polymers. Recently, there has been much effort to make theoretical predictions of nanoscale structures, both for use in mesoscale simulations and

microscopic engineering design problems, and also for the pure intellectual challenge of working with these large molecular structures.<sup>[1–4]</sup>

## OVERVIEW

Many systems are envisioned of being made up of repeating subunits that can be assembled into the desired structure. In the case of proteins, the subunits can be considered as the set of amino acids, or perhaps even larger morphological structures such as alpha helices.<sup>[1]</sup> In molecular machines, these subunits can be structures such as buckyballs, carbon nanotubes, or polymer particles, which have recently been employed in designed structures.<sup>[5–8]</sup> It has been suggested that instead of treating the full atomistic problem, inherent with many degrees of freedom, it may be possible to replace the system with a simplified framework, where it suffices to describe only the interactions between the various subunits in the structure.

Such an approximation could have great utility, for instance, in the case of polymer particles composed of thousands of monomer units, one could replace each of the pairwise distances for thousands of monomer units with a single pairwise difference between two particles, and perhaps 5 more degrees of freedom for the positional orientation between the particles. In addition, internal bending, stretching, and torsional coordinates within the individual polymer strands could be neglected, reducing the total number of degrees of freedom treated in the calculation from tens of thousands, to perhaps tens. In essence, the individual structural subunits are replaced by subunits with some

average property. Such a technique is frequently employed in so-called “multibody dynamics” analysis of structures.<sup>[9]</sup>

In the present entry, we seek to address whether the mechanics of the approximate system resembles that of the full system by studying the vibrational normal modes of complicated polymer particle structures. The most direct approximation to these motions is to examine the vibrational motion of structures composed of individual subunits. In the case of the aforementioned polymer particle structures, the “multibody” analysis would be to consider a system of interacting polymer sphere subunits, whereas the full system would include all the motions of the individual monomer units within the polymer spheres.

The natural question in this case can be rephrased in terms of the vibrational motions of a coupled system. In the present case, we ask whether the eigenmodes of the full system represent the vibrations of the multimode system. In particular, the very large systems have motion that rapidly becomes chaotic<sup>[10,11]</sup> and we suspect the behavior of the simplified system may be significantly less so.

## NORMAL MODE ANALYSIS

When transforming the more complicated system to a simplified one, we must naturally neglect many specific interactions. A number of fundamental questions arise. First among them is the question of whether the mechanics of the approximate system resembles that of the full system. This is a particularly difficult question to approach, because the full system tests the limits of computability, while the approximate system remains quite simple. In addition, one must try to account for the size-dependent properties of nanoscale building blocks.

The two sets of normal modes are quite different, and we require a simple method by which they can be compared. The fundamental idea of normal mode analysis is to express the total vibrational motion  $Q_j$  as a linear combination over a set of linearly independent motions,  $q_i$ ,<sup>[12,13]</sup>

$$Q_j(t) = \sum_i c_{i,j} q_i(t) \quad (1)$$

## SIMPLIFIED NORMAL MODE ANALYSIS

In the simplified model, there are naturally fewer degrees of freedom, so the set of vibrational modes is similarly smaller. We require a mapping from the smaller set of vibrational modes onto the larger set, and ask whether one of the “multimodes” may, in fact,

be a sum of linearly independent eigenmodes for the whole system. As it turns out, this can only be the case when the eigenmodes for the whole system are degenerate in frequency, otherwise there will be rapid dephasing, and after a few cycles of the periodic behavior the motion will no longer be coherent. For mismatched modes of this type, the recurrence time is lengthy, and chaotic behavior ensues. As a result, any correspondence between the two sets of eigenmodes should be dominated by a single mode in each case, and the correspondence should be apparent from a simple and direct inspection. Using this correspondence, one can immediately evaluate the efficacy and any possible limitations of the multibody approximation.

From an engineering perspective, the concept of multibody dynamics is well founded.<sup>[9]</sup> Machines are made of interconnected rigid parts, and the machine operates by the interactions of these parts. Recently, however, there has been much interest in building well-defined structures on the nanoscale out of blocks that are only a few micrometers in dimension. For instance, it is now possible to design and construct polymer structures from individual polymer nanoparticles isolated in an electromagnetic trap and manipulated with the influence of a linear quadrupole placement device.<sup>[14]</sup> These systems can be designed specifically for their optical and mechanical properties.<sup>[15]</sup> As opposed to devices built on macroscopic scales where one expects components to be structurally rigid, at the molecular scale one expects that the particles may be subject to significant deformation, or “softness.” As a result, we have undertaken the study of these structures on the nanoscale.

## METHODS AND COMPUTATION

The theory of the computation of normal modes of molecules is well known and has been reviewed extensively elsewhere,<sup>[12,16–19]</sup> so we provide only a brief summary here of the results that are important to the present study. The essence of normal mode analysis is the solution of the secular equation,

$$|\mathbf{F} - \lambda\mathbf{I}| = 0 \quad (2)$$

where  $\lambda$  are the eigenvalues and  $\mathbf{F}$  is the force constant matrix in mass-weighted Cartesian coordinates. The squares of the frequencies of vibration are given by the eigenvalues,  $\lambda$ . As the eigenvalues are the squares of real numbers, they should all be positive or zero in an accurate calculation. (The eigenvalues that have a frequency of zero are termed “indifferent modes” and correspond to the physical translations and rotations of the entire system in space.)<sup>[13]</sup> The force constant matrix is obtained from the second derivatives

of the potential function,  $V$ ,

$$\mathbf{F} = \mathbf{M}^{-1/2}(\nabla^2 V)\mathbf{M}^{-1/2} \quad (3)$$

where  $\mathbf{M}$  is a diagonal matrix composed of the masses. In a traditional normal coordinate analysis (NCA) calculation for a large molecule, there are numerous negative eigenvalues that correspond to imaginary frequencies, which are in contrast to the assumption that the system is at a local minimum.

To examine the types of vibrational modes within a multibody system, computations consisting of several steps must be performed. The first step is the construction of the particle structures by molecular dynamics simulation, followed by annealing of the structures to a local minimum on the potential surface via a molecular mechanics procedure. The minimized configuration is used to generate a trajectory averaged Hessian matrix, which is diagonalized using sparse matrix techniques to yield the eigenvalues (frequencies) and eigenvectors (displacements) of the molecular normal modes. Finally, the eigenvectors are searched to evaluate their character as consisting largely of inter- or intraparticle motions. Each of these procedures is discussed in some detail in the following sections. In this study we have examined the vibrational structures of polymer particle dimers, which we have discussed extensively elsewhere,<sup>[20,21]</sup> and also polymer particle trimers in bent and approximately linear configurations, as well as a hexagonal arrangement composed of six polymer particles in a near plane geometry, similar to one that has been constructed experimentally (M. D. Barnes, private communication).

## Molecular Dynamics

For the purposes of the present entry, we discuss the motions and interaction forces between individual polymer particles both before and after interactions take place. The details of the geometric statement function approach developed by several of the authors are described more fully elsewhere.<sup>[22]</sup>

Polymer particles have been treated with a molecular dynamics approach,<sup>[23,24]</sup> integrating Hamilton's equations of motion in time,

$$\dot{q}_i = \frac{\partial H}{\partial p_i} \quad (4)$$

$$-\dot{p}_i = \frac{\partial H}{\partial q_i} \quad (5)$$

where  $H$  is the Hamiltonian of the system and the  $q_i$  and  $p_i$  represent the coordinates and their conjugate

momenta. In the present case, we have treated coordinates and momenta in the Cartesian frame, where the total kinetic energy is diagonal. Integration of the equations of motion was accomplished by use of novel symplectic integrators developed in our laboratory.<sup>[25]</sup>

As a simplification we have collapsed the  $\text{CH}_2$  and  $\text{CH}_3$  units of the polyethylene chain into a single monomer of mass 14.5 amu. By neglecting the internal structure of these groups, the number of coordinates and thus the number of equation of motion for the system are greatly reduced. The model has been shown to be useful to study the low-temperature behavior of the system where the effects of the hydrogens have little effect on the heat capacity and entropy of the system.<sup>[26]</sup>

The Hamiltonian for the system is specified as.<sup>[26,27]</sup>

$$H = T + \sum V_{2b} + \sum V_{3b} + \sum V_{4b} + \sum V_{nb} \quad (6)$$

where  $T$  is the kinetic energy component, expressed in terms of Cartesian coordinates, and the terms  $V_{2b}$ ,  $V_{3b}$ , and  $V_{4b}$  represent the 2-, 3-, and 4-body terms for monomer units in an individual polymer strand, respectively, and  $V_{nb}$  is the non-bonded interaction between individual monomer units separated by 4 or more monomer units along the chain, and within a spherical cutoff of 10 Å. The functional forms of the potentials are given by<sup>[26,28–31]</sup>

$$V_{2b} = D\{1 - \exp[-\alpha(r_{ij} - r_e)]\}^2 \quad (7)$$

$$V_{3b} = \frac{1}{2}\gamma(\cos \theta - \cos \theta_e)^2 \quad (8)$$

$$V_{4b} = 8.77 + a \cos \tau + b \cos^3 \tau \quad (9)$$

$$V_{nb} = 4\epsilon \left[ \left( \frac{\sigma}{r_{ij}} \right)^{12} - \left( \frac{\sigma}{r_{ij}} \right)^6 \right] \quad (10)$$

with the values of the constant terms given in Table 1. The distances between the various monomer units,  $r_{ij}$ , are given by the standard Cartesian relation,

$$r_{ij} = \sqrt{(x_i - x_j)^2 + (y_i - y_j)^2 + (z_i - z_j)^2} \quad (11)$$

In the present case, initial conditions for the trajectories composed the coordinates of individual amorphous polymer particles composed of 60 chains of 100 monomer units, which had previously been obtained by annealing.<sup>[32]</sup> Momenta were chosen randomly in the radial coordinate so as not to excite internal

**Table 1** Potential parameters for polyethylene particle systems

Two-body bonded constants <sup>a</sup>	
$D$	$= 334.72 \text{ kJ/mol}$
$r_e$	$= 1.53 \text{ \AA}$
$\alpha$	$= 199 \text{ \AA}^{-1}$
Three-body bonded constants <sup>b</sup>	
$\gamma$	$= 130.122 \text{ kJ/mol}$
$\theta_e$	$= 113^\circ$
Four-body bonded constants <sup>a</sup>	
$a$	$= -18.4096 \text{ kJ/mol}$
$b$	$= 26.78 \text{ kJ/mol}$
Two-body non-bonded constants <sup>a</sup>	
$\epsilon$	$= 0.4937 \text{ kJ/mol}$
$\sigma$	$= 4.335 \text{ \AA}$

<sup>a</sup>Refs.<sup>[30,31]</sup><sup>b</sup>Refs.<sup>[28,29]</sup>

angular momentum. The randomly chosen momenta were rescaled to produce the appropriate temperature for the simulation,

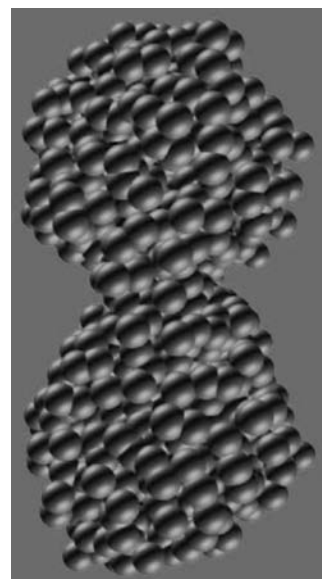
$$\sum_i \frac{1}{2m_i} p_i^2 = \frac{3}{2} k_B T \quad (12)$$

These thermalized particles are then placed in proximity and given an initial impulse to drive them together. Several types of collisions are observed. At high kinetic energies (high relative velocities of the particles) particles are observed to fracture and break apart. At high kinetic energies and orbital angular momenta one observes glancing collisions resulting in either particle fracture or chain transfer between the particles.<sup>[33–35]</sup> In the present case, however, we are interested in building structures of particles, so the range of relative collision velocities has been selected to produce collisions where the particles stick together.

## Soft Matter, Multiparticle Structures

### Dimer structure

The thermalized particles (with an initial temperature of 5 K) offset in the  $z$  coordinate so that their minimum edge to edge distance was 5.75 Å. The particles were then given an initial impulse toward each other of 0.25 Å/ps to induce a collision of the particles. The molecular dynamics simulation was allowed to run for a minimum of 100 ps to allow the particles to equilibrate and relax to their final configuration. The particle dimers formed were then subjected to potential minimization, described below (Fig. 1).

**Fig. 1** Particle dimer composed of two particles each with 60 chains of 100 monomer units.

### Trimer structure

Particle trimers were formed by using three preformed thermalized particles and aligning them along the  $z$  axis in the coordinate system. The centers of mass of the three particles were located at such that the minimum distance between  $z$  coordinates in the two particles was 5.75 Å. The initial  $z$ -velocities of the particles were established at 0.25, 0, and  $-0.25$  Å/ps to induce a collision and coalescence of the particles. Two simulations were run, one in a linear configuration and the other with an offset of 35 Å in the  $x$  coordinate of the middle particle, to produce linear and bent configurations (Fig. 2). The two structures were then subjected to potential minimization, described below.

### Hexmer structure

We have also simulated a hexagon of polymer particles, similar to that which has been designed and constructed experimentally. The structure was created by arranging six preformed and thermalized polymer particles with centers of mass locations given by

$$x = R \cos \frac{n\pi}{3} \quad (13)$$

$$y = R \sin \frac{n\pi}{3} \quad (14)$$

where  $n = 0, \dots, 5$  and  $R = 2R_{\max}$ , where  $R_{\max}$  is the maximum particle radius for an individual particle. An impulse of 0.25 Å/ps was given toward the origin of the system for each of the particles, and the simulation was



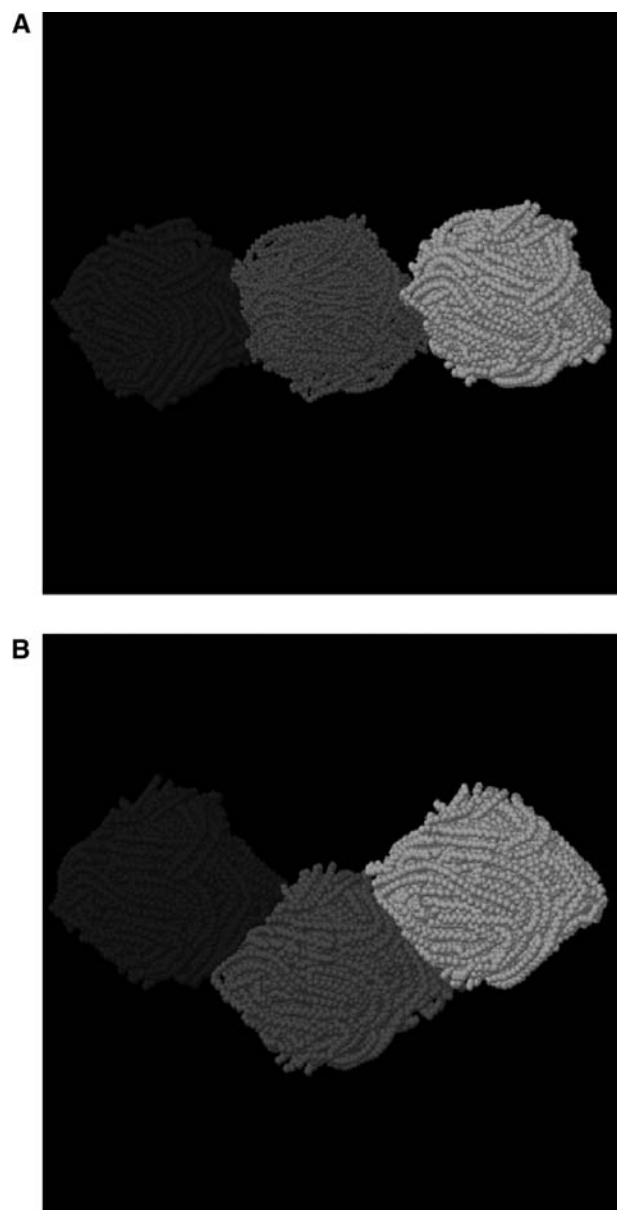


**Fig. 2** Particle trimers in (A) linear and (B) bent configurations. Each of the individual particles is composed of 60 chains of 100 monomer units.

run for 300 ps, where partial coalescence of the particles into a ringlike structure was observed. Structures were then subjected to potential minimization, described below, to find a local minimum (Fig. 3).

### Potential Energy Minimization

The premise behind normal mode calculations is that the structure resides at a local minimum that can be treated in the harmonic approximation. The collisions between particles do not necessarily correspond to a local minimum, as there is a considerable amount of

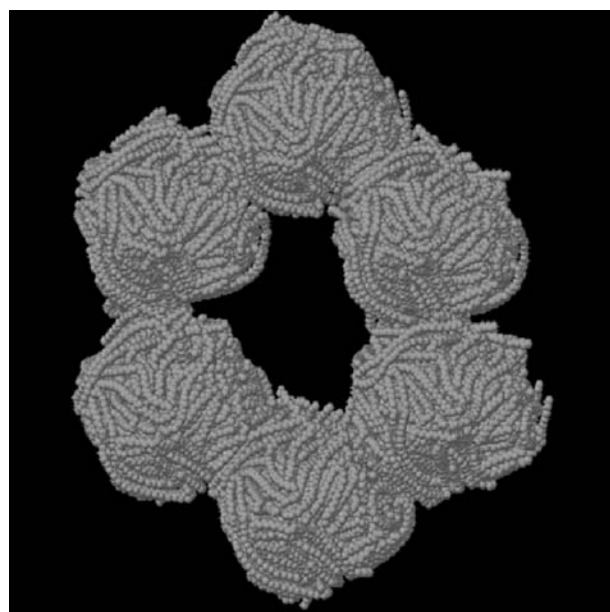


**Fig. 3** Ringlike structure composed of six particles. Each particle is comprised of 60 chains of 100 monomer units.

excess kinetic energy in the initial conditions that may be converted to potential energy in the collision, resulting in a large displacement from a local minimum. Thus, subsequent to creation of the particle structure, it is necessary to establish suitable equilibrium positions for each of the monomer units in the structure, finding the local potential minimum. The method employed in the present approach is a hybrid molecular dynamics–molecular mechanics simulation using the Broyden, Fletcher, Goldfarb, and Shannon (BFGS) quasi-newton minimization algorithm and simulated annealing via classical trajectories (a short trajectory in which the momenta are periodically quenched to zero).<sup>[36]</sup> The resulting structures are shown in Figs. [1–3].

### Hessian Matrix Evaluation

The usual method for normal coordinate analysis is to choose a single configuration and to evaluate and diagonalize the Hessian matrix for this configuration. Since finding the exact minimum of the potential is difficult, such an approach invariably leads to obtaining the Hessian away from the minimum, leading to numerous negative eigenvalues. These negative eigenvalues correspond to imaginary vibrational frequencies and are clearly not physically realistic. This problem is particularly pervasive in the low-frequency modes, as a small computational error can shift an eigenvalue from positive to negative.

In the past, methods to alleviate this problem have included averaging and performing a shift in the

eigenvalues,<sup>[16,17]</sup> which yields positive eigenvalues, but suffers from being an ad hoc solution with little physical justification. In a recent development, it has been shown that the matrix elements of the Hessian for coordinates obtained by sampling over a classical trajectory in the vicinity of the local minimum randomly fluctuate about the true value. As a result, it is possible to employ the average value of the Hessian over a short trajectory, rather than the value of the Hessian at a fixed configuration.<sup>[37]</sup> The accurate integration of the trajectories for polymer systems and calculation of the Hessian matrix is rendered particularly rapidly due to expressions for analytic derivatives that have evolved in our laboratory.<sup>[38,39]</sup>

### Sparse Matrix Diagonalization

We have used a modified version of ARPACK to compute the lowest vibrational modes of the sparse matrix representing the time averaged Hessian matrix. The ARPACK software is based on a variant of the Arnoldi process<sup>[40]</sup> and for symmetric matrices is equivalent to the Lanczos algorithm. Essentially, the method relies on constructing and refining an orthonormal basis for a small dimensional subspace of the full, sparse matrix. The method employed in the present study involves implicitly restarting the algorithm using a method for modifying the initial starting guess in the iterative Lanczos method to accelerate convergence to the desired solution.<sup>[41]</sup> The exact details of the computations employed in our computations have been described and reviewed extensively elsewhere.<sup>[37,42–44]</sup>

### NORMAL MODES OF MULTIPARTICLE SOFT MATTER SYSTEMS

The eigenvectors corresponding to the lowest 100 frequencies were explicitly visualized in order to observe characteristic behaviors. Modes corresponding to higher vibrational frequencies did not have any readily discernible characteristic behavior, with the exception of modes in which the majority of the motion was restricted to a single particle (local or “spectator” vibrations).

#### Indifferent Modes

Each of the systems was observed to have six true “indifferent” modes, corresponding to overall translations and rotations of the system.<sup>[12,13]</sup> As expected, these normal modes are the first six modes, and have eigenvalues quite close to zero, with the exception of a small amount of numerical round-off error. These

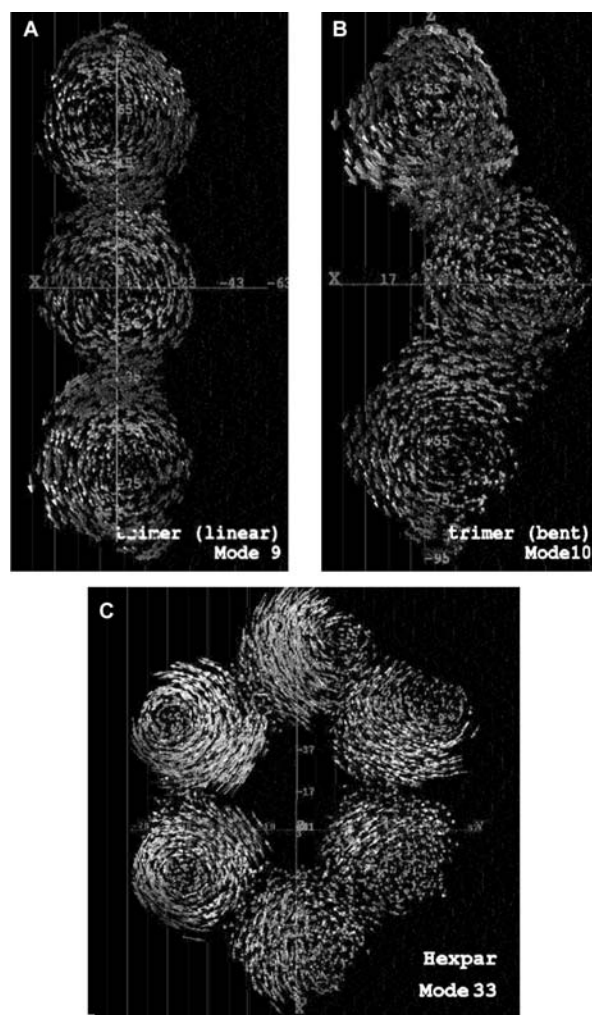


**Fig. 4** Normal modes composed of coupled particle rotations. Examples are chosen for each of the structures represented in Figs. [1–3].

modes are as one would expect and are not illustrated to save space.

#### Coupled Rotational Modes

For each of the systems there are several modes that could be described as “coupled rotations.” Essentially, these modes correspond to gearlike motions of individual polymer particles with respect to each other. These modes are likely to be well described in the multimode approximation as torsional vibrations because the modes appear to preserve the volume of the individual particles (Fig. 4).

#### Spectator Modes

Another class of modes that we observe are those we deem to be “spectator modes.” These are modes where

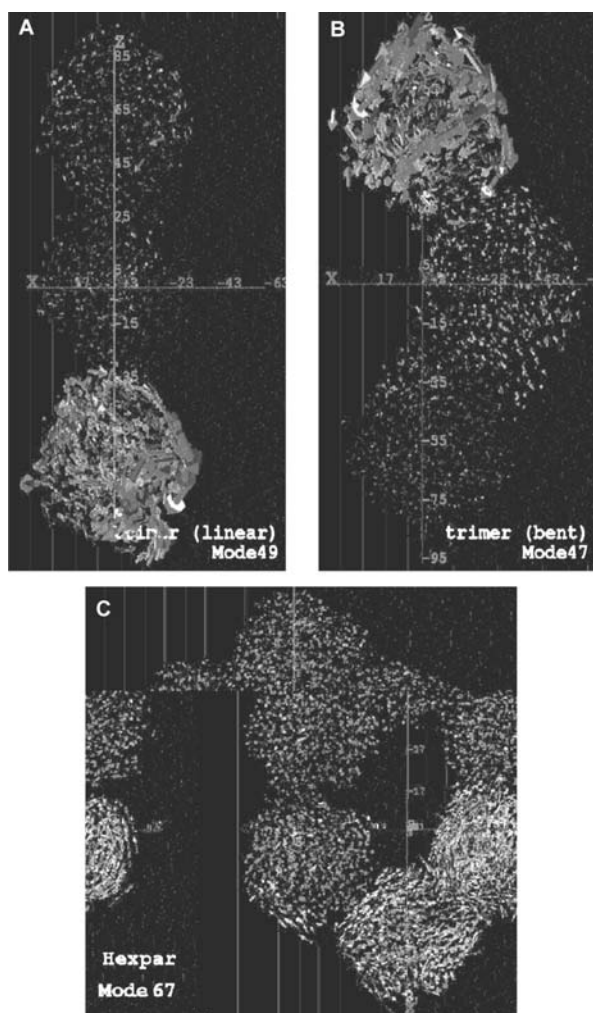


**Fig. 5** Normal modes composed of “spectator vibrations,” where the majority of motion is restricted to a small subset of particles. Examples are chosen for each of the structures represented in Figs. [1–3].

all of the dynamical motion is constrained largely to one part of the structure, with the remaining parts of the structure largely immobile (with the exception of small shifts to leave the center of mass invariant.) These modes are likely to be poorly described by multibody vibrations because they are largely dependent on the internal elasticity of the subunits where the motion is confined (Fig. 5).

### Particle Vibrational Modes

In the context of multibody dynamics, one expects to see modes that are vibrations of the individual particles connected by a single force constant. In the case of the dimer particles, we would expect to see a vibration that essentially amounts to a displacement of the center of mass separation of the two particles. In the case of

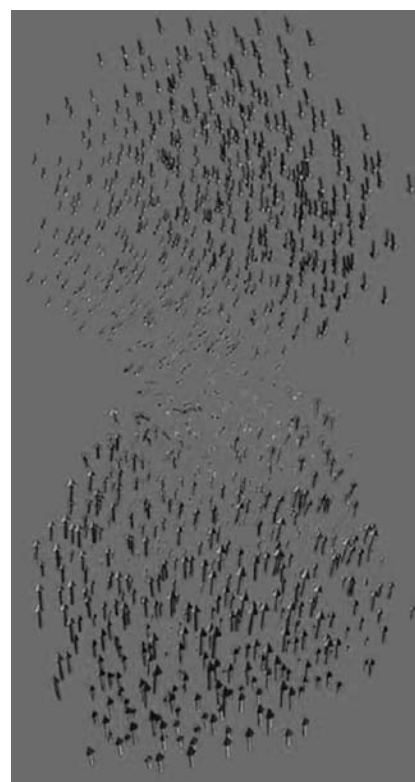


**Fig. 6** Normal mode approximating a dimer “stretch” in the particle dimer system. The center of mass separation motion is coupled to the internal elasticity of the particle.

the linear and bent trimers, we would expect to find bending and stretching normal modes reminiscent of the vibrations of carbon dioxide or water. In the case of the six-member ring, we might expect normal modes similar to benzene.

We do not observe such pure stretching modes. In the case of the dimer system, there are some modes that are similar to the displacement of the center of mass, but it is by no means a pure dimer stretch, and this mode is strongly coupled to the internal elasticity of the particles (Fig. 6). These modes are not well described in a multibody context, as multibody vibrations insist on the preservation of the volume of the individual subunits in the structure and neglect the internal compressibility of the particles.

### CONCLUSION

The goal in the present study was to identify and characterize interparticle vibrational modes and to relate them to characteristic multibody vibrational modes. In a multibody treatment, for “free” joints, there should be six degrees of freedom for each connection between particles<sup>[9]</sup> (if we fix the position of the first subunit to remove overall translations and rotations).

This reduced number of degrees of freedom, if applicable, represents a huge savings in computational effort and provides a direct avenue for interpretation of the vibrational motion of the structure.

What we find in the present investigation is a lack of “pure” multibody stretching modes. These modes are apparently strongly coupled to the internal elasticity of the particles.

At the same time, however, we do observe a number of modes that can be interpreted in the multibody context. These modes are “particle torsional modes,” or modes that involve coupled rotations of the particles and are absent of any internal vibrational structure within the particles. We also observe a number of so-called “spectator modes,” where the dynamical behavior is largely localized within a single particle, or a small collection of particles. In the multibody dynamics context, these modes consist of intrabody vibrations, largely decoupled from the interbody vibrations.

Whereas it appears that there is some promise to the multibody technique for vibrational analysis, the present study indicates that in the present case where the subunits in the structure are composed of “soft matter,” it is necessary to modify the treatment to allow for the internal elasticity of the particles, because the particles deform significantly and couple the vibrational motion between subunits with internal compression of the particles. This class of substances includes both polymers and biopolymers (e.g., proteins). Although the internal elasticity of these types of substances must undoubtedly be accounted for, particles that are substantially more rigid and with definitive chemical structures, such as metal oxide particles or structures with a rigid chemically bonded network, such as structures based on derivatives of buckminsterfullerenes, may not undergo gross defects in particle structure that couple the vibrational modes. These types of particles require additional study to determine the extent to which the internal and overall motions of the structures are coupled.

## ACKNOWLEDGMENTS

This work was sponsored by the Division of Computer Science and Mathematics and the Division of Materials Sciences, Office of Basic Energy Sciences, U.S. Department of Energy under Contract DE-AC05-00OR22725 with UT-Battelle at Oak Ridge National Laboratory (ORNL), using resources of the Center for Computational Sciences at Oak Ridge National Laboratory. We would like to thank Ross Toedte of the ORNL Visualization Group for assistance in producing figures for the manuscript.

## REFERENCES

- Goddard, W.A.; Cagin, T.; Blanco, M.; Vaidehi, N.; Dasgupta, S.; Floriano, W.; Belmares, M.; Kua, J.; Zamanakos, G.; Kashihara, S.; Iotov, M.; Gao, G.H. Strategies for multiscale modeling and simulation of organic materials: Polymers and biopolymers. *Comput. Theor. Polymer Sci.* **2001**, *11* (5), 329–343.
- Gao, G.; Cagin, T.; Goddard, W.A. Energetics, structure, mechanical and vibrational properties of single-walled carbon nanotubes. *Nanotechnology* **1998**, *9* (3), 184–191.
- Cagin, T.; Wang, G.F.; Martin, R.; Zamanakos, G.; Vaidehi, N.; Mainz, D.T.; Goddard, W.A. Multiscale modeling and simulation methods with applications to dendritic polymers. *Comput. Theor. Polymer Sci.* **2001**, *11* (5), 345–356.
- Cagin, T.; Wang, G.; Martin, R.; Breen, N.; Goddard, W.A. Molecular modelling of dendrimers for nanoscale applications. *Nanotechnology* **2000**, *11* (2), 77–84.
- Merkle, R.C. Molecular building blocks and development strategies for molecular nanotechnology. *Nanotechnology* **2000**, *11* (2), 89–99.
- Merkle, R.C. A new family of six degrees of freedom positional devices. *Nanotechnology* **1997**, *8* (2), 47–52.
- Cagin, T.; Jaramillo-Botero, A.; Gao, G.; Goddard, W.A. Molecular mechanics and molecular dynamics analysis of Drexler–Merkle gears and neon pump. *Nanotechnology* **1998**, *9* (3), 143–152.
- Mahurin, S.M.; Mehta, A.; Barnes, M.D.; Hathorn, B.; Sumpter, B.G.; Noid, D.W.; Runge, K. Photonic polymers: A new class of photonic wire structure from intersecting polymer-blend microspheres. *Opt. Lett.* **2002**, *27* (8), 610–612.
- Huston, R.L. *Multibody Dynamics*; Butterworth-Heinemann: Boston, MA, 1990.
- Newman, D.E.; Watts, C.; Sumpter, B.G.; Noid, D.W. On the determination and ramifications of chaos in manybody systems: A model study of polyethylene. *Macromol. Theory Simul.* **1997**, *6* (2), 577–590.
- Tuzun, R.E.; Sumpter, B.G.; Noid, D.W. On the correspondence between classical and quantum mechanics in macromolecular systems: Too much classical chaos. *Macromol. Theory Simul.* **1998**, *7* (2), 203–209.
- Wilson, E.B.; Decius, J.C.; Cross, P.C. *Molecular Vibrations*; Dover: New York, 1955.
- Goldstein, H. *Classical Mechanics*, 2nd Ed.; Addison-Wesley: Reading, MA, 1980.
- Ng, K.C.; Ford, J.V.; Jacobson, S.C.; Ramsey, J.M.; Barnes, M.D. Polymer microparticle arrays from electrostatically focused microdroplet streams. *Rev. Sci. Instrum.* **2000**, *71* (6), 2497–2499.
- Barnes, M.D.; Ng, K.C.; Fukui, K.; Sumpter, B.G.; Noid, D.W. Probing phase-separation behavior in polymer-blend microparticles: Effects of particle size and polymer mobility. *Macromolecules* **1999**, *32* (21), 7183–7189.
- Brooks, B.R.; Janezic, D.; Karplus, M. Harmonic analysis of large systems I: Methodology. *J. Comput. Chem.* **1995**, *16* (12), 1522–1542.

17. van Vlijmen, H.W.T.; Karplus, M. Analysis of calculated normal modes of a set of native and partially unfolded proteins. *J. Phys. Chem., B* **1999**, *103* (15), 3009–3021.
18. Painter, P.C.; Coleman, M.M.; Koenig, J.L. *The Theory of Vibrational Spectroscopy and Its Applications to Polymeric Materials*; Wiley: New York, 1982.
19. Meister, A.G.; Cleveland, F.F. *Am. J. Phys.* **1946**, *14*, 13.
20. Hathorn, B.C.; Sumpter, B.G.; Noid, D.W.; Tuzun, R.E.; Yang, C. Computational simulation of polymer particle structures: Vibrational normal modes using the time averaged normal coordinate analysis method. *Polymer* **2003**, *44* (13), 3761–3767.
21. Hathorn, B.C.; Sumpter, B.G.; Noid, D.W.; Tuzun, R.E.; Yang, C. Vibrational normal modes of polymer nanoparticle dimers using the time averaged normal coordinate analysis method. *J. Phys. Chem., A* **2002**, *106* (40), 9174–9180.
22. Noid, D.W.; Sumpter, B.G.; Wunderlich, B.; Pfeffer, G.A. Molecular dynamics simulations of polymers—Methods for optimal FORTRAN programming. *J. Comput. Chem.* **1990**, *11* (2), 236–241.
23. Hoover, W.G. Non-equilibrium molecular dynamics. *Annu. Rev. Phys. Chem.* **1983**, *34*, 103–127.
24. Klein, M.L. Computer simulation studies of solids. *Annu. Rev. Phys. Chem.* **1985**, *36*, 525–548.
25. Gray, S.K.; Noid, D.W.; Sumpter, B.G. Symplectic integrators for large scale molecular dynamics simulations—A comparison of several explicit methods. *J. Chem. Phys.* **1994**, *101* (5), 4062–4072.
26. Sumpter, B.G.; Noid, D.W.; Wunderlich, B. Computer experiments on the internal dynamics of crystalline polyethylene—Mechanistic details of conformational disorder. *J. Chem. Phys.* **1990**, *93* (9), 6875–6889.
27. Otaigbe, J.U.; Barnes, M.D.; Fukui, K.; Sumpter, B.G.; Noid, D.W. Generation, characterization, and modeling of polymer micro- and nano-particles. *Adv. Polym. Sci.* **2001**, *154*, 1–86.
28. Weber, T.A. Simulation of normal butane using a skeletal alkane model. *J. Chem. Phys.* **1978**, *69* (6), 2347–2354.
29. Weber, T.A. Relaxation of a n-octane fluid. *J. Chem. Phys.* **1979**, *70* (9), 4277–4284.
30. Sorensen, R.A.; Liau, W.B.; Boyd, R.H. Prediction of polymer crystal structures and properties—A method utilizing simultaneous inter-molecular and intramolecular energy minimization. *Macromolecules* **1988**, *21* (1), 194–199.
31. Boyd, R.H. Method for calculation of conformation of minimum potential energy and thermodynamic functions of molecules from empirical valence-force potentials. Application to cyclophanes. *J. Chem. Phys.* **1968**, *49* (6), 2574.
32. Fukui, K.; Sumpter, B.G.; Barnes, M.D.; Noid, D.W. Molecular dynamics simulation of polymer fine particles. Physical and mechanical properties. *Polym. J.* **1999**, *31* (8), 664–671.
33. Hathorn, B.C.; Sumpter, B.G.; Barnes, M.D.; Noid, D.W. Molecular dynamics simulation of polymer nanoparticle collisions: Internal reorganization and translation–vibration coupling. *Macromolecules* **2002**, *35* (3), 1102–1108.
34. Hathorn, B.C.; Sumpter, B.G.; Barnes, M.D.; Noid, D.W. Molecular dynamics simulation of polymer nanoparticle collisions: Orbital angular momentum effects. *Polymer* **2002**, *43* (10), 3115–3121.
35. Hathorn, B.C.; Sumpter, B.G.; Barnes, M.D.; Noid, D.W. Molecular dynamics simulation of collinear polymer nanoparticle collisions: Reaction and scattering. *J. Phys. Chem., B* **2001**, *105* (46), 11468–11473.
36. Fletcher, R. *Practical Methods of Optimization*; John Wiley and Sons: New York, 1987.
37. Noid, D.W.; Fukui, K.; Sumpter, B.G.; Yang, C.; Tuzun, R.E. Time-averaged normal coordinate analysis of polymer particles and crystals. *Chem. Phys. Lett.* **2000**, *316* (3–4), 285–296.
38. Tuzun, R.E.; Noid, D.W.; Sumpter, B.G. Efficient computation of potential energy first and second derivatives for molecular dynamics, normal coordinate analysis, and molecular mechanics calculations. *Macromol. Theory Simul.* **1996**, *5* (4), 771–788.
39. Tuzun, R.E.; Noid, D.W.; Sumpter, B.G. Efficient treatment of out-of-plane bend and improper torsion interactions in MM2, MM3, and MM4 molecular mechanics calculations. *J. Comput. Chem.* **1997**, *18* (14), 1804–1811.
40. Arnoldi, W.E. *Q. Appl. Math.* **1951**, *9*, 17.
41. Lehoucq, R.B.; Sorensen, D.C.; Yang, C. *ARPACK Users' Guide Solution of Large-Scale Eigenvalue Problems with Implicitly Restarted Arnoldi Methods*; SIAM: Philadelphia, PA, 1999.
42. Fukui, K.; Noid, D.W.; Sumpter, B.G.; Yang, C.; Tuzun, R.E. Large-scale normal coordinate analysis of macromolecular systems: Thermal properties of polymer particles and crystals. *J. Phys. Chem., B* **2000**, *104* (3), 526–531.
43. Fukui, K.; Sumpter, B.G.; Yang, C.; Noid, D.W.; Tuzun, R.E. Spectra analysis for macromolecular systems: Chain-length effects in polymer particles. *J. Polym. Sci., Polym. Phys.* **2000**, *38* (13), 1812–1823.
44. Fukui, K.; Sumpter, B.G.; Yang, C.; Noid, D.W.; Tuzun, R.E. Analysis of eigenvalues and eigenvectors of polymer particles: Random normal modes. *Comput. Theor. Polymer Sci.* **2001**, *11* (3), 191–196.

# Computational Analysis of Switchable Catenanes

Xiange Zheng  
Karl Sohlberg

Department of Chemistry, Drexel University, Philadelphia, Pennsylvania, U.S.A.

## INTRODUCTION

The first synthesis of a catenane was reported in the 1960s.<sup>[1,2]</sup> Since then, the chemistry of topologically non-trivial macromolecular systems such as knots, catenanes, and rotaxanes<sup>[3–23]</sup> has attracted considerable attention. With the surge of interest in nanoscience since 1990, this attention has focused on their promise for the fabrication of molecular devices. The design, synthesis, and characterization of nanodevices and molecular devices are now grand challenges to the scientific and engineering communities.<sup>[24–28]</sup> Consequently, reports of novel catenanes are appearing with increased frequency.

Catenanes form a subset of a special class of topologically complex host/guest complexes where the host and guest components are chemically independent but mechanically interlocked with each other. Catenanes are an entirely different class of mechanically interlocked molecules from their close relatives—the rotaxanes. In particular, a catenane is a complex comprising two (or more) macrocyclic rings interlocked like adjacent links of a chain. The two (or more) macrocycles are not linked covalently to each other; rather, their dissociation is prevented only mechanically. The associated co-conformations are stabilized by intercomponent non-covalent interactions, and interconversion among these co-conformations requires the circumrotation of the macrocycle rings. In a switchable catenane, the relative populations of these co-conformations are controllable reversibly by an external stimulus such as complexation/decomplexation by metal ions, protonation/deprotonation, or oxidation/reduction process. Like the rotaxane systems discussed in the accompanying entry entitled “Computational Analysis of Switchable Rotaxanes,” switchable catenanes have recently become the subject of intense interest because of their potential to form components of nanodevices and molecular devices.

## BACKGROUND

The dissociation of catenanes requires the breaking of covalent bond(s). The synthesis of such systems often

relies on the presence of molecular recognition sites in the components, and on the use of transition metal templates or complementary  $\pi$ -electron-rich and  $\pi$ -electron-deficient recognition segments to enable the construction process. For the construction of catenanes, it has been suggested that the most rational construction strategy is through the clipping of one macrocycle onto another preformed one.<sup>[29]</sup>

A characteristic example, [2]catenane ([2] indicates the number of chemically independent subcomponents), may be found in Ref.<sup>[30]</sup>, which reports complexes constructed from a  $\pi$ -electron-deficient bipyridinium-based cyclophane, cyclobis(paraquat-*p*-phenylene), and a  $\pi$ -electron-rich dioxoarene-based and/or dithioarene-based macrocyclic polyether. In this way, the system is designed with intercomponent non-covalent bonding interactions. Ref.<sup>[30]</sup> gives several examples of such interactions including:  $\pi$ - $\pi$  stacking (Ref. 4 in Ref.<sup>[30]</sup>), [CH $\cdots$ O] (Ref. 5 in Ref.<sup>[30]</sup>), and [CH $\cdots$  $\pi$ ] interactions (Ref. 6 in Ref.<sup>[30]</sup>). It was suggested that self-assembly processes might be facilitated by non-covalent interactions between complementary recognition sites on the constituent components.<sup>[30]</sup> For mechanically interlocked molecules, an understanding of the self-assembly processes is an issue of considerable interest. Here, we review theoretical and computational studies of switchable catenanes.

## OVERVIEW OF COMPUTATIONAL METHODS AND TECHNIQUES

In general, there are three classes of theoretical modeling methods for investigating molecular properties. In approximate order of increasing computational expense, they are: molecular mechanics (MM) methods, classical molecular dynamics (MD) methods, and quantum mechanical (QM) methods. The last can be divided into two categories: semiempirical and ab initio techniques. The selection of a method to model supermolecular systems is dominated by consideration of the computational expense. For catenanes (and rotaxanes, as discussed in the accompanying entry entitled “Computational Analysis of Switchable Rotaxanes”), it is also important to choose



a model that reliably represents the non-covalent interactions involved in these systems that hold their constituent components together, often hydrogen bonding and/or  $\pi$ - $\pi$  interactions.

The MM methods, also known as force field methods, attempt to describe molecular structure with an empirical potential energy function that, while often containing physically motivated terms, is not based on fundamental theories of physics or chemistry. The potential is expressed as a function of the internal coordinates of the system. Finding molecular conformations and co-conformations is thereby reduced to finding the minima of the potential function. Because function evaluation is simply an algebraic procedure, computational implementations of MM are very fast and used in the qualitative description of large molecular systems comprising hundreds or even thousands of atoms. MD methods are concerned with molecular motion. They employ similar empirical potential energy functions to the MM methods, but solve the classical differential equations of motion based on this potential function (typically in the Hamiltonian or Newtonian formulation) given an assumed set of initial atomic positions and momenta. In addition to providing dynamical information about molecular motion, MD can also facilitate searching of the potential energy surface for minima. Obviously, carrying out classical trajectories based on a potential function is computationally more demanding than simple optimization to the nearest local minimum, but classical trajectories can aid in finding unknown and unsuspected minima. The general idea is that, based on the ergodic hypothesis, in the absence of resonant frequencies, a classical trajectory will eventually sample all of the energetically allowed configuration spaces. A solvent can also be explicitly included in an MD simulation by including adjacent solvent molecules. This is termed the “discrete solvent model.” This brings further complications and increases the computational expense. An alternative method of modeling a solvent is to replace the dielectric value of vacuum with that appropriate for the selected solvent. This is known as a “continuum solvent model.” Both general classes of solvent models exist in varying degrees of sophistication.

When one concentrates on electronic and/or spectroscopic properties, QM methods need to be employed because they explicitly treat the electronic degrees of freedom. These methods attempt a solution of the time-independent Schrödinger equation (TISE) for the system of interest. In ab initio quantum chemical methods, the molecular Hamiltonian is generally written in matrix form, and all integrals over basis functions are exactly evaluated in the calculation. Such methods are, in principle, applicable to any molecular system, but in practice are limited in that ab initio

calculations are extremely computationally demanding, especially for large molecular systems. In this respect, semiempirical quantum chemical methods are often a more appropriate choice for the modeling of large molecule systems. Like MM, they use empirical parameters (often derived by fitting the results to experimental data), but like ab initio methods, they solve the TISE. They are computationally faster than ab initio methods because many of the difficult integrals are neglected or empirically approximated.

Because of the large size of catenane complexes, consideration of the compromise between modeling accuracy and computational expense is paramount. Therefore MM methods and semiempirical procedures are finding wide applications in the modeling of catenanes. Some theoretical studies of catenanes have investigated the fundamental basis that underlies the co-conformational isomerism and switching mechanisms of such systems, such as metal-ligand interactions,<sup>[31,32]</sup> [C-H...O] hydrogen bonds, and [C-H... $\pi$ ] and [ $\pi$ - $\pi$ ] stacking interactions.<sup>[33,34]</sup> The modeling of catenane systems is generally even more challenging than that of rotaxanes due, in part, to the more frequent involvement of  $\pi$ - $\pi$  interactions.

## COMPUTATIONAL STUDIES OF SWITCHABLE CATENANES

### Structural Fundamentals

Hydrogen bonding is typically the dominant intercomponent interaction in mechanically interlocked molecules. Raymo et al.<sup>[35]</sup> carried out a study to determine the magnitude of [C-H...O] hydrogen bonding. Ab initio MP2/6-311++G\*\* calculations were used for an accurate description of these intercomponent interactions. Because the treatment of catenane and rotaxane systems with ab initio methods is computationally prohibitive owing to their large molecular size, representative structures were modeled. The structures considered were charged and uncharged complexes containing the following components: *N*-methylpyridinium cation, dimethyl ether, and dimethyl phosphate anion. It was found that the main non-bonded contacts involve [C-H...O] bonds on electron-deficient species and oxygen atoms on electron-rich species. The results provided quantitative measures of the large stabilization energies resulting from [C-H...O] interactions in charged systems, which were identified as responsible for the self-assembly of bipyridinium-based catenanes and rotaxanes.

To investigate host/guest chemistry, Kaminski and Jorgensen<sup>[36]</sup> modelled several highly charged catenanes and rotaxanes in the gas phase and in liquid CH<sub>3</sub>CN solution. Methods of MM and Monte Carlo

(MC) statistical mechanics were used. The gas-phase optimizations and MC simulations were carried out using the BOSS program, version 3.6, which was modified to account for the polarization interactions. The torsional energy was expressed as a Fourier cosine expansion, including all terms through  $\cos(4\phi)$ , where  $\phi$  is the torsional angle.<sup>[37]</sup> Explicit polarization was considered for these charged complexes through the use of a polarizable all-atom force field with and without non-additive electrostatic polarization terms. The modeling reproduced the observation from experiments that polarization generally strengthens the interactions in gas phase, but has a modest effect on the complex structures and their binding energies in solution.

Because of the extensive computational resources required for ab initio calculations on catenanes, few studies have been undertaken in which ab initio techniques were adopted. Exceptions include cases where the property of interest is a manifestation of the system's electronic structure, such as circular dichroism (CD) spectra and nuclear magnetic resonance (NMR) chemical shifts. Modeling in these cases requires an explicit electronic calculation. Dobrowolski and Mazurek<sup>[38]</sup> reported ab initio calculations of the qualitative theoretical <sup>13</sup>C NMR chemical shifts ( $\delta$ ) of model carbyne catenanes and knots including C<sub>10</sub>C<sub>30</sub> and C<sub>20</sub>C<sub>30</sub> (Hopf links). They found that the chemical shift ( $\delta$ ) tends to alternate from one carbon atom to the next along the catenane ring backbone or a knot branch. The  $\delta$  fluctuation relies on the redistribution of C≡C triple bond  $\pi$ -electrons, which arises from the repulsion between catenane components or knot branches. The polarization of the  $\pi$ -electron resulting from the repulsion occurs so that a carbon atom located closer to the perturbation is deshielded and, one placed further away, is more shielded.

For properties that require a true electronic structure description, semiempirical methods have been used more frequently than ab initio methods in the study of catenane systems because of the lower computational cost. For example, Fanti et al.<sup>[39]</sup> have reported semiempirical MNDO calculations of the infrared (IR) and Raman spectra of a benzylic amide, [2]catenane, to investigate its vibrational properties. A high sensitivity of the vibrational spectra of the catenane to the environment was revealed, and it was concluded that “the ability to tune this remarkable property of the catenane to modify its vibrational response under rather small perturbations may lead to a vibrationally based sensors [sic].”

## Dynamics of Catenane Systems

A detailed understanding of the factors that govern the relative motion of the components in a switchable

catenane is prerequisite to developing schemes for external control of the kinetics and thermodynamics of macrocyclic ring rotation—a critical issue for practical molecular devices.

Pioneering investigations of the mechanisms of macrocycle circumrotation in enzylic amide catenanes were reported by Leigh et al.<sup>[40]</sup> Based on the <sup>1</sup>H NMR energy barrier measurements in different types of solvent, circumrotation was thought to occur as a cooperative process of assembly and disassembly of hydrogen bonds,  $\pi$ - $\pi$  stacking interactions, and phenyl-phenyl “T-shaped herringbone interactions” (see below; Fig. 1). Given the large number of variables, they devised a reduced complexity computational approach to unravel the complex features. The potential energy surface was explored in terms of stationary points, local energy minima, and transition states. The calculations were performed for isolated molecules with the Tinker suite of programs<sup>[41–44]</sup> using the MM3 force field.<sup>[45–47]</sup> No attempt was made to include polarization and viscosity effects. Therefore the results were compared with the NMR data obtained in apolar solvents. It was reported that the interlocked macrocycle dynamics is governed by a balance of steric effects, intermacrocyclic arrays of hydrogen bonds,  $\pi$ - $\pi$  stacking, and “T herringbone-type interactions.” T herringbone-type  $\pi$ - $\pi$  interactions are phenyl-phenyl interactions in the geometry of a distorted “T.” Fig. 1 presents the schematic drawing of the T herringbone interaction geometry. It was found that a cascade of hydrogen bond ruptures and formations occurs during circumrotation, and that these are accompanied by a series of cooperative conformational and co-conformational rearrangements that help to stabilize the energy of the molecule. The

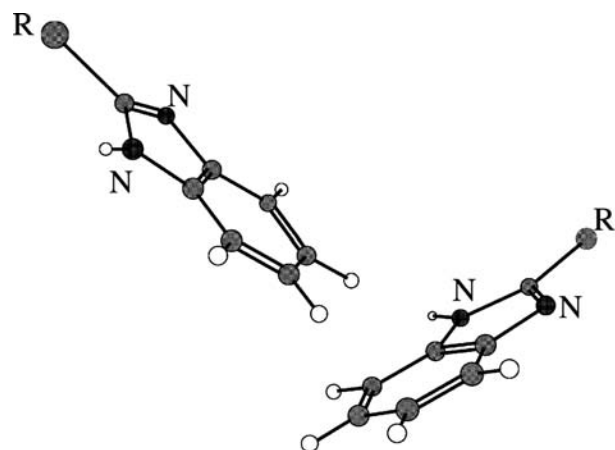


**Fig. 1** Schematic drawing of the T herringbone interaction geometry. *R* and *R'* are functional groups attached to the aromatic rings. All other atoms not labeled are carbon atoms (solid gray circles) and hydrogen atoms (open circles). Source: From Ref.<sup>[74]</sup>.

polarity of the environment was also reported to play a role in determining the inter-ring dynamics.

As noted in the accompanying entry about rotaxane systems, entitled “Computational Analysis of Switchable Rotaxanes,” the accurate simulation of inelastic neutron scattering (INS) spectra provides a description of the atomic motions in a system. Leigh et al.<sup>[48]</sup> demonstrated the application of INS spectroscopy, in combination with MD simulations, to investigate the dynamics of catenane systems. They noted<sup>[48]</sup> that owing to its large incoherent scattering length, hydrogen atoms dominate the INS response of organic molecules. Therefore INS spectra are a monitor of the amount of motion of the hydrogen atoms. This is particularly valuable in benzylic amide catenanes because they form a number of inter-ring hydrogen bonds. All calculations were performed with the Tinker program<sup>[41–44]</sup> and the MM3 force field.<sup>[45–47]</sup> MD calculations were run on isolated systems and after applying boundary conditions to reproduce the crystal structure. The INS spectroscopy for the catenane systems was compared with simulated spectra obtained from the MD simulations, and a good agreement with experiments was achieved for the spectra of the two catenanes for the location of the most prominent bands. This report and other successes<sup>[48–50]</sup> establish that the combination of INS and MD is becoming a powerful tool for the study of catenane and rotaxane systems.

Leigh, Troisi, and Zerbetto<sup>[13,51]</sup> reported a low-dimensional QM modeling of circumrotation in benzylic amide [2]catenanes, with a model similar to that used in their studies of ring shuttling in catenanes. The goal was to demonstrate that low-dimensional QM modeling is able to produce rate constants and barriers similar to those obtained by temperature-dependent NMR experiments, by appropriately fitting the parameters in the analytic potential form to match the symmetry and energy properties of the system. Both non-hydrogen bond-disrupting (e.g., CDCl<sub>3</sub>) and hydrogen bond-disrupting (e.g., [D6]DMSO) solvents are considered. The successful simulation of the rates of circumrotation was achieved by employing transition state theory (TST) in the harmonic approximation, therefore validating this QM model.

Ceroni et al.<sup>[52]</sup> reported an investigation of the electrochemistry of a benzylic amide [2]catenane and its topological subcomponents. They proposed that the redox behavior of the catenane could be understood in terms of the electrochemistry of smaller molecular fragments and simple molecular orbital considerations. Semiempirical quantum chemical (MNDO) calculations were performed on both neutral and doubly charged catenane species. The authors noted some uncertainty specifying the atomic connectivity in the doublet state. (Such connectivity information is

required for an empirical potential calculation, but “connectivity” is essentially a chemist’s book-keeping scheme. Given a chemically reasonable starting geometry, specified only by atomic coordinates, geometry optimization with a true electronic structure method will yield a minimum energy co-conformation. Identification of the *global* minimum energy co-conformation remains a challenging problem indeed.) The results from the calculations were compared with the analysis from experimental electrochemical data. Their electrochemical study and theoretical considerations suggested that the amide carbonyl groups predominantly control the reductive behavior of the catenane. It was suggested that the formation of a C–C bond between two reduced carbonyl groups, because of the close proximity caused by macrocyclic ring rotation, prohibits further macrocyclic ring circumrotation. They termed this as “soldered structure.” In fact, if a chemical bond forms between the different macrocycles of the catenane on electrochemical reduction, the reduction transforms the catenane into a polycyclic molecule. This may provide a useful means of switching “on” and “off” the dynamics of such interlocked macrocycles.

An INS spectroscopy study and complementary MD simulations (simulated annealing) were performed by Caciuffo et al.<sup>[50]</sup> The simulations were based on calculations of the normal modes of the isolated catenane. Anharmonic and crystal effects were neglected. This study suggested that the combination of INS spectroscopy and MD can distinguish between different proposed structures in large interlocked molecular systems, and that this combination of techniques is particularly suitable for accessing the strength of intramolecular and intermolecular hydrogen bonds, which dominate the dynamics of such systems.

Deleuze, Leigh, and Zerbetto<sup>[53]</sup> reported a computational study on the structure and dynamics of the three benzylic amide catenanes shown in Fig. 2. The objective of the study was to describe the relative rotation of the benzylic amide [2]catenane rings. MM and unimolecular reaction rate theory were employed. The study provided a theoretical description of the

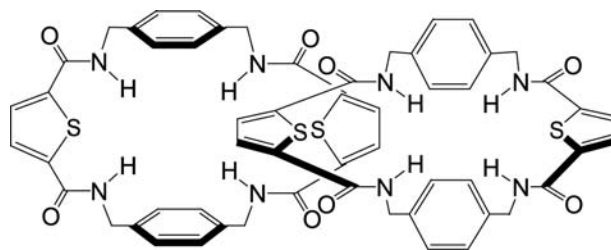


**Fig. 2** Chemical structure of the benzylic amide thiophenyl catenane investigated by Deleuze et al. *Source:* From Ref.<sup>[53]</sup>. ©American Chemical Society, 1999.

lowest energy pathway for the circumrotation of macrocycles in a catenane system. It showed that the circumrotation process involves several cooperative large-amplitude motions. These motions include rearrangements to minimize steric and electrostatic interactions through hydrogen bonding, form  $\pi$ - $\pi$  stacking structures, facilitate phenyl-phenyl T-shaped interactions, and accomplish amide rotamer interconversions. The calculations of rate constants provided insights into the dynamics of these catenanes. Important results include the observation that the rate-determining step is not necessarily the passage of the bulkiest groups, and that the rotations of the rings are cooperative (i.e., rotation of one macrocyclic ring facilitates rotation of the other ring).

### Origin of Binding Site Selectivity

For the purpose of understanding the factors that govern the equilibrium populations of translational isomers and the nature of  $\pi$ - $\pi$  stacking interactions in catenane systems, Raymo, Houk and Stoddart<sup>[30]</sup> carried out a computational investigation on several unsymmetrical [2]catenanes by using empirical force field and ab initio QM methods. MC conformational searching<sup>[54]</sup> was performed individually on each of those catenane complexes and its individual components, which were then energy-minimized with the AMBER force field<sup>[55]</sup> and the GB/SA solvation model for H<sub>2</sub>O and CHCl<sub>3</sub> as implemented in Macromodel 5.0.<sup>[56]</sup> Single-point (SP) calculations were performed in vacuum at the HF/6-31G\*\* level

by using the program Spartan 4.1<sup>[57]</sup> to determine the electrostatic potential (calculated on the surface of the aromatic units) and the energies of the highest occupied molecular orbitals. It was proposed that the more stable translational isomers of the [2]catenane complex do not necessarily correlate to the more stable structures of its components. Both the calculated and experimental population ratios for the translational isomers could be correlated with the dielectric constant of the solvent. Binding was observed to be electrostatic. Therefore translational isomerism was interpreted to arise from the balance between two factors: "1) by the electrostatic effects which govern the  $\pi$ - $\pi$  stacking interactions between the 'inside'  $\pi$ -electron-rich unit and the sandwiching bipyridinium recognition sites; and 2) by the solvation energies of the two translational isomers."<sup>[30]</sup>

### Co-conformational Isomerism in Catenanes

Hydrogen bonding, especially [C-H...O] interactions, plays an important role in biological systems and the self-assembly of many mechanical interlocked molecules. Houk et al.<sup>[58]</sup> presented computational studies of two [3]catenanes presented in Fig. 3, which incorporate  $\pi$ - $\pi$  stacking and [C-H...O] hydrogen bonding. Conformational analyses were performed using the AMBER\* force field and ab initio QM calculations to evaluate the binding affinity of bipyridinium-based guest to catenane hosts. The calculations showed that the combined strength of numerous [C-H...O] hydrogen bonds is quite large and quantitatively much more

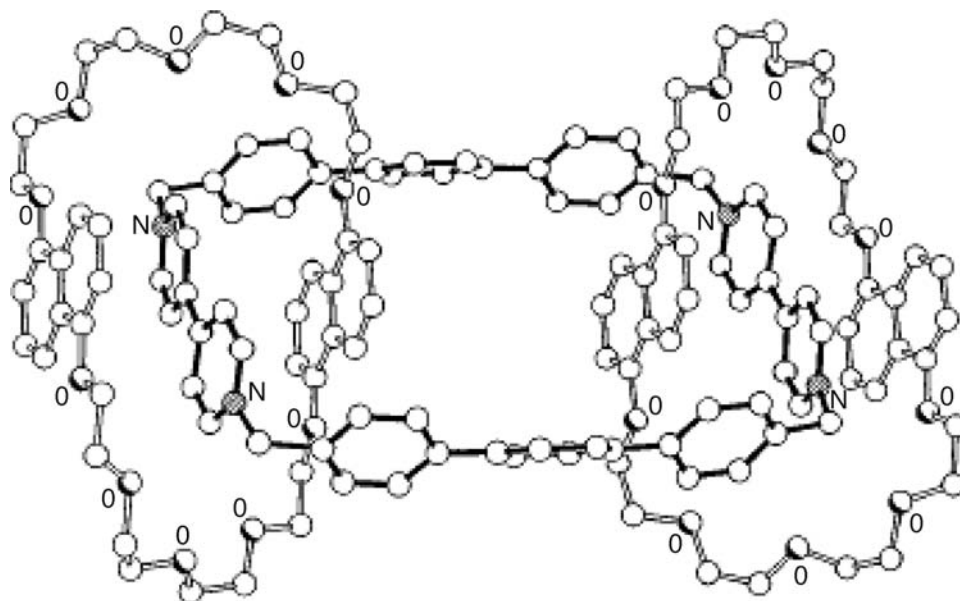


**Fig. 3** The schematic showing the [3]catenane structure investigated by Houk et al. *Source:* From Ref.<sup>[58]</sup>. ©American Chemical Society, 1999.

important than that of  $\pi$ - $\pi$  stacking interactions in these particular systems. This finding is consistent with experimental observations, showing again that hydrogen bonding plays a controlling role.

Rauwolf and Strabner<sup>[59]</sup> carried out computational investigations on several host/guest systems, including catenanes, to examine the concept of self-organization. Conformational searching was performed by the MLTOR option in PCMODEL 3.0,<sup>[60]</sup> and resulting conformers were minimized with the MM2 force field.<sup>[61,62]</sup> The force field minimization was followed by a full optimization without constraints using the semiempirical PM3 Hamiltonian,<sup>[63,64]</sup> together with the EF optimizer.<sup>[65]</sup> They reported that for inclusion complexes with experimentally identified structures, their computed structures agreed with those determined experimentally. The driving forces responsible for the formation of those molecular complexes were determined to be  $\pi$ - $\pi$  stacking and electrostatic interactions.

Hu et al.<sup>[66]</sup> conducted force field (MM2) calculations for a novel [2]catenane to obtain information about the behavior of catenane in solution. A continuum dielectric constant of  $\epsilon = 30$  was used to mimic acetonitrile as the solvent. The model revealed that the catenane exhibits  $C_2(2)$  crystal point symmetry, whereas the ([2]catenane)ruthenium(ii) complex adopts conformers with different sensitizer-acceptor distances and an extended macrocyclic polyether unit because of weakened  $\pi$ - $\pi$  interactions and electrostatic repulsion. This observation was confirmed by X-ray analysis.

Cyclobis(paraquat-1,5-naphthalene) has been prepared by a template-directed synthesis. It can exist in three different stereoisomers—an achiral (*RS*) form and two chiral forms, (*RR*) and (*SS*)—because of the presence of the two chiral planes formed by its 1,5-disubstituted naphthalene residues. Ashton et al.<sup>[67]</sup> assessed the relative stabilities of the two diastereoisomeric forms. MC conformational searching was performed. The calculations showed that the chiral *RR* and *SS* forms are preferred over the achiral *RS* one. In addition, the energy of the tetracationic cyclophane was calculated as a function of the dihedral angle of the bond linking one of the methylene groups and its adjacent naphthalene spacer. The interconversion barrier of the achiral form into the chiral form was predicted to be 21.7 kcal/mol (for back interconversion, it was found to be 23.0 kcal/mol). These observations were consistent with results of <sup>1</sup>H NMR studies.

Brouwer et al.<sup>[68]</sup> proposed that for material science applications, the properties of interest for catenanes might be electronic and vibroelectronic. Such properties require a theoretical model that explicitly addresses electronic degrees of freedom. They conducted the calculations on a benzylic amide [2]catenane to study its

electronic states through a combination of experimental and theoretical techniques. Semiempirical quantum chemical calculations were performed with the CNDO/S method.<sup>[69,70]</sup> The results showed partial delocalization of electronic states over the many chromophores of the catenane. This study is notable because it is (to the authors' knowledge) the only QM study of a catenane or rotaxane to date that includes configuration interaction.

Recently, Zheng and Sohlberg<sup>[71]</sup> carried out a computational investigation of an electrochemically switchable [2]catenane consisting of a tetracationic cyclophane and a cyclic polyether, which was experimentally realized by Collier et al.<sup>[72]</sup> The purpose of this study was to validate the applicability of a modeling procedure,<sup>[73]</sup> previously developed for a rotaxane system (the procedure is reviewed in the accompanying entry), to modeling the multistability structural- vs.-energy profile and switching mechanism of a catenane. An ensemble of >5000 structures of the catenane was generated by conformational searching on the polyether followed by translation and rotation of the cyclophane with respect to the ring backbone of the polyether. SP semiempirical calculations were then carried out for all of the structures that were found to be chemically reasonable to correlate the interlocking position of the two rings with energy. The resulting structure-energy relationship identified by the SP calculations was further refined by geometrical optimizations for a select subset (~3%) of the structures. The calculations not only confirmed the structural preferences previously inferred experimentally, but also gave insights into the fundamental basis of the switching mechanism and resolved earlier ambiguities concerning the connectivity of the TTF unit in the polyether ring. It was reported that the conformation of the TTF unit differs in the catenane from that in isolated TTF. Such changes in the conformation of subunits on incorporation into a catenane or rotaxane have been reported previously.<sup>[30]</sup>

## CONCLUSION

Stimuli-responsive molecular “shuttles” based on mechanically interlocked molecules are attracting considerable attention because of their potential for application in nanoscience and nanotechnology. Computational investigations of switchable catenane (and rotaxane) systems are a major challenge because of their large size, but studies employing a wide range of theoretical methods have been reported and useful capabilities are starting to emerge. For example, identifying the dominant co-conformations at thermal equilibrium, the corresponding factors that determine binding site selectivity, and the dynamics of the

switching process is an issue that has been successfully treated with theoretical calculations. The systems described above provide strong evidence that for structural information, force field methods are of considerable value, particularly after one acquires experience in their application to mechanically interlocked molecules. For systems that involve multiple charge and/or electronic states, and for the investigation of properties that are inherently QM, semiempirical calculations are capable of predicting molecular device characteristics that are consistent with measured properties. Although computationally expensive, for fundamental studies of intercomponent interactions, the accuracy and flexibility of ab initio methods are proving valuable. Computational studies provide details complementary to experimental results. Therefore the development of computational approaches to studying catenane and rotaxane systems will undoubtedly open up new areas of interest and new directions for research.

## ACKNOWLEDGMENT

Our molecular devices research is funded, in part, by the NSF–NER program, startup funds from the Drexel University, and Dupont Corp. in the form of a Dupont Young Professor award to K. S.

## REFERENCES

1. Wasserman, E. The preparation of interlocked rings: A catenane. *J. Am. Chem. Soc.* **1960**, *82* (16), 4433–4434.
2. Schill, G. *Catenanes, Rotaxanes, and Knots*; Academic Press: New York, 1971.
3. Asakawa, M.; Brancato, G.; Fanti, M.; Leigh, D.A.; Shimizu, T.; Slawin, A.M.Z.; Wong, J.K.Y.; Zerbetto, F.; Zhang, S.W. Switching “on” and “off” the expression of chirality in peptide rotaxanes. *J. Am. Chem. Soc.* **2002**, *124* (12), 2939–2950.
4. Chambron, J.C.; Sauvage, J.P.; Mislou, K.; De Cian, A.; Fischer, J. A [2]catenane and a [2]rotaxane as prototypes of topological and Euclidean molecular “rubber gloves”. *Chem. Eur. J.* **2001**, *7* (19), 4085–4096.
5. Reuter, C.; Schmieder, R.; Vogtle, F. From rotaxanes to knots: Templating, hydrogen bond patterns, and cyclo-chirality. *Pure Appl. Chem.* **2000**, *72* (12), 2233–2241.
6. Chiu, S.H.; Rowan, S.J.; Cantrill, S.J.; Ridvan, L.; Ashton, P.R.; Garrell, R.L.; Stoddart, J.F. Making molecular-necklaces from rotaxanes. *Tetrahedron* **2002**, *58* (4), 807–814.
7. Biscarini, F.; Cavallini, M.; Leigh, D.A.; Leon, S.; Teat, S.J.; Wong, J.K.Y.; Zerbetto, F. The effect of mechanical interlocking on crystal packing: Predictions and testing. *J. Am. Chem. Soc.* **2002**, *124* (2), 225–233.
8. Gunter, M.J.; Bampos, N.; Johnstone, K.D.; Sanders, J.K.M. Thermodynamically self-assembling porphyrin-stoppered rotaxanes. *New J. Chem.* **2001**, *25* (1), 166–173.
9. Hunter, C.A.; Low, C.M.R.; Packer, M.J.; Spey, S.E.; Vinter, J.G.; Vysotsky, M.O.; Zonta, C. Noncovalent assembly of [2]rotaxane architectures. *Angew. Chem., Int. Ed. Engl.* **2001**, *40* (14), 2678–2682.
10. Jeppesen, J.O.; Perkins, J.; Becher, J.; Stoddart, J.F. Slow shuttling in an amphiphilic bistable [2]rotaxane incorporating a tetrathiofulvalene unit. *Angew. Chem., Int. Ed. Engl.* **2001**, *40* (7), 1216–1221.
11. Schalley, C.A.; Beizai, K.; Vogtle, F. On the way to rotaxane-based molecular motors: Studies in molecular mobility and topological chirality. *Acc. Chem. Res.* **2001**, *34* (6), 465–476.
12. Li, Z.T. Rotaxane: From supramolecular self-organization to molecular devices. *Chin. J. Org. Chem.* **2000**, *20* (5), 655–662.
13. Leigh, D.A.; Troisi, A.; Zerbetto, F. A quantum-mechanical description of macrocyclic ring rotation in benzylic amide [2]catenanes. *Chem. Eur. J.* **2001**, *7* (7), 1450–1454.
14. Jun, S.I.; Lee, J.W.; Sakamoto, S.; Yamaguchi, K.; Kim, K. Rotaxane-based molecular switch with fluorescence signaling. *Tetrahedron Lett.* **2000**, *41* (4), 471–475.
15. Shukla, R.; Deetz, M.J.; Smith, B.D. [2]Rotaxane with a cation-binding wheel. *Phys. Chem. Chem. Phys.* **2000**, *2* (23), 2397–2398.
16. Ashton, P.R.; Ballardini, R.; Balzani, V.; Credi, A.; Dress, K.R.; Ishow, E.; Kleverlaan, C.J.; Kocian, O.; Preece, J.A.; Spencer, N.; Stoddart, J.F.; Venturi, M.; Wenger, S. A photochemically driven molecular-level abacus. *Chem. Eur. J.* **2000**, *6* (19), 3558–3574.
17. Gibson, H.W.; Bryant, W.S. Rotaxane assemblies: Threading the beads. *Abstr. Pap. Am. Chem. Soc.* **1999**, *218*. 102-ORGN, Part 2.
18. Sohlberg, K.; Sumpter, B.G.; Noid, D.W. Semi-empirical study of a prototype rotaxane-based molecular shuttle. *J. Mol. Struct., Theochem* **1999**, *491* (1–3), 281–286.
19. Amabilino, D.B.; Ashton, P.R.; Balzani, V.; Brown, C.L.; Credi, A.; Frechet, J.M.J.; Leon, J.W.; Raymo, F.M.; Spencer, N.; Stoddart, J.F.; Venturi, M. Self-assembly of [n]rotaxanes bearing dendritic stoppers. *J. Am. Chem. Soc.* **1996**, *118* (48), 12012–12020.
20. Asakawa, M.; Ashton, P.R.; Iqbal, S.; Quick, A.; Stoddart, J.F.; Tinker, N.D.; White, A.J.P.; Williams, D.J. Functionalized [2]rotaxanes. *Isr. J. Chem.* **1996**, *36* (4), 329–340.
21. Lee, J.W.; Kim, K.P.; Kim, K. A kinetically controlled molecular switch based on bistable [2]rotaxane. *Chem. Commun.* **2001**, (11), 1042–1043.
22. Osswald, F.; Vogel, E.; Safarowsky, O.; Schwanke, F.; Vogtle, F. Rotaxane assemblies with dendritic architecture. *Adv. Synth. Catal.* **2001**, *343* (3), 303–309.
23. Kanamathareddy, S.; Gutsche, C.D. Synthesis and conformational properties of calix[6]arenes bridged on the lower rim—Self-anchored rotaxanes. *J. Am. Chem. Soc.* **1993**, *115* (15), 6572–6579.
24. Collin, J.P.; Dietrich-Buchecker, C.; Sauvage, J.P. Towards molecular machines and motors. *Actual. Chim.* **2001**, (6), 27–32.



25. Collin, J.P.; Gavina, P.; Heitz, V.; Sauvage, J.P. Construction of one-dimensional multicomponent molecular arrays: Control of electronic and molecular motions. *Eur. J. Inorg. Chem.* **1998**, (1), 1–14.
26. Amabilino, D.B.; Stoddart, J.F. Interlocked and intertwined structures and superstructures. *Chem. Rev.* **1995**, *95* (8), 2725–2828.
27. Pease, A.R.; Stoddart, J.F. Computing at the molecular level. *Mol. Mach. Mot.* **2001**, *99*, 189–236.
28. Philp, D.; Stoddart, J.F. Self-assembly in natural and unnatural systems. *Angew. Chem., Int. Ed. Engl.* **1996**, *35* (11), 1155–1196.
29. Ballardini, R.; Balzani, V.; Credi, A.; Gandolfi, M.T.; Venturi, M. Molecular-level artificial machines based on photoinduced electron-transfer processes. *Mol. Mach. Mot./Struct. Bond.* **2001**, *99*, 163–188.
30. Raymo, F.M.; Houk, K.N.; Stoddart, J.F. Origins of selectivity in molecular and supramolecular entities: Solvent and electrostatic control of the translational isomerism in [2]catenanes. *J. Org. Chem.* **1998**, *63* (19), 6523–6528.
31. Jimenez, M.C.; Dietrich-Buchecker, C.; Sauvage, J.P. Towards synthetic molecular muscles: Contraction and stretching of a linear rotaxane dimer. *Angew. Chem., Int. Ed. Engl.* **2000**, *39* (18), 3284–3287.
32. Fujita, M. Self-assembly of [2]catenanes containing metals in their backbones. *Acc. Chem. Res.* **1999**, *32* (1), 53–61.
33. Hamilton, D.G.; Montalti, M.; Prodi, L.; Fontani, M.; Zanello, P.; Sanders, J.K.M. Photophysical and electrochemical characterisation of the interactions between components in neutral pi-associated [2]catenanes. *Chem. Eur. J.* **2000**, *6* (4), 608–617.
34. Balzani, V.; Credi, A.; Raymo, F.M.; Stoddart, J.F. Artificial molecular machines. *Angew. Chem., Int. Ed. Engl.* **2000**, *39* (19), 3349–3391.
35. Raymo, F.M.; Bartberger, M.D.; Houk, K.N.; Stoddart, J.F. The magnitude of [C–H center dot center dot center dot O] hydrogen bonding in molecular and supramolecular assemblies. *J. Am. Chem. Soc.* **2001**, *123* (38), 9264–9267.
36. Kaminski, G.A.; Jorgensen, W.L. Host–guest chemistry of rotaxanes and catenanes: Application of a polarizable all-atom force field to cyclobis(paraquat-*p*-phenylene) complexes with disubstituted benzenes and biphenyls. *J. Chem. Soc., Perkin Trans. 2* **1999**, (11), 2365–2375.
37. Jorgensen, W.L. *BOSS Version 3.6*; Yale University: New Haven, CT, 1995.
38. Dobrowolski, J.C.; Mazurek, A.P. On the qualitative theoretical NMR chemical shifts of model carbyne catenanes and knots. *Chem. Phys. Lett.* **2001**, *348* (1–2), 60–66.
39. Fanti, M.; Fustin, C.A.; Leigh, D.A.; Murphy, A.; Rudolf, P.; Caudano, R.; Zamboni, R.; Zerbetto, F. High-frequency vibrations of the simplest benzylic amide [2]catenane. *J. Phys. Chem., A* **1998**, *102* (29), 5782–5788.
40. Leigh, D.A.; Murphy, A.; Smart, J.P.; Deleuze, M.S.; Zerbetto, F. Controlling the frequency of macrocyclic ring rotation in benzylic amide [2]catenanes. *J. Am. Chem. Soc.* **1998**, *120* (26), 6458–6467.
41. Ponder, J.W. *Software Tools for Molecular Design*; Version 3.9, ©1990–2001, <http://dasher.wustl.edu/tinker/>.
42. Dudek, M.J.; Ponder, J.W. Accurate modeling of the intramolecular electrostatic energy of proteins. *J. Comput. Chem.* **1995**, *16* (7), 791–816.
43. Kundrot, C.E.; Ponder, J.W.; Richards, F.M. Algorithms for calculating excluded volume and its derivatives as a function of molecular-conformation and their use in energy minimization. *J. Comput. Chem.* **1991**, *12* (3), 402–409.
44. Ponder, J.W.; Richards, F.M. An efficient Newton-like method for molecular mechanics energy minimization of large molecules. *J. Comput. Chem.* **1987**, *8*, 1016–1024.
45. Allinger, N.L.; Yuh, Y.H.; Lii, J.-H. Molecular mechanics. The MM3 force field for hydrocarbons, Part 1. *J. Am. Chem. Soc.* **1989**, *111* (23), 8551–8565.
46. Lii, J.H.; Allinger, N.L. Molecular mechanics. The MM3 force field for hydrocarbons: 2. Vibrational frequencies and thermodynamics. *J. Am. Chem. Soc.* **1989**, *111* (23), 8566–8575.
47. Lii, J.H.; Allinger, N.L. Molecular mechanics. The MM3 force field for hydrocarbons: 3. The van der Waals potentials and crystal data for aliphatic and aromatic hydrocarbons. *J. Am. Chem. Soc.* **1989**, *111* (23), 8576–8582.
48. Leigh, D.A.; Parker, S.F.; Timpel, D.; Zerbetto, F. The inelastic neutron scattering of two benzylic amide [2]catenanes. *J. Chem. Phys.* **2001**, *114* (11), 5006–5011.
49. Bottari, G.; Caciuffo, R.; Fanti, M.; Leigh, D.A.; Parker, S.F.; Zerbetto, F. Solid-state fingerprints of molecular threading detected by inelastic neutron scattering. *ChemPhysChem* **2002**, *3* (12), 1038–1041.
50. Caciuffo, R.; Degli Esposti, A.D.; Deleuze, M.S.; Leigh, D.A.; Murphy, A.; Paci, B.; Parker, S.; Zerbetto, F. Inelastic neutron scattering of large molecular systems: The case of the original benzylic amide [2]catenane. *J. Chem. Phys.* **1998**, *109* (24), 11094–11100.
51. Leigh, D.A.; Troisi, A.; Zerbetto, F. Reducing molecular shuttling to a single dimension. *Angew. Chem., Int. Ed. Engl.* **2000**, *39* (2), 350–353.
52. Ceroni, P.; Leigh, D.A.; Mottier, L.; Paolucci, F.; Roffia, S.; Tetard, D.; Zerbetto, F. Electrochemically-induced dynamics of a benzylic amide [2]catenane. *J. Phys. Chem., B* **1999**, *103*, 10171–10179.
53. Deleuze, M.S.; Leigh, D.A.; Zerbetto, F. How do benzylic amide [2]catenane rings rotate? *J. Am. Chem. Soc.* **1999**, *121* (11), 2364–2379.
54. Chang, G.; Guida, W.C.; Still, W.C. An internal coordinate Monte Carlo method for searching conformational space. *J. Am. Chem. Soc.* **1989**, *111* (12), 4379–4386.
55. Weiner, S.J.; Kollman, P.A.; Case, D.A.; Singh, U.C.; Ghio, C.; Alagona, G.; Profeta, S.J.; Weiner, P. A new force field for molecular mechanical simulation of nucleic acids and proteins. *J. Am. Chem. Soc.* **1984**, *106* (3), 765–784.
56. Mohamadi, F.; Richards, N.G.J.; Guida, W.C.; Liskamp, R.; Lipton, M.; Caufield, C.; Chang, G.; Hendrickson, T.; Still, W.C. MacroModel—An integrated software system for modeling organic and

- bioorganic molecules using molecular mechanics. *J. Comput. Chem.* **1990**, *11*, 440–467.
57. SPARTAN Program System. *PC Spartan Plus*; Wavefunction, Inc.: Irvine, CA, 1997.
58. Houk, K.N.; Menzer, S.; Newton, S.P.; Raymo, F.M.; Stoddart, J.F.; Williams, D.J. Molecular meccano: 47. [C–H...O] interactions as a control element in supramolecular complexes: Experimental and theoretical evaluation of receptor affinities for the binding of bipyridinium-based guests by catenated hosts. *J. Am. Chem. Soc.* **1999**, *121* (7), 1479–1487.
59. Rauwolf, C.; Strabner, T. Modeling of self-organizing systems. *J. Mol. Model.* **1997**, *3*, 1–16.
60. PCMODEL 3.0, Serena Software; Bloomington, 1988.
61. Allinger, N.L. Conformational analysis 130. MM2. A hydrocarbon force field utilizing V1 and V2 torsional terms. *J. Am. Chem. Soc.* **1977**, *99* (25), 8127–8134.
62. Burkert, U.; Allinger, N.L. Pitfalls in the use of the torsion angle driving method for the calculation of conformational interconversions. *J. Comput. Chem.* **1982**, *3*, 40.
63. Stewart, J.J.P. Optimization of parameters for semi-empirical methods: I. Method. *J. Comput. Chem.* **1989**, *10*, 209–220.
64. Stewart, J.J.P. Optimization of parameters for semi-empirical methods: II. Applications. *J. Comput. Chem.* **1989**, *10*, 221.
65. Baker, J. An algorithm for the location of transition states. *J. Comput. Chem.* **1986**, *7*, 385–395.
66. Hu, Y.Z.; Bossmann, S.H.; van Loyen, D.; Schwarz, O.; Durr, H. A novel 2,2'-bipyridine[2]catenane and its ruthenium complex: Synthesis, structure, and intramolecular electron transfer—A model for the photosynthetic reaction center. *Chem. Eur. J.* **1999**, *5* (4), 1267–1277.
67. Ashton, P.R.; Boyd, S.E.; Menzer, S.; Pasini, D.; Raymo, F.M.; Spencer, N.; Stoddart, J.F.; White, A.J.P.; Williams, D.J.; Wyatt, P.G. Molecular meccano: Part 23. Self-assembling cyclophanes and catenanes possessing elements of planar chirality. *Chem. Eur. J.* **1998**, *4* (2), 299–310.
68. Brouwer, A.M.; Buma, W.J.; Caudano, R.; Fanti, M.; Fustin, C.A.; Leigh, D.A.; Murphy, A.; Rudolf, P.; Zerbetto, F.; Zwier, J.M. Experimental and theoretical studies of the low-lying electronic states of the simplest benzylic amide [2]catenane. *Chem. Phys.* **1998**, *238* (3), 421–428.
69. Bene, J.D.; Jaffe, H.H. CNDO parameterized for spectra (including correlation). *J. Chem. Phys.* **1968**, *48*, 1807.
70. Mataga, N.Z.; Nishimoto, K. Electronic structure and spectra of nitrogen heterocycles. *Z. Phys. Chem.* **1957**, *13*, 140–157.
71. Zheng, X.E.; Sohlberg, K. Modeling bistability and switching in a [2]catenane. *Phys. Chem. Chem. Phys.* *in press* (submitted for publication).
72. Collier, C.P.; Mattersteig, G.; Wong, E.W.; Luo, Y.; Beverly, K.; Sampaio, J.; Raymo, F.M.; Stoddart, J.F.; Heath, J.R. A [2]catenane-based solid state electronically reconfigurable switch. *Science* **2000**, *289* (5482), 1172–1175.
73. Zheng, X.G.; Sohlberg, K. Modeling of a rotaxane-based molecular device. *J. Phys. Chem., A* **2003**, *107* (8), 1207–1215.
74. <http://www.chem.umass.edu/~lahti/Xtl/herring.jpg>.

# Computational Analysis of Switchable Rotaxanes

Xiange Zheng  
Karl Sohlberg

*Department of Chemistry, Drexel University, Philadelphia, Pennsylvania, U.S.A.*

## INTRODUCTION

A rotaxane is an assembly of interlocked molecules in which a dumbbell-shaped component is encycled by one (or more) chemically independent ring component(s). For example, a [2]rotaxane is created when a cyclodextrin or another ring molecule such as a crown ether (called the “shuttle” or “ring”) is threaded with a linear molecule (called the “shaft” or “chain”). The shaft terminates with a bulky substituent on each end to prevent its unthreading, and is therefore sometimes referred to as a “dumbbell” because of its appearance. A rotaxane with multiple rings upon a single shaft is a polyrotaxane. In some rotaxanes, the macrocyclic component can shuttle back and forth between binding sites on the dumbbell component. Such a system constitutes a molecular shuttle. With appropriate molecular design, the shuttling process can be controlled reversibly by external stimuli, including light, electrons, pH, and the chemistry of the environment,<sup>[1–5]</sup> thereby endowing the system with the essential characteristics of a mechanical machine or device, but on the molecular scale.

A pseudorotaxane is closely related to a rotaxane. This type of complex also consists of a chain component threaded through a macrocyclic ring, but unlike a rotaxane, a pseudorotaxane can undergo dissociation into its components without breaking any covalent bonds. A pseudorotaxane in which this threading and unthreading can be controlled with an external stimulus has the essential characteristics of a piston and cylinder, and external inputs are converted into cyclical translational motion.

Early reports of switchable rotaxanes include the thermally switched system reported in 1991 by Anelli, Spencer, and Stoddart<sup>[6]</sup> and the electrochemically switched system prepared by Bissell et al. in 1994,<sup>[7]</sup> which is shown in Fig. 1. Since then, the construction of rotaxane-based molecular shuttles has produced numerous schemes for shifting the ring between two or more “stations” on the linear chain in response to external stimuli.<sup>[6–24]</sup>

Particularly attractive for the construction of molecular machines are rotaxanes with a redox- and/or photo-active unit present in one or more of their constituent components.<sup>[1–5]</sup> The synthesis of such

systems often relies on the presence of molecular recognition sites in the components, and on the use of transition metal templates or complementary  $\pi$ -electron-rich and  $\pi$ -electron-deficient recognition segments to enable the construction process. Three approaches have been proposed for the construction of rotaxanes:<sup>[25]</sup> 1) threading of a long molecule through a ring, followed by capping the end(s) of the thread with stoppers; 2) slipping of a preformed ring over the stoppers of a preformed dumbbell-shaped component; 3) clipping of a preformed dumbbell with a suitable U-type component, which is subsequently cyclized. Technically, the complex formed through the second approach is a pseudorotaxane, because the ring can slip onto and off the thread without breaking any chemical bonds. However, if the barrier to the slipping process is sufficiently high, the rate of decomposition will be exceedingly slow and the system is effectively a rotaxane.

Theoretical studies of rotaxanes are warranted to elucidate the fundamental basis underlying the stability and switching mechanisms of these interlocked molecules, such as metal–ligand interactions,<sup>[26,27]</sup> [C–H...O] hydrogen bonds, and [C–H... $\pi$ ] and [ $\pi$ – $\pi$ ] stacking interactions.<sup>[28,29]</sup> The accompanying entry, entitled “Computational Analysis of Switchable Catenanes,” contains an in-depth discussion of the various theoretical and computational techniques that have been employed for modeling switchable catenanes, and rotaxanes as well, including the relative strengths of these techniques. While a wide range of theoretical techniques has been brought to bear on the modeling of rotaxanes, because of the consideration of computational expense (the simplest prototype rotaxane-based molecular devices involve nearly 200 atoms), structural studies have overwhelmingly employed molecular mechanics (MM) methods, and semiempirical procedures are finding considerable use in the modeling of electronic and/or spectroscopic properties.

For theory-accelerated design of molecular device systems, computational models are needed that accurately capture the multiple stabilities and switching mechanisms of switchable rotaxanes and similar systems. The modeling of such molecular-based devices is a great challenge to computational chemistry because

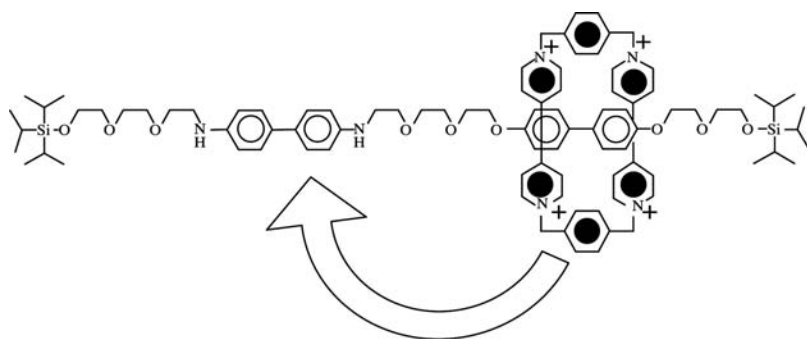


**Fig. 1** The switchable rotaxane designed by Bissell et al. *Source:* Adapted from Ref.<sup>[7]</sup>. © 1994, with permission from Nature ([www.nature.com](http://www.nature.com)) and the author.

of their large molecular size; nevertheless, modeling efforts are reaping success. In this work, some of the most recent achievements in the field of computational modeling of rotaxane systems will be reviewed.

## COMPUTATIONAL STUDIES OF SWITCHABLE ROTAXANES

### Structural Fundamentals

In 1994, Ricketts, Stoddart, and Hann<sup>[30]</sup> presented one of the first attempts at modeling interlocked molecules. They noted that, over time, chemical systems of interest tend to increase in structural complexity and molecular size. They argued that as a consequence, existing experimental analysis techniques such as <sup>1</sup>H nuclear magnetic resonance (NMR) and X-ray crystallography would eventually become less effective. They proposed a technique that combines molecular mechanics and semiempirical methods to determine structures and binding energies. Test applications of the method predicted structures of inclusion complexes and mechanically interlocked molecules in agreement with those obtained by using X-ray crystallographic methods.<sup>[30]</sup> Trends in binding energies were detected and non-covalent binding interactions consistently agreed with those found by experiments.

Pozuelo and coworkers<sup>[31]</sup> reported molecular dynamics (MD) simulations in vacuo for “channel-type” polyrotaxanes, one of which is presented in Fig. 2. In these polyrotaxanes, alpha-cyclodextrins ( $\alpha$ CDs) are threaded onto poly(ethylene glycol) (PEG) chains. Molecular dynamics trajectories were computed by using the Sybyl 6.0 software from Tripos Associates (St. Louis, MO)<sup>[32]</sup> and the Tripos Force Field 5.2,<sup>[33]</sup> at a fixed concentration and *T*. The strengths of the intra- and intermolecular hydrogen bonds and of the van der Waals interactions were evaluated by averaging each property over all classical trajectories. Based on the simulations, they concluded that van der Waals interactions are the main source of the stabilization of these polyrotaxanes. Hydrogen

bonds between successive  $\alpha$ CDs slightly favor head-to-head, tail-to-tail sequences over head-to-tail sequences. Here head-to-head and tail-to-tail sequences mean that the adjacent cyclodextrin rings are threaded onto the polymer chain in the opposite direction. More recently, they carried out molecular dynamic simulations<sup>[34]</sup> on the two polyrotaxane systems, shown in Fig. 3, to determine their preferred configurations. Both of the polyrotaxanes consist of two polymeric chains threaded into the channel formed by eight stacked  $\alpha$ CDs. The simulations were performed by using the Sybyl<sup>[32]</sup> molecular modeling package and the Tripos Force Field<sup>[33]</sup> at 500 K in vacuum, and the results were compared with those of the isolated polymer chain. It was shown that the rotaxane structure is stabilized with respect to the separated chain and alpha cyclodextrins, principally by van der Waals interactions. This stabilization upon threading is noted in several studies reviewed below, and appears to be quite general. As rotaxane assembly is almost certainly entropically unfavorable, generally speaking, the internal energy of a rotaxane must be lower than that of its isolated components to achieve thermodynamically spontaneous self-assembly. We will note below several other instances where theoretical calculations have revealed this result.

The change in the nature and strength of the inter-component hydrogen-bonding interactions in a rotaxane can induce the macrocycle(s) to move along the thread between two or more discrete stations. Altieri et al.<sup>[35]</sup> reported a molecular modeling study of three rotaxane-based molecular shuttles to address this effect. They used simulated annealing, followed by geometrical optimization, to identify the positional preference between the two binding states and the population distribution of the coconformers. The MM3 force field,<sup>[36–38]</sup> as implemented in the Tinker program,<sup>[39–42]</sup> was used in the simulation. The calculations consistently reproduced results in agreement with experimental ones, and evoked the following explanation for the positional discrimination in the rotaxane systems: When certain sites are not occupied, they may hydrogen bond to themselves and thus two possible

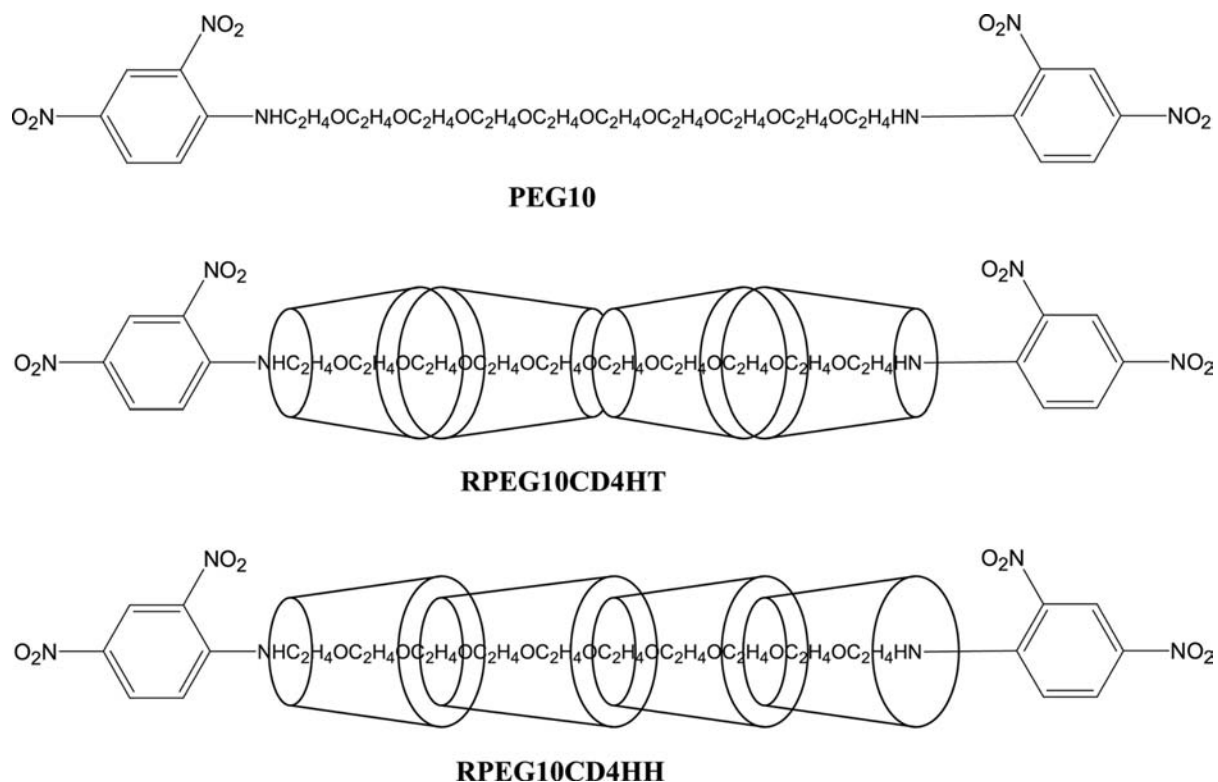


**Fig. 2** The system investigated by Pozuelo et al., with the cyclodextrin rings, which are represented by tori, oriented head-to-tail in the upper molecule and head-to-head or tail-to-tail in the lower one. *Source:* Reprinted with permission from Ref.<sup>[31]</sup>. © 1997, American Chemical Society.

hydrogen bonding sites (carbonyl and NH) are used to form just one hydrogen bond. The translational isomers with such stations unoccupied have at least one hydrogen bond fewer than isomers with those stations occupied. It was concluded that, in molecular machines powered by weak noncovalent interactions, the use of such “self-binding” in unoccupied stations is a common driving force for submolecular motion.

### Studies of Rotaxane Dynamics (MD)

An important aspect of the design of a multicomponent molecular device is the prediction of its dynamic

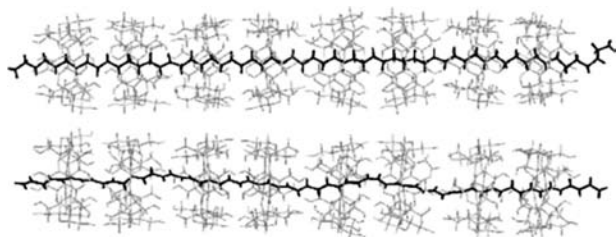


**Fig. 3** The two polyrotaxanes studied by Pozuelo et al. Shown are two minimum energy conformations obtained during MD simulations. *Source:* Reprinted from Ref.<sup>[34]</sup>. © 2002, with permission from Elsevier.

behavior. Molecular device dynamics are often studied using classical molecular dynamics (MD) methods. Most of the existing computational studies of the dynamical behavior of switchable rotaxanes have been devoted to systems with cyclodextrins as the macrocycle.<sup>[31,34,43–46]</sup> In these studies, one primary goal has been to rationalize the driving forces responsible for the preferred arrangement of the macrocyclic component on the threaded chain and its interconversion between binding stations.

Experimental investigations performed by Amabilino et al.<sup>[47]</sup> on [2]rotaxanes bearing dendritic stoppers (Fig. 4), reveal a strong dependence of the shuttling

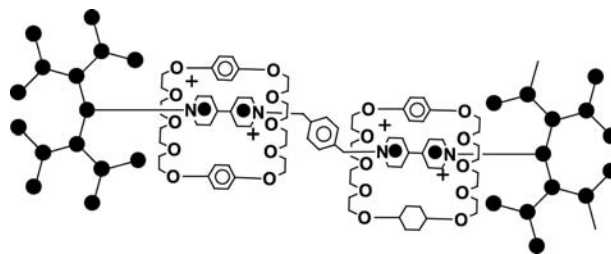


**Fig. 4** The [3]rotaxane containing dendritic stoppers investigated by Amabilino et al. *Source:* Reprinted with permission from Ref.<sup>[47]</sup>. © 1996, American Chemistry Society.

process on the polarity of the solvent. To investigate the origin of this dependence, they carried out molecular dynamic simulations on the [2]rotaxanes, with  $\text{CHCl}_3$  and  $\text{Me}_2\text{CO}$  solvents, as included in the form of the GB/SA<sup>a</sup> solvation model.<sup>[48]</sup> The simulations were performed both with and without the inclusion of acetate counterions. The molecular modeling package Macro-model 5.0 was used.<sup>[49]</sup> Estimations of the approximate size of the rotaxanes based on these simulations suggested that extending the rotaxane shaft with an additional bipyridinium recognition site increases the end-to-end length by about 1.5 nm. Total lengths ranged from 3 to 6 nm, and the molecular volumes from about 4 to 6 nm<sup>3</sup>. Significant conformational changes were found to occur upon changing the polarity of the solvent. Folding of the structure occurred in  $\text{CHCl}_3$  even in the presence of counterions, which was assumed to minimize the exposure of the rotaxane to a low-polarity solvent. The resulting folded structure of the rotaxane complex in  $\text{CHCl}_3$  solvent presents a large steric and electronic hindrance to the shuttling process, revealing a significant solvent dependence of the rotaxane dynamics. The activation energy for the shuttling process was determined to be higher in  $\text{CHCl}_3$  than in  $\text{Me}_2\text{CO}$ . The results of the simulations were consistent with the experimentally observed dependence of the rate of the *shuttling* process on the polarity of the solvent. Therefore, the simulations suggested that the dramatic solvent dependence of the rate is a result of conformational changes induced by varying the solvent polarity.

Inelastic neutron scattering (INS) allows for the observation of motions present in a system and is therefore ideally coupled with MD simulations. Bottari et al.<sup>[50]</sup> reported that the INS spectra of a benzylic amide rotaxane, and of the isolated chain that results from the removal of the benzylic amide macrocycle, show significant differences in some regions. To understand qualitatively the origin of this spectral difference, they carried out molecular dynamics (MD) simulations based on an MM force field. The calculations were performed with the MM3 force field<sup>[36–38]</sup> as implemented in the Tinker program.<sup>[39–42]</sup> Molecular dynamics were run on isolated systems with boundary conditions applied to reproduce the crystal structure. The experimental spectra were compared with the calculated ones. While there were some shifts in the positions of the bands, their number and shape were well reproduced. The shaft features present, inferred from the experimental spectrum of the rotaxane complex

relative to those for the isolated thread, were confirmed by the simulation. This was presented as a “fingerprint” of the ring threading.

The hopping model, which was proposed by Herrmann, Keller, and Wenz,<sup>[51]</sup> was demonstrated to have the potential for investigating the threading process. In this model, the threading movement is assumed to take place by a consecutive hopping of the ring over a series of distinct binding sites on the chain. Compared to the diffusional model proposed by Meier et al.,<sup>[52]</sup> where the movement of rings along the polymer chains is treated as one-dimensional Fickian diffusion, they believed the hopping model to be more suitable for polymers. Horsky<sup>[43]</sup> applied this model with modifications to several pseudorotaxanes, in order to identify the central features of cyclodextrin threading, and to identify the cooperative interactions between adjacent rings. Pseudopolyrotaxane formation was treated. Stochastic simulation was used to address the problems of time evolution of threading and transport across connected sites. The simulation based on the hopping model showed that completely regular head-to-head/tail-to-tail arrangement could not be expected. This is consistent with the result reported by Pozuelo, Mendicuti, and Mattice<sup>[31]</sup> reviewed above. The orientational preference of adjacent rings is not sufficiently strong to guarantee a completely ordered assembly.

Grabuleda and Jaime<sup>[53]</sup> applied molecular mechanics and molecular dynamics methods to model the switching processes of [2] rotaxanes. The MM3 and MM3\* force fields were chosen, which they noted model non-bonded interactions reasonably well. The simulation of the rotaxanes was performed by using the MM3 force field, and the solvent effects were taken into account by changing the dielectric constant. Complementary computations were carried out by using the MM3\* force field, which showed less reliable and, reportedly, sometimes wrong behavior in the prediction of stability between different coconformers.<sup>[53]</sup> The molecular mechanics studies on the rotaxanes showed that electrostatic and van der Waals interactions are the major factors controlling the energy minima. This conclusion is probably generally true for large macrocycles containing highly electronegative atoms.<sup>[54]</sup> MD computations showed qualitative agreement with MM computations in estimates of the shuttling barrier, and the results supported those from experiments for the preferred translational isomers. Additionally, the MD computations provided information regarding [C–H...O] hydrogen-bonding interactions throughout the shuttling process. In comparison,  $\pi$ - $\pi$  stacking interactions were found to be considerably less important. More recently, similar calculations on pseudorotaxanes<sup>[55]</sup> studied their structures and energies, with the intent to establish a

<sup>a</sup>Represents a method which combines the generalized Born (GB) method of interpreting the electrostatic contribution to the solvation free energy with a solvent-accessible-Surface-Area (SA) determination of the hydrophobic contribution to the solvation free energy.



computational procedure for investigating the shuttling process in rotaxanes. The SANDER module of the AMBER v.5 program,<sup>[56]</sup> the parm94 force field<sup>[57]</sup> with RESP charges, and an explicit solvent model for acetonitrile were employed. Here RESP represents Restrained ElectroStatic Potential, which fits the quantum mechanically calculated electrostatic potential (esp) at molecular surfaces using an atom-centered point charge model. Reportedly, the experimental results were reproduced by the computational model. It was concluded that the AMBER force field with RESP charges and the explicit solvent model for acetonitrile<sup>[58]</sup> provide a useful computational scheme for studying pseudorotaxanes, and that they can further be applied for modeling [2]rotaxanes.

### Studies of Rotaxane Dynamics (Quantum)

Leigh, Troisi, and Zerbetto<sup>[59]</sup> reported quantum-mechanical modeling of the shuttling in a rotaxane. A one-dimensional quartic potential was used to describe the potential energy variation with shuttle movement along the shaft of the rotaxane. The parameters of the quartic function were set to yield a double well potential, each well corresponding to one of two ring binding stations on the shaft separated by a potential barrier. The coefficients on the quadratic and quartic terms in the potential were adjusted to reproduce the observed shuttling rate at 298 K. Such a model affords a reduced-dimensionality analysis of the contributions of quantum effects to the shuttling dynamics. It was found that energies slightly exceeding the barrier to binding site interconversion correspond to very high quantum number eigenstates. In such high-lying vibrational eigenstates, the probability distribution approaches the classical limit, i.e., at these energies the shuttle will be found with the greatest probability in the vicinity of the classical turning points on the barrier. High probability of finding the ring at one of the ring binding stations only occurs at energies far below that of the barrier.

There is considerable interest in the possible use of nested carbon nanotubes in molecular-bearing and molecular-motor applications.<sup>[60–62]</sup> In fact, nested carbon nanotubes form a pseudorotaxane. Sohlberg et al.<sup>[63]</sup> carried out rigid-body dynamics and semiclassical mechanics calculations of a nested carbon nanotube molecular bearing to demonstrate the utility of rigid-body dynamics for studying the dynamical properties of nanosystems. In this rigid-body approximation, the entire body (bearing shaft in this case) was allowed to translate and rotate, but all of its internal coordinates are frozen in their equilibrium positions. This avoids the zero-point energy problem of fully atomistic classical molecular dynamics simulations,

i.e., the unphysical pooling of large amounts of zero-point energy into a single mode. Simulations were carried out for a model consisting of a pair of nested carbon nanotubes, with the outer nanotube (sleeve) held in place, while the inner nanotube (shaft) is held in position only in its longitudinal direction. This represents a bearing in application where the shaft axis is fixed in position by the construction of the machine. The simulations demonstrated that, for certain operational conditions, particularly where the bulk of the system kinetic energy is contained in rotation of the shaft, the rotation of the shaft is smooth exhibiting quasiperiodic motion. For other conditions, especially with low shaft rotational kinetic energy, the motion is chaotic. Semiclassical analysis of these dynamical trajectories revealed a significant difference in the level spacing of rotational and processional quantum eigenstates.

### Coconformational Isomerism in Rotaxanes

MD techniques can also identify low-energy configurations of the system. The principle of this application of MD is that a dynamic trajectory will eventually sample all of the energetically accessible configuration space. In a practical calculation, any trajectory must be finite in time; nevertheless, this is often an efficient way to sample configuration space. MD methods have been employed with considerable success in this manner in the study of molecular and nanodevices.

Mayer et al.<sup>[45]</sup> conducted a computational study on the formation of a molecular necklace (a class of polyrotaxane), formed by threading cyclodextrins onto a block copolymer. Allinger's MM3-92 force field was employed in all calculations. A dynamic Monte Carlo (DMC) routine<sup>[64,65]</sup> was used within the program package MultiMize<sup>[66]</sup> to locate low-energy coconformations. It was shown that the formation of the intermolecular hydrogen bonds between adjacent cyclodextrin rings contributes significantly to the overall stability of the molecular necklace. The preferential intramolecular and intermolecular interactions result in the formation of the stable and highly ordered multicomponent complex. This somewhat contrasts to the results of Pozuelo, Mendicuti, and Mattice<sup>[31]</sup> and Horsky,<sup>[43]</sup> both of which reported the ordering preference to be insufficiently weak to guarantee highly ordered stacking of the macrocycles in a polyrotaxane. Indeed, the degree of ordering probably varies from system to system. It should, in principle, be possible to take an experimental measurement of the degree of ordering and convert it to a difference in stacking energy between head-to-head and head-to-tail ordering, but such an analysis has not, to the author's knowledge, been reported.

Fradera et al.<sup>[67]</sup> presented a molecular dynamics study of a [2]rotaxane using the molecular mechanics/Poisson Boltzmann-surface area (MM/PB-SA) strategy developed by Srinivasan et al.,<sup>[68]</sup> to determine its conformational preference and to evaluate the influences of cations and solvation on coconformation. Solvents considered include chloroform, dimethyl sulfoxide (DMSO), and water with the MST<sup>b</sup> continuum solvent model.<sup>[69–71]</sup> It was observed that in chloroform solution, the [2]rotaxane system exists as a mixture of coconformations with intercomponent hydrogen bonds. In DMSO solvent, no coconformation with such hydrogen bonding was found because of the formation of hydrogen bonds between the macrocycle NH group on the rotaxane with solvent molecules. It was found that the insertion of a Na<sup>+</sup> ion into the crown ether, where it coordinates to the ester C=O group, restricts coconformational exchange. Overall, it was demonstrated that the nature of the solvent, the addition of salts, and changing the flexibility of the rotaxane shaft all change the dynamic processes of the rotaxane.

Sohlberg and Tarbet<sup>[72]</sup> carried out a semiempirical investigation of a light-driven rotaxane-based molecular shuttle synthesized and characterized by Murakami et al.<sup>[73]</sup> Some preliminary structural optimizations on the cyclodextrin and shaft components were carried out with the MM<sup>+</sup> molecular mechanics method<sup>[74]</sup> to generate starting structures, followed by the full geometry optimizations assuming the semiempirical AM1<sup>[75]</sup> Hamiltonian. The results of the semiempirical calculations support the experimental results obtained by Murakami et al.<sup>[73]</sup> As an isolated molecule the rotaxane shaft shows twofold symmetry, but in both rotaxane conformers, the symmetry is broken. The loss of symmetry upon inclusion into the cyclodextrin was also observed experimentally.<sup>[73]</sup> Of the *cis* and *trans* coconformers of the rotaxane, the *cis* coconformer was energetically more stable, in agreement with the experimental findings of Murakami et al.,<sup>[73]</sup> where a 2:1 distribution of the *cis/trans* conformers at 278 K was reported. In the rotaxane *trans* conformer, the shaft is very nearly centered in the cyclodextrin cavity, as Murakami et al.<sup>[73]</sup> inferred from induced circular dichroism spectra. In the *cis* conformer, the shaft is off-center. This was suggested as the source of the shuttling action. Additionally, the *cis* conformer of the rotaxane structure displays a kink in the shaft and therefore the conformational isomerism from *trans* to *cis* (or vice versa) involves significant structural transformation. The barrier to conformational isomerization was estimated to be  $\geq 11$  kcal/mol. It

<sup>b</sup>A polarizable continuum model that was originally developed by Miertus, Scrocco, and Tomasi.

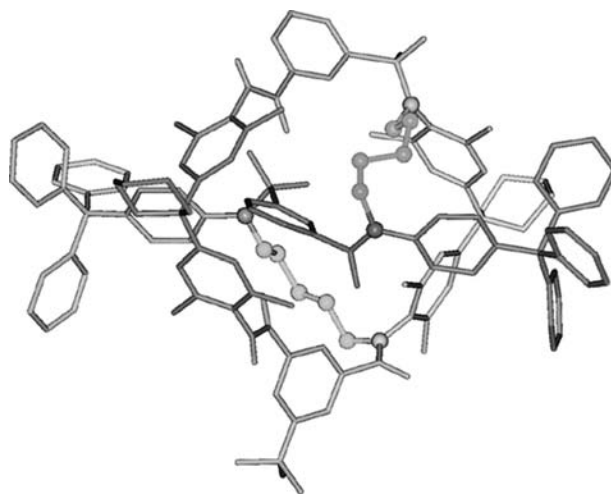


**Fig. 5** The “molecular 8” shaped [1]rotaxane investigated by Reuter et al. *Source:* Reprinted from Ref.<sup>[76]</sup>. © 2001, with permission from WILEY-VCH, STM-copyright & Licenses.

was noted that a significant structural transformation and a large energy barrier are consistent with the experimentally observed<sup>[73]</sup> very slow rate of isomerization at room temperature.

A new type of [1]rotaxane containing two aliphatic bridges between the “shaft” and “ring” was first obtained by Reuter et al.,<sup>[76]</sup> who noted that this system, shown in Fig. 5, is reminiscent of a self-intertwining chiral “molecular 8.” This system is topologically no different from a bridged macrocycle (bicyclic compound), but the “bridge” is very long and contains bulky substituents that lock the molecule into an interesting “intertwined” configuration. To locate the structure of the preferred isomer, they performed a molecular dynamic calculation at 360 K,<sup>[76]</sup> using the Amber\* force field implemented as in the Macro-model 6.5 software package.<sup>[49]</sup> The dominant conformation and the position of the two bridges of the [1]rotaxane, as predicted by the simulations were consistent with data from MS and NMR experiments.<sup>[76]</sup>

Biscarini et al.<sup>[77]</sup> carried out the molecular mechanics-based solid-state calculations on 25 rotaxanes and 1 catenane, to test which types of benzylic amide macrocycle-containing rotaxanes possess mobile components in the crystalline phase, and therefore have the potential to form the basis of solid-state molecular devices. The MM3 model<sup>[36–38]</sup> implemented in the TINKER package was used. Complete Ewald summation was used for the electrostatic interaction. The rotaxanes structures were optimized starting from structures determined by X-ray diffraction. Reoptimization of the X-ray structures was performed to set the positions of the hydrogen atoms, which are not revealed by X-ray analysis. For each minimized

structure, several physical properties were calculated: the packing energy, the molecular van der Waals surface, volume, and the ratio of the occupied volume to total volume of the cell (Kitaigorodski packing coefficient). For comparison with previous work, the same procedure was applied to other non-interlocked systems, similar to the rotaxanes and catenanes of consideration. These comparisons yielded calculated physical parameters in good agreement with literature results. The calculations showed that the experimentally determined rotational barriers and steric energies could be recovered by computations for these types of interlocked molecules.<sup>[77]</sup> The authors proposed their computational method for selecting rotaxanes that contain a macrocycle component that is highly mobile even in the solid phase.

Modeling studies of rotaxanes and catenanes often use an X-ray crystal structure as the starting geometry. However, in many cases, no crystal structure is available owing to experimental difficulties in the isolation of crystals of these complex species. Frankfort and Sohlberg addressed this issue in a semiempirical electronic structure study of a switchable rotaxane that was demonstrated experimentally by MartinezDiaz, Spencer, and Stoddert.<sup>[23]</sup> A starting structure of the rotaxane molecule was constructed from its principle subcomponents.<sup>[78]</sup> There are three subcomponent structures: the ring, shaft, and stopper. Low-energy conformations were identified for each subcomponent and optimized using the AM1 semiempirical method. The rotaxane was then assembled from the optimized subcomponents by computationally mimicking the S<sub>N</sub>2 mechanism by which it is synthesized. The computations showed that internal energy of the system decreases during construction. This result is consistent with the findings of Pozuelo, Mendicuti, and Mattice<sup>[31]</sup> for the assembly of alpha-cyclodextrin polyrotaxanes based on MM studies and also with MD studies of the process of nesting carbon nanotubes.<sup>[79]</sup> Again, we note that this result is confirmed for a wide range of systems and with multiple computational techniques, and undoubtedly has broad implication. In fact, as the association of the shaft and macrocycle is most probably entropically unfavorable, an accompanying decrease in internal energy is presumably necessary for a practical synthetic mechanism.

A second issue in modeling switchable rotaxanes is the involvement of multiple electronic and/or charge states of the system. In the switchable rotaxane reported by MartinezDiaz, Spencer, and Stoddert,<sup>[23]</sup> ring shuttling is initiated by a change in pH. Protonation or deprotonation of the amine functionality on the rotaxane shaft changes the preferred binding site of the ring. For techniques such as MM and classical MD, which are based on empirical molecular potential energy functions, the functions must be reparameterized for

each charge state. By contrast, electronic structure based techniques may be applied without reparameterization. For their study of the switchable rotaxane reported by MartinezDiaz, Spencer, and Stoddert,<sup>[23]</sup> Frankfort and Sohlberg selected the semiempirical AM1 Hamiltonian. After construction of a starting structure, they tracked the shuttling action of the [2]rotaxane by correlating the energy of the system to the position of the ring in both the protonated and deprotonated states.<sup>[78]</sup> For both the protonated and deprotonated species, 95 separate trial structures of the rotaxane were fully optimized at the AM1<sup>[75]</sup> level of theory. To generate these trial structures, the initial rotaxane structure (from the S<sub>N</sub>2-mimicking construction) was modified by translating and rotating the ring about the shaft. For the fully assembled rotaxane in the protonated state, the heavily dominant structure places the ring around the dialkylammonium station. This structure accounts for 64% of the total population at 300 K; the second and third lowest energy structures essentially constitute all of the remaining 36%. The most highly populated structure is representative of all three because they differ only by a slight translation of the macrocycle around the dialkylammonium center. Upon deprotonation, the ring is driven to the opposite side of the shaft where the bipyridinium station is located. The calculations identify three deprotonated structures that represent 86% of the population at 300 K. In all of these structures, the ring is oriented asymmetrically around the bipyridinium station. The bipyridinium station contains a nitrogen atom on either end. The macrocycle associates with either of these two nitrogen atoms, rather than being symmetrically positioned between the two. This asymmetric positioning around the bipyridinium station in the deprotonated state is in agreement with the experimental results based on proton NMR.<sup>[23]</sup> As shown by the energetic data for the structures, the addition of the proton to the dibenzylamine station is energetically favorable, which is also in accordance with experimental results. The calculations further show that relatively little structural change in the shaft accompanies the shuttling action.

In parallel experimental findings,<sup>[23]</sup> the semiempirical AM1 calculations predict that the DB24C8 ring initially resides on the NH<sub>2</sub><sup>+</sup>, and upon deprotonation with a base, the preference of the ring location changes to the bipyridinium station. Frankfort and Sohlberg proposed that such calculations may be useful for predicting the effect of proposed structural modifications on the shuttling action, and therefore, such calculations may be used in the presynthesis design of switchable rotaxanes.<sup>[78]</sup>

Zheng and Sohlberg<sup>[80]</sup> presented a procedure for modeling a photo-induced, redox-switchable, rotaxane-based molecular device that is designed to capture the

critical device-like features, and demonstrated it on an experimentally realized example. The system consists of a benzylic amide macrocycle mechanically locked onto a thread featuring two potential hydrogen bonding stations, a succinamide (*succ*) and a 3,6-di-tert-butyl-1,8-naphthalimide (*ni*) unit separated by a C<sub>12</sub> alkyl spacer. The system, which has been studied experimentally,<sup>[81]</sup> exhibits extremely fast and fully reversible shuttling motion.

The computational procedure consists of three main steps: 1) conformational searching over the full torsional space of the rotaxane; 2) single-point semiempirical calculations for all coconformations in their neutral singlet, triplet, and anionic doublet states; and 3) statistical analysis to correlate the structural features with energy in each state. Results were checked by repeating the analysis on a subset of coconformations (~1%) that were subjected to full geometry optimization.

Constructing the profile of structure vs. energy from a large sample of semiempirical single-point energy calculations is dramatically less expensive computationally than carrying out full structural optimizations at the semiempirical level for each trial structure. For large structures such as rotaxanes and catenanes, which require 1000 or more optimization steps, the computational expense decreases on the order of  $\times 10^3$ . Zheng and Sohlberg<sup>[80]</sup> proposed that as long as the trial structures generated from the systematic conformational search are “chemically reasonable,” the use of single-point calculations will produce a structure-vs.-energy profile that is qualitatively consistent with what would be obtained if each structure were fully optimized. The mathematical basis of their argument is as follows and is shown schematically in Fig. 6:

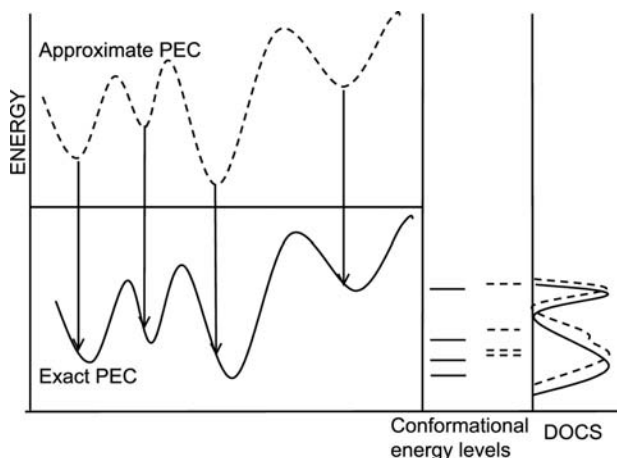


**Fig. 6** Schematic density of conformational states (DOCS) resulting from the exact potential energy curve (PEC) and from evaluation of energy on the exact curve using coordinates from an approximate PEC.

Suppose that the molecular potential energy function is  $f(\alpha_i)$ , where  $\alpha_i$  represents the independent internal coordinates, of which there are  $M$ . (The potential energy function is shown on the left panel in Fig. 6, where the upper curve is the approximate one and the lower curve is the exact one.) The local minima are indexed  $n$ . In the harmonic approximation (widely used in computational chemistry)<sup>[82]</sup> in the vicinity of any particular minimum  $n$ , the function can be expanded in a quadratic polynomial in the parameters  $\alpha_i$

$$f(\alpha_i^n) \approx c^n + \sum_i [\alpha_i^n - \alpha_i^{0n}]^2 \frac{k_i^n}{2} \quad (1)$$

where  $c^n$  and  $k_i^n$  are constants, and  $\alpha_i^{0n}$  are the values of coordinates  $\alpha_i$  at the true minima  $n$ . The superscripts  $n$  refers to an expansion about the  $n$ th minimum. There are four minima shown in Fig. 6; in practice there are thousands.

The function  $G(f)$  is then defined as the number of minima of  $f(\alpha_i)$  with function value  $\leq f$ .  $G'(f) = [dG(f)]/df$  is the density of conformational states function (DOCS).

When minima  $n$  are approximately located (as by conformational searching with MM), mathematically this means that the  $\alpha_i^{0n}$  are determined with finite accuracy. (In Fig. 6, the evaluation of the energy on the exact curve using the minima on the approximate curve translates the uncertainty in the coordinates into uncertainty in the energy.) The uncertainty in  $\alpha_i^{0n}$  translates by propagation of errors into uncertainty in  $f(\alpha_i)$  at the minimum  $n$ , and ultimately into uncertainty in  $G'(f)$ . Error propagation analysis can then be used to find the influence of error in prediction of  $\alpha_i^{0n}$  on error in the energy profile of the system  $G'(f)$ .

By the definition of the derivative,  $G'(f)$  may be written

$$G'(f) = \left. \frac{G(f + \Delta f) - G(f)}{\Delta f} \right|_{\lim \Delta f \rightarrow 0} \quad (2)$$

where,

$$\begin{aligned} f(\alpha_i^n) &\approx c^n + \sum_i [\alpha_i^n - \alpha_i^{0n}]^2 \frac{k_i^n}{2} \\ &= c^n + \sum_{i=1}^M [(\alpha_i^n)^2 - 2\alpha_i^n \alpha_i^{0n} + (\alpha_i^{0n})^2] \frac{k_i^n}{2} \end{aligned} \quad (3)$$

In Eq. (3), the uncertainties in  $c^n$  and  $k_i^n$  are zero. Writing,  $(\alpha_i^{0n} = \alpha_i^{0n} \pm \delta_i^n)$ , the uncertainty in function  $f(\alpha_i)$  is the sum over  $i$  ( $i = 1 \rightarrow M$ ) of the uncertainty in  $(\alpha_i^n)^2$  which is 0, in  $2\alpha_i^n \alpha_i^{0n}$ , which is  $\pm \delta_i^n$ , and in

$(\alpha_i^{on})^2$ , which is  $\pm 2\alpha_i^{on}\delta_i^n$ . This may be written,

$$\begin{aligned}\Delta f &= \sum_{i=1}^M [4(\alpha_i^{on})^2(\delta_i^n)^2 + (\delta_i^n)^2]^{1/2} \\ &= \sum_{i=1}^M \delta_i^n [4(\alpha_i^{on})^2 + 1]^{1/2}\end{aligned}\quad (4)$$

Suppose the upper limit on the uncertainties in  $\alpha_i^n$  ( $i = 1 \rightarrow M$ ) is  $\pm\delta_i^n$ . The operation of the summarization in Eq. (4) becomes:

$$\Delta f = \delta_i^n \sqrt{M} [4(\alpha_i^{on})^2 + 1]^{1/2} \quad (5)$$

As long as  $G'(f)$  is slowly varying, the formula

$$\Delta G = \Delta f G'(f) \quad (6)$$

holds. It follows from Eq. (2) that the uncertainty in  $G'(f)$  is

$$\Delta G'(f) = [(\Delta f G'(f))^2 + (\Delta f G'(f))^2]^{1/2} \quad (7)$$

$$= \sqrt{2} \Delta f G'(f) \quad (8)$$

Finally, based on formula (4), where  $\Delta f = \delta_i^n \sqrt{M} [4(\alpha_i^{on})^2 + 1]^{1/2}$ ,

$$\frac{\Delta G'(f)}{G'(f)} = Q \delta_i^n \quad (9)$$

where

$$Q = \sqrt{2} \sqrt{M} [4(\alpha_i^{on})^2 + 1]^{1/2} \quad (10)$$

Because  $Q$  is independent of the uncertainties, *the relative uncertainty in the DOCS is linearly proportional to the uncertainty in the values of the independent parameters at the minima.* (In Fig. 6, this is shown as the DOCS based on the approximate energies being skewed to higher energy from the correct DOCS.) Zheng and Sohlberg concluded that if values of the  $\alpha_i^{on}$  are “chemically reasonable,” as long as  $f(\alpha_i^n)$  is computed accurately at these *approximate* minima, the resulting DCOS will be chemically reasonable as well.

In their studies of a photo-induced redox-switchable rotaxane, Zheng and Sohlberg<sup>[80]</sup> computed single-point energy and radius of gyration for 10,118 rotaxane structures. It was found that coconformations with ring binding at the *succ* site predominate in the low-energy regime for singlet and triplet species, with preference for the shaft component being extended.<sup>[80]</sup> Doublet species prefer to adopt coconformations with ring binding at the *ni* site in low-energy structures, with coiled and extended shaft conformations being energetically competitive. Effectively, the same results

were obtained by geometrical optimizations of a subset of coconformations, and were also in excellent agreement with previous experimental observations.<sup>[81]</sup>

## Computation as an Aid to Rotaxane Synthesis

Raymo, Houk, and Stodart<sup>[83]</sup> studied a series of  $[n]$ rotaxanes, each consisting of a bipyridinium-based backbone, encircled by one or more dioxyarene-based macrocyclic components. One of the structures is presented in Fig. 7. Syntheses were attempted for various functional R groups. Systematic variations in the R group attached to one of the phenyl rings of the tetraarylmethane-based stopper considerably affected the yields. When certain R groups are used, no rotaxane was isolated leading to the observed “all-or-nothing” substituent effect. A computational study was undertaken to explain this substituent effect, and to search for the transition state of the slipping-off process. The four compounds were constructed with Macromodel<sup>[49]</sup> 5.0, and followed individually by energy minimization using the Polak–Ribiere conjugate gradient (PRCG) algorithm.<sup>[84]</sup> The AMBER\* force field<sup>[85]</sup> was used with the GB/SA H<sub>2</sub>O model<sup>[48]</sup> to resemble a polar solvent. The study revealed two main energy barriers for the slipping-off of the macrocycle over the stoppers.<sup>[86]</sup> (The fact that the ring can slip off the shaft without breaking any chemical bonds means that these systems could be classified as pseudorotaxanes, but given a sufficiently large barrier to slipping, such a distinction is merely semantic.) Note also that if stabilization occurs upon assembly, i.e.,  $\Delta E < 0$ , the activation energy barrier to dissociation will be greater than that for association, and dissociation may therefore be kinetically forbidden even if the assembly process has an appreciable rate. The trend in calculated energy barriers agreed with experimental yields of the corresponding rotaxanes, and the abrupt substituent effect was a result of steric hindrance. This work provides an example of theory and computation yielding qualitative trends and insight that allows for targeted synthesis, thus accelerating the development process.

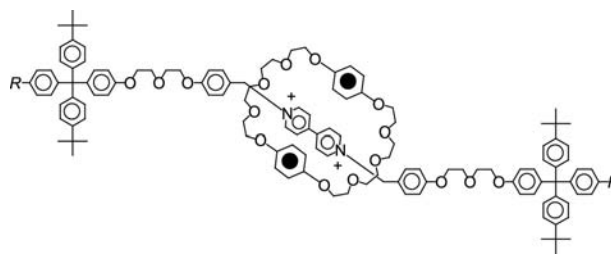


**Fig. 7** The rotaxane system studied by Raymo et al. *Source:* Reprinted with permission from Ref.<sup>[83]</sup>. © 1998, American Chemical Society.

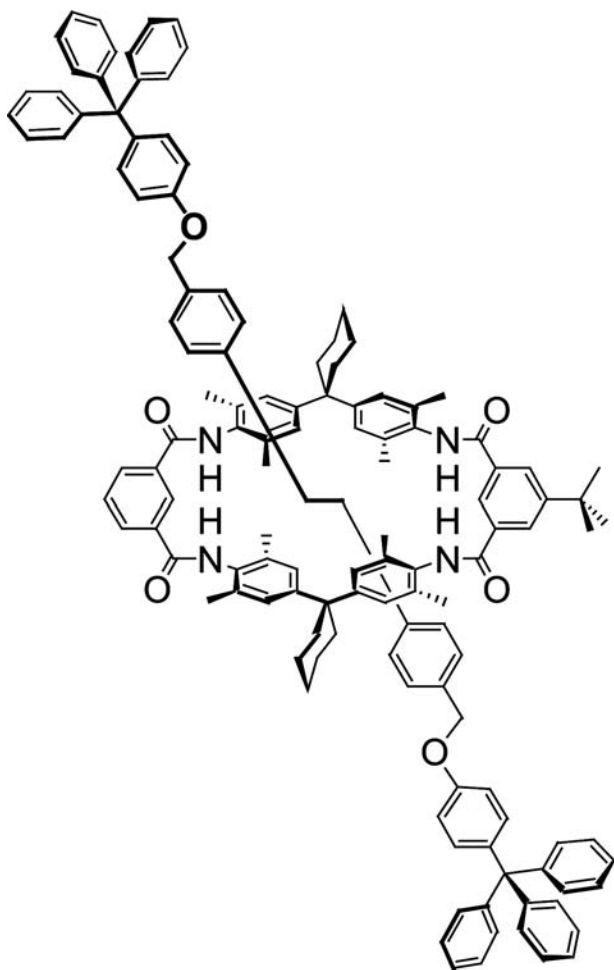


**Fig. 8** Schematic layout of Schalley et al.'s rotaxane system. Source: From Ref.<sup>[87]</sup>.

Schalley et al.<sup>[87]</sup> synthesized a set of rotaxanes with shafts of varying lengths. As in the work of Raymo, Houk, and Stodart,<sup>[83]</sup> they also reported that during the synthesis of these rotaxanes, the yield depends on the nature of the stopper. To examine the steric requirements of the stopper–ring complexes in detail, Schalley et al.<sup>[87]</sup> carried out force-field calculations of the rotaxane molecule shown in Fig. 8, using the Amber\* force field<sup>[85,88,89]</sup> incorporated in the MacroModel 7.1 program package.<sup>[90]</sup> Monte Carlo simulations were performed, and results suggested that rotaxane ring “acts as a noncovalently bound ‘protecting group’ for the stopper nucleophile.”<sup>[87]</sup> The findings based on the modeling suggested an improved synthetic scheme.

### Peptide Rotaxanes

There have been several descriptions of rotaxanes and molecular shuttles based on dipeptide threads and benzylic amide macrocycles.<sup>[59,91–94]</sup> Asakawa et al.<sup>[95]</sup>

reported hydrogen bond-assembled chiral peptide rotaxanes constructed by threading an achiral benzylic amide macrocycle onto a chiral dipeptide shaft. To elucidate the effect of external stimuli on the magnitude and sign of the chiral optical response for peptide rotaxanes, with the general structure GlyX, where X is a chiral amino acid, they performed modeling of the rotaxane circular dichroism (CD) spectra.<sup>[95]</sup> Optimized geometries for each rotaxane were obtained by taking X-ray crystal structures as starting geometries and optimizing with the MM3<sup>[36–38]</sup> method as implemented in the TINKER<sup>[39–42]</sup> program. MM techniques were used for structural optimization, but CD is a purely electronic structure effect, requiring an explicit electronic structure description of the system. The CD spectra were simulated by using the semiempirical INDO/S<sup>[96,97]</sup> procedure. The simulation reproduced the shape of the experimental curves of CD spectra. The expression of chirality was shown to be a non-linear effect that can be transmitted over long distances.

Asakawa et al.<sup>[95]</sup> made the bold claim that, “. . . the switching ‘on’ and ‘off’ of the expression of chirality in peptide rotaxanes by controlling intercomponent interactions, i.e., through the ‘mechanical bond,’ may be a general phenomenon, not limited to a simple optical response.” This novel insight could be conceivably far-reaching. It might be applicable to other areas where chiral transmission from one molecule to another can be beneficially used, such as for asymmetric synthesis.

### Metal-Containing and Metal-Templated Rotaxanes

Organometallic chemistry is finding use in the production of novel rotaxanes and catenanes.<sup>[98–102]</sup> Whelan et al.<sup>[103]</sup> modeled the adsorption of the prototypical benzylic amide macrocycle on a [2]rotaxane onto a gold surface. Molecular mechanics calculations with charge equilibration were performed. Intramolecular interactions, gold–gold interactions, and gold–adsorbate interactions were taken into account. The MM3 model,<sup>[36–38]</sup> as implemented in the Tinker package,<sup>[39–42]</sup> was used for the molecular mechanics aspect of the calculations. Whelan et al. showed that the initial stages of film growth proceed by chemisorption of the amide functions onto the metal surface with the bonding interaction located in two carbonyl groups. They also found that macrocycle–macrocycle interactions are responsible for the difference in the behavior of two carbonyls with respect to the other two.

Li et al.<sup>[98]</sup> noted three sources of broad interest in the complexes of copper: 1) their roles in the catalytic



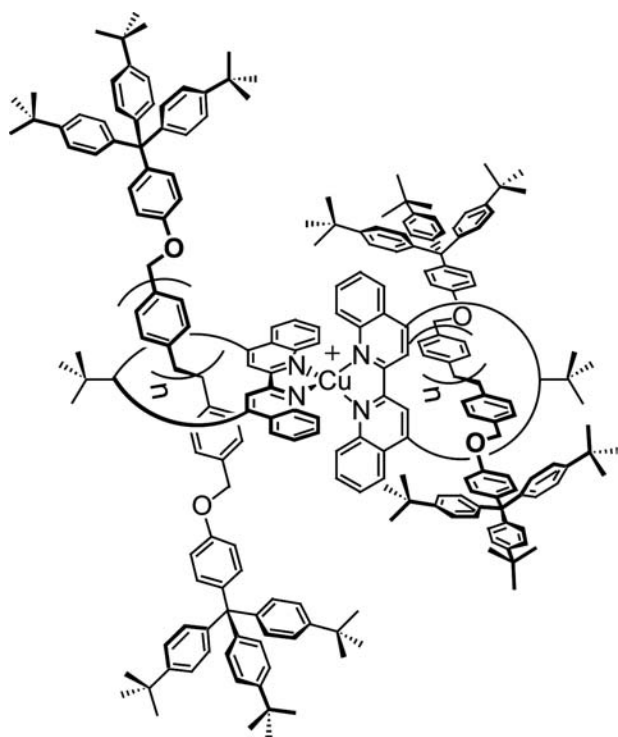


**Fig. 9** Schematic of a dimeric copper-complexed rotaxane. Source: Reprinted from Ref.<sup>[98]</sup>. © 2003, with permission from WILEY-VCH, STM-Copyright & Licenses.

reduction of dioxygen,<sup>[104]</sup> 2) their ability to transfer energy,<sup>[105,106]</sup> and 3) their activity in biological systems.<sup>[107,108]</sup> Li et al. carried out molecular dynamic calculations on three copper-complexed rotaxanes and catenanes,<sup>[98]</sup> one of which is presented in Fig. 9, to identify the lowest energy conformers. The Macro-Model program and the MM2 force field implemented in the CACHE 5.0 program were employed in the calculations. The compounds were predicted to take conformations that are flexible enough to enable the rotation of the four amide groups into an “in” or an “out” conformation, without the occurrence of large energy differences between different conformers. These findings from the molecular modeling studies supported the structural assignments made experimentally.

## CONCLUSION

Despite the very considerable computational challenge, theoretical and computational investigations of switchable rotaxanes are emerging at an accelerating pace. Good success has been reported in modeling structural properties and switching mechanisms. These studies are contributing to a substantially improved understanding of the fundamental nature of these topologically nontrivial molecular complexes. Complementary

application of computational and experimental methods is especially powerful. Inelastic neutron scattering coupled with molecular dynamics simulation is one such synergistic marriage of theory and experiment for the study of switchable rotaxanes. Close on the heels of these successes, examples of theory-accelerated synthesis of molecular shuttles by design are starting to emerge. The development of robust computational approaches to the modeling of such systems will undoubtedly facilitate new research on these systems, and ultimately the design of true molecular and nanodevices.

## ACKNOWLEDGMENT

Our molecular devices research is funded in part by the NSF–NER program, startup funds from Drexel University, and Dupont Corp. in the form of a Dupont Young Professor award to KS.

## REFERENCES

1. Leigh, D.A.; Murphy, A. Molecular tailoring: the made-to-measure properties of rotaxanes. *Chem. Ind.* **1999**, (5), 178–183.
2. Kaifer, A.E. Interplay between molecular recognition and redox chemistry. *Acc. Chem. Res.* **1999**, *32* (1), 62–71.
3. Sauvage, J.P. Transition metal-containing rotaxanes and catenanes in motion: toward molecular machines and motors. *Acc. Chem. Res.* **1998**, *31* (10), 611–619.
4. Balzani, V.; Gomez-Lopez, M.; Stoddart, J.F. Molecular machines. *Acc. Chem. Res.* **1998**, *31* (7), 405–414.
5. Balzani, V.; Credi, A.; Venturi, M. *Supramolecular Science: Where It Is and Where It Is Going*; Kluwer Academic: Dordrecht, 1999.
6. Anelli, P.L.; Spencer, N.; Stoddart, J.F. A molecular shuttle. *J. Am. Chem. Soc.* **1991**, *113* (13), 5131–5133.
7. Bissell, R.A.; Cordova, E.; Kaifer, A.E.; Stoddart, J.F. A chemically and electrochemically switchable molecular shuttle. *Nature* **1994**, *369* (6476), 133–137.
8. Amabilino, D.B.; Stoddart, J.F. Interlocked and intertwined structures and superstructures. *Chem. Rev.* **1995**, *95* (8), 2725–2828.
9. Pease, A.R.; Stoddart, J.F. Computing at the molecular level. *Mol. Mach. Motors* **2001**, *99*, 189–236.
10. Philp, D.; Stoddart, J.F. Self-assembly in natural and unnatural systems. *Angew. Chem., Int. Ed. Engl.* **1996**, *35* (11), 1155–1196.
11. Ashton, P.R.; Ballardini, R.; Balzani, V.; Credi, A.; Dress, K.R.; Ishow, E.; Kleverlaan, C.J.; Kocian, O.; Preece, J.A.; Spencer, N.; Stoddart, J.F.; Venturi, M.; Wenger, S. A photochemically driven molecular-level abacus. *Chem. Eur. J.* **2000**, *6* (19), 3558–3574.
12. Asakawa, M.; Ashton, P.R.; Iqbal, S.; Quick, A.; Stoddart, J.F.; Tinker, N.D.; White, A.J.P.; Williams,

- D.J. Functionalized [2]rotaxanes. *Isr. J. Chem.* **1996**, *36* (4), 329–340.
13. Kanamathareddy, S.; Gutsche, C.D. Synthesis and conformational properties of calix[6]arenes bridged on the lower rim—Self-anchored rotaxanes. *J. Am. Chem. Soc.* **1993**, *115* (15), 6572–6579.
  14. Ashton, P.R.; Bissell, R.A.; Gorski, R.; Philp, D.; Spencer, N.; Stoddart, J.F.; Tolley, M.S. Towards controllable molecular shuttles. 2. *Synlett* **1992**, (11), 919–922.
  15. Ashton, P.R.; Bissell, R.A.; Spencer, N.; Stoddart, J.F.; Tolley, M.S. Towards controllable molecular shuttles. 3. *Synlett* **1992**, (11), 923–926.
  16. Ashton, P.R.; Johnston, M.R.; Stoddart, J.F.; Tolley, M.S.; Wheeler, J.W. The template-directed synthesis of porphyrin-stoppered [2]rotaxanes. *J. Chem. Soc., Chem. Commun.* **1992**, (16), 1128–1131.
  17. Ashton, P.R.; Philp, D.; Spencer, N.; Stoddart, J.F. A new design strategy for the self-assembly of molecular shuttles. *J. Chem. Soc., Chem. Commun.* **1992**, (16), 1124–1128.
  18. Ashton, P.R.; Bissell, R.A.; Spencer, N.; Stoddart, J.F.; Tolley, M.S. Towards controllable molecular shuttles. 1. *Synlett* **1992**, (11), 914–918.
  19. Benniston, A.C.; Harriman, A. A light-induced molecular shuttle based on a [2]rotaxane-derived triad. *Angew. Chem., Int. Ed. Engl.* **1993**, *32* (10), 1459–1461.
  20. Cantrill, S.J.; Rowan, S.J.; Stoddart, J.F. Rotaxane formation under thermodynamic control. *Org. Lett.* **1999**, *1* (9), 1363–1366.
  21. Cao, J.G.; Fyfe, M.C.T.; Stoddart, J.F.; Cousins, G.R.L.; Glink, P.T. Molecular shuttles by the protecting group approach. *J. Org. Chem.* **2000**, *65* (7), 1937–1946.
  22. Glink, P.T.; Oliva, A.I.; Stoddart, J.F.; White, A.J.P.; Williams, D.J. Template-directed synthesis of a [2]rotaxane by the clipping under thermodynamic control of a crown ether like macrocycle around a dialkylammonium ion. *Angew. Chem., Int. Ed.* **2001**, *40* (10), 1870–1875.
  23. MartinezDiaz, M.V.; Spencer, N.; Stoddart, J.F. The self-assembly of a switchable [2]rotaxane. *Angew. Chem., Int. Ed. Engl.* **1997**, *36* (17), 1904–1907.
  24. Pasini, D.; Raymo, F.M.; Stoddart, J.F. Self-assembling catenanes and rotaxanes. *Gazz. Chim. Ital.* **1995**, *125* (9), 431–443.
  25. Ballardini, R.; Balzani, V.; Credi, A.; Gandolfi, M.T.; Venturi, M. Molecular-level artificial machines based on photoinduced electron-transfer processes. *Mol. Mach. Motors/Struct. Bond.* **2001**, *99*, 163–188.
  26. Jimenez, M.C.; Dietrich-Buchecker, C.; Sauvage, J.P. Towards synthetic molecular muscles: contraction and stretching of a linear rotaxane dimer. *Angew. Chem., Int. Ed.* **2000**, *39* (18), 3284–3287.
  27. Fujita, M. Self-assembly of [2]catenanes containing metals in their backbones. *Acc. Chem. Res.* **1999**, *32* (1), 53–61.
  28. Hamilton, D.G.; Montalti, M.; Prodi, L.; Fontani, M.; Zanello, P.; Sanders, J.K.M. Photophysical and electrochemical characterisation of the interactions between components in neutral pi-associated [2]catenanes. *Chem. Eur. J.* **2000**, *6* (4), 608–617.
  29. Balzani, V.; Credi, A.; Raymo, F.M.; Stoddart, J.F. Artificial molecular machines. *Angew. Chem., Int. Ed.* **2000**, *39* (19), 3349–3391.
  30. Ricketts, H.G.; Stoddart, J.F.; Hann, M.M. *Computational Approaches in Supramolecular Chemistry*; Wipff, G., Ed.; Kluwer Academic Publishers: Netherlands, 1994; 377–390.
  31. Pozuelo, J.; Mendicuti, F.; Mattice, W.L. Inclusion complexes of chain molecules with cycloamyloses. 2. Molecular dynamics simulations of polyrotaxanes formed by poly(ethylene glycol) and alpha-cyclodextrins. *Macromolecules* **1997**, *30* (12), 3685–3690.
  32. Sybyl 6.6 from Tripos Associated, I. St. Louis, MO, USA.
  33. Clark, M.; Cramer, R., III; Van Opdenbosch, N. Validation of the general purpose Tripose 5.2 force field. *J. Comput. Chem.* **1989**, *10*, 982–1012.
  34. Pozuelo, J.; Mendicuti, F.; Saiz, E. Conformations and mobility of polyethylene and *trans*-polyacetylene chains confined in alpha-cyclodextrins channels. *Polymer* **2002**, *43* (2), 523–531.
  35. Altieri, A.; Bottari, G.; Dehez, F.; Leigh, D.A.; Wong, J.K.Y.; Zerbetto, F. Remarkable positional discrimination in bistable light- and heat-switchable hydrogen-bonded molecular shuttles. *Angew. Chem., Int. Ed.* **2003**, *42* (20), 2296–2300.
  36. Allinger, N.L.; Yuh, Y.H.; Lii, J.-H. Molecular mechanics. The MM3 force field for hydrocarbons. 1. *J. Am. Chem. Soc.* **1989**, *111* (23), 8551–8565.
  37. Lii, J.H.; Allinger, N.L. Molecular mechanics. The MM3 force field for hydrocarbons. 2. Vibrational frequencies and thermodynamics. *J. Am. Chem. Soc.* **1989**, *111* (23), 8566–8575.
  38. Lii, J.H.; Allinger, N.L. Molecular mechanics. The MM3 force field for hydrocarbons. 3. The van der Waals' potentials and crystal data for aliphatic and aromatic hydrocarbons. *J. Am. Chem. Soc.* **1989**, *111* (23), 8576–8582.
  39. Dudek, M.J.; Ponder, J.W. Accurate modeling of the intramolecular electrostatic energy of proteins. *J. Comput. Chem.* **1995**, *16* (7), 791–816.
  40. Ponder, J.W. *Software Tools for Molecular Design. Version 3.9*. Copyright © 1990–2001. <http://dasher.wustl.edu/tinker/>.
  41. Kundrot, C.E.; Ponder, J.W.; Richards, F.M. Algorithms for calculating excluded volume and its derivatives as a function of molecular-conformation and their use in energy minimization. *J. Comput. Chem.* **1991**, *12* (3), 402–409.
  42. Ponder, J.W.; Richards, F.M. An efficient Newton-like method for molecular mechanics energy minimization of large molecules. *J. Comput. Chem.* **1987**, *8*, 1016–1024.
  43. Horsky, J. Cooperative threading of asymmetric rings onto a linear chain. *Macromol. Theory Simul.* **2000**, *9* (9), 759–771.
  44. Kaminski, G.A.; Jorgensen, W.L. Host-guest chemistry of rotaxanes and catenanes: Application of a polarizable all-atom force field to cyclobis(paraquat-*p*-phenylene) complexes with disubstituted benzenes

- and biphenyls. *J. Chem. Soc., Perkin Trans. 2* **1999**, (11), 2365–2375.
45. Mayer, B.; Klein, C.T.; Topchieva, I.N.; Kohler, G. Selective assembly of cyclodextrins on poly(ethylene oxide)-poly(propylene oxide) block copolymers. *J. Comput.-Aided Mol. Des.* **1999**, *13* (4), 373–383.
  46. Pozuelo, J.; Mendicuti, F.; Mattice, W.L. Inclusion complexes of chain molecules with cycloamyloses—III. Molecular dynamics simulations of polyrotaxanes formed by poly(propyleneglycol) and beta-cyclodextrins. *Polym. J.* **1998**, *30* (6), 479–484.
  47. Amabilino, D.B.; Ashton, P.R.; Balzani, V.; Brown, C.L.; Credi, A.; Frechet, J.M.J.; Leon, J.W.; Raymo, F.M.; Spencer, N.; Stoddart, J.F.; Venturi, M. Self-assembly of [n]rotaxanes bearing dendritic stoppers. *J. Am. Chem. Soc.* **1996**, *118* (48), 12,012–12,020.
  48. Still, W.C.; Tempczyk, A.; Hawley, R.C.; Hendrickson, T. A general treatment of solvation for molecular mechanics. *J. Am. Chem. Soc.* **1990**, *112*, 6127–6129.
  49. Mohamadi, F.; Richards, N.G.J.; Guida, W.C.; Liskamp, R.; Lipton, M.; Caufield, C.; Chang, G.; Hendrickson, T.; Still, W.C. MacroModel—an integrated software system for modeling organic and bioorganic molecules using molecular mechanics. *J. Comput. Chem.* **1990**, *11*, 440–467.
  50. Bottari, G.; Caciuffo, R.; Fanti, M.; Leigh, D.A.; Parker, S.F.; Zerbetto, F. Solid-state fingerprints of molecular threading detected by inelastic neutron scattering. *ChemPhysChem* **2002**, *3* (12), 1038–1041.
  51. Herrmann, W.; Keller, B.; Wenz, G. Kinetics and thermodynamics of the inclusion of ionene-6,10 in alpha-cyclodextrin in an aqueous solution. *Macromolecules* **1997**, *30* (17), 4966–4972.
  52. Meier, L.P.; Heule, M.; Caseri, W.R.; Shelden, R.A.; Suter, U.W.; Wenz, G.; Keller, B. Adsorption of polymeric inclusion compounds on muscovite mica. *Macromolecules* **1996**, *29* (2), 718–723.
  53. Grabuleda, X.; Jaime, C. Molecular shuttles. A computational study (MM and MD) on the translational isomerism in some [2]rotaxanes. *J. Org. Chem.* **1998**, *63* (26), 9635–9643.
  54. Shirts, R.B.; Stolworthy, L.D. Conformational sensitivity of polyether macrocycles to electrostatic potential-partial atomic charges, molecular mechanics, and conformational prediction. *J. Incl. Phenom. Mol. Recognit. Chem.* **1994**, *20* (4), 297–321.
  55. Grabuleda, X.; Ivanov, P.; Jaime, C. Computational studies on pseudorotaxanes by molecular dynamics and free energy perturbation simulations. *J. Org. Chem.* **2003**, *68* (4), 1539–1547.
  56. Case, D.A.; Pearlman, D.A.; Caldwell, J.W.; Cheatham, T.E., III; Ross, W.S.; Simmerling, C.L.; Darden, T.A.; Merz, K.M.; Stanton, R.V.; Cheng, A.L.; Vincent, J.J.; Crowley, M.; Ferguson, D.M.; Radmer, R.J.; Seibel, G.L.; Singh, U.C.; Weiner, P.K.; Kollman, P.A. *AMBER 5*; University of California–San Francisco: San Francisco, 1977.
  57. Cornell, W.D.; Cieplak, P.; Bayly, C.I.; Gould, I.R.; Merz, K.M., Jr.; Ferguson, D.M.; Spellmeyer, D.C.; Fox, T.; Caldwell, J.W.; Kollman, P.A. A second generation force field for the simulation of proteins and nucleic acids. *J. Am. Chem. Soc.* **1995**, *117* (19), 5179–5197.
  58. Grabuleda, X.; Jaime, C.; Kollman, P.A. Molecular dynamics simulation studies of liquid acetonitrile: new six-site model. *J. Comput. Chem.* **2000**, *21* (10), 901–908.
  59. Leigh, D.A.; Troisi, A.; Zerbetto, F. Reducing molecular shuttling to a single dimension. *Angew. Chem., Int. Ed.* **2000**, *39* (2), 350–353.
  60. Merkle, R.C. A proof about molecular bearings. *Nanotechnology* **1993**, *4* (2), 86.
  61. Tuzun, R.E.; Noid, D.W.; Sumpter, B.G. The dynamics of molecular bearings. *Nanotechnology* **1995**, *6* (2), 64.
  62. Tuzun, R.E.; Noid, D.W.; Sumpter, B.G. Dynamics of a laser driven molecular motor. *Nanotechnology* **1995**, *6* (2), 52–63.
  63. Sohlberg, K.; Tuzun, R.E.; Sumpter, B.G.; Noid, D.W. Application of rigid-body dynamics and semiclassical mechanics to molecular bearings. *Nanotechnology* **1997**, *8* (3), 103–111.
  64. Metropolis, N.; Rosenbluth, A.W.; Rosenbluth, M.N.; Teller, A.H.; Teller, E. Equation of state calculation by fast computing machines. *J. Chem. Phys.* **1953**, *21*, 1087–1092.
  65. Kirkpatrick, S.; Gelatt, C.D.; Vecchi, M.P. Optimization by simulated annealing. *Science* **1983**, *220*, 671–680.
  66. Mayer, B. Program Package MultiMize; MultiMize provides a dynamic Monte Carlo framework including various force fields (AMBER4.0, ECEPP/3, GRO-MOS-87, MM3-92), routines to calculate solvation energies based on a continuum approximation, and routines to calculate the induced circular dichroism of host-guest systems as well as of peptides. **1997**.
  67. Fradera, X.; Marquez, M.; Smith, B.D.; Orozco, M.; Luque, F.J. Molecular dynamics study of [2]rotaxanes: Influence of solvation and cation on co-conformation. *J. Org. Chem.* **2003**, *68* (12), 4663–4673.
  68. Srinivasan, J.; Miller, J.; Kollman, P.A.; Case, D.A. Continuum solvent studies of the stability of RNA hairpin loops and helices. *J. Biol. Struct. Dyn.* **1998**, *16*, 671–682.
  69. Curutchet, C.; Orozco, M.; Luque, F.J. Solvation in octanol: parametrization of the continuum MST model. *J. Comput. Chem.* **2001**, *22* (11), 1180–1193.
  70. Luque, F.J.; Zhang, Y.; Alema'n, C.; Bachs, M.; Gao, J.; Orozco, M. Solvent effects in chloroform solution: parametrization of the MST/SCRF continuum model. *J. Phys. Chem.* **1996**, *100* (10), 4269–4276.
  71. Bachs, M.; Luque, F.J.; Orozco, M. Optimization of solute cavities and van-der-Waals parameters in ab-initio MST-SCRF calculations of neutral molecules. *J. Comput. Chem.* **1994**, *15* (4), 446–454.
  72. Sohlberg, K.; Tarbet, B. Computational prediction of trends in the selectivity of macrocyclic receptors for anions. *J. Incl. Phenom.* **1995**, *20*, 203.
  73. Murakami, H.; Kawabuchi, A.; Kotoo, K.; Kunitake, M.; Nakashima, N. A light-driven molecular shuttle based on a rotaxane. *J. Am. Chem. Soc.* **1997**, *119* (32), 7605–7606.

74. Allinger, N.L. Conformational analysis 130. MM2. A hydrocarbon force field utilizing V1 and V2 torsional terms. *J. Am. Chem. Soc.* **1977**, *99* (25), 8127–8134.
75. Dewar, M.J.S.; Zoebisch, E.G.; Healy, E.F.; Stewart, J.J.P. Development and use of quantum mechanical molecular models. 76. AM1: A new general purpose quantum mechanical molecular model. *J. Am. Chem. Soc.* **1985**, *107* (13), 3902–3909.
76. Reuter, C.; Wienand, W.; Schmuck, C.; Vögtle, F. A self-threaded “molecular 8”. *Chem. Eur. J.* **2001**, *7* (8), 1728–1733.
77. Biscarini, F.; Cavallini, M.; Leigh, D.A.; Leon, S.; Teat, S.J.; Wong, J.K.Y.; Zerbetto, F. The effect of mechanical interlocking on crystal packing: predictions and testing. *J. Am. Chem. Soc.* **2002**, *124* (2), 225–233.
78. Frankfort, L.; Sohlberg, K. Semi-empirical study of a pH-switchable [2] rotaxane. *J. Mol. Struct., Theochem.* **2003**, *621* (3), 253–260.
79. Tuzun, R.E.; Sohlberg, K.; Noid, D.W.; Sumpter, B.G. Docking envelopes for the assembly of molecular bearings. *Nanotechnology* **1998**, *9* (1), 37–48.
80. Zheng, X.G.; Sohlberg, K. Modeling of a rotaxane-based molecular device. *J. Phys. Chem., A* **2003**, *107* (8), 1207–1215.
81. Brouwer, A.M.; Frochot, C.; Gatti, F.G.; Leigh, D.A.; Mottier, L.; Paolucci, F.; Roffia, S.; Wurpel, G.W.H. Photoinduction of fast, reversible translational motion in a hydrogen-bonded molecular shuttle. *Science* **2001**, *291* (5511), 2124–2128.
82. Scott, A.P.; Radom, L. Harmonic vibrational frequencies: an evaluation of Hartree–Fock, Moller–Plesset, quadratic configuration interaction, density functional theory, and semiempirical scale factors. *J. Phys. Chem.* **1996**, *100* (41), 16502–16513.
83. Raymo, F.M.; Houk, K.N.; Stoddart, J.F. The mechanism of the slippage approach to rotaxanes. Origin of the “all-or-nothing” substituent effect. *J. Am. Chem. Soc.* **1998**, *120* (36), 9318–9322.
84. Polak, E.; Ribiere, G. Note sur la convergence de méthodes de directions conjuguées. *Rev. Fr. Inf. Rech. Oper.* **1969**, *16-R1*, 35–43.
85. Weiner, S.J.; Kollman, P.A.; Case, D.A.; Singh, U.C.; Ghio, C.; Alagona, G.; Profeta, S.J.; Weiner, P. A new force field for molecular mechanical simulation of nucleic acids and proteins. *J. Am. Chem. Soc.* **1984**, *106* (3), 765–784.
86. Asakawa, M.; Ashton, P.R.; Ballardini, R.; Balzani, V.; Belohradsky, M.; Gandolfi, M.T.; Kocian, O.; Prodi, L.; Raymo, F.M.; Stoddart, J.F.; Venturi, M. The slipping approach to self-assembling [n]rotaxanes. *J. Am. Chem. Soc.* **1997**, *119* (2), 302–310.
87. Schalley, C.A.; Silva, G.; Nising, C.F.; Linnartz, P. Analysis and improvement of an anion-templated rotaxane synthesis. *Helv. Chim. Acta* **2002**, *85* (6), 1578–1596.
88. Weiner, S.J.; Kollman, P.A.; Nguyen, D.T.; Case, D.A. An all atom force field for simulations of proteins and nucleic acids. *J. Comput. Chem.* **1986**, *7* (2), 230.
89. Ferguson, D.M.; Kollman, P.A. Can the Lennard–Jones 6–12 function replace the 10–12 form in molecular mechanics calculations? *J. Comput. Chem.* **1991**, *12* (5), 620–626.
90. McDonald, D.Q.; Still, W.C. AMBER\* torsional parameters for the peptide backbone. *Tetrahedron Lett.* **1992**, *33*, 7743
91. Wurpel, G.W.H.; Brouwer, A.M.; van Stokkum, I.H.M.; Farran, A.; Leigh, D.A. Enhanced hydrogen bonding induced by optical excitation: unexpected subnanosecond photoinduced dynamics in a peptide-based [2]rotaxane. *J. Am. Chem. Soc.* **2001**, *123* (45), 11,327–11,328.
92. Clegg, W.; Gimenez-Saiz, C.; Leigh, D.A.; Murphy, A.; Slawin, A.M.Z.; Teat, S.J. “Smart” rotaxanes: shape memory and control in tertiary amide peptido[2] rotaxanes. *J. Am. Chem. Soc.* **1999**, *121* (17), 4124–4129.
93. Lane, A.S.; Leigh, D.A.; Murphy, A. Peptide-based molecular shuttles. *J. Am. Chem. Soc.* **1997**, *119* (45), 11,092–11,093.
94. Leigh, D.A.; Murphy, A.; Smart, J.P.; Slawin, A.M.Z. Glycylglycine rotaxanes—the hydrogen bond directed assembly of synthetic peptide rotaxanes. *Angew. Chem., Int. Ed. Engl.* **1997**, *36* (7), 728–732.
95. Asakawa, M.; Brancato, G.; Fanti, M.; Leigh, D.A.; Shimizu, T.; Slawin, A.M.Z.; Wong, J.K.Y.; Zerbetto, F.; Zhang, S.W. Switching “on” and “off” the expression of chirality in peptide rotaxanes. *J. Am. Chem. Soc.* **2002**, *124* (12), 2939–2950.
96. Del Bene, J.; Jaffe, H.H. Use of the CNDO method in spectroscopy: I. Benzene, pyridine, and the diazines. *J. Chem. Phys.* **1968**, *48*, 1807–1813.
97. Mataga, N.Z.; Nishimoto, K. Electronic structure and spectra of nitrogen heterocycles. *Z. Phys. Chem.* **1957**, *13*, 140–157.
98. Li, X.Y.; Illigen, J.; Nieger, M.; Michel, S.; Schalley, C.A. Tetra- and octalactam macrocycles and catenanes with exocyclic metal coordination sites: versatile building blocks for supramolecular chemistry. *Chem. Eur. J.* **2003**, *9* (6), 1332–1347.
99. Raehm, L.; Kern, J.M.; Sauvage, J.P.; Hamann, C.; Palacin, S.; Bourgoin, J.P. Disulfide- and thiol-incorporating copper catenanes: synthesis deposition onto gold, and surface studies. *Chem. Eur. J.* **2002**, *8* (9), 2153–2162.
100. Ashton, P.R.; Balzani, V.; Clemente-Leon, M.; Colonna, B.; Credi, A.; Jayaraman, N.; Raymo, F.M.; Stoddart, J.F.; Venturi, M. Ferrocene-containing carbohydrate dendrimers. *Chem. Eur. J.* **2002**, *8* (3), 673–684.
101. McArdle, C.P.; Irwin, M.J.; Jennings, M.C.; Vittal, J.J.; Puddephatt, R.J. Self-assembly of gold(I) rings and reversible formation of organometallic [2]catenanes. *Chem. Eur. J.* **2002**, *8* (3), 723–734.
102. Padilla-Tosta, M.E.; Fox, O.D.; Drew, M.G.B.; Beer, P.D. Self-assembly of a mixed-valence copper(II)/copper(III) dithiocarbamate catenane. *Angew. Chem., Int. Ed.* **2001**, *40* (22), 4235–4239.

103. Whelan, C.M.; Cecchet, F.; Francesca, C.M.; Cecchet, F.; Baxter, R.; Zerbetto, F.; Clarkson, G.J.; Leigh, D.A.; Rudolf, P. Adsorption of a benzylic amide macrocycle on a solid substrate: XPS and HREELS characterization of thin films grown on Au(111). *J. Phys. Chem., B* **2002**, *106* (34), 8739–8746.
104. Lei, Y.B.; Anson, F.C. Dynamics of the coordination equilibria in solutions containing copper(II), copper(I), and 2,9-dimethyl-1,10-phenanthroline and their effect on the reduction of O<sub>2</sub> by Cu(I). *Inorg. Chem.* **1995**, *34* (5), 1083–1089.
105. Ruthkosky, M.; Castellano, F.N.; Meyer, G.J. Photo-driven electron and energy transfer from copper phenanthroline excited states. *Inorg. Chem.* **1996**, *35* (22), 6406–6412.
106. Castellano, F.N.; Ruthkosky, M.; Meyer, G.J. Photo-driven energy-transfer from cuprous phenanthroline derivatives. *Inorg. Chem.* **1995**, *34* (1), 3–4.
107. Meijler, M.M.; Zelenko, O.; Sigman, D.S. Chemical mechanism of DNA scission by (1,10-phenanthroline) copper. Carbonyl oxygen of 5-methylenefuranone is derived from water. *J. Am. Chem. Soc.* **1997**, *119* (5), 1135–1136.
108. Sigman, D.S.; Bruice, T.W.; Mazumder, A.; Sutton, C.L. Targeted chemical nucleases. *Acc. Chem. Res.* **1993**, *26* (3), 98–104.

# Conducting Polymer Nanopatterns

**Shaun F. Filocamo**

*Department of Chemistry, Duke University, Durham, North Carolina, U.S.A.*

**Mark W. Grinstaff**

*Departments of Chemistry and Biomedical Engineering, Boston University, Boston, Massachusetts, U.S.A.*

## INTRODUCTION

Nanotechnology is an emerging field that studies fundamental nanoscale processes and the exploitation of those processes in the development and function of nanodevices.<sup>[1]</sup> To date, development has been hampered by the need for materials and processes that can perform reproducibly at the nanometer scale. Although at present nanodevice development is dominated by materials made from SiO<sub>2</sub> or metals, these materials can suffer from a lack of processability.<sup>[2]</sup> As an alternative that has met with some success, organic-based materials can be easily processed by a variety of methods including spin coating, evaporation, and printing.<sup>[3]</sup> Organic and organic/inorganic hybrid materials have been developed for organic light-emitting diodes (OLEDs), field-effect transistors, and other devices.<sup>[4–6]</sup> However, organic devices usually suffer from a short lifetime as a consequence of poor mechanical and thermal stability associated with small organic molecules.<sup>[5]</sup> Although organic/inorganic hybrid materials have better mechanical and thermal stability,<sup>[7–9]</sup> there still exists an inherent lack of component compatibility, leading to difficulties in processing, and intercomponent communication.<sup>[9]</sup>

A promising class of materials for nanodevice application is conducting polymers (Fig. 1). Their thermal and environmental stability facilitates use in devices for photochemical and electrochemical applications,<sup>[10–12]</sup> and their physical and chemical properties can be easily tailored for specific functions.<sup>[13,14]</sup> When conducting polymers were first introduced, their poor solubility in common processing solvents limited their versatility.<sup>[11]</sup> However, this issue has been addressed through modifying the backbone of the polymer with side chains, such as alkyl and alkoxy groups. With this approach, processing of these materials in either aqueous or organic media has expanded the utility of conducting polymers in OLEDs, electrochromic displays, and coatings for more sensitive materials.<sup>[6,15–17]</sup> Numerous articles are found in the literature reporting

devices in the micrometer regime made with conducting polymers.<sup>[2,3,18–21]</sup>

Although Moore's law predicts a doubling in the number of transistors per chip approximately every 18 months,<sup>[22]</sup> the limits of traditional patterning techniques are threatening to hinder this advancement. The feature size required to continue this trend is in the <100 nm regime, where control over feature size is critical and difficult to achieve. New procedures and variations on current methods need to be developed to break this regime barrier. In this article, we will review current approaches to creating conducting polymer nanopatterns, from "template synthesis" to lithography. We discuss the advantages and disadvantages of each method and highlight the unique nanostructures formed with these techniques. These materials are likely to enhance the emerging field of nanoelectronics, while complementing current technology.

## TEMPLATE SYNTHESIS

The first reported patterning of conducting polymer nanostructures used template synthesis, a method developed by Penner and Martin<sup>[23]</sup> in the mid-1980s. They reported the electrochemical polymerization of pyrrole in the pores of a polycarbonate membrane. Template synthesis, as the name implies, utilizes the microporous or nanoporous structure of materials as a template for the electrochemical or oxidative synthesis of conducting polymer nanotubules and nanofibrils.<sup>[24]</sup> This technique can also be used to form nanotubes and nanofibrils of metals, carbon, and semiconductors.<sup>[24,25]</sup>

### Template Materials

The most common template materials used are "track-etch" membranes and alumina membranes.<sup>[26]</sup> Track-etch membranes are formed by bombarding a



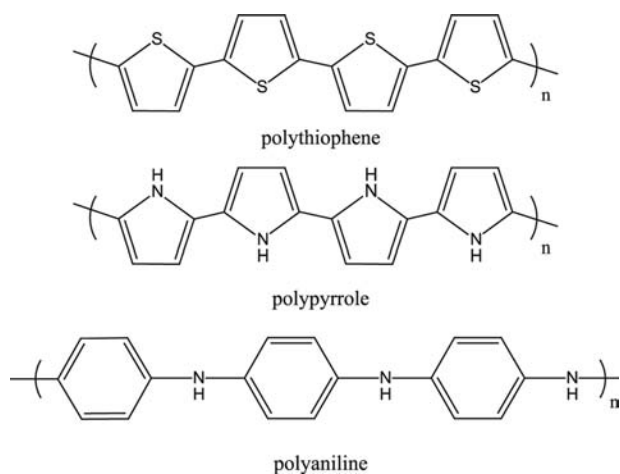


**Fig. 1** Examples of conducting polymers.

nonporous membrane with nuclear fission fragments.<sup>[27]</sup> These membranes are typically polycarbonate or polyester. The tracks that are formed are subsequently chemically etched to produce pores in the material. The size of the uniform pores can be as small as 10 nm in diameter with pore densities as high as  $10^9$  pores/cm<sup>2</sup>.<sup>[26]</sup> The bombardment occurs randomly, which, at small pore diameters and high pore densities, can cause intersections of the pores.<sup>[26]</sup> If these intersections are not desired, alumina or other membranes can be used because the processes used to form these membranes are more controlled.

Porous alumina membranes are formed from the anodization of Al metal in acidic solution. The uniform pores are cylindrical, with pore densities as high as  $10^{11}$  pores/cm<sup>2</sup> and a size range from >100 down to <5 nm.<sup>[26]</sup> Because of the nature of pore formation in the alumina membranes, interconnects do not develop between pores,<sup>[25]</sup> affording a template material that can form isolated nanostructures. Membranes, including SiO<sub>2</sub>, zeolites, and other nanoporous solids, have also been used as template materials, although to a lesser extent.<sup>[25]</sup>

### Mechanism for Template Synthesis

The polymerization mechanism for conducting polymers using template synthesis is either electrochemical or oxidative. The most common electrochemical method is to plate one surface of the membrane with a conducting metal thin film and use this film as the anode in an electroplating process.<sup>[28]</sup> The polymer first nucleates on the walls of the pore, and subsequent deposition yields a well-ordered polymer outer layer that becomes more disordered as the tubule wall thickens.<sup>[29]</sup> In the oxidative method, the template is immersed in a solution containing monomer and a polymerization reagent, such as an aqueous iron(III) salt.<sup>[30,31]</sup> The deposition occurs in a manner similar to the electrochemical method, resulting in a similar polymer-order gradient for the nanostructures (Fig. 2).

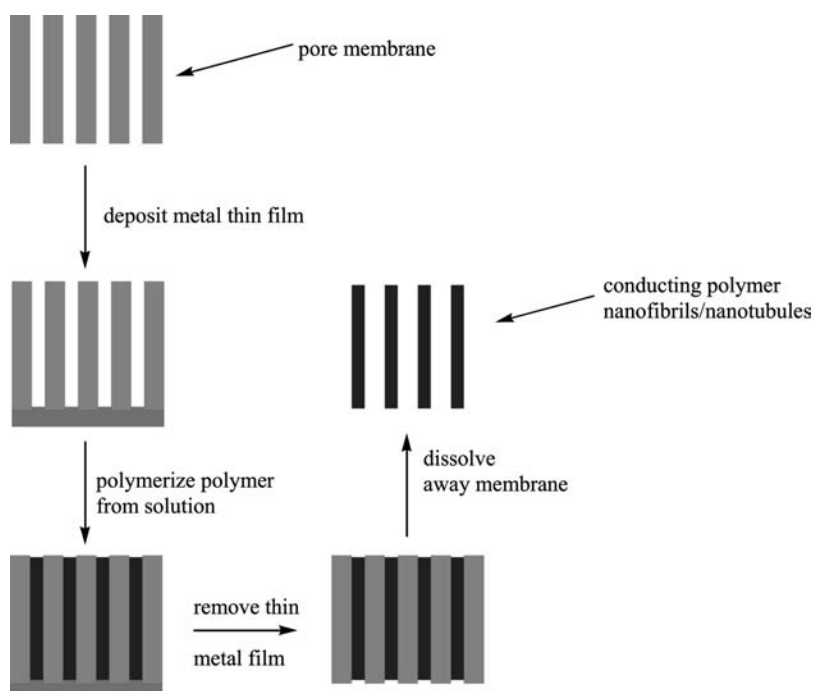


**Fig. 2** Schematic of template synthesis.

### Physical Properties of Conducting Polymer Nanotubules/Nanofibrils

Early studies of polypyrrole chain order in nanofibrils (closed tubules) used polarized infrared absorption spectroscopy (PIRAS) to examine a range of fibril diameters from 30 to 600 nm. In addition, X-ray diffraction was used to observe 30 and 400 nm fibrils.<sup>[32]</sup> In the X-ray diffraction studies, 400-nm fibrils showed diffractograms similar to amorphous conducting polymer, while the 30-nm fibrils exhibited diffractograms similar to stretched polymer, suggesting an alignment of the polymer chains in these small-diameter fibrils.<sup>[32]</sup>

The PIRAS experiment supported the X-ray diffraction evidence that polymer chain alignment in a fibril increases as the diameter decreases. In a typical PIRAS experiment, the absorbance is measured for light polarized parallel and perpendicular to the major axis of a material (Fig. 3). In the case of a polymer fibril, if the polymer chain alignment is completely random, then the absorbance of light parallel to the pore axis will be the same as the absorbance of light perpendicular to the pore axis and will give a dichroic ratio (ratio of absorbances parallel and perpendicular to the pore axis) of 1. Smaller fibrils had dichroic ratios significantly different from 1, with the fibrils preferentially absorbing one polarization over another.<sup>[32]</sup> Amorphous polymer and large-diameter fibrils do not absorb polarized light preferentially, giving dichroic values very close to 1.<sup>[32,33]</sup>

Polarized infrared absorption spectroscopy experiments were also performed on polycarbonate membranes; the polycarbonate was also found to be stretch-oriented.<sup>[32]</sup> Studies have shown that conducting polymers can be induced to align with the orientation of the substrate.<sup>[34–36]</sup> This orientation is lost as the thickness of the deposited polymer film grows. Similarly, the outer walls of conducting polymer

tubules and fibrils deposited in stretch-oriented polycarbonate membranes align with the axis of the membrane, but this alignment is slowly lost as polymerization continues and the walls thicken. Wall thickness is controlled by the polymerization time.<sup>[25]</sup>

The thickness of the polymer walls is also correlated with the conductivity of the tubule. While thick-walled nanotubules had conductivities similar to bulk material, the narrow-walled nanotubules had significantly higher values.<sup>[35]</sup> One explanation for this phenomenon is that the alignment in the polymer chains increases the conjugation length of the polymer, enhancing the electronic properties of the material. As the walls thicken, the overall randomness of the structure increases, decreasing the conjugation length and hence the conductivity.<sup>[35]</sup> This method provides a means to control the conductivity of the material through polymerization time. It has been postulated that the walls in a polycarbonate membrane nucleate the ordered polymer in two ways: 1) as the polymerization commences, the polycationic oligomers forming are not as soluble as the monomer units and 2) there is a coulombic attraction between the anionic walls of the membrane and the forming cationic polymer.<sup>[26]</sup>

Recently, this “greater ordering” claim has been disputed. Most of the above studies of polypyrrole nanotubules were performed with a polycarbonate membrane; Mativetsky and Datar<sup>[37]</sup> used an alumina membrane to form nanotubules of polypyrrole oxidatively and found the tubules to have a highly irregular morphology. Indeed, PIRAS studies with alumina membranes have shown no preferential polarized absorption (dichroic ratios near 1).<sup>[37]</sup> Because there are no charged sites in an alumina membrane, the nucleation occurs more randomly in the alumina pores. Polypyrrole then grows radially outward from each nucleation site until it encounters an obstacle: that of the pore wall or another “polypyrrole mass,” disrupting

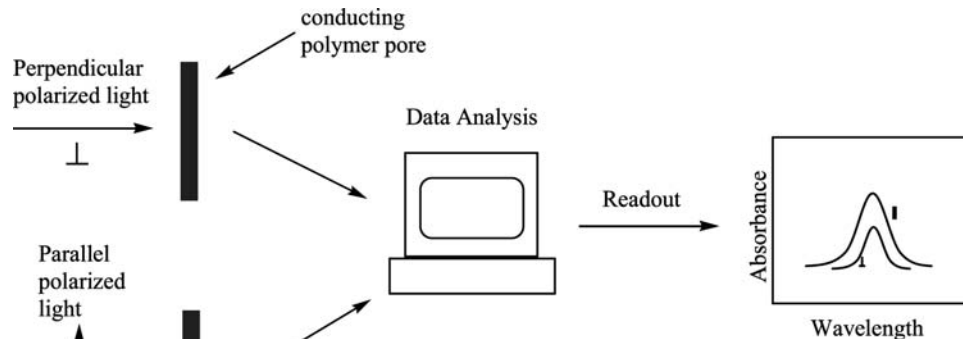


Fig. 3 Schematic of a typical PIRAS experiment.

order. Although Mativetsky and Datars<sup>[37]</sup> were not able to measure conductivity directly, their measurements suggest that the conductivity of these random fibrils is comparable to the fibrils of similar size formed from a polycarbonate membrane. They therefore concluded that the enhanced conductivity of these nanotubules is not a result of increased order imposed by the polycarbonate walls.

### Applications of Template Synthesis

Conducting polymer nanofibrils and nanotubules have a wide variety of potential applications. They are highly permeable, and studies have shown that they can be highly selective for certain gas mixtures; the high-density conducting polymer fibrils could be used as a gas permeation membrane.<sup>[38]</sup> Conducting polymer nanotubules are also well suited for encapsulated sensors because the polymerization process can be stopped at any time, thus controlling the size of the cavity. Researchers have encapsulated a variety of enzymes and chemical species in thin-walled tubules and have found that their activity is greater than that of enzymes trapped in a thin polymer film.<sup>[30,39,40]</sup> These reactions could be carried out in aqueous or organic solvents because the conducting polymer “microreactor” is isolated from the environmental surroundings by the walls of the conducting polymer, utilizing the relative insolubility of the polymer in common solvents.<sup>[30]</sup> The surface area for enzyme/substrate interaction can be adjusted by changing the porosity of the membrane, producing a microreactor with a high loading capability.<sup>[30]</sup>

With the enhanced conductive properties of these materials, numerous groups have reported using nanotubules to form a variety of novel systems. For example, Granstrom, Berggren, and Inganas<sup>[41]</sup> polymerized 3,4-ethylene-dioxythiophene (EDOT) in polycarbonate membranes with pore sizes of 10 nm and 100 nm for the preparation of a hole-injection contact in a polymeric light-emitting diode (PLED). An electroluminescent layer was spin-coated on the surface of the membrane, followed by an Al/Ca layer for the electron-injecting contact. Although the PLED tested had a very low efficiency, with optimization, the authors believed that increased efficiencies up to 1–10% could be obtained.<sup>[41]</sup> The advantage of this technique is in the sheer quantity of nano-LEDs that can be formed at one time.

In other applications, polyaniline tubules have been studied for use as microscale/nanoscale transistors and for field emission because of their excellent switching properties and mechanical stability (Fig. 4).<sup>[42,43]</sup> Polymer composites have been made to blend physical properties, and many have been found to enhance

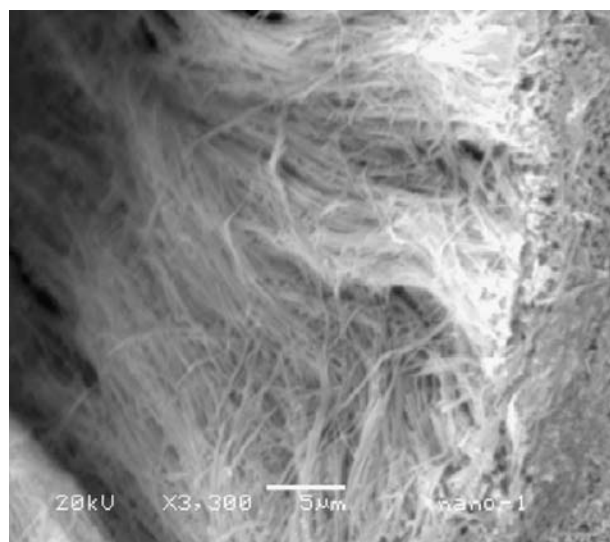


**Fig. 4** Scanning electron microscope image of polyaniline nanofibrils formed from a porous alumina membrane using template synthesis. *Source:* From Ref.<sup>[42]</sup>. © (2001), with permission from Elsevier Science.

desirable characteristics, such as conductivity and “rectification effect.”<sup>[31,44–46]</sup>

### Inverse Opal Formation

A variation of template synthesis is to use microspheres and nanospheres of polymers as templates for the formation of macroporous 2-D and 3-D polymer structures, called inverse opals. A typical experiment involves assembling a template of colloidal microspheres or nanospheres on a conductive metal electrode surface by slow evaporation from a weight percent solution of colloidal particles on an electrode surface. The particles of materials such as poly(styrene) or silica will assemble themselves as the solvent evaporates. Once the structure is dry and mechanically immobilized, it is immersed in a solution containing the desired monomer units. Electropolymerization of the conducting polymer has been favored in the literature over the oxidative method, with many groups citing a greater control over the polymer growth rate and deposition than with the oxidative method (Fig. 5).<sup>[47,48]</sup> The templates are then etched (silica) or dissolved away (colloidal polymer), leaving conducting polymer patterned into a “honeycomb” structure.

This technique has been used to create nanostructures of polypyrrole,<sup>[47–49]</sup> polyaniline,<sup>[49–51]</sup> polythiophene,<sup>[47,49]</sup> and poly(phenylenevinylene) (PPV).<sup>[52]</sup> Nanostructure sizes as low as 50 nm have been reported with polypyrrole,<sup>[48]</sup> where it was found that the pore size can be controlled by the amount and time of applied voltage and by the size of the colloidal

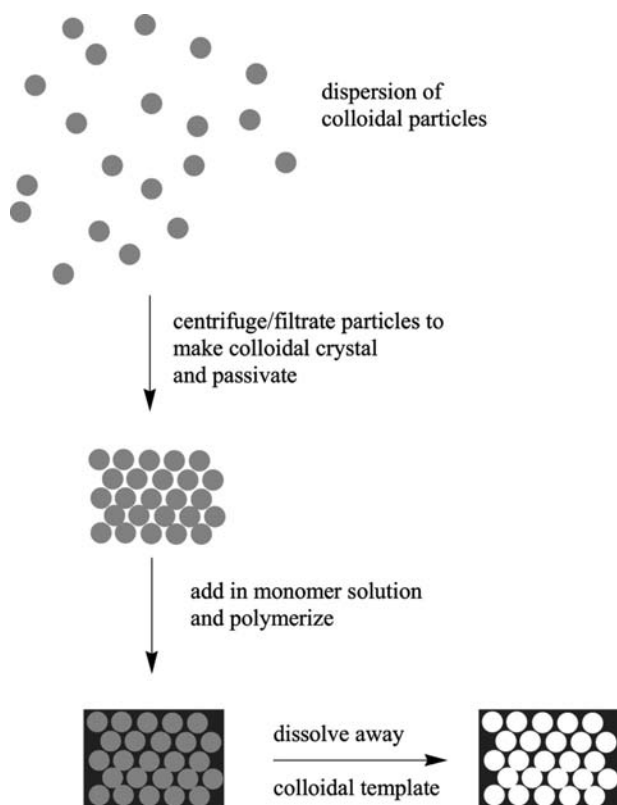


Fig. 5 Schematic of “inverse opal” synthesis.

particle utilized. Han et al.<sup>[50]</sup> used polystyrene nanospheres that were coated with increasing layers of a polyelectrolyte (PE) to see what effect the size of the nanoparticle would have on the resulting conducting polymer film (Fig. 6). The pore size actually decreased upon increasing the number of PE layers, leveling off after 4 PE layers, and the structure shrank less upon extraction of the template, improving mechanical stability.<sup>[50]</sup>

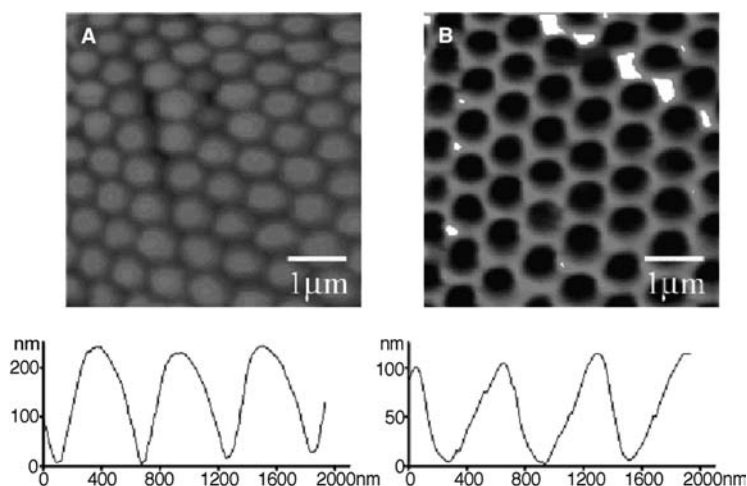


Fig. 6 A) Assembly of PS particles with 2 PE layers on a Au surface. B) Polyaniline honeycomb nanostructure formed in the interstitial voids of the particles. Source: From Ref.<sup>[50]</sup>. © (2002) American Chemical Society.

The tunability of these systems has attracted interest in the field of photonic bandgap crystals.<sup>[47,51,52]</sup> They have been shown to exhibit the property of reflecting certain wavelengths of light, spanning the visible and near-infrared (NIR) regions of the spectrum. The conductivities of these 2-D and 3-D structures are similar to those of bulk conducting polymer.<sup>[49]</sup>

## LITHOGRAPHY AND MASK TECHNIQUES

Lithography is the process of writing a free-form or replicated pattern on a surface by electrical (applied voltage), photochemical (UV, X-ray beam), or physical (diamond etching) means. Lithography has been very successful at creating structures at the micrometer scale, but there are significant challenges and obstacles to forming structures of <100 nm in dimension. Ultimately, the lithography techniques developed must be reliable, accurate, and efficient. Development over the past 10 years has dealt with these issues, and the next few sections describe these advances. As nanolithography is still a relatively young field, many of the techniques described below are unoptimized.

## Solvent-Assisted Micromolding

Solvent-assisted micromolding (SAMIM) is a “soft lithography” technique that provides a simple, fast way to form patterns on a surface. The mold is made out of an elastomeric material [usually poly(dimethylsiloxane) (PDMS)]; it is coated by wetting the mold itself with a thin layer of a solvent appropriate for the polymer or precursor substrate. The mold is then brought into contact with the substrate, and the solvent dissolves (or swells) the substrate, allowing the substrate to flow into the recesses of the mold.

As the solvent evaporates, the polymer hardens, but maintains the shape of the mold (Fig. 7).<sup>[53]</sup> Kim et al.<sup>[54]</sup> first utilized this method to form features down to 50 nm in height and 60 nm in width on polymeric photoresists. Solvent-assisted micromolding was used to create polymeric light-emitting diodes (PLEDs) using a precursor to poly(phenylenevinylene) (PPV) and methanol as a solvent.<sup>[55]</sup> Although the features formed were larger than 100 nm, the potential of this technique to form very small devices of interest has been demonstrated.

### Micromolding in Capillaries

Micromolding in capillaries (MIMIC) is a technique related to SAMIM. A prepatterned stamp made out of an elastomer such as PDMS is placed on a clean, flat substrate and a drop of solution of the desired patterning material is placed at the edge of the stamp. Through capillary action, the drop migrates into the grooves of the stamp. As the solution dries, the material is patterned on the substrate, and the stamp is subsequently removed.<sup>[53]</sup> This technique has been used to form nanowire and nanodot patterns of poly-(3,4-ethylenedioxythiophene) (PEDOT) doped with poly(4-styrenesulfonate) (PEDOT-PSS).<sup>[56]</sup> By varying the size of the capillary channel and the solution concentration, nanowires of 6 nm in height and nanodots of 10 nm in height were formed on the substrate.<sup>[56]</sup>

### Scanning Tunneling Microscopy Lithography

Scanning Tunneling Microscopy (STM) and related techniques have been used for surface modification for about 15 years. The first example of conducting polymer deposition was reported by Wu, Fan, and Bard<sup>[57]</sup> using a scanning electrochemical microscope (SECM), “which maintains a constant faradaic current between a tip electrode and a metal surface electrode.” In this procedure, Nafion<sup>®</sup> film was first deposited on the Pt surface and immersed in an anilinium sulfate solution to saturate the film. In this system, the platinum is the surface electrode and tungsten is used as the tip electrode. A positive potential was applied to the Pt surface to oxidize the aniline at the Pt / Nafion interface, and deposition of the resulting polymer was localized around the tip electrode (Fig. 8). The features formed were larger than 100 nm, which was attributed to tip size, thickness of the Nafion film, and electric field distribution. Control over these parameters was predicted to give smaller features.<sup>[57]</sup> Borgwarth et al.<sup>[58]</sup> utilized SECM to form polythiophene by oxidizing bromide to bromine, which locally diffused to the conductive substrate and oxidatively polymerized the thiophene monomer.

Using a gold electrode, Yang, Evans, and Hendrickson<sup>[59]</sup> reported the formation of polypyrrole nanostructures from a tetrafluoroborate/pyrrole solution. The Pt/Ir STM tip was coated with Apiezon<sup>®</sup> to insulate most of the tip, helping to control the size

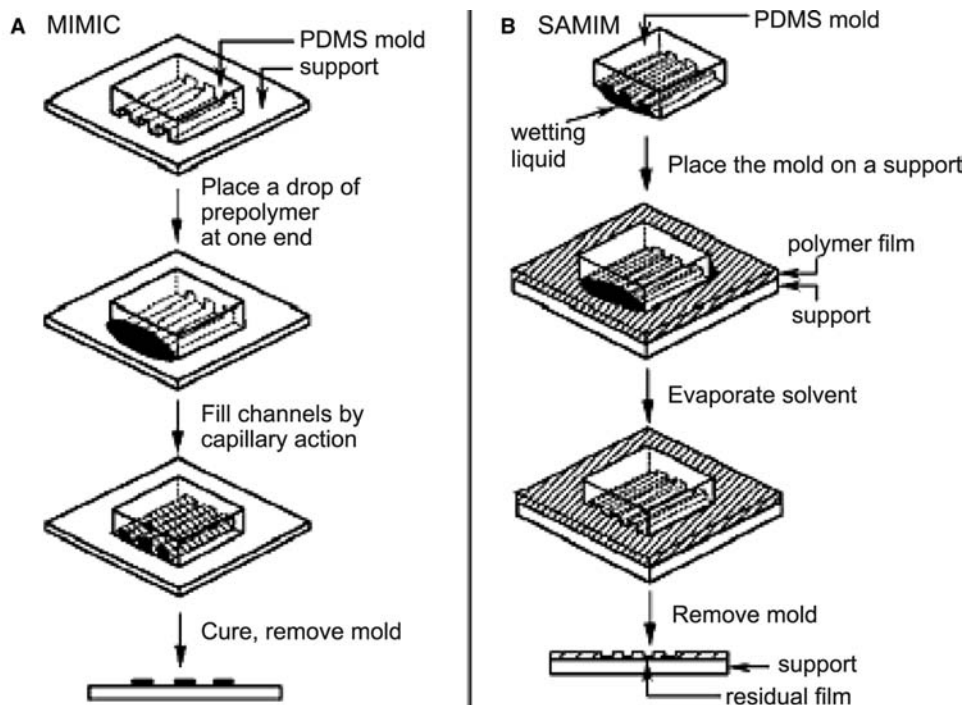


Fig. 7 A) Schematic of MIMIC. B) Schematic of SAMIM. Source: From Ref.<sup>[53]</sup> by Annual Reviews.

of the nanofeature deposited on the surface. Polymer dots were deposited on the surface, and then the ability to remove the polymer dots was demonstrated by “blasting” the polymer dot from the surface with higher voltage.<sup>[59]</sup> This technique was used to “write” the word *science* using dots of 5–10 nm in diameter (Fig. 9). The variation in diameter was attributed to thermal evaporation and consequent concentration of monomer solution during operation, and to the local variation of surface roughness, affecting the movement of the tip as it maintains a constant distance above the surface.<sup>[59]</sup> A polymer line with a width of 10 nm and a circle with a diameter of 6 nm were formed by controlling the translation of the tip on the surface using a simple computer program.<sup>[59]</sup>

Highly oriented pyrolytic graphite (HOPG) has also been used as the conductive surface for forming conducting polymer nanostructures with an STM tip. Yaniv and McCormick<sup>[60]</sup> reported nanofeatures as small as 50 nm in diameter and 4 nm in height, formed from a 0.1 M KCl/0.1 M pyrrole solution. They found that no deposition occurred with potentials below 7.5 V, and control of the features could only be achieved with pulses below 100 nsec. Above this pulse duration, deposition became scattered over the scanned area.<sup>[60]</sup> Nyffenegger and Penner<sup>[61]</sup> studied qualitatively the mechanism of nanostructure formation using a similar setup. They concluded that the bias pulse forms defects in the basal plane of the HOPG within a few microseconds, and then aniline monomer diffuses to the edge of the defect and is oxidized.

As this process proceeds, the cationic aniline oligomers become insoluble and nucleate in the defect.<sup>[61]</sup>

### Atomic Force Microscope Lithography

The first example of atomic force microscopy (AFM) being used for patterning conducting polymer nanostructures was reported by Cai et al.<sup>[62]</sup> The electrochemical polymerization of pyrrole and aniline on an HOPG substrate was locally altered using an AFM tip. Depending on when the AFM scanning was activated, the amount of polymer could be decreased or enhanced in the scanning area. When the AFM tip is scanned over the surface before the application of a potential, any oligomers that are formed once the potential is applied are “swept” to the edges of the scanning area. Indeed, there is an enhancement in the amount of polymer at the edges of the scanning area. When the AFM tip is scanned after polymerization has commenced, the vertical force exerted on the developing polymer both creates a denser film and forces oligomers downward toward the polymer, increasing the local concentration of oligomers and thus the rate of polymerization.<sup>[62]</sup>

Dip-pen nanolithography (DPN) was developed by Piner et al.<sup>[63]</sup> and, as the name suggests, it uses the AFM tip as a pen, dipped in the desired patterning material. The AFM tip is then brought in close proximity to the surface. A water meniscus forms, which facilitates transport of the material from the

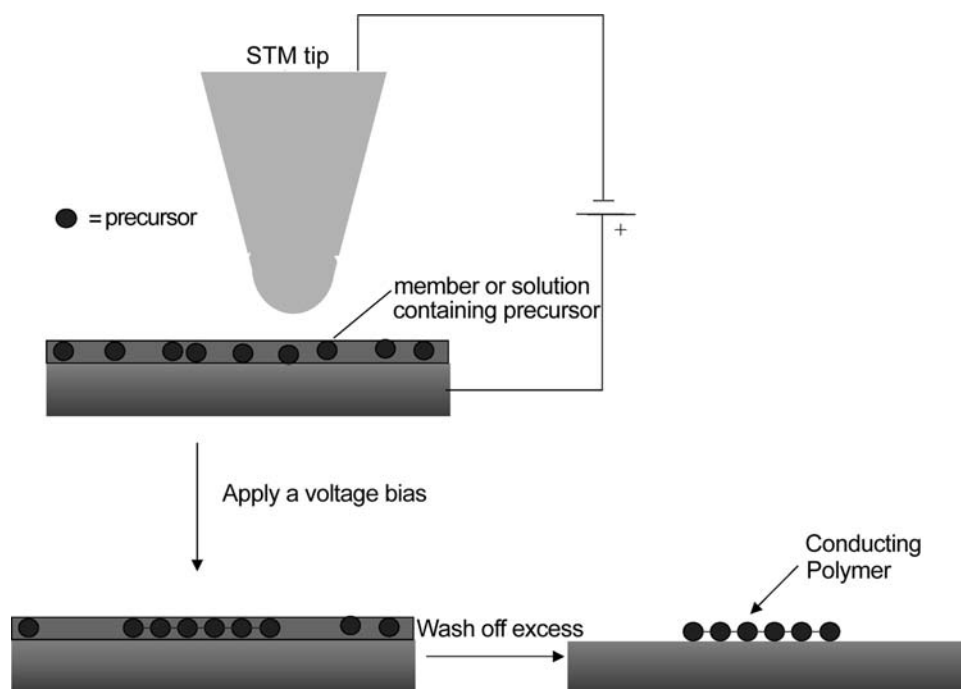


Fig. 8 Schematic of a typical STM lithography experiment.





**Fig. 9** The word “science” formed using STM nanolithography. Source: From Ref.<sup>[59]</sup>. © (1995) American Chemical Society.

tip to the surface. This method has been utilized to pattern a variety of materials to the surface such as DNA and thiols.<sup>[63–65]</sup> The Noy group utilized this method to deposit poly[2-methoxy-5-2'-ethylhexyloxy-1,4-phenylenevinylene] (MEH-PPV) on a glass surface.<sup>[66]</sup> The method was coupled with scanning confocal microscopy to obtain luminescent images of the deposited polymer nanostructures. Although the deposition was successful, more studies are needed to determine the extent of nanowire alignment and continuity.<sup>[66]</sup>

A technique that combines aspects from previous STM tip techniques is electrochemical dip-pen nanolithography (E-DPN), which has been used to deposit metal and conducting polymer nanostructures on a surface.<sup>[67,68]</sup> The tapping mode AFM tip is dipped in the desired monomer or metal salt solution, and as the tip engages the surface in a preprogrammed pattern, a potential is applied between the tip and the surface. This potential reduces the metal salt or electrochemically polymerizes the monomer and deposits the resulting nanostructure on the surface through the meniscus (Fig. 10).<sup>[67,68]</sup> In this way, polymers of 3,4-ethylenedioxythiophene,<sup>[68]</sup> pyrrole, and aniline<sup>[69]</sup> have been formed and deposited on a Si(111) surface with feature sizes as small as 30 nm in width and up to 5 nm in height.

The size of the nanostructures formed depends on a variety of factors, including humidity, speed of translation, and applied voltage, and it has been found that these factors are monomer-dependent. For example, it is easier to draw lines of polyaniline at lower humidity, while other polymers were less affected by the humidity. Aniline has a measurable solubility in water at 25°C (1 g in 28.6-mL water), and upon formation of the water meniscus, capillary action could disperse the aniline before a voltage is applied.

The height of the line can be controlled by the speed of translation of the tip as it deposits.<sup>[68]</sup> Two lines of poly(ethylenedioxythiophene) (PEDOT) were drawn at 10 and 1 nm/sec, and the line drawn at 1 nm/sec was significantly higher than the line drawn at 10 nm/sec (Fig. 11). Applied voltage along with

humidity controls the width of the line. A larger water meniscus covers a larger surface area, leading to a larger area of deposition.

The voltage applied depends, in part, on the potential of the monomer being used and on the native oxide layer that exists on the Si wafer. As the thickness of the oxide layer increases, so does the necessity of higher voltages for polymerization and deposition. Bias voltages ranged from  $-7$  to  $-15$  V. At such a high bias voltage, it is important to ensure that polymer, and not  $\text{SiO}_2$ , is being deposited.

After depositing PEDOT, an oxide layer was formed next to the polymer, and etching studies were performed. Upon exposure to HF, the  $\text{SiO}_2$  was etched from the surface, but the PEDOT line remained. Conversely, when exposed to a strongly oxidizing solution of 1:2  $\text{H}_2\text{O}_2$ : $\text{H}_2\text{SO}_4$ , the PEDOT line was removed while the  $\text{SiO}_2$  remained. Similar etching studies were performed with polyaniline and polypyrrole, and the results were consistent with the PEDOT studies. Interconnects also have been formed with a single polymer and with two different polymers using this technique. The ability to pattern these nanostructures precisely will be important toward the development of nanodevices.

## Masks

Seo, Pyo, and Cho<sup>[70]</sup> reported a mask method for the formation of polypyrrole micropatterns and nanopatterns using domains formed from polymer blends and block copolymers as the template. It is known that in thin films of polystyrene (PS) and poly(4-vinylpyridine) (4PV), microphase-separated domains are formed, and that thin films of block poly(styrene-*b*-4-vinylpyridine) (PS-*b*-4PV) form nanometer-separated domains.<sup>[70]</sup> The mask is formed from protonating the pyridine ring and immersing in a solution of sodium dodecyl sulfate

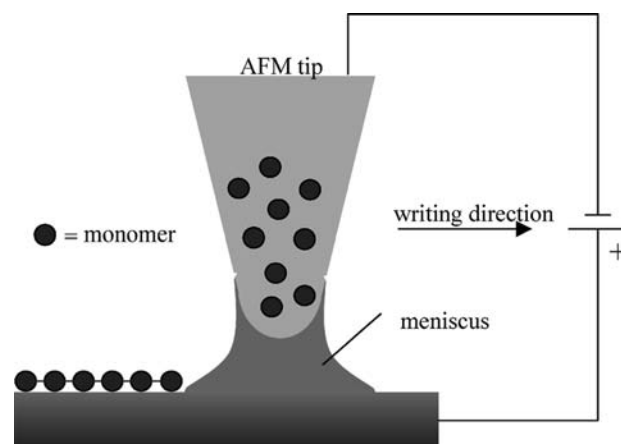


**Fig. 10** Schematic of E-DPN.

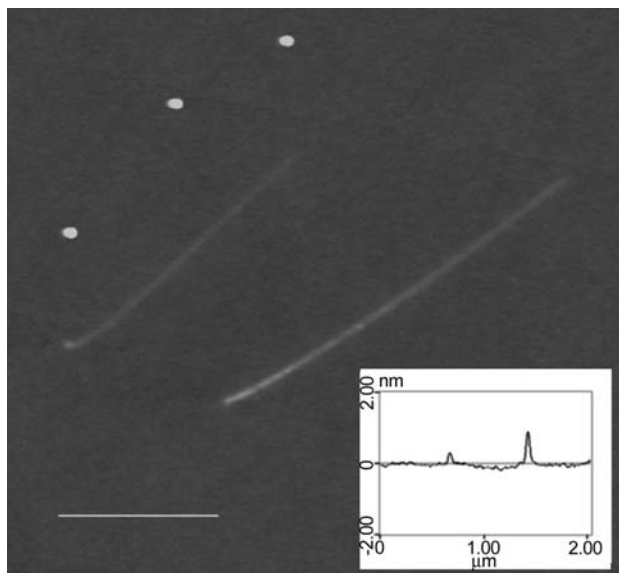


**Fig. 11** Atomic force microscope image of PEDOT lines drawn at 10 and 1 nm/sec. Inset shows height difference of the two lines. *Source:* From Ref.<sup>[67]</sup>. © (2001) American Chemical Society.

(SDS), which will form a bilayer with the pyridine and itself through ionic and hydrophobic interactions, respectively. Although SDS forms a monolayer with the PS through hydrophobic interactions, the polypyrrole nucleates preferentially on PS and displaces the SDS monolayer, but cannot displace the SDS bilayer. Using this method, nanopatterns as small as 50 nm were obtained (Fig. 12).<sup>[70]</sup> The pattern formed is not well defined, and additional research is needed to control pattern size and alignment.

## CONCLUSION

The ability to pattern nanostructures has opened up the field of nanoelectronics, and conducting polymers will play a significant role in the development of this field. The complementarity of these techniques is already apparent and represents a strength in the field. At the nanoscale, control and quantity will be immensely important, highlighting the advantages of both template synthesis and lithography. Today, template synthesis can afford numerous repetitive nanostructures, and lithography can yield nanostructures with precise size at a specific location. Unfortunately, most of the lithography techniques that work so effectively at the micrometer scale have yet to break the nanoscale barrier because of physical limits and methods used to form lithographic masks. Template synthesis is still a “bulk synthesis” technique because it has not been demonstrated that this technique can accurately deposit one or a few nanostructures.

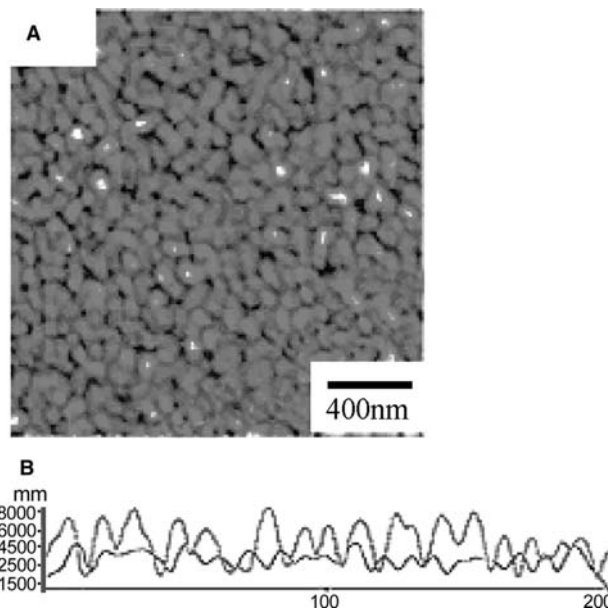


**Fig. 12** A) Atomic force microscope image of nanopatterns formed with polypyrrole on PS-*b*-4PV nanometer-separated domains. B) Cross section showing height difference before (blue) and after (red) polypyrrole formation. *Source:* From Ref.<sup>[69]</sup>. © (2002) American Chemical Society.

Numerous applications have already been demonstrated for these new materials, from encapsulators for biosensors to photonic bandgap crystals. In addition, the potential for use in fabrication of nano-device components and interconnects is great, although high-throughput methods may be some years away. The success of many research groups in circumventing the current chemical, physical, and engineering challenges has encouraged an increasing number of researchers to study fundamental nanoscale processes. Such further research and innovation will likely lead to nanoelectronics playing an integral role in the development of future commercial applications.

## ACKNOWLEDGMENTS

The authors would like to thank the Army Research Office (Grant 2000-ARG-0041) and NSF. M.W.G. gratefully acknowledges the NSF Career Award, the Dreyfus Foundation for a Camille Dreyfus Teacher-Scholar, and the Alfred P. Sloan Foundation for a Research Fellowship.

## REFERENCES

1. Xia, Y.; Rogers, J.A.; Paul, K.E.; Whitesides, G.M. Unconventional methods for fabricating and patterning nanostructures. *Chem. Rev.* **1999**, *99* (7), 1823–1848.

- Gurunathan, K.; Murugan, A.V.; Marimuthu, R.; Mulik, U.P.; Amalnerkar, D.P. Electrochemically synthesized conducting polymeric materials for applications towards technology in electronics, optoelectronics and energy storage devices. *Mater. Chem. Phys.* **1999**, *61*, 173–191.
- Bao, Z.; Rogers, J.A.; Katz, H.E. Printable organic and polymeric semiconducting materials and devices. *J. Mater. Chem.* **1999**, *9*, 1895–1904.
- Tour, J.M. Conjugated macromolecules of precise length and constitution. Organic synthesis for the construction of nanoarchitectures. *Chem. Rev.* **1996**, *96* (1), 537–553.
- Armonk, J.; Mitzi, D.B.; Chondroudis, K.; Kagan, C.R. Organic–inorganic electronics. *IBM J. Res. Develop.* **2001**, *45* (1), 29–45.
- Dodabalapur, A. Organic light emitting diodes. *Solid State Commun.* **1997**, *102* (2–3), 259–267.
- Walcarius, A. Electrochemical applications of silica-based organic–inorganic hybrid materials. *Chem. Mater.* **2001**, *13* (10), 3351–3372.
- Yano, S.; Iwata, K.; Kurita, K. Physical properties and structure of organic–inorganic hybrid materials produced by sol-gel process. *Mater. Sci. Eng., C* **1998**, *6*, 75–90.
- Mitzi, D.B. Thin-film deposition of organic–inorganic hybrid materials. *Chem. Mater.* **2001**, *13* (10), 3283–3298.
- Kumar, D.; Sharma, R.C. Advances in conductive polymers. *Eur. J. Polym. Chem.* **1998**, *34* (8), 1053–1060.
- Heeger, A.J. Semiconducting and metallic polymers: The fourth generation of polymeric materials. *J. Phys. Chem., B* **2001**, *105* (36), 8475–8491.
- MacDiarmid, A.G. Polyaniline and polypyrrole: Where are we headed?. *Synth. Met.* **1997**, *84*, 27–34.
- McCullough, R.D. The chemistry of conducting polythiophenes. *Adv. Mater.* **1998**, *10* (2), 93–116.
- Stanforth, S.P. Catalytic cross-coupling reactions in biaryl synthesis. *Tetrahedron* **1998**, *54*, 263–303.
- Rosseinsky, D.R.; Mortimer, R.J. Electrochromic systems and the prospect for devices. *Adv. Mater.* **2001**, *13* (11), 783–793.
- Le Barny, P.; Dentan, V.; Facoetti, H.; Vergnolle, M.; Veriot, G.; Servet, B.; Pribat, D. Application of organic electroluminescent materials in visualization. *C. R. Acad. Sci. Paris.* **2000**, *1* (4), 493–508.
- Tallman, D.E.; Spinks, G.; Dominis, A.; Wallace, G.G. Electroactive conducting polymers for corrosion control. *J. Solid State Electrochem.* **2002**, *6*, 73–84.
- Granlund, T.; Nyberg, T.; Roman, L.S.; Svensson, M.; Inganas, O. Patterning of polymer light-emitting diodes with soft lithography. *Adv. Mater.* **2000**, *12* (4), 269–273.
- Jager, E.W.H.; Smela, E.; Inganas, O. Microfabricating conjugated polymer actuators. *Science* **2000**, *290*, 1540–1545.
- Urban, G. Microstructuring of organic layers for microsystems. *Sens. Actuators* **1999**, *74*, 219–224.
- Hohnholz, D.; MacDiarmid, A.G. Line patterning of conducting polymers: New horizons for inexpensive, disposable electronic devices. *Synth. Met.* **2001**, *121*, 1327–1328.
- Weldon, M.K.; Queoney, K.T.; Eng, J., Jr.; Raghavachari, K.; Chabal, Y.J. The surface science of semiconductor processing: Gate oxides in the ever-shrinking transistor. *Surf. Sci.* **2002**, *500*, 859–878.
- Penner, R.M.; Martin, C.R. Controlling the morphology of electronically conductive polymers. *J. Electrochem. Soc.* **1986**, *133* (10), 2206–2207.
- Martin, C.R. Membrane-based synthesis of nanomaterials. *Chem. Mater.* **1996**, *8* (8), 1739–1746.
- Huczko, A. Template-based synthesis of nanomaterials. *Appl. Phys., A Mater. Sci. Eng.* **2000**, *70*, 365–376.
- Hulteen, J.C.; Martin, C.R. A general template-based method for the preparation of nanomaterials. *J. Mater. Chem.* **1997**, *7* (7), 1075–1087.
- Fleisher, R.L.; Price, P.B.; Walker, R.M. *Nuclear Tracks in Solids*; University of California Press: Berkeley, CA, 1975.
- Chakarvarti, S.K.; Vetter, J. Template synthesis—A membrane based technology for generation of nano-/micro materials: A review. *Radiat. Meas.* **1998**, *29* (2), 149–159.
- Jerome, C.; Demoustier-Champagne, S.; Legras, R.; Jerome, R. Electrochemical synthesis of conjugated polymer wires and nanotubules. *Chem. Eur. J.* **2000**, *6* (17), 3089–3093.
- Parthasarathy, R.V.; Martin, C.R. Enzyme and chemical encapsulation in polymeric microcapsules. *J. Appl. Polym. Sci.* **1996**, *62*, 875–886.
- Lu, M.; Li, X.-H.; Li, H.-L. Synthesis and characterization of conducting copolymer nanofibrils of pyrrole and 3-methylthiophene using the template-synthesis method. *Mater. Sci. Eng., A* **2002**, *334*, 291–297.
- Cai, Z.; Lei, J.; Liang, W.; Menon, V.; Martin, C.R. Molecular and supermolecular origins of enhanced electronic conductivity in template-synthesized polyheterocyclic fibrils. 1. Supermolecular effects. *Chem. Mater.* **1991**, *3* (5), 960–967.
- Liang, W.; Martin, C.R. Template-synthesized polyacetylene fibrils show enhanced supermolecular order. *J. Am. Chem. Soc.* **1989**, *112* (26), 9666–9668.
- Wittmann, J.C.; Smith, P. Highly oriented thin-films of poly(tetrafluoroethylene) as a substrate for oriented growth of materials. *Nature* **1991**, *352* (6334), 414–417.
- Martin, C.R. Nanomaterials: A membrane-based synthetic approach. *Science* **1994**, *266*, 1961–1966.
- Yuan, G.-L.; Kuramoto, N. Chemical synthesis of optically active polyaniline in the presence of dextran sulfate as molecular template. *Chem. Lett.* **2002**, *5*, 544–545.
- Mativetsky, J.M.; Datars, W.R. Properties of alumina membrane-templated polypyrrole nanostructures. *Solid State Commun.* **2002**, *122*, 151–154.
- Kuwabata, S.; Martin, C.R. Investigation of the gas-transport properties of polyaniline. *J. Membr. Sci.* **1994**, *91*, 1–12.
- Koopal, C.G.L.; Feiters, M.C.; Nolte, R.J.M.; de Ruiter, B.; Schasfoort, R.B.M.; Czajka, R.; Van Kempen, H. Polypyrrole microtubules and their use in the construction of a third generation biosensor. *Synth. Met.* **1992**, *51*, 397–405.

40. Martin, C.R.; Parthasarathy, R.V. Polymeric microcapsule arrays. *Adv. Mater.* **1995**, *7* (5), 487–488.
41. Granstrom, M.; Berggren, M.; Inganas, O. Micrometer- and nanometer-sized polymeric light-emitting diodes. *Science* **1995**, *267*, 1479–1481.
42. Wang, C.; Wang, Z.; Li, M.; Li, H. Well-aligned polyaniline nano-fibril array membrane and its field emission property. *Chem. Phys. Lett.* **2001**, *341*, 431–434.
43. Sukeerthi, S.; Contractor, A.Q. A study of polyaniline microtubules: Toward superior transducing abilities. *Chem. Mater.* **1998**, *10* (9), 2412–2418.
44. Fu, M.; Chen, F.; Zhang, J.; Shi, G. Electrochemical fabrication of aligned microtubular heterojunctions of poly(*p*-phenylene) and polythiophene. *J. Mater. Chem.* **2002**, *12*, 2331–2333.
45. Li, X.; Zhang, X.; Li, H. Preparation and characterization of pyrrole/aniline copolymer nanofibrils using the template-synthesis method. *J. Appl. Polym. Sci.* **2001**, *81*, 3002–3007.
46. Yang, J.; Hou, J.; Zhu, W.; Xu, M.; Wan, M. Substituted polyaniline–polypropylene film composites: Preparation and properties. *Synth. Met.* **1996**, *80*, 283–289.
47. Cassagneau, T.; Caruso, F. Semiconducting polymer inverse opals prepared by electropolymerization. *Adv. Mater.* **2002**, *14* (1), 34–38.
48. Sumida, T.; Wada, Y.; Kitamura, T.; Yanagida, S. Electrochemical preparation of macroporous polypyrrole films with regular arrays of interconnected spherical voids. *Chem. Commun.* **2000**, *17*, 1613–1614.
49. Bartlett, P.N.; Birkin, P.R.; Ghanem, M.A.; Toh, C.-S. Electrochemical syntheses of highly ordered macroporous conducting polymers grown around self-assembled colloidal templates. *J. Mater. Chem.* **2001**, *11* (3), 849–853.
50. Han, S.; Briseno, A.L.; Shi, X.; Mah, D.A.; Zhou, F. Polyelectrolyte-coated nanosphere lithographic patterning of surfaces: Fabrication and characterization of electropolymerized thin polyaniline honeycomb films. *J. Phys. Chem., B* **2002**, *106* (25), 6465–6472.
51. Wang, D.; Caruso, F. Fabrication of polyaniline inverse opals via templating ordered colloidal assemblies. *Adv. Mater.* **2001**, *13* (5), 350–353.
52. Deutsch, M.; Vlasov, Y.A.; Norris, D.J. Conjugated-polymer photonic crystals. *Adv. Mater.* **2002**, *12* (16), 1176–1180.
53. Xia, Y.; Whitesides, G.M. Soft lithography. *Annu. Rev. Mater. Sci.* **1998**, *28*, 153–184.
54. Kim, E.; Xia, Y.; Zhao, X.-M.; Whitesides, G.M. Solvent-assisted microcontact molding: A convenient method for fabricating three-dimensional structures on surfaces of polymers. *Adv. Mater.* **1997**, *9* (8), 651–654.
55. Rogers, J.A.; Bao, Z.; Dhar, L. Fabrication of patterned electroluminescent polymers that emit in geometries with feature sizes into the submicron range. *Appl. Phys. Lett.* **1998**, *73* (3), 294–296.
56. Zhang, F.; Nyberg, T.; Inganas, O. Conducting polymer nanowires and nanodots made with soft lithography. *Nano Lett.* **2002**, *2* (12), 1373–1377.
57. Wu, Y.-M.; Fan, F.-R.F.; Bard, A.J. High resolution deposition of polyaniline on Pt with the scanning electrochemical microscope. *J. Electrochem. Soc.* **1989**, *136* (3), 885–886.
58. Borgwarth, K.; Ricken, C.; Ebling, D.G.; Heinze, J. Surface characterization and modification by the scanning electrochemical microscope (SECM). *Ber. Bunsenges. Phys. Chem.* **1995**, *99* (11), 1421–1426.
59. Yang, R.; Evans, D.F.; Hendrickson, W.A. Writing and reading at nanoscale with a scanning tunneling microscope. *Langmuir* **1995**, *11* (1), 211–213.
60. Yaniv, D.R.; McCormick, L.D. Polypyrrole nanoplating on HOPG utilizing an STM tip (biosensor fabrication). *Nanotechnology* **1992**, *3* (1), 44–47.
61. Nyffenegger, R.M.; Penner, R.M. Nanometer-scale electropolymerization of aniline using the scanning tunneling microscope. *J. Phys. Chem.* **1996**, *100* (42), 17041–17049.
62. Cai, X.W.; Gao, J.S.; Xie, Z.X.; Xie, Y.; Tian, Z.Q.; Mao, B.W. Nanomodification of polypyrrole and polyaniline on highly oriented pyrolytic graphite electrodes by atomic force microscopy. *Langmuir* **1998**, *14* (9), 2508–2514.
63. Piner, R.D.; Zhu, J.; Xu, F.; Hong, S.H.; Mirkin, C.A. “Dip-pen” nanolithography. *Science* **1999**, *283* (5402), 661–663.
64. Maynor, B.W.; Li, Y.; Liu, J. Au “ink” for AFM “dip-pen” nanolithography. *Langmuir* **2001**, *17* (9), 2575–2578.
65. Demers, L.M.; Ginger, D.S.; Park, S.J.; Li, Z.; Chung, S.W.; Mirkin, C.A. Direct patterning of modified oligonucleotides on metals and insulators by dip-pen nanolithography. *Science* **2002**, *296* (5574), 1836–1838.
66. Noy, A.; Miller, A.E.; Klare, J.E.; Weeks, B.L.; Woods, B.W.; DeYoreo, J.J. Fabrication of luminescent nanostructures and polymer nanowires using dip-pen nanolithography. *Nano Lett.* **2002**, *2* (2), 109–112.
67. Li, Y.; Maynor, B.W.; Liu, J. Electrochemical AFM “dip-pen” nanolithography. *J. Am. Chem. Soc.* **2001**, *123* (9), 2105–2106.
68. Maynor, B.W.; Filocamo, S.F.; Grinstaff, M.W.; Liu, J. Direct-writing of polymer nanostructures: Poly-(thiophene) nanowires on semiconducting and insulating surfaces. *J. Am. Chem. Soc.* **2002**, *124* (4), 522–523.
69. Filocamo, S.F.; Maynor, B.M.; Liu, J.; Grinstaff, M.W. Submitted.
70. Seo, I.; Pyo, M.; Cho, G. Micrometer to nanometer patterns of polypyrrole thin films via microphase separation and molecular mask. *Langmuir* **2002**, *18* (20), 7253–7257.

# Conducting Polymer Nanotubes

Seung Il Cho  
Sang Bok Lee

*Department of Chemistry and Biochemistry, University of Maryland,  
College Park, Maryland, U.S.A.*

## INTRODUCTION

Conducting polymers with metallic and polymeric properties are indispensable materials for the development of organic electronic devices, such as batteries, light-emitting diodes, and displays. The electrochemical fabrication of conducting polymer nanostructures, especially nanotubular structures, can enhance their performance by improving charge transport rate as well as surface area. However, the understanding of the electrochemically synthesized conducting polymer nanotubes is lacking in spite of their importance and high applicability. Here, we discuss the electrochemical synthesis, synthetic mechanism, and structural characterization of the conducting polymer nanotubes. The application of conducting polymer nanotubes is also discussed in the development of ultrafast flexible electrochromic device with low power consuming features.

## BACKGROUND

One of the most exciting challenges in recent research fields is the development of organic electronic devices including batteries, organic electronic memory, organic light emitting diode, lasers, and displays.<sup>[1–9]</sup> Conducting polymers, such as polyaniline, polypyrrole, polythiophene, and poly(*p*-phenylene vinylene) classes, are indispensable material in fabricating organic electronic devices because they have the electrical, electronic, electrochemical, and optical properties of a metal as well as the mechanical properties of a conventional polymer.<sup>[1–16]</sup> In optical properties, for example, polythiophene is red (or blue) in the reduced (or oxidized) state, whereas polymethylthiophene is purple (or pale blue) in the reduced (or oxidized) state.<sup>[17]</sup> All these unique characteristics of conducting polymers offer innumerable applicability to organic electronic devices.

Usually, conducting polymers are used in organic devices in three forms: thin film, nanofibrillar form,

and nanotubular form. The film is the most popular in organic devices, acting as electrodes or light controlling materials.<sup>[3,6,7,9]</sup> Oxidative chemical polymerization method is frequently used to fabricate pinhole-free homogenous thin film by spin-coating on a conductive or even insulating surface. Nanofibrils or tubes are used in the devices, which require higher surface area and sensitivity such as sensors or batteries.<sup>[1,2,18]</sup> Template synthesis, as shown in Fig. 1, is one of the most frequently adopted techniques to fabricate nanostructures of the conducting polymers since Penner and Martin pioneered the electrochemical synthesis of polypyrrole nanofibrils using a nucleopore (polycarbonate) membrane in 1986.<sup>[18–26]</sup> Alumina membranes (Fig. 2) and track-etched polycarbonate membranes were frequently used as a template owing to their well-defined pore structures.<sup>[18]</sup> The outer shape of the deposited material is usually determined by the inner structure of the membrane pores. Most of the conducting polymer nanostructures were synthesized by the chemical oxidation method because of its simplicity.<sup>[18,21–23,26]</sup> The polymerization conditions such as polymerization time and monomer concentrations determine whether the resulting inner structures are hollow tubes or completely filled fibrils.

For the electrochemical synthesis of conducting polymer nanofibril/nanotube in the porous template, a conductive substrate should be used at one side of the membrane as an electrode to deposit the polymer in the pores.<sup>[27–30]</sup> The mechanism for the nanostructure growth is more complicated compared to the chemical method. However, the electrochemical method has advantages over the chemical method in that the nanotube length can be easily controlled by changing polymerization time. The electrochemically polymerized nanotubes have also better electrochromic properties such as color vividness and switching rates.<sup>[19,20,27]</sup> For the application of conducting polymers to sensors and organic electronic devices, the tubular form of conducting polymer provides more advantages than the film or fibrillar

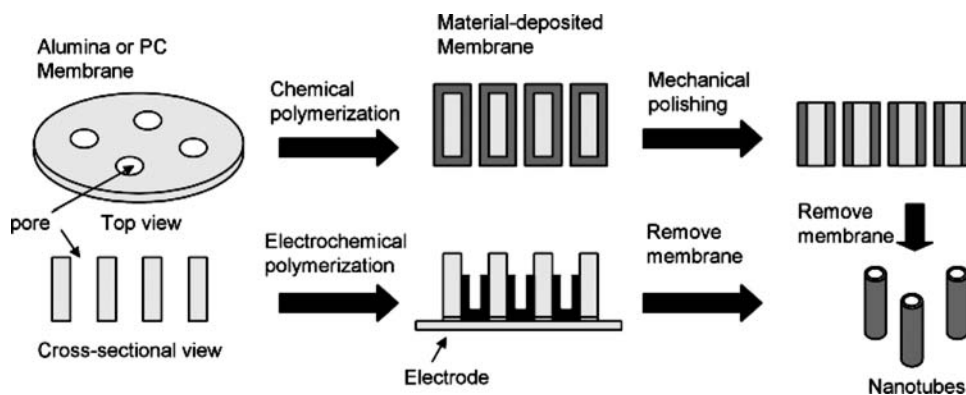


Fig. 1 Schematic of template synthesis of conducting polymer nanotubes chemically (top) and electrochemically (bottom).

form: possibility of inner modification, high surface area, fast response, etc.<sup>[18,27]</sup> Surprisingly, however, the studies on electrochemical synthesis of conducting polymer nanotubes are not many. Here, we discuss the electrochemical synthesis, synthetic mechanism,

structural characterization, and application of conducting polymer nanotubes using the template synthesis.

## METHODS OF ELECTROCHEMICAL SYNTHESIS

Electrochemical polymerization is normally carried out using a standard three-electrode configuration in a solution containing monomer and a supporting electrolyte. Three kinds of methods, potentiostatic, galvanostatic, or potentiodynamic, are used in electrochemical synthesis. Generally, potentiostatic conditions are recommended to obtain thin films, while galvanostatic conditions are recommended to obtain thick films. In the potentiodynamical method, a relatively firm polymer structure is expected because oxidation and reduction cycles are repeated during polymerization. For electrochemical synthesis, one face of the porous membrane is sputter-coated with a thin layer of conducting materials such as gold or indium-doped tin oxide (Fig. 1). This side, acting as a working electrode, is connected to a power source, the potentiostat. Electrochemical potential is defined by a reference electrode such as Ag/AgCl or saturated calomel electrode (SCE).

To make the nanotubular structure, two strategies can be used: one is the direct growth of conducting polymer nanotubes in the membrane pores and the other is the metal layer deposition on the surface of the pores and then the electrochemical growth of the conducting polymer.<sup>[21,22,26–31]</sup> The latter is useful to make nanotubes with very small diameters because the deposited metal layer reduces the inner diameter of pore. However, it is not easy to fabricate the polymer nanotubes with a good shape because the chemically deposited metal surface is very rough. On the other hand, better nanotubular structures are obtained with the direct growth method and the length of the polymer nanotube can be controlled.

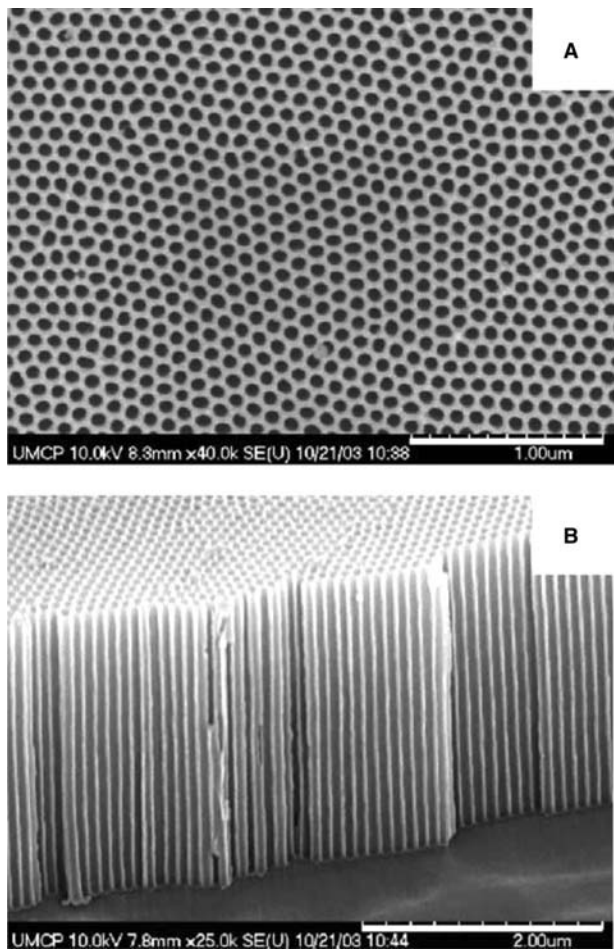


Fig. 2 Scanning electron micrographs of a porous alumina membrane (pore diameter: 60 nm): (A) top view and (B) cross-sectional view.



## CHARACTERIZATION OF NANOTUBE STRUCTURES

To characterize the tubular structures, three methods have been used: observation of end morphology of nanotubes using scanning electron microscopy (SEM), indirect observation of the microtomed section of nanotubes embedded in a membrane, or direct observation of the individual nanotube using transmission electron microscopy (TEM).<sup>[19,22,26–29]</sup> The first method, SEM, is relatively unreliable because it is very hard to differentiate the complete hollow nanotubes with the partially filled nanotubes or nanowires with small pit structures at the end. For example, Duvail et al. reported that the outer structures of poly(3,4-ethylenedioxythiophene) (PEDOT) in a SEM image for the top ends of the nanomaterials were shown like tubular forms with thick walls, while the inner structures in a TEM image were proven to be an almost filled concave shape with an open end.<sup>[30]</sup> Li et al. reported that the TEM image of  $\text{LiMn}_2\text{O}_4$  nanostructures showed tubular structures while the SEM image of their top ends showed fibrillar forms.<sup>[32]</sup> The microtoming is a useful technique to prove inner tubular structures. The nanotubes embedded in a membrane are sliced in a slanted angle. If the tubules within the membrane have a partially filled structure, the TEM image of this thin microtomed slice will show plugged pores as well as unplugged pores containing rings of conducting polymer. In this method, we do not need to remove the template but require an additional instrument to cut the membrane. Direct observation of tubular structure using TEM will be most reliable, although the template should be removed.

## ELECTROCHEMICALLY SYNTHESIZED CONDUCTING POLYMER NANOTUBES

### Polypyrroles

Martin et al. reported the first electrochemical synthesis of the tubular structure of conducting polymer with *N*-methylpyrrole in a nucleopore membrane (1.0  $\mu\text{m}$  pores) chemically or electrochemically (current density of 1.0  $\text{mA}/\text{cm}^2$ ) in 0.5 M *N*-methylpyrrole in an acetonitrile solution.<sup>[22]</sup> They proposed a mechanism for nanotube formation. The key to this process is the interaction of the nascent polyheterocyclic chain with the pore wall. The nascent cationic heterocyclic polymers are adsorbed to the anionic membrane wall by electrostatic attraction, which resulted in the preferential growth of conducting polymers as a tubular form. Demoustier-champagne and coworkers have also investigated the electrochemical synthesis of

polypyrrole nanotubes in a track-etched polycarbonate membrane (pore diameter of 35–200 nm).<sup>[28,29]</sup> The polymerization was carried out at +0.8 V SCE in 0.05–0.1 M pyrrole aqueous solution. The nanostructures were proven using the TEM images of a microtomed section of polypyrrole nanotubes.<sup>[28]</sup> They investigated the importance of the limited diffusion of monomers to nanotube formation using pulsed chronoamperometry technique. However, they concluded that the diffusion of monomer inside the pores is not the determinant parameter leading to the formation of tubes because no changes were found in tube wall thickness as the monomer concentration changed in the range of 0.05–0.35 M or pulsed polymerization was applied with various delay times. Yamada, Gasparac, and Martin prepared a gold/polypyrrole composite microtube membrane to investigate the transport properties of bottlenecked polypyrrole microtubes.<sup>[31]</sup> The pyrroles were electropolymerized by using cyclic voltammetry after electroless deposition of gold on the surface of a polycarbonate membrane. The effective inner diameter of the polypyrrole nanotubes was adjusted by controlling the number of polymerization cycles. As expected, decreasing the pore diameters reduced the transported phenols. Granstrom and coworkers have investigated the electrochemical polymerization of conducting polymer fibrillar structures including polypyrrole and polythiophenes.<sup>[33–35]</sup> The conducting polymer fibrils, synthesized in the pores of a membrane, have higher conductivity and longer conjugation length compared to a conventional polymer film. Higher conductivity was observed for conducting polymer fibrils grown at higher monomer concentration and in smaller pores, as observed by Martin's group in the chemically synthesized nanofibrils of polypyrrole, polymethylthiophene, and polyacetylene.<sup>[21,23]</sup>

### Polyanilines

Demoustier-Champagne and coworkers have synthesized polyaniline nanotubes chemically and electrochemically.<sup>[36]</sup> They used track-etched porous polycarbonate membranes with different pore diameters ranging from 20 to 220 nm. The pore diameter of the membrane is one of the important parameters to have an effect on the growth rate of the polyaniline nanotubes: as the pore diameter of a membrane was reduced, the polyaniline growth rate in the longitudinal direction (along the pore wall) was decreased owing to the limited diffusion of monomers into narrower pores. They also observed that the nanotubes, grown in a membrane with smaller pore diameters, exhibit larger values of conductivity, which has contributed to more ordered structures in smaller-diameter nanotubes.

Szklarczyk et al. investigated the mechanism for the electrochemical formation of poly(*o*-methoxyaniline) nanostructures using in situ atomic force and electron microscopies.<sup>[37]</sup> The polymerization was carried out potentiodynamically by cycling potentials between 0.0 and 1.0 V. Based on an atomic force micrograph, however, it was hard to determine whether the synthesized nanostructures were nanofibrils or end-capped nanotubes. X-ray energy dispersive spectroscopic study showed that the metallic layer, sputtered to make one surface of a membrane conductive, was also present on the walls of the pores. They proposed that this metallic layer on the wall results in the simultaneous growth of nanostructures on the pore wall and on its bottom.

### Polythiophenes

Duvail et al. tried to synthesize PEDOT nanotubes potentiodynamically (cyclic voltammetry) or potentiostatically (chronoamperometry). Unlike polypyrroles and polyanilines, PEDOT was likely to be electrochemically synthesized as nanowires instead of hollow nanotubes in a porous membrane. They remarked that the preferential growth along the pore walls in PEDOT is much less important compared to other conducting polymers.

Recently, we have synthesized PEDOT nanotubes electrochemically using an alumina membrane as a template.<sup>[27]</sup> The tubular structure of PEDOT, grown in a porous alumina film, was investigated by SEM and TEM. Polymerization was performed potentiostatically at 1.2–1.8 V vs. Ag/AgCl in an acetonitrile solution of 20 mM in 3,4-ethylenedioxythiophene (EDOT) and 100 mM in LiClO<sub>4</sub>. After completely removing the alumina template with phosphoric acid (25 wt%), nanotubes were then separated and characterized to prove their hollow tubular structures and to measure their wall thicknesses by using TEM. Key

variables in the growth of the tubular structure of PEDOT are monomer concentration and applied potential. Various nanostructures of PEDOT, including completely tubular, partially filled, and completely filled nanostructures (Fig. 3), were obtained by controlling both the applied potentials and the monomer concentrations.

These phenomena were difficult to explain using only the previous mechanism, that is, the interaction between the wall surface and polymers.<sup>[18,22]</sup> To explain the formation of hollow nanotubes as well as partially filled nanotubes, we proposed an additional mechanism as well as the mechanism by attraction between the polymers and the pore walls: The polymerization reaction of PEDOT in the pores is limited by the diffusion of monomer at highly applied potential that leads to high electrochemical reaction rate in the pores (Fig. 4).

Another important parameter in electrochemically synthesizing nanotubes is the electropolymerization time. In the beginning, very thin nanotubes are formed because of the strong interaction of the membrane wall surface and polymers, as mentioned above. Fig. 5A shows very thin tubular structures with an average length of 3 μm, synthesized at 1.5 V for 20 sec in 50 mM EDOT. As the polymer becomes long, a little voltage drop is expected because of the resistance of polymer. This leads to thickening of the tube wall rather than continuous nanotube elongation. The PEDOT tubes are almost filled in 100 sec and have about 6 μm length (Fig. 5B). Even though the electropolymerization time increased five times, the total length of nanotubes increased twice because most of the diffused monomers are consumed to fill the nanotubes. Further increasing the electropolymerization time leads to completely filled nanowires. Therefore, electropolymerization time as well as monomer concentration and applied potential have to be considered to fully understand the phenomena of nanotube formation.

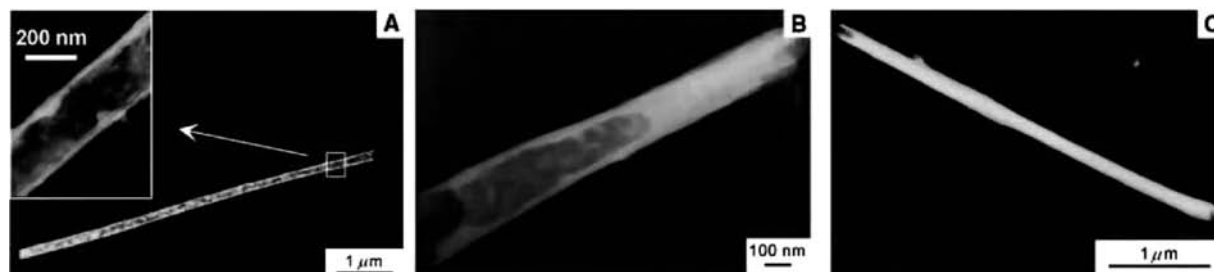


**Fig. 3** Transmission electron microscopy images of the PEDOT nanotube or nanowire synthesized at the constant voltage of (A) 1.5 V, (B) 1.3 V, and (C) 1.2 V vs. Ag/AgCl in 20 mM EDOT using an alumina template (pore diameter: 200 nm). Source: From Ref.<sup>[27]</sup>.

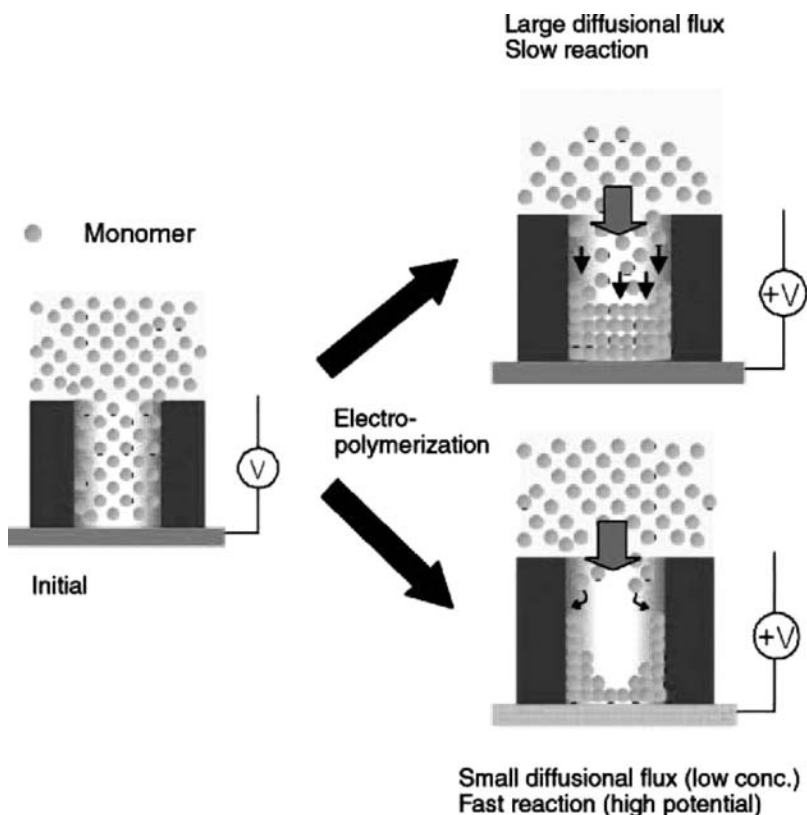


**Fig. 4** Schematic mechanism of the electrochemical synthesis of conducting polymer nanowire (top) or nanotube (bottom) using template synthesis. Large diffusional flux (high monomer concentration) and slow reaction (low potential) resulted in nanowire structure while small diffusional flux (low monomer concentration) and fast reaction (high potential) resulted in nanotubular structure.

### APPLICATIONS

During the past decade, there have been many reports about potentially practical applications of conducting polymers to various fields such as batteries, organic electronic memory, sensors, organic light emitting diode, lasers, and organic display, etc.<sup>[1-9,15,16,38]</sup> However, the applications of the tubular shape of the conducting polymer have been reported rarely. For

example, Kanungo, Kumar, and Contractor fabricated microtubule sensors based on polyaniline microtubules, which were polymerized in the pores of track-etched polycarbonate membrane (pore diameter of 1.2  $\mu\text{m}$ ).<sup>[39]</sup> The poly(styrene sulfonate)-polyaniline was deposited by potentiostatic (+1.0 V; pH 5.0) or potentiodynamic (potential cycles between -0.2 and 0.8 V vs. SCE; scan rate of 50 mV/sec; pH 0.5) method. The enzymes were immobilized by physical adsorption

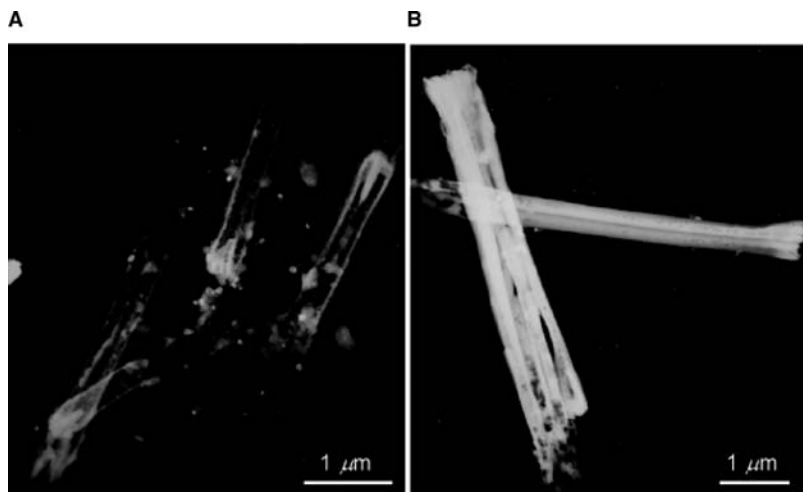


**Fig. 5** The effect of electropolymerization time on nanostructures. Transmission electron microscopy images of the PEDOT nanotubes synthesized at the constant voltage of 1.5 V (vs. Ag/AgCl) for (A) 20 sec and (B) 100 sec in 50 mM EDOT using an alumina template (pore diameter: 200 nm).

after polymerization. The sensor response was improved by about 100 times compared to conventional sensors based on polyaniline film.

One of the fascinating properties of the conducting polymer is the electrochromic effect. PEDOT of the conducting polymers has had much attraction because of its good electrochromic effect in color changes, which can be applied to electronic paper or flexible display. One of the problems in current electrochromic display is the slow color-switching rate, which is limited by the diffusion rate of counterions into the film during the redox process.<sup>[9,27,40–44]</sup> The diffusion time ( $t$ ) of ions to reach a saturation concentration in a polymer film, which implies switching time, is proportional to the square of the film thickness ( $x$ ):  $t \propto x^2/D$ , where  $D$  is the diffusion coefficient of an ion in a polymer film.<sup>[45,46]</sup> Therefore, the simplest way to overcome the slow switching rates is to decrease the diffusion distance of ions, that is, to reduce film thickness.<sup>[47–50]</sup> Based on the reported switching time of 2.2 sec for a 300 nm-thick PEDOT film, we expect the switching time to be about 10 msec for a 20 nm thick film.<sup>[40]</sup> However, the coloration of such a thin film is never sufficient for display applications. That is, there is always a trade-off between the coloration and switching time as the film thickness varies.

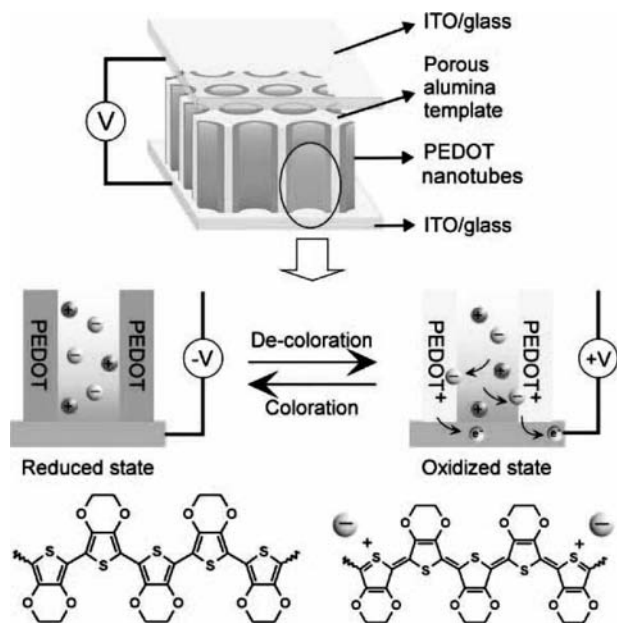


**Fig. 6** Schematic diagram of the ultrafast electrochromic device based on PEDOT nanotube arrays. Counteranions (negatively charged grey balls) diffuse into a thin layer of PEDOT nanotube wall (less than 20 nm in wall thickness to provide the short diffusion distance) when PEDOT nanotubes are oxidized by applying positive potential on the indium-doped tin oxide glass electrode. The color of PEDOT turns from a deep blue to a transparent pale blue. *Source:* From Ref.<sup>[27]</sup>.

To improve the color switching rate without the loss of color contrasts, we developed the electrochromic device based on the PEDOT nanotube arrays. Fig. 6 illustrates that the thin wall thickness of PEDOT nanotubes (less than 20 nm) can provide ions with short diffusion pathways, which allows very fast switching rates, while the micrometer length of the PEDOT nanotubes in an array structure can produce strong coloration for the display system.

In fact, there have been similar examples showing fast charge transport rates with nanofibrillar or nanotubular structures of conducting polymers and inorganic materials.<sup>[32,51,52]</sup> Li et al. demonstrated that the rate capabilities could be improved by reducing the wall thickness of the nanotubes, which decrease the distance for Li ion transport into nanostructured  $\text{LiMn}_2\text{O}_4$  electrodes, compared to a conventional film structure.<sup>[32]</sup> Van Dyke and Martin have reported the significantly increased charge transport rates (five times) in fibrillar polypyrrole compared to conventional polypyrrole films (1  $\mu\text{m}$  in thickness).<sup>[24,25]</sup> However, the charge transport rate was still in a second range owing to not having tubular structure but nanowire structure with 200 nm diameter. Chien and Schlenoff showed that the time to charge and discharge polyacetylene fibrils can be accelerated by reducing the fibril diameter.<sup>[2]</sup>

An electrochromic window with PEDOT nanotube arrays was designed as shown above. The device was switched from pale blue (decoupled and oxidized state of PEDOT) to deep blue (colored and reduced state of PEDOT) by applying alternating square potentials between 1.0 and  $-1.0$  V on PEDOT nanotube arrays

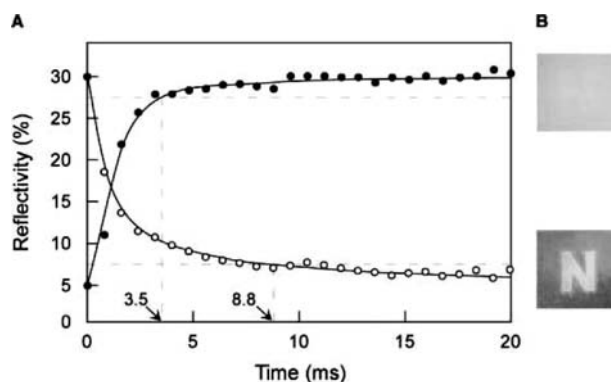


**Fig. 7** (A) Plots of reflectivity of electrochromic window ( $1\text{ cm}^2$ ) monitored at 530 nm for coloration (open circle) and decoloration (solid circle) upon potential-switching between  $-1.0$  and  $1.0$  V, respectively. (B) Patterned letter 'N' on the PEDOT nanotube arrayed film. The alternating square potentials between  $-1.0$  V (lower image) and  $1.0$  V (upper image) were applied on the background area after  $1.0$  V was applied on the letter "N" (decoupled state). *Source:* From Ref.<sup>[27]</sup>.

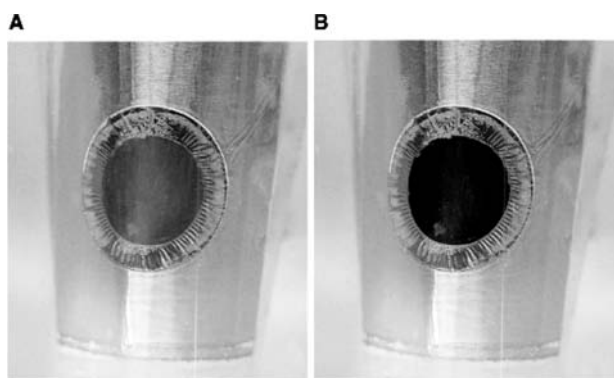


**Fig. 8** Flexible electrochromic display in (A) oxidized or (B) reduced state, which was fabricated using conducting polymer nanotubes in a polycarbonate membrane.

vs. the upper transparent electrode. The switching speed was measured optically from reflectivity responses as a function of time at the applied potentials (Fig. 7A). Both the coloring and decoloring processes show switching times of less than 10 msec. Movie film is usually played at a speed of 24 frames/sec, which corresponds to display switching times of about 40 msec. Furthermore, the patterned letter “N” showed good color contrast of 6 as shown in Fig. 7(B). Therefore, PEDOT nanotubes, exhibiting switching times of <10 msec and good contrast, are excellent candidate material for moving image displays.

The above design is not suitable for a flexible display because the alumina template is highly fragile. Thus, we used a flexible template, a porous polycarbonate membrane. PEDOT nanotubes were grown electrochemically after sputtering a thin layer of gold on one face of the polycarbonate membrane as an electrode. Fig. 8 shows a highly flexible electrochromic device in an electrolyte solution, 100 mM LiClO<sub>4</sub> in acetonitrile. The oxidized and reduced PEDOT usually shows transparent pale blue and deep blue, respectively. However, the color of the device was gold in the oxidized state (Fig. 8A) while it was dark bluish in the reduced state (Fig. 8B) because of the sputtered gold layer. Due to the high flexibility of a polycarbonate template, the electrochromic device can be rolled easily.

## CONCLUSIONS

We investigated the electrochemical syntheses of conducting polymer nanotubes. A variety of parameters influence the nanotube formations, such as applied potential, monomer concentration, pore diameters, electropolymerization time, etc. However, the more detailed mechanism still needs to be investigated.

Tubular structures have many advantages over fibrillar structures including the possibility of inner modification, the high surface area, and the fast charge diffusion. As an application of conducting polymer nanotubes, we introduced ultrafast electrochromic displays with switching speeds compatible with moving image display technology and low power consuming features. The thin wall thickness (less than 20 nm) of nanotubes renders the diffusion path length of counter-ions extremely short, which leads to ultrafast switching speed (<10 msec). The long-nanotube arrays provide a strong coloration. As only a primitive form of a flexible electrochromic display has been demonstrated, we are currently investigating the possibility of demonstrating a flexible display capable of showing color text and images on a rewritable medium by making pixelated nanotube arrays on thin plastic substrates.<sup>a</sup>

## REFERENCES

1. Karasz, F.E.; Chien, J.C.W.; Galkiewicz, R.; Wnek, G.E.; Heeger, A.J.; MacDiarmid, A.G. Nascent morphology of polyacetylene. *Nature* **1979**, *282*, 286–288.
2. Chien, J.C.W.; Schlenoff, J.B. Limiting battery performance parameters for polyacetylene. *Nature* **1984**, *311*, 362–363.
3. Moller, S.; Perlov, C.; Jackson, W.; Taussig, C.; Forrest, S.R. A polymer/semiconductor write-once read-many-times memory. *Nature* **2003**, *426*, 166–169.
4. Forrest, S.R. The path to ubiquitous and low-cost organic electronic appliances on plastic. *Nature* **2004**, *428*, 911–918.
5. Gross, M.; Muller, D.C.; Nothofer, H.-G.; Scherf, U.; Neher, D.; Brauchle, C.; Meerholz, K. Improving the performance of doped  $\pi$ -conjugated polymers for use in organic light-emitting diodes. *Nature* **2000**, *405*, 661–665.
6. Friend, R.H.; Gymer, R.W.; Holmes, A.B.; Burroughes, J.H.; Marks, R.N.; Taliani, C.; Bradley, D.D.C.; Dos Santos, D.A.; Bredas, J.L.; Logdlund, M.; Salaneck, W.R. Electroluminescence in conjugated polymers. *Nature* **1999**, *397*, 121–128.
7. Roman, L.S.; Inganas, O. Modifying interface to semiconducting polymers: PEDOT in polymer microelectronics. In *Conjugated Polymer and Molecular Interfaces*; Salaneck, W.R., Seki, K., Kahn, A., Pireaux, J.-J., Eds.; Marcel Dekker: New York, 2002; 777–792.
8. Scherf, U.; Riechel, S.; Lemmer, U.; Mahrt, R.F. Conjugated polymers: lasing and stimulated emission. *Curr. Opin. Solid State Mater. Sci.* **2001**, *5* (2/3), 143–154.
9. Andersson, P.; Nilsson, D.; Svensson, P.-O.; Chen, M.; Malmstrom, A.; Remonen, T.; Kugler, T.; Berggren, M. Active matrix displays based on all-organic

<sup>a</sup>Reprinted in part from Ref.<sup>[27]</sup>.

- electrochemical smart pixels printed on paper. *Adv. Mater.* **2002**, *14* (20), 1460–1464.
10. MacDiarmid, A.G. “Synthetic Metals”: A novel role for organic polymers. *Angew. Chem. Int. Ed.* **2001**, *40* (14), 2581–2590.
  11. Shirakawa, H. The discovery of polyacetylene film: the dawning of an era of conducting polymers. *Angew. Chem. Int. Ed.* **2001**, *40* (14), 2574–2580.
  12. Heeger, A.J. Semiconducting and metallic polymers: the fourth generation of polymeric materials. *J. Phys. Chem.* **2001**, *105* (36), 8475–8491.
  13. Stenger-Smith, J.D. Intrinsically electrically conducting polymers. Synthesis, characterization, and their applications. *Prog. Polym. Sci.* **1998**, *23* (1), 57–79.
  14. Malinauskas, A. Chemical deposition of conducting polymers. *Polymer* **2001**, *42* (8), 3957–3972.
  15. McQuade, D.T.; Pullen, A.E.; Swager, T.M. Conjugated polymer-based chemical sensors. *Chem. Rev.* **2000**, *100*, 2537–2574.
  16. Wallace, G.G.; Smyth, M.; Zhao, H. Conducting electroactive polymer-based biosensors. *Trends Anal. Chem.* **1999**, *18* (4), 245–251.
  17. Rowley, N.M.; Mortimer, R.J. New electrochromic materials. *Sci. Prog.* **2002**, *85* (3), 243–262.
  18. Martin, C.R. Nanomaterials: a membrane-based synthetic approach. *Science* **1994**, *266*, 1961–1966.
  19. Penner, R.M.; Martin, C.R. Controlling the morphology of electronically conductive polymers. *J. Electrochem. Soc.* **1986**, *133* (10), 2206–2207.
  20. Penner, R.M.; Martin, C.R. Electronically conductive composite polymer membranes. *J. Electrochem. Soc.* **1986**, *133* (2), 310–315.
  21. Cai, Z.; Martin, C.R. Electronically conductive polymer fibers with mesoscopic diameters show enhanced electronic conductivities. *J. Am. Chem. Soc.* **1989**, *111* (11), 4138–4139.
  22. Martin, C.R.; Van Dyke, L.S.; Cai, Z.; Liang, W. Template synthesis of organic microtubules. *J. Am. Chem. Soc.* **1990**, *112* (24), 8976–8977.
  23. Liang, W.; Martin, C.R. Template-synthesized polyacetylene fibrils show enhanced supermolecular order. *J. Am. Chem. Soc.* **1990**, *112* (26), 9666–9668.
  24. Van Dyke, L.S.; Martin, C.R. Fibrillar electronically conductive polymers show enhanced rates of charge transport. *Synth. Methods* **1990**, *36* (2), 275–281.
  25. Van Dyke, L.S.; Martin, C.R. Electrochemical investigations of electronically conductive polymers. 4. *Langmuir* **1990**, *6* (6), 1118–1123.
  26. Parthasarathy, R.V.; Martin, C.R. Template-synthesized polyaniline microtubules. *Chem. Mater.* **1994**, *6* (10), 1627–1632.
  27. Cho, S.I.; Kwon, W.J.; Choi, S.-J.; Kim, P.; Park, S.-A.; Kim, J.; Son, S.J.; Xiao, R.; Kim, S.-H.; Lee, S.B. Nanotube-based ultrafast electrochromic display. *Adv. Mater.* **2005**, *17* (2), 171–175.
  28. Demoustier-Champagne, S.; Ferain, E.; Jerome, C.; Jerome, R.; Legras, R. Electrochemically synthesized polypyrrole nanotubes: effects of different experimental conditions. *Eur. Polym. J.* **1998**, *34* (12), 1767–1774.
  29. Demoustier-Champagne, S.; Stavaux, P.-Y. Effect of electrolyte concentration and nature on the morphology and the electrical properties of electropolymerized polypyrrole nanotubules. *Chem. Mater.* **1999**, *11* (3), 829–834.
  30. Duvail, J.L.; Retho, P.; Garreau, S.; Louarn, G.; Godon, C.; Demoustier-Champagne, S. Transport and vibrational properties of poly(3,4-ethylenedioxythiophene) nanofibers. *Synth. Methods* **2002**, *131* (1/3), 123–128.
  31. Yamada, K.; Gasparac, R.; Martin, C.R. Electrochemical and Transport properties of templated gold/polypyrrole composite microtube membranes. *J. Electrochem. Soc.* **2004**, *151* (1), E14–19.
  32. Li, N.; Patrissi, C.J.; Che, G.; Martin, C.R. Rate capabilities of nanostructured LiMn<sub>2</sub>O<sub>4</sub> electrodes in aqueous electrolyte. *J. Electrochem. Soc.* **2000**, *147* (6), 2044–2049.
  33. Granstrom, M.; Inganas, O. Studies of structure and conductivity in poly(pyrrole) and poly(thiophene-octylthiophene) grown microporous membranes. *Synth. Methods* **1993**, *55* (1), 460–465.
  34. Granstrom, M.; Inganas, O. Electronically conductive polymer fibres with mesoscopic diameters: 1. Studies of structure and electrical properties. *Polymer* **1995**, *36* (15), 2867–2872.
  35. Granstrom, M.; Carberg, J.C.; Inganas, O. Electronically conductive polymer fibres with mesoscopic diameters: 2. Studies of polymerization behavior. *Polymer* **1995**, *36* (16), 3191–3196.
  36. Delvaux, M.; Duchet, J.; Stavaux, P.-Y.; Legras, R.; Demoustier-Champagne, S. Chemical and electrochemical synthesis of polyaniline micro- and nano-tubules. *Synth. Methods* **2000**, *113* (3), 275–280.
  37. Szklarczyk, M.; Strawski, M.; Donten, M.L.; Donten, M. A study of tubular nanostructures formation in the pores of membrane electrode. *Electrochem. Commun.* **2004**, *6* (9), 880–886.
  38. Kros, A.; van Hovell, S.W.F.M.; Sommerdijk, N.A.J.M.; Nolte, R.J.M. Poly(3,4-ethylenedioxythiophene)-based glucose biosensors. *Adv. Mater.* **2001**, *13* (20), 1555–1557.
  39. Kanungo, M.; Kumar, A.; Contractor, A.Q. Microtubule sensors and sensor array based on polyaniline synthesized in the presence of poly(styrene sulfonate). *Anal. Chem.* **2003**, *75* (21), 5673–5679.
  40. Kumar, A.; Welsh, D.M.; Morvant, M.C.; Piroux, F.; Abboud, K.A.; Reynolds, J.R. Conducting poly(3,4-alkylenedioxythiophene) derivatives as fast electrochromics with high-contrast ratios. *Chem. Mater.* **1998**, *10* (3), 896–902.
  41. Sapp, S.A.; Sotzing, G.A.; Reynolds, J.R. High contrast ratio and fast-switching dual polymer electrochromic devices. *Chem. Mater.* **1998**, *10* (8), 2101–2108.
  42. Sankaran, B.; Reynolds, J.R. High-contrast electrochromic polymers from alkyl-derivatized poly(3,4-ethylenedioxythiophenes). *Macromolecules* **1997**, *30* (9), 2582–2588.
  43. Schwendeman, I.; Hickman, R.; Sonmez, G.; Schottland, P.; Zong, K.; Welsh, D.M.; Reynolds, J.R. Enhanced contrast dual polymer electrochromic devices. *Chem. Mater.* **2002**, *14* (7), 3118–3122.
  44. Cirpan, A.; Argun, A.A.; Grenier, C.R.G.; Reeves, B.D.; Reynolds, J.R. Electrochromic devices based on soluble



- and processable dioxothiophene polymers. *J. Mater. Chem.* **2003**, *13* (10), 2422–2428.
45. Monk, P.M.S.; Mortimer, R.J.; Rosseinsky, D.R. Electrochromic systems: electrochemistry, kinetics, and mechanism. In *Electrochromism: Fundamentals and Applications*; VCH: Weinheim, 1995; 22–41.
  46. Beniere, F.; Haridoss, S.; Louboutin, J.P.; Aldissi, M.; Fabre, J.M. Doping of polyacetylene by diffusion of iodine. *J. Phys. Chem. Solids* **1981**, *42*, 649–654.
  47. Diaz, A.F.; Castillo, J.I.; Logan, J.A.; Lee, W.-Y. Electrochemistry of conducting polypyrrole films. *J. Electroanal. Chem.* **1981**, *129* (1/2), 115–132.
  48. Osaka, T.; Naoi, K.; Ogano, S.; Nakamura, S. Dependence of film thickness on electrochemical kinetics of polypyrrole and on properties of lithium/polypyrrole battery. *J. Electrochem. Soc.* **1987**, *134* (9), 2096–2102.
  49. Cutler, C.A.; Bouguettaya, M.; Reynolds, J.R. PEDOT polyelectrolyte based electrochromic films via electrostatic adsorption. *Adv. Mater.* **2002**, *14* (9), 684–688.
  50. Penner, R.M.; Van Dyke, L.S.; Martin, C.R. Electrochemical evaluation of charge-transport rates in electronically conductive polymers. *Solid State Ionics* **1989**, *32/33* (1), 553–566.
  51. Nishizawa, M.; Mukai, K.; Kuwabata, S.; Martin, C.R.; Yoneyama, H. Template synthesis of polypyrrole-coated spinel  $\text{LiMn}_2\text{O}_4$  nanotubules and their properties as cathode active materials for lithium batteries. *J. Electrochem. Soc.* **1997**, *144* (6), 1923–1927.
  52. Li, N.; Martin, C.R. A high-rate, high-capacity, nanostructured Sn-based anode prepared using sol-gel template synthesis. *J. Electrochem. Soc.* **2001**, *148* (2), A164–A170.

# Controlled Size and Shape Supramolecular Aggregates on Solid Surfaces

Takashi Yokoyama

Graduate School of Integrated Science, Yokohama City University, Yokohama, Japan, and  
National Institute for Materials Science, Tsukuba, Japan

Toshiya Kamikado

Shiyoshi Yokoyama

Shinro Mashiko

Communications Research Laboratory, Kobe, Japan

## INTRODUCTION

Molecule-based nanodevices with advanced functions have been attracting much attention, because the size of microelectronic circuit components will soon reach the scale of atoms or molecules.<sup>[1,2]</sup> The idea that one, or a few molecules, could perform the basic functions of electronics was first introduced in 1978.<sup>[3]</sup> Aviram and Ratner<sup>[3]</sup> suggested that a molecular diode should be obtained by a donor–spacer–acceptor structure, when it is placed between two electrodes. Such molecular-scale electronic devices differ radically from bulk-scale devices, because one or a few molecules work as a circuit component.<sup>[4]</sup> In addition, it should be noted that the structure and function of molecular building blocks are rationally controlled by chemical synthesis, and that each molecular component can be aggregated into a larger structure by self-assembly.

To realize molecular-scale devices, the development of new approaches should be required to construct desired molecular nanostructures on a suitable substrate. Whereas large functional molecules have been directly obtained by chemical synthesis,<sup>[5,6]</sup> supramolecular assembly is a realistic way to create nanoscale molecular structures.<sup>[7]</sup> The supramolecular approach, starting from molecular building blocks, can lead to controlled aggregates, which is achieved by selective and directional intermolecular interactions. When non-covalent attractive interactions such as hydrogen bonding are introduced into functional molecules, the selective aggregation results in the controlled formation of molecular nanostructures, which has been widely studied.<sup>[7]</sup> However, these structures have been obtained exclusively in crystals or dissolved structures. For the use of the molecular nanodevices, the supramolecule should be supported on a suitable surface. The surface-supported supramolecules should be located at suitable positions.

On solid surfaces, scanning probe microscopy, particularly scanning tunneling microscopy (STM),<sup>[8]</sup> has proven to be a powerful tool for the real-space investigation of adsorbed functional molecules, allowing to directly determine the arrangement, configuration, and conformation of adsorbed molecules with submolecular resolution. Using the technique of STM, several groups have reported on self-assembled structures of adsorbed molecules on metal surfaces.<sup>[9–11]</sup> To realize molecular nanodevices, further control of their size and shape should become an important step. Here we demonstrate the controlled supramolecular aggregation of porphyrin derivatives formed on a gold surface. First, we describe the structure of porphyrin and substrate surface used. After the adsorption properties of the porphyrin on the gold surface are described in detail, the supramolecular aggregation of cyano-substituted porphyrins is reported.

## PORPHYRIN AND GOLD SURFACE

Porphyrins and other closely related tetrapyrrolic pigments are a class of naturally occurring macrocycles, which play very important roles in various biological processes including hemes, chlorophylls, and several others.<sup>[12]</sup> Thus porphyrin derivatives have been widely studied both in basic research and for functional applications.<sup>[13]</sup> In the present work, we have used 5,10,15,20-tetrakis-(3,5-di-tertiarybutylphenyl) porphyrin ( $H_2$ -TBPP)<sup>[14,15]</sup> as a basic molecule, which is composed of a free-base porphyrin and four di-tertiarybutylphenyl (tBP) substituents (Fig. 1). Fig. 2 shows an ideal shape of  $H_2$ -TBPP obtained from molecular orbital calculations.<sup>[16]</sup> The molecule exhibits a planar macrocyclic conformation of the central porphyrin through 60–90° rotations of four phenyl rings with respect to the porphyrin mean plane. Because of the phenyl-ring

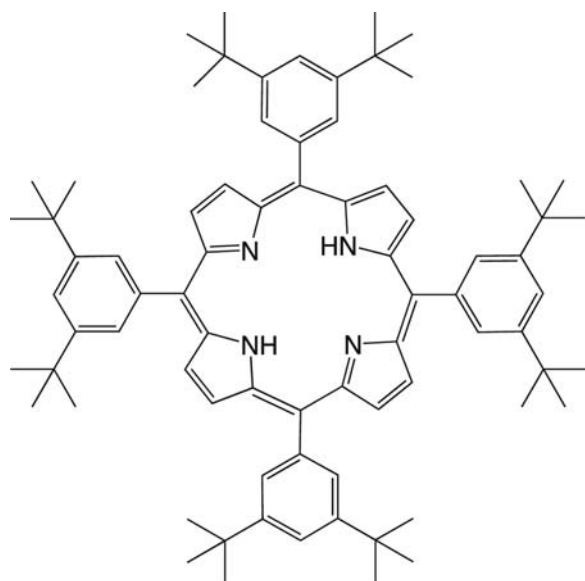


**Fig. 1** Structural formula of H<sub>2</sub>-TBPP, which includes the central free-base porphyrin and four tBP substituents.

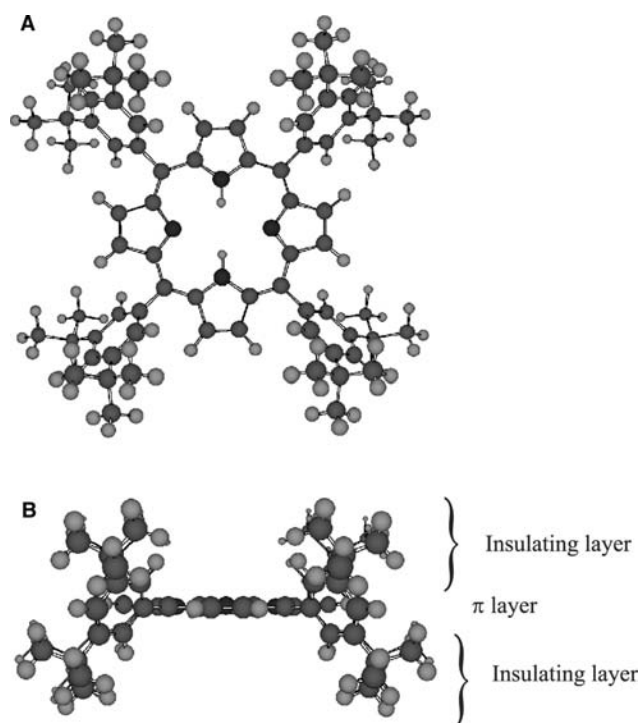


**Fig. 2** (A) Top and (B) side views of the calculated conformation of H<sub>2</sub>-TBPP, obtained from semiempirical molecular orbital method with the AM1 Hamiltonian. The about 65° rotations of phenyl rings result from steric hindrance between the porphyrin and phenyl rings. As shown in the side view, the insulating tBP groups prevent direct interaction between the central porphyrin and substrate surface, when the molecule is adsorbed on a surface.

rotations, the insulating tBP substituents should prevent the direct interactions between the central porphyrin and the surface, even when the H<sub>2</sub>-TBPP molecule is adsorbed onto a surface. As the characteristic features of the central porphyrin should be conserved even for molecules supported on surfaces, this isolation fulfills the requirements for the molecular nanoelectronic or optoelectronic devices.<sup>[14,15]</sup>

To ensure selective molecular aggregation, we used a gold(111) surface as the substrate because of its inertness and its properties of surface reconstruction. The Au(111) was formed by deposition of gold on a mica substrate in ultrahigh vacuum (UHV) and was prepared by repeated cycles of Ar ion sputtering and annealing at 700 K. After the procedure, the starting Au(111) clean surface was obtained as shown in the STM image of Fig. 3A. This STM image was obtained at 63 K in UHV and revealed a characteristic “herringbone” surface reconstruction. As there are 23 surface atoms within 22-unit cells in the [110] direction<sup>[17]</sup> as shown in the atomic-resolved STM image of Fig. 3B,

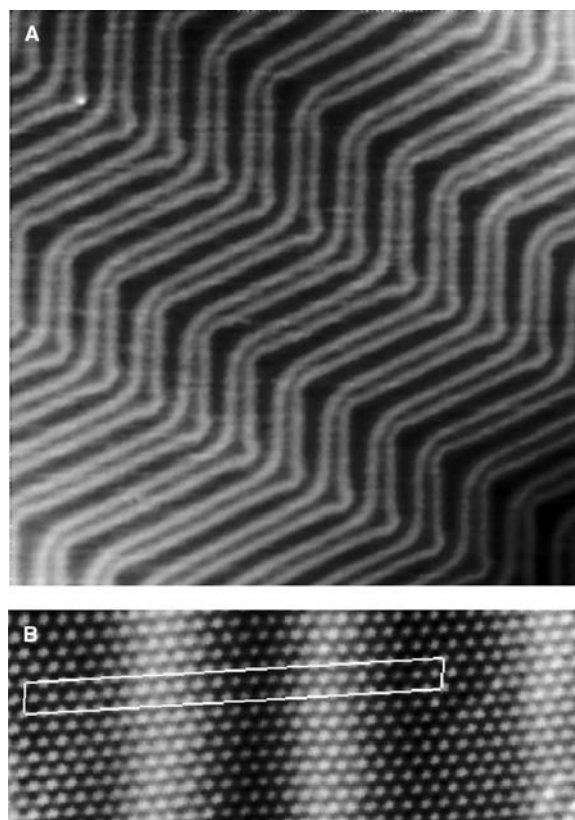


**Fig. 3** (A) STM image (82 × 82 nm) of a Au(111) surface obtained at 63 K, in which periodic rotations of bright stripes result in the formation of herringbone pattern. (B) Atomically resolved STM image (3.5 × 8.6 nm) of the Au(111) surface. Within 22-unit cells of the bulk lattice, indicated by a white rectangle, there are 23 surface atoms, so that the bright stripes are induced by lattice distortion in the surface layer.

the reconstruction of the Au(111) surface results from alternating face-centered cubic (fcc) and hexagonal close-packed (hcp) stacking of the surface atoms with respect to the bulk lattice. In the STM image, brighter stripes correspond to the transition region between hcp and fcc stackings, and periodic rotations of the uniaxial domains result in the formation of long-range herringbone patterns.<sup>[17]</sup> Here it should be noted that a point dislocation of the surface lattice occurs at each elbow of this pattern, and the preferential nucleation of adsorbates at the elbows has been reported in various systems.<sup>[10,18]</sup> It is very important for individual molecules to be selectively positioned at specific sites of the surface.

### CONFORMATION AND ARRANGEMENT OF ADSORBED TBPP

As the conformation of adsorbed molecules is occasionally different from the ideal conformation and is responsible for the molecular functions, the detailed analysis of the conformational change upon adsorption is one of the fundamental steps to realize the selective assembly of adsorbed molecules.<sup>[15]</sup> To directly observe individual molecules using STM, H<sub>2</sub>-TBPP molecule was deposited onto the Au(111) at room temperature by sublimation from a Knudsen cell kept at about 530 K in UHV. The sample was then subsequently transferred to the cold STM stage for direct observations. Fig. 4A shows a STM image of the Au(111) surface after a small amount of H<sub>2</sub>-TBPP deposition, which reveals regular arrays of isolated single molecules. These molecules are located at the elbows of the herringbone patterns, indicating that each molecule is preferentially nucleated at the point dislocations (defects). This selective molecular positioning allows direct imaging of isolated molecules without intermolecular interactions.

Fig. 4B shows a high-resolution STM image of a single H<sub>2</sub>-TBPP molecule on the Au(111) surface, which exhibits four paired lobes surrounding two oblong protrusions.<sup>[19]</sup> From the molecular dimension, we assign each lobe as one of the tBP substituents, and the appearance of the paired lobes suggests that the phenyl rings are oriented close to the porphyrin macrocyclic plane, different from the ideal shape of H<sub>2</sub>-TBPP shown in Fig. 2 where the phenyl rings are rotated by 60–90°. By comparing the STM results with the molecular model, we have derived the dihedral angle between the porphyrin and phenyl rings to be about 20°, where the four phenyl rings are alternately rotated with respect to the porphyrin mean plane. In the STM image, the brighter lobe should correspond to the upper tertiarybutyl group within a tBP substituent. The rotations of the phenyl–porphyrin bonds have

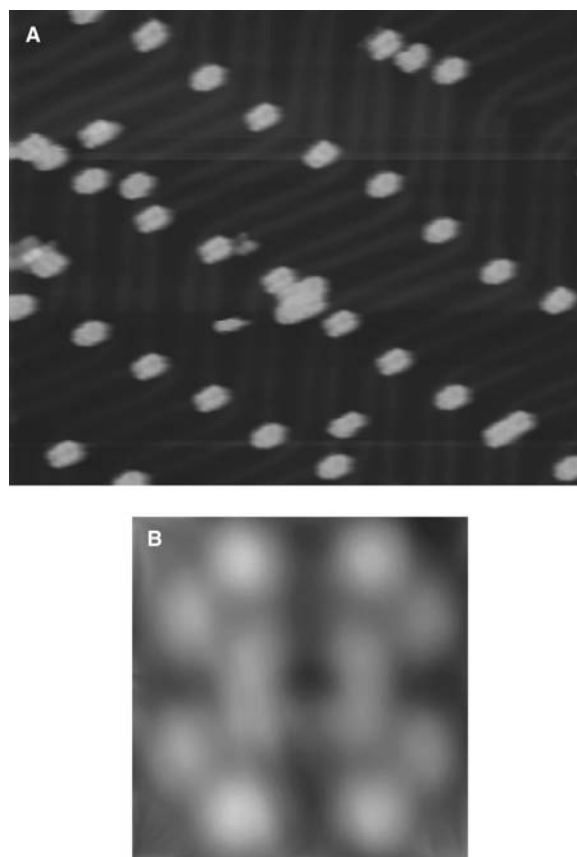


**Fig. 4** (A) STM image (86 × 104 nm) of a Au(111) surface at 63 K after a small amount of H<sub>2</sub>-TBPP deposition. Individual molecules are selectively located at the elbows of the herringbone pattern. (B) Submolecular resolution STM image (2.1 × 2.1 nm) of H<sub>2</sub>-TBPP, which shows four paired lobes surrounding two oblong protrusions.

been reported for adsorbed Cu-TBPP molecules on several metal surfaces, which depend on the substrate structures. These results indicate that the rotational flexibility of the phenyl–porphyrin bonds allows the tertiarybutyl substituents to fit into the surface geometry, leading to the conformational changes.

The most distinguishing feature for the H<sub>2</sub>-TBPP molecules on the Au(111) surface is that the internal structure of the central porphyrin macrocycle has been resolved in the STM images, which is composed of two oblong protrusions. As the  $\pi$  electrons are expanded over the central porphyrin macrocycle, no corrugated structure is expected in the STM image of the central region when the porphyrin exhibits a planar conformation. Thus the oblong protrusions should be associated with the non-planar macrocyclic conformation (deformation) of the central porphyrin.

To confirm the non-planar deformation, we performed a semiempirical molecular orbital calculation with the AM1 Hamiltonian.<sup>[16]</sup> Fig. 5 shows the calculated conformation of H<sub>2</sub>-TBPP with fixed 20°

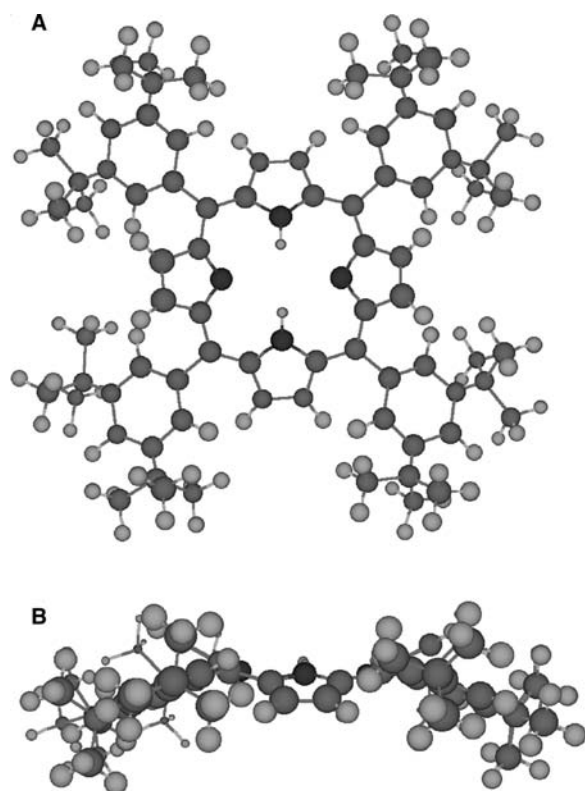


**Fig. 5** (A) Top and (B) side views of calculated conformation of H<sub>2</sub>-TBPP with 20° rotations of phenyl rings, obtained by semiempirical molecular orbital method with the AM1 Hamiltonian. In this structure, the dihedral angle between the porphyrin and phenyl rings has been fixed at 20°, where the four phenyl rings were alternately rotated with respect to the porphyrin mean plane. In the central porphyrin, the saddle-shaped deformation is characterized by alternate tilting of the pyrrole rings above and below the mean plane, which is induced by the steric hindrance with the rotated phenyl rings.

rotations of the four phenyl rings. The converged structure shows that the 20° rotations of the phenyl rings introduce nonplanar deformation of the central porphyrin macrocycle, whereas the ground state planar conformation is formed through 60–90° rotations as shown in Fig. 2. In this non-planar conformation, the saddle-shaped deformation of the central porphyrin is characterized by alternate tilting of the pyrrole rings above and below the mean plane, which is induced by steric hindrance with the rotated phenyl substituents. The maximum deviation of the porphyrin macrocycle from the mean plane is estimated to be about 0.95 Å, which is roughly consistent with the STM corrugation of 0.6 Å. In the high-resolution STM image of Fig. 4B, the two oblong protrusions should be associated with the tilt-up pyrrole rings of the non-planar porphyrin macrocycle, whereas the tilt-down pyrrole rings weakly appear as bridges between two oblong protrusions.

In addition to the direct imaging of molecular structures, STM is also applied for tunneling spectroscopy of adsorbed molecules, which allows probing the electronic properties on an STM resolution. Tunneling spectra  $[(dI/dV)/(I/V)]$ , which are numerically derived from current–voltage ( $I$ – $V$ ) characteristics at a typical tip–sample separation, almost represent the local density of electronic states at the tip position.<sup>[20]</sup> Fig. 6 shows the tunneling spectrum obtained on an adsorbed H<sub>2</sub>-TBPP molecule on the Au(111) surface at 63 K. In this tunneling spectrum of H<sub>2</sub>-TBPP, there are two characteristic peaks of occupied states at  $V = -1.1$  V and at an unoccupied state at 0.9 V, which should correspond to the highest occupied molecular orbital (HOMO) and the lowest unoccupied molecular orbital (LUMO) states of the central porphyrin, respectively. The obtained HOMO–LUMO gap of about 2 eV is in agreement with that of the porphyrin, estimated from optical absorption spectroscopy, which indicates that the electronic properties of H<sub>2</sub>-TBPP remain mostly unchanged even after adsorption and deformation.

With increasing coverage, two-dimensional islands are formed through self-assembled aggregation of the H<sub>2</sub>-TBPP molecules on the Au(111) surface. As shown in Fig. 7A, we have observed larger islands even without thermal annealing above 300 K, suggesting that the diffusion barrier for molecules on this surface is low at room temperature. In the islands, the non-planar

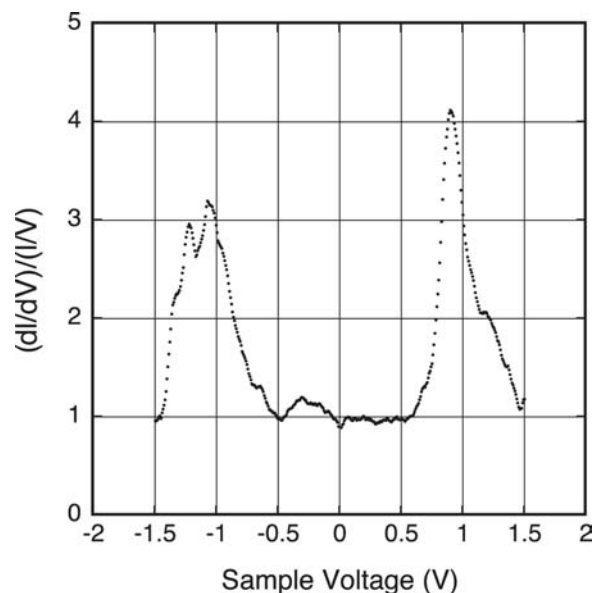


**Fig. 6** Tunneling spectrum of H<sub>2</sub>-TBPP adsorbed on the Au(111) surface at 63 K, which represents the local density of the electronic states of the molecule. In this spectrum, the negative sample voltage corresponds to the occupied electronic states, whereas the positive voltage corresponds to the unoccupied states.

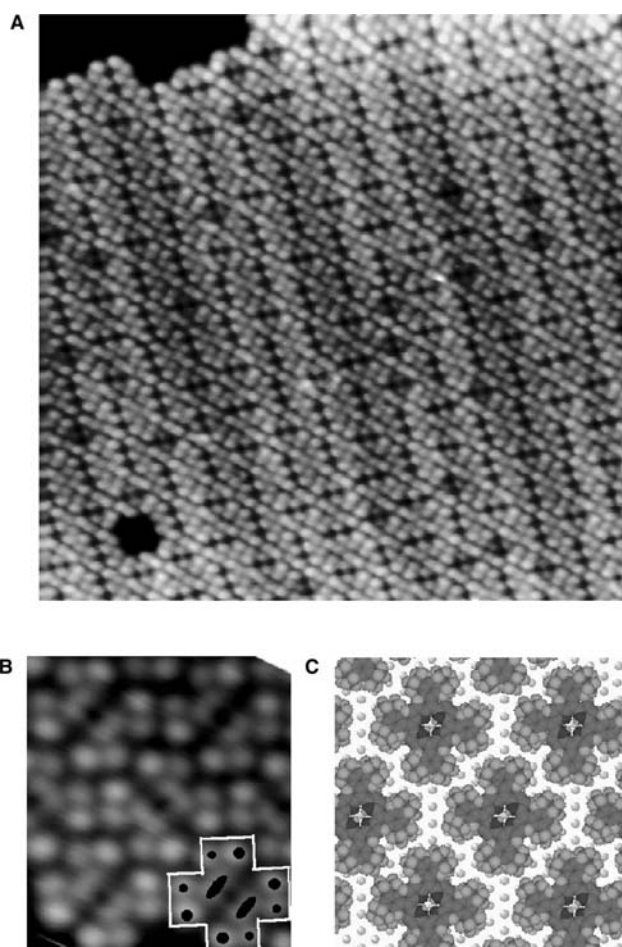


**Fig. 7** (A) STM image ( $33 \times 33$  nm) of a two-dimensional  $H_2$ -TBPP island formed on the Au(111) surface. The Au(111) surface is almost covered with the  $H_2$ -TBPP molecules. (B) High-resolution STM image ( $5.3 \times 5.3$  nm) and (C) its model of the  $H_2$ -TBPP island. The molecules are well ordered into an  $11 \times 5\sqrt{3}$  superstructure with respect to the surface lattice.

macrocyclic conformation of the central porphyrin remains, and the molecules are ordered into a close-packed arrangement [Fig. 7B]. A detailed analysis of the STM image indicates that the molecular arrangement exhibits an  $11 \times 5\sqrt{3}$  superstructure, commensurate with the underlying substrate lattice of Au(111).<sup>[19]</sup> Fig. 7C shows the model of the  $H_2$ -TBPP island formed on the Au(111)- $1 \times 1$  structure, where the symmetric intermolecular interaction should be governed by van der Waals forces between tBP substituents.

### SELECTIVE INTERMOLECULAR INTERACTIONS

A large number of different selective and directional intermolecular connections have been developed in

supramolecular chemistry.<sup>[7]</sup> In this work, we have used a cyanophenyl substituent to control molecular aggregation,<sup>[21]</sup> because it has a simple and symmetric structure as well as an asymmetric charge distribution at the cyano group. Within the cyano group, the nitrogen atom is negatively charged and the carbon atom is positively charged, so that the asymmetric charge distribution should induce a large dipole moment, resulting in the introduction of dipole–dipole interactions between neighboring cyanophenyl substituents. Fig. 8 shows the optimized arrangements of a cyanobenzene dimer and trimer obtained from ab initio molecular

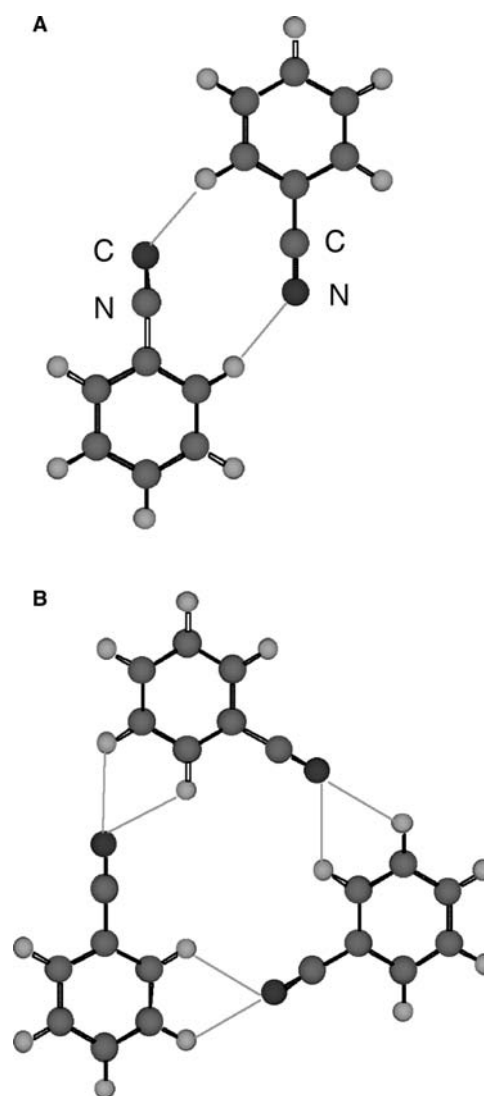


**Fig. 8** Structure of the molecular aggregates of a (A) cyanobenzene dimer and (B) trimer, obtained from ab initio molecular orbital calculations. In the dimer structure, an antiparallel configuration is formed between cyano groups, whereas a cyclic configuration is formed in the trimer structure. These structures are formed by the dipole–dipole interactions of the cyano groups, and further stabilized by  $CN \dots HC$  hydrogen bonding.



calculations at the MP2/6-31G\* level.<sup>[22]</sup> In the aggregated structures, an antiparallel configuration of the cyano groups is stabilized in the dimer, whereas a cyclic arrangement is formed in the trimer.<sup>[23]</sup> The antiparallel and cyclic configurations are in good agreement with the classical dipole–dipole arrangements. In addition, the length of the CH...NC contacts is about 2.39 and 2.65 Å for the dimer and trimer, respectively, which is shorter than the van der Waals distance of about 2.7 Å. The interaction energies were estimated to be  $-7.12$  and  $-12.40$  kcal/mol for the dimer and trimer, respectively. These results indicate that these cluster structures are further stabilized by CH...NC hydrogen bonding.

To introduce the characteristic interaction of the cyanophenyl groups, we have synthesized cyano-substituted porphyrins. When a tBP group of H<sub>2</sub>-TBPP is replaced with a cyanophenyl substituent, (cyanophenyl)-tris(di-tertiarybutyl-phenyl) porphyrin (CTBPP) is

obtained as shown in Fig. 9A. Because of the absence of a di-tertiarybutyl group, three paired lobes appear in the STM image of a single CTBPP molecule on the Au(111) surface as shown in Fig. 9B, in agreement with the chemical structure. At low coverage, most CTBPP molecules assemble into triangular clusters on the Au(111) surface. As shown in Fig. 10A, identical clusters are located separately at the elbows of the herringbone patterns, and the high-resolution STM image of Fig. 10B shows that the triangular cluster is a CTBPP trimer. The cyanophenyl substituents are assembled into a cyclic configuration in the trimer structure, in good agreement with the cyanobenzene trimer aggregation. In addition, we observed that the trimer clusters were ordered to form two-dimensional islands by further deposition, suggesting that the trimer works as a single molecule on the surface.

Compared with the characteristic trimer aggregation of CTBPP, we have not observed such supramolecular

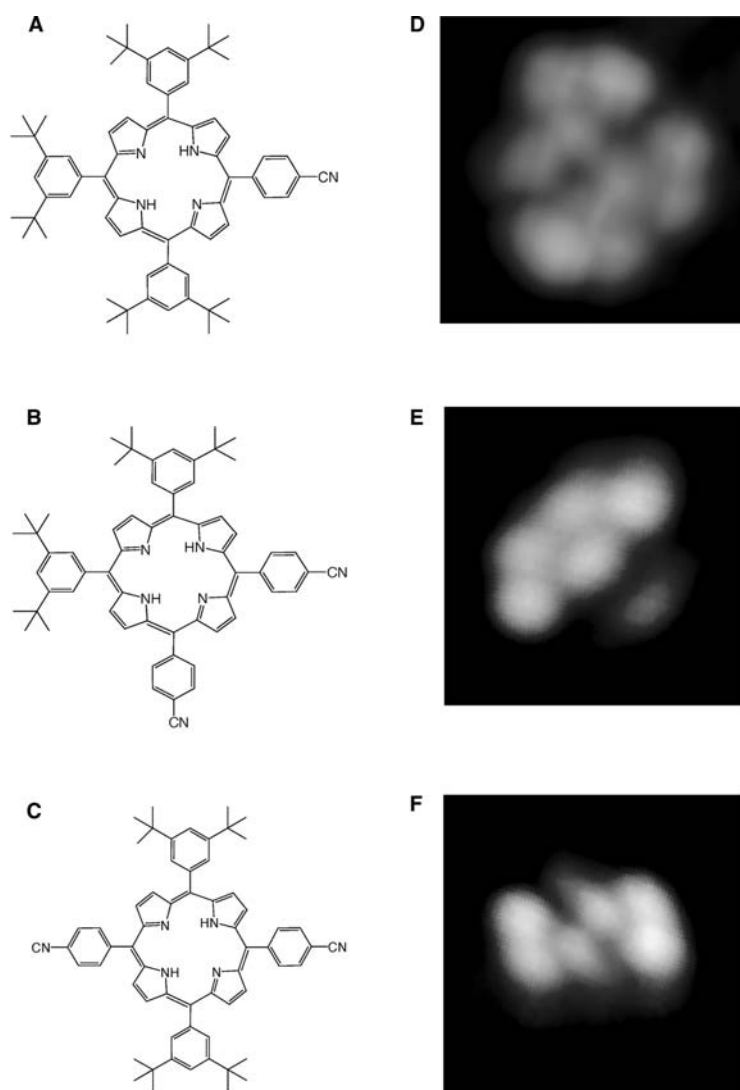


**Fig. 9** Structural formula of cyano-substituted porphyrins. (A) CTBPP, where a tBP substituent of H<sub>2</sub>-TBPP is replaced with a cyanophenyl substituent. (B) *cis*-BCTBPP molecule, where two cyanophenyl groups are substituted at the *cis* position. (C) *trans*-BCTBPP, where two cyanophenyl groups are substituted at the *cis* position. High-resolution STM images of (D) CTBPP, (E) *cis*-BCTBPP, and (F) *trans*-BCTBPP.

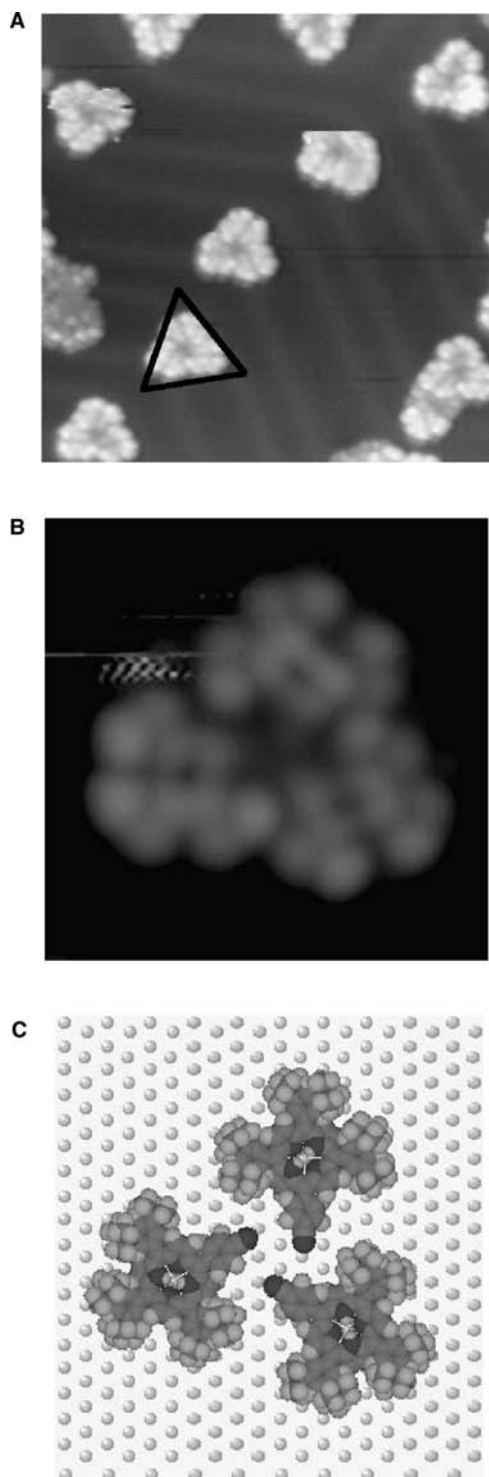


**Fig. 10** (A) STM image at 63 K of CTBPP molecules on Au(111). Identical triangular clusters are formed on the surface. (B) High-resolution STM image of a triangular cluster and (C) its model. This cluster is composed of three molecules, in which cyclic configuration of cyano groups is formed at the center.

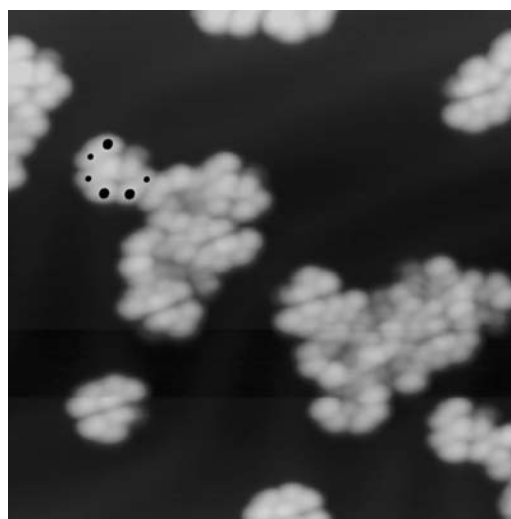


**Fig. 11** STM image at 63 K of (phenyl)-tris(di-tertiarybutyl-phenyl) porphyrin on Au(111). In this molecule, the cyano group was removed from CTBPP. Within two-dimensional islands, the directions of the phenyl groups are randomly distributed.

clusters, when the cyano group was removed from the CTBPP molecule. Fig. 11 shows a small island of (phenyl)-tris(di-tertiarybutyl-phenyl) porphyrins formed on the Au(111) surface, in which the molecular orientations are randomly distributed on the surface, indicating no selective aggregation. This result confirms that the supramolecular aggregation is dominated by the cyano groups.

One more cyano group was substituted to further probe the supramolecular aggregation on the Au(111) surface. When two tBP groups were replaced with cyanophenyl substituents, bis(cyanophenyl)-bis(di-tertiarybutyl-phenyl) porphyrin (BCTBPP) was obtained, which forms two types of isomers (*cis* and *trans*) with respect to the configuration of two cyanophenyl substituents. Figs. 12A and 13A show STM images of single *cis*- and *trans*-BCTBPP molecule, respectively. The disappearance of paired lobes at the cyanophenyl substituents agrees well with the chemical structures. At small coverage of the *cis*-BCTBPP molecules, identical clusters appear as four-leaf clovers as shown in Fig. 12B and C, which are located at the elbows of the surface reconstruction. From the molecular model of Fig. 12C, we find that the *cis*-BCTBPP molecules are aggregated into a supramolecular tetramer on the Au(111) surface. In this structure, the antiparallel intermolecular connections of all the cyanophenyl substituents lead to a macrocyclic arrangement of the porphyrin molecules, forming a molecular ring.

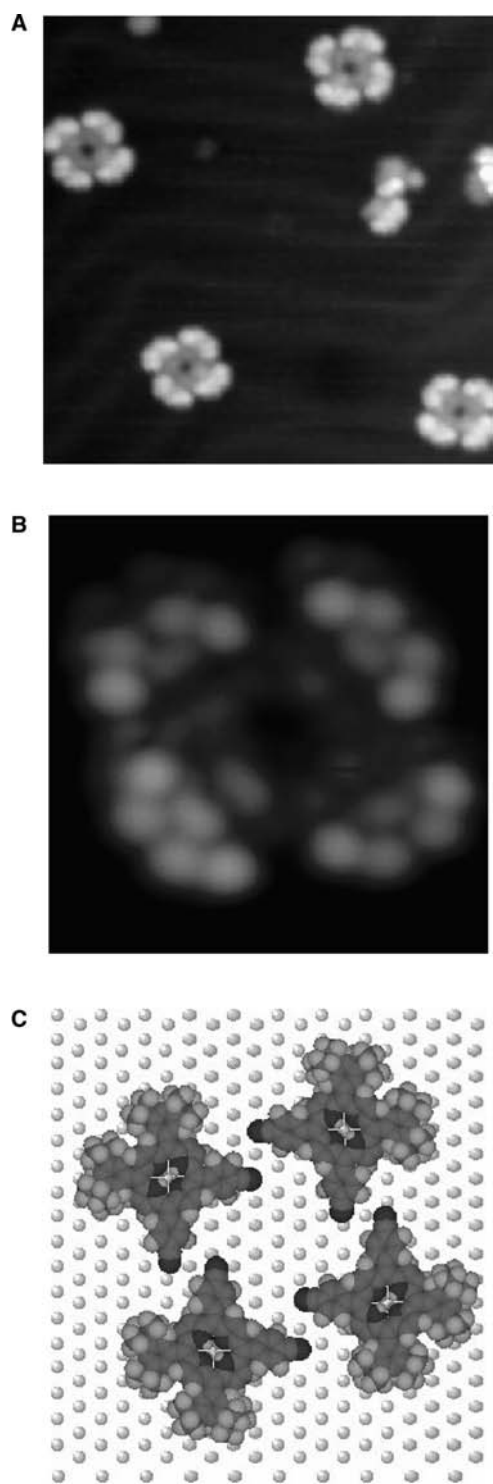


**Fig. 12** (A) STM image at 63 K of *cis*-BCTBPP molecules on Au(111). Identical clusters appear as four-leaf clover. (B) High-resolution STM image of a cluster and (C) its model. This cluster is composed of four molecules, in which antiparallel configuration between cyano groups is formed.

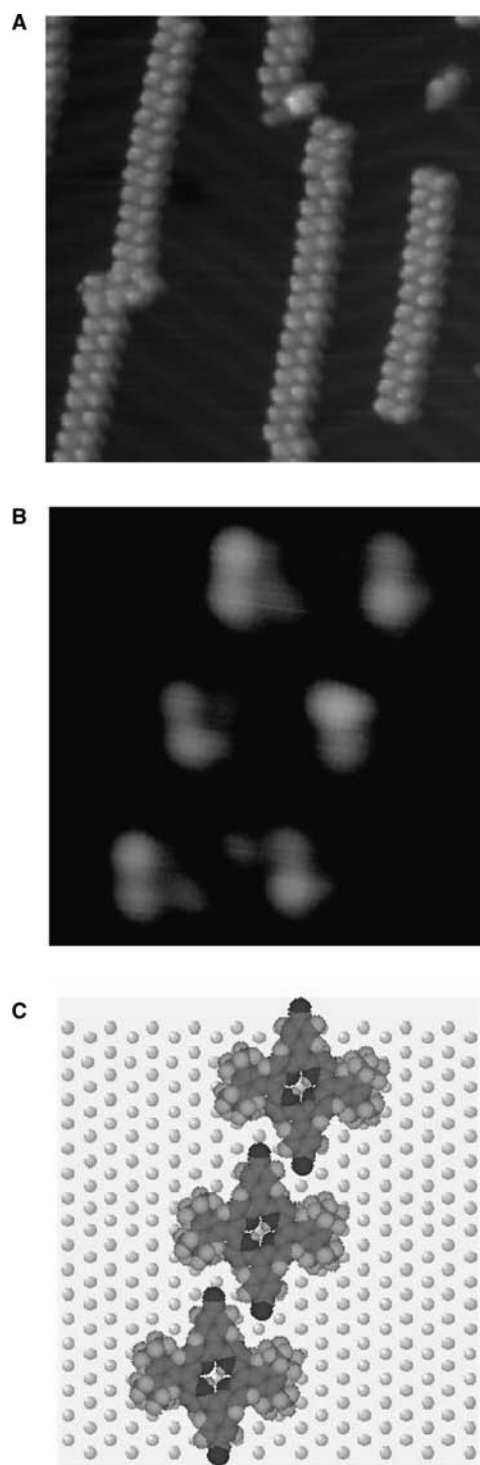


**Fig. 13** (A) STM image at 63 K of *trans*-BCTBPP molecules on Au(111). Linear long wires are formed. (B) High-resolution STM image of a wire and (C) its model. This wire is formed by the antiparallel interaction between cyano groups.

The diameter of the macrocyclic ring is roughly estimated to be about 3.8 nm.

In contrast to the macrocyclic clusters of CTBPP and *cis*-BCTBPP, sequential aggregation was achieved for the *trans*-BCTBPP molecules, where two cyano-phenyl groups were substituted at the *trans* positions. Fig. 13 shows supramolecular wires of *trans*-BCTBPP formed on the Au(111) surface. In this structure, the antiparallel configuration between the cyanophenyl substituents results in a linear arrangement of the molecules. The maximum length of the straight wires is above 100 nm, comparable with the length scale of the present silicon devices. In addition, most of the individual wires extended across the elbows of the heringbone patterns, whereas some branches are also formed because of the three-fold symmetry of Au(111). This is because the molecules were initially nucleated at the elbows, so that it is easy to connect these molecules in the direction across the elbows.

The selective aggregation of the porphyrin molecules results from the antiparallel or cyclic configurations of the cyano substituents. From the high-resolution STM images and related models, we estimated the length of CH...NC contacts between cyanophenyl substituents to be about 2.6 and 2.5 Å for the antiparallel and cyclic configurations, respectively. These values are almost identical to those of the calculated cyanobenzene clusters, indicating that the obtained clusters are stable on the surface.

## CONCLUSION

In this work, we have presented the formation of surface-supported supramolecular structures with controlled size and shape by using the dipole-dipole interactions of the cyano group. On the Au(111) surface, monomer, trimer, tetramer, or wire-like aggregations of porphyrins were controlled only by changing the number and position of the cyanophenyl substituent. It should be emphasized that these porphyrins find one another on the surface and link together spontaneously. Because a large number of substituents have been reported for non-covalent bonding, further controls of selective aggregation should be feasible on surfaces.

In molecular electronic nanodevices, these supramolecular aggregates should be linked to the outside world through microscopic electrodes, and a semiconducting or insulating substrate should be more useful. As some substituents are likely to connect to metal atoms, selective adsorption of substituted molecules at metal electrodes will be easy to obtain on an inert insulating surface. By further selective assembly, supramolecular nanostructures (such as wires) should be constructed between metal electrodes, in which the

structures are electrically coupled with the electrodes because of the metal-substituent connections.

## ACKNOWLEDGMENTS

This work was supported by the Ministry of Education, Culture, Sports, Science, and Technology (MEXT) through Organized Research Combination System.

## REFERENCES

1. Wada, Y.; Tsukada, M.; Fujihira, M.; Matsushige, K.; Ogawa, T.; Haga, M.; Tanaka, S. Prospects and problems of single molecule information devices. *Jpn. J. Appl. Phys.* **2000**, *39*, 3825–3846.
2. Joachim, C.; Gimzewski, J.K.; Aviram, A. Electronics used hybrid-molecular and mono-molecular devices. *Nature* **2000**, *406*, 48–51.
3. Aviram, A.; Ratner, M. Molecular rectifiers. *Chem. Phys. Lett.* **1974**, *29*, 277–283.
4. Nakamura, T.; Matsumoto, T.; Tada, H.; Sugiura, K.-I. *Chemistry of Nanomolecular Systems*; Springer, 2002.
5. Sugiura, K.; Tanaka, H.; Matsumoto, T.; Kawai, T.; Sakata, Y. A Mandala-patterned bandanna-shaped porphyrin oligomer. *Chem. Lett.* **1999**, 1193–1194.
6. Tsuda, A.; Osuka, A. Fully conjugated porphyrin tapes with electronic absorption bands that reach into infrared. *Science* **2001**, *293*, 79–82.
7. Lehn, J.-M. *Supramolecular Chemistry: Concept and Perspectives*; VCH: Weinheim, 1995.
8. Binning, G.; Rohrer, H.; Gerber, Ch.; Weibel, E. Surface studies by scanning tunneling microscopy. *Phys. Rev. Lett.* **1982**, *49*, 57–61.
9. Furukawa, M.; Tanaka, H.; Sugiura, K.; Sakata, Y.; Kawai, T. Fabrication of molecular alignment at the specific sites on Cu(111) surface using self-assembly phenomena. *Surf. Sci.* **2000**, *445*, L58–L63.
10. Barth, J.V.; Weckesser, J.; Gunter, P.; Burgi, L.; Jeandepoux, O.; Kern, K. Building supramolecular nanostructures at surfaces by hydrogen bonding. *Angew. Chem., Int. Ed. Engl.* **2000**, *39*, 1230–1234.
11. Bohringer, M.; Morgenstern, K.; Schneider, W.-D.; Berndt, R.; Mauri, F.; Vita, A.D.; Car, R. Two-dimensional self-assembly of supramolecular clusters and chains. *Phys. Rev. Lett.* **1999**, *83*, 324–327.
12. Milgrom, L.R. *The Color of Life. An Introduction to the Chemistry of Porphyrins and Related Compounds*; Oxford University Press, 1997.
13. Kadish, K.M.; Smith, K.M.; Guillard, R. *The Porphyrin Handbook*; Academic Press, 2000.
14. Sugiura, K.; Iwasaki, K.; Umishita, K.; Hino, S.; Ogata, H.; Miyajima, S.; Sakata, T. X-ray photoelectron spectroscopy of metallo porphyrins having bulky substituents: standard values of core ionization potentials. *Chem. Lett.* **1999**, 841–842.

15. Jung, T.A.; Schlittler, R.R.; Gimzewski, J.K. Conformational identification of individual adsorbed molecules with the STM. *Nature* **1997**, *386*, 696–698.
16. Dewar, M.J.S.; Zebisch, E.G.; Healy, E.F.; Stewart, J.J.P. AM1: A new general purpose quantum mechanical molecular model. *J. Am. Chem. Soc.* **1985**, *107*, 3902.
17. Barth, J.V.; Brune, H.; Ertl, G.; Behm, R.J. Scanning tunneling microscopy observations on the reconstructed Au(111) surface: atomic structure, long-range superstructure, rotational domains, and surface defects. *Phys. Rev., B* **1990**, *42*, 9307–9318.
18. Chambliss, D.D.; Wilson, R.J.; Chiang, S. Nucleation of ordered Ni island arrays on Au(111) by surface-lattice dislocations. *Phys. Rev. Lett.* **1991**, *66*, 1721–1724.
19. Yokoyama, T.; Yokoyama, S.; Kamikado, T.; Mashiko, S. Nonplanar adsorption and orientational ordering of porphyrin molecules on Au(111). *J. Chem. Phys.* **2001**, *115*, 3814–3818.
20. Hamers, R.J. Atomic-resolution surface spectroscopy with the scanning tunneling microscope. *Annu. Rev. Phys. Chem.* **1989**, *40*, 531–559.
21. Yokoyama, T.; Yokoyama, S.; Kamikado, T.; Okuno, Y.; Mashiko, S. Selective assembly on a surface of supramolecular aggregates with controlled size and shape. *Nature* **2001**, *413*, 619–621.
22. Frish, M.; Trucks, G.W.; Schlegel, H.B.; Scuseria, G.E.; Rob, M.A.; Cheeseman, J.R.; Zakrzewski, V.G.; Montgomery, J.A., Jr.; Statmann, R.E.; Burant, J.C.; Dapprich, S.; Millam, J.M.; Daniels, A.D.; Kudin, R.; Mennucci, B.; Pomelli, C.; Adamo, C.; Clifford, S.; Ortiz, J.V.; Baboul, A.G.; Stefanov, B.B.; Liu, G.; Liashenko, A.; Piskorz, P.; Komaromi, I.; Gomperts, R.; Martin, R.L.; Fox, D.J.; Keith, T.; Al-Laham, M.A.; Peng, C.Y.; Nanayakkara, A.; Gonzalez, C.; Challacombe, M.; Gill, P.M.W.; Johnson, B.G.; Chen, W.; Wong, M.W.; Andres, J.L.; Gonzalez, C.; Head-Gordon, M.; Replogle, E.S.; Pople, J.A. *Gaussian 98, Revision A.7*; Gaussian Inc: Pittsburgh, PA, 1988.
23. Okuno, Y.; Yokoyama, T.; Yokoyama, S.; Kamikado, T.; Mashiko, S. Theoretical study of benzonitrile clusters in the gas phase and their adsorption onto a Au(111) surface. *J. Am. Chem. Soc.* **2002**, *124*, 7218–7225.

# Coordination Framework Topology

Neil R. Champness

Neil S. Oxtoby

School of Chemistry, University of Nottingham, Nottingham, U.K.

## INTRODUCTION

This entry describes the use of multimodal ligands in constructing solid-state molecular materials, in particular coordination frameworks. It will be demonstrated that such ligands have advantages over simpler, more traditional unimodal ligands in controlling the topology of coordination frameworks at the molecular level. This gives rise to the hope of a high degree of design of coordination frameworks for subsequent use as advanced materials.

The construction of crystal-engineered frameworks using either coordinative-bonding or hydrogen-bonding interactions is an extremely topical area of inorganic and materials chemistry.<sup>[1–3]</sup> The strong interest in this area arises because the synthetic procedure used to construct these materials allows, in principle, a high degree of design. New materials with tunable properties have been developed from coordination frameworks over recent years and as synthetic procedures become more advanced so the properties of these materials become more highly evolved.

In particular, new framework materials with host-guest properties, similar to those observed with zeolites, have been reported. The potential advantage of using coordination frameworks is that the components of the framework, metal, ligand, and anion can be readily chosen and designed to allow specific manipulation of the dimensions and shape of channels or pores. Component design gives rise to not only shape-selective inclusion but also the possibility of chemoselectivity. Recent examples include very high methane adsorption<sup>[4]</sup> within a coordination framework and also rare example of dioxygen adsorption in which the dimensions of the framework channels give rise to a highly ordered O<sub>2</sub> array.<sup>[5]</sup> Examples of new materials with interesting magnetic<sup>[6]</sup> and non-linear optical<sup>[7]</sup> properties have also been reported. It is even possible to incorporate more than one of these properties within a single material and this gives rise to highly novel and advanced materials such as a nanoporous molecular magnet with reversible solvent-induced mechanical and magnetic properties<sup>[8]</sup> and a coordination-framework-based material that exhibits coexisting ferromagnetism and metallic conductivity.<sup>[9]</sup>

## COORDINATION FRAMEWORK DESIGN: THE BUILDING BLOCK METHODOLOGY

The high degree of design in these systems arises from the coupling of the well-understood coordination properties of individual metal ions and the highly developed organic chemistry of ligand synthesis. Indeed, notable advances have been made in the synthesis of coordination frameworks and in understanding the factors that influence network topology using the building block methodology as originally advanced by Robson et al.<sup>[1]</sup> The building block methodology can be used to design molecular frameworks by using the geometric properties of the framework components. For example, by linking building blocks through simple linear rods (connecting units) the geometric properties of the building block are expressed throughout three-dimensional space. In the case of coordination frameworks one may like to consider the properties of a transition metal ion. Thus if one links metal cations with a linear coordination geometry through a simple connecting unit, a one-dimensional chain will be constructed. Similarly, a square-planar metal cation can be linked to generate a two-dimensional sheet structure. Three-dimensional architectures can be achieved by linking non-linear or non-planar metal centers. Perhaps the most commonly studied example of a three-dimensional coordination framework is that constructed from tetrahedral metal centers, such as Cu(I), and linear bridging ligands, including 4,4'-bipyridine,<sup>[10]</sup> or *trans*-1,2-bis(4-pyridyl) ethene.<sup>[11]</sup> In this case the metal nodes will be linked such that the tetrahedral geometry of the cation is expressed in three dimensions to generate a structure with a diamond-like structure (Fig. 1). The geometry of the ligand can also be readily adapted and in principle combinations of different building block geometric properties may be combined to generate increasingly complex multidimensional architectures.

This concept of using building block geometries to develop extended arrays is highly adaptable, but framework structures can be readily influenced by weaker supramolecular forces,<sup>[2]</sup> and the situation is not as simple as it may at first appear. Indeed, the



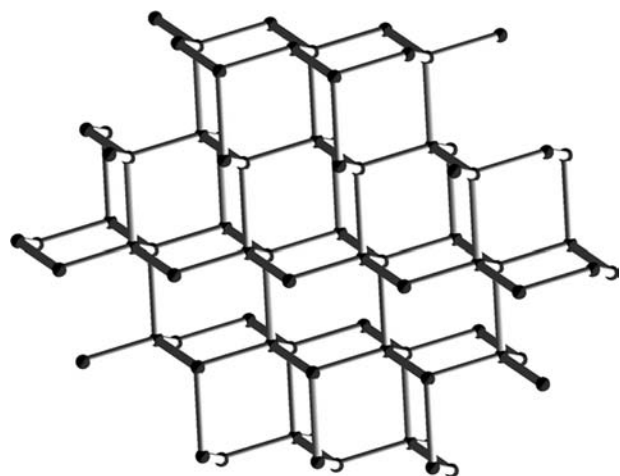
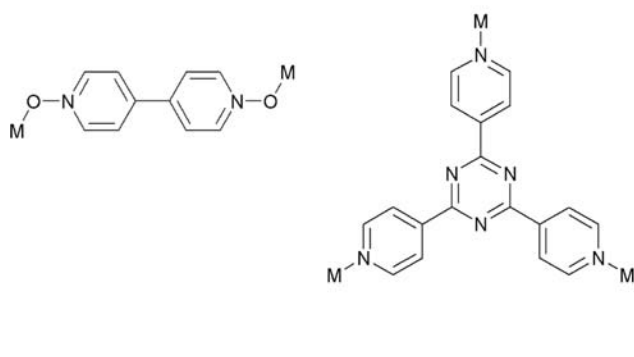


**Fig. 1** Schematic representation of a diamond-like structure which can be generated by linking tetrahedral metal nodes through bidentate bridging ligands, such that the tetrahedral geometry of the cation is expressed in three dimensions.

individual components of a network system cannot be treated separately, but the network must be thought of as a combined entity drawing upon the unified properties of the building blocks used in its construction.

The majority of coordination frameworks reported thus far have used relatively simple ligand systems using bridging ligands that provide two,<sup>[12]</sup> three,<sup>[13]</sup> or four<sup>[14]</sup> monodentate donors in a predefined geometry (Scheme 1). Such ligands give rise to a vast range of structural types but are limited in their influence of network structure in two ways.

Firstly, as the ligands use only monodentate donors they offer little control over the interaction between the ligand and the metal center. The ligand is able to occupy a single metal coordination site offering influence over the rest of the metal center only through steric crowding or through more subtle electronic effects. Secondly, the ligand can bridge metal centers in only a single manner (Scheme 1). This means that the ligand is controlling the network structure only by means of the ligand length or potentially via steric bulk or weaker supramolecular interactions.

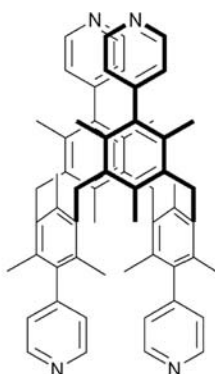


This is not to belittle the contribution of such systems. Indeed, the chemistry of coordination frameworks has advanced so rapidly using precisely these simple ligands and it is a perfect example of how a complicated approach is not always the most useful or applicable to a given problem.

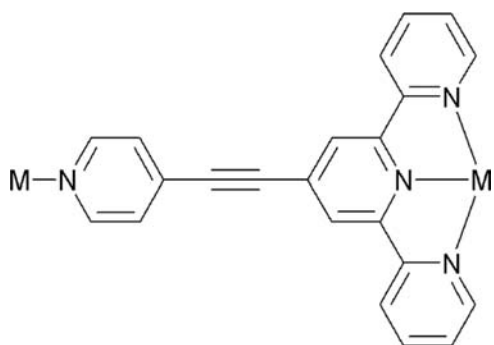
However, the principles and complexity of ligand synthesis strategies offer the supramolecular chemist the possibility of a much higher degree of building-block design. This potentially leads to a greater control of network structure, topology,<sup>[15]</sup> and ultimately functional properties. One way in which coordination network structure can be influenced is by using multimodal ligands.

## MULTIMODAL LIGANDS VS. UNIMODAL LIGANDS

Multimodal ligands differ from simpler unimodal systems in that they offer both more than one binding site, usually both monodentate and chelating bidentate donor sites and in some cases more than one bridging mode. A simple example of a multimodal ligand is 2,4-di(2-pyridyl)-6-(ethynyl-4-pyridyl)pyridine (Scheme 2), which contains both a tridentate, terpyridyl site and a monodentate pyridyl site, both of which are capable of binding to a suitable metal center.<sup>[16]</sup> The tridentate site is expected to be the most strongly coordinating unit, reflecting the simple chelate effect, and reaction with  $\text{Co}(\text{ClO}_4)_2$  affords a mononuclear complex in which the  $\text{Co}(\text{II})$  center is coordinated by two terpyridyl sites. However, in the presence of counteranion with a greater coordinating ability, such as chloride, the metal center is coordinated by two  $\text{Cl}^-$  ligands leaving four residual coordination sites at the octahedral metal center. A terpyridyl ligand and a monodentate pyridyl donor from a second ligand occupy these four sites, and this results in the formation of a one-dimensional coordination polymer (Fig. 2). Thus using appropriate design protocols the multimodal ligand can be used to assemble either a discrete complex or a one-dimensional polymeric system.



**Scheme 1** Examples of unimodal bridging ligands that provide two, three, or four monodentate donors in a predefined geometry. Source: From Refs.<sup>[12–14]</sup>.



**Scheme 2** A simple example of a multimodal ligand, 2,4-di(2-pyridyl)-6-(ethynyl-4-pyridyl)pyridine.

It is evident from this example that the combination of more than one type of coordinating mode within a single ligand offers the potential for control over the coordination sphere of a metal within a self-assembled coordination architecture. Thus when a single tridentate unit is coordinated to the metal center the number and orientation of the remaining coordination sites on a given metal are defined for other ligands. The ligand thus defines, to some extent, the orientation of ligands used in coordination polymer propagation.

Multimodal ligands also differ from simpler unimodal ligands in that they specifically control the relative positions of the donor groups with respect to each other and thus offer more than one method of bridging metal centers within an extended array. This differs from unimodal ligands in which a single bridging mode is typically observed even when using tri- or tetradentate ligands. This point will be elaborated further below.

## COORDINATION PREFERENCES OF MULTIMODAL LIGANDS

As multimodal ligands possess more than one type of coordination site there will inherently be a degree of competition between donor groups within a single ligand. This is illustrated by the example of the 2,4-di(2-pyridyl)-6-(ethynyl-4-pyridyl)pyridine–Cobalt(II) system discussed above (Fig. 2) for which the ligand exhibits two distinct coordination modes, using either just one or both of the available coordination sites.<sup>[16]</sup>

As multimodal ligands often combine both bi- or tridentate groups and monodentate donors the chelating, multidentate unit regularly dominates the

coordinating ability of the ligand following simple thermodynamic principles. This is illustrated by the reaction of pyrazino[2,3-*f*]quinoxaline (pyq) with  $\text{AgBF}_4$  in acetonitrile, which yields discrete complexes of the form  $[\text{Ag}(\text{pyq})_2](\text{BF}_4)$  in which the chelating bidentate fragment of the ligand coordinates, the Ag(I) center, and the monodentate donors remains uncoordinated (Fig. 3).<sup>[17]</sup>

However, it is not always the case that the multidentate site dominates the coordination sphere. Indeed, in one particularly rare case the ligand 2,2'-bi-1,6-naphthyridine reacts with  $\text{M}(\text{SCN})_2$  salts ( $\text{M} = \text{Co}, \text{Zn}, \text{Cd}$ ) to yield polymeric complexes,  $[\text{M}(\text{SCN})_2(2,2'\text{-bi-1,6-naphthyridine})_2]_\infty$ , in which the metal centers are coordinated exclusively by the monodentate groups of this ligand (Fig. 4).<sup>[18]</sup> Thus each metal center is coordinated by four distinct ligands, with the remaining metal sites occupied by the  $\text{SCN}^-$  ligands, and the ligands bridge metal centers to generate a two-dimensional sheet structure of (4,4) topology.<sup>[15]</sup> In this instance the bidentate units remain uncoordinated, which is surprising considering that these groups should be much better donors for the metal centers in comparison to the monodentate donors. The reason for the preference of this particular system to adopt this unexpected coordination mode is unclear, but may possibly be explained by the observed products being a kinetic rather than thermodynamic product. Such a phenomenon has been previously observed for coordination polymer structures for which insolubility of a kinetic product may be an important factor.<sup>[19]</sup> It is interesting to note that if one considers a hypothetical product in which the bidentate unit of this ligand is coordinated to the metal center, there would be a maximum of three such groups coordinated to the metal which would lead to an entirely different architecture.

In most cases the coordination preferences of the metal center will strongly influence the coordinating preferences of the ligand. Typically, a metal center will have a strong thermodynamic preference for a given geometry and ligand type, and for most metals this will result in multimodal ligands coordinating via their chelating groups in preference to a combination of donors unless a specific system is carefully designed, as is the case for the 2,4-di(2-pyridyl)-6-(ethynyl-4-pyridyl)pyridine–Cobalt(II) system discussed above.<sup>[16]</sup> However, certain metal centers do not exhibit strong coordination preferences and only small energy barriers exist

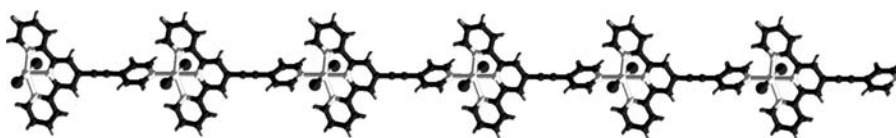


**Fig. 2** View of the one-dimensional coordination polymer formed by  $\{\text{CoCl}_2[2,4\text{-di}(2\text{-pyridyl})\text{-6-(ethynyl-4-pyridyl)pyridine}]\}_2$ . Source: From Ref.<sup>[16]</sup>.

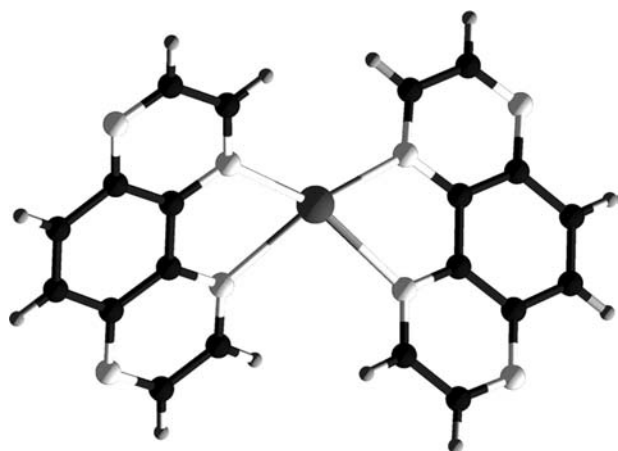


**Fig. 3** View of the structure of  $[Ag(pyq)_2](BF_4)$  in which the chelating bidentate fragment of the ligand coordinates the Ag(I) center, and the monodentate donors remains uncoordinated, pyq = pyrazino[2,3-*f*]quinoxaline.

between multiple coordination geometries. This is particularly noticeable for Ag(I) whose  $d^{10}$  electronic configuration results in a highly flexible and coordinatively labile metal center. Ag(I) compounds are particularly susceptible to variation in reaction conditions, including reaction solvent, and also to the nature of the counteranion that is used. However, in many instances reactions between multimodal ligands and Ag(I) salts will result in the metal center adopting what may be considered a uniform coordination environment within a coordination polymer. In other words, all of the metal centers adopt the same number and types of donor and similar relative orientations. The rest of this entry will concentrate on how the use of multimodal ligands can lead to the development of interesting coordination architectures with Ag(I) cations and how the multimodal ligands contrast with simpler unimodal systems.

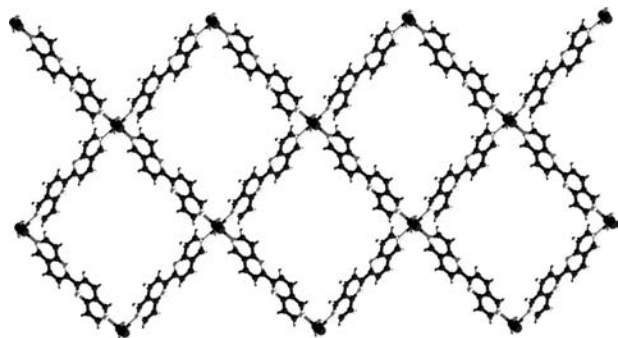


**Fig. 4** View of the two-dimensional coordination polymer formed by  $[M(SCN)_2(2,2'\text{-bi-1,6-naphthyridine})_2]_\infty$  ( $M = Co, Zn, Cd$ ) illustrating that the metal centers are coordinated exclusively by the monodentate groups of the 2,2'-bi-1,6-naphthyridine ligand.

## AG(I) COORDINATION POLYMERS WITH MULTIMODAL LIGANDS

Ag(I)-based coordination polymers are capable of generating one-,<sup>[20]</sup> two-,<sup>[17,21–24]</sup> or three-dimensional structures<sup>[17,21,24–28]</sup> depending on the nature of the other building blocks employed and have been particularly well studied with multimodal ligands.<sup>[17,21,23,24,29,30]</sup> For multimodal ligands, one-dimensional structures are less common, and so to illustrate the influence of such ligands this article will concentrate on three- and two-dimensional architectures.

### Three-Dimensional Architectures

The reaction of Ag(I) salts,  $AgBF_4$  or  $AgPF_6$ , with the multimodal ligand 2,2'-bipyrazine (bpyz) has been extensively studied.<sup>[17,21]</sup> When the reaction is performed using nitromethane as a solvent, three-dimensional coordination polymers are formed,  $\{[Ag(bpyz)](BF_4)\}_\infty$ <sup>[17,21]</sup> or  $\{[Ag(bpyz)](PF_6)\}_\infty$ <sup>[17]</sup> both of which crystallize in the chiral tetragonal space group  $P4_32_12$ . In both polymers the same Ag(I) coordination environment and topological arrangement are observed. The Ag(I) center adopts a “uniform” coordination sphere throughout the polymeric architecture being coordinated by three bpyz ligands, one chelating and two monodentate N-donors, in a pseudo-tetrahedral geometry. Each Ag(I) center is linked to four nearest-neighbor Ag(I) centers, two via the chelating ligand and two more through two peripheral monodentate N-donors forming a distorted diamond-like array (Fig. 5). The chirality of the framework can be most readily understood if one inspects the extended lattice along the crystallographic *c* axis. This view shows that the structure forms two distinct channels that represent different helices running through the network (Fig. 6). The larger square-shaped channel constructs a  $4_3$  helix in which each Ag(I) center is linked to the next Ag(I) center along the helix via a short, single pyrazine bridging mode. In contrast, the smaller rhomboid-shaped channel forms a  $2_1$  helix in which adjacent Ag(I) centers are linked through a longer bridging mode via two peripheral N-donors of a bpyz ligand. In contrast to a conventional diamond lattice in which adjacent helices have opposing hands and are chemically identical, in  $\{[Ag(bpyz)](BF_4)\}_\infty$  adjacent antiparallel helices are chemically distinct, displaying different bridging modes and resulting in the chirality demonstrated by these architectures.

The role of the multimodal ligand is crucial in influencing the architecture of these compounds and in inducing the chirality of the framework that is observed. To fully appreciate the role of the ligands one must consider a related structure constructed using a unimodal

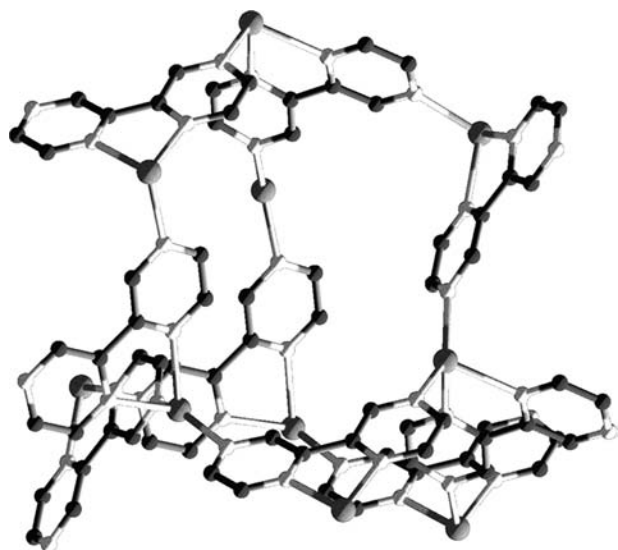


**Fig. 5** View of the three-dimensional structure formed by  $\{[\text{Ag}(\text{bpyz})](\text{BF}_4)\}_\infty$  illustrating an adamantane-shaped unit which forms a portion of the extended diamond-like structure.

ligand. The closest, unimodal analogue to 2,2'-bipyrazine would be two pyrazine ligands (Scheme 3). Unfortunately, the reactions of pyrazine with Ag(I) salts are extremely complex leading to a plethora of different products, and direct comparisons are not valuable.<sup>[22,25,26]</sup> However, comparison with the highly related bridging, bidentate unimodal ligand

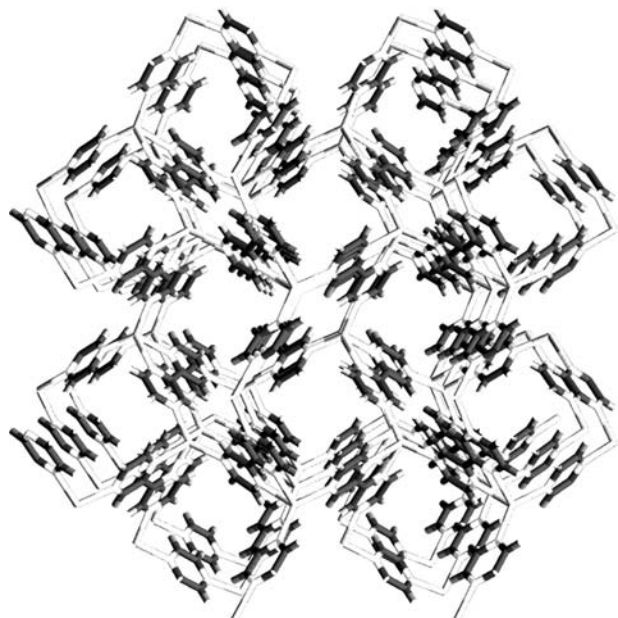


**Fig. 6** View along the crystallographic  $c$  axis of  $\{[\text{Ag}(\text{bpyz})](\text{BF}_4)\}_\infty$  showing the two distinct channels that represent different helices running through the network.

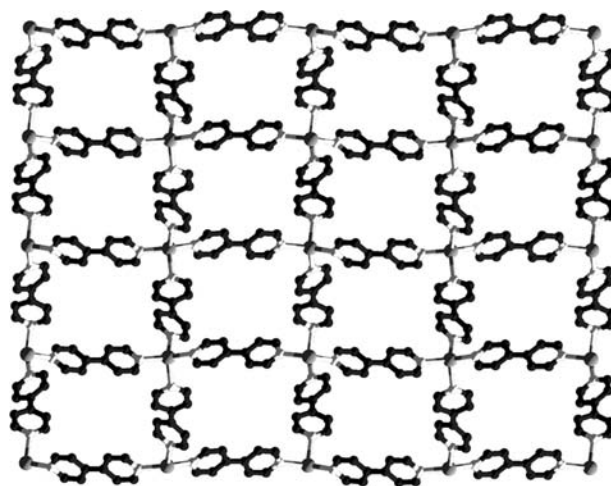
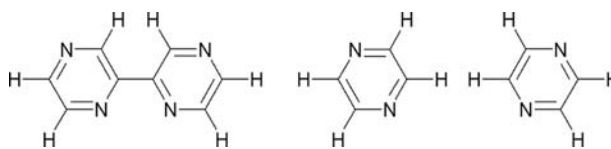


**Fig. 7** View of the conventional diamond structure formed by  $\{[\text{Ag}(4,4'\text{-bipyridine})_2](\text{CF}_3\text{SO}_3)\}_\infty$ , which adopts a single type of channel around which a single type of helix is observed.

4,4'-bipyridine does provide a useful evaluation of the influence of multimodal ligands. Reaction of  $\text{Ag}(\text{CF}_3\text{SO}_3)$  with 4,4'-bipyridine forms a conventional diamond-like structure,  $\{[\text{Ag}(4,4'\text{-bipyridine})_2](\text{CF}_3\text{SO}_3)\}_\infty$ , which crystallizes in the centrosymmetric, achiral space group  $Pbca$ .<sup>[27]</sup> The conventional diamond structure formed by  $\{[\text{Ag}(4,4'\text{-bipyridine})_2](\text{CF}_3\text{SO}_3)\}_\infty$  forms a single type of channel around which a single type of helix is observed (Fig. 7). The uniformity of channel periphery is a result of the unimodal nature of the 4,4'-bipyridine bridging ligand which can only coordinate metal centers through one type of donor and crucially is only capable of bridging metal centers through a single mode. Thus it can be seen that by using a multimodal ligand, such as 2,2'-bipyrazine, the three-dimensional architecture of a coordination polymer can be significantly altered, and in the example of  $\{[\text{Ag}(\text{bpyz})](\text{BF}_4)\}_\infty$  chirality can be introduced to a framework structure.<sup>[17,21]</sup>

The role of the multimodal ligand is key in this system. By possessing multiple bridging modes, 2,2'-bipyrazine can disrupt the homogeneity of channels in the diamond-like array. Such a reduction in homogeneity may prove useful in controlling the properties of materials. For example, in this example the two different channels may ultimately be useful for chemical



**Scheme 3** Comparison of the multimodal ligand, 2,2'-bipyrazine, and two unimodal pyrazine ligands.



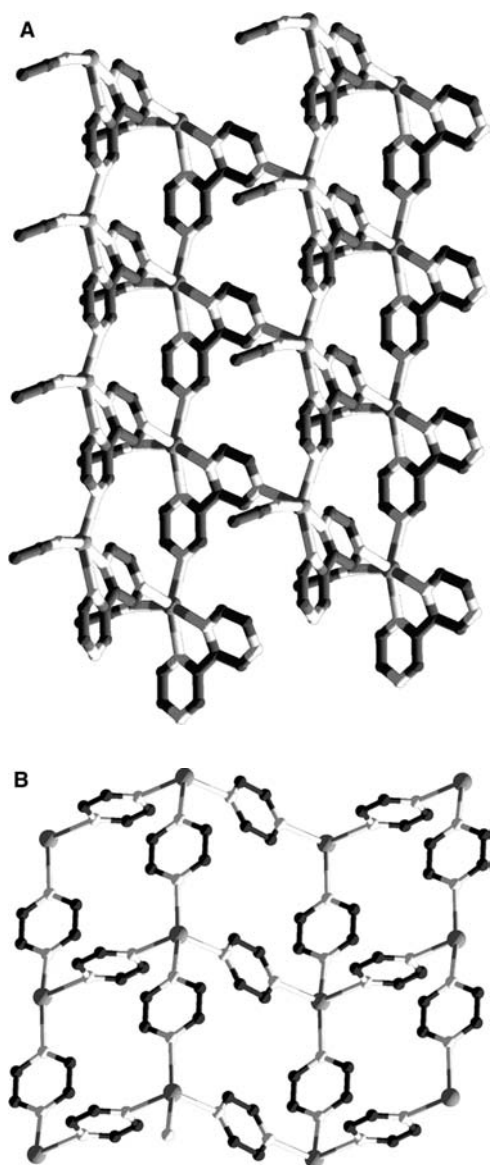


**Fig. 8** View of the two-dimensional sheet structures formed by (A)  $\{[\text{Ag}(\text{bpyz})(\text{MeCN})]\text{BF}_4\}_\infty$  and (B)  $\{[\text{Ag}(\text{pyrazine})_2]\text{PF}_6\}_\infty$ .

separation. Reduction in homogeneity and hence symmetry is also more likely to lead to polar or chiral materials, such as  $\{[\text{Ag}(\text{bpyz})](\text{BF}_4)\}_\infty$ , an area of specific interest for crystal engineering of materials with non-linear optical properties.<sup>[7]</sup>

### Two-Dimensional Architectures

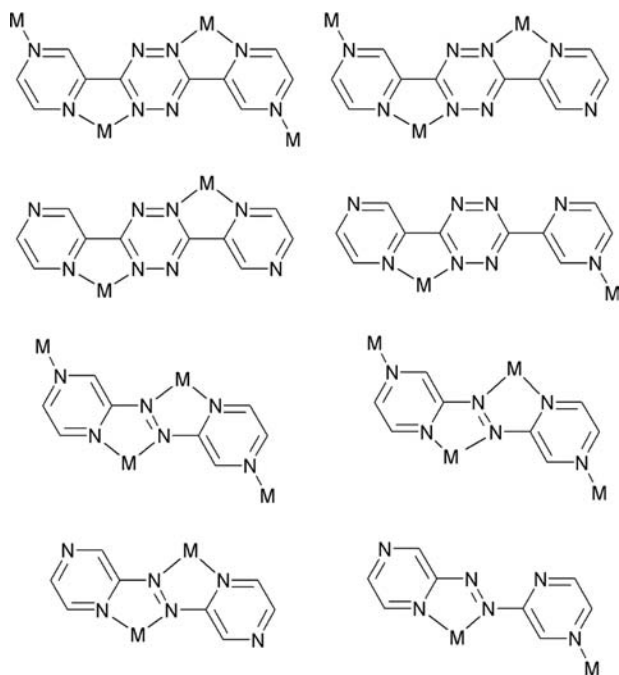
It is also possible to generate two-dimensional coordination polymer architectures using Ag(I) cations and multimodal ligands, including 2,2'-bipyrazine.<sup>[17,21]</sup> Reaction between  $\text{AgBF}_4$  and bpyz using an acetonitrile

solvent results in the formation of an extended two-dimensional sheet structure,  $\{[\text{Ag}(\text{bpyz})(\text{MeCN})]\text{BF}_4\}_\infty$ . In  $\{[\text{Ag}(\text{bpyz})(\text{MeCN})]\text{BF}_4\}_\infty$  all of the Ag(I) cations adopt a uniform coordination sphere with one chelating bidentate bpyz ligand, two monodentate bpyz ligands, and an additional coordinated acetonitrile ligand (Fig. 8A). The acetonitrile ligand plays no role in polymer propagation but does serve to cap the Ag(I) coordination sphere allowing the adoption of a two-dimensional sheet-like structure.

In this instance a comparable pyrazine-based structure has been reported,  $\{[\text{Ag}(\text{pyrazine})_2]\text{PF}_6\}_\infty$ , although a different counteranion,  $\text{PF}_6^-$ , is employed.<sup>[22]</sup> Counteranions can have a very significant impact upon the extended structures of coordination polymers and this is most certainly the case for Ag(I)-based systems.<sup>[17,26,28,31]</sup> However, if one considers the topology of the cationic coordination polymer framework alone, valuable insight into the role of multimodal ligands is still valid. The structure of  $\{[\text{Ag}(\text{pyrazine})_2]\text{PF}_6\}_\infty$  consists of four connected Ag(I) nodes bridged by pyrazine ligands to afford an extended two-dimensional sheet of (4,4) topology that is highly undulating due to a distorted geometry at the Ag(I) center (Fig. 8B).  $\{[\text{Ag}(\text{bpyz})(\text{MeCN})]\text{BF}_4\}_\infty$  adopts a highly related structure in which each Ag(I) cation is linked to four others to give a two-dimensional structure which may be viewed as a (4,4)-grid structure if one considers solely the metal centers as nodes.

Comparison of the structures of the above examples illustrates that the multimodal 2,2'-bipyrazine ligand subtly influences the extended framework structure. In both  $\{[\text{Ag}(\text{bpyz})(\text{MeCN})]\text{BF}_4\}_\infty$  and  $\{[\text{Ag}(\text{pyrazine})_2]\text{PF}_6\}_\infty$ , individual tetranodal units comprise four Ag(I) centers and four aromatic, pyrazyl or pyrazine rings. However, in the case of  $\{[\text{Ag}(\text{bpyz})(\text{MeCN})]\text{BF}_4\}_\infty$  two pyrazine edges of the tetranodal units are linked using the interpyrazyl C–C bond of the 2,2'-bipyrazine ligands. This results in a subtle modification of the tetranodal units contracting two of the angles to make a rhomboid-shaped unit rather than a square-shaped unit (Fig. 8A). Thus it can be seen that using a multimodal ligand, 2,2'-bipyrazine, rather than the unimodal ligand, pyrazine, allows subtle control over the coordination network structure.

The principle of manipulation of two-dimensional sheets can be extended further by using more complex multimodal ligands such as 3,6-di-pyrazin-2-yl-(1,2,4,5)-tetrazine (dpztz)<sup>[23]</sup> or 2,2'-azobispyrazine (azpyz).<sup>[24]</sup> Both of these ligands have the capability to coordinate up to four metal centers, two via chelating sites and two via monodentate sites (Scheme 4), and thus can potentially manipulate the internal arrangement of a two-dimensional sheet to a higher degree.



**Scheme 4** Schematic view of how more complex multimodal ligands, such as 3,6-di-pyrazin-2-yl-(1,2,4,5)-tetrazine (dpptz) or 2,2'-azobispyrazine (azpyz), can bind up to four metal centers.

The single-crystal X-ray structure of  $\{[\text{Ag}(\text{dpptz})]\text{PF}_6\}_\infty$ <sup>[23]</sup> shows each Ag(I) center adopting a five-coordinate geometry (Fig. 9), with two chelating and one monodentate dpptz ligands. Each dpptz ligand coordinates only three Ag(I) cations rather than the potential maximum of four metals, leaving a pendant, uncoordinated pyrazyl donor. The two-dimensional sheet structure can be viewed as a distorted (4,4) grid-type structure akin to those observed for  $\{[\text{Ag}(\text{bpyz})(\text{MeCN})]\text{BF}_4\}_\infty$  and  $\{[\text{Ag}(\text{pyrazine})_2]\text{PF}_6\}_\infty$ . In  $\{[\text{Ag}(\text{dpptz})]\text{PF}_6\}_\infty$  two different tetranodal units are

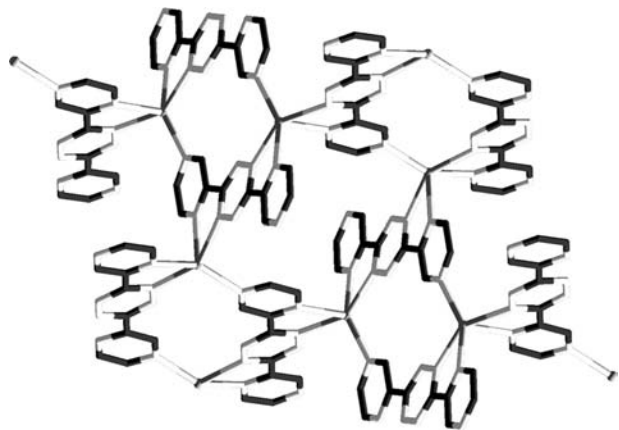


**Fig. 9** View of the two-dimensional sheet structure formed by  $\{[\text{Ag}(\text{dpptz})]\text{PF}_6\}_\infty$ .

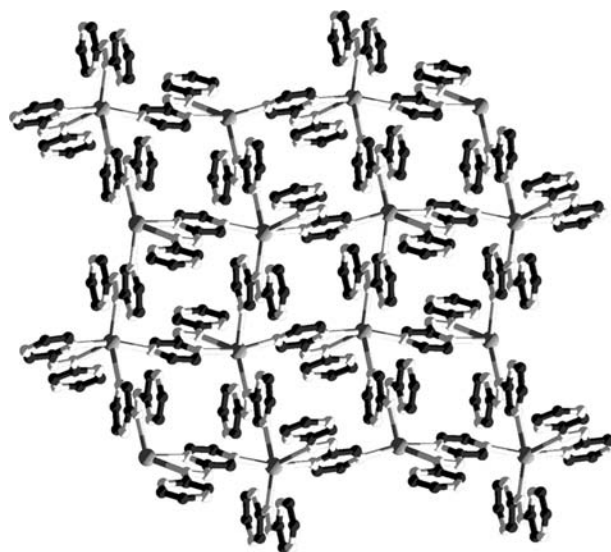


**Fig. 10** View of the two-dimensional sheet structure formed by  $\{[\text{Ag}(\text{azpyz})_2]\text{SbF}_6\}_\infty$ .

observed. In the smaller ring the sides of the unit consist of two tetrazine rings and two pyrazyl rings, thus two of the angles of this tetranodal unit are “pinched” by the intraligand C–C bonds. In the other tetranodal unit the edges also consist of two tetrazine and two pyrazyl groups. However, in this larger unit none of the angles is pinched as no two edges of the tetranodal unit are linked through an intra-dpptz covalent bond. As with  $\{[\text{Ag}(\text{bpyz})(\text{MeCN})]\text{BF}_4\}_\infty$  and  $\{[\text{Ag}(\text{pyrazine})_2]\text{PF}_6\}_\infty$  the sheet is highly undulating, with a depth of ca. 13.0 Å.

Azpyz also reacts to form a structure that adopts a two-dimensional (4,4) grid sheet structure.<sup>[24]</sup> Reaction between azpyz and  $\text{AgSbF}_6$  affords  $\{[\text{Ag}(\text{azpyz})_2]\text{SbF}_6\}_\infty$  in which each Ag(I) center adopts an unusually distorted, trigonal, prismatic, six-coordinate geometry and is coordinated by two chelating azpyz ligands and two monodentate pyrazyl donors (Fig. 10). Each Ag(I) center is bridged to four other via a pyrazyl group that does not participate in a chelating coordination mode and so the tetranodal units in this structure are not distorted by the ligand and a conventional (4,4) grid is observed.

The complexity, and sometimes unpredictable nature, of systems that involve multimodal ligands is illustrated by the structure that is formed from the reaction of  $\text{AgSbF}_6$  with dpptz which forms  $\{[\text{Ag}_2(\text{dpptz})_3](\text{SbF}_6)_2\}_\infty$ .<sup>[23]</sup> As with  $\{[\text{Ag}(\text{azpyz})_2]\text{SbF}_6\}_\infty$ ,  $\{[\text{Ag}_2(\text{dpptz})_3](\text{SbF}_6)_2\}_\infty$  forms a two-dimensional sheet structure that contains Ag(I) cations in a distorted, trigonal, prismatic geometry (Fig. 11). However, in this case the Ag(I) cation is coordinated by three chelating units and the final structure does not form a (4,4) grid structure but rather a (6,3) structure which may be thought of as a brick-wall structure (topologically related to honeycomb arrangements).



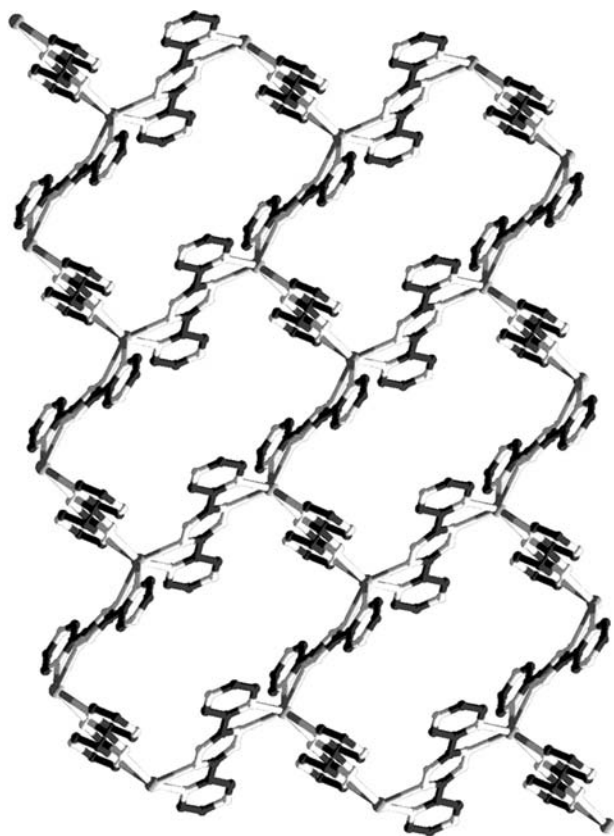


**Fig. 11** View of the two-dimensional sheet structure formed by  $\{[Ag_2(dpztz)_3](SbF_6)_2\}_\infty$ .

## CONCLUSION

It is clear from the brief examples reported here that multimodal ligands can be used to influence the structure of solid-state molecular materials such as coordination frameworks. In many ways such ligands have advantages over simpler, more traditional ligands in controlling the topology of coordination frameworks at the molecular level and give rise to the hope of a high degree of design of coordination frameworks.

## REFERENCES

- Robson, R.; Abrahams, B.F.; Batten, S.R.; Gable, R.W.; Hoskins, B.F.; Liu, J.P. Crystal engineering of novel materials composed of infinite 2-dimensional and 3-dimensional frameworks. *ACS Symp. Ser.* **1992**, *499*, 256–273.
- Blake, A.J.; Champness, N.R.; Hubberstey, P.; Li, W.S.; Withersby, M.A.; Schröder, M. Inorganic crystal engineering using self-assembly of tailored building-blocks. *Coord. Chem. Rev.* **1999**, *183*, 117–138.
- Moulton, B.; Zaworotko, M.J. From molecules to crystal engineering: supramolecular isomerism and polymorphism in network solids. *Chem. Rev.* **2001**, *101* (6), 1629–1658.
- Noro, S.; Kitagawa, S.; Kondo, M.; Seki, K. A new, methane adsorbent, porous coordination polymer  $\{[CuSiF_6(4,4'-bipyridine)_2](n)\}$ . *Angew. Chem. Int. Ed.* **2000**, *39*, 2082–2084.
- Kitaura, R.; Kitagawa, S.; Kubota, Y.; Kobayashi, T.C.; Kindo, K.; Mita, Y.; Matsuo, A.; Kobayashi, M.; Chang, H.C.; Ozawa, T.C.; Suzuki, M.; Sakata, M.; Takata, M. Formation of a one-dimensional array of oxygen in a microporous metal-organic solid. *Science* **2002**, *298*, 2358–2361.
- Kahn, O. Chemistry and physics of supramolecular magnetic materials. *Acc. Chem. Res.* **2000**, *33*, 647–657.
- Evans, O.R.; Lin, W. Crystal engineering of NLO materials based on metal-organic coordination networks. *Acc. Chem. Res.* **2002**, *35*, 511–522.
- Maspoch, D.; Ruiz-Molina, D.; Wurst, K.; Domingo, N.; Cavallini, M.; Biscarini, F.; Tejada, J.; Rovira, C.; Veciana, J. A nanoporous molecular magnet with reversible solvent-induced mechanical and magnetic properties. *Nat. Mater.* **2003**, *2*, 190–195.
- Coronado, E.; Galan-Mascaros, J.R.; Gomez-Garcia, C.J.; Laukhin, V. Coexistence of ferromagnetism and metallic conductivity in a molecule-based layered compound. *Nature* **2000**, *408*, 447–449.
- Macgillivray, L.R.; Subramanian, S.; Zaworotko, M.J. Interwoven 2-dimensional and 3-dimensional coordination polymers through self-assembly of Cu(I) cations with linear bidentate ligands. *J. Chem. Soc., Chem. Commun.* **1994**, 1325–1326.
- Blake, A.J.; Champness, N.R.; Chung, S.S.M.; Li, W.-S.; Schröder, M. Control over interpenetration of independent networks in three-dimensional copper(I) adamantoid arrays. *Chem. Commun.* **1997**, 1005–1006.
- Long, D.-L.; Blake, A.J.; Champness, N.R.; Wilson, C.; Schroder, M. Unprecedented seven- and eight-connected lanthanide coordination networks. *Angew. Chem. Int. Ed.* **2001**, *40*, 2444–2447.
- Abrahams, B.F.; Batten, S.R.; Grannas, M.J.; Hamit, H.; Hoskins, B.F.; Robson, R. Ni(tpt)(NO<sub>3</sub>)<sub>2</sub>—a three-dimensional network with the exceptional (12,3) topology: a self-entangled single net. *Angew. Chem. Int. Ed.* **1999**, *38*, 1475–1477.
- Klein, C.; Graf, E.; Hosseini, M.W.; De Cian, A. Design and structural analysis of interpenetrated 3-D coordination networks formed by self-assembly using tetrapyrrolinecyclophane and silver cations. *New J. Chem.* **2001**, *25*, 207–209.
- Wells, A.F. *Structural Inorganic Chemistry*, 5th Ed.; Clarendon Press: Oxford, 1984.
- Jouaiti, A.; Jullien, V.; Hosseini, M.W.; Planeix, J.-M.; De Cian, A. Controlling the formation of discrete complexes or a 1-D directional coordination network by the binding ability of anions. *Chem. Commun.* **2001**, 1114–1115.
- Blake, A.J.; Champness, N.R.; Cooke, P.A.; Nicolson, J.E.B.; Wilson, C. Multimodal bridging ligands; effects of ligand functionality, anion and crystallisation solvent in silver(I) coordination polymers. *J. Chem. Soc., Dalton Trans.* **2000**, 3811–3819.
- Wu, H.P.; Janiak, C.; Uehlin, L.; Klufers, P.; Mayer, P. 2,2'-bi-1,6-Naphthyridine metal complexes: a new

- ligand and a novel  $2 \times 2$  inclined interpenetration of (4,4) nets or formation of helicoidal chains. *Chem. Commun.* **1998**, 2637–2638.
19. Khlobystov, A.N.; Brett, M.T.; Blake, A.J.; Champness, N.R.; Wilson, C.; Schröder, M. Stereoselective association of binuclear metallacycles in coordination polymers. *J. Am. Chem. Soc.* **2003**, *125*, 6753–6761.
  20. Khlobystov, A.N.; Blake, A.J.; Champness, N.R.; Lemenovskii, D.A.; Majouga, A.G.; Zyk, N.V.; Schroder, M. Supramolecular design of one-dimensional coordination polymers based on silver(I) complexes of aromatic nitrogen-donor ligands. *Coord. Chem. Rev.* **2001**, *222*, 155–192.
  21. Blake, A.J.; Champness, N.R.; Cooke, P.A.; Nicolson, J.E.B. Synthesis of a chiral adamantoid network—the role of solvent in the construction of new co-ordination networks with silver(I). *Chem. Commun.* **2000**, 665–666.
  22. Carlucci, L.; Ciani, G.; Proserpio, D.M.; Sironi, A. 2D Polymeric silver(I) complexes consisting of markedly undulated sheets of squares. X-ray crystal structures of  $[\text{Ag}(\text{ppz})_2](\text{BF}_4)$  and  $[\text{Ag}(\text{pyz})_2](\text{PF}_6)$  (ppz = piperazine, pyz = pyrazine). *Inorg. Chem.* **1995**, *34*, 5698–5700.
  23. Oxtoby, N.S.; Blake, A.J.; Champness, N.R.; Wilson, C. Using multimodal ligands to influence network topology in silver(I) coordination polymers. *Proc. Natl. Acad. Sci. U. S. A.* **2002**, *99*, 4905–4910.
  24. Carlucci, L.; Ciani, G.; Proserpio, D.M.; Rizzato, S. Silver(I) polymeric coordination frameworks assembled with the new multimodal ligand 2,2'-azobispyrazine. *New J. Chem.* **2003**, *27*, 483–489.
  25. Carlucci, L.; Ciani, G.; Proserpio, D.M.; Sironi, A. 1-, 2-, and 3-Dimensional polymeric frames in the coordination chemistry of  $\text{AgBF}_4$  with pyrazine. The first example of three interpenetrating 3-dimensional triconnected nets. *J. Am. Chem. Soc.* **1995**, *117*, 4562–4569.
  26. Carlucci, L.; Ciani, G.; Proserpio, D.M.; Sironi, A. Novel networks of unusually coordinated silver(I) cations: the wafer-like structure of  $[\text{Ag}(\text{pyz})_2][\text{Ag}_2(\text{pyz})_3](\text{PF}_6)_3 \cdot 2\text{G}$  and the simple cubic frame of  $[\text{Ag}(\text{pyz})_3](\text{SbF}_6)$ . *Angew. Chem., Int. Ed. Engl.* **1995**, *34*, 1895–1898.
  27. Carlucci, L.; Ciani, G.; Proserpio, D.M.; Sironi, A. Interpenetrating diamondoid frameworks of silver(I) cations linked by *N,N*-bidentate molecular rods. *J. Chem. Soc., Chem. Commun.* **1994**, 2755–2756.
  28. Hirsch, K.A.; Wilson, S.R.; Moore, J.S. Coordination networks of 3,3'-dicyanodiphenylacetylene and silver(I) salts: structural diversity through changes in ligand conformation and counterion. *Inorg. Chem.* **1997**, *36*, 2960–2968.
  29. Wu, H.-P.; Janiak, C.; Rheinwald, G.; Lang, H. 5,5'-Dicyano-2,2'-bipyridine silver complexes: discrete units or coordination polymers through a chelating and/or bridging metal–ligand interaction. *J. Chem. Soc., Dalton Trans.* **1999**, 183–190.
  30. Janiak, C.; Uehlin, L.; Wu, H.-P.; Klufers, P.; Piotrowski, H.; Scharmann, T.G. Co-ordination engineering: when can one speak of an “understanding”? Case study of the multidentate ligand 2,2'-dimethyl-4,4'-bipyrimidine. *J. Chem. Soc., Dalton Trans.* **1999**, 3121–3131.
  31. Carlucci, L.; Ciani, G.; Proserpio, D.M.; Rizzato, S. Coordination networks from the self-assembly of silver salts and the linear chain dinitriles  $\text{NC}(\text{CH}_2)_n\text{CN}$  ( $n = 2$  to 7): a systematic investigation of the role of counterions and of the increasing length of the spacers. *CrystEngComm.* **2002**, *4*, 413–425.

# Core–Shell Hydrogel Nanoparticles

Clinton D. Jones

L. Andrew Lyon

School of Chemistry and Biochemistry, Georgia Institute of Technology,  
Atlanta, Georgia, U.S.A.

## INTRODUCTION

This contribution introduces the synthesis of poly (*N*-isopropylacrylamide) (pNIPAm)-based core/shell microgels and gives an overview of investigations involving the physical properties of such systems. Core/shell microgels are created via two-stage “seed-and-feed” precipitation polymerization. Core particles serve as preexisting nuclei onto which a hydrogel-forming polymer of a different composition (the shell) is added. The physical properties of the resultant particles are then analyzed with photon correlation spectroscopy (PCS) and fluorescence resonance energy transfer (FRET). Investigations herein show how the overall particle behavior differs between core and core/shell systems. Addition of a shell impacts the swelling behavior of the core component and varies with shell thickness. Particle behavior can be explained by considering the preparation method, where a radial crosslinker density gradient is created, resulting in a distribution of polymer network densities in the core and shell components.

## ENVIRONMENTALLY RESPONSIVE MICROGELS

Responsive hydrogel nanoparticles (microgels) are crosslinked, spherical, colloids normally ranging in diameter from 10 to 1000 nm, and are individually composed of a network of randomly oriented polymer chains having the ability to exist in a swollen or collapsed state depending on local environmental conditions.<sup>[1,2]</sup> The microgels investigated in this contribution are composed of the environmentally responsive polymer poly(*N*-isopropylacrylamide) (pNIPAm)<sup>[3]</sup> and are crosslinked with *N,N*-methylene (bisacrylamide) (BIS) shown in Fig. 1. Particles of this type were first prepared by Pelton and Chibante in 1986,<sup>[4]</sup> and the field has expanded significantly in recent years.<sup>[1,2]</sup> Because of the chemical versatility and physical properties of pNIPAm-based microgels, particle design has continued to attract attention for potential applications in such fields as sensing,<sup>[5,6]</sup> drug

delivery,<sup>[7]</sup> biomaterials,<sup>[8,9]</sup> catalysis,<sup>[10]</sup> and pollution control.<sup>[11]</sup> Part of the appeal of these materials stems from the varied physical properties of pNIPAm particles that are modulated by their phase transition, including hydrophobicity,<sup>[12]</sup> particle size,<sup>[13,14]</sup> porosity,<sup>[15]</sup> refractive index, colloidal stability,<sup>[16]</sup> scattering cross section,<sup>[17,18]</sup> electrophoretic mobility,<sup>[19–21]</sup> and rheology.<sup>[22,23]</sup>

There has been a growing interest into responsive lattices possessing a more advanced architecture and are hence multifunctional. The creation of particles having differing polymer combinations in the core and shell components increases the ability of operators to manipulate the resultant properties multifold. Numerous responsive core/shell or core/corona particles have been synthesized either to introduce spatially localized chemical functionalities to the particle,<sup>[24–26]</sup> to impart thermoresponsivity to non-responsive particles,<sup>[27]</sup> or to modify a specific physical property of the latex.<sup>[22,28,29]</sup> Many of these core/shell particles contain both a responsive and a non-responsive component. However, there are many potential applications of multiresponsive core/shell particles that are composed of two or more environmentally sensitive polymers. Such materials present a potentially diverse chemo–mechanical system for study, as these particles would be expected to display very complex phase transition behavior. This is especially true in core/shell systems where one polymer has a chemical or mechanical influence over the swelling of the other polymeric component.

## CORE/SHELL MICROGEL SYNTHESIS AND CHARACTERIZATION

Crosslinked pNIPAm microgels undergo a reversible temperature-induced volume phase transition (VPT) at 31°C, the intrinsic lower critical solution temperature (LCST) of the parent polymer.<sup>[2]</sup> The particles contain ~98% water by volume below the polymer LCST and ~20% or less water by volume when phase-separated.<sup>[30]</sup> In the hydrophilic swollen state, water molecules surround and fill individual microgels, where hydrogen bonding occurs between water and

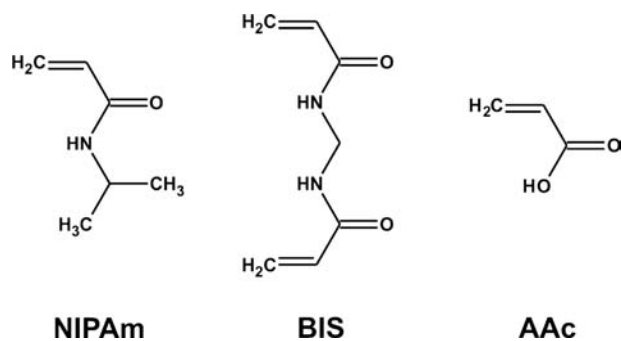


**Fig. 1** Chemical structures of the common monomers employed for these investigations. *N*-Isopropylacrylamide (NIPAm), *N,N'*-methylene(bisacrylamide) (BIS), acrylic acid (AAc).

amide groups along individual polymer chains. However, hydrogen bonding is disrupted as the local solution temperature is increased from below to above the polymer LCST. The entropically favored expulsion of water from the polymer matrix, along with hydrophobic and hydrogen bonding interactions between neighboring polymer chains, induce the particles to undergo a large-magnitude volume change.<sup>[1,31–33]</sup>

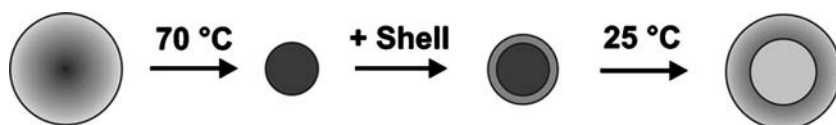
PNIPAm core/shell microgels are synthesized via two-stage precipitation polymerization in aqueous solution.<sup>[34]</sup> This synthetic approach takes full advantage of the physical properties of the polymeric system<sup>[3]</sup> to form monodisperse colloids, and is quite versatile for manipulating the resultant particle behavior. Precipitation polymerization involves the preparation of a polymer that is insoluble in its monomer, or in the presence of a non-solvent for the polymer.<sup>[35]</sup> The procedure for synthesizing core/shell microgels can be referred to as “seed-and-feed” precipitation polymerization. Collapsed core particles, produced in a prior polymerization, serve as preexisting hydrophobic nuclei (the seed) onto which precipitating polymer in solution grows (the feed) to form a shell. In fact, this protocol is fully extendable for adding multiple shells to particles by repeating the shell synthesis on core/shell particles.

First, core microgel particle formation occurs in water at 70°C upon addition of the free-radical initiator ammonium persulfate (APS). At this temperature, APS cleaves homogeneously to form free-radical species that attack olefin groups on the monomers present in the continuous water phase. Water-soluble monomers then begin to polymerize and form oligomer chains that are insoluble upon reaching a certain

critical chain length. Chains reaching this critical length undergo hydrophobically favorable coil-to-globule phase transitions.<sup>[36]</sup> These globules aggregate with one another to form precursor particles, which then have a choice of two competing processes: they can aggregate and grow to form colloiddally stable microgel particles or deposit onto existing colloiddally stable particles in solution. Free radicals located on the growing particle surface capture growing oligomer chains from the continuous phase adding to the particle size. Stabilization occurs due to both surfactant adsorption and charge incorporated on the growing particles from the initiator fragments.<sup>[2,37]</sup> The surfactant employed in these investigations is sodium dodecyl sulfate (SDS) at concentrations well below the critical micelle concentration; therefore, the role of the surfactant is only to stabilize particles during growth and not to “template” particle growth.<sup>[38]</sup> Particle synthesis is normally carried out at 70°C under nitrogen for at least 5 hr. These inert conditions eliminate a majority of dissolved oxygen molecules, which may act as free-radical quenchers.

Shell addition synthesis is performed under monomer-flooded conditions by using the same physical conditions described for the core. A monomer solution, usually differing in composition of the core, is added to the previously synthesized core component in the presence of APS to form the shell.<sup>[39]</sup> This procedure involves diluting the original core solution by 80% in the final aqueous reaction solution in the presence of SDS. The constituent shell monomers are dissolved in H<sub>2</sub>O in a separate solution. After 1 hr of degassing the core solution, the shell monomer solution is heated to approximately the same temperature (70°C) before addition. After thorough mixing and degassing for at least 15 min, APS initiator is then added to begin polymerization. At this temperature, the core particles are fully collapsed and act as preexisting hydrophobic nuclei, which capture growing polymer (the shell) from the continuous phase to form the shell. This process is illustrated in Scheme 1.

The results of core/shell synthesis can easily be realized by comparing the size differences between the original core and resultant core/shell particles via PCS. Fig. 2 shows the results of polymerizing a pNIPAm shell onto a pNIPAm core. Although this particle is not interesting from a functional standpoint, the data illustrate that core/shell particles are larger in size and exhibit the same volume phase transition (VPT) behavior as the original core. PCS analysis also reveals



**Scheme 1** Core/shell synthesis on deswollen seed particles. Source: From Ref.<sup>[39]</sup>. © 2003, Am. Chem. Soc.

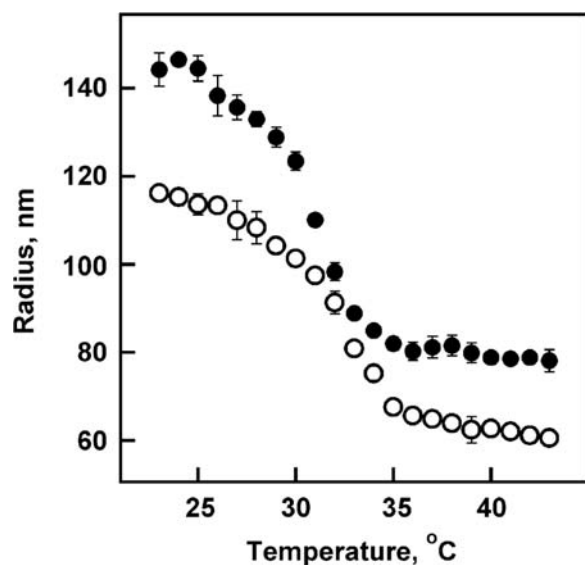


**Fig. 2** PCS analysis of 2 mol% BIS crosslinked pNIPAm core (open circles) and pNIPAm core/pNIPAm shell (filled circles) particles in H<sub>2</sub>O. The core/shell particles are larger than the original core at all temperatures, showing that polymer was added during shell polymerization. Both systems undergo a volume change at approximately the same temperature of 31°C.

that the size distribution between the core and core/shell particles is the same, between 15% and 20%. Furthermore, there is no indication of a new particle population created from the second polymer synthesis step.<sup>[40]</sup> This information supports the contention that the oligoradical capture rate of the core is greater than the propensity of growing polymer chains to form new particles during shell polymerization.

The most interesting core/shell microgels are those in which the hydrogel polymer in the core and shell components differ in composition. Visualization of the core/shell structure is possible when a pNIPAm core is used for subsequent polymerization of a pNIPAm-co-acrylic acid (pNIPAm-co-AAc) shell. The results of this core/shell polymer combination can be seen in the transmission electron micrograph (TEM) image shown in Fig. 3; selective staining of the AAc groups with uranyl acetate allows for easy visualization of the core/shell structure.<sup>[34]</sup> Only one population of particles is shown in the figure, again illustrating that no new particles are formed in solution during the second step of polymerization. This image also suggests that the interface between the two materials is fairly sharp and not highly interpenetrated. It should be noted that the particle size measured by this technique is somewhat unreliable as the particles may have a tendency to flatten and spread on the TEM grid during the sample preparation. This can also lead to a larger apparent polydispersity; individual particles

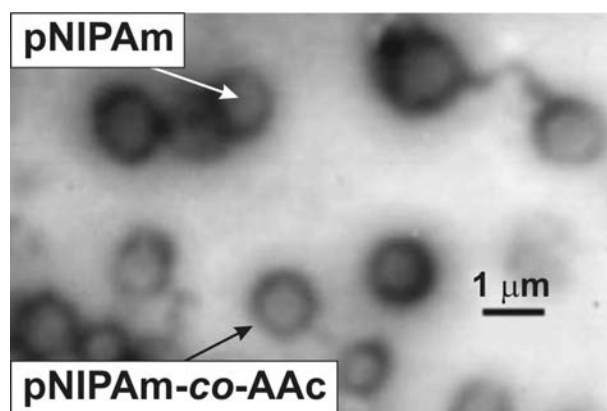


**Fig. 3** Transmission electron micrograph of pNIPAm (core)/pNIPAm-co-AAc (shell) hydrogel particles. The AAc component of the particles was preferentially stained with uranyl acetate to visualize the core/shell structure of the particles. *Source:* From Ref.<sup>[34]</sup>. © 2000, Am. Chem. Soc.

are not expected to interact with the substrate in a homogeneous fashion. It is for these reasons that particle sizing is performed via the less perturbing method of PCS.

### THERMODYNAMIC PROPERTIES OF CORE/SHELL MICROGELS

The copolymer system of pNIPAm-co-AAc is considered to be a multiresponsive polymer because of its sensitivity to both temperature and pH; the  $pK_a$  value of AAc is 4.25.<sup>[41]</sup> This copolymer combination has been shown to undergo a temperature-induced volume change at much higher values ( $\sim 60^\circ\text{C}$ ) than homogeneous pNIPAm under pH conditions where the majority of acid groups are deprotonated.<sup>[42]</sup> The deswelling behavior of the pNIPAm core/pNIPAm-co-AAc shell particles shown in Fig. 3 were investigated via PCS as a function of temperature and solution pH.<sup>[34]</sup> The pH-insensitive pNIPAm core displays a volume phase transition at  $\sim 31^\circ\text{C}$ , the characteristic LCST of the parent polymer as shown in Fig. 2.<sup>[2]</sup> However, the pH-sensitive core/shell particles exhibit value-added properties, where the resultant thermodynamic properties are not a simple summation of the individual hydrogel components. At pH 3.5, where the majority of AAc groups are protonated, the VPT behavior is the same as that of pNIPAm microgels. However, when the AAc groups are deprotonated at pH 6.5, multiple phase transitions occur as a result of both components of the particle collapsing as shown in Fig. 4.<sup>[34]</sup> Size changes as a function of pH can be attributed to both an increased osmotic pressure resulting from counterion ingress, as well as

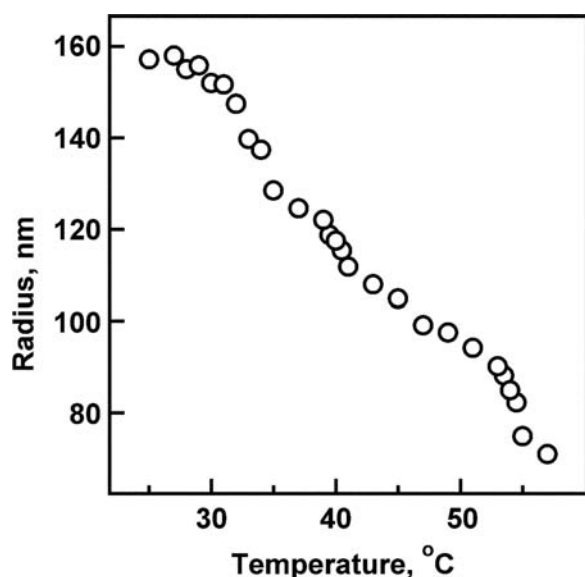


**Fig. 4** PCS data of pNIPAm core/pNIPAm-co-AAc shell particles at pH 6.5. Under these pH conditions, the acrylic acid groups are deprotonated. Deswelling of both the core and the shell leads to multiple volume phase transitions across this temperature range. *Source:* From Ref.<sup>[34]</sup>. © 2000, Am. Chem. Soc.

chain-chain Coulombic repulsion resulting in an increase in the average interchain distance.<sup>[21,42]</sup>

### MECHANICAL INTERACTIONS BETWEEN THE CORE AND SHELL

One aspect of microgel synthesis that is an essential consideration of core/shell particle behavior is the creation of a radially distributed crosslinker density gradient during particle formation. It has been shown that during particle growth, the crosslinker is statistically incorporated faster than other constituent monomers, leading to the creation of a radial distribution of crosslinks.<sup>[1,2,37,43,44]</sup> An illustrative model of the resultant particle morphology is shown in Fig. 5. Because the crosslinker is incorporated fastest, polymer chains toward the particle interior possess a greater number of crosslinking points per chain than those toward the particle exterior. However, this same population of loosely crosslinked chains will be hindered from reaching their fully extended state in the presence of added polymer (e.g., shell). The average number of chains that will be perturbed will differ according to the initial crosslinker concentration, with lower mol% crosslinked particles having a higher average number of loosely crosslinked chains near the periphery than highly crosslinked particles that do not have a gradient morphology.<sup>[45,46]</sup>

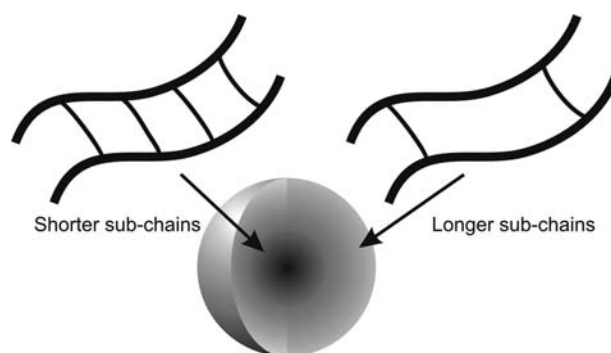


**Fig. 5** The synthesis of pNIPAm microgels via precipitation polymerization creates a radial crosslinker density gradient. Polymer chains near the particle periphery have fewer crosslinker points between chains than those located toward the interior. The various subchain lengths between crosslinking points affect particle deswelling as described in the text.

Because the synthetic conditions used for the core are the same for shell addition, a radial crosslinking density gradient is expected in the shell component as well, with the greatest network density being located at the interface of the core and shell. As illustrated in Scheme 1, collapsed core particles serve as preexisting hydrophobic nuclei and capture growing oligomers from solution that form the shell. Upon particle reswelling at 25°C following shell addition, the rigid interior (more highly crosslinked portion) of the shell component prohibits the core from expanding to its maximum volume, which it possessed prior to shell addition.

The thermodynamic and morphological impact of a hydrogel shell on a hydrogel core particle can be studied with a chosen experimental design relying on a pH- and temperature-responsive core particle, upon which a temperature-responsive, pH-innocent material is added. In this fashion, the shell-induced modulation of the pH response and thermoresponsivity of the core particle can be studied. The well-investigated pH/thermo-responsive hydrogel, pNIPAm-co-AAc, was chosen as the core material and a pH-innocent pNIPAm shell was added. The core/shell particles used for illustration are simply the inverse of those discussed above. In this previous case, the thermodynamics of particle deswelling was investigated, whereas the mechanical properties of this core/shell system are now being presented.

As shown in Fig. 6, a size decrease is observed at all temperatures and at pH 6.5 for these core particles following shell addition, suggesting that the pH-induced swelling of the core is now restricted by the presence of the shell. Indeed, below 31°C, the volume of the core/shell particle is only 40% of the parent core particle volume at pH 6.5. In addition to mediating the solvation of the core, the added pNIPAm shell also



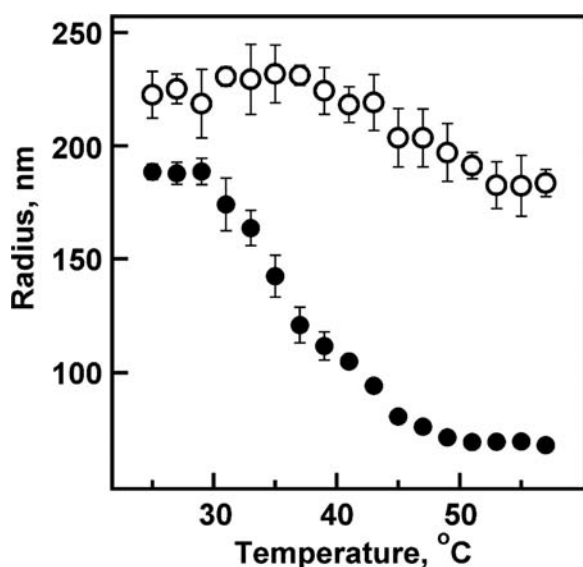
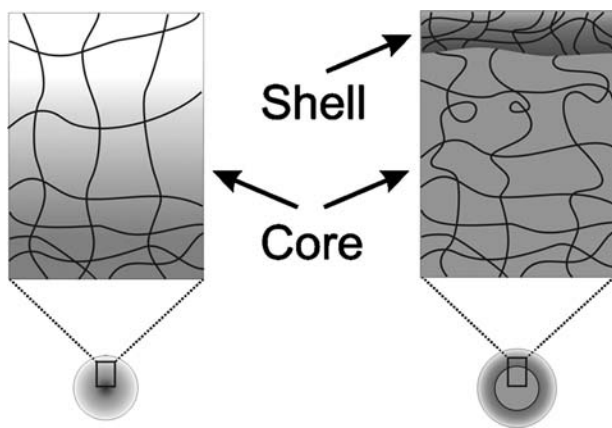


**Fig. 6** Volume phase transition behavior of pNIPAm-co-AAc core (open circles) and pNIPAm-co-AAc core/pNIPAm shell (filled circles) microgels at pH 6.5. The size of the core/shell microgels is smaller than the parent core at all temperatures, suggesting restricted swelling of the core component by the added shell. *Source:* From Ref.<sup>[39]</sup>. © 2003, Am. Chem. Soc.

controls the overall particle deswelling behavior above the polymer LCST by forcing the charged microgel core to undergo a volume phase transition. The added shell compresses the charged core at the LCST of neutral pNIPAm, despite the resistance of the parent core particle to deswelling when the AAc moieties are deprotonated.

A depiction of this core/shell interface is shown in Scheme 2 and illustrates that the loosely crosslinked polymer chains near the core periphery are not allowed to expand to their preshell state because of the added



**Scheme 2** Impact of core and shell crosslinker density gradients on core compression. *Source:* From Ref.<sup>[39]</sup>. © 2003, Am. Chem. Soc.

presence of the highly crosslinked network in the shell. If heterogeneity were not present within both the core and shell in the form of a radial crosslinking density gradient, one would not expect to see the effects observed here, as the core and shell would have the same average and local crosslinker concentration.

## SHELL THICKNESS DEPENDENCE

The thickness of the shell component also impacts the restricted swelling and compression of the core, because it is apparently the nature of the network density in the shell that modulates such behavior. Particles having a pNIPAm-co-AAc core and a pNIPAm shell were used to investigate the effects of shell thickness variation.<sup>[40]</sup> Shell thickness can be controlled by modulating the amount of polymer added to the core during the shell synthesis, which is carried out by simply varying the total monomer concentration present in the shell monomer solution. More monomer present for polymerization directly correlates with the amount of material added and therefore the resultant thickness of the shell. As shown in Fig. 7, the particle size increases with increased shell monomer concentration providing evidence of increasing shell thickness. The average particle polydispersity index

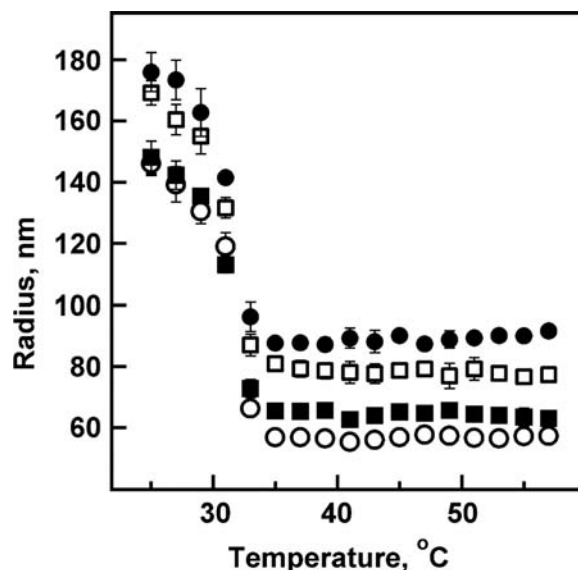


**Fig. 7** PCS results for BIS crosslinked pNIPAm-co-AAc (core)/pNIPAm (shell) particles with varying shell thickness under pH 3.5 solution conditions. Shell thickness is controlled by the initial monomer concentration present in the shell addition synthesis: (open circles) 0 mM, (filled squares) 20 mM, (open squares) 40 mM, (filled circles) 80 mM total shell monomer. The particle size increases relative to the core as the thickness of the shell increases. *Source:* From Ref.<sup>[40]</sup>. © 2003, Am. Chem. Soc.

for all samples varied randomly between 15% and 20% as measured by PCS for all temperatures investigated. These data were taken under pH 3.5 solution conditions (0.001 M total ion), where the core component is not significantly charged. Thus the volume phase transition behavior of each particle should be nearly identical to that of typical pNIPAm homopolymer microgels. Indeed, the VPT temperature (VPTT) is approximately the same for the core and core/shell particles. Recent results using a non-responsive poly(butyl methacrylate) core with varying thickness of a pNIPAm shell also show independence of the VPTT as a function of shell thickness when interrogated via PCS.<sup>[47]</sup>

The data in Fig. 8 show the results of modulated swelling behavior of the core in the presence of increasing shell thickness. These data were collected under pH 6.5 solution conditions (0.001 M total ion), where the acidic groups are fully deprotonated and thus the core component is charged. In each case, the size decrease is greater than the apparent shell thickness observed in Fig. 7, indicating that increasing the thickness of the shell concurrently decreases the ability of the parent core to swell to its original volume. These data indicate that the network structure in the shell changes with shell thickness, thus affecting the swelling ability of the core and the entire core/shell particle. The cross-linking density gradient in thicker shells may have a more gradual persistence toward the particle periphery,

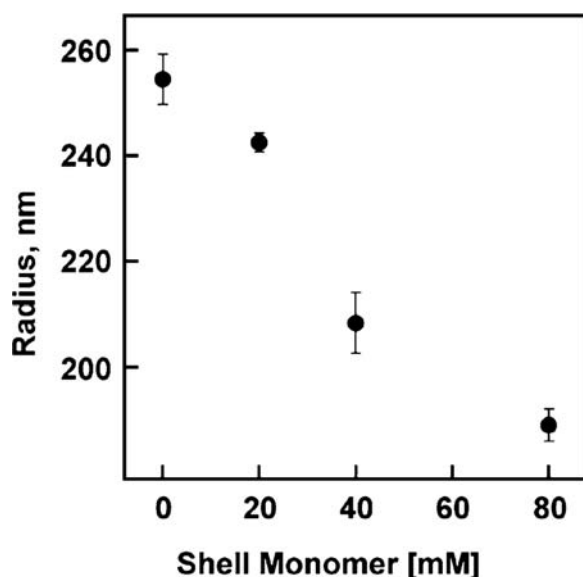


**Fig. 8** PCS results for BIS crosslinked pNIPAm-*co*-AAc (core)/pNIPAm (shell) particles with varying shell thickness under pH 6.5 solution conditions below the VPT temperature of the particles. The core/shell particles show a smaller volume than the core despite the increasing shell thickness. These data indicate that increasing the thickness of the shell directly impacts the phenomenon of restricted swelling of the core component.

thereby decreasing the overall hydrodynamic radius as interrogated via PCS.

## FLUORESCENCE ANALYSIS OF CORE/SHELL NANOPARTICLES

Complimentary to the PCS analysis of restricted swelling and compression of the core by the shell component, the FRET technique can be used to probe the swelling behavior of hydrogel polymer chains inside the core component of core/shell hydrogel nanoparticles. FRET is a distance-dependent process requiring that two fluorophores, termed the donor and the acceptor, have overlapping emission and excitation spectra, respectively. Energy transfer occurs from excited donor molecules to acceptor molecules when the two are within a certain characteristic distance referred to as the Förster radius, and is the result of long-range dipole-induced dipole interactions.<sup>[48]</sup> The Förster radius is typically in the range of 20–60 Å and the efficiency of this process is inversely proportional to the sixth power of the donor–acceptor distance ( $R_0^{-6}$ ). For these investigations, the sulfoindocyanine-based dyes Cy5 and Cy5.5 (Amersham Biosciences) were chosen as the donor and acceptor molecules, respectively.<sup>[49]</sup>

Microgels composed of a pNIPAm core and a homogeneous pNIPAm shell were employed for this study. The core was copolymerized with a small percentage of amine groups for postpolymerization modification with *N*-hydroxysuccinimidyl (NHS) ester functionalized cyanine dyes. Both the core and shell components are lightly crosslinked with 2 mol% *N,N'*-methylene(bisacrylamide) (BIS). The amount of energy transfer occurring between the cyanine FRET pair in the core component is monitored by comparing the emission intensity of the donor and acceptor molecules in the absence and presence of the added shell over a range of temperature values. In the absence of the shell, only a small degree of energy transfer is observed in the core when it is fully swollen below the pNIPAm lower critical solution temperature (LCST) of 31°C. Addition of a pNIPAm shell produces a significant degree of FRET under the same conditions, illustrating that the polymer chains in the core are in a constrained conformation relative to their fully swollen state.

Because of the VPT behavior of pNIPAm microgels, a decrease in the average donor/acceptor distances will occur as the temperature is increased, leading to energy transfer between the molecules. Fig. 9 shows fluorescence data of the donor/acceptor labeled core microgels below (23°C) and above (43°C) the LCST. The sample was excited at 646 nm in both cases. When the microgels are in the fully swollen state at 23°C,

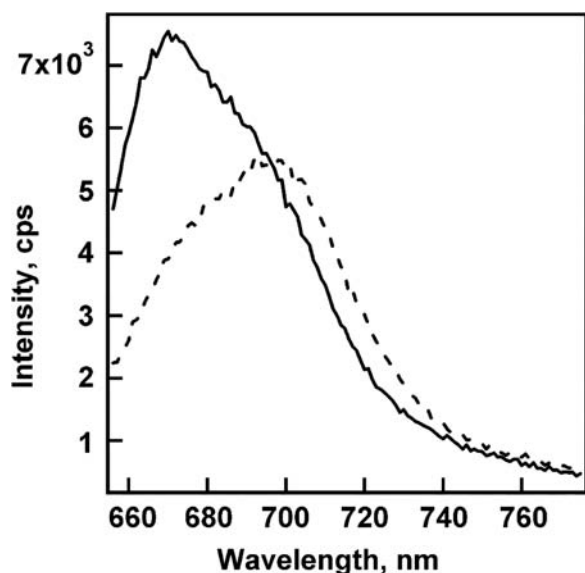


**Fig. 9** Fluorescence emission spectra of core microgels containing both Cy5 donor and Cy5.5 acceptor dyes excited at 646 nm. In the swollen state at 23°C (solid line), there is a small degree of energy transfer, as evidenced by the non-zero Cy5.5 emission intensity. Above the phase transition temperature at 43°C (dashed line), the average donor-to-acceptor distance is decreased, resulting in an increase in the donor/acceptor intensity ratio.

there is a small amount of energy transfer occurring. A significant amount of energy transfer occurs as the temperature is raised to 43°C. The high temperature fluorescence spectrum shows a broadening because of a decrease in the donor emission intensity at 671 nm and a simultaneous increase in the acceptor emission intensity at 697 nm because of FRET.

The VPT behavior of the core microgels can be monitored with FRET by comparing the ratio of the donor and acceptor emission intensities as a function of temperature. As shown in Fig. 10, the FRET analysis exactly coincides with the change in particle size as a function of temperature. These data indicate that the two dyes are homogeneously incorporated throughout the microgel core particle. Thus the amine monomer must also be homogeneously distributed initially within the polymer matrix. Previous investigations indicate that homogeneous incorporation can be expected for this particular amine monomer at the low concentrations used in this study.<sup>[50]</sup> The accepted temperature-induced deswelling mechanism of microgels suggests that the particles collapse beginning at the periphery and continue toward the inside.<sup>[43]</sup> Because of the inverse relationship between the coil to globule phase transition temperature and chain length, loosely crosslinked subnetworks toward the periphery will undergo a phase transition at a lower temperature than highly crosslinked chains near the

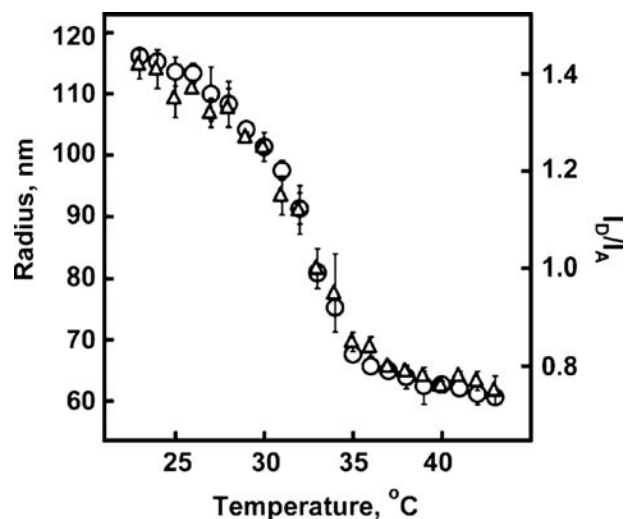


**Fig. 10** A comparison of photon correlation spectroscopy analysis (circles) and fluorescence resonance energy transfer analysis (triangles) of core microgels containing both Cy5 donor and Cy5.5 acceptor molecules in deionized H<sub>2</sub>O. The donor to acceptor emission intensities were monitored at 671 and 697 nm, respectively; samples were excited at 646 nm.

center of the particle.<sup>[36,44]</sup> Accordingly, the continuous phase transition of pNIPAm microgels, such as that in Figs. 2, 4, 6 and 7, can be viewed as a collection of discontinuous phase transitions of the radial distribution of crosslinked networks existing in the particle. If the donor and acceptor groups were not homogeneously distributed inside the polymer matrix, then the FRET analysis would not overlap the PCS data. For instance, energy transfer would not occur until late in the volume decrease and the magnitude of FRET would be substantially less if the dyes were crowded toward the inner portion of the particle. If the dyes were located near the periphery, then a majority of the energy transfer would occur early in the volume decrease.

FRET analysis of the VPT behavior between the core and core/shell is presented in Fig. 11A. In comparison to the degree of FRET in the core, the core/shell particles exhibit significant energy transfer at 23°C. This behavior shows that the shell restricts the core from reswelling to its original state, as shown in Fig. 6 above. The ratio between the donor and acceptor emission intensity at 23°C for the core/shell particles is approximately the same as that for the core particles at 31°C. Fig. 11B shows a spectral comparison between these two sets of data. The two spectra illustrate that amount of energy transfer between donor and acceptor chromophores is approximately the same for each case by observing the shape of the fluorescence emission spectrum. A semiquantitative value of the amount of restricted swelling can be gathered by noting that the core alone undergoes a volume decrease of 40% at 31°C when interrogated via PCS. If

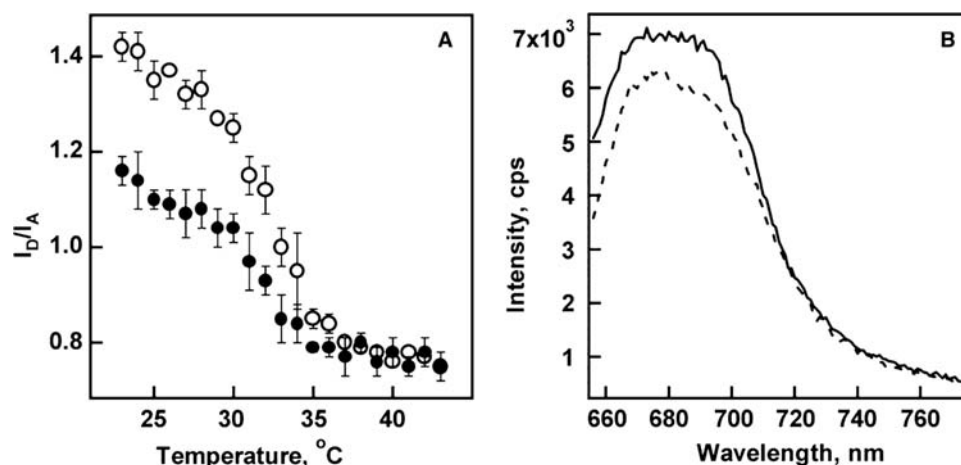


**Fig. 11** (A) Fluorescence resonance energy transfer analysis of Cy5 donor/Cy5.5 acceptor labeled core (open) and core/shell (solid) microgels in H<sub>2</sub>O. These core/shell microgels were excited at 646 nm and exhibit a greater degree of energy transfer than the original core below 33°C. (B) Fluorescence analysis of core particles at 31°C (solid line) and the core/shell particles at 23°C (dashed line). The two spectra show that approximately the same amount of energy transfer is occurring for each system at these temperatures.

the same volume change in the core produces the same amount of FRET in both the original core at 31°C and the core/shell at 23°C, then it may be assumed that the core is restricted from swelling to only 60% of its original volume in the presence of the shell. Indeed, the core is swollen to some extent in the core/shell particles, as FRET does increase as the temperature is raised above the pNIPAm VPT temperature.

## CONCLUSION

The synthesis and characterization of pNIPAm-based microgels possessing a core/shell morphology have been presented. Core particles are first synthesized via precipitation polymerization and serve as preexisting nuclei in a subsequent polymerization containing monomer of a different composition to form the shell. The core/shell structure can be visualized with electron microscopy and the physical properties of the systems are investigated via photon correlation spectroscopy and fluorescence spectroscopy. The presence of the shell impacts the swelling behavior of the core component, which is elucidated by using these analytical techniques. Fundamental understanding of the swelling properties is important for the development of applications-based materials.

## ACKNOWLEDGMENTS

LAL gratefully acknowledges financial support from the National Science Foundation, Division of Materials Research (DMR-0203707). CDJ gratefully acknowledges partial support from the Georgia

Institute of Technology Molecular Design Institute under prime contract N00014-95-1-1116 from the Office of Naval Research, as well as a National Science Foundation Trainee Fellowship in Environmental Sciences and from the Polymer Education Research Center at the Georgia Institute of Technology.

## REFERENCES

1. Saunders, B.R.; Vincent, B. Microgel particles as model colloids: theory, properties and applications. *Adv. Colloid Interface Sci.* **1999**, *80*, 1–25.
2. Pelton, R. Temperature-sensitive aqueous microgels. *Adv. Colloid Interface Sci.* **2000**, *85*, 1–33.
3. Heskins, M.; Guillet, J.E. Solution properties of poly(*N*-isopropylacrylamide). *J. Macromol. Sci., Chem.* **1968**, *A2*, 1441–1455.
4. Pelton, R.H.; Chibante, P. Preparation of aqueous lattices with *N*-isopropylacrylamide. *Colloids Surf.* **1986**, *20*, 247–256.
5. Holtz, J.H.; Holtz, J.S.W.; Munro, C.H.; Asher, S.A. Intelligent polymerized crystalline colloidal arrays: Novel chemical sensor materials. *Anal. Chem.* **1998**, *70*, 780–791.
6. Hu, Z.; Chen, Y.; Wang, C.; Zheng, Y.; Li, Y. Polymer gels with engineered environmentally responsive surface patterns. *Nature* **1998**, *393*, 149–152.
7. Hoffman, A.S. Hydrogels for biomedical applications. *Adv. Drug Deliv. Rev.* **2002**, *54*, 3–12.
8. Chen, G.; Ito, Y.; Imanishi, Y. Regulation of growth and adhesion of cultured cells by insulin conjugated with thermoresponsive polymers. *Biotechnol. Bioeng.* **1997**, *53*, 339–344.
9. Shiroya, T.; Yasui, M.; Fujimoto, K.; Kawaguchi, H. Control of enzymic activity using thermosensitive polymers. *Colloids Surf., B* **1995**, *4*, 275–285.

10. Bergbreiter, D.E.; Case, B.L.; Liu, Y.S.; Caraway, J.W. Poly(*N*-isopropylacrylamide) soluble polymer supports in catalysis and synthesis. *Macromolecules* **1998**, *31*, 6053–6062.
11. Morris, G.E.; Vincent, B.; Snowden, M.J. Adsorption of lead ions onto *N*-isopropylacrylamide and acrylic acid copolymer microgels. *J. Colloid Interface Sci.* **1997**, *190*, 198–205.
12. Kawaguchi, H.; Fujimoto, K.; Mizuhara, Y. Hydrogel microspheres. III. Temperature-dependent adsorption of proteins on poly(*N*-isopropylacrylamide) hydrogel microspheres. *Colloid Polym. Sci.* **1992**, *270*, 53–57.
13. Saunders, B.R.; Vincent, B. Thermal and osmotic deswelling of poly(NIPAM) microgel particles. *J. Chem. Soc., Faraday Trans.* **1996**, *92*, 3385–3389.
14. Saunders, B.R.; Crowther, H.M.; Morris, G.E.; Mears, S.J.; Cosgrove, T.; Vincent, B. Factors affecting the swelling of poly(*N*-isopropylacrylamide) microgel particles: fundamental and commercial implications. *Colloids Surf., A Physicochem. Eng. Asp.* **1999**, *149*, 57–64.
15. Thiagarajan, V.S.; Huang, Z.; Scriven, L.E.; Schottel, J.L.; Flickinger, M.C. Microstructure of a biocatalytic latex coating containing viable *Escherichia coli* cells. *J. Colloid Interface Sci.* **1999**, *215*, 244–257.
16. Snowden, M.J.; Vincent, B., Eds. *Flocculation of Poly(N-Isopropylacrylamide) Latices in the Presence of Nonadsorbing Polymer*; American Chemical Society: Washington, DC, 1993; Vol. 532.
17. Yi, Y.D.; Oh, K.S.; Bae, Y.C. Phase transition of submicron sized *N*-alkylacrylamide-derivative copolymer particles: applicability of photon correlation spectroscopy. *Polymer* **1997**, *38*, 3471–3476.
18. Yi, Y.D.; Bae, Y.C. Volume-phase transition of submicron-sized *N*-isopropylacrylamide/*N*-*tert*-butylacrylamide particles by photon correlation spectroscopy. *J. Appl. Polym. Sci.* **1998**, *67*, 2087–2092.
19. Rasmussen, M.; Vincent, B.; Marston, N. The electrophoresis of poly(*N*-isopropylacrylamide) microgel particles. *Colloid Polym. Sci.* **2000**, *278*, 253–258.
20. Fernandez-Nieves, A.; Fernandez-Barbero, A.; de las Nieves, F.J.; Vincent, B. Motion of microgel particles under an external electric field. *J. Phys., Condens. Matter* **2000**, *12*, 3605–3614.
21. Fernandez-Nieves, A.; Fernandez-Barbero, A.; Vincent, B.; de las Nieves, F.J. Charge controlled swelling of microgel particles. *Macromolecules* **2000**, *33*, 2114–2118.
22. Senff, H.; Richtering, W.; Norhausen, C.; Weiss, A.; Ballauff, M. Rheology of a temperature sensitive core-shell latex. *Langmuir* **1999**, *15*, 102–106.
23. Senff, H.; Richtering, W. Temperature sensitive microgel suspensions: colloidal phase behavior and rheology of soft spheres. *J. Chem. Phys.* **1999**, *111*, 1705–1711.
24. Duracher, D.; Sauzedde, F.; Elaissari, A.; Pichot, C.; Nabzar, L. Cationic amino-containing *N*-isopropylacrylamide-styrene copolymer particles: 2—surface and colloidal characteristics. *Colloid Polym. Sci.* **1998**, *276*, 920–929.
25. Duracher, D.; Sauzedde, F.; Elaissari, A.; Perrin, A.; Pichot, C. Cationic amino-containing *N*-isopropylacrylamide-styrene copolymer latex particles: 1—particle size and morphology vs. polymerization process. *Colloid Polym. Sci.* **1998**, *276*, 219–231.
26. Zhou, G.; Elaissari, A.; Delair, T.; Pichot, C. Synthesis and characterization of surface-cyanofunctionalized poly(*N*-isopropylacrylamide) latexes. *Colloid Polym. Sci.* **1998**, *276*, 1131–1139.
27. Matsuoka, H.; Fujimoto, K.; Kawaguchi, H. Stimuli-response of microsphere having poly(*N*-isopropylacrylamide) shell. *Polym. J.* **1999**, *31*, 1139–1144.
28. Kato, T.; Fujimoto, K.; Kawaguchi, H. Permeation control by thermosensitive shell layer of submicron microspheres. *Polym. Gels Netw.* **1994**, *2*, 307–313.
29. Hazot, P.; Pichot, C.; Maazouz, A. Synthesis of hairy acrylic core-shell particles as toughening agents for epoxy networks. *Macromol. Chem. Phys.* **2000**, *201*, 632–641.
30. Wang, J.; Gan, D.; Lyon, L.A.; El-Sayed, M.A. Temperature-jump investigations of the kinetics of hydrogel nanoparticle volume phase transitions. *J. Am. Chem. Soc.* **2001**, *123*, 11,284–11,289.
31. Flory, P.J. *Principles of Polymer Chemistry*; Cornell University Press: London, 1953.
32. Tanaka, T. Collapse of gels and the critical endpoint. *Phys. Rev. Lett.* **1978**, *40*, 820–823.
33. Tanaka, T.; Swislow, G.; Ohmine, I. Phase separation and gelation in gelatin gels. *Phys. Rev. Lett.* **1979**, *42*, 1556–1559.
34. Jones, C.D.; Lyon, L.A. Synthesis and characterization of multiresponsive core-shell microgels. *Macromolecules* **2000**, *33*, 8301–8306.
35. Billmeyer, F. *Textbook of Polymer Science*; John Wiley & Sons: New York, 1984.
36. Wu, C. A comparison between the “coil-to-globule” transition of linear chains and the “volume phase transition” of spherical microgels. *Polymer* **1998**, *39*, 4609–4619.
37. Wu, X.; Pelton, R.H.; Hamielec, A.E.; Woods, D.R.; McPhee, W. The kinetics of poly(*N*-isopropylacrylamide) microgel latex formation. *Colloid Polym. Sci.* **1994**, *272*, 467–477.
38. Hara, K.; Suzuki, H.; Takisawa, N. High-pressure studies of a fluorescence probe for the critical micelle concentration in sodium dodecyl-sulfate. *J. Phys. Chem.* **1989**, *93*, 3710–3713.
39. Jones, C.D.; Lyon, L.A. Shell-restricted swelling and core compression in poly(*N*-isopropylacrylamide) core-shell microgels. *Macromolecules* **2003**, *36*, 1988–1993.
40. Jones, C.D.; Lyon, L.A. Dependence of shell thickness on core compression in acrylic acid modified poly(*N*-isopropylacrylamide) core/shell microgels. *Langmuir* **2003**, *19*, 4544–4547.
41. Lide, D.R., Ed.; *The CRC Handbook of Chemistry and Physics*, 74th; CRC Press: Boca Raton, 1994; Vol. 124.

42. Ito, S.; Ogawa, K.; Suzuki, H.; Wang, B.L.; Yoshida, R.; Kokufuta, E. Preparation of thermosensitive submicrometer gel particles with anionic and cationic charges. *Langmuir* **1999**, *15*, 4289–4294.
43. Gan, D.J.; Lyon, L.A. Interfacial nonradiative energy transfer in responsive core-shell hydrogel nanoparticles. *J. Am. Chem. Soc.* **2001**, *123*, 8203–8209.
44. Wu, C.; Zhou, S.Q. Volume phase transition of swollen gels: Discontinuous or continuous? *Macromolecules* **1997**, *30*, 574–576.
45. Varga, I.; Gilanyi, T.; Meszaros, R.; Filipcsei, G.; Zrinyi, M. Effect of cross-link density on the internal structure of Poly(*N*-isopropylacrylamide) microgels. *J. Phys. Chem., B* **2001**, *105*, 9071–9076.
46. Guillermo, A.; Addad, J.P.C.; Bazile, J.P.; Duracher, D.; Elaissari, A.; Pichot, C. NMR investigations into heterogeneous structures of thermosensitive microgel particles. *J. Polym. Sci., B, Polym. Phys.* **2000**, *38*, 889–898.
47. Gan, D.J.; Lyon, L.A. Fluorescence nonradiative energy transfer analysis of crosslinker heterogeneity in core-shell hydrogel nanoparticle. *Anal. Chim. Acta*, *in press*.
48. Lakowicz, J.R. *Principles of Fluorescence Spectroscopy*, 2nd Ed.; Kluwer Academic: New York, 1999.
49. Schobel, U.; Egelhaaf, H.J.; Brecht, A.; Oelkrug, D.; Gauglitz, G. New-donor-acceptor pair for fluorescent immunoassays by energy transfer. *Bioconjug. Chem.* **1999**, *10*, 1107–1114.
50. Meunier, F.; Elaissari, A.; Pichot, C. Preparation and characterization of cationic poly(*N*-isopropylacrylamide) copolymer latexes. *Polym. Adv. Technol.* **1995**, *6*, 489–496.



# Core–Shell Nanospheres, Hollow Capsules, and Bottles

**Gang Zhang**

*Department of Chemistry, Jilin University, Changchun, China*

**Kai Zhang**

*Key Lab of Supramolecular Structure and Materials, Jilin University, Changchun, China*

**Yi Yu**

*Key Laboratory of Excited Process of Physics, Chinese Academy of Sciences, Changchun, China*

**Bai Yang**

*College of Chemistry, Jilin University, Changchun, China*

## INTRODUCTION

The design and synthesis of nanoscale materials is important in the fabrication of advanced devices for optics, electronics, and biotechnology.<sup>[1–6]</sup> Over the past decade, considerable effort has been devoted to the design and controlled fabrication of nanostructured materials with functional properties. The interest in nanoscale materials comes from the fact that their properties (optical, electrical, or chemical, etc.) are the functions of their size, composition, and structural order. Colloidal particles represent attractive building blocks from which to create ordered and complex materials. They are also of widespread interest in chemical engineering, biological, and pharmaceutical applications.<sup>[7]</sup> In biotechnology, the encapsulation and delivery of proteins and DNA into cells has led to the implementation of intracellular medicinal therapies such as gene therapy.<sup>[8,9]</sup> Completion of the human genome project has ensured the former, leaving the synthesis of encapsulation and delivery materials as perhaps the single most important challenge in intracellular medicinal therapies. Recently, core-shell particles and micro- or nanosized capsules have received considerable attentions for their technological importance in many fields.<sup>[10–25]</sup> There have been many efforts to fabricate core-shell colloidal materials with tailored structural, surface, and optical properties.<sup>[26–28]</sup> The creation of core-shell colloidal particles is also of interest from a fundamental viewpoint, especially in the areas of colloid and interface science. They can be utilized as model systems to investigate factors governing colloidal interactions and stabilization and to gain valuable information on the properties of concentrated dispersions.<sup>[29,30]</sup>

## OVERVIEW

The synthesis of core-shell particles typically involves tailoring the surface properties of particles, often accomplished by coating or encapsulating them within a shell of a preferred material. The shell can alter the charge, functionality, and reactivity of the surface, and can enhance the stability and dispersibility of the colloidal core. Optical, magnetic, or catalytic functions may be readily imparted to the dispersed colloidal matter depending on the properties of the coating. Encapsulating colloids in a shell of different composition may also protect the core from extraneous chemical and physical changes.<sup>[31,32]</sup> Core-shell particles often exhibit improved physical and chemical properties over their single-component counterparts and, hence, are potentially useful in a broader range of applications. Optimization of the surface characteristics of particles through coating processes is also of primary importance for the successful application of composite particles. Recent methods offer new alternatives for the controlled synthesis of novel, stable, and functional core-shell type materials.

An important extension of core-shell particles is the subsequent removal of the core by either thermal or chemical means (selective etching with a solvent or calcination in air), forming hollow spheres. A variety of procedures currently used to fabricate a wide range of stable hollow capsules of various compositions have been reported.<sup>[33]</sup> Hollow capsules of nanometer to micrometer dimensions constitute an important class of materials that are employed in various technological applications, such as encapsulate agents for delivery of cosmetic, drug, catalysis, and protecting sensitive agents. They may also provide some immediate advantages over their solid counterparts because of their

relatively low densities and as fillers with low dielectric constant in electronic components. Using various chemical and physicochemical methods nowadays routinely produces hollow capsules comprising polymer, glass, metal, and ceramic.

As particular examples, hollow spheres with mesoporous wall have been synthesized from gel composite;<sup>[34,35]</sup> however, large entities such as macromolecules usually cannot penetrate such microspheres. It would be desirable to leave a hole on the shell surface for transporting various molecules. Lin and coworkers synthesized a vesicular hollow microspheres that possess a pair of holes of submicron size on exactly opposite sides.<sup>[36]</sup> Recently, our group obtained the nanobottles through the removal of template functional polymer and silica cores through programmed calcination at high temperature and solution etching, respectively. Because there is an opening on the hollow cavity of silica nanobottle, it can afford both a channel for transmission and a container for storage. So the nanobottles can be used as an extremely small container for encapsulation, as well as a nano-sized carrier and reactor for catalysis and microreaction. Furthermore, the encapsulation of rare earth complex in the nanobottles reveals a potential application for nanotechnology.

This entry provides an overview of the various methods used to synthesize core-shell particles, hollow capsules, and bottles in the nanometer to the micrometer size range, detailing early and very recent developments in the above area.

## NANOSIZED CORE-SHELL SPHERES

### Nanosized Core-Shell Spheres with Polymer Shell

Polymer-coated spheres offer interesting prospects in a broad spectrum of applications, ranging from catalysis to additives and dyes, where they are exploited in the manufacture of cosmetics, inks, and paints. The synthetic routes that have been developed in order to produce polymer-coated spheres fall into two main classes: polymerization at the sphere surface or adsorption onto the spheres. Hofman-Caris has comprehensively reviewed the processes used to obtain spheres that consist of an inorganic core and a polymer shell through polymerization and chemical coupling procedures prior to 1994.<sup>[28]</sup> We will deal with more recent strategies used to coat spheres with polymers, polymerization approaches, and the self-assembly of polymers from solution.

A number of polymerization-based methods have been employed to produce spheres that consist of solid cores coated with a shell of polymeric materials. These include monomer adsorption onto spheres followed by

subsequent polymerization,<sup>[37–42]</sup> heterocoagulation-polymerization,<sup>[43]</sup> and emulsion polymerization.<sup>[28,44]</sup> In the first approach, one of the most frequently employed to achieve polymer coatings on solid spheres, the polymerization reaction can be catalyzed either by an initiator to promote the process or by the colloidal spheres themselves.

Atom transfer radical polymerization (ATRP) is a versatile technique, which offers several advantages over other polymerization routes including control over molecular weight and molecular weight distribution.<sup>[45,46]</sup> Also, the polymers can be end-functionalized or block copolymerized upon the addition of other monomers.<sup>[46]</sup> Not only does this feature offer tailorability of the polymer coating with a variety of compositions and functionalities, but also this feature may be important in biomedical applications to modify the polymer shell with biological moieties for specific cellular interactions. ATRP has been able to form PMMA and PS shells on silica nanoparticles,<sup>[45]</sup> and provides magnetic core-shell nanospheres with size <15 nm. Magnetic studies show a decrease in coercivity, which is consistent with the reduction of magnetic surface anisotropy upon polymer coating. Certainly the magnetic core of these core-shell nanospheres can be selected, depending upon the desired super paramagnetic properties for specific applications such as in data storage and MRI contrast enhancement.<sup>[47]</sup> Moreover, the resulting core-shell nanospheres are within the biological size restrictions and may potentially be modified for a particular biospecificity.

Matijevic et al. reported the coating of aluminum hydrous oxide-modified silica spheres with poly(divinylbenzene) (PDVB) layers by pretreatment of the inorganic cores with coupling agents such as 4-vinylpyridine or 1-vinyl-2-pyrrolidone, followed by subsequent admixing of divinylbenzene and a radical initiator.<sup>[37]</sup> Polymer layers of poly(vinylbenzyl chloride) (PVBC), copolymers of PDVB–PVBC, and double shells of PDVB and PVBC were also synthesized around inorganic spheres using a similar approach.<sup>[38]</sup>

The use of electrochemical or soluble initiators can be eliminated by utilizing catalytically active cores to effect the polymerization of monomers adsorbed on the surface of spheres. This approach was employed to obtain poly(pyrrole) coatings on a range of inorganic cores by using the active sites on the metal oxide surfaces to initiate the polymerization of pyrrole.<sup>[39]</sup> Hematite, silica-modified hematite, and cerium(IV) oxide (CeO<sub>2</sub>) were coated with poly(pyrrole) by exposing the inorganic cores to the polymerization medium of pyrrole in an ethanol/water mixture and heating to 100°C.

Möller et al. presented a work directed toward the formation of core-shell particles consisting of a nanocrystal of Au surrounded by a shell of conducting polymer, e.g., polypyrrole.<sup>[48]</sup> Because of the different

chemical nature of the two materials, charge transfer might be expected at the interface and the optical functions of both materials should be drastically different from the corresponding bulk materials.<sup>[49]</sup> Preliminary experiments using solutions of tetrachloroauric acid (HAuCl<sub>4</sub>) and pyrrole, without diblock copolymer, have demonstrated the formation of PPY and Au. However, in this case it was not possible to prevent the macroscopic segregation of the polymer and the metal phase. Macroscopic segregation can be prevented efficiently if the composite particles are formed within the cores of the micelles of a diblock copolymer. Fig. 1 shows the micrograph recorded after annealing the film at 130°C. Uniform Au particles with a diameter of 7 nm formed within the micelles. The figure indicates that the originally indistinct ultrasmall clusters of elementary gold coalesced upon treatment above the glass transition temperature of both blocks. When the same annealing procedure was applied to an Au-loaded micellar film that had not been treated with pyrrole, larger Au particles were formed and the micellar organization was destroyed. Thus the presence of polypyrrole or pyrrole oligomers is essential to yield a single Au particle within each spherical microdomain.

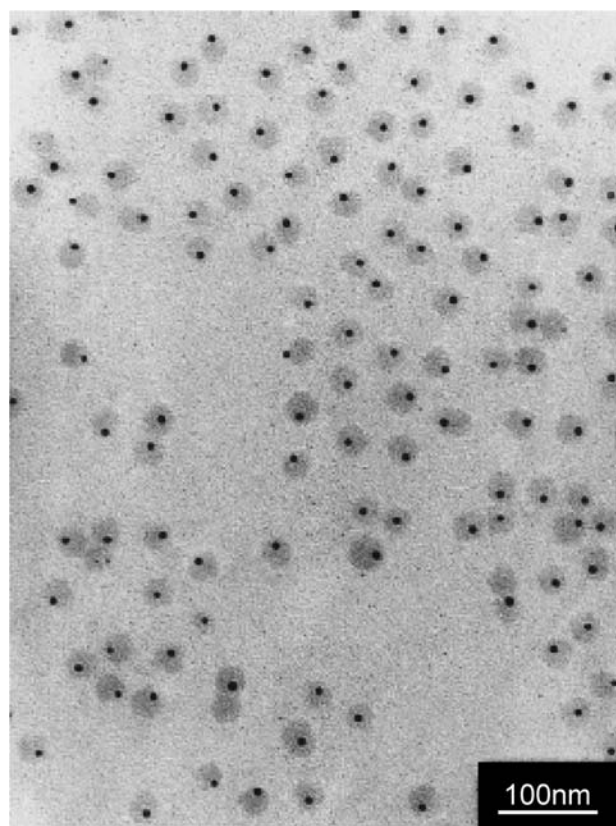


**Fig. 1** TEM micrograph of a colloidal polymer film ([PY]/[HAuCl<sub>4</sub>] = 3.0) after annealing at 130°C for 140 min, exhibiting 7 nm wide Au clusters in each micelle encapsulated by PPY. *Source:* From Ref.<sup>[48]</sup>.

Methods to coat a polymer shell with a controllable thickness on magnetic nanoparticles may aid in the development of ordered arrays of magnetic nanoparticles. The formation of polymeric shells is essential for biomedical applications of magnetic nanoparticles such as magnetic targeting drug delivery and magnetic resonance imaging (MRI) contrast enhancement. Many methods usually create micrometer-sized magnetic polymer spheres, which are large for in vivo applications.<sup>[50]</sup> A less than 20-nm size has been suggested for the efficient diffusion of nanoparticles through tissue in MRI applications.<sup>[51]</sup> An emulsion polymerization of poly(methyl methacrylate) (PMMA) on ~10-nm core of mixed-phase iron oxides has made improvement; the particle size is still >130 nm.<sup>[52,53]</sup> Polystyrene (PS) is easy to synthesize for testing various strategies of coating nanoparticles with polymer shells. Zhang et al. reported the formation of magnetic MnFe<sub>2</sub>O<sub>4</sub> PS nanoparticles using ATRP yielding a core-shell nanoparticle with size <15 nm.<sup>[54]</sup> Most polymer-coating studies on magnetic nanoparticles form the nanoparticle core (typically Fe, Fe<sub>2</sub>O<sub>3</sub>, or Fe<sub>3</sub>O<sub>4</sub>) at the same time as that of polymerization.<sup>[55]</sup> The MnFe<sub>2</sub>O<sub>4</sub> nanoparticles as the magnetic core were separately prepared by a reverse micelle microemulsion procedure.<sup>[56]</sup> Polymerization initiators are chemically attached onto the surface of nanoparticles. The modified nanoparticles are then used as macro-initiators in the subsequent polymerization reaction. This approach provides great flexibility in the selection of magnetic core. Consequently, magnetic tunability can be introduced into these core-shell nanosphere systems to achieve the desired super paramagnetic response.<sup>[57]</sup>

Inspired by the nanosized, amphiphilic core-shell structure of lipoproteins, shell cross-linked nanoparticles with a hydrophobic core, contained within a hydrogel network, were prepared by the self-assembly of amphiphilic block copolymers followed by intramolecular cross-linking between the polymeric chains located within the shell.<sup>[58]</sup> The control over size, shape, and composition of these nanoparticles holds great potential in drug delivery applications.<sup>[59,60]</sup> Intracellular cross-linking of the polymer chains within the shells of polystyrene-*b*-poly(acrylic acid) micelles by reaction with difunctional poly(ethylene oxide) afforded unimolecular amphiphilic core-shell nanospheres (50 nm hydrodynamic radius).<sup>[61]</sup>

The controlled release of polymer chains from the core by adjusting the cross-link density of the shell opens the possibilities of designing polymeric nanoparticles with specific shell permeabilities, capable of delivery of large guests. This approach may provide a solution to some of the delivery problems posed by biologically active molecules, such as peptides and proteins, genes and oligonucleotides. The results of this study also provide a foundation for better understanding

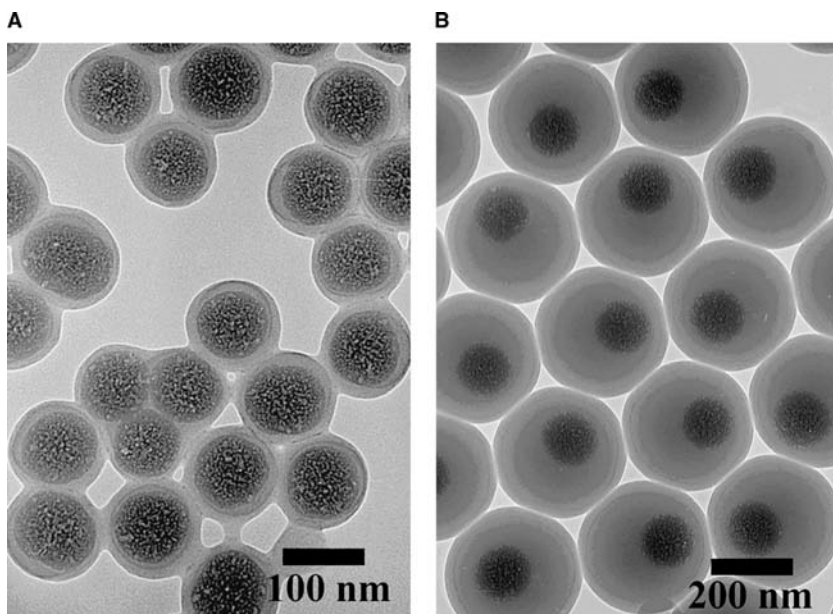


**Fig. 2** TEM images of silica-PMMA (left), silica-PS core-shell spheres (right). *Source:* From Ref.<sup>[64]</sup>.

of the porosity of the cross-linked shell.<sup>[62]</sup> This represents a methodology to probe the permeability of nanoscopic membranes and a means for applications in the controlled release of macromolecular species.

Our group described a flexible method for preparing monodisperse silica-PS core-shell microspheres. In this method, silica nanoparticles grafted with 3-(trimethoxysilyl) propyl methacrylate (MPS) was employed in an emulsion polymerization as seeds. The thickness of the shells could be changed through varying the amount of monomer and emulsifier. The monodispersity and diameters of the core-shell microspheres were found to depend on the size of grafted silica nanoparticles and the concentration of emulsifier.

The monodisperse silica microspheres with average radii ranging from 35 to 90 nm were prepared in ethanol according to the Stöber method<sup>[63]</sup> at ambient temperature. In order to obtain a functionalized surface, MPS with C=C bond was added and reacted with the Si-OH group on the surface of the silica by hydrolysis. Monodisperse silica-polymer core-shell microspheres were obtained through emulsion polymerization of styrene (St) or methyl methacrylate (MMA), while grafted silica particles dispersed in ethanol, which acts as “seeds” in the polymerization process.<sup>[64]</sup>

Fig. 2 shows the TEM images of the resulting silica-PMMA (left) and silica-PS (right) core-shell microspheres. The spherical particles show obvious core-shell structures, light shells (PMMA or PS) coat the dark grafted silica microspheres cores, and over about 90% of these core-shell microspheres have only one single core. The average radius of the monodisperse core-shell microspheres varies from 45 to 150 nm for silica-PMMA and from 80 to 210 nm for silica-PS, which have been confirmed by the TEM.

A series of TEM images of core-shell microspheres prepared by increasing the amount of styrene (St) prove that the grafted silica nanoparticles act as “seeds” in the emulsion polymerization.<sup>[64]</sup> The “raspberry” morphology of core-shell microspheres was seen, and it was clearly visible that the surfaces of shells became smoother and the shells thickened with increasing the amount of monomer; the core-shell microspheres were still monodisperse.

### Nanosized Core-Shell Spheres with Inorganic and Composite Shell

Various procedures have been employed in the fabrication of inorganic/hybrid coatings on particles, allowing a broad range of materials with different properties to be prepared. The specific methods of solid-core inorganic/hybrid-shell sphere preparation can be classified into two general categories: precipitation and surface reactions, and the controlled deposition of preformed inorganic colloids.

Previous investigations have demonstrated that polymeric and inorganic particles dispersed in aqueous solutions can be coated with layers of various inorganic materials either by precipitation of the coating materials onto the cores or by direct surface reactions utilizing specific functional groups on the cores to induce coating.<sup>[17,27,31,65–76]</sup> The inorganic coatings prepared using these approaches include silica,<sup>[17,27,31,65–73]</sup> yttrium basic carbonate, titania,<sup>[74–76]</sup> and polyelectrolytes onto particles via the layer-by-layer (LbL) and LB techniques. Early work focused on the coating of titania microparticles with silica layers; however, significant particle clumping and coalescence took place

during silica deposition. Using the precipitation method, in which the coating material is precipitated directly onto the core, Ohmori and Matijevic optimized the coating conditions and coated spindle-shaped hematite ( $\alpha$ - $\text{Fe}_2\text{O}_3$ ) particles with silica layers by hydrolysis of the alkoxide tetraethoxysilane (TEOS) in 2-propanol.<sup>[31,65,77]</sup> Uniform silica coatings on individual  $\alpha$ - $\text{Fe}_2\text{O}_3$  particles were obtained when the kinetics of the TEOS hydrolysis was properly controlled. Dispersions of uniform sub-micrometer spherical particles consisting of silica cores and yttria coatings, as well as yttria cores with silica coatings, were also prepared by a similar method.

Electrostatic interactions between nanoparticles and larger particles via solution self-assembly have been widely exploited to prepare core-shell materials.<sup>[66,78–82]</sup> Homola et al. reported the coating of  $\gamma$ - $\text{Fe}_2\text{O}_3$  particles with preformed smaller silica particles by combining the particle mixtures under conditions where the two types of particles are oppositely charged. This resulted in better dispersion and less aggregation of the magnetic particles. Similarly, nanosized silica was deposited on a range of larger inorganic particles, thus forming a protective layer. Nanocomposite multilayers can be assembled on particle surfaces by using the LbL method based on colloidal templates.

Lu et al. described a sol-gel approach for the coating of super paramagnetic iron oxide nanoparticles with uniform shells of amorphous silica.<sup>[83]</sup> The coating process has been successfully applied to particles contained in a commercial ferrofluid and those synthesized through a wet chemical process. The thickness of the silica coating could be conveniently controlled in the range of 2–100 nm by changing the concentration of the sol-gel solution. Fluorescent dyes could also be incorporated into these silica shells through a covalent coupling between these organic dyes and the sol-gel precursor. Also, they and Liz-Marzan et al. demonstrated that gold nanoparticles could be directly coated with uniform shells of amorphous silica using a sol-gel process (Fig. 3).<sup>[27,83,84]</sup> The thickness of such a conformal coating could be changed from tens to several hundred nanometers by controlling the concentration

of TEOS precursor or the deposition time. The potential use of these spherical, core-shell colloids in fabricating photonic devices has been illustrated with two examples: photonic crystals and plasmonic waveguides. These demonstrations suggest that Au-SiO<sub>2</sub> core-shell particles with well-controlled sizes are promising building blocks for nanoscale integrated optics, in which the dimensions of structures for guiding and modulating photons will no longer be limited by the wavelength of light.

Stable colloidal core-shell particles consisting of a PS core and a titania coating were prepared in one step by the hydrolysis of a titanium alkoxide in the presence of a cationic PS latex.<sup>[85]</sup> Although this study used PS as a core, it should be possible to replace it with other polymer colloids that can be given cationic surface groups or with negatively charged particles that can be made positive by coating with a polyelectrolyte. This results in unusually smooth and uniform titania shells that can be made as thin as a few nanometers. This is attributed to a very rapid collection of the negatively charged titania oligomers by the positively charged surfaces. The coatings are very smooth and uniform and can be varied in thickness from just a few nanometers to at least 50 nm. Thicker coatings should also be possible but only through a multistep seeded growth process. The coated spheres have the same monodispersity as the starting latex, allowing them to form colloidal crystals.

Novel fine polymer particles containing ultrafine Pd, Pt, or Rh metal dispersed on the core-shell-type sphere were prepared by the emulsifier-free emulsion polymerization, followed by the addition of a mixture of  $\text{Ln}(\text{NO}_3)_3$  and  $\text{NaH}_2\text{PO}_4$ .<sup>[86]</sup> Rogach et al. and Caruso et al. report on the fabrication of 3-D colloidal photonic crystals by the self-organization of submicrometer-sized PS latex spheres covered via the consecutive electrostatic adsorption of charged polyelectrolytes and luminescent semiconductor nanocrystals (Fig. 1).<sup>[82]</sup> CdTe and CdTe(S) nanocrystals,<sup>[87]</sup> capped on the surface with different thiols and with sizes ranging from 2.5 to 5 nm, have been prepared by a wet

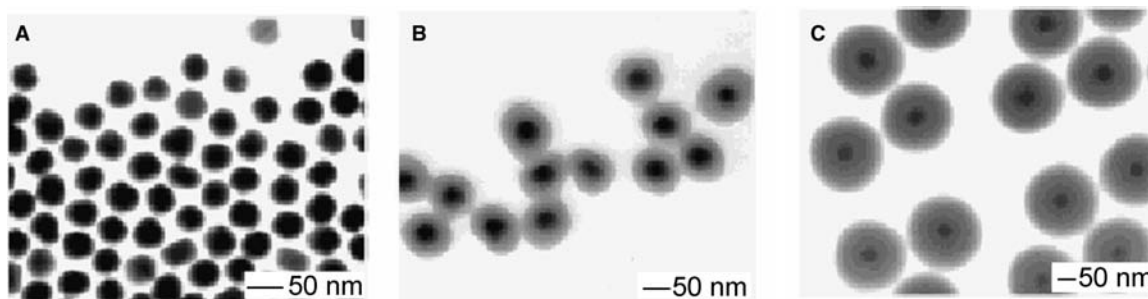


**Fig. 3** (A) TEM image of gold nanoparticles with an average diameter of 50 nm. (B,C) TEM images of such gold nanoparticles after their surfaces had been coated with amorphous silica shells of  $\sim 20$  and  $\sim 80$  nm in thickness, respectively. *Source:* From Ref.<sup>[83]</sup>.

chemical route.<sup>[88]</sup> They show a pronounced size dependence on the position of their electronic transitions and luminescence maxima due to the quantum confinement effect. Relatively narrow and reasonably strong “excitonic” luminescence occurs close to the onset of absorption and is tunable between 530 and 680 nm.

Highly monodispersed CdSe–CdS core-shell nanoparticles have been prepared by a novel route involving thermolysis in TOPO in a one-pot synthesis.<sup>[89]</sup> This route is a simple and convenient route to produce reasonable quantities of high-quality, monodispersed core-shell nanoparticles. The precursors are easy to synthesize and store and give high yields of TOPO-capped quantum dots.

Submicrometer-sized anionic PS latexes have been coated with uniform layers of iron compounds by aging, at elevated temperature. Dispersions of the polymer colloid in the presence of aqueous solutions of ferric chloride, urea, hydrochloric acid, and polyvinylpyrrolidone have been produced.<sup>[25]</sup> The thickness of the deposited layers could be altered by suitable adjustment of the reactant concentrations, and they could also be increased by further aging of the coated particles in the presence of aqueous solutions of ferric chloride. Hollow colloidal spheres of iron compounds were obtained by calcinations of the so-coated PS latexes at elevated temperature in air. Different chemical compositions of hollow colloidal spheres were obtained by heating them in hydrogen.

## HOLLOW CAPSULES AND NANOBOTTLES

Hollow spheres are useful in a variety of areas. They can be used in catalysis, delivery of drugs, development of artificial cells, or protection of biologically active agents (such as proteins, enzymes, or DNAs). Hollow spheres may also provide some immediate advantages over their solid counterparts because of their relatively low densities. In a typical procedure, hollow spheres are prepared by the removal of the “cores” (via selective etching with a solvent or calcination in air) from core-shell structure nanospheres. There are a variety of methods currently used to fabricate a wide range of stable, hollow spheres of various compositions. These methods include nozzle reactor systems,<sup>[90–92]</sup> emulsion/phase separation techniques coupled with sol-gel processing,<sup>[73,93,94]</sup> sacrificial core procedures,<sup>[77,95–97]</sup> and LbL technique (consecutively assembling inorganic nanoparticles and polymer onto colloids and subsequently removing the templated colloid).<sup>[1,10–15,98–102]</sup> There have been some successful examples for the preparation of different kinds of hollow microsphere materials (such as silica,<sup>[12,16–21,80]</sup> zirconium<sup>[16]</sup> hydroxide, yttrium compounds,<sup>[15,22,23]</sup> titania,<sup>[75,99–101]</sup> copper

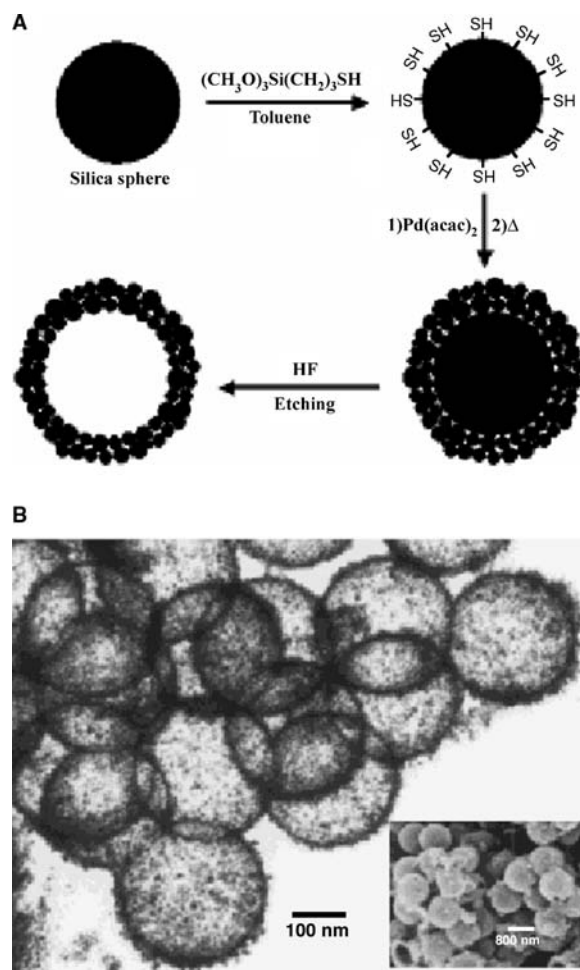


**Fig. 4** TEM and SEM (inset) of hollow palladium spheres. *Source:* From Ref.<sup>[105]</sup>.

compounds,<sup>[102]</sup> zeolite,<sup>[103]</sup> and magnetic nanoparticles.<sup>[17,24,25,104]</sup> Yin et al. synthesized mesoscopic hollow microspheres of ceramic materials with functionalized interior surfaces.<sup>[96]</sup> Kim et al. fabricated hollow palladium microspheres and successfully applied them to the recyclable heterogeneous catalyst for Suzuki coupling reactions (Fig. 4).<sup>[105]</sup> Caruso and coworkers prepared many kinds of inorganic and hybrid hollow spheres (SiO<sub>2</sub>, TiO<sub>2</sub>, Fe<sub>3</sub>O<sub>4</sub>, luminescent polyelectrolyte, etc.) by consecutively assembling inorganic nanoparticles and polymer onto colloids (LbL technology) and subsequently removing the templated colloid (Fig. 5).<sup>[106]</sup>

## Polymer Hollow Capsules and Nanobottles

Recent advances in supramolecular chemistry have given chemists unprecedented control over the composition and shape of nanoscopic objects. An example of such development is the synthesis of nanometer-sized organic hollow spheres, which can find numerous



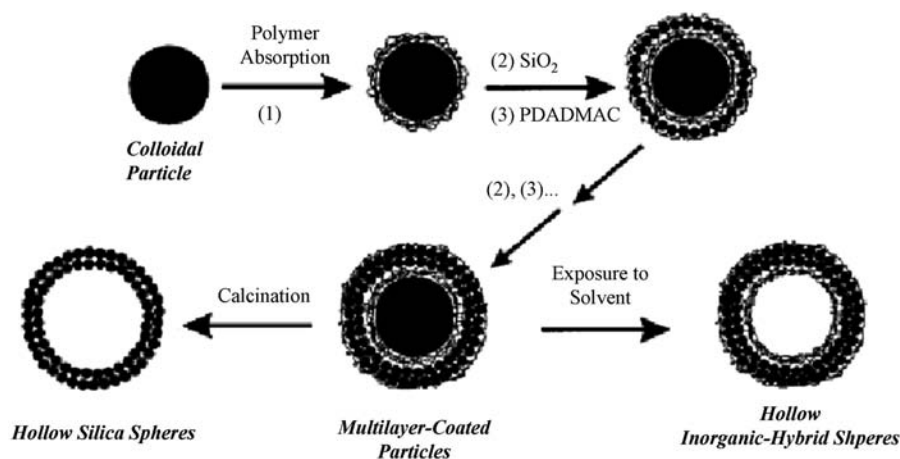


**Fig. 5** Illustration of procedures for preparing inorganic and hybrid hollow spheres. The scheme is shown for PS latex particles. Source: From Ref.<sup>[106]</sup>.

applications in drug delivery/targeting, extraction and as nanoreactors. Sun et al. described a new strategy for synthesizing nanometer-scale organic hollow spheres using Au colloids as templates.<sup>[107]</sup> The whole structure is held together by S–S bonds. Oxidation of gold nanoparticles protected by thiolated cyclodextrin molecules leads to the formation of water-soluble polycyclodextrin nanocapsules held together by S–S bonds. They are currently working on broadening the described strategy to other substrates/templates and probing the encapsulation properties of the hollow spheres.

Marinakos et al. described new methods for synthesizing nanometer-sized hollow capsules of poly(pyrrole), poly(*N*-methylpyrrole), and polyalkenes.<sup>[41,42]</sup> These methods utilized nanometer-sized gold particles as templates from which to grow polymer shells. Dissolution of the template particles yielded structurally intact hollow polymer capsules with interior volume and shell thickness governed by the diameter of the template particle and the polymerization time, respectively. Moreover, they showed that alkanethiols were encapsulated in the hollow polymer core by attaching them to the gold template particles prior to polymerization and particle etching, and small molecule diffusion rates through the pyrrole-based polymer capsules depended on polymer oxidation state. They also described a method for converting alkylthiolate monolayers on gold particles into hollow polymer capsules.<sup>[108]</sup> The synthetic design of the tripodal ligand provides the potential to ultimately control the functionality present on the surface of the particle as well as that present internally.

Marinakos et al. show that small molecules and enzymes can be trapped inside poly(pyrrole), poly(*N*-methylpyrrole), and poly-(3-methylthiophene) capsules synthesized using the gold particle template method.<sup>[1]</sup> Diffusion coefficients of small molecules through the capsule shell were found to vary by almost 3 orders of magnitude depending on the polymer, polymer oxidation state, and counter anion incorporated

during polymer synthesis. A small molecule (anthraquinone) and an enzyme (horseradish peroxidase) were trapped inside hollow capsules by attaching them to the template particle prior to polymerization and particle etching. A thin poly(pyrrole) shell protected the enzyme two times longer in neat toluene compared to unencapsulated enzyme. Finally, the potential for using conductive polymer nanoparticles for intracellular delivery or diagnostics was examined by administering particle suspensions to 3T3 murine fibroblasts. Particles ranging in size from 25 to 100 nm were engulfed by fibroblasts without compromising cell viability.<sup>[1]</sup>

Hollow polymer spheres synthesized from a vesicle-directed polymerization can be dried and redispersed in water using a variety of non-ionic ethoxylated alcohol surfactants as stabilizers.<sup>[109]</sup> The final dispersions consist of both polymer shells and surfactant micelles, which remain together in colloidal suspension for at least several months. Small-angle neutron scattering (SANS) is used to measure the polymer shell thickness (6.3 nm) and core radius (56 nm) of the surfactant-stabilized hollow polymer spheres in the presence of surfactant micelles.

Hollow polymer microsphere latexes were synthesized according to polymer–polymer core-shell emulsion polymerization then removing the core by selective solvents.<sup>[41]</sup> Kamata et al. have demonstrated a practical route to the facile synthesis of spherical hollow colloids of PBzMA that contained movable cores of Au nanoparticles (Fig. 6).<sup>[110]</sup> This procedure should be extendable to many other systems that involve the use of different combinations of materials for the core and the shell. These core-shell colloids may also find use as building blocks to form colloidal crystals with photonic band gap properties different from those of conventional core-shell or hollow particles.

Water-soluble polyelectrolyte nanocapsules as pH-sensitive nanocontainers can be synthesized by vesicular or emulsion polymerization via core-shell latexes.<sup>[111]</sup> These particles show a reversible pH and

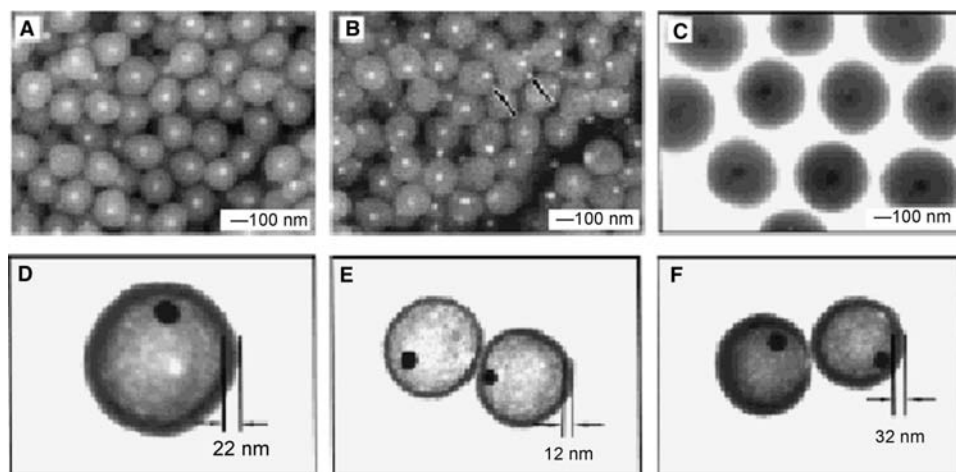


**Fig. 6** (A,B) Backscattering SEM and (C,D) TEM images of Au-SiO<sub>2</sub>-PBzMA particles before (A,C) and after (B,D) HF etching. The polymerization time was 4 hr, and the polymer shell was ~22 nm thick. (E,F) TEM images of Au-Air-PBzMA particles synthesized using different polymerization times: (E) 3 hr and (F) 6 hr. The polymer shells were ~12 and ~32 nm in thickness, respectively. *Source:* From Ref.<sup>[110]</sup>.

ionic strength-dependent swelling transition causing a considerable increase (decrease) of their radius. During this transition, gated pores are opened (closed) in the spherical polymer shells, which enable free molecular exchange between the interior of the hollow sphere and the bulk medium. This pH-switchable control of the permeability of the polyelectrolyte envelopes can be used to trigger the release of encapsulated materials from their central cavity.

### Inorganic Hollow Capsules and Nanobottles

Previous studies have provided successful procedures for the preparation of composite particles consisting of inorganic and organic cores covered with shells of other inorganic materials by controlled surface precipitation processes.<sup>[85,112–114]</sup> Such composite particles may be useful in many applications because the properties (magnetic, optical, electric, adsorptive, etc.) of these particles can be altered by appropriate coatings. Other studies have also shown that these procedures can be used for the preparation of polymer particles covered with yttrium, zirconium, iron, and titanium compounds by controlled surface precipitation processes, which makes it possible to extend the use of these colloids to different areas of high technology.

Owing to their lower density, large specific surface area, and optical properties, hollow particles have been of interest as fillers, coatings, catalysts, capsule agents, etc. In a novel approach, it was shown that hollow inorganic colloidal spheres of narrow size distribution could be obtained by thermal decomposition of the polymer core of PS particles coated with yttrium,

zirconium, iron, and titanium compounds. Kawahashi and Shiho described the application of these processes to other systems. Thus, under certain conditions, copper compounds can be deposited uniformly on PS latexes by precipitation using solutions of the corresponding salts in the presence of urea. Hollow metallic copper and copper oxide particles of a narrow size distribution can be obtained by calcination of particles coated in this manner at elevated temperatures in nitrogen and air, respectively.<sup>[102]</sup>

Calcination of sulfate-stabilized PS latexes coated with nanoparticle/polymer multilayers results in the production of hollow silica spheres.<sup>[11,84]</sup> The calcination process removes the organic matter (the colloidal core and bridging polymer) during heating to 450°C, as confirmed by thermogravimetric analysis.

Hollow spheres of zeolite b and silicalite-1 with different sizes were fabricated efficiently and conveniently through LbL self-assembly of nanozeolite-polymer multilayers on PS latex, coupled with the removal of the core by calcination.<sup>[103]</sup> The pH and ionic strength of the colloidal solution, crystal size of nanozeolites, and size of PS latex templates are factors affecting the fabrication of hollow zeolite spheres. Hollow spheres of other zeolites such as ZSM-5 and TS-1 have also been successfully fabricated in the same manner. Currently, the application of these novel materials in catalysis, separation and delivery systems is in progress in our laboratory.

Fowler et al. prepared hollow silica microspheres in high yields by a one-step facile synthesis under ambient conditions.<sup>[34]</sup> By controlling the rate of TEOS hydrolysis specifically at the droplet/water interface, intact microspheres with uniform wall thickness and thermal stability can be routinely synthesized. The

procedure can be readily extended to the synthesis of organo-functionalized silica shells, microspheres with encapsulated organic pigment, and hollow silica capsules with submicrometer dimensions. Such materials could have a wide range of uses in diverse materials applications. And they reported the facile synthesis of thermally stable hollow spherical shells with ordered mesoporous walls, approximately 20 nm or less in thickness. The structures were synthesized at room temperature by hydrolysis and condensation of TEOS in an aqueous solution of cetyltrimethyl ammonium bromide (CTABr), which was subjected to rapid quenching by dilution followed by pH neutralization after an induction period.<sup>[35]</sup>

Novel fine polymer particles containing ultrafine Pd particles dispersed on the surface of core-shell [core, poly(styrene-*co*-acrylic acid); shell, PrPO<sub>4</sub>]-type microspheres were prepared by the emulsifier-free emulsion polymerization of styrene with acrylic acid followed by the addition of PdCl<sub>2</sub> and a mixture of Pr(NO<sub>3</sub>)<sub>3</sub> and NaH<sub>2</sub>PO<sub>2</sub>. Pyrolysis of the resulting polymer particles at 900°C provides organic polymer-free hollow capsules composed of Pd metal and PrPO<sub>4</sub>.<sup>[115]</sup>

Most work in this area has been focused on the development of synthetic methodologies. Very little attention has been directed toward the functionalization of the interiors of these hollow particles. In addition, there are only limited sets of reports that address the diffusion of chemical reagents across the shells of hollow particles. Yin et al. described a method based on template-directed synthesis for generating ceramic hollow spheres whose interior surfaces could be functionalized with the prespecified, nanoscopic objects.<sup>[96]</sup> The templates involved in this process were crystalline lattices of monodispersed polymer beads whose surfaces had been derivatized with functional objects such as nanoparticles, quantum dots, or other nanoscale objects. These nanoscopic objects were left behind on the interior surfaces of the hollow spheres when the templates were selectively removed through etching or calcination (Fig. 7).

On the other hand, nanosized hollow inorganic spheres with a hole in the wall (denoted as nanobottle) had been successfully prepared from the assembly of functional polymer nanosphere with tetraethoxysilane or tetrabutyl titanate, coupled with the removal of the cores by programmed calcination. Cross-linked polymer nanospheres with quaternary ammonium species on the surface were synthesized using an emulsifier-free emulsion copolymerization. The polymerization and purification were carried out according to a published procedure,<sup>[116]</sup> and cross-linked polymer nanospheres with a uniform size of about 45 nm were obtained. As-synthesized silica-coated polymer nanospheres were hydrothermally prepared from chemical assembly of TEOS with the functional polymer nanospheres.

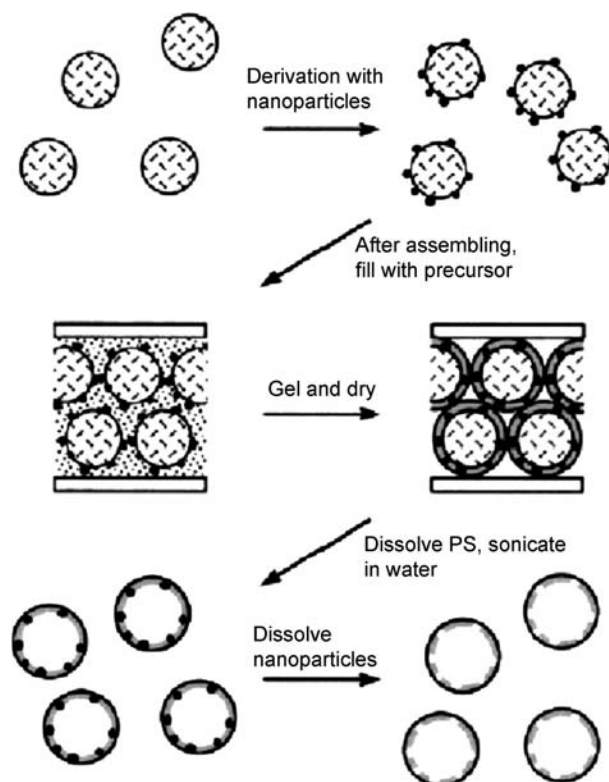


**Fig. 7** Schematic outline of the experimental procedure. The polymer template could be either dissolved with a solvent or burnt out through calcination at elevated temperatures. *Source:* From Ref.<sup>[96]</sup>.

After calcination at 550°C, the polymer template was removed and hollow silica spheres were obtained (named as silica nanobottles). Figure 8 shows the TEM images of functional polymer nanospheres from emulsion polymerization process, as-synthesized silica microspheres, and calcined hollow silica samples. After the self-assembly of the silica gel with the functional polymer nanospheres, the as-synthesized silica microspheres also show a very uniform size at 52–55 nm (B), which are nearly 10 nm thicker than the polymer nanospheres.<sup>[117–120]</sup> Calcination of the as-synthesized silica spheres results in the complete removal of the polymer nanospheres, forming hollow nanospheres with the size of 50–53 nm (C). As shown in Fig. 8D, a hole with the size of 5–8 nm can be seen on the surface of some hollow silica microspheres. These results may suggest that the holes in the silica hollow microspheres are formed in the following steps: Calcination at 550°C leads to decomposition of polymer nanospheres to smaller gas molecules, which have high pressure in the closed hollow microspheres. Then the gaseous molecules with high pressure break through the shells of the hollow microspheres, and the hole in the silica hollow microsphere is formed (scheme as

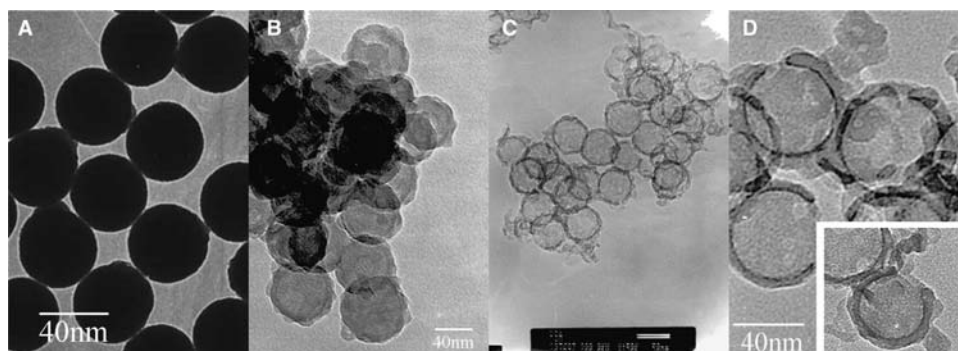


**Fig. 8** TEM images of (A) polymer spheres, (B) silica spheres before calcination, (C) hollow silica spheres after calcinations, and (D) magnification of silica nanobottles. *Source:* From Ref.<sup>[121]</sup>.

Fig. 9). Therefore these silica hollow microspheres with the hole are referred to as *silica nanobottles*.<sup>[121]</sup>

The AFM observation of functional polymer nanospheres, as-synthesized silica microspheres, and calcined silica samples were carried out. Similar to the TEM images, the functional polymer nanospheres have a uniform size of 52–56 nm and as-synthesized silica microspheres show a bigger size of 58–62 nm (not shown here). In addition, it can be seen clearly in Fig. 10 that the surface of every shell contains one hole of 9–12 nm in diameter. Obviously, the sample size characterized by AFM is slightly larger than that by TEM technique, which could be explained by assuming that the probe does not follow the microsphere's surface precisely because of the blunt scanning tip. Interestingly, the AFM images also show that there are holes on the hollow microspheres and each hollow microsphere possesses only one hole, which is in good agreement with the images observed by TEM. These results further confirmed that the sample is a kind of *silica nanobottles*. The nitrogen adsorption–desorption isotherms of silica nanobottles and uncalcined silica-coated polymer microspheres are well measured.

The comparisons of adsorption results suggest that the calcined sample is a kind of opening hollow nanosphere (nanobottles). The relatively larger pore volume of silica nanobottles may be potentially useful for the encapsulation of functional compounds in the silica nanobottles.

### Composite Capsules

Hollow inorganic–organic composite spheres can be obtained by selection of a solvent that decomposes the templated core but leaves the polymer bridging the nanoparticles in the shell. The choice of solvent depends on the type of core employed; for example, acidic or dimethyl sulfoxide solutions cause the removal of MF polymer latex core templates, tetrahydrofuran the removal of some PS cores, and highly oxidizing solutions decompose proteinaceous cores.

Similar to the pure polymer shells, the nanoparticle/polymer multiplayer shell assembled onto MF particles obtained upon decomposition of the MF core by acid assumes a rather flat confirmation on the substrate

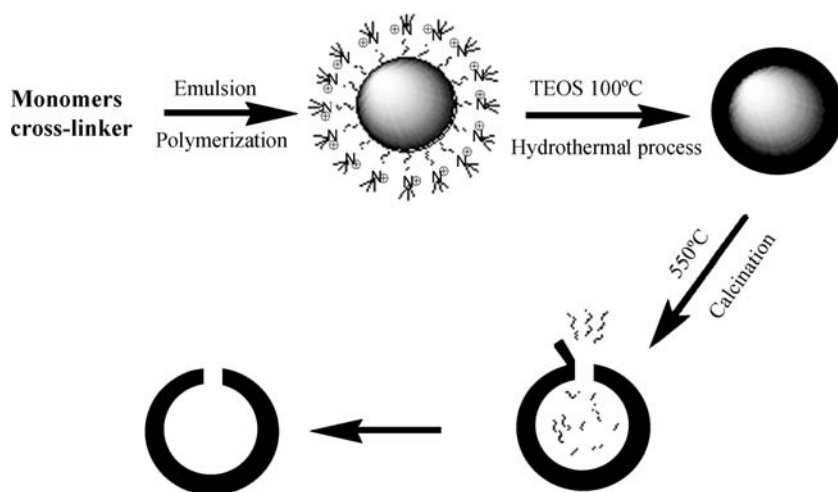


**Fig. 9** The procedure for preparation of silica nanobottles. *Source:* From Ref.<sup>[121]</sup>.

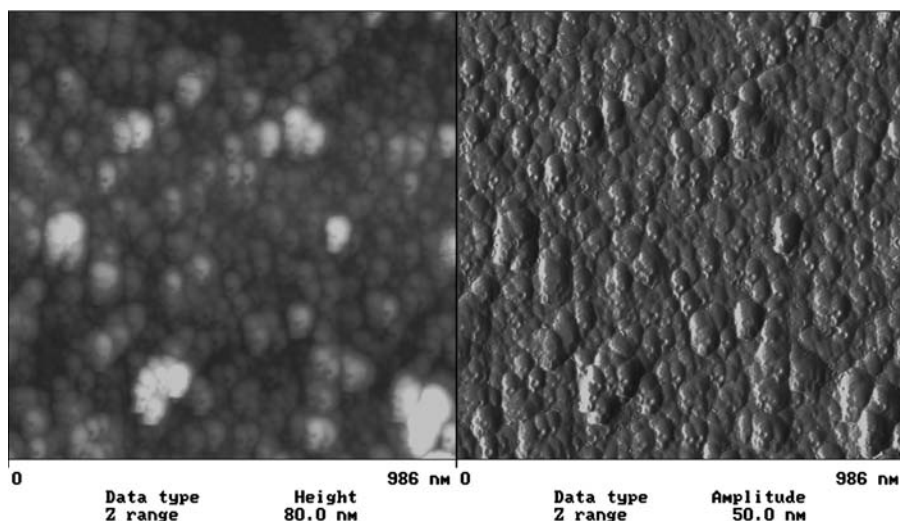


**Fig. 10** AFM height and amplitude images of silica nanobottles. *Source:* From Ref.<sup>[121]</sup>.

when dried.<sup>[84]</sup> Confocal microscopy images of the hollow composite microspheres again show that the shells often maintain their spherical shape in solution. Interestingly, permeating the nanoparticle/polymer shell still readily expels the oligomers produced as a result of decomposing the MF particles. Higher magnification TEM reveals that the shell is composed of nanoparticles embedded in the polymer matrix.

Nanoparticle/polymer-coated biocolloids (gluteraldehyde-fixed echinocytes) can also be utilized for the production of composite hollow structures. The template has a jagged and highly structured surface. After the removal of the core by exposure to deproteinizer, hollow composite silica/polymer capsules are obtained. Unlike the polymer or nanoparticle/polymer shells produced by the removal of MF-templated cores by acid solutions, these hollow structures mimic the original shape, including the secondary structure (spikes) of the templates, and do not significantly spread-out on the surface when dried. This is most probably due to the gelation of the silica particles as a result of the decomposing solution. SEM experiments confirmed that these structures were hollow.

### ENCAPSULATION OF RARE EARTH COMPLEX IN NANOBOTTLES

The abovementioned silica bottles are nanosized materials and there is a hole on the surface of it, which may be useful for further encapsulations. Rare earth (RE) complex  $\text{Eu}(\text{TTA})_3(\text{TPPO})_2$  (TTA: 1-(2-thenoyl)-3,3,3-trifluoroacetate, TPPO: triphenyl phosphineoxide) was selected as a guest molecule. After the modification of silica nanobottles with APTES ( $\text{NH}_2-(\text{CH}_2)_3\text{Si}(\text{OC}_2\text{H}_5)_3$ ),<sup>[122]</sup> the RE complex was mixed

with the silica nanobottles in chloroform, followed by filtering and washing with chloroform until the filter liquors gave no luminescence under UV radiation.

After RE complex encapsulation, the SEM images of silica nanobottles give most like morphology as before encapsulation, indicating that the silica nanobottles still remained after the encapsulation of RE complex. Furthermore, the encapsulation of  $\text{Eu}(\text{TTA})_3(\text{TPPO})_2$  in nanobottles was characterized by energy dispersive X-ray analysis (EDX). The results indicate that RE complex still exists in silica nanobottle samples after careful washing. Fig. 11 shows UV-visible absorption

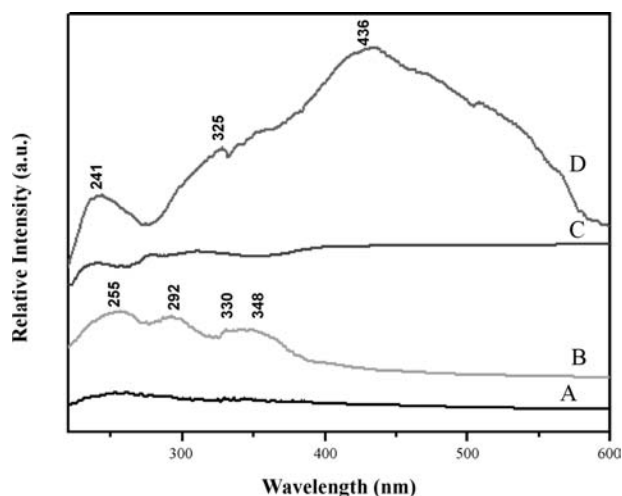


**Fig. 11** UV-Visible absorption spectra for (A) the modified silica nanobottles itself, (B) the assembly of  $\text{Eu}(\text{TTA})_3(\text{TPPO})_2$  in modified silica nanobottles, (C)  $\text{Eu}(\text{TTA})_3(\text{TPPO})_2$  absorbed on the outer surface of as-synthesized silica-coated polymer spheres (after washing with chloroform many times), and (D) RE complex  $\text{Eu}(\text{TTA})_3(\text{TPPO})_2$ . *Source:* From Ref.<sup>[121]</sup>.

spectra of silica nanobottles, RE complex  $\text{Eu}(\text{TТА})_3(\text{TPPO})_2$  encapsulated in silica nanobottles, and  $\text{Eu}(\text{TТА})_3(\text{TPPO})_2$  adsorbed on the outer surface of as-synthesized silica-coated polymer microspheres (after washing with chloroform many times) as well as RE complex  $\text{Eu}(\text{TТА})_3(\text{TPPO})_2$  itself. The spectrum of silica nanobottles does not show any absorption in the region of 200–800 nm (a); the sample spectrum of RE complex encapsulated in silica nanobottles shows clear peaks at near 255, 292, 330, and 348 nm (b); the spectrum of RE complex adsorbed on the outer surface of silica nanobottles only shows very weak absorptions after careful washing, and is similar to that of RE complex (c); the spectrum of  $\text{Eu}(\text{TТА})_3(\text{TPPO})_2$  shows typical peaks at 241, 325, and 436 nm (d). From the contrast of the above spectra, it can be confirmed that RE complex adsorbed both the inner and outer surface of the hollow microspheres. In addition, the peaks of RE complex are shifted to a lower wavelength in silica nanobottles. This phenomenon is possibly assigned to the encapsulation of RE complex in silica nanobottles, which is consistent with those of RE complex entrapped in mesopores of MCM-41 and in microcages of zeolite Y.<sup>[123,124]</sup>

## CONCLUSION

Research efforts over the last decade have led to a host of new strategies being developed for the modification of particle surfaces. Earlier methods have primarily focused on achieving single-component coatings on particles through surface chemical modification and conventional polymerization and precipitation reactions. More recent approaches, particularly those based on solution self-assembly, have been shown to be highly effective in producing multicomposite, nanostructured coatings. These methods permit remarkable control over the coating uniformity and thickness, and thus the assembled components and experimental conditions can be readily manipulated to prevent the aggregation of the coated colloids. Although the method of choice highly depends on the coating required and the end use of the composite particles, the synthetic approaches outlined provide a high level of flexibility, thus allowing the design, structure, and properties of the resultant particles to be varied tremendously. In addition, combinations of these methods are likely to allow new functional and composite layers to be manufactured on the surfaces of particles. Accordingly, nanoengineered core-shell particles are expected to find new and exciting applications in the chemistry, bioscience, and materials science fields. Core-shell particles have already been assembled into colloidal crystals for photonic

applications, used as heterogeneous catalysts and multienzyme biocatalysts, and in surface enhanced Raman scattering applications.

An interesting extension of the composite particles is the production of hollow capsules by the removal of the core particle; these hollow materials may find applications in drug delivery, or as reactor or specific recognition systems. The successful production of such hollow capsules opens many new and exciting avenues in the areas of chemistry, biotechnology, and materials science. They are potentially suitable for a variety of applications including the loading of drugs, as confined environment reactor systems, and for targeting by utilization of the surface functionalities on the capsule walls to attach specific receptors. Controlling the thickness and composition of the capsule walls should allow selective and switchable permeation for the encapsulation and release of various substances. The use of cross-linkable, pH- or temperature-sensitive polymers as capsule wall constituents are attractive candidates for controlling and varying the permeability, while the incorporation of specific reactive groups inside the capsule walls would allow specific chemistry to be carried out in these systems. Coupling of biospecies to the surfaces of the capsules through functional groups would provide biofunctionalized capsules.

Some experiments demonstrate that it is possible to coat the outer and inner surfaces of hollow polymer capsules with phospholipid bilayers. The polymer capsules are permeable to small low molecular weight dyes, but not to polyelectrolytes with molecular weights greater than 4000 or molecules larger than 5–10 nm in diameter. The phospholipid coating reduces the permeability to small organic dyes. The precipitation of small organic dye molecules inside polymer capsules has been achieved, as has the solubilization of various organic solvents. Functional biomolecules have also been encapsulated at a very high loading capacity in polymer capsules; these systems are expected to be used in enzyme catalysis applications. The coating technique is currently being extended to inorganic templates to create novel hollow capsules of nanometer size and to emulsion-based systems. A luminescent RE complex is successfully encapsulated in silica nanobottles, showing this material has potential nanotechnology applications.

## ACKNOWLEDGMENTS

This work was supported by NSFC (29925412) and the Major State Basic Research Development Program (G2000078102).



## REFERENCES

1. Marinakos, S.M.; Anderson, M.F.; Ryan, J.A.; Martin, L.D.; Feldheim, D.L. *J. Phys. Chem., B* **2001**, *105*, 8872.
2. Hostetler, M.J.; Templeton, A.C.; Murray, R.W. *Langmuir* **1999**, *15*, 3782.
3. Foss, C.A., Jr.; Tierney, M.J.; Martin, C.R. *J. Phys. Chem.* **1992**, *96*, 9001.
4. Sandrock, M.L.; Pibel, C.D.; Geiger, F.M.; Foss, C.A., Jr. *J. Phys. Chem., B* **1999**, *103*, 2668.
5. Mirkin, C.A.; Letsinger, R.L.; Mucic, R.C.; Storhoff, J. *J. Nat.* **1996**, *382*, 607.
6. Freeman, R.G.; Grabar, K.C.; Allison, K.J.; Bright, R.M.; Davis, J.A.; Guthrie, A.P.; Hommer, M.B.; Jackson, M.A.; Smith, P.C.; Walter, D.G.; Natan, M. *J. Sci.* **1995**, *267*, 1629.
7. Caruso, F. *Adv. Mater.* **2001**, *13*, 11.
8. Bateman, A.R.; Harrington, K.J.; Melcher, A.A. *Expert Opin. Investig. Drugs* **2000**, *9*, 2799.
9. Garcia-Blanco, M.A.; Puttaraju, M.; Mansfield, S.G.; Mitchell, L.G. *Gene Ther. Reg.* **2000**, *1*, 141.
10. Caruso, F. *Chem. Eur. J.* **2000**, *6*, 413.
11. Caruso, F.; Caruso, R.A.; Mohwald, H. *Science* **1998**, *282*, 1111.
12. Giersig, M.; Ung, T.; Liz-Marzan, L.M.; Mulvaney, P. *Adv. Mater.* **1997**, *9*, 570.
13. Philpse, A.P.; van Bruggen, M.P.B.; Pathmamanoharan, C. *Langmuir* **1994**, *10*, 92.
14. Chang, S.Y.; Liu, L.; Asher, S.A. *J. Am. Chem. Soc.* **1994**, *116*, 6739.
15. Ung, T.; Liz-Marzan, L.M.; Mulvaney, P. *Langmuir* **1998**, *14*, 3740.
16. Kawahashi, N.; Persson, C.; Matijevic, E. *J. Mater. Chem.* **1991**, *1*, 577.
17. Kawahashi, N.; Matijevic, E. *J. Colloid Interface Sci.* **1991**, *143*, 103.
18. Bamnolker, H.; Nitzan, B.; Gura, S.; Margel, S. *J. Mater. Sci. Lett.* **1997**, *16*, 1412.
19. Walsh, D.; Mann, S. *Nature* **1995**, *377*, 320.
20. Garg, A.; Matijevic, E. *J. Colloid Interface Sci.* **1988**, *126*, 243.
21. Correa-Duarte, M.A.; Giersig, M.; Liz-Marzan, L.M. *Chem. Phys. Lett.* **1998**, *286*, 497.
22. Kawahashi, N.; Matijevic, E. *J. Colloid Interface Sci.* **1990**, *138*, 534.
23. Gieshe, H.; Matijevic, E. *J. Mater. Res.* **1994**, *9*, 436.
24. Shiho, H.; Manabe, Y.; Kawahashi, N. *J. Mater. Chem.* **2000**, *10*, 333.
25. Shiho, H.; Kawahashi, N. *J. Colloid Interface Sci.* **2000**, *226*, 91.
26. Davies, R.; Schurr, G.A.; Meenan, P.; Nelson, R.D.; Bergna, H.E.; Brevett, C.A.S.; Goldbaum, R.H. *Adv. Mater.* **1998**, *10*, 1264.
27. Liz-Marzan, L.M.; Giersig, M.; Mulvaney, P. *Langmuir* **1996**, *12*, 4329.
28. Hofman-Caris, C.H.M. *New J. Chem.* **1994**, *18*, 1087.
29. Antelmi, D.A.; Spalla, O. *Langmuir* **1999**, *15*, 7478.
30. Bartsch, E.; Frenz, V.; Baschnagel, J.; Schaertl, W.; Silescu, H. *J. Chem. Phys.* **1997**, *106*, 3743.
31. Ohmori, M.; Matijevic, E. *J. Colloid Interface Sci.* **1993**, *160*, 288.
32. Goia, D.V.; Matijevic, E. *New J. Chem.* **1998**, 1203.
33. Donath, E.; Sukhorukov, G.B.; Caruso, F.; Davis, S.A.; Mohwald, H. *Angew. Chem., Int. Ed. Engl.* **1998**, *37*, 2201.
34. Fowler, C.E.; Khushalani, D.; Mann, S. *J. Mater. Chem.* **2001**, *11*, 1968.
35. Fowler, C.E.; Khushalani, D.; Mann, S. *Chem. Commun.* **2001**, 2028.
36. Lin, H.P.; Mou, C.Y.; Liu, S.B.; Tang, C.Y. *Chem. Commun.* **2001**, 1970.
37. Oyama, H.T.; Sprycha, R.; Xie, Y.; Partch, R.E.; Matijevic, E. *J. Colloid Interface Sci.* **1993**, *160*, 298.
38. Sprycha, R.; Oyama, H.T.; Zelenev, A.; Matijevic, E. *Colloid Polym. Sci.* **1995**, *273*, 693.
39. Partch, R.; Gangolli, S.G.; Matijevic, E.; Cai, W.; Aaraj, S. *J. Colloid Interface Sci.* **1991**, *144*, 27.
40. Marinakos, S.M.; Brousseau, L.C.; Jones, A.; Feldheim, D.L. *Chem. Mater.* **1998**, *10*, 1214.
41. Marinakos, S.M.; Shultz, D.A.; Feldheim, D.L. *Adv. Mater.* **1999**, *11*, 34.
42. Marinakos, S.M.; Novak, J.P.; Brousseau, L.C.; House, A.B.; Edeki, E.M.; Feldhaus, J.C.; Feldheim, D.L. *J. Am. Chem. Soc.* **1999**, *121*, 8518.
43. Ottewill, R.H.; Schofield, A.B.; Waters, J.A.; Williams, N.S. *J. Colloid Polym. Sci.* **1997**, *275*, 274.
44. Quaroni, L.; Chumanov, G. *J. Am. Chem. Soc.* **1999**, *121*, 10642.
45. Von Werne, T.; Patten, T.E. *J. Am. Chem. Soc.* **2001**, *123*, 7497.
46. Patten, T.E.; Matyjaszewski, K. *Adv. Mater.* **1998**, *10*, 901.
47. Sun, S.; Murray, C.B.; Weller, D.; Folks, D.; Moser, A. *Science* **2000**, *287*, 1989.
48. Selvan, S.T.; Spatz, J.P.; Klok, H.A.; Möller, M. *Adv. Mater.* **1998**, *10*, 132.
49. Godovski, D.Y. *Adv. Polym. Sci.* **1995**, *119*, 79.
50. Go'mez-Lopera, S.A.; Plaza, R.C.; Delgado, A.W. *J. Colloid Interface Sci.* **2001**, *240*, 40.
51. Portet, D.; Denizot, B.; Rump, E.; Lejeune, J.J.; Jallot, P. *J. Colloid Interface Sci.* **2001**, *238*, 37.
52. Xu, X.; Friedman, G.; Humfeld, K.D.; Majetich, S.A.; Asher, S.A. *Adv. Mater.* **2001**, *13*, 1681.
53. Xu, X.; Friedman, G.; Humfeld, K.D.; Majetich, S.A.; Asher, S.A. *Chem. Mater.* **2002**, *14*, 1249.
54. Vestal, C.R.; Zhang, Z.J. *J. Am. Chem. Soc.* **2002**, *124*, 14312.
55. Srikanth, H.; Hajndl, R.; Chirinos, C.; Sanders, J.; Sampath, A.; Sudarshan, T.S. *Appl. Phys. Lett.* **2001**, *79*, 3503.
56. Liu, C.; Zou, B.; Rondinone, A.J.; Zhang, Z.J. *J. Phys. Chem., B* **2000**, *104*, 1141.
57. Liu, C.; Zou, B.; Rondinone, A.J.; Zhang, Z.J. *J. Am. Chem. Soc.* **2000**, *122*, 6263.

58. Huang, H.; Kowalewski, T.; Remsen, E.E.; Gertsmann, R.; Wooley, K.L. *J. Am. Chem. Soc.* **1997**, *119*, 11653.
59. Bütün, V.; Billingham, N.C.; Armes, S.P. *J. Am. Chem. Soc.* **1998**, *120*, 12135.
60. Zhang, Q.; Remsen, E.E.; Wooley, K.L. *J. Am. Chem. Soc.* **2000**, *122*, 3642.
61. Huang, H.; Remsen, E.E.; Wooley, K.L. *Chem. Commun.* **1998**, 1415.
62. Murthy, K.S.; Ma, Q.; Clark, C.G.; Remsen, E.E.; Wooley, K.L. *Chem. Commun.* **2001**, 773.
63. Stöber, W.; Fink, A. *J. Colloid Interface Sci.* **1968**, *26*, 62.
64. Zhang, K.; Chen, H.; Chen, X.; Chen, Z.; Cui, Z.; Yang, B. *Macromol. Mater. Eng.* **2003**, *288*, 380.
65. Ohmori, M.; Matijevic, E. *J. Colloid Interface Sci.* **1992**, *150*, 594.
66. Liz-Marzan, L.M.; Giersig, M.; Mulvaney, P. *Chem. Commun.* **1996**, 731.
67. Dokoutchaev, A.; James, J.T.; Koene, S.C.; Pathak, S.; Prakash, G.K.S.; Thompson, M.E. *Chem. Mater.* **1999**, *11*, 2389.
68. Liu, Q.; Xu, Z.; Finch, J.A.; Egerton, R. *Chem. Mater.* **1998**, *10*, 3936.
69. Liz-Marzan, L.M.; Philipse, A.P. *J. Colloid Interface Sci.* **1995**, *176*, 459.
70. Ung, T.; Liz-Marzan, L.M.; Mulvaney, P. *J. Phys. Chem., B* **1999**, *103*, 6770.
71. Bruggen, M.P.B. *Langmuir* **1998**, *14*, 2245.
72. Hall, S.R.; Davis, S.A.; Mann, S. *Langmuir* **2000**, *16*, 1454.
73. Hardikar, V.V.; Matijevic, E. *J. Colloid Interface Sci.* **2000**, *221*, 133.
74. Hanprasopwattana, A.; Srinivasan, S.; Sault, A.G.; Datye, A.K. *Langmuir* **1996**, *12*, 3173.
75. Guo, X.C.; Dong, P. *Langmuir* **1999**, *15*, 5535.
76. Pastoriza-Santos, I.; Koktysh, D.S.; Mamedov, A.A.; Giersig, M.; Kotov, N.A.; Liz-Marzan, L.M. *Langmuir* **2000**, *16*, 2731.
77. Stober, W.; Fink, A.; Bohn, E. *J. Colloid Interface Sci.* **1968**, *26*, 62.
78. Keller, S.W.; Johnson, S.A.; Brigham, E.S.; Yonemoto, E.H.; Mallouk, T.E. *J. Am. Chem. Soc.* **1995**, *117*, 12879.
79. Caruso, F.; Lichtenfeld, H.; Giersig, M.; Mohwald, H. *J. Am. Chem. Soc.* **1998**, *120*, 8523.
80. Caruso, F.; Mohwald, H. *Langmuir* **1999**, *15*, 8276.
81. Caruso, F.; Susha, A.S.; Giersig, M.; Moehwald, H. *Adv. Mater.* **1999**, *11*, 950.
82. Rogach, A.; Susha, A.; Caruso, F.; Sukhorukov, G.; Kornowski, A.; Kershaw, S.; Möhwald, H.; Eychmüller, A.; Weller, H. *Adv. Mater.* **2000**, *12*, 333.
83. Lu, Y.; Yin, Y.; Mayers, B.T.; Xia, Y. *Nano Lett.* **2002**, *2*, 183.
84. Caruso, F.; Caruso, R.A.; Mohwald, H. *Chem. Mater.* **1999**, *11*, 3309.
85. Imhof, A. *Langmuir* **2001**, *17*, 3579.
86. Tamai, H.; Ikeya, T.; Nishiyama, F.; Yasuda, H. *J. Mater. Sci.* **2000**, *35*, 4945.
87. Susha, A.S.; Caruso, F.; Rogach, A.L.; Sukhorukov, G.B.; Kornowski, A.; Möhwald, H.; Giersig, M.; Eychmüller, A.; Weller, H. *Colloids Surf., A* **2000**, *163*, 39.
88. Gao, M.; Kirstein, S.; Möhwald, H.; Rogach, A.L.; Kornowski, A.; Eychmüller, A.; Weller, H. *J. Phys. Chem., B* **1998**, *102*, 8360.
89. Revaprasadu, N.; Malik, M.A.; O'Brien, P.; Wakefield, G. *Chem. Commun.* **1999**, 1573.
90. Lu, Y.; Fan, H.; Stump, A.; Ward, T.L.; Rieker, T.; Brinker, C. *J. Nat.* **1999**, *398*, 223.
91. Bruinsma, P.J.; Kim, A.Y.; Liu, J.; Baskaran, S. *Chem. Mater.* **1997**, *9*, 2507.
92. Iida, M.; Sasaki, T.; Watanabe, M. *Chem. Mater.* **1998**, *10*, 3780.
93. Pekarek, K.J.; Jacob, J.S.; Mathiowitz, E. *Nature* **1994**, *367*, 258.
94. Liu, J.G.; Wilcox, D.L. *J. Mater. Res.* **1995**, *10*, 84.
95. Hubert, D.H.W.; Jung, M.; Frederik, P.M.; Bowmans, P.H.H.; Meuldijk, J.; German, A.L. *Adv. Mater.* **2000**, *12*, 1286.
96. Yin, Y.D.; Lu, Y.; Gates, B.; Xia, Y.N. *Chem. Mater.* **2001**, *13*, 1146.
97. Rhodes, K.H.; Davis, S.A.; Caruso, F.; Zhang, B.; Mann, S. *Chem. Mater.* **2000**, *12*, 2832.
98. Decher, G. *Science* **1997**, *277*, 1232.
99. Zhong, Z.; Yin, Y.; Gates, B.; Xia, Y.N. *Adv. Mater.* **2000**, *12*, 206.
100. Caruso, R.A.; Susha, A.; Caruso, F. *Chem. Mater.* **2001**, *13*, 400.
101. Shiho, H.; Kawahashi, N. *J. Colloid Polym. Sci.* **2000**, *278*, 270.
102. Kawahashi, N.; Shiho, H. *J. Mater. Chem.* **2000**, *10*, 2294.
103. Wang, X.D.; Yang, W.L.; Tang, Y.; Wang, Y.J.; Fu, S.K.; Gao, Z. *Chem. Commun.* **2000**, 2161.
104. Caruso, F.; Spasova, M.; Susha, A.; Giersig, M.; Caruso, R.A. *Chem. Mater.* **2001**, *13*, 109.
105. Kim, S.W.; Kim, M.; Lee, W.Y.; Hyeon, T. *J. Am. Chem. Soc.* **2002**, *124*, 7642.
106. Caruso, F.; Caruso, R.A.; Möhwald, H. *Science* **1998**, *282*, 6.
107. Sun, L.; Crooks, R.M.; Chechik, V. *Chem. Commun.* **2001**, 359.
108. Wu, M.; O'Neill, S.A.; Brousseau III, L.C.; McConnell, W.; Shultz, D.A.; Feldheim, D.L.; Linderman, R. *J. Chem. Commun.* **2000**, 775.
109. McKelvey, C.A.; Kaler I, E.W. *J. Colloid Interface Sci.* **2001**, *245*, 68.
110. Kamata, K.; Lu, Y.; Xia, Y.N. *J. Am. Chem. Soc.* **2003**, *125*, 2384.
111. Sauer, M.; Streich, D.; Meier, W. *Adv. Mater.* **2001**, *13*, 1649.
112. Garg, A.; Matijevic, E. *Langmuir* **1988**, *4*, 38.
113. Aiken, B.; Matijevic, E. *J. Colloid Interface Sci.* **1988**, *126*, 645.
114. Furusawa, K.; Anzai, C. *Colloids Surf.* **1992**, *63*, 103.
115. Tamai, H.; Ikeya, T.; Yasuda, H. *J. Colloid Interface Sci.* **1999**, *218*, 217.

116. Chen, X.; Cui, Z.; Chen, Z.; Zhang, K.; Lu, G.; Zhang, G.; Yang, B. *Polymer* **2002**, *43*, 4147.
117. Beck, J.S.; Vartuli, J.C.; Roth, W.J.; Leonowicz, M.E.; Kresge, C.T.; Schmitt, K.D.; Chu, C.T.W.; Olson, D.H.; Sheppard, E.W.; McCullen, S.B.; Higgins, J.B.; Schlenker, J.L. *J. Am. Chem. Soc.* **1992**, *114*, 10834.
118. Zhao, D.Y.; Feng, J.L.; Huo, Q.S.; Melosh, N.; Fredrickson, G.H.; Chmelka, B.F.; Stucky, G.D. *Science* **1998**, *279*, 548.
119. Xiao, F.S.; Han, Y.; Yu, Y.; Meng, X.J.; Yang, M.; Wu, S. *J. Am. Chem. Soc.* **2002**, *124*, 888.
120. Zhang, Z.T.; Han, Y.; Xiao, F.S.; Qiu, S.L.; Zhu, L.; Wang, R.W.; Yu, Y.; Zhang, Z.; Zou, B.S.; Wang, Y.Q.; Sun, H.P.; Zhao, D.Y.; Wei, Y. *J. Am. Chem. Soc.* **2001**, *123*, 5014.
121. Zhang, G.; Yu, Y.; Chen, X.; Han, Y.; Di, Y.; Yang, B.; Xiao, F.; Shen, J. *J. Colloid Interface Sci.* **2003**, *263*, 467.
122. Liu, C.J.; Li, S.G.; Pang, W.Q.; Che, C.M. *Chem. Commun.* **1997**, 65.
123. Xu, Q.H.; Li, L.S.; Li, B.; Yu, J.H.; Xu, R.R. *Microporous Mesoporous Mater.* **2000**, *38*, 351.
124. Rose, I.L.V.; Serra, O.A.; Nassa, E.J. *Lumin* **1997**, *72*, 532.

# Cubosomes: Bicontinuous Liquid Crystalline Nanoparticles

Patrick T. Spicer

Complex Fluids Research, Procter & Gamble Company,  
West Chester, Ohio, U.S.A.

## INTRODUCTION

Surfactants, lipids, and polymer molecules that have both polar and non-polar components are termed amphiphilic. The hydrophobic effect drives amphiphilic molecules in polar solvents to spontaneously self-assemble into a rich array of thermodynamically stable lyotropic liquid crystalline phases with characteristic lengths on the nanometer scale. Liquid crystalline phases possess a sufficient average degree of molecular orientational order to be characterized by their structural symmetry, despite their liquid state, and often form in aqueous surfactant systems at relatively high amphiphile concentrations. An interesting example of contemporary interest is the bicontinuous cubic liquid crystalline phase.

Bicontinuous cubic phases are optically isotropic, very viscous, solidlike liquid crystals with cubic crystallographic symmetry. Prior to their structural characterization, these phases were termed “viscous isotropic phases” and considered quite a nuisance in industrial processes. Bicontinuous cubic phases consist of two separate, continuous but non-intersecting hydrophilic regions divided by a lipid bilayer that is contorted into a periodic minimal surface with zero average curvature. The phase’s regular structural connectivity results in a very high viscosity, whereas its tortuosity is useful for slowing diffusion in controlled transport applications. The bicontinuous nature of such cubic phases distinguishes them from the so-called micellar or discontinuous cubic phases containing micelles packed in cubic symmetry. In this work, all references to cubic phases refer to bicontinuous cubic phases, unless otherwise noted.

The last several decades have brought about a great understanding of the properties of cubic phases and a realization of their relevance in areas such as medicine, biology, and chemistry. An intriguing property of the cubic phases formed by certain classes of amphiphiles is their ability to be dispersed into particles, termed cubosomes. Cubosomes are liquid crystalline nanostructured particles with the same unique properties of the bulk cubic phase, although cubosome dispersions have much lower viscosity. Although fundamental research has been focused sharply on bulk cubic phases, it is commercial applications that drive much

of the existing and still very active research into cubosomes. This entry reviews historical research into cubic phases and cubosomes, describing the initial discovery and the realization that differential geometry allows the mathematical characterization of cubic phase structures. Cubosome properties are reviewed in the context of particle formation and applications. Where appropriate, interesting open problems are cited and discussed.

## CUBIC PHASE STRUCTURE

Luzzati and Husson<sup>[1]</sup> and Luzzati et al.<sup>[2]</sup> first recognized the existence of cubic phases in lipid–water systems using x-ray scattering measurements. Fontell, Mandell, and Ekwall<sup>[3]</sup> drew similar conclusions regarding cubic phases in ternary systems of amphiphiles, oils, and water. In parallel, although without apparent awareness of the lipid work, biologists began documenting structures with cubic symmetry in plant leaf plastid membranes,<sup>[4]</sup> identical to what is now accepted as cubic liquid crystalline phase structures. Around the same time, Lutton<sup>[5]</sup> published a comprehensive study of the aqueous phase behavior of monoglycerides. Monoglycerides are polar lipids with poor water solubility that exhibit aqueous phase behavior, reflecting their structural similarity to nonionic surfactants. Fig. 1 shows a schematic of Lutton’s results for monoglycerides with hydrocarbon chain lengths between  $C_{12}$  and  $C_{22}$ . Of particular interest is the large region of cubic phase exhibited by each of the aqueous monoglyceride systems, with the largest being that of monoolein, the unsaturated  $C_{18}$  monoglyceride (Fig. 2). Cubic phases are often found sandwiched between lamellar and hexagonal liquid crystalline phases, especially in nonionic surfactant systems.<sup>[6]</sup> However, the monoolein–water system uniquely possesses a cubic phase region spanning large compositional and temperature ranges. It is not entirely clear why monoolein forms cubic phases in such broad compositional and temperature ranges, but surfactant packing concepts offer some conceptual approaches. Monoolein has a slightly larger cross-sectional area of its hydrophobic tail region, leading to a ratio of the hydrophobic tail group area to the

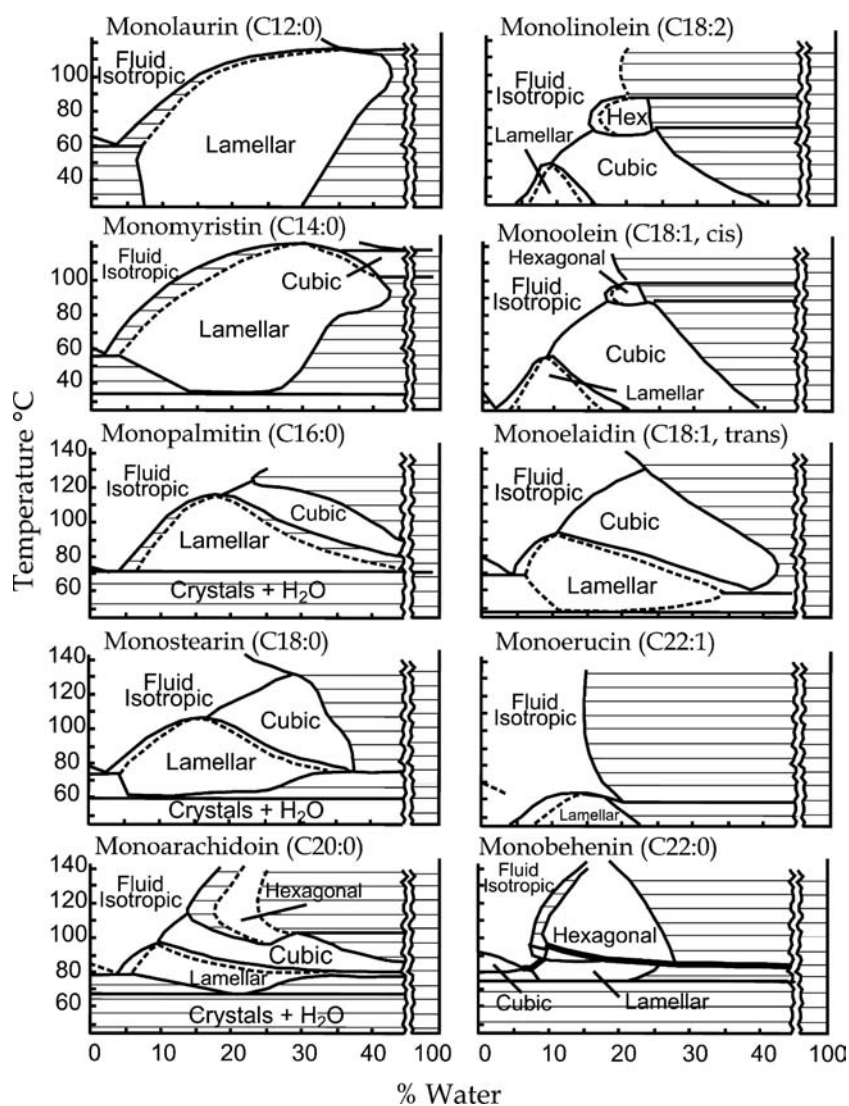


**Fig. 1** Schematic of the aqueous phase behavior of the monoglycerides showing the regions of cubic phase formation. Source: From Ref.<sup>[5]</sup>. © American Oil Chemists' Society, 1965.

hydrophilic head group area slightly larger than one ( $\sim 1.03$ ,<sup>[7]</sup>). As a result, the cubic phases are often referred to as reversed or inverse cubic phases, indicating the curvature of the constituent bilayers toward the polar medium. Shortly after Lutton's study, Larsson began to systematically examine the structure of aqueous monoglyceride cubic phases using x-ray diffraction. He found, using nuclear magnetic resonance (NMR) and x-ray, that the cubic phases have continuous regions of both hydrophobic and hydrophilic nature<sup>[8]</sup> leading to the conclusion that the cubic phase structures can be described using the concepts of differential geometry and periodic minimal surfaces.<sup>[9]</sup>

Minimal surfaces are best described by analogy with their most readily observed natural form: soap films. The surface formed by a soap film between two rings is a catenoid, a simple form of minimal surface whose two principal curvatures are equal but opposite in sign at every point, resulting in an average curvature of zero and a negative Gaussian curvature.<sup>[10]</sup> Fig. 3 shows approximate plots of the three most commonly studied minimal surfaces in cubic phases. The surfaces in Fig. 3 are particularly fascinating because their discovery was purely mathematical, prior to knowledge of the structures' existence in cubic phases. The P-surface (or primitive surface) and the D-surface (or diamond surface) were both discovered mathematically by Schwarz

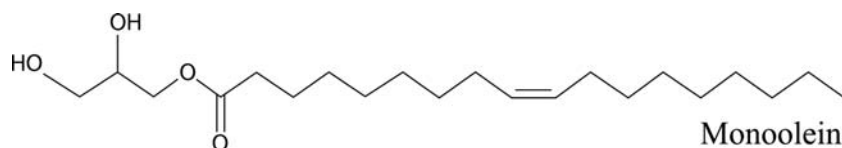


**Fig. 2** Molecular structure of monoolein, the lipid most commonly used to form cubosomes.

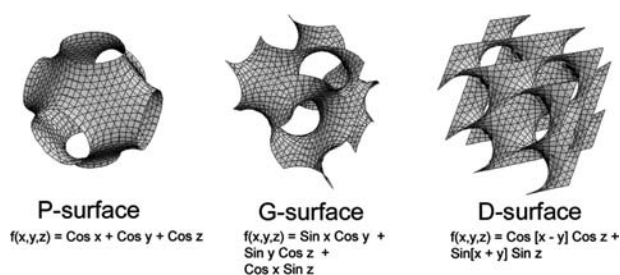


**Fig. 3** Unit cubes of the P-surface, G-surface, and D-surface formed in bicontinuous amphiphilic systems.

in 1890, whereas the G-surface (or gyroid surface) was only discovered by Schoen<sup>[11]</sup> in the 1960s. In cubic phases, the minimal surface is formed by the self-assembled bilayer that occurs as the hydrophobic or hydrophilic portions of the surfactant molecules line up to minimize their interaction with their opposites. The three structures are all bicontinuous (i.e., they divide space into two continuous but non-intersecting regions); in the case of cubic phases, two separate regions of hydrophilic material (water channels) form. Following suggestions by Scriven<sup>[12]</sup> that minimal surfaces could explain liquid crystal structure, Larsson, Fontell<sup>[9]</sup> applied the minimal surface description to the cubic phase observed in the monoolein–water system and noted the connection to the structures formed in plastid systems. However, Longley and McIntosh<sup>[13]</sup> found evidence of an alternative symmetry in the monoolein–water cubic phase, leading Larsson<sup>[14]</sup> to realize that two cubic phases are formed, both with minimal surface structures. The monoolein–water system forms the D-surface at high water levels and the G-surface at lower levels, as shown in the phase diagram in Fig. 4.<sup>[15]</sup> Qiu and Caffrey<sup>[16]</sup> later updated

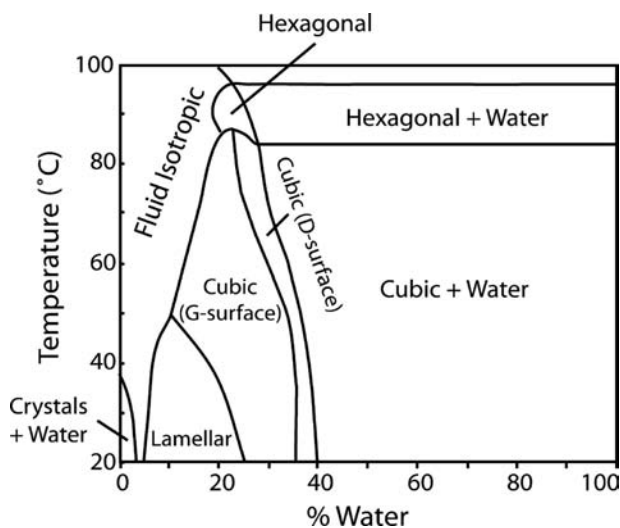


**Fig. 4** Aqueous phase behavior of the monoolein–water system, updated to reflect the existence of two cubic phases. Source: From Ref.<sup>[23]</sup>. © American Chemical Society, 1989.

elements of the monoolein–water phase diagram, but the version put forth by Larsson (Fig. 4) remains the benchmark. The P-surface is formed in the monoolein–water system, but only when a third component, such as caseins<sup>[17]</sup> or amphiphilic block copolymers,<sup>[18]</sup> is added. The strength of the minimal surface approach to cubic phase characterization is its quantitative mathematical basis. Unfortunately, the analytical representation of minimal surfaces in Fig. 3 is still mathematically very difficult. A significant advance came in the discovery that nodal surfaces are closely related to minimal surfaces and offer a simple equation that can be used to plot and study cubic phase structures.<sup>[19]</sup> The structures plotted in Fig. 3 are generated using nodal surfaces and the equations used are also shown. Extensive reviews of the history and mathematical description of bicontinuous phases are given in Refs.<sup>[20]</sup> and <sup>[21]</sup>, whereas a more recent review<sup>[22]</sup> generally discusses bicontinuous geometry in amphiphilic systems. Contemporary with the discovery of minimal surface applicability to cubic phases was the realization that, in certain cases, the cubic phases can exist in a particulate form, possessing the same bicontinuous structure as the bulk cubic phase.

## CUBOSOMES—DISPERSED CUBIC PHASE PARTICLES

Dispersed particles of bicontinuous cubic phases were first observed during studies of fat digestion that simulated stomach contents by combining oil with lipase and bile salts.<sup>[23]</sup> Olive oil droplets, mainly triolein, in contact with lipase formed small particles of cubic phases as the enzyme broke the triglyceride down into monoolein that then hydrated. Lindstrom et al.<sup>[24]</sup> studied the phenomenon further, observing that sodium cholate bile salts provided dispersion and colloidal stability of the cubic phase particles formed by monoolein and water, and that such particles formed in other ternary systems as well. One of the first published instances of the word “cubosome” appears in a review by Larsson<sup>[25]</sup> of the implications of bicontinuous cubic phases to biological membranes. Later research on cubosomes focused on the ternary phase behavior of the Poloxamer 407 (a PEO<sub>99</sub>–PPO<sub>67</sub>–PEO<sub>99</sub> block copolymer)–monoolein–water system because of the polymer’s utility at providing colloidal stability to cubosomes against recoalescence to bulk cubic phase.<sup>[18]</sup> The PPO region of the block copolymer exists either at the surface of the cubic phase particles, or within the bilayer structure, whereas the PEO chains remain in the bulk water phase. Landh<sup>[18]</sup> observed cubosome formation in a three-phase region including disordered bicontinuous ( $L_3$  or sponge) phase, cubic phase, and water. Cubosome structures,



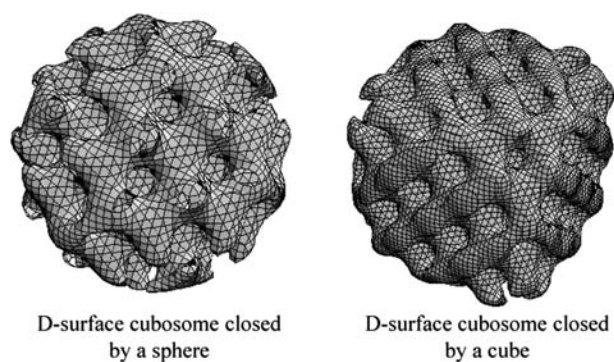


**Fig. 5** Calculated nodal surface representations of a D-surface cubosome closed off on its surface with a sphere and a cube.

such as bulk cubic phases, are critical elements of some biological processes and occur naturally in bacterial cells, for example.<sup>[26]</sup>

Just as bulk cubic phases can be mathematically characterized using nodal surface approximations, so, too, can cubosomes. Andersson et al.<sup>[27]</sup> model different cubosome structures by extending nodal surface descriptions<sup>[19]</sup> to describe closed-off surfaces such as those formed by cubosomes. Fig. 5 shows two examples of such simulated cubosomes, in this case a D-surface that has been closed off on its surface by a sphere and by a cube. A comprehensive overview of the structures that can be simulated by such techniques is given by Jacob and Andersson.<sup>[28]</sup> Many experimental studies of cubosomes utilize cryo-transmission electron microscopy (TEM) micrographs that allow the visualization of cubosome particles and the verification of their lattice symmetry, although x-ray measurements are required to confirm phase structures. Cryo-TEM allows the visualization of hydrated phase structures by vitrifying, instead of freezing, the sample in a thin film suspended between polymer-coated grid struts.<sup>[29,30]</sup> Insight into bulk cubic phase structure has also been gained in some cases by freeze-fracture electron microscopy.<sup>[31,32]</sup> More recent work has shown the possibility of *in situ* study of cubosomes using atomic force microscopy.<sup>[33]</sup>

Although small amounts of cubosomes are apparently produced by simple addition of dispersing agents such as sodium cholate to bulk cubic phase,<sup>[24]</sup> mechanical dispersion of bulk cubic phase is the most studied and most direct cubosome formation technique. Gustafsson et al.<sup>[34,35]</sup> formed cubosomes by high shear microfluidization and ultrasonication of bulk cubic phase in contact with aqueous Poloxamer 407. The cubosomes produced exhibit the P-surface structure based on x-ray diffraction and, interestingly, resemble cubes despite their nonsolid nature. The molecular-scale cubic symmetry of the lipid bilayer comprising

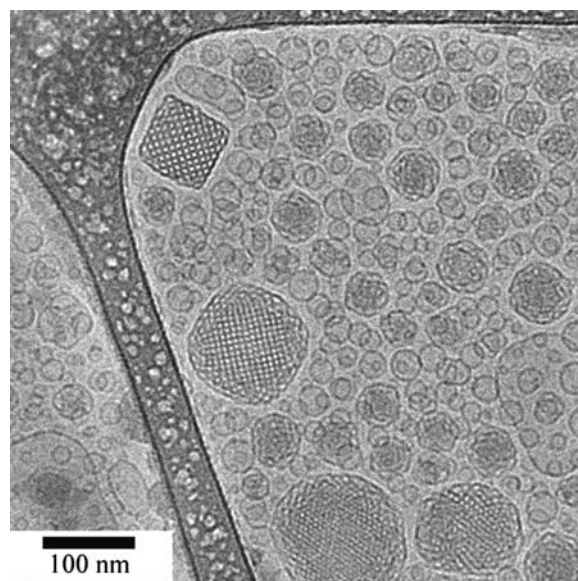


**Fig. 6** Cryo-TEM micrograph of cubosomes and vesicles formed by ultrasonic dispersion of bulk cubic phase in aqueous Poloxamer 407 solution. *Source:* From Ref.<sup>[36]</sup>. © American Chemical Society, 2001.

cubosomes is thus manifested in the nanometer-scale cubosome particles, although their appearance is often orientation-dependent.<sup>[34,36]</sup> An example of the different types of particles formed by ultrasonication of bulk cubic phase in aqueous Poloxamer 407 solution is seen in Fig. 6, a cryo-TEM micrograph of the dispersion. The particles range in size from about 10 to 500 nm in diameter. Cubosomes are immediately identifiable as square particles with a well-defined cubic lattice of dots. Each dot corresponds to the presence of a pore-containing aqueous phase. Along with well-formed cubosomes, more disordered cubosomes that have a more spherical shape are also visible. Gustafsson et al.<sup>[34]</sup> point out that the absence of grain boundaries in the cubosomes indicates they are single-crystal structures. Unilamellar vesicles, dispersed lamellar liquid crystalline phase particles, are also visible in Fig. 6. Increased polymer-to-monoolein ratios lead to the formation of larger ratios of vesicles to cubosomes. Such vesicles often form during the dispersion of bulk cubic phase, despite the fact that the lamellar phase is not an equilibrium phase at these conditions. Ultrasonication of bulk cubic phase produces mostly vesicles<sup>[34]</sup> that, over the course of several weeks, transform into cubosomes, likely via membrane fusion. Such metastability is characteristic of cubosome systems because of the slow transport processes involved in forming the high-viscosity crystalline structure and the high-energy input required to fragment bulk cubic phase. Distinct from the dispersed vesicles, the surfaces of some of the cubosome particles have

hemispherical vesicle structures that are thought to block the exposure of the hydrophobic bilayer at the termination of the cubosome edge structure but may also aid in colloidal stabilization of the cubosomes.<sup>[35,37]</sup> Gustafsson et al.<sup>[35]</sup> were able to shift the cubosome structure between the P-surface and the D-surface by varying Poloxamer 407 concentration. Although cubosomes have been feasibly produced in various laboratory settings for years, the desire to apply cubosomes in various commercial products spurs current research interest in cubosome production.

## CUBOSOME MANUFACTURE

At its most basic, the production of cubosomes entails the formation of nanoparticles. Two distinct nanoparticle production routes exist: top-down and bottom-up techniques. Most cubosome research over the last two decades has focused on top-down techniques, whereby bulk cubic phase is first produced and then dispersed by high-energy processing into cubosome nanoparticles. No systematic study exists of the effect of power input on bulk cubic phase dispersion, but existing rheological work offers some insight into the energy required to form cubosomes.

Bulk cubic phase resembles a clear rigid gel formed by water-swollen cross-linked polymer chains, but cubic phases differ in that they are a single thermodynamic phase and display periodic liquid crystalline structure. Studies<sup>[38,39]</sup> of the P-surface and D-surface cubic phases formed by several didodecyldimethylammonium bromide (DDAB)-oil-water systems found the phases to behave as viscoelastic fluids that exhibit relatively constant modulus values until the lattice structures break down around 1–5% strain. Rupture of the cubic phases occurs in a direction parallel to the shear direction and the energy required is proportional to the number of tubular network branches that rupture. Warr and Chen<sup>[40]</sup> found that rupture of the cubic phase occurs as the bilayer breaks under applied shear stresses and flows along slip planes. The cubic phases exhibit a yield stress that increases with increasing amounts of bilayer-forming surfactants and oils, and that is inversely proportional to the crystalline unit cell dimension.<sup>[40]</sup> Warr and Chen<sup>[40]</sup> also suggested but could not confirm that cubic phases may behave as lamellar phases do during dispersion with increasing shear: dispersed liquid crystalline particles form at intermediate shear rates, whereas a defect-free bulk phase re-forms at higher shear rates. At high oscillatory frequencies, cubic phases become highly elastic<sup>[38]</sup> and may be more apt to fracture than deform. A worthwhile study would be the correlation of energy input with the cubic phase breakage

mechanism most feasible for a given deformation rate. Different breakage mechanisms could correlate with cubosome yield.

Unfortunately, most existing studies provide little insight into the mechanisms underlying cubosome formation by energetic dispersion of bulk cubic phases. Comparison of the dispersions produced by sonication and high-pressure homogenization suggests the formation of complex dispersions containing vesicles and cubosomes with time-dependent ratios of each particle type. Coarse cubosomes on the micron scale possess the same D-surface cubic structure as their originating bulk cubic phase,<sup>[41]</sup> but after homogenization, the P-surface dominates, either because of the added polymer or other factors.<sup>[34]</sup> Based on such studies, it has been suggested that high-energy dispersion processes destroy the structure of bulk cubic phases, creating vesicles that then must fuse their bilayers to form ordered cubosomes.<sup>[41]</sup> However, no quantitative conclusion can be drawn without a systematic study of the effects of the fundamental parameters of a dispersion process. Fluid shear stresses, temperature changes induced by sonication, and pressure<sup>[42,43]</sup> all affect cubic phase and thus cubosome formation in different ways.

More recent work has examined the development of bottom-up methods of cubosome formation, allowing cubosomes to form and crystallize from precursors on the molecular length scale. Almgren et al.<sup>[30]</sup> discuss the formation of cubosomes by dispersion of L<sub>2</sub> or inverse micellar phase droplets in water at 80°C, then by slow cooling to allow the droplets to gradually crystallize into cubosomes. Large-scale production of cubosomes and products containing them requires more robust processes. Spicer et al.<sup>[36]</sup> developed a room temperature process to produce cubosomes by simply diluting monoolein-ethanol (or other hydrotrope) solutions with aqueous Poloxamer 407 solutions. The cubosomes have been shown to form by spontaneous emulsification,<sup>[44]</sup> producing nanoparticle dispersions in the near absence of energy input beyond that required for simple blending of the two liquids. Smaller and more stable cubosomes are produced than those by high-energy processes, but some vesicles are also produced.<sup>[36]</sup> A second process was also developed to allow cubosome production from a powdered precursor.<sup>[45]</sup> Spray-dried powders comprising monoolein coated with starch or dextran form cubosomes on simple hydration. Colloidal stabilization of the cubosomes is immediately provided by the polymers. An example of a cubosome formed in such systems is shown in Fig. 7. The large unfolded bilayers that form in such cases may be stabilized by polymer-induced osmotic, steric, or viscous forces,<sup>[45]</sup> identical to the higher fraction of surface vesicles observed in the Poloxamer 407-Monoolein-water system.<sup>[35]</sup>

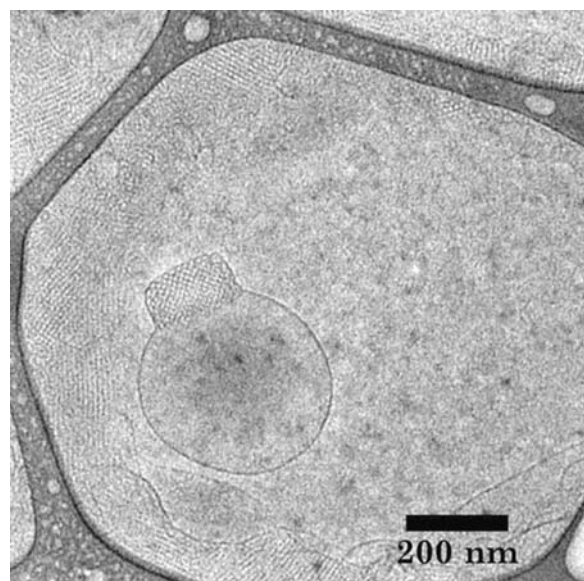


**Fig. 7** Cryo-TEM micrograph of cubosome formed by hydrating starch-encapsulated monoolein particles. *Source:* From Ref.<sup>[45]</sup>. © Kluwer Academic Publishers, 2002.

## SYSTEMS FORMING CUBOSOMES

The formation of cubosomes is possible in binary and ternary systems with a sufficiently large miscibility gap between the cubic phase and the solvent. Colloidal stabilization of cubosomes is good when Poloxamer 407 is used to provide steric stabilization against aggregation and coalescence, but other suitable polymers can be used as well. Earlier studies<sup>[37]</sup> advocate mixing vesicles and cubosomes produced by fragmentation of bulk lamellar and cubic liquid crystalline phases in excess water, respectively. The coating of cubosomes with lamellar bilayer “caps” covers the cubic bilayer openings formed by fragmentation, preventing exposure of hydrocarbon chains to water and providing limited colloidal stability. Coating the cubosomes with solid crystalline bilayers provides superior colloidal stability to lamellar liquid crystalline coatings, although such rigid coatings limit the lowest diameter of the cubosomes to 100 nm, rather than the absolute minimum of 50 nm, because of curvature restrictions.<sup>[37]</sup> In addition, coatings of the sponge phase have been proposed as a stabilizing coating for cubosomes.<sup>[37]</sup> Figs. 8 and 9 show schematics of the two general forms of ternary phase diagrams exhibited by systems forming cubosomes. For ternary systems of lamellar phase-forming polar lipids, cubic phase-forming polar lipids, and water (Fig. 8), cubosomes form in the two-phase region of equilibrium between the cubic phase and water or solvent, whereas vesicles form in the two-phase region between the lamellar phase and water. The three-phase region between the lamellar,

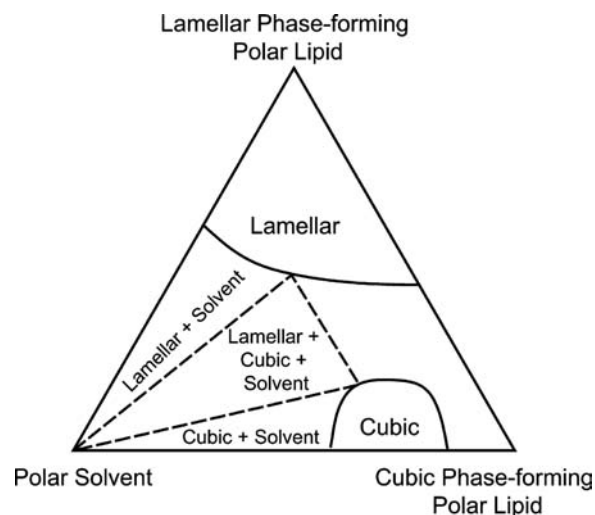


**Fig. 8** Schematic of the typical ternary phase diagram exhibited by systems containing a lamellar phase-forming polar lipid, a cubic phase-forming polar lipid, and water. *Source:* From Ref.<sup>[37]</sup>.

cubic, and water phases is likely to contain both vesicles and cubosomes. Similarly, for ternary systems containing cubic phase-forming polar lipids, a non-aqueous polar solvent or an active ingredient (such as a drug), and water, a sponge phase often forms in the general area indicated in Fig. 9.<sup>[46]</sup> In such cases, cubosomes form in the two-phase region of equilibrium between the cubic phase and water or solvent, whereas cubosomes, vesicles, and/or sponge phase particles may form in the multiphase regions between the cubic phase, sponge phase, lamellar phase, and water.<sup>[36]</sup> Currently, the only well-documented instances of cubosome formation are in systems containing monoolein. There is no reason why other

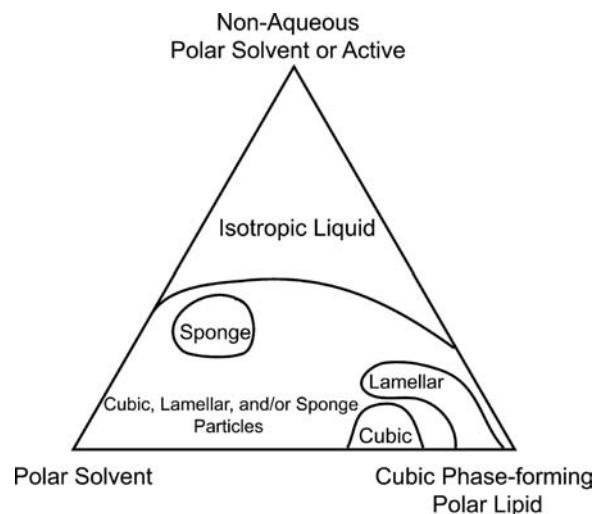


**Fig. 9** Generalized ternary phase diagram for systems containing a cubic phase-forming polar lipid, a non-aqueous polar solvent, and water.

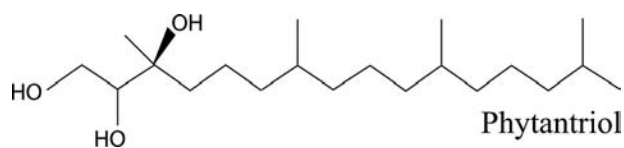


**Fig. 10** Molecular structure of phytantriol, the second most commonly used amphiphile for forming cubosomes.

similar surfactant systems should not form cubosomes, provided that a sufficient miscibility gap exists between the bicontinuous cubic phase and the solvent. One molecule with great potential for cubosome formation is phytantriol (Fig. 10), a commonly used additive in consumer products such as sunscreens. Several patents have emerged citing the formation of cubosomes in phytantriol–water systems,<sup>[47–49]</sup> but no published phase diagram is known. However, a simple swelling experiment offers insights into the aqueous phase behavior of phytantriol. Figs. 11 and 12 show partially polarized light micrographs of the interfaces formed on contacting a small droplet of monoolein (Fig. 11) and phytantriol (Fig. 12) with excess water. In both cases, interfaces that separate the amphiphile from the optically birefringent lamellar phase, and two distinct optically isotropic cubic phase regions are visible. Although such experiments are qualitative, the similarity between monoolein and phytantriol is striking and fortuitous, suggesting the need for more quantitative assessment (e.g., using the Diffusive Interfacial Transport (DIT) technique<sup>[50]</sup>) of the phytantriol–water system. Some glycolipids<sup>[51,52]</sup> also exhibit the cubic–water miscibility gap required for cubosome formation, and confirmation should be relatively simple. Ultimately, much of the future work on

cubosomes will be driven by the most financially compelling applications.

## APPLICATIONS

### Controlled-Release Drug Delivery

Controlled release of solubilized actives is the most popular application pursued by cubosome researchers, and excellent reviews exist of attempted delivery applications as well as pharmaceutical actives that have been solubilized in bulk cubic phase<sup>[53]</sup> and cubosomes.<sup>[54]</sup> Cubic phase is attractive for controlled release because of its small pore size (ca. 5–10 nm); its ability to solubilize hydrophobic, hydrophilic, and amphiphilic molecules; and its biodegradability by simple enzyme action.<sup>[55]</sup> Cubic phase is strongly bioadhesive<sup>[56]</sup> and is thought to be a skin penetration enhancer,<sup>[57]</sup> suggesting excellent compatibility with topical and mucosal deposition and delivery of active ingredients. Recent studies<sup>[58,59]</sup> have emphasized similarities between the bicontinuous structures formed in human skin layers and those comprising cubic phases, offering the promise of better skin transport understanding and treatment. The tortuous structure of cubic phase lends itself well to slowing diffusive release of solubilized actives. Theory predicts the minimum reduction of a solute's free solution diffusivity by 33%.<sup>[60]</sup> Experimental measurements of small molecule diffusivity in cubic phases give values on the order of  $10^{-10}$  m<sup>2</sup>/sec.<sup>[61]</sup> No commercial applications of cubic phase delivery vehicles are known other than a treatment developed for periodontal disease that is based on triglyceride–monoolein mixtures combined with

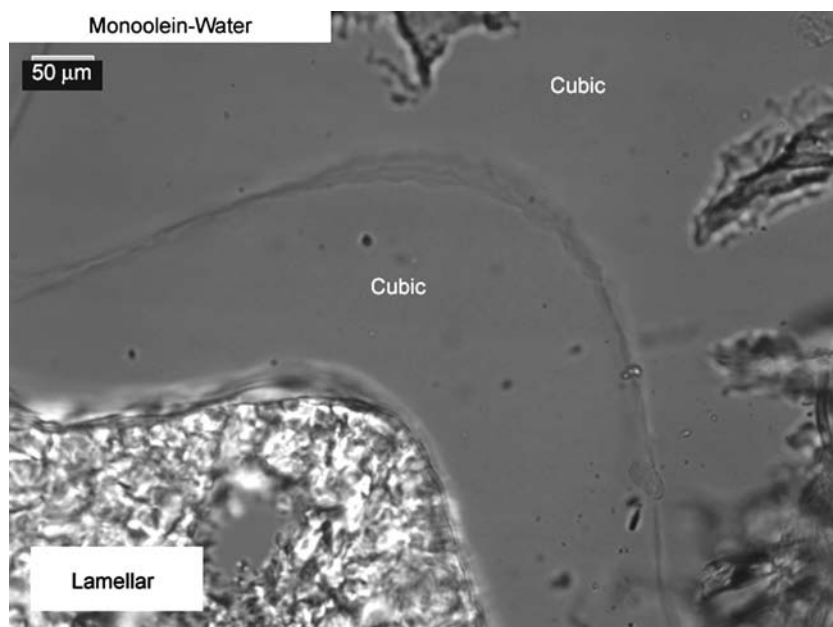


**Fig. 11** Polarized light micrographs of the aqueous phase progression exhibited by monoolein in excess water.

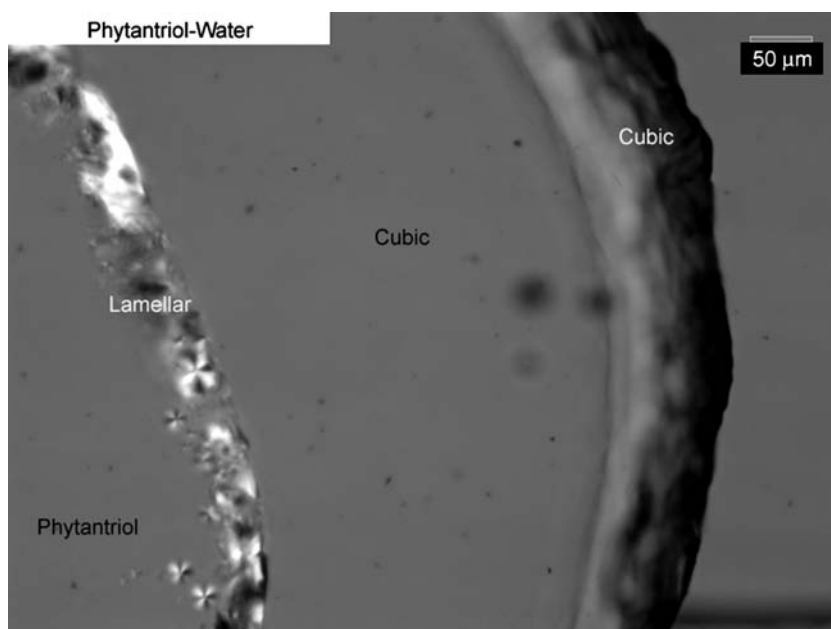


**Fig. 12** Aqueous phase progression of phytantriol in excess water. The sequence of phases is qualitatively identical to that of monoolein (Fig. 11).

the drug metronidazole.<sup>[62]</sup> The lipid–drug mixture forms a low-viscosity liquid that, when applied to the gums and placed in contact with saliva, hydrates to form a bulk cubic phase that then delivers the drug to the gum. Despite the potential of bulk cubic phase as a delivery vehicle, some applications are not compatible with the extremely high viscosity of the bulk cubic phase and require the use of cubosomes.

Cubosomes prepared in dispersions possess a nanometer-scale structure identical to bulk cubic phase, but the dispersion itself has a much lower, waterlike viscosity. Compared to liposomes or vesicles, cubosomes possess much higher bilayer area-to-particle volume ratios as well as higher viscous resistance to rupture. Although bulk cubic phase has sufficient length scale to allow controlled release of solutes, cubosomes are too small and have too high a surface area for such performance, exhibiting instead burst release.<sup>[63]</sup> Turning this concept around, cubosomes should be quite useful for *uptake* instead of release because they can rapidly absorb pollutants (e.g., for water treatment or cosmetic skin protection) and retain an amount determined by the solute partition coefficient.<sup>[47–49]</sup> For example, oleic acid-containing cubosomes change from cubic phase to hexagonal phase with a drop in pH, indicating a relatively rapid response of the cubosome interior to the outer fluid environment.<sup>[64,65]</sup> Although the above controlled-release limitations exist for small molecule solutes and unmodified cubosomes, other routes may still exist for controlled-release applications of cubosomes. For example, large poly(amidoamine) dendrimer molecules exhibit a 100 × reduction in free diffusivity when entrapped in cubic phases.<sup>[66]</sup> Modification of the cubic

phase environment is also a potential method of regulating solute transport. Puvvada et al.<sup>[67]</sup> find that aqueous alginate molecules can be gelled in cubic phase pores by ionic strength changes, increasing local viscosity and drastically slowing active release. Other studies have found that the partitioning and release kinetics of ionic solutes in cubic phases are significantly altered by incorporating oppositely charged surfactants into the cubic bilayers.<sup>[68,69]</sup> In such cases, the functionalizing surfactant must be chosen carefully to avoid disturbing the cubic phase structure, but guidelines exist for additive selection.<sup>[69]</sup> The contorted but regular structure of the cubic phases is also of interest to material science researchers as a template for complex solid materials.

## Materials Synthesis

From a materials science perspective, the creation of ordered structures with nanoscale pore geometries is of great interest to numerous fields including electronics, photonics, catalysis, and medicine. The creation of solid structures using cubic phases as a template usually entails either polymerization or reaction to form solids from precursors that are solubilized in, or comprise, the cubic phase matrix. One of the earliest and most successful materials formed in a cubic phase template is the aluminosilicate zeolite MCM-48,<sup>[70]</sup> used for catalytic processing of petroleum. Yang, O'Brien, and Marder<sup>[71]</sup> successfully carried out polymerization inside cubosomes, yielding a solid nanostructured particle with cubic symmetry. Such particles hold promise for use in photonic and



semiconductor applications.<sup>[72]</sup> Lu et al.<sup>[73]</sup> have developed novel aerosol processes that create particles with nanometer-scale structure by evaporation of solvent from isotropic phase liquid droplets, simultaneously driving them into cubic phase structures and solidifying the particles. As sophistication in the cubic phase template area builds, optimization of the structures will be a leading interest area. Along these lines, Larson<sup>[74]</sup> suggests the possibility of aligning the cubic phases by steady or large-amplitude oscillatory shearing prior to templating, forming materials with unique and highly anisotropic properties. Beautiful structures have been formed using careful growth of faceted cubosomes in the  $C_{12}E_2$ -water system,<sup>[75]</sup> offering future promise of multiple-decade length-scale control over the morphology of particles formed from such templates.

## OPEN PROBLEMS

The creation of cubosomes and other liquid crystalline nanoparticles is still an open and active area of research. Numerous applications as well as fundamental insights into behavior and performance regularly emerge. As a result, many open problems remain to be examined and solved by intrepid researchers, including some described in the above sections. An especially interesting area is the formation of dispersions of other liquid crystalline phases besides cubosomes. Studies of such dispersions, excluding vesicles, are sparse. Dispersions of hexagonal liquid crystalline phase<sup>[35]</sup> and sponge phase<sup>[76]</sup> have been reported, usually in coexistence with cubosomes. Such dispersion mixtures may provide multiple modes of controlled release, whereas their structures are compelling templates for solid nanoparticle synthesis, but more work is needed. As more becomes known about bicontinuous mesh and intermediate phases,<sup>[77,78]</sup> it may become possible to find stable, dispersed forms of these structures as well, liberally broadening liquid crystalline nanoparticle applications. Probably the most compelling direction of research into these systems seeks to understand the interactions between bicontinuous structures and biological systems in general. Enormous potential exists for the expansion of the current understanding of biological processes and medical treatment.

## CONCLUSION

Cubosome nanoparticles formed from cubic liquid crystalline phases are a unique and intriguing self-assembled material with enormous potential in areas as diverse as medicine, materials science, and consumer products. The relatively recent discovery of cubosomes has spurred a broad level of investigation that, as proposed

applications become financially attractive, will continue to narrow and fill in many of the current gaps in our knowledge of cubosome formation and performance. Interdisciplinary research in engineering, biology, medicine, and chemistry will be especially crucial to tie together existing cubosome research and to provide a consistent understanding of these fascinating particles.

## ACKNOWLEDGMENTS

I am indebted to my collaborators at the Procter & Gamble Company, Matthew Lynch and Janet Burns (Corporate Research), and Kristin Hayslip, Bill Small, and David Piatt (Corporate Engineering). Invaluable advice and mentoring have been and continue to be received from Stig Friberg (Clarkson University, retired), Eric Kaler (University of Delaware), Robert Prud'homme (Princeton University), and Robert Laughlin (Procter & Gamble Company, retired). The support of management at the Procter & Gamble Company, in particular Richard Owens, has been crucial throughout our work in the area of cubosomes.

## REFERENCES

1. Luzzati, V.; Husson, F. The structure of the liquid-crystalline phases of lipid-water systems. *J. Cell Biol.* **1962**, *12*, 207-219.
2. Luzzati, V.; Tardieu, A.; Gulik-Krzywicki, T.; Rivas, E.; Reiss-Husson, F. Structure of the cubic phases of lipid-water systems. *Nature* **1968**, *220*, 485-488.
3. Fontell, K.; Mandell, L.; Ekwall, P. Some isotropic mesophases in systems containing amphiphilic compounds. *Acta Chem. Scand.* **1968**, *22*, 3209-3223.
4. Gunning, B.E.S. The greening process in plastids: 1. The structure of the prolamellar body. In *Protoplasma*; Höfler, K., Porter, K.R., Eds.; Springer-Verlag: New York, 1965; 111-139.
5. Lutton, E.S. Phase behavior of aqueous systems of monoglycerides. *J. Am. Oil Chem. Soc.* **1965**, *42*, 1068-1070.
6. Sjöblom, J.; Stenius, P.; Danielsson, I. Phase equilibria of nonionic surfactants and the formation of microemulsions. Phase equilibria of nonionic surfactants and the formation of microemulsions. In *Nonionic Surfactants: Physical Chemistry*; Schick, M.J., Ed.; Marcel Dekker: New York, 1987; Vol. 23, 369-434.
7. Angelov, B.; Ollivon, M.; Angelova, A. X-ray diffraction study of the effect of the detergent octyl glucoside on the structure of lamellar and nonlamellar lipid/water phases of use for membrane protein reconstitution. *Langmuir* **1999**, *15*, 8225-8234.
8. Lindblom, G.; Larsson, K.; Johansson, L.; Fontell, K.; Forsen, S. The cubic phase of monoglyceride-water systems. Arguments for a structure based upon lamellar bilayer units. *J. Am. Chem. Soc.* **1979**, *101* (19), 5465-5470.



9. Larsson, K.; Fontell, K.; Krog, N. Structural relationships between lamellar, cubic, and hexagonal phases in monoglyceride–water systems. Possibility of cubic structures in biological systems. *Chem. Phys. Lipids* **1980**, *27*, 321–328.
10. Lovett, D. *Demonstrating Science with Soap Films*; Institute of Physics: Bristol, 1994.
11. Schoen, A.H. *Infinite Periodic Minimal Surfaces Without Self-Intersections*; NASA Technical Note D-5541; NASA, 1970.
12. Scriven, L.E. Equilibrium bicontinuous structure. *Nature* **1976**, *263*, 123–125.
13. Longley, W.; Mcintosh, T.J. A bicontinuous tetrahedral structure in a liquid-crystalline lipid. *Nature* **1983**, *303*, 612–614.
14. Larsson, K. Two cubic phases in monoolein–water system. *Nature* **1983**, *304*, 664.
15. Hyde, S.T.; Andersson, S.; Ericsson, B.; Larsson, K. A cubic structure consisting of a lipid bilayer forming an infinite periodic minimal surface of the gyroid type in the glycerolmonooleat–water system. *Z. Kristallogr.* **1984**, *168*, 213–219.
16. Qiu, H.; Caffrey, M. The phase diagram of the monoolein/water system: metastability and equilibrium aspects. *Biomaterials* **2000**, *21*, 223–234.
17. Buchheim, W.; Larsson, K. Cubic lipid–protein–water phases. *J. Colloid Interface Sci.* **1987**, *117* (2), 582–583.
18. Landh, T. Phase behavior in the system pine oil monoglycerides–Pluronic 407–water at 20°C. *J. Phys. Chem.* **1994**, *98*, 8453–8467.
19. Von Schnering, H.G.; Nesper, R. Nodal surfaces of Fourier series: Fundamental invariants of structured matter. *Z. Phys., B* **1991**, *83*, 407–412.
20. Anderson, D.M. Periodic surfaces of prescribed mean curvature. *Adv. Chem. Phys.* **1990**, *77*, 337–396.
21. Hyde, S.; Andersson, A.; Larsson, K.; Blum, Z.; Landh, T.; Lidin, S.; Ninham, B.W. *The Language of Shape*, 1st Ed. Ed.; Elsevier: New York, 1997.
22. Schwarz, U.; Goppper, G. Bicontinuous surfaces in self-assembling amphiphilic systems. *Lect. Notes Phys.* **2002**, *600*, 107–151.
23. Patton, J.S.; Carey, M.C. Watching fat digestion. *Science* **1979**, *204*, 145–148.
24. Lindstrom, M.; Ljusberg-Wahren, H.; Larsson, K.; Borgstrom, B. Aqueous lipid phases of relevance to intestinal fat digestion and absorption. *Lipids* **1981**, *16* (10), 749–754.
25. Larsson, K. Cubic lipid–water phases: structures and biomembrane aspects. *J. Phys. Chem.* **1989**, *93*, 7304–7314.
26. Meyer, H.W.; Richter, W.; Gumpert, J. Periodically curved bilayer structures observed in hyphal cells or stable L-form cells of a *Streptomyces* strain, and in liposomes formed by the extracted lipids. *Biochim. Biophys. Acta* **1990**, *1026*, 171–178.
27. Andersson, S.; Jacob, M.; Ladin, S.; Larsson, K. Structure of the cubosome—a closed lipid bilayer aggregate. *Z. Kristallogr.* **1995**, *210* (5), 315–318.
28. Jacob, M.; Andersson, S. *The Nature of Mathematics and the Mathematics of Nature*; Elsevier: Amsterdam, 1998.
29. Bellare, J.R.; Davis, H.T.; Scriven, L.E.; Talmon, Y.J. Controlled environment vitrification system: an improved sample preparation technique. *Electron Microsc. Technol.* **1988**, *10*, 87–98.
30. Almgren, M.; Edwards, K.; Gustafsson, J. Cryotransmission electron microscopy of thin vitrified samples. *Curr. Opin. Colloid Interface Sci.* **1996**, *1* (2), 270–278.
31. Gulik-Krzywicki, T.; Delacroix, H. Combined use of freeze–fracture electron microscopy and x-ray diffraction for the structure determination of three-dimensionally ordered specimens. *Biol. Cell* **1994**, *80*, 193–201.
32. Gulik-Krzywicki, T.; Aggerbeck, L.P.; Larsson, K. The use of freeze–fracture and freeze–etching electron microscopy for phase analysis and structure determination of lipid systems. In *Surfactants in Solution*; Mittal, K., Lindman, B., Eds.; Plenum Press: New York, 1984; 237–257.
33. Neto, C.; Aloisi, G.; Baglioni, P.; Larsson, K. Imaging soft matter with the atomic force microscope: cubosomes and hexosomes. *J. Phys. Chem., B* **1999**, *103* (19), 3896–3899.
34. Gustafsson, J.; Ljusberg-Wahren, H.; Almgren, M.; Larsson, K. Cubic lipid–water phase dispersed into submicron particles. *Langmuir* **1996**, *12* (20), 4611–4613.
35. Gustafsson, J.; Ljusberg-Wahren, H.; Almgren, M.; Larsson, K. Submicron particles of reversed lipid phases in water stabilized by a nonionic amphiphilic polymer. *Langmuir* **1997**, *13*, 6964–6971.
36. Spicer, P.T.; Hayden, K.L.; Lynch, M.L.; Ofori-Boateng, A.; Burns, J.L. Novel process for producing cubic liquid crystalline nanoparticles (cubosomes). *Langmuir* **2001**, *17* (19), 5748–5756.
37. Ljusberg-Wahren, H.; Nyberg, L.; Larsson, K. Dispersion of the cubic liquid crystalline phase—structure, preparation, and functionality aspects. *Chim. Oggi* **1996**, *14* (6), 40–43.
38. Radiman, S.; Toprakcioglu, C.; Mcleish, T. Rheological study of ternary cubic phases. *Langmuir* **1994**, *10*, 61–67.
39. Jones, J.L.; Mcleish, T.C.B. Concentration fluctuations in surfactant cubic phases: theory, rheology, and light scattering. *Langmuir* **1999**, *15* (22), 7495–7503.
40. Warr, G.G.; Chen, C.-M. Steady shear behavior of ternary bicontinuous cubic phases. In *Structure and Flow in Surfactant Solutions*; Herb, C.A., Prud'homme, R.K., Eds.; American Chemical Society: Washington, 1994; Vol. 578, 306–319.
41. Siekmann, B.; Bunjes, H.; Koch, M.H.J.; Westesen, K. Preparation and structural investigations of colloidal dispersions prepared from cubic monoglyceride–water phases. *Int. J. Pharm.* **2002**, *244* (1–2), 33–43.
42. Squires, A.M.; Templer, R.H.; Seddon, J.M.; Woenckhaus, J.; Winter, R.; Finet, S.; Theyencheri, N. Kinetics and mechanism of the lamellar to gyroid inverse bicontinuous cubic phase transition. *Langmuir* **2002**, *18* (20), 7384–7392.
43. Pisani, M.; Bernstorff, S.; Mariani, P. Pressure induced cubic-to-cubic phase transition in monoolein hydrated system. *J. Phys. Chem., B* **2001**, *105* (15), 3109–3119.
44. Spicer, P.T. Cubosome formation via dilution—kinetic effects and consumer product implications. In *Mesoscale Phenomena in Liquid Systems*; Case, F., Alexandridis, P., Eds.; ACS, 2003.

45. Spicer, P.T.; Small, W.B.; Lynch, M.L.; Burns, J.L. Dry powder precursors of "soft" cubic liquid crystalline nanoparticles (cubosomes). *J. Nanopart. Res.* **2002**, *4* (4), 297–311.
46. Engström, S.; Alfons, K.; Rasmusson, M.; Ljusberg-Wahren, H. Solvent-induced sponge ( $L_3$ ) phases in the solvent–monoolein–water system. *Prog. Colloid Polym. Sci.* **1998**, *108*, 93–98.
47. Ribier, A.; Biatry, B. Oily Phase in an Aqueous Phase Dispersion Stabilized by Cubic Gel Particles and Method of Making. US Patent 5,756,108.
48. Biatry, B. Cosmetic and Dermatological Emulsion Comprising Oily and Aqueous Phase. Eur. Pat. Appl. 968,704.
49. Biatry, B. Use of Phytantriol as Anti-Pollution Agent in a Cosmetic Composition. Eur. Pat. Appl. 1,161,938.
50. Lynch, M.L.; Kochvar, K.A.; Burns, J.L.; Laughlin, R.G. Aqueous phase behavior and cubic phase-containing emulsions in the  $C_{12}E_2$ –water system. *Langmuir* **2000**, *16* (7), 3537–3542.
51. Hato, M.; Minamikawa, H.; Tamada, K.; Baba, T.; Tanabe, Y. Self-assembly of synthetic glycolipid/water systems. *Adv. Colloid Interface Sci.* **1999**, *80* (3), 233–270.
52. Attard, G.S.; Blackaby, W.P.; Leach, A.R. The aggregation behaviour of two structurally isomeric glycolipids. *Chem. Phys. Lipids* **1994**, *74*, 83–91.
53. Shah, J.C.; Sadhale, Y.; Chilukuri, D.M. Cubic phase gels as drug delivery systems. *Adv. Drug Deliv. Rev.* **2001**, *47*, 229–250.
54. Drummond, C.J.; Fong, C. Surfactant self-assembly objects as novel drug delivery vehicles. *Curr. Opin. Colloid Interface Sci.* **2000**, *4*, 449–456.
55. Borne, J.; Nylander, T.; Khan, A. Effect of lipase on monoolein-based cubic phase dispersion (cubosomes) and vesicles. *J. Phys. Chem., B* **2002**, *106* (40), 10,492–10,500.
56. Geraghty, P.B.; Attwood, D.; Collett, J.H.; Sharma, H.; Dandiker, Y. An investigation of the parameters influencing the bioadhesive properties of Myverol 18-99/water gels. *Biomaterials* **1997**, *18*, 63–67.
57. Lee, J.; Kellaway, I.W. Combined effect of oleic acid and polyethylene glycol 200 on buccal permeation of [D-Ala<sub>2</sub>, D-Leu<sub>5</sub>]enkephalin from a cubic phase of glyceryl monooleate. *Int. J. Pharm.* **2000**, *204*, 137–144.
58. Norlen, L. Skin barrier formation: the membrane folding model. *J. Invest. Dermatol.* **2001**, *117*, 823–829.
59. Norlen, L. Skin barrier structure and function: the single gel phase model. *J. Invest. Dermatol.* **2001**, *117*, 830–836.
60. Anderson, D.M.; Wennerström, H. Self-diffusion in bicontinuous cubic phases,  $L_3$  phases, and microemulsions. *J. Phys. Chem.* **1990**, *94*, 8683–8694.
61. Mattisson, C.; Nylander, T.; Axelsson, A.; Zacchi, G. Diffusivity measurements using holographic laser interferometry in a cubic lipid–water phase. *Chem. Phys. Lipids* **1996**, *84*, 1–12.
62. Norling, T.; Lading, P.; Engstrom, S.; Larsson, K.; Krog, N.; Nissen, S.S. Drug delivery system based on a mixture of monoglycerides and triglycerides for use in treatment of periodontal disease. *Proc. Int. Symp. Control. Release Bioact. Mater.* **1997**, *23*, 294–295.
63. Boyd, B. Characterisation of drug release from cubosomes using the pressure ultrafiltration method. *Int. J. Pharm.* **2003**, *260*, 239–247.
64. Nakano, M.; Sugita, A.; Matsuoka, H.; Handa, T. Small-angle x-ray scattering and <sup>13</sup>C NMR investigation on the internal structure of "cubosomes". *Langmuir* **2001**, *17*, 3917–3922.
65. Nakano, M.; Teshigawara, T.; Sugita, A.; Leesajakul, W.; Taniguchi, A.; Kamo, T.; Matsuoka, H.; Handa, T. Dispersions of liquid crystalline phases of the monoolein/oleic acid/pluronic F127 system. *Langmuir* **2002**, *18* (24), 9283–9288.
66. Jeong, S.W.; O'Brien, D.F.; Oraedd, G.; Lindblom, G. Encapsulation and diffusion of water-soluble dendrimers in a bicontinuous cubic phase. *Langmuir* **2002**, *18* (4), 1073–1076.
67. Puvvada, S.; Qadri, S.B.; Naciri, J.; Ratna, B. Ionotropic gelation in a bicontinuous cubic phase. *J. Phys. Chem.* **1993**, *97*, 11,103–11,107.
68. Lindell, K.; Engblom, J.; Jonstromer, M.; Carlsson, A.; Engstrom, S. Influence of a charged phospholipid on the release pattern of timolol maleate from cubic liquid crystalline phases. *Prog. Colloid Polym. Sci.* **1998**, *108*, 111–118.
69. Lynch, M.L.; Ofori-Boateng, A.; Hippe, A.; Kochvar, K.; Spicer, P.T. Enhanced loading of water-soluble actives into bicontinuous cubic phase liquid crystals using cationic surfactants. *J. Colloid Interface Sci.* **2003**, *260*, 404–413.
70. Kresge, C.T.; Leonowicz, M.E.; Roth, W.J.; Vartuli, J.C.; Beck, J.S. Ordered mesoporous molecular sieves synthesized by a liquid-crystal template mechanism. *Nature* **1992**, *359* (6397), 710–712.
71. Yang, D.; O'Brien, D.F.; Marder, S.R. Polymerized bicontinuous cubic nanoparticles (cubosomes) from a reactive monoacylglycerol. *J. Am. Chem. Soc.* **2002**, *124* (45), 13,388–13,389.
72. Yang, J.; Ratna, B. Formation of Nanocrystalline Semiconductor Particles Within a Bicontinuous Cubic Phase. US Patent Appl. 841957.
73. Lu, Y.; Fan, H.; Stump, A.; Ward, T.L.; Rieker, T.; Brinker, C.J. Aerosol-assisted self-assembly of mesostructured spherical nanoparticles. *Nature* **1999**, *398* (6724), 223–226.
74. Larson, R. *The Structure and Rheology of Complex Fluids*; Oxford University Press: New York, 1999; 590–610.
75. Pieranski, P.; Sittler, L.; Sotta, P.; Imperor-Clerc, M. Growth and shapes of a cubic lyotropic liquid crystal. *Eur. Phys. J., E* **2001**, *5*, 317–328.
76. Gustafsson, J.; Nylander, T.; Almgren, M.; Ljusberg-Wahren, H. Phase behavior and aggregate structure in aqueous mixtures of sodium cholate and glycerol monooleate. *J. Colloid Interface Sci.* **1999**, *211*, 326–335.
77. Hyde, S.T. Interfacial architecture in surfactant–water mixtures: beyond spheres, cylinders and planes. *Pure Appl. Chem.* **1992**, *64* (11), 1617–1622.
78. Hyde, S.T. Microstructure of bicontinuous surfactant aggregates. *J. Phys. Chem.* **1989**, *93*, 1458–1464.

# Cyanogels: Processing by Spin Coating

**Shu Zhu**

*Business Development, PLIVA Inc., East Hanover, New Jersey, U.S.A.*

**Andrew B. Bocarsly**

*Department of Chemistry, Princeton University, Princeton, New Jersey, U.S.A.*

## INTRODUCTION

Small particles with high surface-to-volume ratio composed of bimetallic alloys are extensively used as catalysts<sup>[1,2]</sup> and magnetic recording media<sup>[3,4]</sup> in the chemical and information technology industries. Current research has been focused on reducing particle size, preferably to the nanometer scale, to achieve both improved catalytic activity<sup>[5]</sup> and higher areal density for information storage.<sup>[6]</sup> Both physical and chemical methods have been developed for such purpose, albeit with many shortcomings. Gonsalves, Rangarajan, and Wang<sup>[7]</sup> have provided an excellent review of those methods, with emphasis on chemical approaches. Physical methods such as gas condensation or mechanical deformation are very energy-intensive and tend to produce heterogeneous size populations.<sup>[7,8]</sup> Chemical approaches offer better control over alloy composition and homogeneity. Chemical reduction of metallic salts is the most generally applied approach. Reducing agents based on borohydrides have been extensively used,<sup>[7]</sup> while recently, organic reducing agents are receiving more attention.<sup>[9,10]</sup> Nanosized alloys can also be prepared through thermal decomposition reactions.<sup>[7]</sup> In its finer form, the thermal treatment is performed sonochemically in numerous minute reactors created through supersonic radiation.<sup>[11]</sup> Chemical preparations of nanoalloys usually suffer from tough, demanding environments (airless and water-free conditions in some reactions), contamination from reducing agents, and the limited choice of starting agents (metal carbonyls for thermalization and supersonication). In addition, chemical reduction routes are flawed by an intrinsic limit that the reduction rates of both metal cations need to be similar; otherwise, a core-shell structure rather than real alloys will prevail.<sup>[12]</sup>

Sol-gel processing has been widely used to prepare nanomaterials, especially composites.<sup>[13–15]</sup> However, to date, this approach has not been applied to the formation of nanoalloys. This method offers the advantage of high chemical purity as well as product homogeneity. Moreover, this technique excels in fabricating thin films, which are actually preferred in the

forementioned applications. However, current sol-gel processing is based on the hydrolysis of metal alkoxides, a method applicable to only  $d^0$  transition metal cations.<sup>[16]</sup> More importantly, a large amount of oxygen exists in the backbone of the gel polymer, from which only ceramics can be prepared through subsequent sintering treatment. We have found two cases<sup>[13,14]</sup> that consider the synthesis of nanometal alloys through sol-gel processing. In fact, in both studies, it was the silica matrix that underwent the sol-gel process and the alloys were prepared through hydrogen reduction.

The transition metal cyanogel polymers introduced in the following section are proposed to have a star polymer structure given in Fig. 1. For the case of a palladium/cobalt cyanogel as shown in the model, a  $Pd^{II}$  center is coordinated by two cyano groups and two chlorides in a trans configuration, while every Co center is coordinated octahedrally by six cyano groups. Usually synthesized in aqueous media, nascent cyanogel polymers are hydrogels containing 98 wt.% water. The water is not chemically bound and therefore evaporates when cyanogels are oven-dried ( $\sim 90^\circ C$ ) to produce a solid-state xerogel having no oxygen element in or near the polymer network. The sol-gel processing of cyanogels has been proven to be a very convenient method to prepare various bulk materials.<sup>[17–19]</sup> It is also an extremely versatile route as cyanogels containing almost all the transition metals can be prepared.<sup>[20,21]</sup> These attributes render the sol-gel processing of cyanogels ideal for nanoalloy fabrication.

## BACKGROUND

Sol-gel processing of metal-oxo polymers has developed into a standard technology for the formation and mechanical shaping of ceramics and metal oxide glasses.<sup>[16]</sup> Here we suggest that a similar approach using hydrogels based on novel transition metal coordination polymers provides an attractive route to the formation of metal alloy particles in the nanometer size range. The sol-gel approach offers

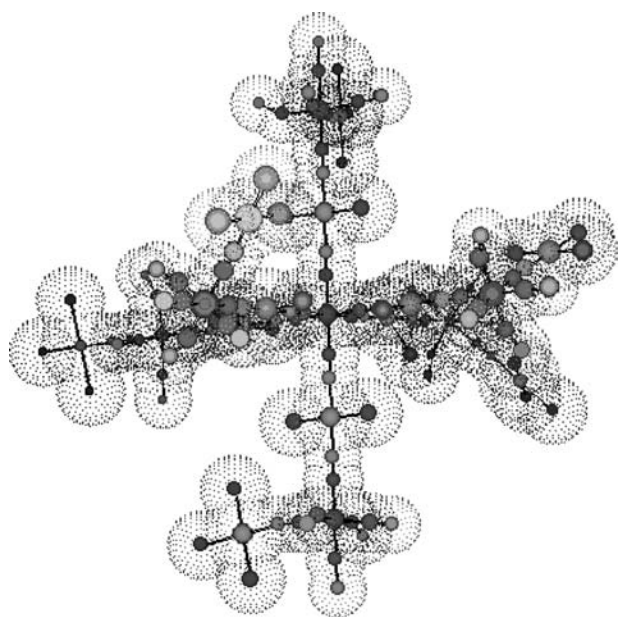


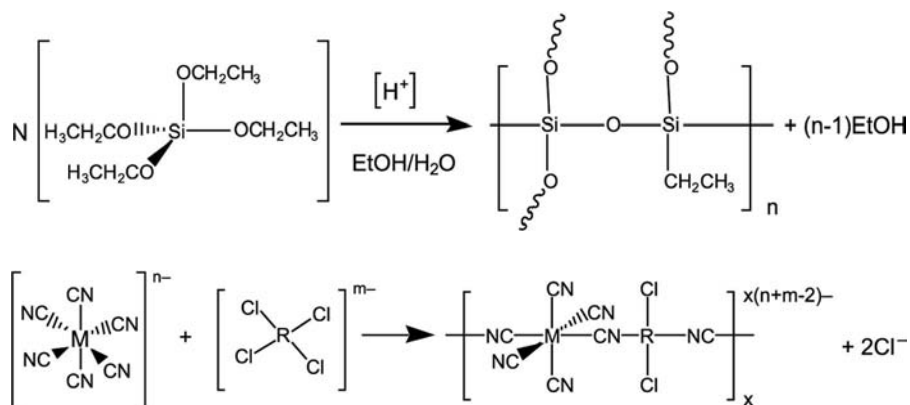
**Fig. 1** Proposed tar polymer structure model of the Pd/Co cyanogel based on elemental analysis, FTIR data, and TGA.

advantages of low processing temperatures and improved chemical homogeneity of the product when compared with standard high-temperature solid-state synthesis techniques. In addition, because simple molding of the gel state allows formation of a “green-body” product (i.e., a mechanically soft intermediate structure that can be annealed to form a product having the density of the crystalline state), machining to form a technologically useful shape can often be minimized or eliminated. Central to sol-gel processing is the formation of a hydrogel as the key intermediate product. This material consists of two continuous intermingled phases: an aqueous phase and a continuous network or polymeric phase. Both phases completely fill the container utilized forming a macroscopically homogeneous material.

In general, sol-gel processing has been limited to the formation of inorganic “polymers” having metal-oxygen linkages as the defining polymer structure

motif. Most typically, the metalloid species involved is silicon and the final product is a silica-type glass. For example, in the case of silica gel, an initial polymer phase can be generated by the acid catalyzed reaction of  $\text{Si}(\text{OCH}_2\text{CH}_3)_4$  [tetraethoxysilane-TEOS] in an aqueous alcoholic solvent (Eq. (1), below). This reaction leads to a hydrogel system containing a continuous polysiloxane phase and a continuous aqueous phase. Upon heating, one observes the loss of the aqueous phase and fracture of the remaining solid-state polymer phase to generate a xerogel composed of particulates of the initial polymer. Continued heating of the xerogel causes loss of ethoxy moieties as ethanol from the silane centers forming a solid-state silica. Thus from a simple stoichiometric point of view, sol-gel processing of metal-oxo polymers is just the densification of a metal oxide system via loss of chemically bonded solvent molecules. That is, there is no significant change in chemical composition as the systems move from a molecular state to a solid-state product. Most typically, the metalloid species involved is silicon leading to the formation of a silica-type glass, although several other ceramic materials based on early transition metal-oxo polymers, such as those of titanium and vanadium, have also been utilized to produce dense ceramic materials. The science and engineering of such systems has been carefully reviewed in Brinker and Scherers’s<sup>[16]</sup> text, “Sol-Gel Science.”

In contrast to this chemistry, we have reported that a sol-gel system can be generated by the reaction of  $[\text{M}'\text{Cl}_x]^{m-}$  complexes (where  $\text{M}' = \text{Pt}, \text{Pd}, \text{Ru},$  or  $\text{Ir}$ ) with  $[\text{M}(\text{CN})_x]^{n-}$  complexes (where  $\text{M}$  is a transition metal,  $x = 4, 6,$  or  $8$ ) in aqueous solution.<sup>[22]</sup> This reaction forms an oxygen-free polymer utilizing bridging cyanide linkages for the bonding motif as illustrated by Eq. (2) (below). Upon formation, the aqueous polymer undergoes a classic sol-gel transition to form a hydrogel that is referred to as a “cyanogel” to highlight the central role of the cyanide ligand and the lack of an oxygen-based polymer. Likewise, the sol phase is referred to as a “cyanosol.”



Cyanogels can be thermally processed to generate a wide variety of solid-state materials including alloys, nitrides, sulfides, and ceramics.<sup>[17,19]</sup> When compared with classic sol-gel processing, one intriguing aspect of cyanogel processing is that the solid-state product can have a different chemical composition from the starting polymer. Thus, for example, if a cyanogel formed from  $[\text{PdCl}_4]^{2-}$  and  $[\text{Co}(\text{CN})_6]^{3-}$  is thermalized in the presence of oxygen, the ceramic  $\text{PdCoO}_2$  having the delafossite structure is obtained. Thus in this system, one observes both the loss of an integral polymer component ( $\text{CN}^-$ ) and the addition of gas phase oxygen to the final product.<sup>[17,20,23]</sup> Broad-based experience with cyanogel systems indicates that this is a general property of such systems. Therefore unlike classic sol-gel processing, cyanogel processing is not limited to densification of the initial polymer, but gives rise to a rich and extensive materials chemistry that allows for the synthesis of a wide variety of materials. Of particular interest to the present discussion is the finding that thermal processing of a cyanogel under an inert atmosphere leads to the formation of pure metallic alloys. For instance, previous research has indicated that a Pd/Co alloy<sup>[17]</sup> is formed by sintering of the cyanogel noted above at temperatures as low as 375°C under an argon atmosphere, although a 650°C reaction temperature is found to be more convenient because only a short reaction time is needed. The traditional alternative is to co-mix the two metals at 1800°C.<sup>[4]</sup>

If the polymer system is trapped in the cyanosol state and then thermally processed, a new methodology for the synthesis of nanocrystalline metal alloys is accomplished. In the present study, Pd/Co cyanosols were spin cast to form thin films, which were then sintered to prepare nanometer-scale alloys. The Pd/Co cyanogel thin film was found to have an intrinsic thickness of approximately 40 nm. Infrared spectroscopy indicated that only bridging cyano groups exist inside the cyanogel thin film, in contrast to the bulk gel counterpart. Transmission electron microscopy revealed that the films were composed of uniform size (2–3 nm) gel particles which formed either clusters or superlattices. Sintering of this thin film under an inert atmosphere produced nanosized Pd/Co alloys. By manipulating polymerization and thin film fabrication conditions, one is able to control the size and distribution of prepared nanoalloys. Currently, nanosized Pd/Co alloy particles (10-nm mean diameter) with near monodisperse size distribution (20%) can be prepared through this method. To the best of our knowledge, this is the first example of the controlled preparation of nanosized metal alloys through sol-gel processing and is by far the simplest method for such purpose.

## EXPERIMENTAL

### Preparation

Aqueous solutions using deionized, reverse osmosis purified water of 0.06 M  $\text{Na}_2\text{PdCl}_4$  (Pressure Chemical Corporation) and 0.06 M  $\text{K}_3\text{Co}(\text{CN})_6$  (Aldrich) were mixed in a 3:1 ratio to form a cyanosol solution at the designated temperatures. Immediately after mixing, the cyanosol solution was quickly spin-coated onto a substrate using a Chemat Tech. KW-4A spin-coater to form a thin film. These films were sintered under Ar using a Carbolite 2416-cm<sup>3</sup> three-zone furnace. A variety of substrates were employed including Pyrex glass, pyrolytic graphite, nickel TEM grids, single crystal calcium fluoride, and single crystal silicon.

*Warning:* Hazardous gases, HCN and  $(\text{CN})_2$ , can be evolved during the heating of the gels above 200°C. Therefore while doing the thermogravimetric and calorimetric analyses, it is important to trap all product gases using two dispersion bubblers in series; the first one should contain bleach, while the terminal one should contain aqueous sodium hydroxide.

### Film Characterization

Fourier transform infrared (FTIR) spectra of sol-gel thin films coated on optical quality  $\text{CaF}_2$  disks (International Crystal Laboratories) were taken using a Nicolet 730 spectrometer. Multilayer (up to 9) cyanogel thin films were prepared by repeated spin coating and characterized by IR spectroscopy after each new layer was added. The surface and cross-section morphology of Pd/Co cyanogel thin film coated on microcover glasses (VWR Scientific) were characterized by scanning electron microscopy (SEM) using a Philips XL30 FEG-SEM. The thickness of the Pd/Co cyanogel thin film coated on single crystal silicon wafer was measured by ellipsometric analysis (laser wavelength: 632.8 nm) using an AutoEL III ellipsometer (Rudolph Technologies, Inc.). Sintered films were characterized by transmission electron microscopy (TEM) using either a Philips CM200 FEG-TEM or a Zeiss 910 TEM.

## RESULTS AND DISCUSSION

Figure 2 shows the IR spectrum of a Pd/Co cyanogel thin film prepared at room temperature. The absorption at 2200  $\text{cm}^{-1}$  is assigned to the stretching vibration of bridging cyano groups. This feature confirms the formation of the coordination polymer under spin-coating conditions. The bonding situation in the thin film is significantly different from that found in bulk

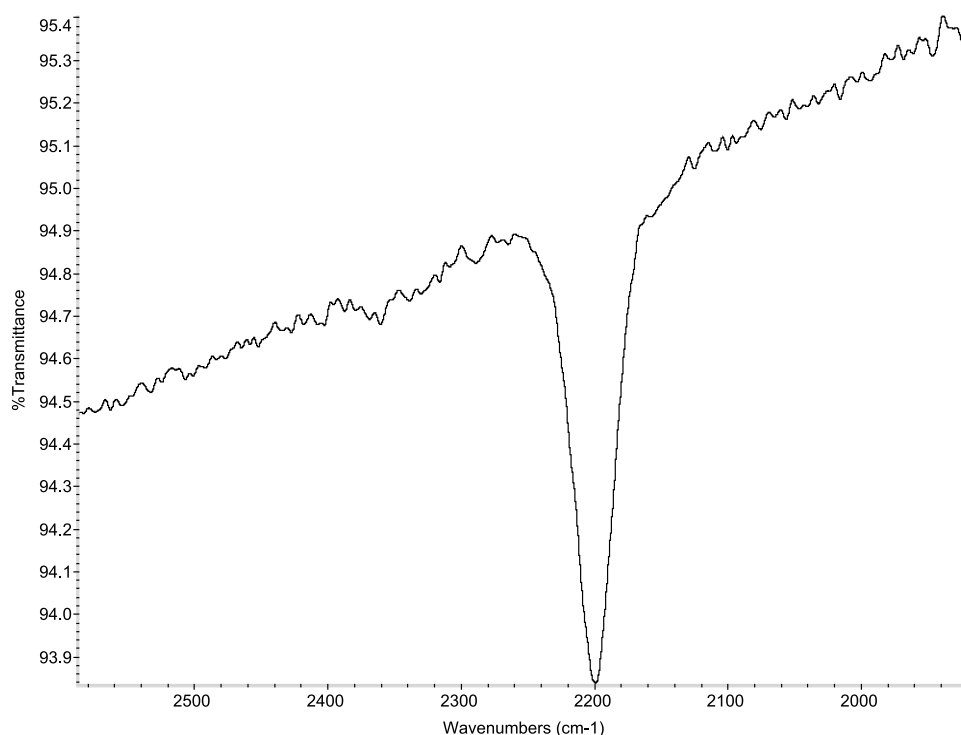


**Fig. 2** The FTIR spectrum of a Pd/Co cyanogel thin film showing no terminal cyanide stretches but intense bridging cyanide.

Pd/Co cyanogels. Bulk gels exhibit both terminal and bridging cyano groups. During the gelation reaction, the nitrogen end of a cyano ligand in the  $[\text{Co}(\text{CN})_6]^{3-}$  complex coordinates to the Pd center of a  $[\text{PdCl}_4]^{2-}$  complex through the displacement of a chloride ligand. On average, two chlorides are lost per Pd center allowing the formation of bridging cyanide ligands in a trans configuration about the palladiums. This forms a chain structure of metal centers (Pd and Co) bridged by cyano groups. Because the Co(III) center is coordinated octahedrally by six cyano groups, the same chain pattern branches into six directions from the Co(III) center forming a star polymer structure. Essentially no terminal cyano groups can be detected by IR spectroscopy; this suggests  $O_h$  geometry. The highly ordered ideal structure shown in Fig. 1 is difficult to achieve in reality. Small-angle X-ray scattering analysis indicates the surface fractal nature of bulk cyanogels.<sup>[18]</sup> This implies that short-range order rather than long-range order prevails in the bulk cyanogel polymer, and this situation is expected to apply in the thin film systems considered here. Infrared spectroscopy of bulk gel structures always indicates a fair amount of terminal cyano groups. Therefore the IR of the Pd/Co cyanogel thin film shown in Fig. 2 is surprising and suggests that the thin film environment is much more ideal from a structural point of view than the bulk gel environment.

The as-prepared Pd/Co cyanogel thin film is transparent and visually indistinguishable from the substrate. The surface morphology of the thin film is homogeneous at the level of SEM observation (Fig. 3A). A cross section of a thin film membrane is shown in Fig. 3B. Because of the strong electron scattering property of high atomic number elements, the palladium content of the thin film causes it to appear as the bright fine line at the top of the cross section. Measurement of this feature yields a film thickness of 40 nm. Ellipsometric analysis indicates the thickness to be  $14 \pm 1$  nm as detailed in Table 1. Both thickness and refractive index from three different points are self-consistent, again demonstrating the homogeneity of the thin film. The thickness obtained through ellipsometric analysis is of the same magnitude as SEM measurement. The discrepancy between these two measurements may be explained by the different choices of substrates when the thin films were prepared. The SEM measurements are obtained by forming a cyanogel thin film on a borosilicate glass substrate, while the ellipsometric measurements utilize a single crystal silicon substrate. Examination of multilayer cyanogel thin films formed on a  $\text{CaF}_2$  substrate by IR indicates that the same thickness per layer ( $\sim 40$  nm) is reproduced during repeated spin coating of cyanogel layers on top of each other for at least 10 layer thickness ( $\sim 400$  nm). This is demonstrated in Fig. 4 by a plot of IR absorbance corresponding to bridging cyano



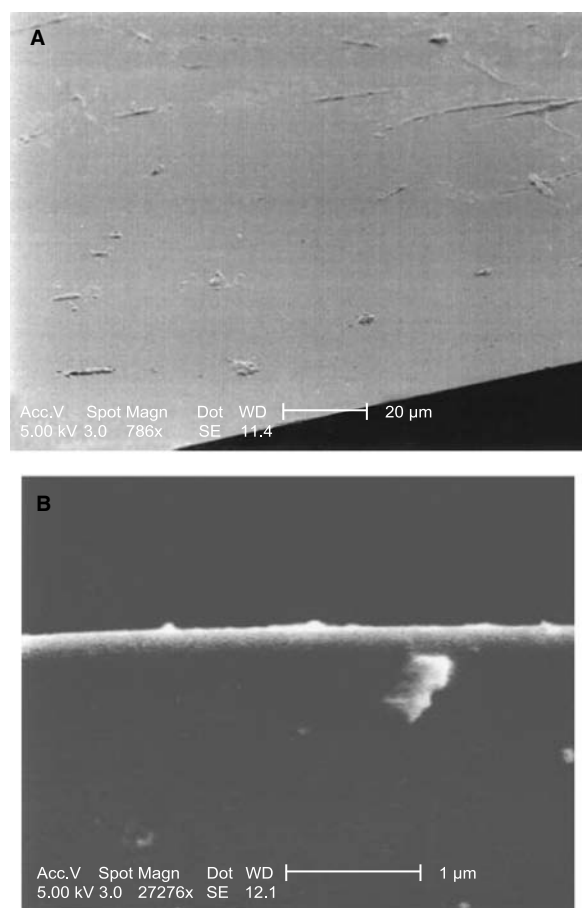


**Fig. 3** Scanning electron micrograph of the surface (A) and cross-section (B) morphology of a cyanogel thin film.

groups vs. the number of layers showing a linear dependence. Based on this data, a Beer's law plot yields an absorption coefficient for the vibration of the bridging cyano groups of  $1000 \text{ cm L mol}^{-1}$ , which agrees with the literature value.<sup>[24]</sup>

Transmission electron microscopy characterization furnishes more information on the microstructure of the thin film. Fig. 5A provides a nanometer-resolved image of a Pd/Co cyanogel thin film. On this length scale, the film is observed to be composed of uniform size (3 nm) cyanosol particles, which form both clusters and superlattices. The formation of a superlattice is often observed with nanoparticles when a monodispersed distribution is

**Table 1** The ellipsometry analysis of Pd/Co cyanogel thin film

	Point 1#	Point 2#	Point 3#	Average
Thickness (nm)	13.7	14.7	13.7	14.0
Refractive index	1.61	1.58	1.61	1.60

present. In the current study, we believe that Coulomb repulsions between the negatively charged sol particles are also a factor.

It is worth pointing out that the spin-coating technique plays a rather unconventional role in this study. As noted earlier, the thin films were fabricated immediately after the mixing of reactant solutions. During spin coating, the solvent (water) is rapidly removed, effectively "freezing" the reaction. Therefore the polymerization reaction is truncated when compared with bulk cyanogel synthesis, leaving isolated sol particles as the final product. Consequently, in addition to serving as a thin film fabrication technique, the spin-coating method also intervenes and alters the chemistry of cyanogel formation. The Pd/Co polymer thin film is therefore both physically and chemically different from its bulk counterpart.

It was demonstrated previously in our lab that bulk Pd/Co alloys could be prepared by sintering 3-D samples of Pd/Co cyanogels.<sup>[17]</sup> A novel process for alloy preparation, the sol-gel processing of cyanogels is actually very intuitive. Within the framework of the cyanogel, Pd and Co cationic centers are homogeneously mixed at the atomic level. As shown in reaction 3, subsequent heat treatment induces a redox reaction between the metal ions and the cyanide ligands, producing bulk alloy systems and gas phase cyanogen. This reaction initiates at temperatures as low as  $\sim 350^\circ\text{C}$  and proceeds at fairly rapid rates above  $\sim 500^\circ\text{C}$ .

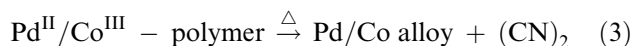
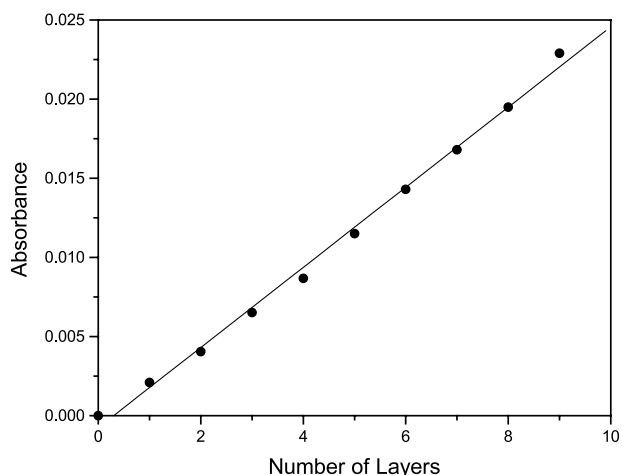
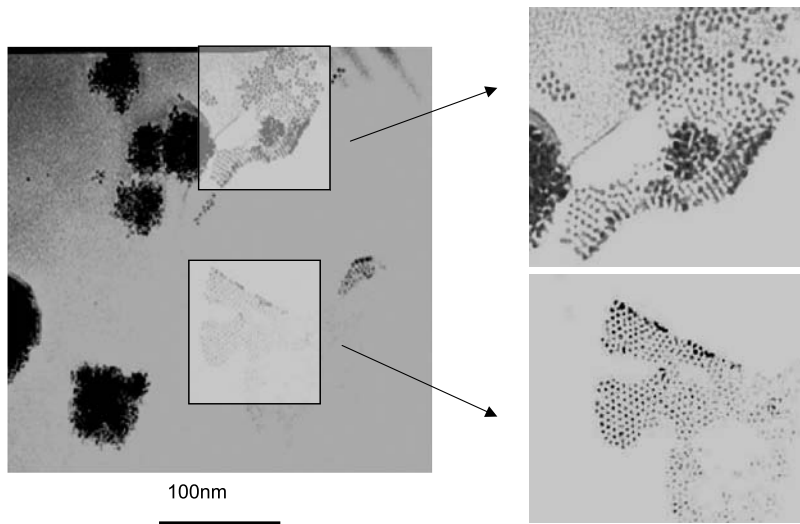


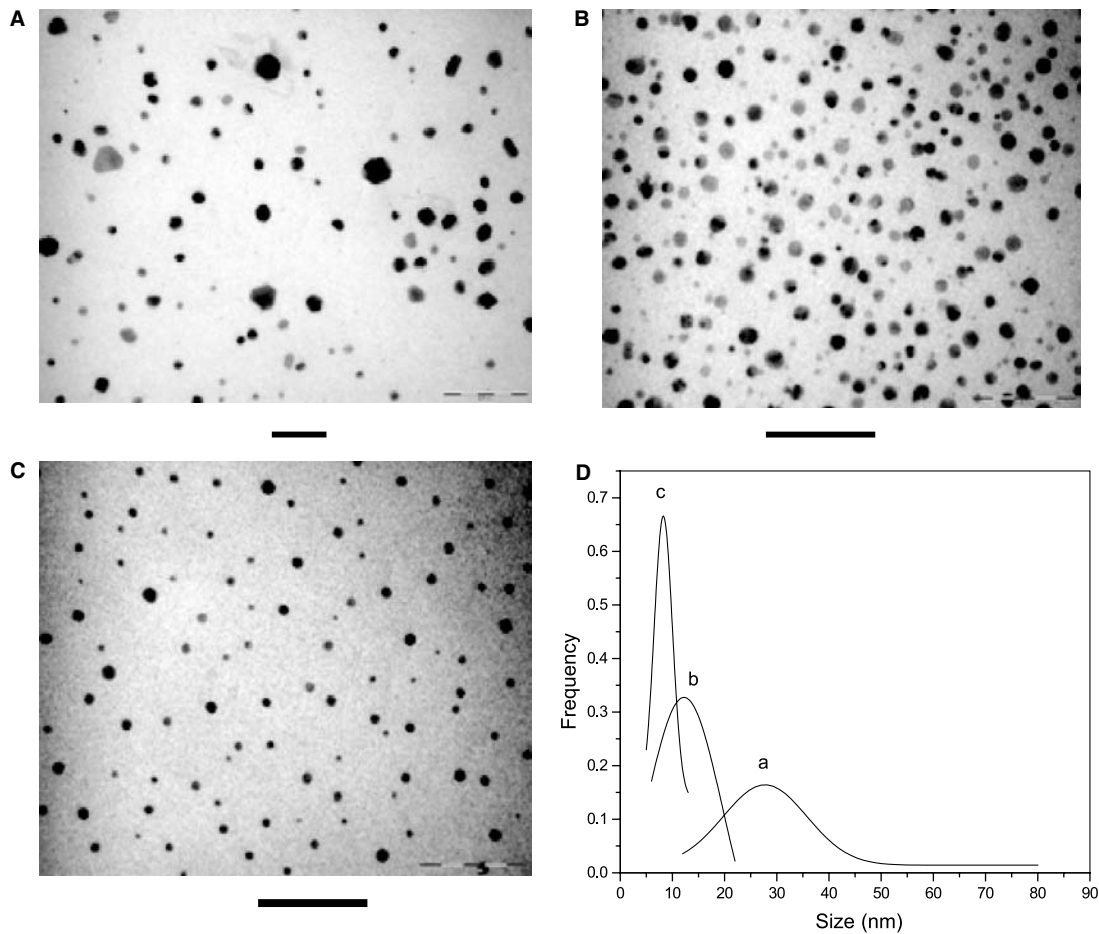
Figure 6A shows alloys prepared by sintering at  $650^\circ\text{C}$  a 60 mM Pd/Co cyanogel thin film that was



**Fig. 4** Plot of IR absorbance at  $2200 \text{ cm}^{-1}$  vs. number of layers of Pd/Co cyanogel thin films spin-coated. The plot is well fit by Beer's law (solid line) yielding a molar extinction coefficient of  $10^3 \text{ cm L mol}^{-1}$ .



**Fig. 5** A TEM micrograph of the Pd/Co cyanogel thin film showing monodispersed sol particles that form both clusters and superlattices.



Scale bar represents 100nm.

**Fig. 6** Transmission electron microscopy analysis of nanoalloys prepared by sintering Pd/Co cyanogel thin films synthesized under conditions as follows: (A) Room temperature, 60 mM reactants, 3000 rpm spin-coating rate; (B) 0°C, 60 mM reactants, 3000 rpm spin-coating rate; (C) 0°C, 1 mM reactants, 4000 rpm spin-coating rate; (D) Size distribution analysis of the nanoalloy particles presented in micrographs A–C.

formed by spin coating at 3000 revolutions per minute (rpm) at room temperature. The Pd–Co alloy crystallites show clean crystal symmetries, bearing hexagonal or trigonal shapes. The sizes of the observed alloy particles are widely distributed, ranging from 10 to 80 nm with a median size of 32 nm. The sol–gel processing can be divided roughly into two steps: thin film fabrication and sintering. The sintering temperature and time are predetermined because exact conditions in bulk cyanogel processing are used. On the other hand, thin film fabrication through spin coating can be influenced by at least three variables: reactant concentration, reaction temperature, and spin-coating rate. During sintering, gel particles coalesce to form alloy particles while losing non-metal elements. To prepare smaller and more homogeneous nanoalloys, it is desirable to prepare cyanosol thin films composed of well-dispersed colloidal particles. In such thin films, there are similar numbers of particles in any given area, which tend to form alloy particles of similar sizes. In addition, because there will be few areas with higher than usual particle density, extremely large alloy particles are less likely to be produced. Such cyanosol thin films can be prepared by either increasing the spin rate or slowing down the polymerization rate, which can be realized by lowering reaction temperature or reactants concentration. Therefore we prepared a 60 mM Pd/Co cyanogel thin film by coating at 3000 rpm a cyanosol solution cooled to 0°C in ice–water mixture. Figure 6B shows the nanoalloy prepared by sintering this thin film at 650°C. Sizes of these alloy particles range from 6 to 25 nm with a median value of 14 nm, significantly smaller than those found in Fig. 6A. These alloy particles are, for the most part, spherical because of the minimization of surface energy. A further decrease in polymerization rate can be obtained by lowering the reactant concentration; Fig. 6C shows a nanoalloy prepared by sintering a 1 mM Pd/Co cyanogel thin film prepared at 0°C and 4000 rpm. The spherical alloy particles range from 6 to 12 nm with the median at 10 nm. The size distribution plots of nanoalloy particles prepared from three different cyanogel thin films are shown in Fig. 6D. They clearly indicate that smaller and more uniformly sized alloy particles are yielded when cyanogel polymerization rate is slowed or spin rate is increased, approaching monodispersed samples when the polymerization rate is minimized and the water removal rate is maximized.

## CONCLUSION

A novel method was developed for the fabrication of nanosized bimetal alloys utilizing sol–gel processing of cyanogel thin films. Two exceptional advantages are associated with this method: access to most transition metals via cyanometalate reagents and easy

control of alloy size distribution. In addition, this is by far the simplest method for such purpose.

## ACKNOWLEDGMENT

We thank Mr. Allan Chang and Prof. Steven Chow for ellipsometry measurements; This work was supported by the National Science Foundation under award number CHE-0079169.

## REFERENCES

1. Ponec, V.; Bond, G.C. *Catalysis by Metals and Alloys*; Elsevier Science B.V.: Amsterdam, 1995.
2. Ponec, V. Alloy catalysts: The concepts. *Appl. Catal., A* **2001**, *222*, 31–45.
3. Bate, G. Magnetic recording materials since 1975. *J. Magn. Mater.* **1991**, *100* (1–3), 413–424.
4. Bozorth, R.M. et al. Ferromagnetism in dilute solutions of cobalt in palladium. *Phys. Rev.* **1961**, *122*, 1157–1160.
5. Schmidt, G. Metals. In *Nanoscale Materials in Chemistry*; Klabunde, K.J., Ed.; John Wiley & Sons, Inc.: New York, 2001; 15–60.
6. Yeack-Scranton, C.E. *Nanomagnetism*; Hernando, A., Ed.; Kluwer Academic Publishers: Dordrecht, 1993; 1–6.
7. Gonsalves, K.E.; Rangarajan, S.P.; Wang, J. Chemical Synthesis of Nanostructured Materials and Nanotechnology. In *Handbook of Nanostructured Materials and Nanotechnology*; Nalwa, H.S., Ed.; Academic Press: San Diego, 2000; 1–55.
8. Suryanarayana, C. Mechanical alloying and milling. *Prog. Mater. Sci.* **2001**, *46* (1–2), 1–184.
9. Mayers, B. et al. Large-scale synthesis of monodisperse nanorods of Se/Te alloys through a homogeneous nucleation and solution growth process. *Adv. Mater.* **2001**, *13* (18), 1380–1384.
10. Sun, S. et al. Monodisperse FePt nanoparticles and ferromagnetic FePt nanocrystal superlattices. *Science* **2000**, *287*, 1989–1992.
11. Suslick, K.; Price, G.J. Applications of ultrasound to materials chemistry. *Annu. Rev. Mater. Sci.* **1999**, *29*, 295–326.
12. Park, J.; Cheon, J. Synthesis of “solid solution” and “core-shell” type cobalt–platinum magnetic nanoparticles via transmetalation reactions. *J. Am. Chem. Soc.* **2001**, *123*, 5743–5746.
13. Gwak, J.; Kim, S.; Lee, M. Sol–gel preparation of AuCu and Au<sub>4</sub>Cu nanocluster alloys in silica thin films. *J. Phys. Chem., B* **1998**, *102*, 7699–7704.
14. Mattei, G. et al. Synthesis, structure, and magnetic properties of Co, Ni, and Co–Ni alloy nanocluster-doped SiO<sub>2</sub> films by sol–gel processing. *Chem. Mater.* **2002**, *14*, 3440–3447.
15. Roy, R. Nanocomposites: Retrospect and Prospect. In *Nanophase and Nanocomposite Materials*; Komarneni, S., Parker, J.C., Thomas, G.J., Eds.; Materials Research Society: Pittsburgh, 1993; 241–251.

16. Brinker, C.J.; Scherer, G.W. *Sol-Gel Science The Physics and Chemistry of Sol-Gel Processing*; Academic Press, Inc.: San Diego, 1990.
17. Heibel, M. et al. Use of sol-gel chemistry for the preparation of cyanogels as ceramic and alloy precursors. *Chem. Mater.* **1996**, *8*, 1504–1511.
18. Sharp, S.L.; Bocarsly, A.B.; Scherer, G.W. Bulk properties of a cyanogel network: Toward an understanding of the elastic, mechanical, and physical processes associated with sol-gel processing of cyanide-bridged gel systems. *Chem. Mater.* **1998**, *10*, 825–832.
19. Sharp, S.L. et al. Formation and structure of a tin-iron oxide solid-state system with potential applications in carbon monoxide sensing through the use of cyanogel chemistry. *Chem. Mater.* **1998**, *10*, 880–885.
20. Heibel, M. Sol-Gel Chemistry of the New Inorganic Polymers-Cyanogels. In *Chemistry*; University of Ljubljana: Ljubljana, Slovenia, 1996.
21. Sharp, S.L. The Physical Characterization and Sol-Gel Chemistry of the Cyanogel System. In *Chemistry*; Princeton University: Princeton, 2000.
22. Pfennig, B.W.; Bocarsly, A.B.; Prud'homme, R.K. Synthesis of a novel hydrogel based on a coordinate covalent polymer network. *J. Am. Chem. Soc.* **1993**, *115*, 2661–2665.
23. Wilson, J. Cyanogel: An Investigation into Their Fractal Nature, Syneresis Processes, and Their Sol-Gel Processing into Solid-State Materials. In *Chemistry*; Princeton University: Princeton, 2001; 126.
24. Kral, K.; Dobiasova, L.; Rysava, N. Intensities of the infrared absorption in TCNQ salts. *Lect. Notes Phys.* **1977**, *65*, 529–531.

# Cyclic Peptides: Self-Assembly in Hydrogen-Bonded Nanotubes

Roberto J. Brea

Juan R. Granja

*Department of Organic Chemistry, Universidad de Santiago de Compostela, Santiago de Compostela, Spain*

## INTRODUCTION

The numerous potential applications of tubular molecules or supramolecules in such fields as biosensing, pharmacology, or catalysis continue to drive the search for new strategies for their construction. This entry reviews the design, preparation, characterization, and application status of nanotubular structures obtained from cyclic peptides by self-assembly.

## OVERVIEW

### Nanotubes and Supramolecular Chemistry

The novel properties of nanostructures have given rise to enormous current interest in the development of nanostructured devices and materials for equally novel applications.<sup>[1–3]</sup> Nanotubes<sup>[4,5]</sup> are of particular interest because of their potential applications—sometimes inspired by the biological roles of natural tubules—in fields including ion sensing, molecular inclusion and separation, catalysis, nanocomposites, optics, electronics, chemotherapy, transmembrane transport, and drug delivery. In these contexts, nanotubes have been constructed that consist of, or are based on, zeolites, graphite, inorganic, lipids, and cyclodextrins.<sup>[6–11]</sup> In most cases, however, it is not yet possible to guarantee uniform prespecified internal tube diameter, a property that, together with its length, will be essential for success in many potential applications.

Nanotubes composed of the materials mentioned above are mostly covalently bonded. Although great advances have been made in this area, non-covalently bonded nanotubes offer significant advantages, including high synthetic convergence, built-in error correction, control through unit design, and, most importantly, self-organization. In non-covalently bonded nanotubes the component molecules are held together by mechanisms such as hydrogen bonding,

$\pi$ - $\pi$  stacking, electrostatic or van der Waals forces, and hydrophobic interactions.<sup>[12,13]</sup> These interactions are much weaker than covalent bonds but determine many of the physical properties of molecules, such as solubility and organization in aggregates, and their exploitation for the formation of structures with well-defined composition, shape, and chemical, physical, and biological properties can constitute a viable alternative to covalent synthesis. Lehn coined the term “supramolecular chemistry” for this field,<sup>[14]</sup> which is beginning to have an enormous impact on materials science and nanotechnology. In supramolecular chemistry, molecules are designed and synthesized for their ability to interact specifically with more or less well-specified target molecules (“molecular recognition”) or spontaneously to form larger aggregates with well-defined pattern or structure (“self-assembly” or “self-organization”).<sup>[15–17]</sup>

In this entry we review the history and current situation of one of the most successful approaches to the preparation of non-covalently bonded self-assembling nanotubes, to wit, the aggregation of cyclic polypeptides in stacks stabilized by hydrogen bonds.

### Nanotubes Designs and Peptide Nanotubes

Programs for the preparation of non-covalently bonded self-organizing nanotubes have aimed at a variety of different structures (many inspired by natural structures), including hollow bundles of rod-like units, helically folded linear species, rolled-up sheets, helically juxtapositioned truncated wedges, and stacked rings (Fig. 1A–E, respectively).<sup>[11]</sup> The last of these schemes (Fig. 1E) is particularly attractive in that the internal diameter of the nanotube is determined solely by that of the unit rings, and can therefore be controlled more easily than in the other cases.

Self-assembling peptide nanotubes (SPN)<sup>[18]</sup> are formed by stacking cyclic peptides, the stacking interactions being backbone–backbone hydrogen bonds

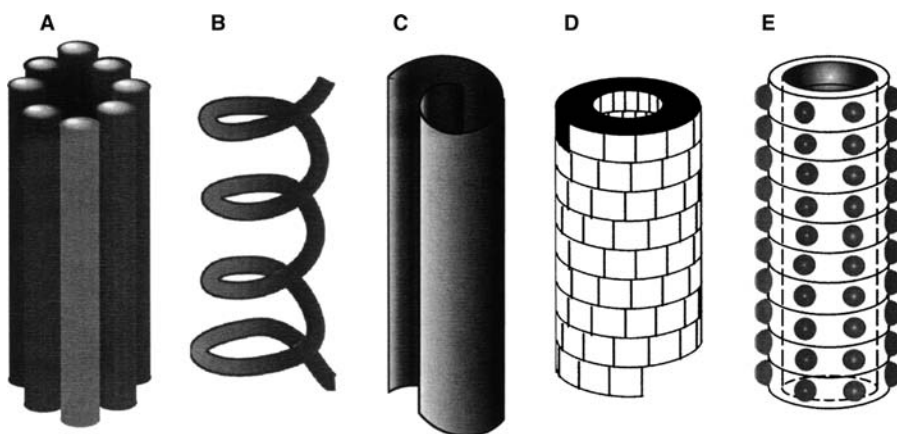


**Fig. 1** Various strategies for the self-organization of simple components as tubular structures.

(Fig. 2). Suitable peptides are those in which the ring can adopt a flat conformation in which all the amino acid side chains have a pseudo-equatorial outward-pointing orientation and the carbonyl and amino groups of the peptide bonds are oriented perpendicular to the ring, the carbonyl of each peptide bond on one side of the ring and the corresponding N-H group on the other (Fig. 3). Achievement of this kind of conformation depends on the number of amino acid residues per ring and on their kind ( $\alpha$ ,  $\beta$ , etc.) and

chirality (R, S); it perfectly positions the carbonyl and amino groups of neighboring rings for the formation of hydrogen bonds that link the rings into tubes like rolled-up  $\beta$ -sheets. Appropriate cyclic peptides can be synthesized by connecting the ends of a linear peptide constructed by successive addition of either individual amino acids or small peptide sequences.<sup>[19]</sup>

The cyclic peptide approach to nanotubes has two crucial advantages over all others that have so far been tried: firstly, the diameter of the polypeptide rings, and

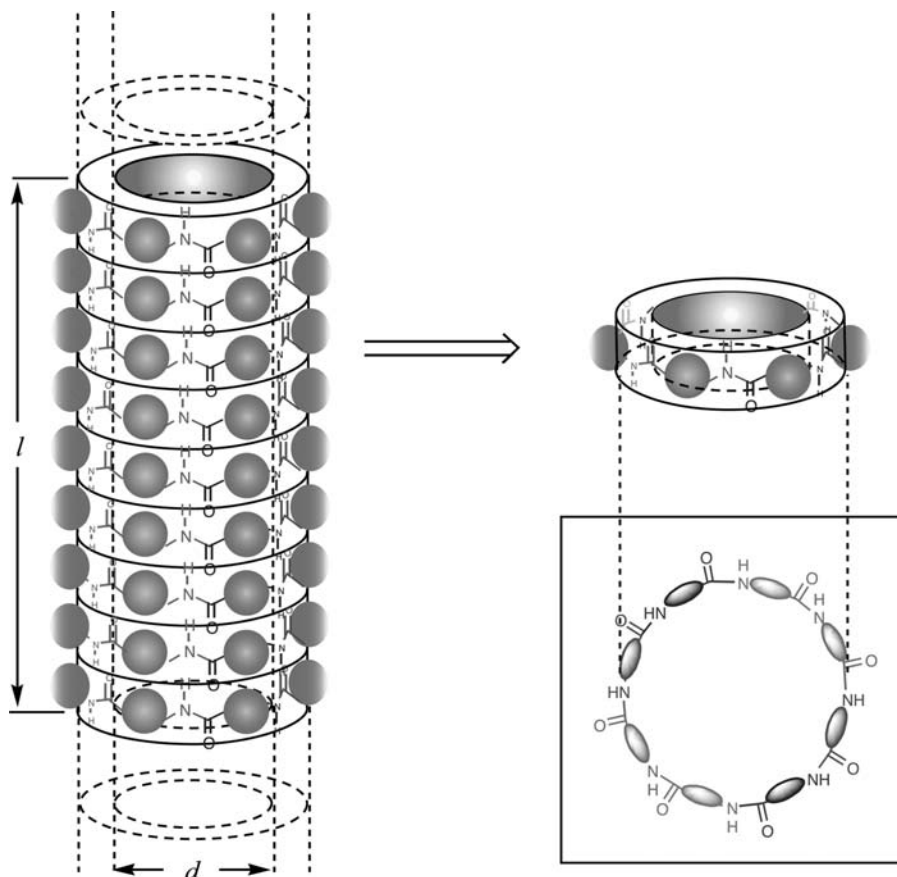


**Fig. 2** Schematic representations of the general strategy for nanotube formation stacking cyclic peptides.



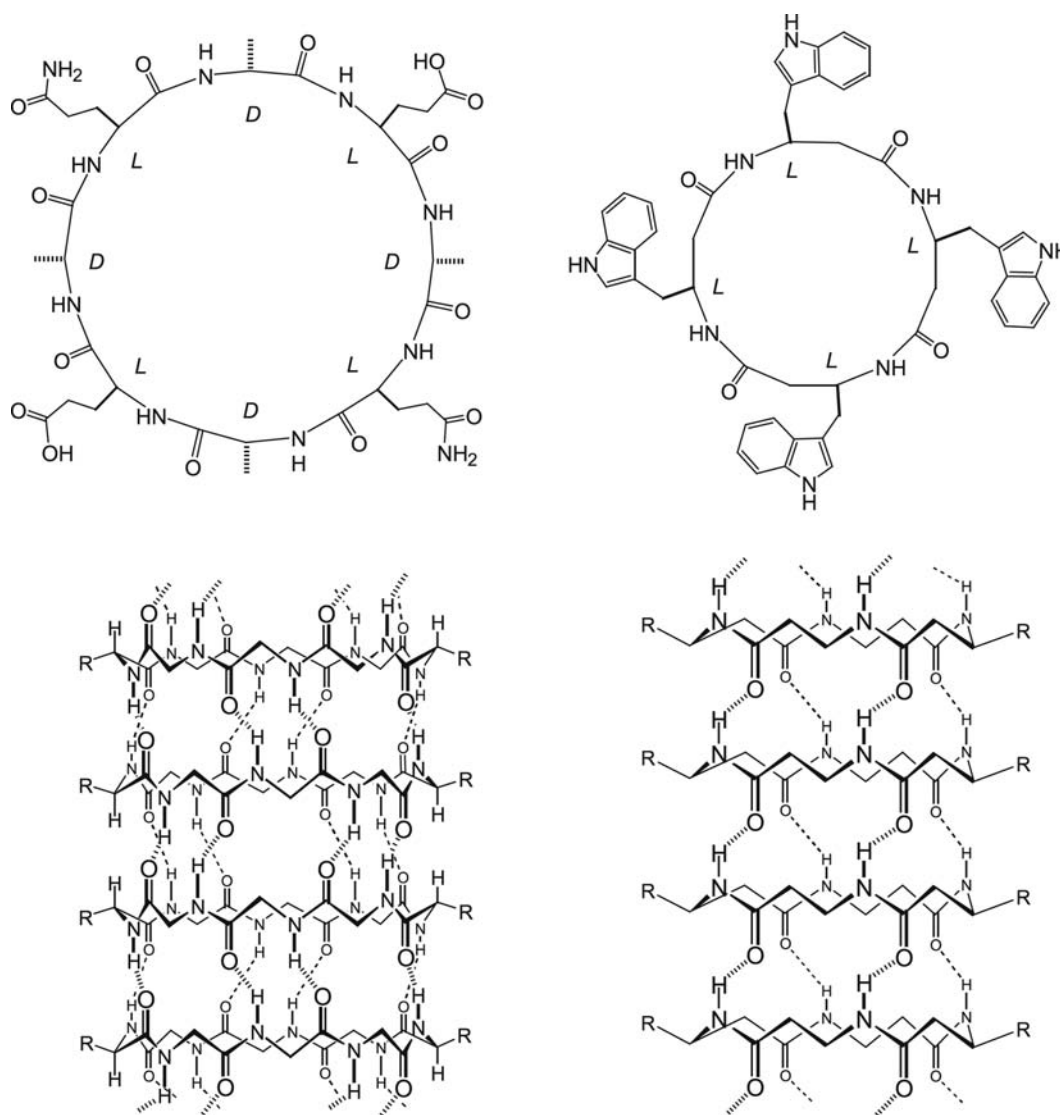


**Fig. 3** Schematic representations of nanotubes (bottom) formed by self-assembly from cyclic D,L- $\alpha$ - or  $\beta$ -peptides (top left and top right, respectively) (for clarity most side chains are omitted).

hence the internal diameter of the nanotube, is easily controlled by varying the number of amino acid residues in each ring; and secondly, the properties of the outer surface of the nanotube can easily be modified by varying the amino acid side chains. For example, self-assembly in lipidic or aqueous media can be promoted by endowing the cyclic units with hydrophobic or hydrophilic groups, respectively, so as to stabilize the flat conformation required for ring stacking. Appropriate unit design and optimization of conditions for self-assembly allows the properties of the resulting nanotubes to be tailored for specific applications. Thanks to this, SPN can be used as or in porous solid materials, soluble cylindrical supermolecules, ion channels and other transmembrane pores, solid-supported ion sensors, antimicrobial and cytotoxic agents, and nanocluster composites.<sup>[11,20]</sup>

## TYPES OF PEPTIDE NANOTUBE

### Introduction

The assembly of nanotubes by stacking cyclic peptides was first suggested in 1972 by Hassall, who envisaged that cyclic tetrapeptides composed of alternating  $\alpha$ - and  $\beta$ -amino acid residues would assemble through backbone-backbone hydrogen bonding.<sup>[21]</sup> This hypothesis was verified in 1975 by the analysis of the crystal structure of the tetrapeptide *cyclo*[L-Ser(O-*t*-Bu)- $\beta$ -Ala-Gly-L- $\beta$ -Asp(OMe)].<sup>[22]</sup> However, although the peptide rings were found to adopt the required conformation and stack above one another in the crystal lattice, neighboring rings were linked by only two hydrogen bonds instead of four. The use of hybrid rings composed of mixed  $\alpha$ - and  $\beta$ -amino acid residues is currently in

abeyance, and in this review we concentrate on cyclic D,L- $\alpha$ -peptides, cyclic  $\beta$ -peptides, and other peptide rings.

## Tubular Ensembles of Cyclic D,L- $\alpha$ -Peptides

### Preliminary studies

In 1974, on the basis of theoretical analysis, De Santis et al. concluded that peptides composed of an even number of alternating D- and L-amino acid residues would form closed rings capable of stacking through backbone-backbone hydrogen bonding.<sup>[23]</sup> The resulting supramolecular tubes would be closely related to the  $\beta$ -helical conformations adopted by linear D,L-peptides. Initial attempts to verify these predictions experimentally were inconclusive because of the poor solubility of the peptides employed.<sup>[24]</sup> For example, in 1989 an X-ray crystallographic study of diverse cyclic peptides by Lorenzi and coworkers failed to find the expected associations between the basic units, each peptide instead being hydrogen-bonded to several cocrystallized solvent molecules.<sup>[25]</sup> However, in 1993 Ghadiri and coworkers took advantage of the pH-dependent ionization of the glutamic acid side chain to control nanotube formation, as described in the next subsection.<sup>[18]</sup>

### Solid-state ensembles: microcrystalline peptide nanotubes

The first well-characterized peptide nanotube was prepared using the octapeptide *cyclo*-[(L-Gln-D-Ala-L-Glu-D-Ala)<sub>2</sub>], which was chosen because it would favor solubility in basic aqueous solution, where coulombic repulsion among its negatively charged carboxylate side chains would prevent premature ring stacking.<sup>[18]</sup> Controlled acidification of the basic solution of this peptide led to microcrystalline aggregates that were characterized by transmission electron microscopy (TEM), electron diffraction, Fourier transform infrared spectroscopy (FT-IR), and molecular modeling. These analyses showed, as expected, ordered hollow tubes formed by cyclic units stacked through antiparallel  $\beta$ -sheet-type hydrogen bonding, the between-ring distance being 4.73 Å and the internal tube diameter 7.5 Å (Fig. 4).

Proton-controlled self-assembly also allowed the preparation of microcrystalline aggregates of nanotubes with an internal diameter of 13 Å composed of *cyclo*-[(L-Gln-D-Ala-L-Glu-D-Ala)<sub>3</sub>] units,<sup>[26]</sup> which confirmed that the internal diameter of the nanotube could be determined just by varying the number of amino acid residues in the cyclic unit. Ghadiri's group has also prepared solid nanotubular assemblies using

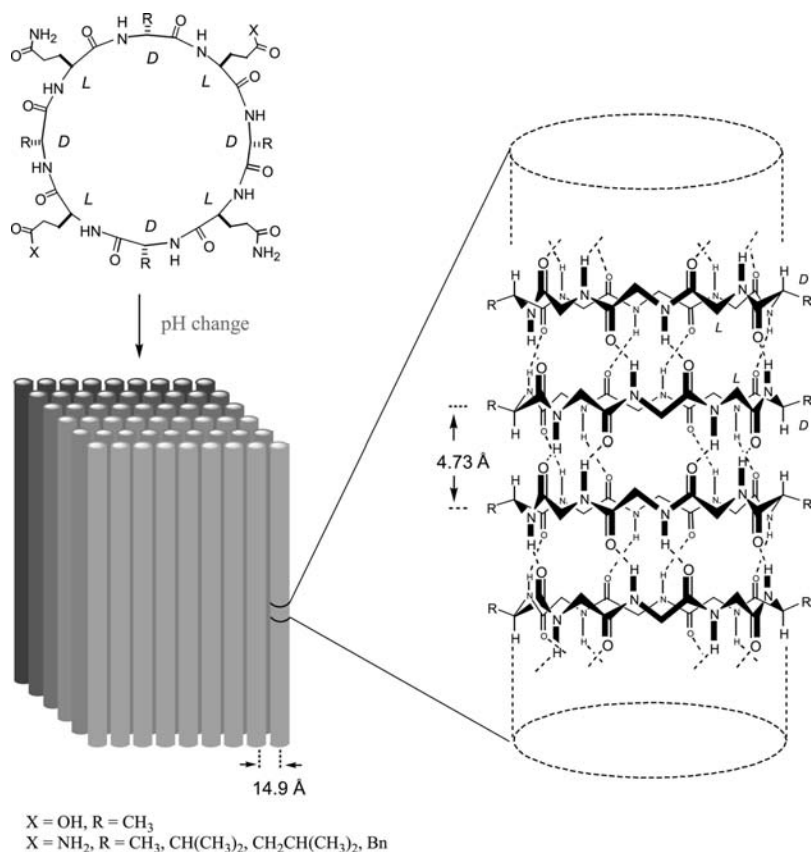


**Fig. 4** Dimensions of *cyclo*-[(L-Gln-D-Ala-L-Glu-D-Ala)<sub>2</sub>]-based nanotubes in crystal arrays, as deduced by TEM, electron diffraction, FT-IR, and molecular modeling.

various uncharged cyclic octapeptides to explore the effects of intertubular hydrophobic packing interactions on crystal formation; FT-IR, cryoelectron microscopy, and electron diffraction analyses show the expected cylindrical structures, with between-ring distances of about 4.8 Å and all the characteristic features of an antiparallel  $\beta$ -sheet-like structure.<sup>[27]</sup> More recently, Lambert and coworkers have employed pH-controlled self-assembly to synthesize nanotubular microcrystals of the cyclic D,L- $\alpha$ -octapeptide *cyclo*-[(L-Asn-D-Phe-L-Asp-D-Phe-)]<sub>2</sub>.<sup>[28]</sup>

### Solution-phase studies of dimerization

The basic step in all the above self-assembly processes, the association of cyclic peptides by antiparallel- $\beta$ -sheet-type hydrogen bonding, has been investigated in water by fluorescence quenching methods, which confirm that ring–ring association with the previously reported stacking parameters occurs in solution and is not just a consequence of crystallization.<sup>[29]</sup> To obtain a better understanding of this stacking interaction, and to carry out preliminary exploration of various ways of stabilizing the resulting nanotube structures, toy systems were designed and studied in

which complications associated with unlimited stacking (such as poor solubility) are avoided by allowing only the formation of two-ring structures (hereinafter, “tubelets”). This restriction is achieved by selective alkylation of the amino groups on one face of the peptide ring (those of amino acid residues with the same chirality).<sup>[30]</sup> For example, in deuteriochloroform *cyclo*-[(L-Phe-D-<sup>Me</sup>N-Ala-)]<sub>4</sub> associates as dimeric tubelets with an association constant of about 2540 M<sup>-1</sup>, but these structures grow no further because their *N*-methyl groups prevent hydrogen bonding to a third peptide ring (Fig. 5).<sup>[31]</sup> X-ray analysis shows that crystals obtained in methylenechloride/hexanes are composed of similar dimers, the hydrophilic nature of the cavity of which is confirmed by their containing water molecules. Solution-phase nuclear magnetic resonance (NMR) and FT-IR studies of this and other *N*-methylated peptides support the proposed structures and have begun to elucidate the thermodynamics of nanotube formation. These studies suggest that each hydrogen bond contributes 0.5–0.8 kcal mol<sup>-1</sup> to the enthalpy of formation. *N*-Methylated cyclic hexapeptides such as *cyclo*-[(L-<sup>Me</sup>N-Leu-D-Leu-)]<sub>3</sub> dimerize with smaller association constants,<sup>[32]</sup> but deca- and dodecapeptides fail to do so because of the difficulty to adopt the required flat conformation.<sup>[29–31]</sup> *N*-Propyl

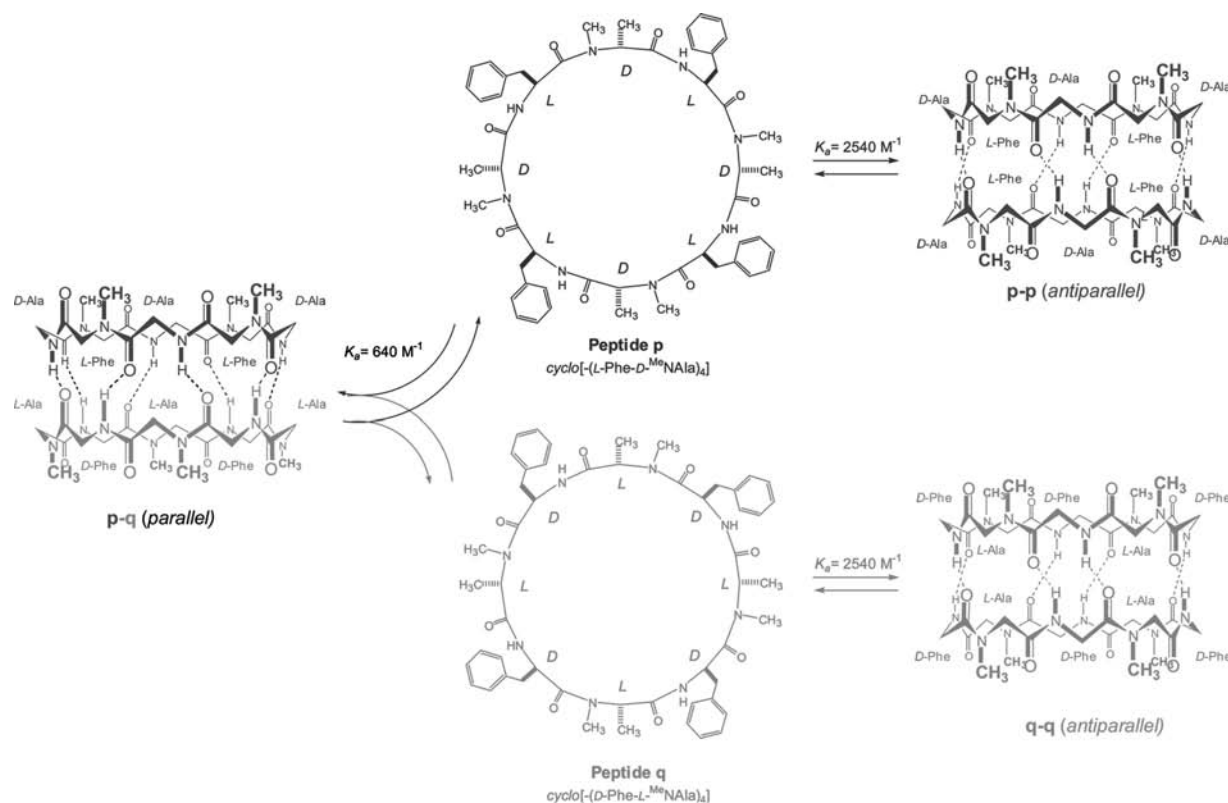


**Fig. 5** Parallel (*p*–*q*) and antiparallel (*p*–*p* and *q*–*q*)  $\beta$ -sheet structures of dimeric tubelets composed of *cyclo*-[(L-Phe-D-<sup>Me</sup>N-Ala-)]<sub>4</sub> (*p*) and/or *cyclo*-[(D-Phe-L-<sup>Me</sup>N-Ala-)]<sub>4</sub> (*q*), with the corresponding dimerization constants.

and allyl groups can also be used to prevent ring stacking from proceeding beyond the dimer stage.

Studies of sidechain–sidechain interactions have shown that  $\gamma$ -branched side chains are more favorable for dimerization than unbranched chains. Recently, aromatic side chain–side chain interactions in cyclic peptides containing homophenylalanine were used to induce crystal growth orthogonal to the tubulet axis through the prevalent effect of dimer formation in the crystal nucleation.<sup>[33]</sup>

Dimeric tubelets have also allowed easy comparison of the stabilities of parallel and antiparallel  $\beta$ -sheet structures in solution.<sup>[34]</sup> Using the enantiomeric cyclic peptides *cyclo*-[(L-Phe-D-MeN-Ala)<sub>4</sub>] and *cyclo*-[(D-Phe-L-MeN-Ala)<sub>4</sub>], it was found that antiparallel  $\beta$ -sheet structures (*p-p* and *q-q* in Fig. 5) are more stable than parallel structures (*p-q*) by 0.8 kcal mol<sup>-1</sup>.

Finally, further confirmation of  $\beta$ -sheet-type hydrogen bonding has been obtained by covalent consolidation of non-covalently constituted cyclic peptide dimers. In non-polar solvents the olefin-bearing peptide *cyclo*-[(L-Phe-D-MeN-Ala-L-Hag-D-MeN-Ala)<sub>2</sub>] (X = CH<sub>2</sub>-CH=CH<sub>2</sub> in Fig. 6; Hag = homoallylglycine)

forms equal proportions of two kinds of dimer, one of which undergoes selective hydrogen-bond-mediated olefin metathesis to afford covalently stabilized  $\beta$ -sheet peptide tubelets (see legend in Fig. 6).<sup>[35]</sup> Subsequent work has extended this general strategy to other covalent links, such as disulfide bonds:<sup>[36]</sup> for example, with *cyclo*-[(L-Phe-D-MeN-Ala-L-Cys-D-MeN-Ala)<sub>2</sub>] (X = SH in Fig. 6) S-H...S hydrogen bonds appear to stabilize the reactive dimer prior to formation of the disulfide bond. Studies of this kind, using dimers as toy systems, are paving the way for the preparation of stable polymeric nanotubes composed of cyclic peptides with backbone-unalkylated amino groups.

### Artificial transmembrane ion channels

As was emphasized above, the major advantage of peptide nanotubes over others is the ease with which their external surface properties and internal diameters can be controlled by the use of cyclic peptides with appropriate side chains and numbers of amino acid residues. In 1994, Ghadiri's group created the first

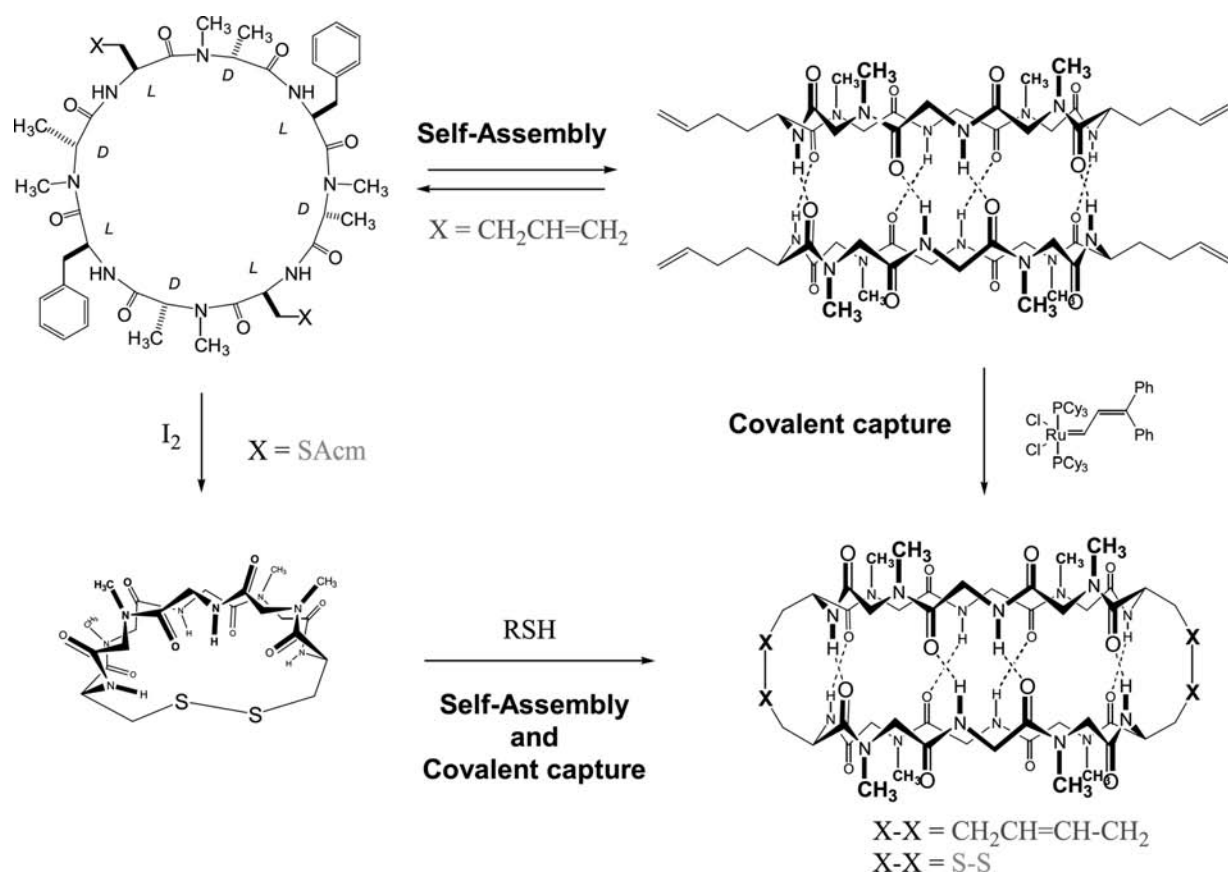


**Fig. 6** Consolidation of cyclic peptide dimers by covalent bonding between their constituent rings using olefinic or thiolic side chains. Of the two dimers formed by *cyclo*-[(L-Phe-D-MeN-Ala-L-Hag-D-MeN-Ala)<sub>2</sub>] (Hag = homoallylglycine; X = CH<sub>2</sub>-CH=CH<sub>2</sub> in the figure), only the isomer in which CH<sub>2</sub>-CH=CH<sub>2</sub> groups of different peptide rings face each other can undergo covalent stabilization.

transmembrane nanotube to self-assemble in a lipid bilayer, a feat that depended on the hydrophobic side chains of the cyclic  $D,L$ - $\alpha$ -peptide *cyclo*-[L-Gln-(D-Leu-L-Trp)<sub>3</sub>-D-Leu-] (Fig. 7,  $x = H$ ).<sup>[37]</sup> Since then, several similar structures have been studied by liposome-based proton transport assays, computational methods, FT-IR spectroscopy, grazing-angle reflection/absorption, polarized attenuated total reflectance (ATR), and single-channel conductance measurements.<sup>[38,39]</sup> In all cases, when the amino acid sequence is dominated by hydrophobic amino acids, the resulting nanotube is oriented nearly parallel to the lipid alkyl chains, as required for a transmembrane channel.<sup>[39]</sup> While peptide nanotubes formed from amphipathic cyclic peptides lay parallel to the membrane plane. Increasing the size of the cyclic peptide, for example by using *cyclo*-[L-Gln-(D-Leu-L-Trp)<sub>4</sub>-D-Leu-], provides channels with larger pores. Both *cyclo*-[L-Gln-(D-Leu-L-Trp)<sub>3</sub>-D-Leu-] and *cyclo*-[L-Gln-(D-Leu-L-Trp)<sub>4</sub>-D-Leu-]-based channels have prodigious alkaline ion transport activities. Molecular dynamics simulations suggest that these high rates of transport may be due largely to the way in which water molecules are ordered in the lumen.<sup>[38]</sup> However, even larger cation conductances (10–15% larger for 20 mM  $K^+$ ) can be achieved by oriented heterodimer-based nanotubes in which the

ring at the end facing the  $K^+$  source, *cyclo*-[(L-Glu-D-Leu)<sub>4</sub>], is negatively charged at the working pH.<sup>[40]</sup>

Ab initio calculations have suggested that band conduction may occur through the between-ring hydrogen bonds of peptide nanotubes as a result of delocalization of electrons and holes toward the tube axis.<sup>[41]</sup>

### Tubular Ensembles of Cyclic $\beta$ -Peptides

$\beta$ -Peptides are an emerging class of non-natural biopolymers that in solution adopt a variety of secondary structures analogous to those of  $\alpha$ -peptides, including pleated sheets, turns, hairpins, and a variety of helical conformations of differing chirality and radius.<sup>[42]</sup> Their ability to resist enzymatic degradation and their favorable conformational properties suggest that  $\beta$ -peptides may have interesting applications. Molecular modeling and X-ray crystallography have shown that in the solid state, cyclic tetrapeptides composed of chiral  $\beta^3$ -amino acid residues can adopt flat-ring conformations and stack to form nanotubes in the same way as cyclic  $D,L$ - $\alpha$ -peptides, and that in the case of  $\beta$ -peptides this is possible with peptide rings composed of homochiral  $\beta$ -amino acid residues as well as with rings of residues of alternating chirality (Fig. 3).<sup>[43]</sup>

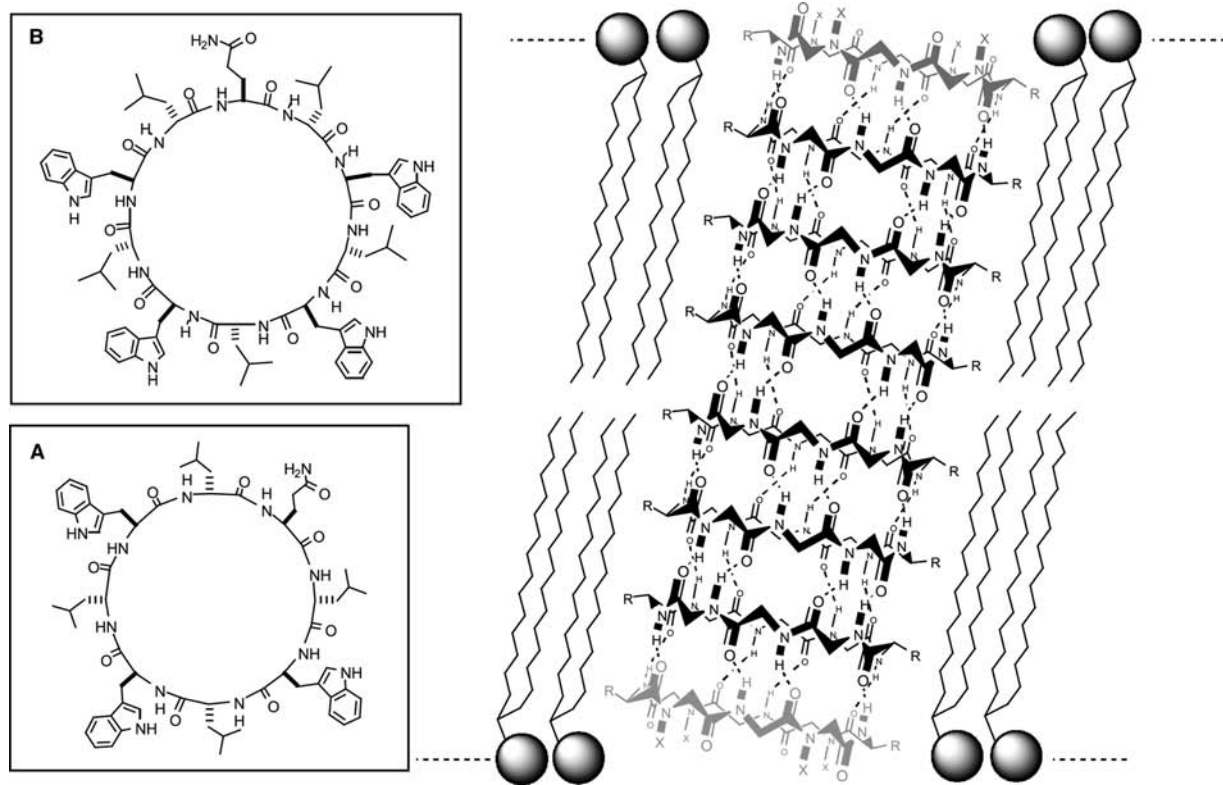


**Fig. 7** Schematic representation of a peptide nanotube self-assembled in a lipid bilayer by association of cyclic peptide units. Peptides used by Ghadiri and coworkers in transport experiments are shown at the left ( $x = H$ ). Source: From Ref.<sup>[38,39]</sup>

Like their D,L- $\alpha$  counterparts, cyclic  $\beta^3$ -peptides with appropriate hydrophobic side chains can associate in lipid bilayers to form efficient self-assembled artificial transmembrane ion channels.<sup>[44]</sup> In the cases of *cyclo*-[( $\beta^3$ -HTrp-)<sub>4</sub>]- and *cyclo*-[( $\beta^3$ -HTrp- $\beta$ -Hleu-)<sub>2</sub>]-based channels assembled in planar lipid bilayers, single-channel conductance measurements have shown activities similar to those of D,L- $\alpha$ -peptide-based channels, with K<sup>+</sup> transport rates of  $1.9 \times 10^7$  ions sec<sup>-1</sup>, greater than that of gramicidin A under similar conditions. It is thought that the unnatural backbones of channel-forming cyclic  $\beta^3$ -peptides will have interesting consequences for the corresponding channels and channel formation processes. In particular, as linear  $\beta$ -peptides resist digestion by proteases because of their unnatural backbone, the same is expected to be true of cyclic  $\beta^3$ -peptides, which should therefore be able to

form ion channels with potential antimicrobial effects in the presence of these enzymes; a mechanism of this kind is thought to be responsible for the known antimicrobial activity of helical linear  $\beta$ -peptides.<sup>[45]</sup>

### Tubular Ensembles of Cyclic Peptides Containing $\gamma$ -Amino Acid Residues

The inner faces of D,L- $\alpha$ - and  $\beta$ -peptide-based nanotubes are hydrophilic (and some of their potential applications depend on this). It is not possible to modify their pore properties by introducing functional groups on their inner faces, because all their amino acid side chains point outward and substitution at C $_{\alpha}$  or C $_{\beta}$  would interfere with nanotube assembly. However, this shortcoming disappears if cyclic hybrid

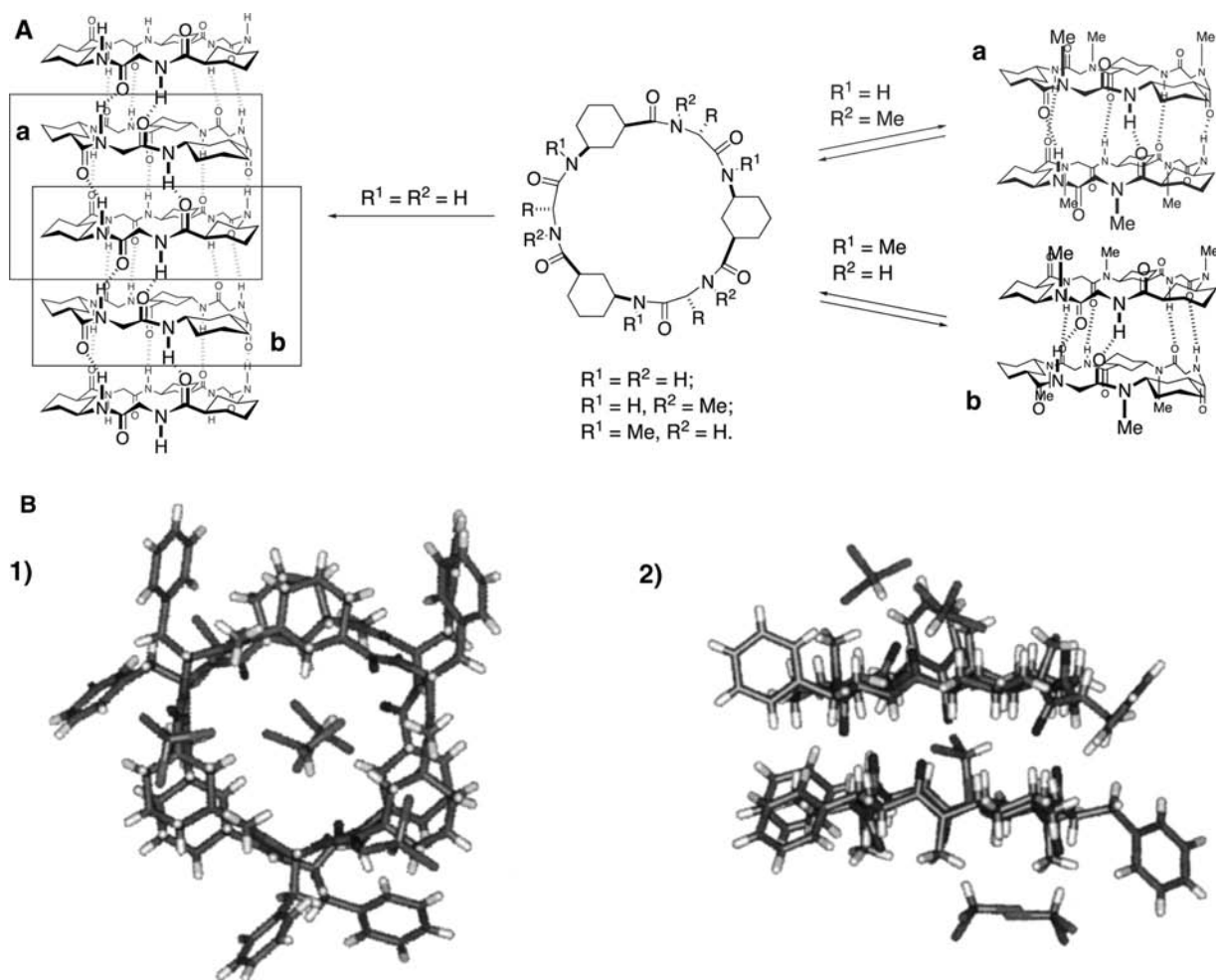


**Fig. 8** A cyclic peptide composed of alternating  $\alpha$ -amino acids and *cis*-3-aminocyclohexanecarboxylic acid ( $\gamma$ -Ach) that can stack to form nanotubes with hydrophobic regions in the lumen around the cyclohexane  $\beta$ -methylenes. A) The two types of hydrogen bond involved in nanotube formation (left, a and b) and their separate realizations in N-methylated dimeric tubelets (right). B) Silicon representations (1, top view; 2, side view) of the crystal structure of dimeric *cyclo*-[(D-Phe-(1R,3S)-<sup>Me</sup>N- $\gamma$ -Ach-)<sub>3</sub>], which crystallized in association with five molecules of chloroform, one of them occupying the central cavity of the dimer.



$\alpha,\gamma$ -peptides are used as the basic units for nanotube construction. Our group has recently designed, synthesized, and characterized a new cyclic peptide, composed of alternating  $\alpha$ -amino acids and *cis*-3-aminocyclohexanecarboxylic acid ( $\gamma$ -Ach), that can adopt the flat conformation required for the formation of nanotubes consisting of hydrogen-bonded stacks of alternately oriented rings (Fig. 8).<sup>[46]</sup> In these rings the  $\beta$ -methylene of each cyclohexane projects into the lumen, creating a hydrophobic region. That these rings can indeed stack as desired was verified by using the backbone methylation strategy (see “[Solution-Phase Studies of Dimerization](#)”) to prepare hydrogen-bonded dimers of each of the two types required for nanotube formation (one bonded via the  $\alpha$ -amino acid residues of each component cyclic peptide, the other via their  $\gamma$ -Ach moieties; Fig. 8A, frames a and b). Nuclear magnetic resonance, Fourier transform infrared spectroscopy, and X-ray diffraction studies conclusively confirmed the formation of these dimers and showed that the dimer bonded via  $\alpha$ -amino acid residues are extremely stable in non-polar solvents, with  $K_a$ 's  $> 10^5$ . It should be possible to functionalize the inner surface of nanotubes composed of these hybrid  $\alpha,\gamma$ -peptides by introducing substituents on the  $\beta$ -methylene, something that, as noted above, is impossible for nanotubes based on cyclic  $\alpha$ - or  $\beta$ -peptides. The ability to functionalize nanotube cavities would give the chemist greater capacity to design selective ion channels, selective molecular inclusion devices, or molecular and catalytic containers.

### Tubular Ensembles of Other Cyclic Peptides

The  $\alpha$ -,  $\beta$ - and  $\gamma$ -amino-acid-based peptides discussed above do not exhaust the kinds of cyclic peptide that

have already been examined as potential basic units for nanotube construction. Dori and coworkers synthesized a tripeptide that crystallized as bundles of nanotubes.<sup>[47]</sup> It is composed of  $\alpha,\beta$ -unsaturated  $\delta$ -amino acid residues that, because of the *trans* geometry of the vinyl group, adopt the flat conformation required for self-assembly of nanotubes (Fig. 9). Because the peptide backbone has an even number of atoms between the carbonyl and amino groups of each residue, all the carbonyl groups are oriented in the same direction (as in the  $\beta$ -peptide-based nanotube of Fig. 2), which gives the nanotubes a large dipole moment resulting in highly anisotropic crystals.

Guichard and coworkers have reported the design, synthesis, and structural analysis of cyclic oligopeptides consisting of homochiral residues with proteinogenic side chains.<sup>[48]</sup> These units crystallize as hydrogen-bonded polar nanotubes with electron density in the tubular cavity.

Macrocyclic bisureas prepared from cystine have been used by Ranganathan and coworkers, as well as the analogous bisamides (Fig. 10A).<sup>[49]</sup> Despite their flexibility, these molecules crystallize in tubular arrays of uniform shape and internal diameter, adjacent rings being bound together by two hydrogen bonds in the bisamides and four in the bisureas. The tubular structure may additionally be stabilized by the hydrophobic collapse of the alkyl bridge.

Finally, Ranganathan and coworkers have also explored the nanotube-forming possibilities of a quite different kind of cyclic unit, cyclodepsipeptides in which the amide groups lie in the ring plane and solid-state ring–ring stacking is due to  $\pi$ – $\pi$  interactions between phenyl and carbonyl rings included in the depsipeptide backbones of the rings of neighboring tubes, which interdigitate as shown in Fig. 10B.<sup>[50]</sup>

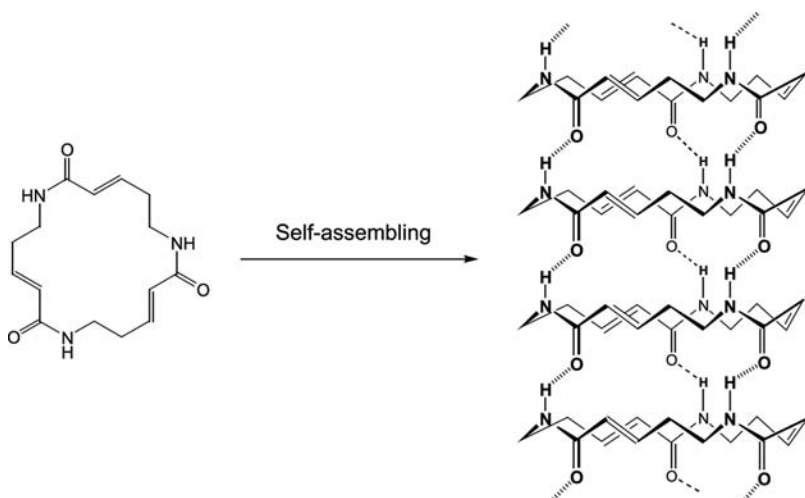


**Fig. 9** Self-association of a rigid lactamic  $\gamma$ -tripeptide as a nanotube.

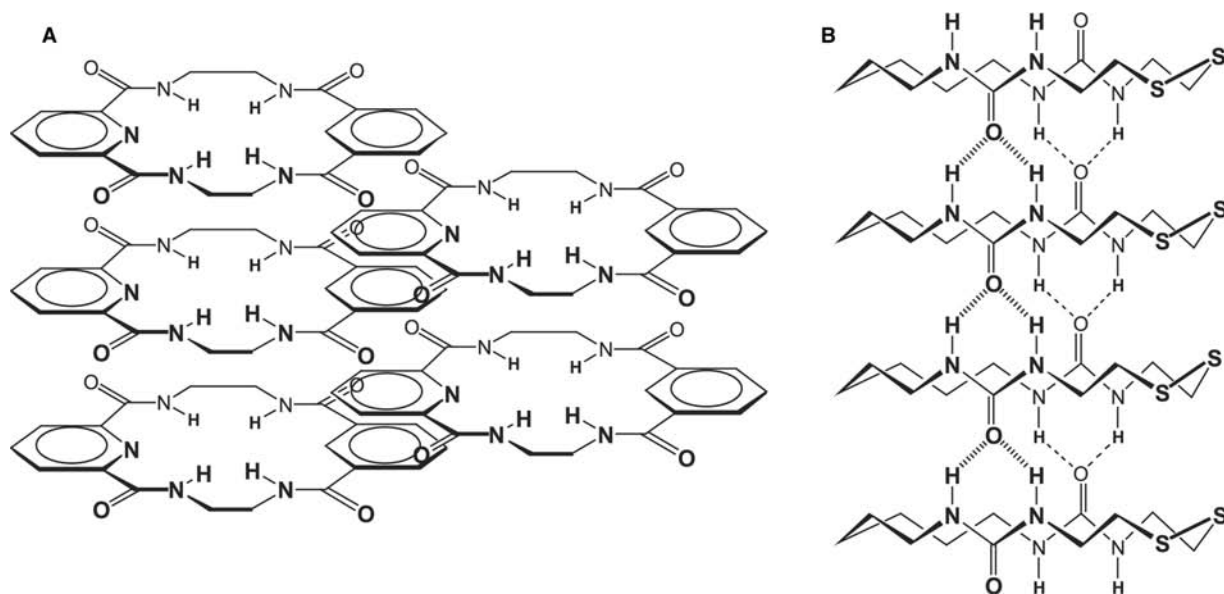


**Fig. 10** Self-assembled nanotubes investigated by Ranganathan and coworkers. A) Self-assembly by association of cysteine-based macrocyclic bisureas. B) Self-assembly through  $\pi$ - $\pi$  interactions between interdigitating aromatic rings included in the backbones of the cyclodepsipeptides constituting neighboring nanotubes.<sup>[49,50]</sup>

## APPLICATION STATUS OF PEPTIDE NANOTUBES (FIG. 11)

### As Selective Transmembrane Transport Channels

Naturally occurring transmembrane channels are chemically diverse molecules performing molecular transport and selection and ion-flow trafficking.<sup>[51,52]</sup> Synthetic peptide nanotubes that are internally hydrophilic and externally endowed with appropriate characteristics can mimic certain transmembrane channel functions. As noted above, the first such nanotubes, designed to explore the possibility of self-assembly in lipid bilayers, were composed of *cyclo*-[L-Gln-(D-Leu-L-Trp)<sub>3</sub>-D-Leu-] units (Fig. 7) and had ion conductivities greater than  $10^7$  ions  $\text{sec}^{-1}$ .<sup>[37]</sup> The incorporation of the constituent peptide rings into lipid bilayers was shown by absorption and fluorescence spectroscopy, and their spontaneous assembly into hydrogen-bonded nanotubes by FT-IR spectroscopy, while ion conductance studies using patch clamp techniques found  $\text{K}^+$  and  $\text{Na}^+$  transport rates about three times faster than those of the naturally occurring channel gramicidin A (Fig. 12).

These artificial peptide transmembrane channels are naturally size selective. For example, the passage of glucose, which is estimated to require a pore diameter somewhat larger than 9 Å, is not allowed by the octapeptide nanotubes described above, but nanotubes built of the decapeptide *cyclo*-[(L-Trp-D-Leu)<sub>4</sub>-L-Gln-D-Leu-], which have an internal diameter of 10 Å, pass

both glucose and glutamic acid very efficiently.<sup>[53,54]</sup> These decapeptide nanotubes also transport ions with similar efficiency, but with mean opening times that are shorter than with octapeptide channels because of their greater conformational freedom. Potential applications of these artificial transmembrane channels include biosensing and size-selective molecular delivery.

Recently, a heterodimeric peptide nanotube architecture that displays altered conductance and rectification properties has been described, (Fig. 7, e.g.,  $x = \text{CH}_2\text{COOH}$ ).<sup>[40]</sup> by taking advantage of the different properties (mode of interaction and microenvironment in which they reside) of the two subunits that reside at the ends of the channel assembly (caps). The local electrostatic perturbations brought by the cap subunits bearing ionizable functionalities were used to modulate the ion selectivity and conductance of the transmembrane channel. For example, an increase in conductance (10–15% in 20 mM KCl) was observed when a negative charged (*cyclo*-[(L-Glu-D-Leu)<sub>4</sub>]) cap was used because of the inherent cation selectivity of the resulting channel.

Likewise as noted above, the cyclic  $\beta^3$ -peptides *cyclo*-[( $\beta^3$ -HTrp)<sub>4</sub>] and *cyclo*-[( $\beta^3$ -HTrp- $\beta$ -HLeu)<sub>2</sub>] can also associate tubewise in lipid bilayers (Fig. 13), forming channels with  $\text{K}^+$  transport rates of  $1.9 \times 10^7$  ions  $\text{sec}^{-1}$ .<sup>[44]</sup> It is worth pointing out that these channels are anisotropic, as all the component rings of  $\beta$ -peptide nanotubes stack with the same orientation. This leaves all the amide NH groups pointing toward one end of the nanotube and all the C=O groups pointing toward the other end, giving

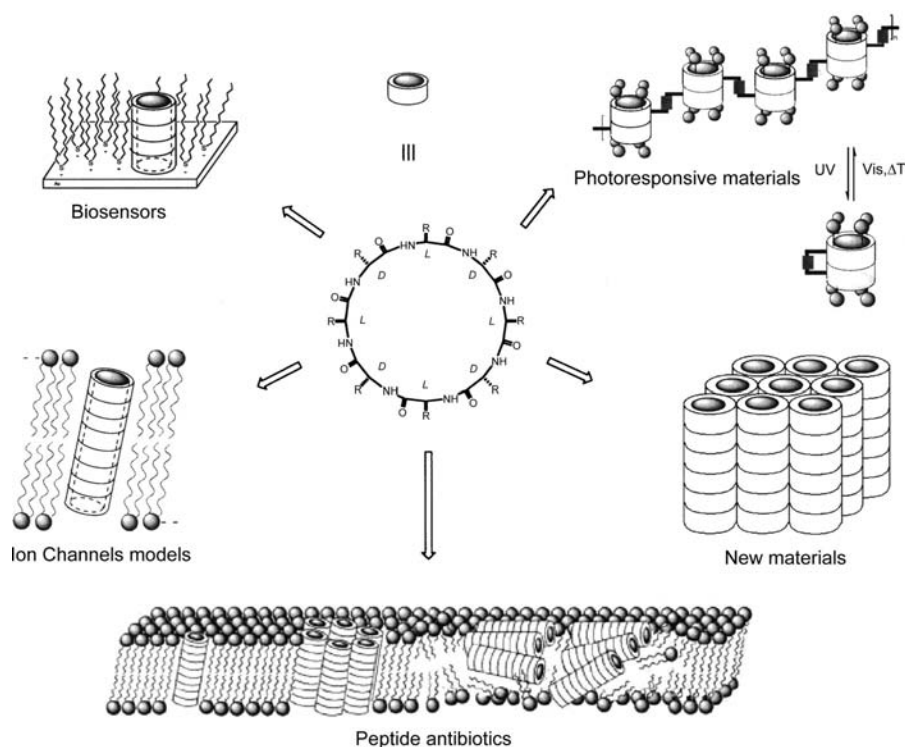


**Fig. 11** Potential applications of peptide nanotubes that are currently being investigated.

the entire tube a dipole moment that should result in its being oriented parallel to an applied electric field and in its exhibiting voltage-gating behavior. Moreover, the formation of the nanotube itself should also be facilitated by the application of an electric field, which should cause all the peptide rings to adopt the correct orientation for stacking.

### As Antibiotics

The proliferation of antibiotic-resistant bacteria in recent years has intensified the need for new antibiotics with novel modes of action.<sup>[55,56]</sup> Many naturally occurring peptide antibiotics act by creating pores in bacterial membranes, which kills the bacterium by

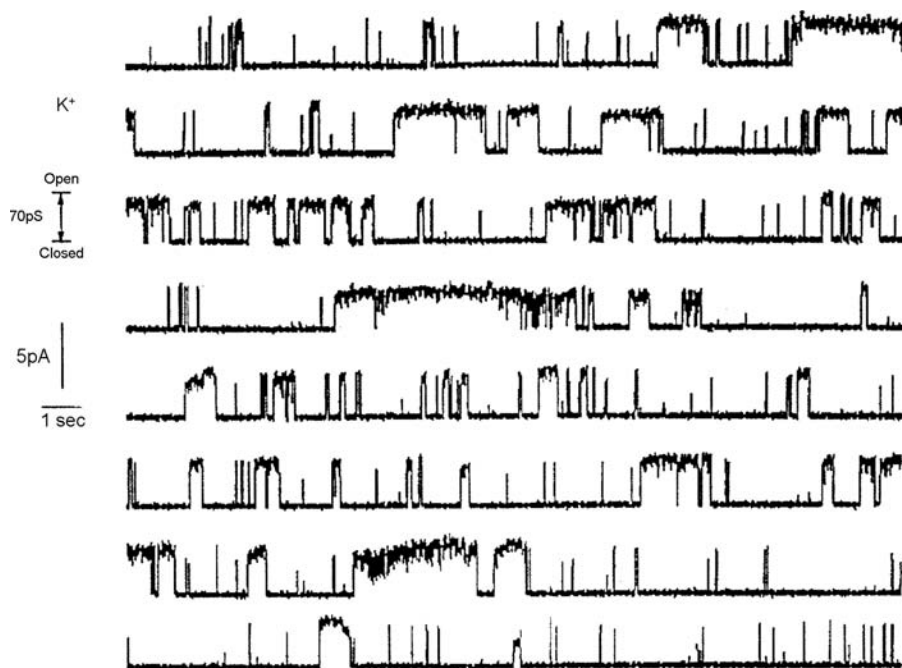


**Fig. 12** Micro-patch-clamp measurements of ion conduction by nanotubes self-assembled from *cyclo*-[L-Gln-(D-Leu-L-Trp)<sub>3</sub>-D-Leu] in lipid bilayers. The figure shows a 140-sec continuous record of single-channel K<sup>+</sup> conduction under an applied voltage drop of 50 mV. Closure of the ion channels is due to thermal disruption of their constituent hydrogen bonds. *Source:* From Ref.<sup>[37]</sup>; © 1993, Macmillan Magazines Ltd.

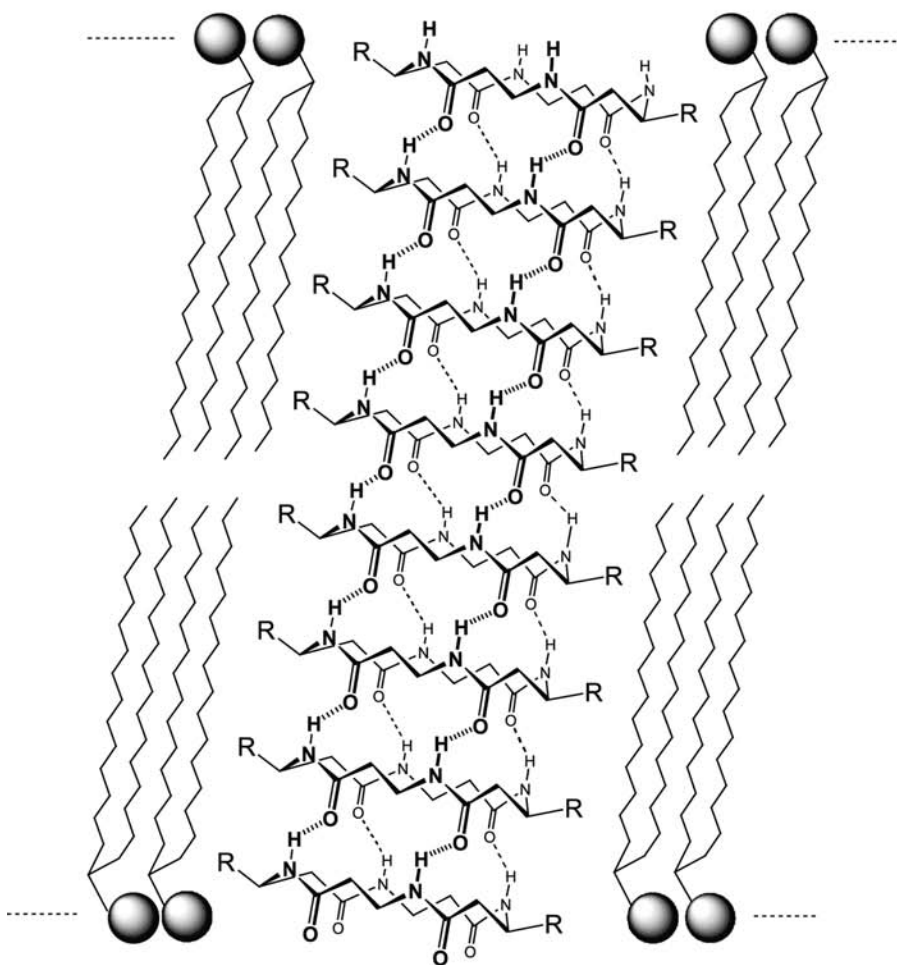
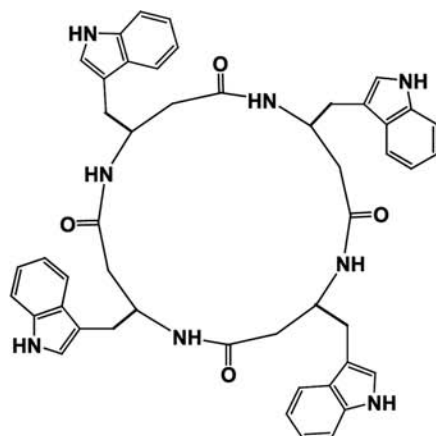


**Fig. 13** Schematic representation of a transmembrane ion channel self-assembled in a lipid bilayer from *cyclo*-[( $\beta^3$ -HTrp-)<sub>4</sub>].

destabilizing electric potential and ion gradients.<sup>[57]</sup> Approaches to novel antibiotics mimicking this mode of action include the use of peptide rings capable of stacking in the membrane to form transmembrane pores (Fig. 14).<sup>[58,59]</sup> In particular, amphipathic cyclic D,L-octa- and hexapeptides with at least one positively charged amino acid residue (included to interact with negatively charged bacterial membranes) have been shown to infiltrate the bacterial membrane and

associate as nanotubes oriented at an angle of 20° to the membrane plane, suggesting the formation of nanotube “carpets” causing extensive membrane damage.<sup>[58]</sup> An important aspect of this approach is that peptide rings can be designed to associate as nanotubes selectively in bacterial rather than mammalian membranes. Such peptides exhibit significant antibacterial activity *in vitro*, and their preferential action against bacterial cells has been demonstrated in mice, in which

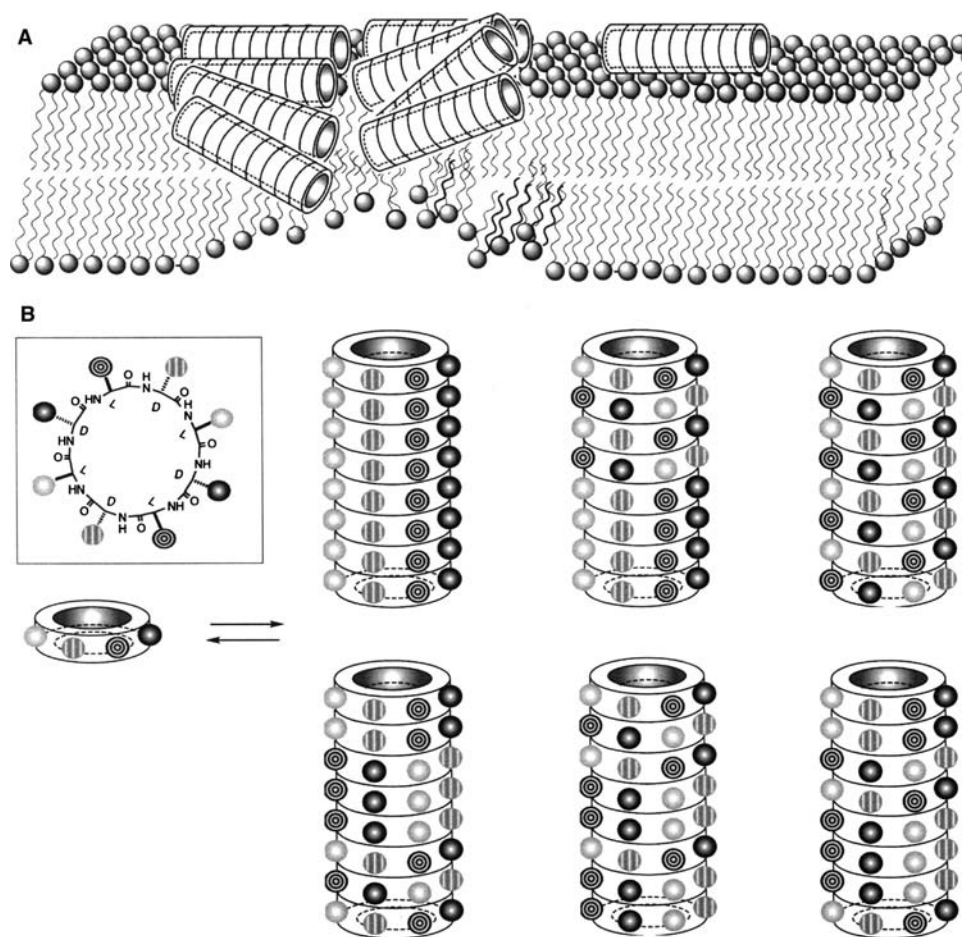


**Fig. 14** Schematic representation of the formation of lethal ion channels in bacterial membranes. A) Proposed carpet-like mode of action of peptide nanotube, showing the greater potential for membrane discrimination due to its polyvalent display of surface-exposed hydrophilic side chains to interact with various membrane constituents. B) Schematic representation of multiple nanotube assemblies formation with different surface presentation from a given cyclic peptide.

they exhibit activity against a broad spectrum of bacteria, including methicillin-resistant *Staphylococcus aureus*.

The design of new supramolecular drugs based on the principles shown for these antibiotic peptides may be the 21st century drugs and a step toward combating the development of drug-resistance. The actual molecular approach to drug design of lead compounds based on the narrow sequence space between the pharmacophore and the molecular target (receptors, enzymes, or nucleic acids) makes very easy its inactivation just by only a few structural changes. The supramolecular approach would have a large sequence space, maintaining their mode of action despite gross structural changes. The potential of the supramolecular approach to drug design is illustrated in Fig. 14; from a given cyclic  $D,L$ - $\alpha$ -peptide sequence it is possible to generate several different nanotube assemblies with different surface presentations through variations in the relative rotations of the cyclic subunits.

### As Biosensors

The feasibility of diffusion-limited size-selective ion sensing using supported nanotubes has been shown in studies using a cyclic  $D,L$ - $\alpha$ -octapeptide that self-associated as nanotubes embedded in self-assembled organosulfur monolayers supported on gold films (Fig. 11).<sup>[60,61]</sup> The functional properties of this arrangement were studied by cyclic voltammetry and impedance spectroscopy, showing, for example, selective redox activity for the smaller  $[\text{Fe}(\text{CN})_6]^{3-}$  complex compared to  $[\text{Mo}(\text{CN})_8]^{4-}$ , because of the presence of peptide channels. The studies have demonstrated the feasibility of diffusion-limited size-selective ion sensing based on supported tubular biomaterials. Variations in the type of cyclic peptide, diameter, and their channel selectivity toward different species, along with the differences in the chain length of the alkyl group of the organosulfur adsorbates, are expected to increase the repertoire of the sensor applications.

## As Biomaterials

Inspired by natural mineralization processes thought to involve interaction with oriented groups on natural polymers, Ghadiri's group has also investigated the formation and stabilization of metal nanoclusters on the surface of SPN crystals composed of *cyclo*-[(L-Gln-D-Ala-L-Gln-D-Ala-)<sub>2</sub>]-based nanotubes (J.D. Hartgerink, M.R. Ghadiri, personal communication).<sup>[11,62]</sup> The array of carboxyl groups on the outer nanotube surface served to nucleate the deposition of copper(I) oxide. The resulting nanocomposite material was characterized by high-resolution TEM and electron energy loss spectroscopy (EELS). It is thought that regular nanotube-borne functional group arrays may also serve to nucleate mineral crystallization processes.

## As Photoresponsive Materials

Molecules that can be reversibly switched between two states using light have been extensively studied in

recent decades,<sup>[63–65]</sup> especially with a view to their application as optical data storage devices. Ghadiri and coworkers have investigated a system in which *N*-methylated cyclic D,L-peptide dimers can be switched between one state in which the two rings in each dimer are connected covalently by an azobenzene link in *Z* conformation and another in which the *E* conformation of this link connects neighboring dimers (Fig. 15).<sup>[66,67]</sup> Interconversion between the two states can be effected both in solution and in thin films at the air–water interface; the *E*–*Z* isomerization is the faster process. Further research in this direction may lead to materials capable of modifying their macroscopic properties in response to light.

## Other Potential Applications

The ease with which the size and external properties of peptide nanotubes can be controlled, and the fact that their outer surfaces present regularly oriented arrays of functional groups, suggests that other fields in which these supermolecules may find application include

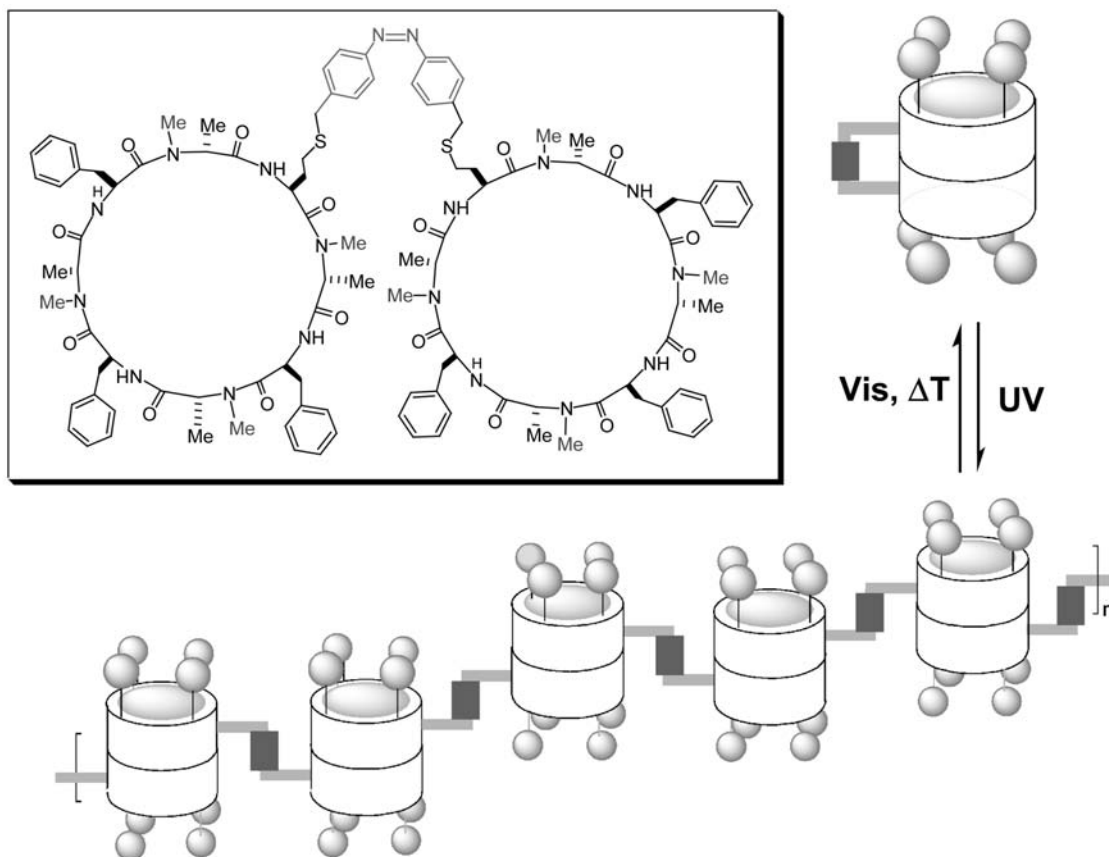


**Fig. 15** An azo-linked cyclic peptide dimer that can be reversibly switched between isolated-dimer and interconnected-dimer forms using radiation of different frequencies.



catalysis, anticancer therapy, and electronic, optical, and molecular engineering.<sup>[68,69]</sup>

## CONCLUSION

Although covalent bonds constitute the strongest kind of connection between atoms, weaker interactions such as hydrogen bonds, hydrophobic interactions, and salt bridges can be decisive for molecular organization and properties, as first became apparent in studies of biological systems. Supramolecular chemistry, the study of supramolecular structures formed by non-covalent interactions among covalently bound components, investigates, inter alia, the behavior of simple component units designed to self-associate non-covalently to form ordered supramolecular structures with prespecified properties. In this entry we have surveyed aspects of the supramolecular chemistry of cyclic peptides, which under appropriate conditions interact via hydrogen bonds to form nanoscale tubular structure–peptide nanotubes. Crucial for this interaction is the adoption of a flat conformation in which the amino acid side chains of the peptide rings have a pseudo-equatorial outward-pointing orientation and the carbonyl and amino groups of the peptide bonds are oriented perpendicular to the ring, the carbonyl on one side of the ring and the corresponding amino group on the other. This conformation can be achieved by cyclic peptides with a variety of amino acid compositions, including alternating D- and L- $\alpha$ , alternating  $\alpha$  and  $\gamma$ ,  $\beta$ , and  $\delta$ . Peptide rings composed of amino acid residues with an even number of carbons between the amino and carboxyl groups stack with all rings having the same orientation, so creating nanotubes with strong dipole moments, while rings composed of  $\alpha$ - and  $\gamma$ -amino acids stack with alternating orientations and lack this natural directedness. In all cases, the resulting nanotubes have well-defined uniform internal diameters and external surfaces that can be easily endowed with specific properties by modification of the amino acid side chains; to quote Ghadiri, “a reliable repeat unit can be exploited to place functionality in a supramolecular lattice with molecular precision.”<sup>[70]</sup> Once the nanotube has been formed, it can be consolidated by the formation of covalent bonds between adjacent peptide rings. Recent work has also paved the way to the modification of the properties of the inner nanotube surface, which in previous peptide nanotubes had always been bare and hydrophilic. Peptide nanotubes are currently being actively investigated with regard to their application as selective transmembrane ion or molecular transport channels, antimicrobial and cytotoxic devices, ion sensors, porous solid materials, nanocluster composites, and photoresponsive materials.

## REFERENCES

1. Special issue. Engineering a small world. *Science* **1991**, 254 (5036), 1300–1335.
2. Klabunde, K.J. Introduction to Nanotechnology. In *Nanoscale Materials in Chemistry*; Klabunde, K.J., Ed.; John Wiley & Sons, Inc.: New York, **2001**; 1–13.
3. Rao, C.N.R.; Cheetham, A.K. Science and technology of materials: Current status and future prospects. *J. Mater. Chem.* **2001**, 11 (12), 2887–2894.
4. Terrones, M.; Hsu, W.K.; Kroto, H.W.; Walton, D.R.M. Nanotubes: A revolution in materials science and electronics. *Top. Curr. Chem.* **1999**, 199, 189–234.
5. Ghadiri, M.R. Self-assembled nanoscale tubular ensembles. *Adv. Mater.* **1995**, 7 (7), 675–677.
6. Langley, P.J.; Hulliger, J. Nanoporous and mesoporous structures: New openings for material research. *Chem. Soc. Rev.* **1999**, 28 (5), 279–291.
7. Wolfgang, T. Inorganic nanotubes. *Angew. Chem. Int. Ed.* **1999**, 38 (15), 2175–2179.
8. Baughman, R.H.; Zakhidov, A.A.; de Heer, W.A. Carbon nanotubes—the route toward applications. *Science* **2002**, 297 (5582), 787–792.
9. Huo, Q.S.; Margolese, D.I.; Ciesla, U.; Feng, P.; Gier, T.E.; Sieger, P.; Leon, R.; Petroff, P.M.; Schüth, F.; Stucky, G.D. Generalized synthesis of periodic surfactant/inorganic composite materials. *Nature* **1994**, 368 (6469), 317–321.
10. Patzke, G.R.; Krumeich, F.; Nesper, R. Oxidic nanotubes and nanorods—Anisotropic modules for a future nanotechnology. *Angew. Chem. Int. Ed.* **2002**, 41 (14), 2446–2462.
11. Bong, D.T.; Clark, T.D.; Granja, J.R.; Ghadiri, M.R. Self-assembling organic nanotubes. *Angew. Chem. Int. Ed.* **2001**, 40 (6), 988–1011.
12. Special issue. Supramolecular chemistry and self-assembly. *Science* **2002**, 295 (5564), 2395–2421.
13. Special issue. Supramolecular chemistry and self-assembly special feature. *PNAS* **2002**, 99 (8), 4762–5188.
14. Lehn, J.M. Supramolecular chemistry—Scope and perspectives. *Molecules, supermolecules and molecular devices*. *Angew. Chem. Int. Ed.* **1988**, 27 (1), 89–112.
15. Cram, D.J. The design of molecular hosts, guests, and their complexes. *Angew. Chem. Int. Ed.* **1988**, 27 (8), 1009–1020.
16. Pedersen, C.J. The discovery of crown ethers. *Angew. Chem. Int. Ed.* **1988**, 27 (8), 1021–1027.
17. Philp, D.; Stoddart, J.F. Self-assembly in natural and unnatural systems. *Angew. Chem. Int. Ed.* **1996**, 35 (11), 1155–1196.
18. Ghadiri, M.R.; Granja, J.R.; Milligan, R.A.; McRee, D.E.; Khazanovich, N. Self-assembling organic nanotubes based on a cyclic peptide architecture. *Nature* **1993**, 366 (6453), 324–327.
19. Kates, S.A., Albericio, F., Eds.; *Solid-Phase Synthesis*; Marcel Dekker, Inc.: New York, 2000.
20. Granja, J.R.; Ghadiri, M.R. Self-assembling peptide nanotubes. In *NMR in Supramolecular Chemistry*; Pons, M., Ed.; Kluwer Academic Publishers: Netherlands, 1999; 61–66.

21. Hassall, C.H. Chemistry and Biology of Peptides. In *Proceedings of the Third American Peptide Symposium*; Meienhofer, J., Ed.; Ann Arbor: Michigan, 1972; 153–157.
22. Karle, I.L.; Handa, B.K.; Hassall, C.H. The conformation of the cyclic tetrapeptide L-Ser(O-*t*-Bu)- $\beta$ -Ala-Gly-L- $\beta$ -Asp(OMe) containing a 14-membered ring. *Acta Crystallogr.* **1975**, *B31* (2), 555–560.
23. De Santis, P.; Morosetti, S.; Rizzo, R. Conformational analysis of regular enantiomeric sequences. *Macromolecules* **1974**, *7* (1), 52–58.
24. Tomasic, L.; Lorenzi, G.P. Some cyclic oligopeptides with S<sub>2n</sub> symmetry. *Helv. Chim. Acta* **1987**, *70* (4), 1012–1016.
25. Pavone, V.; Benedetti, E.; Di Blasio, B.; Lombardi, A.; Pedone, C.; Lorenzi, G.P. Structural versatility of peptides from C $\alpha$ , $\alpha$  dialkylated glycines: Linear Ac<sub>3</sub>c oligopeptides. *Biopolymers* **1989**, *28* (1), 215–223.
26. Khazanovich, N.; Granja, J.R.; Milligan, R.A.; McRee, D.E.; Ghadiri, M.R. Nanoscale tubular ensembles with specified internal diameters. Design of a self-assembled nanotube with a 13-Å pore. *J. Am. Chem. Soc.* **1994**, *116* (13), 6011–6012.
27. Hartgerink, J.; Granja, J.R.; Milligan, R.A.; Ghadiri, M.R. Self-assembling peptide nanotubes. *J. Am. Chem. Soc.* **1996**, *118* (1), 43–50.
28. Polaskova, M.E.; Ede, N.J.; Lambert, J.N. Synthesis of nanotube-forming cyclic octapeptides via an Fmoc strategy. *Aust. J. Chem.* **1998**, *51* (7), 535–540.
29. Karlström, A.; Uden, A. Association of cyclic peptides in aqueous solution measured by fluorescence quenching. *Biopolymers* **1997**, *41* (1), 1–4.
30. Ghadiri, M.R.; Kobayashi, K.; Granja, J.R.; Chadha, R.K.; McRee, D.E. The structural and thermodynamic basis for the formation of self-assembled peptide nanotubes. *Angew. Chem., Int. Ed. Engl.* **1995**, *34* (1), 93–95.
31. Clark, T.D.; Buriak, J.M.; Kobayashi, K.; Isler, M.P.; McRee, D.E.; Ghadiri, M.R. Cylindrical  $\beta$ -sheet peptide assemblies. *J. Am. Chem. Soc.* **1998**, *120* (35), 8462–8499.
32. Sun, X.C.; Lorenzi, G.P. On the stacking of  $\beta$ -rings: The solution self-association behavior of two partially *N*-methylated cyclo(hexaleucines). *Helv. Chim. Acta* **1994**, *77* (6), 1520–1526.
33. Bong, D.T.; Ghadiri, M.R. Self-assembling cyclic peptide cylinders as nuclei for crystal engineering. *Angew. Chem. Int. Ed.* **2001**, *40* (11), 2163–2166.
34. Kobayashi, K.; Granja, J.R.; Ghadiri, M.R.  $\beta$ -Sheet peptide architecture: Measuring the relative stability of parallel vs. antiparallel  $\beta$ -sheets. *Angew. Chem., Int. Ed. Engl.* **1995**, *34* (1), 95–98.
35. Clark, T.D.; Ghadiri, M.R. Supramolecular design by covalent capture. Design of a peptide cylinder via hydrogen-bond-promoted intermolecular olefin metathesis. *J. Am. Chem. Soc.* **1995**, *117* (49), 12364–12365.
36. Clark, T.D.; Kobayashi, K.; Ghadiri, M.R. Covalent capture and stabilization of cylindrical  $\beta$ -sheet peptide assemblies. *Chem. Eur. J.* **1999**, *5* (2), 782–792.
37. Ghadiri, M.R.; Granja, J.R.; Buehler, L.K. Artificial transmembrane ion channels from self-assembling peptide nanotubes. *Nature* **1994**, *369* (6478), 301–304.
38. Engels, M.; Bashford, D.; Ghadiri, M.R. Structure and dynamics of self-assembled peptide nanotubes and channel-mediated water organization and self-diffusion. A molecular dynamics study. *J. Am. Chem. Soc.* **1995**, *117* (36), 9151–9158.
39. Kim, H.S.; Hartgerink, J.D.; Ghadiri, M.R. Oriented self-assembly of cyclic peptide nanotubes in lipid membranes. *J. Am. Chem. Soc.* **1998**, *120* (18), 4417–4424.
40. Sanchez-Quesada, J.; Isler, M.P.; Ghadiri, M.R. Modulating ion channel properties of transmembrane peptide nanotubes through heteromeric supramolecular assemblies. *J. Am. Chem. Soc.* **2002**, *124* (34), 10004–10005.
41. Fukasaku, K.; Takeda, K.; Shiraishi, K. Electronic structures of protein nanotubes. *J. Phys. Soc. Jpn.* **1997**, *66* (11), 3387–3390.
42. Appella, D.H.; Christianson, L.A.; Klein, D.A.; Powell, D.R.; Huang, X.; Barchi, J.J.; Gellman, S.H. Residue-based control of helix shape in  $\beta$ -peptide oligomers. *Nature* **1997**, *387* (6631), 381–384.
43. Seebach, D.; Matthews, J.L.; Meden, A.; Wessels, T.; Baerlocher, C.; McCusker, L.B. Cyclo- $\beta$ -peptides. Structure and tubular stacking of cyclic tetramers of 3-aminobutanoic acid as determined from powder diffraction data. *Helv. Chim. Acta* **1997**, *80* (1), 173–182.
44. Clark, T.D.; Buehler, L.K.; Ghadiri, M.R. Self-assembling cyclic  $\beta^3$ -peptide nanotubes as artificial transmembrane ion channels. *J. Am. Chem. Soc.* **1998**, *120* (4), 651–656.
45. Porter, E.A.; Wang, X.; Lee, H.S.; Weisblum, B.; Gellman, S.H. Antibiotics: Non-hemolytic  $\beta$ -amino acid oligomers. *Nature* **2000**, *404* (6778), 565
46. Amorín, M.; Castedo, L.; Granja, J.R. New cyclic peptide assemblies with hydrophobic cavities: The structural and thermodynamic basis of a new class of peptide nanotubes. *J. Am. Chem. Soc.* **2003**, *125* (10), 2844–2845.
47. Gauthier, D.; Baillargeon, P.; Drouin, M.; Dory, Y.L. Self-assembly of cyclic peptides into nanotubes and then into highly anisotropic crystalline materials. *Angew. Chem. Int. Ed.* **2001**, *40* (24), 4635–4638.
48. Semetey, V.; Didierjean, C.; Briand, J.P.; Aubry, A.; Guichard, G. Self-assembling organic nanotubes from enantiopure cyclo-*N,N*-linked oligoureas: Design, synthesis, and crystal structure. *Angew. Chem. Int. Ed.* **2002**, *41* (11), 1895–1898.
49. Ranganathan, D.; Lakshmi, C.; Karle, I.L. Hydrogen-bonded self-assembled peptide nanotubes from cystine-based macrocyclic bisureas. *J. Am. Chem. Soc.* **1999**, *121* (26), 6103–6107.
50. Ranganathan, D.; Haridas, V.; Gilardi, R.; Karle, I.L. Self-assembling aromatic-bridged serine-based cyclo-depsipeptides (serinophanes): A demonstration of tubular structures formed through aromatic  $\pi$ - $\pi$  interactions. *J. Am. Chem. Soc.* **1998**, *120* (42), 10793–10800.
51. Eisenberg, B. Ionic channels in biological membranes: Natural nanotubes. *Acc. Chem. Res.* **1998**, *31* (3), 117–123.
52. Bayley, H. Designed membrane channels and pores. *Curr. Opin. Biotechnol.* **1999**, *10* (1), 94–103.
53. Granja, J.R.; Ghadiri, M.R. Channel-mediated transport of glucose across lipid bilayers. *J. Am. Chem. Soc.* **1994**, *116* (23), 10785–10786.

54. Sanchez-Quesada, J.; Kim, H.S.; Ghadiri, M.R. A synthetic pore-mediated transmembrane transport of glutamic acid. *Angew. Chem. Int. Ed.* **2001**, *40* (13), 2503–2506.
55. Neu, H.C. The crisis in antibiotic resistance. *Science* **1992**, *257* (5073), 1064–1073.
56. Coates, A.; Hu, Y.; Bax, R.; Paged, C. The future challenges facing the development of new antimicrobial drugs. *Nat. Drug Discover* **2002**, *1*, 895–910.
57. Huang, H.W. Action of antimicrobial peptides: Two-state model. *Biochemistry* **2000**, *39* (29), 8347–8352.
58. Fernández-López, S.; Kim, H.S.; Choi, E.C.; Delgado, M.; Granja, J.R.; Khasanov, A.; Kraehenbuehl, K.; Long, G.; Weinberger, D.A.; Wilcoxon, K.M.; Ghadiri, M.R. Antibacterial agents based on the cyclic D,L-peptide architecture. *Nature* **2001**, *412* (6845), 452–455.
59. Ganz, T. Rings of destruction. *Nature* **2001**, *412* (6845), 392–393.
60. Motesharei, K.; Ghadiri, M.R. Diffusion-limited size-selective ion sensing based on SAM-supported peptide nanotubes. *J. Am. Chem. Soc.* **1997**, *119* (46), 11306–11312.
61. Motesharei, K.; Ghadiri, M.R. Diffusion-limited size-selective ion sensing based on SAM-supported peptide nanotubes [Erratum to document cited in CA128:32011]. *J. Am. Chem. Soc.* **1998**, *120* (6), 1347
62. Hartgerink, J.D.; Clark, T.D.; Ghadiri, M.R. Peptide nanotubes and beyond. *Chem. Eur. J.* **1998**, *4* (8), 1367–1372.
63. Sekkat, Z.; Knoll, W. Photoreactive organic thin films in the light of bound electromagnetic waves. *Adv. Photochem.* **1997**, *22*, 117–195.
64. Willner, I. Photoswitchable biomaterials: En route to optobioelectronic systems. *Acc. Chem. Res.* **1997**, *30* (9), 347–356.
65. Delaire, J.A.; Nakatani, K. Linear and nonlinear properties of photochromic molecules and materials. *Chem. Rev.* **2000**, *100* (5), 1817–1845.
66. Vollmer, M.S.; Clark, T.D.; Steinem, C.; Ghadiri, M.R. Photoswitchable hydrogen-bonding in self-organized cylindrical peptide systems. *Angew. Chem. Int. Ed.* **1999**, *38* (11), 1598–1601.
67. Steinem, C.; Janshoff, A.; Vollmer, M.S.; Ghadiri, M.R. Reversible photoisomerization of self-organized cylindrical peptide assemblies at air–water and solid interfaces. *Langmuir* **1999**, *15* (11), 3956–3964.
68. Okamoto, H.; Kasahara, M.; Takeda, K.; Shiraishi, K. In *Theoretical Possibility of Semiconductive Properties in Peptide Nanotubes*, Proceedings of the 25th International Conference on the Physics of Semiconductors, Osaka, Japan, Sept., 17–22, 2000; Miura, N., Ando, T., Eds.; Springer: Berlin, 2001; ia457FC1 (I041).
69. Okamoto, H.; Kasahara, M.; Takeda, K.; Shiraishi, K. Theoretical possibility of semiconductive properties in peptide nanotubes. *Springer Proc. Phys.* **2001**, *87*, 1637–1638.
70. Rouhi, A.M. Bacteria: Beware! *C&EN* **2001**, *79* (32), 41–43.

# Dendritic Nanocatalysts

**Kiyotomi Kaneda**

**Masahiko Ooe**

*Department of Chemical Science and Engineering, Osaka University, Osaka, Japan*

**Makoto Murata**

*Osaka University, Osaka, Japan*

**Tomoo Mizugaki**

**Kohki Ebitani**

*Department of Chemical Science and Engineering, Osaka University, Osaka, Japan*

## INTRODUCTION

Dendrimers are three-dimensional, highly branched, monodispersed macromolecules,<sup>[1,2]</sup> which are obtained by an iterative sequence of reaction steps, giving precisely defined branching structures. The possibility of designing these well-defined macromolecules (e.g., by choosing specific functional end groups, or certain multifunctional monomers) is a very powerful tool that enables the exploration and development of a wide variety of applications. One of the most promising applications of dendrimers is in catalysis.<sup>[3,4]</sup> In general, organometallic dendrimers offer potentials in combining the advantages of both homogeneous and heterogeneous catalyses<sup>[5–8]</sup> because of their structurally well-defined and specific number of active sites, as well as their advantage of facile recovery by nanofiltration<sup>[9,10]</sup> or solvent precipitation.<sup>[11]</sup>

Active sites can be introduced specifically at: a) the surface, b) the core, c) branches, and d) inner cavities of dendrimers in a controlled manner (Fig. 1), although it is difficult to control the number and location of active metal species in traditionally supported metal catalysts using linear or cross-linked polymers. The active sites at the periphery of dendrimers are readily available for catalytic reactions because of their globular shapes. However, when catalytic species are incorporated at the core of dendrimers, these dendrimers are applied as shape-selective, size-selective, or enantioselective catalysts. Catalytic groups can be anchored to the branches of the interior, giving rise to catalysts with both high loading of catalytic sites and control of the nanoenvironment around the active species. Moreover, dendrimers serve as host-type “nanoreactors” for metal guest molecules. Encapsulation of catalytic sites into the cavities of dendrimers leads to both active site isolation and substrate size selectivity.

We describe here the unique catalytic properties of both periphery-functionalized dendrimer-bound Pd(II)<sup>[12]</sup>

and Pd(0)<sup>[13]</sup> complexes, and dendrimer-encapsulated Pd(0) nanoparticles<sup>[14]</sup> based on poly(propylene imine) dendrimers. The dendrimer-bound Pd(II) complex has higher catalytic activity for selective hydrogenation of conjugated dienes to monoenes, than those of the corresponding low-molecular-weight Pd complex. Moreover, the dendrimer-bound Pd(II) complex is easily recovered and reused without any loss of activity. The dendrimer-bound Pd(0) complex showed high stereoselectivity in the allylic substitution reaction. Facile recovery of dendritic Pd complexes can be achieved by the use of a thermomorphic system.<sup>[8]</sup> The size-selective and substrate-specific hydrogenation of olefins is achieved by dendrimer-encapsulated Pd(0) nanoparticles. Unique catalysis is attributed to hydrogen bonding between the internal amino groups of the dendrimers and substrates.

## APPLICATION

### Dendrimer-Bound Pd(II) and Pd(0) Complexes

Surface functional groups on dendrimers can be easily modified with various ligands capable of binding metal complexes to give a number of metal-containing dendrimers.<sup>[15]</sup> Transition metal complexes at the surface of dendrimers will be readily available for catalytic reactions. The high local concentration of catalysts greatly affects catalytic performance in either a positive or a negative sense.

### Preparation and Characterization of the Dendrimer-Bound Pd(II) and Pd(0) Complexes

Double phosphinomethylation of primary amino groups on the first, third, fourth, and fifth generations

	A	B	C	D
metal loading	high	low	high	low / high
control of solubility	difficult	easy	easy	easy
control of environment around active sites	difficult	easy	easy	easy

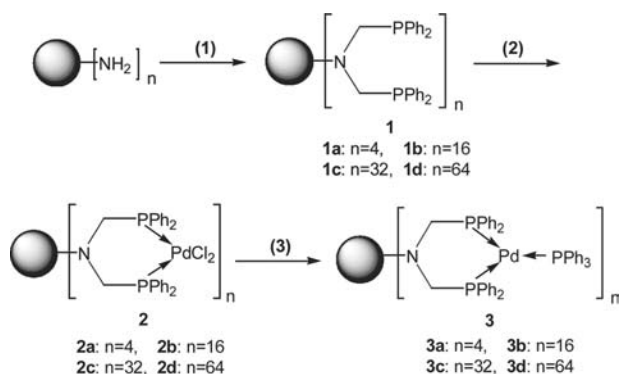
**Fig. 1** Comparison of different types of metal-functionalized dendrimer catalysts: (A) periphery, (B) core, (C) interior branches, and (D) inner cavities of dendrimers.

of poly(propylene imine) dendrimers was carried out, giving 4, 16, 32, and 64 chelate phosphines on the periphery (**1a–d**), respectively, as shown in Scheme 1.<sup>[11]</sup> Treatment of the dendrimers **1a–d** with  $\text{PdCl}_2(\text{PhCN})_2$  afforded dendrimer-bound  $\text{PdCl}_2$  complexes **2a–d**. Subsequently, the reduction of **2** with hydrazine monohydrate in the presence of two equivalents of  $\text{PPh}_3$ <sup>[16]</sup> led to the formation of dendritic  $\text{Pd}(0)$  complexes **3a–d**, respectively, with retention of parent dendritic structures.  $\text{PhN}(\text{CH}_2\text{PPh}_2)_2\text{PdCl}_2$  (**4**) as a low-molecular-weight analogue of **2** was synthesized by literature procedure.<sup>[17,18]</sup> These dendritic Pd complexes were characterized by  $^1\text{H}$ ,  $^{13}\text{C}\{^1\text{H}\}$ ,  $^{31}\text{P}\{^1\text{H}\}$  nuclear magnetic resonance (NMR), Fourier transform infrared spectroscopy (FTIR), and X-ray photoelectron spectroscopy (XPS). The  $^{31}\text{P}\{^1\text{H}\}$  NMR spectrum of **2** did not show any signal for the residual free phosphine at  $\delta -27$  but only one singlet at  $\delta 8$ . The infrared spectrum of **2** had broad bands at  $294\text{ cm}^{-1}$  assigned as terminal *cis* Pd–Cl stretching bands, which were

similar to those observed in **4**.<sup>[19]</sup> Elemental analysis of **2** gave a Pd:P:Cl ratio of 1:2:2, which strongly supports the complete complexation of the chelate phosphine to Pd in a *cis* form. After the reduction of **2**, the above  $^{31}\text{P}$  NMR resonance at  $\delta 8$  was fully replaced by a new one around  $\delta 27$ . XPS analyses of **2** showed two bands at 343 and 338 eV because of Pd  $3d_{3/2}$  and  $3d_{5/2}$ , respectively, and the binding energy of Cl 2p was 198 eV. In the case of **3**, the binding energies of 341 and 336 eV for  $3d_{3/2}$  and  $3d_{5/2}$ , respectively, were observed. The above values of binding energies were comparable with those of **4**, typical Pd complexes of  $\text{PdCl}_2(\text{PPh}_3)_2$  and  $\text{Pd}(\text{PPh}_3)_4$ . From these results, the structure of dendritic Pd complexes **2** and **3** can be determined as shown in Scheme 1, respectively.

### Selective Hydrogenation of Conjugated Dienes to Monoenes with Dendrimer-Bound Pd(II) Complex Catalyst

The catalytic activity of **2** was examined in the hydrogenation of cyclopentadiene under an atmospheric pressure of  $\text{H}_2$  in EtOH, compared with those of **4**, Pd/C, and Pd/ $\text{Al}_2\text{O}_3$ . The time courses of hydrogen uptakes are shown in Fig. 2. In the case of **2**, hydrogen uptake drastically dropped after cyclopentadiene was consumed completely. At that time, high selectivity for the formation of cyclopentene was observed; cyclopentane was the only product without cyclopentane. Using Pd/C and Pd/ $\text{Al}_2\text{O}_3$  catalysts, rates of hydrogenation remained constant after perfect consumption of the diene without such a turning point of hydrogen uptake. The rate of hydrogenation of **4** was extremely low among the Pd catalysts used. It has been reported that such a selective hydrogenation of dienes to monoenes using homogeneous Pd catalysts required high pressures of  $\text{H}_2$  and  $\text{SnCl}_2$  as activating agents.<sup>[20,21]</sup>



**Scheme 1** Preparation of dendritic Pd(II) complexes **2** and Pd(0) complexes **3**. Reagents and conditions: (1) HCHO, HPPH<sub>2</sub>, toluene, 60°C; (2) PdCl<sub>2</sub>(PhCN)<sub>2</sub>, toluene, room temperature; and (3) H<sub>2</sub>NNH<sub>2</sub>·H<sub>2</sub>O, PPh<sub>3</sub>, EtOH, room temperature.

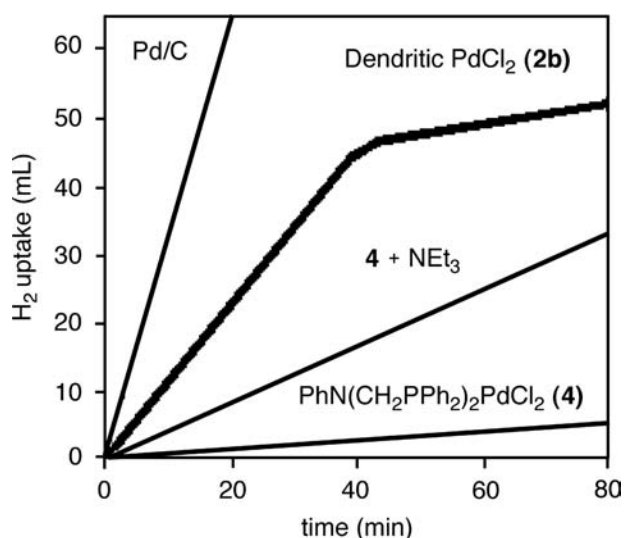
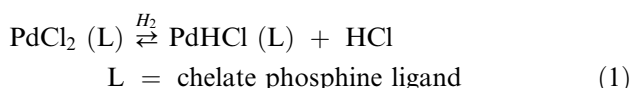


Fig. 2 Time courses of  $H_2$  uptakes using various Pd catalysts in the hydrogenation of cyclopentadiene.

Presumably, an active species for this hydrogenation may be a Pd(II) hydride species derived from the following scheme (Eq. (1))



based on hydrogenation using the polystyrene-bound Pd(II) catalyst.<sup>[22]</sup> According to the above equilibrium equation, the generation of Pd–H can be accelerated by the presence of bases. In a separate experiment, addition of triethylamine to the corresponding low-molecular-weight catalyst **4** increased rates of hydrogenation, as shown in Fig. 2. The high catalytic performance of **2** would be because of the dendrimer structure containing many amino moieties, compared with **4**. It has been also reported that dendritic metal complex catalysts had lower activities than analogous monomeric complexes in many organic reactions.<sup>[23–25]</sup>

Interestingly, the solubility of **2** in various solvents did not strongly influence catalytic activities. Hydrogenation was very efficient in EtOH in which **2** was insoluble, whereas it was slow in *N,N*-dimethylformamide (DMF) in which it was soluble. Because all active sites of **2** are located on the dendrimer surface, substrates easily gain access to active sites on the surface without steric hindrance and diffusion limitation, which might lead to efficient hydrogenation even in the heterogeneous system using an EtOH solvent. Generally, heterogenization of metal complexes using organic polymers has disadvantages such as lowered reactivity induced by diffusion limitation of substrates, catalyst leaching, steric hindrance, and inability to totally mimic reactivity and selectivity attainable with the corresponding homogeneous ones.<sup>[8]</sup>

Initial rates of  $H_2$  uptake in the hydrogenation of various cyclic conjugated dienes are summarized in Fig. 3. Notably, the rates increase in the order of  $C_5 < C_6$ – $C_8$ . The fact that the molecular size of dienes did not affect the hydrogenation rate could be explained by the above unique character of the functionalized dendrimer ligand. These phenomena are a sharp contrast to the results of our previous hydrogenation using the polystyrene-bound Pd complex;<sup>[22]</sup> to swell polystyrene support, a mixed solvent of benzene and ethanol must be used because many Pd active sites exist within the polystyrene matrix.

Recycling of **2** was carried out in the heterogeneous hydrogenation of 1,3-COD in EtOH. After hydrogenation, the dendritic catalyst was separated from the reaction mixture by centrifugation and washed with EtOH in air, then dried in vacuo.<sup>a</sup> The spent Pd catalyst was used in the hydrogenation for the second run while keeping the activity and selectivity for hydrogenation.

### Stereoselective Allylic Amination Reactions with Dendrimer-Bound Pd(0) Catalysts

The prominent catalysis of dendritic Pd(0) complexes **3** was investigated in the allylic amination<sup>[26,27]</sup> of *cis*-3-acetoxy-5-carbomethoxycyclohex-1-ene with morpholine. Notably, the stereoselectivity for a *cis* product increased with increasing generation (third to fifth) of dendrimers, as depicted in Fig. 4: A high *cis* selectivity of 94% was obtained with **3d**, whereas Pd(PPh<sub>3</sub>)<sub>4</sub> as a typical monomeric Pd(0) catalyst led to a slight excess of *cis* products. The first and third generations of the dendritic catalysts **3a** and **3b** showed moderate *cis* selectivity, respectively. To clarify the origin of stereoselectivity, <sup>13</sup>C spin–lattice relaxation times ( $T_1$ ) of the phosphinated dendrimers **1a–d** were measured (Fig. 4).<sup>b</sup> The  $T_1$  value of peripheral phenyl groups on **1a–d** decreased with increasing generation of dendrimers, and this phenomenon shows that the dendrimer surface becomes more congested for higher generations.<sup>[28,29]</sup> In the case of **3d**, attaining high stereoselectivity of substitution reactions can be explained by steric steering of nucleophilic attack to a surface ( $\pi$ -allyl) Pd intermediate (i.e., the active sites would be strongly shielded from the *endo* attack of the nucleophile). The moderate selectivity with **3a** and **3b** might be due to the loosely packed dendrimer surface, which would allow the partial dissociation of chelate phosphine ligands.<sup>[30]</sup> Trost and Keinan,<sup>[31]</sup> Trost and

<sup>a</sup>In the case of homogeneous hydrogenation in DMF solvents, **2** could be recovered as precipitates by adding an excess of ether to the reaction mixtures.

<sup>b</sup>Because of the low solubility of dendrimers **3**,  $T_1$  for dendrimers **1** in place of **3** was measured by the inversion–recovery method.



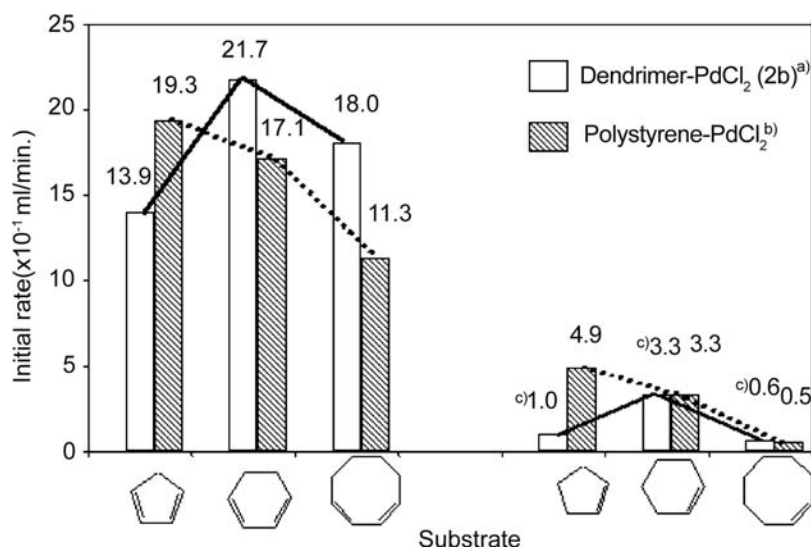


**Fig. 3** Substrate size dependence on initial rate in the hydrogenation of cyclic dienes and monoenes using the dendrimer PdCl<sub>2</sub> and the polystyrene PdCl<sub>2</sub>. (A) Reaction conditions: substrate, 1.3 mmol; EtOH, 5.0 mL; catalyst 2, 0.01 mmol Pd; H<sub>2</sub>, 1 atm; 25 ± 1°C. (B) Reaction conditions: substrate, 4.3 mmol; benzene–EtOH (1:1), [13 – (volume of substrate)] mL; catalyst, 0.04 mmol Pd; H<sub>2</sub>, 1 atm; 25 ± 1°C. Source: From Ref.<sup>[26]</sup>. (C) Reaction temperature, 40 ± 1°C.

Verhoeven,<sup>[32]</sup> and Bäckvall, Granberg, and Heumann<sup>[33]</sup> have also reported similar stereoselective performances in allylic amination because of the steric hindrance of solid supports with polystyrene-bound and silica-bound Pd(0) complex catalysts.

Recycling of dendritic metal complex catalysts was attempted by membrane filtration<sup>[9,10]</sup> or solvent precipitation,<sup>[11]</sup> which often results in some losses of catalytic activities during the recovery and reuse processes. Fortunately, our dendritic Pd(0) catalysts **3** could be easily recycled by using a biphasic system of DMF and heptane, and the system does not need any special procedures such as membrane filtration.

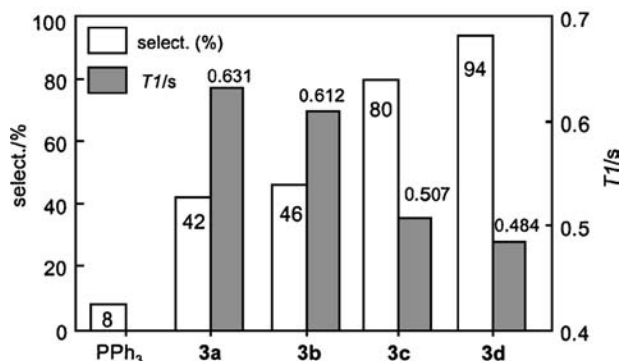


**Fig. 4** Generation dependence on stereoselectivity in the allylic amination of *cis*-3-acetoxy-5-carbomethoxycyclohex-1-ene with morpholine. Stereoselectivity for *cis* isomers was compared at 30% conversion of the substrate. Selectivity (%) = [(*cis* – *trans*)/(*cis* + *trans*)] × 100. T<sub>1</sub> values were calculated for the C<sub>4</sub> carbon (128 ppm) in the phenyl groups of corresponding dendrimers **1**, respectively.

**Fig. 5** shows a thermomorphic biphasic system containing **3**. An extremely low solubility of **3** in the heptane solvent meant that the catalysts were completely transferred to DMF and the catalyst solution could be recycled after decantation of the heptane phase containing products. For example, in the allylic substitution of *trans*-cinnamyl acetate with dibutylamine, the high catalytic activity was retained during three reuse experiments: Yields of the allylic amine in the heptane phase were 66%, 99%, 99%, and 99% for the first, second, third, and fourth runs, respectively. In the above reactions, no Pd leaching in the heptane phase was observed during recycle experiments. This is the first application of surface-functionalized dendritic catalysts in a thermomorphic system.

### Dendrimer-Encapsulated Pd Nanoparticles

The unique architecture of dendrimers provides special opportunities for host–guest chemistry<sup>[34]</sup> initially proposed as the concept of the dendritic box in which organic dyes are encapsulated through electrostatic interactions.<sup>[29]</sup> Ooe et al.<sup>[14]</sup> Crooks et al.<sup>[35]</sup> Balogh and Tomalia,<sup>[36]</sup> and Esumi et al.<sup>[37]</sup> reported on the preparation of transition metal nanoparticles such as Cu, Pt, Ag, Au, and Pd within the definite internal cavity of dendrimers to prevent the agglomeration of metal nanoparticles. In catalysis, dendrimers act as nanoreactors containing metal nanoparticles.<sup>[14,35,38]</sup>

### Preparation and Characterization of Dendrimer-Encapsulated Pd(0) Nanoparticles

Third-generation to fifth-generation PPI dendrimers were selected to construct nanocapsules because of

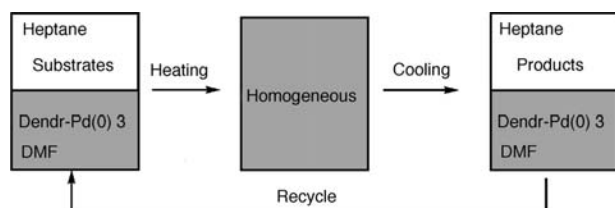


**Fig. 5** Schematic illustration of thermomorphic allylic amination using dendrimer-bound Pd(0) complex **3**.

their compact molecular sizes and the high density of amino groups within their dendritic structures. Treatment of the above PPI dendrimers with 3,4,5-triethoxybenzyl chloride gave surface-functionalized dendrimer **5** (**5a** = G3, **5b** = G4, and **5c** = G5), as illustrated in Fig. 6.<sup>[14]</sup> Pd nanoparticles were prepared within **5** by the following sequence: A predetermined quantity of aqueous Pd<sup>2+</sup> was extracted into the interior of **5** to give preorganized Pd<sup>2+</sup> dendrimers **6**, which were reduced with KBH<sub>4</sub> to yield Pd nanoparticles encapsulated within the dendrimers **7**.

The <sup>1</sup>H NMR spectrum of **6b** in chloroform showed that the signals of  $\alpha$ -methylene protons of amino groups were broadened. In <sup>14</sup>N NMR spectra, the broad signal of amino groups for **5b** shifted from  $-348.5$  to  $-347.2$  ppm after treatment with Pd<sup>2+</sup>, whereas amide signal at  $-278.8$  ppm remained unchanged.<sup>[39,40]</sup> These results suggest that Pd ions are coordinated to amino groups within dendrimers. The incorporation of Pd ions into dendrimers was also confirmed by the color change of liquid phases: When an aqueous solution containing 10  $\mu\text{mol}$  Pd<sup>2+</sup> ions was added to 0.72  $\mu\text{mol}$  **5b** in chloroform, the light brown color of aqueous Pd<sup>2+</sup> solution completely disappeared and then shifted to the chloroform solution. Using a 30:1 molar ratio of Pd<sup>2+</sup> to **5b**, a pale yellow color remained in the aqueous phase. Inductively coupled plasma (ICP) measurements of the aqueous phase revealed that the number of extracted Pd ions per dendrimer was 24.<sup>c</sup> The number of extracted Pd<sup>2+</sup> corresponds to the total number of N<sup>3</sup> and N<sup>4</sup> nitrogen atoms, where tertiary amino groups in  $n$ th shell were labeled as N <sup>$n$</sup>  ( $n = 1-5$ ) from the core to the  $n$ th shell, as shown in Fig. 6. The above phenomena were also observed in the case of **5a** and **5c**, respectively.

Treatment of **6** with KBH<sub>4</sub> in chloroform gave homogeneous dark brown solutions. XPS spectra of **6** showed two bands at 343.0 and 337.9 eV because of Pd 3d<sub>5/2</sub> and 3d<sub>3/2</sub>, respectively. After reduction with

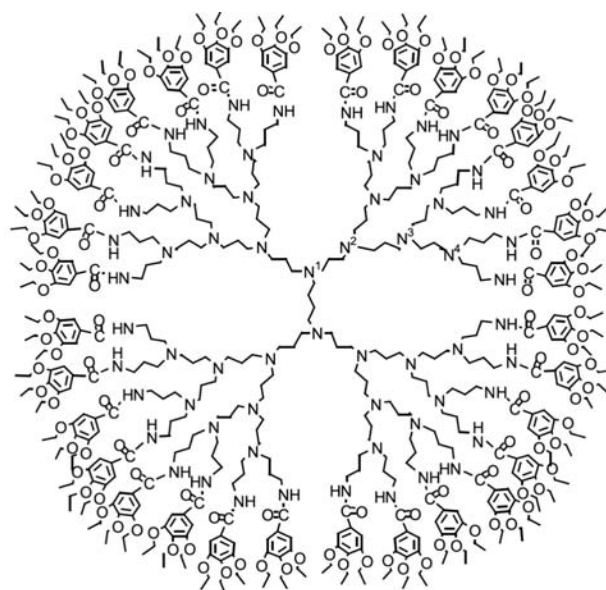


**Fig. 6** Structure of triethoxybenzamide dendrimer (**5b**).

KBH<sub>4</sub>, the above two bands shifted to 340.6 (Pd 3d<sub>5/2</sub>) and 335.3 eV (Pd 3d<sub>3/2</sub>), which provides evidence for the complete reduction of Pd<sup>2+</sup> to Pd<sup>0</sup> species. A transmission electron microscopy (TEM) image of **7c** in Fig. 7 reveals the formation of roughly spherical and nearly monodispersed Pd nanoparticles. For **7a**, **7b**, and **7c**, the Pd particle diameters were  $2.6 \pm 0.6$ ,  $2.4 \pm 0.6$ , and  $2.3 \pm 0.4$  nm, respectively, which are smaller than the diameters of **5a** (3.9 nm), **5b** (4.3 nm), and **5c** (4.9 nm), respectively. All the above Pd(0) nanoparticles were so stable that no aggregates of Pd particles were observed for several months in the solution.

By comparing the size of dendrimers with that of Pd(0) nanoparticles, we found that the dendrimers,

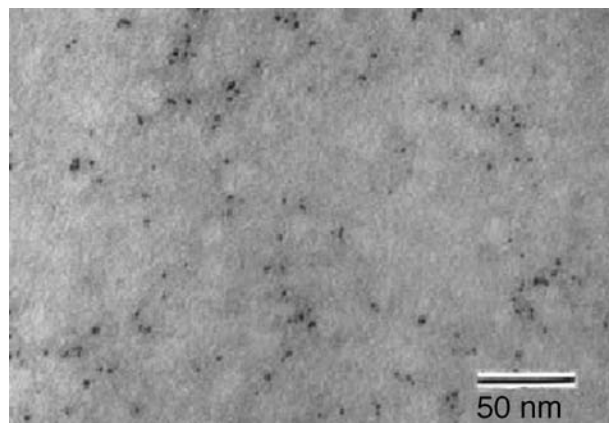


**Fig. 7** High-resolution transmission electron microscopy image of **7c** nanocomposites. The average particle size and distribution of Pd particles were determined by counting 100 particles.

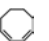


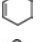
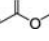
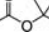
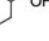
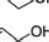
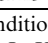
<sup>c</sup>The amount of Pd ions extracted with **4b** in chloroform was calculated from the difference of Pd concentrations in the aqueous phase between that before and that after the extraction.

especially **5c**, encapsulate the Pd(0) nanoparticles. Yeung and Crooks<sup>[41]</sup> have also prepared Pd(0) nanoparticles 2–3 nm in diameter by the chemical reduction of Pd<sup>2+</sup> species within the perfluorinated polyether-derivatized PPI dendrimer.

### Substrate-Specific Hydrogenation of Dendrimer-Encapsulated Pd(0) Nanoparticles

The catalytic performance of the dendrimer-encapsulated Pd(0) nanoparticles **7** was tested in the hydrogenation of various olefins, as shown in Table 1. Hydrogenation rates decreased with increasing generation of dendrimers from G<sub>3</sub> to G<sub>5</sub>. A conjugated diene of 1,3-cyclooctadiene was selectively hydrogenated to cyclooctene in >99% yield, and its initial hydrogenation rates using **7a**, **7b**, and **7c** were 5.4, 4.1, and 2.9, respectively (entry 1). In the case of Pd/C catalyst, cyclooctene was formed together with a 19% yield of cyclooctane as an overhydrogenation product at a complete consumption of 1,3-cyclooctadiene. High selectivity for the monoene has been also reported in the catalytic hydrogenation using poly-(amido amine) (PAMAM) dendrimer-encapsulated Pd nanoparticles<sup>[35]</sup> and poly(*N*-vinyl-2-pyrrolidone)-stabilized Pd colloids.<sup>[42]</sup> The ring size effect of substrates on hydrogenation rates was remarkable in the case of **7c**. Initial rates for the hydrogenation of cyclic conjugated dienes decreased in the order of cyclopentadiene > 1,3-cyclohexadiene > 1,3-cyclooctadiene (entries 1–3). The substrate size effect was also observed for the hydrogenation of acrylates and allylic alcohols (entries 6, 7, 9, and 10). However, using Pd/C catalysts, the hydrogenation

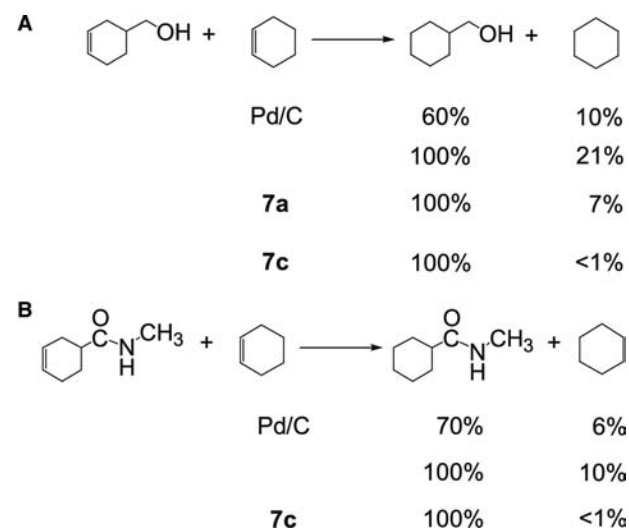
**Table 1** Hydrogenation of olefins using dendrimer-encapsulated Pd nanoparticles<sup>a</sup>

Entry	Substrates	Initial rate [ $\times 10^{-1}$ mL/min]			
		<b>7a</b>	<b>7b</b>	<b>7c</b>	Pd/C
1		5.4	4.1	2.9	12.0
2		9.8	8.7	7.2	11.8
3		9.2	9.0	8.3	10.3
4		0.92	0.80	0.70	2.8
5		9.5	9.0	7.6	10.0
6		5.5	4.5	3.1	9.1
7		1.5	1.2	0.86	2.4
8		12.1	11.5	11.2	11.6
9		5.8	4.2	3.8	9.3

<sup>a</sup>Reaction conditions: catalyst, 5.0  $\mu$ mol Pd; substrate, 1.0 mmol; toluene, 12.5 mL; H<sub>2</sub>, 1 atm; 30°C.

rates were not strongly affected by substrate size. A similar ring size effect using **7** was also obtained in our previous hydrogenation catalyzed by the polystyrene-bound Pd complex, where the active sites are buried within the polystyrene matrix.<sup>[22]</sup> On the contrary, when the phosphinated dendrimer-bound Pd(II) complex catalyst having active species located on the periphery of the dendrimers was used, hydrogenation rates were not strongly dependent on substrate size.<sup>[12]</sup> Thus it can be concluded that the surface congestion of dendrimers, especially for **5c**, suppresses the penetration of large substrates into encapsulated Pd nanoparticles.

Notably, in the hydrogenation of an equimolar mixture of 3-cyclohexene-1-methanol and cyclohexene using **7c**, cyclohexanemethanol was obtained exclusively without the formation of cyclohexanes. However, the selectivity for cyclohexanemethanol decreased in the case of **7a**; cyclohexane was obtained in 7% yield at a complete consumption of 3-cyclohexene-1-methanol. The use of Pd/C resulted in the formation of 60% yield of cyclohexanemethanol together with cyclohexane in 10% yield. A similar substrate specificity for polar substrates was also obtained in a competitive hydrogenation between *N*-methyl-3-cyclohexene-1-carboxamide and cyclohexene; an olefinic bond of the carboxamide was exclusively reduced to give *N*-methyl-cyclohexanecarboxamide without contamination of cyclohexane. These results are summarized in Scheme 2. To the best of our knowledge,



**Scheme 2** Competitive hydrogenation of (A) 3-cyclohexene-1-methanol and cyclohexene (B) *N*-methyl-3-cyclohexene-1-carboxamide and cyclohexene using various Pd catalysts. (A) Reaction conditions: 3-cyclohexene-1-methanol, 0.5 mmol; cyclohexene, 0.5 mmol; catalyst, 5.0  $\mu$ mol Pd; toluene, 12.5 mL; H<sub>2</sub>, 1 atm; 30°C. (B) Reaction conditions: *N*-methyl-3-cyclohexene-1-carboxamide, 0.5 mmol; cyclohexene, 0.5 mmol.

this is the first example of substrate-specific catalysis on dendrimer-metal nanocomposites reported to date.

The interaction between dendrimers and substrates was examined by NMR and FTIR. The  $^1\text{H}$  NMR spectra show that the  $\alpha$ -methylene proton signal of the tertiary amino groups for **5c** at 2.17 ppm shifted downfield to 2.20 ppm in the presence of 3-cyclohexene-1-methanol, whereas there was no change in the proton signals of **5c** in cyclohexene. In FTIR spectra of 3-cyclohexene-1-methanol, the free hydroxyl band at  $3621\text{ cm}^{-1}$  disappeared when **5c** coexisted. These data clearly show that hydrogen bonding between the hydroxyl group of the substrate and the amino group exists within the dendrimers. Hydrogen bonding plays an important role in the preferential penetration of polar substrates into the dendrimers, which could lead to the above remarkable substrate specificity. We think that complete encapsulation of Pd nanoparticles within the  $G_5$  dendrimer can promote substrate specificity for 3-cyclohexene-1-methanol and *N*-methyl-3-cyclohexene-1-carboxamide. The lower selectivity observed for the polar substrates in the case of **7a** could be attributed to partly exposed Pd nanoparticles that bulged out from the polar nanoenvironment inside the dendrimers.<sup>d</sup>

## CONCLUSION

This study demonstrated the preparation and catalyses of both periphery-functionalized dendritic catalysts and dendrimer-encapsulated metal catalysts. The location of catalytic sites and their spatial separation are very important for unique catalyses. Various dendritic effects in catalysis have been observed, including increased/decreased activity, selectivity, and stability. The high local concentration of catalytic active sites on the periphery can lead to accessibility of substrates to active metallic sites without the influence of substrate size. Moreover, these dendritic catalysts enable the easy recovery of catalysts from reaction mixtures by centrifugation and reuse without loss of activity. On the contrary, the encapsulation of catalytic species gave not only the stability of the active species but also the size selectivity by nanofiltration. Moreover, the nanoenvironment inside the dendrimers provided substrate-specific selectivity based on H-bonding. We believe that the dendrimers can contribute to the development of tailor-made catalysts with high substrate selectivity as obtained by enzymes based on molecular recognition.

<sup>d</sup>Large aggregates of Au and Pt were observed when low-generation PPI dendrimers were used (see Ref.<sup>[43]</sup>).

## REFERENCES

- Newkome, G.R.; Moorefield, C.N.; Vögtle, F. *Dendrimers and Dendrons: Concepts, Syntheses, Applications*; Wiley-VCH: Weinheim, 2001.
- Fréchet, J.M.J., Tomalia, D.A., Eds. *Dendrimers and Other Dendritic Polymers*; John Wiley and Sons: New York, 2001.
- Astruc, D.; Chardac, F. Dendritic catalysts and dendrimers in catalysis. *Chem. Rev.* **2001**, *101* (9), 2991–3023.
- van Heerbeek, R.; Kamer, P.C.J.; van Leeuwen, P.W.N.M.; Reek, J.N.H. Dendrimers as support for recoverable catalysts and reagents. *Chem. Rev.* **2002**, *102* (10), 3717–3756.
- Panster, P.; Wieland, S. *Recent Developments in Homogeneous Catalysis. Applied Homogeneous Catalysis with Organometallic Compounds*; Cornils, B., Herrmann, W.A., Eds.; VCH: Weinheim, 1996; Vol. 2, 605–623.
- Iwasawa, Y. *Tailored Metal Catalysts*; Reidel: Dordrecht, 1986.
- Leadbeater, N.E.; Marco, M. Preparation of polymer-supported ligands and metal complexes for use in catalysis. *Chem. Rev.* **2002**, *102* (10), 3217–3274.
- Bergbreiter, D.E. Using soluble polymers to recover catalysts and ligands. *Chem. Rev.* **2002**, *102* (10), 3345–3384.
- de Groot, D.; Eggeling, E.B.; de Wilde, J.C.; Kooijman, H.; van Haaren, R.J.; van der Made, A.W.; Spek, A.L.; Vogt, D.; Reek, J.N.H.; Kamer, P.C.J.; van Leeuwen, P.W.N.M. Palladium complexes of phosphine functionalized carbosilane dendrimers as catalysts in a continuous flow membrane reactor. *Chem. Commun.* **1999**, (17), 1623–1624.
- Eggeling, E.B.; Hovestad, N.J.; Jastrzebsky, J.T.B.H.; Vogt, D.; van Koten, G. Phosphino carboxylic acid ester functionalized carbosilane dendrimers: Nanoscale ligands for the Pd-catalyzed hydrovinylation reaction in a membrane reactor. *J. Org. Chem.* **2000**, *65* (26), 8857–8865.
- Reetz, M.T.; Lohmer, G.; Schwickardi, R. Synthesis and catalytic activity of dendritic diphosphane metal complexes. *Angew. Chem., Int. Ed. Engl.* **1997**, *36* (13/14), 1526–1529.
- Mizugaki, T.; Ooe, M.; Ebitani, K.; Kaneda, K. Catalysis of dendrimer-bound Pd (II) complex—Selective hydrogenation of conjugated dienes to monoenes. *J. Mol. Catal., A Chem.* **1999**, *145* (1–2), 329–333.
- Mizugaki, T.; Murata, M.; Ooe, M.; Ebitani, K.; Kaneda, K. Novel catalysis of dendrimer-bound Pd(0) complexes: Sterically steered allylic amination and the first application for a thermomorphic system. *Chem. Commun.* **2002**, (7), 52–53.
- Ooe, M.; Murata, M.; Mizugaki, T.; Ebitani, K.; Kaneda, K. Dendritic nanoreactors encapsulating Pd particles for substrate-specific hydrogenation of olefins. *Nano Lett.* **2001**, *1* (9), 14–17.
- Twyman, L.J.; King, A.S.H. Catalysis using peripherally functionalized dendrimers. *J. Chem. Res., Synop.* **2002**, (2), 43–59; 201–242.
- Terasawa, M.; Kaneda, K.; Imanaka, T.; Teranishi, S. A coordinatively unsaturated, polymer-bound palladium(0)

- complex. Synthesis and catalytic activities. *J. Organomet. Chem.* **1978**, *162* (3), 403–414.
- Balch, A.L.; Olmstead, M.M.; Rowley, S.T. Preparation and structural characterization of rhodium and palladium complexes of mixed phosphine/amine ligands with methylene spacers between donor atoms. *Inorg. Chim. Acta* **1990**, *168* (2), 255–264.
  - Fawcett, J.; Hoye, P.A.T.; Kemmitt, R.D.W.; Law, D.J.; Russell, D.R. Synthesis of bis(phosphinomethyl)amines via bis(hydroxymethyl)phosphonium salts. Isolation of 9,9-bis-(hydroxymethyl)-9-phosphoniabicyclo[3.3.1]nonane hydrogen sulfate and chloride salts, and the crystal structures of  $[\text{PPh}_2(\text{CH}_2\text{OH})_2]^+ \text{Cl}^-$  and  $[(\text{C}_6\text{H}_{11})_2\text{PCH}_2]_2\text{-NCHMePh}$ . *J. Chem. Soc. Dalton Trans.* **1993**, (17), 2563–2568.
  - Maitlis, P.M.; Espinet, P.; Russel, M.J.H. *Palladium: Introduction and General Principles. Comprehensive Organometallic Chemistry*; Wilkinson, G., Ed.; Pergamon: Oxford, 1982; Vol. 6, 238.
  - Fujii, Y.; Bailar, J.C., Jr. The selective hydrogenation of 1,5-cyclooctadiene with bis(triphenylphosphine) dichloropalladium and the formation of a  $\pi$ -allylic reaction intermediate. *J. Catal.* **1978**, *55* (2), 146–157.
  - Itatani, H.; Bailar, J.C., Jr. Homogeneous catalysis in the reactions of olefinic substances: V. Hydrogenation of soybean oil methyl ester with triphenylphosphine and triphenylarsine palladium catalysts. *J. Am. Oil Chem. Soc.* **1967**, *44* (2), 147–151.
  - Terasawa, M.; Kaneda, K.; Imanaka, T.; Teranishi, S. Study of hydrogenation of olefins catalyzed by polymer-bound palladium (II) complexes. *J. Catal.* **1978**, *51* (3), 406–421.
  - Mak, C.C.; Chow, H.-F. Dendritic catalysts: Reactivity and mechanism of the dendritic bis(oxazoline)metal complex catalyzed Diels–Alder reaction. *Macromolecules* **1997**, *30* (4), 1228–1230.
  - Rheiner, P.B.; Sellner, H.; Seebach, D. Dendritic styryl TADDOLs as novel polymer crosslinkers. First application in an enantioselective  $\text{Et}_2\text{Zn}$  addition mediated by a polymer-incorporated titanate. *Helv. Chim. Acta* **1997**, *80* (7), 2027–2032.
  - Knapen, J.W.J.; Made, A.W.; Wilde, J.C.; Leeuwen, P.W.N.M.; Wijkens, P.; Grove, D.M.; van Koten, G. Homogeneous catalysts based on silane dendrimers functionalized with arylnickel(II) complexes. *Nature* **1994**, *372* (6507), 659–663.
  - Johannsen, M.; Jørgensen, K.A. Allylic amination. *Chem. Rev.* **1998**, *98* (4), 1689–1708.
  - Heumann, A. *Transition Metal-Catalyzed Reactions. In Transition Metals for Organic Synthesis: Building Blocks and Fine Chemicals*; Beller, M., Bolm, C., Eds.; Wiley-VCH: Weinheim, 1998; Vol. 1, 251–264.
  - Nayler, A.M.; Goddard, W.A., III; Kiefer, G.E.; Tomalia, D.A. Starburst dendrimers: 5. Molecular shape control. *J. Am. Chem. Soc.* **1989**, *111* (6), 2339–2341.
  - Jansen, J.F.G.A.; de Brabander-van den Berg, E.M.M.; Meijer, E.W. Encapsulation of guest molecules into a dendritic box. *Science* **1994**, *266* (5188), 1226–1229.
  - Csakai, Z.; Skoda-Fördes, R.; Kollár, L. NMR investigation of Pd(II)–Pd(0) reduction in the presence of mono- and ditertiary phosphines. *Inorg. Chim. Acta* **1999**, *286* (1), 93–97.
  - Trost, B.M.; Keinan, E. Steric steering with supported palladium catalysts. *J. Am. Chem. Soc.* **1978**, *100* (24), 7779–7781.
  - Trost, B.M.; Verhoeven, T.R. Allylic alkylation. Palladium-catalyzed substitution of allylic carboxylates. Stereo- and regiochemistry. *J. Am. Chem. Soc.* **1980**, *102* (14), 4730–4743.
  - Bäckvall, J.E.; Granberg, K.L.; Heumann, A. On the mechanism of palladium(0)-catalyzed reactions of allylic substrates with nucleophiles. Origin of the loss of stereospecificity. *Isr. J. Chem.* **1991**, *31* (1), 17–24.
  - Lehn, J.-M. *Supramolecular Chemistry: Concepts and Perspectives*; VCH: New York, 1995.
  - Crooks, R.M.; Zhao, M.; Sun, L.; Chechik, V.; Yeung, L.K. Dendrimer-encapsulated metal nanoparticles: Synthesis, characterization, and application to catalysis. *Acc. Chem. Res.* **2001**, *34* (3), 181–190, and references therein.
  - Balogh, L.; Tomalia, D.A. Poly(amidoamine) dendrimer-templated nanocomposites: 1. Synthesis of zerovalent copper nanoclusters. *J. Am. Chem. Soc.* **1998**, *120* (19), 7355–7356.
  - Esumi, K.; Suzuki, A.; Aihara, N.; Usui, K.; Torigoe, K. Preparation of gold colloids with UV irradiation using dendrimers as stabilizer. *Langmuir* **1998**, *14* (12), 3157–3159.
  - Niu, Y.; Yeung, L.K.; Crooks, R.M. Size-selective hydrogenation of olefins by dendrimer-encapsulated palladium nanoparticles. *J. Am. Chem. Soc.* **2001**, *123* (28), 6840–6846.
  - Gupta, R.R.; Lechner, M.D. *Chemical Shifts and Coupling Constants for Fluorine-19 and Nitrogen-15*; Springer: Berlin, 1998.
  - Kooper, G.J.M.; van Genderen, M.H.P.; Elissen-Román, C.; Baars, M.W.P.L.; Meijer, E.W.; Borkovec, M. Protonation mechanism of poly(propylene imine) dendrimers and some associated oligo amines. *J. Am. Chem. Soc.* **1997**, *119* (28), 6512–6521.
  - Yeung, L.K.; Crooks, R.M. Heck heterocoupling within a dendritic nanoreactor. *Nano Lett.* **2001**, *1* (1), 14–17.
  - Hirai, H.; Chawanya, H.; Toshima, N. Selective hydrogenation of cyclooctadienes catalyzed by colloidal palladium in poly(*N*-vinyl-2-pyrrolidone). *Macromol. Chem., Rapid Commun.* **1981**, *2* (1), 99–103.
  - Michels, J.J.; Huskens, J.; Reinhoudt, D.N.J. Dendrimer–cyclodextrin assemblies as stabilizers for gold and platinum nanoparticles. *J. Chem. Soc., Perkin Trans. 2* **2002**, (1), 102–105.

# Dimensionally Graded Semiconductor Nanoparticle Films

**Arif A. Mamedov**

*Oklahoma State University and Nomadics, Inc., Stillwater, Oklahoma, U.S.A.*

**Nicholas A. Kotov**

*Department of Chemical Engineering, University of Michigan, Ann Arbor, Michigan, U.S.A.*

**Nataliya N. Mamedova**

*Department of Chemistry, Oklahoma State University, Stillwater, Oklahoma, U.S.A.*

## INTRODUCTION

Nanometer-sized particles of II–VI semiconductors and their size-dependent physical and chemical properties are currently an object of interest in various areas of chemistry and physics.<sup>[1–8]</sup> The high luminescence (quantum yield 15–20%) of CdTe nanoparticles, stabilized with thioglycolic acid (TGA), along with their size-dependent optical properties, makes them a promising material for the engineering of nanoelectronic devices. CdTe nanoparticles have already been found to be useful as components of X-ray and  $\gamma$ -detectors,<sup>[9]</sup> photodiodes,<sup>[5]</sup> and solar cells.<sup>[10]</sup> For any possible use of such particles in thin films, especially for LED devices, it is necessary to obtain a high density of particles to facilitate charge transfer between them.<sup>[11,12]</sup>

## OVERVIEW

Simplicity and high universality of the layer-by-layer (LBL) assembly method along with the possibility to control the structure of growing films at each deposition step allows for the preparation of stratified thin composite materials with specific predetermined order of the inner nanometer-thick layers.<sup>[13–36]</sup> This method consists in cyclic deposition of oppositely charged species from their aqueous colloidal solutions. Each deposition cycle results in the formation of bilayer or two monolayers bounded together mainly due to electrostatic attraction of opposite charges. At the optimized conditions of the LBL deposition the packing and thickness of nanoparticles (NP) is reproduced from layer to layer, and there is little (if any) restructuring of the NP layer during the polyelectrolyte deposition. These conditions should change a little or not change at all when NP of different sizes are used. This makes possible the

preparation of thin films with an asymmetric internal structure by varying the LBL deposition sequence. The order of the layers can be used as a powerful tool for optimizing the diverse functional properties of the layered nanostructured materials from biological to electronic. However, the interpenetration of layers and relatively small size of most semiconductor NP (2–6 nm) may not give the possibility to distinguish separate layers inside of the film. To visualize them, one can deposit strata by assembling several bilayers of the same type of particles before assembling the next type of particles to satisfy the resolution limits of the microscopy equipment and to overcome a substantial degree of disorder in each adsorption layer.

The preparation of graded semiconductors with the methods commonly used for this task, such as molecular beam epitaxy and plasma-enhanced chemical vapor deposition,<sup>[37,38]</sup> is difficult, expensive, complex, and sometimes hazardous. The simple and universal LBL deposition method makes it possible to build graded semiconducting materials from a stable aqueous dispersion of semiconductor NP.

The objective of the current work was to apply the regularities of the LBL assembly to the optimization of the conditions for the LBL deposition of thiol-stabilized CdTe nanoparticles and to prepare graded film, based on these particles. Because of their size-dependent luminescence and, supposedly, size-independent assembly conditions, they are one of the best choices for the preparation and characterization of one-dimensionally graded films. Graded films, prepared by sequential assembly of thiol-capped CdTe nanoparticles will also be discussed in this chapter. Such films demonstrate the possible use as photodetectors, bipolar transistors, waveguides, light-emitters, and non-linear optical, magneto-optical, and high-speed devices.<sup>[38]</sup> These types of materials also reveal new phenomena in charge injection, charge carrier dynamics, and light trapping.<sup>[37]</sup>



## EXPERIMENTAL PROCEDURE

### Materials

Poly(dimethyldiallylammonium chloride) (PDDA,  $M_w = 200,000$ – $350,000$ ; 20 wt.% in water) and poly(acrylic acid) (PAA,  $M_w = 450,000$ ) used as organic components in the LBL assembly as well as cadmium perchlorate hydrate ( $\text{Cd}(\text{ClO}_4)_2 \cdot 2\text{H}_2\text{O}$ ), sodium hydroxide (NaOH), and thioglycolic acid (TGA), needed for CdTe nanoparticles synthesis, were bought from Aldrich (Milwaukee, WI). Aluminum telluride ( $\text{Al}_2\text{Te}_3$ ), used in the same synthesis, was purchased from Gerao Inc. (Milwaukee, WI). Sulfuric acid ( $\text{H}_2\text{SO}_4$ ) was obtained from EM Science (Gibbstown, NJ).  $\text{N}_2$  gas was obtained from Airgas (Stillwater, OK). LR-white embedding resin, used for transmission electron microscopy (TEM) sample preparation, was obtained from London Resin Company Ltd. (Berkshire, England). All chemicals were used without further purification. De-ionized water ( $> 18.0 \text{ M}\Omega \text{ cm}$ , Barnstead, E-pure system), with an unadjusted pH of approximately 5.5, was exclusively used in all solutions and rinsing procedures.

### Synthesis of CdTe Nanoparticles

Cadmium telluride (CdTe) NP, stabilized with TGA, were prepared according to the procedure described elsewhere.<sup>[4,5]</sup> Briefly, they were prepared by adding a NaHTe solution to a  $\text{Cd}(\text{ClO}_4)_2 \cdot 2\text{H}_2\text{O}$  aqueous solution in the presence of TGA as the stabilizing agent. The molar ratio of  $\text{Cd}^{2+}/\text{Te}^{2-}/\text{TGA}$  was 1:0.47:2.43. The 0.05 M solution of NaHTe was prepared by titration of a 0.05 M NaOH solution with an excess amount of hydrogen telluride ( $\text{H}_2\text{Te}$ ) at  $0^\circ\text{C}$  under an inert atmosphere.  $\text{H}_2\text{Te}$  gas, needed for this reaction, was generated by the direct reaction of  $\text{Al}_2\text{Te}_3$  with a 0.5 M  $\text{H}_2\text{SO}_4$  solution. After the titration was complete, the excess amount of hydrogen telluride was removed by bubbling the reaction mixture with  $\text{N}_2$  gas for 30 min. All initial components of the reaction mixture were saturated with  $\text{N}_2$  to obtain an oxygen-free media.

After the reaction was complete, the resulting solution was heated at  $96^\circ\text{C}$ . Such a treatment allows for the tuning of the size of the obtained CdTe nanoparticles by varying the heating time. For example, heating the reaction mixture for 30 min yielded nanocrystals with a luminescent maxima at 485–505 nm with an average particle size of 2.0–3.0 nm, while extension of the heating time to several hours produced a 5.0–6.0-nm nanoparticles with a luminescent maxima at 605–620 nm. CdTe nanocrystals with emission peaks at 485–505, 530–545, 570–585, and 605–630 nm display green, yellow, orange, and red luminescence, respectively, and will be denoted so accordingly.

### Layer-by-Layer Assembly of CdTe Nanoparticles

As substrates for CdTe nanoparticles LBL assembly, glass slides, silicon wafers, and cellulose acetate (CA) films were used. Transparent substrates were needed for UV-visible spectroscopy and luminescence measurements. Because glass does not absorb light at wavelengths higher than 320 nm, it was suitable as a substrate for such types of measurements. Silicon wafer substrates were used for the atomic force microscopy (AFM) study of the LBL-assembled films. Both the silicon wafers and glass slides were cleaned with a hot Nochromix solution in concentrated  $\text{H}_2\text{SO}_4$  followed by a rinsing with DI water. The surface of a flexible cellulose acetate film, needed for the TEM study of the graded film, was partially hydrolyzed with 0.1 M NaOH for 5 min to facilitate the LBL assembly, and then thoroughly rinsed with DI water.

As organic components of a LBL assembly system, positively charged PDDA and negatively charged PAA were used. A typical deposition step consisted of 1) deposition of the PDDA from its 1% aqueous solution (pH = 9) for 10 min; 2) two rinses with DI water for 1 min each; 3) deposition for 20 min of CdTe nanoparticles from as-synthesized dispersion (pH = 9–10); and 4) two rinses with DI water for 1 min each. To enhance the LBL assembly of the CdTe NP, the precursor bilayer of the PDDA/PAA was deposited on a clean substrate surface in the same fashion that was used for the LBL assembly of magnetic NP. This layer formed a uniform surface coating, providing better adsorption for subsequent NP layers. Poly(acrylic acid) was assembled from its 1% aqueous solution (pH = 3.5).

The graded LBL assembled films were prepared on glass slides and cellulose acetate substrates from “green,” “yellow,” “orange,” and “red” nanoparticles to produce a model of NP rainbow. Typically, 5–10 PDDA/NP bilayers of each of four luminescent colors were deposited. The precursor bilayer of PDDA/PAA was assembled before carrying out the preparation of the graded film. The surface of the cellulose acetate film was partially hydrolyzed with NaOH to add additional charges to it.

### Luminescence Spectroscopy

The progress of nanoparticle growth in the reaction media as well as the progress of their LBL assembly was monitored with Fluorolog 3 and Fluoromax 2 from JY SPEX by registering the luminescence spectra of the particles. During the nanocrystal growth step, the spectra were taken every 15–20 min. To check the growth of the graded CdTe film, fluorospectra were taken after the deposition of PDDA/CdTe bilayers of each color. The right-angle registration mode with no intermediate filters was utilized in these measurements.

## Transmission Electron Microscopy

Transmission electron microscopy and high-resolution transmission electron microscopy (HRTEM) images were taken on a Philips CM 12 instrument, equipped with super twin high-resolution lenses and Zeiss digital camera. The instrument was operated at 120 kV. A graded CdTe film was embedded in a LR-white embedding resin according to the specifications recommended by the manufacturer. The embedded film was cross sectioned utilizing a Reichert Ultracut E ultramicrotome (Leica) with "Diatome" diamond knife. The obtained 25–30-nm sections were placed on a 200-mesh copper grid coated with formvar and then dried in a desiccator for 30 min before being placed in the microscope.

## Confocal Laser Scanning Microscopy

The graded CdTe film was checked with a confocal laser scanning microscopy. The micrographs were taken with a Leica TCS SP microscope, equipped with 63 × Plan APO 1.32 NA water immersion and 100 × Plan APO 1.4 NA oil immersion objectives. The CdTe nanoparticles of the film were excited with an Ar-UV laser. The images were processed with Leica TCS NT software.

## RESULTS AND DISCUSSION

### Synthesis of CdTe Nanoparticles

The aqueous solutions of nanoparticles obtained according to the procedure described in the experimental part of this entry have narrow and symmetric peaks ranging from 495 nm for "green" CdTe to 620 nm for "red" CdTe NP (Fig. 1). The set of vessels, shown in Fig. 1A, contain solutions of TGA-stabilized CdTe excited with a UV lamp ( $\lambda_{\text{ex}} = 368$  nm). The average particle size gradually increases from 2.0–3.0 nm for "green" NP to 5.0–6.0 nm for "red" NP as determined by HRTEM. The arrows indicate the solutions from which the luminescence spectra (Fig. 1B) were taken. A wider peak for the "yellow" CdTe solution can be attributed to the higher polydispersity of CdTe nanoparticles compared to "green," "orange," and "red" solutions.

### Layer-by-Layer Deposition of CdTe Nanoparticles

The LBL deposition of CdTe nanoparticles was performed on glass slides and silicon wafers. The progress of the assembly was monitored by UV-visible spectroscopy and AFM. Fig. 2 shows the UV-visible spectra of a growing film of "green" CdTe nanoparticles. The spectra show the UV-visible adsorption peaks

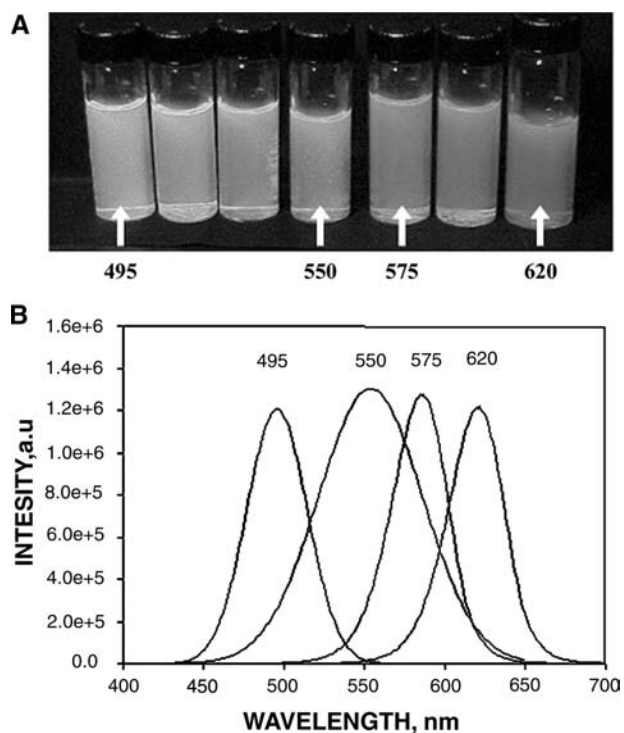


**Fig. 1** (A) Optical image of vessels, containing aqueous dispersions of CdTe nanoparticles excited with UV lamp. The average particle size changes gradually from 2.0–3.0 nm for the solution exhibiting green luminescence (emission peak at 495 nm) to 5.0–6.0 nm for the solution exhibiting red luminescence (emission peak at 620 nm). Arrows indicate the solutions from which the luminescence spectra (B) were taken.

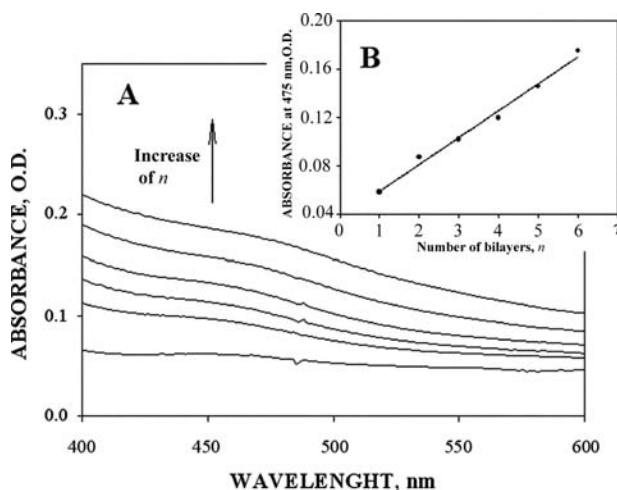


**Fig. 2** (A) UV-visible adsorption spectra of "green" nanoparticles with glass slide as a substrate. (B) Dependence of O.D. at 475 nm of growing film on the number of absorbed PDDA/CdTe bilayers. Only NP absorb light at this wavelength.

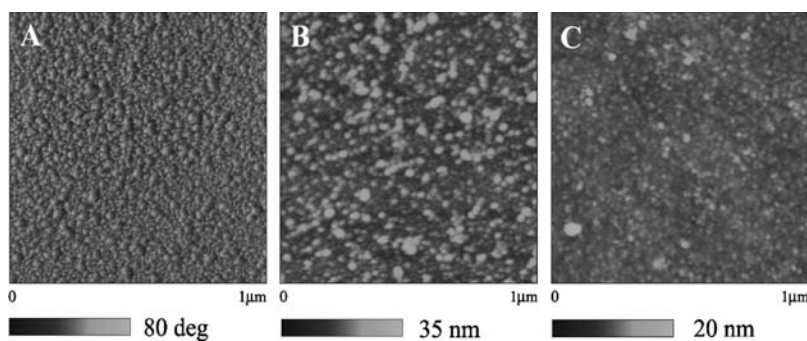


**Fig. 3** AFM phase (A) and topography (B,C) images of PDDA/CdTe (A,B) and PDDA/CdTe/PDDA (C), adsorbed on precursor PDDA/PAA bilayer.

coinciding with those for the CdTe nanoparticles in the film. As in the case of the assembly of the magnetic nanoparticles the linear dependence of the increment of optical density with the number of adsorption cycles was observed (Fig. 2B). The linear dependence correlates with data published elsewhere for the LBL assembly of the semiconductor NP.<sup>[6,12]</sup> Observation of the growing film with AFM revealed a completely covered surface with a dense packing of CdTe nanoparticles after the deposition of one PDDA/CdTe bilayer, adsorbed on a precursor PDDA/PAA bilayer (Fig. 3A,B). When a layer of PDDA was adsorbed on top of the CdTe NP (Fig. 3C), the roughness of the growing film was reduced. This can be attributed to a greater number of the negative charges in the spaces between the closely packed nanoparticles, which leads to the preferential polymer adsorption (Fig. 3D).

#### Graded Films From CdTe Nanoparticles: Preparation

The assembly of a graded CdTe film started with a deposition of a precursor PDDA/PAA bilayer on

a substrate. This procedure resulted in a uniform coating, which resulted in a successful LBL growth of the film. The assembly of the NP started with an adsorption of five bilayers of PDDA/“green” CdTe NP, followed by five bilayers of PDDA/“yellow,” “orange,” and “red” CdTe NP, respectively. A sketch of the structure of the obtained film, along with the corresponding band-gap progression of the CdTe NP inside of the film, is shown in Fig. 4. With the complete addition of new layers of bigger nanoparticles, a luminescence spectrum of the LBL stack was taken (Fig. 5). When CdTe nanoparticles of a bigger size were added to the film, the luminescence of the assembly broadened and shifted toward the red part of the electromagnetic spectra. Finally, after the addition of NP of each of four colors, the luminescence spectra of the film had a plateau appearance with almost equal emission intensity in a wide range of wavelengths. The red shift of the fluorescence in comparison to the original spectra of CdTe nanoparticles (Fig. 1) can be attributed to the excitation energy transfer from smaller NP to larger ones.<sup>[39,40]</sup>

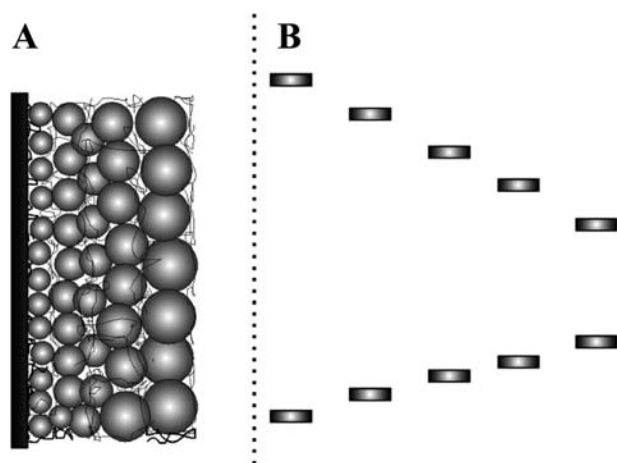


**Fig. 4** Schematic view of (A) a gradient film and (B) corresponding band-gap progression.

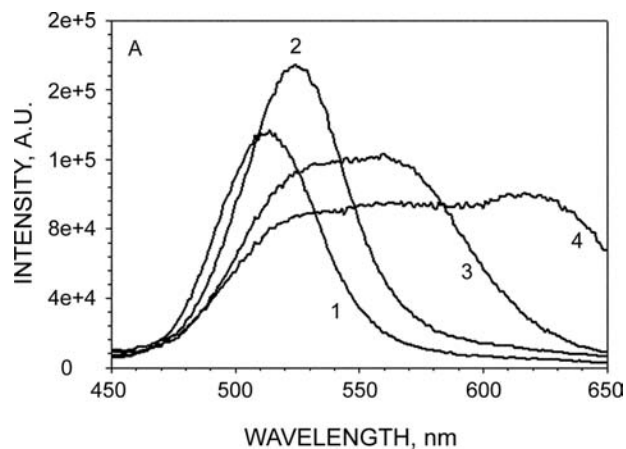


**Fig. 5** Luminescence spectra of thin films obtained after the sequential deposition of five bilayers of (1) “green,” (2) “yellow,” (3) “orange,” and (4) “red” CdTe nanoparticles.

### Graded Films from CdTe Nanoparticles: Evaluation of the Internal Structure

To evaluate the internal structure of a gradient CdTe film, it was assembled on a flexible CA substrate. Then the LBL stack along with substrate was embedded into epoxy resin and then cross sectioned. The choice of a CA substrate can be rationalized by the fact that it does not require a complicated slicing procedure. This makes a thin and flexible CA film preferable to those of traditional glass or silicon wafers. The surface of the CA was pretreated by partial hydrolysis with 0.1 M NaOH. Such pretreatment resulted in greater adsorption rate during the LBL assembly process.<sup>[28]</sup> A graded film consisting of five bilayers of PDDA and each of “green,” “yellow,” and “red” CdTe nanoparticles was assembled in the manner described above. Embedding and cross sectioning of the LBL stack resulted in 25-nm-thick slices, which were analyzed with TEM.

The asymmetry of the obtained film is visualized as the difference in image density on the “red” and “green” sides of the LBL stack. The side of the film containing bigger “red” CdTe nanoparticles appears to be darker. This is explained by a greater percentage of heavier elements (Cd and Te) on this side of the assembly, leading to the stronger electron beam

scattering (Fig. 6A). HRTEM images of the “green,” “yellow,” and “red” parts of the film (Fig. 6B–D) show the presence of CdTe nanoparticles inside of a polyelectrolyte matrix with an average diameter of 2–4 nm for the “green” and “yellow” and 5–6 nm for the “red” sides of the assembly. This correlates with the emission wavelength of the particles. The low contrast of HRTEM micrographs, as well as the impossibility of distinguishing the differences in sizes of the “green” and “yellow” CdTe nanoparticles inside of the LBL stack, should be attributed to a stacking of at least 3–4 “red” and 6–10 “green” and “yellow” nanoparticles on top of each other inside of the slice.

The gradient nature of the resulting CdTe film was confirmed using confocal laser scanning microscopy. The sample consisting of 10 bilayers of PDDA and each of “green,” “yellow,” “orange,” and “red” nanoparticles was assembled on a CA film. The stacks of multilayers, made from NP of the same color, were separated from each other by additional interbilayers of PDDA/PAA. A series of luminescence images were obtained at different focus depths inside the assembly when the CdTe nanoparticles in the film were excited with a UV laser. The images were processed with standard Leica TCS NT software and a cross-sectional image was obtained without physical sectioning of the film (Fig. 7A). The gradual change of luminescence

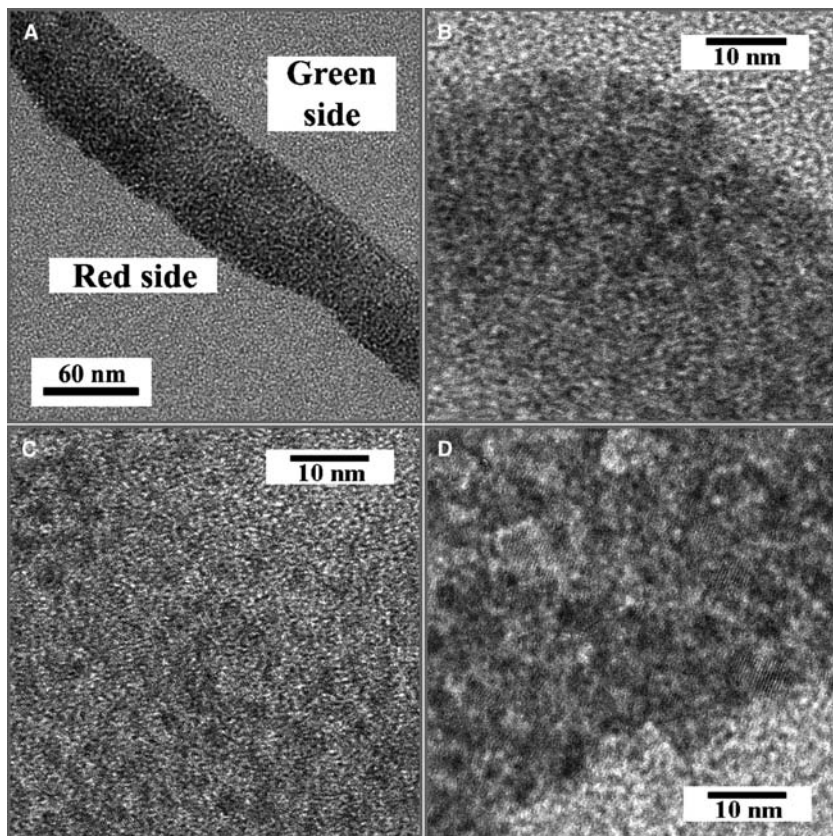


**Fig. 6** (A) TEM image of cross sections of a graded CdTe film made from five bilayers of “green,” “yellow,” and “red” nanoparticles. (B–C) HRTEM images of “green” (B), “yellow” (C), and “red” (D) parts of LBL assembly.

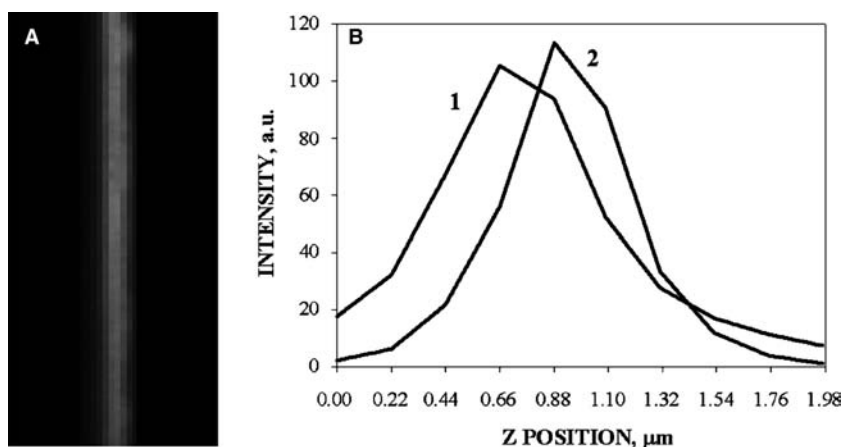


**Fig. 7** (A) Cross-sectional confocal microscopy image of the graded film, made from 10 bilayers of “green,” “yellow,” “orange,” and “red” CdTe nanoparticles. Additional interlayers of PDDA/PAA separate stacks made of nanoparticles of the same size. (B) Dependence of green (1) and red (2) luminescence signals intensity on focus depth during cross-sectional analysis.

color from green on one side to red on the other side of the film, as the corresponding size of the NP inside of the film increases, can be clearly seen. The absence of well-separated color layers inside of the obtained “nanorainbow” results mainly from the low resolution of the technique used. There is a certain degree of interpenetration of the separate nanoparticle layers, which may also influence the cross-sectional image.

By the difference in the positions of the maxima for the red and green channels of intensity vs. the Z-position (focus depth) plot (Fig. 7B) the thickness of the obtained CdTe assembly was estimated to be  $220 \pm 20$  nm. This correlates quite well with the expected thickness of the film. One dipping cycle during an assembly results in the formation of a 3–7-nm-thick PDDA/CdTe bilayer depending on the size of the particles used. The average thickness of a PDDA/CdTe bilayer can be estimated to be 5 nm. Poly(acrylic acid), assembled on top of PDDA, forms a 5-nm-thick bilayer as determined by ellipsometry. The thickness of graded film can be estimated by adding up these numbers:  $5 \times 40 + 3 \times 5 = 215$  nm, which matches surprisingly well the thickness estimate from the confocal study. It is important to mention that because the maximum possible magnification of the confocal microscope was  $100 \times$  with an oil immersion objective, the correct thickness estimation for the CdTe-graded film can be done for relatively thick samples.

## CONCLUSION

Layer-by-layer assembled multilayers of luminescent CdTe nanoparticles have been prepared on a number of substrates. UV–visible monitoring of the assembly process shows a linear dependence of the optical density on the number of deposited bilayers. Nanoparticles completely covered the substrate surface and formed uniform closely packed layers as was

demonstrated by AFM. Sequential assembly of the CdTe nanoparticles of different sizes, ranging from 2–3 to 5–6 nm, opens the possibility of preparing films with the gradient structures utilizing the LBL assembly method. The combination of quantum-size effects with the gradient nature of the obtained CdTe films gives the opportunity to study new physical and optical effects, as well the optimization of existing applications using nanoparticle thin films based on charge transfer. At the same time it should be mentioned that the characteristic distance for CdTe LBL films, at which a change in properties can be programmed, should exceed 100 nm. This number is significantly greater than the average thickness of one bilayer or the diameter of nanoparticles. However, this observation does not prevent the organization of the NP on a much smaller scale. It is possible to tune some parameters, such as polarizability and the refractive index, on the molecular level in such asymmetric assemblies, which may lead to the discovery of unique photonic and electronic devices.

## ACKNOWLEDGMENTS

The authors are grateful to Dr. Michael Giersig (Hahn-Meitner-Institut, Berlin, Germany) for assistance with TEM and Jim Henthorn (Oklahoma University Health Sciences Center, Oklahoma City, OK, USA) for aid with confocal microscopy.

## REFERENCES

1. Eychmueller, A.; Mews, A.; Weller, H. A quantum dot quantum well: cadmium sulfide/mercuric sulfide/cadmium sulfide. *Chem. Phys. Lett.* **1993**, *208* (1–2), 59–62.
2. Mews, A.; Eychmueller, A.; Giersig, M.; Schooss, D.; Weller, H. Preparation, characterization, and photophysics of the quantum dot quantum well system cadmium



- sulfide/mercury sulfide/cadmium sulfide. *J. Phys. Chem.* **1994**, *98* (3), 934–941.
3. Rockenberger, J.; Troger, L.; Kornowski, A.; Vossmeier, T.; Eychmuller, A.; Feldhaus, J.; Weller, H. Size dependence of structural and dynamic properties of CdS nanoparticles. *Ber. Bunsen-Ges.* **1997**, *101* (11), 1613–1616.
  4. Rogach, A.L.; Katsikas, L.; Kornowski, A.; Su, D.; Eychmuller, A.; Weller, H. Synthesis and characterization of thiol-stabilized CdTe nanocrystals. *Ber. Bunsen-Ges.* **1996**, *100* (11), 1772–1778.
  5. Rogach, A.L.; Katsikas, L.; Kornowski, A.; Su, D.; Eychmuller, A.; Weller, H. Synthesis, morphology, and optical properties of thiol-stabilized CdTe nanoclusters in aqueous solution. *Ber. Bunsen-Ges.* **1997**, *101* (11), 1668–1670.
  6. Gao, M.; Kirstein, S.; Rogach, A.L.; Weller, H.; Mohwald, H. Photoluminescence and electroluminescence of CdSe and CdTe nanoparticles. *Adv. Sci. Technol.* **1999**, *27*, 347–358.
  7. Talapin, D.V.; Haubold, S.; Rogach, A.L.; Kornowski, A.; Haase, M.; Weller, H. A novel organometallic synthesis of highly luminescent CdTe nanocrystals. *J. Phys. Chem., B* **2001**, *105* (12), 2260–2263.
  8. Talapin, D.V.; Rogach, A.L.; Mekis, I.; Haubold, S.; Kornowski, A.; Haase, M.; Weller, H. Synthesis and surface modification of amino-stabilized CdSe, CdTe and InP nanocrystals. *Colloids Surf., A: Physicochem. Eng. Asp.* **2002**, *202* (2–3), 145–154.
  9. Redus, R.; Squillante, M.; Gordon, J.; Knoll, G.; Wehe, D. A combined video and gamma ray imaging system for robots in nuclear environments. *Nucl. Instrum. Methods Phys. Res., Sect. A* **1994**, *353* (1–3), 324–327.
  10. Ferekides, C.; Britt, J. CdTe solar cells with efficiencies over 15%. *Solar Energy Mater. Solar Cells* **1994**, *35* (1–4), 255–262.
  11. Lesser, C.; Gao, M.; Kirstein, S. Highly luminescent thin films from alternating deposition of CdTe nanoparticles and polycations. *Mater. Sci. Eng., C: Biom. Supramol. Syst.* **1999**, *C8–C9*, 159–162.
  12. Sun, J.; Gao, M.; Feldmann, J. Electric field directed layer-by-layer assembly of highly fluorescent CdTe nanoparticles. *J. Nanosci. Nanotechnol.* **2001**, *1* (2), 133–136.
  13. Aliev, F.; Correa-Duarte, M.; Mamedov, A.; Ostrander, J.W.; Giersig, M.; Liz-Marzan, L.; Kotov, N. Layer-by-layer assembly of core-shell magnetite nanoparticles: effect of silica coating on interparticle interactions and magnetic properties. *Adv. Mater.* **1999**, *11* (12), 1006–1010.
  14. Ariga, K.; Lvov, Y.; Ichinose, I.; Kunitake, T. Ultrathin films of inorganic materials (SiO<sub>2</sub> nanoparticle, montmorillonite microplate, and molybdenum oxide) prepared by alternate layer-by-layer assembly with organic polyions. *Appl. Clay Sci.* **1999**, *15* (1–2), 137–152.
  15. Cassier, T.; Lowack, K.; Decher, G. Layer-by-layer assembled protein/polymer hybrid films: nanoconstruction via specific recognition. *Supramol. Sci.* **1998**, *5* (3–4), 309–315.
  16. Decher, G.; Lehr, B.; Lowack, K.; Lvov, Y.; Schmitt, J. New nanocomposite films for biosensors: Layer-by-layer adsorbed films of polyelectrolytes, proteins or DNA. *Biosens. Bioelectron.* **1994**, *9* (9/10), 677–684.
  17. Decher, G. Fuzzy nanoassemblies toward layered polymeric multicomposites. *Science* **1997**, *277*, 1232–1237.
  18. Decher, G.; Hong, J.D. Buildup of ultrathin multilayer films by a self-assembly process: II. Consecutive adsorption of anionic and cationic bipolar amphiphiles and polyelectrolytes on charged surfaces. *Ber. Bunsen-Ges., Phys. Chem.* **1991**, *95* (11), 1430–1434.
  19. Decher, G.; Hong, J.D. Buildup of ultrathin multilayer films by a self-assembly process: I. Consecutive adsorption of anionic and cationic bipolar amphiphiles on charged surfaces. *Macromol. Chem., Macromol. Symp.* **1991**, *46*, 321
  20. Ichinose, I.; Mizuki, S.; Ohno, S.; Shiraishi, H.; Kunitake, T. Preparation of cross-linked ultrathin films based on layer-by-layer assembly of polymers. *Polym. J. (Tokyo)* **1999**, *31* (11–2), 1065–1070.
  21. Jiang, X.; Hammond, P.T. Selective deposition in layer-by-layer assembly: functional graft copolymers as molecular templates. *Langmuir* **2000**, *16* (22), 8501–8509.
  22. Kotov, N.A.; Magonov, S.; Tropsha, E. Layer-by-layer self-assembly of aluminosilicate-polyelectrolyte composites: mechanism of deposition, crack resistance, and perspectives for novel membrane materials. *Chem. Mater.* **1998**, *10* (3), 886–895.
  23. Kotov, N.A.; Dekany, I.; Fendler, J.H. Layer-by-layer self-assembly of polyelectrolyte-semiconductor nanoparticle composite films. *J. Phys. Chem.* **1995**, *99* (35), 13,065–13,069.
  24. Lee, G.S.; Lee, Y.J.; Yoon, K.B. Layer-by-layer assembly of zeolite crystals on glass with polyelectrolytes as ionic linkers. *J. Am. Chem. Soc.* **2001**, *123* (40), 9769–9779.
  25. Liu, Y.; Wang, A.; Claus, R.O. Layer-by-layer electrostatic self-assembly of nanoscale Fe<sub>3</sub>O<sub>4</sub> particles and polyimide precursor on silicon and silica surfaces. *Appl. Phys. Lett.* **1997**, *71* (16), 2265–2267.
  26. Lvov, Y.; Ariga, K.; Kunitake, T. Layer-by-layer assembly of alternate protein/polyion ultrathin films. *Chem. Lett.* **1994**, *23* (12), 2323–2326.
  27. Mamedov, A.; Ostrander, J.; Aliev, F.; Kotov, N.A. Stratified assemblies of magnetite nanoparticles and montmorillonite prepared by the layer-by-layer assembly. *Langmuir* **2000**, *16* (8), 3941–3949.
  28. Mamedov, A.A.; Kotov, N.A. Free-standing layer-by-layer assembled films of magnetite nanoparticles. *Langmuir* **2000**, *16* (13), 5530–5533.
  29. Ostrander, J.; Mamedov, A.A.; Correa-Duarte, M.A.; Liz-Marzan, L.M.; Aliev, F.; Kotov, N.A. Stratified thin film materials prepared by the layer-by-layer assembly of nanoparticles. In *Book of Abstracts*, 218th ACS National Meeting, New Orleans, Aug., 22–26, 1999.
  30. Rogach, A.L.; Koktysh, D.S.; Harrison, M.; Kotov, N.A. Layer-by-layer assembled films of HgTe nanocrystals with strong infrared emission. *Chem. Mater.* **2000**, *12* (6), 1526–1528.
  31. Sukhorukov, G.B.; Donath, E.; Lichtenfeld, H.; Knippel, E.; Knippel, M.; Budde, A.; Mohwald, H. Layer by layer self assembly of polyelectrolytes on colloidal particles. *Colloids Surf., A* **1998**, *137*, 253–266.



32. L'vov, Y.M.; Decher, G. Assembly of multilayer ordered films by alternating adsorption of oppositely charged macromolecules. *Kristallografiya* **1994**, *39* (4), 696–716.
33. Kotov, N.A.; Dekany, I.; Fendler, J.H. Ultrathin graphite oxide polyelectrolyte composites prepared by self assembly transition between conductive and non-conductive states. *Adv. Mater.* **1996**, *8*, 637.
34. Schuetz, P.; Caruso, F. Multilayer thin films based on polyelectrolyte-complex nanoparticles. *Colloids Surf., A: Physicochem. Eng. Asp.* **2002**, *207* (1–3), 33–40.
35. Yang, W.; Trau, D.; Renneberg, R.; Yu, N.T.; Caruso, F. Layer-by-layer construction of novel biofunctional fluorescent microparticles for immunoassay applications. *J. Colloid Interface Sci.* **2001**, *234* (2), 356–362.
36. Caruso, F. Nanoengineering of particle surfaces. *Adv. Mater.* **2001**, *13* (1), 11–22.
37. Vlaev, S.; Velasco, V.R.; Garcia-Moliner, F. Tight-binding calculation of electronic states in an inverse parabolic quantum well. *Phys. Rev., B: Condensed Mater.* **1995**, *51* (11), 7321–7324.
38. Aigouy, L.; Mathet, V.; Liaci, F.; Gil, B.; Briot, O.; Briot, N.; Cloitre, T.; Averous, M.; Aulombard, R.L. Optical spectroscopy in (Zn,Cd)Se–ZnSe graded-index separate-confinement heterostructures. *Phys. Rev., B: Condensed Mater.* **1996**, *53* (8), 4708–4721.
39. Kagan, C.R.; Murray, C.B.; Bawendi, M.G. Long-range resonance transfer of electronic excitations in close-packed CdSe quantum-dot solids. *Phys. Rev., B: Condensed Mater.* **1996**, *54* (12), 8633–8643.
40. Kagan, C.R.; Murray, C.B.; Nirmal, M.; Bawendi, M.G. Electronic energy transfer in CdSe quantum dot solids. *Phys. Rev. Lett.* **1996**, *76* (9), 1517–1520.

# Dip-Pen Nanolithography: Applications and Functional Extensions

Björn T. Rosner

Linette M. Demers

Nanolnk Inc., Chicago, Illinois, U.S.A.

## INTRODUCTION

In many areas of modern technology, from biotechnology to solid-state device fabrication, two-dimensional patterning techniques are used to define structures and boundaries. These patterning techniques ultimately determine features size and density and thus unit performance and price. Much is developed upon the well-known techniques of resist lithography, yet to achieve extreme spatial resolution or chemical versatility other techniques are better suited.

Dip-Pen Nanolithography (DPN<sup>TM</sup>) is a widely used scanning probe lithography (SPL) method. Here, a sharp tip is coated with a functional molecule (the “ink”) and brought into contact with a surface where it deposits ink via a water meniscus. The DPN process is a direct-write pattern transfer technique with nanometer resolution and is inherently general with respect to usable inks and substrates.

This entry serves to outline the basics of DPN writing and discusses its most important applications as well as new technological advances in DPN instrumentation.

## BACKGROUND

The invention of scanning tunneling microscopy (STM) in the early 1980s by Binnig and Rohrer<sup>[1]</sup> and the subsequent development of other scanning probe microscopy (SPM) techniques, most notably atomic force microscopy (AFM),<sup>[2]</sup> made much of nanotechnology accessible. The field of nanotechnology can be split into three major components: One is based on the ability to directly observe structures at atomic and molecular dimensions; another is involved in the direct measurement of a myriad of physical properties at the smallest scale; and the third deals with the fabrication of nanoscale structures with unique properties. Among the many techniques to produce nanoscale features, SPL techniques are of particular interest because of their inherent flexibility.<sup>[3–5]</sup> In all

instances of SPL, a proximal probe is used to locally modify the surface. These surface modification techniques can be further divided into categories found in their molecular-scale chemical synthesis counterparts<sup>[6]</sup>—that is, additive lithography (e.g., oxidation lithography<sup>[7–9]</sup>), subtractive lithography (e.g., scratching lithography<sup>[10–12]</sup>), and substitutive lithography (e.g., nanografting<sup>[13,14]</sup>).

The most intuitive type of additive lithography is the direct deposition of material from a solid stylus.<sup>[15]</sup> Indeed, writing with pen on paper is one of the oldest methods to create patterns. In 1999, researchers of Chad Mirkin’s group in Northwestern University succeeded in controllable deposition of dots and lines and invented the DPN process as a result.<sup>[16,17]</sup> DPN patterning is now a patented<sup>[18–20]</sup> and commercialized<sup>[21]</sup> process.

## POSITIONING OF DPN

An overview comparison between most popular patterning techniques is shown in Table 1. Today’s most commonly employed patterning technique is photolithography, which has very high throughput due to its parallel nature but it is also very expensive if small to medium quantities of each design are desired: Exposure of a photoresist is facilitated through a photomask that—depending on required resolution—can command up to a six digit US dollar price tag. Other techniques directly borrow concepts from photolithography, enabling their convenient use as a replacement tool, however giving them the same disadvantage regarding operation costs due to mask fabrication. These techniques include nano-imprint lithography (NIL)<sup>[22]</sup> and micro-contact printing ( $\mu$ CP).<sup>[23–25]</sup> Because of the need for molds or stamps, these techniques also show little patterning flexibility and long turnaround time from pattern inception to pattern creation. On the other hand, probe- and beam-based techniques such as electron beam patterning, STM-based lithography and DPN writing allow

**Table 1** Comparison of popular nanolithography techniques

Nanopatterning technique	Serial/parallel	Material flexibility	Patterning operation flexibility	Resolution	Registration accuracy	Speed	Cost	
							Equipment	Use
Photolithography	Parallel	No	No	~90 nm	High	Very fast	\$10M++	High
E-Beam lithography	Serial	No	Yes	~15 nm	Very high	Medium	\$500k–\$5M	High
Nanoimprint lithography (NIL)	Parallel	No	No	~10 nm	High	Fast	\$1.6M	High
Dip-pen nanolithography (DPN)	Serial or parallel pens	Yes	Yes	14 nm	Extremely high	Slow, but highly scalable	\$200k	Low
Microcontact printing ( $\mu$ CP)	Parallel	Yes	No	~100 nm	Low	Fast	~\$300k?	High
Scanning tunneling microscopy (STM)	Serial	Limited	Yes	Atomic/molecular	Extremely high	Very slow	~\$200k–\$1M	Low

for a very flexible and transparent hand-off between design and patterning. E-beam lithography, which also exposes a resist as masking material, is often used instead of photolithography for concept and low-volume work and is the most commonly used method for producing high-resolution masks for mask-based techniques. E-beam lithography is reasonably fast and well developed and offers a metrology aspect in the same instrument comparable to DPN printing, but it is specialized to high-vacuum operation and resist patterning. On the other hand, the DPN process has the unique combination of material flexibility, extremely high registration accuracy<sup>[26]</sup> between patterns consisting of multiple inks, low overall cost, and ambient environmental operation. This makes DPN writing often the choice for applications involving rapid prototyping and patterning with biomolecules at the nanoscale, while its parallel probe capability holds the promise of substantially increased throughput, when required. Its excellent registration accuracy of better than 50 nm not only allows very exact registration between multiple layers, possibly with multiple inks, it also allows alignment of DPN patterns with ultrahigh precision to previously existing surface structures (e.g., microelectronic structures produced via photolithography). In the last years, an array of good review articles on general nanoscale patterning and imaging has been published.<sup>[3–5,27,28]</sup> Therefore, the following discussion focuses exclusively on DPN methods.

## BASICS OF DPN

DPN patterning is a direct deposition technique where one or more chemically coated “pens” (usually a scanning force microscopy tip) deposit a material (“ink”) with nanometer precision to form a stable pattern

feature onto a substrate (the “paper”),<sup>[16]</sup> see Fig. 1. Typically, contact mode is used for the underlying AFM operation although patterning in AC mode (e.g., non-contact mode) has also been demonstrated.<sup>[29]</sup> In a typical DPN experiment, a conventional AFM probe tip is coated with a molecule, or “ink,” by dipping the tip in a solution of the molecules. The AFM probes used are typically made of single crystal silicon or a thin film of silicon-rich silicon nitride. They have a sharp conical or pyramidal tip that ends in an apex with an effective radius of only 10–15 nm. By contacting the tip with the surface, molecules are deposited via a water meniscus that naturally condenses at the tip–substrate contact under ambient conditions. Because so many different inks can be processed via DPN printing, as explained elsewhere in this entry, it is not possible to give a clear set of deposition control parameters for all possible chemistries. However, for all processes that are fully or

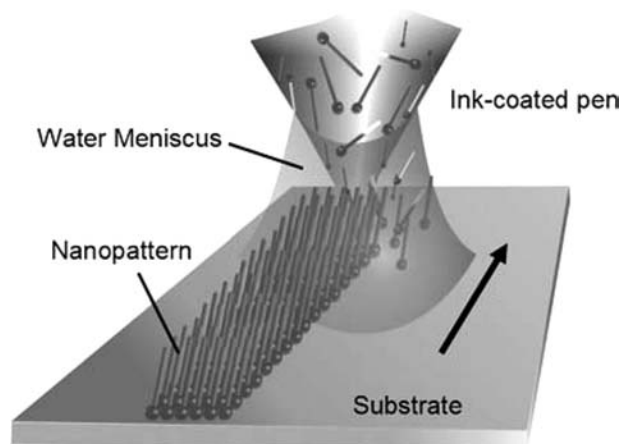


**Fig. 1** The principle of DPN. A sharp pen, coated with a functional ink, is scanned across a surface and deposits material through a water meniscus.

partially based on chemical diffusion, longer tip-substrate dwell times lead to larger pattern spot areas or wider lines, see Fig. 2.<sup>[16,30,31]</sup> Lines and dots of 14 nm width or diameter have been demonstrated using 16-mercaptohexadecanoic acid (MHA) on polycrystalline gold while a clear connection between tip sharpness and achievable patterning resolution was observed.<sup>[32]</sup> Besides contact time, environmental humidity and temperature are the most important factors that change ink deposition characteristics.<sup>[33–36]</sup> Among others, an entry in this encyclopedia treats these effects in detail.<sup>[37]</sup> Because DPN ink transport onto the surface is due to highly complex yet reproducibly controllable interactions between ink and surface molecules as well as the environment, DPN printing can be used not only as a patterning technique but also as a research tool for material interactions at the nanoscale.<sup>[38–40]</sup> After patterning an ink, the same instrument can be used as an AFM in contact or AC mode to inspect the written patterns, either by using the writing tip at high scanning speeds, such that ink deposition is negligible, or by using a special reading pen in a multipen array, as described later in this entry. It is in these passive multipen array applications, as well as multi-ink writing scenarios, that the extremely high registration accuracy of scanning-probe-based instruments adds value. Another possibility to image previously written features is by mounting a fresh, un-inked probe. As features get smaller and smaller on samples that still must be easy to handle, finding the nanoscale features with a new probe becomes equivalent to searching for a pin in a haystack, especially if prototype work involves writing only a few features. In the instance of the dedicated DPN instrument NSCRIPTOR by NanoInk Inc., a two-level

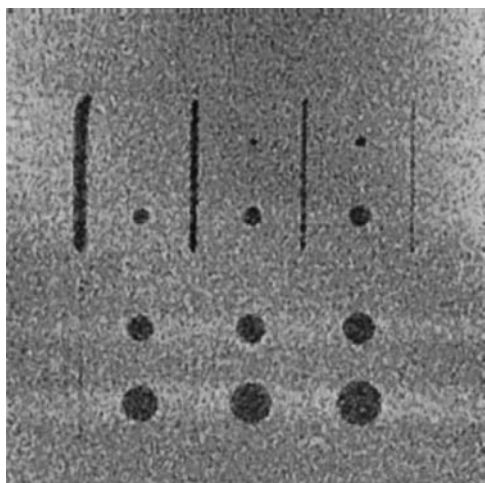


**Fig. 2** A calibration run using an alkanethiol on gold substrate and the InkCal software by NanoInk. Longer dwell times and slower scan speeds result in bigger spots and wider lines, respectively.

routine allows alignment of a new scanning tip to features on the surface, first on the microscale and then on the nanoscale. With this and other useful routines, such as semiautomated ink diffusion calibration, the DPN process becomes a reliable and easy-to-use lithography technique that does not require expert knowledge to produce results.

## APPLICATIONS

### DNA Patterning

Microarrays, especially genetic arrays, are gaining acceptance as an important tool in many areas of medical research and are becoming the discovery tool of choice in the pharmaceutical community.<sup>[41]</sup> The use of microarrays can potentially save money and time in bringing a therapeutic to market by accelerating the cycle of target discovery, candidate lead validation, and toxicity studies. Genomic and proteomic microarrays are particularly powerful in this context because they facilitate high-throughput screening of vast libraries of molecules. Further developing microarrays into nanoarrays brings with it various advantages;<sup>[42]</sup> for example, reduced cost due to less usage of reagents and analytes, and higher information content on the same sample area. Balancing these improvements is the challenge of developing appropriate high-resolution screening tools. Among patterning techniques that have the potential for operation at sub-micrometer dimensions, there are two major strategies for the fabrication of bioarrays. One method employs indirect patterning by locally altering the chemical or physical properties of a surface in order to selectively immobilize or build up biomolecules. In the other method one locally deposits the molecules or materials of interest using a nanoscale delivery device. In the past, these delivery devices have taken the form of a pin, pipette, or a non-contact jetting device and typically produce spots many micrometers in diameter. This technique is preferred because several different kinds of molecules can be deposited without exposing the patterned molecules to harsh solvents, chemical etchants, ultraviolet, or electron radiation and vacuum conditions and without risking cross-contamination—the desired chemistry is carried out exactly, and only where it is desired. DPN writing is the only technology that can directly deposit biological molecules to form multiple, sub-micrometer chemically diverse patterns with ultrahigh precision and registration. DNA patterning via DPN writing can be highly controllable in terms of pattern size and shape, resulting in immobilized DNA that is functional and accessible to specific binding of labeled targets.<sup>[43]</sup> Initial studies showed that in addition to tip-coating

and humidity, a judicious choice of ink–substrate combination can facilitate the DPN process. For example, hexanethiol-modified oligonucleotides were used to directly pattern gold substrates with features ranging from 30 nm to several micrometers in size. For nanoarrays on oxidized silicon wafers or glass surfaces, acrylamide-modified oligonucleotides were deposited directly via DPN patterning onto activated (mercaptopropyl-trimethoxysilane) substrates where subsequent reaction formed a covalent link to the surface, Fig. 3A. Non-specific binding of target oligonucleotides was minimized by passivating the unpatterned regions of the substrate by reaction with buffered acrylic acid monomer at pH 10. The feature size of individual DNA spots was controllable over a range of several orders of magnitude via the tip–surface dwell time and by tuning the relative humidity inside the patterning chamber. For micrometer-sized features on silicon substrates, the binding selectivity and function of patterned oligonucleotides was verified by hybridizing complementary fluorophore-labeled DNA.<sup>[43]</sup> For example, a two-component DNA pattern was characterized by binding complementary

fluorophore-tagged complements under hybridization conditions. Importantly, the only epi-fluorescence signals detected on the sample corresponded to the complementary targets on the patterned area. An overlay of the red and green images shows the positions of the two different sequences, Fig. 3B. In a second experiment involving sub-micrometer sized features, two different DNA sequences were identified by selectively binding two different sizes of DNA-modified gold nanoparticles to the respective patterns of DNA. AFM topography was used to show that the gold particles reacted only with the correct oligonucleotide spots. Thus, the patterned oligonucleotide was accessible for hybridization and the hybridization was selective. In these preliminary experiments, spot shape, size, and emission intensity were extremely uniform within individual features and from spot to spot. With this technique, DNA spots with diameters as small as 50 nm were prepared, i.e., 10,000 times smaller (in terms of area density) than those in conventional microarrays formed by robotic spotting. With this resolution, arrays with  $\sim 100,000$  oligonucleotide spots can be generated within an area the size of a typical AFM scanner ( $100 \times 100 \mu\text{m}^2$ ), making it possible to investigate scanned probe methods of microarray readout.

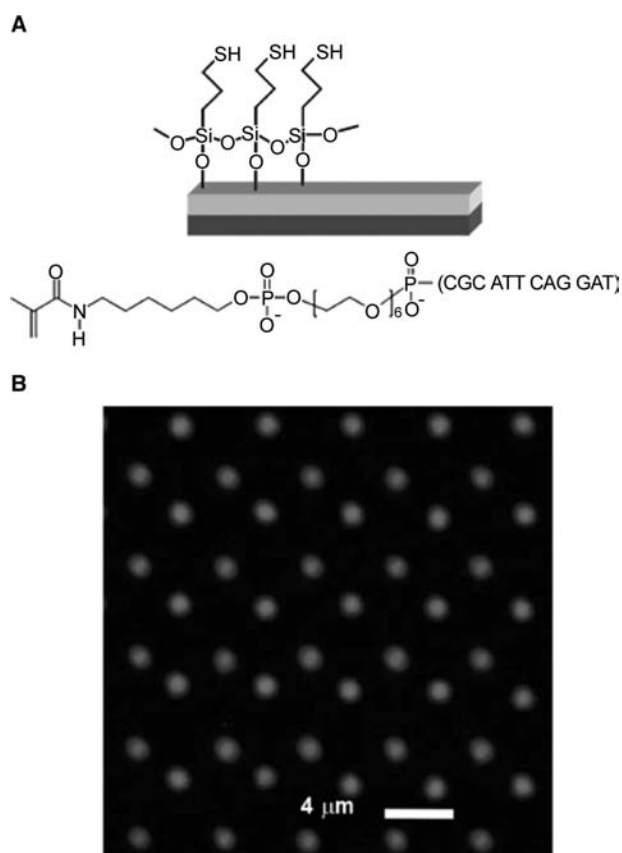


**Fig. 3** (A) Surface and oligonucleotides functionalization for covalent attachment. (B) Epi-fluorescence image of an area containing two different DNA sequences. *Source:* Reprinted with permission from Ref.<sup>[43]</sup>. © 2002 AAAS.

### Protein Patterning

The DPN technique has also been extended to direct deposition of proteins. Kaplan and Mirkin were the first to directly pattern thiolated collagen and collagen-like peptides onto gold surfaces.<sup>[44]</sup> The researchers concluded that the DPN deposition process promotes the formation of native collagen fiber on the surface. Further reports of direct protein patterning include deposition of human chorionic gonadotropin antibody onto (3-glycidioxy-)propyltrimethoxysilane modified glass surfaces as well as a number of immunoproteins, enzymes, and viruses<sup>[45–51]</sup> Although DPN writing is an extremely gentle lithographic technique, surface interactions and covalent or non-covalent attachment chemistry could potentially denature some classes of proteins. Therefore, significant effort has been directed toward studying the complex issues involved in preserving the biological activity of immunoproteins such as IgG during a DPN experiment.<sup>[47]</sup> Additives such as glycerin were used in the protein patterning solution to enhance patterning capabilities when depositing human IgG and rabbit IgG nanostructures. The activity and identity of the immobilized proteins were confirmed by binding fluorescently tagged antibodies specific for the two different nanopatterns.<sup>[47]</sup> The resulting two-color fluorescence images revealed specific biological activity and indicated that the patterns

exhibited acceptable amounts of rabbit–human cross-reactivity. In these and other initial studies,<sup>[37,48]</sup> researchers used fluorescence microscopy to detect the patterned molecules. For dot spacing below 500 nm such optical detection technologies are no longer appropriate due to resolution limits imposed by the diffraction of light. In these cases other methods of detecting binding interactions must be developed. As shown for the DNA nanopatterning work presented in the previous section, nanoparticle probes can be particularly useful for selectively labeling proteins in nanoscale binding assays.<sup>[52]</sup> The binding of metal nanoparticles in particular can be detected optically, electrically, or using AFM topographic imaging.<sup>[53–55]</sup> Nanoarrays printed via DPN present another exciting opportunity: label-free screening. Monitoring label-free signals such as height, friction, and electrostatic changes can lead to high-sensitivity detection methods based on AFM imaging and on-chip electronic circuitry. Researchers at Northwestern University showed that selective binding of antibodies to these protein nanoarrays can be detected without the use of labels by monitoring small (5–15 nm) topographical height increases in AFM images,<sup>[45]</sup> see Fig. 4. A two-component array consisting of nanoscale spots of rabbit IgG protein and lysozyme enzyme was deposited on a gold substrate. When the patterned substrate was exposed to a solution containing anti-IgG and then scanned by AFM, a height increase of 5.5 nm was observed in the position of the IgG features while no height increase was observed at the site of the lysozyme features used as control, see Fig. 5.

## Other Applications

DPN writing has become a diverse research tool in the past years.<sup>[56]</sup> Thus, it comes as no surprise that the

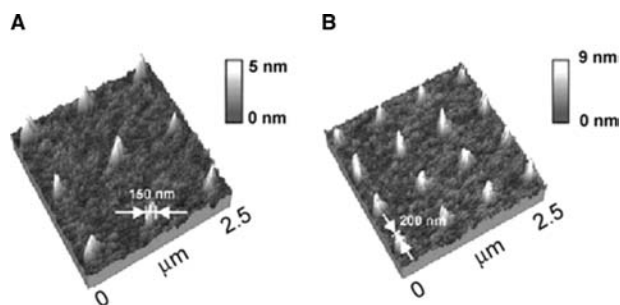


**Fig. 4** Contact AFM images of protein nanodot arrays prepared via DPN patterning: (A) image of lysozyme nanodot array; (B) image of IgG nanodot array. *Source:* Reprinted with permission from Ref.<sup>[45]</sup>. © 2003 American Chemical Society.

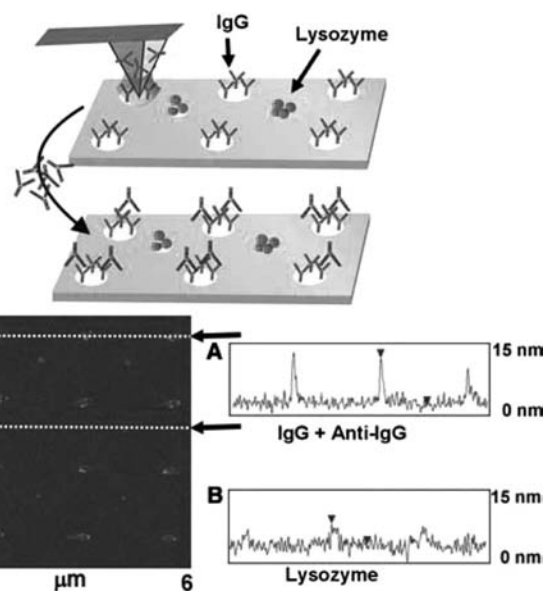


**Fig. 5** Two-component DPN-generated protein pattern after reaction with anti-IgG. Top, scheme showing label-free detection method; Bottom, a height increase of  $5.5 \pm 0.9$  nm in the IgG features is observed by tapping mode AFM. Note that no height increase is observed on lysozyme pattern. *Source:* Reprinted with permission from Ref.<sup>[45]</sup>. © 2003 American Chemical Society.

materials deposited and applications pursued with DPN patterning are equally diverse. Here, a look at the main application fields of DPN writing besides the biotech sector discussed above, namely polymers, hard materials, and etch resist applications, should suffice as a starting point for further literature research by the inclined reader. Finally, recently developed advanced DPN techniques are discussed as well.

## Polymer patterning

Starting in 2002, a series of papers was published that explored patterning of various polymeric materials using DPN. It was found that it is not necessary to rely on covalent bonding between ink and substrate as driving force for ink diffusion and dependable ink transfer. Instead, DPN writing also works on molecules that use weaker attraction forces to the substrate such as electrostatic attraction<sup>[57]</sup> and possibly even van der Waals forces.<sup>[48,58]</sup> Writing electrically conductive lines on the nanoscale is a significant step for nanotechnology, especially if the materials used merge electric conductivity with optically active behavior. The group of J. De Yoreo was able to pattern a luminescent conductive polymer, MEH-PPV,<sup>[37,48]</sup> using DPN deposition and observed its optical activity using its fluorescence response. Using optical intensity rather than topographic line width, the group demonstrated a



diffusion curve similar to those observed when using alkanethiol inks on gold. These and other researchers<sup>[59]</sup> also demonstrated writing and optical imaging of various organic dyes. Conducting polymers were also deposited by Lim and Mirkin.<sup>[57]</sup> Here, two different materials, self-doped sulfonated polyaniline (SPAN) and doped polypyrrole (PPy), were deposited using water as solvent. It was found that the negatively charged SPAN polymer could be patterned in a controlled fashion on a positively charged surface, modified with diethylene-triamine, while positively charged PPy showed similar behavior on negatively charged piranha-treated substrates. It was not possible to produce controlled deposition when switching the substrate between the two polymers or when using unmodified silicon surfaces. It was therefore concluded that the electrostatic interaction served as driving force for DPN patterning for the materials. Another approach was chosen by Maynor et al.<sup>[60]</sup> where electrically biased DPN deposition, further explained below, was used to deposit polythiophene nanowires, a polymeric material that possesses interesting electrical and electrooptical properties. Unfortunately, because of the small size of the deposited structures, none of the above-mentioned researchers attempted to measure electrical characteristics of the patterned materials. The group of V. Dravid at Northwestern University has gone one step further<sup>[61]</sup> and was able to measure a distinct electrooptical response from the deposited material. In short, the researchers developed an ink containing pyrrole monomer and a polymerizing agent and patterned the ink onto an electrode gap. After curing, the patterned features exhibited clear photosensitive behavior, documented by measured  $I$ - $V$  curves with and without illumination and temporal resistance profiles with changing illumination, see Fig. 6. McKendry et al.<sup>[62]</sup> studied writing with dendrimers on silicon surfaces and produced lines down to 100 nm width. These versatile materials have potential applications, for example, in the fields of chemical sensors and photosensitive materials. The researchers investigated DPN patterning with two different classes of dendrimers and dendrimers of varying molecular weight. They found that molecular weight is an important factor in material delivery rate when comparing equally functionalized molecules. In addition, the type of surface functionalization is an important parameter for ink delivery as well. Finally, the group of C. Mirkin also demonstrated a DPN technique to produce small but diverse libraries of nanoscale polymer brushes that comprise large numbers of structurally distinct compounds.<sup>[63]</sup> This technique using surface and site-specific ring-opening metathesis polymerization is a formidable example of the use of DPN writing to produce combinatorial libraries of many different materials.

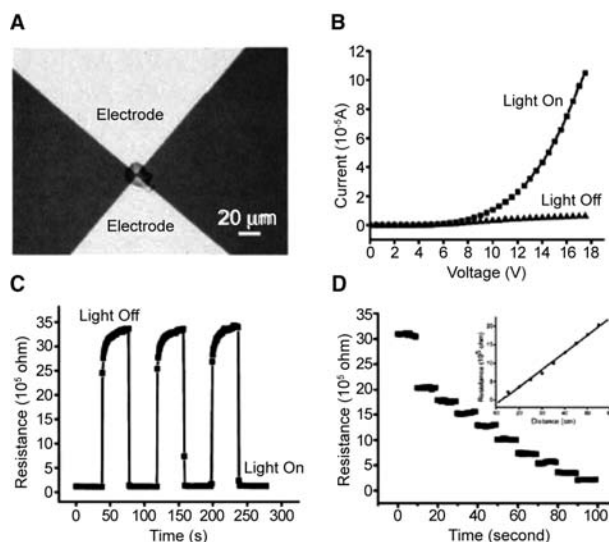


**Fig. 6** (A) Optical micrograph of a patterned conducting polymer structure between a 2  $\mu\text{m}$  wide electrode gap. (B)  $I$ - $V$  curve of the patterned structure in dark and illuminated states. (C) Repeated photoresponses of a patterned structure. (D) The dependence of resistance to the relative light intensity. Source: Reprinted with permission from Ref.<sup>[61]</sup>.

### Hard material patterning

In addition to polymers, so-called “hard” materials have received much attention in recent years from the DPN community. Typically, “hard” materials as defined for the purpose of this review have Young’s moduli near and above 80 GPa and are patterned not in a single-molecular layer but in some form of bulk deposition or discrete particle attachment. One of the most exciting techniques of particle patterning is to use structures patterned by DPN as templates for subsequent particle self-assembly. As mentioned above, Demers et al.<sup>[52]</sup> used alkylamine-modified DNA linked to DPN-patterned MHA as templating material and nanoparticles functionalized with complementary DNA in a solution as self-assembly agent. Two differently sized and functionalized types of nanoparticles were used to assemble on the respective complementarily modified areas. A most important realization stemming from this work was that it is indeed possible to create orthogonal assemblies of nanoparticles using the specificity of DNA as linking agent, resulting in small amounts of non-specific binding. The technique of templating was also ported to patterning magnetic nanostructures. Several publications exist in this field with obvious potential applications in magnetic high-density data recording. Using templating of magnetically active iron oxide ( $\text{Fe}_3\text{O}_4$ ) particles with 4–16 nm particle diameter on MHA templates, Liu et al.<sup>[64]</sup> were able to create sub-100 nm magnetic dots. Other researchers<sup>[65]</sup> used a sol containing  $\gamma\text{-Fe}_2\text{O}_3$

nanocrystals as ink and produced lines of less than 200 nm width by direct patterning on multiple substrate materials. Fu et al.<sup>[66]</sup> also used a sol-gel-based technique to produce magnetic nanostructures. Here, a BaFe precursor solution was written via DPN and then cured at 950°C. The resulting barium hexaferrite nanostructures contained polygonal single-crystalline particles with 35 nm mean diameter. Lines of less than 100 nm linewidth could be drawn while the annealed crystals were shown to have reasonably high coercivity and remnant magnetization. Su et al. were able to further make use of their development work on sol-based ink patterning<sup>[67]</sup> and produced a functional chemical sensor array.<sup>[68]</sup> The individual chemical sensors consisted of two current-carrying electrodes and a DPN-patterned dot of metal-doped SnO<sub>2</sub> connecting the electrodes. Chloroform, toluene, and acetonitrile were introduced into the atmosphere and were clearly distinguishable due to the characteristic resistance changes on the eight different sensor materials. Importantly, the sensor exhibited rapid response and fast recovery due to the small size and nanoporous structure of the patterned material.

As a last field of “hard” material DPN, patterning of metallic structures should be surveyed here. Metals have been patterned with DPN using a multitude of approaches. The group of J. Liu developed electrochemical DPN (E-DPN)<sup>[69]</sup> where an electric field is supplied between the patterning tip and the substrate. In this instance, the water meniscus that carries the ink also acts as a miniature electrochemical cell and allows for example for reduction of metal salts and deposition as elemental metal. This technique was not only used on conducting polymers<sup>[60]</sup> as mentioned above, but also to pattern a variety of metals and semiconductors including Pt, Au, Ag, and Cu using a corresponding metal salt as starting material. The same group also showed<sup>[70]</sup> that a gold metal salt can be deposited as elemental gold without the use of E-DPN on certain surfaces such as silicon, through surface-induced reduction. Such metal salts were also used to pattern catalyst sites for GaN nanowire growth.<sup>[71]</sup> Another approach to metal patterning, viable also on insulating materials, is the direct deposition of a metal precursor ink that can be converted to a metallic film at relatively low annealing temperatures. NanoInk-internal development work has yielded encouraging results<sup>[72]</sup> using this approach, see also Fig. 7. In particular, it was possible to measure electrical properties of such lines: A 5 μm wide version of the trace shown in Fig. 7 exhibited a resistivity of only 4.3 μΩ cm, making this ink formulation a good candidate for further studies into miniaturization. It is also possible to deposit metallic nanoparticles as was shown by Ben Ali et al.<sup>[73]</sup> using thiol-capped gold nanoclusters. In a further refinement of this approach, the

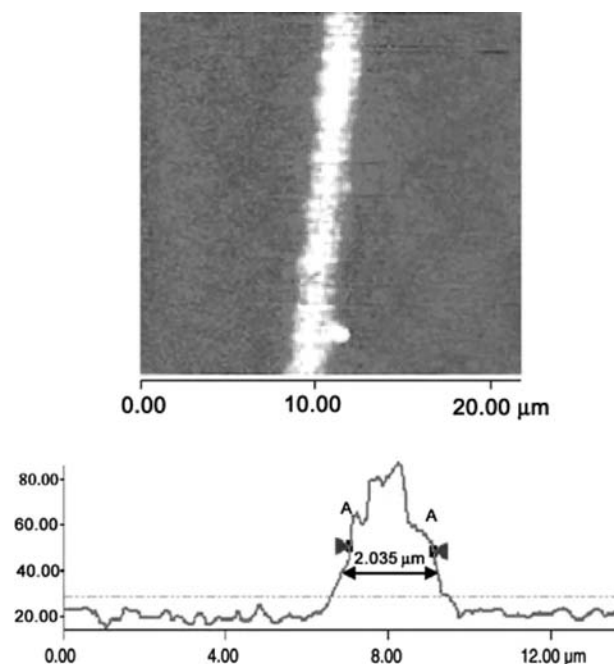


**Fig. 7** A metallic line deposited via DPN writing. It is 2 μm wide (see AFM scan on top) and 6 nm high (line scan below).

group of C.N.R. Rao used aqueous metal nanocrystal dispersions<sup>[74]</sup> with particle sizes of about 3 nm and produced lines of width as small as 30 nm with one to three layers of nanocrystals in height.

### Etch resist patterning

DPN patterning can also be used in a more traditional way to selectively mask an underlying material for certain further processing steps, equivalent in function to a layer of exposed and developed photoresist in traditional photolithographic microfabrication. In the first publication reporting this application by Weinberger et al.<sup>[75]</sup> 1-octadecanethiol (ODT) was patterned via DPN onto a gold-coated silicon substrate. The monolayer formed by this alkanethiol is known to protect the underlying Au from etching during certain chemical wet etching procedures.<sup>[23]</sup> Thus, using a standard ferri/ferrocyanide etchant, only the gold layer unprotected by the patterned ODT is removed. In a subsequent wet etching step, KOH attacks the silicon wafer where it is not protected by gold. This dual-resist technique results in a three-dimensional relief structure etched into the silicon with height 55 nm and top line width down to 50 nm, see Fig. 8. Importantly, this basic technique can be used to quickly and inexpensively produce molds or stamps used for NIL or μCP. Using this approach but omitting the second etch step, it is also possible to produce

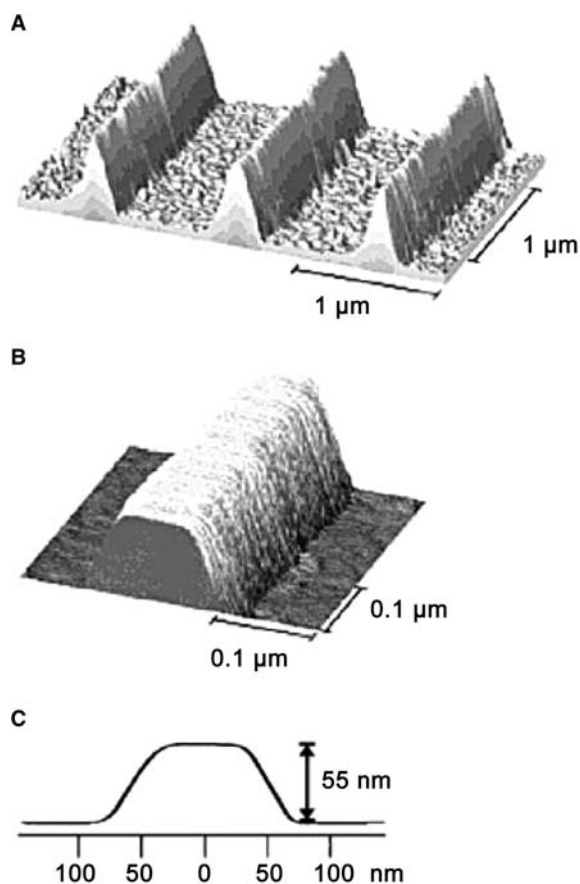


**Fig. 8** (A and B) AFM topography images of DPN-patterned and wet etched silicon wafer. (C) Cross-sectional topography trace taken from image (B). *Source:* Reprinted with permission from Ref.<sup>[75]</sup>.

metal nanostructures, very similar to the way photoresist can be used together with chemical wet etchants on an underlying continuous metal thin film. Such nanoscopic structures are of interest for the study of surface-enhanced Raman spectroscopy, plasmon optical coupling, and nanoparticle-based biodiagnostics. Zhang et al. have perfected this patterning technique to produce gold structures in the sub-50 nm regime and nanogaps from 12 to 100 nm.<sup>[76]</sup> They also extended the patterning and etch protocols to include silver and palladium<sup>[77]</sup> structures in addition to gold. Finally, the group of Chad Mirkin also introduced an electrochemical desorption strategy<sup>[78]</sup> that reduces the size of already patterned structures by “whittling” them down in size from the outside. It was found that by holding the potential of a gold-patterned substrate at a value of  $-750$  mV against an Ag/AgCl electrode, DPN-generated MHA patterns were slowly reduced in size by electrochemical desorption, resulting in dots as small as 30 nm in diameter. There are indications that this technique can be well combined with the

aforementioned dual-resist technique in order to increase feature resolution.

## FUNCTIONAL EXTENSIONS OF DPN

### Passive Pen Arrays

One of the most valuable properties of DPN writing for high-volume applications is its force independence. It was shown<sup>[17]</sup> that the tip contact force for single-pen writing has no or little effect on the ink diffusion speed in the case of alkanethiol inks. This could well be an effect of binary on-off behavior due to the capillary force acting through the water meniscus, which can be orders of magnitude larger than the “contact force” of the AFM cantilever probe. Thanks to this effect, slight variations of contact force across an array of writing probes that is introduced by minute misleveling of the array with respect to the sample surface does not affect the writing process. Writing identical structures in parallel with a multipen array becomes possible as demonstrated by Hong and Mirkin<sup>[17]</sup> In this first report, a series of standard AFM probes were used together in parallel. One pen was used with AFM feedback while the others followed passively, thus the term “passive pen array.” In order to fill a large area with parallel-written features without gaps, the individual pens must be spaced not wider than the AFM scanner range, which is typically 100  $\mu\text{m}$ . Thus, microfabricated pen arrays are needed. Such microelectromechanical systems (MEMS) based parallel cantilevered pen arrays were pioneered by the group of C. Quate and used for both imaging and lithographic applications.<sup>[79,80]</sup> In recent years, the group of Chang Liu worked closely together with the original inventors of DPN to produce such passive probe arrays and report on parallel writing.<sup>[81]</sup> The same group also reported on conductivity-based contact sensing to improve probe leveling.<sup>[82]</sup> Independently, NanoInk also developed passive pen arrays customized for DPN patterning requirements and the NSCRIPTOR instrument, using 2–26 parallel pens. Among the features offered are dedicated reader and writer probes, a variety of cantilever-to-cantilever gaps, and multiple spring constants for use with different inks and substrates. Fig. 9 shows an SEM image of such an array. To increase the level of parallel DPN writing even more and make good use of the linear scaling of throughput with number of pens, two-dimensional arrays of probes are of great interest. However, they pose unique challenges in terms of leveling and contact force management. MEMS fabrication of such devices has already been demonstrated by different research groups.<sup>[83,84]</sup> NanoInk produced a 1.3 million cantilever array on a 4 in. wafer footprint using conventional

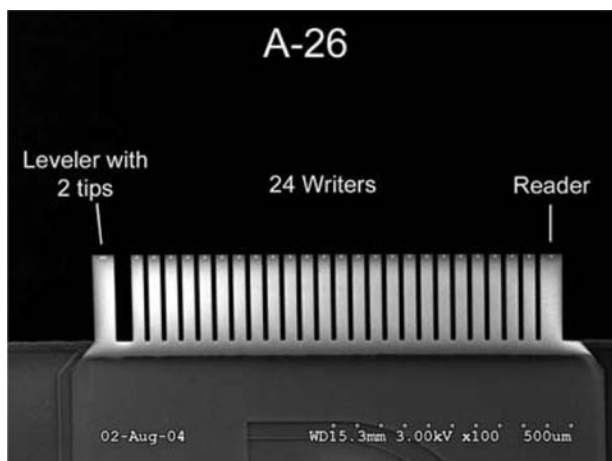


**Fig. 9** SEM micrograph of NanoInk passive pen array A-26. Twenty-four writer pens are equally spaced and flanked by one wider reader tip and an additional cantilever used for array leveling.

fabrication techniques also used for NanoInk's commercial offerings of silicon nitride cantilevers, see Fig. 10A. This array was used with a fluorescent ink formulation described elsewhere<sup>[59]</sup> to pattern a large area by repeating a manual "stamp and translate" process several times. Imaging of these dots using a fluorescence microscope showed large areas of uniformly patterned dots as seen in Fig. 10B and some defect sites as well.

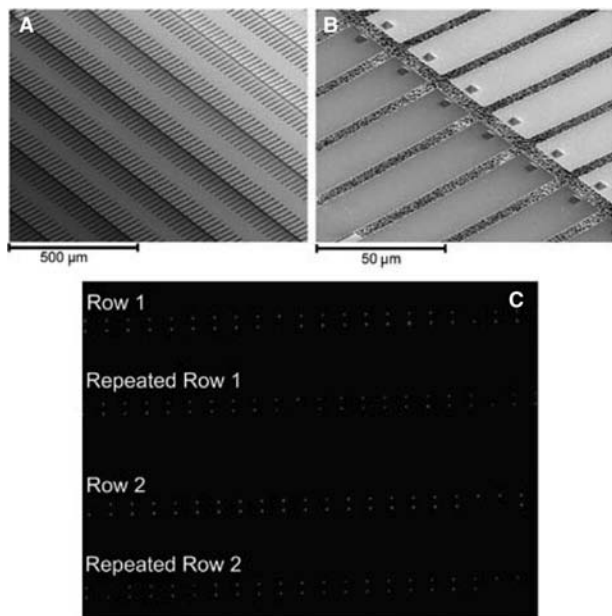


**Fig. 10** (A) SEM images of a 1.3 million pen array fabricated by NanoInk, showing multiple double-rows of cantilevers. (B) A zoom-in on opposing pens. (C) Fluorescence image acquired after stamp-and-repeat operation with the inked array.

## Ink Delivery

In the most basic DPN process, the entire AFM pen is submerged and then removed from the ink solution. In many cases excess ink and solvent are removed with a high-pressure blast of air or gas. While this technique can produce good results in skilled hands, it is advantageous to have a more reproducible approach to inking the pen. Various research groups have worked on developing a writing pen with continuous ink supply as it can be found in a macroscopic fountain pen.<sup>[85–87]</sup> However, these probes cannot produce line widths of less than a few hundred nanometers and are quite limited in the types of ink that can be transported. The other possibility is to introduce the ink by dipping the pen into an inkwell. For reproducible ink transfer, it is advantageous to only let the sharp tip get in contact with the liquid and not submerge the entire cantilever. This also reduces feedback laser reflection problems because spilled ink on the top side of the cantilever can reduce reflected laser intensity and produce interference effects. Most importantly, it also paves the way for inking multiple pens with different inks to allow writing multiple inks in the same session. NanoInk's approach, inspired by early work by Chang Liu at UIUC, is to produce microfabricated devices (inkwells) that carry ink and can be brought in contact with the pen to transfer ink onto the pen. These inkwells have the same lateral spacing as existing multipen arrays and consist of large ink reservoirs and distribution channels so that adjacent pens can be supplied with different inks without cross-contamination, as shown in Fig. 11. One additional and important use for microfluidic ink delivery is to not supply ink to specified probes while adjacent

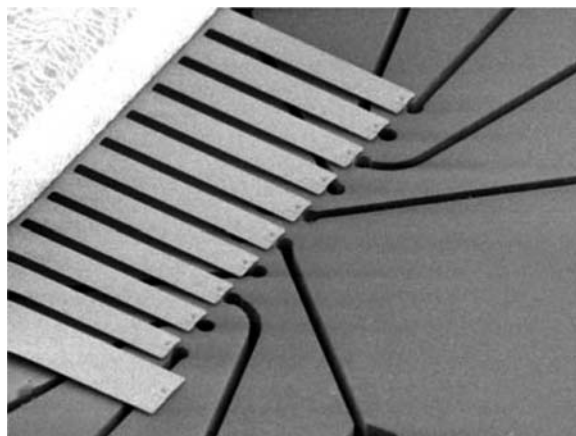


**Fig. 11** SEM image of a NanoInk passive pen array A-11 aligned to an inkwell. Ten manually fillable larger reservoirs lead through microfluidic channels to 10 microwells that can ink the tips. The wider reader probe at the bottom remains uninked.

probes receive ink, as explained in the following: In the case of single-pen DPN operation, the inked probe is also used for inspection of the written pattern. While it is commonly assumed that ink transfer is negligible at very high probe scan speed, it can be very advantageous to use an adjacent, non-inked probe for pattern inspection. This allows for slower scan speed with possibly better image quality and less contamination onto the finished pattern. The inkwells were designed to deliver at least four different aqueous inks (e.g., for genomic applications) into an appropriately spaced inkwell array. Fluid transport occurs by open channel meniscus driven flow (wicking) in microchannels, which distribute liquid from reservoirs into an array of terminal inkwells connected by tributaries. The flow rates in the microchannels were calculated from a balance of the capillary and viscous forces (neglecting inertial forces).<sup>[88,89]</sup> It is important to note that proper ink containment is a function of the wetting properties of the various surfaces as well as the overall three-dimensional geometry of the pen-inkwell system. Correctly chosen parameters result in well-contained ink delivery as seen in Fig. 12. The pens could be used immediately for patterning, Fig. 13.

### Active Pens

The next advance in DPN technology, after adding the capability of using multiple parallel pens and the use of various different inks in parallel, is the move from arrays of passive probes to individually actuated pens. Passive probe arrays are limited to writing the same structure with all pens. This increases throughput  $n$ -fold with  $n$  pens if the desired final pattern is a repetition of any single pen pattern, each pattern spaced from each other by the probe pitch. For more complex and large-scale patterns, active pens are the enabling technology to use: If the actuated probes are spaced

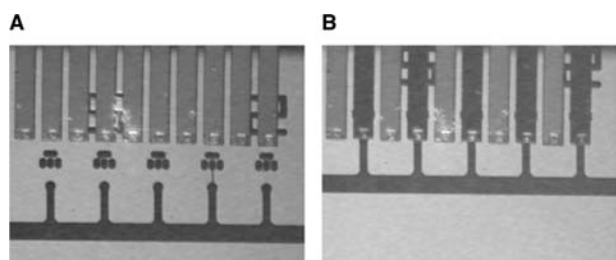


**Fig. 12** (A) Video image of a probe array leveled and rotationally aligned with filled microwell array below. (B) Video image of the same setup during inking process. Here, cantilevers that are positioned on top of microwells are deflected toward the liquid filled microwells. This changes the apparent brightness since light reflects off-axis. *Source:* Reprinted with permission from Ref.<sup>[89]</sup>.

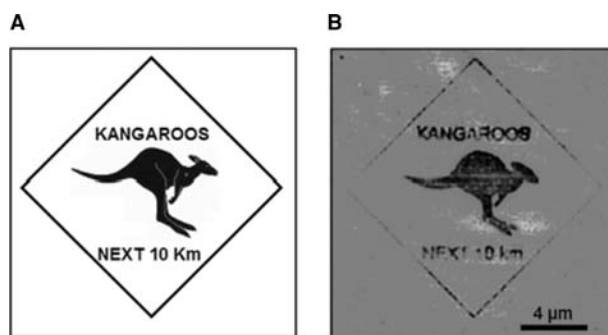


**Fig. 13** (A) Original bitmap used as source for the pattern. (B) After conversion to DPN instructions, this pattern was written using a NanoInk NSCRIPTOR, immediately after inking the probe in an inkwell as shown in Fig. 12.

apart as far as the scanner area is across, the patterning area is effectively increased by a factor of  $n$ . If they are closer together, they have an overlapping area where multiple inks can be overlaid into a single writing space (i.e., the scanner range). In contrast to passive pens, active probe arrays can be used to produce arbitrarily complex patterns of multiple inks over large areas. In particular, complex patterns can be drawn with a succession of single adjacent linear paths. In this “raster write” approach, the complexity of the pattern rests in the programming and timing of pen actuation rather than the complicated movement of a single pen or a passive multiprobe array.

Various actuation principles were explored, but most research to date focuses on thermal actuation. Thermal actuation of a cantilever is readily implemented using a bimorph design, where heating of a double layer of thin films of different materials will result in bending if the materials have sufficiently different thermal expansion coefficients. Furthermore, thermal bimorphs have already been used previously in MEMS design, with applications ranging from data storage<sup>[90]</sup> to AC-mode AFM<sup>[91]</sup> to wafer probe cards.<sup>[92]</sup> On the downside, thermal actuation can lead to increased cross-talk between adjacent pens as well as detrimental

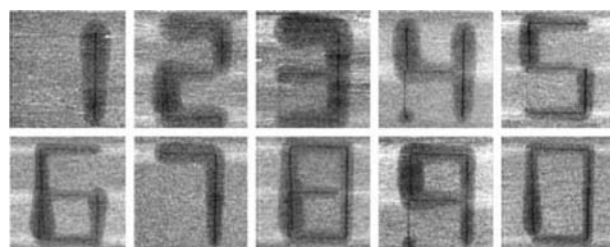


**Fig. 14** Lateral force microscopy scans,  $8 \mu\text{m}^2$ , of 10 simultaneously generated ODT patterns on a gold surface, using thermomechanical active pens. Writing speed was  $1 \mu\text{m}/\text{sec}$ . *Source:* Reprinted with permission from Ref.<sup>[94]</sup>.



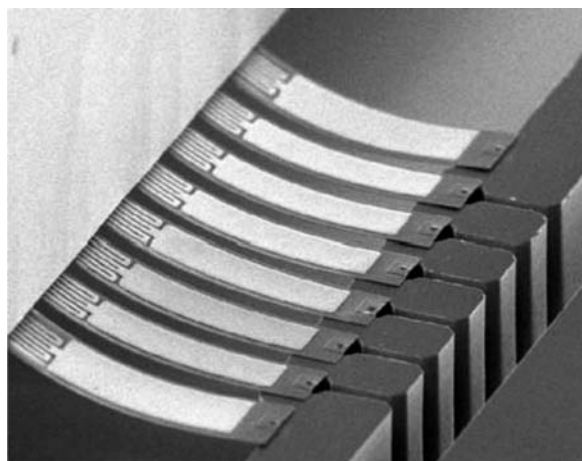


**Fig. 15** SEM micrograph of a NanoInk active pen array aligned to an inkwell. On top of the cantilever, the serpentine resistive heater and large area heat spreader can be clearly seen.

heating of the ink; so particular care has to be taken in the design of the pen array with these issues in mind. Sheehan et al. have shown that the heated tip can also be used to advantage.<sup>[93]</sup> Using tip temperature control, they demonstrated “thermal DPN,” or tDPN, the controlled deposition of an ink that only becomes liquid and deposits once the tip is heated. When using active pens for non-thermal DPN writing, the goal is nonetheless to keep the tip at the lowest temperature possible. Therefore, the bimorph should be kept as far away from the tip as possible. The group of Liu produced a body of work<sup>[94–96]</sup> describing the fabrication, integration, and application of a 10-pen active parallel array. The group used rigorous analytical and numerical thermomechanical modeling to optimize the design. They produced active pen arrays based on silicon nitride<sup>[95]</sup> and silicon<sup>[96]</sup> cantilevers. Notably, the group was able to write 10 numerals, each one with one active pen, using ODT as ink,<sup>[94]</sup> see Fig. 14. NanoInk also produces commercially available active pen arrays that also use thermal bimorph actuation. Notably, the two designs differ in that they have opposite actuation directions. NanoInk active pens actuate toward the substrate, which is particularly useful if the duty cycle of each single pen is expected to be less than 50%. The NanoInk bimorph design consists of the silicon nitride cantilever and an evaporated Cr/Pt/Au thin film. Fig. 15 shows such an array aligned to and approached into an inkwell array.

## CONCLUSIONS

In this review, we presented the basics of the DPN process as well as the positioning of DPN writing with

regards to other popular nanolithography techniques. Applications of DPN were surveyed, starting with biomolecule patterning, such as DNA and protein writing. Polymer and hard material patterning were also reviewed, as was the use of DPN writing to produce structures that can act as etch resists. Finally, technology developments specific to DPN methods such as passive pen arrays, active pen arrays, and inkwells were discussed.

DPN is a nanolithography technique with excellent potential. Besides continued use in research laboratories worldwide, to investigate nanoscale patterning of almost any material, it is expected that DPN writing will also find success in industrial use. Its ink-general nature, high resolution, and direct-write operation make it a good candidate for defect repair applications such as photomask repair. At the same time, it can be envisioned that DPN printing finds use in patterning applications such as producing nanoimprint lithography masters because of its scalability and fast turnaround from design to finished pattern. Continued research on inks and methods by the international research community will see these and other applications become reality.

## ACKNOWLEDGMENTS

The authors gratefully thank all employees at NanoInk Inc. for their contributions and support. In particular, thanks are due to Jason Haaheim for nanolithography technique comparisons and Dr Nabil Amro for work and images on inkwell-inked pens.

## REFERENCES

1. Binnig, G.; Rohrer, H. Scanning tunneling microscopy. *Helv. Phys. Acta* **1982**, *55* (6), 726–735.
2. Binnig, G.; Quate, C.F.; Gerber, C. Atomic force microscope. *Phys. Rev. Lett.* **1986**, *56* (9), 930–933.
3. Kramer, S.; Fuierer, R.; Gorman, C. Scanning probe lithography using self-assembled monolayers. *Chem. Rev.* **2003**, *103* (11), 4367–4418.
4. Wouters, D.; Schubert, U. Nanolithography and nanotechnology: probe-related patterning techniques and chemical modification for nanometer-sized devices. *Angew. Chem. Int. Ed.* **2004**, *43* (19), 2480–2495.
5. Nyffenegger, R.M.; Penner, R.M. Nanometer-scale surface modification using the scanning probe microscope: progress since 1991. *Chem. Rev.* **1997**, *97*, 1195–1230.
6. Kramer, S.; Fuierer, R.R.; Gorman, C.B. Scanning probe lithography using self-assembled monolayers. *Chem. Rev.* **2003**, *103* (11), 4367–4418.
7. Sugimura, H.; Nakagiri, N. AFM lithography in constant current mode. *Nanotechnology* **1997**, *8*, A15–A18.



8. Avouris, P.; Hertel, T.; Martel, R. Atomic force microscope tip-induced local oxidation of silicon: kinetics, mechanism, and nanofabrication. *Appl. Phys. Lett.* **1997**, *71* (2), 285–287.
9. Sigrist, M.; Fuhrer, A.; Ihn, T.; Ensslin, K.; Driscoll, D.C.; Gossard, A.C. Multiple layer local oxidation for fabricating semiconductor nanostructures. *Appl. Phys. Lett.* **2004**, *85* (16), 3558–3560.
10. Sohn, L.; Willett, R. Fabrication of nanostructures using atomic-force-microscope-based lithography. *Appl. Phys. Lett.* **1995**, *67* (11), 1552–1554.
11. Hsu, J.; Lin, C.; Lin, H. Fabrication of metallic nanostructures by atomic force microscopy nanomachining and lift-off process. *J. Vac. Sci. Technol. B* **2004**, *22*, 2768–2771.
12. Porter, L.; Ribbe, A.; Buriak, J. Metallic nanostructures via static plowing lithography. *Nano Lett.* **2003**, *3* (8), 1043–1047.
13. Xu, S.; Liu, G.Y. Nanometer-scale fabrication by simultaneous nanoshaving and molecular self-assembly. *Langmuir* **1997**, *13* (2), 127–129.
14. Amro, N.; Xu, S.; Liu, G. Patterning surfaces using tip-directed displacement and self-assembly. *Langmuir* **2000**, *16* (7), 3006–3009.
15. Jaschke, M.; Butt, H.-J. Deposition of organic material by the tip of a scanning force microscope. *Langmuir* **1995**, *11* (4), 1061–1064.
16. Piner, R.; Zhu, J.; Xu, F.; Hong, S.; Mirkin, C. “Dip-pen” nanolithography. *Science* **1999**, *283* (5402), 661–663.
17. Hong, S.; Mirkin, C. A nanoplotter with both parallel and serial writing capabilities. *Science* **2000**, *288* (5474), 1808–1811.
18. Mirkin, C.A.; Piner, R.D.; Hong, S. Methods Utilizing Scanning Probe Microscope Tips and Products Therefor or Products Thereby. U.S. Patent 6,635,311, 2003.
19. Mirkin, C.A.; Piner, R.; Hong, S. Methods Utilizing Scanning Probe Microscope Tips and Products Therefor or Produced Thereby. U.S. Patent 6,827,979, 2004.
20. Liu, C.; Zhang, M.; Bullen, D. Parallel, Individually Addressable Probes for Nanolithography. U.S. Patent 6,642,129, 2003.
21. NanoInk Inc., 1335 W. Randolph St., Chicago, IL 60607, [www.nanoink.net](http://www.nanoink.net).
22. Chou, S.Y.; Krauss, P.R.; Renstrom, P.J. Nanoimprint lithography. *J. Vac. Sci. Technol. B* **1996**, *14* (6), 4129–4133.
23. Kumar, A.; Whitesides, G.M. Features of gold having micrometer to centimeter dimensions can be formed through a combination of stamping with an elastomeric stamp and an alkanethiol “ink” followed by chemical etching. *Appl. Phys. Lett.* **1993**, *63* (14), 2002–2004.
24. Xia, Y.; Whitesides, G. Soft lithography. *Angew. Chem. Int. Ed.* **1998**, *37*, 550–575.
25. Wilbur, J.L.; Kumar, A.; Biebuyck, H.A.; Kim, E.; Whitesides, G.M. Microcontact printing of self-assembled monolayers: applications in microfabrication. *Nanotechnology* **1996**, *7* (4), 452–457.
26. Hong, S.; Zhu, J.; Mirkin, C. Multiple ink nanolithography: toward a multiple-pen nano-plotter. *Science* **1999**, *286* (5439), 523–525.
27. Colton, R. Nanoscale measurements and manipulation. *J. Vac. Sci. Technol. B* **2004**, *22* (4), 1609–1635.
28. Marrian, C.R.K.; Tennant, D.M. Nanofabrication. *J. Vac. Sci. Technol. A* **2003**, *21* (5), S207–S215.
29. Agarwal, G.; Sowards, L.; Naik, R.; Stone, M. Dip-pen nanolithography in tapping mode. *J. Am. Chem. Soc.* **2003**, *125* (2), 580–583.
30. Ivanisevic, A.; Mirkin, C. “Dip-pen” nanolithography on semiconductor surfaces. *J. Am. Chem. Soc.* **2001**, *123* (32), 7887–7889.
31. Demers, L.; Mirkin, C. Combinatorial templates generated by dip-pen nanolithography for the formation of two-dimensional particle arrays. *Angew. Chem. Int. Ed.* **2001**, *40* (16), 3069–3071.
32. Haaheim, J.; Eby, R.; Nelson, M.; Fragala, J.; Rosner, B.; Zhang, H.; Athas, G. Dip Pen Nanolithography (DPN): process and instrument performance with NanoInk’s NSCRIPTOR system. *Ultramicroscopy* **2005**, *103*, 117–132.
33. Schwartz, P. Molecular transport from an atomic force microscope tip: a comparative study of dip-pen nanolithography. *Langmuir* **2002**, *18* (10), 4041–4046.
34. Sheehan, P.; Whitman, L. Thiol diffusion and the role of humidity in “dip pen nanolithography”. *Phys. Rev. Lett.* **2002**, *88* (15), 156, 104.
35. Weeks, B.; Noy, A.; Miller, A.; De Yoreo, J. Effect of dissolution kinetics on feature size in dip-pen nanolithography. *Phys. Rev. Lett.* **2002**, *88* (25), 255, 505.
36. Rozhok, S.; Piner, R.; Mirkin, C. Dip-pen nanolithography: what controls ink transport? *J. Phys. Chem.* **2003**, *107* (3), 751–757.
37. Weeks, B.L.; Noy, A.; Miller, A.E.; Klare, J.E.; Woods, B.W.; De Yoreo, J.J. Dip-pen nanolithography: optical inks. In *Dekker Encyclopedia of Nanoscience and Nanotechnology*, 2E; Schwarz, J.A., Contescu, C.I., Putyera, K., Eds.; Taylor & Francis: New York, NY, 2009; Vol. 2, 1084–1092.
38. Jang, J.; Hong, S.; Schatz, G.; Ratner, M. Self-assembly of ink molecules in dip-pen nanolithography: a diffusion model. *J. Chem. Phys.* **2001**, *115* (6), 2721–2729.
39. Jang, J.; Schatz, G.; Ratner, M. Liquid meniscus condensation in dip-pen nanolithography. *J. Chem. Phys.* **2002**, *116* (9), 3875–3886.
40. Jang, J.; Schatz, G.; Ratner, M. How narrow can a meniscus be? *Phys. Rev. Lett.* **2004**, *92* (8), 85, 504.
41. Debouck, C.; Goodfellow, P.N. DNA microarrays in drug discovery and development. *Nat. Genet.* **1999**, *21*, 48–50.
42. Nicolau, D.V.; Demers, L.; Ginger, D.S. Nanoarrays. In *Microarray Technology and its Applications*; Springer: New York, 2005; 89–118.
43. Demers, L.; Ginger, D.; Park, S.; Li, Z.; Chung, S.; Mirkin, C. Direct patterning of modified oligonucleotides on metals and insulators by dip-pen nanolithography. *Science* **2002**, *296*, 1836–1838.
44. Wilson, D.; Martin, R.; Hong, S.; Cronin-Golomb, M.; Mirkin, C.; Kaplan, D. Surface organization and nanopatterning of collagen by dip-pen nanolithography. *Proc. Natl. Acad. Sci. USA* **2001**, *98* (24), 13,660–13,664.

45. Lee, K.; Lim, J.; Mirkin, C. Protein nanostructures formed via direct-write dip-pen nanolithography. *J. Am. Chem. Soc.* **2003**, *125* (19), 5588–5589.
46. Lee, K.; Park, S.; Mirkin, C.; Smith, J.; Mrksich, M. Protein nanoarrays generated by dip-pen nanolithography. *Science* **2002**, *295* (5560), 1702–1705.
47. Lim, J.; Ginger, D.; Lee, K.; Nam, J.; Mirkin, C. Direct-write dip-pen nanolithography of proteins on modified silicon oxide surfaces. *Angew. Chem. Int. Ed.* **2003**, *42* (20), 2309–2312.
48. Noy, A.; Miller, A.; Klare, J.; Weeks, B.; Woods, B.; DeYoreo, J. Fabrication of luminescent nanostructures and polymer nanowires using dip-pen nanolithography. *Nano Lett.* **2002**, *2* (2), 109–112.
49. Hyun, J.; Ahn, S.; Lee, W.; Chilkoti, A.; Zauscher, S. Molecular recognition-mediated fabrication of protein nanostructures by dip-pen lithography. *Nano Lett.* **2002**, *2* (11), 1203–1207.
50. Hyun, J.; Kim, J.; Craig, S.; Chilkoti, A. Enzymatic nanolithography of a self-assembled oligonucleotide monolayer on gold. *J. Am. Chem. Soc.* **2004**, *126* (15), 4770–4771.
51. Hyun, J.; Lee, W.; Nath, N.; Chilkoti, A.; Zauscher, S. Capture and release of proteins on the nanoscale by stimuli-responsive elastin-like polypeptide “switches”. *J. Am. Chem. Soc.* **2004**, *126* (23), 7330–7335.
52. Demers, L.; Park, S.; Taton, T.; Li, Z.; Mirkin, C. Orthogonal assembly of nanoparticle building blocks on dip-pen nanolithographically generated templates of DNA. *Angew. Chem. Int. Ed.* **2001**, *40* (16), 3071–3073.
53. Park, S.J.; Taton, T.A.; Mirkin, C.A. Array-based electrical detection of DNA with nanoparticle probes. *Science* **2002**, *295*, 1503–1506.
54. Taton, T.A.; Lu, G.; Mirkin, C.A. Two-color labeling of oligonucleotide arrays via size-selective scattering of nanoparticle probes. *J. Am. Chem. Soc.* **2001**, *123* (21), 5164–5165.
55. Taton, T.A.; Mirkin, C.A.; Letsinger, R.L. Scanometric DNA array detection with nanoparticle probes. *Science* **2000**, *289*, 1757–1760.
56. Ginger, D.; Zhang, H.; Mirkin, C. The evolution of dip-pen nanolithography. *Angew. Chem. Int. Ed.* **2004**, *43* (1), 30–45.
57. Lim, J.; Mirkin, C. Electrostatically driven dip-pen nanolithography of conducting polymers. *Adv. Mater.* **2002**, *14* (20), 1474–1477.
58. Manandhar, P.; Jang, J.; Schatz, G.; Ratner, M.; Hong, S. Anomalous surface diffusion in nanoscale direct deposition processes. *Phys. Rev. Lett.* **2003**, *90* (11), 115505-1–115505-4.
59. Su, M.; Dravid, V. Colored ink dip-pen nanolithography. *Appl. Phys. Lett.* **2002**, *80* (23), 4434–4436.
60. Maynor, B.W.; Filocamo, S.F.; Grinstaff, M.W.; Liu, J. Direct-writing of polymer nanostructures: poly-(thiophene) nanowires on semiconducting and insulating surfaces. *J. Am. Chem. Soc.* **2002**, *124* (4), 522–523.
61. Su, M.; Aslam, M.; Fu, L.; Wu, N.; Dravid, V.P. Dip-pen nanopatterning of photosensitive conducting polymer using a monomer ink. *Appl. Phys. Lett.* **2004**, *84* (21), 4200–4202.
62. McKendry, R.; Huck, W.; Weeks, B.; Florini, M.; Abell, C.; Rayment, T. Creating nanoscale patterns of dendrimers on silicon surfaces with dip-pen nanolithography. *Nano Lett.* **2002**, *2* (7), 713–716.
63. Liu, X.; Guo, S.; Mirkin, C. Surface and site-specific ring-opening metathesis polymerization initiated by dip-pen nanolithography. *Angew. Chem. Int. Ed.* **2003**, *42* (39), 4785–4789.
64. Liu, X.G.; Fu, L.; Hong, S.H.; Dravid, V.P.; Mirkin, C.A. Arrays of magnetic nanoparticles patterned via “dip-pen” nanolithography. *Adv. Mater.* **2002**, *14* (3), 231–234.
65. Gundiah, G.; John, N.; Thomas, P.; Kulkarni, G.; Rao, C. Dip-pen nanolithography with magnetic Fe<sub>2</sub>O<sub>3</sub> nanocrystals. *Appl. Phys. Lett.* **2004**, *84* (26), 5341–5343.
66. Fu, L.; Liu, X.; Zhang, Y.; Dravid, V.; Mirkin, C. Nanopatterning of “hard” magnetic nanostructures via dip-pen nanolithography and a sol-based ink. *Nano Lett.* **2003**, *3* (6), 757–760.
67. Su, M.; Liu, X.; Li, S.; Dravid, V.; Mirkin, C. Moving beyond molecules: patterning solid-state features via dip-pen nanolithography with sol-based inks. *J. Am. Chem. Soc.* **2002**, *124* (8), 1560–1561.
68. Su, M.; Li, S.; Dravid, V. Miniaturized chemical multiplexed sensor array. *J. Am. Chem. Soc.* **2003**, *125*, 9930–9931.
69. Li, Y.; Maynor, B.W.; Liu, J. Electrochemical AFM “dip-pen” nanolithography. *J. Am. Chem. Soc.* **2001**, *123* (9), 2105–2106.
70. Maynor, B.; Li, Y.; Liu, J. Au “ink” for AFM “dip-pen” nanolithography. *Langmuir* **2001**, *17* (9), 2575–2578.
71. Li, J.; Lu, C.; Maynor, B.; Huang, S.; Liu, J. Controlled growth of long GaN nanowires from catalyst patterns fabricated by “dip-pen” nanolithographic techniques. *Chem. Mater.* **2004**, *16* (9), 1633–1636.
72. Rosner, B.; Amro, N.; Disawal, S.; Demers, L.; Zhang, H.; Rendlen, J.; Duenas, T.; Shile, R.; Fragala, J.; Elghanian, R. Dip pen nanolithography<sup>TM</sup> and its potential for nanoelectronics. In Fourth IEEE Conference on Nanotechnology, Munich, Germany, August, 2004, TU2-2-2.
73. Ben Ali, M.; Ondarcuhu, T.; Brust, M.; Joachim, C. Atomic force microscope tip nanoprinting of gold nanoclusters. *Langmuir* **2002**, *18*, 872–876.
74. Thomas, P.J.; Kulkarni, G.U.; Rao, C.N.R. Dip-pen lithography using aqueous metal nanocrystal dispersions. *J. Mater. Chem.* **2004**, *14*, 625–628.
75. Weinberger, D.; Hong, S.; Mirkin, C.; Wessels, B.; Higgins, T. Combinatorial generation and analysis of nanometer- and micrometer-scale silicon features via “dip-pen” nanolithography and wet chemical etching. *Adv. Mater.* **2000**, *12* (21), 1600–1603.
76. Zhang, H.; Chung, S.; Mirkin, C. Fabrication of sub-50-nm solid-state nanostructures on the basis of dip-pen nanolithography. *Nano Lett.* **2003**, *3* (1), 43–45.
77. Zhang, H.; Mirkin, C. DPN-generated nanostructures made of gold, silver, and palladium. *Chem. Mater.* **2004**, *16* (8), 1480–1484.

78. Zhang, Y.; Salaita, K.; Lim, J.; Mirkin, C. Electrochemical whittling of organic nanostructures. *Nano Lett.* **2002**, *2* (12), 1389–1392.
79. Chow, E.M.; Yaralioglu, G.G.; Quate, C.F.; Kenny, T.W. Characterization of a two-dimensional cantilever array with through-wafer electrical interconnects. *Appl. Phys. Lett.* **2002**, *80* (4), 664–666.
80. Sulchek, T.; Grow, R.J.; Yaralioglu, G.G.; Minne, S.C.; Quate, C.F.; Manalis, S.R.; Kiraz, A.; Aydine, A.; Atalar, A. Parallel atomic force microscopy with optical interferometric detection. *Appl. Phys. Lett.* **2001**, *78* (12), 1787–1789.
81. Zhang, M.; Bullen, D.; Chung, S.W.; Hong, S.; Ryu, K.S.; Fan, Z.F.; Mirkin, C.A.; Liu, C. A MEMS nanoplotter with high-density parallel dip-pen nanolithography probe arrays. *Nanotechnology* **2002**, *13* (2), 212–217.
82. Zou, J.; Bullen, D.; Wang, X.; Liu, C.; Mirkin, C. Conductivity-based contact sensing for probe arrays in dip-pen nanolithography. *Appl. Phys. Lett.* **2003**, *83* (3), 581–583.
83. Kawakatsu, H.; Saya, D.; Kato, A.; Fukushima, K.; Toshiyoshi, H.; Fujita, H. Millions of cantilevers for atomic force microscopy. *Rev. Sci. Instr.* **2002**, *73* (3), 1188–1192.
84. Zou, J.; Wang, X.; Bullen, D.; Ryu, K.; Liu, C.; Mirkin, C.A. A mould-and-transfer technology for fabricating scanning probe microscopy probes. *J. Micromech. Microeng.* **2004**, *14*, 204–211.
85. Deladi, S.; Tas, N.R.; Berenschot, J.W.; Krijnen, G.J.M.; De Boer, M.J.; De Boer, J.H.; Peter, M.; Elwenspoek, M.C. Micromachined fountain pen for atomic force microscope-based nanopatterning. *Appl. Phys. Lett.* **2004**, *85* (22), 5361–5363.
86. Kim, K.-H.; Moldovan, N.; Ke, C.; Espinosa, H.D. A novel AFM chip for fountain pen nanolithography—design and microfabrication. *Mater. Res. Soc. Symp. Proc.* **2004**, *782*, 267–272.
87. Taha, H.; Marks, R.S.; Gheber, L.A.; Rousso, I.; Newman, J.; Sukenik, C.; Lewis, A. Protein printing with an atomic force sensing nanofountainpen. *Appl. Phys. Lett.* **2003**, *83* (5), 1041–1043.
88. Banerjee, D.; Fragala, J.; Duenas, T.; Shile, R.; Rosner, B. Planar capillary pumped ink delivery apparatus for dip pen nanolithography. In 7th International Conference on Miniaturized Chemical and Biochemical Analysis Systems (Micro Total Analysis Systems 2003), Squaw Valley, California USA; Vol. 1, 57.
89. Rosner, B.; Duenas, T.; Banerjee, D.; Shile, R.; Amro, N.; Rendlen, J. Active probes and microfluidic ink delivery for Dip Pen Nanolithography<sup>TM</sup>. *Proc. SPIE* **2004**, *5275*, 213–222.
90. Vettiger, P.; Cross, G.; Despont, M.; Drechsler, U.; Durig, U.; Gotsmann, B.; Haberle, W.; Lantz, M.A.; Rothuizen, H.E.; Stutz, R.; Binnig, G.K. The “millipede”—nanotechnology entering data storage. *IEEE Trans. Nanotechnol.* **2002**, *1* (1), 39–55.
91. Hillier, A.C.; Bard, A.J. AC-mode atomic force microscope imaging in air and solutions with a thermally driven bimetallic cantilever probe. *Rev. Sci. Instr.* **1997**, *68* (5), 2082–2090.
92. Zhang, Y.; Zhang, Y.; Marcus, R.B. Thermally actuated microprobes for a new wafer probe card. *IEEE J. Microelectromech. Syst.* **1999**, *8* (1), 43–49.
93. Sheehan, P.; Whitman, L.; King, W.; Nelson, B. Nanoscale deposition of solid inks via thermal dip pen nanolithography. *Appl. Phys. Lett.* **2004**, *85* (9), 1589–1591.
94. Bullen, D.; Chung, S.; Wang, X.; Zou, J.; Mirkin, C.; Liu, C. Parallel dip-pen nanolithography with arrays of individually addressable cantilevers. *Appl. Phys. Lett.* **2004**, *84* (5), 789–791.
95. Bullen, D.; Wang, X.; Zou, J.; Chung, S.W.; Mirkin, C.A.; Liu, C. Design, fabrication, and characterization of thermally actuated probe arrays for dip pen nanolithography. *J. Micromech. Syst.* **2004**, *13* (4), 594–602.
96. Wang, X.; Bullen, D.; Zou, J.; Liu, C. Thermally actuated probe array for parallel dip-pen nanolithography. *J. Vac. Sci. Technol. B* **2004**, *22* (6), 2563–2567.

# Dip-Pen Nanolithography: Optical Inks

**Brandon L. Weeks**

*Biosecurity Support Laboratory, Lawrence Livermore National Laboratory,  
Livermore, California, U.S.A.*

**Aleksandr Noy**

**Abigail E. Miller**

**Jennifer E. Klare**

**Bruce W. Woods**

**James J. De Yoreo**

*Lawrence Livermore National Laboratory, Livermore, California, U.S.A.*

## INTRODUCTION

Many capillarity-related phenomena originate from the well-documented formation of water films on surfaces.<sup>[1]</sup> Thin water films have been studied by a variety of techniques including ellipsometry,<sup>[2]</sup> adsorption isotherms,<sup>[3]</sup> and atomic force microscopy (AFM).<sup>[4]</sup> These investigations have shown that the films are often just a few monolayers in thickness. When a water meniscus forms between an AFM tip and a surface, it has a profound effect on tip-sample interactions, both degrading image quality and interfering with force measurements.<sup>[5]</sup> However, the meniscus formed between the tip and surface has been proposed as the crucial feature that enables the AFM tip to be used as a tool for controlled deposition of molecules on surfaces in dip-pen nanolithography (DPN),<sup>[6,7]</sup> while other groups have suggested that the meniscus plays no or little role in the DPN process.<sup>[8,9]</sup>

We investigated the effects of humidity, tip speed, and dwell time on feature size during DPN using alkanethiol “ink” on gold “paper.” Our results indicate two distinct deposition regimes. The dwell time at which the transition between the two regimes occurs is independent of ambient humidity. In addition, while the feature size increases with humidity, the relative increase is independent of dwell time. The observed behavior is described using a deposition model that takes into account the kinetics of alkanethiol detachment and attachment at the tip. The model suggests that, at short dwell times and high tip speeds, the most important parameter controlling the feature size is the activation energy for detachment of the ink molecules. Additional results will be presented for luminescent molecules on a combined atomic force/scanning confocal microscope. We show that this method can be used successfully to push the limits of DPN down to controlled deposition of single molecules. We also demonstrate that this method is able to create and

visualize protein patterns on surfaces. Finally, we show that our method can be used to fabricate polymer nanowires of controlled size using conductive polymers.

## FACTORS AFFECTING DIP-PEN NANOLITHOGRAPHY

To perform DPN, an AFM tip is “inked” with a chemical of interest and brought into contact with a surface. The ink molecules flow from the tip onto the surface analogous to the actions of a fountain pen. This method is capable of producing nanostructures down to 15 nm in diameter and separated by as little as 5 nm.<sup>[10]</sup> While, in principle, nearly any ink or paper can be used, as has been demonstrated with dendrimers, conducting polymers, organic dyes, antibodies, and gold on silicon,<sup>[11–13]</sup> by far the most common application of DPN is the patterning of thiol “inks” on gold “paper.”

A variety of factors could determine the feature size achieved during DPN. These factors include dwell time, writing speed, temperature, concentration of the ink, interfacial tension, and humidity.<sup>[14]</sup> Thus a complete picture of the physical processes and materials parameters that control transfer and deposition has not yet emerged. Here we report the results of an experimental investigation of the effects of humidity, tip speed, and dwell time on feature size during DPN using mercaptohexadecanoic acid (MHA), a carboxyl-terminated alkanethiol. We analyze these results using a model that accounts for both the effect of humidity on meniscus height and the dissolution dynamics at the tip. We show that there is a transition from a dissolution-dominated to a diffusion-dominated regime, that the dwell time at which the transition occurs is independent of meniscus height, and that, for fabrication of small features, the most

important materials parameter controlling feature size is the activation energy of detachment from the tip.

## EXPERIMENTAL

### Humidity Dependence of MHA

Experiments were performed with a Digital Instruments multimode AFM enclosed in a custom-built humidity controlled box. The relative humidity was increased by ultrasonic evaporation of water or decreased by flowing dry air through the chamber. Sharpened microlever AFM probes were used as supplied by TM Microscopes. Gold substrates were prepared by sputtering 2–5 nm of titanium on silicon for improved adhesion followed by sputtering of 100 nm of gold. Inking of the cantilevers was accomplished by bringing them in contact with a soft membrane inoculated with the MHA solution under an optical microscope. All experiments were conducted at room temperature between 22°C and 23°C.

### Optically Active Inks

For the optical studies, our instrument combines AFM and scanning confocal microscopy. A bioscope AFM head (Digital Instruments, Santa Barbara, CA) is mounted on a Nikon Eclipse 300 inverted microscope equipped with a custom-built stage that incorporates a closed-loop piezo scanner (PolytecPI, Germany). The scanning stage is used in both the lithography procedure and confocal imaging. The fluorescence excited by a 514 line of Ar-Ion laser (Coherent Innova-70) is collected with  $100 \times 1.4$  NA lens, passed through a 50- $\mu\text{m}$  pinhole to reject stray light and then detected by an avalanche photodiode (Perkin Elmer Optoelectronics, Santa Clara, CA). Excitation light was rejected by a long-pass filter (Omega Optical, VT).

For both MHA and optical inks, arrays of dots and lines were fabricated by bringing an inked cantilever into contact with a freshly prepared gold surface. To minimize the transfer of ink from the tip to the substrate, the sample was rastered at speeds greater than 4 Hz. To make a dot, the raster scanning was stopped and the tip allowed to dwell at a specific location for a given time. The tip was then moved quickly to the next position and the process was repeated. In order to image the resulting pattern, the sample was rastered while recording the friction (lateral force) signal from the AFM. Fig. 1 shows a typical friction image for an array of MHA dots deposited on gold. In addition to the friction signal, for optical inks, the confocal arrangement provides a method of imaging fluorescent molecules (Fig. 2).

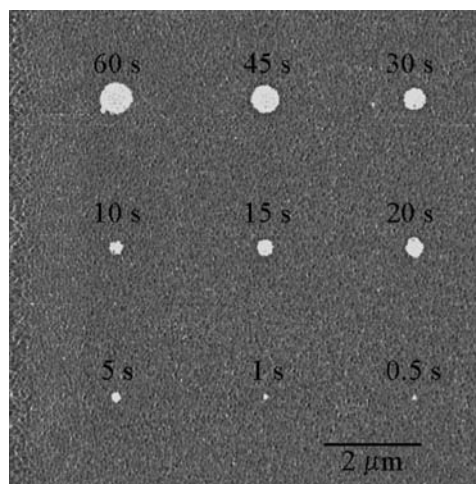


**Fig. 1** Friction-force image of MHA dots on gold fabricated with the indicated dwell times. *Source:* From Ref.<sup>[14]</sup>.

## RESULTS

### Model of Ink Transfer (MHA)

The first experiments performed were to determine whether the applied force on the tip could affect the patterning behavior and feature size. Experiments were conducted by varying the force from a few micro-Newtons down to negative forces. In order to obtain a negative force, the tip was first brought into contact with a positive force and then the set point was adjusted to a point below the resting position of the cantilever. No effect of contact force on feature size was observed, even at negative forces. The reason for this is that the water meniscus that forms at the tip–surface contact causes a substantial capillary force between the tip and the sample surface. In fact,

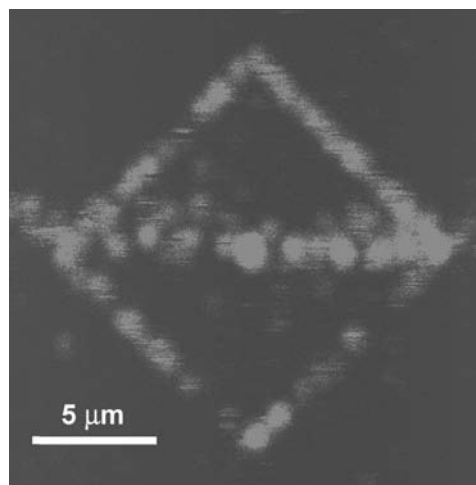


**Fig. 2** Scanning confocal image of Rhodamine 6G patterned with DPN on a glass substrate.

capillary adhesion is much larger than the force applied by the AFM cantilever and, consequently, capillarity dominates the total load force. The measured capillary adhesion force was typically  $\sim 120$  nN, as compared to the externally applied load, which was typically on the order of 10 to 20 nN. We can estimate the typical tip-sample contact area using a Hertz model of contact mechanics. For the contact of a sphere with a flat plate the contact area is given by:

$$\text{Area} = \pi a^2 = \pi \left( \frac{RP_0}{K} \right)^{2/3}$$

where  $a$  is the radius of the contact area,  $R$  is the probe radius of curvature,  $P_0$  is the applied load, and  $K$  is the elastic constant for the contact of gold and silicon nitride. For our experiments,  $R$  typically ranges from 20 to 40 nm.  $K$  can be estimated as  $8.85 \cdot 10^{10}$  Pa. For these values, the contact area at the applied load of 130 nN will be equal to  $39 \text{ nm}^2$ , which corresponds to the radius of 3.5 nm. Both values are small compared to our typical values for dot area and line width. Tip convolution did not affect the measurements of feature size except at the smallest sizes because of the small contact radius.

To determine the effects of humidity on size we placed the AFM in an environmental chamber and fabricated MHA dots at a relative humidity,  $H$ , varying between 15% and 55%. At a relative humidity at or below 15% reproducible features were not observed for the shortest contact times (0.5 sec and below), while for longer contact times we were able to produce features systematically. We initially proposed that at that humidity the meniscus does not form between the tip and the sample, thus the ink transport to the surface is inhibited. However, subsequent experiments have shown that the meniscus takes time to form and that a meniscus can form even at low humidity. Another possible explanation is that the gold used in these experiments was sputtered making grains that are larger than the smallest patterned features. Because we do not have complete data sets for the shortest contact times at low humidity, our results will be presented from 20% relative humidity. Fig. 3A shows the dependence of the dot area on dwell time for times between 0.5 and 60 sec and humidities ranging from 20% to 54%. Fig. 3B shows the dependence of dot size on humidity for three different dwell times. Three features are evident. First, the dependence of the square of the dot radius on dwell time is well fit by two linear regions separated by a sharp transition zone which occurs over the same range of dwell times for all humidities. Second, from 20% to 45% the spot size increases while above 45% there is little change in the diameter of the spot. Third, the dependence of feature size on humidity

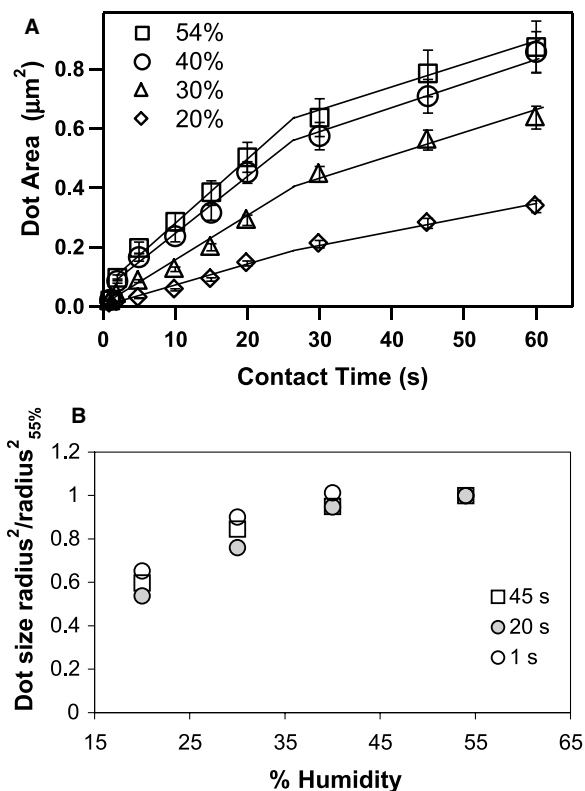


**Fig. 3** (A) Dependence of radius squared on dwell time as a function of relative humidity. (B) Dependence of dot radius squared on humidity for three different dwell times normalized by the maximum radius squared at  $H = 55\%$ . Source: From Ref.<sup>[14]</sup>.

is the same for all dwell times. However, we observed that at the highest humidity, the precision of the measurements decreased and the edges of the dots became less well defined.

These results are consistent with those observed by Xu et al.<sup>[15]</sup> while investigating force distance curves on wet mica surfaces. In the low humidity range ( $< 20\%$ ) only a relatively small and uniform adhesion force was observed. This indicates that capillary forces did not play an important role likely because of an incomplete coverage of water on the surface. Between 20% and 45%, a steep increase in the adhesion was measured as the surface coverage of the water increased and a meniscus formed between the tip and sample. Above 45%, water formed on the surface became more “bulk-like,” showing evidence of flow dynamics and adding complexity to the measurements. Similar results have been observed with lateral force microscopy.<sup>[16]</sup>

In addition to dot fabrication, DPN can be used to write lines. In contrast to the case of dot generation where the tip is held stationary for the deposition time, during the fabrication of lines the tip continuously moves along the sample. In order to make a



comparison between the controls on dot size and line width, we fabricated a series of lines such as those shown in Fig. 4A at tip speed,  $v$ , ranging from about 0.1 to 1  $\mu\text{m}/\text{sec}$ . The dependence of line width,  $W$ , on inverse speed,  $1/v$ , is presented in Fig. 4B. The data show a linear increase down to a speed of about 0.2  $\mu\text{m}/\text{sec}$  where the dependence weakens significantly. Data on line widths for the lines of poly-[2-methoxy-5-(2'-ethyl-hexyloxy)-*p*-phenylene-vinylene] (MEH-PPV),<sup>[17]</sup> a luminescent polymer, drawn on  $\text{SiO}_2$  are also given in the inset to show that this behavior is not peculiar to MHA.

To understand our experimental results we consider the following model for ink transfer to the surface (Fig. 5). The tip moves at constant speed,  $v$ , which is zero for fabrication of dots, through a water film of thickness,  $\delta$ , on the surface. Because of a nonzero contact angle at the tip, the height,  $h$ , of the meniscus at the tip is different from  $\delta$ . Thiol molecules dissolve from the tip into the meniscus, diffuse through the meniscus, and attach to the surface making a continuous self-assembled monolayer (SAM). After a time,  $\tau$ , the tip is removed from the water film. At this time, thiol molecules are both attached to the surface and dissolved in the meniscus. Through diffusion, the

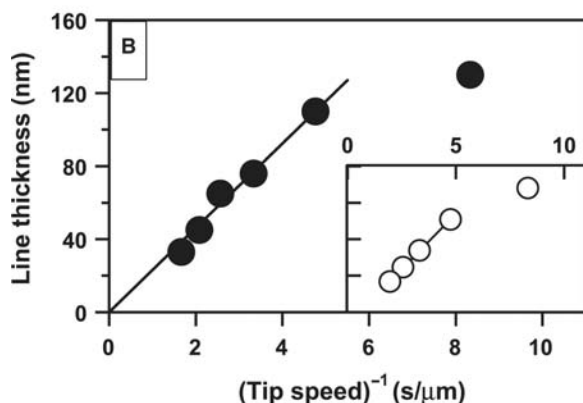
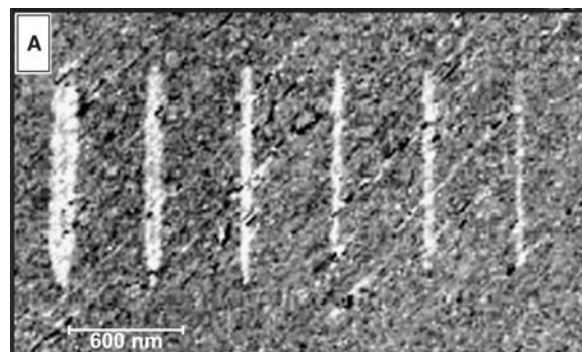


**Fig. 4** (A) Friction-force image of MHA lines on gold fabricated at tip speeds between 0.1 and 1  $\mu\text{m}/\text{sec}$ . (B) Dependence of line width on inverse tip speed for both MHA and MEH-PPV (inset). Source: From Ref.<sup>[14]</sup>.

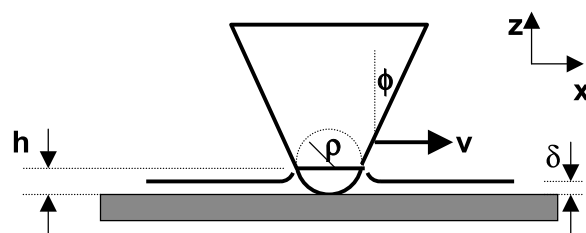


**Fig. 5** Schematic of the physical model for molecular transfer from AFM tip to substrate through meniscus of height  $h$ . Source: From Ref.<sup>[14]</sup>.

dissolved thiols will eventually reach the edge of the SAM and attach to the substrate, contributing to the final feature size. Regardless of the tip-meniscus geometry, the magnitude of the diffusion constant, or the dissolution rate, the total number of molecules,  $N$ , transferred to the surface will be given by the integral of the transfer rate over the total tip-surface contact time  $\tau$ .

We start by considering the case of dot fabrication. Two terms contribute to  $dN/dt$ : First, molecules dissolve from the tip through thermal activated detachment at a rate:

$$\left(\frac{dN}{dt}\right)_+ = \frac{A}{\pi a^2} \beta_+ = \frac{A}{\pi a^2} \nu e^{-E_D/kT} \quad (1)$$

where  $A$  is the contact area between the tip and the meniscus,  $\pi a^2$  is the average area per thiol ink molecule,  $E_D$  is the activation energy for ink detachment,  $k$  is Boltzmann's constant,  $T$  is the temperature, and  $\nu$  is an attempt frequency. In this case, the ink molecules are not detaching from the surface of a silicon nitride tip, rather they are detaching from the surface of a bulk alkanethiol solid that has precipitated onto the tip during the inking process. Second, molecules return to the tip simply because of impingement and attachment at a rate given by:

$$\left(\frac{dN}{dt}\right)_- = A\beta_- C_0 \approx A \left(\frac{kT}{2\pi m}\right)^{1/2} e^{-E_A/kT} C_0 \quad (2)$$

where  $m$  is the mass of a thiol,  $E_A$  is the activation energy for attachment, and  $C_0$  is the concentration of thiols in solution adjacent to the tip. The right-hand side of Eq. (2) assumes a gas kinetic expression for the impinging flux. A more complicated description would modify the factors in  $\beta_-$ , but will not change the dependence on  $C_0$ . (Note that in the absence of diffusion,  $C_0$  will simply increase until it reaches the equilibrium solubility,  $C_e$ , at which time,  $(dN/dt)_+ = (dN/dt)_-$ .)

The dot radius is related to  $N$  through  $\pi R^2 = N\pi a^2$ . Combining this relationship with Eqs. (1) and (2)

and integrating gives:

$$R^2 = A \left( \beta_+ \tau - \pi a^2 \beta_- \int_0^\tau C_0(t) dt \right) \quad (3)$$

Similar arguments lead to an expression for the dependence of line-width on tip speed. Assuming the tip moves over a distance  $l$  at a speed  $v$ , we write:

$$N = \int_0^l \left( \frac{dN}{dt} \right) \left( \frac{dt}{dx} \right) dx = \frac{1}{v} \int_0^l \left( \frac{dN}{dt} \right) dx \quad (4)$$

The expressions for  $(dN/dt)_+$  and  $(dN/dt)_-$  remain the same as for dots, except that  $C_0$  is now expressed as a function of  $v$  instead of  $t$ . Recognizing that  $C_0(v)$  and  $\beta_-$  are both independent of  $x$  and that the line width  $W = N\pi a^2/l$ , Eq. (4) becomes:

$$W = \left( \frac{A}{v} \right) (\beta_+ - \pi a^2 \beta_- C_0(v)) \quad (5)$$

For both dots and lines, the exact form of  $C_0$  depends on a number of factors including the tip-meniscus geometry, surface attachment probability and the diffusivity, but because  $C_0$  is small at short contact times or high tip speeds, two regimes emerge. For small  $\tau$  (high  $v$ ),  $C_0 \approx 0$  and the dot size (line width) is given by the first term in Eq. (3).<sup>[5]</sup> That is  $R^2 \sim A\tau$  and  $W \sim A/v$ . This is the regime in which surface kinetics dominates the transfer process. For long contact times/slow tip speeds,  $C_0$  reaches a limiting value  $C_0$  that is less than  $C_c$ . Once again,  $R^2 \sim A\tau$  and  $W \sim A/v$ , but the slopes of these linear relationships are reduced. In this regime the transfer process is controlled by diffusion. We observed very similar dependencies in our experiments for both dot and line fabrication (Figs. 3 and 4).

The effect of humidity comes into this model through the impact of meniscus height,  $h$ , on contact area,  $A$ . The tip can be approximated by a cone terminated by a hemisphere of radius  $\rho$ . If  $h \gg \rho$ ,  $A$  is approximately equal to that of a conical tip with half-cone angle  $\phi$ , and height  $h$ , which is  $\pi h^2 \sin \phi$ . In contrast, for  $h < \rho$ ,  $A = 4\rho^2 \cos^{-1}(1 - h/\rho)$ .

For  $h \ll \rho$ , this has an  $h^{0.5}$  dependence, while for  $h \approx \rho$ , it is linear in  $h$ . Consequently, as the humidity is increased from 15% to 50%, we expect the dot size to increase with a dependence that ranges from  $h^{0.5}$  to  $h^2$ . Furthermore, because  $A$  is a multiplicative factor for both terms in Eqs. (3) and (5), in agreement with our measurements, the transition from dissolution-dominated to diffusion-dominated deposition should be independent of the humidity and the functional form of the dependence of dot radius on humidity should be the same for all dwell times (Fig. 3B).

An investigation of water film thickness performed on gold surfaces using scanning tunneling microscopy<sup>[18]</sup> concluded that the film consisted of 30–50-nm islands that increased in thickness from about 2 nm at  $H = 20\%$  to 10 nm at  $H = 45\%$ . Coincidentally, the increases in film thickness from that study, which are about a factor of four between  $H$  of 20% and 30% and about 1.4 between  $H$  of 30% and 40%, match our measured increases in dot size with humidity assuming an  $h^{0.5}$  dependence in the low range, and an  $h^2$  dependence in the high range.

Some questions remain on the height of the meniscus formed when the AFM tip is brought in contact with the surface. By using the Kelvin equation, the meniscus height predicted is only 2 nm at 60% relative humidity and a tip radius of 20 nm.<sup>[8]</sup> Because this proposed meniscus height is less than the height of MHA monolayer, it does not seem that a meniscus can facilitate transport. However, by imaging an AFM tip in an environmental scanning electron microscope (ESEM) in contact with a surface, we can directly visualize the height of the meniscus formed (Fig. 6). The results clearly show that the meniscus height is far greater than expected from the Kelvin equation alone.

We can quantitatively test the sensibility of this model to some degree by examining the low  $\tau$ /high  $v$  dependence of dot size and line width. In this regime, the slopes of  $R^2$  vs.  $\tau$  and  $W$  vs.  $1/v$  are both given by  $A\beta_+$ . An upper limit for the attempt frequency,  $\nu$ , is given by  $kT/h_p$ , where  $h_p$  is Planck's constant. This value is appropriate for simple atomic solids. In the case of chain-like molecules such as alkane thiols, the

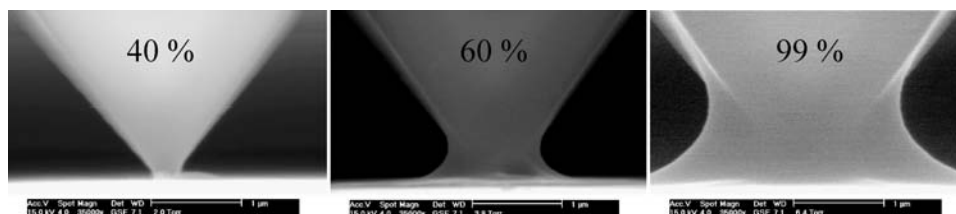


**Fig. 6** ESEM images of an AFM tip in contact with a gold substrate. The relative humidity is noted in each image. The same tip was used for all images. The meniscus formed at 60% is approximately 400 nm high while at 100% is nearly 2  $\mu\text{m}$ . We cannot verify whether a meniscus forms at the low humidity range because of the resolution limit of the ESEM (approximately 75 nm under these conditions).

attempt frequency is smaller. Although no detailed calculations of the appropriate frequency factor for these systems exist, models of idealized chain-like molecules lead to an estimate for  $\nu$  which is one to two orders of magnitude smaller. Taking the data for 20% to 54% relative humidity, using a range for  $n$  of  $10^{10}$  to  $6 \times 10^{12} \text{ sec}^{-1}$ , and assuming the film thickness of 2 to 10 nm from Freund, Halbritter, and Horber<sup>[18]</sup> gives  $E_D = 45\text{--}60 \text{ kJ/mol}$  for both the dots and the lines. This number should be greater than or equal to the heat of solution for MHA in water. Literature values for the heat of solution of a number of alkanes range from 25 to 40 kJ/mol.<sup>[19,20]</sup>

Other than the comparison between the predicted value of  $E_D$  from the short-time data with the heat of solution, the other potential comparisons include 1) direct comparison of Eq. (3) with the experimental data; 2) comparison of the observed crossover time to the prediction of Eq. (3); and 3) comparison of the predicted slope of the second term in Eq. (3) with the measured slope from the long-time data. The first two involve an estimate of both  $\nu$  and  $E_D$ . As  $E_D$  goes in the exponential term, even an error of a factor of two would produce a discrepancy of an order of magnitude. As  $\nu$  is also known only to within an order of magnitude, the comparisons stated in 1) and 2) are only good to within about two orders of magnitude. The final comparison also has errors, but at least some estimate is possible. At long times, the slope should be given by  $A\pi a^2 \beta_- C_0$ . Taking  $\beta_-$  to be given by the Brownian flux (on the right-hand side of Eq. (2)), with  $T = 298 \text{ K}$ ,  $m = 4.79 \times 10^{-22} \text{ g}$  per MHA molecule,  $A = 220 \text{ nm}^2$  (meniscus height of 10 nm at 45% humidity), and  $C_0$  to be given by the equilibrium concentration of MHA in water (estimated to be  $10^{-7} \text{ M}$ ), the slope from the long-time data predicts a value for the sticking coefficient,  $e^{-E_A/kT}$  of 0.005, or  $E_A = 0.13 \text{ eV/molecule}$ . The uncertainties in the terms that define the flux as well as our lack of knowledge about the detailed tip-meniscus geometry and diffusivity in nanometer-scale films make this comparison of limited value. Although this appears to be a reasonable number, there is no literature value with which to compare it.

## Optical Inks

### Deposition of single molecules

Conventional DPN with alkanethiol inks relies on the formation of a chemical bond between the ink and the substrate to facilitate the ink transfer from the tip to the sample surface. However, recent works demonstrated that even weaker interactions such as van der Waals interactions are often sufficient to facilitate the

transfer of matter from the tip to the sample.<sup>[11,12]</sup> We have used dilute solutions of Rhodamine 6G (R6G) dye as the writing “ink” to create luminescent nanoscale patterns. Lithography was performed immediately after the “inking.” R6G has strong affinity for negatively charged glass surfaces; therefore we did not use any surface treatments to promote the transfer of the “ink.” All patterns were fabricated at ambient humidity.

Fig. 7 shows a fluorescent confocal microscopy image of a pattern of R6G deposited on glass. Several features of this image are noteworthy. First, the apparent width of the lines in the image does not reflect the actual line width of the deposited dye. Rather, image line width is determined by the size of the confocal microscope probing beam (in our case  $\sim 600 \text{ nm}$ ). Second, several features in the optical image do not show a continuous line but rather are composed of a number of spots. Moreover, these spots showed features that are characteristic of a single molecule emission pattern, such as a striped pattern and abrupt emission cessation that is indicative of a dye molecule going in and out of dark states and finally photobleaching.<sup>[21]</sup> Likewise, as we continued to image our pattern, it rapidly degraded from photobleaching. From these observations we concluded that our pattern was composed of a number of isolated single molecules deposited in a straight line by the AFM tip. Notably, we did not observe any evidence of the pattern in normal or lateral force AFM images. Therefore the amount of the material deposited on the surface was not sufficient to cause a height change or an appreciable surface free energy change. This observation is also consistent with a pattern that is composed of only a number of single molecules. It is

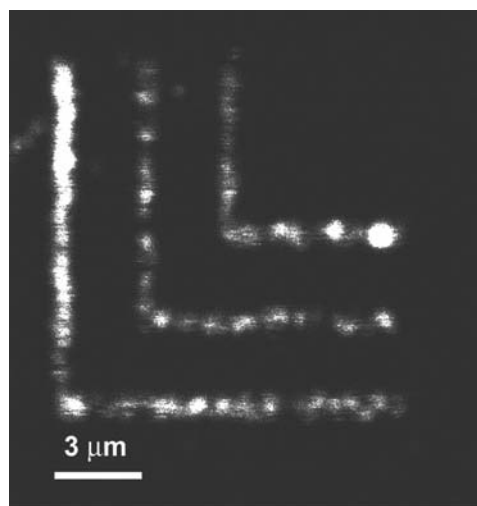


**Fig. 7** Scanning confocal microscopy image of a Rhodamine 6G patterned in a series of lines on glass surface. Probe translation speed was  $0.2 \mu\text{m/sec}$ . Source: From Ref.<sup>[13]</sup>.

impossible to say how well the single molecules are aligned within the pattern line because the optical image does not provide nearly enough resolution to answer this question. However, we can speculate that the dye molecules are confined laterally at least within the typical line width attainable with alkanethiol DPN. Such width is  $\sim 30$  nm in our case, but other groups have reported the patterns with line widths as small as 15 nm.<sup>[8]</sup> However, this limit may simply reflect the fact that lateral force microscopy cannot visualize thiol lines smaller than 15 nm, even if they can be fabricated by DPN. Changing the concentration of the dye solution used for inking along with careful adjustment of ambient humidity can control the average spacing between the molecules along the written line. For our sample we estimated this spacing to be  $566 \pm 210$  nm. We expect that further improvements in the deposition process such as smaller probes, rigorous humidity control, and careful choice of the writing ink will result in smaller line widths and more regular deposition patterns. These improvements will permit better alignment of single molecules on the sample for studies of the proximity effects in single molecule interactions.

### Protein patterns

One of the promising potential applications of nanolithography is fabrication of ultrahigh density protein patterns for use in “biochips.” Some of the current approaches use soft lithography or “nanografting” to create reactive sites in a SAM.<sup>[22]</sup> Proteins then attach to these reactive sites via a chemical reaction. Both of these methods are complex multistage processes and use chemical attachment, which is always complicated by the problem of nonspecific adsorption. Dip-pen nanolithography provides a simple and straightforward way for creating protein patterns as features can be directly written onto the surface. Significantly, this method provides a route to avoid the complications associated with nonspecific binding in many instances. If the protein is tagged by a specific fluorophore, then the pattern can be easily identified and verified using optical imaging. To demonstrate the feasibility of this approach we fabricated patterns of human chorionic gonadotropin (HCG) antibody tagged with tetramethylrhodamine (TMR) dye on the glass surface (Fig. 8). A glass surface was pre-treated with 3-glycidoxypropyltrimethoxysilane to introduce the epoxy groups that facilitate protein adhesion to the surface. Reliable fabrication of protein chips will require the ability to deposit proteins at high surface concentration. To demonstrate this capability, we used a high concentration of the protein “ink” [ $\sim 2 \cdot 10^{-5}$  M (1 mg/ml) solution in PBS buffer] for fabrication of the pattern in Fig. 7. In addition, each line

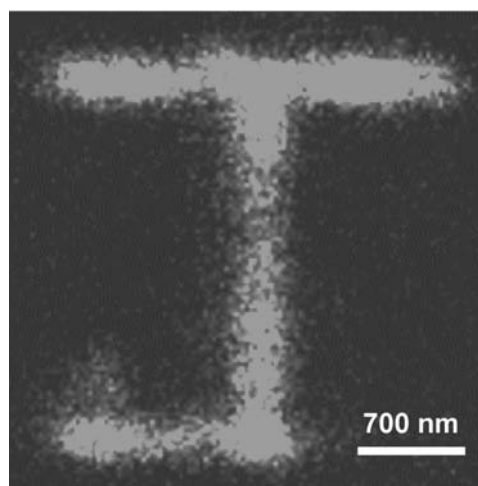


**Fig. 8** Scanning confocal microscopy image of a HCG antibody pattern fabricated on glass. Probe translation speed was  $0.2 \mu\text{m}/\text{sec}$ . Each line in the pattern was overwritten 10 times to maximize the protein surface density.

in the pattern was overwritten 10 times to enhance the surface concentration of the protein. The lines in the optical image on Fig. 7 appear continuous and no sufficient photobleaching was observed during scanning. The absence of single molecule behavior suggests that we have achieved large protein density in our lines.

Optical detection of a written pattern provides a straightforward way to generalize the process for creating patterns that incorporate many different proteins. Such patterns can be successfully fabricated and imaged by using a set of protein inks tagged with different fluorophores in a manner analogous to DPN with multiple inks.

### Fabrication of polymer nanowires

We have used our apparatus to fabricate and image nanowires of luminescent conductive polymers. These materials have long been under investigation as potential components of polymer light-emitting diodes (LEDs)<sup>[23]</sup> and fabrication of nanometer-scale polymer structures is a potentially significant step for creating nano-LED device prototypes. In addition, nanowires of these polymers present an ideal system for studying photoluminescence and electron transport in organic one-dimensional materials. Polymer nanowires have previously been fabricated using template-directed synthesis<sup>[24]</sup> and stretching of polymer bridges.<sup>[25]</sup> However, these methods do not allow good control over the size and position of a nanowire, or any way to assemble these nanowires in a predetermined configuration. Dip-pen nanolithography with its ability to create surface patterns is ideally suited for solving these problems. We demonstrated controlled deposition procedure by writing a series of polymer lines

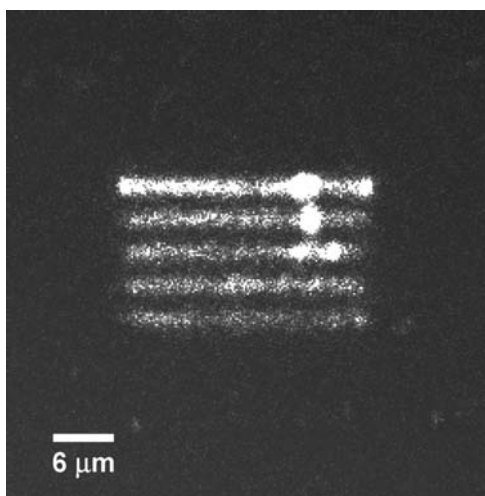


**Fig. 9** Scanning confocal microscopy image of a series of MEH-PPV polymer nanowires fabricated on glass surface. A plot of the average fluorescence intensity of a polymer wire vs. inverse probe translation speed used can be found in Fig. 4B. Source: From Ref.<sup>[13]</sup>.

on a glass surface (Fig. 9) using a  $10^{-7}$  M solution of MEH-PPV in chloroform as ink. Only the following three factors limit the length of these nanowires: 1) the available range of the force microscope scanner; 2) the amount of material on the probe tip; and 3) the ability of the tip to deliver continuous ink flow. As in the two experiments that we discussed earlier, the apparent width of the structure in the image does not correspond to the real width of the nanowire; instead, it is determined by the size of the confocal microscope excitation beam. Besides the tip size, the major variable in controlling the nanowire thickness is the tip translation speed. We found that the amount of material deposited in the line during nanolithography decreases with the increase in tip translation speed. The observed trends confirm that at constant humidity the amount of material deposited on the surface is effectively controlled by the probe translation speed (Fig. 4B).

## CONCLUSION

In summary, we have used dip-pen nanolithography combined with scanning confocal optical microscopy to create and image luminescent surface patterns of arbitrary shape. We demonstrated that this method affords a robust and versatile way to pattern a variety of photoluminescent materials on the surface. Significantly, we showed that dip-pen nanolithography could be used to deposit increasingly small amounts of material down to single isolated molecules. We also showed that a combination of dip-pen nanolithography

and optical detection could be used to create and identify protein patterns on the surface, while avoiding the problem of non-specific adsorption. We demonstrated that dip-pen nanolithography affords a direct and flexible route to creating polymer nanowires of a predetermined size and shape on surfaces. We also presented a simple kinetic model that captures the main physics of the deposition process. Our model takes into account the kinetics of dissolution as well as the effect of humidity on the thickness of the adsorbed water layer. This model predicts the dependencies of feature size on dwell time and tip speed that are in agreement with the measured dependencies, as well as a transition from a kinetic to a diffusive regime. Below that transition, the fundamental material parameter that controls the feature size for a given contact time or tip speed is the activation energy for detachment of the ink into the meniscus.

These results open up several possibilities for fundamental and applied research. Further refinements in the control of the spacing between isolated single molecules will present an ideal model system for studying proximity effects in the interactions between isolated fluorophores. The ability to fabricate arrays of single molecules with controlled spacing will allow studies of collective behavior in such systems. Patterning optically tagged proteins could provide a direct route to fabrication of prototype “biochips” once the protein surface attachment chemistry is refined. In addition to significant reduction in the feature size, dip-pen nanolithography simplifies the fabrication process because it eliminates the multiple protection/deprotection steps necessary for conventional lithographic manufacturing of such chips. Finally, fabrication of conductive polymer nanowires could open up numerous possibilities for fundamental studies of electron transfer and photoconductivity in such structures. In addition, fine control over the size and shape and position of these wires will greatly facilitate their incorporation into prototype optoelectronic devices.

## ACKNOWLEDGMENTS

The authors gratefully thank Jose Saleta (UCSB) for ESEM time. This work was performed under the auspices of the U.S. Department of Energy by the University of California, Lawrence Livermore National Laboratory under Contract No. W-7405-Eng-48.

## REFERENCES

1. Thiel, P.A.; Madey, T.E. The interaction of water with solid-surfaces—Fundamental-aspects. *Surf. Sci. Rep.* **1987**, *7* (6–8), 211–385.

2. Beaglehole, D.; Christenson, H.K. Vapor adsorption on mica and silicon-entropy effects, layering, and surface forces. *J. Phys. Chem.* **1992**, *96* (8), 3395–3403.
3. Pashley, R.M. Multilayer adsorption of water on silica—An analysis of experimental results. *J. Colloid Interface Sci.* **1980**, *78* (1), 246–248.
4. Xu, L.; Lio, A.; Hu, J.; Ogletree, D.F.; Salmeron, M. Wetting and capillary phenomena of water on mica. *J. Phys. Chem.* **1998**, *102* (3), 540–548.
5. Grigg, D.A.; Russell, P.E.; Griffith, J.E. Tip sample forces in scanning probe microscopy in air and vacuum. *J. Vac. Sci. Technol., A* **1992**, *10* (4), 680–683.
6. Piner, R.D.; Zhu, J.; Xu, F.; Hong, S.; Mirkin, C.A. “Dip-pen” nanolithography. *Science* **1999**, *283* (5402), 661–663.
7. Mirkin, C.A.; Hong, S.; Demers, L. Dip-pen nanolithography: Controlling surface architecture on the sub-100 nanometer length scale. *ChemPhysChem* **2001**, *2* (1), 37–39.
8. Sheehan, P.E.; Whitman, L.J. Thiol diffusion and the role of humidity in “dip pen nanolithography”. *Phys. Rev. Lett.* **2002**, *88* (15), 156104.
9. Schwartz, P.V. Molecular transport from an atomic force microscope tip: A comparative study of dip pen nanolithography. *Langmuir* **2002**, *18* (10), 4041–4046.
10. Hong, S.H.; Zhu, J.; Mirkin, C.A. Multiple ink nanolithography: Toward a multiple-pen nano-plotter. *Science* **1999**, *286* (5439), 523–525.
11. McKendry, R.; Huck, W.T.S.; Weeks, B.; Fiorini, M.; Abell, C.; Rayment, T. Creating nanoscale patterns of dendrimers on silicon surfaces with dip-pen nanolithography. *Nano Lett.* **2002**, *2* (7), 713–716.
12. Maynor, B.W.; Li, Y.; Liu, J. Au ‘ink’ for AFM “dip-pen” nanolithography. *Langmuir* **2001**, *17* (9), 2575–2578.
13. Noy, A.; Miller, A.E.; Klare, J.E.; Weeks, B.L.; Woods, B.W.; De Yoreo, J.J. Fabrication and imaging of luminescent nanostructures and nanowires using dip-pen nanolithography. *Nano Lett.* **2002**, *2* (2), 109–112.
14. Weeks, B.L.; Noy, A.; Miller, A.E.; De Yoreo, J.J. Effect of dissolution kinetics on feature size in dip-pen nanolithography. *Phys. Rev. Lett.* **2002**, *88* (25), 255505.
15. Xu, L.; Lio, A.; Hu, J.; Ogletree, D.F.; Salmeron, M. Wetting and capillary phenomena of water on mica. *J. Phys. Chem. B* **1998**, *102* (3), 540.
16. Piner, R.D.; Mirkin, C.A. Effect of water on lateral force microscopy in air. *Langmuir* **1997**, *13* (26), 6864–6868.
17. Huser, T.; Yan, M.; Rothberg, L.J. Single chain spectroscopy of conformational dependence of conjugated polymer photophysics. *Proc. Natl. Acad. Sci. U. S. A.* **2000**, *97* (21), 11187–11191.
18. Freund, J.; Halbritter, J.; Horber, J.K.H. How dry are dried samples? Water adsorption measured by STM. *Microsc. Res. Tech.* **1999**, *44* (5), 327–338.
19. Tsonopoulos, C. Thermodynamic analysis of the mutual solubilities of normal alkanes and water. *Fluid Phase Equilib.* **1999**, *156* (1–2), 21–33.
20. Tsonopoulos, C. Thermodynamic analysis of the mutual solubilities of hydrocarbons and water. *Fluid Phase Equilib.* **2001**, *186* (1–2), 185–206.
21. Weiss, S. Fluorescence spectroscopy of single biomolecules. *Science* **1999**, *283* (5408), 1676–1683.
22. Mrksich, M.; Whitesides, G.M. Patterning self-assembled monolayers using microcontact printing—A new technology for biosensors. *Trends Biotechnol.* **1995**, *13* (6), 228–235.
23. Friend, R.H.; Gymer, R.W.; Holmes, A.B.; Burroughes, J.H.; Marks, R.N.; Taliani, C.; Bradley, D.D.C.; Dos Santos, D.A.; Bredas, J.L.; Logdlund, M.; Salaneck, W.R. Electroluminescence in conjugated polymers. *Nature* **1999**, *397* (6715), 121–128.
24. Wu, C.G.; Bein, T. Conducting carbon wires in ordered, nanometer-sized channels. *Science* **1994**, *266* (5187), 1013–1015.
25. He, H.X.; Li, C.Z.; Tao, N.J. Conductance of polymer nanowires by a combined electrodeposition and mechanical break junction method. *Appl. Phys. Lett.* **2001**, *78* (6), 811–813.



# Dissymmetrical Nanoparticles

**Stéphane Reculosa**

*Centre de Recherche Paul Pascal, CNRS, Pessac, France*

**Christophe Mingotaud**

*Laboratoire des IMRCP, Université Paul Sabatier, Toulouse, France*

**Etienne Duguet**

*Institut de Chimie de la Matière Condensée de Bordeaux, CNRS, Pessac Cedex, France*

**Serge Ravaine**

*Centre de Recherche Paul Pascal, CNRS, Pessac, France*

## Abstract

Half-way between molecular and materials chemistries lies the field of colloidal chemistry where the shape, the size, and the morphology of supramolecular assemblies are key parameters that determine their intrinsic properties, such as their interfacial behavior, surface chemistry, density, and so on. In this review, we aim to gather some of the most significant works carried out within the last few years and dealing with particles wherein the spatial distribution of these properties is not isotropic. Therefore, we present some interesting synthetic routes suggested by researchers all around the world and leading to dumbbell-like, snowman-like or Janus-like nanoparticles whose potential remarkable properties are also discussed.

## INTRODUCTION

Probably since the very first days of the mankind, symmetry has been considered as an evidence of aestheticism and harmony and consequently as a main criteria for beauty, not only in arts, but also in science. To give a single example of a field where symmetry has played and still plays a major role, one can consider the case of chemistry and highly recommend the reading of books from Magdolna and Istvan Hargittai who have thoroughly studied the matter.<sup>[1]</sup> Given all the positive influences of symmetry in so different areas of knowledge, it may be surprising that some people could be attracted by the mysteries of dissymmetry. In 1848, Louis Pasteur was probably the most famous scientist to raise the question while studying what he called the “molecular dissymmetry,” later recognized as the foundation of the stereochemistry. One of the main conclusions of his works was that only natural substances are dissymmetrical and optically active, what he summarized by “la vie est fonction de la dissymétrie de l’Univers (life is a function of the dissymmetry of the Universe).”<sup>[2]</sup> A few years later, around 1880, Pierre Curie began to study the relationship between symmetry and properties of crystals. From his early observations, he concluded that a physico-chemical phenomenon, like piezoelectricity, could not occur without a change in the symmetry elements of the system, and he summed up the idea saying that “c’est la dissymétrie qui crée le phénomène (dissymmetry creates the phenomenon).”<sup>[3]</sup>

Since these pioneering studies, dissymmetry at the molecular or crystalline scale has been thoroughly explored. Until recent years, this has not been extended to supramolecular systems and particularly colloids. In this entry, we aim to demonstrate that the specific geometry or design of dissymmetrical sub-micrometer particles should be as worthy of interest as symmetrical particles in several applications of the modern physical and chemical sciences.

## DISSYMMETRY AGAINST SYMMETRY

As quoted before, dissymmetry was historically first studied at the molecular level and this research led to tremendous applications, mainly in the field of drugs. The interest in the matter remains strong, however, and the origin of the homochirality—and therefore dissymmetry—of the biomolecules is one of the current main issues in prebiotic chemistry. As an example, the reasons why proteins comprise almost entirely “left-handed” amino acids, whereas nucleic acids contain “right-handed” sugars, are still an intriguing problem.

At the macromolecular scale, many advances have been carried out recently in the field of dendrimers and several syntheses of “unsymmetrical” structures resulting from the combination of two chemically different dendrons have been reported.<sup>[4,5]</sup> Elaboration of unimolecular micelles made of a cross-linked core

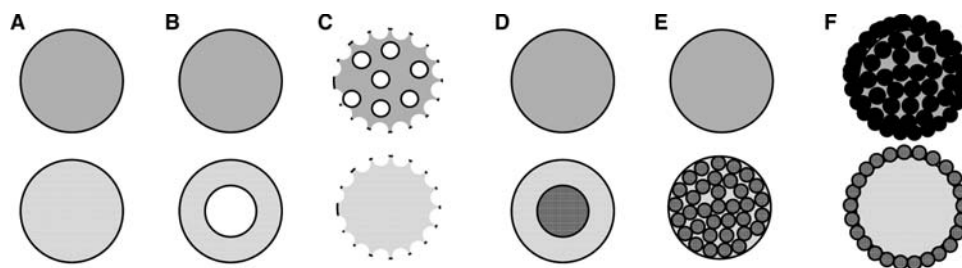


**Fig. 1** Schematic representation of some symmetrical particles (with outside views, top, and cross-sections, bottom): spherical (A), void or hollow (B), golf ball-like (C), core-shell (D), composite (E), and raspberry-like (F).

and a hairy shell with two different hemispheres also proved to be a novel amphiphilic system able to reorganize in supermicelles<sup>[6]</sup> whereas asymmetric star-block copolymer architectures have also been described.<sup>[7]</sup> Although interesting, these studies are, however, a limit case in the matter of interest of this entry since the so-formed objects are intermediate between molecules and colloidal particles.

Whereas the terms asymmetrical, unsymmetrical, or dissymmetrical are intuitive enough for a molecule, this is no more the case when dealing with particles and no effort has been made, until now, to standardize the nomenclature. So far, few authors were indeed interested in the elaboration of such “non-symmetrical” particles. The main aim of this entry is to collect these works and to classify the so-formed objects, describing and comparing their synthetic routes and discussing about their current and potential applications in chemistry, physics, biology, or medicine. To make it clear, only particles deriving from spherical and isotropic objects will be discussed in the rest of this paper.

Three main parameters should be taken into account to determine whether a particle is symmetrical or not. First, the particle shape, the more evident since the term “symmetry” is commonly associated to geometric considerations, second, the chemical composition of the particle bulk, and third, the chemical composition of its surface. In Fig. 1 are presented several examples of particles previously described in the literature and that should be considered as symmetrical. They are monophasic or not, solid or hollow, homogeneously surface-modified by chemical functions or again surface-decorated by smaller particles and their morphology is often described through very colorful terms such as core-shell, golf ball-like, raspberry-like particles, etc.

In comparison, the classification of dissymmetrical particles is more complex because their dissymmetry may be related to the shape, or the chemical composition of the bulk, or the chemical composition of the surface, or any combination of these three modes. This variety is illustrated in Fig. 2 where literature examples are classified according to these criteria.

The few researchers who have reported the synthesis and the properties of such particles have also used the terms asymmetrical, unsymmetrical, non-symmetrical, non-centrosymmetrical, or they just talked about anomalous morphologies or shapes. Nevertheless, these terms are most of the time inadequate since asymmetry, for instance, which means a complete lack of symmetry, is sometimes used to describe a particle that still retained symmetry elements after the modification process.

From the viewpoint of the applications, dissymmetrical particles should be very promising when compared with symmetrical ones. Indeed, such objects may present original properties such as (i) an amphiphilic character if a hydrophilic hemisphere may be combined with a hydrophobic one, (ii) a giant dipole moment if the surface charges may segregate onto separate poles, or (iii) a discriminatory reactive behavior if two types of chemical functions may be concentrated onto separate hemispheres. So, synthesis and properties

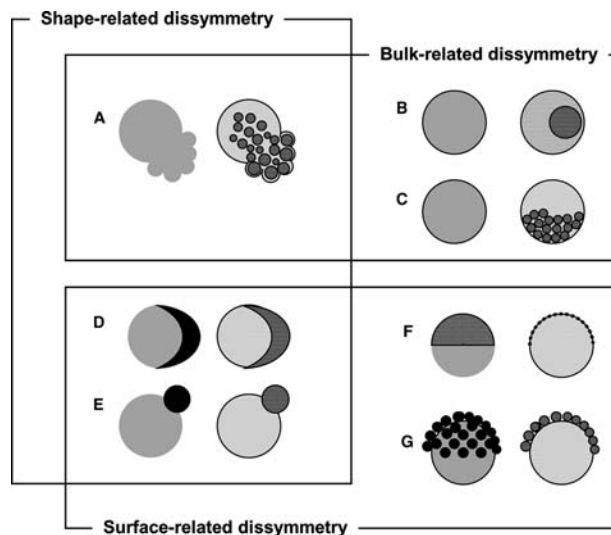


**Fig. 2** Examples of dissymmetrical particles (outside views and cross-sections) classified according to their dissymmetry modes: octopus ocellatus-like (A), decentered core-shell (B), loaded dice-like (C), half moon-like (D), snowman-like (E), Janus-like (F), and half-raspberry-like (G).

of dissymmetrical particles will be more extensively described in the following sections.

## SYNTHESIS AND CHARACTERIZATION

In the most general case, dissymmetrical particles are prepared from symmetrical ones and several dissymmetrization procedures, i.e. chemical or physico-chemical processes altering the symmetry elements of a precursor particle, are available. In the following paragraphs, different surface modification processes as well as one-pot chemical syntheses and polymerization reactions, which historically led to surface-dissymmetrical or bulk-dissymmetrical particles, are being discussed.

### Surface-dissymmetrical Particles through Toposelective Surface Modification Techniques

#### Partial contact with reactive media

As far as we know, the oldest and most intuitive way to elaborate a dissymmetrical particle is to place a pristine symmetrical particle along an interface, where it may most likely undergo different chemical reactions or physico-chemical processes, depending on the nature of the media separated by this interface and the position of the particle at this interface.

The very first example was reported in 1988 by Casagrande and Veyssié,<sup>[8]</sup> who described the elaboration of “Janus particles”, i.e. glass beads whose one hemisphere is naturally hydrophilic and the other one hydrophobic after a regioselective chemical surface modification. This well-chosen terminology was first employed by de Gennes<sup>[9]</sup> and refers to the god of the doors (literally janus in Latin) that is most commonly represented with a two-headed face, one looking at the past and the other one at the future and also considered as a representation of beginning and end (what explains that January is the first month of the year), war and peace, or life and death.

In the work of Casagrande and Veyssié, glass microspheres (around 50  $\mu\text{m}$  in diameter) were deposited on a solid support covered with a cellulose varnish film of controllable thickness protecting one part of the spheres whereas the other one was treated with octadecyltrichlorosilane, which is commonly used to make a surface hydrophobic. After removal of the varnish that let the protected surface hydrophilic, amphiphilic particles were obtained. Indeed, optical microscopy experiments showed a discriminatory behavior of adsorbed water with the formation of small droplets onto the hydrophobic part and a continuous film onto the hydrophilic one. Although

interesting for large particles, the technique is unsuitable for nanoparticles, because the control of the varnish layer thickness below 1  $\mu\text{m}$  would be rather difficult.

More recently, Fujimoto et al. have exploited techniques using air–liquid and liquid–solid interfaces to make polymer microspheres<sup>[10]</sup> and nanoparticles<sup>[11]</sup> dissymmetrical. In the latter case, after spreading and compression at the air–water interface of a Langmuir trough, a fluorine-containing (and consequently hydrophobic) terpolymer monolayer was transferred onto polymer particles (around 200 nm in diameter) previously deposited onto a glass substrate. Initially, the particles were hydrophilic owing to the presence of amine groups at their surface and became amphiphilic after the transfer. To give evidence of the fact, contact angle measurement were carried out as well as X-ray Photoelectron Spectroscopy analyses showing that fluorine atoms were only present onto one hemisphere, the one being covered with the terpolymer.

During the same period, a similar route was investigated for silica particles whose diameter was less than 100 nm.<sup>[12,13]</sup> Taking advantage of both Langmuir technique and chemical affinity between gold colloids and amine functions, silica nanoparticles were dissymmetrically decorated by gold clusters (diameter close to 8–10 nm). Transmission electron microscopy (TEM) observations show that adsorption of metallic colloids occurred only onto the immersed surface of the initial silica particle. More precisely, statistical calculations from TEM micrographs showed that about 40% of the final silica particles were obviously dissymmetrical, i.e. with a gold coverage onto one single hemisphere. Nevertheless, about 30% extra appeared to be homogeneously covered and were in fact probably badly positioned onto the TEM grid.

“Janus” gold nanoparticles with an average diameter of 2 nm were very recently prepared by ligand exchange reactions, using an air–water interface as dissymmetrization tool.<sup>[14]</sup> Hydrophilic thiol derivatives were injected into the water subphase after compression of a Langmuir film of hydrophobic alkanethiolate-passivated gold nanoparticles. The ligand place-exchange reactions only occurred on the side of the nanoparticles facing the aqueous phase, leading to the formation of nanoparticles that exhibit hydrophobic character on the one side and hydrophilic one on the other. This amphiphilic character was confirmed by contact angle measurements, FTIR, UV–visible, and NMR spectroscopies.

By using the so-called particle lithography technique, Yake and co-workers<sup>[15]</sup> have produced dissymmetrical nanoparticles. The essence of the method is to adhere particles to a surface and then to use the surface to mask one or more regions on the particle surface as the particle is coated by smaller nanoparticles (Fig. 3A). The diameter of the lithographed region ( $D$ ) is a function

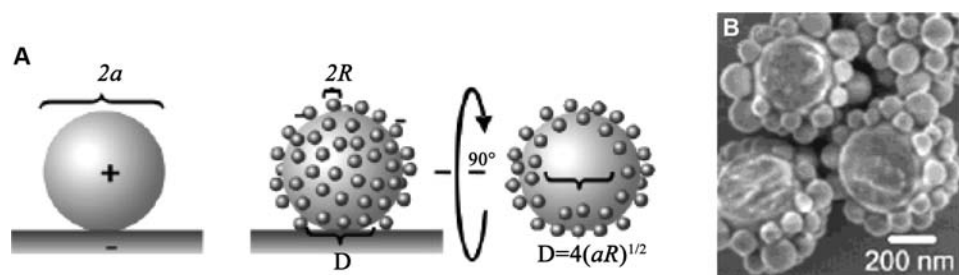


**Fig. 3** (A) Schematic of patterning colloidal particles with particle lithography. Positively charged colloidal particles are electrostatically adhered to a negatively charged glass surface. The result is a monolayer of positively charged particles adhered to the surface. Negatively charged nanoparticles of the same or different material are placed in solution and allowed to electrostatically adhere to the positively charged, adhered larger particles. The nanoparticles adhere in all areas except where the larger particles are masked off by being adhered to the glass surface. (B) Field emission scanning electron microscope image of 520-nm amidine-functionalized polystyrene latex patterned with particle lithography using smaller 170-nm silica nanoparticles. *Source:* Reprinted with permission from Ref.<sup>[15]</sup>.

of the core particles radius ( $a$ ) and the coating radius ( $R$ ). Simple geometry shows that:  $D = 4(aR)^{1/2}$ . Fig. 3B shows that amidine-functionalized polystyrene latex with size as small as 520 nm was dissymmetrically patterned with silica nanocolloids.

#### Directional fluxes and fields

Takei and Shimizu<sup>[16]</sup> have been the first to describe an easy method to prepare surface-dissymmetrical particles by evaporating gold on one side of latex microspheres (diameter of 20–50  $\mu\text{m}$ ). If this route could also be described as using a reactive interface (gas–solid interface), it seems more logical to consider this type of dissymmetrization process as the result of a surface modification in a directional flux, i.e. the direction from the gold target to the substrate-particles. This technique was applied recently to produce dissymmetrical sub-micrometer silica spheres.<sup>[17]</sup> Monolayers of 600 nm silica beads were prepared by drop-casting aqueous suspensions of particles onto glass slides. An adhesion layer of Ti/W alloy was deposited on the templates by electron-beam evaporation, followed by a thin film of gold. After the deposition of the metallic film, the thermal annealing of the coated particles led to a great increase in the mobility of gold atoms. Each gold half-shell beaded up by dewetting from its edge where it was the thinnest, inducing the transformation into a gold microcrystal sitting atop of the silica bead.

More recently, bimetallic silica nanospheres were synthesized by depositing gold and nickel on opposite hemispheres of the same particle.<sup>[18]</sup> Because of the magnetic functionality, these dissymmetrical colloids could be used as building blocks to fabricate one-dimensional assemblies, which are less accessible for traditional materials.

#### Towards larger interfaces

In all these previously described works, dissymmetry was brought to a symmetric pristine particle through oriented surface reactions. The low amount of produced particles is, however, the main limitation for further applications. In the current state of the art, a rough calculation allows to evaluate the production (in a reasonable duration) of dissymmetrical particles from few tens of particles in the case of laser-induced dissymmetry (which operates particle by particle) to few milligrams in the Langmuir film-inspired technique (assuming a trough surface of  $1\text{ m}^2$  and that every particle may be recovered).

So, the industrial future of these routes, in particular those involving a reactive interface, will mainly depend on the development of processes involving interfaces with very large surface areas. The most promising outcomes will mainly be the use of emulsions or microparticulate solid substrates. Indeed, for a perfect dissymmetry, the interface has to be theoretically infinitely flat. But, for the dissymmetrization of nanoparticles, it is reasonable to anticipate that closed interfaces, such as droplets or particles of few tens of micrometers in diameter and dispersed in a liquid medium, would be promising tools. Moreover, since the pioneering works of Pickering,<sup>[19]</sup> organic or inorganic particles are known for their ability to place themselves at liquid–liquid interfaces and therefore stabilize some emulsions.<sup>[20]</sup>

A French patent was initially published according to these goals.<sup>[21]</sup> The whole principle was to place initially symmetrical oxide nanoparticles at the surface of silicon oil droplets dispersed in water. Not taking into account the stabilization parameter, it was assumed that particles adsorbed at this interface, even during a short period of time, were able to react with molecules dissolved in the oil phase. When the reaction

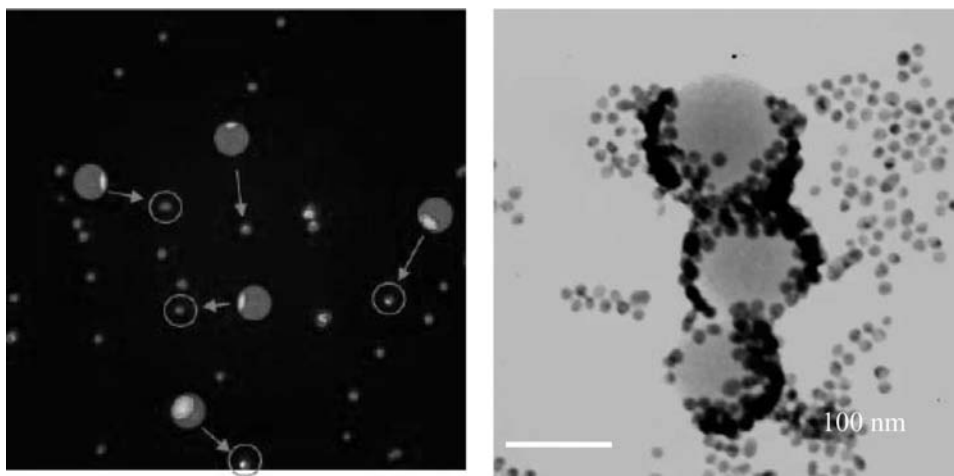


**Fig. 4** (Left) Epifluorescence of Janus-modified particles in an aqueous suspension. They are positively charged around the sphere but fluorescent on one hemisphere only. The particle diameter was  $1.5\ \mu\text{m}$ . *Source:* Reprinted with permission from Ref.<sup>[24]</sup>. (Right) TEM image of “Janus” 110-nm silica particles whose amine grafted area is decorated by gold nanoparticles.

was supposed to be completed, the so-modified particles were recovered through several centrifugation cycles. Following a similar strategy, Gu and co-workers have fabricated heterodimers by exploiting the partial protection of  $\text{Fe}_3\text{O}_4$  nanoparticles, which were placed at a liquid–liquid interface during the growth of silver nanoparticles at their surface.<sup>[22]</sup>

To avoid any rotation of the nanoparticles adsorbed at the liquid/liquid interface, molten paraffin wax was chosen as the oil phase. The emulsion was prepared at a temperature where wax was molten, and then it was cooled to room temperature to “lock” particles at frozen wax-aqueous surfaces, preventing particle rotation and facilitating subsequent chemical modification and purification. “Janus” silica particles with size ranging from  $2\ \mu\text{m}$ ,<sup>[23]</sup>  $1.5\ \mu\text{m}$ , and  $800\ \text{nm}$ ,<sup>[24]</sup> to  $110\ \text{nm}$  were thus obtained in large quantity, as shown in Fig. 4

Concerning the use of microparticles as solid substrates for making nanoparticles dissymmetrical, pioneer experiments concerned the use of commercial trityl resins, formyl polystyrene, and poly(methylmethacrylate) (PMMA) beads.<sup>[25]</sup> The first step consisted in the covalent grafting of amino-functionalized silica nanoparticles ( $100\text{--}200\ \text{nm}$  in diameter) at their surface. After a thorough washing, these raspberry-like particles were stirred in a gold colloidal solution and washed again. The more delicate step concerned the cleavage reactions for removing the silica particles.

Since then, the same strategy was followed to create “Janus” 10-nm magnetite nanoparticles<sup>[26]</sup> and heterodimers.<sup>[27]</sup> Water-dispersible hybrid nanotubes composed of an inorganic nanotube surrounded by a hydrophobic polymer layer (HPL) with water-soluble polymer chains grafted on the outer surface of the

HPL was recently used as a dissymmetrization tool during a reaction of polymerization.<sup>[28]</sup> Figure 5 shows that this process led to the formation of amphiphilic “Janus” particles in which water-soluble polymer chains are grafted on one side of a hydrophobic sphere. The “Janus” particles were found to self-assemble in water into supermicelles with a narrow size distribution. Under suitable conditions, the supermicelles can dissociate into individual nanosized “Janus” particles.

### Bulk-dissymmetrical Particles through Batch Polymerization Reactions

#### Phase separation processes

Several authors have studied the formation of dissymmetrical morphologies as the consequence of phase

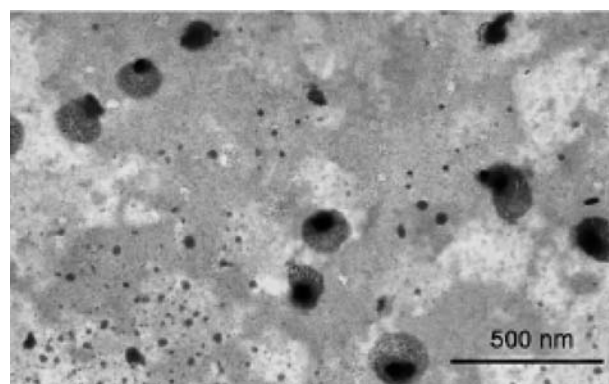


**Fig. 5** TEM image of amphiphilic polymeric Janus nanoparticles stained with  $\text{RuO}_4$ . *Source:* Reprinted with permission from Ref.<sup>[28]</sup>.

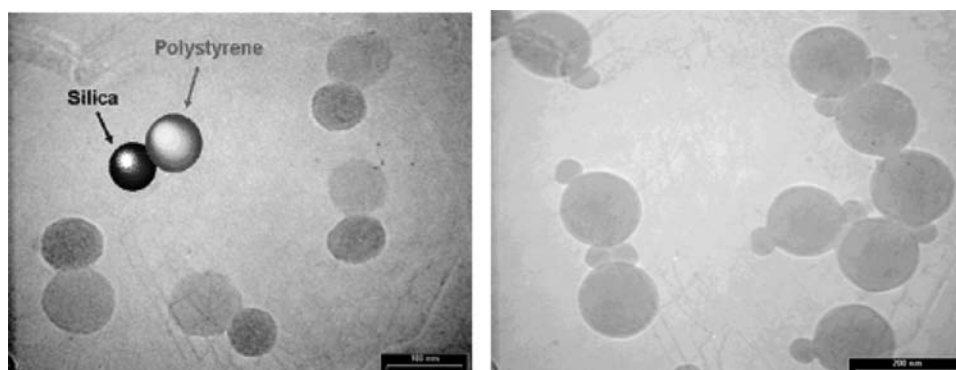


**Fig. 6** TEM images of: (Left) dumbbell-like and (Right) snowman-like hybrid nanoparticles synthesized through polystyrene growth onto silica seeds. *Source:* Reprinted with permission from Ref.<sup>[40]</sup>.

separation phenomena during some growth-seeded polymerization processes.<sup>[29–37]</sup> By varying the nature of the seeds and the monomer mixture, exotic structures were obtained as ovoid-like and red blood corpuscle-like,<sup>[29]</sup> golf ball-like,<sup>[30]</sup> raspberry-like and octopus-like.<sup>[32]</sup> Theoretical explanations taking into account geometrical as well as thermodynamical considerations have been proposed to predict the final particle morphology.<sup>[33,34]</sup>

Nevertheless, Cho and Lee<sup>[36]</sup> reported that in specific conditions, the styrene emulsion polymerization in the presence of PMMA-based seeds led to biphasic latex particles, such as half moon-like particles offering simultaneously bulk-related and surface-related dissymmetries or sandwich-like particles, which were in addition dissymmetrical from the viewpoint of their shape. What is also remarkable is the final particle size, around 500 nm in the larger dimension, this being interesting for some applications, as it is shown later.

Similarly, Pfau and co-workers<sup>[37]</sup> synthesized mushroom-like nanoparticles (around 200 nm in diameter) with a poly(*n*-butyl acrylate) (PnBA) core partially capped with PMMA through successive emulsion polymerization reactions. As it is often the case, SEM and TEM are privileged techniques to characterize the so-formed polymeric objects. More unusually, atomic force microscopy experiments in tapping mode (AFM-TM) were carried out. They gave evidence for a preferential organization of the dissymmetrical particles depending on the chemical nature of the substrate surface: When the substrate was hydrophilic muscovite mica, an orientational ordering of the hydrophilic PMMA caps toward the surface was observed.

#### Controlled surface nucleation

Dissymmetrical morphologies were also reported in some experiments initially dedicated to the micro-encapsulation of inorganic particles in polymer shells.

In general, such techniques derive from heterogeneous polymerization techniques, such as emulsion, dispersion, suspension, and miniemulsion techniques.<sup>[38]</sup>

Conventional emulsion polymerization involves the use of monomers insoluble or sparingly soluble in water, surfactant, and water-soluble initiator. Polymerization normally takes place in monomer-swollen micelles and surfactant-stabilized polymer particles formed by nucleation in aqueous medium. The encapsulation of non-swellable particles such as inorganic particles is successful if the nucleation step is favored at particle surface and it depends not only on interfacial properties of inorganic seeds, but also on details of nucleation and stabilization of newly formed polymer particles. If core-shell particles are generally obtained, raspberry-like,<sup>[39]</sup> dumbbell-like, and snowman-like<sup>[40]</sup> shapes based on silica and polystyrene particles were recently reported (see Fig. 6). Mushroom-like and swaddle-like nanocomposite particles<sup>[41]</sup> were also prepared via one-step miniemulsion polymerization of styrene in the presence of locally surface-modified silica particles<sup>[42,43]</sup> as seeds.

On the basis of the concept that a removable mask can temporarily protect a part of an object in a reactive medium, “Janus” silica nanoparticles were synthesized through the selective functionalization of the unprotected mineral part of the snowman-like particles and the subsequent removal of the protecting polymer mask.<sup>[44]</sup>

Dissymmetrical nanoparticles were also obtained by the controlled growth of metals or metal oxides on metallic seeds. For instance, the decomposition of iron pentacarbonyl over the surface of gold nanoparticles, followed by oxidation under air, led to dumbbell-like Au-Fe<sub>3</sub>O<sub>4</sub> nanoparticles of various sizes (Fig. 7).<sup>[45]</sup> The Au-Fe<sub>3</sub>O<sub>4</sub> structure is most likely derived from the epitaxial growth of Fe<sub>3</sub>O<sub>4</sub> on the Au seeds as Au has a face-centered-cubic structure with a lattice parameter *a* of 4.08 Å, while Fe<sub>3</sub>O<sub>4</sub> has a cubic structure with *a* = 8.35 Å, which is within 3% of being



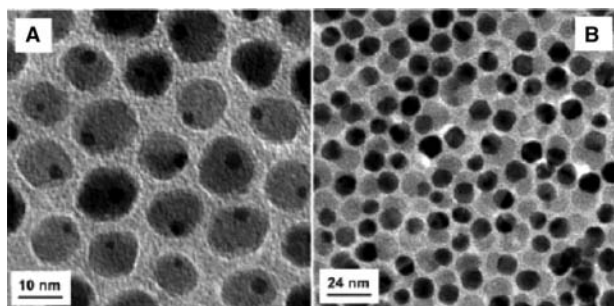


**Fig. 7** TEM images of Au-Fe<sub>3</sub>O<sub>4</sub> particles of different sizes: (A) 3–14 nm; (B) 8–14 nm. *Source:* Reprinted with permission from Ref.<sup>[45]</sup>.

exactly double. Once the Fe<sub>3</sub>O<sub>4</sub> starts to nucleate on an Au seed, the free electrons from the Au particle must compensate for the charge induced by the polarized plane at the interface. As the Au particle has only a very limited source of electrons, this compensation makes all other facets of the Au nanoparticle electron deficient and unsuitable for multi-nucleation, giving only the dumbbell structure.

Co<sub>9</sub>S<sub>8</sub>/PdS<sub>x</sub> acorn- or peanut-shaped nanoparticles (Fig. 8) were also recently synthesized through the anisotropical growth of Co<sub>9</sub>S<sub>8</sub> phases from preformed PdS<sub>x</sub> seeds.<sup>[46,47]</sup> A thorough study of the growth process of the Pd–Co–Pd sulfide structures revealed that the “nanopeanuts” resulted from the fusion of the “nanoacorns” when the amount of passivating agent, C<sub>18</sub>SH, was small.

## POTENTIAL APPLICATIONS

When compared with symmetrical particles, the indisputable advantages of dissymmetrical ones are the additional degrees of freedom related to the anisotropy of the properties or the chemical bifunctionality confined on single particles. These non-conventional nanoparticles possess original properties and the aim of this part is to present those which have been already noticed and checked and those which are expected so far.

## Stabilization of Complex Media

The behavior of amphiphilic Janus particles at water/oil interfaces was first studied by Casagrande and Veyssié.<sup>[8]</sup> During the synthesis of these particles, the authors managed to control the surface coverage of hydrophilic and hydrophobic domains by adjusting the varnish layer thickness, giving evidence that a parallel with the Bankroft rule, well known for amphiphilic molecules that can lead to either direct or inverse emulsions, was possible.<sup>[48–50]</sup> Moreover, as shown successfully by Ondarçuhu et al.,<sup>[49]</sup> such Janus particles are very likely to stay at oil–water interfaces, provided that they are specifically functionalized with both hydrophilic and hydrophobic groups onto separate parts of their surface. These particles can be thus considered as colloidal surfactants.

## Electronic Displays

Dissymmetrical particles could also be of interest in the field of electronics, assuming that they have a dipolar moment and are able to react to an applied electric field. Typically, the gradient sensitive microscopic probes synthesized by Takei and Shimizu<sup>[16]</sup> are a good example of such an application. Whether an electric field can be applied specifically onto one dissymmetrical particle supporting a gold cap on one hemisphere (this generating the dipole moment) and bare on the other side, one can orientate the particle as desired.

## Biology and Medicine

Dissymmetrical nanoparticles with hemispheres coated with two different species may exhibit a behavior sensitive to the gradient of physico-chemical (pH, ionic strength...) or biological environments. Therefore, these objects can be used as nanoscopic probes and may find a wide ranging utility in biological studies. Furthermore, if the species grafted onto the two sides are an antibody and a drug, for instance, potential applications of these objects in biomedicine may include a powerful recognition of the targeted cell and an improved drug delivery.

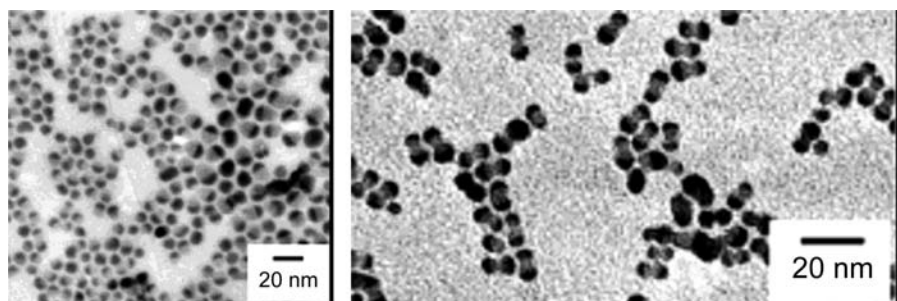


**Fig. 8** TEM images of: (Left) Co<sub>9</sub>S<sub>8</sub>/PdS<sub>x</sub> acorn-shaped nanoparticles. (Right) Pd–Co–Pd sulfide peanut-shaped nanoparticles. *Source:* Reprinted with permission from Ref.<sup>[46]</sup>. Reprinted with permission from Ref.<sup>[47]</sup>.

## Bio-inspired Systems

In the last fields of application, the use of surface-dissymmetrical particles may require large quantities of material, involving consequently mass production processes. However, techniques of elaboration leading to small amounts of product, such as those previously described while discussing about surface-dissymmetrical particles, may be of interest for some specific studies and for instance in biochemistry.<sup>[51]</sup>

## CONCLUSION AND PROSPECTS

The current trend in materials science is to elaborate “smart” functional nanomaterials, which often requires the control of the organization and therefore of the assemblies of molecules or particles. Such a control may be gained by a careful choice of complementary chemical or biochemical functions and a well-defined localization of those groups. Dissymmetrization is a powerful tool to control such a preferential localization and can be easily used to induce one-dimensional assemblies from nanoparticles. Recent extension of this process to tetrapods with a size in the nanometer range<sup>[52]</sup> now opens a way toward multi-functional materials that could be organized in a two- or three-dimensional fashion, as desired.

## REFERENCES

- Hargittai, I.; Hargittai, M. *Symmetry Through the Eyes of a Chemist*, 2nd Ed.; Plenum Press: New York, 1995.
- Pasteur, L. *Leçons de chimie professées en 1860*; Hachette, Ed.; Paris, 1861: 1–48.
- Curie, P. Sur la symétrie dans les phénomènes physiques, symétrie d'un champ électrique et d'un champ magnétique. *Journal de Physique Théorique et Appliquée* **1894**, *3* (1), 393–414.
- Wooley, K.L.; Hawker, C.J.; Fréchet, J.M.J. Unsymmetrical three-dimensional macromolecules: preparation and characterization of strongly dipolar dendritic macromolecules. *J. Am. Chem. Soc.* **1993**, *115* (24), 11,496–11,505.
- Bo, Z.; Rabe, J.P.; Schlüter, A.D. A poly(paraphenylene) with hydrophobic and hydrophilic dendrons: prototype of an amphiphilic cylinder with the potential to segregate lengthwise. *Ang. Chem. Int. Ed.* **1999**, *15* (13), 2370–2372.
- Erhardt, R.; Böker, A.; Zettl, H.; Kaya, H.; Pyckhout-Hintzen, W.; Krausch, G.; Abetz, V.; Müller, A.H.E. Janus micelles. *Macromolecules* **2001**, *34* (4), 1069–1075.
- Hadjichristidis, N.; Pitsikalis, M.; Pispas, S.; Iatrou, H. Polymers with complex architecture by living anionic polymerization. *Chem. Rev.* **2001**, *101* (12), 3747–3792.
- Casagrande, C.; Veyssié, M. “Grains Janus”: réalisation et premières observations des propriétés interfaciales. *C. R. Acad. Sci. Paris* **1988**, *306* (II), 1423–1425.
- de Gennes, P.G. Nanoparticles and dendrimers: hopes and illusions. *Croatica Chemica Acta* **1998**, *71* (4), 833–836.
- Fujimoto, K.; Nakahama, K.; Shidara, M.; Kawaguchi, H. Preparation of unsymmetrical microspheres at the interfaces. *Langmuir* **1999**, *15* (13), 4630–4635.
- Nakahama, K.; Kawaguchi, H.; Fujimoto, K. A novel preparation of nonsymmetrical microspheres using the Langmuir-Blodgett technique. *Langmuir* **2000**, *16* (21), 7882–7886.
- Petit, L.; Sellier, E.; Duguet, E.; Ravaine, S.; Mingo-taud, C. Dissymmetric silica nanospheres: a first step to difunctionalized nanomaterials. *J. Mater. Chem.* **2000**, *10*, 253–254.
- Petit, L.; Manaud, J.-P.; Mingo-taud, C.; Ravaine, S.; Duguet, E. Sub-micrometer silica spheres dissymmetrically decorated with gold nanoclusters. *Mat. Lett.* **2001**, *51*, 478–484.
- Pradhan, S.; Xu, L.-P.; Chen, S. Janus nanoparticles by interfacial engineering. *Adv. Funct. Mater.* **2007**, *17*, 2385–2392.
- Yake, A.M.; Snyder, C.E.; Velegol, D. Site-specific functionalization on individual colloids: size control, stability, and multilayers. *Langmuir* **2007**, *23*, 9069–9075.
- Takei, H.; Shimizu, N. Gradient sensitive microscopic probes prepared by gold evaporation and chemisorption on latex spheres. *Langmuir* **1997**, *13* (7), 1865–1868.
- Lu, Y.; Xiong, H.; Jiang, X.; Xia, Y. Asymmetric dimers can be formed by dewetting half-shells of gold deposited on the surfaces of spherical oxide colloids. *J. Am. Chem. Soc.* **2003**, *125*, 12,724–12,725.
- Correa-Duarte, M.A.; Rodriguez-Gonzalez, B.; Liz-Marzan, L.M.; Salguero-Maceira, V.; Kosiorek, A.; Kandulski, W.; Giersig, M. Asymmetric functional colloids through selective hemisphere modification. *Adv. Mater.* **2005**, *17*, 2014–2018.
- Pickering, S.U. Emulsions. *J. Chem. Soc.* **1907**, *91*, 2001–2021.
- Böker, A.; He, J.; Emrick, T.; Russell, T.P. Self-assembly of nanoparticles at interfaces. *Soft Matter* **2007**, *3*, 1231–1248.
- Chane Ching, J.Y. Agents tensioactifs formés par des particules minérales de dimension nanométrique de surface modifiée. French Patent FR 2 808 704, May 10, 2000 (Rhodia Chimie)
- Gu, H.; Yang, Z.; Gao, J.; Chang, C.K.; Xu, B. Heterodimers of nanoparticles: formation at a liquid-liquid interface and particle-specific surface modification by functional molecules. *J. Am. Chem. Soc.* **2005**, *127*, 34–35.
- Perro, A.; Reculosa, S.; Ravaine, S.; Bourgeat-Lami, E.; Duguet, E. Design and synthesis of Janus micro- and nanoparticles. *J. Mater. Chem.* **2005**, *15*, 3745–3760.
- Hong, L.; Jiang, S.; Granick, S. Simple method to produce Janus colloidal particles in large quantity. *Langmuir* **2006**, *22*, 9495–9499.

25. Poncet-Legrand, C.; Petit, L.; Reculosa, S.; Mingotaud, C.; Duguet, E.; Ravaine, S. Dissymmetrical gold tagging on spherical silica nanoparticles. *Prog. Colloid Polym. Sci.* **2004**, *123*, 240–244.
26. Lattuada, M.; Hatton, T.A. Preparation and controlled self-assembly of Janus magnetic nanoparticles. *J. Am. Chem. Soc.* **2007**, *129*, 12,878–12,889.
27. Ohnuma, A.; Abe, R.; Shibayama, T.; Ohtani, B. Commun. Heterodimeric particle assemblies: preparation of anisotropically connected spherical silica particles via surface-bound gold nanoparticles. *Chem. Commun.* **2007**, *33*, 3491–3493.
28. Nie, L.; Liu, S.; Shen, W.; Chen, D.; Jiang, M. One-pot synthesis of amphiphilic polymeric Janus particles and their self-assembly into supermicelles with a narrow size distribution. *Angew. Chem. Int. Ed.* **2007**, *46*, 6321–6324.
29. Okubo, M.; Minami, H.; Morikawa, K. Production of micron-sized, monodisperse, transformable rugby-ball-like-shaped polymer particles. *Colloid Polym. Sci.* **2001**, *279*, 931–935.
30. Okubo, M.; Fujiwara, T.; Yamaguchi, A. Morphology of anomalous polystyrene/polybutyl acrylate composite particles produced by seeded emulsion polymerization. *Colloid Polym. Sci.* **1998**, *276*, 186–189.
31. Okubo, M.; Yamashita, T.; Minami, H.; Konishi, Y. Preparation of micron-sized monodispersed highly monomer-“adsorbed” polymer particles having snowman shape by utilizing the dynamic swelling method with tightly cross-linked seed particles. *Colloid Polym. Sci.* **1998**, *276*, 887–892.
32. Okubo, M.; Kanaida, K.; Matsumoto, T. Production of anomalously shaped carboxylated polymer particles by seeded emulsion polymerization. *Colloid Polym. Sci.* **1987**, *265*, 876–881.
33. Chen, Y.C.; Dimonie, V.; El-Aasser, M.S. Interfacial phenomena controlling particle morphology of composite latexes. *J. Appl. Polym. Sci.* **1991**, *42*, 1049–1063.
34. Durant, Y.G.J.; Guillot, J. Some theoretical aspects on morphology development in seeded composite latexes. I. Batch conditions below monomer saturation. *Colloid Polym. Sci.* **1993**, *271*, 607–615.
35. Sheu, H.R.; El-Aasser, M.S.; Vanderhoff, J.W. Uniform nonspherical latex particles as model interpenetrating polymer networks. *J. Polym. Sci.: Part A* **1990**, *28*, 653–667.
36. Cho, I.; Lee, K.W. Morphology of latex particles formed by poly(methyl methacrylate)-seeded emulsion polymerization of styrene. *J. Appl. Polym. Sci.* **1985**, *30*, 1903–1926.
37. Pfau, A.; Sander, R.; Kirsch, S. Orientational ordering of structured polymeric nanoparticles at interfaces. *Langmuir* **2002**, *18* (7), 2880–2887.
38. Bourgeat-Lami, E. Organic-inorganic nanocomposites by multiphase polymerization. In *Dendrimers, Assemblies, Nanocomposites*; Arshady, R., Guyot, A., Eds.; Citus Book: London, 2002; The MML Series Vol. 5, 149–194.
39. Reculosa, S.; Poncet-Legrand, C.; Ravaine, S.; Mingotaud, C.; Duguet, E.; Bourgeat-Lami, E. Syntheses of raspberry-like silica/polystyrene materials. *Chem. Mater.* **2002**, *14* (5), 2354–2359.
40. Reculosa, S.; Poncet-Legrand, C.; Perro, A.; Duguet, E.; Bourgeat-Lami, E.; Mingotaud, C.; Ravaine, S. Hybrid dissymmetrical colloidal particles. *Chem. Mater.* **2005**, *17*, 3338–3344.
41. Qiang, W.; Wang, Y.; He, P.; Xu, H.; Gu, H.; Shi, D. Synthesis of asymmetric inorganic/polymer nanocomposite particles via localized substrate surface modification and miniemulsion polymerization. *Langmuir* **2008**, *24*, 606–608.
42. Takahara, Y.K.; Ikeda, S.; Ishino, S.; Tachi, K.; Ikeue, K.; Sakata, T.; Hasegawa, T.; Mori, H.; Matsumara, M.; Ohtani, B. Asymmetrically modified silica particles: a simple particulate surfactant for stabilization of oil droplets in water. *J. Am. Chem. Soc.* **2005**, *127*, 6271–6275.
43. Ikeda, S.; Kowata, Y.; Ikeue, K.; Matsumara, M.; Ohtani, B. Asymmetrically modified titanium(IV) oxide particles having both hydrophobic and hydrophilic parts of their surfaces for liquid–liquid dual-phase photocatalytic reactions. *Appl. Catal. A* **2004**, *265*, 69–74.
44. Perro, A.; Reculosa, S.; Pereira, F.; Delville, M.-H.; Mingotaud, C.; Duguet, E.; Bourgeat-Lami, E.; Ravaine, S. Towards large amounts of Janus nanoparticles through a protection-deprotection route. *Chem. Commun.* **2005**, *44*, 5542–5543.
45. Yu, H.; Chen, M.; Rice, P.M.; Wang, S.X.; White, R.L.; Sun, S. Dumbbell-like bifunctional Au-Fe<sub>3</sub>O<sub>4</sub> nanoparticles. *Nano Lett.* **2005**, *5*, 379–382.
46. Teranishi, T.; Inoue, Y.; Saruyama, M.; Nakaya, M.; Kanehara, M. Anisotropically phase-segregated Co<sub>9</sub>S<sub>8</sub>/PdS<sub>x</sub> nanoacorns: stability improvement and new heterostructures. *Chem. Lett.* **2007**, *36* (4), 490–491.
47. Teranishi, T.; Saruyama, M.; Nakaya, M.; Kanehara, M. Anisotropically phase-segregated Pd–Co–Pd sulfide nanoparticles formed by fusing two Co–Pd sulfide nanoparticles. *Angew. Chem. Int. Ed.* **2007**, *46*, 1713–1715.
48. Casagrande, C.; Fabre, P.; Raphaël, E.; Veyssié, M. “Janus beads”: realization and behaviour at water/oil interfaces. *Europhys. Lett.* **1989**, *9* (3), 251–255.
49. Ondarçuhu, T.; Fabre, P.; Raphaël, E.; Veyssié, M. Specific properties of amphiphilic particles at fluid interfaces. *J. Phys. France* **1990**, *51*, 1527–1536.
50. Binks, B.P.; Fletcher, P.D.I. Particles adsorbed at the oil-water interface: A theoretical comparison between spheres of uniform wettability and “Janus particles”. *Langmuir* **2001**, *17* (16), 4708–4710.
51. Bernheim-Groswasser, A.; Wiesner, S.; Golsteyn, R.M.; Carlier, M.F.; Sykes, C. The dynamics of actin-based motility depend on surface parameters. *Nature* **2002**, *417*, 308–311.
52. Liu, H.; Alivisatos, P.A. Preparation of asymmetric nanostructures through site selective modification of tetrapods. *Nano Lett.* **2004**, *4*, 2397–2401.

# DNA-Based Nanoinstrument Design

**Alexander Hillisch**

*Structural Bioinformatics and Drug Design, EnTec GmbH,  
Jena, Germany*

**Stephan Diekmann**

*Abteilung Molekularbiologie, Institut für Molekulare Biotechnologie, Jena, Germany*

## INTRODUCTION

The formation of protein–DNA complexes is a crucial step in many biological processes. Structural information on such complexes originates mainly from X-ray crystallography and nuclear magnetic resonance (NMR) spectroscopy. However, only few experimental techniques are available to deduce structural information on larger flexible protein–DNA complexes. We have designed DNA-based nanoinstruments that enable us to measure DNA deformation in solution.

Using bioinformatics and conformational search force field methods, we designed DNA molecules with one, two, and three  $dA_5$  bulges separated by double-stranded sections of DNA to be used as substrates for DNA–protein binding assays. The molecules were synthesized and 5'-end-labeled with 6-fluorescein (Fl) and 5-tetramethylrhodamine (TMRh) dyes. These large DNA molecules adopt a nearly planar conformation in aqueous solution with their helix ends being close in space. Fluorescence resonance energy transfer (FRET) between dyes was used to measure end-to-end distances and monitor the binding of proteins such as catabolite activator protein (CAP). The changes in the FRET efficiency of three-bulge DNA structures containing the specific binding sequence of CAP demonstrated significant deformation of the DNA upon binding of CAP.

In addition, the NMR solution structure of the  $dA_5$  bulge DNA fragment was solved.<sup>2</sup> This structure together with explicit positions of the dyes at the DNA helix ends allowed us to translate the measured FRET data into precise structural information.<sup>3</sup> This was demonstrated with two further DNA-binding proteins, high-mobility-group protein (HMG-D) and integration host factor (IHF). The concept of DNA-based nanoinstruments detecting DNA deformations can be used in solution, in gels, and at surfaces. It allows one to measure the influence of the DNA sequence itself, of proteins, and of environmental factors.

## BACKGROUND

Structure and function are key items in the world of biomolecules as well as in the world of physical techniques. Molecular biology and physical nanofabrication both essentially deal with nanostructures. During the last few years, biomolecular science and physics of microfabrication have come together in the geometrical dimensions of the considered objects: The world of single molecules and the world of lithographic patterning and physical manipulation are no longer separated by their size domains.

Over the last years, modern biotechnology has added fascinating new concepts and ideas for their application. By learning how nature performs wonders and how molecules can play tricks, we are discovering novel solutions to our scientific and daily problems. Since molecules are doing the work, the machinery consequently becomes very small—in the nanometer scale. Nanotechnology seems to be the ultimate domain, as atoms by themselves cannot perform complex working steps. Molecular biologists gain detailed insight into the structures of organization mechanisms of large biomolecules and functional molecular complexes. Confocal techniques and scanning probe instruments make the detection and manipulation of single molecules possible.

Advanced methods of physical nanopatterning and molecular biotechnology are fused to use the advantages of both method repertoires. Biomolecules such as nucleic acids and proteins (e.g., enzymes) seem to be particularly suitable candidates for such trials since they are defined in geometry and function and can be treated by enzymes that serve as biogenic tools. Molecular biology, genetic engineering, chemistry, and supramolecular construction contribute to the new development, as well as solid-state technology and nanolithography, surface sciences, and ultramicroscopy. The application of biomolecules in biomedical diagnostics, in the development of new drugs, and in other fields of molecular biotechnology reflects a pioneering function for the development of nanosystems.

The biomolecules and biomolecular systems used are optimized in natural evolution for their biological function within their natural environment and not for the solution of technical problems, such as physical signal transduction, mechanical motion, energy conversion, or data storage and transmission. We think that future molecular developments will supply new materials and artificial molecular tools—probably from organic chemistry—adapted to the physical and chemical problems of nanosystems that are optimally designed for their technical purposes and economical restrictions. Future molecularly based nanotechnical systems might have similarities with natural systems; in general, however, they will not be identical to them. Soon, further progress will guide nanofabrication by means of biomolecules from technically adapted biomolecules to a biomimetic molecular nanotechnology. This leads us to well-organized, completely artificial molecular nanosystems.

The nanometer-range molecular distances within biomolecular complexes are hardly measurable by biophysical techniques in solution. Three-dimensional information on nucleo- and multiprotein complexes originates mainly from X-ray crystallography and NMR spectroscopy; both techniques are labor-intensive and require large amounts of material. The resolution of light microscopy is limited to distances larger than about 200 nm, although new optical techniques reduce the resolution down to a few tenths of nanometers. Cryo electron microscopy allows us to deduce global structural features of large protein-DNA complexes,<sup>[1]</sup> but does not directly yield information of low Ångstrom resolution. Atomic force microscopy (AFM)<sup>[2]</sup> is generally limited to surfaces.

One technique yielding distance information in the low nanometer range is FRET. FRET provides

distance information for labeled macromolecules in the range 1 to 10 nm. Energy is transmitted from a donor dye to an acceptor dye that emits at a longer wavelength. The efficiency of this energy transfer is related to the distance between the dyes. If these dyes are specifically linked to known sites at macromolecules, molecular distances can be measured. The position of the dye cyanine-3 (Cy3) is known at the helical ends of DNA with atomic resolution, and evidence is accumulated on the position of fluorescein and rhodamine. This allows one to deduce absolute distance values with small errors. The measured FRET efficiency is transformed into distance values of particular precision when the dyes are separated in the range of the Förster distance  $R_0$ . This is not a general limitation since, as we have shown, by introducing structural elements such as bulges, nucleic acids can be constructed such that the helix ends come close in space. FRET efficiencies can also be quantitatively determined in polyacrylamide gels and by using fluorescent proteins in fusion. FRET is unique in its ability to provide accurate distance information (1–10 nm) in solution under physiological conditions. Recent advances make FRET a powerful tool for structural molecular biology and the construction of nanoinstruments.

In this entry we describe approaches and concepts of how FRET can be used in bionanotechnology to detect structural changes in DNA.

## MEASUREMENT PRINCIPLE

Compared to other particles such as electrons, photons are nice reporters because they have no charge. In a particular energy range, they can be easily distinguished by their color. However, in the nanometer

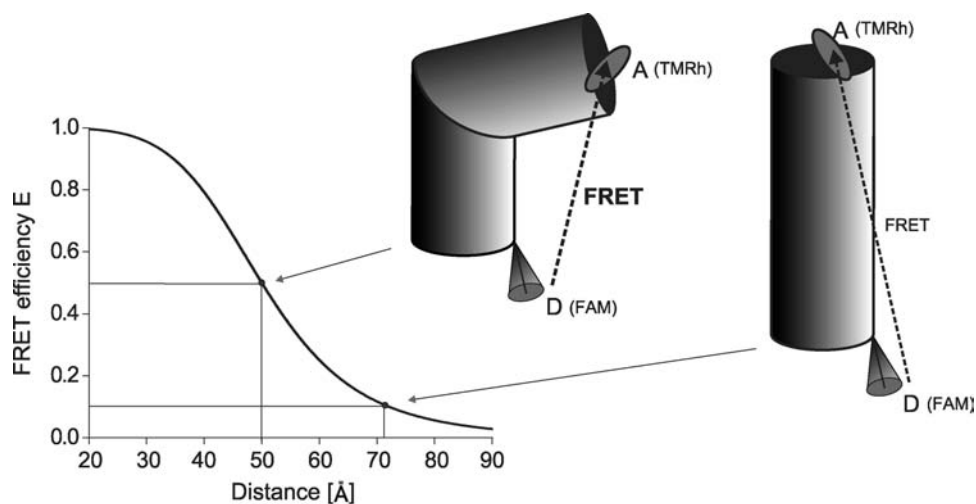


**Fig. 1** Change of FRET efficiency  $E$  due to DNA deformation. Gray cylinder: DNA, donor dye (D) Fl, and acceptor dye (A) TMRh.

range molecular distances cannot be measured because in a normal optical microscope the resolution is determined by the wavelength (>200 nm). Nevertheless, tricks exist that help to circumvent these physical principles. Fluorescence resonance energy transfer is one of them.

### Principles of Fluorescence Resonance Energy Transfer Measurements

FRET is a photophysical process by which energy is transferred from a fluorophore (the energy donor D) in an excited state to another chromophore (the energy acceptor A). The transfer of energy is a non-radiative, long-range (10 to 100 Å) dipole–dipole coupling process.<sup>[3]</sup> The particular advantage of FRET is the dependence (and thus sensitivity) of the energy transfer efficiency ( $E$ ) on the sixth power of the distance ( $R$ ) between the chromophores (Fig. 1).<sup>[4]</sup>

$$E = \frac{R_0^6}{R_0^6 + R^6}$$

The Förster distance ( $R_0$ ) is a dye pair-dependent parameter in the range up to 70 Å.<sup>[5]</sup>

### Multibulge DNA Constructs for Measuring Protein-Induced DNA Deformation

The distance sensitivity of the FRET efficiency is strongest when this distance is about  $R_0$  (i.e., about 5 nm). However, this is also the size domain of many biomolecules to be studied (e.g., the DNA binding domain of many proteins): The difference in the end-to-end distance of a straight 32-base-pair (bp) DNA before (10.8 nm) (Fig. 2A) and after (Fig. 2B) binding to the catabolite gene activator protein (CAP) is small and cannot be well detected with FRET.<sup>[6]</sup> In addition, undesirable dye–protein interactions could occur (Fig. 2B, \*). These problems can be circumvented by using (multi)bulge DNA molecules with helix ends close in space (Fig. 2C).<sup>[7]</sup> This molecular construction offers three advantages: 1) the FRET signal is measured in the distance range ( $R_0$ ) of highest sensitivity rather independent of the size of the biomolecule or complex, 2) dye–protein interactions can be avoided, and 3) the DNA after the framing bulges become “reporter arms” that amplify the sometimes small DNA deformation, further increasing the sensitivity enormously.<sup>[8]</sup>

### Labeling Biopolymers with Dyes

Often FRET is used to measure distances in protein structures and their assemblies in solution.<sup>[9]</sup> Proteins

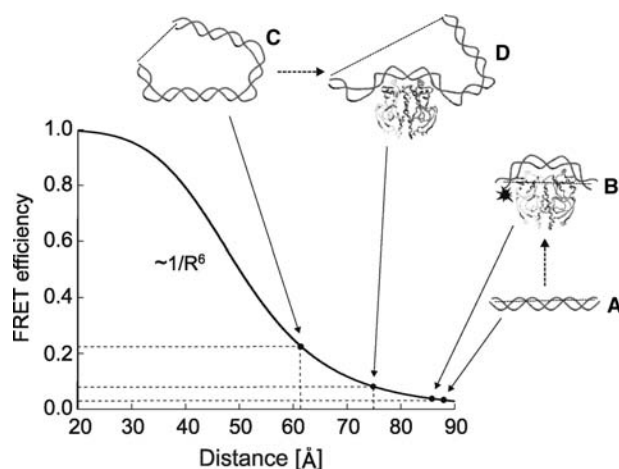


**Fig. 2** Detection and characterization of DNA bending utilizing DNA molecules with helix ends close in space. Straight 32-bp DNA before (A) and after (B) binding to the catabolite gene activator protein (CAP), potential dye–protein interactions (\*). Use of three-bulge DNA molecules (C, D) for bound (D) and unbound (C) DNA. The DNA structural changes due to CAP binding are amplified using these constructs.

contain intrinsic fluorophores (tryptophan and tyrosine). In addition, they can be labeled with dyes at defined sites such as cysteine residues. However, multiple occurrence of intrinsic fluorophores and tethering sites for dyes reduce the interpretability of FRET data obtained with these chromophores.

The known helical structure of double-stranded DNA and RNA can be exploited for measuring the global structure of nucleic acids and nucleoprotein complexes. Well-defined sequences of DNA and RNA oligomers are now routinely synthesized and fluorescently labeled at the 3'- or 5'-termini as well as within the DNA sequence. Dyes binding to the minor groove of DNA have also been used in FRET studies.<sup>[10]</sup> The end labeling has three main advantages (if the shortest possible DNA is used): 1) the dyes can be spatially separated from the binding protein to avoid protein–dye interactions, 2) the DNA end sequence can be specifically designed to provide an identical chemical environment and thus, identical fluorescence properties of the dyes in a series of molecules, and 3) the exact location of Cy3 on the DNA is known<sup>[11]</sup> and evidence is accumulated on the position of fluorescein and rhodamine.<sup>[12]</sup> In most studies, fluorescein and rhodamine have been attached to the 5'-ends. Because of its improved absorption and fluorescence properties, Cy3 will largely replace rhodamine as acceptor in FRET studies. Additionally and in contrast to rhodamine, Cy3 can directly be attached to the oligonucleotides during synthesis.



### Positions of the Dye Molecules on DNA Helix Ends

In FRET experiments, the energy transfer efficiency is not only dependent on the distance between the two dyes, but also on the orientation of the transition dipoles of the dyes. For an easy quantitative representation, at least one of the dyes should have rotational freedom<sup>[13]</sup> so that all dipole orientations appear with equal probability. To achieve this flexibility, the dyes are chemically attached to biopolymers via linear alkyl chains (two to six carbon atoms). Because of the flexibility of the dyes and the associated uncertainty in the dye positions, so far it has not been possible to use dye-to-dye distances as exact restraints comparable to nuclear overhauser effect (NOE) restraints in NMR spectroscopy (Fig. 3).

Norman and coworkers solved this problem for the dye pair fluorescein/Cy3. They determined the NMR structure of Cy3 tethered to the 5'-end of a 10-bp DNA duplex.<sup>[11]</sup> The resulting geometry of the dye-DNA adduct shows Cy3 stacked on top of the DNA

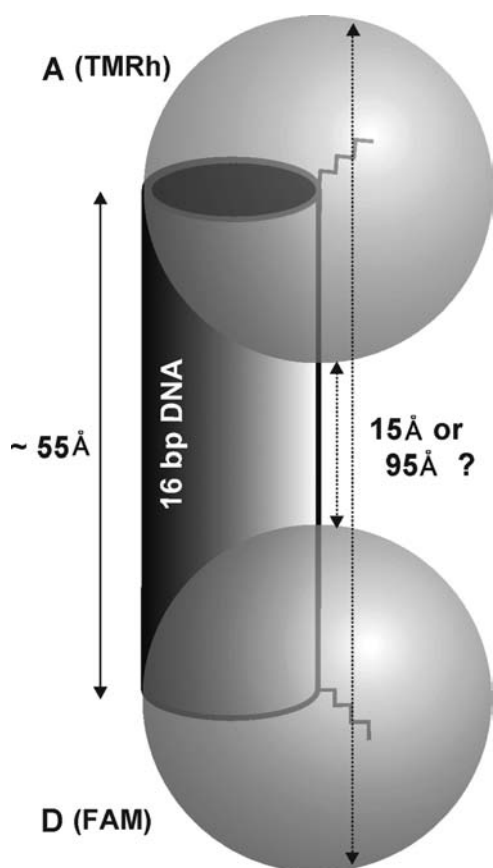


**Fig. 3** Dyes Fl (D, green) and TMRh (A, red) attached to the DNA (gray cylinder) via linkers. The positional space available to the dyes is shown as colored spheres, the minimal (1.5 nm) and maximal (9.5 nm) distance is indicated.

helix end, similar to an additional base pair (Fig. 4). The location of fluorescein is given by a maximally extended linker conformation.

We calculated the distribution of fluorescein (Fl) and rhodamine (TMRh) conformations at the DNA duplex ends using conformational sampling and energy minimization.<sup>[12,14]</sup> Most of the fluorescein conformers are pointing away from the DNA with an extended linker conformation because of the electrostatic repulsion of the twofold negatively charged dye and the poly-anionic DNA. The calculated averaged position is located 10 Å from the 5'-termini in a virtual elongation of the DNA backbone. This result is in concord with anisotropy measurements,<sup>[15]</sup> indicating that fluorescein freely rotates in solution. However, most of the calculated TMRh conformers either interact with the DNA in the major groove or stack on top of the DNA helix<sup>[16]</sup> (Fig. 4). The interaction of TMRh with the DNA is confirmed by anisotropy measurements,<sup>[17]</sup> and burst-integrated fluorescence lifetime (BIFL) experiments show direct contacts of TMRh with only the last base pair of the DNA helix (C. Seidel, personal communication). For the stacked conformation we obtained further evidence from FRET measurements of a complex of 55-bp DNA with the protein IHF.<sup>[16]</sup> Thus, TMRh, like Cy3, seems to stack on top of the DNA helix end (Fig. 4).

### DNA DEFORMATION MEASURED IN SOLUTION

Here we describe nanosystems that allow the detection of the DNA deformation in solution, in gels, or at surfaces.

#### Deformation Due to Protein Binding

The DNA deformation monitored by FRET can be used as a detection tool for the presence of those DNA-binding proteins that deform the DNA on binding. We also describe DNA constructions, either by specific proteins or DNA bulges, which yield in long reporter arms amplifying small changes in DNA structure.

#### Bending and kinking

Several proteins are known to bend or kink DNA. Some of them (e.g., TATA binding protein [TBP], PAPI, HMGs, IHF, and CAP) have been studied using FRET techniques.

*TBP*: The conformational change of a 14-bp, dye-labeled DNA upon binding of TBP has been studied in solution with FRET.<sup>[18]</sup> A strong decrease in the dye-to-dye distances was observed in the complex

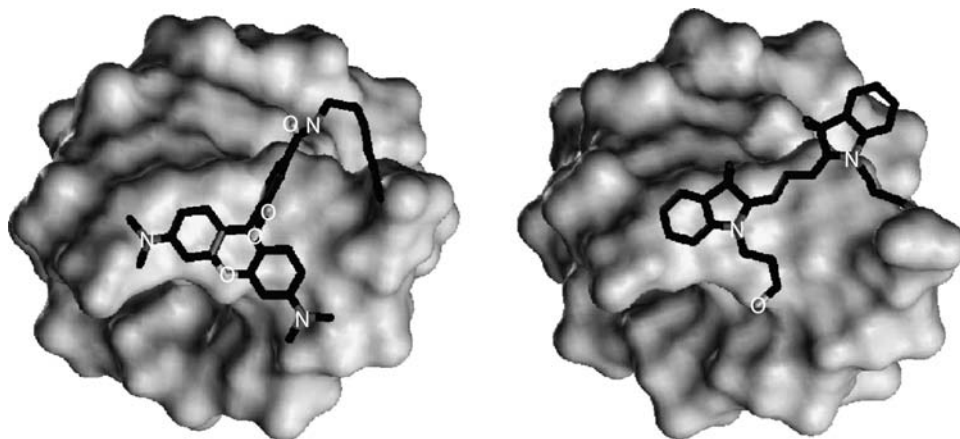


**Fig. 4** Position of the dyes TMRh (left) and Cy3 (right) on DNA helix ends. The molecular surface of the DNA is shown in gray; the dyes are represented as stick models in black. The location of Cy3 with respect to a 10-bp self-complementary DNA duplex was determined using two-dimensional homonuclear NMR experiments.<sup>[11]</sup> The position of TMRh attached with a six-carbon linker to the 5'-end of a DNA heptamer was modeled using systematic conformational search techniques. *Source:* From Ref.<sup>[12]</sup>.

compared to the naked DNA. The FRET data are in accord with a three-dimensional structure determined by X-ray crystallography.<sup>[19]</sup> A detailed kinetic study that used FRET revealed two intermediate complex species with similarly bent DNA. TBP binding and DNA bending were shown to occur simultaneously.<sup>[20]</sup>

**PAP1:** The conformational change of a 26-bp DNA upon binding of PAP1, a basic region leucine zipper motif containing transcription factor homologous to human c-Jun, has been studied in solution.<sup>[21]</sup> The authors conclude that the DNA adopts a bent conformation characterized by a bending angle of about 26°.

**HMG:** The HMG box is an 80-amino-acid domain found in many DNA-binding proteins and transcription factors. For reviews, see Refs.<sup>[22,23]</sup> In several studies the interaction of HMG proteins with DNA was analyzed using FRET.<sup>[24–28]</sup> The transcription factors, sex-determining region Y (SRY) and lymphoid enhancer-binding factor 1 (LEF-1), bind sequence specifically to DNA and induce a bend of 80–120°, as shown by NMR.<sup>[29,30]</sup> However, other HMG proteins bind less sequence specifically. These show elevated affinity to DNA distorted by cisplatinum,<sup>[31]</sup> to bulged DNA,<sup>[32]</sup> or to four-way junctions.<sup>[33]</sup>

Heyduk et al.<sup>[24]</sup> studied the interaction of the *Chironomus* HMG1a to a 30-bp double-stranded DNA using FRET between a europium chelate complex as donor and terminally attached cyanine-5 (Cy5). They estimated a DNA bending angle of 150° in the complex. We studied the binding of the *Drosophila* HMG-D and protein homologues to a dA<sub>2</sub> bulge containing 18-bp DNA 5'-labeled with fluorescein and rhodamine.<sup>[25]</sup> Molecular modeling was used to interpret the FRET data and to deduce a bending angle of 95°.<sup>[34]</sup> This value compares well with a bending

angle of 110° in the X-ray structure of HMG-D binding to a 12-bp DNA.<sup>[35]</sup> Further structural details predicted by our model (which were based on NMR data, footprinting results, and FRET) (Fig. 5) were confirmed by the subsequently published X-ray structure.

**IHF:** The interaction of DNA with the protein IHF was studied in solution with FRET. The crystal structure of this protein<sup>[36]</sup> complexed with a 35-bp DNA fragment containing a nick shows that IHF induces a U-shaped DNA conformation. To check if the DNA in the “physiological” complex (with intact DNA) adopts a similar conformation as revealed by the X-ray structure, the end-to-end distances of nicked and intact 55-bp DNA oligomers in the presence of IHF were measured using FRET.<sup>[16]</sup> For nicked

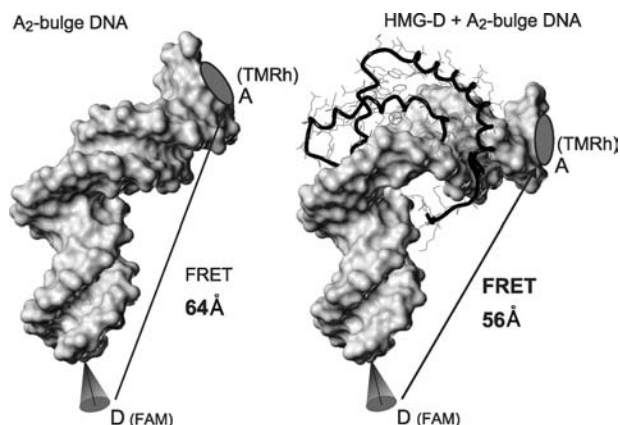


**Fig. 5** HMG-D binding (right) to dye-labeled, 18-bp, dA<sub>2</sub>-bulged DNA (naked DNA: left). Upon binding the protein increases the bend angle and reduces the dye distance from 6.4 to 5.6 nm.

DNA, the experimental dye-to-dye distance agrees, within 1–2 Å, with the distance between the dyes in a model based on the X-ray. The measured dye-to-dye distance of intact DNA is 4 Å larger than that of nicked DNA, suggesting a slightly different conformation of the IHF complex in solution for intact compared to nicked DNA (Fig. 6).

**CAP:** Catabolite activator protein binding to straight DNA (see Figs. 2 and 7) leads to a significant bending of the nucleic acid molecule.<sup>[37]</sup> Using an iterative approach of molecular modeling, DNA synthesis, and FRET measurements, we designed 22- to 65-bp-long DNA molecules with two or three dA<sub>5</sub> bulges each separated by double-stranded sections of B-DNA.<sup>[7]</sup> A molecular model of a two-bulge DNA molecule with close helix ends is shown in Fig. 8. Double-helical B-DNA regions can be used as substrates for protein binding. DNA molecules 65 bp long and containing three dA<sub>5</sub> bulges (and the CAP binding site in between) were constructed, 5'-end labeled, and used to monitor the binding of CAP by measuring FRET.

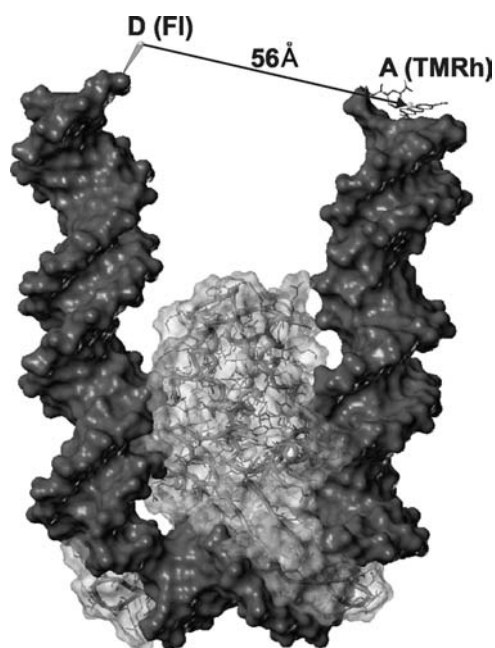


**Fig. 6** FRET analysis of IHF in complex with an intact 55-bp DNA.<sup>[16]</sup> The model building was based on the X-ray structure of IHF with a nicked 35-bp DNA oligomer.<sup>[36]</sup> Explicit positions for 5'-labeled dyes F1 (green) and TMRh (red) are shown. DNA strands are colored according to the covalently attached dyes, the protein is depicted in blue. Large spheres indicate the hypothetical range of locations for the dyes. Without knowledge of the exact dye positions, the end-to-end distance of the DNA could in principle be interpreted to range between 10 and 90 Å. FRET measurements show a distance of 55 Å, which is in agreement with a dye-to-dye distance of 56 Å (black arrow) in this model.

A decrease of Förster transfer efficiencies from 21% with CAP to 8% without CAP was observed (Fig. 7 and 2).<sup>[7]</sup> To be able to interpret the FRET data on a high-resolution level, we determined the NMR structure of a dA<sub>5</sub> bulge containing DNA fragment<sup>[38]</sup> and modeled the multiple bulge molecules (Fig. 8).

We constructed a series of double- and triple-bulged DNA molecules with different linker and reporter arm lengths to select those molecules that are (close to) planar and show maximal FRET efficiency<sup>[7]</sup> (Fig. 9). Because of handling reasons, the large triple-bulge DNA constructs (Fig. 9E and F) contain a nick.

### DNA twist

We constructed large triple-bulged DNA molecules not only to study the effects of CAP (see Figs. 2, 7, and 9) but also those of *EcoRI* binding (Fig. 10). Upon binding, *EcoRI* induces a twist into the DNA helix.<sup>[39]</sup> This subtle change can in principle be detected by labeled reporter arms (Fig. 10). Larger triple-bulge constructs are required to guarantee a sufficiently long and undistorted DNA binding site. The planar molecule (Fig. 10, left) is predicted to be twisted out of plane (Fig. 10, right) by *EcoRI*, increasing the dye distance and reducing FRET efficiency.<sup>[12]</sup>

### Influence of the Environment on DNA Deformation: Electrostatic Interaction of Double-Stranded DNA Strands

In the U-shaped DNA molecule, the two double-stranded arms are parallelly oriented<sup>[12]</sup> and the dyes are close to one another. The bulge–turn–bulge “linker” fixes the distance of the two helices at the “bottom” of the U. Thus, at this end the distance of the two strands is known (Fig. 3). The distance at the open end of the U-shaped molecule is measured by FRET in solution. This construction allows one, e.g., to measure the electrostatic interaction between the two negatively charged DNA double-stranded arms.

Because of the negatively charged phosphate backbones, the two roughly parallel helices repel each other. The electrostatic interaction between the two DNA arms was changed in two alternative ways: 1) the charge of the DNA arms was reduced by introducing methylphosphonates replacing backbone phosphates and 2) the salt concentration was increased. In the first case, the electrostatic repulsion is reduced because of the lower charge of the DNA backbone. Here, the FRET measurements can be performed under identical buffer conditions so that buffer influences on the properties of the dyes can be excluded. With increasing salt concentration, the additional mono- (Na<sup>+</sup>) and divalent (Mg<sup>2+</sup>) cations shield the DNA phosphate

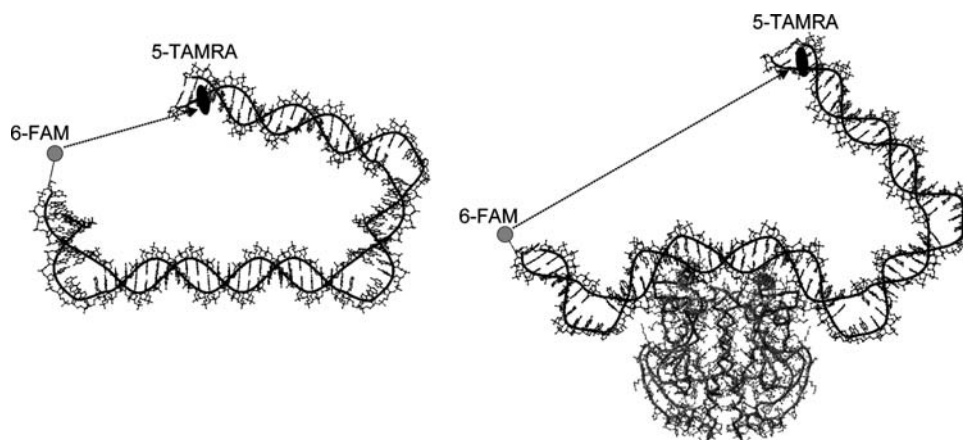


**Fig. 7** CAP binding to three-bulged DNA (left: naked DNA, right: CAP–DNA complex). Upon binding, CAP bends the DNA. Because of the reporter arms, the increase in end-to-end distance is large.

charges and reduce the electrostatic repulsion between the arms. Because of the increased salt concentration, buffer conditions change, and the influence of the buffer on the properties of the dyes has to be taken into account. Both procedures result in a shortened end-to-end distance between the DNA helix ends and thus in an increased FRET efficiency.

Such U-shaped DNA molecules with two nearly parallel DNA helices were constructed by introducing two  $dA_5$  bulges into the DNA helix that are separated by 9 bp of double-stranded DNA. The U-shaped structure and sequence is shown in Fig. 11. Four DNA

molecules were synthesized using increasing amounts of methylphosphonates. We compared the FRET efficiencies of a native, fully charged DNA with three partially uncharged DNA structures with 2, 4, or 6 methylphosphonate groups in the DNA backbone. The positions of the substituted nucleotides are shown in Fig. 11. The electrostatic effect of these methyl groups was maximized by placing them inside the U-turn facing each other at closest distances.

The fully charged U-shaped DNA molecule and its three less charged variants containing 2, 4, and 6 methylphosphonates were analyzed by measuring the

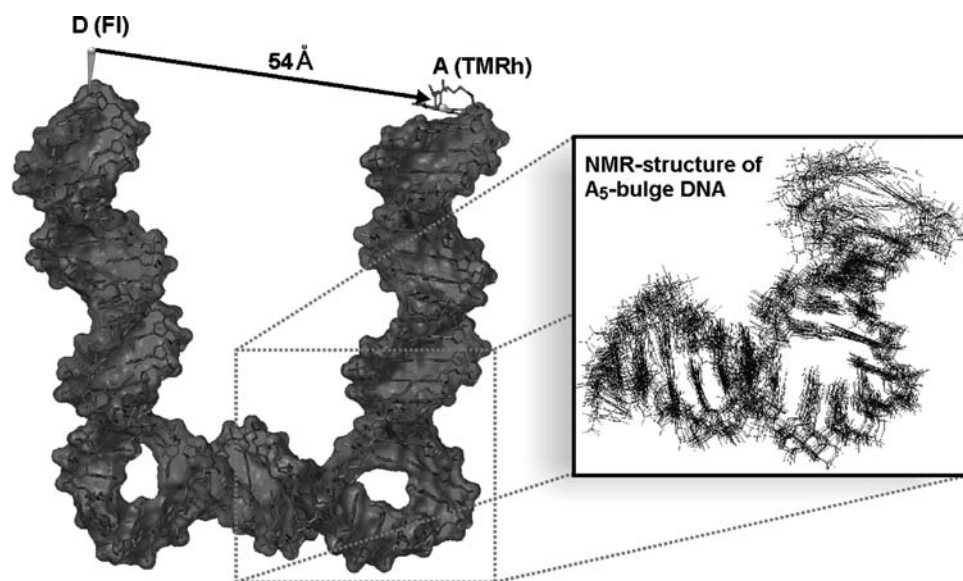


**Fig. 8** Atomic model of a DNA molecule containing two  $dA_5$  bulges. The molecule consists of three double-helical stems (16-, 9-, and 17-bp length). The longer FI-labeled strand is composed of 52 bases and colored green in the model; the shorter 42-base strand is labeled with TMRH and is depicted in red. The model is based on the NMR structure<sup>[38]</sup> of the  $dA_5$  bulge and FRET measurements.<sup>[7]</sup> Combining local (NMR) and global (FRET) structure information with the use of molecular modeling allows one to deduce this detailed model of a large DNA molecule in solution.



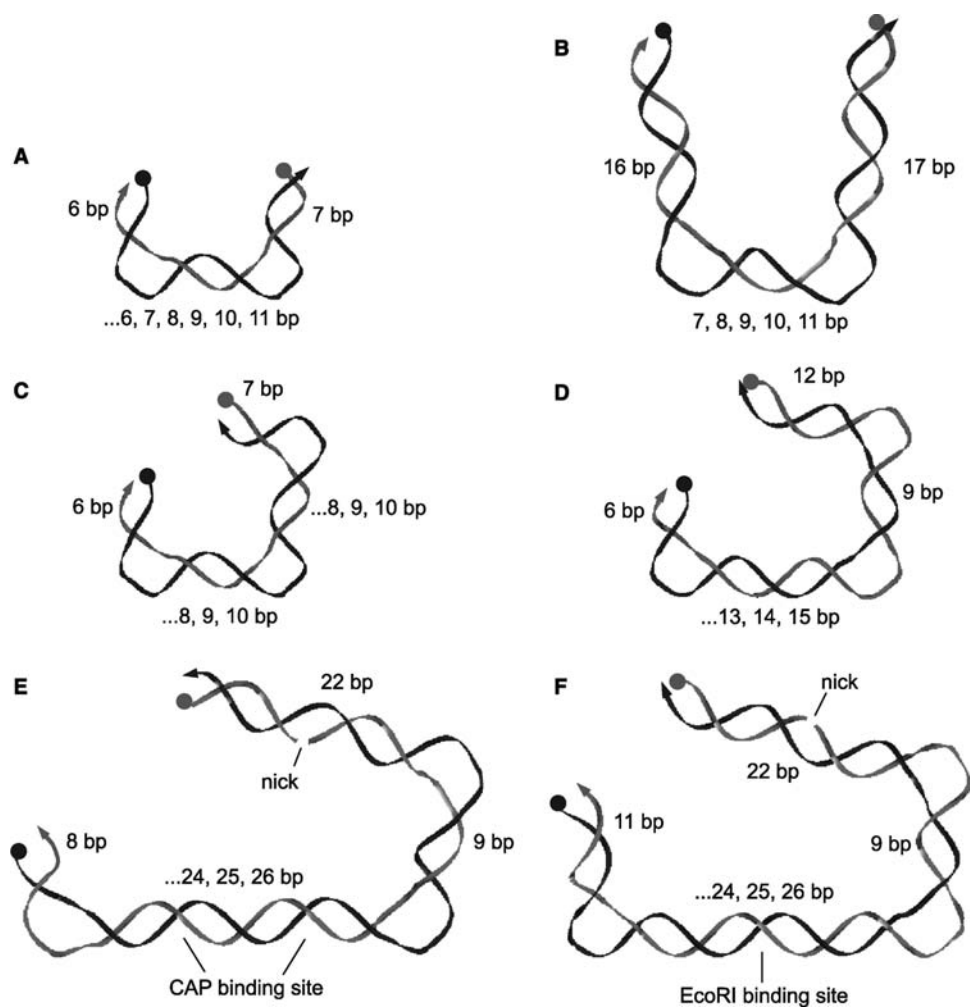


**Fig. 9** DNA constructs including two or three  $A_5$  bulges leading to close helix ends and thus a high FRET efficiency between end-labeled dyes. Fl-labeled strands are colored green and TMRh labeled are shown in red. A and B contain two  $A_5$  bulges and double-helical sections with different lengths flanking the bulges. The length of the double-helical section between the two bulges was varied between 7 and 11 bp. C, D, E, and F contain three  $A_5$  bulges. In addition, E and F have a CAP and *EcoRI* binding site in the longest stem and contain a nick.

FRET efficiency in the presence of 50 mM Tris-borate, pH 7.9, with increasing NaCl and  $MgCl_2$  concentrations. We found the FRET efficiency  $E$  strongly increasing with salt concentration (Fig. 12).

The strong increase of  $E$  levels off above about 200 mM NaCl or, alternatively, 10 mM  $MgCl_2$ , and shows only a moderate increase of  $E$  above these concentrations.

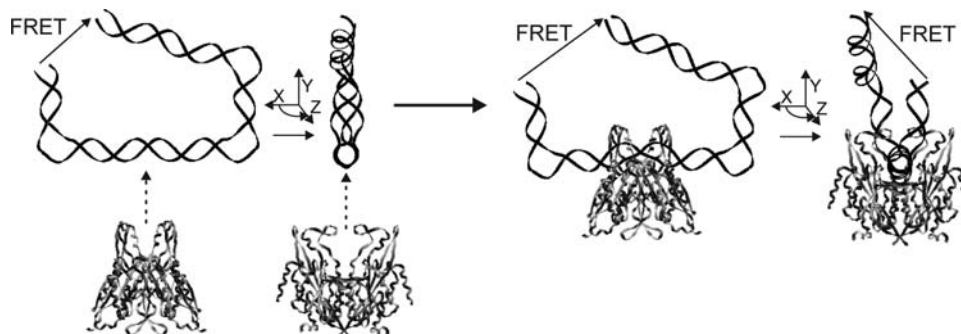


**Fig. 10** *EcoRI* binding to a triple-bulged DNA construct. *EcoRI* twists the DNA out of plane. This deformation can in principle be measured by these DNA nanoinstruments.

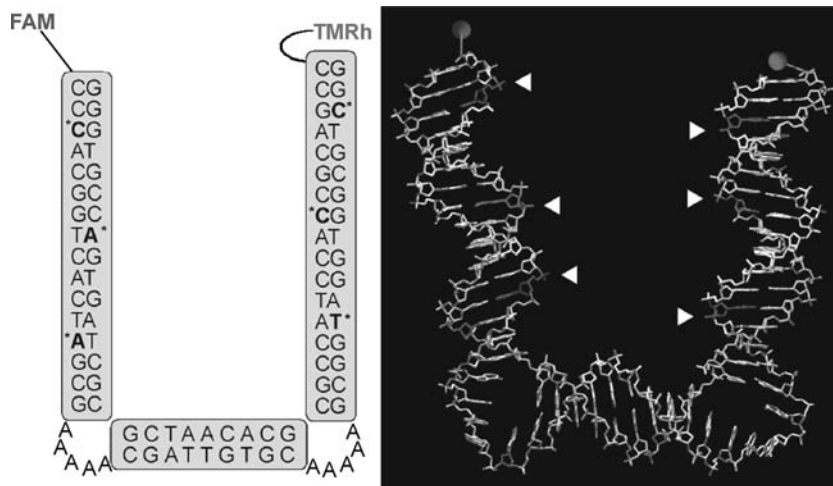


**Fig. 11** Sequence and global structure of the double-bulge DNA molecules. The positions of the methylphosphonates are shown in bold with an asterisk (left side) and shown in green and red for fluorescein and TMRh-labeled oligonucleotide, respectively, and pointed at by arrowheads (right side). The methylphosphonates are placed inside the U-turn facing each other. The dyes fluorescein (FI) and tetramethylrhodamine (TMRh) are shown in green and red, respectively.

The control experiments indicate that the increase of the FRET efficiencies of the double-bulge and the single-bulge molecules is due to structural changes of the DNA and not to changes of the dye properties or

positions. The strong increase at low salt concentrations is due to structural changes in the bulge (see single-bulge control, Fig. 12). The slightly increased FRET efficiency from 0.30 to 0.36 of the double-bulge molecules above 130 mM NaCl or 5 mM MgCl<sub>2</sub> is induced by reduced electrostatic repulsion of the two nearly parallel DNA helices.

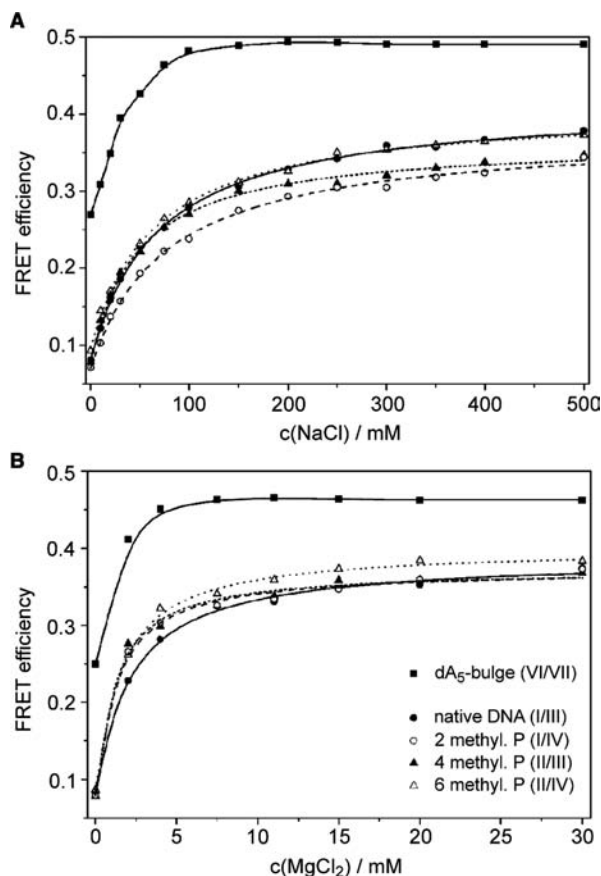


**Fig. 12** FRET efficiency dependence of the double-bulge constructs and, as control, a single bulge molecule on NaCl (A) and MgCl<sub>2</sub> (A) concentration. The roman numbers indicate the different DNA oligomers that were annealed for double-strand formation.

### Influence of the DNA Sequence on DNA Deformation

Dye-labeled, U-shaped DNA molecules can also be used for the very sensitive study of structural details of particular DNA sequences. When different sequences are placed between the two bulges, structural differences of these sequence stretches are strongly amplified and thus sensitively reported by the two helix arms. FRET between dyes attached to the helix arm ends can be used to measure twist and curvature changes.

### DETECTION OF DNA DEFORMATION IN POLYACRYLAMIDE GELS

The FRET efficiency can also be determined quantitatively in polyacrylamide gels<sup>[40]</sup> (Fig. 13). We labeled the two 5'-ends of the double-stranded substrate DNA with fluorescein and tetramethylrhodamine and measured the increase of FRET by binding of two proteins, either the HMG protein NHP6a or IHF; both proteins bend the DNA. In the gel, fluorescein retains its free rotational flexibility. However, the quantum yield is reduced, which can be taken into account by a different Förster distance  $R_0$  in the gel compared to solution. From the FRET increase, we determined the dye-to-dye distances in the protein-DNA complexes from polyacrylamide gel data<sup>[40]</sup> (Fig. 13),



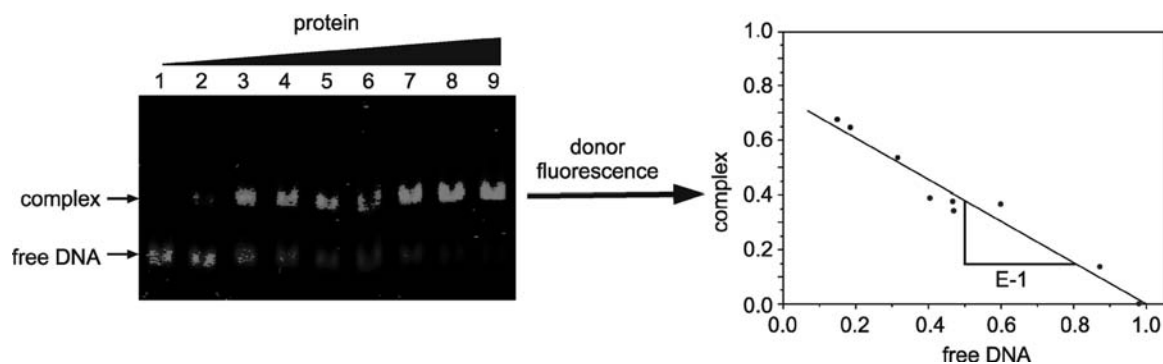


**Fig. 13** Determination of FRET efficiency  $E$  by the gel-based fluorescence assay “FRET in polyacrylamide gel electrophoresis (PAGE).”<sup>[40]</sup> Constant amounts of double-labeled DNA are incubated with increasing amounts of protein. The free DNA is separated from the complex in a polyacrylamide gel. In the complex, the DNA is bent and, thus, the dyes attached to the DNA helix ends are close to one another in space allowing for energy transfer. The donor fluorescence is quenched compared to free DNA. By plotting the donor fluorescence intensity of the complex vs. free DNA, a straight line is obtained with a slope ( $E - 1$ ) yielding the energy transfer efficiency  $E$ .

yielding global structural information on the complexes such as DNA bending angles.

#### DETECTION OF DNA DEFORMATION AT SURFACES

Often it is of advantage when molecular detection systems are bound to surfaces. For example, immobilized constructions allow for washing procedures. Such a

requirement does not exclude our detection concept. If one or two of the  $90^\circ$  bends in the DNA structure are due to protein binding by TBP or IHF, respectively (e.g., replacing one or two of the DNA bulges), and these proteins are linked to a surface by classical protein immobilization techniques, the detection principles and systems described above are applicable. For example, when a one-bulge DNA molecule including a TATA-box sequence in the longer stem (Fig. 14, left) binds to TBP (being immobilized to a surface) FRET

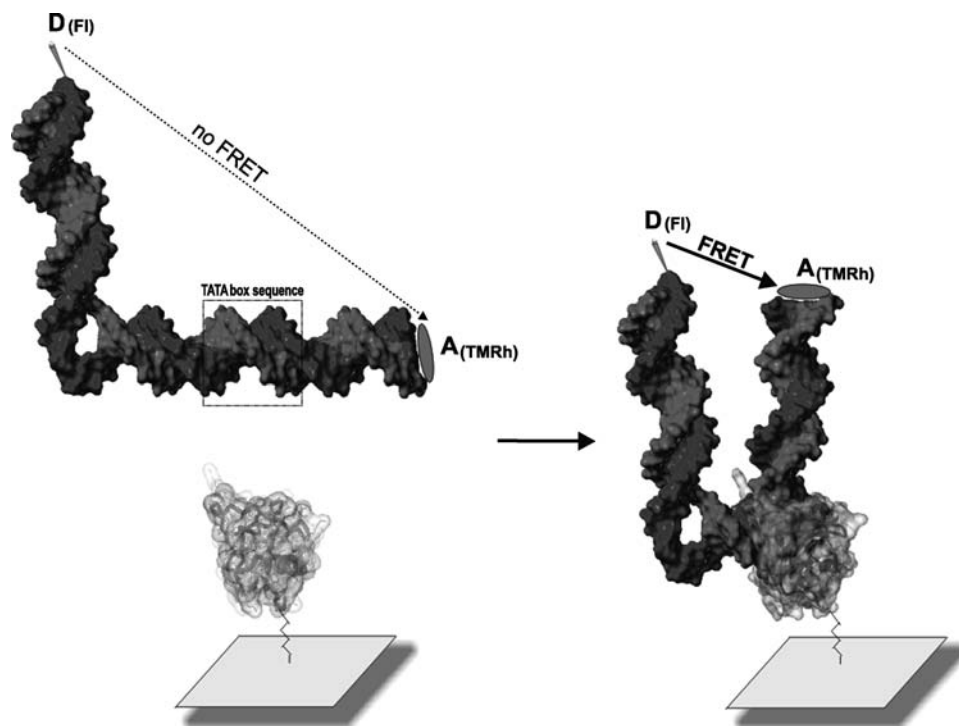


**Fig. 14** One-bulge DNA with TATA box sequence without (left) and with bound TBP (right). TBP is immobilized to a surface. Upon binding, TBP induces a DNA bend of approximately  $90^\circ$  leading to a strong FRET signal.

occurs due to the bending of the longer stem, resulting in a close dye distance (Fig. 14, right).

## CONCLUSION

We have shown that DNA-based nanoinstruments, designed by molecular modeling and realized by linear chemical synthesis, can be valuable tools for detecting and quantifying DNA bending and kinking, e.g., by proteins binding to DNA. Since those constructs allow one to bring dyes in a certain distance to each other, a new measurement principle was generated. For future work, these DNA molecules may not only carry dyes, but other molecules (enzymes, small organic compounds, catalysts, etc.) that work only in defined distances from each other. Such constructs could be switched on and off by modifying the structure of the DNA resulting in controllable nanomachines.

## ACKNOWLEDGMENTS

We thank Frank Stühmeier, Robert Clegg, Andrew Travers, and Mike Lorenz for a great collaboration.

## ABBREVIATIONS

A	acceptor
BIFL	burst-integrated fluorescence lifetime
bp	base pair
Cy3	cyanine-3
Cy5	cyanine-5
D	donor
Fl	6-fluorescein
FRET	fluorescence resonance energy transfer
HMG	high mobility group
IHF	integration host factor
LEF-1	lymphoid enhancer-binding factor 1
NOE	nuclear overhauser effect
PAGE	polyacrylamide gel electrophoresis
$R_0$	Förster distance
SRY	sex-determining region Y
TBP	TATA binding protein
TMRh	5-tetramethylrhodamine

## REFERENCES

1. Stuijver, M.H.; Bergsma, W.G.; Arnberg, A.C.; van, A.H.; van, G.R.; van der Vliet, P.C. Structural alterations of double-stranded DNA in complex with the adenovirus DNA-binding protein. Implications for its function in DNA replication. *J. Mol. Biol.* **1992**, *225*, 999–1011.
2. Engel, A.; Schoenenberger, C.A.; Muller, D.J. High resolution imaging of native biological sample surfaces using scanning probe microscopy. *Curr. Opin. Struct. Biol.* **1997**, *7*, 279–284.
3. Förster, T. Energiewanderung und Fluoreszenz. *Naturwissenschaften* **1946**, *6*, 166–175.
4. Stryer, L. Fluorescence energy transfer as a spectroscopic ruler. *Annu. Rev. Biochem.* **1978**, *47*, 819–846.
5. Wu, P.; Brand, L. Resonance energy transfer: Methods and applications. *Anal. Biochem.* **1994**, *218*, 1–13.
6. Heyduk, T.; Lee, J.C. Solution studies on the structure of bent DNA in the CAMP receptor protein–lac DNA complex. *Biochemistry* **1992**, *31*, 5165–5171.
7. Stühmeier, F.; Hillisch, A.; Clegg, R.M.; Diekmann, S. Fluorescence energy transfer analysis of DNA structures containing several bulges and their interaction with CAP. *J. Mol. Biol.* **2000**, *302*, 108–1100.
8. Hillisch, A.; Lorenz, M.; Diekmann, S. Recent advances in FRET: Distance determination in protein–DNA complexes. *Curr. Opin. Struct. Biol.* **2001**, *11*, 201–207.
9. Mendelsohn, A.R.; Brent, R. Protein interaction methods—Toward an endgame. *Science* **1999**, *284*, 1948–1950.
10. Loontjens, F.G.; McLaughlin, L.W.; Diekmann, S.; Clegg, R.M. Binding of Hoechst 33258 and 4',6'-diamidino-2-phenylindole to self-complementary decadeoxynucleotides with modified exocyclic base substituents. *Biochemistry* **1991**, *30*, 182–189.
11. Norman, D.G.; Grainger, R.J.; Uhrin, D.; Lilley, D.M. Location of cyanine-3 on double-stranded DNA: Importance for fluorescence resonance energy transfer studies. *Biochemistry* **2000**, *39*, 6317–6324.
12. Hillisch, A. *Computer Aided Design and Structure Verification of Single- and Multiple-Bulge DNA Molecules*. Ph.D. Thesis; 1998.
13. Clegg, R.M. Fluorescence resonance energy transfer and nucleic acids. *Methods Enzymol.* **1992**, *211*, 353–388.
14. Stühmeier, F.; Hillisch, A.; Clegg, R.M.; Diekmann, S. Practical aspects of fluorescence resonance energy transfer (FRET) and its applications in nucleic acid biochemistry. In *DNA-Protein Interactions*; Travers, A., Buckle, M., Eds.; Oxford University Press: Oxford, 2000. Chapter 6.
15. Stühmeier, F.; Welch, J.B.; Murchie, A.I.; Lilley, D.M.; Clegg, R.M. Global structure of three-way DNA junctions with and without additional unpaired bases: A fluorescence resonance energy transfer analysis. *Biochemistry* **1997**, *36*, 13530–13538.
16. Lorenz, M.; Hillisch, A.; Goodman, S.D.; Diekmann, S. Global structure similarities of intact and nicked DNA complexed with IHF measured in solution by fluorescence resonance energy transfer. *Nucleic Acids Res.* **1999**, *27*, 4619–4625.
17. Vámosi, G.; Gohlke, C.; Clegg, R.M. Fluorescence characteristics of 5-carboxytetramethylrhodamine linked covalently to the 5' end of oligonucleotides: Multiple conformers of single-stranded and double-stranded dye–DNA complexes. *Biophys. J.* **1996**, *71*, 972–994.

18. Parkhurst, K.M.; Brenowitz, M.; Parkhurst, L.J. Simultaneous binding and bending of promoter DNA by the TATA binding protein: Real time kinetic measurements. *Biochemistry* **1996**, *35*, 7459–7465.
19. Kim, Y.; Geiger, J.H.; Hahn, S.; Sigler, P.B. Crystal structure of a yeast TBP/TATA-box complex. *Nature* **1993**, *365*, 512–520.
20. Parkhurst, K.M.; Richards, R.M.; Brenowitz, M.; Parkhurst, L.J. Intermediate species possessing bent DNA are present along the pathway to formation of a final TBP–TATA complex. *J. Mol. Biol.* **1999**, *289*, 1327–1341.
21. Ozaki, H.; Iwase, N.; Sawai, H.; Kodama, T.; Kyogoku, Y. Detection of DNA bending in a DNA–PAP1 protein complex by fluorescence resonance energy transfer. *Biochem. Biophys. Res. Commun.* **1997**, *231*, 553–556.
22. Bustin, M.; Reeves, R. High-mobility-group chromosomal proteins: Architectural components that facilitate chromatin function. *Prog. Nucleic Acid Res. Mol. Biol.* **1996**, *54*, 35–100.
23. Travers, A. Recognition of distorted DNA structures by HMG domains. *Curr. Opin. Struct. Biol.* **2000**, *10*, 102–109.
24. Heyduk, E.; Heyduk, T.; Claus, P.; Wisniewski, J.R. Conformational changes of DNA induced by binding of *Chironomus* high mobility group protein 1a (CHMG1a). Regions flanking an HMG1 box domain do not influence the bend angle of the DNA. *J. Biol. Chem.* **1997**, *272*, 19763–19770.
25. Lorenz, M.; Hillisch, A.; Payet, D.; Buttinelli, M.; Travers, A.; Diekmann, S. DNA bending induced by high mobility group proteins studied by fluorescence resonance energy transfer. *Biochemistry* **1999**, *38*, 12150–12158.
26. Jamieson, E.R.; Jacobson, M.P.; Barnes, C.M.; Chow, C.S.; Lippard, S.J. Structural and kinetic studies of a cisplatin-modified DNA icosamer binding to HMG1 domain B. *J. Biol. Chem.* **1999**, *274*, 12346–12354.
27. Wisniewski, J.R.; Krohn, N.M.; Heyduk, E.; Grasser, K.D.; Heyduk, T. HMG1 proteins from evolutionary distant organisms distort b-DNA conformation in similar way. *Biochim. Biophys. Acta* **1999**, *1447*, 25–34.
28. Slama-Schwok, A.; Zakrzewska, K.; Leger, G.; Leroux, Y.; Takahashi, M.; Kas, E.; Debey, P. Structural changes induced by binding of the high-mobility group I protein to a mouse satellite DNA sequence. *Biophys. J.* **2000**, *78*, 2543–2559.
29. Werner, M.H.; Bianchi, M.E.; Gronenborn, A.M.; Clore, G.M. NMR spectroscopic analysis of the DNA conformation induced by the human testis determining factor SRY. *Biochemistry* **1995**, *34*, 11998–12004.
30. Love, J.J.; Li, X.; Case, D.A.; Giese, K.; Grosschedl, R.; Wright, P.E. Structural basis for DNA bending by the architectural transcription factor LEF-1. *Nature* **1995**, *376*, 791–795.
31. Pil, P.M.; Lippard, S.J. Specific binding of chromosomal protein HMG1 to DNA damaged by the anticancer drug cisplatin. *Science* **1992**, *256*, 234–237.
32. Payet, D.; Travers, A. The acidic tail of the high mobility group protein HMG-D modulates the structural selectivity of DNA binding. *J. Mol. Biol.* **1997**, *266*, 66–75.
33. Bianchi, M.E.; Beltrame, M.; Paonessa, G. Specific recognition of cruciform DNA by nuclear protein HMG1. *Science* **1989**, *243*, 1056–1059.
34. Payet, D.; Hillisch, A.; Lowe, N.; Diekmann, S.; Travers, A. The recognition of distorted DNA structures by HMG-D: A footprinting and molecular modelling study. *J. Mol. Biol.* **1999**, *294*, 79–91.
35. Murphy, F.V.; Sweet, R.M.; Churchill, M.E. The structure of a chromosomal high mobility group protein–DNA complex reveals sequence-neutral mechanisms important for non-sequence-specific DNA recognition. *EMBO J.* **1999**, *18*, 6610–6618.
36. Rice, P.A.; Yang, S.; Mizuuchi, K.; Nash, H.A. Crystal structure of an IHF–DNA complex: A protein-induced DNA U-turn. *Cell* **1996**, *87*, 1295–1306.
37. Passner, J.M.; Steitz, T.A. The structure of a CAP–DNA complex having two CAMP molecules bound to each monomer. *Proc. Natl. Acad. Sci. U. S. A.* **1997**, *94*, 2843–2847.
38. Dornberger, U.; Hillisch, A.; Gollmick, F.A.; Fritzsche, H.; Diekmann, S. Solution structure of a five-adenine bulge loop within a DNA duplex. *Biochemistry* **1999**, *38*, 12860–12868.
39. Kim, Y.C.; Grable, J.C.; Love, R.; Greene, P.J.; Rosenberg, J.M. Refinement of EcoRI endonuclease crystal structure: A revised protein chain tracing. *Science* **1990**, *249*, 1307–1309.
40. Lorenz, M.; Diekmann, S. Quantitative distance information on protein–DNA complexes determined in polyacrylamide gels by fluorescence resonance energy transfer. *Electrophoresis* **2001**, *22*, 990–998.

# DNA-Conjugated Metal Nanoparticles: Chip Detection Applications

Wolfgang Fritzsche

Department of Biotechnical Microsystems, Institute for Physical High Technology (IPHT),  
Jena, Germany

## INTRODUCTION

Metal nanoparticles exhibit interesting optical, electronic, and catalytic properties, which are primarily based on their small size and their high surface-to-bulk ratio. By the application of standard processes of chemical synthesis, large numbers of particles with a narrow size distribution can be prepared in a size range between 1 and 100 nm. The properties of these nanoparticles are often different from bulk materials of the same kind and are usually influenced by the particle size. A typical example is the color of gold nanoparticles, as apparent in colored glass from the middle ages or in the labeling solutions used in light and electron microscopy. Other examples are the quantized behavior of electrons tunneling onto gold nanoparticles under low-temperature conditions, and the surface enhancement of Raman spectroscopy for molecules adsorbed onto the surface of metal particles.

To access these interesting properties, an integration of the nanoparticles in technological systems is needed. This integration could be based on the long tradition of bioconjugated nanoparticles in biological microscopy, which is explained in details in this entry. Thus DNA-modified nanoparticles could play an important part in DNA chip detection and, furthermore, establish a novel, multidisciplinary approach in molecular nanotechnology (Fig. 1).

## PREPARATION OF BIOCONJUGATED METAL NANOPARTICLES

The need for electron-dense labels for nanometer structures in electron microscopy leads to the development of bioconjugated particles. Monodisperse colloidal gold can be produced by several methods in a size range of less than 2 nm up to 150 nm and more.<sup>[1]</sup> Therefore proteins were adsorbed onto gold particles, induced by hydrophobic interactions and/or the binding of thiol groups (present in the protein) to the gold surface. This thiol-gold binding is an important principle for the connection to gold surfaces in fields as diverse as molecular labeling or molecular

nanotechnology.<sup>[2]</sup> The interaction of thiol-containing molecules with gold surfaces was extensively studied in the case of self-assembly monolayers (SAMs). It is based on the high affinity between sulfur and gold, and results in a covalent bond. The experiences of these fields regarding gold binding of proteins were also extended to DNA. The stability of an unmodified gold solution is based on intercolloidal electrostatic repulsion and is sensitive against higher salt concentrations. This sensitivity increases with larger particle diameter. By modification of the gold with DNA, a significant stabilization of the colloid because of increased charging of the surface (induced by the negatively charged DNA backbone) is observed, which is a prerequisite for further (bio)chemical or molecular-biological manipulations.

## NETWORKS IN SOLUTION BASED ON SPECIFIC DNA BINDING

Material sciences are driven by the search for new materials with preferably customized properties. One approach is the synthesis of such materials starting from elemental building blocks. By adjusting the parameters of the building blocks, the properties of the resulting bulk material should be determined. Because of their size and their adjustable parameters (size, composition), nanoparticles present ideal candidates for these building blocks. As demonstrated in electron and light microscopy, metal nanoparticles can be positioned because of specific molecular interactions of conjugated biomolecules. This principle can also be used for the fabrication of nanoparticle-based materials utilizing bioconjugated particles. It applies a binding pair of biomolecules, so that each of two batches of nanoparticles is conjugated to one of these partners. After mixing both batches, specific bonds are established. This process results in a network of particles interconnected because of specific binding of the molecules.<sup>[3,4]</sup>

These networks exhibit an interesting optical behavior. Solutions of statistically distributed gold nanoparticles (with or without attached biomolecules)

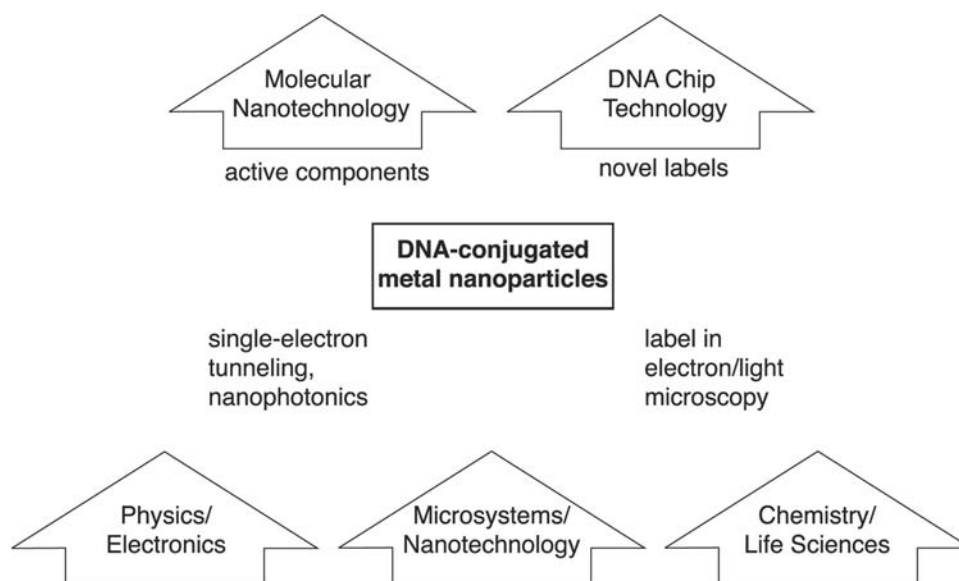


**Fig. 1** Nanoparticles exhibit interesting properties as, for example, regarding single-electron tunneling and nanophotonics. This potential is complemented by decades of experiences with bioconjugated nanoparticles in microscopy, and will result in active components for molecular nanotechnology (with the potential for integration) as well as in novel labels for DNA chip detection.

show at a certain concentration a visible color, ranging from yellow for small particles (<5 nm diameter) over reddish (about 20–40 nm) to increasingly violet (>60 nm). However, if these solutions aggregate, as it is the case after increasing the salt concentration (because of higher screening of the electrostatic repulsion as stabilizing factor), a dark fallout can be observed. The colors are induced by surface plasmon effects, a result of the interactions of photons with the highly localized electrons in the nanoparticles. This effect is influenced by the average distance of neighboring particles, and can be used for macroscopical detection of DNA-based nanoparticle networks. Therefore two batches of nanoparticles were modified with each DNA molecule with a sequence A' or B' (A' is non-complementary to B'). If these two batches are mixed, the purple color of the solution remains unchanged. However, after the addition of DNA linker molecules that exhibit sequences A and B (complementary to A' and B', respectively), the solution changes its color to blue. This color change is indicative of the creation of networks of nanoparticles connected

by the linker DNA, as shown in the scheme in Fig. 2. For better visibility, the reaction solution can be transferred to a solid substrate (e.g., to a reverse-phase silica plate).<sup>[5]</sup>

The constructions with nanoparticles of the same size (homogeneous systems) were extended toward systems combining particles of different sizes.<sup>[6]</sup> Therefore two batches with gold particles of 8 and 31 nm diameter, respectively, were modified with thiolated oligonucleotides in a way that each of both batches had a different sequence. A nanoparticle satellite structure was created after the addition of a DNA linker (which bridges the sequences on the particles, comparable to the scheme in Fig. 2). Transmission electron microscopy (TEM) images of such structures show extended aggregates of two different-sized particles with (large particle/small particle) periodicity. The demonstrated use of the recognition properties of oligonucleotides to direct the placement of two different particle types within extended particle assemblies should be expandable beyond size differences (e.g., to building blocks that differ in chemical composition).

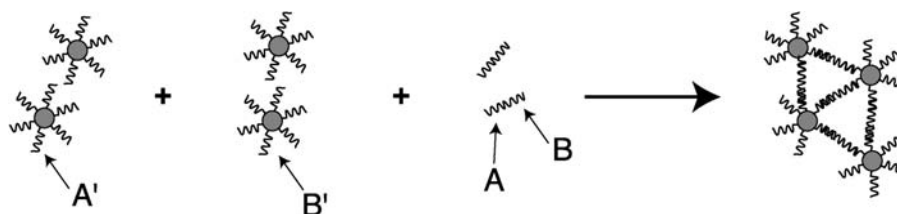


**Fig. 2** A network of DNA-interconnected particles results when a connecting linker DNA molecule AB is added to a mixture of nanoparticles with sequences A' or B' (A and B are complementary to A' and B', respectively).

## IMMOBILIZATION ONTO SOLID SUBSTRATES

### Microscopical Marker Applications

The localization of specific molecules (antigens) in microscopical preparations using labeled molecules, which bind specifically to the molecule of interest, is a basic technique in numerous microscopical techniques. Typically, antibodies against the molecule of interest are labeled with a marker molecule or substance, and after the binding of the antibody, the conjugated marker is detected. Thus the position of the antibody and of the molecule of interest is identified. Gold colloids are an example for such a label. They have a long tradition as markers in electron and light microscopy (e.g., by using their high electron contrast for tissue<sup>[7]</sup> or single-particle<sup>[8]</sup> identification). Large numbers of particles are detectable by optical microscopy (e.g., for cell labeling).<sup>[1]</sup> An interesting extension of gold labeling is the silver enhancement method, which amplifies the signal for better detection.<sup>[9]</sup> Therefore a stabilized silver solution is used, which leads to a specific silver deposition on gold surfaces. Thus the gold nanoparticles increase in size because of silver deposition, resulting in a stronger signal in the optical or electron contrast.

### Applications in Molecular Nanotechnology

Immobilized DNA–nanoparticle construction exhibits several advantages over the complexes created in solution. For nanotechnology, the integration of the fabricated molecular structures into materials or devices is seriously hampered by the difficult access to the individual structures floating in solution. Technology is only possible with structures integrated into technical systems, allowing for defined access. For example, the envisioned use of electronically active molecules needs techniques for the inclusion of such molecules in a defined manner into electrical circuits. Because of the small size, conventional microstructuring techniques are not applicable. Thus self-assembly principles have been proposed to provide an answer to these problems. These techniques rely on the specific interactions of binding pairs, comparable to the antibody–antigen pairing. DNA is of special interest for such approaches because it provides an easily accessible and well-studied system with a large variety of different binding pairs because of its sequence variability. Thus DNA–nanoparticle complexes coupled to DNA-modified surfaces present an interesting model system for the demonstration of the feasibility of DNA-based connection and/or positioning of inorganic structures for molecular nanotechnology.

### Chemical immobilization strategies for DNA

The binding of DNA-conjugated nanoparticles to surfaces via specific DNA–DNA interactions requires the immobilization of single-stranded (ss) DNA on the surface, which acts as a capture molecule (Fig. 3D). This procedure is comparable to the techniques used in the preparation of DNA microarrays and DNA chips. In principle, there are two approaches regarding the kind of binding, namely, a non-specific adsorption and a defined terminal covalent binding. The so-called non-specific adsorption is usually based on electrostatic interactions between the rather positively charged surfaces and the negative charges in the phosphate backbone of the DNA. Another less defined interaction is the binding of DNA to surfaces with an affinity to amino groups, resulting in covalent bonds to such groups inside the DNA molecule. However, defined terminal bonds with much higher efficiency are possible using similar amino-binding surfaces and terminal amino-modified DNA, or utilizing the beforementioned affinity between gold surfaces and thiol-modified DNA (Fig. 3A). The latter binding pair is well studied and highly efficient,<sup>[10]</sup> but it shows some serious disadvantages. First, thiol modification of DNA is difficult and expensive. Moreover, especially the interesting optical or electronic properties of gold nanoparticles are hardly, or not, accessible after immobilization onto gold substrates. Thus other substrates are required, which allow optical transmission or which are electrical isolators. Glass provides ideal optical properties and can be used for DNA immobilization. Controlled DNA immobilization onto glass can be achieved by the modification of the activated glass surface (inducing OH groups) with substituted silanes, which bind to the glass and provide a coupling group for modified DNA (Fig. 3B). A standard system is the application of amino-modified DNA and 3'-aminopropyltrimethoxy-silane (APTES) or 3'-glycidoxy-propyltrimethoxy-silane (GOPS) as described elsewhere.<sup>[11]</sup> Because of the similar chemical composition, silicon oxide surfaces as found on oxidized silicon wafers are accessible by the same techniques (Fig. 3C).

### Immobilization techniques

A straightforward method for DNA immobilization is the incubation of the whole substrate (e.g., glass) with the required solutions. As a result, the substrate is covered by immobilized DNA (Fig. 4A). For instance, this approach was used for the fabrication of glass substrates for the immobilization of nanoparticle-labeled DNA prior to silver enhancement and optical readout.<sup>[12]</sup> Although simple and robust, this technique



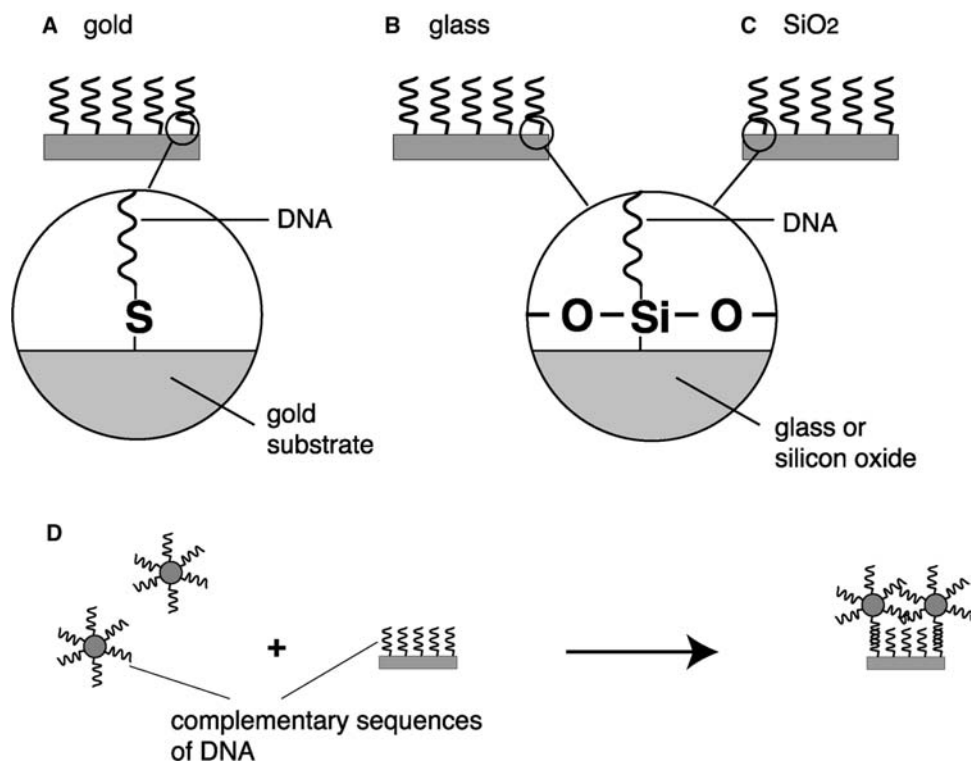


**Fig. 3** Strategies for surface immobilization of DNA. (A) The high affinity of thiols to gold surfaces is used by the utilization of thiolated DNA. (B,C) The standard chemistry for the modification of glass or silicon oxide surfaces to bind DNA is based on silanization. Silanes with functional groups able to bind, for example, amino-modified DNA directly or via a linker molecule are used. (D) Scheme for binding of DNA-conjugated nanoparticles onto surfaces modified with complementary DNA.

does not meet the requirements of either molecular nanotechnology or chip detection for a variety of different sequences on one substrate. For molecular construction, the DNA has to be further aligned in binding spots and should not cover the whole surface. On the other side, DNA chips exhibit an array of different sequences for detection purposes; this quantity is a key advantage of DNA chip technology. These requirements for multiple-sequence substrates are realizable using spotting techniques. Therefore, applying similar chemical strategies as described above, substrates are usually modified and/or activated before small quantities (droplets) of a solution of modified DNA are applied to this surface for immobilization (Fig. 4B). Typical dimensions of an area modified with DNA according to such an approach are 100  $\mu\text{m}$ .

Although this is quite sufficient for today's DNA chips, it blocks both further integration of DNA detection schemes and nanotechnological applications. Another shortcoming is the low reproducibility and homogeneity of the DNA layers realized by this method. A highly efficient way to achieve immobilization is the on-chip synthesis in a DNA synthesizer.<sup>[13]</sup> This technique results in a homogeneous, high-density coverage of the surface, and is compatible with microstructuring techniques. Thus a predefined pattern of DNA-modified regions with a resolution in the lower micrometer range is possible (Fig. 4C). However, only one sequence of DNA is synthesized on each substrate, which prevents the inclusion of on-chip control sequences or the high integration regarding DNA chip applications.

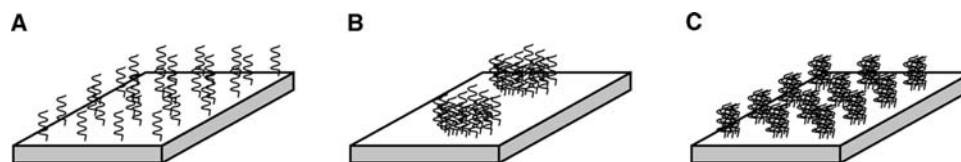


**Fig. 4** Immobilization techniques. (A) Whole substrate incubation. (B) Spotting of DNA. (C) microstructured surfaces for DNA immobilization.

A hybrid approach combining microstructuring and manual spotting provides  $1 \times 1$  mm windows in a hydrophobic passivation layer for the manual deposition of DNA solution for immobilization.<sup>[14]</sup> Thus different DNA sequences can be arranged on the same substrate without the need for spotting equipment. Moreover, the typical problems with the inhomogeneous signal of spotted DNA (because of drying artifacts and insufficient binding of the DNA) are minimized in this approach because the microstructured windows serve as a reservoir for the incubated droplets and minimize drying and the associated artifacts. Another advantage is the defined geometry and position of the signal, so that the required readout algorithms are streamlined and the image processing is simplified by standard masking procedures.

### MARKER APPLICATION FOR DNA CHIP READOUT

The previous paragraphs introduced typical setups for a chip-based DNA detection: DNA molecules immobilized on a substrate, with a sequence complementary to DNA of interests. When the latter molecules are present in a solution, which is applied onto the chip surface, specific binding occurs and the molecules of interest are bound to the surface. To detect this binding event, the surface-bound molecule of interest has to be labeled. Typical labels (beside the extremely sensitive but complicate radioactive substances) are fluorescence dyes. They exhibit a high sensitivity and allow a fast and spatially resolved readout as needed for highly integrated DNA arrays and chips. However, they require a sophisticated scanner with a high price tag and need expert knowledge to measure/process/interpret the results. Moreover, the fluorescence signal depends on the local chemical environment, so that chip-to-chip comparisons or calibrations are hampered. Another problem is bleaching, an irreversible process resulting in a decay of the fluorescence signal. Gold nanoparticles are a possible complement to, or even replacement for, the fluorescent readout mainly because of their signal stability. In the optical contrast (both transmission and reflection), an ensemble of

nanoparticles induces a detectable signal, which does not depend on the chemical environment and which will not significantly decrease over time. For medium surface densities of particles and microstructured binding areas in the medium micrometer range, this signal is already detectable by the naked eye.<sup>[13]</sup> Microscopical images demonstrate the excellent contrast in plain optical contrasts as transmission and reflection. However, the dynamic range is limited. There seems to be a saturation limit before a monolayer of particles can be achieved,<sup>[15]</sup> which is probably based on electrostatic interactions between the particles. On the other side, lower surface concentrations of nanoparticles are hardly detectable by optical means. The detection limit of nanoparticle labeling was significantly enhanced by the introduction of metal enhancement procedures (Fig. 5), as known from optical and electron microscopical applications of gold nanoparticles.<sup>[9]</sup> Thus the signal is enhanced and allows detection in a standard flatbed scanner, without the requirement for a microscope.<sup>[12]</sup> But the metal layer induced by the metal enhancement results not only in a much stronger optical signal, it also allows for a quite different detection principle: an electrical detection based on the resistivity change between two electrodes, which are connected by this layer.<sup>[16,17]</sup> Such an electrical detection represents a significant development regarding future point-of-care applications of DNA analytics and their requirements of easy and stable assays in connection with low equipment costs (Fig. 6).<sup>[18]</sup>

### NANOPARTICLES IN MOLECULAR NANOTECHNOLOGY

Molecular nanotechnology describes a field, which uses a molecular approach for the fabrication of novel materials and devices. Molecular units are utilized, so that the addressable dimensions reach the molecular scale. This potential makes molecular nanotechnology a promising candidate for complementing, or maybe even replacing, the traditional, silicon-based microelectronics. However, there is still a long way to go until realistic concepts for this revolutionary new field

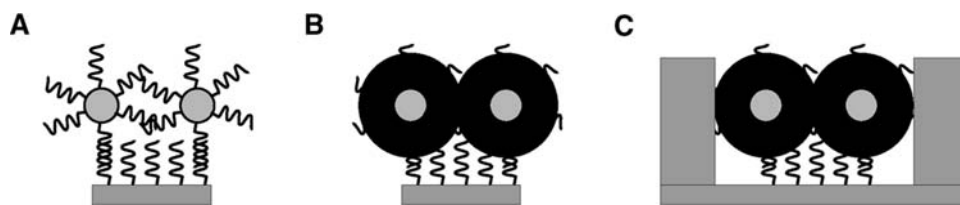


**Fig. 5** Metal enhancement of immobilized nanoparticles. Nanoparticles specifically bound to substrates by DNA–DNA interactions (A) can be enhanced by a chemical metal enhancement step, resulting in the deposition of, for example, silver on the gold nanoparticles (B). This effect can be applied to create a conductive layer between prestructured microelectrodes (C).



**Fig. 6** System for electrical readout of DNA hybridization.<sup>[18]</sup> Top row: An array of micrometer-sized gaps (left, center) of microstructured gold electrodes for DNA detection (cf. Fig. 5C) is arranged on a half-inch chip (right). Bottom row: A chip holder (left) is part of the reader (right) that contains measurement electronics controlled by an embedded PC. © 2003 American Institute of Physics.

of electronics are worked out. One problem is the missing technology for interconnections, which is needed for the integration of molecular devices into an electronic setup. To develop first demonstrators, hybrid approaches are needed, which use molecular parts in a still conventional (macroscopical/microscopical) technological environment. But what are the active parts in such hybrid setups, as long as molecules with interesting electronic or optical properties are not directly accessible? Thus nanometer-sized structures are needed, which represent active parts but are already addressable today. Metal nanoparticles are an optimal candidate for such structures because they combine small size with interesting physical properties. Nanoparticles are promising replacements for the electron confinements in single-electron tunneling structures in quantum electronics,<sup>[19,20]</sup> and they show potential as nanoconverters of photonic energy to thermal energy.<sup>[21]</sup> Moreover, complexes of bioconjugated

metal nanoparticles with biomolecules based on specific molecular binding used for decades in microcopy demonstrated the use of nanoparticles in biomolecular assemblies. This points to a possibility to overcoming the interconnectivity problem, namely, using specific molecular binding. In microscopical applications, antibody-conjugated nanoparticles attach in a highly specific manner onto complementary surface regions of the specimen. This process can be reversed; instead of detecting the location of complementary regions, predefined complementary regions can be utilized to direct the nanoparticles to the selected location. Although such molecularly modified surface regions can be created, the anchored molecular structure is still not accessible by two contacts, as needed for a variety of applications (e.g., the molecular-based electronic switch,<sup>[22]</sup> lasers,<sup>[23]</sup> etc.). One approach for a two-sided terminal binding is based on very small (lower nanometer range) electrode gaps, and applies electrostatic

trapping<sup>[24]</sup> or specific binding<sup>[25]</sup> of molecular structures. Because the fabrication of such structures is complicated, other ways for the integration of molecules were proposed. One possibility is the use of a long DNA molecule, with each end specifically connected to an electrode modified with complementary DNA.<sup>[26]</sup> This structure can be used as base for further assemblies by relying on specific attachment of short ssDNA to a location along the long immobilized DNA,<sup>[27]</sup> following the standard technique used for in situ hybridization in cytogenetics. Additionally, the short DNA can be coupled to an interesting molecular structure, such as a nanoparticle. A single-electron tunneling structure utilizing this scheme to position a DNA-conjugated nanoparticle along a micrometer-long DNA molecule that is stretched between pre-structured microelectrodes on a chip surface was proposed.<sup>[28]</sup> Key steps in this project, as the attachment of the nanoparticle to DNA including microscopical characterization as well as the positioning of individual DNA molecules in a microstructured gap, could already be demonstrated.<sup>[29]</sup>

## CONCLUSION

DNA-conjugated metal nanoparticles represent a unique class of nanomaterials with applications both in molecular diagnostics (DNA chip detection technology) and molecular nanotechnology. In both fields, these complexes of nanoparticles with DNA combine many advantages and could demonstrate the large potential of nanotechnology by the realization of a demonstrator system. Thus molecular diagnostics could reach high sensitivity combined with highly stable and low-cost equipment. On the other side, because of their DNA handles, nanoparticles have a realistic chance of serving as active elements in nanotechnological setups, which are assembled by self-assembly principles.

## ACKNOWLEDGMENTS

I would like to thank the colleagues at the IPHT in the field of DNA-conjugated nanoparticles for their contributions: A. Csaki, R. Möller, J. M. Köhler, G. Maubach, G. -J. Zhang, and J. Reichert. This work was funded by the DFG (Fr 1348/1-4) and the Volkswagen Foundation.

## REFERENCES

- Horisberger, M. Colloidal gold: a cytochemical marker for light and fluorescent microscopy and for transmission and scanning light microscopy. *Scanning Electron Microsc.* **1981**, *II*, 9–31.
- Nuzzo, R.G.; Allara, D.L. Adsorption of bifunctional organic disulfides on gold surfaces. *J. Am. Chem. Soc.* **1983**, *105*, 4481–4483.
- Alivisatos, A.P.; Johnsson, K.P.; Peng, X.; Wilson, T.E.; Loweth, C.J.; Bruchez, M.P., Jr.; Schultz, P.G. Organization of 'nanocrystal molecules' using DNA. *Nature* **1996**, *382*, 609–611.
- Mirkin, C.A.; Letsinger, R.L.; Mucic, R.C.; Storhoff, J.J. A DNA-based method for rationally assembling nanoparticles into macroscopic materials. *Nature* **1996**, *382* (6592), 607–609.
- Elghanian, R.; Storhoff, J.J.; Mucic, R.C.; Letsinger, R.L.; Mirkin, C.A. Selective colorimetric detection of polynucleotides based on the distance-dependent optical properties of gold nanoparticles. *Science* **1997**, *277* (5329), 1078–1081.
- Mucic, R.C.; Storhoff, J.J.; Mirkin, C.A.; Letsinger, R.L. DNA-directed synthesis of binary nanoparticle network materials. *J. Am. Chem. Soc.* **1998**, *120* (48), 12,674–12,675.
- DeMey, J. Colloidal gold as marker and tracer in light and electron microscopy. *EMSA Bull.* **1984**, *14*, 54–66.
- Tanaka, K.; Mitsushima, A.; Yamagata, N.; Kashima, Y.; Takayama, H. Direct visualization of colloidal gold-bound molecules and a cell-surface receptor by ultrahigh-resolution scanning electron microscopy. *J. Microsc.* **1991**, *161* (3), 455–461.
- Hacker, G.W. Silver-enhanced colloidal gold for light microscopy. In *Colloidal Gold: Principles, Methods, and Applications*; Hayat, M.A., Ed.; Academic Press, 1989; 297–321.
- Csáki, A.; Möller, R.; Straube, W.; Köhler, J.M.; Fritzsche, W. DNA monolayer on gold substrates characterized by nanoparticle labeling and scanning force microscopy. *Nucleic Acids Res.* **2001**, *29* (16), e81.
- Möller, R.; Csáki, A.; Köhler, J.M.; Fritzsche, W. DNA probes on chip surfaces studied by scanning force microscopy using specific binding of colloidal gold. *Nucleic Acids Res.* **2000**, *28* (20), e91.
- Taton, T.A.; Mirkin, C.A.; Letsinger, R.L. Scanometric DNA array detection with nanoparticle probes. *Science* **2000**, *289* (5485), 1757–1760.
- Reichert, J.; Csáki, A.; Köhler, J.M.; Fritzsche, W. Chip-based optical detection of DNA-hybridization by means of nanobead labeling. *Anal. Chem.* **2000**, *72* (24), 6025–6029.
- Zhang, G.-J.; Möller, R.; Csaki, A.; Fritzsche, W. Optical detection of DNA constructs based on nanoparticles and silver enhancement. In *DNA-Based Molecular Construction*; Fritzsche, W., Ed.; AIP Conference Proceedings; American Institute of Physics, 2002; Vol. 640, 13–21.
- Csaki, A.; Möller, R.; Fritzsche, W. Gold nanoparticles as novel label for DNA diagnostics. *Exp. Rev. Mol. Diagn.* **2002**, *2*, 187–193.
- Möller, R.; Csáki, A.; Köhler, J.M.; Fritzsche, W. Electrical classification of the concentration of bio-conjugated metal colloids after surface adsorption and silver enhancement. *Langmuir* **2001**, *17* (18), 5426–5430.

17. Park, S.J.; Taton, T.A.; Mirkin, C.A. Array-based electrical detection of DNA with nanoparticle probes. *Science* **2002**, *295* (5559), 1503–1506.
18. Urban, M.; Möller, R.; Fritzsche, W. A paralleled read-out system for an electrical DNA-hybridization assay based on a microstructured electrode array. *Rev. Sci. Instrum.* **2003**, *74*, 1077–1081.
19. Soldatov, E.S.; Khanin, V.V.; Trifonov, A.S.; Presnov, D.E.; Yakovenko, S.A.; Khomutov, G.B.; Gubin, C.P.; Koleslov, V.V. Room temperature molecular single-electron transistor. *JETP Lett.* **1996**, *64*, 556.
20. Davidovic, D.; Tinkham, M. Coulomb blockade and discrete energy levels in Au nanoparticles. *Appl. Phys. Lett.* **1998**, *73* (26), 3959–3961.
21. Kurita, H.; Takami, A.; Koda, S. Size reduction of gold particles in aqueous solution by pulsed laser irradiation. *Appl. Phys. Lett.* **1998**, *72*, 789–791.
22. Chen, J.; Reed, M.A.; Rawlett, A.M.; Tour, J.M. Large on–off ratios and negative differential resistance in a molecular electronic device. *Science* **1999**, *286*, 1550–1552.
23. Duan, X.; Huang, Y.; Agarwal, R.; Lieber, C.M. Single-nanowire electrically driven lasers. *Nature* **2003**, *421* (6920), 241–245.
24. Bezryadin, A.; Dekker, C.; Schmid, G. Electrostatic trapping of single conducting nanoparticles between nanoelectrodes. *Appl. Phys. Lett.* **1997**, *71* (9), 1273–1275.
25. Reed, M.A.; Zhou, C.; Muller, C.J.; Burgin, T.P.; Tour, J.M. Conductance of a molecular junction. *Science* **1997**, *278*, 252–254.
26. Braun, E.; Eichen, Y.; Sivan, U.; Ben-Yoseph, G. DNA-templated assembly and electrode attachment of a conducting silver wire. *Nature* **1998**, *391*, 775–778.
27. Bier, F.F.; Gajovic-Eichelmann, N.; Hölzel, R. Oriented immobilization of single DNA molecules as a nanostructuring tool. In *DNA-Based Molecular Construction*; Fritzsche, W., Ed.; AIP Conference Proceedings; American Institute of Physics, 2002; Vol. 640, 61–69.
28. Fritzsche, W.; Maubach, G.; Born, D.; Köhler, J.M.; Csaki, A. A Construction scheme for a SET device based on self-assembly of DNA and nanoparticles. In *DNA-Based Molecular Construction*; Fritzsche, W., Ed.; AIP Conference Proceedings; 2002; Vol. 640, 83–92.
29. Csáki, A.; Maubach, G.; Born, D.; Reichert, J.; Fritzsche, W. DNA-based molecular nanotechnology. *Single Mol.* **2002**, *3*, 275–280.

# DNA Hybridization: Electronic Control

**Kimberly Hamad-Schifferli**

*Department of Mechanical Engineering and Division of Biological Engineering,  
Massachusetts Institute of Technology, Cambridge, Massachusetts, U.S.A.*

## INTRODUCTION

Nature has created a multitude of biological molecules that perform tasks with remarkable efficiency, accuracy, and precision. Increasingly these systems are being viewed more and more as machines because of the complexity of their function. In an effort to harness the engineering of Nature, many scientists and engineers are going beyond characterizing biological systems by investigating methods for direct manipulation. This effort has been promoted by the enormous progress in understanding the complex mechanisms and structures of biological systems. This knowledge, largely fueled by the advances in biological and biochemical tools and characterization techniques such as X-ray crystallography and NMR, has reached a point where one can describe the structure and mechanisms of large biological molecules in molecular detail. Consequently, direct manipulation of biomolecular activity is an attractive avenue for the development of new types of systems that utilize the engineering of Nature. Deoxyribonucleic acid (DNA) hybridization is a simple process that has been investigated as an interface for control, assembly, and computation. The ideal method for controlling hybridization in many of these applications would display a high degree of specificity (to control target DNA strands and leave others unaffected) and reversibility, and allow for control *in vivo*. Many novel methods of controlling hybridization have been developed, such as by electric field direction of DNA hybridization on a chip and optical triggering, yet each of them has limitations concerning these criterion. Here we describe a form of electronic control that directly interfaces to a DNA molecule in solution.<sup>[1]</sup> The DNA is covalently linked to a metal nanoparticle, which can be inductively heated by a radiofrequency magnetic field (RFMF). The nanoparticle transfers heat to the DNA, denaturing it and thus switching on or off its activity. Heat dissipation into solution is rapid so once the field is turned off, the DNA can renature. This technique has been demonstrated to be both reversible and specific.

## BACKGROUND

DNA is the universal carrier of hereditary information for all cellular life. It is the molecule responsible for

transmission and conservation of genetic information. Its sequence of nucleotides contains the program for life for an organism. DNA also contains information for gene regulation, which permits organisms to respond to various environmental conditions such as stress.<sup>[2]</sup> In addition, Nature has created a system that can self-replicate so that the genetic information can be passed on to the next generation. By an ingenious construct, replication is semiconservative, in that DNA serves as a template for itself. The machinery of replication does so with high efficiency and speed (3000 bases/min in eukaryotes). Because the fidelity of the message is crucial for organisms, mechanisms for error correction exist, resulting in an overall error rate of 1 per  $10^5$  bases. This efficiency, speed, and reliability is what makes DNA and the machinery that interact with it attractive systems to control.

These properties have been determined by DNA's unique structure and chemical composition. The structure of DNA was determined to be double helical in which two strands align in an antiparallel configuration such that the bases along the backbone pair with one another by hydrogen bonds.<sup>[3-5]</sup> Its structure confirmed its function as a carrier of hereditary information. The double helix is stabilized by the stacking energy of the base pairs. Hydrogen bonds between bases provide specificity (G pairing with C, A pairing with T).<sup>[5]</sup> Remarkably, the combinations of four different bases are all that is needed to encode life.

## MANIPULATION OF DEOXYRIBONUCLEIC ACID

Enormous progress has been made in developing the tools for DNA manipulation and characterization such as cloning, synthesis, and sequencing. Many of these processes are now fully automated, permitting exploration into the genetic analysis of complex cellular systems and organisms. Structural characterization and analytical techniques for separation, purification, cloning, etc. are now widespread and often commercially available. DNA sequencing has made enormous progress in terms of efficiency and speed, thus enabling full characterization of the human genome<sup>[6]</sup> and of other organisms. Automated chemical synthesis of artificial nucleic acid oligos is now commercially available and



can be done with high accuracy for short pieces. Chemical modifications of the backbone or bases with a variety of functional groups can also be incorporated, which allow oligos to be linked to other molecules in inorganic systems such as bulk macroscopic surfaces and also nanoparticles. This has greatly furthered research and the development of pharmaceutical applications and permitted exploration of interdisciplinary studies with biology.

In addition to these analytical and synthetic techniques, there has been recent interest in manipulating and utilizing DNA as an information medium or a machine. DNA is an attractive system for this purpose as it has exquisite recognition properties in base pairing. In addition, DNA is involved in many information transfer processes in a cell such as self-replication. All the processes necessary for life are contained in DNA, as this is what is passed on from parent to offspring. Engineered into the DNA are complex information components such as promoter and repressor elements that can turn on or off expression of a particular gene, allowing the cell or organism to react to DNA environment. As a result, controlling its hybridization is one simple way to access the machinery of biology. In addition, with the sequencing of the human genome, the formidable task of gene profiling has generated interest in developing rapid, inexpensive, and high-throughput characterization and manipulation tools. Described below are just a few examples of the tools developed for studying and manipulating DNA.

### Microarray Chips

Recently, there has been tremendous interest in using gene chips to study genes for analysis of behavior of an organism. In order to study the presence of genes, multiple probe strands complementary to a given target strand are chemically tethered to a substrate. The slide is incubated with the set of target DNA strands, which hybridize to the corresponding probe strands. A reporter strand complementary to the overhang of the target strand is added.<sup>[7]</sup> The reporter strand has fluorophore chemically attached to it, so when the target is present fluorescence increases. Because of the multitude of groups and companies using this technology, the generation of DNA microarrays by automated spotters and their analysis of large numbers of them has been standardized. As a result, thousands of genes can be probed simultaneously, enabling high-throughput analysis of an entire genome on a single chip.

Some groups have taken this further by developing methods for spatially controlling hybridization on an array by using an electric field.<sup>[8,9]</sup> A DNA probe is chemically tethered to a site above an electrode on a surface. A voltage applied to the electrode attracts

negatively charged DNA complement, thereby directing where the DNA is hybridized with single nucleotide resolution. Electric field interfacing to DNA on a surface has the advantages of multiplex control of hybridization events. Other electronic interfaces to DNA molecules for the purposes of control include orientation of DNA helices on metal surfaces by an applied electric field.<sup>[10]</sup>

### Assembly of Nanoscale Structures in Solution or on Surfaces

Manipulation of DNA is attractive for purposes of assembly on the nanometer scale because of its dimension and high degree of specificity in base pairing. It is a unique structure for interfacing to nanoscale systems because DNA is in the same size range as nanoparticles in one dimension ( $\sim 2$  nm in width) but can be very long in the other (micrometers to millimeters)<sup>[11]</sup> so macroscopic and microscopic systems can be interfaced to it electronically. Many have explored the possibility of utilizing it not only as a nanoscale wire but also as a recognition medium for assembling patterns of inorganic nanoparticles and wires. In this case, the DNA serves as a chemical linker to a nanoparticle and also a tether that can recognize a specific set of electrodes that interface to the nanoparticle.<sup>[12,13]</sup>

In addition, DNA has great potential for assembling programmed structures.<sup>[14-17]</sup> The assembly is “programmed” in that one designs a structure by choosing appropriate sequences of the DNA and allowing them to self-assemble in solution. By harnessing biology’s use of self-assembly, which has the potential to create something as complex as an organism, one can construct complex biological/inorganic hybrid structures by supramolecular assembly. Consequently, DNA is being used to design and assemble in two and three dimensions,<sup>[15,17]</sup> also with nanometer-scale inorganic materials such as gold nanocrystals<sup>[18]</sup> that can act as colorimetric sensors for the hybridization event.<sup>[14,19,20]</sup> Eventually this will result in new classes of materials that possess properties unique from the corresponding bulk inorganic materials. Inorganic-biological composites that occur in nature such as abalone shell have remarkable properties such as strength and toughness. Combining nanometer inorganic structures with organization via DNA programmed assembly will result in new materials with designable properties that are unique from each component alone.

### DNA as a Computational Medium

Within the past decade, DNA has been recognized as a computing medium. DNA hybridization is a process in which a strand recognizes its complement according to

the code programmed in the strands, often with a resolution of a single base pair. Considerable effort has gone into investigating how to take advantage of the attractive properties of DNA and the machinery that edits and creates it such as self-replication, error correction, and recognition. Other factors that make DNA attractive as a computing mechanism emerge directly from comparison to silicon. Its size is smaller than current silicon design rules, which would result in an information density and potential processing power several orders of magnitude higher than traditional computers.

Many approaches to DNA computing involve exploiting the exquisite accuracy in which a strand of DNA can recognize its complement. To date, DNA has been used successfully to solve a model problem that is intractable for traditional computers. The answer to a simple version of the traveling salesman problem has been experimentally determined for DNA in solution.<sup>[21]</sup> In addition, other problems have been explored using DNA hybridization.<sup>[16,17,22–25]</sup> From these experiments, it has been determined that DNA computational operations are several orders of magnitude higher in efficiency than standard computers, close to thermodynamic limit. In addition, DNA is an attractive computational medium as the process of finding the answer is the oligos finding their respective complements in solution. This process is massively parallel because each type of molecule in solution can sample a large number of complements simultaneously. This results in a processing speed many times that of current computers. Other forms for DNA computers have examined systems on a surface<sup>[23]</sup> and also utilized transcriptional machinery to create binary logic elements such as a ring oscillator and toggle switches.<sup>[26,27]</sup>

### DNA as a Nanoscale Machine

Other work has used the hybridization properties of DNA to create a nanoscale machine.<sup>[28]</sup> Oligos in solution have been designed to be DNA “tweezers” that can be mechanically opened or closed depending on the presence of a third “fuel” strand. The fuel strand has a sequence such that it is complementary to the tweezers in such a way that when it hybridizes with it, the tweezers are forced to the closed position. Addition of a strand complementary to the fuel strand removes it from the tweezers, allowing the tweezers to revert to the open position. Readout of the motion was done by fluorophore–quencher pairs linked directly to the DNA strands. The opening and closing of the DNA tweezers has been shown to be completely reversible. This system represents a type of molecular tweezers or motor that requires only DNA for fuel.

This would be entirely specific as only a strand complementary to tweezers can open/close the tweezers. Similar work involves the construction of a nanomechanical device of DNA that undergoes a chemically induced structural transition between the B and Z forms.<sup>[29]</sup>

In addition, optical control of DNA hybridization has been investigated. Typically, these approaches use a chromophore such as azobenzene, which can isomerize between the cis and trans forms depending on the excitation wavelength. Higher-energy light ( $\lambda < 300$  nm) converts the molecule to the cis state, whereas lower-energy light ( $\lambda > 300$  nm) or heating converts it back to the trans state. This isomerization results in a dramatic structural change in the molecule. Azobenzene can be chemically incorporated into nucleotide sites and thus sterically destabilize hybridization. This isomerization has been utilized to control triplex formation of DNA. When the azobenzene is switched to the cis configuration, the triplex is destabilized and the observed melting temperature is decreased by as much as 13°C.<sup>[30,31]</sup> Photoexcited denaturation via azobenzene has been used to control the hybridization of nucleic acid antisense strands that block parts of the message for transcription *in vitro*, which is the machinery that replicates DNA.<sup>[32]</sup> The azobenzene-containing oligonucleotide is hybridized to its message, preventing polymerase from reaching the end of the template. This forces transcription of an abbreviated message. When the system is exposed to light, the blocking oligonucleotide is dehybridized from the template, and the full message is transcribed. This strategy of phototriggering azobenzene to disrupt conformation in a biomolecule has been extended to ribonuclease S for control of enzymatic activity.<sup>[33–35]</sup>

## ELECTRONIC CONTROL OF DNA HYBRIDIZATION

### Background

The basic goal of this work is to develop a means of controlling hybridization of nucleic acids. In general, such a technique should utilize some form of an electronic interface but also be applicable to systems *in vivo* where more complex and interesting processes occur. In addition, the method of control should be selective, reversible, direct, and externally addressed. Finally, it should be universal so that it can be applied not just to nucleic acids but to any biomolecule.

In designing a technique for control, the question of the interface between the biological and inorganic systems arises. In general, it is difficult to interface electronically to biological systems. Typically, it has been achieved by putting the biomolecule onto a fabricated

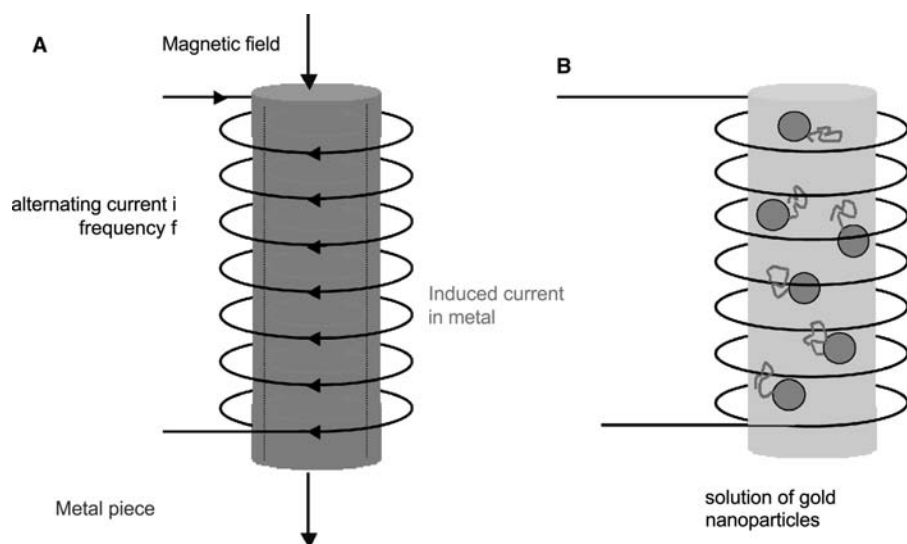


**Fig. 1** Induction heating of a metal sample (A) and of nanometer-sized gold particles in solution (B) covalently linked to the DNA or biomolecule to be controlled.

two-dimensional surface, an unnatural environment. Issues such as denaturation and subsequent loss of function can often be overcome, but biological systems do not exist solely in two dimensions. As a result, extension to controlling individual biological molecules in a cell or organism faces many challenges. Here we describe how one can interface between the biological and inorganic systems by using a nanoparticle.<sup>[1,36]</sup>

Control of DNA hybridization involves disrupting the hydrogen bonds between complementary strands. Chemical means of disrupting these bonds is achieved by introducing a denaturant. In addition, lowering the salt concentration of the solution decreases charge screening and thus the negatively charged DNA strands tend to repel each other, prohibiting hybridization. As a result, melting temperatures in low salt content are lower than at physiological levels. Hydrogen bonds can also be disrupted by heat. In general, heat disrupts the noncovalent bonds that hold together proteins, and denaturation by heat is a general effect in biology. Control via nanoparticles exploits this property where the nanoparticle is used as a heat source to initiate dehybridization of DNA. Metal nanoparticles can be heated by induction heating, which utilizes an alternating magnetic field to heat conductors. A rapidly alternating magnetic field induces alternating eddy currents in the metal that generates heat by the joule effect. This is an industrial method of heating bulk metals in a rapid and noncontact manner (Fig. 1A).<sup>[37,38]</sup> Here its use is extended to metal nanoparticles that are covalently linked to DNA in solution (Figs. 1B and 2). The alternating magnetic field is used to heat the metal nanoparticle, which transfers its heat to the DNA, dehybridizing it. Once the alternating magnetic field is turned off, the DNA dissipates the heat into solution rapidly,<sup>[39]</sup> and thus can rehybridize, so the denaturation is reversible. In addition, because

the nanoparticle is small (nm), heat is fairly localized, so biomolecules can be heated selectively without affecting neighboring molecules. Because the phenomenon by which the biomolecule is controlled is heat, this technique can be applied to nearly any biomolecule as heat denaturation is universal. For example, it can be attached to a protein to denature it slightly, turning off its activity. If the temperature rise is kept within a certain range, the biological molecule can renature and recover its activity.

Induction heating of metal conductors is characterized by a skin depth effect that results from partial cancellation of the external magnetic field by the generated magnetic field. Consequently, most of the power absorbed by the conductor is concentrated in the surface of the conductor to a depth of  $d_0$ , where  $d_0$  is defined by

$$d_0 = \frac{1}{2\pi} \sqrt{\frac{\rho \times 10^7}{\mu_r \mu_0 f}} \quad (1)$$

where  $\mu_r$  = magnetic permeability,  $\mu_0$  = permeability of free space,  $\rho$  = material resistivity, and  $f$  = frequency of the applied alternating magnetic

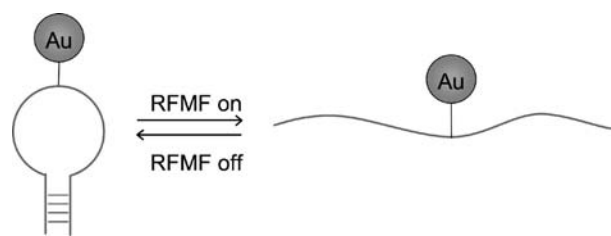


**Fig. 2** Basic mechanism for controlling the hybridization state of a DNA loop/hairpin molecule by a covalently linked 1.4-nm gold nanoparticle.

field. The power density  $P$ , which is a measure of how much heat can be generated in the sample, depends on the skin depth

$$P = 4\pi H_c^2 \mu_0 \mu_r f F \frac{d_0}{d} \quad (2)$$

where  $d$  = sample diameter,  $H_c$  = magnetic field strength, and  $F$  a transmission factor that has a sigmoidal dependence on  $(d/d_0)$ . As a result, it has been determined that optimal power absorption and heating occur when  $d/d_0 = 3.5$ . To inductively heat a gold nanoparticle with  $d = 1.4$  nm optimally, higher frequencies in the radio frequency to microwave range are required (1–10<sup>2</sup> GHz). However, because of experimental limitations the highest frequency achievable was 1 GHz. It should be of note that the inductively heating nanometer particles have not been explored extensively and will be the subject of future investigations.

### Nanoparticle Incorporation into Biological Systems

Nanoparticles are particles that are nanometers in diameter (1–100 nm) that contain about 10<sup>2</sup>–10<sup>4</sup> atoms (Fig. 3). Nanoparticles can be synthesized in a variety of inorganic materials, and have been predominantly semiconductors (group II–VI, III–V, and IV) such as CdS, CdSe, InP, InAs, GaN, Si, Ge, etc. They can also be made of metals such as Au, Ag, Cu, Pt, Pd, etc. In addition, they can be made of organic materials (polymers, dendrimers are nanoparticles) and often used as drug delivery agents. Materials in the nanometer size range can be synthesized by several different methods. The wet chemical route has been quite successful in producing high-quality particles that are tunable in size, monodisperse, crystalline, and soluble.<sup>[40–42]</sup> They typically have an organic capping ligand passivating the surface; Fig. 3 shows the coordinating ligand of R = trioctylphosphine oxide. Other methods for creating soluble nanoparticles include gas phase laser ablation followed by capping with solvent, or by crystallization on Langmuir–Blodgett surfaces.<sup>[43]</sup>

Nanocrystals are typically spherical although a variety of other shapes can be achieved through control of the wet-chemical synthesis yielding nanorods, core-shell structures, pyramids, dodecahedrons, “inorganic dendrimers.”<sup>[44]</sup> They also display physical properties (optical, magnetic, structural, chemical) that differ from bulk systems and vary with the size of the particle. This has fueled considerable interest in the study of the physical properties.<sup>[45,46]</sup> Furthermore, many applications of nanoparticles are being actively pursued as their size is of relevance to the electronic device industry, as transistors are now sub-100 nm in size. Device applications being explored that utilize nanoparticles include photovoltaics, LEDs,<sup>[47,48]</sup> photonic materials,<sup>[49]</sup> and sensors.<sup>[50]</sup>

In addition, nanoparticles have been utilized for biological applications.<sup>[51]</sup> They are ideally suited for incorporation into biological systems because their size approximates the lower range of proteins and DNA (nm). In addition, the chemistry to link nanoparticles to biological molecules has been explored.<sup>[18–20,52,53]</sup> Nanoparticle solubility permits ingestion into a cell/tissue for in vivo applications possible, and surface modification by ligand exchange or encapsulation has resulted in nanoparticles that are fully biocompatible. Besides the inherent compatibility with DNA, nanocrystals have unique properties, such as the scaling of physical properties by size. For example, the size-dependent fluorescent of nanoparticles has been exploited for use as fluorescent tags in biology.<sup>[52,54–57]</sup> Because of the broad absorption and narrow emission lines of semiconductor nanocrystals, one can excite multiple sizes of nanocrystals with a single laser line, facilitating a multicolor experiment. They also offer advantages over typical dyes as they can be made robust to photobleaching by careful choice of overcoats and capping groups, and exhibit enhanced lifetimes.

A nanocrystal can be covalently attached to DNA by chemical linkages synthesized onto the DNA backbone or on a base at a site not involved in base pairing. There has been extensive work on developing a chemical linkage to nanocrystals, some of which are shown in Fig. 4. This can be achieved by using a thiol on

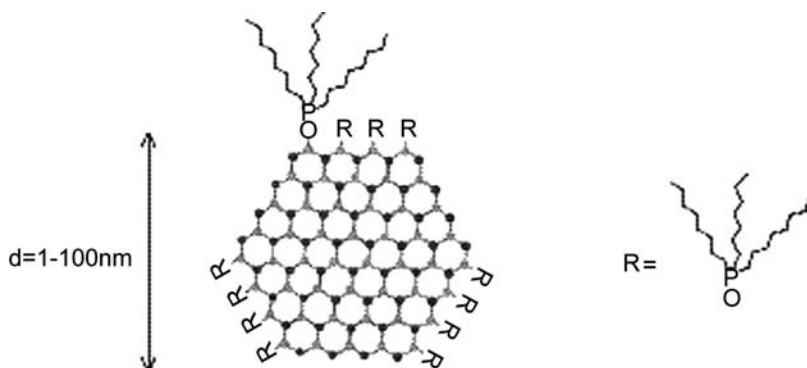
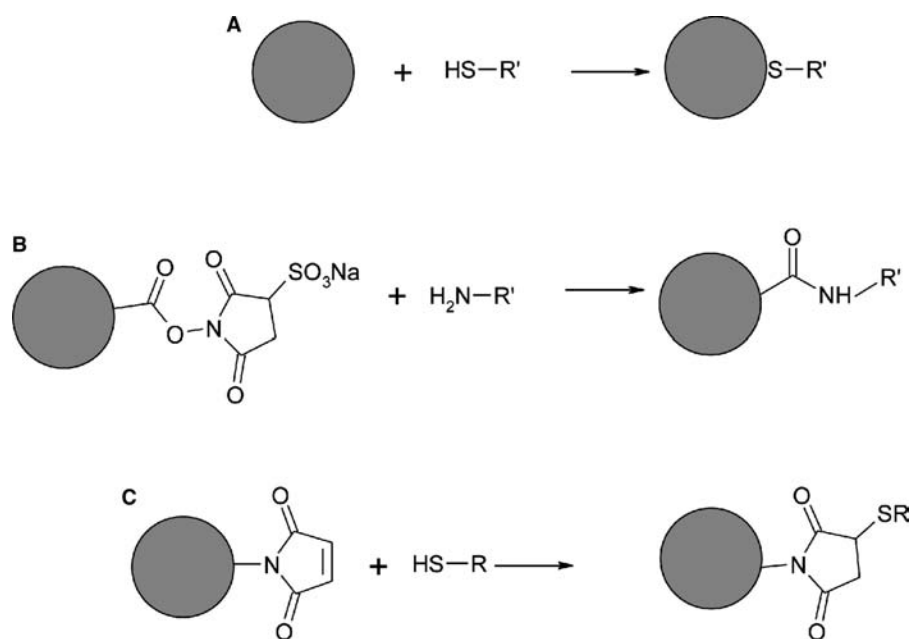


Fig. 3 Schematic of a nanoparticle.



**Fig. 4** Three different schemes for covalently linking a nanoparticle to a biomolecule (R'). (A) The thiol group on the biomolecule reacts with the gold nanocrystal directly, gold-thiol, (B) NHS ester with a primary amine, (C) maleimide group-thiol.

the DNA to form a gold-thiol bond directly with the gold nanoparticle. In addition, the nanoparticle can be refunctionalized to have a different chemical identity on the surface such as a reactive group that can specifically react with a group on the DNA. A primary amine on the DNA can react with an *N*-hydroxysuccinimido ester (NHS ester) to form a peptide bond.<sup>[14,18,51,58]</sup> Alternatively, the nanoparticle can be functionalized with a maleimide group, which can react with a thiol on the DNA to form a thioether bond.<sup>[58]</sup>

### Controlling DNA Hybridization via Nanoparticles: Experiments and Results

This section describes in detail the experiments using nanoparticles to control DNA hybridization. DNA oligonucleotides, purchased commercially, were synthesized via solid phase synthesis during which terminal groups (biotins, fluorophores) and internal amines were incorporated. Uncharged gold nanocrystals (1.4 nm) functionalized with a single sulfo NHS ester were purchased commercially (Nanoprobes). The nanoparticles were linked to the DNA oligos by incubation for 1 hr at room temperature in solution. Nanoparticles were used in large excess to ensure labeling of all of the DNA oligos. Excess nanoparticles were purified away by either ethanol precipitation or solid phase extraction of the desired product, with multiple washes with buffer (1 × phosphate-buffered solution, PBS).

Alternating magnetic fields were generated by applying an alternating current to coils that had 5–35 turns. Coils were wrapped around a plastic cuvette/

tube holder with open structures to maximize light passage and had a cross section of  $\sim 1 \text{ cm}^2$  so that microfuge tubes could fit inside. An RF signal generator (Hewlett Packard 8648C) generated currents at 1 GHz with an output of 1 mW, which were sent through an amplifier to result in an ultimate output power tunable from 0.4 to 4 W. This is an estimate as losses can occur from setup architecture. To eliminate effects from heating of the sample by the coil, the entire coil was placed in a large water bath at room temperature ( $T = 22^\circ\text{C}$ , volume  $\sim 1 \text{ L}$ ). Samples were heated in either quartz cuvettes or PCR tubes and had volumes of 180–200  $\mu\text{L}$ .

The first system used to demonstrate heating of the particle and transfer of the heat to the attached DNA was a molecular beacon, or a loop/hairpin,<sup>[59]</sup> which is single-stranded DNA with a sequence that is self-complementary on the ends for seven bases (see Fig. 5). Molecular beacons have become popular for applications of quantifying PCR products as they fluoresce when hybridized to its complement. The nanocrystal was attached to the DNA by a C6 primary amine off one of carbon 2 of a thymidine in the loop region. A 1- $\mu\text{M}$  solution of the DNA-nanoparticle conjugate in 1 × PBS was put in a cuvette in a coil that had an alternating current run through it. Using the hyperchromicity of DNA, its optical absorbance was simultaneously monitored to measure dehybridization of the hairpin structure. Fig. 5 shows the response in absorbance with the application of the RFMF. The RFMF was applied at 15-sec intervals, and each time the field was on the absorbance increased, suggesting dehybridization. When DNA alone was put into the solution at

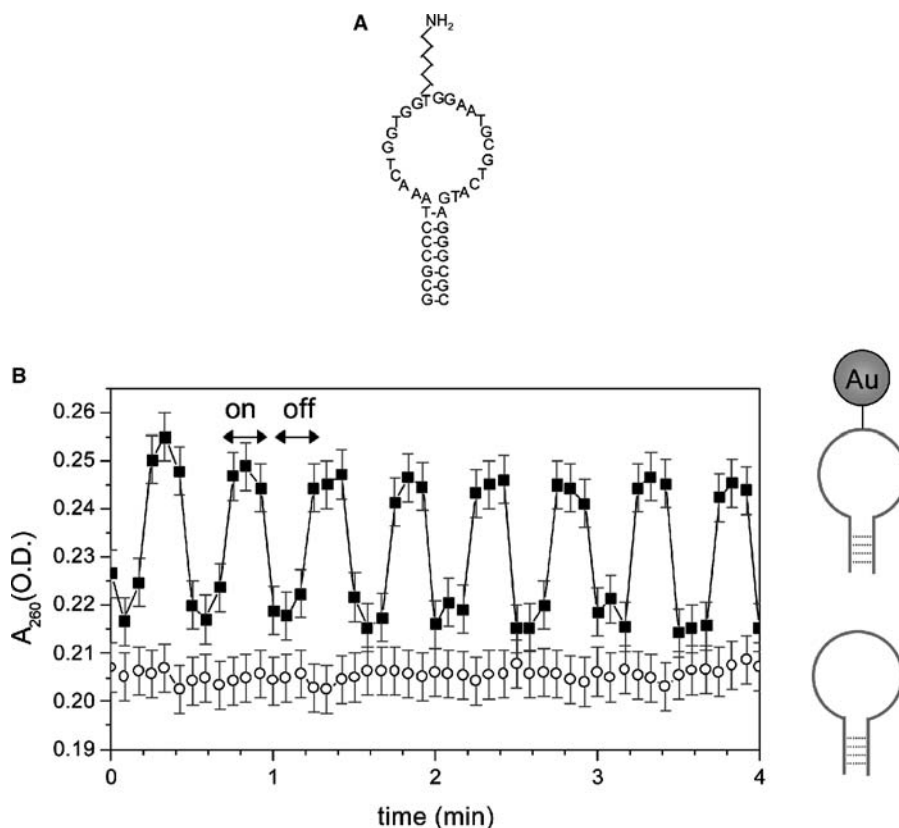


**Fig. 5** Inductive coupling to nanoparticles linked to DNA (A) and evidence of dehybridization (B). *Source:* Reprinted by permission from Ref.<sup>[1]</sup>. © 2002, Macmillan Publishers Ltd.

a comparable concentration, the absorbance did not increase with the RFMF, indicating that the nanocrystals must be present for the absorbance to change. It is of note that the optical absorbance did increase in the presence of nanocrystals alone, which was probably a result of the perturbing of the plasmon resonance in the particles by the alternating magnetic field. However, the change in OD with the nanocrystals in the RFMF is much less than that of the DNA, and the plot in Fig. 5 has this contribution subtracted out.

Evidently the nanocrystals create a higher temperature that may be localized to the DNA oligo. To determine this effective temperature increase, samples that were exposed to the alternating magnetic field were compared to those exposed to fixed global temperatures. In this case, a two-phase system was utilized to avoid temperature-dependent effects on optical properties. Nanocrystals were linked to a 12mer of DNA that had the 5' end functionalized with a fluorophore, which served as a means to count the oligo. It was hybridized to a solid surface, which was done by using a complement that had a biotin on one end that could be captured onto streptavidin agarose bead. Because the beads were large (diameter  $\sim 100 \mu\text{m}$ ), they settled to the bottom of the tube, comprising the solid phase. The supernatant above it served as the solution phase. If the oligo was dehybridized by either heat or the RFMF, it can diffuse into the supernatant,

which can be removed and measured by fluorescence spectroscopy.

One sample of the two-phase system was prepared and aliquoted into separate tubes. Each tube was exposed to a fixed global temperature using a 1-L water bath, and one tube was placed in the coil with the RFMF at room temperature. Following heat or RFMF, the samples were spun down and the supernatant was removed. Each supernatant was then measured by fluorescence spectroscopy, which yielded a relative concentration of DNA present in the sample. Fig. 6 shows the spectra from the supernatants. The fluorophore, FAM, has an emission maximum at 515 nm. For samples exposed to higher temperatures, the fluorescence intensity increased as more DNA was dehybridized. The sample that was exposed to the RFMF (thick black line) had a fluorescence intensity between that of the 30° and 50°C samples. To quantify the effective temperature of the RFMF sample, the fluorescence intensity peaks were integrated and plotted as a function of incubation temperature (dots), shown in Fig. 6. The curve is fit to a sigmoidal (line) characteristic of DNA melting curves. The intensity for the RFMF sample was extrapolated (dotted line) to a temperature of 35°C, or 13°C above ambient temperature. This is the effective temperature increase the DNA oligo experiences from the RFMF. It is important to note that this temperature jump is



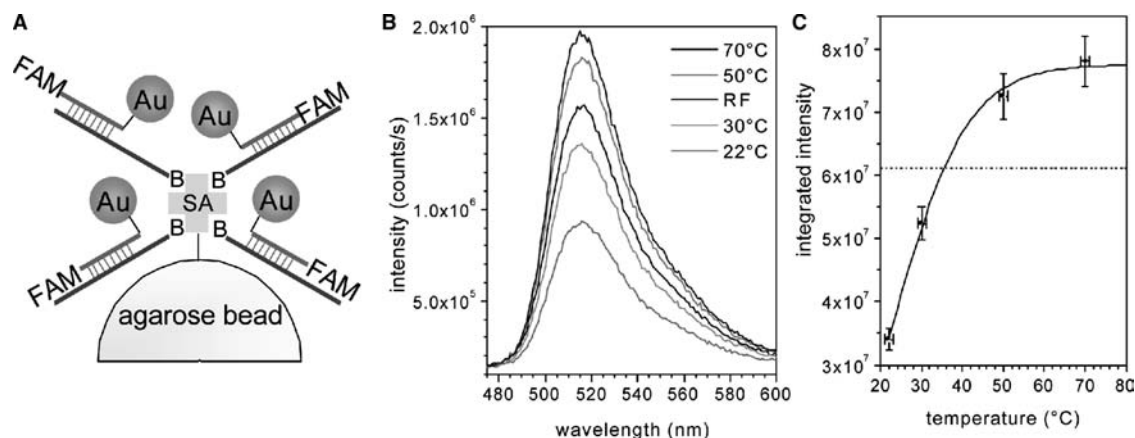


**Fig. 6** Determination of effective temperature from inductive coupling to a gold nanoparticle linked to DNA. (A) The two-phase system. (B) Supernatant fluorescence spectra. (C) Integrated peak intensity of the supernatant fluorescence spectra shown in (B) (squares) and a sigmoidal fit (solid line) and the intensity of the sample exposed to RFMF (dotted line). *Source:* Reprinted by permission from Ref.<sup>[1]</sup>. © 2002, Macmillan Publishers Ltd.

sufficient to partially denature many proteins in biology. However, using this technique to dehybridize longer strands of DNA that have elevated melting temperatures may be difficult using the parameters utilized in the experiments described here. One way to achieve denaturation of longer oligos would be to increase the delivered power to the coil, which would increase the heating of the nanoparticle. In addition, using multiple nanocrystals along the backbone can distribute heating along the DNA. However, functionalization becomes difficult as the only available points in the middle of the chain are off the bases themselves and nanoparticles attached to these sites may interfere with hybridization.

Next we tested if the heating of the nanoparticle could be localized to the strand to which it was linked. This property is crucial if nanoparticle antennas are to be utilized for specific control in real biological environments. The environment inside cells is crowded, with concentrations greater than 300 mg/mL. This results in very little space between proteins.<sup>[60]</sup> We used a mixture of oligos to test if the heating of the nanoparticle was localized using the two-phase system described above. The oligo to be dehybridized was mixed with another oligo. This second oligo was identical in sequence but had a fluorophore instead of a nanoparticle attached to the 3' end. The fluorophore for this second oligo was tetramethylrhodamine (TMR), which is spectroscopically distinct from FAM ( $\lambda_{\text{emission}} = 563 \text{ nm}$ ) and thus can be distinguished in fluorescence spectroscopy (Fig. 7). One sample was exposed to a 70°C water bath, and the other was exposed to the RFMF. Fluorescence spectra are shown in Fig. 7 where the ratio of the fluorescence intensity at 515 and 563 nm are compared. The globally heated sample had a higher ratio of TMR:FAM,

while the sample that was exposed to the RFMF had a lower ratio. Integration of the peaks to quantify the ratios showed that the sample exposed to the global heating has approximately 50:50 gold- vs. TMR-labeled oligos, while the RFMF sample has a ratio of 80:20. This signifies that dehybridization of the gold-labeled molecule was enhanced in the RFMF. One possible explanation for the dehybridization not to be completely specific is that streptavidin has the capacity to bind four biotins and thus four oligos, which on average would be a mixture of gold-labeled and TMR-labeled oligos. As a result, the TMR-labeled oligos were estimated to be about 10 nm or less away from a gold-labeled oligo. At these distances, it is expected that through-solution heating will occur, resulting in nonspecific dehybridization.

### Advantages and Weaknesses

Although the experiments described here are in vitro, the use of nanoparticle antennas to control molecules in highly disorganized environments in vivo shows promise. Because of the solubility properties of nanoparticles, they can be attached to proteins in solution or in cells. Incorporation of inorganic nanoparticles (CdSe, Au, Ag, Fe<sub>3</sub>O<sub>4</sub>, etc.) into cellular systems<sup>[61]</sup> and even living organisms have been successful.<sup>[57]</sup> Additionally, because the means of externally addressing the nanoparticles does not require light, it does not require transparent samples like optical techniques. Consequently, it avoids the problem of needing long-wavelength (>800 nm) excitable transducers so that the excitation can penetrate tissue. In addition, the nanoparticle antennas do not suffer short lifetimes or photobleaching that optical chromophores undergo.

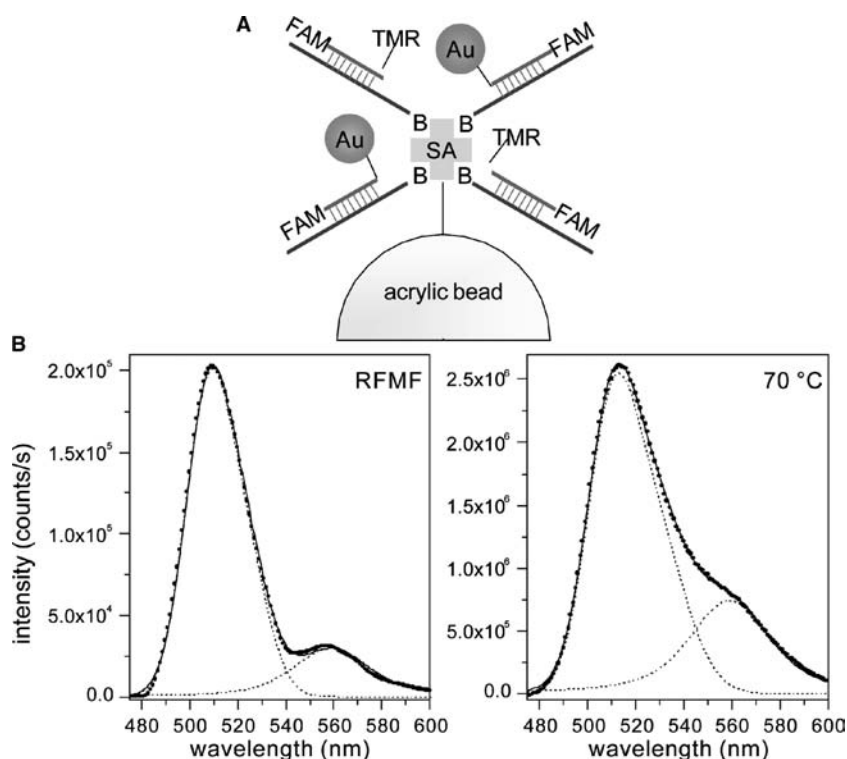


**Fig. 7** (A) Two-phase system for testing selectivity. Another (B) difference fluorescence spectra (dots) (after dehybridization by heat/RFMF minus before dehybridization), individual fluorescence peak fits (dashes), and composite fit (lines). Sample exposed to RFMF (left) and to 70°C (right). *Source:* Reprinted by permission from Ref.<sup>[1]</sup>. © 2002, Macmillan Publishers Ltd.

However, there are considerable challenges that this technique faces. Because it is still being developed, it has not yet been fully explored, and limitations in sensitivity and resolution have not yet been quantified. In addition, it requires a coil placed around the sample to be addressed unlike lasers, which can address things from afar. Furthermore, unlike lasers, alternating magnetic fields cannot be focused to microscopic dimensions, although focusing to centimeters has been possible.<sup>[62]</sup> Finally, short- and long-term biological side effects of both the RFMF and the nanoparticles have yet to be tested.

### Future Work

To utilize nanoparticle antennas for controlling real biological systems, it is necessary to have a fundamental understanding of the electromagnetic heating mechanism of the nanoparticles and also the process of heat transfer to its surroundings. The degree of localization of the heating needs to be characterized. It is expected that the spatial extent of the heat from the nanoparticle is localized based on calculations for a sphere.<sup>[63,64]</sup> As a result, temperature drop-offs around the nanoparticle are expected to be rather sharp, as high as 95% by 10 nm, which is the approximate size of a protein. Therefore, spatial localization within complex environments such as a cell may be possible. In addition, the effect of localized heating on the structure of the DNA duplex can also be investigated.

Control by nanoparticle antennas can be easily extended to systems other than DNA such as proteins, since many proteins denature with heat. However, protein systems are much more challenging to control as placement of the nanoparticle is key to the switching of its activity. It must be linked to a section of the protein so that it does not normally affect the functioning of the protein. However, it should be at a site from which the heat can distort the shape of the active site. This relies on the enormous progress made in the molecular-level characterization of both the structures and mechanisms of proteins by X-ray crystallography or NMR combined with site-directed mutagenesis.

Magnetic particles have been used to heat tissues *in vivo*, in particular for tumor ablation, or hyperthermia. Because tumors are macroscopic objects (up to millimeters in diameter), the magnetic particles used to heat them are often much larger (up to 10  $\mu\text{m}$  in diameter), and are often used *en masse* to heat a large region of tissue rather than an individual molecule. The technique described here strives to have control of individual molecules so that selectivity is permitted, rather than heating a large bulk of molecules. This finer, molecular level of control imparts the potential to regulate more complex processes.

### CONCLUSION

The technique described above is just the beginning of only one way to control electronically biomolecular

activity. Other efforts in controlling biological systems show much promise in reaching goals of creating “biomolecular machines.” In the future, one would like to unite these methods to the myriad of biological phenomena that involve nucleic acids for applications in therapy and diagnostics. Control of DNA could lead to manipulation of the passage of the behavior of simple organisms and information transfer between them. Even control of the hybridization of a short oligonucleotide can have profound ramifications on the physical behavior of a cell or organism, as in antisense therapy or RNA interference. In addition, interfacing to biological systems is desirable for applications in computation and self-assembly. Direct manipulation of biological machinery would allow one to take advantage of the engineering inherent in the systems that Nature has built.

## ACKNOWLEDGMENTS

This work was supported by DARPA and the MIT Media Lab TTT consortium. I would like to acknowledge J. Jacobson and S. Zhang for support.

## REFERENCES

- Hamad-Schifferli, K.; Schwartz, J.J.; Santos, A.; Zhang, S.; Jacobson, J.M. Remote electronic control of DNA hybridization through inductive heating of an attached metal nanocrystal. *Nature* **2002**, *415* (6868), 152–155.
- Ptashne, M. *A Genetic Switch: Phage and Higher Organisms*; Blackwell Science Inc., 1992.
- Watson, J.D.; Crick, F.H.C. Molecular structure of nucleic acids: A structure for deoxyribose nucleic acid. *Nature* **1953**, *171*, 737–738.
- Cantor, C.R.; Schimmel, P. *Biophysical Chemistry Part I: The Conformation of Biological Macromolecules*; W. H. Freeman: San Francisco, 1980.
- Bloomfield, V.A.; Crothers, D.M.; Tinoco, I., Jr. *Nucleic Acids: Structures, Properties and Functions*; University Science Books: Sausalito, 2000.
- Consortium, I.H.G.S. Initial sequencing and analysis of the human genome. *Nature* **2001**, *409* (6822), 860–921.
- Shoemaker, D.D.; Schadt, E.E.; Armour, C.D.; He, Y.D.; Garrett-Engel, P.; McDonagh, P.D.; Loerch, P.M.; Leonardson, A.; Lum, P.Y.; Cavet, G.; Wu, L.F.; Altschuler, S.J.; Edwards, S.; King, J.; Tsang, J.S.; Schimmack, G.; Schelter, J.M.; Koch, J.; Ziman, M.; Marton, M.J.; Li, B.; Cundiff, P.; Ward, T.; Castle, J.; Krolewski, M.; Meyer, M.R.; Mao, M.; Burchard, J.; Kidd, M.J.; Dai, H.; Phillips, J.W.; Linsley, P.S.; Stoughton, R.; Scherer, S.; Boguski, M.S. Experimental annotation of the human genome using microarray technology. *Nature* **2001**, *409* (6822), 922–927.
- Gilles, P.N.; Wu, D.J.; Foster, C.B.; Dillon, P.J.; Chanock, S.J. Single nucleotide polymorphic discrimination by an electronic dot blot assay on semiconductor microchips. *Nat. Biotechnol.* **1999**, *17*, 365–370.
- Westin, L.; Xu, X.; Miller, C.; Wang, L.; Edman, C.F.; Nerenberg, M. Anchored multiplex amplification on a microelectronic chip array. *Nat. Biotechnol.* **2000**, *18*, 199–204.
- Kelley, S.O.; Barton, J.K.; Jackson, N.M.; McPherson, L.D.; Potter, A.B.; Spain, E.M.; Allen, M.J.; Hill, M.G. Orienting DNA helices on gold using applied electric fields. *Langmuir* **1998**, *14* (24), 6781–6784.
- Braun, E.; Eichen, Y.; Sivan, U.; Ben-Yoseph, G. DNA-templated assembly and electrode attachment of a conducting silver wire. *Nature* **1998**, *391*, 775–778.
- Park, S.-J.; Taton, A.T.; Mirkin, C.A. Array-based electrical detection of DNA with nanoparticle probes. *Science* **2002**, *295*, 1503–1506.
- Berven, C.A.; Wybourne, M.N.; Clarke, L.; Hutchison, J.E.; Brown, L.O.; Mooster, J.L.; Schmidt, M.E. The use of biopolymer templates to fabricate low-dimensional gold particle structures. *Superlattices Microstruct.* **2000**, *27*, 489–493.
- Mitchell, G.P.; Mirkin, C.A.; Letsinger, R.L. Programmed assembly of DNA functionalized quantum dots. *J. Am. Chem. Soc.* **1999**, *121* (35), 8122–8123.
- LaBean, T.H.; Yan, H.; Kopatsch, J.; Liu, F.; Winfree, E.; Reif, J.H.; Seeman, N.C. Construction, analysis, ligation, and self-assembly of DNA triple crossover complexes. *J. Am. Chem. Soc.* **2000**, *122*, 1848–1860.
- Mao, C.; LaBean, T.H.; Reif, J.H.; Seeman, N.C. Logical computation using algorithmic self-assembly of DNA triple-crossover molecules. *Nature* **2000**, *407*, 493–496.
- Winfree, E.; Liu, F.; Wenzler, L.; Seeman, N. Design and self-assembly of two-dimensional DNA crystals. *Nature* **1998**, *394* (6693), 539–544.
- Loweth, C.J.; Caldwell, W.B.; Peng, X.; Alivisatos, A.P.; Schultz, P.G. DNA-based assembly of gold nanocrystals. *Angew. Chem., Int. Ed. Engl.* **1999**, *38* (12), 1808–1812.
- Taton, A.T.; Mirkin, C.A.; Letsinger, R.L. Scanometric DNA array detection with nanoparticle probes. *Science* **2000**, *289*, 1757–1760.
- Elghanian, R.; Storhoff, J.J.; Mucic, R.C.; Letsinger, R.L.; Mirkin, C.A. Selective colorimetric detection of polynucleotides based on the distance-dependent optical properties of gold nanoparticles. *Science* **1997**, *277*, 1078–1081.
- Adleman, L.M. Molecular computation of solutions to combinatorial problems. *Science* **1994**, *266*, 1021–1024.
- Sakamoto, K.; Gouzu, H.; Komiyama, K.; Kiga, D.; Yokoyama, S.; Yokomori, T.; Hagiya, M. Molecular computation by DNA hairpin formation. *Science* **2000**, *288*, 1223–1226.
- Liu, Q.; Wang, L.; Frutos, A.G.; Condon, A.E.; Corn, R.M.; Smith, L.M. DNA computing on surfaces. *Nature* **2000**, *403*, 175–179.
- Forbes, N. Biologically inspired computing. *Comput. Sci. Eng.* **2000**, *2* (6), 83–87.
- Faulhammer, D.; Cukras, A.R.; Lipton, R.J.; Landweber, L.F. Molecular computation: RNA solutions

- to chess problems. Proc. Natl. Acad. Sci. U. S. A. **2000**, *97* (4), 1385–1389.
26. Elowitz, M.B.; Leibler, S. A synthetic oscillatory network of transcriptional regulators. *Nature* **2000**, *403* (6767), 335–338.
  27. Gardner, T.S.; Cantor, C.R.; Collins, J.J. Construction of a genetic toggle switch in *Escherichia coli*. *Nature* **2000**, *403* (6767), 339–342.
  28. Yurke, B.; Turberfield, A.J.; Mills, J.; Allen, P.; Simmel, F.C.; Neumann, J.L. A DNA-fuelled molecular machine made of DNA. *Nature* **2000**, *406* (6796), 605–608.
  29. Mao, C.; Sun, W.; Shen, Z.; Seeman, N.C. A nanomechanical device based on the B-Z transition of DNA. *Nature* **1999**, *397* (6715), 144–146.
  30. Asanuma, H.; Yoshida, T.; Ito, T.; Komiyama, M. Photo-responsive oligonucleotides carrying azobenzene at the 2'-position of uridine. *Tetrahedron Lett.* **1999**, *40*, 7995–7998.
  31. Asanuma, H.; Liang, X.; Yoshida, T.; Yamazawa, A.; Komiyama, M. Photocontrol of triple-helix formation by using azobenzene-bearing oligo(thymidine). *Angew. Chem., Int. Ed. Engl.* **2000**, *39* (7), 1316–1318.
  32. Yamazawa, A.; Liang, X.; Asanuma, H.; Komiyama, M. Photoregulation of the DNA polymerase reaction by oligonucleotides bearing an azobenzene. *Angew. Chem., Int. Ed. Engl.* **2000**, *39* (13), 2356–2357.
  33. James, D.A.; Burns, D.C.; Woolley, G.A. Kinetic characterization of ribonuclease S mutants containing photoisomerizable phenylazophenylalanine residues. *Protein Eng.* **2001**, *14* (12), 983–991.
  34. Kumita, J.R.; Smart, O.S.; Woolley, G.A. Photo-control of helix content in a short peptide. Proc. Natl. Acad. Sci. U. S. A. **2000**, *97* (8), 3803–3808.
  35. Liu, D.; Karanicolas, J.; Yu, C.; Zhang, Z.; Woolley, G.A. Site-specific incorporation of photoisomerizable azobenzene groups into ribonuclease S. *Bioorg. Med. Chem. Lett.* **1997**, *7* (20), 2677–2680.
  36. Direct electronic control of biomolecular systems: Using nanocrystals as antennas for regulation of biological activity. In *Synthesis, Functional Properties, and Applications of Nanostructures: Symposium Held April 17–20, 2001, San Francisco, California, U.S.A.*; Hamad-Schifferli, K.; Schwartz, J.J.; Santos, A.T.; Zhang, S.; Jacobson, J.M. Hahn, H.W., Feldhelm, D.L., Kubiak, C.P., Tannenbaum, R., Siegel, R.W., Eds.; Materials Research Society: Warrendale, PA, 2002. Mater. Res. Soc. Proc., 2001. Y8.43.1-6 (San Francisco).
  37. Orfeuil, M. *Electric Process Heating: Technologies/Equipment/Applications*; Battelle Press: Columbus, OH, 1987.
  38. Davies, E.J. *Conduction and Induction Heating*; P. Pergin Ltd. on behalf of the Institution of Electrical Engineers: London, 1990.
  39. Lian, T.; Locke, B.; Kholodenko, Y.; Hochstrasser, R.M. Energy flow solute to solvent probed by femtosecond IR spectroscopy: Malachite green and heme protein solutions. *J. Phys. Chem.* **1994**, *98*, 11648–11656.
  40. Murray, C.B.; Norris, D.J.; Bawendi, M.G. Synthesis and characterization of nearly monodisperse CdE (E = S, Se, Te) semiconductor nanocrystallites. *J. Am. Chem. Soc.* **1993**, *115*, 8706–8715.
  41. Peng, Z.A.; Peng, X. Formation of high-quality CdTe, CdSe, and CdS nanocrystals using CdO as precursor. *J. Am. Chem. Soc.* **2001**, *123*, 183–184.
  42. Peng, X.; Manna, L.; Yang, W.; Wickham, J.; Scher, E.; Kadavanich, A.K.; Alivisatos, A.P. Shape control of CdSe nanocrystals. *Nature* **2000**, *404* (6773), 59–61.
  43. Fendler, J.H. Monolayer interfaces as templates for particle growth. *Colloids Surf., A* **1993**, *71*, 309–315.
  44. Manna, L.; Scher, E.; Alivisatos, A.P. Synthesis of soluble and processable rod-, arrow-, teardrop-, and tetrapod-shaped CdSe nanocrystals. *J. Am. Chem. Soc.* **2000**, *122*, 12700–12706.
  45. Alivisatos, A.P. Semiconductor clusters, nanocrystals, and quantum dots. *Science* **1996**, *271* (5251), 933–937.
  46. Bawendi, M.G.; Steigerwald, M.L.; Brus, L.E. The quantum mechanics of larger semiconductor clusters (quantum dots). *Annu. Rev. Phys. Chem.* **1990**, *41*, 477–496.
  47. Colvin, V.L.; Schlamp, M.C.; Alivisatos, A.P. Light-emitting diodes made from cadmium selenide nanocrystals and a semiconducting polymer. *Nature* **1994**, *370*, 354–357.
  48. Coe, S.; Woo, W.-K.; Bawendi, M.G.; Bulovic, V. Electroluminescence from single monolayers of nanocrystals in molecular organic devices. *Nature* **2002**, *420*, 800–803.
  49. Norris, D.J.; Vlasov, Y.A. Chemical approaches to three-dimensional semiconductor photonic crystals. *Adv. Mater.* **2001**, *13* (6), 371–376.
  50. Vossmeier, T.; Guse, B.; Besnard, I.; Bauer, R.E.; Mullen, K.; Yasuda, A. Gold nanoparticle/polyphenylene dendrimer composite films. Preparation and vapor-sensing properties. *Adv. Mater.* **2002**, *14* (3), 238–242.
  51. Niemeyer, C.M. Nanoparticles, proteins, and nucleic acids: Biotechnology meets materials science. *Angew. Chem., Int. Ed. Engl.* **2001**, *40*, 4128–4158.
  52. Mattoussi, H.; Mauro, J.M.; Goldman, E.R.; Anderson, G.P.; Sundar, V.C.; Mikulec, F.V.; Bawendi, M.G. Self-assembly of CdSe–ZnS quantum dot bioconjugates using an engineered recombinant protein. *J. Am. Chem. Soc.* **2000**, *122* (49), 12142–12150.
  53. Zanchet, D.; Micheel, C.M.; Parak, W.J.; Gerion, D.; Alivisatos, A.P. Electrophoretic isolation of discrete Au nanocrystal/DNA conjugates. *Nano Lett.* **2001**, *1* (1), 32–35.
  54. Bruchez, M.; Moronne, M.; Gin, P.; Weiss, S.; Alivisatos, A.P. Semiconductor nanocrystals as fluorescent biological labels. *Science* **1998**, *281* (5385), 2013–2016.
  55. Chan, W.C.W.; Nie, S. Quantum dot bioconjugates for ultrasensitive nonisotopic detection. *Science* **1998**, *281* (5385), 2016–2018.
  56. Rosenthal, S.J.; Tomlinson, I.; Adkins, E.M.; Schroeter, S.; Adams, S.; Swafford, L.; McBride, J.; Wang, Y.; DeFelice, L.J.; Blakely, R.D. Targeting cell surface receptors with ligand-conjugated nanocrystals. *J. Am. Chem. Soc.* **2002**, *124*, 4586–4594.
  57. Dubertret, B.; Skourides, P.; Norris, D.J.; Noireaux, V.; Brivanlou, A.H.; Libchaber, A. In vivo imaging of

- quantum dots encapsulated in phospholipid micelles. *Science* **2002**, *298*.
58. Hermanson, G.T. *Bioconjugate Techniques*; Academic Press: San Diego, 1996.
  59. Tyagi, S.; Krame, F.R. Molecular beacons: Probes that fluoresce upon hybridization. *Nat. Biotechnol.* **1996**, *14*, 303–308.
  60. Kuthan, H. Self-organisation and orderly processes by individual protein complexes in the bacterial cell. *Prog. Biophys. Mol. Biol.* **2001**, *75*, 1–17.
  61. Parak, W.J.; Boudreau, R.; Le Gros, M.; Gerion, D.; Zanchet, D.; Micheel, C.M.; Williams, S.C.; Alivisatos, A.P.; Larabell, C. Cell motility and metastatic potential studies based on quantum dot imaging of phagokinetic tracks. *Adv. Mater.* **2002**, *14* (12), 882–885.
  62. Boddie, A.W.J.; Yamanashi, W.S.; Frazer, J.; McBride, C.M.; Martin, R. Field focusing and focal heating patterns using a hybrid radiofrequency hyperthermia system. *Med. Instrum.* **1983**, *17*, 358–364.
  63. Goldenberg, H.; Tranter, C.J. Heat flow in an infinite medium heated by a sphere. *Br. J. Appl. Phys.* **1952**, *3*, 296–298.
  64. Hüttman, G.; Serbin, J.; Radt, B.; Lange, B.I.; Birngruber, R. Proceedings of SPIE: Laser–Tissue Interaction XII: Photochemical, Photothermal, and Photomechanical; Duncan, D.D., Jacques, S.L., Johnson, P.C., Eds.; SPIE, 2001, 398–409.

# DNA Interactions with Functionalized Emulsions

Thierry Delair

CNRS-bioMérieux, École Normale Supérieure de Lyon, Lyon, France

## INTRODUCTION

Synthetic colloidal DNA carriers have been under intense investigation lately as they represent one of the safer alternatives<sup>[1]</sup> to viral-mediated gene delivery. Moreover, in vaccination purposes, the group of Singh has demonstrated that DNA adsorbed onto particle surface could be a potent immunogene.<sup>[2]</sup> Colloidal carriers include particles, i.e., hard spherical objects made from polymers, and emulsions, dispersions of a liquid nonsoluble in the continuous phase, which most of the time are “soft objects.” Depending on the size of the droplets, the emulsions will be named macro-, micro-, or nanoemulsions. Emulsions are thermodynamically unstable, except for micro- or nanoemulsions, which can form spontaneously, upon mixing the appropriate amounts of components, in particular with a high concentration of surfactants. Emulsions are oil-in-water (O/W) dispersions or the reverse (water-in-oil, W/O) very often stabilized with phospholipids as surface active agent. They structurally differ from liposomes which consist in phospholipidic bilayers (ideally one) surrounding an aqueous core.

In clinics, emulsions have long been used for parenteral nutrition and later for drug delivery, as a means to reduce the toxicity of the active substance.<sup>[3]</sup> So, a solid technical background exists for the production at high scale and low cost of safe carriers for in vivo applications. Moreover, compared to related DNA particulate vectors, the manufacture of emulsions does not require the use of solvents, and components are well tolerated by the body, as for instance lipids such as triglycerides or olive oil, etc.

For DNA delivery, nanotechnologies are expected to develop formulations of nanocomposites capable of interactions with nucleic acids and transport to the targeted site. The nanometer-size range of these carriers allows a better uptake by cells and even offers the capability to cross the blood–brain barrier.<sup>[4]</sup> Moreover, nanoparticles can be administrated into the systemic circulation with no risk of aggregation and blockage of fine blood capillaries. In some applications, it may be essential to target not only a tissue, but as well a specific compartment of the cells.<sup>[4]</sup> Hence this chapter will be devoted to the elaboration of nanosized

emulsions, their interactions with DNA, and various applications of these composite objects.

## ELABORATION OF NANOEMULSIONS

### High-Pressure Homogenization

This technique has been developed for the emulsions for parenteral nutrition and thus much technical background is available and high-scale production lines exist. Both oils and solid lipids can be used, although the latter have to be processed under the molten form.<sup>[3]</sup> First, one preemulsion is obtained by mixing the oil and lipid containing surfactants such as lecithin, for instance, with the aqueous phase. Then, the homogenization step occurs by applying a pressure of up to 500 bars.<sup>[5]</sup> For sterilization purposes, the emulsions can be filtered through 0.22- $\mu\text{m}$  filters and eventually autoclaved (121°C, 15 min). This process can be applied to oil-based emulsions stabilized by cationic surfactants<sup>[6,7]</sup> or with a polysaccharide<sup>[8,9]</sup> and for solid lipids.<sup>[3]</sup>

### Emulsification-Based Methods

These methods rely on the emulsification of the oily phase in the aqueous phase using milder emulsification conditions than the process described above. Dissolved in an organic solvent, the oil containing phospholipid surfactants can be dried and then redispersed after hydration in an aqueous buffer. With this approach, cationic emulsions in the 170–250-nm range were obtained in the presence of a nonionic stabilizer for gene-transfer purposes.<sup>[10]</sup> In another approach, the phospholipids can be directly emulsified in the aqueous phase using ultrasounds or added as an alcoholic solution, subsequently added to the oil phase and sonicated—or microemulsified—to yield the emulsions.<sup>[11,12]</sup> The key parameters of the process are the interfacial properties of the emulsions which can be controlled by the nature and concentration of the phospholipid surfactants and the properties of the oil (surface tension, viscosity). It appears that for a high



colloidal stability, a high surface tension and a low viscosity were most favorable.<sup>[12]</sup>

### Solvent-Based Processes

In order to avoid processes involving long and high shearing steps, the emulsification of two low viscosity nonmiscible phases has been investigated. Moreover, the following approaches can be performed at room temperature, even with solid lipids.

The lipid matrix, dissolved in a volatile water insoluble solvent, chloroform, or dichloromethane, can be emulsified in an aqueous phase often containing a stabilizer or a surfactant. In the last step, the solvent is removed under reduced pressure or by stirring overnight, yielding the final emulsion, whose average droplet diameter, in the 30–100-nm range,<sup>[13]</sup> depends on the fat load and emulsifier concentration. Solvents such as acetone, ethyl acetate benzyl alcohol, butyl lactate, etc., less toxic than the halogenated ones, can be used, but their water miscibilities have to be reduced. This is achieved by mutual saturation of both phases (organic by the aqueous and vice-versa). Thus the water saturated organic phase, containing the hydrophobic compounds, can be emulsified in the organic solvent-saturated aqueous phase. This emulsion is then added to a large amount of water under gentle stirring, as a result, the solvent can diffuse in the continuous phase (Fig. 1). Concentration by ultradialysis or under reduced pressure allows solvent

elimination. In this process, Trotta et al. showed that the natures of the emulsifiers were essential to obtain submicronic dispersions—160–320 nm depending on the solvent.<sup>[13]</sup>

Solvent displacement is a technically very simple process to obtain functionalized emulsions. In a water miscible solvent, the hydrophobic compounds are dissolved and slowly added to an aqueous solution containing a nonionic surfactant (Fig. 2). The diffusion of the solvent in the continuous phase allows the formation of emulsions (self-emulsification). This procedure was originally developed for the formation of nanocapsules<sup>[14]</sup> and was used by Trimaille et al. to obtain functionalized submicrometric particles by surface nanodeposition of amphiphilic functional copolymers.<sup>[15]</sup>

Nanocapsules made of a hydrophilic core and a solid lipid shell can be prepared by the water-in-oil-in-water (W/O/W) double emulsion technique. The primary W/O emulsion was obtained by emulsification of water, as the inner core of the capsules, in dichloromethane as the main continuous phase containing tripalmitin (10% w), and different amounts of lecithin. This emulsion was then emulsified in a 2% w of Poloxamer (nonionic surfactant) aqueous solution. Solvent evaporation allowed the formation of the solid lipid shell of the capsules, whose submicrometric diameter ranged from 200 to 395 nm.<sup>[16]</sup> In the hydrophilic core, water soluble active compounds could be incorporated.

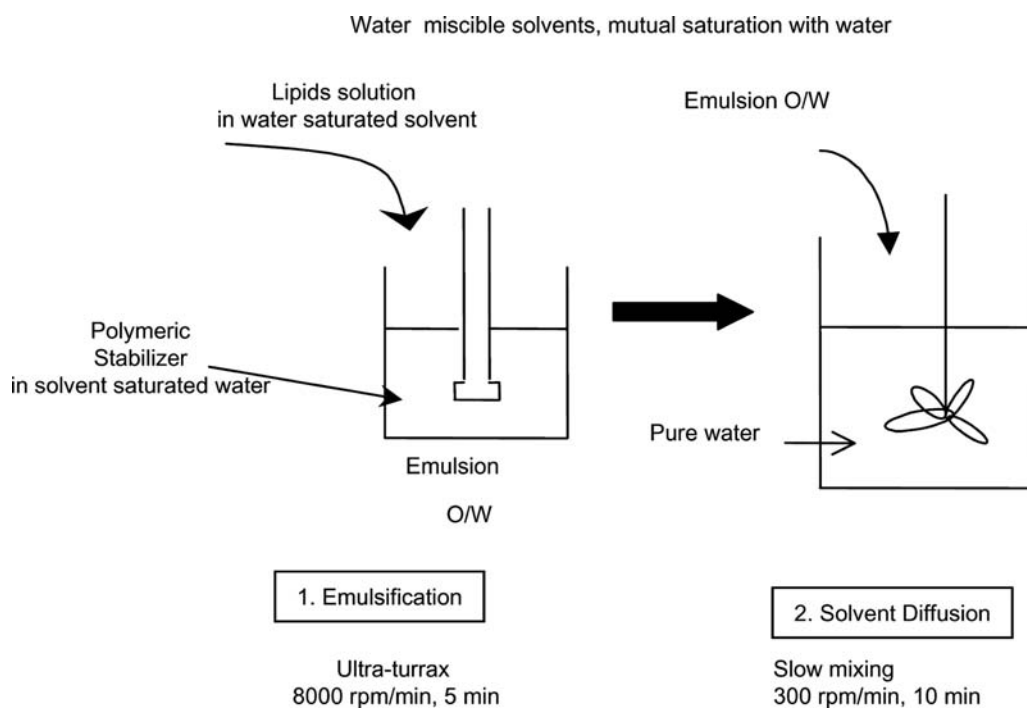


**Fig. 1** Schematic representation of the emulsification diffusion process.

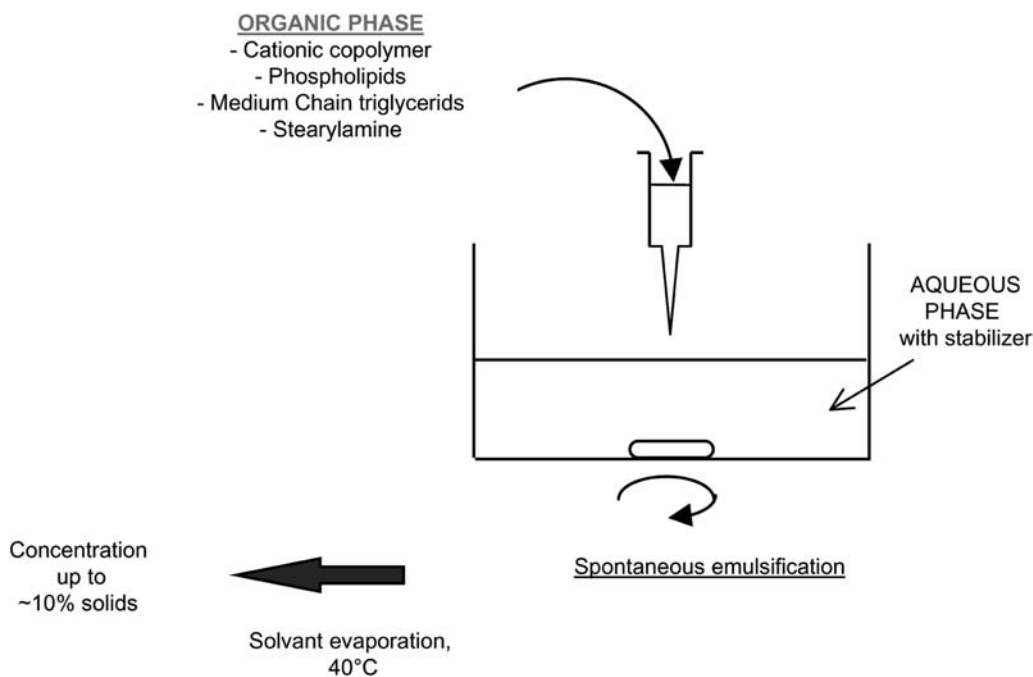


Fig. 2 Schematic representation of the solvent displacement process.

## Microemulsions

The development of the microemulsion procedures relied on the following advantages: 1) all ingredients can be potentially biocompatible and no solvent is needed; 2) the process can be adapted to include various excipients, as no damaging mechanical mixing, microfluidization, nor homogenization is required. Moreover, the method can be used with solid lipids to form particles. On a practical standpoint, a milky dispersion of the lipid is obtained in water, then, the appropriate amount of surfactant is added until a clear O/W microemulsion is formed. Cationic nanoparticles were obtained by this procedure using wax as the hydrophobic core and cetyltrimethylammonium bromide (CTAB) as a surfactant. The emulsion was formed with molten wax leading to droplets with a mean diameter of around 50 nm. On cooling, the wax solidified into particles of less than 100 nm in diameter. The main factors to control were the nature of the oily core and the CTAB concentration.<sup>[17,18]</sup> Applying a similar methodology, ethanol-in-fluorocarbon microemulsions containing DNA have been obtained in the presence of a fluorosurfactant.<sup>[19]</sup>

One of the major drawbacks of this procedure is the use of large amounts of surfactant to obtain the microemulsion. To remove the excess, gel filtration can be used.<sup>[17,18]</sup> Heydenreich et al. compared ultrafiltration, ultracentrifugation, and dialysis and found the latter method to be the best choice at yielding dispersions with reduced toxicity and improved physical stability.<sup>[20]</sup>

## Water-In-Oil Nanoemulsions

Water-in-oil nanoemulsions are stable liquid isotropic dispersions, which form spontaneously at defined stoichiometric ratios of ingredients. Thus, no shear and no toxic components need to be used, which makes this approach quite attractive for the encapsulation of DNA into nanoemulsions. To the oily phase constituted of olive oil containing a mixture of nonionic surfactants, a buffered solution of DNA was added. Gentle mixing leads to a DNA containing emulsion of droplet mean size of ca. 42 nm as compared to 32 nm in the absence of nucleic acid.<sup>[21]</sup>

## Interfacial Modification of Emulsions with Polymers

Nonionic polymers have been added to the formulation of emulsions in order to increase their colloidal stability in various media, in particular in the presence of serum. Castor oil-<sup>[10]</sup> or squalene-based<sup>[22]</sup> cationic dispersions have had their performances improved by the use of polyoxyethylene surfactants. Nonetheless, similar results were obtained when the polyoxyethylene chains were anchored in the bilayer via modified phospholipids.<sup>[6]</sup>

Chitosan,  $\alpha(1-4)$  2 amino 2-deoxy  $\beta$ -Dglucan, was used to obtain positively charged nanoemulsions. The polysaccharide was solubilized in an acidic aqueous phase to which was added the oily phase composed

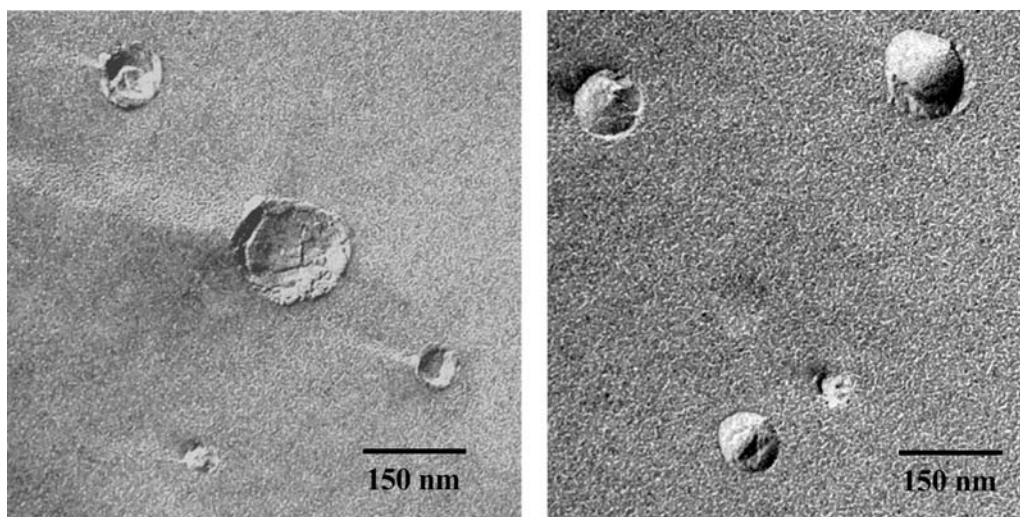


**Fig. 3** Transmission electron microscopy after cryofracture. *Source:* From Ref.<sup>[15]</sup>.

of phospholipids and surfactants. After high-pressure homogenization, positively charged nanoemulsions of mean diameter of 150–200 nm were obtained (dispersities of 0.15–0.2), considered by the authors as monodisperse.<sup>[9]</sup>

Trimaille et al. used reactive polyanhydride copolymers<sup>[15]</sup> or poly *N*-hydroxysuccinimide macromolecules<sup>[23]</sup> as precursor backbones to obtain amphiphilic comb-like polymers, for the interfacial modification of nanoemulsions. The triglyceride nanoparticles were formed by the solvent displacement method using increasing amounts of amphiphilic polymers. The hydrophobic components of the emulsions were dissolved in acetone or ethanol, along with the modified copolymers. On addition of the organic phase to water, the spontaneous formation of the emulsions was observed, with a concomitant deposition of the amphiphilic structure at the interface. The presence of the polymer at the surface of the nanoemulsions was demonstrated by the alteration of the zeta-potentials of the functionalized emulsions compared to the bare ones and by <sup>1</sup>H NMR experiments.<sup>[23]</sup>

#### Nanoemulsion characterizations

Particle size and interfacial charge have to be measured to characterize nanoemulsions on a fundamental standpoint, but also for quality control in production.<sup>[8]</sup> The routine method used for diameter measurement is dynamic light scattering, or quasi-elastic light scattering known as well as photon correlation spectroscopy (PCS). The intensity of scattered light is measured at a 90° angle and the fluctuations of the intensity with time, due to the motion of the particles, lead to the hydrodynamic radius of the particles, i.e., the sum of the real

diameter of the object plus the strongly solvated molecules and ions.

Field flow fractionation (FFF) allows separation according to size, depending on the diffusion coefficient of the colloids. The fractionation is achieved with a field pressure, for instance, perpendicular to the direction of the flow of the mobile phase transporting the colloids. This method is rather well suited for solid lipid particles.<sup>[3]</sup>

Electron microscopy is a very powerful tool for the visualization of the colloids. In order to minimize the alterations of the samples due to experimental conditions, in particular because soft emulsions are fragile objects, cryofracture electron microscopy is an appropriate technique (Fig. 3).<sup>[8,15]</sup>

#### DNA–NANOEMULSION INTERACTIONS

DNA, as a hydrophilic, negatively charged macromolecule, is very water soluble, hence it is almost impossible to dissolve in any organic solvent, unless the organic phase has an elevated hydrophilic/lipophilic balance (HLB) as shown by Teixeira et al. for short oligonucleotides.<sup>[24]</sup> Thus a widely used strategy to tether DNA to emulsion droplets is to take advantage of the electrostatic interactions between positively charged nanoemulsions and polyanionic nucleic acids. Nonetheless, a few strategies have been described, based on the encapsulation of DNA within emulsions.

#### DNA Encapsulated Within Emulsions

To achieve an effective encapsulation, the use of W/O nanoemulsions has been reported fairly recently.<sup>[21]</sup>

The DNA solution was emulsified by spontaneous microemulsification using olive oil, polyoxyethylene 20 sorbitan monooleate (Tween® 80), sorbitan monooleate (Span® 80), and 1,2-Dioleoyl-3-trimethylammonium propane (DOTAP) as a cationic surfactant. The clear resulting nanoemulsion was sterilized by filtration for further in vivo transfection studies. A similar approach described for topical administration of DNA was reported. Ethanol-in-fluorocarbon microemulsions were obtained by gentle stirring of predefined mixtures of 40% w of pentadecafluorooctanoic acid and 60% w of perfluorooctyl bromide as the oily phase, and an 80% v of ethanol solution containing the DNA to be encapsulated, as a hydrophilic phase.<sup>[19]</sup> As these formulations were established to form stable dispersions, all the DNA is therefore within the emulsified aqueous phase.

Encapsulation of DNA within an O/W nanoemulsion requires either to use high HLB oils or to hydrophobize the nucleic acid to increase its solubility in apolar media. In the first approach, not so many oils are capable of dissolving DNA apart from octanol as reported in Ref.<sup>[24]</sup>. But the toxicity of this solvent is such that no in vivo application can be expected from this strategy. Hydrophobization of DNA and its incorporation in an O/W nanoemulsion was reported as an approach toward virus-mimicking nonviral vectors. Cationic derivatives of cholesterol were used to interact with the nucleic acid to form hydrophobic complexes in a chloroform/methanol/water (1:2.1:1)

mixture. The complex was extracted in the organic phase and subsequently added to the oily phase as a solution in chloroform. The emulsion was obtained by a rehydration/emulsification process, with 65% efficacy of DNA incorporation.<sup>[25]</sup>

## DNA Adsorption onto Emulsions

The strategy that consists in adsorbing DNA onto the surface of emulsion droplets is widely investigated and can be related to the approach using cationic liposomes. One advantage foreseen of emulsions vs. liposomes was the greater physical stability of the former over the latter. It has been shown that most liposomal preparations aggregate on interaction with DNA, which can cause embolism if administered systemically.<sup>[6]</sup> Moreover, in vitro, liposomal preparations suffer from a lack of stability in the presence of serum.<sup>[10]</sup>

Emulsion–DNA interactions have to be investigated in terms of droplet size, surface charge or zeta potential, loading capacity and efficiency, stability of the interactions, and release from the carrier. Finally, the overall cell activity of the DNA–emulsion complexes will have to be assessed in vitro or in vivo. As seen in Table 1, various formulations are capable of binding DNA with a fair level of colloidal stability (the particle mean size should not dramatically increase on immobilizing the nucleic acid). In some formulations, the global charge is inverted, which is a prerequisite as in

**Table 1** An overview of various formulations used for DNA binding

Emulsion composition	Emulsion mean diameter (nm)	Emulsion zeta potential (mV)	Emulsion/DNA complex mean diameter (nm)	Emulsion/DNA complex zeta potential (mV)	DNA loading (mg DNA/g oily phase)	References
Wax/CTAB	90–140 depending on CTAB concentration	+60	280–300	–25/ +22 depending on formulation	Calculated as in the 50–75 mg/g range	[17,18]
Solid lipid/EQ1	101	+42	Bi population aggregates	–10/ –16	Calculated as 50 mg/g	[5]
Castor oil/DOPE:DC-CHOL	187–194	NR	384–410	NR	Calculated as 30 mg/g	[10]
Soy bean oil/DOPE:DOTAP	180	+50	175–180	+40	Calculated as 27 mg/g	[6]
MCT/SA	183	+28	202–311	+33	Calculated as 16 mg/g	[26]
MCT/SA:polymer	185	+60	185	–30/ –40	70 mg/g at saturation	[23]
Squalene/DOTAP	180	+54	180	+32	ND	[34]

DOTAP: 1,2 dioleoyl-*sn*-glycero-3-trimethylammonium propane; DOPE: 1,2 dioleoyl-*sn*-glycero-3-phosphoethanolamine; EQ1: *N,N*-di-( $\beta$ -stearoyl-ethyl)-*N,N*-diethylammonium; DC-Chol: 3 $\beta$ -[*N,N,N'*-dimethylaminoethane] carbamoyl cholesterol; MCT: medium chain triglycerides; SA: stearylamine; NR: not reported; ND: not determined.

Ref.<sup>[23]</sup> to maintain the colloidal stability, but it may remain positive as in Ref.<sup>[26]</sup>. Surprisingly, not all positively charged emulsions bind DNA. Olbrich's group investigated four different formulations leading to cationic dispersions and only one could immobilize DNA, as visualized by agarose gel electrophoresis, although all emulsions had similar size and zeta potential. To obtain the most efficient formulation, the nature of the oily core and of the cationic surfactant had to be optimized.<sup>[5]</sup> The interfacial properties of emulsions can be modulated by varying the nature of the surface active compound and the concentration of cationic surfactants<sup>[18,26]</sup> or of functionalized polymers.<sup>[23]</sup> Even negatively charged emulsions can interact with short-chain, single-stranded oligonucleotides, but, in that case, interactions are too weak and a massive release was observed in phosphate buffer saline (PBS) pH 7.1.<sup>[24]</sup> Adsorption isotherms, which relate the amount of adsorbed DNA to the input, can provide further information on DNA–emulsion interactions. The adsorption process can be monitored using agarose gel electrophoresis<sup>[5,6,23]</sup> or by quantifying the amount of free DNA in the continuous phase

by UV adsorption, which, by difference with the input, gives access to the amount of complexed nucleic acid. In Fig. 4, a complete set of data obtained for polymer functionalized emulsions is reported,<sup>[23]</sup> the isotherm was established by UV (Fig. 4A), confirmed by agarose gel electrophoresis (Fig. 4B), and the charge inversion was controlled by zeta potential measurements (Fig. 4C).

The conformation of the plasmid at the surface of the emulsion droplets can be assessed by the experiment named ethidium bromide (EB) displacement (Fig. 5). EB is an intercalant which becomes fluorescent on binding with double-stranded DNA. As a result of complexation with a polycation, DNA is compacted and EB is expelled into the aqueous phase provoking a drop in the fluorescence signal. At maximal compaction, only 10% of the original fluorescence remains. Fig. 5 gives the results for emulsion functionalized with an amphiphilic copolymer bearing spermine pendant groups (polymer T2). With the free polymer, a drastic loss in fluorescence was observed revealing a high compaction of the DNA; for emulsions functionalized with the same polymer, the loss in signal was far

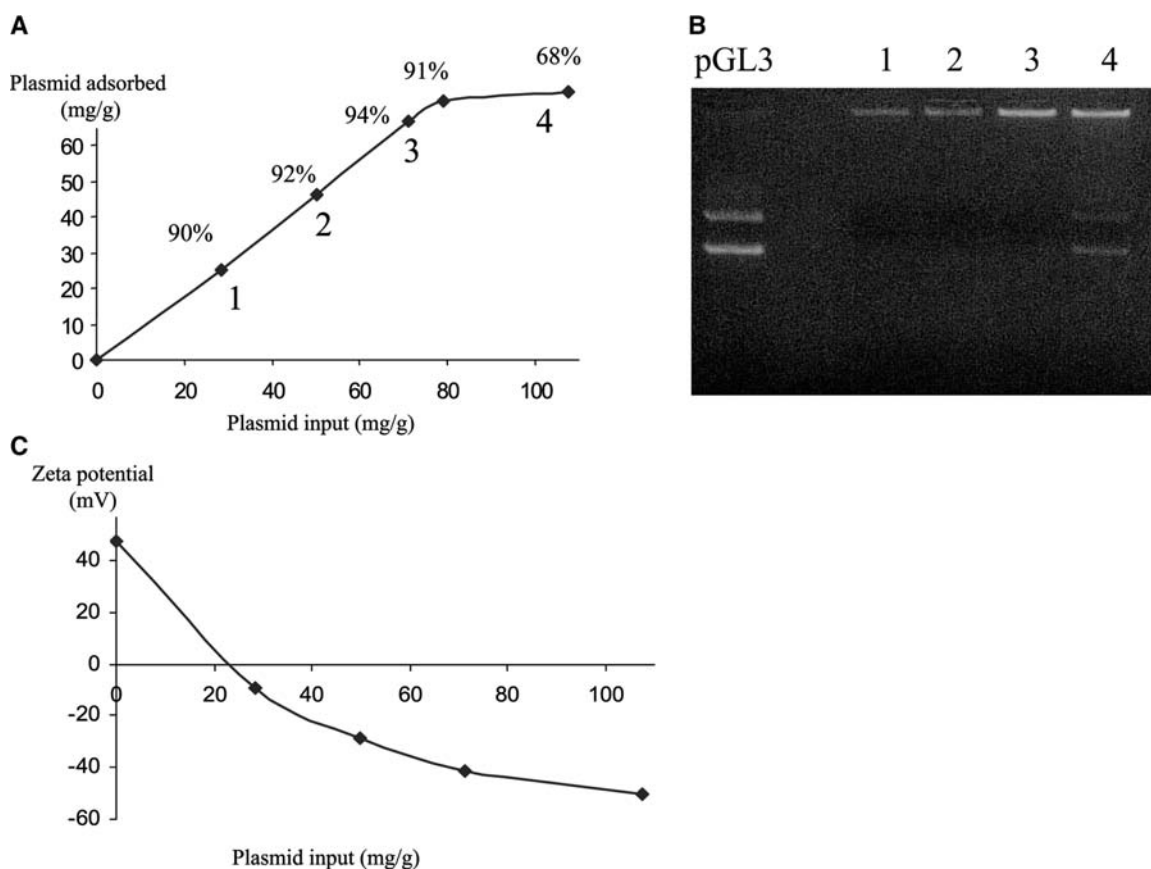


**Fig. 4** Complexation isotherm and associated zeta potential measurement for the complexation of DNA onto cationic emulsions. A) isotherm obtained by UV and the subtraction method; B) agarose gel electrophoresis and EB staining; C) zeta potential measurements. *Source:* From Ref.<sup>[36]</sup>.

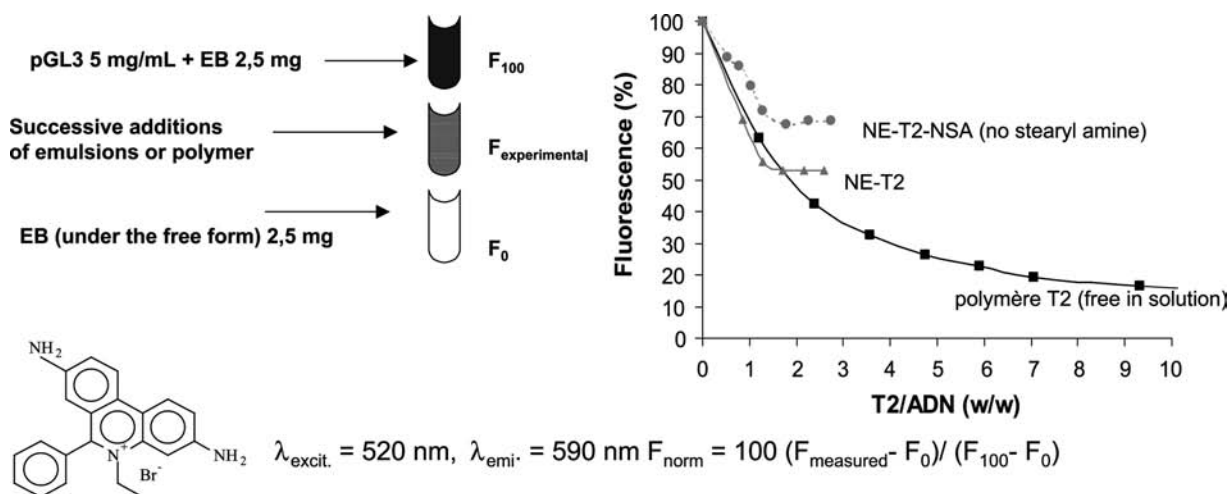


Fig. 5 Ethidium bromide displacement method. Source: From Ref.<sup>[23]</sup>.

less, although, at the plateau, all the DNA had been complexed as checked by agarose gel electrophoresis. Thus the DNA adsorbed onto emulsions was rather expanded toward the aqueous phase. Another way to study the accessibility of immobilized DNA is to measure the amount of intercalating EB after the complexation of the DNA had occurred on the colloidal carriers. The authors showed that on increasing the emulsion content, the DNA was less and less accessible, to a plateau value that corresponded to the plateau determined by agarose gel.<sup>[5]</sup>

The stability of the complexation of DNA onto cationic emulsions was investigated by Teixeira et al. for the particular case of synthetic single-stranded oligonucleotide (ODN) in an antisense strategy. The authors used fluorescence energy transfer (FRET), surface tension measurements, cryomicroscopy to elucidate the fast oligonucleotide release from the carrier. It appeared that the ODN was released under the form of a complex with the cationic lipids, which ensured a protection against DNAs,<sup>[24,27]</sup> even in solution.

## APPLICATIONS OF DNA-NANOEMULSIONS COMPLEXES

DNA carriers have been designed for gene transfer applications aiming at delivering an exogenous gene either in vitro or in vivo. For biotechnologies, in vitro cell transfection is a means to produce recombinant proteins and highly performing transfection agents are required. Clinical applications of gene transfer are gene therapy and DNA vaccine. For gene therapy, expression of the foreign gene should take place in the right organ, for a prolonged period of time, in order to

substitute a defective one. In DNA vaccine, the expression of the gene will allow the production of the antigen, for which an immune response is looked for. Hence the endogenously expressed antigenic protein will be able to elicit both protective and cytotoxic immunity, which is a key advantage over conventional protein or attenuated virus-based vaccines.<sup>[18]</sup> Related to gene transfer is the delivery of oligonucleotides in an antisense strategy for the correction of genetic diseases, suppression of oncogenes, and eradication of viral infections.<sup>[28]</sup>

## In Vitro Cell Transfection

The production of papers dealing with in vitro cell transfection is very intense but because of lack of standards and normalized references, it is not easy to compare interexperiment performances. Apparently, the stability of the emulsion is an important factor in gene transfer and this can be achieved also by choosing the appropriate oil. With squalene, stable dispersions were obtained whose transfection properties were 30 times better than liposomes.<sup>[12]</sup> Solid lipid nanoparticles (120 nm in diameter) coated with plasmid DNA (220 nm after coating) were more powerful at transfecting cell lines than naked DNA, although they ranked average in comparison with some commercially available transfer agents. No toxicity was observed with these emulsions which was far to be the case with other carriers.<sup>[5]</sup> Cationic emulsions stabilized with nonionic surfactant are efficient transfer agents.<sup>[10,29]</sup> According to the authors, it seems that Tween<sup>®</sup> 80 seems the most efficient nonionic compound both for transfection efficiencies, which was confirmed later,<sup>[22]</sup> and for stability toward serum.<sup>[6]</sup>



## In Vivo Transfections

In vivo transfection in mice is the first step in preclinical evaluations. Emulsions elaborated according to Ref.<sup>[6]</sup> were tested as mucosal gene carriers and proved to be better performing than liposomes, thanks probably to a better stability of emulsions in contact with the nasal cavity mucosa.<sup>[30]</sup>

## Topical Transfection

Noninvasive delivery of active substances through the skin is quite attractive, as no needle is needed, the administration protocol is simple and safe. However, in order to efficiently deliver genes via the skin, it is necessary to circumvent its inherent barrier function. The presence of hair follicles and associated structures may allow local delivery to skin cells. With W/O nanoemulsions, the deposition of plasmid DNA was found to be primarily in follicular keratinocytes. Transgene expression was optimal at 24 hr following a single-dose application. No toxicity nor irritation was observed on the treated skins.<sup>[21]</sup>

## Emulsions as Adjuvants in DNA Immunization

It has been shown that naked plasmid DNA could induce strong T-helper type 1 (Th1) immune responses as proved by the production of interleukin-2 (IL-2) and interferon- $\gamma$  (IFN- $\gamma$ )<sup>[31,32]</sup> leading to a cytotoxic response. Protein-based vaccine tends to induce a Th2-type response with production of IL-4 and IL-10, associated to antibody production. The main limitation of the naked DNA approach is the large doses of plasmid required to obtain potent response in humans,<sup>[33]</sup> hence the need for powerful delivery systems.

Cationic emulsions based on squalene, Tween<sup>®</sup> 80, and DOTAP, prepared by microfluidization, could efficiently complex DNA on surface, up to 95%. After immunization, both mice and rabbits showed strong antibody titers in serum, 14- to 18 folds higher than with naked DNA, with a fair Th1 polarization of the response in mice. A similar orientation of the response was observed with particles engineered from warm O/W microemulsions using wax and CTAB.<sup>[18]</sup>

Skin is the body's front line for immunosurveillance as the viable epidermis contains Langerhans and dendritic cells which are effective antigen presenting cells. Moreover, these cells cover over 25% of the total skin area, making topical immunization very attractive.<sup>[35]</sup> Using either wax particles from microemulsions<sup>[17]</sup> or ethanol-in-fluorocarbon nanoemulsions,<sup>[19]</sup> the authors observed a 45-fold

enhancement of the total antibody titer as compared to naked DNA, with a strong Th1-type response. This result is also interesting in the sense that objects in the 100–200-nm size range can efficiently convey adsorbed DNA through the skin to the antigen presenting cells (although more work seems to be needed as mice were shaved prior to application. Shaving can generate microalterations of the skin integrity). When compared with intramuscular injection of DNA, which is the established route for naked pDNA, the overall response remains greater for the i.m. route, but the Th1 character was more important for the topical administration.

## CONCLUSION

Nanoengineered emulsion-based DNA vectors have been obtained by interaction of functionalized emulsions and DNA. Some manufacturing processes are already available for high-scale production using cheap and generally regarded as safe (GRAS) materials. Other elaboration methods are presently under investigation in order to improve the performances of the carriers, by increasing their colloidal stabilities and modulating their physico-chemical properties. Surface functionalization is an essential means for improving emulsion-based vectors and investigators use surfactants (cationic, nonionic) or polymers, for which the choice seems only limited by the researchers' imagination. The interactions of DNA with emulsions need more thorough investigations; fundamental knowledge on this aspect would be quite profitable for further applications.

Nanoemulsion–DNA complexes can serve as synthetic vectors for in vitro and in vivo purposes. In vitro cell transfection with DNA either coated on or adsorbed within emulsions has been well established, although performances are still modest. In vivo transfections were observed but gene expression was transient. More impressive were the results obtained by immunization. A strong immune response, including antibodies and cytotoxicity, was obtained in mice and rabbits. Moreover, nanoemulsion–DNA complexes could be either injected or applied onto the skin for topical administration. These appear to be sound results for the development of a fully synthetic DNA vaccine.

## REFERENCES

1. Christiano, R. Viral and non-viral vectors for cancer gene therapy. *Anticancer Res.* **1998**, *18*, 3241–3246.

2. Singh, M.; Briones, M.; Ott, G.; O'Hagan, D. Cationic microparticles: A potent delivery system for DNA vaccines. *Proc. Natl. Acad. Sci. U. S. A.* **2000**, *97*, 811–816.
3. Müller, R.H.; Mäder, K.; Gohla, S. Solid lipid nanoparticles (SLN) for controlled drug delivery—A review of the state of the art. *Eur. J. Pharm. Biopharm.* **2000**, *50*, 161–177.
4. Panyam, J.; Labhasetwar, V. Biodegradable nanoparticles for drug and gene delivery to cells and tissue. *Adv. Drug Deliv. Rev.* **2003**, *55*, 329–347.
5. Olbrich, C.; Bakowsky, U.; Lehr, C.M.; Müller, R.H.; Kneuer, C. Cationic solid-lipid nanoparticles can efficiently bind and transfect plasmid DNA. *J. Control. Release* **2001**, *77*, 345–355.
6. Yi, S.W.; Yune, T.Y.; Kim, T.W.; Chung, H.; Choi, Y.W.; Kwon, I.C.; Lee, E.B.; Jeong, S.Y. A cationic emulsion/DNA complex as a physically stable and serum-resistant gene delivery system. *Pharm. Res.* **2000**, *17* (3), 314–320.
7. Jumaa, M.; Müller, B.W. The effect of oil components and homogenization conditions on the physicochemical properties and stability of parenteral fat emulsions. *Int. J. Pharm.* **1998**, *163*, 81–89.
8. Jumaa, M.; Müller, B.W. Physicochemical properties of chitosan-lipid emulsions and their stability during the autoclaving process. *Int. J. Pharm.* **1999**, *183*, 175–184.
9. Jumaa, M.; Müller, B.W. A new lipid emulsion formulation with high antimicrobial efficacy using chitosan. *Eur. J. Pharm. Biopharm.* **2002**, *53*, 115–123.
10. Liu, F.; Yang, J.; Huang, L.; Liu, D. Effect of non-ionic surfactants on the formation of DNA/emulsion complexes and emulsion-mediated gene transfer. *Pharm. Res.* **1996**, *13* (11), 1642–1646.
11. Elbaz, E.; Zeevi, A.; Klang, S.; Benita, S. Positively charged submicron emulsions—A new type of colloidal carrier. *Int. J. Pharm.* **1993**, *96*, R1–R6.
12. Chung, H.; Kim, T.W.; Kwon, M.; Kwon, I.C.; Jeong, S.Y. Oil components modulate physical characteristics and function of the natural oil emulsions as drug or gene delivery system. *J. Control. Release* **2001**, *71*, 339–350.
13. Trotta, M.; Debernardi, F.; Caputo, O. Preparation of solid lipid nanoparticles by a solvent emulsification–diffusion technique. *Int. J. Pharm.* **2003**, *257*, 153–160.
14. Fessi, H.; Puisieux, F.; Devissaguet, J.Ph.; Ammoury, N.; Benita, S. Nanocapsule formation by interfacial polymer deposition following solvent displacement. *Int. J. Pharm.* **1989**, *55*, R1–R4.
15. Trimaille, T.; Chaix, C.; Delair, T.; Pichot, C.; Dubernet, C.; Couvreur, P. Interfacial deposition of functionalized copolymers onto nanoemulsions produced by the solvent displacement method. *Colloid Polym. Sci.* **2001**, *279*, 784–792.
16. Garcia-Fuentes, M.; Torres, D.; Alonso, M.J. Design of lipid nanoparticles for the oral delivery of hydrophilic macromolecules. *Colloids Surf., B Biointerfaces* **2002**, *27*, 159–168.
17. Cui, Z.; Mumper, J.R. Topical immunization using nanoengineered genetic vaccines. *J. Control. Release* **2002**, *81*, 173–174.
18. Cui, Z.; Mumper, J.R. Genetic immunization using nanoparticles engineered from microemulsion precursors. *Pharm. Res.* **2002**, *19* (7), 939–946.
19. Cui, Z.; Fountain, W.; Clark, M.; Jay, M.; Mumper, J.R. Novel ethanol-in-fluorocarbon microemulsions for topical genetic immunization. *Pharm. Res.* **2003**, *20* (1), 16–23.
20. Heydenreich, A.V.; Westmeier, R.; Pedersen, N.; Poulsen, H.S.; Kristensen, H.G. Preparation and purification of cationic solid lipid nanospheres—Effects on particle size, physical stability and cell toxicity. *Int. J. Pharm.* **2003**, *254*, 83–87.
21. Wu, H.; Ramachandran, C.; Bielinska, A.U.; Kingzett, K.; Sun, R.; Weiner, N.D.; Roessler, B.J. Topical transfection using plasmid DNA in a water-in-oil nanoemulsion. *Int. J. Pharm.* **2001**, *221*, 23–34.
22. Kim, T.W.; Kim, Y.J.; Chung, H.; Kwon, I.C.; Sung, H.C.; Jeong, S.Y. The role of non-ionic surfactants on cationic lipid mediated gene transfer. *J. Control. Release* **2002**, *82*, 455–465.
23. Trimaille, T.; Chaix, C.; Pichot, C.; Delair, T. Polymer functionalized submicrometric emulsions as potential DNA carriers. *J. Colloid Interface Sci.* **2003**, *258*, 135–145.
24. Teixeira, H.; Dubernet, C.; Rosilio, V.; Laigle, A.; Deverre, J.R.; Scherman, D.; Benita, S.; Couvreur, P. Factors influencing the oligonucleotides release from O/W submicron cationic emulsions. *J. Control. Release* **2001**, *70*, 243–255.
25. Hara, T.; Tan, Y.; Huang, L. In vitro gene delivery to the liver using reconstituted chylomicron remnants as a novel nonviral vector. *Proc. Natl. Acad. Sci. U. S. A.* **1997**, *94*, 14547–14552.
26. Teixeira, H.; Dubernet, C.; Puisieux, F.; Benita, S.; Couvreur, P. Submicron cationic emulsions as a new delivery system for oligonucleotides. *Pharm. Res.* **1999**, *16* (1), 30–36.
27. Teixeira, H.; Rosilio, V.; Laigle, A.; Alepault, J.; Erk, I.; Scherman, D.; Benita, S.; Couvreur, P.; Dubernet, C. Characterization of oligonucleotide/lipid interactions in submicron cationic emulsions: Influence of the cationic lipid structure and the presence of PEG-lipids. *Biophys. Chemist.* **2001**, *92*, 169–181.
28. Rojanasakul, Y. Antisense oligonucleotide therapeutics: Drug delivery and targeting. *Adv. Drug Deliv. Rev.* **1996**, *18*, 952–960.
29. Liu, F.; Yang, J.; Huang, L.; Liu, D. Effect of non-ionic surfactants on the formation of DNA/emulsion complexes and emulsion-mediated gene transfer. *Pharm. Res.* **1996**, *13* (12), 1856–1860.
30. Kim, T.W.; Chung, H.; Kwon, I.C.; Sung, H.C.; Jeong, S.Y. In vivo gene transfer to the mouse nasal cavity

- mucosa using a stable cationic lipid emulsion. *Mol. Cells* **2000**, *10* (2), 142–147.
31. Barry, M.A.; Johnston, A. Biologic features of genetic immunization. *Vaccine* **1997**, *15*, 788–791.
  32. Robinson, L.H.; Torres, C.T. DNA vaccines. *Semin. Immunol.* **1997**, *9*, 271–283.
  33. Mac Gregor, R.R.; Boyer, J.; Gluckman, S.J.; Bagarazzi, M.L.; Chattergoon, M.A.; Baine, Y.; Higgins, T.J.; Ciccar-elli, R.B.; Coney, L.R.; Ginsberg, R.S.; Weine, D.B. First human trial of a DNA-based vaccine for treatment of human immunodeficiency virus type 1 infection: Safety and host responses. *J. Infect. Dis.* **1998**, *178*, 92–100.
  34. Ott, G.; Singh, M.; Kazzaz, J.; Briones, M.; Soenawan, E.; Ugozzoli, M.; O'Hagan, D.T. A cationic sub-micron emulsion (MF59/DOTAP) is an effective delivery system for DNA vaccines. *J. Control. Release* **2002**, *79*, 1–5.
  35. Banchereau, J.; Steinman, R.M. Dendritic cells and the control of immunity. *Nature* **1998**, *392*, 245–252.
  36. Trimaille, T. Elaboration de Colloïdes Fonctionnalisés par des Polymères: Nouveaux Vecteurs Potentiels d'acides Nucléiques. In *Ph.D. Thesis*; Université Claude Bernard: Lyon I, 2001.

# Dynamic AFM on Heterogeneous Surfaces

Ijeoma M. Nnebe  
James W. Schneider

*Department of Chemical Engineering, Carnegie Mellon University,  
Pittsburgh, Pennsylvania, U.S.A.*

## INTRODUCTION

Since the development of the atomic force microscope (AFM) in 1986,<sup>[1]</sup> it has become a widely used and versatile tool in both the nanoscale imaging of surfaces<sup>[2–7]</sup> and in the measurement of many intermolecular and surface forces.<sup>[8–15]</sup> In AFM, forces between a probe and the relevant surface are measured through changes in the deflection of a flexible cantilever attached to the probe. For image collection, it is assumed that changes in sample topography affect the probe–sample interaction profile and therefore affect the response of the cantilever. The feedback control required to maintain a constant deflection of the cantilever is then used to reconstruct a three-dimensional image of the surface. In force measurements, the feedback control is disabled, and the deflections of the cantilever are measured as a function of normal probe–sample separation. Often, the interpretation of AFM images is assisted through force measurement results.

While there are currently numerous modes of AFM operation, they can be separated into two major categories—the dc or static method and the dynamic methods. In the dc mode of operation (also known as contact-mode AFM), the static deflection of the cantilever is the measured and controlled signal. The cantilever can be treated as a simple Hookian spring with its deflection proportional to the force acting on the probe. This was the first established AFM mode and is still the most commonly used one for force measurements. Dynamic AFM methods are more recent expansions of the technique and involve forced oscillation of the cantilever and the measurement and control of the dynamic response through quantities such as the cantilever's amplitude of oscillation, its resonance frequency, and its phase lag from the driving signal. Commonly used dynamic methods include noncontact mode (NC) AFM,<sup>[16]</sup> tapping mode (TM) or intermittent-contact (IC) AFM,<sup>[17]</sup> frequency modulation (FM) AFM,<sup>[18]</sup> and force modulation AFM.<sup>[19]</sup> With the exception of force modulation that uses small-amplitude oscillation of a tip or sample<sup>[20]</sup> in contact to measure local variations in material viscoelasticity, the other dynamic methods are less-invasive

methods of force measurement and imaging. In these methods, the cantilever is oscillated at large amplitudes and at frequencies close to or at its resonance frequency ( $\sim$  kHz). The NC and FM modes are operated out of contact with the sample (in the attractive regime). Frequency modulation measures the resonance frequency shift at constant amplitude operation, while NC measures changes in the oscillation amplitude at a fixed driving frequency. In both techniques, probe–sample interactions can be obtained from the frequency shift or from the change in the amplitude of oscillation. Tapping mode operation is similar to NC; however, the cantilever is forced to oscillate at larger amplitudes resulting in intermittent contact with the sample. As a result, the probe–sample interaction potential changes nonlinearly during each oscillation cycle. Because the dynamic quantities measured are averages over the whole oscillation cycle, it is non-trivial to directly relate the observed changes to the probe–sample interaction in TM. This makes the interpretation of both TM images and force measurement results more difficult. A recent review by García and Pérez<sup>[21]</sup> contains detailed information about the interpretation and application of these dynamic methods in air and vacuum.

Regardless of the complexities, TM is a valuable tool in the gentle and non-destructive imaging of soft and easily deformable surfaces such as biologically relevant surfaces<sup>[6,22,23]</sup> and soft polymer interfaces.<sup>[24,25]</sup> Contact loads in TM can be comparable to those in the conventional dc mode; however, it is the reduction of lateral shear of the sample, the brief probe–sample contact time, and the small contact area that enable it to be a less-destructive technique.<sup>[26,27]</sup> Some researchers have also hypothesized that soft biological materials undergo hardening under high frequency, making them less susceptible to deformation and damage upon impact.<sup>[28]</sup> Although TM is now used fairly extensively as an imaging tool, its force measurement capabilities have not been thoroughly exploited especially in nonambient environments appropriate for many surfaces of interest. Potentially, the gentle properties of the TM image process are shared in TM force measurements. Additionally, a

dynamic mode of measurement would offer increased sensitivity with the retention of lateral resolution and early detection of the sample before significant indentation takes place. It is these capabilities of TM AFM that we believe will make it a unique tool in the force measurement of heterogeneous biomaterial surfaces. We thus present a review of the common method of modeling TM force measurements in air and extend this method toward TM force measurement in liquid. We will report on the few studies aimed at understanding and improving TM in liquid and will focus on the importance of hydrodynamics in the system. Additionally, we will discuss the application of TM in liquid to the measurement of interactions occurring on biomaterial surfaces.

### TAPPING MODE ATOMIC FORCE MICROSCOPE: OBTAINING THE PROBE-SAMPLE INTERACTION

Unlike its dc counterpart, there is no direct method of obtaining the probe-sample interaction from TM force curves. Instead, an equation of motion that includes all the factors that affect the dynamics of the oscillator must be solved to obtain the full oscillatory behavior of the cantilever as a function of the equilibrium probe-sample separation,  $D$ . In air, the dynamics of the tapping cantilever can be suitably modeled using the forced damped harmonic oscillator (FDHO) model.<sup>[29–32]</sup> The cantilever is thus treated as a Hookian spring with some overall effective mass. Upon displacement from its equilibrium position, its inertia causes acceleration in the direction of the displacement, while its restoring force opposes the acceleration to return it to its equilibrium position. In the absence of external forces, the spring will oscillate for an infinitely long period of time with an amplitude,  $A$ , determined from its mass,  $m$ , and spring constant,  $k_c$  (harmonic oscillation). In real environments, a drag force caused by the viscous medium dampens the oscillations. Therefore to sustain oscillation, an external continuous energy supply is provided to the spring, and in most commercial AFMs, this is achieved with an external sinusoidal drive. All these contributions appear in the classical FDHO model. In TM experiments, however, probe-sample interactions exist that perturb the harmonic oscillation and, henceforth, we will refer to this as the *perturbed oscillator* [Eq. (1)]. In air, this probe-sample interaction is typically modeled as a long-range attractive van der Waals force and short-range contact mechanics that may include surface adhesion, and the contact mechanics usually dominate the cantilever response. Capillary-based attractive forces can also arise, but instabilities in cantilever motion caused by

this force are usually overcome through the use of very stiff cantilevers ( $k_c \sim 40$  N/m). The governing equation of motion that describes the cantilever motion is:

$$m \frac{d^2x}{dt^2} + \gamma \frac{dx}{dt} + k_c(x - D) = F_{\text{drive}} + F_{\text{P-S}}(x) \quad (1)$$

where  $\gamma$  is the viscous damping coefficient,  $F_{\text{drive}}$  is the external driving force, and  $F_{\text{P-S}}$  is the probe-sample interaction. The relevant positions of the oscillator are its instantaneous distance from the sample,  $x$ , and its equilibrium separation,  $D$  (Fig. 1). The FDHO model was derived for oscillations of a point mass; however, the distributed mass of the cantilever can still be lumped and approximated as a single vibrating mass because the vibration amplitude at the fundamental frequency is consistently at least an order of magnitude larger than the vibration amplitudes of higher harmonics.<sup>[33,34]</sup>

The mass of the cantilever is not a directly accessible parameter, so it is more convenient to write Eq. (1) in terms of the parameters that are usually measured:

$$\frac{d^2x}{dt^2} + \frac{\omega_o}{Q} \frac{dx}{dt} + \omega_o^2(x - D) = \omega_o^2 a_d \sin(\omega t) + \frac{\omega_o^2 F_{\text{P-S}}(x)}{k_c} \quad (2)$$

In the above equation, the relationships 1)  $\omega_o = (k_c/m)^{1/2}$  and 2)  $\gamma = m\omega_o/Q$ <sup>[35]</sup> were used to eliminate  $m$  and to replace  $\gamma$  with the term  $Q$  (quality factor) that is a descriptor of the viscous damping in the system and is obtained from the shape of the resonance curve.  $\omega_o$  is the resonance frequency of the cantilever for *free* oscillation (separations when the probe-sample interaction is negligible),  $\omega$  is the drive frequency, and  $a_d$

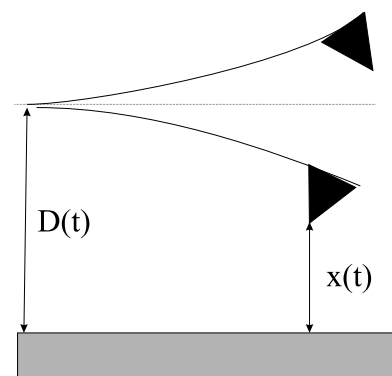


**Fig. 1** Schematic of the oscillating cantilever in TM AFM.  $x(t)$  is the instantaneous tip separation and  $D(t)$  is the equilibrium cantilever separation from the sample (grey box).

is the drive amplitude. In TM operation in air,  $Q$  is commonly on the order of 200–400 and  $f_o = \omega_o/2\pi \sim 400$  kHz.  $k_c$  can be calibrated experimentally with a variety of methods.<sup>[36–38]</sup> In most instances, the cantilever maintains approximately sinusoidal oscillation even when probe–sample interactions are significant. This oscillation is of the form  $A \sin(\omega t + \phi)$ , where  $\phi$  is the phase lag between the drive and the cantilever response.

The effect of probe–sample interactions on  $A(D)$  can be partially understood from frequency modulation studies.<sup>[39,40]</sup> In these studies, it has been shown that probe–sample interactions alter the overall spring constant of the system,  $k_o$ , thereby shifting the oscillator's resonance frequency. The frequency shift,  $\Delta\omega_r$ , arising from the interaction can be determined from the force gradient ( $\partial F_{p-s}/\partial x$ ) as long as this gradient is constant over the whole range of tip motion.<sup>[41]</sup>

$$\Delta\omega_r(D) = \frac{\omega_o}{2k_c} \frac{-\partial F_{p-s}}{\partial x} \quad (3)$$

Although this assumption is not strictly valid for TM operation, the general relationship derived is useful in understanding the cantilever response in TM force measurements. To illustrate this more clearly, Fig. 2 plots the total energy profile of the unperturbed harmonic oscillator and the perturbed oscillator. An attractive force (positive force gradient) lowers the potential energy of the oscillator ( $1/2 k_o x^2$ ) and corresponds to a decrease in  $k_o$ , while a repulsive force (negative force gradient) has the opposite effect. Because the oscillator's resonance frequency is proportional to the spring constant:  $\omega_p = (k_o/m)^{1/2}$ ,

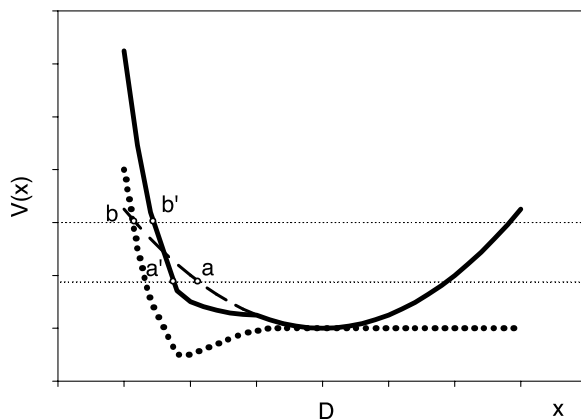


**Fig. 2** Theoretical energy profile of the oscillator. Dotted line is the probe–sample interaction energy profile; dashed line is the unperturbed oscillator and solid line is the perturbed oscillator.  $A$ , at a specific energy, is defined as  $(D - x)$ , where  $x$  can be  $a$ ,  $a'$ ,  $b$ , or  $b'$ .

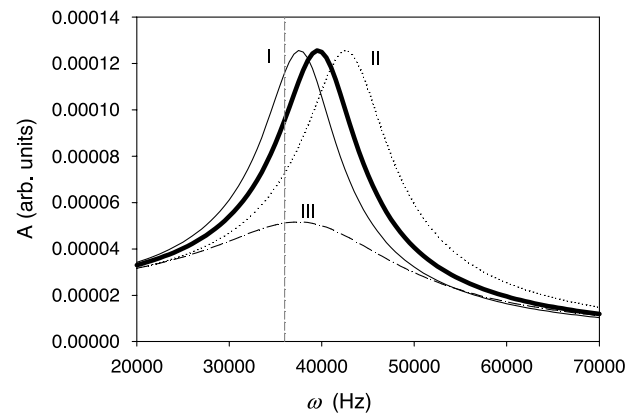


**Fig. 3** Theoretical resonance curve [ $A(\omega)$ ] of an unperturbed oscillator (thick solid line) and of the perturbed oscillator affected by an attractive probe–sample interaction (I), a repulsive probe–sample interaction (II), and additional damping (III). The driving frequency is the dashed line.

where  $\omega_p$  is now the resonance frequency of the perturbed system, decreasing  $k_o$  will result in a decrease in  $\omega_p$  or  $\Delta\omega_r = (\omega_p - \omega_o) < 0$ , while increasing  $k_o$  yields  $\Delta\omega_r > 0$ . In TM force measurements, where the drive frequency is fixed, frequency shifts cause an increase in  $A$  with attractive interactions or a decrease with repulsive ones (Fig. 3). Bielefeldt and Giessibl<sup>[42]</sup> have shown that the above analysis can be used to generate the linear decay in amplitude with separation that is observed experimentally on non-deformable samples such as silicon. On these samples, the contact stiffness is large and is the dominant interaction. Because the cantilever cannot penetrate the sample and is approximately symmetric in its oscillation, the amplitude decreases linearly with a linear decrease in the probe–sample separation.

In many TM experiments in air, the  $A(D)$  curves contain stepwise discontinuities that cannot be explained using the analysis presented earlier.<sup>[43,44]</sup> Using a variational principle approach to analytically solve Eq. (2) (assuming a van der Waals interaction), Nony, Boisgard, and Aime<sup>[45]</sup> and Aime et al.<sup>[46]</sup> have directly related these discontinuities to two possible stable oscillation states for the cantilever caused by the strong attractive potential. This bistability is observed as a jump in the  $A(D)$  curve that occurs because of the transition from one oscillation state to the other<sup>[32]</sup> (Fig. 4). The concept of bistability is perhaps more easily understood by examining the dependence of amplitude on frequency [ $A(\omega)$ ]. For perfectly harmonic systems, only one possible amplitude exists for each oscillation frequency (Fig. 3); however, with strong attractive potentials, the  $A(\omega)$  curve becomes distorted leading to two possible amplitudes at certain frequencies<sup>[45]</sup> (Fig. 5). Analytical solutions to Eq. (2) prove useful in elucidating the origins of specific



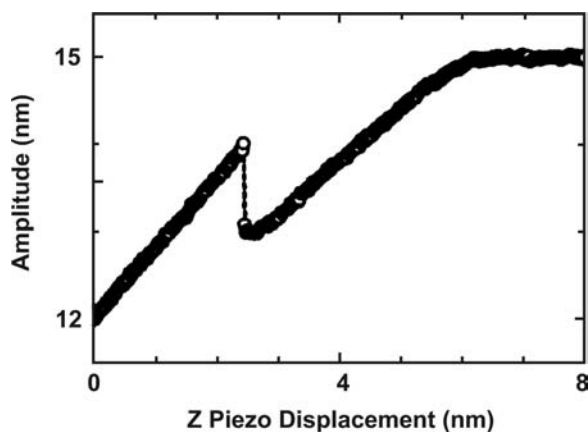


**Fig. 4** Bistable oscillation (manifested as a jump in the amplitude–displacement curve) observed experimentally in measurements involving a silicon tip tapping on a semiconductor surface. *Source:* From Ref.<sup>[48]</sup>.

features in the amplitude vs. distance,  $A(D)$ , and phase vs. distance,  $\phi(D)$ , force curves.<sup>[42,47,48]</sup> However, this method of solution is only valid if the probe–sample interaction is linear and if one assumes that the cantilever motion remains sinusoidal at all probe–sample separations. In most cases, the interaction is nonlinear in TM and deviations from sinusoidal motion can arise because of the stiffness of the impact. Therefore quantitative modeling is not possible using analytical approaches, and a numerical solution to Eq. (2) must be undertaken.

In the numerical solution, the probe–sample interactions are obtained by solving the inverse problem. This requires a fairly good understanding of the relevant interactions on the sample being studied. Fortunately, many intermolecular/intersurface interactions have been studied using dc AFM, and good agreement has

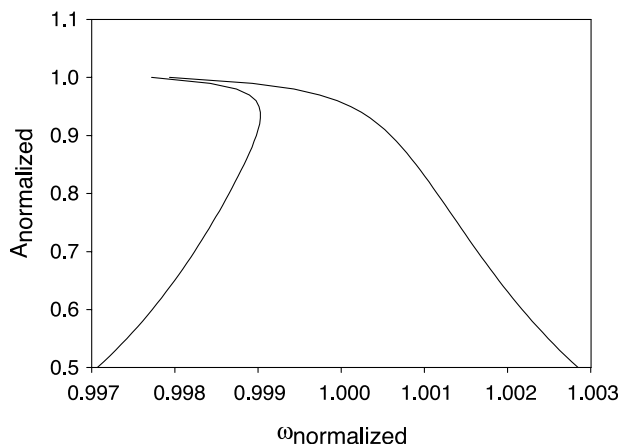


**Fig. 5** Distorted theoretical resonance curve when strong attractive interactions are incorporated into the probe–sample interaction. *Source:* From Ref.<sup>[49]</sup>.

been obtained between experiment and theory. Therefore the general force laws for many interactions are well described theoretically.<sup>[49]</sup> Anczykowski et al.<sup>[30]</sup> simulated tapping on silicon in air using the MYD/BHW (Muller-Yushenko-Derjaguin/Burgess-Hughnes White) model that combines a long-range attractive interaction with a short-range elastic repulsion at contact separations and observed fair agreement between the experiment and simulation results. They did note that quantitative agreement was highly sensitive to the exact form of surface potential applied and discouraged the use of linearized models to describe the surface potential. Bar et al.<sup>[50]</sup> reproduced experimental force curves on elastomers using contact forces that accounted for surface adhesion. They showed that bistability was not present during tapping on compliant samples and that sinusoidal oscillation was maintained even at small probe–sample separations, thereby validating the harmonic approximation. The work of Dubourg and Aime,<sup>[51]</sup> however, has shown that bistability can occur on elastomers when both elastic and glassy domains are present, but reproduction of experimental data was achievable with the correct form of surface adhesion in the interaction. Through analytical and numerical efforts by these and other groups, there is now a good understanding of how probe–sample interactions affect the dynamics of the cantilever in air and how to extract these interactions from  $A(D)$  curves. In principle, much of the analysis that is relevant to TM in air should be applicable to TM force measurement in liquid; however, we will discuss in the next section the added complexities associated with this form of measurement.

Although not yet discussed, another useful quantity that can be measured is the phase lag  $\phi$ . This is often used to determine the amount of energy dissipated by the cantilever during tapping<sup>[52]</sup> and can be a good measure of local material viscoelasticity or anisotropy.<sup>[27,53,54]</sup> Energy dissipation causes an increase in  $\phi$ ; however,  $\phi$  can also be affected by conservative tip–sample interactions<sup>[55]</sup> (Fig. 6). The phase lag is particularly useful in TM imaging where  $A$  is maintained at a constant value. As such, changes in  $\phi$  can be attributed solely to changes in the material-induced dissipation in the system.<sup>[56]</sup> If  $A$  is not constant, then the energy dissipated cannot be obtained from the phase information alone.<sup>[27]</sup> An additional advantage in collecting the phase signal is to identify whether the cantilever is operating in a primarily attractive (non-contact) or repulsive (intermittent contact) regime when the cantilever is driven at its resonance frequency.<sup>[27]</sup> Unfortunately, in TM in liquid, the phase signal is difficult to interpret as it is affected by the presence of other resonances in the system. The origin of these spurious resonances will be discussed in the next section.

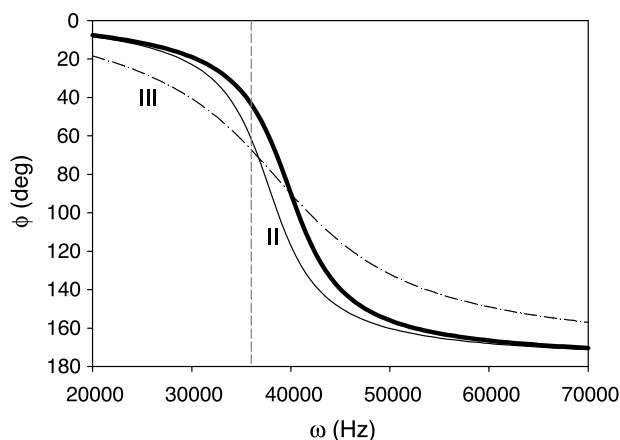


**Fig. 6** Theoretical phase lag,  $\phi$ , of an unperturbed oscillator (thick solid line), the oscillator perturbed by an attractive probe–sample interaction (||), and the oscillator affected by additional damping (|||).

### EXTENSION OF THE FORCED DAMPED HARMONIC OSCILLATOR MODEL TO TAPPING IN LIQUID

Tapping mode in liquid<sup>[28,57]</sup> is not an extensively studied technique, although it is practical for the imaging of biofunctionalized surfaces.<sup>[22,58,59]</sup> In liquid, images of molecules in their physiological state can be obtained and the intermolecular interactions that occur in these conditions can be measured. Here cantilevers with spring constants that are comparable to those used in dc force measurements ( $k_c \sim 0.1\text{--}1\text{ N/m}$ ) are used, as stiff cantilevers are no longer needed because of the absence of capillary forces.

There are several intrinsic complications that arise from TM operation in liquid. The first is dependent on the mode of cantilever excitation. The most common method of forcing cantilever oscillation is through acoustic excitation. Here the cantilever oscillation is promoted through the vibration of the fluid cell at high frequencies. This gives rise to spurious resonances from the coupled oscillations of various parts of the cell that cloud the identification of the fundamental resonance of the cantilever<sup>[60]</sup> (Fig. 7). As mentioned previously, these spurious resonances complicate the measured phase signal in TM in liquid. It is no longer sigmoidal but can have multiple maxima and minima because of neighboring resonances (Fig. 7). If the form of cantilever excitation is changed to one that is more direct, such as directly oscillating a magnetized cantilever using an oscillating magnetic field (MAC-mode AFM),<sup>[61]</sup> the presence of these spurious resonances can be attenuated.

Because most commercial AFMs utilize acoustic excitation to drive the cantilever, we will only discuss operation with this mode of excitation. The thermal

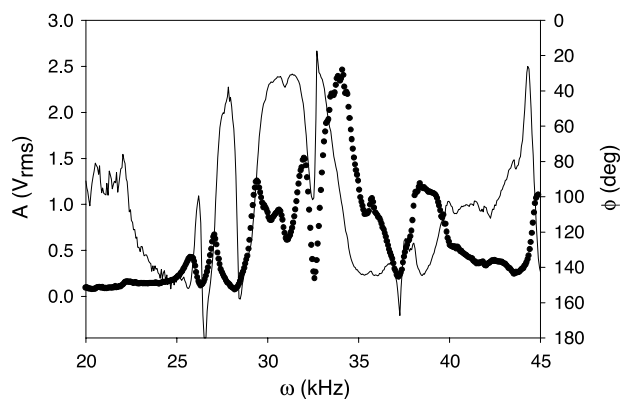


**Fig. 7** Resonance behavior obtained by an acoustically excited silicon nitride ( $\text{Si}_3\text{N}_4$ ) cantilever ( $k_c \sim 0.5\text{ N/m}$ ) in water. Thick dotted line is the  $A(\omega)$  data and the solid line is the  $\phi(\omega)$  data.

noise spectrum of the cantilever<sup>[59,62]</sup> can be used to assist in the identification of the resonance of the cantilever. Additionally, it is common that the resonance of the cantilever exhibits the highest vibrational amplitude in the frequency sweep. However, further verification can be obtained from the initial phase lag when probe–sample interactions are negligible. Fig. 8 shows  $\phi$  for a cantilever oscillated at a frequency close to its resonance frequency and at a frequency off a neighboring spurious resonance. In the latter case,  $\phi \sim 90^\circ$ , whereas  $\phi > 90^\circ$  when the oscillating frequency is on the true cantilever resonance. When the cantilever is driven on or close to its resonance, we expect  $\phi$  to be sensitive to the damping environment of the cantilever, and a value  $>90^\circ$  indicating increased damping/energy dissipation closer to the surface is expected because of the presence of hydrodynamic forces. Some authors have also observed that

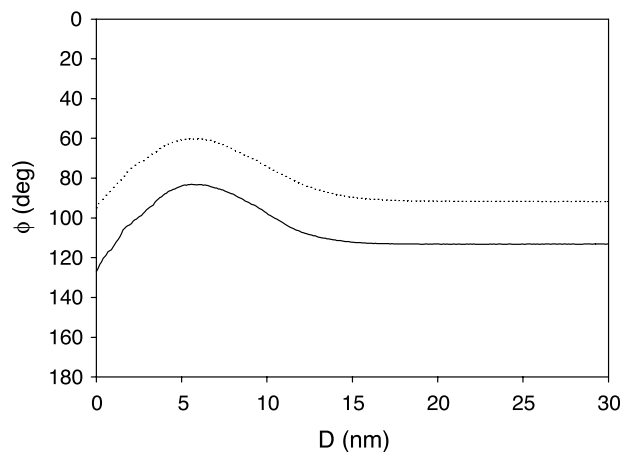


**Fig. 8**  $\phi(D)$  of the  $\text{Si}_3\text{N}_4$  cantilever ( $k_c \sim 0.5\text{ N/m}$ ) driven close to its fundamental resonance (solid line) and driven off a spurious resonance (dotted line) in water.

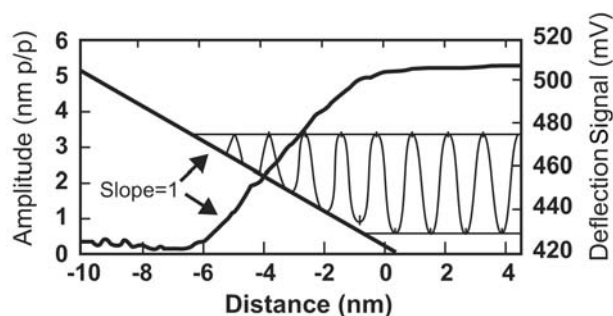


**Fig. 9**  $A(D)$  of a magnetically excited silicon nitride cantilever ( $k_c \sim 0.6$  N/m) with a silicon tip tapping against a mica surface. Additionally plotted is the instantaneous position of the cantilever (deflection signal). The drive frequency used (1 kHz) was much smaller than the resonance frequency of the cantilever (14.8 kHz). *Source:* From Ref. [67].

if the cantilever is driven at a frequency that is not close to its fundamental resonance, the oscillations do not decay symmetrically with tapping.<sup>[28,31,63]</sup> Instead, the lower turning point of oscillation varies, while the upper turning point remains constant (Fig. 9). The perturbed FDHO model does not describe this type of oscillatory response as Burnham et al. have shown.<sup>[31]</sup>

With the true resonance of the cantilever appropriately selected, a more significant complication with regards to modeling TM in liquid is the large hydrodynamic damping of cantilever oscillation. Resonance frequencies are now 3–4 times lower than those in air because of the added mass of liquid that moves with the oscillating cantilever<sup>[64–66]</sup> and  $Q$  is of order 1. These low-quality factors compromise the sensitivity of TM force measurements as they result in broader resonance curves and smaller  $\Delta A/\Delta D$  changes with probe–sample interaction (Fig. 3). Additionally, sample-induced dissipation becomes difficult to measure because of the dominance of hydrodynamic damping. To circumvent these problems caused by low-quality factors, Humphris, Tamayo, and Miles<sup>[67]</sup> have developed a positive feedback control loop system, known as active  $Q$  control, that increases the effective quality factor of the system to values that are more comparable with those obtained in air operation ( $>100$ ).  $Q$  control can also assist in the identification of the fundamental cantilever resonance in acoustically excited systems.

Hydrodynamic damping not only affects the free oscillation of the cantilever, but can also be distance-dependent through squeeze damping.<sup>[64]</sup> Squeeze damping can occur between the cantilever or probe and surface and is caused by an increase in hydrostatic pressure that develops because of the film of liquid that must be squeezed out of the gap between the relevant approaching surfaces.<sup>[68]</sup> Its onset scales with the size of the approaching object. Hosaka, Ito, and

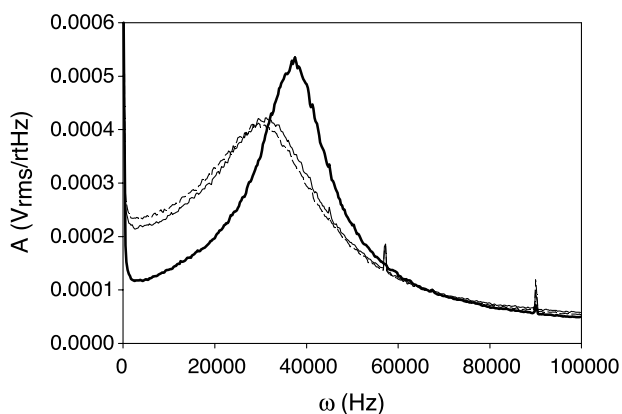


**Fig. 10** Resonance behavior of an oscillating  $\text{Si}_3\text{N}_4$  cantilever ( $k_c \sim 0.5$  N/m) in water at  $D \sim 50$   $\mu\text{m}$  (thick solid line),  $D \sim 0.5$   $\mu\text{m}$  (solid line), and  $D \sim 0.05$   $\mu\text{m}$  (dashed line).

Kuroda<sup>[69]</sup> have derived the squeeze force for beam-shaped cantilevers by modeling the cantilever as a string of spheres and have shown that it varies with  $D^{-3}$ . However, Alcaraz et al.<sup>[70]</sup> have shown experimentally that the squeeze force varies more as  $D^{-1}$  for both rectangular and V-shaped cantilevers. For the probe (assuming a spherical geometry), the squeeze force is proportional to  $D^{-1}$  (Reynolds equation).<sup>[64,71]</sup> The theoretical models for the squeeze force are only valid for laminar flow within the squeeze film, i.e.,  $Re \ll 1$  in the film, for ideal geometries, for oscillation amplitudes that are very small relative to the gap distance, and for constant velocity approach of the object to the surface. Because many AFM cantilevers and probes (usually conical tips) have complex geometry and are inclined at a small angle, deviations from these models are not unreasonable. Additionally, in TM,  $A$  is comparable to the gap distance, making the analysis of the squeeze force more difficult.

In their study of solvation forces near a graphite surface, O'Shea and Welland<sup>[64]</sup> observed squeeze damping at tip–sample separations on the order of tens of microns for all the cantilevers used. This damping has also been observed in the aqueous solutions used in our work (Fig. 10). At smaller separations ( $<1$   $\mu\text{m}$ ) (while maintaining noncontact with the substrate), they observe no significant additional damping and conclude that squeeze effects between the tip apex and the surface are negligible in their experiments. This conclusion is consistent with the Reynolds model that predicts a tip squeeze-drag coefficient that is about 3 orders of magnitude smaller than the cantilever squeeze-drag coefficient, making the cantilever the dominant contributor to distance-dependent damping. O'Shea and Welland do observe a huge increase in damping at  $D < 2.5$  nm that they ascribe to the solvation layer becoming more viscoelastic because of confinement.

O'Shea and Welland's characterization of hydrodynamic damping was conducted at noncontact separations, and their separation calibration was affected by drift of the piezo and other experimental limitations. For TM force measurements, the form of damping must be known accurately for separation changes on the order of the resolution of the force measurement acquisition ( $\Delta D \leq 1$  nm). Additionally, it is possible that the tip-squeeze contribution is much larger in TM than in NC because of the very small squeeze gaps ( $< 1$  nm) created during oscillation. We therefore investigate how  $Q$  varies with  $D$  using *Fourier spectroscopy*.<sup>[72]</sup> This involves high-speed collection of the cantilever deflection signal during force measurement and discrete Fourier transformation of subsets of the signal (Hanning window) to obtain the resonance curve of the cantilever,  $A(\omega)$ , at various  $D$ . This method allows us to overcome effects such as piezo-drift because of the continuous acquisition involved, allowing accurate separation calibration. From the  $A(\omega)$  curves, we can obtain  $Q$  from the steady-state analytical solution of Eq. (2), in which the probe-sample interaction is accounted for through an average value,  $r[A]$ .<sup>[48]</sup>

$$A = \frac{a_d}{\sqrt{(1 - \omega^2/\omega_0^2 - r[A])^2 + \frac{\omega^2/\omega_0^2}{Q^2}}} \quad (4)$$

Several authors have shown that the cantilever oscillation is anharmonic in TM in liquid.<sup>[28,31,73]</sup> Indeed, the cantilever deflection has been observed to deviate fairly significantly from sinusoidal oscillation during intermittent contact that Chen et al.<sup>[65]</sup> attribute to cantilever buckling caused by motion of the fluid. Despite the anharmonicity, Eq. (4) still adequately fits the resonance curves of our tapping cantilever even up to small separations (Fig. 11A). Fig. 11B shows how  $Q$  varies with  $D$  for various drive amplitudes in tapping on silicon in water using a tip as the probe. The distance axis has been normalized using the free peak amplitude,  $A_{p,o}$ . All the curves collapse on top of each other, indicating that additional dissipation only ensues when the probe starts to intermittently contact the surface (onset of strong repulsive interaction observed through a more negative  $r[A]$ ). Because oscillation amplitude is a key factor in determining both the onset and extent of additional damping, we can only obtain  $Q$  averaged over the whole oscillation cycle,  $Q(D)$ , instead of  $Q(x)$ . In this analysis,  $D = 0$  is defined as the onset of constant oscillation amplitude in the approach curve after intermittent contact occurs. It is important to note that the point of zero separation is always ambiguous with AFM force measurements, as only the deflection of the cantilever is monitored in the technique. In dc operation, the point of zero

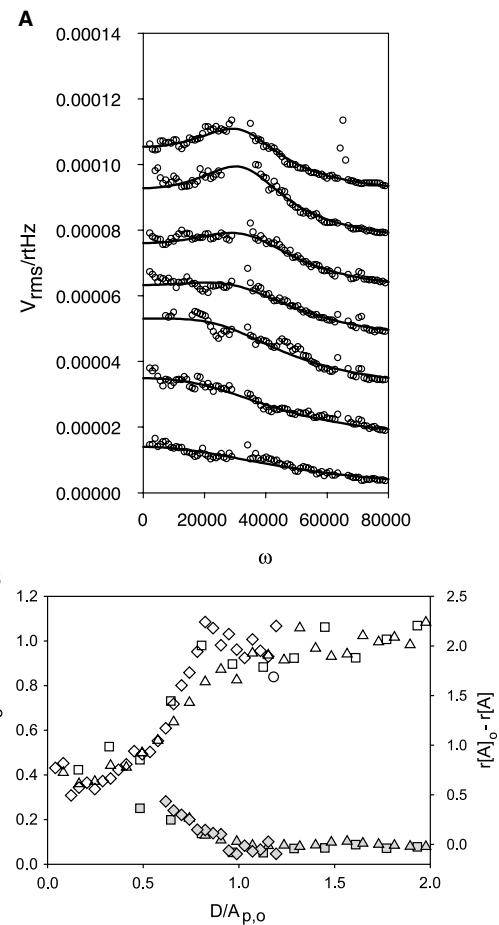


**Fig. 11** (A) Theoretical fit of  $A(\omega)$  curves [Eq. (2)] obtained using Fourier spectroscopy at various  $D$  for a free peak amplitude,  $A_{p,o}$  of 6.1 nm. The bottom curve is for  $D = 0$ , and each subsequent curve is +1.6 nm away from the previous curve. (B) Fitted  $Q$  (unfilled symbols) and  $r[A]$  (shaded symbols) as a function of normalized separation,  $D/A_{p,o}$  for different  $A_{p,o}$ .  $Q$  and  $r[A]$  have also been normalized by their free values (for negligible probe-sample interactions).  $A_{p,o}$  was 0.4 nm (circles), 3.1 nm (squares), 6.1 nm (triangles), and 12.2 nm (diamonds).

separation/contact is usually calibrated from the onset of linearity in the cantilever deflection. Equivalently in TM, one can define an equilibrium zero probe-sample separation,  $D = 0$ .

The results and discussion presented show that hydrodynamic forces are a key component of force measurements in liquid. Experiments using solutions of different viscosities<sup>[72]</sup> have illuminated that the origin of the  $Q$  decay that occurs in our TM force measurements with intermittent contact is not a result of squeeze damping. Instead, we hypothesize that the origin of the dissipation is a result of frictional losses associated with both cantilever buckling<sup>[73]</sup> and lateral sliding of the tip upon contact.<sup>[54]</sup> If we allow for the occurrence of this intermittent contact-induced

dissipation, introduced in the FDHO model through a decaying  $Q(D)$ , a more accurate simulation of TM force measurements in liquid is achieved.<sup>[72]</sup>

## DYNAMIC MEASUREMENTS OF STERIC FORCES FROM DIFFUSE POLYMER LAYERS

Physically and chemically adsorbed polymer layers are used to modify surface properties, such as charge and wettability, as well as to prevent adsorption of molecules onto the surfaces. On biomaterials, such polymer layers are commonly used as antifouling coatings as they exert repulsive steric forces that prevent contaminant adsorption. The polymer steric interactions arise from the osmotic penalties associated with confining the polymer segments.<sup>[74]</sup>

There have been a number of dynamic studies<sup>[75,76]</sup> focused on characterizing the viscoelastic properties of adsorbed or constrained polymer layers on surfaces using AFM. Traditionally, these studies were conducted using the surface forces apparatus (SFA),<sup>[77–79]</sup> where the interaction area of the approaching surface is many orders of magnitude larger than the probes used in AFM. Both techniques involve oscillating the sample at frequencies in the 10–1000 Hz range and looking at changes in the phase lag and the amplitude to obtain both the storage and loss moduli of the system through the Voigt model. A slightly different approach that has been taken to study the properties of swollen grafted polymer layers is to observe changes in the dynamic properties from the thermal noise fluctuations of the cantilever. This technique has been exploited by Gelbert et al.<sup>[80,81]</sup> to study the viscoelastic properties of various tethered polymer layers and offers advantages to forced oscillation because of the small oscillation amplitudes that ensure the dynamic responses are linear.

One of the few AFM studies involving high-frequency, large amplitude probing of polymer layers is Overney et al.'s<sup>[82]</sup> compliance measurement of a grafted polystyrene brush. In their work, oscillation was mediated through modulation of the cantilever at a free oscillation amplitude of 5.5 nm and a modulation frequency of 3 kHz. From storage modulus vs. distance profiles for both a bare silicon substrate and the polystyrene brush, a brush layer height was calculated that compared favorably to neutron reflectivity experiments and dc force measurements. The storage modulus is the elastic contribution from the compression of the polymer segments and is analogous to the steric repulsion exerted by the brush. Overney et al.'s polystyrene brush system is an ideal one in that the layer is dense enough to resist compression before significant penetration into the layer occurs, making escape transitions unlikely.<sup>[83,84]</sup>

Simulations<sup>[83,85]</sup> have shown that when sparsely grafted polymer layers undergo continuous compression from sharp tips, the polymer chains splay or escape away from the tip to minimize their energy of confinement. These events are frequently observed in dc force measurements<sup>[13]</sup> and result in an underestimation of the magnitude of the steric repulsion that would be experienced between the layer and an adsorbing molecule. It would be interesting to compare the sensitivities of dynamic and dc force measurements for sparsely grafted systems using a modulation frequency close to the cantilever's resonance to enhance sensitivity. Grafted polymer systems are ideal to study because they display an exponential resistance to compression that is well described theoretically<sup>[74]</sup> and they are commonly used in biotechnical applications because of the covalent form of attachment that increases stability.

We have explored the sensitivity of TM AFM force measurements on grafted poly(ethylene glycol), PEG, layers on silicon at two grafting densities using the integrated tips on the cantilevers as probes. Fig. 12A and B shows the results of dc force measurements on the two PEG layers for cantilevers of differing spring constant ( $k_{c1} \sim 0.01$  N/m and  $k_{c2} \sim 0.5$  N/m). For the sparsely grafted layer, the onset of deflection of the stiffer cantilever ( $k_{c2}$ ) is more short-ranged than that observed with the more flexible cantilever ( $k_{c1}$ ). This suggests that polymer chains are splaying/escaping from the tip of the stiffer cantilever (because of the high compression load), resulting in significant penetration of the tip through the layer before a detectable resistance to compression is measured. After a certain amount of compression, escape transitions become less favorable because the polymer is constrained at one end and the stretching penalty associated with the chain completely escaping from under the tip is too great.<sup>[85]</sup> Therefore segments will start to resist compression. Confirming this, we observe two compression regimes in the force profiles on this layer. Only one compression regime is observed on the densely grafted layer because the osmotic penalty for chain escape as a result of the proximity of neighboring chains is large enough to prevent escape despite the large compression loads.

Tapping mode force measurements on the same surfaces described earlier are shown in Fig. 13. These force measurements were conducted with the stiff cantilevers, but the onset of deflection is comparable to the onset obtained from dc measurements with cantilevers of  $k_{c1}$  (Table 1). Therefore we can conclude that TM force measurements are more sensitive than their dc counterparts. This increased sensitivity is attributed to the large oscillation amplitude that allows the polymer layer to be sensed before significant compression occurs and the high frequency of oscillation

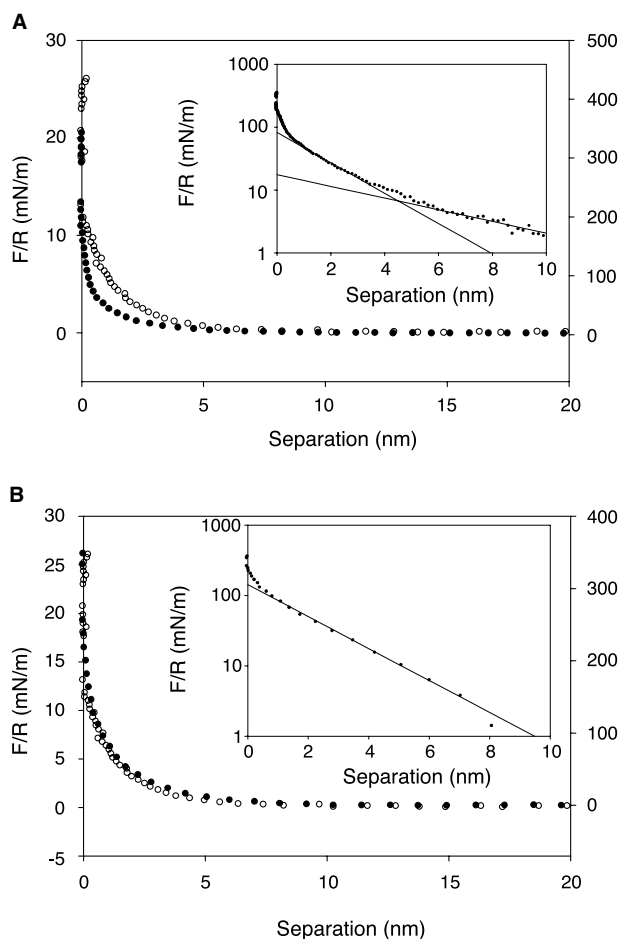


**Fig. 12** Interaction energy profiles measured on (A) a sparsely grafted PEG layer and (B) a densely grafted PEG layer using d.c. force measurements with  $\text{Si}_3\text{N}_4$  cantilevers of  $k_{c1}$  (unfilled symbols) and  $k_{c2}$  (filled symbols) (insets are the energy profiles for  $k_{c2}$  plotted on a semilog scale).

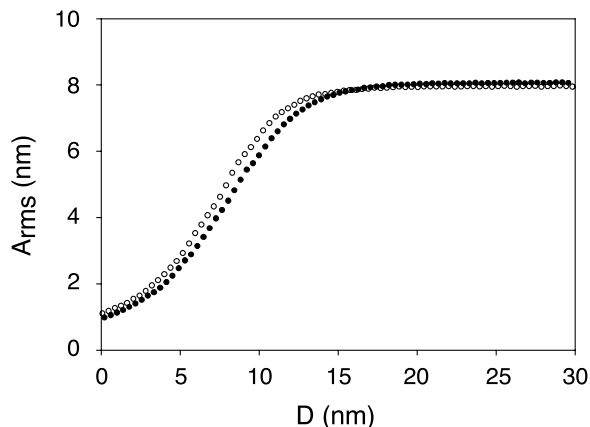


**Fig. 13** TM  $A(D)$  curves obtained on the sparsely grafted PEG layer (unfilled symbols) and the densely grafted PEG layer (filled symbols) using a  $\text{Si}_3\text{N}_4$  cantilever of  $k_{c2}$ .

**Table 1** Values indicate 5% deviation from the overall measured change

Experiment	Detection of change ( $D$ ) (nm)
dc: sparse PEG layer, $k_{c1}$	4.3
dc: sparse PEG layer, $k_{c2}$	2.85
dc: dense PEG layer, $k_{c1}$	3.5
dc: dense PEG layer, $k_{c2}$	4
TM: sparse PEG layer, $k_{c2}$	14
TM: dense PEG layer, $k_{c2}$	14.8

that possibly prevents slower events such as polymer escape from occurring.

## DYNAMIC MEASUREMENTS OF RECEPTOR-LIGAND INTERACTIONS

Much of biological activity and cellular response is mediated through specific interactions termed receptor-ligand interactions. These interactions are short-ranged ( $\sim 1-2$  nm) and occur because of a combination of hydrogen bonding, van der Waals interactions, and hydrophobic attractions between complementary sites on molecules.<sup>[86]</sup> Dc force measurements have been used extensively to measure the binding strength between receptor-ligand pairs.<sup>[14,15,87,88]</sup> In these measurements, the force of unbinding is determined by the amount the cantilever deflects because of the receptor-ligand attraction during retraction from the surface. Because biological interactions are, by nature, dynamic, many researchers have also investigated the dependence of the receptor-ligand binding strengths on the loading and unloading rate.<sup>[89-91]</sup> To our knowledge, only a few authors have investigated the feasibility of high-frequency dynamic probing of these interactions.

In particular, Raab et al.<sup>[92]</sup> have used MAC-mode AFM to conduct successful antibody recognition imaging using a functionalized AFM tip. In their work, they attached the antibody to a flexible polymer tether and carefully controlled both oscillation amplitude and driving frequency to optimize the contact time such that binding between the antibody and antigen was feasible. Liu Leuba, and Lindsay<sup>[93]</sup> have also examined single molecule stretching behavior with both dynamic and static AFM measurements. Additionally, a new tool named molecular recognition force microscopy (MRFM) that uses magnetic excitation of the cantilever has emerged in recent years. Here the tip is functionalized with a flexible cross-linker carrying a ligand that will complex to its complementary receptor on the surface. The oscillation responses of the cantilever and tip are then recorded as a function of frequency. Pastushenko et al.<sup>[94]</sup> and Schindler et al.<sup>[95]</sup> used a



theoretical analysis of the damped oscillator model to investigate the conditions necessary for the most sensitive detection of the receptor–ligand complexation (maximizing  $\Delta A$ ) with the lowest possible compressive load. They determined that if  $Q > 1$ , MRFM experiments are more sensitive than dc experiments and that driving below  $\omega_0$  offers greater sensitivity than driving above  $\omega_0$ . Their analysis, as they duly noted, did not rigorously account for the viscous interactions that affect the cantilever response in liquid; however, it is still a useful guide in optimizing dynamic MRFM experiments.

There is a lower limit to the flexibility of the cantilevers that can be used for these studies to increase the sensitivity of the measurement. With very flexible cantilevers (usually of larger dimension), hydrodynamic forces become too great<sup>[96]</sup> and result in  $\omega_0$  in liquid that occur within the noise frequencies of the instrument. Huge drive amplitudes are also needed to sustain oscillation, thereby increasing the impact force on the sample. In our experiments, stable tapping could only be achieved using cantilevers with  $k_c \geq 0.1$  N/m. However, it may be possible to drive the cantilever at frequencies off its higher eigenmodes of vibration that arise from its secondary bending and twisting states.<sup>[97]</sup>

## CONCLUSION

The interactions that we have discussed are relevant to many biomaterial surfaces<sup>[98–102]</sup> on which receptor–ligand interactions are used for the specific recruitment of biomolecules/analytes to the surface and polymer steric forces are used to prevent fouling of the surface by noncomplementary contaminants. In nature, carbohydrates that protrude out of the plasma membrane on the cell surface are responsible for imparting steric repulsion.<sup>[103]</sup> Understanding the interplay between these interactions will aid in the comprehension of important cellular processes such as cell adhesion and in the design of various biomaterials. The potential of TM AFM as a tool in the gentle, simultaneous probing of these interactions in physiological conditions is promising.

We have shown that hydrodynamics and other forms of energy dissipation that are independent of the probe–sample interactions play a very important role in TM in liquid. Full characterization of this dissipation is necessary before accurate quantitative extraction of the relevant probe–sample interactions is possible. This can be achieved for each force measurement using the Fourier spectroscopy technique that we proposed.

As with all AFM methods, the ambiguity associated with the knowledge of absolute zero separation is a

major limitation to the technique. This uncertainty affects quantitative reproduction of experimental data and accurate knowledge of the acting probe–sample interaction. Additionally, the dynamic signal measured is not specific to the motion of the probe, but reflects the overall motion of the cantilever. In TM in liquid, where the fluid can cause secondary bending and rotation of the cantilever, this complicates interpretation of the measured signal and limits the applicability of the FDHO model that treats the cantilever as a unified mass. We hope that with growing utility of this mode of measurement, these problems will be addressed in the future.

## ACKNOWLEDGMENTS

We would like to thank Dr. Tomasz Kowalewski for useful discussions on the physics behind AFM operation, and we would also like to thank all the scientists cited for their contributions toward the advancement of knowledge about AFM operation. Our personal work has been supported by the ACS Petroleum Research Fund and NSF-CTS-0210205.

## REFERENCES

1. Binnig, G.; Gerber, C.; Quate, C. Atomic force microscope. *Phys. Rev. Lett.* **1986**, *56*, 930.
2. Drake, B.; Prater, C.B.; Weisenhorn, A.L.; Gould, S.A.; Albrecht, T.R.; Quate, C.F.; Cannell, D.S.; Hansma, H.G.; Hansma, P.K. Imaging crystals, polymers, and processes in water with the atomic force microscope. *Science* **1989**, *243*, 1586–1589.
3. Radmacher, M.; Fritz, M.; Hansma, P.K. From molecules to cells: imaging soft samples with the atomic force microscope. *Science* **1992**, *257*, 1900–1905.
4. Döppenschmidt, A.; Kappl, M.; Butt, H.-J. Surface properties of ice studied by atomic force microscopy. *J. Phys. Chem., B* **1998**, *102*, 7813–7819.
5. Magonov, S. Visualization of polymers at surfaces and interfaces with atomic force microscopy. *Handb. Surf. Interface Mater.* **2001**, *2*, 393–430.
6. Hansma, H.G.; Revenko, I.; Kim, K.; Laney, D.E. Atomic force microscopy of long and short double-stranded, single-stranded and triple-stranded nucleic acids. *Nucleic Acids Res.* **1996**, *24* (4), 713–720.
7. Le Grimmelc, C.; Lesniewska, E.; Giocondi, M.-C.; Finot, E.; Vié, V.; Goudonnet, J.-P. Imaging of the surface of living cells by low-force contact-mode atomic force microscopy. *Biophys. J.* **1998**, *75*, 695–703.
8. Franz, V.; Butt, H.-J. Confined liquids: solvation forces in liquid alcohols between solid surfaces. *J. Phys. Chem., B* **2002**, *106* (7), 1703–1708.
9. Hartley, P.G.; Scales, P.J. Electrostatic properties of polyelectrolyte modified surfaces studied by direct force measurement. *Langmuir* **1998**, *14*, 6948–6955.

10. Kohonen, M.M.; Karaman, M.E.; Pashley, R.M. Debye length in multivalent electrolyte solutions. *Langmuir* **2000**, *16*, 5749–5753.
11. Biggs, S. Non-equilibrium interaction forces between adsorbed polymer layers. *J. Chem. Soc., Faraday Trans.* **1996**, *92*, 2783–2789.
12. Braithwaite, G.J.C.; Howe, A.; Luckham, P.F. Interactions between poly(ethylene oxide) layers adsorbed to glass surfaces probed by using a modified atomic force microscope. *Langmuir* **1996**, *12*, 4224–4237.
13. Kelley, T.W.; Schorr, P.A.; Johnson, K.D.; Tirrell, M.; Frisbie, C.D. Direct force measurements at polymer brush surfaces by atomic force microscopy. *Macromolecules* **1998**, *31*, 4297–4300.
14. Florin, E.-L.; Moy, V.T.; Gaub, H.E. Adhesion forces between individual ligand–receptor pairs. *Science* **1994**, *264*, 415–417.
15. Hinterdorfer, P.; Baumgartner, W.; Gruber, H.J.; Schilcher, K.; Schindler, H. Detection and localization of individual antibody–antigen recognition events by atomic force microscopy. *Proc. Natl. Acad. Sci. U. S. A.* **1996**, *93*, 3477–3481.
16. Martin, Y.; Williams, C.C.; Wickramasinghe, H.K. Atomic force microscope–force mapping and profiling on a sub 100-Å scale. *J. Appl. Phys.* **1987**, *61*, 4723–4729.
17. Zhong, Q.; Inniss, D.; Kjoller, K.; Elings, V.B. Fractured polymer/silica fiber surface studied by tapping-mode AFM. *Surf. Sci. Lett.* **1993**, *290*, L688.
18. Albrecht, T.R.; Grütter, P.; Home, D.; Rugar, D. Frequency modulation detection using high-Q cantilevers for enhanced force microscope sensitivity. *J. Appl. Phys.* **1991**, *69*, 668–673.
19. Maivald, P.; Butt, H.-J.; Gould, S.A.C.; Prater, C.B.; Drake, B.; Gurley, J.A.; Elings, V.B.; Hansma, P.K. Using force modulation to image surface elasticities with the atomic force microscope. *Nanotechnology* **1991**, *2*, 103–106.
20. Oulevey, F.; Burnham, N.A.; Kulik, A.J.; Gallo, P.J.; Gremaud, G.; Benoit, W. Mechanical properties studied at the nanoscale using scanning local-acceleration microscopy (SLAM). *J. Phys. (Paris IV)* **1996**, *6*, 731–734.
21. García, R.; Pérez, R. Dynamic atomic force microscopy methods. *Surf. Sci. Rep.* **2002**, *47*, 197–301.
22. Hallett, P.; Tskhovrebova, L.; Trinick, J.; Offer, G.; Miles, M.J. Improvements in atomic force microscopy protocols for imaging fibrous proteins. *J. Vac. Sci. Technol., B* **1996**, *14* (2), 1444–1448.
23. Vié, V.; Giocondi, M.-C.; Lesniewska, E.; Finot, E.; Goudonnet, J.-P.; Le Grimellec, C. Tapping-mode atomic force microscopy on intact cells: optimal adjustment of tapping conditions by using the deflection signal. *Ultramicroscopy* **2000**, *82*, 279–288.
24. Betley, T.A.; Banaszak Holl, M.M.; Orr, B.G.; Swanson, D.R.; Tomalia, D.A.; Baker, J.R., Jr. Tapping mode atomic force microscopy investigation of poly(amidoamine) dendrimers: Effects of substrate and pH on dendrimer deformation. *Langmuir* **2001**, *17* (9), 2768–2773.
25. Musselman, I.H.; Gray, K.H.; Leasure, R.M.; Meyer, T.J.; Linton, R.W. Scanning probe microscopy and sputter depth profiling of conductive polymer thin films. *Microbeam Anal.* **1993**, *2* (6), 297–310.
26. Tamayo, J.; García, R. Deformation, contact time, and phase contrast in tapping mode scanning force microscopy. *Langmuir* **1996**, *12*, 4430–4435.
27. Cleveland, J.P.; Anczykowski, B.; Schmid, A.E.; Elings, V.B. Energy dissipation in tapping-mode atomic force microscopy. *Appl. Phys. Lett.* **1998**, *72* (20), 2613–2615.
28. Putman, C.A.J.; van der Werf, K.O.; De Grooth, B.G.; Van Hulst, N.F.; Greve, J. Tapping mode atomic force microscopy in liquid. *Appl. Phys. Lett.* **1994**, *64* (18), 2454–2456.
29. Chen, J.; Workman, R.K.; Sarid, D.; Höper, R. Numerical simulations of a scanning force microscope with a large-amplitude vibrating cantilever. *Nanotechnology* **1994**, *5*, 199–204.
30. Anczykowski, B.; Krueger, D.; Babcock, K.L.; Fuchs, H. Basic properties of dynamic force spectroscopy with the scanning force microscope in experiment and simulation. *Ultramicroscopy* **1997**, *66*, 251–259.
31. Burnham, N.A.; Behrend, O.P.; Oulevey, F.; Gremaud, G.; Gallo, P.-J.; Gourdon, D.; Dupas, E.; Kulik, A.J.; Pollock, H.M.; Briggs, G.A.D. How does a tip tap? *Nanotechnology* **1997**, *8*, 67–75.
32. García, R.; San Paulo, A. Dynamics of a vibrating tip near or in intermittent contact with a surface. *Phys. Rev., B* **2000**, *61* (20), R13381–R13384.
33. Stark, R.W.; Heckl, W.M. Fourier transformed atomic force microscopy: tapping mode atomic force microscopy beyond the Hookian approximation. *Surf. Sci.* **2000**, *457*, 219–228.
34. Tamayo, J. Energy dissipation in tapping-mode scanning force microscopy with low quality factors. *Appl. Phys. Lett.* **1999**, *75* (22), 3569–3571.
35. Fowles, G.R. The harmonic oscillator. In *Analytical Mechanics*, 4th Ed.; Saunders College Publishing: Philadelphia, 1986; 64–76.
36. Cleveland, J.P.; Manne, S.; Bocek, D.; Hansma, P.K. A nondestructive method for determining the spring constant of cantilevers for scanning force microscopy. *Rev. Sci. Instrum.* **1993**, *64* (2), 403–405.
37. Tortonese, M.; Kirk, M. Characterization of application specific probes for SPMs. *Proc. SPIE.* **1997**, *3009*, 53–60.
38. Hutter, J.L.; Bechhoefer, J. Calibration of atomic-force microscope tips. *Rev. Sci. Instrum.* **1993**, *64* (7), 1868–1873.
39. Giessibl, F.J. Forces and frequency shifts in atomic-resolution dynamic force microscopy. *Phys. Rev., B* **1997**, *56* (24), 16010–16015.
40. Giessibl, F.J.; Bielefeldt, H. Physical interpretation of frequency-modulation atomic force microscopy. *Phys. Rev., B* **2000**, *61* (15), 9968–9971.
41. Giessibl, F.J. A direct method to calculate tip-sample forces from frequency shifts in frequency-modulation atomic force microscopy. *Appl. Phys. Lett.* **2001**, *78* (1), 123–125.

42. Bielefeldt, H.; Giessibl, F.J. A simplified but intuitive analytical model for intermittent-contact-mode force microscopy based on Hertzian mechanics. *Surf. Sci.* **1999**, *440* (3), L863–L867.
43. Kühle, A.; Sørensen, A.H.; Bohr, J. Role of attractive forces in tapping tip force microscopy. *J. Appl. Phys.* **1997**, *81* (10), 6562–6569.
44. García, R.; San Paulo, A. Amplitude curves and operating regimes in dynamic atomic force microscopy. *Ultramicroscopy* **2000**, *82*, 79–83.
45. Nony, L.; Boisgard, R.; Aime, J.P. Nonlinear dynamical properties of an oscillating tip-cantilever system in the tapping mode. *J. Chem. Phys.* **1999**, *111* (4), 1615–1627.
46. Aime, J.P.; Boisgard, R.; Nony, L.; Couturier, G. Influence of noncontact dissipation in the tapping mode: attempt to extract quantitative information on the surface properties with the local force probe method. *J. Chem. Phys.* **2001**, *114* (11), 4945–4954.
47. Boisgard, R.; Michel, D.; Aime, J.P. Hysteresis generated by attractive interaction: oscillating behavior of a vibrating tip-microlever system near a surface. *Surf. Sci.* **1998**, *401* (2), 199–205.
48. Gauthier, M.; Tsukada, M. Damping mechanism in dynamic force microscopy. *Phys. Rev. Lett.* **2000**, *85* (25), 5348–5351.
49. Burnham, N.A.; Kulik, A.J. Surface forces and adhesion. In *Handbook of Micro/Nanotribology*; Bhushan, B., Ed.; CRC Press: Boca Raton, 1998.
50. Bar, G.; Delineau, L.; Brandsch, R.; Ganter, M.; Whangbo, M.-H. Hysteresis in the distance-sweep curves of elastomers and its implications in tapping-mode atomic force microscopy. *Surf. Sci.* **2000**, *457*, L404–L412.
51. Dubourg, F.; Aime, J.P. Role of the adhesion between a nanotip and a soft material in tapping mode AFM. *Surf. Sci.* **2000**, *466*, 137–143.
52. Tamayo, J.; García, R. Relationship between phase shift and energy dissipation in tapping-mode scanning force microscopy. *Appl. Phys. Lett.* **1998**, *73* (20), 2926–2928.
53. Chen, X.; Davies, M.C.; Roberts, C.J.; Tendler, S.J.B.; Williams, P.M.; Davies, J.; Dawkes, A.C.; Edwards, J.C. Interpretation of tapping mode atomic force microscopy data using amplitude-phase-distance measurements. *Ultramicroscopy* **1998**, *75* (3), 171–181.
54. Marcus, M.S.; Carpick, R.W.; Sasaki, D.Y.; Eriksson, M.A. Material anisotropy revealed by phase contrast in intermittent contact atomic force microscopy. *Phys. Rev. Lett.* **2002**, *88* (22), 226103-1–226103-4.
55. Whangbo, M.-H.; Bar, G.; Brandsch, R. Description of phase imaging in tapping mode atomic force microscopy by harmonic approximation. *Surf. Sci.* **1998**, *411*, L794–L801.
56. Kopp-Marsaudon, S.; Leclere, P.; Dubourg, F.; Lazzaroni, R.; Aime, J.P. Quantitative measurement of the mechanical contribution to tapping-mode atomic force microscopy images of soft materials. *Langmuir* **2000**, *16* (22), 8432–8437.
57. Hansma, P.K.; Cleveland, J.P.; Radmacher, M.; Walters, D.A.; Hillner, P.E.; Bezanilla, M.; Fritz, M.; Vie, D.; Hansma, H.G. Tapping mode atomic force microscopy in liquids. *Appl. Phys. Lett.* **1994**, *64* (13), 1738–1740.
58. Fritz, M.; Radmacher, M.; Cleveland, J.P.; Allersma, M.W.; Stewart, R.J.; Gieselmann, R.; Janmey, P.; Schmidt, C.F.; Hansma, P.K. Imaging globular and filamentous proteins in physiological buffer solutions with tapping mode atomic force microscopy. *Langmuir* **1995**, *11* (9), 3529–3535.
59. Revenko, I.; Proksch, R. Magnetic and acoustic tapping mode microscopy of liquid phase phospholipid bilayers and DNA molecules. *J. Appl. Phys.* **2000**, *87* (1), 526–533.
60. Schaeffer, T.E.; Cleveland, J.P.; Ohnesorge, F.; Walters, D.A.; Hansma, P.K. Studies of vibrating atomic force microscope cantilevers in liquid. *J. Appl. Phys.* **1996**, *80* (7), 3622–3627.
61. Han, W.; Lindsay, S.M.; Jing, T. A magnetically driven oscillating probe microscope for operation in liquids. *Appl. Phys. Lett.* **1996**, *69* (26), 4111–4113.
62. Roters, A.; Johannsmann, D. Distance-dependent noise measurements in scanning force microscopy. *J. Phys., B* **1996**, *8* (41), 7561–7577.
63. Lantz, M.; Liu, Y.Z.; Cui, X.D.; Tokumoto, H.; Lindsay, S.M. Dynamic force microscopy in fluid. *Surf. Interface Anal.* **1999**, *27*, 354–360.
64. O'Shea, S.J.; Welland, M.E. Atomic force microscopy at solid-liquid interfaces. *Langmuir* **1998**, *14* (15), 4186–4197.
65. Chen, G.Y.; Warmack, R.J.; Thundat, T.; Allison, D.P. Resonance response of scanning force microscopy cantilevers. *Rev. Sci. Instrum.* **1994**, *65* (8), 2532–2537.
66. Sader, J.E. Frequency response of cantilever beams immersed in viscous fluids with applications to the atomic force microscope. *J. Appl. Phys.* **1998**, *84* (1), 64–76.
67. Humphris, A.D.L.; Tamayo, J.; Miles, M.J. Active quality factor control in liquids for force spectroscopy. *Langmuir* **2000**, *16* (21), 7891–7894.
68. Williams, J.A. *Engineering Tribology*; Oxford University Press: Oxford, 1994.
69. Hosaka, H.; Itao, K.; Kuroda, S. Damping characteristics of beam-shaped micro-oscillators. *Sens. Actuators, A, Phys.* **1995**, *A49*, 87–95.
70. Alcaraz, J.; Buscemi, L.; Puig-de-Morales, M.; Colchero, J.; Baro, A.; Navajas, D. Correction of microrheological measurements of soft samples with atomic force microscopy for the hydrodynamic drag on the cantilever. *Langmuir* **2002**, *18* (3), 716–721.
71. Craig, V.S.J.; Neto, C. In situ calibration of colloid probe cantilevers in force microscopy: hydrodynamic drag on a sphere approaching a wall. *Langmuir* **2001**, *17* (19), 6018–6022.
72. Nnebe, I.; Schneider, J.W. Energy dissipation in tapping-mode atomic force microscopy in liquid. *Langmuir* (Submitted).
73. Chen, G.Y.; Warmack, R.J.; Oden, P.I.; Thundat, T. Transient response of tapping scanning force microscopy in liquids. *J. Vac. Sci. Technol., B* **1996**, *14* (2), 1313–1317.
74. Israelachvili, J. *Intermolecular and Surface Forces*; Academic Press: New York, 1992; 299 pp.

75. Friedenber, M.C.; Mate, C.M. Dynamic viscoelastic properties of liquid polymer films studied by atomic force microscopy. *Langmuir* **1996**, *12* (25), 6138–6142.
76. Braithwaite, G.J.C.; Luckham, P.F. The simultaneous determination of the forces and viscoelastic properties of adsorbed polymer layers. *J. Colloid Interface Sci.* **1999**, *218*, 97–111.
77. Montfort, J.P.; Hadziioannou, G. “Equilibrium” and dynamic behavior of thin films of a perfluorinated polyether. *J. Chem. Phys.* **1988**, *88* (11), 7187–7196.
78. Dhinojwala, A.; Granick, S. Surface forces in the tapping mode: solvent permeability and hydrodynamic thickness of adsorbed polymer brushes. *Macromolecules* **1997**, *30* (4), 1079–1085.
79. Luckham, P.F.; Manimaaran, S. A nanorheological study of adsorbed polymer layers. *Macromolecules* **1997**, *30*, 5025–5033.
80. Gelbert, M.; Roters, A.; Schimmel, M.; Ruhe, J.; Johannsmann, D. Viscoelastic spectra of soft polymer interfaces obtained by noise analysis of AFM cantilevers. *Surf. Interface Anal.* **1999**, *27*, 572–577.
81. Gelbert, M.; Biesalski, M.; Ruehe, J.; Johannsmann, D. Collapse of polyelectrolyte brushes probed by noise analysis of a scanning force microscope cantilever. *Langmuir* **2000**, *16* (13), 5774–5784.
82. Overney, R.M.; Leta, D.P.; Pictroski, C.F.; Rafailovich, M.H.; Liu, Y.; Quinn, J.; Sokolov, J.; Eisenberg, A.; Overney, G. Compliance measurements of confined polystyrene solutions by atomic force microscopy. *Phys. Rev. Lett.* **1996**, *76* (8), 1272–1275.
83. Murat, M.; Grest, G. Molecular dynamics simulations of the force between a polymer brush and an AFM tip. *Macromolecules* **1996**, *29*, 8282–8284.
84. Sevick, E.M.; Williams, D.R.M. A polymer end-tethered to a potential stripe: a simple example of an escape transition. *Macromolecules* **1999**, *32*, 6841–6846.
85. Guffond, M.C.; Williams, D.R.M.; Sevick, E.M. End-tethered polymer chains under AFM tips: Compression and escape in theta solvents. *Langmuir* **1997**, *13*, 5691–5696.
86. Leckband, D.; Israelachvili, J. Intermolecular forces in biology. *Q. Rev. Biophys.* **2001**, *34*, 105–267.
87. Boland, T.; Ratner, B.D. Direct measurement of hydrogen bonding in DNA nucleotide bases by atomic force microscopy. *Proc. Natl. Acad. Sci. U. S. A.* **1995**, *92* (12), 5297–5301.
88. Lo, Y.-S.; Simons, J.; Beebe, T.P., Jr. Temperature dependence of the biotin-avidin bond-rupture force studied by atomic force microscopy. *J. Phys. Chem., B* **2002**, *106* (38), 9847–9852.
89. Merkel, R.; Nassoy, P.; Leung, A.; Ritchie, K.; Evans, E. Energy landscapes of receptor–ligand bonds explored with dynamic force spectroscopy. *Nature* **1999**, *397*, 50–53.
90. Yuan, C.; Chen, A.; Kolb, P.; Moy, V.T. Energy landscape of streptavidin–biotin complexes measured by atomic force microscopy. *Biochemistry* **2000**, *39* (33), 10219–10223.
91. Kienberger, F.; Kada, G.; Gruber, H.J.; Pastushenko, V.Ph.; Riener, C.; Trieb, M.; Knaus, H.-G.; Schindler, H.; Hinterdorfer, P. Recognition force spectroscopy studies of the NTA-His6 bond. *Single Mol.* **2000**, *1* (1), 59–65.
92. Raab, A.; Han, W.; Badt, D.; Smith-Gill, S.J.; Lindsay, S.M.; Schindler, H.; Hinterdorfer, P. Antibody recognition imaging by force microscopy. *Nat. Biotechnol.* **1999**, *17* (9), 902–905.
93. Liu, Y.Z.; Leuba, S.H.; Lindsay, S.M. Relationship between stiffness and force in single molecule pulling experiments. *Langmuir* **1999**, *15*, 8547–8548.
94. Pastushenko, V.P.; Hinterdorfer, P.; Kienberger, F.; Borcken, C.; Schindler, H. Effects of viscoelastic cantilever–sample interaction on laser beam deflection in MAC mode MRFM. *Single Mol.* **2000**, *1* (2), 165–170.
95. Schindler, H.; Badt, D.; Hinterdorfer, F.; Kienberger, P.; Raab, A.; Wielert-Badt, S.; Pastushenko, V.P. Optimal sensitivity for molecular recognition MAC-mode AFM. *Ultramicroscopy* **2000**, *82*, 227–235.
96. Walters, D.A.; Cleveland, J.P.; Thomson, N.H.; Hansma, P.K.; Wendman, M.A.; Gurley, G.; Elings, V. Short cantilevers for atomic force microscopy. *Rev. Sci. Instrum.* **1996**, *67* (10), 3583–3590.
97. Stark, R.W.; Drobek, T.; Heckl, W.M. Tapping-mode atomic force microscopy and phase imaging in higher eigenmodes. *Appl. Phys. Lett.* **1999**, *74* (22), 3296–3298.
98. Metzger, S.W.; Natesan, M.; Yanavich, C.; Schneider, J.; Lee, G.U. Development and characterization of surface chemistries for silicon-based biosensors. *J. Vac. Sci. Technol., A* **1999**, *17*, 2623–2628.
99. Edelstein, R.L.; Tamana, C.R.; Sheehan, P.E.; Miller, M.M.; Baselt, D.R.; Whitman, L.J.; Colton, R.J. The BARC biosensor applied to the detection of biological warfare agents. *Biosens. Bioelectron.* **2000**, *14*, 805–813.
100. Tziampazis, E.; Kohn, J.; Moghe, P.V. PEG-variant biomaterials as selectively adhesive protein templates: model surfaces for controlled cell adhesion and migration. *Biomaterials* **2000**, *21*, 511–520.
101. Bronich, T.K.; Solomatin, S.V.; Yaroslavov, A.A.; Eisenberg, A.; Kabanov, V.A.; Kabanov, A.V. Steric stabilization of negatively charged liposomes by cationic graft copolymer. *Langmuir* **2000**, *16*, 4877–4881.
102. Brunner, S.; Schuller, S.; Kircheis, R.; Wagner, E. PEGylated DNA/transferrin–PEI complexes: reduced interaction with blood components, extended circulation in blood and potential for systemic gene delivery. *Gene Ther.* **1999**, *6*, 595–605.
103. Voet, D.; Voet, J.G. *Biochemistry*, 1st Ed.; John Wiley & Sons: New York, 1990.

# Electrical Double-Layer Formation

**Kun-Lin Yang**

*Georgia Institute of Technology, Atlanta, Georgia, U.S.A.*

**Sotira Yiacoumi**

*School of Civil and Environmental Engineering, Georgia Institute of Technology, Atlanta, Georgia, U.S.A.*

**Costas Tsouris**

*Separations and Materials Research Group, Oak Ridge National Laboratory, Oak Ridge, Tennessee, U.S.A.*

## INTRODUCTION

When a surface is immersed or created in an aqueous solution, a discontinuity is formed at the interface where such physicochemical variables as electrical potential and electrolyte concentration change significantly from the aqueous phase to another phase. Because of the different chemical potentials between the two phases, charge separation often occurs at the interfacial region.<sup>[1]</sup> This interfacial region, together with the charged surface, is usually known as the electrical double layer (EDL). This layer, which can extend as far as 100 nm in a very dilute solution to only a few angstroms in a concentrated solution,<sup>[2]</sup> plays an important role in electrochemistry,<sup>[3,4]</sup> colloid science, and surface chemistry. Applications of the electrical double layer can be found in energy-storing devices in the form of capacitors, electrosorption of metal ions, purification of drinking water, nanomaterial processing, and sensor assembly.

The importance of the EDL has led to numerous studies, and many models were proposed in the past. The best known is the Gouy–Chapman model,<sup>[2]</sup> in which ions are considered as point charges and water is considered as a continuum. The electrical potential distribution and the concentration profiles can be predicted simply by using the Poisson–Boltzmann (P–B) equation. This theory, which has been proven very successful at low electrolyte concentrations and low surface charge densities,<sup>[5–7]</sup> has been applied to many EDL problems, such as heavy metal adsorption<sup>[8]</sup> and ion transport through membrane channels.<sup>[9,10]</sup> For higher concentrations of ions and higher surface charge densities, a better description of the EDL can be obtained by using primitive models,<sup>[5,7,11,12]</sup> in which water is still considered as a continuum but ions are considered as hard spheres with a point charge embedded at their centers. Various theoretical approaches such as molecular dynamics,<sup>[13]</sup> modified P–B equations,<sup>[14]</sup> integral equation theories,<sup>[15–19]</sup>

and Monte Carlo simulations<sup>[6,7]</sup> have been employed to study the primitive model. These studies confirm that the primitive model and the Gouy–Chapman model provide similar results for dilute solutions and low surface charge densities. However, the agreement between these two models becomes worse when a high ion concentration or a high surface charge density is encountered, especially if an asymmetric electrolyte is present in the solution.<sup>[7]</sup> A more realistic EDL model would be the non-primitive model,<sup>[13,20–27]</sup> in which water is considered as individual molecules instead of a continuum. For example, in the solvent primitive model (the simplest form of a non-primitive model),<sup>[23,24]</sup> water molecules are considered as neutral hard spheres. Because of the steric effect caused by water molecules, the ion concentration profile in the EDL shows strong oscillations, which cannot be observed in the primitive model. In this study, the results of Monte Carlo simulations used to compare the primitive and nonprimitive EDL models with the classical Gouy–Chapman model in 10- and 20-Å slit-type nanopores are reported.

## EDL AND SURFACE PROPERTIES

Because not all of interfaces are of the same kind, the characteristic behavior of the EDL depends on the properties of the particular interface. Ideally, such interfaces can be characterized either as polarizable or non-polarizable, depending on the interfacial resistance.<sup>[1]</sup> This idea can be better explained by the concept of an equivalent circuit. As shown in Fig. 1, the entire interfacial region can be represented by an equivalent circuit composed of an electrical double-layer capacitor (EDLC), an interfacial resistance, and a solution resistance, where  $C_{dl}$ ,  $R_f$ , and  $R_s$  represent the double-layer capacitance, the faradaic resistance, and the solution resistance, respectively. If  $R_f$  is very large (such as in metal–solution interfaces), the

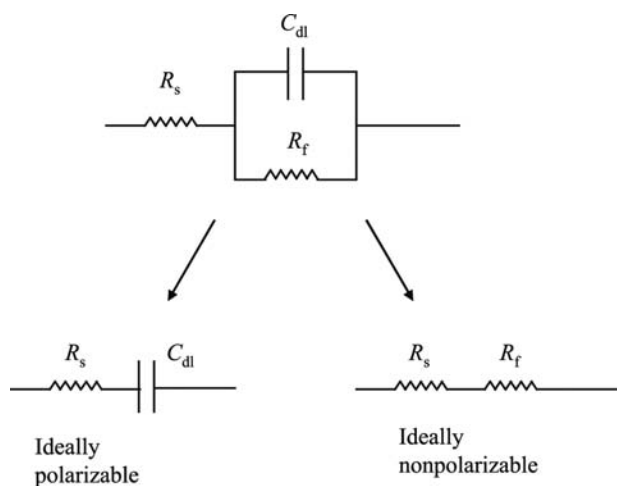


**Fig. 1** Equivalent circuit of the interface and two ideal cases: ideally polarizable and nonpolarizable interfaces.

equivalent circuit can be simplified as a double-layer capacitor in series with a solution resistance. Therefore any increase in electrical potential on the surface will cause counterions to accumulate in the EDLC, preventing electric current from passing through the interface. In this case, the interface is characterized as ideally polarizable. On the other hand, if  $R_f$  is very small, such as in the case of a Ag/AgCl surface in contact with NaCl solution, the equivalent circuit can be simplified as solution and faradaic resistances in series. In this situation, any slight change in the electrical potential on the surface results in the flow of electric current across the interface. Therefore such an interface is characterized as ideally non-polarizable. Although the non-polarizable interface has its own importance in areas such as reference electrodes, only the polarizable interface is a good EDLC.<sup>[1]</sup> Accordingly, the following discussion focuses on the polarizable interface and all of the interfaces investigated in the study are assumed to be ideally polarizable.

A schematic diagram of an ideally polarizable interface is shown in Fig. 2, in which the interface can be further divided by the inner Helmholtz plane (IHP) and outer Helmholtz plane (OHP). By definition, the IHP is the locus of the centers of specifically adsorbed dehydrated ions, while the OHP is the plane of closest approach of hydrated counterions.<sup>[2]</sup> The ions in the layer outside the OHP are mobile, and their distribution depends on the balance between the electrostatic interaction and the thermal diffusion; therefore, this layer is called the diffuse layer, or Gouy–Chapman layer. On the other hand, ions inside the OHP are immobilized because they are strongly bound with the charged surface (specific adsorption). The immobile ions constitute the Stern layer, or the Helmholtz layer.

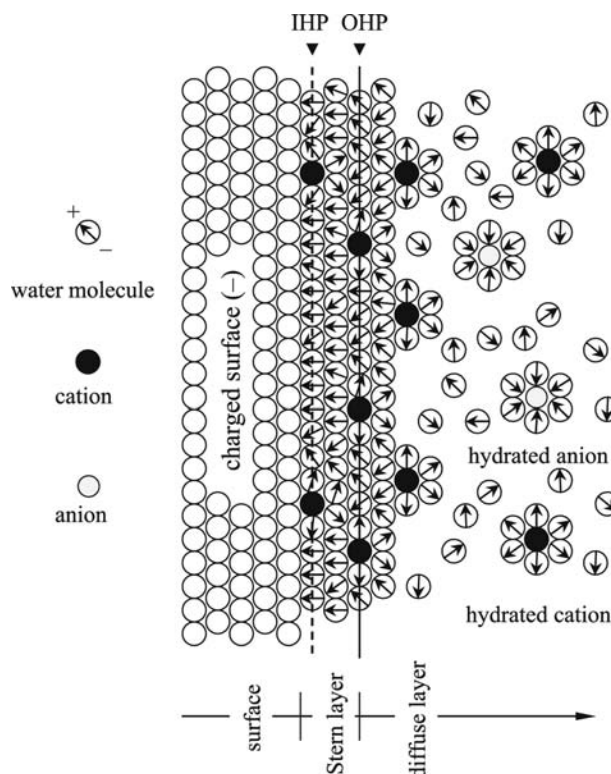


**Fig. 2** Schematic model of the EDL, showing the specifically adsorbed cations and the fully hydrated anions and cations on a negatively charged surface.

The EDL behaves like an electrical capacitor. When the surface potential is increased, the surface charge density increases as well. Because the Stern layer is very different from the diffuse layer, it is better to separate the entire EDL capacitor into a series of diffuse-layer and Stern-layer capacitors. Therefore the relationship between the double-layer, Stern-layer, and diffuse-layer capacitances can be written in the form

$$\frac{1}{C_{dl}} = \frac{1}{C_s} + \frac{1}{C_d} \quad (1)$$

where  $C_s$  and  $C_d$  are the Stern-layer and diffuse-layer capacitances, respectively.

Results of the EDL experiment involving NaF on the mercury surface<sup>[28]</sup> indicate that  $C_s$  has only a minimal dependency on the surface charge density or electrolyte concentration; therefore, it is customary to assume that  $C_s$  is constant at low surface charge density and low electrolyte concentration. On the other hand,  $C_d$  shows strong dependency on the surface charge density and electrolyte concentration. This capacitance has a minimum value when the surface charge density is zero and increases exponentially with the surface charge density and electrolyte concentration. Therefore under high electrolyte



concentration, the value of  $C_d$  is much larger than that of  $C_s$ , making the Stern layer more important than the diffuse layer. Because the overall capacitance is always determined by the smaller of two capacitors in series,  $C_{dl}$  is determined solely by  $C_s$  under such conditions. On the other hand, the diffuse layer is more important than the Stern layer for low electrolyte concentration and low surface charge density, and  $C_{dl}$  is determined solely by  $C_d$  in this case. Accordingly, by measuring  $C_{dl}$  at two extreme conditions (very concentrated and very dilute solutions),  $C_s$  and  $C_d$  can be determined independently. The experimental value of  $C_d$  can be compared with the theoretical value of  $C_d$  that is determined by using the classical Gouy–Chapman theory, which is described in the following section.

### GOUY–CHAPMAN THEORY

In order to maintain the overall electroneutrality of the system, an excess of charge on the surface side of the interface must attract an equal amount of oppositely charged ions in the diffuse layer, in which the electrical potential distribution is given by the Poisson equation:

$$\nabla^2\psi = -\frac{\rho}{\varepsilon} \quad (2)$$

where  $\nabla^2$  is the Laplacian operator,  $\psi$  is the relative electrical potential between the diffuse layer and the bulk phase,  $\varepsilon$  is the dielectric constant of the medium, and  $\rho$  is the volume charge density given by

$$\rho = \sum_i N_i z_i e \quad (3)$$

In this expression,  $z_i$  is the valence of ions of type  $i$ ,  $e$  is the elementary charge, and  $N_i$  is the number of ions of type  $i$ . According to the Boltzmann distribution,  $N_i$  can be expressed as

$$N_i = N_{i0} \exp\left[-\frac{z_i e(\phi - \phi_b)}{kT}\right] \quad (4)$$

where  $k$  is the Boltzmann constant,  $T$  is the absolute temperature,  $N_{i0}$  is the bulk concentration of ions, and  $\phi$  and  $\phi_b$  are the absolute electrical potentials in the double-layer region and in the bulk phase, respectively. It is convenient to define the reference electrical potential located in the bulk phase; therefore,  $\phi_b = 0$  and  $\phi$  can be represented by  $\psi$ . When Eqs. (2), (3), and (4) are combined, the Poisson–Boltzmann equation is then obtained:

$$\nabla^2\psi = -\frac{e}{\varepsilon} \sum_i N_{i0} z_i e \exp\left(\frac{-z_i e\psi}{kT}\right) \quad (5)$$

If the solution contains only single  $z:z$ -type electrolyte, Eq. (5) can be further simplified for a one-dimensional EDL system:

$$\frac{d^2\psi}{dx^2} = \frac{2N_0 z e}{\varepsilon} \sinh\left(\frac{ze\psi}{kT}\right) \quad (6)$$

The second-order differential equation given by Eq. (6) can be integrated by multiplying both sides by  $2(d\psi/dx)$ , followed by an integration with respect to  $x$ :

$$\int \frac{d}{dx} \left(\frac{d\psi}{dx}\right)^2 dx = \int \frac{4N_0 z e}{\varepsilon} \sinh\left(\frac{ze\psi}{kT}\right) d\psi \quad (7)$$

Integrating from the bulk solution where  $\psi = 0$  and  $d\psi/dx = 0$  up to some point in the double layer yields the first-order differential equation of  $\psi$ .

$$\frac{d\psi}{dx} = \frac{-2\kappa kT}{ze} \sinh\left(\frac{ze\psi}{2kT}\right) \quad (8)$$

where  $\kappa = (2N_A I e^2 / \varepsilon kT)^{1/2}$  is the Debye–Hückel parameter for a symmetrical 1:1 electrolyte,  $I$  is the ionic strength, and  $N_A$  is Avogadro's number.

The charge density in the diffuse layer,  $\sigma_d$ , is related to the volume charge density,  $\rho$ , by

$$\sigma_d = \int_d^\infty \rho dx \quad (9)$$

From Eq. (2),  $\rho$  can also be expressed as a second-order derivative of the electrical potential for a one-dimensional system; therefore,

$$\sigma_d = \int_\infty^d \varepsilon \frac{d^2\psi}{dx^2} dx = \varepsilon \left[\frac{d\psi}{dx}\right]_\infty^d \quad (10)$$

Because  $\psi = 0$  as  $x \rightarrow \infty$ , the derivative  $(d\psi/dx)_{x \rightarrow \infty} = 0$  and  $\sigma_d = \varepsilon(d\psi/dx)_{x=d}$ . From Eq. (8), a useful relationship between  $\psi_d$  and  $\sigma_d$  can be obtained:

$$\sigma_d = \frac{-2\varepsilon\kappa kT}{ze} \sinh\left(\frac{ze\psi_d}{2kT}\right) \quad (11)$$

By definition, the differential capacitance of the diffuse double layer,  $C_d$ , can be expressed as

$$C_d = -\frac{d\sigma_d}{d\psi_d} \quad (12)$$

Taking the derivative of Eq. (11) with respect to  $\psi_d$ , the expression of  $C_d$  can therefore be obtained as

$$C_d = \varepsilon\kappa \cosh\left(\frac{ze\psi_d}{2kT}\right) \quad (13)$$

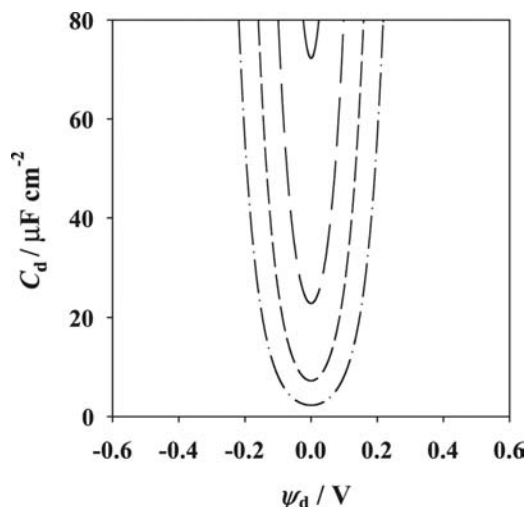


**Fig. 3** Diffuse-layer capacitance of the EDL as a function of diffuse-layer potential for several concentrations based on Eq. (13): solid line, 0.1 M; long-dashed line, 0.01 M; short-dashed line, 0.001 M; dot-dashed line, 0.0001 M.

Based on Eq. (13), Fig. 3 plots the values of  $C_d$  as a function of  $\psi_d$ . As shown in the figure,  $C_d$  is very small at very low electrolyte concentration; therefore, according to Eq. (1),  $C_{dl}$  is determined solely by  $C_d$  at low concentration. On the other hand,  $C_d$  is very large at high electrolyte concentration. In this case,  $1/C_d$  becomes insignificant and  $C_{dl}$  is solely determined by  $C_s$ .

## EDL IN NANOPORES

### Gouy–Chapman Model

In the discussion of EDL formation adjacent to a single charged surface, only one side of the interface is considered and the boundary condition,  $\psi = 0$  as  $x \rightarrow \infty$ , is always true. However, if the EDL is confined by two charged surfaces such as in a slit-type pore, this boundary condition is valid only when the separation distance between these two charged surfaces, or the diameter of the pore in case of a cylindrical pore, is large enough. When the separation distance is decreased, the EDLs of the two surfaces begin to overlap in the central region as shown in Fig. 4. In this case, Eq. (6) still applies to the system but with a new boundary condition:

$$\frac{d\psi}{dx} = 0 \text{ and } \psi = \psi_m \text{ at } x = \frac{D}{2} \quad (14)$$

where  $\psi_m$  is the electrical potential at the midplane and  $D$  is the separation distance between the two identical charged surfaces. Thus the diffuse-layer charge density can be written as

$$\sigma_d = -\sqrt{4\varepsilon RTI} \left[ \cosh\left(\frac{e\psi_0}{kT}\right) - \cosh\left(\frac{e\psi_m}{kT}\right) \right]^{1/2} \quad (15)$$

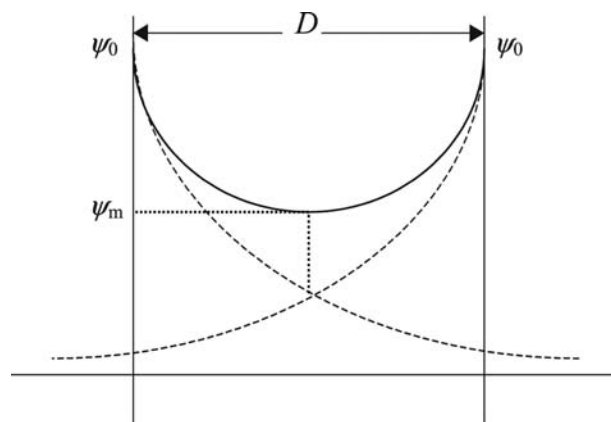


**Fig. 4** The overlap of two diffuse layers in a nanopore. The electrical potential distribution adjacent to a single double layer is represented by the dashed line; the solid line is the electrical potential distribution that results from the overlapping of two EDLs; and  $\psi_0$  and  $\psi_m$  are the surface and midplane potentials, respectively.

where  $R$  is the ideal gas constant. The second term inside the bracket is the contribution from the overlapping of EDLs. When the two charged surfaces are far away from one another,  $\psi_m$  approaches zero and the second term becomes unity. If this condition is satisfied, then Eq. (15) can be simplified to Eq. (11), and the two charged surfaces can be viewed as two independent charged surfaces. Therefore the overlapping effect becomes important as the distance between two charged interfaces decreases, as in the case for a nanopore. When the overlapping increases to the extent that make  $\psi_0 = \psi_m$ , the EDLs no longer exist in the nanopore and  $\sigma_d = 0$ . In practical applications, especially for nanoporous materials, it is doubtful that the microporosity ( $< 2$  nm) contributes to EDL capacitance, because the effect of overlapping is too strong.<sup>[29]</sup> Moreover, it is questionable whether the P–B equation and the Gouy–Chapman model are applicable at a very small length scale.

### Primitive Model and Grand Canonical Monte Carlo (GCMC) Simulations

As indicated in the ‘‘Introduction’’, a better approach to the EDL problem would be the primitive model combined with Monte Carlo simulations, especially the GCMC. The advantage of the GCMC method is that the chemical potential, rather than the total number of ions, is kept constant. This feature is very important for the EDL problem because the number of counterions increases and the number of coions decreases considerably in the EDL region. Therefore only GCMC can provide an unambiguous way to determine the total number of ions in the EDL. Generally, a GCMC step includes two types of options. The first is a move in the canonical

ensemble, in which a randomly selected ion is moved from an initial position  $r_i$  to a new position  $r_j$ , and the move is accepted with a probability of  $f_{ij}$ , which is given by

$$f_{ij} = \min\{1, Y \exp[-\beta(U_j - U_i)]\} \quad (16a)$$

where  $Y = 1$ ,  $\beta = (kT)^{-1}$ , and  $U_i$  and  $U_j$  are the configurational energies at positions  $i$  and  $j$ , respectively. The second option involves the addition or deletion of a pair of positive and negative ions (so that the electroneutrality is still maintained during the addition/deletion processes). If a pair of ions is inserted in configuration  $i$  to reach configuration  $j$ , then the number of positive ions and the number of negative ions in state  $j$  are  $N_j^+ = N_i^+ + 1$  and  $N_j^- = N_i^- + 1$ , respectively. The transition probability from configuration  $i$  to  $j$  is given by Eq. (16a), with a different value assigned to  $Y$ :

$$Y = \frac{N_+ N_-}{N_j^+ N_j^-} \gamma_{\pm}^2 \quad (16b)$$

where  $N_+$  and  $N_-$  are the original numbers of positive and negative ions in the bulk phase of the same volume, respectively, and  $\gamma_{\pm}$  is the mean ionic activity coefficient in the McMillan–Mayer system at solution concentration  $C_0$ . In the primitive model, the activity coefficient,  $\gamma_{\pm}$ , was found to be  $-0.127$  for 1.0 M electrolyte concentration.<sup>[30]</sup>

The total potential energy,  $U_T$ , of an electrolyte system is the sum of the single-ion energy  $U_1$ , and the two-ion energy,  $U_2$ :

$$U_T = U_1 + U_2 \quad (17)$$

The only single-ion energy term,  $U_1$ , is the electrostatic interaction between an ion and the two charged surfaces. Thus  $U_1$  can be expressed as<sup>[20]</sup>

$$U_1 = \infty, \quad z_1, z_2 < d/2 \quad (18a)$$

$$U_1 = \frac{1}{4\pi\epsilon_0\epsilon_r} \sum_{i=1}^N q_i [\sigma_1 u(z_1, W) + \sigma_2 u(z_2, W)], \quad z_1, z_2 \geq d/2 \quad (18b)$$

$$u(z, W) = \left\{ 4W \ln\left(\frac{0.5 + r_1}{r_2}\right) - |z| \left[ 2\pi - 4 \tan^{-1} \frac{4|z|r_1}{W} \right] \right\} \quad (18c)$$

where  $W$  is the width and height of the square charged surfaces, and  $z_1$  and  $z_2$  are the distances between an ion carrying charge  $q_i$  and the first and second charged surfaces, respectively. The charge densities of these two charged surfaces are  $\sigma_1$  and  $\sigma_2$ , respectively. The

parameters  $r_1$  and  $r_2$  are given by

$$r_1 = \sqrt{0.5 + \left(\frac{z}{W}\right)^2} \quad (18d)$$

and

$$r_2 = \sqrt{0.25 + \left(\frac{z}{W}\right)^2} \quad (18e)$$

The two-ion energy,  $U_2$ , is basically the pair interaction between two ions. However, because the long-range electrostatic interaction is extended far beyond the small simulation box, an additional term needs to be used to properly account for the long-range effect. Therefore periodic boundary conditions are imposed in the dimensions  $x$  and  $y$ , and the traditional minimum image method is used.<sup>[31]</sup> In the  $z$  dimension, the long-range interaction is handled by a modified charged-sheet (CS) method proposed by Boda and Chan,<sup>[20]</sup> in which each ion forms an infinite CS minus the central square hole occupied by the simulation box. Therefore the two-particle energy is the sum of Coulombic interaction between two ions inside the simulation box and the interaction between one ion and the CS formed by another ion. The term  $U_2$  can be expressed as

$$U_2 = \infty, \quad r_{ij} < d \quad (19a)$$

and

$$U_2 = \frac{1}{4\pi\epsilon_0\epsilon_r} \left\{ \sum_{i=1}^{N-1} \sum_{j=i+1}^N \frac{q_i q_j}{r_{ij}} + \frac{q_i q_j}{W^2} \sum_{i=1}^N \sum_{j=1}^N [u(z_{ij}, \infty) - u(z_{ij}, W)] \right\}, \quad r_{ij} \geq d \quad (19b)$$

In this expression,  $r_{ij}$  is the magnitude of the vector  $\mathbf{r}_{ij}$  between the  $i$ -th and  $j$ -th ions, and  $z_{ij}$  is the  $z$  component of  $\mathbf{r}_{ij}$ .

Without loss of generality, both surfaces were assumed to be negatively charged, and an equal amount of excessive counterions in the solution phase was used to balance the charge on the surfaces. Moreover, the water is considered as a continuum with a dielectric constant  $\epsilon_r = 78.5$ , and the ions are considered as hard spheres with diameter  $d = 4.25$  Å as in the case for other primitive models found in the literature.<sup>[30]</sup> In the GCMC simulations, an equal probability of 1/3:1/3:1/3 was used to insert, delete, or move an ion. The maximum traveling distance between  $(-\eta_{\max}, \eta_{\max})$  was adjusted every 10 passes to maintain an acceptance ratio of 0.5. More details of the GCMC

simulation procedure for electrolyte systems can be found elsewhere.<sup>[6,7]</sup>

### Nonprimitive Model and Canonical Monte Carlo (CMC) Simulations

In the non-primitive model of the EDL, the water is considered as individual molecules instead of a continuum. To better describe the properties of water, the TIP4P-FQ water model,<sup>[32–34]</sup> in which the charge on each atomic site is allowed to fluctuate in response to its surrounding environment, is employed. A single water molecule has four atomic sites: one O, two H, and one M, representing oxygen, hydrogen, and an imaginary charged site, respectively. The oxygen atomic site, O, is the only Lennard–Jones (LJ) center for the water molecule and carries no charge. The negative charge of  $-1.04 e$  is carried by the imaginary site M, which is located  $0.15 \text{ \AA}$  away from the oxygen atom, along the bisector of the angle of the H–O–H bond. Two hydrogen atomic sites carry charges of  $+0.52e$  to balance the negative charge on the M site. The angle of the H–O–H bond is  $104.52^\circ$ , and its length is  $0.9572 \text{ \AA}$ .

The interaction energy between ion and ion, and ion and water can be divided into LJ and electrostatic energy. The total LJ energy,  $U_{LJ}$ , between any two water molecules, any two ions, or between one water molecule and one ion can be expressed as

$$U_{LJ} = \sum_{i=1}^{N-1} \sum_{j=i+1}^N \left( \frac{LJA}{r_{ij}^{12}} - \frac{LJC}{r_{ij}^6} \right) \quad (20)$$

where  $N$  is the number of water molecules plus the number of ions and LJA and LJC are the LJ parameters. In the current study, sodium and chloride ions are selected as representative cations and anions, respectively. LJ parameters between the same species are found in the literature for water,<sup>[35]</sup> sodium ion, and chloride ion,<sup>[36]</sup> otherwise, they can be obtained by the Lorentz–Berthelot mixing rule. All LJ parameters used in the simulations are listed in Table 1.

The electrostatic energy includes single-atom and two-atom interaction energies. The interaction energy between charged surfaces and atoms or ions constitutes the single-atom term in the system, and its value can be calculated by using Eqs. (18a) and (18b) with the dielectric constant,  $\epsilon_r$ , as unity and  $N$  becoming the total number of charged atomic sites of water molecules and ions. Similarly,  $d$  is the equivalent hard-sphere diameter of water molecule or ions, which is assumed to be  $2.5 \text{ \AA}$  for water and  $2.0 \text{ \AA}$  for ions. The use of Eqs. (18a) and (18b) implies that the CS method is used to calculate the long-range electrostatic

**Table 1** Lennard–Jones parameters used in eq. (20) for pair interactions

Type	LJC (kcal $\text{\AA}^6/\text{mol}$ )	LJA $\times 10^{-3}$ (kcal $\text{\AA}^{12}/\text{mol}$ )
O ... O	1138.0	1131.0
Na <sup>+</sup> ... Na <sup>+</sup>	300.0	14.0
Cl <sup>-</sup> ... Cl <sup>-</sup>	3500.0	26,000.0
O ... Na <sup>+</sup>	584.3	125.8
O ... Cl <sup>-</sup>	1995.7	5422.0
Na <sup>+</sup> ... Cl <sup>-</sup>	1024.7	603.3

interaction. Traditionally, the use of Ewald sum<sup>[31]</sup> has proven to be more accurate in the non-primitive model; however, the computational cost is very high. On the other hand, although the CS technique is easy to implement and the computational cost is relatively low, it shows strong size dependency when the box size is too small<sup>[37]</sup>. In the current study, the CS method is preferred because only the EDL in a slit-type nanopore is of interest; therefore, the width of the simulation box can be chosen to be large enough ( $W = 100 \text{ \AA}$ ) to avoid the problem of size dependency. More importantly, using CS allows a simulation to be performed more effectively. Therefore a larger simulation box can be used and the artificial periodicity can be reduced.

The two-atom term includes the intermolecular (ion–ion and ion–water) and the intramolecular interaction within the same water molecule. The former can be calculated by Eq. (19b), with  $N$  becoming the total number of charged atomic sites of water and ions, and the latter,  $U_3$ , can be calculated by

$$U_3 = \sum_{i=1}^N \sum_{\alpha} \sum_{\beta} (J_{\alpha\beta} q_{i\alpha} q_{i\beta}) \quad (21)$$

where  $q_{i\alpha}$  and  $q_{i\beta}$  are the charges of atoms  $\alpha$  and  $\beta$  on the same water molecule  $i$  and  $J_{\alpha\beta}$  is a constant that is derived elsewhere.<sup>[32]</sup> In this study,  $J_{OH}$  and  $J_{HH}$  are  $286.4$  and  $203.6 \text{ kcal}/(\text{mol } e^2)$ , respectively.

Because charge fluctuation occurs among different atomic sites within a water molecule, the asymmetric distribution of partial charge at different atomic sites has to be accounted for by an additional energy term,  $U_{FQ}$ :

$$U_{FQ} = \sum_{i=1}^N \sum_{\alpha} \left( \bar{\chi}_{\alpha}^0 q_{i\alpha} + \frac{1}{2} J_{\alpha\alpha}^0 q_{i\alpha}^2 \right) \quad (22)$$

where  $\bar{\chi}_{\alpha}^0$  is the Mulliken electronegativity parameter of the isolated atom  $\alpha$  and  $J_{\alpha\alpha}^0$  is twice the hardness of the electronegativity of an atom. The parameters used in this study are  $(\bar{\chi}_{O}^0 - \bar{\chi}_{H}^0) = 68.49 \text{ kcal}/(\text{mol } e)$ ,  $J_{OO}^0 = 371.6 \text{ kcal}/(\text{mol } e^2)$ , and  $J_{HH}^0 = 353.0 \text{ kcal}/(\text{mol } e^2)$ .

More detailed discussion of the TIP4P-FQ model can be found elsewhere.<sup>[32]</sup>

The total number of ions in the simulation box is obtained from the GCMC simulations. Water molecules are then added to achieve a bulk water density of  $1.0 \text{ g/cm}^3$ . However, partial volume in the simulation is occupied by hydrated ions; therefore, the total volume available to water molecules is the volume of the simulation box minus the volume occupied by the ions in their hydrated form. The radii of hydrated sodium and chloride ions are found to be 2.3 and 3.2 Å, respectively, which correspond to an excluded volume of 51.0 and  $137.3 \text{ Å}^3$  for a single hydrated sodium and chloride ion, respectively.

Metropolis Monte Carlo simulations based on the canonical ensemble ( $N, V, T$ ), that is, CMC simulations, were then carried out for an electrolyte system including TIP4P-FQ water molecules and ions between two charged surfaces. The dimensions of the simulation box in the  $x, y, z$  directions ( $W \times W \times L$ ) were  $100 \times 100 \times 10 \text{ Å}$  (for a 10-Å nanopore) and  $100 \times 100 \times 20 \text{ Å}$  (for a 20-Å nanopore), respectively, and periodic boundary conditions similar to those employed in GCMC simulations were also used here. For each step, a water molecule or a single ion was allowed to move a random distance between  $(-\eta_{\max}, \eta_{\max})$ . Water molecules were also rotated at an angle between  $(-\phi_{\max}, \phi_{\max})$  around three randomly chosen axes and each charge was randomly fluctuated between  $(-\delta_{\max}, \delta_{\max})$ , while intramolecular electroneutrality was maintained. The maximum degree of rotation,  $\phi_{\max}$ , and the maximum amount of charge allowed to fluctuate,  $\delta_{\max}$ , were also adjusted every 10 passes in the program to reach an average acceptance ratio of 0.5.

## RESULTS AND DISCUSSION

All simulations were carried out on either an IBM SP with a total of 18 nodes and 72 CPUs or on SGI-Origin 3400 supercomputer with 16 CPUs. The original computer code was written in FORTRAN 95 and parallelized by OPEN-MP.<sup>[38]</sup> In the Monte Carlo simulations, every single simulation started from an initial configuration with randomly distributed ions and water molecules (only in the non-primitive model). Initial configurations were preequilibrated until fluctuations of the total energy were stabilized. In the GCMC simulations, 2 million passes were performed. The final 500 K passes were used to calculate the ensemble average of the total number of ions and the ion concentration profiles. For the final ion configuration, CMC simulations were performed for another 500 K (for a 10-Å pore) or 100 K passes (for a 20-Å pore). The final 20% of the passes were then used to calculate the ensemble average.

## Grand Canonical Monte Carlo (GCMC) Simulations of the Primitive Model

Two simulation boxes were used in the GCMC simulations. A smaller box ( $W \times W \times L = 200 \times 200 \times 10 \text{ Å}$ ) was used to simulate the EDL in a 10-Å slit-type nanopore, while a larger one ( $200 \times 200 \times 20 \text{ Å}$ ) was used to simulate a 20-Å nanopore. Four different initial conditions used in the simulations are summarized in Table 2. Comparisons of the ion concentration profiles for the Gouy–Chapman and primitive models in the nanopore at  $-0.05$  and  $-0.1 \text{ C/m}^2$  are presented in Fig. 5A and B, respectively. As shown in Fig. 5A, the maximum concentration adjacent to the charged surfaces is slightly overestimated by the Gouy–Chapman model because the steric effect is neglected. Moreover, because more counterions accumulate at the surface and a stronger shielding effect occurs as a result, the coion concentration at the central region predicted by the Gouy–Chapman model is also higher than that predicted by the primitive model. Nevertheless, the Gouy–Chapman model still gives a fairly good approximation of the ion concentration profile in the entire range. For a higher surface charge density ( $-0.1 \text{ C/cm}^2$ ), as shown in Fig. 5B, the counterion concentration is higher than that shown in Fig. 5A and the coion concentration is lower. This feature implies an ion-exclusion effect in nanopores—most coions are pushed out of the pores by strong electrostatic force and, therefore, only counterions can exist.

In the case of a larger pore, 20 Å for example, the counterion concentration is still higher than the coion concentration throughout the entire pore space, as shown in Fig. 6A and B. However, their values are closer in the central region, meaning that equal numbers of both ions exist in this region and the bulk phase can be reproduced. Again, the Gouy–Chapman model gives a very good approximation for a larger-size pore as well, and no significant difference can be observed between the primitive and the Gouy–Chapman models. Because the effect of pore size is more pronounced than that of the surface charge density,

**Table 2** Average number ( $\text{Avg}N$ ) of ions in the EDL as calculated by the primitive model and GCMC simulations at different conditions

Run no.	$W$ (Å)	$L$ (Å)	$dN^a$	$\sigma_1, \sigma_2$ ( $\text{C/m}^2$ )	$\text{Avg}N$
1	200	10	256	-0.05	364
2	200	10	512	-0.1	554
3	200	20	256	-0.05	812
4	200	20	512	-0.1	962

<sup>a</sup>The difference between the numbers of counterions and coions. The initial number of ions in the nonprimitive model is calculated based on the average number of ions listed in this table.

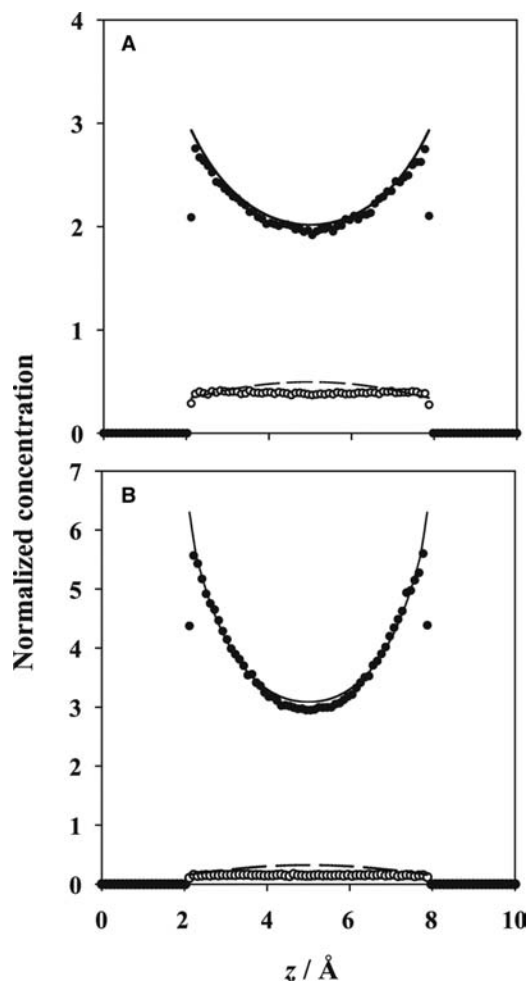


**Fig. 5** Comparison of ion concentration profiles in a 10-Å slit-type nanopore, based on the Gouy–Chapman and primitive models at surface charge densities of (A)  $-0.05 \text{ C/m}^2$  and (B)  $-0.1 \text{ C/m}^2$ . The solid and dashed lines are the normalized concentrations of counterion and coion, respectively, based on the Gouy–Chapman model; the solid and open circles are the normalized concentrations of counterion and coion, respectively, in the primitive model. The concentration profiles are also subject to two hard-sphere exclusion regions. *Source:* From 0 to 2.125 Å on the left and from 7.875 to 10 Å on the right. ©American Institute of Physics.

only the effect of pore size and ion species was studied in the non-primitive model; therefore, the total number of ions obtained in Run 1 and Run 3 (Table 2) are used in the CMC simulations of the non-primitive model.

### Canonical Monte Carlo (CMC) Simulations of the Non-primitive Model

To demonstrate that water molecules do play an important role in the formation of EDL and to understand

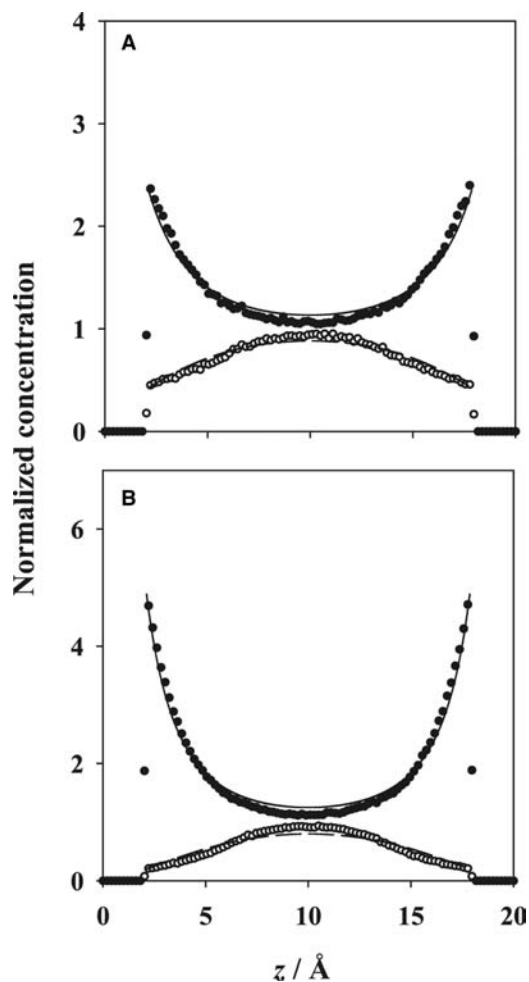


**Fig. 6** Comparison of ion concentration profiles in a 20-Å slit-type nanopore, based on the Gouy–Chapman and primitive models at surface charge densities of (A)  $-0.05 \text{ C/m}^2$  and (B)  $-0.1 \text{ C/m}^2$ . The solid and dashed lines are the normalized concentrations of counterion and coion, respectively, based on the Gouy–Chapman model; the solid and open circles are the normalized concentrations of counterion and coion, respectively, in the primitive model. *Source:* ©American Institute of Physics.

the effect of pore size and ion species on EDL, a non-primitive model together with CMC simulations was used to study this problem for several initial conditions (Table 3). An illustration of a single CMC simulation of both electrolyte (NaCl) and water molecules in a 20-Å negatively charged nanopore (Run 3) is shown in Fig. 7. A brief look at this figure reveals that the charged surface is covered by water molecules rather than counterions, as suggested in the classical Gouy–Chapman model. This observation is further confirmed in the following discussion.

Results in Fig. 8A show the comparison of ion concentration profiles for the Gouy–Chapman and the nonprimitive models in a 10-Å pore, with a surface



**Table 3** Initial conditions used in the CMC simulations of the non-primitive model

Run no.	$W$ (Å)	$L$ (Å)	$\sigma_1, \sigma_2$ (C/m <sup>2</sup> )	$N_p$	$N_n$	$N_w$
1	100	10	-0.05	77	13	2331
2	100	10	+0.05	13	77	2134
3	100	20	-0.05	133	69	5333
4	100	20	+0.05	69	133	5136

The number of ions was obtained from the GCMC study.  $N_p$  is the number of positive ions,  $N_n$  is the number of negative ions, and  $N_w$  is the number of water molecules used in the simulations.

charge density of  $-0.05$  C/m<sup>2</sup> on both surfaces (Run 1). The Gouy–Chapman model predicts that an excess number of positive ions (i.e., sodium ions) accumulate adjacent to the negatively charged surfaces and then decay exponentially toward the center. However, it is surprising to see that this is not the case predicted by the nonprimitive model. In fact, in the latter case, the maximum counterion concentration is located at the center and then decays toward the surfaces. This unique feature can be explained by a strongly adsorbed water layer at the charged surfaces. Because water molecules are polar, they tend to compete with other charged species and cause the approaching ions to remain in the diffuse layer rather than be adsorbed on the charged surfaces.<sup>[26,39]</sup> When compared with the water distribution shown in Fig. 8B, distinct water peaks are shown in the region adjacent to the charged surfaces. Thus it is sufficiently clear that water molecules are more favored at the charged surfaces than ionic species are.

A similar argument that ions accumulate at the center of a nanopore was also made by Williams et al.,<sup>[40]</sup> who conducted a neutron diffraction experiment involving vermiculite clay. Williams et al. observed that the negatively charged clay surfaces were covered by two layers of partially ordered water molecules and that the concentration of counterion ( $C_3H_7NH_3^+$ ) reached a maximum at the center of the interlayer

region. This observation was supported by theoretical analysis of a one-dimensional adsorption model and the competition between water and counterions.<sup>[41]</sup> The results showed that fewer than 15% of the sites are bound with counterions. This feature may have important implications for ion transport through a charged nanochannel, an issue that has relevance for many physical, chemical, and biological problems. If water molecules keep ions from being adsorbed on the charged surface of a nanochannel, the ion transport should be faster than expected because ions are not constrained by the charged surface. As a result, higher ionic mobility can be expected.

Another discrepancy between the non-primitive and Gouy–Chapman models is that the ion concentration predicted by the non-primitive model is much higher than that predicted by the Gouy–Chapman model. This discrepancy can be explained by the strongly adsorbed water layer as well. Because water molecules cover the negatively charged surfaces, the effective volume of the nanopores to accommodate ions is reduced. The initial number of ions in the nonprimitive model is estimated from the primitive model, which does not take this layer of water into account; therefore, the initial number of counterions is overestimated. This effect may not be critical in a mesopore or macropore, but is considerably larger in a 10-Å nanopore. If a water molecule is considered as a hard sphere with a 2.5-Å diameter, 50% of the pore volume is occupied by a compact layer of strongly adsorbed water molecules and the number of ions should be decreased at least 50%.

When both surfaces are switched from negatively charged to positively charged, more anions (chloride ions in this case) will be present in the solution phase (Table 3, Run 2). In the primitive or Gouy–Chapman model, cations and anions are treated as similar hard spheres, except for the fact that the charges are of opposite sign. Therefore changing the sign of the surface charge does not change the counterion

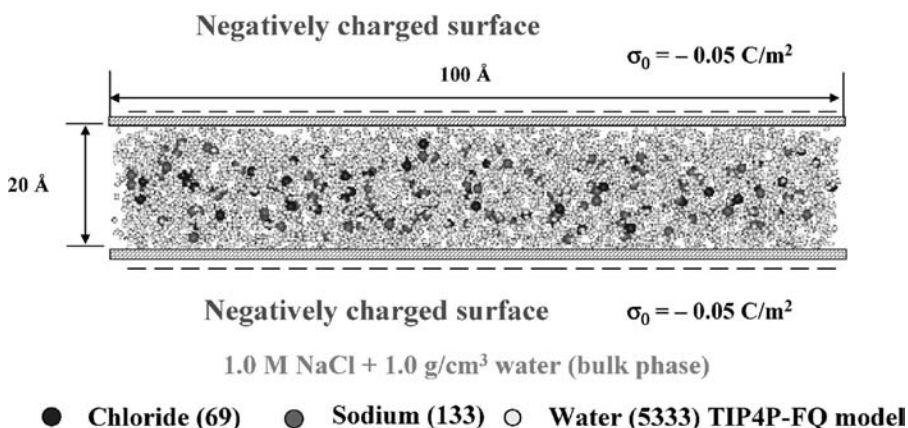


**Fig. 7** A Monte Carlo simulation of a 1.0 M NaCl electrolyte solution in a 20-Å charged nanopore. The surface charge density on each surface is  $-0.05$  C/m<sup>2</sup>, and the numbers of chloride, sodium, and water molecules are 69, 133, and 5333, respectively.

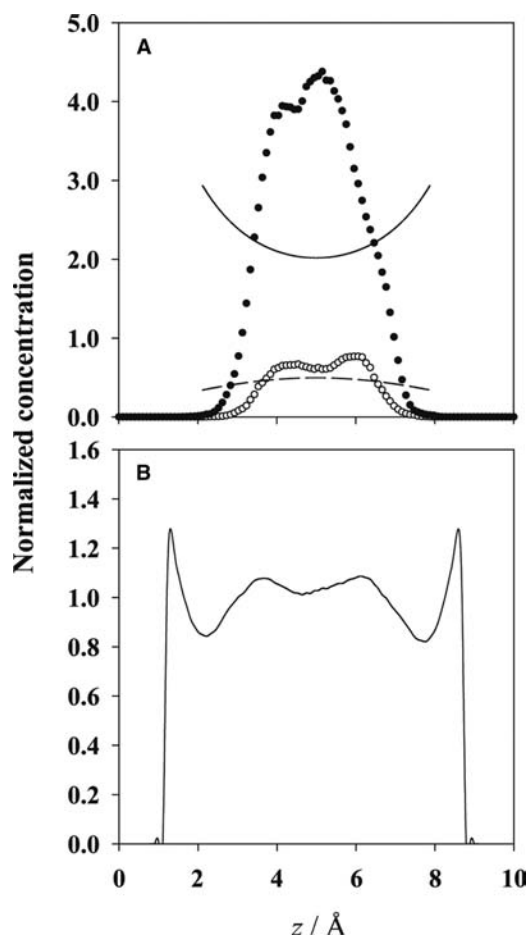


**Fig. 8** Ion and water concentration profiles in a 10-Å slit-type nanopore with a surface charge density of  $-0.05 \text{ C/m}^2$ . (A) Ion profiles: The solid and open circles are the normalized concentrations of sodium ion (counterion) and chloride ion (coion), respectively, based on the non-primitive model and CMC simulations. The solid and dashed lines are the normalized concentrations of counterion and coion, respectively, based on the Gouy–Chapman model, provided for comparison. (B) Water profile: The solid line is the normalized concentration of water based on the location of the oxygen atom. *Source:* ©American Institute of Physics.

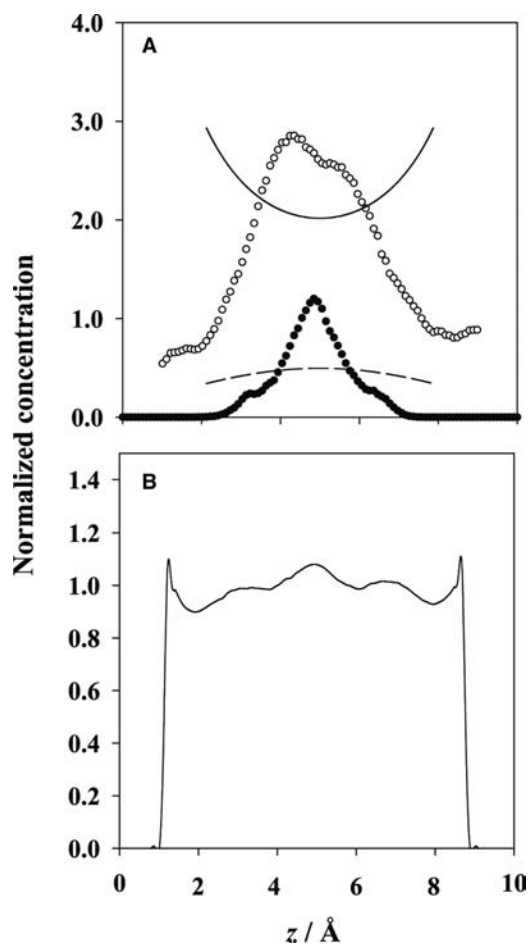


**Fig. 9** Ion and water concentration profiles in a 10-Å slit-type nanopore with a surface charge density of  $+0.05 \text{ C/m}^2$ . (A) Ion profiles: The solid and open circles are the normalized concentrations of chloride ion (counterion) and sodium ion (coion), respectively, based on the non-primitive model and CMC simulations. The solid and dashed lines are the concentration profiles of counterion and coion, respectively, based on the Gouy–Chapman model, provided for comparison. (B) Water profile: The solid line is the normalized concentration of water based on the location of the oxygen atom. *Source:* ©American Institute of Physics.

concentration profile; as a result, the solid and dashed lines in Figs. 8A and 9A are identical. However, in the non-primitive model, each species is unique. As shown in Table 1, the LJ parameters for the chloride ion differ greatly from those of the sodium ion. Consequently, the concentration profile of chloride ions in Fig. 9A is also considerably different from that of sodium ions in Fig. 8A. Because of the larger volume of the chloride ion and the lower hydration energy, a small amount of chloride ion is specifically adsorbed on the charged surfaces, which can be observed from the non-zero concentration at 2 and 8 Å in Fig. 9A. This point can be further demonstrated by observing the water density profile in Fig. 9B. In this figure, the water peaks near

the charged surfaces are less obvious than those shown in Fig. 8B. This feature implies that the chloride ions tend to compete with water molecules for adsorption and that contact adsorption of chloride is also energetically favorable.

Different adsorption behaviors of sodium and chloride ions can be explained by their hydration radii and the pair-distribution functions with water molecules. The ion–oxygen pair-distribution function and the accumulated number of water molecules are shown in Fig. 10A and B, respectively. As shown in Fig. 10A, the sodium ions are smaller (hydrated radius: 2.3 Å) than the chloride ions (hydrated radius: 3.2 Å). Water molecules are associated with the sodium ion in a very

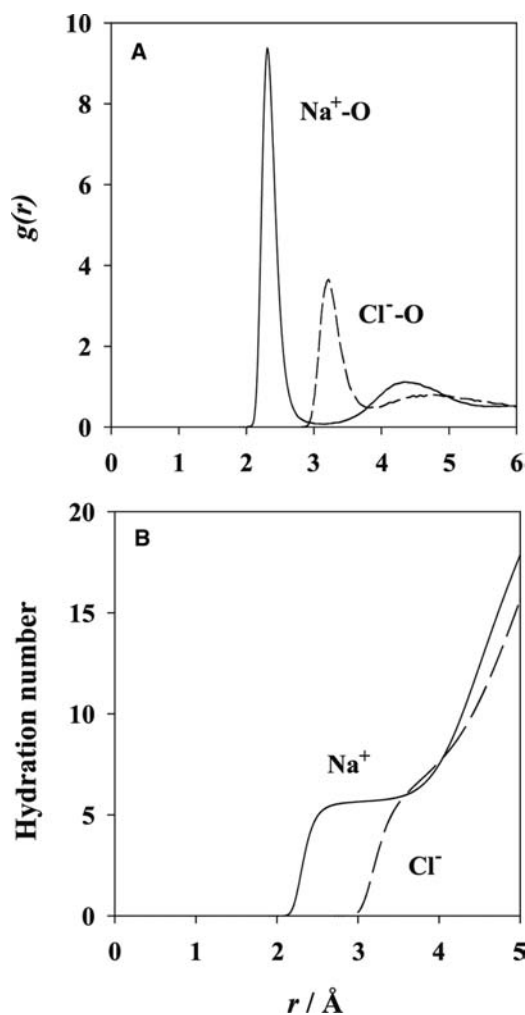


**Fig. 10** Comparison of the hydration radius and the hydration number of sodium and chloride ions. (A) Ion–water pair-distribution function,  $g(r)$ : the solid line represents sodium ion, and the dashed line represents chloride ion. The hydration radius for sodium ions is estimated to be 2.3 Å, while that for chloride ions is 3.2 Å. (B) Hydration number: For sodium ion (solid line) and chloride ion (dashed line), the hydration numbers are estimated to be 6 and 7, respectively. *Source:* ©American Institute of Physics.

compact hydrated shell (sharp peak) when compared with the loose hydrated shell (broad peak) surrounding the chloride ion. The number of hydrated water molecules can be estimated from Fig. 10B, in which the number of hydrated water molecules around a sodium ion is approximately 6, while that of a chloride ion is about 7. Because water molecules are loosely bound with chloride ions, chloride ions are more likely than sodium ions to lose their hydration water when both approach a charged surface. This phenomenon explains the contact adsorption of chloride ions at the charged surfaces. However, the bulky hydrated chloride ions prevent other chloride ions from forming a dense layer at the charged surfaces. Thus only a small

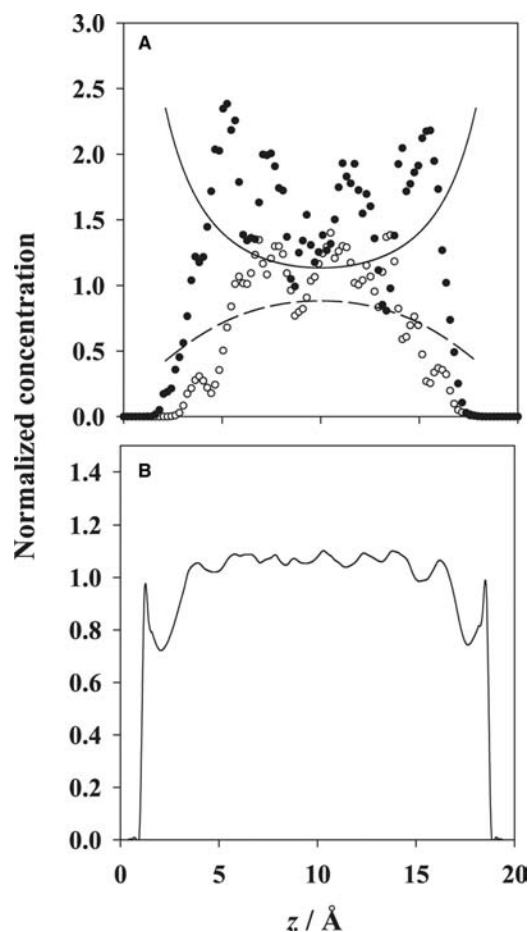


**Fig. 11** Ion and water concentration profiles in a 20-Å slit-type nanopore with a surface charge density of  $-0.05 \text{ C/m}^2$ . (A) Ion profiles: The solid and open circles are the normalized concentrations of sodium ion (counterion) and chloride ion (coion), respectively, based on the non-primitive model and CMC simulations. The solid and dashed lines are the normalized concentration of counterion and coion, respectively, based on the Gouy–Chapman model, provided for comparison. (B) Water profile: The solid line is the normalized concentration of water based on the location of the oxygen atom. *Source:* ©American Institute of Physics.

number of chloride ions are adsorbed on the charged surfaces, and the maximum concentration in Fig. 9A is still located in the central region.

Simulation results of the EDL formation in a 20-Å pore with a surface charge density of  $-0.05 \text{ C/m}^2$  (Run 3) are shown in Fig. 11A for the ion concentration profiles and in Fig. 11B for the water concentration profile. The concentration profiles for both counterions and coions in Fig. 11A are oscillatory. For counterions, two major peaks at 5 and 15 Å are followed by smaller peaks at 7.5 and 12.5 Å, respectively. For coions, in addition to the two major peaks at 7.5 and 12.5 Å are two smaller adsorption peaks at 4 and 16 Å. These oscillatory patterns can be attributed to the steric effect caused by water molecules, which

can be seen in Fig. 11B. A similar pattern was also observed in other non-primitive models, such as in the solvent primitive model.<sup>[23]</sup> On the other hand, such an effect cannot be observed if water is treated as a continuum, such as in the Gouy–Chapman or primitive model. In both cases, smooth concentration profiles for counterions and coions were obtained. For a positively charged 20-Å pore, the concentration profiles of ions and water are shown in Fig. 12A and B, respectively. As shown in Fig. 12A, oscillatory ion concentration profiles similar to those shown in Fig. 11A are obtained; however, the peaks of counterion concentration are less apparent in Fig. 12A. This observation can be explained by the loose hydration shell and

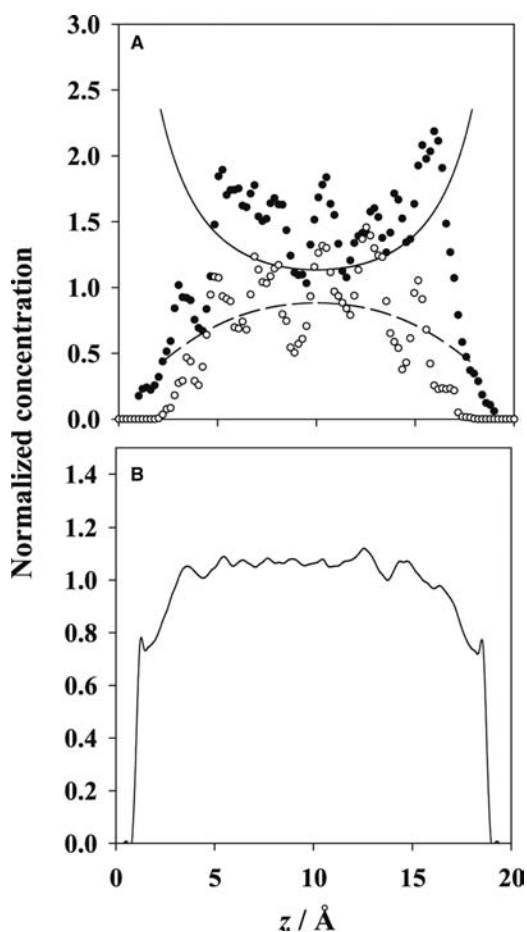


**Fig. 12** Ion and water concentration profiles in a 20-Å slit-type nanopore with a surface charge density of  $+0.05 \text{ C/m}^2$ . (A) Ion profiles: The solid and open circles are the normalized concentrations of chloride ion (counterion) and sodium ion (coion), respectively, based on the non-primitive model and CMC simulations. The solid and dashed lines are the normalized concentrations of counterion and coion, respectively, based on the Gouy–Chapman model, provided for comparison. (B) Water profile: The solid line is the normalized concentration of water based on the location of the oxygen atom. *Source:* ©American Institute of Physics.

less-pronounced steric effect for chloride ions. The first water peak also becomes much smaller, as shown in Fig. 12B, as a result of the competition on the surface site between water molecules and chloride ions.

The difference between the primitive and Gouy–Chapman models generally becomes smaller in a larger pore, and the characteristic behaviors caused by different counterions also become less significant because the space occupied by adsorbed water molecules accounts for a smaller percentage in the pore. Moreover, the prediction of the ion concentration profiles by the Gouy–Chapman and the primitive models becomes more satisfactory in a larger pore, as shown in Figs. 11A and 12A. Therefore, it is believed that when the separation distance between two charged surfaces is increased, the system behaves more and more like a classical EDL system, and it becomes reasonable to treat individual ions as indifferent ions, as in the primitive and Gouy–Chapman models. In these cases, ions are always in their hydrated form and remain in the diffuse double layer. However, this is not the case when the confined effect becomes dominant in a small nanopore. Adsorption of water molecules and ions downplays the importance of the diffuse double layer, and only the non-primitive model can provide a viable way to simulate these effects.

## CONCLUSION

In this study, Monte Carlo simulations are used to compare the primitive and non-primitive EDL models with the classical Gouy–Chapman model in 10- and 20-Å slit-type nanopores. The Gouy–Chapman and primitive models generally give similar results, except that the primitive model shows some steric effects at high surface charge density. However, the non-primitive model gives a very different view of the EDL in a 10-Å nanopore. Sodium ions tend to form a very compact hydration shell with 6 water molecules, and contact adsorption with the charged surfaces is prevented. Therefore the charged surfaces are covered by a strongly adsorbed water layer instead of sodium ions, which means that the maximum sodium ion concentration occurs at the center. This interesting phenomenon cannot be seen by using the classical Gouy–Chapman model or even the primitive model. On the other hand, the chloride ions are able to form a small portion of contact adsorption layer with the charged surfaces because their hydration energy with 7 water molecules is much lower than that of sodium ions. However, the maximum chloride ion concentration is still located at the center of the pore for the simulation conditions of this work.

For a 20-Å pore, the discrepancy between the non-primitive model and the primitive and Gouy–Chapman

models decreases, except that the concentration profile obtained in the non-primitive model has an oscillatory behavior. For larger pores or in an open space (e.g., one charged surface), the classical theories are still reliable. The agreement of all these models in open space explains why classical theories are still successful and viable for resolving many EDL problems.

## ACKNOWLEDGMENTS

Support for this research was provided by the National Science Foundation through a Career Award (BES-9702356 to S.Y.), and support to C.T. was provided by the Office of Basic Sciences, Division of Chemical Sciences, U.S. Department of Energy, under contract DE-AC05-00OR22725 with UT-Battelle, LLC. The authors also gratefully acknowledge partial support of this project by the Georgia Institute of Technology Molecular Design Institute, under prime contract N00014-95-1-1116 from the Office of Naval Research. Computations were supported by the Center for Computational Molecular Science and Technology at the Georgia Institute of Technology and partially funded through a Shared University Research (SUR) grant from IBM and the Georgia Institute of Technology. Computations were also supported by the High Performance Computing Center at the Georgia Institute of Technology.

## REFERENCES

- Gileadi, E. *Electrode Kinetics for Chemists, Chemical Engineers, and Materials Scientists*; VCH: New York, 1993.
- Hunter, R.J. *Foundations of Colloid Science*; Oxford University: New York, 1985; Vol. I.
- Ying, T.-Y.; Yang, K.-L.; Yiacoumi, S.; Tsouris, C. Electrosorption of ions from aqueous solutions by nanostructured carbon aerogel. *J. Colloid Interface Sci.* **2002**, *250*, 18–27.
- Yang, K.-L.; Ying, T.-Y.; Yiacoumi, S.; Tsouris, C.; Vittoratos, E.S. Electrosorption of ions from aqueous solutions by carbon aerogel: an electrical double-layer model. *Langmuir* **2001**, *17*, 1961–1969.
- Torrie, G.M.; Valleau, J.P. A Monte Carlo study of an electrical double layer. *Chem. Phys. Lett.* **1979**, *65*, 343–346.
- Torrie, G.M.; Valleau, J.P. Electrical double layer. I. Monte Carlo study of a uniformly charged surface. *J. Chem. Phys.* **1980**, *73*, 5807–5816.
- Torrie, G.M.; Valleau, J.P. Electrical double layers. 4. Limitations of the Gouy–Chapman theory. *J. Phys. Chem.* **1982**, *86*, 3251–3257.
- Yiacoumi, S.; Tien, C. *Kinetics of Metal Ion Adsorption from Aqueous Solutions: Models, Algorithms, and Applications*; Kluwer: Norwell, MA, 1995.
- Weetman, P.; Goldman, S.; Gray, C.G. Use of the Poisson–Boltzmann equation to estimate the electrostatic free energy barrier for dielectric models of biological ion channels. *J. Phys. Chem., B* **1997**, *101*, 6073–6078.
- Jordan, P.C.; Bacquet, R.J.; McCammon, J.A.; Tran, P. How electrolyte shielding influences the electrical potential in transmembrane ion channels. *Biophys. J.* **1989**, *55*, 1041–1052.
- Vlachy, V.; Haymet, A.D.J. Salt exclusion from charged and uncharged micropores. *J. Electroanal. Chem.* **1990**, *283*, 77–85.
- Vlachy, V.; Marshall, C.H.; Haymet, A.D.J. Highly asymmetric electrolytes: a comparison of Monte Carlo simulations and the HNC integral equation. *J. Am. Chem. Soc.* **1989**, *111*, 4160–4166.
- Lo, W.Y.; Chan, K.-Y.; Mok, K.L. Molecular dynamics simulation of ions in charged capillaries. *J. Phys., Condens. Matter* **1994**, *6*, A145–A149.
- Hribar, B.; Vlachy, V.; Bhuiyan, L.B.; Outhwaite, C.W. Ion distributions in a cylindrical capillary as seen by the modified Poisson–Boltzmann theory and Monte Carlo simulations. *J. Phys. Chem.* **2000**, *104*, 11,522–11,527.
- Lozada-Cassou, M.; Diaz-Herrera, E. Three point extension for hypernetted chain and other integral equation theories: Numerical results. *J. Chem. Phys.* **1990**, *92*, 1194–1210.
- Lozada-Cassou, M.; Henderson, D. A new method of deriving electrical double layer equations from electrolyte theories. *J. Chem. Phys.* **1981**, *75*, 1412–1421.
- Lozada-Cassou, M.; Olivares, W.; Sulbaran, B. Violation of the electroneutrality condition in confined charged fluids. *Phys. Rev., E* **1996**, *53*, 522–530.
- Lozada-Cassou, M.; Saavedra-Barrera, R.; Henderson, D. Application of the hypernetted chain approximation to the electrical double layer: comparison with Monte Carlo results for symmetric salts. *J. Chem. Phys.* **1982**, *77*, 5150–5156.
- Yeomans, L.; Feller, S.E.; Sanchez, E.; Lozada-Cassou, M. The structure of electrolytes in cylindrical pores. *J. Chem. Phys.* **1993**, *98*, 1436–1450.
- Boda, D.; Chan, K.-Y. Monte Carlo simulation of an ion–dipole mixture as a model of an electrical double layer. *J. Chem. Phys.* **1998**, *109*, 7362–7371.
- Lo, W.Y.; Chan, K.-Y.; Henderson, D. Improved Monte Carlo simulations of the structure of ion–dipole mixtures. *Mol. Phys.* **1993**, *80*, 1021–1029.
- Lo, W.Y.; Chan, K.-Y.; Lee, M.; Mok, K.L. Molecular simulation of electrolytes in nanopores. *J. Electroanal. Chem.* **1998**, *450*, 265–272.
- Zhang, L.; Davis, H.T.; White, H.S. Simulations of solvent effects on confined electrolytes. *J. Chem. Phys.* **1993**, *98*, 5793–5799.
- Zhang, S.Q.; Wang, J.; Shen, J.; Deng, Z.S.; Lai, Z.Q.; Zhou, B.; Attia, S.M.; Chen, L.Y. The investigation of the adsorption character of carbon aerogel. *Nanostruct. Mater.* **1999**, *11*, 375–381.
- Carvalho, R.J.F.L.; Skipper, N.T. Atomistic computer simulation of the clay–fluid interface in colloidal laponite. *J. Chem. Phys.* **2001**, *114*, 3727–3733.

26. Crozier, P.S.; Rowley, R.L.; Henderson, D. Molecular-dynamics simulations of ion size effects on the fluid structure of aqueous electrolyte systems between charged model electrodes. *J. Chem. Phys.* **2001**, *114*, 7513–7517.
27. Crozier, P.S.; Rowley, R.L.; Henderson, D. Molecular dynamics calculations of the electrochemical properties of electrolyte systems between charged electrodes. *J. Chem. Phys.* **2000**, *113*, 9202–9207.
28. Grahame, D.C. Differential capacity of mercury in aqueous sodium fluoride solutions. I. Effect of concentration. *J. Am. Chem. Soc.* **1954**, *76*, 4819–4823.
29. Mayer, S.T.; Pekala, R.W.; Kaschmitter, J.L. The aerocapacitor: an electrochemical double-layer energy-storage device. *J. Electrochem. Soc.* **1993**, *140*, 446–451.
30. Valleau, J.P.; Cohen, L.K. Primitive model electrolytes. I. Grand canonical Monte Carlo computations. *J. Chem. Phys.* **1980**, *72*, 5935–5941.
31. Allen, A.P.; Tildesley, D.J. *Computer Simulation of Liquid*; Oxford University: New York, 1987.
32. Rick, S.W.; Stuart, S.J.; Berne, B.J. Dynamical fluctuating charge force fields: application to liquid water. *J. Chem. Phys.* **1994**, *101*, 6141–6156.
33. Yang, K.-L.; Yiacoumi, S.; Tsouris, C. Canonical Monte Carlo simulations of the fluctuating-charge molecular water between charged surfaces. *J. Chem. Phys.* **2002**, *117*, 337–345.
34. Yang, K.-L.; Yiacoumi, S.; Tsouris, C. Monte Carlo simulation of electrical double-layer formation in nanopores. *J. Chem. Phys.* **2002**, *117*, 8499–8507.
35. Rick, S.W. Simulations of ice and liquid water over a range of temperatures using the fluctuating charge model. *J. Chem. Phys.* **2001**, *114*, 2276–2283.
36. Chandrasekhar, J.; Spellmeyer, D.C.; Jorgensen, W.L. Energy component analysis for dilute aqueous solutions of  $\text{Li}^+$ ,  $\text{Na}^+$ ,  $\text{F}^-$ , and  $\text{Cl}^-$  ions. *J. Am. Chem. Soc.* **1984**, *106*, 903–910.
37. Crozier, P.S.; Rowley, R.L.; Spohr, E.; Henderson, D. Comparison of charged sheets and corrected 3D Ewald calculations of long-range forces in slab geometry electrode systems with solvent molecules. *J. Chem. Phys.* **2000**, *112*, 9253–9257.
38. Chandra, R.; Dagum, L.; Kohr, D.; Maydan, D.; McDonald, J.; Menon, R. *Parallel Programming in Open MP*; Morgan Kaufmann: San Francisco, 1997.
39. Rose, A.D.; Benjamin, I. Adsorption of  $\text{Na}^+$  and  $\text{Cl}^-$  at the charged water–platinum interface. *J. Chem. Phys.* **1993**, *98*, 2283–2290.
40. Williams, G.D.; Soper, A.K.; Skipper, N.T.; Smalley, M.V. High resolution structural study of an electrical double layer by neutron diffraction. *J. Phys. Chem., B* **1998**, *45*, 8945–8949.
41. Schmitz, K.S. Distribution of water and counterions in vermiculite clays. *J. Phys. Chem., B* **1999**, *103*, 8882–8887.



# Electrically Functional Nanostructures

**Orlin D. Velev**

*Department of Chemical Engineering, North Carolina State University,  
Raleigh, North Carolina, U.S.A.*

**Simon O. Lumsdon**

*Particle Science and Technology, DuPont Central Research and Development,  
Wilmington, Delaware, U.S.A.*

## INTRODUCTION

The use of nanoparticles in advanced technological applications has surged because of their unusual properties, such as enormous surface-to-volume ratio, specific interactions, and confinement effects on the nanoscale. Most of the present practical applications use the nanoparticles as suspensions, material fillers, and in coatings. As knowledge and complexity in nanoscience and nanotechnology progress, nanoparticle assemblies are expected to find use in more complex photonic and electronic devices on the microscale. In this entry, we will focus on methods for the assembly of nanoparticles suspended in liquids into electrically functional devices and will present examples of such assemblies and their potential applications. First, nanoparticle assemblies can work as simple electrical conductors, transmitting currents on chips and in liquids to make microscopic circuits. More complex functions can be realized by utilizing the non-linear properties of such nanoparticle conductors in the fabrication of sensors, photocells, light-emitting diodes, electronic elements, and quantum electronics. Electrical functionality can also be imparted by modulating the properties of the nanoparticle assemblies via electrical fields and using the response for the manipulation of currents and light in displays and for transport and mechanical actuation on the microscale.

## ELECTRICAL FIELD-INDUCED FORCES IN COLLOIDAL SUSPENSIONS

Nanoparticle self-assembly can be effected by a variety of colloidal forces, including electrostatic repulsion and van der Waals attraction, capillary forces acting on fluid surfaces, hydrodynamic liquid drag, biospecific interactions, and others. One very convenient way to realize the electrical functionality of nanoparticle suspensions is to subject them to the action of electrical fields via external electrodes. External fields can easily

manipulate the particles in suspension and can be used for rapid and controllable assembly of structures. Suspended colloidal particles can be manipulated by applying constant (d.c.) or alternating (a.c.) voltage to electrodes in contact with the liquid.<sup>[1]</sup> Three general types of forces can be distinguished (Fig. 1):

1. The electrophoretic (EP) force,  $F_{EP}$ , operating on a particle in a d.c. electric field,  $E$ , is proportional to its charge  $q$

$$\vec{F}_{EP} = q\vec{E} \quad (1)$$

The particles move toward the electrode of opposite sign. A common problem in using d.c. fields in ionic media (such as water) is the electrophoretic mobility of the liquid adjacent to the walls. The moving liquid can drag the particles in arbitrary direction or distort the assembled structures. The assembly process can also be disrupted by electrolysis.

2. The dielectrophoretic (DEP) force is driven by the application of an a.c. field across the suspension. As the sign of the electrode polarization changes constantly, the particles are not attracted by direct charge-electrode electrostatic interactions (apart from oscillations at low frequencies on the order of tens of hertz). Instead, the DEP force arises via interaction of the induced dipoles with the gradient of the field. Its sign and magnitude are dependent on the effective polarizability of the particle, which is given by the real part of the Clausius-Mossotti function,  $K$

$$Re|K| = \frac{\epsilon_2 - \epsilon_1}{\epsilon_2 + 2\epsilon_1} + \frac{3(\epsilon_1\sigma_2 - \epsilon_2\sigma_1)}{\tau_{MW}(\sigma_2 + 2\sigma_1)^2(1 + w^2\tau_{MW}^2)} \quad (2)$$

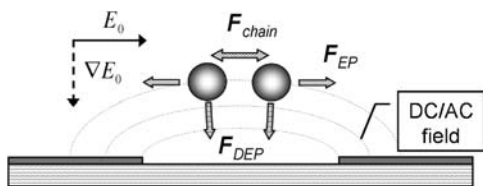


**Fig. 1** Electrical forces exerted on a charged dielectric particle by a.c. or d.c. fields applied to two coplanar electrodes. The electrophoretic force,  $F_{EP}$ , in d.c. fields attracts the particle toward the electrode of opposite charge in the direction of the field  $E$ . The dielectrophoretic force,  $F_{DEP}$ , in a.c. fields moves the particle along the field gradient,  $\nabla E$ . In this configuration, the DEP and EP forces act in perpendicular directions. The chaining force,  $F_{chain}$ , brings the particles together along the field lines.

where  $\varepsilon_1$  and  $\sigma_1$  are the dielectric permittivity and conductivity of the media and  $\varepsilon_2$  and  $\sigma_2$  are the dielectric permittivity and conductivity of the particles, respectively. Metallic particles are always attracted to the regions of high-field gradient. For dielectric particles, this function changes sign (that is, the force changes from attractive to repulsive) at a crossover frequency of  $\omega_C = (\tau_{MW})^{-1}$ , where  $\tau_{MW}$  is the Maxwell-Wagner charge relaxation time.

$$\tau_{MW} = \frac{\varepsilon_2 + \varepsilon_1}{\sigma_2 + 2\sigma_1}$$

Such a frequency-dependent change of sign of the interactions is commonly observed with polymer microspheres in water<sup>[2-4]</sup> and allows a high degree of control.

The resultant force,  $F_{DEP}$ , is dependent on the gradient,  $\nabla E$ , caused by inhomogeneities in the field and the radius of the particle,  $r$ .<sup>[2-6]</sup>

$$\vec{F}_{DEP} = 2\pi\varepsilon_1 R e[\underline{K}(w)] |r^3 \nabla E_{rms}^2 \quad (3)$$

The use of alternating voltage allows manipulation of virtually any type of particle in any type of media and has the advantage of permitting high-field strengths without water electrolysis and electro-osmotic currents.

- The “chaining” force,  $F_{chain}$ , originates between the particles in the suspension when the dipoles induced in them by either a.c. or d.c. fields interact with each other. This force is dependent on the field strength,  $E$ . A generalized expression for the force between adjacent particles is

$$F_{chain} = -C\pi\varepsilon r^2 K^2 E^2 \quad (4)$$

where the coefficient  $C$  ranges from 3 to  $>10^3$  depending on the distance between the particles

and the length of the particle chain. This force can provide directional orientation during the colloidal assembly as the particle chains are always aligned along the field lines.

## FABRICATION OF ELECTRICAL CIRCUITS VIA COLLOIDAL ASSEMBLY

The mature electronics industry possesses a very well developed set of tools for fabrication of electrical circuits at almost any length scale, from wiring and soldering on millimeter scale to micropatterning and microfabrication of integrated circuits with features smaller than 100 nm. Yet the current lithographic techniques work poorly for applications where electrical circuits have to be fabricated in complex 3-D configurations. Another domain that is not accessible for conventional lithographic patterning and soldering is the fabrication of electrical circuits in liquids and specifically in water. In this section, we will first discuss how capillary forces can be used to assemble 3-D circuits and how electrical connections in liquid can be made via directed electrochemical deposition of metals. The main focus will then be placed on electrical-field-driven assembly of nanoparticles into microwires and their use in making in situ electrical connections in liquids.

### Assembly of Electrical Circuits by Capillary Forces

One of the major requirements for self-assembly of electrical circuits from prefabricated components is the use of forces that could bring together the elements of the circuit in predefined, directional patterns. Most of the colloidal forces, such as the electrostatic and van der Waals, do not provide directionality and may be too weak to align electronic components. However, the “capillary forces” generated by the action of interfacial tension on bodies wetted by liquid can provide the long-range attraction and alignment required to assemble objects of up to a millimeter scale.<sup>[7-11]</sup> This technique has been pioneered by the group of Bowden et al.<sup>[12]</sup> originally for the self-assembly of topologically complex, millimeter-sized objects. When these objects are suspended on a water-oil interface, they assemble into designed close-packed, or loose, ordered structures. Structures fabricated by this method include arrays and gratings with different symmetry, “host-guest” templated structures, or even analogs of bio-recognition and DNA doublets.<sup>[12-17]</sup>

This technique has enabled the fabrication of 3-D electrical circuits from self-assembling blocks in density-matched liquids.<sup>[18-25]</sup> The assembly blocks

in this method are prefabricated octagons or prisms of millimeter size. Some of the facets of these blocks are fabricated with a pattern of solder patches that match the pattern on the opposing units only in certain orientation(s). The assembly is carried out by capillary attraction of liquefied low-melting point solder wetting the connector patches. The process is carried out by tumbling the elements in heated liquid whose density matches the one of the blocks. Only configurations of complementary match of the patterns are held strongly enough by the capillary forces of the molten solder to stay together during the tumbling, and thus the elements self-assemble into the designed circuit rejecting wrong orientations during the process. The capillary assembly method has been used to fabricate arrays of small light-emitting diodes (LEDs) on the surfaces of cylindrical substrates with rows of addressable electrodes.<sup>[26]</sup> The complex cylindrical displays obtained in this way illustrate the potential of self-assembly in fabrication of 3-D circuits.

### Formation of Electrical Circuits by Chemical and Electrochemical Deposition

The engineering of self-assembled electrical circuits often requires particles with specific shape and electrical properties. A simple and elegant method for synthesis of rod-like metallic and semiconductor particles has been reported by Martin<sup>[27]</sup> and Alkawlawi, Liu, and Moskovits.<sup>[28]</sup> It is based on electrochemical reduction inside uniform cylindrical micropores of alumina membranes. The process begins by vapor deposition of a metal layer on the branched side of the membrane, which closes the pore openings on that side and serves as a substrate electrode for electrodeposition inside the pores. The diameters of the metallic rods formed are equal to the diameter of the membrane micropores and typically are in the range of 200–300 nm. The rods are released into suspension by dissolving the templating alumina membrane in basic aqueous solution. A variety of precisely structured rods from different metals, semiconductors, and polymers have been fabricated.<sup>[29–35]</sup>

These suspensions of complex microscopic rods can be assembled in specific patterns and interfaced with electrical circuits. Chemical functionalization of the tips of the microrods during the process can be used to bind them to surfaces or to each other. The molecular layer can be attached by using agents with a terminal cyanide group (binding to Au and Pt) or thiol group (very strong binding to Au);<sup>[29,32]</sup> either the whole surface or only the tips of the rods can be functionalized.<sup>[34]</sup> The attachment of DNA and biomolecules is of specific importance,<sup>[34]</sup> as it allows the assembly of rod-particle structures or the application of the barcode

rods in highly selective bioassays.<sup>[30]</sup> The rods can be oriented and manipulated by external electric and magnetic fields to interface electrodes on surfaces.<sup>[35,36]</sup> Once the rods are positioned onto the electrode pads, they can be electrically connected to the probe by metal evaporation on top, allowing precise measurement of their current–voltage characteristics.<sup>[35]</sup>

Direct metal reduction and deposition, either by chemical or electrochemical reduction, is one of the simplest techniques for making electrical connections in liquids and can be used in template-directed growth of electrically conductive wires. Direct electrical connections between electrodes have been created via electrodeposition<sup>[37]</sup> and electropolymerization.<sup>[38,39]</sup> Electrochemical reduction of metal has been utilized for the fabrication of direct electrical connections between metallic beads in electrolyte solutions.<sup>[40]</sup> Such controllably deposited wires can be used to make connections on circuit boards and electrical circuits.<sup>[41–43]</sup> The bipolar electrochemistry method, however, is relatively slow and has limitations in terms of the voltages and distances between the connected particles.

Another electrodeposition method used for electrochemical fabrication of metallic nanowires is the selective reduction of molybdenum and palladium upon natural 2-D templates provided by the step edges of materials such as graphite.<sup>[44,45]</sup> The Mo wires are created by a two-step chemical process. At first, molybdenum oxides ( $\text{MoO}_x$ ) are electrodeposited on the step edges of cleaved molecularly smooth graphite. In the second step, the oxides are reduced to metal by hydrogen reduction at 500°C. The Pd mesowires are directly reduced on the graphite steps from a solution containing  $\text{Pd}^{2+}$  ions. The thickness of these hemicylindrical metallic nanowires and mesowires ranges from tens to hundreds of nanometers; their length can be larger than hundreds of micrometers. These metallic structures can be embedded in polymers such as polystyrene and cyanoacrylate, lifted off the graphite substrate, and their resistance and electrical response can be measured after metallic electrodes are deposited on the two sides of the plastic substrate spanned by the wires (Fig. 2). The conductivity and mechanical resiliency of the Mo wires are similar to those of bulk molybdenum. The Pd nanoparticle wires can be used as sensors and will be discussed in the corresponding section below. The simple fabrication principle may be extended to other metals and devices. The major disadvantage is the inability to create the structures directly in the desired conformations in electrical circuits.

The complementarity of DNA pairing has been one of the most efficient tools for the designed assembly of nanoparticles into microstructures and prototype nanomechanical devices.<sup>[46–51]</sup> Designed DNA strands have also been used as templates for metal deposition

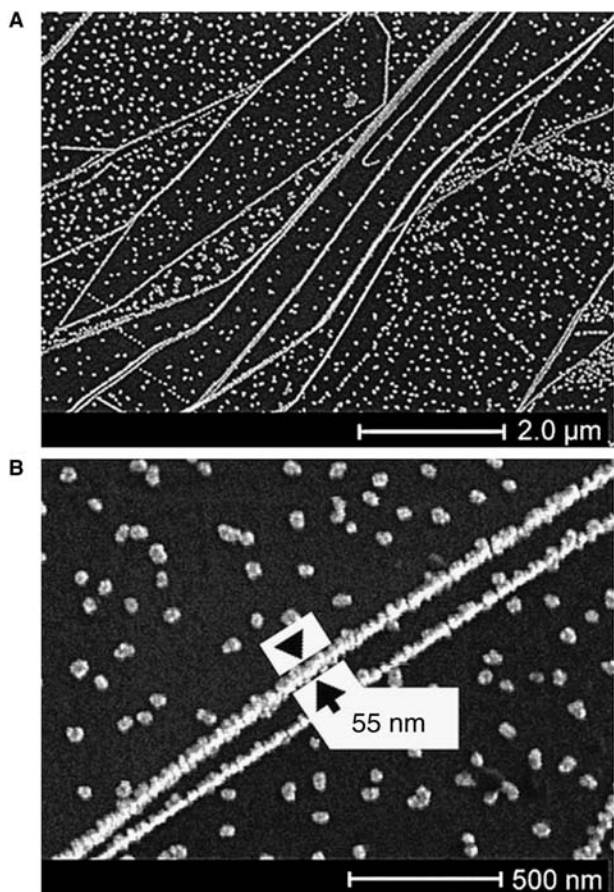


**Fig. 2** Scanning electron micrographs (SEMs) of Pd mesowires prepared by electrodeposition (A) from aqueous 2.0 mM PdCl<sub>2</sub> and 0.1 M HCl and (B) from aqueous 2.0 mM Pd(NO<sub>3</sub>)<sub>2</sub> and 0.1 M HClO<sub>4</sub>.<sup>[45]</sup> Note that the wires are composed of multiple metallic grains. Such mesowires can act as sensitive hydrogen sensors and switches. *Source:* From Ref.<sup>[45]</sup>. © American Association for the Advancement of Science, 2001.

and creation of microscopic electrical connectors.<sup>[52]</sup> The connection is achieved by chemical reduction of silver nanocrystals on top of the DNA chain. In the first step, a DNA bridge is assembled in the 12–16 μm gap between two gold electrodes from three complementary strands. The two terminal oligonucleotides are attached to the gold surface by thiol chemistry. The third DNA segment has “sticky” ends that are complementary to the two immobilized segments and attaches to them to complete the bridge. The metallic silver is deposited on the DNA surface via electroless reduction of a silver salt. The Ag<sup>+</sup> ions attracted to the surface of the DNA molecule nucleate the metallic nanocrystals, so the polynucleotide bridge becomes encrusted into a dense shell of 30–50 nm large nanoparticles. The electrical current through the nanoparticle shell is originally a nonlinear function of the voltage, but the structure can be “annealed” by

applying a higher voltage, resulting in wires of ohmic properties and of resistance in the megaohm region. The technique has been used for making DNA-guided metallic microwires from palladium<sup>[53]</sup> and platinum,<sup>[54]</sup> and the properties of these structures have been characterized in detail.<sup>[55–57]</sup> It is expected that DNA pairing could be used in the creation of more complex electrically functional nanodevices.

### Assembly of Electrical Circuits from Nanoparticles

Fabrication of electrical wires by metal ion reduction in solution can be problematic because of the chemical reactivity of the reagents or the relatively slow speed of deposition. An alternative technique for making such connectors is to assemble the wires from metallic particles. The directional chaining of particles in an external electric field [Eq. (4)], similar to that found in electrorheological fluids, can be used to make simple electrical connections. When the particles in such fluids are conductive, the chain will form a kind of conductive wire between the electrodes. Dueweke, Dierker, and Hubler<sup>[58]</sup> have studied the assembly of millimeter-sized steel spheres in castor oil under the action of d.c. voltages on the order of 20 kV. The spheres organize into a chain in a few tens of seconds, bridging the gap between the electrodes submerged in the oil. Average growth times are proportional to the distance between the electrodes. The authors also noted that these connections are self-repairing with new spheres assembling at the ends of open chains and have discussed the “Hebbian learning” in such systems, i.e., the easier restoration of previously built chains because of the presence of agglomerated particles in the gaps.<sup>[59]</sup>

Chaining and column formation of conductive particles has also been studied experimentally by Wen, Lu, and Zheng<sup>[60,61]</sup> for system of 65-μm copper particles suspended in silicone oil. The chains are grown between planar and coaxial electrodes and between vertical plates. The particles form fractal agglomerates of dimension between 1.2 and 2, increasing with the volume fraction of the Cu particles. In analogy to the diffusion-limited aggregation (DLA), responsible for the formation of fractal aggregates in colloidal suspensions, the concept of electric-field-induced diffusion-limited aggregation (EDLA) has been extended. This concept, however, has been indirectly questioned by a theoretical study by Kun and Pál,<sup>[62]</sup> who have performed lattice simulations of the growth of aggregates under similar conditions and have found out that the Brownian diffusion of the particles does not play a crucial role in structure formation. This work confirms the power law dependence of the fractal dimensions on the sphere concentration and points out the importance

of particle–particle interactions for structure growth. The assembly of electrical circuits is not specifically discussed, but the potential to use the structures as electrically conductive wires is obvious. One major disadvantage of these structures is the disassembly of the chains when the electric field is removed, which limits their potential to be used in microscopic circuits or as permanent connectors inside liquid environments.

To overcome the above restrictions, a truly versatile technique for direct wire assembly should be based on dispersion of conductive nanoparticles in water. We have recently described a new class of electrically functional microwires assembled by dielectrophoresis from suspensions of metallic nanoparticles in water.<sup>[63]</sup> Microwires are assembled from a suspension of 15–30 nm gold nanoparticles enclosed within a thin chamber above planar metallic electrodes on a glass surface. An alternating voltage of 50–250 V and frequency of 50–200 Hz is applied to the planar electrodes (resulting in a field intensity of ca. 250 V/cm), causing thin metallic fibers to grow on the electrode edge facing the gap (Fig. 3A). The wires are of diameter on the order of a micrometer and can grow longer than a centimeter with a speed that is typically  $\approx 50 \mu\text{m}/\text{sec}$ , but, in some cases, can be up to an order of magnitude

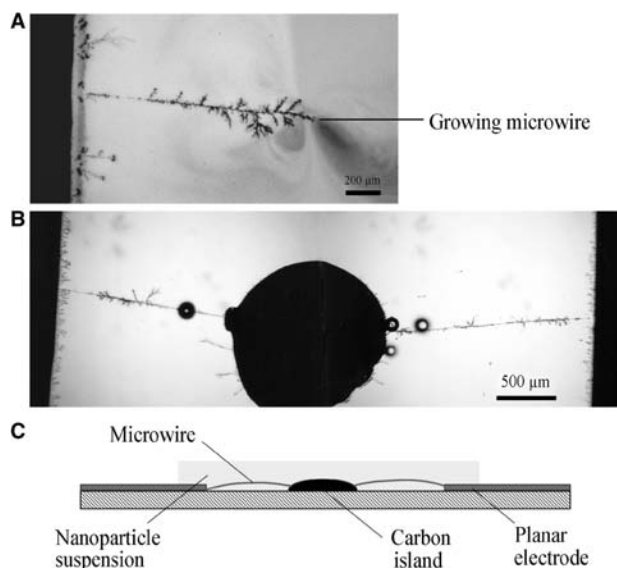


**Fig. 3** (A) Optical micrograph of a DEP assembly process of a microwire from suspension of metallic nanoparticles. The wire is growing from the edge of a planar electrode. Note the high concentration of particles at the tip of the wire and the depleted region behind. (B) Optical micrograph of two wires that have connected the two electrodes, wiring in the process an island of conductive carbon paint in the middle of the gap. (C) Schematic illustration of the experimental configuration. *Source:* © American Association for the Advancement of Science, 2001.

higher. When the wire is completely assembled, the electrodes become effectively short-circuited (Fig. 3B).

The finding that dielectrophoretic forces can readily assemble nanometer-sized metallic particles from aqueous suspensions into long, electrically conductive microwires is not directly predicted by theory. The dipole–dipole interaction energy between 15 and 30 nm particles separated by a gap of a few nanometers is smaller than  $10^{-2}kT$  ( $kT$  being the thermal energy) and therefore insignificant. Instead of direct chaining, the assembly is driven by the DEP force arising from the interaction of the particle dipoles with the non-uniform a.c. field. The tip of a growing microwire creates local fields of high intensity and gradient, attracting and concentrating the particles at the end. Purple coronas of highly concentrated areas in front of the tips of the growing wire and depletion zones behind them are clearly observed at low nanoparticle concentrations (Fig. 3A). The concentrated particles aggregate at the tip of the fibers, sustaining the growth toward the opposite electrode. Thus the microwire formation is a collective effect whereby the nanoparticles are highly concentrated at the tip and subsequently aggregate to extend the wire in the direction of the field gradient.

The microwire growth direction can be steered via inhomogeneities in the electric field by introducing objects of high dielectric permittivity in the gap between the electrodes. For example, when small islands of (conductive) carbon paint are deposited in the gap, the wires grow in their direction and spontaneously connect these islands to both electrodes (Fig. 3B and C). More complex structures involving multiple connections between multiple conductive pads can be formed. The field strength and particle concentration are also key variables, as they must exceed a threshold value in order for the wire to start growing. This threshold behavior emphasizes the collective nature of the assembly, as it shows that aggregation occurs only at sufficiently high concentration of particles accumulated near the end of the wire.

The porous nature of the wires was confirmed by scanning electron microscopy (SEM). When the field is removed, the wires remain intact, which enables SEM analysis of the dried structures. Fig. 4A shows a wire formed from 25-nm diameter gold particles in low electrolyte solution ( $5 \times 10^{-4} \text{ M NaCl}$ ). The wire has a high surface area and an even growth pattern under these conditions. In higher electrolyte concentration ( $1 \times 10^{-3} \text{ M NaCl}$ , Fig. 4B), the wire structure is more uneven consisting of large particle aggregates that form because of the suppressed electrostatic interactions between the particles in the bulk liquid.

The resistivity of the microwires was measured by adding a second pair of electrodes to the cell, which allows for compensation of the electrolyte conductance



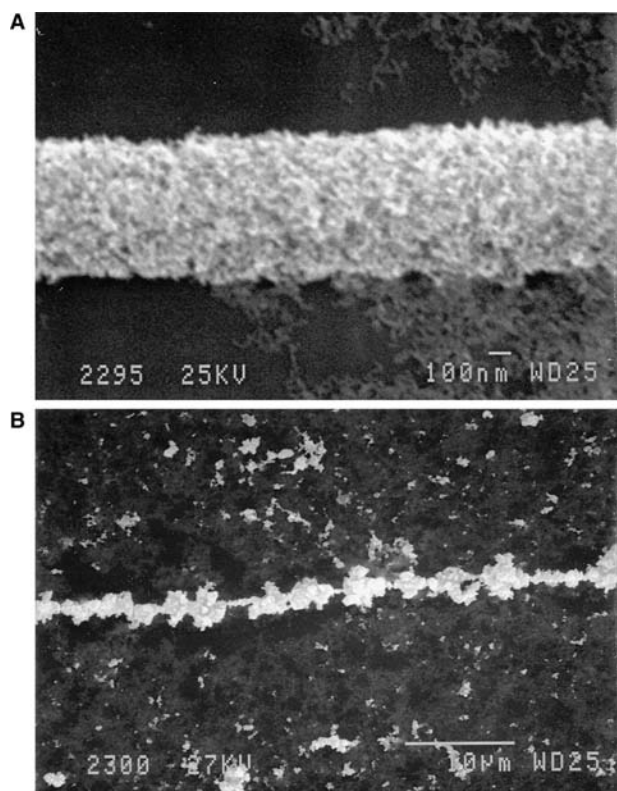


**Fig. 4** (A) Scanning electron micrograph of the tip of a wire grown in low electrolyte solution ( $5 \times 10^{-4}$  M NaCl) that highlights the uniform growth and high surface area of the structure. (B) Scanning electron micrograph of a wire grown in high electrolyte solution ( $1 \times 10^{-3}$  M NaCl) containing large particle aggregates that form because of the suppressed electrostatic interactions. *Source:* © American Association for the Advancement of Science, 2001.

in the surrounding medium (Fig. 5A). The wires have linear (ohmic) current-to-voltage response for both a.c. and d.c. voltages, with specific resistances that depend on the conditions of assembly and ranges from  $3 \times 10^{-6}$  to  $20 \times 10^{-6} \Omega\text{m}$  (Fig. 5B). This resistivity is 2 to 3 orders of magnitude higher than that of bulk solid gold because of the porosity and small interparticle contact areas in the microwires, yet it is comparable to that of good electrical conductors. Wires formed under identical conditions have highly reproducible resistivities, and despite being highly porous, they also possess good mechanical stability.

The self-assembling conductive wires can quickly and simply connect electrical circuits in water. In Fig. 6A, a light-emitting diode is attached to one of the planar electrodes and the aqueous gold suspension is placed in the gap between them. When voltage is applied, a single wire grows and energizes the LED (Fig. 6B). As mentioned previously for the large particle chains, these self-assembling electrical connections are also self-repairing. When the current applied to the single microwire is increased, the structure will

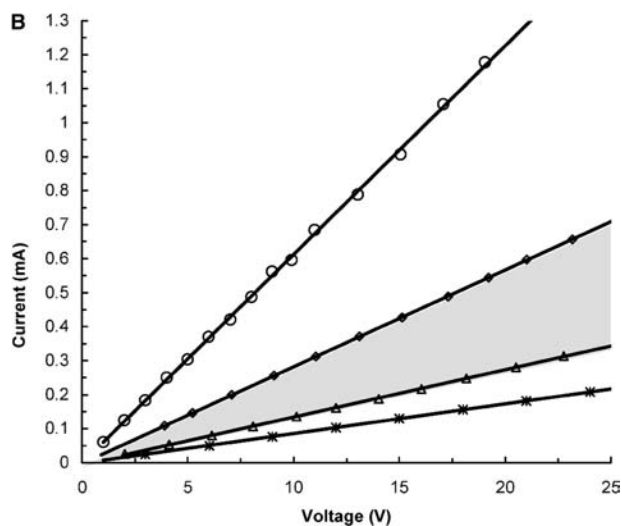
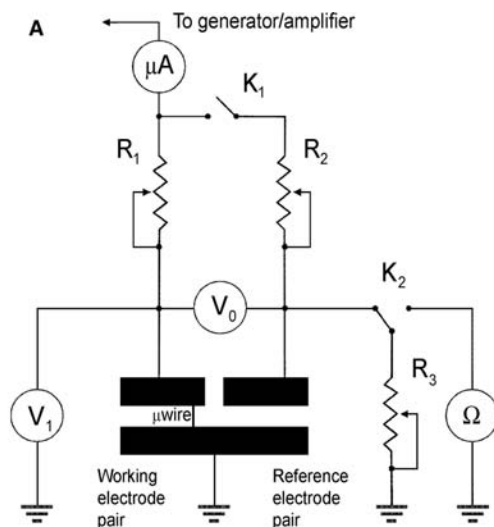


**Fig. 5** (A) Schematic of the bridge mode circuit that enables accurate measurement of the wire resistivity in situ by compensating for the conductivity of the surrounding medium. (B) Plot of the current ( $I$ ) to voltage ( $V$ ) response of a selection of microwires assembled under various experimental conditions. The shaded area highlights the region where the majority (>75%) of the responses are found. *Source:* © American Association for the Advancement of Science, 2001.

eventually break and snap open. It is immediately restored, however, by the build up of particles from the surrounding medium in the region of high-field intensity between the broken wire ends. This often results in the assembly of a second wire, which allows more current to flow through the circuit so that the LED shines with brighter intensity (Fig. 6C).

A further example of how the wires can form, break, and re-form electrical connections on chips is shown in Fig. 7. Wires are grown in the 18- $\mu\text{m}$  gaps between three pairs of electrodes in Fig. 7A. These connectors are burned open in Fig. 7B by substituting the gold



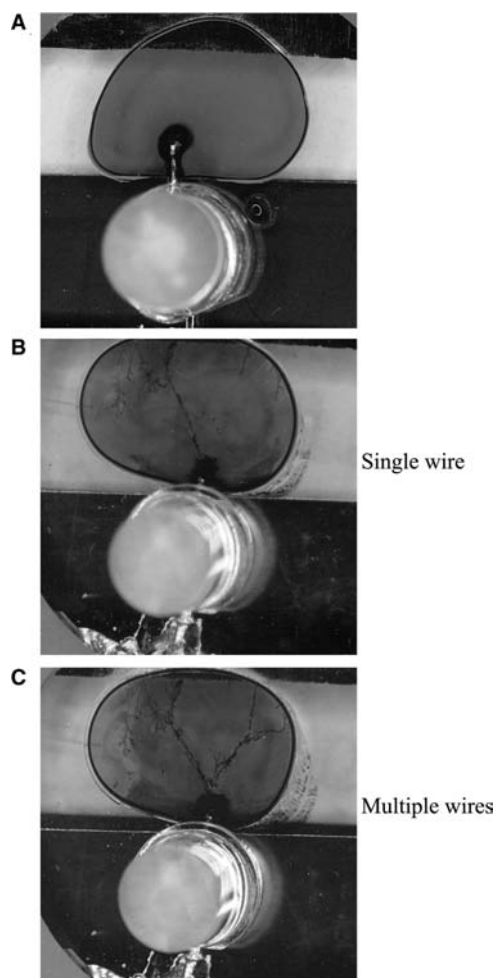


**Fig. 6** Example of assembling rudimentary electrical circuits in liquid. (A) Before the voltage is applied, the colloidal gold suspension is placed in the gap between a planar electrode and one of the electrodes of a commercial LED. (B) After the a.c. field is applied, a single wire connects between the electrodes and the LED starts to glow. (C) At higher voltages, a second wire is formed, providing more current to the LED and brighter light emission. *Source:* © American Association for the Advancement of Science, 2001.

suspension with pure water and applying a high voltage. Four pairs of wires are then reassembled in Fig. 7C by applying a voltage across a fresh gold suspension. Such wiring and rewiring could, in principle, be used to store bits of information on a chip and post-production reconfiguring of electrical microcircuits.

Dielectrophoresis is also capable of assembling more complex core-shell metallo-dielectric microwires from mixtures of metallic particles and submicrometer polystyrene latex spheres (Fig. 8). In this case, both types of particles are attracted to the tip of the growing wire resulting in a core of metallic particles that are surrounded by a shell of polymer spheres. The resistivity of this structure is comparable to a metallic wire grown under identical conditions in the absence of the

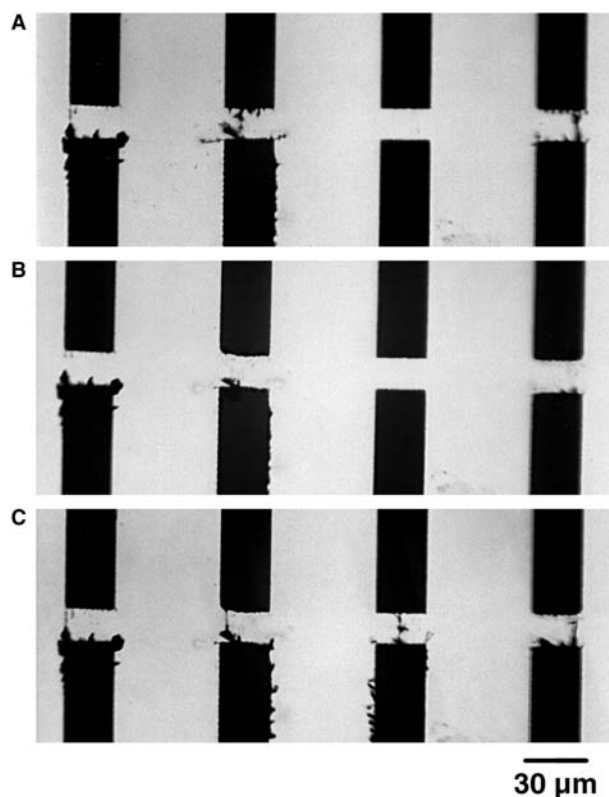


**Fig. 7** Example of using microwires as reconfigurable on-chip connections and memory storage. Wires grown in an 18- $\mu\text{m}$  gap between electrodes deposited on a microchip (A) are burnt open at high voltage (B) and reassembled in a different configuration (C). *Source:* © American Association for the Advancement of Science, 2001.

polymer beads. A variety of similar structures can potentially be assembled by this method, possibly enlarging the scope of applications for this technology. An illustration of the use of the microwires in chemical sensors is presented in the next section.

## ELECTRICALLY FUNCTIONAL MICROSTRUCTURES FROM COLLOIDAL PARTICLES

In this section, we will present a few examples that demonstrate the potential of the nanoparticle assemblies as microscopic electrically functional devices modulating electrical currents. The most obvious and important application of nanoparticle structures interfacing liquid flows and electrical circuits is as chemical and biological sensors.

### Chemical Sensors

One of the characteristic properties of nanoparticles and nanowires is their enormous surface area. This

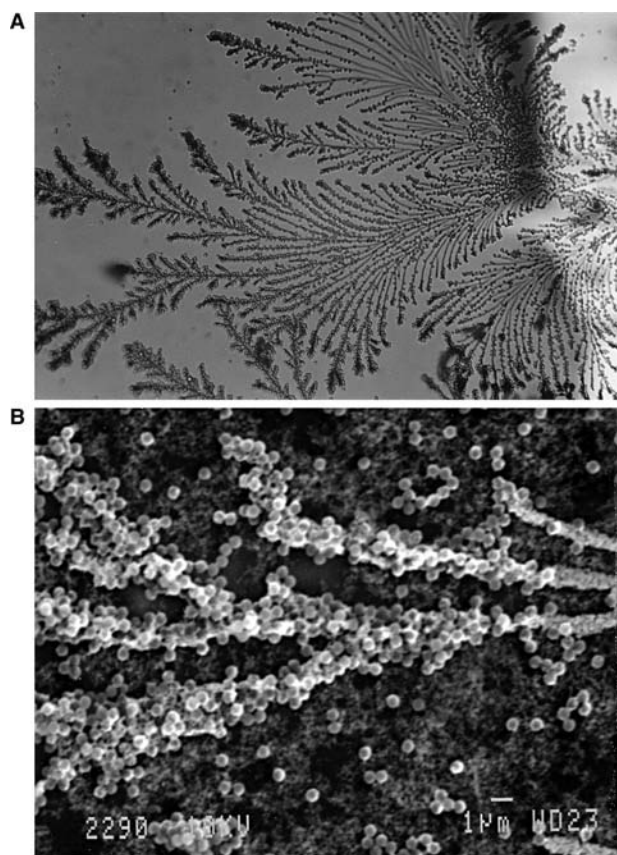


**Fig. 8** (A) Optical micrograph of a composite wire consisting of a fractal gold structure surrounded by a half-shell of micron-sized latex particles. (B) Scanning electron micrograph of the latex-coated wire; the gold core in the middle is resolved by its higher intensity. *Source:* © American Association for the Advancement of Science, 2001.

property makes the nanowires very sensitive to changes in the environment that might affect their surface composition and properties. Any modification would be easily detected by a shift in the electrical characteristics of the wire. Similar “chemiresistance” effects can be observed in both gaseous and liquid media. The phenomenon has been extensively studied theoretically and experimentally for the cases of ultrathin metallic films and wires.<sup>[64–68]</sup> For example, the conductance of nanoscopic gold films and wire junctions has been shown to be sensitive to adsorbates ranging from  $N_2$  to ethanol, to pyridine, mercaptans, and thiols.<sup>[64,65]</sup> Chemiresistance substrates for sensors can also be made from metallic nanoparticles.<sup>[69–71]</sup> The particles are capped with a thiolated ligand and are deposited by drying or spraying of suspension on top of interdigitated electrodes. The resistance of such nanoparticle films changes two times or more in the presence of vapors of organic compound such as aliphatic and aromatic hydrocarbons, alcohols, and even water. The response of this type of sensor to organic

vapors is roughly proportional to the partial vapor pressure and depends on the core size of the nanoparticles and the chemical nature of the linking molecules in the shells. The response is fast (less than a second), reversible, and selective to vapor molecules that have strong interaction and sorption on the nanoparticle film. Detection limits below 1 ppmv have been reported.<sup>[71]</sup>

Electrically conductive nanowires and microwires can also serve as active elements in chemical sensors. The method of Zach, Ng, and Penner<sup>[44]</sup> and Favier et al.<sup>[45]</sup> for electrochemical reduction of palladium mesowires on graphite step edges has allowed the formation of a novel type of hydrogen sensor. The Pd wires consist of polycrystalline metallic grains of sizes from 10 to 300 nm (Fig. 2). Arrays of these mesowires have shown remarkable sensitivity to gaseous  $H_2$ , acting as switches that short-circuit the gap in the presence of hydrogen and disconnect the current in its absence. The hydrogen-sensing effect is based on the swelling and shrinking of the grains making or breaking the electrical contacts between them. Hydrogen sensors with characteristics comparable, or superior, to the ones based on alternative principles have been made.<sup>[45]</sup>

The technique for DEP microwire assembly described above<sup>[63]</sup> also presents a simple and efficient way to make electrically interfaced nanoparticle sensors. The properties of microwires formed between planar electrodes in a 170- $\mu$ l flow cell have been measured in bridge mode (Fig. 4A) as a function of organic solutes added to the liquid. The ionic conductivity of all samples of the analytes has been adjusted constantly. An easily resolvable and concentration-dependent increase of the resistivity of the microwires has been observed after exposure to analytes that adsorb and modify the gold surface such as 2-(dimethylamino)ethanethiol hydrochloride and sodium cyanide (Table 1). The percentage shift of the response in the table denotes the difference between the initial voltage and the voltage measured after 10 min of flushing with the sample. The residual response is the compensated resistance of the wire, measured after the bridge has been balanced. The resistivity is shown to increase by  $\approx 2$ –12% after treatment with thiol solutions at increasing concentrations and  $\approx 5\%$  after treatment with NaCN at pH 11.<sup>[63]</sup> This signal possibly results from a decrease in the surface conductivity of the gold nanoparticles in the wire structure as they become covered by an organic layer. No signal was measured from solutions containing the protein lysozyme, which adsorbs on the gold surface without significantly affecting its surface conductivity. This demonstrates that the signal is specific to analytes that intimately modify the counterionic layer around the gold nanoparticles. In comparison to conventional gold nanoparticle assemblies on surfaces, the microwires can

**Table 1** Example of the response of the nanoparticle microwires as chemiresistance sensors

Analyte	Concentration	Response (% shift)	Residual response after refluxing (%)
Dimethylamino ethanethiol	$0.5 \times 10^{-4}$ M	+1.6	+1.6
	$2.5 \times 10^{-4}$ M	+9.0	+8.4
	$6.25 \times 10^{-4}$ M	+12.1	+11.3
Cyanide at pH 11	500 ppb	+4.7	+4.7
Protein lysozyme	1 mg/ml	0	0

The changes in resistance result in voltage drop changes on the order of a few volts, and thus the response is easily and reliably detectable. For additional details, see the supplementary material to Ref.<sup>[63]</sup>.

provide a quick response by virtue of their very high surface-to-volume ratio and easy analyte adsorption from the bulk of the surrounding solution. These sensors can potentially be tailored to specific analytes by surface functionalization with self-assembled monolayers (SAMs), which may specifically bind ions and small molecules. The conductivity response of the wires is sensitive to the presence and state of adsorption monolayers, so it is likely that it will also be sensitive to the presence of small charged molecules that specifically bind to the surface of such monolayers.

## Biological Sensors

Biosensors and bioarrays with direct electrical interfacing between electronic chips and particle assemblies have a number of potential advantages compared with the present technologies based on optical detection. The particle assemblies are the essential element that interfaces the wet 3-D biological environment with the dry 2-D electronic circuits. A pioneering example of how microscopic electrically readable sensors can be assembled by DEP in situ from microparticles and nanoparticles has been presented by Velev and Kaler.<sup>[72]</sup> The method is schematically shown in Fig. 9. The sensors are assembled on glass substrates with four pairs of photolithographically fabricated gold electrodes separated by gaps of  $30 \times 12 \mu\text{m}$ . Micron-sized latex particles, of the type used in agglutination assays, are assembled between the electrodes by positive dielectrophoresis at relatively low frequencies (1–5 kHz). The latexes are stabilized by electrostatic or steric interactions, so they immediately disassemble when the field is removed. A particle immobilization step is therefore necessary to decrease the repulsive interactions. Addition of an oppositely charged surfactant causes the charged particles to coagulate by neutralizing the charge on their surface. Particles stabilized by non-ionic surfactant are easily bound together by washing away the adsorbed steric protective layer. The assembly procedure can be repeated many times by exchanging the particle suspension and addressing

different gaps so that different microscopic sensors can be assembled on the same “chip.”

The model target molecule for these sensors has been human immunoglobulin (IgG). Immunoglobulin binds specifically to the protein A on the latex and is detected by tagging the molecules with colloidal gold conjugated to a secondary antibody, antihuman IgG. To ensure that the binding of IgG is specific, the immobilized latex particles are washed with a saline solution containing serum protein and a nonionic surfactant, which restore the steric coating to the particles. The gold particles in the shells are enlarged and fused together by a silver layer deposited from a metastable solution of silver salts (Fig. 9). This short-circuits the electrodes (Fig. 10), and the electronic readout is obtained by simply measuring the resistance. The size of these sensors has been a state of the art in miniaturization, and the experimentally estimated lower limit of detection (LOD) is on the order of the better IgG agglutination assays and immunosensors available. Further miniaturization of the sensor would increase the sensitivity of the active elements, possibly as low as a few tens of hundreds of molecules. This method could potentially be optimized by using easily assembled latexes with customized interactions, increasing the speed and sensitivity by generating an electro-osmotic flux over the sensor area, and by micromachining a microscopic sample chamber.

The electrical detection method utilizing nanoparticle short-circuiting of electrodes has recently been extended to miniaturized DNA assays by Möller et al.<sup>[73]</sup> and Park, Taton, and Mirkin.<sup>[74]</sup> In both of these studies, oligonucleotide strands are chemically immobilized on the surface between the electrodes. Gold nanoparticles become bound only if a complementary match between the DNA fragments is found; the complementary strands were either bound to the gold particles<sup>[73]</sup> or bridge the strands on the surface and the ones on the gold particles.<sup>[74]</sup> Some degree of quantification of the DNA concentration in the sample has been made possible by measuring the time required to short-circuit the electrodes after the enhancer is introduced. The ability to fabricate parallel microscopic

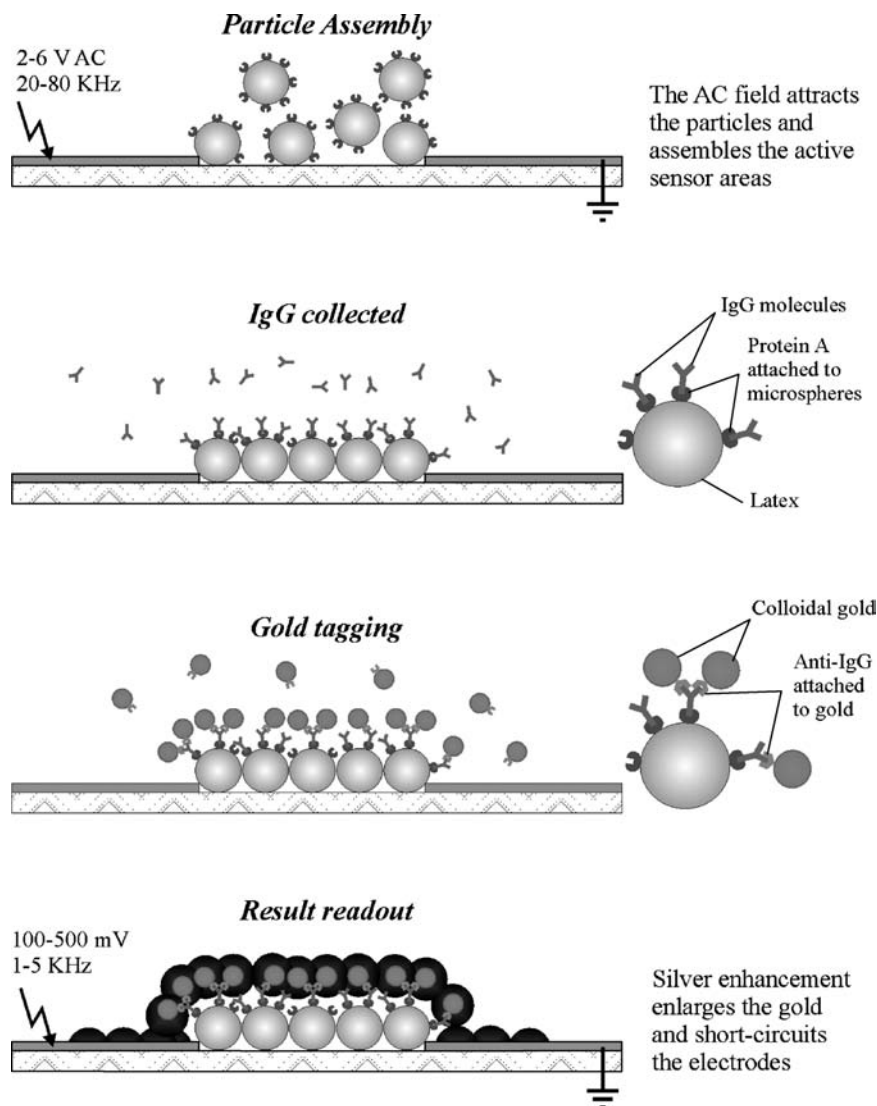


**Fig. 9** Schematics of formation of microscopic biosensor patches via DEP assembly of latex particles and direct electric readout of the results via gold tagging and silver enhancement.<sup>[72]</sup> The procedure is illustrated on the basis of IgG detection. *Source:* © American Chemical Society, 1999.

arrays of detectors for specific genetic markers is promising for the biotechnology and medical diagnostics industries.

### Quantum Electronics Nanoparticle Devices

Very interesting effects are observed when the nanoparticles assembled on chips are less than a few nanometers in diameter and insulated from the electrodes (and each other) by a layer of surfactant. The tunneling current increases in discrete steps as a function of the number of electrons injected inside the nanoparticle.<sup>[75–81]</sup> The incremental electron tunneling manifests itself in the so-called “coulomb staircase” current–voltage dependence. These quantum-based effects can, in principle, be used to store bits of information within a single nanoparticle and to make miniature lasers.<sup>[79–83]</sup> The assembly of such quantum dots in larger-scale structures is likely to produce devices

bridging the domains of molecular electronics and semiconductor technologies. This very promising area occupies a large research domain of its own, so we will not go into detailed overview and discussion here.

### ELECTRICAL FUNCTIONALITY VIA FIELD-DRIVEN ASSEMBLY OF PHOTONIC AND OPTICALLY ACTIVE STRUCTURES

The electrical functionality of nanoparticle and micro-particle assemblies can also be realized in areas beyond conducting and modulating electrical currents. Very active research is focused on the formation of colloidal crystals via the use of electric fields. As long as the products of the assembly process, 2-D and 3-D periodic structures, can act as photonic crystals, the process itself is an example of electrically imparted functionality in nanoparticle structures. The reversible assembly



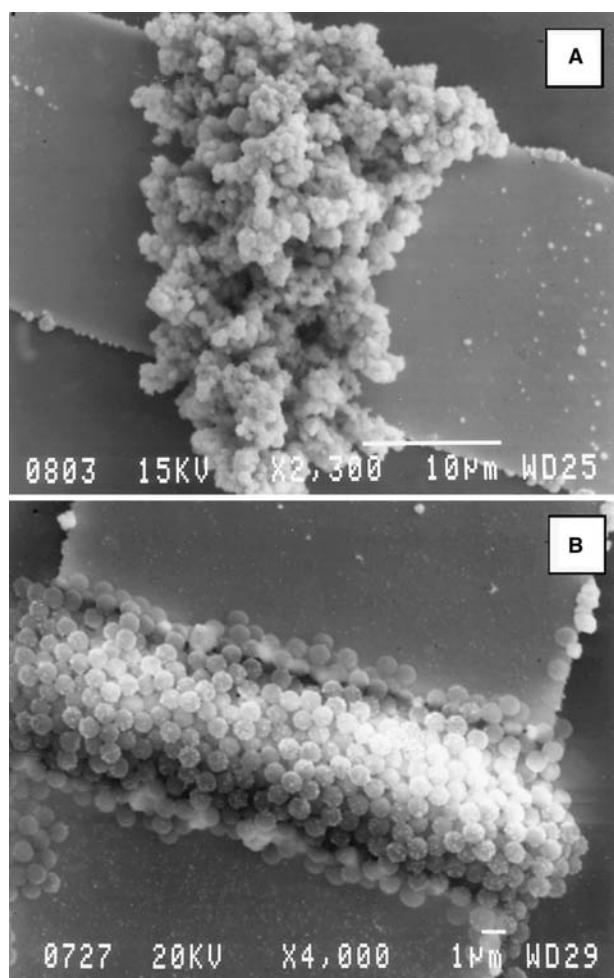


**Fig. 10** Scanning electron micrograph of a 10- $\mu\text{m}$  patch from functionalized latex spheres in the miniature immunosensors with direct electronic readout.<sup>[72]</sup> (A) Functionalized latexes heavily coated by deposited metal that short-circuits the electrodes. (B) The nonfunctionalized particles in the negative control patches are only marginally tagged by deposited metal. *Source:* © American Chemical Society, 1999.

can eventually be used in switchable electro-optical devices. Another broadly similar application of enormous practical importance is the use of nanoparticle structures in displays and “electronic paper.” Nanoparticles can also find application in active elements of light-emitting diodes. A brief overview of these research areas will be given in this section (Fig. 11).

### Assembly of Colloidal Crystals by Electrophoretic Forces

Dielectric particles in water such as latex and silica microspheres always possess some degree of surface charge, which prevents them from coagulating. Electrophoretic (d.c.) attraction toward electrodes can be

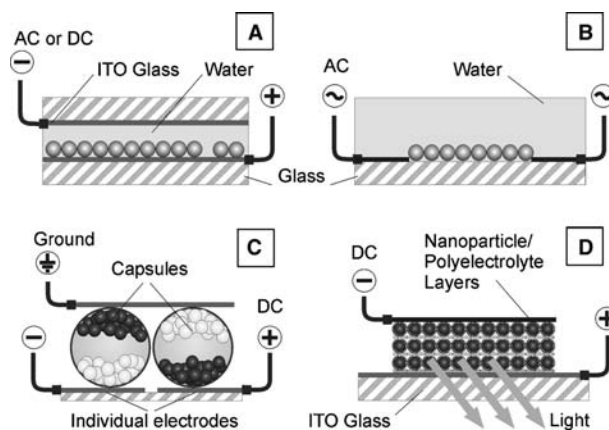


**Fig. 11** Schematics of four different devices where photonic or optical function of particle assemblies is imparted by electric field. (A) Two-dimensional colloidal crystals assembled by d.c. field in thin cells with opposing electrodes. (B) Oriented two-dimensional colloidal crystals assembled by DEP between coplanar electrodes on a surface. (C) Electronic ink by electrophoretic segregation of colored particles in microcapsules. (D) Light-emitting diodes assembled from layers of oppositely charged semiconductor particles and polyelectrolyte.

used efficiently for concentrating the particles near the oppositely charged surface and for colloidal crystallization. The process can be viewed as speeding up the deposition of dense particle crystals that may otherwise be formed under gravity. The use of electrophoretic forces in the deposition of ordered arrays of gold and latex particles onto carbon-coated copper grid surfaces has been reported by Giersig and Mulvaney.<sup>[84]</sup> The process takes place in field intensities on the order of 1–5 V/cm. Holgado et al.<sup>[85]</sup> achieved direct electrophoretic control of the deposition speed of silica spheres for the fabrication of high-quality crystals. The d.c. field is applied in the vertical direction in cylinders with sedimenting spheres, controlling the speed at which the spheres deposit on the bottom. The electrophoretic deposition method has been used to prepare a variety of crystals and multilayered deposits.<sup>[86–90]</sup>

Functionality that is potentially usable in devices can be achieved when the particle suspensions are enclosed in thin films between electrodes a few micrometers to tens of micrometers apart (Fig. 11A). This configuration can be used for quick, potentially reversible, assembly of 2-D crystalline structures. The dynamics of electrophoretic particle deposition and ordering onto conductive surfaces has been observed microscopically by Trau, Saville, and Aksay<sup>[91,92]</sup> and Böhmer.<sup>[93]</sup> When the potential applied between the cell electrodes exceeds ca. 0.5 V d.c., the microspheres move toward the oppositely charged electrode, forming ordered 2-D clusters on its surface. The microspheres

also exhibit lateral attraction forces, which, at higher potentials (1–2 V), act at distances exceeding a few particle diameters. Because of that lateral attraction, the 2-D ordered aggregates can attract to, and merge with, other aggregates until the electrode is covered with a complete monolayer or multilayer of crystalline array. The ordered sphere arrays formed, however, are multicrystalline and made up of domains with different orientation, which may restrict their application in photonic structures.

Electrophoretic 2-D colloidal crystallization has been observed with latex, silica, and gold particles, suspended in deionized water or in moderate electrolyte, in both d.c. and a.c. fields. The high-field intensity in the thin gap leads to the appearance of electrohydrodynamic currents around the particles and lateral dipole–dipole interactions. The electrohydrodynamic flows are generated because the counterionic atmosphere around the colloidal particles disturbs the concentration polarization layer onto the electrode, leading to emergence of local flow streams perpendicular to the cell wall. The hydrodynamic interaction of the flows around the microspheres leads to attraction between the particles and their aggregation into ordered patterns. Electrohydrodynamic models have been developed that explain the reversibility of the process and the “softness” of the incurred attractive forces that allow the lateral rearrangement of the particles into ordered arrays.<sup>[92,94–97]</sup>

The electrophoretic method, concurrently with the photosensitivity of indium tin oxide (ITO) layers, has been used to make optically tunable micropatterns from colloidal crystals.<sup>[98]</sup> The microspheres slowly migrate to the regions illuminated through a mask to form patterns from ordered arrays. The particles diffuse back to an unordered state when the voltage is turned off. If the particles in the illuminated patterns are pushed beyond the coagulation threshold by increased current, the assembled patterned arrays are permanently immobilized onto the electrode. Electrophoretic patterning has also been used to deposit live cells on surfaces.<sup>[99]</sup>

### Assembly of Colloidal Crystals by Alternating Current Chaining and Dielectrophoretic Forces

Particle chaining as a result of interaction between dipoles directed along the electric field [Eq. (4)] can be used for reversible assembly and alignment of ordered colloidal structures. Dipolar chaining has been used for a long time in electrorheological and magnetorheological fluids, which drastically increase their viscosity and become rigid when the particles stick together in the field.<sup>[100,101]</sup> It has been found that particles in

electrorheological fluids commonly arrange into 3-D body-centered tetragonal (bct) crystals.<sup>[101–104]</sup> This field-driven structure formation can be used to assemble and align colloidal crystals. Various stable and metastable crystalline phases formed in electrorheological suspensions of silica spheres have been reported by Dassanayake, Fraden, and van Blaaderen.<sup>[104]</sup> The chaining effect can also be used to induce annealing and large-scale orientation of colloidal crystals formed by conventional sedimentation.<sup>[105]</sup> Structures other than colloidal crystals can be fabricated by modifications of the method.<sup>[106]</sup>

The confinement of suspensions in thin closed cells can make use of chaining and DEP effects in colloidal crystallization. The first observation of particle clustering in thin cells was described by Richetti, Prost, and Barois<sup>[107]</sup> who reported that above a certain threshold magnitude of the a.c. voltage, the spheres are attracted to the surfaces of the electrodes and exhibit lateral attraction, forming ordered 2-D aggregates. The ordered structure “melts” at frequencies higher than  $\approx 5$  kHz. The electrophoretic mobility at frequencies below 100 Hz can cause particle compression and long-range crystallization in highly deionized systems.<sup>[108,109]</sup> The a.c. field-induced particle interactions in thin films can also be repulsive for certain combinations of cell thickness and particle sizes. Gong and Marr<sup>[110]</sup> have studied the “strictly confined” system where the thin gap between the electrodes is just ca. 20% larger than the particle size. The high-intensity fields induce strong dipoles in the microspheres, and as these dipoles are parallel, they repel each other (in contrast to the case of chaining, where the dipoles are colinear). The strongly repelling microspheres organize into 2-D crystals with long-range separation between the particles. The lack of friction, the relatively high mobility, and the long-range repulsion lead to rapid formation of relatively large crystal domains.

Combinations between DEP and chaining forces can be used for controlled colloidal crystallization above planar electrodes on a surface. Lumsdon et al.<sup>[111]</sup> have recently studied the reversible formation of crystals in suspensions of latex or silica microspheres subjected to an a.c. field in a gap above two coplanar electrodes (Fig. 11B). In this geometry, positive DEP forces attract the particles to the gap as predicted by Eq. (3). The chaining forces assemble the particles in the direction of the field as explained above. Formation of specifically oriented 2-D hexagonal crystals with areas above  $25 \text{ mm}^2$  has been observed. The transitions between ordered and disordered states take place within seconds and can be repeated tens of times. The laser diffraction patterns of all consecutively formed crystals are identical, which can be used to make rudimentary optical switches (Fig. 12). Various combinations of DEP, EP, and



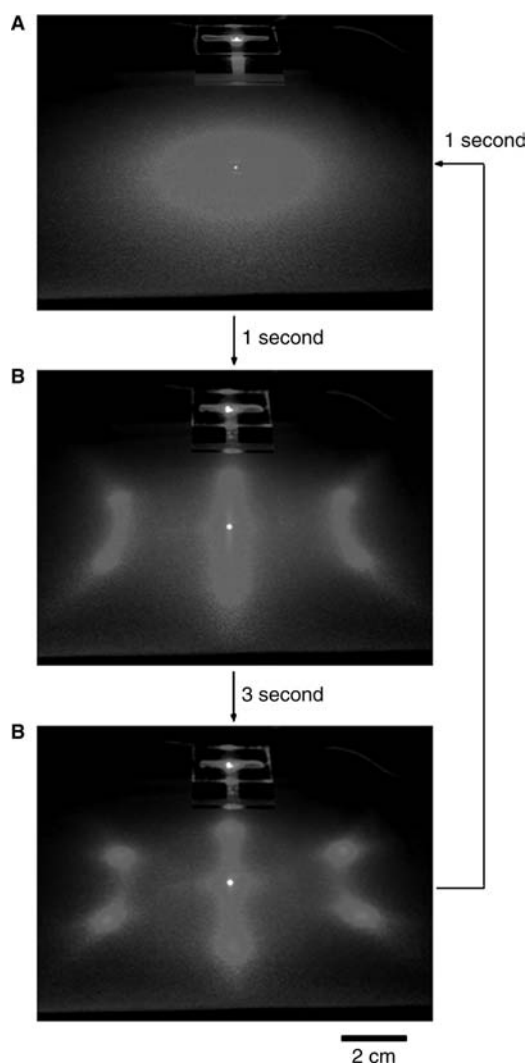


**Fig. 12** Diffraction pattern of a laser beam directed through a 2-D crystallization cell with planar electrodes similar to the one in Fig. 11B.<sup>[111]</sup> (A) Diffuse scattering from a suspension of 0.7- $\mu\text{m}$  latex particles before the electric field is applied; (B) 1 sec after a.c. voltage is applied, the particles align in chains diffracting in parallel lines; (C) 3 sec after voltage is applied, the particles crystallize into hexagonal close packed array. The process is fully reversible and can be used in beam splitters. *Source:* © American Institute of Physics, 2003.

chaining forces are likely to find more elaborate applications in the reversible assembly of ordered structures inside electrically controlled devices.

### Electrical Displays Based on Nanoparticle Manipulation

The optical properties of colloidal structures can be modulated even more simply by using microparticles of different color and moving them to face the observer or backward. This principle could be used in display

technologies based on colloidal particles that are a competitive alternative to the common liquid crystal displays. One very promising research area is the development of microencapsulated electrophoretic inks for electronic “paper.”<sup>[112,113]</sup> This “ink” is made from thousands of capsules 30–300  $\mu\text{m}$  in diameter, incorporating a suspension of white and black microparticles in the size range of 1–5  $\mu\text{m}$ . The white and black particles carry opposite charges and are protected from heterocoagulation via a polymeric adsorption layer around their surfaces. Alternatively, only white particles suspended in dark liquid can be used.

The microcapsules are spread in a thin layer and addressable electrodes from ITO and silver-doped polymer are applied from top and bottom, respectively. To switch the color on and off, potential fields of a few volts per micrometer are applied across the electrodes. The particles move to oppositely charged electrodes, separating into black mass on one side of the capsule and white on the other side (Fig. 11C). If the electrode potential is reversed, the position of the black and white particles changes, reversing the color of the capsule. Such displays exhibit high optical reflectance and contrast and wide viewing angle.<sup>[114]</sup> Potential for achieving resolutions as high as 1200 dots per inch has been suggested. The displays may be made flexible and can retain the displayed information after the electric field is turned off. Recent commercial development of this technology has led to the fabrication of color displays of relatively low cost and low energy consumption. The commercialization of such displays is intertwined with the development of technologies for fabrication of inexpensive organic transistors and electronic circuits by printing on flexible plastic films.<sup>[115,116]</sup>

### Photovoltaic Cells and Light-Emitting Diodes

Conductor and semiconductor nanoparticles have found application in light-emitting diodes and photovoltaic cells, the active junctions of which are created by self-assembly instead of vacuum evaporation and ion implantation. Ultrathin structures of semiconductor nanoparticles can form electronic elements similar to the heterojunctions of doped semiconductors used in solid-state electronics. One convenient method for the assembly of thin layer-by-layer structures is nanoparticle adsorption onto oppositely charged polyelectrolytes.<sup>[117–120]</sup> The delicate balance of the forces in layers of alternating charge allows sequential deposition of particle layers of various types. The particles/polyelectrolyte layers are assembled on a metallic surface acting as the first electrode, and a layer of another metal is coated on top of the structure to form the second electrode (Fig. 11D). This technique has been used in the fabrication of prototypes of

nanoparticle-based rectifying and Zenner diodes.<sup>[121,122]</sup> Optically active elements such as LEDs<sup>[123–131]</sup> and photovoltaic cells can also be fabricated.<sup>[132,133]</sup> The size and the chemical composition of the nanoparticles can be used as a means to tune the emission wavelength of the electroluminescence. Additional advantages offered by the nanoparticle layering technique are simple processing, precise control of the layer thickness, choice of a wide range of semiconductor nanoparticle types (e.g., CdSe, CdS, Si, TiO<sub>2</sub>, ZnO, etc.), and the ability to tune and improve the electrical characteristics of the devices via polyelectrolytes and self-assembled monolayers.<sup>[120,128,129]</sup>

## CONCLUSION

We show in this entry how simple nanoparticles and microparticles suspended in water can be assembled in a variety of structures, which can act as electrical connectors in liquid and as active elements in biological and chemical sensors or in optical devices. The assembly of the nanoparticles can be driven by a variety of colloidal forces; however, among the most convenient tools for controlled assembly are external a.c. and d.c. electrical fields applied to on-chip electrodes. The diverse scientific results reviewed here are by no means inclusive of all exciting developments in related research areas. Carbon nanotubes and semiconductor nanowires form a large research topic not reviewed in detail here because of the higher complexity of these “nanoparticles,” which are rarely used in aqueous environments. We have also not reviewed the exciting field of quantum and molecular electronics, which deals with electrical structures smaller than the nanoparticle scale.

The field of creating electrically functional nanoparticle structures is still in its infancy, and exciting and important developments can be expected in the near future by bringing together new techniques and interdisciplinary research. For example, the combination of electrically functional nanostructures with microfluidics is likely to bring forward novel sensors and bio-electronic devices. The combination of the techniques and structures presented here with biomolecules, molecular electronics, and carbon and semiconductor nanotubes is almost unexplored yet and holds enormous possibilities for nanotechnology applications. Novel electrically functional nanostructures are likely to find practical applications in the near future.

## ACKNOWLEDGMENTS

The authors' research reviewed here was carried out in collaboration with Eric Kaler, Kevin Hermanson, and Jacob Williams. The financial support from the

Camille and Henry Dreyfus Foundation, from Oak Ridge Associated Universities, and from NSF (IBN-0210656) are gratefully acknowledged.

## REFERENCES

1. Russell, W.B.; Saville, D.A.; Schowalter, W.R. *Colloidal Dispersions*; Cambridge Univ. Press: Cambridge, 1999.
2. Pethig, R.; Huang, Y.H.; Wang, X.B.; Burt, J.P.H. Positive and negative dielectrophoretic collection of colloidal particles using interdigitated castellated microelectrodes. *J. Phys., D, Appl. Phys.* **1992**, *25*, 881–888.
3. Müller, T.; Gerardino, A.; Schnelle, T.; Shirley, S.G.; Bordoni, F.; DeGasperis, G.; Leoni, R.; Fuhr, G. Trapping of micrometre and sub-micrometre particles by high-frequency electric fields and hydrodynamic forces. *J. Phys., D, Appl. Phys.* **1996**, *29*, 340–349.
4. Fuhr, G.; Müller, T.; Schnelle, T.; Hagedorn, R.; Voigt, A.; Fiedler, S.; Arnold, W.M.; Zimmermann, U.; Wagner, B.; Heuberger, A. Radio-frequency microtools for particle and live cell manipulation. *Naturwissenschaften* **1994**, *81*, 528–535.
5. Pohl, H.A. *Dielectrophoresis*; Cambridge Univ. Press: Cambridge, 1978.
6. Jones, T.B. *Electromechanics of Particles*; Cambridge Univ. Press: Cambridge, 1995.
7. Paunov, V.N.; Kralchevsky, P.A.; Denkov, N.D.; Nagayama, K. Lateral capillary forces between floating submillimeter particles. *J. Colloid Interface Sci.* **1993**, *157*, 100–112.
8. Velev, O.D.; Denkov, N.D.; Paunov, V.N.; Kralchevsky, P.A.; Nagayama, K. Direct measurement of lateral capillary forces. *Langmuir* **1993**, *9*, 3702–3709.
9. Paunov, V.N. On the analogy between lateral capillary interactions and electrostatic interactions in colloid systems. *Langmuir* **1998**, *14*, 5088–5097.
10. Kralchevsky, P.A.; Nagayama, K. *Particles at Fluid Interfaces and Membranes*; Elsevier: Amsterdam, 2001.
11. Kralchevsky, P.A.; Denkov, N.D. Capillary forces and structuring in layers of colloid particles. *Curr. Opin. Colloid Interface Sci.* **2001**, *6*, 383–401.
12. Bowden, N.; Terfort, A.; Carbeck, J.; Whitesides, G.M. Self-assembly of mesoscale objects into ordered two-dimensional arrays. *Science* **1997**, *276*, 233–235.
13. Choi, I.S.; Bowden, N.; Whitesides, G.M. Shape selective recognition and self-assembly of mm-scale components. *J. Am. Chem. Soc.* **1999**, *121*, 1754–1755.
14. Choi, I.S.; Bowden, N.; Whitesides, G.M. Macroscopic, hierarchical, two-dimensional self-assembly. *Angew. Chem. (Int. Ed.)* **1999**, *38*, 3078–3081.
15. Choi, I.S.; Weck, M.; Xu, B.; Jeon, N.L.; Whitesides, G.M. Mesoscopic, templated self-assembly at the fluid–fluid interface. *Langmuir* **2000**, *16*, 2997–2999.
16. Weck, M.; Choi, I.S.; Jeon, N.L.; Whitesides, G.M. Assembly of mesoscopic analogues of nucleic acids. *J. Am. Chem. Soc.* **2000**, *122*, 3546–3547.

17. Bowden, N.B.; Weck, M.; Choi, I.S.; Whitesides, G.M. Molecule-mimetic chemistry and meso-scale self-assembly. *Acc. Chem. Res.* **2001**, *34*, 231–238.
18. Terfort, A.; Bowden, N.; Whitesides, G.M. Three-dimensional self-assembly of millimetre-scale components. *Nature* **1997**, *386*, 162–164.
19. Tien, J.; Breen, T.L.; Whitesides, G.M. Crystallization of millimeter-scale objects with use of capillary forces. *J. Am. Chem. Soc.* **1998**, *120*, 12670–12671.
20. Breen, T.L.; Tien, J.; Oliver, S.R.J.; Hadzic, T.; Whitesides, G.M. Design and self-assembly of open, regular, 3D mesostructures. *Science* **1999**, *284*, 948–951.
21. Whitesides, G.M.; Boncheva, M. Beyond molecules: self-assembly of mesoscopic and macroscopic components. *Proc. Natl. Acad. Sci. U. S. A.* **2002**, *99*, 4769–4774.
22. Terfort, A.; Whitesides, G.M. Self-assembly of an operating electrical circuit based on shape complementarity and the hydrophobic effect. *Adv. Mater.* **1998**, *10*, 470–473.
23. Gracias, D.H.; Tien, J.; Breen, T.L.; Hsu, C.; Whitesides, G.M. Forming electrical networks in three-dimensions by self-assembly. *Science* **2000**, *289*, 1170–1172.
24. Gracias, D.H.; Boncheva, M.; Omoregie, O.; Whitesides, G.M. Biomimetic self-assembly of helical electrical circuits using orthogonal capillary interactions. *Appl. Phys. Lett.* **2002**, *80*, 2802–2804.
25. Boncheva, M.; Gracias, D.H.; Jacobs, H.O.; Whitesides, G.M. Biomimetic self-assembly of a functional asymmetrical electronic device. *Proc. Natl. Acad. Sci. U. S. A.* **2002**, *99*, 4937–4940.
26. Jacobs, H.O.; Tao, A.R.; Schwartz, A.; Gracias, D.H.; Whitesides, G.M. Fabrication of a cylindrical display by patterned assembly. *Science* **2002**, *296*, 323–325.
27. Martin, C.R. Membrane-based synthesis of nanomaterials. *Chem. Mater.* **1996**, *8*, 1739–1746.
28. Alkawlawi, D.; Liu, C.Z.; Moskovits, M. Nanowires formed in anodic oxide nanotemplates. *J. Mater. Res.* **1994**, *9*, 1014–1018.
29. Martin, B.R.; Dermody, D.J.; Reiss, B.D.; Fang, M.M.; Lyon, L.A.; Natan, M.J.; Mallouk, T.E. Orthogonal self-assembly on colloidal gold–platinum nanorods. *Adv. Mater.* **1999**, *11*, 1021–1025.
30. Nicewarner-Pena, S.R.; Freeman, R.G.; Reiss, B.D.; He, L.; Pena, D.J.; Walton, I.D.; Cromer, R.; Keating, C.D.; Natan, M.J. Submicrometer metallic barcodes. *Science* **2001**, *294*, 137–141.
31. Kovtyukhova, N.I.; Martin, B.R.; Mbindyo, J.K.N.; Smith, P.A.; Razavi, B.; Mayer, T.S.; Mallouk, T.E. Layer-by-layer assembly of rectifying junctions in and on metal nanowires. *J. Phys. Chem., B* **2001**, *105*, 8762–8769.
32. Mbindyo, J.K.N.; Mallouk, T.E.; Mattzela, J.B.; Kratochvilova, I.; Razavi, B.; Jackson, T.N.; Mayer, T.S. Template synthesis of metal nanowires containing monolayer molecular junctions. *J. Am. Chem. Soc.* **2002**, *124*, 4020–4026.
33. Yu, J.S.; Kim, J.Y.; Lee, S.; Mbindyo, J.K.N.; Martin, B.R.; Mallouk, T.E. Template synthesis of polymer-insulated colloidal gold nanowires with reactive ends. *Chem. Commun.* **2000**, *24*, 2445–2446.
34. Mbindyo, J.K.N.; Reiss, B.D.; Martin, B.R.; Keating, C.D.; Natan, M.J.; Mallouk, T.E. DNA-directed assembly of gold nanowires on complementary surfaces. *Adv. Mater.* **2001**, *13*, 249–254.
35. Sapp, S.A.; Mitchell, D.T.; Martin, C.R. Using template-synthesis micro- and nanowires as building blocks for self-assembly of supramolecular architectures. *Chem. Mater.* **1999**, *11*, 1183–1185.
36. Smith, P.A.; Nordquist, C.D.; Jackson, T.N.; Mayer, T.S.; Martin, B.R.; Mbindyo, J.; Mallouk, T.E. Electric-field assisted assembly and alignment of metallic nanowires. *Appl. Phys. Lett.* **2000**, *77*, 1399–1401.
37. Gurtner, C.; Sailor, M.J. Selective construction of electrical connections using an organic charge-transfer salt. *Adv. Mater.* **1996**, *8*, 897–899.
38. Sailor, M.J.; Curtis, C.L. Conducting polymer connections for molecular devices. *Adv. Mater.* **1994**, *6*, 688–692.
39. Curtis, C.L.; Ritchie, J.E.; Sailor, M.J. Fabrication of conducting polymer interconnects. *Science* **1993**, *262*, 2014–2016.
40. Bradley, J.C.; Chen, H.M.; Crawford, J.; Eckert, J.; Ernazarova, K.; Kurzeja, T.; Lin, M.D.; McGee, M.; Nadler, W.; Stephens, S.G. Creating electrical contacts between metal particles using directed electrochemical growth. *Nature* **1997**, *389*, 268–271.
41. Bradley, J.C.; Crawford, J.; Ernazarova, K.; McGee, M.; Stephens, S.G. Wire formation on circuit boards using spatially coupled bipolar electrochemistry. *Adv. Mater.* **1997**, *9*, 1168–1171.
42. Bradley, J.C.; Ma, Z.M.; Clark, E.; Crawford, J.; Stephens, S.G. Programmable hard-wiring of circuitry using spatially coupled bipolar electrochemistry. *J. Electrochem. Soc.* **1999**, *146*, 194–198.
43. Bradley, J.C.; Ma, Z.M.; Stephens, S.G. Electric field directed construction of diodes using free-standing three-dimensional components. *Adv. Mater.* **1999**, *11*, 374–378.
44. Zach, M.P.; Ng, K.H.; Penner, R.M. Molybdenum nanowires by electrodeposition. *Science* **2000**, *290*, 2120–2123.
45. Favier, F.; Walter, E.C.; Zach, M.P.; Benter, T.; Penner, R.M. Hydrogen sensors and switches from electrodeposited palladium mesowire arrays. *Science* **2001**, *293*, 2227–2231.
46. Alivisatos, A.P.; Johnsson, K.P.; Peng, X.G.; Wilson, T.E.; Loweth, C.J.; Bruchez, M.P.; Schultz, P.G. Organization of ‘nanocrystal molecules’ using DNA. *Nature* **1996**, *382*, 609–611.
47. Loweth, C.J.; Caldwell, W.B.; Peng, X.G.; Alivisatos, A.P.; Schultz, P.G. DNA-based assembly of gold nanocrystals. *Angew. Chem. (Int. Ed.)* **1999**, *38*, 1808–1812.
48. Connolly, S.; Fitzmaurice, D. Programmed assembly of gold nanocrystals in aqueous solution. *Adv. Mater.* **1999**, *11*, 1202–1205.
49. Willner, I.; Patolsky, F.; Wasserman, J. Photoelectrochemistry with controlled DNA-cross-linked CdS nanoparticle arrays. *Angew. Chem. (Int. Ed.)* **2001**, *40*, 1861–1864.

50. Mao, C.D.; Sun, W.Q.; Shen, Z.Y.; Seeman, N.C. A nanomechanical device based on the B-Z transition of DNA. *Nature* **1999**, *397*, 144–146.
51. Seeman, N.C. DNA engineering and its application to nanotechnology. *Trends Biotechnol.* **1999**, *17*, 437–443.
52. Braun, E.; Eichen, Y.; Sivan, U.; Ben-Yoseph, G. DNA-templated assembly and electrode attachment of a conducting silver wire. *Nature* **1998**, *391*, 775–778.
53. Richter, J.; Seidel, R.; Kirsch, R.; Mertig, M.; Pompe, W.; Plaschke, J.; Schackert, H.K. Nanoscale palladium metallization of DNA. *Adv. Mater.* **2000**, *12*, 507–510.
54. Ford, W.E.; Harnack, O.; Yasuda, A.; Wessels, J.M. Platinated DNA as precursors to templated chains of metal nanoparticles. *Adv. Mater.* **2001**, *13*, 1793–1797.
55. Richter, J.; Mertig, M.; Pompe, W.; Monch, I.; Schackert, H.K. Construction of highly conductive nanowires on a DNA template. *Appl. Phys. Lett.* **2001**, *78*, 536–538.
56. Gu, J.H.; Tanaka, S.; Otsuka, Y.; Tabata, H.; Kawai, T. Self-assembled dyed-DNA network and its photoinduced electrical conductivity. *Appl. Phys. Lett.* **2002**, *80*, 688–690.
57. Rakitin, A.; Aich, P.; Papadopoulos, C.; Kobzar, Y.; Vedenev, A.S.; Lee, J.S.; Xu, J.M. Metallic conduction through engineered DNA: DNA nanoelectronic building blocks. *Phys. Rev. Lett.* **2001**, *86*, 3670–3673.
58. Dueweke, M.; Dierker, U.; Hubler, A. Self-assembling electrical connections based on the principle of minimum resistance. *Phys. Rev., E* **1996**, *54*, 496–506.
59. Sperl, M.; Chang, A.; Weber, N.; Hubler, A. Hebbian learning in the agglomeration of conducting particles. *Phys. Rev., E* **1999**, *59*, 3165–3168.
60. Wen, W.; Lu, K. Electric field induced diffusion limited aggregation. *Phys. Rev., E* **1997**, *55*, R2100–R2103.
61. Wen, W.; Zheng, D.W.; Tu, K.N. Fractal chain transition of field induced colloid structure. *Phys. Rev., E* **1998**, *58*, 7682–7685.
62. Kun, F.; Pál, K.F. Simulating fractal pattern formation in metal–oil electrorheological fluids. *Phys. Rev., E* **1998**, *57*, 3216–3220.
63. Hermanson, K.D.; Lumsdon, S.O.; Williams, J.P.; Kaler, E.W.; Velev, O.D. Dielectrophoretic assembly of electrically functional microwires from nanoparticle suspensions. *Science* **2001**, *294*, 1082–1086.
64. Li, C.Z.; Sha, H.; Tao, N.J. Adsorbate effect on conductance quantization in metallic nanowires. *Phys. Rev., B* **1998**, *58*, 6775–6778.
65. Zhang, Y.; Terrill, R.H.; Bohn, P.W. In-plane resistivity of ultra-thin gold films: a high sensitivity, molecularly differentiated probe of Mercaptan chemisorption at the liquid–metal interface. *J. Am. Chem. Soc.* **1998**, *120*, 9969–9970.
66. He, H.X.; Tao, N.J. Interactions of molecules with metallic quantum wires. *Adv. Mater.* **2002**, *14*, 161–164.
67. Li, C.Z.; He, H.X.; Bogozzi, A.; Bunch, J.S.; Tao, N.J. Molecular detection based on conductance quantization of nanowires. *Appl. Phys. Lett.* **2000**, *76*, 1333–1335.
68. Tobin, R.G. Mechanisms of adsorbate induced surface resistivity—experimental and theoretical developments. *Surf. Sci.* **2002**, *502–503*, 374–387.
69. Wohltjen, H.; Snow, A.W. Colloidal metal–insulator–metal ensemble chemiresistor sensor. *Anal. Chem.* **1998**, *70*, 2856–2859.
70. Han, L.; Daniel, D.R.; Maye, M.M.; Zhong, C.J. Core-shell nanostructured nanoparticle films as chemically sensitive interfaces. *Anal. Chem.* **2001**, *73*, 4441–4449.
71. Krasteva, N.; Besnard, I.; Guse, B.; Bauer, R.E.; Mullen, K.; Yasuda, A.; Vossmeier, T. Self-assembled gold nanoparticle/dendrimer composite films for vapor sensing applications. *Nano Lett.* **2002**, *2*, 551–555.
72. Velev, O.D.; Kaler, E.W. In-situ assembly of colloidal particles into miniaturized biosensors. *Langmuir* **1999**, *15*, 3693–3698.
73. Möller, R.; Csaki, A.; Kohler, J.M.; Fritzsche, W. Electrical classification of the concentration of bioconjugated metal colloids after surface adsorption and silver enhancement. *Langmuir* **2001**, *17*, 5426–5430.
74. Park, S.J.; Taton, T.A.; Mirkin, C.A. Array-based electrical detection of DNA with nanoparticle probes. *Science* **2002**, *295*, 1503–1506.
75. Andres, R.P.; Bein, T.; Dorogi, M.; Feng, S.; Henderson, J.I.; Kubiak, C.P.; Mahoney, W.; Osifchin, R.G.; Reifenberger, R. “Coulomb staircase” at room temperature in a self-assembled molecular nanostructure. *Science* **1996**, *272*, 1323–1325.
76. Markovich, G.; Leff, D.V.; Chung, S.W.; Soye, H.M.; Dunn, B.; Heath, J.R. Parallel fabrication and single electron charging of devices based on ordered, two-dimensional phases of organically functionalized metal nanocrystals. *Appl. Phys. Lett.* **1997**, *70*, 3107–3109.
77. Feldheim, D.L.; Grabar, K.C.; Natan, M.J.; Mallouk, T.E. Electron-transfer in self-assembled inorganic polyelectrolyte/metal nanoparticle heterostructures. *J. Am. Chem. Soc.* **1996**, *118*, 7640–7641.
78. Sato, T.; Ahmed, H. Observation of a coulomb staircase in electron transport through a molecularly linked chain of gold colloidal particles. *Appl. Phys. Lett.* **1997**, *70*, 2759–2761.
79. Klein, D.L.; Roth, R.; Lim, A.K.L.; Alivisatos, A.P.; McEuen, P.L. A single-electron transistor made from a cadmium selenide nanocrystal. *Nature* **1997**, *389*, 699–701.
80. Feldheim, D.L.; Keating, C.D. Self-assembly of single electron transistors and related devices. *Chem. Soc. Rev.* **1998**, *27*, 1–12.
81. Schiffrin, D.J. Capped nanoparticles as potential electronic components with nanoscale dimensions. *MRS Bull.* **2001**, *26*, 1015–1019.
82. Fendler, J.H. Chemical self-assembly for electronic applications. *Chem. Mater.* **2001**, *13*, 3196–3210.
83. Shipway, A.N.; Katz, E.; Willner, I. Nanoparticle arrays on surfaces for electronic, optical and sensor applications. *ChemPhysChem* **2000**, *1*, 18–52.
84. Giersig, M.; Mulvaney, P. Preparation of ordered colloid monolayers by electrophoretic deposition. *Langmuir* **1993**, *9*, 3408–3413.
85. Holgado, M.; García-Santamaría, F.; Blanco, A.; Ibisate, M.; Cintas, A.; Míguez, H.; Serna, C.J.; Molpeceres, C.; Requena, J.; Mifsud, A.; Meseguer, F.; López, C. Electrophoretic deposition to control artificial opal growth. *Langmuir* **1999**, *15*, 4701–4704.

86. Rogach, A.L.; Kotov, N.A.; Koktysh, D.S.; Ostrander, J.W.; Ragoisha, G.A. Electrophoretic deposition of latex-based 3D colloidal photonic crystals: a technique for rapid production of high-quality opals. *Chem. Mater.* **2000**, *12*, 2721–2726.
87. Bailey, R.C.; Stevenson, K.J.; Hupp, J.T. Assembly of micropatterned colloidal gold thin films via micro-transfer molding and electrophoretic deposition. *Adv. Mater.* **2000**, *12*, 1930–1934.
88. Sun, J.Q.; Gao, M.Y.; Feldmann, J. Electric field directed layer-by-layer assembly of highly fluorescent CdTe nanoparticles. *J. Nanosci. Nanotechnol.* **2001**, *1*, 133–136.
89. Gao, M.Y.; Sun, J.Q.; Dulkeith, E.; Gaponik, N.; Lemmer, U.; Feldmann, J. Lateral patterning of CdTe nanocrystal films by the electric field directed layer-by-layer assembly method. *Langmuir* **2002**, *18*, 4098–4102.
90. Gu, Z.Z.; Hayami, S.; Kubo, S.; Meng, Q.B.; Einaga, Y.; Tryk, D.A.; Fujishima, A.; Sato, O. Fabrication of structured porous film by electrophoresis. *J. Am. Chem. Soc.* **2001**, *123*, 175–176.
91. Trau, M.; Saville, D.A.; Aksay, I.A. Field-induced layering of colloidal crystals. *Science* **1996**, *272*, 706–709.
92. Trau, M.; Saville, D.A.; Aksay, I.A. Assembly of colloidal crystals at electrode interfaces. *Langmuir* **1997**, *13*, 6375–6381.
93. Böhmer, M. In-situ observation of 2-dimensional clustering during electrophoretic deposition. *Langmuir* **1996**, *12*, 5747–5750.
94. Solomentsev, Y.; Bohmer, M.; Anderson, J.L. Particle clustering and pattern formation during electrophoretic deposition: A hydrodynamic model. *Langmuir* **1997**, *13*, 6058–6068.
95. Solomentsev, Y.; Guelcher, S.A.; Bevan, M.; Anderson, J.L. Aggregation dynamics for two particles during electrophoretic deposition under steady fields. *Langmuir* **2000**, *16*, 9208–9216.
96. Sides, P.J. Electrohydrodynamic particle aggregation on an electrode driven by an alternating electric field normal to it. *Langmuir* **2001**, *17*, 5791–5800.
97. Kim, J.; Guelcher, S.A.; Garoff, S.; Anderson, J.L. Two-particle dynamics on an electrode in ac electric fields. *Adv. Colloid Interface Sci.* **2002**, *96*, 131–142.
98. Hayward, R.C.; Saville, D.A.; Aksay, I.A. Electrophoretic assembly of colloidal crystals with optically tunable micropatterns. *Nature* **2000**, *404*, 56–59.
99. Brisson, V.; Tilton, R.D. Self-assembly and two-dimensional patterning of cell arrays by electrophoretic deposition. *Biotechnol. Bioeng.* **2002**, *77*, 290–295.
100. Gast, A.P.; Zukoski, C.F. Electrorheological fluids as colloidal suspensions. *Adv. Colloid Interface Sci.* **1989**, *30*, 153–202.
101. Parthasarathy, M.; Klingenberg, D.J. Electrorheology: Mechanisms and models. *Mater. Sci. Eng., R* **1996**, *17*, 57–103.
102. Tao, R.; Sun, J.M. Three-dimensional structure of induced electrorheological solid. *Phys. Rev. Lett.* **1991**, *67*, 398–401.
103. Martin, J.E.; Odinek, J.; Halsey, T.C.; Kamien, R. Structure and dynamics of electrorheological fluids. *Phys. Rev., E* **1998**, *57*, 756–775.
104. Dassanayake, U.; Fraden, S.; van Blaaderen, A.J. Structure of electrorheological fluids. *J. Chem. Phys.* **2000**, *112*, 3851–3858.
105. van Blaaderen, A.J.; Velikov, K.P.; Hoogenboom, J.P.; Vossen, D.L.J.; Yethiraj, A.; Dullens, R.; van Dillen, T.; Polman, A. *Photonic Crystals and Light Localization in the 21st Century*; Soukoulis, C.M., Ed.; Kluwer: Amsterdam, 2001.
106. Trau, M.; Sankaran, S.; Saville, D.A.; Aksay, I.A. Electric-field-induced pattern-formation in colloidal dispersions. *Nature* **1995**, *374*, 437–439.
107. Richetti, P.; Prost, J.; Barois, P. Two-dimensional aggregation and crystallization of a colloidal suspension of latex spheres. *J. Physique, Lett. (Paris)* **1984**, *45*, 1137–1143.
108. Larsen, A.E.; Grier, D.G. Melting of metastable crystallites in charge stabilized colloidal suspensions. *Phys. Rev. Lett.* **1996**, *76*, 3862–3865.
109. Larsen, A.E.; Grier, D.G. Like-charge attractions in metastable colloidal crystallites. *Nature* **1997**, *385*, 230–233.
110. Gong, T.; Marr, D.W.M. Electrically switchable colloidal ordering in confined geometries. *Langmuir* **2001**, *17*, 2301–2304.
111. Lumsdon, S.O.; Williams, J.P.; Kaler, E.W.; Velev, O.D. Dielectrophoretic assembly of oriented and switchable two-dimensional photonic crystals. *Appl. Phys. Lett.* **2003**, *82*, 949–951.
112. Comiskey, B.; Albert, J.D.; Yoshizawa, H.; Jacobson, J. An electrophoretic ink for all-printed reflective electronic displays. *Nature* **1998**, *394*, 253–255.
113. Sheridan, N.K.; Berkovitz, M.A. Gyricon—Twisting ball display. *Proc. SID.* **1977**, *18*, 289–293.
114. Kazlas, P.T.; McCreary, M.D. Paperlike microencapsulated electrophoretic materials and displays. *MRS Bull.* **2002**, *27*, 894–897.
115. Rogers, J.A.; Bao, Z.; Baldwin, K.; Dodabalapur, A.; Crone, B.; Raju, V.R.; Kuck, V.; Katz, H.; Amudson, K.; Ewing, J.; Drazic, P. Paper-like electronic displays: Large-area rubber-stamped plastic sheets of electronics and microencapsulated electrophoretic inks. *Proc. Natl. Acad. Sci. U. S. A.* **2001**, *98*, 4835–4840.
116. Dimitrakopoulos, C.D.; Malenfant, P.R.L. Organic thin film transistors for large area electronics. *Adv. Mater.* **2002**, *14*, 99–117.
117. Lvov, Y.; Haas, H.; Decher, G.; Mohwald, H.; Kalachev, A. Assembly of polyelectrolyte molecular films onto plasma-treated glass. *J. Phys. Chem.* **1993**, *97*, 12835–12841.
118. Keller, S.W.; Kim, H.N.; Mallouk, T.E. Layer-by-layer assembly of intercalation compounds and heterostructures on surfaces: Toward molecular “beaker” epitaxy. *J. Am. Chem. Soc.* **1994**, *116*, 8817–8818.
119. Fendler, J.H. Self-assembled nanostructured materials. *Chem. Mater.* **1996**, *8*, 1616–1624.
120. Decher, G.; Eckle, M.; Schmitt, J.; Struth, B. *Curr. Opin. Colloid Interface Sci.* **1998**, *3*, 32–39.
121. Cassagneau, T.; Mallouk, T.E.; Fendler, J.H. Layer-by-layer assembly of thin film Zener diodes from conducting polymers and CdSe nanoparticles. *J. Am. Chem. Soc.* **1998**, *120*, 7848–7859.

122. Sweryda-Krawiec, B.; Cassagneau, T.; Fendler, J.H. Ultrathin electroactive junctions assembled from silicone nanocrystallites and polypyrrole. *Adv. Mater.* **1999**, *11*, 659–664.
123. Colvin, V.L.; Schlamp, M.C.; Alivisatos, A.P. Light-emitting-diodes made from cadmium selenide nanocrystals and a semiconducting polymer. *Nature* **1994**, *370*, 354–357.
124. Gao, M.Y.; Gao, M.L.; Zhang, X.; Yang, Y.; Yang, B.; Shen, J.C. Constructing PbI<sub>2</sub> nanoparticles into a multilayer structure using the molecular deposition (MD) method. *J. Chem. Soc., Chem. Commun.* **1994**, *24*, 2777–2778.
125. Onitsuka, O.; Fou, A.C.; Ferreira, M.; Hsieh, B.R.; Rubner, M.F. Enhancement of light emitting diodes based on self-assembled heterostructures of poly(*p*-phenylene vinylene). *J. Appl. Phys.* **1996**, *80*, 4067–4071.
126. Fou, A.C.; Onitsuka, O.; Ferreira, M.; Rubner, M.F.; Hsieh, B.R. Fabrication and properties of light emitting diodes based on self-assembled multilayers of poly(*p*-phenylene vinylene). *J. Appl. Phys.* **1996**, *79*, 7501–7509.
127. Kumar, N.D.; Joshi, M.P.; Friend, C.S.; Prasad, P.N.; Burzynski, R. Organic–inorganic heterojunction light emitting diodes based on poly(*p*-phenylene vinylene)/cadmium sulfide thin films. *Appl. Phys. Lett.* **1997**, *71*, 1388–1390.
128. Carter, S.A.; Scott, J.C.; Brock, P.J. Enhanced luminance in polymer composite light emitting devices. *Appl. Phys. Lett.* **1997**, *71*, 1145–1147.
129. Liu, Y.J.; Claus, R.O. Blue light emitting nanosized TiO<sub>2</sub> colloids. *J. Am. Chem. Soc.* **1997**, *119*, 5273–5274.
130. Gao, M.Y.; Lesser, C.; Kirstein, S.; Mohwald, H.; Rogach, A.L.; Weller, H. Electroluminescence of different colors from polycation/CdTe nanocrystal self-assembled films. *J. Appl. Phys.* **2000**, *87*, 2297–2302.
131. Eckle, M.; Decher, G. Tuning the performance of layer-by-layer assembled organic light emitting diodes by controlling the position of isolating clay barrier sheets. *Nano Lett.* **2001**, *1*, 45–49.
132. Oregan, B.; Gratzel, M. A low-cost, high-efficiency solar-cell based on dye-sensitized colloidal TiO<sub>2</sub> films. *Nature* **1991**, *353*, 737–740.
133. Lahav, M.; Gabriel, T.; Shipway, A.N.; Willner, I. Assembly of Zn (II)–porphyrin–bipyridinium dyad and Au-nanoparticle superstructures on conductive surfaces. *J. Am. Chem. Soc.* **1999**, *121*, 258–259.



# Electrochemical Langmuir Trough

Natalia Varaksa  
Thomas F. Magnera  
Josef Michl

*University of Colorado, Boulder, Colorado, U.S.A.*

## INTRODUCTION

The term electrochemical Langmuir trough is used to describe a modification of the original Langmuir trough in which compression isotherms and thus surface areas per molecule can be measured at the interface between two conducting liquids at a controlled electrical potential. The instrument has been used to investigate molecular surface areas as a function of applied potential and to examine insoluble monolayers on mercury surface. These include films built from trigonal connectors and believed to have an open grid structure.

## THE LANGMUIR TROUGH

The Langmuir trough<sup>[1–3]</sup> was introduced by Irving Langmuir<sup>[4]</sup> and co-worker Katherine Blodgett<sup>[5]</sup> for the investigation of the behavior of amphiphilic molecules on a water–air interface. Such molecules contain hydrophilic and hydrophobic parts and tend to organize on the surface with their hydrophilic groups directed toward the aqueous phase. In a typical experiment, a solution of an amphiphile in a volatile solvent is spread on water, and the solvent is allowed to evaporate, leaving the water-insoluble molecules broadly dispersed on the water surface. A moving compression barrier is then used to reduce the surface area, until a closely packed and organized monolayer is formed in favorable cases. During the compression the two-dimensional interfacial material often goes through several phase transformations: from a dilute gas-like phase to a liquid-like phase, and finally to a condensed, solid-like phase. Those transitions are clearly reflected in the surface pressure ( $\pi$ ), which can be measured as a resistance to further compression. It is conveniently determined using a platinum plate attached to an electrobalance and partly immersed in a liquid (Wilhelmy plate). The net force acting on a Wilhelmy plate is composed of gravity, surface tension, and buoyancy. In surface pressure measurements the gravity and buoyancy components, invariant with surface areas, are subtracted out, leaving the surface tension as the

only surface-area-dependent variable. If the plate is completely wetted by a liquid (i.e., contact angle is zero), the resulting surface pressure depends only on the surface tension changes normalized to the perimeter of the plate in contact with a liquid.

The plot of  $\pi$  against the surface area  $A$  is known as the Langmuir isotherm (Fig. 1). To deduce the area per molecule at the interface, several compression isotherms are measured with different numbers  $N$  of amphiphile molecules on the surface. The steeply rising part of each isotherm is extrapolated to zero surface pressure, giving the compressed monolayer area  $A$ . The plot of areas  $A$  against  $N$  is linear and its slope corresponds to the area per molecule  $\sigma$ .

The compressed film can often be transferred to a solid substrate by passing the substrate through the water surface. Depending on the direction of the passage and the nature of the solid surface, the hydrophilic or the hydrophobic end of the molecules can face the solid. Multilayers can be deposited upon multiple passage. The transfer technique was worked out by Blodgett,<sup>[5]</sup> and the resulting thin films are known as Langmuir–Blodgett monolayers or multilayers. A horizontal transfer is also possible (Schaefer transfer).<sup>[6]</sup>

Traditionally, the liquid phase is pure water or aqueous electrolyte solutions, but mercury has also been used.<sup>[7–9]</sup>

## ELECTROCHEMICAL LANGMUIR TROUGH

This is a modification of the Langmuir trough in which the water–air interface is replaced by a mercury–electrolyte interface, kept at a well-defined potential. Solid films on mercury drop electrodes have been studied for a long time,<sup>[10]</sup> and electrochemical measurements permit a determination of  $\sigma$ , the surface area per redox center. The electrochemical Langmuir trough provides a complementary capability for such studies, the determination of surface area per molecule.

As mercury is easily oxidized in the presence of atmospheric oxygen and moisture, the electrochemical

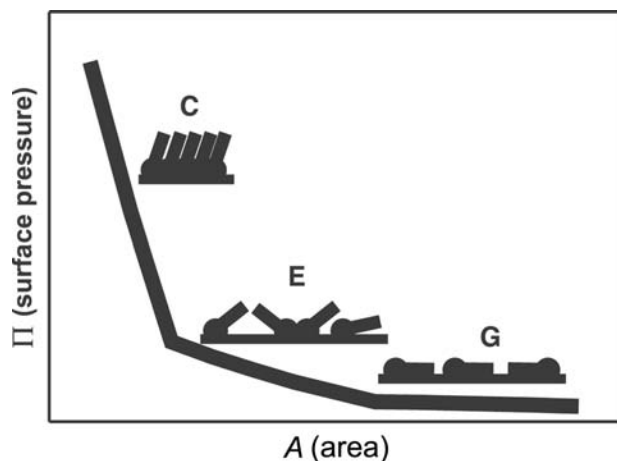


**Fig. 1** Schematic plot of monolayer transformations from the “gaseous” (G) to the expanded (E) and to the condensed phase (C), and their effect on surface pressure changes.

Langmuir trough must be used under an inert atmosphere, which is usual in most electrochemical studies. As mercury reflects electromagnetic radiation, it is relatively easy to perform grazing incidence spectroscopy of the interfacial material during compression. It is also possible to make standard electrochemical measurements such as cyclic voltammetry at various stages of compression, but special precautions are necessary because of the large area of the working electrode.

A schematic design of our latest version of the electrochemical Langmuir trough is shown in Fig. 2.

A rectangular Teflon trough has inside dimensions of 40 cm × 5 cm × 1 cm and a deeper well on one side, intended for the transfer of an interfacial film onto a solid substrate. A platinum barrier slides along the trough edges, and it is operated via a gearing system coupled to an electric motor. Once amalgamated, the surface of platinum is wetted by mercury, which forms a convex meniscus, preventing leakage of surface layers under the barrier and assuring proper monolayer compression.

Before each experiment, the mercury surface is swept with the barrier, and any contaminants present are compressed at one end of the trough and aspirated with a pipette into a mercury reservoir attached to the trough. The reservoir is designed to separate waste products from clean mercury by gravity, as the impurities concentrate in the upper layer in the reservoir. Fresh mercury from the bottom of reservoir is delivered to the trough, allowing circulation of mercury within the apparatus and the automatic adjustment of the mercury level in the trough.

During electrochemical experiments an electrolyte layer is added above the mercury pool and is provided with a counterelectrode (CE) (a platinum wire running along the inner perimeter of the mercury trough) and a reference electrode (RE). A common electrolyte is CH<sub>3</sub>CN/Bu<sub>4</sub>NPF<sub>6</sub>, with Ag/0.01 M AgNO<sub>3</sub>/0.1 M Bu<sub>4</sub>NPF<sub>6</sub> in CH<sub>3</sub>CN as the reference electrode. However, all potentials reported below are referred to the aqueous Ag/AgCl/1 M LiCl electrode via the intermediacy of the ferrocene/ferricinium couple. The electrical potential of the mercury pool is controlled with a

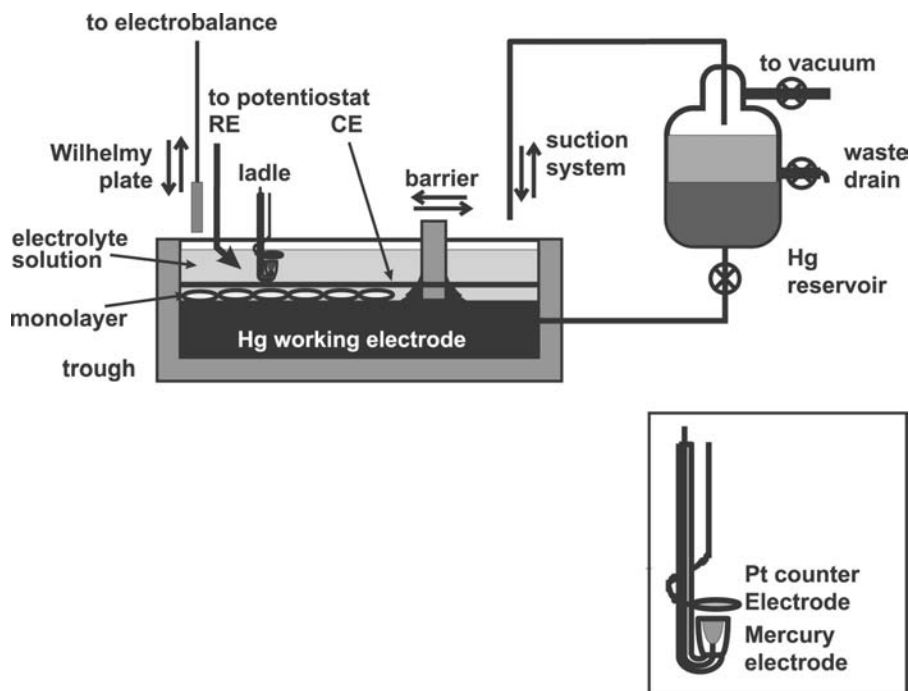


**Fig. 2** Schematic drawing of the electrochemical Langmuir trough. Inset: the ladle electrode.

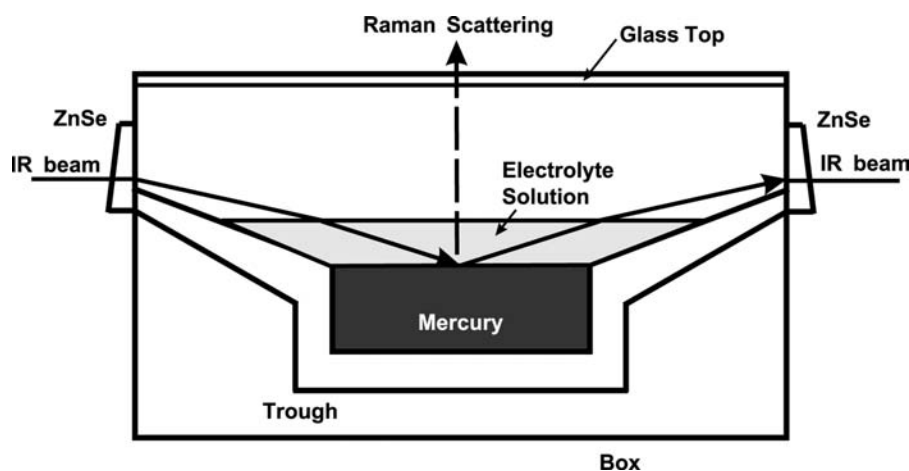


Fig. 3 Cross section of the electrochemical Langmuir trough with extended wings for spectroscopy of compressed monolayers.

potentiostat, connected to the trough through sealed leads. The trough along with the barrier driving system and the electrobalance with an attached Wilhelmy plate are enclosed in a purgeable airtight stainless steel box. For IR spectroscopy an IR beam enters in a direction perpendicular to the long axis of the trough at grazing incidence and exits through a pair of wedged ZnSe windows (Fig. 3). The instrument also has a removable transparent glass top, used for viewing and for Raman spectroscopic measurements. The communication between the trough and a potentiostat, as well as the control of the barrier movements and the electrobalance readings (interface unit/software), is accomplished via sealed electrical connectors installed in the body of the steel box. The glass top accommodates several airtight ports. Three ports with replaceable septum pads (inserts) are used for the introduction of solutions and solvents into the system from a syringe. Another port is used for a reference electrode and yet another for a ladle working electrode (See Fig. 2, inset). The box also has inlet and outlet ports for purging with inert gas.

In a typical experiment, a solution of a compound of interest is spread on the mercury and the solvent is allowed to evaporate on a cleaned mercury surface. Electrolyte solution is then added, and the desired potential is applied simultaneously to enable electrochemical control. After a short pause, the surface pressure-area isotherm is recorded by moving the barrier toward the Wilhelmy plate position. Spectra are taken concurrently if desired. In the grazing incidence IR measurement, the beam is polarization modulated, removing all contributions to the spectrum from species not located at the interface.

Because of the large size of the working electrode, the mercury surface potential is not entirely uniform, but it appears that a small potential gradient can be tolerated in the isotherm measurement. For accurate electrochemical measurements on the monolayers, such as cyclic voltammetry, constant-potential coulometry,

or double-layer capacitance determination, a separate “ladle electrode” with a  $0.1\text{-cm}^2$  surface area is used. It consists of a long vertical glass handle carrying an insulating cup at the lower end, with a conductive contact at the bottom. Initially, the cup is fully immersed in the mercury pool. Before an electrochemical measurement, the handle is pulled up until the top of the cup emerges into the electrolyte and separates a small volume of mercury along with a portion of the surface carrying the partially or fully compressed film. After breaking the mercury surface, the ladle stays in the electrolyte solution, but the scooped portion of mercury with a monolayer is electrically insulated from the rest of the mercury pool electrode. The small amount of mercury in the ladle then serves as a separate working electrode. A circular platinum foil positioned above the top of the cup and parallel to it is used as a counter-electrode.

## EXAMPLES OF APPLICATION

### A Molecular Conformation [Ref.<sup>[11]</sup>]

Metal sandwich complexes provided with sulfur-containing substituents adsorb firmly on a mercury surface over a considerable range of potentials.<sup>[12]</sup> The compounds studied on the electrochemical Langmuir trough were tetraphenylcyclobutadienecyclopentadienylcobalt complexes with five “tentacles” attached to the cyclopentadienyl ring. In general, they form a chemisorbed layer at the least negative potentials, are merely physisorbed at intermediate potentials, and are not adsorbed at all at the most positive potentials, but there is considerable variation.

The compression isotherms (Fig. 4, right inset) for molecules with short tentacles containing a single sulfur atom (Fig. 5A) confirm that at potentials less negative than  $\sim -0.55\text{ V}$  a firmly chemisorbed surface layer is formed. The slope of the plot of extrapolated

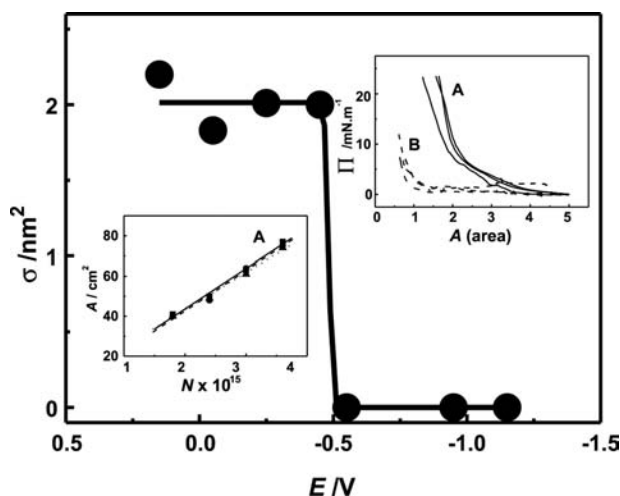


**Fig. 4** Molecular surface areas of connectors of Fig. 5A as a function of applied potential. Insets: right, compression isotherms at  $-0.50$  to  $+0.15$  V (A) and at  $-1.15$  to  $-0.55$  V (B); left, extrapolated surface areas of connectors (A) vs. the number of molecules ( $N$ ) at the mercury/electrolyte solution interface (potential range  $-0.5$  to  $+0.55$  V).

monolayer areas for different numbers of molecules at the interface (Fig. 4, left inset) yields an area per molecule of  $\sim 2 \text{ nm}^2$ . At potentials more negative than  $\sim -0.55$  V the physisorbed molecules show no resistance to compression, and instead leave the surface and move into the supernatant solution. In a cyclic voltammogram,<sup>[12]</sup> a mercury redox peak occurs at  $-0.69$  V, and it seems that the formation of a firmly adsorbed layer is associated with the availability of mercury cations at the less negative potentials. Apparently, these bridge sulfur atoms that are located in different tentacles and produce an insoluble polymeric network.

When the substituents on the cyclopentadienyl ring are longer and each contains two sulfur atoms (Fig. 5B), the results are different. Now, the mercury redox peak appears at  $-1.14$  V in the cyclic voltammogram,<sup>[12]</sup> and

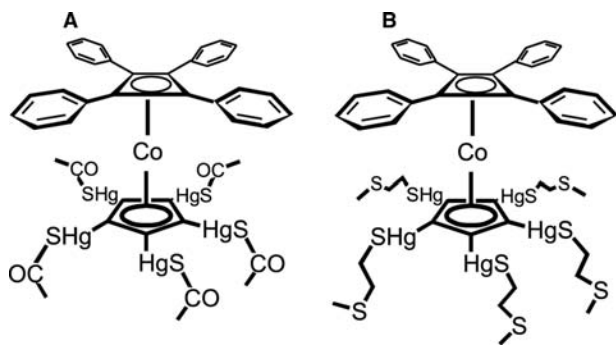


**Fig. 5** Molecular structures of tetraphenylcyclobutadienylcyclopentadienylcobalt complexes with a single (A) and with two (B) sulfur atoms per tentacle.

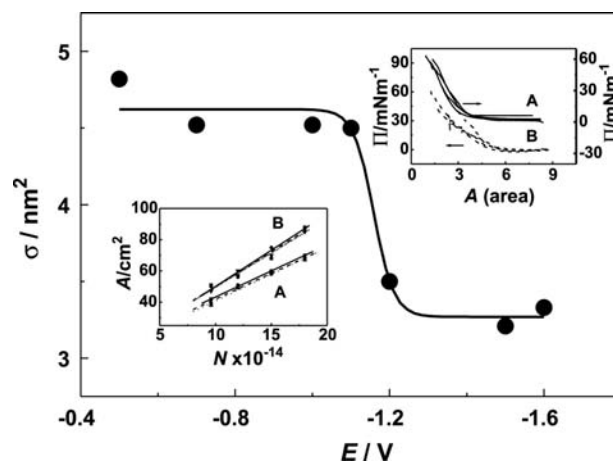


**Fig. 6** Molecular surface areas of connectors of Fig. 7B as a function of applied potential. Insets: right, compression isotherms of connectors at  $-1.6$  V (A) and at  $-1.0$  V (B); left, extrapolated surface areas of connectors (A) vs. the number of molecules ( $N$ ) at the mercury/electrolyte solution interface at  $-1.6$  to  $-1.2$  V (A) and at  $-1.1$  to  $-0.5$  V (B).

the compression isotherms show that the molecules are firmly adsorbed on the mercury surface both at potentials less negative and those more negative than  $\sim -1.15$  V, but the areas per molecule are different in the two regions (Fig. 6). At less negative potentials, the connectors seem to be adsorbed with both sulfur atoms in each tentacle, with the tentacles fully stretched on the surface and a surface area per molecule equal to  $\sim 4.5 \text{ nm}^2$ . At more negative potentials, the tentacles seem to contract and the surface area per molecule is only  $\sim 3.3 \text{ nm}^2$ . It is again likely that the conformation change is related to the availability of mercury cations.

Measurements of a doubled sandwich complex (Fig. 7) at  $-0.8$  V yield twice the surface area ( $8 \text{ nm}^2$ ), suggesting that the mode of absorption of these molecules on a mercury surface is analogous.

### Open Grids [Ref.<sup>[13]</sup>]

The fabrication of regular two-dimensional molecular grids<sup>[14–17]</sup> of desired structure, dimensions, and chemical functionalization is motivated by their potential use as molecular-scale separation membranes and selective barrier materials, and as organized surfaces for mounting molecular functionalities in a plane in a regular fashion. The building units of such grids are star-shaped monomers adhering to the surface with their arms. The arms can be tailored to control the lateral spacing and the nature of interactions between monomers. Given an ability to control the potential applied to the mercury/electrolyte interface, the grid structure can be governed and manipulated. Specifically, if mercury cations participate in grid formation by providing

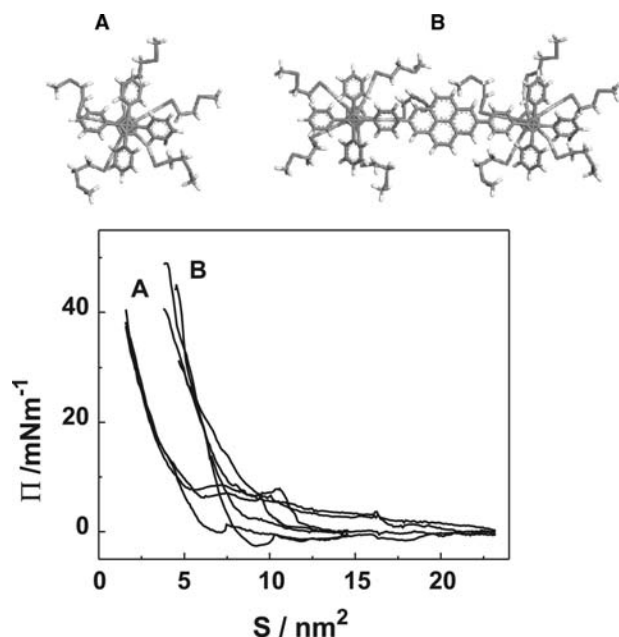


**Fig. 7** Molecular structures and compression isotherms of tetraphenylcyclobutadienecyclopentadienylcobalt complexes of Fig. 7B (A) and of altitudinal rotor molecules (B) at  $-0.8$  V.

links between neighboring arms, the use of the electrode potential to control their presence offers opportunities for defect annealing.

The adsorption and self-assembly of the trigonal connector, 1,3,5-tris[10-(3-ethylthiopropyl)dimethylsilyl-1,10-dicarba-*closo*-decaboran-1-yl]benzene, on a mercury surface under controlled electrochemical conditions have been examined and are compatible with the formation of a two-dimensional hexagonal grid (Fig. 8).<sup>[13]</sup> No adsorption is observed at potentials more negative than  $\sim -0.85$  V, physisorption takes place between  $\sim -0.85$  and 0 V, and at positive potentials anodic dissolution of mercury promotes the

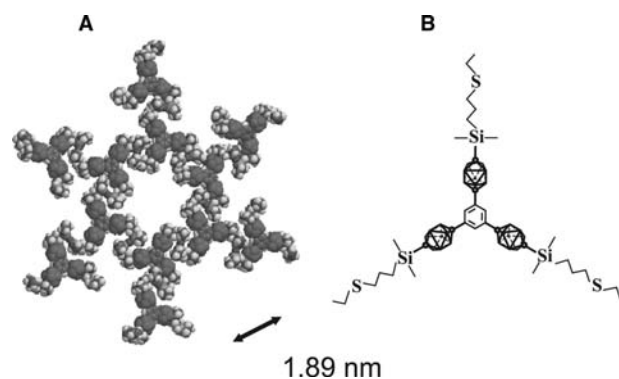


**Fig. 8** AM1 optimized structure of the proposed hexagonal grid (A) and the chemical structure of the trigonal connector (B).

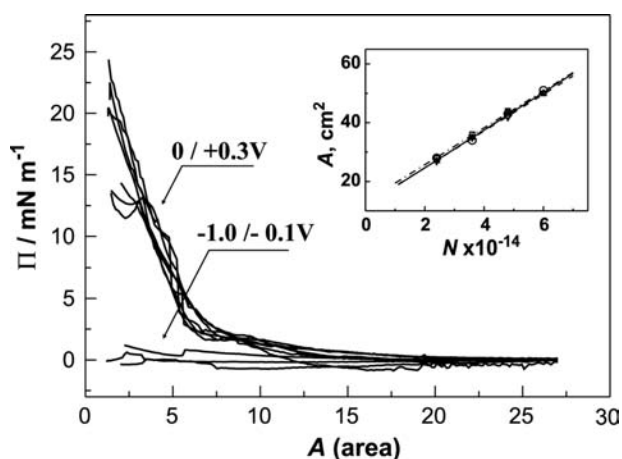


**Fig. 9** Compression isotherms of trigonal connectors under potential control. Inset: extrapolated areas ( $A$ ) vs. the number of molecules ( $N$ ) at the mercury/electrolyte solution interface.

mutual binding of thioether-containing arms through surface mercury cations.

Langmuir compression isotherms (Fig. 9) show that at potentials more negative than the mercury reduction peak, trigonal connectors offer no significant resistance to compression. At potentials more positive than the mercury redox peak, the trigonal connectors form an insoluble adsorbed surface layer on mercury. The areas per molecule at various potentials are shown as dark circles in Fig. 10. The average number is  $6.20$  nm<sup>2</sup>, and this fits fairly well with the area expected from a semiempirical AM1 geometry optimization of a perfect hexagonal grid (Fig. 8). The benzene rings are at the vertices of a hexagon, and mercury cations are midway between each pair of benzene rings. The S–Hg–S or S–Hg–Hg–S line is roughly perpendicular to the edge of a planar hexagon. After unconstrained optimization, the structure is nearly planar and almost sixfold symmetric. Assuming the S–Hg–S structure, the edge length is  $1.89$  nm, which corresponds to an area of  $4.64$  nm<sup>2</sup> per connector molecule. This is less than the  $6.2$  nm<sup>2</sup> deduced from the electrochemical Langmuir isotherm, but the result agrees closely with the electrochemical data of Ref. <sup>[13]</sup> (area per molecule  $4.4$  nm<sup>2</sup>), suggesting that the number of electrons exchanged per redox center is 2, and the binding cations are Hg<sup>2+</sup> or Hg<sub>2</sub><sup>2+</sup> (not Hg<sup>+</sup>).

A noteworthy peculiarity of this hexagonal network on mercury is the existence of a bistable state up to the potential  $-0.85$  V. When the monolayer is formed at  $+0.1$  V, and then the potential is stepped to a more negative value, the surface layer remains on the mercury surface and resists the compression. The areas per molecule of trigonal connectors deduced from the corresponding compression isotherms



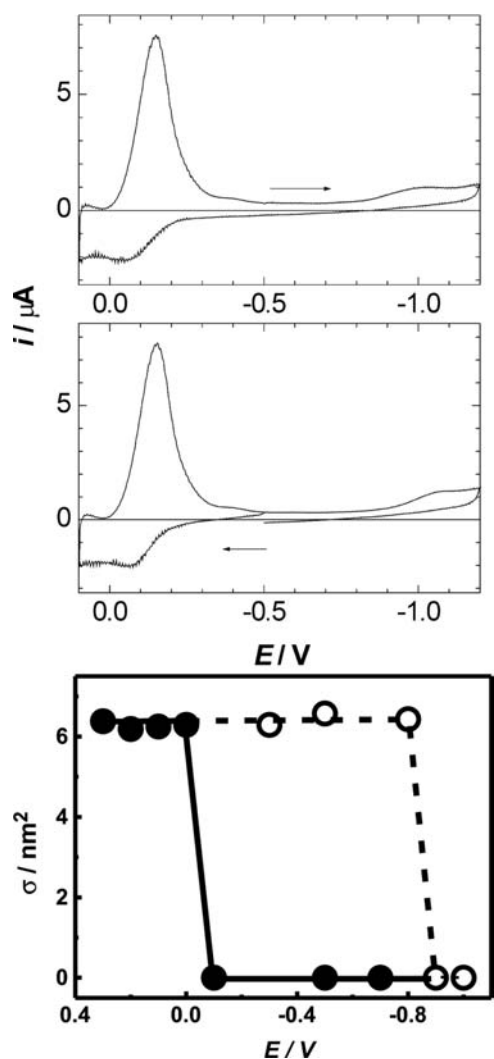


**Fig. 10** Bottom: Trigonal connector footprints ( $\sigma$ ) vs. potential ( $E$ ). Hollow circles represent an alternative long-term stable state of adsorbed molecules. Top: cyclic voltammograms of trigonal connectors on a static mercury drop electrode, scanned in both directions.

average  $\sim 6.20 \text{ nm}^2$ , the same as obtained at potentials more negative than the redox peak. It is not clear why the self-assembled layer remains ordered after the structure-defining mercury cations have been reduced. Although complexes of  $\text{Hg}(0)$  are known to exist,<sup>[18]</sup> it is unlikely that the mercury atoms stay in place, continuing to bridge the thioether arms. Perhaps  $\text{Li}^+$  ions from the supporting electrolyte perform the same function as the mercury cations do at more positive potentials.

## CONCLUSION

The electrochemical Langmuir trough combines two powerful methods to permit the manipulation of

molecules on the surface of liquid mercury through the simultaneous control of the electrochemical potential and surface density. The technique has been demonstrated to be useful for monitoring the molecular conformation of adsorbed molecules as a function of electrical potential and for the assembly and characterization of open and regular two-dimensional molecular grids. The ability to synthesize regular two-dimensional molecular grids with precise control represents progress in the development of new nanoporous ultrathin membrane materials.

## REFERENCES

1. Gaines, G.L. *Insoluble Monolayers at Liquid-Gas Interface*; Wiley-Interscience: New York, 1966.
2. Roberts, G. *Langmuir-Blodgett Films*; Plenum Press: New York, 1990.
3. Ulman, A. *Ultrathin Organic Films*; Academic Press: San Diego, 1991.
4. Langmuir, I. The mechanism of the surface phenomena of flotation. *Trans. Faraday Soc.* **1920**, *15*, 62–64.
5. Blodgett, K.B. Films built by depositing successive monomolecular layers on a solid surface. *J. Am. Chem. Soc.* **1935**, *57*, 1007–1022.
6. Langmuir, I.; Schaefer, V.J. Activities of urease and pepsin monolayers. *J. Am. Chem. Soc.* **1938**, *60*, 1351–1360.
7. Ellison, A.H. Surface pressure-area properties of organic monolayers on mercury. *J. Phys. Chem.* **1962**, *66*, 1867–1872.
8. Smith, T. Monomolecular films on mercury. *Adv. Colloid Interface Sci.* **1972**, *3*, 161–221.
9. Yoshimura, H.; Matsumoto, M.; Endo, S.; Nagayama, K. Two-dimensional crystallization of proteins on mercury. *Ultramicroscopy* **1990**, *32*, 265–274.
10. De Levie, R. The dynamic double layer: Two-dimensional condensation at the mercury–water interface. *Chem. Rev.* **1988**, *88*, 599–609.
11. Varaksa, N.; Pospíšil, L.; Janoušek, Z.; Grüner, B.; Wang, B.; Pecka, J.; Harrison, R.; Noll, B.; Michl, J. Tentacled 1,3,5-tris(1,10-dicarba-*closo*-decarboran-1-yl)benzene as a trigonal connector for molecular tinkertoys: Network formation on a mercury electrode—unpublished results.
12. Brotin, T.; Pospíšil, L.; Fiedler, J.; King, B.T.; Michl, J. Toward a square grid polymer: Electrochemistry of tentacled tetragonal star connectors,  $\text{C}_4\text{R}_4\text{Co}-\text{C}_5(\text{HgY})_5$ , on mercury. *J. Phys. Chem.* **1998**, *B102*, 10062–10070.
13. Varaksa, N.; Pospíšil, L.; Magnera, T.F.; Michl, J. Self-assembly of a metal-ion-bound monolayer of trigonal connectors on mercury: An electrochemical Langmuir trough. *Proc. Natl. Acad. Sci. U. S. A.* **2002**, *99*, 5012–5017.



14. Harrison, R.M.; Magnera, T.F.; Vacek, J.; Michl, J. Towards Designer Solids. In *Modular Chemistry*; Michl, J., Ed.; Kluwer: Dordrecht, The Netherlands, 1997; 1–16.
15. Magnera, T.F.; Pecka, J.; Vacek, J.; Michl, J. Synthesis and Handling of Single Sheets of a Covalent Monolayer Square Grid Polymer. In *Nanostructural Materials: Clusters, Composites and Thin Films*; Moskovits, M., Shalaev, V., Eds.; Am. Chem. Soc.: Washington, DC, 1997; 213–220.
16. Magnera, T.F.; Pecka, J.; Michl, J. Synthesis of a Covalent Square Grid. In *Science and Technology of Polymers & Advanced Materials*; Prasad, P.N., Mark, J.E., Kandil, S.H., Eds.; Plenum: New York, 1998; 385–391.
17. Michl, J.; Magnera, T.F. Two-dimensional supramolecular chemistry with molecular Tinkertoys. *Proc. Natl. Acad. Sci. U. S. A.* **2002**, *99*, 4788–4792.
18. Catalano, V.J.; Malwitz, M.A.; Noll, B.C. A linearly coordinated Hg(0) trapped in a gold(1) metallocryptand cage. *Chem. Commun.* **2001**, 581–582.

# Electrochemical Sensors: Functionalized Silica

Yuehe Lin

Wassana Yantasee

Glen E. Fryxell

*Pacific Northwest National Laboratory, Richland, Washington, U.S.A.*

## INTRODUCTION

Nanostructured materials allow the development of miniature sensing devices that are compact, low-cost, low-energy-consuming, and easily integrated into field-deployable units. This article reviews our recent successful development of electrochemical sensors that are solid-state and mercury-free by using nanostructured materials. Specifically, thiol- or acetamide phosphonic acid-functionalized nanoporous silica materials have been incorporated in carbon paste electrodes for the detection of uranium,<sup>[2]</sup> and the simultaneous detection of lead/mercury,<sup>[1]</sup> and copper/lead/cadmium.<sup>[3]</sup> Thiol-functionalized mesoporous silica thin film has been immobilized on gold electrode arrays for the detection of lead ions.<sup>[4]</sup> The electrochemical sensors based on functionalized nanoporous silica yield reproducible measurements with excellent detection limits (at a few ppb of metal ions) and require little or no regeneration of electrode materials. Other advantages of our approaches, compared to those of current sensor technology, will also be discussed.

## BACKGROUND

There is enormous current interest in exploiting nanostructured materials in the developments of electrochemical sensors of metal ions.<sup>[1-14]</sup> Nanostructured materials are defined as materials that have at least one dimension smaller than 100 nm. The unique properties (e.g., electrical, optical, magnetic properties) of the nanomaterials, obtained as the particle sizes approach molecular dimensions, make them very useful for specific applications.<sup>[14]</sup> Nanostructured materials allow the development of miniature sensing devices that are compact, low-cost, low-energy-consuming, and easily integrated into field-deployable units.

Currently, quantification of heavy metals at surface and subsurface hazardous waste sites relies upon the collection of liquid discrete samples for subsequent laboratory analysis using techniques such as inductively coupled plasma mass spectrometry (ICP-MS) and

atomic absorption spectroscopy (AAS). Sensors for obtaining real-time ppb-level heavy metal concentrations would reduce time and costs associated with the characterization and treatments of hazardous waste sites. Desirable characteristics of the metal ion sensors include specificity for targeted metal ions, enhanced measurement frequency and precision, robustness, inexpensiveness, and infrequent regeneration of sensor material. Electrochemical sensors based on stripping voltammetry appear to be a promising technique that meets these requirements.

Adsorptive stripping voltammetry (AdSV) is an extremely sensitive electrochemical technique for measuring trace species. Its remarkable sensitivity is attributed to the combination of a selective preconcentration step with advanced measurement procedures that generate an extremely favorable signal-to-background ratio. AdSV usually involves preconcentration of metal ions at an electrode surface, followed by quantification of the accumulated species by voltammetric methods. Preconcentration of metal ion species at an electrode surface prior to the detection step allows the sensitive detection of the metal species that may be present at extremely low levels (ppb) in contaminated groundwater or wastewater. Preconcentration of metal species at mercury drop or mercury film electrodes has been available for decades; however, mercury drop electrodes have the disadvantage of being mechanically unstable during various steps of the assay procedure, and thus, they are less desirable than solid-state sensors in routine field applications.<sup>[15,16]</sup> In addition, all mercury-based electrodes have issues related to the use and disposal of toxic mercury.

We have focused on developing mercury-free, solid-state electrochemical sensors, in which the preconcentration of metal species at the electrodes modified with functional ligands uses the specific binding properties of the ligand (toward the target metal ions) to accumulate the metal ions via coordination or chelation onto the electrode without applying any potential. These ligand-modified electrodes have several advantages: 1) they can preconcentrate metal ions that cannot be

reductively accumulated such as species that require excessively large negative reduction potentials; 2) electrolytes are not required in the preconcentration solution, thus reducing the risk of introduction of contaminants (i.e., trace metal impurity in chemical reagents) or competing ligands; and 3) with the appropriate ligand, the overall selectivity of the analysis for the targeted metal ions may increase.

Chemically (ligand) modified electrodes (CMEs) have been fashioned by immobilizing functional ligands on electrode surfaces using thin-polymeric films,<sup>[9,10]</sup> self-assembled monolayer (SAM) thin films,<sup>[11,12]</sup> or by immobilizing suitable functional ligands on an electrically conductive porous matrix.<sup>[17–24]</sup> One major limitation for CMEs based on polymeric films is slow diffusion across the films. CMEs based on SAM thin films can effectively remove this limitation. This approach has shown to provide a reproducible method for the sensitive and selective determination of trace cadmium<sup>[11]</sup> and chromium(VI).<sup>[12]</sup> The potential drawback of CMEs modified with SAM thin films is that the total number of binding sites in SAM thin films is limited, which may lead to a narrow linear range of the calibration curves.

Chemically modified carbon paste electrodes are often used in AdSV because they have low background currents, have a large potential domain, are low cost, and are easy to prepare and regenerate. Carbon paste electrodes modified with functional ligands have been employed to detect heavy metal ions.<sup>[17–24]</sup> However, the ligands in these sensors are in loose association with the conductive carbon matrix, thus the sensors may easily degrade over time from depletion of ligand-bearing material. In our work,<sup>[1–3]</sup> suitable ligands were first immobilized via covalent bonding through the self-assembly process onto a high surface area mesoporous silica substrate (MCM-41) prior to embedding the self-assembled monolayer on mesoporous silica (SAMMS) in a carbon graphite matrix. Thus the chemical functionality of the sensor is retained despite diffusion or abrasive wear.

The use of carbon paste electrodes modified with functional groups grafted on mesoporous silica supports for the detection of metal ions is a relatively new research area. Several unmodified silica materials were incorporated into carbon paste electrodes for copper(II)<sup>[5]</sup> and mercury(II)<sup>[6]</sup> detection by exploiting the silanol groups inherent in the MCM-41 silica materials. By using unmodified mesoporous silica materials, specificity for the targeted metal ions was limited to the silanol groups of the silica materials. In the pH range of 4–7, only metal hydroxides of mercury(II) are soluble enough to reach and react with silanol groups of the MCM-41 via a condensation process.<sup>[6]</sup> Metal species that are not hydroxylated can only bind with silanolate groups, which are formed in significant

amounts at above pH 7. Therefore ammoniacal medium was used as a preconcentration medium so that the silanolate groups could accumulate positively charged species such as  $\text{Cu}(\text{NH}_3)_4^{2+}$ .<sup>[5]</sup> Polysiloxane-immobilized amine ligands<sup>[7]</sup> and aminopropyl-grafted silica gel<sup>[8]</sup> were later used successfully by Walcarius and co-workers as electrode modifiers in order to study the uptake of copper(II) from an aqueous solution. Both functionalized MCM-41 materials show very promising results as electrode modifiers. Two factors believed to affect voltammetric detection responses of copper ions are the number of immobilized functional groups and the structure of the organically modified silicates, the latter of which governs the accessibility to the binding sites and the diffusivity of the copper ions.<sup>[5,7]</sup> However, amine functional groups are highly selective mainly for copper ions. Using this class of materials as the electrode modifiers for other toxic metal ions has therefore become our main research focus.

## FUNCTIONALIZED NANOPOROUS SILICA FOR SELECTIVE ADSORPTION OF METAL SPECIES

Self-assembled monolayer on mesoporous silica is a new class of nanostructured sorbent materials developed at the Pacific Northwest National Laboratory (PNNL) through the marriage of nanoporous ceramic science with self-assembly chemistry.<sup>[25–36]</sup> Self-assembled monolayers provide a simple and direct method of chemically derivatizing ceramic oxide surfaces. These nanoporous hybrid materials with particle sizes of 5–200  $\mu\text{m}$  and a nominal pore size of 5 nm<sup>[35]</sup> are highly efficient sorbents. The high surface area (up to 1000  $\text{m}^2/\text{g}$ ) of nanoporous ceramic backbone coupled with the dense monolayer coating promises a high loading capacity. The close proximity of the binding sites allows for multiligand chelation of the target ion in the monolayer interface, enhancing the binding affinity and stability. The open pore structure that allows facial diffusion into the nanoporous matrix and the rigid ceramic backbone that prevents pore closure due to solvent swelling result in fast sorption kinetics.<sup>[31]</sup> The interfacial chemistry of SAMMS has been fine-tuned to selectively sequester a specific target species, including lanthanides,<sup>[32]</sup> actinides,<sup>[34]</sup> heavy and transition metal ions,<sup>[25–28,35]</sup> and oxometallate anions.<sup>[29,33]</sup> Two SAMMS materials have been investigated in our laboratory, first as sorbent materials and further as modifiers for electrochemical sensors for metal ions including thiol-terminated self-assembled monolayer on mesoporous silica (SH-SAMMS) and self-assembled acetamide phosphonic acids on mesoporous silica (Ac-Phos SAMMS). The schematics of both materials are shown in Fig. 1.

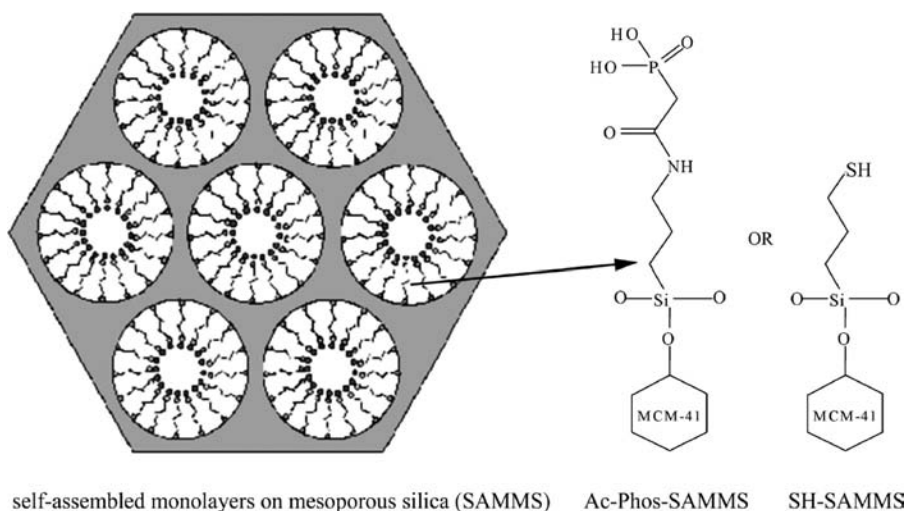


**Fig. 1** Schematics of thiol (SH)-SAMMS and acetamide phosphonic acid (Ac-Phos) SAMMS.

The SH-SAMMS was designed to be an excellent sorbent for lead and mercury.<sup>[36]</sup> With thiol coverage of up to 82%, the SH-SAMMS has a loading capacity for Hg of 0.64 g Hg/g.<sup>[28]</sup> From batch competitive adsorption experiments previously performed at PNNL,<sup>[25]</sup> in the presence of Ag, Cr, Zn, Ba, and Na, the SH-SAMMS has demonstrated the mass-weighted distribution coefficients ( $K_d$ ) of Hg and Pb on the order of  $10^5$  at neutral pH. Background ions, such as Na, Ba, and Zn, although present at high concentrations (i.e., 350 times higher concentrations than Hg and Pb), did not bind to the SH-SAMMS. Other transition metals such as Cd, Cu, Ag, and Au may bind to the SH-SAMMS, but not as effectively as Hg and Pb. The  $K_d$  values of Cu and Cd, for instance, are about 25 times lower than those of Hg. The presence of other anions (i.e.,  $\text{CN}^-$ ,  $\text{CO}_3^{2-}$ ,  $\text{SO}_4^{2-}$ ,  $\text{PO}_4^{3-}$ ) did not significantly interfere either with the adsorption of lead and mercury ions onto the SH-SAMMS.<sup>[36]</sup> The high selectivity of SAMMS material toward Hg and Pb is a combined effect of the suitable stereochemistry of the ligand, size of the chelation cavity, and hardness/softness of the metal ion and ligand field.

Similarly, the Ac-Phos SAMMS material was designed to be highly selective for hard Lewis acids such as actinide ions<sup>[37]</sup> by pairing a “hard” anionic Lewis base with a suitable synergistic ligand. The Ac-Phos SAMMS material displays excellent selectivity for actinide ions with virtually no competition from a wide variety of transition metal and alkaline earth cations.<sup>[31]</sup> In the absence of actinides, the Ac-Phos SAMMS is a good sorbent material for heavy and transition metal ions such as Cu, Pb, and Cd.<sup>[35]</sup> With a functional group density of 2.0 mmol phosphonic acid/g, the Ac-Phos SAMMS has a loading capacity of 0.3 mmol Cd/g and is able to uptake 99% of 2 mg/L  $\text{Cd}^{2+}$  within 1 min at a solution-to-solids ratio of 200.<sup>[35]</sup>

## ELECTROCHEMICAL SENSORS BASED ON FUNCTIONALIZED NANOPOROUS SILICA

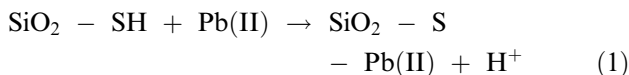
### Electrochemical Sensors Based on SAMMS-Modified Carbon Paste Electrodes

The high loading capacity and high selectivity of SAMMS materials are desirable for metal ion detection based on the AdSV technique because they minimize the competition for the binding sites of the nontarget species, thereby reducing the interferences and preserving the signal intensity of the target metal ions. In addition, as SAMMS particles are not conductive, the high surface of the material does not contribute to the charging current when the material is used as electrode modifiers, leading to the low background current for measurements. Self-assembled monolayer chemistry readily allows installation of a wide variety of chemical monolayers that can be tailored to specific metal ion detection needs when used as electrode modifiers. Our sensors that are based on different functionalized mesoporous silica materials are summarized as follows.

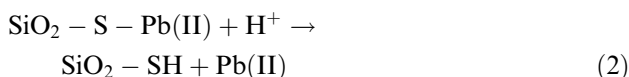
#### Thiol-terminated self-assembled monolayer on mesoporous silica

The anodic stripping voltammetry at a carbon paste electrode modified with a SH-SAMMS provides a new sensor for simultaneous detection of lead ( $\text{Pb}^{2+}$ ) and mercury ( $\text{Hg}^{2+}$ ) in aqueous solutions.<sup>[1]</sup> The overall analysis involved a two-step procedure: an accumulation step at an open circuit, followed by medium exchange to a pure electrolyte solution for the stripping analysis. For example, the reactions that occur between Pb(II) and an SH-SAMMS ( $\text{SiO}_2\text{-SH}$ )-modified electrode during each step in AdSV experiments can be summarized as follows.

Preconcentration of Pb(II) ions under an open circuit (Eq. (1)):



Because SAMMS is an electronic insulator, desorption of  $\text{Pb}^{2+}$  previously accumulated on the SH-SAMMS to the electrode/solution interface must occur for the voltammetric detection to be possible (Eq. (2)).



Then the desorbed  $\text{Pb}^{2+}$  may be detected directly by reduction from lead ions to elemental lead ( $\text{Pb(II)} \rightarrow \text{Pb(0)}$ ). However, it is more sensitive and quantitative to first perform a thorough electrolysis by applying a negative potential to deposit  $\text{Pb(0)}$  on the electrode surface (Eq. (3)),



followed by performing anodic stripping voltammetry to oxidize the previously reduced  $\text{Pb(0)}$  to  $\text{Pb(II)}$  (Eq. (4)).



Factors affecting the performance of the SH-SAMMS modified electrodes were investigated. The most sensitive and reliable electrode contained 20% SH-SAMMS and 80% carbon paste. The optimal operating conditions were a sequence with a 2-min preconcentration period, then a 60-sec electrolysis period of the preconcentrated species in 0.2 M nitric acid, followed by square

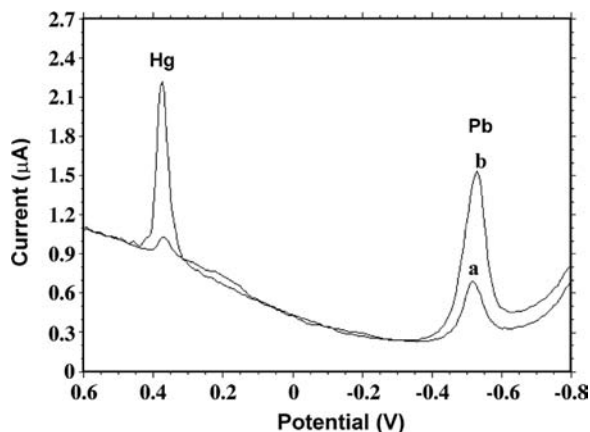


**Fig. 2** The voltammetric responses of  $\text{Pb}^{2+}$  and  $\text{Hg}^{2+}$  (A) measured after 2 min of preconcentration in 30 ppb  $\text{Pb}^{2+}$ /160 ppb  $\text{Hg}^{2+}$  solution and (B) measured after 20 min of preconcentration in 1.5 ppb  $\text{Pb}^{2+}$ /3 ppb  $\text{Hg}^{2+}$  solution. *Source:* From Ref.<sup>[1]</sup>.

wave anodic stripping voltammetry from  $-1.0$  to  $0.6$  V in 0.2 M nitric acid. Fig. 2 shows that the  $\text{Pb}^{2+}$  and  $\text{Hg}^{2+}$  anodic peaks appear at  $-0.5$  and  $0.4$  V, respectively; the large differential potential ( $\Delta E$ ) of 0.9 V enables  $\text{Pb}^{2+}$  and  $\text{Hg}^{2+}$  to be detected simultaneously without interference with each other. Table 1 summarizes the detection limits and the parameters for the calibration curves of metal ions measured by various types of SAMMS-modified electrodes, including the SH-SAMMS-modified carbon paste electrode for simultaneous detection of  $\text{Hg}^{2+}$ / $\text{Pb}^{2+}$ . After 2 min of preconcentration, the area of each anodic peak of  $\text{Pb}^{2+}$  and  $\text{Hg}^{2+}$  was proportional to their concentrations in the range of 10–1500 ppb  $\text{Pb}^{2+}$  and 20–1600 ppb  $\text{Hg}^{2+}$ , respectively. The experimental detection limit for  $\text{Pb}^{2+}$  was 10 ppb after a 2-min preconcentration period and improved significantly to 0.5 ppb after a 20-min preconcentration period. Similarly, the detection limit for  $\text{Hg}^{2+}$  was 20 ppb after a 2-min preconcentration period and improved to 3 ppb after a 20-min preconcentration period.

#### Self-assembled acetamide phosphonic acids on mesoporous silica

Because of its excellent selectivity for actinide ions, the Ac-Phos SAMMS was used to modify a carbon paste electrode for uranium detection.<sup>[2]</sup> One issue for stripping voltammetric detection of uranium is the potential interferences from heavy and transition metal ions existing at higher concentrations in most wastes. The superior selectivity for actinides over heavy and transition metal ions of the Ac-Phos SAMMS greatly improves the selectivity for uranium sensing. Compared to propyl gallate (PG)<sup>[16]</sup> and trioctylphosphine oxide (TOPO),<sup>[38]</sup> carbamoyl methyl phosphine oxide (CMPO) is a more notable class of ligands in which a carbonyl amide and a  $\text{P}=\text{O}$  double bond are arranged in a suitable fashion to chelate actinide cations.<sup>[34,39–41]</sup> The characteristic of the  $\text{C}=\text{O}$  methyl  $\text{P}=\text{O}$  moiety in the Ac-Phos SAMMS (Fig. 1) plays an important role just like the CMPO, which leads to high selectivity for actinide binding.

Uranium in aqueous solution will form complexes with ligands that may vary as a function of solution pH. Speciation can greatly affect the voltammetric responses of uranium (matrix effect). The type and concentration of anions, the concentration of uranium, and the pH of the solution are factors that determine which uranium complex will be preferentially formed in the solution. Sensors based on cathodic stripping voltammetry techniques rely on electrodeposition of metal–ligand complexes on electrode surfaces before detecting the metal within the same solution, hence the presence of ligands in the sample matrix can affect both deposition and detection steps. Using SAMMS-based electrodes with medium exchange in

**Table 1** Summary of the detection limits and calibration curve parameters of SAMMS-based electrodes

Modifier	Electrode	Metal ion	Detection Limit Detection limit (preconcentration time)	Calibration Curve		
				Linear range (preconcentration time)	Slope (area or current/concentration)	$R^2$
SH-SAMMS	Carbon paste	Hg/Pb	0.5 ppb Pb <sup>2+</sup> / 3 ppb Hg <sup>2+</sup> (20 min)	10–1500 ppb Pb <sup>2+</sup> (2 min)	0.0011 V $\mu$ A/ppb Pb <sup>2+</sup>	0.98
			10 ppb Pb <sup>2+</sup> / 20 ppb Hg <sup>2+</sup> (2 min)	20–1600 ppb Hg <sup>2+</sup> (2 min)	0.0006 V $\mu$ A/ppb Hg <sup>2+</sup>	0.98
Ac-Phos-SAMMS	Carbon paste	Cu/Pb/Cd	0.5 ppb Cu <sup>2+</sup> / Pb <sup>2+</sup> /Cd <sup>2+</sup> (20 min)	10–200 ppb Cu <sup>2+</sup> (2 min)	0.200 $\mu$ A/ppb Cu <sup>2+</sup>	0.99
			10 ppb Cu <sup>2+</sup> / Pb <sup>2+</sup> /Cd <sup>2+</sup> (2 min)	10–200 ppb Pb <sup>2+</sup> (2 min)	0.246 $\mu$ A/ppb Pb <sup>2+</sup>	0.99
			10–200 ppb Cd <sup>2+</sup> (2 min)	0.303 $\mu$ A/ppb Cd <sup>2+</sup>	0.99	
Ac-Phos-SAMMS	Carbon paste	U	1 ppb U(VI) (20 min)	25–500 ppb U(VI) (5 min)	0.0065 $\mu$ A/ppb U(VI)	1.00
			25 ppb U(VI) (5 min)			
SH-FMS thin film	Gold Microelectrode– Pb array	Pb	25 ppb Pb <sup>2+</sup> (30 min)	250–5000 ppb Pb <sup>2+</sup> (5 min)	0.0031 $\mu$ A/ppb Pb <sup>2+</sup>	0.99
			250 ppb Pb <sup>2+</sup> (5 min)			

the detection step after uranium preconcentration can overcome the matrix effect and ligand interference.

The pH of the solution was predicted to affect the distribution of uranyl complexes with acetate, hydroxyl, and carbonate ligands as shown in Fig. 3A using 500 ppb U(VI) in 0.05 M CH<sub>3</sub>COONa open to atmosphere. Fig. 3B shows the effect of pH on the voltammetric responses of 500 ppb U(VI) in 0.05 M CH<sub>3</sub>COONa. In the pH range of 2–5, the dominant uranyl species is one with positive or neutral charge (e.g., UO<sub>2</sub><sup>2+</sup>, UO<sub>2</sub>(Ac)<sup>+</sup>), and its binding strength to phosphonic acid (on Ac-Phos SAMMS) increased with increasing pH, leading to an increasing amount of uranium being preconcentrated, and hence increasing voltammetric responses with increasing pH. Above pH 6, uranyl species with negative charge appear to cause repulsive forces, resulting in low uranium adsorption onto binding sites and correspondingly low voltammetric responses. A series of experiments at varied aqueous U(VI) concentrations in 0.05 M CH<sub>3</sub>COONa (pH 5) showed that, after a 5-min preconcentration period, the current of the anodic peak of uranium (appearing at –0.37 V) was proportional to the U(VI) concentration in the range of 25–500 ppb (Fig. 4). The uranium detection limit, obtained experimentally, improved significantly from 25 ppb, after a 5-min preconcentration period, to 1 ppb, after a 20-min preconcentration period (parameters are reported in Table 1).

Ac-Phos SAMMS has been used to modify a carbon paste electrode for simultaneous detection of cadmium

(Cd<sup>2+</sup>), copper (Cu<sup>2+</sup>), and lead (Pb<sup>2+</sup>) in the absence of actinides.<sup>[3]</sup> Most of the operating conditions (e.g., electrode compositions, electrolysis/stripping media conditions, electrolysis time) for heavy metal ion detection obtained by using SH-SAMMS-modified electrodes can be used effectively with the Ac-Phos SAMMS (and other SAMMS)-modified electrodes. The Cu, Pb, and Cd peaks appeared at –0.2, –0.5, and –0.75 V, respectively. The voltammetric responses of 50 ppb Pb<sup>2+</sup> increased linearly with the preconcentration time from 1 to 30 min. Fig. 5 shows that the voltammetric responses of Cu<sup>2+</sup>, Pb<sup>2+</sup>, and Cd<sup>2+</sup> after 2 min of preconcentration were linear with respect to metal ion concentrations ranging from 10 to 200 ppb (parameters are reported in Table 1). At any given concentration below 200 ppb, the copper peak response obtained from the multicomponent metal ion solution was not significantly different from that obtained from the single-component Cu<sup>2+</sup> solution (Fig. 6). Therefore one can infer that the electrochemical responses for copper ions were not affected by the presence of lead and cadmium in the concentration range studied, owing to the high loading capacity of the SAMMS materials. At 200 ppb Cu<sup>2+</sup>/Pb<sup>2+</sup>/Cd<sup>2+</sup>, the total moles of metal ions in the solution corresponded to approximately 0.0004% of the total number of binding sites (phosphonic acids).<sup>[3]</sup> Above 200 ppb, the detection of each Cu<sup>2+</sup>, Pb<sup>2+</sup>, and Cd<sup>2+</sup> started to interfere with each other because of the insufficient anodic potential difference between two adjacent metal peaks



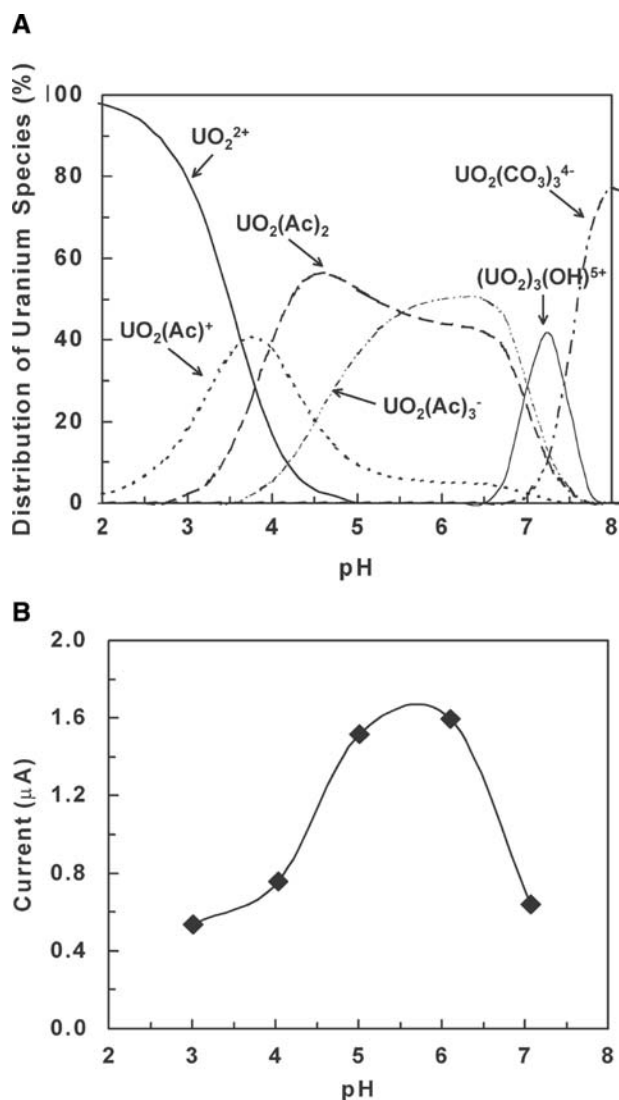


**Fig. 3** The effects of pH on (A) uranium speciation, as predicted by MINEQL+ for conditions of 500 ppb U(VI) in 0.05 M  $\text{CH}_3\text{COONa}$  and open to atmosphere ( $\text{Ac} = -\text{COOCH}_3$ ), and (B) uranium voltammetric responses, measured after 5 min of preconcentration with 500 ppb U(VI) in 0.05 M  $\text{CH}_3\text{COONa}$ . Source: From Ref.<sup>[2]</sup>.

(i.e.,  $\Delta E_{\text{Cu-Pb}} = 0.3 \text{ V}$ ,  $\Delta E_{\text{Pb-Cd}} = 0.25 \text{ V}$ ), and not because of their competition for the binding sites on SAMMS.

The binding between SAMMS and metal ions is reversible, therefore the SAMMS-modified carbon paste electrodes can be easily regenerated without damaging the ligand monolayer by desorption of the preconcentrated species in an acidic solution. By choosing an appropriate acid solution (i.e., 0.2 M  $\text{HNO}_3$ ) as a stripping medium, the electrodes usually are ready for reuse after the stripping voltammetric measurement. We found that SH-SAMMS electrodes were reliable even after 80 consecutive runs with no need for surface renewal.

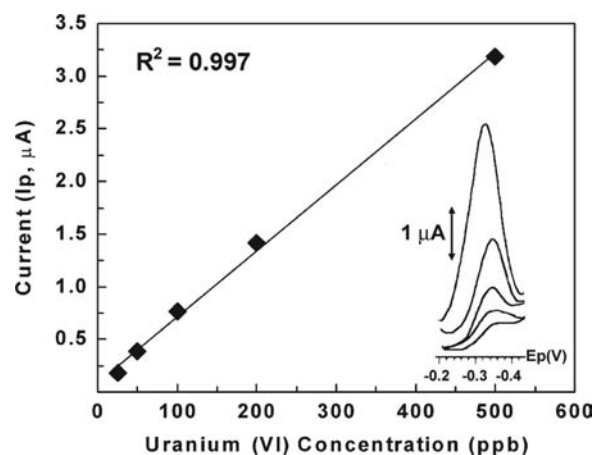


**Fig. 4** Uranium voltammetric responses as a function of U(VI) concentration in 0.05 M  $\text{CH}_3\text{COONa}$  (pH 5), measured after 5 min of preconcentration. Inset shows the voltammograms with varied U(VI) concentration (in the ascending order) from 25, 50, 100, 200 to 500 ppb. Source: From Ref.<sup>[2]</sup>.

### Electrochemical Sensors Based on a Microelectrode Array Modified with a Functionalized Nanoporous Silica Thin Film

Most electrode modifications with mesoporous silica (MCM-41) have been accomplished via composite coating of the silica materials on electrode surfaces<sup>[42,43]</sup> or mixing of the silica materials with conductive materials such as graphite powder.<sup>[1-3,5-8]</sup> These techniques often rely on graphite powder as a

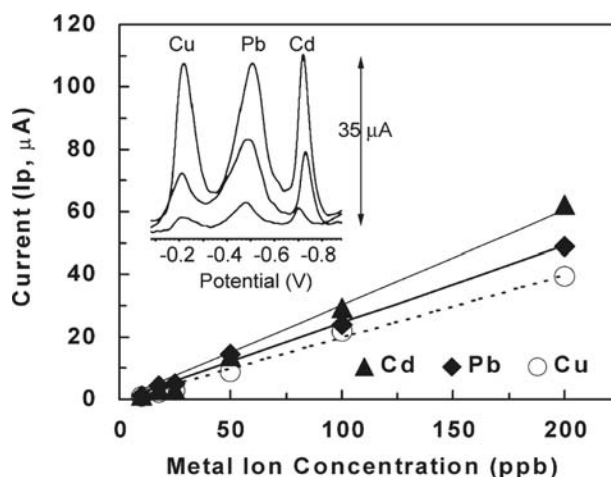


**Fig. 5** The voltammetric responses of  $\text{Cu}^{2+}$ ,  $\text{Pb}^{2+}$ , and  $\text{Cd}^{2+}$  measured after a 2-min preconcentration period in multicomponent  $\text{Cu}^{2+}/\text{Pb}^{2+}/\text{Cd}^{2+}$  solutions with concentrations ranging from 10 to 200 ppb of each metal ion. Inset shows representative voltammograms in the ascending order of 25, 50, and 100 ppb (each)  $\text{Cu}^{2+}/\text{Pb}^{2+}/\text{Cd}^{2+}$  solutions. Source: From Ref.<sup>[3]</sup>.

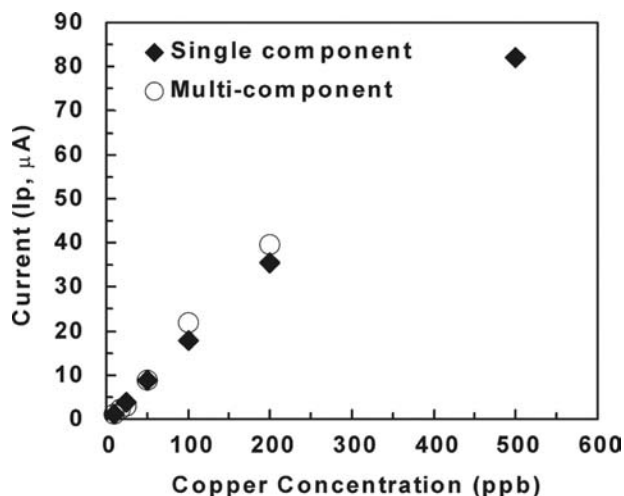


**Fig. 6** The voltammetric responses of  $\text{Cu}^{2+}$  measured after a 2-min preconcentration period in 10–500 ppb single-component  $\text{Cu}^{2+}$  solutions and in multicomponent  $\text{Cu}^{2+}/\text{Pb}^{2+}/\text{Cd}^{2+}$  solutions with concentrations ranging from 10 to 200 ppb of each metal ion. *Source:* From Ref.<sup>[3]</sup>.

conductive additive or polystyrene as a binder between the mesoporous silica materials and the electrode surfaces. Therefore we have focused on a method for preparation of mesoporous silica thin film-modified electrodes through an interfacial silica-surfactant self-assembly process that does not require additives or binders.<sup>[4]</sup> The self-assembly process allows surface layers to be constructed in a manner that is highly reproducible which is very important for any two-dimensional surface reaction to be successful.<sup>[44]</sup>

Mesoporous silica films with pore sizes of up to 100 Å have been synthesized from spin-coated silica sol-gels (normally consisting of silica precursor, acid solution, organic solvent, and water) by a surfactant-templating process in which the pores are formed upon removal of the surfactant by calcinations.<sup>[45–49]</sup> The precise design and control of pore structure, pore size/volume, and pore orientation of the silica films

can be achieved by using structure-directing agents, such as the nonionic surfactant Pluronic F-127 ( $\text{EO}_{106}\text{PO}_{70}\text{EO}_{106}$ ), as in our case. By controlling the film thickness (e.g., changing the composition of the precursor solution, spin rate, calcination conditions), a continuous, defect-free, mesoporous silica thin film is produced. However, spin-coated silica thin films have been found to be unstable in basic aqueous solutions but stable in pure water and acidic electrolyte solutions.<sup>[50]</sup> The instability is caused by the dissolution of the mesoporous framework, which increases with increasing pH. Because electrodes modified with these silica films cannot be used in basic solutions, the silanol groups, inherent to the nanoporous silica, are not useful in binding with metal ions in the preconcentration step of AdSV. Silanol groups must be ionized in a basic solution (e.g., ammoniacal medium) in order to accumulate positively charged ion species.<sup>[5]</sup> Therefore, without functional ligands attached, the spin-coated films of mesoporous silicas are often used as molecular sieves in electrodes by either blocking or improving the voltammetric responses of the analyte species.<sup>[50]</sup>

To remove this limitation, we have immobilized organic thiol ( $-\text{SH}$ ) functional groups onto the nanopore surfaces of the silica thin film through a self-assembly process, subsequently after the film was attached onto the surface of a gold microelectrode array by the spin-coating of the silica sol-gel.<sup>[4]</sup> Fig. 7 shows the schematics (top and side views) of the thiol functionalized mesoporous silica (SH-FMS) thin-film-modified gold microelectrode array. The modified microelectrode array was then used for detection of lead ions by employing the AdSV technique. To our knowledge, this is the first time that a microchip-based electrode modified with functionalized mesoporous silica thin film for metal ion detection based on AdSV has been investigated. With the SH-FMS thin film-modified electrode array, the preconcentration step can be performed in slightly acidic electrolyte solutions or neutral nonelectrolyte solutions as long as the thiol

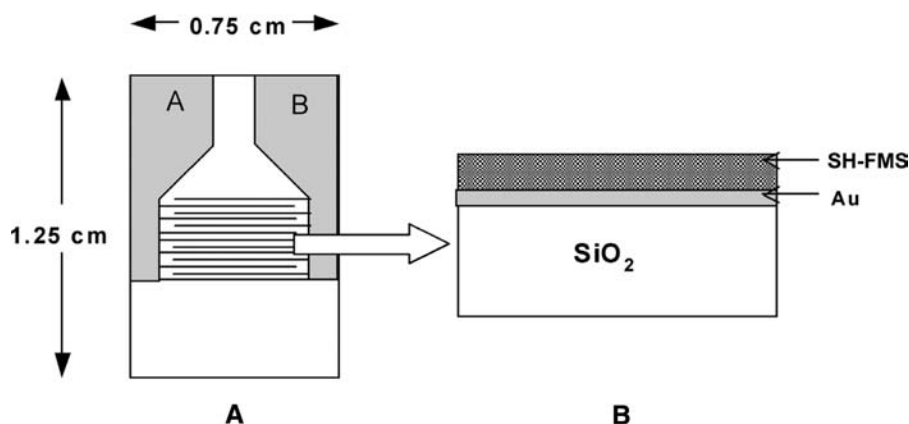


**Fig. 7** A schematic of the gold electrode array with the SH-FMS thin film: (A) top-view of the array and (B) side-view of the three-layer sensor ( $\text{SiO}_2/\text{Au}/\text{SH-FMS}$ ). *Source:* From Ref.<sup>[4]</sup>.

ligands can adsorb the target analyte, based on a previous pH study using batch adsorption experiments.<sup>[25]</sup> In nonbasic solutions, the mesoporous silica films are more likely to remain stable for a long period of time.

Several surface characterization methods were performed on the mesoporous silica thin film before and after thiol functionalization. TEM measurement of the SH-FMS film shows short-range ordered mesopores. The nitrogen adsorption/desorption isotherms of the untreated SiO<sub>2</sub> thin film are of type IV with a clear H<sub>2</sub>-type hysteresis loop, which is consistent with the film's large ratio of pore size to pore spacing<sup>[51,52]</sup> and cubic arrangement of pores.<sup>[53]</sup> From BET analysis, the calcined film had a large primary pore diameter of 77 Å, a porosity of 60%, and a high BET surface area of 613 m<sup>2</sup>/g. The FTIR spectra indicate that organic thiol monolayers were successfully immobilized inside the nanopores of the mesoporous silica. After the thiol immobilization, the refractive index of the mesoporous silica film increased from 1.16 to 1.36, corresponding to the decrease in film porosity from 66% to 23%. However, both XRD patterns of the film before and after thiol functionalization were alike, indicating that the structure of mesoporous film remained unchanged after the thiols attachment.

When the SH-FMS thin film-modified electrode array was tested for Pb<sup>2+</sup> detection, the electrode behaved in a similar fashion with the powdered SH-SAMMS-modified carbon paste electrodes. For example, the optimum cathodic electrolysis, corresponding to optimum voltammetric response, was obtained at 60 sec; the lead voltammetric responses were poorer at lower than 60 sec due to the incomplete electrolysis process and at 120-sec electrolysis period, perhaps due to the generation of H<sub>2</sub> bubbles on electrode surface, which affected the stability of the signals. Fast electrolysis (60 sec) is evidence of a fast desorption rate and diffusion of Pb<sup>2+</sup> species out of the mesoporous silica to reach the conducting substrate, owing to the suitable surface chemistry (e.g., hydrophilicity) and pore geometry of SAMMS. The voltammetric responses for 1 ppm Pb<sup>2+</sup> increased linearly with the preconcentration time from 1 to 30 min. Fig. 8 shows that the responses also increased linearly with Pb<sup>2+</sup> concentrations ranging from 250 to 5000 ppb after 5 min of preconcentration and from 25 to 100 ppb after 30 min of preconcentration (parameters are reported in Table 1). The large dynamic range for lead ion sensing is a result of the functionalized mesoporous thin film having a high binding site density due to the high surface area of mesoporous silica. This solves a potential drawback of AdSV based on conventional chemically modified thin-film electrodes that the total number of binding sites in the thin films is limited, leading to a narrow linear range of the calibration (preconcentration time and concentration)

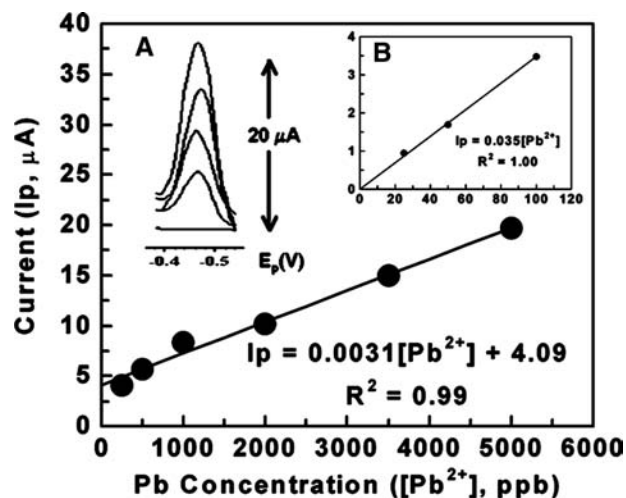


**Fig. 8** The calibration curve for Pb<sup>2+</sup>, measured after a 5-min preconcentration period, with inset (A) showing the representative voltammograms of Pb<sup>2+</sup> concentrations (in ascending order) of 0, 500, 2000, 3500, and 5000 ppb Pb<sup>2+</sup>, and inset (B) showing the low-concentration-range calibration curve measured after a 30-min preconcentration period. All experiments were performed with a 60-sec electrolysis period and 0.1 M HNO<sub>3</sub> as electrolysis/stripping media. Source: From Ref.<sup>[4]</sup>.

curves. In addition, high binding site density in FMS thin film is extremely important for miniaturized sensors because it provides sufficient sensitivity at the electrodes of limited size.

Similar to the powdered-SAMMS-modified carbon paste electrodes, the SH-FMS thin-film-modified gold microelectrode has many appealing aspects: it has excellent stability (i.e., data were collected for several weeks using the same electrode) because the ligands are immobilized via covalent bonding onto silica substrates, it has low maintenance requirements (no activation and regeneration were required during this testing). The advantages of SH-FMS thin-film-modified microelectrode array over powdered SAMMS-modified carbon paste electrodes are that the SH-FMS electrode arrays are easier to be mass-produced with highly reproducible surface properties and low costs as well as easier to be incorporated into portable sensing devices. Manipulating the pore structure and pore orientation as well as the thickness of the silica film to improve the detection limits of metal ions and reduce the detection time will require further investigation.

## CONCLUSION

Nanostructured self-assembled monolayers on mesoporous supports (SAMMS) materials reported here are highly effective as electrode modifiers in the forms

of powder and thin film. The interfacial chemistry of SAMMS can be fine-tuned to selectively sequester a specific target metal ion. The functional groups in SAMMS materials allowed the preconcentration of metal ions to be accomplished without the aid of mercury, adding supporting electrolytes, or applying an electrodeposition potential. The high loading capacity and high selectivity of SAMMS materials are desirable for metal ion detection based on the AdSV technique because they minimize the competition for the binding sites of the nontarget species, thereby reducing the interferences and preserving the signal intensity of the target metal ions. The covalent bonding between the functional groups and the surface of silica prevents sensors from degradation over time due to the depletion of ligand-bearing materials. The reversible binding between metal ions and ligands on SAMMS enables many successive uses of SAMMS-based electrodes with virtually no requirements for surface regeneration and renewal.

Our future work will be focused on using other class of SAMMS materials to construct electrochemical sensors for other ion detection needs. For example, SAMMS that is synthesized from installation of copper(II) ethylenediamine (Cu-EDA) on silica pore walls will be investigated for the detection of chromate and pertechnetate ions. Interfacial chemistry and electrochemistry of metal species on surfaces of SAMMS-based electrodes will also be studied: this fundamental knowledge is required for predicting how the sensors will perform in real wastes that consist of many interferences and ligands at a broad spectrum of pH levels. The best electrodes for each specific waste constituent will be integrated onto our patented portable microfluidic/electrochemical sensor systems<sup>[54]</sup> specifically designed for field-deployed detections.

## ACKNOWLEDGMENTS

This work was supported by the SERDP Program, U.S. Department of Defense; DOE-EMSP program, and NIH/NIEHS R01 (#1 R01 ES010976-01A2). Pacific Northwest National Laboratory (PNNL) is operated by Battelle Memorial Institute for the U.S. Department of Energy (DOE). The research was performed in part at the Environmental Molecular Sciences Laboratory (EMSL), a national scientific user facility sponsored by the DOE's Office of Biological and Environmental Research and located at PNNL.

The authors thank Dr. Mychailo Toloczko for reviewing this manuscript.

## REFERENCES

1. Yantasee, W.; Lin, Y.; Zemanian, T.S.; Fryxell, G.E. Voltammetric detection of lead(II) and mercury(II) using a carbon paste electrode modified with thiol self-assembled monolayer on mesoporous silica (SAMMS). *Analyst* **2003**, *128* (5), 467–472.
2. Yantasee, W.; Lin, Y.; Fryxell, G.E.; Wang, Z. Acetamide phosphonic acid-modified carbon paste electrode: A new sensor for uranium detection. *Electroanal*, *in press*.
3. Yantasee, W.; Lin, Y.; Fryxell, G.E.; Busche, B.J. Simultaneous detection of cadmium(II), copper(II), and lead(II) using a carbon paste electrode modified with carbamoyl-phosphonic acid self-assembled monolayer on mesoporous silica (SAMMS). *Anal. Chim. Acta*, *in press*.
4. Yantasee, W.; Lin, Y.; Li, X.; Fryxell, G.E.; Zemanian, T.S.; Viswanathan, V. Nanoengineered electrochemical sensor based on mesoporous silica thin-film functionalized with thiol-terminated monolayer. *Analyst* **2003**, *128* (7), 899–904.
5. Walcarius, A.; Despas, C.; Bessière, J. Selective monitoring of Cu-(II) species using a silica modified carbon paste electrode. *Anal. Chim. Acta* **1999**, *385* (1–3), 79–89.
6. Walcarius, A.; Bessière, J. Electrochemistry with mesoporous silica: Selective mercury(II) binding. *Chem. Mater.* **1999**, *11* (11), 3009–3011.
7. Walcarius, A.; Lüthi, N.; Blin, J.-L.; Su, B.-L.; Lamberts, L. Electrochemical evaluation of polysiloxane-immobilized amine ligands for the accumulation of copper(II) species. *Electrochim. Acta* **1999**, *44* (25), 4601–4610.
8. Etienne, M.; Bessiere, J.; Walcarius, A. Voltammetric detection of copper(II) at a carbon paste electrode containing an organically modified silica. *Sens. Actuators, B, Chem.* **2001**, *76* (1–3), 531–538.
9. de Jesus, D.P.; Neves, C.A.; do Lago, C.L. Determination of boron by using a quartz crystal resonator coated with *N*-methyl-D-glucamine-modified poly(epichlorohydrin). *Anal. Chem.* **2002**, *74* (14), 3274–3280.
10. Akmal, N.; Zimmer, H.; Mark, H.B. Strontium ion-selective electrode based on a conducting poly(dibenzo-18-crown-6) film. *Anal. Lett.* **1991**, *24* (8), 1431–1443.
11. Turyan, I.; Mandler, D. Self-assembled monolayers in electroanalytical chemistry—Application of omega-mercaptopropionic acid monolayers for electrochemical determination of ultralow levels of cadmium(II). *Anal. Chem.* **1994**, *66* (1), 58–63.
12. Turyan, I.; Mandler, D. Selective determination of Cr(VI) by a self-assembled monolayer-based electrode. *Anal. Chem.* **1997**, *69* (5), 894–897.
13. Tu, Y.; Lin, Y.; Ren, Z.F. Nanoelectrode arrays based on low site density aligned carbon nanotubes. *Nano Lett.* **2003**, *3* (1), 107–109.
14. Martin, C.R.; Mitchell, D.T. Nanomaterials in analytical chemistry. *Anal. Chem. News Featur.* May 1 **1998**, *70* (9), 322A–327A.
15. Wang, J.; Wang, J.; Tian, B.; Jiang, M. Adsorptive stripping measurements of chromium and uranium at iridium based mercury electrodes. *Anal. Chem.* **1997**, *69* (8), 1657–1661.
16. Wang, J.; Lu, J.; Larson, D.D.; Olsen, K. Voltammetric sensor for uranium based on the propyl gallate-modified carbon-paste electrode. *Electroanalysis* **1995**, *7* (3), 247–250.
17. Prabhu, S.V.; Baldwin, R.P.; Kryger, L. Chemical preconcentration and determination of copper at a

- chemically modified carbon-paste electrode containing 2,9-dimethyl-1,10-phenanthroline. *Anal. Chem.* **1987**, *59* (8), 1074–1078.
18. Baldwin, R.P.; Christensen, J.K.; Kryger, L. Voltammetric determination of traces of nickel(II) at a chemically modified electrode based on dimethylglyoxime-containing carbon paste. *Anal. Chem.* **1986**, *58* (8), 1790–1798.
  19. Navratilova, Z. Hg(II) voltammetry on a 1,5-diphenylcarbazine containing carbon paste electrode. *Electroanalysis* **1991**, *3* (8), 799–802.
  20. Svegl, I.G.; Kolar, M.; Ogorevc, B.; Pihlar, B. Vermiculite clay mineral as an effective carbon paste electrode modifier for the preconcentration and voltammetric determination of Hg(II) and Ag(I) ions. *Fresenius J. Anal. Chem.* **1998**, *361* (4), 358–362.
  21. Ijeri, V.S.; Srivastava, A.K. Voltammetric determination of lead at chemically modified electrodes based on crown ethers. *Anal. Sci.* **2001**, *17* (5), 605–608.
  22. Mousavi, M.F.; Rahmani, A.; Golabi, S.M.; Shamsipur, M.; Sharghi, H. Differential pulse anodic stripping voltammetric determination of lead(II) with a 1,4-bis(-prop-2'-enyloxy)-9,10-anthraquinone modified carbon paste electrode. *Talanta* **2001**, *55* (2), 305–312.
  23. Degefa, T.H.; Chandravanshi, B.S.; Alemu, H. Differential pulse anodic stripping voltammetric determination of lead(II) with *N-p*-chlorophenylcinnamohydroxamic acid modified carbon paste electrode. *Electroanalysis* **1999**, *11* (17), 1305–1311.
  24. Ogorevc, B.; Cai, X.H.; Grabec, I. Determination of traces of copper by anodic-stripping voltammetry after its preconcentration via an ion-exchange route at carbon-paste electrodes modified with vermiculite. *Anal. Chim. Acta* **1995**, *305* (1–3), 176–182.
  25. Feng, X.D.; Fryxell, G.E.; Wang, L.Q.; Kim, A.Y.; Liu, J.; Kemner, K. Functionalized monolayers on mesoporous supports. *Science* **1997**, *276*, 923–926.
  26. Liu, J.; Feng, X.D.; Fryxell, G.E.; Wang, L.Q.; Kim, A.Y. Hybrid mesoporous materials with functionalized monolayers. *Adv. Mater.* **1998**, *10* (2), 161–165.
  27. Mattigod, S.V.; Feng, X.D.; Fryxell, G.E.; Liu, J.; Gong, M. Separation of complexed mercury from aqueous wastes using self-assembled mercaptan on mesoporous silica. *Sep. Sci. Technol.* **1999**, *34* (12), 2329–2345.
  28. Chen, X.B.; Feng, X.D.; Liu, J.; Fryxell, G.E.; Gong, M. Mercury separation and immobilization using self-assembled monolayers on mesoporous supports (SAMMS). *Sep. Sci. Technol.* **1999**, *34* (6&7), 1121–1132.
  29. Fryxell, G.E.; Liu, J.; Hauser, T.A.; Nie, Z.; Ferris, K.F.; Mattigod, S.V.; Feng, X.; Gong, M.; Hallen, R.T. Design and synthesis of selective mesoporous anion traps. *Chem. Mater.* **1999**, *11* (8), 2148–2154.
  30. Liu, J.; Fryxell, G.E.; Qian, M.X.; Wang, L.Q.; Wang, Y. Interfacial chemistry in self-assembled nanoscale materials with structural ordering. *Pure. Appl. Chem.* **2000**, *72* (1–2), 269–279.
  31. Fryxell, G.E.; Lin, Y.; Wu, H.; Kemner, K.M. Environmental Applications of Self-Assembled Monolayers on Mesoporous Supports (SAMMS). In *Studies in Surface Science and Catalysis*; Sayari, A., Jaroniec, M., Eds.; Elsevier Science: Amsterdam, The Netherlands, 2002; 141, 583–590.
  32. Lin, Y.; Fryxell, G.E.; Wu, H.; Engelhard, M. Selective sorption of cesium using self-assembled monolayers on mesoporous supports (SAMMS). *Environ. Sci. Technol.* **2001**, *35* (19), 3962–3966.
  33. Kelly, S.D.; Kemner, K.M.; Fryxell, G.E.; Liu, J.; Mattigod, S.V.; Ferris, K.F. An X-ray absorption fine structure spectroscopy study of the interactions between contaminant tetrahedral anions to self-assembled monolayers on mesoporous supports. *J. Phys. Chem., B* **2001**, *105* (27), 6337–6346.
  34. Birnbaum, J.C.; Busche, B.; Lin, Y.; Shaw, W.; Fryxell, G.E. Synthesis of carbamoylphosphonate silanes for the selective sequestration of actinides. *Chem. Commun.* **2002**, *13*, 1374–1375.
  35. Yantasee, W.; Lin, Y.; Fryxell, G.E.; Busche, B.J.; Birnbaum, J.C. Removal of heavy metals from aqueous solution using novel nanoengineered sorbents: Self-assembled carbamoylphosphonic acids on mesoporous silica. *Sep. Sci. Technol.* **2003**, *38* (15), 3809–3825.
  36. Fryxell, G.E.; Liu, J.; Mattigod, S.V.; Wang, L.Q.; Gong, M.; Hauser, T.A.; Lin, Y.; Ferris, K.F.; Feng, X. *Environmental Issues and Waste Management Technologies in the Ceramic and Nuclear Industries V*; Ceramic Transactions; Chandler, G.T., Feng, X., Eds.; The American Ceramic Society: Westerville, OH, USA, 2000; 107, 29–37.
  37. Pearson, R.G. Hard and soft acids and bases. *J. Am. Chem. Soc.* **1963**, *85* (22), 3533–3539.
  38. Lubert, K.H.; Schnurrbusch, M.; Thomas, A. Preconcentration and determination of uranyl ions on electrodes modified by tri-normaloctylphosphine oxide. *Anal. Chim. Acta* **1982**, *144*, 123–136.
  39. Michael, K.M.; Rizvi, G.H.; Mathur, J.N.; Kapoor, S.C.; Ramanujam, A.; Iyer, R.H. Recovery of plutonium and americium from laboratory acidic waste solutions using tri-*n*-octylamine and octylphenyl-*N,N*-diisobutylcarbamoylmethylphosphine oxide. *Talanta* **1997**, *44* (11), 2095–2102.
  40. Horwitz, E.P.; Chiarzia, R. Liquid Extraction, the TRUEX Process-Experimental Studies. In *Separation Techniques in Nuclear Waste Management*; Carleson, T.E., Chipman, N.A., Wai, C.M., Eds.; CRC Press: Boca Raton, FL, USA, 1995; 3–33.
  41. Horwitz, E.P.; Schulz, W.W. Solvent Extraction in the Treatment of Acidic High-Level Liquid Waste: Where Do We Stand?. In *Metal Ion Separation and Preconcentration: Progress and Opportunities*; ACS Symposium Series; Bond, A.H., Dietz, M.L., Rogers, R.D., Eds.; ACS: Washington, DC, 1999; 716, 390–400.
  42. Jiang, Y.X.; Song, W.B.; Liu, Y.; Wei, B.; Cao, X.C.; Xu, H.D. Electrochemical characterization of the host-guest nanocomposite material MCM-41-based iron and ruthenium complexes with bipyridine and phenanthroline. *Mater. Chem. Phys.* **2000**, *62* (2), 109–114.
  43. Villemure, G.; Pinnavaia, T.J. Cyclic voltammetry of tris(2,2'-bipyridyl)ruthenium(II) cations adsorbed in electrodes modified with mesoporous molecular sieve silicas. *Chem. Mater.* **1999**, *11* (3), 789–794.
  44. Gooding, J.J.; Praig, V.G.; Hall, E.A.H. Platinum-catalyzed enzyme electrodes immobilized on gold using self-assembled layers. *Anal. Chem.* **1998**, *70* (11), 2396–2402.

45. Yang, H.; Kuperman, A.; Coombs, N.; MamicheAfara, S.; Ozin, G.A. Synthesis of oriented films of mesoporous silica on mica. *Nature* **1996**, *379* (6567), 703–705.
46. Yang, H.; Coombs, N.; Sokolov, I.; Ozin, G.A. Free-standing and oriented mesoporous silica films grown at the air–water interface. *Nature* **1996**, *381* (6583), 589–592.
47. Aksay, I.A.; Trau, M.; Manne, S.; Honma, I.; Yao, N.; Zhou, L.; Fenter, P.; Eisenberger, P.M.; Gruner, S.M. Biomimetic pathways for assembling inorganic thin films. *Science* **1996**, *273* (5277), 892–898.
48. Zhao, D.Y.; Huo, Q.S.; Feng, J.L.; Chmelka, B.F.; Stucky, G.D. Nonionic triblock and star diblock copolymer and oligomeric surfactant syntheses of highly ordered, hydrothermally stable, mesoporous silica structures. *J. Am. Chem. Soc.* **1998**, *120* (24), 6024–6036.
49. Zhao, D.Y.; Feng, J.L.; Huo, Q.S.; Melosh, N.; Fredrickson, G.H.; Chmelka, B.F.; Stucky, G.D. Triblock copolymer syntheses of mesoporous silica with periodic 50 to 300 angstrom pores. *Science* **1998**, *279* (5350), 548–552.
50. Song, C.; Villemure, G. Electrode modification with spin-coated films of mesoporous molecular sieve silicas. *Microporous Mesoporous Mater.* **2001**, *44* (Sp. Iss.), 679–689.
51. Luzzati, V.; Delacroix, H.; Gulik, A. The micellar cubic phases of lipid-containing systems: Analogies with foams, relations with the infinite periodic minimal surfaces, sharpness of the polar apolar partition. *J. Phys. II.* **1996**, *6* (3), 405–418.
52. Huo, Q.; Leon, R.; Petroff, P.M.; Stucky, G.D. Mesostructure design with Gemini surfactants-Supercage formation in a 3-dimensional hexagonal array. *Science* **1995**, *268* (5215), 1324–1327.
53. Zhao, D.; Yang, P.; Melosh, N.; Feng, J.; Chmelka, B.F.; Stucky, G.D. Continuous mesoporous silica films with highly ordered large pore structures. *Adv. Mater.* **1998**, *10* (16), 1380–1385.
54. Lin, Y.; Timchalk, C.A.; Wu, H.; Matson, D.W.; Thrall, K.D. *Biomed. Microdevices* **2001**, *3*, 331



# Electrochemical Toxicity Sensors

**James F. Rusling**

*Department of Chemistry, University of Connecticut, Storrs, Connecticut, U.S.A.*

## INTRODUCTION

Medical abnormalities from exposure to toxic chemicals constitute a critical public health problem in our modern world. The use of toxic chemicals in agriculture, heavy industry, and other human endeavors throughout the past century has led to widespread pollution of our environment with potential disease-causing substances.<sup>[1]</sup> New drugs also have important toxicity issues. Twenty years ago, Singer and Grunberger<sup>[2]</sup> estimated that 65,000 chemicals were commonly used in modern society, and over 200,000 new chemicals were discovered each year. Since that time, advances in automated methods of chemical synthesis including combinatorial techniques<sup>[3]</sup> have led to an explosion into the millions of new chemicals produced each year for end-use applications including drugs, agriculture, personal care, and nutrition. While only a fraction of these new compounds will turn out to be acutely toxic, those that do may have long-term possibilities of causing cancer and reproductive damage.

A major mechanism of chemical toxicity involves activation of chemicals by catalytic oxidation mediated by cytochrome P450 (cyt P450) enzymes in the liver.<sup>[4–6]</sup> Lipophilic molecules bioactivated in this way often damage genetic material (i.e., DNA). They include styrene, benzo[a]pyrene, naphthylamines, and many others.<sup>[7–11]</sup> Covalent DNA adducts of these activated molecules with DNA bases are important biomarkers of cancer risk in humans exposed to toxic molecules.<sup>[12–14]</sup>

Conventional toxicity evaluation of new chemicals proceeds from microbiological testing to animal testing and is expensive and time consuming. While advances in speed and automation of microbiological test are on the horizon, simple, inexpensive chemical screening protocols that could be used at early stages of commercial consideration would be very useful. One such scheme could be based on enzyme bioactivation of the chemicals with detection of DNA damage from the resulting metabolites. Sensors built on this principle could be used to screen chemicals and metabolites that clearly damage DNA. These compounds could

then be eliminated from further commercial consideration and testing. Such a screening process could decrease the cost of bringing new drugs and agricultural chemicals to the marketplace by eliminating toxic candidates early in their commercial development and lightening the burden on toxicity bioassays. Of course, new commercially viable chemicals would still need to be subjected to microbiological and animal testing before final marketing.

## OVERVIEW

Nanoscience can be harnessed to make sensors featuring active metabolic enzymes and double-stranded DNA in films of nanometer-scale thickness<sup>[15]</sup> for toxicity screening. Early in the quest for such toxicity sensors, we evaluated a number of film formation strategies. (For an overview, see Ref.<sup>[16]</sup>.) We found that the excellent films for these applications could be made by a layer-by-layer construction method developed over the past decade.<sup>[17–20]</sup> The films are assembled by electrostatic adsorption of alternately charged layers of macromolecular ions and provide films with good stability, excellent enzyme activity, and control of thickness and architecture on the nanometer scale. Film construction relies on a series of steps in which the oppositely charged macromolecules (e.g., DNA, enzymes, and polyions) are adsorbed alternately from solutions onto an electrode. Iron heme enzymes in these films, such as cyt P450s, are easily activated for catalysis by addition of hydrogen peroxide along with substrate to a reaction solution.<sup>[15]</sup> The resulting DNA damage can be monitored by a variety of electroanalytical methods and by electrochemiluminescence, as will be seen below.

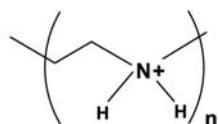
## CONSTRUCTING ENZYME–DNA FILMS

Preparation of enzyme–DNA films one layer at a time provides excellent control over the thickness of films designed to the specifications of the builder. Films containing two layers each of enzyme and DNA that

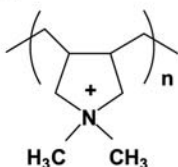
are 20–40 nm thick are easily made. Alternate adsorption of layers of biomolecules and polyions is a general method that has been developed over the past decade by Lvov et al.<sup>[17–20]</sup> The technique has been used to make ultrathin films of a wide variety of proteins and oppositely charged polyions including DNA. Some polyions that have been used to make such films are shown below.

### Some ionic polymers used for film formation

#### Polycations

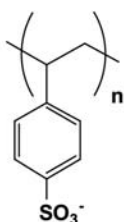


poly(ethylene imine) (PEI)



poly(diallyldimethylamine) (PDDA)

#### Polyanions



poly(styrenesulfonate) (PSS)



nanoparticles:

TiO<sub>2</sub> MnO<sub>2</sub>  
SiO<sub>2</sub> Clay

A DNA/enzyme film grown on a rough pyrolytic graphite electrode is illustrated in Fig. 1. The pyrolytic graphite has a negative charge by virtue of oxygenic functional groups on its surface, and oxidizing the surface can enhance this negative charge. The films are made as follows. First, the negatively charged electrode is immersed into a 2 mg mL<sup>-1</sup> solution of positively charged PDDA. The polycations adsorb at roughly monolayer coverage in about 15–20 min,<sup>[18–20]</sup> effectively reversing the charge on the solid surface.

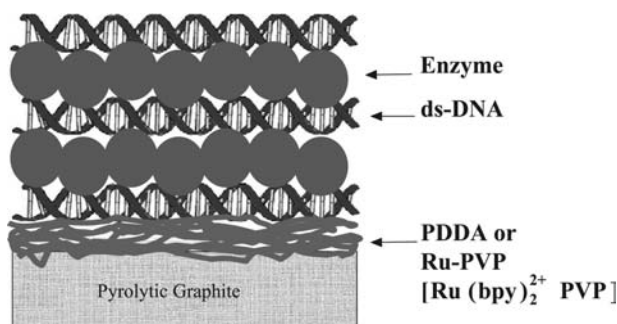


**Fig. 1** Conceptual representation of DNA/enzyme films used for toxicity sensing.

The electrode is rinsed with water, then immersed in a 2 mg mL<sup>-1</sup> solution of double-stranded (ds) DNA, and now the surface develops a negative charge. This surface is rinsed again, then immersed into a solution of enzyme (1–3 mg mL<sup>-1</sup>) in a buffer of pH lower than the enzyme's isoelectric point to assure a positive charge. An enzyme layer adsorbs, and the surface becomes positive. The latter two adsorption steps can be repeated as many times as desired to obtain a film of reproducible alternating layers of enzyme and DNA in a multilayer assembly. In practice, protein does not even have to be positively charged because charge patches on protein surfaces often enable good binding to oppositely charged polyions.<sup>[21]</sup> While there is extensive intermixing of neighboring layers,<sup>[17–20]</sup> this does not adversely affect the performance of most devices.

In the initial stages of developing new films, it is important to monitor layer growth during or after each adsorption step with quartz crystal microbalance (QCM) weighing, surface plasmon resonance (SPR), spectroscopy, or voltammetry. Fig. 2 illustrates QCM monitoring during the construction of DNA/enzyme films on gold-quartz resonators. The frequency of the QCM resonator decreases in direct proportion to the

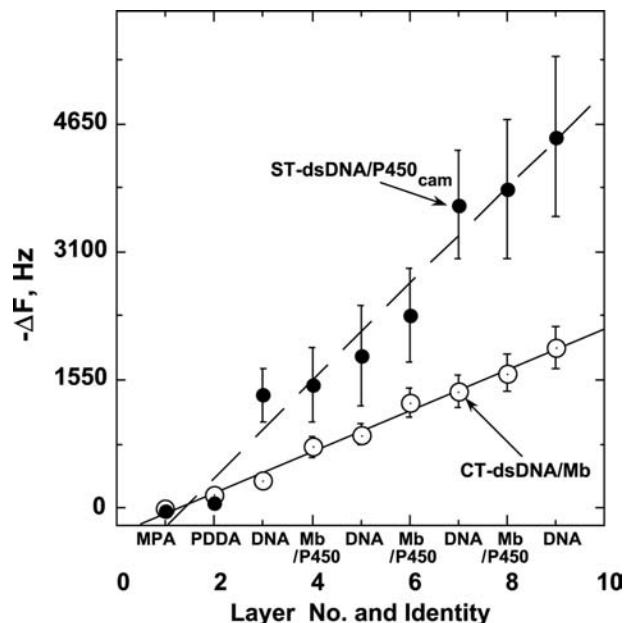


**Fig. 2** Quartz crystal microbalance frequency shifts for cycles of alternate myoglobin/ds-DNA and cytochrome P450<sub>cam</sub>/ds-DNA adsorption on gold resonators coated with mixed monolayers of mercaptoproionic acid/mercaptopropanol as first layer and PDDA as second layer. DNA was from salmon testes (ST) and calf thymus (CT). Average values are shown for five replicates of [Mb/ST ds-DNA] (○) and four replicates of [cyt P450<sub>cam</sub>/ST ds-DNA] (●) films. Source: From Ref.<sup>[15]</sup> with permission. © American Chemical Society.

mass on its gold coating, provided the viscoelasticity of the interface does not change.<sup>[22]</sup> Estimates of the weight of each layer and of the repeatability of the multiple adsorption steps can be obtained from QCM of dry films. Drying minimizes bias from interfacial viscoelasticity changes and absorbed water. For 9-MHz quartz resonators, mass per unit area  $M/A$  ( $\text{g cm}^{-2}$ ) of the film is related to the QCM frequency shift  $\Delta F$  (Hz) by:

$$M/A = -\Delta F / (1.83 \times 10^8) \quad (1)$$

where the area is that of the metal disk on the resonator in  $\text{cm}^2$ . Direct scaling between  $\Delta F$  and nominal film thickness ( $d$ ) is given by:<sup>[18–20]</sup>

$$d(\text{nm}) \approx -(0.016 \pm 0.002)\Delta F \text{ (Hz)} \quad (2)$$

To mimic the PG electrode surface for QCM measurements of layers adsorbed on the gold-quartz resonators, we first chemisorb a mixed monolayer of mercaptopropionic acid/mercaptopropanol. This layer is represented by the first point in Fig. 2, labeled MPA. The second layer is PDDA. Quartz crystal microbalance frequency decreasing in a roughly linear fashion and at regular intervals for the multiple adsorption steps demonstrates repeatable adsorption for the two DNA/enzyme films. Relative precision of layer formation on multiple resonators within  $\pm 15\%$  can be achieved. Film thicknesses and component weights in Table 1 were obtained by analyzing the QCM data with Eqs. (1) and (2).

## ELECTROANALYTICAL METHODS FOR DETECTING DNA DAMAGE

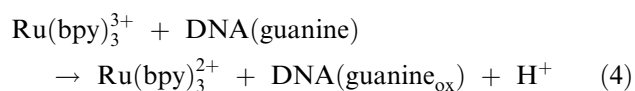
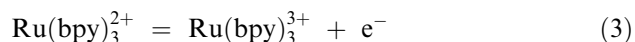
### Electrochemistry of DNA

Fundamental studies of the electrochemistry of DNA have shown that single-stranded (ss) DNA is more easily oxidized at guanine and adenine base sites than double-stranded (ds) DNA.<sup>[23–25]</sup> The double helical ds-DNA structure does not allow ready access of the bases to the electrode or to catalytic oxidizing agents. However, unwinding of the double helix frees the bases for closer access by oxidants, leading to faster reaction rates. Voltammetry has been applied to detecting

DNA damage from strong acids,<sup>[26]</sup> strand cleavage agents,<sup>[27]</sup> and hydroxyl radicals<sup>[28]</sup> after adsorbing the DNA onto mercury electrodes. In a similar experimental approach, damage to DNA from ionizing radiation and detected by linear sweep voltammetry<sup>[29]</sup> and alkylation was monitored by a.c. voltammetry.<sup>[30]</sup> In these methods, the DNA in solution was damaged and then accumulated on the electrodes by adsorption prior to analysis. Guanine and adenine bases in ss-DNA can also be oxidized on *solid* electrodes,<sup>[31]</sup> such as glassy carbon and pyrolytic graphite. Damage from ionizing radiation to DNA adsorbed onto carbon electrodes was detected by chronopotentiometry.<sup>[32]</sup>

Guanine, with a formal potential at pH 7 of  $\sim 1.3$  V vs. normal hydrogen electrode (NHE) (1.06 V vs. saturated calomel electrode (SCE)), is the most easily oxidized of the four DNA bases.<sup>[33]</sup> The other bases have formal potentials up to 0.5 V more positive. Detecting nucleic acids by electrochemical oxidation depends on structure, with double-stranded (ds) DNA giving only trace oxidation peaks at best and single-stranded (ss) DNA giving irreversible oxidation peaks at about 1.0–1.2 V vs. SCE on carbon electrodes.

Enhanced electrochemical signals for DNA can be obtained by catalytic electrochemical oxidation using transition metal complexes.<sup>[34]</sup> Studies by Thorp et al.<sup>[35–40]</sup> showed that  $\text{Ru}(\text{bpy})_3^{2+}$  (bpy = 2,2'-bipyridine) is an efficient electrochemical catalyst that oxidizes only guanine bases in DNA and oligonucleotides. The reaction follows the catalytic pathway below:



$\text{DNA}(\text{guanine}_{\text{ox}})$  represents a guanine radical site<sup>[41,42]</sup> on DNA.  $\text{Ru}(\text{bpy})_3^{3+}$  formed by oxidation at the electrode is cycled back to  $\text{Ru}(\text{bpy})_3^{2+}$  by the fast chemical step in Eq. (4), which provides greatly enhanced voltammetric current over that of  $\text{Ru}(\text{bpy})_3^{2+}$  or DNA alone. The peak current depends on the rate of the chemical step in Eq. (4). In oversimplified terms, the faster the rate of the chemical step, the larger the peak. Guanine accessibility is important in these catalytic

**Table 1** Average characteristics of protein/DNA films from QCM results

Film	Total thickness (nm)	wt. DNA ( $\mu\text{g cm}^{-2}$ )	wt. Protein ( $\mu\text{g cm}^{-2}$ )
DNA(Mb/CT-ds-DNA) <sub>2</sub>	20	3.1	3.6
DNA(Mb/ST-ds-DNA) <sub>2</sub>	30	5.8	4.9
DNA(Cyt P450 <sub>cam</sub> /ST-ds-DNA) <sub>2</sub>	40	15	2.9

oxidations as in direct electrochemical oxidation; that is, guanine in ss-DNA reacts much more rapidly than in ds-DNA. In addition, the reaction rate at a given guanine site is dependent on the sequence of neighboring bases in the DNA.

### Electrochemical Methods for Toxicity Sensing

Against the backdrop of the electrochemical research on DNA summarized above, we set out to develop methods to detect chemical DNA damage as the basis for toxicity screening. Our first attempts involved derivative square wave voltammetric (SWV) analysis of films of double-stranded (ds) DNA and ionomers Eastman AQ38S or Nafion.<sup>[43,44]</sup> Square wave voltammetric analysis was used because of its inherent high sensitivity and resolution. DNA-ionomer films were incubated with styrene oxide, which reacts with guanine bases and disrupts the DNA double helix.<sup>[7,8]</sup> Damage to DNA in these films resulted in multiple oxidation peaks that developed during the reaction. This damage was confirmed by capillary electrophoresis detection of DNA base adducts in hydrolyzed DNA reacted with styrene oxide under these same conditions. Total integrals of the derivative SWV oxidation peaks increased with time of incubation with styrene oxide.

Unfortunately, direct electrochemical detection of DNA damage in films suffered from poor signal to noise ratios and data analysis that required derivative or other background corrections. Thus we explored catalytic methods of DNA oxidation (cf. Eqs. (3) and (4)) to improve signal to noise in SWV detection.<sup>[45]</sup> At the same time, we began to realize that layer-by-layer growth of films had clear advantages in versatility, stability, and thickness control and so was used to make films of DNA and the polycation PDDA. The best sensitivity was found with ds-DNA as the outer layer of the film and at low salt concentration. Quartz crystal microbalance of (PDDA/ds-DNA)<sub>2</sub> on gold resonators showed that the average thickness was 6 nm and that each film contained 0.23 μg of ds-DNA. [The (PDDA/ds-DNA)<sub>2</sub> terminology represents two bilayers of PDDA/DNA.]

(PDDA/ds-DNA)<sub>2</sub> films on oxidized PG electrodes were reacted with styrene oxide, then the electrodes were washed and transferred into pH 5.5 buffer containing 50 μM Ru(bpy)<sub>3</sub><sup>2+</sup> as the catalyst. The SWV oxidation peaks increased with incubation time with saturated styrene oxide (Fig. 3). Control (PDDA/ds-DNA)<sub>2</sub> electrodes incubated in buffer or saturated toluene showed much smaller peaks characteristic of intact ds-DNA layers in the films. Average peak current for catalytic SWV oxidation of the ds-DNA films increased with incubation time for 30 min, then

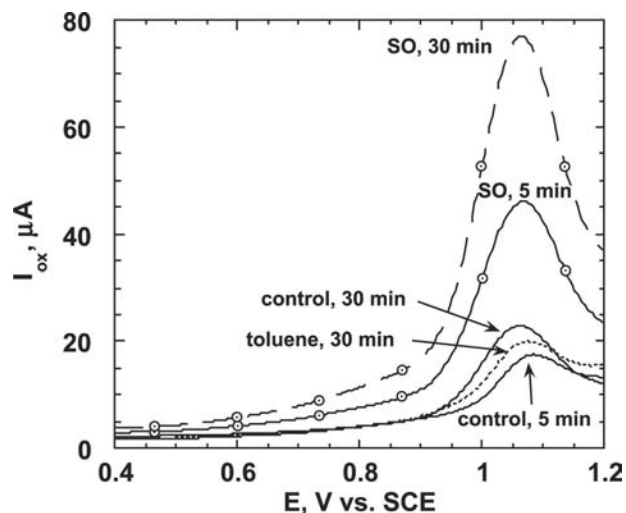


**Fig. 3** Square wave voltammetric of (PDDA/ds-DNA)<sub>2</sub> films on oxidized PG electrodes in pH 5.5 acetate buffer containing 50 mM NaCl, with 50 μM Ru(bpy)<sub>3</sub><sup>2+</sup> in buffer and after incubations at 37°C with saturated styrene oxide (SO) or unreactive toluene. *Source:* From Ref.<sup>[45]</sup> with permission. © American Chemical Society.

decreased slightly (Fig. 4). Each point represents a single electrode, and error bars reflect electrode-to-electrode variability. Incubation of films with toluene, for which no chemical reactions with DNA have been reported, gave catalytic oxidation peaks that showed no trends with reaction time. Catalytic SWV oxidation with Ru(bpy)<sub>3</sub><sup>2+</sup> provided more sensitive

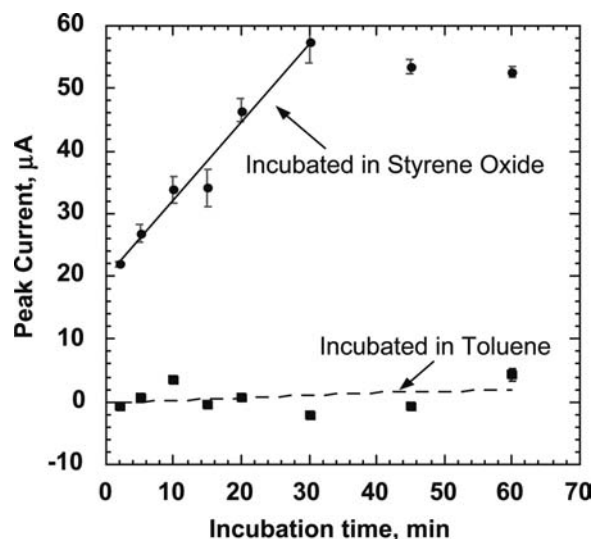


**Fig. 4** The influence of incubation time with saturated styrene oxide and toluene in pH 5.5 buffer on the average catalytic peak current (less current for controls) for 5 to 15 trials per data point for (PDDA/ds-DNA)<sub>2</sub> films. Error bars represent standard deviations. *Source:* From Ref.<sup>[45]</sup> with permission. © American Chemical Society.

detection of DNA damage than direct SWV oxidation. Studies of DNA and polynucleotides in solutions and films suggested that oxidation of guanine and chemically damaged adenine in partly unraveled damaged DNA were the most likely contributors to the catalytic peaks.<sup>[45]</sup>

Another method to monitor DNA damage in films employed a cationic electroactive probe that binds better to ds-DNA than to damaged DNA.  $\text{Co}(\text{bpy})_3^{3+}$  was used to probe films of  $(\text{PDDA}/\text{ds-DNA})_2$  grown layer-by-layer on PG electrodes first coated with a layer of PSS.<sup>[46]</sup> After incubation of  $(\text{PDDA}/\text{ds-DNA})_2$  films with styrene oxide, electrodes were rinsed, placed into  $20\ \mu\text{M}$   $\text{Co}(\text{bpy})_3^{3+}$ , and the  $\text{Co}^{\text{III}}/\text{Co}^{\text{II}}$  reduction peak at  $0.04\ \text{V}$  vs. SCE from the DNA-bound complex was monitored by SWV. Peak current decreased with increasing time of reaction with styrene oxide because of the decreasing ability of the damaged outer layer of DNA to bind  $\text{Co}(\text{bpy})_3^{3+}$ . A single electrode can be used to measure the incubation time course. Denoting the initial SWV peak current as  $I_{\text{p,initial}}$  and the peak current after incubation as  $I_{\text{p,final}}$ , plots of the peak current ratio  $I_{\text{p,initial}}/I_{\text{p,final}}$  vs. incubation time (Fig. 5) were used to monitor DNA damage rates. This ratio helps correct for electrode-to-electrode variations.  $I_{\text{p,initial}}/I_{\text{p,final}}$  increased for ds-DNA electrodes with increasing incubation time with styrene oxide solutions. No significant variations were found for controls with or without toluene.

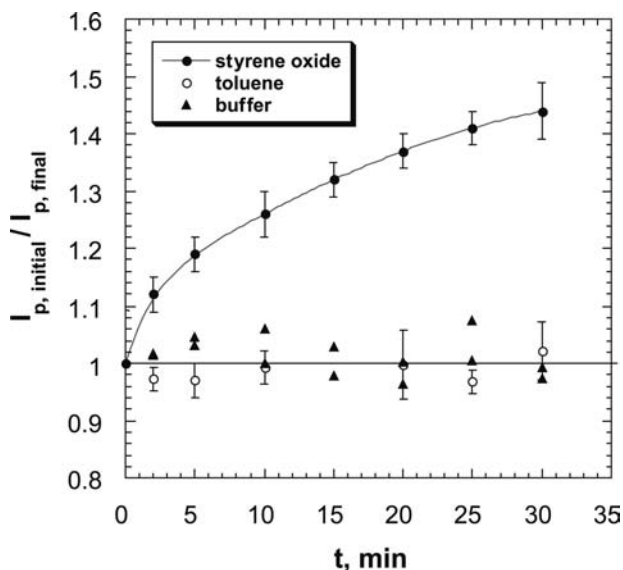
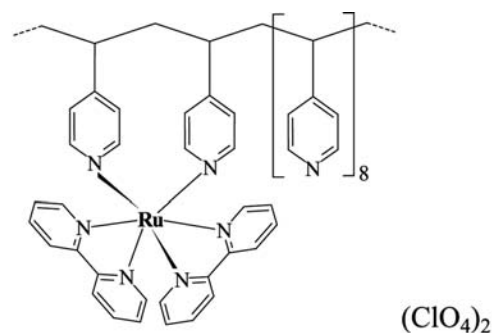


**Fig. 5** Influence of incubation time on average SWV peak current ratios for  $(\text{PDDA}/\text{ds-DNA})_2$  films in  $20\ \mu\text{M}$   $\text{Co}(\text{bpy})_3^{3+}$  at pH 5.5 after incubations with styrene oxide, toluene, or pure buffer.  $I_{\text{p,final}}$  corresponds to the peak current after each incubation;  $I_{\text{p,initial}}$  corresponds to peak current before incubation. Source: From Ref.<sup>[46]</sup> with permission. © 2002 Wiley-VCH.

Building films a layer at a time allowed us to incorporate catalytic metallopolyion catalysts for DNA oxidation into “reagentless” toxicity biosensors. Two polyions containing  $\text{Ru}(\text{bpy})_2^{2+}$  were used that are capable of catalytically oxidizing guanines in DNA. The one shown below, denoted Ru-PVP, has 6 Ru-N bonds and reversible oxidation at  $1.15\ \text{V}$  vs. SCE.



**Structure of catalytic metallopolymer  $[\text{Ru}(\text{bpy})_2(\text{PVP})_{10}](\text{ClO}_4)_2$**

A related polymer denoted RuCl-PVP has 5 Ru-N bonds with chloride as the sixth Ru ligand. It is reversibly oxidized at  $0.75\ \text{V}$  vs. SCE<sup>[47–49]</sup> and provided clearer peaks on a flatter background for the catalytic reaction at this lower voltage without sacrificing very much sensitivity. Use of this catalytic polymer is illustrated in Fig. 6A, showing an increase in catalytic SWV peaks of RuCl-PVP in PSS/RuCl-PVP/DNA/PDDA/DNA films after incubation with styrene oxide.

PSS/RuCl-PVP/DNA/PDDA/DNA films were also incubated with methylating agents dimethyl sulfate (DMS), a confirmed human carcinogen, and suspected carcinogen methyl methanesulfonate (MMS).<sup>[50]</sup> Films incubated with DMS or MMS gave increases in the peak current that suggested DNA damage. Fig. 6B shows changes with reaction time in the ratio of final SWV peak current of the films to the initial peak current for the PSS/RuCl-PVP layers alone. The increase in the ratio is a result of DNA unwinding caused by nucleobases that have been methylated by MMS and DMS.<sup>[51,52]</sup> Damage to DNA under these conditions was confirmed by capillary electrophoresis detection of methylated guanines and adenines in hydrolyzed DNA that had been reacted with MMS or DMS.

Ru-PVP, the more powerful oxidizing agent, was used to develop a new method of DNA detection, direct electrochemiluminescence (ECL). A SWV waveform oxidized the  $\text{Ru}^{\text{II}}$  sites in the metallopolymer to  $\text{Ru}^{\text{III}}$ . Electrochemiluminescence was measured simultaneously with catalytic SWV peaks in a simple apparatus employing an optical fiber to conduct light from the electrode to a photomultiplier detector. The

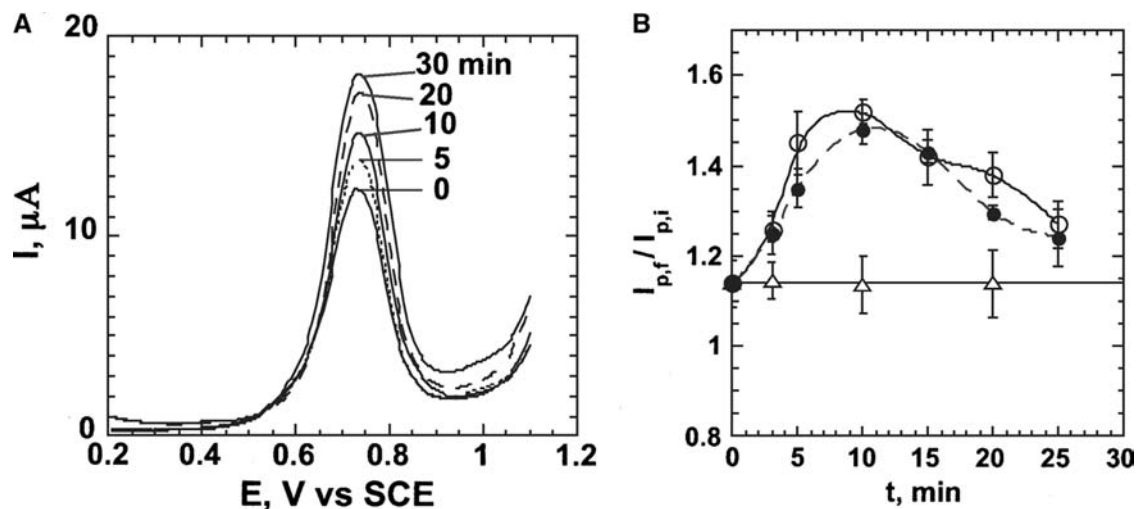


**Fig. 6** Examples of data obtained with catalytic RuCl-PVP layer in films: (A) SWV of PSS/RuCl-PVP/DNA/PDDA/DNA films after incubations at 37°C and pH 5.5 with saturated styrene oxide (SO) for 5, 10, 20, and 30 min, respectively. Incubations in toluene gave no changes in peak current. (B) Influence of reaction time (37°C, pH 6.5) of PSS/RuCl-PVP/DNA/PDDA/DNA films incubated in 2 mM dimethyl sulfate (●), 2 mM methyl methanesulfonate (○), and buffer control (△) on ratio of final SWV peak current to initial peak current of PSS/RuCl-PVP. *Source:* From Ref.<sup>[49]</sup> with permission. © American Chemical Society.

principle is illustrated in Fig. 7, showing the alternating layers of ds-DNA and the ruthenium metallopolymer  $[\text{Ru}(\text{bpy})_2(\text{PVP})_{10}]^{2+}$  used in the film. Direct electrochemiluminescence (ECL) involving DNA oxidation was observed in 10-nm films of Ru-PVP assembled layer-by-layer with DNA.<sup>[53]</sup> The electrode oxidized the  $\text{Ru}^{\text{II}}$  sites in the metallopolymer to  $\text{Ru}^{\text{III}}$  sites that reacted with guanines in the DNA. Electrochemiluminescence was measured simultaneously with catalytic voltammetric peaks at about 1.15 V vs. SCE (Fig. 8). Electrochemiluminescence was observed only when guanines were present on oligonucleotides in the films.

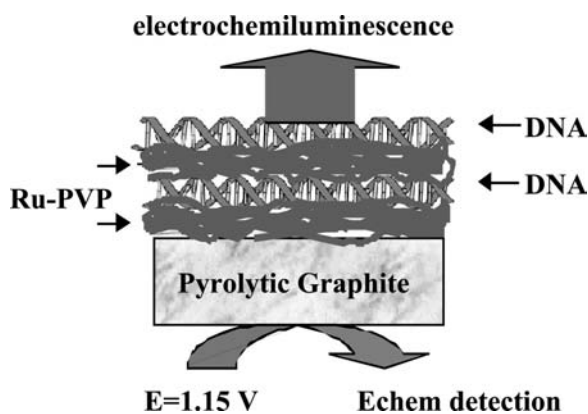


**Fig. 7** Conceptual cartoon of film of ds-DNA and the catalytic metallopolymer  $[\text{Ru}(\text{bpy})_2(\text{PVP})_{10}](\text{ClO}_4)_2$  designed for simultaneous electrochemiluminescent (610 nm) and voltammetric detection of DNA. *Source:* From Ref.<sup>[53]</sup> with permission. © American Chemical Society.

This result along with previously proposed ECL pathways suggests that guanine radicals initially formed by catalytic oxidation of guanines by  $\text{Ru}^{\text{III}}$  react with the metallopolymer to produce electronically excited  $\text{Ru}^{\text{II}*}$  in the film.  $\text{Ru}^{\text{II}*}$  spontaneously emits light at 610 nm and decays to ground-state  $\text{Ru}^{\text{II}}$ . Simultaneous linear

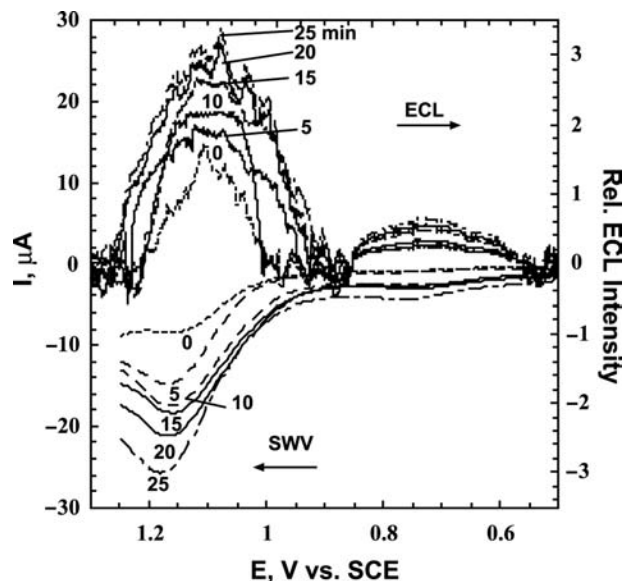


**Fig. 8** Simultaneous SWV (downward curves) and ECL (upward curves) responses for  $(\text{Ru-PVP/ds-CT DNA})_2$  films on PG electrodes in pH 5.5 buffer after incubations at 37°C with saturated styrene oxide. Curve labels are incubation times in min. *Source:* From Ref.<sup>[53]</sup> with permission. © American Chemical Society.



growth of ECL and SWV peaks occurred after incubation with styrene oxide over 20 min. The estimated detection limit was 1 damaged DNA base in 1000, or 0.1% damage. Control incubations of metallopolymer/ds-DNA films in buffer containing unreactive toluene resulted in no significant trends in ECL or SWV peaks with time.

### COMBINING BIOACTIVATION WITH DNA DETECTION

A practical approach for toxicity screening combines bioactivation and DNA damage detection into a single biosensor for toxicity screening. To make these types of sensors, ultrathin films (20–40 nm thick) containing myoglobin or cytochrome P450<sub>cam</sub> and DNA were grown layer-by-layer on electrodes. [Film composition is denoted by listing the components in their order of assembly, e.g., PDDA/ds-DNA/(enzyme/ds-DNA)<sub>2</sub>, where PDDA = polydiallyldimethylammonium ion.] Enzymes in the films were activated by hydrogen peroxide, generating test metabolite styrene oxide from styrene.<sup>[54]</sup> Styrene oxide formed in these nanometer-scale films reacted with double-stranded (ds) DNA in the same film, mimicking metabolism and DNA damage in the human liver. In the first demonstration of this concept, DNA damage was detected by SWV by using catalytic oxidation with dissolved Ru(bpy)<sub>3</sub><sup>2+</sup> or by monitoring the binding of Co(bpy)<sub>3</sub><sup>3+</sup> to the outer DNA layer in the film.<sup>[15]</sup> Later, we also detected DNA damage after enzyme-catalyzed bioactivation by using an inner RuCl-PVP layer in DNA/enzyme films.<sup>[49]</sup>

The SWV peak at 1.05 V vs. SCE for Ru(bpy)<sub>3</sub><sup>2+</sup> increased with time of the DNA damage reaction (Fig. 9). As in the case where enzyme-free films are incubated directly with DNA damage agents, ds-DNA in the film is damaged by styrene oxide. As a result of these reactions, guanines are released from the protection of the double helix, as are adducts of adenine.<sup>[45]</sup> These species are more easily oxidized than the original ds-DNA, and the catalytic oxidation current increases.

Control electrodes incubated in hydrogen peroxide without styrene showed catalytic oxidation peaks of similar heights to freshly prepared films (Fig. 9). Thus the low concentrations of hydrogen peroxide used had no measurable influence on ds-DNA. Only peaks for films that had been activated by hydrogen peroxide and styrene together increased with reaction time.

Similar results were obtained using cyt P450 as the enzyme. DNA/(Cyt P450<sub>cam</sub>/ST-ds-DNA)<sub>2</sub> films were incubated with styrene and hydrogen peroxide, and a rapid increase in SWV peak current in the first 5 min was followed by a slower increase from 5 to 30 min

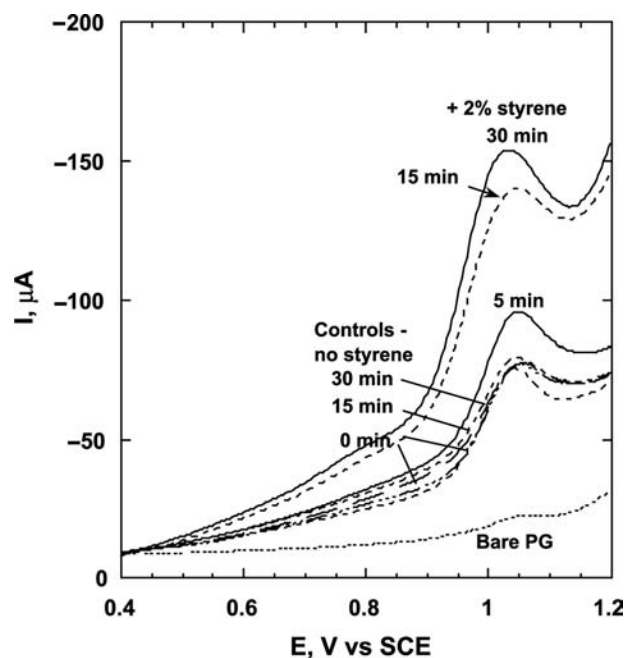


**Fig. 9** Catalytic square wave voltammetry of PDDA/ds-DNA/(Mb/ds-DNA)<sub>2</sub> films on rough PG electrodes before and after incubations at 37°C with 2% styrene (no styrene in controls) and 0.2 mM H<sub>2</sub>O<sub>2</sub> in aerobic buffer (SWV amplitude: 25 mV; frequency: 15 Hz; step height: 4 mV; PDDA = polydiallyldimethylammonium ion). After incubation, electrodes were washed and placed into pH 5.5 buffer containing 50 μM Ru(bpy)<sub>3</sub><sup>2+</sup> for the SWV analysis. *Source:* From Ref.<sup>[15]</sup> with permission. © American Chemical Society.

(Fig. 10A). Capillary electrophoresis and HPLC-MS analyses of DNA in thin films that were reacted with styrene oxide, and then hydrolyzed, confirmed formation of known styrene oxide adducts of DNA bases under similar reaction conditions.

Average SWV peak currents for ds-DNA/Mb films also increased with incubation time with hydrogen peroxide and styrene at relatively larger rates for the first 5 min, then at smaller rates at longer times (Fig. 10B). Slightly larger initial rates of peak growth were found with Mb/ST ds-DNA films than with Mb/CT ds-DNA films (CT = calf thymus, ST = salmon testes). Error bars are mainly the result of film-to-film variability. No significant growth in peak current with reaction time was found for films incubated with toluene and hydrogen peroxide, styrene alone, benzaldehyde, or hydrogen peroxide alone (Fig. 10, controls).

In alternative assays, Co(bpy)<sub>3</sub><sup>3+</sup> was used as an electroactive probe. Co(bpy)<sub>3</sub><sup>3+</sup> reduction peaks at 0.04 V decreased as DNA was damaged by enzyme-generated styrene oxide. Little change in SWV signals was found for incubations of DNA/enzyme films with unreactive organic controls or hydrogen peroxide. The catalytic SWV method was more sensitive than the Co(bpy)<sub>3</sub><sup>3+</sup>

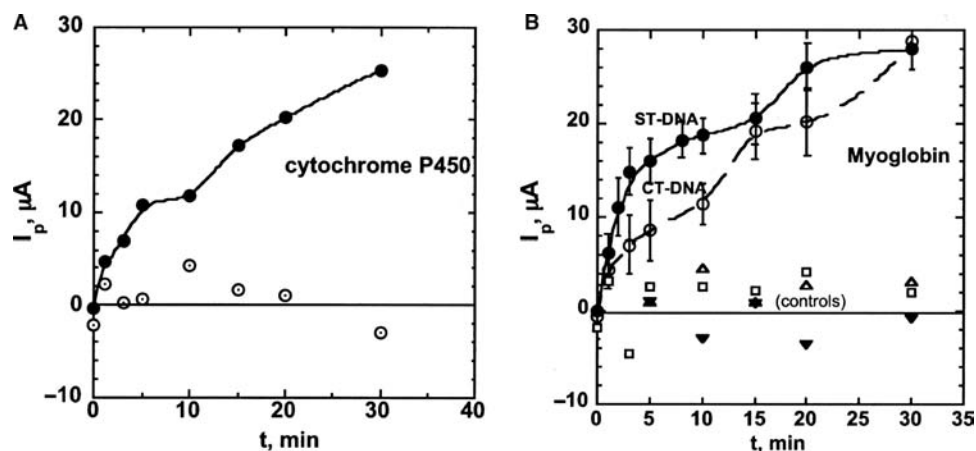


**Fig. 10** The influence of reaction time with 2% styrene + 0.2 mM  $\text{H}_2\text{O}_2$  on catalytic SWV peak in  $50 \mu\text{M Ru}(\text{bpy})_3^{2+}$ : (A) for PDDA/ds-ST-DNA/(cyt P450<sub>cam</sub>/ds-ST-DNA)<sub>2</sub> films (●) in  $50 \mu\text{M Ru}(\text{bpy})_3^{2+}$  solution. Control (○) is for incubation with 0.2 mM  $\text{H}_2\text{O}_2$ . (B) PDDA/ds-DNA/(Mb/ds-DNA)<sub>2</sub> films using CT-DNA (●) and ST-DNA (○) (5–15 trials per data point, CT = calf thymus, ST = salmon testes). Also shown are controls representing incubation of ST-DNA/Mb films with 2% styrene but no  $\text{H}_2\text{O}_2$  (□), 2% toluene + 0.2 mM  $\text{H}_2\text{O}_2$  (▼), and 0.2 mM benzaldehyde + 0.2 mM  $\text{H}_2\text{O}_2$  (△) (average peak current for unreacted DNA/enzyme electrodes was subtracted). Source: From Ref.<sup>[15]</sup> with permission. © American Chemical Society.

binding assay, providing multiple measurements over a 5-min reaction time. However, the  $\text{Co}(\text{bpy})_3^{3+}$  binding assay may be more useful in the presence of potential interferences because of its low measurement voltage where few electroactive species are reduced or oxidized.

## CONCLUSION

This entry described how adsorption of layers or biomolecules and polyions onto electrodes can provide films of nanometer-scale thickness on electrodes for screening the toxicity of chemicals and their metabolites. Such films containing DNA and enzymes enable detection of structural damage to DNA as a basis for the toxicity screening. The most sophisticated versions of these sensors bioactivate chemicals to their metabolites, which may react with DNA. The approach mimics toxicity pathways in the human liver. DNA damage can presently be detected at levels of about 0.1% to 0.5% by methods including catalytic square wave voltammetry using soluble or polymeric catalysts, electrochemically active DNA binding probes, or electrochemiluminescence using a special metallo-polymer. Catalytic polyions can be incorporated into DNA/enzyme films leading to “reagentless” sensors for chemical toxicity. These sensors are suitable for detection of relative DNA damage rates in 5–10 min.

We expect good future progress in applications of enzyme/DNA films to toxicity biosensors. The analytical approaches discussed above may also be adaptable to monitoring DNA oxidation, which has been suggested as a clinical marker for oxidative stress.<sup>[55]</sup> Electrode arrays could be developed to provide many

tests simultaneously. Future sensor arrays could be configured to detect toxicity of metabolites generated by a range of human cyt P450s.

## ACKNOWLEDGMENTS

This author’s research described herein was supported by US PHS grant No. ES03154 from the National Institute of Environmental Health Sciences (NIEHS), NIH, U.S.A. The author thanks students and collaborators named in joint publications, without whom the development of the sensors described would not have been possible.

## REFERENCES

1. Travis, C.C.; Hester, S.T. Global chemical pollution. *Environ. Sci. Technol.* **1991**, *25*, 815–817.
2. Singer, B.; Grunberger, D. *Molecular Biology of Mutagens and Carcinogens*; Plenum: New York, 1983.
3. Borman, S. Combinatorial chemistry. *Chem. Eng. News* November 11, **2002**, *80*, 43–57.
4. Jacoby, W.B., Ed.; *Enzymatic Basis of Detoxification*; Academic: New York, 1980; Vols. I and II.
5. Schenkman, J.B., Greim, H., Eds.; *Cytochrome P450*; Springer-Verlag: Berlin, 1993.
6. Ortiz de Montellano, P.R., Ed.; *Cytochrome P450*; Plenum: New York, 1995.
7. Bond, J.A. Review of the toxicology of styrene. *CRC Crit. Rev. Toxicol.* **1989**, *19*, 227–249.
8. Pauwels, W.; Vodiceka, P.; Servi, M.; Plna, K.; Veulemans, H.; Hemminki, K. Adduct formation on DNA and hemoglobin in mice intraperitoneally

- administered with styrene. *Carcinogenesis* **1996**, *17*, 2673–2680.
- Cavaliere, E.L.; Rogan, E.G.; Devaneshan, P.D.; Cremonesi, P.; Cerny, R.L.; Gross, M.L.; Bodell, W.J. Binding of benzo[a]pyrene to DNA by cytochrome p450 catalyzed one-electron oxidation in rat liver microsomes and nuclei. *Biochemistry* **1990**, *29*, 4820–4827.
  - Latham, G.J.; Zhou, L.; Harris, C.M.; Harris, T.M.; Lloyd, R.S. The replication fate of R- and S-styrene oxide adducts on adenine N<sup>6</sup> is dependent on both the chirality of the lesion and the local sequence content. *J. Biol. Chem.* **1993**, *268*, 23527–23530.
  - Lantham, G.J.; Lloyd, R.S. Deoxynucleotide polymerization by HIV-1 reverse transcriptase is terminated by site-specific styrene oxide adducts after translesion synthesis. *J. Biol. Chem.* **1994**, *268*, 23427–28530.
  - Phillips, D.H.; Farmer, P.B.; Beland, F.A.; Nath, R.G.; Poirier, M.C.; Reddy, M.V.; Turteltaub, K.W. Methods of DNA adduct determination and their application to testing compounds for genotoxicity. *Environ. Mol. Mutagen.* **2000**, *35*, 222–233.
  - Vodicka, P.; Tvrdik, T.; Osterman-Golkar, S. Evaluation of styrene genotoxicity using several biomarkers in a 3-year follow-up study of hand lamination workers. *Mutat. Res.* **1999**, *445*, 205–244.
  - Warren, A.J.; Shields, P.G. Molecular epidemiology: Carcinogen–DNA adducts and genetic susceptibility. *Proc. Soc. Exp. Biol. Med.* **1997**, *216*, 172–180.
  - Zhou, L.; Yang, J.; Estavillo, C.; Stuart, J.D.; Schenkman, J.B.; Rusling, J.F. Toxicity screening by electrochemical detection of DNA damage by metabolites generated in-situ in ultrathin DNA–enzyme films. *J. Am. Chem. Soc.* **2003**, *125*, 1431–1436.
  - Rusling, J.F.; Zhang, Z. Thin Films on Electrodes for Direct Protein Electron Transfer. In *Handbook of Surfaces and Interfaces of Materials*; Nalwa, R.W., Ed.; Biomolecules, Biointerfaces, and Applications, Academic Press, 2001; 5, 33–71.
  - Decher, G. Fuzzy nanoassemblies. *Science* **1997**, *277*, 1231–1237.
  - Lvov, Y. Electrostatic Layer-by-Layer Assembly of Proteins and Polyions. In *Protein Architecture: Interfacing Molecular Assemblies and Immobilization Biotechnology*; Lvov, Y., Mohwald, H., Eds.; Marcel Dekker: New York, 2000; 125–167.
  - Rusling, J.F. Electroactive and Enzyme-Active Protein Polyion Films Assembled Layer-by-Layer. In *Protein Architecture: Interfacing Molecular Assemblies and Immobilization Biotechnology*; Lvov, Y., Mohwald, H., Eds.; Marcel Dekker: New York, 2000; 337–354.
  - Lvov, Y. Thin-Film Nanofabrication by Alternate Adsorption of Polyions, Nanoparticles, and Proteins. In *Handbook of Surfaces and Interfaces of Materials*; Nalwa, R.W., Ed.; Nanostructured Materials, Micelles and Colloids, Academic Press: San Diego, 2001; Vol. 3, 170–189.
  - Schenkman, J.B.; Jansson, I.; Lvov, Y.; Rusling, J.F.; Boussaad, S.; Tao, N.J. Charge-dependent sidedness of cytochrome P450 forms studied by QCM and AFM. *Arch. Biochem. Biophys.* **2001**, *385*, 78–87.
  - Buttry, D.A.; Ward, M.D. Measurement of interfacial processes at electrode surfaces with the electrochemical quartz crystal microbalance. *Chem. Rev.* **1992**, *92*, 1355–1379.
  - Palecek, E. From polarography of DNA to microanalysis with nucleic acid-modified electrodes. *Electroanalysis* **1996**, *8*, 7–14.
  - Palecek, E.; Fojta, M. Detecting DNA hybridization and damage. *Anal. Chem.* **2001**, *73*, 74A–83A.
  - Palecek, E.; Jelen, F. Electrochemistry of nucleic acids and development of DNA sensors. *Crit. Rev. Anal. Chem.* **2002**, *32*, 261–270.
  - Jelen, F.; Fojta, M.; Palecek, E. Adsorptive stripping square-wave voltammetry of DNA. *J. Electroanal. Chem.* **1997**, *427*, 49–56.
  - Fojta, M.; Stankova, V.; Palecek, E.; Koscielniak, P.; Mitas, J. A supercoiled DNA-modified mercury electrode-based biosensor for the detection of DNA strand cleaving agents. *Talanta* **1998**, *46*, 155–161.
  - Fojta, M.; Palecek, E. Supercoiled DNA-modified mercury electrode: A highly sensitive tool for the detection of DNA damage. *Anal. Chim. Acta* **1997**, *342*, 1–12.
  - Sequaris, J.-M.; Valenta, P.; Nurnberg, H.W. A new electrochemical approach for the in vitro investigation of damage in native DNA by small G-radiation doses. *Int. J. Radiat. Res.* **1982**, *42*, 407–415.
  - Sequaris, J.-M.; Valenta, P. AC voltammetry: A control method for the damage to DNA caused in vitro by alkylating mutagens. *J. Electroanal. Chem.* **1987**, *227*, 11–20.
  - Wang, J.; Cai, X.; Wang, J.; Johnsson, C.; Palecek, E. Trace measurements of RNA by potentiometric stripping analysis at carbon paste electrodes. *Anal. Chem.* **1995**, *67*, 4065–4075.
  - Wang, J.; Rivas, G.; Ozsoz, M.; Grant, D.H.; Cai, X.; Parrado, C. Microfabricated electrochemical sensor for the detection of radiation-induced DNA damage. *Anal. Chem.* **1997**, *69*, 1457–1460.
  - Steenken, S.; Jovanovic, S.V. How easily oxidizable is DNA: One-electron oxidation potentials of adenosine and guanosine radicals in aqueous solution. *J. Am. Chem. Soc.* **1997**, *119*, 617–618.
  - Thorp, H.H. Cutting out the middleman: DNA biosensors based on electrochemical oxidation. *Trends Biotechnol.* **1998**, *16*, 117–121.
  - Johnston, D.H.; Glasgow, K.C.; Thorp, H.H. Electrochemical measurement of the solvent accessibility of nucleobases using electron transfer between DNA and metal complexes. *J. Am. Chem. Soc.* **1995**, *117*, 8933–8938.
  - Napier, M.E.; Thorp, H.H. Modification of electrodes with dicarboxylate self-assembled. *Langmuir* **1997**, *13*, 6342–6344.
  - Sistare, M.F.; Codden, S.J.; Heimlich, G.; Thorp, H.H. Effects of base stacking on guanine electron transfer: Rate constants for G and GG sequences of oligonucleotides from catalytic electrochemistry. *J. Am. Chem. Soc.* **2000**, *122*, 4742–4749.
  - Yang, I.V.; Thorp, H.H. Kinetics of metal-mediated one-electron oxidation of guanine in polymeric DNA and in oligonucleotides containing trinucleotide repeat sequences. *Inorg. Chem.* **2000**, *39*, 4969–4976.

39. Armistead, P.M.; Thorp, H.H. Oxidation kinetics of guanine in DNA molecules adsorbed onto ITO electrodes. *Anal. Chem.* **2001**, *73*, 558–564.
40. Onkto, A.C.; Armistead, P.M.; Kircus, S.R.; Thorp, H.H. Electrochemical detection of single-stranded DNA using polymer-modified electrodes. *Inorg. Chem.* **1999**, *38*, 1842–1846.
41. Weatherly, S.C.; Yang, I.V.; Thorp, H.H. Proton-coupled electron transfer in duplex DNA. *J. Am. Chem. Soc.* **2001**, *123*, 1236–1237.
42. Weatherly, S.C.; Yang, I.V.; Armistead, P.A.; Thorp, H.H. Proton-coupled electron transfer in guanine oxidation: Effect of isotope, solvent, and chemical modification. *J. Phys. Chem., B* **2003**, *107*, 372–378.
43. Mbindyo, J.; Zhou, L.; Zhang, Z.; Stuart, J.D.; Rusling, J.F. Detection of chemically-induced DNA damage by derivative square-wave voltammetry. *Anal. Chem.* **2000**, *72*, 2059–2065.
44. Rusling, J.F.; Zhou, L.; Munge, B.; Yang, J.; Estavillo, C.; Schenkman, J.B. Applications of polyion films containing biomolecules to sensing toxicity. *Faraday Discuss.* **2000**, *116*, 77–87.
45. Zhou, L.; Rusling, J.F. Detection of chemically-induced DNA damage in layered films by catalytic square wave voltammetry using  $\text{Ru}(\text{bpy})_3^{2+}$ . *Anal. Chem.* **2001**, *73*, 4780–4786.
46. Yang, J.; Zhang, Z.; Rusling, J.F. Detection of chemically-induced damage in layered DNA films with  $\text{Co}(\text{bpy})_3^{3+}$  by square wave voltammetry. *Electroanalysis* **2002**, *14*, 1494–1500.
47. Mugweru, A.; Rusling, J.F. Catalytic square-wave voltammetric detection of DNA with reversible metallopolymer-coated electrodes. *Electrochem. Commun.* **2001**, *3*, 406–409.
48. Mugweru, A.; Rusling, J.F. Square wave voltammetric detection of chemical DNA damage with catalytic poly(4-vinylpyridine)- $\text{Ru}(\text{bpy})_2^{2+}$  films. *Anal. Chem.* **2002**, *74*, 4044–4049.
49. Wang, B.; Rusling, J.F. Catalytic voltammetric sensor for DNA damage using  $[\text{Ru}(\text{bpy})_2\text{Poly}-(4\text{-Vinylpyridine})_{10}\text{Cl}]^+$  in layered DNA films. Damage from methylating agents and an enzyme-generated epoxide. *Anal. Chem.* **2003**, *75*, 4229–4235.
50. Lewis, R.J. *Carcinogenically Active Chemicals: A Reference Guide*; Lewis, R.J., Ed.; Van Nostrand Reinhold: New York, 1990.
51. Veld, C.W.; Jansen, J.; Zdzienicka, M.Z.; Vrieling, H.; Van Zeeland, A.A. Methyl methanesulfonate-induced hprt mutation spectra in the Chinese hamster cell line CHO9 and its xrccl-deficient derivative EM-C11. *Mutat. Res.* **1998**, *398*, 83–92.
52. Adams, S.P.; Laws, G.M.; Storer, R.D.; Deluca, J.G.; Nichols, W.W. Detection of DNA damage induced by human carcinogens in acellular assays: Potential application for determining genotoxic mechanisms. *Mutat. Res.* **1996**, 235–248.
53. Dennany, L.; Forster, R.J.; Rusling, J.F. Simultaneous direct electrochemiluminescence and catalytic voltammetry detection of DNA in ultrathin films. *J. Am. Chem. Soc.* **2003**, *125*, 5213–5218.
54. Munge, B.; Estavillo, C.; Schenkman, J.B.; Rusling, J.F. Optimizing electrochemical and peroxide-driven oxidation of styrene with ultrathin polyion films containing cytochrome P450cam and myoglobin. *ChemBioChem* **2003**, *4*, 82–89.
55. Shigenaga, M.K.; Ames, B.N. Assays for 8-hydroxy-2'-deoxyguanosine: A biomarker of in-vivo oxidative DNA damage. *Free Radic. Biol. Med.* **1991**, *10*, 211–216.

# Electron Microscopy at Very High Resolution

**Klaus van Benthem**

Center for Nanophase Materials Sciences, Oak Ridge National Laboratory, Oak Ridge, Tennessee, U.S.A., and Department of Chemical Engineering and Materials Science, University of California–Davis, Davis, California, U.S.A.

**Stephen J. Pennycook**

Materials Science and Technology Division, Oak Ridge National Laboratory, Oak Ridge, Tennessee, U.S.A.

## Abstract

Transmission electron microscopy (TEM) is one of the most frequently used tools for the characterization of nanomaterials. Aberration-correction has revolutionized the field of electron microscopy and now equipment is commercially available providing sub-Ångström resolution and single atom sensitivity for atomic, electronic, and chemical structure analyses. In this entry, aberration-corrected scanning transmission electron microscopy and related techniques are reviewed in the framework of nanomaterials sciences. Three examples from the areas of catalysis, hydrogen storage, and nanoscale thin films, are used to demonstrate experimental capabilities and current resolution limits.

## INTRODUCTION

The characterization of structure and electronic properties of materials is a key issue in modern nanotechnology. Electron microscopy techniques, especially transmission electron microscopy (TEM), are probably the most important tools for the investigation of nanomaterials since many properties can be directly accessed with very high spatial resolution.<sup>[1,2]</sup> The Royal Swedish Academy of Sciences named the electron microscope as “*one of the most important inventions*” of the 20th century.<sup>[3]</sup> Ever since the invention of the electron microscope in 1932,<sup>[4]</sup> technical advances have brought higher and higher resolution limits all the way to the ultimate limit for materials sciences: the imaging and identification of a single isolated atom. This development in increasing the spatial resolution for materials sciences is illustrated in Fig. 1. Already in 1936, it was recognized by Scherzer that lens aberrations occur in electron optical round lenses as a result of physics rather than purely due to imperfections,<sup>[5]</sup> hence limiting the achievable resolution orders of magnitude apart from the electron’s wavelength. In his famous lecture entitled “*There’s Plenty of Room at the Bottom*,” Feynman directly addressed the development of electron microscopes by asking “*Is there no way to make the electron microscope more powerful?*”<sup>[6]</sup> He suggested to break axial symmetries to overcome spherical aberrations and, thus, improve the resolution limits so that one could “*see individual atoms distinctly*.” Even though first designs of aberration-correctors already existed,<sup>[7]</sup> it was not until the advance of fast computers that aberration-correction became suitable for the electron microscope.

Tuning and focusing correction elements for electron optics requires the alignment of many multipole lenses with accuracies of the order of  $10^{-7}$ , resulting in a parameter space with more than 40 dimensions.

Today, aberration-correction is successfully applied to both TEM and scanning transmission electron microscopy (STEM), and enables the discrimination of two objects separated by less than 1 Å with both techniques. In addition, the high spatial resolution can be combined with spectroscopy techniques to determine local chemical compositions and electronic structures. Therefore, TEM and STEM are invaluable tools for modern nanomaterials research and provide structural and chemical information with unprecedented detail and sensitivity.

In the following, basic concepts of TEM and different techniques for nanocharacterization will be reviewed. Emphasis will be laid on aberration-correction in STEM. Afterwards, different examples from nanomaterials research will be reviewed, which could only be obtained through the application of aberration-corrected STEM. Finally, an outlook to future developments in TEM/STEM in connection to nanomaterials sciences and technology will be offered.

## Transmission Electron Microscopy

The main focus of this entry lies on scanning transmission electron microscopy, in which a fine electron probe is scanned across the sample and signals provided by transmitted electrons are collected serially as a function of position on the sample. In contrast to STEM, conventional TEM uses a parallel illumination

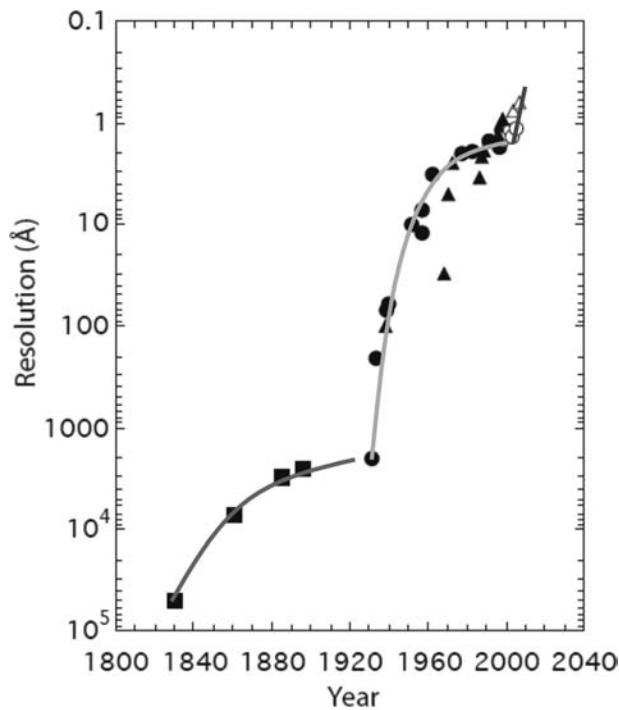


**Fig. 1** The evolution of spatial resolution in microscopy since the early 1800s. Squares represent light microscopy, circles TEM, triangles STEM. Solid symbols refer to results obtained before aberration-correction, while open symbols denote studies after correction. Red, green, and blue lines, respectively, have been added to show overall trends. *Source:* Figure created from Ref.<sup>[8]</sup>.

of the electron transparent specimens. For the coherent electron beam conditions in TEM, contrast is mainly achieved through the use of apertures in the back focal plane of the objective lens to select or interfere diffracted beams, referred to respectively as diffraction contrast or phase contrast imaging.<sup>[1]</sup> Figure 2 shows

a sketch of the electron ray diagrams for STEM and TEM operation modes and compares the essential optical elements in both instruments for one picture element, i.e. image pixel. As can be inferred from Fig. 2, the bright field STEM and TEM ray diagrams are equivalent when read in opposite directions of electron propagation.<sup>[1]</sup> This equivalence is often referred to as the theory of reciprocity, which was formulated for light optics by Stokes, Lorentz, Helmholtz, and others in the 19<sup>th</sup> century.<sup>[9]</sup> The principle of reciprocity in the context of electron wave optics is based on time-reversal symmetry of the electron propagation process. The STEM collector aperture  $\beta_{\text{STEM}}$  is, therefore, equivalent to the TEM condenser aperture  $\alpha_{\text{TEM}}$  while the objective aperture  $\alpha_{\text{STEM}} = \beta_{\text{TEM}}$  remains the same. For clarification, apertures passed by the electron beam before interaction with the sample are denoted with angles  $\alpha$ , while post-specimen apertures are called  $\beta$ . Note, however, in a combined TEM/STEM instrument the STEM objective (i.e. probe-forming) aperture is usually the same aperture used as condenser aperture in the TEM mode. The difference in the two operating conditions is that in STEM, the image pixels are recorded serially while in TEM they are all acquired at once. It is important to recognize that when identical apertures  $\alpha_{\text{STEM}} = \beta_{\text{TEM}}$  and  $\beta_{\text{STEM}} = \alpha_{\text{TEM}}$  are used, and provided that  $\beta_{\text{STEM}}$  is coherently and  $\beta_{\text{TEM}}$  is incoherently illuminated, the principle of reciprocity results in identical image contrast for bright field STEM and TEM.<sup>[1]</sup>

In an STEM instrument, electrons are accelerated from a source and focused into a small probe onto the specimen by a set of condenser lenses and an objective lens. The objective aperture limits the maximum angle under which electrons contribute to the electron probe, which is scanned across the sample by a set of scan coils.

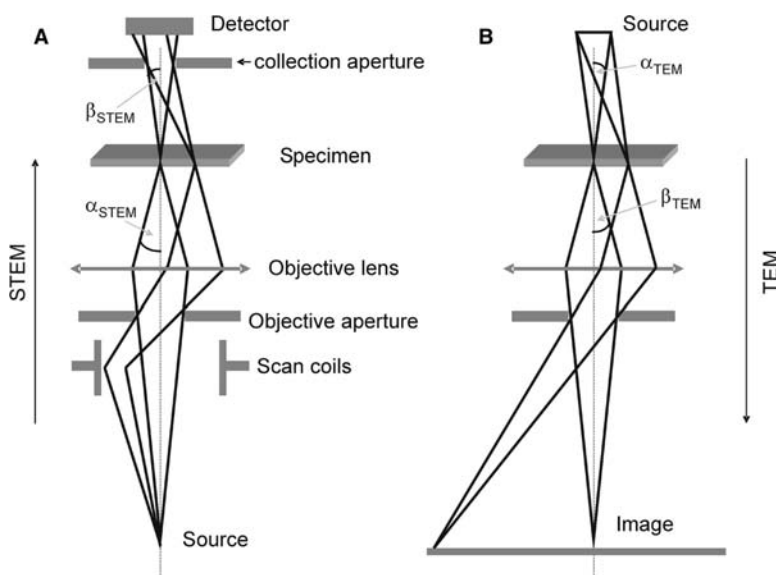


**Fig. 2** Theorem of reciprocity between (A) STEM and (B) TEM in terms of electron ray diagrams connecting the intermediate source and image. *Source:* From Ref.<sup>[1]</sup>.



Images are formed by recording electrons transmitted by the specimen as a function of probe position. Electrons scattered into high-angles are recorded with an annular detector. The cross-section for electrons scattered into high angles over a large angular range is roughly proportional to the squared atomic number of the scattering element.<sup>[1]</sup> For large enough scattering angles, coherent effects between, e.g., atomic columns average out. Hence, the scattering process itself can be considered purely incoherent, which bypasses the phase problem that complicates interpretation of conventional high-resolution TEM using phase contrast imaging. High-angle annular dark field (HAADF) imaging is often referred to as *Z*-contrast imaging because of the atomic number dependence of the scattering cross-section. Consequently, the HAADF technique is most sensitive to heavy elements, and images provide a high degree of chemical information in addition to structural details.<sup>[10]</sup>

Those electrons scattered into small angles can be collected “*on-axis*” by a bright field detector, or they can be analyzed with respect to their kinetic energy to form electron energy-loss spectra to investigate inelastic scattering events. In addition, secondary electron detectors, energy-dispersive X-ray detectors, cathodoluminescence detectors, etc. can also be attached to the microscope. Consequently, STEM provides the simultaneous acquisition of multiple different image and spectroscopy signals while scanning the electron probe across the specimen or pointing it directly onto different defect structures, such as, for instance, point defects, grain boundaries, or heterophase interfaces.<sup>[10]</sup> Figure 3A shows a schematic drawing of the main components of a dedicated STEM instrument. As an example, Fig. 3B is a picture of the VG Microscopes HB603 U dedicated STEM operated at 300 keV accelerating voltage, which is located at Oak Ridge National Laboratory.

The spatial resolution of an STEM experiment is determined by the diameter of the electron probe. Therefore, the probe formation is the critical aspect determining interaction volumes inside the sample. To increase the spatial resolution, aberration-correctors have recently been developed to overcome limitations due to lens imperfections and aberrations. In the following section, some basics of the concepts for aberration-correction will be reviewed.

### Lens aberrations

Aberration-correction is most likely the most exciting recent development in electron optics and microscopy. Ideal lenses focus a point source to a single image point, as sketched in Fig. 4A. Scherzer, however, first recognized that every rotationally symmetric lens will always suffer from both spherical and chromatic aberrations.<sup>[5]</sup> Spherical aberrations cause electrons traveling at higher angles to the optical axis to be focused more strongly than those at smaller angles (cf. Fig. 4B). Chromatic aberrations describe the spread in focus of a lens dependent on the kinetic energy spread of the electron wave (Fig. 4B). Consequently, both types of lens aberrations lead to a blurring of the electron beam in the back focal plane and, hence, a degradation of the spatial resolution. The practical limit to the achievable spatial resolution in modern electron microscopes is determined by these lens aberrations and instrument instabilities to about 50 times the electron wavelength  $\lambda$ .

The aberration is an error in the optical path length between the actual wave front and the perfect sphere, and is commonly expressed as a Taylor expansion in angle  $\theta$ . When ignoring all non-rotationally symmetric

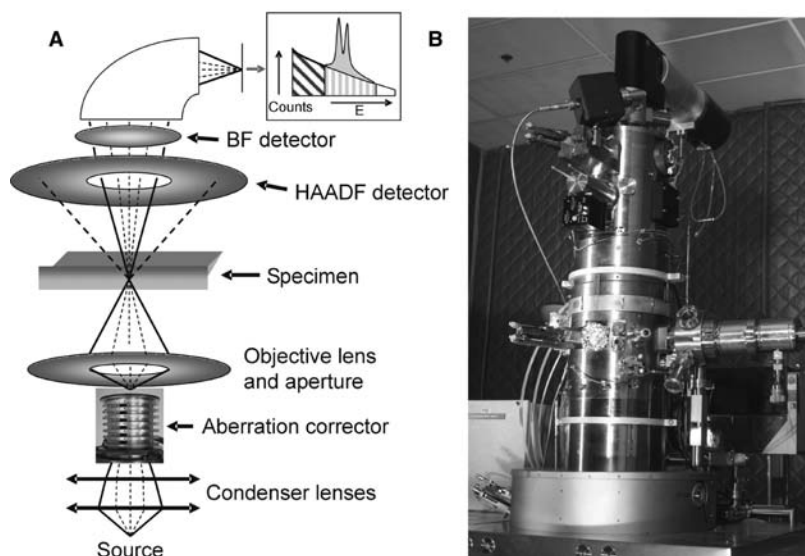


**Fig. 3** (A) Schematic drawing of the main components of an aberration-corrected scanning transmission electron microscope. The geometric setup allows simultaneous recording of different detector signals. (B) Picture of the Oak Ridge VG Microscopes HB603 U dedicated STEM.

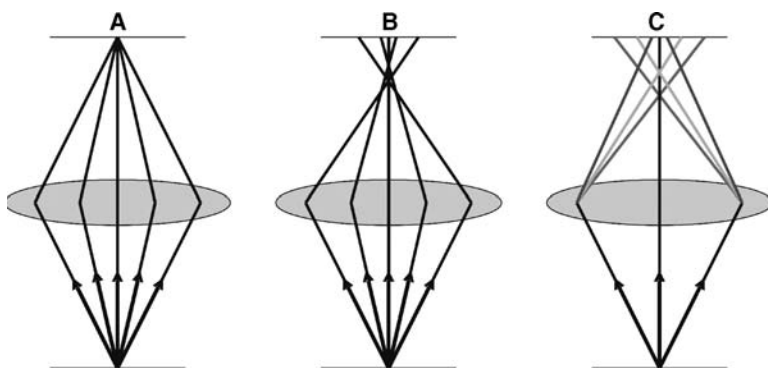


**Fig. 4** Schematic drawing of main lens aberrations. (A) A perfect lens focuses a point source to a single image point. (B) Geometric aberrations such as the spherical aberration bring electron rays at different angles to different focus points. The chromatic aberration (C) focuses the electron beam at different positions as a function of energy blur. *Source:* Adapted and reprinted, with permission, from Ref.<sup>[10]</sup>.

aberrations, the aberration function  $X(\theta)$  becomes

$$X(\theta) = \frac{1}{2}\Delta f\theta^2 + \frac{1}{4}C_3\theta^4 + \frac{1}{6}C_5\theta^6 + \frac{1}{8}C_7\theta^8 + \dots, \quad (1)$$

where  $\Delta f$  is the defocus,  $C_3 = C_s$ ,  $C_5$ , and  $C_7$  are the coefficients of third-, fifth-, and seventh-order spherical aberrations, respectively. For round magnetic lenses, these coefficients are all positive and have dimensions of length. At first, the order of the aberration coefficients seems counter-intuitive to Eq. (1). However, geometric aberrations lead the electron rays at different angles towards the different focus points along the optical axis, causing a lateral displacement in the Gaussian focal plane. The lateral displacements are proportional to the gradient of the aberration function  $\text{grad}_\theta X(\theta)$ .<sup>[11]</sup> Therefore,  $C_s$  is often referred to as a third-order spherical aberration.

Similar notations as used in Eq. (1) can be used for non-round aberrations, such as astigmatism, by introducing the dependence on the azimuthal angle. The description of general lens imperfection to fifth order would need 25 aberration coefficients to be included in the expression of the aberration function.<sup>[12,13]</sup> Fortunately, most of these coefficients are small in round lenses and can be kept small by suitable lens designs and microscope column alignments.

### Aberration-correctors

In practice, every optical lens exhibits aberrations. The underlying principle used by aberration-correctors is to generate an identical but negative aberration coefficient, which cancels out with the one introduced by the actual lens itself. The fundamental strategy to achieve this has been laid out by Scherzer in 1947 when he proposed to break rotational symmetry to eliminate spherical and chromatic aberrations.<sup>[7]</sup> Consequently, non-round optical elements, so-called multipoles, have been used to facilitate aberration-correction for round lenses. At the time of writing, there are two main types

of aberration-correctors commercially available: the quadrupole–octupole corrector from Nion<sup>[12–14]</sup> and the round-lens-hexapole corrector from CEOS.<sup>[15,16]</sup> Both types of correctors consist of either octupoles or hexapoles as correction elements, and quadrupoles or round lenses as steering elements for the electron trajectories inside the corrector. The two different designs have certain advantages and disadvantages when compared with each other. A discussion of the two different strategies is well beyond the scope of this entry. However, it should be noted that the round-lens-hexapole design can not only be used for the probe-forming lenses in STEM, but also was initially introduced to the imaging optics of high-resolution TEM instruments to achieve sub-Ångström resolution.<sup>[17,18]</sup> In STEM, direct imaging of a crystal lattice with sub-Ångström resolution has been achieved initially with the quadrupole–octupole corrector design (see Fig. 5).<sup>[19,20]</sup> Similar results were reproduced shortly thereafter with the hexapole corrected STEM.<sup>[18]</sup>

### Effects of aberration-correction

The initial goal of all efforts to correct lens aberrations in electron microscopy was to increase the spatial resolution, i.e. to decrease the electron probe diameter in the case of STEM. That this goal has been achieved is demonstrated with today's sub-Ångström spatial resolution imaging conditions (see Figs. 1 and 5). However, in STEM aberration-correction provides two additional effects: single atom sensitivity<sup>[21]</sup> and drastically increased depth sensitivity.<sup>[20,22]</sup>

Figure 6 shows calculated electron probe profiles before and after aberration-correction. For both simulations, the number of electrons, i.e. the electron beam current, is conserved. It becomes immediately evident that not only the probe diameter becomes significantly smaller, but at the same time the intensity increases dramatically. In HAADF imaging, the signal scales with the square power of the reciprocal probe diameter, while the background scales with the square power of the diameter itself. Therefore, the strongly

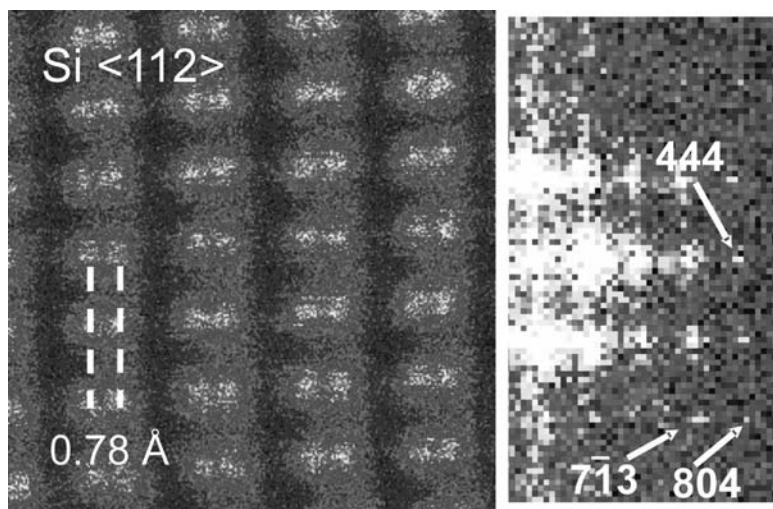


**Fig. 5** HAADF image directly recorded from a silicon single crystal, which was oriented with its <112> direction parallel to the optical axis. Columns of Si atoms only 0.78 Å apart from each other were clearly resolved. The right panel shows a part of the Fourier transform of the same image revealing information transfer to 0.61 Å.<sup>[22]</sup> Source: Figure reproduced with permission from Ref.<sup>[19]</sup>.

increased beam current density after aberration-correction conveys higher sensitivity for annular dark field imaging, which enables single atom sensitivity in annular dark field images.<sup>[21]</sup>

The depth of field  $T$  in STEM can be expressed as the quotient of lateral spatial resolution  $\delta_s = 0.61 \cdot \lambda / \alpha$  and the probe-forming angle  $\alpha$ <sup>[11]</sup>

$$T = \frac{\delta_s}{\alpha} = 0.61 \frac{\lambda}{\alpha^2} \tag{2}$$

Equation (2) shows that the availability of larger illumination angles because aberration-correction decreases the depth of field much faster than it improves the lateral resolution. The major consequence of the smaller depth of field is that only very thin slices of the specimen come into focus at a time. Hence, a through-focal series acquisition of images can provide optical sectioning of the sample along the optical axis in a manner comparable to confocal optical microscopy.<sup>[22]</sup>

Such depth sectioning techniques have recently been established<sup>[20,23,24]</sup> and represent an additional avenue to tilt-series tomography<sup>[25,26]</sup> to deduce three-dimensional information from TEM samples.

The achievable three-dimensional spatial resolution, however, is highly anisotropic. As discussed above, aberration-corrected STEM has demonstrated sub-Ångström resolution in the lateral, i.e. in-plane directions. For the 300 keV VG HB603 U STEM at Oak Ridge, the depth of focus following Eq. (2) ranges around 3–4 nm.<sup>[22–24]</sup> Two atoms vertically displaced by the depth of focus  $T$  reveal total image intensity as shown in Fig. 7, which is, because of the incoherent nature of ADF imaging, a superposition of the contributions from each individual atom. Figure 7 demonstrates that in this case, the atoms cannot be discriminated using the depth-sectioning technique. For vertical distances equal to  $1.75T$ , the resulting image intensity plateaus, which is formally equivalent to a resolution criterion by Sparrow.<sup>[27,28]</sup> Both atoms can clearly be

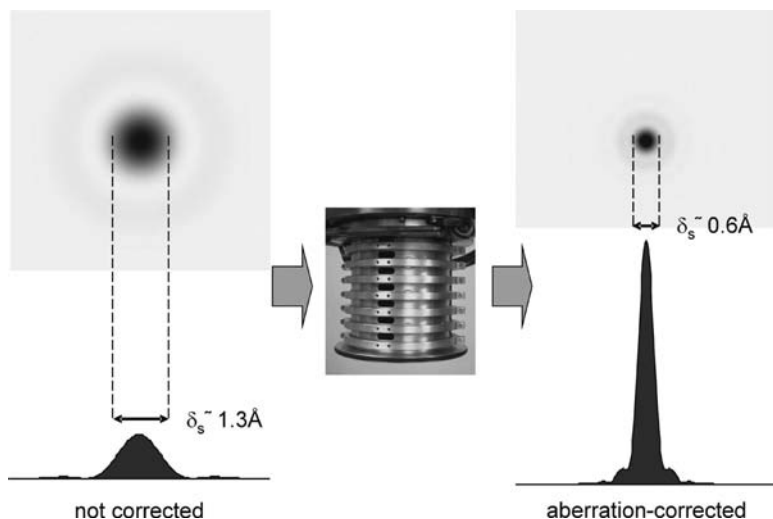


**Fig. 6** Simulated images and intensity line profiles of the electron probe before and after aberration-correction. The number of electrons is identical in both cases. Source: Adapted with permission from Ref.<sup>[10]</sup>.

Dynamic –  
Electronic

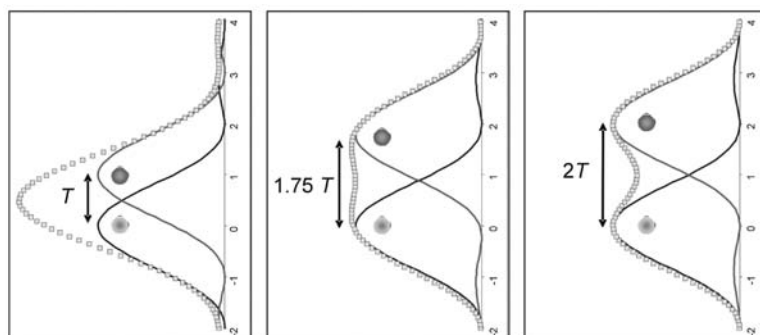


**Fig. 7** Sketch of two isolated atoms vertically separated by  $1\times$ ,  $1.75\times$ , and  $2\times$  the depth of field  $T$ . At the position of each atom, a simulated vertical probe profile is plotted. The dotted line is a superposition of the two corresponding profiles and represents the resulting image intensity as a function of defocus. *Source:* Adapted from Ref.<sup>[24]</sup> with permission from Elsevier.

discriminated along the optical axis for vertical displacements of  $2T$ , for which the resulting image intensity reveals a contrast variation of about 20% between the atoms. Therefore, this condition has been chosen as a criterion for vertical resolution. It is equivalent to the lateral resolution criterion formulated by Lord Raleigh in that, in the absence of aberrations, one atom is placed at the first zero of the diffracted intensity of the other.<sup>[11,28,29]</sup>

Examples and applications of single atom sensitivity in STEM imaging and depth sectioning techniques, both of which are direct consequences of aberration-correction, will be discussed further.

## MICROSCOPY OF NANOMATERIALS

In the following sections, three applications of aberration-corrected STEM to functional nanomaterials, results obtained from activated carbon fibers, catalyst nanoparticles, and alternate gate dielectrics, will be reviewed.

### Activated Carbon Fibers for Hydrogen Storage

Nanostructured carbon materials, such as carbon fibers, are lightweight inexpensive materials, which exhibit hydrogen storage capabilities.<sup>[30–33]</sup> Physisorption of  $H_2$  on nanoporous carbon, although significant at cryogenic temperatures, is weak at room temperatures<sup>[30]</sup> and does not satisfy the current goals established by the US Department of Energy. However, on physical activation with  $CO_2$ <sup>[31]</sup> or doping with catalyst materials,<sup>[32]</sup> the hydrogen uptake can be enhanced when compared with unmodified carbons.

Recently, it was shown that significant enhancements of  $H_2$  adsorption can be achieved at room temperature and 20 bar for activated carbon fibers (ACF) modified with Pd catalyst particles.<sup>[33]</sup> To control such processes in greater detail, and to further enhance the hydrogen uptake capacity, it is necessary to understand the fundamental atomistic mechanisms of metal-assisted

hydrogen storage on nanostructured carbon fibers, and in particular, on how processing conditions affect the microstructure of Pd-doped activated carbon fibers.<sup>[34]</sup>

The following results were obtained from a sample processed at Clemson University.<sup>[35]</sup> An isotropic pitch precursor was mixed with about 1% Pd salt before melt-spinning. The traditional subsequent carbonization and activation processes were combined into a single-stage process of *direct carbonization and activation* in pure  $CO_2$ , and samples with various levels of burn-off were generated.<sup>[35]</sup> The particular material used for the results presented is characterized by a burn-off level of 40%. Further details of the materials processing and the effect on materials properties can be found in Refs.<sup>[34,35]</sup>. The hydrogen storage characteristics are not the subject of this entry and are reported elsewhere.<sup>[33]</sup> Details on the microscopy results reviewed in the following are the object of a separate publication.<sup>[36]</sup>

As described above, ADF images are very sensitive to heavy elements since the scattering cross-section is roughly proportional to the squared atomic number of the illuminated species. However, bright field (BF) images, which are very sensitive to light elements in the sample, can be recorded simultaneously (see Fig. 3). Aberration-correction in STEM leads to “slower” oscillations of the phase contrast transfer function so that larger BF detectors can be used.<sup>[37]</sup> This directly results into BF images with enhanced signal when compared with the uncorrected case, which, according to the theorem of reciprocity, are equivalent to phase-contrast images. The simultaneous acquisition of ADF and BF images with pixel-to-pixel correlation at very high resolution becomes a very powerful tool for the investigation of carbon microstructures in the presence of catalytic Pd particles.<sup>[36]</sup>

Figure 8 shows a pair of ADF and BF images, which were acquired with an aberration-corrected VG Microscopes HB603 U STEM operated at 300 keV. The microscope is equipped with a Nion third-order aberration-corrector (cf. Fig. 1). Bright spot-like contrasts in the ADF image represent small Pd clusters and, in many cases, even single isolated Pd atoms



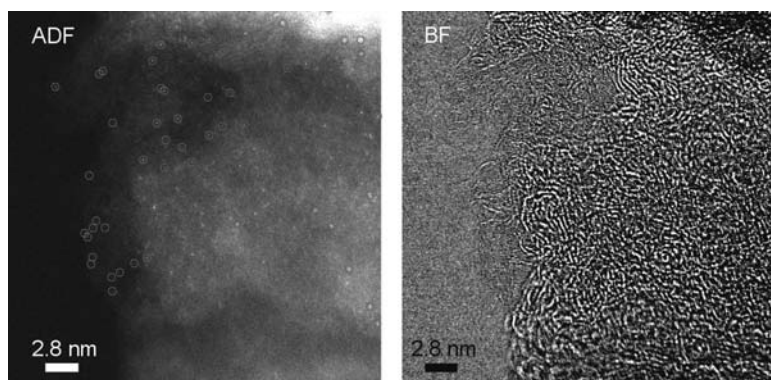


**Fig. 8** Simultaneously acquired pair of ADF and BF images using the 300 keV aberration corrected dedicated STEM. The frames have pixel-to-pixel correlation, so that the location of single Pd atoms in the ADF images (encircled) can be superimposed on the BF image, which reveals the local carbon microstructure. *Source:* Image adapted from Ref.<sup>[36]</sup>.

distributed throughout the carbon microstructure. Through-focal series acquisition of ADF images was used to confirm that the observed bright regions are due to single Pd atoms.<sup>[37]</sup> Pd atoms became very mobile due to illumination with the electron beam and could in many cases not be imaged at the exact same location in a subsequently acquired frame but at a nearby position.

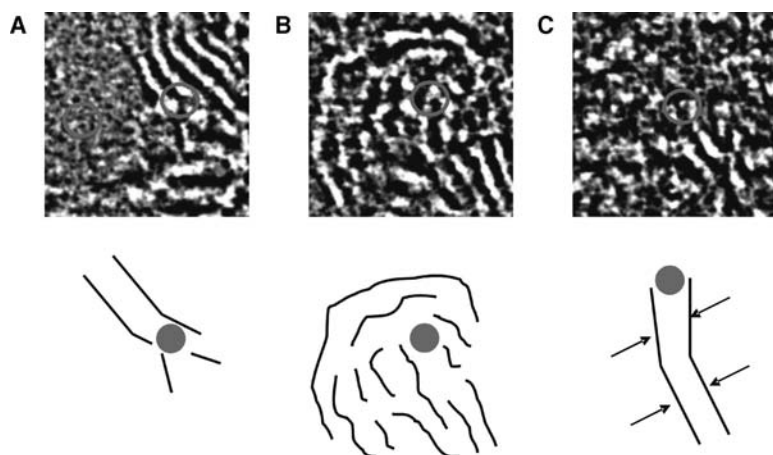
The simultaneously acquired BF image clearly reveals the carbon microstructure exhibiting graphene sheets in various different orientations. It is evident that the carbon fiber material is somewhat disordered on a larger length scale. However, some structural ordering with parallel but bent graphene layers can be observed. The overall contrast in the ADF image varies in steps from dark on the left to lighter gray on the right side, indicating different specimen thicknesses in the direction parallel to the electron beam. In the upper right corner, the ADF image shows a bright contrast region, which appears significantly dark in the BF image. This contrast is due to a larger Pd particle extending into the field of view when this set of images was acquired.

Figure 9 shows three magnified areas extracted from the BF image shown in Fig. 8. In Fig. 9A, one Pd atom is located within a highly disordered, probably amorphous region, while a second Pd atom

is terminating one graphene sheet located in between two others. Figure 9B shows a configuration in which a Pd atom is surrounded by concentric graphene sheets. A third configuration was observed in which Pd atoms are located in between two quasi-parallel sheets, which reveal slightly increased distances at and close to the Pd atom location. Such bending of atomic planes and the corresponding local straining reveals nanosized voids or pores inside the carbon microstructure correlated with the presence of single catalyst atoms. Previous investigations<sup>[38–40]</sup> indicate that nanosized pores are highly effective for hydrogen storage so that the configurations identified by STEM (Fig. 9) may represent local storage sites for atomic hydrogen after a spillover process,<sup>[41]</sup> encouraged by the presence of the metal catalyst. Such fundamental understanding of atomic-scale processes accessible by high-resolution STEM correlated with materials functionality, such as increased hydrogen gas uptake, can lead to more effective design of future storage materials.

### Catalyst Particles

In the previous section, it was shown that single isolated atoms can be detected and laterally localized



**Fig. 9** Three different areas extracted from the BF image in Fig. 8 with the positions of single Pd atoms transferred from the corresponding ADF images encircled. In the schematics underneath, the location of white BF contrasts is sketched as black lines, while the Pd atoms are marked by filled circles. *Source:* BF intensities are discussed in detail in Ref.<sup>[36]</sup>, from which this figure was adapted.

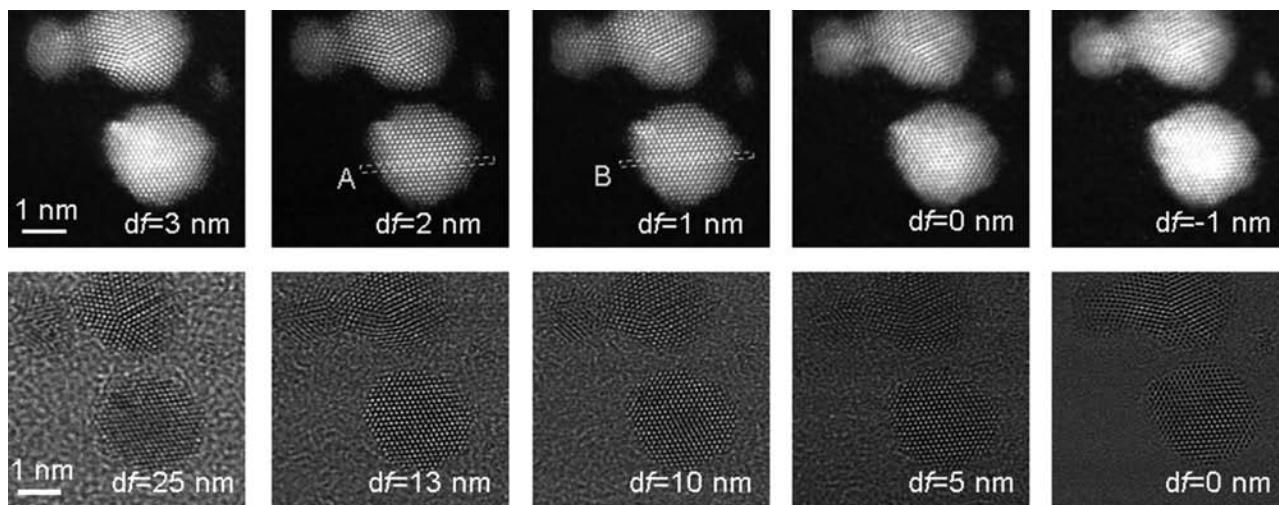


**Fig. 10** ADF (top row) and BF (lower row) images extracted from a through-focal series of Au nanoclusters supported by an amorphous carbon film. The defocus ( $df$ ) at which the images were taken is listed. *Source:* Figure reproduced from Ref.<sup>[42]</sup> with permission from Materials Research Society.

using aberration-corrected STEM. However, often times image quantification is desired to determine the absolute number of atoms forming, for instance, a catalyst particle. Since STEM typically provides a projection view of the investigated sample, the quantification of image contrast could in principle be used to determine specimen thickness.

Figure 10 shows a number of frames extracted from a through-focal series of simultaneously acquired ADF (upper row) and BF images (lower row) recorded from Au catalyst particles supported by an amorphous carbon film. The micrographs show four gold particles. The ADF image clearly exhibits lattice contrast for the crystalline particles while the carbon support film is almost invisible due to the Z-dependence of the scattering cross-section and, therefore, the large contrast differences. The corresponding bright-field images, however, clearly show the typical speckle pattern for amorphous carbon, whose contrast depends on the defocus value during image acquisition. Furthermore, the BF images also reveal lattice information of the Au clusters but with different contrast when compared with the ADF images.<sup>[1]</sup> The BF intensities change with defocus and even show contrast reversal, which is a typical feature of phase contrast imaging.<sup>[1]</sup> However, in this case the contrast inversion in the area of the amorphous carbon support film was used to calibrate the defocus scale.<sup>[42]</sup> Owing to the incoherent conditions for large inner detector angles, no reversal of contrast occurs for any defocus value in ADF imaging.

The ADF micrographs in Fig. 10 clearly exhibit regions with spot-like bright contrasts, which extend over multiple image pixels, and therefore represent single Au atoms in the vicinity of the larger Au clusters

(see, e.g., frames labeled  $df = 2$  nm and  $df = 3$  nm). In Fig. 11, two intensity line profiles A and B are plotted as a function of relative distance across one of the Au particles. The direction and exact location from which these profiles were extracted are marked in Fig. 10. Arrows in Fig. 11A highlight three different locations where minimal but identical image intensities of about 350 counts/pixel above the background level can be observed. These intensities represent single Au atoms.

Complimentary ADF image simulations were performed using parameters as determined by the aberration-corrector to calculate quantitative image intensities as a function of specimen thickness, i.e. number of Au atoms in a column. For the calculations an Au crystal was oriented with the  $\langle 111 \rangle$  zone-axis parallel to the incoming beam direction, resembling the experimental conditions as observed for the lower Au cluster in Fig. 10. It was found that the incoherent ADF signal is *linear* with the number of Au atoms for columns containing up to 6 atoms (see Fig. 12). Beyond 6 atoms, the ADF signal flattens out and channeling effects complicate the image quantification.

Based on the calculated calibration curve in Fig. 12, ADF image intensities were analyzed quantitatively. For each atomic column, the number of Au atoms along the electron beam direction was assigned. The results for line profile B are included in Fig. 11B. The anomalous background between the atomic columns could result from the so-called Stobbs factor.<sup>[43]</sup> Effects of chromatic aberrations or increased Debye–Waller factors due to a lower melting point of nanocrystalline Au clusters did not contribute to this background according to the image simulations.<sup>[42]</sup>



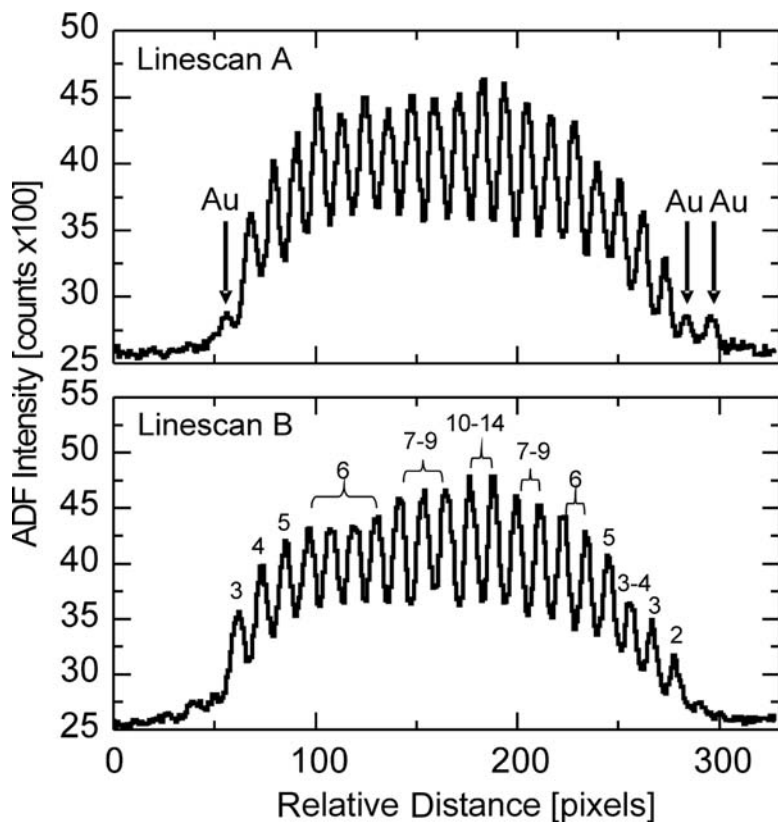


**Fig. 11** ADF intensity line profiles as extracted from the areas marked in Fig. 10. The net counts per single Au atoms were extracted from linescan labeled A, and the number of Au atoms in each column for the profile labeled B was assigned. *Source:* Original data are published in Ref.<sup>[42]</sup>. Figure reproduced from Ref.<sup>[42]</sup> with permission from Materials Research Society.

The number of atoms in each individual column of an atomically resolved catalyst particle can thus be determined with very high accuracy, which, in the case discussed here, is  $\pm 1$  atom for columns containing up

to 6 atoms, and  $\pm 2-4$  atoms for columns extending 2–4 nm along the beam direction. For the interpretation of catalytic activities, however, the true three-dimensional shape of the particle and its faceting is

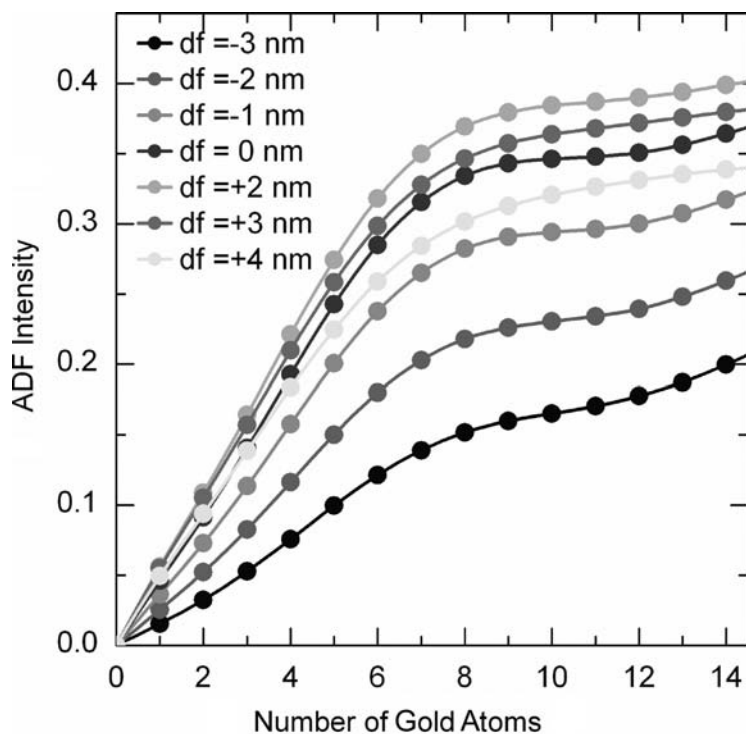


**Fig. 12** Calculated fractional ADF intensities for different defocus values as a function of the number of Au atoms along the beam direction. The ADF intensity scales linearly with the number of atoms up to a thickness of 6–7 atoms.<sup>[42]</sup> *Source:* Figure reproduced from Ref.<sup>[42]</sup> with permission from Materials Research Society.

Dynamic –  
Electronic

of critical importance. Such aspects, though at smaller resolution, can be addressed by tilt-series electron tomography of single catalyst particles.<sup>[26]</sup> In a recent study, Huang et al. have combined ADF image quantification as described earlier with statistical data for crystal shapes to determine the true three-dimensional shape of Au nanoparticles<sup>[44]</sup> and how many Au atoms they contain. In the future, a combination of these techniques might reveal more detailed information about faceting and shaping of nanoparticles with single atom accuracy.

## Nanoscale Thin Films

It is well recognized that the macroscopic properties of polycrystalline or composite materials are determined to a large extent by their internal two-dimensional defect structures such as heterophase interfaces and grain boundaries.<sup>[45]</sup> Most structural and functional ceramics, for example, exhibit intergranular films with thicknesses around 1 nm (see, e.g., Ref.<sup>[46]</sup> and references therein). Composite materials provide their functionality through thin films with thicknesses in the nanometer regime. Very prominent examples are complex oxide structures exhibiting colossal magnetoresistance<sup>[47]</sup> or superconductivity properties.<sup>[48]</sup> Other examples include high-*k* dielectric films present in many semiconductor devices. Here, shrinking dimensions<sup>[49,50]</sup> demand material replacements to maintain device performance even though critical structures have dimensions of only a few atoms.<sup>[51,52]</sup> It is, therefore, of utmost importance to gain a fundamental understanding of interface structures and, hence, thin film properties.

HfO<sub>2</sub> is a prominent candidate as a replacement for SiO<sub>2</sub> as a high-*k* dielectric in semiconductor device structures. For the study reviewed in the following, 3 nm of HfO<sub>2</sub> were grown on the (100) surface of a silicon substrate using atomic layer deposition at 320°C. Afterwards, the thin film was capped with polycrystalline silicon by chemical vapor deposition techniques

and rapidly thermally annealed at 950°C in N<sub>2</sub> atmosphere for 30s. Cross-sectional TEM samples of the interface structure were prepared by mechanical wet-polishing<sup>[22]</sup> until electron transparency was reached. Figure 13 shows a pair of ADF and BF images simultaneously recorded from the interface structure. The TEM sample was oriented with the <110> direction in the silicon substrate parallel to the optical axis. Owing to the relatively high atomic number of Hf (*Z* = 72), the crystalline HfO<sub>2</sub> film appears with bright contrast in the ADF image. The typical silicon “dumbbell” spacing of 1.36 Å in this orientation is clearly observable in the ADF image. The BF image reveals an 8 Å wide amorphous interlayer between the HfO<sub>2</sub> thin film and the substrate. This interlayer was found to be a sub-stoichiometric silicon oxide.<sup>[53,54]</sup>

A through-focal series acquisition of ADF images revealed that within the SiO<sub>x</sub> interlayer, bright spot-like features come into focus in various different areas at different focus settings. Figure 14 shows nine frames extracted from a through-focal series. It was found that these contrast features are due to single isolated Hf atoms embedded inside the interlayer,<sup>[22]</sup> which can hence be located laterally with sub-Å precision and vertically with better than 0.5 nm accuracy owing to the focal increment of 0.5 nm/frame during the data acquisition.<sup>[22,24]</sup> According to the increased depth sensitivity discussed earlier, the recorded stack of images from the through-focal series acquisition contains three-dimensional information about the interface structure. A 3D representation of the imaging data was created by surface and volume rendering techniques<sup>[22]</sup> and is shown in Fig. 15. The HfO<sub>2</sub> film is represented by bold yellow color. Columns of Si atoms can be observed in addition to five representative Hf atoms located in the interlayer, which was not color-coded. Overall, a concentration of  $1.40 \pm 0.11$  atoms/nm<sup>3</sup> was found inside the interlayer.<sup>[22]</sup> A systematic investigation of the growth and annealing conditions during the interface formation revealed that the concentration of Hf atoms in the interlayer critically depends on the

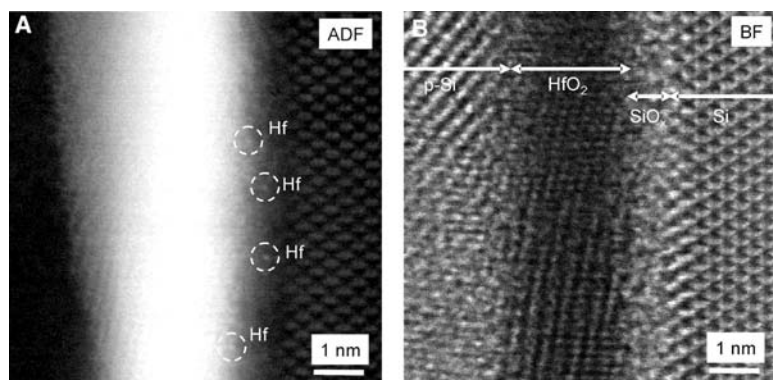


**Fig. 13** Simultaneously acquired ADF (A) and BF (B) images of the alternate gate stack consisting of a HfO<sub>2</sub> layer deposited on a silicon substrate. The BF image reveals an amorphous interlayer formed between the alternate gate dielectric and the substrate. The ADF image exposes single Hf atoms within this interlayer. *Source:* Reprinted with permission from Ref.<sup>[42]</sup>.

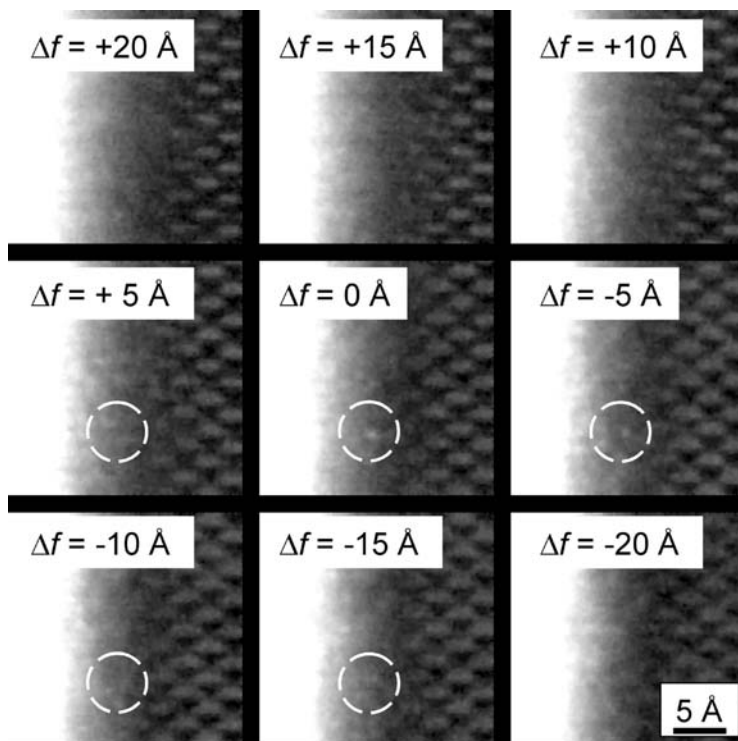


**Fig. 14** ADF images extracted from a through-focal series showing spot-like bright contrasts representing single Hf atoms coming into focus at different locations.<sup>[24,55]</sup> Source: Figure reproduced from Ref.<sup>[42]</sup> with permission from Elsevier.

quality, i.e. stoichiometry, of the silicon oxide before the annealing process<sup>[54]</sup> and the oxygen affinity of the alternative high-*k* material.<sup>[54,56]</sup> Hf atoms diffuse into the suboxide interlayer during the rapid thermal

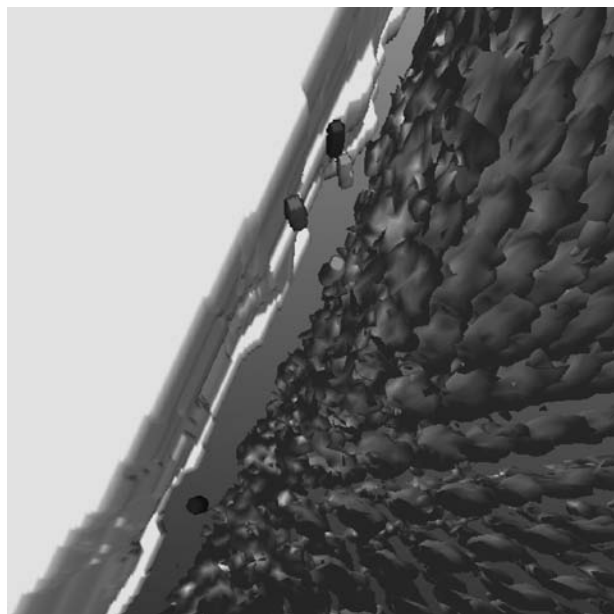


**Fig. 15** 3D reconstruction of the HfO<sub>2</sub>/SiO<sub>x</sub>/Si interface structure. The HfO<sub>2</sub> film is represented by bold yellow on the left while columns of Si atoms can (gold color) can be observed on the right. Five Hf atoms are reconstructed with black, green, blue, and red colors inside the interlayer (not color-coded). Source: Reprinted with permission from Ref.<sup>[42]</sup>.

annealing process owing to oxygen vacancy formation.<sup>[54,56]</sup> This ultimately creates states in the silicon band gap and can thus affect electron mobilities along or leakage across the gate channel.<sup>[56,57]</sup> The detection, identification and location of individual stray atoms and a fundamental understanding of their impact on the macroscopic materials properties is a critical aspect for the design and future application of functional nanomaterials.

## CONCLUSIONS AND FUTURE DIRECTIONS

In this entry, it was illustrated how aberration-corrected STEM can be applied for the characterization of a wide variety of nanostructured materials. The STEM represents an invaluable tool for the structural and chemical investigation of nanostructures using a variety of different imaging and spectroscopy tools. Aberration-correction has revolutionized electron microscopy by enabling the formation of electron probes with diameters well below 1 Å and enhanced depth sensitivity by reducing the depth of field. A resulting consequence is that STEM data can no longer be interpreted as a simple two-dimensional projection of a three-dimensional structure, but provides three-dimensional information with the ultimate sensitivity down to one single atom. Three different materials systems have been discussed here for which STEM techniques provided insights into atomic and electronic structures with heretofore unprecedented detail. Even

though many of the unanswered questions in the field of materials sciences can be addressed with lower resolution imaging capabilities than reported here, it is the sensitivity down to a single atom that is ultimately important and critical.

The availability of atomic resolution imaging and spectroscopy in combination with single atom sensitivities in all three dimensions stimulates a renewed interest in *in situ* capabilities. If it were possible to maintain the resolution limits on heating or cooling of the sample or changing the gas pressure and atmosphere during the experiments, new fundamental insights could be gained to understand critical processes in functional materials on the atomic length scale in their anticipated working environments. Such advances in electron microscopy will probably lead to an over-achievement of Feynman's request for a "better electron microscope."

## ACKNOWLEDGMENTS

Discussions with A.R. Lupini, A.Y. Borisevich, M.F. Chisholm, M.P. Oxley, Y. Peng, N.D. Gallego, S.N. Rashkeev, and S.T. Pantelides are gratefully acknowledged. This work was funded by the U.S. Department of Energy, Division of Scientific User Facilities (KvB) and Division of Materials Sciences and Engineering (SJP). Partial financial funding from the Alexander-von-Humboldt Foundation (KvB) is gratefully acknowledged.

## REFERENCES

1. Reimer, L. *Transmission Electron Microscopy*, 4th Ed.; Springer: Berlin, Heidelberg, New York, 1997.
2. Williams, D.B.; Carter, C.B. *Transmission Electron Microscopy*; Plenum Press: New York, USA, 1996 and London, UK.
3. [http://nobelprize.org/nobel\\_prizes/physics/laureates/1986/press.html](http://nobelprize.org/nobel_prizes/physics/laureates/1986/press.html); (accessed January 2008).
4. Knoll, M.; Ruska, E. Das Elektronenmikroskop. *Z. Physik* **1932**, *78*, 318–339.
5. Scherzer, O. Über einige Fehler von Elektronenlinsen. *Zeit. Phys.* **1936**, *101*, 593–603.
6. Feynman, R.P. There's plenty of room at the bottom. *Eng. Sci.* **1960**, *23*, 22–36.
7. Scherzer, O. Sphärische und kromatische Korrektur von Elektronen-Linsen. *Optik* **1947**, *2*, 114–132.
8. Rose, H. Correction of aberrations, a promising means for improving the spatial and energy resolution of energy-filtering electron microscopes. *Ultramicroscopy* **1994**, *56*, 11–25.
9. Potton, R.J. Reciprocity in optics. *Rep. Prog. Phys.* **2004**, *67*, 717–754.
10. Varela, M.; Lupini, A.R.; van Benthem, K.; Borisevich, A.Y.; Chisholm, M.F.; Shibata, N.; Abe, E.; Pennycook, S.J. Materials characterization in the aberration-corrected scanning transmission electron microscope. *Ann. Rev. Mater. Res.* **2005**, *35*, 539–569.
11. Born, M.; Wolf, E. *Principles of Optics*; Pergamon Press: Oxford, UK, 1980.
12. Dellby, N.; Krivanek, O.L.; Nellist, P.D.; Batson, P.E.; Lupini, A.R. Progress in aberration-corrected scanning transmission electron microscopy. *J. Electron Microscopy* **2001**, *50*, 177–185.
13. Krivanek, O.L.; Dellby, N.; Lupini, A.R. Towards sub-angstrom electron beams. *Ultramicroscopy* **1999**, *78*, 1–11.
14. [www.nion.com](http://www.nion.com) (accessed January 2008).
15. Rose, H. Outline of a spherically corrected semiplanatic medium-voltage transmission electron microscope. *Optik* **1990**, *85*, 19–24.
16. [www.ceos-gmbh.de](http://www.ceos-gmbh.de) (accessed January 2008).
17. Haider, M.; Rose, H.; Uhlemann, S.; Schwan, E.; Kabius, B.; Urban, K. A spherical-aberration-corrected 200 kV transmission electron microscope. *Ultramicroscopy* **1998**, *75*, 53–60.
18. O'Keefe, M.A.; Allard, L.F.; Blom, D.A. HRTEM imaging of atoms at sub-Ångstrom resolution. *J. Electron Microscopy* **2005**, *54*, 169–180.
19. Nellist, P.D.; Chisholm, M.F.; Dellby, N.; Krivanek, O.L.; Murfitt, M.F.; Szilagy, Z.S.; Lupini, A.R.; Borisevich, A.Y.; Sides, W.H.; Pennycook, S.J. Direct sub-Ångstrom imaging of a crystal lattice. *Science* **2004**, *305*, 1741.
20. Borisevich, A.Y.; Lupini, A.R.; Travaglini, S.; Pennycook, S.J. Depth sectioning of aligned crystals with the aberration-corrected scanning transmission electron microscope. *J. Electron Microscopy* **2006**, *55*, 7–12.
21. Wang, S.W.; Borisevich, A.Y.; Rashkeev, S.N.; Glazoff, M.V.; Sohlberg, K.; Pennycook, S.J.; Pantelides, S.T. Dopants adsorbed as single atoms prevent degradation of catalysts. *Nature Mater.* **2004**, *3*, 143–146.
22. van Benthem, K.; Lupini, A.R.; Kim, M.; Baik, H.S.; Doh, S.J.; Lee, J.-H.; Oxley, M.P.; Findlay, S.D.; Allen, L.J.; Pennycook, S.J. Three-dimensional imaging of individual hafnium atoms inside a semiconductor device. *Appl. Phys. Lett.* **2005**, *87*, 034104.
23. Borisevich, A.Y.; Lupini, A.R.; Pennycook, S.J. Depth-sectioning with the aberration-corrected scanning transmission electron microscope. *Proc. Natl. Acad. Sci.* **2006**, *103*, 3044–3048.
24. van Benthem, K.; Lupini, A.R.; Oxley, M.P.; Findlay, S.D.; Allen, L.J.; Pennycook, S.J. Three dimensional ADF imaging of individual atoms by through-focal series scanning transmission electron microscopy. *Ultramicroscopy* **2006**, *106*, 1062–1068.
25. Midgley, P.A.; Weyland, M. 3D electron microscopy in the physical sciences: the development of Z-contrast and EFTEM tomography. *Ultramicroscopy* **2003**, *96*, 413–431.
26. Arslan, I.; Yates, T.J.V.; Browning, N.D.; Midgley, P.A. *Science* **2005**, *309*, 2195–2198.
27. Sparrow, C.M. Spectroscopic resolving power. *Astrophys. J.* **1916**, *44*, 76–86.
28. den Dekker, A.J.; von den Bos, A. Resolution: a survey. *J. Opt. Soc. Am. A* **1997**, *14*, 547–557.

29. Lord Raleigh Investigations in optics, with special reference to the spectroscope. *Philos. Mag.* **1879**, *8*, 261–274, 403–411, 477–486.
30. David, E. An overview of advanced materials for hydrogen storage. *J. Mater. Process. Technol.* **2005**, *162/163*, 169.
31. Panella, B.; Hirscher, M.; Roth, S. Hydrogen adsorption in different carbon nanostructures. *Carbon* **2005**, *43*, 2209–2214.
32. Anson, A.; Lafuente, E.; Urriolabeitia, E.; Navarro, R.; Benito, A.M.; Maser, W.; Martinez, M.T. Hydrogen capacity of palladium-loaded carbon materials. *J. Phys. Chem. B* **2006**, *110*, 6643–6648.
33. Contescu, C.I.; Gallego, N.C.; Wu, X.; Tekinalp, H.L.; Edie, D.D.; Baker, F.S. Extended abstract to CARBON '07, International Carbon Conference, Seattle, WA, USA, July 15–20, 2007.
34. Wu, X.; Gallego, N.C.; Contescu, C.I.; Tekinalp, H.; Bhat, V.; Baker, F.S.; Thies, M.C.; Edie, D.D. The effect of processing conditions on microstructure of Pd-containing activated carbon fibers. *Carbon* **2008**, *46*, 54–61.
35. Tekinalp, H.L.; Cervo, E.; Edie, D.D.; Thies, M.C.; Contescu, C.I. *Extended abstract to CARBON '07*, International Carbon Conference, Seattle, WA, USA, July 15–20, 2007.
36. van Benthem, K.; Pennycook, S.J.; Contescu, C.I.; Gallego, N.D. in preparation.
37. Lupini, A.R.; Rashkeev, S.N.; Varela, M.; Borisevich, A.Y.; Oxley, M.P.; van Benthem, K.; Peng, Y.; de Jonge, N.; Veith, G.M.; Chisholm, M.F.; Pennycook, S.J. Scanning transmission electron microscopy. In *Nanocharacterization*; Kirkland, A.I., Hutchinson, J.L., Eds.; Royal Society of Chemistry: London, UK, 2007.
38. de la Casa-Lillo, M.A.; Lamari-Darkrim, F.; Cazorla-Amorós, D.; Linares-Solano, A. Hydrogen storage in activated carbons and activated carbon fibers. *J. Phys. Chem. B* **2002**, *106*, 10,930–10,934.
39. Zhao, X.; Villar-Rodil, S.; Fletcher, A.J.; Thomas, K.M. Kinetic isotope effect for H<sub>2</sub> and D<sub>2</sub> quantum molecular sieving in adsorption/desorption on porous carbon materials. *J. Phys. Chem. B* **2006**, *110*, 9947–9955.
40. Aga, R.S.; Fu, C.L.; Krčmar, M.; Morris, J.R. Theoretical investigation of the effect of graphite interlayer spacing on hydrogen absorption. *Phys. Rev. B* **2007**, *76*, 165404.
41. Lueking, A.D.; Yang, R.T. Hydrogen spillover onto carbon: Inference of spillover hydrogen on optimization for hydrogen storage. *Appl. Catal. A: General* **2004**, *265*, 259–268.
42. van Benthem, K.; Peng, Y.; Pennycook, S.J. Tomographic imaging of nanocrystals vs aberration-corrected scanning transmission electron microscopy. *Mat. Res. Soc. Symp. Proc.* **2005**, *839*, 3–8.
43. Hÿtch, M.J.; Stobbs, W.M. Quantitative comparison of high-resolution TEM images and image simulations. *Ultramicroscopy* **1994**, *53*, 191–203.
44. Huang, B.; Wang, W.; Bates, M.; Zhuang, X. Three-dimensional super-resolution imaging by stochastic optical reconstruction microscopy. *Science* **2008**: DOI: 10.1126/science.1153529.
45. Sutton, A.P.; Balluffi, R.W. *Interfaces in Crystalline Materials*; Clarendon Press: Oxford, UK, 1996.
46. Hoffmann, M.J.; Petzow, G.; Eds. *Tailoring of Mechanical Properties of Si<sub>3</sub>N<sub>4</sub> Ceramics*; NATO ASI Series E 267; Kluwer Acad. Publ.: Dordrecht, 1994.
47. Jin, S.; Tiefel, T.H.; McCormack, M.; Fastnacht, R.A.; Ramesh, R.; Chen, L.H. Thousandfold change in resistivity in magnetoresistive La-Ca-Mn-O films. *Science* **1994**, *264*, 413–415.
48. Triscone, J.-M.; Fischer, Ø. Rep. Superlattices of high-temperature superconductors: synthetically modulated structures, critical temperatures and vortex dynamics. *Prog. Phys.* **1997**, *60*, 1673–1721.
49. Moore, G. Cramming more components into integrated circuits. *Electronics* **1965**, 38.
50. Packan, P.A. Pushing the limits. *Science* **1999**, *285*, 2079–2081.
51. Semiconductor Industry Association. The National Technology Roadmap for Semiconductors 71–81, Sematech, Austin, TX, 1997.
52. Muller, D.A.; Sorsch, T.; Moccio, S.; Baumann, F.H.; Evans-Lutterodt, K.; Timp, G. The electronic structure at the atomic scale of ultra-thin gate oxides. *Nature* **1999**, *399*, 758–761.
53. van Benthem, K.; Rashkeev, S.N.; Pennycook, S.J. Atomic and electronic structure investigations of HfO<sub>2</sub>/SiO<sub>2</sub>/Si gate stacks using aberration-corrected STEM. *AIP Conf. Proc.* **2005**, *788*, 79–84.
54. van Benthem, K.; Pennycook, S. Imaging and spectroscopy of defects in semiconductors using aberration-corrected STEM. *Appl. Phys. A* **2008** (in press).
55. Corrigendum to reference 23, in preparation.
56. Bersuker, G.; Park, C.S.; Barnett, J.; Lysaght, P.S.; Kirsch, P.D.; Young, C.D.; Choi, R.; Lee, B.H.; Foran, B.; van Benthem, K.; Pennycook, S.J.; Lenahan, P.M.; Ryan, J.T. The effect of interfacial layer properties on the performance of Hf-based gate stack devices. *J. Appl. Phys.* **2006**, *100*, 094108.
57. Rashkeev, S.N.; van Benthem, K.; Pantelides, S.T.; Pennycook, S.J. Single Hf atoms inside the ultrathin SiO<sub>2</sub> interlayer between an HfO<sub>2</sub> dielectric film and the Si substrate: How do they modify the interface? *Microelectron. Eng.* **2005**, *80*, 416–419.

## BIBLIOGRAPHY

1. Peng, Y.; Oxley, M.P.; Lupini, A.R.; Chisholm, M.F.; Pennycook, S.J. Spatial resolution and information transfer in scanning transmission electron microscopy. *Microsc. Microanal.* **2008**, *14*, 36–47.



# Electronic Switches

Richard J. Nichols

David J. Schiffrin

Wolfgang Haiss

*Department of Chemistry, University of Liverpool, Liverpool, U.K.*

## INTRODUCTION

The fundamental building block of modern electronic circuits is the switching element, typically a transistor, which can be used to perform computational operations when assembled into digital circuits. The number of devices on such circuits, or chips, has increased at a staggering rate, even exceeding the expectations of Moore's law, which predicts a doubling in areal density of devices about every 2 years. Devices are now routinely manufactured with submicron precision using the top-down approaches of photolithography, masking, and etching to produce complex circuits in silicon. A contemporary microprocessor produced by such methodology can have in excess of 40 million transistors, and this figure is likely to grow at least in accordance with Moore's law in the next 5 to 10 years. However, can this phenomenon continue beyond then? Beyond that horizon, the further downsizing of silicon devices throws up some seemingly insurmountable problems. The cost of manufacturing devices approaching nanoscale dimensions using top-down methodologies may well be prohibitive, but physical as well as financial constraints may prevail. Semiconductor junctions and oxide barriers may not have satisfactory performance when minimized to nanometer dimensions. For instance, ultrathin oxide barriers leak charge, or semiconductor junctions may not exhibit sufficiently developed band structure. In addition, thermal dissipation is already a problem for state-of-the-art chips and these problems will become more difficult to solve as the areal density of silicon-based devices is increased.

Given these problems on the horizon of the silicon industries road map for future miniaturization, many believe that there should be a paradigm shift in the architecture of devices.<sup>[1]</sup> Such an approach would be the use of bottom-up methodology, in which molecular wires, nanoparticles, nanotubes, and other molecular structures are organized into functional units, using the methods of synthetic chemistry and self-assembly. Richard P. Feynman, in his classic talk, "There Is Plenty of Room at the Bottom," envisaged the development of nanotechnologies, and these bottom-up

methodologies may help us in understanding how this "room at the bottom" may be exploited.<sup>[2]</sup> Needless to say, the wiring, addressing, and organization of large-scale arrays of nanodevices will provide immense challenges. As a result, nanotechnology is more likely to first appear in hybrid technologies that integrate elements of nanometer devices with conventional micrometer technologies. Indeed, magnetic nanoparticles are already working their way into magnetic storage technologies.

## OVERVIEW

Recent years have seen a variety of often highly imaginative ways of fabricating chemically designed nanoscale components. This has been coupled with the development of techniques and devices in which electronic transport measurements can be made on molecular wires and nanostructures. It should be noted that this quest for practical nanodevices also yields important fundamental science on the behavior of mesoscopic aggregates of molecules and nanoparticles. Indeed, such an understanding is a requisite if functional nanodevices are to be exploited.

The most commonly featured building blocks for nanoscale devices include nanoparticles, carbon nanotubes, molecular "wires" and bridges, and redox molecules. In the following section, some of the basic architectures in which these units have been used for the construction of nanodevices with an electronic function will be reviewed.

## Nanoparticles and Quantum Dots

Nanometer-sized metallic or semiconductor particles are fundamental building blocks for the construction of electronic devices of nanometer dimensions. They can be used as the basis of single-electron information processing, in the attachment of molecular wires in forming ohmic or tunneling junctions, or they can be used to measure charge down to tiny fractions of an electron charge. Monolayer-capped clusters (MPCs)



have proven to be particularly attractive building blocks, in that they can be assembled into 2- or even 3-dimensional superlattices using the techniques of chemical self-assembly.<sup>[3–9]</sup> Such a self-assembled superlattice of Au nanoparticles with a narrow size distribution between 3 and 5 nm is shown in Fig. 1.<sup>[10]</sup> One particularly attractive feature of nanoparticles is the possibility of forming individual particles or even superlattices whose properties can be tuned through chemical control of the particles size, composition, and, in the case of superlattices, spacing.

Sub-10-nm particles lie in the interesting mesoscopic size range where unusual electronic, structural, and optical properties can arise because of their small size.<sup>[11,12]</sup> One interesting property that can be exploited is their unusual charging behavior for sufficiently small sizes. When the electrostatic charging energy for adding an electron to a nanoparticle sufficiently exceeds  $k_B T$ , then single-electron charging phenomena can be observed. This behavior could form the basis of a nanodevice capable of processing single electrons.

The electrostatic energy ( $E_{es}$ ) required to charge a nanoparticle of capacitance  $C$  by one electron is given by

$$E_{es} = \frac{e^2}{C}$$

The condition for observing single-electron tunneling behavior at room temperature is  $e^2/C > k_B T = 26$  meV, where  $k_B$  is the Boltzmann constant. Single-electron tunneling phenomena have now been observed in a wide range of nanostructures at both low and room temperature. Examples include nanosized metal islands, nanoparticles and monolayer-capped

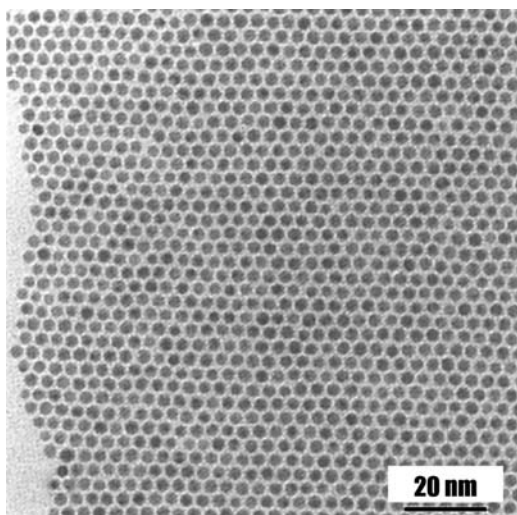


**Fig. 1** Transmission electron microscopy image of a hexagonal raft of alkanethiol-derivatised gold nanoparticles, with a narrow size distribution between 3 and 5 nm. *Source:* From Ref.<sup>[10].)</sup>

nanoparticles on supports,<sup>[13–15]</sup> single metal or semiconducting nanocrystals placed between closely spaced metallic or semiconducting leads<sup>[16,17]</sup> and even kinked carbon nanotubes placed between contacts.<sup>[18]</sup> Single-electron tunneling for these nanoscopic systems has been measured using a variety of methods. Nanocrystals, both metallic and semiconducting, have been anchored through molecular spacers.<sup>[19,20]</sup> Typically dithiol-based self-assembling monolayers have been used to anchor nanoparticles to well-defined surfaces, as illustrated in Fig. 2.<sup>[20]</sup> Tunneling through such devices has been monitored using a scanning tunneling microscope (STM). In one such configuration using  $\sim 1.8$ -nm Au clusters and aryl dithiol self-assembled monolayers (SAMs) ( $\alpha$ ,  $\alpha'$ -xylyldithiol and 4,4'-biphenyldithiol) single-electron tunneling phenomena were observed.<sup>[20,21]</sup> For these measurements, localized  $I$ - $V$  responses were recorded with the STM tip positioned above the nanoparticle. The observation of current steps as the voltage is swept is a clear indication of Coulomb staircase behavior. This system can be modeled as a double junction: The Au surface–nanoparticle and nanoparticle–tip junctions can then be simplified as a coupled parallel RC circuit 1 and 2, as illustrated in Fig. 2.<sup>[20]</sup> The parameters  $R_1$ ,  $R_2$ ,  $C_1$ ,  $C_2$ , and  $Q_0$  (the fractional charge on the cluster) may be obtained with the standard semiclassical model of the Coulomb blockade. Single-electron tunneling for such nanoparticle system can be tuned by adjusting the RC junctions that connect the nanoparticle to the external circuits or by adjusting the particle size.<sup>[22–24]</sup>

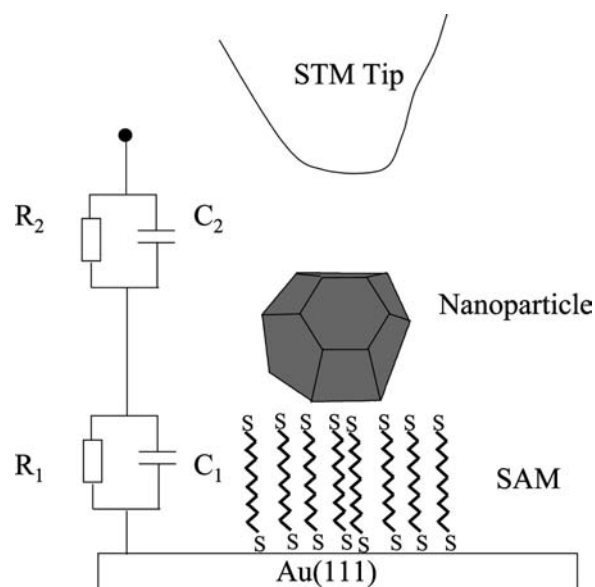


**Fig. 2** Schematic diagram illustrating the STM measurement of Coulomb blockade behavior of a nanoparticle adsorbed onto a self-assembled monolayer of alkane-dithiol. The equivalent electrical circuit is shown on the left. *Source:* From Ref.<sup>[20].)</sup>

Other device structures have been used to monitor single-electron phenomena in nanostructures. Individual nanoparticles have been placed between two metallic leads created by mechanically forming break junctions in one approach, shown in Fig. 3.<sup>[16]</sup> This enables the isolation of individual nanostructures between metallic contacts for analysis of their electrical properties. In another approach, ensembles of nanoparticles have been sandwiched between electrodes covered with insulating dielectric layers.<sup>[25]</sup> Both approaches have enabled determination of single-electron transistor (SET) behavior at low temperature.

Another approach to observing single-electron tunneling phenomena has been to create quantum dots (QDs), which are typically confined semiconducting islands.<sup>[11]</sup> Semiconducting QDs have been produced using modern semiconductor fabrication techniques. For example, it has been possible to sandwich 10-nm-thick GaAs films between AlGaAs barrier layers. Electrons can be confined in movement within and parallel to these GaAs “quantum wells.” By placing electrostatic gates above and below the structure, electrons are confined laterally as well to create “quantum dots.” Electron transport to and from these QDs is governed by quantum mechanical phenomena and can be probed by monitoring the gate voltages at which individual electrons can be added successively to the dot. Great sensitivity could be achieved by probing the admittance changes with a 100 kHz a.c. signal as the d.c. gate voltage is changed. Spikes in the a.c.

admittance represent individual electrons entering the quantum dot.<sup>[11]</sup> Another particularly interesting feature of semiconducting QDs is the ability to control their electronic structure by tuning their size. However, even clusters of metal atoms, when sufficiently small and at sufficiently low temperatures, start to lose the characteristic electronic band structure of the metallic state in the size range between 1 and 4 nm and start to form discrete energy levels, which are determined by quantum physical phenomena.

This sensitivity of either quantum dots or nanoparticle-based structures shows the ability of these devices to record single-electron events, opening the possibility of electronic devices for processing single electrons. The energy for single-electron events increases as the device size is shrunk, clearly emphasizing the importance of developing reliable nanofabrication methods if SETs are to be practically implemented.

### Molecular Wires and Switches

The use of molecules as components to assemble electrical devices is an idea that has attracted many researchers since the subject was conceptually broached by Aviram and Ratner in 1974.<sup>[26]</sup> More recently, methods have become available to connect individual molecules between contacts and measure their electrical behavior.<sup>[27–31]</sup> Molecules have been attached to metallic probes through a variety of end groups including sulfur, selenium, tellurium, and isonitrile.<sup>[32]</sup> Molecules assembled into structures in such a way have been termed “molecular wires.” This term, wire, may be appropriate to thin metallic rods or conductive carbon nanotubes that exhibit an ohmic behavior arising from an extended band structure. However, as pointed out by Whitesides, the term “molecular wire” is misleading when describing the electrical properties of molecular devices because it implies metallic or ohmic conductivity, whereas electron transport through molecules is often far from ohmic.<sup>[33]</sup> Indeed, it is the non-linear electrical behavior of molecules that is of interest if they are to take up the function of electrical components such as switches, diodes, transistors, or logic gates.

Measuring and theoretically understanding the non-linear electrical behavior of molecules is a central question in molecular electronics.<sup>[34–38]</sup> Although there is a very long and extensive history of both theoretically and experimentally studying electron transfer processes, it is only more recently that electron transport across defined molecular films has been realized and still more recently that single molecule contacts and electrical measurements have been established.<sup>[27–31]</sup> A detailed understanding of charge transport through molecular films and single molecules is mandatory if

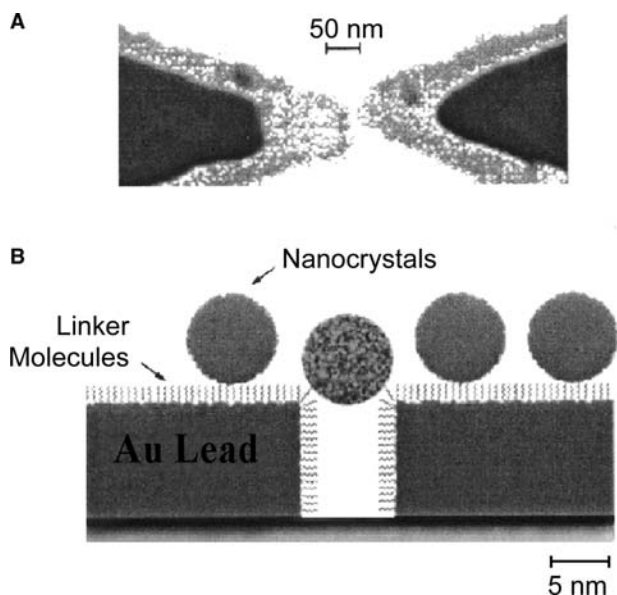


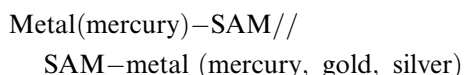
**Fig. 3** (A) A field electron microscopy image of the two leads and gap before the nanoparticles are introduced. (B) A schematic illustration of the immobilization of nanoparticles through dithiol linker molecules to the leads. *Source:* From Ref.<sup>[16]</sup>.

molecules are to be integrated into devices. Pioneering work in molecular electronics was conducted by Mann and Kuhn, who studied transport through molecular films.<sup>[39]</sup> More recently, electron transport across well-defined SAMs with redox active species at a fixed distance from the metal electrode surfaces has been studied by electrochemical means.<sup>[40]</sup> In these experiments, the rate of electron transfer from the electrode surface for redox active species such as ferrocene has been measured as a function of length and nature of the bridge. For simple alkanethiol monolayers, this rate has been found to depend exponentially on the thickness of the molecular layer, following a simple tunneling relationship:

$$I = I_0 e^{-\beta d}$$

where  $\beta$  is the attenuation factor, which depends on the medium in the tunneling gap between the contacts.

More recently, solid-state junctions have been formed by sandwiching two self-assembled monolayers between metal electrodes to give a junction of the form:



By using this approach,  $\beta$  was found to be structure dependent, with values of  $0.87 \pm 0.1 \text{ \AA}^{-1}$  for alkanethiols and  $0.6 \pm 0.1 \text{ \AA}^{-1}$  for oligophenylene thiols. These values for the attenuation factor can be rationalized in terms of tunneling theories, which are well developed for molecules in solution of the kind D–B–A, where electrons can be shuttled across a molecular bridge (B) from donor (D) to acceptor (A). This is somewhat analogous to a molecular bridge between two metal leads in which the donor and acceptor states take the place of the leads. The rate of electron transfer is determined by the coupling between donor and acceptor wave functions, and one of the simplest models for describing the distance dependence is superexchange. In this scheme electronic coupling is through high energy states in the bridge groups, which cause the electronic wave functions to fall off more slowly than if D and A were separated by vacuum, hence lowering  $\beta$ . However, it is also well recognized that the tunneling electrons may interact and strongly couple with nuclear degrees of freedom of the bridge molecules.<sup>[41]</sup> In superexchange there is only weak coupling and the electron transport can be envisaged as a “wavelike” electronic flow. On the other hand, the electron transfer may be sequential, in which it is best described by two or more consecutive electronic transitions. It is clear then that nuclear relaxation and thermal dissipation in the molecular bridge can play a determining role in the charge transport.

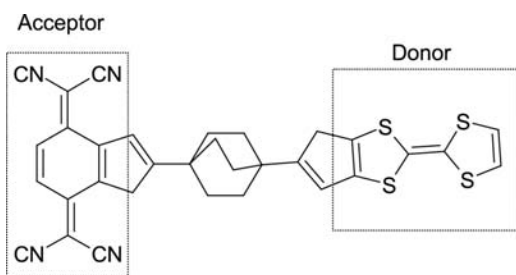
Another factor of importance in determining charge transport through a molecular bridge between two

metal leads is the degree of coupling between the metal contacts and the molecule, which will depend in a sensitive manner on the bonding between the molecule and the junction, the position of the Fermi level of the contacts, and the molecular and electronic structure of the bridging molecule. The variation of the electrochemical potential across the molecular bridge is also of significance. For instance, if the complete potential drop occurs solely at the interface between the molecule and the metal contacts, the electronic structure of the molecule is expected to be only slightly perturbed by the voltage drop. On the other hand, if a significant fraction of the voltage drop occurs across the molecule then electron transport across the molecule can be very sensitive to the profile of local electrochemical potential along the length of the bridge.

The direct measurement of the electronic factor  $\beta$  and hence the “conductivity” of individual molecules recently has been made possible with the development of the scanning probe microscope.<sup>[27–31]</sup> In experiments conducted by the group of Lindsay, molecules have been embedded into an insulating layer of thiol molecules attached to a gold electrode.<sup>[27–30]</sup> The molecules were then connected to gold nanoparticles so that a molecular bridge was formed between the gold electrode and the nanoparticle. Tunneling currents were measured with a conducting AFM probe by making direct electrical contact between the tip and nanoparticle. Values of  $\beta$  for alkanethiol molecule of about  $0.8 \text{ \AA}^{-1}$  have been obtained, as compared to  $2 \text{ \AA}^{-1}$  for vacuum tunneling. Both these single-molecule measurements and the measurements of electron transport across alkanethiol SAMs show the reduction in the electronic factor for tunneling across the alkanethiol bridge.

However, reduction of  $\beta$  alone in a molecule bridging two contacts is not sufficient for the generation of non-linear devices such as nanoscale switches. The involvement of molecular levels, charge trapping, or asymmetric contact geometries can all promote a non-linear response. In 1974, Aviram and Ratner predicted that molecules could act as diodes based on their non-linear electrical response.<sup>[26]</sup> They theoretically predicted rectification for the molecular system shown in [Scheme 1](#) on the basis of electron tunneling mediated through acceptor lowest unoccupied molecular orbitals (LUMO) and donor highest occupied molecular orbital (HOMO) levels of the donor–acceptor system. Because substantially larger threshold voltage was expected for alignment of the levels under negative bias than positive bias, an asymmetric  $I$ – $V$  response and, hence, rectification was expected.

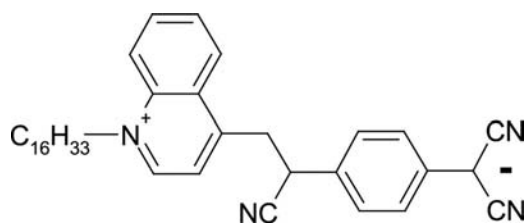
Metzger et al. have made Langmuir–Blodgett (LB) films of the donor–acceptor molecule shown in [Scheme 2](#).<sup>[42]</sup> The LB films were sandwiched between aluminum electrodes and electrical measurements



Scheme 1

demonstrated strong rectification, Fig. 4A. The rectification may be explained in the schematic model shown in Fig. 4B.<sup>[42,43]</sup> This model shows electron transfer under forward and reverse bias. The asymmetry in the  $I$ - $V$  behavior arises from the orientation of the donor-acceptor molecule in between the electrodes and intramolecular electron transfer within the molecule, as illustrated in Fig. 4B. Intervalence transfer (IVT) favors current flow in the forward bias direction, while it impedes it in the reverse bias direction. Although these experiments have been performed on extended LB films, they show the potential for the use of molecules in switching devices, where the rectifying behavior can be tuned by the electronic and molecular structure of orientated molecules.

More recently Chen et al. have shown that highly non-linear  $I$ - $V$  behavior can be achieved in molecular devices.<sup>[44,45]</sup> They self-assembled  $\sim 1000$  molecular wires containing nitroamine redox centers in a micro-fabricated device that could be used to measure conductivity of the monolayer.<sup>[45]</sup> A schematic representation of the nitroamine-based molecules used in the monolayers and their reduction is shown in Fig. 5A.  $I$ - $V$  responses of the device at 60 K shows negative differential resistance (NDR) with an on-off peak-to-valley ratio (PVR) of about 1000:1, as shown in Fig. 5B. This switching is attributed to the one-electron reduction of the molecule to the radical anion, which provides a conductive state for electron transfer across the molecular bridge.<sup>[45]</sup> A further increase in voltage leads to a second reduction to form the dianion, which is insulating, switching the device off. The authors note that the NDR switching could have



Scheme 2

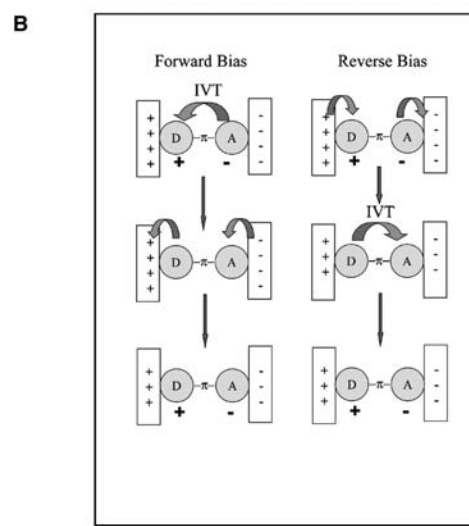
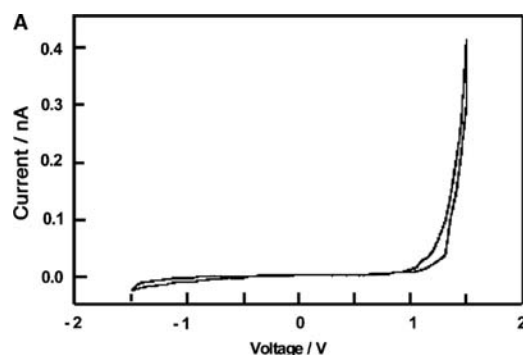


**Fig. 4** (A) An  $I$ - $V$  curve for a Langmuir-Blodgett film of the donor-acceptor molecule shown in Scheme 2 sandwiched between two aluminum electrodes. These electrical measurements demonstrate strong rectification.<sup>[42,43]</sup> (B) A model for electrical transport through and rectification by the donor-acceptor molecule (D- $\pi$ -A). Source: From Ref.<sup>[42]</sup>

numerous applications in either two- or three-terminal electronic devices.<sup>[45]</sup>

Redox active molecules can also be incorporated into nanoscale devices and “wired” to nanometer-sized metal particles. Gittins et al. noted that films consisting of 6-nm-sized Au nanoparticles and redox active viologen dithiol molecules can exhibit current rectification when assembled onto gold electrode surfaces.<sup>[46–48]</sup> This observation was noted when recording rates of electron transfer through such films using electrochemical methods. They have further shown that these redox active molecules can be wired to nanoparticles in individual nanostructures as illustrated in Fig. 6.<sup>[47]</sup> Recent measurements have shown that a double tunneling structure is formed between the redox active viologen center isolated in the middle of an insulating molecular wire and the gold contacts on either end of the molecule. This work shows the potential for incorporation of highly reversible redox couples into nanometer-sized tunneling devices.

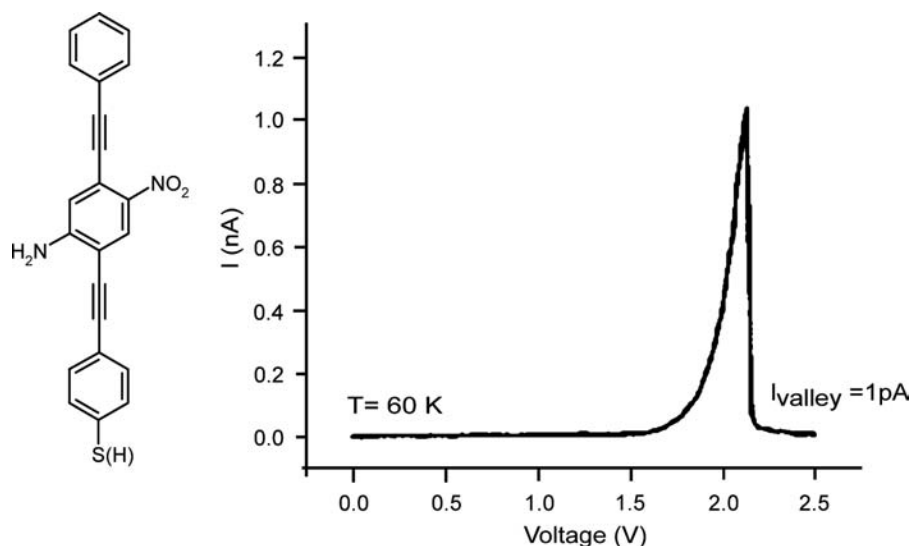


**Fig. 5** (A) Schematic representation of the nitroamine-based molecules used in the monolayers of the molecular device showing NDR. (B)  $I$ - $V$  responses of the device at 60 K. *Source:* From Ref.<sup>[45]</sup>.

Although two-terminal connections to molecules can be used to create devices with rectifying or NDR behavior, the three-terminal transistor is the fundamental element of modern integrated circuit technology. Several studies have shown how nanometer-sized objects, such as CdSe nanocrystals<sup>[49]</sup> or carbon nanotubes,<sup>[18,50–52]</sup> can be functional elements in field-effect transistors, with these nanostructures being tethered between two contact leads and a third semiconductor gate underlying an insulating SiO<sub>2</sub> layer. However, reliable direct wiring of three or more metallic contacts to an individual molecule is certainly more tricky because it requires close proximity of at least three leads. Clearly, these contacts would have

to be of nanometer dimensions to accommodate the size of target molecules. Proposed multicontact-point molecules have been suggested that rely on thiol (or thioacetate)-based end groups, which form the relatively strong gold–thiolate bond. A three-terminal molecular device proposed by Wada is shown in Fig. 7.<sup>[43,53,54]</sup> Thiol groups attach the molecule to three gold electrodes that form the source, drain, and gate, respectively. These are individually linked by polythiophene-based molecular wires to an oligothiophene “dot,” which is isolated from the molecular wires by methylene spacers. However, the challenge exists to build, interconnect, and test junctions of this kind.

These selected examples show that great advances have been made in a relatively short period of time in the fabrication of molecular devices and in understanding electron transport across them. Great heterogeneity has been displayed in the electrical behavior ranging from ohmic to highly nonlinear responses. Molecular and electronic structure can be varied in a sensitive manner through organic synthesis and reactions can be scaled up to synthesize large quantities. However, some formidable challenges remain, including the need to arrange molecular devices in large, interconnected arrays that can be individually addressed.

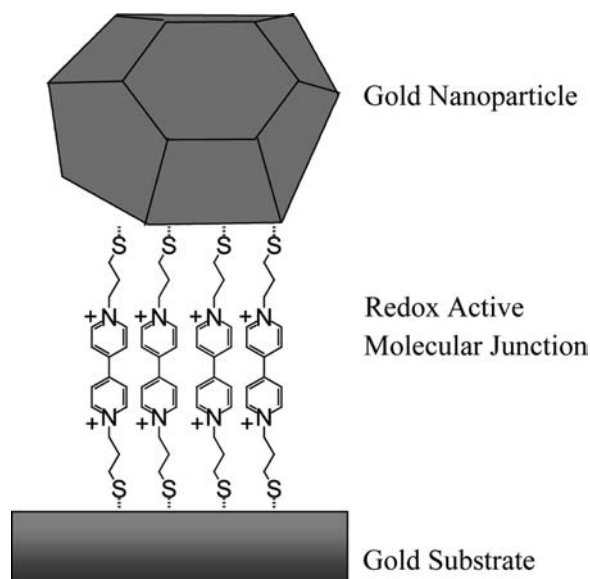


**Fig. 6** A schematic representation of a nanoscale device consisting of Au nanoparticles and redox active viologen dithiol molecules. *Source:* From Refs.<sup>[46–48]</sup>.

### Carbon Nanotubes

Like metal or semiconducting nanoparticles, carbon nanotubes show promise as versatile components in the molecular electronics toolbox and in the construction of nanoscale switches.<sup>[18,51,55–60]</sup> Carbon nanotubes can be envisaged as sheets of graphite that have been rolled up into a seamless cylinder.<sup>[56,59]</sup> Both single-walled carbon nanotubes (SWCNTs) and

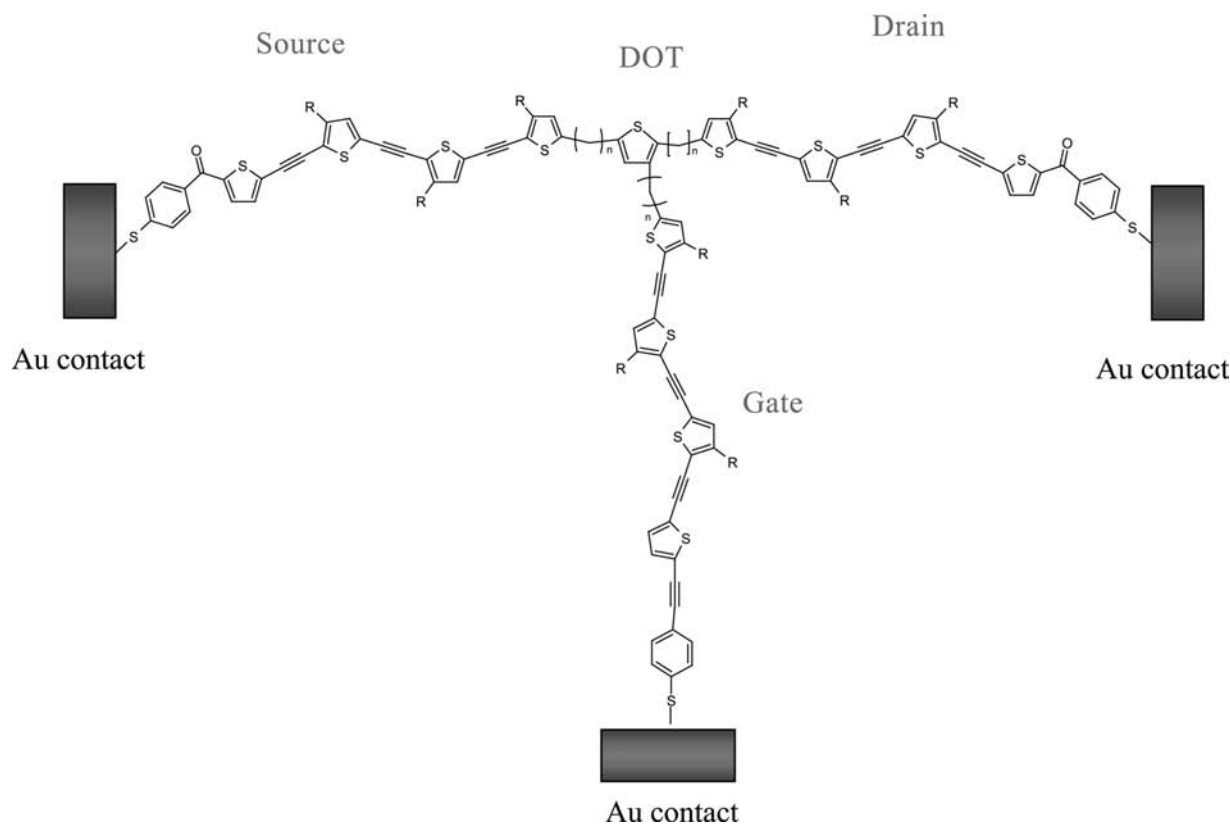


**Fig. 7** A nanoscale switching device proposed by Wada,<sup>[43,53,54]</sup> with thiol groups forming contacts to three gold pads that form the source, drain, and gate, respectively. Each arm of the molecular device is individually linked by polythiophene-based molecular wires to an oligothiophene “dot,” which is isolated from the molecular wires by methylene spacers. *Source:* From Ref.<sup>[53]</sup>.

multiwalled carbon nanotubes (MWCNT) can be produced, in the later case with diameters exceeding 50 layers.<sup>[60–62]</sup> SWCNTs are defined by a chirality vector whose indices  $(n, m)$  are given by the folding of the graphene sheet into a cylinder.<sup>[56,59,60]</sup> In an  $(n, m)$  nanotube the beginning and end of an  $(n, m)$  lattice vector in the graphene plane join together. An extended graphene sheet is metallic in six wave vector directions; however, for SWCNTs it is also necessary to consider the confinement of electrons around the tubes' circumference. On analysis, it is found that when  $n = m$  or  $n - m = 3i$  (where  $i$  is an integer) the tubes are metallic, whereas when  $n - m \neq 3i$ , the tubes are semiconducting. Thus, by tuning the diameter and the wrapping angle the conductivity can be altered in a sensitive manner. Another feature of the electronic structure of metallic SWCNTs is the confinement of electrons, which allows motion along only two directions of  $k$  space, making them model 1-D conductors. An important consequence of this is the reduced probability for carrier scattering. This combined with their high heat conductance and bond stability allows them to carry extremely high current densities ( $\sim 10^8$ – $10^9$  A/cm<sup>2</sup>), well above that of a metal, which would suffer severe electromigration at these current levels.<sup>[63]</sup>

Carbon nanotubes also have exceptional tensile strength and rigidity, making them good candidates for molecular wires and nanoscale electronic devices. Disadvantages include difficulty in selective synthesis of particular SWCNTs and formation of contacts and junctions with, for instance, nanoparticles or electrical leads. In the absence of scattering, ideally the resistance of a perfectly conductive ballistic nanotube connected to metal leads should be about  $h/4e^2 = 6.5$  k $\Omega$ .<sup>[59,63]</sup> This resistance is a quantum mechanical contact resistance caused by a mismatch in the number of conduction channels of the metallic SWCNT ( $N = 2$ ) and the relatively huge number of conduction channels in the metal leads.<sup>[59]</sup> However, other types of contact resistance can dominate the electrical transport of carbon nanotubes. Poor metal–nanotube contacts, in the form of interfacial barriers, or poor coupling between the CNTs and leads, led in some early transport measurements to high resistance values in the order of megaohms. However, these high contact resistances, much larger than the resistance quantum, when coupled with the sufficiently low capacitance of long SWCNTs provide good conditions for the observation of single-electron charging or Coulomb blockade behavior at sufficiently low



temperatures. Coulomb blockage behavior has been observed for micron-long nanotubes at liquid helium temperatures. Low-contact-resistance junctions between SWCNTs and metallic leads have also been achieved, approaching in some cases the quantum mechanical contact resistance. Resistances as low as  $12\text{ k}\Omega$  have been recorded for  $3\text{-}\mu\text{m}$ -long SWCNTs contacted by Ti electrodes evaporated onto the nanotubes.<sup>[60]</sup>

Three-terminal switching devices exhibiting transistor behavior have been fabricated in a number of ways from carbon nanotubes. Semiconducting carbon nanotubes have been incorporated into a device illustrated in the inset in Fig. 8.<sup>[60]</sup> The carbon nanotube is contacted at both ends by metal electrodes that form the source and drain. A highly doped and conducting silicon gate electrode is separated from the nanotube by a sufficiently thick insulating silicon oxide layer. The source–drain current across such a nanotube device as a function of gate voltages is shown in Fig. 8. This  $I\text{-}V_{\text{gate}}$  curve shows that by applying a sufficiently positive gate voltage the nanotube can be switched from a conducting to an insulating state.<sup>[60]</sup> The p-type behavior of these nanotubes results in hole depletion at positive gate voltages where the device is switched off.

Recently a novel approach has been adopted for fabricating single-electron devices from individual carbon nanotubes.<sup>[18]</sup> The concept used is to create a nanoscale “electron trap” within a double tunneling junction, similar to the approach used for QDs, but in this case individual metallic single-wall carbon

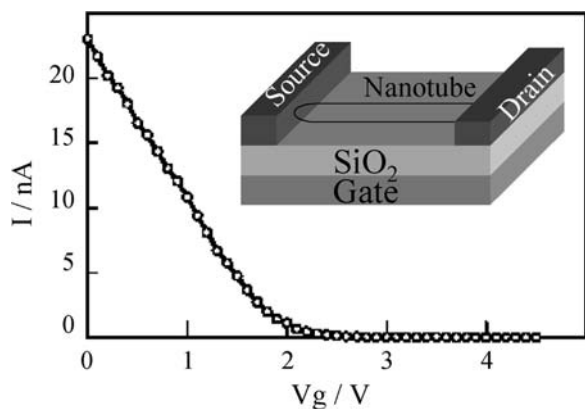


**Fig. 8** The inset shows a “transistor” based on semiconducting carbon nanotubes.<sup>[60]</sup> The carbon nanotube is contacted at both ends by metal electrodes that form the source and drain, respectively. A highly doped and conducting silicon gate electrode is separated from the nanotube by a sufficiently thick insulating silicon oxide layer. The graph shows the source–drain current across such a nanotube device as a function of gate voltage. This  $I\text{-}V_{\text{gate}}$  curve shows that by applying a sufficiently positive gate voltage the nanotube can be switched from a conducting to an insulating state. *Source:* From Ref.<sup>[60]</sup>.

nanotubes form the basis of the structure. An AFM image of the structure is shown in Fig. 9.<sup>[18]</sup> A double kink is introduced into the nanotube by mechanical manipulation with an atomic force microscope. The double kink induces two local barriers, leading to an “island” within the nanotube, which is connected at both ends to two metal terminals. This whole structure is assembled on top of a Si/SiO<sub>2</sub> substrate to provide a three-terminal device. Energy of 120 meV has been recorded for single-electron addition, rendering this a functional single-electron transistor device at room temperature with operation akin to a field-effect transistor.

In constructing complex logic systems it is necessary to create large arrays of devices and to interconnect them into a network. Rueckes et al. have indicated one possible way by which this might be achieved.<sup>[64]</sup> It is proposed that semiconducting SWCNTs are arranged into a parallel array with a set of perpendicular nanotubes suspended above them on a periodic array of supports, as illustrated in Fig. 10. The two sets of arrays consist of p- and n-doped carbon nanotubes, respectively. The nanotubes serve two functions; they form the wires as well as the individual devices. Device elements are at points where the wires cross. By applying a transient voltage between the respective CNTs the wires can be switched from being separated by a gap (“OFF”) to touching (“ON”) where the conductivity is higher.<sup>[64]</sup> The voltage pulse causes charging of the semiconducting nanotubes, resulting in attractive electrostatic forces and contact between the tubes. The OFF state with separation of the tubes can be regenerated by application of a restorative current transient. The operation of this electromechanical

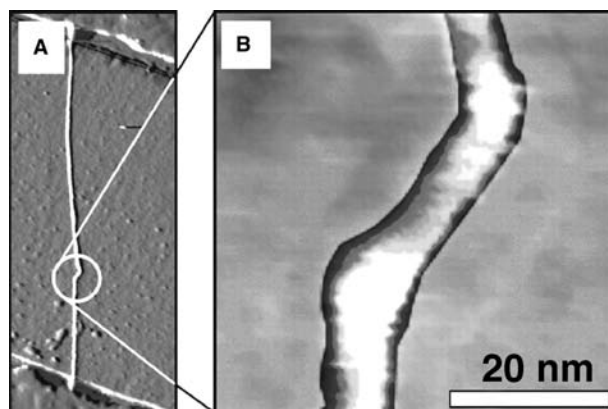


**Fig. 9** An AFM image of a double kink introduced into a carbon nanotube by mechanical manipulation with the tip. This structure forms a nanoscale “electron trap” within the double tunneling junction created by the kink. This whole structure is assembled on top of a Si/SiO<sub>2</sub> substrate to provide a three-terminal device with single-electron transistor behavior at room temperature. *Source:* From Ref.<sup>[18]</sup>.

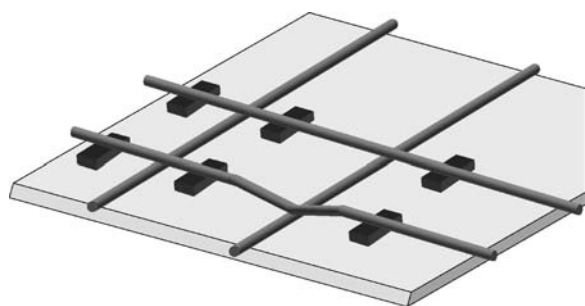


**Fig. 10** A schematic representation showing four junctions between two parallel pairs of carbon nanotubes. The bottom right junction is ON, with both nanotubes touching, while the other three junctions are OFF. The lower tubes lie directly on a thin dielectric layer (e.g.,  $\text{SiO}_2$ ), which is itself on top of a conducting layer (e.g., highly doped silicon). The upper nanotubes are suspended above the substrate by periodic supports (dark gray blocks). Each nanotube is contacted at the end (contacts not shown). *Source:* From Ref.<sup>[64]</sup>.

switch relies on the excellent mechanical properties of the SWCNT, which can withstand the high strain. Measurements demonstrating the principle of operation have been made on a single pair of crossed SWCNTs assembled into position through mechanical manipulation. This switching device showed a 10 times current difference between ON and OFF states for reversible operation and this was increased to  $10^5$  for irreversible operation. This shows how nanoscale switching elements can be interconnected through molecular scales wires, with operation of individual elements in an array of switches through the application of voltage pulses at the ends of respective wires. This integrated approach to nanoscale electronics shows a promising way forward, although great challenges still exist in the fabrication and addressing of reliable and sufficiently large arrays.

### Molecular Actuators

Another approach to electronic switching at the nanoscale level has been to exploit changes in the electronic structure of molecules that accompany major conformation or orientational changes. A molecular actuator

has been constructed around bistable catenane-based molecules.<sup>[65–67]</sup> Oxidation and subsequent reduction of this molecule induces the circumrotation of the molecule shown in Fig. 11, which forms the basis of the device. Fabrication is achieved by anchoring the catenane-based single monolayers with amphiphilic phospholipid counterions and sandwiching this between an n-type silicon electrode and a Ti/Al counter electrode. Oxidation of the molecular structure at +2.0 V opens the switch, while subsequent reduction at –2.0 V closes it. Reading was performed at between 0.1 and 0.3 V and the switch could be recycled many times. Although the solid-state devices used for examining the electrical properties were macroscopic, the bistable switching is, in theory, scalable to the nanoscale because it is based on defined molecular events.

Joachim and Gimzewski have demonstrated another approach by which large and reversible changes in effective conductance of a single molecule could be achieved.<sup>[68,69]</sup> The active element of their device was a single  $\text{C}_{60}$  molecule, which was compressed between the tip and a Cu(111) surface. They found that the conductance of  $\text{C}_{60}$  molecule increased by more than two orders of magnitude with increasing tip pressure.<sup>[69]</sup> The origin of the increase is perturbation of the tails of the LUMO and HOMO of the  $\text{C}_{60}$  molecule resulting from structural deformation. They used this as a basis of a single-molecule “electromechanical amplifier” demonstrating an amplification factor of 5, and as such showing another method by which nanoscale structures might be used as switching elements.<sup>[69]</sup>

Changes in the orientation of molecules at surfaces could also be used for devices based on conductance switching. Donhauser et al. have observed with an STM the stochastic reorientation of single and bundled phenylene ethynylene oligomers isolated in matrices of relatively nonconducting alkanethiolate monolayers.<sup>[70]</sup> The inserted molecules were observed to undergo reorientation or reconfiguration from a state that exhibited low contrast to one with high contrast in the STM. This bistability between the ON and OFF states exhibited a stochastic behavior with persistence times ranging from seconds to tens of hours.

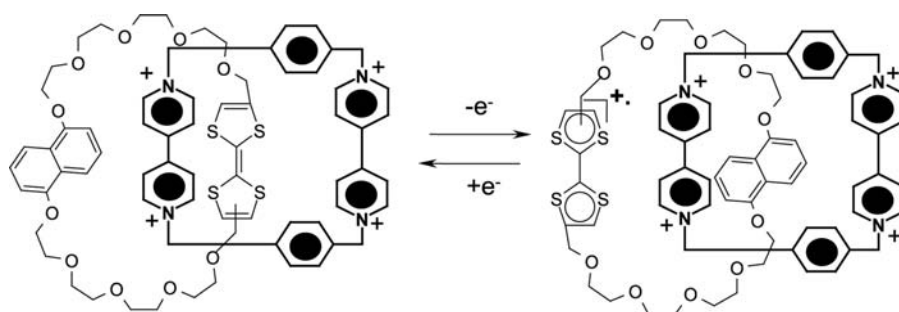


**Fig. 11** Molecular structures of the two conformers forming the basis of a bistable device. The switching is based on the voltage-actuated circumrotation of co-conformer  $[\text{A}^0]$  to co-conformer  $[\text{B}^+]$ . *Source:* From Ref.<sup>[66]</sup>.

Recently, Haiss et al. have demonstrated that molecular reorientation and accompanying large conductivity changes can be driven by an electric field between an STM tip and a gold surface.<sup>[71]</sup> This conductance switching was achieved for viologen dithiol molecules and is illustrated in Fig. 12. In their flat-lying state, molecular layers of viologen dithiol (Fig. 12A and B) have subnanometer thickness. However, reorientation can be used to bridge distances between conductors of over 3 nm and the molecular bridges formed provide the switch ON high-conduction state (the formation of one “molecular bridge” is shown in Fig. 12B). The reorientation is induced by

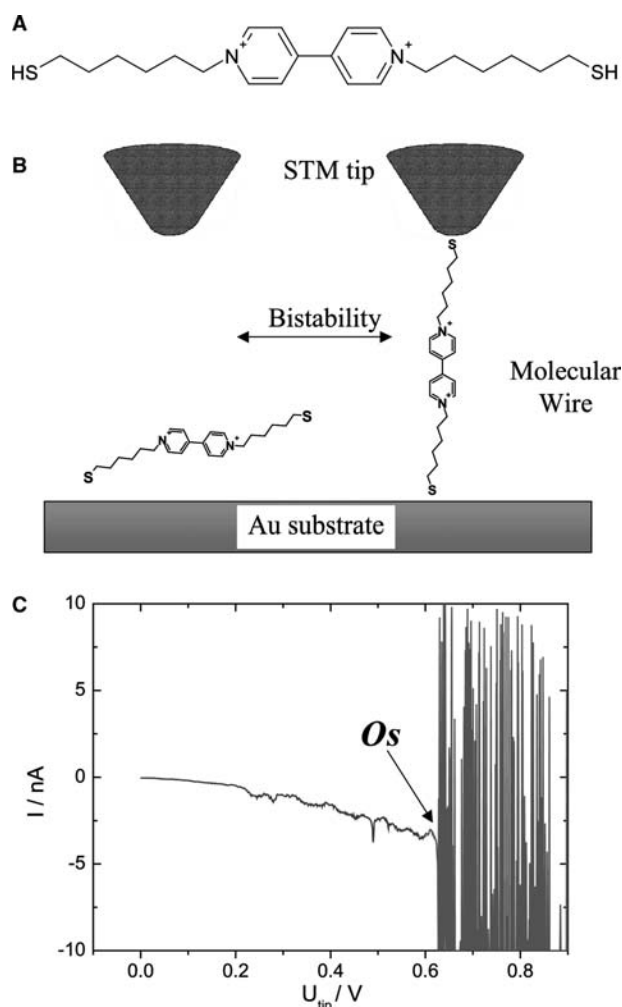


**Fig. 12** (A) Molecular structure of 6V6. (B) The bistability exhibited for 6V6 results from flipping between a flat-lying adsorbed phase and a vertically oriented phase in which the molecule bridges the gap between the Au substrate and the STM tip provide a higher conductivity path. (C) Current vs. tip voltage as measured in the STM configuration shown in (B). Oscillation occurs at  $U_{\text{tip}} > 0.6$  V and results from the formation and cleavage of molecular wires between the STM tip and substrate. *Source:* From Refs.<sup>[31,71]</sup>

the electric field between the STM tip and the substrate and results in oscillatory behavior at sufficiently high bias where a large number of molecules in the gap ( $\geq 20$ ) may partake.<sup>[31,71]</sup> It has been proposed that the oscillatory behavior results from thermal effects, where the molecular wires break following inelastic tunneling at a threshold voltage and subsequently reform after cooling in a cyclic process. This ON–OFF oscillatory switching behavior and the resulting a.c. signal measured at high fields could form the basis of a novel bistable device.

## CONCLUSION

A great deal has been learned in recent years about the manipulation, assembly, and properties of devices with nanoscale dimensions. In particular, there are a growing number of architectures in which molecular wires, nanotubes, nanoparticles, and quantum dots have been assembled into structures that can perform basic switching functions. The methods of chemical synthesis, self-organization, and self-assembly, as well as state-of-the-art microfabrication techniques have all played a role in the fabrication of such structures.

It is clear that substantial work lies ahead before nanofabricated devices could work their way into any practical electronic device. However, a great deal of new physics that underlies the behavior of mesoscopic structures has been learned from studying the properties of such systems and other nanofabricated devices. Notable examples include insights into the rich quantum mechanical behavior of electrons in quantum dots, quantification of thermal conductance in nanodevices, and a further understanding of charge transport through molecular wires. This demonstrates the contribution to the understanding of basic science that has been achieved in the quest for functional nanostructures.

## ACKNOWLEDGMENTS

We thank EPSRC for financial support under the Nanoscale Switch-Project, grant GR/R07684/01.

## REFERENCES

1. Lieber, C.M. The incredible shrinking circuit—researchers have built nanotransistors and nanowires. Now they just need to find a way to put them all together. *Sci. Am.* **2001**, 285, 58–64.
2. <http://www.zyvex.com/nanotech/feynman.html>.

3. Hostetler, M.J.; Murray, R.W. Colloids and self-assembled monolayers. *Curr. Opin. Colloid Interface Sci.* **1997**, *2*, 42–50.
4. Green, S.J.; Stokes, J.J.; Hostetler, M.J.; Pietron, J.; Murray, R.W. Three-dimensional monolayers: nanometer-sized electrodes of alkanethiolate-stabilized gold cluster molecules. *J. Phys. Chem., B* **1997**, *101*, 2663–2668.
5. Brust, M.; Walker, M.; Bethell, D.; Schiffrin, D.J.; Whyman, R. Synthesis of thiol-derivatized gold nanoparticles in a 2-phase liquid–liquid system. *J. Chem. Soc., Chem. Commun.* **1994**, 801–802.
6. Brust, M.; Fink, J.; Bethell, D.; Schiffrin, D.J.; Kiely, C. Synthesis and reactions of functionalized gold nanoparticles. *J. Chem. Soc., Chem. Commun.* **1995**, 1655–1656.
7. Bethell, D.; Brust, M.; Schiffrin, D.J.; Kiely, C. From monolayers to nanostructured materials: an organic chemist's view of self-assembly. *J. Electroanal. Chem.* **1996**, *409*, 137–143.
8. Schiffrin, D.J.; Brust, M.; Horswell, S.; Baum, T.; Bethell, D. Electrochemistry of nanostructured systems. *Abstr. Pap. - Am. Chem. Soc.* **1998**, *215*, 126-COLL.
9. Korgel, B.A.; Fitzmaurice, D. Condensation of ordered nanocrystal thin films. *Phys. Rev. Lett.* **1998**, *80*, 3531–3534.
10. Fink, J.; Kiely, C.J.; Bethell, D.; Schiffrin, D.J. *Institute of Physics Conference Series, Electron Microscopy and Analysis 1997*; 1997; 601–604.
11. Ashoori, R.C. Electrons in artificial atoms. *Nature* **1996**, *379*, 413–419.
12. Schmid, G. The role of big metal clusters in nanoscience. *J. Chem. Soc., Dalton Trans.* **1998**, 1077–1082.
13. Amman, M.; Field, S.B.; Jaklevic, R.C. Coulomb-blockade spectroscopy of gold particles imaged with scanning-tunneling-microscopy. *Phys. Rev., B* **1993**, *48*, 12,104–12,109.
14. Schonberger, C.; Vanhouten, H.; Donkersloot, H.C. Single-electron tunneling observed at room-temperature by scanning-tunneling microscopy. *Europhys. Lett.* **1992**, *20*, 249–254.
15. Hartmann, E.; Marquardt, P.; Ditterich, J.; Radojkovic, P.; Steinberger, H. Characterization and utilization of the context-dependent physical properties of nanoparticles for nanostructures investigated by scanning tunneling microscopy. *Appl. Surf. Sci.* **1996**, *107*, 197–202.
16. Klein, D.L.; McEuen, P.L.; Katari, J.E.B.; Roth, R.; Alivisatos, A.P. An approach to electrical studies of single nanocrystals. *Appl. Phys. Lett.* **1996**, *68*, 2574–2576.
17. Guo, L.J.; Leobandung, E.; Chou, S.Y. A silicon single-electron transistor memory operating at room temperature. *Science* **1997**, *275*, 649–651.
18. Postma, H.W.C.; Teepen, T.; Yao, Z.; Grifoni, M.; Dekker, C. Carbon nanotube single-electron transistors at room temperature. *Science* **2001**, *293*, 76–79.
19. Banin, U.; Cao, Y.W.; Katz, D.; Millo, O. Identification of atomic-like electronic states in indium arsenide nanocrystal quantum dots. *Nature* **1999**, *400*, 542–544.
20. Andres, R.P.; Bein, T.; Dorogi, M.; Feng, S.; Henderson, J.I.; Kubiak, C.P.; Mahoney, W.; Osifchin, R.G.; Reifenberger, R. “Coulomb staircase” at room temperature in a self-assembled molecular nanostructure. *Science* **1996**, *272*, 1323–1325.
21. Andres, R.P.; Datta, S.; Dorogi, M.; Gomez, J.; Henderson, J.I.; Janes, D.B.; Kolagunta, V.R.; Kubiak, C.P.; Mahoney, W.; Osifchin, R.F.; Reifenberger, R.; Samanta, M.P.; Tian, W. Room temperature Coulomb blockade and Coulomb staircase from self-assembled nanostructures. *J. Vac. Sci. Technol., A, Vac. Surf. Films* **1996**, *14*, 1178–1183.
22. Hanna, A.E.; Tinkham, M. Variation of the Coulomb staircase in a 2-junction system by fractional electron charge. *Phys. Rev., B* **1991**, *44*, 5919–5922.
23. Amman, M.; Wilkins, R.; Benjacob, E.; Maker, P.D.; Jaklevic, R.C. Analytic Solution for the current–voltage characteristic of 2-mesoscopic tunnel-junctions coupled in series. *Phys. Rev., B* **1991**, *43*, 1146–1149.
24. Wang, B.; Wang, H.Q.; Li, H.X.; Zeng, C.G.; Hou, J.G.; Xiao, X.D. Tunable single-electron tunneling behavior of ligand-stabilized gold particles on self-assembled monolayers. *Phys. Rev., B* **2001**, *6303*.
25. Markovich, G.; Leff, D.V.; Chung, S.W.; Soyez, H.M.; Dunn, B.; Heath, J.R. Parallel fabrication and single-electron charging of devices based on ordered, two-dimensional phases of organically functionalized metal nanocrystals. *Appl. Phys. Lett.* **1997**, *70*, 3107–3109.
26. Aviram, A.; Ratner, M.A. Molecular rectifiers. *Chem. Phys. Lett.* **1974**, *29*, 277
27. Cui, X.D.; Primak, A.; Zarate, X.; Tomfohr, J.; Sankey, O.F.; Moore, A.L.; Moore, T.A.; Gust, D.; Harris, G.; Lindsay, S.M. Reproducible measurement of single-molecule conductivity. *Science* **2001**, *294*, 571–574.
28. Lindsay, S.M. Single molecule electronics and tunneling in molecules. *Jpn. J. Appl. Phys. Part 1, Regul. Pap. Short Notes Rev. Pap.* **2002**, *41*, 4867–4870.
29. Cui, X.D.; Primak, A.; Zarate, X.; Tomfohr, J.; Sankey, O.F.; Moore, A.L.; Moore, T.A.; Gust, D.; Nagahara, L.A.; Lindsay, S.M. Changes in the electronic properties of a molecule when it is wired into a circuit. *J. Phys. Chem., B* **2002**, *106*, 8609–8614.
30. Cui, X.D.; Zarate, X.; Tomfohr, J.; Sankey, O.F.; Primak, A.; Moore, A.L.; Moore, T.A.; Gust, D.; Harris, G.; Lindsay, S.M. Making electrical contacts to molecular monolayers. *Nanotechnology* **2002**, *13*, 5–14.
31. Haiss, W.; Nichols, R.J.; Higgins, S.J.; Bethell, D.; Hobenreich, H.; Schiffrin, D.J. Wiring nanoparticles with redox molecules. *Faraday Discuss.* **2003**, *125*, *in press*.
32. Tour, J.M. Molecular electronics. Synthesis and testing of components. *Accounts Chem. Res.* **2000**, *33*, 791–804.
33. Rampi, M.A.; Whitesides, G.M. A versatile experimental approach for understanding electron transport through organic materials. *Chem. Phys.* **2002**, *281*, 373–391.
34. Tian, W.D.; Datta, S.; Hong, S.H.; Reifenberger, R.; Henderson, J.I.; Kubiak, C.P. Conductance spectra of molecular wires. *J. Chem. Phys.* **1998**, *109*, 2874–2882.
35. Stokbro, K.; Taylor, J.; Brandbyge, M.; Mozos, J.L.; Ordejon, P. Theoretical study of the nonlinear conductance of di-thiol benzene coupled to Au[111] surfaces via thiol and thiolate bonds. *Comput. Mater. Sci.* **2003**, *27*, 151–160.

36. Ness, H.; Fisher, A.J. Quantum inelastic conductance through molecular wires. *Phys. Rev. Lett.* **1999**, *83*, 452–455.
37. Burin, A.L.; Berlin, Y.A.; Ratner, M.A. *Molecular Electronics II*; 2002; Vol. 960, 240–247.
38. Emberly, E.; Kirczenow, G. Electrical conductance of molecular wires. *Nanotechnology* **1999**, *10*, 285–289.
39. Mann, B.; Kuhn, H. Tunneling through fatty acid salt monolayers. *J. Appl. Phys.* **1971**, *42*, 4398.
40. Chidsey, C.E.D. Free-energy and temperature-dependence of electron-transfer at the metal–electrolyte interface. *Science* **1991**, *251*, 919–922.
41. Kuznetsov, A.M.; Ulstrup, J. *Electron Transfer in Chemistry and Biology: An Introduction to the Theory*; Wiley: Chichester, 1999.
42. Metzger, R.M.; Chen, B.; Hopfner, U.; Lakshminantham, M.V.; Vuillaume, D.; Kawai, T.; Wu, X.L.; Tachibana, H.; Hughes, T.V.; Sakurai, H.; Baldwin, J.W.; Hosch, C.; Cava, M.P.; Brehmer, L.; Ashwell, G.J. Unimolecular electrical rectification in hexadecylquinolinium tricyanoquinodimethanide. *J. Am. Chem. Soc.* **1997**, *119*, 10,455–10,466.
43. Carroll, R.L.; Gorman, C.B. The genesis of molecular electronics. *Angew. Chem., Int. Ed.* **2002**, *41*, 4379–4400.
44. Chen, J.; Wang, W.; Reed, M.A.; Rawlett, A.M.; Price, D.W.; Tour, J.M. Room-temperature negative differential resistance in nanoscale molecular junctions. *Appl. Phys. Lett.* **2000**, *77*, 1224–1226.
45. Chen, J.; Reed, M.A.; Rawlett, A.M.; Tour, J.M. Large on–off ratios and negative differential resistance in a molecular electronic device. *Science* **1999**, *286*, 1550–1552.
46. Gittins, D.I.; Bethell, D.; Nichols, R.J.; Schiffrin, D.J. Redox-connected multilayers of discrete gold particles: a novel electroactive nanomaterial. *Adv. Mater.* **1999**, *11*, 737–740.
47. Gittins, D.I.; Bethell, D.; Schiffrin, D.J.; Nichols, R.J. A nanometre-scale electronic switch consisting of a metal cluster and redox-addressable groups. *Nature* **2000**, *408*, 67–69.
48. Gittins, D.I.; Bethell, D.; Nichols, R.J.; Schiffrin, D.J. Diode-like electron transfer across nanostructured films containing a redox ligand. *J. Mater. Chem.* **2000**, *10*, 79–83.
49. Klein, D.L.; Roth, R.; Lim, A.K.L.; Alivisatos, A.P.; McEuen, P.L. A single-electron transistor made from a cadmium selenide nanocrystal. *Nature* **1997**, *389*, 699–701.
50. Bachtold, A.; Hadley, P.; Nakanishi, T.; Dekker, C. Logic circuits with carbon nanotube transistors. *Science* **2001**, *294*, 1317–1320.
51. Tans, S.J.; Verschueren, A.R.M.; Dekker, C. Room-temperature transistor based on a single carbon nanotube. *Nature* **1998**, *393*, 49–52.
52. Martel, R.; Schmidt, T.; Shea, H.R.; Hertel, T.; Avouris, P. Single- and multi-wall carbon nanotube field-effect transistors. *Appl. Phys. Lett.* **1998**, *73*, 2447–2449.
53. Wada, Y. A prospect for single molecule information processing devices. *Pure Appl. Chem.* **1999**, *71*, 2055–2066.
54. Wada, Y. Proposal of atom/molecule switching devices. *J. Vac. Sci. Technol., A, Vac. Surf. Films* **1999**, *17*, 1399–1405.
55. Robertson, N.; McGowan, C.A. A comparison of potential molecular wires as components for molecular electronics. *Chem. Soc. Rev.* **2003**, *32*, 96–103.
56. Ouyang, M.; Huang, J.L.; Lieber, C.M. Fundamental electronic properties and applications of single-walled carbon nanotubes. *Accounts Chem. Res.* **2002**, *35*, 1018–1025.
57. Collins, P.C.; Arnold, M.S.; Avouris, P. Engineering carbon nanotubes and nanotube circuits using electrical breakdown. *Science* **2001**, *292*, 706–709.
58. Avouris, P. Molecular electronics with carbon nanotubes. *Accounts Chem. Res.* **2002**, *35*, 1026–1034.
59. Avouris, P. Carbon nanotube electronics. *Chem. Phys.* **2002**, *281*, 429–445.
60. Dai, H.J. Carbon nanotubes: opportunities and challenges. *Surf. Sci.* **2002**, *500*, 218–241.
61. McEuen, P.L. Single-wall carbon nanotubes. *Phys. World* **2000**, *13*, 31–36.
62. Schonenberger, C.; Forro, L. Multiwall carbon nanotubes. *Phys. World* **2000**, *13*, 37–41.
63. Yao, Z.; Kane, C.L.; Dekker, C. High-field electrical transport in single-wall carbon nanotubes. *Phys. Rev. Lett.* **2000**, *84*, 2941–2944.
64. Rueckes, T.; Kim, K.; Joselevich, E.; Tseng, G.Y.; Cheung, C.L.; Lieber, C.M. Carbon nanotube-based nonvolatile random access memory for molecular computing. *Science* **2000**, *289*, 94–97.
65. Pease, A.R.; Jeppesen, J.O.; Stoddart, J.F.; Luo, Y.; Collier, C.P.; Heath, J.R. Switching devices based on interlocked molecules. *Accounts Chem. Res.* **2001**, *34*, 433–444.
66. Collier, C.P.; Mattersteig, G.; Wong, E.W.; Luo, Y.; Beverly, K.; Sampaio, J.; Raymo, F.M.; Stoddart, J.F.; Heath, J.R. A 2 catenane-based solid state electronically reconfigurable switch. *Science* **2000**, *289*, 1172–1175.
67. Collier, C.P.; Jeppesen, J.O.; Luo, Y.; Perkins, J.; Wong, E.W.; Heath, J.R.; Stoddart, J.F. Molecular-based electronically switchable tunnel junction devices. *J. Am. Chem. Soc.* **2001**, *123*, 12,632–12,641.
68. Joachim, C.; Gimzewski, J.K. A nanoscale single-molecule amplifier and its consequences. *Proc. IEEE* **1998**, *86*, 184–190.
69. Joachim, C.; Gimzewski, J.K. An electromechanical amplifier using a single molecule. *Chem. Phys. Lett.* **1997**, *265*, 353–357.
70. Donhauser, Z.J.; Mantoosh, B.A.; Kelly, K.F.; Bumm, L.A.; Monnell, J.D.; Stapleton, J.J.; Price, D.W.; Rawlett, A.M.; Allara, D.L.; Tour, J.M.; Weiss, P.S. Conductance switching in single molecules through conformational changes. *Science* **2001**, *292*, 2303–2307.
71. Haiss, W.; van Zalinge, H.; Nichols, R.J.; Higgins, S.J.; Bethell, D.; Hobenreich, H.; Schiffrin, D.J. *Unpublished results.*

# Enantioselectivity on Surfaces

David M. Rampulla

Andrew J. Gellman

Department of Chemical Engineering, Carnegie Mellon University,  
Pittsburgh, Pennsylvania, U.S.A.

## INTRODUCTION

Chirality is a critical property of amino acids that form proteins, the building blocks of life, and of DNA, which encodes the genetic traits passed from one generation to the next. Furthermore, chirality can be observed throughout nature in objects ranging from spiral seashells to the human hands. If an object and its mirror image are non-superimposable, then they have the property of chirality. This property is found in nearly every biological molecule and in many synthetic bioactive molecules such as pharmaceuticals and agrochemicals. From a practical perspective, the importance of molecular chirality arises from the fact that the two mirror images of a chiral molecule, known as enantiomers, can have vastly different physiological impacts when ingested by living organisms. As a result, it is necessary to produce many chiral compounds in enantiomerically pure form.<sup>[1]</sup> Understanding chirality and enantioselectivity is critical to the development of the separations and reactions used to achieve enantiopurity.

Many processes used in chemical production involve solid surfaces and can be made enantioselective by using chiral surfaces. There are three common types of chiral surfaces: surfaces modified by chiral organic adsorbates, surfaces of any naturally chiral bulk crystalline solid, and chiral surfaces prepared from achiral bulk crystals. A number of studies have shown that such chiral surfaces exhibit enantiospecific properties when exposed to chiral species in either the gas phase or in solution. Although chirality is simply a symmetry property of an object or an extended lattice, the enantiospecificity of surfaces is derived from the local structure of nanoscale features such as molecular adsorbates, or specific arrangements of atoms at a crystal surface. Experimental and theoretical work to elucidate the properties of these nanostructured surfaces is an active area of research in surface chemistry. Although a number of aspects of the enantioselectivity of chiral surfaces are now understood, many unanswered questions remain as topics of ongoing research in the field.

## CHIRALITY OF MOLECULES, SOLIDS, AND SURFACES

The simplest molecules exhibiting chirality are those containing a carbon atom tetrahedrally coordinated to four different substituents. Such molecules are not superimposable on their mirror images. Fig. 1 shows the tetrahedral arrangement of a simple, chiral carbon-centered molecule. The handedness of a chiral center or carbon atom is denoted *R* for rectus (right-handed) or *S* for sinister (left-handed) based on a convention conceived by Cahn, Ingold, and Prelog.<sup>[2]</sup> Biologically relevant molecules can be very complex and tend to have multiple chiral centers. Although possession of one or more tetrahedral carbon atoms having four different substituents is sufficient to render a molecule chiral, it is not a necessary condition. Chiral centers can also exist in molecular structures such as allenes ( $R'RC=CR'R$ ) and *trans*-cycloalkenes, which do not have tetrahedrally coordinated carbon atoms as their chiral centers.

Chirality can arise in crystalline solids because either the unit cell is chiral, or the basis of an achiral unit cell is chiral. Examples of the former case include all solids based on monoclinic unit cells. Examples of the latter case could be crystals of enantiomerically pure compounds. Of the 230 space groups into which all crystals can be classified, 65 are chiral.<sup>[3]</sup> Because mirror planes, inversion centers, and glide planes in crystal structures render them achiral, the chiral space groups can only contain screw axes and rotational axes as symmetry elements.

Surfaces can have structures that are chiral in the sense that they are non-superimposable on their mirror images. One of the most common and versatile approaches to preparing a chiral surface is to adsorb an enantiomerically pure chiral compound onto the surface of an otherwise achiral substrate (Fig. 2A). The mere presence of such a chiral modifier or template renders the surface chiral. The second obvious class of chiral surfaces is those produced by cleaving any solid having a chiral bulk structure. Many oxides have chiral bulk structures and thus expose chiral



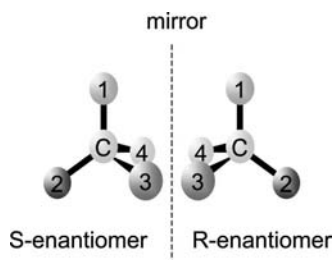


**Fig. 1** The mirror images of chiral molecules are not superimposable on each other, thus simple molecules based on tetrahedrally coordinated carbon atoms with four different substituents are chiral.

surfaces (Fig. 2B). Although it is somewhat counterintuitive, it is also possible to create chiral surfaces from crystalline solids with achiral bulk structures. Metals have either face-centered cubic (fcc), body-centered cubic (bcc), or hexagonal close-packed (hcp) bulk structures, all of which are achiral. Nonetheless, many of their high Miller index surfaces have monoclinic lattices and thus are chiral. The fcc(643) surface shown in Fig. 2C is composed of terrace–step–kink features, which render it chiral. On all three types of chiral surfaces, the features that give rise to chirality have nanometer dimensions. This nanostructure is critical to their utility in enantioselective chemistry. In order for adsorbate–surface interactions to be enantiospecific, the length scale of the chiral structures on the surface must roughly match the length scale of the chiral features of the adsorbed molecule.

## IMPORTANCE OF CHIRAL SURFACES

The two enantiomers of a chiral compound are structurally related simply by mirror symmetry and, thus,

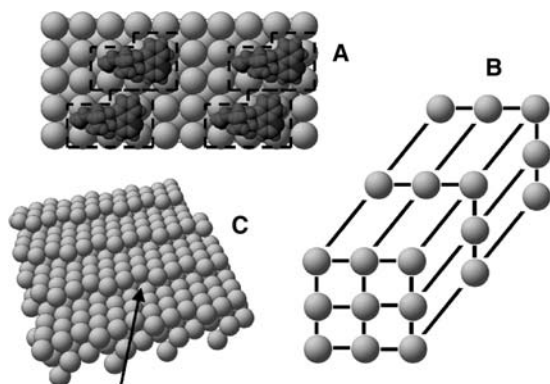


**Fig. 2** Chiral surfaces: (A) modification of an achiral surface with chiral organic molecules renders the surface chiral; (B) cleavage of bulk chiral solids exposes surfaces with chiral structures; and (C) cleavage of an achiral fcc metal along a high Miller index plane generates a surface with chiral kinks.

enantiomerically pure compounds have bulk properties such as density, melting point, heat of phase change, etc. that are truly identical. The properties of two enantiomers are only differentiated in a chiral environment and, in particular, in a chiral environment in which the length scale of the chiral features is on the nanoscale matching molecular dimensions. Living organisms constitute chiral environments because the proteins that perform most biochemical functions in living organisms are chiral and exist as single enantiomers. As a result, the physiological impact of the two enantiomers of a chiral compound will be different. Appreciation of this fact could have prevented one of the greatest tragedies in medical history. In the late 1950s, the chiral drug thalidomide was administered as a racemic mixture (equimolar concentrations of both enantiomers) to pregnant women to abate morning sickness and to act as a general sedative. Unfortunately, only the *R*-enantiomer has the desired therapeutic effect whereas the *S*-enantiomer is a teratogen and caused birth defects in thousands of infants born in that period of time.<sup>[4]</sup> As a consequence of this problem and related issues associated with the use of many chiral pharmaceuticals, the production of enantiomerically pure drugs has grown to be a large concern for the pharmaceutical industry. The current market for enantiomerically pure pharmaceuticals is estimated to be in excess of US\$100 billion per year.<sup>[5]</sup>

As a result of the fact that the physical properties of the two enantiomers of chiral compounds are identical, most chemical syntheses lead to the production of equimolar or racemic mixtures of both enantiomers. If one desires an enantiomerically pure product, the racemic mixture must be separated. The separation of mixed products of a chemical synthesis is commonplace and can be achieved by a number of means; however, the separation of racemic mixtures is very difficult. The most common separation methods exploit differences in physical properties such as boiling point, melting point, or density; however, in achiral environments, these properties are identical for two enantiomers. Separation of racemic mixtures must be performed in chiral environments that differentiate the properties of the two enantiomers. For example, mixing two enantiomers  $R_1$  and  $S_1$  with a single enantiomer of a second chiral compound ( $R_2$ ) can result in the formation of diastereomeric complexes  $R_1R_2$  and  $S_1R_2$  (molecules with more than one chiral center that are not mirror images). These complexes are not enantiomers of one another and thus can be separated by exploiting differences in their physical properties.<sup>[6]</sup> Once the two complexes are separated,  $R_2$  can be removed and separated to produce pure samples of  $R_1$  and  $S_1$ . The desired enantiomer can then be used, whereas the undesired enantiomer is either discarded or, if possible, racemized and subjected to further

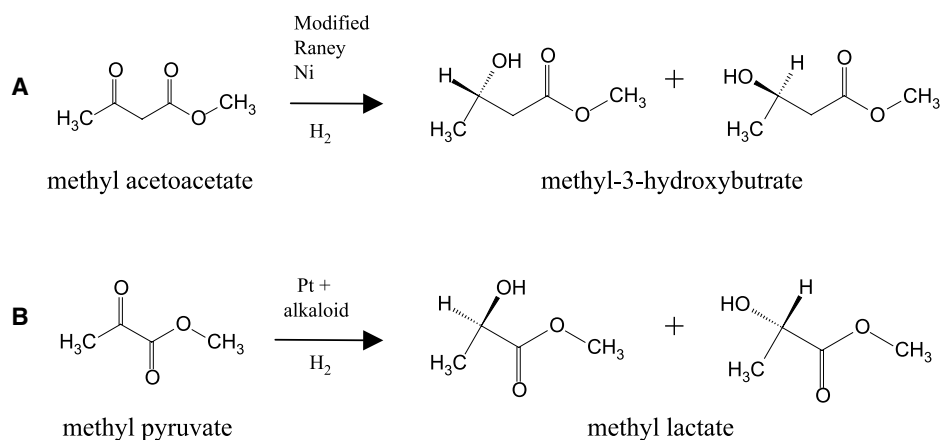


**Fig. 3** The asymmetric hydrogenations of methyl acetoacetate on Ni (A) and methyl pyruvate on Pt (B) are the two most widely studied enantioselective reactions catalyzed by chirally templated surfaces.

enantioselective purification by complexation with  $R_2$ .<sup>[6]</sup> The point is that the addition of the pure enantiomer  $R_2$  to the racemic mixture constitutes the creation of a chiral environment in which  $R_1$  and  $S_1$  can be separated.

Most enantiomerically pure substances are formed by homogeneous syntheses and then separated using techniques such as the aforementioned creation of diastereomers. Direct enantiospecific syntheses or simpler separation methods would, of course, be preferable. Many such processes, including heterogeneous catalyses and chromatographic separations, are commonly performed using solid surfaces. The types of chiral surfaces that are the subject of this entry have many potential applications in enantiospecific chemical processing.

## TYPES OF CHIRAL SURFACES

Three types of nanostructured chiral surfaces will be described in this entry: those produced by chiral templating with an organic ligand, surfaces derived from chiral bulk structures, and those produced from achiral bulk structures such as metals. In all three cases, the length scale of the chiral features is that of nanometers and thus they can interact enantiospecifically with chiral adsorbates.

### Surfaces Templated with Chiral Organic Modifiers

The adsorption of enantiomerically pure chiral molecules on achiral surfaces yields surfaces that are chiral, provided that the adsorbed molecule retains its chirality. Such surfaces can be used for enantioselective heterogeneous catalysis<sup>[7,8]</sup> or enantioselective chromatography.<sup>[9,10]</sup> The most successful chirally templated, enantioselective heterogeneous catalyst has been Ni templated with tartaric acid, which is used for the asymmetric hydrogenation of  $\beta$ -ketoesters and Pt templated with cinchonidine used for hydrogenation of  $\alpha$ -ketoesters (see

Fig. 3). Many of the underlying issues encountered with these catalysts are common to other template/substrate systems, so this section will focus on these two examples.

### Hydrogenation of $\beta$ -ketoesters on nickel

The enantioselective hydrogenation of  $\beta$ -ketoesters on chirally templated Raney Ni catalysts has been reviewed extensively by Izumi.<sup>[11]</sup> Most works have used Raney Ni and nickel powder as catalysts; however, some have used Ni particles supported on high-surface-area materials such as silica and alumina.<sup>[12]</sup> These catalysts have demonstrated enantioselectivity for the hydrogenation of methyl acetoacetate to methyl-3-hydroxybutyrate, yielding enantiomeric excesses as high as  $ee = 95\%$ .<sup>[13]</sup>

The enantioselectivity of the catalytic hydrogenation of  $\beta$ -ketoesters is influenced by the nature of the Ni used as the catalyst, by the nature of the chiral modifier, and, in some cases, by the nature of a comodifier. In addition to tartaric acid, which has been shown to be the most promising modifier,  $\alpha$ -amino acids have been used. The superiority of tartaric acid is believed to arise from its ability to stereospecifically orient the reacting  $\beta$ -ketoesters on the surface via hydrogen bonding.<sup>[14]</sup> One model has been suggested to explain the enantioselectivity in which chiral five-member chelate rings are formed by the bonding of the tartaric acid to Ni through a carboxylate oxygen atom and the oxygen atom of the  $\beta$ -hydroxyl group.<sup>[15]</sup>

In addition to the nature of the chiral modifier, another factor that determines the enantioselectivity of Ni-based catalysts is the size of the Ni particles. During the modification process of the Ni particles, tartaric acid has been shown to selectively dissolve catalyst particles with diameters less than 2 nm. The tartaric acid creates the pores that contain the hydrogenation sites, and the longer a particle is leached, the more pores it will have. This supports earlier results showing that larger nickel particles yield higher enantioselectivity.<sup>[15–17]</sup>

Comodifiers can also influence the enantioselectivity of chirally templated surfaces. Typically, NaBr is used as the comodifier and is thought to poison the racemic sites, reaction sites that have no enantioselective bias for hydrogenation, thus increasing the net enantiomeric excess.<sup>[18]</sup> However, it has also been proposed that the NaBr modifies the stereochemistry of the product-determining surface complex between the reactant and the chiral template.<sup>[19]</sup>

### Hydrogenation of $\alpha$ -ketoesters on platinum

The most highly studied enantioselective reaction over a chirally modified heterogeneous catalyst is the

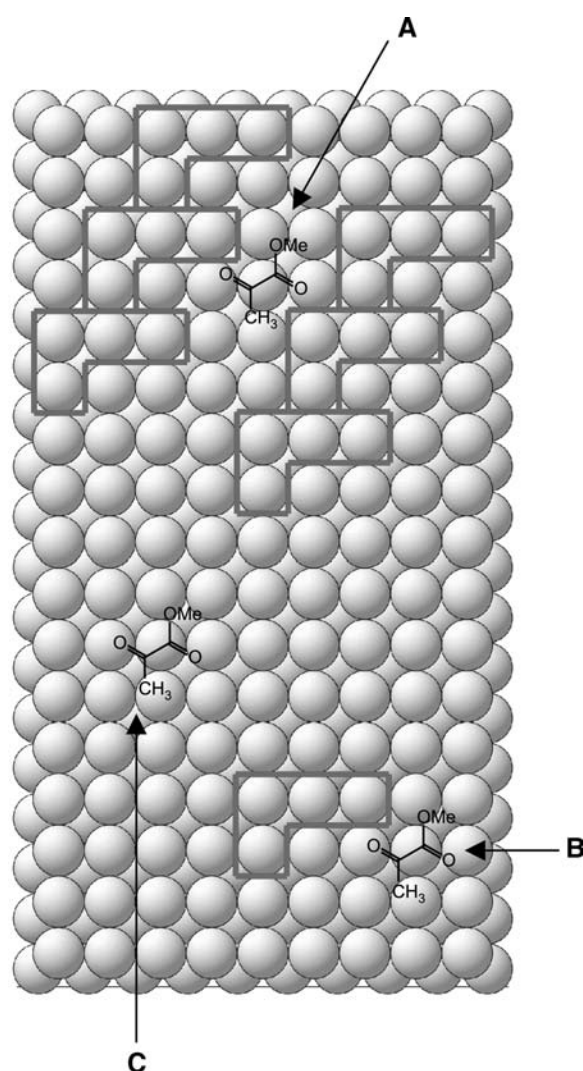


**Fig. 4** It has been proposed that the L-shaped structure of the cinchona alkaloid creates three possible reaction sites when adsorbed on a surface. Sites A and B allow the methyl pyruvate to interact with the adsorbed modifier and thus promote enantioselective hydrogenation. Site C is achiral and does not promote enantioselective hydrogenation.

hydrogenation of  $\alpha$ -ketoesters over Pt templated with cinchonidine. Studies of this reaction began in 1978 when Orito et al.<sup>[20]</sup> enantioselectively hydrogenated methyl pyruvate to *R*-(+)-methyl lactate in the presence of adsorbed cinchonidine. As in the case of the enantioselective hydrogenation on modified Ni catalysts, a variety of factors influence the enantioselectivity, including: temperature, the nature of the solvent, modifier concentration, and the size of the Pt particles.

One important aspect of the chirality of the cinchona-templated Pt surface is the structure and adsorption geometry of the cinchona alkaloid<sup>[21]</sup> illustrated in Figs. 4 and 5. There are three available sites for reaction. The first is the chiral cavity where the methyl pyruvate is bound to two or three cinchonidine molecules in an ordered array, the second is the 1:1 interaction between methyl pyruvate and a single cinchonidine molecule, and the third is a racemic site. One important characteristic of cinchonidine is its L-shaped configuration. Studies have shown that replacing the modifier with a chemically similar alkaloid that is not L-shaped, while increasing the reaction rate, eliminates enantioselectivity.<sup>[22]</sup>

Despite the large number of factors influencing the enantioselectivity of templated Pt catalysts, excellent results have been achieved by empirical tuning of pH, solvents, particle sizes, and comodifiers as was done with the Ni/tartaric acid system. Blaser, Jalett, and Wien<sup>[23]</sup> obtained an *ee* = 94% for the hydrogenation of methyl pyruvate. As in the case of the hydrogenation of  $\beta$ -ketoesters on Ni, the exact impact of

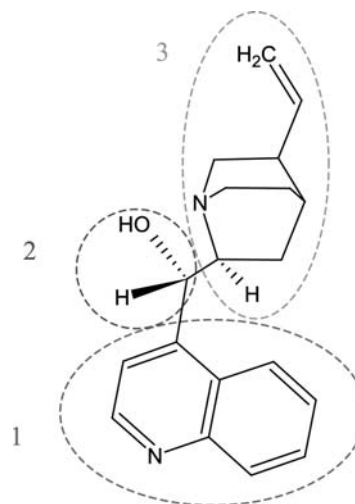


**Fig. 5** It has been suggested that three features of the cinchonidine structure are necessary to impart enantioselectivity. First, the quinoline ring system (1) is believed to anchor the modifier to the surface; second, the chirality of the reaction product is directed by the chiral region between the quinoline and the quinuclidine rings (2); and, third, the tertiary nitrogen in the quinuclidine ring (3) interacts with the C=O in the reacting ketoester.

these parameters must ultimately be elucidated to attain enantioselectivities approaching 100%.

### Other chiral templates

Three structural features of the cinchona modifier are thought to impart chirality to the Pt surface.<sup>[7]</sup> First,  $\pi$ -bonding through the quinoline ring system is believed to anchor the modifier to the surface; second, the chirality of the product is directed by the chiral region between the quinoline and quinuclidine rings; and, third, the tertiary nitrogen in the quinuclidine ring interacts with the C=O in the ketoester (Fig. 5). Based on this model for the origin of the enantioselectivity of catalysts templated with cinchonidine, new modifiers based on the cinchona alkaloid, such as dihydroapovincamic acid ethyl ester,<sup>[24]</sup> strychnine,<sup>[25]</sup> and others,<sup>[26,27]</sup> have been identified and have been shown to work with varying degrees of success.

Amino acids have also been identified as potentially useful chiral modifiers for catalytic surfaces.<sup>[25]</sup> In particular, the adsorption of glycine<sup>[28–30]</sup> and alanine<sup>[31,32]</sup> has been studied on Cu(110). These amino acids form well-ordered arrays whose structure is driven by hydrogen bonding. Alanine has been shown to be a promising modifier on Cu(110) because of the existence of a homochiral, two-dimensional phase that extends across the surface.<sup>[32]</sup>

### Surfaces Based on Bulk Chiral Materials

In addition to chiral surfaces that have been templated with chiral ligands, naturally chiral surfaces can be derived from inherently chiral bulk crystalline structures. This can be performed either by exposing a surface of a crystal of an enantiomerically pure organic compound, or by exposing a surface of a naturally chiral crystal. It has been postulated that the chirality of certain naturally occurring minerals may have been critical to the homochiral evolution of life on Earth. The homochirality of naturally occurring biomolecules (i.e., the preference for L-amino acids and D-sugars) may have arisen from enantioselective adsorption on naturally chiral crystal surfaces.<sup>[33]</sup>

#### Surfaces of bulk enantiomerically pure compounds

The crystallization of an enantiomerically pure sample of an organic compound will produce a crystal structure that must be chiral. Similarly, the surfaces of such a crystal must be chiral and should have enantiospecific properties. This ought to offer an excellent avenue for the study of enantiospecific interactions between chiral molecules; however, there do not seem to have been any significant attempts to study the surface chemistry of such materials.

#### Surfaces of bulk enantiomorphous crystals

Intrinsically chiral surfaces can be produced from crystalline materials with inherently chiral bulk structures. One of the most common chiral materials is quartz, whose bulk structure is formed by a helical arrangement of corner-sharing SiO<sub>4</sub> tetrahedra. This helical structure is chiral and renders quartz chiral. There have been some studies of the enantioselectivity of the surfaces of quartz crystals. However, much of this work has used powdered samples, which expose a variety of different crystallographic planes, each of which will have different adsorption characteristics for the same chiral species.<sup>[34,35]</sup> Bonner et al.<sup>[36,37]</sup> studied enantioselectivity on quartz powders prepared from enantiomerically pure crystals. By comparing the adsorbed concentrations of D-alanine and L-alanine on the same faces of quartz, a preferential enantioselective adsorption of approximately 1.4% was observed for D-alanine on right-handed quartz and for L-alanine on left-handed quartz. In another demonstration of enantiospecific surface chemistry, synthesis of pyramidal alkanols with an enantiomeric excess of *ee* > 90% was initiated using quartz and sodium chlorate crystals.<sup>[38]</sup>

Obviously, any material with a bulk chiral structure can expose chiral enantioselective surfaces; however, even achiral minerals can expose chiral surfaces. In an achiral environment, these would have equal surface energies and would be present in equal areas. However, it is possible to prepare achiral minerals, which expose surfaces with net chiral excess when grown in the presence of chiral molecules. When grown in the presence of chiral organic compounds, gypsum displayed an asymmetric growth.<sup>[39]</sup> Calcite, another achiral crystal, has also displayed asymmetric growth in the presence of chiral amino acids.<sup>[40]</sup>

The origin of homochirality in living systems is one of the most intriguing aspects of the development of life on Earth. It has been proposed that the enantioselective processes that must have led to this homochirality occurred on chiral surfaces. To study the origin of the homochirality of life on Earth, Hazen, Filley, and Goodfriend<sup>[41]</sup> have chosen to use calcite, an achiral mineral, which can expose chiral surfaces. Figure 6 shows the chiral facets of crystalline calcite. This mineral was abundant during the Archaean Era, a time in

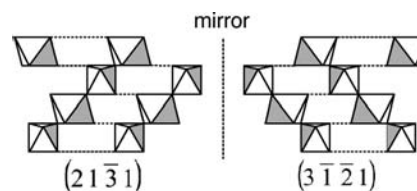


**Fig. 6** On certain faces of calcite, the CaO<sub>6</sub> octahedra are arranged in a chiral structure.

the Earth's history when the homochirality of life is thought to have originated. Furthermore, amino acids have particularly high heats of adsorption on calcite. The naturally chiral  $(2\ 1\ \bar{3}\ 1)$  and  $(3\ \bar{1}\ \bar{2}\ 1)$  faces showed 10% enantioselective adsorption of D-aspartic acid and L-aspartic acid, respectively. A control experiment using the achiral  $(1\ 0\ \bar{1}\ 1)$  face displayed no preference for aspartic acid adsorption.

Most of the known crystalline materials with naturally chiral bulk structures are covalent inorganic solids such as oxides, which have surfaces with low chemical reactivity. One approach to enhancing their reactivity while maintaining enantioselectivity is through deposition of a transition metal film on their surfaces. Terent'ev, Klabunovskii, and Patrikeev<sup>[42]</sup> and Klabunovskii and Patrikeev<sup>[43]</sup> created a nickel-coated quartz catalyst that enantioselectively hydrogenated  $\alpha$ -phenyl cinnamic acid. The mechanism by which the chiral substrate imparts enantioselectivity to the metal is not clear. On one hand, it may induce chirality in the structure of the metal film. Alternatively, the quartz might orient the reactant enantiospecifically at the edges of Ni particles where they may be hydrogenated. In principle, metal deposition onto chiral substrates is widely applicable to chiral surfaces with low reactivity; however, few works have been done in this field.

### Chiral Surfaces from Achiral Bulk Crystal Structures

Although it may seem counterintuitive, chiral surfaces can be formed from crystalline materials with otherwise achiral bulk structures. This type of chiral surface is created by exposing a high Miller index plane with indices  $(hkl)$  such that  $h \neq k \neq l$  and  $h \cdot k \cdot l \neq 0$ . Most of such surfaces have structures formed of terraces, steps, and kinks, as shown in Fig. 2C. It is the kinks on such surfaces that impart chirality. Each kink is formed by the intersection of three low Miller index microfacets ( $\{111\}$ ,  $\{100\}$ , and  $\{110\}$ ) with different structures.<sup>[44]</sup> The chirality of the kink arises from the sense of rotational progression among the three microfacets when viewed from above the surface. Like chiral molecules, the handedness of chiral surfaces can be denoted by using a modified Cahn–Ingold–Prelog convention based on microfacet priority.<sup>[44]</sup> For fcc metals, the order of priority is  $\{111\} > \{100\} > \{110\}$  and surfaces with a counterclockwise progression of microfacets when viewed from above are denoted  $(hkl)^S$ , whereas surfaces with a clockwise progression are denoted  $(hkl)^R$ . The naming convention and microfacet structure are illustrated in Fig. 7.

If one considers the high Miller index surfaces with terrace–step–kink structures and recognizes that these

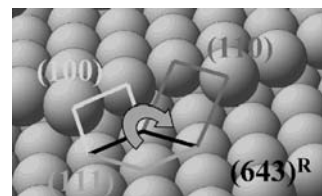


**Fig. 7** A kink on a high Miller index surface of an fcc structure is formed by the intersection of three dissimilar low Miller index microfacets ( $\{111\}$ ,  $\{100\}$ , and  $\{110\}$ ). Its handedness is dictated by the direction of rotational progression of the microfacets about the surface normal.

are formed by the intersection of three different low Miller index microfacets, it is clear that there are six types of chiral terrace–step–kink structures that can be formed on the surfaces of achiral bulk structures. The full set of surfaces that can be derived from an fcc bulk structure is usually represented by the stereographic projection shown in Fig. 8. The points on the perimeter of the stereographic projection represent surfaces that are achiral. The six types of chiral kinks divide the interior of the stereographic projection into six regions. The differences in the structures of the surfaces within each region are the lengths of the steps that separate the kinks and the widths of the terraces that separate the steps. The points along the dashed lines of Fig. 8 that separate the regions with different types of kinks represent surfaces with structures that have kinks formed of single unit cells of the low Miller index microfacets. They are also chiral but cannot be thought of as having structures with long step edges separating the kinks. Finally, at the center of the stereographic projection is the  $(531)$  surface with a structure that is formed of single unit cells of the  $(111)$ ,  $(100)$ , and  $(110)$  microfacets. It is also chiral but cannot be thought of as having a terrace–step–kink structure. In summary, the high Miller index surfaces of cubic lattices have structures that expose chiral kinks of a small number of types. These chiral kinks are based on the nanoscale arrangements of atoms at the intersections of microfacets.

### Roughening of naturally chiral surfaces

The ideal chiral surface structures that one obtains by simple cleavage of an fcc lattice along a high Miller index plane are formed of terrace–step–kink structures with nanoscale dimensions. The chiral kinks on the ideal surfaces are always single atom kinks along the step edge. These ideal structures will be destroyed by any amount of atomic motion or diffusion across the surface. A real chiral surface deviates from the ideal surface because of thermal roughening as seen in Fig. 9. Simulations by Sholl, Asthagiri, and Dower,<sup>[45]</sup> Asthagiri, Feibelman, and Sholl<sup>[46]</sup> and Power,



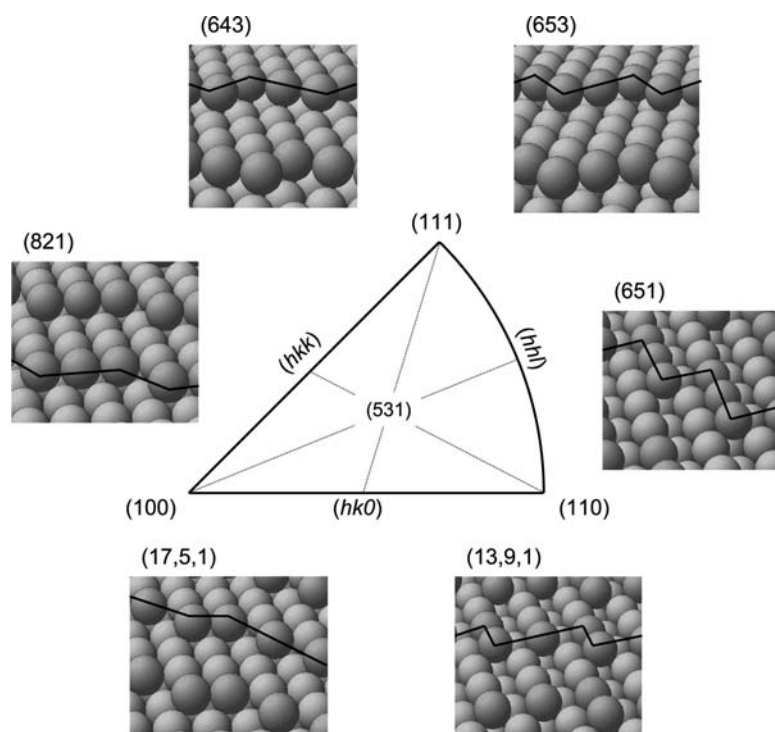


**Fig. 8** The stereographic projection allows a representation of all possible surfaces exposed by cleavage of an fcc structure. The points on the perimeter of the triangle represent achiral surfaces. The points contained within the triangle represent surfaces with kinked structures that are chiral. The dashed lines divide the triangle into six regions containing surfaces with six different kink structures represented by the examples shown in the ball diagrams. At the center of the triangle is the (531) surface, which is comprised of single unit cells of the (111), (100), and (110) microfacets and has the highest kink density of all the chiral surfaces.

Asthağiri, and Sholl<sup>[47]</sup> show that chiral surfaces roughen to form structures with nonideal kinks formed by the intersections of long step edges. Scanning tunneling microscopy of the Cu(5, 8, 90) surface has revealed such roughening of the step edges because of thermal diffusion of the kinks.<sup>[48]</sup> However, it is important to realize that the nonideal kinks generated by step roughening are still chiral because they are formed by the intersections of three different low Miller index microfacets. Equally important, the net chirality of the surface is preserved because the kinks present on the roughened surface are predominantly of the same chirality as the kinks on the ideal high Miller index surface from which it evolved.

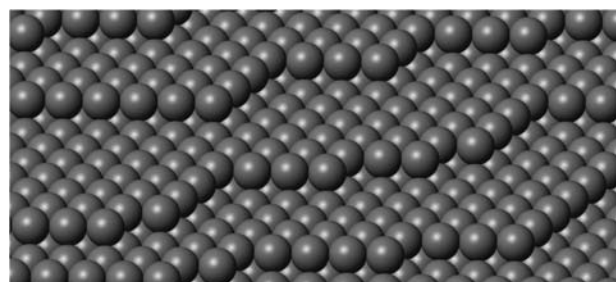


**Fig. 9** A thermally roughened surface no longer exhibits the periodic kink structure seen in Fig. 2C. Because of kink coalescence, a thermally roughened surface has fewer kinks than an ideal surface, and these kinks are now formed by the intersection of longer step edges. Despite roughening, the surface maintains its chirality.

### Enantioselectivity of naturally chiral metal surfaces

McFadden, Cremer, and Gellman<sup>[49]</sup> first postulated that the naturally chiral, high Miller index planes of fcc metals ought to exhibit enantiospecific surface chemistry. Atomistic simulations by Sholl<sup>[50]</sup> of the interactions of small chiral hydrocarbons with chiral platinum surfaces demonstrated that such enantioselectivity should occur and that enantiospecific adsorption energies for chiral molecules on chiral surfaces should be observable. Recently, temperature-programmed desorption studies of *R*-propylene oxide and *S*-propylene oxide<sup>[51,52]</sup> and *R*-3-methyl-cyclohexanone<sup>[52,53]</sup> on the Cu(643)<sup>R</sup> and Cu(643)<sup>S</sup> surfaces have revealed enantiospecific adsorption energies. The enantiospecific differences in the adsorption energies of propylene oxide and 3-methyl-cyclohexanone on the Cu(643) surfaces are  $\Delta\Delta E_{\text{ads}} = 0.06$  kcal/mol and  $\Delta\Delta E_{\text{ads}} = 0.22$  kcal/mol, respectively. It is these types of differences in energetics that ultimately lead to enantioselective separations and enantioselective catalytic reactions on chiral surfaces. Such an enantioselective separation of racemic 3-methyl-cyclohexanone has been demonstrated on the Cu(643) surface.<sup>[53]</sup>

In addition to influencing the energetics of adsorption and desorption, the handedness of naturally chiral surfaces can influence the kinetics of surface reactions. Cyclic voltammetry has been used to study the electro-oxidation kinetics of glucose and other sugars on an array of naturally chiral platinum electrode surfaces in aqueous solutions.<sup>[44,54–56]</sup> These studies have shown



that the rates of D-glucose and L-glucose oxidation on naturally chiral Pt electrodes can differ by as much as a factor of three. As in the case of enantioselective hydrogenation on the chirally templated Pt catalysts, the enantioselectivities of glucose oxidation are influenced by the presence of modifiers adsorbed from solutions. In particular, the enantioselectivity of glucose oxidation increases in the presence of sulfuric acid, but decreases in the presence of perchloric acid.

#### Enantiomorphic heteroepitaxial growth of metals on chiral oxides

The nanoscale kinks present on the high Miller index metal surfaces have clearly been shown to exhibit enantiospecific surface chemistry. However, the ultimate utility of surfaces with such chiral structures is dependent on their being produced with high surface area. One approach is to use the chiral surfaces of relatively cheap metal oxides as the substrates for deposition of otherwise expensive catalytic metals such as Pt.<sup>[57]</sup> This is analogous to the enantioselective catalyst mentioned above that was created by the deposition of Ni onto quartz.<sup>[42,43]</sup> In principle, the metal films could be grown epitaxially on metal oxides and, if the metal oxide substrates are prepared with chiral terrace-step-kink structures, the metal film may grow enantiomorphically and retain the chirality of the substrate. Initial work on this problem has suggested that enantiomorphic heteroepitaxial growth of metals on naturally chiral oxide surfaces can be achieved and may serve as a route to inexpensive naturally chiral metal surfaces.

#### Adsorbate-induced formation of naturally chiral surfaces

An adsorbed chiral molecule imparts chirality to a surface merely by its presence. However, it is possible that adsorbate-induced reconstruction of achiral metal surfaces can yield homochiral high Miller index facets with nanoscale kink structures that are naturally chiral. This method of inducing chirality in a surface is distinct from chiral templating in the sense that the chirality of the substrate could be retained even if the adsorbate were removed. This can be thought of as chiral imprinting. Imprinting could serve as a potential route to the inexpensive production of high area chiral surfaces. An example of chiral imprinting arises during amino acid adsorption on the otherwise achiral Cu(100) surface.<sup>[58–60]</sup> Step bunching on the Cu(100) surface in the presence of adsorbed L-lysine causes the formation of a homochiral set of {3, 1, 17} facets. The chirality of the facets is dictated by the chirality of the L-lysine. Although achiral amino acids will induce the formation of {3, 1, 17} facets on the Cu(100) surface, they are present in both *R* and *S* forms.

## TECHNOLOGICAL IMPACT OF CHIRAL SURFACES

The potential technological impact of chiral surfaces is enormous because they can, in principle, play an important role in the processing of chiral pharmaceuticals worth an estimated US\$100 billion per year. At this point in time, the most highly developed application is as stationary phases for chiral chromatography. Chiral columns are often formed by templating of materials such as silica with enantiomerically pure chiral ligands.<sup>[9,10]</sup> Templating has also been shown to produce enantioselective heterogeneous catalysts, which, in principle, offer some advantages over homogeneous catalysts during scaleup. Thus chiral templating of surfaces is a demonstrated technology with growing opportunities for application in pharmaceuticals production.

The study of the enantioselective surface chemistry of naturally chiral surfaces and, in particular, those derived from kinked high Miller index metal surfaces is in its infancy. In principle, they offer potential advantages over templated surfaces in that they may be more thermally and chemically robust because they do not rely on organic ligands as the source of chirality. Another opportunistic niche that the naturally chiral surfaces may fill is in the development of microscale reactors. In reactors based on single-crystalline Si, it is easy to imagine that one could make channels that expose naturally chiral surfaces, and that such an element in a microreactor might then be used for enantioselective chemical processes. Although the impact of naturally chiral surfaces is yet to be determined, there are a number of exciting opportunities. Furthermore, the possible role that naturally chiral surfaces may have played in dictating the origins of the homochirality of life on Earth makes their study intrinsically intriguing.

## CONCLUSION

Of the three types of chiral surfaces described in this article, the most well developed are those that are produced by templating with chiral organic modifiers. Although the mechanisms and adsorbate/substrate interactions that impart enantioselectivity on these surfaces are not understood in great detail, some such surfaces have been highly optimized to give highly enantioselective separations and catalytic reactions. Naturally chiral surfaces can be generated from materials that are chiral in bulk, or achiral materials cleaved to expose surface structures that are chiral at the nanoscale. The crystalline nature of these structures makes them good candidates for a detailed study of the origins of enantiospecificity on their surfaces.

Furthermore, they have demonstrated high enantioselectivity for both reactions and separations. The limitation in their practical use is the need for methods of preparation that yield naturally chiral surfaces in high area form. Although possible routes exist, these have yet to be explored.

## ACKNOWLEDGMENTS

We would like to thank Prof. David Sholl and Prof. Greg Rohrer for their helpful discussions. The authors' work on naturally chiral crystals is supported by the NSF through grant no. CTS-0216170 and by the DOE through grant no. DMR-0079996.

## REFERENCES

- Chiral Reactions in Heterogeneous Catalysis, Proceedings of the First European Symposium on Chiral Reactions in Heterogeneous Catalysis, Brussels, Belgium, October, 25–26; Jannes, G., Dubois, V., Eds.; Plenum Publishers, 1993; 5.
- Jones, M. *Organic Chemistry*; W. W. Norton & Company: New York, 1997.
- Hahn, T., Ed.; *International Tables for Crystallography* 2nd Ed.; Space Group Symmetry, Kluwer Academic Publishers: Dordrecht, 1989; 4pp.
- Federsel, H.J. Drug chirality—scale-up, manufacturing, and control. *Chemtech* **1993**, *23* (12), 24–33.
- Stinson, S.C. Chiral Drugs. *Chem. Eng. News* **1994**, *19*, 38.
- Nugent, W.A.; Rajan Babu, T.V.; Burk, M.J. Beyond nature's chiral pool: Enantioselective catalysis in industry. *Science* (Washington, DC) **1993**, *259* (5094), 479–483.
- Smith, G.V.; Notheisz, F. *Heterogeneous Catalysis in Organic Chemistry*; Academic Press: San Diego, 1999.
- Webb, G.; Wells, P.B. Asymmetric hydrogenation. *Catal. Today* **1992**, *12* (2–3), 319–337.
- Pirkle, W.H.; Pochapsky, T.C. Considerations of chiral recognition relevant to the liquid chromatography separation of enantiomers. *Chem. Rev.* (Washington, DC) **1989**, *89* (2), 347–362.
- Francotte, E.R. Enantioselective chromatography as a powerful alternative for the preparation of drug enantiomers. *J. Chromatogr., A* **2001**, *906* (1–2), 379–397.
- Izumi, Y. Modified Raney nickel (MRNi) catalyst: Heterogeneous enantiodifferentiating (asymmetric) catalyst. *Adv. Catal.* **1983**, *32*, 215–271.
- Hoek, A.; Sachtler, W.M.H. Enantioselectivity of nickel catalysts modified with tartaric acid or nickel tartrate complexes. *J. Catal.* **1979**, *58* (2), 276–286.
- Hoek, A.; Woerde, H.M.; Sachtler, W.M.H. Enantioselectivity of nickel catalysts modified with tartaric acid or nickel tartrate complexes. *Stud. Surf. Sci. Catal.* **1981**, *7*, 376–389.
- Keane, M.A. Adsorption of optically pure alanine on silica-supported nickel and the consequent catalytic enantioselectivity. *Langmuir* **1994**, *10* (12), 4560–5.
- Fu, L.; Kung, H.H.; Sachtler, W.M.H. Particle size effect on enantioselective hydrogenation of methyl acetoacetate over silica-supported nickel catalyst. *J. Mol. Catal.* **1987**, *42* (1), 29–36.
- Nitta, Y.; Imanaka, T.; Teranishi, S. Preparation chemistry of precipitated nickel–silica catalysts for enantioselective hydrogenation. *J. Catal.* **1985**, *96* (2), 429–438.
- Nitta, Y.; Utsumi, T.; Imanaka, T.; Teranishi, S. Effect of preparation variables on morphological and catalytic properties of precipitated nickel–silica catalysts. *Chem. Lett.* **1984**, *8*, 1339–1342.
- Harada, T.; Izumi, Y. Improved modified Raney nickel catalyst for enantioface-differentiating (asymmetric) hydrogenation of methyl acetoacetate. *Chem. Lett.* **1978**, *11*, 1195–1196.
- Bostelaar, L.J.; Sachtler, W.M.H. The role of alkali halides in the enantioselective hydrogenation of a prochiral keto compound over modified nickel catalysts. *J. Mol. Catal.* **1984**, *27* (3), 387–395.
- Orito, Y.; Imai, S.; Niwa, S.; Nguyen Gia, H. Asymmetric hydrogenation of methyl benzoylformate using platinum–carbon catalysts modified with cinchonidine. *Yuki Gosei Kagaku Kyokai* **1979**, *37* (2), 173–174.
- Sutherland, I.M.; Ibbotson, A.; Moyes, R.B.; Wells, P.B. Enantioselective hydrogenation. I. Surface conditions during methyl pyruvate hydrogenation catalyzed by cinchonidine-modified platinum/silica (EUROPT-1). *J. Catal.* **1990**, *125* (1), 77–88.
- Meheux, P.A. University of Hull, 1991.
- Blaser, H.U.; Jalett, H.P.; Wiehl, J. Enantioselective hydrogenation of alpha-keto esters with cinchona-modified platinum catalysts: Effect of acidic and basic solvents and additives. *J. Mol. Catal.* **1991**, *68* (2), 215–222.
- Tungler, A.; Mathe, T.; Tarnai, T.; Fodor, K.; Toth, G.; Kajtar, J.; Kolossvary, I.; Herenyi, B.; Sheldon, R.A. (–)-Dihydroapovincaminic acid ethyl ester, preparation and use as a chiral modifier in enantioselective heterogeneous catalytic hydrogenations. *Tetrahedron: Asymmetry* **1995**, *6* (9), 2395–2402.
- Blaser, H.U. The chiral pool as a source of enantioselective catalysts and auxiliaries. *Chem. Rev.* (Washington, DC) **1992**, *92* (5), 935–952.
- Baiker, A. Progress in asymmetric heterogeneous catalysis: Design of novel chirally modified platinum metal catalysts. *J. Mol. Catal., A Chem.* **1997**, *115* (3), 473–493.
- Schurch, M.; Heinz, T.; Aeschmann, R.; Mallat, T.; Pfaltz, A.; Baiker, A. Design of new modifiers for the enantioselective hydrogenation of ethyl pyruvate. *J. Catal.* **1998**, *173* (1), 187–195.
- Barlow, S.M.; Kitching, K.J.; Haq, S.; Richardson, N.V. A study of glycine adsorption on a Cu{110} surface using reflection absorption infrared spectroscopy. *Surf. Sci.* **1998**, *401* (3), 322–335.
- Booth, N.A.; Woodruff, D.P.; Schaff, O.; Giessel, T.; Lindsay, R.; Baumgartel, P.; Bradshaw, A.M. Determination of the local structure of glycine adsorbed on Cu(110). *Surf. Sci.* **1998**, *397* (1–3), 258–269.
- Nyberg, M.; Hasselstrom, J.; Karis, O.; Wassdahl, N.; Weinelt, M.; Nilsson, A.; Pettersson, L.G.M. The electronic structure and surface chemistry of glycine adsorbed on Cu(110). *J. Chem. Phys.* **2000**, *112* (12), 5420–5427.

31. Williams, J.; Haq, S.; Raval, R. The bonding and orientation of the amino acid L-alanine on Cu{110} determined by RAIRS. *Surf. Sci.* **1996**, *368* (1–3), 303–309.
32. Raval, R.; Baddeley, C.J.; Haq, S.; Louafi, S.; Murray, P.; Murny, C.; Lorenzo, M.O.; Williams, J. Complexities and dynamics of the enantioselective active site in heterogeneous catalysis. *Stud. Surf. Sci. Catal.* **1999**, *122*, 11–22 (Reaction Kinetics Development of Catalytic Processes).
33. Lahav, N. *Biogenesis: Theories of Life's Origins*; Oxford University Press: New York, 1999.
34. Tsuchida, R.; Kobayashi, M.; Nakamura, A. Asymmetric adsorption of complex salts on quartz. *J. Chem. Soc. Jpn.* **1935**, *56*, 1339–1345.
35. Karagounis, G.; Coumonlos, G. A new method for resolving a racemic compound. *Nature* **1938**, *142*, 162–163.
36. Bonner, W.A.; Kavasmaneck, P.R.; Martin, F.S.; Flores, J.J. Asymmetric adsorption of alanine by quartz. *Science* **1974**, *186* (4159), 143–144.
37. Bonner, W.A.; Kavasmaneck, P.R.; Martin, F.S.; Flores, J.J. Asymmetric adsorption by quartz. Model for the prebiotic origin of optical activity. *Orig. Life* **1975**, *6* (3), 367–376.
38. Soai, K.; Sato, I.; Shibata, T. Asymmetric autocatalysis and the origin of chiral homogeneity in organic compounds. *Chem. Rec.* **2001**, *1* (4), 321–332.
39. Cody, A.M.; Cody, R.D. Chiral habit modifications of gypsum from epitaxial-like adsorption of stereospecific growth inhibitors. *J. Cryst. Growth* **1991**, *113* (3–4), 508–519.
40. Orme, C.A.; Noy, A.; Wierzbicki, A.; McBride, M.T.; Grantham, M.; Teng, H.H.; Dove, P.M.; DeYoreo, J.J. Formation of chiral morphologies through selective binding of amino acids to calcite surface steps. *Nature (London)* **2001**, *411* (6839), 775–779.
41. Hazen, R.M.; Filley, T.R.; Goodfriend, G.A. Selective adsorption of L- and D-amino acids on calcite: Implications for biochemical homochirality. *Proc. Natl. Acad. Sci. U. S. A.* **2001**, *98* (10), 5487–5490.
42. Terent'ev, A.P.; Klabunovskii, E.I.; Patrikeev, V.V. Asymmetric synthesis with the aid of catalysts deposited on right and left quartz. *Dokl. Akad. Nauk Souza Sov. Social. Resp., A* **1950**, *74*, 947–950.
43. Klabunovskii, E.I.; Patrikeev, V.V. Mechanism of the asymmetrizing effect of metal catalysts deposited on right and left quartz. *Dokl. Akad. Nauk Souza Sov. Social. Resp., A* **1951**, *78*, 485–487.
44. Ahmadi, A.; Attard, G.; Feliu, J.; Rodes, A. Surface reactivity at “chiral” platinum surfaces. *Langmuir* **1999**, *15* (7), 2420–2424.
45. Sholl, D.S.; Asthagiri, A.; Power, T.D. Naturally chiral metal surfaces as enantiospecific adsorbents. *J. Phys. Chem., B* **2001**, *105* (21), 4771–4782.
46. Asthagiri, A.; Feibelman, P.J.; Sholl, D.S. Thermal fluctuations in the structure of naturally chiral Pt surfaces. *Top. Catal.* **2002**, *18* (3–4), 193–200.
47. Power, T.D.; Asthagiri, A.; Sholl, D.S. Atomically detailed models of the effect of thermal roughening on the enantiospecificity of naturally chiral platinum surfaces. *Langmuir* **2002**, *18* (9), 3737–3748.
48. Dieluweit, S.; Ibach, H.; Geisen, M.; Einstein, T.L. Orientation dependence of step stiffness: Failure of SOS and ising models to describe experimental data. *Phys. Rev. Lett.*, *in press*.
49. McFadden, C.F.; Cremer, P.S.; Gellman, A.J. Adsorption of chiral alcohols on “chiral” metal surfaces. *Langmuir* **1996**, *12* (10), 2483–2487.
50. Sholl, D.S. Adsorption of chiral hydrocarbons on chiral platinum surfaces. *Langmuir* **1998**, *14* (4), 862–867.
51. Horvath, J.D.; Gellman, A.J. Enantiospecific desorption of R- and S-propylene oxide from a chiral Cu(643) surface. *J. Am. Chem. Soc.* **2001**, *123* (32), 7953–7954.
52. Horvath, J.D.; Gellman, A.J. Enantiospecific desorption of chiral compounds from chiral Cu(643) and achiral Cu(111) surfaces. *J. Am. Chem. Soc.* **2002**, *124* (10), 2384–2392.
53. Horvath, J.; Kamakoti, P.; Sholl, D.S.; Gellman, A.J. Enantioselective separation on a naturally chiral surface. *Nature*, *in press*.
54. Attard, G.A.; Ahmadi, A.; Feliu, J.; Rodes, A.; Herrero, E.; Blais, S.; Jerkiewicz, G. Temperature effects in the enantiomeric electro-oxidation of D- and L-glucose on Pt{643}S. *J. Phys. Chem., B* **1999**, *103* (9), 1381–1385.
55. Attard, G.A. Electrochemical studies of enantioselectivity at chiral metal surfaces. *J. Phys. Chem., B* **2001**, *105* (16), 3158–3167.
56. Attard, G.A.; Harris, C.; Herrero, E.; Feliu, J. The influence of anions and kink structure on the enantioselective electro-oxidation of glucose. *Faraday Discuss.* **2002**, *121*, 253–266. (Dynamic Electrode Surface).
57. Asthagiri, A.; Sholl, D.S. First principles study of Pt adhesion and growth on SrO- and TiO<sub>2</sub>-terminated SrTiO<sub>3</sub>(100). *J. Chem. Phys.* **2002**, *116* (22), 9914–9925.
58. Zhao, X.; Gai, Z.; Zhao, R.G.; Yang, W.S.; Sakurai, T. Adsorption of glycine on Cu(001) and related step faceting and bunching. *Surf. Sci.* **1999**, *424* (2–3), L347–L351.
59. Zhao, X.; Zhao, R.G.; Yang, W.S. Adsorption of alanine on Cu(001) studied by scanning tunneling microscopy. *Surf. Sci.* **1999**, *442* (2), L995–L1000.
60. Zhao, X.; Zhao, R.G.; Yang, W.S. Scanning tunneling microscopy investigation of L-lysine adsorbed on Cu(001). *Langmuir* **2000**, *16* (25), 9812–9818.

# Environmental Electron Microscopy Imaging

**Satoshi Utsunomiya**

*Department of Nuclear Engineering and Radiological Sciences, University of Michigan, Ann Arbor, Michigan, U.S.A.*

**Christopher S. Palenik**

*Department of Geological Sciences, University of Michigan, Ann Arbor, Michigan, U.S.A.*

**Rodney C. Ewing**

*Departments of Geological Sciences, Material Science and Engineering, and Nuclear Engineering and Radiological Science, University of Michigan, Ann Arbor, Michigan, U.S.A.*

## INTRODUCTION

Nanoparticles and nanodomains are omnipresent in low-temperature environments at the Earth's surface, including the hydrosphere and the atmosphere. This part of the Earth is often referred to as the "critical zone"<sup>[1]</sup> because this zone experiences the greatest impact from human activities. The relatively low temperatures (<100°C) of the critical zone are conducive to the formation and survival of nanoparticles.<sup>[2]</sup> Many trace elements are toxic (Pb, Hg, and As), and their release and mobilization at the nanoscale can cause serious health effects.<sup>[3]</sup> However, other trace elements (e.g., Se) are essential for life forms and have an important impact on the success of different organisms in different ecological systems.<sup>[4]</sup> In addition, the speciation and distribution of trace elements have important implications for geologic processes, such as the formation of ore deposits, environmental contaminations, and geologic age dating using isotopes (e.g., U, Th, and Pb).<sup>[5]</sup> Trace elements in the critical zone are frequently present as dispersed nanoparticles, or in nanodomains that contain the elements at relatively high concentration. Finally, at the nanoscale, the chemical, thermal, and electronic properties of materials can change dramatically from bulk values as a function of size.<sup>[6,7]</sup>

For our understanding of nanoparticles in environmental and geological sciences to continue to develop, our ability to directly study the chemical and structural forms of these particles at continually shorter length scales becomes evermore critical.<sup>[8]</sup> This brief review of traditional analytical techniques illustrates a few of these techniques, their applications, and their limitations. The remainder of this article will focus on the application of high-angle annular dark field scanning transmission electron microscopy (HAADF-STEM)

and associated high-resolution analytical techniques by presenting four examples. These examples will focus on heavy trace elements of importance in the fields of geological and environmental sciences.

## CONVENTIONAL TECHNIQUES

Scanning electron microscopy (SEM) can provide submicrometer morphological information, but the coupled elemental analysis through an energy-dispersive spectrometer (EDX) or a wavelength-dispersive spectrometer (WDS) on an electron microprobe analyzer (EMPA) is limited to a volume of several cubic micrometers. Atomic force microscopy (AFM) and scanning tunneling microscopy (STM) provide surface information at the atomic scale; however, elemental data cannot be obtained except in the case of well-controlled, simple experiments.<sup>[9]</sup> Other techniques that are useful in analyzing ultrafine particles—such as electron energy loss spectroscopy (EELS), which provides elemental and valence information, and secondary ionization mass spectrometry (SIMS), which provides isotopic information—both have beam sizes that cannot resolve individual nanoparticles.<sup>[10,11]</sup> Each of the above techniques, under proper conditions, can provide information about nanoparticle characteristics; however, none of these techniques is capable of locating or providing direct chemical and structural information about an individual particle.

In contrast, transmission electron microscopy (TEM) has become recognized as the most powerful and appropriate technique for the direct investigation of nanoscale particles. Coupled with EDX, STEM has been applied to the characterization of colloids.<sup>[12,13]</sup> With traditional STEM resolution, the size of particles studied is typically

limited to the range of 100–1000 nm, and only major element compositions can be routinely determined. For smaller particles (<100 nm), conventional transmission electron microscopy (CTEM) and associated spectroscopies have been commonly applied to the structural and elemental characterization of nanoparticles.<sup>[14–16]</sup> The major limitation to CTEM is that image contrast is minimal (except at the highest magnifications and, subsequently, the smallest field of view). This makes locating specific nanoparticles (i.e., those that host the elements of interest) in a bulk sample extremely difficult. The difficulty in locating the element of interest limits the utility of CTEM to real-world environmental samples that contain only trace concentrations of an element of interest (e.g., a few parts per million).

In such cases, when the particles of interest consist of relatively heavy elements situated in a lighter matrix material, HAADF-STEM is a powerful method for locating and studying the nanoparticles of interest, as the image contrast is strongly correlated with atomic number.

## ANALYTICAL TECHNIQUES

To study a sample by TEM, a sample must be made thin enough to allow transmission of the electron beam. Sample preparation for advanced TEM is a critical step that can affect the ultimate resolution and the ability to perform the desired analyses on a given sample. For particulate samples, a fine size fraction of particles (<1  $\mu\text{m}$ ) is dispersed onto a 3-mm grid that is covered by a film of lacey carbon. The carbon, which is transparent to the electron beam, acts as a support for the particles. For rock or mineral samples, the sample is mechanically polished to a thickness of  $\sim 10 \mu\text{m}$ . Final thinning is carried out using an ion milling system where a beam of Ar ions bombards the sample to create a nanometer-scale thin edge on the sample.

Samples illustrated in this article were studied using a JEOL JEM2010F high-resolution transmission electron microscopy analytical electron microscopy (HRTEM-AEM) with HAADF-STEM imaging. Fig. 1 shows a schematic illustration of the HAADF-STEM.

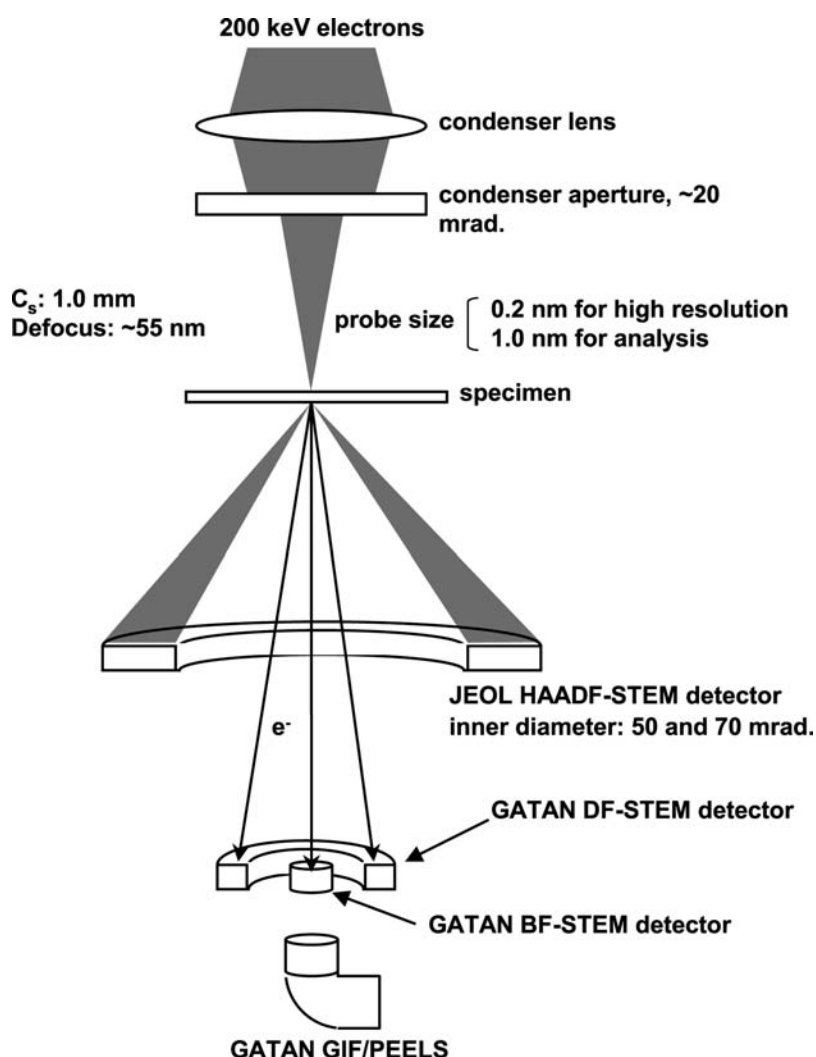


**Fig. 1** Schematic illustration of the electron microscope configuration used in the HAADF-STEM mode (JEOL JEM2010F). Source: From Ref.<sup>[17]</sup>.

In contrast to CTEM mode where elastically scattered electrons are diffracted by the sample to create an image, an HAADF image is created by electrons that are scattered by thermal diffuse scattering. The amount of scattering is dependent on the average atomic number of the scatterer (i.e., the sample). As shown in Fig. 1, the HAADF detector is an annular dark-field detector that collects electrons scattered at an angle between 50 and 110 mrad. The final image is produced by rastering the electron beam across the sample in two dimensions to produce an image in which contrast is proportional to atomic mass. The intensity profile in HAADF-STEM for some elements was simulated<sup>[17]</sup> with the code developed by Kirkland<sup>[18]</sup> (Fig. 2). In general, a heavier element shows a higher signal in an HAADF-STEM image; however, other factors that can affect the HAADF-STEM image contrast include: 1) specimen thickness: a thicker area shows a brighter contrast; 2) crystal structure: an amorphous domain will produce less contrast than a crystalline phase of similar concentration. The lack of structural configuration results in a loss of efficient thermal diffuse scattering; and 3) density: low-density areas produce less contrast than high-density regions of similar composition. A more rigorous treatment of HAADF theory is given in Kirkland.<sup>[18]</sup>

Elemental data are collected using an EDX detector, which collects X-rays emitted from the sample as a result of the sample–electron beam interaction. The energy of an X-ray emitted is characteristic of the generating atom. Elemental data can be collected from a single point as small as 0.2 nm, or the beam can be moved across the sample in a grid to create an elemental map. While collecting an elemental map, TEM samples have a tendency to drift. To minimize the effect of specimen drift, a computer-controlled drift

correction mode is used to track sample movement during mapping.

## EXAMPLES

### Uranium Nanocrystals in Atmospheric Particulates

The first example is uranium in an urban aerosol.<sup>[19]</sup> Public exposure to ionizing radiation comes mostly from natural sources, accounting for over 80% of the average individual dose of less than 4 mSv/year. The principal source of radioactivity is from radionuclides in the decay chains of <sup>238</sup>U, <sup>235</sup>U, and <sup>232</sup>Th. Fly ash from coal combustion is one of the major sources of release of radioactive elements. Although the total radioactivity of these nuclides is low and accounts for only a small fraction of the radiation exposure from natural sources, the radioactivity associated with uranium and thorium in airborne particulates continues to be of concern. In addition, recent results have shown that very-fine-sized particulates (less than 2.5 μm in diameter) in air pollution can produce significant effects on health.<sup>[20]</sup> Thus it is important to develop an understanding of the association of radioactive elements with atmospheric particulates. The questions of importance are: 1) What is the solid-state speciation of radioactive elements in the atmosphere? 2) In what size range of particulates are the radioactive elements associated? 3) How are the trace elements associated with particulates? Ultimately, these data are required for the determination of pathways of the exposure of the public to technogenic sources of radioactivity. To address these questions, atmospheric particulates from an area of Detroit, MI were examined in detail using advanced TEM techniques. Previous success in directly studying such samples has been largely limited because of the low concentrations (less than 10 ppm) and extremely small particle size (a few tens of nanometers) of the aerosol samples. However, because the radioactive elements of interest are relatively heavy elements (i.e., U and Th), HAADF-STEM could be used to scan relatively large areas of the sample to search for particles of interest.

The sample studied was composed of mainly quartz, gypsum, clays, and Fe oxides with a measured bulk U concentration of 9.2 ppm (0.25 ng/m<sup>3</sup>). This U concentration is comparable to average crustal compositions in the Earth<sup>[21]</sup> and is lower than the concentration of U in soot from coal-fired power plants.<sup>[22]</sup> Based on correlation analysis using the other elements analyzed, both coal combustion and traffic pollution have contributed significantly to the material collected in these samples.

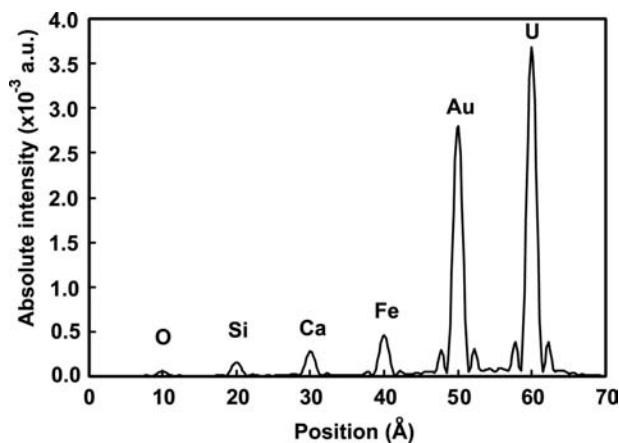
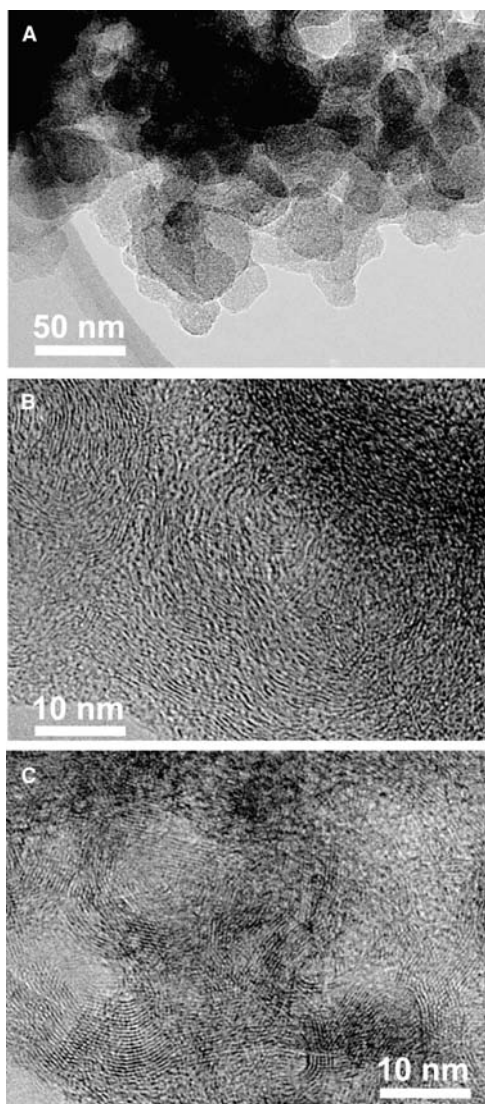


Fig. 2 Simulated contrast profile in HAADF-STEM calculated for some elements. The atoms of a given element were placed in a row at 1-nm intervals. Source: From Ref.<sup>[17]</sup>.



TEM analysis revealed a considerable amount of soot (carbonaceous matter) at the surface of the mineral particles. The soot particles in these aerosol samples were a few tens of nanometers in size and had rounded shapes (Fig. 3A). Using HRTEM, each soot particle showed a range in crystallinity from nearly amorphous to highly crystalline carbonaceous matter (Fig. 3B and C). The crystallinity of carbon depends on the ambient environment of formation, especially the temperature and cooling history. In general, higher temperatures produce a more crystalline form of carbon.<sup>[23]</sup> The varying degrees of crystallinity of the samples from Detroit suggest that these particulates have experienced a variety of



**Fig. 3** Carbonaceous matter in the soot of aerosol (A). Rounded carbon particles from a connected mass form larger particles. HRTEM of the carbonaceous matter shows various degrees of crystallinity from a small amount of rounded fringes (B) to the very crystalline carbon (C). *Source:* From Ref.<sup>[19]</sup>.

thermal histories, thus consistent with a variety of sources. Of particular interest are HRTEM images (Fig. 3B and C) of crystalline soot that show a lattice fringe spacing of  $\sim 0.35$  nm, which is comparable to those of either graphite or fullerene.

The HAADF-STEM image showed a high density of bright-contrast particles less than 10 nm in size (Fig. 4A). STEM-EDX maps of the square region in the HAADF-STEM image reveal that the particles consist of uranium and oxygen (Fig. 4A). Further analysis using HRTEM reveals that U-bearing particles were encapsulated in a well-crystallized carbonaceous graphite or spherical fulleroid matrix, as shown in Fig. 4B. By HRTEM, it was established that the uranium-bearing particles are individual nanocrystallites (Fig. 5A) of uraninite ( $\text{UO}_{2+x}$ ,  $x = 0-0.25$ ;  $Fm\bar{3}m$ ), based on lattice spacings in the image and diffraction maximum in the fast Fourier transform (FFT) (Fig. 5C) of the boxed region in the HRTEM image (Fig. 5B).

The encapsulated uraninite in this “fulleroid shell” appears to be partially protected from ambient oxidizing

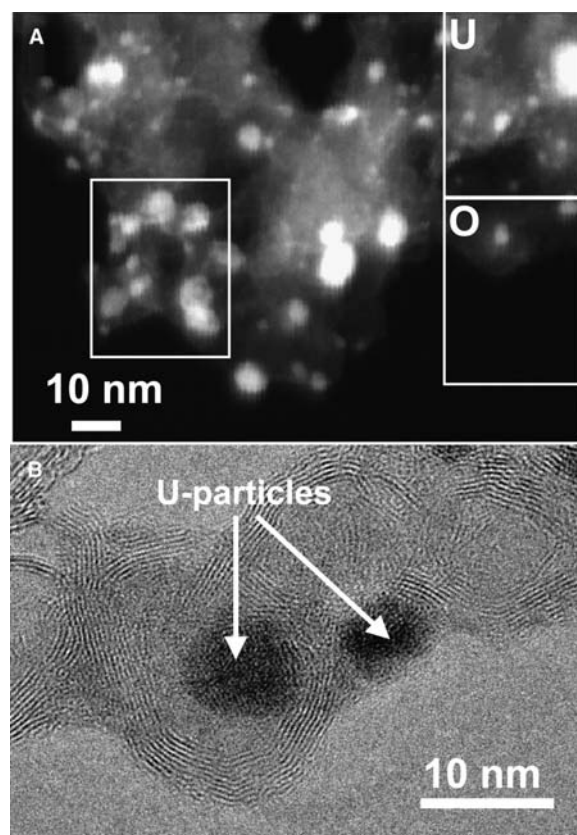


**Fig. 4** (A) HAADF-STEM image reveals the occurrence of many heavy particles less than 10 nm in size. The insets are elemental maps of uranium and oxygen by STEM-EDX. (B) HRTEM images show that U-bearing nanoparticles are encapsulated in the “cage” structure of fulleroid. *Source:* From Ref.<sup>[19]</sup>.

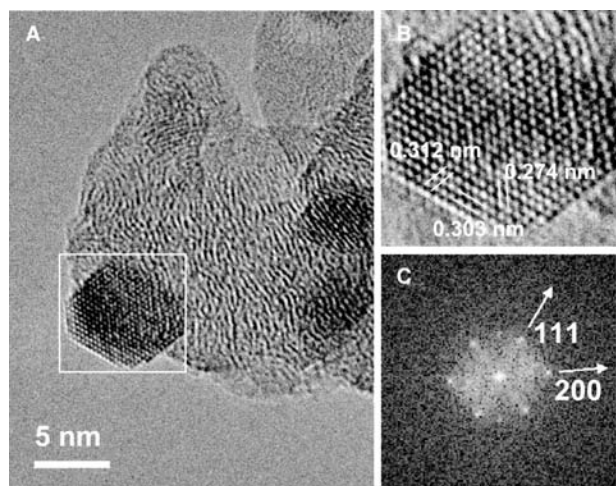


**Fig. 5** (A) HRTEM of the U particle. The matrix carbon has lost its structure after the STEM mode analysis because of the focused electron probe. (B) Wiener-filtered image of the white square portion of panel (A). In the FFT image (C), the main diffraction maxima were indexed to be those of uraninite. *Source:* From Ref.<sup>[19]</sup>.

conditions of the atmosphere. This further reduces mobility in the environment, as oxidized species of uranium are much more mobile in solution. The present results provide the basis for a detailed determination of uranium bioavailability, and also new insights into the process of transportation of uranium by aerosols.

### Heavy Element Colloids at the Nevada Test Site

Migration of plutonium and other radiotoxic elements is a serious issue in the disposal of radioactive waste in a geologic repository. In general, colloids, which are defined as particles less than 10  $\mu\text{m}$  in diameter, are thought to play an important role in the migration of elements through groundwater systems.<sup>[24–26]</sup> Thus the adsorption of radionuclides on colloids has been extensively studied.<sup>[27–29]</sup> Recently, the ratio of  $^{240}\text{Pu}/^{239}\text{Pu}$  in the groundwater from a well (ER-20-5) that is located 1.3 km away from the Benham nuclear test site was determined to have the same ratio of  $^{240}\text{Pu}/^{239}\text{Pu}$  as Pu at the Benham site.<sup>[30]</sup> This evidence suggests that Pu had been transported through the groundwater at least 1.3 km in 35 years, far faster than the rate predicted by groundwater flow models. Radiochemical analysis of filtered colloids from the well suggested that colloids in the groundwater have absorbed important radioactive elements such Co, Cs, Eu, and Pu.<sup>[30]</sup> However, an important question remained: What is the form of the radioactive elements associated with the colloids? In an attempt to locate and characterize the phase containing these heavy elements in a sample with such low concentrations of the elements of interest

(<math>10^{-14}</math> M of Pu in groundwaters), HAADF-STEM was applied. Samples consisted of solid colloids filtered out of the groundwaters from the same contaminated well at the Nevada test site. Three important and potentially radionuclide elements (Co, Cs, and Eu) were identified in the sample. Based on HRTEM images, Co was identified to exist with Mo and Cr in the structure of awaruite ( $\text{Ni}_2\text{Fe}$ ) (Fig. 6A). The Cs-bearing phase consisted of Cs, O, and U, possibly forming a Cs uranate (Fig. 6B). The Eu-bearing phase was monazite (Fig. 6C). The interesting result is that the three potentially radioactive elements were present not as adsorbed surface species, but structurally incorporated into a mineral. Although Pu has not been detected yet, these results show that the HAADF-STEM is useful for investigating such colloids associated with radioactive trace elements.

### Gold Nanocrystals in a Gold Ore Deposit

The Carlin trend in Nevada hosts some of the largest gold deposits in the United States.<sup>[17,31,32]</sup> Despite the economic and scientific interest these deposits have generated, the large concentrations of gold are present at relatively low concentrations in the host rock (30–150 ppm Au) and have never been directly observed—an attribute that has led to the term “invisible gold” being commonly applied to the gold-bearing rocks of Carlin-type deposits.<sup>[33,34]</sup> The majority of gold in the ore have been shown to be associated with hydrothermally formed arsenian pyrite overgrowths that have formed over pyrite ( $\text{FeS}_2$ ) grains.

Although the presence of gold in the arsenic-bearing rim has been established, the mineralogical state of gold remains in question. In particular, is the gold present structurally incorporated into the mineral, or is it present as native gold inclusions at the nanoscale? The HAADF-STEM image clearly revealed a heterogeneous occurrence of heavy element nanoparticles less than 30 nm in diameter embedded in a matrix containing relatively lighter elements (As, Fe, and S) (Fig. 7A). The EDX mapping of an area containing the bright nanoparticles clearly revealed that Au nanodomains occur within the pyrite matrix (Fig. 7B). HAADF-STEM was also able to show the lattice image of gold nanoparticles in high-resolution mode (Fig. 7C). The lattice image of gold domains showed a perfect array of gold atoms, suggesting that gold atoms do not exist in an interatomic site of pyrite but as gold metal crystals. The FFT image of the high-resolution HAADF-STEM was indexed and determined to be structurally consistent with elemental gold. In this example, the occurrence and form of gold nanoparticles in high enough concentrations to account for the majority of gold in the rim were, for the first time, directly established in samples from a Carlin-type gold deposit.

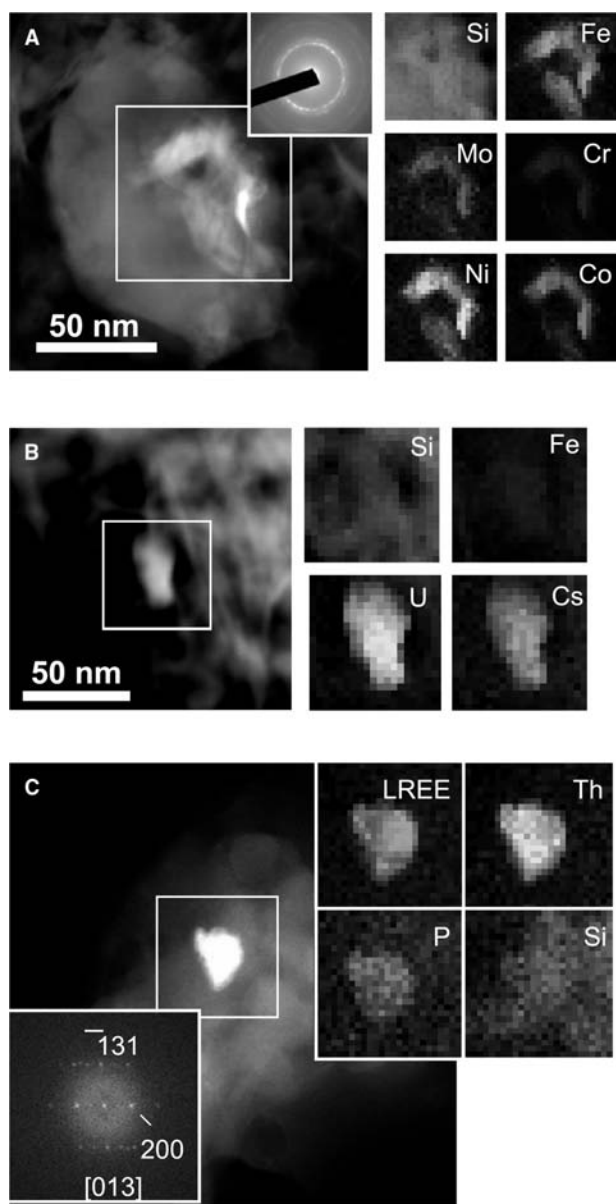


**Fig. 6** HAADF-STEM image and the elemental maps of groundwater colloids bearing potential fissiogenic elements from the ER-20-5 well at the Nevada test site. (A) A Co-bearing colloid. Cobalt associated with other metallic compounds Ni, Mo, Cr, and Fe. The structure is similar to the alloy phase, awaruite, based on the diffraction pattern. (B) A Cs-bearing colloid. Cesium is associated with only U, whereas Fe and Si maps are derived from background phases. The Cs phase is anticipated to be cesium uranate. (C) An Eu-bearing phosphate phase with a monazite structure contained the other light rare earth elements.

### Lead in an Early Archean Zircon

Zircon ( $\text{ZrSiO}_4$ ) is one of the most thoroughly studied natural phases because of its predominant use in geochronology<sup>[5]</sup> and other isotopic studies.<sup>[35–37]</sup> Zircon has also been proposed as a waste form for

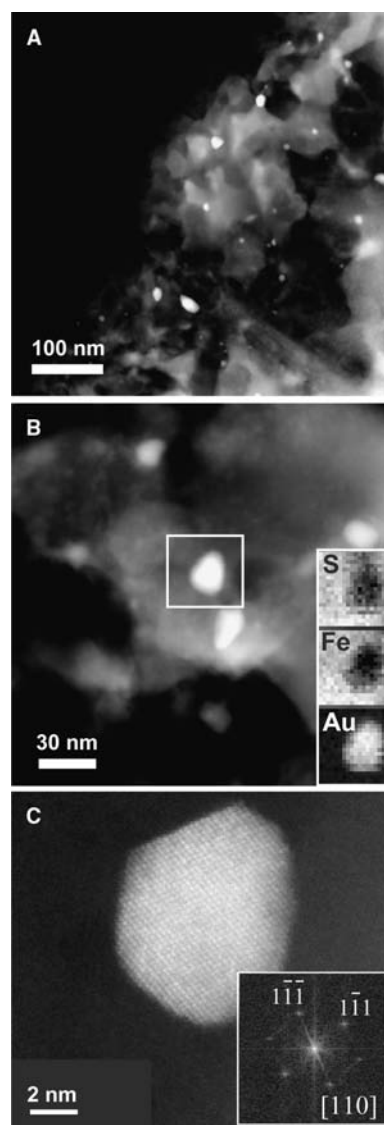


**Fig. 7** (A) A HAADF-STEM image of arsenian pyrite rim developing over pyrite grains from Twin Creeks, NV shows that many bright particles are embedded in arsenian pyrite matrix. (B) The elemental maps indicate that the nanodomains consist of Au. (C) A HR-HAADF-STEM image of a bright nanodomain reveals evidence of crystalline of gold at an atomic scale. Inset: The FFT showing an indexed pattern consistent with native gold. *Source:* Panels a and b from Ref.<sup>[17]</sup>.

immobilization of plutonium from dismantled nuclear weapons<sup>[38]</sup> because it is so physically and chemically durable.<sup>[38]</sup> In each of these applications, the loss of trace elements, in particular U, Pb, and Pu, is of critical interest. Furthermore, elemental loss may be more enhanced by radiation damage caused by the  $\alpha$ -decay of constituent actinides  $^{232}\text{Th}$ ,  $^{235}\text{U}$ ,  $^{238}\text{U}$ , and radionuclides in their decay series.<sup>[39]</sup> The fate of Pb is critical in U–Th–Pb isotopic dating because Pb loss caused by radiation-enhanced



alteration of zircon is a common cause of discordant dates.<sup>[40,41]</sup> Thus the diffusion of Pb, coupled with the diffusion of U and Th, has been extensively studied, and the Pb diffusion rate is generally considered to be faster than that of the tetravalent actinides U, Th, and Pu.<sup>[42,43]</sup>

Although a previous study<sup>[43]</sup> has pointed out that the valence of Pb in zircon must affect the Pb diffusion rate, the form of Pb in zircon has never been determined because of its relatively low concentration in zircon. In this study, zircon crystals from the Jack Hills meta-sedimentary belt, representative of some of the oldest minerals of the Earth (sample 01-JH-54: age range 4.4–3.3 Ga),<sup>[44]</sup> were investigated using advanced TEM techniques. Because zircon is relatively resistant to electron beam effects and the mass of Pb is considerably greater than the elements comprising the zircon matrix (Zr, Si, and O), high-resolution HAADF-STEM and nanoelemental mapping were used to determine the location and distribution of Pb within zircon.

In a well-crystalline area of the zircon sample, HAADF-STEM imaging provides a Z-contrast image in which Pb-rich regions will appear brighter against the lower average atomic mass of the zircon matrix. This technique revealed some relatively high-contrast patches (~5 nm in the diameter) (Fig. 8A), and nano-scale elemental maps confirmed higher concentrations of Pb in these areas. The Zr content was significantly depleted in the Pb-rich region, whereas the Si distribution in the same region did not show any detectable depletion (Fig. 8A). Semiquantitative analyses indicated that the concentration of Pb in the white spots was ~3 wt.% (elemental) (Fig. 8C). High-resolution (HR) HAADF-STEM images of a Pb-rich region show a continuous zircon structure without distortion across the Pb-rich region (Fig. 8C). Because the HR-HAADF-STEM image is formed by an incoherent imaging process,<sup>[45]</sup> the Pb atoms simply appear as brighter spots than Zr, although Zr atoms appear as relatively bright spots compared with Si and O (Fig. 8D and E). The FFT image of Fig. 8C was

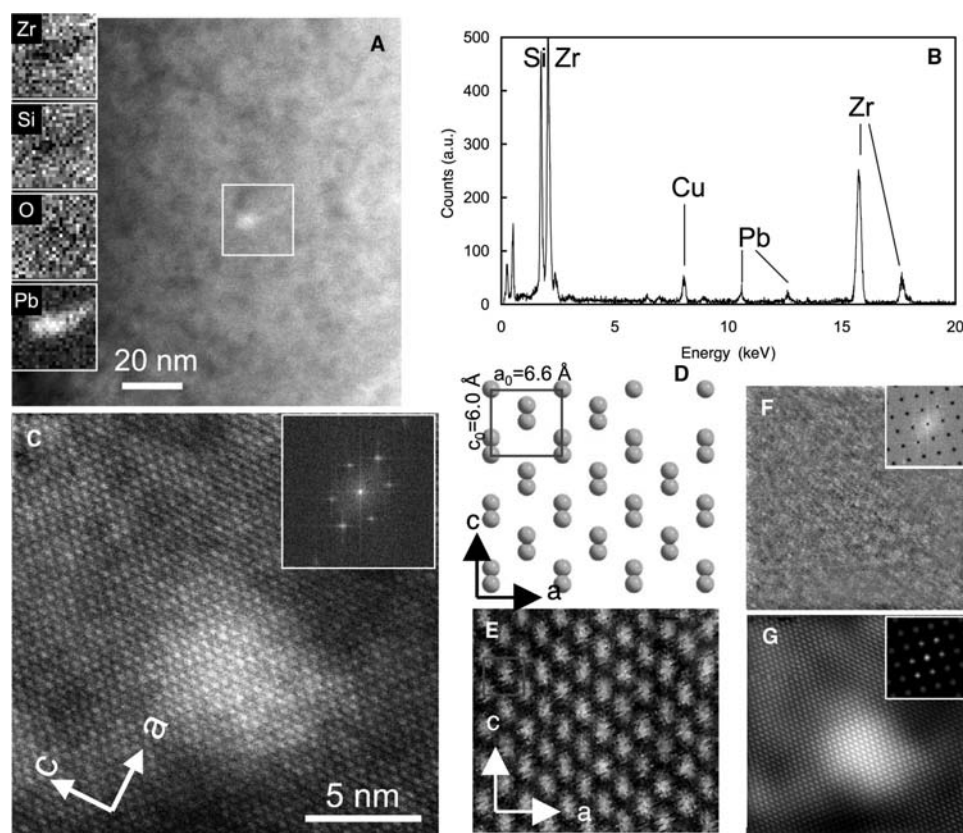


**Fig. 8** Patchy concentrations of Pb in zircon. (A) HAADF-STEM image with elemental maps of the boxed region. (B) The EDX spectrum of the bright region in (A) analyzed by a nanoprobe (1 nm in the diameter). Copper peak is derived from Cu grid. (C) HR-HAADF-STEM image from the view along [010] with the inset of the FFT image. (D) The projected position of Zr atoms in zircon structure along [010], based on the configuration of Zr atoms in zircon.<sup>[42]</sup> The radius of the ball is scaled to the ionic radius of  $\text{Zr}^{4+}$ . The box represents the unit cell. (E) A typical image of pure zircon using HR-HAADF-STEM. The relatively heavier element, Zr, shows the brightest contrast compared to Si and O. (F) The inverse FFT image from the opaquely masked the diffraction pattern (inset). (G) The inverse FFT image from the masked diffraction (inset). *Source:* From Ref.<sup>[35]</sup>.

masked to extract structural information (Fig. 8F and G). The filtered image suggest that: 1) Pb atoms were incorporated directly into the zircon structure; and 2) there is no other phase that contains Pb (Fig. 8F and G). Based on the distribution of Pb in this area (Fig. 8A) and the structural information provided by HR-HAADF-STEM (Fig. 8B), we conclude that the Pb substitutes directly for Zr in the zircon structure. The replacement of Zr by Pb without distortion of the zircon lattice requires that the ionic radius of the incorporated Pb be comparable to that of  $Zr^{4+}$ , implying that Pb in zircon is tetravalent. However, the Pb–O system is dominated by PbO under typical geological conditions, with a small stability field for native Pb, whereas the stability field for  $PbO_2$  exists only at far more oxidizing conditions.<sup>[46]</sup> One explanation for the incorporation of tetravalent Pb into the zircon structure is that the compatibility of the size and charge with  $Zr^{4+}$  results in an expansion of the  $Pb^{4+}$  stability field.

In addition to the patchy occurrence of Pb, numerous fission tracks (<5 nm width) created by high-energy (~100 MeV) heavy particles from spontaneous fission events were imaged (Fig. 9A and B). The majority of the fission tracks showed a dark contrast in the HAADF-STEM images; however, one fission track showed bright contrast throughout the length of the entire track (Fig. 9C). The elemental maps indicated that the fission track had a higher concentration of Pb than

the matrix. The HR-HAADF-STEM image of this area (Fig. 9D) indicates that: 1) the edge of the zircon lattice (arrow 1) shows a lattice image with higher contrast than the bulk zircon matrix, suggesting the incorporation of Pb atoms in the zircon lattice adjacent to the fission track. The incorporation of Pb in the surrounding zircon matrix could be caused by diffusion from accumulated Pb in the fission track; 2) there is no continuous lattice within the track (arrow 2). The interface between the zircon matrix and the fission track (arrow 3) shows a disordered array of bright contrast, suggesting that the accumulated Pb is not in a crystalline phase, or, if crystalline, is without any preferred orientation relative to the surrounding zircon structure. In addition, the oxygen distribution in this area does not show any evidence of O depletion in the fission track, which indicates that Pb is not present as elemental Pb.

The occurrence of Pb in the fission track is obviously not original because spontaneous fission occurred after zircon formation. Thus Pb accumulated in the track by diffusion, which, in the case of the images shown in Fig. 9C and D, appears to be at the end of the fission track. A similar texture of U or Th accumulation in the fission track was not observed. In general, fission tracks are amorphous regions,<sup>[47]</sup> as anticipated by irradiation experiments using highly energetic heavy ions.<sup>[39]</sup> The Pb that has accumulated in the fission track observed here suggests that Pb has diffused through the amorphous

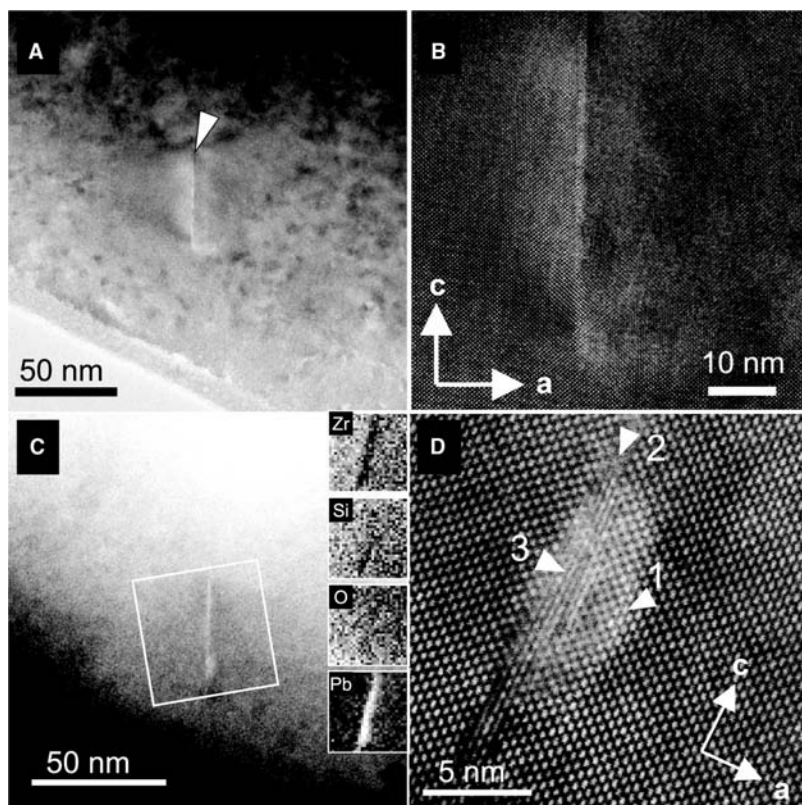


**Fig. 9** Pb accumulation in a fission track. (A) Bright-field TEM image of a fission track. (B) HRTEM image of the fission track from the view along [010]. The direction of the fission track is parallel to the (010) plane. (C) HAADF-STEM image of the fission track with the elemental maps of the boxed area. (D) HR-HAADF-STEM image of the fission track (the boxed area in panel C) from the view along [010]. Source: From Ref.<sup>[35]</sup>.

volumes, such as fission tracks, as well as metamict domains resulting from the accumulation of  $\alpha$ -decay event damage. In fact, previous experiments<sup>[48,49]</sup> on the Pb diffusion rate in zircon have predicted that Pb diffusion through highly damaged paths would increase the diffusion rate. These results show the importance of Pb diffusion through amorphous domains that result from radiation damage.

## CONCLUSION

Each of these briefly described examples demonstrates that HAADF-STEM is a powerful technique for the investigation and identification of trace elements in nanoscale particles (either crystalline or amorphous). This is a particularly useful technique when relatively heavy elements occur at extremely low bulk concentrations (parts per billion to parts per million). When there is a relatively large difference in atomic mass among constituent elements, HR-HAADF-STEM can provide useful information on the elemental distribution at the near-atomic scale. Once the nanoparticles are located by HAADF-STEM, characterization can be also completed using HRTEM. The combination of HAADF-STEM, STEM-EDX mapping, and HRTEM is presently the only method that can provide a complete characterization of each heavy trace element at the nanoscale. HAADF-STEM-EDX is a breakthrough technique that will have many applications in nanogeoscience and environmental science.

## ACKNOWLEDGMENTS

The authors are grateful to Drs. M. Kawasaki and S. Johnson (JEOL USA, Inc.) for technical advice in the use of the HAADF-STEM. Profs. S. E. Kesler and G. J. Keeler (University of Michigan) and Dr. A. B. Kersting (Lawrence Livermore National Laboratory) kindly provided the samples. We thank Drs. J. F. Mansfield and C. J. Wauchope for daily maintenance of 2010F. Electron microscopy was completed at the Electron Microbeam Analysis Laboratory (EMAL) at the University of Michigan. This work was supported by the University of Michigan's GeoScience and Engineering Initiative and the Environmental Management Sciences Program of DOE (DE-FG07-97ER14816).

## REFERENCES

- Hochella, M.F., Jr. There's plenty of room at the bottom: Nanoscience in geochemistry. *Geochim. Cosmochim. Acta* **2002**, *66* (5), 735–743.
- Banfield, J.F.; Zhang, H. Nanoparticles in the Environment. In *Nanoparticles and the Environment*; Reviews in Mineralogy and Geochemistry; Banfield, J.F., Navrotsky, A., Eds.; Mineralogical Society of America: Washington, DC, 2001; Vol. 44, 1–58.
- Fergusson, J.E. *The Heavy Elements, Chemistry, Environmental Impact and Health Effects*; Pergamon: New York, 1990.
- Nriagu, J. Heavy metals and the origin of life. *J. Phys.*, **IV** **2003**, *107*, 969–974.
- Krogh, T.E. Improved accuracy of U–Pb zircon ages by the creation of more concordant system using an air abrasion technique. *Geochim. Cosmochim. Acta* **1982**, *46* (4), 637–649.
- Buffat, P.; Borel, J.P. Size effect on the melting temperature of gold. *Phys. Rev., A* **1976**, *13*, 2287–2298.
- Halperin, W.P. Quantum size effects in metal particles. *Rev. Mod. Phys.* **1986**, *58*, 533–606.
- McCrone, W.C. Ultra-microanalysis. Part. *Anal.* **1968**, *1*, 49–59.
- Becker, U.; Hochella, M., Jr.; Vaughan, D.J. The adsorption of gold to galena surfaces: calculation of adsorption/reduction energies, reaction mechanisms, XPS spectra, and STEM images. *Geochim. Cosmochim. Acta* **1997**, *61* (17), 3565–3585.
- Maynard, A.D. Overview of methods for analyzing single ultrafine particles. *Philos. Trans. R. Soc. Lond., A* **2000**, *358*, 2593–2610.
- Xhoffer, C.; Wouters, L.; Artaxo, P.; Van Put, A.; Van Grieken, R. Characterization of individual environmental particles by beam techniques. In *Environmental Particles*; Buffle, J., van Leeuwen, H.P., Eds.; Lewis Publishers: Chelsea, MI, 1992; Vol. 1.
- Mavrocordatos, D.; Mondy-Couture, C.; Atteia, O.; Leppard, G.G.; Perret, D. Formation of a distinct class of Fe–Ca(C<sub>org</sub>)-rich particles in a complex peat–karst system. *J. Hydrol.* **2000**, *237* (3–4), 234–247.
- Couture, C.; Mavrocordatos, D.; Atteia, O.; Perret, D. The genesis and transformation of organo-mineral colloids in a drained peatland area. *Phys. Chem. Earth* **1998**, *23* (2), 153–157.
- Wells, M.L.; Goldberg, E.D. Occurrence of small colloids in sea-water. *Nature* **1991**, *353* (6342), 342–344.
- Hochella, M.F., Jr.; Moore, J.N.; Golla, U.; Putnis, A. A TEM study of samples from acid mine drainage systems: metal–mineral association with implications for transport. *Geochim. Cosmochim. Acta* **1999**, *63* (19–20), 3395–3406.
- Suzuki, Y.; Kelly, S.D.; Kemner, K.M.; Banfield, J.F. Nanometre-size products of uranium bioreduction. *Nature* **2002**, *419* (6903), 134.
- Utsunomiya, S.; Ewing, R.C. Application of high-angle annular dark field scanning transmission electron microscopy, scanning transmission electron microscopy–energy dispersive X-ray spectrometry, and energy-filtered transmission electron microscopy to the characterization of nanoparticles in the environment. *Environ. Sci. Technol.* **2003**, *37* (4), 786–791.
- Kirkland, E.J. *Advanced Computing in Electron Microscopy*, 1st Ed.; Plenum Press: New York, 1998.



19. Utsunomiya, S.; Jensen, K.A.; Keeler, G.J.; Ewing, R.C. Uraninite and fullerene in atmospheric particulates. *Environ. Sci. Technol.* **2002**, *36* (23), 4943–4947.
20. Pope, C.A., III; Burnett, R.T.; Thun, M.J.; Galle, E.E.; Krewski, D.; Ito, K.; Thurston, G.D. Lung cancer, cardiopulmonary mortality, and long-term exposure to fine particulate air pollution. *JAMA, J. Am. Med. Assoc.* **2002**, *287* (9), 1132–1142.
21. Greenwood, N.N.; Earnshaw, A. *Chemistry of the Elements*; Pergamon Press: Oxford, 1984.
22. Smith, K.L.; Smoot, L.D.; Fletcher, T.H. *Fundamentals of Coal Combustion: For Clean and Efficient Use*; Coal Science and Technology Series; Smoot, L.D., Ed.; Elsevier: Amsterdam, 1993; 20, 131–234.
23. Katrinak, K.A.; Rez, P.; Buseck, P.R. Structural variations in individual carbonaceous particles from and urban aerosol. *Environ. Sci. Technol.* **1992**, *26* (10), 1967–1976.
24. Stumm, W. Coagulation and filtration in water and wastewater treatment become more efficiency of collisions between particles and particles and filter grains. *Environ. Sci. Technol.* **1977**, *11* (12), 1066–1070.
25. McCarthy, J.F.; Zachara, J.M. Subsurface transport of contaminants. *Environ. Sci. Technol.* **1989**, *23* (5), 496–502.
26. Traexler, K.A.; Ewing, R.C. *Colloid Formation and the Potential Effects on Radionuclide Transport in a Geologic Repository for Spent Nuclear Fuel*; Department of Energy, 2002. (DOE/SNF/REP-070).
27. Nelson, D.M.; Penrose, W.R.; Karttunen, J.O.; Mehlhaff, P. Effects of dissolved organic carbon on the adsorption properties of plutonium in natural waters. *Environ. Sci. Technol.* **1985**, *19* (2), 127–131.
28. Kim, J.I. Actinide colloid generation in groundwater. *Radiochim. Acta* **1991**, *52/53*, 71–81.
29. Silva, R.J.; Nitsche, H. Actinide environmental chemistry. *Radiochim. Acta* **1995**, *70/71*, 377–396.
30. Kersting, A.B.; Efurud, D.W.; Finnegan, D.L.; Rokop, D.J.; Smith, D.K.; Thompson, J.L. Migration of plutonium in ground water at the Nevada test site. *Nature* **1999**, *393* (6714), 56–59.
31. Palenik, C.S.; Utsunomiya, S.; Reich, M.; Kesler, S.E.; Ewing, R.C. Invisible gold revealed: direct imaging of gold nanoparticles from a carlin-type deposit. *Am. Mineral*. Submitted.
32. Simon, G.; Kesler, S.E.; Ghryssoulis, S. Geochemistry and texture of gold-bearing arsenian pyrite, twin creeks, Nevada: implications for deposition of gold in carlin-type deposits. *Econ. Geol. Bull. Soc.* **1999**, *94* (3), 405–422.
33. He, M.S. Occurrence and distribution of invisible gold in a carlin-type gold deposit in China. *Am. Mineral.* **1991**, *76* (11–12), 1964–1972.
34. Pals, D.W.; Spry, P.G.; Chryssoulis, S. Invisible gold and tellurium in arsenic-rich pyrite from the Emperor gold deposit, Fiji; implications for gold distribution and deposition. *Econ. Geol. Bull. Soc.* **2003**, *98* (3), 479–493.
35. Utsunomiya, S.; Palenik, C.S.; Valley, J.W.; Cavosie, A.; Wilde, S.A.; Ewing, R.C. Fate of Pb in an Archean zircon. *Geochim. Cosmochim. Acta*. Submitted.
36. Wilde, S.A.; Valley, J.W.; Peck, W.H.; Graham, C.M. Evidence from detrital zircons for the existence of continental crust and oceans on the Earth 4.4 Gyr ago. *Nature* **2001**, *409* (6817), 175–178.
37. Valley, J.W. Oxygen Isotopes in Zircon. In *Zircon; Reviews in Mineralogy and Geochemistry*; Hanchar, J.M., Hoskin, P.W.O., Eds.; Mineralogical Society of America: Washington, DC, 2003; Vol. 53, *in press*.
38. Ewing, R.C. Nuclear waste forms for actinides. *Proc. Natl. Acad. Sci. U. S. A.* **1999**, *96*, 3432–3439.
39. Ewing, R.C.; Meldrum, A.; Wang, L.M.; Weber, W.J.; Corrales, L.R. *Zircon; Reviews in Mineralogy and Geochemistry*; Hanchar, J.M., Hoskin, P.W.O., Eds.; Mineralogical Society of America: Washington, DC, 2003; Vol. 53, *in press*.
40. Pidgeon, R.T.; O'Neil, J.R.; Silver, L.T. Uranium and lead isotopic stability in a metamict zircon under experimental hydrothermal condition. *Science* **1966**, *154* (3756), 1538–1540.
41. Craig, H. Zircon lead loss—A kinetic mode. *Science* **1968**, *159* (3813), 447.
42. Lee, J.K.W.; Williams, I.S.; Ellis, D.J. Pb, U and Th diffusion in natural zircon. *Nature* **1997**, *390* (6656), 159–162.
43. Cherniak, D.J.; Watson, E.B. Pb diffusion in zircon. *Chem. Geol.* **2000**, *172* (1–2), 5–24.
44. Cavosie, A.J.; Valley, J.W.; Liu, D.; Wilde, S.A.; Grant, M. In *3.7 Ga Overgrowths on a 4.33 Ga Zircon from Jack Hills: Evidence of Early Crustal Recycling*, Annual Meeting of Geological Society of America, Denver, CO, Oct., 27–30, 2002; Geological Society of America: Denver, 2002; Vol. 34, 365.
45. Pennycook, S.J.; Jesson, D.E. High-resolution incoherent imaging of crystals. *Phys. Rev. Lett.* **1990**, *64* (8), 938–941.
46. Watson, E.B.; Cherniak, D.J.; Hanchar, J.M.; Harrison, T.M.; Wark, D.A. The incorporation of Pb into zircon. *Chem. Geol.* **1997**, *141* (1–2), 19–31.
47. Yada, K.; Tanji, T.; Sunagawa, I. Application of lattice imagery to radiation damage investigation in natural zircon. *Phys. Chem. Miner.* **1981**, *7* (1), 47–52.
48. Cherniak, D.J.; Lanford, W.A.; Ryerson, F.J. Lead diffusion in apatite and zircon using ion implantation and Rutherford backscattering techniques. *Geochim. Cosmochim. Acta* **1991**, *55* (6), 1663–1673.
49. Cherniak, D.J. Lead diffusion in titanite and preliminary results on the effects of radiation damage on Pb transport. *Chem. Geol.* **1993**, *110* (1–3), 177–194.

# Environmental Nanoparticles

Alexandra Navrotsky

Department of Chemical Engineering and Materials Science, University of California–Davis, Davis, California, U.S.A.

## INTRODUCTION

Nanoparticles have no exact definition, but they are aggregates of atoms bridging the continuum between small molecular clusters of a few atoms and dimensions of 0.2–1 nm and chunks of solid containing millions of atoms and having the properties of macroscopic bulk material. In water, nanoparticles include colloids; in air, they include aerosols. Nanoparticles are ubiquitous. We pay to have them. We pay more to not have them. They occur as dust in the air, as suspended particles that make river water slightly murky, in soil, in volcanic ash, in our bodies, and in technological applications ranging from ultratough ceramics to microelectronics. They both pollute our environment and help keep it clean. Microbes feast on, manufacture, and excrete nanoparticles.

Understanding nanoparticle formation and properties requires sophisticated physics, chemistry, and materials science. Tailoring nanomaterials to specific applications requires both science and Edisonian inventiveness. Applying them to technology is state-of-the-art engineering. Tracing their transport and fate in the environment invokes geology, hydrology, and atmospheric science. Applying them to improving soil fertility and water retention links soil science and agriculture to surface chemistry. Understanding their biological interactions brings in fields ranging from microbiology to medicine. Probing the impact of nanoparticles on humans and of human behavior on the production and control of nanoparticles requires the behavioral and social sciences, e.g., in dealing with issues of automotive pollution. The purpose of this review is to describe some of the unique features of nanoparticles and to discuss their occurrence and importance in the natural environment.

Although we often think of the natural environment as that part of the planet which we can see, a somewhat broader definition includes the “critical zone”: the atmosphere, hydrosphere, and shallow portion of the solid earth that exchange matter on a geologically short time scale, on the order of tens to thousands of years. This critical zone affects us directly, and our activities influence it. Because of the active chemical reactions continuously taking place in the critical zone, and because its temperatures and pressures are

relatively low and it is dominated by water, solids are constantly being formed and decomposed. Many of these solids start out as nanoparticles; many remain so. In a yet broader sense, our entire planet from crust to core, the solar system, and the galaxy are part of our environment.

## PHYSICAL CHEMISTRY OF NANOPARTICLES

A major feature of nanoparticles is their high surface-to-volume ratio. Fig. 1 shows the volume fraction within 0.5 nm of the surface for a spherical particle of radius  $r$ . One can think of this fraction either as the fraction of atoms likely to be influenced by processes at the surface, or as the fraction of the volume of a material that could be taken up by a 0.5-nm coating of another material. In the first case, because the surface dominates chemical reactivity, the increased surface to volume ratio means that nanoparticles dominate chemical reactions. In the second case, the ability to carry a substantial coating offers a mechanism for the transport of nutrients or pollutants.

Many oxides are *polymorphic*, exhibiting several crystal structures as a function of pressure and temperature. Often, nanosized oxide particles crystallize in structures different from that of large crystals of the same composition.<sup>[1]</sup> Examples are  $\gamma$ -Al<sub>2</sub>O<sub>3</sub>, a defect spinel rather than  $\alpha$ -Al<sub>2</sub>O<sub>3</sub>, corundum,  $\gamma$ -Fe<sub>2</sub>O<sub>3</sub>, the defect spinel maghemite rather than  $\alpha$ -Fe<sub>2</sub>O<sub>3</sub>, hematite, and the anatase and brookite forms of TiO<sub>2</sub> rather than rutile. From arguments based on transformation sequences and the occurrence of phases, it was long argued that there may be a crossover in phase stability at the nanoscale if the structure which is metastable for large particles has a significantly lower surface energy.<sup>[2]</sup> This has been proven for alumina and titania in recent calorimetric studies (Fig. 2).<sup>[3,4]</sup> The resulting transformation enthalpies and surface energies, and those of other related systems are shown in Table 1. Another interesting feature is that the hydrous phases AlOOH boehmite and FeOOH goethite have significantly lower surface energies than their anhydrous counterparts, Al<sub>2</sub>O<sub>3</sub> and Fe<sub>2</sub>O<sub>3</sub>.<sup>[5,6]</sup> Whether this is a general feature of hydrous minerals with hydroxylated surfaces is not yet known.

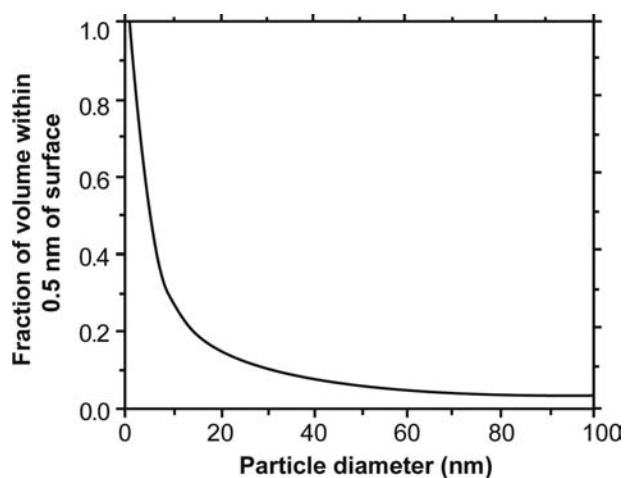


**Fig. 1** Volume fraction of a nanoparticle within 0.5 nm of the surface as a function of particle radius. *Source:* From Ref.<sup>[41]</sup>. Kluwer Academic Publishers.

As particles become less than about 10 nm in size, their X-ray diffraction patterns are broadened sufficiently that they begin to appear “X-ray amorphous” (Fig. 3). This term lacks exact definition. High-resolution electron microscopy may still detect periodicity, and short-range order is certainly present.<sup>[7]</sup> The identification of structure in 1–10 nm particles is very difficult, and phases are empirically described as, for example, “two line ferrihydrite,” based on x-ray diffraction patterns.<sup>[8]</sup>

## NANOPARTICLES IN SOIL AND WATER

Soil is a complex aggregate of inorganic, organic, and biological material.<sup>[9]</sup> Its constituents of largest size are rocks and gravel, small animals, plant roots, and other debris. Smaller mineral grains, clumps of organic matter, and microorganisms make up an intermediate size fraction. The smallest particles, ranging into the nanoscale, are clays, iron oxides, and other minerals. These are often heterogeneous and coated by other minerals and organic matter. The entire composite is porous and hydrated. The percolation of water in soil transports both nanoparticles and dissolved organic and inorganic species. The texture and porosity, as well as the chemical composition and pH, are crucial to biological productivity. The surfaces of nanoparticles provide much of the chemical reactivity for both biological and abiotic processes.

Major aluminosilicate minerals in soils include clays, zeolites, and poorly crystalline phases (Table 2). These can change their water content in response to ambient conditions, often swelling in wet seasons, and shrinking in dry seasons. These nanophase materials are major controllers of soil moisture and

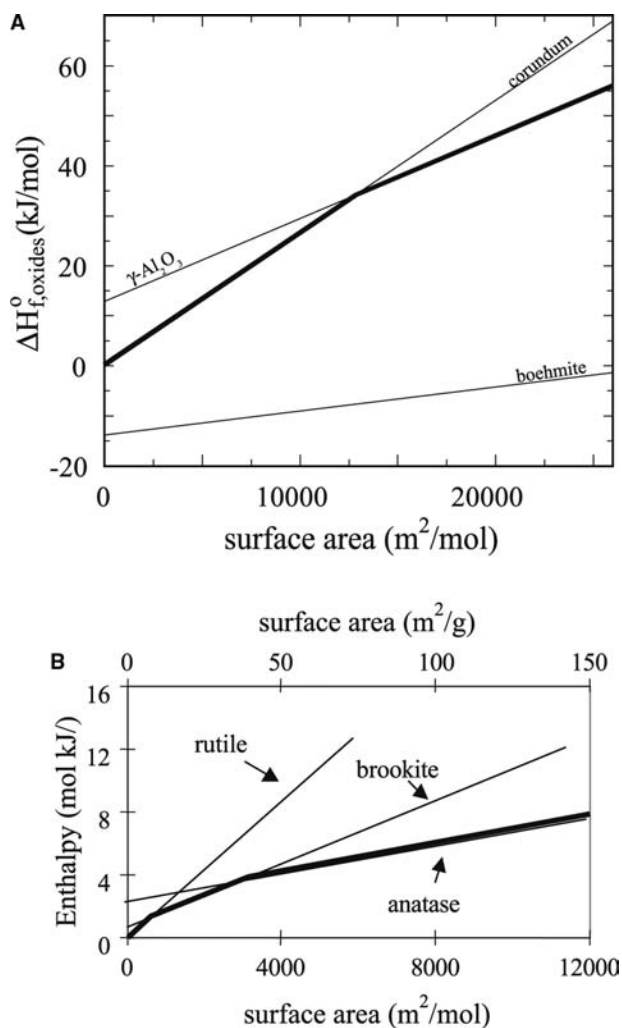


**Fig. 2** (A) Enthalpies of alumina polymorphs as a function of surface area. *Source:* From Ref.<sup>[3]</sup>. (B) Enthalpies of titania polymorphs as a function of surface area. The heavy lines show the stable polymorphs in each size range. *Source:* From Ref.<sup>[4]</sup>. PNAS.

permeability. Iron and manganese oxides are another class of major soil minerals. Their extensive polymorphism at the nanoscale makes them highly variable. They sequester and/or transport and make available the essential plant nutrient iron, as well as other essential transition metals (cobalt, copper, zinc, etc.). They frequently carry coatings of other metal oxides and oxyhydroxides, including toxic metals such as lead and chromium. They also frequently have organic coatings. Sulfates, including the jarosite–alunite family of hydrated [(K, Na), (Al, Fe)] sulfates, are another important constituent. In alkaline and arid environments, other sulfates and halides form, and their formation, dissolution, and transport is a major issue in heavily irrigated regions. How much these processes are controlled by nanoscale phenomena is not known.

**Table 1** Energetic parameters for oxide and oxyhydroxide polymorphs

Formula	Polymorph	Metastability (kJ/mol)	Surface energy (J/m <sup>2</sup> )
Al <sub>2</sub> O <sub>3</sub> <sup>a</sup>	Corundum ( $\alpha$ )	0	2.6
	Spinel ( $\gamma$ )	13.4	1.7
Fe <sub>2</sub> O <sub>3</sub> <sup>b</sup>	Hematite	0	0.8
	Maghemite	20	0.8
TiO <sub>2</sub> <sup>c</sup>	Rutile	0	2.2
	Brookite	0.7	1.0
	Anatase	2.6	0.4
AlOOH <sup>d</sup>	Diaspore	0	?
	Boehmite	4.9	0.5
FeOOH <sup>b</sup>	Goethite	0	0.3
	Lepidocrocite		0.3

<sup>a</sup>From Ref.<sup>[3]</sup>.<sup>b</sup>From Ref.<sup>[6]</sup>.<sup>c</sup>From Ref.<sup>[4]</sup>.<sup>d</sup>From Ref.<sup>[5]</sup>.

Groundwater is constantly in touch with soil and rock, and minerals are dissolving and precipitating as it flows. The load of fine sediments in streams and groundwater can be substantial, especially during spring floods. The Missouri River is called “the Big Muddy” because of its load of particulate matter, a large fraction of which is of nanoscale dimensions. The yearly flooding of the Nile, depositing fertile soil with its large nanoparticle content, made ancient

Egyptian civilization flourish. Today, one of the major concerns of our system of dams, especially in the arid western United States, is interference with the normal cycle of sediment transport and “silt up” of the lakes behind the dams. Silt is partly nanoparticles.

Contaminants and pollutants in water can be transported as aqueous ions (dimensions <0.5 nm), as molecular clusters (0.5–2 nm), as nanoparticles (2–100 nm), as larger colloids (100–1000 nm), and as macroscopic particles (>1  $\mu$ m). These size range distinctions are rather arbitrary and serve to illustrate the continuity between the dissolved and the solid state. Several examples illustrate this complexity. Aluminum oxyhydroxide particles can transport transition metals such as nickel, cobalt, and zinc, seemingly as adsorbed coatings. Initially thought to be loosely bound metal complexes at the surface of the aluminum oxyhydroxide mineral grain, these are now realized to be precipitates, only a few atomic layers thick, of mixed double hydroxides of the hydrotalcite family, in which anions such as carbonate play an essential role.<sup>[10]</sup> The transport of plutonium through groundwater is a concern in old plutonium processing facilities such as the Hanford, WA atomic energy reservation, in the Nevada nuclear test site, and in the planned nuclear waste repository at Yucca Mountain, Nevada. There remain questions of permeability and the adhesion of particles to the rock and engineered barrier walls, of colloid transport, of biological transport, and of mineral precipitation which can change the rate of progress of a contamination plume. Linking laboratory scale, field

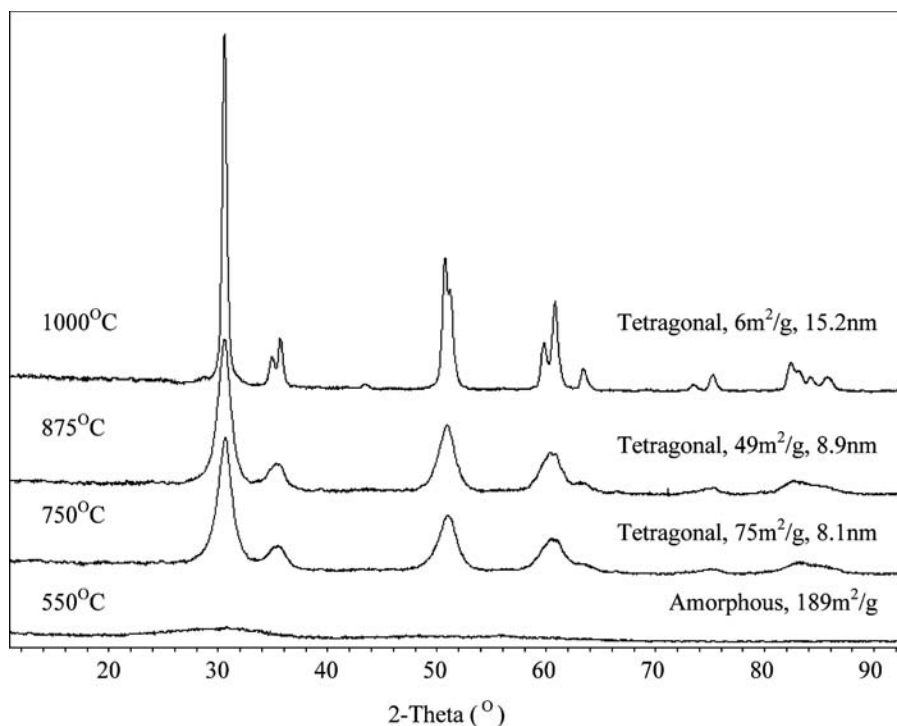


**Fig. 3** Powder X-ray diffraction patterns of sol-gel zirconia heated at various temperatures. The structure and average particle diameters are indicated. *Source:* M. Pitcher and A. Navrotsky, unpublished data.

**Table 2** Major soil minerals and constituents

Type	Composition	Structures
Clay	Hydrated aluminosilicate	Layered
Zeolite	Hydrated aluminosilicate	Three-dimensional porous
Salts	NaCl, Na <sub>2</sub> SO <sub>4</sub> , CaSO <sub>4</sub>	Ionic crystals
Carbonates	CaCO <sub>3</sub> –MgCO <sub>3</sub> –FeCO <sub>3</sub>	Calcite, dolomite, others
Allophane	Hydrated aluminosilicate gel	Amorphous
Iron oxides	Fe <sub>2</sub> O <sub>3</sub> , FeOOH	Various polymorphs
Aluminum oxides	AlOOH, Al(OH) <sub>3</sub>	Various polymorphs
Quartz	SiO <sub>2</sub>	Quartz
Manganese oxides	Mn <sub>2</sub> O <sub>3</sub> , MnOOH, MnO <sub>2</sub>	Various polymorphs
H <sub>2</sub> O	H <sub>2</sub> O	Water, ice, vapor
Organics	C–H–N–O	Large surface area amorphous colloids
Jarosite–alunite	Alkali (Fe, Al) sulfates	Ionic double salts

scale, and simulation studies of nanoparticle transport is an essential area of research for understanding radioactive and chemical contamination and geologic processes involving uranium and other actinides.<sup>[11]</sup>

When particles are below 5 nm in size, several other effects must be considered. Whereas for larger particles, most of the atoms are in specific planes or faces, for smaller ones, an increasing number of surface atoms must sit at the intersection of facets, in presumably even higher energy sites. An alternate, more macroscopic way of describing this is to consider the surface as curved, rather than as a series of planes. Then the surface energy per unit area is no longer a constant, but potentially increases quite rapidly with decreasing particle size. This unfavorable energy may be relaxed by the adsorption of various molecules on the surface, and there is evidence that the adsorption coefficient of organics rises steeply at very small particle size.<sup>[12]</sup>

The flocculation of colloids depends on the surface charge; the pH of which the surface is neutral is the “point of zero charge.”<sup>[13]</sup> Does this depend on particle size? This is an area of active research.

How do nanocrystals form from solution? The classical picture of nucleation and growth by addition of single atoms or ions is probably inadequate.<sup>[14]</sup> There is increasing evidence for clusters of atoms or ions in solution which contain 5–50 atoms and clearly show some of the structural features of the solid. An example is the Keggin-molecular cluster containing 13 aluminum atoms shown in Fig. 4.<sup>[16]</sup> It appears stable over a wide range of neutral to basic pH, and is probably a major precursor to and a dissolution product of aluminum oxyhydroxides.<sup>[17]</sup> The growth of TiO<sub>2</sub> anatase may occur by the oriented attachment of ~3-nm particles.<sup>[18]</sup> The growth of zeolites templated by organics may involve 3-nm cuboctahedral clusters.<sup>[19]</sup> Nanoclusters have been invoked in

the growth of sulfides in ore-forming solutions.<sup>[20]</sup> Characterization of such nanoscale precursors in aqueous solutions remains a major challenge.

The coarsening and phase transformation of nanoscale precipitates upon heating is equally important to the sol–gel synthesis of ceramics and the geologic compaction and diagenesis of buried sediments. Loss of water, loss of surface area, and phase transformations to the stable bulk polymorph are closely interlinked.<sup>[14]</sup> A nanoparticle with dimensions below 5 nm probably cannot maintain defects or dislocations; they can migrate to the surface and be annihilated.<sup>[21]</sup> An aggregate of such single domain nanocrystals, with disorder and impurities at their surfaces, may be a common morphology in nature. Such aggregates give smaller average particle size from X-ray peak broadening than from gas adsorption [Brunauer–Emmett–Teller (BET)] measurements.

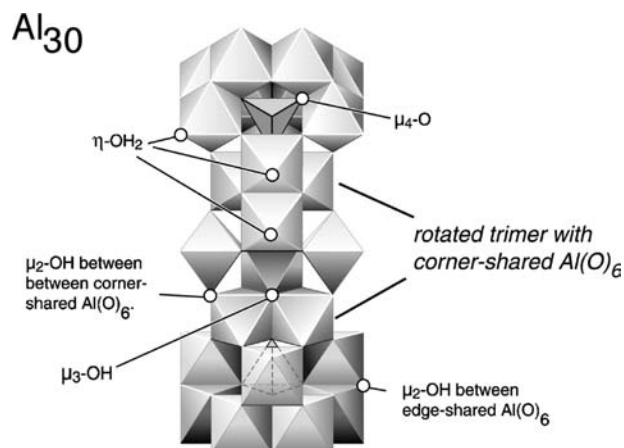


**Fig. 4** Al<sub>2</sub>O<sub>8</sub>Al<sub>28</sub>(OH)<sub>56</sub>(H<sub>2</sub>O)<sub>24</sub><sup>18+</sup>(aq) (often called Al<sub>30</sub>) cluster of 2 nm dimensions, which is intermediate in structure and properties between isolated ions and solid aluminum. Source: W.H. Casey, personal communications. From Ref.<sup>[15]</sup>.

Magnetic nanoparticles cannot hold a direction of magnetization for a long time because of thermal fluctuations.<sup>[22]</sup> The magnetic iron oxides found in magnetotactic bacteria, which are single domain particles, neither too large nor too small, provide orientation in the Earth's magnetic field (see below). On a geologic time scale (millions of years), magnetization of largely nanophase iron oxides provides a record of the variation of the Earth's magnetic field through time, including periodic reversals of north and south poles. Thus the ability or inability of nanoparticle oxides to retain magnetization is of critical importance.

## NANOPARTICLES IN THE ATMOSPHERE

Atmospheric particles include dust (rock and soil), sea salt, acids including sulfuric, organics (especially carbon), inorganics, and, of course, water and ice (Table 3). The atmosphere can carry particles of spherical equivalent diameters from 1 to  $10^5$  nm. Often, a trimodal distribution of particle sizes, with peaks in number density near 5, 50, and 300 nm, is seen.<sup>[23]</sup> The smaller particles account for most of the reactive surface area but little of the total mass.

Atmospheric particles affect the environment in many ways.<sup>[23,24]</sup> They reduce visibility (smog, haze) primarily through light scattering. They act as nuclei for water vapor condensation and cloud formation.

**Table 3** Atmospheric nanoparticles

Liquid droplets
Water
Sulfuric acid
Nitric acid
Sea water and other salt solutions
Organics
Solid particles
Ice (H <sub>2</sub> O)
NaCl
Na <sub>2</sub> SO <sub>4</sub>
CaSO <sub>4</sub> · 2H <sub>2</sub> O
NaNO <sub>3</sub>
H <sub>2</sub> SO <sub>4</sub> · 4H <sub>2</sub> O
HNO <sub>3</sub> · 3H <sub>2</sub> O
C (graphite, amorphous, fullerenes, nanotubes)
SiO <sub>2</sub>
Iron oxides
Clays
Organics
Many particles have core-shell structures and coatings

They are involved in radiative forcing, changing the ratio of absorbed sunlight to reflected sunlight. Thus they are implicated in global climate change. Their effect on radiative forcing can be positive (more energy adsorbed) or negative (more energy reflected), leading to warming or cooling, respectively.<sup>[23,24]</sup> Their net effect is a subject of vigorous research and controversy.

Anthropogenic particles contribute disproportionately to the fine particle fractions.<sup>[23]</sup> These may have very significant effects on climate and (see below) health. Soot (carbon) from burning coal and oil and from automobile (especially diesel) emissions contribute greatly to the atmospheric load of nanoparticles.

Particles in the atmosphere travel a long way. Dust from Africa is seen in Florida; industrial emissions from China are detected in North America. Particles are removed from the atmosphere by diffusion and gravitational settling (aided by small particles coalescing into larger ones) and by rain. The residence time of nanoparticles in the atmosphere ranges from minutes to days.<sup>[23]</sup>

Atmospheric nanoparticles are more involved in gas phase reactions than particles in soil and water.<sup>[24]</sup> Their formation may involve combustion synthesis, as in industrial or automobile emission. Mineral nanoparticle surfaces may catalyze the oxidation of SO<sub>2</sub> and NO<sub>2</sub>, leading to sulfuric and nitric acid. These acids can exist as gaseous species, liquids, or solid hydrates at low temperature. Nanoparticles are invoked in the depletion of atmospheric ozone by catalytic production of reactive chlorine compounds. Changes of phase (liquid to solid) are critical to the chemistry of sodium chloride and sodium nitrate particles, with their water content being controlled by available humidity.

Mineral dust particles may provide critical nutrients (e.g., iron) to the surface of the ocean far from land. The ocean's biological productivity is often limited by the availability of these nutrients; thus such inorganic nanoparticles may significantly influence the global cycling of carbon through ocean biomass.<sup>[25]</sup>

## NANOPARTICLES IN SEDIMENTS, ROCKS, AND THE DEEP EARTH

The debris of rock weathering is brought down river to the ocean in sediments consisting of nanoscale particles of clay, small quartz grains, and other minerals. Indeed, the terms "clay" and "silt" have a classic connotation of size fraction, although the former also implies a structural group of minerals, the layered aluminosilicates. In the ocean, carbonates precipitate, dissolve, and reprecipitate as a complex function of depth.<sup>[26]</sup> Both silica and various polymorphs of calcium carbonate (calcite, aragonite, vaterite) are produced by organisms such as diatoms, foraminifera, and



corals. Their debris rains down on the ocean bottom, forming sediments which often show annual cycles in composition and texture and which bear records of climate change, shifts in ecosystems, and catastrophic events such as meteor impacts.<sup>[27]</sup> These sediments start off largely nanoscale. They coarsen and dehydrate with time and depth of burial. The evolution of their organic matter leads to petroleum. The evolution of their minerals, involving coarsening and compaction, called diagenesis, leads to rocks such as limestones and shales. The nanoscale processes that take place (dehydration and organic loss, phase transformation, coarsening and densification) are natural analogs of ceramic processing which starts with nanoscale precipitates or gels.

Natural processes involving changes in temperature, pressure, acidity, and oxygen fugacity cause the concentration of trace metals into ore deposits. These often occur in hydrothermal systems, spatially contained circulations of hot, pressurized, metal-rich aqueous solutions. Our ability to mine low-grade deposits by chemical leaching techniques brings us into the world of nanoparticles and reactions at mineral surfaces. There is increasing evidence that microorganisms play an active role in ore deposition.<sup>[28,29]</sup> Hot springs at the surface produce deposits of nanoscale amorphous silica and other minerals, which may also be closely linked to microbial activity.<sup>[30]</sup>

At temperatures above a few hundred degrees Centigrade and pressures above a few kilobars, coarse-grained metamorphic and igneous rocks predominate. The interior of the Earth is layered, with seismic discontinuities delineating the crust, upper mantle, transition zone, lower mantle, and core. These discontinuities represent regions of rapidly changing density, mineralogy, and chemistry.<sup>[31]</sup> Ongoing phase transitions and chemical reactions can decrease the grain size of a material and render it easier to deform.<sup>[32]</sup> Thus nanoscale phenomena, occurring at specific locations, may play a disproportionate role in processes such as subduction, plate tectonics, earthquake generation, and volcanism. Shock processes, (e.g., meteor impact, nuclear detonation) also produce nanoparticles.

When a volcano erupts explosively, a plume of dust particle is sent into the atmosphere, sometimes reaching the stratosphere. These particles make beautiful sunsets but they also exert a significant cooling effect on climate for several years and pose a significant aviation hazard. Combining sedimentation, coarsening, subduction, volcanism, and weathering, there is an ongoing global geochemical cycle of nanoparticles, analogous in some ways to global geochemical cycles of elements such as carbon. However, the mass balances, or imbalances, in global nanoparticle production and consumption through time have not been characterized.

## NANOPARTICLES BEYOND THE EARTH

In the early stages of planet formation, dilute and more or less uniform gas condensed to form a series of mineral particles, with the order of condensation described by thermodynamic calculations based on the volatility and stability of these phases.<sup>[37]</sup> The more refractory oxides condensed earlier than those with higher volatility. These particles accreted, under the influence of gravity, to form our solar system. What was the nature of these initial particles? What was their size distribution? Were they crystalline or amorphous? Were metastable polymorphs formed? While the initial high temperatures might argue against such metastability, the low pressures and condensation from a vapor argue for it. In technological processes, chemical vapor deposition produces nanoscale amorphous silica “snow,” and combustion produces soot and inorganic nanoparticles. The role of nanoparticles in planetary accretion has not yet been explored. The change in stability at the nanoscale, which will be different for various compositions and polymorphs, may alter the sequence of condensation of phases. Are the particles now present in space as interplanetary dust partly or mostly nanoparticles?

The surfaces of the Moon and Mars, subject to “space weathering” by bombardment with meteorites of all sizes, contain an extensive fine grained dust or soil layer.<sup>[32]</sup> Samples of lunar soil, brought back by the Apollo missions, contain a distribution of particle sizes of spherules and irregular shards. Their particle size distribution appears not to have been a subject of active interest, but clearly a significant number are in the nanoregime. The red surface of Mars appears to be dominated by various fine-grained or nanophase iron oxides. Until Martian sample return missions, planned to occur in the next decade or two, bring some of this material to Earth, we must rely on remote sensing technology (spectroscopic techniques) and instrumentation on Martian landers (possibly Mossbauer spectroscopy, X-ray fluorescence, and X-ray diffraction) to obtain information on the composition and structure of Martian soil. Considering the difficulty of characterizing iron oxide nanoparticles in the best laboratories on Earth, definitive conclusions about the nature of Martian soil are unlikely until we have some samples in hand. Meteorites believed to be from Mars contain micron-sized spherules, which were proposed to be biological in origin. This sparked much recent controversy and it is by no means settled whether these structures are fossil microorganisms or the product of inorganic nanoscale crystal growth processes.<sup>[33,34]</sup>

## NANOPARTICLES AND LIFE

Microbial communities are rich in the production and utilization of nanoparticles.<sup>[35]</sup> Table 4 lists some examples. In addition to aerobic respiration (the enzymatic oxidation of carbohydrates and other organics with molecular oxygen to produce water, carbon dioxide, and energy stored as high-energy phosphate linkages) organisms use many other strategies to extract energy from the environment. The following biological reactions produce or consume nanoparticles. Dissolved Mn(II) or Fe(II) can be oxidized by oxygen, producing Mn(III), Mn(IV), or Fe(III) oxide nanoparticles, while organics can be oxidized by manganese or iron oxides, producing soluble Mn(II) and Fe(II) species. Some bacteria can also utilize the U(IV)–U(VI) couple as an energy source. Because hexavalent uranium is much more soluble than tetravalent, biological processes that accelerate its production are of concern in modeling nuclear waste leaching. The sum of these two groups of redox processes is the oxidation of organics by oxygen, akin to respiration. The important difference is that the organic food source and the oxygen source can be spatially separated in the sharp gradients in oxygen and organic contents that frequently occur in sediments, and different communities of organisms participate in the two processes. In marine sediments, sulfate is the dominant biological electron acceptor and is more important than oxygen. Bacterial sulfate reduction produces sulfide which often precipitates as nanophase metal sulfide minerals. Sulfide and sulfur oxidizing bacteria typically live in specialized environments where there is enough oxygen to oxidize sulfur but not so much that chemical oxidation swamps biological oxidation. This oxidation consumes solid sulfur and sulfides, and produces soluble sulfate.

Organisms utilize nanoparticles in processes other than respiration. Bacterial precipitation of sulfide minerals, e.g., ZnS and UO<sub>2</sub>, may also be a mechanism

of detoxification.<sup>[36]</sup> Similar detox processes may occur in plants. Magnetotactic bacteria synthesize and align single domain magnetic iron oxide and iron sulfide particles in structures called magnetosomes.<sup>[37]</sup> Such bacteria align themselves both north–south and vertically in the Earth's magnetic field. The navigational (homing) capabilities of bees, pigeons, and probably other higher organisms utilize magnetic field orientation sensed by magnetic iron oxide particles in their brains. Similar particles, although at lower abundance, occur in many mammals, including *Homo sapiens*.<sup>[38]</sup> There has been a debate in the public sector whether the magnetic fields produced by high-voltage power lines are potentially dangerous to human health. In contrast, the use of magnets in alternative medicine, and the market for magnetic pillows, back supports, etc. suggests, or at least hopes for, a beneficial effect of the interaction of magnetic fields with animals. Key to either harmful or helpful biological effects is a mechanism for the magnetic field to interact with living cells. Interaction with biological magnetic nanoparticles may provide such a mechanism, but very little is known at present.

Nanoparticles have other documented health effects.<sup>[39]</sup> When inhaled into the lungs, particles cause an inflammatory response, which contributes to allergies, asthma, and cancer.<sup>[48]</sup> The detailed mechanism of this response, and how it depends on surface area, particle size, or specific particle chemistry, is not clear. The harmful effects of inhaled particles may be enhanced by other pollutants, particularly ozone, typically present in smog. Nanoparticles penetrate deep into the lungs. Many are returned with exhaled air, some stick to the surfaces of the alveoli, and some may even penetrate into general blood circulation and be transported to other organs. Studies linking detailed nanoparticle characterization, biochemical and physiological processes, and health effects are just beginning to be carried out. It is likely that not all particles have

**Table 4** Example of interactions of microorganisms and nanoparticles

Class of organisms	Example	Nanoparticle interaction
Iron and manganese oxidizing bacteria	<i>Thiobacillus</i>	Oxidize soluble Mn <sup>2+</sup> and Fe <sup>2+</sup> to insoluble higher oxides
Iron and manganese reducing bacteria	<i>Shewenella</i>	Reduce insoluble Mn and Fe oxides to soluble forms oxidize sulfide to sulfate to sulfide precipitate
Sulfur reducing bacteria	<i>Thiobacillus</i>	Reduce sulfate to sulfur in sulfide
Magnetotactic bacteria	<i>Aquaspirillum magnetotacticum</i>	Nanoparticles of Fe <sub>2</sub> O <sub>3</sub> , Fe <sub>3</sub> O <sub>4</sub> , and/or iron sulfides
Uranium reducing bacteria	<i>Geobacter, shewenella</i>	Soluble U <sup>6+</sup> → insoluble U <sup>4+</sup>
Fungi	Specific strains unknown	Oxidize Mn <sup>2+</sup> , precipitate MnO <sub>2</sub>
Diatoms	Various	Precipitate silica
Foraminifera	Various	Precipitate CaCO <sub>3</sub> calcite and aragonite

comparable effects, and understanding which are the most dangerous could lead to rational, rather than arbitrary, emission standards for automotive and industrial particulates.

In the early Earth, prebiotic processes culminated in the origin of life.<sup>[40]</sup> Because the synthesis of complex organic molecules competes with their destruction by hydrolysis and other degradation, it is possible that the most successful synthesis could have occurred in sheltered and catalytic environments, such as those provided by mineral surfaces, nanoparticle surfaces, and pores within mineral grains. Present-day organisms utilize a wide variety of elements (e.g., Fe, Co, Ni, Cr, Zn, Se) in specific enzymes. Although large amounts of such elements are toxic, trace amounts are essential. The active centers in enzymes utilizing these trace elements often consist of clusters of metal atoms, sometimes associated with sulfide. Are these fine-tuned by evolution from earlier simpler metal clusters and nanoparticles existing in the environment? Thus nanoparticles may play a role not just in the sustenance of life but in its origin.

## CONCLUSIONS

Nanoparticles play diverse roles in the environment and are involved in both abiotic and biologically mediated chemical and physical processes. Their high surface area, chemical reactivity, polymorphism, and unique properties involve nanoparticles in a disproportionately large fraction of the chemical reactions occurring on and in the Earth and other planets. Understanding this involvement is itself evolving into a new field of study in the environmental and Earth sciences, which is beginning to be called "nanogeoscience." Nanogeoscience will take its place alongside other new areas such as astrobiology and biogeochemistry, fields that link physical, chemical, and biological processes viewed in the context of the long time and distance scales natural to the Geosciences.

## REFERENCES

1. Navrotsky, A. Thermochemistry of Nanomaterials. In *Nanoparticles and the Environment*; Reviews in Mineralogy and Geochemistry; Banfield, J.F., Navrotsky, A., Eds.; Mineralogical Society of America: Washington, DC, 2001; Vol. 44, 73–103.
2. Garvie, R.C. The occurrence of metastable tetragonal zirconia as a crystallite size effect. *J. Phys. Chem.* **1965**, *69*, 1238–1243.
3. McHale, J.M.; Auroux, A.; Perrotta, A.J.; Navrotsky, A. Surface energies and thermodynamic phase stability in nanocrystalline alumina. *Science* **1997**, *277*, 788–791.
4. Ranade, M.R.; Navrotsky, A.; Zhang, H.Z.; Banfield, J.F.; Elder, S.H.; Zaban, A.; Borse, P.H.; Kulkarni, S.K.; Doran, G.S.; Whitfield, H.J. Energetics of nanocrystalline TiO<sub>2</sub>. *Proc. Natl. Acad. Sci.* **2002**, *99* (Suppl. 2), 6476–6481.
5. Majzlan, J.; Navrotsky, A.; Casey, W.H. Surface enthalpy of boehmite. *Clays Clay Miner.* **2000**, *48*, 699–707.
6. Majzlan, J. Ph.D. Thesis; University of California at Davis, 2002.
7. Janney, D.E.; Cowley, J.M.; Buseck, P.R. Structure of synthetic 2-line ferrihydrite by electron nanodiffraction. *Am. Mineral.* **2002**, *85* (9), 1180–1187.
8. Schwertmann, U.; Cornell, R.M. *Iron Oxides in the Laboratory*, 2nd Ed.; Wiley-VCH, 2000; 188 pp.
9. Singer, M.J.; Munns, D.N. *Soils: An Introduction*, 3rd Ed.; Simon and Schuster Company: Upper Saddle River, NJ, 1991.
10. Thompson, H.A.; Parks, G.A.; Brown, G.E., Jr. Ambient-temperature synthesis, evolution, and characterization of cobalt–aluminum hydrotalcite-like solids. *Clays Clay Mater.* **1999**, *47*, 425–438.
11. Ragnarsdottir, K.V.; Charlet, L. Uranium behavior in natural environments. *Environ. Mineral.* **2000**, *9*, 245–289.
12. Zhang, H.; Penn, R.L.; Hamers, R.J.; Banfield, J.F. Enhanced adsorption of molecules on surfaces of nanocrystalline particles. *J. Phys. Chem., B* **1999**, *103*, 4656–4662.
13. Hunter, R.J. *Foundations of Colloid Science*; Oxford University Press: New York, 1993; Vol. 1.
14. Banfield, J.F.; Zhang, H. Nanoparticles in the Environment. In *Nanoparticles and the Environment*; Reviews in Mineralogy and Geochemistry; Banfield, J.F., Navrotsky, A., Eds.; Mineralogical Society of America: Washington, DC, 2001; Vol. 44, 2–58.
15. Rowsell, J.; Nazar, L.F. Speciation and thermal transformation in alumina sols: Structures of the polyhydroxyoxoaluminum cluster [Al<sub>30</sub>O<sub>8</sub>(OH)<sub>56</sub>(H<sub>2</sub>O)<sub>26</sub>]<sup>18+</sup> and its Keggin moeité. *J. Am. Chem. Soc.* **2000**, *122*, 3777–3778.
16. Casey, W.H.; Phillips, B.L.; Furrer, F. Aqueous Aluminum Polynuclear Complexes and Nanoclusters: A Review. In *Nanoparticles and the Environment*; Reviews in Mineralogy and Geochemistry; Banfield, J.F., Navrotsky, A., Eds.; Mineralogical Society of America: Washington, DC, 2001; Vol. 44, 167–190.
17. Furrer, G.F.; Phillips, B.L.; Ulrich, K.U.; Poethig, R.; Casey, W.H. The origin of aluminum flocs in polluted streams. *Science* **2002**, *in press*.
18. Penn, R.L.; Banfield, J.F. Oriented attachment and growth, twinning, polytypism, and formation of metastable phases: Insights from nanocrystalline TiO<sub>2</sub>. *Am. Mineral.* **1998**, *83*, 1077–1082.
19. de Moor, P.P.E.A.; Beelen, T.P.M.; Komanshek, B.U.; Beck, L.W.; Wagner, P.; Davis, M.E.; Van Santen, R.A. Imaging the assembly process of the organic-mediated synthesis of a zeolite. *Chem. Eur. J.* **1995**, *5*, 2083–2088.
20. Luther, G.W.; Theberge, S.M.; Richard, D.T. Evidence for aqueous clusters as intermediates during zinc sulfide formation. *Geochim. Cosmochim. Acta* **1999**, *64*, 579.

21. Jacobs, K.; Alivisatos, A.P. Nanocrystals as model systems for pressure-induced structural phase transitions. In *Nanoparticles and the Environment*; Reviews in Mineralogy and Geochemistry; Banfield, J.F., Navrotsky, A., Eds.; Mineralogical Society of America: Washington, DC, 2001; Vol. 44, 59–104.
22. Rancourt, D.G. Magnetism of Earth, Planetary, and Environmental Nanomaterials. In *Nanoparticles and the Environment*; Reviews in Mineralogy and Geochemistry; Banfield, J.F., Navrotsky, A., Eds.; Mineralogical Society of America: Washington, DC, 2001; Vol. 44, 217–292.
23. Anastasio, C.; Martin, S.T. Atmospheric Nanoparticles. In *Nanoparticles and the Environment*; Reviews in Mineralogy and Geochemistry; Banfield, J.F., Navrotsky, A., Eds.; Mineralogical Society of America: Washington, DC, 2001; Vol. 44, 293–349.
24. Ramanathan, V.; Crutzen, P.J.; Kiehl, J.T.; Rosenfeld, D. Aerosols, climate, and the hydrological cycle. *Science* **2001**, *294*, 2119–2124.
25. Martin, J.H.; Coale, K.H.; Johnson, K.S.; Fitzwater, S.E.; Gordon, R.M.; Tanner, S.J.; Hunter, C.N.; Elrod, V.A.; Nowicki, J.L.; Coley, T.L.; Barber, R.T.; Lindley, S.; Watson, A.J.; Vanscoy, K.; Law, C.S.; Liddicoat, M.I.; Ling, R.; Stanton, T.; Stockel, J.; Collins, C.; Anderson, A.; Bidigare, R.; Ondrusek, M.; Latasa, M.; Millero, F.J.; Lee, K. Testing the iron hypothesis in ecosystems of the equatorial Pacific Ocean. *Nature* **1994**, *371*, 123–129.
26. Millero, F.J. *Chemical Oceanography*, 2nd Ed.; CRC: Boca Raton, FL, 1996.
27. Broecker, W.S. *The Great Ocean Conveyor*; AIP Conference Proceedings; Columbia University Palisades: New York, 1992; Vol. 347, 129–161.
28. Labrenz, M.; Druschel, G.K.; Thomsen-Ebert, T.; Gilbert, B.; Welch, S.A.; Kemner, K.M.; Logan, G.A.; Summons, R.E.; de Stasio, G.; Bond, P.L.; Lai, B.; Kelly, S.D.; Banfield, J.F. Formation of sphalerite (ZnS) deposits in natural biofilms of sulfate-reducing bacteria. *Science* **2000**, *290*, 1744–1745.
29. Ehrlich, H.L. Microbes as geologic agents: Their role in mineral formation. *Geomicrobiol. J.* **1999**, *16*, 135–153.
30. Konhauser, K.O.; Phoenix, V.R.; Bottrell, S.H.; Adams, D.G.; Head, I.M. Microbial–silica interactions in Icelandic hot spring sinter: Possible analogues for some Precambrian siliceous stromatolites. *Sedimentology* **2001**, *48*, 415–433.
31. Anderson, D.L. *Theory of the Earth*; Blackwell Scientific Publications: Brookline Village, MA, 1989.
32. Karato, S.; Li, P. Diffusion creep in perovskite: Implications for the rheology of the lower mantle. *Science* **1992**, *255*, 1238–1240.
33. Sasaki, S.; Nakamura, K.; Hamabe, Y.; Kurahashi, E.; Hiroi, T. Production of iron nanoparticles by laser irradiation in a simulation of lunar-like space weathering. *Nature* **2001**, *410*, 555–557.
34. Buseck, P.R.; Dunin-Borkowski, R.E.; Devouard, B.; Frankel, R.B.; McCartney, M.R.; Midgley, P.A.; Posfai, M.; Weyland, M. Magnetite morphology and life on Mars. *Proc. Natl. Acad. Sci. U. S. A.* **2001**, *98* (24), 13490–13495.
35. Gibson, E.K.; McKay, D.S.; Thomas-Keprta, K.L.; Wentworth, S.J.; Westall, F.; Steele, A.; Romanek, C.S.; Bell, M.S.; Toporski, J. Life on Mars: Evaluation of the evidence within Martian meteorites ALH84001, Nakhla, and Shergotty. *Precambrian Res.* **2001**, *106* (1–2), 15–34.
36. Nealson, K.H.; Stahl, D.A. Microorganisms and Biogeochemical Cycles: What Can We Learn from Layered Microbial Communities? In *Geomicrobiology: Interaction Between Microbes and Minerals*; Review in Mineralogy; Banfield, J.F., Nealson, K.H., Eds.; Mineralogical Society of America: Washington, DC, 1997; Vol. 35, 5–34.
37. Suzuki, Y.; Banfield, J.F. Geomicrobiology of Uranium. In *Uranium: Mineralogy, Geochemistry and the Environment*; Review in Mineralogy; Burns, P.C., Finch, R., Eds.; Mineralogical Society of America: Washington, DC, 1999; Vol. 38, 388–432.
38. Stolz, J.F. Magnetotactic Bacteria: Biomineralization, Ecology, Sediment Magnetism, Environmental Indicator. In *Biomineralization Process of Iron and Manganese: Modern and Ancient Environments*; Catena Supplement 21; Skinner, H.C.W., Fitzpatrick, R.W., Eds.; Destedt. Germany, 1992; 133–146.
39. Kirschvink, J.L.; Walker, M.M.; Diebel, C.E. Magnetite-based magnetoreception. *Curr. Opin. Neurobiol.* **2001**, *11* (4), 462–467.
40. Guthrie, G.D.; Mossman, B.T. *Health Effects of Mineral Dusts*; Reviews in Mineralogy; Mineralogical Society of America: Chelsea, MI, 1993; Vol. 28.
41. Navrotsky, A. Nanomaterials in the environment, agriculture, and technology (NEAT). *J. Nanopart. Res.* **2000**, *2*, 321–323.

## BIBLIOGRAPHY

1. Nakashima, S.; Ikoma, M.; Shiota, D.; Nakazawa, K.; Maruyama, S. Geochemistry and the origin and evolution of life: A tentative summary and future perspectives. *Precursors Chall. Investig. Ser.* **2001**, *2*, 329–344.

# Enzymatic Synthesis of Nanostructured Polymers and Composites

**Christy Ford**  
**Vijay T. John**  
**Gary McPherson**  
**Jibao He**

*Chemistry Department, Tulane University, New Orleans, Louisiana, U.S.A.*

**Joseph Akkara**

*National Science Foundation, Arlington, Virginia, U.S.A.*

**David Kaplan**

*Chemical Engineering Department, Tufts University, Medford, Massachusetts, U.S.A.*

**Arijit Bose**

*Department of Chemical Engineering, University of Rhode Island, Kingston, Rhode Island, U.S.A.*

## INTRODUCTION

Surfactant microstructures provide a unique environment for the enzymatic synthesis of polymers. Surfactants can create large oil–water interfaces, which can be exploited for biocatalysis where the enzyme is resident in the aqueous phase and the monomer is resident in the oil phase or at the oil–water interface. The polymerization of substituted phenols using an oxidative enzyme, horseradish peroxidase (HRP), is explored. The surfactant microstructures used in enzymatic synthesis include the system of bis(2-ethylhexyl) sodium sulfosuccinate (AOT) water-in-oil microemulsions, cetyltrimethylammonium bromide (CTAB) micelles, and a novel gel system formed by the addition of lecithin and water to AOT water-in-oil microemulsions. The monomers partition to the oil–water interface, and polymerization is extremely feasible.

The use of enzymes in synthesis represents an inherently environmentally benign approach to chemical processing. In addition to catalytic function at or near ambient conditions, the exquisite specificity of enzyme biocatalysis can be potentially exploited to develop processes with minimal side products. Advances in large-scale enzyme production and purification, and synthetic enzyme mimetic chemistry, are eventually expected to lead to enzyme-based processes that are economically viable.<sup>[1]</sup> The use of enzymes to synthesize polymers is one such area of research undergoing rapid development.<sup>[2]</sup> Enzymatic polymerization

exhibits a wonderful aspect of biomimetics, as enzymes function in the biological world in the synthesis and degradation of polysaccharides, proteins, polyphenols, and polynucleic acids. If such enzyme action can be exploited in the *in vitro* synthesis of polymers with commercial significance, it may be possible to obtain polymers with unique material properties that are inherently biodegradable and in specific cases, biocompatible. Examples of enzyme biocatalysis for polymer synthesis include the use of lipases for polyester synthesis,<sup>[3]</sup> peroxidases for polyphenol synthesis,<sup>[4]</sup> and cellulases for polysaccharide synthesis.<sup>[5]</sup>

In developing enzymes for synthesis, the reaction environment plays a vital role in determining the activity and catalytic efficiency of the enzyme. The ability of enzymes to function in nonaqueous environments when properly conditioned has brought about the development of an entire field of biocatalysis in organic solvents.<sup>[6]</sup> A parallel development is the field of enzyme chemistry in surfactant systems, in particular the system of water-in-oil microemulsions, conventionally referred to as reversed micelles.<sup>[7]</sup>

## OVERVIEW

In this entry, a variety of self-assembled surfactant systems are investigated for enzymatic synthesis of nanostructured polymers and polymer–ceramic composites. Specifically, reversed micelles, micelles, and a novel

surfactant gel mesophase are used as templating environments to generate conjugated polymers with conductive and luminescent properties. Finally, enzymatic polymerization is coupled with mesoporous silica synthesis to fabricate structured polymer–ceramic nanocomposites.

### ENZYMATIC SYNTHESIS OF POLYPHENOLS AND POLYAROMATIC AMINES

The concepts of enzymatic polymer synthesis in surfactant systems with a focus on the synthesis of polyphenols and polyaromatic amines are presented. Phenolic polymers have a variety of conventional applications in making resins for coatings, laminates, etc.<sup>[8]</sup> The traditional technology for making these polymers involves a formaldehyde-based high-temperature process, where undesirable side reactions lead to poor control of polymer structure and molecular weight. In addition, concern over the toxicity of

formaldehyde necessitates the study of alternative technologies to produce such polymers. The enzymatic approach using an oxidative enzyme such as horseradish peroxidase eliminates the need for formaldehyde. The reaction has a mechanistic analogy to the synthesis of lignin<sup>[9]</sup> and is illustrated through the simplified mechanism shown in Fig. 1A, where reaction is initiated by the addition of H<sub>2</sub>O<sub>2</sub>. Phenoxy radical centers initially formed on the monomer or growing chains migrate to the ortho positions (the para position, although mechanistically allowed, is less favored) after which coupling through condensation occurs. A molecular space-filling model of polyphenol illustrates the curvature of the chains obtained when the hydroxyl groups lie on the same side of the polymer backbone. In the unfolded state, the polymer assumes an open structure.

A variety of monomers can be used in the synthesis of modified phenolic polymers and copolymers with novel functional characteristics (Fig. 1C). As an example, the multiring naphthol and hydroxypyrene

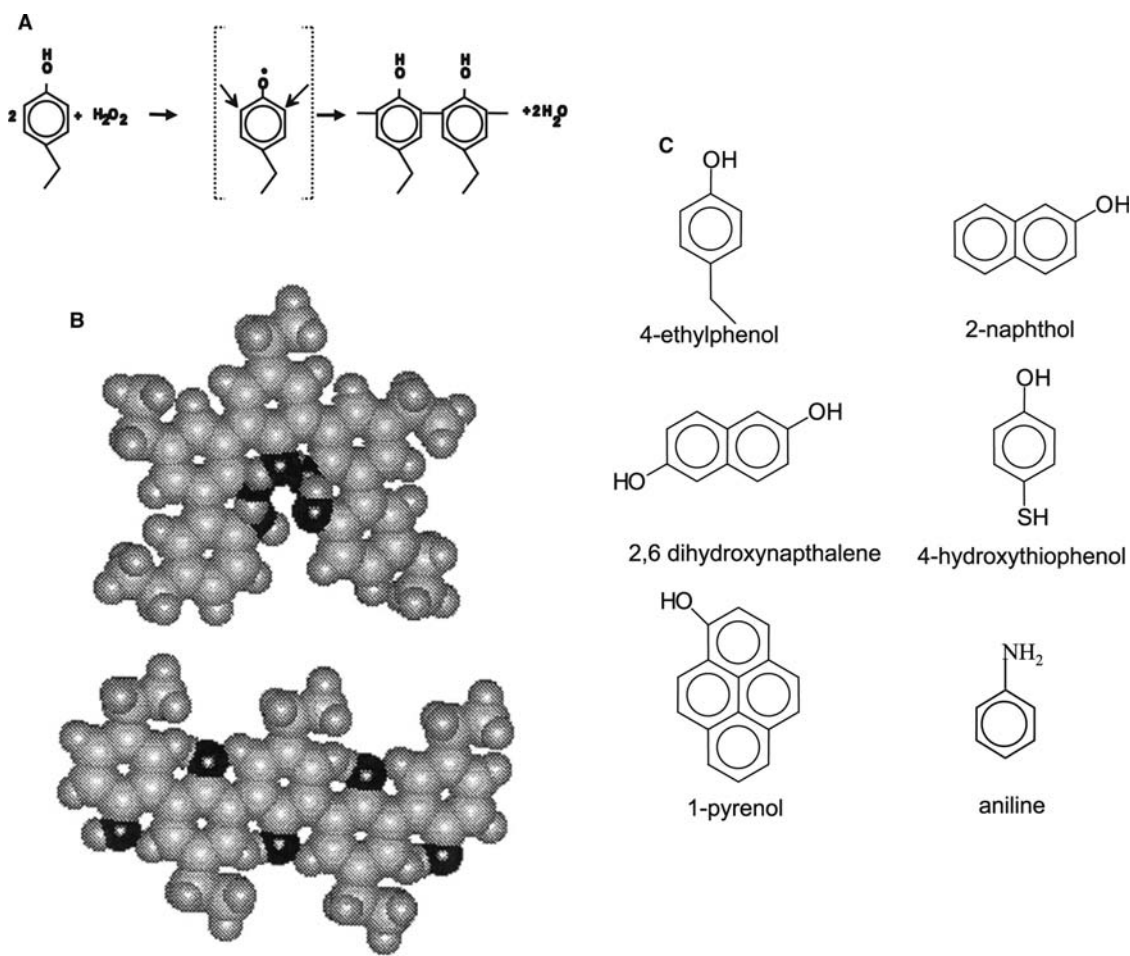


**Fig. 1** (A) Simplified schematic of the polymerization of alkyl substituted phenols. The arrows (in the phenoxy radical) indicate coupling in the ortho position. (B) Molecular model of polyphenol folding due to monomer alignment at an oil–water interface. (C) Various monomers that can be used for the synthesis of functional polymers.



based polymers are intrinsically photoluminescent.<sup>[11]</sup> Since these polymers are conjugated, there may be opportunities to develop new classes of electroluminescent and photoluminescent polymers. The use of monomers such as hydroxythiophenol allows the synthesis of polymers that are capable of binding to inorganic sulfide nanoclusters (e.g., CdS, PbS) with semiconductor properties.<sup>[12]</sup> This may lead to new possibilities in the preparation of polymer–nanoparticle films and composites with electrooptical properties. Polymers made with dihydroxynaphthalene may be redox active and may have electrochemical applications in battery and sensor development.<sup>[13]</sup>

In principle, the enzymatically synthesized polyphenolics have similar applications to the phenol–formaldehyde resins that are chemically synthesized.<sup>[14]</sup> However, there are unique aspects related to the enzymatically synthesized material. In contrast to phenol–formaldehyde polymers, these polyphenolics lack the intervening methylene bridge between the aromatic groups, as illustrated in the simplified mechanistic scheme of Fig. 1A. The polymer is therefore conjugated and thus has a variety of potential applications in electro-optics.<sup>[15]</sup> A specific property that is being investigated is the use of these materials in non-linear optics (NLO), in particular for applications based on the optical third-order non-linear susceptibilities ( $\chi^{(3)}$ ).<sup>[4,15]</sup> In such materials, higher-order terms become significant in the expansion of the material polarization ( $P$ ) in terms of an applied electric field ( $E$ ).

$$P = \chi^{(1)}E + \chi^{(2)}E^2 + \chi^{(3)}E^3 + \dots$$

While details of the physics behind NLO materials can be found in several excellent sources (e.g., Prasad and Williams),<sup>[16]</sup> the relevance of NLO polymers to applications in optical switching, waveguide technology, laser protection, etc. is well recognized. Thus, the enzymatically synthesized polymers have some useful applications in electro-optics.<sup>[17]</sup> The polyaromatic amines synthesized through the enzymatic process are especially promising as materials with high  $\chi^{(3)}$  values of up to  $10^{-7}$  esu, among the highest reported for organic materials.<sup>[17]</sup>

A unique and suitable environment for the enzymatic synthesis of polyphenols and polyaromatic amines is needed. The monomers are typically water insoluble, and therefore intrinsically incompatible with the water-soluble enzyme. Therefore, a unique system in which both enzyme and monomer are contacted efficiently is needed. One approach involves using a two-phase oil and water system; however, the agitation needed to enhance enzyme–monomer contact may shear-deactivate the enzyme. A second approach entails activating the enzyme in organic solvents, feasible for polyphenol synthesis.<sup>[4,6]</sup> A third approach

encompasses the use of surfactants to incorporate water into an organic phase (or vice versa). This approach has the advantage that the enzyme and the monomer reside in close proximity and the enzyme experiences minimal agitation.

## POLYMER SYNTHESIS IN REVERSE MICELLES

The AOT water-in-oil microemulsion system represents an effective system to synthesize polyphenolics and polyaromatic amines. Fig. 2 illustrates the system and the rationale for synthesis in this medium. The enzyme is catalytically active in the water core, and the organic bulk phase sustains the monomer and the surfactant hydrocarbon chains. An interesting aspect of synthesis in reversed micelles is the partitioning of the polar monomer to the oil–water interface (depicted by the arrow of Fig. 2 with the head of the arrow representing the hydroxyl moieties of the monomer). In addition, hydrogen bonding between the surfactant headgroup and the monomer influences monomer orientation and partitioning at the water–oil interface. A strong indication of such hydrogen bonding is the perturbation of the vibrational frequencies of the surfactant C=O groups on addition of the monomers.<sup>[18]</sup> Such partitioning may result in a prealignment of the monomers before synthesis and may provide a means of monomer replenishment to the vicinity of the enzyme. In addition, the surfactant–monomer

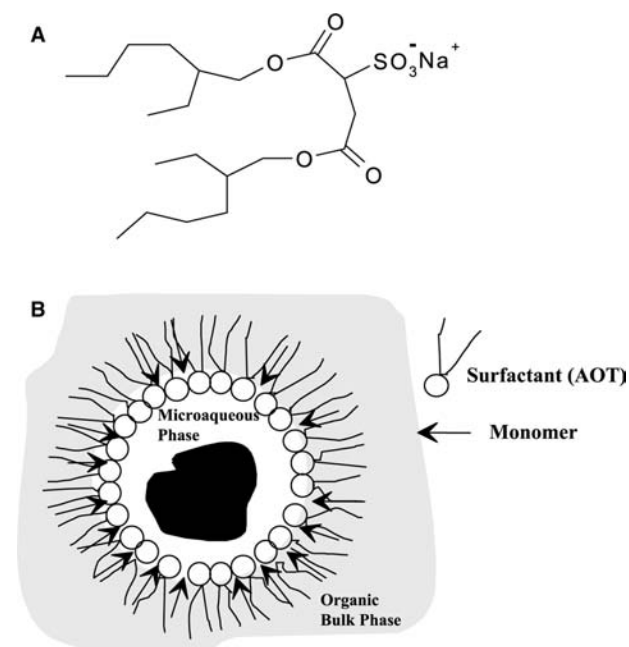


**Fig. 2** (A) Chemical structure of the anionic surfactant sodium bis(2-ethylhexyl) sulfosuccinate. (B) Schematic of enzyme solubilized in the micelle and monomer partitioning to the micelle interface. The arrow refers to the monomer.

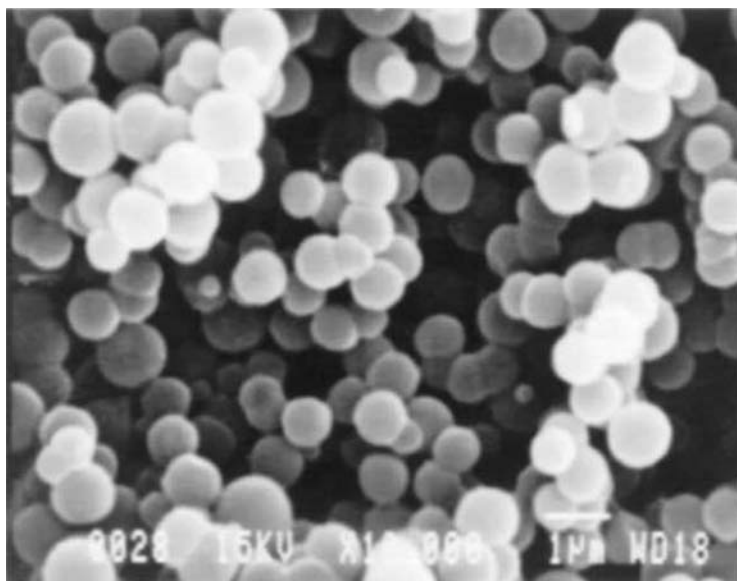


**Fig. 3** Scanning electron micrograph of polymer microspheres prepared through synthesis in reverse micelles.

interactions significantly enhance monomer solubility in the reaction medium. The implication is that the hydroxyl groups are on the same side of the polymer backbone as simply illustrated in Fig. 1, noting that the actual C–C bond between aromatic rings has an angle of  $120^\circ$ . In simple molecular models, ortho coupling with proximal hydroxyls on the same side of the backbone induces a natural curvature to the polymer. Indeed, intramolecular hydrogen bonding leads to polymer folding when most of the hydroxyls lie on the same side of the backbone.<sup>[19]</sup> We will return to the concept of polymer curvature in the interpretation of the observations.

Enzymatic polymerization in reverse micelles is a simple procedure.<sup>[20]</sup> In a typical experiment, the enzyme (HRP) dissolved in 0.01 M HEPES buffer (pH 7.5) is added to a dry reversed micellar solution of AOT in isooctane, followed by the addition of the monomer, 4-ethylphenol (EP). The enzyme concentration in the buffer is adjusted so that the final enzyme concentration in the micellar solution is 0.5 mg/mL. The reaction mixture typically has the overall composition 0.5 M AOT, 0.15 M EP, 0.5 mg/mL HRP and a  $w_0$  of 15 ( $w_0$  is the water-to-surfactant molar ratio). The reaction is initiated by the addition of  $H_2O_2$  in aliquots to minimize enzyme deactivation. The reaction is rapid, and within 5–10 min of reaction initiation, over 80% of monomer conversion occurs, with the polymer precipitating out of solution.<sup>[20]</sup>

Fig. 3 illustrates the fascinating microsphere morphology of polymers synthesized and precipitated from reaction in reversed micellar solutions. We have found that as long as the initial surfactant-to-monomer ratio is 2:1 or higher (preferably 3:1) the polymer precipitates in the morphology of microspheres.<sup>[20]</sup> Many of the microspheres are not independent, but

are connected to each other. Although it would appear that the microspheres are a consequence of polymerization around micelle interfaces, the size of these microspheres (0.5–1  $\mu\text{m}$ ) are significantly larger than the micelle size (0.5–5 nm depending on the water level in the micelle).

The large sizes of the microspheres in comparison to micelle dimensions indicate the lack of a direct templating effect produced by synthesis at the micelle oil–water interface. However, in studying the growth characteristics of these microspheres, we have found that they initially have a very low internal density. The microspheres appear to be made up of minute interconnected spherical patches,<sup>[11]</sup> which may have their origin from reaction on the micelle periphery (Fig. 4A). The scanning electron micrograph of Fig. 4B where the shell of a microsphere is broken by gentle sonication correlates well with the initially low internal density of the microsphere. In fact, the internal density of the microspheres can be controlled by adjustment of reaction time and  $H_2O_2$  addition due to remaining enzyme and unreacted monomer in the microspheres. Polymerization continues even after the overall morphology has been achieved, leading to densification. Over a period of about 24 hr, all microspheres fully densify.<sup>[11]</sup> At the other extreme, at very early reaction times (<5 min), sampling of the polymer simply indicates interconnected patches with no overall defined spherical morphologies. The internal morphology and densification characteristics of the microspheres suggest the following mechanism. The initial dense patches are a consequence of reaction at the oil–water interface. The polymer is “sticky” because of the large number of hydroxyl groups, and the hydroxyl groups are capable of hydrogen bonding both within the chain and between

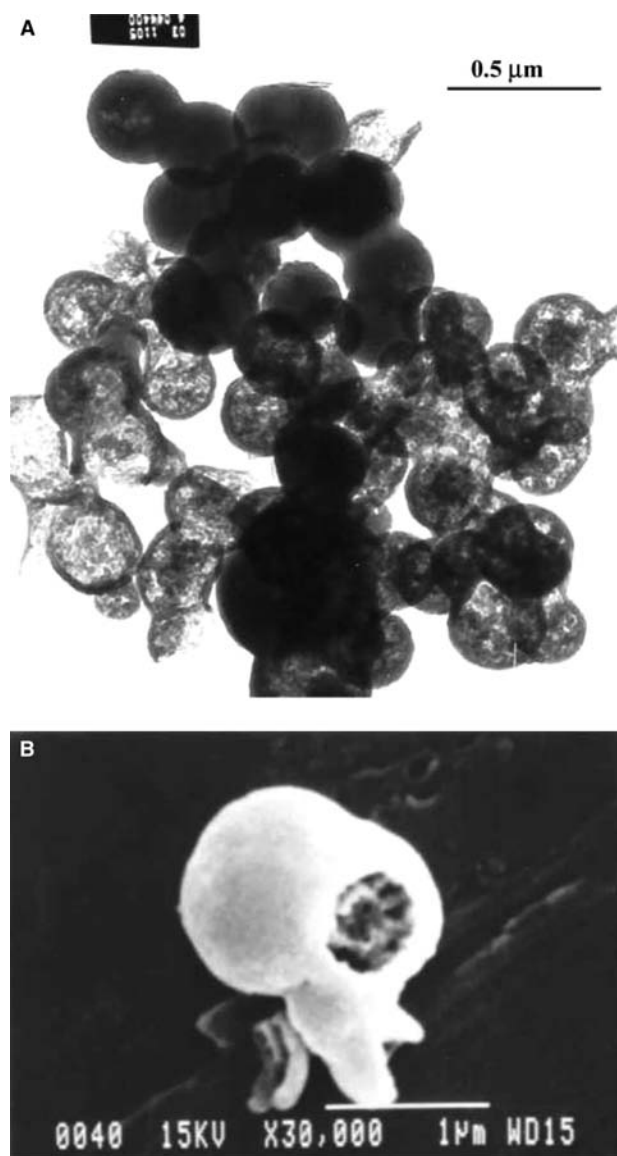


**Fig. 4** (A) Transmission electron micrograph of a polymer microsphere at an initial stage (5 min reaction time) illustrating the low internal density. (B) Scanning electron micrograph illustrating the internal structure of a polymer microsphere.

chains. The intrachain hydrogen bonding may lead to the curvature of the chain, whereas interchain hydrogen bonding can create the connections to polymer growing on separate micelles during micelle collisions. The interplay between these effects leads to the interconnected patches.

The second interesting observation is that during precipitation, the polymer also encapsulates solutes located in the water core of the micelle. The densification observation is clearly a consequence of peroxidase becoming encapsulated in the microspheres. Realizing this, we have attempted to exploit the phenomenon to synthesize polymer–nanoparticle composites. We

propose utilizing these reversed micelles as a microenvironment in which to synthesize inorganic materials that do not grow beyond the nanometer size range.<sup>[22]</sup> Enhanced band gap semiconductor materials (CdS, TiO<sub>2</sub>), magnetic particles, etc. are examples of novel nanoparticles that have been synthesized in reversed micelles. We have attempted to make polymer–nanoparticle composites by first synthesizing the nanoparticles in the micelles, then adding monomer, enzyme, and H<sub>2</sub>O<sub>2</sub> to initiate polymer synthesis. When the polymer precipitates (in spherical morphologies) it incorporates a significant amount of the nanoparticles. For example, we have synthesized superparamagnetic iron oxide in reversed micelles.<sup>[23,24]</sup> In such synthesis, the particle size approaches magnetic domain size, leading to thermally induced randomization of magnetic dipole orientations. The particles therefore do not exhibit magnetic characteristics in the absence of a field (the term superparamagnetism is usually applied to particles that are non-magnetic in the absence of a field as paramagnetic materials are, but on application of an external field exhibit magnetization far in excess of paramagnetic materials). We have then incorporated these particles into the polymer as described earlier, allowing the particles to become dense. Fig. 5 shows a cut section transmission electron micrograph of a polymer particle. The dark specks are the ferrite particles uniformly distributed across the section. The cut section also indicates a significant amount of ferrite entrapment (up to 6% of the polymer weight). We also note that the particle size increases on incorporation of the nanoparticles. The particle deformation in the micrograph is a consequence of the cut section procedure.

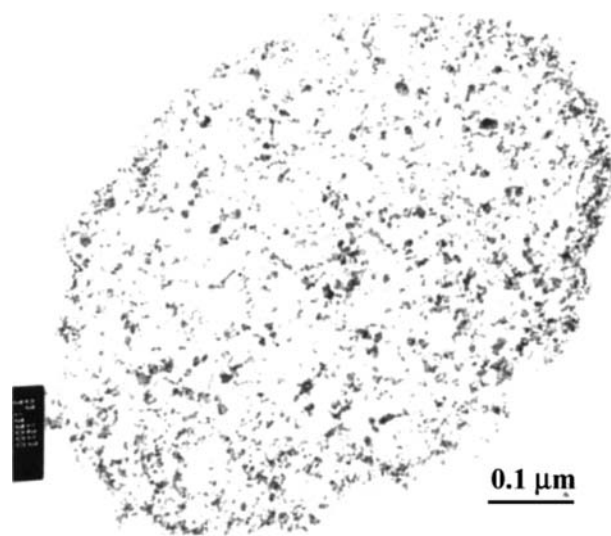


**Fig. 5** Cut section transmission electron micrograph of ferrite nanoparticles within a polymer microsphere. The ellipsoidal cross section is induced by the cut section procedure.

## POLYMER SYNTHESIS IN A NOVEL SURFACTANT GEL MESOPHASE

As described in the previous section, synthesis in reversed micelles leads to microspherical polymer particles that precipitate. In an effort to maintain polymer solubility in the reaction medium, we have exploited a surfactant-based gel system to sustain the polymer during synthesis. A rigid, surfactant gel mesophase is formed by a novel transformation from low-viscosity AOT water-in-oil microemulsions to a highly viscous, rigid state. Specifically, we have found that the addition of lecithin (phosphatidylcholine) to the AOT water-in-oil microemulsions results in the formation of a rigid gel when additional water is added to the system. These gel systems are a significant variant of the fascinating organogels discovered by Luisi and coworkers<sup>[25]</sup> based on the system lecithin/water/cyclohexane, and extensively characterized through various spectroscopy and scattering techniques.<sup>[26–28]</sup> Luisi and coworkers used less than 10 wt.% water in the gel system. In the present system, the amount of water can be greater than 50 wt.% with retention of gel stability. In other words, the surfactant gel phase can be sustained with equal volume fractions of water and the organic phase implying the presence of spatially immobilized extended hydrophilic and hydrophobic microstructures. A typical gel has the composition AOT/lecithin/isooctane/water 15/14/29/42 (wt.%).

Fig. 6 illustrates the zero shear viscosity and conductivity trends as the water content of the system is varied. The measurements were performed by adding

water to a system containing 0.8 M AOT and 0.4 M lecithin in isooctane. The quantity  $w_0$  is the molar ratio of water to AOT, and is the quantity typically used to characterize the water content in AOT water-in-oil microemulsions. As Fig. 6 indicates, gelation starts at a  $w_0$  50 with a rigid gel formed at  $w_0$  value of 65. The zero shear viscosity increase of six to seven decades indicates the magnitude of rigidification from a low-viscosity solution. It is also interesting to note that the gelation point correlates rather well with a significant increase in electrical conductivity. The sharp increase in electrical conductivity indicates the formation of percolating water channels in the gel. Small angle neutron scattering (SANS) data indicate that the surfactant gel assumes a columnar hexagonal microstructure at lower water contents and a lamellar microstructure at higher water contents.<sup>[29]</sup>

This novel surfactant gel is hypothesized to serve as a medium in which aqueous synthesis can be combined with organic synthesis, leading to structured composite materials with novel application possibilities. As an example, the organic phase could be used in the synthesis of hydrophobic polymers whereas the aqueous phase can be used in the synthesis of hydrophilic polymers or inorganic materials. Thus, this system may allow the possibility of obtaining structured polymer-polymer nanocomposites or polymer-ceramic nanocomposites. The oil-water interface in these systems may also be exploited in interfacial polymerization. The microaqueous phase may also be used to sustain biomolecules leading to novel systems for enzyme biocatalysis or drug delivery. If synthesis is

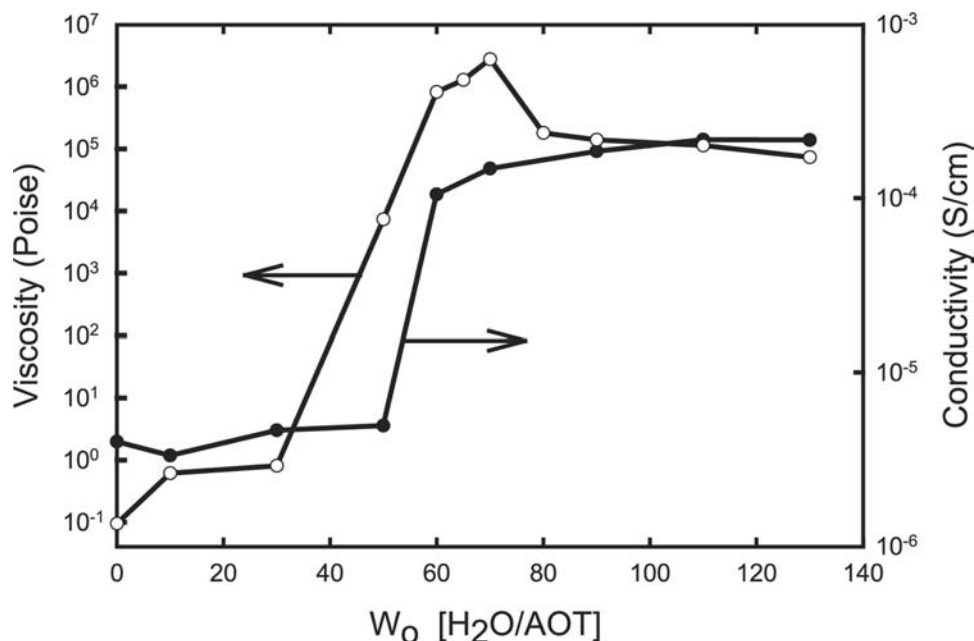


**Fig. 6** Viscosity and electrical conductivity data illustrating the conversion from liquid to gel systems upon adding water to AOT + lecithin systems.

performed in simply one of the microphases (organic or aqueous), there is the possibility of generating materials with structured porosities, leading to membrane and separations applications.

Our objective in conducting enzymatic polymerization in these systems is to sustain polymer solubility in the reaction phase. Monomer and enzyme are loaded into the gel, the monomer being soluble in the organic phase (isooctane) and the enzyme being encapsulated in the percolating microaqueous phase. The schematic method is illustrated in Fig. 7, where the hydroxyl moieties of the monomer are represented by an arrowhead. The polymerization is initiated through the addition of hydrogen peroxide in two ways. In one approach, the components to form a surfactant gel (isooctane, AOT, lecithin), 4-ethylphenol, and horseradish peroxidase are combined to form a surfactant gel loaded with monomer and enzyme. After the surfactant gel forms, hydrogen peroxide is injected via a needle several times. After injecting hydrogen peroxide into the gel media, a thin, tan line of poly(4-ethylphenol) (PEP) formed where the needle pierced the gel. As the polymerization reaction continued in the gel system, the tan polymer lines broaden. However,

the polymer remains in the spikes from the hydrogen peroxide injection and does not grow throughout the gel media uniformly. The polymer appears to be initially constrained to the cavities created by the needle, and then slowly grows outward from the cavities. As a second approach to grow polymer throughout the surfactant gel media, the components to form a surfactant gel (isooctane, AOT, lecithin), 4-ethylphenol, and horseradish peroxidase are combined followed by addition of hydrogen peroxide. The solution is then mixed to form a surfactant gel. The hydrogen peroxide is added before gel formation with the intention that the hydrogen peroxide will become better distributed throughout the gel media and encourage the growth of longer polymer chains. During the mixing process, a transition from dark green-blue to blue to gray was observed as the solution forms into a gel. The color change pattern is similar to the color change pattern observed for poly(4-ethylphenol) synthesis in the AOT reversed micellar system. Enzymatic polymerization appears feasible via this method, and this method seems to allow the polymer to grow uniformly throughout the gel media. In addition, the polymer remains suspended during the polymerization reaction.

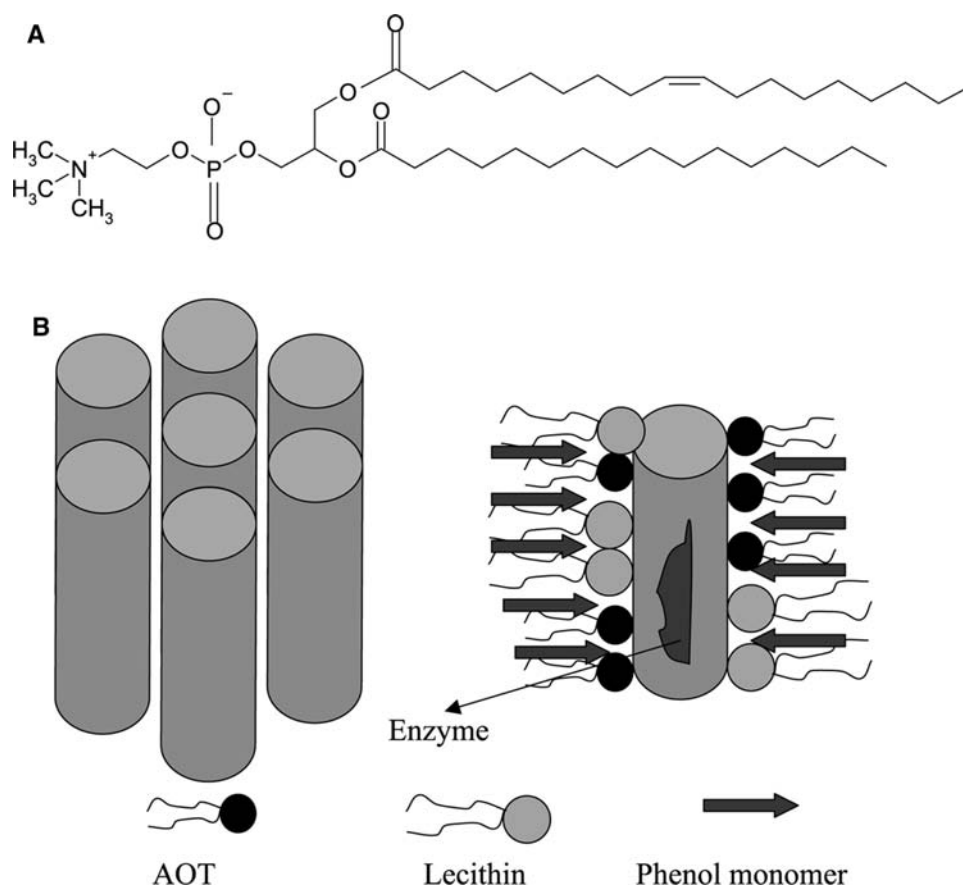


**Fig. 7** (A) Chemical structure of zwitterionic surfactant phosphatidylcholine (lecithin). (B) Schematic of enzyme solubilized in AOT and lecithin surfactant gel. Monomer partitions to micelle interface (monomer represented by arrow).

Scanning electron micrographs of poly(4-ethylphenol) synthesized in the surfactant gel via both hydrogen peroxide addition methods show polymer particles with spherical morphology (Fig. 8). The polymer particles are well defined and are similar in morphology to poly(4-ethylphenol) synthesized in an AOT water-in-oil microemulsion previously studied in our laboratory. Uniform-sized spherical particles in the range of 0.1 to 1.4  $\mu\text{m}$  are observed for varying water contents. At higher water content, polymer particles synthesized in the surfactant gels show a greater extent of agglomeration, where several particles fuse together forming links and clusters. The AOT and lecithin surfactant gel system is unique in that it produces polymer with a spherical morphology. The molecular weight of polymer synthesized in the surfactant gel system is approximately  $3 \times 10^3$ , comparable to poly(4-ethylphenol) synthesized in AOT reversed micelles. The polymer exhibits a polydispersity of approximately 1.

Fourier transform infrared (FTIR) analysis indicates the formation of polymer in the surfactant gel mesophase. Strong retention of the hydroxyl group is observed. The monomer shows a strong, single C–H bend vibration at  $821\text{ cm}^{-1}$ , indicative of two adjacent hydrogen atoms on an aromatic ring and suggestive of 1,4-disubstituted aromatic rings. The polymer exhibits two C–H out-of-plane bend vibration at  $821$  and  $870\text{ cm}^{-1}$ . The C–H bending vibrations are indicative of an isolated hydrogen on an aromatic ring and a 1,2,4,6-tetra-substituted aromatic ring and ortho-ortho coupling of the repeat units.

To supplement our understanding of the polymer synthesized in the surfactant gel, we shift our focus to investigating the microstructural integrity of the surfactant gel after polymerization. The surfactant gel Wo 90, the surfactant gel Wo 90 containing 4-ethylphenol,

and the surfactant gel Wo 90 containing poly(4-ethylphenol) were examined by polarized light microscopy at  $400\times$  magnification. The surfactant gel Wo 90 has a hexagonal microstructure arrangement. The surfactant gel Wo 90 showed fanlike structures indicative of hexagonal microstructures. Fanlike structures are quite distinct for the surfactant gel Wo 90 containing 4-ethylphenol, suggesting that the microstructure of the surfactant gel is preserved upon the incorporation of the monomer. It is striking that after polymerization in the surfactant gel Wo 90, fanlike structures are observed. The preservation of the fanlike structures throughout enzymatic polymerization indicates that the synthesis of poly(4-ethylphenol) does not appear to destroy the surfactant gel microstructure. In addition to polarized light microscopy, SANS study was performed to further determine the stability of the surfactant gel during the polymerization reaction. SANS data were collected before and after the enzymatic polymerization of poly(4-ethylphenol). The SANS profile without polymerization has a  $q_m$  and a  $q_{ho}$  at 0.052 and  $0.09\text{ \AA}^{-1}$ , respectively, and is in the hexagonal columnar phase. After PEP polymerization, the SANS profile has a  $q_m$  at  $0.048\text{ \AA}^{-1}$  and a  $q_{ho}$  at  $0.085\text{ \AA}^{-1}$  and remains in the hexagonal columnar phase. In terms of overall appearance, the profile has changed very little over the course of the poly(4-ethylphenol) synthesis implying that the microstructure of the gel has changed only slightly after the poly(4-ethylphenol) has been formed. Hence, the polymerization reaction does not disrupt the microstructure of the surfactant gel, which suggests that the surfactant gel system retains its templating effect throughout the polymerization reaction.

In monophasic organic solvents, the enzyme-catalyzed polyphenol synthesis does not lead to a unique morphology. In contrast, synthesis in self-assembled surfactant systems leads to the microsphere morphology, thus revealing that monomer prealignment may lead to oriented chains that fold as a consequence of bond geometry leading to initial dense patches. Interactions between the patches and the continued tendency of the chains to fold may lead to the microspheres.

## POLYMER SYNTHESIS IN MICELLES

Cylindrical micelles have attracted considerable attention because of their unique viscoelastic properties.<sup>[30,31]</sup> Cetyltrimethylammonium bromide (CTAB) forms cylindrical micelles and has gained widespread interest as a template for assembly and subsequent condensation of silicate ions to form hexagonally arranged mesoporous materials such as MCM-41 (siliceous molecular sieve).<sup>[32,33]</sup> The MCM-41S family of mesoporous materials has promising applications

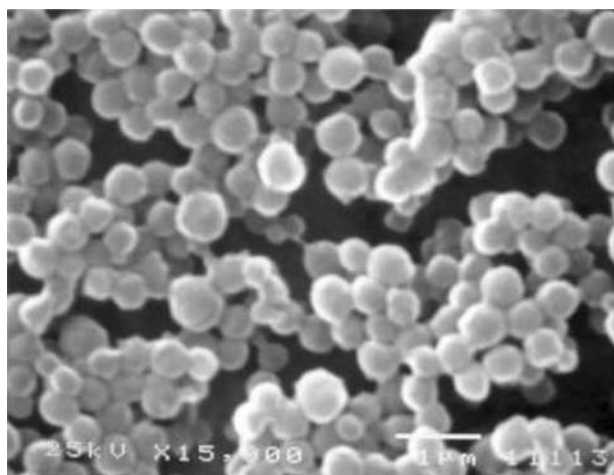


**Fig. 8** Scanning electron micrograph of poly(4-ethylphenol) upon recovery of the polymer from the gel phase.



in separation and selective adsorption,<sup>[34,35]</sup> catalysis,<sup>[36]</sup> and the development of functional materials.<sup>[37]</sup> Researchers have performed extensive studies to fine-tune the pore size of the mesoporous materials. The pore size has been controlled by increasing the length of the alkyl chain of the surfactant and using block copolymers,<sup>[38]</sup> restructuring of the mesopores under mild aqueous conditions,<sup>[39]</sup> and adding auxiliary organic molecules to the synthesis mixture.<sup>[40,41]</sup>

We investigate the feasibility of enzymatic polymerization in CTAB micelles and the effect of polymerization on CTAB micelles. Polyaniline and poly(4-ethylphenol) were polymerized via enzymatic polymerization in CTAB micelles. The polymer is stable in the micellar solution and does not precipitate. Upon polymerization, a color change in the solution is observed and this color change is typical of enzymatic polymerization. Remarkably, the polymer is stable in the micellar solution at high monomer-to-surfactant molar ratios; the polymer does not precipitate even when the moles of monomer exceed the moles of surfactant by six times. A weight average molecular weight of 2300 with a polydispersity of 1.45 is obtained.

FTIR and nuclear magnetic resonance (NMR) analysis provide evidence of the formation of polymer. FTIR analysis shows strong preservation of the OH functional group of poly(4-ethylphenol). FTIR also indicates the presence of two C–H out-of-plane bend vibrations at 821 and 876 cm<sup>-1</sup> for the poly(4-ethylphenol). In comparison, the monomer exhibits only one strong, single C–H bend vibration at 821 cm<sup>-1</sup>, indicative of 1,4-disubstituted aromatic rings. The two C–H bending vibrations observed for the polymer imply that the aromatic groups are 1,2,4,6-tetrasubstituted aromatic rings and the repeat units are linked through ortho–ortho coupling. Both <sup>13</sup>C NMR spectra and <sup>1</sup>H NMR spectra show linewidth broadening in the aromatic region for poly(4-ethylphenol) as compared to the monomer. NMR data provide further evidence of ortho–ortho coupling of the repeat units. Thermogravimetric analysis indicates the polymer synthesized in CTAB micelles is stable until 220°C. In comparison, the monomer shows a 100% weight loss at 150°C. A 15% weight loss at 220°C and a 60% weight loss at 600°C are observed for the polymer.

### BIOMOLECULAR APPROACH TO POLYMER ENCAPSULATION IN MESOPOROUS MATERIALS

Mesoporous materials may serve as host guest molecules for the preparation of nanomaterials with unique properties. Encapsulated conducting polymers exhibit increased mechanical, thermal, and chemical performance compared with pure polymer.<sup>[42]</sup>

Conjugate systems with appropriate end groups<sup>[43]</sup> and confined aromatic systems<sup>[44]</sup> can transfer excitations upon photon absorption or after reduction or oxidation. The desire to miniaturize displays, electronic circuits, and microchips drives the development of mesoporous materials containing conductive polymers.<sup>[45]</sup>

The internal channels of MCM-41 have been exploited as catalytic reactors for the fabrication of aligned polymer fibers<sup>[46–50]</sup> and metal nanowires.<sup>[51,52]</sup> The high pore volume and uniform pore size of MCM-41 allows high polymer loading. Researchers have demonstrated that MCM-41-type structures can serve as a mold for polymerization of ethylene,<sup>[47]</sup> aniline,<sup>[48]</sup> acrylonitrile,<sup>[53]</sup> methyl methacrylate,<sup>[54]</sup> and phenol–formaldehyde.<sup>[55]</sup> In these techniques, the monomers are adsorbed from the gas phase into the mesoporous material, MCM-41, and then polymerized within the mesoporous framework using benzoyl peroxide or anhydrous HCl vapor as initiators. These hybrid materials have the advantages of compositional stability and mechanical strength over their small molecular analogues. A major limitation of this approach has been the low polymer loading and non-uniform distribution of polymer within the mesoporous channels.<sup>[56,57]</sup>

Based on our discovery that polymer is stable in CTAB micelles, we explore the concept of condensing silica around CTAB micelles swollen with polymer. Specifically, the idea of forming polymer in CTAB micelles and then forming silica may lead to a novel composite material with high polymer loading. Polymerization in CTAB micelles is performed as described previously, followed by the addition of a silica precursor such as tetramethyl orthosilicate (TMOS). After silica condensation, a tan slurry forms for mesoporous silica/poly(4-ethylphenol) composites and a reddish slurry forms for mesoporous silica/polyaniline

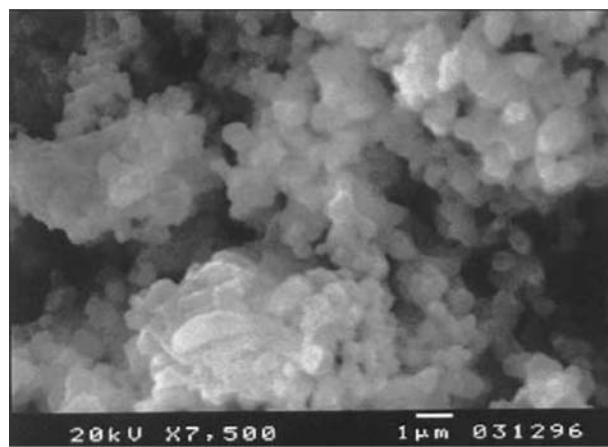


**Fig. 9** Scanning electron micrograph of poly(4-ethylphenol)/mesoporous silica composites with monomer-to-surfactant molar ratios = 3.

composites. When the slurry settles, the supernatant is clear while the precipitate retains the color of the polymer, suggestive of polymer encapsulation. Fig. 9 shows a typical SEM micrograph of mesoporous silica/polymer composites with varying monomer-to-surfactant ratios.

Powder X-ray diffraction (XRD) of the polymer/mesoporous silica composites was performed to determine ordered structure. XRD data of mesoporous silica without polymer and polymer/mesoporous silica composite are shown in Fig. 10. Before polymer encapsulation, four main peaks at  $2\theta = 2.167^\circ$ ,  $3.736^\circ$ ,  $4.283^\circ$ , and  $5.694^\circ$  exist, corresponding to the  $d$  spacing of

4.125 ( $d_{100}$ ), 2.383 ( $d_{110}$ ), 2.079 ( $d_{200}$ ), and 1.554 nm ( $d_{210}$ ). At ethylphenol-to-CTAB molar ratios equal to 1, the polymer/mesoporous silica composite was observed to have a hexagonal structure, as indicated by the four-peak pattern with reciprocal peak spacings,  $1/d_{hk}$ , ratios of 1,  $\sqrt{3}$ , 2, and  $\sqrt{7}$ . The polymer/mesoporous composite with a monomer-to-surfactant ratio of 1 exhibited four main peaks at  $2\theta = 2.321^\circ$ ,  $3.939^\circ$ ,  $4.659^\circ$ , and  $6.08^\circ$ , corresponding to the  $d$  spacing of 3.806 ( $d_{100}$ ), 2.241 ( $d_{110}$ ), 1.895 ( $d_{200}$ ), and 1.454 nm ( $d_{210}$ ).

A transmission electron microscopy (TEM) micrograph of MCM-41 without polymer shows the hexagonal pore structure consistent with the literature,

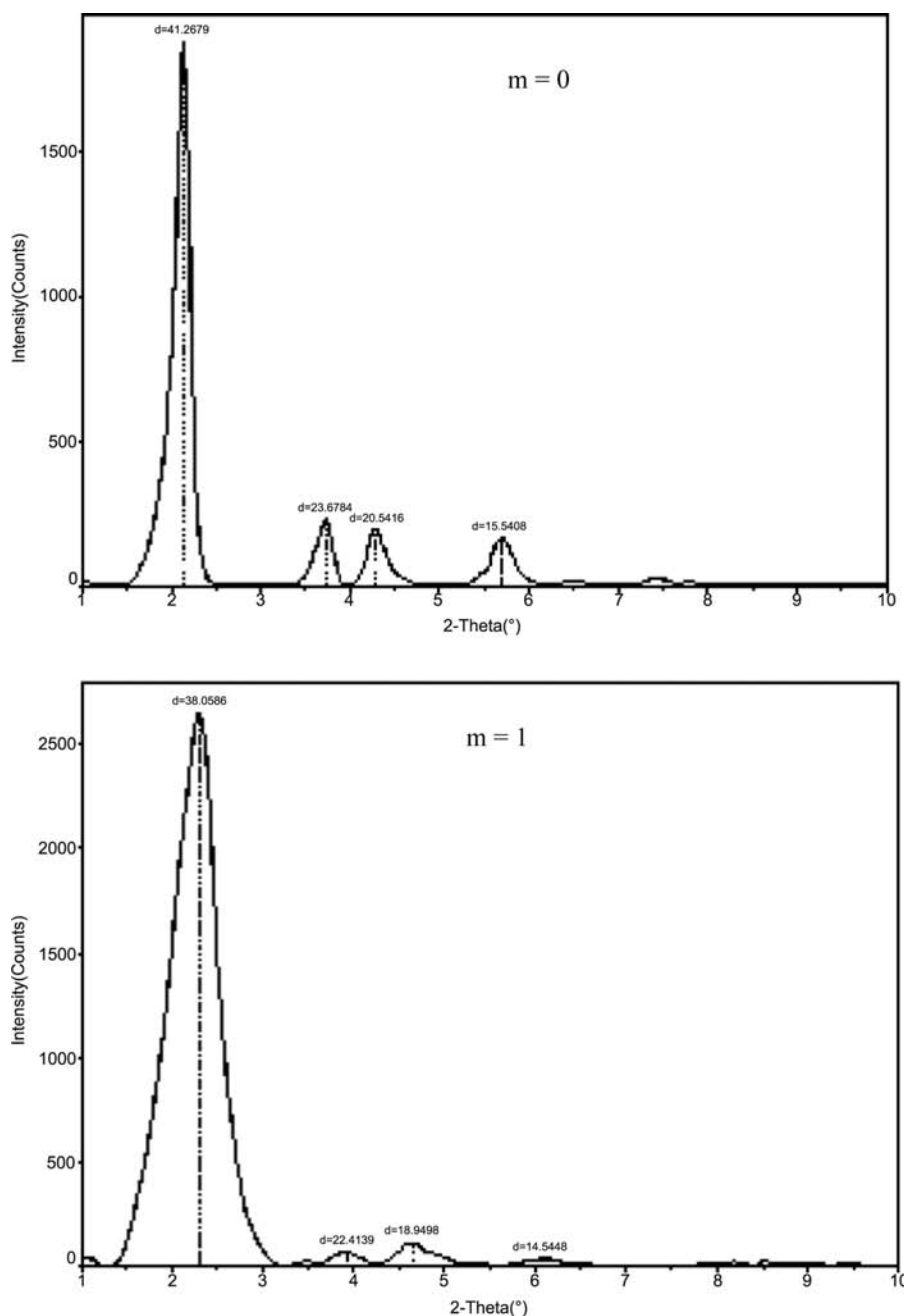


**Fig. 10** Powder X-ray diffraction of mesoporous silica containing polymer showing retention of ordered structure after polymer encapsulation, where  $m$  is the molar ratio of monomer to surfactant.

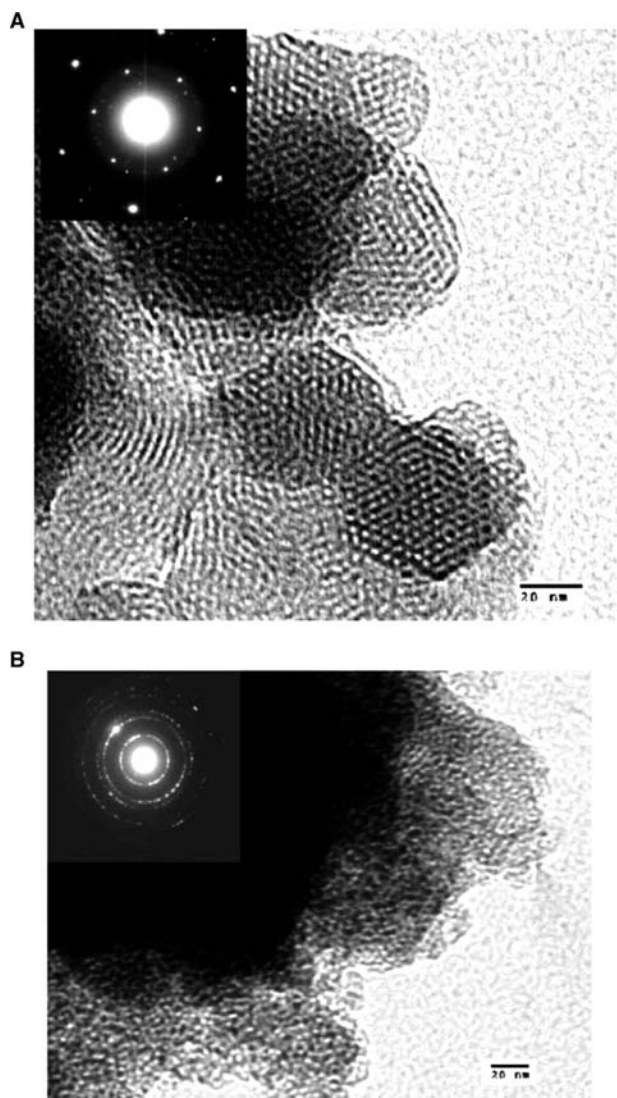


**Fig. 11** Transmission electron micrographs of (A) mesoporous silica without polymer and (B) mesoporous silica/polymer composite with monomer-to-surfactant ratio = 1. Hexagonal structure observed before and after incorporating polymer in silica.

where the pore size is approximately 3.6 nm (Fig. 11A). MCM-41/polymer composites with monomer-to-surfactant ratio of 1 show ordered pores and the electron diffraction pattern shows concentric rings characteristic of a hexagonal arrangement, ratio of radii 1, 3, 4, and 7 (Fig. 11B). The appearance of rings rather than distinctive dots indicates polycrystallinity.

Mesoporous silica without polymer exhibits a large surface area ( $1098 \text{ m}^2/\text{g}$ ) and high pore volume ( $0.65 \text{ cm}^3/\text{g}$ ), similar to reported values in the literature for MCM-41. The total surface area and the pore volume decreases when polymer is incorporated into mesoporous silica. Adsorption/desorption isotherms of nitrogen on mesoporous silica containing poly(4-ethylphenol) indicate the preservation of mesoporosity.

Comparing calcined mesoporous silica/polymer composites to mesoporous silica/polymer composites that are washed with distilled water and not calcined offers critical information about the localization of polymer in the mesoporous silica. The washed composite shows a noticeable disappearance of the adsorption step, a decrease in surface area, and decrease in volume absorbed as compared with the calcined composite. In comparison, mesoporous silica not containing polymer that was washed with distilled water and not calcined showed only a slight decrease in surface area. These observations suggest that the pores are blocked and imply that the mesoporous pores are filled with polymer.

## CONCLUSION

Self-assembled surfactant systems can be exploited in the biocatalytic synthesis of structured polymers with unique properties that are a consequence of chemical structure and/or morphology. Although a precise templating effect from the surfactant microstructure may not be immediately evident, it is clear that the surfactant self-assembly plays an important role in the development of polymer morphology. These systems may be exploited in the development of a variety of polymer-polymer and polymer-ceramic composites. For example, enzymatic polymer synthesis could be coupled with traditional free radical polymer synthesis with vinyl monomers to make novel structured composites. It is also possible to combine enzymatic polymer synthesis with inorganic cluster synthesis to make structured polymer-ceramic nanocomposites. An immobilized surfactant gel phase may offer a simple approach to encapsulating nanoparticles within polymer. Upon polymerization and polymer folding, the polymer may entrap inorganic molecules that are immobilized in the surfactant gel. Continuing work seeks to systematize these studies to develop clear correlations between surfactant microstructure and materials morphology.

## ACKNOWLEDGMENTS

Funding from NASA, the U.S. Army, and the National Science Foundation for various aspects of this work, is gratefully acknowledged.

## REFERENCES

1. Dordick, J. *Biocatalysts for Industry*; Plenum Press: New York, 1991.
2. Gross, R.A.; Kaplan, D.; Swift, G. *Enzymes in Polymer Synthesis*; ACS Symposium Series; ACS: Washington, DC, 1998; 684 pp.

3. Chaudhary, A.K.; Beckman, E.J.; Russell, A.J. *Enzymes in Polymer Synthesis*; ACS Symposium Series; Gross, R.A., Kaplan, D., Swift, G., Eds.; ACS: Washington, DC, 1998; 684 pp.
4. Akkara, J.A.; Senecal, K.J.; Kaplan, D.L. Synthesis and characterization of polymers produced by horseradish peroxidase in dioxane. *J. Polym. Sci., A, Polym. Chem.* **1991**, *29* (11), 1561–1574.
5. Kobayashi, S.; Kasiwa, K.; Kawaskai, T.; Shoda, S. Novel method for polysaccharide synthesis using an enzyme: the first in vitro synthesis of cellulose via a non-biosynthetic path utilizing cellulase as catalyst. *J. Am. Chem. Soc.* **1991**, *113*, 3079–3084.
6. Dordick, J.; Marletta, M.A.; Klibanov, A.M. Polymerization of phenols catalyzed by peroxidase in nonaqueous media. *Biotechnol. Bioeng.* **1987**, *30*, 31–36.
7. Barbaric, S.; Luisi, P.L. Micellar solubilization of biopolymers in organic solvents. 5. Activity and conformation of alpha-chymotrypsin in isooctane-AOT reverse micelles. *J. Am. Chem. Soc.* **1981**, *103*, 4239–4244.
8. Kopf, P.W. *Encyclopedia of Polymer Science and Engineering*; John Wiley & Sons: New York, 1985; 11 pp.
9. Halliwell, B.; Gutteridge, J.M.C. *Free Radicals in Biology and Medicine*; Clarendon Press: Oxford, 1989.
10. Premchandran, R.; Banerjee, S.; John, V.T.; McPherson, G.L.; Akkara, J.A.; Kaplan, D.L.; Ayyagari, M. Enzymatic synthesis of fluorescent naphthol-based polymers. *Macromolecules* **1996**, *29*, 6452–6460.
11. Banerjee, S.; Rammannair, P.; Wu, K.; John, V.T.; McPherson, G.; Akkara, J.A.; Kaplan, D.L. *Enzymes in Polymer Synthesis*; ACS Symposium Series; Gross, R.A., Kaplan, D., Swift, G., Eds.; ACS: Washington, DC, 1998; 684, 125–143.
12. Premchandran, R.; Banerjee, S.; John, V.T.; McPherson, G.L.; Akkara, J.; Kaplan, D.L. The enzymatic synthesis of thiol-containing polymers to prepare polymer–CdS nanocomposites. *Chem. Mater.* **1997**, *9*, 1342–1347.
13. Wang, N.; Martin, B.D.; Parida, S.; Rethwisch, D.G.; Dordick, J.S. Multienzymic synthesis of poly(hydroquinone) for use as a redox polymer. *J. Am. Chem. Soc.* **1995**, *117*, 12,885–12,886.
14. Millis, G.A.; Mark, H.M.; Othmer, D.F. *Kirk–Othmer Encyclopedia of Chemical Technology*; John Wiley & Sons: New York, 1979; 5 pp.
15. Ayyagari, M.; Bruno, F.; Tripathy, S.; Marx, K.; Kaplan, D.; Akkara, J.; Rao, D. *Polymers and Other Advanced Materials: Emerging Technologies and Business Opportunities*; Prasad, P.N., Mark, J.E., Fai, T.J., Eds.; Plenum Press: New York, 1996; 667–675.
16. Prasad, P.N.; Williams, D.J. *Introduction to Nonlinear Optical Effects in Molecules and Polymers*; John Wiley & Sons: New York, 1991.
17. Akkara, J.A.; Aranda, F.A.; Rao, D.V.G.L.N.; John, V.T. Nonlinear optical properties of bioengineered materials. In *Plastics Engineering*; Electrical and Optical Polymer Systems; Marcel Dekker: New York, 1998; 45, 453–465.
18. Rao, A.M.; John, V.T.; Gonzalez, R.D.; Akkara, J.A.; Kaplan, D.L. Catalytic and interfacial aspects of enzymic polymer synthesis in reversed micellar systems. *Biotechnol. Bioeng.* **1993**, *41*, 531–540.
19. Banerjee, S.; Premachandran, R.; Tata, M.; John, V.; McPherson, G.; Akkara, J.; Kaplan, D. Polymer precipitation using a micellar nonsolvent: The role of surfactant–polymer interactions and the development of a microencapsulation technique. *Ind. Eng. Chem. Res.* **1996**, *35*, 3100–3109.
20. Karayigitoglu, C.; Kommareddi, N.; John, V.; McPherson, G.; Akkara, J.; Kaplan, D. The morphology of phenolic polymers enzymatically synthesized in surfactant microstructures. *Mater. Sci. Eng., C* **1995**, *2*, 165–171.
21. Xu, X.; Kommareddi, N.; McCormick, M.; John, V.T.; McPherson, G.L.; Akkara, J.A.; Kaplan, D.L. The microstructure of polymers enzymatically synthesized in a self-assembling environment. *Mater. Sci. Eng., C* **1996**, *4*, 161–169.
22. Pileni, M.P. Reverse micelles as microreactors. *J. Phys. Chem.* **1993**, *97*, 6961–6973.
23. Kommareddi, N.; Tata, M.; Karyigitoglu, C.; John, V.T.; McPherson, G.L.; Herman, M.F.; O'Connor, C.J.; Lee, Y.S.; Akkara, J.; Kaplan, D.L. Enzymic polymerization using surfactant microstructures and the preparation of polymer–ferrite composites. *Appl. Biochem. Biotechnol.* **1995**, *51/52*, 241–252.
24. Kommareddi, N.; Tata, M.; Karayigitoglu, C.; John, V.T.; McPherson, G.L.; Herman, M.F.; O'Connor, C.J.; Lee, Y.S.; Akkara, J.; Kaplan, D.L. Synthesis of superparamagnetic polymer–ferrite composites using surfactant microstructures. *Chem. Mater.* **1996**, *8*, 801–809.
25. Luisi, P.L.; Scartazzini, R.; Haering, G.; Schurtenburger, P. Organogels from water-in-oil microemulsions. *Colloid Polym. Sci.* **1990**, *356*, 268–274.
26. Schurtenberger, P.; Majid, L.J.; Lindner, P.; Luisi, P.L. Cylindrical structure and flexibility of polymerlike lecithin reverse micelles. *J. Phys. Chem.* **1991**, *95*, 4173–4176.
27. Capitani, D.; Rossi, E.; Segre, A.L.; Guistini, M.; Luisi, P.L. Lecithin microemulsion gels: an NMR study. *Langmuir* **1993**, *9*, 685–689.
28. Capitani, D.; Segre, A.L.; Dreher, F.; Walde, P.; Luisi, P.L. Multinuclear NMR investigation of phosphatidylcholine organogels. *J. Phys. Chem.* **1996**, *100*, 15,211–15,217.
29. Simmons, B.A.; Irvin, G.C.; Agarwal, V.; Bose, A.; John, V.T.; McPherson, G.L.; Balsara, N.P. Small angle neutron scattering study of microstructural transitions in a surfactant-based gel mesophase. *Langmuir* **2001**, *18* (3), 624–632.
30. Hassan, P.A.; Candau, S.J.; Kern, F.; Manohar, C. Rheology of wormlike micelles with varying hydrophobicity of the counterion. *Langmuir* **1998**, *14*, 6025–6029.
31. Soltero, J.F.A.; Puig, J.E.; Manero, O. Rheology of the cetyltrimethylammonium tosylate–water system. 2. Linear viscoelastic regime. *Langmuir* **1996**, *12*, 2654–2662.
32. Kresge, C.T.; Leonowicz, M.E.; Roth, W.J.; Vartuli, J.C.; Beck, J.S. Ordered mesoporous molecular sieves

- synthesized by a liquid-crystal template mechanism. *Nature* **1992**, *359*, 710–712.
33. Beck, J.S.; Vartuli, J.C.; Roth, W.J.; Leonowicz, M.E.; Kresge, C.T.; Schmitt, K.T.; Chu, C.T.-W.; Olson, D.H.; Sheppard, E.W.; McCullen, S.B.; Higgins, J.B.; Schlenker, J.L. A new family of mesoporous molecular sieves prepared with liquid crystal templates. *J. Am. Chem. Soc.* **1992**, *114*, 10,834–10,843.
  34. Morishige, K.; Shikimi, M. Adsorption hysteresis and pore critical temperature in a single cylindrical pore. *J. Chem. Phys.*, **B 1998**, *108*, 7821–7824.
  35. Sonwane, C.G.; Bhatia, S.K.; Calos, N. Experimental and theoretical investigations of adsorption hysteresis and criticality in MCM-41: studies with O<sub>2</sub>, Ar, and CO<sub>2</sub>. *Ind. Eng. Chem. Res.* **1998**, *37*, 2271–2283.
  36. Tanev, P.T.; Chibwe, M.; Pinnavaia, T.J. Titanium-containing mesoporous molecular sieves for catalytic oxidation of aromatic compounds. *Nature* **1994**, *368*, 321–323.
  37. Sayari, A.; Hamoudi, S. Periodic mesoporous silica-based organic–inorganic nanocomposite materials. *Chem. Mater.* **2001**, *13*, 3151–3168.
  38. Matos, J.R.; Kruk, M.; Mercuri, L.P.; Jaroniec, M.; Asefa, T.; Coombs, N.; Ozin, G.A.; Kamiyama, T.; Terasaki, O. Periodic mesoporous organosilica with large cage-like pores. *Chem. Mater.* **2002**, *14*, 1903–1905.
  39. Khushalani, D.; Kuperman, A.; Ozin, G.; Tanaka, K.; Garces, J.; Olken, M.; Coombs, N. Metamorphic materials. Restructuring siliceous mesoporous materials. *Adv. Mater.* **1995**, *7*, 842–846.
  40. Lind, A.; Andersson, J.; Karlsson, S.; Agren, P.; Bussian, P.; Amenitsch, H.; Linden, M. Controlled solubilization of toluene by silicate-cationic surfactant mesophases as studied by in situ and ex situ XRD. *Langmuir* **2002**, *18*, 1380–1385.
  41. Sayari, A.; Yang, Y.; Kruk, M.; Jaroniec, M. Expanding the pore size of MCM-41 silicas: Use of amines as expanders in direct synthesis and postsynthesis procedures. *J. Phys. Chem.*, **B 1999**, *103*, 3651–3658.
  42. Gomez-Romero, P. Hybrid organic–inorganic materials—in search of synergic activity. *Adv. Mater.* **2001**, *13*, 163–174.
  43. Arrhenius, S.; Blanchard, D.M.; Dvolaitzky, M.; Lehn, J.M.; Malthete, J. Molecular devices: carviologens as an approach to molecular wires—synthesis and incorporation into vesicle membranes. *Proc. Natl. Acad. Sci. U.S.A.* **1986**, *83*, 5355–5359.
  44. Kopelman, R.; Parus, S.J.; Prasad, J. Exciton reactions in ultrathin molecular wires, filaments and pores: a case study of kinetics and self-ordering in low dimensions. *Chem. Phys.* **1988**, *128*, 209–217.
  45. Carter, C. *Molecular Electronic Devices*; Marcel Dekker: New York, 1982.
  46. Lin, V.S.-Y.; Radu, D.R.; Han, M.; Deng, W.; Shigeki, K.; Shanks, B.H.; Pruski, M. Oxidative polymerization of 1,4-diethynylbenzene into highly conjugated poly(phenylene butadiynylene) within the channels of surface-functionalized mesoporous silica and alumina materials. *J. Am. Chem. Soc.* **2002**, *124*, 9040–9041.
  47. Kageyama, K.; Tamazawa, J.; Aida, T. Extrusion polymerization: catalyzed synthesis of crystalline linear polyethylene nanofibers within a mesoporous silica. *Science* **1999**, *285*, 2113–2115.
  48. Wu, C.G.; Bein, T. Conducting polyaniline filaments in a mesoporous channel host. *Science* **1994**, *264*, 1757–1759.
  49. Li, Z.F.; Ruckenstein, E. Intercalation of conductive polyaniline in the mesostructured V<sub>2</sub>O<sub>5</sub>. *Langmuir* **2002**, *18*, 6956–6961.
  50. Wu, J.; Gross, A.F.; Tolbert, S. Host–guest chemistry using an oriented mesoporous host: alignment and isolation of a semiconducting polymer in the nanopores of an ordered silica matrix. *J. Phys. Chem.*, **B 1999**, *103*, 2374–2384.
  51. Zhang, Z.; Dai, S.; Blom, D.A.; Shen, J. Synthesis of ordered metallic nanowires inside ordered mesoporous materials through electroless deposition. *Chem. Mater.* **2002**, *14*, 965–968.
  52. Fukuoka, A.; Sakamoto, Y.; Guan, S.; Inagaki, S.; Sugimoto, N.; Fukushima, Y.; Hirahra, K.; Iijima, S.; Ichikawa, M. Novel templating synthesis of necklace-shaped mono- and bimetallic nanowires in hybrid organic–inorganic mesoporous material. *J. Am. Chem. Soc.* **2001**, *123*, 3373–3374.
  53. Wu, C.G.; Bein, T. Conducting carbon wires in ordered, nanometer-sized channels. *Science* **1994**, *266*, 1013–1015.
  54. Moller, K.; Bein, T.; Fischer, R.X. Entrapment of PMMA polymer strands in micro- and mesoporous materials. *Chem. Mater.* **1998**, *10*, 1841–1852.
  55. Johnson, S.A.; Khushalani, D.; Coombs, N.; Mallouk, T.E.; Ozin, G.A. Polymer mesofibers. *J. Mater. Chem.* **1998**, *8*, 13–14.
  56. Pereira, C.; Kokotailo, G.T.; Gorte, R.J. Acetylene polymerization in a H-ZSM-5 zeolite. *J. Phys. Chem.* **1991**, *95*, 705–709.
  57. Cox, S.D.; Stucky, G.D. Polymerization of methylacetylene in hydrogen zeolites. *J. Phys. Chem.* **1991**, *95*, 710–720.

# Epoxy-Layered Silicate Nanocomposites

**Chenggang Chen**

*Nonmetallic Division, University of Dayton Research Institute,  
Dayton, Ohio, U.S.A.*

**Tia Benson Tolle**

*Plastic Composites/Military Organic Matrix Composites, Air Force Research Laboratory,  
Wright-Patterson Air Force Base, Ohio, U.S.A.*

## INTRODUCTION

Research on polymer nanocomposites based on layered silicates has exploded over the last decade,<sup>[1–5]</sup> ever since the pioneering work of the organoclay–nylon nanocomposite by Toyota.<sup>[6]</sup> The dispersion of the silicate nanolayer with its high aspect ratio, large surface area, and high stiffness within a polymer matrix results in significant improvement of the properties of polymeric materials, including mechanical properties,<sup>[7]</sup> barrier properties,<sup>[8]</sup> resistance to solvent swelling,<sup>[9]</sup> ablation performance,<sup>[10]</sup> thermal stability,<sup>[11]</sup> fire retardancy,<sup>[11]</sup> controlled release of drugs,<sup>[12]</sup> anisotropic electrical conductivity,<sup>[13]</sup> and photoactivity.<sup>[14]</sup> Layered-silicate nanocomposites have great potential for applications, ranging from automotive and aerospace to food packaging and tissue engineering. Cost and processability are as important to many applications as the property improvements.

Epoxy materials have been widely used in adhesives, coatings, electronic encapsulants, and advanced composites. Since the Pinnavaia group first extended the nanocomposite concept to epoxy systems,<sup>[15]</sup> extensive research on layered-silicate epoxy nanocomposites has been carried out.<sup>[16–45]</sup> This entry is the summary of some of the past research and latest research in our group, which focus on layered-silicate epoxy nanocomposites for aerospace applications. The aerospace epoxy used in the study is made from Shell Epon 862 with Epi-Cure curing agent W. This epoxy system has a high glass transition temperature ( $T_g$ ), good mechanical and physical performance characteristics, and low viscosity, and involves non-4,4'-methylenedianiline aromatic amines. The compatibility of organoclays with aerospace epoxy resin and the preparation of the nanocomposite were studied. Small-angle x-ray scattering (SAXS) and transmission electron microscopy (TEM) were used to characterize the morphology of the nanocomposites. The properties of the nanocomposite, including the dynamic and

static mechanical property and survivability in aggressive environments such as oxygen plasma, were measured. The integrated study of in situ SAXS, differential scanning calorimetry (DSC), and rheology provides information about the viscosity development and processing window, as well as the morphology development and exfoliation mechanism. Morphology development behavior for the epoxy nanocomposites as a function of curing agents, including Jeffamine and curing agent W, is discussed. In addition, epoxy nanocomposites as primer layer for aircraft coatings for improved anticorrosion properties are described.

## LAYERED SILICATE AND LAYERED ORGANOSILICATE

There are many layered silicates, including montmorillonite, illite, vermiculite, hectorite, beidellite, magadiite, kenyaite, kanemite, and crystalite. Among them, montmorillonite is the most popular choice for layered-silicate polymer nanocomposites. Natural sodium montmorillonite is an aluminosilicate composed of two silica tetrahedral sheets and one alumina octahedral sheet with strong covalent bonding within the sheets and weak bonding between the layers. Sodium montmorillonite is hydrophilic in nature and is not compatible with generally hydrophobic organic polymers. However, the weak bonding between the layers makes the cations in the gallery of the layered silicate easily exchangeable. Cations are typically used for nanocomposites with alkyl ammonium. The organic ammonium pendent group on these exchanged cations renders the layered silicate hydrophobic, thus compatible with the polymer matrix. One measure of the hydrophilic or hydrophobic nature of materials is the value of surface tension  $\gamma^-$  (electron donor).<sup>[46]</sup> Materials that have a  $\gamma^{LW}$  (Lifshitz–van der Waals) value of about 40 mJ/m<sup>2</sup> with  $\gamma^-$  higher than 28 mJ/m<sup>2</sup> are hydrophobic; at  $\gamma^-$  smaller



than 28 mJ/m<sup>2</sup>, they are hydrophobic.<sup>[46]</sup> For Wyoming sodium montmorillonite (SWy-1), the  $\gamma^{\text{LW}}$  and  $\gamma^-$  values are 42.9 and 36.7 mJ/m<sup>2</sup>; thus this material is hydrophilic in nature and is incompatible with epoxy. When the native sodium cation is exchanged with an ammonium cation, the charged end of the ammonium cation maintains contact with the silicate nanolayer surface, whereas the alkyl tail is directed away from the silicate nanolayer surface. This results in a reduction of  $\gamma^-$  value. The actual reduction depends on the alkyl chain length. For SWy-1, the  $\gamma^{\text{LW}}$  and  $\gamma^-$  values are 41.7 and 36.2 mJ/m<sup>2</sup> for NH<sub>4</sub><sup>+</sup>-montmorillonite, 41.2 and 9.8 mJ/m<sup>2</sup> for *n*-C<sub>6</sub>H<sub>12</sub>NH<sub>3</sub><sup>+</sup>-montmorillonite, 39.4 and 7.7 mJ/m<sup>2</sup> for *n*-C<sub>8</sub>H<sub>17</sub>NH<sub>3</sub><sup>+</sup>-montmorillonite, and 39.6 and 6.0 mJ/m<sup>2</sup> for *n*-C<sub>12</sub>H<sub>25</sub>NH<sub>3</sub><sup>+</sup>-montmorillonite.<sup>[46]</sup> Thus it appears that the organoclay with six-carbon alkyl chain length can still be compatible with epoxy, although it is generally thought that longer alkyl chains in the pendent group are preferred for compatibility with polymers.

Based on this, an investigation of the effect of alkyl chain length on interplanar spacings of layered-silicate epoxy nanocomposites was conducted on four synthetic organoclays, including SC6 (*n*-C<sub>6</sub>H<sub>13</sub>NH<sub>3</sub><sup>+</sup>-montmorillonite), SC8 (*n*-C<sub>8</sub>H<sub>17</sub>NH<sub>3</sub><sup>+</sup>-montmorillonite), SC12 (*n*-C<sub>12</sub>H<sub>25</sub>NH<sub>3</sub><sup>+</sup>-montmorillonite), and SC18 (*n*-C<sub>18</sub>H<sub>37</sub>NH<sub>3</sub><sup>+</sup>-montmorillonite), and on one commercial organoclay, I.30E, from Nancor. Organoclays SC6, SC8, SC12, and SC18 were prepared by the treatment of sodium montmorillonite with HCl and primary amine (*n*-hexylamine or *n*-octylamine or *n*-dodecylamine or *n*-octadecylamine, respectively). Wide-angle x-ray diffraction (WAXD) studies show that the interplanar spacings of original sodium montmorillonite (SNA), SC6 (*n*-C<sub>6</sub>H<sub>13</sub>NH<sub>3</sub><sup>+</sup>-montmorillonite), SC8 (*n*-C<sub>8</sub>H<sub>17</sub>NH<sub>3</sub><sup>+</sup>-montmorillonite), SC12 (*n*-C<sub>12</sub>H<sub>25</sub>NH<sub>3</sub><sup>+</sup>-montmorillonite), and SC18 (*n*-C<sub>18</sub>H<sub>37</sub>NH<sub>3</sub><sup>+</sup>-montmorillonite) are 12.1, 13.0, 13.2, 16.5, and 18.7 Å, respectively. The interplanar spacings of these organoclays increase with increasing alkyl chain length of the pendent group.

## AEROSPACE EPOXY NANOCOMPOSITES

There are three typical morphologies when a polymer is associated with organically modified layered silicates:<sup>[1–5]</sup> 1) traditional microcomposite—the polymer chain cannot penetrate inside the gallery of the layered silicate, resulting in a phase-separated composite; 2) intercalated nanocomposite—the polymer chains penetrate inside the gallery of the layered silicate and expand the nanolayers, resulting in a well-ordered multilayer morphology with alternating polymeric and silicate layers; and 3) exfoliated nanocomposite—the individual silicate nanolayers are completely separated and uniformly dispersed in a continuous polymer matrix. This is an ideal situation and perfect

morphology. Among the most reported exfoliated nanocomposites, there exist mixed morphologies with combinations of exfoliation and intercalation. The morphology can be determined by x-ray diffraction and transmission electronic microscopy.

There are three main approaches to fabricating layered-silicate polymer nanocomposites:<sup>[3,4]</sup> 1) in situ intercalative polymerization—the organosilicate is swollen in the liquid monomer, the monomer penetrates inside the gallery of the layered silicate, and the polymerization takes place inside the gallery; 2) exfoliation adsorption (solvent-assisted)—the organosilicate is mixed with the solvent, which can penetrate inside the gallery of the organosilicate, enlarge the gallery of the silicate nanolayers to expansion, or delaminate the silicate nanolayers. Simultaneously, the polymer can also dissolve in this solvent. When the mixture of organosilicate and solvent is combined with the polymer, the polymer can penetrate inside the gallery of the silicate nanolayers. The solvent can then be evaporated, leaving the nanocomposite; and 3) melt intercalation—the polymer is heated into the molten state and then mixed with organosilicate. The polymer will penetrate inside the gallery of the silicate nanolayers to expand the gallery to form the nanocomposite. In situ intercalative polymerization involves chemical reactions, whereas exfoliation adsorption and melt intercalation are primarily physical. Epoxy nanocomposites are generally prepared by in situ intercalative polymerization.<sup>[15–45]</sup>

The aerospace epoxy used in the study to be referenced is made from Shell Epon 862 (diglycidylbisphenol-F) with Epi-Cure curing agent W (diethyltoluenediamine). The desired amount of organoclay was added to the Epon 862. The organoclay/Epon 862 mixture was stirred at elevated temperature, then the stoichiometric amount of curing agent W was added to the mixture. The resulting mixture was degassed, cast in the mold, and cured at 121°C for 2 hr and at 177°C for another 2 hr, then cooled to room temperature overnight. DSC studies confirm that all of the nanocomposites were fully cured. All the organoclays, including SC6, SC8, SC12, SC18, and I.30E, can form transparent nanocomposites with the epoxy resin confirming the good compatibility of these organoclays with the Epon 862/W system. It appears that the six-carbon alkyl chain length can render the clay nanolayers sufficiently hydrophobic to be compatible with the epoxy resin, consistent with what the  $\gamma^-$  of the SC6 indicates.

## MORPHOLOGY CHARACTERIZATION

WAXD studies show no peak with  $2\theta$  down to 2° for all of the aerospace epoxy nanocomposite samples even with organoclay loading as high as 15%, indicating a

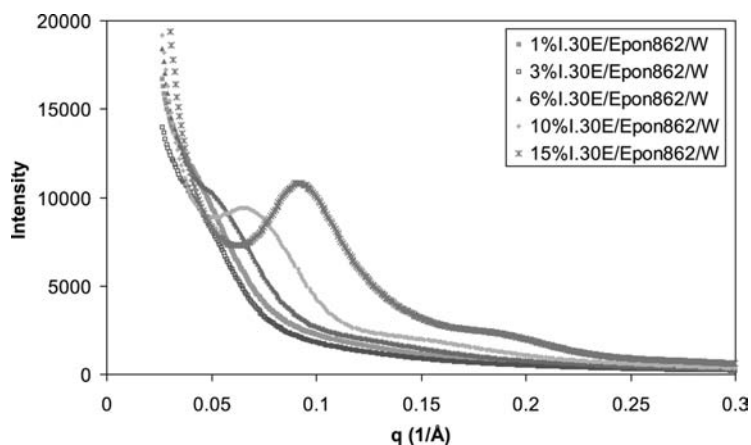


**Fig. 1** SAXS of Epon 862/curing agent W with different concentrations of I.30E (1%, 3%, 6%, 10%, and 15%).

large interplanar spacing ( $>44 \text{ \AA}$ ). The SAXS of Epon 862/curing agent W with different concentrations of I.30E (1%, 3%, 6%, 10%, and 15%) is shown in Fig. 1. SAXS study indicates that the interplanar spacings of all the nanocomposites with 3% and 6% different organoclay loadings are more than  $100 \text{ \AA}$ , and are 88 and  $69 \text{ \AA}$  for 10% I.30E/Epon 862/W and 15% for I.30E/Epon 862/W nanocomposites, whereas the original interplanar spacing of the organoclays is in the range of  $13\text{--}23 \text{ \AA}$ . The large increase in the interplanar spacing is because of the penetration of the epoxy resin inside the gallery and the expansion of the gallery of the organoclay. This also demonstrates that the dispersion of the nanolayers of the organoclay in the epoxy matrix is pretty good. Even at 10% I.30E loading, which is generally considered a very high loading in nanocomposites, the SAXS data still indicate good dispersion of clays in the matrix.

TEM provides direct imaging of the morphology of nanocomposites. The TEM image of cured 10% I.30E/Epon 862/W nanocomposites is shown in Fig. 2. The dark lines are the cross sections of the silicate nanolayers. The original aggregates of the organoclay were disrupted, and the nanometer-thick individual sheets were well dispersed in the epoxy resin. Although some nanolayers are disordered, others preserve the original ordered structure separated by approximately  $10 \text{ nm}$ , consistent with the SAXS results. The image also indicates that there still exist some ordered structures with disordered structure and some pure polymer domains. The TEM image of the cured 3% SC6/Epon 862/W nanocomposite is shown in Fig. 3. The interplanar spacing between the nanolayers of the ordered gallery is  $\sim 15 \text{ nm}$ , consistent with the SAXS results (a weak 001 reflection at  $140 \text{ \AA}$ ). The dispersions of the layers are very good. However, it is still not strictly an exfoliated nanostructure; rather, it is partially exfoliated with some intercalated structures of very large interplanar spacings ( $\sim 15 \text{ nm}$ ).

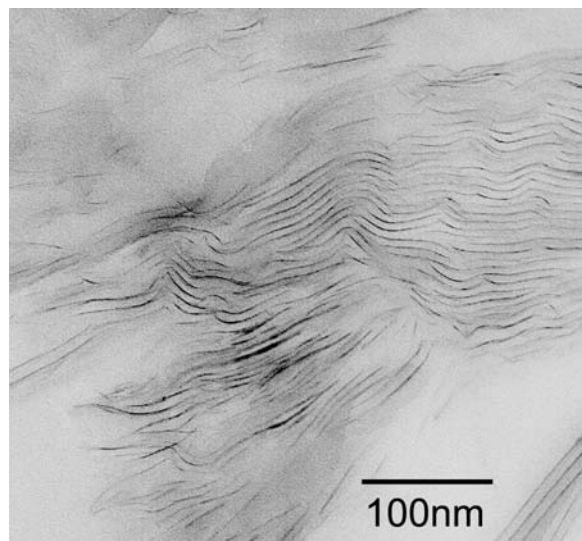


**Fig. 2** TEM image of cured 10% I.30E/Epon 862/W nanocomposite.

## PROPERTIES OF AEROSPACE EPOXY NANOCOMPOSITES

The storage modulus and  $\tan \delta$  curves obtained through dynamic mechanical analysis (DMA) of pure Epon 862/W and 1% I.30E/Epon 862/W, 6% I.30E/Epon 862/W, and 10% I.30E/Epon 862/W nanocomposites are shown in Figs. 4 and 5. The DMA data indicate that the increase in the storage modulus of the nanocomposites with different organoclays (1%, 3%, 6%, 10%, and 15% I.30E; 3% SC6; 6% SC8; 6% SC12; and 6% SC18) ranges from 15% to 35% in the glass state and from 15% to 300% in the rubber state. The increase of the storage modulus is attributed to the high aspect ratio and relatively high stiffness of the silicate nanolayers in the epoxy matrix. Based

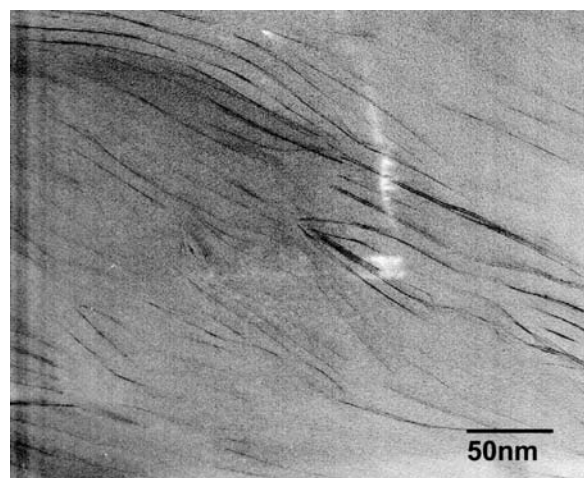


**Fig. 3** TEM images of cured 3% SC6/Epon 862/W nanocomposite.

on the  $\tan \delta$  curve, the glass transition temperatures of the nanocomposites are from 152°C to 155°C, compared with 154°C of the pure Epon 862/W, except for the 143°C for the 15% I.30E/Epon 862/W nanocomposite. The decrease for the 15% I.30E/Epon 862/W nanocomposite perhaps is caused by the less homogeneous dispersion of the organoclay because of the high concentration of I.30E in the nanocomposite and plasticization effect from the organoclay.

Flexural data from three-point flex testing performed at room temperature and at high temperature (250°F) are shown in Figs. 6 and 7. The flexural modulus of the epoxy is significantly increased because of the organoclays by as much as 85%, with 10% I.30E loading. The improvement in modulus is perhaps because of the good dispersion of the stiffer clay nanolayers in the epoxy matrix, which may transfer and carry more load. However, the strength of the nanocomposites is decreased compared with that of the pristine epoxy resin. The results are similar to the those for the epoxy system reported by Zerda and Lesser<sup>[26]</sup>

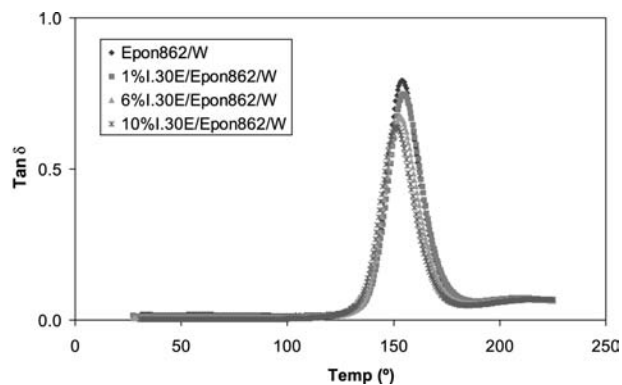


**Fig. 5**  $\tan \delta$  curve of cured pure Epon 862/W and 1% I.30E/Epon 862/W, 6% I.30E/Epon 862/W, and 10% I.30E/Epon 862/W nanocomposites.

and Yasmin, Abot, and Daniel<sup>[44]</sup> Strength is more sensitive to the interface and to defects than modulus. The small reduction of strength may be partially attributed to the weak interface between the clay nanolayer and the epoxy because there is no covalent bonding in the interface between the nanoclay and the epoxy matrix. One of the key factors to improving the strength of the nanocomposite is the enhancement of the interfacial interaction between the polymer matrix and the layered silicates. Another possible reason for the reduction is the possible existence of nanovoids inside the nanocomposite system.<sup>[44]</sup> The data also show that the reduction of flex strength of the nanocomposites at elevated temperature is much smaller than that seen by the pristine polymer. Interestingly, the strength of some of the nanocomposites is higher than that of pure resin at 250°F. The cause for this significant phenomenon is under investigation.

The survivability of the nanocomposites in extreme environments may be improved and was assessed here via exposure to oxygen plasma.<sup>[47]</sup> Oxygen plasma contains many species that are extremely strong oxidants and to which polymeric materials are vulnerable. The

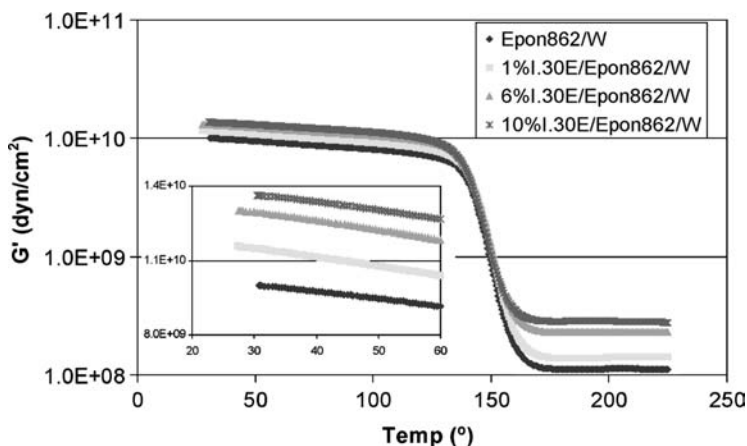


**Fig. 4** Storage modulus vs. temperature of cured pure Epon 862/W and 1% I.30E/Epon 862/W, 6% I.30E/Epon 862/W, and 10% I.30E/Epon 862/W nanocomposites.

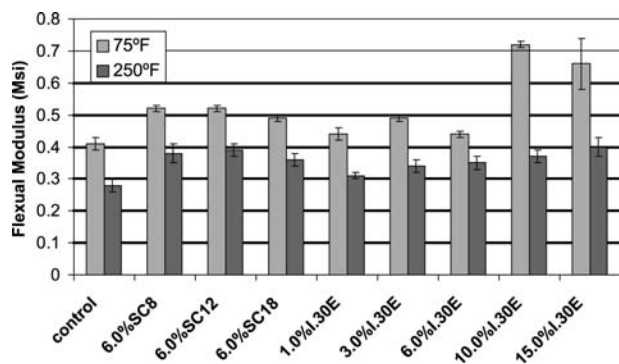


Fig. 6 Flexural modulus of the pure Epon 862/W and nanocomposites at room temperature and 250°F.

surface erosion thicknesses after a 5-hr exposure to oxygen plasma are 34 and 22  $\mu\text{m}$  for the pure Epon 862/W and 6% for the I.30E/Epon 862/W nanocomposites, respectively, when they were exposed to oxygen plasma. Under this environment, the surface erosion rate of the nanocomposite is retarded compared with that of pure epoxy resin. A possible mechanism for the improved survivability is the ability of the nanocomposite to form intact inorganic layers when exposed to oxygen plasma.<sup>[47]</sup> The preferential oxidation of polymers and the corresponding enrichment of the nanoscale-layered silicates on the surface result in the formation of a ceramic-like inorganic layer, which retards the penetration of the oxygen plasma, thus slowing further degradation. Thus the incorporating organoclays in polymer matrices could increase the survivability of resulting composites in aggressive aerospace environments.

## PROCESSING AND MORPHOLOGY DEVELOPMENT

DSC studies show that the onset temperatures of polymerization are much lower for the Epon 862/W with

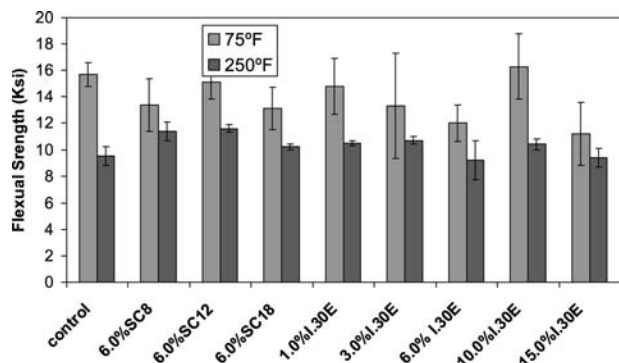
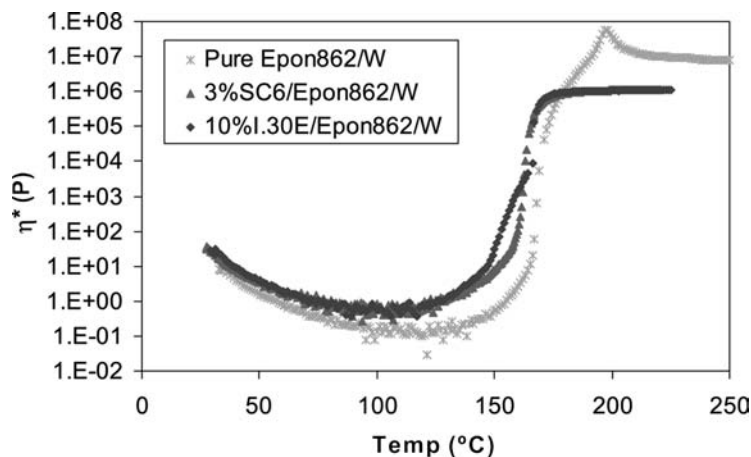


Fig. 7 Flexural strength of the pure Epon 862/W and nanocomposites at room temperature and 250°F.

organoclays than those for pure Epon 862/W ( $\sim 65$ – $100^\circ\text{C}$  vs.  $122^\circ\text{C}$ ). The catalytic effect is likely because of the acidity from the ammonium ( $\text{RNH}_3^+$ ) group of the pendent group from the organomontmorillonite.<sup>[15,18,19,39,40]</sup> The mechanism for the catalytic effect that the organoclay has on the epoxy polymerization may be explained as follows: The proton from the ammonium ( $\text{RNH}_3^+$ ) forms a cation with the glycidyl group, causing the functional group to become more electrophilic, which becomes more easily attacked by the nucleophilic curing agent amine. Thus the pendent group ( $\text{RNH}_3^+$ ) inside the gallery will catalyze the polymerization of the epoxy resin, resulting in cross-linking of the epoxy resin inside the gallery at relatively lower temperatures than those outside the gallery.

The addition of particles to a polymer generally increases its viscosity. If the organoclay significantly increases the viscosity of the epoxy resin, processing rates for aerospace composites, such as in resin transfer molding, may be difficult. The viscosity-vs.-temperature curves of the Epon 862/W mixture, the 3% SC6/Epon 862/W mixture, and the 10% I.30E/Epon 862/W mixture, when heated at  $2^\circ\text{C}/\text{min}$ , is shown in Fig. 8. The complex viscosity of the epoxy resin with organoclays (23 P for 3% SC6/Epon 862/W and 30 P for 10% I.30E/Epon 862/W mixture at  $30^\circ\text{C}$ ) is slightly higher than that of Epon 862/W (11 P at  $30^\circ\text{C}$ ). For the sample with 3% SC6 loading, the viscosity is increased very slightly from 0.6 P at  $90^\circ\text{C}$  to 2.7 P at  $140^\circ\text{C}$ , increased significantly from 7.6 P at  $150^\circ\text{C}$  to 108 P at  $160^\circ\text{C}$ , and increased very rapidly from 254 P at  $161^\circ\text{C}$  to 90,200 P at  $165^\circ\text{C}$  and to  $4.6 \times 10^5$  P at  $170^\circ\text{C}$ . This trend is similar to that seen for the 10% I.30E/Epon 862/W mixture. The viscosity is increased slightly from 0.7 P at  $90^\circ\text{C}$  to 4.2 P at  $140^\circ\text{C}$ , increased significantly from 8.4 P at  $145^\circ\text{C}$  to 110 P at  $152^\circ\text{C}$ , and increased again rapidly from 377 P at  $155^\circ\text{C}$  to 1900 P at  $160^\circ\text{C}$  and to  $6.2 \times 10^5$  P at  $170^\circ\text{C}$ . For the sample of pure Epon 862/W mixture, the complex viscosity is increased very slightly to 2.1 P at  $160^\circ\text{C}$ , increased significantly from 2.1 P at  $160^\circ\text{C}$  to 43 P at  $167^\circ\text{C}$ , and very rapidly from 430 P at  $168^\circ\text{C}$  to 13,192 P at  $170^\circ\text{C}$  and to  $5.9 \times 10^5$  P at  $180^\circ\text{C}$ . The rapid increase of the viscosity for the 3% SC6/Epon 862/W and 10% I.30E/Epon 862/W mixture at relatively low temperatures is related to the catalytic effect for the polymerization from the organoclay. Therefore, the incorporation of the organoclay into the epoxy resin does increase the viscosity not only because of the expected effect of particles, but also through the catalytic effect of the organoclays. However, the increase of the complex viscosity is limited and the processing window for the 3% SC6/Epon 862/W mixture and 10% I.30E/Epon 862/W mixture is still quite wide. This is important for subsequent composite processes.



**Fig. 8** Complex viscosity of the mixtures of pure Epon 862/W, 3% SC6/Epon 862/W, and 10% I.30E/Epon 862/W heated at 2°C/min.

In situ SAXS can be used to monitor the morphology development of the nanocomposites; here, some typical data of a 3% SC6/Epon 862/W mixture heated up at 2°C/min obtained at the National Synchrotron Light Source at the Brookhaven National Laboratory on Beamline X27C are shown in Fig. 9. SAXS data show that the initial interplanar spacing of the mixture is  $\sim 85$  Å compared with the original interplanar spacing of SC6 at 13.0 Å. This increase of the interplanar spacing is because of the penetration of epoxy resin into and the expansion of the gallery of the organoclay. The larger expansion of the interplanar spacing for 3% SC6/Epon 862/W mixture (85 Å), compared with that of 3% SC12/Epon 862/W mixture (35 Å),<sup>[40]</sup> is due perhaps to the smaller pendent group of SC6, which makes the migration of the epoxy resin inside the gallery relatively easier. SAXS data coupled with thermal analysis can provide insights into the morphology development mechanisms during the curing process of layered-silicate epoxy nanocomposites. When the temperature is elevated from 60°C to 80°C, the peak corresponding to the interplanar spacing between the nanolayers remains fairly constant. During this period, there is almost no polymerization

occurring, and the heating role in the expansion of the gallery of the nanoclay is very limited. From 80°C to 100°C, the increase of the interplanar spacing is still fairly limited. This is not unexpected as the onset temperature of curing for this mixture occurs at approximately 85°C based on DSC studies; polymerization is just beginning in this temperature region. From 100°C to 170°C, the peak corresponding to the interplanar spacing is shifted first gradually and then quickly from  $\sim 97$  to  $\sim 176$  Å, and the intensity of the peaks increases gradually as well. The quick polymerization in the intragallery because of the catalytic effect from the pendent group in the intragallery results in the consumption of the epoxy monomer inside the gallery and enhances the migration of more epoxy monomers from extragallery to intragallery, thus enhancing the continued expansion of the intragallery. In addition, the exothermal heat of curing provides additional energy to that from the process-imposed heating to help expand the nanoclay sheets. Based on rheological studies (Fig. 8), the viscosities for the 3% SC6/Epon 862/W mixture are 0.8 P at 100°C, 0.9 P at 120°C, 1.1 P at 130°C, 7.6 P at 150°C, 108 P at 160°C, 254 P at 161°C, 1303 P at 162°C, and 90,200 P

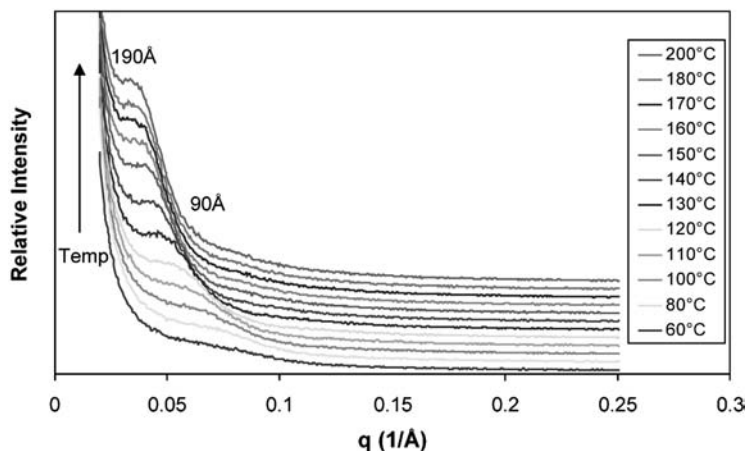


**Fig. 9** The in situ SAXS of the mixture of 3% SC6/Epon 862/W heated at 2°C/min.



at 165°C. The low viscosity of the epoxy resin from 100°C to 160°C guarantees that the epoxy resin can easily migrate from extragallery to intragallery. With an increase in temperature, curing of the epoxy resin both intragallery and extragallery results in increasingly high viscosities ( $4.6 \times 10^5$  P at 170°C, and  $8.7 \times 10^5$  P at 180°C). The epoxy is eventually almost fully cured with a viscosity of  $1.0 \times 10^6$  P at 190°C, and the material surrounding the nanolayers of the organoclay at this point is rigid. Ultimately, the interplanar spacing between the nanolayers is around 190 Å at 200°C.

Differences in the nanostructural evolution between the above-discussed SC6/Epon 862/W mixture and the previously studied SC12/Epon 862/W can be observed. The nanostructural or morphological evolution for the SC6-based nanocomposite was via a gradual ordered expansion of the galleries. In contrast, the SC12/Epon 862/W mixture morphological evolution occurs in stages, and experiences a transition from ordered to disordered and then back to order structure.<sup>[39]</sup> For the SC12/Epon 862/W system, the initial interplanar spacing is 35 Å after mixing. During initial curing, the silicate layers are distorted as the intragallery epoxy polymerizes and the outside resin infuses into the gallery through the tactoids edges. The SAXS data show an apparent loss of the peak associated with the initial spacing as the number of ordered scatterers is reduced because of resulting curvature of the nanosheets. As more and more epoxy migrates, the gallery makeup becomes more homogenous, the curvature is reduced, and the ordered (registered) structure is regained. For the SC6/Epon 862/W system, the original interplanar spacing is on the order of ~85 Å after mixing. In this case, the mixing step brings sufficient epoxy into the galleries as the epoxy is less impeded by the shorter alkyl chains (six-carbon chain in SC6 vs. 12-carbon chain in SC12); this results in an almost homogeneously filled gallery prior to heating. Therefore at the onset of polymerization, no distortion occurs and registry is maintained as the organoclay tactoid expands.

In summary, based on in situ SAXS studies, the exfoliation mechanism is seen to take place during curing. This important phenomenon enables low viscosity during the mixing processes and the ultimate formation of the nanoscale morphology during the curing steps of a process. This is vital to ultimate processability and manufacturability of nanotailored reinforced composites for aerospace applications.

### MORPHOLOGY DEVELOPMENT OF EPOXY NANOCOMPOSITES WITH DIFFERENT CURING AGENTS

The nature of the selected curing agent plays a role in the morphology development of epoxy nanocomposites.

When Epon 828 is mixed with organoclay SC18, Epon 828 penetrates inside the gallery of the organoclay. The SC18/Epon 828 mixture has a very ordered intercalated structure with an interplanar spacing of ~35 Å compared with the original interplanar spacing of ~18 Å of the SC18. When the mixture of SC18/Epon 828 was mixed with Jeffamine D230 or Jeffamine D400 curing agents and held for 30 min at room temperature, SAXS showed no peaks (Fig. 10). This indicates that Jeffamine D230 can easily penetrate into the gallery of the organoclay, therefore causing separation of the nanolayers and exfoliation. The SAXS shows the same pattern for fully cured systems. When the SC18/Epon 828 mixture was mixed with Jeffamine D2000 and held for 30 min at room temperature, SAXS showed the ordered nanolaminated structure with interplanar spacings of ~55 Å (Fig. 10), again because of the penetration of the Jeffamine D2000 into the gallery of the organoclays and the expansion of the gallery. However, the larger molecular weight of Jeffamine D2000 and the size of the molecule reduced its mobility and penetration into the gallery; therefore an intercalated—instead of an exfoliated—structure is obtained. When the SC18/Epon 828/D2000 mixture was held in 60°C for 3 hr, SAXS showed no peaks (Fig. 10). The high temperature increased the mobility of the Jeffamine D2000 molecule, easing penetration of the gallery and causing the separation of the nanolayers. For the mixture of SC18/Epon 828 with curing agent W, SAXS indicates almost no change of the ordered nanolaminated structure and the interplanar spacings remain essentially constant at ~35 Å (Fig. 10). This suggests that curing agent W is not compatible with the gallery of organoclays, and that there is no or very little penetration of it into the gallery. Exfoliation for the SC18/Epon 828/W system took place during heatup. These observations demonstrate the role that curing agents may play in morphology development. Curing agent W is an aromatic amine containing an aromatic group, whereas the Jeffamine is a polyoxypropyleneamine curing agent containing oxygen with a more flexible chain. Simultaneously, the organoclay contains siloxane backbone with many oxygen atoms inside, which perhaps makes it more compatible with Jeffamine. Such properties and nature of different curing agents cause different exfoliation behaviors for epoxy nanocomposites.

### EPOXY NANOCOMPOSITE AS PRIMER LAYER FOR AIRCRAFT COATING

Nanocomposites offer significant barrier properties, as observed by many researchers to date. Corrosion protection requirements of modern aircraft coating systems become increasingly demanding, and environmental as well as performance enhancements are sought.



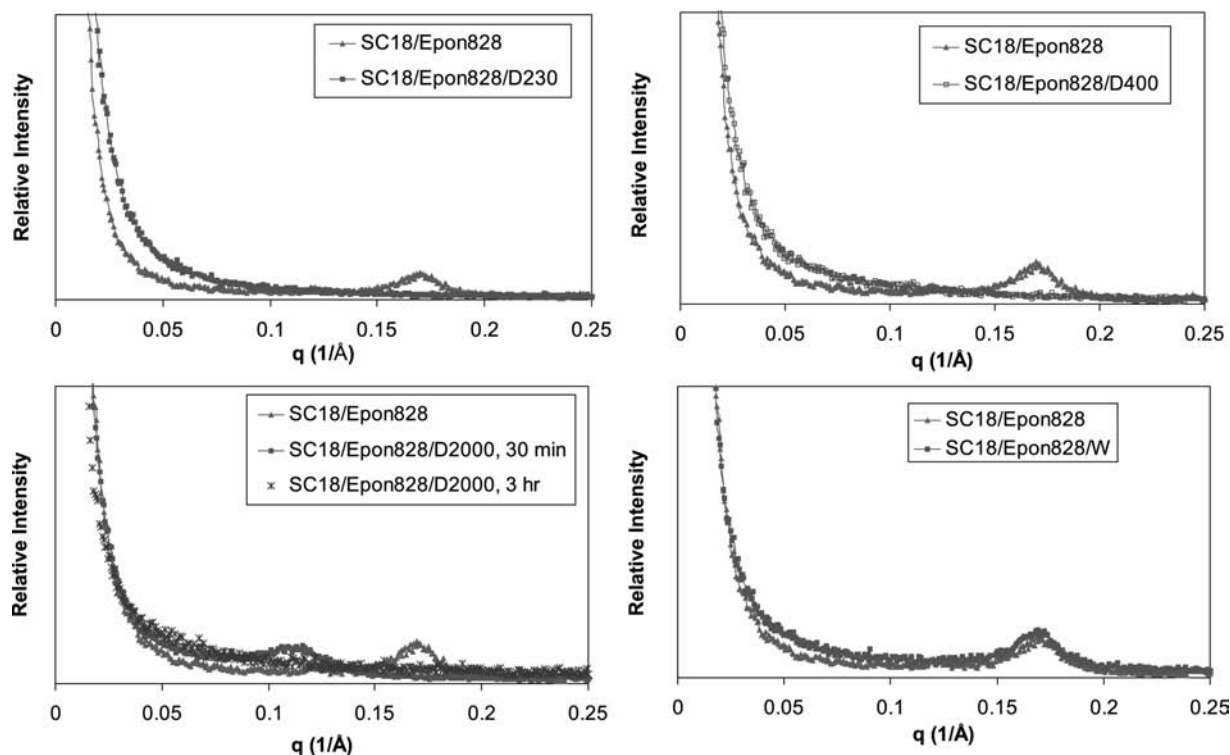


**Fig. 10** SAXS of SC18/Epon 828 with SC18/Epon 828/D230, SC18/Epon 828 with SC18/Epon 828/D400, SC18/Epon 828 with SC18/Epon 828/D2000 after 30 min and 3 hr, and SC18/Epon 828 with SC18/Epon 828/W.

The incorporation of nanoclays into epoxy primers offers opportunities to develop environmentally benign, improved anticorrosion protection, which may provide new applications for nanocomposites. The most common primer layer for aircraft coatings is epoxy based on Epon 828 (diglycidylbisphenol-A) with Epi-Cure curing agent 8290-Y-60 [polyethylene polyamine adduct (60) and 2-propoxyethanol (40)]. Epon 828 with Jeffamine D400 curing agent is a model for such primers, and a 2.5% SC18/Epon 828/D400 nanocomposite achieves an essentially exfoliated morphology. This system has very high barrier resistance for anticorrosion protection and can be cured at room temperature within a week, similar to the Epon 828/curing agent 8290-Y-60 system. Corrosion performance was assessed through exposure of AA2024-T3-coated panels to dilute Harrison's solution (a mixture of 0.05% sodium chloride and 0.35% ammonium sulphate) for 24 hr, followed by potentiodynamic polarization scans.<sup>[45]</sup> The corrosion current was 0.4 pA for pure Epon 828/D400, which is representative of very good barrier properties. The 2.5% SC18/Epon 828/D400 nanotailored coating exceeded the epoxy with a corrosion current of 0.2 pA. The improvement in the barrier properties of the SC18/Epon 828/D400 coating is attributed to the dispersion of the platy nanolayers in the epoxy matrix and the resulting tortuous path that they provide for fluids. Nanotailored epoxies and

nanocomposites offer promise for anticorrosion coatings as well as any polymeric material that requires improved barrier properties or reduced permeability.

## CONCLUSION

Both commercially available organoclay (I.30E) and synthetic organoclays (SC6, SC8, SC12, and SC18) are compatible with aerospace epoxy resins such as those studied here. Characterizations of the nanocomposites from WAXD, SAXS, and TEM confirm that their nanostructure can achieve interplanar spacings larger than 100 Å—5–10 times the original organoclay spacings. Even loadings as high as 10% (I.30E) can reach relatively large interplanar spacings as confirmed by scattering and TEM studies. Selection of organoclay treatment is critical because it can affect both the math of morphology development during cure processing as well as the final interplanar spacings. Selection of curing agent can also affect nanostructure morphology. Nanomodified epoxies offer properties that are appropriate to many aerospace applications. The modulus of the nanocomposite is significantly increased over the baseline epoxy from 15% to 35% in the glass state and to 300% in the rubber state, depending on loading as expected. The increase of the storage modulus is attributed to the high aspect

ratio and high stiffness of the silicate nanolayers in the epoxy matrix. The change in the  $T_g$  for the nanocomposite compared with the pure epoxy resin is insignificant.

For the materials reported here, the flex strength of the nanocomposites is decreased compared with that of the pristine epoxy resin. This reduction of strength is perhaps attributed to the weak interface between the clay nanolayer and the epoxy resin—an area to be further addressed. Surprisingly, the strength at high temperature (250°F) of some nanocomposites can be greater than that of pure resin, which may allow for more effective utilization of polymer composites in high-temperature environments. The survivability of aerospace epoxy resins under oxygen plasma and perhaps other extreme environments can be improved through nanotailoring by organoclays as the resulting nanocomposite materials can form inorganic barrier layers. Anticorrosion and other permeability-dependent properties may lead to some near-term aerospace applications. For all properties, nanostructure morphology plays a role.

Processability of nanotailored resins is a factor for many current advanced composite fabrication methods. Initial in-depth studies indicate that nanostructural evolution and viscosity development lend themselves to composite processes. The quick polymerization in the intragallery because of the catalytic effect from the pendent group results in the consumption of the epoxy monomer inside the gallery and makes the migration of more epoxy monomers from extragallery to intragallery, thus causing the expansion of the intragallery during the early stages of processing when viscosity is low. In addition, the exothermal heat from curing provides extra energy, in addition to energy from heating, to help expand the nanoclay sheets. Because the development of exfoliated morphology takes place during the cure for epoxy, as opposed to during the mixture processing step as in the case of thermoplastics, the impact of the organoclay on viscosity during the processing of epoxy nanocomposites is minimized. This is a very attractive attribute from the viewpoint of processing.

Ultimate control of properties through fundamental understanding of process morphology and nanoscale morphology properties is key to aerospace applications. Although there are many opportunities that may open up as a result of the insight into nanotailoring of epoxies through organoclays obtained through studies such as those reported and referenced here, many material developments will be required to fully exploit nanocomposites for the aerospace community, such as interface modifications, and validated analytical predictive tools will eventually be required to guide such material development as well as to predict their long-term performance.

## ACKNOWLEDGMENTS

This work is supported by the Air Force Office of Scientific Research and Air Force Research Laboratory, Materials and Manufacturing Directorate (contract no. F33615-00-D-5006). The authors would like to thank Dr. Charles Lee, Dr. David Curliss, and Mr. Brian Rice for their support and help.

## REFERENCES

1. Giannelis, E.P. Polymer-layered silicate nanocomposites. *Adv. Mater.* **1996**, *8*, 29–35.
2. LeBaron, P.C.; Wang, Z.; Pinnavaia, T.J. Polymer-layered silicate nanocomposites: An overview. *Appl. Clay Sci.* **1999**, *15*, 11–29.
3. Alexandre, M.; Dubois, P. Polymer-layered silicate nanocomposites: Preparation, properties and use of a new class of materials. *Mater. Sci. Eng., R Rep.* **2000**, *28*, 1–63.
4. Pinnavaia, T.J.; Beall, G.W. *Polymer-Clay Nanocomposites*; John Wiley and Sons, Ltd.: Chichester, UK, 2000.
5. Krishnamoorti, R.; Vaia, R.A. *Polymer Nanocomposites: Synthesis, Characterization and Modeling*; ACS Symposium Series; American Chemical Society: Washington, DC, 2002; Vol. 804.
6. Usuki, A.; Kojima, Y.; Okada, A.; Fukushima, Y.; Kurauchi, T.; Kamigaito, O. Synthesis of nylon 6–clay hybrid. *J. Mater. Res.* **1993**, *8*, 1179–1184.
7. Kojima, Y.; Usuki, A.; Kawasumi, M.; Okada, A.; Fukushima, Y.; Kurauchi, T.; Kamigaito, O.J. Mechanical properties of nylon 6–clay hybrid. *Mater. Res.* **1993**, *8*, 1185–1189.
8. Yano, K.; Usuki, A.; Okada, A.; Kurauchi, T.; Kamigaito, O.J. Synthesis and properties of polyimide–clay hybrid. *Polym. Sci., A* **1993**, *31* (10), 2493–2498.
9. Burnside, S.D.; Giannelis, E.P. Synthesis and properties of new poly(dimethylsiloxane) nanocomposites. *Chem. Mater.* **1995**, *7* (9), 1597–1600.
10. Vaia, R.A.; Price, G.; Ruth, P.N.; Nguyen, H.; Lichtenhan, J. Polymer/layered silicate nanocomposites as high performance ablative materials. *Appl. Clay Sci.* **1999**, *15*, 67–92.
11. Gilman, J.W. Flammability and thermal stability studies of polymer layered-silicate (clay) nanocomposites. *Appl. Clay Sci.* **1999**, *15*, 31–49.
12. Cypes, S.H.; Saltzman, W.M.; Giannelis, E.P. Organosilicate–polymer drug delivery systems: Controlled release and enhanced mechanical properties. *J. Control. Release* **2003**, *90* (2), 163–169.
13. Mehrota, V.; Giannelis, E.P. Metal–insulator molecular multilayers of electroactive polymers—Intercalation of polyaniline in mica-type layered silicate. *Solid State Commun.* **1991**, *77* (2), 155–158.
14. Ogawa, M.; Kuroda, K.; Kato, C. Layered silicate–organic intercalation compounds as photofunctional materials. *Stud. Surf. Sci. Catal.* **1994**, *83*, 171–178.
15. Wang, M.S.; Pinnavaia, T.J. Clay–polymer nanocomposites formed from acidic derivatives of montmorillonite and an epoxy resin. *Chem. Mater.* **1994**, *6*, 468–474.

16. Messersmith, P.B.; Giannelis, E.P. Synthesis and characterization of layered silicate-epoxy nanocomposites. *Chem. Mater.* **1994**, *6*, 1719–1725.
17. Lan, T.; Pinnavaia, T.J. Clay-reinforced epoxy nanocomposites. *Chem. Mater.* **1994**, *6*, 2216–2219.
18. Lan, T.; Kavirayna, P.D.; Pinnavaia, T.J. Mechanism of clay tactoid exfoliation in epoxy-clay nanocomposites. *Chem. Mater.* **1995**, *7*, 2144–2150.
19. Lan, T.; Kavirayna, P.D.; Pinnavaia, T.J. Epoxy self-polymerization in smectite clays. *J. Phys. Chem. Solids* **1996**, *57*, 1005–1010.
20. Wang, Z.; Lan, T.; Pinnavaia, T.J. Hybrid organic-inorganic nanocomposites formed from an epoxy polymer and a layered silicic acid (magadiite). *Chem. Mater.* **1996**, *8*, 2200–2204.
21. Wang, Z.; Pinnavaia, T.J. Hybrid organic-inorganic nanocomposites: Exfoliation of magadiite nanolayers in an elastomeric epoxy polymer. *Chem. Mater.* **1998**, *10*, 1820–1826.
22. Zilg, C.; Mulhaupt, R.; Finter, J. Morphology and toughness/stiffness balance of nanocomposites based upon anhydride-cured epoxy resins and layered silicate. *Macromol. Chem. Phys.* **1998**, *200*, 661–670.
23. Zilg, C.; Thomann, R.; Finter, J.; Mulhaupt, R. The influence of silicate modification and compatibilizers on mechanical properties and morphology of anhydride-cured epoxy nanocomposite. *Macromol. Mater. Eng.* **2000**, *280/281*, 41–46.
24. Ke, Y.; Lu, J.; Yi, X.; Zhao, J.; Qi, Z. The effects of promoter and curing process on exfoliation behavior of epoxy/clay nanocomposites. *J. Appl. Polym. Sci.* **2000**, *78*, 808.
25. Brown, J.B.; Curliss, D.; Vaia, R.A. Thermoset-layered silicate nanocomposites. Quaternary ammonium montmorillonite with primary diamine cured epoxies. *Chem. Mater.* **2000**, *12*, 3376.
26. Zerda, A.S.; Lesser, A.J. Intercalated clay nanocomposites: Morphology, mechanics, and fracture behavior. *Polymer* **2001**, *42*, 1137–1146.
27. Kornmann, X.; Lindberg, H.; Berglund, L. Synthesis of epoxy-clay nanocomposites: Influence of the nature of the clay on structure. *Polymer* **2001**, *42*, 1303–1310.
28. Kornmann, X.; Lindberg, H.; Berglund, L. Synthesis of epoxy-clay nanocomposites: Influence of the nature of the curing agent on structure. *Polymer* **2001**, *42*, 4493–4499.
29. Chen, C.; Curliss, D. Resin matrix composites: Organoclay-aerospace epoxy nanocomposites, Part II. *SAMPE J.* **2001**, *37* (5), 11–18.
30. Chin, I.J.; Thurn-Albrecht, T.; Kim, H.C.; Russell, T.P.; Wang, J. On exfoliation of montmorillonite in epoxy. *Polymer* **2001**, *42*, 5947–5952.
31. Chen, J.S.; Poliks, M.D.; Ober, C.K.; Zhang, Y.; Wiesner, U.; Giannelis, E.P. Study of the interlayer expansion mechanism and thermal-mechanical properties of surface-initiated epoxy nanocomposites. *Polymer* **2002**, *43*, 4895–4904.
32. Benson Tolle, T.; Anderson, D.P. Morphology development in layered silicate thermoset nanocomposites. *Comput. Sci. Tech.* **2002**, *62* (7–8), 1033–1041.
33. Xu, W.; Bao, S.; He, P. Intercalation and exfoliation behavior of epoxy resin/curing agent/montmorillonite nanocomposite. *J. Appl. Polym. Sci.* **2002**, *84* (4), 842–849.
34. Park, S.-J.; Seo, D.-I.; Lee, J.-R. Surface modification of montmorillonite on surface acid-base characteristics of clay and thermal stability of epoxy/clay nanocomposite. *J. Colloid Interface Sci.* **2002**, *251*, 160–165.
35. Chen, K.H.; Yang, S.M. Synthesis of epoxy-montmorillonite nanocomposite. *J. Appl. Polym. Sci.* **2002**, *86* (2), 414–421.
36. Triantafyllidis, C.S.; LeBaron, P.C.; Pinnavaia, T.J. Thermoset epoxy-clay nanocomposites: The dual role of alpha, omega-diamines as clay surface modifiers and polymer curing agents. *J. Solid State Chem.* **2002**, *167*, 354–362.
37. Becker, O.; Varley, R.; Simon, G. Morphology, thermal relaxations and mechanical properties of layered silicate nanocomposites based upon high-functionality epoxy resins. *Polymer* **2002**, *43* (16), 4365–4373.
38. Triantafyllidis, C.S.; LeBaron, P.C.; Pinnavaia, T.J. Homostructured mixed inorganic-organic ion clays: A new approach to epoxy polymer-exfoliated clay nanocomposites with a reduced organic modifier content. *Chem. Mater.* **2002**, *14* (10), 4088–4095.
39. Chen, C.; Curliss, D. Processing and morphological development of montmorillonite epoxy nanocomposites. *Nanotechnology* **2003**, *14* (6), 643–648.
40. Kong, D.; Park, C.E. Real time exfoliation behavior of clay layers in epoxy-clay nanocomposites. *Chem. Mater.* **2003**, *15*, 19–424.
41. Breker, O.; Cheng, Y.-B.; Varley, R.J.; Simon, G.P. Layered silicate nanocomposites based on various high-functionality epoxy resins: The influence of cure temperature on morphology, mechanical properties, and free volume. *Macromolecules* **2003**, *36* (5), 1616–1622.
42. Park, J.H.; Jana, S.C. Mechanism of exfoliation of nanoclay particles in epoxy-clay nanocomposites. *Macromolecules* **2003**, *36*, 2758–2768.
43. Luo, J.-J.; Daniel, I.M. Characterization and modeling of mechanical behavior of polymer/clay nanocomposites. *Comput. Sci. Tech.* **2003**, *63* (11), 1607–1616.
44. Yasmin, A.; Abot, J.L.; Daniel, I.M. Processing of clay/epoxy nanocomposites by shear mixing. *Scr. Mater.* **2003**, *49* (1), 81–86.
45. Chen, C.; Khobaib, M.; Curliss, D. Epoxy layered-silicate nanocomposite. *Prog. Org. Coat.* *in press*.
46. Giese, R.F.; van Oss, C.J. *Colloid and Surface Properties of Clays and Related Minerals*; Marcel Dekker, Inc.: New York, 2002.
47. Hao, F.; Vaia, R.A.; Sanders, J.H.; Lincoln, D.; Vreugdenhil, A.J.; Liu, W.; John, B.; Chen, C. Self-passivation of polymer-layered silicate nanocomposites. *Chem. Mater.* **2001**, *13*, 4123–4129.

# Ethane-Preferred Conformation

Lionel Goodman

Department of Chemistry, Rutgers University, New Brunswick, New Jersey, U.S.A.

Vojislava Pophristic

Center for Molecular Modeling, Department of Chemistry,  
University of Pennsylvania, Philadelphia, Pennsylvania, U.S.A.

## INTRODUCTION

In chemistry (as well as biology and medicine), the concept of molecular structure is axiomatic; its status is essentially that of a cornerstone for predicting and understanding diverse molecular phenomena. Consequently, a lot of attention has been paid to developing molecular geometry predictive computational methods.<sup>[1]</sup> Despite the ability of modern large-scale *ab initio* calculations to accurately predict molecular geometries (in small-size and medium-size molecules), the forces that control the preferred conformer shape remain only partially appreciated.

## ETHANE

Single bonds allow facile rotation around the bond, leading to an abundance of conformations for molecules with many such bonds (e.g., alkanes, sugars, and polymers). It is noteworthy that the formulation of fundamental chemical concepts, including that of molecular structure, originated in the framework of carbon chemistry. The simplest model molecule for studying C–C bond rotation is ethane (C<sub>2</sub>H<sub>6</sub>). It is the textbook example of a molecule that can rotate internally around one or more of its bonds so that during a full 360° rotation, it changes between unstable and relatively stable conformations. The equilibrium structure is the staggered (S) structure in which the two methyl (CH<sub>3</sub>) groups are stacked so that the hydrogen atoms are maximally separated (Fig. 1A). As one of its two methyl groups rotates once around the central carbon–carbon bond, the molecule will alternate three times between the preferred staggered conformation (Fig. 1A) and a ~3-kcal/mol<sup>[2,3]</sup> higher-energy unstable eclipsed (E) conformation (Fig. 1B). Schreiner<sup>[4]</sup> has given a careful account of the rich history behind the conviction for hindered rotation in ethane. Ebert and Wagner<sup>[6]</sup> appear to have been the first to propose ethane-hindered rotation in 1929 and 1931, respectively. Their molar heat capacity measurements led to recognition—in the early years of

quantum theory—by Nielson<sup>[5]</sup> and Teller and Weigert<sup>[6]</sup> of the quantum mechanical nature of internal rotation. However, the magnitude of the barrier remained in dispute and it was not until 1936 that Kemp and Pitzer<sup>[7]</sup> established definitively, from precise thermodynamic measurements, that the rotational barrier is appreciable, close to the now-accepted 3 kcal/mol. Wilson,<sup>[8]</sup> realizing that elucidation of rotational barrier origins would lead to an in-depth understanding of the relationship between electronic and molecular structures, published many papers (ethane included) on this topic. More details of the ethane internal rotation history, with additional references, have been given by Payne and Allen<sup>[9]</sup> and Veillard.<sup>[10]</sup>

Early work on the staggered structural preference focussed on the change in exchange repulsion (basically the Pauli principle leading to a tendency of electrons to avoid occupying the same space).<sup>[11]</sup> In this intuitively satisfying model, while ethane rotates toward an eclipsed structure, the electrons in C–H bonds on the different carbon atoms draw closer to each other (Fig. 1B) and experience increased repulsion, which destabilizes the eclipsed structure. Other conjectures included classical electrostatics, van der Waals (dispersion) forces, d-orbital and f-orbital participation, and hyperconjugation.<sup>[12]</sup> A more recent proposal involves quadrupole polarization of the C–C bond density in the eclipsed conformation.<sup>[13]</sup> Hyperconjugation is the term given to stabilizing delocalization effects caused by  $\sigma$ – $\sigma^*$  interactions, analogous to the  $\pi$ -conjugation present in unsaturated molecules.<sup>a</sup> Mulliken,<sup>[15]</sup> as early as 1939, concluded that  $\sigma_{\text{CH}}$ – $\sigma_{\text{CH}}^*$  hyperconjugation plays a role in the torsional potential of ethanelike molecules. However, Mulliken's estimate of the hyperconjugation effect at that time was necessarily crude, seeming to suggest that it was too small to account for the observed 3.0-kcal/mol

<sup>a</sup>Mulliken, Rieke, and Brown<sup>[14]</sup> originally labeled such extended  $\sigma$ -delocalization arising from  $\pi$ – $\sigma^*$  and  $\sigma$ – $\pi^*$  interactions in unsaturated systems as hyperconjugation. The extension to  $\sigma$ – $\sigma^*$  delocalization in fully saturated molecules<sup>[15]</sup> is sometimes termed “secondary hyperconjugation.”

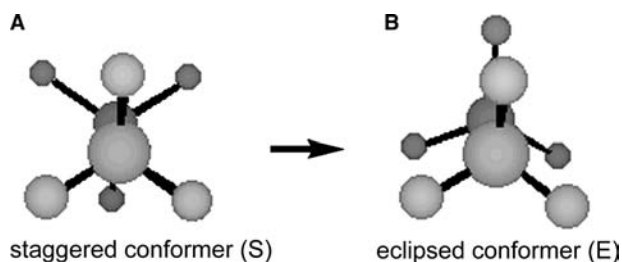


Fig. 1 Ethane internal rotation.

staggered–eclipsed energy difference. This idea was largely forgotten until the simple Huckel molecular orbital (MO) studies of Lowe,<sup>[16,17]</sup> and the analysis in terms of semilocalized orbitals, by England and Gordon<sup>[18]</sup> in the early 1970s, rekindled interest in hyperconjugation as a factor in the ethane torsional barrier.

Building on England and Gordon's finding that overlap between the tails of incompletely localized CH bond orbitals is important in energy analysis, Brunck and Weinhold,<sup>[19]</sup> using semiempirical MOs, showed how the staggered–eclipsed energy difference can arise simply from the change in the overlap of vicinal  $\sigma_{\text{CH}}$  and  $\sigma_{\text{CH}^*}$  orbitals in the *anti* and *syn* arrangements of the staggered and eclipsed conformers (Fig. 2). It is clear that the donor–acceptor interactions are sharply reduced in the *syn* arrangement compared to *anti* because of unfavorable cancellation in the latter case, as the nodal plane of the CH antibond cuts through the main lobe of the CH bond orbital. This visual estimate is confirmed by the overlap integral magnitudes shown in Fig. 2, which strongly favor larger hyperconjugative stabilization in the staggered conformer.

Thus by the turn of the century (i.e., 21st century), the two surviving models for the ethane staggered preference were: 1) lower steric and electrostatic repulsion; and 2) higher hyperconjugative stabilization than for the eclipsed structure. The latter model, although advocated by a substantial segment of the theoretical chemistry community, remained controversial and virtually every undergraduate organic chemistry textbook in 2000 favored the intuitively seductive steric repulsion model. Almost all omitted any mention of the hyperconjugation explanation.<sup>b</sup> Even so, a key step had been made in 1980, which had the potential for allowing a decisive choice to be made between the two models: Brunck and Weinhold's formulation of natural bond orbital (NBO) theory.<sup>[19]</sup> Lowdin<sup>[21]</sup> defined a set of “natural orbitals” describing a system

<sup>b</sup>An exception is Ref.<sup>[20]</sup>, but this volume is rarely used in undergraduate courses.

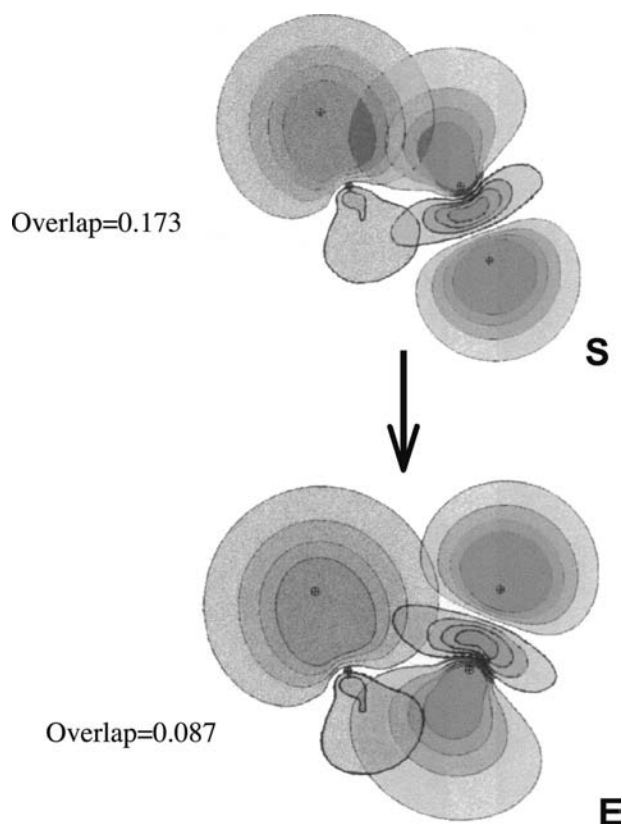


Fig. 2 Leading vicinal  $\sigma_{\text{CH}}-\sigma_{\text{CH}^*}$  hyperconjugative donor–acceptor interaction in the staggered (S) and eclipsed (E) conformers of ethane. Dark shading: antibonding orbitals; light shading: bonding orbitals.

as the unique complete set of orthonormal maximum occupancy orbitals possible within the general double occupancy Pauli restriction. Natural bond orbitals represent an extension of natural orbitals: they are two-centered transforms of MOs into almost doubly occupied bonding orbitals (bonds) and nearly unoccupied antibonding orbitals (antibonds), which fulfill the natural orbital restrictions. They retain the energetic accuracy of MOs; however, they have the desirable property of being able to describe properties of a system in localized terms that are well hidden in the complex forms of MOs.

The NBO scheme allowed  $\sigma-\sigma^*$  delocalization effects, essentially buried in the ethane MOs, to be pinpointed. The resulting energetic analysis favored the hyperconjugative model,<sup>[22]</sup> but a complication arises in evaluating the steric and electrostatic interactions. Steric energetics inherently involve a collective response of the entire N-electron system to the spatial region and, consequently, is sensitive to the details of the staggered  $\rightarrow$  eclipsed torsional coordinate.<sup>[23]</sup> Thus a central point in eliminating repulsive interactions as a factor in determining the staggered structure is including skeletal expansion, explicitly C–C

bond lengthening (i.e., torsion in ethane is not pure rotation).<sup>[24]</sup> Wanting to get away from the pitfalls of energy analysis, Pophristic and Goodman<sup>[25]</sup> carried out a series of ethane geometry optimizations by successive removal of hyperconjugative, Pauli exchange, and repulsive electrostatic interactions (with and without the skeletal relaxations).

Because an individual hyperconjugative interaction is expressed as a charge (electron) transfer between selected bond and antibonds in the NBO description, specific hyperconjugative interactions that influence structural preference can be pinpointed. Table 1 shows the result of geometry optimization with selected charge transfers absent. If the inversion of conformational preference occurs on removal of a specific charge transfer interaction, the controlling factor for ethane's staggered structure has been identified. The "no hyperconjugation" entry in Table 1 shows that preference for the staggered conformation is lost on removal of all charge transfers. Furthermore, the equilibrium conformer of ethane with only the vicinal hyperconjugation (i.e., charge transfer between NBOs on adjacent carbon atoms) removed ("no vicinal hyperconjugation" entry) is eclipsed. If only the geminal hyperconjugation (i.e., charge transfers between the orbitals originating on the same carbon atom) is deleted, the inversion of conformational preference does not occur. The conclusion is that vicinal charge transfer interactions are the ones that keep the molecule in the staggered conformation. By this argument, it is the hyperconjugatively induced preferential stabilization that controls the ethane structure.

Where does this leave the repulsion model? Repulsion involves two types of interactions: exchange, necessarily a short-range effect because of the orbital overlap requirement, and electrostatic or Coulomb involving classical  $1/R$  repulsion between charges. Taken together, these are frequently regarded as "steric repulsion." Figure 3 considers two cases: the real ethane molecule with all interactions present, and a hypothetical one with all of the exchange repulsions removed. One potential curve

**Table 1** Conformational dependence on hyperconjugative interactions<sup>a</sup>

Deleted hyperconjugative interactions	Torsional angle (°)	Corresponding conformer
No deletion	60.0	S
No hyperconjugation	0.0	E
No vicinal hyperconjugation	0.0	E
No geminal hyperconjugation	60.0	S

<sup>a</sup>HF/6-311G(3df,3pd) geometry optimization. These trends are found to be basis set-independent.

Source: Ref.<sup>[25]</sup>.

(with all interactions present) represents the energy of the real molecule; the other curve represents the energy of the hypothetical molecule with exchange repulsion absent. The conclusion from Fig. 3 is that the minima of both curves coincide at the staggered conformation, establishing that the staggered conformation is preferred regardless of the presence of exchange repulsion.

The effect of electrostatic repulsion can be understood by comparing its torsional angle dependence for three cases: rigid rotation (i.e., pure rotation, all skeletal relaxations frozen), partially relaxed rotation (only C–C bond lengthening included), and fully relaxed rotation (all skeletal flexings taken into account). Figure 4 shows that for rigid rotation, both electron and nuclear Coulomb repulsions increase as the torsional angle incrementally increases to the eclipsed conformer. However, when C–C bond lengthening is included as part of the rotational process as it is in fully relaxed rotation, both repulsions decrease, agreeing with Bader et al.<sup>[13]</sup> Thus the central bond stretching that is an intrinsic part of the rotational coordinate, which takes ethane from the staggered structure to eclipsed, reduces the strain that is accumulated in the molecule by rotation alone. The 0.014-Å C–C bond lengthening leads to a large decrease in Coulomb repulsion energies. Therefore electrostatic repulsion does not explain the staggered structural preference in ethane.

The conclusion is that ethane adopts the eclipsed conformation when the vicinal charge transfers are absent, and no inversion of structure occurs on the removal of Coulombic and exchange repulsions. This shows decisively that it is hyperconjugation, not repulsive forces, that determines the staggered equilibrium structure of ethane. A central point in eliminating

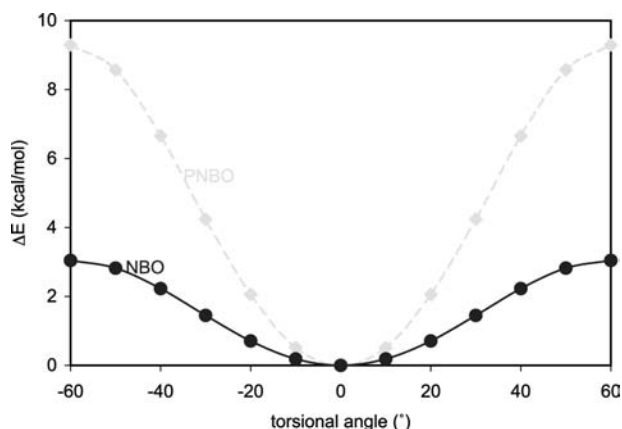


**Fig. 3** Torsional angle dependencies of energy of real ethane (solid curve) and hypothetical ethane with exchange repulsion absent (dashed curve). Zero degrees denotes the staggered conformer;  $\pm 60^\circ$  denotes the eclipsed conformer. Source: From Ref.<sup>[25]</sup>.



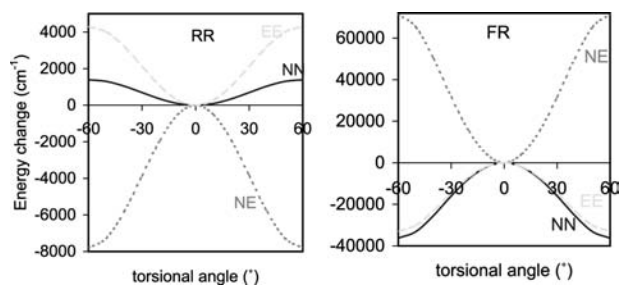


**Fig. 4** Torsional dependence of nuclear–nuclear (NN; full line), electron–electron (EE; long dash line) repulsion, and nuclear–electron (NE; short dash line) attraction energy changes for rigid (RR) and fully relaxed (FR) rotation in ethane. Corresponding curves for the partially relaxed model (C–C bond lengthening included) are indistinguishable from the FR ones on the figure scale.

repulsive interactions as a factor in determining the staggered structure is the necessity to take into account skeletal expansion, explicitly C–C bond lengthening (i.e., internal rotation is not pure rotation).

## DISILANE AND DIGERMANE

The interest in silicon and germanium group IV analogs of ethane, disilane ( $\text{SiH}_3\text{SiH}_3$ ), and digermane ( $\text{GeH}_3\text{GeH}_3$ ) stems from a combination of two factors. One is the increased separation of the rotating groups (the central Si–Si and Ge–Ge bonds are 0.84 and 0.92 Å, respectively, longer than in ethane; Table 2) and the other is the X–H (X = Si and Ge, respectively) polarity reversal from ethane. These changes are expected to cause hyperconjugative interactions between the  $\text{XH}_3$  groups to become small, if not negligible. An analysis of these ethane congener interactions allows a deepening of the hyperconjugative conformational preference conclusion drawn for ethane itself. Although experiments have not established their equilibrium conformer structure (H atoms contribute little to electron diffraction patterns),<sup>[26]</sup> all calculations conclude that both digermane and disilane exhibit a staggered conformational preference. As expected from the hyperconjugative diminution, the rotational barriers are strongly reduced (Table 3).<sup>[27–32]</sup> As pointed out, these molecules can be thought of as stretched ethanes enriched by additional electrons.

Figure 5 illustrates that hyperconjugative stabilization, the principal barrier forming interaction in ethane, falls to a small fraction of the ethane value (Table 3), as seen from the related reduced overlap between the  $\sigma-\sigma^*$  hyperconjugating orbitals. The absence of significant backside lobe overlap with the middle lobe of the antibond is particularly conspicuous. Is the barrier attenuation primarily because of

**Table 2** MP2/6-311G(3df,2p) optimized geometries of ethane, disilane, and digermane conformers

	X–X bond length <sup>a,b</sup>	X–H bond length <sup>a,b</sup>	$\angle\text{HXH}^{\text{a,b}}$
<i>Ethane</i>			
S	1.523	1.089	107.6
E	1.537	1.088	107.1
<i>Disilane</i>			
S	2.344	1.479	108.7
E	2.358	1.479	108.5
<i>Digermane</i>			
S	2.444	1.539	108.7
E	2.454	1.539	108.5

Bond lengths in angstroms; bond angles in degrees.

<sup>a</sup>X represents carbon atom in ethane, silicon in disilane, and germanium in digermane.

<sup>b</sup>Bond lengths rounded off to the nearest 0.001 Å; bond angles rounded off to the nearest 0.1°.

Source: Ref.<sup>[32]</sup>.

the larger Si–Si and Ge–Ge bond lengths, or because of the X–H polarity reversal? That the attenuation is mostly because of the larger bond lengths can be seen from the barrier energies in two phantom molecules created by expanding ethane to the more open structures of disilane and digermane, respectively, without any electron configuration change (Table 4). These phantom molecules have C–H bonds instead of the Si–H and Ge–H ones in the real molecules. The calculated barrier energies are reduced to even lower values than those found for real disilane and digermane.<sup>[31,32]</sup>

The effect of hyperconjugation alone is sufficient to keep disilane from exhibiting free rotation (Table 2).<sup>[31]</sup> However, the 0.3-kcal/mol hyperconjugation energy, by itself, is insufficient to prevent digermane from going into free rotation. Nevertheless, the role that hyperconjugation plays in rigidizing the digermane equilibrium conformer is shown clearly by the internal rotation potential curves with and without this interaction given in Fig. 6. The 0.3-kcal/mol delocalization energy is substantially smaller than the Boltzmann energy at 300 K. The total energy is actually only

**Table 3** Internal rotation barriers and delocalization energy changes in ethane,<sup>[31]</sup> disilane,<sup>[31]</sup> and digermane<sup>[32]</sup> (kcal/mol)<sup>a</sup>

	$\Delta E_{\text{barrier}}$	$\Delta E_{\text{deloc}}$
Ethane	3.03	6.61
Disilane	1.03	0.68
Digermane	0.74	0.32

<sup>a</sup>HF/6-311G(3df,2p) geometries and energy calculations, except for digermane geometries (MP2/6-311G(3df,2p)).

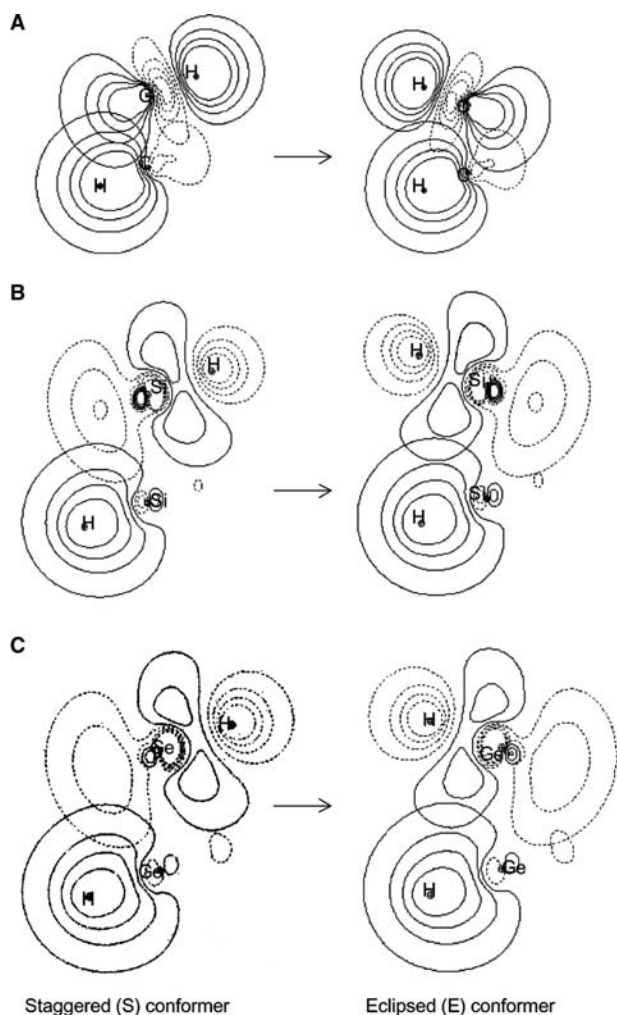


**Fig. 5** C–H/C–H\*, Si–H/Si–H\*, and Ge–H/Ge–H\* bond/antibond overlaps for the *anti* (staggered conformer) and *syn* (eclipsed conformer) arrangements in ethane (A), disilane (B), and digermane (C). *Source:* From Ref.<sup>[32]</sup>.

greater than the Boltzmann energy when the torsional angle exceeds 40°. Thus digermane is expected to exhibit large amplitude (~80°) torsional oscillations at room temperature. If vicinal hyperconjugation is removed (dashed curve in Fig. 6), digermane is predicted to go into free rotation at this temperature.

**Table 4** Barrier energies for ethane and phantom molecules (kcal/mol)<sup>a,b,c</sup>

	$\Delta E_{\text{barrier}}$
Ethane	3.17
(ET) <sub>DS</sub>	0.28
(ET) <sub>DG</sub>	0.23

<sup>a</sup>(ET)<sub>DS</sub> = disilane geometry, ethane electronic configuration; (ET)<sub>DG</sub> = digermane geometry, ethane electronic configuration.

<sup>b</sup>See footnote <sup>a</sup>, Table 3.

<sup>c</sup>Rigid rotation barriers are used to reduce the number of variables.

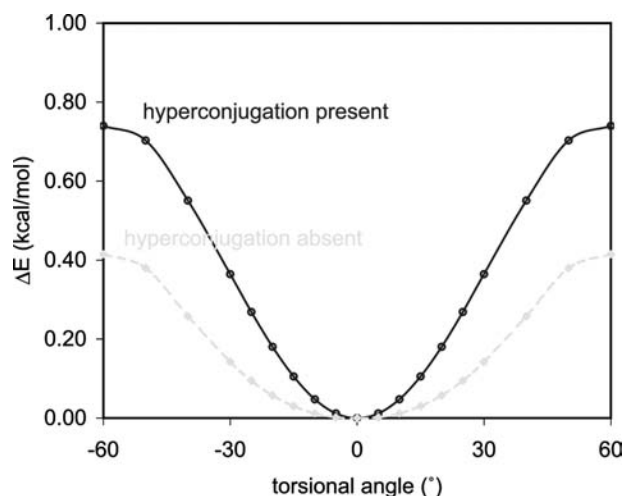


**Fig. 6** Torsional potential curves for real digermane (full curve) and hypothetical digermane with hyperconjugation absent (dashed curve). Zero degrees denotes the staggered conformer;  $\pm 60^\circ$  denotes the eclipsed conformer. *Source:* From Ref.<sup>[32]</sup>.

## CONCLUSION

The weight of evidence (particularly direct structural optimizations with missing interactions) indicates that vicinal hyperconjugation controls the staggered structure of ethane. A central point in eliminating repulsive interactions as a factor in determining the staggered structure is the effect of the C–C bond lengthening that accompanies internal rotation (i.e., internal rotation in ethane is not pure rotation). The group IV congeners, disilane and digermane, show greatly attenuated hyperconjugative interactions. In digermane, hyperconjugation stabilization is predicted to be so weakened that it is insufficient to give much rigidity to the molecule at room temperature.

## REFERENCES

1. Fogarasi, G.; Zhou, X.; Taylor, P.W.; Pulay, P. The calculation of Ab initio molecular geometries: efficient optimization by natural internal coordinates and empirical correction by offset forces. *J. Am. Chem. Soc.* **1992**, *114*, 8191–8201, and references therein.
2. Moazzen-Ahmadi, N.; Gush, H.P.; Halpern, M.; Jagannath, H.; Leung, A.; Ozier, I. The torsional spectrum of CH<sub>3</sub>CH<sub>3</sub>. *J. Chem. Phys.* **1988**, *88*, 563–577.
3. Lee, J.S. Accurate theoretical prediction of relative energy: barriers to linearity, inversion and internal rotation in polyatomic molecules. *J. Phys. Chem.* **1997**, *101*, 8762–8767.

- Schreiner, P.R. Teaching the right reasons: lessons from the mistaken origin of the rotational barrier in ethane. *Angew. Chem., Int. Ed. Engl.* **2002**, *41*, 3579–3581.
- Nielson, H.H. The torsion oscillator–rotator in the quantum mechanics. *Phys. Rev.* **1932**, *40*, 445–456.
- The Ebert, Wagner, and Teller and Weigert articles are not generally available. Journal and page citations for the interested reader are given in Ref.<sup>[4]</sup>.
- Kemp, J.D.; Pitzer, K.S. Hindered rotation of methyl groups in ethane. *J. Chem. Phys.* **1936**, *4*, 749.
- Wilson, J.E.B. The problem of barriers to internal rotation in molecules. *Adv. Chem. Phys.* **1959**, *2*, 367–393.
- Payne, P.W.; Allen, L.C. Barriers to Rotation and Inversion. In *Methods of Electronic Structure Theory*; Schaefer, H.F., Ed.; Plenum: New York, 1977; Vol. 3, 29–108.
- Veillard, A. Origin of internal rotation barriers. In *Internal Rotation in Molecules*; Orville-Thomas, W.J., Ed.; John Wiley and Sons: London, 1974.
- Sovers, O.J.; Kern, C.W.; Pitzer, R.M.; Karplus, M. Bond-function analysis of rotational barriers: Ethane. *J. Chem. Phys.* **1968**, *49*, 2592–2599.
- Pitzer, R.M. The barrier to internal rotation in ethane. *Acc. Chem. Res.* **1983**, *16*, 207–210.
- Bader, R.F.W.; Cheeseman, J.R.; Laidig, K.E.; Wiberg, K.B.; Breneman, C. Origin of rotation and inversion barriers. *J. Am. Chem. Soc.* **1990**, *112*, 6530–6536.
- Mulliken, R.S.; Rieke, C.A.; Brown, W.G. Hyperconjugation. *J. Am. Chem. Soc.* **1941**, *63*, 41–56.
- Mulliken, R.S. Intensities of electronic transition in molecular spectra: IV. Cyclic dienes and hyperconjugation. *J. Chem. Phys.* **1939**, *7*, 339–352.
- Lowe, J.P. A simple molecular orbital explanation for the barrier to internal rotation in ethane and other molecules. *J. Am. Chem. Soc.* **1970**, *92*, 3799–3800.
- Lowe, J.P. The barrier to internal rotation in ethane. *Science* **1973**, *179*, 527–532.
- England, W.; Gordon, M.S. Localized charge distributions: I. General theory, energy partitioning and the internal rotation barrier in ethane. *J. Am. Chem. Soc.* **1971**, *93*, 4649–4657.
- Brunck, T.K.; Weinhold, F. Quantum mechanical studies on the origin of barriers to internal rotation about single bonds. *J. Am. Chem. Soc.* **1979**, *101*, 1700–1709.
- Eliel, E.L.; Wilen, S. *Stereochemistry of Organic Molecules*; John Wiley and Sons: New York, 1994. Monograph.
- Lowdin, P.O. Quantum theory of many-particle systems, I. *Phys. Rev.* **1955**, *97*, 1474–1489.
- Reed, A.E.; Weinhold, F. Natural bond orbital analysis of internal rotation barriers and related phenomena. *Isr. J. Chem.* **1991**, *31*, 277–285.
- Goodman, L.; Gu, H. Flexing analysis of steric exchange repulsion accompanying ethane internal rotation. *J. Chem. Phys.* **1998**, *109*, 72–78.
- Goodman, L.; Pophristic, V.; Weinhold, F. Origin of methyl internal rotation barriers. *Acc. Chem. Res.* **1999**, *32*, 983–993.
- Pophristic, V.; Goodman, L. Hyperconjugation not steric repulsion leads to the staggered structure of ethane. *Nature* **2001**, *411*, 565–568.
- Beagley, B.; Conrad, A.R.; Freeman, J.M.; Monaghan, J.J.; Norton, B.G.; Holywell, G.C. Electron diffraction studies of the hydrides Si<sub>2</sub>H<sub>6</sub> and P<sub>2</sub>H<sub>4</sub>. *J. Mol. Struct.* **1972**, *11*, 371–380.
- Gordon, M.S.; Neubauer, L. Second row molecular orbital calculations. Geometries, internal rotation barriers, and dipole moments of methylsilane, disilane, methyl mercaptan, and methylphosphine. *J. Am. Chem. Soc.* **1974**, *96*, 5690–5693.
- Durig, J.R.; Church, J.S. Vibrational spectra of crystalline disilane and disilane-d<sub>6</sub>, barrier to internal rotation and some normal coordinate calculations on disilane, silylisocyanate, and silylthioisocyanate. *J. Chem. Phys.* **1980**, *73*, 4784–4797.
- Schleyer, P.V.R.; Kaupp, M.; Hampel, F.; Bremer, M.; Mislow, K. Relationships in the rotational barriers of all group 14 ethane congeners H<sub>3</sub>X–YH<sub>3</sub> (X, Y = C, Si, Ge, Sn, Pb). Comparisons of Ab initio pseudopotential and all-electron results. *J. Am. Chem. Soc.* **1992**, *114*, 6791–6797.
- Cho, S.G.; Rim, O.K.; Park, G. Rotational barriers of disilane, hexafluorodisilane, and hexamethyldisilane: Ab initio, density functional, and molecular mechanics (MM3) studies. *J. Comp. Chem.* **1997**, *18*, 1523–1533.
- Pophristic, V.; Goodman, L. Disilane internal rotation. *J. Phys. Chem.* **2001**, *105*, 7454–7459.
- Goodman, L.; Pophristic, V.; Wang, W. Does digermane exhibit free rotation? A test of barrier theory. *Int. J. Quantum Chem.* **2002**, *90*, 657–662.

# Fluorescence-Voltage Single Molecule Spectroscopy

## Young Jong Lee

Polymers Division, National Institute of Standards and Technology (NIST),  
Gaithersburg, Maryland, U.S.A.

## Andre J. Gesquiere

Nanoscience Technology Center and Department of Chemistry,  
University of Central Florida, Orlando, Florida, U.S.A.

## So-Jung Park

Department of Chemistry, Nanoscale Materials and Surface Chemistry,  
University of Pennsylvania, Philadelphia, Pennsylvania, U.S.A.

## Paul F. Barbara

Department of Chemistry and Biochemistry, University of Texas at Austin,  
Austin, Texas, U.S.A.

## INTRODUCTION

Single molecule spectroscopy (SMS) has been recently used extensively to study semiconductor nanomaterials, including semiconductor nanocrystals,<sup>[1–4]</sup> and nanostructured conjugated polymers.<sup>[5–13]</sup> SMS has made the complex photophysical processes accessible on these heterogeneous materials that are often obscured in ordinary ensemble measurements. For example, the molecular structure and photophysical dynamics of single isolated polymer chains (molecules) of conjugated polymers have been successfully investigated using SMS,<sup>[5,7–12,14–19]</sup> because the spectroscopy of single polymer chains, as opposed to the bulk material, has the advantage of tremendously reducing the size and complexity.

A new SMS technique has recently been introduced for investigation of functional nanomaterials by involving simultaneously controllable oxidation/reduction or charge injection in an electronic device. The new technique denoted by fluorescence-voltage SMS (*F-V/SMS*) is analogous to current-voltage (*I-V*) measurements for devices and electrochemical cells. *F-V/SMS* has been proven to be a powerful tool for studying the photophysics and charge-transfer processes of conjugated polymers, giving new insights into the complex interaction of excited and charged species that exist in a device environment.

## BACKGROUND

Conjugated polymers are widely used as active materials in a broad range of electronic devices including organic light emitting diodes (OLEDs), photovoltaic devices, thin-film transistors, and chemical sensors.<sup>[20–22]</sup> Fig. 1 portrays a simplified device architecture and associated energy level diagram of a typical two-layer OLED, where electrons and holes are injected from the cathode and anode, recombine close to the interface between the electron/hole transport layers, and electroluminescence is generated from the resulting excitons (excited states). Unfortunately, however, it is extremely difficult to unravel the complex and heterogeneous kinetics in such a device. First, there are many different types of singlet excitons ( $S_1$ ), triplet excitons ( $T_1$ ), and charged species (polarons) in a device, leading to large spatial variations and fluctuations in the kinetics of these species. Second, conjugated polymers have a complex nanostructure associated with morphological features (polymer chain folding, packing, and aggregation), which can seriously impact the operation of a device.<sup>[23]</sup> Third, various dynamical processes involving the exciton–exciton and exciton–polaron interactions (e.g.,  $S_1$ – $S_1$  annihilation,  $T_1$ – $T_1$  annihilation,  $S_1$  quenching by  $T_1$ ,  $S_1$  quenching by holes, and  $T_1$  quenching by holes) make it difficult to analyze the photophysics in organic devices.

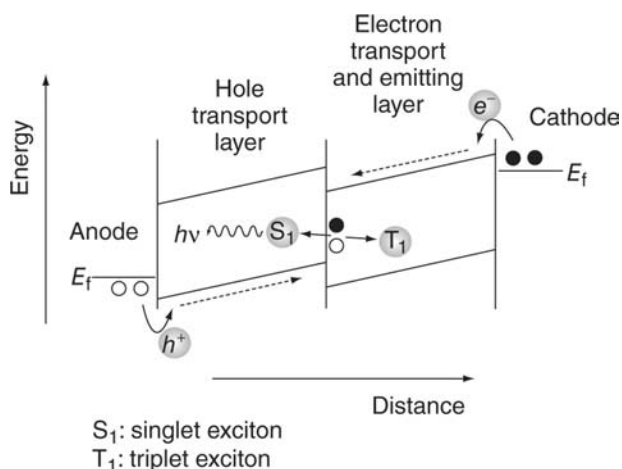


**Fig. 1** A schematic band energy diagram for a two-layer OLED.

Recently, the complicated interaction of excitons and polarons has been successfully approached by using a new technique that allows for SMS in a device environment.<sup>[24–27]</sup> This method involves simultaneous single molecule fluorescence spectroscopy while controlling oxidation/reduction of individual molecules or nanoparticles in an electronic device (Fig. 2B). The technique, which is denoted by *F-V/SMS*, where “*F*” signifies fluorescence intensity, is analogous in several ways to *I-V* measurements for devices and

electrochemical cells. For example, *F-V/SMS* data at different sweep rates can be analyzed to obtain information on both energetics and kinetics of charge transfer (oxidation/reduction) processes involving single molecules. This is achieved by recording the single molecule fluorescence intensity as a function of device bias, which controls the population of polarons. This method also offers a unique means for characterizing the chemical nature of the poorly understood photochemically induced intermediate states of conjugated polymers that are responsible for fluorescence “blinking” and “flickering,” i.e., intermittency. By studying the bias dependence of the SMS during the lifetime of the fluorescence “flickering” intermediate, information on the *oxidation/reduction properties* (e.g., HOMO energies) of the intermediate can be determined.

### *F-V/SMS*

An *F-V/SMS* example is presented in Fig. 3, which shows the fluorescence intensity of a single isolated conjugated polymer molecule as a function of the bias voltage  $V$ .<sup>[24,25,27]</sup> The *F-V/SMS* data reveal that a single positive charge (hole) injected from the device induces a significant fluorescence quenching of poly[2-methoxy,5-(2'-ethyl-hexyloxy)-P-phenylene-vinylene]

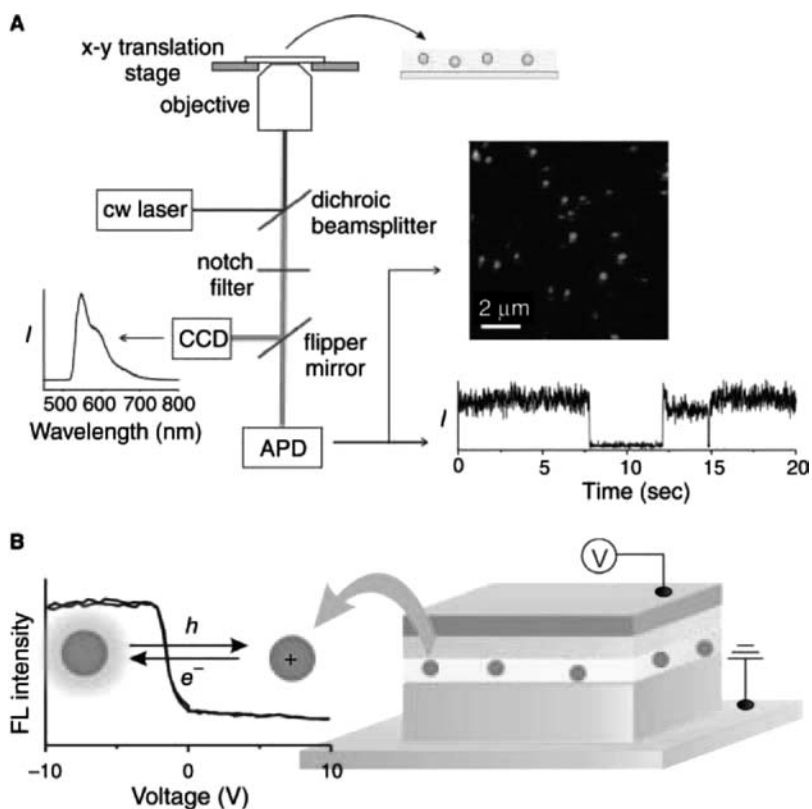


**Fig. 2** (A) Typical single molecule fluorescence spectroscopy apparatus. (B) Configuration of a typical *F-V/SMS* setup and *F-V/SMS* data.



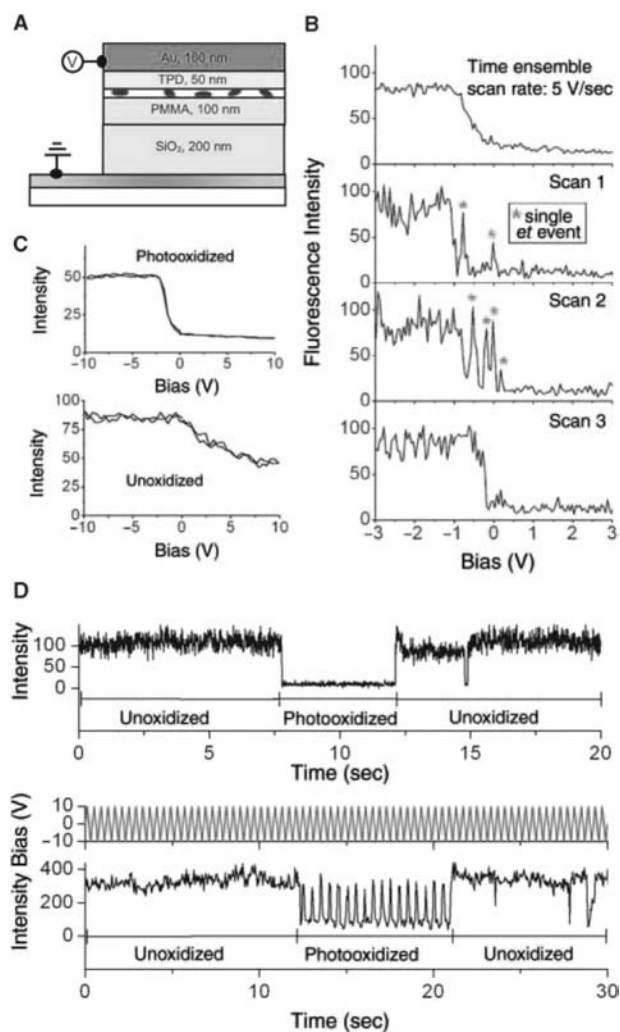


**Fig. 3** (A) A diagram of a capacitor-like hole-injection device. (B)  $F$ - $V$ /SMS time ensemble and individual scans of an MEH-PPV molecule. (C) Two typical bias-dependent modulation behaviors;  $F$ - $V$  curves collected from (top) a photo-oxidized molecule showing a discrete fluorescence quenching by a hole injection, and (bottom) a unoxidized molecule showing a gradual fluorescence quenching by TPD holes. (D) Intensity vs. time transients of a single MEH-PPV molecule (top) with no bias and (bottom) with triangle wave bias applied.

(MEH-PPV). The capacitor-like hole injection device employed for this study is described in Fig. 3A. In the device configuration, holes are injected from the Au electrode to the hole transport layer of *N,N*-bis(3-methylphenyl)-*N,N'*-diphenylbenzidine (TPD) at positive bias. In typical experiments, fluorescence intensity vs. time transients of isolated single MEH-PPV molecules are collected (Fig. 3D) while a triangular wave bias voltage sequence is repeatedly applied to the device and then the SMS data are averaged over many cycles and replotted in the form of time ensemble  $F$ - $V$  curve (Fig. 3C). The time-ensemble and single  $F$ - $V$

**Table 1** Best-fit kinetic parameters for different MEH-PPV molecules in an inert polymer matrix<sup>a</sup>

Molecule	$k'_{isc}/s$	$k_{QST}/s$
1	$6.0 \times 10^3$	$7.8 \times 10^9$
2	$6.4 \times 10^3$	$1.1 \times 10^{11}$
3	$3.8 \times 10^3$	$3.4 \times 10^{11}$
4	$4.0 \times 10^3$	$1.2 \times 10^{10}$

<sup>a</sup>In the fitting procedures a quantum yield of intersystem crossing of 1.25% was used for MEH-PPV. (From Ref.<sup>[15]</sup>)

scans in Fig. 3B show that the electron transfer process definitely involves a single electron transfer per molecule. The intensity fluctuations at the transition region reflect the stochastic nature of electron transfer, not photon shot noise, which is much smaller.  $F$ - $V$ /SMS data of this type can be used to sort out the complex mechanism of charge transport, interface charging, and actual electron transfer, on a molecule-by-molecule, and a location-by-location basis in a device. The dynamics for oxidation/reduction of MEH-PPV single molecules are controlled by various factors including filling of deep hole traps in the charge transporting layer of the device,<sup>[28,29]</sup> the oxidation/reduction chemical “state” of the MEH-PPV molecule,<sup>[24,25]</sup> and the molecular scale heterogeneity of the device.<sup>[30]</sup> At zero bias, fluorescence vs. time traces from MEH-PPV molecules incorporated in a device were indistinguishable from the molecules in an inert polymer matrix, poly(methyl methacrylate) (PMMA), and showed discrete intensity fluctuations (e.g., Fig. 2A) (Table 1). This behavior is relatively rare in freshly prepared, oxygen-depleted samples, but becomes more common as the sample ages in ambient conditions and oxygen diffuses through pinholes in the Au electrode.<sup>[6,31]</sup> The fluorescence flickering in single conjugated polymer molecules has been attributed to efficient energy funneling to a photo-oxidation-induced quencher site.<sup>[5,6,14,32,33]</sup>

For typical unoxidized MEH-PPV molecules, fluorescence quenching was observed at positive bias (Fig. 3C). The relatively gradual dependence of the quenching efficiency on bias for the unoxidized molecules is consistent with the  $S_1$  quenching by hole polarons present in the hole transport TPD layer. Significantly, while molecules are at the fluorescence flickering intermediate state (photo-oxidized), an extraordinary repairing of photo-bleaching was observed for negative bias, Fig. 3C. The sigmoidal  $F$ - $V$ /SMS data of photo-oxidized molecules near  $-1.5$  V are indicative of a reversible single electron transfer event. This behavior indicates that the long-lived quencher sites can be reversibly oxidized and reduced, and that the photobleached form of the polymer is a charged species such as a MEH-PPV<sup>+</sup>/anion complex. Such a complex could be formed by photo-induced



electron transfer between MEH-PPV and oxygen, forming  $\text{MEH-PPV}^+/\text{O}_2^-$ , which could further react with water, a common impurity, resulting in a more stable anion,  $\text{OH}^-$ . The reversible oxidation/reneutralization and extraordinary bias-induced repair process exclude typical  $S_1$  oxygen oxidation products such as dioxetanes and endoperoxides, as these latter species would be expected to exhibit non-reversible reduction/oxidation by charge carriers. Photo-induced electron transfer is indeed consistent with well-known, but poorly understood, persistent photoconductivity of conjugated polymers owing to exposure to air.

### FV-TR-SMS

Several papers have described how  $S_1$  can be quenched by hole polarons, leading to a reduction of the electroluminescence efficiency of a device.<sup>[34,35]</sup> In contrast, the quenching of  $T_1$  by hole polarons has received much less attention. Recently, there has been a growing appreciation that dynamical processes involving the interaction of  $T_1$  with polarons can play an important role in the performance of polymer OLED and related organic electronic devices. For example, it has been shown that  $T_1$  can be “harvested” in OLEDs using  $T_1$  emitters to improve electroluminescence efficiencies.<sup>[36,37]</sup>  $T_1$  can also deteriorate device performance by quenching  $S_1$  and sensitizing  $S_1$  oxygen formation.<sup>[38–40]</sup> Gesquiere, Park, and Barbara<sup>[30]</sup> have used a technique, FV-TR-SMS to obtain quantitative information on the mechanisms and rates of hole polaron-induced quenching of  $T_1$  and  $S_1$ .<sup>[30]</sup> This approach measures the fluorescence intensity of a single molecule embedded in an electronic device while simultaneously modulating the irradiation intensity (Fig. 4A) and the bias on the device (Fig. 4B).

FV-TR-SMS data in Fig. 4C were obtained for a single MEH-PPV nanoparticle in contact with the hole transport layer (TPD) of a hole-injection capacitor-like device structure described in Fig. 3A. The observed FV-TR-SMS data varied for different MEH-PPV molecules but were constant over time for any individual molecule. Negative-bias device environment results are similar to the inert polymer host measurements, consistent with the expectation that at negative bias, the capacitor device is depleted of polarons. This demonstrates that MEH-PPV  $S_1$  and  $T_1$  are not significantly perturbed by the contact with the TPD hole-transport layer. For biases above the threshold for hole injection ( $\sim 1$  V), the FV-TR-SMS data reveal evidence of  $T_1$  quenching by TPD hole polarons ( $p^+$ ),

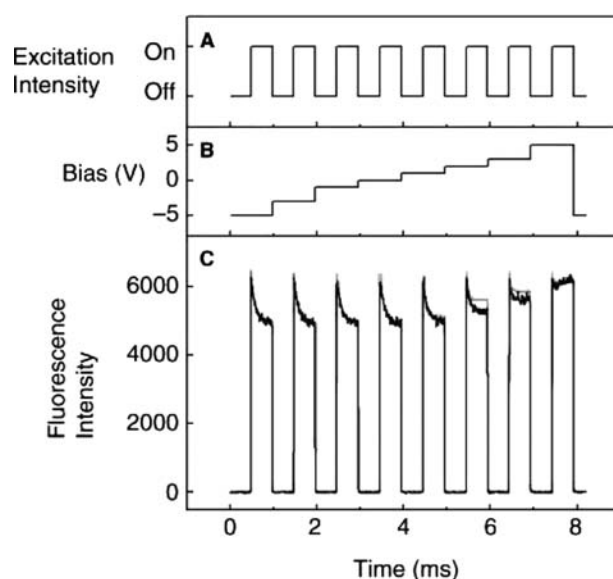


**Fig. 4** Fluorescence intensity collected for single MEH-PPV molecules while simultaneously modulating (A) the excitation laser intensity and (B) the device bias. This process is repeated over many of these cycles while the data are synchronously time averaged (C).

which presumably occurs by a charge transfer mechanism, perhaps involving the intermediacy of an MEH-PPV hole polaron.  $S_1$  quenching by TPD hole polarons was also observed in these devices.



This mechanism may involve spin-allowed energy transfer or charge transfer.

The data are well fit by our previously described kinetic model<sup>[15,16,30]</sup> (parameters in Table 2) with the exception of the slowly varying intensity changes during each pulse region at positive bias ( $V > V_0$ ). The slowly varying regions are assigned to a non-instantaneous response of the local quasi-Fermi-potential in the device because of the filling of deep hole traps in the hole transporting layer of the device.

A significant result from this study is the observation that  $T_1$  are much more efficiently quenched than  $S_1$ . This is summarized in Table 2, where the efficiency of  $T_1$  and  $S_1$  quenching by hole polarons,  $E_{QT}$  and  $E_{QS}$ , is shown for  $V(t) = 5$  V for various molecules. The more efficient quenching of  $T_1$  occurs despite the fact that the  $T_1$  quenching rate constant ( $k_{QT}$ ) is in fact several orders of magnitude slower than that for  $S_1$  ( $k_{QS}$ ). The more efficient quenching of  $T_1$  is probably owing to a factor of  $10^6$  greater lifetime for the  $T_1$  compared to the  $S_1$ . This result suggests that  $S_1$  and  $T_1$  quenching by hole polarons occurs by different mechanisms. The  $S_1$  quenching process can in principle

**Table 2** Best-fit kinetic parameters for different MEH-PPV molecules in a capacitor device environment.<sup>a</sup>

Molecule	$k'_{isc}/s$	$k_{QST}/s$	$k_{QT}/mol/s$	$k_{QS}/mol/s$	$E_{QT} (%)^d$	$E_{QS} (%)^e$
1	$6.0 \times 10^3$	$7.0 \times 10^9$	$1.1 \times 10^7$	$(3.0 \times 10^6)^c$	100	0
2	$6.0 \times 10^3$	$5.3 \times 10^9$	$1.1 \times 10^9$	$1.6 \times 10^{11}$	100	24
3	$4.0 \times 10^3$	$4.3 \times 10^9$	$1.1 \times 10^9$	$1.1 \times 10^{12}$	100	70
4	$6.0 \times 10^3$	$3.8 \times 10^9$	<sup>b</sup>	<sup>b</sup>	0	0

<sup>a</sup>In the fitting procedures a quantum yield of intersystem crossing of 1.25% was used for MEH-PPV.

<sup>b</sup>No polarons are interacting with the molecule, so no rate constant is reported.

<sup>c</sup>This value is an upper limit for  $k_{QS}$ .

<sup>d</sup>Defined as  $[F(\text{plateau})_{V=5V} - F(\text{plateau})_{V<V_0}]/[F(\text{initial}) - F(\text{plateau})]_{V<V_0}$  in the case of  $T_1$  quenching only. When  $S_1$  quenching is observed the  $T_1$  quenching efficiency is 100%.

<sup>e</sup>Defined as  $[F(\text{initial})_{V<V_0} - F(\text{initial})_{V=5V}]/F(\text{initial})_{V<V_0}$ .

occurs by a spin-allowed energy transfer process, analogous to that described above for the quenching of  $S_1$  by  $T_1$ . The quenching of  $T_1$  by polarons is a spin-forbidden process, and a slower charge transfer mechanism is probably operating for  $T_1$ .

### Probing a Molecular Interface in a Functioning Organic Diode

OLEDs have a multilayer structure that comprises morphologically heterogeneous materials and interfaces. Owing to several complex and poorly understood factors, OLEDs are much less amenable to modeling and simulation than inorganic devices. These devices contain a complex set of polarons and excitons during operation, and are complicated by processes such as interfacial charge transfer, charge trapping by deep acceptor-like states, and electrochemical-like effects owing to impurities. Lee et al.<sup>[26]</sup> have used  $F$ - $V$ /SMS to study a hole-injection/hole-transport interface within a functioning organic diode (Fig. 5). MEH-PPV single molecules were dispersed at the interface between the hole injection and hole transport layers to create and probe  $S_1$  and  $T_1$  at the heterojunction. Fig. 5 shows representative  $F$ - $V$  curves from single molecules along with  $I$ - $V$  data of the diode. Efficient exciton quenching is observed at high forward bias owing to a buildup of interfacial polaron density, Figs. 5A and B. Additionally, for some diodes (denoted as Type II), an unexpected quenching process was also observed at reverse bias, which is ascribed to hole charging of the interface owing to leakage current, Figs. 5C and D.

More quantitative information on the rates of hole polaron-induced quenching of  $T_1$  and  $S_1$  was acquired by the FV-TR-SMS. The fact that the  $T_1$  decay at early times is entirely absent indicates that the  $T_1$  lifetime is much shorter than 1  $\mu$ s (the instrument resolution) at 5 V (Figs. 6C and D) owing to highly efficient quenching of  $T_1$  by hole polarons that was accumulated at the [poly(3,4-ethylenedioxythiophene):poly(styrenesulfonate)/ $N,N'$ -diphenyl- $N,N'$ -bis(3-methylphenyl)-1,1'-biphenyl-4,4'-diamine] (PEDOT : PSS) interface.

### CONCLUSIONS

This entry is focused on development of the recently introduced  $F$ - $V$ /SMS technique for semiconductor nanoparticle research. In addition, FV-TR-SMS has shown potential to unravel complex interactions among excitons and polarons in organic devices. Furthermore, these new  $F$ - $V$ /SMS techniques are successfully used to investigate the interfaces in a

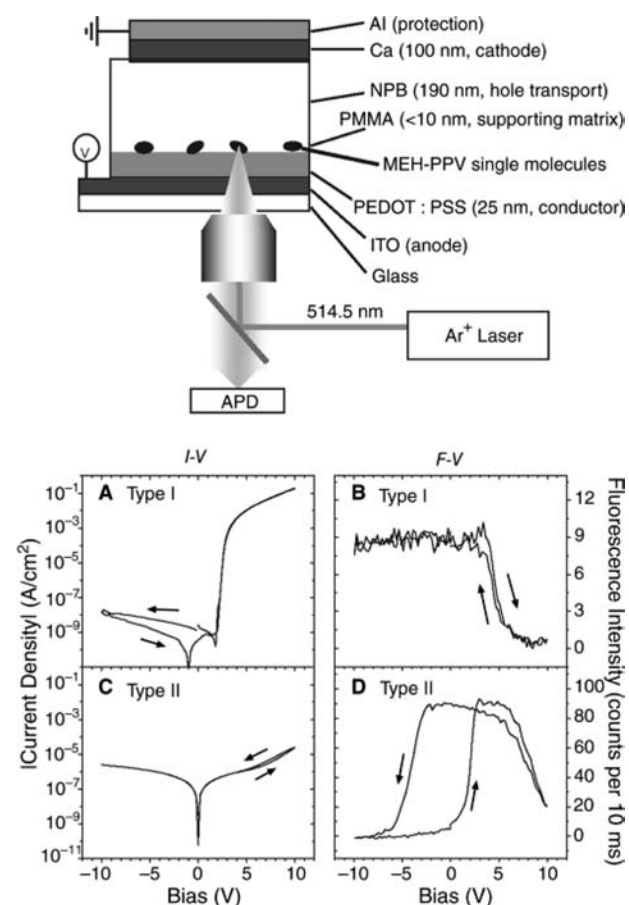


**Fig. 5** Basic structure of a hole-only organic diode and  $I$ - $V$  and  $F$ - $V$  data of two different types of diodes.

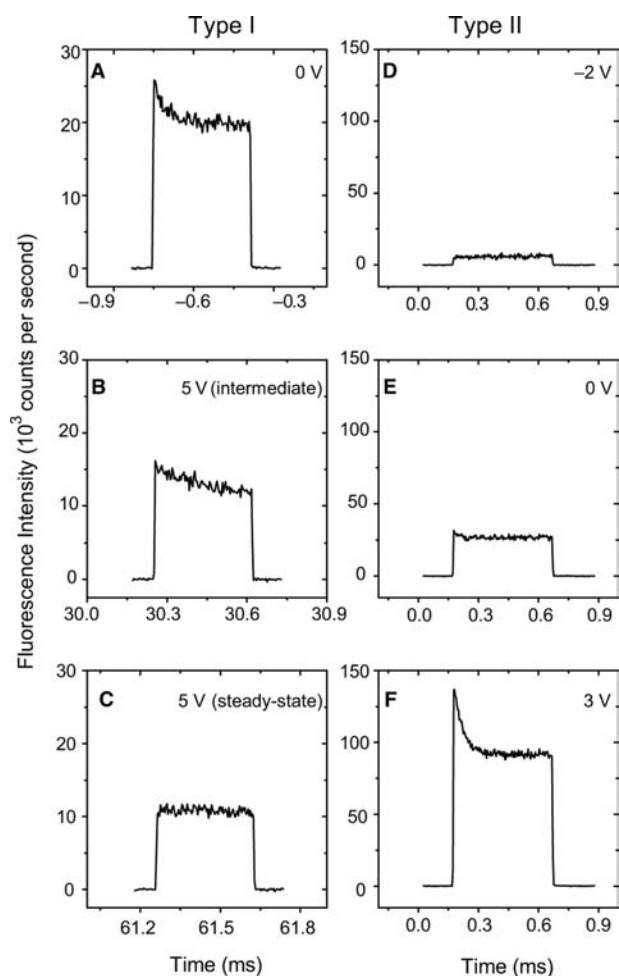


**Fig. 6** FV-TR-SMS data of MEH-PPV embedded in the two types of organic diodes.

functioning organic diode, leading to new insights on the charging/discharging processes.

## ACKNOWLEDGMENTS

Financial support from the National Science Foundation, the Welch Foundation, and the Keck Foundation is gratefully acknowledged.

## REFERENCES

- Nirmal, M.; Dabbousi, B.O.; Bawendi, M.G.; Macklin, J.J.; Trautman, J.K.; Harris, T.D.; Brus, L.E. Fluorescence intermittency in single cadmium selenide nanocrystals. *Nature* **1996**, *383*, 802.
- Kuno, M.; Fromm, D.P.; Hamann, H.F.; Gallagher, A.; Nesbitt, D.J. Nonexponential "blinking" kinetics of single CdSe quantum dots: a universal power law behavior. *J. Chem. Phys.* **2000**, *112*, 3117.
- Koberling, F.; Mews, A.; Basche, T. Oxygen-induced blinking of single CdSe nanocrystals. *Adv. Mater.* **2001**, *13*, 672.
- Brokmann, X.; Hermier, J.P.; Messin, G.; Desbiolles, P.; Bouchaud, J.P.; Dahan, M. Statistical aging and non-ergodicity in the fluorescence of single nanocrystals. *Phys. Rev. Lett.* **2003**, *90*, 120601.
- Vanden Bout, D.A.; Yip, W.-T.; Hu, D.; Fu, D.-K.; Swager, T.M.; Barbara, P.F. Discrete intensity jumps and intramolecular electronic energy transfer in the spectroscopy of single conjugated polymer molecules. *Science* **1997**, *277*, 1074.
- Yu, J.; Hu, D.; Barbara, P.F. Unmasking electronic energy transfer of conjugated polymers by suppression of O<sub>2</sub> quenching. *Science* **2000**, *289*, 1327.
- Hu, D.H.; Yu, J.; Wong, K.; Bagchi, B.; Rossky, P.J.; Barbara, P.F. Collapse of stiff conjugated polymers with chemical defects into ordered, cylindrical conformations. *Nature* **2000**, *405*, 1030.
- Hu, D.H.; Yu, J.; Padmanaban, G.; Ramakrishnan, S.; Barbara, P.F. Spatial confinement of exciton transfer and the role of conformational order in organic nanoparticles. *Nano. Lett.* **2002**, *2*, 1121.
- Guillet, T.; Berrehar, J.; Grousson, R.; Kovensky, J.; Lapersonne-Meyer, C.; Schott, M.; Voliotis, V. Emission of a single conjugated polymer chain isolated in its single crystal monomer matrix. *Phys. Rev. Lett.* **2001**, *87*, 087401.
- Huser, T.; Yan, M.; Rothberg, L.J. Single chain spectroscopy of conformational dependence of conjugated polymer photophysics. *Proc. Natl. Acad. Sci. U.S.A.* **2000**, *97*, 11,187.
- Bartko, A.P.; Dickson, R.M. Three-dimensional orientations of polymer-bound single molecules. *J. Phys. Chem. B* **1999**, *103*, 3053.
- Kumar, P.; Mehta, A.; Dadmun, M.D.; Zheng, J.; Peyser, L.; Bartko, A.P.; Dickson, R.M.; Thundat, T.; Sumpter, B.G.; Noid, D.W.; Barnes, M.D. Narrow-bandwidth spontaneous luminescence from oriented semiconducting polymer nanostructures. *J. Phys. Chem. B* **2003**, *107*, 6252.
- Barbara, P.F.; Gesquiere, A.J.; Park, S.-J.; Lee, Y.J. Single molecule spectroscopy of conjugated polymers. *Acc. Chem. Res.* **2005**, *38*, 602.
- Yu, Z.; Barbara, P.F. Low-temperature single-molecule spectroscopy of MEH-PPV conjugated polymer molecules. *J. Phys. Chem. B* **2004**, *108*, 11,321.
- Yu, J.; Lammi, R.K.; Gesquiere, A.J.; Barbara, P.F. Singlet-triplet and triplet-triplet interactions in conjugated polymer single molecules. *J. Phys. Chem. B* **2005**, *109*, 10,025.
- Gesquiere, A.J.; Lee, Y.J.; Yu, J.; Barbara, P.F. Single molecule modulation spectroscopy of conjugated polymers. *J. Phys. Chem. B* **2005**, *109*, 12,366.
- Grey, J.K.; Kim, D.Y.; Lee, Y.J.; Gutierrez, J.J.; Luong, N.; Ferraris, J.P.; Barbara, P.F. Single molecule studies of electronic energy transfer in a diblock conjugated polymer. *Angew. Chem. Int. Ed.* **2005**, *44*, 6202.
- Lammi, R.K.; Fritz, K.P.; Scholes, G.D.; Barbara, P.F. Ordering of single conjugated polymers in a nematic liquid crystal host. *J. Phys. Chem. B* **2004**, *108*, 4593.

19. Link, S.; Hu, D.; Chang, W.-S.; Scholes, G.D.; Barbara, P.F. Nematic solvation of segmented polymer chains. *Nano. Lett.* **2005**, *5*, 1757.
20. Wang, H.L.; MacDiarmid, A.G.; Wang, Y.Z.; Gebler, D.D.; Epstein, A.J. Application of polyaniline (emeraldine base, EB) in polymer light-emitting devices. *Synth. Met.* **1996**, *78*, 33.
21. Hide, F.; Diazgarcia, M.A.; Schwartz, B.J.; Heeger, A.J. New developments in the photonic applications of conjugated polymers. *Acc. Chem. Res.* **1997**, *30*, 430.
22. Friend, R.H.; Gymer, R.W.; Holmes, A.B.; Burroughes, J.H.; Marks, R.N.; Taliani, C.; Bradley, D.D.C.; Dos Santos, D.A.; Bredas, J.L.; Logdlund, M.; Salaneck, W.R. Electroluminescence in conjugated polymers. *Nature* **1999**, *397*, 121.
23. Vanden Bout, D.A.; Kerimo, J.; Higgins, D.A.; Barbara, P.F. Near-field optical studies of thin-film mesostructured organic materials. *Acc. Chem. Res.* **1997**, *30*, 204.
24. Park, S.-J.; Gesquiere, A.J.; Yu, J.; Barbara, P.F. Charge injection and photooxidation of single conjugated polymer molecules. *J. Am. Chem. Soc.* **2004**, *126*, 4116.
25. Gesquiere, A.J.; Park, S.-J.; Barbara, P.F. *F-V/SMS*: a new technique for studying the structure and dynamics of single molecules and nanoparticles. *J. Phys. Chem. B* **2004**, *108*, 10,301.
26. Lee, Y.J.; Park, S.-J.; Gesquiere, A.J.; Barbara, P.F. Probing a molecular interface in a functioning organic diode. *Appl. Phys. Lett.* **2005**, *87*, 051906.
27. Gesquiere, A.J.; Park, S.-J.; Barbara, P.F. Photochemistry and kinetics of single organic nanoparticles in the presence of charge carriers. *Eur. Polym. J.* **2004**, *40*, 1013.
28. Nguyen, P.H.; Scheinert, S.; Berleb, S.; Brutting, W.; Paasch, G. The influence of deep traps on transient current-voltage characteristics of organic light-emitting diodes. *Org. Electron.* **2001**, *2*, 105.
29. Paasch, G.; Scheinert, S. Simulation and modeling of C-V curves of OLEDs with trap states for the holes. *Synth. Met.* **2001**, *122*, 145.
30. Gesquiere, A.J.; Park, S.J.; Barbara, P.F. Hole-induced quenching of triplet and singlet excitons in conjugated polymers. *J. Am. Chem. Soc.* **2005**, *127*, 9556.
31. English, D.S.; Furube, A.; Barbara, P.F. Single-molecule spectroscopy in oxygen-depleted polymer films. *Chem. Phys. Lett.* **2000**, *324*, 15.
32. Hu, D.; Yu, J.; Barbara, P. Single-molecule spectroscopy of the conjugated polymer MEH-PPV. *J. Am. Chem. Soc.* **1999**, *121*, 6936.
33. Kim, D.Y.; Grey, J.K.; Barbara, P.F. A bimodal density of states for conjugated polymers. **2005**, *156*, 336.
34. Young, R.H.; Tang, C.W.; Marchetti, A.P. Current-induced fluorescence quenching in organic light-emitting diodes. *Appl. Phys. Lett.* **2002**, *80*, 874.
35. Ran, G.Z.; Wu, Z.L.; Ma, G.L.; Xu, A.G.; Qiao, Y.P.; Wu, S.K.; Yang, B.R.; Qin, G.G. Improvement of the charge imbalance caused by the use of a p-type silicon anode in an organic light-emitting diode. *Chem. Phys. Lett.* **2004**, *400*, 401.
36. Baldo, M.A.; O'Brien, D.F.; You, Y.; Shoustikov, A.; Sibley, S.; Thompson, M.E.; Forrest, S.R. Highly efficient phosphorescent emission from organic electroluminescent devices. *Nature* **1998**, *395*, 151.
37. Yang, X.H.; Neher, D.; Hertel, D.; Daubler, T.K. Highly efficient single-layer polymer electrophosphorescent devices. *Adv. Mater.* **2004**, *16*, 161.
38. Wilkinson, F.; McGarvey, D.J.; Olea, A.F. Factors governing the efficiency of singlet oxygen production during oxygen quenching of singlet and triplet-states of anthracene-derivatives in cyclohexane solution. *J. Am. Chem. Soc.* **1993**, *115*, 12,144.
39. Grewer, C.; Brauer, H.D. Mechanism of the triplet-state quenching by molecular-oxygen in solution. *J. Phys. Chem.* **1994**, *98*, 4230.
40. Scurlock, R.D.; Wang, B.J.; Ogilby, P.R.; Sheats, J.R.; Clough, R.L. Singlet oxygen as a reactive intermediate in the photodegradation of an electroluminescent polymer. *J. Am. Chem. Soc.* **1995**, *117*, 10,194.

# Fluorofullerenes

**Olga V. Boltalina**

*Chemistry Department, M.V. Lomonosov Moscow State University, Moscow, Russia*

**Steven H. Strauss**

*Department of Chemistry, Colorado State University, Fort Collins, Colorado, U.S.A.*

## INTRODUCTION

Since the soccer-ball-shaped molecule  $C_{60}$  and other fullerenes became available in macroscopic quantities, a wide variety of derivatives with multiple C–F bonds have been generated and observed in the gas phase. A significant number of these have also been isolated in weighable amounts and characterized by spectroscopic, electrochemical, and diffraction techniques. Those that have had their structures unambiguously determined by single-crystal X-ray diffraction include the fluorofullerenes  $C_{60}F_{18}$ ,  $C_{60}F_{36}$ , and  $C_{60}F_{48}$ ; the trifluoromethyl derivative  $C_{60}F_{17}(CF_3)$ ; the oxafuorofullerene  $C_{60}F_{18}O$ ; and the organofluorofullerene  $C_{60}F_{15}[CBr(CO_2Et)_2]_3$ . In this entry, the major developments in fluorofullerene chemistry will be reviewed, including the synthesis and characterization of selectively fluorinated fullerenes and their physical properties and chemical reactivities that will be important in their consideration for technological applications.

## BACKGROUND

Fluorination was among the first derivitizations proposed for buckminsterfullerene,  $C_{60}$ , the new allotrope of carbon discovered in laser-vaporized graphite in 1985.<sup>[1]</sup> Although it was only known as a gas-phase species at the time, the discoverers speculated that the preparation of fully fluorinated “Teflon-like” ball bearings (e.g.,  $C_{60}F_{60}$ ) might lead to a new era of “superlubricating” materials. Not surprisingly, when  $C_{60}$  became available in macroscopic quantities in 1991,<sup>[2]</sup> its reaction with  $F_2$  was immediately investigated.<sup>[3]</sup> Extensive experimental work followed, with dozens of publications from experts in the specialized and technically demanding field of fluorine chemistry.<sup>a</sup>

<sup>a</sup>Space limitations preclude a complete bibliography of the earliest fluorination papers in this entry.

The history of fluorofullerene (FF) chemistry can be divided into two periods, the first being the initial exploration period from 1991 to 1994. Commonly available fluorinating reagents and well-known methodologies were employed during this time.<sup>a</sup> The substrate for these seminal papers was either a few milligrams of pure  $C_{60}$  or larger amounts of the so-called “fullerene extract,” which was predominantly  $C_{60}$  with the bulk of the remainder being  $C_{70}$ . The purported FF products proved difficult to characterize. Nevertheless, approximate numbers of F-atom substituents (formerly referred to as F-atom addends)<sup>[4]</sup> were reported. Also reported were relative stabilities in various solvents, thermal stabilities, relative solubilities, and, to a limited extent, chemical reactivities, although these early FF products were not pure compounds of definite composition. They were complex, often intractable mixtures, in most cases containing a broad distribution of  $C_{60}F_x$  and  $C_{70}F_x$  molecules. Furthermore, it is now known that some early samples contained significant amounts of oxafuorofullerenes,  $C_{60}F_xO_y$  ( $y = 1$ , 2<sup>[5]</sup> or  $y = 1-18$ <sup>[6]</sup>), making the product mixtures even more complex than originally thought. For these reasons, the early literature should be examined with skepticism and cited with caution. The frequently cited *Nature* paper “No Lubricants from Fluorinated  $C_{60}$ ” is a good example.<sup>[7]</sup> The rapid hydrolysis and low stability of FF samples was reported, but it was the abundant, much more reactive  $C_{60}F_xO_y$  “impurities,” and not the simple  $C_{60}F_x$  FFs, that turned out to be thermally labile and to undergo rapid hydrolysis.<sup>[6]</sup> Another example is a current website that describes the putative  $C_{60}F_{60}$  FF as a “colorless,” “crystalline solid” with a “melting point of 287°C,”<sup>[8]</sup> although the original reports of its preparation and isolation are now widely believed to be incorrect.<sup>[9]</sup> As discussed below, the most highly fluorinated [60]fullerene that has been isolated is  $C_{60}F_{48}$ . The hypothetical molecule containing a closed  $C_{60}$  cage and having one F atom attached to each C atom has not been shown to exist, reports of its aforementioned physical properties (and pending commercial availability!) notwithstanding.

The second period, from 1994 to the present, has been a period of deliberate improvements and innovations in synthetic strategies that resulted in the isolation and complete characterization of several FFs that are 90 + % compositionally pure, including one that is also isomerically pure to within the limit of detection.<sup>b</sup> The breakthrough that inspired this work was the synthesis and <sup>19</sup>F nuclear magnetic resonance (NMR) characterization of ~70% compositionally pure C<sub>60</sub>F<sub>48</sub> from C<sub>60</sub> and F<sub>2</sub> (i.e., direct fluorination).<sup>[10]</sup> Its detailed structure (i.e., the positions of the 48 C–F bonds and the 6 remaining C=C double bonds) could not be unambiguously determined from the NMR data. Assuming, as the authors correctly did, that C<sub>60</sub>F<sub>48</sub> was an intact C<sub>60</sub> cage with 48 F atoms attached to 48 of the 60 C atoms, 14 different isomers were consistent with the NMR data (the total number of possible isomers for C<sub>60</sub>F<sub>48</sub> is greater than 20,000,000). They suggested that the two most likely structures, one with D<sub>3</sub> symmetry and one with S<sub>6</sub> symmetry, were the two predicted by MO calculations to be the most stable thermodynamically, although it was not known whether the fluorination reaction was under thermodynamic or kinetic control. The importance of this paper, overlooking the low yield and poor compositional purity, is that two important features of FF chemistry that served to inspire others had been determined: 1) the final product of direct fluorination is C<sub>60</sub>F<sub>48</sub>, so previously reported products with fewer than 48 F atoms represented incomplete fluorinations; and 2) fluorinated products of certain stable compositions can, in principle, be obtained. Further study of C<sub>60</sub> direct fluorination led to the high-yield preparation of macroscopic amounts of compositionally pure C<sub>60</sub>F<sub>48</sub>,<sup>[11]</sup> which made possible its complete characterization by a battery of physicochemical techniques including X-ray crystallography<sup>[12]</sup> and combustion calorimetry, the latter providing the first experimentally determined enthalpy of formation for any fullerene derivative.<sup>[13]</sup>

The next important development in the preparation of selectively fluorinated fullerenes was reported in 1995 by chemists at the Moscow State University. They used transition-metal fluorides as fluorinating reagents and observed the formation of the selectively fluorinated fullerenes C<sub>60</sub>F<sub>18</sub> and C<sub>60</sub>F<sub>36</sub>.<sup>[14]</sup> This was followed by papers describing the laborious chromatographic separation of dozens of less-abundant products, including FFs with  $x = 2, 4, 6, 8, 16,$  and  $20$ ,<sup>[15–21]</sup> as well as oxafuorofullerenes<sup>[22–24]</sup> and fullerenes containing both F atoms and CF<sub>3</sub> groups.<sup>[23,25]</sup>

<sup>b</sup> *Compositional purity* is the mol% of molecules with a specific molecular formula in a given sample. *Isomeric purity* is the mol% of a specific isomer in a sample having a specific molecular formula.

For the first time, detailed studies of the physical and chemical properties of gram quantities of individual, compositionally pure FF compounds could be carried out, studies that must precede the development of commercial applications of any new compound.

## SYNTHESIS OF FLUOROFULLERENES

### From C<sub>60</sub> and F<sub>2</sub>, XeF<sub>2</sub>, KrF<sub>2</sub>, ClF<sub>3</sub>, or BrF<sub>5</sub>

Until 1995, direct fluorination with F<sub>2</sub> was the most extensively studied method of C<sub>60</sub> fluorination.<sup>[26]</sup> Many different experimental conditions were investigated: reaction temperatures from 25°C to 355°C; a 1-atm continuous-flow reactor or a high-pressure batch reactor; and reaction times from hours to months. In some cases, the in situ mass uptake of the sample was recorded<sup>[3]</sup> or the volatile products were monitored by mass spectrometry<sup>[27]</sup> or infrared (IR) spectroscopy.<sup>[3]</sup> In others, color changes from black to brown to pale yellow to white were noted.<sup>[28,29]</sup>

Direct fluorination occurred slowly at 25°C (weeks), affording mixtures of unreacted C<sub>60</sub> and C<sub>60</sub>F<sub>*x*</sub> FFs with even *x* values from 36 to 46.<sup>[30]</sup> Similar results, but with higher overall conversions, were obtained at 130–250°C.<sup>[29,31]</sup> A complicated two-stage direct fluorination at 250–275°C in the presence of NaF afforded a 56% yield of FF material in 50 hr that was 70 mol% C<sub>60</sub>F<sub>48</sub> according to mass spectrometry.<sup>[10]</sup> In contrast, a one-stage direct fluorination in a flow reactor at 315–355°C afforded a 70% yield of FFs in 3–10 hr that was 95 mol% C<sub>60</sub>F<sub>48</sub> according to electron-ionization mass spectrometry (EI-MS).<sup>[31]</sup> This is still the highest compositional purity reported to date for C<sub>60</sub>F<sub>48</sub>.

Use of the noble gas fluorides XeF<sub>2</sub> and KrF<sub>2</sub>, which are more powerful fluorinating reagents than F<sub>2</sub>, did not afford compositionally pure C<sub>60</sub>F<sub>48</sub>. In the case of XeF<sub>2</sub>, complex mixtures of FFs were isolated.<sup>[28,32]</sup> In the case of KrF<sub>2</sub>, a mass spectrum of the complex mixture of fluorocarbon products showed the presence of non-fullerene C<sub>60</sub>F<sub>*x*</sub> species with  $x > 60$ , which requires C<sub>60</sub> cage rupture and the formation of CF<sub>2</sub> and/or CF<sub>3</sub> groups.<sup>[33]</sup> Such hyperfluorinated species had been previously observed as products of the direct fluorination of C<sub>60</sub> under UV radiation.<sup>[34]</sup>

The use of the reactive interhalogens ClF<sub>3</sub> and BrF<sub>5</sub> did not result in significant yields of any compositionally pure FF.<sup>[5]</sup> To further complicate matters, many products containing multiple Cl or Br atoms in addition to F atoms were obtained based on IR spectroscopy and elemental analysis. It was also reported that “IF<sub>7</sub> did not react [with C<sub>60</sub>] in the gaseous phase.”<sup>[5]</sup>



The reaction of C<sub>60</sub> dissolved in liquid Br<sub>2</sub> (which is known to produce C<sub>60</sub>Br<sub>24</sub>) with BrF<sub>3</sub> was reported to yield C<sub>60</sub>F<sub>24</sub>.<sup>[35]</sup> The stoichiometry was based on the ratio of C 1s and F 1s XPS (X-ray photoelectron spectroscopy) intensities. However, new, unpublished mass spectrometric evidence indicates that the product actually consisted of a distribution of C<sub>60</sub>F<sub>x</sub> compositions with an average *x* value of 24 (N.F. Yudanov and O.V. Boltalina, unpublished data, 2001).

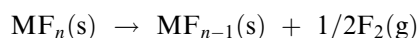
The reaction of C<sub>60</sub> with IF<sub>5</sub> in liquid CCl<sub>4</sub> was reported to yield chlorofluorofullerenes, including C<sub>60</sub>Cl<sub>18</sub>F<sub>14</sub>.<sup>[36]</sup> However, the only method of characterization was low-resolution mass spectrometry, and these data were inconclusive. For example, a sample of C<sub>60</sub>Cl<sub>24</sub> and a sample purported to be C<sub>60</sub>Cl<sub>18</sub>F<sub>14</sub> exhibited similar complex distributions of ions with *m/z* at 1534 ± 2 Da, 1464 ± 2 Da, 1394 Da, 1322 ± 2 Da, etc.

### From C<sub>60</sub> and High-Valent Metal Fluorides

A conceptual breakthrough in the synthesis of selectively fluorinated fullerenes was discovered in 1995, not by synthetic chemists but by mass spectrometrists at Moscow State University (MSU) who were studying the thermochemistry of gaseous ions.<sup>[14]</sup> They used a magnetic-sector mass spectrometer equipped with a Knudsen effusion cell as a chemical reactor. Solid state reactions of fullerenes with various high-valent transition-metal and rare-earth-metal fluorides as fluorinating reagents resulted in the simultaneous generation and mass-spectrometric detection of the volatile products. Because the temperature was programmed to increase over time, a wealth of information on the dynamics of formation and distribution of combinatorial-like mixture of products as a function

of temperature was obtained for each pair of reagents and stoichiometric ratio studied. Significantly, a large fraction of the products formed at a given temperature were condensed on a specially designed collection plate, which allowed for the further characterization of new derivatives by a variety of spectroscopic techniques.<sup>[15,16]</sup>

The Knudsen-cell technique was largely responsible for the rapid development of synthetic fluorofullerene chemistry. It was discovered that heating a 1 : 36 mole ratio mixture C<sub>60</sub> and MnF<sub>3</sub> afforded a 60–70% yield of 90 + % compositionally pure C<sub>60</sub>F<sub>36</sub>.<sup>[37]</sup> Another paper reported that mixtures of C<sub>60</sub> and the ternary metal fluoride K<sub>2</sub>PtF<sub>6</sub> resulted in the selective formation of C<sub>60</sub>F<sub>18</sub> (also with 90 + % compositional purity and in 60–70% yield) with only trace quantities of C<sub>60</sub>F<sub>36</sub> and several other FFs with fewer than 18 F atoms present.<sup>[38]</sup> In general, reactions with high-valent metal fluorides gave products with high compositional purity or, at worst, a narrow distribution of C<sub>60</sub>F<sub>x</sub> compositions. In general, it was also found that the average number of F atoms added to C<sub>60</sub> is correlated with the relative fluorinating strength of the metal fluoride, which to a first approximation increases as the enthalpy change for the reaction



becomes less positive or more negative.<sup>[39]</sup> Additionally, it was found that, for a given metal fluoride, higher temperatures favored the selective formation of FFs with fewer F atoms per C<sub>60</sub> cage. Some representative data are listed in Table 1.

A recent paper reported a series of reactions of C<sub>60</sub> with ternary metal fluorides other than K<sub>2</sub>PtF<sub>6</sub>.<sup>[40]</sup> This is potentially a significant next step for two reasons. First, ternary metal fluorides are more numerous than

**Table 1** Values of *x* for the C<sub>y</sub>F<sub>x</sub> or C<sub>59</sub>NF<sub>x</sub> major products of fullerene fluorinations<sup>a</sup>

Fullerene substrate	Fluorination reagent (temperature range, °C)				
	F <sub>2</sub> (25–300)	AgF <sub>2</sub> (330–500)	MnF <sub>3</sub> (380–500)	CeF <sub>4</sub> (420–520)	K <sub>2</sub> PtF <sub>6</sub> (450–520)
C <sub>60</sub>	48	44	36	36	36, 18
C <sub>70</sub>	56/54		40/38/36		
C <sub>74</sub>		48/46	40/38/36		38, 18
C <sub>76</sub>	54/52		40/38	42/40/38	38/36, 20
C <sub>84</sub>	58/56		44/42	42/40	40/38, 24
C <sub>59</sub> N <sup>b</sup>			37/35/33	35/33	33/31, 17
Percentage of occupancy, ( <i>x</i> / <i>y</i> ) × 100% <sup>c</sup>	67–80	62–73	49–60	48–60	24–30

<sup>a</sup>Slashes separate *x* values for a distribution of species observed under a given set of conditions. Commas separate *x* values for different species or different distributions of species observed under two different sets of conditions.

<sup>b</sup>The substrate for these fluorinations was (C<sub>59</sub>N)<sub>2</sub>, but the *x* values listed are for a single azafullerenes, which, with an odd number of F atoms, are closed-shell species.

<sup>c</sup>In those cases where products from two different sets of conditions are listed, the percentages of occupancy are for the species with the smallest number of F atoms.

the corresponding binary transition metal fluorides (consider  $K_2MnF_6$  and  $Rb_2MnF_6$  vs.  $MnF_4$  and  $Cs_2PbF_6$  and  $Cs_3PbF_6$  vs.  $PbF_4$ ), so a wider variety of reagents has become available to the synthetic chemist. Second, these ternary compounds are generally weaker fluorinating reagents (i.e., less reactive) than the parent binary metal fluoride. This feature makes them easier to handle in the laboratory environment and, more importantly, opens up the possibility of isolating FFs with lower degrees of fluorination.

The reaction of  $C_{60}$  with  $WF_6$ ,  $TaF_5$ ,  $NbF_5$ , and  $TiF_4$ , which are not particularly strong fluorinating reagents, only produced “adducts” of unknown structure [e.g.,  $C_{60}(MF_n)_x$ ].<sup>[41]</sup> No fluorofullerenes were observed.

### Fluorination of Higher Fullerenes and Some $C_{60}$ Derivatives

Fluorination of the higher fullerenes  $C_{74}$ ,  $C_{76}$ ,  $C_{78}$ , and  $C_{84}$  and of  $C_{60}$  derivatives such as  $(C_{59}N)_2$ ,  $C_{60}Cl_x$ , and  $C_{60}Br_x$  were investigated as these compounds became available in macroscopic quantities. As far as the higher fullerenes and  $(C_{59}N)_2$  are concerned, EI-MS characterization of volatile products generated by the Knudsen-cell technique showed that specific compositions, or narrow ranges of compositions, could be attained with a given high-valent metal fluoride and a given reaction temperature.<sup>[42–44]</sup> Representative data are listed in Table 1. Note that the percentage of occupancy for the  $C_yF_x$  and  $C_{59}NF_x$  compounds with the smaller of the listed  $x$  values parallels the percentage of occupancy for the  $C_{60}F_x$  products with the same fluorination reagent. Some individual higher FFs and  $C_{59}NF_x$  compounds have been isolated, but none has been extensively characterized. Nevertheless, the fact that different  $x$  values or narrow ranges of  $x$  values were observed in each case means that certain  $C_yF_x$  and  $C_{59}NF_x$  compounds may possess a special kinetic or thermodynamic stability similar to the special stabilities possessed by  $C_{60}F_{18}$ ,  $C_{60}F_{36}$ , and  $C_{60}F_{48}$ . Based on this reasoning, likely structures of  $C_{74}F_{38}$  and  $C_{76}F_{20}$ <sup>[44]</sup> and several  $C_{59}NF_x$  compounds<sup>[45]</sup> have been proposed.

Reactions of the halofullerenes  $C_{60}Br_6$ ,  $C_{60}Br_8$ ,  $C_{60}Br_{24}$ ,  $C_{60}Cl_6$ , and  $C_{60}Cl_{24}$  with either  $F_2$  or  $XeF_2$  were reported to produce a variety of FFs, mixed fluorohalofullerenes, and/or oxafuorofullerenes.<sup>[36]</sup> Another study of the reactions of  $C_{60}Br_8$  and  $C_{60}Br_{24}$  with  $XeF_2$  reported similar findings.<sup>[32]</sup> An important goal of these studies was to prepare compositionally pure FFs such as  $C_{60}F_6$ ,  $C_{60}F_8$ , and  $C_{60}F_{24}$  that have not yet been prepared by other methods. However, to date, there is no convincing example of a direct, high-yield  $C_{60}X_x \rightarrow C_{60}F_x$  transformation ( $X = Cl, Br$ ).

## STRUCTURAL CHARACTERIZATION OF FLUOROFULLERENES

### X-Ray Crystallography

The fluorofullerenes and fluorofullerene derivatives that have been structurally characterized by single-crystal X-ray diffraction are all derivatives of  $C_{60}$ . The complete list includes the three FFs,  $C_{60}F_{18}$ ,  $C_{60}F_{36}$ , and  $C_{60}F_{48}$ , and the three FF derivatives,  $C_{60}F_{17}(CF_3)$ ,  $C_{60}F_{18}O$ , and  $C_{60}F_{15}[CBr(CO_2Et)_2]_3$ . From these few structures, an analysis of F-atom addition patterns and of interatomic distances and angles has provided some insight into the mechanisms by which F atoms and other atoms or groups of atoms are added to a given starting material or intermediate. An assessment of the distances and angles also provides insight into the steric and electronic reasons that the underlying  $C_{60}$  cage is distorted, in some cases significantly distorted, from the nearly spherical  $I_h$  symmetry of native  $C_{60}$ .

### $C_{60}F_{18}$

This was the first FF to be structurally characterized.<sup>[46]</sup> Seven different modifications have been studied, a solvent-free modification,<sup>[38]</sup> a toluene solvate,<sup>[46]</sup> and five other arene solvates.<sup>[47]</sup> They all contain the same  $C_{3v}$  isomer of  $C_{60}F_{18}$ . A ball-and-stick plot (BSPlot) of the  $C_{60}F_{18}$  molecule present in the toluene solvate, and its Schlegel diagram, are shown in Fig. 1. The molecule has all 18 F atoms situated on one hemisphere. This undoubtedly makes it highly polar (calculated dipole moments range from 12 to 16 D).<sup>[46]</sup> The Schlegel diagram shows that the 18 F atoms have been added to a contiguous set of C atoms, a common feature of hydrofullerenes but uncommon when larger substituents are present, as in chlorofullerenes and bromofullerenes.<sup>[48]</sup> The Schlegel diagram also shows that the fluorinated hemisphere contains a central, nearly planar, fully aromatic benzenoid ring, with six nearly identical C–C distances, separated from the remainder of the fullerene  $\pi$ -electron system by a belt of  $sp^3$  C atoms each bearing a C–F bond. The BSPlot shows that the fluorinated hemisphere is significantly flattened, so much so that if the unfluorinated hemisphere is superimposed on a molecule of  $C_{60}$ , the C atoms of the benzenoid ring are ca. 0.6 Å closer to the center of the  $C_{60}$  molecule than the C atoms of the antipodal hexagonal ring. The C–F distances are normal. The  $C(sp^3)$ – $C(sp^3)$  distances, many of which are greater than 1.62 Å, are significantly longer than typical organic C–C distances but are not unusual for highly fluorinated or perfluorinated hydrocarbons.<sup>[46]</sup>

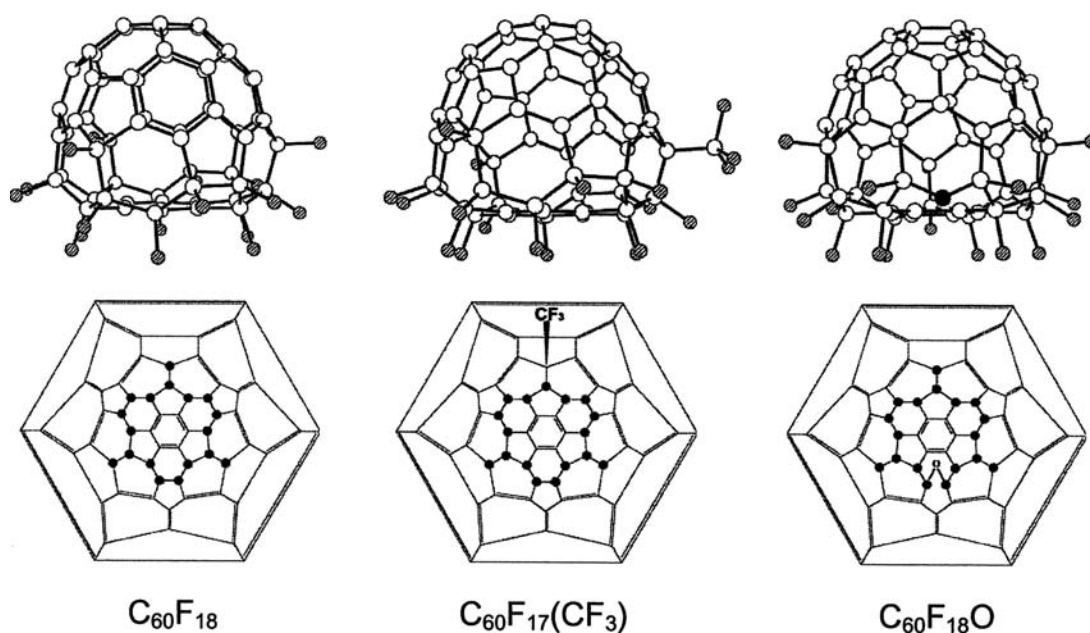


**Fig. 1** Ball-and-stick plots and Schlegel diagrams for three structures determined by X-ray crystallography. The open and hatched circles in the plots represent C and F atoms, respectively. The solid circle in the plot of  $C_{60}F_{18}O$  represent the O atom. The solid circles in the Schlegel diagrams represent C–F bonds.

### $C_{60}F_{17}(CF_3)$

This compound was a by-product of  $C_{60}$  fluorination with  $K_2PtF_6$ . It was originally believed to be  $C_{60}F_{18}(CF_2)$ , with the  $CF_2$  group incorporated into a cyclopropane ring.<sup>[49]</sup> The true nature of the structure was revealed by X-ray diffraction analysis. Crystals of this compound were found, both by X-ray and  $^{19}F$  NMR analysis, to contain a  $C_s$  isomer (ca. 68%), the Schlegel diagram of which is shown in Fig. 1, and a pair of  $C_1$  enantiomers (ca. 16% each) having the  $CF_3$  group attached instead to one of the six symmetry-related  $sp^3$  C atoms that are not directly bonded to the central benzenoid ring.<sup>[50]</sup> All of the isomers exhibit threefold rotational disorder in the solid state. Nevertheless, a reasonable structure solution was possible. A BSPlot of the major isomer is shown in Fig. 1. The molecule exhibits the same flattening observed in the structure of  $C_{60}F_{18}$ . It may be mechanistically significant that the major isomer of  $C_{60}F_{17}(CF_3)$  has the  $CF_3$  group attached to the least sterically demanding  $sp^3$  C atoms.

### $C_{60}F_{18}O$

As was the case with  $C_{60}F_{17}(CF_3)$ , the X-ray diffraction analysis of the oxafuorofullerene  $C_{60}F_{18}O$  settled a long-standing problem concerning its structure. It was also a by-product of  $C_{60}$  fluorination with  $K_2PtF_6$ . It had been originally formulated as an epoxide,<sup>[6]</sup> an interpretation that remained unchallenged nearly a decade later.<sup>[20,51–53]</sup> The structure, shown in

Fig. 1, revealed that it is an ether formed (conceptually, not necessarily mechanistically) by the insertion of an O atom into a  $C(sp^3)–C(sp^3)$  bond of  $C_{60}F_{18}$ .<sup>[22]</sup> The structure shown is the major isomer of  $C_{60}F_{18}O$ ; two other isomers were separated by high-performance liquid chromatography (HPLC) and are presumably also ethers, with the O atom inserted into different  $C(sp^3)–C(sp^3)$  bonds. Note that in the major isomer, the O atom has been inserted into one of the three longest  $C(sp^3)–C(sp^3)$  bonds, which average 1.67 Å in  $C_{60}F_{18}$ . The two remaining such bonds in  $C_{60}F_{18}O$  are probably also extremely long, but the threefold rotational disorder in these crystals makes distances and angles involving these C atoms unreliable.

### $C_{60}F_{15}[CBr(CO_2Et)_2]_3$

This compound, originally prepared and characterized by mass spectrometry (A.L. Mirakyan, personal communication to O.V. Boltalina, 2000), was later purified and structurally characterized by single-crystal X-ray diffraction.<sup>[54]</sup> Its structure is related to that of  $C_{60}F_{18}$  except that the three bulky organic substituents are not attached to C atoms contiguous with the belt of 15  $sp^3$  C atoms.

### $C_{60}F_{36}$

There are three isomers known for this composition. The two major isomers have  $C_3$  (>90%) and  $T$  (<10%) symmetry.<sup>[55]</sup> A BSPlot and Schlegel diagram

of the *T* isomer are shown in Fig. 2.<sup>[56]</sup> This structure is severely disordered, so much so that all 36 C–F bonds had to be constrained to have the same distance. There were other constraints imposed on the two independent  $C_{60}F_{36}$  molecules in the asymmetric unit. Nevertheless, four salient features were unambiguously determined. First, this isomer of  $C_{60}F_{36}$  does indeed have idealized (although not crystallographic) *T* symmetry, in agreement with predictions based on  $^{19}F$  NMR spectra.<sup>[55,57]</sup> In accordance with its proper rotational symmetry, *T*- $C_{60}F_{36}$  is chiral and exists as a pair of enantiomers. Second, the 36 F atoms were added to a contiguous set of C atoms, which is consistent with the addition patterns extant in  $C_{60}F_{18}$ ,  $C_{60}F_{17}(CF_3)$ , and  $C_{60}F_{18}O$ . Third, there are four isolated benzenoid rings in this isomer, each of which is planar to within  $\pm 0.02$  Å. The Schlegel diagram in Fig. 2 shows that any three of the four benzenoid rings are symmetrically related by a  $C_3$  axis perpendicular to the plane of the remaining ring. Fourth, the molecule is severely distorted from the nearly spherical structure of  $C_{60}$ . The four benzenoid rings are much closer to the geometric center of the molecule than the corresponding six-membered rings in  $C_{60}$ , while the  $C_6F_6$  hexagons

opposite the benzenoid rings are much farther away from the geometric center. In  $C_{60}$ , the distance from each C atom to the geometric center is 3.57 Å; in *T*- $C_{60}F_{36}$ , the corresponding distances from the geometric center to the benzenoid C atoms and to the antipodal  $C_6F_6$  C atoms are 3.0–3.1 and 3.9–4.0 Å, respectively.

The structure of the  $C_3$  isomer has not yet been determined by X-ray diffraction. Its likely structure, deduced from a careful analysis of 1-D and 2-D  $^{19}F$  NMR spectra, has three benzenoid rings and three isolated C=C double bonds arising from a contiguous addition of F atoms.<sup>[57]</sup> If one of the double bonds were moved by just one C atom, the  $C_3$  axis would be lost and the molecule would have  $C_1$  symmetry. This isomer has recently been isolated and structurally characterized by X-ray diffraction.<sup>[58]</sup>

### $C_{60}F_{48}$

Single crystals of this compound, grown from mesitylene solution, were found to contain nearly equal amounts of  $D_3$  and  $S_6$  isomers. The X-ray diffraction analysis was further complicated by the fact that both isomers appeared to be statistically disordered over two positions. The structure was eventually solved,

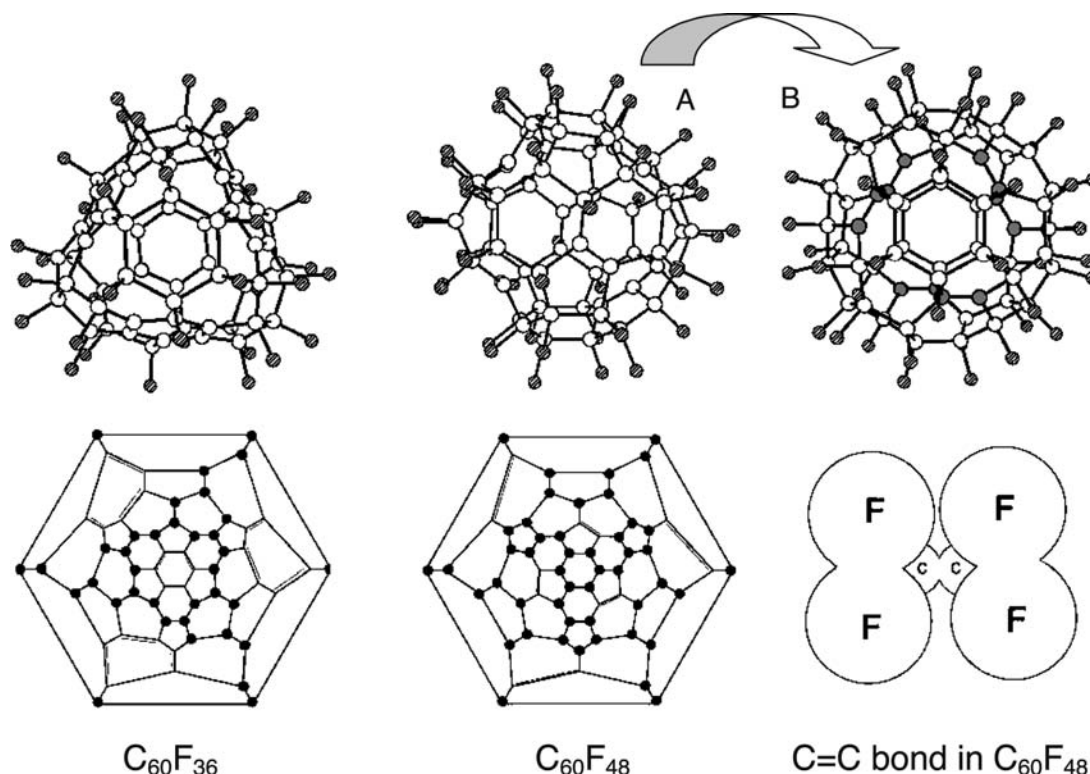


**Fig. 2** Ball-and-stick plots and Schlegel diagrams for the *T*-symmetry isomer of  $C_{60}F_{36}$  and the  $D_3$ -symmetry structure of  $C_{60}F_{48}$ , both determined by X-ray crystallography. Two different rotational orientations, A and B, are shown for  $C_{60}F_{48}$ . In orientation B, looking down the  $C_3$  axis, the 12 remaining  $sp^2$  C atoms are represented as grey circles and form the six isolated C=C double bonds, three in the upper hemisphere and three in the lower hemisphere. Elsewhere, the open and hatched circles represent C and F atoms, respectively. The solid circles in the Schlegel diagrams represent C–F bonds. Also shown is the local structure around one of the C=C bonds in  $D_3$ - $C_{60}F_{48}$ . The size of each F atom in this drawing corresponds to its van der Waals radius.

and a BSPlot and Schlegel diagram of the  $D_3$  isomer are shown in Fig. 2.<sup>[12]</sup> As in the other FFs and FF derivatives that have been structurally characterized, the 48 F atoms have been added to  $C_{60}$  in a contiguous manner. There are only 12 remaining  $sp^2$  C atoms distributed over six isolated C=C bonds, each of which is a common edge to a hexagon and a pentagon, the same as for the three isolated C=C bonds in the  $C_1$  and  $C_3$  isomers of  $C_{60}F_{36}$ . Similar to the structure of  $T-C_{60}F_{36}$ , the structure of  $C_{60}F_{48}$  is severely distorted. The distances between the 12  $sp^2$  C atoms and the geometric center are all ca. 3.05 Å, while the distances between  $sp^3$  C atoms that are bonded only to other  $sp^3$  C atoms are all ca. 3.9 Å.

Perhaps the most interesting feature of the structure is that the six remaining C=C bonds are well shielded from external reagents, both by the distortion that draws them closer to the molecular center and by their four adjacent C–F bonds. A diagram showing one of the isolated C=C bonds in  $C_{60}F_{48}$  and its four closest F atoms is also shown in Fig. 2. The size of each F atom corresponds to its van der Waals radius. The four F atoms are nearly coplanar and form an idealized rectangle having two sides of 2.6 Å, two sides of  $3.3 \pm 0.2$  Å, and two diagonals of 4.1 Å. It is rather obvious that the addition of more than 48 F atoms to an intact  $C_{60}$  cage must have a high kinetic barrier if not a high thermodynamic barrier.

Neither the  $D_3$  nor the  $S_6$  isomer has a permanent dipole moment. Therefore  $C_{60}F_{48}$  may be the closest approximation to a spherical “Teflon-like” ball prepared to date. It will be interesting to see what lubricating properties, if any, it possesses.

### Fluorine-19 Nuclear Magnetic Resonance Spectroscopy

Many more FFs have been studied by NMR spectroscopy than by X-ray crystallography, both because many compounds have not yet yielded suitable crystals and because NMR spectra of mixtures can be, in many cases, readily interpreted. Although NMR analysis cannot, in general, lead to unambiguous structure elucidation, it can rule out many structure possibilities on the basis of symmetry (number and intensities of peaks) and coupling-constant patterns.

Nuclear magnetic resonance studies that simply support the results of X-ray structure determinations discussed above will not be included here because of space limitations.

#### $C_{60}F_x$

Small amounts of the FFs  $C_{60}F_2$ ,  $C_{60}F_4$ ,  $C_{60}F_6$ ,  $C_{60}F_8$ ,  $C_{60}F_{16}$ , and  $C_{60}F_{20}$  were isolated by HPLC from the

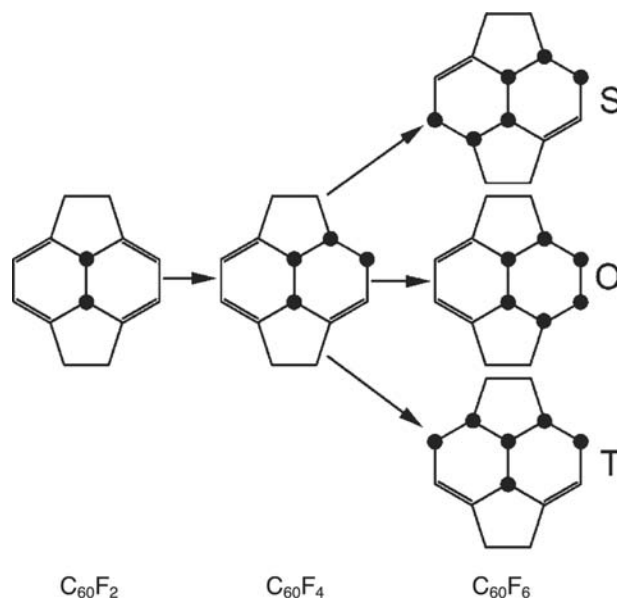


**Fig. 3** Diagrams showing likely F-atom addition patterns for  $C_{60}F_2$  and  $C_{60}F_4$  and three possible F-atom addition patterns  $C_{60}F_6$ . The solid circles represent C–F bonds. The  $^{19}F$  NMR spectrum of  $C_{60}F_6$  is consistent with the diagram labeled S.

crude reaction products of  $C_{60}$  fluorinations with  $K_2PtF_6$ .<sup>[15–19,21]</sup> Their  $^{19}F$  NMR spectra are consistent with sequential, contiguous addition patterns that result from a series of 1,2 additions of F atoms. Diagrams showing these additions for  $C_{60}F_2$ ,  $C_{60}F_4$ , and  $C_{60}F_6$  are shown in Fig. 3. Note that NMR spectroscopy is a particularly suitable technique for distinguishing between the three patterns shown for  $C_{60}F_6$ . Structure S would result in an NMR spectrum with three equal intensity peaks (this was what was observed), structure O would result in a spectrum with one peak, and structure T would result in a spectrum with four peaks with relative intensities 1:1:2:2. Even in cases where the number of peaks and their relative intensities cannot distinguish between two different patterns, a distinction based on coupling constant patterns may still be possible.

The  $^{19}F$  NMR spectrum of  $C_{60}F_{20}$  is interesting because of its simplicity. It consists of a single peak, requiring that all 20 F atoms are symmetrically related.<sup>[19]</sup> The only possible contiguous addition structure has  $D_{5d}$  symmetry with the 20 C–F bonds arranged on the “equator” of a  $C_{60}$  cage. The structure, shown in Fig. 4, is reminiscent of the planet Saturn, and  $C_{60}F_{20}$  has been tentatively named saturnene.

#### $C_{60}F_xO_y$

The isolation and  $^{19}F$  NMR analysis of small quantities of the oxafuorofullerenes  $C_{60}F_2O$ ,  $C_{60}F_4O$ ,  $C_{60}F_6O$ ,  $C_{60}F_8O$ ,  $C_{60}F_{16}O$ , and several isomers of



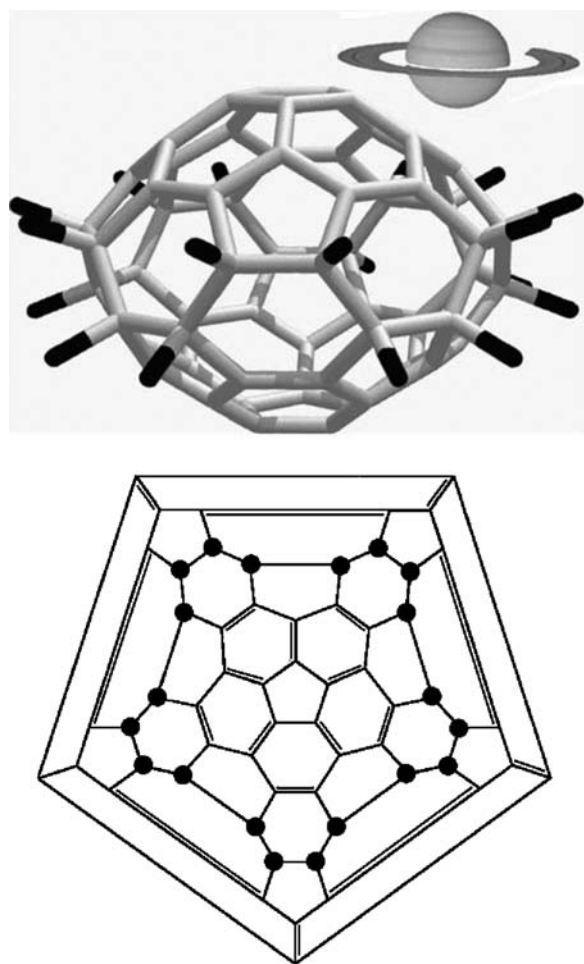


**Fig. 4** Schlegel diagram and an artist's rendition of the proposed structure of  $C_{60}F_{20}$  (saturnene). The structure has  $D_{5d}$  symmetry; therefore all 20 F atoms are equivalent. The solid circles in the Schlegel diagrams represent C–F bonds.

$C_{60}F_{18}O$  led to the conclusion that they are all intramolecular ethers like the isomer of  $C_{60}F_{18}O$  that had been structurally characterized.<sup>[18]</sup> Schlegel diagrams for the likely structures of  $C_{60}F_2O$ ,  $C_{60}F_4O$ ,  $C_{60}F_6O$ ,  $C_{60}F_8O$ , based on the distinctive chemical shifts of F atoms on the two ether C atoms, are shown in Fig. 5. The contiguous pattern of F atom addition is clearly seen, and the O atom is always inserted into the weakest  $C(sp^3)-C(sp^3)$  bond.

## PHYSICAL PROPERTIES OF FLUOROFULLERENES

### Solubilities in Organic Solvents

The statement that FFs are more soluble than their parent fullerene can be found in a growing number of publications. Not only is this statement incorrect in many instances, the quantitative data on which it

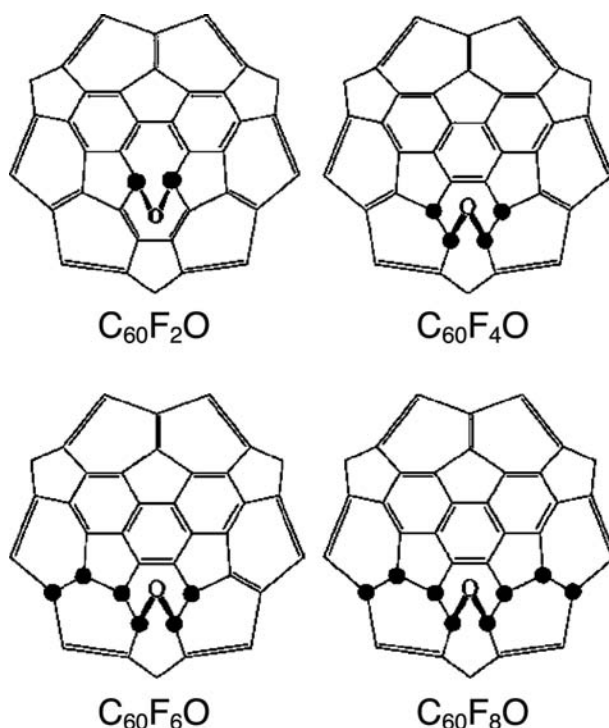


**Fig. 5** Schlegel diagrams showing likely F- and O-atom addition patterns for  $C_{60}F_2O$ ,  $C_{60}F_4O$ ,  $C_{60}F_6O$ , and  $C_{60}F_8O$  based on  $^{19}F$  NMR spectra. The solid circles represent C–F bonds.

would be properly based have not yet been published in the open literature. Quantitative solubilities could only be measured after selectively fluorinated fullerenes became available in macroscopic amounts. Some of the recently measured solubilities of  $C_{60}F_{36}$  and  $C_{60}F_{48}$  in hydrocarbon solvents are listed in Table 2.<sup>[59]</sup>

It was found that the solubilities of  $C_{60}F_{48}$  in aromatic hydrocarbon solvents were lower, not higher, than the corresponding solubility of  $C_{60}$ . The solubilities for  $C_{60}F_{18}$  were even lower than those for  $C_{60}F_{48}$ . Nevertheless, the solubilities are high enough so that toluene can be used as the eluent for HPLC purifications. On the other hand, the solubilities of  $C_{60}F_{48}$  in aliphatic hydrocarbon solvents were orders of magnitude higher than for  $C_{60}$ , and those for  $C_{60}F_{36}$  were ca. 10–50 times higher than for  $C_{60}$ . In contrast to the solubility of FFs in aliphatic and aromatic hydrocarbon solvents, bromofullerenes have such low solubilities that little synthetic work with them can be anticipated in common organic solvents.<sup>[9]</sup>

Whenever a FF is crystallized from an aromatic hydrocarbon or halogenated aromatic hydrocarbon solvent, one or more solvent molecules per FF are strongly bound in the lattice (see the “[X-Ray Crystallography](#)” section). For example, crystals containing one toluene molecule per  $C_{60}F_{18}$  are stable up to 190°C, at which temperature the solvent evaporates,



**Table 2** Solubilities of fluorofullerenes in hydrocarbon solvents at 25°C<sup>a</sup>

Solvent	Solubility (mmol L <sup>-1</sup> )		Solubility ratio		
	C <sub>60</sub> F <sub>36</sub>	C <sub>60</sub> F <sub>48</sub>	C <sub>60</sub> F <sub>48</sub> /C <sub>60</sub> F <sub>36</sub>	C <sub>60</sub> F <sub>36</sub> /C <sub>60</sub>	C <sub>60</sub> F <sub>48</sub> /C <sub>60</sub>
<i>n</i> -Pentane	0.26(4)	11.9(1)	46	46	2.2 × 10 <sup>3</sup>
<i>n</i> -Hexane	0.36(4)	7.1(1)	20	6.7	1.3 × 10 <sup>2</sup>
<i>n</i> -Heptane	0.43(3)	6.6(1)	15	6.7	1.0 × 10 <sup>2</sup>
<i>n</i> -Decane	0.43(1)	5.5(1)	13	4.5	57
Benzene		0.91(1)			0.44
Toluene		0.86(1)			0.22
Mesitylene		0.19(1)			0.09

<sup>a</sup>Solubilities are reported in mmol fullerene per liter of solvent. The molar masses of C<sub>60</sub>, C<sub>60</sub>F<sub>36</sub>, and C<sub>60</sub>F<sub>48</sub> are 720, 1404, and 1632 g mol<sup>-1</sup>.

leaving behind solvent-free C<sub>60</sub>F<sub>18</sub>.<sup>[47]</sup> The structure of C<sub>60</sub>F<sub>48</sub> discussed above was determined with a crystal-line modification containing two mesitylene molecules per FF. A drawing of the formula unit is shown in Fig. 6. The two symmetry-related mesitylene molecules

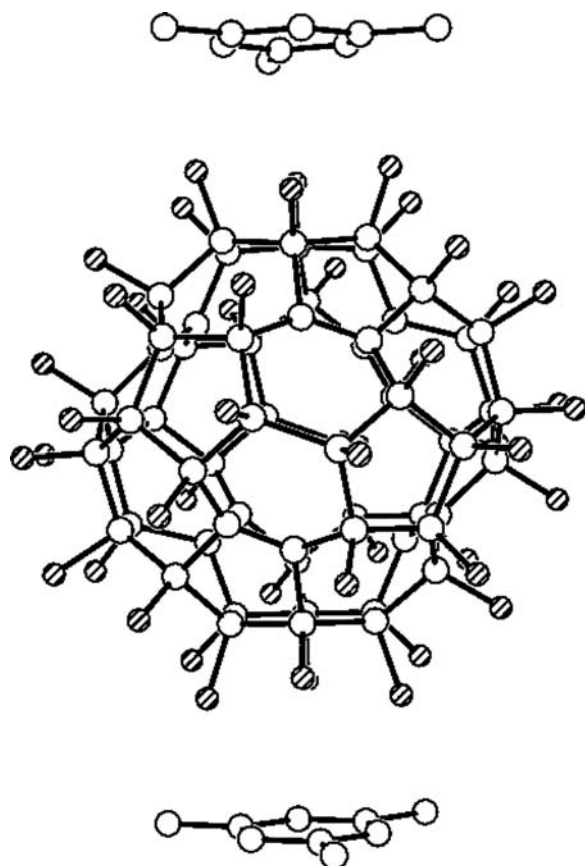


**Fig. 6** Ball-and-stick plot of the C<sub>60</sub>F<sub>48</sub> · 2 C<sub>6</sub>H<sub>3</sub>Me<sub>3</sub> formula unit determined by X-ray crystallography (C<sub>6</sub>H<sub>3</sub>Me<sub>3</sub> = 1,3,5-C<sub>6</sub>H<sub>3</sub>Me<sub>3</sub> = mesitylene). Hydrogen atoms on the mesitylene molecules have been omitted for clarity. The open and hatched circles represent C and F atoms, respectively. The distances between the three molecules are to scale.

lie directly above and below the molecule along the C<sub>3</sub> symmetry axis. Further solid state and solution studies will be needed to more fully understand the relative solubilities of fullerenes and FFs.

As far as oxygenated solvents are concerned, the early literature must, once again, be approached with caution. For example, acetone and tetrahydrofuran (THF) were used in the early 1990s to extract FFs from reaction vessels.<sup>[28,29]</sup> It was later found that these solvents, as well as methanol, completely degrade FFs with 36 or more F atoms, even to the point of rupturing the C<sub>60</sub> cage.<sup>[60]</sup> The decomposition rate in THF increased as the residual water content of the solvent increased. On the other hand, C<sub>60</sub>F<sub>18</sub> has recently been found to be stable for weeks in carefully dried THF or 1,2-dimethoxyethane.<sup>[61]</sup>

### Thermodynamic Properties

The compositional purity, thermal stability, and availability of gram quantities of C<sub>60</sub>F<sub>18</sub>, C<sub>60</sub>F<sub>36</sub>, and C<sub>60</sub>F<sub>48</sub> have allowed some of their thermodynamic properties to be investigated. Selected data are listed in Table 3.<sup>[13,62–65]</sup>

The vaporization properties of all three compounds have been studied<sup>[66,67]</sup> and parallel the sublimation enthalpies listed in Table 3. The vapor pressure of C<sub>60</sub>F<sub>48</sub> is marginally higher than that of C<sub>60</sub>F<sub>36</sub> (e.g., 0.45 vs. 0.17 Pa, respectively, at 560 K).<sup>[68]</sup> The major isomers of these compounds are either non-polar or have negligible polarity; they are spheroidal, essentially non-polarizable, fluorocarbon nanoparticles with weak intermolecular interactions. In contrast, the vapor pressures of C<sub>60</sub> and C<sub>60</sub>F<sub>18</sub> are orders of magnitude lower, but for different reasons. The extended  $\pi$ -electron system in C<sub>60</sub> renders its polarizable, which leads to a relatively large sublimation enthalpy. On the other hand, the large dipole moment of C<sub>60</sub>F<sub>18</sub> leads to strong intermolecular interactions and a large sublimation enthalpy.

**Table 3** Thermodynamic properties (kJ mol<sup>-1</sup>) of fluorofullerenes and C<sub>60</sub>

Compound	$\Delta_f H_m^o(c)^a$	$\Delta_{\text{sub}} H_m^o b$	$\Delta_f H_m^o(g)^c$	Ave. BDE(C-F)
C <sub>60</sub> F <sub>48</sub>	-7563 ± 166	130 ± 7	-7454 ± 166	287 ± 4
C <sub>60</sub> F <sub>36</sub>	-5362 ± 201	139 ± 8	-5223 ± 201	295 ± 6
C <sub>60</sub> F <sub>18</sub>		202 ± 10	-1450 <sup>d</sup>	302
C <sub>60</sub>	-2355 ± 15	174 ± 6	-2586 ± 14	

$\Delta_f H_m^o(c)$  = standard molar enthalpy of formation of the crystalline solid;  $\Delta_{\text{sub}} H_m^o$  = standard molar enthalpy of sublimation;  $\Delta_f H_m^o(g)$  = standard molar enthalpy of formation of the gaseous substance; Ave. BDE(C-F) = average C-F bond dissociation energy.

<sup>a</sup>Data from Refs.<sup>[13]</sup> (C<sub>60</sub>F<sub>48</sub>),<sup>[63]</sup> (C<sub>60</sub>F<sub>36</sub>), and <sup>[62]</sup> (C<sub>60</sub>).

<sup>b</sup>Data from Refs.<sup>[64,66]</sup>.

<sup>c</sup>Sum of the values in the first two columns except for C<sub>60</sub>F<sub>18</sub>.

<sup>d</sup>Average of the two theoretical values (-1400 and -1500 kJ mol<sup>-1</sup>) reported in Ref.<sup>[65]</sup>.

Combustion calorimetry was used to measure standard molar enthalpies of formation,  $\Delta_f H_m^o$ , both in the solid state and in the gas phase (the two values differ only by the standard molar enthalpies of sublimation).<sup>[13,62,63]</sup> The importance of these measurements is that it allowed the average C-F bond dissociation energies, ca. 290 kJ mol<sup>-1</sup>, to be determined. Temperature-dependent heat capacity measurements for C<sub>60</sub>F<sub>36</sub> revealed an order-disorder phase transition at 329.6 K ( $\Delta_{\text{trs}} H^o = 7$  kJ mol<sup>-1</sup>).<sup>[69,70]</sup> An ordered body-centered tetragonal to plastic face-centered cubic phase transition was also observed in a variable temperature X-ray diffraction study.<sup>c</sup>

### Properties of Fluorofullerene Ions

Ionic properties of FFs have been of particular interest to both gas-phase and solution chemists as the expectation was that addition of many electronegative F atoms should significantly enhance the electron accepting ability of the fullerene. Indeed, the very first measurements of EA(C<sub>60</sub>F<sub>2</sub>)<sup>[71]</sup> and EA(C<sub>60</sub>F<sub>46,48</sub>)<sup>[72]</sup> showed them to be 2.72 and 4.06 eV, respectively, higher than EA(C<sub>60</sub>), which is 2.67 eV.<sup>[73]</sup> Even more remarkable was the discovery made by gas-phase scientists that FFs formed doubly charged anions in the gas phase either under high-energy collisions of C<sub>60</sub>F<sub>x</sub><sup>-</sup> with inert gases<sup>[74]</sup> or as the result of a thermal desorption electron-capture process.<sup>[69,70]</sup> In the latter case, C<sub>60</sub>F<sub>48</sub><sup>2-</sup> was found to be exceptionally stable toward ejection of the second electron under collision conditions, or in the process of metastable decay, this was explained by the existence of the Coulomb barrier to the removal of the excess electron. The ability to form stable negative ions is a manifestation of the exceptional electron-withdrawing character of FFs. Another manifestation was observed in electrochemical studies of C<sub>60</sub>F<sub>48</sub>,<sup>[75]</sup> C<sub>60</sub>F<sub>36</sub>,<sup>[76]</sup> and C<sub>60</sub>F<sub>18</sub>,<sup>[77]</sup> with reported

$E_{\text{red}}$  values of 1.38, 0.58 and 0.04 V, respectively, vs. SCE [cf.  $E_{\text{red}}(\text{C}_{60}) = -0.43$  V vs. SCE].<sup>[77]</sup> The FF C<sub>60</sub>F<sub>48</sub> is believed to have the most positive  $E_{\text{red}}$  among known organic electron acceptors. A comparison of EAs<sup>[77]</sup> and  $E_{\text{red}}$  values shows that, as expected, the electron-accepting ability of FFs increases as the number of F atoms increases.

## CHEMICAL PROPERTIES OF FLUOROFULLERENES

### Formation of Oxafluorofullerenes

In a series of earlier papers,<sup>[5,6,78]</sup> considerable attention was paid to the presence of oxygenated fluorofullerene species C<sub>60</sub>F<sub>x</sub>O<sub>y</sub> in the products of some fluorination reactions (with F<sub>2</sub>, interhalogens, or XeF<sub>2</sub>). The origin of these by-products was believed to be either exposure of fluorofullerenes in air or formation during the synthesis because of the presence of adventitious O<sub>2</sub> or H<sub>2</sub>O. However, the first hypothesis was not confirmed as solid FFs can be kept in open air for years without any change in chemical composition (O.V. Boltalina, unpublished data). The latter reason seems more feasible; moreover, this is confirmed by direct observations by the MSU group of the increased content of C<sub>60</sub>F<sub>34</sub>O (or C<sub>60</sub>F<sub>18</sub>O) in the crude product of reaction between C<sub>60</sub> and MnF<sub>3</sub> (or K<sub>2</sub>PtF<sub>6</sub>), used for large-scale preparation of C<sub>60</sub>F<sub>36</sub> (or C<sub>60</sub>F<sub>18</sub>) under reduced pressure of 10<sup>-2</sup> Torr, in comparison with the product obtained in situ in a mass spectrometer (pressure 10<sup>-6</sup> Torr).<sup>[79]</sup> A similar effect, i.e., the enhanced formation of oxygen-containing species, also occurred in the presence of hydrolysis products of some fluorinating reagents, such as high-valent metal fluorides.

### Addition Reactions

The chemistry of C<sub>60</sub> includes the attachment of pairs of atoms or groups of atoms across double bonds,

<sup>c</sup>Poster presented by O.V. Boltalina et al. at 15th International Conference on Chemical Thermodynamics, Porto, Portugal (July, 2001).

resulting in  $C_{60}X_x$  derivatives, and various types of cycloadditions yielding monoadducts, bisadducts, or polyadducts.<sup>[9]</sup> If a fullerene derivative with some of its reaction sites occupied is used in an addition reaction, one might expect a more restricted set of products with fewer added functional groups. The simplest examples that can be found in the literature are further fluorinations of FF substrates with specific compositions:  $C_{60}F_{18}$ ,<sup>[80]</sup>  $C_{60}F_{36}$ ,<sup>[81]</sup> and  $C_{60}F_{48}$ .<sup>[82]</sup> The latter substrate was used in a reaction with  $F_2$  in an attempt to achieve a higher degree of fluorination. However, the reaction led to the rupture of the fluorofullerene cage. In case of fluorinations of  $C_{60}F_{18}$  with  $MnF_3$  and  $C_{60}F_{36}$  with  $F_2$  or  $XeF_2$ , selective formation of  $C_{60}F_{36}$  and  $C_{60}F_{48}$ , respectively, with the expected isomer compositions, were reported. This is another piece of evidence confirming the stability of specific isomers of [60]fullerenes with 36 and 48 F atoms.

At present,  $C_{60}F_{18}$ , with its bare hemisphere, and other FFs with relatively few F atoms, appear to be the most suitable substrates for addition chemistry. The availability of these compounds allows one to explore reactions similar to those carried out with pristine  $C_{60}$ . At present, only a few examples have been reported: reactions of anthracene with  $C_{60}F_{18}$  and  $C_{60}F_{20}$ <sup>[83,84]</sup> and reaction of  $C_{60}F_{18}$  with tetrathiafulvalene (TTF).<sup>[85]</sup> In the reaction with anthracene, only 1:1 cycloaddition products were formed with both FFs because of steric hindrance caused by the presence of F atoms on the cage, while  $C_{60}$  itself formed monoadducts and several bisadducts in similar reactions. In the case of addition of TTF to  $C_{60}F_{18}$ , six-electron cycloaddition occurred through the terminal C=C bond in the fulvalene (accompanied by elimination of two F atoms) and yielded as a main product an asymmetric  $C_{60}F_{16} \cdot TTF$  monoadduct. Another recent example concerns the  $CF_3$ -radical addition to  $C_{60}F_{18}$ , with silver trifluoroacetate used as source of trifluoromethyl radicals. Gas-phase species with up to six attached trifluoromethyl groups to  $C_{60}F_{18}$  were observed by mass spectrometry.<sup>[44]</sup>

## Substitution Reactions

Earlier reports on the chemical reactivity of FFs involved impure mixtures, so isolation and characterization of the products was not achieved. These studies concerned introduction of the phenyl and methyl groups<sup>[86]</sup> or the formation of various hydroxides and oxides from hydrolysis reaction of relatively compositionally pure  $C_{60}F_{36}$ , although characterization of those products was not complete.<sup>[87]</sup> Two types of substitution reactions were more systematically studied using  $C_{60}F_{18}$  as a substrate: electrophilic substitutions into aromatics in the presence of Lewis acid catalyst

and nucleophilic substitutions. The first study of the phenylation of  $C_{60}F_{18}$ , in which  $FeCl_3$  was used as the catalyst, resulted in the formation of a triphenylated derivative.<sup>[51]</sup> This was followed by a more extensive study of a variety of aromatic addends.<sup>[88]</sup> Monosubstituted, disubstituted, and trisubstituted products  $C_{60}F_{18-n}Ar_n$  were isolated ( $n = 1-3$ ) for  $Ar = 4$ -tolyl, 4-methoxyphenyl, 4-phenoxyphenyl, and 4-chlorophenyl. In all cases, substitution occurred at the three least sterically hindered F atoms (the F atoms outside of the 15-F-atom belt in  $C_{60}F_{18}$ ). For the bulky substituents  $Ar = 2$ -fluorenyl, 2-biphenyl, and 1- and 2-naphthyl, monoadducts  $C_{60}F_{17}Ar$  were the dominant products. The Lewis acids  $SbF_5$  and  $TiCl_4$  were also found to be effective catalysts for these reactions.

The reaction of a fluorofullerene with a bromomalonate diester (Bingel reaction) was first studied by MALDI mass spectrometry and resulted in the substitution of up to three F atoms with bromomalonate groups (A.L. Mirakyan, personal communication to O.V. Botalina, 2000). Later isolation and spectroscopic and crystallographic characterization of the monosubstituted, disubstituted, and trisubstituted products revealed that instead of the expected (by analogy with similar reaction of  $C_{60}$ ) methanofullerene formation, nucleophilic substitution of up to three bromomalonate groups for F atoms in  $C_{60}F_{18}$  occurred, with the three F atoms leaving from the least sterically hindered positions. The trisadduct had a prominent emerald-green color because of the formation of  $18\pi$  annulene belt of electrons with high conjugation.<sup>[54]</sup> This new type of fluorofullerene derivative with various electron-donor substituents was extensively studied with the goal of designing of donor-acceptor systems to be probed in photovoltaic devices.<sup>[89]</sup> Mono- and bis-addition products of the Prato reaction with  $C_{60}F_{18}$  ([3 + 2] dipolar cycloaddition with aldehydes and amino acids) were obtained, with a much greater variety of isomeric products than in the case of Prato reactions with  $C_{60}$ .<sup>[90]</sup>

## CONCLUSION

The first decade of the fluorine chemistry of fullerenes has passed. Joint efforts of research chemists worldwide laid the foundation for further developments in this fascinating branch of fullerene chemistry. At present, fluorine-containing fullerenes represent the largest group of derivatives with the same single substituent that have been synthesized in macroscopic amounts, isolated into specific compositionally and/or isomerically pure compounds, and fully or partially structurally characterized. Fundamental physical quantities such as formation enthalpies, vapor pressures, heat capacities,

reduction potentials, ionization energies, and electron affinities were determined for few specific fluorofullerenes, which constitutes the basis for more advanced theoretical and experimental physical-chemical and chemical studies with these compounds. Developments of new non-conventional approaches to the preparation of fluorine-containing derivatives provides hope that compounds with new compositions and structures will be obtained in the future.

Basic physical properties such as solubility, stability, thermal resistance, and resistance toward light and moisture were studied, all showing that fluorofullerenes represent a promising class of new chemical materials, sufficiently robust to be probed/examined/used for various practical applications. Although the high price remains an obstacle for advancing these materials, as it does for other fullerene-related applications, recent activities of large international companies as well as small nanotech businesses should bring down the prices of fullerenes once planned ton-scale production facilities come on line.

As for the possible applications of fluorinated fullerenes that were discussed in the past decade, which include their use as cathode materials in Li-batteries, as lubricants, and as oxidizing and fluorinating reagents, more research with pure materials under controlled conditions is needed (early reports on the performance of FFs in batteries or as lubricants were based on studies with complex mixtures of FFs contaminated with various oxafuorofullerenes). Current interest in the use of FFs in photovoltaic devices is based on their ability to function as good electron acceptors. In this regard, the report that the charge-transfer lifetime of a complex of  $C_{60}F_{18}$  and tetrathiofulvalene is 780 nsec is very promising.<sup>[91]</sup> The possibility that FFs might be useful in lithography technologies has also been suggested recently.<sup>[92]</sup>

## REFERENCES

- Kroto, H.W.; Heath, J.R.; O'Brien, S.C.; Curl, R.F.; Smalley, R.E.  $C_{60}$ : buckminsterfullerene. *Nature* **1985**, *318*, 162–163.
- Kratschmer, W.; Lamb, L.D.; Fostiropoulos, K.; Huffman, D.R. Solid  $C_{60}$ : a new form of carbon. *Nature* **1990**, *347*, 354.
- Selig, H.; Lifshitz, C.; Peres, T.; Fischer, J.E.; McGhie, A.R.; Romanov, W.J.; McCauley, J.P.; Smith, A.B. Fluorinated fullerenes. *J. Am. Chem. Soc.* **1991**, *113*, 5475–5476.
- Powell, W.H.; Cozzi, F.; Moss, G.P.; Thilgen, C.; Hwu, R.J.-R.; Yerin, A. Nomenclature for the  $C_{60}-I_h$  and  $C_{70}-D_{5h}(6)$  fullerenes (IUPAC recommendations 2002). *Pure Appl. Chem.* **2002**, *744*, 629–695.
- Selig, H.; Kniaz, K.; Vaughan, G.B.M.; Fischer, J.E.; Smith, A.B. Fluorinated fullerenes: Synthesis and characterization. *Macromol. Symp.* **1994**, *82*, 89–97.
- Taylor, R.; Langley, G.J.; Bridson, A.K.; Holloway, J.H.; Hope, E.G.; Kroto, H.W.; Walton, D.R.M. Highly oxygenated derivatives of fluorinated  $C_{60}$ , and the mode of fragmentation of the fluorinated cage under electron impact ionization conditions. *J. Chem. Soc., Chem. Commun.* **1993**, 875–878.
- Taylor, R.; Avent, A.G.; Dennis, T.J.; Hare, J.P.; Kroto, H.W.; Walton, D.R.M.; Holloway, J.H.; Hope, E.G.; Langley, J.J. No lubricants from fluorinated  $C_{60}$ . *Nature* **1992**, *355*, 27.
- [www.webelements.com/webelements/compounds/text/C/C60F60-134929592.html](http://www.webelements.com/webelements/compounds/text/C/C60F60-134929592.html) (accessed March 2003).
- Wilson, S.R.; Schuster, D.I.; Nuber, B.; Meier, M.S.; Maggini, M.; Prato, M.; Taylor, R. Organic chemistry of fullerenes. In *Fullerenes: Chemistry, Physics, and Technology*; Kadish, K.M., Ruoff, R.S., Eds.; Wiley-Interscience: New York, 2000; 91–176.
- Gakh, A.A.; Tuinman, A.A.; Adcock, J.L.; Sachleben, R.A.; Compton, R.N. Selective synthesis and structural characterization of  $C_{60}F_{48}$ . *J. Am. Chem. Soc.* **1994**, *116*, 819–820.
- Bagryantsev, V.F.; Zapol'skii, A.S.; Boltalina, O.V.; Galeva, N.A.; Sidorov, L.N. Synthesis of  $C_{60}F_{48}$  in the reaction of  $C_{60}$  with molecular fluorine. *Dokl. Akad. Nauk* **1997**, *3574*, 487–489.
- Troyanov, S.I.; Troshin, P.A.; Boltalina, O.V.; Ioffe, I.N.; Sidorov, L.N.; Kemnitz, E. Two isomers of  $C_{60}F_{48}$ : an indented fullerene. *Angew. Chem., Int. Ed.* **2001**, *4012*, 2285–2287.
- Papina, T.S.; Kolesov, V.P.; Lukyanova, V.A.; Boltalina, O.V.; Galeva, N.A.; Sidorov, L.N. The standard molar enthalpy of formation of fluorofullerene  $C_{60}F_{48}$ . *J. Chem. Thermodyn.* **1999**, *3110*, 1321–1328.
- Boltalina, O.V.; Markov, V.Y.; Lukonin, A.Y.; Avakjan, T.V.; Ponomarev, D.B.; Sorokin, I.D.; Sidorov, L.N. Mass spectrometric measurements of the equilibrium constants of ion molecular reactions of fullerenes, fluorine derivatives and endohedrals. electron and fluorine affinity estimates. In *Recent Advances in the Chemistry and Physics of Fullerenes and Related Materials*; Kadish, K.M., Ruoff, R.S., Eds.; Electrochemical Society: Pennington, NJ, 1995; Vol. 95-10, 1395–1408.
- Boltalina, O.V.; Borschevskii, A.Y.; Sidorov, L.N.; Street, J.M.; Taylor, R. Preparation of  $C_{60}F_{36}$  and  $C_{70}F_{36/38/40}$ . *Chem. Commun.* **1996**, 529–530.
- Boltalina, O.V.; Markov, V.Y.; Taylor, R.; Waugh, M.P. Preparation and characterization of  $C_{60}F_{18}$ . *Chem. Commun.* **1996**, 2549–2550.
- Boltalina, O.V.; Lukonin, A.Y.; Street, J.M.; Taylor, R.  $C_{60}F_2$  exists! *Chem. Commun.* **2000**, 1601–1602.
- Boltalina, O.V.; Darwish, A.D.; Street, J.M.; Taylor, R.; Wei, X.W. Isolation and characterization of  $C_{60}F_4$ ,  $C_{60}F_6$ ,  $C_{60}F_8$ ,  $C_{60}F_7CF_3$  and  $C_{60}F_2O$ , the smallest oxahomofullerene; the mechanism of fluorine addition to fullerenes. *J. Chem. Soc., Perkin Trans. 2* **2002**, 251–256.
- Boltalina, O.V.; Markov, V.Y.; Troshin, P.A.; Darwish, A.D.; Street, J.M.; Taylor, R.  $C_{60}F_{20}$ : “Saturnene,” an extraordinary squashed fullerene. *Angew. Chem., Int. Ed.* **2001**, *404*, 787–789.

20. Boltalina, O.V.; Lukonin, A.Y.; Avent, A.G.; Street, J.M.; Taylor, R. Formation and characterization of  $C_{60}F_8O$ ,  $C_{60}F_6O$ , and  $C_{60}F_4O$ ; the sequential pathway for addition to fullerenes. *J. Chem. Soc., Perkin Trans. 2* **2000**, 683–686.
21. Avent, A.G.; Boltalina, O.V.; Lukonin, A.Y.; Street, J.M.; Taylor, R. Isolation and characterization of  $C_{60}F_{16}$ ; a key to understanding fullerene addition patterns. *J. Chem. Soc., Perkin Trans. 2* **2000**, 1359–1361.
22. Boltalina, O.V.; de La Vaissiere, B.; Lukonin, A.Y.; Fowler, P.W.; Abdul-Sada, A.K.; Street, J.M.; Taylor, R. Isolation and characterisation of bis(oxahomo)fullerene derivatives of  $C_{60}F_{18}$ . *J. Chem. Soc., Perkin Trans. 2* **2001**, 550–556.
23. Boltalina, O.V.; de La Vaissiere, B.; Fowler, P.W.; Lukonin, A.Y.; Abdul-Sada, A.K.; Street, J.M.; Taylor, R. Isolation and characterization of two oxahomofullerene derivatives of  $C_{60}F_{18}$ . *J. Chem. Soc., Perkin Trans. 2* **2000**, 2212–2216.
24. Boltalina, O.V.; Troshin, P.A.; de La Vaissiere, B.; Fowler, P.W.; Sandall, J.P.B.; Hitchcock, P.B.; Taylor, R.  $C_{60}F_{18}O$ , the first characterised intramolecular fullerene ether. *Chem. Commun.* **2000**, 1325–1326.
25. Avent, A.G.; Boltalina, O.V.; Goryunkov, A.A.; Darwish, A.D.; Markov, V.Y.; Taylor, R. Isolation and characterisation of  $C_{60}(CF_3)_2$ . *Fuller. Nanotub. Carbon Nanostruct.* **2002**, *103*, 235–241.
26. Boltalina, O.V.; Galeva, N.A. Direct fluorination of fullerenes. *Russ. Chem. Rev.* **2000**, *69*, 609–621.
27. Chilingarov, N.S.; Nikitin, A.V.; Rau, J.V.; Golyushevskii, I.V.; Kepman, A.V.; Spiridonov, F.M.; Sidorov, L.N. Selective formation of  $C_{60}F_{18}(g)$  by reaction of [60]fullerene with molecular fluorine. *J. Fluorine Chem.* **2002**, *113*, 219–226.
28. Holloway, J.H.; Hope, E.G.; Taylor, R.; Langley, G.J.; Avent, A.G.; Dennis, T.J.; Hare, J.P.; Kroto, H.W.; Walton, D.R.M. Fluorination of buckminsterfullerene. *J. Chem. Soc., Chem. Commun.* **1991**, 966–969.
29. Tuinman, A.A.; Muckherjee, P.; Adcock, J.L.; Hettich, R.L.; Compton, R.N. Characterization and stability of highly fluorinated fullerenes. *J. Phys. Chem.* **1992**, *96*, 7584–7589.
30. Matsuo, Y.; Nakajima, T.; Kasamatsu, S. Synthesis and spectroscopic study of fluorinated fullerene,  $C_{60}$ . *J. Fluorine Chem.* **1996**, *78*, 7–13.
31. Bagryantsev, V.F.; Zapol'skii, A.S.; Boltalina, O.V.; Galeva, N.A.; Sidorov, L.N. Reactions of fullerenes with difluorine. *Zh. Neorg. Khim.* **2000**, *457*, 1121–1127.
32. Denisenko, N.I.; Streletskii, A.V.; Boltalina, O.V. Investigation of fluorination reactions of the  $C_{60}Br_{24}$  bromofullerene with xenon difluoride. *Phys. Solid State* **2002**, *443*, 539–541.
33. Boltalina, O.V.; Abdul-Sada, A.K.; Taylor, R. Hyperfluorination of [60]fullerene by krypton difluoride. *J. Chem. Soc., Perkin Trans. 2* **1995**, 981–985.
34. Tuinman, A.A.; Gakh, A.A.; Adcock, J.L. [[Hyperfluorination of  $C_{60}$ ]]. *J. Am. Chem. Soc.* **1993**, *115*, 5885.
35. Bulusheva, L.G.; Okotrub, A.V.; Yudanov, N.F. Investigation of the electronic structure of  $C_{60}F_{24}$ . *J. Phys. Chem.* **1997**, *101*, 10,018–10,028.
36. Adamson, A.J.; Holloway, J.H.; Hope, E.G.; Taylor, R. Halogen and interhalogen reactions with [60]fullerene: Preparation and characterization of  $C_{60}Cl_{24}$  and  $C_{60}Cl_{18}F_{14}$ . *Fuller. Sci. Technol.* **1997**, *54*, 629–642.
37. Lukonin, A.Y.; Markov, V.Y.; Boltalina, O.V. Synthesis of fluorofullerenes by reaction with inorganic fluorides. *Vestn. Mosk. Univ., Ser. 2 Khim.* **2001**, *421*, 3–16.
38. Goldt, I.V.; Boltalina, O.V.; Kemnitz, E.; Troyanov, S.I. Synthesis and structure of solvent-free  $C_{60}F_{18}$ . *Solid State Sci.* **2002**, *4*, 1395–1401.
39. Goryunkov, A.A.; Markov, V.Y.; Boltalina, O.V.; Zemva, B.; Abdul-Sada, A.K.; Taylor, R. Reaction of silver(I) and -(II) fluorides with  $C_{60}$ : thermodynamic control over fluorination level. *J. Fluorine Chem.* **2001**, *1122*, 191–196.
40. Troshin, P.A.; Boltalina, O.V.; Polyakova, N.V.; Klinkina, Z.E. Novel synthetic route to fluorofullerenes: reaction with binary and complex lead fluorides. *J. Fluorine Chem.* **2001**, *1102*, 157–163.
41. Hamwi, A.; Latouche, C.; Burteaux, B.; Dupuis, J. Preparation and characterization of inorganic fluorides—fullerene compounds. *Fuller. Sci. Technol.* **1996**, *46*, 1213–1226.
42. Boltalina, O.V.; Avakyan, T.V.; Markov, V.Y.; Dennis, T.J.S.; Abdul-Sada, A.K.; Taylor, R. Formation of  $C_{76}F_{38}$ ,  $C_{78}F_{38}$ ,  $C_{82}F_{44}$ ,  $C_{84}F_{40}$ , and  $C_{84}F_{44}$ . *J. Phys. Chem., B* **1999**, *10338*, 8189–8191.
43. Abdul-Sada, A.K.; Avakyan, T.V.; Boltalina, O.V.; Markov, V.Y.; Street, J.M.; Taylor, R. Isolation and characterisation of fluorinated derivatives of [76]- and [78]fullerenes. *J. Chem. Soc., Perkin Trans. 2* **1999**, 2659–2666.
44. Boltalina, O.V.; Goryunkov, A.A.; Markov, V.Y.; Ioffe, I.N.; Sidorov, L.N. In situ synthesis and characterization of fullerene derivatives by Knudsen-cell mass spectrometry. *Int. J. Mass Spectrom.* **2003**, *228*, 807–828.
45. Abdul-Sada, A.K.; Darwish, A.D.; Taylor, R.; Boltalina, O.V.; Markov, V.Y.; Hirsch, A.; Reuther, U.; Street, J.M. Fluorination and hydrogenation of aza[60]fullerene ( $C_{59}N$ )<sub>2</sub>. In *Fullerenes: The Exciting World of Nanocages and Nanotubes*; Kamat, P.V., Guldi, D.M., Kadish, K.M., Eds.; Electrochem. Soc.: Pennington, NJ, 2002; Vol. 2002-12, 242–252.
46. Neretin, I.S.; Lyssenko, K.A.; Antipin, M.Y.; Slovokhotov, Y.L.; Boltalina, O.V.; Troshin, P.A.; Lukonin, A.Y.; Sidorov, L.N.; Taylor, R.  $C_{60}F_{18}$ , a flattened fullerene: alias a hexasubstituted benzene. *Angew. Chem., Int. Ed.* **2000**, *3918*, 3273–3276.
47. Troyanov, S.I.; Boltalina, O.V.; Kouvytchko, I.V.; Troshin, P.A.; Kemnitz, E.; Hitchcock, P.B.; Taylor, R. Molecular and crystal structure of the adducts of  $C_{60}F_{18}$  with aromatic hydrocarbons. *Fuller. Nanotub. Carbon Nanostruct.* **2002**, *103*, 243–259.
48. Clare, B.W.; Kepert, D.L. Early stages in the addition to  $C_{60}$  to form  $C_{60}X_n$ ,  $X = H, F, Cl, Br, CH_3, C_4H_9$ . *J. Mol. Struct., Theochem.* **2003**, *621*, 211–231.
49. Avent, A.G.; Boltalina, O.V.; Lukonin, A.Y.; Street, J.M.; Taylor, R. Isolation and spectroscopic characterization of  $C_{60}F_{18}CF_2$ , the first difluoromethano[60]fullerene. *J. Chem. Soc., Perkin Trans. 2* **2000**, 1–3.

50. Boltalina, O.V.; Hitchcock, P.B.; Troshin, P.A.; Street, J.M.; Taylor, R. Isolation and spectroscopic characterization of  $C_{60}F_{17}CF_2CF_3$  and isomers of  $C_{60}F_{17}CF_3$ ; insertion of  $:CF_2$  into fluorofullerene C–F bonds. *J. Chem. Soc., Perkin Trans. 2* **2000**, 2410–2414.
51. Boltalina, O.V.; Holloway, J.H.; Hope, E.G.; Street, J.M.; Taylor, R. Isolation of oxides and hydroxides derived from fluorofullerenes. *J. Chem. Soc., Perkin Trans. 2* **1998**, 1845–1850.
52. Avent, A.G.; Boltalina, O.V.; Fowler, P.W.; Lukonin, A.Y.; Pavlovich, V.K.; Sandall, J.P.B.; Street, J.M.; Taylor, R.  $C_{60}F_{18}O$ : isolation, spectroscopic characterization and structural calculations. *J. Chem. Soc., Perkin Trans. 2* **1998**, 1319–1322.
53. Chowdhury, S.W.; Cameron, S.D.; Cox, D.M.; Kniaz, K.; Strongin, R.A.; Cichy, M.A.; Fischer, J.E.; Smith, A.B. Mass-spectrometric investigation of polyfluorinated  $C_{60}$  evidence for the existence of  $C_{60}F_{2n}$  ( $n = 0–30$ ). *Org. Mass Spectrom.* **1993**, *28*, 860–866.
54. Wei, X.-W.; Darwish, A.D.; Boltalina, O.V.; Hitchcock, P.B.; Street, J.M.; Taylor, R. The remarkable stable emerald green  $C_{60}F_{15}[CBr(CO_2Et)_2]_3$ : the first [60]fullerene that is also the first [18]trannulene. *J. Chem. Soc., Perkin Trans. 2* **2001**, 2989–2992.
55. Boltalina, O.V.; Street, J.M.; Taylor, R.  $C_{60}F_{36}$  consists of two isomers having  $T$  and  $C_3$  symmetry. *J. Chem. Soc., Perkin Trans. 2* **1998**, 649–654.
56. Hitchcock, P.B.; Taylor, R. Single crystal X-ray structure of tetrahedral  $C_{60}F_{36}$ : the most aromatic and distorted fullerene. *Chem. Commun.* **2002**, 2078–2079.
57. Gakh, A.A.; Tuinman, A.A. Structure of  $C_{60}F_{36}$ . *Tetrahedron Lett.* **2001**, *42*, 7137–7139.
58. Avent, A.G.; Clare, B.W.; Hitchcock, P.B.; Kepert, D.L.; Taylor, R.  $C_{60}F_{36}$ : there is a third isomer and it has  $C_1$  symmetry. *Chem. Commun.* **2002**, 2370–2371.
59. Makeev, Y.A. Physico-Chemical Properties of the Fluorofullerene-Organic Solvent Systems. Ph.D. Dissertation; Moscow State University, 2001.
60. Boltalina, O.V.; Sidorov, L.N.; Bagryantsev, V.F.; Seredenko, V.A.; Zapol'skii, A.S.; Street, J.M.; Taylor, R. Formation of  $C_{60}F_{48}$  and fluorides of higher fullerenes. *J. Chem. Soc., Perkin Trans. 2* **1996**, 2275–2278.
61. Boltalina, O.V.; Ioffe, I.N.; Makeev, Y.A.; Denisenko, N.I.; Goryunkov, A.A.; Markov, V.Y.; Streletskii, A.S. Stabilities, hydrolysis reactions and further fluorinations of  $C_{60}F_x$  compounds. Book of Abstract, 201st Electrochemical Society Meeting, **2002**, Abstract 932.
62. Kolesov, V.P.; Pimenova, S.M.; Pavlovich, V.K.; Tamm, N.B.; Kurskaya, A.A. Enthalpies of combustion and formation of fullerene  $C_{60}$ . *J. Chem. Thermodyn.* **1996**, *28*, 1121–1125.
63. Papina, T.S.; Kolesov, V.P.; Lukyanova, V.A.; Boltalina, O.V.; Lukonin, A.Y.; Sidorov, L.N. Enthalpy of formation and C–F bond enthalpy of fluorofullerene  $C_{60}F_{36}$ . *J. Phys. Chem., B* **2000**, *10423*, 5403–5405.
64. Gigli, G.; Nunziante, C.S.; Rau, J.V.; Goldt, I.V.; Markov, V.Y.; Goryunkov, A.A.; Popov, A.A.; Boltalina, O.V.; Sidorov, L.N. Recent Thermodynamic and Spectroscopic Studies of  $C_{60}F_{18}$ . In *Fullerenes*; Guldi, D., Kamat, P.V., Kadish, K.M., Eds.; Electrochemical Society: Pennington, NJ, 2003; Vol. 2003-13.
65. Cioslowski, J.; Rao, N.; Szarecka, A.; Pernal, K. Theoretical thermochemistry of the  $C_{60}F_{18}$ ,  $C_{60}F_{36}$  and  $C_{60}F_{48}$  fluorofullerenes. *Mol. Phys.* **2001**, *99*, 1229–1232.
66. Boltalina, O.V.; Markov, V.Y.; Borchshevskii, A.Y.; Galeva, N.A.; Pavlovich, V.K.; Sidorov, L.N.; Gigli, G.; Balducci, G.; Bardi, G. Saturated vapor pressure of  $C_{60}F_{36}$ . *Mol. Cryst. Liq. Cryst. Sci. Technol., Sect. C* **1998**, *101-4*, 225–228.
67. Boltalina, O.V.; Markov, V.Y.; Borschevskii, A.Y.; Galeva, N.A.; Sidorov, L.N.; Gigli, G.; Balducci, G. Saturated vapor pressure and sublimation enthalpy of fluorine derivatives of  $C_{60}$ . *J. Phys. Chem., B* **1999**, *103*, 3828–3832.
68. Sidorov, L.N.; Boltalina, O.V. Endohedral metal derivatives and exohedral fluorine derivatives of fullerenes. *Russ. Chem. Rev.* **2002**, *717*, 535–561.
69. Druzhinina, A.I.; Galeva, N.A.; Varushchenko, R.M.; Boltalina, O.V.; Sidorov, L.N. The low temperature heat capacities and thermodynamic functions of fluorofullerenes  $C_{60}F_{48}$  and  $C_{60}F_{46}$ . In *Recent Advances in the Chemistry and Physics of Fullerenes and Related Materials*; Kadish, K.M., Ruoff, R.S., Eds.; Electrochem. Soc.: Pennington, NJ, 1998; Vol. 98-8, 1203–1211.
70. Druzhinina, A.I.; Galeva, N.A.; Varushchenko, R.M.; Boltalina, O.V.; Sidorov, L.N. The low temperature heat capacities of fluorofullerenes. *J. Chem. Thermodyn.* **1999**, *31*, 1469–1482.
71. Boltalina, O.V.; Sidorov, L.N.; Sukhanova, E.V.; Sorokin, I.D. Observation of difluorinated higher fullerene anions by Knudsen cell mass spectrometry and determination of electron affinities of  $C_{60}F_2$  and  $C_{70}F_2$ . *Chem. Phys. Lett.* **1994**, *2306*, 567–570.
72. Jin, C.; Hettich, R.L.; Compton, R.N.; Tuinman, A.; Derecskei-Kovacs, A.; Marynick, D.S.; Dunlap, B.I. Attachment of two electrons to  $C_{60}F_{48}$ : Coulomb barriers in doubly charged anions. *Phys. Rev. Lett.* **1994**, *73*, 2821–2824.
73. Brink, C.; Andersen, L.H.; Hvelplund, P.; Mathur, D.; Voldstad, J.D. Laser photodetachment of  $C_{60}^-$  and  $C_{70}^-$  ions cooled in a storage ring. *Chem. Phys. Lett.* **1995**, *233*, 52.
74. Boltalina, O.V.; Hvelplund, P.; Jorgensen, T.J.D.; Larsen, M.C.; Larsson, M.O.; Sharoitchemko, D.A. Electron capture by fluorinated fullerene anions in collisions with Xe atoms. *Phys. Rev., A* **2000**, *62*, 023202-1-023202-7.
75. Zou, F.; Van Berkel, G.J.; Donovan, B.T. Electron transfer reactions of  $C_{60}F_{48}$ . *J. Am. Chem. Soc.* **1994**, *116*, 5485–5486.
76. Liu, N.; Y., M.; Okino, F.; Touhara, H.; Boltalina, O.V.; Pavlovich, V.K. Electrochemical properties of  $C_{60}F_{36}$ . *Synth. Met.* **1997**, *86*, 2289–2290.
77. Ohkubo, K.; Taylor, R.; Boltalina, O.V.; Ogo, S.; Fukuzumi, S. Electron transfer reduction of a highly electron-deficient fullerene,  $C_{60}F_{18}$ . *Chem. Commun.* **2002**, 1952–1953.
78. Hamwi, A.; Fabre, C.; Chaurand, P.; Della-Nega, S.; Ciot, C.; Djurado, D.; Dupuis, J.; Rassat, A. Preparation and characterization of fluorinated fullerenes. *Fuller. Sci. Technol.* **1993**, *1*, 499–535.



79. Lukonin, A.Y. Synthesis of Fluorofullerenes in Reactions with Inorganic Fluorides and Some Physical Chemical Properties. Ph.D. Dissertation; Moscow State University, 2002.
80. Boltalina, O.V.; Buhl, M.; Khong, A.; Saunders, M.; Street, J.M.; Taylor, R. The  $^3\text{He}$  NMR spectra of  $\text{C}_{60}\text{F}_{18}$  and  $\text{C}_{60}\text{F}_{36}$ ; the parallel between hydrogenation and fluorination. *J. Chem. Soc., Perkin Trans. 2* **1999**, 1475–1479.
81. Gakh, A.A.; Tuinman, A.A. ‘Fluorine dance’ on the fullerene surface. *Tetrahedron Lett.* **2001**, *42*, 7137–7139.
82. Gakh, A.A.; Tuinman, A.A. Chemical fragmentation of  $\text{C}_{60}\text{F}_{48}$ . *J. Phys. Chem., A* **2000**, *104*, 5888–5891.
83. Avent, A.G.; Boltalina, O.V.; Street, J.M.; Taylor, R.; Wei, X.-W. The [4 + 2] cycloaddition of anthracene with  $\text{C}_{60}\text{F}_{18}$ ; anthracene goes ring walking. *J. Chem. Soc., Perkin Trans. 2* **2001**, 994–997.
84. Avent, A.G.; Boltalina, O.V.; Street, J.M.; Taylor, R.; Troshin, P.A.; Wei, X.-W. The reaction of  $\text{C}_{60}\text{F}_{20}$  with anthracene: formation of an oxidised-anthracene 1:1 complex. *Fuller. Nanotub. Carbon Nanostruct.* **2002**, *103*, 227–233.
85. Darwish, A.D.; Avent, A.G.; Boltalina, O.V.; Gol’dt, I.V.; Kuvytko, I.V.; da Ros, T.; Taylor, R. Formation of novel sulphur-containing  $\text{C}_{60}\text{F}_{16}$  cycloadducts through reaction of etraethiofulvalene with  $\text{C}_{60}\text{F}_{18}$ . *Chem. Eur. J.* **2003**, *9*, 2008–2012.
86. Mickelson, E.T.; Hauge, R.H.; Margrave, J.I. Methylated and phenylated  $\text{C}_{60}$  from fluorinated fullerene precursors. *J. Fluorine Chem.* **1998**, *92*, 59–62.
87. Boltalina, O.V.; Taylor, R.; Street, J.M. Formation of triumphene,  $\text{C}_{60}\text{F}_{15}\text{Ph}_3$ : first member of a new trefoil-shaped class of phenylated [60]fullerenes. *Chem. Commun.* **1998**, 1827–1828.
88. Darwish, A.D.; Avent, A.G.; Abdul-Sada, A.K.; Boltalina, O.V.; Kuvytko, I.V.; Hitchcock, P.B.; Taylor, R. Electrophilic aromatic substitution by the fluorofullerene  $\text{C}_{60}\text{F}_{18}$ . *J. Chem. Soc., Perkin Trans. 2* **2003**, *in press*.
89. Burley, G.A.; Avent, A.G.; Boltalina, O.V.; Drewello, T.; Gol’dt, I.V.; Marcaccio, M.; Paolucci, D.; Street, J.M.; Taylor, R. Synthesis of 18- $\pi$ -annulenic fluorofullerenes from tertiary carbanions: Size matters! **2003**, *1*, 2015–2024.
90. Burley, G.A.; Avent, A.G.; Boltalina, O.V.; Gol’dt, I.V.; Guldi, D.; Marcaccio, M.; Pauloucci, F.; Paolucci, D.; Taylor, R. A light-harvesting fluorinated fullerene donor–acceptor ensemble. Long-lived charge separation. *Chem. Commun.* **2003**, 148–149.
91. Fujikawa, Y.; Sadowski, J.T.; Kelly, K.F.; Nakayama, K.C.; Mickelson, E.T.; Hauge, R.H.; Margrave, J.I.; Sakurai, T.J. Adsorption of fluorinated  $\text{C}_{60}$  on the Si(111)-(7  $\times$  7) surface studied by scanning tunneling microscopy and high-resolution electron-energy loss spectroscopy. *J. Appl. Phys.* **2002**, *41*, 245–249.
92. Wei, X.-W.; Avent, A.G.; Boltalina, O.V.; Street, J.M.; Taylor, R. Products from the reaction of  $\text{C}_{60}\text{F}_{18}$  with sarcosine and aldehydes: the Prato reaction. *J. Chem. Soc., Perkin Trans. 2* **2002**, 47–52.

# Fullerenes and Carbon Nanotubes

Laszlo Mihaly

Department of Physics and Astronomy, State University of New York at Stony Brook,  
Stony Brook, New York, U.S.A.

## INTRODUCTION

The Nobel Prize winning discovery of fullerenes<sup>[1]</sup> initiated a new era in carbon chemistry. In addition to the two well-known allotropes, graphite and diamond, a large number of carbon structures were synthesized.<sup>[2–7]</sup> Here we will first discuss the structure of single- and multiwalled nanotubes and the nanotube “ropes.” The fullerene molecule (primarily the most abundant fullerene, C<sub>60</sub>), the polymerized, and doped fullerenes will be considered. We will review some of the physical properties, mostly focusing on the electronic structure: electrical conduction, superconductivity, and magnetism.

## MOLECULAR STRUCTURE

Conceptually, the new structures<sup>[1–7]</sup> can be derived from graphene, an sp<sup>2</sup>-bonded honeycomb lattice of carbon atoms, which is the basic element in the structure of graphite.<sup>[8]</sup> Assume each carbon atom is connected to three neighbors, the bond lengths are fixed to be the same, but the bond angles are a bit variable. If a long strip of graphene is cut out and bent into a cylinder, so that loose carbon bonds match up, we get a nanotube. The matching carbon atoms can be labeled by a chiral vector  $\mathbf{C}_h$ . This vector is represented by two basic vectors ( $\mathbf{a}_1$  and  $\mathbf{a}_2$ ) and by two integers ( $n_1$  and  $n_2$ );  $\mathbf{C}_h = n_1\mathbf{a}_1 + n_2\mathbf{a}_2$  (Fig. 2). Accordingly, the structure of every nanotube is unambiguously characterized by the  $\mathbf{C}_h$  vector; in a shorthand notation  $\mathbf{C}_h = (n_1, n_2)$ , so that  $n_1 \geq n_2$ . Based on the patterns visible on the nanotube they may be called “zigzag” (for  $n_2 = 0$ ; Fig. 1), “arm-chair” (for  $n_1 = n_2$ ), or “chiral” (for any other, see, for example, Fig. 2). The diameter of the nanotube is given by  $d = (a/\pi) [3(n_1^2 + n_1n_2 + n_2^2)]^{1/2}$ , where  $a = 0.144$  nm is the carbon–carbon distance. There is no upper limit on the size of the nanotube, although at large diameter the structure becomes very soft [except for multiwalled nanotubes (MWNT), see later]. For small diameter the carbon–carbon bonds are more strained, and the thinnest stable nanotube corresponds to  $\mathbf{C}_h = (5,5)$  (Fig. 3).

The nanotubes derived from a single graphene strip are called single-walled nanotubes (SWNT).<sup>[4,5]</sup> If a set of subsequently smaller diameter nanotubes are stacked like concentric cylinders, a MWNT is obtained. The distance between the carbon layers in an MWNT is about the same as the distance between the graphene layers in graphite. MWNTs are produced more commonly, and the very first report of nanotubes by Iijima was about MWNTs.<sup>[3]</sup>

A nanotube rope<sup>[10]</sup> is a parallel arrangement of SWNTs in a crystalline order, as shown in Fig. 4. The rope is held together by weak van der Waals forces (just like graphite), but it is extremely strong along the long direction. SWNT strands as long as a few centimeters have been produced.<sup>[11]</sup>

Fullerenes can be viewed as fully closed graphene sheets. The guiding principle is that each carbon atom is connected to three neighbors, and the bond angles must remain close to 120°. The perfect honeycomb lattice satisfies this requirement, as the building blocks are ideal hexagons. However, in order to get closed surfaces, one has to allow for an occasional pentagon in the structure, just as in the domes designed by the architect Buckminster Fuller (hence are the names of “fullerene” and “buckyball”). There is a simple geometrical principle, Euler’s theorem, that connects the number of faces ( $f$ ), vertices ( $v$ ), and edges ( $e$ ) of a closed three-dimensional polyhedron,  $f + v - e = 2$ . If only hexagons and pentagons are allowed, one can easily prove that the number of pentagons is always 12.

The smallest fullerene, C<sub>36</sub>, has the shape of a dodecahedron, with exactly 12 pentagons, and no hexagons. However, this molecule is very reactive,<sup>[12]</sup> as the bond angles are quite stretched. If we look for surfaces where no two pentagons can be nearest neighbor we get the smallest and most abundant stable fullerene, C<sub>60</sub> (Fig. 1). In this molecule the carbon nuclei reside on a sphere of about 0.7 nm diameter, with the electronic wavefunctions extending inside and outside by about 0.15 nm. The diameter of the molecule is approximately 1.0 nm, and there is a 0.4-nm-diameter cavity inside. This molecule still has the same symmetry properties as the dodecahedron (described by the icosahedral symmetry group, I<sub>h</sub>), and the symmetry is preserved even if not all bond lengths are exactly the

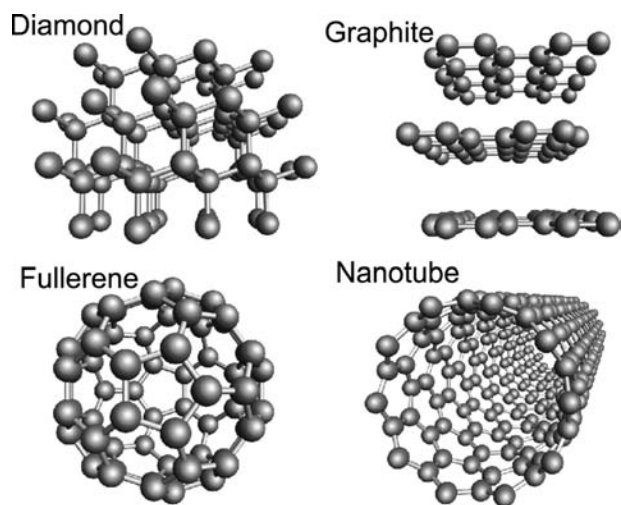


**Fig. 1** Four carbon structures, representing diamond, graphite, a typical fullerene ( $C_{60}$ ), and a typical nanotube (10,0 zigzag, see discussion later).

same. In fact, in  $C_{60}$  the edges that separate two hexagonal faces are slightly shorter (0.140 nm) than the edges separating a pentagonal and a hexagonal face (0.146 nm). The chemical bond along the shorter edge is sometimes considered double bond, whereas the others are single bonds. Notice, however, the single bond distance in diamond is 0.154 nm (much longer than 0.146 nm), and the typical double bond in molecules is 0.135 nm (much shorter than 0.140 nm). This already indicates that the simple bond picture does not work for  $C_{60}$ , and the  $\pi$  electrons are, at least partially, delocalized.

The most abundant fullerene higher than  $C_{60}$  is  $C_{70}$ . Its structure can be constructed by adding a “belt” of five hexagons in one of the equatorial planes of  $C_{60}$ . Other fullerenes, such as  $C_{76}$ ,  $C_{78}$ ,  $C_{80}$ , and up, have also been prepared and purified. The number of

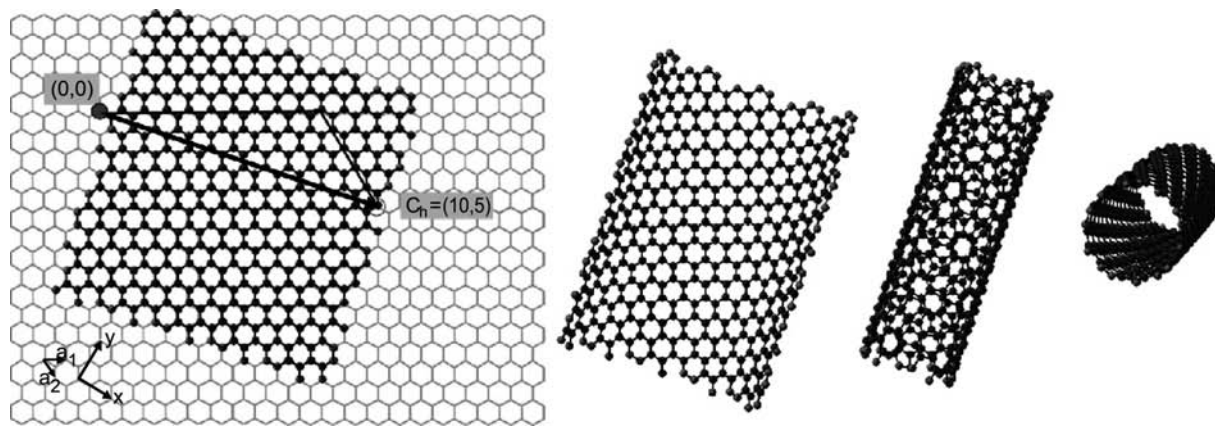


**Fig. 2** Schematic illustration of deriving a nanotube structure from graphene. The unit vectors  $\mathbf{a}_1$  and  $\mathbf{a}_2$ , and the chiral vector  $\mathbf{C}_n$  are indicated in the first panel. Bending the graphene strip results in the nanotube shown in the last panel. *Source:* From Shigeo Maruyama, University of Tokyo, [www.photon.t.u-tokyo.ac.jp/~maruyama](http://www.photon.t.u-tokyo.ac.jp/~maruyama).

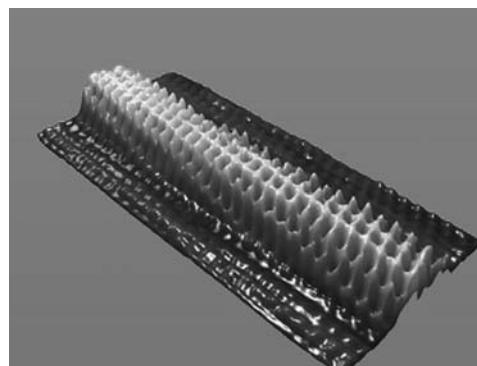


**Fig. 3** Scanning tunneling microscope image of a nanotube. The peaks correspond to individual carbon atoms; the chirality of the structure is quite visible. *Source:* From Cees Dekker; TU Delft, <http://www.mb.tn.tudelft.nl/nanotubes.html>, see also Ref.<sup>[9]</sup>.

isomers increases rapidly with the increasing fullerene size, representing some difficulty for the determination of their structure (mainly by NMR measurements and theoretical calculations). It is interesting to note that one of the isomers of  $C_{80}$  has the exact shape of an icosahedron (there are also six other isomers with lower symmetry).

Nanotubes with closed ends can be obtained by capping the open ends with a fullerene fragment of appropriate size and shape. For example, the (5,5) nanotube can be capped at the two ends with the two halves of a  $C_{60}$  molecule. Adding more “belts” of hexagons to  $C_{70}$  yields the same structure. In this sense the distinction between nanotubes and fullerenes is somewhat artificial.

## SYNTHESIS

Once synthesized in the laboratory, fullerenes were also discovered in common sooth and in natural minerals,

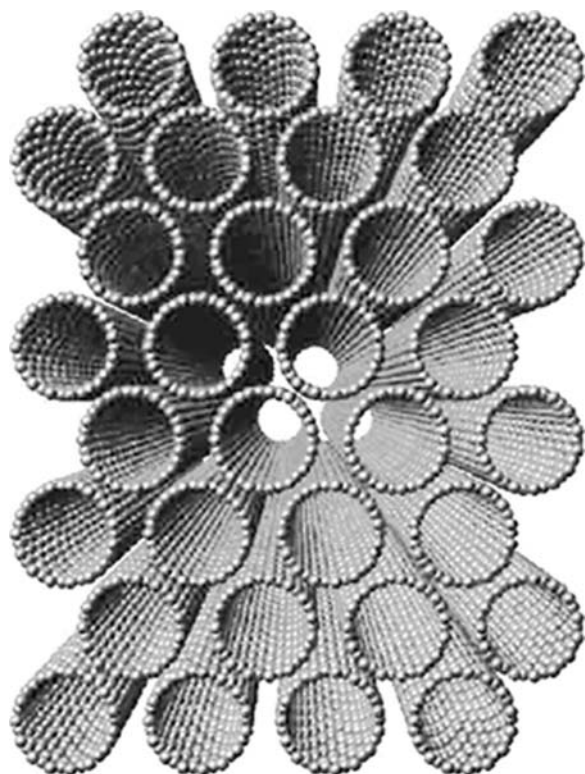


**Fig. 4** Cross-sectional view of a nanotube rope. *Source:* From Don Noid and Bobby Sumpter, ORNL, [http://www.csm.ornl.gov/SC98/viz/noid\\_multi.jpg](http://www.csm.ornl.gov/SC98/viz/noid_multi.jpg).

but it is still more productive to make them in the laboratory. The most common way of preparing fullerenes and nanotubes is the arc discharge method. The typical apparatus<sup>[2]</sup> consists of a high current source (e.g., and arc welding machine) and a vacuum jar, where a partial pressure (about 100–200 Torr) of He is maintained. Inside the jar two carbon rods are brought into contact to form an arc. A constant distance should be maintained between the rods as the material is gradually converted into carbon soot. In one version of the apparatus the weight of one of the carbon rods maintains a loose contact between the rods. The soot is collected from the inside surface of the jar, and from other parts.

A more precisely controlled preparation method involves laser ablation of carbon.<sup>[1,10]</sup> The graphite target is kept at high temperature (1200°C) in a furnace. A high power laser (typically a Nd:YAG laser operating at several hundred millijoules of power) is aimed at the target and produces a carbon plasma. A flow of inert gas carries the end products and deposits them in a colder part of the apparatus.

In both cases the reaction products are mixtures of various fullerenes, nanotubes, and amorphous carbon, although by properly setting and controlling the preparation conditions the relative quantity of the end

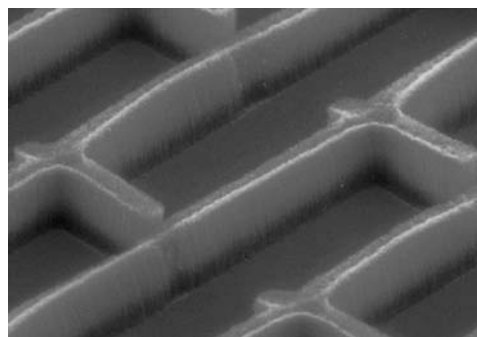


**Fig. 5** Nanotubes grown by chemical vapor deposition on a pattern of catalyst deposited on a substrate. *Source:* Laszlo Forro, EPFL, Lausanne.

products can be influenced greatly. Nevertheless, the separation and purification of the components is a critical part of the process. Various organic solvents (such as toluene or tetrahydrofuran) can be used to dissolve fullerenes or disperse the nanotubes. High-performance liquid chromatography (HPLC) is used to separate the different fractions. Once a solid phase is obtained fullerenes can be further purified by sublimation (e.g., C<sub>60</sub> sublimates at 430°C). Smaller quantities of higher fullerenes can also be purified by gas-phase separation methods.

A third approach, primarily used in the production of SWNTs, is based on chemical vapor deposition (CVD). This method involves a carefully prepared catalyst, and it can be used to grow large quantities of ordered nanotubes.<sup>[13]</sup> It is generally believed that SWNTs are more readily obtained if the reaction temperature is not too high. Note that in the arc discharge method the reaction happens at temperatures larger than 3000°C, whereas in CVD the temperature of the reaction can be kept below 1000°C. Fig. 5 shows a pattern of “nanotube forest” synthesized by CVD.

## MOLECULAR PROPERTIES

The unsaturated nature of the sp<sup>2</sup> bonds is responsible for several interesting properties of fullerenes and nanotubes. Functionalization (attaching other molecules with desirable properties) can be carried out easily. A pretty good description of the electronic properties can be obtained by assuming that three of the four valence electrons of each carbon are tied up in the three  $\sigma$  bonds, and by considering the behavior of the remaining one electron. There is a large body of literature dealing with these issues (see, for example, Refs.<sup>[6,7]</sup>); we will focus on one of the fullerenes, C<sub>60</sub>. We will also discuss the electronic states in a single SWNT.



## Electronic States in C<sub>60</sub>

C<sub>60</sub> has 240 valence electrons, but each carbon atom has three sigma bonds to its neighbors, using up a total of 180 electrons for this purpose. The energy of these electrons is well below the Fermi surface. They stabilize the structure, but they will not contribute to the conduction. The remaining 60 electrons are distributed around the molecule on orbitals that originate from the (much less tight) carbon-carbon  $\pi$  orbitals. There are two important differences between these orbitals and the  $\pi$  electrons of a graphene plane. First, the three bonds around a carbon atom in C<sub>60</sub> (or in any other fullerene) do not make a plane. Whereas in graphene the electrons had equal probability of being “below” and “above” the plane, in fullerenes the  $\pi$  electrons tend to spend more time outside of the ball than inside. Second, in C<sub>60</sub> the C–C bond lengths are not uniform, the  $\pi$  electrons are not truly delocalized around the six-member carbon rings (like in benzene or graphene), but they are distributed over 30 “bulges” of electronic orbits that stick out of the C<sub>60</sub> molecule. A somewhat lower electron density belongs to the other 60 orbits connecting the carbon pairs with longer bond lengths.

The first insight to the nature of the molecular orbitals can be obtained by borrowing ideas from the early days of nuclear physics, when the quantum mechanics of particles confined into a spherical potential well was first considered. In this case the states are still labeled by quantum numbers  $n$ ,  $l$ , and  $m$ , just like in the hydrogen atom, but the peculiar degeneracy of the different angular momentum states, which characterizes the textbook treatment of the hydrogen atom, does not apply. In steep-walled potential well (like in a nucleus or in a C<sub>60</sub> molecule) the lower  $l$  states will have lower energy.

Let us consider 60, noninteracting electrons, confined to a sphere on a high  $n$  orbit with various  $l$ 's. The first two electrons will fill up  $l = 0$  state. Proceeding to higher  $l$ , one has to count the number of available states,  $N = 2(2l + 1)$  (where the first factor of 2 stands for spin). It is easy to see that by reaching  $l = 4$  altogether 50 electrons are consumed. The remaining 10 electrons will all go to the  $l = 5$  state.

In reality the situation is much more complex. The potential does not have the spherical symmetry; each carbon atom creates its own potential well for the electrons. Nevertheless, a more exact treatment of the electrons (e.g., a Hückel molecular orbital calculation) shows that the above arguments work well for  $l = 0, 1, 2, 3, 4$ . For higher energies the “spherical potential” approximation does not work anymore. In order to go any further we need to look at the energy splitting due to the true atomic potentials. In the real

C<sub>60</sub>  $l$  is not a good quantum number, and the electronic orbitals should be labeled according to the irreducible representations of the icosahedral symmetry group. The orbitals available for the remaining 10 electrons are, in the order of increasing energy, the  $h_u$ , the  $f_{1u}$ , and the  $f_{1g}$  levels. The degeneracy of these levels (including spin) is 10, 6, and 6, respectively. The  $h_u$  level is completely filled by the 10 remaining electrons, becoming the highest occupied molecular orbit (HOMO), and the  $f_{1u}$  level becomes the lowest unoccupied molecular orbit (LUMO). The HOMO–LUMO gap is about 2 eV.

The energy gap between the filled and empty electronic states causes the molecule to be non-reactive, and it accounts for the insulating nature of the C<sub>60</sub> solid. The empty  $f_{1u}$  level can hold six electrons, and a proper addition of electrons to the molecule (sometimes called “doping”, in analogy to adding electrons to a pure superconductor) should result in dramatic changes in the properties, including higher reactivity and metallic character. Two possible ways will be discussed here shortly: adding an atom inside the C<sub>60</sub> cage (endohedral doping) and exchanging a carbon atom to another one (on-site doping; Fig. 6). The third (and most fruitful) method, exohedral doping, when the donor atom is placed in-between the C<sub>60</sub> molecules, will be considered later.

Endohedral C<sub>60</sub> molecules can be prepared by a “brute-force” method, where ions of atoms are accelerated and implanted to the C<sub>60</sub> cage.<sup>[14]</sup> The ions should have just enough energy to open up the cage and enter. The first collision should absorb and redistribute a good part of the initial kinetic energy so that the atom does not escape the cage. Endohedral molecules of M–C<sub>60</sub> with M = N, P, Li, Ca, Na, K, Rb were produced this way in small quantities. A larger yield can be achieved by coevaporation<sup>[15]</sup> of the carbon and the metal in an arc-discharge chamber (typical for fullerene production). In this process mostly higher endohedral fullerenes, such as M–C<sub>82</sub> (where M is a metal atom), can be extracted from the soot on a chromatographic column.

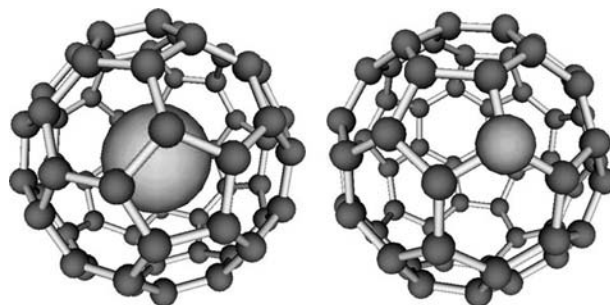


Fig. 6 Endohedral and on-site doping of a C<sub>60</sub> molecule.

Electron spin resonance spectroscopy (ESR) studies and detailed quantum chemical calculations show that the endohedral dopant atom does not always transfer its charge to the cage. If the dopant remains neutral, it stays in the center of the cage, like in  $N-C_{60}$ .<sup>[16]</sup> Compounds such as  $La-C_{60}$  are very interesting, as complete charge transfer from La to the  $C_{60}$  cage results in a triply charged molecule.

On-ball doping has been achieved by replacing one carbon atom with a nitrogen atom obtaining  $C_{59}N$  (azafullerenes).<sup>[17]</sup> The replacement of N for C adds one extra electron to the cage, changes the structure locally, lowers the symmetry of the molecule, and splits the degeneracy of the electronic orbitals. Furthermore, this chemical substitution renders the molecule very reactive with a high electron affinity. At ambient temperature the  $C_{59}N$  exists only in a dimerized phase.

### Electrical Conduction in Nanotubes

In order to understand the electrical properties of a nanotube, we first have to look at a single graphene sheet. Graphene is on the borderline of being metallic: the band structure calculation results in a “zero-gap semiconductor” behavior.<sup>[18]</sup> Fig. 7 shows an illustration of the electron energy as a function of the two-dimensional wave vector. The Brillouin zone of graphene is a hexagon, and the allowed electronic states (wave vectors) correspond to the points inside the hexagon; the electronic bands reach the Fermi level

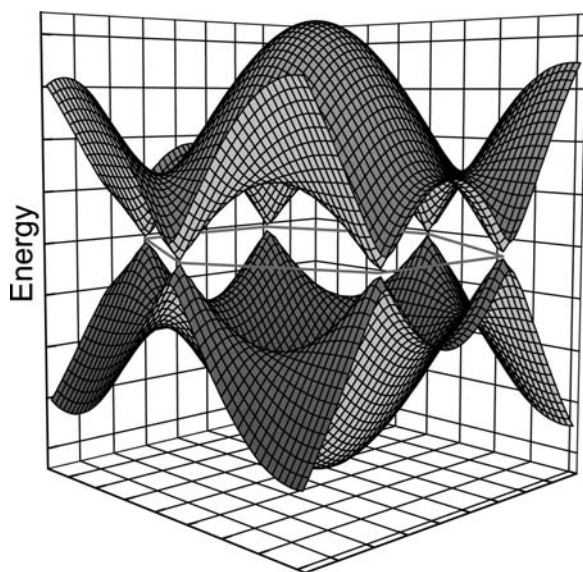


**Fig. 7** Schematic representation of the energy bands in graphene. The possible electron states are constrained in a hexagon in the base plane. The lower band is full, the upper band is empty. The energy of the electrons is zero (equal to the Fermi energy) at the six corners of the hexagon.

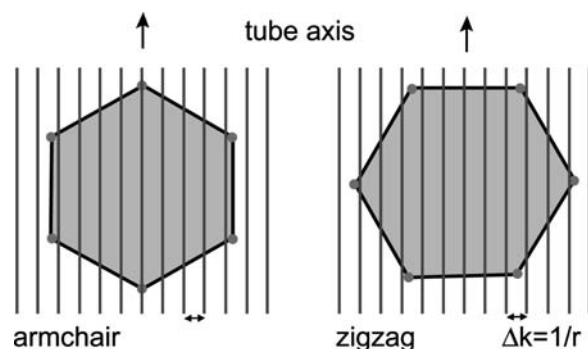


**Fig. 8** The six corners of the hexagon correspond to electronic states available for conduction. The lines represent the allowed electronic states in a zigzag and an armchair nanotube.

at the six corners of the hexagon. Therefore the Fermi “surface” consists of six points, as indicated in the two panels in Fig. 8. (In graphite the influence of the neighboring layers causes the bands to cross the Fermi level, and there will be finite Fermi surface, yielding a semimetallic behavior.)

By bending the graphene sheet into a nanotube the most drastic change will be the constraint introduced due to the periodic boundary condition along the circumference of the cylinder. Accordingly, in the direction perpendicular to the tube axis the allowed wave vectors will be constrained to lines. The larger the diameter of the nanotube the more dense are the lines. Naturally, for a very large diameter nanotube the allowed wave vectors are just about the same as for the graphite, and the properties are also similar. However, for smaller diameters the constraint is really important. As shown in the two panels of Fig. 8, the relative orientation of the lines corresponding to the allowed states is sensitive to the actual structure of the nanotube.<sup>[8,19]</sup> For armchair nanotubes one of the lines always intersects the corner of the hexagon, therefore these nanotubes are metallic; for the zigzag structure it is possible that the lines miss the corners, and in those cases the nanotube is semiconducting. By carrying out this analysis in more detail, we obtain that a nanotube is metallic if the integers in the chiral vector describing the structure  $C_h = (n_1, n_2)$  satisfy  $n_1 - n_2 = 3j$ , where  $j$  is an arbitrary integer. More detailed calculations, taking into account the curvature of the graphene sheet, lead to the conclusion that for  $n_1 = n_2$  (armchair) the nanotubes are metallic, for  $n_1 - n_2 = 3j$  there is a tiny gap at the Fermi surface, and for all other cases the gap is large.

Much progress has been made in the experimental test of these predictions.<sup>[20]</sup> One prefers to work with a SWNT, because for a MWNT it is unlikely that all of the component nanotubes are of the same type (metal or semiconductor). The first conductance



measurements were done on a nanotube rope, a collection of similar SWNTs. Several single SWNTs of various chirality have been tested later. The measurements largely support the conclusions drawn above. For the complete interpretation of the experimental results one needs to step beyond the simple theory of bulk metals: the electrical leads to the nanotube must be treated as tunneling contacts. The resonance between higher quantum levels and the Coulomb repulsion of electrons on the nanotube play important roles.<sup>[21,22]</sup>

## FULLERENE SOLID

The vast majority of research on the fullerene-based solids was done on  $C_{60}$ . The molecule dissolves in various solvents. Crystallization from solution usually yields a structure that includes the solvent molecules.<sup>[23]</sup> However, sublimation in vacuum or inert gas atmosphere may yield pure  $C_{60}$  crystals of several millimeters or even centimeter size. In the solid form the centers of the fullerene molecules are ordered in a face-centered cubic (fcc) crystal lattice (Fig. 9).

At room temperature the fullerene molecules rapidly and randomly rotate between various orientations.<sup>[24]</sup> In time average the molecules look like spheres and all of the molecular sites are equivalent. (The well-defined molecular center and a nearly free molecular rotation are not a unique property of the fullerene molecule. It is characteristic to many organic solids, where the binding is due to van der Waals forces, and the molecule has “rounded” symmetric shape, like solid  $CH_4$  and  $CCl_4$ .)

The nearest neighbor  $C_{60}$ – $C_{60}$  distance corresponds to the diameter of the molecule. At room temperature the size of the cubic unit cell is 1.417 nm, and the nearest neighbor distance is 1.002 nm. As the temperature is lowered, the rotation of the molecules stops. The center of the molecules remains in about the same place, but the incompatibility of the icosahedral molecular symmetry and the cubic lattice symmetry makes it impossible to describe the structure in terms of the

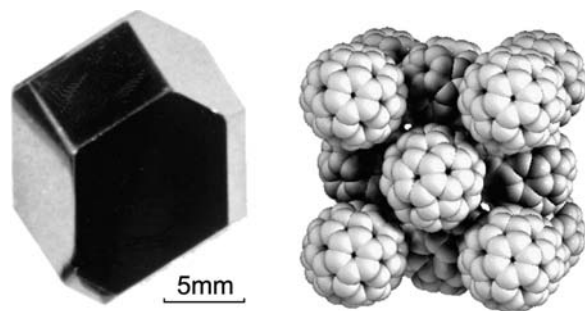


**Fig. 9** A pure fullerene crystal, and the illustration of the structure of the fullerene solid. *Source:* From Ref.<sup>[33]</sup>.

simple fcc lattice, with one  $C_{60}$  molecule of fixed orientation each unit cell. The freezing of the rotational motion actually happens in two stages. First, at 261 K the rotational axis of each molecule becomes constrained. The building block of the new structure consists of four  $C_{60}$  molecules arranged at the vertices of a tetrahedron, with each one of them spinning around a different, but well-defined axis.<sup>[25–28]</sup> Then, at lower temperatures, the rotation around these axes slows down and stops gradually. Below about 90 K the molecules are entirely frozen, but they never order perfectly.

## Doped Fullerenes

The linear size of a fullerene molecule is 10 times larger than a typical atom. Even in a close-packed fcc structure, large empty spaces between the molecules are freely available for smaller atoms, ions, or molecules. Because of the unsaturated character of the C–C bonds on the fullerene, there are plenty of electronic states to accept electrons from appropriate donors. The combination of alkali and alkaline earth elements with fullerenes results in an unusual variety of  $A_nC_{60}$  materials that are mostly near-stoichiometric (A can stand for Na, K, Rb, Cs, Ca, Sr, and Ba). Organic and inorganic molecules were also used to produce charge transfer salts with fullerenes. The term “doped fullerene” is often used to describe the product (although in its original sense, “doping” means a small, nonstoichiometric amount of charge transfer, typically in a semiconductor).

In the fcc structure the interstitial sites have either octahedral or tetrahedral symmetry. The tetrahedral sites are smaller, and there are twice as many of them as octahedral sites. A series of  $A_nC_{60}$  (with  $n = 0, 1, 2, 3, 4, 6, 10$ ) materials are based on the original fcc structure of pure  $C_{60}$ . Several other compounds are known where the  $C_{60}$  abandons the close-packed structure.<sup>[29–34]</sup> Two of these, the body-centered tetragonal  $A_4C_{60}$  and the body-centered cubic  $A_6C_{60}$ , are illustrated in Fig. 10. There is also a series of compounds with alkaline earth metals. Based on the simple

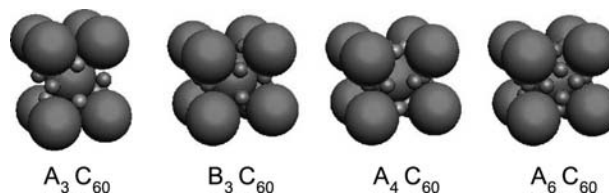


**Fig. 10** The leftmost structure corresponds to  $A_3C_{60}$ , with  $A = K, Rb, Cs$ , (or a mixture of these). If the dopant is an alkaline-earth metal (denoted by B), the structure is  $B_3C_{60}$ . The  $A_4C_{60}$  and  $A_6C_{60}$  structures shown here are known to exist with  $A = K, Rb$ , and  $Cs$ .

electron band arguments, the HOMO level of the  $C_{60}$  can accept a total of six electrons. Anything less than that should result in a partially occupied electron band and lead to a metallic behavior in the solid state. Surprisingly, at room temperature and ambient pressure, only  $AC_{60}$ , and  $A_3C_{60}$  are metals (for a review, see Ref.<sup>[33]</sup>).

### Superconductivity and Magnetism in Fullerenes

A class of alkali-metal-doped fullerenes, with chemical composition  $A_3C_{60}$ , is metallic at room temperature<sup>[35]</sup> and turns into superconductor at low temperature.<sup>[36]</sup> The transition temperature is unusually large; for example, in  $Rb_3C_{60}$  it is 32 K.<sup>[37]</sup> In contrast to other exotic superconductors (such as the copper-oxide-based high-temperature superconductors), the superconductivity in fullerides is well understood in terms of the theory developed in the 1960s by Bardeen, Cooper, and Schrieffer (BCS). The formation of Cooper pairs (two electrons that are held together by some attractive force) is the key element of the BCS theory. In the  $A_3C_{60}$  fullerides the conduction electrons are donated by the alkali metal atoms to the  $C_{60}$  molecules, the electrons easily hop between the molecules (because of the overlap of the molecular orbitals), and the attractive interaction is mediated by the deformation of the molecule induced by the presence of the electron.

When  $C_{60}$  is combined with the strong electron acceptor tetrakis(diethylamino)ethylene (TDAE) each fullerene molecule loses an electron. It was expected that this material will also be a metal, and perhaps a superconductor, too. Instead, it turned out to be an insulator, but when it was cooled to low temperature a strong magnetism was detected.  $(TDAE)C_{60}$  is a ferromagnetic compound with a Curie temperature of 16-K.<sup>[38,39]</sup> It is very rare to find ferromagnetic behavior with no transition metal (such as iron or nickel) in the chemical formula.  $(TDAE)C_{60}$  held the record of being the highest temperature truly organic ferromagnet.

### Polymerization of Fullerenes

The ability of the  $C_{60}$  molecule to form covalently bonded polymers was first noticed in laser-irradiated thin films of  $C_{60}$ .<sup>[40]</sup> The polymerization happens in a Diels–Alder-type (2 + 2) cycloaddition reaction when the double bonds on two fullerenes are broken up and cross links are formed. This reaction has a large activation energy, and at room temperature it is extremely slow. It is believed that (2 + 2) cycloaddition also occurs in high-pressure/high-temperature polymerization of fullerenes.<sup>[41]</sup> Some of these high-pressure synthesized disordered polymers are very attractive

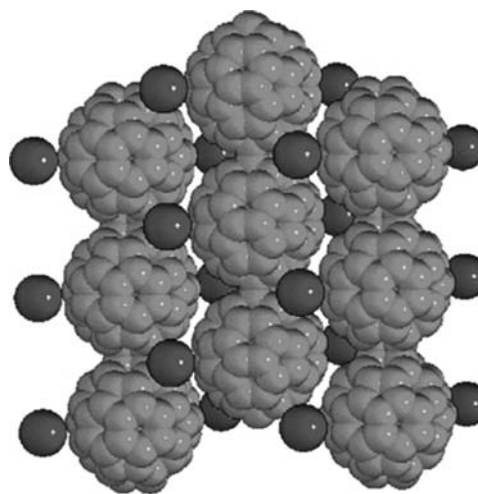


**Fig. 11** The low-temperature structure of  $RbC_{60}$ . The polymerized  $C_{60}$  chains are quite visible. *Source:* From Joseph Lauher, SUNY, Stony Brook, <http://sbchem.sunysb.edu/msl/fullerene.html>.

for applications, as they can exhibit mechanical properties stronger than diamond.

In doped fullerenes polymerization can happen without exposing the material to light, high temperature, or pressure. The best known examples are  $KC_{60}$  and  $RbC_{60}$ , where the fullerene molecules form linear chain structures (Fig. 11). The formation of these chains happens spontaneously as the material is cooled slightly below room temperature.<sup>[42]</sup> There are dramatic changes in the electrical conductivity and in the other properties; most notably the material becomes stable in air (otherwise all alkali-doped fullerene compounds decompose rapidly in air). This is a reversible transition, and the material turns back to the monomeric form if the temperature is raised. A slightly different polymer is formed in  $Na_4C_{60}$ . In this compound, sheets of  $C_{60}$  molecules are formed so that there is a single bond between the nearest neighbors.

### CONCLUSION

Inorganic fullerenes and nanotubes have been prepared in binary composition; for example, the graphite-like solid lubricant  $MoS_2$  served as the basis for a series of compounds.<sup>[43]</sup> However, only carbon has the extraordinary chemical flexibility to serve as the sole basic unit of such a variety of compounds. The materials discussed here are testing grounds for important concepts in condensed matter theory; at the same time there is a constant effort to find potentially useful applications. Fullerene-like structures are known in more complex materials, including biologically important molecules,

including the HIV virus.  $C_{60}$  was investigated as a potential drug delivery agent, it may have antiviral activity,<sup>[44]</sup> and endohedral  $C_{60}$  compounds can be possibly used as a spin label (or relaxation agent) in magnetic resonance spectroscopy.<sup>[45]</sup> Bulk quantities of nanotubes are considered for reinforcement additives in metals and for storage of hydrogen gas.<sup>[46]</sup> In scanning tunneling and force microscopy the nanotubes may serve as the sharpest possible microscope tip. Single nanotubes were shown to work as single-electron transistors, reaching the ultimate limit of nanoscale electronics.<sup>[47,48]</sup> Electron emission and light emission from the tips of the nanotubes have been seen at relatively low applied voltages, and according to a recent press release from Motorola, the nanotube-based “nanoemissive display (NED) technology enables manufacturers to design large flat panel displays that exceed the image quality characteristics of plasma and LCD screens.” The strange structures, discovered during the search for new molecules in the interstellar medium,<sup>[1]</sup> may have a real impact on our everyday life in the not-too-distant future.

## REFERENCES

- Kroto, H.W.; Heath, J.R.; O'Brien, S.C.; Curl, R.F.; Smalley, R.E.  $C_{60}$  buckminsterfullerene. *Nature* **1985**, *318*, 162.
- Kratschmer, W.; Lamb, L.D.; Foristopoulos, K.; Huffman, D.R. Solid  $C_{60}$ : a new form of carbon. *Nature* **1990**, *347*, 354.
- Iijima, S. Helical microtubules of graphitic carbon. *Nature* **1991**, *354*, 56.
- Iijima, S.; Ichihashi, T. Single-shell carbon nanotubes of 1-nm diameter. *Nature* **1993**, *363*, 603.
- Bethune, D.S.; Kiang, C.H.; DeVries, M.S.; Gorman, G.; Savoy, R.; Beyers, R. Cobalt-catalysed growth of carbon nanotubes with single-atomic-layer walls. *Nature* **1993**, *363*, 605.
- Dresselhaus, M.S.; Dresselhaus, G.; Eklund, P.C. *Science of Fullerenes and Carbon Nanotubes*; Academic Press: San Diego, 1996.
- Carbon nanotubes: synthesis, structure, properties and applications. Dresselhaus, M.S., Dresselhaus, G., Avouris, Ph., Eds.; *Topics in Applied Physics*, Springer: Berlin, 2001; Vol. 80.
- Hamada, N.; Sawada, S.; Oshiyama, A. New one-dimensional conductors: graphite microtubules. *Phys. Rev. Lett.* **1992**, *68*, 1579.
- Wildoer, J.W.G.; Venema, L.C.; Rinzler, A.G.; Smalley, R.E.; Dekker, C. Electronic structure of atomically resolved carbon nanotubes. *Nature* **1998**, *391*, 59.
- Thess, A.; Lee, R.; Nikolaev, P.; Dai, H.; Petit, P.; Robert, J.; Xu, C.; Lee, Y.H.; Kim, S.G.; Colbert, D.T.; Scuseria, G.; Tománek, D.; Fischer, J.E.; Smalley, R.E. Crystalline ropes of metallic carbon nanotubes. *Science* **1996**, *273*, 483.
- Zhu, H.W.; Xu, C.L.; Wu, D.H.; Wei, B.Q.; Vajtai, R.; Ajayan, P.M. Direct synthesis of long single-walled carbon nanotube strands. *Science* **2002**, *296*, 884.
- Piskoti, C.; Yager, J.; Zettl, A.  $C_{36}$ : A new carbon solid. *Nature* **1998**, *393*, 771.
- Kong, J.; Cassell, A.M.; Dai, H.J. Chemical vapor deposition of methane for single-walled carbon nanotubes. *Chem. Phys. Lett.* **1998**, *292*, 567.
- Murphy, T.A.; Pawlik, Th.; Weidinger, A.; Hohne, M.; Alcalá, R.; Spaeth, J.M. Observation of atomlike nitrogen in nitrogen-implanted solid  $C_{60}$ . *Phys. Rev. Lett.* **1996**, *77*, 1075.
- Yannoni, C.S.; Hoinkins, M.; de Vries, M.S.; Bethune, D.S.; Salem, J.R.; Crowder, M.S.; Johnson, R.D. Scandium clusters in fullerene cages. *Science* **1992**, *256*, 1191.
- Dietel, E.; Hirsch, A.; Pietzak, B.; Waiblinger, M.; Lips, K.; Weidinger, A.; Gruss, A.; Dinse, K.P. Atomic nitrogen encapsulated in fullerenes: effects of cage variations. *J. Am. Chem. Soc.* **1999**, *121*, 2432.
- Hummelen, J.C.; Knight, B.; Pavlovich, J.; Gonzalez, R.; Wudl, F. Isolation of the heterofullerene  $C_{59}N$  and its dimmer  $(C_{59}N)_2$ . *Science* **1995**, *269*, 1554.
- Reich, S.; Maultzsch, J.; Thomsen, C.; Ordejon, P. Tight-binding description of graphene. *Phys. Rev., B* **2002**, *66*, 035412.
- Saito, R.; Dresselhaus, G.; Dresselhaus, M.S. Electronic structure of chiral graphene tubules. *Appl. Phys. Lett.* **1992**, *60*, 2204.
- Tans, S.J.; Devoret, M.H.; Dai, H.; Thess, A.; Smalley, R.E.; Geerligs, L.J.; Dekker, C. Individual single-wall carbon nanotubes as quantum wires. *Nature* **1997**, *386*, 474.
- Bockrath, M.; Cobden, D.H.; McEuen, P.L.; Chopra, N.G.; Zettl, A.; Thess, A.; Smalley, R.E. Single-electron transport in ropes of carbon nanotubes. *Science* **1997**, *275*, 1922.
- Buitelaar, M.R.; Belzig, W.; Nussbaumer, T.; Babic, B.; Bruder, C.; Schönberger, C. Multiple andreev reflection in a carbon nanotube quantum dot. *Phys. Rev. Lett.* **2003**, *91*, 057005.
- Faigel, G.; Bortel, G.; Oszlányi, G.; Pekker, S.; Stephens, P.W.; Liu, D. Low-temperature phase transition in  $C_{60}$ -*n*-pentane. *Phys. Rev., B* **1994**, *49*, 9186.
- Stephens, P.W.; Mihaly, L.; Lee, P.A.; Whetten, R.L.; Huang, S.M.; Kaner, R.; Diederich, F.; Holczer, K. Structure of single phase, superconducting  $K_3C_{60}$ . *Nature* **1991**, *351*, 632.
- Tycko, R.; Dabbagh, G.; Fleming, R.M.; Haddon, R.C.; Makhija, A.V.; Zahurak, S.M. Molecular dynamics and the phase transition in solid  $C_{60}$ . *Phys. Rev. Lett.* **1991**, *67*, 1886.
- Heiney, P.A.; Fischer, J.E.; McGhie, A.R.; Romanow, W.J.; Denenstien, A.M.; McCauley, J.P., Jr.; Smith, A.B.; Cox, D.E. Orientational ordering transition in solid  $C_{60}$ . *Phys. Rev. Lett.* **1991**, *66*, 2911.reply to comment **1991**, *67*, 1468.
- David, W.I.F.; Ibberson, R.M.; Dennis, T.J.S.; Hare, J.P.; Prassides, K. Structural phase-transitions in the fullerene  $C_{60}$ . *Europhys. Lett.* **1991**, *18*, 735.
- Harris, A.B.; Sachidanandam, R. Orientational ordering of icosahedra in solid  $C_{60}$ . *Phys. Rev., B* **1992**, *46*, 4944.

29. Stephens, P.W.; Bortel, G.; Faigel, G.; Tegze, M.; Jánossy, A.; Pekker, S.; Oszlányi, G.; Forró, L. Polymeric fullerene chains in  $\text{RbC}_{60}$  and  $\text{KC}_{60}$ . *Nature* **1994**, *370*, 636.
30. Yildirim, T.; Fischer, J.E.; Harris, A.B.; Stephens, P.W.; Liu, D.; Brard, L.; Strongin, R.M.; Smith, A.B., III. Orientational phase transition in  $\text{Na}_x\text{C}_{60}$  ( $1 < x < 3$ ). *Phys. Rev. Lett.* **1993**, *71*, 1383.
31. Stephens, P.W.; Mihaly, L.; Lee, P.L.; Whetten, R.L.; Huang, S.-M.; Kaner, R.; Diederich, F.; Holczer, K. Structure of single-phase superconducting  $\text{K}_3\text{C}_{60}$ . *Nature* **1991**, *351*, 632.
32. Rosseinsky, M.J.; Murphy, D.W.; Fleming, R.M.; Tycko, R.; Ramirez, A.P.; Siegrist, T.; Dabbagh, G.; Barrett, S.E. Structural and electronic properties of sodium-intercalated C-60. *Nature* **1992**, *356*, 416.
33. Forro, L.; Mihaly, L. Electronic properties of doped fullerenes. *Rep. Prog. Phys.* **2001**, *64*, 649.
34. <http://buckminster.physics.sunysb.edu>.
35. Haddon, R.C.; Hebard, A.F.; Rosseinsky, M.J.; Murphy, D.W.; Duclos, S.J.; Lyons, K.B.; Miller, B.; Rosamilia, J.M.; Fleming, R.M.; Kortan, R.M.; Glarum, S.H.; Makhija, A.V.; Muller, A.J.; Eick, R.H.; Zahurak, S.M.; Tycko, R.; Dabbagh, G.; Thiel, F.A. Conducting films of  $\text{C}_{60}$  and  $\text{C}_{70}$  by alkali metal doping. *Nature* **1991**, *350*, 320.
36. Hebard, A.F.; Rosseinsky, M.J.; Haddon, R.C.; Murphy, D.W.; Glarum, S.H.; Palstra, T.T.M.; Ramirez, A.P.; Kortan, A.R. Superconductivity at 18K in potassium doped  $\text{C}_{60}$ . *Nature* **1991**, *350*, 600.
37. Holczer, K.; Klein, O.; Huang, S.-M.; Kaner, R.B.; Fu, K.-J.; Whetten, R.L.; Diederich, F. Alkali-fulleride superconductors: Synthesis, composition and diamagnetic shielding. *Science* **1991**, *252*, 1154.
38. Allemand, P.-M.; Khemani, K.C.; Koch, A.; Wudl, F.; Holczer, K.; Donovan, S.; Gruner, G.; Thompson, J.D. Organic molecular soft ferromagnetism in  $\text{C}_{60}$ . *Science* **1991**, *253*, 301.
39. Stephens, P.W.; Cox, D.; Lauher, J.W.; Mihaly, L.; Wiley, J.B.; Allemand, P.M.; Hirsch, A.; Holczer, K.; Li, Q.; Thompson, J.D.; Wudl, F. Lattice structure of the fullerene ferromagnet TDAE- $\text{C}_{60}$ . *Nature* **1991**, *355*, 331.
40. Rao, A.M.; Zhou, P.; Wang, K.; Hager, G.T.; Holden, J.M.; Wang, Y.; Lee, W.-T.; Bi, X.; Eklund, C.; Cornett, D.S.; Duncan, M.A.; Amster, I.J. Photoinduced polymerization of solid  $\text{C}_{60}$  films. *Science* **1993**, *259*, 955.
41. Nunez-Regueiro, M.; Marques, L.; Hodeau, J.-L.; Bethoux, O.; Perroux, M. Polymerized fullerite structures. *Phys. Rev. Lett.* **1995**, *74*, 278.
42. Pekker, S.; Janossy, A.; Mihaly, L.; Chauvet, O.; Carrard, M.; Forro, L. Single crystalline  $(\text{KC}_{60})_n$ —conducting linear alkali fulleride polymer. *Science* **1994**, *265*, 1077.
43. Feldman, Y.; Wasserman, E.; Srolovitz, D.J. High-rate gas-phase growth of  $\text{MoS}_2$  inorganic fullerenes and nanotubes. *Science* **1995**, *267*, 222.
44. Friedman, S.H.; Schinazi, R.F.; Wudl, F.; Hill, C.L.; DeCamp, D.L.; Sijbesma, R.P.; Kenyon, G.L. Water Soluble Fullerenes with Antiviral Activity. US #5,811,460 (1998) US #6,204,391, 2001.
45. Mikawa, M.; Kato, H.; Okumura, M.; Narazaki, M.; Kanazawa, Y.; Miwa, N.; Shinohara, H. Paramagnetic water-soluble metallofullerenes having the highest relaxivity for MRI contrast agents. *Bioconj. Chem.* **2001**, *12*, 510.
46. Dillon, A.C.; Jones, K.M.; Bekkendahl, T.A.; Kiang, C.H.; Bethune, D.S.; Heben, M.J. Storage of hydrogen in single-walled carbon nanotubes. *Nature* **1997**, *386*, 377.
47. Collins, P.C.; Arnold, M.S.; Avouris, P. Engineering carbon nanotubes and nanotube circuits using electrical breakdown. *Science* **2001**, *292*, 706.
48. Bachtold, A.; Hadley, P.; Nakanishi, T.; Dekker, C. Logic circuits with carbon nanotube transistors. *Science* **2001**, *294*, 1317

## BIBLIOGRAPHY

1. Mintmire, J.W.; Dunlap, B.I.; White, C.T. Are fullerene tubules metallic? *Phys. Rev. Lett.* **1992**, *68*, 631.

# Fullerenes: Chemistry

Mark S. Meier

Department of Chemistry, University of Kentucky,  
Lexington, Kentucky, U.S.A.

## INTRODUCTION

Fullerenes are the most exciting new set of chemical structures discovered in the last part of the 20th century. The advent of these novel structures has led to fascinating new scientific questions and to intriguing potential applications. This article provides an overview of the structures of the common members of the fullerene class of carbon allotropes and introduces the essentials of fullerene reactivity. Specific types of reactivity discussed herein include reactions of fullerenes with nucleophiles and electrophiles, oxidations and reductions, as well as reactions with metals and cycloaddition reactions. A glimpse of the potential applications of these fascinating molecules is also provided. The focus will be on the chemistry of  $C_{60}$  as it is the most available and the best-understood member of an expanding set of chemical structures. The chemistry of  $C_{70}$  is discussed briefly as well, demonstrating how strain directs the reactivity of this less-symmetrical structure.

## STRUCTURE

Fullerenes are hollow clusters of carbon atoms. The name fullerene is a shortened form of *buckminsterfullerene*, a name that pays homage to the designer of the geodesic dome.<sup>a</sup> The structure of  $C_{60}$  is reminiscent of that famous dome, being a near-perfect sphere formed from a set of fused rings in the same manner as a soccer ball.  $C_{70}$  is similar, having the same general structure with an extra “belt” of 10 carbon atoms. Common members of this class of structures include  $C_{60}$ ,  $C_{70}$ ,  $C_{76}$ , and  $C_{84}$ , although small amounts of larger structures (“higher fullerenes”) are formed along with the more common species. As the number of carbon atoms increases, the number of possible structures increases, and indeed multiple isomers of several of the higher fullerenes have been observed.<sup>b</sup> New fullerene species

have been prepared from other fullerenes, albeit in low yield.<sup>c</sup>

The  $C_{60}$  cage ( $I_h$  symmetry) measures 7 Å across. The  $C_{70}$  “rugbyball” shape ( $D_{5h}$  symmetry) is 7 Å across and 10 Å long. These highly curved structures place carbon in a strained geometry. Trivalent carbon ( $sp^2$  hybridization) typically leads to a planar geometry. In fullerenes, the bonding arrangement at carbon is far from planar—the three bonds form a shallow pyramid.<sup>[4,5]</sup> The strain in  $C_{60}$  is significant (over 400 kcal/mol) and is responsible for much of the reactivity of fullerenes.<sup>[6]</sup>

The bonding pattern in these molecules may be better illustrated through a “Schlegel” diagram, which is a flattened projection of the three-dimensional structures shown in Fig. 1. In these diagrams, the pattern of 5-membered and 6-membered rings is easily seen.

Only the pattern of  $\sigma$  bonds is shown in Figs. 1 and 2. There is an extensive (and critically important) set of  $\pi$  bonds that involves every carbon atom in the molecule. It is clear from the reactivity of  $C_{60}$  as well as from theory that these bonds are not localized between pairs of carbon atoms, but are instead delocalized over the surface of the fullerene cage. There is some debate over whether fullerenes can be properly classified as aromatic.<sup>[7]</sup> Aromaticity is normally associated with significant electronic ring currents, diminished reactivity, and diminished bond length alternation. Fullerenes display a degree of bond length alternation. The bonds that form the fusion of a 6-membered ring with a 5-membered ring are somewhat longer (bond length of 1.46 Å) than the bonds that form the fusion of two 6-membered rings (1.40 Å), but this amount of bond length alternation is also found in some molecules commonly considered to be aromatic (Fig. 3).

Fullerenes are much more reactive toward addition reactions than are classical aromatic compounds such as benzene. This likely reflects the relatively poor overlap of p-orbitals (splayed apart as a result of the curvature of structure), as well as the tremendous release of strain that results from conversion of carbon atoms

<sup>a</sup>For a detailed discussion of fullerene nomenclature, see Ref.<sup>[1]</sup>.

<sup>b</sup>For an example, see Ref.<sup>[2]</sup>.

<sup>c</sup>For an example, see Ref.<sup>[3]</sup>.

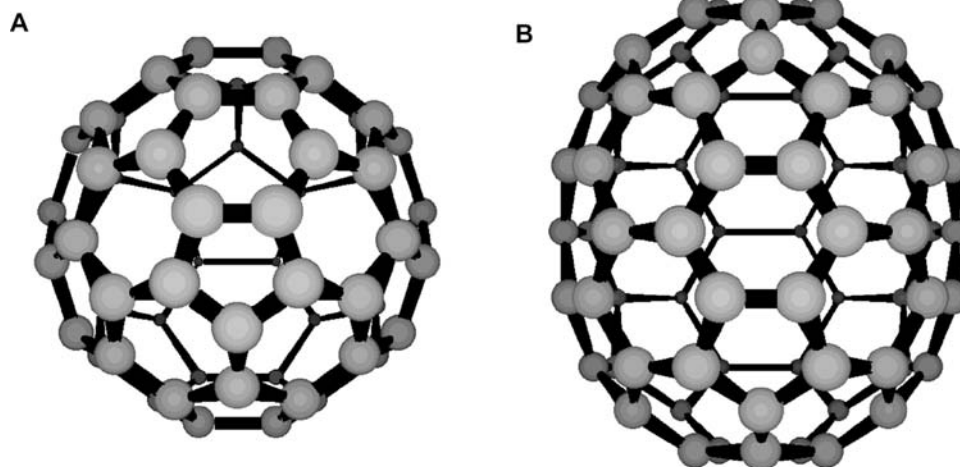


Fig. 1 The two most common fullerenes: (A)  $C_{60}$  and (B)  $C_{70}$ .

from highly strained  $sp^2$  geometry to a much less strained  $sp^3$  geometry. Ring currents in fullerenes are segregated into opposing diamagnetic and paramagnetic currents that sum to 0 in the case of  $C_{60}$  and to small values for the other fullerenes. It is clear that traditional notions of aromaticity and indeed some of the traditional hallmarks of aromaticity, which were originally developed for planar, monocyclic systems, are not easily applied in the case of these spherical, polycyclic structures. A novel  $2(N + 1)^2$  rule has been proposed as a guideline for aromaticity in spherical systems.<sup>[8]</sup>

$C_{60}$  has three degenerate Lowest Unoccupied Molecular Orbitals (LUMOs) and can be reduced to the

$C_{60}^{n-}$  anions, where  $n$  is 1–6. The reduction can be achieved electrochemically, by electron transfer from various anions, or by direct reduction with metals. Reviews on electron-transfer reactions of fullerenes<sup>[9]</sup> and of the preparation and properties of the anions (fullerides) and the less well-known cations (fullerenium ions) have been published.<sup>[10]</sup>

### Synthesis

These beautiful molecules were first detected in the plume above a laser-evaporated carbon target and have also been formed on a large scale in electric arcs

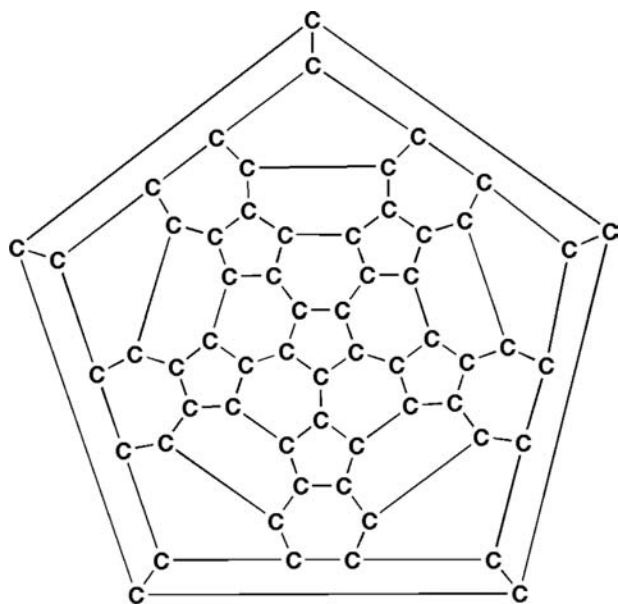


Fig. 2 Planar projection of  $C_{60}$ , showing the pattern of 5- and 6-membered rings.

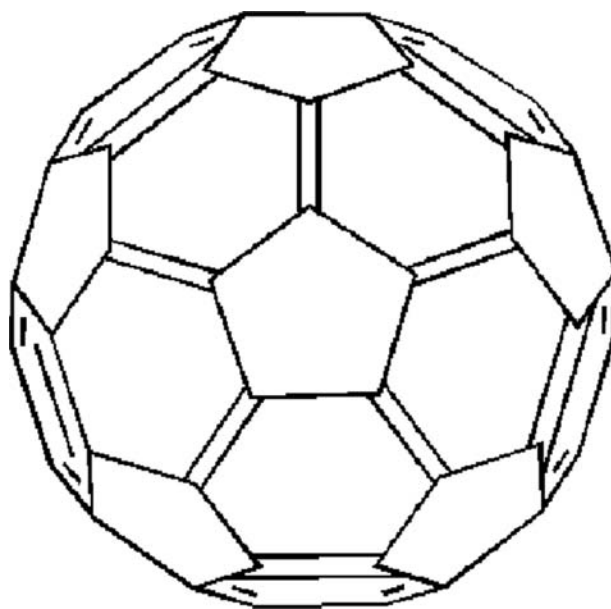


Fig. 3 A common type of drawing of  $C_{60}$ , showing double bonds at the site of the shortest bonds and not showing the back side of the ball.



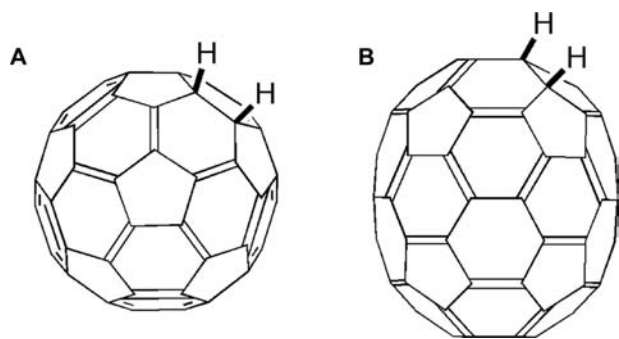


Fig. 4 (A)  $C_{60}H_2$  and (B)  $C_{70}H_2$ .

between carbon electrodes and in particular types of flames.<sup>[11–13]</sup> The precise mechanism by which fullerenes form is not known, but they seem to occur during the condensation of carbon plasmas. There has been a total synthesis of  $C_{60}$  reported,<sup>[14]</sup> but the ease, low cost, and scalability of arc and of flame methods clearly make these the preferred routes. In essentially all cases, the dominant fullerene formed is  $C_{60}$ , and the amounts of the higher fullerenes ( $C_{70}$  and higher) diminish rapidly, to the point where miniscule amounts of fullerenes larger than  $C_{84}$  are formed. In 2003, a large-scale facility dedicated to fullerene production was established, using the flame method.

Purification of fullerenes is usually accomplished by chromatography, and numerous methods have proven effective. On large scales, short silica/carbon columns are most appropriate. On smaller scales, sublimation can be used to produce highly pure, solvent-free fullerenes.

Fullerenes are typically dark, sometimes lustrous, solids. The liquid phase has not been observed, but the solids sublime well under high vacuum. The solubility of fullerenes is negligible in hydrocarbon solvents, but reasonable in aromatic and halogenated aromatic solvents.<sup>d</sup> Larger fullerenes are typically less soluble than smaller ones.

## CHEMICAL REACTIVITY

When macroscopic amounts of fullerenes became available for study around 1990, it did not take long to discover that these molecules were quite reactive.<sup>e</sup> Because fullerenes themselves have no chemical groups available for substitution, they can react only in

<sup>d</sup>For an extensive list of the solubility of  $C_{60}$  in different solvents, see Ref.<sup>[15]</sup>.

<sup>e</sup>A number of key early studies of the chemical reactivity of fullerenes are contained in Ref.<sup>[16]</sup>.

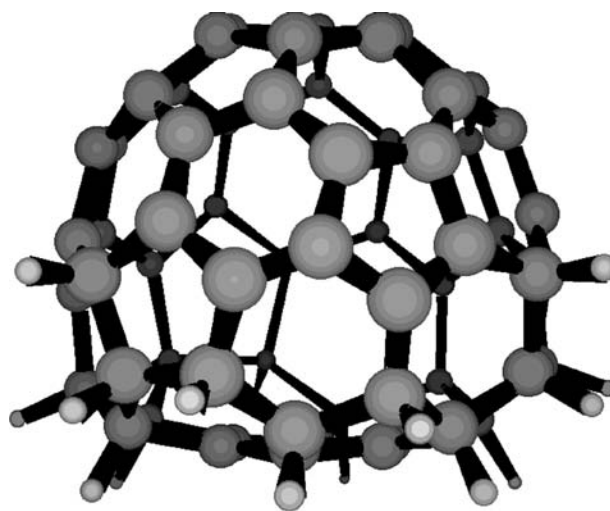


Fig. 5 The structure of  $C_{60}H_{18}$ .

addition reactions.<sup>[17]</sup> The driving force for these reactions is provided (in part) by the release of strain from pyramidalization. The chemistry of fullerenes has turned out to be very rich.<sup>f</sup>

## Hydrogenation

Hydrogenation of fullerenes is easily accomplished under a variety of conditions. The simplest hydrogenated fullerenes,  $C_{60}H_2$  and  $C_{70}H_2$  (Fig. 4), have been made by reduction with  $BH_3$ , with Zn, with diimide, and with other reagents.<sup>g</sup> In both of these cases, the two hydrogen atoms are bonded to adjacent carbons, as this arrangement is more stable than arrangements that place the hydrogen atoms farther apart. Interestingly,  $C_{60}H_2$  is a remarkably acidic compound for a hydrocarbon, with a  $pK_a$  below 5.

As expected, more highly hydrogenated compounds can be obtained, and compounds out to  $C_{60}H_{36}$  have been prepared, using transfer hydrogenation,  $Li/NH_3$ , or high-pressure catalytic hydrogenation. While  $C_{60}H_{18}$  is isolated as a single species,  $C_{60}H_{36}$  is isolated as a mixture of isomers. The structure of  $C_{60}H_{18}$  has been established as having a “turtle-shell” shape (Fig. 5).

## Oxidation

Treatment of  $C_{60}$  with most oxidizing agents results in the formation of  $C_{60}O$ . This compound is less soluble than  $C_{60}$  itself and less chromatographically mobile. Multiple oxidations occur with excess oxidizing agent,

<sup>f</sup>Excellent reviews include Refs.<sup>[18–22]</sup>.

<sup>g</sup>For reviews of hydrogenated fullerenes, see Refs.<sup>[23,24]</sup>.

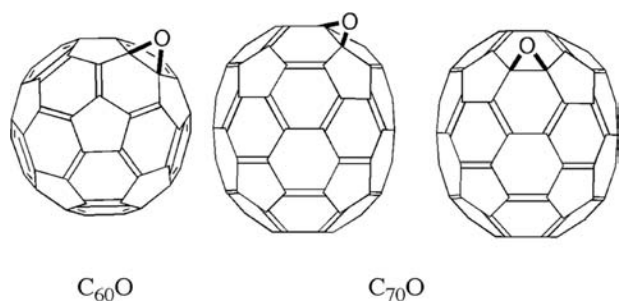


Fig. 6 The monooxides of  $C_{60}$  and  $C_{70}$ .

and multiple isomers of the  $C_{60}O_x$  product are formed. These oxides are increasingly insoluble and difficult to characterize. Oxidation of  $C_{70}$  is somewhat more complex, as multiple isomers of the monoadduct are possible. The two predominate isomers formed are shown in Fig. 6.

### Cycloadditions

Fullerenes react readily in a variety of different cycloadditions.<sup>h</sup> These reactions often proceed at room temperature, although multiple additions occur. In most cases, a single cycloaddition to  $C_{60}$  will produce a single isomer of monoadduct, but a second cycloaddition produces a mixture of isomeric diadducts. Reactions on less-symmetrical higher fullerenes are even more problematic. In practice, reactions are usually limited to less than 50% conversion to maximize the yield of monoadduct.

A number of different [2 + 2] cycloadditions have been reported. For example, benzyne adds in a [2 + 2] manner to produce a new 4-membered ring fused to  $C_{60}$  (Fig. 7). This reaction is thermal, although there are analogous photochemical reactions between fullerenes themselves, for example, the photopolymerization of  $C_{60}$ . While strong dienophiles will react with  $C_{60}$ , they do so in a [2 + 2] manner rather than the [4 + 2] manner of the classical Diels–Alder reaction.

A number of different [3 + 2] cycloadditions have been reported, leading to a rich variety of products. Nitrile oxides add to  $C_{60}$  to form isoxazolines, azomethine ylids add to form pyrrolidines, and diazoalkanes add to form pyrazolines. The latter case is one of the most important reactions in fullerene chemistry, and the  $C_{60}$ –pyrazoline adduct is thermally unstable and decomposes to new products. In the case of  $Ph_2CN_2$ , the primary product is the methanofullerene. However, in the case of  $CH_2N_2$ , the product is a novel compound  $C_{61}H_2$ , known as a homofullerene or

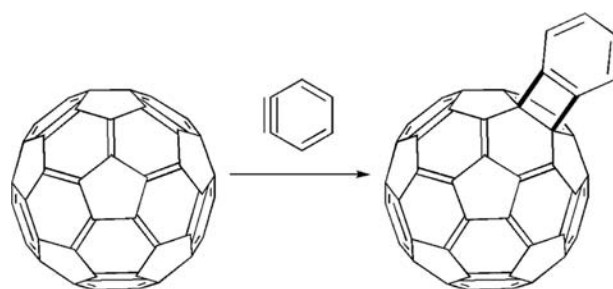


Fig. 7 The [2 + 2] cycloaddition of benzyne to  $C_{60}$ .

a “fulleroid.”<sup>i</sup> Fulleroids are fullerenes that have been “inflated” by the addition of a carbon atom and the opening of one of the original C–C bonds in the cage. The opened bond is typically the bond that formed the fusion of a 5-membered ring with a 6-membered ring (Fig. 8).

Similar chemistry occurs with alkyl azides, leading to the formation of azafulleroids. Azafulleroids have served as the starting material for the formation of  $C_{59}N$ -based species, a rare example of a fullerene cage with a heteroatom replacing one of the carbon atoms<sup>[26]</sup> (Fig. 9).

Fullerenes undergo a number [4 + 2] cycloadditions, with the fullerene functioning as the 2-electron component. Reaction with dienes such as cyclopentadiene yields adducts, and, as is often the case, multiple additions can occur.

Of the various 1,3-dipolar cycloaddition reactions that have been demonstrated on fullerenes, the addition of azomethine ylids has proven to be particularly versatile. This reaction converts a fullerene into a fulleropyrrolidine (Fig. 10). The nitrogen atom provides a convenient point of attachment for a host of different groups.

A tandem [4 + 4]/[2 + 2 + 2] cycloaddition route has been used to generate a novel fullerene ( $C_{62}$ ) that is not formed in significant amounts in arc reactors (Fig. 11).

### Addition of Nucleophiles

Fullerenes react in a manner not unlike electron-deficient alkenes. Strong nucleophiles add readily and often add repeatedly if conditions are not carefully controlled. Examples of carbon nucleophiles that react with  $C_{60}$  include alkyl lithium reagents, alkyl magnesium (Grignard) reagents, acetylide anions, and cyanide. Addition of several equivalents of nucleophile is a common side reaction. Organocuprates also add readily, resulting in a symmetrical cyclopentadienyl pattern. Heteroatom nucleophiles, including amines, are also known to add to  $C_{60}$ .

<sup>h</sup>For a review of cycloadditions of fullerenes, see Ref.<sup>[21]</sup>.

<sup>i</sup>For a detailed discussion of the nomenclature of fullerenes (including homofullerenes), see Ref.<sup>[25]</sup>.

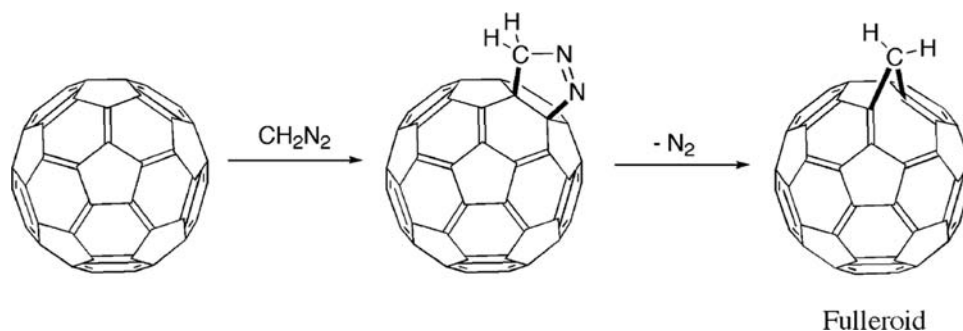


Fig. 8 Formation of a fulleroid via addition of diazomethane to  $C_{60}$ .

One of the most useful reactions in all of fullerene chemistry is the addition of dialkyl bromomalonate anion. This reaction, often called the Bingel reaction, results in formation of a cyclopropane (Fig. 12). Most likely, this reaction involves addition of the enolate nucleophile, followed by displacement of the bromide ion by the resulting fulleride anion. This reaction has produced  $T_d$ -symmetrical species that display luminescence. Luminescence from fullerenes and fullerene derivatives is uncommon.<sup>[27]</sup>

### Addition of Radicals

Radicals add readily and repeatedly to fullerenes.<sup>[28]</sup> Alkyl radicals can add over 30 times to  $C_{60}$ . Sulfur- and nitrogen-based radicals have been observed to add to fullerenes. The tendency for multiple additions and multiple isomers has limited the synthetic utility of this reaction. However, radical addition to fullerenes has been used as method for covalent incorporation of fullerenes into polymers.

### Addition of Electrophiles

Halogenation of fullerenes is easily accomplished with a variety of reagents. The resulting compounds are reactive under a variety of conditions, establishing the halogenated compounds as useful synthetic

intermediates. Addition of  $F_2$ ,  $Br_2$ , and  $Cl_2$  to  $C_{60}$  are all known, but addition of  $I_2$  is not favorable. Reaction of  $C_{60}$  with neat  $Br_2$  produces  $C_{60}Br_8$  and  $C_{60}Br_{24}$  (Fig. 13).<sup>[29]</sup> The addition is reversible, as both products lose  $Br_2$  upon heating.

Chlorination with  $ICl$  produces  $C_{60}Cl_6$ , an interesting compound with an isolated cyclopentadienyl substructure. The presence of chlorines opens up new chemical possibilities, and these atoms have been substituted by methoxide and by aromatic rings.<sup>[30]</sup> Dissolving  $C_{60}Cl_6$  in benzene with  $AlCl_3$  brings about a classical Friedel–Crafts reaction, producing  $C_{60}Ph_5Cl$  (Fig. 14).<sup>[31]</sup> This compound has been used to make metal–cyclopentadienyl complexes.

Fluorination has resulted in a number of different highly fluorinated species (up to  $C_{60}F_{48}$ ),<sup>[32]</sup> and these are typically reactive toward nucleophiles, including weak nucleophiles such as water. In many cases, the addition patterns seen in fluorination reactions mimic the pattern seen in hydrogenation.

Fuming sulfuric acid adds to  $C_{60}$  to produce cyclic sulfates. These can be hydrolyzed to produce polyhydroxylated compounds known as fullerols. These compounds are usually isolated as complex mixtures, containing species with different numbers of hydroxyl groups and numerous isomers for each molecular formula. Fullerols are notable as one of the few classes

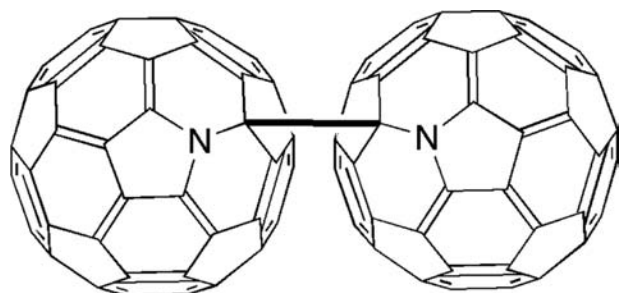


Fig. 9 The  $C_{59}N$  dimer.



Fig. 10 A fulleropyrrolidine.

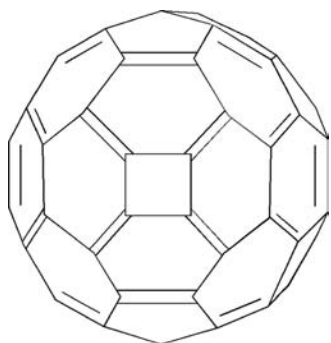


Fig. 11 The structure of  $C_{62}$ .

of fullerene derivatives that are commonly water-soluble.

### Electrophilic Substitution

The chemistry of most aromatic hydrocarbons is characterized by substitution reactions, in which an attacking electrophile replaces a peripheral hydrogen. The lack of peripheral groups (the lack of a periphery!) makes it impossible to do a true substitution reaction on a fullerene, but fullerene derivatives can participate in these reactions. The halides have proven to be useful in electrophilic aromatic substitution reactions. Dissolving  $C_{60}Cl_6$  in benzene with  $AlCl_3$  brings about a classical Friedel–Crafts reaction, producing  $C_{60}Ph_5Cl$ .

### Multiple Additions

While a single isomer results from addition of one group to  $C_{60}$ , addition of a second group can result in large number of different isomers. Two isomers are the most common, but in most cases, complex mixtures of many isomers result.

A template-directed approach has been used to address this problem. This approach relies on the initial addition that connects a template to the fullerene. The template bears reactive groups that lead to additional reactions on the fullerene, but only at sites that can be reached by the template.<sup>j</sup>

### Metal Complexes

Fullerenes form complexes with a wide array of transition metals,<sup>[34,35]</sup> essentially always in a  $\eta - 2$  manner.<sup>k</sup> These complexes are often very insoluble,

<sup>j</sup>For an example, see Ref.<sup>[33]</sup>.

<sup>k</sup>For an example of a pentahapto metal complex, see Ref.<sup>[36]</sup>.

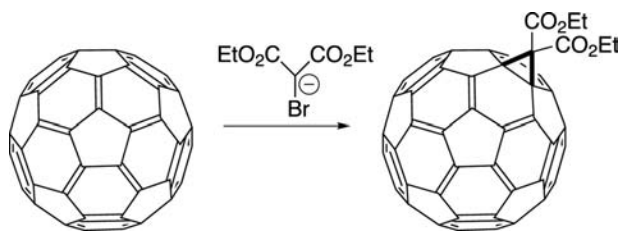


Fig. 12 Cyclopropanation of  $C_{60}$ .

but a number have been crystallographically characterized. Complexes with platinum and iridium are common, and a typical example is shown in Fig. 15.

Alkali metals and alkaline earth metals generally undergo electron-transfer reactions with fullerenes, leading to  $M_xC_{60}$  species, where  $x$  depends on how strongly reducing the metal is. In solution, the exact species formed depends on the metal and on the solvent.

The most novel aspect of the organometallic chemistry of fullerenes is the chemistry of endohedral fullerenes. Endohedral complexes of fullerenes are composed of one or more atoms *inside* of a carbon shell. Such species are commonly denoted as “ $M@C_{60}$ ,” meaning atom  $M$  *inside*  $C_{60}$ .<sup>[37,38]</sup> There is very little free space inside of a fullerene, so only individual atoms or small groups of atoms can be accommodated.

Endohedral fullerenes can be prepared in a number of different ways. It is possible to drive small inert gas atoms directly into the interior of a fullerene. This is the common synthetic route for species such as

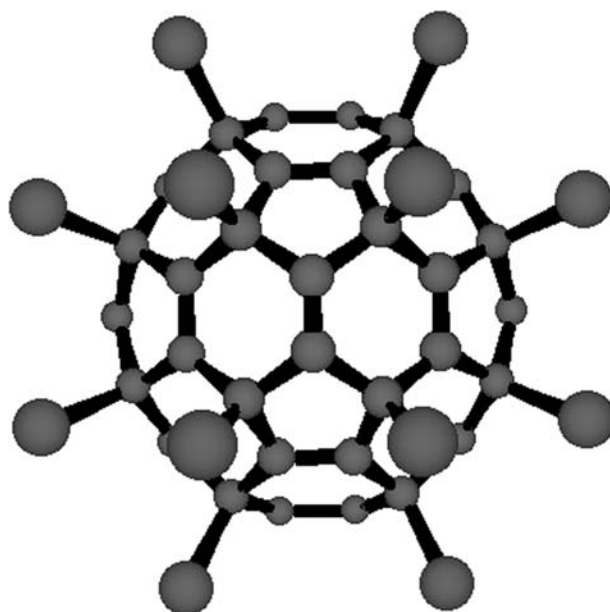


Fig. 13  $C_{60}Br_{24}$ , showing one side of the structure.

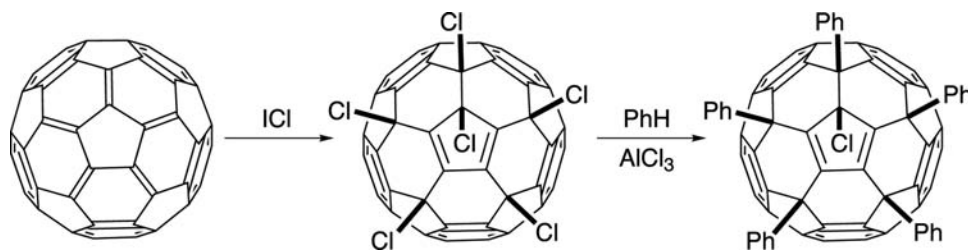


Fig. 14 Preparation and reactions of  $C_{60}Cl_6$ .

$^3He@C_{60}$  and  $^3He@C_{70}$ . This procedure requires high temperature ( $>600^\circ C$ ) and pressures ( $>2000$  atm) and results in low ( $\leq 0.1\%$ ) incorporation.<sup>[39]</sup> Regardless of the difficulty, these  $^3He$  complexes have proven invaluable for the  $^3He$  NMR signal, which has been used to determine the number of isomers of a fullerene (or fullerene derivative) present in a sample and as a probe of the internal electronic environment.

A second route to endohedral fullerenes is to form the fullerene around the endohedral atom(s). This is most commonly performed by using a metal-doped carbon rod in an arc reactor. The resulting endohedral complexes are then isolated from the resulting soot and purified by chromatography. A wide range of endohedral complexes has been formed by this method, and the carbon shell formed around the metal is often (usually) not a  $C_{60}$  or a  $C_{70}$  shell.

The most common members of this class of compound are species such as  $La@C_{82}$ . Much larger shells and much smaller shells have been observed ( $La_3@C_{106}$ ,  $U@C_{28}$ ). Multiple atoms can be encapsulated, including a mixture of metals and non-metals ( $Sc_3N@C_{82}$ ).

### The Chemistry of Higher Fullerenes

Higher fullerenes ( $C_{70}$  and larger fullerenes) have received much less attention than has  $C_{60}$ .<sup>[40,41]</sup> The

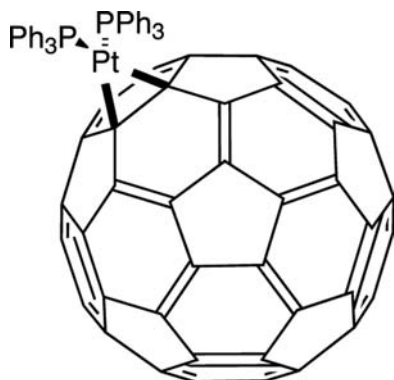


Fig. 15 A typical transition metal complex of  $C_{60}$ ,  $(Ph_3P)_2PtC_{60}$ .

limited availability and high price of these molecules have made it difficult to undertake extensive studies of their chemistry. Thankfully, the reactivity of the higher fullerenes is very similar to that of  $C_{60}$ . However, because  $C_{70}$  and the higher fullerenes are less symmetrical than  $C_{60}$ , there are more options for the site of the first addition, for the second addition, and so on. Hirsch–Bingel reactions on  $C_{70}$  have been used to identify the most reactive site, the second reactive site, and so on.<sup>[42]</sup> As expected, the most reactive site on  $C_{70}$  is the  $C=C$  bond between the most pyramidalized carbons in the molecule. The second most reactive site is typically at the opposite pole of the molecule. The last to react are usually the carbons closest to the equator.

There are exceptions to this rule. Addition of chlorine, as well as reduction with  $Zn(Cu)$ , results in addition near the equatorial belt. This pattern may result from a different mechanism (radical?) than is operating. As a result, reactions on the poles and near the equatorial belt are known.

### APPLICATIONS

A variety of applications have been proposed for fullerenes based on the potential exploitation of the electronic or optical properties. The quantum yield for production of the triplet excited state of  $C_{60}$  is nearly unity, and  $C_{60}$  is an efficient sensitizer for producing singlet oxygen. The high molar absorptivity and absorption at the long-wavelength end of the visible spectrum, coupled with being an efficient sensitizer, makes fullerenes good candidates in photodynamic therapy. Fullerenes exhibit non-linear optical behavior, and so optical limiting applications are possible.<sup>[43]</sup> Fullerene derivatives have also been used in enzyme inhibitors, and fullerene derivatives have shown activity against a number of tumor cells lines.<sup>[44]</sup> Fullerenols have shown some promise as MRI contrast agents.

Most of the potential applications lay in the electronic and materials areas. Transistors have been made from  $C_{60}$  films and from  $C_{70}$  films.<sup>[45]</sup> Much excitement was generated when the superconductive  $M_3C_{60}$

species were discovered, and these fulleride films and  $T_c$ 's as high as 33 K have been measured in  $Cs_2RbC_{60}$ . While some advances beyond 33 K have been reported, to date, the  $T_c$ 's of fullerene-based superconductors have not surpassed copper oxide-based materials.

## CONCLUSION

Fullerenes are closed shells formed of carbon atoms. The chemistry of these novel forms of carbon is similar to electron-deficient alkenes, in that the fullerenes react with nucleophiles faster than with electrophiles. The chemistry of fullerenes is largely addition chemistry, and a host of reagents is known to add to  $C_{60}$  and other fullerenes. Most addition reactions will proceed multiple times, and conversions are typically limited to ~50% to produce the highest yield of mono-adduct. Multiple additions generally result in complex mixtures of isomers. Higher fullerenes ( $C_{70}$  and larger) pose even more daunting regiochemical problems. Template-directed methods can help produce di-adducts, triadducts, and higher adducts with predictable regiochemistry.

## REFERENCES

- Powell, W.H.; Cozzi, F.; Moss, G.P.; Thilgen, C.; Hwu, R.J.-R.; Yerin, A. Nomenclature for the  $C_{60-I_h}$  and  $C_{70-D_{5h(6)}}$  fullerenes. *Pure Appl. Chem.* **2002**, *74*, 629–695.
- Diederich, F.; Whetten, R.L.; Thilgen, C.; Ettl, R.; Chao, I.; Alvarez, M.M. Fullerene isomerism: isolation of  $C_{2v-C_{78}}$  and  $D_3-C_{78}$ . *Science* **1991**, *254*, 1768–1770.
- Qian, W.; Bartberger, M.D.; Pastor, S.J.; Houk, K.N.; Wilkins, C.L.; Rubin, Y.  $C_{62}$ , a non-classical fullerene incorporating a four-membered ring. *J. Am. Chem. Soc.* **2000**, *122*, 8333–8334.
- Haddon, R.C. Comment on the relationship of the pyramidalization angle at a conjugated carbon to the  $\sigma$  bond angles. *J. Phys. Chem., A* **2001**, *105*, 4164–4165.
- Haddon, R.C. Measure of nonplanarity in conjugated molecules: which structurally characterized molecule displays the highest degree of pyramidalization? *J. Am. Chem. Soc.* **1990**, *112*, 3385–3389.
- Haddon, R.C. Chemistry of the fullerenes: the manifestation of strain in a class of continuous aromatic molecules. *Science* **1993**, *261*, 1545–1550.
- Gomes, J.A.N.F.; Mallion, R.B. Aromaticity and ring currents. *Chem. Rev.* **2001**, *101*, 1349–1383.
- Bühl, M.; Hirsch, A. Spherical aromaticity of fullerenes. *Chem. Rev.* **2001**, *101*, 1153–1183.
- Fukuzumi, S.; Guldi, D.M. Electron-transfer chemistry of fullerenes. *Electron Trans. Chem.* **2001**, *2*, 270–337.
- Reed, C.A.; Bolskar, R.D. Discrete fulleride anions and fullerenium cations. *Chem. Rev.* **2000**, *100*, 1075–1119.
- Kroto, H.W.; Fischer, J.E.; Cox, D.E., Eds. *The Fullerenes*; Pergamon Press: Oxford, UK, 1993.
- Krätschmer, W.; Lamb, L.D.; Fostiropoulos, K.; Huffman, D.R. Solid  $C_{60}$ : a new form of carbon. *Nature* **1990**, *347*, 354–358. Arc method: 1.
- Howard, J.B.; McKinnon, J.T.; Makarovskiy, Y.; Lafleur, A.L.; Johnson, M.E. Fullerenes  $C_{60}$  and  $C_{70}$  in flames. *Nature* **1991**, *352*, 139–141.
- Boorum, M.M.; Vasil'ev, Y.V.; Drewello, T.; Scott, L.T. Groundwork for a rational synthesis of  $C_{60}$ : cyclodehydrogenation of a  $C_{60}H_{30}$  polyarene. *Science* **2001**, *294*, 828–831.
- Ruoff, R.S.; Tse, D.S.; Malhotra, R.; Lorents, D.C. Solubility of  $C_{60}$  in a variety of solvents. *J. Phys. Chem.* **1993**, *97*, 3379–3383.
- Hammond, G.S.; Kuck, V.J., Eds. *Fullerenes: Synthesis, Properties, and Chemistry of Large Carbon Clusters*; American Chemical Society Press: Washington, DC, 1992; 481.
- Hirsch, A. Addition reactions of buckminsterfullerene ( $C_{60}$ ). *Synthesis* **1995**, 895–913.
- Hirsch, A., Ed.; *Principles of Fullerene Chemistry*; Topics in Current Chemistry; Springer, 1999; 199, 1–65.
- Fullerene chemistry. *Tetrahedron Symp. Print* **1996**, *52*, 4925–5261.
- Diederich, F.; Thilgen, C. Covalent fullerene chemistry. *Science* **1996**, *271*, 317–323.
- Taylor, R., Ed. *The Chemistry of the Fullerenes*; World Scientific Books, 1994; Vol. 4.
- Hirsch, A. *The Chemistry of the Fullerenes*; Thieme: Stuttgart, 1994.
- Nossal, J.; Saini, R.K.; Alemany, L.B.; Meier, M.S.; Billups, W.E. The synthesis and characterization of fullerene hydrides. *Eur. J. Chem.* **2001**, *7*, 4167–4180.
- Gol'dshleger, N.F.; Moravshii, A.P. Fullerene hydrides: synthesis, properties, and structure. *Russ. Chem. Rev.* **1997**, *66*, 323–342.
- Powell, W.H.; Cozzi, F.; Moss, G.P.; Thilgen, C.; Hwu, R.J.-R.; Yerin, A. Nomenclature for the  $C_{60-I_h}$  and  $C_{70-D_{5h(6)}}$  fullerenes. *Pure Appl. Chem.* **2002**, *74*, 629–695.
- Hummelen, J.C.; Bellavia-Lund, C.; Wudl, F. Heterofullerenes. *Top. Curr. Chem.* **1999**, *199*, 93–134.
- Arbogast, J.W.; Darmanyan, A.P.; Foote, C.S.; Rubin, Y.; Diederich, F.N.; Alvarez, M.M.; Anz, S.J.; Whetten, R.L. Photophysical properties of  $C_{60}$ . *J. Phys. Chem.* **1991**, *95*, 11–12.
- Morton, J.R.; Negri, F.; Preston, K.F. Addition of free radicals to  $C_{60}$ . *Acc. Chem. Res.* **1998**, *31*, 63–69.
- Tebbe, F.N.; Harlow, R.L.; Chase, D.B.; Thorn, D.L.; Campbell, G.C.; Calabrese, J.C.; Herron, N.; Young, R.J.; Wasserman, E. Synthesis and single crystal X-ray structure of a highly symmetrical  $C_{60}$  derivative,  $C_{60}Br_{24}$ . *Science* **1992**, *256*, 822–825.
- Birkett, P.R.; Avent, A.G.; Darwish, A.D.; Hahn, I.; Kroto, H.W.; Langley, G.J.; O'Loughlin, J.; Taylor, R.; Walton, D.R.M. Arylation of [60]fullerene via electrophilic aromatic substitution involving the electrophile  $C_{60}Cl_6$ : front side nucleophilic substitution of fullerenes. *J. Chem. Soc., Perkin Trans. 2* **1997**, 1121–1125.



31. Avent, A.G.; Birkett, P.R.; Crane, J.D.; Darwish, A.D.; Langley, G.J.; Kroto, H.W.; Taylor, R.; Walton, D.R.M. The structure of  $C_{60}Ph_5Cl$  and  $C_{60}Ph_5H$ , formed via electrophilic aromatic substitution. *J. Chem. Soc., Chem. Commun.* **1994**, 1463–1464.
32. Taylor, R. Progress in fullerene fluorination. *Russ. Chem. Bull.* **1998**, *47*, 823–832.
33. Cardullo, F.; Isaacs, L.; Diederich, F.; Gisselbrecht, J.-P.; Boudon, C.; Gross, M. Regiospecific templated synthesis of  $D_{2h}$ -symmetrical tetrakis-adduct  $C_{64}(COOEt)_8$  by reversible tether-directed remote functionalization of  $C_{60}$ . *J. Chem. Soc., Chem. Commun.* **1996**, 797–799.
34. Sokolov, V.I., Ed. *Special Issue: Organometallic Chemistry of Fullerenes*; J. Organomet. Chem.; Elsevier, 2000; 599 (1).
35. Birkett, P.R. Fullerenes. In *Annual Reports on the Progress of Chemistry, Section A: Inorganic Chemistry*; The Chemical Society: London, 2000; 96, 467–490.
36. Sawamura, M.; Iikura, H.; Nakamura, E. The first pentahaptofullerene metal complexes. *J. Am. Chem. Soc.* **1996**, *118*, 12850–12851.
37. Shinohara, H. *Fullerenes: Chemistry, Physics, and Technology*; Kadish, K.M., Ruoff, R.S., Eds.; John Wiley and Sons: New York, 2000; 357 pp.
38. Hirsch, A. New cages and unusual guests: Fullerene chemistry continues to excite. *Angew. Chem., Int. Ed. Engl.* **2001**, *40*, 1195–1197.
39. Saunders, M.; Jimenez-Vazquez, H.A.; Cross, R.J.; Mroczkowski, S.; Gross, M.L.; Giblin, D.E.; Poreda, R.J. Incorporation of helium, neon, argon, krypton, and xenon into fullerenes using high pressure. *J. Am. Chem. Soc.* **1994**, *116*, 2193–2194.
40. Diederich, F.; Whetten, R.L. Beyond  $C_{60}$ : the higher fullerenes. *Acc. Chem. Res.* **1992**, *25*, 119–126.
41. Diederich, F.; Ettl, R.; Rubin, Y.; Whetten, R.L.; Beck, R.; Alvarez, M.; Anz, S.; Sensharma, D.; Wudl, F.; Khemani, K.C.; Koch, A. The higher fullerenes: isolation and characterization of  $C_{76}$ ,  $C_{84}$ ,  $C_{90}$ ,  $C_{94}$ , and  $C_{70-O}$ , an Oxide of  $D_{5h}-C_{70}$ . *Science* **1991**, *252*, 548–551.
42. Herrmann, A.; Ruettimann, M.; Thilgen, C.; Diederich, F. Multiple cyclopropanations of  $C_{70}$ . Synthesis and characterization of bis-, tris-, and tetrakis-adducts and chiroptical properties of bis-adducts with chiral addends, including a recommendation for the configurational description of fullerene derivatives with a chiral addition pattern. *Helv. Chem. Acta* **1995**, *78*, 1673–1704.
43. Signorini, R.; Bozio, R.; Prato, M. Optical limiting applications. *Dev. Fuller. Sci.* **2002**, *4*, 295–326.
44. Schuster, D.I.; Wilson, S.R.; Schinazi, R.F. Anti-human immunodeficiency virus activity and cytotoxicity of derivatized buckminsterfullerenes. *Bioorg. Med. Chem. Lett.* **1996**, *6*, 1253–1256.
45. Haddon, R.C.  $C_{70}$  thin film transistors. *J. Am. Chem. Soc.* **1996**, *118*, 3041–3042.

# Fullerenes: Isomer Identification

Guangyu Sun

National Cancer Institute, National Institute of Health (NIH),  
Frederick, Maryland, U.S.A.

## INTRODUCTION

Buckminsterfullerene  $C_{60}$  was first detected in the time-of-flight mass spectrometer from the product of laser vaporization of graphite<sup>[1]</sup> and later obtained in large quantity from electric arc resistive heating of graphite rods.<sup>[2,3]</sup> The four characteristic peaks in the infrared (IR) spectrum of  $C_{60}$  revealed its truncated icosahedron structure,<sup>[3]</sup> which was further confirmed by nuclear magnetic resonance (NMR) spectroscopy.<sup>[4-6]</sup> Separation and characterization of fullerenes  $C_{70}$ ,<sup>[4,5,7]</sup>  $C_{76}$ ,<sup>[8]</sup>  $C_{78}$ ,<sup>[9-12]</sup>  $C_{82}$ ,<sup>[11]</sup> and those with even higher carbon atom counts followed. High-performance liquid chromatography (HPLC) has proved to be a powerful technique to separate fullerene isomers, while  $^{13}C$  NMR is the method of choice to characterize them.

The cage-like structure of a fullerene consists of 12 five-membered rings and a number of six-membered rings depending on the number of carbon atoms.<sup>[13]</sup> It was postulated that the five-membered rings need to be separated from each other to reduce the localization of the strain caused by the bending of the  $sp^2$ -hybridized carbon atoms. This is the essence of the isolated pentagon rule (IPR),<sup>[13]</sup> which dramatically reduces the possible number of isomers for a given fullerene family. Fig. 1 shows the major isomers of fullerenes  $C_{60}$  to  $C_{84}$ . On the other hand, it is still common that several IPR isomers of a fullerene have same point-group symmetry and have same  $^{13}C$  NMR patterns. For instance, isomers **1**, **5**, **21**, and **22** of fullerene  $C_{84}$  all have  $D_2$  symmetry and give 21 NMR peaks with equal intensity. One of the two major isomers of  $C_{84}$  has  $D_2$  symmetry as observed in experiment, but its structure cannot be determined from the one-dimensional (1-D) NMR spectrum.<sup>[11,12]</sup> Relative energies calculated using quantum mechanics are helpful, but not definitive in determination of the molecular structure. Accurate theoretical chemical shifts predicted by high-level quantum mechanical calculations have been shown to result in unambiguous assignment for those isomers.<sup>[14,15]</sup>

This entry reviews the identification of the fullerene isomers based on theoretical  $^{13}C$  NMR chemical shifts. All the studied isomers have been separated by HPLC

and characterized by NMR spectroscopy, and their NMR chemical shifts are taken from literature. We first briefly review the experimental aspects of the generation, separation, and characterization of fullerene isomers and earlier theoretical attempts to assign these isomers. Subsequently, the predicted NMR spectra for nine isomers of fullerenes  $C_{70}$ ,  $C_{76}$ ,  $C_{78}$ ,  $C_{80}$ , and  $C_{84}$  are compared with experimental data, demonstrating the accuracy of the density functional theory (DFT) calculated chemical shifts and, at the same time, confirming the experimental structural assignment. The discrepancy between experiment and theory in the NMR spectra of the  $D_{5d}$  isomer of fullerene  $C_{80}$  is discussed. Then the predicted NMR spectra for fullerenes  $C_{82}$  to  $C_{90}$  are summarized, and the identification of 11 previously unassigned isomers is achieved for which good experimental spectra are available. The reported results on theoretical NMR chemical shifts for charged and substituted fullerenes are also briefly reviewed. Finally, the relationship between chemical shift and local connectivity, and the energetics of the stable fullerene isomers are discussed.

## EXPERIMENTAL ISSUES

Fullerenes were first detected in the product of laser vaporization of graphite.<sup>[1]</sup> Although this method gave sufficient amounts of fullerenes for mass spectroscopic measurement, it is not suitable to produce samples large enough for separation. Gram-scale samples of fullerenes were obtained by resistive heating,<sup>[2,3]</sup> electric arc discharge,<sup>[16]</sup> and plasma discharge of graphite.<sup>[17]</sup> Fullerenes up to  $C_{108}$  have also been obtained from the condensable material from flat premixed benzene/oxygen/argon flames.<sup>[18,19]</sup> Recently, the rational chemical synthesis of  $C_{60}$  has been achieved by laser irradiation<sup>[20]</sup> of polycyclic aromatic hydrocarbon  $C_{60}H_{30}$  and later in isolable quantities by flash vacuum pyrolysis<sup>[21]</sup> of  $C_{60}H_{27}Cl_3$  at  $1100^\circ C$ . Because no other fullerenes were produced as byproducts, this method raised the possibility of producing fullerenes by target-specific synthesis.

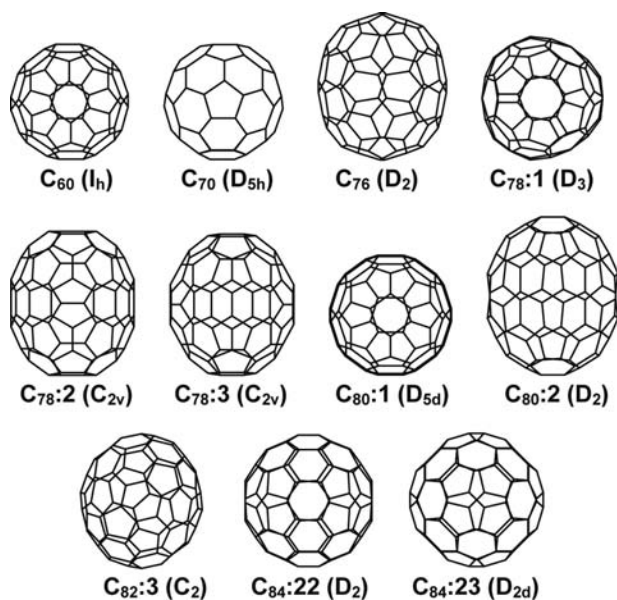


**Fig. 1** The major isomers of fullerenes  $C_{60}$ ,  $C_{70}$ ,  $C_{76}$ ,  $C_{78}$ ,  $C_{80}$ ,  $C_{82}$ , and  $C_{84}$ .

The resulting fullerenes are normally first extracted using various organic solvents, then separated by HPLC. Characterization of the fullerenes includes mass spectrum, UV-Vis, IR, and NMR measurements. Among the characterization techniques, 1-D  $^{13}\text{C}$  NMR spectrum is easily obtained and directly related to the molecular structure, thus commonly used for fullerenes. The  $^3\text{He}$  NMR spectra have also been used to distinguish among isomers as well as to probe the magnetic shielding environment inside the fullerene cavity.<sup>[22,23]</sup> We will focus in this entry on the identification of fullerene isomers based on 1-D NMR spectra.

## EARLIER THEORETICAL ATTEMPTS

Much attention was focused on the energetic aspects of fullerenes, while considerably less effort has been paid to their magnetic properties. The magnetic susceptibility of buckminsterfullerene  $C_{60}$  was studied in the early theoretical studies<sup>[24–26]</sup> before the fullerene samples were obtained. After fullerene samples became available, the prediction of NMR chemical shifts has been an active subject to identify the observed isomers. Fowler and Manolopoulos<sup>[13,27]</sup> presented all mathematically possible structures for fullerenes  $C_{60}$ – $C_{100}$  and compiled the structures for all IPR-abiding isomers. Häser et al.<sup>[28]</sup> used the gauge-independent atomic orbital-coupled perturbed Hartree-Fock (GIAO-CPHF/DZP) method to calculate the chemical shifts of  $C_{60}$  and  $C_{70}$ . In the first attempt to identify the observed  $D_2$  isomer of  $C_{84}$ , Schneider et al.<sup>[29]</sup> calculated the NMR spectra for isomers **5**, **22**, and **23**

(isomer numbering after Fowler and Manolopoulos,<sup>[13]</sup> which will be followed here) using the GIAO-SCF/TZP level of theory. They concluded that isomer **22** was the most likely structure because the spectral span of isomer **5** was much larger than that of the observed isomer and isomer **22** was favored over isomer **21** on energetic grounds. The calculated NMR spectral spans were used to rule out the  $D_2(I_h)$  isomer of  $C_{80}$  as the experimentally observed  $D_2$  isomer.<sup>[30]</sup> Heine et al.<sup>[31]</sup> used the individual gauge for local orbitals-density functional based tight binding (IGLO-DFTB) method to study fullerenes  $C_{70}$ ,  $C_{76}$ ,  $C_{78}$ , five isomers of  $C_{84}$ ,  $(C_{36})_2$ , and  $(C_{60})_2$ . Qualitative agreement with experiment was achieved for the experimentally distinguished isomers, and assignment of the  $D_2$  isomer as **22** was supported. A full survey of the 24 isomers of  $C_{84}$  was later reported.<sup>[32]</sup> The structure of  $C_{70}$  was solved by Hedberg et al.<sup>[33]</sup> in gas-phase electron diffraction experiments with the help of NMR chemical shifts calculated at the GIAO-SCF/TZP level of theory. Accurate chemical shifts of  $C_{60}$  and  $C_{70}$  were calculated using Hartree-Fock (HF) and DFT methods by Bühl et al.<sup>[34]</sup>

## COMPUTATIONAL METHOD

While the relative energies of the fullerene isomers calculated from total electronic energies by various quantum mechanical methods play an important role in determining the structures of the observed isomers, it is not definitive because the observed isomers have to survive the high temperature used in the production process. Direct comparison between accurate theoretical chemical shifts and experimental values is necessary to assign the observed fullerenes as NMR is the commonly used characterization technique and chemical shift directly relates to the chemical environment of the nucleus. In early 1998, it appeared to us that the calculation of NMR chemical shifts for molecules of the size of fullerenes became practical using ab initio or DFT methods with medium basis sets. Because the DFT method<sup>[35]</sup> in the form of B3LYP<sup>[36,37]</sup> hybrid functional had been shown to give better geometries and vibrational frequencies for a wide range of molecules than ab initio HF method, it was tested to predict the NMR chemical shifts of isomers **22** and **23** of fullerene  $C_{84}$ .<sup>[15]</sup> The results were in very good agreement with experimental data and led to the prediction of NMR chemical shifts for other fullerenes and subsequent assignment of their isomers. The calculation of NMR properties of fullerenes has recently been reviewed by Heine.<sup>[38]</sup>

To perform NMR calculations, good geometry is required.<sup>[39]</sup> Starting from model building or downloaded coordinates,<sup>[40]</sup> we first optimized the

geometries using the PM3 semiempirical method.<sup>[41]</sup> Frequency analyses were normally performed at this level to ensure that the structures are indeed minima. The structures corresponding to true minima were further optimized using B3LYP functional<sup>[36,37]</sup> and the STO-3G, 3-21G, and 6-31G\* (or 6-31G for C<sub>86</sub>, C<sub>88</sub>, and C<sub>90</sub>) basis sets. The main purpose of this practice is to save computer time by always starting from the best available geometry; it also gives structures and energy values at the intermediate theoretical levels. Geometry optimizations normally converge after about ten cycles at the B3LYP/STO-3G level and after about four or five cycles with larger basis sets. Because the numbers of IPR isomers for the large fullerenes are very large (46 for C<sub>90</sub>),<sup>[13]</sup> we have limited the calculations using the larger basis sets on the isomers of fullerenes C<sub>86</sub>, C<sub>88</sub> and C<sub>90</sub> that have relative energies less than 25 kcal/mol at the B3LYP/STO-3G level. The default settings for convergence criteria and the default integration grid were used. All geometry optimizations were performed using Gaussian 98 program.<sup>[42]</sup>

The NMR shielding tensors were evaluated employing the GIAO method<sup>[43]</sup> at the geometries optimized at the highest level. The 6-31G\* or 6-31G basis sets were used for all fullerene isomers depending on the basis set used for geometry optimization. A larger 6-311G\*\* basis set was also used for selected isomers. The NMR calculations were carried out using the PQS program.<sup>[44]</sup> The <sup>13</sup>C NMR chemical shifts were obtained by converting the isotropic shielding constant by the following formula:

$$\delta(i) = \delta(C_{60}) + \sigma(C_{60}) - \sigma(i) \quad (1)$$

where the experimental chemical shift of C<sub>60</sub>,  $\delta(C_{60})$ , is taken as 143.15 ppm, after Avent et al.,<sup>[45]</sup>  $\sigma(C_{60})$  is the calculated chemical shielding for C<sub>60</sub>, and  $i$  is the carbon atom under consideration. The experimental chemical shift of C<sub>60</sub> is used as a second reference to correct the systematic error of about 4 ppm in the calculated chemical shifts when only TMS is used as the reference.<sup>[14]</sup>

### VALIDATION OF PREDICTED <sup>13</sup>C NMR CHEMICAL SHIFTS FOR FULLERENES

In this section, we show that the DFT-calculated <sup>13</sup>C NMR chemical shifts for fullerenes agree well with experimental values for the fullerene isomers that can be identified based on the 1-D NMR pattern. It is shown that the spectral span, grouping of the peaks, and the relative positions of the half-intensity peaks with respect to those of full-intensity peaks are important features in comparing theoretical and experimental NMR spectra. An empirical trend emerges to

indicate that the NMR peaks above 140 ppm are better reproduced than peaks below 140 ppm.

### Buckminsterfullerene C<sub>60</sub>

The icosahedral symmetry of fullerene C<sub>60</sub> renders all of its 60 carbon atoms equivalent, giving one signal in the NMR spectrum. The observed chemical shift for C<sub>60</sub> ranges from 142.68<sup>[4]</sup> to 143.2 ppm.<sup>[5,8,10]</sup> The chemical shift predicted at the B3LYP/6-31G\* level is 138.72 ppm.<sup>[14]</sup> This is in very good agreement with experiment, considering that <sup>13</sup>C NMR signal spread over a wide range of 0–200 ppm. The deviation between our prediction and experiment is 3.96 to 4.48 ppm depending on which experimental value is used. This difference is comparable to deviations of earlier theoretical values,<sup>[34]</sup> ranging from ~6 ppm for GIAO-HF to ~1 ppm for GIAO-UDFT-BPW91 methods. Because this deviation is mainly systematic for fullerenes,<sup>[31]</sup> we use the chemical shift of C<sub>60</sub> as a second reference in calculating chemical shifts for other fullerenes.

### Fullerene C<sub>70</sub>

Fullerene C<sub>70</sub> has D<sub>5h</sub> symmetry that gives five different sets of atoms. Five NMR peaks were observed in experiment and assigned to the five sets of atoms based on both 1-D and 2-D NMR measurements.<sup>[4,5,7]</sup> The NMR spectrum of C<sub>70</sub> calculated at the B3LYP/6-31G\* level of theory correctly shows the required two full-intensity peaks and three half-intensity peaks.<sup>[14]</sup> Fig. 2 shows the experimental and predicted NMR spectra for C<sub>70</sub>. The calculated spectral span and the distribution of the peaks are in good agreement with experiment. Similar results were also reported by Bühl et al.<sup>[34]</sup> and Heine et al.<sup>[31,32]</sup> Because all five peaks have been experimentally assigned, the case of C<sub>70</sub>

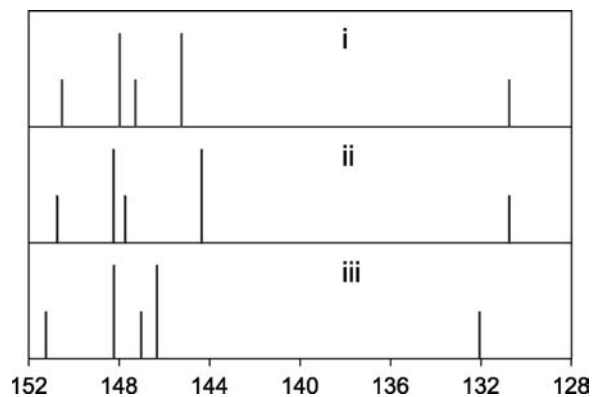


**Fig. 2** <sup>13</sup>C NMR spectra of C<sub>70</sub> by (i) experiment,<sup>[4]</sup> (ii) experiment,<sup>[10]</sup> and (iii) calculated by B3LYP/6-31G\*. All spectra are referenced to C<sub>60</sub> at 143.15 ppm. Source: From Ref.<sup>[14]</sup>. © 2000 American Chemical Society.

presents a unique example to assess the quality of the predicted chemical shifts. A one-to-one comparison gives 0.70, 0.24, -0.26, 1.09, and 1.32 ppm deviations with respect to the experimental values of Taylor et al.<sup>[4]</sup> Because the chemical shifts are referenced with respect to the experimental value of C<sub>60</sub> at 143.15 ppm and this is the center of the normal spectral span of fullerenes, it is expected that peaks far away from the spectral center have larger deviations than those close to the center. It seems, however, that the peaks below 140 ppm have larger deviations from experimental values than those peaks above 140 ppm. In the case of C<sub>70</sub>, the deviation for the most upfield peak (1.32 ppm) is almost twice that for the most downfield peak (0.70 ppm). This trend becomes clear when we consider more NMR spectra of fullerenes. Therefore we expect a 1–2 ppm overestimation for peaks below 140 ppm and a much better comparison for peaks above 140 ppm.

### Fullerene C<sub>76</sub>

Two IPR structures are possible for fullerene C<sub>76</sub>,<sup>[13]</sup> but only one isomer with D<sub>2</sub> symmetry has closed-shell electronic configuration, thus stable under normal conditions. Experimentally, 19 NMR peaks have been reported with equal intensity.<sup>[8]</sup> The 19 peaks form five groups from downfield to upfield, containing 1, 6, 8, 3, and 1 peaks. These five groups and the spectral span were well reproduced in the predicted NMR spectrum,<sup>[14]</sup> as shown in Fig. 3. Fifteen peaks occurring between 140 and 150 ppm appear to agree with experiment much better than the four peaks below 140 ppm. Overestimations of chemical shifts of as much as 2.22 ppm from experiment were calculated for the four

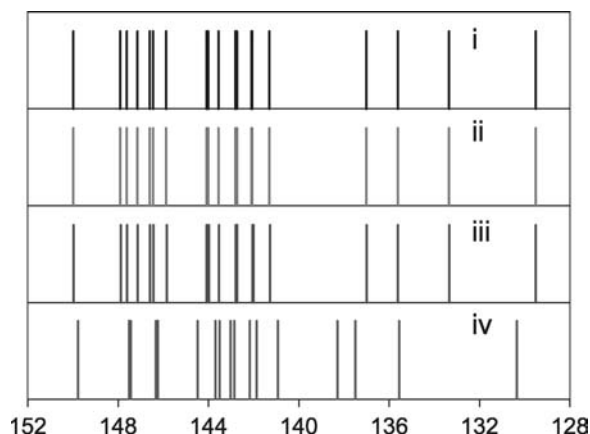


**Fig. 3** <sup>13</sup>C NMR spectra of C<sub>76</sub>:1 by (i) experiment,<sup>[8]</sup> (ii) experiment,<sup>[10]</sup> (iii) experiment,<sup>[12]</sup> and (iv) calculated by B3LYP/6-31G\*. All spectra are referenced to C<sub>60</sub> at 143.15 ppm. Source: From Ref.<sup>[14]</sup>. © 2000 American Chemical Society.

peaks below 140 ppm. The chemical shifts of C<sub>76</sub> earlier predicted by IGLO-DFTB were able to give a good estimate on the spectral span but failed to show the subtle distribution of the peaks.<sup>[31,32]</sup> A one-to-one assignment of the NMR peaks based on our predicted chemical shifts was not possible because of the crowdedness of the spectrum. It is, however, obvious that the NMR chemical shifts calculated at the B3LYP/6-31G\* level are accurate enough to determine the isomeric structure when good experimental spectrum from isomer-pure sample is available.

### Fullerene C<sub>78</sub>

Three of the five IPR isomers of C<sub>78</sub> have been characterized by NMR spectroscopy.<sup>[9–12]</sup> Isomer **1** (D<sub>3</sub>) has 13 NMR peaks with equal intensity, which can be divided into four groups with 2, 2, 7, and 2 peaks from downfield to upfield. The predicted NMR chemical shifts gave good agreement with experiment in terms of distribution of peaks and spectral span.<sup>[14]</sup> It became obvious from our theoretical result that two NMR peaks occur in the 132–135 ppm region instead of three as reported in Ref.<sup>[10]</sup> The deviations from experiment for the two most downfield peaks, 0.18 and -0.17 ppm, are much smaller than those for the two most upfield peaks, 1.70 and 0.89 ppm, illustrating the much better reproduced chemical shifts for peaks above 140 ppm.

Isomers **2** and **3** both have C<sub>2v</sub> symmetry, but show different NMR patterns: the ratio of full-intensity peaks:half-intensity peaks is 18:3 for isomer **2** and 17:5 for isomer **3**. The spectral spans were well reproduced for these two isomers by our DFT calculations.<sup>[14]</sup> The distribution of the peaks was also in agreement with experiment, thus confirming earlier assignment of the isomeric structures. Also reported were the chemical shifts for isomers **4** and **5** of C<sub>78</sub>, which could facilitate their identification if they are observed.

### Fullerene C<sub>80</sub>

The NMR spectra of six IPR isomers of C<sub>80</sub> predicted by DFT calculations have been reported, including isomers **1–5** and a D<sub>2</sub> distorted form of isomer **7**(I<sub>h</sub>).<sup>[46]</sup> The NMR spectra of isomer **2** (D<sub>2</sub>) show good agreement between theory and experiment.<sup>[30]</sup> At the downfield end, a group of three peaks were well reproduced in the spectra calculated using B3LYP hybrid functional and the 6-31G, 6-31G\*, and 6-311G\*\* basis sets. Sixteen peaks occurring at the middle of the spectrum in the calculated spectra also agree with experiment. One peak at the upfield end tends to be underestimated by large basis set than by medium basis

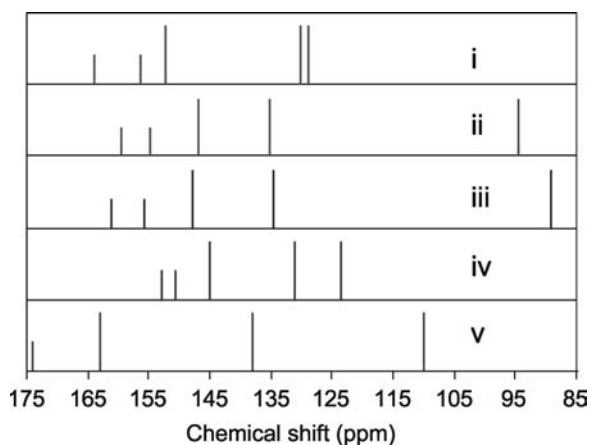


**Fig. 4**  $^{13}\text{C}$  NMR spectra of  $\text{C}_{80}:1$  by (I) experiment,<sup>[47]</sup> (II) calculated by B3LYP/6-31G\*, (III) by B3LYP/6-311G\*\*, (IV) HF/6-31G\*, and (V) BP86/SVP.<sup>[49]</sup> All spectra are referenced to  $\text{C}_{60}$  at 143.15 ppm.

set. Overall, the distribution for most of the peaks was well reproduced.

The NMR spectrum of another observed isomer,  $\text{C}_{80}:1$ , shows large discrepancy between DFT results<sup>[46]</sup> and experiment,<sup>[47]</sup> as shown in Fig. 4. This isomer has  $D_{5d}$  symmetry, thus shows three full-intensity peaks and two half-intensity peaks. The DFT-predicted spectrum shows that the two half-intensity peaks occur at downfield positions than the full-intensity peaks, which is consistent with experiment. The separation within the four downfield peaks seems to be comparable with that in experiment. However, one full-intensity peak in the DFT results occurs at around 90 ppm, far below the normal NMR ranges for fullerenes. Switching to a gradient-corrected pure functional such as BLYP did not improve the result.<sup>[48]</sup> Furche and Ahlrichs<sup>[49]</sup> also reported similar chemical shifts for the  $D_{5d}$  isomer of  $\text{C}_{80}$  using the BP86 functional.

To solve the apparent discrepancy, we have carried out NMR calculations at the HF/6-31G\* level.<sup>[48]</sup> The chemical shifts are all in the 120–155 ppm range that is normal for fullerenes, and the peak positions are in good agreement with experiment. On the energetic aspect, isomer **1** is predicted at the B3LYP/6-31G\* level to be 2.20 kcal/mol less stable than isomer **2**, but its HOMO-LUMO gap is only 0.986 eV, which is much smaller than that of isomer **2** (1.346 eV). At the HF level, its HOMO-LUMO gap is 4.56 eV, still slightly smaller than that (4.97 eV) of isomer **2**, but much larger than those (~3.2 eV) of isomers **3–5**. This shows that the wrong chemical shifts from DFT calculations can be related to the severely underestimated HOMO-LUMO gap.

Isomers **3**, **4**, and **5** have small HOMO-LUMO gaps and high relative energies at both DFT and HF levels.<sup>[46,48]</sup> These isomers also have NMR peaks at

beyond the normal 120–160 ppm range, suggesting that the electron distribution in the molecule is less optimal.

### Fullerene $\text{C}_{84}$ : Two Major Isomers

Two major isomers of  $\text{C}_{84}$  were among the first observed fullerene species<sup>[11,12,50]</sup> and have drawn much research interest. Because isomer **23** ( $D_{2d}$ ) can be uniquely identified by 1-D NMR spectrum among the 24 possible IPR isomers<sup>[13]</sup> and isomer **22** ( $D_2$ ) has been identified by 2-D NMR experiment on the  $^{13}\text{C}$ -enriched sample,<sup>[51]</sup> they represent interesting testing cases for the DFT-calculated chemical shifts.

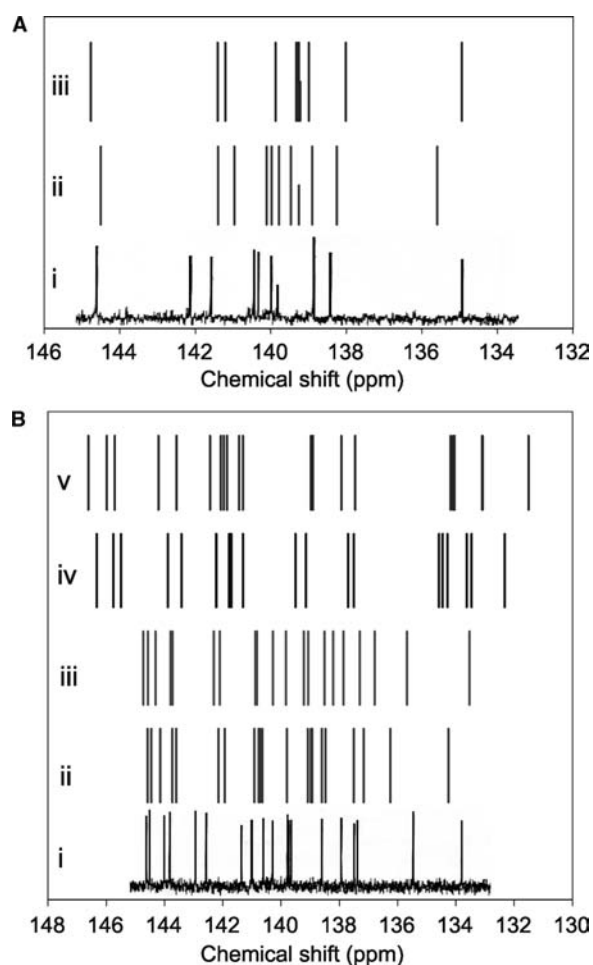


**Fig. 5** Theoretical and experimental  $^{13}\text{C}$  NMR spectra of  $\text{C}_{84}$ . (A) Spectra of **23**( $D_{2d}$ ) by experiment (i), B3LYP/6-31G\* (ii), and B3LYP/6-311G\*\* (iii). (B) Spectra of **22**( $D_2$ ) by experiment (i), B3LYP/6-31G\* (ii), and B3LYP/6-311G\*\* (iii), and of **21**( $D_2$ ) by B3LYP/6-31G\* (iv), and B3LYP/6-311G\*\* (v). Experimental spectra reproduced from Ref.<sup>[53]</sup>. Source: From Ref.<sup>[15]</sup>. © 2000, The Royal Society of Chemistry and the Centre National de la Recherche Scientifique.



We used density functional theory at the B3LYP level with the 6-31G\* and 6-311G\*\* basis sets to predict the chemical shifts for these two isomers and isomer **21** ( $D_2$ ).<sup>[15]</sup> Isomers **22** and **23** were isoenergetic and both have large HOMO-LUMO gaps. Fig. 5 shows their theoretical NMR spectra in comparison with experiment. Both DFT results for isomer **23** are in very good agreement with experiment in terms of the spectral span and peak positions. The rms deviation calculated for all 11 chemical shifts were 0.464 and 0.556 ppm for 6-31G\* and 6-311G\*\* basis sets, respectively. We note that because one-to-one peak assignment was not possible, the rms deviation will likely be larger when the peaks are assigned. However, the change would be small and thus it would not affect our conclusion. It is evident that the accuracy of the calculated chemical shifts allows identification of isomeric structures of fullerenes.

Earlier calculated NMR results could not unambiguously distinguish between isomers **21** and **22**.<sup>[29,31,32]</sup> Our DFT-calculated chemical shifts, as shown in Fig. 5B, clearly differentiate these two isomers.<sup>[15]</sup> Both spectral span and peak distribution conclusively favor isomer **22** over isomer **21** as the observed species. The rms deviations of chemical shifts between theory and experiment were 1.944 and 0.512 ppm for isomers **21** and **22** at the B3LYP/6-31G\* level, respectively. Essentially same values of rms deviation were obtained from calculations using a larger basis set 6-311G\*\*. Again, we note that, while the rms deviation values will likely change when all NMR peaks are assigned, the conclusion will hold. This assignment was further supported by the large differences in the relative energies (16.04 kcal/mol) and the HOMO-LUMO gaps of isomers **21** and **22**.

## IDENTIFICATION OF FULLERENE ISOMERS BY NMR SPECTRA

As the results for the nine observed isomers of fullerenes  $C_{70}$  to  $C_{84}$  have shown, the DFT-calculated NMR chemical shifts are accurate enough to determine the molecular structures for the observed fullerene isomers. In the mean time, care needs to be taken in the cases where the DFT-calculated HOMO-LUMO gap is too small. In the following section, we summarize theoretical NMR results for fullerenes  $C_{82}$  to  $C_{90}$  and for charged and substituted fullerene species, focusing on the identification of the observed isomers when experimental spectra of good quality are available. The calculated NMR chemical shifts for the isomers that have not been isolated have also been reported in the literature and should facilitate in determining the molecular structures when new isomers are observed.

## Fullerene $C_{82}$

Fullerene  $C_{82}$  poses the first challenge to successively identify an isomer based on theoretical  $^{13}C$  NMR chemical shifts. One major isomer having  $C_2$  symmetry was observed in experiment with some minor isomers whose symmetry could not be determined.<sup>[11]</sup> Of the three  $C_2$  isomers (**1**, **3**, and **5**), isomer **3** was predicted to have the lowest energy and a large HOMO-LUMO gap from our DFT calculations.<sup>[52]</sup> Its predicted chemical shifts compare favorably with experiment, as shown in Fig. 6. The two NMR peaks at the downfield end of the spectrum are well separated from the rest in both theory and experiment. The separation of a group of six peaks at the upfield end from the group at the middle of the spectrum is less obvious in the 6-31G\* results than in the 6-31G results. The spectral spans from theoretical results of both basis sets also show isomer **3** as the observed isomer. Thus the excellent agreement of the NMR spectrum together with the low energy and large gap allowed us to identify the observed  $C_2$  isomer as isomer **3**.

The predicted chemical shifts of isomers **1**, **2**, **4**, and **5** fell in the normal range for fullerenes, whereas the chemical shifts of isomer **6** have values as low as 113.50 ppm.<sup>[52]</sup> Because the four isomers have relatively low energy and large HOMO-LUMO gaps, their observation may be possible and the predicted chemical shifts could facilitate their identification.

## Fullerene $C_{84}$

Nine isomers have been obtained and characterized by NMR spectroscopy.<sup>[11,12,50,53–55]</sup> As discussed above,

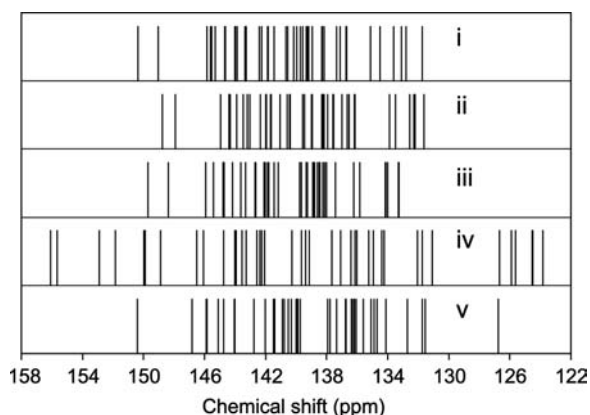


**Fig. 6**  $^{13}C$  NMR spectra of  $C_2$  isomers of fullerene  $C_{82}$  for (i) isomer **3** by experiment,<sup>[11]</sup> (ii) isomer **3** calculated by B3LYP/6-31G, (iii) isomer **3** calculated by B3LYP/6-31G\*, (iv) isomer **1** calculated by B3LYP/6-31G\*, and (v) isomer **5** calculated by B3LYP/6-31G\*. All spectra are referenced to  $C_{60}$  at 143.15 ppm. Source: From Ref.<sup>[52]</sup>. © 2001 American Chemical Society.

structures of the two major isomers **22** ( $D_2$ ) and **23** ( $D_{2d}$ ) of fullerene  $C_{84}$  have been assigned,<sup>[15]</sup> and here we look at the minor isomers.

A second  $D_{2d}$  isomer of  $C_{84}$  was observed and assigned as isomer **4** based on the ratio of the full-intensity peaks:half-intensity peaks.<sup>[54]</sup> In our DFT results at the B3LYP/6-31G\* level, isomer **4** has a relative energy of 14.64 kcal/mol and a HOMO-LUMO gap of 2.13 eV.<sup>[56]</sup> The predicted NMR chemical shifts were in good agreement with experiment. Three full-intensity peaks are well separated from each other at the 131–138 ppm region, while the rest of the full-intensity peaks are found at 143–149 ppm. The half-intensity peaks are all above 140 ppm, consistent with experiment.

A second  $D_2$  isomer was tentatively assigned as isomer **5**.<sup>[54]</sup> Its experimental NMR spectrum has a single peak well separated from others at the downfield end and four peaks separated at the upfield end. Our theoretical spectrum of isomer **5** reproduced these features very well, confirming the earlier assignment.<sup>[56]</sup> The calculated spectral span, 21.17 ppm, is in excellent agreement with the measured value (22.10 ppm). Similarly, good agreement was also obtained for the spectral span (15.13 ppm) of the observed  $C_2$  isomer and that of isomer **11** (15.15 ppm), whereas the calculated spectral spans for other  $C_2$  isomer are much larger.

Two  $C_s$  isomers were isolated from graphite soot of DC arc discharge.<sup>[54]</sup> Both isomers have two half-intensity peaks and 41 full-intensity peaks, which suggests that they are isomers **14** and **16** but no final assignment could be reached. The spectral spans are very close, being 15.29 and 15.51 ppm for  $C_s(a)$  and  $C_s(b)$ , respectively, and the full-intensity peaks are very crowded. Because of this, the assignment of these isomers has to be based on the chemical shifts of the half-intensity peaks. The two half-intensity peaks of isomer **14** occur at 132.22 and 148.49 ppm in our B3LYP/6-31G\* results,<sup>[56]</sup> in good agreement with those of  $C_s(b)$  occurring at 134.33 and 148.44 ppm. On the other hand, the two half-intensity peaks of isomer **16** occur at 136.12 and 141.01 ppm, consistent with those of  $C_s(a)$  appearing at 137.03 and 141.76 ppm. Thus isomer  $C_s(a)$  is isomer **16** and isomer  $C_s(b)$  has the structure of isomer **14**.

Two highly symmetric isomers, **19** ( $D_{3d}$ ) and **24** ( $D_{6h}$ ), have also been characterized.<sup>[55]</sup> The predicted general pattern of the six full-intensity peaks of isomer **19** was in agreement with the experiment.<sup>[56]</sup> The two half-intensity peaks appear at 133.85 and 136.86 ppm, which is different from experimental values of 136.39 and 147.81 ppm. Other authors have suggested that the half-intensity peak at downfield region is misassigned.<sup>[32]</sup> This appears to be likely because the measurement was taken from mixture samples. For

isomer **24**, the two full-intensity peaks are in fair agreement between theory and experiment,<sup>[56]</sup> whereas the position of one of the three half-intensity peaks is shown to be misassigned in experiment. Future NMR measurement on isomer-pure samples is highly desirable for these isomers.

### Fullerene $C_{86}$

Two isomers of  $C_{86}$  with  $C_2$  and  $C_s$  point group symmetry have been isolated using the multistage HPLC method.<sup>[57]</sup> Based on earlier energy calculations,<sup>[58]</sup> they were provisionally assigned as isomers **17**( $C_2$ ) and **16**( $C_s$ ), respectively. Our calculated NMR chemical shifts at the B3LYP/6-31G level confirmed this assignment.<sup>[59]</sup> The calculated spectral span, 20.25 ppm, of isomer **17** is in excellent agreement with the experimental value, 20.28 ppm. The other  $C_2$  isomers (**2**, **3**, **4**, **6**, and **14**) all have much larger spectral spans. A single isolated peak at the downfield end, a single isolated peak at the upfield end, and the crowded middle part of the NMR spectrum are well reproduced in our theoretical results for isomer **17**.

Two  $C_s$  IPR isomers, **15** and **16**, have the ratio of full-intensity peaks/half-intensity peaks<sup>[13]</sup> that was observed in experiment. In addition to the low energy and large HOMO-LUMO gap, isomer **16** has a calculated spectral span of 17.73 ppm, in good agreement with experimental value of 17.99 ppm for the  $C_s$  isomer. The distribution of the NMR peaks also supports the experimental assignment.<sup>[59]</sup>

### Fullerene $C_{88}$

Three isomers of  $C_{88}$  were separated and characterized by NMR as  $C_{88-1}(C_s)$ ,  $C_{88-2}(C_2)$ , and  $C_{88-3}(C_2)$ .<sup>[57]</sup> Isomer **17**( $C_s$ ) has the lowest energy and a large HOMO-LUMO gap in our DFT results.<sup>[60]</sup> The chemical shifts of isomer **17** calculated by B3LYP/6-31G have two distinct half-intensity peaks at the downfield end, which is consistent with experimental spectrum. The 42 full-intensity peaks occur within the 130–147 ppm range in theory, comparing well with the experimental range of 131–148 ppm. Similar comparison was also obtained for the 6-31G\* results.

Of the five  $C_2$  isomers studied, isomers **7** and **33** have low energies and have been proposed as the observed isomers.<sup>[57]</sup> All  $C_2$  isomers have 44 NMR peaks with equal intensity. The spectral spans for isomers **7** and **33** are 20.68 and 18.29 ppm,<sup>[60]</sup> respectively, suggesting that they correspond to  $C_{88-2}$  and  $C_{88-3}$ , respectively. Detailed comparison on the peak positions shows that two peaks at the downfield end of the B3LYP/6-31G\*-calculated spectrum of isomer **7** are separated from others, which agrees with the

spectrum of  $C_{88-2}$ . The downfield end of the predicted NMR spectrum of isomer **33** is crowded, in consistency with the spectrum of  $C_{88-3}$ . Thus our DFT results strongly suggest  $C_{88-2}$  as isomer **7** and  $C_{88-3}$  as isomer **33**.

### Fullerene $C_{90}$

Isomer **45**( $C_2$ ) of  $C_{90}$  is the most stable isomer in our DFT results, while isomers **28**( $C_2$ ), **30**( $C_1$ ), **32**( $C_1$ ), **35**( $C_s$ ), **40**( $C_2$ ), and **46**( $C_{2v}$ ) show significant stabilities.<sup>[61]</sup> The chemical shifts for these isomers all occur in the normal range of 125–155 ppm for fullerenes. Isomers of  $C_{90}$  have been observed only in mixture, and this prevents the determination of molecular structures because of the large number of NMR peaks. Five weak experimental NMR peaks were reported in literature, which led to the speculation of the existence of isomer **36**( $C_{2v}$ ).<sup>[62]</sup> Our DFT calculations show that isomer **36** has very high energy, thus unlikely to be the source of the observed weak NMR peaks. A comparison of the predicted chemical shifts suggests that the five weak peaks are more likely from the stable isomers **35** and **46**.<sup>[61]</sup> Future measurements on isomer-pure samples are needed to elucidate the ground-state structures of fullerene  $C_{90}$ .

### Charged and Substituted Fullerenes

Besides the pristine fullerenes, the charged and substituted fullerenes have also been subjected to theoretical

NMR studies using DFT methods, and the NMR chemical shifts calculated at B3LYP/6-31G\* or comparable levels of theory have been used for identification of the fullerene species. The hexa-anions of fullerenes  $C_{76-D_2}$ ,  $C_{78-D_3}$ ,  $C_{78-C_{2v}}$ ,  $C_{84-D_2}$ , and  $C_{84-D_{2d}}$  have been recently obtained from lithium reduction of neutral fullerenes and characterized by NMR spectroscopy.<sup>[63]</sup> DFT-calculated chemical shifts were used to assist the determination of the reduction states of the multiply charged anions. The chemical shifts of the hexa-anions are deshielded comparing to the neutral fullerenes.

The carbocation  $C_{59}N^+$  has recently been obtained from the oxidation of  $(C_{59}N)_2$  by crude hexabromo(*N*-phenyl)carbazole and characterized by MS, X-ray, NMR, UV-Vis, and infrared spectroscopy.<sup>[64]</sup> Theoretical NMR chemical shifts calculated at the B3LYP/6-311G\*\* level are in good agreement with experiment. The majority of the NMR peaks cluster around 144 ppm, showing the overall positive charge of the cation.

The  $^{13}C$  NMR chemical shifts of the proposed aza[60]fullerene  $C_{48}N_{12}$ <sup>[65]</sup> have been recently predicted using DFT method.<sup>[66]</sup> Compared with  $C_{60}$ , most NMR peaks of  $C_{48}N_{12}$  have lower chemical shifts.

### NMR CHEMICAL SHIFTS AND LOCAL GEOMETRY

Nuclear magnetic resonance chemical shifts are determined by the electronic configuration of the molecule and are affected by the local structure close to the

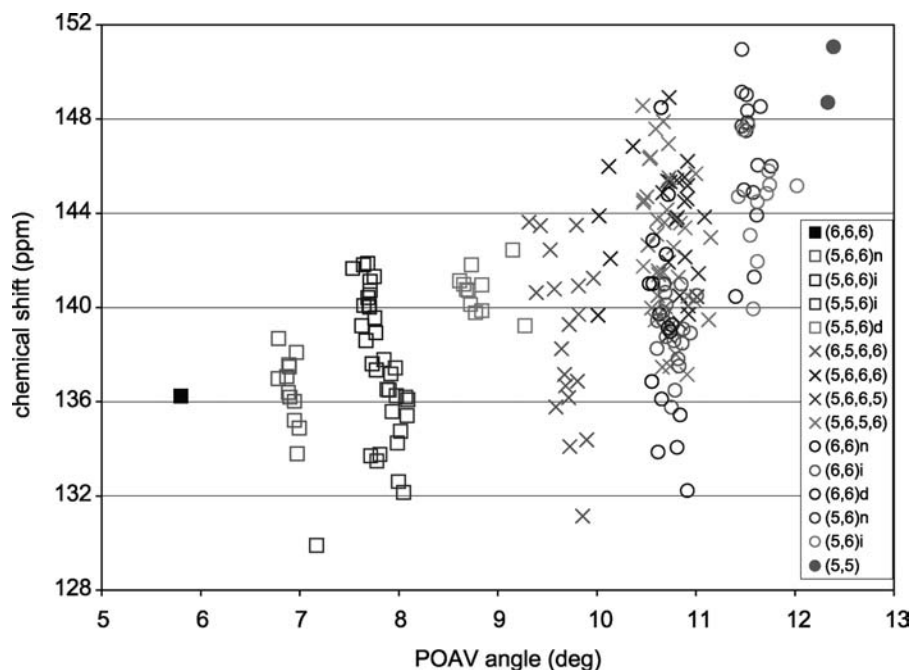


**Fig. 7** Theoretical  $^{13}C$  NMR chemical shifts and POAV angles of isomers **4**, **5**, **11**, **14**, **16**, **19**, and **22–24** of fullerene  $C_{84}$  calculated by B3LYP/6-31G\*. The py-type carbons are represented by squares, the cor type are represented by crosses, and the pc type are represented by circles. *Source:* From Ref.<sup>[56]</sup>. © 2001 American Chemical Society.

atom. Diederich et al.<sup>[8,10]</sup> have suggested that the carbon site in fullerenes be divided into three types: pyracylene (type 1, pc), corannulene (type 2, cor), and pyrene (type 3, py). The chemical shifts should fall in the pc > cor > py order. Heine et al.<sup>[31,32]</sup> plotted the chemical shifts against the  $\pi$ -orbital axis vector (POAV) angle<sup>[67]</sup> and found a marked upward trend of chemical shifts with increasing POAV angle for pc and cor sites but no apparent trend for py sites.

We have also studied the relationship between chemical shift and local geometry in the context of POAV angle.<sup>[14,46,52,56]</sup> The chemical shifts are, in general, larger for type pc than cor, which in turn are larger than py. There is, however, no clear range where each type will occur and the chemical shifts of different types are in fact often mixed. To thoroughly study the relationship between chemical shift and local geometry, we have considered further neighbors of a given atom and arrived at 15 structural motifs.<sup>[56]</sup> Fig. 7 shows the graph of chemical shifts vs. POAV angles for the nine observed isomers of C<sub>84</sub>. Distinct ranges of POAV angles and chemical shifts are seen for each of the five motifs of the py type. Two and three groups of POAV angles are obvious for the cor and pc types, respectively, but the chemical shifts for these sites occur throughout the 130–150 ppm range.

## ENERGETICS OF STABLE FULLERENES

We have been using low relative energy and large HOMO-LUMO gap as indicators of the stability of

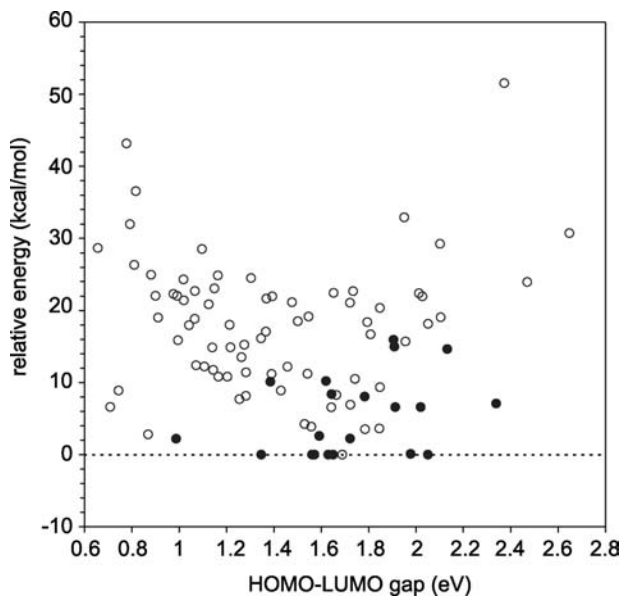


**Fig. 8** The relative energy and HOMO-LUMO gap for the isomers of fullerenes C<sub>78</sub> to C<sub>90</sub>. The observed isomers are represented by solid circles.

fullerene isomers. Here we show a statistical graph of the energy and gaps for the observed isomers in Fig. 8. The majority of the observed isomers have relative energies less than 10 kcal/mol at the B3LYP/6-31G\* level. The highest energy of the observed isomers is for C<sub>84</sub>:5 with 15.94 kcal/mol. The HOMO-LUMO gaps for observed isomers are all in the range 1.35–2.34 eV. Note that the gap (0.99 eV) for C<sub>80</sub>:1 is wrong in the DFT calculations. Therefore for a fullerene isomer to be isolable, it should have a low relative energy and large HOMO-LUMO gap.

## CONCLUSION

Theoretical NMR chemical shifts calculated using density functional theory at the B3LYP/6-31G\* level have been shown to be accurate to unambiguously determine the molecular structures of the observed fullerene isomers. For the isomers of fullerenes C<sub>70</sub>, C<sub>76</sub>, C<sub>78</sub>, C<sub>80</sub>, and some isomers of C<sub>84</sub> where the NMR spectral patterns uniquely correspond to the structures, the predicted chemical shifts are in very good agreement with experiment. The spectral spans and the distribution of the NMR peaks are well reproduced for these cases. Comparing the predicted and experimental chemical shifts of isomers **22** and **23** of fullerene C<sub>84</sub>, rms deviations were 0.464 and 0.512 ppm, respectively. The calculated NMR chemical shifts allowed the identification of the previously unassigned fullerene isomers: C<sub>82</sub>:3, C<sub>84</sub>:5, C<sub>84</sub>:11, C<sub>84</sub>:14, C<sub>84</sub>:16, C<sub>84</sub>:22, C<sub>86</sub>:16, C<sub>86</sub>:17, C<sub>88</sub>:7, C<sub>88</sub>:17, and C<sub>88</sub>:33. The calculated NMR chemical shifts also proved necessary in determining the charge status of the charged and substituted fullerene species. The local geometry at the sp<sup>2</sup>-hybridized carbon in fullerenes has been shown to have some effect on the chemical shift, but lack any linear relationship. The observed fullerene isomers all have low energies and large HOMO-LUMO gaps among the set of possible IPR isomers for each fullerene family. Because of the high accuracy of the DFT-calculated chemical shifts, we expect the calculation of NMR chemical shifts to be performed commonly in various areas of chemical research because the computers are becoming faster and the programs capable of calculating chemical shifts are becoming easier to use.

## ACKNOWLEDGMENT

The author thanks Prof. Miklos Kertesz of Georgetown University for continued encouragement and insightful discussions. A Visiting Fellowship Award from the National Cancer Institute at Frederick, NIH to the author is gratefully acknowledged.

## REFERENCES

1. Kroto, H.W.; Heath, J.R.; O'Brien, S.C.; Curl, R.F.; Smalley, R.E. C<sub>60</sub>: Buckminsterfullerene. *Nature* **1985**, *318*, 162–163.
2. Kratschmer, W.; Fostiropoulos, K.; Huffman, D.R. The infrared and ultraviolet-absorption spectra of laboratory-produced carbon dust—evidence for the presence of the C<sub>60</sub> molecule. *Chem. Phys. Lett.* **1990**, *170*, 167–170.
3. Kratschmer, W.; Lamb, L.D.; Fostiropoulos, K.; Huffman, D.R. Solid C<sub>60</sub>—a new form of carbon. *Nature* **1990**, *347*, 354–358.
4. Taylor, R.; Hare, J.P.; Abdulsada, A.K.; Kroto, H.W. Isolation, separation and characterization of the fullerenes C<sub>60</sub> and C<sub>70</sub>—the 3rd form of carbon. *J. Chem. Soc., Chem. Commun.* **1990**, 1423–1424.
5. Ajie, H.; Alvarez, M.M.; Anz, S.J.; Beck, R.D.; Diederich, F.; Fostiropoulos, K.; Huffman, D.R.; Kratschmer, W.; Rubin, Y.; Schriver, K.E.; Sensharma, D.; Whetten, R.L. Characterization of the soluble all-carbon molecules C<sub>60</sub> and C<sub>70</sub>. *J. Phys. Chem.* **1990**, *94*, 8630–8633.
6. Johnson, R.D.; Meijer, G.; Bethune, D.S. C<sub>60</sub> has icosahedral symmetry. *J. Am. Chem. Soc.* **1990**, *112*, 8983–8984.
7. Johnson, R.D.; Meijer, G.; Salem, J.R.; Bethune, D.S. 2D nuclear-magnetic-resonance study of the structure of the fullerene C<sub>70</sub>. *J. Am. Chem. Soc.* **1991**, *113*, 3619–3621.
8. Ettl, R.; Chao, I.; Diederich, F.; Whetten, R.L. Isolation of C<sub>76</sub>, a chiral (D<sub>2</sub>) allotrope of carbon. *Nature* **1991**, *353*, 149–153.
9. Diederich, F.; Whetten, R.L.; Thilgen, C.; Ettl, R.; Chao, I.; Alvarez, M.M. Fullerene isomerism— isolation of C<sub>2v</sub>-C<sub>78</sub> and D<sub>3h</sub>-C<sub>78</sub>. *Science* **1991**, *254*, 1768–1770.
10. Diederich, F.; Whetten, R.L. Beyond C<sub>60</sub>: The higher fullerenes. *Accounts Chem. Res.* **1992**, *25*, 119–126.
11. Kikuchi, K.; Nakahara, N.; Wakabayashi, T.; Suzuki, S.; Shiromaru, H.; Miyake, Y.; Saito, K.; Ikemoto, I.; Kainosho, M.; Achiba, Y. NMR characterization of isomers of C<sub>78</sub>, C<sub>82</sub> and C<sub>84</sub> fullerenes. *Nature* **1992**, *357*, 142–145.
12. Taylor, R.; Langley, G.J.; Avent, A.G.; Dennis, T.J.S.; Kroto, H.W.; Walton, D.R.M. <sup>13</sup>C NMR-Spectroscopy of C<sub>76</sub>, C<sub>78</sub>, C<sub>84</sub> and mixtures of C<sub>86</sub>–C<sub>102</sub>—anomalous chromatographic behavior of C<sub>82</sub>, and evidence for C<sub>70</sub>H<sub>12</sub>. *J. Chem. Soc., Perkin Trans.* **1993**, *2*, 1029–1036.
13. Fowler, P.W.; Manolopoulos, D.E. *An Atlas of Fullerenes*; Oxford University Press Inc.: New York, 1995.
14. Sun, G.Y.; Kertesz, M. Theoretical <sup>13</sup>C NMR spectra of IPR isomers of fullerenes C<sub>60</sub>, C<sub>70</sub>, C<sub>72</sub>, C<sub>74</sub>, C<sub>76</sub>, and C<sub>78</sub> studied by density functional theory. *J. Phys. Chem., A* **2000**, *104*, 7398–7403.
15. Sun, G.Y.; Kertesz, M. Theoretical evidence for the major isomers of fullerene C<sub>84</sub> based on <sup>13</sup>C NMR chemical shifts. *New J. Chem.* **2000**, *24*, 741–743.
16. Haufler, R.E.; Conceicao, J.; Chibante, L.P.F.; Chai, Y.; Byrne, N.E.; Flanagan, S.; Haley, M.M.; O'Brien, S.C.; Pan, C.; Xiao, Z.; Billups, W.E.; Ciufolini, M.A.; Hauge, R.H.; Margrave, J.L.; Wilson, L.J.; Curl, R.F.; Smalley, R.E. Efficient production of C<sub>60</sub> (Buckminsterfullerene), C<sub>60</sub>H<sub>36</sub>, and the solvated buckide ion. *J. Phys. Chem.* **1990**, *94*, 8634–8636.
17. Parker, D.H.; Wurz, P.; Chatterjee, K.; Lykke, K.R.; Hunt, J.E.; Pellin, M.J.; Hemminger, J.C.; Gruen, D.M.; Stock, L.M. High-yield synthesis, separation, and mass-spectrometric characterization of fullerenes C<sub>60</sub> to C<sub>266</sub>. *J. Am. Chem. Soc.* **1991**, *113*, 7499–7503.
18. Howard, J.B.; McKinnon, J.T.; Makarovskiy, Y.; Lafleur, A.L.; Johnson, M.E. Fullerenes C<sub>60</sub> and C<sub>70</sub> in flames. *Nature* **1991**, *352*, 139–141.
19. Richter, H.; Labrocca, A.J.; Grieco, W.J.; Taghizadeh, K.; Lafleur, A.L.; Howard, J.B. Generation of higher fullerenes in flames. *J. Phys. Chem., B* **1997**, *101*, 1556–1560.
20. Boorum, M.M.; Vasil'ev, Y.V.; Drewello, T.; Scott, L.T. Groundwork for a rational synthesis of C<sub>60</sub>: Cyclodehydrogenation of a C<sub>60</sub>H<sub>30</sub> polyarene. *Science* **2001**, *294*, 828–831.
21. Scott, L.T.; Boorum, M.M.; McMahon, B.J.; Hagen, S.; Mack, J.; Blank, J.; Wegner, H.; deMeijere, A. A rational chemical synthesis of C<sub>60</sub>. *Science* **2002**, *295*, 1500–1503.
22. Saunders, M.; Jimenezvazquez, H.A.; Cross, R.J.; Mroczkowski, S.; Freedberg, D.I.; Anet, F.A.L. Probing the interior of fullerenes by <sup>3</sup>He NMR Spectroscopy of endohedral <sup>3</sup>He@C<sub>60</sub> and <sup>3</sup>He@C<sub>70</sub>. *Nature* **1994**, *367*, 256–258.
23. Saunders, M.; Jimenezvazquez, H.A.; Cross, R.J.; Billups, W.E.; Gesenberg, C.; Gonzalez, A.; Luo, W.; Haddon, R.C.; Diederich, F.; Herrmann, A. Analysis of isomers of the higher fullerenes by <sup>3</sup>He NMR spectroscopy. *J. Am. Chem. Soc.* **1995**, *117*, 9305–9308.
24. Elser, V.; Haddon, R.C. Icosahedral C<sub>60</sub>—an aromatic molecule with a vanishingly small ring current magnetic-susceptibility. *Nature* **1987**, *325*, 792–794.
25. Fowler, P.W.; Lazzeretti, P.; Zanasi, R. Electric and magnetic-properties of the aromatic sixty-carbon cage. *Chem. Phys. Lett.* **1990**, *165*, 79–86.
26. Haddon, R.C.; Elser, V. Icosahedral C<sub>60</sub> revisited—an aromatic molecule with a vanishingly small ring current magnetic-susceptibility—Comment. *Chem. Phys. Lett.* **1990**, *169*, 362–364.
27. Manolopoulos, D.E.; Fowler, P.W. Molecular graphs, point groups, and fullerenes. *J. Chem. Phys.* **1992**, *96*, 7603–7614.
28. Häser, M.; Ahlrichs, R.; Baron, H.P.; Weis, P.; Horn, H. Direct computation of 2nd-order scf properties of large molecules on workstation computers with an application to large carbon clusters. *Theor. Chim. Acta* **1992**, *83*, 455–470.
29. Schneider, U.; Richard, S.; Kappes, M.M.; Ahlrichs, R. Ab-Initio <sup>13</sup>C NMR shifts of several C<sub>84</sub> isomers. *Chem. Phys. Lett.* **1993**, *210*, 165–169.
30. Hennrich, F.H.; Michel, R.H.; Fischer, A.; Richard-Schneider, S.; Gilb, S.; Kappes, M.M.; Fuchs, D.; Burk, M.; Kobayashi, K.; Nagase, S. Isolation and

- characterization of C<sub>80</sub>. *Angew. Chem., Int. Ed. Engl.* **1996**, *35*, 1732–1734.
31. Heine, T.; Seifert, G.; Fowler, P.W.; Zerbetto, F. A tight-binding treatment for <sup>13</sup>C NMR spectra of fullerenes. *J. Phys. Chem., A* **1999**, *103*, 8738–8746.
  32. Heine, T.; Bühl, M.; Fowler, P.W.; Seifert, G. Modelling the <sup>13</sup>C NMR chemical shifts of C<sub>84</sub> fullerenes. *Chem. Phys. Lett.* **2000**, *316*, 373–380.
  33. Hedberg, K.; Hedberg, L.; Buhl, M.; Bethune, D.S.; Brown, C.A.; Johnson, R.D. Molecular structure of free molecules of the fullerene C-70 from gas-phase electron diffraction. *J. Am. Chem. Soc.* **1997**, *119*, 5314–5320.
  34. Bühl, M.; Kaupp, M.; Malkina, O.L.; Malkin, V.G. The DFT route to NMR chemical shifts. *J. Comput. Chem.* **1999**, *20*, 91–105.
  35. Kohn, W.; Sham, L.J. Self-consistent equations including exchange and correlation effects. *Phys. Rev.* **1965**, *140*, 1133–1138.
  36. Becke, A.D. Density-functional thermochemistry .3. The role of exact exchange. *J. Chem. Phys.* **1993**, *98*, 5648–5652.
  37. Lee, C.T.; Yang, W.T.; Parr, R.G. Development of the Colle–Salvetti correlation-energy formula into a functional of the electron-density. *Phys. Rev., B* **1988**, *37*, 785–789.
  38. Heine, T. Fullerenes. In *Calculation of NMR and EPR Parameters: Theory and Applications*; Kaupp, M., Bühl, M., Malkin, V.G., Eds.; VCH Wiley: Weinheim, Germany, 2004.
  39. Cheeseman, J.R.; Trucks, G.W.; Keith, T.A.; Frisch, M.J. A comparison of models for calculating nuclear magnetic resonance shielding tensors. *J. Chem. Phys.* **1996**, *104*, 5497–5509.
  40. Yoshida, M. Maintains a Website at that has the cartesian coordinates of all the fullerene isomers presented in the book. In *An Atlas of Fullerenes*; Fowler and Manolopoulos.
  41. Stewart, J.J.P. Optimization of parameters for semiempirical methods .1. Method. *J. Comput. Chem.* **1989**, *10*, 209–220.
  42. Frisch, M.J.; Trucks, G.W.; Schlegel, H.B.; Scuseria, G.E.; Robb, M.A.; Cheeseman, J.R.; Zakrzewski, V.G.; Montgomery, J.A.; Stratmann, R.E.; Burant, J.C.; Dapprich, S.; Millam, J.M.; Daniels, R.E.; Kudin, K.N.; Strain, M.C.; Farkas, O.; Tomasi, J.; Barone, V.; Cossi, M.; Cammi, R.; Mennucci, B.; Pomelli, C.; Adamo, C.; Clifford, S.; Ochterski, J.; Petersson, G.A.; Ayala, P.Y.; Cui, Q.; Morokuma, K.; Malick, D.K.; Rabuck, A.D.; Raghavachari, K.; Foresman, J.B.; Cioslowski, J.; Ortiz, J.V.; Stefanov, B.B.; Liu, G.; Liashenko, A.; Piskorz, P.; Komaromi, I.; Gomperts, R.; Martin, R.L.; Fox, D.J.; Keith, T.; Al-Laham, M.A.; Peng, C.Y.; Nanayakkara, A.; Gonzalez, C.; Challacombe, M.; Gill, P.M.W.; Johnson, B.; Chen, W.; Wong, M.W.; Andres, J.L.; Gonzalez, C.; Head-Gordon, M.; Pople, J.A. *GAUSSIAN 98 (Rev. A.5)*; Gaussian Inc.: Pittsburgh, PA, USA, 1998.
  43. Wolinski, K.; Hinton, J.F.; Pulay, P. Efficient implementation of the gauge-independent atomic orbital method for NMR chemical-shift calculations. *J. Am. Chem. Soc.* **1990**, *112*, 8251–8260.
  44. *Parallel Quantum Solutions*: Fayetteville, Ar, 1998.
  45. Avent, A.G.; Dubois, D.; Penicaud, A.; Taylor, R. The minor isomers and IR spectrum of [84]fullerene. *J. Chem. Soc., Perkin Trans.* **1997**, *2*, 1907–1910.
  46. Sun, G.Y.; Kertesz, M. Theoretical <sup>13</sup>C NMR spectra of IPR isomers of fullerene C<sub>80</sub>: A density functional theory study. *Chem. Phys. Lett.* **2000**, *328*, 387–395.
  47. Wang, C.R.; Sugai, T.; Kai, T.; Tomiyama, T.; Shinohara, H. Production and isolation of an ellipsoidal C<sub>80</sub> fullerene. *Chem. Commun.* **2000**, 557–558.
  48. Sun, G.Y. *Structures and Properties of New Carbon Allotropes: Fullerene and Single-Walled Carbon Nanotubes*. Ph.D. Dissertation; Georgetown University: Washington, DC, 2002.
  49. Furche, F.; Ahlrichs, R. Fullerene C<sub>80</sub>: Are there still more isomers?. *J. Chem. Phys.* **2001**, *114*, 10362–10367.
  50. Manolopoulos, D.E.; Fowler, P.W.; Taylor, R.; Kroto, H.W.; Walton, D.R.M. An end to the search for the ground-state of C<sub>84</sub>. *J. Chem. Soc., Faraday Trans.* **1992**, *88*, 3117–3118.
  51. Kikuchi, K.; Miyake, Y.; Achiba, Y. Carbon Cluster News **1994**, *2*, 34.
  52. Sun, G.Y.; Kertesz, M. Identification for IPR isomers of fullerene C<sub>82</sub> by theoretical <sup>13</sup>C NMR spectra calculated by density functional theory. *J. Phys. Chem., A* **2001**, *105*, 5468–5472.
  53. Dennis, T.J.S.; Kai, T.; Tomiyama, T.; Shinohara, H. Isolation and characterisation of the two major isomers of [84]fullerene. *Chem. Commun.* **1998**, 619–620.
  54. Dennis, T.J.S.; Kai, T.; Asato, K.; Tomiyama, T.; Shinohara, H.; Yoshida, T.; Kobayashi, Y.; Ishiwatari, H.; Miyake, Y. et al. Isolation and characterisation by <sup>13</sup>C NMR spectroscopy of [84]fullerene minor isomers. *J. Phys. Chem., A* **1999**, *103*, 8747–8752.
  55. Tagmatarchis, N.; Avent, A.G.; Prassides, K.; Dennis, T.J.S.; Shinohara, H. Separation, isolation and characterisation of two minor isomers of the [84]fullerene. *Chem. Commun.* **1999**, 1023–1024.
  56. Sun, G.Y.; Kertesz, M. Isomer identification for fullerene C<sub>84</sub> by <sup>13</sup>C NMR spectrum: A density-functional theory study. *J. Phys. Chem., A* **2001**, *105*, 5212–5220.
  57. Miyake, Y.; Minami, T.; Kikuchi, K.; Kainosho, M.; Achiba, Y. Trends in structure and growth of higher fullerenes isomer structure of C<sub>86</sub> and C<sub>88</sub>. *Mol. Cryst. Liquid Cryst.* **2000**, *340*, 553–558.
  58. Slanina, Z.; Lee, S.L.; Adamowicz, L. C<sub>80</sub>, C<sub>86</sub>, C<sub>88</sub>: Semiempirical and ab initio SCF calculations. *Int. J. Quantum Chem.* **1997**, *63*, 529–535.
  59. Sun, G.Y.; Kertesz, M. <sup>13</sup>C NMR spectra for IPR isomers of fullerene C<sub>86</sub>. *Chem. Phys.* **2002**, *276*, 107–114.
  60. Sun, G.Y. Assigning the major isomers of fullerene C<sub>88</sub> by theoretical <sup>13</sup>C NMR spectra. *Chem. Phys. Lett.* **2002**, *367*, 26–33.



61. Sun, G.Y. Theoretical  $^{13}\text{C}$  NMR chemical shifts of the stable isomers of fullerene  $\text{C}_{90}$ . *Chem. Phys.* **2003**, *289*, 371–380.
62. Slanina, Z.; Zhao, X.; Lee, S.L.; Osawa, E.  $\text{C}_{90}$  temperature effects on relative stabilities of the IPR isomers. *Chem. Phys.* **1997**, *219*, 193–200.
63. Sternfeld, T.; Thilgen, C.; Chen, Z.F.; Siefken, S.; Schleyer, P.V.; Thiel, W.; Diederich, F.; Rabinovitz, M. Fullerene anions of different sizes and shapes: A  $^{13}\text{C}$  NMR and density-functional study. *J. Org. Chem.* **2003**, *68*, 4850–4854.
64. Kim, K.C.; Hauke, F.; Hirsch, A.; Boyd, P.D.W.; Carter, E.; Armstrong, R.S.; Lay, P.A.; Reed, C.A. Synthesis of the  $\text{C}_{59}\text{N}^+$  carbocation. A monomeric azafullerene isoelectronic to  $\text{C}_{60}$ . *J. Am. Chem. Soc.* **2003**, *125*, 4024–4025.
65. Hultman, L.; Stafstrom, S.; Czigany, Z.; Neidhardt, J.; Hellgren, N.; Brunell, I.F.; Suenaga, K.; Colliex, C. Cross-linked nano-anions of carbon nitride in the solid phase: Existence of a novel  $\text{C}_{48}\text{N}_{12}$  aza-fullerene. *Phys. Rev. Lett.* **2001**, *8722*, art. no.-225503.
66. Schimmelpfennig, B.; Agren, H.; Csillag, S. Theoretical  $^{13}\text{C}$  and  $^{15}\text{N}$  NMR spectra for the  $\text{C}_{48}\text{N}_{12}$  azafullerene. *Synth. Met.* **2003**, *132*, 265–268.
67. Haddon, R.C.; Scott, L.T. Pi-orbital conjugation and rehybridization in bridged annulenes and deformed molecules in general—Pi-orbital axis vector analysis. *Pure Appl. Chem.* **1986**, *58*, 137–142.

# Fullerenes: Magnetic Behavior

T. L. Makarova

Department of Experimental Physics, Institute of Physics, Umeå University, Umeå, Sweden

## Abstract

The discovery of fullerenes opened new possibilities in design and synthesis of new materials, and particularly exciting have been the substances exhibiting different types of collective behavior: superconductivity, ferromagnetism, antiferromagnetism, and spin density wave. This review collects the experimental studies of the following fullerene-based magnets: complexes of fullerenes with organic and organometallic donors; fullerene-containing supramolecular complex substances; rare earth elements intercalated compounds; endohedral fullerenes; polymerized and hydrogenated fullerenes. The ability of polymerized fullerene matrix to act as a magnetic coupling unit between paramagnetic centers is presented. Applications of magnetic fullerenes in nano- and biotechnological areas are briefly described.

## INTRODUCTION

Fullerenes are among the most non-magnetic known substances: they do not exhibit either strong paramagnetism or strong diamagnetism. The foretellers<sup>[1]</sup> and discoverers<sup>[2]</sup> of spherical carbon molecules expected a strong diamagnetic response owing to the ring currents around the cage. It was found, however, that C<sub>60</sub> fullerene exhibits five times smaller magnetic susceptibility than benzene.<sup>[3]</sup> At room temperature, the specific magnetic susceptibility ( $\chi_{1/g}$ ) of the C<sub>60</sub> fullerene is  $\chi_{1/g}(C_{60}) = -0.35 \times 10^{-6} \text{ cm}^3/\text{g}$  and molar susceptibility  $\chi_M(C_{60}) = -252 \times 10^{-6} \text{ cm}^3/\text{mol}$ .<sup>[4]</sup>

There are still debates whether fullerenes can be classified as a novel class of aromatic compounds.<sup>[5]</sup> From the point of view of a physicist, fullerenes possess a three-dimensional delocalized electronic structure, and all 60  $\pi$ -electrons equally contribute to the transport and polarization phenomena. From the chemical point of view, the bond length alternation, high chemical reactivity, and the enthalpy of formation values speak against aromaticity.<sup>[6]</sup> The existence of different types of bonds in fullerenes indicates that there is a partial localization of the  $\pi$ -orbitals. The extensive cyclic delocalization of electrons determines the magnetic properties of fullerenes. Extremely small diamagnetism of fullerenes arises from the cancellation effect between paramagnetic currents around the pentagons and diamagnetic ring currents around the hexagons.<sup>[7]</sup> Ring currents induced by the presence of an external magnetic field have been investigated in polymerized fullerenes. Extremely large ring currents are obtained in polymerized molecules with a particular number of molecules in a polymerized pattern.<sup>[8]</sup>

During the storage of fullerene in air, the magnetic properties change: a noticeable increase in paramagnetic term at low-temperature appears. This paramagnetic Curie-term is usually explained by the absorption

of oxygen, but recent experiments have shown that the paramagnetic properties of an O<sub>2</sub> molecule disappear when oxygen is incorporated into the fullerene lattice, and the paramagnetic term arises from the low-temperature chemical interaction of oxygen with fullerene.<sup>[9]</sup> The source of the paramagnetic response could be stable defects, such as a C<sub>60</sub><sup>+</sup> or C<sub>60</sub><sup>-</sup> ions observed in many EPR experiments. Addition of charge drastically changes the magnetic properties of fullerenes, and they demonstrate different types of collective behavior: superconductivity, ferromagnetism, antiferromagnetism, and spin density wave.

## MAGNETISM OF FULLERENE CHARGE-TRANSFER COMPLEXES

The studies of the reduction of fullerene C<sub>60</sub> with strong organic donors has led to the discovery of the compound tetrakis(dimethylamino) ethylene-C<sub>60</sub> (TDAE-C<sub>60</sub>), which showed a ferromagnetic transition at a temperature of 16 K, thus demonstrating that high-temperature  $\pi$ -electron magnetism is a reality.<sup>[10]</sup> The discovery of ferromagnetic transition in TDAE-C<sub>60</sub> appeared to be the first fact that disproved the opinion that strong magnetism is a property of elements with d and f electrons. Later, magnetic transitions were discovered in (NH<sub>3</sub>) K<sub>3</sub>C<sub>60</sub> antiferromagnet, and the AC<sub>60</sub> and Na<sub>2</sub>AC<sub>60</sub> (A = K, Rb, Cs) polymers (reviewed in Ref.<sup>[11]</sup>).

Tetrakis(dimethylamino) ethylene-C<sub>60</sub> behaves as a soft ferromagnet with a very small coercive force and remnant magnetization (2 Oe and  $M_r \sim 3 \times 10^{-4} \text{ emu/g}$  correspondingly).<sup>[12]</sup> The ultimate proof for the ferromagnetism of this compound came from the  $\mu\text{SR}$  experiments,<sup>[13]</sup> which showed the presence of an internal field, and also demonstrated strong inhomogeneity of

the field. The samples exhibited strange aging effects: ferromagnetism increased during the sample storage. The reason for both inhomogeneity and aging was understood later: it was shown experimentally and theoretically<sup>[14]</sup> that a direct connection exists between the orientation of C<sub>60</sub> molecules and the magnetic interactions in the system. In the as-prepared polycrystalline samples, the molecules were randomly oriented, and thus the system simultaneously exhibited the properties of both soft ferromagnet and a spin glass. The orientational dependence of fullerene magnetism was clarified by the experiments on single crystals. It was shown that this compound has two modifications: ferromagnetic  $\alpha$ -TDAE-C<sub>60</sub> and paramagnetic  $\alpha'$ -TDAE-C<sub>60</sub> modification. The  $\alpha'$  modification is metastable and transforms into the stable  $\alpha$  modification by thermal treatment. Thus, the riddle of the coexistence of the long-range ferromagnetic order and the short-range spin-glass disorder was resolved.

The microscopic understanding of TDAE-C<sub>60</sub> magnetism started from the fact that this compound appears in two modifications. The difference between  $\alpha'$  and  $\alpha$ -TDAE-C<sub>60</sub> is in relative rotation of C<sub>60</sub> molecules around their threefold axis.<sup>[15]</sup> Thus, it was shown that the magnetic properties of the compound are dictated by the relative orientation of the fullerene molecules. Magnetic resonance data provided evidence for the correlation between spin and orientational ordering of Jahn–Teller-distorted C<sub>60</sub> ions.<sup>[16]</sup>

The discovery of ferromagnetism in TDAE-C<sub>60</sub> initiated the works in the following directions: (i) reduction of higher fullerenes with TDAE; (ii) reduction of C<sub>60</sub> with other strong donors; (iii) producing C<sub>60</sub>-containing supramolecular complex substances; (iv) combining C<sub>60</sub> with rare earth elements.

## REDUCTION OF HIGHER FULLERENES WITH TDAE

Until now, the role of TDAE in the magnetism is not quite clear because the TDAE<sup>+</sup> spins are mutually cancelled in both  $\alpha'$  and  $\alpha$ -TDAE-C<sub>60</sub>. The attempts to create a ferromagnet from higher fullerenes reduced with TDAE were unsuccessful: C<sub>70</sub>, C<sub>84</sub>, C<sub>90</sub>, and C<sub>96</sub> readily form the charge-transfer complexes with TDAE,<sup>[17]</sup> but ferromagnetism was never observed. Moreover, the experiment with the molecular alloys TDAE-(C<sub>60</sub>)<sub>1-x</sub>(C<sub>70</sub>)<sub>x</sub> showed that the magnetic properties of the alloys were monotonically changing from ferromagnetic TDAE-C<sub>60</sub> to paramagnetic TDAE-C<sub>70</sub>. The Curie temperature  $T_c$  also linearly decreased with the increase in C<sub>70</sub> content. These experiments confirmed once more that it is C<sub>60</sub> rather than TDAE, which plays the role of magnetic unit in this ferromagnetic organic compound. Fullerene

C<sub>60</sub> doped with a strong organic donor TDAE is the only fullerene that shows bulk ferromagnetism.

## REDUCTION OF C<sub>60</sub> WITH ORGANIC OR ORGANOMETALLIC DONORS

The number of organic and organometallic donors that are able to ionize the fullerene molecules is limited.<sup>[18]</sup> metallocenes, porphyrines, and unsaturated amines, the most known representative of the latter is the above-mentioned TDAE.

There were attempts to combine C<sub>60</sub> with other organic or organometallic donors to form charge-transfer (CT) salts. Other amines similar to tertiary amine TDAE did not produce magnetic substances. For example, tertiary amine diazobicyclononene (DBN) and diazobicycloundecene (DBU) formed covalent bonds with C<sub>60</sub>, and therefore, only a few percent of spins survived. Nevertheless, in the case of DBU-C<sub>60</sub>, these residual spins showed a short-range magnetic order below 70 K.<sup>[19]</sup>

It was reported that the CT complexes with metallocenes: decamethylferrocene (Cp<sub>2</sub><sup>+</sup>Fe), cobaltocene (Cp<sub>2</sub>Co), and nickelocene (Cp<sub>2</sub>Ni) showed ferromagnetic characteristics,<sup>[20,21]</sup> but the synthesis and magnetic properties of charge-transfer complexes of C<sub>60</sub> with the metallocenes were not reproducible.

The next attempt to create fullerene-based magnets was functionalizing of C<sub>60</sub> and subsequent combining with organic or organometallic donors to form charge-transfer complexes. The first compound of this type, dinitro-spiromethanofullerene (C<sub>61</sub>“NO<sub>2</sub>”) doped with bicyclopentadiene cobalt (Cp<sub>2</sub>Co or cobaltocene) showed the ferromagnetic transition at 8 K.<sup>[22]</sup> Another cobaltocene C<sub>60</sub> derivative, 1-(3-aminophenyl)-1H-methanofullerene[C<sub>60</sub>], became magnetic below 19 K, and this temperature was higher than for TDAE-C<sub>60</sub>.<sup>[23]</sup> These studies contributed to the understanding of ferromagnetism in TDAE-C<sub>60</sub>, where the role of TDAE remained unknown. In the cobaltocene derivatives, the cobaltocene is present in its oxidized state Cp<sub>2</sub>Co<sup>+</sup>. It has spin  $S = 0$  and does not contribute to the magnetic signal. Magnetic ordering in the fullerene ferromagnets is established by the  $S = 1/2$  on fullerene moieties.

## IONIC MULTI-COMPONENT COMPLEXES

A novel approach for ionizing the C<sub>60</sub> molecule has been suggested.<sup>[24]</sup> This method produces ionic multi-component complexes, which consist of a charged fullerene and two donors, D1 and D2. The first donor D1 forms a supramolecular packing pattern and the second donor D2 ionizes the fullerene molecule.

The method was used for obtaining porphyrin-based and TDAE-based complexes, as well as tetrabenzylphenylenediamine (TBPDA) complexes.<sup>[25]</sup>

An example of this approach is shown in the work<sup>[26]</sup> in which the donors D2 in different spin states (0,  $1/2$ ,  $3/2$ ) were considered. A neutral part of these complexes, i.e. D1 is TBPDA. For the role of the second donor D2, several donors were chosen: 1) decamethylchromocene ( $\text{Cp}^*_2\text{Cr}$ ) with the spin  $3/2$ ; 2) decamethylcobaltocene ( $\text{Cp}^*_2\text{Co}$ ), which is diamagnetic ( $s = 0$ ); 3) TDAE with  $s = 1/2$ . In the case of a diamagnetic donor, the EPR signal was attributed to  $\text{C}_{60}^{\bullet-}$  ( $\text{Cp}^*_2\text{Co}^+$  is diamagnetic), whereas for the paramagnetic donors, the EPR line demonstrates a resonating signal between  $\text{C}_{60}^{\bullet-}$  and the cation owing to indirect coupling. The EPR signals from cobaltocene-complex and TDAE-complex are split into two components below 50 and 60 K. The magnetic moments of all three compounds decrease below 50–100 K. Both effects are associated with the formation of field-induced short-range antiferromagnetically ordered clusters. For all compounds, it was shown that D1 cations do not noticeably affect the antiferromagnetic interaction of spins due to their isolation by the benzyl groups of TBPDA. Large distances between the fullerenes is a reason for relatively weak antiferromagnetic interactions between the spins residing on  $\text{C}_{60}$ .

### INTERCALATION OF MAGNETIC IONS

The tetrahedral and octahedral voids of the  $\text{C}_{60}$  lattice are able to incorporate foreign atoms. Intercalation of alkali metals into  $\text{C}_{60}$  crystal leads to superconductivity, and it was expected that intercalation of rare earth ions like europium and cerium will produce novel magnetic substances. Europium has a magnetic moment of  $7\mu_B$  in the divalent state, while it is non-magnetic in the trivalent state. In a fulleride  $\text{Eu}_6\text{C}_{60}$ , europium ions are in the divalent state and they order ferromagnetically below 12 K. Below  $T_c$ , this compound shows giant magnetoresistance.<sup>[27]</sup> Substitution of Eu with non-magnetic Sr ions in  $\text{Eu}_{6-x}\text{Sr}_x\text{C}_{60}$  ( $x = 1-5$ ) has not influenced the transition temperature,  $T_c$ . In addition,  $\text{Eu}_6\text{C}_{60}$  showed a huge negative magnetoresistance at and below  $T_c$ . Evidently, there exists a strong interaction between conduction carriers and localized magnetic moments, namely, the strong  $\pi$ - $f$  interaction in  $\text{Eu}_6\text{C}_{60}$ . This fact indicates that the ferromagnetism in  $\text{Eu}_6\text{C}_{60}$  comes from the indirect exchange interaction via  $\text{C}_{60}$  molecules, which is quite in contrast with the case of magnetic semiconductor  $\text{EuO}$ .

Magnetic properties of the cerium-intercalated compounds are complicated: the competition of superconductivity and ferromagnetism has been observed.<sup>[28]</sup> This compound exhibits the superconducting behavior

with the transition temperature 13.5 K. However, very weak magnetic field (2 Oe) destroys superconductivity, and this compound shows a transition to ferromagnetic ground state at 15 K. Superconductivity is suggested to be a property of the doped  $\text{C}_{60}$  subsystem, whereas ferromagnetism is ascribed to the superexchange interactions between  $\text{Ce}^+$  ions.

Intercalation of  $\text{C}_{70}$  with europium affords two kinds of magnetic compounds, a canted antiferromagnet  $\text{Eu}_x\text{C}_{70}$  ( $x$  approximates 3) and a ferromagnet  $\text{Eu}_x\text{C}_{70}$  ( $x$  approximates 9) with transition temperatures of 5 and 38 K, respectively.<sup>[29]</sup>

### HIGH-TEMPERATURE FERROMAGNETISM IN FULLERENE COMPOUNDS

Ferromagnetism in  $\text{C}_{60}$ -containing macromolecular polymer was first reported in 1994<sup>[30]</sup> and magnetism has been ascribed to the radical adducts represented as  $\text{C}_{60}\text{R}_n$  ( $\text{R} = \text{H}, \text{F}, \text{CF}_3$ ), where  $n$  is odd. The films were produced by ultrasonic dispersion of  $\text{C}_{60}$  in dimethylformamide solution of polyvinylidene fluoride and subsequent vacuum evaporation of the solution. The Curie point and magnetization were 370 K and 0.210 emu/g. The contamination with Fe, Mn, Cr, Co, and Ni were less than 0.001, 0.0005, 0.001, 0.002, and 0.005 wt.%, respectively, and it could not account for the observed magnetization.

Room-temperature ferromagnetism in fullerene hydride  $\text{C}_{60}\text{H}_{36}$  has been reported with  $M_s = 0.04 \text{ emu/g}$ <sup>[31]</sup> and in  $\text{C}_{60}\text{H}_{24}$  with  $M_s = 0.046, 0.054,$  and  $0.16 \mu_B/\text{C}_{60}$  (i.e.  $1.2 \text{ emu/g}$ ).<sup>[32]</sup> Measured by the atomic-emission analysis, the concentration of all detected metals in the sample with the highest magnetization of  $0.16 \mu_B/\text{C}_{60}$  was the following: Fe: 0.01; Ni: 0.002; Pd: 0.01; Al: 0.05; Cu: 0.1 (wt.%). Seeing that the magnetization due to the metallic impurities could be only on the level of a few percents from the observed value, the magnetic ordering is an intrinsic property of hydrofullerites. A circumstantial evidence of the intrinsic nature of ferromagnetism is aging: one-year storage brings the samples to a diamagnetic state.

Room-temperature ferromagnetism of fullerenes photopolymerized in the presence of oxygen was first reported in 1996.<sup>[33]</sup> Polymerized fullerene is a specific form of pure carbon in which spheroidal carbon molecules are connected by covalent bonds. The samples of commercial  $\text{C}_{60}$  powder were exposed to oxygen under the action of strong visible light. This process leads to photo-induced polymerization of  $\text{C}_{60}$  units within a surface layer of the crystallites. The thickness of the photo-transformed layer is controlled by the light penetration depth and is of the order of  $0.5 \mu\text{m}$ . The saturation value for the partially polymerized sample was only

$1.4 \times 10^{-2}$  emu/g corresponding to  $0.001 \mu_B/C_{60}$ . However, the residue of the solution in toluene, i.e., a photo-polymerized part of the sample, exhibited a hundred times larger magnetization corresponding to  $0.1 \mu_B/C_{60}$ .

Another group<sup>[34]</sup> verified the existence of a ferromagnetic phase in fullerene photopolymers by three methods: SQUID measurements, ferromagnetic resonance, and low-field non-resonance derivative EPR signal. The room temperature value of saturation magnetization for photolyzed  $C_{60}$  is 0.04 emu/g. The experiments were conducted in a chamber with flowing oxygen, which excludes any possibility of penetration of metallic particles during the experiment. The impurity concentration was measured by means of inductively coupled plasma, which indicated that the signals from all metals were below 100 parts per  $10^9$ ; independent analysis by the plasma-induced atomic absorption spectroscopy confirmed the iron level to be a few parts per  $10^9$ .

In a number of papers,<sup>[35,36]</sup> magnetism of fullerenes polymerized by high-temperature-high-pressure treatment has been reported. A systematic study of synthesis conditions for the production of the ferromagnetic phase<sup>[35]</sup> showed that the phase is formed in the vicinity of fullerene collapse. Gradual transformation of polymerized fullerenes from a paramagnetic through a ferromagnetic (with magnetic moment  $0.34 \mu_B$  per  $C_{60}$  molecule) to a diamagnetic state, as a function of preparation temperature, was monitored.<sup>[35]</sup>

However, studies performed after the first publication revealed considerable (174 ppm) iron content measured locally by the PIXE on some parts of the surface of samples reported in Ref.<sup>[34]</sup>. These findings are described in detail in Refs.<sup>[37,38]</sup>. Later part of the authors retracted from this paper because the Curie temperature of about 500 K is close to that of iron carbide,  $Fe_3C$ .<sup>[39]</sup> Anyway, the  $Fe_3C$  scenario of Ref.<sup>[40]</sup> cannot give the universal interpretation of the literature data such as the trend in the synthesis condition, influence of heat treatment on magnetic behavior, and the observation of the magnetism up to 800 K both in pressure-polymerized and photo-polymerized fullerenes. The temperature stability of magnetic fullerenes exceeds the depolymerization temperature for polymeric phase, and a theoretical approach to give explanation to this fact is developed in Ref.<sup>[40]</sup>. In all described cases, the authors note that the samples do not demonstrate bulk ferromagnetism, but instead contain islands of magnetic phase in a non-magnetic matrix.

## FULLERENES AS A MAGNETIC COUPLING UNIT

Several scenarios that account for (or predict) the magnetism of fullerenes have been suggested. In the models

of ferromagnetic fullerenes, the following possibilities are considered: (i) a fraction of the fullerene cages are broken, and, thus, unpaired electrons appear at the dangling bonds; (ii) the shape of the fullerene cage changes as a result of Stone–Wales transformations; and (iii) fullerenes remain intact, but unpaired electrons are formed at interfullerene links. In an alternative approach (iv), a high-spin ground state of fullerene polymer is considered.

Theoretically, the ability of  $C_{60}$ -fullerene to act as a magnetic coupling unit between radical centers has been evaluated using ab initio method. The results indicate that functionalized  $C_{60}$ -fullerenes have a very good potential to couple radical centers. Depending on the relative position of the two radical centers, the resulting interaction is ferro- or antiferromagnetic.<sup>[41,42]</sup>

A scenario in which structural defects (vacancies) and  $sp^3$ -hybridized atoms interact is described in a series of works.<sup>[43,44]</sup> A correlation should exist between spin moments for magnetic ordering to appear. Since the defects are widely spaced, interaction between them is indirect and needs a mediator. The dipole moment induced by a vacancy can play the role of such a mediator. The Coulomb interaction between localized charges and electric dipoles ensures a means for the exchange interaction between magnetic moments.

Long-range spin coupling has been considered through the investigation of an infinite, periodic system of polymerized  $C_{60}$  network.<sup>[45]</sup> It was shown that chemically bonded hydrogen plays a vital role, providing a necessary pathway for the ferromagnetic coupling of the considered defect structure.<sup>[46]</sup>

A model of fullerene ferromagnetism, which does not require ad hoc constructed defects, has been suggested.<sup>[47]</sup> In this model, the presence of some paramagnetic impurities in fullerene matrix (e.g. hydrogen, fluorine, as well as carbon from partially destroyed fullerenes) leads to a formation of the paramagnetic fullerene ions  $C_{60}^\pm$  as a result of the reaction with charge and spin transfer. Paradoxically, this is an impurity-based model, and at the same time this model is based on intrinsic properties of fullerene matrix. Paramagnetic impurities play only the passive role of net charges and spin sources. According to this model, diamagnetic  $C_{60}$  molecules transform into stable paramagnetic species ( $C_{60}^\pm$  ions or fullerene radical adducts  $C_{60}R$ ) and become magnetically active due to the charge and spin transfer from dopants. Whether the electron comes from a donor to a  $C_{60}$  or goes from  $C_{60}$  to an acceptor, its spin is transferred to the fullerene in any case being well localized at the lattice site. The model is supported by ab initio calculations, the main result of which is that in the  $[2 + 2]$ -cycloadduct polymerized phase, the effective exchange interaction between the paramagnetic fullerene ions is ferromagnetic, strong, and of long range. The coupling between paramagnetic species

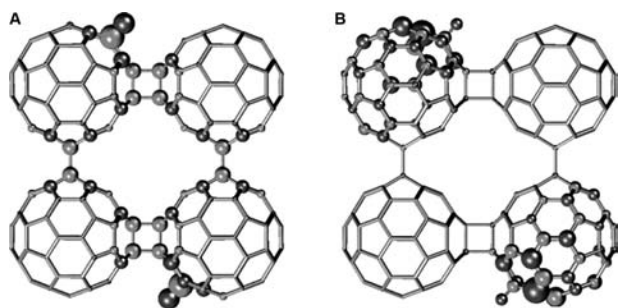


**Fig. 1** The charge (A) and spin (B) density spatial distribution in the triplet spin state of the tetragonally polymerized fullerene  $C_{60}$  doped with hydrogen.

(nearest neighbours and next nearest neighbours) in polymerized fullerene matrix is examined, and it is shown that exchange integral is of the order of several tenths of an electronvolt.<sup>[53]</sup> Figure 1 illustrates this model for the case of tetragonally polymerized fullerene and for the case when the spins are situated at the next nearest neighbors (rather than the nearest neighbors). Figure 1A shows the Mulliken charge distribution, and Fig. 1B depicts the spin distribution.

Remarkably, the spin density is zero on the bonds bridging the molecules, so that one can assign a spin to each of the doped buckyballs. Thus, the spin of an individual charged molecule is well defined, and  $C_{60}$  molecules play the role of the sites on which spins reside. The ab initio calculations for this pattern give large positive splitting between the triplet and singlet ground states, and its value  $E_{\uparrow\uparrow} - E_{\downarrow\downarrow} = 0.68$  eV is enough to account for the high-temperature ferromagnetism.

Analysis of various experimental data, including pure organic ferromagnetic substance TDAE- $C_{60}$ , antiferromagnetic ground states encountered in various alkali or lanthanide fulleride salts,  $\pi$ - $f$  interactions through  $C_{60}$  in metal-intercalated fullerenes, magnetism of polymeric networks, and other experimental examples show that in many cases, fullerene  $C_{60}$  works either as a magnetic unit, or a magnetic coupling unit.

## FULLERENES IN MAGNETIC RESONANCE IMAGING

One of the main reasons for studying the magnetic properties of fullerenes is the perspective applications in medicine, as carbon is a biocompatible element. At present, progress is made for the Gd-based water-soluble metallofullerenes. They are regarded as a possible new generation of magnetic resonance imaging (MRI) contrast agents, sensibilizers for the photodynamic therapy of tumors. Their proton relaxivities are greater than those of commercially available MRI contrast agents, but the

main advantage is that they offer a safe alternative to the existing substances. Toxic gadolinium is isolated from the tissues by the carbon cages. For these purposes, water-soluble Gd-based endohedral metallofullerenes ( $Gd@C_{82}(OH)_x$ ,  $Gd@C_{60}(OH)_x$ , and  $Gd@C_{60}[C-(COOH)_{10}]$ ) have been extensively studied.<sup>[48]</sup> Other water-soluble multi-hydroxyl lanthanoid (La, Ce, Gd, Dy, and Er) endohedral metallofullerenes [metallofullerenols,  $M@C-82(OH)(n)$ ] have been synthesized and characterized for the use of MRI contrast agents<sup>[49]</sup> or an X-ray contrast material.<sup>[50]</sup>

A novel photosensitizer with magnetic resonance imaging activity was designed from fullerene ( $C_{60}$ ) for efficient photodynamic therapy of tumor.<sup>[51]</sup> Gadolinium-based compound  $C_{60}$ -PEG-Gd (where PEG is polyethylene glycol) maintained an enhanced MRI signal at the tumor tissue. Injection of  $C_{60}$ -PEG-Gd plus light irradiation showed significant tumor PDT effect, which depended on the timing of light irradiation. Trimetallic nitride endohedral metallofullerene  $Gd_3N@C-80$ <sup>[52]</sup> showed MR imaging relaxivity markedly higher than that for commercial agents (e.g., gadodiamide). The use of functionalized  $Gd_3N@C-80$  at concentrations an order of magnitude lower resulted in equivalent visualization in comparison with commercial agents.

Paramagnetic  $Gd@C_{82}$  fullereneol was tested as a contrast agent.<sup>[53]</sup> Cellular labeling with  $Gd@C_{82}$  is feasible and can produce T1-enhanced cells on magnetic resonance imaging. This study suggests that further investigation of Gd fullereneols for tracking studies of viable cells, including stem cells, is warranted. Thus, fullerenes bring to medicine a new type of magnetic agents, which are water-soluble and non-toxic.

## FULLERENE-BASED QUANTUM COMPUTER

Recently, an interest in the magnetic properties of endohedral fullerenes was renewed when a concept for a spin quantum computer based on the endohedral fullerenes has been proposed.<sup>[54,55]</sup> This computer uses the electron spin of a doped atom, i.e., nitrogen or phosphorus, caged in a fullerene. The carbon cage protects the spin and keeps it in the symmetrical environment; hence, the spin system is highly shielded from the environment. Combined electron and nuclear spin pseudo-entangled states can be prepared in the multi-level quantum system of a nitrogen atom with electron spin  $3/2$  and nuclear spin  $1/2$  encaged in the endohedral fullerene.<sup>[56]</sup>

Two types of endohedral fullerenes are considered as building blocks for the quantum computer,  $^{15}N@C_{60}$  and  $^{31}P@C_{60}$ . In these fullerenes, the nuclear spin of the encapsulated atom is a spin  $1/2$ . It is coupled to three uncoupled electrons located in the



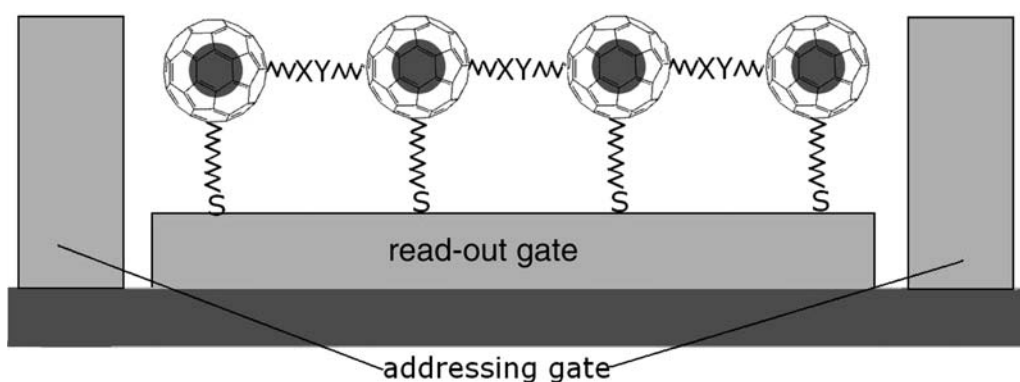


**Fig. 2** Graphical visualization of the solid-state spin quantum computer based on endohedral fullerenes. *Source:* Adapted from Ref.<sup>[60]</sup>.

highest energy level of the encapsulated atom. In a system of aligned fullerenes, the two neighboring spin sites communicate via electronic coupling. The entire system is exposed to a static and homogeneous magnetic field, and the interaction with this field induces a Zeeman splitting in the nuclei and electrons, which can be measured by the resonance techniques.

This approach has real promises to become a reality because the state-of-the-art technology is able to provide the necessary components and processes: (i) fullerene technology including the endohedral ones is mature; (ii) manipulation of fullerene molecules is fairly easy; (iii) writing and reading procedures are performed via pulsed electron-spin resonance; (iv) addressing is provided by local magnetic fields or field gradients; (v) the qubit–qubit interaction is mediated by magnetic dipolar coupling and can be controlled via the direction of the magnetic field with respect to the distance vector of the qubits. Figure 2 illustrates the computer design.

Many experimental and theoretical efforts were made to create a technology based on endohedral fullerenes.<sup>[57]</sup> In one of the projects, the construction of the quantum computer requires linear chains of endohedral fullerenes, which can be achieved by embedding them in a liquid crystal matrix.<sup>[58]</sup> The readout of a qubit in fullerene-based quantum computing can be made using the scanning tunneling microscope.<sup>[59]</sup> A scheme was proposed to implement the two-qubit gates and to compose a universal set of quantum gates in fullerene-based quantum computation.<sup>[60]</sup>

## CONCLUSIONS

Fullerenes in their pristine and polymerized form are diamagnetic substances. Doped with donors, they exhibit different types of magnetic behavior, including

soft ferromagnetism, antiferromagnetism, spin density wave, and superconductivity. In all cases, fullerenes play an active role in the establishment of the collective behavior. In the charge-transfer salts, the ferromagnetic or antiferromagnetic ordering is established by the  $S = 1/2$  on fullerene moieties. In the metal-intercalated fullerenes, superconductivity arises due to the doped  $C_{60}$  subsystem, whereas ferromagnetism is due to the superexchange interactions between metallic ions mediated by the  $C_{60}$  molecules. There have been reports about high-temperature ferromagnetism in polymerized and hydrogenated fullerenes and some charge-transfer salts, but these samples do not demonstrate bulk ferromagnetism, and instead contain islands of magnetic phase in a non-magnetic matrix, which complicates the identification of the magnetic unit. These reports initiated a large number of theoretical investigations, which showed that intrinsic high-temperature magnetism of fullerenes is a feasible possibility.

It is difficult to expect practical applications for the superconducting fullerenes, because they are unstable in air, or for magnetic charge-transfer salts, which have low transition temperatures. Magnetic properties of fullerenes have recently found an unexpected usage as the basic module for quantum computers. It is expected that fullerenes will be applied in diverse fields varying from nano- to biotechnological areas, to magnetic resonance imaging, photodynamic therapy of tumors, drug delivery for the treatment of brain tumors, and quantum computing.

## REFERENCES

1. Osawa, E. Superaromaticity. *Kagaku (Kyoto)* **1970**, 25, 843–863 (in Japanese).
2. Kroto, H.W.; Heath, J.R.; O'Brien, S.C.; Curl, R.F.; Smalley, R.E.  $C_{60}$ : buckminsterfullerene. *Nature* **1985**, 318, 162–163.

3. Elser, V.; Haddon, R.C. Icosahedral C<sub>60</sub> – an aromatic molecule with a vanishingly small ring current magnetic susceptibility. *Nature* **1987**, *325*, 792–794.
4. Haddon, R.C.; Schneemeyer, L.F.; Waszczak, J.V.; Glarum, S.H.; Tycko, R.; Dabbagh, G.; Kortan, A.R.; Muller, A.J.; Mujsce, A.M.; Rosseinsky, M.J.; Zahurak, S.M.; Makhija, A.V.; Thiel, F.A.; Raghavachari, K.; Cocayne, E.; Elser, V. Experimental and theoretical determination of the magnetic susceptibility of C<sub>60</sub> and C<sub>70</sub>. *Nature* **1991**, *350*, 46–47.
5. Buhl, M.; Hirsch, A. Spherical aromaticity of fullerenes. *Chem. Rev.* **2001**, *101* (5), 1153–1184.
6. Poater, J.; Fradera, X.; Duran, M.; Sola, M. An insight into the local aromaticities of polycyclic aromatic hydrocarbons and fullerenes. *Chem. A Europ. J.* **2003**, *9*, 1113–1122.
7. Pasquarello, A.; Schlüter, M.; Haddon, R.C. Ring currents in icosahedral C<sub>60</sub>. *Science* **1992**, *257*, 1660–1661.
8. Lopez-Urias, F.; Rodriguez-Manzo, J.A.; Terrones, M.; Terrones, H. Induced ring currents in polymerized C<sub>60</sub> and C<sub>70</sub> molecules. *J. Comput. Theor. Nanosci.* **2007**, *4* (2), 257–263.
9. Shul'ga, Yu.M.; Martynenko, V.M.; Shestakov, A.F.; Baskakov, S.A.; Kulikov, S.V.; Vasilets, V.N.; Makarova, T.L.; Morozov, Yu.G. Doping of fullerite with molecular oxygen at low temperature and pressure. *Russ. Chem. Bull.* **2006**, *55* (4), 687–696.
10. Allemand, P.-M.; Khemani, K.C.; Koch, A.; Wudl, F.; Holczer, K.; Donovan, S.; Grüner, G.; Thompson, J.D. Organic molecular soft ferromagnetism in a fullerene C<sub>60</sub>. *Science* **1991**, *253*, 301–303.
11. Arcon, D.; Prassides, K. Magnetism in fullerene derivatives. *Struct. Bond.* **2001**, *100*, 129–162.
12. Suzuki, A.; Suzuki, T.; Whitehead, R.J.; Maruyama, R. Evidence of spontaneous magnetic order in the C<sub>60</sub> complex with tetrakis(dimethylamini)ethylene. *Chem. Phys. Lett.* **1994**, *223*, 517.
13. Lappas, A.; Prassides, K.; Vavekis, K.; Arcon, D.; Blinc, R.; Cevc, P.; Amato, A.; Feyerherm, R.; Gygax, F.N.; Schenck, A. Spontaneous magnetic ordering in the fullerene charge-transfer salt TDAE-C<sub>60</sub>. *Science* **1995**, *267*, 1799.
14. Michailovich, D.; Arcon, D.; Venturini, P.; Blinc, R.; Omerzu, A.; Cevc, P. Orientational and magnetic ordering of buckyballs in TDAE-C<sub>60</sub>. *Science* **1995**, *268* (5209), 400–402.
15. Narymbetov, B.; Omerzu, A.; Kabanov, V.V.; Tokumoto, M.; Kobayashi, H.; Mihailovic, D. Origin of ferromagnetic exchange interactions in a fullerene-organic compound. *Nature* **2000**, *407*, 883.
16. Arcon, D.; Blinc, R. Role of Jahn-Teller effect in fullerene ferromagnetism. Fullerene-based materials: structure and bonding **2004**, *109*, 231–276.
17. Tanaka, K.; Sato, T.; Yamabe, T.; Yoshizawa, K.; Okahara, K.; Zakhidov, A.A. Weak suppression of ferromagnetism in tetrakis(dimethylamino)ethylene-(C<sub>60</sub>)(1-x)(C<sub>70</sub>)(x). *Phys. Rev. B* **1994**, *51*, 990.
18. Balch, A.L.; Olmstead, M.M. Reactions of transition metal complexes with fullerenes (C<sub>60</sub>, C<sub>70</sub>, etc) and related materials. *Chem. Rev.* **1998**, 2123–2165.
19. Klos, H.; Rystau, I.; Schutz, W.; Gotschy, W.; Skiebe, A.; Hirsch, A. Doping of C<sub>60</sub> with tertiary amines – TDAE, DBU, DBN – a comparative study. *Chem. Phys. Lett.* **1994**, *224* (3–4), 333–337.
20. Otsuka, A.; Teramoto, T.; Sugita, Y.; Ban, T.; Saito, G. Preparation and physical properties of some C<sub>60</sub> charge transfer complexes. *Synth. Met.* **1995**, *70* (1–3), 1423.
21. Wang, W.-J.; Lay, Y.L.; Chang, C.-S.; Chiu, H.-S.; Chuang, K.-S.; Wang, B.-C. Synthesis, spectroscopic and magnetic properties of the charge-transfer complex Bifc.C<sub>60</sub>. *Synth. Met.* **1997**, *86*, 2293.
22. Venturini, P.; Krasevec, V.; Mihailovic, D.; Eiermann, M.; Srdanov, G.; Sariciftci, N.S.; Li, C.; Wudl, F. Proceedings of International Winterschool on Electronic Properties of Novel Materials; World Scientific, Singapore, 1994, 514–517.
23. Mrzel, A.; Omerzu, A.; Umek, P.; Mihailovic, D.; Jaglicic, Z.; Trontelj, Z. Ferromagnetism in a cobaltocene-doped fullerene derivative below 19 K due to unpaired spins only on fullerene molecules. *Chem. Phys. Lett.* **1998**, *298* (4–6), 329–334.
24. Konarev, D.V.; Khasanov, S.S.; Otsuka, A.; Yoshida, Y.; Lyubovskaya, R.N.; Saito, G. The interaction of fullerenes C<sub>60</sub>, C<sub>70</sub>, and C<sub>60</sub>(CN)<sub>2</sub> radical anions with cobalt(II) tetraphenylporphyrin in solid multicomponent complexes. *Chem. Eur. J.* **2003**, *9*, 3837–3848.
25. Konarev, D.V.; Khasanov, S.S.; Saito, G.; Lyubovskaya, R.N. Ionic multi-component complexes of fullerenes: structures and magnetic properties. *Fuller. Nanot. Car. Nan.* **2006**, *14* (2–3), 349–356.
26. Konarev, D.V.; Neretin, I.S.; Saito, G.; Slovokhotov, Yu.L.; Otsuka, A.; Lyubovskaya, R.N. Ionic multi-component complexes containing TDAE and C<sub>60</sub> radical ions and neutral D1 molecules. *Dalton Trans.* **2003**, *20*, 3886–3891.
27. Ishii, K.; Fujiwara, A.; Suematsu, H.; Kubozono, Y. Ferromagnetism and giant magnetoresistance in the rare-earth fullerides Eu<sub>6-x</sub>Sr<sub>x</sub>C<sub>60</sub>. *Phys. Rev. B* **2002**, *65*, 134431-1.
28. Maruyama, Y.; Motohashi, S.; Sakai, N.; Watanabe, M.; Suzuki, K.; Ogata, H.; Kubozono, Y. Possible competition of superconductivity and ferromagnetism in Ce<sub>x</sub>C<sub>60</sub> compounds. *Solid State Commun.* **2002**, *123*, 229–233.
29. Takenobu, T.; Chi, D.H.; Margadonna, S.; Prassides, K.; Kubozono, Y.; Fitch, A.N.; Kato, K.; Iwasa, Y. Synthesis, structure, and magnetic properties of the fullerene-based ferromagnets Eu<sub>3</sub>C<sub>70</sub> and Eu<sub>9</sub>C<sub>70</sub>. *J. Amer. Chem. Soc.* **2003**, *125* (7), 1897–1904.
30. Ata, M.; Machida, M.; Watanabe, H.; Seto, J. Polymer-C<sub>60</sub> composite with ferromagnetism. *Jpn. J. Appl. Phys.* **1994**, *33*, 1865–1871.
31. Lobach, A.S.; Shul'ga, Y.M.; Roshchupkina, O.S.; Rebrov, A.I.; Perov, A.A.; Morozov, Y.G.; Spector, V.N.; Ovchinnikov, A.A. C<sub>60</sub>H<sub>18</sub>, C<sub>60</sub>H<sub>36</sub>, and C<sub>70</sub>H<sub>36</sub> fullerene hydrides: study by methods of IR, NMR, XPS, EELS and magnetochemistry. *Fullerene Sci. Technol.* **1998**, *6* (3), 375–391.
32. Antonov, V.E.; Bashkin, I.O.; Khasanov, S.S.; Moravsky, A.P.; Morozov, Yu.G.; Shulga, Yu.M.;

- Ossipyan, Yu.A.; Ponyatovsky, E.G. Magnetic ordering in hydrofullerite  $C_{60}H_{24}$ . *J. Alloys Comp.* **2002**, *330*, 365–368.
33. Murakami, Y.; Suematsu, H. Magnetism of  $C_{60}$  induced by photo-assisted oxidation. *Pure Appl. Chem.* **1996**, *68* (7), 1463–1467.
34. Owens, F.J.; Iqbal, Z.; Belova, L.; Rao, K.V. Evidence for high temperature ferromagnetism in photolyzed  $C_{60}$ . *Phys. Rev. B* **2004**, *69*, 033403.
35. Makarova, T.L.; Sundqvist, B.; Esquinazi, P.; Höhne, R.; Kopelevich, Y.; Scharff, P.; Davydov, V.A.; Kashevarova, L.S.; Rakhmanina, A.V. Magnetic carbon. *Nature* **2001**, *413*, 718–720.
36. Wood, R.A.; Lewis, M.H.; Lees, M.R.; Bennington, S.M.; Cain, M.G.; Kitamura, N. Ferromagnetic fullerene. *J. Phys.: Condens. Matter* **2002**, *14* (22), L385–L391.
37. Hohne, R.; Esquinazi, P. Can carbon be ferromagnetic? *Adv. Mater.* **2002**, *14*, 753.
38. Han, K.-H.; Spemann, D.; Höhne, R.; Setzer, A.; Makarova, T.; Esquinazi, P.; Butz, T. Observation of intrinsic magnetic domains in  $C_{60}$  polymer. *Carbon* **2003**, *41*, 785.
39. Makarova, T.L.; Sundqvist, B.; Esquinazi, P.; Höhne, R.; Kopelevich, Y.; Scharff, P.; Davydov, V.A.; Kashevarova, L.S.; Rakhmanina, A.V. Magnetic carbon, retraction. *Nature* **2005**, *436*, 1200.
40. Owens, F.W. Stability of  $(C-60)_2$  and epoxide dimers,  $(C-60)_2O-N$ , and their anions. *J. Comput. Chem.* **2005**, *26*, 803–806.
41. Ribas-Ariño, J.; Novoa, J.J. The origin of the magnetic moments in compressed crystals of polymeric  $C_{60}$ . *Angew. Chem. Int. Ed.* **2004**, *43*, 577–580.
42. Ribas-Ariño, J.; Novoa, J.J. Generalized Stone-Wales transformation as the possible origin of ferromagnetism in polymeric  $C_{60}$ : a density-functional theory study. *J. Chem. Phys.* **2006**, *125* (17), 174312.
43. Andriotis, A.N.; Sheetz, R.M.; Menon, M. Doping and the unique role of vacancies in promoting the magnetic ground state in carbon nanotubes and  $C-60$  polymers. *Phys. Rev. B* **2006**, *74* (15), 153403.
44. Andriotis, A.N.; Sheetz, R.M.; Menon, M.; Chernozatonskii, L.A. Magnetic properties of  $C_{60}$  polymers. *Phys. Rev. Lett.* **2003**, *90*, 026801.
45. Chan, J.A.; Montanari, B.; Chan, W.L.; Harrison, N.M. Hybrid density functional study of organic magnetic crystals: Bi-metallic Cr-III cyanides and rhombohedral  $C_{60}$ . *Mol. Phys.* **2005**, *103* (18), 2573–2585.
46. Chan, J.A.; Montanari, B.; Gale, J.D.; Bennington, S.M.; Taylor, J.W.; Harrison, N.M. Magnetic properties of polymerized  $C_{60}$ : the influence of defects and hydrogen. *Phys. Rev. B* **2004**, *70* (4), 041403.
47. Kvyatkovskii, O.E.; Zakharova, I.B.; Shelankov, A.L.; Makarova, T.L. Spin-transfer mechanism of ferromagnetism in polymerized fullerenes: ab initio calculations. *Phys. Rev.* **2005**, *72* (21), 214426.
48. Toth, E.; Bolskar, R.D.; Borel, A.; Gonzalez, G.; Helm, L.; Merbach, A.E.; Sitharaman, B.; Wilson, L.J. Water-soluble gadofullerenes: Toward high-relaxivity, pH-responsive MRI contrast agents. *J. Amer. Chem. Soc.* **2005**, *127* (2), 799–805.
49. Kato, H.; Kanazawa, Y.; Okumura, M.; Taninaka, A.; Yokawa, T.; Shinohara, H. Lanthanoid endohedral metallofullerenols for MRI contrast agents. *J. Amer. Chem. Soc.* **2003**, *125* (14), 4391–4397.
50. Miyamoto, A.; Okimoto, H.; Shinohara, H.; Shibamoto, Y. Development of water-soluble metallofullerenes as X-ray contrast media. *Europ. Radiol.* **2006**, *16* (5), 1050–1053.
51. Liu, J.; Ohta, S.; Akinaga Sonoda, A.; Yamada, M.; Yamamoto, M.; Nitta, N.; Murata, K.; Tabata, Y. Preparation of PEG-conjugated fullerene containing  $Gd^{3+}$  ions for photodynamic therapy. *J. Controlled Release* **2007**, *17* (1), 104–110.
52. Fatouros, P.P.; Corwin, F.D.; Chen, Z.J.; Broaddus, W.C.; Tatum, J.L.; Kettenmann, B.; Ge, Z.; Gibson, H.W.; Russ, J.L.; Leonard, A.P.; Duchamp, J.C. In vitro and in vivo imaging studies of a new endohedral metallofullerene nanoparticle. *Radiology* **2006**, *240* (3), 756–764.
53. Anderson, S.A.; Lee, K.K.; Frank, J.A. Gadolinium-fullerenol as a paramagnetic contrast agent for cellular imaging. *Invest. Radiol.* **2006**, *41* (3), 332–338.
54. Harneit, W. Fullerene-based electron-spin quantum computer. *Phys. Rev. A* **2002**, *65* (3), 032322.
55. Suter, D.; Lim, K. Scalable architecture for spin-based quantum computers with a single type of gate. *Phys. Rev. A* **2002**, *65*, 052309.
56. Mehring, M.; Scherer, W.; Weidinger, A. Pseudoentanglement of spin states in the multilevel  $15N@C60$  system. *Phys. Rev. Lett.* **2004**, *93* (20), 206603.
57. Benjamin, S.C.; Ardavan, A.; Briggs, A.D.; Britz, D.A.; Gunlycke, D.; Jefferson, J.; Jones, M.A.G.; Leigh, D.F.; Lovett, B.W.; Khlobystov, A.N.; Lyon, S.A.; Morton, J.J.L.; Porfyrakis, K.; Sambrook, M.R.; Tyryshkin, A.M. Towards a fullerene-based quantum computer. *J. Phys.: Condens. Matter* **2006**, *18*, S867–S883.
58. Meyer, C.; Harneit, W.; Weidinger, A.; Lips, K. Experimental steps towards the realization of a fullerene quantum computer. *Phys. Stat. Sol. B* **2002**, *233* (3), 462–466.
59. Feng, M.; Dong, G.J.; Hu, B. The readout of fullerene-based quantum computing by a scanning tunnelling microscope. *New J. Phys.* **2006**, *8*, 252–256.
60. Suter, D.; Ju, C.; Du, J. Two-qubit gates between noninteracting qubits in endohedral-fullerene-based quantum computation. *Phys. Rev. A* **2007**, *75*, 012318.

# Fullerenes: Topology and Structure

G. Benedek

M. Bernasconi

*Dipartimento di Scienza dei Materiali, Università di Milano Bicocca,  
Milan, Italy*

## INTRODUCTION

The discovery of fullerenes<sup>[1,2]</sup> has disclosed a new wide area of research in fundamental condensed matter physics,<sup>[3,4]</sup> as well as in chemistry<sup>[2,5]</sup> and materials science,<sup>[6]</sup> confirming carbon as the most versatile element of nature. Fullerenes constitute a family of cage-like carbon molecules where each carbon atom is threefold coordinated and forms covalent  $sp^2$  bonds with the three nearest neighbors like in a single graphite sheet. The atoms of fullerenes lie on a closed surface topologically equivalent to a sphere. The actual shapes of fullerene clusters are polyhedra whose structural features can be largely understood from pure topological arguments. The number  $N$  of atoms of a fullerene molecule vary from a minimum of 20 to indefinite large values, presumably in the range of several thousands, although the far most stable fullerene is made of 60 atoms ( $C_{60}$ ) and takes the shape of a soccer ball, otherwise known as a truncated icosahedron. The shape of this highly symmetric polyhedron, having 60 equivalent vertices that can be generated by the 60 operations of the icosahedral point group, was well known to ancient Greek mathematicians, notably to Archimedes who described the 13 possible semiregular polyhedra. Semiregular polyhedra, otherwise known as the Archimedean polyhedra, are made of two different kinds of regular polygons and are obtained by vertex truncation of the five regular (Platonic) polyhedra. The first known representations of the truncated icosahedron have been given by the celebrated Renaissance artists and scholars Piero della Francesca and Leonardo da Vinci (Fig. 1).

In this entry, the structural and topological features of graphite-like carbon are described, with special emphasis on the novel families of graphene materials that have been discovered and thoroughly investigated after the first identification of the fullerenes  $C_{60}$  and  $C_{70}$ . In “Historical Background,” an overview is given on the historical development and the scientific and technical motivations of studies on the different forms of graphite-like carbon. The topology of graphene structures is presented in “Graphene Topology.” This section contains an elementary introduction to the

general topological properties of graphenes, which allows for a classification of the graphene families in terms of topological connectivity. This is followed by four subsections describing the main graphene families: fullerenes, nanotubes, schwarzites, and amorphous  $sp^2$  carbon. “Topology vs. Total Energy and Growth Processes” shows that the energetics and the growth processes of graphene structures can also be related to and, to some extent, understood from general topological arguments.

## HISTORICAL BACKGROUND

The first idea that graphite sheets could be bent, at the cost of replacing a number of six-membered rings with five-membered ones, so as to form graphite balloons, dates back to the mid-1960s and is due to D. E. H. Jones.<sup>a</sup> The conjecture that 60 carbon atoms could arrange themselves in a stable molecule having the shape of a truncated icosahedron was investigated in 1970 by the Japanese chemist Eiji Osawa and confirmed shortly after by the Russian chemists Bochvar and Galpern with a Hückel calculation (1973) and by R. A. Davidson (1980) by means of a group theoretical analysis. It is now recognized that fullerenes are rather frequent in nature, especially in soot and probably in interstellar dust. However, it was in 1985 that the cluster  $C_{60}$  was experimentally identified by Robert F. Curl, Harold W. Kroto, and Richard E. Smalley with their graduate students J. R. Heath and S. C. O'Brien at Rice University.<sup>[1]</sup> The molecule was recognized among the various products of a cluster beam experiment where carbon clusters were generated by laser vaporization of graphite—a technique developed by E. A. Rohlfing, D. M. Cox, and A. Kaldor a year before and then adopted by Richard Smalley for his experiments at Rice. The large abundance of  $C_{60}$  in the cluster beam, as signaled by mass spectra, was indicative of its exceptional stability whereas the

<sup>a</sup>References to this and following historical works are found in Sir H. W. Kroto's introductory paper in Ref.<sup>[2]</sup>.

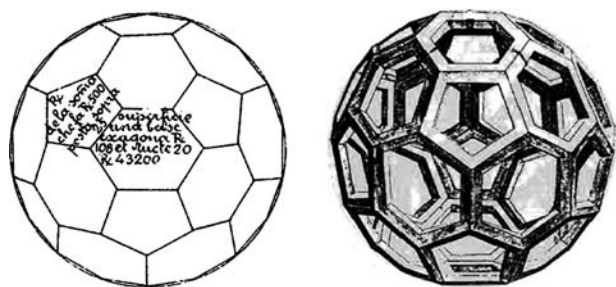


**Fig. 1** The truncated icosahedron according to Piero della Francesca (*Libellus de Quinque Corporibus Regularibus*, 1492 manuscript at Bibliotheca Vaticana) and Leonardo da Vinci (in L. Pacioli, *De Divina Proportione*, Bologna 1498).

occurrence of a single line in the nuclear magnetic resonance spectrum suggested that all 60 atoms are equivalent, which led to one single possible geometry for the molecule, the truncated icosahedron. Although the number of possible fullerene isomers rapidly increases with the cluster size and many isomers have a comparable cohesive energy per atom, the truncated icosahedron is definitely the most stable form of  $C_{60}$  among its 1812 possible isomers. The resemblance of these new molecules with the geodetic domes invented by the renowned architect Buckminster Fuller led to the general name of buckminsterfullerenes, subsequently abbreviated into fullerenes.

A further breakthrough in the chemistry and physics of fullerenes was made by Wolfgang Krätschmer and Donald R. Huffman (1990) who devised a method for the production of fullerenes in gram quantities.<sup>[7]</sup> This allowed for the growth of fullerene crystals, either pure (fullerite) or in a compound form with other elements (fullerides), and led to the discovery of superconductivity in alkali fullerides at moderately high temperatures (1991).<sup>[8]</sup> Carbon clusters can also be considered as the building blocks for a large variety of carbon-based, cluster-assembled materials and novel nanostructured carbon forms.<sup>[9]</sup> Quite often clusters have peculiar properties, originating from the low dimensionality, which are frustrated in the corresponding three-dimensional solid. The concept behind cluster assembling is that some of the interesting properties and functions that occur in the composing clusters may be preserved in a three-dimensional robust structure. Much of the materials science based on fullerenes relies on their peculiar chemistry and on various functionalization and polymerization processes that have been discovered and extensively studied starting from the early 1990s.<sup>[10]</sup> The chemistry of fullerenes also includes the synthesis of endohedral fullerenes having the formula  $C_n@Me$ , where Me stands for a metal atom inside the fullerene cage. Indeed, these studies have suggested enormous potentialities and a wide range of applications for carbon-based materials,

thanks to the possibility of tailoring their physical properties and performances. It was suggested, for example, that the superconducting critical temperature of doped fullerite increases with the curvature of fullerene cages, namely with the reduction of the cluster size from  $C_{60}$  down to  $C_{36}$ ,<sup>[11]</sup> and perhaps  $C_{28}$  and  $C_{20}$ . Moreover, an unexpected ferromagnetic behavior has been recently described in fullerene materials.<sup>[12]</sup>

The surprising wealth of physical and chemical properties found in fullerenes has stimulated an extensive search for additional forms of carbon.<sup>[13]</sup> The peculiar cage-like geometry of fullerenes has provided a new ingredient for the structural analysis and growth of some widely studied forms of aggregation of  $sp^2$  carbon, such as carbon blacks, which are currently obtained by dehydrogenation of hydrocarbons and modeled as concentric shells of graphitic segments.<sup>[14]</sup> Indeed, single fullerenes may work as templates for the formation of a highly idealized form of  $sp^2$  carbon nanoparticles known as carbon onions. Carbon onions consist of concentric hollow carbon spheres that are produced with a strong electron beam irradiation of carbon nanoparticles such as those present in carbon blacks. Carbon onions have been found to act as precursors for the formation of diamond under suitable high-temperature electron beam irradiation. The low-density aggregation of  $sp^2$  clusters leads to the formation of highly porous, low-density carbon phases (carbon aerogels). Among these structures, schwarzites, discussed below, are of special interest from the topological point of view.

Another important class of  $sp^2$  carbon materials is that of carbon fibers, which can be viewed as assemblies of closely connected carbon nanotubes. A single-wall carbon nanotube (SWCNT) consists of graphite sheet rolled up to form a cylinder of a given constant diameter and indefinite length. The diameter can be as small as about 0.7 nm. When a nanotube is closed (capped) at both extremities, the nanotube can be viewed as a very elongated fullerene, and is indeed topologically equivalent to a fullerene. A single-wall nanotube can be dressed by other coaxial nanotubes in the very same way as a carbon onion grows around a fullerene and forms a multiwall carbon nanotube (MWNT). Carbon nanotubes have been discovered by high-resolution transmission electron microscopy (TEM) by S. Iijima in 1991<sup>[15]</sup> and since then have stimulated an enormous interest for their great mechanical robustness combined with excellent transport properties and potential applications in field emitters, supercapacitors, nanoelectronics, etc. Carbon nanotubes can be grown from the decomposition of hydrocarbons on metal nanoparticles acting as catalysts. Like endohedral fullerenes, nanotubes can be filled with metal ions that modify their one-dimensional properties; for example, their electrical behavior and

functions as nanowires. Indeed, nanotubes are considered as elementary components for nanocircuits, T- and Y-shaped junctions, and possibly semiconducting n-p junctions where the difference between the two sides of the junction is achieved either with two unequal nanotube structures or through doping, e.g., with endohedral metal atoms.

Other exotic morphologies of  $sp^2$  carbon that have been obtained with the use of different catalytic metal particles, laser-ablation processes, or simply by flash chemical vapor deposition techniques are carbon parallelepipeds,<sup>[16]</sup> single-wall<sup>[17]</sup> and multiwall<sup>[18]</sup> ring-shaped nanotubes, graphitic nanocones,<sup>[19]</sup> carbon nanohorns,<sup>[20]</sup> and nanotrees.<sup>[21]</sup> Nanotubes as well as cones and similar morphologies can be obtained in principle by a continuous bending of a graphite sheet without breaking any bond, namely without introducing disclinations. As will be explained in the next sections, from the topological point of view, this kind of deformation keeps the Gauss curvature of the surface constant, in this case zero as for the originally flat graphite sheet. For comparison, the bending of a graphite sheet and its closure into a fullerene implies a change of the Gauss curvature from zero to a positive value and the creation of a certain number of positive disclinations associated with the conversion of some hexagonal rings into smaller polygons.

The synthesis of new  $sp^2$  carbon forms, such as fullerenes and nanotubes, and the observation of important properties, such as superconductivity in alkali metal-doped fullerenes,<sup>[22]</sup> field-emission,<sup>[23]</sup> and supercapacitance<sup>[24]</sup> from arrays of nanotubes, are opening fascinating perspectives for nanostructured carbon as a novel, all-purpose material. However, fullerenes and nanotubes, as well as graphite, aggregate into van der Waals three-dimensional (3-D) solids. For many technological applications, there is a need of highly connected, fully covalent  $sp^2$ -bonded carbon forms, combining the valuable properties of fullerenes and nanotubes with a robust 3-D architecture. A basic question is whether a graphite sheet can be transformed into a surface characterized by a negative Gauss curvature everywhere through the creation of a sufficient number of negative disclinations where some hexagonal rings transform into larger polygons. A special case of negative Gauss curvature occurs when the mean curvature is zero everywhere, which corresponds to what is known in differential geometry as a minimal surface. The conjecture that a minimal surface is particularly stable has stimulated much theoretical work on hypothetical graphite sheets (graphenes) with the shape of a periodic minimal surface.<sup>[25–31]</sup> These structures have been called schwarzites, after the name of the mathematician H. A. Schwarz, who investigated the differential geometry of this class of surfaces at the end of the 19th century.<sup>[32]</sup>

Similar theoretical  $sp^2$  carbon structures such as polybenzenes<sup>[33]</sup> and hollow graphites<sup>[34,35]</sup> can be ascribed to the general family of schwarzites. In the late 1990s, possible routes to the synthesis of schwarzites through the assembling of small carbon clusters in supersonic cluster beam deposition (SCBD) experiments<sup>[36,37]</sup> have been theoretically investigated by means of classical molecular dynamics.<sup>[37,38]</sup> Indeed, there is a clear evidence that *random schwarzites*, characterized by a highly porous, fully 3-D graphite-like carbon, are formed under special conditions.<sup>[28,39]</sup> Recently, periodic structures, with a porosity on the mesoscopic scale and fascinating perspectives in optoelectronics, have been synthesized by chemical methods.<sup>[40]</sup>

While most of the theoretical studies concerned periodic schwarzites, experimental evidence has been recently obtained for an amorphous schwarzitic form of carbon corresponding to the random schwarzite previously envisaged by various authors.<sup>[28,41,42]</sup> This new structure, which is fully covalent in three dimensions, represents the fourth form of  $sp^2$  carbon; the first form, fullerite, is the aggregation of zero-dimensional objects (fullerenes); the second form, nanotubes bundles, is the aggregation of one-dimensional objects (nanotubes); and the third form, graphite, is the aggregation of two-dimensional objects (the graphite sheets or graphenes). Random schwarzites have been obtained by supersonic cluster beam deposition (SCBD) of carbon clusters in the presence of very small catalyst nanoparticles,<sup>[39]</sup> and look like a highly porous spongy carbon. The numerical simulation of the TEM images suggests that random schwarzites grow in the form of a self-affine minimal surface, with relevant and not yet fully understood topological features. The topology and structural properties of the different classes of  $sp^2$  carbon are discussed in “Graphene Topology.”

Supersonic cluster beam deposition experiments have also shown that by increasing the energy per atom of the beam clusters, an increasing  $sp^3$ -to- $sp^2$  bond ratio is observed in the SCBD carbon. A natural question was whether carbon is able to form other *fully covalent, fully three-dimensional*  $sp^3$  solids besides diamond and lonsdaleite, which can be obtained from the coalescence of fullerene cages. Much theoretical work and speculations have been made about the possible geometries and structure of carbon clathrates originating from the coalescence of small fullerenes,<sup>[43–46]</sup> but no experimental synthesis of these interesting materials has been obtained so far. Similar structures, characterized by only a partial saturation of bonds (mixed  $sp^3/sp^2$  forms), have been recently synthesized by linking together through covalent bonds  $C_{36}$  clusters<sup>[11]</sup> or  $C_{20}$  clusters.<sup>[47]</sup> The topology of clathrates is discussed in general terms in Refs.<sup>[48,49]</sup> while some topological algorithms that



generate complex and even fractal clathrate structures can be found in Refs.<sup>[46,50]</sup> together with some topological algorithms that generate complex and even fractal clathrate structures.

## GRAPHENE TOPOLOGY

From the topological point of view, fullerenes as well as graphite sheets, nanotubes, and schwarzites [which we shall group under the general family name of *graphenes* (Fig. 2)] are here described as polygonal tilings of surfaces with only hexagons, pentagons, and heptagons, where each vertex corresponds to a carbon atom, each edge corresponds to a covalent bond, and each polygon corresponds to a carbon ring. The generalization to structures with larger and/or smaller polygons is straightforward. Each atom has a threefold coordination. The surface, covered by a polygonal tiling of carbon rings, defines the shape of a graphene and is characterized by its connectivity or order of connection  $k$ . According to Hilbert and Cohn-Vossen,<sup>[51]</sup> the order of connection is the number plus one of the close cuts that can be made on the given surface without breaking it apart in two pieces. The

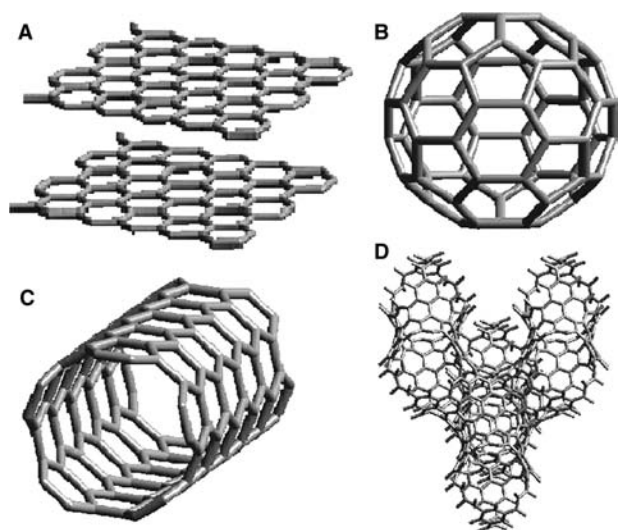


**Fig. 2** The four allotropic forms of graphite-like carbon, which are characterized by  $sp^2$  bonds and threefold coordination and are grouped under the general name of *graphenes*: (A) Two lattice planes of graphite crystal, where each plane represents an ideal graphene with only hexagonal rings. (B) The fullerene  $C_{60}$ , formed by 12 pentagons and 20 hexagons. (C) A nanotube, having a cylindrical shape and an indefinite length. (D) A three-periodic, D-type schwarzite, characterized by a lattice with the diamond structure. While the crystalline forms of fullerenes, nanotubes, and graphite are held together by van der Waals forces in three, two, and one space directions, respectively, schwarzite is entirely covalent in three dimensions.

surface topology may be alternatively characterized by the Euler–Poincaré characteristic  $\chi = 3 - k$  or the genus  $g = (k - 1)/2$ . For example, a simple (one-hole) torus can be cut along two closed lines without splitting it in two pieces, and therefore  $k = 3$  or  $\chi = 0$ ,  $g = 1$ . For a sphere,  $k = 1$  ( $g = 0$ ,  $\chi = 2$ ), whereas for an  $n$ -hole torus,  $k = 1 + 2n$ ,  $\chi = 2(1 - n)$ , and  $g = n$ . Thus the genus represents the number of “holes” (or “handles”) of a generalized torus.

While fullerenes are represented by a closed surface topologically equivalent to a sphere ( $k = 1$ ), uncapped nanotubes, graphite sheets, and schwarzites are open surfaces with an infinite extension in one, two, or three dimensions, respectively. However, graphenes characterized by a periodic atomic structure can be conveniently reduced to a closed surface by applying cyclic boundary conditions. In this way, uncapped nanotubes and graphite sheets become topologically equivalent to an ordinary (one-hole) torus ( $k = 3$ ). On the other hand, the connectivity of an infinite periodic surface is infinite. However, if cyclic boundary conditions are applied on a finite portion of the periodic surface, the connectivity is finite, although dependent on the actual number of unit cells of the periodic structure. Thus it is convenient to define the connectivity per unit cell. This is obtained by closing the portion of surface contained in the unit cell on itself as implied by the cyclic boundary conditions, and the number  $g_{\text{cell}}$  of handles generated by the closure operation gives the order of connection per unit cell as

$$k_{\text{cell}} = 2g_{\text{cell}} + 1 \quad (1)$$

There is a fundamental relationship, known as the Gauss–Bonnet theorem, which links the topological properties of a closed surface, expressed by the Euler–Poincaré characteristic, to its differential geometrical properties, expressed by the principal curvature radii  $R_1$  and  $R_2$ :

$$\int_S \frac{dS}{R_1 R_2} = 2\pi\chi \quad (2)$$

where the integral extends over the whole surface  $S$ . For a periodic surface, the theorem applies to any portion of it, notably to a single unit cell, after closure through the periodic boundary conditions. The two principal radii are usually replaced by two more convenient variables, the mean curvature  $H$  and the Gauss curvature  $K$ , defined by

$$H = \frac{1}{2} \left( \frac{1}{R_1} + \frac{1}{R_2} \right), \quad K = \frac{1}{R_1 R_2} \quad (3)$$

respectively, with the convention that radii have a positive or a negative sign according to whether they are oriented on one side of the surface or the other. Thus according to the Gauss–Bonnet theorem, the Euler–Poincaré characteristic is the average Gauss curvature times  $S/2\pi$ .

According to Euler's theorem, the tiling of a closed surface with a Euler–Poincaré characteristic  $\chi$  fulfils the equation

$$v - e + f = \chi = 3 - k = 2(1 - g) \quad (4)$$

where  $v$  is the number of vertices (atoms),  $e$  is the number of edges (bonds) and  $f$  is the number of polygonal faces (atom rings). We shall indicate by  $f_j$  the number of  $j$ -membered rings present in the tiling, so that

$$f = \sum_j f_j \quad (5)$$

and

$$v = \sum_j jf_j/3 = \frac{2}{3}e \quad (6)$$

By inserting Eqs. (5) and (6) into Eq. (4), one obtains

$$\sum_j (6 - j)f_j = 6(3 - k) = 12(1 - g) \quad (7)$$

For a given connectivity (genus) of the surface, this equation provides a condition among the numbers of polygons. It appears that this condition is independent of the number of hexagons, which is therefore arbitrary.

Special cases are the *Platonic tilings*, with a single kind of polygons, and the *Archimedean tilings*, with two different kinds of polygons, one of which is, in the present discussion, the hexagon. In both cases

$$f_j = 6(3 - k)/(6 - j) \quad (8)$$

for  $j \neq 6$ , whereas the number of hexagons is zero for Platonic tilings or any other number  $>1$  for Archimedean tilings. If, besides hexagons, the tiling also includes pentagons and heptagons, then

$$f_5 - f_7 = 6(3 - k) \quad (9)$$

From this equation, it appears that pentagon–heptagon pairs may be added to (or cancelled from) a tiling within the same topology of the surface. Thus if a hexagon is replaced by a pentagon in some thermally induced or stress-induced defect formation process, a heptagon must be formed as well in some other place of the graphene network.

To replace a hexagon in a flat graphite layer with a pentagon with no bond stretching, a whole sector  $60^\circ$ -wide of the surrounding hexagonal lattice has to be removed. This transforms the original flat lattice into a cone truncated by the pentagonal face, where the continuous surface encompassing the atoms acquires a positive Gaussian curvature: The perimeter of a circle of radius  $R$  lying on the surface and centered at the pentagon center is shorter than  $2\pi R$ . This defect is an example of a *positive disclination*. In a similar way, a hexagon can be replaced by a heptagon with no bond stretching by inserting a  $60^\circ$ -wide sector, which transform the original flat lattice into a saddle around the heptagonal face, with a negative Gaussian curvature: The perimeter of a circle of radius  $R$  lying on the surface and centered at the heptagon center is longer than  $2\pi R$ . This defect is an example of a *negative disclination*.

The creation of pentagon–heptagon defect pairs occurs, for example, when a cylindrical nanotube is bent. An ideally infinite cylindrical nanotube is a perfect hexagonal tiling. An elbow bending produces a positive Gauss curvature on the external side and a negative Gauss curvature on the internal side of the elbow, and this is accommodated by the creation of pentagon and heptagon defects on the two sides, respectively. These arguments are easily extended to the case where octagons are considered instead of, or in addition to, heptagons.

The topological features of graphenes are relevant to their cohesive energy and electronic structure. Intuitively, the number of topologically different close electron orbits increases with the order of connection of the graphene surface. The topological structure of the electronic eigenfunctions in graphenes, notably in schwarzites, has been theoretically investigated in some recent works by Aoki et al.<sup>[52]</sup> The electronic energy levels and their degeneracy depend also, and more specifically, on the local point symmetries. The subtle links between topological and point-symmetry properties have been elucidated by Fowler, Ceulemans, and coworkers in a series of seminal works.<sup>[53–56]</sup>

## Fullerenes

For fullerenes ( $k = 1$ ), Eq. (8) gives  $f_5 = 12$  or  $f_4 = 6$  or  $f_3 = 4$ . By excluding energetically unfavorable three- and four-membered rings, it turns out that Archimedean fullerenes must always contain 12 five-membered rings, and the number of atoms grows with the number of six-membered rings as

$$v = 20 + 2f_6 \quad (10)$$

Therefore the most common fullerenes  $C_{60}$  and  $C_{70}$  have 20 and 25 six-membered rings, respectively,

whereas the smallest fullerene is the Platonic dodecahedron  $C_{20}$ . In general, fullerenes with abutting pentagons are less stable. To avoid abutting pentagons, each pentagon must be surrounded by five hexagons, and each hexagon cannot have more than three adjacent pentagons. Thus the smallest fullerene with no abutting pentagons must have  $12 \times 5/3 = 20$  hexagons, and this explains the high stability of  $C_{60}$  in its isomeric form with the 12 pentagons regularly spaced at the vertices of an icosahedron. On the other hand, the carbon atom at the trihedral vertex of three abutting pentagons has three bonds forming angles of  $108^\circ$  and can therefore easily go in an approximate  $sp^3$  configuration as long as its outward dangling bond is saturated, say, by a hydrogen atom, which leads to rather stable forms of hydrogenated fullerenes. Thus  $C_{20}H_{20}$ ,  $C_{28}H_4$ , etc. are particularly stable molecules, unlike the corresponding pure fullerenes that have a very low stability. As regards the possible isomeric forms, even restricting the fullerene isomers to those exclusively made of five- and six-membered rings, their number rapidly increases with  $v$ . As shown by Fowler et al.<sup>[57,58]</sup> in some basic works, the enumeration of isomers and the classification of their electronic structures can be achieved through the so-called spiral algorithm and leapfrog rules. Thus for  $C_{28}$ , there are only two isomers; for  $C_{40}$  this number is 40, whereas for  $C_{60}$  there are 1812 spectrally distinct isomers. Fortunately, because of the geometrical conditions discussed above, there is, in general, at least for not too large fullerenes, only a small number of particularly stable isomers that are largely favored with respect to the others. They are the isomers with no abutting pentagons: only one isomer for  $C_{60}$ , but five for  $C_{78}$ , seven for  $C_{80}$ , etc. The most stable isomers approximate as much as possible the spherical shape to minimize the distortion of the bonds from the ideal  $sp^2$  configuration. For approximately spherical fullerenes, the average diameter  $d_v$  can be evaluated from the equation

$$\pi d_v^2 \cong \frac{f_6 S_6}{1 - S_6/S_p} + \frac{12 S_5}{1 - S_5/S_p} \quad (11)$$

where  $S_5 \cong 1.720r_5^2$  and  $S_6 \cong 2.598r_6^2$  are the areas of pentagons and hexagons of average edge length  $r_5$  and  $r_6$ , respectively, and  $S_p = 12S_5 + f_6S_6$  is the surface area of the fullerene polyhedron. For  $r_5$  and  $r_6$  equal to the bond length in graphite  $r_0 = 0.142$  nm, the diameter of  $C_{60}$  estimated from this equation is  $d_{60} \cong 0.694$  nm, whereas the experimental value is  $0.704$  nm. This small discrepancy is fully accounted for by using the actual average bond lengths  $r_5 = 0.145$  nm and  $r_6 = 0.142$  nm.

Giant fullerenes, with  $v$  in the range  $10^2$ – $10^3$ , are believed to approach an icosahedral shape with the

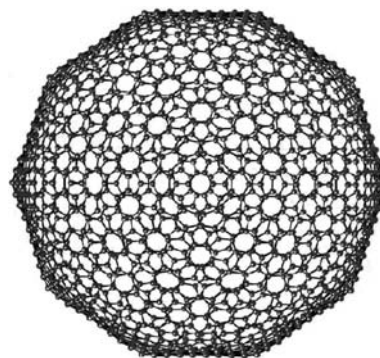


**Fig. 3** A giant fullerene of 1620 carbon atoms. Rather than spherical, the structure is approximately icosahedral as a result of the positive disclinations induced by the 12 pentagonal rings requested by Euler's theorem and located at the vertices. *Source:* From Ref.<sup>[59]</sup>.

12 five-membered rings at the vertices and the 20 triangular faces made by graphite sheets (Fig. 3). In this limit, the fullerene may be viewed as obtained by folding a single graphite sheet through the insertion of 12 positive disclinations. However, capped nanotubes may also be viewed as giant fullerenes where the 12 five-membered rings are concentrated in the caps, six on each side.

## Nanotubes

A single-wall carbon nanotube can be constructed by rolling up a portion of a graphite sheet into a cylinder so as to bring an atomic site in the unit cell  $(L, M)$  of the graphite sheet to coincide with its equivalent site in the origin unit cell  $(0, 0)$  (Fig. 4A). The structure of the nanotube is entirely defined by the pair of integer numbers  $(L, M)$ . The diameter is given by.<sup>[60,61]</sup>

$$d_{L,M} = \frac{\sqrt{3}}{\pi} r_0 (L^2 + LM + M^2)^{1/2} \quad (12)$$

On pure geometrical grounds, the smallest open-ended nanotube is  $(3, 0)$ ; however, with the requirement of end capping with six pentagons on each side, the smallest possible nanotube is  $(5, 0)$  with a diameter of about  $0.39$  nm.

Nanotubes are classified into three types depending on the indices  $(L, M)$  (Fig. 4B–D): *parallel* nanotubes, with indices  $(L, 0)$  or  $(0, M)$ , where one third of the interatomic bonds is parallel to the nanotube axis; *perpendicular* nanotubes, with indices  $(L, L)$ , where one third of the interatomic bonds is normal to the nanotube axis; and *chiral* nanotubes with either  $L > M > 0$  (right-handed) or  $M > L > 0$  (left-handed).

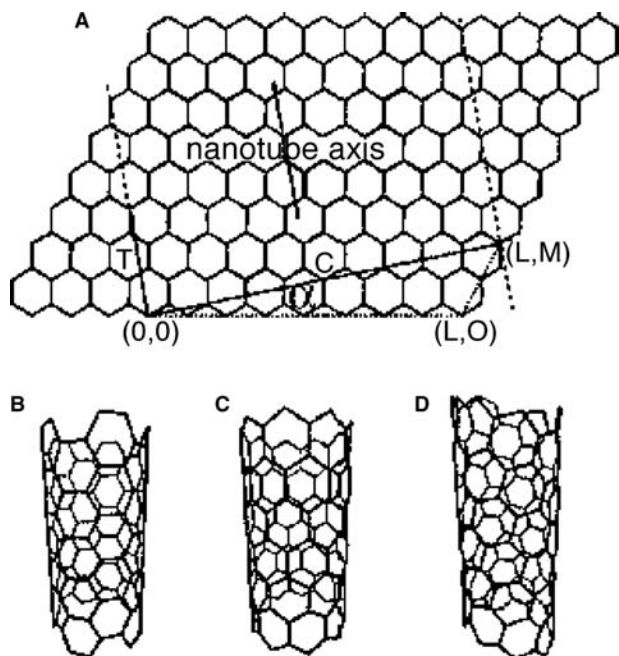


**Fig. 4** (A) A single-wall carbon nanotube can be obtained by folding a graphite sheet so as to bring the point  $(L,M)$  to coincide with the origin  $(0,0)$ . The vector  $T$ , orthogonal to the circumference  $C$ , defines the periodicity in the axial direction. In this example  $(L,M) = (4,1)$ . (B) An achiral perpendicular nanotube of indices  $(5,5)$ . (C) An achiral parallel nanotube of indices  $(9,0)$ . (D) A chiral  $(7,3)$  nanotube. (Ph. Lambin, private communication.)

From the symmetry point of view, the nanotube axis is a rotation axis of order  $L$  for both parallel  $(L,0)$  and perpendicular  $(L,L)$  nanotubes, whereas chiral nanotubes have a screw axis. In the direction parallel to the axis, nanotubes are periodic with a period of  $3r_0$  for the parallel type,  $\sqrt{3}r_0$  for the perpendicular type and  $\pi d_{LM}/\sqrt{3}D(L,M)$  for the chiral type, where  $D(L,M)$  is the greatest common divisor of  $L$  and  $M$ . Thus for prime pairs, for which  $D(L,M) = 1$ , the period along the axis is  $1/\sqrt{3}$  times the circumference.

Multiple-wall nanotubes grow by sequential addition of layers on an original single-wall nanotube. The interlayer distance is constant and is about 0.34 nm, with a tolerance that keeps, for energetic reasons, within about 1%. Thus the diameters of a multi-wall nanotube with the concentric nanotubes labeled in the outward direction by  $n = 1, 2, 3, \dots$  are given by

$$d_{L'M'} = d_{LM} + 2(n - 1)(0.34 \text{ nm}) \quad (13)$$

It turns out that each layer has indices  $(L',M')$  that differ from the indices  $(L,M)$  of the template ( $n = 1$ ) layer, their values being those that better simultaneously fulfill Eqs. (12) and (13) within a 1% tolerance (Fig. 5).

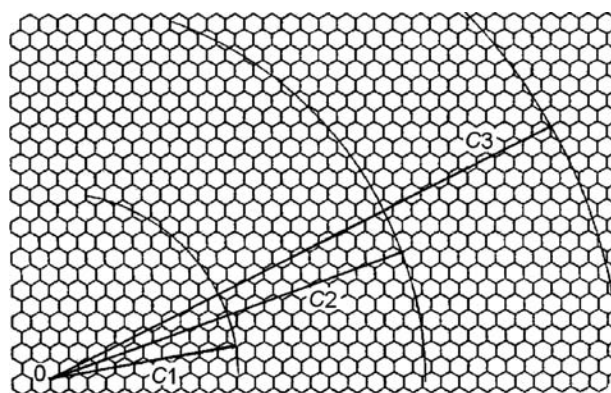


**Fig. 5** A multiwall nanotube is grown around an initial single-wall  $(9,2)$  nanotube of circumference  $C_1$  by the addition of further layers of circumferences  $C_2 = C_1 + 2\pi$  (0.34 nm),  $C_3 = C_2 + 2\pi$  (0.34 nm), etc. The indices of second, third, etc. layers are those that better match the respective radii with some interatomic distance:  $(15,8)$  and  $(19,16)$  in the present example. (Ph. Lambin, private communication.)

Apart from caps, which contain 12 pentagons each, ideal straight nanotubes are exclusively made of hexagonal rings as in the graphite sheet, with a good conjugation among interatomic bonds. However, as explained above, nanotubes can be bent with the addition of pentagon–heptagon pairs that introduce pairs of disclinations of opposite sign. In particular, an open-ended nanotube can be closed on itself to give a toroidal shape. Ring-shaped and even coiled nanotubes have been experimentally observed.<sup>[17,62]</sup>

Non-ideal nanotubes may have a variety of defects as in ordinary graphite. Of special interest here are the topological defects in which some hexagons are replaced by other polygons preserving the threefold coordination at each atom. Since the connectivity must not change, the number  $f_j^d$  of polygons replacing hexagons in each defect must fulfill the equation

$$\sum_j (6 - j)f_j^d = 0 \quad (14)$$

as a consequence of Eq. (7). The simplest topological defect, which can be entirely accommodated within a 14-membered ring with no alteration outside, is constituted by two pentagon–heptagon pairs ( $f_5^d = f_7^d = 2$ ) and is generated by the so-called Stone–Wales transformation (Fig. 6).

### Periodic Schwarzites

The fourth form of  $sp^2$  (graphite-like) carbon, which we have called schwarzite, may be defined on a pure topological basis as a graphene with a negative average

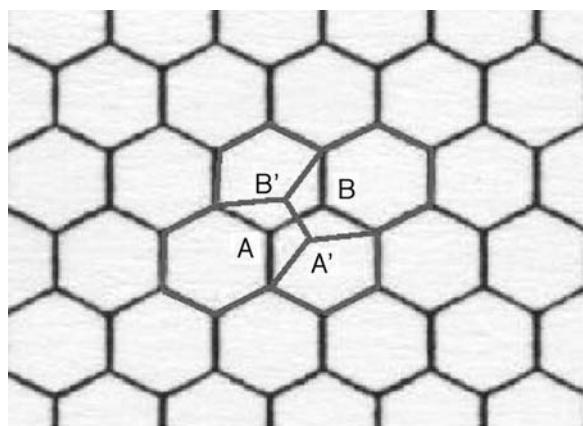


**Fig. 6** Illustration of the simplest topological defect in a nanotube originating from the rotation of the AB bond into A'B'. This operation, known as Stone–Wales transformation, reduces by one the edge number of polygons having AB in common and increases by one the edge number of the two adjacent polygons.

Gauss curvature ( $\chi < 0$ ), unlike fullerenes and capped nanotubes, having  $\chi > 0$ , and graphite, open and toroidal tubulenes, having  $\chi = 0$ . Any periodic surface with a periodicity in two or three space directions has a unit cell that can be closed by the periodic boundary conditions with two or three handles, respectively, and therefore the average Gauss curvature is always negative. As proved in “Topology vs. Total Energy and Growth Processes,” the highest stability of a graphene with a negative  $\chi$  occurs for a shape corresponding to a minimal surface, namely when the principal radii fulfil the condition

$R_1 = -R_2$  everywhere, or equivalently the mean curvature  $H$  vanishes at any point of the surface. Among the possible shapes of minimal surfaces, special attention has been given to branched tubular structures, as an obvious generalization of nanotubes,<sup>[30]</sup> which form two disjoint labyrinths, one complementary to the other. For this special feature, periodic schwarzites have been pictorially termed as the *plumber’s nightmares*.<sup>[30]</sup>

Periodic schwarzites are generated by covalent connections of identical units (elements). The unit cell may contain one or more such elements. The centers of the elements can be viewed as the nodes of a corresponding *dual lattice*. One of the two labyrinths, assumed as the internal one, contains the dual lattice. The dual lattice with the four-coordinated diamond structure defines an important class of cubic schwarzites, with two elements per unit cell (*bielemental* schwarzites). They are tessellations of a D-type Schwarz minimal surface<sup>[28]</sup> (Fig. 7A). *Monoelemental* cubic schwarzites with a *sc*, or *bcc* or *fcc* dual lattice are also possible, in principle, although the negative curvature of the elements becomes large and energetically unfavorable because of the increasing dual-lattice coordination (6, 8 and 12, respectively). However, *sc*(P-type) schwarzites (Fig. 7B) include a special class of structures known as polybenzenes, which have been predicted to be rather stable.<sup>[33]</sup>

Minimal surfaces can be analytically defined by means of the complex Weierstrass–Enneper representation.<sup>[63,64]</sup> However, for visual representation purposes, a minimal three-periodic surface can indeed be sufficiently well approximated by a trigonometric expression corresponding to the lowest-order terms

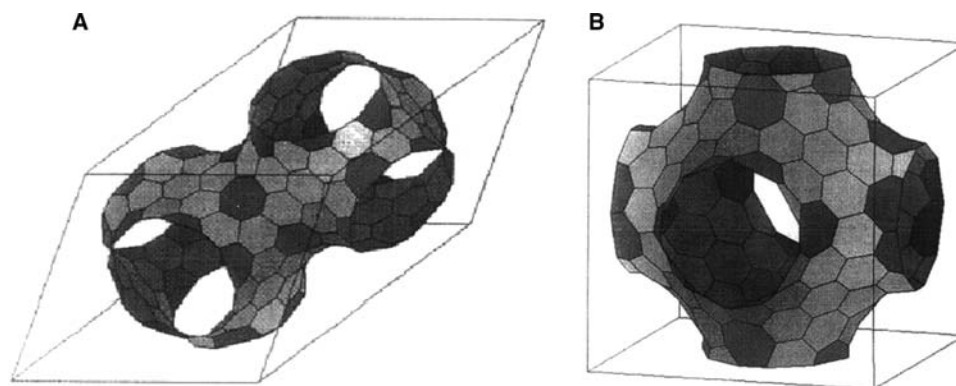


**Fig. 7** The unit cells of D-type (A) and P-type (B) schwarzites with a tessellation of hexagonal and heptagonal tiles. Schwarzites are three-periodic minimal surfaces. According to Euler’s theorem, heptagons (darker grey) must be 24 in the unit cell of both types, whatever is the number of hexagons (except 1). D-type schwarzites have the structure of a diamond lattice so that the unit cell can be split into two identical elements having 12 heptagons each, whereas P-type schwarzites have the structure of a simple cubic lattice. In principle, schwarzites can be associated to any kind of lattice, either periodic or amorphous (random schwarzites). *Source:* From Ref.<sup>[28]</sup>.



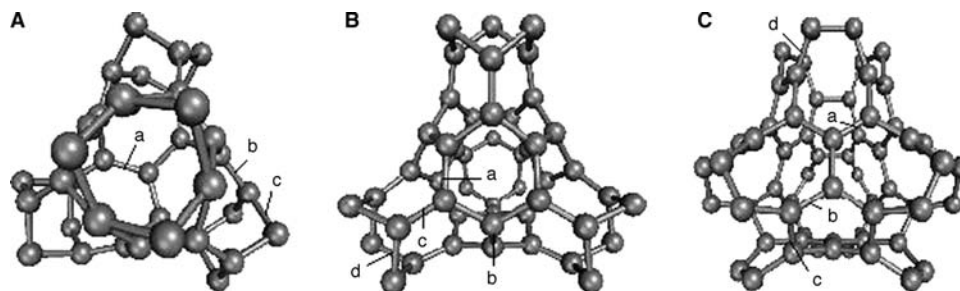


**Fig. 8** The atomic structure of the elements of the smallest D-type schwarzites with a tetrahedral symmetry: (A)  $(C_{28})_2$  with 12 heptagons per element and no hexagon; (B)  $(C_{36})_2$  with 4 hexagons per element; (C)  $(C_{40})_2$  with 6 hexagons per element. The unit cell of D-type schwarzites contains two elements. Note that  $(C_{28})_2$  has a chirality that allows for two enantiomeric lattices, whereas  $(C_{36})_2$  and  $(C_{40})_2$  are achiral.

of a Fourier expansion. For example, D- and P-type surfaces are well described in the  $(x, y, z)$  space by

$$\cos(x) \cos(y) \cos(z) + \sin(x) \sin(y) \sin(z) = 1 \quad (15)$$

$$\cos(x) + \cos(y) + \cos(z) = 0 \quad (16)$$

respectively (Fig. 7).

In D-type schwarzites, each element is linked to four identical elements and therefore has four open terminations. Correspondingly, the unit cell, containing two elements, has six terminations. The closure procedure transforms a single element into a two-hole torus ( $k_{el} = 5$ ), and the unit cell into a three-hole torus ( $k_{cell} = 7$ ). Thus the Platonic tiling of a D type, according to Eq. (8), is obtained with either 12 heptagons or 6 octagons or 4 non-agons per element, and 28, 16, or 12 atoms per element, respectively. The corresponding numbers per unit cell are twice as much.

Each Platonic tiling is the zeroth element of an infinite series of larger schwarzites obtained by inserting in each element an arbitrary number ( $f_6 > 1$ ) of hexagons. The number of atoms per element increases by two units for each additional hexagon (Eq. (6)). Thus the D-type schwarzites with only heptagons and hexagons form a family of crystals with  $2(28 + 2f_6)$  atoms in the unit cell. However, only certain values of  $f_6$ , given by

$$f_6 = 4(3n + m) + 6l \quad (17)$$

with  $l, n$  any integer  $\geq 0$  and  $m = 0, 1$ , are compatible with the tetrahedral symmetry and give a *fcc* crystal. Therefore the smallest member of this family is *fcc*- $(C_{28})_2$  ( $l = n = m = 0$ ). The second member is *fcc*- $(C_{36})_2$  ( $l = n = 0$  and  $m = 1$ ) with 36 atoms per element and four hexagons in each element lying on the faces of the tetrahedron. The third member is *fcc*- $(C_{40})_2$  ( $l = 1$  and  $m = n = 0$ ) with 40 atoms per element and six hexagons lying on the edges of

the tetrahedron, etc. The respective elements are shown in Fig. 8A–C: While the elements of *fcc*- $(C_{36})_2$  and *fcc*- $(C_{40})_2$  have a full tetrahedral point symmetry ( $T_d$ ) with six mirror planes, *fcc*- $(C_{28})_2$  shows an intriguing chirality ( $T$  point group) that allows for two enantiomeric lattice forms. Fig. 9 depicts a portion of the *fcc*- $(C_{36})_2$  lattice.<sup>[65]</sup>

Isomeric forms of schwarzites are possible with rules similar to those applied to fullerenes, although no systematic analysis is presently available. Also, in this case, isomers with non-abutting heptagons are expected to be more stable. The smallest D-type schwarzite with non-abutting heptagons requires seven hexagons around each heptagon and three heptagons adjacent to each hexagon. This makes  $f_6 = 12(7/3) = 28$  hexagons per element, corresponding to the lattice formula *fcc*- $(C_{84})_2$ . Indeed, this structure, analogous to  $C_{60}$  for being the smallest structure with non-abutting odd polygons, was theoretically predicted to be very stable.<sup>[30]</sup> The lattice constant  $a(f_6)$  of the cubic cell for D-type *fcc* schwarzites with only heptagons and hexagons is approximately given by

$$\frac{a(f_6)}{a(0)} \cong \left(1 + \frac{f_6 S_6}{24 S_7}\right)^{1/2} \quad (18)$$

where  $a(0) = 1.5$  nm is the lattice constant of the Platonic member of the family and  $S_7 = 3.634r_7^2$  is the area of the heptagons. It is a simple exercise to extend the above analysis to the family of schwarzites with only octagons and hexagons of both D and P types.

### Amorphous $sp^2$ Carbon

Among the various forms of amorphous graphite-like carbon, random schwarzites are of special interest here for their topological features as well as for the fact that they have been recently synthesized. The synthesis was achieved through SCBD in the presence of a metallorganic catalyst.<sup>[39]</sup> More information can be found in



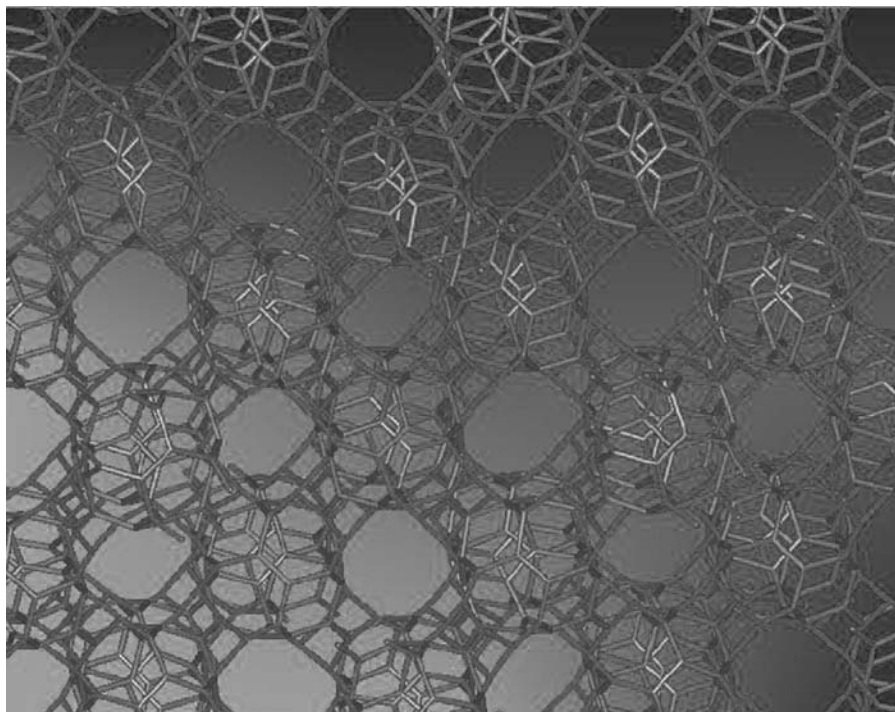


**Fig. 9** The structure of the D-type schwarzite ( $C_{36}$ )<sub>2</sub> shows the distinct features of a face-centered cubic diamond lattice as seen along the  $\langle 100 \rangle$  direction.

“Fullerenes and Carbon Nanotubes,” p. 1322. The SCBD experiments relied on a number of previous theoretical studies based on classical molecular dynamics of the aggregation process of carbon clusters in a gaseous phase<sup>[38]</sup> or during a cluster beam deposition on a substrate.<sup>[37]</sup> The aggregation process can be conveniently understood from a topological point of view, e.g., by following the evolution of the order of connection  $k$  as a function of time, namely as a function of the time step.

Two examples of such simulations, starting from different cluster distributions in the gas phase, are displayed in Fig. 10. The insets show the initial distributions of carbon clusters and the aggregation obtained at the end of the molecular dynamics simulations and after different changes of temperature.<sup>[38]</sup> Although the condensed phases obtained at the end of the simulation look qualitatively similar, the evolution of  $k$  follows different behaviors. In both cases,

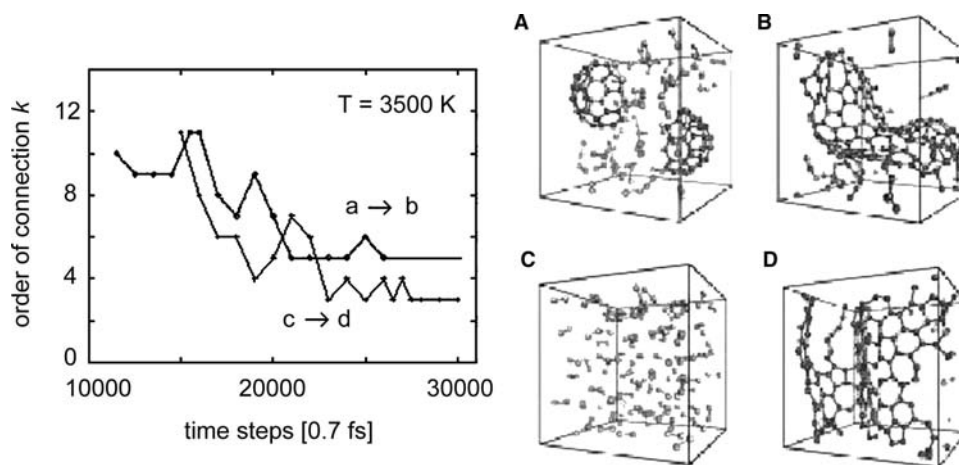


**Fig. 10** Simulations by classical molecular dynamics of the condensation process of carbon clusters of various sizes (a) or carbon dimers (c) into a connected graphene structure (b,d). The final condensation temperature is 3500 K. The time evolution, expressed in time steps of 0.7 fsec, of the order of connection  $k$ , allows to distinguish between ill-condensed and well-condensed matter, according to whether the connectivity oscillates or is stable. While a distribution of clusters including fullerene fragments leads to a connectivity corresponding to a schwarzite structure, the dimer gas condenses into graphite (or open nanotube) sheets. The simulation cells shown in A–D should be periodically repeated in three dimensions.

the connectivity, after large oscillations, becomes stabilized at a limit value  $k_{\text{lim}}$ , which is 3 for the aggregation of carbon dimers, or 5 for the aggregation of larger clusters. The first value corresponds to a graphitic layer (or open nanotube); the second value corresponds to a schwarzite. These structures can be better visualized by periodically repeating, in three dimensions, the cubic simulation cells shown in Fig. 10. The clear distinction between two regimes, with either an oscillating or a constant connectivity, has been viewed as the topological definition of an ill-condensed and a well-condensed phase, respectively. However, a constant value of  $k$  does not mean that the system does not evolve any more. However, the interatomic bonds keep breaking and reforming in a way that the connectivity remains constant. In fact, any change of  $k$  would require the sudden creation/annihilation of a fixed number of pentagons/heptagons, as a consequence of Euler's theorem, and this has a substantial cost in terms of free energy. In principle, the evolution at constant  $k = 3, 5$  may gradually transform the above disordered structures into an ideal graphite layer (or an open-ended nanotube) or an ideal schwarzite, respectively.

These examples show that the topological connectivity is a useful parameter for characterizing and monitoring the evolution of a condensed amorphous phase. Another application of this concept is illustrated in Fig. 11 where the thermal dissociation of the D-type schwarzite  $fcc\text{-}(C_{36})_2$  lattice is signaled by the sudden drop at  $T_c = 3800$  K of the order of connection  $k$  from 19, corresponding to eight elements within the cubic

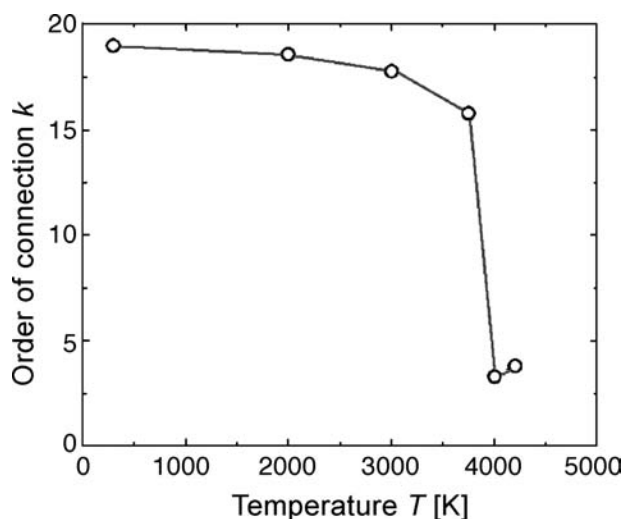


**Fig. 11** Thermal evolution of the D-type schwarzite  $(C_{36})_2$  as monitored by the connectivity for the simulation cell of Fig. 8. By heating up to 3700 K, the connectivity shows a small decrease as a result of a random break of bonds; but suddenly above that temperature, the connectivity drops to a small value, which is indicative of a transition leading to graphitization.

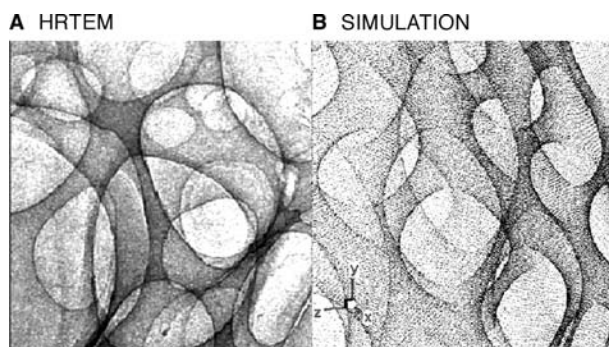


**Fig. 12** (A) A high-resolution transmission electron microscope (HRTEM) image of random schwarzite obtained by supersonic cluster beam deposition compared with (B) an image simulation constructed through a self-affine distortion of an analytical expression for a P-type minimal surface.

simulation cell, to 3, corresponding to a graphite sheet.<sup>[65]</sup> Thus the topological analysis reveals that transition at  $T_c$  corresponds to a graphitization process. This example shows that the order of connection can provide a sort of order parameter and a useful topological picture of a structural phase change.

Series of high-resolution transmission electron microscope (HRTEM) images of this material, such as the one reproduced in Fig. 12A, suggested a novel form of nanostructured carbon consisting of three-dimensional, fully connected  $sp^2$  networks. This form of carbon seemingly consists of multiply connected graphene sheets forming a spongy structure with meso- and macroporosity, and appears to be fully covalent in three dimensions, which ensures a certain robustness as compared to fullerite and nanotube bundles, which are held together by van der Waals forces. An atomic force microscopy (AFM) analysis indicated that SCBD carbon films grow in a fractal self-affine structure<sup>[66–68]</sup> characterized by a growth exponent  $\beta$  of the order of 0.5.

In general, the reconstruction of the detailed three-dimensional structure is not possible from HRTEM images, but a useful comparison can be made with simulated images originating from the projection of a model analytical surface with suitable topological requisites. To simulate extended regions of the observed graphene surfaces as they appear in HRTEM images, analytical surfaces have been generated by applying a self-affine distortion along a given axis  $z$ , assumed as the growth direction, to the approximate Eqs. (15) and (16) for D-type or P-type three-periodic schwarzites through the coordinate transformation

$$x \rightarrow xz^\beta, y \rightarrow yz^\beta, z \rightarrow z^{\beta-1}/(\beta - 1) \quad (19)$$

where the coordinates  $x, y, z$  are in units of a conventional length  $a_0 = 1$  nm and  $\beta = 0.5$ . The direct comparison of the HRTEM images with the simulated

ones (Fig. 12B) gives a convincing evidence that the observed SCBD spongy carbon can be ascribed to a random schwarzite, more precisely a form of fractal self-affine schwarzite.

## TOPOLOGY VS. TOTAL ENERGY AND GROWTH PROCESSES

It has been shown<sup>[69]</sup> that the total energy of a curved single-walled graphene can be written in the form proposed by Helfrich for membranes and foams.<sup>[70–72]</sup>

$$E = \int_S dS(\gamma + \kappa H^2 - \bar{\kappa}K) \quad (20)$$

where  $S$  is the (portion of the) surface which the total energy refers to and  $\gamma = 2.82 \text{ eV}/\text{\AA}^2$  is the energy for a unitary flat surface (a graphite sheet).<sup>[61]</sup> The constants  $\kappa$  and  $\bar{\kappa}$  are two elastic constants associated with cylindrical and elliptical/hyperbolic deformations of the surface, respectively. Density functional calculations in the local density approximation for nanotubes of variable radius  $R$  [where  $H = 1/(2R)$  and  $K = 0$ ]<sup>[73]</sup> and  $C_{60}$  (where  $H = 1/R$  and  $K = 1/R^2$ )<sup>[61]</sup> permit to extract the values  $\kappa = 3.1 \text{ eV}$  and  $\bar{\kappa} = 1.7 \text{ eV}$ . Consistently, a value of  $\bar{\kappa} = 1.5 \text{ eV}$  can be obtained from the available calculations of the cohesive energy of schwarzites<sup>[28,30,42,65]</sup> by means of the Gauss–Bonnet theorem (Eq. (2)). This shows that the above Helfrich's form for the total energy approximately holds also for graphenes. The total energy expressed by Eq. (20) has the important property, if  $\bar{\kappa}$  is constant, that a minimal surface corresponds to a stable local minimum, because for  $\kappa > 0$ , the integral on  $H^2$  is always positive unless  $H = 0$ , while the integral over  $K$  is, according to Gauss–Bonnet theorem, independent of any small continuous deformation of the surface. Thus graphenes taking the shape of a minimal surface, such as schwarzites, are stable forms, up to effects of the contour where  $\kappa$  and  $\bar{\kappa}$  may change, as discussed below. If the negative disclinations yielding a negative Gauss curvature are exclusively because of heptagons, the number of disclinations  $N_d$  is fixed by the Euler characteristic as  $N_d = 6(2 - \chi)$  independently of the length scale of the surface.<sup>[74]</sup> On the other hand, if the Gaussian surface energy density  $-\bar{\kappa}K$  is roughly assumed to be nonzero only at pentagons or heptagons, a local definition of  $\bar{\kappa}$  is obtained as

$$\bar{\kappa} \simeq \frac{\gamma}{2K_5} \frac{5S_6 - 6S_5}{5S_6 + 3S_5} \simeq \frac{\gamma}{2K_7} \frac{7S_6 - 6S_7}{7S_6 + 3S_7} \quad (21)$$

where  $K_5 = 0.0808 \text{ \AA}^{-2}$  and  $K_7 = -0.0783 \text{ \AA}^{-2}$  are the Gaussian curvatures at a pentagon and a heptagon

surrounded by five or seven hexagons, respectively.<sup>[27]</sup> With the polygon areas given above, Eq. (21) yields  $\bar{\kappa} = 2.1 \text{ eV}$  for both pentagons and heptagons. The consistency of this value with that deduced from density-functional calculations for the various types of graphenes confirms the validity of the Helfrich's form of total energy for graphenes of any shape. The residual discrepancy of  $0.4 \text{ eV}$  may be ascribed to the crude approximations implied in Eq. (21), although this equation is useful because it relates  $\bar{\kappa}$  to the actual size of the polygons generating the disclinations, hence to the local electronic structure. The values of  $\kappa$  and  $\bar{\kappa}$  give general indications about whether the growth process of  $sp^2$  carbon preferentially leads to fullerenes, nanotubes, or schwarzites. In an incipient growth process from an initial radius  $R_1$  on the surface of a catalyst, the second principal radius  $R_2$  corresponding to a local energy minimum is obtained from Eqs. (3) and (20) as

$$\frac{R_1}{R_2} = \frac{2\bar{\kappa}}{\kappa} - 1 \quad (22)$$

The surface deformation energy densities for (spherical) fullerenes ( $R_1 = R_2 \equiv R$ ), nanotubes ( $R_1 \equiv R$ ,  $R_2 \rightarrow \infty$ ), and schwarzites ( $R_1 = -R_2 \equiv R$ ) are  $(\kappa - \bar{\kappa})/R^2$ ,  $\kappa/4R^2$  and  $\bar{\kappa}/R^2$ , respectively. Therefore, for any given  $R_1$ , the values of  $\kappa$  and  $\bar{\kappa}$  define three different topological domains: schwarzites are favored for  $\bar{\kappa} < 1/4\kappa$ , nanotubes for  $1/4\kappa < \bar{\kappa} < 3/4\kappa$  and fullerenes for  $\bar{\kappa} > 3/4\kappa$ . When  $\bar{\kappa} \approx \kappa/2$ , as found from density-functional calculations, nanotubes are more likely to occur. However, the local values of  $\bar{\kappa}$  and  $\kappa$  either at the surface termination into vacuum, where the growth takes place by cluster addition, or at the contact with a catalyst where the growth process starts, may be quite different from the above values (which have been fitted to ideal close structures), and therefore other forms can be favored. The expected local changes in the electronic structure, e.g., a  $\pi$  bond-charge depletion or accretion, can substantially modify  $\bar{\kappa}$ . The fact that the growth of schwarzites supersedes that of nanotubes when metallorganic precursors are used<sup>[39]</sup> suggests that the charge redistribution produced by a catalyst, and the consequent change of the incipient  $\bar{\kappa}/\kappa$  ratio, generally depend on the actual size (and shape) of catalyst nanoparticles. Once the growth has started as either a nanotube or a schwarzite, it is likely to proceed within the same topological domain. As mentioned above, simulations of the aggregation process of a fixed number of carbon clusters have shown that after the initial condensation process, the Euler–Poincaré characteristic  $\chi$  stabilizes at a given value (for either the topology of a nanotube or a schwarzite, depending on the initial conditions) during all the subsequent morphological evolution.

On the other hand, the growth of a fully connected schwarzite in the open space with a constant addition of atoms results in a progressive branching and joining of schwarzitic elements with an increase in connectivity and a corresponding stepwise increase  $\Delta\chi$  of  $\chi$ . The process leading to an increase in connectivity is actually favored if the corresponding total energy increase  $-2\pi\kappa\Delta\chi$  is overcompensated by the total energy decrease associated with the reduction in the free contour length. The geometrical constraints on the surface derivatives associated with the minimality conditions and topology (via Gauss–Bonnet theorem) lead to apparently well organized, albeit amorphous structures, through a fairly deterministic, low-entropy process.

## CONCLUSION

Fullerenes, nanotubes, and schwarzites, when considered from the topological point of view, provide a paradigmatic example of the close link between topology and various physical aspects, ranging from thermodynamic stability to electronic and transport properties. In the particular case of schwarzites, the surface minimality condition, implied by the Helfrich form for the total energy, leads to the far-reaching consequence that an extensive property  $E$  (for example, the total energy) is minimal if and only if a local (intensive) condition  $I$  (for example, a vanishing mean curvature) is fulfilled everywhere. If the kinetics of a growth process are such that condition  $I$  is fulfilled at any step, then the property  $E$  turns out to be automatically minimal at any stage of the process. In this case the evolution of the system occurs along the valley bottom of the energy landscape.

The intriguing similarity between graphenes and foams, based on the Helfrich form for the total energy, suggests the existence of a wider class of systems, where the calculation of the total energy can be reduced, through a variable transformation, to the calculation of a surface area. For all of them the search for the stability conditions can be reformulated in the well-established mathematical realm of minimal surfaces. Many complex chemical systems such as supramolecular structures, nanoporous materials, biomembranes, and many other objects which are crowding into the rapidly growing fields of nanostructures and mesoscopic physics are characterized by complicated, highly connected surfaces with a large specific area and a large surface-free energy. A challenging question is whether the morphology and the stability of each of these systems can be reduced to a problem of minimal surfaces and solved with the tools of differential geometry.

## REFERENCES

1. Kroto, H.W.; Heath, J.R.; O'Brien, S.C.; Curl, R.F.; Smalley, R.E.  $C_{60}$ : Buckminsterfullerene. *Nature* **1985**, *318*, 162–163.
2. Kroto, H.W., Fischer, J.E., Cox, D.E., Eds. *The Fullerenes*; Pergamon Press: Oxford, UK, 1993.
3. Billups, W.E., Ciufolini, M.A., Eds. *Buckminsterfullerenes*; VCH Publishing: New York, 1993.
4. Dresselhaus, M.S.; Dresselhaus, G.; Eklund, P.C. *Science of Fullerenes and Carbon Nanotubes*; Academic Press: Boston, USA, 1996.
5. Andreoni, W., Ed. *The Chemical Physics of Fullerenes 10 Years Later*; Kluwer Academic Publ.: Dordrecht, The Netherlands, 1996.
6. Bernier, P.; Bethune, D.S.; Chiang, L.J.; Ebbesen, T.W., Metzger, R.M., Mintmire, J.W., Eds. *Science and Technology of Fullerene Materials*; MRS Symposium Proceedings; Materials Research Society: Pittsburgh, USA, 1995; Vol. 359.
7. Kratschmer, W.; Lamb, L.D.; Fostiropoulos, K.; Huffman, D.R. Solid  $C_{60}$ : A new form of carbon. *Nature* **1990**, *347*, 354–358.
8. Hebard, A.F.; Rosseinsky, M.J.; Haddon, R.C.; Murphy, D.W.; Glarum, S.H.; Palstra, T.T.M.; Ramirez, A.P.; Koltran, A.M. Superconductivity at 18 K in potassium-doped  $C_{60}$ . *Nature* **1991**, *350*, 600–601.
9. Benedek, G., Milani, P., Ralchenko, V.G., Eds. *Nanostructured Carbon for Advanced Applications*; Kluwer Academic Publishers: Dordrecht, The Netherlands, 2001.
10. Olah, G.A.; Bucsi, I.; Aniszfeld, R.; Surya Prakash, G.K. Chemical Reactivity and Functionalization of  $C_{60}$  and  $C_{70}$ . In *The Fullerenes*; Kroto, H.W., Fischer, J.E., Cox, D.E., Eds.; Pergamon Press: Oxford, UK, 1993; 65–73.
11. Grossman, G.C.; Louie, S.G.; Cohen, M.L. *Phys. Rev. B* **1999**, *60*, R6941–R6944.
12. Makarova, T.L.; Sundqvist, B.; Höhne, R.; Esquinazi, P.; Kopelevich, K.; Scharff, P.; Davydov, V.A.; Kashevarova, L.S.; Rakhmanina, A.V. Magnetic carbon. *Nature* **2001**, *413*, 716–718.
13. Rao, A.M.; Dresselhaus, M.S. Nanostructured Forms of Carbon: An Overview. In *Nanostructured Carbon for Advanced Applications*; Benedek, G., Milani, P., Ralchenko, V.G., Eds.; Kluwer Academic Publishers: Dordrecht, The Netherlands, 2001; 3–24.
14. Donnet, J.B.; Bansal, R.C.; Wang, M.J. *Carbon Black*; Marcel Dekker: New York, 1993.
15. Iijima, S. Helical microtubules of graphitic carbon. *Nature* **1991**, *324*, 56–58.
16. Saito, Y.; Matsumoto, T. Carbon nano-cages created as cubes. *Nature* **1998**, *392*, 237.
17. Martel, R.; Shea, H.R.; Avouris, P. Rings of single-walled carbon nanotubes. *Nature* **1999**, *398*, 299.
18. Ahlskog, M.; Seynaeve, E.; Vullers, R.J.M.; Van Haesendonck, C.; Fonseca, A.; Hernadi, K.; Nagy, J.B. Ring formations from catalytically synthesized carbon nanotubes. *Chem. Phys. Lett.* **1999**, *300*, 202–206.

19. Krishnan, A.; Dujardin, E.; Treacy, M.M.J.; Hugdahl, J.; Lynum, S.; Ebbesen, T.W. Graphitic cones and the nucleation of curved carbon surfaces. *Nature* **1997**, *388*, 451–454.
20. Iijima, S.; Yudasaka, M.; Yamada, R.; Bandow, S.; Suenaga, K.; Kokai, F.; Takahashi, K. Nano-aggregates of single-walled graphitic carbon nano-horns. *Chem. Phys. Lett.* **1999**, *309*, 165–170.
21. Ajayan, P.M.; Nugent, J.M.; Siegel, R.W.; Wei, B.; Kohler-Redlich, Ph. Growth of carbon micro-trees. *Nature* **2000**, *404*, 243.
22. Rotter, L.D.; Schlesinger, Z.; McCauley, J.P.; Coustel, N.; Fisher, J.E.; Smith, A.B., III. Infrared reflectivity measurements of a superconducting energy scale in  $\text{Rb}_3\text{C}_{60}$ . *Nature* **1992**, *355*, 532–534.
23. Wang, H.; Setlur, A.A.; Lauerhaas, J.M.; Dai, J.W.; Seelig, E.W.; Chang, R.P.H. A nanotube-based field-emission flat panel display. *Appl. Phys. Lett.* **1998**, *72*, 2912–2913.
24. Niu, C.; Sichel, E.K.; Hoch, R.; Moy, D.; Tennent, H. High power electrochemical capacitors based on carbon nanotube electrodes. *Appl. Phys. Lett.* **1997**, *70*, 1480–1482.
25. MacKay, A.L. Periodic minimal surfaces. *Nature* **1985**, *314*, 604–606.
26. MacKay, A.L. Two-dimensional space-groups with sevenfold symmetry. *Acta Crystallogr.* **1986**, *A42*, 55–56.
27. Terrones, H.; MacKay, A.L. The Geometry of Hypothetical Curved Graphite Structures. In *The Fullerenes*; Kroto, H.W., Fischer, J.E., Cox, D.E., Eds.; Pergamon Press: Oxford, UK, 1993; 113–122.
28. Lenosky, T.; Gonze, X.; Teter, M.; Elser, V. Energetics of negatively curved graphitic carbon. *Nature* **1992**, *355*, 333–335.
29. MacKay, A.L.; Terrones, H. Diamond from graphite. *Nature* **1991**, *352*, 762.
30. Vanderbilt, D.; Tersoff, J. Negative-curvature fullerene analog of  $\text{C}_{60}$ . *Phys. Rev. Lett.* **1992**, *68*, 511–513.
31. Gaito, S.; Colombo, L.; Benedek, G. A theoretical study of the smallest tetrahedral carbon schwarzites. *Europhys. Lett.* **1998**, *44*, 525–530.
32. Schwarz, H.A. *Gesammelte Mathematische Abhandlungen*; Springer: Berlin, 1890; Vols. 1–2.
33. O’Keeffe, M.; Adams, G.B.; Sankey, O.F. Predicted new low energy forms of carbon. *Phys. Rev. Lett.* **1992**, *68*, 2325–2328.
34. Benedek, G.; Colombo, L.; Gaito, S.; Galvani, E.; Serra, S. Prediction of new  $\text{sp}^2$  and  $\text{sp}^2/\text{sp}^3$  hollow carbon crystals. *J. Chem. Phys.* **1997**, *106*, 2311–2316.
35. Coté, M.; Grossman, J.C.; Cohen, M.L.; Louie, S.G. Theoretical study of a three-dimensional all- $\text{sp}^2$  structure. *Phys. Rev., B* **1998**, *58*, 664–668. The two structures proposed by these authors are identical to the hollow graphites  $\text{fcc-C}_{20}$  and  $\text{fcc-C}_{22}$  first described and calculated by G. Benedek et al. [34].
36. Milani, P.; Iannotta, S. Cluster Beam Synthesis of Nanostructured Materials. In *Springer Series in Cluster Physics*; Springer: Berlin, 1999.
37. Donadio, D.; Colombo, L.; Milani, P.; Benedek, G. Growth of nanostructured carbon films by cluster assembly. *Phys. Rev. Lett.* **1999**, *83*, 776–779.
38. Spadoni, S.; Colombo, L.; Milani, P.; Benedek, G. Routes to carbon schwarzites from fullerene fragments. *Europhys. Lett.* **1997**, *39*, 269–274.
39. Barborini, E.; Piseri, P.; Milani, P.; Benedek, G.; Ducati, C.; Robertson, J. Negatively curved spongy carbon. *Appl. Phys. Lett.* **2002**, *81*, 3359–3361.
40. Zakhidov, A.A.; Baughman, R.H.; Iqbal, Z.; Cui, C.; Khayrullin, I.; Dantas, S.O.; Marti, J.; Ralchenko, V.G. Carbon structures with three-dimensional periodicity at optical wavelengths. *Science* **1998**, *282*, 897–901.
41. Jones, D. Ghostly graphite. *Nature* **1991**, *351*, 526.
42. Townsend, S.J.; Lenosky, T.; Muller, D.A.; Nichols, C.S.; Elser, V. Negatively curved graphitic sheet model of amorphous carbon. *Phys. Rev. Lett.* **1992**, *69*, 921–924.
43. O’Keeffe, M.; Adams, G.B.; Sankey, O.F. Duals of Frank–Kasper structures as C, Si and Ge clathrates: Energetics and structure. *Philos. Mag. Lett.* **1998**, *78*, 21–28.
44. Adams, G.B.; O’Keeffe, M.; Demkov, A.A.; Sankey, O.F.; Huang, Y. Wide-band-gap Si in open fourfold-coordinated clathrate structures. *Phys. Rev., B* **1994**, *49*, 8048–8053.
45. Benedek, G.; Galvani, E.; Sanguinetti, S. Hollow diamonds—stability and elastic properties. *Chem. Phys. Lett.* **1995**, *244*, 339–344.
46. Benedek, G.; Colombo, L. Hollow Diamonds from Fullerenes. In *Cluster Assembled Materials*; Sattler, K., Ed.; Trans. Tech. Publ.: Winthertur, Switzerland, 1997; 247–273.
47. Iqbal, Z.; Zhang, Y.; Grebel, H.; Lahamer, A.; Benedek, G.; Bernasconi, M.; Cariboni, J.; Spagnolatti, I.; Sharma, R.; Owens, F.W.; Kozlov, M.E.; Rao, K.V.; Muhammed, M. Evidence for a solid phase of dodecahedral  $\text{C}_{20}$ . *Eur. Phys. J., B* **2003**, *31*, 509–515.
48. O’Keeffe, M. Crystal Structures as Periodic Foams and Vice Versa. In *Foams and Emulsions*; Sadoc, J.F., Rivier, N., Eds.; Kluwer: Dordrecht, The Netherlands, 1998; 403–422.
49. O’Keeffe, M.; Hyde, B.G. *Crystal Structures I: Patterns and Symmetry*; Min. Soc. America: Washington, DC, 1996.
50. Benedek, G.; Colombo, L.; Gaito, S.; Serra, S. Exotic Diamonds from Topology and Simulation. In *The Physics of Diamond*; Paoletti, A., Tucciarone, A., Eds.; IOS Press: Amsterdam, The Netherlands, 1997; 575–598.
51. Hilbert, D.; Cohn-Vossen, S. *Anschauliche Geometrie*; Springer: Berlin, 1932.
52. Aoki, H.; Koshino, M.; Takeda, D.; Morise, H.; Kuroki, K. Electronic structure of periodic curved surfaces: Topological band structure. *Phys. Rev., B* **2001**, *65*, 035102.
53. Ceulemans, A.; Fowler, P.W. Extension of Euler theorem to symmetry properties of polyhedra. *Nature* **1991**, *353*, 52–54.
54. Fowler, P.W.; Rassat, A.; Ceulemans, A. Symmetry generalisation of the Euler–Schläfli theorem for multi-shell polyhedra. *J. Chem. Soc., Faraday Trans.* **1996**, *92*, 4877–4884.
55. Ceulemans, A.; Szopa, M.; Fowler, P.W. Homology groups, symmetry representations and polyhedral clusters. *Europhys. Lett.* **1996**, *36*, 645–649.

56. Ceulemans, A.; Chibotaru, L.F.; Fowler, P.W.; Szopa, M. Symmetry extensions of Euler's polyhedral theorem and the band theory of solids. *J. Chem. Phys.* **1999**, *110*, 6916–6926.
57. Fowler, P.W.; Manopoulos, D.E. Magic numbers and stable structures for fullerenes, fullerides and fullerenium ions. *Nature* **1992**, *355*, 428–430.
58. Fowler, P.W.; Manopoulos, D.E.; Ryan, R.P. Isomerization of the Fullerenes. In *The Fullerenes*; Kroto, H.W., Fischer, J.E., Cox, D.E., Eds.; Pergamon Press: Oxford, UK, 1993; 97–112. And references therein.
59. Wang, C.Z.; Ho, K.M.; Chan, C.T. Material research with tight-binding molecular dynamics. *Comp. Mater. Sci.* **1994**, *2*, 93–102.
60. Lucas, A.A.; Moreau, F.; Lambin, Ph. Diffraction by Carbon-Based Tubular Helical Structures. In *Nanos-structured Carbon for Advanced Applications*; Benedek, G., Milani, P., Ralchenko, V.G., Eds.; Kluwer Academic Publishers: Dordrecht, The Netherlands, 2001; 129–147.
61. White, C.T.; Mintmire, J.W.; Mowrey, R.C.; Brenner, D.W.; Robertson, D.H.; Harrison, J.A.; Dunlap, B.I. Predicting Properties of Fullerenes and Their Derivatives. In *Buckminsterfullerenes*; Billups, W.E., Ciufolini, M.A., Eds.; VCH Publ.: New York, 1993; 125–184.
62. Bernaerts, D.; Zhang, X.B.; Zhang, X.F.; Amelinckx, S.; van Tenderloo, G.; van Landuyt, J.; Ivanov, V.; B'Nagi, J. Electron-microscopy study of coiled carbon tubules. *Philos. Mag.* **1995**, *A71*, 605–630.
63. Hyde, S.T. *Sponges Foams and Emulsions*; Sadoc, J.F., Rivier, N., Eds.; Kluwer: Dordrecht, The Netherlands, 1999; 437–469.
64. Hoffman, D. Geometry—A new turn for Archimedes. *Nature* **1996**, *384*, 28–29.
65. Rosato, V.; Celino, M.; Benedek, G.; Gaito, S. Thermodynamic behavior of the carbon schwarzite fcc (C<sub>36</sub>)<sub>2</sub>. *Phys. Rev., B* **1999**, *60*, 16928–16933.
66. Buzio, R.; Gnecco, E.; Boragno, C.; Valbusa, U.; Piseri, P.; Barborini, E.; Milani, P. Self-affine properties of cluster-assembled carbon thin films. *Surf. Sci.* **2000**, *444*, L1–L6.
67. Bogana, M.; Donadio, D.; Benedek, G.; Colombo, L. Simulation of atomic force microscopy of fractal nano-structured carbon films. *Europhys. Lett.* **2001**, *54*, 72–76.
68. Barabasi, A.L.; Stanley, H.E. *Fractal Concepts in Surface Growth*; Cambridge University Press: Cambridge, USA, 1983.
69. Benedek, G.; Vahedi-Tafreshi, H.; Barborini, E.; Piseri, P.; Milani, P.; Ducati, C.; Robertson, J. The structure of negatively curved spongy carbon. *Diamond Rel. Mater.* **2003**, *12*, 768–773.
70. Helfrich, W. Possible chromatographic effect of liquid-crystalline. *Z. Naturforsch.* **1973**, *28*, 1967.
71. Aste, T.; Weaire, D. *The Pursuit of Perfect Packing*; IOP Publishing Ltd.: Bristol, UK, 2000.
72. Sullivan, J.M. The Geometry of Bubbles and Foam. In *Foams and Emulsions*; Sadoc, J.F., Rivier, N., Eds.; Kluwer: Dordrecht, The Netherlands, 1999; 379–401.
73. Robertson, D.H.; Brenner, D.W.; Mintmire, J.W. Energetics of nanoscale graphitic tubules. *Phys. Rev., B* **1992**, *45*, 12592–12595.
74. Sadoc, J.-F. Curved Spaces and Geometrical Frustration. In *Foams and Emulsions*; Sadoc, J.F., Rivier, N., Eds.; Kluwer: Dordrecht, The Netherlands, 1999; 511–525.



# Functionalization of Surface Layers on Ceramics

Toshihiro Ishikawa

Functional Materials Research Department, Ube Research Laboratory,  
Yamaguchi, Japan

## INTRODUCTION

Ceramics are often prepared with surface layers of different composition from the bulk,<sup>[1,2]</sup> to impart a specific functionality to the surface or to act as a protective layer for the bulk material.<sup>[3,4]</sup> Here I describe a general process by which functional surface layers with a nanometer-scale compositional gradient can be readily formed during the production of bulk ceramic components. The first concept regarding this process was established by Ishikawa et al. in 1998.<sup>[5]</sup> The basis of this approach is to incorporate selected low-molecular-mass additives into either the precursor polymer from which the ceramic forms, or the binder polymer used to prepare bulk components from ceramic powders. Thermal treatment of the resulting bodies leads to controlled phase separation (“bleed out”) of the additives, analogous to the normally undesirable outward loss of low-molecular-mass components from some plastics;<sup>[6–10]</sup> subsequent calcination stabilizes the compositionally changed surface region, generating a functional surface layer. This approach is applicable to a wide range of materials and morphologies, and should find use in catalysts, composites, and environmental barrier coatings.

## PREVIOUS METHODS TO OBTAIN SURFACE GRADIENT STRUCTURES

To avoid the concentration of thermomechanical stress at the interface between the surface layer and the bulk material, many materials were developed that had gradually varying properties as the distance into the material increases.<sup>[11]</sup> Such materials can contain gradients in morphology or in composition. For example, gradients in morphology can result in materials that have a graded distribution of pore sizes on a monolith of silica aerogel, and a type of integral plastic. These materials were created by strictly controlling the vaporization of the volatile during the production process.<sup>[12,13]</sup> Gradients in chemical composition have been achieved, for example: 1) chemical vapour deposition;<sup>[14,15]</sup> 2) powder methods such as slip cast or dry processing;<sup>[16]</sup> 3) various coating methods;<sup>[17]</sup> and 4) thermal chemical reaction.<sup>[2,18]</sup> Of these, 1) and 4)

are relatively expensive, complicated and result in damage to bulk substrates. Items 2) and 3) produce stepped gradient structures, and it is difficult to control the thickness of each layer to less than 100 nm. Furthermore, most of these processes are not easily adapted to coating samples in the form of fiber bundles, fine powders, or other materials with complicated shapes.

## A NEW PROCESS FOR CREATING SURFACE FUNCTIONAL LAYERS

We have addressed the issue of establishing an inexpensive and widely applicable process for creating a material with a compositional gradient and excellent functionality. A schematic representative of our new in situ formation process for functional surface layers, which have a gradient-like structure toward the surface, is shown in Fig. 1. The important feature of this method is that the surface layer of the ceramic is not deposited on the substrate, but is formed during the production of the bulk ceramic. We confirmed that our process is applicable to any type of system as long as, in the green-body (that is, not calcined) state, the system contains a resin and a low-molecular-mass additive that can be converted into a functional ceramic at high temperatures. Here the resin is a type of precursor polymer (polycarbosilane, polycarbosilazane, polysilastyrene, methylchloropolysilane, and so on) or binder polymer used for preparing green bodies from ceramic powders.<sup>[19]</sup> Although the former case (using precursor polymers) is explained in detail in this paper, the latter case, using binder polymers, was also confirmed by treating a  $\text{Si}_3\text{N}_4$  body with a TiN surface layer.  $\text{Si}_3\text{N}_4$  can exhibit excellent thermal stability and wear resistance in the high-speed machining of cast iron, but shows poor chemical wear resistance in the machining of steel.<sup>[20]</sup> To avoid this problem, TiN coating, via expensive chemical vapor deposition, was often performed on previously prepared  $\text{Si}_3\text{N}_4$  substrates. But if our new process is appropriately applied, formation of the TiN surface layer could be achieved during the sintering process of the  $\text{Si}_3\text{N}_4$  green body. In this case, titanium(IV) butoxide and polystyrene are used as the low-molecular-mass additive and binder polymer, respectively. By a combination of sufficient

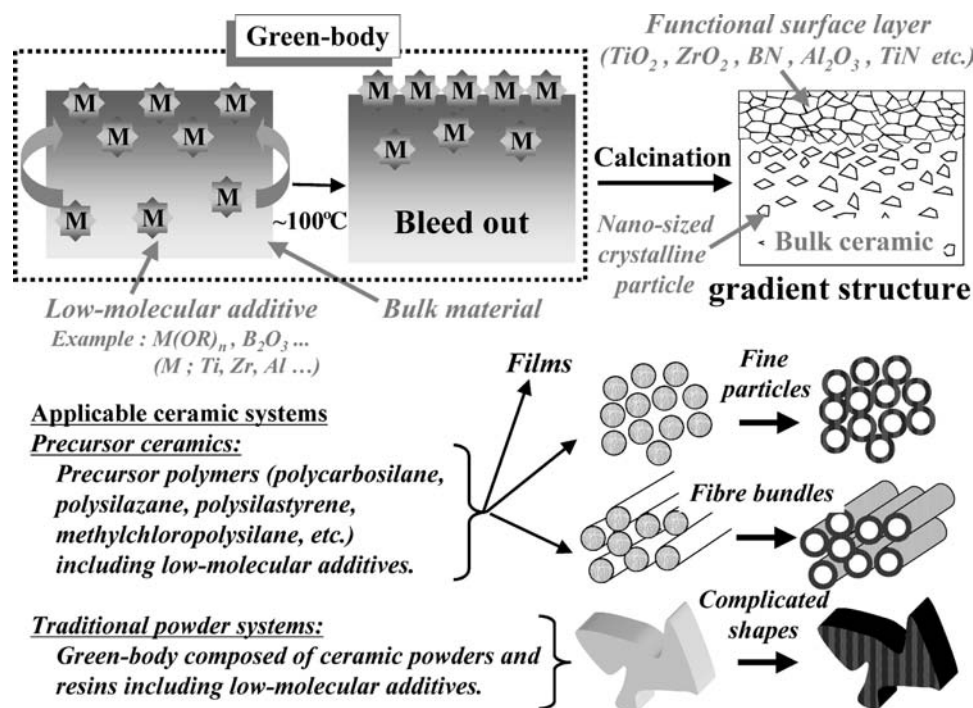


Fig. 1 Schematic diagram of a general process for in situ formation of functional surface layers on ceramics.

maturation (in air at  $100^\circ\text{C}$ ) and subsequent sintering (in  $NH_3 + H_2 + N_2$  at  $1200^\circ\text{C}$ ),  $Si_3N_4$  covered with TiN is successfully produced. This technology would be very useful for producing ceramic materials with complicated shapes and various coating layers. Moreover, our process is advantageous for preparing precursor ceramics (particularly fine particles, thin fibrous ceramics and films). The systems to which our concept is applicable are shown in Fig. 1.

Here I give a detailed account of the results for the precursor ceramic obtained by using polycarbosilane. Polycarbosilane ( $-SiH(CH_3)-CH_2-$ )<sub>n</sub> is a representative preceramic polymer for preparing SiC ceramics—for example, Hi-Nicalon fiber<sup>[21]</sup> and Tyranno SA fiber.<sup>[22]</sup> Furthermore, oxide or nitride can also be produced from the polycarbosilane by firing in air or ammonia, respectively. Our new technology makes full use of the bleed-out phenomenon<sup>[6–10]</sup> of additives intentionally mixed in the polycarbosilane. Here we treated a polycarbosilane with  $Ti(OC_4H_9)_4$  or  $Zr(OC_4H_9)_4$ , and created a strong, fibrous photocatalyst with a surface  $TiO_2$  layer, or a highly alkali-resistant SiC-based fiber with a surface  $ZrO_2$  layer.

#### PHOTOCATALYTIC FIBER PRODUCED BY THIS NEW PROCESS

The preceramic polymer containing  $Ti(OC_4H_9)_4$  (50 wt.%) was shaped into a fiber by melt spinning.

The fiber was then matured in air at  $70^\circ\text{C}$  for 100 h; during this process, the titanium compound oozed from the preceramic polymer. The bleed-out phenomenon was confirmed by using electron spectroscopy for chemical analysis (ESCA). After the maturation, the fiber material was cured in air at  $200^\circ\text{C}$ . The cured material was then calcined in air at  $1200^\circ\text{C}$  to obtain a silica fiber covered with titania. This production process is schematically shown in Fig. 2.

Fig. 3 shows Auger electron spectroscopy (AES) depth analysis of the surface layer of the fiber. The thickness of the surface layer can be controlled in the range 5–500 nm by changing the temperature ( $70$ – $100^\circ\text{C}$ ) and time (10–200 h) of the maturation.<sup>[23]</sup> Furthermore, the composition of the surface layer

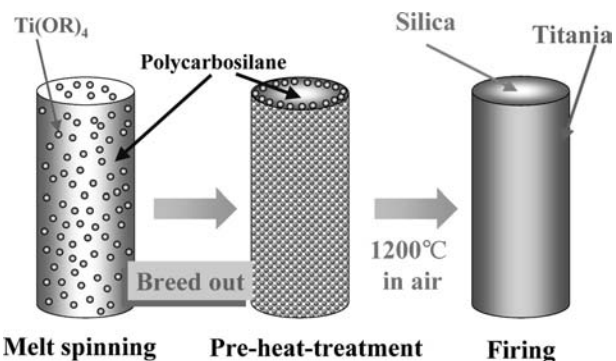


Fig. 2 A new process for producing strong photocatalytic fiber with gradient structure.

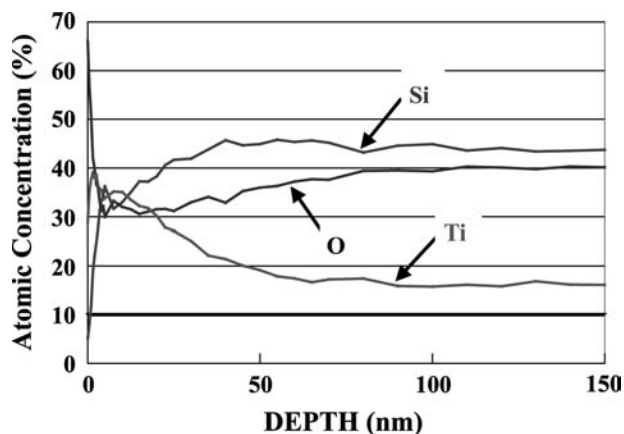


Fig. 3 Surface gradient compositions of the photocatalytic fiber.

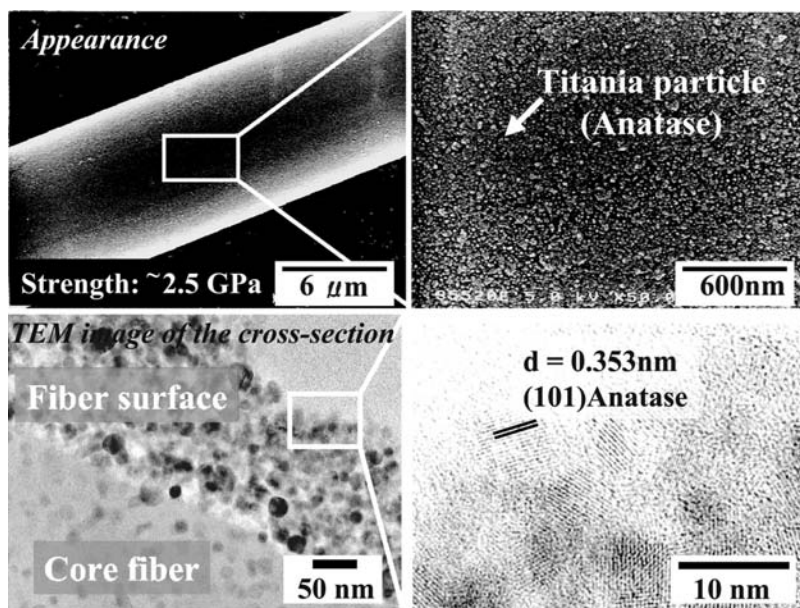
reflects the composition of the low-molecular-mass additives.

According to the results of X-ray diffraction analysis, these fibers were composed of anatase  $\text{TiO}_2$  and an amorphous  $\text{SiO}_2$  phase. Investigation by scanning electron microscopy (SEM) showed that the outer surface of the fiber prepared via maturation for 100 h appeared to be smooth (Fig. 4A) and was covered with titania particles (Fig. 4B). Furthermore, the transmission electron microscopy (TEM) image of the cross section near the surface showed a  $\text{TiO}_2$ -sintered surface and particle-dispersed bulk structures (Fig. 4C). Most of the surface  $\text{TiO}_2$  crystals (crystalline size: 8 nm, Fig. 4D) were directly sintered (directly sintered structure), whereas the internal  $\text{TiO}_2$  crystals were bound

with the amorphous  $\text{SiO}_2$  phase (liquid-phase sintered structure). This result corresponds to the gradient composition shown in the AES data. The gradient-like structure resulted in strong adhesion between the surface  $\text{TiO}_2$  layer and the bulk material, which is different from the behavior of other coating layers formed on substrates via conventional methods. Although in the case of the other  $\text{TiO}_2$ -covered silica fiber, the  $\text{TiO}_2$  layer was easily peeled off, and our  $\text{TiO}_2$ -sintered surface definitely did not drop off after heat-cycling, washing, or rubbing.

Furthermore, a strengthening effect of the fine particles (<10 nm) dispersed in the bulk ceramics can be achieved at the same time by using our technology. Tensile testing of the monofilaments according to the ASTM D3379-75 standard with a 25-mm-gauge length demonstrated that the strength was markedly higher (>2.5 GPa) than that of ordinary sol-gel  $\text{TiO}_2/\text{SiO}_2$  fibers (<1 GPa).<sup>[24]</sup> At present, the reason for this is not clear, but it was assumed that this was caused by less stress concentration at the surface region because of the gradient structure toward the surface.

We subsequently confirmed the objective function (photocatalytic activity) of the above-mentioned fiber (titania fiber) as follows. We prepared a quartz tubular reactor (inner volume:  $7 \text{ cm}^3$ ) with an ultraviolet (UV) lamp. The tubular reactor was filled with 2 g of the felt material (Fig. 5) made of the titania fiber. The photocatalytic activity was confirmed by using air containing 140 ppm of acetaldehyde, at a flow rate of 1 L/min, and UV light at an intensity of  $1\text{--}5 \text{ mW cm}^{-2}$  (wavelength, 352 nm). Under these conditions (single pass), the acetaldehyde was effectively decomposed



*Bleed out, inorganicization, crystallization, and sintering competitively proceed. → Grain growth was prevented.*

Fig. 4 Surface appearances and cross sections of the  $\text{TiO}_2/\text{SiO}_2$  photocatalytic fiber.

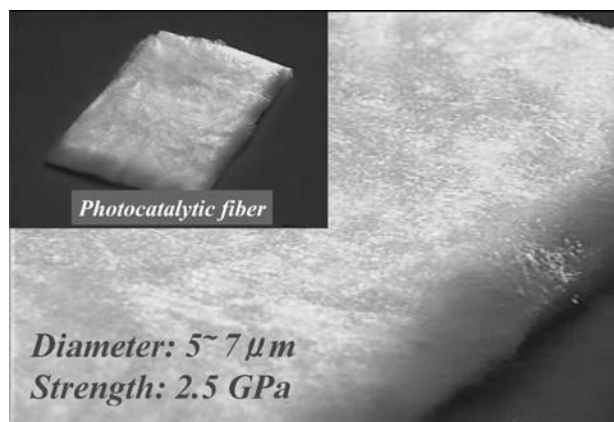
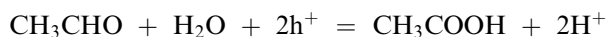


Fig. 5 Felt material of the photocatalytic fiber.

accompanied by the generation of  $\text{CO}_2$ . The results are shown in Fig. 6.

It is well known that the catalytic effect of  $\text{TiO}_2$  is attributed to the generation of a strong oxidant, hydroxyl radicals. Following this theory, the quantum efficiency of the felt material prepared from the above titania fiber was calculated from a decrease in the acetaldehyde. In this case, if the number of molecules is significantly larger than the number of photon, acetaldehyde is oxidized to  $\text{CH}_3\text{COOH}$  as follows:



\*Semiconductor (such as  $\text{TiO}_2$ )

+  $h\nu$  (energy of photon)

=  $\text{e}^-$  (electron) +  $\text{h}^+$  (hole)

In this case, the apparent quantum efficiency (QE) of the felt material prepared from the aforementioned

titania fiber is calculated by the following equation:

$$\text{QE} = 2 \times (\text{Number of decomposed molecules}) / (\text{Number of incident photons})$$

$$\begin{aligned} \text{Wavelength} &= 352 \times 10^{-9} \text{ m, Intensity of UV light} \\ &= 1 \text{ mW/cm}^2 = 10 \text{ J/sec/m}^2 \end{aligned}$$

$$\text{Actual irradiation area} = 8.33 \times 10^{-4} \text{ m}^2$$

The calculation result using these values showed an extremely high QE value even at room temperature (over 37%). It is believed that this higher value at high temperatures is attributable to the evaporation of the formed acetic acid adsorbed on the fiber surface. These excellent QE values could be realized by the dense existence of very fine anatase- $\text{TiO}_2$  crystals (8 nm) on the surface. These fine crystals are considered to facilitate the diffusion of excited electrons and holes toward the surface before their recombination.

We also confirmed the coliform-sterilization ability of this fiber as follows. Our fiber (0.2 g) was placed in wastewater (20 mL) containing coliform at a concentration of  $1 \times 10^6 \text{ mL}^{-1}$ . Irradiation by UV light (wavelength: 352 nm,  $2 \text{ mW cm}^{-2}$ ) was performed at room temperature, and a small amount of the wastewater was extracted. After cultivation using the extracted water, the amount of active coliform was calculated from the number of colonies formed. In this experiment, using the desirable fiber covered with very fine titania crystals (8 nm), all of the coliform in the wastewater was completely sterilized within 5 hr, accompanied by the generation of  $\text{CO}_2$ . In the comparative study, using undesirable fibers covered with large titania crystals (9–11 nm), sterilization of

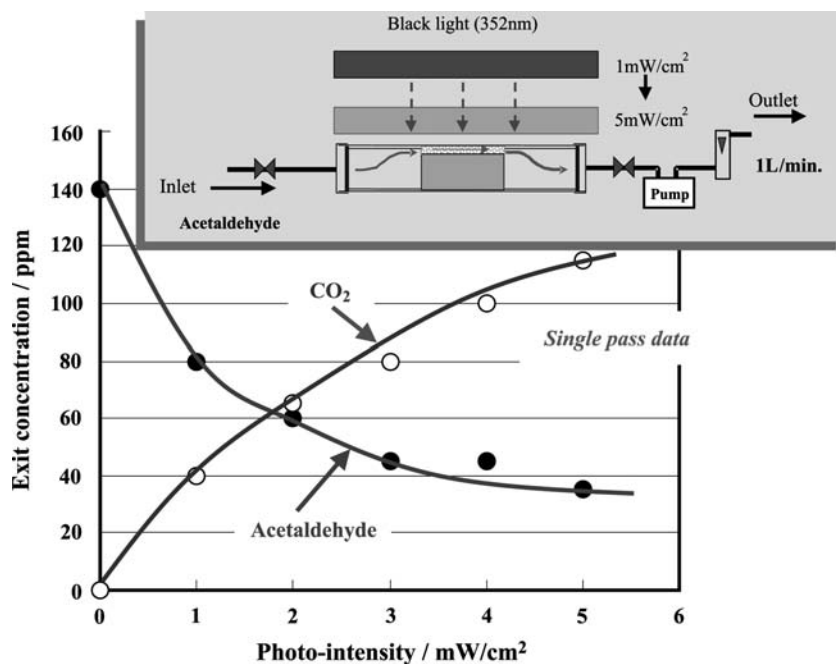


Fig. 6 Decomposition of acetaldehyde using the photo-catalytic fiber with UV irradiation.



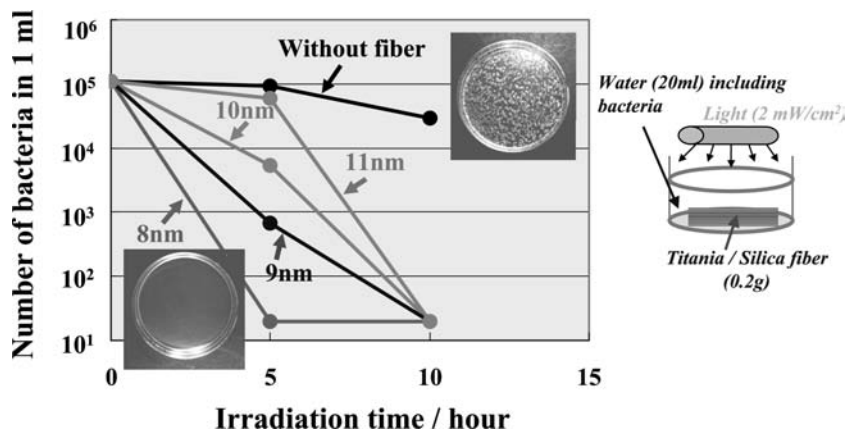


Fig. 7 The results of extinction activity of coliform using the photocatalytic fiber with UV irradiation.

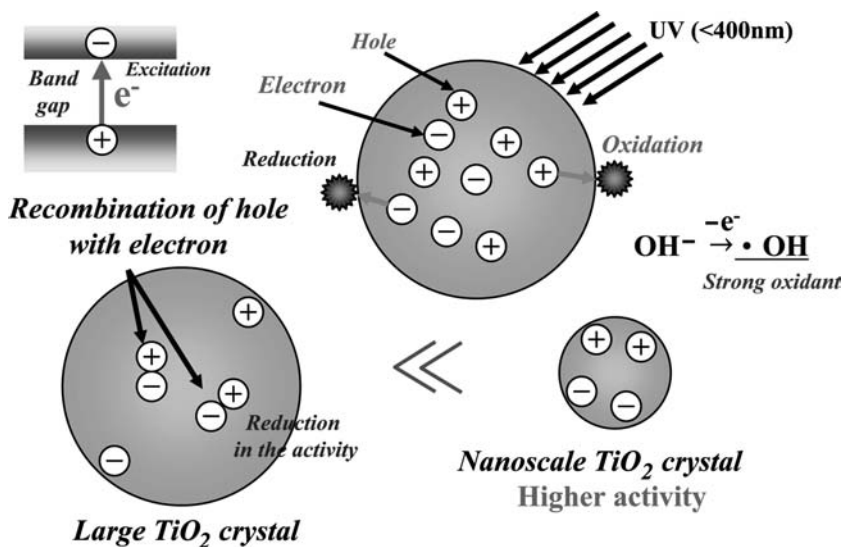


Fig. 8 The relationship between the photocatalytic activity and the size of a titania crystal.

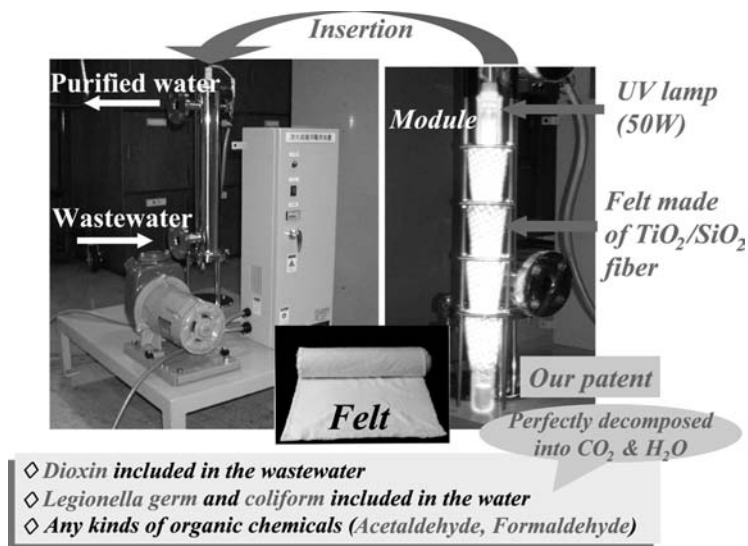
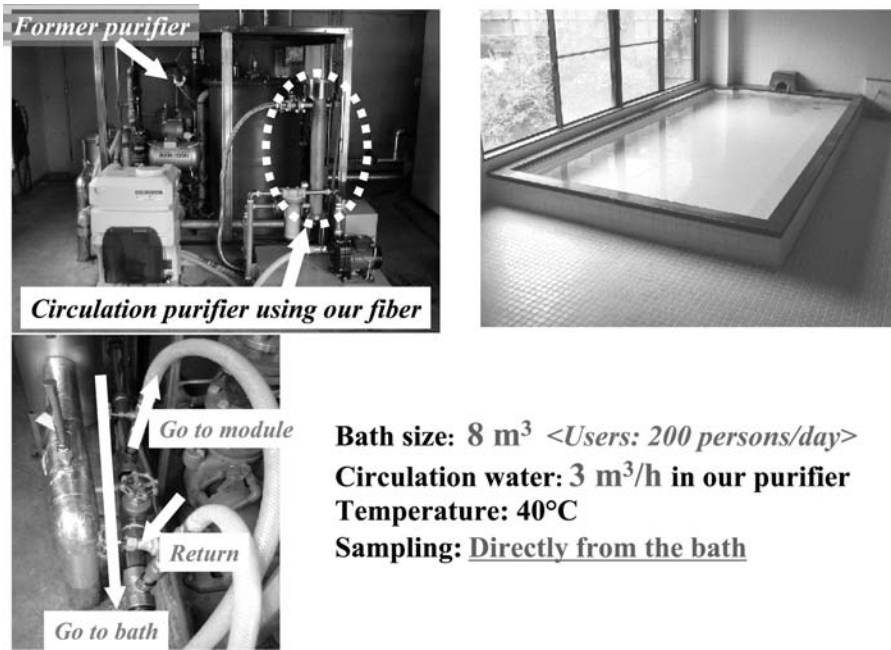


Fig. 9 Circulation purifier for pollutants using photocatalytic fiber with a UV lamp.



**Bath size: 8 m<sup>3</sup> <Users: 200 persons/day>**  
**Circulation water: 3 m<sup>3</sup>/h in our purifier**  
**Temperature: 40°C**  
**Sampling: Directly from the bath**

**Fig. 10** Purification test of the water of a circulation bath system using the circulation purifier.

the coliform was markedly slow (Fig. 7). From the results, the size of the titania crystal is found to be closely related to the photocatalytic activity. It is assumed that, in the case of large crystals, the recombination (inactivation) of the hole and excited electron generated by UV irradiation easily occurs (Fig. 8). To suppress the recombination and obtain the good

photocatalytic activity, the creation of the smaller titania crystals is very important. The new process described in this paper is very desirable for controlling the size of fine crystals, because both the bleed-out phenomenon of the low-molecular-mass additive and the crystallization of the led functional material proceed competitively.

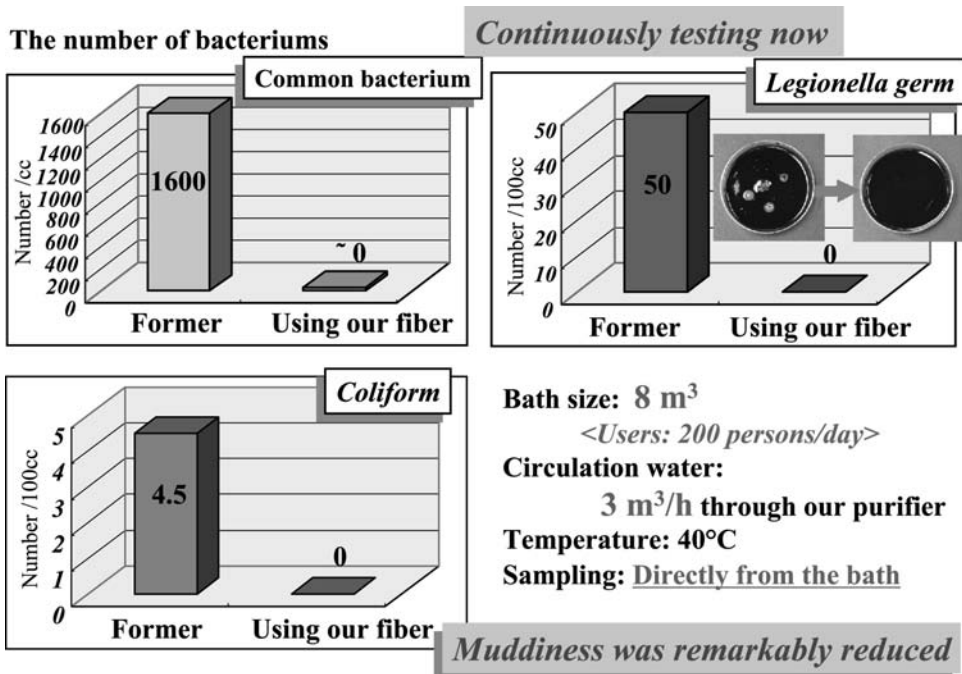


**Fig. 11** The results of the purification test using the circulation purifier.



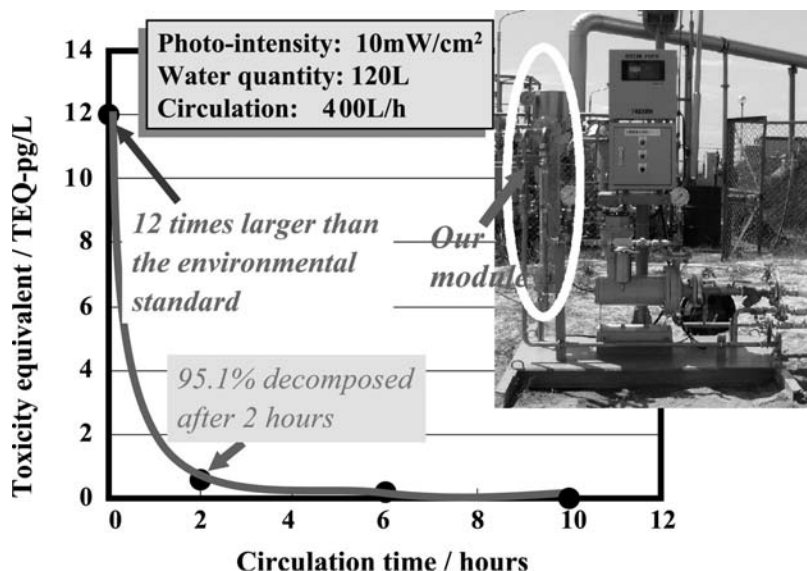


Fig. 12 Decomposition of dioxin using the circulation purifier.

### INDUSTRIAL APPLICATION OF THE PHOTOCATALYTIC FIBER WITH A GRADIENT TITANIA LAYER

A circulation purifier for pollutants (Fig. 9) was developed by using the felt material made of the aforementioned photocatalytic fiber. This is a very simple purifier with a module composed of the cone-shaped felt material (made of the photocatalytic fiber) and UV lamp. Purification of the bath water of a circulation bath system was performed by using the above purifier (Fig. 10). Many bacteria (common bacterium, legionera germ, and coliform), which existed in the bath water before the purification, were perfectly decomposed into  $\text{CO}_2$  and  $\text{H}_2\text{O}$  by using the above purifier (Fig. 11).

Furthermore, the photocatalytic fiber can be used for the purification of the many types of wastewater. Fig. 12 shows the result regarding a decomposition

of dioxin contained in a wastewater. In this case, 95.1% of the dioxin was found to be decomposed after only 2 hr.

### FORMATION OF THE ALKALI-RESISTANT SURFACE LAYER ON SiC

The next fiber was prepared from polycarbosilane containing  $\text{Zr}(\text{OC}_4\text{H}_9)_4$  by the same process as that used for the  $\text{TiO}_2/\text{SiO}_2$  fiber material (the aforementioned photocatalytic fiber), except that the calcination was performed in Ar atmosphere at  $1300^\circ\text{C}$ . In this case, the polycarbosilane and  $\text{Zr}(\text{OC}_4\text{H}_9)_4$  were effectively converted into SiC-based bulk ceramic and zirconium oxide (cubic zirconia), respectively (X-ray diffraction results are given in Fig. 13). Before the conversion, bleed-out of the zirconium compound proceeded effectively. AES depth analysis of the fiber surface showed an increase in the concentration of zirconium toward the surface. This construction was confirmed by the TEM image of the cross section near the fiber surface (Fig. 14A and B). This indicates the direct production of an SiC-based fiber covered with a  $\text{ZrO}_2$  surface layer, which has a gradient-like composition toward the surface. In general, amorphous fibers covered with ceramic crystal do not show high strength.<sup>[25]</sup> However, this fiber showed relatively high strength (2.5 GPa) compared with other SiC fiber (2.1 GPa) coated with zirconia nanocrystals via the sol-gel method. The initial strength of the SiC fiber used for the comparative study was 3.1 GPa. The  $\text{ZrO}_2$  surface layer, a basic oxide material, can provide better alkali resistance for SiC ceramics.

To confirm the better alkali resistance for our  $\text{ZrO}_2$ -covered SiC fiber, the following experiment was

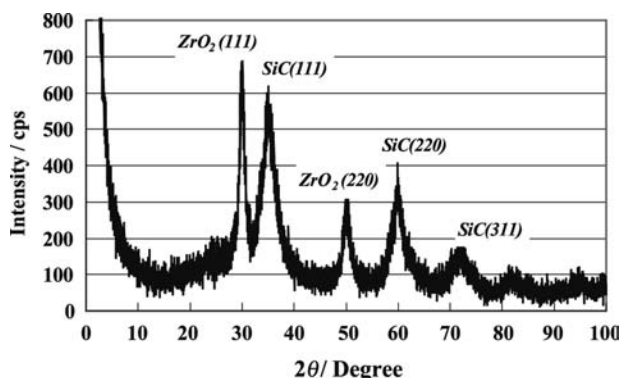
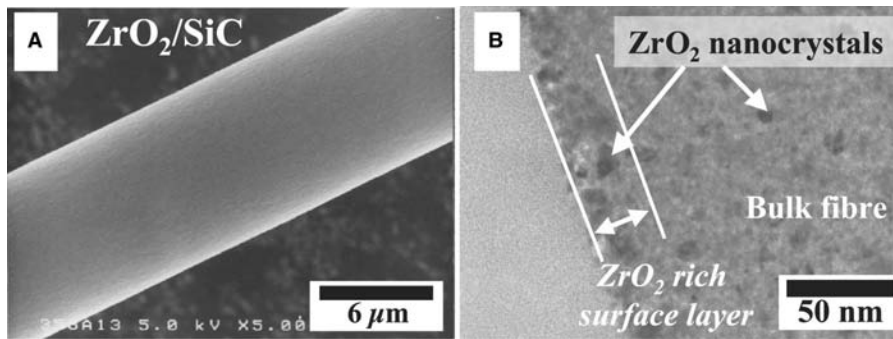


Fig. 13 X-ray diffraction pattern of the SiC fiber covered with zirconia.



**Fig. 14** Surface appearances and cross sections of the SiC fiber covered with  $ZrO_2$ .

performed. The fiber material was immersed for 15 min in deionized water saturated with potassium acetate and then annealed at  $800^\circ\text{C}$  for 100 hr in air after drying. Comparative studies were conducted by using the SiC-based fiber prepared from polycarbosilane, which did not contain zirconium (IV) butoxide, as well as commercial SiC fibers, namely, Hi-Nicalon and an alkali-resistant sintered SiC fiber<sup>[22]</sup> (Tyranno SA fiber). Fig. 15 shows the fractured surfaces of the tested fiber bundles, obtained by using field-emission scanning electron microscopy (FE-SEM). As can be seen from the micrographs, only the  $ZrO_2$ -covered SiC fiber, which was obtained by using our method, retained its intact fibrous shape, whereas the other SiC fibers were extensively oxidized and then bonded together.

## CONCLUSION

Fundamentally, this new process can be applied for preparing functional ceramics with gradient, nano-sized surface structures as long as in the green-body state, the system contains both a polymer component and a low-molecular-mass additive which can be converted into a functional ceramic by heat treatment at high temperatures. Namely, this process does not care about the shape of the precursor materials. Fine particles, thin fibrous ceramics and films ( $\text{SiC}$ ,  $\text{Si}_3\text{N}_4$ ,  $\text{SiO}_2$ ) covered with functional layers ( $\text{BN}$ ,  $\text{TiN}$ ,  $\text{TiO}_2$ ,  $\text{ZrO}_2$ ,  $\text{Al}_2\text{O}_3$ ) could also be synthesized by sufficiently maturing and firing the precursor powders of polycarbosilane or polysilazane including the corresponding additives. The atmosphere and temperature during

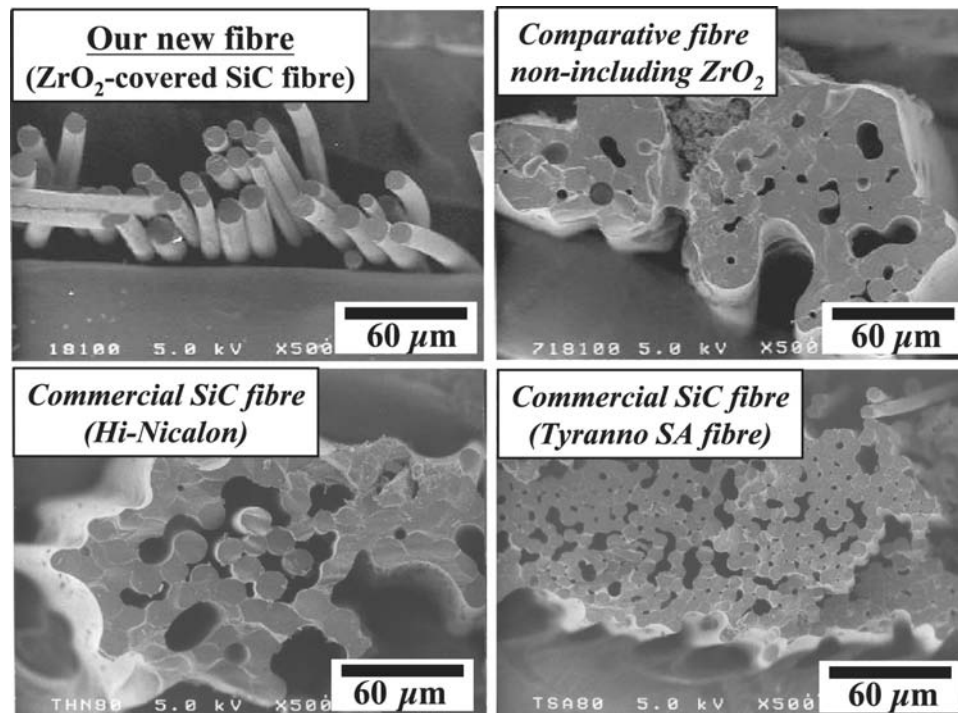


**Fig. 15** Alkali resistance of the SiC fiber covered with  $ZrO_2$  with comparative results.

firing would need to be strictly controlled. This process is applicable to a wide range of materials and morphologies, and should find use in catalysts, composites, and environmental barrier coatings.

## REFERENCES

- Singh, R.K.; Gilbert, D.R.; Fitz-Gerald, J.; Harkness, S.; Lee, D.G. Engineered interfaces for adherent diamond coatings on larger thermal-expansion coefficient mismatched substrate. *Science* **1996**, *272*, 396–398.
- Gogotsi, Y.G.; Yoshimura, M. Formation of carbon films on carbides under hydrothermal conditions. *Nature* **1994**, *367*, 628–630.
- Roy, R. Ceramics by the solution–sol–gel route. *Science* **1987**, *238*, 1664–1669.
- Besmann, T.M.; Sheldon, B.W.; Lowden, R.A.; Stinton, D.P. Vapor-phase fabrication and properties of continuous-filament ceramic composites. *Science* **1991**, *253*, 1104–1109.
- Ishikawa, T.; Yamaoka, H.; Harada, Y.; Fujii, T.; Nagasawa, T. A general process for in situ formation of functional surface layers on ceramics. *Nature* **2002**, *416* (6876), 64–67.
- Kerk, S.L.; Tay, S.C.; Hu, S.J. Effect of inherent deformations of leadframes on bleedability of plastic dip. *J. Electron. Mater.* **1989**, *18*, 117–121. Part 1.
- Perovic, A. Morphological instability of poly(ethylene terephthalate) cyclic oligomer crystals. *J. Mater. Sci.* **1985**, *20*, 1370–1374.
- Perovic, A.; Murti, D.K. The effect of coatings on the surface precipitation of oligomeric crystals in poly(ethylene terephthalate) films. *J. Appl. Polym. Sci.* **1984**, *29*, 4321–4327. Part 2.
- Needles, H.L.; Berns, R.S.; Lu, W.C.; Alger, K.; Varma, D.S. Effect of nonionic surfactant and heat on selected properties on polyester. *J. Appl. Polym. Sci.* **1980**, *25*, 1737–1744.
- Perovic, A.; Sundararajan, P.R. Crystallization of cyclic oligomers in commercial poly(ethylene terephthalate) films. *Polym. Bull.* **1982**, *6*, 277–283.
- Neubrand, A.; Rodel, J. Gradient materials: an overview of a novel concept. *Z. Met.kd.* **1997**, *88*, 358–371.
- Gladden, L.F. Structural studies of high surface area silicas. *J. Non-Cryst. Solids* **1992**, *139*, 47–59.
- Dariel, M.P.; Levin, L.; Frage, N. Graded ceramic preforms: various proceeding approaches. *Mater. Chem. Phys.* **2001**, *67*, 192–198.
- Fischbach, D.B.; Lemoine, P.M. Influence of a CVD carbon coating on the mechanical property stability of nicalon silicon carbide fiber. *Compos. Sci. Technol.* **1990**, *37*, 55–61.
- Li, J.X.; Matsuo, Y.; Kimura, S. Improvement of thermal stability of SiC fiber by CVD-C.SiC coating. *Bull. Ceram. Soc., Jpn.* **1991**, *99*, 1207–1211.
- Moya, J.S.; Sanchez-Herencia, M.R.; Pena, P.; Requena, J. *Layered Ceramic Composites: A New Family of Advanced Materials*; Third Euro-Ceramics, Duran, P., Fenandez, J.F., Eds.; Feenza Editrica Iberica: Spain, 1993; Vol. 3, 289–300.
- Sidky, P.S.; Hocking, M.G. Review of inorganic coatings and coating processes for reducing wear and corrosion. *Br. Corros. J.* **1999**, *34*, 171–183.
- Somiya, S.; Ed.; *Hydrothermal Reactions for Materials Science and Engineering*; Elsevier: London, 1989.
- Varaprasad, D.V.; Wade, B.; Venkatasubramanian, N.; Desai, P.; Abhiraman, A.S. Critical requirements in the formation of continuous ceramic fiber precursors. *Ind. J. Fiber Textile Res.* **1991**, *16*, 73–82.
- Bhat, D.G.; Rebenne, H.E.; Strandberg, C. Analysis of coating interlayer between silicon nitride cutting tools and titanium carbide and titanium nitride coatings. *J. Mater. Sci.* **1991**, *26*, 4567–4580.
- Takeda, M.; Sakamoto, J.; Saeki, A.; Imai, Y.; Ichikawa, H. High performance silicon carbide fiber Hi-Nicalon for ceramic matrix composites. *Ceram. Eng. Sci. Proc.* **1995**, *16*, 37–44.
- Ishikawa, T.; Kohtoku, Y.; Kumagawa, K.; Yamamura, T.; Nagasawa, T. High-strength alkali-resistant sintered SiC fiber stable to 2,200°C. *Nature* **1998**, *391*, 773–775.
- Yamaoka, H.; Harada, Y.; Fujii, T. Inorganic Fiber Including Zirconia and Its Production Process. Japanese Patent Application No. 2001-167679, 2001.
- Abe, Y.; Gunji, T.; Hikita, M. Preparation of SiO<sub>2</sub>-TiO<sub>2</sub> fibers from polytitanosiloxanes. *Yogyo Kyokaiishi* **1986**, *94* (12), 1243–1245.
- Shen, L.; Tan, B.J.; Willis, W.S.; Galasso, F.S.; Suib, S.L. Characterization of dip-coated boron nitride on silicon carbide fibers. *J. Am. Ceram. Soc.* **1994**, *77*, 1011–1016.

# Gecko-Inspired Adhesives: Nanofabrication

**Aránzazu del Campo**

*Max-Planck-Institut für Metallforschung, Stuttgart, Germany, and Functional Surfaces, Leibniz-Institut für Neue Materialien (INM), Saarbrücken, Germany*

**Eduard Arzt**

*Leibniz-Institut für Neue Materialien (INM), Saarbrücken, Germany*

## Abstract

The attachment pads of some beetles, spiders, flies, and geckos are covered by a dense array of long hairs with characteristic geometries. This curious surface topography allows them to firmly attach to and easily release from almost any kind of surfaces. In a technological context, such reversible adhesion could enable robots to walk along walls or ceilings, or lead to new medical devices, disposable plasters, reusable adhesive tapes, etc. Artificial fibrillar surfaces mimicking nature's design have been recently fabricated. This chapter describes the micro- and nanofabrication strategies that have been applied to generate such systems.

## INTRODUCTION

The ability of some insects and geckos to firmly attach to and rapidly detach from varied types of surfaces in diverse conditions has gathered the attention of zoologists for many centuries.<sup>[1–6]</sup> Microscopic examination of their attachment pads has revealed a complex surface hyperstructure consisting of long hairs, sometimes organized in a hierarchical arrangement spanning the millimeter to nanometer range (Fig. 1). These hairs have characteristic sizes and geometries depending on the animal, and their small dimension seems to be the key factor enabling their strong but reversible adhesion.<sup>[7]</sup> In the particular case of the gecko foot, which shows the best adhesion performance, the keratinous hairs (“setae”) are typically 30–130  $\mu\text{m}$  long and contain hundreds of projections terminating in 200–500 nm spatula-shaped structures.

Recent innovations in the area of micro and nanofabrication with polymeric materials have created a unique opportunity for mimicking natural attachment systems as a new generation of moderately strong but reversible adhesives.<sup>[8–10]</sup> Increasing efforts are being made to establish fabrication technologies, which allow the production of polymeric structured surfaces with greater geometrical complexity, closer to the natural systems in design and performance. These include patterns made of polymer materials possessing elongated fibers (high aspect ratio), ordered in a tilted arrangement, exhibiting several hierarchy levels, or 3D spatula-like terminals. This entry describes a number of micro and nanofabrication approaches that have been applied to generate such structures. The methods are classified attending to the dimensions and complexity of the produced structures (micro-metric, nanometric, hierarchical, or 3D). At the end,

recent developments in the area of switchable adhesives based on structured surfaces and responsive materials will be described.

## MICROSTRUCTURED ADHESIVE SURFACES

### Soft Lithography

The term soft lithography is applied to a collection of pattern-replication methods, which rely on an elastomeric mold.<sup>[11]</sup> This is a negative replica of a micro or nanostructured hard master and is prepared by casting and thermal curing a liquid prepolymer (mostly poly(dimethylsiloxane), PDMS) on the master. The PDMS replica can be considered the final patterned surface (Fig. 2A), or it can also be used as mold (or stamp) for patterning other polymeric materials in subsequent replication processes (Fig. 2B and 2C). The elastomeric character allows the PDMS stamp to be released easily from the master (or molded polymer), even in the presence of complex and fragile structures, like high-aspect ratio fibers. Moreover, its low interfacial free energy and chemical inertness reduce mold sticking.

A prerequisite for soft-molding is the access to masters with the desired geometry. Masters for bioinspired fibrillar adhesives consisting of arrays of holes with predefined dimensions have been typically fabricated by photolithography.<sup>[12–15]</sup> Alternatively, masters have been produced by indenting a wax surface with an AFM tip,<sup>[16]</sup> or by laser ablation of a metallic surface.<sup>[17]</sup> Photolithography using SU-8 photoresist has been proven to be particularly suited for obtaining regular, model surfaces in which the influence of the

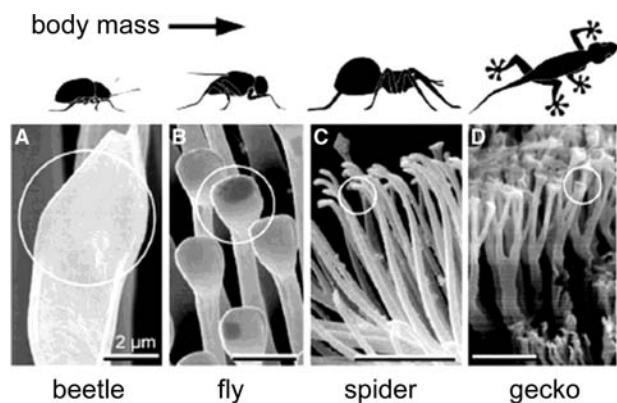


**Fig. 1** Terminal elements (circles) in animals with hairy design of attachment pads. Note that heavier animals exhibit finer adhesion structures. Scale bar represents 2  $\mu\text{m}$ . Source: Reused with permission from Ref.<sup>[7]</sup>.

different geometrical parameters in adhesion can be characterized and quantified.<sup>[14]</sup> This resist material has been specially formulated to obtain high-aspect-ratio features, like holes that are required for obtaining long PDMS fibers in the replication process.<sup>[18]</sup> Arrays of fibers with radius between 1 and 25  $\mu\text{m}$  and lengths between 5 and 80  $\mu\text{m}$  have been reported over 25  $\text{cm}^2$  areas (Fig. 3A).<sup>[14]</sup> These systems have been used to analyze the influence of contact radius and aspect ratio of the fibers in the final adhesion performance of the artificial adhesive surface.<sup>[14]</sup>

In theory, soft-molding allows fabrication of fibers of any dimensions. In reality, the aspect ratio of the fibers is limited by the low mechanical stability of PDMS, and fiber collapse typically occurs in microsized fibers with

aspect ratios exceeding 4 (Fig. 3B). This fact is more critical in nanosized fibers and their fabrication requires the use of harder materials.

Soft PDMS stamps can be also applied to generate fibrillar micropatterns of different materials by soft-molding polymer melts, polymer solutions, or polymer precursors (Fig. 2B). For example, PDMS stamps were used to soft-mold liquid polyurethane precursors and fibers with 20  $\mu\text{m}$  diameter, 40–100  $\mu\text{m}$  length, and 40  $\mu\text{m}$  spacing were obtained.<sup>[19]</sup> In addition, PDMS is transparent and can be used to mold UV-curable prepolymers (Fig. 2C). Using this method, hard polyurethane patterns with fibrils of 0.5–4  $\mu\text{m}$  height and diameters between 1 and 4  $\mu\text{m}$  have been generated.<sup>[15]</sup>

Tilted fibrillar structures are required if reversible gecko-inspired adhesives need to be fabricated. The tilted disposition of the fibers allows peeling-off the adhesive and, therefore, easy removal.<sup>[20]</sup> Tilted SU-8 fibrils have been obtained by photolithography by tilting the mask and resist film with respect to the beam during exposure using a tilting stage (Fig. 4A). Soft-molding polyurethane precursors with a PDMS negative replica of the SU-8 master yielded arrays of polyurethane microfibers with a tilting angle of 25 (Fig. 4B).<sup>[19]</sup>

## NANOSTRUCTURED ADHESIVE SURFACES

### Hot Embossing

Thermoplastic materials can be patterned by hot-embossing (Fig. 5). This involves the shaping of a

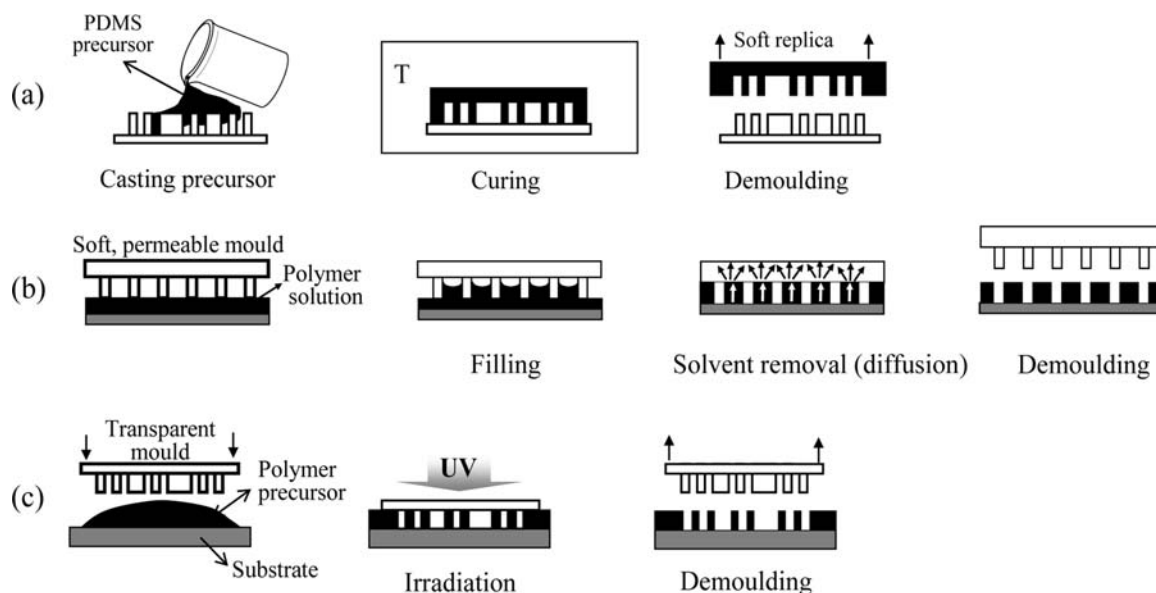


**Fig. 2** (A) Replication by soft lithography. (B) Soft molding polymer solutions using PDMS stamps. (C) Soft-molding UV curable prepolymers.



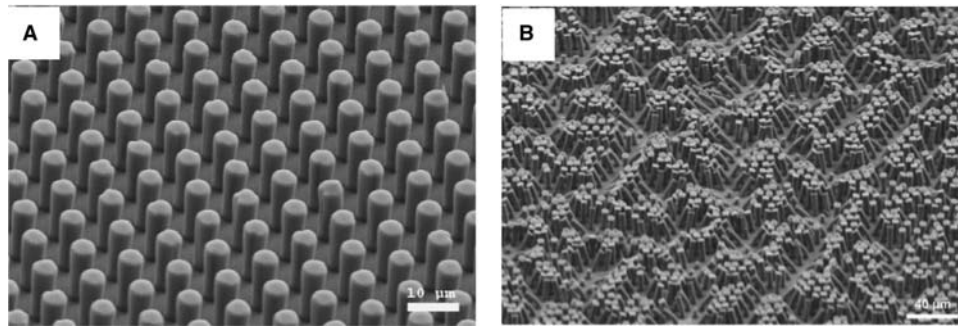


**Fig. 3** SEM micrographs showing arrays of fibers made by soft-molding PDMS onto SU-8 photolithographic templates. (A) Fibers have a radius of  $2.5\ \mu\text{m}$  and a height of about  $20\ \mu\text{m}$ . The minimum interpillar distance is  $5\ \mu\text{m}$ . (B) PDMS pillar with higher aspect ratios collapse after demolding due to the low mechanical stability of PDMS. *Source:* Reprinted with permission from Ref.<sup>[14]</sup>.

polymer melt by conformal contact of a micro or nanostructured mold using heat and pressure. The polymer melt is able to flow and fill the mold cavities in the processing conditions. The filling depends on the viscosity, wetting properties, and pattern geometry, as well as on applied pressure or vacuum. Solidification of the polymer after filling is achieved by cooling below the crystallization temperature in semicrystalline polymers, or below the glass transition temperature in amorphous polymers. Removal of the mold releases a structured polymer with features reproducing its particular geometry. This can be done by peeling off (demolding) or by selective dissolution of the template. Demolding is preferred since it permits use of the same mold for additional molding processes. An example of embossed poly(methyl methacrylate) (PMMA) fibrillar surface is given in Fig. 5. The embossing process was performed at temperatures above the glass transition of PMMA ( $\sim 120^\circ\text{C}$ ) using a polyurethane acrylate mold. Arrays of fibers with  $150\ \text{nm}$  diameter and up to  $500\ \text{nm}$  height were obtained.<sup>[21,22]</sup>

The fabrication of high-quality molds is one of the most important requirements in performing successful embossing. These are typically made of silicon or silicon

dioxide by dry etching technologies, or by deposition of nickel or other metals on patterned resist substrates (LIGA process). Mold fabrication is the most time- and cost-consuming step involved in these patterning techniques, and is very likely to constitute the biggest limitation in potential industrial applications.

### Filling Nanoporous Membranes

Track-etched polycarbonate (PC) and anodic alumina (AA) membranes have been used as low-cost alternatives to expensive molds for producing arrays of long, nanosized fibers.<sup>[16,23,24]</sup> These membranes are commercially available with pore sizes ranging from a few nm to a few  $\mu\text{m}$  and different spacings and thicknesses. The pores of the membrane can be filled with polymer precursors, solutions of melts to obtain a structured polymer film possessing cylinders with dimensions reproducing those of the pores (Fig. 6).

PC membranes containing randomly distributed cylindrical pores of  $0.6\ \mu\text{m}$  diameter and spacings  $< 5\ \mu\text{m}$  have been filled with poly(imide) (PI) solutions.<sup>[23]</sup> Since the PC membrane is flexible, it can be

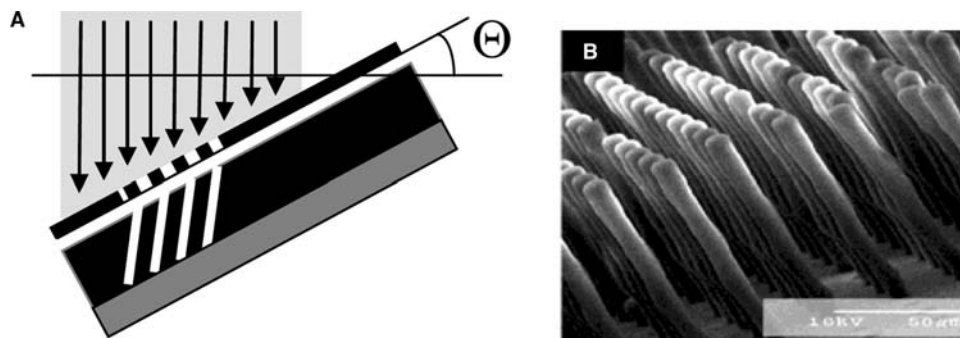


**Fig. 4** Fabrication of tilted fibers by inclined lithography. The SEM picture shows tilted polyurethane pillars obtained after soft-molding with the photolithographic SU-8 masters. Pillars have high aspect ratio, a diameter of  $8\ \mu\text{m}$  and a tilting angle of  $25^\circ$ . *Source:* Reprinted with permission from Ref.<sup>[17]</sup>.



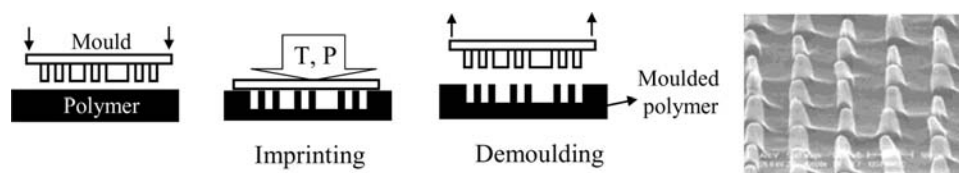


**Fig. 5** Hot-embossing and example of fabricated PMMA fibers with this method. Fibers are 150 nm at base end and 50 nm at top, and 500 nm height.<sup>[22]</sup>

peeled off from the solidified PI film to release dense arrays of high aspect ratio nanofibers. Owing to their large aspect ratio, these fibers were shown to collapse laterally and therefore reduced adhesion is expected. AA membranes with pores between 200 and 400 nm have been also filled with two-parts epoxy resin,<sup>[23]</sup> with a PS solution,<sup>[25]</sup> and with UV curable precursors.<sup>[26]</sup> Because of their rigidity, AA membranes cannot be removed from the polymer by peeling off but need to be selectively dissolved in NaOH solution. This represents a strong disadvantage for fabrication, since the template is destroyed and dissolution takes long times and may cause polymer swelling. In addition, wet etching is followed by a drying step during which capillary forces usually may cause fiber's lateral collapse and, consequently, reduced adhesion (Fig. 6).<sup>[26]</sup>

### e-Beam Lithography

Arrays of PI fibers have also been microfabricated using electron-beam lithography followed by pattern transfer by dry etching in oxygen plasma (Fig. 7A).<sup>[27]</sup> The etching step is necessary to obtain high aspect ratio structures, since the maximum penetration depth of low energy electrons is about 100 nm. Fiber diameters ranged between 0.2 and 4  $\mu\text{m}$ , heights from 0.15 to 2  $\mu\text{m}$ , and spacings from 0.4 to 4.5  $\mu\text{m}$ . This method is appropriate to obtain model nanostructures with smaller dimensions than those obtained by optical photolithography.

However, patterning is slow and restricted to small areas, and requires the availability of e-beam facility.

### Carbon Nanotubes

Microfabrication techniques strongly restrict material's selection to a few resists, all of them quite expensive. In addition, patterning can only be performed in specialized laboratories and requires costly equipment and long processing times. For this reason, scientists have started to look for alternative patterning techniques, which do not require a template (e.g. the mold in soft-lithography or the mask in photolithography). Arrays of vertically aligned carbon nanotubes (CNTs) have been reported as an interesting alternative (Fig. 7B).<sup>[28–31]</sup> Carbon nanotubes have smaller diameters (10–20 nm) than gecko spatulae ( $\sim 200$  nm) and can be made very long (above 65  $\mu\text{m}$ ).<sup>[29]</sup> Having an extremely high aspect ratio, exceptional mechanical strength, and excellent electronic and thermal properties, the CNTs show great potential for dry adhesion applications with additional electrical/thermal management capabilities (e.g., electroswitching, through-thickness thermal transport, high temperature use).<sup>[28]</sup> Arrays of CNTs are fabricated by chemical vapour deposition on Si substrates. In the reported systems, the nanotubes aligned almost normal to the substrate surface and have a fairly uniform tubular length. However, they tend to stick to their closest neighbors

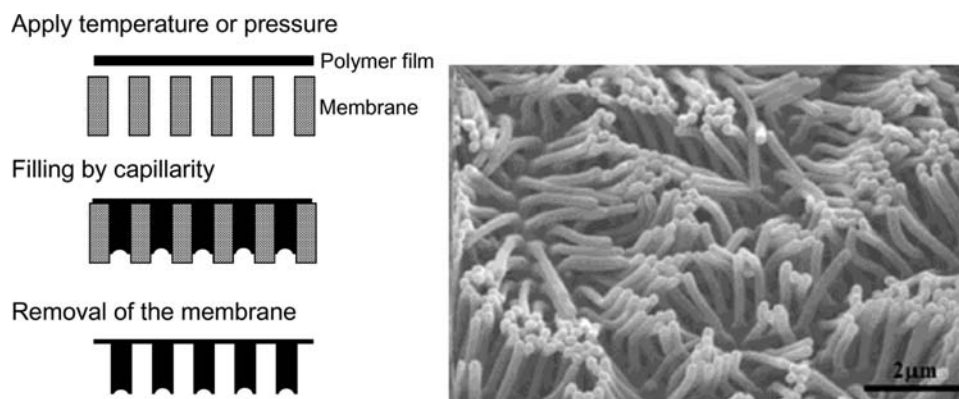


**Fig. 6** Fabrication of high aspect ratio fibers by filling porous AA membranes. Fibers collapse after removal of the membrane (dissolution) because of the large capillary forces acting during the drying process. *Source:* Reprinted from Ref.<sup>[26]</sup> with kind permission of Springer Science and Business Media.

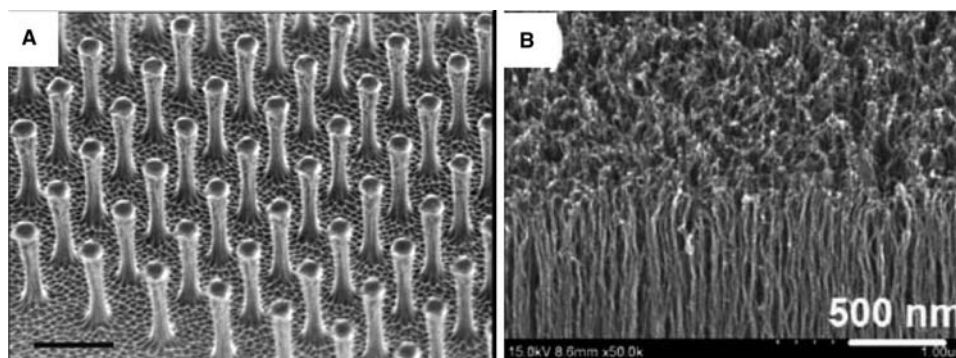


**Fig. 7** SEM micrographs of fibrillar surfaces fabricated by different methods. (A) Arrays of PI pillars fabricated using e-beam lithography and pattern transfer by dry etching.<sup>[27]</sup> Source: Reprinted by permission from Macmillan Publishers Ltd.: Nature Materials. (B) Side-top view of an array of CNTs.<sup>[28]</sup>

forming loosely packed “bundles.” This reduces the overall adhesion force of the CNT layer owing to the reduced number of contact points.

The array of CNTs can be transferred from the Si wafer to flexible backing substrates.<sup>[29,30]</sup> For this purpose, the patterned silicon wafer was embedded in a polymer precursor. After curing, the CNTs were peeled off from the wafer. By etching the silicon-facing side of the polymer matrix by solvents or plasma treatment, a smooth layer of CNTs on a flexible backing was generated.

### Drawing Polymer Fibers

Arrays of nanofibers have been obtained by drawing fibers from polymer drops on non-wettable surfaces by contacting them with a hot plate and then moving both surfaces apart.<sup>[32]</sup> The process is based on surface tension and capillary forces and is available in a number of versions. For example, films of thermoplastic polymers can be brought in contact with a hot structured master possessing pillars. When pulling the master apart, fibers will be drawn from the contacting points (Fig. 8). Alternatively, structured polymer films with large features can be brought in contact with a hot surface and then removed to obtain elongated fibers on the top of the features.<sup>[32]</sup> Other authors have miniaturized this method by using an AFM tip to draw nanosized fibers from a melt polymer film.<sup>[33]</sup> These fabrication

methods seem to be more suitable for large area patterning, and are therefore more likely to be applied in manufacture. However, this requires severe alignment between hot plate (or a roll) and the polymer film across large areas, if nanosized fibers need to be obtained.

An ingenious alternative has been reported recently, which allows alignment problems by combining molding and fiber drawing processes to obtain high aspect ratio nanofibers from thin PS and PMMA films.<sup>[34]</sup> This was achieved by performing the demolding step at temperatures above the glass transitions of the materials. Capillary forces induced deformation of the polymer melt into the void spaces of the mold, and the filled nanofibers were elongated on removal of the mold because of tailored adhesive force at the mold/polymer interface (Fig. 8).

### HIERARCHICAL ADHESIVE SURFACES

A hierarchical organization of fibers over different length scales (mm to nm) mimicks the multiple levels of compliance present in the gecko setae, which is required for adaptability and adhesion to rough surfaces of any kind.

### Multistep Exposure in Photolithography

Lithographic fabrication by superposition of coating and irradiation steps enables fabrication of structures



**Fig. 8** Fabrication of structured surfaces by fiber drawing method. The SEM picture shows an example of obtained PMMA fibrillar surface. Source: Reprinted with permission from Ref.<sup>[34]</sup>.

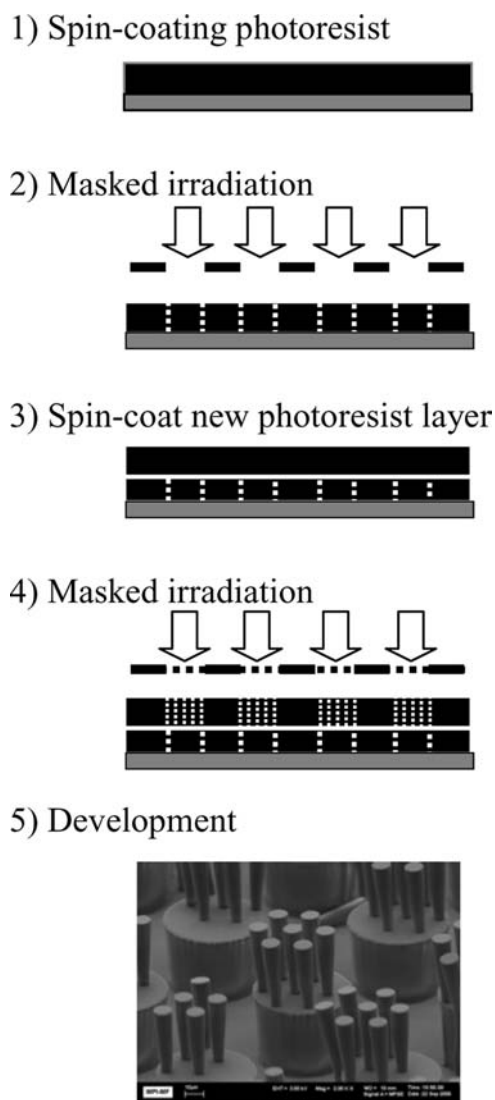


**Fig. 9** Hierarchical structures by double exposure photolithography.

with several organization levels using traditional 2D setups and alignment markers on the mask for guiding superposition. Figure 9 shows the fabrication procedure and an example of micrometric adhesive structure with two hierarchical levels obtained by SU-8.<sup>[18]</sup> Additional levels are possible by just increasing the number of coating and irradiation steps. Geometries are not restricted to cylindrical fibers and depend only on the mask used for irradiation. This can also be replicated using soft-molding methods and transferred to other materials.

### Microfabrication Technologies

Hierarchical structured surfaces have also been obtained by combining photolithography and dry etching methods, as typically used in MEMS fabrication.<sup>[35,36]</sup> Single

crystal silicon posts (1  $\mu\text{m}$  in diameter and height up to 50  $\mu\text{m}$ ) supporting microsized silicon dioxide platforms (2  $\mu\text{m}$  thick and 100–150  $\mu\text{m}$  on a side) were coated by photoresist fibers with  $\sim 250$  nm diameter and  $\sim 4$   $\mu\text{m}$  height in average (Fig. 10A and 10B).

### Filling Stacked Membranes

Hierarchical patterns were also obtained by filling stacked micro and nanoporous AA membranes with different pore diameters.<sup>[37]</sup> The nanoporous membrane (pore diameter  $\approx 60$  nm and interpore distance  $\approx 100$  nm) was generated by the anodization of an aluminum film in an oxalic acid solution. The microporous alumina was produced by conventional lithography and anisotropic chemical etching of the thick film of anodic alumina pores. The micro- and nanoporous alumina membranes were subsequently brought into intimate contact and filled with PMMA solution. Hierarchical polymeric microfibrils (fibril diameter  $\approx 10$   $\mu\text{m}$ ; fibril length  $\approx 70$   $\mu\text{m}$ ) with nanofibril arrays at their tips were obtained after removal of the solvent by heating and selective etching of the AA membranes (Fig. 10C and 10D).<sup>[37]</sup> The nanofibril has a lateral dimension of approximately 60 nm with length-to-diameter aspect ratios as high as 100:1.

### Two-Step Embossing

By performing two sequential embossing steps, hierarchical patterns with micrometric fibers decorated with nanosized fibers of various sizes and spacings were obtained (Fig. 10E and 10F).<sup>[21]</sup> A PMMA film was patterned with microfibers using a PDMS stamp. Subsequently, nanofibers were patterned on the top of the preformed microfibers using a hard polyurethane acrylate (PUA) mold. The PUA mold replaces the PDMS mold for sub-100 nm lithography since high-aspect ratio sub-100 nm features in a PDMS mold do not retain dimensional stability due to the low Young's modulus of PDMS. The resulting micro/nanoscale combined structures were robust and demonstrated enhanced water-repellent properties as a consequence of the hierarchical arrangement.

### 3D STRUCTURED ADHESIVE SURFACES

The 3D geometry of the tip seems to be crucial for the adhesion performance of the fibrillar surface. Spherical, conical, filament-like, band-like, sucker-like, spatula-like, flat, and toroidal tip shapes have been observed in different animals.<sup>[38]</sup> The role of the contact geometry has been analyzed in artificial

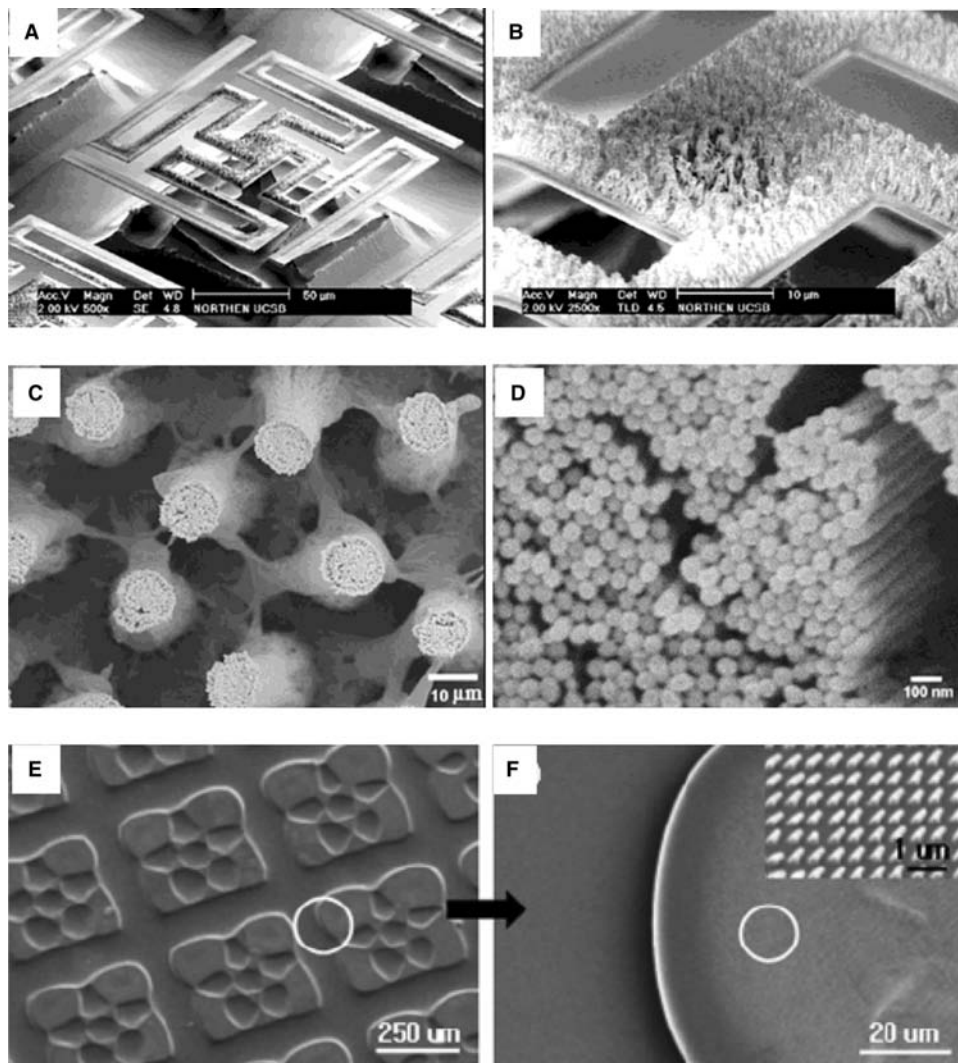


**Fig. 10** (A) Multiscale microfabricated structures consisting of single crystal silicon pillars supporting a silicon dioxide platform and coated by nanometer-sized polymer fibers (B). (C) Hierarchical microfibril array fabricated by filling porous AA. Microfibers are  $10\ \mu\text{m}$  wide and  $70\ \mu\text{m}$  long, and each branches into nanofibrils about  $60\ \text{nm}$  wide and  $0.5\ \mu\text{m}$  long (D). (E) and (F) Hierarchical PMMA pattern fabricated by superposition of two embossing steps. *Source:* Reprinted from Ref.<sup>[36]</sup>. Reprinted with permission from Ref.<sup>[37]</sup>. Reprinted with permission from Ref.<sup>[21]</sup>.

model systems.<sup>[39]</sup> Using a modification of the soft-molding method, arrays of PDMS fibers with spherical and spatula-like tips have been reported.<sup>[39–41]</sup> Figure 11 shows the fabrication methods. Arrays of pillars with spherical and spatular tips were obtained by inking PDMS fibrillar surfaces (Fig. 11A) in a thin film of PDMS precursor. A small drop of precursor remained on the top of the pillars. Curing of the array in upside-down orientation yielded hemispherical tips as a consequence of gravity and surface tension acting on the fluid drop (Fig. 11B). Alternatively, the inked stamp can be pressed against a flat substrate and then cured. This renders pillars with a flexible and flat roof with a diameter that depends on the thickness of the spin-coated film. The roofs can be symmetric or asymmetric depending on the tilt

of the substrate during curing (Fig. 11C and 11D). Other authors have used this method to obtain a continuous thin film of PDMS on the top of a fibrillar surface, which also seems to be advantageous for adhesion purposes.<sup>[42]</sup>

Spatula-like fibers have also been fabricated by filling prefabricated 3D masters with the negative profile with Teflon, followed by etching the master away.<sup>[43]</sup>

## SWITCHABLE ADHESIVE SURFACES MADE OF RESPONSIVE MATERIALS

Patterning technologies can be combined with responsive polymer materials to create microstructured surfaces with switchable adherence. Application of an

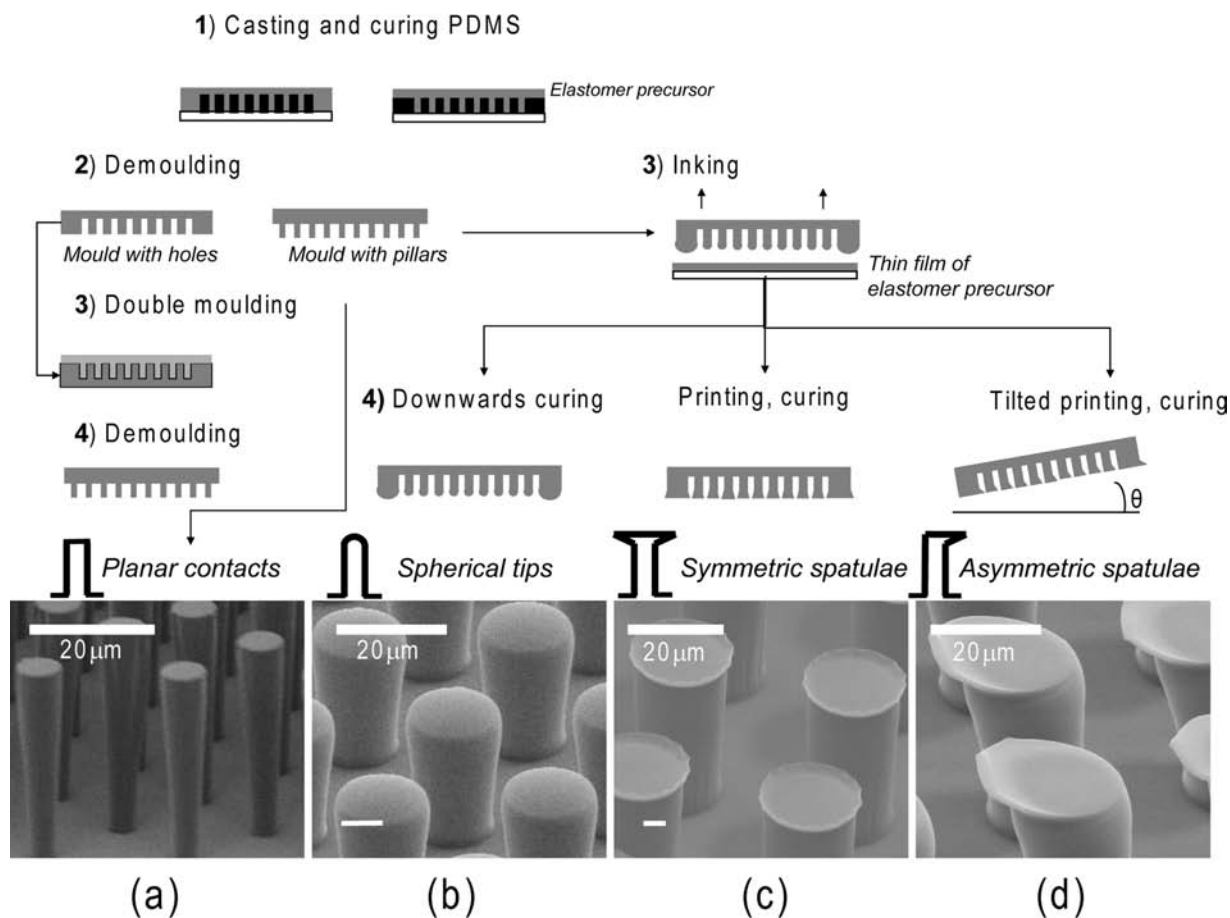


Fig. 11 3D structuring methods.<sup>[40]</sup>

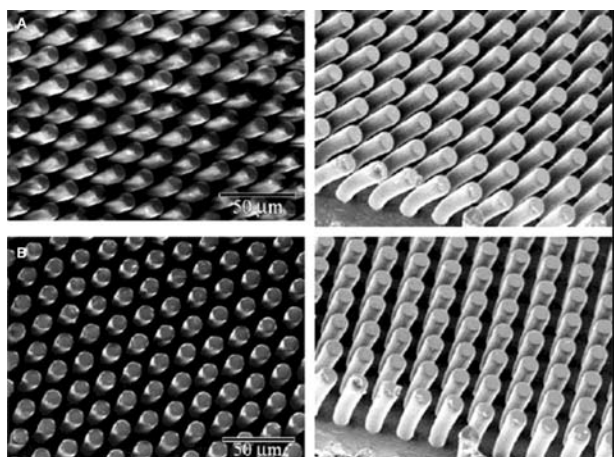


Fig. 12 SEM images of pillars made by soft molding a shape memory polymer with a masters with holes of radius of  $10\ \mu\text{m}$ , height of  $100\ \mu\text{m}$ , and  $20\ \mu\text{m}$  interpillar spacing.<sup>[44]</sup> (A) Top and side views of tilted pillars after deformation above the shape memory transition temperature and fixation in the deformed state by cooling (non-adhesive state). (B) Top and side views of recovered pillars after reheating the sample above the transition temperature (adhesive state).

external field (e.g. temperature) causes changes in the topographical design and this influences the final adhesion performance. A shape memory polymer was selected for this purpose. Arrays of microfibers with diameters between  $0.5$  and  $50\ \mu\text{m}$  and heights between  $10$  and  $100\ \mu\text{m}$  were patterned by soft molding in the molten state.<sup>[44]</sup> Mechanical deformation of this topography at the shape-memory transition temperature, followed by cooling to room temperature in the deformed position yielded a temporary non-adhesive surface consisting of pillars in a tilted position (Fig. 12A). By reheating above the transition temperature, the patterned surface switches from the temporary non-adhesive state to a permanent adhesive surface with at least a 200-fold increase in adherence (Fig. 12B).

## CONCLUSIONS

Fibrillar adhesive surfaces with increasing complexity have been generated by different micro and nanofabrication methods. The achieved geometries still represent

a coarse simplification of natural systems and this may limit their adhesion performance. Combination of different techniques is required if the geometrical design spans over three dimensions and in different length scales (from mm to nm). Material parameters like the viscosity during embossing, or the mechanical stability of the fibers after processing, also limit the fabrication procedure. Large-scale manufacture has not yet been demonstrated with any of the reported technologies.

## REFERENCES

- Hiller, U. Untersuchungen zum feinaufbau und zur funktion der haftborsten in reptilien. *Zeitschrift für morphologie der Tiere* **1968**, *62*, 307–362.
- Gorb, S.; Scherge, M. Biological microtribology: anisotropy in frictional forces of orthopteran attachment pads reflects the ultrastructure of a highly deformable material. *Proc. Roy. Soc. Lond. B Biol.* **2000**, *267* (1449), 1239–1244.
- Gorb, S.; Gorb, E.; Kastner, V. Scale effects on the attachment pads and friction forces in syrphid flies. *J. Exp. Biol.* **2001**, *204* (8), 1421–1431.
- Gorb, S.N.; Beutel, R.G.; Gorb, E.V.; Jiao, Y.K.; Kastner, V.; Niederegger, S.; Popov, V.L.; Scherge, M.; Schwarz, U.; Votsch, W. Structural design and biomechanics of friction-based releasable attachment devices in insects. *Integr. Comp. Biol.* **2002**, *42* (6), 1127–1139.
- Autumn, K. How gecko toes stick. *Am. Sci.* **2006**, *94*, 124–132.
- Autumn, K.; Peattie, A.M. Mechanisms of adhesion in geckos. *Integr. Comp. Biol.* **2002**, *42* (6), 1081–1090.
- Arzt, E.; Gorb, S.; Spolenak, R. From micro to nano contacts in biological attachment devices. *Proc. Natl. Acad. Sci. USA* **2003**, *100* (19), 10,603–10,606.
- Gates, B.D.; Xu, Q.B.; Stewart, M.; Ryan, D.; Willson, C.G.; Whitesides, G.M. New approaches to nanofabrication: molding, printing, and other techniques. *Chem. Rev.* **2005**, *105* (4), 1171–1196.
- Geissler, M.; Xia, Y.N. Patterning: principles and some new developments. *Adv. Mater.* **2004**, *16* (15), 1249–1269.
- del Campo, A.; Arzt, E. Fabrication approaches for generating complex micro and nanopatterns on polymeric surfaces. *Chem. Rev.* *in press*.
- Xia, Y.N.; Whitesides, G.M. *Soft lithography*. *Angew. Chem. Int. Edit.* **1998**, *37* (5), 551–575.
- Crosby, A.J.; Hageman, M.; Duncan, A. Controlling polymer adhesion with “pancakes”. *Langmuir* **2005**, *21* (25), 11,738–11,743.
- Glassmaker, N.J.; Jagota, A.; Hui, C.Y.; Kim, J. Design of biomimetic fibrillar interfaces: I. Making contact. *J. Roy. Soc. Interface* **2004**, *1* (1), 23–33.
- Greiner, C.; del Campo, A.; Arzt, E. Adhesion of bio-inspired micropatterned surfaces: effects of pillar radius, aspect ratio and preload. *Langmuir* **2007**, *23* (7), 3495–3502.
- Lamblot, M.; Verneuil, E.; Vilmin, T.; Buguin, A.; Solberzan, P.; Léger, L. Adhesion enhancement through micropatterning at polydimethylsiloxane-acrylic adhesive interfaces. *Langmuir* **2007**, *23*, 6966–6974.
- Sitti, M.; Fearing, R.S. Synthetic gecko foot-hair micro/nano-structures as dry adhesives. *J. Adh. Sci. Technol.* **2003**, *17* (8), 1055–1073.
- Peressadko, A.; Gorb, S.N. When less is more: experimental evidence for tenacity enhancement by division of contact area. *J. Adhesion* **2004**, *80* (4), 247–261.
- del Campo, A.; Greiner, A. SU-8: A photoresist for high-aspect-ratio and 3D submicron lithography. *J. Micromech. Microeng.* **2007**, *17* (R81–R95).
- Aksak, B.; Murphy, M.P.; Sitti, M. Adhesion of biologically inspired vertical and angled polymer microfiber arrays. *Langmuir* **2007**, *23*, 3322–3332.
- Federle, W. Why are so many adhesive pads hairy? *J. Exp. Biol.* **2006**, *209*, 2611–2621.
- Jeong, H.E.; Lee, S.H.; Kim, J.K.; Suh, K.Y. Nanoengineered multiscale hierarchical structures with tailored wetting properties. *Langmuir* **2006**, *22* (4), 1640–1645.
- Yoon, E.S.; Singh, R.A.; Kong, H.; Kim, B.; Kim, D.H.; Jeong, H.E.; Suh, K.Y. Tribological properties of biomimetic nano-patterned polymeric surfaces on silicon wafer. *Tribol. Lett.* **2006**, *21* (1), 31–37.
- Majidi, C.; Groff, R.E.; Fearing, R. Clumping and packing of hair arrays manufactured by nanocasting. Presented at IEEE-NANO, San Francisco, 2003.
- Jin, M.; Feng, X.; Feng, L.; Sun, T.; Zhai, J.; Li, T.; Jiang, L. Superhydrophobic aligned polystyrene nanotube films with high adhesive force. *Adv. Mater.* **2005**, *17* (16), 1977–1981.
- Jin, M.H.; Feng, X.J.; Feng, L.; Sun, T.L.; Zhai, J.; Li, T.J.; Jiang, L. Superhydrophobic aligned polystyrene nanotube films with high adhesive force. *Adv. Mater.* **2005**, *17* (16), 1977–1981.
- Kim, D.S.; Lee, H.S.; Lee, J.; Kim, S.; Lee, K.H.; Moon, W.; Kwon, T.H. Replication of high-aspect-ratio nanopillar array for biomimetic gecko foot-hair prototype by UV nano embossing with anodic aluminium oxide mold. *Microsyst. Technol.* **2007**, *13* (5), 601–606.
- Geim, A.K.; Dubonos, S.V.; Grigorieva, I.V.; Novoselov, K.S.; Zhukov, A.A.; Shapoval, S.Y. Microfabricated adhesive mimicking gecko foot-hair. *Nat. Mater.* **2003**, *2* (7), 461–463.
- Qu, L.; Dai, L. Gecko-foot-mimetic aligned single-walled carbon nanotube dry adhesives with unique electrical and thermal properties. *Adv. Mater.* **2007**, *19*, 3844–3849.
- Yurdumakan, B.; Ravavikar, N.R.; Ajayan, P.M.; Dhinojwala, A. Synthetic gecko foot-hairs from multi-walled carbon nanotubes. *Chem. Commun.* **2005**, (30), 3799–3801.
- Ge, L.; Sethi, S.; Ci, L.; Ajayan, P.M.; Dhinojwala, A. Carbon nanotube-based synthetic gecko tapes. *Proc. Natl. Acad. Sci. USA* **2007**, *104* (26), 10,792–10,795.
- Zhao, Y.; Tong, T.; Delzeit, L.; Kashani, A.; Meyyappan, M.; Majumdar, A. Interfacial energy and strength of multiwalled-carbon-nanotube-based dry adhesive. *J. Vac. Sci. Technol. B* **2006**, *24* (1), 331–335.



32. La Spina, G.; Stefanini, C.; Menciassi, A.; Dario, P. A novel technological process for fabricating micro-tips for biomimetic adhesion. *J. Micromech. Microeng.* **2005**, *15* (8), 1576–1587.
33. Harfenist, S.A.; Cambron, S.D.; Nelson, E.W.; Berry, S.M.; Isham, A.W.; Crain, M.M.; Walsh, K.M.; Keynton, R.S.; Cohn, R.W. Direct drawing of suspended filamentary micro- and nanostructures from liquid polymers. *Nano Lett.* **2004**, *4* (10), 1931–1937.
34. Jeong, H.E.; Lee, S.H.; Kim, P.; Suh, K.Y. Stretched polymer nanohairs by nanodrawing. *Nano Lett.* **2006**, *6* (7), 1508–1513.
35. Northen, M.T.; Turner, K.L. A batch fabricated biomimetic dry adhesive. *Nanotechnology* **2005**, *16*, 1159–1166.
36. Northen, M.T.; Turner, K.L. Meso-scale adhesion testing of integrated micro-and nano-scale structures. *Sensor Actuator A-Phys.* **2006**, *130–131*, 583–587.
37. Kustandi, T.S.; Samper, V.D.; Ng, W.S.; Chong, A.S.; Gao, H. Fabrication of a gecko-like hierarchical fibril array using a bonded porous alumina template. *J. Micromech. Microeng.* **2007**, *17*, N75–N81.
38. Spolenak, R.; Gorb, S.; Gao, H.J.; Arzt, E. Effects of contact shape on the scaling of biological attachments. *Proc. Roy. Soc. Lond. A Mater.* **2005**, *461* (2054), 305–319.
39. del Campo, A.; Greiner, C.; Arzt, E. Contact shape controls adhesion of bioinspired fibrillar surfaces. *Langmuir* **2007**, *23* (20), 10,235–10,243.
40. del Campo, A.; Greiner, C.; Álvarez, I.; Arzt, E. Patterned surfaces with pillars with controlled and 3D tip geometry mimicking bioattachment devices. *Adv. Mater.* **2007**, *19*, 1973–1977.
41. del Campo, A.; Álvarez, I.; Filipe, S.; Wilhelm, M. 3D microstructured surfaces obtained by soft-lithography using fast-crosslinking elastomeric precursors and 2D masters. *Adv. Funct. Mater.* **2007**, *17* (17), 3590–3597.
42. Glassmaker, N.J.; Jagota, A.; Hui, C.Y.; Noderer, W.L.; Chaudhury, M.K. Biologically inspired crack trapping for enhanced adhesion. *Proc. Natl. Acad. Sci. USA* **2007**, *104* (26), 10,786–10,791.
43. Kim, S.; Sitti, M. Biologically inspired polymer microfibers with spatulate tips as repeatable fibrillar adhesives. *Appl. Phys. Lett.* **2006**, *89*, 261911.
44. Reddy, S.; Arzt, E.; Del Campo, A. Bioinspired surfaces with switchable adhesion. *Adv. Mater.* **2007**, *19*, 3833–3837.

# Gene Delivery via Polymer Nanoparticles

Jie Wen

Kam W. Leong

*Department of Biomedical Engineering, Johns Hopkins University School of Medicine, Baltimore, Maryland, U.S.A.*

## INTRODUCTION

Gene therapy, a therapeutic modality designed to introduce an extraneous gene into the patient's cells to produce a specific protein, potentially can treat a variety of inherited and acquired diseases. Gene medicines are composed of a gene expression vector that encodes a therapeutic protein and a gene delivery system that delivers the gene to the desired tissue and subcellular compartments. The specific and efficient delivery of DNA to the diseased sites and to the nuclei of particular cell populations is the key for successful gene therapy. Gene delivery system plays a central role in fulfilling this mission.

## OVERVIEW

Traditionally, DNA delivery systems fall into two categories, viral-mediated and non-viral-mediated. In addition, naked DNA can be directly injected into the target tissue to produce the transgenes. Viral vectors such as retrovirus, adenovirus, adeno-associated virus, lentil virus, and herpes-simplex virus are usually much more efficient than non-viral vectors in both gene delivery and expression because of their highly evolved and specialized mechanisms in infecting cells. However, viral vectors have inherent disadvantages such as immunogenicity, restricted targeting of specific cell types, size limit of the DNA packaged into a virus, and scale-up difficulties.<sup>[1]</sup> The safety issue takes on new significance in light of the tragic event in recent clinical trial.<sup>[2]</sup> Consequently, non-viral delivery systems have been increasingly proposed as alternatives to viral systems. However, non-viral systems are inefficient and produce only transient transgene expression.

Nonviral gene delivery systems rely on condensing DNA to a compact size that can be internalized by cell and protecting the DNA from enzymatic degradation until the DNA reaches the nucleus. However, this tight binding and protection must be balanced by the ability of the gene carrier to release the DNA. The non-viral gene carriers include cationic liposomes, cationic

polymers, and neutral polymers. They are able to condense DNA to nanoparticles with a size of 20–500 nm in diameter for cellular internalization. The term nanoparticle is used in this review to cover particulate carrier systems that are less than 1  $\mu\text{m}$  in size and normally below 500 nm, including liposomes and solid nanocapsules.

Most cationic liposome formulations are composed of a cationic lipid and a neutral helper lipid. The cationic lipid binds the DNA through electrostatic interaction to form a complex termed lipoplex, while the helper lipid helps to stabilize the liposome and improve the cytoplasmic delivery of DNA.<sup>[3]</sup> Cationic polymers are usually nitrogen-rich polymers and have been used in much the same way as cationic liposomes with the polymer interacting electrostatically with DNA to yield a transfection-competent complex, termed polyplex. Polyplex is generally more stable than lipoplex in a physiological environment. The neutral polymer system usually involves encapsulating DNA in nanoparticles using biodegradable polymers, such as PLA and PLGA, to obtain sustained release characteristics. Recently, an inorganic system based on calcium phosphate nanoparticle has also been reported for gene delivery.<sup>[4]</sup>

Although most non-viral gene carriers can efficiently condense and protect the DNA, delivering the intact DNA to the nucleus remains a major challenge in the field. Poor mechanistic understanding of the whole gene transfer process makes it difficult to develop an optimal delivery system with all the desirable features for gene delivery. This review focuses on the application of cationic polymer-based nanoparticles for gene delivery.

## NANOPARTICLE FORMATION

Because of large electrostatic repulsion, free or naked DNA remains in an expanded state. Free DNA is too large and too polar a molecule to cross cell membranes by passive diffusion. The condensation of DNA into compacted nanoparticles is essential for

the transport of DNA through the cell membrane, although recent studies suggest that naked DNA can be taken up by muscle cells via receptor-mediated endocytosis.<sup>[5]</sup> Multivalent cations such as polyamines, positively charged polymers, and peptides are known to be capable of condensing DNA via electrostatic interaction with the negatively charged phosphate groups of DNA. A valence of  $\geq 3$  is required for the multivalent cations to condense DNA because the Coulombic interactions should be stronger than the entropic interactions so the entropy loss can be overcome.<sup>[6]</sup> The condensed DNA nanoparticles appear as rods, toroids, or spheroids under electron microscope.<sup>[7]</sup>

In understanding the mechanism of DNA condensation, the most extensive work has been conducted using small cations, such as spermidine [ $\text{H}_2\text{N}(\text{CH}_2)_3\text{NH}(\text{CH}_2)_4\text{NH}_2$ ],<sup>[8]</sup> spermine [ $\text{H}_2\text{N}(\text{CH}_2)_3\text{NH}(\text{CH}_2)_4\text{NH}(\text{CH}_2)_3\text{NH}_2$ ],<sup>[9]</sup> and cobalt hexamine [ $\text{Co}(\text{NH}_3)_6^{3+}$ ].<sup>[10]</sup> A variety of techniques, such as microscopy, light scattering, fluorescence, and calorimetry, have been used. Two models, the spool model and the constant loop model, have been proposed to explain how the DNA is compacted within the toroid.<sup>[9,11]</sup> The cations instigate localized bending or distortion of DNA at a critical extent of charge neutralization, which facilitates the formation of rods and toroid-like structures.<sup>[12,13]</sup> The cations can also induce DNA condensation by rendering the DNA-solvent interactions less favorable.<sup>[14,15]</sup> Formation of a highly ordered liquid crystalline phase of DNA is believed to be involved in DNA condensation.<sup>[16]</sup>

Many factors affect the formation of DNA nanoparticles, such as chemical structure of cations, ionic strength of the medium, and molar ratio of the

polycation and DNA. The study on the structural arrangement of DNA condensed by polyamine homologues indicates that the number of positive charges and the charge density of polyamine molecules affect the size of DNA nanoparticles as well as the ability to induce the formation of liquid crystalline phase of DNA.<sup>[17,18]</sup> In high ionic strength solution, DNA nanoparticles may aggregate because the salt overcomes the repulsive interaction between particles. Excess positive charge on the surface can prevent the nanoparticles from aggregating under the salt condition. The surface charge of the nanoparticles is characterized by  $\zeta$ -potential and can be adjusted by changing the reactant ratio of DNA to polycations.

A better understanding of the relationship between the physicochemical properties of the DNA nanoparticles, their ability to be taken up by cells, and the chemical structure of agents that cause the condensation of DNA is needed for the development of non-viral gene delivery vehicles.

## DELIVERY OBSTACLES FOR NON-VIRAL SYSTEMS

Ultimately, DNA has to be delivered to the nucleus for successful gene expression, after overcoming a number of obstacles on the way (Fig. 1). These delivery obstacles are both extracellular as well as intracellular. The biodistribution of nanoparticles in the extracellular space is determined by their interaction with the physiological environment, based on their physicochemical and biological properties, such as size, electrical charge, hydrophilicity-hydrophobicity, and possible ligand conjugation.

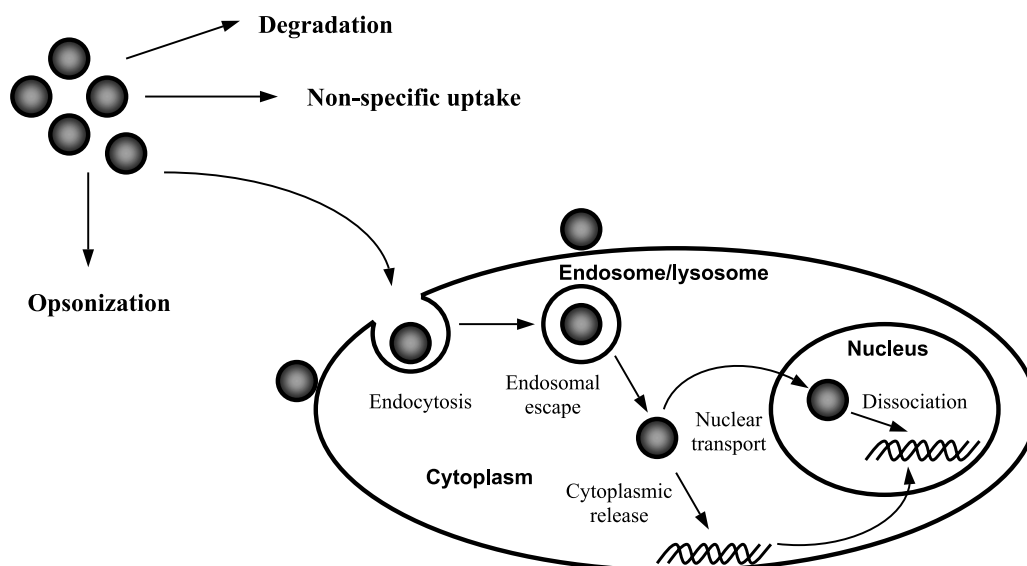


Fig. 1 Obstacles of nonviral gene delivery.

Of all the properties, particle size is of crucial importance in determining the biodistribution.<sup>[19]</sup> Any particle aggregation during the gene delivery is detrimental for DNA to get to the final site, the nucleus. In fact, negatively charged proteins such as albumin tend to bind with the positively charged nanoparticles, leading to a size increase of the particles and a reduced positive charge on the particle surface, which may diminish the affinity of the nanoparticles to the negatively charged cell surface. Therefore the nanoparticles must first be stable in the extracellular fluid so that they can be delivered to the target tissue or cells. It should be noted that the immune cells might recognize the particles as foreign materials and phagocytose them, which may be attractive for genetic vaccination but may not be desirable for other gene therapy applications.

Once the nanoparticles reach the target cells, they bind with the negatively charged cell membrane and are subsequently taken up by endocytosis. The rate of entry into the cells varies with cell type and is relatively slow.<sup>[20]</sup> In order to achieve cell-specific gene transfer, cell-specific targeting ligands such as monoclonal antibodies, peptides, and sugars can be conjugated to the gene carriers to promote receptor-mediated endocytosis. After the non-specific or receptor-mediated endocytosis, most DNA complexes are internalized into the endosomes/lysosomes and are eventually degraded. Cytoplasmic release of the DNA complex is the first barrier in the intracellular transport. Efficient destabilization of the endosomes/lysosomes is believed to enhance gene expression. Some endosomolytic reagents such as chloroquine,<sup>[21]</sup> lipids,<sup>[22]</sup> and peptides<sup>[23]</sup> have been used to disrupt the endosome membrane, leading to an enhanced gene expression. The buffering capacity of amine-containing polymers has also proved to reduce the acidification of the endosome, triggering endosome swelling and rupture or collapse.<sup>[24]</sup> Some anionic lipids in the endosome may compete with the DNA and dissociate the DNA complexes, leading to the release of the DNA into the cytoplasm.<sup>[25]</sup>

Cytosol is not a friendly environment for DNA because of the presence of nuclease. Microinjected plasmid DNA is rapidly degraded in the cytoplasm with an apparent half-life of 50–90 min.<sup>[26]</sup> The translocation of released or “unpacked” DNA from cytosol to nucleus is probably through diffusion, a relatively slow process compared to cytoplasmic degradation. It is understandable that the DNA would be more stable in cytosol if it were still complexed with cationic carrier. However, only certain synthetic polymers, such as polyethylenimine (PEI), can show protection of DNA in the cytoplasm and also promote nuclear transport. The pathway of the transport of DNA complexes from cytoplasm to nucleus is not well understood. Some hypothesis leans toward the involvement of

anionic phospholipids. The inclusion of viral nuclear localization signals (NLS) has been demonstrated to be an efficient strategy to facilitate nuclear transport.<sup>[27,28]</sup> Typically comprising several positively charged lysines and arginines, a NLS is a peptide signal sequence that directs a protein from the cytosol into the nucleus.

As stated above, eventually the DNA has to be released from the complexes to allow transcription. The dissociation of complexes may occur either in the endosome, cytosol, or nucleus. Other than enzymatic degradation of the gene carrier, anionic membrane components and other intracellular substances may also be responsible for the dissociation by carrier substitution.

## POLYMERIC GENE CARRIERS

The poor transfer efficiency and transient gene expression of polymer–DNA complexes continue to stimulate the development of more effective and less-toxic polymeric gene carriers. A number of polycations have been tested to transfer genes *in vitro* or *in vivo*, including poly-L-lysine (PLL) (Fig. 2A), PEI (Fig. 2B), polyamidoamine (PAMAM) dendrimers (Fig. 2C), poly( $\alpha$ -(4-aminobutyl)-L-glycolic acid) (PAGA) (Fig. 2D), poly((2-dimethylamino)ethyl methacrylate) (PDMAEMA) (Fig. 2E), chitosan (Fig. 2F), etc. Our group has been interested in investigating polyphosphoester as a new polycationic gene carrier (Fig. 2G).

### Poly-L-Lysine

Poly-L-lysine has been widely used in the early days as a gene delivery carrier because of its excellent DNA condensation ability and efficient protection of DNA from nuclease digestion. However, its cytotoxicity and low transfection problems remain to be solved. Moreover, PLL–DNA complexes tend to aggregate under physiological conditions. Efforts have focused on improving the solubility of PLL by the introduction of hydrophilic groups, such as dextran<sup>[29]</sup> and PEG.<sup>[30,31]</sup> Both PEG-g-PLL and PEG-b-PLL have shown lower cytotoxicity and enhanced transfection efficiency than PLL. A polymeric micelle, PLGA-g-PLL has also been proposed as an effective carrier for gene delivery.<sup>[32]</sup>

### Polyethylenimine

Polyethylenimine–DNA complex is one of the most potent synthetic gene transfer vectors. They can also transfect a wide variety of cells. The high transfection efficiency of PEI has been postulated to relate to its buffering capacity, which leads to the accumulation



cell membranes. Moreover, PEI is not degradable and high molecular weight PEI may accumulate in the body. Several approaches have been explored to reduce the cytotoxicity, such as PEGylation<sup>[34]</sup> and conjugation of low molecular weight PEI with cleavable cross-links such as disulfide bonds, which can be cleaved in the reducing environment of the cytoplasm.<sup>[35]</sup>

### Polyamidoamine Dendrimers

Starburst polyamidoamine dendrimers with either ammonia or ethylenediamine as core molecules have been used for gene delivery. These molecules are highly defined in terms of molecular weight and geometry. They are spherical polymers, with primary amine groups on the surface, which can be used to condense DNA. Dendrimers can transfect a wide variety of cells in culture,<sup>[36]</sup> with an efficiency matching that of PEI under optimal conditions. The higher generation dendrimers (G6 and G7) are effective at disrupting anionic vesicle membranes, which may explain the high transfection efficiency.<sup>[37]</sup> The advantage of these dendrimers over PEI remains to be established.

### Poly( $\alpha$ -(4-aminobutyl)-L-glycolic acid)

Poly( $\alpha$ -(4-aminobutyl)-L-glycolic acid) is an analogue of PLL with a degradable ester linkage in the main chain.<sup>[38]</sup> Poly( $\alpha$ -(4-aminobutyl)-L-glycolic acid) efficiently condenses and protects DNA and shows enhanced transfection efficiency in culture compared to other PLL-based systems. It is also less cytotoxic than Lipofectamine and SuperFect (a dendrimers). Although PAGA generates positive results in producing cytokines as an immunoadjuvant in a murine cancer model, its biodegradation rate of the polymer may be too rapid for some in vivo gene transfer applications.<sup>[39]</sup>

### Poly((2-Dimethylamino)Ethyl Methacrylate)

Poly((2-dimethylamino)ethyl methacrylate) is a water-soluble cationic polymer capable of binding plasmid DNA and transfecting different cell types.<sup>[40]</sup> The complexes with a slightly positive  $\zeta$ -potential (25–30 mV) and a size around 200 nm possess the highest transfection efficiency.<sup>[41]</sup> Study on the structure–activity relationship of a number of water-soluble cationic methacrylate/methacrylamide polymers with structures closely related to PDMAEMA shows that among these polymers, PDMAEMA has the highest transfection efficiency and cytotoxicity.<sup>[42]</sup> The high transfection efficiency of PDMAEMA is probably due to its high buffering capacity to destabilize endosome, combined with its ability to release the DNA in the cytosol

and/or the nucleus. Its strength and shortcomings are similar to those of PEI.

### Chitosan

Chitosan, a biodegradable polysaccharide composed of D-glucosamine repeating units, has been explored by several research groups as a non-viral gene carrier.<sup>[43–45]</sup> Chitosan can efficiently bind DNA and protect DNA from nuclease degradation. Moreover, chitosan has good biocompatibility and toxicity profile, rendering it a safe biomedical material for clinical applications. Chitosan–DNA nanoparticles can transfect several different cell types. However, the transfection efficiency is relatively poor. Chitosan can be readily modified. For example, trimethylated chitosan can be prepared with different quarternization degree to increase the solubility of chitosan at neutral pH,<sup>[46]</sup> or chitosan can be conjugated with deoxycholic acid to become a colloidal gene carrier.<sup>[47]</sup> Both quaternarized chitosan and deoxylic acid-modified chitosan can efficiently transfect COS-1 cells. Chitosans with different molecular weights have different DNA binding affinities and exhibit different transfection efficiencies, indicating that particle stability may be one of the rate-limiting steps in the overall transfection process.<sup>[43]</sup> The effect of degree of deacetylation on the stability of chitosan–DNA nanoparticles is being investigated.<sup>[48]</sup>

### Polyphosphoester

We have been working on polyphosphoesters (PPE) for more than 15 years, particularly the ones with a backbone analogous to nucleic acids and teichoic acids. They show promise in different biomedical applications because of their biocompatibility, biodegradability, and pendent chain functionality. Several polyphosphoesters with positive charges either in the backbone or in the side chain were synthesized and evaluated as non-viral gene carriers.<sup>[49–51]</sup> These polyphosphoesters can efficiently bind DNA and protect DNA from nuclease degradation. Efficient transfection was found in a number of cell lines, with some of them comparable to Lipofectamine. The transfection is cell-type dependant and can be improved with the incorporation of chloroquine. All the polyphosphoesters exhibit a significantly lower cytotoxicity than PLL or PEI in vitro and in vivo. With the structural versatility, polyphosphoester can be designed to have different hydrophilicity–hydrophobicity properties. One interesting feature is that the PPE can provide extracellular sustained release of the DNA, leading to prolonged and enhanced transgene expression in the muscle compared to naked DNA administration.<sup>[50]</sup> An amphiphilic polyphosphoester,



poly{[(cholesteryl oxocarbonylamido ethyl) methyl bis(ethylene) ammonium iodide] ethyl phosphate} (PCEP), was synthesized and investigated for gene delivery.<sup>[51]</sup> Carrying a positive charge in its backbone and a lipophilic cholesterol structure in the side chain, PCEP self-assembles into micelles in aqueous solution at room temperature with an average size of 60–100 nm. This is one of the few polymeric lipids for gene delivery that are biodegradable.

## TARGETING

Drug targeting can be achieved with different levels of sophistication: first-, second-, and third-order targeting. First-order targeting can be defined as the delivery of a drug to a particular organ; second-order targeting is where the drug is internalized in a specific cell type; and third-order targeting is where the drug is localized in a specific cellular compartment.<sup>[52]</sup> Gene delivery is indeed a third-order targeting challenge with nucleus as the targeting site.

The use of polymeric nanoparticles for targeted drug and gene delivery system has gained increasing attention and importance.<sup>[53]</sup> Targeting can be achieved either by passive route, where the particles are captured by a physiological uptake mechanism such as filtration or macrophage sequestration, or by active route, where the particles are recognized by the host molecule through the targeting moiety conjugated on the surface of the particles.

### Passive Targeting

Normally, after the nanoparticles are injected into the blood stream, they are rapidly coated by circulation elements, such as plasma proteins and glycoproteins. This process renders the particles easily recognized by the major defense system of the body, the reticuloendothelial system. The macrophage (Kupffer) cells of the liver play a critical role in removing these coated foreign particles.<sup>[54]</sup> Thus Kupffer cells specificity can be achieved by passive targeting. Particles with a more hydrophobic surface, which can be efficiently coated with plasma elements, are more desirable for this targeting. This strategy can be used to achieve gene delivery to the blood circulation.

The lymph nodes are of great interest because of their vital role in the staging of anticancer and anti-infection immune responses.<sup>[52]</sup> A subcutaneous administration of nanoparticles can be an efficient way of reaching local draining lymph nodes. Particle size and surface property are two decisive parameters for such targeting. Generally, particles with a size less than 100 nm are preferable for such targeting. The

particles with intermediate hydrophilicity–hydrophobicity in nature appear to have the most lymph node accumulation. This type targeting is particularly useful for DNA vaccination applications.

### Active Targeting

To increase the specificity of DNA uptake by target cells, transferrin,<sup>[55]</sup> monoclonal antibodies,<sup>[56]</sup> mannose,<sup>[57]</sup> galactose,<sup>[58]</sup> lactose,<sup>[59]</sup> folic acid,<sup>[60]</sup> low-density lipoproteins,<sup>[61]</sup> and RGD peptides<sup>[62]</sup> have been conjugated to the polymer backbone to achieve receptor-mediated endocytosis. Poly-L-lysine and PEI are popular candidates for the conjugation because of the readily available primary amine groups. After endocytosis, the DNA nanoparticles are internalized in the vesicles within the cells. Two strategies are used to help cytoplasmic release of DNA. One is to use fusogenic peptides derived from fusion-active virus to destabilize the endosomal membrane. Another approach is to use a carrier with a high buffering capacity to promote the escape of the complexes into the cytosol, with mechanisms discussed above. The next target is then the nucleus. The cut-off size of nuclear pores is 9–10 nm, which allows proteins up to 60 kDa and nucleotides up to 300 bp to enter freely.<sup>[63]</sup> However, larger molecules can still get through the nuclear pores via an active process, which can be modulated by NLS. Enhanced gene transfection efficiency has been achieved by the conjugation of NLS peptide to the gene carriers such as PLL<sup>[64]</sup> and PDMAEMA,<sup>[65]</sup> or plasmid itself.<sup>[66]</sup> If the NLS peptide is conjugated to the gene carrier, the DNA has to stay complexed before nuclear translocation takes place. It has been reported that the number of NLS peptides conjugated to DNA plays an important role in the nuclear transport. Too many NLS peptides may actually inhibit nuclear translocation.<sup>[67]</sup>

## IN VIVO APPLICATION

Targeted delivery is the ultimate goal of gene therapy. Local administration so far presents a more feasible approach as systemic barriers are bypassed. Significant gene expression has been found in a variety of tissues/organs, such as muscle, lung, liver, brain, tumor, and gastrointestinal (GI) tract using polymeric gene carriers.

### Muscle

Muscle has been of interest as a target for gene therapy since Wolff et al. demonstrated that intramuscularly injected naked plasmid DNA can be expressed in myofibers in 1990.<sup>[68]</sup> Naked DNA has poor bioavailability in muscle due to the degradation by extracellular nucleases and the rapid elimination from the muscle.

In order to protect DNA from degradation cationic agents are used to condense DNA. However, the use of condensed DNA particles to achieve higher transfection in muscle rather than naked DNA has not been successful. This is possibly because the connective tissue surrounding myofibers and muscle fasciculus could limit the diffusion of rigid condensed DNA particles through the muscle.<sup>[69]</sup> Recently, a sustained release system using PPE-EA as a carrier has been proved to enhance gene expression in mouse muscle compared to naked DNA.<sup>[50]</sup> Lower N/P ratios of 0.5 and 1 were used in the study. The intramuscular delivery of plasmid encoding antigens can induce antibody and cytotoxic T-lymphocyte (CTL) responses, which is desirable for DNA vaccination.

## Lung

Gene delivery to the lung has the potential to treat several life-threatening genetic diseases such as cystic fibrosis (CF) and  $\alpha_1$ -antitrypsin ( $\alpha_1$ AT) deficiency. Cystic fibrosis is the result of mutations in a single gene (CF transmembrane conductance regulator, CFTR), and the gene delivery target is the airway epithelial cell.  $\alpha_1$ AT is another lung disease resulting from a single gene mutation; however,  $\alpha_1$ AT is a secreted product that does not need to be expressed in lung epithelium. Pulmonary gene delivery can be achieved through different administration methods, such as lung instillation, aerosol delivery, and intravenous injection. The method of application greatly influences the extent of gene expression in the lung as well as the cell type that is transfected. Instillation usually leads to significant but inhomogeneous gene expression in epithelial cells lining the bronchioles and distal airways, while aerosol delivery enables a more uniform distribution of gene expression.<sup>[70,71]</sup> By intravenous injection, transfection is mainly restricted to pulmonary endothelium.<sup>[72]</sup> Cationic polymers such as PEI and PAMAM have been proposed for pulmonary gene therapy.<sup>[73,74]</sup> Several problems including avoidance of biological barriers, suppression of immune response, and increase of transfection efficiency and specificity need to be solved before successful pulmonary gene therapy becomes a reality.

## Tumor

Cancer gene therapy can take the form of the administration of a good copy of a mutated tumor suppressor gene, a gene encoding an enzyme that activates an anticancer prodrug, or a gene that encodes an antigen designed to generate a protective immune response.<sup>[75]</sup> There are two general methods for tumor treatment. One is the direct injection of DNA particles into

arterial blood vessels that supply the tumor. Another method is the direct injection of the particles into the tumor.<sup>[76]</sup> In this case, the mobility of the particles within the tissue is very important to the transfection efficiency and is affected by the particle size, charge, and concentration. Liposomal and naked DNA formulations are two intensively investigated intratumoral gene delivery systems. Polyethylenimine,<sup>[77]</sup> poly( $\alpha$ -(4-aminobutyl)-L-glycolic acid),<sup>[78]</sup> and poly-amidoamine<sup>[79]</sup> have been the polymeric gene carriers studied for cancer gene therapy.

## Liver

Gene delivery to the liver involves intravenous administration of DNA containing formulations, either into a systemic or the portal vein. The stability of DNA complexes in the blood and the dilution of DNA dose by the blood are two major challenges for this application. Interestingly, naked DNA has been found to transfect hepatocytes by intravenous delivery under some special circumstances. Hydrodynamic injection of a large volume of naked DNA solution via the tail vein in 5–8 sec can induce potent gene expression in internal organs, especially the liver.<sup>[5]</sup> Significant gene expression can also be achieved in the liver by transiently restricting blood flow through the liver immediately after peripheral intravenous injection of naked DNA.<sup>[80]</sup> The hypothesis is that naked DNA is taken up by hepatocytes through receptor-mediated pathway and pressure can increase cellular uptake. However, these methods are not practical in clinical application. Condensed systems, such as poly-L-lysine<sup>[81]</sup> and PEI,<sup>[82]</sup> have been reported to achieve transfection in the liver.

## Brain

Gene therapy of the brain is hindered by the presence of the blood–brain barrier (BBB), which only allows permeation of small lipophilic molecules. Exogenous genes have been expressed in the brain after invasive routes of administration, such as craniotomy<sup>[83]</sup> or intracarotid arterial infusion of noxious agents causing BBB disruption.<sup>[84]</sup> Taking advantage of receptor-mediated transport, a non-invasive gene delivery system using transferrin as receptor to cross the BBB has been described.<sup>[85]</sup> PEI has been shown to be a versatile and efficient vector in the mammalian brain.<sup>[86,87]</sup> As neurons are capable of taking up exogenous particulates from the muscles they innervate, a non-invasive strategy for gene delivery to the brain stem has been developed via peripheral intramuscular injection of PEI/DNA complexes. It is hypothesized that the complexes can reach the neuronal cell bodies in the

brain stem by retrograde axonal transport after being internalized by nerve terminals in the tongue muscle.<sup>[88]</sup>

## Gastrointestinal Tract

Oral gene delivery is by far the most attractive of administration. The efficiency of chitosan–DNA nanoparticles has been explored as an oral gene delivery system in a peanut allergy vaccine model.<sup>[44]</sup> The study demonstrates that transgene expression can be achieved in the small intestine of the mouse after oral administration of chitosan/DNA nanoparticles. Using pCMVArh2 plasmid encoding a dominant anaphylaxis-inducing antigen identified in mice sensitized with peanut, nanoparticle immunization elicits a relatively high IgG2a immune response and protects the animals from an allergic challenge.

## CONCLUSION

Successful non-viral gene therapy will rely on the development of efficient vectors that can overcome the multitude of delivery barriers, including targeted cellular uptake, cytoplasmic release, and nuclear transport. An ideal non-viral vector would be non-immunogenic, non-toxic, biodegradable, able to condense DNA into nanoparticles, and amenable to conjugation of ligands, endosomolytic agents, and NLS peptides. The DNA complex should possess stability before and after cellular uptake, but instability after nuclear transport. Although significant progress has been made in the development of DNA condensing agents, poor understanding of the relationship between the structure of gene carriers and transfection efficiency has rendered the design of non-viral gene delivery systems suboptimal. Systematic mechanistic studies to identify the rate-limiting steps in the non-viral gene transfer process will undoubtedly produce the next generation of efficient and safe non-viral vectors.

## REFERENCES

1. Lee, R.J.; Huang, L. Folate-targeted, anionic liposome-entrapped polylysine-condensed DNA for tumor cell-specific gene transfer. *J. Biol. Chem.* **1996**, *271*, 8481–8487.
2. Marshall, E. Gene therapy death prompts review of adenovirus vector. *Science* **1999**, *286*, 2244–2245.
3. Felgner, J.H.; Kumar, R.; Sridhar, C.N.; Wheeler, C.J.; Tsai, Y.J.; Border, R.; Ramsey, P.; Martin, M.; Felgner, P.L. Enhanced gene delivery and mechanism studies with a novel series of cationic lipid formulations. *J. Biol. Chem.* **1994**, *269*, 2550–2561.
4. Roy, I.; Mitra, S.; Maitra, A.; Mozumdar, S. Calcium phosphate nanoparticles as novel non-viral vectors for targeted gene delivery. *Int. J. Pharm.* **2003**, *250*, 25–33.
5. Budker, V.; Budker, T.; Zhang, G.; Subbotin, V.; Loomis, A.; Wolff, J.A. Hypothesis: Naked plasmid DNA is taken up by cells in vivo by a receptor-mediated process. *J. Gene Med.* **2000**, *2*, 76–88.
6. Bloomfield, V.A. DNA condensation. *Curr. Opin. Struct. Biol.* **1996**, *6*, 334–341.
7. Vijayanathan, V.; Thomas, T.; Thomas, T.J. DNA nanoparticles and development of DNA delivery vehicles for gene therapy. *Biochemistry* **2002**, *41*, 14085–14094.
8. Fang, Y.; Hoh, J.H. Early intermediates in spermidine-induced DNA condensation on the surface of mica. *J. Am. Chem. Soc.* **1998**, *120*, 8903–8909.
9. Bottcher, C.; Endisch, C.; Fuhrhop, J.H.; Catterall, C.; Eaton, M. High-yield preparation of oligomeric C-type DNA toroids and their characterization by cryoelectron microscopy. *J. Am. Chem. Soc.* **1998**, *120*, 12–17.
10. Widom, J.; Baldwin, R.L. Monomolecular condensation of lambda-DNA induced by cobalt hexamine. *Biopolymers* **1983**, *22*, 1595–1620.
11. Hud, N.V.; Downing, K.H.; Balhorn, R. A constant radius of curvature model for the organization of DNA in toroidal condensates. *Proc. Natl. Acad. Sci. U. S. A.* **1995**, *92*, 3581–3585.
12. Rouzina, I.; Bloomfield, V.A. DNA bending by small, mobile multivalent cations. *Biophys. J.* **1998**, *74*, 3152–3164.
13. Golan, R.; Pietrasanta, L.I.; Hsieh, W.; Hansma, H.G. DNA toroids: Stages in condensation. *Biochemistry* **1999**, *38*, 14069–14076.
14. Bloomfield, V.A. DNA condensation by multivalent cations. *Biopolymers* **1997**, *44*, 269–282.
15. Li, A.Z.; Marx, K.A. The iso-competition point for counterion competition binding to DNA: Calculated multivalent versus monovalent cation binding equivalence. *Biophys. J.* **1999**, *77*, 114–122.
16. Saminathan, M.; Thomas, T.; Shirahata, A.; Pillai, C.K.; Thomas, T.J. Polyamine structural effects on the induction and stabilization of liquid crystalline DNA: Potential applications to DNA packaging, gene therapy and polyamine therapeutics. *Nucleic Acids Res.* **2002**, *30*, 3722–3731.
17. Hud, N.V.; Downing, K.H. Cryoelectron microscopy of lambda phage DNA condensates in vitreous ice: The fine structure of DNA toroids. *Proc. Natl. Acad. Sci. U. S. A.* **2001**, *98*, 14925–14930.
18. Saminathan, M.; Antony, T.; Shirahata, A.; Sigal, L.H.; Thomas, T.; Thomas, T.J. Ionic and structural specificity effects of natural and synthetic polyamines on the aggregation and resolubilization of single-, double-, and triple-stranded DNA. *Biochemistry* **1999**, *38*, 3821–3830.
19. Nishikawa, M.; Huang, L. Nonviral vectors in the new millennium: Delivery barriers in gene transfer. *Hum. Gene Ther.* **2001**, *12*, 861–870.
20. Zabner, J.; Fasbender, A.J.; Moninger, T.; Poellinger, K.A.; Welsh, M.J. Cellular and molecular barriers to gene transfer by a cationic lipid. *J. Biol. Chem.* **1995**, *270*, 18997–19007.

21. Midoux, P.; Mendes, C.; Legrand, A.; Raimond, J.; Mayer, R.; Monsigny, M.; Roche, A.C. Specific gene transfer mediated by lactosylated poly-L-lysine into hepatoma cells. *Nucleic Acids Res.* **1993**, *21*, 871–878.
22. El Ouahabi, A.; Thiry, M.; Pector, V.; Fuks, R.; Ruyschaert, J.M.; Vandenbranden, M. The role of endosome destabilizing activity in the gene transfer process mediated by cationic lipids. *FEBS Lett.* **1997**, *414*, 187–192.
23. Sosnowski, B.A.; Gonzalez, A.M.; Chandler, L.A.; Buechler, Y.J.; Pierce, G.F.; Baird, A. Targeting DNA to cells with basic fibroblast growth factor (FGF2). *J. Biol. Chem.* **1996**, *271*, 33647–33653.
24. Bousif, O.; Lezoualc'h, F.; Zanta, M.A.; Mergny, M.D.; Scherman, D.; Demeneix, B.; Behr, J.P. A versatile vector for gene and oligonucleotide transfer into cells in culture and in vivo: Polyethylenimine. *Proc. Natl. Acad. Sci. U. S. A.* **1995**, *92*, 7297–7301.
25. Xu, Y.; Szoka, F.C., Jr. Mechanism of DNA release from cationic liposome/DNA complexes used in cell transfection. *Biochemistry* **1996**, *35*, 5616–5623.
26. Lechardeur, D.; Sohn, K.J.; Haardt, M.; Joshi, P.B.; Monck, M.; Graham, R.W.; Beatty, B.; Squire, J.; O'Brodovich, H.; Lukacs, G.L. Metabolic instability of plasmid DNA in the cytosol: A potential barrier to gene transfer. *Gene Ther.* **1999**, *6*, 482–497.
27. Branden, L.J.; Mohamed, A.J.; Smith, C.I. A peptide nucleic acid-nuclear localization signal fusion that mediates nuclear transport of DNA. *Nat. Biotechnol.* **1999**, *17*, 784–787.
28. Ziemienowicz, A.; Gorlich, D.; Lanka, E.; Hohn, B.; Rossi, L. Import of DNA into mammalian nuclei by proteins originating from a plant pathogenic bacterium. *Proc. Natl. Acad. Sci. U. S. A.* **1999**, *96*, 3729–3733.
29. Maruyama, A.; Watanabe, H.; Ferdous, A.; Katoh, M.; Ishihara, T.; Akaike, T. Characterization of interpolyelectrolyte complexes between double-stranded DNA and polylysine comb-type copolymers having hydrophilic side chains. *Bioconjug. Chem.* **1998**, *9*, 292–299.
30. Choi, Y.H.; Liu, F.; Kim, J.S.; Choi, Y.K.; Park, J.S.; Kim, S.W. Polyethylene glycol-grafted poly-L-lysine as polymeric gene carrier. *J. Control. Release* **1998**, *54*, 39–48.
31. Wolfert, M.A.; Schacht, E.H.; Toncheva, V.; Ulbrich, K.; Nazarova, O.; Seymour, L.W. Characterization of vectors for gene therapy formed by self-assembly of DNA with synthetic block co-polymers. *Hum. Gene Ther.* **1996**, *7*, 2123–2133.
32. Jeong, J.H.; Park, T.G. Poly(L-lysine)-g-poly(D-L-lactico-glycolic acid) micelles for low cytotoxic biodegradable gene delivery carriers. *J. Control. Release* **2002**, *82*, 159–166.
33. Wightman, L.; Kircheis, R.; Rossler, V.; Carotta, S.; Ruzicka, R.; Kurs, M.; Wagner, E. Different behavior of branched and linear polyethylenimine for gene delivery in vitro and in vivo. *J. Gene Med.* **2001**, *3*, 362–372.
34. Nguyen, H.K.; Lemieux, P.; Vinogradov, S.V.; Gebhart, C.L.; Guerin, N.; Paradis, G.; Bronich, T.K.; Alakhov, V.Y.; Kabanov, A.V. Evaluation of polyether-polyethyleneimine graft copolymers as gene transfer agents. *Gene Ther.* **2000**, *7*, 126–138.
35. Gosselin, M.A.; Guo, W.; Lee, R.J. Efficient gene transfer using reversibly cross-linked low molecular weight polyethylenimine. *Bioconjug. Chem.* **2001**, *12*, 989–994.
36. Kukowska-Latallo, J.F.; Bielinska, A.U.; Johnson, J.; Spindler, R.; Tomalia, D.A.; Baker, J.R., Jr. Efficient transfer of genetic material into mammalian cells using Starburst polyamidoamine dendrimers. *Proc. Natl. Acad. Sci. U. S. A.* **1996**, *93*, 4897–4902.
37. Zhang, Z.Y.; Smith, B.D. High-generation polycationic dendrimers are unusually effective at disrupting anionic vesicles: Membrane bending model. *Bioconjug. Chem.* **2000**, *11*, 805–814.
38. Lim, Y.B.; Han, S.O.; Kong, H.U.; Lee, Y.; Park, J.S.; Jeong, B.; Kim, S.W. Biodegradable polyester, poly-[alpha-(4-aminobutyl)-L-glycolic acid], as a non-toxic gene carrier. *Pharm. Res.* **2000**, *17*, 811–816.
39. Maheshwari, A.; Mahato, R.I.; McGregor, J.; Han, S.; Samlowski, W.E.; Park, J.S.; Kim, S.W. Soluble biodegradable polymer-based cytokine gene delivery for cancer treatment. *Mol. Ther.* **2000**, *2*, 121–130.
40. Cherng, J.Y.; van de Wetering, P.; Talsma, H.; Crommelin, D.J.; Hennink, W.E. Effect of size and serum proteins on transfection efficiency of poly((2-dimethylamino)ethyl methacrylate)-plasmid nanoparticles. *Pharm. Res.* **1996**, *13*, 1038–1042.
41. vandeWetering, P.; Cherng, J.Y.; Talsma, H.; Hennink, W.E. Relation between transfection efficiency and cytotoxicity of poly(2-(dimethylamino)ethyl methacrylate)/plasmid complexes. *J. Control. Release* **1997**, *49*, 59–69.
42. van de Wetering, P.; Moret, E.E.; Schuurmans-Nieuwenbroek, N.M.; van Steenbergen, M.J.; Hennink, W.E. Structure-activity relationships of water-soluble cationic methacrylate/methacrylamide polymers for nonviral gene delivery. *Bioconjug. Chem.* **1999**, *10*, 589–597.
43. MacLaughlin, F.C.; Mumper, R.J.; Wang, J.J.; Tagliaferri, J.M.; Gill, I.; Hinchcliffe, M.; Rolland, A.P. Chitosan and depolymerized chitosan oligomers as condensing carriers for in vivo plasmid delivery. *J. Control. Release* **1998**, *56*, 259–272.
44. Roy, K.; Mao, H.Q.; Huang, S.K.; Leong, K.W. Oral gene delivery with chitosan-DNA nanoparticles generates immunologic protection in a murine model of peanut allergy. *Nat. Med.* **1999**, *5*, 387–391.
45. Richardson, S.C.; Kolbe, H.V.; Duncan, R. Potential of low molecular mass chitosan as a DNA delivery system: Biocompatibility, body distribution and ability to complex and protect DNA. *Int. J. Pharm.* **1999**, *178*, 231–243.
46. Thanou, M.; Florea, B.I.; Geldof, M.; Junginger, H.E.; Borchard, G. Quaternized chitosan oligomers as novel gene delivery vectors in epithelial cell lines. *Biomaterials* **2002**, *23*, 153–159.
47. Lee, K.Y.; Kwon, I.C.; Kim, Y.H.; Jo, W.H.; Jeong, S.Y. Preparation of chitosan self-aggregates as a gene delivery system. *J. Control. Release* **1998**, *51*, 213–220.
48. Kiang, T.; Wen, J.; Lim, H.; Leong, K.W. Degree of Deacetylation of Chitosan: Effect on Gene Transfection Efficiency In vivo, Proceedings of 29th Annual Meeting of the Controlled Release Society, Seoul, Korea, July, 20–25, 2002.

49. Wang, J.; Mao, H.Q.; Leong, K.W. A novel biodegradable gene carrier based on polyphosphoester. *J. Am. Chem. Soc.* **2001**, *123*, 9480–9481.
50. Wang, J.; Zhang, P.C.; Mao, H.Q.; Leong, K.W. Enhanced gene expression in mouse muscle by sustained release of plasmid DNA using PPE-EA as a carrier. *Gene Ther.* **2002**, *9*, 1254–1261.
51. Wen, J.; Mao, H.Q.; Lin, K.; Li, W.; Leong, K.W. Novel Biodegradable Polyphosphoester Micelles as Gene Carriers, Proceedings of 3rd Annual Meeting of the American Society of Gene Therapy, Denver, CO, May 31–June 4, 2000.
52. Davis, S.S. Biomedical applications of nanotechnology-implications for drug targeting and gene therapy. *Trends Biotechnol.* **1997**, *15*, 217–224.
53. Poznansky, M.J.; Juliano, R.L. Biological approaches to the controlled delivery of drugs: A critical review. *Pharmacol. Rev.* **1984**, *36*, 277–336.
54. Patel, H.M. Serum opsonins and liposomes: Their interaction and opsonophagocytosis. *Crit. Rev. Ther. Drug Carr. Syst.* **1992**, *9*, 39–90.
55. Wagner, E.; Cotten, M.; Foisner, R.; Birnstiel, M.L. Transferrin-polycation-DNA complexes: The effect of polycations on the structure of the complex and DNA delivery to cells. *Proc. Natl. Acad. Sci. U. S. A.* **1991**, *88*, 4255–4259.
56. Puls, R.; Minchin, R. Gene transfer and expression of a non-viral polycation-based vector in CD4<sup>+</sup> cells. *Gene Ther.* **1999**, *6*, 1774–1778.
57. Diebold, S.S.; Lehrmann, H.; Kursa, M.; Wagner, E.; Cotten, M.; Zenke, M. Efficient gene delivery into human dendritic cells by adenovirus polyethylenimine and mannose polyethylenimine transfection. *Hum. Gene Ther.* **1999**, *10*, 775–786.
58. Mahato, R.I.; Takemura, S.; Akamatsu, K.; Nishikawa, M.; Takakura, Y.; Hashida, M. Physicochemical and disposition characteristics of antisense oligonucleotides complexed with glycosylated poly(L-lysine). *Biochem. Pharmacol.* **1997**, *53*, 887–895.
59. Kollen, W.J.; Mulberg, A.E.; Wei, X.; Sugita, M.; Raghuram, V.; Wang, J.; Foskett, J.K.; Glick, M.C.; Scanlin, T.F. High-efficiency transfer of cystic fibrosis transmembrane conductance regulator cDNA into cystic fibrosis airway cells in culture using lactosylated polylysine as a vector. *Hum. Gene Ther.* **1999**, *10*, 615–622.
60. Leamon, C.P.; Weigl, D.; Hendren, R.W. Folate copolymer-mediated transfection of cultured cells. *Bioconjug. Chem.* **1999**, *10*, 947–957.
61. Kim, J.S.; Maruyama, A.; Akaike, T.; Kim, S.W. Terplex DNA delivery system as a gene carrier. *Pharm. Res.* **1998**, *15*, 116–121.
62. Harbottle, R.P.; Cooper, R.G.; Hart, S.L.; Ladhoff, A.; McKay, T.; Knight, A.M.; Wagner, E.; Miller, A.D.; Coutelle, C. An RGD-oligolysine peptide: A prototype construct for integrin-mediated gene delivery. *Hum. Gene Ther.* **1998**, *9*, 1037–1047.
63. Ludtke, J.J.; Zhang, G.; Sebestyen, M.G.; Wolff, J.A. A nuclear localization signal can enhance both the nuclear transport and expression of 1 kb DNA. *J. Cell. Sci.* **1999**, *112* (Pt. 12), 2033–2041.
64. Chan, C.K.; Jans, D.A. Enhancement of polylysine-mediated transferrin infection by nuclear localization sequences: Polylysine does not function as a nuclear localization sequence. *Hum. Gene Ther.* **1999**, *10*, 1695–1702.
65. van Dijk-Wolthuis, W.N.; van de Wetering, P.; Hinrichs, W.L.; Hofmeyer, L.J.; Liskamp, R.M.; Crommelin, D.J.; Hennink, W.E. A versatile method for the conjugation of proteins and peptides to poly-[2-(dimethylamino)ethyl methacrylate]. *Bioconjug. Chem.* **1999**, *10*, 687–692.
66. Sebestyen, M.G.; Ludtke, J.J.; Bassik, M.C.; Zhang, G.; Budker, V.; Lukhtanov, E.A.; Hagstrom, J.E.; Wolff, J.A. DNA vector chemistry: The covalent attachment of signal peptides to plasmid DNA. *Nat. Biotechnol.* **1998**, *16*, 80–85.
67. Zanta, M.A.; Belguise-Valladier, P.; Behr, J.P. Gene delivery: A single nuclear localization signal peptide is sufficient to carry DNA to the cell nucleus. *Proc. Natl. Acad. Sci. U. S. A.* **1999**, *96*, 91–96.
68. Wolff, J.A.; Malone, R.W.; Williams, P.; Chong, W.; Acsadi, G.; Jani, A.; Felgner, P.L. Direct gene transfer into mouse muscle in vivo. *Science* **1990**, *247*, 1465–1468.
69. Mumper, R.J.; Wang, J.; Klakamp, S.L.; Nitta, H.; Anwer, K.; Tagliaferri, F.; Rolland, A.P. Protective interactive noncondensing (PINC) polymers for enhanced plasmid distribution and expression in rat skeletal muscle. *J. Control. Release* **1998**, *52*, 191–203.
70. Uychi, L.S.; Gagne, L.; Thurston, G.; Szoka, F.C., Jr. Mechanism of lipoplex gene delivery in mouse lung: Binding and internalization of fluorescent lipid and DNA components. *Gene Ther.* **2001**, *8*, 828–836.
71. Guillaume, C.; Delepine, P.; Droal, C.; Montier, T.; Tymen, G.; Claude, F. Aerosolization of cationic lipid-DNA complexes: Lipoplex characterization and optimization of aerosol delivery conditions. *Biochem. Biophys. Res. Commun.* **2001**, *286*, 464–471.
72. Bragonzi, A.; Boletta, A.; Biffi, A.; Muggia, A.; Sersale, G.; Cheng, S.H.; Bordignon, C.; Assael, B.M.; Conese, M. Comparison between cationic polymers and lipids in mediating systemic gene delivery to the lungs. *Gene Ther.* **1999**, *6*, 1995–2004.
73. Trubetskoy, V.S.; Wong, S.C.; Subbotin, V.; Budker, V.G.; Loomis, A.; Hagstrom, J.E.; Wolff, J.A. Recharging cationic DNA complexes with highly charged polyanions for in vitro and in vivo gene delivery. *Gene Ther.* **2003**, *10*, 261–271.
74. Kukowska-Latallo, J.F.; Raczka, E.; Quintana, A.; Chen, C.; Rymaszewski, M.; Baker, J.R., Jr. Intravascular and endobronchial DNA delivery to murine lung tissue using a novel, nonviral vector. *Hum. Gene Ther.* **2000**, *11*, 1385–1395.
75. Brown, M.D.; Schatzlein, A.G.; Uchegbu, I.F. Gene delivery with synthetic (non viral) carriers. *Int. J. Pharm.* **2001**, *229*, 1–21.
76. Merdan, T.; Kopecek, J.; Kissel, T. Prospects for cationic polymers in gene and oligonucleotide therapy against cancer. *Adv. Drug Deliv. Rev.* **2002**, *54*, 715–758.
77. Aoki, K.; Furuhashi, S.; Hatanaka, K.; Maeda, M.; Remy, J.S.; Behr, J.P.; Terada, M.; Yoshida, T.

- Polyethylenimine-mediated gene transfer into pancreatic tumor dissemination in the murine peritoneal cavity. *Gene Ther.* **2001**, *8*, 508–514.
78. Maheshwari, A.; Han, S.; Mahato, R.I.; Kim, S.W. Biodegradable polymer-based interleukin-12 gene delivery: Role of induced cytokines, tumor infiltrating cells and nitric oxide in anti-tumor activity. *Gene Ther.* **2002**, *9*, 1075–1084.
  79. Sato, N.; Kobayashi, H.; Saga, T.; Nakamoto, Y.; Ishimori, T.; Togashi, K.; Fujibayashi, Y.; Konishi, J.; Brechbiel, M.W. Tumor targeting and imaging of intraperitoneal tumors by use of antisense oligo-DNA complexed with dendrimers and/or avidin in mice. *Clin. Cancer Res.* **2001**, *7*, 3606–3612.
  80. Liu, F.; Huang, L. Improving plasmid DNA-mediated liver gene transfer by prolonging its retention in the hepatic vasculature. *J. Gene Med.* **2001**, *3*, 569–576.
  81. Zhang, X.; Collins, L.; Sawyer, G.J.; Dong, X.; Qiu, Y.; Fabre, J.W. In vivo gene delivery via portal vein and bile duct to individual lobes of the rat liver using a polylysine-based nonviral DNA vector in combination with chloroquine. *Hum. Gene Ther.* **2001**, *12*, 2179–2190.
  82. Yamazaki, Y.; Nango, M.; Matsuura, M.; Hasegawa, Y.; Hasegawa, M.; Oku, N. Polycation liposomes, a novel nonviral gene transfer system, constructed from cetylated polyethylenimine. *Gene Ther.* **2000**, *7*, 1148–1155.
  83. Culver, K.W.; Ram, Z.; Wallbridge, S.; Ishii, H.; Oldfield, E.H.; Blaese, R.M. In vivo gene transfer with retroviral vector-producer cells for treatment of experimental brain tumors. *Science* **1992**, *256*, 1550–1552.
  84. Nilaver, G.; Muldoon, L.L.; Kroll, R.A.; Pagel, M.A.; Breakefield, X.O.; Davidson, B.L.; Neuwelt, E.A. Delivery of herpesvirus and adenovirus to nude rat intracerebral tumors after osmotic blood–brain barrier disruption. *Proc. Natl. Acad. Sci. U. S. A.* **1995**, *92*, 9829–9833.
  85. Shi, N.; Pardridge, W.M. Noninvasive gene targeting to the brain. *Proc. Natl. Acad. Sci. U. S. A.* **2000**, *97*, 7567–7572.
  86. Abdallah, B.; Hassan, A.; Benoist, C.; Goula, D.; Behr, J.P.; Demeneix, B.A. A powerful nonviral vector for in vivo gene transfer into the adult mammalian brain: polyethylenimine. *Hum. Gene Ther.* **1996**, *7*, 1947–1954.
  87. Goula, D.; Remy, J.S.; Erbacher, P.; Wasowicz, M.; Levi, G.; Abdallah, B.; Demeneix, B.A. Size, diffusibility and transfection performance of linear PEI/DNA complexes in the mouse central nervous system. *Gene Ther.* **1998**, *5*, 712–717.
  88. Wang, S.; Ma, N.; Gao, S.J.; Yu, H.; Leong, K.W. Transgene expression in the brain stem effected by intramuscular injection of polyethylenimine/DNA complexes. *Molec. Ther.* **2001**, *3*, 658–664.



# Germanium Nanoparticles

Boyd R. Taylor

Louisa J. Hope-Weeks

*Chemistry and Chemical Engineering Directorate, Lawrence Livermore National Laboratory, Livermore, California, U.S.A.*

## INTRODUCTION

The interest in semiconductor nanoparticles is primarily because of disparities in electronic properties from the bulk material they exhibit because of their extremely small size. However, the preparation method used and the ability to manipulate them make an enormous impact on the applications of semiconductor nanoparticles. In the case of Ge nanoparticles, interest in their preparation and properties traces back to the proposal by Canham<sup>[1]</sup> in 1990 that the luminescence of porous Si was caused by quantum confinement (QC) of charge carriers. Because both bulk Si and Ge are diamond-lattice semiconductors with indirect band gaps in the near infrared, it seemed natural that the great interest in Si nanoparticles triggered by Canham's paper would cause a similar interest in Ge nanoparticles. This level of interest has not materialized because of the desire to link with the microelectronics community, which focuses so intensely on Si. Physically, the larger exciton Bohr radius of Ge of 11.5 nm,<sup>[2]</sup> its higher dielectric constant, and its higher refractive index make Ge the material of choice for some applications. Unlike Si, very little work has been performed on nanoparticles derived from porous Ge<sup>[3,4]</sup> or spark processed Ge.<sup>[5]</sup> The purpose of this entry is to discuss methods for preparation of Ge nanoparticles by colloidal chemistry; we will first discuss the initial methods and point out their strengths and weaknesses. A discussion of more recent preparation methods will follow. Finally, a comparison of the recent methods will point to some possible improvements in the colloidal preparation of Ge nanoparticles.

## PREPARATION OF Ge NANOPARTICLES

The preparation methods of Ge nanoparticles, such as those of other semiconductors, separate naturally into physical or "top-down" approaches and colloidal chemistry or "bottom-up" approaches. The colloidal chemistry approach mentioned here refers to preparing

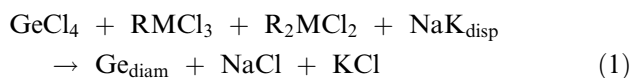
the nanoparticles using conventional synthetic chemistry and preparing a suspension of them in a solvent. The dividing line between a colloidal suspension and a solution is literally a murky one because one may think of a solution as a suspension that shows minimal light scattering. In the case of the very small particles considered here, the strong scattering characteristic of most colloids is seen only at high concentrations, where they agglomerate. Colloidal preparation of nanoparticles offers several advantages; the colloidal chemistry offers better control over the surface chemistry of the nanoparticles and their size distribution, and the particles are produced with no surrounding matrix. Because surface effects can change the properties of nanoparticles, control over the surface chemistry is vital to understanding their properties. To date, physical preparation methods such as various chemical vapor deposition (CVD) techniques and co-sputtering rely heavily on clean high-vacuum conditions to exclude impurities from the nanoparticles produced. These "top-down" techniques were developed to prepare thin films of bulk materials. Layers of nanoparticles were produced only by mixing these films with an inert matrix. Although many different techniques have been developed to both control and narrow the size distribution of semiconductor nanoparticles prepared by "top-down" methods, the best systems prepared through colloidal chemistry are nearly monodisperse,<sup>[6]</sup> far better than particles prepared by physical methods. In the case of compound semiconductors, particularly the II–VI semiconductors, the colloidal chemistry approach has been much more successful in preparing nanoparticles than "top-down" methods. The colloidal chemistry preparation of Si and Ge nanoparticles is much more difficult because of the greater sensitivity to oxidation and the difficulty of preparing anions with these elements.

Because there is enough literature on the preparation of Ge nanoparticles to infer an interest in this area, one might naturally ask why there is an interest. This question has been partially addressed previously. Because the microelectronics industry drives a continuing interest in Si as a semiconductor, and QC is widely

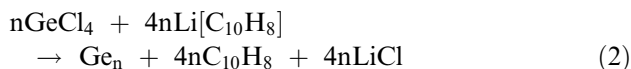
seen as a way of obtaining visible light from Si, the desire to integrate optical and electronic components drove early work on Si nanoparticles. Because Ge has a larger dielectric constant than Si (15.9 vs. 11.5) and smaller effective masses for the electron and hole, which give it a larger exciton Bohr radius, QC effects should be easier to observe in Ge nanoparticles than Si nanoparticles. Additionally, colloids of Ge nanoparticles have been predicted to have exceptional non-linear optical properties.<sup>[7,8]</sup>

### Colloidal Preparative Methods

Several methods have been used to prepare colloidal suspensions of Ge nanoparticles. Previous colloidal synthesis of both Ge quantum dots and wires has been reported to utilize the reduction of alkylchlorogermanes by NaK alloy.<sup>[9–11]</sup>



where  $\text{NaK}_{\text{disp}}$  means a dispersion of NaK alloy in hexane and  $\text{Ge}_{\text{diam}}$  means diamond-cubic Ge, the crystal structure of bulk Ge. The NaK dispersion was prepared by sonicating NaK alloy under anaerobic conditions. This reduction was performed in a bomb at 275°C and 200 atm, rather harsh synthetic conditions. Additionally, the reaction offered little control over size or surface termination, typically produced mixtures of quantum dots and wires, and had relatively low recoveries of Ge as nanoparticles. Previous attempts at liquid solution synthesis of Ge, Si, or SiGe quantum dots under less-forcing conditions all led to amorphous material. Another interesting liquid solution synthesis of Ge nanoparticles used ruby laser light to crystallize amorphous Ge particles from a colloidal solution after terminating the surface of the particles with alkylsilanes.<sup>[12]</sup> The reaction used to produce a colloidal solution of Ge particles was



The particles initially produced are amorphous, requiring annealing with ruby laser light to crystallize. However, this reaction takes place at 60°C and atmospheric pressure, and the resulting particles show some evidence of size selection because particles between 6 and 10 nm absorb the laser light, heating, and annealing. The amorphous particles still present must be separated, but the crystalline particles are produced in a reasonably narrow size range.

### Recent Colloidal Preparations

More recent colloidal preparative methods for Ge nanoparticles include the metathesis of  $\text{GeCl}_4$  with the Zintl salts NaGe, KGe, and  $\text{Mg}_2\text{Ge}$  and the reduction of  $\text{GeCl}_4$  in inverse micelles. Both methods offer the ability to prepare Ge nanoparticles in quantity. The Zintl salt metathesis permits reasonable control over the surface termination and limited control over size distribution.<sup>[13]</sup> The reduction of  $\text{GeCl}_4$  in inverse micelles permits excellent control over size distribution, but limited control over surface chemistry.<sup>[14]</sup> Because these more recently developed colloidal preparations offer better control over size distribution and surface chemistry than the previously mentioned methods, more detailed examination of both methods is in order.

#### Zintl salt metathesis

Zintl salts<sup>[15]</sup> are named for Eduard Zintl, who first prepared and characterized them in the 1930s. They consist of polyanions of elements to the right of the Zintl line, which divides groups 13 and 14 with cations from the left of the Zintl line.<sup>[16]</sup> These polyanions follow the octet rule, with cations from groups 1, 2, or the lanthanides providing charge balance. Zintl characterized these unusual air-sensitive compounds by X-ray diffraction (XRD) of the crystalline phases prepared and potentiometric titrations of solutions of Zintl salts in liquid ammonia.<sup>[15]</sup> It must be kept in mind that the structure of the polyanions in the crystalline phases need not closely resemble the structure of anionic clusters in solutions prepared from them.

To begin the Zintl salt metathesis, a suspension of the salt in a glyme (ethylene glycol dimethyl ether) is prepared under water- and air-free conditions by heating to reflux. While the Zintl salts used to prepare Ge nanoparticles, NaGe, KGe,  $\text{Mg}_2\text{Ge}$ , and CaGe, do not dissolve well in the glyme solvents used, enough dissolves to support the metathesis reaction with  $\text{GeCl}_4$ . Because the Cl-terminated Ge nanoparticles produced by the initial reaction dissolve freely in glyme solvents, the reaction is driven to completion. The reaction between the Zintl salts and a 3-fold excess of  $\text{GeCl}_4$  takes from 4 to 6 hr in diglyme and from 1/2 to 2 hr in triglyme, judged by the suspension changing from opaque gray-blue to clear and colorless. A 3-fold excess of  $\text{GeCl}_4$  is needed to drive the reaction to completion, and both the Zintl salt used and the  $\text{GeCl}_4$  are consumed in the reaction. It is not known why a 3-fold excess of  $\text{GeCl}_4$  is needed to drive the reaction to completion, but neither reactions performed with a 10-fold excess of  $\text{GeCl}_4$  nor those performed with less than a 3-fold excess of  $\text{GeCl}_4$  reacted completely. The ability

of Li alkyls and Grignard reagents to alkylate the surface of the nanoparticles also points to the chloride termination of the surface mentioned above.

Of course, reaction with Li alkyls and Grignard reagents has permitted surface termination with more interesting groups than alkyls. To date, surfaces with methyl, butyl, octyl,<sup>[13,17]</sup> *p*-chlorophenyl,<sup>[18]</sup> vinyl, and allyl groups have been prepared with varying success. Ge nanoparticles with alkyl-terminated surfaces are remarkably stable and relatively simple to separate. Nanoparticles with vinyl- and allyl-terminated surfaces have been proven to be both unstable and difficult to purify. The primary failing of this preparative method is the limited control over size distribution and the difficulty of separating sizes. While different concentrations of reactants, reaction time, or reaction temperature changed the mean nanoparticle size, no control over size distribution is apparent.

### Reduction in inverse micelles

In the inverse micelle preparation of Ge nanoparticles, both size control and size separation are incorporated into the preparative method. The partial separation of the halide salt and reductant into hydrophilic and hydrophobic regions of the inverse micelles permits some control over size distribution, which is greatly enhanced by the use of high-performance liquid chromatography (HPLC) to size-separate the nanoparticles. In essence, GeX<sub>4</sub> (X = Cl, Br, or I) was more soluble in the tetrahydrofuran (THF) portion of inverse micelles formed in THF/octane or THF/decane mixtures than in the hydrocarbon portion of the reaction mixture. The micelles form at the interface of the THF and alkane phases, with aliphatic polyethers or quaternary ammonium salts acting as phase transfer catalysts and stabilizing the micellar phase. Small regions of THF/GeX<sub>4</sub> are formed with octane or decane separating them. This was followed by the introduction of the reductant, typically 1 M LiAlH<sub>4</sub> in THF. The micelles determine the size of nanoparticles produced, although thinking of micelles as pores or cavities is an oversimplification. Rather than act as cavities, which directly limit the size of the nanoparticles, the micelles slow the rate of reaction, perhaps separating crystallite nucleation from growth. Similar to all of the other reactions discussed, this reduction was carried out under water-free, anaerobic conditions. However, the use of alkaline N<sub>2</sub>H<sub>4</sub> as a reductant was suggested, indicating that as long as hydrolysis was slower than reduction, the presence of a small amount of water could be tolerated. Although no attempt to characterize or manipulate the surface chemistry has yet been made for Ge nanoparticles prepared with this method, the surface is most likely terminated by H. The strengths of this method are that it is generally

applicable to main group nanoparticles and that the reaction mixture can be size-separated by HPLC. However, because the nanoparticles produced are terminated by H, they are not stable in air, making characterization difficult.

## DISCUSSION

### Quantum Confinement

Because most of the interest in Si nanoparticles can be traced back to Canham's proposal that quantum confinement is responsible for the observed photoluminescence in porous Si, it may be assumed that most of the interest in Ge nanoparticles also arises from an interest in QC. Because the changes in electronic properties as a result of QC are observable only at radii  $\leq R_{\text{Bohr}}$  of the exciton, or equivalently, when the particle size is approximately the same as the mean free path of charge carriers in the material, measuring the size of the nanoparticles produced is crucial.

Quantum confinement changes all of the electronic properties of nanoparticles relative to the bulk material. The best-known example of this is the change in optical properties. The absorption onset of bulk Ge lies in the near infrared, at 0.67 eV, and it photoluminesces in the near infrared, with an efficiency of less than 10<sup>-4</sup>%. Quantum confinement predicts that the band gap, the photoluminescence (PL), and the photoluminescence excitation (PLE) maxima will shift to higher energies with decreasing size. It also predicts that the efficiency of an optical transition will increase with decreasing size.

### Size Measurement

Because the properties of nanoparticles depend primarily on size, measurement of both the mean size and size distribution is vital to understanding their properties. It has been proven to be more difficult than expected to establish reliable size measurements. Size measurements of Ge nanoparticles have been made by high-resolution transmission electron microscopy (HRTEM), selected area electron diffraction (SAED), X-ray diffraction (XRD), or atomic force microscopy (AFM). Size measurements by HRTEM have been used most widely because one may image the d-spacing of the lattice of the nanoparticles while imaging them. This ability to measure d-spacing and obtain an image simultaneously permits looking for a phase change at extremely small sizes. Size measurements based on diffraction rely on the broadening of diffraction lines for both XRD and SAED observations. However, the need to assume a particle shape in the Debye-Scherrer

formula and the low intensity of diffraction maxima for these measurements make them uncertain and difficult. More importantly, line-broadening measurements provide no information about the size distribution. Atomic force microscopy provides a quick measurement of both mean size and size distribution, providing that the nanoparticles are equiaxial because AFM measurements are precise only in  $Z$ .

### Surface Termination

The issue of surface termination is often overlooked because most of the interesting properties of nanoparticles depend primarily on their size. However, particles from 2 to 10 nm in diameter, which is the size range of interest for quantum-confined nanoparticles, have enormous surface areas. They also oxidize more rapidly than bulk material because they have so many atoms near the surface. To prevent the nanoparticles from oxidizing, one must passivate the surface in some way. Unlike Si nanoparticles, the surface oxide of Ge does not effectively passivate the nanoparticle surface. For Ge nanoparticles prepared by the Zintl salt metathesis, reacting the chlorides on the surface with Grignard reagents or Li alkyls is a natural method of passivating the surface. For Ge nanoparticles prepared in inverse micelles, some other coupling chemistry must be devised. Hydrogen-terminated Si surfaces have been prepared by reaction with 1-alkenes.<sup>[19]</sup> Similar chemistry should work on Ge nanoparticles with H-terminated surfaces.

### RESULTS

As predicted by quantum confinement models, the optical properties of quantum-confined nanoparticles differ greatly from those of the bulk material. The plot of absorption onsets vs. mean diameter in Fig. 1 demonstrates the change in absorption onset with size for Ge nanoparticles prepared by the Zintl salt metathesis. Although the UV-Vis spectra in this figure are not presented as measurements of band gaps, the absorption onsets seen in this figure are of similar energy and scale inversely with mean particle size as expected from quantum confinement models. The size-selected PL spectra in Fig. 2 demonstrate luminescence in the blue-to-violet region of the spectrum. The shift in energy of the PL maxima is over 2 eV. However, this large energy shift is reproducible and consistent between samples of similar mean size. While some of the shift may be a result of surface effects, it is primarily because of quantum confinement. Ge nanoparticles 2–4 nm in diameter prepared in inverse micelles using  $\text{LiAlH}_4$  as a reductant show a similar shift in

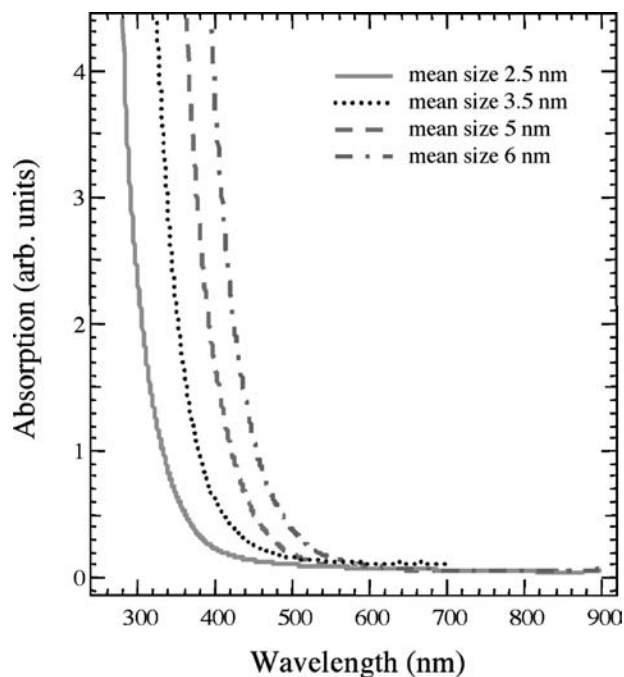


**Fig. 1** Absorption onset vs. mean diameter for alkyl-terminated Ge nanoparticles.

energy in PL spectra.<sup>[14]</sup> Recent X-ray absorption measurements of butyl-terminated Ge nanoparticles prepared by the Zintl salt metathesis also showed approximately a 2-eV shift of the conduction band.<sup>[20]</sup> The XAS data do not rule out solvent-nanoparticle interactions, defects, or electronic transitions involving the butyl groups, but the resemblance of the XAS spectra of the nanoparticles to bulk Ge rather than

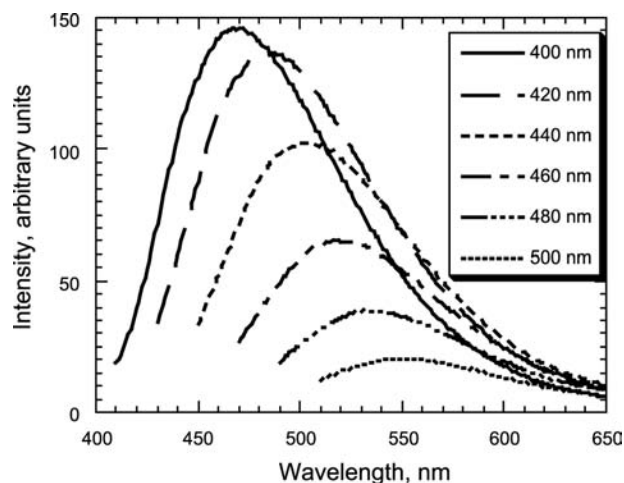


**Fig. 2** Size-selected photoluminescence spectra of butyl-terminated Ge nanoparticles. The figure legend labels the excitation wavelength of each spectrum. The wide range of photoluminescence wavelengths is due to a broad range of sizes for this sample.

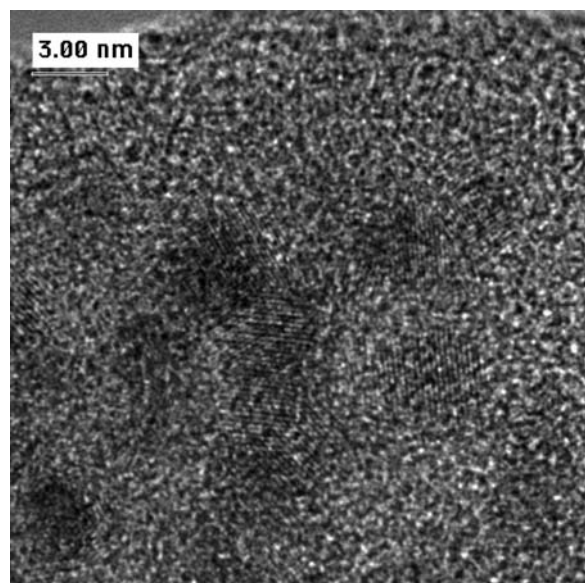


**Fig. 3** High-resolution TEM image of butyl-terminated Ge nanoparticles. The lattice spacing is 3.27 Å, as expected for the  $\langle 111 \rangle$  face for bulk Ge.

Ge oxide or carbide supports quantum confinement as the primary cause of the large conduction band shift.

Transmission electron microscopy (TEM) is the most widely used size measurement for nanoparticles because diffraction and chemical information are available in tandem with the images obtained. High-resolution TEM (HRTEM) permits direct imaging of the lattice spacing of the nanoparticles, providing some composition information. The HRTEM micrograph in Fig. 3 of several Ge nanoparticles shows the  $\langle 111 \rangle$  plane of the crystallites, with a d-spacing of 3.27 Å,

as expected for bulk Ge. This lattice plane is both the easiest to image by HRTEM because of its relatively large d-spacing and the most commonly seen plane for a diamond cubic lattice. A phase change from diamond cubic to tetragonal has been predicted in Ge nanoparticles and observed in nanoparticles prepared in co-sputtered Ge/SiO<sub>2</sub> at diameters  $\leq 4$  nm.<sup>[21]</sup> However, no such phase change has been observed in Ge nanoparticles prepared colloiddally. There is no evidence for this cubic-to-tetragonal phase change in colloidal Ge nanoparticles.

An atomic force microscope (AFM) measurement of butyl-terminated Ge nanoparticles is presented in Fig. 4. The height measurements by AFM were performed in tapping mode, on colloid spin-coated onto mica substrates, which provided a nearly atomically flat surface. Another sample from this same preparation had a mean diameter of 6.5 nm by HRTEM compared with 6.1 nm by AFM. Because HRTEM imaging is based on interference<sup>[22]</sup> and will inherently overestimate the size of objects, some size difference is to be expected. The agreement between HRTEM and AFM measurements is surprising and suggests equiaxial, although not necessarily spherical nanoparticles.

The surface termination of Ge nanoparticles prepared from the Zintl salt metathesis is seen clearly in Fig. 5. This Fourier transform infrared (FTIR) spectrum of butyl-terminated Ge nanoparticles was obtained by evaporating a hexane colloid onto a CsI plate followed by heating to 120°C in air for 4 hr. The alkyl stretches and bends are clearly seen, while there is no evidence of GeO<sub>2</sub> in the spectrum. The absence of the broad, intense peak for GeO<sub>2</sub> at 870–940 cm<sup>-1</sup> in this FTIR spectrum does not rule out the presence of small amounts of surface oxide in the

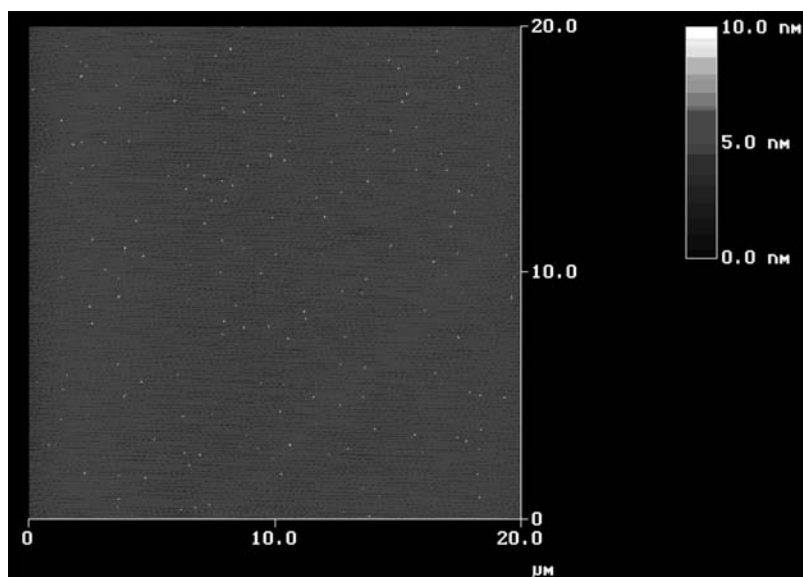


**Fig. 4** Atomic force micrograph of butyl-terminated Ge nanoparticles with a mean height of 6.1 nm. The nanoparticles appear as small bright spots against the mica substrate.

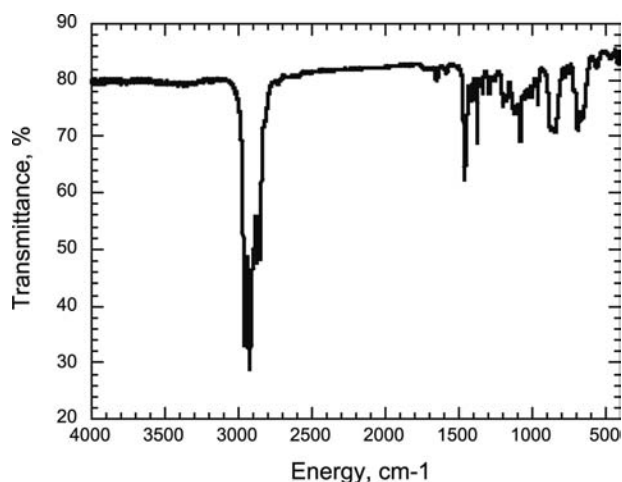


**Fig. 5** FTIR spectrum of a film of butyl-terminated Ge nanoparticles on a CsI plate. The vibrations correspond closely to those of  $\text{Ge}(n\text{-C}_4\text{H}_9)_4$ .

nanoparticles. However, the ability to handle the nanoparticles in air and heat them for several hours at  $T > 100^\circ\text{C}$  demonstrates excellent surface termination.

## CONCLUSION

Most semiconductor nanoparticles are prepared by colloidal chemistry because of the superior optical properties and control of size distribution. Colloidal preparation of Ge nanoparticles is far more difficult than the compound semiconductors. The early colloidal preparation methods for Ge nanoparticles offered low yields and little or no control over size and surface termination. More current colloidal preparation methods offer better yields; nearly 80% of the Ge in the reaction was recovered in the inverse micelle synthesis, and yields as high as 60% have been obtained for the Zintl salt metathesis. The inverse micelle synthesis also permits good control over the size distribution, which is greatly enhanced by HPLC. The Zintl salt metathesis offers limited control over size distribution, but good control over surface termination, according to the choice of reagents used. While no perfect method for colloidal Ge nanoparticle preparation yet exists, progress continues in this area.

## ACKNOWLEDGMENTS

This work was performed under the auspices of the U.S. Department of Energy by University of California Lawrence Livermore National Laboratory under contract No. W-7405-Eng-48. B. Taylor wishes

to thank Prof. Susan M. Kauzlarich for assistance in the preparation of Zintl salts and Gil Delgado for assistance with optical spectroscopy.

## REFERENCES

1. Canham, L.T. Silicon quantum wire array fabrication by electrochemical and chemical dissolution of wafers. *Appl. Phys. Lett.* **1990**, *57*, 1046–1048.
2. Ashcroft, N.W.; Mermin, N.D. *Solid State Physics*, 1st Ed.; Saunders College Publishing: Orlando, 1976.
3. Miyazaki, S.; Sakamoto, K.; Shiba, K.; Hirose, M. Photoluminescence from anodized and thermally anodized porous germanium. *Thin Solid Films* **1995**, *255*, 99–102.
4. Bayliss, S.; Zhang, Q.; Harris, P. Network dimensionality of porous Si and Ge. *Appl. Surf. Sci.* **1996**, *102*, 390–394.
5. Chang, S.-S.; Choi, G.J.; Hummel, R.E. Optical properties of spark-processed Ge. *Mater. Sci. Eng., B* **2000**, *B76*, 237–240.
6. Murray, C.B.; Norris, D.J.; Bawendi, M.G. Synthesis and characterization of nearly monodisperse CdE ( $E = \text{S}, \text{Se}, \text{Te}$ ) semiconductor nanocrystallites. *J. Am. Chem. Soc.* **1993**, *115*, 8706–8715.
7. Wang, L.-W.; Zunger, A. Pseudopotential Theory of Nanometer Silicon Quantum Dots. In *Nanocrystalline Semiconductor Materials*; Kamat, P.V., Meisel, D., Eds.; Elsevier Science, 1996; 1–41.
8. Wang, Y. Nonlinear optical properties of nanometer-sized semiconductor clusters. *Acc. Chem. Res.* **1991**, *24*, 133–139.
9. Heath, J.R.; LeGoues, F.K. A liquid solution synthesis of single crystal germanium quantum wires. *Chem. Phys. Lett.* **1993**, *208*, 263–268.
10. Heath, J.R.; Shiang, J.J.; Alivisatos, A.P. Germanium quantum dots: Optical properties and synthesis. *J. Chem. Phys.* **1994**, *101*, 1607–1615.
11. Heath, J.R.; Seidler, P.F. Separation of nucleation and crystallization in the solution-phase synthesis of group IV quantum structures. *Mater. Res. Soc. Symp. Proc.* **1993**, *298*, 91–98.
12. Kornowski, A.; Giersig, M.; Vogel, R.; Chemseddine, A.; Weller, H. Nanometer-sized colloidal germanium particles: Wet-chemical, laser-induced crystallization and particle growth. *Adv. Mater.* **1993**, *5*, 634–636.
13. Taylor, B.R.; Kauzlarich, S.M.; Lee, H.W.H.; Delgado, G.R. Solution synthesis and characterization of quantum confined Ge nanoparticles. *Chem. Mater.* **1999**, *11*, 2493–2500.
14. Wilcoxon, J.P.; Provencio, P.N.; Samara, G.A. Synthesis and optical properties of colloidal germanium nanocrystals. *Phys. Rev., B* **2001**, *64*, 035417(9).
15. Kauzlarich, S.M.; Chan, J.Y.; Taylor, B.R. Exploitation of Zintl Phases in the Pursuit of Novel Magnetic and Electronic Materials. In *Inorganic Materials Synthesis*; Winter, C.H., Hoffman, D.M., Eds.; American Chemical Society: Washington, DC, 1999; Vol. 727, 15–27.



16. Müller, U. Polyanionic and Polycationic Compounds, "Zintl Phases". In *Inorganic Structural Chemistry*; Wiley: New York, 1993; 116–138.
17. Taylor, B.R.; Kauzlarich, S.M.; Lee, H.W.H.; Delgado, G.R. Solution synthesis of germanium nanocrystals demonstrating quantum confinement. *Chem. Mater.* **1998**, *10*, 22–24.
18. Taylor, B.R.; Hope-Weeks, L.J.; Fox, G.A.; Maxwell, R.; Kauzlarich, S.M.; Lee, H.W.H. Solution preparation of Ge nanoparticles with chemically tailored surfaces. *Mater. Sci. Eng., B* **2002**.
19. Linford, M.R.; Fenter, P.; Eisenberger, P.M.; Chidsey, C.E.D. Alkyl monolayers on silicon prepared from 1-alkenes and hydrogen-terminated silicon. *J. Am. Chem. Soc.* **1995**, *117*, 3145–3155.
20. van Buuren, T.; Bostedt, C.; Taylor, B.R.; Willey, T.M.; Hope-Weeks, L.J.; Weeks, B.; Terminello, L.J. X-ray absorption study of colloidal Ge quantum dots. *SPIE Proc.* **2002**, *4807*, 1–9.
21. Kanemitsu, Y.; Uto, H.; Masumoto, Y.; Maeda, Y. On the origin of visible photoluminescence in nanometer-size Ge crystallites. *Appl. Phys. Lett.* **1992**, *61*, 2187–2189.
22. Reimer, L. Crystal Structure Imaging. In *Transmission Electron Microscopy Physics of Image Formation and Microanalysis*, 3rd Ed.; Hawkes, P.W., Ed.; Springer-Verlag: New York, 1993; Vol. 36, 545 pp.

# Gold Nanoclusters: Structural Disorder

Ignacio L. Garzón

*Instituto de Física, Universidad Nacional Autónoma de México, Mexico City, Mexico*

## INTRODUCTION

One of the main goals of researchers working on Nanoscience and Nanotechnology is the design and the fabrication of nanostructured materials with novel and perhaps unexpected properties.<sup>[1]</sup> These systems are defined as materials constructed from structural elements (clusters, crystallites, or molecules) with dimensions in the range of 1–100 nm. The case of gold-based nanostructured materials has been especially relevant because of the potential applications in nanoelectronics<sup>[2]</sup> and in biological diagnostics.<sup>[3]</sup> An important contribution in this area was the self-assembly of two- and three-dimensional superlattices of nanometer-diameter gold particles linked to each other by organic interconnects.<sup>[4–6]</sup> Thiol-passivated gold nanoclusters, assembled in closed-packed arrays, showed interesting electronic transport properties, such as single-electron tunneling at room temperature, and are expected to be useful for the development of nanoscale electronics.<sup>[5,6]</sup> It was also shown that although the self-organization of nanoparticles is a powerful route to grow these materials, imperfections in the superlattice can result from incorrect chemical recognition between the constituents.<sup>[2]</sup> This can be a serious limitation in making nanostructured materials for electronic applications, where long-range order is important. On the other hand, biological systems are able to solve complex recognition problems. In particular, DNA transmits well-defined chemical information through the pairing properties of nucleotide bases. A major advance in controlling the self-assembly of metal particles was achieved by using oligonucleotides to organize colloidal gold nanoclusters into superlattices, allowing for the controlled growth of hybrid DNA-gold nanostructured materials.<sup>[7,8]</sup>

Although the main mechanisms to synthesize and to isolate hybrid DNA-gold nanostructured materials have been discovered,<sup>[7,8]</sup> further studies continue to fully characterize the structural, electronic, optical, transport, and other physical and chemical properties. This research represents a challenge for future investigations in Nanoscience and Nanotechnology because of the complexity of these materials, which are a complex mixture of inorganic and biological structures.<sup>[9]</sup> The first investigations toward a full characterization

of gold-based nanostructured materials have already begun. In a first stage, valuable information on the properties of each subsystem, metal particles and DNA, is being obtained. These separate properties will be fundamental in understanding the behavior of the hybrid materials.<sup>[9]</sup> Along this direction, theoretical and experimental information on the shape and morphology of bare and passivated gold nanoclusters will be fundamental to fully predict and understand their electronic, optical, and other physical and chemical properties. This information is essential to optimizing their utilization as building blocks of the new molecular nanostructured materials.

## OVERVIEW

The objective of this entry is to describe recent theoretical advances on the study of the shape and morphology of bare and passivated gold nanoclusters of different sizes. A detailed knowledge of the most stable structural configurations of these nanostructures is a very active field of research because the cluster geometries are the starting point to study their electronic, optical, and other physical and chemical properties, which are relevant for the design and fabrication of gold-based nanostructured materials. The main trend emerging from recent theoretical studies on structural optimizations of bare Au clusters in the size range up to 200 atoms indicates that many topologically interesting low-symmetry, disordered structures exist with energy near or below the lowest-energy ordered isomer.<sup>[10,11]</sup> Moreover, chiral structures have been obtained as the lowest-energy isomers of bare Au<sub>28</sub> and Au<sub>55</sub> clusters,<sup>[12]</sup> whereas in the size range of 75–212 atoms, defective Marks decahedral structures are nearly degenerate in energy with the ordered symmetrical isomers.<sup>[11,13]</sup> For methylthiol-passivated gold nanoclusters [Au<sub>28</sub>(SCH<sub>3</sub>)<sub>16</sub> and Au<sub>38</sub>(SCH<sub>3</sub>)<sub>24</sub>], structural relaxations have shown that the ligands are not only playing the role of passivating molecules, but their effect is strong enough to distort the metal cluster structure.<sup>[12,14]</sup> These predictions on the existence and the stability of disordered configurations for bare and passivated gold nanoclusters have opened the possibility of constructing gold-based nanostructured

materials, where the amorphous-like character of the gold nanoparticles could generate interesting electronic and optical behavior with potential nanotechnological applications.

In the next section, we briefly describe the theoretical methodologies utilized to study the structural properties of bare and passivated gold nanoclusters, as well as the existing experimental techniques that provide useful information to complement the structural characterization of these systems. The trends on the most stable geometries of bare and passivated gold nanoclusters are then discussed including a recent prediction on the existence of chirality in such systems. Finally, some concluding remarks are presented.

## THEORETICAL AND EXPERIMENTAL METHODOLOGIES

Several experimental studies have reported results on the properties of bare and thiol-passivated gold nanoclusters that constitute the building blocks of gold-based nanostructured materials. For example, structural information of bare and passivated gold nanoclusters of different sizes has been obtained using high-resolution transmission electron microscopy (HRTEM),<sup>[15–19]</sup> X-ray powder diffraction (XRPD),<sup>[20–23]</sup> scanning tunneling microscopy (STM),<sup>[24,25]</sup> and extended X-ray absorption fine structure (EXAFS).<sup>[26,27]</sup> Furthermore, optical spectrum measurements on the smallest gold particles (1–2 nm) have shown discrete electronic transitions indicating the existence of quantum size effects in these systems.<sup>[20]</sup> Despite the existence of these sophisticated experimental tools, several questions concerning the physical and chemical properties of bare and passivated gold nanoclusters remain unsolved or under debate.<sup>[9,11,12,14]</sup> For example, the current approach to determine nanocluster structures is based on the comparison between experimental HRTEM images<sup>[16,19]</sup> or XRPD and EXAFS structure factors<sup>[20,21,26]</sup> with those calculated from geometrical models of these nanostructures. However, the actual experimental resolution is not sufficient to resolve the broad features shown in the XPRD patterns,<sup>[21,23]</sup> neither have the HRTEM images<sup>[16,19]</sup> allowed for a clear discrimination of the atomic positions of gold nanoclusters in the size range of 1–2 nm.

An effective theoretical approach to determine the lowest-energy configuration (global minimum) and the structures of low-energy isomers (local minima) of clusters combines genetic algorithms and many-body potentials (to perform global structural optimizations over the cluster potential energy landscape),<sup>[9–12,28–32]</sup> with first-principles density functional theory (to confirm the stability and the energy ordering of the local minima).<sup>[9–14,33–36]</sup> This method has been recently

utilized to study the structural properties of bare and passivated gold nanoclusters. In the initial stage of this approach, global unconstrained structural optimizations of bare gold nanoclusters of different sizes are performed using semiempirical many-body potentials, such as the Gupta potential,<sup>[37,38]</sup> and a genetic-symbiotic algorithm.<sup>[29,31,39,40]</sup> With this procedure, it is possible to obtain the distribution of lowest-energy isomers in a range of potential energy values for each cluster size.<sup>[28,29]</sup> From this distribution, representative isomers such as those with the lowest energy are selected, together with those isomers that are considered good candidates to be the lowest-energy minima, based on the existence of well-known symmetric structures for certain cluster sizes such as the truncated octahedron, icosahedron, or decahedron configurations.<sup>[12]</sup>

In the second stage of this approach, the first-principles methods, which do not depend on empirical parameterizations and have a reliable predictive power, are used to locally reoptimize the representative isomers obtained at the first stage. Specifically, unconstrained relaxations are performed using the forces calculated from density functional theory (DFT) in the local density (LDA) and generalized-gradient (GGA) approximations. The DFT calculations are performed using scalar relativistic norm conserving pseudopotentials and numerical atomic orbitals<sup>[41]</sup> or plane waves<sup>[42]</sup> as basis sets. For these quantum mechanical calculations, the atomic coordinates of each cluster, obtained from the global optimizations realized at the first stage, are used as initial conditions for the DFT relaxations.

The lowest-energy structures of passivated gold clusters are obtained by performing local relaxations, using the forces calculated from the DFT–LDA–GGA first principles method, and starting from different cluster-ligands configurations.<sup>[9,11,12,14,43–48]</sup> These include the lowest energy bare gold cluster geometries obtained by the procedure described above, with the passivating molecules placed on different adsorption sites (top, bridge, and hollow), as well as on random positions over the metal cluster surface.<sup>[9,11,12,14]</sup> For passivated gold clusters, a global structural optimization, of the type mentioned above for bare gold clusters, is more difficult to perform because of the lack of adequate model potentials that describe appropriately the interaction between the metal cluster and the organic passivating molecules. Nevertheless, some calculations of this kind have been reported in connection with gold-based nanostructured materials.<sup>[49]</sup>

## STRUCTURAL PROPERTIES OF BARE GOLD NANOCLUSTERS

Extensive theoretical studies on the geometrical structures of the most stable isomers of bare gold clusters

have shown that these systems have interesting and perhaps unique peculiarities. For example, in the small-size regime ( $n \leq 13$ ), quantum mechanical calculations of neutral and charged gold clusters<sup>[34,36,50–54]</sup> indicate that the lowest-energy configurations correspond to planar (two-dimensional) structures. These results have been attributed to the non-additivity of the many-body forces existing in small noble metal clusters<sup>[50,51]</sup> and to the strong *sp-d* hybridization caused by the large relativistic effects present in the bonding and structure of gold clusters.<sup>[52,53]</sup> This planarity in the structures of small gold clusters is being considered as an important factor for the appearance of unusual catalytic activity, recently observed in these systems.<sup>[52,53]</sup>

In the intermediate-size regime ( $n = 12–55$ ), structural optimizations of  $Au_n$  clusters have shown that many topologically interesting low-symmetry, disordered structures exist with energy near or below the lowest-energy ordered isomer.<sup>[9–12,29,30,32,33,35,36,55]</sup> This is especially surprising because the calculations include “magic” cluster sizes for which very compact ordered structures exist. Fig. 1 shows the lowest-energy structures calculated for the  $Au_{55}$  cluster.<sup>[55]</sup> In this case, there are several amorphous-like structures, such as those shown in the three upper panels of Fig. 1, that have higher stability than the ordered icosahedral and cuboctahedral structures.

It was shown that the analysis of the cluster local stress can be used to understand the physical origin of the higher stability of disordered clusters with respect to their ordered isomers.<sup>[33,35]</sup> Specifically, it was found that the compact ordered structures are destabilized by the tendency of metallic bonds to contract at the surface because of the decreased coordination. The cluster amorphization is also favored by the relatively low energy associated with bond length and coordination disorder in metals.<sup>[33,35]</sup> Although these are the general effects of the metallic bonding, they are especially large in the case of gold because of the short range of the many-body forces existing in this system as compared with other metals.<sup>[55]</sup> The low spatial symmetry or lack of symmetry at all in the most stable configurations of intermediate-size gold nanoclusters opened the possibility of having distinct electronic and optical properties in such systems that are of interest for the fabrication of gold-based nanostructured materials.<sup>[10]</sup> In fact, the atomic disorder in the gold nanocluster structures is reflected in the broad features present in their vibrational and electronic density of states (DOS), as compared with the sharper structure found in the DOS corresponding to high-symmetry ordered structures.<sup>[10]</sup> Such differences could lead to distinct optical responses according to the cluster size and structural symmetry. Fig. 2 displays a comparison of different physical properties,

including the vibrational and electronic DOS, between disordered and ordered gold nanoclusters of different sizes.<sup>[10]</sup>

In HRTEM studies<sup>[56,57]</sup> on Au and Pd nanoparticles, images of polycrystalline and amorphous structures have been reported in the size range of a few nanometers, providing experimental evidence for the existence and the stability of disordered metal nanoclusters. Further experimental evidence in this direction was obtained through the qualitative agreement between the XRPD patterns measured for  $Au_{38}$  and  $Au_{75}$  clusters and those calculated using their disordered configurations.<sup>[28,29]</sup> It can be noticed in Fig. 3 the level of agreement with the experimental results between the structure factors corresponding to the disordered and ordered clusters. However, the above comparisons are not completely fair because the experimental samples corresponded to thiol-passivated gold nanoclusters, whereas the calculated structures corresponded to bare gold particles. In fact, an obvious question is what the effect is of the thiol-passivating monolayer on the physical and chemical properties of gold nanoclusters.

More recently, it was also found using DFT calculations that in larger gold nanoclusters ( $Au_n$ ,  $n = 75, 101, 146, 192,$  and  $212$ ), defective decahedral structures are nearly degenerate in energy with the highly symmetrical Marks decahedron isomer.<sup>[13]</sup> These results are in agreement with another experimental study on Au clusters of 2–4 nm in size, where complex and defective structures have been detected using XRPD.<sup>[23]</sup>

## STRUCTURAL PROPERTIES OF THIOL-PASSIVATED GOLD NANOCCLUSERS

Several theoretical studies have been performed to investigate the effect of thiol passivation on gold nanoclusters.<sup>[9,11,12,14,43–49]</sup> One approach consists of performing conjugate gradient structural DFT relaxations starting from different cluster-thiol monolayer configurations. Specifically, the  $Au_{28}$  and  $Au_{38}$  clusters coated with 16 and 24 methylthiol ( $SCH_3$ ) molecules, respectively, have been investigated.<sup>[9,11,12,14]</sup> These passivated gold clusters with diameters of 0.8 and 1.1 nm have been isolated and characterized by XRPD and other experimental techniques.<sup>[20,58]</sup> According to the DFT calculations performed on these passivated clusters, the effect of the thiol monolayer is strong enough to drastically distort the structure of the bare gold cluster. In one calculation, a truncated octahedron  $Au_{38}$  cluster (with fcc symmetry) was dramatically distorted upon relaxation with 24 methylthiol molecules, symmetrically positioned on the (111) facets close to the hollow sites.<sup>[14]</sup> The relaxed structure of the  $Au_{38}(SCH_3)_{24}$  cluster corresponds to a disordered,

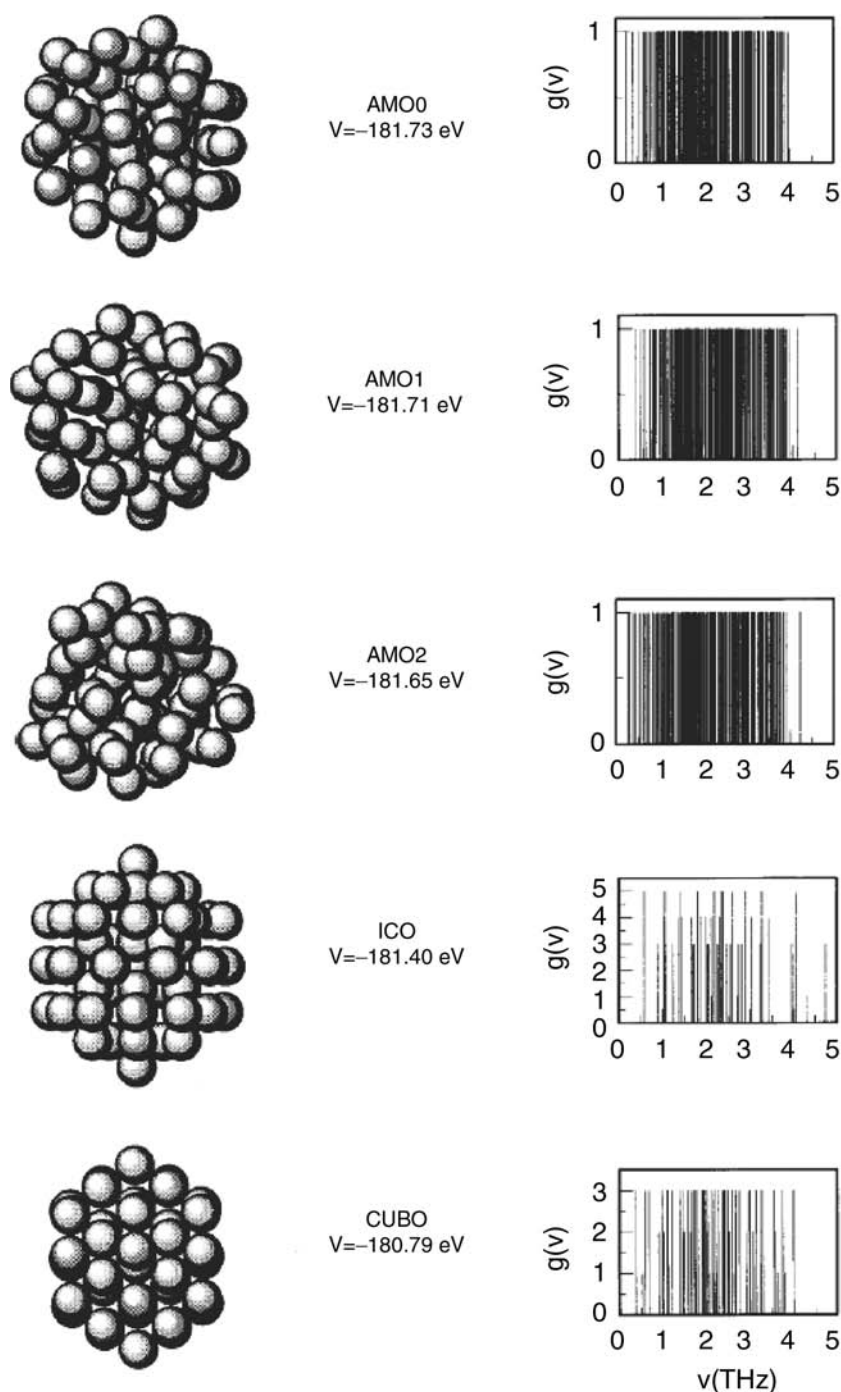


**Fig. 1** Left: stable isomers and their energies (in eV) of the  $\text{Au}_{55}$  cluster. The three upper configurations correspond to amorphous gold clusters. The cluster shown on the top was the lowest-energy configuration obtained in the optimization procedure. The icosahedron and octahedron structures are local minima with higher potential energy. Right: vibrational spectra of the five isomers. The vertical axis shows the degree of degeneracy. *Source:* From Ref.<sup>[55]</sup>.

passivated nanocluster where the sulfur atoms of the thiol heads are incorporated within the cluster surface. Fig. 4 shows the clearly separated gold and sulfur atomic shells of the fcc structure and their distortion and overlap in the disordered configuration.<sup>[14]</sup> Different patterns of charge transfer are expected to occur on this disordered, alloyed cluster surface.<sup>[14]</sup>

The lowest-energy structure obtained from DFT structural relaxations of  $\text{Au}_{28}(\text{SCH}_3)_{16}$  also corresponds to a highly disordered passivated nanocluster with an ill-defined gold–thiol interface.<sup>[12]</sup> It was obtained by

the relaxation of the lowest-energy disordered structure of the bare  $\text{Au}_{28}$  cluster, with the methylthiols placed close to three-atom hollow sites.<sup>[12]</sup> In the top panel of Fig. 5, the gold and sulfur atomic shells of the  $T$  structure and the most stable disordered configuration of the bare  $\text{Au}_{28}$  cluster are compared.<sup>[12]</sup> The bottom panel of Fig. 5 shows the gold and sulfur atomic shells for the most stable disordered configuration of the passivated  $\text{Au}_{28}(\text{SCH}_3)_{16}$  cluster.<sup>[12]</sup> From different DFT studies on thiol–gold cluster systems, it has been found that the main driving force

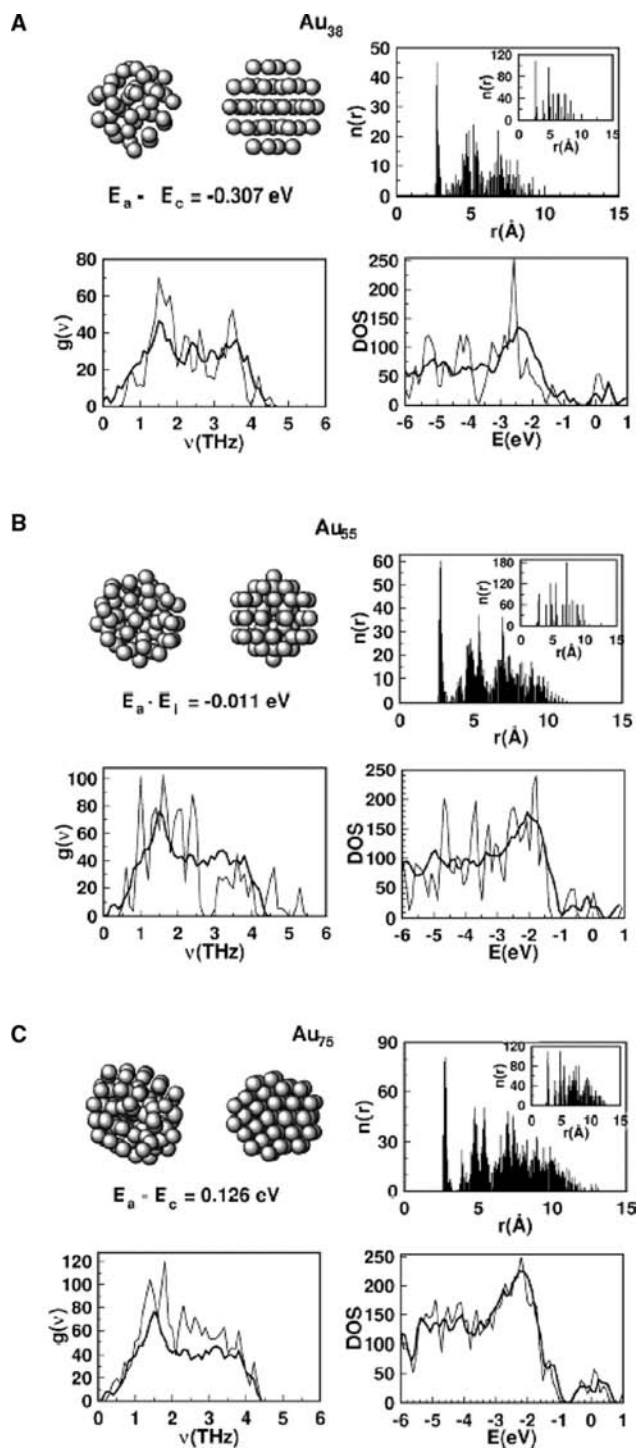


**Fig. 2** Cluster structures, distribution of interatomic distances, vibrational density of states, and total electronic density of states (DOS) for the lowest-energy amorphous and ordered isomers of  $Au_n$  ( $n = 38, 55, 75$ ) nanoclusters. The DFT-LDA calculated difference in cluster energy between the lowest-energy amorphous isomer and the first-ordered structure is shown. The insets show the distribution of interatomic distances of the ordered isomers. Vibrational and electronic DOS results for the ordered isomers are also included for comparison (thinner lines). *Source:* from Ref.<sup>[10]</sup>.

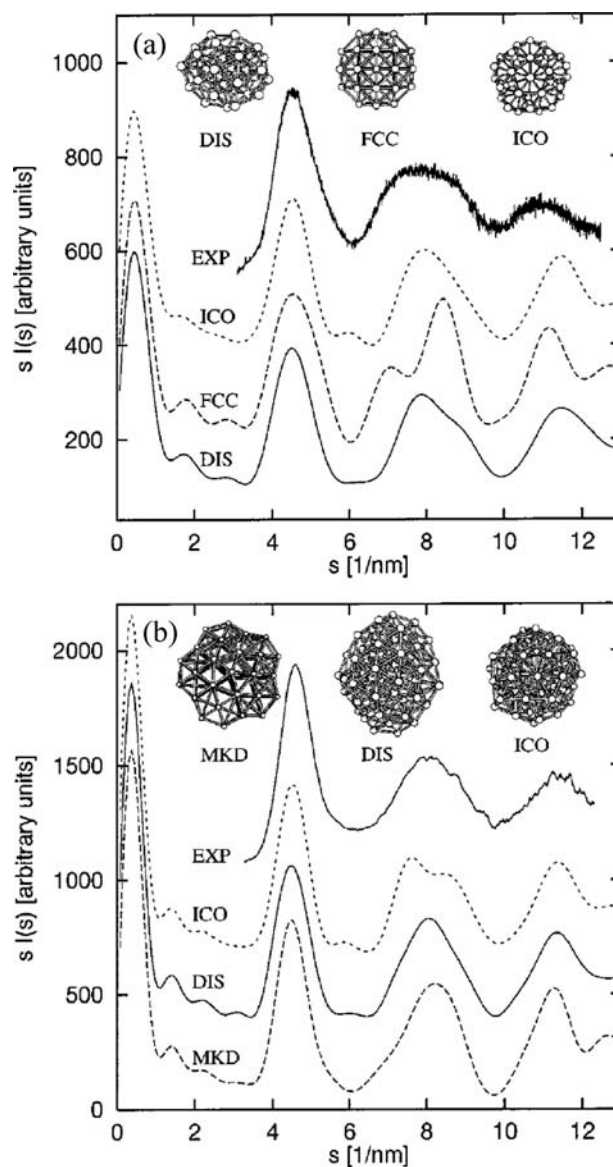


**Fig. 3** Comparison of the experimental structure factors (Refs.<sup>[20,21]</sup>) for  $Au_{38}$  (A) and  $Au_{75}$  (B) with those determined using calculated cluster configurations obtained by global optimization techniques and DFT relaxations. The solid line is for the disordered isomer, the dashed line is for the fcc structure, and the dot-dashed line is for the icosahedral structure. *Source:* From Ref.<sup>[29]</sup>.

producing the metal cluster distortion is the gold-sulfur interaction.<sup>[45-47]</sup> This corresponds to a strong covalent-like (directional) bond between the sulfur atom of the passivating thiol and the gold atoms in the metallic cluster core.<sup>[45-47]</sup>

## CHIRALITY IN GOLD NANOCLUSTERS

Although most of the theoretical results mentioned above on the degeneracy in energy of amorphous or



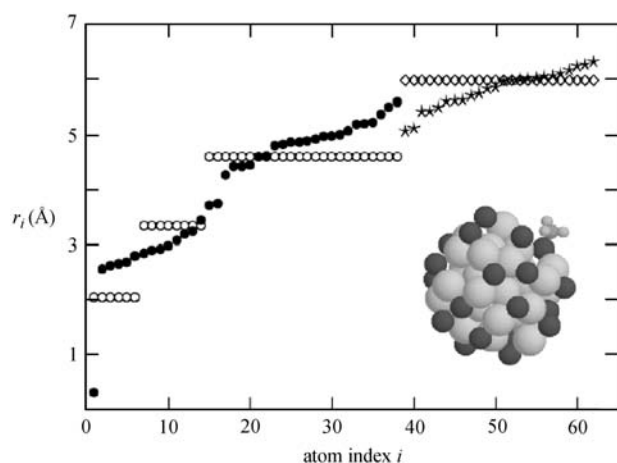


**Fig. 4** Distances of the gold ( $i = 1-38$ ) and sulfur ( $i = 39-62$ ) atoms from the cluster center of mass for the  $\text{Au}_{38}(\text{SCH}_3)_{24}$  nanocluster in the disordered (closed circles and stars) and the truncated octahedron fcc (open circles and diamonds) structures. The inset shows the relaxed disordered structure. Sulfur atoms are depicted as darker spheres and only one  $\text{CH}_3$  group is shown. Source: From Ref.<sup>[14]</sup>.

disordered isomers with ordered structures for intermediate-size gold clusters have been obtained by several research groups,<sup>[9-14,28-33,35,36,55]</sup> and the calculated XRPD structure factors of the disordered gold clusters are in qualitative agreement with the experimental data,<sup>[28,29]</sup> direct confirmation of the existence of bare and thiol-passivated gold nanoclusters with low or no spatial symmetry has not been possible. This is mainly because of the lack of enough experimental resolution in HRTEM and XRPD measurements for cluster in the size range of 1–2 nm.<sup>[20,21]</sup> Nevertheless, a recent study using circular dichroism techniques found strong optical activity in the metal-based electronic transitions (across the near-infrared, visible, and near ultraviolet regions) of size-separated glutathione-passivated gold clusters in the size range of 20–40 atoms.<sup>[58]</sup> In this work, it was pointed out that the most plausible interpretation of these results is that the structure of the metal cluster core of the gold glutathione cluster compound would be inherently chiral.<sup>[58]</sup> Moreover, because the most abundant cluster in the experimental samples corresponds to the passivated cluster  $\text{Au}_{28}(\text{SG})_{16}$ , where SG denote the glutathione adsorbate, a chiral structure with  $T$  point group for the  $\text{Au}_{28}$  cluster was proposed.<sup>[58]</sup>

In earlier studies, several structural, vibrational, and electronic properties of disordered gold nanoclusters have been reported.<sup>[10-12,55,59]</sup> Although an initial quantification of the amount and type of local disorder present in amorphous-like structures of  $\text{Au}_{55}$  was obtained,<sup>[55]</sup> no attempt to theoretically investigate the existence of chirality in gold nanoclusters has been

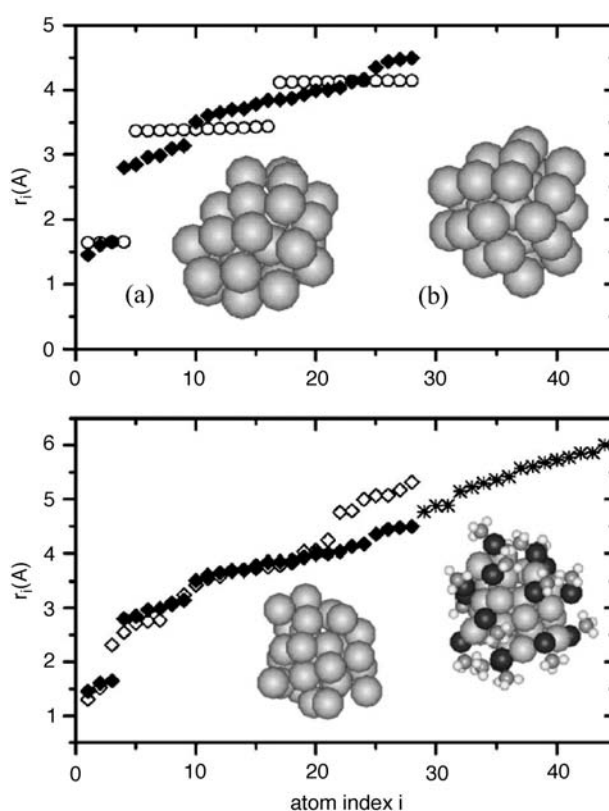


**Fig. 5** Top panel: distances of the gold atoms from the center of mass and cluster geometry for the lowest-energy disordered [closed diamonds and inset (A)] and the  $T$  [open circles and inset (B)] isomers of the bare  $\text{Au}_{28}$  cluster. Bottom panel: distances of the gold (open diamonds) and sulfur (stars) atoms from the center of mass for the lowest-energy structure of the thiol-passivated  $\text{Au}_{28}(\text{SCH}_3)_{16}$  cluster. The closed diamonds denote the same gold atom distances as in the top panel. They are included to show at the same scale the degree of distortion and expansion of the gold metal cluster core upon passivation. The insets show the geometries of the chiral metal cores and the passivated clusters. Sulfur atoms are depicted as darker spheres. Source: From Ref.<sup>[12]</sup>.

reported. Very recently, a theoretical study on the existence and quantification of chirality in bare and thiol-passivated nanoclusters was published.<sup>[11,12]</sup> In this study, the asymmetrical structures corresponding to the lowest-energy configurations of several cluster sizes, obtained by the theoretical approach described above, have been analyzed to calculate their index of chirality.<sup>[11,12]</sup> This information is relevant for a proper interpretation of the circular dichroism measurements performed on glutathione-passivated gold nanoclusters.<sup>[11,12]</sup>

Because chirality is a geometrical property of the system, independent of its chemical and physical manifestations, it is possible to quantify chirality without reference to experimental measurements, but using

the inherent structural symmetry of the clusters. Although in recent years several approaches have been developed to measure chirality,<sup>[60,61]</sup> the Hausdorff chirality measure (HCM) has emerged as the general method of choice for the quantification of chirality.<sup>[62,63]</sup> Within this approach, the degree of chirality is found by calculating the maximum overlap between the actual molecular structure and its mirror image, using the Hausdorff distance between the sets of atomic coordinates. By rotating and translating one structure with respect to the other, the optimal overlap can be calculated. The HCM is a continuous and similarity-invariant function of the molecular shape and is zero only if the molecule is achiral.<sup>[62,63]</sup> The advantage of this approach is that its numerical implementation for large cluster sizes in a three-dimensional space is straightforward.<sup>[11,12]</sup>

The HCM for the lowest-energy structures of the bare and passivated gold nanoclusters can be calculated using their relaxed Cartesian coordinates measured with respect to the cluster center of mass.<sup>[11,12]</sup> Through an inversion operation, the coordinates of the mirror-image clusters are obtained. By calculating the maximum overlap between a given cluster and its mirror image, the HCM is obtained. This corresponds to the minimum value of the Hausdorff distance between the sets of atomic coordinates of both structures. To obtain the minimum Hausdorff distance, the mirror cluster is translated and rotated around the original cluster in the three-dimensional space generating different configurations. For each configuration, the Hausdorff distance with respect to the original cluster is calculated. The minimum of these values, normalized by the largest interatomic distance in the cluster, corresponds to the HCM.<sup>[11,12]</sup>

Chiral structures, with HCM values different from zero, have been obtained for the lowest-energy isomers of bare (Au<sub>28</sub> and Au<sub>55</sub>) and thiol-passivated [Au<sub>28</sub>(SCH<sub>3</sub>)<sub>16</sub> and Au<sub>38</sub>(SCH<sub>3</sub>)<sub>24</sub>] gold nanoclusters using the HCM approach.<sup>[11,12]</sup> For the lowest-energy isomers of bare Au<sub>38</sub> and Au<sub>75</sub> clusters, the HCM index of chirality is zero. These values are expected because the lowest-energy structures corresponding to these sizes have one plane of symmetry and therefore are achiral. By comparing the HCM index of chirality of bare and passivated gold nanoclusters, an interesting theoretical prediction,<sup>[11,12]</sup> to be confirmed experimentally, indicates that the effect of the passivating thiol monolayer is strong enough to distort the bare cluster geometry, producing chiral metal cores that give rise to intense chiroptical activity. This effect could change an achiral cluster into a chiral one as in the Au<sub>38</sub> case or increase the index of chirality in an already chiral structure as in the Au<sub>28</sub> cluster.<sup>[11,12]</sup>

The HCM values calculated for bare and passivated clusters have been compared with the corresponding values of other chiral nanostructures such as the D<sub>2</sub>-C<sub>78</sub> and D<sub>2</sub>-C<sub>84</sub> fullerenes. It shows that the chiral gold clusters are as chiral as those fullerenes.<sup>[11,12]</sup> However, it remains to be seen if clusters with different chirality can be detected experimentally. In this respect, circular dichroism spectroscopy seems to be an appropriate technique to study the above effect, as has been suggested by the optical activity measurements in passivated gold-glutathione cluster compounds.<sup>[58]</sup> At present, it is expected that novel and interesting properties emerge from the chiral character of metal clusters that could be useful for new applications.

## CONCLUSION

Along this entry, several trends and predictions on the most stable configurations of bare and passivated gold nanoclusters, obtained through a theoretical approach that incorporates “state-of-the-art” techniques,<sup>[39–42]</sup> have been discussed. The main conclusion emerging from these studies indicates the existence of many topologically interesting low-symmetry, disordered structures, nearly degenerate in energy.<sup>[9–14,28–36]</sup> Specifically, planar,<sup>[34,36,50–54]</sup> low-symmetry,<sup>[9–12,28–33,35,36,55,59]</sup> chiral,<sup>[11,12]</sup> and defective<sup>[13]</sup> structures have been obtained as the most stable configurations for bare gold clusters in the size range of 3–200 atoms. On the other hand, highly distorted structures were found for gold clusters with 20–40 atoms upon passivation with thiol monolayers.<sup>[9,11,12,14]</sup> Experimental techniques such as HRTEM,<sup>[16,56,57]</sup> XRPD,<sup>[23]</sup> and circular dichroism<sup>[58]</sup> have now been used to provide further evidence to support the above predictions.

The existence and the stability of disordered structures of bare and passivated gold nanoclusters have opened the possibility of using these amorphous-like nanostructures as building-blocks of gold-based nanostructured materials, where the nanoscale disorder may produce interesting behavior with potential nanotechnological applications. Although most of the results on disordered nanostructures described in this entry have focused on gold nanoclusters, other metals may have similar structural behavior as indicated by recent theoretical studies.<sup>[59]</sup> One important characteristic of the structural nanoscale disorder existing in gold clusters is that it is not a result of kinetic or temperature effects,<sup>[64]</sup> but of the complexity of the cluster potential energy landscape generated by the special bonding mechanisms involving Au atoms, where nonadditive,<sup>[50,51]</sup> relativistic,<sup>[52,53]</sup> and strong *sp-d* hybridization<sup>[52,53]</sup> effects are present.

## ACKNOWLEDGMENTS

I have greatly benefited from collaborations with E. Artacho, M.R. Beltrán, G. Bravo-Pérez, A. García, J. Junquera, K. Michaelian, O. Novaro, P. Ordejón, A. Posada-Amarillas, J.A. Reyes-Nava, J.I. Rodríguez-Hernández, C. Rovira, D. Sánchez-Portal, and J.M. Soler.

This work has been supported by DGAPA-UNAM grant IN104402 and DGSCA-UNAM Supercomputing Center.

## REFERENCES

- Moriarty, P. Nanostructured materials. *Rep. Prog. Phys.* **2001**, *64* (3), 297–381.
- Bethell, D.; Schiffrin, D.J. Supramolecular chemistry—nanotechnology and nucleotides. *Nature* **1996**, *382* (6592), 581
- Zanchet, D.; Micheel, C.M.; Parak, W.J.; Gerion, D.; Alivisatos, A.P. Electrophoretic isolation of discrete Au nanocrystal/DNA conjugates. *Nano Lett.* **2001**, *1* (1), 32–35.
- Whetten, R.L.; Khoury, J.T.; Alvarez, M.M.; Murthy, S.; Vezmar, I.; Wang, Z.L.; Stephens, P.W.; Cleveland, C.L.; Luedtke, W.D.; Landman, U. Nanocrystal gold molecules. *Adv. Mater.* **1996**, *8* (5), 428–433.
- Andres, R.P.; Bein, T.; Dorogi, M.; Feng, S.; Henderson, J.I.; Kubiak, C.P.; Mahony, W.; Osifchin, R.G.; Reifengerger, R. Coulomb staircase at room temperature in a self-assembled molecular nanostructure. *Science* **1996**, *272* (5266), 1323–1325.
- Andres, R.P.; Bielefeld, J.D.; Henderson, J.I.; Janes, J.B.; Kolagunta, V.R.; Kubiak, C.P.; Mahony, W.J.; Osifchin, R.G. Self-assembly of a two-dimensional superlattice of molecularly linked metal clusters. *Science* **1996**, *273* (5282), 1690–1693.
- Mirkin, C.A.; Letsinger, R.L.; Mucic, R.C.; Storhoff, J.J. A DNA-based method for rationally assembling nanoparticles into macroscopic materials. *Nature* **1996**, *382* (6592), 607–609.
- Alivisatos, A.P.; Johnsson, K.P.; Peng, X.; Wilson, T.E.; Loweth, C.J.; Bruchez, M.P., Jr.; Schultz, P.G. Organization of nanocrystal molecules using DNA. *Nature* **1996**, *382* (6592), 609–611.
- Garzón, I.L.; Artacho, E.; Beltrán, M.R.; García, A.; Junquera, J.; Michaelian, K.; Ordejón, P.; Rovira, C.; Sánchez-Portal, D.; Soler, J.M. Hybrid DNA-gold nanostructured materials: An ab initio approach. *Nanotechnology* **2001**, *12* (2), 126–131.
- Garzón, I.L.; Michaelian, K.; Beltrán, M.R.; Posada-Amarillas, A.; Ordejón, P.; Artacho, E.; Sánchez-Portal, D.; Soler, J.M. Lowest-energy structures of gold nanoclusters. *Phys. Rev. Lett.* **1998**, *81* (8), 1600–1603.
- Garzón, I.L.; Beltrán, M.R.; González, G.; Gutiérrez-González, I.; Michaelian, K.; Reyes-Nava, J.A.; Rodríguez-Hernández, J.I. Chirality, defects, and disorder in gold clusters. *Eur. Phys. J. D* **2003**, *24* (1-3), 105–109.
- Garzón, I.L.; Reyes-Nava, J.A.; Rodríguez-Hernández, J.I.; Sigal, I.; Beltrán, M.R.; Michaelian, K. Chirality in bare and passivated gold nanoclusters. *Phys. Rev. B* **2002**, *66* (7), 073403.
- Beltrán, M.R.; González, G.; Rodríguez-Hernández, J.I.; Reyes-Nava, J.A.; Michaelian, K.; Garzón, I.L. Defective decahedral structures in gold nanoclusters. In *Book of Abstracts*, 11th International Symposium on Small Particles and Inorganic Clusters: ISSPIC-11, Strasbourg, France, Sept. 9–13, 2002.
- Garzón, I.L.; Rovira, C.; Michaelian, K.; Beltrán, M.R.; Ordejón, P.; Junquera, J.; Sánchez-Portal, D.; Artacho, A.; Soler, J.M. Do thiols merely passivate gold nanoclusters? *Phys. Rev. Lett.* **2000**, *85* (24), 5250–5251.
- Marks, L.D. Experimental studies of small particle structures. *Rep. Prog. Phys.* **1994**, *57* (6), 603–649.
- Ascencio, J.A.; Gutiérrez-Wing, C.; Espinosa, M.E.; Marín, M.; Tehuacanaro, S.; Zorrilla, C.; José-Yacamán, M. Structure determination of small particles by HRTEM imaging: theory and experiment. *Surf. Sci.* **1998**, *396* (1–3), 349–368.
- Zanchet, D.; Moreno, M.S.; Ugarte, D. Anomalous packing in thin nanoparticle supercrystals. *Phys. Rev. Lett.* **1999**, *82* (26), 5277–5280.
- Pauwels, B.; Van Tendeloo, G.; Bouwen, W.; Theil Kuhn, L.; Lievens, P.; Lei, H.; Hou, M. Lowest-energy deposited Au clusters investigated by high-resolution electron microscopy and molecular dynamics simulations. *Phys. Rev. B* **2000**, *62* (15), 10,383–10,393.
- José-Yacamán, M.; Ascencio, J.A.; Liu, H.B.; García-Torresdey, J. Structure, shape, and stability of nanometric sized particles. *J. Vac. Sci. Technol. B* **2001**, *19* (4), 1091–1103.
- Schaaff, T.G.; Shafiqullin, M.N.; Khoury, J.T.; Vezmar, I.; Whetten, R.L.; Cullen, W.G.; First, P.N.; Gutiérrez-Wing, C.; Ascencio, J.A.; José-Yacamán, M. Isolation of smaller nanocrystal Au molecules: Robust quantum effects in optical spectra. *J. Phys. Chem. B* **1997**, *101* (40), 7885–7891.
- Cleveland, C.L.; Landman, U.; Schaaff, T.G.; Shafiqullin, M.N.; Stephens, P.W.; Whetten, R.L. Structural evolution of smaller gold nanocrystals: the truncated decahedral motif. *Phys. Rev. Lett.* **1997**, *79* (10), 1873–1876.
- Cleveland, C.L.; Landman, U.; Shafiqullin, M.N.; Stephens, P.W.; Whetten, R.L. Structural evolution of larger clusters. *Z. Phys. D* **1997**, *40* (1–4), 503–508.
- Zanchet, D.; Hall, B.D.; Ugarte, D. Structure population in thiol-passivated gold nanoparticles. *J. Phys. Chem. B* **2000**, *104* (47), 11,013–11,018.
- Durston, P.J.; Schmidt, J.; Palmer, R.E.; Wilcoxon, J.P. Scanning tunneling microscopy of ordered coated cluster layers on graphite. *Appl. Phys. Lett.* **1997**, *71* (20), 2940–2942.
- Harrell, L.E.; Bigioni, T.P.; Cullen, T.P.; Whetten, R.L.; First, P.N. Scanning tunneling microscopy of passivated Au nanocrystals immobilized on Au(111) surface. *J. Vac. Sci. Technol. B* **1999**, *17* (6), 2411–2416.

26. Zanchet, D.; Tolentino, H.; Matins Alves, M.C.; Alves, O.L.; Ugarte, D. Inter-atomic distance in thiol-passivated gold nanoparticles. *Chem. Phys. Lett.* **2000**, *323* (1–2), 167–172.
27. Benfield, R.E.; Grandjean, D.; Kröll, M.; Pugin, R.; Sawitowski, T.; Schmidt, G. Structure and bonding of gold metal clusters, colloids, and nanowires studied by EXAFS, XANES, and WAXS. *J. Phys. Chem. B* **2001**, *105* (10), 1961–1970.
28. Garzón, I.L.; Michaelian, K.; Beltrán, M.R.; Posada-Amarillas, A.; Ordejón, P.; Artacho, E.; Sánchez-Portal, D.; Soler, J.M. Structure and thermal stability of gold nanoclusters: the Au<sub>38</sub> case. *Eur. Phys. J. D* **1999**, *9* (1–4), 211–215.
29. Michaelian, K.; Rendón, N.; Garzón, I.L. Structure and energetics of Ni, Ag, and Au nanoclusters. *Phys. Rev. B* **1999**, *60* (3), 2000–2010.
30. Li, T.X.; Yin, S.Y.; Yi, Y.L.; Wang, B.L.; Wang, G.H.; Zhao, J.J. A genetic algorithm study on the most stable disordered and ordered configurations of Au<sub>38</sub>–55. *Phys. Lett. A* **2000**, *267* (5–6), 403–407.
31. Michaelian, K.; Beltrán, M.R.; Garzón, I.L. Disordered global-minima structures for Zn and Cd nanoclusters. *Phys. Rev. B* **2002**, *65* (4), 041403(R)
32. Darby, S.; Mortimer-Jones, T.V.; Johnston, R.L.; Roberts, C. Theoretical study of Cu–Au nanoalloy clusters using a genetic algorithm. *J. Chem. Phys.* **2002**, *116* (4), 1536–1550.
33. Soler, J.M.; Beltrán, M.R.; Michaelian, K.; Garzón, I.L.; Ordejón, P.; Sánchez-Portal, D.; Artacho, E. Metal bonding and cluster structure. *Phys. Rev. B* **2000**, *61* (8), 5771–5780.
34. Häkkinen, H.; Landman, U. Gold clusters (Au<sub>N</sub>, 2 ≤ N ≤ 10) and their anions. *Phys. Rev. B* **2000**, *62* (4), R2287–R2290.
35. Soler, J.M.; Garzón, I.L.; Joannopoulos, J.D. Structural patterns of unsupported gold clusters. *Solid State Commun.* **2001**, *117* (10), 621–625.
36. Wang, J.; Wang, G.; Zhao, J. Density-functional study of Au<sub>n</sub> (n = 2–20) clusters: Lowest-energy structures and electronic properties. *Phys. Rev. B* **2002**, *66* (3), 035418
37. Rosato, V.; Guillope, M.; Legrand, B. Thermodynamical and structural properties of fcc transition metals using a simple tight-binding model. *Philos. Mag.*, **A** **1989**, *59* (2), 321–336.
38. Cleri, F.; Rosato, V. Tight-binding potentials for transition metals and alloys. *Phys. Rev. B* **1993**, *48* (1), 22–33.
39. Michaelian, K. A symbiotic algorithm for finding the lowest energy isomers of large clusters and molecules. *Chem. Phys. Lett.* **1998**, *293* (3–4), 202–208.
40. Michaelian, K. Evolving few-ion clusters of Na and Cl. *Am. J. Phys.* **1998**, *66* (3), 231–240.
41. Artacho, E.; Sánchez-Portal, D.; Ordejón, P.; García, A.; Soler, J.M. Linear-scaling ab-initio calculations for large and complex systems. *Phys. Status Solidi B* **1999**, *215* (1), 809–817.
42. Payne, M.C.; Teter, M.P.; Allan, D.C.; Arias, T.A.; Joannopoulos, J.D. Iterative minimization techniques for ab initio total-energy calculations: molecular dynamics and conjugate gradients. *Rev. Mod. Phys.* **1992**, *64* (4), 1045–1097.
43. Häkkinen, H.; Barnett, R.N.; Landman, U. Electronic structure of passivated Au<sub>38</sub>(SCH<sub>3</sub>)<sub>24</sub> nanocrystal. *Phys. Rev. Lett.* **1999**, *82* (16), 3264–3267.
44. Andreoni, W.; Curioni, A.; Grönbeck, H. Density functional theory approach to thiols and disulfides on gold: Au(111) surface and clusters. *Int. J. Quantum Chem.* **2000**, *80* (4–5), 598–608.
45. Krüger, D.; Fuchs, H.; Rosseau, R.; Marx, D.; Parrinello, M. Interaction of short-chain alkane thiols and thiolates with small gold clusters: Adsorption structures and energetics. *J. Chem. Phys.* **2001**, *115* (10), 4776–4786.
46. Larsson, J.A.; Nolan, M.; Greer, J.C. Interactions between thiol molecular linkers and the Au<sub>13</sub> nanoparticle. *J. Phys. Chem. B* **2002**, *106* (23), 5931–5937.
47. Krüger, D.; Fuchs, H.; Rosseau, R.; Marx, D.; Parrinello, M. Pulling monatomic gold wires with single molecules: an ab initio simulation. *Phys. Rev. Lett.* **2002**, *89* (18), 186402.
48. Majumder, C.; Briere, T.M.; Mizuseki, H.; Kawasoe, Y. Structural investigation of thiophene thiol adsorption on Au nanoclusters: influence of back bonds. *J. Chem. Phys.* **2002**, *117* (6), 2819–2822.
49. Luedtke, W.D.; Landman, U. Structure, dynamics, and thermodynamics of passivated gold nanocrystallites and their assemblies. *J. Phys. Chem.* **1996**, *100* (32), 13,323–13,329.
50. Bravo-Pérez, G.; Garzón, I.L.; Novaro, O. Ab initio study of small gold clusters. *J. Mol. Struct., Theochem* **1999**, *493* (1–3), 225–231.
51. Bravo-Pérez, G.; Garzón, I.L.; Novaro, O. Non-additive effects in small gold clusters. *Chem. Phys. Lett.* **1999**, *313* (3–4), 655–664.
52. Häkkinen, H.; Moseler, M.; Landman, U. Bonding in Cu, Ag, and Au clusters: Relativistic effects, trends, and surprises. *Phys. Rev. Lett.* **2002**, *89* (3), 033401.
53. Bonacic-Koutecky, V.; Burda, J.; Mitric, R.; Ge, M.; Zampella, G.; Fantucci, P. Density functional study of structural and electronic properties of bimetallic silver–gold clusters: Comparison with pure gold and silver clusters. *J. Chem. Phys.* **2002**, *117* (7), 3120–3131.
54. Gilb, S.; Weis, P.; Furche, F.; Ahlrichs, R.; Kappes, M.M. Structures of small gold cluster cations (Au<sub>n</sub><sup>+</sup>, n < 14): Ion mobility measurements versus density functional calculations. *J. Chem. Phys.* **2002**, *116* (10), 4094–4101.
55. Garzón, I.L.; Posada-Amarillas, A. Structural and vibrational analysis of amorphous Au<sub>55</sub> clusters. *Phys. Rev. B* **1996**, *54* (16), 11796–11802.
56. Tehuacanero, S.; Herrera, R.; Avalos, M.; Yacamán, M.J. High resolution TEM studies of gold and palladium nanoparticles. *Acta Metall. Mater.* **1992**, *40* (7), 1663–1674.
57. Krakow, W.; José-Yacamán, M.; Aragón, J.L. Observation of quasimelting at the atomic level in

- Au nanoclusters. *Phys. Rev. B* **1994**, *49* (15), 10591–10596.
58. Shaaff, G.T.; Whetten, R.L. Giant gold–glutathione cluster compounds: Intense optical activity in metal-based transitions. *J. Phys. Chem. B* **2000**, *104* (12), 2630–2641.
59. Oviedo, J.; Palmer, R.E. Amorphous structures of Cu, Ag, and Au nanoclusters from first principles calculations. *J. Chem. Phys.* **2002**, *117* (21), 9548–9551.
60. Weinberg, N.; Mislow, K. A unification of chirality measures. *J. Math. Chem.* **1995**, *17* (1), 35–53.
61. Solymosi, M.; Low, R.J.; Grayson, M.; Neal, M.P. A generalized scaling of a chiral index for molecules. *J. Chem. Phys.* **2002**, *116* (22), 9875–9881.
62. Buda, A.B.; Mislow, K. A Hausdorff chirality measure. *J. Am. Chem. Soc.* **1992**, *114* (15), 6006–6012.
63. Buda, A.B.; Auf der Heyde, T.; Mislow, K. On quantifying chirality. *Angew. Chem., Int. Ed. Engl.* **1992**, *31* (6), 989–1007.
64. Baletto, F.; Mottet, C.; Ferrando, R. Reentrant morphology transition in the growth of free silver nanoclusters. *Phys. Rev. Lett.* **2000**, *84* (24), 5544–5547.

# Gold Nanoparticles on Titania: Activation and Behavior

Jose A. Rodriguez

Chemistry Department, Brookhaven National Laboratory,  
Upton, New York, U.S.A.

## INTRODUCTION

Gold nanoparticles supported on titania show a high activity in many catalytic processes, including the oxidation of CO and the destruction of SO<sub>2</sub>. This is a remarkable phenomenon because surfaces of bulk metallic gold are not good catalysts. In recent years, many experimental and theoretical studies have been focused on understanding the high catalytic activity of gold nanoparticles supported on titania. Quantum effects related to the small size of the particles could be responsible for the enhancement in catalytic activity with respect to bulk gold, but it is becoming increasingly clear that interactions between the gold nanoparticles and the titania support plays a very important role. In this contribution, a review is presented of studies dealing with the behavior of a well-defined system such as Au/TiO<sub>2</sub>(110). The edge and corner sites of a gold nanoparticle (i.e., sites having three to four metal atom neighbors) can bond well adsorbates such as CO, O<sub>2</sub>, and SO<sub>2</sub>. They can even perform the catalytic oxidation of CO, but for more demanding reactions, the chemical activity of the isolated Au nanoparticles is not enough. A comparison of the DeSO<sub>x</sub> activity for the Au/TiO<sub>2</sub>(110) and Au/MgO(100) surfaces illustrates the important role played by gold–titania interactions. The titania support is not a simple spectator.

## CATALYTIC ACTIVITY OF BULK GOLD AND GOLD/TITANIA

Bulk metallic gold typically exhibits a very low chemical and catalytic activity.<sup>[1–4]</sup> Among the transition metals, gold is, by far, the least reactive and is often referred to as the “coinage metal.” Fig. 1 shows a valence photoemission spectrum for metallic gold.<sup>[5]</sup> The zero of binding energy represents the Fermi level of the system. States with Au 6s,p character appear from 0 to 2 eV, while the Au 5d states extend from 2 to 8 eV.<sup>[5]</sup> The low reactivity of metallic Au is a

consequence of combining a deep-lying valence 5d band and very diffuse valence 6s,p orbitals.<sup>[3,4,6]</sup>

In the last 10 years, gold has become the subject of considerable attention because of its unusual catalytic properties when dispersed on some oxide supports.<sup>[7–29]</sup> The Au/TiO<sub>2</sub> system is particularly interesting.<sup>[8,14–20,23,25,28,29]</sup> Gold particles supported on titania are active catalysts for the low-temperature oxidation of CO, as shown in Fig. 2. This phenomenon was originally discovered by Haruta and coworkers in the early 1990s,<sup>[8]</sup> and has been corroborated by many subsequent studies.<sup>[7,10,19,25,27,29]</sup> The exact catalytic activity of the Au/TiO<sub>2</sub> system depends on the method of preparation and the dispersion of the metal on the support,<sup>[8,10,25,29]</sup> but in general, Au particles with sizes between 2 and 4 nm display a catalytic activity for CO oxidation much larger than that of bulk metallic gold. New preparation methods aim for the synthesis of very small Au particles (<2 nm) with an extremely high catalytic activity.<sup>[25]</sup> The Au/TiO<sub>2</sub> systems lose catalytic activity over time as a consequence of the sintering of the Au particles.<sup>[8,25]</sup> The smaller the initial size of the particles, the more dramatic the negative effects of sintering.

Au particles supported on titania are also efficient catalysts for the complete oxidation of methane, the selective or partial oxidation of propene, the hydrogenation of CO and olefins, the reduction of NO with hydrocarbons, and the decomposition of SO<sub>2</sub>.<sup>[8,9,11,24,28–31]</sup> Depending on the conditions, Au/TiO<sub>2</sub> is a useful catalysts for the destruction of the three major contaminants produced during the combustion of fossil-derived fuels: CO, NO, and SO<sub>2</sub>.<sup>[8,29,31]</sup> Several models have been proposed for explaining the activation of supported gold:<sup>[8,10,17–19,23,29,31]</sup> ranging from special electronic properties resulting from the limited size of the active gold particles (usually less than 10 nm),<sup>[8,10,19,31]</sup> to the effects of metal–support interactions (i.e., charge transfer between the oxide and gold).<sup>[15,18,23,31]</sup> In principle, the active sites for the catalytic reactions could be located only on the supported Au particles or on the perimeter of



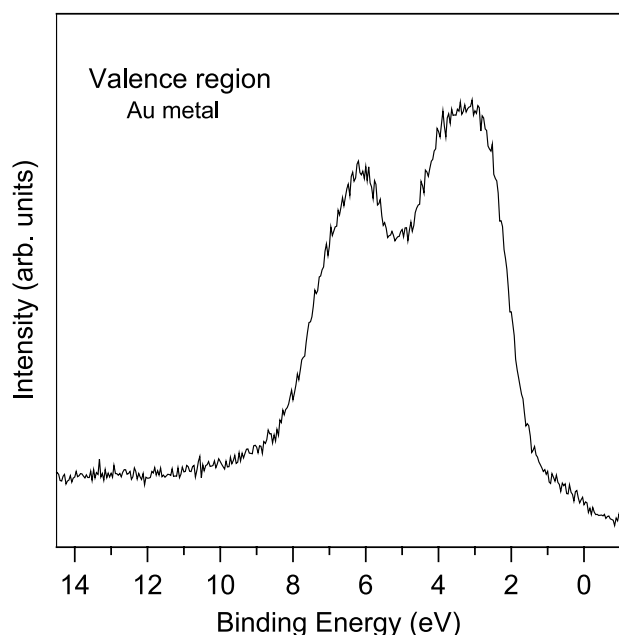


**Fig. 1** Valence photoemission spectrum for metallic gold. *Source:* From Ref.<sup>[5]</sup>.

the gold–oxide interface.<sup>[8,10,12,16,31]</sup> The Au/TiO<sub>2</sub>(110) surface appears as an ideal and well-defined system to examine some of these hypothesis in a controlled manner.<sup>[10,12,14–18,22,23,28]</sup>

## GOLD NANOPARTICLES ON TiO<sub>2</sub>(110)

Fig. 3 shows a schematic model for the (110) face of titania in its rutile phase. The surface exposes pentacoordinated Ti cations, while O atoms are present

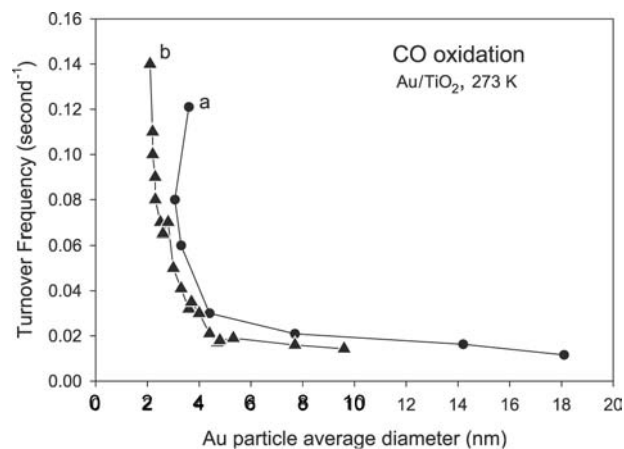


**Fig. 2** Turnover frequencies for CO oxidation at 300 K on Au/TiO<sub>2</sub> as a function of the mean particle diameter of Au. *Source:* From Refs.<sup>[8]</sup> (curve a) and <sup>[29]</sup> (curve b).

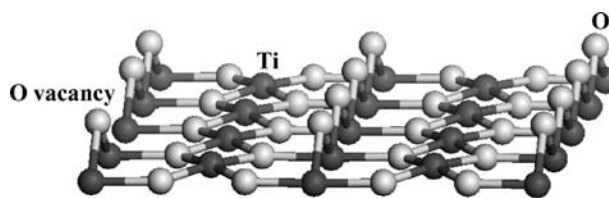


**Fig. 3** Schematic model for the TiO<sub>2</sub>(110) surface. Dark spheres represent Ti atoms, while white spheres represent O atoms.

at in-plane and bridging positions. O vacancies are usually created by the removal of O atoms from bridging positions. Several studies indicate that gold grows on TiO<sub>2</sub>(110) epitaxially, forming two- or three-dimensional particles (Volmer–Weber growth mode).<sup>[10,12,16]</sup> The formation of two-dimensional (2-D) clusters has been detected only at low gold coverages [ $<0.2$  monolayers (ML)] and moderate temperatures ( $<350$  K).<sup>[10,16]</sup> Although, thermodynamically, gold would prefer to form three-dimensional (3-D) islands from the onset of growth, kinetic limitations constrain the growth initially to two-dimensional (2-D) islands.<sup>[16]</sup> The critical gold coverage for a 2-D  $\rightarrow$  3-D transition decreases with temperature, and increases with the defect density of the TiO<sub>2</sub> surface.<sup>[10,16]</sup> At elevated temperatures ( $\sim 750$  K), 3-D particles are usually present on the oxide surface, without encapsulation of the Au islands by Ti suboxides.<sup>[10,12,16]</sup>

Fig. 4 shows an image of scanning tunneling microscopy (STM) for 0.25 ML of Au on TiO<sub>2</sub>(110)

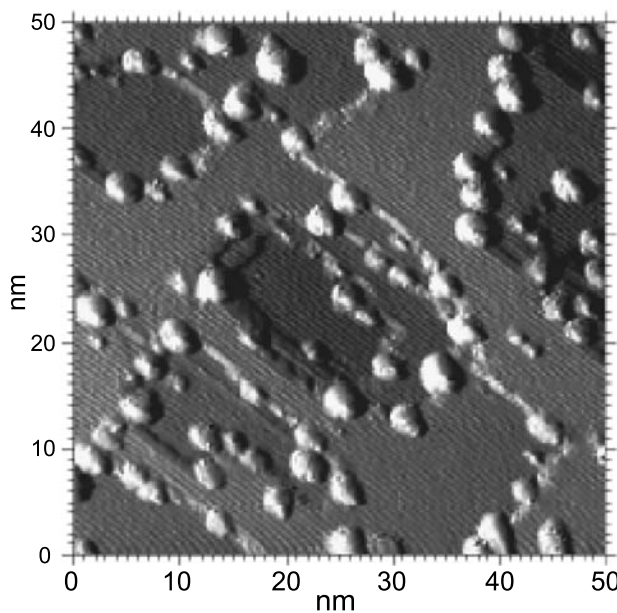


**Fig. 4** STM image for 0.25 ML of Au on TiO<sub>2</sub>(110). *Source:* From Ref.<sup>[10]</sup>.

after deposition of Au at 300 K and annealing at 850 K for 2 min.<sup>[10]</sup> The TiO<sub>2</sub>(110) surface consists of flat (1 × 1) terraces separated by monoatomic steps. The Au clusters are imaged as bright protrusions with a relatively narrow size distribution.<sup>[10]</sup> The clusters preferentially nucleate on the step edges of the TiO<sub>2</sub>(110) substrate and have an average size of ~2.6 nm in diameter and ~0.7 nm in height (two to three atomic layers). Studies of scanning tunneling spectroscopy (STS) indicate that the clusters have a small band gap (0.2–0.6 V) and electronic properties different from those of bulk metallic Au.<sup>[10]</sup> This is important, because such difference could be responsible for the variation in chemical activity when going from the nanoparticles to bulk gold.<sup>[10]</sup>

The nature of the interactions between Au and TiO<sub>2</sub>(110) has been examined in several theoretical studies.<sup>[15,17,18,23]</sup> In agreement with experimental observations, density-functional (DF) calculations show weak bonding interactions between Au atoms and stoichiometric TiO<sub>2</sub>(110). Au–Au bonds are stronger than Au–TiO<sub>2</sub> bonds, which explains the formation of mostly 3-D particles in Fig. 4. The results of STM and DF calculations show that Au adatoms prefer to interact with the O-vacancy sites present on the oxide support.<sup>[18,23,30]</sup> Theoretical studies<sup>[18,23]</sup> and photoemission measurements<sup>[15,23]</sup> indicate that the Au atoms bonded to these sites receive electron density from the oxide substrate. Fig. 5 displays Ti 2p photoemission spectra collected before and after dosing Au to a TiO<sub>2</sub>(110) surface.<sup>[23]</sup> The surface without gold (top) was initially annealed at 750 K for 2 min to induce the formation of O vacancies. In this way, one obtains a distribution of vacancies from the surface to the bulk of the sample. The Ti 2p spectrum for this system is well fitted<sup>[23]</sup> by a set of two doublets with p<sub>3/2</sub> components at 458.03 eV (Ti<sup>4+</sup>) and 455.96 eV (Ti<sup>3+</sup>). Under these conditions, the near surface region contains O vacancies with a density of ~7%. When Au is deposited on this surface at 300 K, the features between 454 and 456 eV gain relative intensity with respect to the main feature at ~458 eV and the resulting Ti 2p spectrum needs three doublets for a good fit (center of Fig 5). The p<sub>3/2</sub> components of these doublets appear at 458.06, 456.93, and 455.41 eV. The first peak is attributable to Ti<sup>4+</sup> cations, the last one corresponds to Ti<sup>3+</sup> species, and the middle one can be assigned to Ti<sup>3+</sup> ions weakly oxidized (Ti<sup>δ+</sup>) by interaction with Au.<sup>[23]</sup> Final annealing of the Au/TiO<sub>2</sub>(110) surface at 750 K produces a clear increase in the signal covering the 454–456 eV region because of a rise in the intensity of the Ti<sup>3+</sup> and Ti<sup>δ+</sup> peaks. This phenomenon is not a consequence of the oxidation of Au, or the evolution of O<sub>2</sub> into gas phase. It originates in the migration of O vacancies or Ti<sup>3+</sup> interstitial sites from the bulk to the surface of the oxide.<sup>[23]</sup> One has a

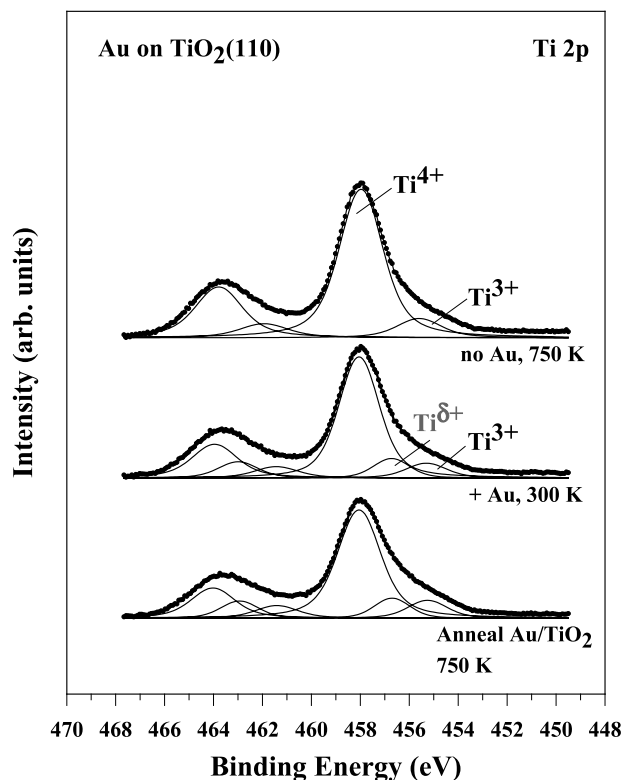


**Fig. 5** Ti 2p photoemission spectra taken before and after dosing 0.5 ML of gold to a TiO<sub>2</sub>(110) surface. In the first step, the clean oxide was annealed at 750 K, and then the top spectrum was recorded. This was followed by the dosing of Au at 300 K, middle, and final heating to 750 K, bottom. *Source:* From Ref.<sup>[23]</sup>.

complex situation, in which the admetal modifies the rate of exchange of defects between the bulk and surface of the oxide, and at the same time, the presence of O vacancies in the surface electronically perturbs the gold, probably making it more chemically active.

### OXIDATION OF CARBON MONOXIDE ON Au/TiO<sub>2</sub>(110)

High surface area Au/TiO<sub>2</sub> catalysts are very efficient for the oxidation of CO.<sup>[8,25]</sup> The top panel in Fig. 6 shows how the CO oxidation activity of a Au/TiO<sub>2</sub>(110) surface changes as a function of particle diameter.<sup>[10]</sup> There is a marked size effect on the catalytic activity, with Au clusters in the range of 3.5 nm exhibiting the maximum reactivity. For this size, most of the particles have a band gap of 0.2–0.6 V according to STS (Fig. 6B and C). Particles with a larger band gap (>1 V) display a lower reactivity, and particles with metallic character (band gap ~0 V) are the least active. Thus there is a correlation between the electronic and chemical properties of the supported Au

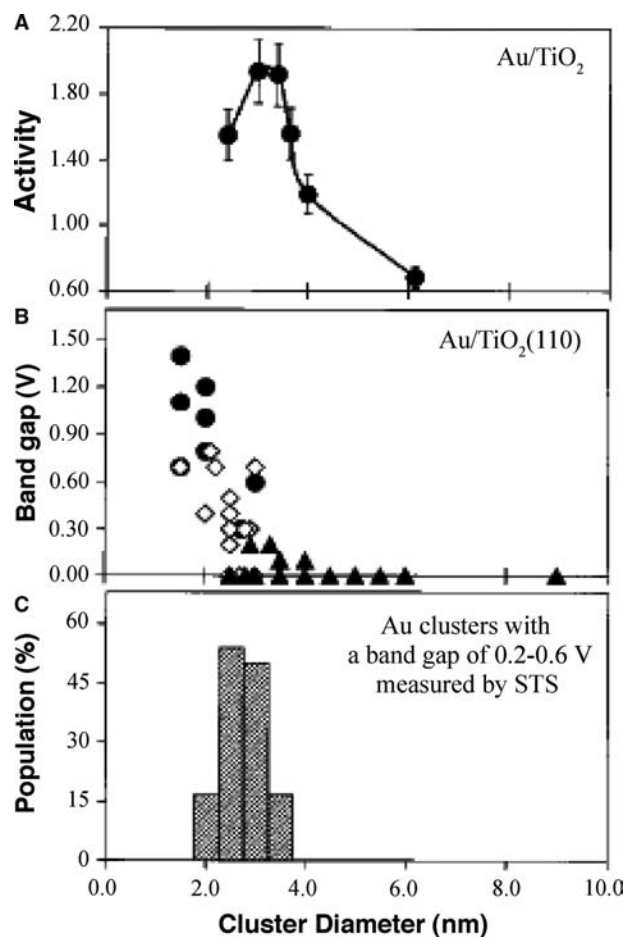


**Fig. 6** (A) The activity for CO oxidation at 350 K as a function of the Au cluster size supported on TiO<sub>2</sub>(110). (B) Cluster band gap measured by STS as a function of the Au cluster size supported on TiO<sub>2</sub>(110). (C) Relative population of the Au clusters that exhibited a band gap of 0.2–0.6 V as measured by STS. *Source:* From Ref.<sup>[10]</sup>.

nanoparticles. Studies of STM indicate that exposure to CO has no effect on the morphology of the Au/TiO<sub>2</sub>(110) surface.<sup>[10]</sup> On the other hand, significant morphological changes occur after exposure to O<sub>2</sub> or CO:O<sub>2</sub> mixtures. In these cases, the Au cluster density is considerably reduced as a result of sintering. The Au/TiO<sub>2</sub>(110) surfaces exhibit an exceptionally high reactivity toward O<sub>2</sub> at 300 K that promotes the sintering of the Au nanocrystallites.<sup>[10,14]</sup> This sintering eventually leads to a decrease in the CO oxidation activity of the Au/TiO<sub>2</sub>(110) systems.<sup>[10]</sup>

A transfer of electrons from the titania support to atoms in the Au nanoparticles could help to explain the high catalytic activity of Au/TiO<sub>2</sub><sup>[10,15,18]</sup> DF calculations have been used to study the CO oxidation process on an isolated (i.e., nonsupported) Au<sub>10</sub> cluster.<sup>[19]</sup> The results are summarized in Fig. 7. Two different reaction paths were considered: one where O<sub>2</sub> dissociates and one where adsorbed O<sub>2</sub> directly reacts

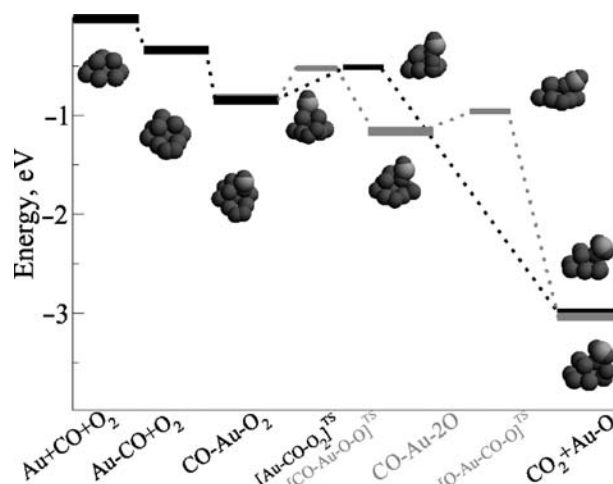


**Fig. 7** Calculated reaction profile for CO oxidation on a Au<sub>10</sub> particle. All energies are given with respect to CO and O<sub>2</sub> in gas phase. Black color, direct path; gray, indirect path. Thicker lines represent stable states, while thinner lines correspond to transition states. Light gray spheres represent Au atoms, dark spheres represent O atoms, and gray spheres represent C atoms. *Source:* From Ref.<sup>[19]</sup>.

with adsorbed CO. Both reactions were found to be extremely facile on the Au<sub>10</sub> particle, with reaction barriers of less than 0.4 eV indicating that the CO oxidation reaction should be possible well below room temperature.<sup>[19]</sup> This is contrary to the behavior found for a Au(111) surface. The small Au<sub>10</sub> cluster offers special geometrical configurations (corner and edge sites) that cannot be found on the extended surface.<sup>[19]</sup> The size and shape of the Au particle are important parameters. Also, the electronic structure of the Au atoms in the cluster is different from that of the Au atoms at the surface of a large crystal. The d states of Au<sub>10</sub> are 0.75 eV higher in energy than the d states of the surface atoms of an Au(111) surface.<sup>[19]</sup> These DF results show that an isolated Au nanoparticle could catalyze the oxidation of CO.

No theoretical study has been published examining the role of the oxide support during the oxidation of CO on Au/TiO<sub>2</sub>(110). Similar studies have been carried out in the case of the Au/MgO(100) system.<sup>[26,27]</sup> It appears that the smallest gold cluster that catalyzes the CO oxidation reaction is Au<sub>8</sub>.<sup>[26]</sup> A key aspect for the reactivity of this particle is its structural fluxionality that allows the adsorption and activation of O<sub>2</sub>.<sup>[26]</sup> DF calculations indicate that the active sites for CO oxidation on Au/MgO(100) involve low-coordinated Au atoms and Mg cations.<sup>[27]</sup> The oxide stabilizes a peroxolike intermediate, CO·O<sub>2</sub>, and then the oxidation reaction proceeds in the metal–oxide interface.<sup>[27]</sup> Such a reaction pathway is consistent with studies for Au/TiO<sub>2</sub> high-surface area catalysts,<sup>[31]</sup> which show that a strong contact between the Au

nanoparticles and oxide support is indispensable for high catalytic activity because the periphery sites probably carry out the oxidation of CO.

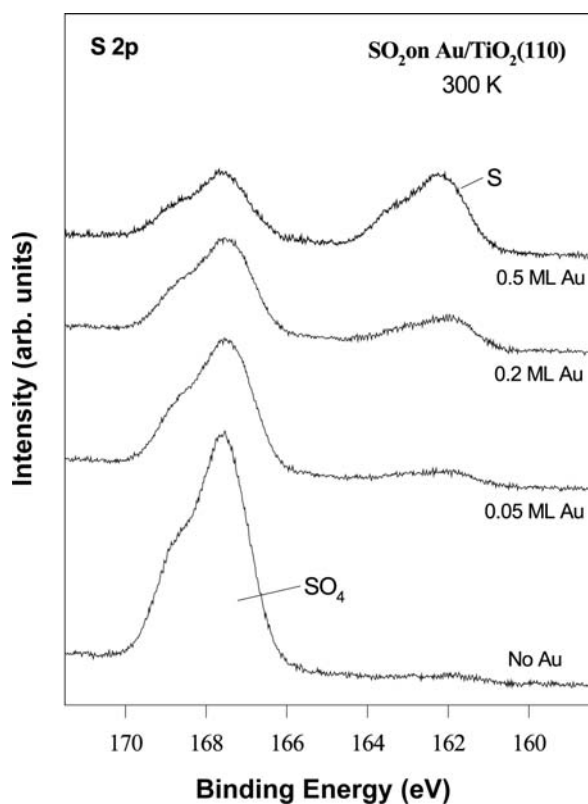
### DECOMPOSITION OF SULFUR DIOXIDE ON Au/TiO<sub>2</sub>(110)

Surfaces of metallic gold interact very weakly with SO<sub>2</sub> and the molecule desorbs intact at temperatures below 200 K.<sup>[23]</sup> Titania is the most common catalyst used in the chemical industry and oil refineries for the removal of SO<sub>2</sub> through the Claus reaction: SO<sub>2</sub> + 2H<sub>2</sub>S → 2H<sub>2</sub>O + 3S<sub>solid</sub>.<sup>[1,2,32]</sup> The main product of the adsorption of SO<sub>2</sub> on stoichiometric TiO<sub>2</sub>(110) are SO<sub>3</sub> and SO<sub>4</sub> species.<sup>[23,33]</sup> A substantial concentration of O vacancies on the oxide surface is necessary to induce the decomposition of SO<sub>2</sub> at high temperatures (>400 K). In contrast, Au/TiO<sub>2</sub>(110) surfaces fully dissociate SO<sub>2</sub> at room temperature.<sup>[23]</sup> Fig. 8 shows S 2p photoemission spectra for the adsorption of SO<sub>2</sub> on TiO<sub>2</sub>(110) and Au/TiO<sub>2</sub>(110) at 300 K. The Au/TiO<sub>2</sub>(110) surfaces were prepared following a procedure similar to that used to obtain the surface in Fig. 4.<sup>[10]</sup> The S 2p spectra indicate that upon adsorption of SO<sub>2</sub> on Au/TiO<sub>2</sub>(110), SO<sub>4</sub> and atomic

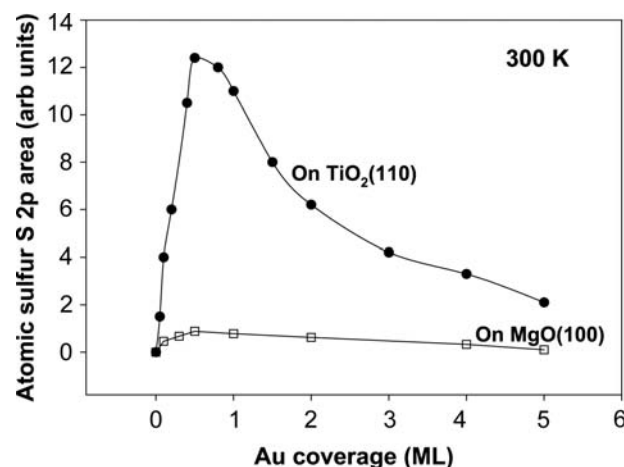
S (produced by the full dissociation of SO<sub>2</sub>) coexist on the surface. For the systems in Fig. 8, the larger the Au coverage on titania (0.05–0.5 ML range), the bigger the amount of atomic S deposited. This trend points to a direct involvement of gold in the dissociation of SO<sub>2</sub>. A large shift in the corresponding Au 4f core level spectra also supports this idea.<sup>[23]</sup>

Fig. 9 compares S 2p areas measured for atomic S after dosing the same amount of SO<sub>2</sub> to Au/TiO<sub>2</sub>(110) and Au/MgO(100) surfaces at 300 K.<sup>[28]</sup> Neither TiO<sub>2</sub>(110) nor MgO(100) is able to dissociate SO<sub>2</sub> on their own. On both oxide supports, the largest activity for the full dissociation of SO<sub>2</sub> is found in systems containing Au coverages smaller than 1 ML when the average diameter of the nanoparticles is below 5 nm.<sup>[10,28]</sup> Clearly, the Au/TiO<sub>2</sub>(110) systems are much more chemically active than the Au/MgO(100) systems. Catalytic tests also show that Au/TiO<sub>2</sub> is substantially more active than Au/MgO for the Claus reaction or the reduction of SO<sub>2</sub> with CO.<sup>[23,28]</sup> These data indicate that titania either play a direct active role in the dissociation of SO<sub>2</sub> or modifies the chemical properties of the supported Au nanoparticles.

DF calculations have been used to examine the adsorption of SO<sub>2</sub> on Au(100) and a series of clusters: Au<sub>6</sub>, Au<sub>8</sub>, and Au<sub>14</sub>.<sup>[28]</sup> Very weak bonding interactions were observed on the extended Au surface with adsorption energies smaller than 0.15 eV. On the other hand, the corner atoms in the Au clusters were able to interact reasonably well with SO<sub>2</sub>, giving adsorption energies of 0.43–0.65 eV. However, none of the isolated clusters was able to dissociate the SO<sub>2</sub> molecule. The DF calculations indicate that such a process is very



**Fig. 8** S 2p photoemission spectra for the adsorption of SO<sub>2</sub> on TiO<sub>2</sub>(110) and Au/TiO<sub>2</sub>(110) at 300 K. *Source:* From Ref.<sup>[23]</sup>.



**Fig. 9** Relative amounts of atomic S formed by the full dissociation of SO<sub>2</sub> on Au/MgO(100) and Au/TiO<sub>2</sub>(110) surfaces at 300 K. Each surface was exposed to the same amount of SO<sub>2</sub>. The S coverage is assumed to be proportional to the area under the corresponding S 2p XPS features. *Source:* From Ref.<sup>[28]</sup>.

endothermic on Au<sub>6</sub>, Au<sub>8</sub>, and Au<sub>14</sub>.<sup>[28]</sup> One of the most favorable cases found is shown in Fig. 10.<sup>[28]</sup> The adsorption of SO<sub>2</sub> on the Au<sub>14</sub> particle is an exothermic process but, upon heating, the molecule should desorb instead of dissociating. The chemistry observed experimentally for SO<sub>2</sub> on Au/MgO(100) seems to reflect mainly the intrinsic reactivity of Au nanoparticles with the oxide support playing only a minor role.<sup>[28]</sup>

Variations in the strength of metal–support interactions are probably the key to the large difference in chemical activity seen in Fig. 9 for Au/MgO and Au/TiO<sub>2</sub>. During the preparation of the active Au/TiO<sub>2</sub>(110) surfaces, the system is annealed to temperatures as high as 700–750 K to induce the formation of O vacancies and migration of bulk defects to the surface of the oxide.<sup>[23]</sup> Au particles like to interact with O vacancies,<sup>[15,18,23,30]</sup> and on these adsorption sites an oxide → gold charge transfer has been predicted from theoretical studies<sup>[15,18,23]</sup> and X-ray photoelectron

spectroscopy (XPS) measurements.<sup>[10,15,23]</sup> The active Au/TiO<sub>2</sub>(110) surfaces combine electronically perturbed Au atoms and an oxide substrate with a significant amount of defects. Both factors probably contribute to the high activity of these surfaces for the dissociation of SO<sub>2</sub>.<sup>[23]</sup> DF calculations for SO<sub>2</sub>/Au/TiO<sub>2</sub>(110) systems show several bonding conformations in which Au- and O-vacancy sites work in a cooperative way to dissociate the SO<sub>2</sub> molecule.<sup>[23]</sup> Thus the active sites should be at the Au–TiO<sub>2</sub> interface. In the case of MgO(100), the formation of O vacancies is a highly endothermic and difficult process.<sup>[34]</sup> In the Au/MgO(100) surfaces, a negligible number of O vacancies is expected and this probably leads to a low activity for the dissociation of SO<sub>2</sub>.

## CONCLUSION

Gold nanoparticles supported on titania show a high activity in many catalytic processes not seen for bulk metallic gold or titania. Quantum effects related to the small size of the particles could be responsible for the enhancement in catalytic activity with respect to bulk gold. The edge and corner sites of a gold nanoparticle have distinctive electronic properties and can bond well adsorbates such as CO, O<sub>2</sub>, and SO<sub>2</sub>. They can even perform the catalytic oxidation of CO, but for more demanding reactions, it is becoming increasingly clear that interactions between the gold nanoparticles and the titania support can play a very important role in determining chemical activity.

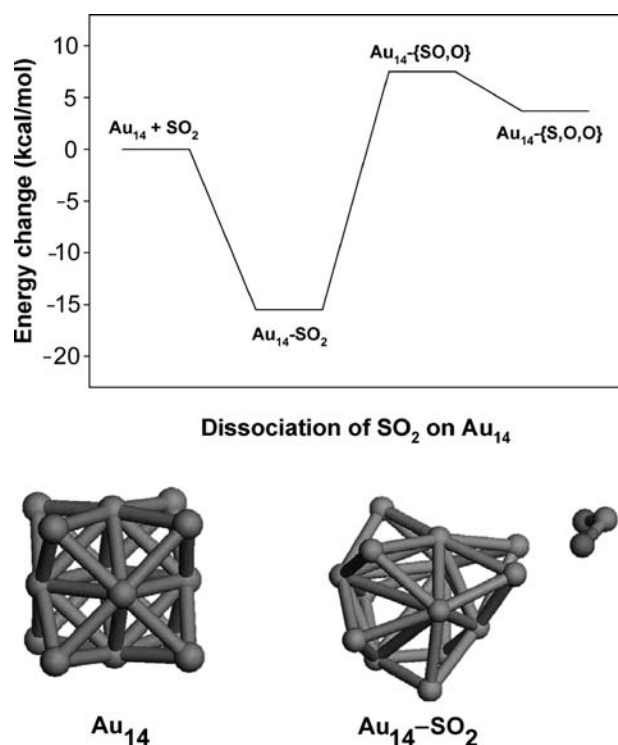


**Fig. 10** Bottom: Diagrams showing an isolated Au<sub>14</sub> cluster and the cluster with the SO<sub>2</sub> molecule bonded. The molecule is bonded via the oxygen atoms ( $\eta^2$ -O,O). Each oxygen atom is bonded to a corner site of the Au<sub>14</sub> cluster. Top: Change in energy for the dissociation of a SO<sub>2</sub> molecule on the Au<sub>14</sub> cluster. The zero of energy corresponds to an initial state with SO<sub>2</sub> and the Au<sub>14</sub> separated. Then, the SO<sub>2</sub> molecule is adsorbed in the configuration shown at the bottom of the figure. This is followed by cleavage of a S–O bond, and at the end, the molecule is fully dissociated into one S and two O atoms. *Source:* From Ref.<sup>[28]</sup>.

## ACKNOWLEDGMENTS

The author would like to thank Profs. D.W. Goodman, M. Haruta, and J. Nørskov for kindly allowing the reproduction of figures from their work. Many of the studies described here were done in collaboration with Z. Chang, J. Dvorak, J. Evans, L. González, J. Hrbek, F. Illas, T. Jirsak, G. Liu, A. Maiti, M. Pérez, and J.M. Ricart. I am very grateful to all of them. This research was supported by the U.S. Department of Energy, Division of Chemical Sciences.

## REFERENCES

1. Thomas, J.M.; Thomas, W. *J. Principles and Practice of Heterogeneous Catalysis*; VCH: New York, 1997.
2. Somorjai, G.A. *Introduction to Surface Chemistry and Catalysis*; Wiley: New York, 1994.
3. Cotton, F.A.; Wilkinson, G. *Advanced Inorganic Chemistry*, 5th Ed.; Wiley: New York, 1988.

4. Huheey, J.E. *Inorganic Chemistry*, 3rd Ed.; Harper & Row: New York, 1983.
5. Rodriguez, J.A.; Kuhn, M. Electronic properties of gold on Mo(110):  $d \rightarrow s,p$  charge redistribution and valence band shifts. *Surf. Sci.* **1995**, *330* (1), L657.
6. Hammer, B.; Nørskov, J.K. Why gold is the noblest of all the metals. *Nature* **1995**, *376* (6537), 238.
7. Haruta, M.; Tsubota, S.; Kobayashi, T.; Kageyama, H.; Genet, M.J.; Delmont, B. Low-temperature oxidation of CO over Gold Supported on  $\text{TiO}_2$ ,  $\alpha\text{-Fe}_2\text{O}_3$ , and  $\text{Co}_3\text{O}_4$ . *J. Catal.* **1993**, *144* (1), 175.
8. Haruta, M. Size- and support-dependency in the catalysis of gold. *Catal. Today* **1997**, *36* (1), 153.
9. Lin, S.D.; Bollinger, M.; Vannice, M.A. Hydrocarbon transformations on supported gold. *Catal. Lett.* **1993**, *17* (3–4), 245.
10. Valden, M.; Lai, X.; Goodman, D.W. Onset of catalytic activity of gold clusters on titania with the appearance of nonmetallic properties. *Science* **1998**, *281* (5383), 1647.
11. Jia, J.; Haraki, K.; Kondo, J.N.; Domen, K.; Tamaru, K. Selective hydrogenation of acetylene over a Au/ $\text{Al}_2\text{O}_3$  catalyst. *J. Phys. Chem., B* **2000**, *104* (47), 11153.
12. Consadey, F.; Zhang, L.; Madey, T.E. Effect of substrate temperature on the epitaxial growth of Au on  $\text{TiO}_2(110)$ . *Surf. Sci.* **2001**, *474* (1), 1.
13. Rodriguez, J.A.; Chaturvedi, S.; Kuhn, M.; van Ek, J.; Diebold, U.; Robbert, P.S.; Geisler, H.; Ventrice, C.A.  $\text{H}_2\text{S}$  adsorption on chromium, chromia, and gold/chromia surfaces: Photoemission studies. *J. Chem. Phys.* **1997**, *107* (21), 9146.
14. Bondzie, V.A.; Parker, S.C.; Campbell, C.T. Oxygen adsorption on well-defined gold particles on  $\text{TiO}_2(110)$ . *J. Vac. Sci. Technol., A* **1999**, *17* (4), 1717.
15. Yang, Z.; Wu, R.; Goodman, D.W. Structural and electronic properties of Au on  $\text{TiO}_2(110)$ . *Phys. Rev., B* **2000**, *61* (20), 14066.
16. Parker, S.C.; Grant, A.W.; Bondzie, V.A.; Campbell, C.T. Island growth kinetics during the vapor deposition of gold onto  $\text{TiO}_2(110)$ . *Surf. Sci.* **1999**, *441* (1), 10.
17. Giordano, L.; Pacchioni, G.; Bredow, T.; Fernández-Sanz, J. Cu, Ag, and Au atoms adsorbed on  $\text{TiO}_2(110)$ : Cluster and periodic calculations. *Surf. Sci.* **2001**, *471* (1), 21.
18. Vijay, A.; Mills, G.; Metiu, H.J. Adsorption of gold on stoichiometric and reduced rutile  $\text{TiO}_2(110)$  surfaces. *J. Chem. Phys.* **2003**, *118* (14), 6536.
19. Lopez, N.; Nørskov, J. Catalytic CO oxidation by a gold nanoparticle: A density functional study. *J. Am. Chem. Soc.* **2002**, *124* (38), 11262.
20. Cunningham, D.A.H.; Vogel, W.; Kageyama, H.; Tsubota, S.; Haruta, M. The relationship between the structure and activity of nanometer size gold when supported on  $\text{Mg}(\text{OH})_2$ . *J. Catal.* **1998**, *177* (1), 1.
21. Sanchez, A.; Abbet, S.; Heiz, U.; Schneider, W.D.; Hakkinen, H.; Barnett, R.N.; Landman, U. When gold is not noble: Nanoscale gold catalysts. *J. Phys. Chem., A* **1999**, *103* (48), 9573.
22. Campbell, C.T. Chemisorption on metal films on oxide surfaces. *Curr. Opin. Solid State Mater. Sci.* **1998**, *3* (5), 439.
23. Rodriguez, J.A.; Liu, G.; Jirsak, T.; Hrbek, J.; Chang, Z.; Dvorak, J.; Maiti, A. Activation of gold on titania: Adsorption and reaction of  $\text{SO}_2$  on Au/ $\text{TiO}_2(110)$ . *J. Am. Chem. Soc.* **2002**, *124* (18), 5242.
24. Okumura, M.; Akita, T.; Haruta, M. Hydrogenation of 1,3-butadiene over highly dispersed Au catalysts. *Catal. Today* **2002**, *74* (3–4), 265.
25. Schumacher, B.; Plzak, V.; Kinne, M.; Behm, R.J. Highly active Au/ $\text{TiO}_2$  catalysts for low-temperature CO oxidation: Preparation, conditioning and stability. *Catal. Lett.* **2003**, *89* (1–2), 109.
26. Molina, L.M.; Hammer, B. Active role of oxide support during CO oxidation at Au/MgO. *Phys. Rev. Lett.* **2003**, *90* (20), 206102.
27. Häkkinen, H.; Abbet, S.; Sanchez, A.; Heiz, U.; Landman, U. Structural, electronic, and impurity-doping effects in nanoscale chemistry: Supported gold nanoclusters. *Angew. Chem., Int. Ed.* **2003**, *42* (11), 1297.
28. Rodriguez, J.A.; Pérez, M.; Jirsak, T.; Evans, J.; Hrbek, J.; González, L. Activation of Au nanoparticles on oxide surfaces: Reaction of  $\text{SO}_2$  with Au/MgO(100). *Chem. Phys. Lett.* **2003**, *378* (4), 526.
29. Evans, J.; Lee, H. Oxide-Based Catalysts for the Reduction of Air Pollution. In *Topics in Environmental Catalysis*; Rao, S.V., Ed.; Interscience: New York, 2001; 187.
30. Wahlstrom, E.; Lopez, N.; Schaub, R.; Thostrup, P.; Rønnau, A.; Africh, C.; Lægsgaard, E.; Nørskov, J.K.; Besenbacher, F. Bonding of gold nanoclusters to oxygen vacancies on rutile  $\text{TiO}_2(110)$ . *Phys. Rev. Lett.* **2003**, *90* (2), 026101.
31. Haruta, M. Catalysis of gold nanoparticles deposited on metal oxides. *Cattech* **2002**, *6* (3), 102.
32. Piéplu, A.; Saur, O.; Lavalley, J.-C.; Legendre, O.; Nédéz, C. Claus catalysis and  $\text{H}_2\text{S}$  selective oxidation. *Catal. Rev., Sci. Eng.* **1998**, *40* (4), 409.
33. Sayago, D.I.; Serrano, P.; Böhme, O.; Goldoni, A.; Paolucci, G.; Roman, E.; Martín-Gago, J.A. Adsorption and desorption of  $\text{SO}_2$  on the  $\text{TiO}_2(110)$  surface: A photoemission study. *Phys. Rev., B* **2001**, *64* (20), 205402.
34. Pacchioni, G.; Pescarmona, P. Structure and stability of oxygen vacancies on sub-surface, terraces, and low-coordinated surface sites of MgO: An Ab initio study. *Surf. Sci.* **1998**, *412/413* (1), 657.



# Guests within Hydrophobic Pockets: Conventional Synthesis

**Bruce C. Gibb**

*Department of Chemistry, University of New Orleans,  
New Orleans, Louisiana, U.S.A.*

## INTRODUCTION

According to Cram, a “guest” is a molecule or ion that possesses divergent binding sites, while a “host” is a molecule containing convergent binding sites.<sup>[1]</sup> The combination of the two is a host–guest complex, an incredibly large number of which have been identified and studied. The paradigm of “guests within large synthetic hydrophobic pockets” represents a small subset of host–guest chemistry. Hence, using the adverb “within” limits the discussion to systems in which the (smaller) guest can actually reside inside the host. Likewise, the adjective “large” narrows the coverage further by focusing on sizable cavities that by the laws of physics bind sizable guests. In this review, “sizable guests” refers to those of at least seven non-hydrogen atoms. The term “hydrophobic” is used to focus only on organic guest molecules undergoing solution phase complexations. Finally, and perhaps most importantly, the term “pocket” narrows the review somewhat to focus on hosts that possess well-defined, highly concave surfaces or enclosed surfaces. An arbitrary value of greater than approximately 50% encapsulation has been set. Thus, crown ethers and other “2-D” macrocycles, as well as simple resorcinarenes, calixarenes, and other bowl-shaped cavities do not fall within the purview of this work. Although setting the bar at this height is undoubtedly subjective, it seems reasonable, bearing in mind that the general movement of the field is toward greater “percent encapsulation” and maximal guest control. Finally, one more proviso must be added. The general topic of hosts binding guests within hydrophobic pockets have been reviewed—albeit in several separate contributions—within the major publication, *Comprehensive Supramolecular Chemistry*.<sup>[2]</sup> This review is therefore primarily interested with the literature since this publication.

For chemists, the underlying rationale for placing molecules or guests within synthetic hydrophobic pockets is straightforward: control. Chemists are interested in placing guest molecules within hydrophobic pockets to gain complete control of the immediate

environment around the guest molecule. Why do this? There is a variety of potential applications: protecting the guest from reacting with the surrounding environment, or at the opposite extreme, orchestrating non-covalent or covalent interactions to affect a precise conversion of the guest into a product. Alternatively, the goal may be to bring about a change in the host so that the guest can be detected. These applications—storage/delivery, catalysis, and detection—are powerful motivators for the field of host–guest chemistry in general.

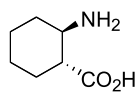
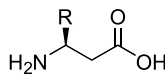
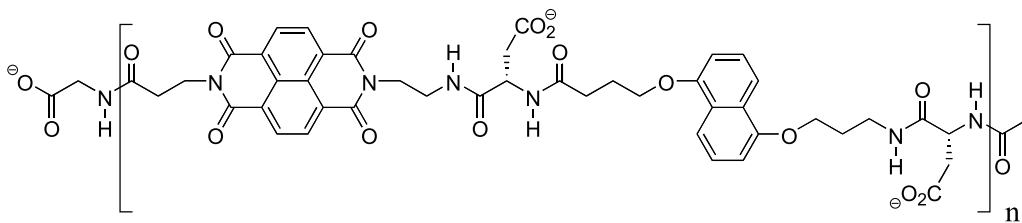
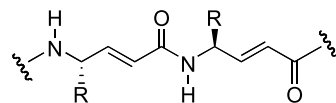
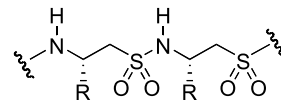
There are three ways in which synthetic hydrophobic pockets can be synthesized. First, they can be constructed in a method analogous to the way Nature does it. In other words, a polymer can be folded into a distinct conformation that possesses the required cavity. At the moment the protein-folding problem is just that, a problem. Consequently, the normal way to build a cavity using polymers is to use one with relatively few conformational degrees of freedom so that some preferred conformation is “guaranteed.” Because there is a distinct qualitative difference between a well-defined hydrophobic pocket and the microenvironment within a dendrimer, dendrimers do not fall under the auspices of this review. Instead, we will focus on systems that possess one principle conformation to define their hydrophobic cavity.

The second approach is to use conventional synthetic techniques and build up the hydrophobic pocket, “brick-by-brick.” This circumnavigates the problem of protein folding and in theory allows precise control of the shape of the cavity. No approach is perfect, however, and this strategy suffers from the problem of hydrophobic pocket collapse. By constructing a “mere” shell to define the pocket, it is hard to build into it design elements that inhibit collapse. The conformational minimum of the target must possess the desired cavity.

The third approach is to use self-assembly. This strategy is treated in a separate review titled “Guest Within Large Hydrophobic Pockets: Synthesis Using Self-Assembly.”

## THE POLYMER APPROACH

The term “foldamer” has been used by Gellman to describe any polymer with a strong tendency to adopt a specific conformation.<sup>[3]</sup> From a hydrophobic pocket perspective, polymers get interesting when they adopt specific conformations that engender a hydrophobic pocket. As we shall see, some polymers need only possess local conformational preferences, or what is called defined secondary structure, to create a pocket. On the other hand, many foldamers cannot form a suitable pocket from secondary structure alone, and these elements of secondary structure must combine to form a tertiary structure. Unfortunately, to date no synthetic polymer with a defined tertiary structure analogous to a compact folded protein has been synthesized. Not that this is a problem if your interests lie out with hydrophobic pocket design. For example,  $\beta$ -peptides, foldamers built from  $\beta$ -amino acids such as *trans*-2-aminocyclohexanecarboxylic acid **1**, or  $\beta$ -homo amino acids **2**, have been intensively studied.<sup>[3–6]</sup> These investigations revealed unusual protease-resistant peptidomimetics,<sup>[7]</sup> novel inhibitors of fat and cholesterol absorption,<sup>[8]</sup> and new antibiotics.<sup>[9]</sup> Other polymer systems with exciting possibilities, including vinylogous peptides **3**,<sup>[10]</sup>  $\beta$ -sulfonepeptides **4**,<sup>[11,12]</sup> and aedamers **5**,<sup>[13–15]</sup> have also been investigated, but if hydrophobic pockets are your goal then more time is needed to develop variations on these themes that possess tertiary structure.

**1****2****5****3****4**

A central theme of the Moore group is the development of foldamers that form hydrophobic pockets.<sup>[16–18]</sup> Thus, all-*meta* phenylacetylene oligomers **6** have been shown to fold into distinct helical conformations when  $n > 8$ . The formation of secondary structure, driven in part by nonspecific solvophobic forces, engenders a cylindrical cavity the length of which is dependent on the number of residues in the polymer. Fig. 1 shows a space-filling model of the polymer ( $n = 18$ ), where the side chain ester groups have been “reduced” to methyls. The binding properties of the corresponding 12-mer have been investigated.<sup>[18]</sup> In mixed water/acetonitrile, the polymer exists as a pair of helical enantiomers (P and M) that possess the requisite pocket for binding small bicycles such as (–)- $\alpha$ -pinene **8** or (+)- $\beta$ -pinene **9**. The binding constants for several enantiopure, chiral guests were recorded at between 1790 and 6830 M<sup>-1</sup>. Each of these  $K_a$ s represent an amalgam of the association constants for the diastereomeric complexes formed when the chiral guest forms a complex with the two helices, e.g., **8**-P and **8**-M. Interestingly, the molecular volume of these guests corresponds to about 55% of the volume of the pocket, a criterion for binding suggested by Rebek.<sup>[19]</sup> Circular dichroism (CD) spectroscopy demonstrated that the ratio of each pair of diastereomeric complexes varied considerably with only small changes in the structure of the guest. Thus, **8** was 20 times more selective for

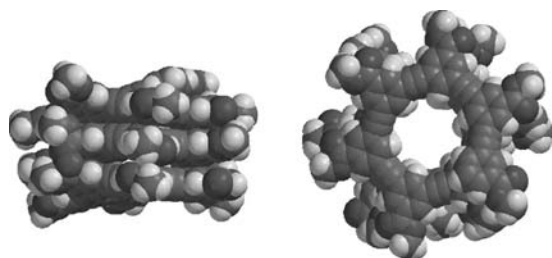
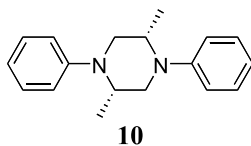
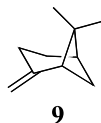
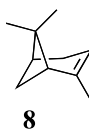
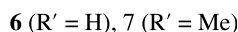
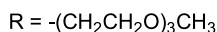
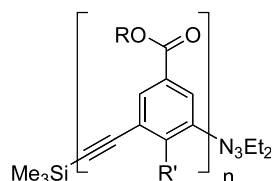


Fig. 1 Perpendicular views of the 18-mer of polymer 6.

one helical enantiomer than **9** was, even though the association constants were very similar. The dynamic nature of these hosts was emphasized by determining the association constants for the same guests to polymer **7**. Although the methyl groups in this derivative essentially fill its pocket, the association constants for the bicycles examined decreased only by two orders of magnitude. In contrast, such changes to less conformationally flexible hosts generally cause a more dramatic drop in association constants.

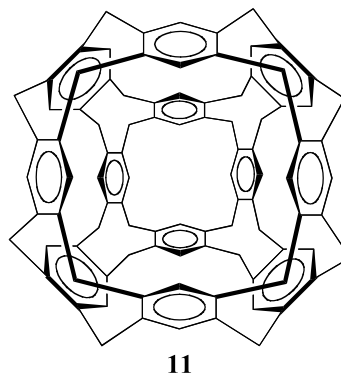


Larger guests can be incorporated into longer *meta*-phenylacetylene polymers. Hence, the association constants between rodlike guest **10** and a range of polymers ranging in length from a 10-mer to a 24-mer

have been determined.<sup>[17]</sup> In these studies, the 10-mer proved to be the weakest host ( $K_a = 5600 M^{-1}$ ), with binding increasing rapidly to 30 times this level for the 20-mer and 22-mer. Binding was weaker for slightly larger hosts. However, even larger *n*-mers will be required to confirm that maximal binding occurs in the region of  $n = 20$  or 22. The volume of guest **10** was calculated to be 58% of the volume of the pocket of the 22-mer, again suggesting that at least to a first approximation, a cavity should be between 1.5 times and twice the volume of the intended guest for maximal binding.

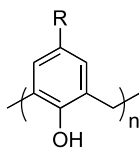
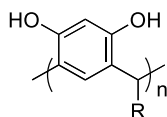
## THE SYNTHESIS APPROACH

In the earlier days of host design, the diversity of approaches to synthesizing hosts was inspiring. The field “scanned” the different possible approaches to host architectures to identify workable systems of molecular curvature. Phase II, for want of a better phrase, built on those systems that proved to be the most utilitarian, those that were easily synthesized and easily adapted. Thus, the bulk of the literature concerning the synthesis of hydrophobic pockets since 1995 has focused in relatively few systems. These are described below.



In 1983, Cram proposed the concept of a molecular container.<sup>[20]</sup> He suggested hypothetical structure **11** as an interesting possible target. An important design feature of **11** is that it cannot readily collapse. Just as an architect must use the known gamut of architectural rules to build, say a dome, so a chemist must carefully choose the different hybridization states and connectivities of the atoms involved to synthesize a cavity that cannot collapse under its own “weight.” The target must be conformationally flexible to bestow it with reasonable solubility and recognition properties, and unless the idea is to permanently entrap a guest, the shell of the cavity must possess at least one portal. At the same time, however, the cavity-possessing

conformer must be at, or close to, the thermodynamic minimum. Since this seminal paper, advances in molecular host design has progressed to the point that new entrants to the field have a range of starting materials with which to induce molecular curvature. Of these different kinds, arguably the two richest sources of molecular curvature are the calixarenes<sup>[21–24]</sup> **12** ( $R =$  various,  $n = 4–20$ ) and the resorcinarenes<sup>[1,23,25]</sup> **13** ( $n = 4$ ). In terms of general utility to supramolecular chemistry, the former has proven most engaging, primarily because they are available in a larger range of sizes. However, for the construction of large hydrophobic pockets the resorcinarenes have perhaps proven of greater utility.

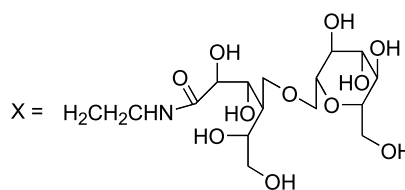
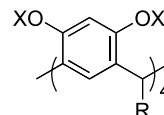
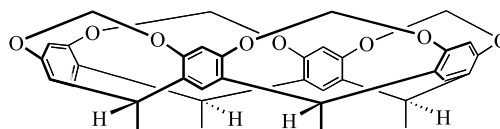
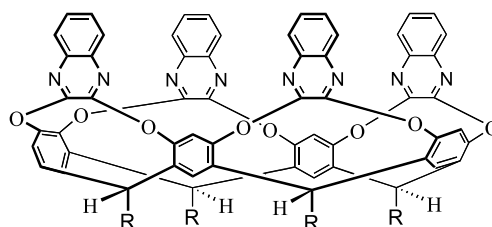
**12****13**

Many of the larger hosts that have been synthesized are obtained by combining multiple copies of molecular subunits in self-assembly processes. These are discussed in the aforementioned accompanying paper. Here the focus is on hosts derived from calixarene or resorcinarenes, as well as other hosts such as the cucurbiturils, which are formed via traditional synthetic means. Note that this is a subjective means of demarcation. If self-assembly is considered in terms of probability,<sup>[26]</sup> cucurbiturils, calixarenes, and resorcinarenes themselves could also be discussed under the banner of self-assembly. Their placement here is the result of their nomenclature; cucurbiturils are considered as monomers, not  $n$ -mers, of glycoluril and resorcinarenes are considered as monomers, not as  $n$ -mers, of resorcinol, etc.

### Hosts Based on Resorcinarenes

Resorcinarenes have themselves been used as hosts for sugars and *bis*-carboxylic acids.<sup>[27–30]</sup> However, the cavity of these hosts is too small to encapsulate large guest molecules. One way to increase the cavity is to add long chains to each phenol oxygen. This produces a poorly preorganized cavity that we will review only

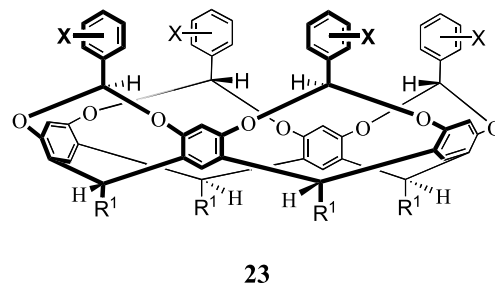
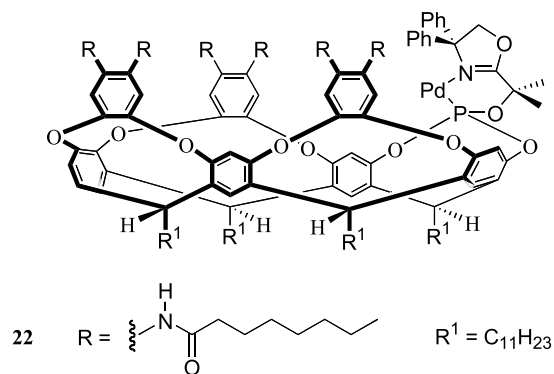
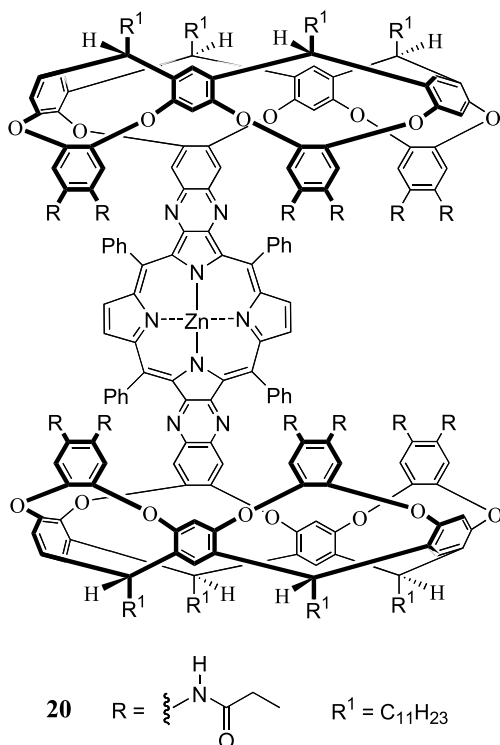
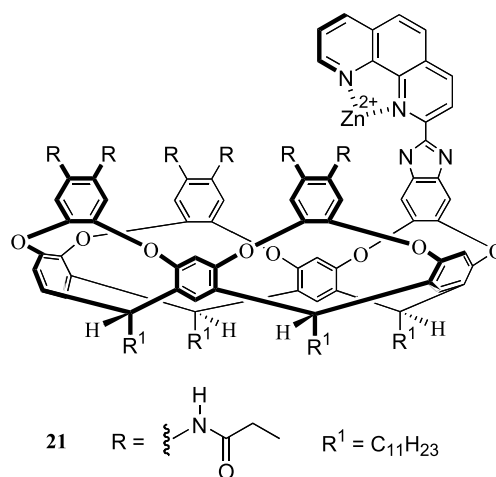
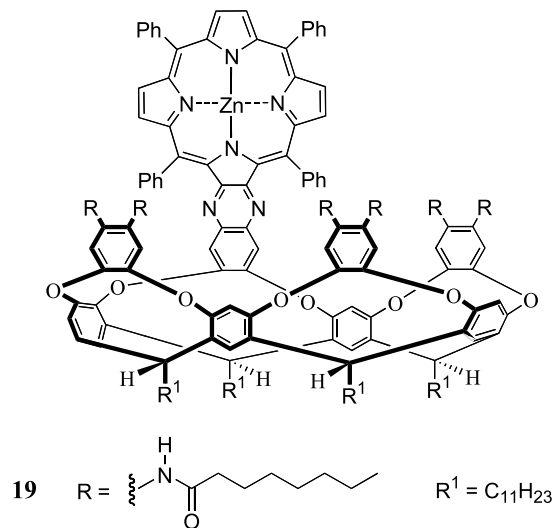
briefly. Hence, by attaching sugar chains to resorcinarenes, the Aoyama group has generated a series of hosts that bind large molecules.<sup>[31–33]</sup> Water-soluble host **14** can bind both nucleotides and 8-anilino-naphthalene-1-sulfonate (ANS). In the latter case, if a quartz plate is immersed in a solution of ANS and the host, the complexed guest is delivered to the quartz surface by the host, as it irreversibly binds. Similar systems have also been used to deliver guests to proteins.<sup>[31]</sup>

**14****15****16**

To synthesize cavities that are more preorganized, the phenol groups of resorcinarenes must be “bridged” to form cavitands, molecules possessing rigid, enforced cavities. The first attempt at bridging was with bromochloromethane and 2,3-dichloro-1,4-diazanaphthalene to give, respectively, **15** and **16** ( $R = \text{Me}$ ).<sup>[34]</sup> Although capable of binding guests,<sup>[35]</sup> the cavity of the former is still rather small. However, the cavity of **16**, the first example of what can be termed a deep-cavity cavitand,<sup>[36]</sup> is capable of binding large guests. One of the obstacles to confirming this point was solubility. Thus, longer “feet,” the  $R$  groups in structure **16**, were appended to these cavitands to bestow them with

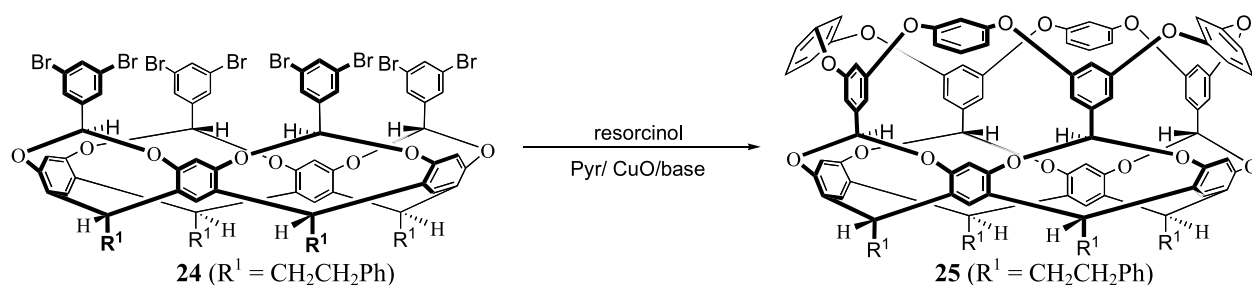


by a porphyrin, also bound suitably shaped guests. Studies revealed that a rod-shaped guest, with an adamantyl group at each end and a pyridine moiety in the center, bound strongly. Interestingly, binding was only slightly stronger than with guests possessing only two (pyridine and adamantyl) recognition points, suggesting that perhaps for entropic reasons the second adamantyl group did not contribute significantly to binding. Host **20** can also form ternary complexes by binding two guests. Variations on this theme of two deep-cavity cavitands tethered together to make a large, nanoscale cavity have also been investigated.<sup>[55,56]</sup>

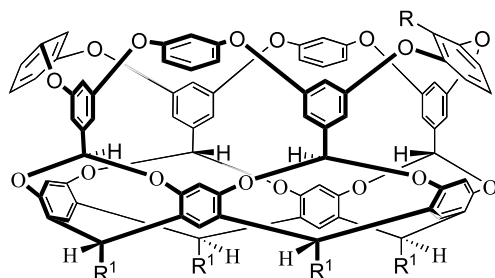


Most recently, these types of cavitands have been modified to include other metal ion binding sites. Cavitand **21** is one such example capable of binding amines that coordinate to the zinc center.<sup>[53]</sup> Going one step further, Gibson and Rebek have also investigated a cavitand that promotes allylic alkylations.<sup>[54]</sup> This palladium(0) cavitand, complex **22**, was shown by mass spectrometry to be capable of subtly discriminating among various allyl acetates of general structure  $R'\text{CH(OAc)CHCH}_2$ . As a result, the rate of 1,4-addition to these substrates, using the conjugate base of dimethyl malonate as nucleophile, was dependent on the nature of the hydrocarbon  $R'$  group.



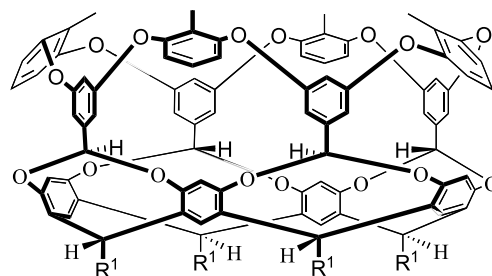
Scheme 1 Synthesis of deep-cavity cavitand **25**.

In the aforementioned examples, hydrogen bonding constrained the aromatic rings in the “second row” to conformations that defined a hydrophobic pocket. An alternative way to preorganizing deep-cavity cavitands is to add a further covalent link between the aromatic rings in the second row. One way that this has been accomplished is to first bridge resorcinarenes with benzal bromides.<sup>[57–59]</sup> The resulting cavitands such as **23** are amenable to a range of strategies for preorganizing their hydrophobic pockets. One approach is to perform an eightfold Ullman ether reaction on octabromide **24** with *bis*-nucleophiles such as resorcinol (Scheme 1).<sup>[60]</sup> The resulting series of hosts, e.g., **25**, possesses highly preorganized cavities that are ca. 1 nm in diameter and depth and capable of binding guests as large as adamantane and camphor derivatives. One of the more significant non-covalent interactions that can form between host and suitably appended guest are C–H···X–R hydrogen bonds.<sup>[60–63]</sup> Each of the benzal hydrogens at the base of the cavity is electron deficient, and the geometry of the array is such that halogen atoms on a guest can fit within it. This is especially true for iodine groups, which snugly fit within the crown and interact with all four benzal hydrogens simultaneously. As a result, guests such as iodoadamantane bind strongly ( $\Delta G^\circ -7.3 \text{ kcal mol}^{-1}$ ) in non-competitive solvents such as DMSO. Binding of such highly complementary guests is enthalpically driven. Smaller guests—down to bromocyclobutane—also bind if DMSO is used to study complexation.<sup>[61,64]</sup>

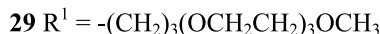
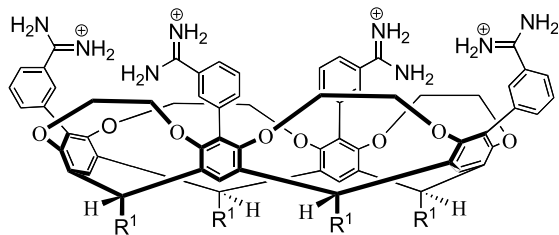


These hosts cannot undergo a “flowering process” to release their guests. Consequently, those guests that are highly complementary to the shape of the cavity exchange in a dissociative mechanism that is slow on the (500 MHz) NMR timescale.<sup>[65]</sup> On the other hand, the small weaker binding guests undergo exchange much more rapidly.

It is relatively straightforward to modify these hosts by dangling functional groups from the rim of the pocket. These can control what type of guest binds in the pocket, how the guest is oriented once inside, and if several orientations are available to the guest, the equilibria between the different isomeric complexes.<sup>[65]</sup> The placement of a methyl group at the rim greatly decreases the strength of association between the resultant host **26** and adamantyl guests. Indeed, binding to **26** is completely shut down if the adamantane guest is so shaped that a substituent is forced to impact the methyl group on the wall of the cavity. On the other hand, host **27** is selective for guests that can form salt bridges or hydrogen bonds with the phenol group. In these situations, the guest binds functional group up. Finally, placing four methyl groups at the rim of cavity drastically alters the properties of the pocket. Thus, tetramethyl cavitand **28** binds halocycloalkanes as large as bromocycloheptane but has a strong preference for halocyclopentanes.<sup>[61]</sup>



A third way in which cavitands can be deepened is to directly add a new layer of moieties to the 3-position of the resorcinol rings. This strategy<sup>[66]</sup> allows cavitands such as *tetra*-amidinium **29** to be synthesized.<sup>[67]</sup> By necessity, the second row of aromatic rings must be at right angles to the first. This makes for a rather



open cavity, which in this case can bind a variety of nucleotides.

### Hosts Based on Calixarenes

Although calixarenes **12** ( $\text{R} = \text{various}$ ) as large as 20-mers have been synthesized and characterized,<sup>[68]</sup> the larger examples are too “ropey” to construct discrete hydrophobic pockets. The smaller calixarenes are capable of binding guests if they are constrained in the cone conformation, a task readily accomplished by the alkylation of the phenols with groups of sufficient size to inhibit the interconversion between the different possible conformations. As was the case with resorcinarenes, simple calixarene hosts are ideally suited for complexing relatively small guests, with some of the most recent endeavors focusing on the development of concave reagents and enzyme mimics.<sup>[69–75]</sup> Readers interested in these examples and the bigger calixarene picture are directed to an excellent resource.<sup>[23]</sup>

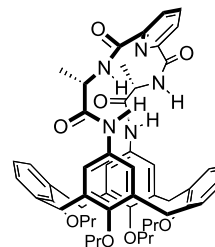
Extending the cavity of calixarenes by attaching amino acids or sugars to their rim leads to a range of fascinating hosts on the verge of this summary. These hosts have been recently reviewed.<sup>[76]</sup> Adding a “roof” to such derivatives makes for a much more defined pocket that can encapsulate guests more fully. By way of example, **30** has been characterized by solution and solid-state techniques and has been shown to bind benzoate ions and N-acyl amino acid derivatives with  $K_{\text{a}}$ s up to  $44,000 \text{ M}^{-1}$ .<sup>[77]</sup> Examples where cavitands<sup>[78]</sup> or porphyrins<sup>[79]</sup> have been used as roofing material have also been reported. As expected, the zinc-containing derivatives of the latter hosts bind Lewis basic guests such as 4-methylpyridine.

Perhaps the most common approach to synthesizing large hydrophobic pockets using calixarenes is to join two or more calixarenes together. Saadioui and Böhmer have recently written an excellent review on this topic.<sup>[80]</sup> The most common strategies are to join two calixarene “hemispheres” via either one or two linking groups. We focus here on illustrative examples

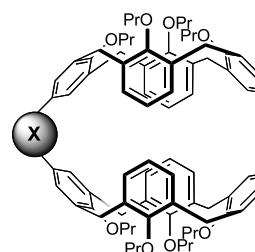
that show a high degree of guest encapsulation. For a more comprehensive review of covalently linked polycalixarenes, readers are directed toward the latest calixarene compendium.<sup>[23]</sup>

Turning first to singly linked calix[4]arenes, compound **31** (Fig. 2) binds methylpyridinium and methylquinolinium guests.<sup>[81]</sup> Binding is strongest for methylpyridinium iodide ( $K_{\text{a}} = 480 \text{ M}^{-1}$ ) while NMR shift data suggest that methyl quinolinium iodide is a little too large to be fully included into the  $\pi$ -rich cavity.<sup>[81]</sup> Related hosts,<sup>[82]</sup> including those from the Arduini group in Parma,<sup>[83]</sup> show similar binding profiles. For example, the olefin-linked calixarene **32** also binds pyridinium and quinolinium guests.<sup>[82]</sup> In contrast, directly connecting calix[4]arenes with an aryl–aryl bond reduces the size of the cavity so that only methylpyridinium species may bind.<sup>[84]</sup> Linking the two hemispheres together with a ferrocenoyl group generates host **33**, capable of sequestering benzoate ions. In this case the aromatic ring binds into the hydrophobic cavity, while the carboxylate group interacts with the ferrocenoyl linker.<sup>[85]</sup>

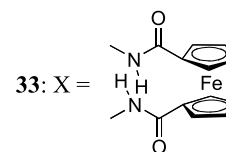
*Bis*-linked calix[4]arenes have more preorganized cavities. Two related examples are **34** and **35** (Fig. 3), both of which are capable of binding methylpyridinium and methylquinolinium guests.<sup>[86,87]</sup> As anticipated, the binding of methylpyridinium iodide to **34**



**30**



**31:**  $\text{X} = \text{CH}_2$



**33:**  $\text{X} =$

**32:**  $\text{X} = \text{CH}=\text{CH}$

**Fig. 2** Mono-linked *bis*-calixarenes.

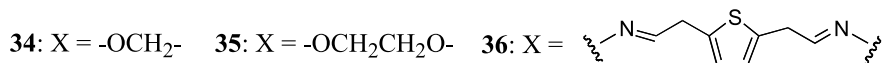
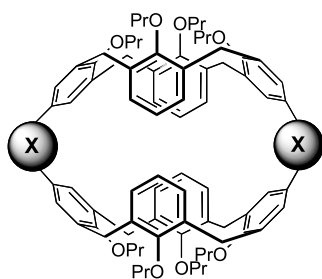


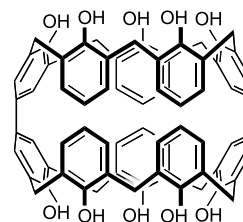
Fig. 3 Bis-linked bis-calixarenes.

is stronger than its association to **31**. Additionally, unlike host **32**, exchange of *N*-methyl- $\gamma$ -picolinium iodide and other guests into and out of the cavity of **34** is slow on the (500 MHz) NMR timescale. It is less feasible for the host to adopt a conformation possessing a large portal for guest entry or egression. NMR peak shifts of the guest suggest that it is predominantly in an orientation in which the methyl group protrudes out of the cavity at the “equator” of the host. The larger cavity of **35** does not bind pyridinium guests strongly. Instead, its preferences are for methylquinolinium guests. Furthermore, because of the larger portals in the host the kinetics of guest exchange are faster than in **34**.

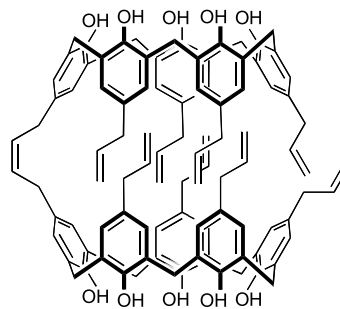
A series of bis-calixarenes with larger and more open cavities has been reported by Kim's group.<sup>[88,89]</sup> In this work, several bis-calixarenes with aromatic linkers were investigated for their ability to bind viologens and other bis-pyridinium derivatives. In this regard, one of the best hosts was bis-thiophene **36** (Fig. 3).

Calix[5]arenes or larger are capable of binding fullerenes. Indeed, the early successes in developing facile means of C<sub>60</sub> purification<sup>[90,91]</sup> resulted in a flurry of activity as analogous methods for purifying other fullerenes were sought. Many open hosts consisting of one calixarene moiety have been investigated, as a recent review by Zhongm Ikeda, and Shinkai will testify to.<sup>[92]</sup> Our focus here is on the less common hosts capable of encapsulating C<sub>60</sub>, rather than binding to the surface of it. Host **37** is one such example.<sup>[93]</sup> This host was shown to weakly bind both C<sub>60</sub> and C<sub>70</sub>; with *K<sub>a</sub>* values of 43 and 233 M<sup>-1</sup>, respectively, the *K<sub>C70</sub>*/*K<sub>C60</sub>* ratio was 5.4. Stronger binding was observed for host **38**. However, the recorded association constants of 1300 and 625 M<sup>-1</sup> for C<sub>60</sub> and C<sub>70</sub>, respectively, gave a *K<sub>C70</sub>*/*K<sub>C60</sub>* ratio of only 0.48. An even stronger binder of C<sub>60</sub> and C<sub>70</sub> is host **39**, which presumably exists in solution as a mixture of interconverting *meso* and enantiomeric stereoisomers.<sup>[94]</sup> In toluene, the association constants for C<sub>60</sub> and C<sub>70</sub> were 76,000 and 163,000 M<sup>-1</sup>, respectively. NMR experiments revealed that the poles of C<sub>70</sub> bind deeply into

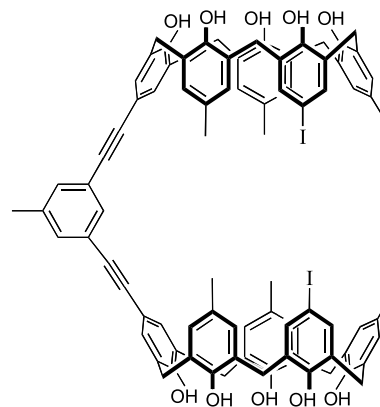
the calixarene cavities of the host. Hence, the spherical C<sub>60</sub> cannot form as intimate a series of contacts as C<sub>70</sub> can. Studies on a closely related host reveal that the complexation of C<sub>60</sub> is entropically penalized.<sup>[95]</sup>



37



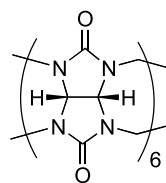
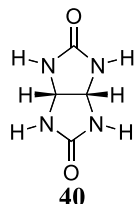
38



39

## Hosts Based on Glycoluril

Another source of molecular curvature is glycoluril **40**. This simple bicycle has been polymerized with formaldehyde to form a series of fascinating, gourdlike macrocycles, the cucurbiturils. It has also served as the foundation for the syntheses of a family of hosts known as molecular clips. We will review each of these in turn.



In 1981, Freeman, Mock, and Shih reported the structure of cyclic hexamer **41**, the main product from the acidic condensation of glycoluril with excess formaldehyde.<sup>[96]</sup> This reaction had been investigated 75 years earlier by Behrend, Meyer, and Rusche<sup>[97]</sup> but without the benefit of modern instrumentation the remarkable structure of what is now termed cucurbit[6]uril could not be identified. More recently, several other cucurbiturils possessing five, seven, and eight glycoluril moieties, have been synthesized and characterized.<sup>[98]</sup> A space-filling model of cucurbit[8]uril is shown in Fig. 4. As a rule, cucurbiturils are rather rigid and so are only significantly soluble in aqueous acidic media or aqueous solutions of alkaline metal salts. In the latter, the capping of each portal with two sodium metal ions is responsible for the noted solubility.<sup>[99]</sup> Because of these solubility limitations, most of the organic guests that have been shown to form host-

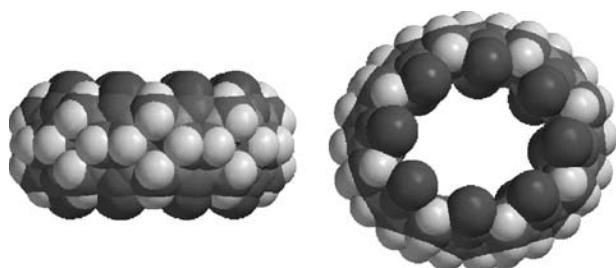
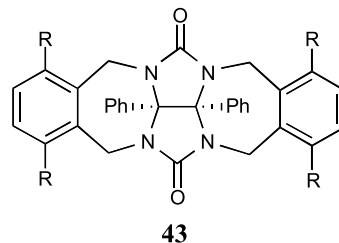
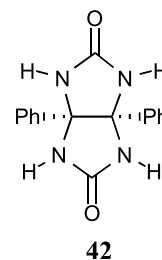


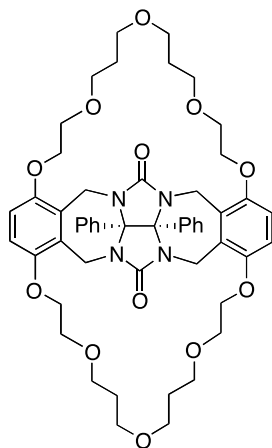
Fig. 4 Space-filling model of cucurbit[8]uril.

guest complexes with cucurbiturils are ammonium species.<sup>[100–104]</sup> For the cyclic hexamer **41**, the largest guests observed in the hydrophobic pocket are *para*-substituted aromatic derivatives such as *p*-methylbenzylammonium. A telltale sign that the cavity of **41** is filled by this guest is that the corresponding *ortho*- and *meta*-substituted isomers do not bind. The *para*-oriented substituents are apparently poking out of the portals when such guests bind. Another indicator is that the  $K_a$  for *p*-methylbenzylammonium is  $3.2 \times 10^2 \text{ M}^{-1}$ , while the strongest binding guests such as  $\alpha,\omega$ -alkanediammonium ions bind with  $K_a$ s in the region of  $2.4 \times 10^6 \text{ M}^{-1}$ . The shell must distort to accommodate the bulkier guest. For these and other guests, the rates of exchange in and out of the pocket is independent of the structure or concentration of the displacing molecule; that is, the rate-determining step is the egression of the occupant. Rate constants varied by seven orders of magnitude depending on the guest. The binding properties of the larger cucurbiturils have also been examined. Cucurbit[7]uril has been shown to bind 4,4-bipyridinium (viologen) dications, guests that can be reduced while bound inside the cavity,<sup>[105]</sup> whereas the larger cucurbit[8]uril has been shown to bind two dissimilar guests that form a charge transfer complex within its cavity.<sup>[106]</sup> The latter has also been shown to bind aza-crowns, which, once bound, can be metalated by treatment with copper or zinc salts. Encapsulation of copper within the aza-crown, within the cucurbituril, stabilizes the Cu(I) state and considerably slows the electron transfer rate between electrode and redox center.<sup>[107]</sup>

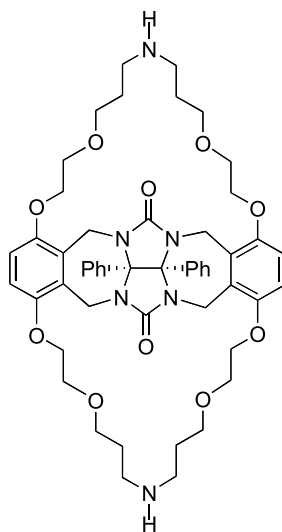


The Nolte group's approach to pocket design is to use glycoluril as a foundation and build up hosts possessing narrow slitlike cavities.<sup>[108–110]</sup> For example, the combination of benzil and urea yields foundation **42**,

whereas a further two-step process leads to hosts **43** ( $R = H, OH, OMe$  or  $OAc$ ).<sup>[111]</sup> The two walls of the cavity of **43** ( $R = H$ ), the *ortho*-xylylene units, can adopt *anti* or *syn* orientations with respect to the phenyl groups. NMR experiments reveal that the host can adopt three possible conformers: *aa* (the conformation with an actual cavity), *as*, or *ss*, but that the former is generally preferred.<sup>[111]</sup> Examining many systems demonstrates that the precise conformer population depends on the structure of the host and occasionally even the type of guest.

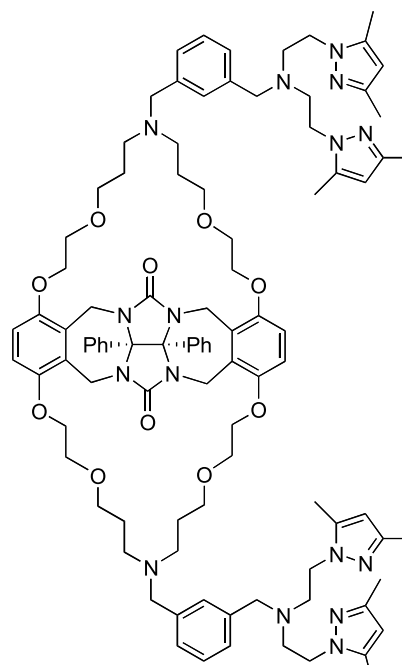
**44**

Host **44** binds metal ions and *bis*-ammonium or paraquat guests,<sup>[112]</sup> while variations on this structure, e.g., **45**, have been shown to bind dihydroxybenzene derivatives.<sup>[113]</sup> The order of guest affinity for **45** is resorcinol > hydroquinone > catechol. Hydrogen bonding and  $\pi$ - $\pi$  stacking are important to binding,

**45**

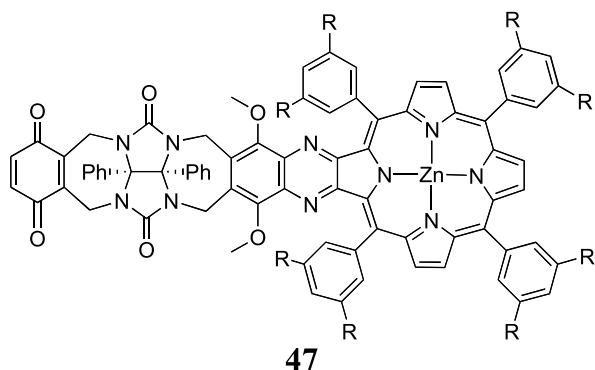
the latter being apparent from color changes upon complexations and the observation that electron-withdrawing groups on the guest increase association. Thus, 2,3-dicyanohydroquinone binds more strongly ( $K_a = 3 \times 10^5 \text{ M}^{-1}$ ) than hydroquinone or even resorcinol. To separate the contributions of hydrogen bonding and  $\pi$ - $\pi$  stacking, complexation has been examined in a series of related hosts.<sup>[114]</sup> By and large, hydrogen bonding is the larger contributor. A “cavity effect,” the result of an entropy effect and a solvation effect, was also found to be important.

The Nolte group has also investigated how their hosts can act as shape-selective catalysts. For example, the copper (II) complex of pyrazole derivative **46** is capable of the shape-selective oxidation of benzyl alcohols.<sup>[115]</sup> Dihydroxybenzene derivatives bind into the cavity of **46**, and if these guests also possess a benzyl alcohol group it is quickly oxidized. The rate of formation of the corresponding aldehyde varies by over  $5 \times 10^4$ , with complementary guests being oxidized fastest.

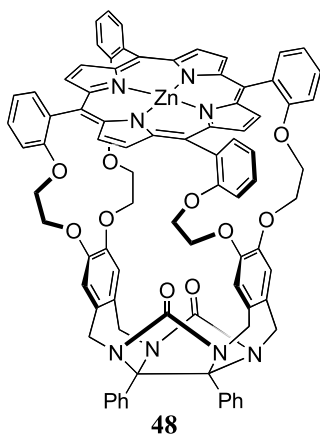
**46**

More recent technologies have allowed the synthesis of a variety of molecular clips possessing two different cavity walls.<sup>[116,117]</sup> This had led to examples such as **47** ( $R = t\text{-Bu}$ ), possessing one porphyrin wall and capable of binding resorcinol derivatives.<sup>[116]</sup> Guest binding was shown to influence both the electrochemistry and the fluorescence of **47**. The latter was quenched upon binding because of a photoinduced electron transfer process, an observation of interest because in the photosynthetic reaction center,

aromatic residues are thought to play a role in the electron transfer process.



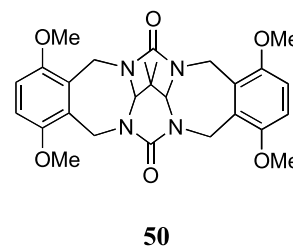
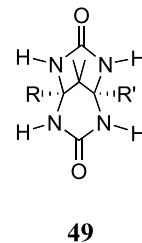
Molecular clips have also been designed and synthesized in which a porphyrin moiety is used to “roof” the cavity. Host **48** is an example.<sup>[118]</sup> The pocket of this molecule is capable of binding viologens, resorcinols, and pyridine derivatives. Some of the strongest binding guests are the viologens, whose pyridinium moieties can interact with the crown ether functionality of the host. Pyridine guests can also bind strongly via N-coordination to the zinc center. 3-Hydroxy pyridine binds particularly strongly as a hydrogen bond between host and guest can also be established. Resorcinols, which can only bind primarily with the aid of hydrogen bonding, bind more weakly.



The Mn(V)-oxo derivative of **48** has been shown to catalyze the epoxidation of alkenes.<sup>[119]</sup> Epoxidation can be accomplished from either porphyrin face. Thus, when pyridine was added to a solution of the Mn(III)-Cl complex, it was shown to enter the cavity and bind axially to the metal. The addition of oxygen and substrate led to epoxidation of the latter on the outer face, and decomposition of the catalyst. In contrast, when a bulky pyridine derivative was used it coordinated to the metal center on the open face of the porphyrin,

and hence epoxidation occurs within the pocket. Under these conditions, the observed conversion rates are intimately tied to the shape of the substrate. For example, *trans*-stilbene was oxidized almost twice as fast as *cis*-stilbene, a reversal of the results observed for the simple porphyrin. Furthermore, under these conditions no decomposition of the catalyst occurred. Related, two-cavity systems in which molecular clips are covalently attached to each face of a porphyrin have also been synthesized.<sup>[120]</sup> One example of these hosts demonstrated negative homotropic allosteric binding; a viologen guest can bind to each compartment, but the binding of the first is 15 kJ mol<sup>-1</sup> stronger than the second.

Recent research from the Nolte group includes the synthesis of alternative hosts. Thus, molecular clips based on propanediurea **49** (R = R' = H, or R = H, R' = Me, or R = R' = Me) have been synthesized and analyzed.<sup>[121,122]</sup> Propanediurea hosts such as **50** possess U-shaped rather than V-shaped clefts. In addition, the distance between the hydrogen bond acceptor carbonyl groups in **50** is ca. 0.3 Å shorter than the glycoluril-based hosts. As a result, these two families of hosts possess slightly different binding properties. Generally, guests can form stronger hydrogen bonds and make more intimate contacts with the walls of **50** than they can in the corresponding glycoluril host **43** (R = OMe). Hence, in CDCl<sub>3</sub> the *K*<sub>a</sub>s between 5-cyanoresorcinol and hosts **50** (R = R' = H) and **43** (R = Me) are 2.4 × 10<sup>6</sup> and 1.0 × 10<sup>5</sup> M<sup>-1</sup>, respectively.



### Hosts Based on Steroids

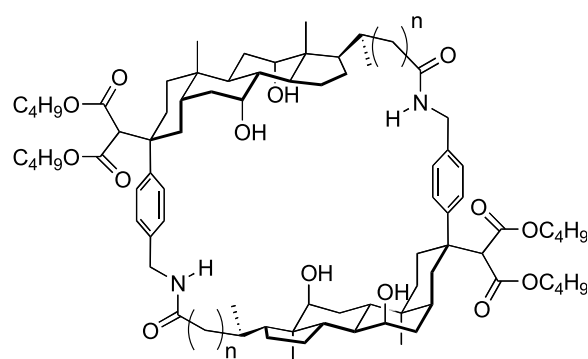
The incidents of steroids in molecular recognition have been reviewed.<sup>[123]</sup> In terms of steroids being used to



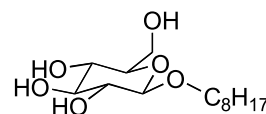
construct hydrophobic pockets, molecular curvature can be introduced by two architectural approaches. If the steroid of choice has all *trans*-A/B, B/C, and C/D ring junctions, then each unit is essentially flat and the curvature must be introduced by the groups that link them together. If on the other hand the steroid possesses, e.g., a *cis*-A/B ring junction, then the steroid framework itself possesses a degree of curvature that can be used to construct hydrophobic pockets. Examples of the latter approach predominate. Many of the steroid-based host systems that have been reported do not form hydrophobic pockets as such. Work from the Regen group is illustrative in this regard, where one of the main thrusts of their research is the synthesis of facial amphiphiles called molecular umbrellas.<sup>[124–126]</sup> Structure **51** is one example that, under aqueous conditions, can envelop guests and transport them across membranes.<sup>[125]</sup>

Steroids have been used to construct large macrocycles. Hosts **52–54** are representative examples of what have been termed cholaphanes, cyclophanes derived from the  $5\beta$  steroid, cholic acid.<sup>[127,128]</sup> These hosts have been shown to bind octyl  $\beta$ -D-glucoside **55** with association constants of 1305, 600, and  $1560\text{ M}^{-1}$ , respectively.<sup>[129]</sup> No binding of **55** to analogues **56**<sup>[130,131]</sup> has been noted, but the corresponding host with a *para*-substituted aromatic ring was noted to bind this guest.<sup>[127]</sup> A triply bridged cholaphane **57** has also been synthesized and its properties examined. This host was shown to bind several guests including *p*-nitrophenol, triethanolamine, benzyloxycarbonyl-protected amino acids, as well as glycoside **55**.<sup>[132]</sup> Smaller guests formed 1:2 complexes, with the second association constant being about one-fourth the value of the first. Cholic acid roofed porphyrin **58**<sup>[133]</sup> has also been examined for their ability to bind several alkyl-chained glycosides.<sup>[134]</sup> In this regard, a

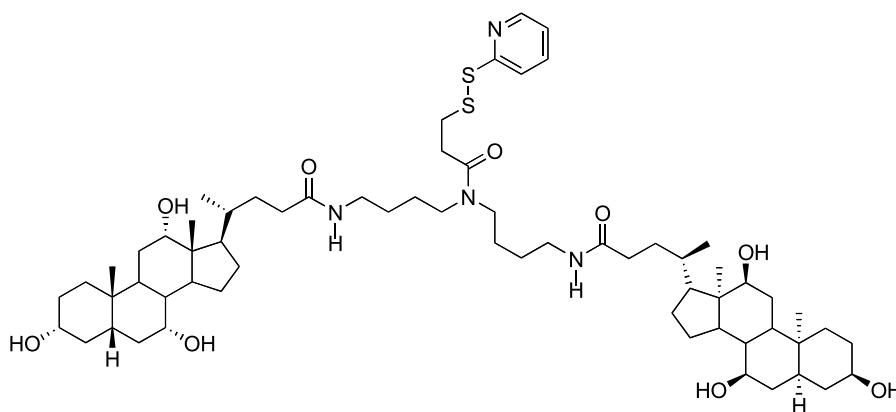
semiquantitative two-point binding model was developed with the strength of binding rationalized in terms of the number of hydrogen bonds between host and guest. An interesting feature of these systems is that glycoside binding was noted to increase in the presence of small traces of methanol or water. A detailed analysis revealed that “gap filling” by the methanol or water was occurring. Host and guest are not perfectly complementary in the 1:1 complex, but the overall fit is greatly improved if a methanol or water molecule joins the glycoside inside the cavity and forms a 1:1:1 complex. The binding properties of porphyrin hosts “roofed” on both faces with *bis*-cholic acid moieties have also been examined in micelles. Chiral discrimination of hydrophobic amino acids was noted.<sup>[135]</sup>



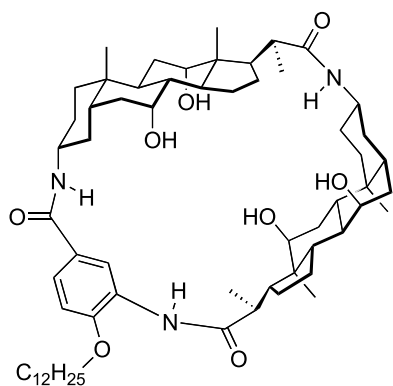
**52** ( $n = 2$ ), **53** ( $n = 1$ ), **54** ( $n = 0$ )



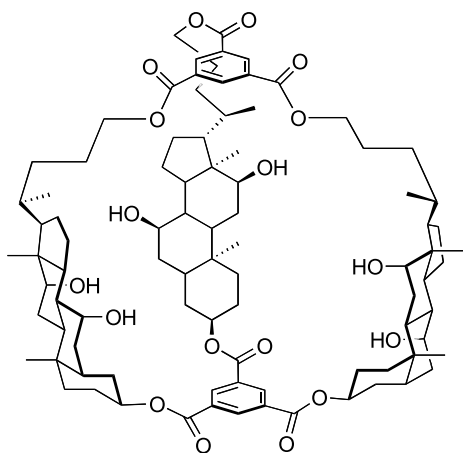
**55**



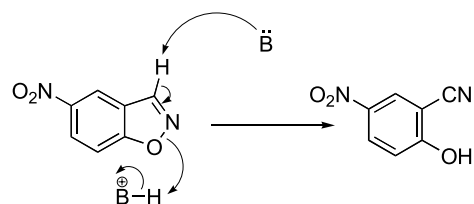
**51**



56

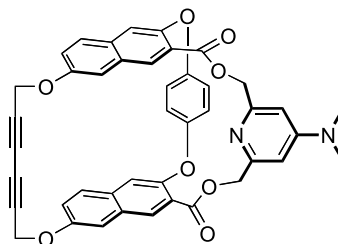


57



**Scheme 2** The base-promoted decomposition of 5-nitrobenzoxazole.

pyridine nitrogen removes the requisite proton and triggers the ring-opening process. The overall reaction can be described in terms of a fast preequilibrium, a slow intramolecular reaction, product release, and subsequent product reuptake. It was shown that the product bound much more strongly to **59** than the starting material. Nevertheless, host **59** accelerated the reaction in question by 6000-fold relative to a cavityless pyridine analogue.

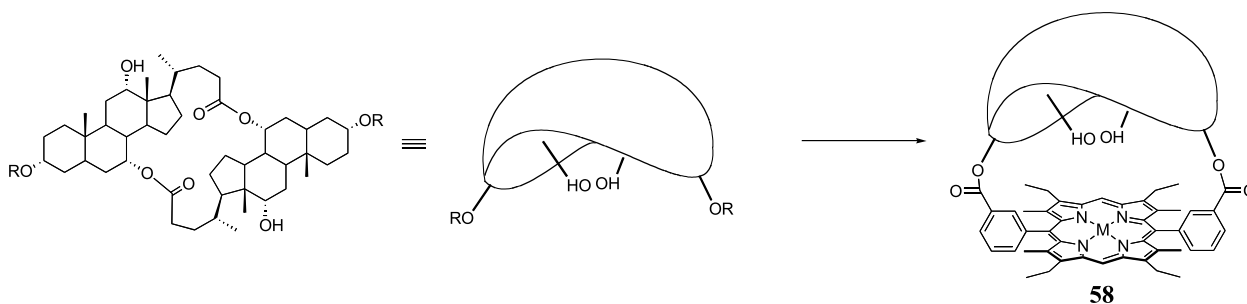


59

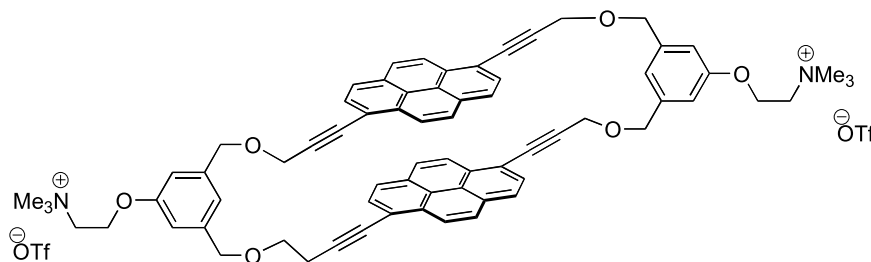
## Cyclophane Hosts

Early cyclophanes were rather open and bound relatively small guests. However, as synthetic approaches to these unique types of hosts have been honed, so have their size and complexity increased.<sup>[2]</sup> Our first example is host **59**, capable of catalyzing the ring opening of isoxazoles (Scheme 2).<sup>[136]</sup> The 5-nitrobenzoxazole binds into the cavity of **59**, whereupon the

Inouye et al. have also recently investigated the properties of cyclophanes. By way of example, they synthesized host **60**.<sup>[137]</sup> The two pyrene rings are held about 4.5 Å apart, just the right distance for binding aromatic rings. Guests that bind to **60** included the four nucleotides: adenine, uracil, guanine, and cytosine. Presumably, the base moiety of each enters the cavity leaving the phosphate sugar free in solution. The strongest binding guest examined was 4-hydroxy-2,7-naphthalenedisulfonic acid sodium salt.



58

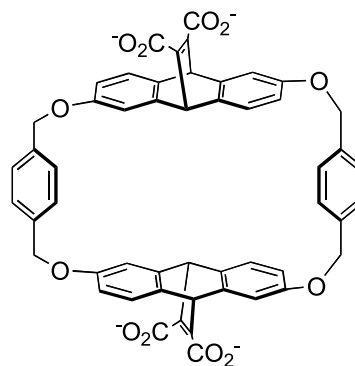


60

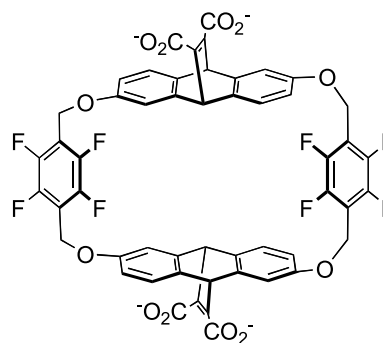
When bound, the naphthalene ring of this “ideal” guest was completely shielded from the water/ethylene glycol solvent, leaving the charged groups at the portals of the cavity.

Cyclophanes have also figured prominently in the recent research endeavors of the Dougherty group. Chiral cyclophane **61** forms the foundation of much of this work.<sup>[138]</sup> Both slim guests such as quinoline and methylquinolinium chloride, as well as more rotund guests such as *N,N,N*-trimethyl-1-adamantanammonium chloride, bind into **61**. The free energy of complexations for these guests,  $\Delta G_{298^\circ} = 5.3, 8.4,$  and  $6.7 \text{ kcal mol}^{-1}$ , respectively, were typical values observed for a wide range of similarly shaped guests. Slim guests bind best, especially so if they possessed a positive charge that interacts with the walls of the cavity. When fluorine atoms are added to the structure of the host, i.e., **62**, binding is reduced relative to **61** by  $2 \text{ kcal mol}^{-1}$  if the guest is charged, and  $1 \text{ kcal mol}^{-1}$  if the guest is neutral.<sup>[139]</sup> This result was attributed to the electron-withdrawing fluorine atoms that essentially reverse the quadrupole moment of the benzene moieties. In other words, the walls of the cavity of **62** are relatively electron deficient and any cation- $\pi$  interaction diminished. Hosts **63** and **64** have also been examined.<sup>[140]</sup> The binding of neutral guests to **63** differed little from host **61**. Thus, even though it is conceivable that the additional carboxylate group would decrease the hydrophobicity of the pocket, this does not seem to be the case. Additionally, a more detailed comparison between **61** and **63** suggested that the carboxylate group had little influence on the conformation of **63**. The strength of association between **63** and cationic guests was generally stronger, but this was not always the case. For some guests, e.g., *N,N,N*-trimethyl-1-adamantanammonium iodide, the salt bridge between the host and guest was not strong in pure water, and the binding of this guest to **61** and to **63** were identical. However, in 10% aqueous acetonitrile, this and other charged guests were noted to bind more strongly to **63**. In contrast to **63**, host **64** showed

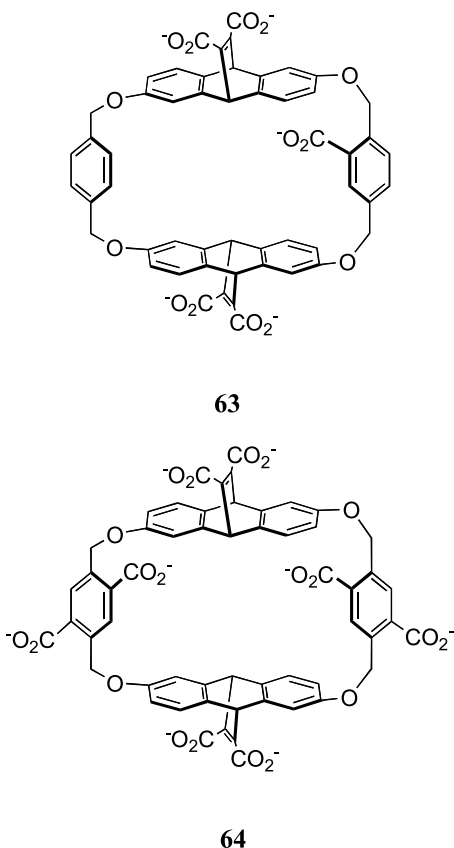
a general decreased affinity for neutral guests, a diminution attributed to a decrease in the hydrophobicity of the cavity. For charged guests complexing with **64**, binding was considerably stronger if the guest was flat, but slightly reduced with quasi-spherical guests. This difference arises because aromatic and adamantyl guests induced different host conformations. The rhomboidal-shaped cavity ideal for binding the former allowed the formation of salt bridges between host and guest, whereas the toroidal form ideal for binding rotund guests did not.



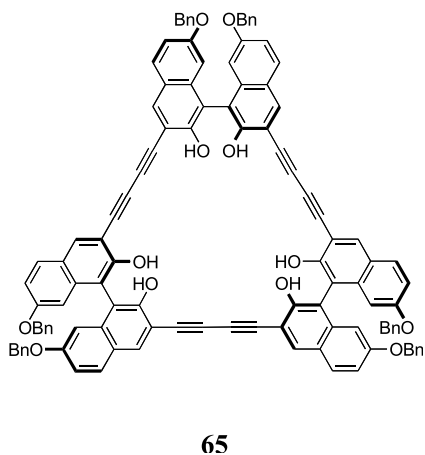
61



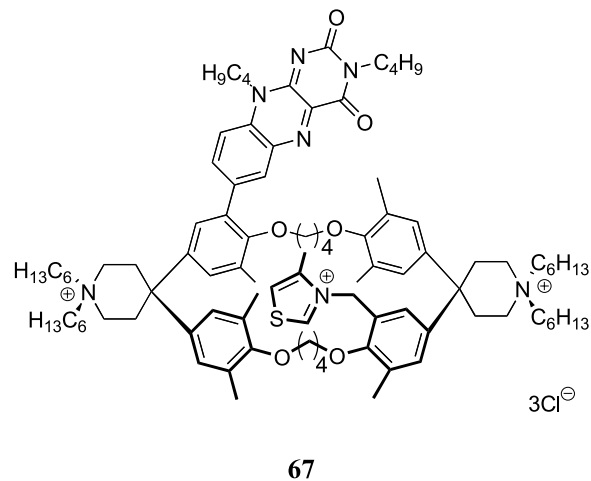
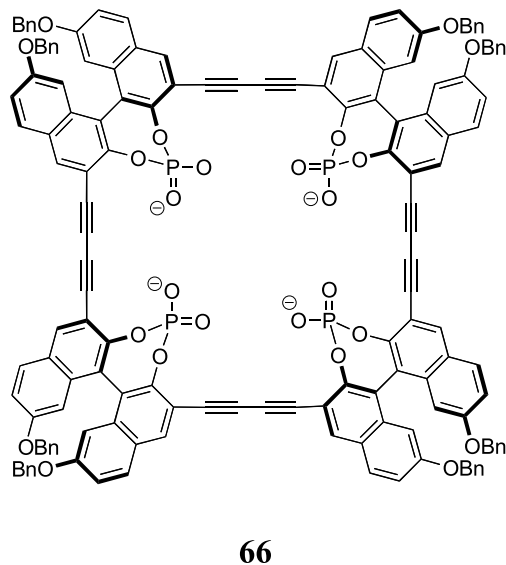
62



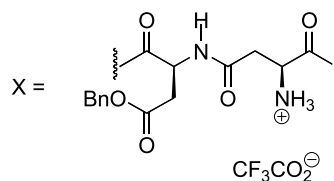
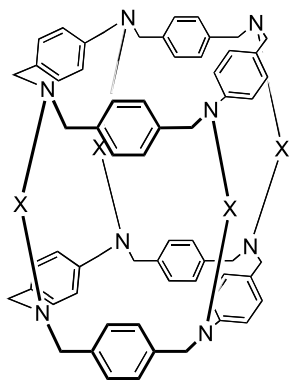
A rather open, chiral cavity is engendered by the unusual structure of host **65** synthesized by the Diederich lab.<sup>[141]</sup> With six converging hydroxy groups, this  $C_3$  symmetry host was designed to recognize pyranosides. Thus, binding of guest **55** and other sugars was demonstrated in  $CDCl_3$ . The addition of phenethyl groups to each naphthalene moiety and the development of a successful strategy to engender  $C_2$  symmetry isomers has expanded the size of the family of these hosts.<sup>[142]</sup> In these cases, guest binding was rather weak. However, stronger binding was realized



with hosts such as **66**. Possessing eight converging phosphodiester groups, this cyclophane was capable of sequestering mono- and disaccharides from deuterated acetonitrile/methanol mixtures. Binding constants as high as  $41,000 M^{-1}$  were recorded.<sup>[143]</sup>



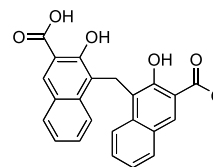
The Diederich group has also synthesized cyclophane **67**.<sup>[144]</sup> This rather complicated host is a mimic of the enzyme pyruvate oxidase, a flavin adenine dinucleotide (FAD)-dependent enzyme that within lactobacteria catalyzes the reaction from pyruvate to acetyl phosphate. The mimic consists of three essential features, the first of which is a slot-shaped cavity for binding aromatic guests. It also possesses two pieces of catalytic machinery “taken” from the enzyme, which in this model study were used to oxidize aldehydes to carboxylic acids/esters. First, it possesses a thiazolium moiety that readily forms an ylide by deprotonating of the C-2 atom. This nucleophile



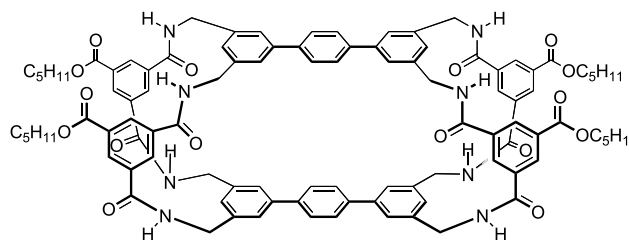
68

initiates conversion by attacking the carbonyl group of the substrate. The mimic also possesses a flavin moiety that oxidizes the resulting intermediate to form an activated ester. In the last step of the reaction either water or an alcohol reacts with this activated ester to generate the product. The naphthalene ring is ideal for binding to **67**. Thus, the binding constant for 2-naphthaldehyde to **67** was  $2900 \text{ M}^{-1}$ . By comparison, binding of 2-naphthaldehyde to the corresponding cyclophane without a thiazolium ring was  $5300 \text{ M}^{-1}$ , indicating a small amount of self-complexation occurs in **67**. In methanol, and in the presence of triethylamine, **67** smoothly converts 2-naphthaldehyde to the corresponding ester. A comparison with reactions using mixtures of the individual components, e.g., a flavinless cyclophane plus flavin, demonstrated the increase in efficiency when all the catalytic machinery are brought together in one reagent. Unfortunately, attempts to complete the catalytic cycle by running the reaction under aerobic conditions to allow reoxidation of the flavin were not successful.

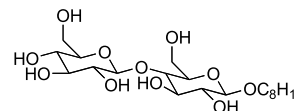
We finish off with some more encapsulating cyclophanes. Host **68** is a water-soluble cyclophane whose conformational motions are relatively slow because of its many amide bonds.<sup>[145]</sup> Its binding properties were examined with fluorescent guests such as ANS. In aqueous acetate buffer, a  $K_a$  between **68** and ANS of  $20,000 \text{ M}^{-1}$  was recorded. The complexation and preferred orientation of the more sizable guest, pamoic acid **69**, was also examined. Related cyclophanes have also been used for complexing steroids.<sup>[146]</sup> Cyclophane **70** is also capable of sequestering sizable guests.<sup>[147]</sup> This host from the Davis group was examined for its ability to bind a range of monosaccharides and disaccharides. Of the different guests examined, the host was shown to bind only the all-equatorially substituted *n*-octyl- $\beta$ -D-cellobioside **71**. Monosaccharides, or disaccharides with axial substituents, did not fit within the cavity.



69



70



71

## CONCLUSION

Both selected polymers and traditional synthetic techniques can engender the formation of discrete hydrophobic pockets. Each approach is associated with considerable diversity and offers many opportunities for new strategies in storage/delivery, catalysis, and detection. Many of these goals are currently being addressed by rather open, solvated, supramolecular tools. And what successes there have been! Nevertheless,

it is surely the case that soon the more encompassing hydrophobic pockets highlighted here will ultimately herald even more powerful supramolecular tools.

## ACKNOWLEDGMENTS

The partial support of the National Science Foundation (CHE 0111133) is greatly acknowledged. Special thanks also to Zachary Laughrey for assistance with the figures, and to Corinne L. D. Gibb for help with library searches.

## REFERENCES

- Cram, D.J.; Cram, J.M. *Container Molecules and Their Guests*, 1st Ed.; Royal Society of Chemistry: Cambridge, 1994.
- Lehn, J.-M.; Atwood, J.L.; Davies, J.E.D.; MacNicol, D.D.; Vögle, F.; Eds. *Comprehensive Supramolecular Chemistry*; Pergamon: New York, 1996.
- Gellman, S.H. Foldamers: a manifesto. *Acc. Chem. Res.* **1998**, *31*, 173–180.
- Cheng, R.P.; Gellman, S.H.; DeGrado, W.F.  $\beta$ -Peptides: from structure to function. *Chem. Rev.* **2001**, *101*, 3219–3232.
- Seebach, D.; Overhand, M.; Kühnle, F.N.M.; Martinoni, B.; Oberer, L.; Hommel, U.; Widmer, H.  $\beta$ -Peptides: synthesis by Arndt–Eistert homologation with concomitant peptide coupling. Structure determination by NMR and CD spectrometry and by x-ray crystallography. Helical secondary structure of a  $\beta$ -hexapeptide in solution and its stability towards pepsin. *Helv. Chim. Acta* **1996**, *79*, 913–941.
- Seebach, D.; Beck, A.K.; Brenner, M.; Gaul, C.; Heckel, A. From synthetic methods to  $\gamma$ -peptides— from chemistry to biology. *Chimia* **2001**, *55*, 831–838.
- Gademann, K.; Ernst, M.; Hoyer, D.; Seebach, D. Synthesis and biological evaluation of a cyclic- $\beta$ -tetrapeptide as a somatostatin analogue. *Angew. Chem., Int. Ed. Engl.* **2001**, *38*, 1223–1226.
- Wender, M.; Hauser, H.; Abele, S.; Seebach, D.  $\beta$ -Peptides as inhibitors of small-intestinal cholesterol and fat absorption. *Helv. Chim. Acta* **1999**, *82*, 1774–1783.
- Porter, E.A.; Wang, X.; Lee, H.-S.; Weisblum, B.; Gellman, S.H. Non-haemolytic  $\beta$ -amino-acid oligomers. *Nature* **2000**, *404*, 565.
- Habihara, M.; Anthony, N.J.; Stout, T.J.; Clardy, J.; Schreiber, S.L. Vinylogous polypeptides: an alternative peptide backbone. *J. Am. Chem. Soc.* **1992**, *114*, 6568–6570.
- Gennari, C.; Longari, C.; Ressel, S.; Salom, B.; Mielgo, A. Synthesis of chiral vinylogous sulfonamido peptides (VS peptides). *Eur. J. Org. Chem.* **1998**, *6*, 945–959.
- Gennari, C.; Salom, B.; Potenza, D.; Longari, C.; Fioravanzo, E.; Carugo, O.; Sardone, N. Conformational studies of vinylogous sulfonamido peptides. *Chemistry* **1996**, *2*, 644–655.
- Cubberley, M.S.; Iverson, B.L. Models of higher-order structure: foldamers and beyond. *Curr. Opin. Chem. Biol.* **2001**, *5*, 650–653.
- Lokey, R.S.; Iverson, B.L. Synthetic molecules that fold into a pleated secondary structure in solution. *Nature* **1995**, *375*, 303–305.
- Cubberley, M.S.; Iverson, B.L.  $^1\text{H}$  NMR Investigation of solvent effects in aromatic stacking interactions. *J. Am. Chem. Soc.* **2001**, *123*, 7560–7563.
- Nelson, J.C.; Saven, J.G.; Moore, J.S.; Wolynes, P.G. Solvophobically driven folding of nonbiological oligomers. *Science* **1998**, *277*, 1793–1796.
- Tanatani, A.; Mio, M.J.; Moore, J.S. Chain length-dependent affinity of helical foldamers for a rod-like guest. *J. Am. Chem. Soc.* **2001**, *123*, 1792–1793.
- Prince, R.B.; Barnes, S.A.; Moore, J.S. Foldamer-based molecular recognition. *J. Am. Chem. Soc.* **2000**, *122*, 2758–2762.
- Rebek, J., Jr. Reversible encapsulation and its consequences in solution. *Acc. Chem. Res.* **1999**, *32*, 278–286.
- Cram, D.J. Cavitands: organic hosts with enforced cavities. *Science* **1983**, *219*, 1177–1183.
- Gutsche, C.D. *Calixarenes Revisited*; Royal Society of Chemistry: London, 2000.
- Gutsche, C.D. *Calixarenes for Separations*; ACS Symposium Series; American Chemical Society (ACS): Washington, D.C., 2000; 757, 2–9.
- Zouhair, A.; Böhmer, V.; Harrowfield, J.; Vicens, J.; Saadioui, M.; Eds. *Calixarenes 2001*; Zouhair, A., Böhmer, V., Harrowfield, J., Vicens, J., Saadioui, M., Eds.; Kluwer Academic Publishers: Dordrecht, 2001.
- Rudkevich, D.M. Nanoscale molecular containers. *Bull. Chem. Soc. Jpn.* **2002**, *75*, 393–413.
- Timmerman, P.; Verboom, W.; Reinhoudt, D.N. Resorcinarenes. *Tetrahedron* **1996**, *52*, 2663–2704.
- Gibb, C.L.D.; Gibb, B.C. Estimating the efficiencies of self-assemblies. *J. Supramol. Chem.* **2001**, *1*, 39–52.
- Yanagihara, R.; Tominaga, M.; Aoyama, Y. Chiral host–guest interaction. A water-soluble calix[4] resorcinarene having L-proline moieties as a non-lanthanide chiral NMR shift reagent for chiral aromatic guests in water. *J. Org. Chem.* **1994**, *59*, 6865–6867.
- Kikuchi, Y.; Kato, Y.; Toi, H.; Aoyama, Y. Molecular recognition and stereoselectivity: geometrical requirements for the multiple hydrogen-bonding interaction of diols with a multidentate polyhydroxy macrocycle. *J. Am. Chem. Soc.* **1991**, *113*, 1349–1354.
- Tanaka, Y.; Kato, Y.; Aoyama, Y. Two-point hydrogen-bonding interaction: a remarkable chain-length selectivity in the binding of dicarboxylic acids with resorcinol–aldehyde cyclotetramer as a multidentate host. *J. Am. Chem. Soc.* **1990**, *112*, 2807–2808.
- Aoyama, Y.; Tanaka, Y.; Sugahara, S. Molecular recognition. 5. Molecular recognition of sugars via hydrogen-bonding interaction with a synthetic polyhydroxy macrocycle. *J. Am. Chem. Soc.* **1989**, *111*, 5397–5404.
- Hayashida, O.; Kato, M.; Akagi, K.; Aoyama, Y. Interaction of sugar and anion in water via hydrogen



- bonding: chain-length dependent agglutination of oligosaccharide clusters induced by multivalent anion binding. *J. Am. Chem. Soc.* **1999**, *121*, 11,597–11,598.
32. Fujimoto, T.; Shimizu, C.; Hayashida, O.; Aoyama, Y. Ternary complexation involving protein. Molecular transport to saccharide-binding proteins using macrocyclic saccharide cluster as specific transporter. *J. Am. Chem. Soc.* **1998**, *120*, 601–602.
  33. Fujimoto, T.; Shimizu, C.; Hayashida, O.; Aoyama, Y. Solution-to-surface molecular-delivery system using a macrocyclic sugar cluster. Sugar-directed adsorption of guests in water on polar solid surfaces. *J. Am. Chem. Soc.* **1997**, *119*, 6676–6677.
  34. Moran, J.R.; Karbach, S.; Cram, D.J. Cavitands: synthetic molecular vessels. *J. Am. Chem. Soc.* **1982**, *104*, 5826–5828.
  35. Gui, X.; Sherman, J.C. Host–guest binding of simple cavitands in water. *Chem. Commun.* **2001**, 2680–2681.
  36. Rudkevich, D.M.; Rebek, J., Jr. Deepening cavitands. *Eur. J. Org. Chem.* **1999**, 1991–2005.
  37. Dalcanale, E.; Soncini, P.; Bacchilega, G.; Ugozzoli, F. Selective complexation of neutral molecules in organic solvents. Host–guest complexes and cavities between cavitands and aromatic compounds. *Chem. Commun.* **1989**, 500–503.
  38. Soncini, P.; Bonsignore, S.; Dalcanale, E.; Ugozzoli, F. Cavitands as versatile molecular receptors. *J. Org. Chem.* **1992**, *57*, 4608–4612.
  39. Moran, J.R.; Ericson, J.L.; Dalcanale, E.; Bryant, J.A.; Knobler, C.B.; Cram, D.J. Vases and kites as cavitands. *J. Am. Chem. Soc.* **1991**, *113*, 5707–5714.
  40. Cram, D.J.; Heung-Jin, C.; Bryant, J.A.; Knobler, C.B. Solvophobic and entropic driving forces for forming velcra, which are four-fold, lock-key dimers in organic media. *J. Am. Chem. Soc.* **1992**, *114*, 7748–7765.
  41. Tucci, F.C.; Rudkevich, D.M.; Rebek, J., Jr. Deeper cavitands. *J. Org. Chem.* **1999**, *64*, 4555–4559.
  42. Rudkevich, D.M.; Hilmersson, G.; Rebek, J., Jr. Intramolecular hydrogen bonding controls the exchange rates of guests in a cavitand. *J. Am. Chem. Soc.* **1997**, *119*, 9911–9912.
  43. Rudkevich, D.M.; Hilmersson, G.; Rebek, J., Jr. Self-folding cavitands. *J. Am. Chem. Soc.* **1998**, *120*, 12,216–12,217.
  44. Shivanyuk, A.; Rissanen, K.; Körner, S.K.; Rudkevich, D.M.; Rebek, J., Jr. Structural studies of self-folding cavitands. *Helv. Chim. Acta* **2000**, *83*, 1778–1791.
  45. Starnes, S.D.; Rudkevich, D.M.; Rebek, J., Jr. Cavitand-porphyrins. *J. Am. Chem. Soc.* **2001**, *123*, 4659–4669.
  46. Ma, S.; Rudkevich, D.M.; Rebek, J., Jr. Supramolecular isomerism in cavitand complexes. *Angew. Chem., Int. Ed. Engl.* **1999**, *38*, 2600–2602.
  47. Haino, T.; Rudkevich, D.M.; Shivanyuk, A.; Rissanen, K.; Rebek, J., Jr. Induced-fit molecular recognition with water-soluble cavitands. *Chem. Eur. J.* **2000**, *6*, 3797–3805.
  48. Ballester, P.; Shivanyuk, A.; Far, A.R.; Rebek, J., Jr. A synthetic receptor for choline and carnitine. *J. Am. Chem. Soc.* **2002**, *124*, 14,014–14,016.
  49. Far, A.R.; Shivanyuk, A.; Rebek, J., Jr. Water-stabilized cavitands. *J. Am. Chem. Soc.* **2002**, *124*, 2854–2855.
  50. Saito, S.; Nuckolls, C.; Rebek, J., Jr. New molecular vessels: synthesis and chiroselective recognition. *J. Am. Chem. Soc.* **2000**, *122*, 9628–9630.
  51. Renslo, A.R.; Rebek, J., Jr. Molecular recognition with introverted functionality. *Angew. Chem., Int. Ed. Engl.* **2000**, *39*, 3281–3283.
  52. Wash, P.L.; Renslo, A.R.; Rebek, J., Jr. Isolation of an acid/base complex in solution puts the brakes on nitrogen inversion. *Angew. Chem., Int. Ed. Engl.* **2001**, *40*, 1221–1222.
  53. Lücking, U.; Chen, J.; Rudkevich, D.M.; Rebek, J., Jr. A self-folding metallocavitand. *J. Am. Chem. Soc.* **2001**, *123*, 9929–9934.
  54. Gibson, C.; Rebek, J., Jr. Recognition and catalysis in allylic alkylations. *Org. Lett.* **2002**, *4*, 1887–1890.
  55. Lücking, U.; Tucci, F.C.; Rudkevich, D.M.; Rebek, J., Jr. Self-folding cavitands of nanoscale dimensions. *J. Am. Chem. Soc.* **2000**, *122*, 8880–8889.
  56. Tucci, F.C.; Renslo, A.R.; Rudkevich, D.M.; Rebek, J., Jr. Nanoscale container structures and their host–guest properties. *Angew. Chem., Int. Ed. Engl.* **2000**, *39*, 1076–1079.
  57. Xi, H.; Gibb, C.L.D.; Stevens, E.D.; Gibb, B.C. Deep-cavity cavitands: the synthesis and solid state structure of host molecules possessing large, bowl-shaped cavities. *Chem. Commun.* **1998**, 1743–1744.
  58. Xi, H.; Gibb, C.L.D.; Gibb, B.C. Functionalized deep-cavity cavitands. *J. Org. Chem.* **1999**, *64*, 9286–9288.
  59. Green, J.O.; Baird, J.-H.; Gibb, B.C. Reduced-symmetry deep-cavity cavitands. *Org. Lett.* **2000**, *2*, 3845–3848.
  60. Gibb, C.L.D.; Stevens, E.D.; Gibb, B.C. C–H...X–R hydrogen bonds drive the complexation properties of a nano-scale molecular basket. *J. Am. Chem. Soc.* **2001**, *123*, 5849–5850.
  61. Laughrey, Z.R.; Gibb, C.L.D.; Senechal, T.; Gibb, B.C. Guest binding and orientation within open molecular hosts possessing deep crowns of acidic C–H groups. *Chem. Eur. J.* **2003**, *9*, 130–139.
  62. Desiraju, G.R. Hydrogen bridges in crystal engineering: interactions without borders. *Acc. Chem. Res.* **2002**, *35*, 565–573.
  63. Desiraju, G.R.; Steiner, T. *The Weak Hydrogen Bond*; Oxford University Press: Oxford, 1999.
  64. Gibb, C.L.D.; Xi, H.; Politzer, P.A.; Concha, M.; Gibb, B.C. The synthesis and binding properties of nano-scale hydrophobic pockets. *Tetrahedron* **2002**, *58*, 673–681.
  65. Gibb, C.L.D.; Li, X.; Gibb, B.C. Adjusting the binding thermodynamics, kinetics, and orientation of guests within large synthetic hydrophobic pockets. *Proc. Natl. Acad. Sci. U. S. A.* **2002**, *99*, 4857–4862.
  66. von dem Bussche-Hünnefeld, C.; Helgeson, R.C.; Bühring, D.; Knobler, C.B.; Cram, D.J. Bowl shaped cavitands dimerize and complex certain organic guests in organic solvents which themselves are poor guests. *Croat. Chem. Acta* **1996**, *69*, 447–458.

67. Sebo, L.; Diederich, F. Tetrakis(phenylamimidinium)-substituted resorcin[4]arene receptors for the complexation of dicarboxylates and phosphates in protic solvents. *Helv. Chim. Acta* **2000**, *83*, 93–113.
68. Stewart, D.R.; Gutsche, C.D. Isolation, characterization and conformation characteristics of *p*-*tert*-butylcalix[9–20]arenes. *J. Am. Chem. Soc.* **1999**, *121*, 4136–4146.
69. Blanchard, S.; Le Clainche, L.; Rager, M.-N.; Tuchagues, J.-P.; Dupart, A.F.; Le Mest, Y.; Reinaud, O. Calixarene-based copper(I) complexes as models for monocopper sites in enzymes. *Angew. Chem., Int. Ed. Engl.* **1998**, *37*, 2732–2735.
70. Rondelez, Y.; Bertho, G.; Reinaud, O. The first water-soluble copper(I) calix[6]arene complex presenting a hydrophobic ligand binding pocket: a remarkable model for active sites in metalloenzymes. *Angew. Chem., Int. Ed. Engl.* **2002**, *41*, 1044–1046.
71. Rondelez, Y.; Rager, M.N.; Duprat, A.; Reinaud, O. Calix[6]arene-based cuprous “funnel complexes”: a mimic for the substrate access channel to metalloenzyme active sites. *J. Am. Chem. Soc.* **2002**, *124*, 1334–1340.
72. Sénèque, O.; Rager, M.-N.; Giorgi, M.; Reinaud, O. Calix[6]arenes and zinc: biomimetic receptors for neutral molecules. *J. Am. Chem. Soc.* **2000**, *122*, 6183–6189.
73. Sénèque, O.; Rager, M.-N.; Giorgi, M.; Reinaud, O. Supramolecular stabilization of a tris(imidazolyl) Zn–aqua complex evidenced by x-ray analysis: a structural model for mono-zinc active sites of enzymes. *J. Am. Chem. Soc.* **2001**, *123*, 8442–8443.
74. Ross, H.; Lüning, U. Concave reagents—23. Synthesis of a calix[6]arene bridged by a 1,10-phenanthroline. *Tetrahedron Lett.* **1997**, *38*, 4539–4542.
75. Ross, H.; Lüning, U. Concave reagents based on calixarenes. *Angew. Chem., Int. Ed. Engl.* **1995**, *34*, 2555–2557.
76. Casnati, A.; Sansone, F.; Ungaro, R. Peptido- and glycolcalixarenes: playing with hydrogen bonds around hydrophobic cavities. *Acc. Chem. Res.* **2003**, *36*, 246–254.
77. Sansone, F.; Baldini, L.; Casnati, A.; Lazzarotto, M.; Ugozzoli, F.; Ungaro, R. Biomimetic macrocyclic receptors for carboxylate anion recognition on C-linked peptidocalix[4]arenes. *Proc. Natl. Acad. Sci. U. S. A.* **2002**, *99*, 4842–4847.
78. Timmerman, P.; Verboom, W.; van Veggel, F.C.J.M.; van Duynhoven, J.P.M.; Reinhoudt, D.N. A novel type of stereoisomerism in calix[4]arene-based carceplexes. *Angew. Chem., Int. Ed. Engl.* **1994**, *33*, 2345–2348.
79. Rudkevich, D.M.; Verboom, W.; Reinhoudt, D.N. Capped bis-calix[4]arene–Zn–porphyrin: metallo-receptor with a rigid cavity. *J. Org. Chem.* **1995**, *60*, 6585–6587.
80. Saadioui, M.; Böhmer, V. *Calixarenes 2001*; Zouhair, A., Böhmer, V., Harrowfield, J., Vicens, J., Saadioui, M., Eds.; Kluwer Academic Publishers: Dordrecht, 2001. Chap. 7.
81. Araki, K.; Hisaichi, K.; Kanai, T.; Shinkai, S. Synthesis of an upper-rim-connected bis-calix[4]arene and its improved inclusion ability based on the cooperative action. *Chem. Lett.* **1995**, 569–570.
82. Lhoták, P.; Shinkai, S. Structural unusual calix[4]arene derivatives generated by intra- and intermolecular McMurry reactions. *Tetrahedron* **1996**, *37*, 645–648.
83. Arduini, A.; Pochini, A.; Secchi, A. Rigid calix[4]arene as a building block for the synthesis of new quaternary ammonium cation receptors. *Eur. J. Org. Chem.* **2000**, 2325–2334.
84. Neri, P.; Bottino, A.; Cunsolo, F.; Piattelli, M.; Gavuzzo, E. 5,5′-Bicalix[4]arene: the bridgeless prototype of double calix[4]arene of the head-to-head type. *Angew. Chem., Int. Ed. Engl.* **1998**, *37*, 166–169.
85. Beer, P.D.; Shade, M. Solvent dependant anion selectivity exhibited by neutral ferrocenyl receptors. *Chem. Commun.* **1997**, 2377–2378.
86. Araki, K.; Hayashida, H. Guest inclusion properties of a novel cage molecule composed of two calix[4]arenes. *Tetrahedron Lett.* **2000**, *41*, 1209–1213.
87. Araki, K.; Hayashida, H. Synthesis and inclusion properties of an upper-rim-connected *bis*-calix[4]arene. *Chem. Lett.* **2000**, 20–21.
88. Hwang, G.T.; Kim, B.H. Synthesis and binding studies of multiple calix[4]arenes. *Tetrahedron* **2002**, *58*, 9019–9028.
89. Hwang, G.T.; Kim, B.H. *Bis*-calix[4]arenes with imine linkages: synthesis and binding study of thiopheno *bis*-calix[4]arene with viologens. *Tetrahedron Lett.* **2000**, *41*, 5917–5921.
90. Atwood, J.L.; Koutsantonis, G.A.; Raston, C.L. Purification of C<sub>60</sub> and C<sub>70</sub> by selective complexation with calixarenes. *Nature* **1994**, *368*, 229–231.
91. Suzuki, T.; Nakashima, K.; Shinkai, S. Very convenient and efficient purification method for fullerene (C<sub>60</sub>) with 5,11,17,23,29,35,41,47-octa-*tert*-butylcalix[8]arene-49,50,51,52,53,54,55,56-octol. *Chem. Lett.* **1994**, 699–702.
92. Zhong, Z.-L.; Ikeda, A.; Shinkai, S. *Calixarenes 2001*; Zouhair, A., Böhmer, V., Harrowfield, J., Vicens, J., Saadioui, M., Eds.; Kluwer Academic Publishers: Dordrecht, 2001. Chap. 26.
93. Wang, J.; Bodige, S.G.; Watson, W.H.; Gutsche, C.D. Complexation of fullerenes with 5,5-bis-calix[5]arene. *J. Org. Chem.* **2000**, *65*, 8260–8263.
94. Haino, T.; Yanase, M.; Fukazawa, Y. Fullerenes enclosed in bridged calix[5]arenes. *Angew. Chem., Int. Ed. Engl.* **1998**, *37*, 997–998.
95. Yanase, M.; Matsuoka, M.; Tatsumi, Y.; Suzuki, M.; Iwamoto, H.; Haino, T.; Fukazawa, Y. Thermodynamic study on supramolecular complex formation of fullerene with calix[5]arenes in organic solvents. *Tetrahedron Lett.* **2000**, *41*, 493–497.
96. Freeman, W.A.; Mock, W.L.; Shih, N.-Y. Cucurbituril. *J. Am. Chem. Soc.* **1981**, *103*, 7367–7368.
97. Behrend, R.; Meyer, E.; Rusche, F. Ueber Condensationsproducte ans Glycoluril und Formaldehyde. *Liebigs Ann. Chem.* **1905**, *339*, 1–37.

98. Kim, J.; Jung, I.-S.; Kim, S.-Y.; Lee, E.; Kang, J.-K.; Sakamoto, S.; Yamaguchi, K.; Kim, K. New cucurbituril homologues: synthesis, isolation, characterization and x-ray crystal structures of cucurbit[n]uril ( $n = 5, 7$  and  $8$ ). *J. Am. Chem. Soc.* **2000**, *122*, 540–541.
99. Jeon, Y.-M.; Kim, J.; Whang, D.; Kim, K. Molecular container assembly capable of controlling binding and release of its guest molecules: reversible encapsulation of organic molecules in sodium ion complexed cucurbituril. *J. Am. Chem. Soc.* **1996**, *118*, 9790–9791.
100. Mock, W.L.; Shih, N.-Y. Host–guest binding capacity of cucurbituril. *J. Org. Chem.* **1983**, *48*, 3618–3619.
101. Mock, W.L.; Shih, N.-Y. Structure and selectivity in host–guest complexes of cucurbituril. *J. Org. Chem.* **1986**, *51*, 4440–4446.
102. Mock, W.L.; Shih, N.-Y. Organic ligand–receptor interactions between cucurbituril and alkylammonium ions. *J. Am. Chem. Soc.* **1988**, *110*, 4707–4710.
103. Mock, W.L.; Shih, N.-Y. Dynamics of molecular recognition involving cucurbituril. *J. Am. Chem. Soc.* **1989**, *111*, 2697–2699.
104. Whang, D.; Park, K.-M.; Heo, J.; Ashton, P.; Kim, K. Molecular necklace: quantitative self-assembly of a cyclic oligorotaxane from nine molecules. *J. Am. Chem. Soc.* **1998**, *120*, 4899–4900.
105. Ong, W.; Gómez-Kaifer, M.; Kaifer, A.E. Cucurbit[7]-uril: a very effective host for viologens and their cationic radicals. *Org. Lett.* **2002**, *4*, 1791–1794.
106. Kim, H.-J.; Heo, J.; Jeon, W.S.; Lee, E.; Kim, J.; Sakamoto, S.; Yamaguchi, K.; Kim, K. Selective inclusion of a hetero-guest pair in a molecular host: formation of stable charge-transfer complexes in cucurbit[8]uril. *Angew. Chem., Int. Ed. Engl.* **2001**, *40*, 1526–1529.
107. Kim, S.-Y.; Jung, I.-S.; Lee, E.; Kim, J.; Sakamoto, S.; Yamaguchi, K.; Kim, K. Macrocycles within macrocycles: cyclen, cyclam, and their transition metal complexes encapsulated in cucurbit[8]uril. *Angew. Chem., Int. Ed. Engl.* **2001**, *40*, 2119–2121.
108. Rowan, A.E.; Elemans, J.A.A.W.; Nolte, R.J.M. Molecular and supramolecular objects from glycoluril. *Acc. Chem. Res.* **1999**, *32*, 995–1006.
109. Sijbesma, R.P.; Nolte, R.J.M. Synthesis of concave receptors derived from diphenylglycoluril. *Recl. Trav. Chim. Pays-Bas* **1993**, *112*, 643–647.
110. Sijbesma, R.P.; Nolte, R.J.M. *Molecular Clips and Cages Derived from Glycoluril Topics in Current Chemistry: Supramolecular Chemistry II—Host Design and Molecular Recognition*; Weber, E., Ed.; Springer: Berlin, 1995; 25–56.
111. Smeets, J.W.H.; Sijbesma, R.P.; van Dalen, L.; Spek, A.L.; Smeets, W.J.J.; Nolte, R.J.M. Synthesis and binding properties of basket-shaped hosts. *J. Org. Chem.* **1989**, *54*, 3710–3717.
112. Schenning, A.P.H.J.; de Bruin, B.; Rowan, A.E.; Kooijman, H.; Spek, A.L.; Nolte, R.J.M. Strong binding of paraquat and polymeric paraquat derivatives by basket-shaped hosts. *Angew. Chem., Int. Ed. Engl.* **1995**, *34*, 2132–2134.
113. Sijbesma, R.P.; Nolte, R.J.M. Binding of dihydroxybenzenes in synthetic molecular clefts. *J. Org. Chem.* **1991**, *56*, 3122–3124.
114. Reek, J.N.H.; Priem, A.H.; Engelkamp, H.; Rowan, A.E.; Elemans, J.A.A.W.; Nolte, R.J.M. Binding features of molecular clips. separation of the effects of hydrogen bonding and  $\pi$ – $\pi$  interactions. *J. Am. Chem. Soc.* **1997**, *119*, 9956–9964.
115. Martens, C.F.; Klein Gebbink, R.J.M.; Feiters, M.C.; Nolte, R.J.M. Shape-selective oxidation of benzylic alcohols by a receptor functionalized with a dicopper(II) pyrazole complex. *J. Am. Chem. Soc.* **1994**, *116*, 5667–5670.
116. Reek, J.N.H.; Rowan, A.E.; Crossley, M.J.; Nolte, R.J.M. Synthesis and photophysical properties of porphyrin-functionalized molecular clips. *J. Org. Chem.* **1999**, *64*, 6653–6663.
117. Reek, J.N.H.; Elemans, J.A.A.W.; Nolte, R.J.M. Synthesis, conformational analysis, and binding properties of molecular clips with two different side walls. *J. Org. Chem.* **1997**, *62*, 2234–2243.
118. Elemans, J.A.A.W.; Claase, M.B.; Aarts, P.P.M.; Rowan, A.E.; Schenning, A.P.H.J.; Nolte, R.J.M. Porphyrin clips derived from diphenylglycoluril. Synthesis, conformational analysis, and binding properties. *J. Org. Chem.* **1999**, *64*, 7009–7016.
119. Elemans, J.A.A.W.; Bijsterveld, E.J.A.; Rowan, A.E.; Nolte, R.J.M. A host–guest epoxidation catalyst with enhanced activity and stability. *Chem. Commun.* **2000**, 2443–2444.
120. Thordarson, P.; Bijsterveld, E.J.A.; Elemans, J.A.A.W.; Kasák, P.; Nolte, R.J.M.; Rowan, A.E. Highly negative homotropic allosteric binding of viologens. *J. Am. Chem. Soc.* **2003**, *125*, 1186–1187.
121. Jansen, R.J.; Rowan, A.E.; de Gelder, R.; Scheeren, H.W.; Nolte, R.J.M. Synthesis, x-ray structure and binding properties of molecular clips based on dimethylpropanediurea. *Chem. Commun.* **1998**, 121–122.
122. Jansen, B.J.; de Gelder, R.; Rowan, A.E.; Scheeren, H.W.; Nolte, R.J.M. Molecular clips based on propanediurea. Exceptionally high binding affinities for resorcinol guests. *J. Org. Chem.* **2001**, *66*, 2643–2653.
123. Willmann, P.; Marti, T.; Fürer, A.; Diederich, F. Steroids in molecular recognition. *Chem. Rev.* **1997**, *97*, 1567–1608.
124. Shawaphun, S.; Janout, V.; Regen, S.L. Chemical evidence for transport movement of molecular umbrellas. *J. Am. Chem. Soc.* **1999**, *121*, 5860–5864.
125. Janout, V.; Staina, I.V.; Bandyopadhyay, P.; Regen, S.L. Evidence for an umbrella mechanism of bilayer transport. *J. Am. Chem. Soc.* **2001**, *123*, 9926–9927.
126. Janout, V.; Jing, B.; Staina, I.V.; Regen, S.L. Selective transport of ATP across a phospholipid bilayer by a molecular umbrella. *J. Am. Chem. Soc.* **2003**, *125*, 4436–4437.
127. Davis, A.P.; Wareham, R.S. Carbohydrate recognition through non-covalent interactions: a challenge for biomimetic and supramolecular chemistry. *Angew. Chem., Int. Ed. Engl.* **1999**, *38*, 2979–2996.

128. Davis, A.P.; Davis, A.P. Cholaphanes et al. Steroids as structural components in molecular engineering. *Chem. Soc. Rev.* **1993**, 243–253.
129. Bhattarai, K.M.; Davis, A.P.; Perry, J.J.; Walter, C.J. A new generation of “cholaphanes”: steroid-derived macrocyclic hosts with enhanced solubility and controlled flexibility. *J. Org. Chem.* **1997**, 62, 8463–8473.
130. Davis, A.P.; Menzer, S.; Walsh, J.J.; Williams, D.J. Steroid-based receptors with tunable cavities; a series of polyhydroxylated macrocycles of varying size and flexibility. *Chem. Commun.* **1996**, 453–455.
131. Davis, A.P.; Walsh, J.J. Steroid-based receptors with tunable cavities; stepwise and direct syntheses of a C<sub>3</sub>-symmetrical prototype. *Chem. Commun.* **1996**, 449–451.
132. Kohmoto, S.; Fukui, D.; Nagashima, T.; Kishikawa, K.; Yamamoto, M.; Yamada, K. Synthesis of steroidal triply-bridged cyclophanes. *Chem. Commun.* **1996**, 1869–1870.
133. Bonar-Law, R.P.; Sanders, J.K.M. Synthesis of cyclocholesterol-capped porphyrins. *J. Chem. Soc., Perkin Trans. 1* **1995**, 3085–3096.
134. Bonar-Law, R.P.; Sanders, J.K.M. Polyol recognition by a steroid-capped porphyrin. Enhancement and modulation of misfit guest binding by added water or methanol. *J. Am. Chem. Soc.* **1995**, 117, 259–271.
135. Bonar-Law, R.P. Recognition by a solubilized receptor: Hydrogen bonding, solvophobic interactions, and solvent engineering inside micelles. *J. Am. Chem. Soc.* **1995**, 117, 12,397–12,407.
136. Kennan, A.J.; Whitlock, H.W. Host-catalyzed isoxazole ring opening: a rationally designed artificial enzyme. *J. Am. Chem. Soc.* **1996**, 118, 3027–3028.
137. Inouye, M.; Fujimoto, K.; Furusyo, M.; Nakazumi, H. Molecular recognition abilities of a new class of water-soluble cyclophanes capable of encompassing a neutral cavity. *J. Am. Chem. Soc.* **1999**, 121, 1452–1458.
138. Forman, J.E.; Barrans, R.E.J.; Dougherty, D.A. Circular dichroism studies of molecular recognition with cyclophane hosts in aqueous media. *J. Am. Chem. Soc.* **1995**, 117, 9213–9228.
139. Ngola, S.M.; Dougherty, D.A. Concerning the effects of aromatic ring fluorination on the cation- $\pi$  interaction and other molecular recognition phenomena in aqueous media. *J. Org. Chem.* **1998**, 63, 4566–4567.
140. Ngola, S.M.; Kearney, P.C.; Mecozzi, S.; Russell, K.; Dougherty, D.A. A selective receptor for arginine in aqueous media. Energetic consequences of salt bridges that are highly exposed to water. *J. Am. Chem. Soc.* **1999**, 121, 1192–1201.
141. Anderson, S.; Neidlein, U.; Gramlich, V.; Diederich, F. A new family of chiral binaphthyl-derived cyclophane receptors: complexation of pyranosides. *Angew. Chem., Int. Ed. Engl.* **1995**, 34, 1597–1600.
142. Bähr, A.; Droz, A.S.; Püntener, M.; Neidlein, U.; Anderson, S.; Seiler, P.; Diederich, F. Molecular recognition of pyranosides by a family of trimeric, 1,1'-binaphthalene-derived cyclophane receptors. *Helv. Chim. Acta* **1998**, 81, 1998.
143. Droz, A.S.; Neidlein, U.; Anderson, S.; Seiler, P.; Diederich, F. Optically active cyclophane receptors for mono- and disaccharides: the role of bidentate ionic hydrogen bonding in carbohydrate recognition. *Helv. Chim. Acta* **2001**, 84, 2243–2289.
144. Mattei, P.; Diederich, F. A flavo-thiazolio-cyclophane as a functional model for pyruvate oxidase. *Angew. Chem., Int. Ed. Engl.* **1996**, 35, 1341–1344.
145. Tanaka, A.; Fujiyoshi, S.; Motomura, K.; Hayashida, O.; Hisaeda, Y.; Murakami, Y. Preparation and host-guest interactions of novel cage-type cyclophanes bearing chiral binding sites provided by dipeptide residues. *Tetrahedron* **1998**, 54, 5187–5206.
146. Murakami, Y.; Kikuchi, J.; Hisaeda, Y.; Hayashida, O. *Chem. Rev.* **1996**, 96, 721–758. For other examples of steroid binding, and a review of steroids in supramolecular chemistry in general, see Willmann, P.; Marti, T.; Fürer, A.; Diederich, F. *Chem. Rev.* **1997**, 97, 1567–1608.
147. Lecollinet, G.; Dominey, A.P.; Velasco, T.; Davis, A.P. Highly selective disaccharide recognition by a tricyclic octaamide cage. *Angew. Chem., Int. Ed. Engl.* **2002**, 41, 4093–4097.

# Guests within Hydrophobic Pockets: Self-Assembly

Bruce C. Gibb

Department of Chemistry, University of New Orleans,  
New Orleans, Louisiana, U.S.A.

## INTRODUCTION

This review focuses on how self-assembly can form hosts capable of binding large guests. Its sister article, “Guests within Large Synthetic Hydrophobic Pockets Synthesized Using Polymer and Conventional Techniques,” reviews like-minded work using either polymers or hosts synthesized by traditional synthetic approaches. As described in more detail in that paper, the focus here is on hosts capable of binding organic molecules of more than seven non-hydrogen atoms. Likewise, a similar definition of a “pocket” is retained, with the focus on hosts possessing well-defined, highly concave or enclosed surfaces. An arbitrary value of greater than approximately 50% encapsulation has been set. “Comprehensive Supramolecular Chemistry” covers much of our discussion topic up to 1995.<sup>[1]</sup> This review is therefore primarily interested with the literature since that time.

Motivators for supramolecular chemists include molecular storage/delivery, the detection of substances, and the conversion of one substance into another via catalytic processes. All these processes include at some point the binding of a guest to a host. The hard part in these endeavors is the synthesis of the host, with all the required functionality gathered in a converging array. One approach uses self-assembly, whereby molecular subunits are designed to merge in a specific pattern that possesses a hydrophobic pocket. In this regard, both self-assembly and self-assembly with covalent modification have been used. As with the polymer and traditional synthetic strategies, the self-assembly approach has pros and cons. Normally, relatively rigid subunits are used and so a common worry in cavity design—hydrophobic pocket collapse—is generally avoided. On the other hand, at our current level of understanding we are limited to relatively symmetrical subunits and assembled structures. Nevertheless, testimony to the power of this approach is found in the large cavities formed, some in the order of thousands of cubic Ångströms.

The bulk of recent self-assembly research has focused on understanding the rules that govern how one product can arise out of a reaction mixture that, if all things were equal, would lead to a highly complex

mixture. Hence in a manner analogous to contemporary polymer research, the emphasis is on understanding how the structure of the product is reached, rather than on understanding the properties of any cavity in the product. As a result, many of the very large cavities created by self-assembly are “simply” filled with a large number of (small) solvent molecules. Such examples are not dealt with explicitly here but can be found in citations throughout the text.

## HOSTS BASED ON RESORCINARENES

In the last seven or so years it has become apparent that resorcinarenes, **1** ( $n = 4$ ), a family of molecules<sup>[2–5]</sup> held in much regard for their hosting properties and their use in the synthesis of a plethora of cavitands, also possess a spectacular flair for self-assembly. Two general assembly products have been identified (Fig. 1). Either two molecules can come together in a pseudo  $C_{4h}$  symmetric host, or six assemble into a pseudo-octahedral array. A second component, usually solvent, is necessary to “glue” the subunits together. The first hint of this supramolecular chemistry was pinpointed by MacGillivray and Atwood, who identified the pseudo-octahedral complex both in the solid and the solution state.<sup>[6]</sup> The total assembly consists of six resorcinarenes, eight water molecules and has a solvent-filled cavity. Shortly thereafter, the dimer, again in part held together by 2-propanol/water molecules, was identified independently by the Rose and Aoki groups.<sup>[7,8]</sup> The latter identified a tetraethylammonium ion within the cavity. A third such structure, this time hosting triethylammonium, was identified shortly thereafter.<sup>[9]</sup> Recently, Atwood, Barbour, and Jerga identified a more robust pseudo-spherical hexamer derived from pyrogallol[4]arenes **2**,<sup>[10]</sup> while Shivanyuk and Rebek have determined that the corresponding dimeric assembly also forms and encapsulates large guests.<sup>[11]</sup> Thus, in deuterated methanol or aqueous acetonitrile, NMR evidence suggests that **2** ( $R = Pr$ ) is monomeric. However, the addition of tropylium tetrafluoroborate results in an intense red color indicating a charge transfer complex between **2** ( $R = Pr$ ) and guest. Furthermore, at host/

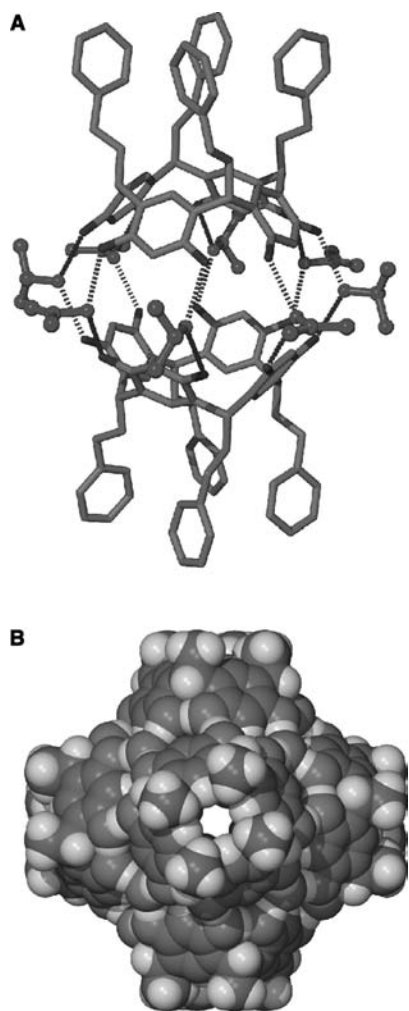
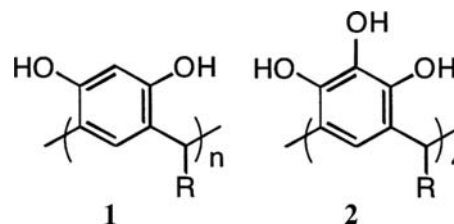


**Fig. 1** Dimeric and hexameric assemblies of resorcin[4]arenes.

guest ratios larger than two, the  $^1\text{H}$  NMR at 233 K demonstrates that a 2:1 complex of **2** ( $\text{R} = \text{Pr}$ ) and tropylium tetrafluoroborate exists. At this temperature, the kinetics of guest exchange is slow on the (600 MHz) NMR time-scale. Further experiments revealed that 1) at higher equivalents of guest a 1:1 complex was formed, and 2) a protic solvent was necessary for assembly of the dimer host. This latter point was noted when more lipophilic **2** ( $\text{R} = \text{C}_{11}\text{H}_{23}$ ) was shown to only assemble in deuterated chloroform when a trace of methanol was present. Interestingly, resorcinarenes **1** ( $\text{R} = \text{Me}$ , or  $\text{Et}$ ) did not undergo this encapsulation of the tropylium ion.

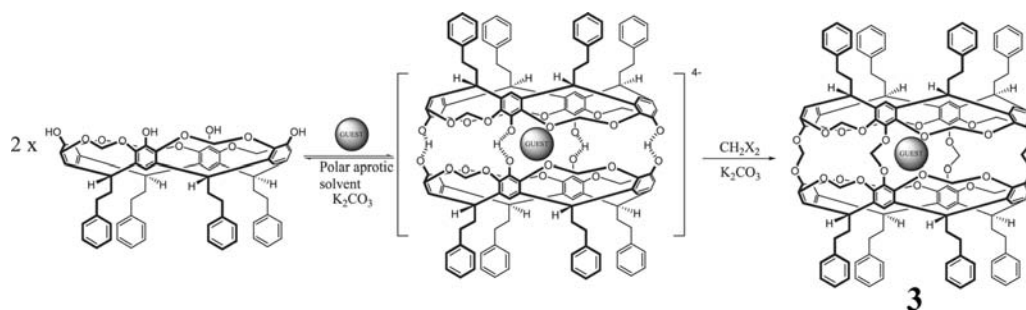
The octahedral assemblies of **1** ( $n = 4$ )<sup>[12,13]</sup> have demonstrated some fascinating encapsulation properties. For example, in water saturated, deuterated chloroform, the hexamer of **1** encapsulates a range of ammonium ions in a manner that is intimately tied to the size and concentration of the guest.<sup>[14]</sup> Tetrahexylammonium bromide is an ideal guest and exchanges slowly, relative to the 600-MHz NMR

time-scale, between cavity and free solution. Nuclear magnetic resonance evidence suggests that the larger guest tetraheptylammonium bromide is cramped within the confines of the assembly, while the still larger tetrahexadecylammonium bromide was not complexed. With smaller guests, things became even more interesting. Thus, in the case of  $\text{Bu}_4\text{N}^+\text{BF}_4^-$ , the small counter ion is coencapsulated along with cation. In such cases, solvent is also present in the cavity but leaves when a more suitable space-filler is present. Hence, at the expense of bound water 4-phenyltoluene is also encapsulated along with  $\text{Bu}_4\text{N}^+\text{BF}_4^-$ . Still smaller ammonium ions instead template the assembly of the dimeric host.  $\text{Bu}_4\text{SbBr}$ , along with a variety of co-encapsulated aromatic guests, is also seen within the hexameric assembly.<sup>[15]</sup> Co-guests included are benzene, *p*-xylene, 4-phenyltoluene, and naphthalene. In contrast, 4,4'-dimethylbiphenyl was not encapsulated with the antimony guest, suggesting that adding an extra methyl group to 4-phenyltoluene was enough to destabilize the complex. Size, however, is not the only important factor for encapsulation. Neither hexafluorobenzene, cyclohexane, nor pentane was coencapsulated. Rather, the antimony guest and presumably some solvent molecules occupied the cavity.

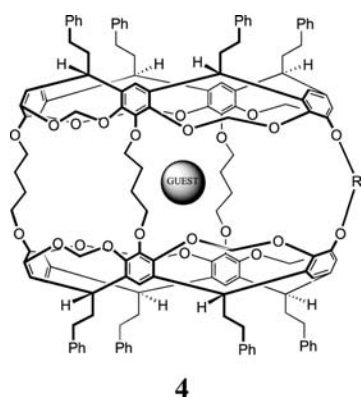


As the basis of cavitands, resorcinarenes have also been instrumental in the synthesis of carceplexes such as **3** (Scheme 1).<sup>[16–18]</sup> As defined by their inventor, Donald Cram, carceplexes are closed surface compounds that permanently entrap guest molecules or ions within their shell, such that guest escape can only occur by rupture of covalent bonds. Since their initial synthesis,<sup>[19]</sup> their self-assembly (with covalent modification) has been intensively investigated; as has the relationship between host shell (the carcerand) and guest. As it transpires, these two facets are intimately tied. Early work focusing on small guests established that templation<sup>[20]</sup> is essential for successful synthesis. The best yields arise when a template stabilizes the transition state of the rate-determining step (rds) for the synthesis. Furthermore, the transition state at the rds has a similar cavity to the product.<sup>[21–29]</sup> Hence good templates for assembly make good guests for the carcerands. In these initial studies, the best guest identified was pyrazine, while the worst guest, and hence the solvent of choice for many of these studies, was *N*-methylpyrrolidinone (NMP).





Scheme 1 Synthesis of carceplex 3.



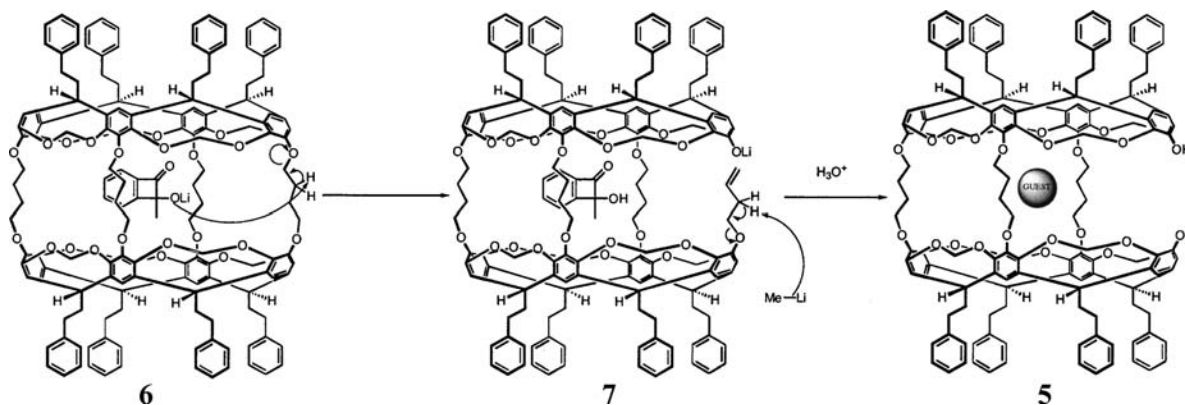
4

Carceplexes can be increased in size to allow the encapsulation of large guests. One way is to use wide-bodied cavitands—cavitands derived from resorcin [5]arenes—in the carceplex reaction.<sup>[30]</sup> Another is to join several “normal”-sized cavitands together.<sup>[31–33]</sup> To date, only relatively small molecules have been observed within hosts synthesized by these methods. A more common approach is to increase the size of the linker groups that join the two “hemispheres” of the shell, i.e., replace bromochloromethane in the synthesis shown in Scheme 1 with a compound with two separate electrophilic centers.<sup>[34]</sup> The resulting products, such as **4** ( $R = -(CH_2)_4-$ ),<sup>[35]</sup> are called hemicarceplexes; so named because the portals in the shell, or hemicarcerand, are large enough for guests to exit or enter the cavity without covalent bond rupturing.<sup>[36]</sup> The ability of over 68 molecules to template the formation of **4** ( $R = -(CH_2)_4-$ ) has been recently studied.<sup>[37]</sup> Of these, 30 proved capable of templation, with the best template *p*-xylene proving to be 3600 times better than the worst *N*-formylpiperidine. However, in contrast to carceplex **3**, the final host structure **4** did not appear to be a reasonable model of the transition state of the rds in its synthesis.

Although many hemicarceplexes can be assembled via templation, most have been synthesized by inserting the desired guest post-assembly. This has provided information about how solvent and the shape of the

portals or guest influence thermodynamic stability, and complexation and decomplexation rates. For example, after synthesizing hemicarceplex **4** ( $R = -(CH_2)_4-$ , guest = solvent), the guest solvent can be exchanged using the law of mass action. Either heating the hemicarceplex in the presence of 100 equivalents of new guest in a solvent too large to enter the cavity, or more simply heating the complex in neat guest, leads to exchange. Using this technique, it is possible to synthesize a range of hemicarceplexes.<sup>[38]</sup> In general, long, thin guests complexed the fastest, while for disubstituted aromatic guests a general order of complexation was demonstrated by the xylene isomers; *p*-xylene  $\gg$  *m*-xylene > *o*-xylene. Computational studies on a related hemicarceplex indicated that two type of gating processes, involving conformational changes in the intra-hemispherical linker groups, affect guest entry or egression.<sup>[39,40]</sup>

How do guests inside the cavity interact with species in free solution? Host **4** ( $R = -(CH_2)_4-$ ) was used to study the first  $S_N2$  reactions of inner-phase guests with outer-phase reactants.<sup>[41]</sup> For example, when the complexes **4** ( $R = -(CH_2)_4-$ , guest = either 4-HOC<sub>6</sub>H<sub>4</sub>OH or 2-HOC<sub>6</sub>H<sub>4</sub>OH or 3-HOC<sub>6</sub>H<sub>4</sub>OH) were exposed to THF/NaH/CH<sub>3</sub>I, three different reaction outcomes were noted. The encapsulated *para*-isomer gave no reaction, the *meta*-isomer was doubly methylated, while the *ortho*-isomer gave a mixture of mono- and dimethylated guest. Different reactivity profiles were noted because each guest prefers a different orientation within the cavity. In the case of the 1,4-isomer for example, the two OH groups can reside deep within the “poles” of the host and cannot be readily alkylated. A similar rationale explains the observed alkyllithium additions and borane reductions of **4** ( $R = -(CH_2)_4-$ , guest = benzaldehyde, benzocyclobutenone, and benzocyclobutenedione).<sup>[42]</sup> If a reactive species is generated within the cavity, it can sometimes react with the hemicarcerand shell. For example, reaction at 0°C between **4** ( $R = -(CH_2)_4-$ , guest = benzocyclobutenedione) and an excess of MeLi gave diol **5** (Scheme 2). Experiments revealed

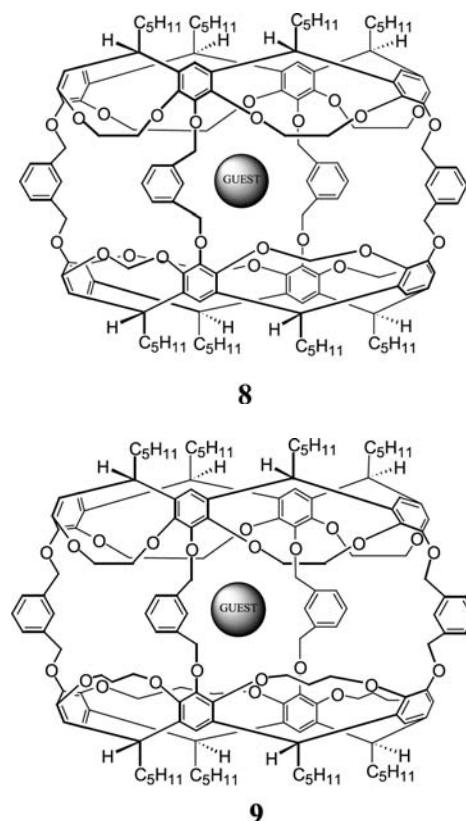


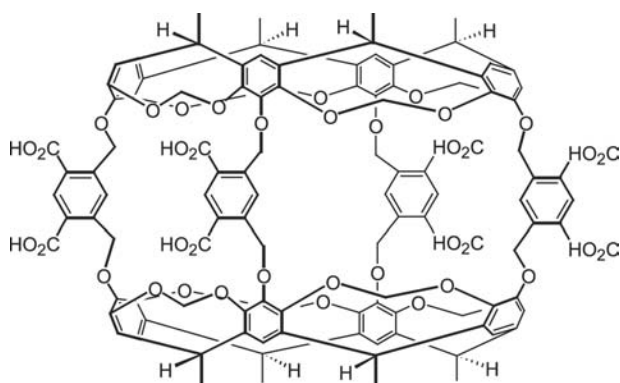
**Scheme 2** Synthesis of diol **5** via an inner-molecular reaction.

that a possible mechanism for this conversion begins with the addition of one equivalent of MeLi to a C=O group of the guest. The basic lithiate complex **6** can then induce a  $\beta$ -elimination in one of the linkers. This produces a butene ether derivative **7** that can then undergo a further elimination to yield the *bis*-phenoxide. Workup yields **5**. The tetramethylene linkers are not the sole reactive sites in this hemicarceand. Thus the methylene bridges in each hemisphere undergo reaction with the guest derived from methyl lithium addition to encapsulated *N*-methyl-2-pyrrolidinone.<sup>[42]</sup>

By carrying out a two-step (hemi)carceplex reaction, lower symmetry hydrophobic pockets can be synthesized.<sup>[43,44]</sup> To point out just two examples, hosts such as **4** (R =  $-\text{CH}_2-$ , or R =  $-(\text{CH}_2)_6-$ ) were synthesized and their corresponding hemicarceplexes examined by X-ray crystallography, NMR, and computational studies.<sup>[45]</sup> As anticipated, introducing a dissimilar linker between the hemispheres altered the shape of the pocket, the orientation of the guest, and hence the thermodynamic and kinetic stability of the corresponding complexes. The kinetics of exchange were measured at different temperatures for 1,4-dimethoxybenzene vacating **4** (R = 1,3- $(\text{CH}_2)_2\text{C}_6\text{H}_4$ ), to show how  $\Delta H^\ddagger$ ,  $\Delta S^\ddagger$ , and hence  $\Delta G^\ddagger$  varied as a function of solvent.<sup>[43]</sup> These studies revealed that solvation plays an important role in decomplexation. Hence decomplexation rates in  $\text{CDCl}_3$  were 800 times faster than in deuterated 1,1,2,2-tetrachloroethane. An examination of different hemicarceplexes showed that the structure of the unique linker also has a considerable effect on egression rates. For example, changing the dissimilar linker R in **4** from pentamethylene to hexamethylene increased the rate constant for egression by a factor of 177. Lower symmetry cavities can also be made by using two different cavitands to construct a hemicarceplex. For example, in hosts **8** and **9** methylene and dimethylene bridges link the phenol oxygens of the former, while dimethylene and

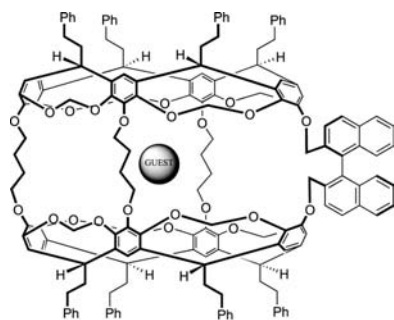
trimethylene linkers are used in the latter.<sup>[46,47]</sup> Nuclear magnetic resonance evidence demonstrates that these subtle changes in the host are manifest in how the guest moves within the pocket. Hence when the guest in **8** is 1,2,3-trimethoxybenzene three signals are observed for the methoxy groups. The 1- and 3-methoxy groups reside within different hemispheres, and the movement of the guest that allows them to exchange is slow on the (500 MHz) NMR time-scale; in contrast, the slightly bigger cavity of **9** means that the corresponding process is fast on the NMR time-scale. Although no simple rules were discernable, the size of the bridges between the phenolic O-atoms undoubtedly influences guest movement and decomplexation rates.





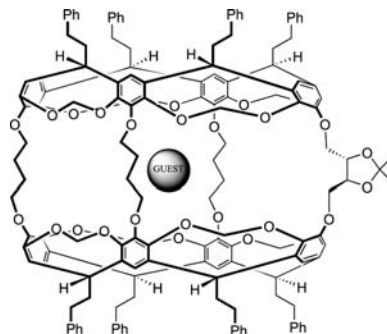
10

Building on these developments, Cram moved the carceplex and hemicarceplex field into the realms of aqueous solution, while at the same time synthesizing chiral hosts. The first water soluble hemicarceplexes were isolated from hemicarcerand **10**.<sup>[48]</sup> In aqueous solution, this host is capable of sequestering a number of guests including naphthalene and 1,3-dimethoxybenzene. Guests such as alkyl ammonium salts that are well solvated by water did not bind. Chiral hemicarceplexes can be synthesized by using the two-step process discussed above. Hosts **11** and **12** are two examples.<sup>[49]</sup> Introducing the chiral linker group of **11** in the presence of a racemic mixture of selected chiral guests resulted in ratios of the diastereomeric complexes of up to 1:1.5. Alternatively, higher diastereomeric ratios could be attained if the chiral hemicarceplex **11** containing chloroform was heated either in the presence of pure, racemic guest, or in diphenylether with an excess of racemic guest. By this approach the highest diastereomeric ratio observed was >20:1 in favor of the *R*-isomer of 4-MeC<sub>6</sub>H<sub>4</sub>-S(O)Me binding to **11**. In contrast, the diastereomeric ratio observed for complexing racemate C<sub>6</sub>H<sub>5</sub>S(O)Me was only 1.6:1 in favor of the *R*-isomer. Overall, the hemicarcerand **12** (guest = chloroform) was less discriminating than **11**. This was attributed to the two “non-chiral,” 26-membered ring portals in **12** being less encumbering than its two chiral portals.



11

As a rule, the shape and functionality of the guest can be transferred through a hemicarceplex shell to the external environment. A simple thin layer chromatography experiment is usually sufficient to demonstrate this point. Furthermore, hemicarceplex shells allow the transfer of triplet energy from aryl ketone guests to free naphthalene.<sup>[50]</sup> These results notwithstanding, guests in carceplexes or hemicarceplexes are in relatively sheltered waters, and this has allowed these unique hosts to be used as storage containers for highly reactive guests.<sup>[34,51,52]</sup> The first example, involving a small guest, was carried out over 12 years ago. Nevertheless, the trapping and room temperature analysis of cyclobutadiene **13** (Fig. 2), the Mona Lisa of organic chemistry as Cram described it, is always worth mentioning.<sup>[34]</sup> Equally as exciting was the trapping by Warmuth of *o*-benzynes **14** inside the cavity of **4** (R = -(CH<sub>2</sub>)<sub>4</sub>-).<sup>[51]</sup> This remarkable feat was accomplished by the photolysis of **4** (R = -(CH<sub>2</sub>)<sub>4</sub>-, guest = benzocyclobutenedione) and allowed its <sup>1</sup>H and <sup>13</sup>C NMR analysis. The former suggested that “free” benzyne would possess <sup>1</sup>H NMR chemical shifts of  $\delta = 7.0$  and 7.6 ppm, while <sup>13</sup>C-<sup>13</sup>C coupling in the latter suggests that **14** is best described as a cumulene. Interestingly, when warmed up to room temperature, the guest reacted with the hemicarcerand in an intermolecular Diels-Alder reaction.<sup>[53]</sup> Following on from this work, Warmuth and Marvel successfully trapped an enantiomeric mixture of 1,2,4,6-cycloheptatriene **15** inside hemicarceplex **4** (R = -(CH<sub>2</sub>)<sub>4</sub>-), by first encapsulating phenyldiazirine and then irradiating the resulting hemicarceplex.<sup>[54]</sup> Protected by the host shell, **15** could not dimerize and was stable for weeks at ambient temperature. By carrying out the same chemistry within chiral host **12**, a 3:2 ratio of the two resulting diastereomeric complexes was formed.<sup>[55]</sup> No coalescence of NMR signals could be observed when heating these complexes up to 100°C, which puts a lower limit to the enantiomerization barrier of >19.6 kcal mol<sup>-1</sup>. This value was collaborated with a parallel experiment using the diastereomeric complex of **12** (guest = **16**). Thus using line broadening analysis



12



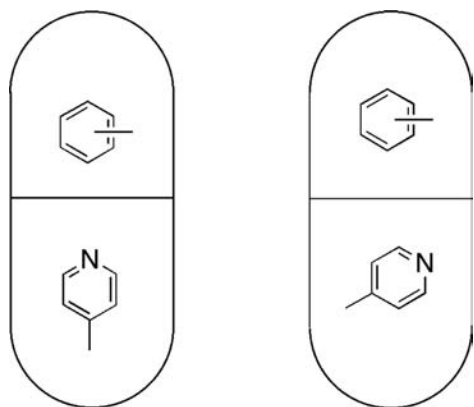
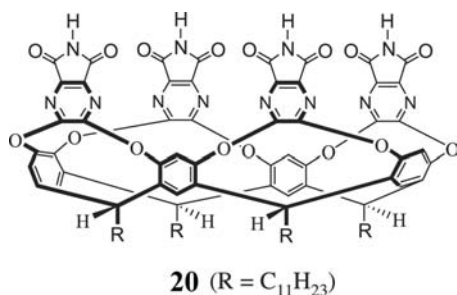


Fig. 3 Cartoon of the two, heterodimeric assemblies in the  $20_2$  toluene and  $\gamma$ -picoline complex.

heterodimeric assemblies is shown in Fig. 3. In these assemblies, each toluene molecule tumbles freely whereas the methyl pyridine can only adopt one of two, thermodynamically equilibrated orientations. Replacing the toluene guest with another guest alters this equilibrium.<sup>[67]</sup> This intriguing supramolecular isomerism is not of course restricted to two guests. For example, in more recent work, the isomers that can result when three guests are encapsulated within the dimer of **20** have also been identified.<sup>[68]</sup>

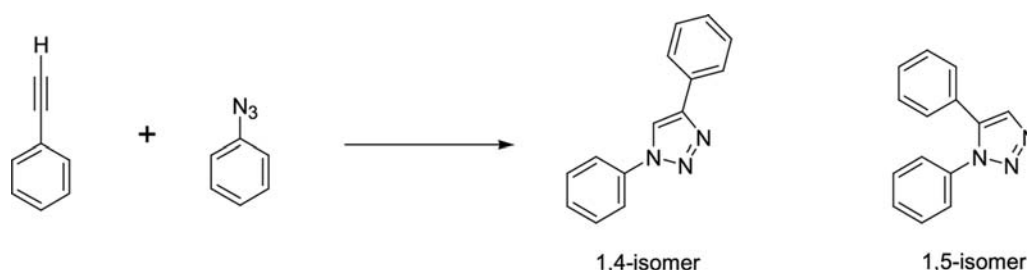


Host **20** can also be used as a means of storage and delivery. Thus, capsule-bound dibenzyl peroxide was shown to be incapable of oxidizing triphenylphosphine. However, normal peroxide reactivity is restored when dimethylformamide is added and the

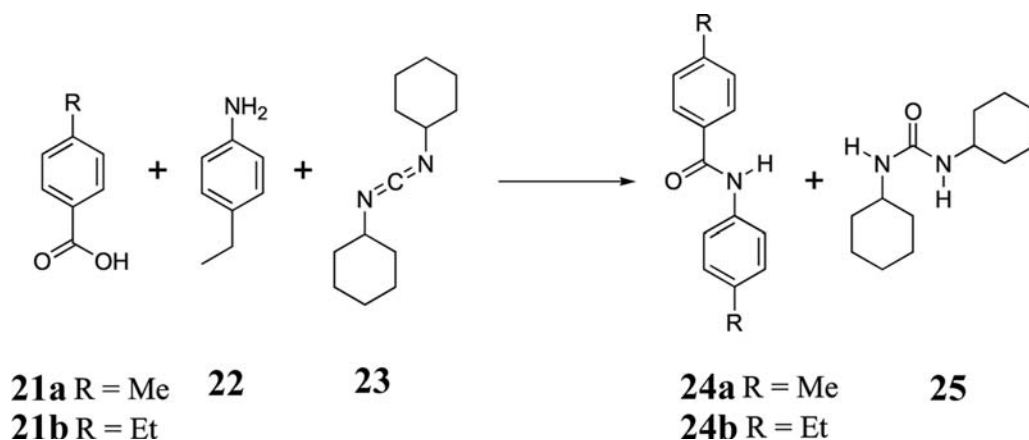
capsular assembly broken.<sup>[63]</sup> The same host can also be used to control the regioselectivity of cycloaddition reactions.<sup>[69]</sup> The 1,3-dipolar cycloaddition between phenylacetylene and phenyl azide can lead to two isomeric triazoles, the 1,4 isomer or the 1,5-isomer (Scheme 4). At ambient temperature and millimolar concentration this reaction is negligible on the human time-scale. In the presence of **20** though, a heteroassembly formed, the effective molarity of the two reactants greatly increased, and the reaction accelerated. Furthermore, the shape of the cavity directs the reaction only toward the 1,4-isomer.

The capsule formed by the dimerization of **20** can engender more complex kinetic systems (Scheme 5).<sup>[70]</sup> When free in solution, acids **21a** and **21b** can react with amine **22** via the activated ester formed between the acid and dicyclohexylcarbodiimide **23**. The main products are amides **24a/24b** and urea **25**. Both acids are observed to react at about the same rate. Adding a stoichiometric amount of **20** slows these reactions down because **23** is encapsulated, leaving little to promote the formation of the amide bond. The two acids **21a** and **21b** do not, however, react at the same rate. The smaller acid **21a** reacts faster because both products **24a** and **25** fit within the confines of the capsule. Indeed, they associate more strongly with the capsule than **23** does. Thus, for each peptide bond formed, two molecules that bind to the capsule are generated and two equivalents of encapsulated reagent **23** are expelled into free solution. In contrast, **24b** is a poor guest, so for each peptide bond made only one molecule of **25** can liberate one carbodiimide **23**. As a result, in the presence of **20**, the formation of **24b** is slower than the formation of **24a**.

The kinetics of exchange into and out of dimer **20** have been examined for both pairs of small guests and singular large guests.<sup>[71]</sup> Using  $^1\text{H}$  magnetization transfer experiments it was shown that the substitution of a benzene guest in the dimer of **20** containing one benzene and one *p*-xylene molecule occurred without the capsule breaking in two. Instead, two walls of one subunit can flap open to allow the guest to be displaced either by an incoming benzene molecule or by the resident *p*-xylene guest. For singular guests, a



Scheme 4 Reaction between phenyl acetylene and phenyl azide.

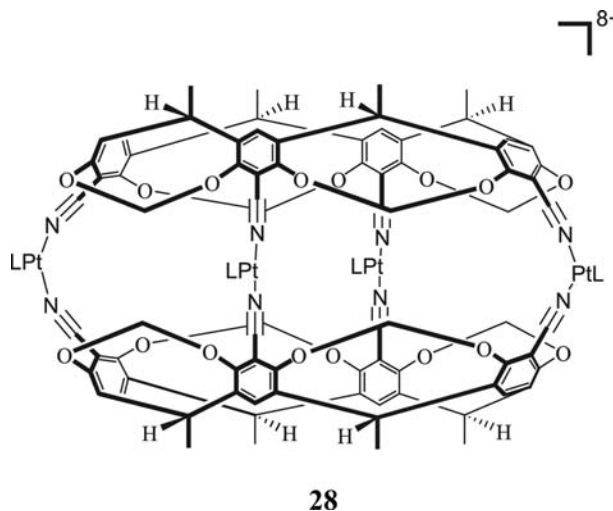
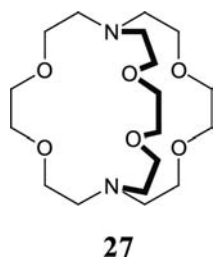
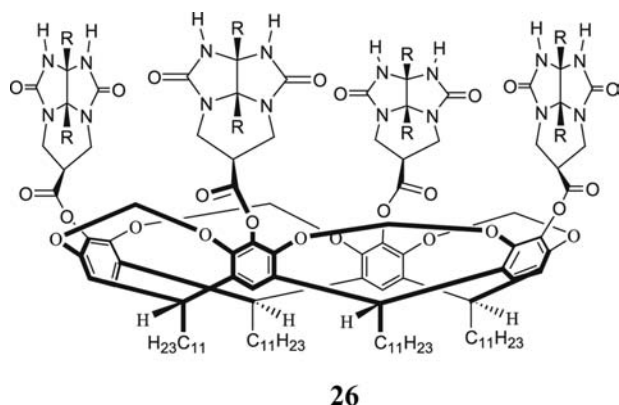
Scheme 5 Synthesis of amides **24a** and **24b**.

mechanism was proposed in which solvent displaces the guest, before it in turn is displaced by either a copy of the original guest or a competing species.

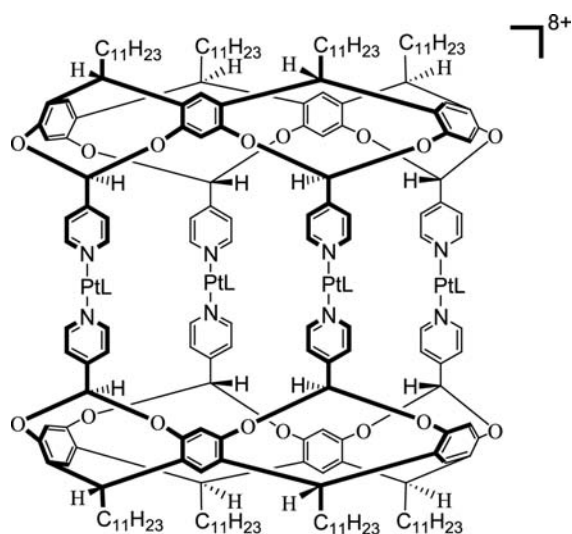
Tetra-glycoluril derivative **26** is another resorcinarene-based host that self-assembles into a hydrophobic cavity.<sup>[72]</sup> The dimer of this molecule features a cavity of volume 950 Å<sup>3</sup>, sufficiently large enough to complex cryptates such as **27**. Furthermore, the potassium thiocyanate salt of **27** is also encapsulated within the dimer of **26** to form a complex within a complex.

Metal ion coordination is a powerful means to synthesize hydrophobic pockets via self-assembly. Most examples utilize planar subunits (vide infra); however,

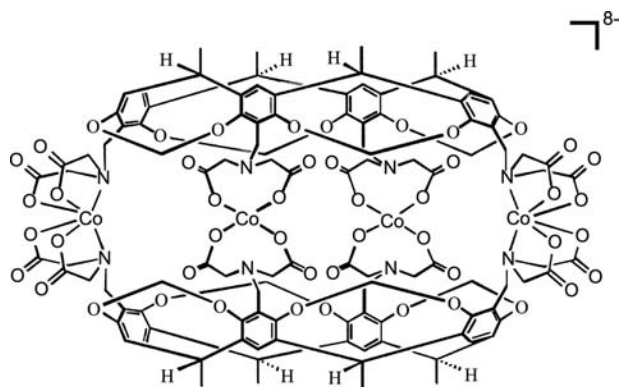
metal ions have also been used to assemble resorcinarenes and calixarenes. The Dalcanale group in Parma investigated several such resorcinarene-based systems, including using palladium ions to assemble **28** and **29**.<sup>[73–75]</sup> To date, however, only triflate ion binding in the former has been reported.<sup>[75]</sup> Related systems have also been developed by the Harrison group. The tetra-cobalt derivative **30**, as well as the corresponding iron complex, has been shown to bind 40 guests.<sup>[76–78]</sup> The largest of these were bromobenzene, *p*-xylene, and their ilk. One interesting feature of **30** is that it acts as a NMR shift reagent. <sup>1</sup>H NMR signals for a guest shift as much as –30 and –40 ppm, and can cover a range of 12 ppm. The Beer group has also been active in this area. Host **31** (R = *n*-butyl or *n*-propyl, M = Cd<sup>2+</sup> or Zn<sup>2+</sup>) possesses a cavity large enough to bind C<sub>60</sub>.<sup>[79]</sup> The binding constants between each variant and C<sub>60</sub> were similar, with the host **31** (R = *n*-propyl, M = Cd<sup>2+</sup>) showing the strongest association (log K<sub>a</sub> > 6).



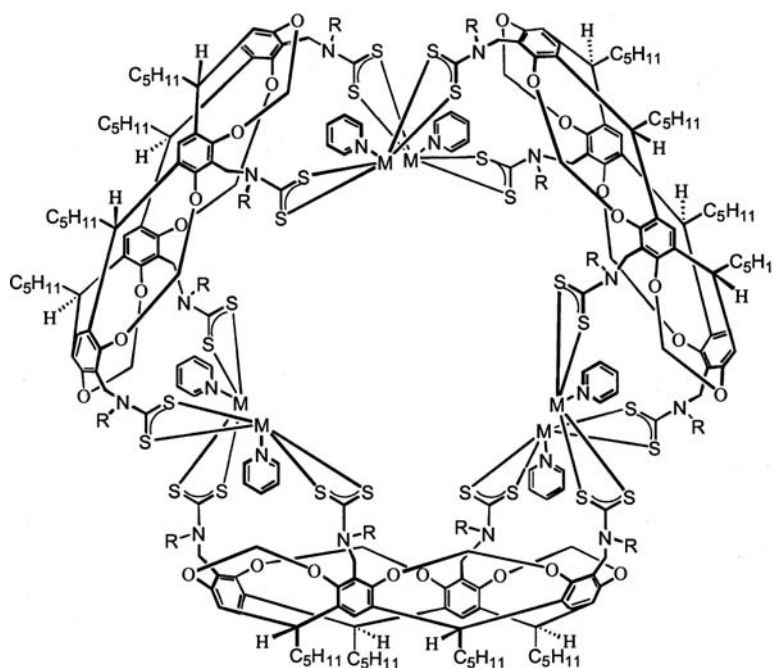




29



30



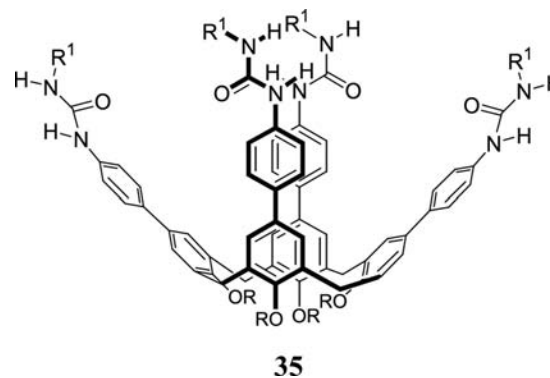
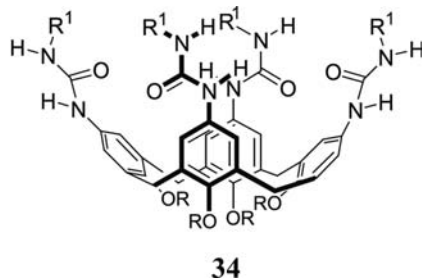
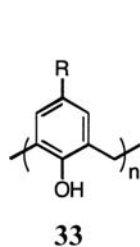
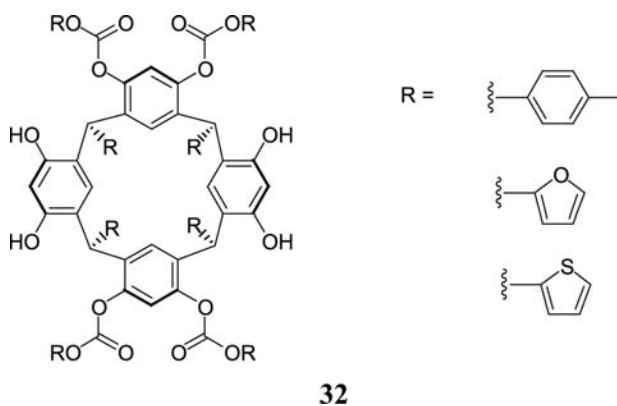
31

Although cavitands have played a large role in the field of self-assembling resorcinarene derivatives, they are not alone. For example, Shivanyuk, Paulusn, and Böhmer, have noted that regioselectively acetylated resorcinarenes also undergo self-assembly.<sup>[80]</sup> Thus in  $\text{CDCl}_3$  tetra ester **32** dimerizes around a templating tropylium salt. The intense red color observed is indicative of a charge transfer complex, and indeed the forces in such a complex are essential for assembly as neither benzene nor toluene is capable of affecting a similar assembly. The combination of the charge transfer forces and eight  $\text{CO}\cdots\text{HO}$  hydrogen bonds (as evidenced by X-ray crystallography) is sufficient to form a thermodynamically and kinetically stable complex.

### HOSTS BASED ON CALIXARENES

The self-assembly of calixarenes, **33** ( $R$  and  $n =$  various), is another active area of cavity synthesis research. Most of this research has utilized calix[4]-arenes ( $n = 4$ ). For example, independently the Rebek and Böhmer groups devised a family of upper-rim, urea-functionalized calixarenes of general structure **34** ( $R$  and  $R^1 =$  various). These molecules dimerize to produce a quasi-spherical host in which the two hemispheres are  $45^\circ$  out of register, and the urea arms interdigitated.<sup>[81,82]</sup> By meshing in this manner, the subunits form interstrand hydrogen bonds between the carbonyl of one strand and the two  $\text{N-H}$  donors

of an adjacent strand. Thus, the host is held together by a circular array of 16 hydrogen bonds. The first examples, **34** ( $R = \text{Bn}$ ,  $R^1 = \text{Ph}$  or *p*-fluorophenyl), were shown to bind both deuterated benzene, deuterated toluene, as well as chlorobenzene and 1,4-difluorobenzene.<sup>[83,84]</sup> More recently, selected ammonium salts, including tetra-alkyl ammonium, pyridinium, and *N*-methylquinuclidinium, were also encapsulated.<sup>[85]</sup> The multitude of noncovalent forces between the three species induces each hemisphere to clamp down on the guest, with the result that guest exchange is slow on the NMR time-scale. At the same time, the conformation of each individual hemisphere is also altered. For example, calixarenes with small *R* groups, e.g., **34** ( $R = \text{Me}$ ), can adopt several conformations because the *R* group can pass through the annulus of the macrocycle. Thus, each of the precursors to **34** ( $R = \text{Me}$ ,  $R^1 = p$ -tolyl) is in partial cone conformations. Contrastingly, each hemisphere in the dimer is 100% cone conformation.<sup>[86]</sup>



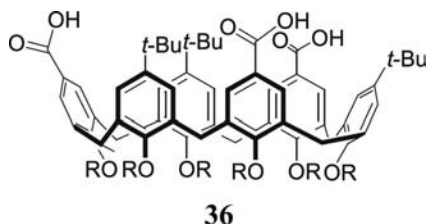
All things being equal, the combination of two different calixarenes should lead to a statistical distribution of the three possible products ( $A_2$ ,  $2 \times AB$ ,  $B_2$ ). However, the combination of **34** ( $R = \text{Me}$ ,  $R^1 = \text{C}_6\text{H}_4$ -*p*- $\text{C}_7\text{H}_{16}$ ) and **34** ( $R = \text{Me}$ ,  $R^1 = \text{SO}_2\text{C}_6\text{H}_4$ -*p*- $\text{CH}_3$ ) led exclusively to the heterodimer; a supramolecule that, because the seam of hydrogen bonds can run in either a clockwise or anticlockwise manner, exists as a pair of enantiomers.<sup>[87]</sup> Encapsulation of a chiral guest

therefore leads the formation of two diastereomeric complexes, complexes that only reach equilibrium at ambient temperature after several days. Chiral calixarenes such as **34** ( $R = \text{C}_{10}\text{H}_{21}$ ,  $R^1 = \text{CH}(\text{Me})\text{Ph}$ ) also dimerize around guests.<sup>[88]</sup> In these cases  $^1\text{H}$  NMR chemical shifts suggested that different heterodimers possessed the opposite sense of directionality to their respective hydrogen-bonding seam. Building on this work, a close examination of the ability of chiral calixarenes to form heterodimers with achiral calixarene **34** ( $R = \text{C}_{10}\text{H}_{21}$ ,  $R^1 = \text{Ph}$ ) was undertaken to determine the influences that control heterodimerization.<sup>[88]</sup> Solvent was found to be important in the percentage of homo- vs. heterodimeric assemblies, with benzene promoting the formation of the latter. Structural influences were subtler, and although selected derivatives were identified for optimal heterodimer formation, pinpointing the rules governing assembly proved elusive.

In an effort to identify a more capacious system, Cho, Rudkevich, and Rebek synthesized calixarene **35** ( $R = \text{CH}_2\text{C}(\text{O})\text{NEt}_2$ ,  $R^1 = p$ -tolyl).<sup>[89]</sup>  $^1\text{H}$  NMR revealed that this calixarene did indeed dimerize in solution. By mixing **35** ( $R = \text{CH}_2\text{C}(\text{O})\text{NEt}_2$ ,  $R^1 = p$ -tolyl) with **35** ( $R = \text{CH}_2\text{C}(\text{O})\text{NEt}_2$ ,  $R^1 = p$ -(*n*-hexyl)-phenyl) and identifying the three possible complexes, it was apparent that dimerization was slow on the NMR time-scale; N-H signals could be observed for each individual dimer. Neutral guests did not bind to these assemblies, but charged species including pyridinium and quinuclidinium salts did. In these cases, exchange rates were faster than the rate of assembly, indicating that guests can vacate the cavity through portals in the host.

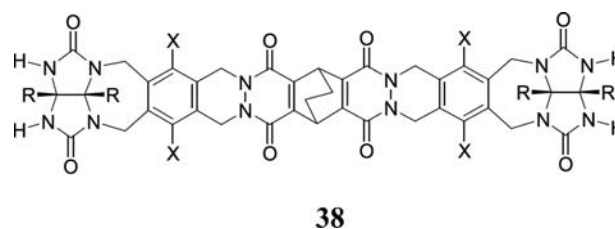
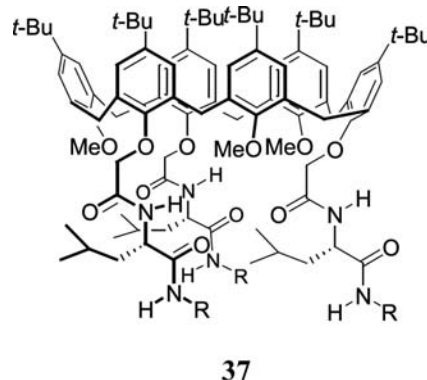
Böhmer's group also investigated dimerizing calix[4]arenes that possess urea functionality at the wide rim. As the first to observe heterodimerization of calixarenes with general structure **34**,<sup>[90]</sup> their research lent credence to the dimer structure initially put forward by Shimizu and Rebek on the basis of N-H and guest NMR signal shifts.<sup>[83]</sup> The case for a dimer assembly was clinched with the crystal structure of the dimer of **34** ( $R = \text{CH}_2\text{C}(\text{O})\text{OEt}$ ,

$R^1 = p\text{-tolyl}$ ).<sup>[82]</sup> Furthermore, the synthesis of a lower symmetry calixarene with two different R groups in an A/C arrangement provided a handle for an intense NMR investigation and the determination of the rate constants for assembly.<sup>[91]</sup> Recent studies show how the nature of the guest influences the rates of assembly. Although the bulk of the  $\Delta G^\ddagger$  for dissociation presumably arises through the breaking of hydrogen bonds, the shape and electronics of the guest nevertheless have a considerable effect. For example, the half-lives of guest exchange for cyclohexane, fluorobenzene, and toluene were measured at 78 days, 3 days, and 4.2 hr, respectively.<sup>[92]</sup> The nature of the  $R^1$  groups influences assembly, with large groups both reducing the range of homo- and heterodimers that can form, as well as slowing down the rate of assembly.<sup>[93]</sup> In deuterated benzene, discerning monomer **34** ( $R = \text{Me}$ ,  $R^1 = \text{trityl}$ ) does not form homodimers, nor heterodimers with calixarenes such as **34** ( $R = \text{Me}$ ,  $R^1 = 3,5\text{-di}(t\text{-butyl})\text{phenyl}$ ). It does, however, form a heterodimer with **34** ( $R = \text{Me}$ ,  $R^1 = 4\text{-tritylphenyl}$ ), one that is particularly stable in deuterated cyclohexane. As well as increasing the kinetic stability of the dimer, increasing the size of the  $R^1$  group also decreases the size of the cavity. Thus, the homodimer of **34** ( $R = \text{Me}$ ,  $R^1 = \text{trityl}$ ) forms a homodimer by encapsulating a relatively small tetramethyl ammonium ion, but the complex is kinetically stable even in neat  $d_6\text{-DMSO}$ .<sup>[94]</sup> The motion within the cavity of such relatively small guests has also been examined.<sup>[95]</sup>



With urea-substituted calix[5]arenes, it has been possible to encapsulate  $C_{60}$ .<sup>[96]</sup> Urea groups are not, however, the only functionality that can be used to promote the assembly of calixarenes. For example, metal ion coordination has also been used to encapsulate both  $C_{60}$  and small chiral amines between assembling homooxacalix[3]arenes.<sup>[97–99]</sup> In addition, carboxylic acids have been used to promote the assembly of calixarenes. Tri-acid **36** is one such example.<sup>[100]</sup> This compound has been shown to dimerize around molecules such as *N*-methyl-4-picolinium iodide, but not *N*-methyl-2-picolinium iodide. Functionalization of the lower rim of calixarenes also leads to subunits capable of self-assembly. Thus **37** ( $R = C_8H_{17}$ ) was shown to dimerize around benzene and toluene.<sup>[101]</sup> In these cases some of the  $^1\text{H}$  NMR signals were broad, an indicator that these

solvents are not good guests. In contrast, the  $^1\text{H}$  NMR signals of the same complex in  $CDCl_3$  were well resolved, suggesting that this guest did complement the cavity.



## HOSTS BASED ON GLYCOLURIL

The Rebek group has worked with a number of glycoluril-based assembly systems for the generation of hydrophobic pockets. One of the richest systems devised is **38**, a molecule possessing 14 fused rings and an overall “C” shape (Fig. 4). In suitable organic solvents, this molecule forms a hollow, pseudo-spherical dimer in which the two halves are held together by hydrogen bonds between the glycoluril termini and the amide carbonyl groups. The first examples of these “soft-ball” hosts, e.g., **38** ( $R = \text{phenyl}$ ,  $X = \text{H}$ ), were shown to bind various guests, the strongest binder being 1-adamantanecarboxylic acid.<sup>[102,103]</sup> Subtle modifications to **38** ( $R = 4\text{-}n\text{-heptylphenyl}$ ,  $X = \text{OH}$ ) generated a self-assembling system that was both more soluble, thanks to the heptyl groups, and more robust, thanks to the phenol groups which contributed to the total number of hydrogen bonds between the subunits.<sup>[104]</sup> As expected, in both these systems assembly and guest complexation was highly dependant on the solvent.<sup>[105]</sup> Interestingly, in all solvents examined, binding of guests was entropically driven. To rationalize this observation it was proposed that two or more solvent molecules occupied the cavity and that the addition of a large guest liberated these. By such a mechanism, the system could become more disordered upon complexation and release up to

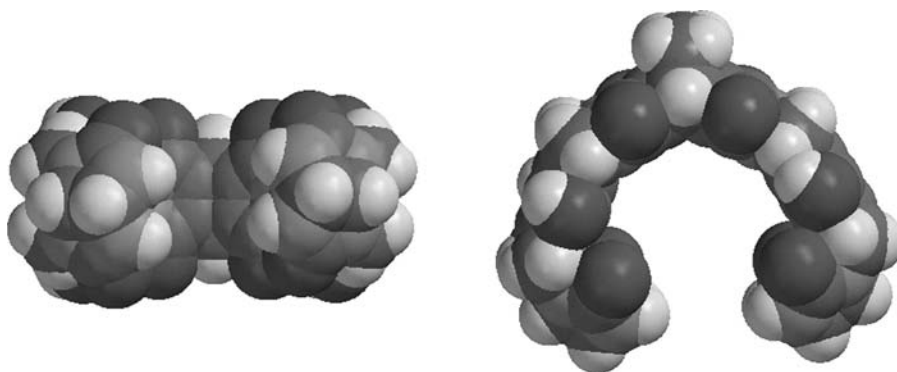


**Fig. 4** Perpendicular views of space filling model of subunit **38** (R groups omitted for clarity, X = OH).

6.0 kcal mol<sup>-1</sup> of free energy when 1-adamantane-methanol was encapsulated. Once a guest is encapsulated, exchanging it for another is a relatively slow process. The mechanism, at least in the case of [2.2]paracyclophane substituting adamantane in a deuterated xylene solvent, has been examined.<sup>[106]</sup> The guest vacates the cavity via a conformational change in one subunit that opens a “flap” in the side of the host. The new guest can then exchange with the resident, potentially via an intermediate that possesses a solvated cavity. One of the remarkable properties of host **38** (R = 4-*n*-heptylphenyl, X = OH) is its ability to accelerate<sup>[107,108]</sup> and even catalyze Diels–Alder reactions.<sup>[109]</sup> The first experiments highlighting these properties involves the reaction in Scheme 6, a process that at millimolar concentrations in xylene has a half-life of about 1 year. In contrast, the reaction greatly accelerates in the presence of capsule **38** (R = 4-*n*-heptylphenyl, X =

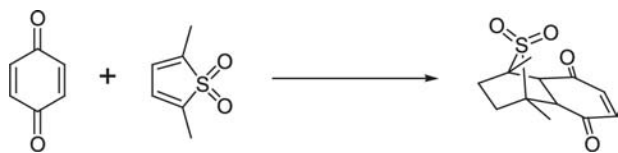
OH) because the host can encapsulate both reagents and hold them at an effective concentration 1000 times that of the free reagents. The capsule is not, however, a catalyst. That bane of catalyst designers, product inhibition, raises its head and prevents catalytic turnover. On the other hand, no such problem was observed with the Diels–Alder reaction involving *p*-quinone and 2,5-dimethylthiophene dioxide (Scheme 7).<sup>[109]</sup> In this system, *p*-quinone binds more strongly to the cavity formed by host **38** (R = 4-*n*-heptylphenyl, X = OH). Consequently, the product is driven out of the cavity by the starting material and so each dimer can induce many transformations.

Analogous systems have also been used for chiral recognition. Host **39** (X = H) possesses one symmetry plane and is therefore achiral ( $C_S$ ).<sup>[110]</sup> In the softball-type assembly, however, the two subunits are orthogonal to each other and each plane bisects and therefore violates the other. The result is a chiral capsule ( $C_2$ ) that racemizes via a process of disassembly and reassembly. Upon the addition of a chiral guest two diastereomeric complexes form, with diastereomeric excesses ranging from 0% for guest **40**, to 35% for the more complementary **41**. The latter value corresponds to  $\Delta\Delta G^\circ$  of 0.4 kcal mol<sup>-1</sup>. A more extensive examination revealed diastereoselective excesses as high as 50%.<sup>[111]</sup>

The additional hydrogen bonds in the dimer of **39** (X = OH) slow its rate of isomerization down somewhat so the  $t_{1/2}$  is approximately 10–20 hr. In contrast, the rate of guest exchange in this system is much faster because the subunits do not need to completely dissociate for exchange to occur. As per **38**, a flap can open to allow guest egression. These points lead to an unusual memory effect. If a deuterated *p*-xylene solution of the dimer of **39** (X = OH) is charged with (+)-pinanediol **41**, then after equilibration an excess of one diastereomeric complex is observed. The addition of an excess of the enantiomer of **41** rapidly leads to guest exchange. As this process is so much quicker than racemization, the enantiomeric shells of the original major and minor complexes find themselves with a mismatched and a matched guest, respectively. The major diastereomeric complex is now the least stable complex, and only through the slow racemization



**Scheme 6** The Diels–Alder reaction between *p*-hydroquinone and cyclohexadiene.

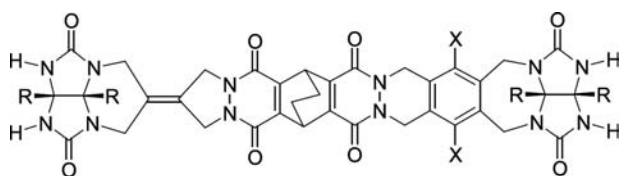


**Scheme 7** The Diels–Alder reaction between *p*-quinone and 2,5-dimethylthiophene dioxide.

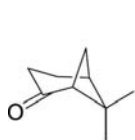
can equilibrium be reestablished. Until then, the system finds itself “remembering” the shape of the first guest.

Another way to introduce chirality is to make assemblies using **38** ( $X = H$ ) in which the pairs of R groups on each glycoluril are different. This approach has to date been less successful in chiral recognition, presumably because the chirality is associated with the outer surface rather than the inner cavity.<sup>[112]</sup>

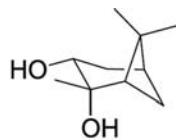
The glycoluril subunit has been used by the Rebek group to synthesize other assembling systems. The “jelly doughnut,” a dimer of *tri*-glycoluril **42**



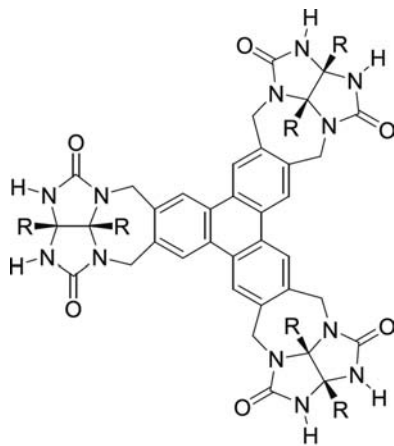
**39**



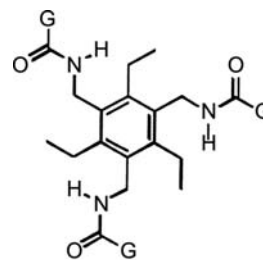
**40**



**41**



**42**

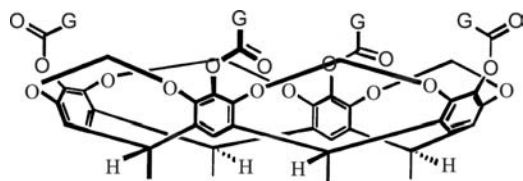


**43**

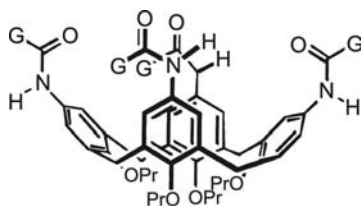
( $R = CO_2$ -*i*-pentyl) capable of encapsulating benzene and cyclohexane, lies at the edge of our review. Readers interested in its hosting properties, and its ability to slow the ring inversion of encapsulated cyclohexane, are directed toward Refs.<sup>[113]</sup> and<sup>[114]</sup>. Building upon these studies, a modular approach to self-assembling subunits such as **43–45** ( $G =$  glycoluril) has been proposed.<sup>[115]</sup> By a combination of NMR and mass spectrometry, the smaller of these three hosts, **43**, was shown to bind *N*-methylquinuclidinium, while the large guests built from cavitands could bind 2,2′bipyridine and metal complexes of cryptates such as **27**.

A final self-assembling host based on glycoluril is built from monomer **46** ( $R = 4$ -*n*-dodecylphenyl,  $X = H$ ).<sup>[116]</sup> This molecule possesses curvature, and at each end, an acidic H-bond donor (the sulfamide N–H) and a basic acceptor (the glycoluril carbonyl). Because the sulfamide N–H/glycoluril C=O hydrogen bond is the strongest possible noncovalent interaction between subunits, the molecules assemble into a barrel-shaped tetramer of  $D_{2d}$  symmetry where each stave is antiparallel to its neighbors. The monomer has low solubility in  $CD_2Cl_2$  and toluene- $d_8$ , but the addition of adamantane derivatives results in a homogeneous solution. Diketone **47** was the strongest binding guest initially screened ( $K_{app} = 3200 M^{-1}$ ), and exchanged slowly (relative to the 600-MHz NMR time-scale) between the free and the bound states. Subsequent competition experiments between neutral guests and cationic species such as **48** revealed that the latter bind more strongly.<sup>[117]</sup> The barrel assembly is chiral ( $D_2$  symmetry) if the staves used to construct it are **46** ( $R = 4$ -*n*-dodecylphenyl,  $X = OH$ ).<sup>[118]</sup> This monomer is itself chiral—it possesses a plane of chirality—and was therefore resolved upon synthesis. Choosing one enantiomer and investigating its ability to bind racemic guests revealed a range of diastereoselective recognitions. For example, the diastereomeric excess in binding ( $\pm$ ) 3-methylcyclohexanone **49** was 60%, while for its constitutional isomer ( $\pm$ ) norcamphor **50** there was no diastereomeric excess. Shape is everything! The binding profiles of these hosts have recently been investigated as a dynamic combinatorial library. By examining mixtures of seven different staves in

the presence of a series of guests, it was possible to identify the different assembly products, often in distributions far from statistical, that arose from matched and mismatched assembly components.<sup>[119]</sup>

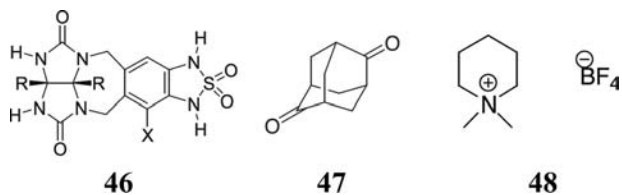


44



45

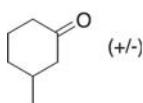
Even larger guests can be encapsulated with the host arising from **51** ( $R = 4$ -*n*-heptylphenyl).<sup>[120]</sup> This monomer again forms a tetrameric, barrel-shaped assembly and is capable of binding guests such as adamantane **52** and congressane **53**. These assemblies are very secure structures in solvents such as  $CD_2Cl_2$  or  $CCl_4$ . In the latter, EXSY NMR experiments revealed a lower limit for the activation energy of the dissociation of tetramer of **51** ( $R = 4$ -*n*-heptylphenyl) containing **52** to be  $20 \text{ kcal mol}^{-1}$ . Two possible mechanisms of this exchange were identified. Either one or two staves flip up to allow the guest to escape, or the barrel breaks in two before the guest enters solution.



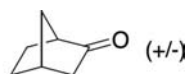
46

47

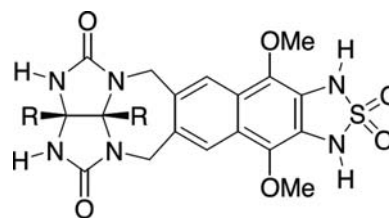
48



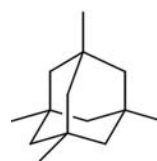
49



50



51



52



53

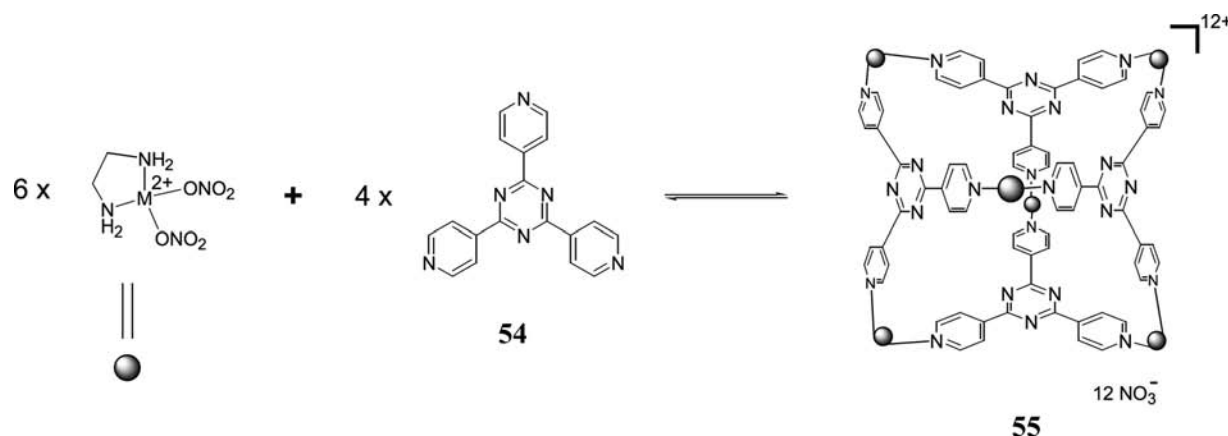
are also many ways that planar subunits can be used to form quasi-spherical hosts. The majority of these assemblies use metal ion coordination to join subunits with Lewis basic sites. As arguably the most powerful approach to self-assembly, an important goal of this field has been to garner the rules that govern assembly.<sup>[121–124]</sup> Thus a great deal of metal coordination assembly has not been directly concerned with guest binding within hydrophobic pockets. Here the focus is on assemblies in which large guest molecule binding properties have been studied. For more general reviews readers are directed to Refs.<sup>[125–131]</sup>

The Fujita group investigates using heterocycles and palladium complexes in self-assembly. Their research has led to some of the largest hydrophobic cavities reported to date.<sup>[127]</sup> A particularly rich seam of research emerged from the triazine-based subunit **54**, which assembles into tetrahedral structure **55** in the presence of palladium or platinum ions (Scheme 8). This host is spacious enough to complex four adamantane guests.<sup>[132]</sup> Guests can be sequestered by stirring an aqueous solution of **55** ( $M = Pd^{2+}$ ) with a saturated hexane solution of the desired target.<sup>[133–135]</sup> Adamantane is one such example; another is tri-*tert*-butylbenzene. The latter is larger than the portals in the host and therefore is encapsulated very slowly. Only at  $80^\circ C$  is the 1:1 complex formed at an appreciable rate. For the smaller guests, a “ship-in-a-bottle” mechanism is in operation whereby each guest enters the cavity sequentially, and the contents of the cavity assembled into the lowest free-energy packing arrangement; an assembly within an assembly! Not all guests can pack with equal efficiency though. Thus in competition experiments between *cis*- and *trans*-dimethylazobenzene only two molecules of the former are taken up by **55** ( $M = Pd^{2+}$ ).<sup>[136]</sup> Residency within

## HOSTS BASED ON PLANAR SUBUNITS

As just described, hydrophobic pocket design via self-assembly often utilizes curved subunits. However, as MacGillivray and Atwood have observed,<sup>[121]</sup> there





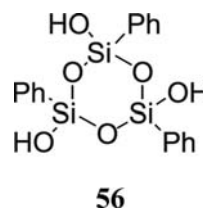
**Scheme 8** The metal-ion assembly of ligand **54** into host **55**.

**55** ( $M = \text{Pd}^{2+}$ ) alters the properties of the *cis*-4,4'-dimethylazobenzene guests, in so much as they do not isomerize to the more stable *trans* form even after a few weeks of exposure to visible light. Interestingly, two molecules of unsubstituted azobenzene do not bind to **55** ( $M = \text{Pd}^{2+}$ ). It was suggested that  $\text{CH}-\pi$  interactions between the methyl protons of the guest and the walls of the cavity are important in the packing process. Host **55** ( $M = \text{Pd}^{2+}$ ) recognized *cis* and not *trans* isomers via shape-recognition. Shape complementarity is not, however, the only important factor in determining guest complexation. For example, although 1,3,5-trimethoxybenzene is a good guest, electron deficient guests such as 1,3,5-tribromobenzene were not taken up by the host.<sup>[134]</sup>

Host **55** ( $M = \text{Pt}^{2+}$ ) has also been used to assemble cyclic siloxanes that are presumed to be ephemeral intermediates in the so-called sol-gel condensation; the polycondensation of trialkoxysilanes that leads to siloxanes.<sup>[137,138]</sup> Guest **56** is one such example. It is a kinetic intermediate en route to a thermodynamic product in the sol-gel process, the cyclic "tetramer." In contrast, **56** is kinetically stable when synthesized inside host **55** ( $M = \text{Pd}^{2+}$ ). This is determined by hydrolyzing phenyltrimethoxysilane in a solution of the host. A NMR spectrum after only 5 min of reaction suggested that three or four molecules of phenyltrihydroxysilane were initially incorporated into the cavity, while within 1 hr NMR spectroscopy demonstrated that the complex **55**·**56** had been formed. Once encapsulated, a consideration of the NMR spectrum of the shell and variable temperature NMR experiments told a good deal about the mobility of the guest.<sup>[139]</sup>

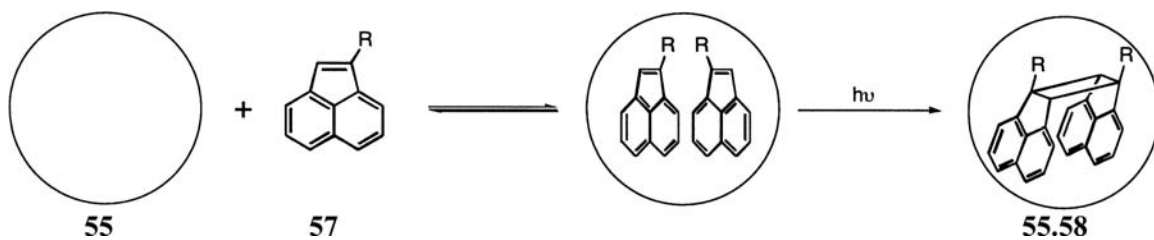
Host **55** ( $M = \text{Pd}^{2+}$ ) can also accelerate and control reactions (Scheme 9).<sup>[140]</sup> When acenaphthylene guest **57** ( $R = \text{H}$ ) was heated with **55**, two guests were encapsulated. Irradiation of this sample led to a near

quantitative yield of *syn*-dimer **58** ( $R = \text{H}$ ), in a considerably shorter time than is required for reaction in free solution. On a related note, normally guest **57** ( $R = \text{Me}$ ) does not undergo dimerization. However, inside **55** ( $M = \text{Pd}^{2+}$ ) the  $C_{2v}$  product was quickly formed in near quantitative yield. No  $C_s$  symmetric dimer was observed. Similar rate accelerations and stereoselectivities were seen for the dimerization of naphthoquinones, and cross-photodimerizations (Scheme 10).<sup>[141]</sup> Thus when 5-ethoxy-naphthoquinone **59** ( $R' = \text{Et}$ ) and acenaphthylene **57** ( $R = \text{H}$ ) were heated with host **55** ( $M = \text{Pd}^{2+}$ ) a 1:1:1 complex formed. Irradiation of this complex gave a 92% yield of the cross *syn* product **60** ( $R = \text{Et}$ ,  $R' = \text{H}$ ). Surprisingly, with **59** ( $R' = \text{Me}$ ) this yield dropped to 44%, and a considerable amount of the homodimers were observed. More dramatically, with **59** ( $R' = \text{H}$ ) only a 35% yield of the cross product was observed, along with 21% of the dimer of **59** and 14% of the dimer of **57**.

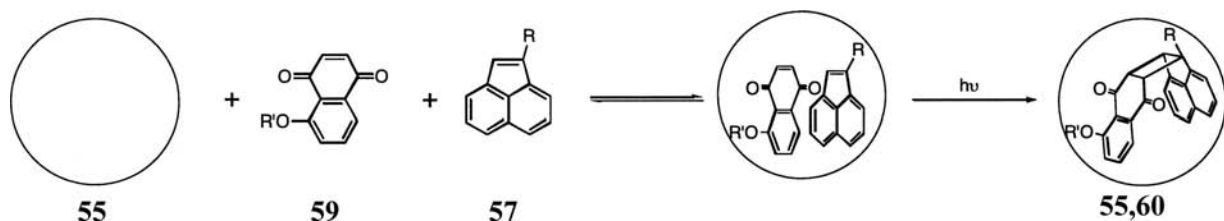


**56**

Another family of subunits from the Fujita group are the oligo(3,5-pyridine)s such as **61** (Scheme 11). In the presence of palladium ions this subunit forms square prism or "nanotube" **62**.<sup>[142-144]</sup> To affect this formation, a rod-like template, e.g., 4,4'-biphenylene-carboxylate **63**, is required. In the final assembly product the dicarboxylate resides within the hydrophobic tube. In fact, it is rather hard to remove. Only at elevated temperatures was (weaker binding) biphenyl



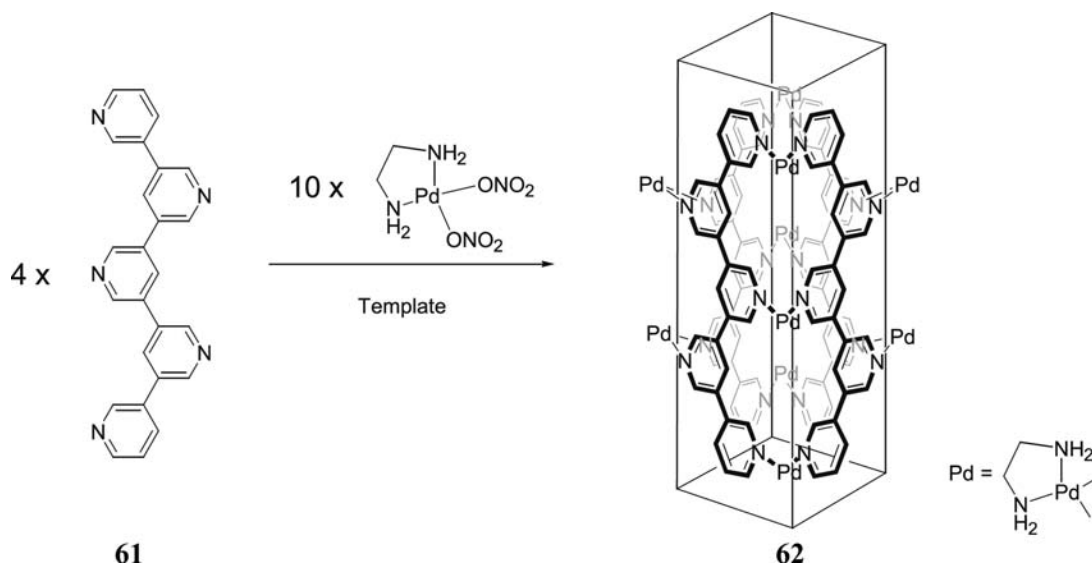
Scheme 9 A [2 + 2] photodimerization of acenaphthylenes.



Scheme 10 A [2 + 2] cross-photodimerization of olefins.

slowly extracted from the pocket by chloroform. The smaller subunit **64** ( $n = 1$ ) undergoes an analogous assembly, whereas the even-numbered pyridine ligand **64** ( $n = 2$ ) forms two assembly products, **65** and **66**. These products have  $C_{2h}$  and  $D_{2h}$  symmetry, respectively, and are formed in a 1:1 ratio in the presence of template **63**.<sup>[143]</sup> The rate of isomerization between **65** and **66** is slow. Two weeks were required for one isolated product to form an equilibrium mixture. The movement of guests within these nanotubes was examined by synthesizing the complex between **62** and

4-phenylbenzoic acid.<sup>[144]</sup> This lower symmetry guest induced desymmetrization of the host framework at room temperature. As the temperature was raised, coalescence of the NMR signals at 47°C demonstrated that the guest vacated the cavity via an activation barrier of 16 kcal mol<sup>-1</sup>. This coalescence temperature varied as a function of guest concentration suggesting two mechanisms of exchange, a dissociative one at low concentrations and an associative mechanism at higher guest concentrations. Guest egression depends on the length of the nanotube—the shorter the tube

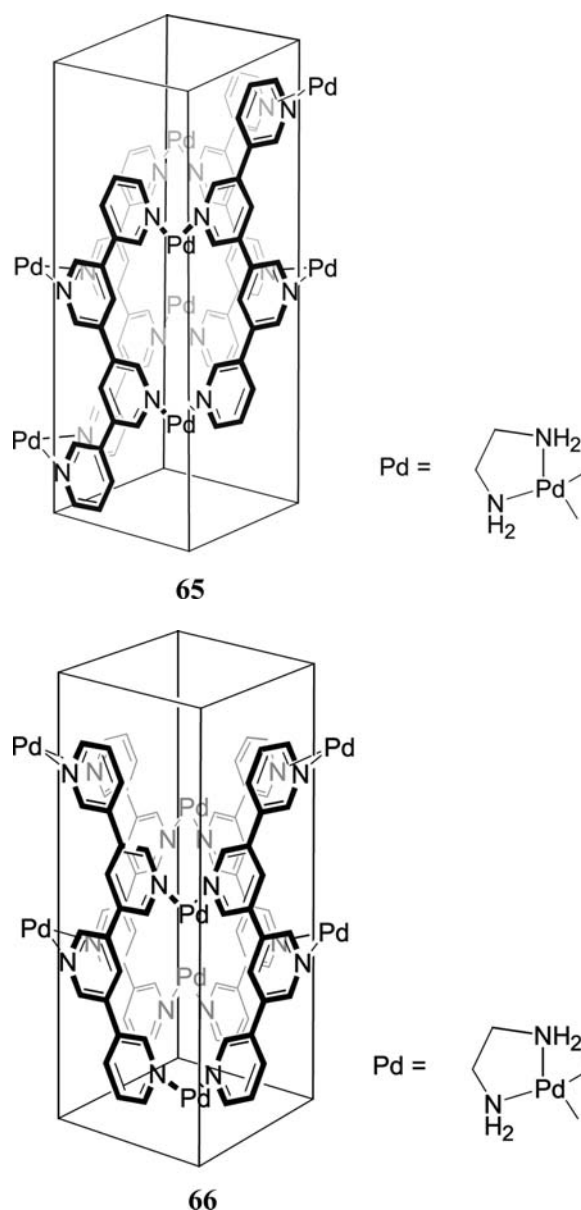
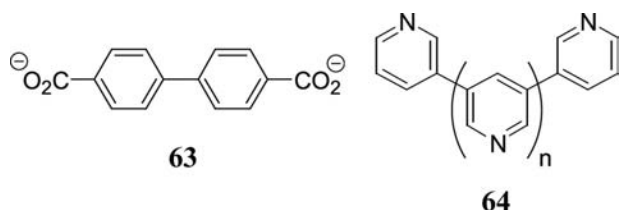
Scheme 11 Assembly of nanotube **62**.

the lower the activation energy—and the nature of the guest.<sup>[138,144]</sup>

A subtle change to **54** leads to a family of bowl-shaped hosts. Thus subunit **67** assembles into cavitand **68** (Scheme 12).<sup>[145]</sup> Binding studies revealed that this host can hold two molecules of *m*-terphenyl.<sup>[146]</sup> At room temperature, guest motion within the cavity is slow on the NMR time-scale. Interestingly, the solid-state structure of this complex revealed a dimeric capsule of **68** encapsulating four guests. Whether this is the case in solution could not be determined. The encapsulation of *cis*-stilbene in **68** was equally interesting. Six molecules were trapped in a dimeric capsule in the solid state. In solution, the garnered evidence suggested that a monomeric host containing one or two guests was in equilibrium with the dimeric capsule containing six. Host **68** has also been used to stabilize sol-gel condensation intermediates, in particular the condensed “dimer” of naphthyltrihydroxysilane.<sup>[138]</sup>

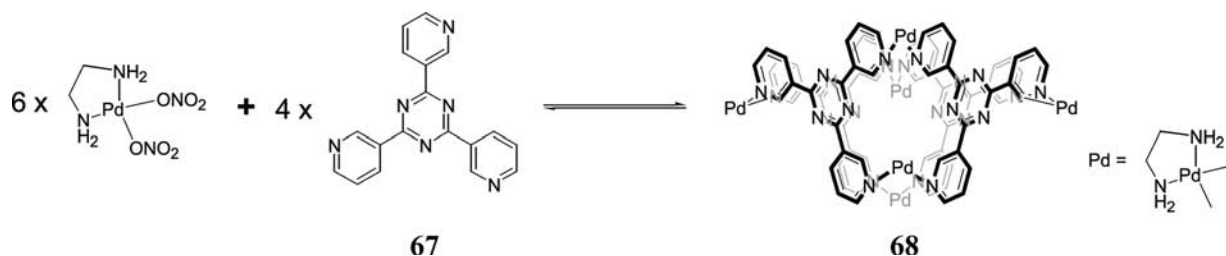
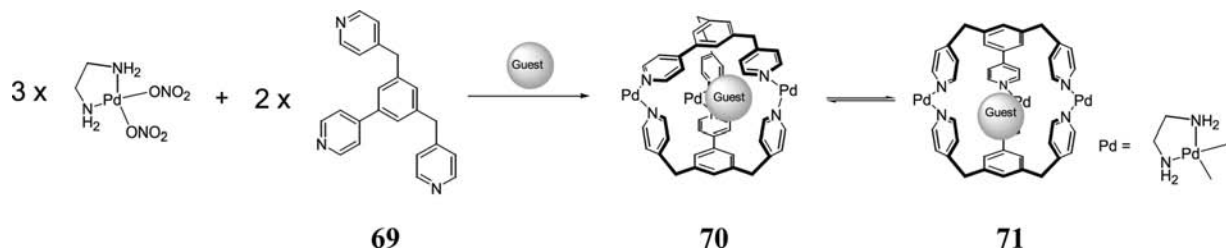
The assembly properties of tripodal ligand **69** have been examined.<sup>[147]</sup> In the presence of palladium ions, this subunit assembles into one of two forms: dimer **70** that exists as a pair of enantiomers, and **71** (Scheme 13). Addition of 1,3,5-benzenetricarboxylic acid to the assembly reaction leads to **70**, whereas addition of a more spherical guest leads to **71** with the more spherical cavity. Furthermore, each assembly product can be converted to the other by the addition of a suitable excess of the requisite guest. Hence this system constitutes a dynamic receptor library. This library can be taken to the “next level” by mixing ligands **69** and **72**. This leads to up to four products whose ratios depend on the guest present in the assembly mixture.<sup>[148]</sup>

Hexahedral capsule **74** (Scheme 14), formed by the assembly of 18 palladium ions and six copies of subunit **73**, is a remarkable structure that, at least for host/guest applications, was designed too well.<sup>[149]</sup> The shell possesses little in the way of portals and, with six connections between each of the organic subunits, is of very high kinetic stability. Guest exchange is hard. For this reason **75**, a subunit that possesses a “N-defect,” was synthesized.<sup>[150]</sup> This molecule assembles into an analogous structure, but with one less coordination site, there are fewer linking groups between each subunit and the shell is a bit more forgiving. To date, only guests as large as CBr<sub>4</sub> have been stored in this capsule.



Subunit **76** follows different assembly paths than **75**. Using four subunits and eight metal ions, this triangular subunit forms either a tetrahedron-shaped capsule, or an open pocket of square pyramidal architecture.<sup>[151]</sup> The assembly is again template dependant. Benzil promotes the formation of the open pocket, which in aqueous conditions is filled with one guest. In contrast, the smaller CBr<sub>4</sub> leads to the sealed, tetrahedral-shaped host. In the absence of a template, two products form in a 3:2 ratio. The major component was tentatively identified as a trimer of **76** possessing an open, trigonal pyramid structure, while the minor component was the open, square pyramidal pocket.

Porphyrin derivative **77** also undergoes self-assembly with palladium ions; three subunits assemble

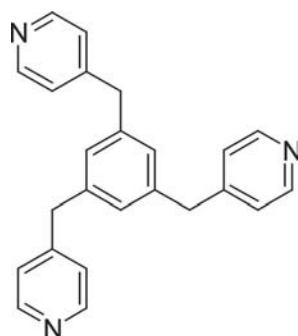
Scheme 12 Assembly of cavitaand **68**.Scheme 13 Assembly of **69** to form **70** and **71**.

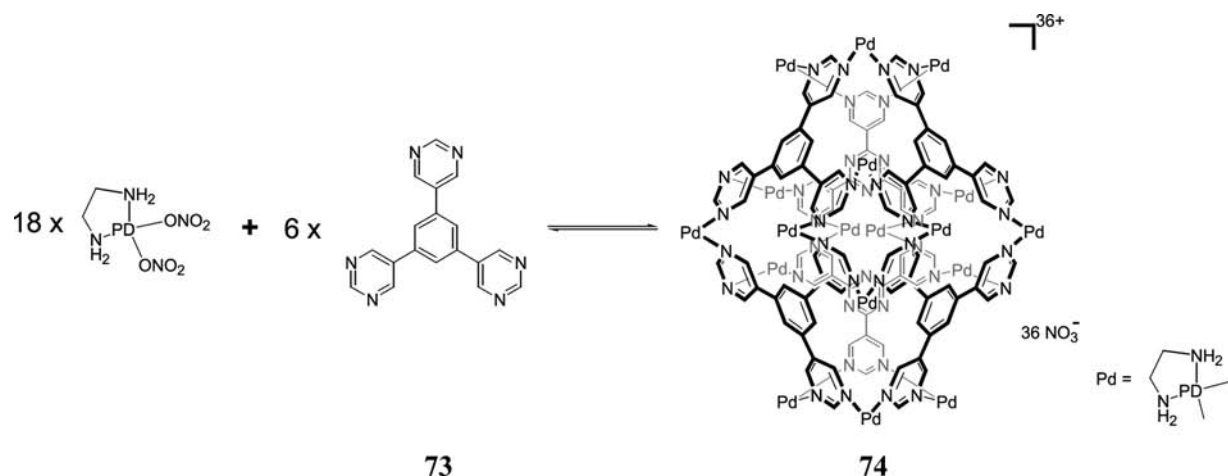
into a trigonal prism capable of encapsulating pyrene.<sup>[152]</sup> Porphyrin dimers have also been reported that bind bipyridines.<sup>[153]</sup> Subunit **78** forms a square prism assembly.<sup>[154]</sup> By using a biphenyl template, it was possible to switch this assembly to a trimer of trigonal prism architecture, while crystallization led to the formation of an alternative (lower symmetry) square pyramid structure.

The Raymond group has also utilized Lewis acid/Lewis base coordination processes to drive the assembly of subunits into hydrophobic pockets. One of their more successful systems in this regard is based on ligand **79**, which, in the presence of a variety of metal ions, assembles into the distorted tetrahedron **80** (Scheme 15). Host **80** is chiral (symmetry group T) and therefore exists as a pair of enantiomers. The helical twist of the three ligands around each metal center induces chirality. In each enantiomer, all these

centers possess the same twist sense,  $\Delta\Delta\Delta\Delta$  or  $\Lambda\Lambda\Lambda\Lambda$ . In the absence of a guest, water fills the cavity of host **80** ( $M = \text{Ga}^{3+}$ ) and the counterion of the base used in the assembly, e.g.,  $\text{K}^+$ , is not incorporated into the cavity.<sup>[155]</sup> If a guest such as  $\text{Et}_4\text{N}^+\text{Cl}^-$  is added to the assembly process, it is encapsulated within the racemic mixture of host.<sup>[156]</sup> As expected, there is a dramatic upfield shift of the  $^1\text{H}$  NMR signals of the encapsulated guest. Furthermore, the signal from each methylene proton, enantiotopic in the free state but diastereotopic in the assembly, appears as a complex multiplet rather than a quartet. Other guests can be encapsulated within the confines of **80**. A study of the entrapment of  $\text{Me}_2\text{Pr}_2\text{N}^+$ ,  $\text{Pr}_4\text{N}^+$ , and  $\text{Me}_2\text{NCH}_2\text{CH}_2\text{NMe}_2\text{H}^+$  revealed that  $\text{Et}_4\text{N}^+$  is the best guest and that the assembly processes were endothermic (for a cation binding to a host of charge  $-12!$ ).<sup>[155]</sup> The endothermic nature of this process was rationalized in terms of the necessity to desolvate both host and guest. However, desolvating the host is not at all bad. As the authors pointed out, the release of the solvating waters from the cavity is probably at the root of the enthalpic gain of guest complexation. A mono-charged guest does, however, appear to be a necessity. Neither  $\text{Et}_4\text{Si}^+$ —isosteric with  $\text{Et}_4\text{N}^+$ —nor doubly charged  $N,N,N',N'$ -tetramethyl-1,3-propanediamine was observed to bind to the cavity of **80** ( $M = \text{Ga}^{3+}$ ).

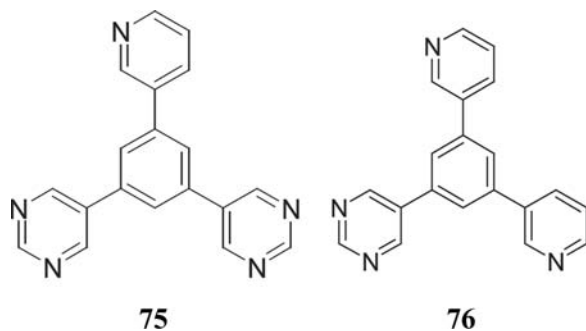
Host **80** ( $M = \text{Ga}^{3+}$ ) is also capable of stabilizing reactive species in aqueous solution. For example, the phosphonium salt  $[\text{Me}_2\text{C}(\text{OH})\text{PEt}_3][\text{Br}]$  has been trapped in its cavity.<sup>[157]</sup> This salt can be formed by the reversible addition of triethylphosphine to acetone

**72**



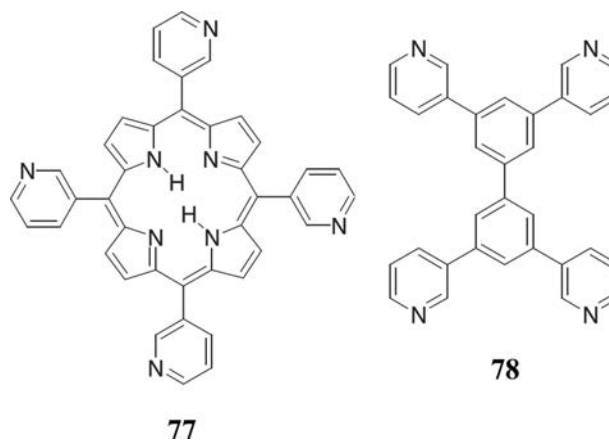
**Scheme 14** Assembly of **73** to form hexahedral cage **74**.

in the presence of HBr, but in an aqueous solution devoid of acetone this compound rapidly decomposes to its constituent parts. The combination of a water-free cavity, a high effective concentration of the components, and shielding by the cavity walls, stabilizes the normally reactive phosphonium salt. The proposed formation involved triethylphosphine entering the confines of the cavity and undergoing reaction with an acetone guest.

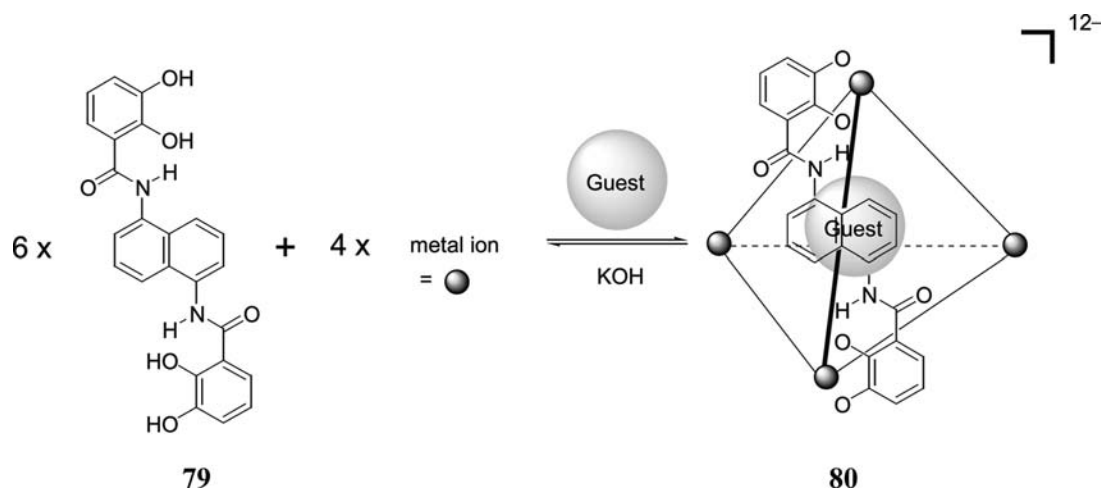


Complex **80** ( $M = \text{Ga}^{3+}$ ) is large enough to act as a host for a host.<sup>[158]</sup> Thus mixing **80** with either [12]crown-4, [15]crown-5, or [18]crown-6 led to the appearance of new  $^1\text{H}$  NMR signals that corresponded to the encapsulated crown ether complex. That the crowns were carrying a metal ion was revealed using  $^7\text{Li}$  NMR on the lithiated host  $\text{Li}_{12}[\text{Ga}_4\text{L}_6]$  containing one of the two smaller crown complexes. In these experiments, with the signal from the crown complex free in solution referenced at 0 ppm, the signal for the encapsulated complexes appeared at  $-4.0$  ppm. The association constants for the three  $\text{Na}^+$  complexes of [12]crown-4, [15]crown-5 and [18]crown-6 binding to **80** ( $M = \text{Ga}^{3+}$ ) were calculated at 2700, 18,  $<0.1 \text{ M}^{-1}$ , respectively. Nuclear magnetic resonance

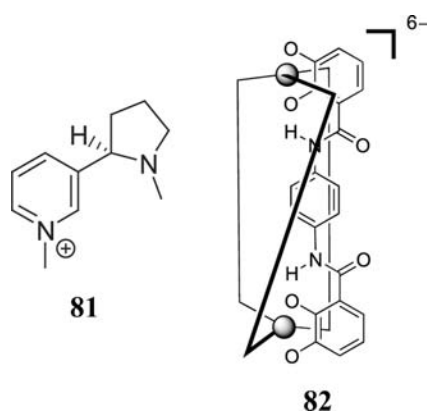
evidence also suggested that one or two water molecules were incorporated into the host along with the crown complex.



As discussed above, host **80** ( $M = \text{Ga}^{3+}$ ) exists as a pair of enantiomers. These do not interconvert with any apparent haste. The activation energy for flipping a tris(catecholate)gallium(III) center from  $\Delta$  to  $\Lambda$  has been measured at about  $67 \text{ kJ mol}^{-1}$ .<sup>[159]</sup> Hence incorporation of a guest that possesses an element of chirality should result in the formation of readily separable diastereomeric complexes. This was accomplished with the guest, *N*-methyl(-)nicotinium **81**.<sup>[160]</sup> The separated complexes were indeed very stable; they retained their diastereomeric purity in alkaline aqueous solution over a period of at least 8 months. The isolation of each enantiomer of **80** ( $M = \text{Ga}^{3+}$ ) allowed experiments that revealed a chiral memory effect.<sup>[161]</sup> Thus host **80** ( $M = \text{Ga}^{3+}$ ) was prepared with the *N*-methyl(-) nicotinium **81** guest, and the  $\Delta\Delta\Delta$  diastereomer isolated. Cation exchange with excess  $\text{Et}_4\text{N}^+$  gave the enantiomerically pure  $\Delta\Delta\Delta$  ( $\text{Et}_4\text{N}^+$ )<sub>12</sub> salt,



Scheme 15 Assembly of **79** to form T-symmetry cage **80**.



with one of the ammonium ions acting as guest by occupying the cavity; guest exchange did not affect the chirality of the shell. Addition of an excess of helicate complex **82** led to the gradual replacement of the naphthyl ligands in **80** with the phenyl biscatecholamide ligands of **82**. The tetraethyl ammonium guest was a good reporter group for this exchange process, but it was CD spectrometry that revealed that the original chirality of host **80** ( $M = \text{Ga}^{3+}$ ) was retained even after all six ligands had been exchanged!

## CONCLUSION

Self-assembly is a powerful technique for hydrophobic pocket design. Although contemporary technologies mean that the pockets so synthesized must be of relatively high symmetry, this strategy allows access to very large host molecules and supramolecules. As a result, inroads are already being made in terms of molecular storage and catalysis. As the field's ability

to synthesize increasing lower symmetry hosts improves, self-assembly is likely to play an increasing role in the development of new tools for molecular-storage/delivery, detection, and catalysis.

## ACKNOWLEDGMENTS

The partial support of the NSF (CHE 0111133) is gratefully acknowledged. Special thanks to Zachary Laughrey for assistance with the figures, and Len Barbour and Jerry Atwood for providing Fig. 1. Many thanks also to Corinne L. D. Gibb for help with library searches.

## REFERENCES

1. Lehn, J.-M.; Atwood, J.L.; Davies, J.E.D.; MacNicol, D.D.; Vögle, F., Eds.; *Comprehensive Supramolecular Chemistry*; Pergamon: New York, 1996.
2. Högberg, A.G.S. Two stereoisomeric macrocyclic resorcinol-acetaldehyde condensation products. *J. Org. Chem.* **1980**, *45*, 4498–4500.
3. Tunstad, L.M.; Tucker, J.A.; Dalcanale, E.; Weiser, J.; Bryant, J.A.; Sherman, J.C.; Helgeson, R.C.; Knobler, C.B.; Cram, D.J. Host-guest complexation: 48. Octol building blocks for cavitands and carcerands. *J. Org. Chem.* **1989**, *54*, 1305–1312.
4. Schneider, H.-J.; Schneider, U. The host-guest chemistry of resorcinarenes[1]. *J. Incl. Phenom. Mol. Recogn. Chem.* **1994**, *19*, 67–83.
5. Timmerman, P.; Verboom, W.; Reinhoudt, D.N. Resorcinarenes. *Tetrahedron* **1996**, *52*, 2663–2704.
6. MacGillivray, L.R.; Atwood, J.L. A chiral spherical molecular assembly held together by 60 hydrogen bonds. *Nature* **1997**, *389*, 469–472.



- Rose, K.N.; Barbour, L.J.; Orr, G.W.; Atwood, J.L. Self-assembly of carcerand-like dimers of calix[4]-resorcinarene facilitated by hydrogen bonded solvent bridges. *Chem. Commun.* **1998**, 407–408.
- Murayama, K.; Aoki, K. Resorcin[4]arene dimer linked by eight water molecules and incorporating a tetraethylammonium ion: guest-driven capsule formation via cation– $\pi$  interactions. *Chem. Commun.* **1998**, 607–608.
- Shivanyuk, A.; Rissanen, K.; Kolehmainen, E. Encapsulation of  $\text{Et}_3\text{NH}^+\cdots\text{H}_2\text{O}$  in a hydrogen-bonded resorcinarene capsule. *Chem. Commun.* **2000**, 1107–1108.
- Atwood, J.L.; Barbour, L.J.; Jerga, A. Hydrogen-bonded molecular capsules are stable in polar media. *Chem. Commun.* **2001**, 2377.
- Shivanyuk, A.; Rebek, J., Jr. Hydrogen-bonded capsules in polar, protic solvents. *Chem. Commun.* **2001**, 2374–2375.
- Shivanyuk, A.; Rebek, J., Jr. Assembly of resorcinarene capsules in wet solvents. *J. Am. Chem. Soc.* **2003**, *125*, 3432–3433.
- Avram, L.; Cohen, Y. Spontaneous formation of hexameric resorcinarene capsule in chloroform solution as detected by diffusion NMR. *J. Am. Chem. Soc.* **2002**, *123*, 15,148–15,149.
- Shivanyuk, A.; Rebek, J., Jr. Reversible encapsulation by self-assembling resorcinarene subunits. *Proc. Natl. Acad. Sci. U. S. A.* **2001**, *98*, 7662–7665.
- Shivanyuk, A.; Rebek, J., Jr. Reversible encapsulation of multiple, neutral guests in hexameric resorcinarene hosts. *Chem. Commun.* **2001**, 2424–2425.
- Jasat, A.; Sherman, J.C. Carceplexes and hemicarceplexes. *Chem. Rev.* **1999**, *99*, 932–967.
- Chapman, R.G.; Sherman, J.C. Templatation and encapsulation in supramolecular chemistry. *Tetrahedron* **1997**, *53*, 15,911–15,945.
- Sherman, J.C. Carceplexes and hemicarceplexes: molecular encapsulation—from hours to forever. *Tetrahedron* **1995**, *51*, 3395–3422.
- Sherman, J.C.; Knobler, C.B.; Cram, D.J. Syntheses and properties of soluble carceplexes. *J. Am. Chem. Soc.* **1991**, *113*, 2194–2204.
- Diederich, F.; Stang, P.J.; Eds.; *Templated Organic Synthesis*; Wiley-VCH: Weinheim, 2000.
- Chapman, R.G.; Chopra, N.; Cochien, E.D.; Sherman, J.C. Carceplex formation: scope of a remarkably efficient encapsulation reaction. *J. Am. Chem. Soc.* **1994**, *116*, 369–370.
- Chapman, R.G.; Sherman, J.C. Study of templatation and molecular encapsulation using highly stable and guest-selective self-assembling structures. *J. Am. Chem. Soc.* **1995**, *117*, 9081–9082.
- Fraser, J.R.; Borecka, B.; Trotter, J.; Sherman, J.C. An asymmetric carceplex and new crystal structure yield information regarding a 1 million-fold template effect. *J. Org. Chem.* **1995**, *60*, 1207–1213.
- Chapman, R.G.; Sherman, J.C. Reversible molecular capsules composed of two cavitands linked via an assortment of charged-hydrogen bonds and covalent bonds. *J. Am. Chem. Soc.* **1998**, *120*, 9818–9826.
- Chapman, R.G.; Sherman, J.C. Restricted motion of guests in carceplexes and capsules. *J. Org. Chem.* **2000**, *65*, 513–516.
- Chapman, R.G.; Sherman, J.C. Templatation in the formation of carceplexes. *J. Org. Chem.* **1998**, *63*, 4103–4110.
- Nakamura, K.; Sheu, C.; Keating, A.E.; Houk, K.N.; Sherman, J.C.; Chapman, R.G.; Jorgensen, W.L. Self-assembly ternary complex stabilities and template ratios in carceplex formation. *J. Am. Chem. Soc.* **1997**, *119*, 4321–4322.
- Chapman, R.G.; Olovsson, G.; Trotter, J.; Sherman, J.C. Crystal structure and thermodynamics of reversible molecular capsules. *J. Am. Chem. Soc.* **1998**, *120*, 6252–6260.
- Chapman, R.G.; Sherman, J.C. Elucidation of “twistomers” in container compounds. *J. Am. Chem. Soc.* **1999**, *121*, 1962–1963.
- Naumann, C.; Place, S.; Sherman, J.C. Synthesis and characterization of a disulfide-linked  $\text{C}_5$ -symmetric [5]carceplex. *J. Am. Chem. Soc.* **2002**, *124*, 16–17.
- Chopra, N.; Sherman, J.C. A bis(carceplex) from a cyclic tetramer of cavitands. *Angew. Chem., Int. Ed. Engl.* **1997**, *36*, 1727–1729.
- Chopra, N.; Sherman, J.C. A giant carceplex permanently entraps three organic molecules. *Angew. Chem., Int. Ed. Engl.* **1999**, *38*, 1955–1957.
- Chopra, N.; Naumann, C.; Sherman, J.C. Bis-capsules: cooperative reversible encapsulation of two molecules in adjacent separate chambers. *Angew. Chem., Int. Ed. Engl.* **2000**, *39*, 194–196.
- Cram, D.J.; Tanner, M.E.; Thomas, R. The taming of cyclobutadiene. *Angew. Chem., Int. Ed. Engl.* **1991**, *30*, 1024–1027.
- Robbins, T.A.; Cram, D.J. Through-shell oxidation and reduction reactions of guests in a hollow container single molecule. *J. Am. Chem. Soc.* **1993**, *115*, 12,199.
- Warmuth, R.; Yoon, J. Recent highlights in hemicarcerand chemistry. *Acc. Chem. Res.* **2001**, *34*, 95–105.
- Makeiff, D.A.; Pope, D.J.; Sherman, J.C. Template effects in the formation of tetramethylene-bridged hemicarceplexes. *J. Am. Chem. Soc.* **2000**, *122*, 1337–1342.
- Robbins, T.A.; Knobler, C.B.; Bellew, D.R.; Cram, D.J. A highly adaptive and strongly binding hemicarcerand. *J. Am. Chem. Soc.* **1994**, *116*, 111–122.
- Sheu, C.; Houk, K.N. Molecular mechanics and statistical thermodynamics studies of complexes of a flexible hemicarcerand with neutral guests. *J. Am. Chem. Soc.* **1996**, *118*, 8056–8070.
- Houk, K.N.; Nakamura, K.; Sheu, C.; Keating, A.E. Gating as a control element in constrictive binding and guest release by hemicarcerands. *Science* **1996**, *273*, 627–629.
- Kurdistani, S.K.; Helgeson, R.C.; Cram, D.J. Stepwise shell closures provide hosts that expose or protect guests from outer-phase reactants. *J. Am. Chem. Soc.* **1995**, *117*, 1659–1660.
- Warmuth, R.; Maverick, E.; Knobler, C.B.; Cram, D.J. Through-shell alkyllithium additions and borane reductions. *J. Org. Chem.* **2003**, *68*, 2077–2088.

43. Yoon, J.; Cram, D.J. Decomplexation rate comparisons of hemicarceplexes whose single unique bridge is changed in length and blocking power. *Chem. Commun.* **1997**, 1505–1506.
44. Yoon, J.; Knobler, C.B.; Maverick, E.F.; Cram, D.J. Dissymmetric new hemicarcerands containing four bridges of different lengths. *Chem. Commun.* **1997**, 1303–1304.
45. Yoon, J.; Sheu, C.; Houk, K.N.; Knobler, C.B.; Cram, D.J. Syntheses, binding properties, and structures of seven new hemicarcerands each composed of two bowls bridged by three tetramethylenedioxy groups and a fourth unique linkage. *J. Org. Chem.* **1996**, *61*, 9323–9339.
46. Helgeson, R.C.; Knobler, C.B.; Cram, D.J. Correlations of structure with binding ability involving nine hemicarcerands hosts and twenty-four guests. *J. Am. Chem. Soc.* **1997**, *119*, 3229–3244.
47. Helgeson, R.C.; Paek, K.; Knobler, C.B.; Maverick, E.F.; Cram, D.J. Guest-assisted and guest-inhibited shell closures provide differently shaped carceplexes and hemicarceplexes. *J. Am. Chem. Soc.* **1996**, *118*, 5590–5604.
48. Yoon, J.; Cram, D.J. The first water-soluble hemicarceplexes. *Chem. Commun.* **1997**, 497–498.
49. Yoon, J.; Cram, D.J. Chiral recognition properties in complexation of two asymmetric hemicarcerands. *J. Am. Chem. Soc.* **1997**, *119*, 11,796–11,806.
50. Farrán, A.; Deshayes, K.; Matthews, C.; Balanescu, I. “Through space” triplet energy transfer: movement of electrons through the hemicarcerand skeleton. *J. Am. Chem. Soc.* **1995**, *117*, 9614–9615.
51. Warmuth, R. *o*-Benzynes: strained alkyne or a cumulene? NMR characterization in a molecular container. *Angew. Chem., Int. Ed. Engl.* **1997**, *37*, 1347–1350.
52. Warmuth, R. Inner-phase stabilization of reactive intermediates. *Eur. J. Org. Chem.* **2001**, 423–437.
53. Warmuth, R. First intramolecular Diels–Alder reaction of *o*-benzynes inside a molecular container compound. *Chem. Commun.* **1998**, 59–60.
54. Warmuth, R.; Marvel, M.A. 1,2,4,6-Cycloheptatetraene: room temperature stabilization inside a hemicarcerand. *Angew. Chem., Int. Ed. Engl.* **2000**, *39*, 1117–1119.
55. Warmuth, R.; Marvel, M.A. Chemistry and properties of cycloheptatetraene in the inner phase of a hemicarcerand. *Chem. Eur. J.* **2001**, *7*, 1209–1220.
56. Warmuth, R. The enantiomerization barrier of 5-methylcyclohepta-1,2,4,6-tetraene. *J. Am. Chem. Soc.* **2001**, *123*, 6955–6956.
57. Kerdelhué, J.L.; Langenwalter, K.J.; Warmuth, R. Mapping the potential energy surface of the tolylcarbene rearrangement in the inner phase of a hemicarcerand. *J. Am. Chem. Soc.* **2003**, *125*, 973–986.
58. Piatnitski, E.L.; Deshayes, K.D. Hemicarceplexes that release guests upon irradiation. *Angew. Chem., Int. Ed. Engl.* **1998**, *37*, 970–972.
59. Hof, F.; Rebek, J., Jr. Molecules within molecules: Recognition through self-assembly. *Proc. Natl. Acad. Sci. U. S. A.* **2002**, *99*, 4775–4777.
60. Rebek, J., Jr. Reversible encapsulation and its consequences in solution. *Acc. Chem. Res.* **1999**, *32*, 278–286.
61. Conn, M.M.; Rebek, J., Jr. Self-assembly capsules. *Chem. Rev.* **1997**, *97*, 1647–1668.
62. Heinz, T.; Rudkevich, D.M.; Rebek, J., Jr. Pairwise selection of guests in a cylindrical capsule of nanometer dimensions. *Nature* **1998**, *394*, 764–766.
63. Körner, S.K.; Tucci, F.C.; Rudkevich, D.M.; Heinz, T.; Rebek, J., Jr. A self-assembled cylindrical capsule: new supramolecular phenomena through encapsulation. *Chem. Eur. J.* **2000**, *6*, 187–195.
64. Hayashida, O.; Sebo, L.; Rebek, J., Jr. Molecular discrimination of *N*-protected amino acid esters by a self-assembled cylindrical capsule: spectroscopic and computational studies. *J. Org. Chem.* **2002**, *67*, 8291–8298.
65. Heinz, T.; Rudkevich, D.M.; Rebek, J., Jr. Molecular recognition within a self-assembled cylindrical host. *Angew. Chem., Int. Ed. Engl.* **1999**, *38*, 1136–1139.
66. Tucci, F.C.; Rudkevich, D.M.; Rebek, J., Jr. Stereochemical relationships between encapsulated molecules. *J. Am. Chem. Soc.* **1999**, *121*, 4928–4929.
67. Shivanyuk, A.; Rebek, J., Jr. Social isomers in encapsulation complexes. *J. Am. Chem. Soc.* **2002**, *124*, 12,074–12,075.
68. Shivanyuk, A.; Rebek, J., Jr. Isomeric constellations of encapsulation complexes store information on the nanometer scale. *Angew. Chem., Int. Ed. Engl.* **2003**, *42*.
69. Chen, J.; Rebek, J., Jr. Selectivity in an encapsulated cycloaddition reaction. *Org. Lett.* **2002**, *4*, 327–329.
70. Chen, J.; Körner, S.; Craig, S.L.; Rudkevich, D.M.; Rebek, J., Jr. Amplification by compartmentalization. *Nature* **2002**, *415*, 385–386.
71. Craig, S.L.; Lin, S.; Chen, J.; Rebek, J., Jr. An NMR study of the rates of single-molecule exchange in a cylindrical host capsule. *J. Am. Chem. Soc.* **2002**, *124*, 8780–8781.
72. Lützen, A.; Renslo, A.R.; Schalley, C.A.; O’Leary, B.M.; Rebek, J., Jr. Encapsulation of ion-molecule complexes: second-sphere supramolecular chemistry. *J. Am. Chem. Soc.* **1999**, *121*, 7455–7456.
73. Pirondini, L.; Bertolini, F.; Cantadori, B.; Ugozzoli, F.; Massera, C.; Dalcanale, E. Design and self-assembly of wide and robust coordination cages. *Proc. Natl. Acad. Sci. U. S. A.* **2002**, *99*, 4911–4915.
74. Fochi, F.; Jacopozzi, P.; Wegelius, E.; Rissanen, K.; Cozzini, P.; Marastoni, E.; Fiscaro, E.; Manini, P.; Fokkens, R.; Dalcanale, E. Self-assembly and anion encapsulation properties of cavitand-based coordination cages. *J. Am. Chem. Soc.* **2001**, *123*, 7539–7552.
75. Jacopozzi, P.; Dalcanale, E. Metal-induced self-assembly of cavitand-based cage molecules. *Angew. Chem., Int. Ed. Engl.* **1997**, *36*, 613–615.
76. Fox, O.D.; Dalley, N.K.; Harrison, R.G. Structure and small molecule binding of a tetranuclear iron (II) resorc[4]arene-based cage complex. *Inorg. Chem.* **1999**, *38*, 5860–5863.
77. Fox, O.D.; Dalley, N.K.; Harrison, R.G. A metal-assembled pH-dependant, resorcinarene-based cage molecule. *J. Am. Chem. Soc.* **1998**, *120*, 7111–7112.

78. Fox, O.D.; Leung, J.F.Y.; Hunter, J.M.; Dalley, N.K.; Harrison, R.G. Metal-assisted cobalt resor[4]arene-based cage molecules that reversibly capture organic molecules from water and act as NMR shift reagents. *Inorg. Chem.* **2000**, *39*, 783–790.
79. Fox, O.D.; Drew, M.G.B.; Wilkinson, E.J.S.; Beer, P.D. Cadmium- and zinc-directed assembly of nano-sized, resorcinarene-based host architectures which strongly bind C<sub>60</sub>. *Chem. Commun.* **2000**, 391–392.
80. Shivanyuk, A.; Paulus, E.F.; Böhmer, V. Guest-controlled formation of a hydrogen-bonded molecular capsule. *Angew. Chem., Int. Ed. Engl.* **1999**, *38*, 2906–2909.
81. Rebek, J., Jr. Host–guest chemistry of calixarene capsules. *Chem. Commun.* **2000**, 637–643.
82. Mogck, O.; Paulus, E.F.; Böhmer, V.; Thondorf, I.; Vogt, W. Hydrogen-bonded dimers of tetraurea calix[4]arenes: unambiguous proof by single crystal analysis. *Chem. Commun.* **1996**, 2533–2534.
83. Shimizu, K.D.; Rebek, J., Jr. Synthesis and assembly of self-complementary calix[4]arenes. *Proc. Natl. Acad. Sci. U. S. A.* **1995**, *92*, 12,403–12,407.
84. Hamann, B.C.; Shimizu, K.D.; Rebek, J., Jr. Reversible encapsulation of guest molecules in a calixarene dimer. *Angew. Chem., Int. Ed. Engl.* **1996**, *35*, 1326–1329.
85. Schalley, C.A.; Castellano, R.K.; Brody, M.S.; Rudkevich, D.M.; Siuzdak, G.; Rebek, J., Jr. Investigating molecular recognition by mass spectrometry: characterization of calixarene-based self-assembling capsule hosts with charged guests. *J. Am. Chem. Soc.* **1999**, *121*, 4568–4579.
86. Castellano, R.K.; Rudkevich, D.M.; Rebek, J., Jr. Tetramethoxy calix[4]arenes revisited: conformational control through self-assembly. *J. Am. Chem. Soc.* **1996**, *118*, 10,002–10,003.
87. Castellano, R.K.; Kim, B.H.; Rebek, J., Jr. Chiral capsules: asymmetric binding in calixarene-based dimers. *J. Am. Chem. Soc.* **1997**, *119*, 12,671–12,672.
88. Castellano, R.K.; Nuckolls, C.; Rebek, J., Jr. Transfer of chiral information through molecular assembly. *J. Am. Chem. Soc.* **1999**, *121*, 11,156–11,163.
89. Cho, Y.L.; Rudkevich, D.M.; Rebek, J., Jr. Expanded calix[4]arene tetraurea capsules. *J. Am. Chem. Soc.* **2000**, *122*, 9868–9869.
90. Mogck, O.; Böhmer, V.; Vogt, W. Hydrogen bonded homo- and heterodimers of tetra urea derivatives of calix[4]arenes. *Tetrahedron* **1996**, *52*, 8489–8496.
91. Mogck, O.; Pons, M.; Böhmer, V.; Vogt, W. NMR studies of the reversible dimerization and guest exchange processes of tetra urea calix[4]arenes using a derivative with lower symmetry. *J. Am. Chem. Soc.* **1997**, *119*, 5706–5712.
92. Vysotsky, M.O.; Böhmer, V. Guest-enhanced kinetic stability of hydrogen-bonded dimeric capsules of tetraurea calix[4]arenes. *Org. Lett.* **2000**, *2*, 3571–3574.
93. Vysotsky, M.O.; Thondorf, I.; Böhmer, V. Self-assembled hydrogen-bonded dimeric capsules with high kinetic stability. *Angew. Chem., Int. Ed. Engl.* **2000**, *39*, 1264–1267.
94. Vysotsky, M.O.; Thondorf, I.; Böhmer, V. Hydrogen bonded calixarene capsules kinetically stable in DMSO. *Chem. Commun.* **2001**, 1890–1891.
95. Vysotsky, M.O.; Pop, A.; Broda, F.; Thondorf, I.; Böhmer, V. Molecular motions within self-assembled dimeric capsules with tetraethylammonium cations as guest. *Chem. Eur. J.* **2001**, *7*, 4403–4410.
96. Yanase, M.; Haino, T.; Fukazawa, Y. A self-assembling molecular container for fullerenes. *Tetrahedron Lett.* **1999**, *40*, 2781–2784.
97. Ikeda, A.; Yoshimura, M.; Tani, F.; Naruta, Y.; Shinkai, S. Construction of a homooxacalix[3]arene-based dimeric capsule cross-linked by a Pd(II)-pyridine interaction. *Chem. Lett.* **1998**, 587–588.
98. Ikeda, A.; Udzu, H.; Yoshimura, M.; Shinkai, S. Inclusion of [60]fullerene in a self-assembled homooxacalix[3]arene-based dimeric capsule constructed by a Pd(II)-pyridine interaction. The Li<sup>+</sup>-binding to the lower rims can improve the inclusion ability. *Tetrahedron* **2000**, *56*, 1825–1832.
99. Ikeda, A.; Udzu, H.; Zhong, Z.; Shinkai, S.; Sakamoto, S.; Yamaguchi, K. A self-assembled homooxacalix[3]arene-based dimeric capsule constructed by a Pd<sup>II</sup>-pyridine interaction which shows a novel chiral twisting motion in response to guest inclusion. *J. Am. Chem. Soc.* **2001**, *123*, 3872–3877.
100. Arduini, A.; Domiano, L.; Oglioni, L.; Pochini, A.; Secchi, A.; Ungaro, R. Self-assembled hydrogen bonded molecular cages of calix[6]arenetricarboxylic acid derivatives. *J. Org. Chem.* **1997**, *62*, 7866–7868.
101. Rincón, A.M.; Prados, P.; De Mendoza, J. A calix[6]-arene dimer linked through amino acid hydrogen bond interactions. *Eur. J. Org. Chem.* **2002**, 640–644.
102. Meissner, R.S.; Rebek, J., Jr.; De Mendoza, J. Autoencapsulation through intermolecular forces: a synthetic self-assembling spherical complex. *Science* **1995**, *270*, 1485–1488.
103. Meissner, R.; Garcias, X.; Mecozzi, S.; Rebek, J., Jr. Synthesis and assembly of new molecular hosts: solvation and the energetics of encapsulation. *J. Am. Chem. Soc.* **1997**, *119*, 77–85.
104. Kang, J.; Rebek, J., Jr. Entropically driven binding in a self-assembling molecular capsule. *Nature* **1996**, *382*, 239–241.
105. Tokunaga, Y.; Rudkevich, D.M.; Santamaría, J.; Hilmersson, G.; Rebek, J., Jr. Solvent controls synthesis and properties of supramolecular structures. *Chem. Eur. J.* **1998**, *4*, 1449–1457.
106. Santamaría, J.; Martín, T.; Hilmersson, G.; Craig, S.L.; Rebek, J., Jr. Guest exchange in an encapsulation complex: a supramolecular substitution reaction. *Proc. Natl. Acad. Sci. U. S. A.* **1999**, *96*, 8344–8347.
107. Kang, J.; Rebek, J., Jr. Acceleration of a Diels–Alder reaction by a self-assembled molecular capsule. *Nature* **1997**, *385*, 50–52.
108. Kang, J.; Hilmersson, G.; Santamaría, J.; Rebek, J., Jr. Diels–Alder reactions through reversible encapsulation. *J. Am. Chem. Soc.* **1998**, *120*, 3650–3656.
109. Kang, J.; Santamaría, J.; Hilmersson, G.; Rebek, J., Jr. Self-assembled molecular capsule catalyzes a Diels–Alder reaction. *J. Am. Chem. Soc.* **1998**, *120*, 7389–7390.

110. Rivera, J.M.; Martín, T.; Rebek, J., Jr. Chiral spaces: dissymmetric capsules through self-assembly. *Science* **1998**, *279*, 1021–1023.
111. Rivera, J.M.; Martín, T.; Rebek, J., Jr. Chiral softballs: synthesis and molecular recognition properties. *J. Am. Chem. Soc.* **2001**, *123*, 5213–5220.
112. Tokunaga, Y.; Rebek, J., Jr. Chiral capsules: 1. Softballs with asymmetric surfaces bind camphor derivatives. *J. Am. Chem. Soc.* **1998**, *120*, 66–69.
113. Grotzfeld, R.M.; Branda, N.; Rebek, J., Jr. Reversible encapsulation of disc-shaped guests by a synthetic, self-assembled host. *Science* **1996**, *271*, 487–489.
114. O'Leary, B.M.; Grotzfeld, R.M.; Rebek, J., Jr. Ring inversion dynamics of encapsulated cyclohexane. *J. Am. Chem. Soc.* **1997**, *119*, 11,701–11,702.
115. O'Leary, B.M.; Szabo, T.; Svenstrup, N.; Schalley, C.A.; Lützen, A.; Schäfer, M.; Rebek, J., Jr. "Flexi-ball" toolkit: A modular approach to self-assembling capsules. *J. Am. Chem. Soc.* **2001**, *123*, 11,519–11,533.
116. Martín, T.; Obst, U.; Rebek, J., Jr. Molecular assembly and encapsulation directed by hydrogen-bonding preferences and the filling of space. *Science* **1998**, *281*, 1842–1845.
117. Schalley, C.A.; Martín, T.; Obst, U.; Rebek, J., Jr. Characterization of self-assembly encapsulation complexes in the gas phase and solution. *J. Am. Chem. Soc.* **1999**, *121*, 2133–2138.
118. Nuckolls, C.; Hof, F.; Martín, T.; Rebek, J., Jr. Chiral microenvironments in self-assembled capsules. *J. Am. Chem. Soc.* **1999**, *121*, 10,281–10,285.
119. Hof, F.; Nuckolls, C.; Rebek, J., Jr. Diversity and selection in self-assembled tetrameric capsules. *J. Am. Chem. Soc.* **2000**, *122*, 4251–4252.
120. Hof, F.; Nuckolls, C.; Craig, S.L.; Martín, T.; Rebek, J., Jr. Emergent conformational preferences of a self-assembling small molecule: structure and dynamics in a tetrameric capsule. *J. Am. Chem. Soc.* **2000**, *122*, 10,991–10,996.
121. MacGillivray, L.R.; Atwood, J.L. Structural classification and general principles for the design of spherical molecular hosts. *Angew. Chem., Int. Ed. Engl.* **1999**, *38*, 1018–1033.
122. Gibb, C.L.D.; Gibb, B.C. Estimating the efficiencies of self-assemblies. *J. Supramol. Chem.* **2001**, *1*, 39–52.
123. Swiegers, G.F.; Malefetse, T.J. Classification of coordination polygons and polyhedra according to their mode of self-assembly. *Chem. Eur. J.* **2001**, *7*, 3637–3643.
124. Swiegers, G.F.; Malefetse, T.J. Classification of coordination polygons and polyhedra according to their mode of self-assembly: 2. Review of the literature. *Coord. Chem. Rev.* **2002**, *225*, 91–121.
125. Seidel, S.R.; Stang, P.J. High-symmetry coordination cages via self-assembly. *Acc. Chem. Res.* **2002**, *35*, 972–983.
126. Leininger, S.; Olenyuk, B.; Stang, P.J. Self-assembly of discrete cyclic nanostructures mediated by transition metals. *Chem. Rev.* **2000**, *100*, 853–908.
127. Fujita, M.; Umemoto, K.; Yoshizawa, M.; Fujita, N.; Kusukawa, T.; Biradha, K. Molecular paneling via coordination. *Chem. Commun.* **2001**, 509–518.
128. Swiegers, G.F.; Malefetse, T.J. New self-assembled structural motifs in coordination chemistry. *Chem. Rev.* **2000**, *100*, 3483–3537.
129. Holliday, B.J.; Mirkin, C.A. Strategies for the construction of supramolecular compounds through coordination chemistry. *Angew. Chem., Int. Ed. Engl.* **2001**, *40*, 2022–2043.
130. Caulder, D.L.; Raymond, K.N. Supermolecules by design. *Acc. Chem. Res.* **1999**, *32*, 975–982.
131. Jones, C.J. Transition metals as structural components in the construction of molecular containers. *Chem. Soc. Rev.* **1998**, *27*, 289–299.
132. Fujita, M.; Oguro, D.; Mlyazawa, M.; Oka, H.; Yamaguchi, K.; Ogura, K. Self-assembly of ten molecules into nanometer-sized organic host frameworks. *Nature* **1995**, *378*, 469–471.
133. Sakamoto, S.; Yoshizawa, M.; Kusukawa, T.; Fujita, M.; Yamaguchi, K. Characterization of encapsulating supramolecules by using CSI-MS with ionization-promoting reagents. *Org. Lett.* **2001**, *3*, 1601–1604.
134. Kusukawa, T.; Fujita, M. Encapsulation of large, neutral molecules in a self-assembled nanocage incorporating six palladium (II) ions. *Angew. Chem., Int. Ed. Engl.* **1998**, *37*, 3142–3144.
135. Kusukawa, T.; Fujita, M. Self-assembled  $M_6L_4$ -type coordination nanocage with 2,2'-bipyridine ancillary ligands. Facile crystallization and x-ray analysis of shape-selective enclathration of neutral guests in the cage. *J. Am. Chem. Soc.* **2002**, *124*, 13,576–13,582.
136. Kusukawa, T.; Fujita, M. "Ship in a bottle" formation of stable hydrophobic dimers of *cis*-azobenzene and -stilbene derivatives in a self-assembled coordination nanocage. *J. Am. Chem. Soc.* **1999**, *121*, 1397–1398.
137. Yoshizawa, M.; Kusukawa, T.; Fujita, M.; Yamaguchi, K. Ship-in-a-bottle synthesis of otherwise labile cyclic trimers of siloxanes in a self-assembled coordination cage. *J. Am. Chem. Soc.* **2000**, *122*, 6311–6312.
138. Yoshizawa, M.; Kusukawa, T.; Fujita, M.; Sakamoto, S.; Yamaguchi, K. Cavity-directed synthesis of labile silanol oligomers within self-assembled coordination cages. *J. Am. Chem. Soc.* **2001**, *123*, 10,454–10,459.
139. Kusukawa, T.; Yoshizawa, M.; Fujita, M. Probing guest geometry and dynamics through host-guest interactions. *Angew. Chem., Int. Ed. Engl.* **2001**, *40*, 1879–1884.
140. Yoshizawa, M.; Takeyama, Y.; Kusukawa, T.; Fujita, M. Cavity directed, highly stereoselective [2 + 2] photodimerization of olefins within self-assembled coordination cages. *Angew. Chem., Int. Ed. Engl.* **2002**, *41*, 1347–1349.
141. Yoshizawa, M.; Takeyama, Y.; Okano, T.; Fujita, M. Cavity-directed synthesis within a self-assembled coordination cage: highly selective [2 + 2] cross-photodimerization of olefins. *J. Am. Chem. Soc.* **2003**, *125*, 3243–3247.

142. Aoyagi, M.; Biradha, K.; Fujita, M. Quantitative formation of coordination nanotubes templated by rodlike guests. *J. Am. Chem. Soc.* **1999**, *121*, 7457–7458.
143. Aoyagi, M.; Tashiro, S.; Tominaga, M.; Biradha, K.; Fujita, M. Spectroscopic and crystallographic studies on the stability of self-assembled coordination nanotubes. *Chem. Commun.* **2002**, 2036–2037.
144. Tominaga, M.; Tashiro, S.; Aoyagi, M.; Fujita, M. Dynamic aspects in host-guest complexation by coordination nanotubes. *Chem. Commun.* **2002**, 2038–2039.
145. Fujita, M.; Yu, S.-Y.; Kusukawa, T.; Funaki, H.; Ogura, K.; Yamaguchi, K. Self-assembly of nanometer-sized macrotricyclic complexes from ten small component molecules. *Angew. Chem., Int. Ed. Engl.* **1998**, *37*, 2082–2085.
146. Yu, S.-Y.; Kusukawa, T.; Biradha, K.; Fujita, M. Hydrophobic assembling of a coordination nanobowl into a dimeric capsule which can accommodate up to six large organic molecules. *J. Am. Chem. Soc.* **2000**, *122*, 2665–2666.
147. Hiraoka, S.; Fujita, M. Guest-selected formation of Pd(II)-linked cages from a prototypical dynamic library. *J. Am. Chem. Soc.* **1999**, *121*, 10,239–10,240.
148. Hiraoka, S.; Kubota, Y.; Fujita, M. Self- and hetero-recognition in the guest-controlled assembly of Pd(II)-linked cages from two different ligands. *Chem. Commun.* **2000**, 1509–1510.
149. Takeda, N.; Umemoto, K.; Yamaguchi, K.; Fujita, M. A nanometer-sized hexahedral coordination capsule assembled from 24 components. *Nature* **1999**, *398*, 794–796.
150. Umemoto, K.; Tsukui, H.; Kusukawa, T.; Biradha, K.; Fujita, M. Molecular paneling by coordination: an  $M_1L_6$  hexahedral molecular capsule having clefts for reversible guest inclusion. *Angew. Chem., Int. Ed. Engl.* **2001**, *40*, 2620–2622.
151. Umemoto, K.; Yamaguchi, K.; Fujita, M. Molecular paneling via coordination: guest-controlled assembly of open cone and tetrahedron structures from eight metals and four ligands. *J. Am. Chem. Soc.* **2000**, *122*, 7150–7151.
152. Fujita, N.; Biradha, K.; Fujita, M.; Sakamoto, S.; Yamaguchi, K. A porphyrin prism: Structural switching triggered by guest inclusion. *Angew. Chem., Int. Ed. Engl.* **2001**, *40*, 1718–1721.
153. Ikeda, A.; Ayabe, M.; Shinkai, S.; Sakamoto, S.; Yamaguchi, K. A self-assembled porphyrin-based dimeric capsule constructed by a Pd(II)-pyridine interaction which shows efficient guest inclusion. *Org. Lett.* **2000**, *2*, 3707–3710.
154. Yamanoi, Y.; Sakamoto, Y.; Kusukawa, T.; Fujita, M.; Sakamoto, S.; Yamaguchi, K. Dynamic assembly of coordination boxes from (en)Pd(II) units and a rectangular panel-like ligand: NMR, CSI-MS and X-ray studies. *J. Am. Chem. Soc.* **2001**, *123*, 980–981.
155. Parac, T.N.; Caulder, D.L.; Raymond, K.N. Selective encapsulation of aqueous cationic guests into a supramolecular tetrahedron  $[M_4L_6]_{12}$ -anionic host. *J. Am. Chem. Soc.* **1998**, *120*, 8003–8005.
156. Caulder, D.A.; Powers, R.E.; Parac, T.N.; Raymond, K.N. The self-assembly of a pre-designed tetrahedral  $M_4L_6$  supramolecular cluster. *Angew. Chem., Int. Ed. Engl.* **1998**, *37*, 1840–1843.
157. Ziegler, M.; Brumaghim, J.L.; Raymond, K.N. Stabilization of a reactive cationic species by supramolecular encapsulation. *Angew. Chem., Int. Ed. Engl.* **2000**, *39*, 4119–4121.
158. Parac, T.N.; Scherer, M.; Raymond, K.N. Host within a host: encapsulation of alkali ion-crown ether complexes into a  $[Ga_4L_6]^{12}$  supramolecular cluster. *Angew. Chem., Int. Ed. Engl.* **2000**, *39*, 1239–1242.
159. Meyer, M.; Kersting, B.; Powers, R.E.; Raymond, K.N. Rearrangement reactions in dinuclear triple helicates. *Inorg. Chem.* **1997**, *36*, 5179–5191.
160. Terpin, A.J.; Ziegler, M.; Johnson, D.W.; Raymond, K.N. Resolution and kinetic stability of a chiral supramolecular assembly made of labile components. *Angew. Chem., Int. Ed. Engl.* **2001**, *40*, 157–160.
161. Ziegler, F.E.; Davis, A.; John, D.; Raymond, K.N. Supramolecular chirality: a reporter of structural memory. *Angew. Chem., Int. Ed. Engl.* **2003**, *42*.

# Halide Transport through Biological Membranes

Lars-Oliver Essen

Department of Chemistry, Philipps University, Marburg, Germany

## INTRODUCTION

The transport of chloride and other halides through lipid membranes is crucial for many cellular processes, but the molecular basis of this important phenomenon is still poorly understood. One reason for this is the lack of small model compounds such as valinomycin or gramicidin A which have played a major role in elucidating the specificity of cation transporters since decades. Of the estimated 19 protein families which are involved in halide transport, structural information exists for three families at high resolution. This review focuses on the recent progress in the structural biology of chloride channels and pumps and what kind of lessons can be learned now for the chemical engineering of synthetic chloride transporters. The design of such chloride-conducting compounds may have profound implications in the treatment of several hereditary diseases such as cystic fibrosis or hypothyroidism.

## CHLORIDE—AN UNUSUAL ANION

Chloride transport through biological membranes might be expected to set different structural restraints on ion translocation pathways than the transport of protons. Proton transport often goes along chains of water molecules and (de)protonable groups via the Grotthus mechanism<sup>[1]</sup> and does not require structural changes in a H<sup>+</sup>-conducting membrane protein per se, except that unidirectionality of H<sup>+</sup> transfer and energy conservation needs to be established. In contrast, chloride ions are sterically rather demanding with a Pauling radius of 1.81 Å and impose high energetic penalties on desolvation.<sup>[2]</sup> Their translocation through lipid bilayers requires at least some dehydration and rearrangement of the hydration shell surrounding the ion. However, the precise structure of the hydration shell around chloride ions in bulk solution is still a matter of debate.<sup>[3]</sup> Several X-ray and neutron diffraction studies suggested coordination numbers of six water molecules, but other reports indicated that the hydration structure around chloride and the more voluminous halides such as Br<sup>-</sup> and I<sup>-</sup> is not so

uniform and might comprise up to 14 water molecules.<sup>[3]</sup> Besides this quantitative uncertainty for the halide solvation shell, several studies of the gas-phase behavior of solvated halides gave conflicting results whether Cl<sup>-</sup> and Br<sup>-</sup> are more stable on the surface of neutral water clusters than in their interiors.<sup>[2]</sup> A preferential surface location of halides on water clusters might be particularly important for transmembrane conductance because it would imply that the partial desolvation of halides in the apolar environments of the transmembrane regions is energetically more favorable as compared to other ion species.

So far, there are only a few theoretical approaches to the structural rearrangements imposed on chloride and its hydration shell during the transfer through biological membranes. Computer simulations of the liquid-to-liquid transfer of hydrated chloride ions from an aqueous to an apolar phase such as 1,2-dichloroethane or CCl<sub>4</sub><sup>[4,5]</sup> might be considered to be representative for the transmembrane transport of halides, because in both cases a transfer of the chloride is firstly implied from a high to a low dielectricity medium (water:  $\epsilon = 81$ , hydrophobic regions of biological membranes:  $\epsilon \approx 2$ ). These simulations showed that the hydration shell is successively reduced and deformed during transfer. The intrusion of chloride into the apolar phase is accompanied by a tailing (“fingering”) of attached water molecules.<sup>[4,5]</sup> Similar calculations using lipid bilayers indicated that the “fingering” effect may increase the permeabilities of membranes by 14 orders of magnitude as compared to a rigid lipid bilayer model.<sup>[6]</sup> As membrane proteins represent natural, for purpose-optimized distortions of the lipid bilayer structure, one may predict that this “fingering” of water molecules will be reflected by their structures.

Another factor besides the effects on halide solvation is the electrostatic contribution of the biological membrane to the transfer process. The arrangement of a dipole layer along the membrane–water interface was postulated to cause a steep electrostatic potential of up to +300 mV in the hydrophobic membrane interior.<sup>[7]</sup> This effect rationalizes why hydrophobic anions partition better to the apolar membrane region



than hydrophobic cations. Consequently, the energetic barrier for anions crossing the lipid bilayer through an integral membrane protein might be considerably smaller than for cations.

Specific interactions between the anion and the membrane protein might be predominantly of enthalpic nature, e.g., by the formation of salt bridges and hydrogen bonds from protein side chains or the peptide backbone in or close to the selectivity filter. Such a stabilization of the transported ion in the transmembrane region of the protein could be further supplemented by size or shape complementarity between the solute and the selectivity filter or by interactions with the electrostatic field of the lipid bilayer. Another theory that deals with the preferential conductance of large over small ions might be relevant for halide selectivity.<sup>[8]</sup> This theory of large-ion selectivity postulates a preferential adsorption of the solute by entropic size exclusion effects which are created by small energetic penalties for the entrance of solvent into the channel. One consequence of the unfavorable water/channel interactions postulated by this theory is that no steric rigidity in the selectivity filter is required to induce large-ion selectivities.<sup>[9]</sup> Furthermore, this theory is also capable to explain the nonlinear conductivities which are particularly often observed for halide channels.

## OVERVIEW OF HALIDE-SPECIFIC MEMBRANE TRANSPORT SYSTEMS

The currently known families of chloride-conducting membrane proteins are summarized in Table 1 using the transporter classification (TC) of Busch and Saier.<sup>[10]</sup> A common functional aspect of these proteins is their rather broad specificity as other halides such as Br<sup>-</sup> or I<sup>-</sup>, or even polyatomic anions such as nitrate, phosphate, or organic acids are often transported. However, chloride is among the most abundant physiological anions and its equilibrium potential of -90 mV is near the resting potential, so that the transport of chloride is energetically not demanding and often contributes to the stabilization of the resting potential.<sup>[11]</sup>

Despite the diversity and the physiological roles of chloride transport, only a few families have been extensively studied in molecular and structural terms. Among the chloride channels (for review, see Ref. <sup>[12]</sup>) whose number of transmembrane spans can be between 1 and 18  $\alpha$ -helices, there are only three major, well-characterized families: the chloride channels of the ClC family (see below), the cystic fibrosis transmembrane regulator (CFTR), which is the only known ion channel of the ABC-transporter family, and the neurotransmitter-gated chloride channels (LIC family) such as the GABA or glycine receptor (Table 1). At least one family, the volume-regulated anion channels

(VAC or VRAC), has not even been cloned, although members of this family are responsible for important cellular responses such as cell volume regulation.<sup>[13]</sup>

Many of the secondary halide transporters exploit the energizing effect of the Na<sup>+</sup>/K<sup>+</sup>-ATPase on the extracellular and intracellular sodium and potassium distribution because these symporters catalyze the electro-neutral symport of K<sup>+</sup> or Na<sup>+</sup> together with halide ions. Symporters such as the (Na<sup>+</sup>/K<sup>+</sup>/2Cl<sup>-</sup>), NaCl, or KCl symporters belong to the CCC family (Table 1),<sup>[14]</sup> but several other transporters such as the NaI-symporter, whose defect may cause congenital hypothyroidism<sup>[15]</sup> or the pendrins, which are implied in hereditary deafness,<sup>[16]</sup> are found in different transporter families (Table 1). Anion-coupled antiporters include the famous HCO<sub>3</sub><sup>-</sup>/Cl<sup>-</sup> exchanger of blood erythrocytes (AE1) or the sodium-driven, electroneutral NaHCO<sub>3</sub>/HCl exchangers of the mammalian tissues (NCBE).

Often, the chloride-conducting channels and the secondary transporters act in concert. For example, the developmentally controlled coexpression of the K<sup>+</sup>/Cl<sup>-</sup> cotransporter KCC2, a member of the CCC family, decides whether the chloride currents mediated by the GABA receptor cause hyperpolarization of neuronal membranes as usually found in the adult or depolarization as found at birth.<sup>[17]</sup> A special class of passive chloride transporters is represented by cryptdin-3 that belongs to the defensin family and appears to be a natural, peptide-based chloride channel maker.<sup>[18]</sup> This peptide, 35 amino acids long, is secreted into the small intestine by the Paneth cells which are located at the base of the crypts. Besides its antimicrobial function, a regulatory role for the intestinal secretion of water and salt was suggested for these small compounds.

Primary active halide transport has been reported several times in animal tissues or algal cells.<sup>[19]</sup> However, evidences for the molecular nature and mechanism of ATP-driven chloride transport are still mostly indirect. In the absence of sequence information, it was concluded from biochemical and electrophysiological data that the chloride-ATPase of the snail *Aplysia* belongs to the P-type,<sup>[19]</sup> whereas such ATPases from the green algae *Acetabularia* were assigned to the F-type.<sup>[20]</sup> Another active chloride transporter that is commonly found in Haloarchaea is halorhodopsin.<sup>[21]</sup> This member of the microbial rhodopsins mediates the conversion of light energy into the intracellular accumulation of chloride and is discussed in detail below.

## STRUCTURALLY CHARACTERIZED HALIDE TRANSPORTERS

Only four structures are now deposited in the RCSB protein database for halide-conducting membrane

**Table 1** Chloride-conducting membrane proteins as classified by Saier's TC nomenclature

TC	Family name	Type	# TM spans	Typical sizes (amino acids)	Occurrence	Comments
1.A.9	Ligand-gated ion channel family of neurotransmitter receptors (LIC)	Channel	4	400–500	Eukaryotes	Pentameric, chloride channels exist for GABA, serotonin, glutamate, glycine as ligands
<b>1.A.11</b>	Chloride channel (ClC)	Channel	18	395–998	Eukaryotes, eubacteria	Dimeric, often voltage-gated
1.A.12	Organelle chloride channel (O-ClC)	Channel	2	241–437	Eukaryotes, eubacteria	Similar to glutathione-S-transferase family, also named as CLIC family
1.A.13	Epithelial chloride channel (E-ClC)	Channel	4	420–917	Eukaryotes, eubacteria	Activated by CaM-dependent protein kinase II
1.A.27	Phospholipid (PLM)	Channel	1	88–92	Eukaryotes	Anion-selective channels formed in planar bilayers
1.A.36	Intracellular chloride channel (ICC)	Channel	4	508	Vertebrates	Only 2 of the 4 $\alpha$ -helices are strongly hydrophobic
<b>1.B.8</b>	Mitochondrial and plastid porin (MPP)	Channel	16 ( $\beta$ -barrel)	275–283	Eukaryotic organelles	Voltage-dependent anion channels (VDAC), several eubacterial homolog, member of porin superfamily
1.C.9	Vacuolating cytotoxin (VacA)	Channel	1	1290	<i>Helicobacter pylori</i>	Channel-forming toxin of <i>H. pylori</i> , also transports $\text{HCO}_3^-$ , pyruvate
1.C.19	Defensin	Channel	?	35–95	Mammals	Cryptdin-3 and -10 form chloride-selective ion channels
2.A.21.5.1	NaI-symporter	Symport	13	643	Animals	Import of sodium iodide, belongs to solute:sodium symporter family (SSS)
2.A.22	Neurotransmitter: sodium symporter (NSS)	Symport	12	600–800	Animals	Some family members cotransport $\text{Cl}^-$
2.A.29	Mitochondrial carrier (MC)	Uniport	6	288	Eukaryotic organelles	Dimeric, only UCP-1 conducts chloride besides other substrates
2.A.30	Cation-chloride cotransporter (CCC)	Symport	12	1000–1200	Eukaryotes, eubacteria	Symport of $\text{Na}^+$ , $\text{K}^+$ , $2\text{Cl}^-$ , or $\text{NaCl}$ or $\text{KCl}$
2.A.31	Anion exchanger (AE)	Antiport	10, 14	900–1250	Animals	Exchange of $\text{HCO}_3^-$ and $\text{Cl}^-$
2.A.53	Sulfate permease (SulP)	Antiport	13–14	434–893	Ubiquitous	A few family members, e.g., the pendrins, catalyze the exchange of $\text{I}^-$ or $\text{Cl}^-$
3.A.1.202	ABC-type chloride channel	Channel	11	1480	Mammals	cAMP-Dependent chloride channel, CFTR defects cause cystic fibrosis
3.A.3	P-type ATPases	Ion pump	?	?	Eukaryotes	No $\text{Cl}^-$ -pump yet cloned, although presence is shown in vivo
<b>3.E.1</b>	Microbial rhodopsins	Ion pump	7	248	Archaea	The trimeric halorhodopsin is the only chloride-transporting member of this family, pump is powered by light energy absorbed by a retinal chromophore

The 9.C.2 family which corresponds to volume-sensitive anion channels (VAC) is not included because this family is not yet characterized on a molecular level. Another family omitted in this table is the bestrophin family for which chloride channel activity was very recently shown.<sup>[77]</sup> Conflicting reports about the number of transmembrane spans exist for the anion exchanger (AE) family. 3-D structural information about the transmembrane domains of halide-conducting membrane proteins is only present for the boldly printed TC-families.

Source: From Ref. <sup>[10]</sup>.

proteins (April '03): the anion-selective porin Omp32 (PDB-code: 1E54), two prokaryotic members of the CIC family of chloride channels (1KPK, 1KPL), and halorhodopsin, the light-driven chloride pump (1E12). A few other structurally well-characterized membrane proteins of the porin family such as PhoE also conduct halides, but they are omitted from further discussion because of their lack of specificity. In the following sections, the different characteristics of these structurally highly diverse membrane proteins are discussed in terms of their structural base for ion specificity and transport.

### Omp32, an Anion-Selective Channel of the Porin Superfamily

Omp32 (molecular weight: 34.7 kDa, 332 amino acids) belongs to the porin superfamily and resides as a trimer in the outer membranes of the eubacterium *Delftia acidovorans*.<sup>[22]</sup> Unlike the unspecific porins which generally facilitate the transport of solutes of a molecular mass of less than 600 Da along large, 10-Å-wide water-filled pores, the Omp32 porin exerts a pronounced selectivity for anions. Its permeability is 17-fold higher for chloride than for potassium cations, at least under low ionic strength conditions.<sup>[23]</sup> The voltage–current curve is nonlinear and varies as a function of the salt concentration. This effect was interpreted as partial shielding of charged residues in the selectivity filter by salt ions. Among the halide-conducting proteins discussed in this review, Omp32 is the least specific case because its *in vivo* role is presumably the transport of nonhalide anions such as organic acids which are the preferred carbon sources of *D. acidovorans*. However, its simple structure exemplifies convincingly several principles of anion selectivity such as electrostatic adaptation and the presence of a selectivity filter.

The 2.1-Å X-ray structure of the Omp32 porin<sup>[22]</sup> shows a 16-stranded, antiparallel  $\beta$ -barrel (Fig. 1A) whose widely opened, water-filled pore narrows down to a cross section of  $5 \times 7$  Å at the central constriction zone of the protein (Fig. 1B). Consequently, steric restriction alone is not considered to be a major factor for the observed anion selectivity of Omp32. In addition to the nonpolar belts which line the extracellular and periplasmic transmembrane regions of the porin, a highly basic girdle is found comprising 10 lysine and 1 arginine residues along the extracellular membrane surface. However, this belt is obviously not important for anion selectivity as its charge is counterbalanced by an almost equal number of acidic residues. This region was hence implied to interact with the anionic head groups of lipopolysaccharides of the outer membrane.<sup>[22]</sup> In contrast, a ladder of four

arginines (R38, R75, R92, and R133) and one lysine residue (K74) transverses the inner side of the  $\beta$ -barrel that lines the pore (Fig. 1B and C). Because of the large positive potential at the constriction site of the Omp32 porin that is devoid of acidic residues, cations are thought to be electrostatically repelled from this selectivity filter, whereas anions should be attracted. The dimension of the constriction zone implies that the permeation of halides proceeds without a loss of their hydration shell. The selectivity filter is partly walled by hydrophobic residues (L94, I132). Whether this serves for enforcing the hydrated ions into closer contact to the charged residues or for imposing a slight energetic penalty for the intrusion of water molecules into the pore<sup>[9]</sup> is unclear.

The electrostatic features of Omp32 might be also at least partially present in the highly related, eukaryotic voltage-dependent anion channel (VDAC) that is present in the outer membranes of mitochondria and shares high sequence similarity with Omp32.<sup>[22]</sup>

### The CIC Family of Chloride Channels

Chloride channels of the CIC family were firstly discovered by Miller in the electric organs of *Torpedo marmorata* during 1979<sup>[24]</sup> and therefrom cloned a decade later.<sup>[25]</sup> CIC-like chloride channels were subsequently found in eubacteria, archaea, and eukaryotes (for concise reviews, see Refs. [12] and [26]). In eukaryotes, the CIC channels have manifold biological functions such as the regulation of electrical membrane excitability, the maintenance of electroneutrality during cation uptake, e.g., for the acidification of endosomal compartments, or the transepithelial chloride transport, e.g., across the nephron segments of kidneys. This range of functions correlates with the presence of at least nine CIC channel isoform in mammals which can be present in either the plasma membrane or the intracellular compartments.<sup>[26]</sup>

Although first structural studies by cryoelectron microscopy utilized the CIC channel EriC from *Escherichia coli*,<sup>[27]</sup> the function of the prokaryotic CIC channels remained enigmatic. Iyer et al.<sup>[28]</sup> recently found that the CIC-like chloride channel of *E. coli* is essential for the extreme acid resistance (XAR). This resistance allows the enterobacteria to survive up to 1 hr under the highly acidic conditions of the stomach (pH 2–3). As XAR apparently depends on the electrogenic countertransport of decarboxylated amino acids (GABA, agmatine) in exchange for glutamate and arginine, the prokaryotic chloride channels act as electrical shunts so that hyperpolarization of the inner membrane is avoided.

Despite the different functions, the prokaryotic and eukaryotic CIC channels share significant sequence

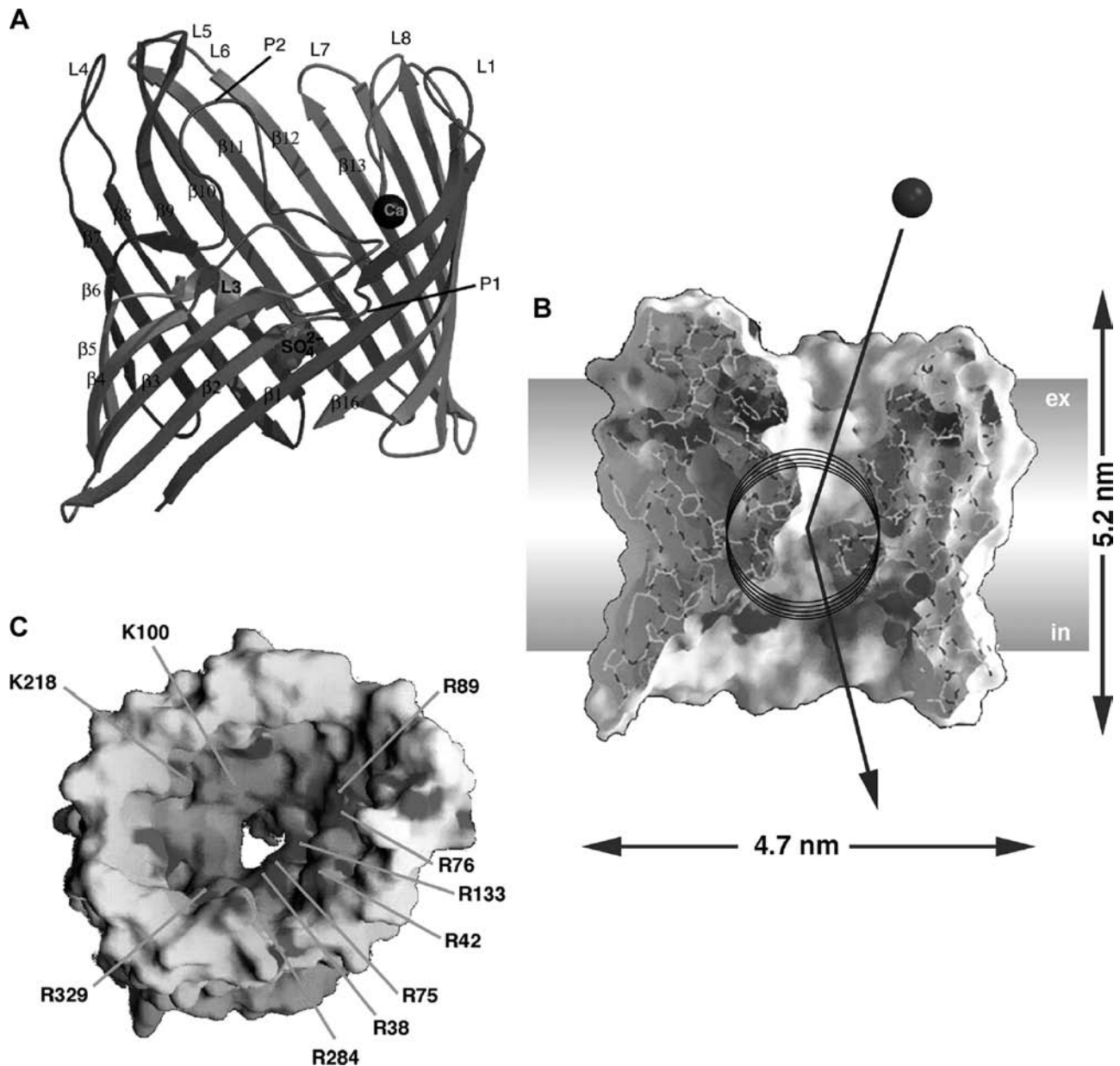


**Fig. 1** The Omp32 anion-selective porin. (A) The  $\beta$ -barrel fold architecture of Omp32. The 16  $\beta$ -strands are successively colored from blue to red. The position of a sulfate anion that is stuck in the selectivity filter is indicated. (B) Cross section through Omp32 with the surfaces colored according to the charge distribution (blue: positive; red: negative electrostatic potential). The constriction zone with the selectivity filter is encircled. (C) View from the periplasmic side to the selectivity filter. *Source:* This figure was modified from Ref. [22] and reproduced with permission of *Structure*.

similarities ( $\approx 21\%$ ) and many of them resemble in their selectivity sequences for anions:  $\text{Cl}^-$ ,  $\text{Br}^- > \text{NO}_3^- > \text{I}^- > \text{F}^-$ .<sup>[29,30]</sup> The observed high conductance for nitrate might be surprising in terms of the structural differences between nitrate and halide anions, but at least in plants, an eminent physiological role of a ClC homologue for nitrate uptake was shown.<sup>[31]</sup> Interestingly, a similar specificity order is observed for the halorhodopsins (see below), which might indicate that the structural restraints for the transport of

partially dehydrated halides and nitrate ions are very similar.

The X-ray structures of the ClC channels from the enterobacteriae *E. coli* and *Salmonella typhimurium* (Fig. 2A) were solved at 3.0- and 3.5-Å resolution by Dutzler et al.<sup>[32]</sup> and confirmed earlier electrophysiological,<sup>[33,34]</sup> biochemical,<sup>[29]</sup> and electron-microscopic reports<sup>[27]</sup> that the ClC channels form dimers with each pore acting independently from each other. Within the membrane, the triangularly shaped



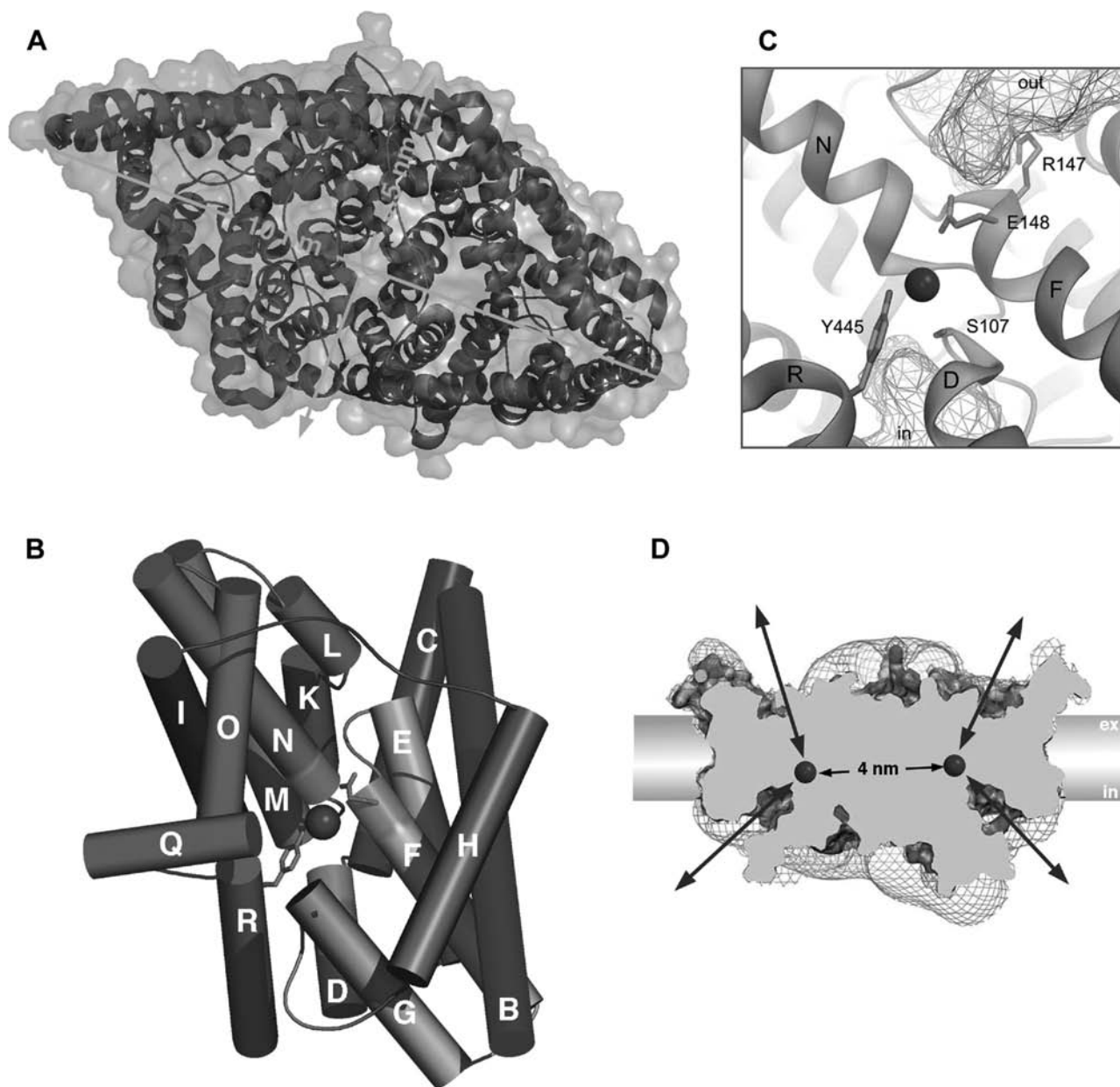


**Fig. 2** The CIC-like chloride channels. (A) Dimeric quaternary structure as viewed from the extracellular side. (B) Pseudotwofold topology of the CIC channel monomer. From N- to C-terminus, the helices of the CIC monomer are successively colored from blue to red. The N-terminal ends of helices D, F, and N are colored in violet to highlight their orientation towards the bound chloride (green). Residues E148 and Y445 of the selectivity gate are shown as yellow sticks. (C) Selectivity gate of the CIC chloride channel. (D) Cross section through the CIC monomer showing the electrostatic potential of the CIC dimer and the access pathways to the selectivity filter. *Source:* The slightly modified figures C and D were reprinted from Ref. [32] with permission of *Nature*.

subunits (*E. coli*—molecular weight: 46.6 kDa, 438 amino acids) form a large dimer interface of about  $2300 \text{ \AA}^2$ . Despite the large dimer interface, a functional interaction between the two 40- $\text{\AA}$  distant pores is restricted to slow gating<sup>[35]</sup> because fast gating is a property of the individual pores.<sup>[12]</sup> The CIC dimer protrudes by at least 15  $\text{\AA}$  from each membrane side and has a rhombus shape with dimensions of  $100 \times 55 \text{ \AA}$  when viewed along the membrane normal.

Compared to other chloride channel families (Table 1), the CIC family excels by a topologically highly complex transmembrane architecture. Each CIC channel subunit comprises 18  $\alpha$ -helices (numbered from A–R). These helices do not assume a simple helical bundle architecture as mostly found for membrane proteins, but are highly inclined relative to the membrane normal and vary in length between 6 and 55  $\text{\AA}$ . Analogously to the structurally unrelated aquaporin

family,<sup>[36]</sup> a pseudo-twofold relates the N- and C-terminal halves of the ClC monomer (Fig. 2B). As a consequence of this complex topology, four  $\alpha$ -helices (D, F, N, and R) point their N-terminal ends toward a central selectivity gate that is occupied in the ClC structures by a single chloride.<sup>[32]</sup> Three of these helices are capped by conserved, but different GxxxP motifs and apparently stabilize the chloride electrostatically by their helix dipole moments because no basic residues are found close to the selectivity gate (Fig. 2C).

Surprisingly, a conserved glutamic acid, E148, positions its carboxylate only 4 Å away from the chloride so that its passage to the extracellular side is blocked. Dutzler et al.<sup>[32]</sup> interpreted this intimate location of two anionic groups in the selectivity filter as the structural base for Cl<sup>-</sup>-dependent gating. According to their model, high concentrations of extracellular chloride cause a displacement of the side chain of E148. In such an open state, two closely spaced chloride ions would be found in the selectivity filter: one from the cytosolic side as observed in the crystal structure and one at the position of the carboxylate group of E148. This intriguing model resembles the mechanism of K<sup>+</sup> selectivity in kcsA-like potassium channels.<sup>[37]</sup> Alternatively, the protonation state of E148 might be a function of the halide concentration, i.e., invasion of extracellular chloride into the selectivity filter would cause protonation of E148 and thereby a disruption of the electrostatic barrier for halide translocation. This model is consistent with the strong pH dependence of the selectivity order Cl<sup>-</sup> > Br<sup>-</sup> > I<sup>-</sup> which can be reversed in several ClC channels by low pH values.<sup>[12]</sup>

Besides the interactions with the helix dipole moments, the chloride forms two hydrogen bonds with the side chains of the conserved residues S107 and Y445 and the amide nitrogens of the peptide bonds next to I356.<sup>[32]</sup> The chloride also contacts the methylene groups of G355 and F357. Because of the low resolution and high average B-factor of the ClC structures, there is no structural information about putative water ligands for the chloride, although the structure provides sufficient space for at least one water ligand. The access to the selectivity gate that is in the midst of a narrow, 12-Å-long tunnel is provided by wide, water-filled vestibules which are partly lined by basic residues (Fig. 2D). This feature is at least analogous to the wide pore architecture of the anion-selective porin Omp32 and obviously provides some electrostatic guidance for incoming anions.

## Halorhodopsin

In 1980, halorhodopsins (HRs) were for the first time described in the plasma membranes of *Halobacterium*

*salinarum*<sup>[38]</sup> and in other haloarchaea such as *Natronomonas pharaonis*. For these haloarchaeal extremophiles, chloride is a crucial growth parameter because the viability of haloarchaea depends on hypersaline environments like salt ponds or salinas. In the cytosol, the high osmolarity of the environment is counterbalanced by almost iso-osmolar KCl concentrations that can be as high as  $\approx 4$  M. During cell growth, the uptake of potassium chloride occurs actively by the combined action of potassium channels and halorhodopsins. The latter energize this process by acting as light-driven, inwardly directed chloride pumps.<sup>[39]</sup> Apparently, the light energy that is converted by HR contributes substantially to the maintenance of an osmotic balance during cell growth. Alternatively, passive salt import can be mediated in the dark by potassium and chloride channels.

Halorhodopsins exert slightly different affinities for the halides (Br<sup>-</sup> > Cl<sup>-</sup>, I<sup>-</sup>) which are pumped against their electrochemical gradients.<sup>[40]</sup> The halorhodopsins of *H. salinarum* and *N. pharaonis* can be produced by homologous and heterologous overexpression in large amounts.<sup>[41,42]</sup> Therefore a plethora of biophysical techniques was applicable in the past to reveal details about the transport mechanism, the photocycle kinetics, and the primary photoreaction of the chromophore (reviewed in Refs. [21], [40], and [43]).

Halorhodopsins define one subfamily of the microbial rhodopsins which also comprise subfamilies like the light-driven, proton-pumping bacteriorhodopsins (BR) and the sensory rhodopsins with sequence identities to each other of 25–35%.<sup>[44]</sup> The structural similarity to other microbial rhodopsins, i.e., an architecture with seven transmembrane  $\alpha$ -helices (numbered from A to G), was initially proven by cryoelectron microscopy on 2-D crystals of halorhodopsins<sup>[45–47]</sup> which were spontaneously formed in vivo during the homologous overexpression in *H. salinarum*.

High-resolution data at 1.8 Å were obtained by X-ray crystallographic analysis of *H. salinarum* halorhodopsin 3-D crystals<sup>[48]</sup> which were grown in a lipidic cubic phase.<sup>[49]</sup> In these crystals, halorhodopsin (molecular weight: 27.0 kDa, 253 amino acids) assembles to trimers (Fig. 3A). The layer-like crystal packing highly resembles the organization of purple membranes which are formed in vivo by bacteriorhodopsin. The quaternary structure of the HR trimer differs significantly from the bacteriorhodopsin trimer because the monomers are tilted by 11° relative to the BR trimer and involve van der Waals packing between the C helices in addition to interactions between the B and D helices.<sup>[48]</sup> The halorhodopsin structure shows that a lipidic plug consisting of the fatty acid palmitate is encircled by the HR trimer (Fig. 3A). This surprising association of halorhodopsin with a fatty acid was shown before by biochemical analysis,<sup>[50]</sup> but its



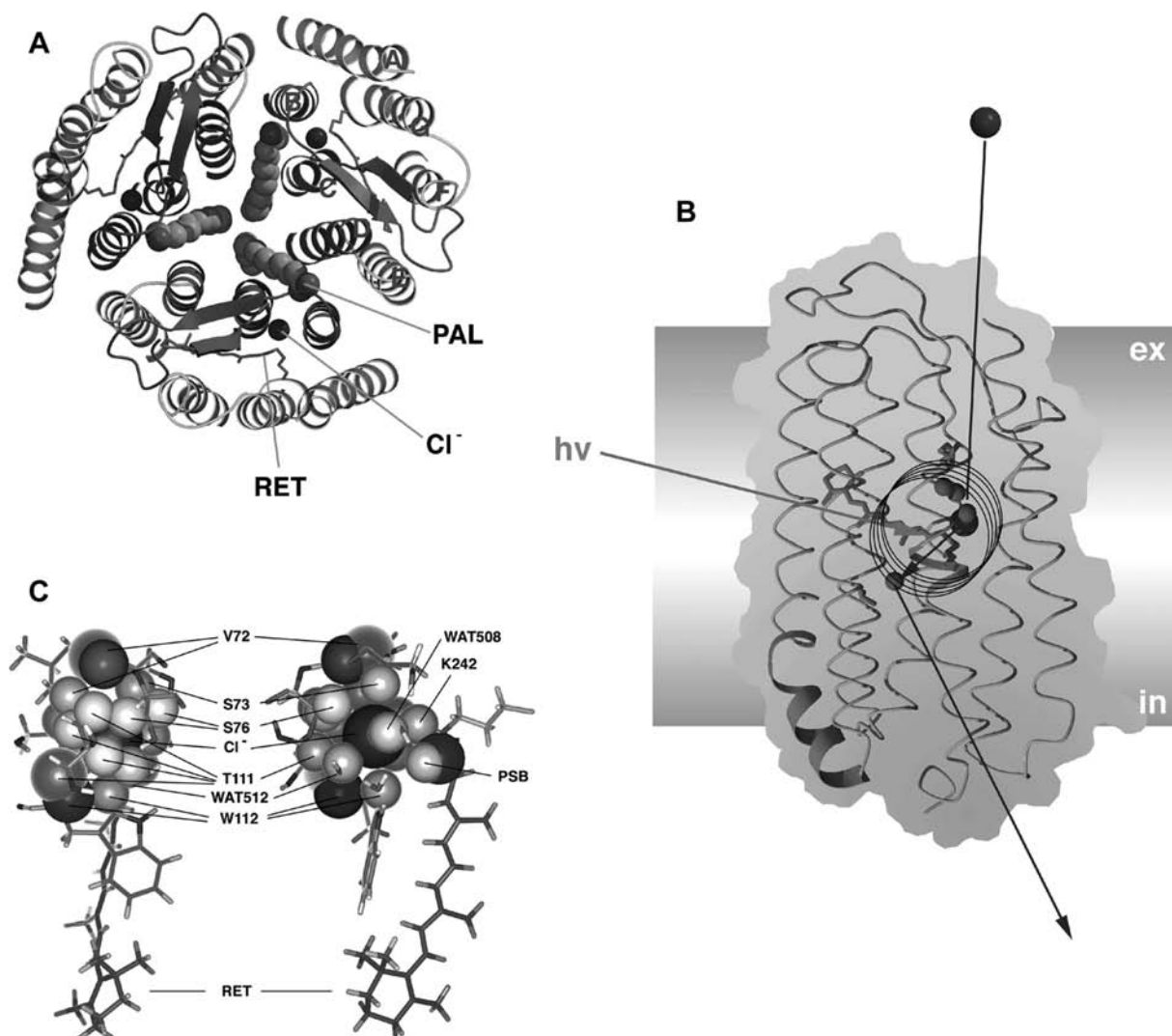


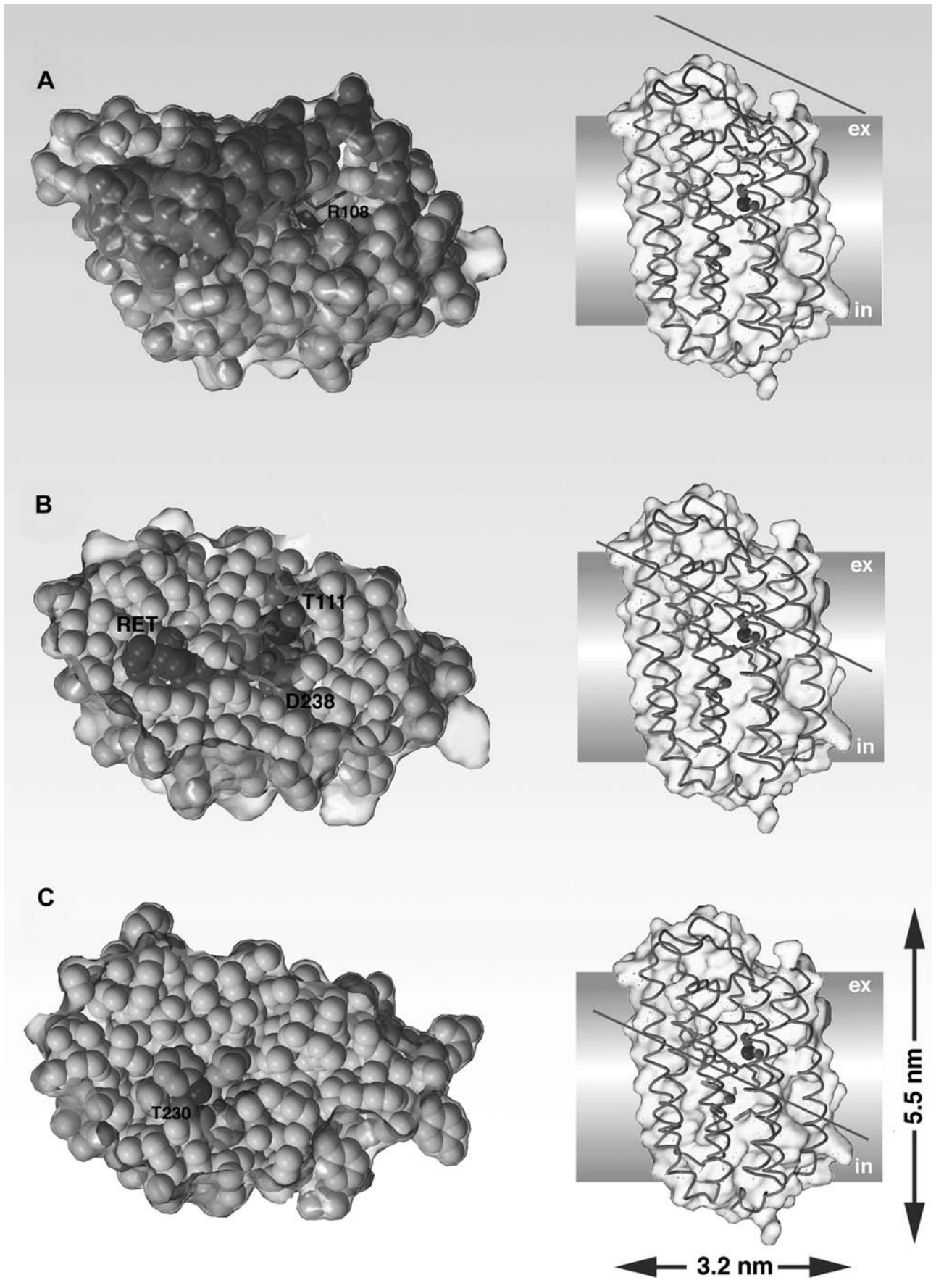
**Fig. 3** Halorhodopsin. (A) Trimeric arrangement of halorhodopsin as viewed from the extracellular side. The bound retinal (stick representation), chloride (green sphere), and palmitate groups (CPK model) are highlighted. Helix assignments are shown in blue. (B) Side view on halorhodopsin showing the translocation pathway of chloride.  $\Pi$ -Helical distortions in the  $\alpha$ -helix bundle are shown in blue. (C) Chemical environment of the chloride that is bound in the transport site. Hydrogens are shown as white spheres, chloride in green, and the nitrogens of the protonated Schiff base (PSB) and W112 in blue. *Source:* Figure C was reprinted with permission of *Nature*.

implication for the action of halorhodopsin is unclear. At least, a change in the photocycle kinetics and the  $pK_a$  of the protonated Schiff base was found upon the removal of palmitate<sup>[51]</sup> whose carboxylate group is approximately 11 Å away from the chloride that is bound to the transport site.<sup>[48]</sup>

The most appealing feature of the ion- and signal-translocating microbial rhodopsins is the presence of

an all-trans retinal chromophore that is bound as a protonated Schiff base to a conserved lysine residue, K242 in helix G (Figs. 3B and 4B). This chromophore causes the purple-like color of the unphotolyzed HR state with an absorbance maximum  $\lambda_{max}$  of 578 nm. Illumination of this HR state causes the formation of a red-shifted intermediate, the K-state ( $\lambda_{max} \approx 600$  nm), by photoisomerization of the retinal from the all-trans to

**Fig. 4** Steric restraints on the chloride translocation pathway through halorhodopsin. The location of the cross sections through halorhodopsin is indicated by a red line. The chloride ion in the transport site is highlighted as green sphere; the retinal chromophore is shown in blue and buried water molecules are shown in red. (A) View from the extracellular side. (B) The transport site for chloride. (C) The putative chloride release site. Surfaces of the internal cavities are marked in purple.



a 13-cis, 15-anti configuration and an accompanying flip of the N–H dipole of the protonated Schiff base. The 23 kcal/mol of remaining photon energy are mostly stored in the K-state by a twisted conformation of the retinal chromophore and drive the on-going conformational changes of the protein which accompany unidirectional ion transport. The flip of the Schiff base N–H dipole was indicated by a small, negative electrogenic charge shift upon K-state formation.<sup>[52]</sup>

The structure of the HR state of halorhodopsin shows that next to the protonated Schiff base a chloride is bound at a distance of 3.8 Å (Fig. 3C,<sup>[48]</sup>). Consequently, pumping of chloride from this transport site to the cytosol is directly linked to conformational changes of the chromophore and its vicinity which are organized in a well-ordered series of spectroscopically distinguishable photointermediates.<sup>[21,40]</sup> The observed electrostatic interactions between the chloride and the protonated Schiff base and another essential residue nearby, R108, were concluded before from the halide dependence of FTIR<sup>[53]</sup> and UV/VIS spectra.<sup>[54,55]</sup>

Because of the long distance and the relative geometrical arrangement, a strong hydrogen bond between the chloride and the Schiff base nitrogen is not expected in the HR state. However, the stabilization of the chloride in this central transmembrane portion involves the additional coordination to a cluster of three water molecules in the transport site (Figs. 3C and 4B). As in the structure of the ClC channel, the partial hydration around the Cl<sup>−</sup> anion is supplemented by an H bond to the hydroxyl of the conserved serine S115 and a cluster of aliphatic hydrogens which are derived from protein side chains (Fig. 3C). Here electrostatic calculations suggested that these aliphatic side chains might contribute enthalpically to halide binding because of the numerous interactions between the C–H dipoles and the chloride.<sup>[48]</sup> However, the affinities of chloride to the transport site of HR are not very high. Chizhov and Engelhard<sup>[56]</sup> estimated them from kinetic experiments to be in the millimolar range (*N. pharaonis*: ≈2.5 mM; *H. salinarum*: 10 mM).

Large conformational changes of the protein are required during the photocycle to open a transient pathway for chloride conduction because the retinal environment and the cytosolic half of HR are tightly packed (Fig. 4B and C). These changes might be transmitted by distortions in three of the  $\alpha$ -helices (Fig. 3B): a  $\Pi$ -helical segment in helix G (V239–F245), a  $\Pi$ -helical segment at the cytosolic end of helix E (A178–W183), and a  $3_{10}$ -like helical segment in helix C (L110–A113). After photoisomerization, the peptide planes of the first  $\Pi$ -helical segment, which are adjacent to K242, reorient and change the H-bonding pattern of the transport site in the early photocycle intermediates. The second  $\Pi$ -helical segment was suggested to be a hinge for the movements of helix F

that accompany the formation of late photocycle intermediates.<sup>[57]</sup>

The only  $\alpha$ -helical distortion that is not found in other microbial rhodopsins is the  $3_{10}$ -like helical segment of helix C.<sup>[21]</sup> This stretch includes T111 which corresponds to D85 in bacteriorhodopsin, the primary proton acceptor. Compared to D85 of bacteriorhodopsin, the T111 residue is retracted by 1.8 Å out of the chloride-occupied transport site of halorhodopsin. Recently, it was suggested that T111 might drive like a piston the chloride toward the cytosolic side of the chromophore by restoring the regular  $\alpha$ -helical H-bonding pattern after photoisomerization.<sup>[21]</sup> Interestingly, the hydroxyl of T111 is not contributing to Cl<sup>−</sup> binding as shown by the crystal structure of HR and transport studies of the T111V mutant.<sup>[58]</sup>

While K-state formation occurs within picoseconds and is too fast to cause a major displacement of the chloride from the transport site, the subsequently, in about 1  $\mu$ sec, reversibly formed *L-state* ( $\lambda_{\max}$  ≈ 520 nm) coincides with the movement of the halide to a second chloride binding site in the cytoplasmic half of HR.<sup>[21,48]</sup> The putative, second chloride binding site is empty in the HR state (Fig. 4C), but borders directly to the Schiff base and is completely occluded from cytosolic access.<sup>[48]</sup> Consequently, after light-triggered movement of a chloride into this cytoplasmic release site, substantial conformational changes are required in the cytoplasmic half to establish free exchange with the cytosolic milieu. In *N. pharaonis* halorhodopsin, the transport site lowers its chloride affinity from 2.5 mM to 1.1 M after photoexcitation,<sup>[56]</sup> while the affinity of the cytoplasmic release site is almost unchanged (≈5.7 M.<sup>[59]</sup>).

Interestingly, the transport specificity Br<sup>−</sup> > Cl<sup>−</sup> arises from the better binding of Br<sup>−</sup> to the cytoplasmic release site, but not to the transport site.<sup>[54]</sup> Alternative or in addition to the piston model, where movements of the T111 residue drive the ion translocation, some form of “ion-dragging” was considered before where the halide ion follows the flipped dipole of the N–H Schiff base bond and keeps a strong hydrogen bond with the protonated Schiff base.<sup>[48]</sup> A subsequent opening of an extracellular pathway from the cytoplasmic release site toward the protein surface was attributed either to a transition between the L2 and O states<sup>[60]</sup> or to a spectroscopically silent transition between two L-like intermediates.<sup>[56,61]</sup> The chloride transport along the extracellular pathway occurs by passive diffusion during the later part of the photocycle.<sup>[62]</sup> However, the precise order of the further photocycle intermediates is still unclear and might be, for halorhodopsin, even a function of the halide concentration and the source organism. Chloride uptake occurs presumably along an access channel whose outer rim on the extracellular side is lined by aliphatic side chains (Fig. 4A)

which may support the deformation of the hydration shell of the incoming halide ion.

### Converting Proton Pumps to Chloride Pumps

A single mutation in bacteriorhodopsin, aspartate 85 to serine or threonine, suffices to convert the specificity of bacteriorhodopsin from proton to chloride transport.<sup>[63]</sup> The photocycles of halorhodopsin and these mutants resemble each other, but the photocycle of the D85T mutant additionally indicates that chloride uptake becomes a rate-limiting step compared to halorhodopsin.<sup>[64,65]</sup> This might be caused by a sterically hindered access of chloride from the extracellular side to the transport site or by the lack of a hydrophobic ridge around the extracellular entrance site as in HR. Besides the 10-fold reduced transport efficiency, the D85T mutant also exhibits a 20-fold relaxed affinity to  $\text{Cl}^-$ ,<sup>[64,65]</sup> for which the structural reasons are not delineated. Furthermore, in the D85T mutant, the  $\text{Cl}^-$  translocation is accompanied by a deprotonation of E204, which belongs to the extracellular proton release group of bacteriorhodopsin but is missing in halorhodopsin, as this residue is there replaced by a neutral threonine.<sup>[21]</sup>

Apart from T203 in halorhodopsin which is predicted to line the cytosolic release site for  $\text{Cl}^-$  (Fig. 4C), no other residues essential for halide transport were identified by mutagenesis in the cytoplasmic half of halorhodopsin<sup>[58]</sup> or the bacteriorhodopsin D85T mutant.<sup>[65]</sup> Consequently, the walling of the postulated cytosolic exit pathway for  $\text{Cl}^-$  can be rather unspecific to promote the passive diffusion of  $\text{Cl}^-$  into the cytosol.<sup>[62]</sup>

Halorhodopsin is converted to an outwardly directed proton pump, if the chloride in the transport site was replaced by an  $\text{N}_3^-$  anion.<sup>[66]</sup> As a result of a  $\text{p}K_a$  of 4.75 in solution, this azide can act as a proton-accepting group such as D85 in bacteriorhodopsin. The possibility to convert the transport specificities of both bacteriorhodopsin and halorhodopsin from proton to chloride transport and vice versa implies that in these proteins, proton and halide transports depend on similar mechanisms. During the L→M transition of bacteriorhodopsin, a proton is transferred from the protonated Schiff base to the deprotonated D85. Among the models that have been suggested to rationalize the unidirectionality of this step (summarized in Ref. [67]), the so-called hydroxide hypothesis can reconcile these observations. This hypothesis states that a water molecule next to the Schiff base becomes firstly deprotonated by D85 after photoisomerization of the chromophore. The hydroxide then moves toward the cytosolic side of the chromophore like  $\text{Cl}^-$  in halorhodopsin.<sup>[67]</sup> There, it abstracts a proton from the protonated Schiff base so that as a net result, a water molecule is pumped inwardly and a proton outwardly.

The hydroxide hypothesis suggests that the ion-translocating archaeal rhodopsins generally catalyze the passage of anionic species across the photoisomerized retinal where only steric and electrostatic properties of the transport site determine the  $\text{OH}^-$  vs.  $\text{Cl}^-$  specificity.

### CONCLUSION

The structural studies on natural, halide-conducting membrane proteins show that halides are stabilized in the central region of lipid bilayers by similar mechanisms as postulated before for the transfer of halides from aqueous to apolar phases, i.e., “fingering” of the aqueous solvent into the transmembrane region and electrostatic compensation of the halide’s charge. The charge compensation involves arginine side chains such as in halorhodopsin or the Omp32 porin or at least the alignment of the dipole moments of several helices toward the bound anion such as in the ClC channels. Apart from this, the chloride binding in these proteins occurs without a highly ordered coordination shell as observed before in cation channels. For the potassium channels, it was noted that  $\text{K}^+$  ions are highly regularly coordinated in the selectivity filter in two alternative coordination geometries:<sup>[37]</sup> a square-antiprismatic coordination sphere with eight oxygen atoms and an octahedral geometry with six oxygen ligands which are derived either from water or from carbonyl groups of the selectivity filter. These coordination geometries coincided with structural data from potassium-selective antibiotics such as nonactin or valinomycin and confirmed that there are common principles for the stabilization and the conductance of cations in lipid bilayers by  $\text{K}^+$ -selective ionophores and channels.

A common feature of the structures discussed above is certainly the partial lining of the selectivity filter by hydrophobic residues. According to the theory of large-ion conductance, such an apolar channel lining might impose an energetic penalty for water intrusion into the selectivity gate and induce the observed anion specificity by excluded volume effects.<sup>[9]</sup> Unfortunately, this theory might be hard to prove by mutagenesis and biophysical analysis of natural membrane proteins because small differences in the geometry of the channel could exert large differences for the energetics of water intrusion. What is needed is hence a much simpler and, in steric terms, more stringently defined system than the ClC-like chloride channels or the porins.

Biochemical and biophysical data about small, natural transporters such as cryptdin-3<sup>[18]</sup> or synthetic model compounds capable of transmembrane halide transport<sup>[68]</sup> have been reported since only a few years

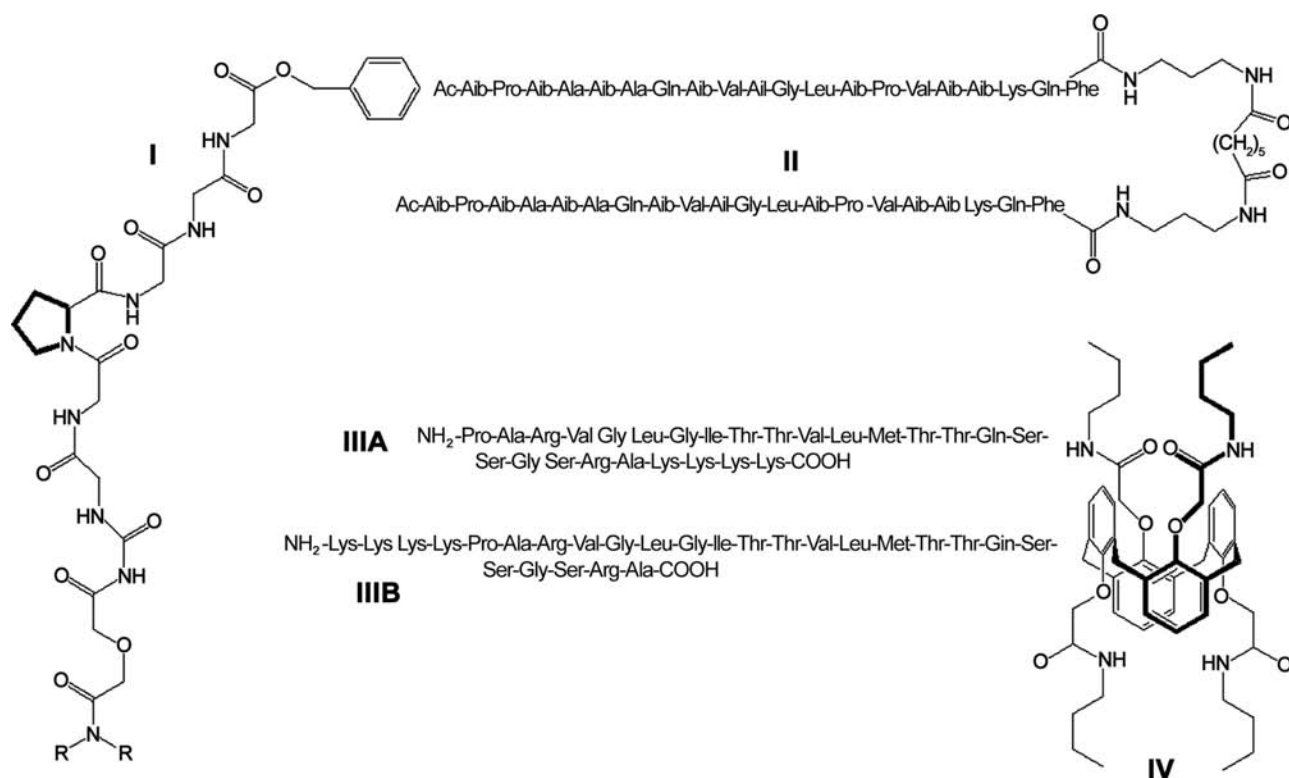


**Fig. 5** Synthetic halide transporters. I = SCMTRs,<sup>[70]</sup> II = alamethicin derivative alm-K16,<sup>[69]</sup> IIIA = C-K<sub>4</sub>-M2GlyR,<sup>[75]</sup> IIIB = N-K<sub>4</sub>-M2GlyR,<sup>[78]</sup> IV = calix[4]arene tetrabutylamide. *Source:* From Ref. [76].

(Fig. 5). The design of most of the synthetic halide transporters is based on peptidic backbones. In the case of a specificity-modified, dimeric alamethicin derivative, a mild anion preference was built in by introducing a lysine residue close to the C-terminal end.<sup>[69]</sup> However, the observed anion preference was caused by a drop of the cation conductance, while anion permeability was unaffected in comparison to the parental alamethicin. Another more promising strategy followed by Schlesinger et al.<sup>[70]</sup> was inspired by the conserved motif GKxGPxxH that is present in the anion pathway of ClC chloride channels. By attaching the heptapeptide GGGPGGG to a lipidic anchor (Fig. 5), these authors obtained chloride conductivities with  $> 10 \text{ Cl}^-/\text{K}^+$  selectivity. Furthermore, they could show that these synthetic chloride membrane transporters (SCMTRs) exhibit voltage gating similar to natural chloride channels. Their conductance crucially depends on the presence of the proline kink<sup>[71]</sup> and the precise length of the lipidic moiety.<sup>[72]</sup> Interestingly, this design lacks a direct electrostatic compensation of the chloride charge. The distortion in the lipid bilayer by the proline kink might hence indicate a mechanism which relies on the “fingering” of partially dehydrated chlorides into the apolar region.

Another evidence for the relaxed structural requirements for transmembrane halide conductance is the observation that peptides which are derived from the transmembrane regions of CFTR or the GABA receptor readily form chloride channels *in vitro*.<sup>[73,74]</sup> As these peptides might have a pharmaceutical potential in the treatment of CFTR deficiency, i.e., cystic fibrosis, they are momentarily subject to further optimization in terms of solubility and conductance properties.<sup>[75]</sup> While these approaches to halide channels used peptidic backbones for the transmembrane region, one of the first successful designs of a nonpeptidic chloride transporter utilized a calix[4]arene as chemical scaffold (Ref. [76], Fig. 5).

Certainly, further high-resolution structural studies on synthetic and natural halide transmembrane transporters will be needed before our view about the transport of halides is similarly concise as it is nowadays for the transport of cations.

## ACKNOWLEDGMENTS

This work was supported by a grant of the German Ministry of Science and Education (BMBF).



## REFERENCES

- Agmon, N. The Grotthus mechanism. *Chem. Phys. Lett.* **1995**, *224*, 456–462.
- Takashima, K.; Riveros, J.M. Gas-phase solvated negative ions. *Mass Spectrom. Rev.* **1998**, *17*, 409–430.
- Ohtaki, H.; Radnai, T. Structure and dynamics of hydrated ions. *Chem. Rev.* **1993**, *93*, 1157–1204.
- Benjamin, I. Mechanism and dynamics of ion transfer across a liquid–liquid interface. *Science* **1993**, *261*, 1558–1560.
- Dang, L.X. Computer simulation studies of ion transport across a liquid/liquid interface. *J. Phys. Chem., B* **1999**, *103*, 8195–8200.
- Wilson, M.A.; Pohorille, A. Mechanism of unassisted ion transport across membrane bilayers. *J. Am. Chem. Soc.* **1996**, *118*, 6580–6587.
- McLaughlin, S. Electrostatic potentials at membrane–solution interfaces. *Curr. Top. Membr. Transp.* **1977**, *9*, 71–144.
- Goulding, D.; Melchionna, S.; Hansen, J.-P. Entropic selectivity of microporous materials. *Phys. Chem., Chem. Phys.* **2001**, *3*, 1644–1654.
- Gillespie, D.; Nonner, W.; Henderson, D.; Eisenberg, R.S. A physical mechanism for large-ion selectivity of ion channels. *Phys. Chem., Chem. Phys.* **2002**, *4*, 4763–4769.
- Busch, W.; Saier, M.H. The transporter classification (TC) system, 2002. *Crit. Rev. Biochem. Mol. Biol.* **2002**, *37*, 287–337.
- Hille, B. *Ion Channels of Excitable Membranes*, 3rd Ed.; Sinauer Associates Incorporated, 2001.
- Nilius, B.; Droogmans, G. Amazing chloride channels: An overview. *Acta Physiol. Scand.* **2003**, *177*, 119–147.
- Strange, K.; Emma, F.; Jackson, P.S. Cellular and molecular physiology of volume-sensitive anion channels. *Am. J. Physiol.* **1996**, *270*, C711–C730.
- Lauf, P.K.; Adragna, N.C. K–Cl cotransport: Properties and molecular mechanism. *Cell. Physiol. Biochem.* **1999**, *10*, 341–364.
- Fujiwara, H.; Tatsumi, K.; Miki, K.; Harada, T.; Miyai, K.; Takai, S.; Amino, N. Congenital hypothyroidism caused by a mutation in the Na<sup>+</sup>/I<sup>-</sup> symporter. *Nat. Genet.* **1997**, *16*, 124–125.
- Everett, L.A.; Glaser, B.; Beck, J.C.; Idol, J.R.; Buchs, A.; Heyman, M.; Adawi, F.; Hazani, E.; Nassir, E.; Baxevanis, A.D.; Sheffield, V.C.; D., G.E. Pendred syndrome is caused by mutations in a putative sulphate transporter gene (PDS). *Nat. Genet.* **1997**, *17*, 411–422.
- Rivera, C.; Voipio, J.; Payne, J.A.; Ruusuvuori, E.; Lahtinen, H.; Lamsa, K.; Pirvola, U.; Saarna, M.; Kaila, K. The K<sup>+</sup>/Cl<sup>-</sup> co-transport KCC2 renders GABA hyperpolarization during neuronal maturation. *Nature* **1999**, *397*, 251–255.
- Yue, G.; Merlin, D.; Selsted, M.E.; Lencer, W.I.; Madara, J.L.; Eaton, D.C. Cryptdin 3 forms anion selective channels in cytoplasmic membranes of human embryonic kidney cells. *Am. J. Physiol.* **2002**, *282*, G757–G765.
- Gerencser, G.A.; Zhang, J. Cl–ATPases: Novel primary active transporters in biology. *J. Exp. Zool.* **2001**, *289*, 215–223.
- Moritani, C.; Ohhashi, T.; Kadowaki, H.; Tagaya, M.; Fukui, T.; Lottspeich, F.; Oesterhelt, D.; Ikeda, M. The primary structure of the Cl–translocating ATPase b subunit of *Acetabularia acetabulum* which belongs to the F-type ATPase family. *Arch. Biochem. Biophys.* **1997**, *339*, 115–124.
- Essen, L.-O. Halorhodopsin: Light-driven ion pumping made simple? *Curr. Opin. Struct. Biol.* **2002**, *12*, 516–522.
- Zeth, K.; Diederichs, K.; Welte, W.; Engelhardt, H. Crystal structure of Omp32, the anion-selective porin from *Comamonas acidovorans*, in complex with a periplasmic peptide at 2.1 Å resolution. *Structure* **2000**, *8*, 981–992.
- Mathes, A.; Engelhardt, H. Nonlinear and asymmetric open channel characteristics of an ion-selective porin in planar lipid membranes. *Biophys. J.* **1998**, *75*, 1255–1262.
- White, M.M.; Miller, C. A voltage-gated anion channel from the electric organ of *Torpedo marmorata*. *J. Biol. Chem.* **1979**, *254*, 10161–10166.
- Jentsch, T.J.; Steinmeyer, K.; Schwarz, G. Primary structure of *Torpedo marmorata* chloride channel isolated by expression cloning in *Xenopus* oocytes. *Nature* **1990**, *348*, 510–514.
- Jentsch, T.J.; Stein, V.; Weinreich, F.; Zdebik, A.A. Molecular structure and physiological function of chloride channels. *Phys. Rev.* **2002**, *82*, 503–568.
- Mindell, J.A.; Maduke, M.; Miller, C.; Grigorieff, N. Projection structure of a ClC-type chloride channel at 6.5 Å resolution. *Nature* **2001**, *409*, 219–223.
- Iyer, R.; Iverson, T.M.; Accardi, A.; Miller, C. A biological role for prokaryotic ClC chloride channels. *Nature* **2002**, *419*, 715–718.
- Maduke, M.; Pheasant, D.J.; Miller, C. High-level expression, functional reconstitution, and quaternary structure of a prokaryotic ClC-type chloride channel. *J. Gen. Physiol.* **1999**, *114*, 713–722.
- Rychkov, G.Y.; Pusch, M.; Roberts, M.L.; Jentsch, T.J.; Bretag, A.H. Permeation and block of the skeletal muscle chloride channel, ClC-1, by foreign anions. *J. Gen. Physiol.* **1998**, *111*, 653–665.
- Geelen, D.; Lurin, C.; Bouchez, D.; Frachisse, J.M.; Lelievre, F.; Courtial, B.; Barbier-Brygoo, H.; Maurel, C. Disruption of putative anion channel gene AtCLC-a in *Arabidopsis* suggests a role in the regulation of nitrate content. *Plant J.* **2001**, *21*, 259–267.
- Dutzler, R.; Campbell, E.B.; Cadene, M.; Chait, B.T.; MacKinnon, R. X-ray structure of a ClC chloride channel at 3.0 Å reveals the molecular basis of anion selectivity. *Nature* **2002**, *415*, 287–294.
- Middleton, R.E.; Pheasant, D.J.; Miller, C. Homodimeric architecture of a ClC-type chloride ion channel. *Nature* **1996**, *383*, 337–340.
- Ludewig, U.; Pusch, M.; Jentsch, T.J. Two physically distinct pores in the dimeric ClC-0 chloride channel. *Nature* **1996**, *383*, 340–343.



35. Weinreich, F.; Jentsch, T.J. Pores formed by single subunits in mixed dimers of different CIC chloride channels. *J. Biol. Chem.* **2001**, *276*, 2347–2353.
36. Sui, H.; Han, B.-G.; Lee, J.K.; Wallan, P.; Jap, B. Structural basis of water-specific transport through the AQP1 water channel. *Nature* **2001**, *414*, 872–878.
37. Morais-Cabral, J.H.; Zhou, Y.; MacKinnon, R. Energetic optimization of ion conduction rate by the K<sup>+</sup> selectivity filter. *Nature* **2001**, *414*, 37–42.
38. Matsuno-Yagi, A.; Mukohata, Y. ATP synthesis linked to light-dependent proton uptake in a red mutant strain of *Halobacterium* lacking bacteriorhodopsin. *Arch. Biochem. Biophys.* **1980**, *199*, 297–303.
39. Schobert, B.; Lanyi, J.K. Halorhodopsin is a light-driven chloride pump. *J. Biol. Chem.* **1982**, *257*, 10306–10313.
40. Oesterhelt, D. Structure and function of halorhodopsin. *Isr. J. Chem.* **1995**, *35*, 475–494.
41. Heymann, J.A.W.; Havelka, W.A.; Oesterhelt, D. Homologous overexpression of a light-driven anion pump in an archaeobacterium. *Mol. Microbiol.* **1993**, *7*, 623–630.
42. Hohenfeld, I.P.; Wegener, A.A.; Engelhard, M. Purification of histidine tagged bacteriorhodopsin, *pharaonis* halorhodopsin and *pharaonis* sensory rhodopsin II functionally expressed in *Escherichia coli*. *FEBS Lett.* **1999**, *442*, 198–202.
43. Varo, G. Analogies between halorhodopsin and bacteriorhodopsin. *Biochim. Biophys. Acta* **2000**, *1460*, 220–229.
44. Mukohata, Y.; Ihara, K.; Tamura, T.; Sugiyama, Y. Halobacterial rhodopsins. *J. Biochem.* **1999**, *125*, 649–657.
45. Kunji, E.R.S.; von Gronau, S.; Oesterhelt, D.; Henderson, R. The three-dimensional structure of halorhodopsin to 5 angstrom by electron crystallography: A new unbending procedure for two-dimensional crystals by using a global reference structure. *Proc. Natl. Acad. Sci. U.S.A.* **2000**, *97*, 4637–4642.
46. Havelka, W.A.; Henderson, R.; Oesterhelt, D. Three-dimensional structure of halorhodopsin at 7 Angstrom resolution. *J. Mol. Biol.* **1995**, *247*, 726–738.
47. Havelka, W.A.; Henderson, R.; Heymann, J.A.W.; Oesterhelt, D. Projection structure of halorhodopsin from *Halobacterium halobium* at 6 Å resolution obtained by electron cryo-microscopy. *J. Mol. Biol.* **1993**, *234*, 837–846.
48. Kolbe, M.; Besir, H.; Essen, L.O.; Oesterhelt, D. Structure of the light-driven chloride pump halorhodopsin at 1.8 angstrom resolution. *Science* **2000**, *288*, 1390–1396.
49. Landau, E.M.; Rosenbusch, J.P. Lipidic cubic phases—A novel concept for the crystallization of membrane proteins. *Proc. Natl. Acad. Sci. U.S.A.* **1996**, *93*, 14532–14535.
50. Colella, M.; Lobasso, S.; Babudri, F.; Corcelli, A. Palmitic acid is associated with halorhodopsin as a free fatty acid: Radiolabeling of halorhodopsin with H-3-palmitic acid and chemical analysis of the reaction products of purified halorhodopsin with thiols and NaBH<sub>4</sub>. *Biochim. Biophys. Acta* **1998**, *1370*, 273–279.
51. Corcelli, A.; Lobasso, S.; Colella, M.; Trotta, M.; Guerrieri, A.; Palmisano, F. Role of palmitic acid on the isolation and properties of halorhodopsin. *Biochim. Biophys. Acta* **1996**, *1281*, 173–181.
52. Ludmann, K.; Ibrón, G.; Lanyi, J.K.; Varo, G. Charge motions during the photocycle of *pharaonis* halorhodopsin. *Biophys. J.* **2000**, *78*, 959–966.
53. Walter, T.J.; Braiman, M.S. Anion–protein interactions during halorhodopsin pumping: Halide binding at the protonated Schiff base. *Biochemistry* **1994**, *33*, 1724–1733.
54. Hutson, M.S.; Shilov, S.V.; Krebs, R.; Braiman, M.S. Halide dependence of the halorhodopsin photocycle as measured by time-resolved infrared spectra. *Biophys. J.* **2001**, *80*, 1452–1465.
55. Scharf, B.; Engelhard, M. Blue halorhodopsin from *Natronobacterium pharaonis*: Wavelength regulation by anions. *Biochemistry* **1994**, *33*, 6387–6393.
56. Chizhov, I.; Engelhard, M. Temperature and halide dependence of the photocycle of halorhodopsin from *Natronobacterium pharaonis*. *Biophys. J.* **2001**, *81*, 1600–1612.
57. Subramaniam, S.; Henderson, R. Molecular mechanism of vectorial proton translocation by bacteriorhodopsin. *Nature* **2000**, *406*, 653–657.
58. Rüdiger, M.; Oesterhelt, D. Specific arginine and threonine residues control anion binding and transport in the light-driven chloride pump halorhodopsin. *EMBO J.* **1997**, *16*, 3813–3821.
59. Okuno, D.; Asaumi, M.; Muneyuki, E. Chloride concentration dependency of the electrogenic activity of halorhodopsin. *Biochemistry* **1999**, *38*, 5422–5429.
60. Hackmann, C.; Guijarro, J.; Chizhov, I.; Engelhard, M.; Rodig, C.; Siebert, F. Static and time-resolved step-scan Fourier transform infrared investigations of the photoreaction of halorhodopsin from *Natronobacterium pharaonis*: Consequences for models of the anion translocation mechanism. *Biophys. J.* **2001**, *81*, 394–406.
61. Chon, Y.S.; Kandori, H.; Sasaki, J.; Lanyi, J.K.; Needleman, R.; Maeda, A. Existence of two L photointermediates of halorhodopsin from *Halobacterium salinarum*, differing in their protein and water FTIR bands. *Biochemistry* **1999**, *38*, 9449–9455.
62. Sato, M.; Kanamori, T.; Kamo, N.; Demura, M.; Nitta, K. Stopped-flow analysis on anion-binding to blue-form halorhodopsin from *Natronobacterium pharaonis*: Comparison with the anion-uptake process during the photocycle. *Biophys. J.* **2002**, *41*, 2452–2458.
63. Sasaki, J.; Brown, L.S.; Chon, Y.S.; Kandori, H.; Maeda, A.; Needleman, R.; Lanyi, J.K. Conversion of bacteriorhodopsin into a chloride ion pump. *Science* **1995**, *269*, 73–75.
64. Tittor, J.; Haupts, U.; Haupts, C.; Oesterhelt, D.; Becker, A.; Bamberg, E. Chloride and proton transport in bacteriorhodopsin mutant D85T-different modes of ion translocation in a retinal protein. *J. Mol. Biol.* **1997**, *271*, 405–416.
65. Paula, S.; Tittor, J.; Oesterhelt, D. Roles of cytoplasmic arginine and threonine in chloride transport by the bacteriorhodopsin mutant D85T. *Biophys. J.* **2001**, *80*, 2386–2395.

66. Bamberg, E.; Tittor, J.; Oesterhelt, D. Light-driven proton or chloride pumping by halorhodopsin. *Proc. Natl. Acad. Sci. U.S.A.* **1993**, *90*, 639–643.
67. Luecke, H. Atomic resolution structures of bacteriorhodopsin photocycle intermediates: The role of discrete water molecules in the function of this light-driven ion pump. *Biochim. Biophys. Acta* **2000**, *1460*, 133–156.
68. Boon, J.M.; Smith, B.D. Synthetic membrane transporters. *Curr. Opin. Chem. Biol.* **2002**, *6*, 749–756.
69. Starostin, A.V.; Butan, R.; Borisenko, V.; James, D.A.; Wenschuh, H.; Sansom, M.S.P.; Woolley, G.A. An anion-selective analogue of the channel-forming peptide alamethicin. *Biochemistry* **1999**, *38*, 6144–6150.
70. Schlesinger, P.H.; Ferdani, R.; Liu, J.; Pajewska, J.; Pajewski, R.; Saito, M.; Shabany, H.; Gokel, G.W. SCMTR: A chloride-sensitive, membrane anchored peptide channel that exhibits voltage-gating. *J. Am. Chem. Soc.* **2002**, *124*, 1848–1849.
71. Schlesinger, P.H.; Ferdani, R.; Pajewski, R.; Pajewska, J.; Gokel, G.W. A hydrocarbon anchored peptide that forms a chloride-selective channel in liposomes. *Chem. Commun.* **2002**, *2002*, 840–841.
72. Schlesinger, P.H.; Djedovic, N.K.; Ferdani, R.; Pajewska, J.; Pajewski, R.; Gokel, G.W. Anchor chain length alters the apparent mechanism of chloride channel function in SCMTR derivatives. *Chem. Commun.* **2003**, *2003*, 308–309.
73. Reddy, G.L.; Iwamoto, T.; Tomich, J.M.; Montal, M. Synthetic peptides and four-helix bundle proteins as model systems for the pore-forming structure of channel proteins. *J. Biol. Chem.* **1993**, *268*, 14608–14615.
74. Oblattmontal, M.; Reddy, G.L.; Iwamoto, T.; Tomich, J.M.; Montal, M. Identification of an ion channel-forming motif in the primary structure of CFTR, the cystic-fibrosis chloride channel. *Proc. Natl. Acad. Sci. U.S.A.* **1994**, *91*, 1495–1499.
75. Wallace, D.P.; Tomich, J.M.; Eppler, J.W.; Iwamoto, T.; Grantham, J.J.; Sullivan, L.P. A synthetic channel-forming peptide induces  $\text{Cl}^-$  secretion: Modulation by  $\text{Ca}^{2+}$ -dependent  $\text{K}^+$  channels. *Biochim. Biophys. Acta* **2000**, *1464*, 69–82.
76. Sidorov, V.; Kotch, F.W.; Abdrakmanova, G.; Mizani, R.; Fetting, J.C.; Davis, J.T. Ion channel formation from a calix[4]arene amide that binds HCl. *J. Am. Chem. Soc.* **2002**, *124*, 2267–2278.
77. Sun, H.; Tsunenari, T.; Yau, K.-W.; Nathans, J. The vitelliform macular dystrophy protein defines a new family of chloride channels. *Proc. Natl. Acad. Sci. U.S.A.* **2002**, *99*, 4008–4013.
78. Broughman, J.R.; Mitchell, K.E.; Sedlacek, R.L.; Iwamoto, T.; Tomich, J.M.; Schultz, B.D. NH<sub>2</sub>-terminal modification of a channel-forming peptide increases capacity for epithelial anion secretion. *Am. J. Physiol., Cell Physiol.* **2001**, *280*, C451–C458.

*Encyclopedia of*

# Nanoscience and Nanotechnology

*Second Edition*

## Volume III

*Pages 1491 through 2210*

*Heterogeneous – Metallomacrocyclic*

Heterogeneous  
– Hydrogel

Ice – Inorganic

Integrated – Island

Lab – Layered

Ligand –  
Luminescence

Magnetic –  
Mesoporous

Metal Clusters  
– Metal Nano

Metal—Oxide  
– Metallo

# Heterogeneous Catalysts: Atomic Scale Studies

**Robert F. Klie**

*Brookhaven National Laboratory, Upton, New York, U.S.A.*

**Kai Sun**

*Department of Physics, University of Illinois at Chicago, Chicago, Illinois, U.S.A.*

**Mark M. Disko**

*Corporate Strategic Research, ExxonMobil Research and Engineering, Annandale, New Jersey, U.S.A.*

**Jingyue Liu**

*Monsanto Company, St. Louis, Missouri, U.S.A.*

**Nigel D. Browning**

*Department of Chemical Engineering and Materials Science, University of California–Davis, Davis, California, U.S.A.*

## INTRODUCTION

In this entry, we will describe an analytical atomic-resolution scanning transmission electron microscopy (STEM) study of supported nanoscale systems. The combination of high-resolution Z-contrast imaging and electron energy loss spectroscopy (EELS) provides an analytical tool with unprecedented chemical and spatial sensitivity that is vital for studying interfaces in heterogeneous catalyst systems. We study three examples of heterogeneous catalyst systems: Pt/SiO<sub>2</sub>, Pd/Al<sub>2</sub>O<sub>3</sub>, and Cu/Al<sub>2</sub>O<sub>3</sub> and the in situ reduction of PdO. In Pt/SiO<sub>2</sub>, the presence of a few monolayers of platinum oxide and changes in the chemistry of the SiO<sub>2</sub> support are characterized as a function of the catalyst preparation conditions. In Pd/Al<sub>2</sub>O<sub>3</sub>, electron transfer from the alumina toward the Pd particles appears to be dependent on the metal particle size that is observed. The Cu/Al<sub>2</sub>O<sub>3</sub>, reduced at various temperatures, exhibits increasing oxidation of the Cu particles upon higher temperature reduction. The in situ reduction of PdO upon heating in the microscope column confirms that the reduction to metallic Pd occurs through a shellwise mechanism, and the effects of beam damage are studied briefly on this system.

Heterogeneous metal catalysts are routinely used in a variety of chemical processes, including dehydrogenation, naphtha reforming, oxidation and automotive exhaust catalysis (e.g., see Ref.<sup>[1]</sup>). Although they have been successfully used for many years, a fundamental understanding of the mechanism behind their activity and selectivity remains elusive. This is

primarily because the bulk materials typically contain a wide range of metallic cluster sizes,<sup>[1–3]</sup> and the majority of experimental techniques, such as infrared absorption spectroscopy extended X-ray absorption fine structure (EXAFS)<sup>[4]</sup> do not have the required combination of spatial resolution (to see individual clusters) and chemical sensitivity (to see changes in composition and bonding). Although accurate information on the electronic structure can be obtained from these techniques, they all lack the ability to define the spatial location from which the information is obtained. The ability to characterize the structure, composition, and properties of individual clusters represents a key advance in the development of a fundamental understanding of existing heterogeneous catalysts and the future engineering of new and improved catalyst systems, as the chemical activity/selectivity in many systems is known to be intimately related to the cluster size.<sup>[5]</sup>

Since it has become increasingly clear that in many cases the core phenomena occur at interfaces between the metal clusters and the support,<sup>[6]</sup> the traditional method of investigating interfaces, transmission electron microscopy (TEM),<sup>[2,7]</sup> is not sensitive to small local changes in composition and electronic structure. There is therefore an “information gap” between what can be learned from spectroscopy and what can be obtained from microscopy. The combination of Z-contrast imaging and EELS can potentially fill this information gap. Here, we describe the combination of Z-contrast imaging<sup>[8]</sup> and EELS<sup>[9]</sup> in the STEM that permits the characterization of individual nanoclusters in heterogeneous catalyst systems on the atomic scale.

The Z-contrast technique routinely provides atomic resolution images of the interface between the support and the metal cluster.<sup>[10]</sup> Using this image to position the probe, one can acquire an energy loss spectrum from any location in and around the interface,<sup>[11,12]</sup> allowing local changes in electronic structure to be correlated directly with the size and composition of the metal cluster. If this analysis is performed on catalysts whose preparation and reaction history is known, then this characterization tool can be used, in conjunction with the surface techniques mentioned above, to derive a fundamental understanding of the mechanism behind activity/selectivity in heterogeneous catalysts.

The metal–support interaction (MSI) is studied in three different systems, Pt/SiO<sub>2</sub>, Pd/Al<sub>2</sub>O<sub>3</sub>, and Cu/Al<sub>2</sub>O<sub>3</sub>. There are two reasons to choose these three systems. One is that they are all important catalysts used in environmental catalytic technologies.<sup>[13–27]</sup> Another is that there are still controversies on some main issues of these catalysts. For example, the activity and selectivity of these Pd catalysts are strongly affected by the support material used.<sup>[28]</sup> Hence, the interaction with the support can alter the electronic properties of palladium. Although a strong metal support interaction (SMSI)<sup>[29,30]</sup> was not seen, it was suggested that the MSI originates from the formation of Pd–Al alloys at the metal–support interface.<sup>[31]</sup>

Furthermore, the reduction behavior of PdO is investigated in situ by EELS to clarify its reduction mechanism. In addition, it is treated as a model system to study the beam effect on the metal oxides in our experiments.

## EXPERIMENTAL TECHNIQUES

The STEM and EELS results presented in this entry were obtained using a JEOL 2010F STEM/TEM, having a Schottky field emission gun source and being operated at 200 kV.<sup>[32–34]</sup> The microscope is equipped with a standard ultra high resolution objective lens pole piece, a JEOL annular dark-field detector, a post column Gatan imaging filter (GIF), and a piezo stage for drift control.<sup>[33,34]</sup> The key to atomic resolution in STEM<sup>[33–35]</sup> is the formation of the smallest possible electron probe with sufficient probe current (~40 pA) to obtain statistically significant images and spectra (Fig. 1). The electron probe is optimized using the electron “Ronchigram,” or “shadow image,”<sup>[33,36]</sup> to obtain a probe size of ~0.2 nm.

The Z-contrast image is formed by collecting the scattered intensity on a high-angle detector (35–100 mrad). The high angles and large angular range of this detector effectively average out the coherent effects in the image, thereby allowing it to be regarded as a simple convolution of the average scattering cross section located at

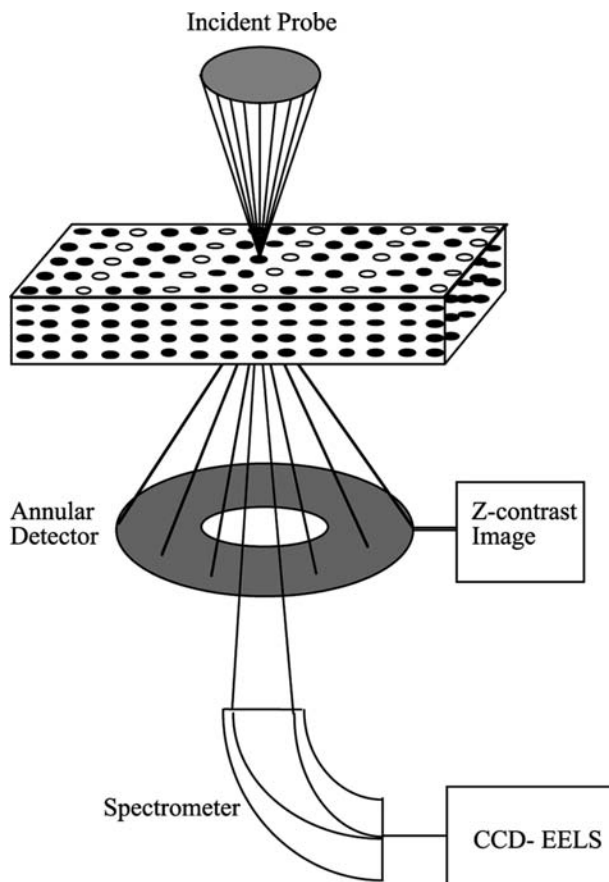


**Fig. 1** Schematic of the detector arrangement for STEM imaging and analysis.

the position of the atomic columns and the incoming electron probe intensity profile.<sup>[34]</sup> As the scattering amplitude at high angles is essentially Rutherford scattering,<sup>[35]</sup> the measured intensity is proportional to the average atomic number of the column (i.e.,  $\sim Z^2$ ). If the atomic spacing in a zone-axis orientation is larger than the probe size, a direct atomic resolution image can be obtained.<sup>[32–35]</sup>

The experimental setup of this microscope allows us to use the low-angle scattered electrons that do not contribute to the Z-contrast image for EELS.<sup>[37]</sup> As the two techniques do not interfere, the Z-contrast images can be used to position the electron probe at the desired spot in the sample to acquire spectra.<sup>[9,33,38]</sup> The physical principle behind EELS relates to the interaction of the fast electrons with the sample to cause either collective excitations of electrons (plasmons), or discrete transitions between atomic energy levels.<sup>[11,12]</sup> Here, only the highly localized, discrete atomic transitions commonly known as core losses, which allow both compositional analysis and the degree of bonding hybridization to be determined, will be considered.

The in situ heating experiments that are performed here utilize a double tilt heating stage with a variable temperature range between 20° and 1000°C. The oxygen partial pressure in the microscope column is  $P_{O_2}^{gas} \sim 5 \times 10^{-8}$  Pa during the experiment, which means that at 300°C the samples are in a highly reducing environment (for a more detailed description see Ref.<sup>[39]</sup>). To compensate for the continuous drift of the heating holder a piezoelectric driver is used. The piezo-stage drift control was originally developed to eliminate the systematic specimen drift in HRTEM imaging mode. The computer-controlled stage can also be used to compensate for drift in STEM mode. Using the Ronchigram,<sup>[33,45]</sup> the autocorrelation algorithm computes and corrects for the specimen drift.

One side effect of irradiation on the sample with high-energy electrons is that ionizing radiation can damage the specimen. Although STEM is generally considered a low-dose technique with beam currents of  $\sim 40$  pA, radiation damage remains the major challenge in analytical high-resolution STEM analyses. Some aspects of beam damage are particularly pronounced at higher voltages. The most common radiation damage mechanism in oxide materials is the loss of oxygen because of the ionization of the bulk structure. We will study this effect on the PdO system. In amorphous support oxides and especially at the metal–oxide interfaces, radiation damage is hard to detect. The only way to monitor radiation damage effects is to acquire a set of EEL spectra with very short exposure times and observe the continuous changes in the near-edge fine structure. Therefore, it remains very difficult to distinguish the genuine reduction of the interfacial support region from radiation damage effects that take place predominately at the interface.

Because of the specimen preparation techniques, the catalyst system exhibits an uneven surface topology. The spherical oxide support and small, suspended

metal cluster cause the region of interest to be at various different heights with respect to the focal plane of the objective lens system. Consequently, the images of particles that are not in the focal plane appear blurred. For regions out of the focal plane, the height of the sample will be changed until it appears in focus rather than changing the objective lens excitation, as changing the objective lens excitation will result in a decreased spatial resolution. The effects of varying sample heights is particularly pronounced at the metal–support interface for larger metal particles, and it is essential that the ideal height is found to obtain the ideal spatial resolution.

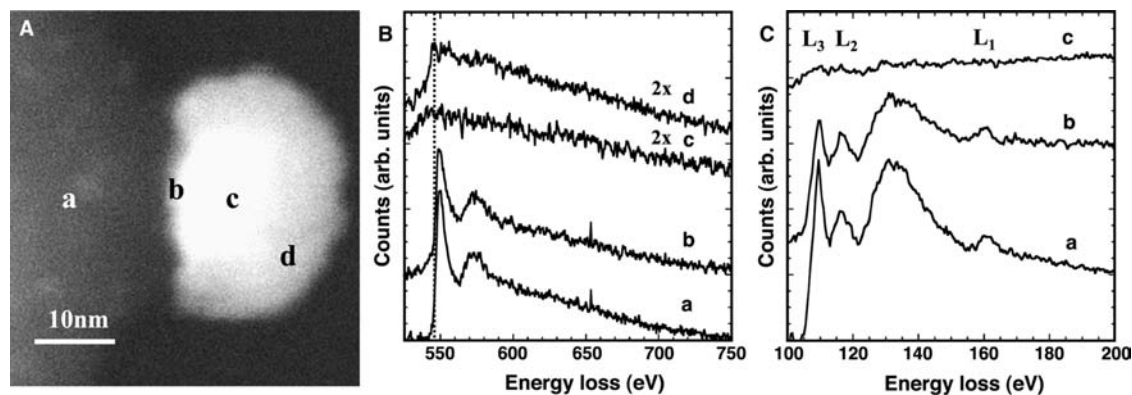
## APPLICATIONS

### Pt/SiO<sub>2</sub>

These catalytic systems were prepared by impregnating colloidal amorphous SiO<sub>2</sub> microspheres (Nissan Chemical Snowtex ZL) of  $\sim 80$  nm diameter with platinum tetraamine hydroxide (pH = 9.3). After an overnight drying at 120°C, the resulting Pt/SiO<sub>2</sub> catalyst was exposed to two different calcination treatments at 350° and 250°C, respectively.

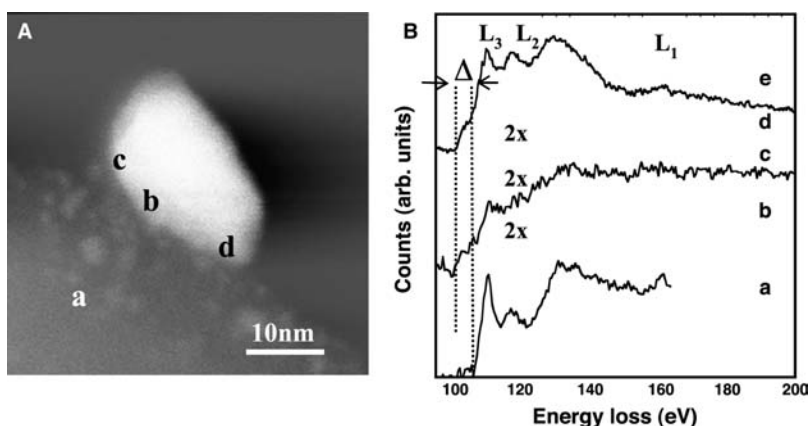
The first set of Pt/SiO<sub>2</sub> sample was heated in an oven to a temperature of 350°C in air. The calcination process was completed after 3 hr and the catalyst was then prepared for TEM analysis. To achieve the appropriate electron transparent samples, the catalyst was crushed to a fine powder. A pure copper grid was then dipped into the fine crushed powder, and a considerable amount of material stuck to the grid for TEM investigations. The average metal particle size is measured by conventional phase contrast imaging to be  $\sim 20$  nm (average dispersion  $\sim 4.5\%$ ).

Fig. 2A shows a high-resolution STEM image of a particle edge on the supporting SiO<sub>2</sub> sphere in a



**Fig. 2** Pt/SiO<sub>2</sub> (calcined at 350°C) at room temperature. (A) Z-contrast image with locations of EELS analysis indicated. (B) EEL spectra showing oxygen K edges with acquisition time  $t = 10$  sec. The dotted lines indicated the edge onsets. Spectra c and d are magnified by a factor of 2. (C) EEL spectra showing Si L edges with acquisition time  $t = 0.3$  sec.





**Fig. 3** Pt/SiO<sub>2</sub> (calcined at 250°C) at room temperature. (A) Z-contrast image with locations of EELS analysis indicated. (B) EEL spectra showing Si L edges with acquisition time  $t = 0.3$  sec. Spectrum e reflects a model spectrum of pure silicon. The interface spectra are magnified by a factor of 2–3 to observe the changes in the fine structure. The dotted lines indicated the edge onsets with an edge-onset shift of  $\Delta = 3.5$  eV.

random orientation (i.e., atomic resolution images of the lattice are not possible). The examination of several edge on particles reveals that the bright core of the particle is surrounded by a darker ring of material that seems to be of a different nature than the center.

A series of EEL spectra (Fig. 2B) were acquired from the positions indicated in Fig. 2A. The spectrum labeled “a” from the bulk of the amorphous SiO<sub>2</sub> sphere has an edge onset of 539 eV. The spectrum taken from the interface does not show any obvious changes, except for a lower intensity of the oxygen peak, which is caused by the decreasing amount of SiO<sub>2</sub> under the beam. The Pt particle bulk spectrum, magnified by a factor of 2, does not show any contribution from oxygen in the spectrum. The spectrum labeled “d” is taken from the lower contrast edge of the particle. In this spectrum, the onset of the edge is shifted toward a lower energy (532 eV) and the main peak is shifted from 548 to 546 eV. The Si L edge spectra (Fig. 2C) are taken from the same positions. The support bulk spectrum displays the fine structure expected for amorphous SiO<sub>2</sub>,<sup>[46]</sup> with an edge onset of 105 eV, and the L<sub>3</sub>, L<sub>2</sub>, and L<sub>1</sub> edges at 108, 112, and 160 eV, respectively. For the interface spectrum b, the same peaks are visible, although the intensity ratios are slightly different. This small change is attributed to the thinner illuminated edge of the SiO<sub>2</sub> sphere. The spectrum c shows no obvious modulation of the background. The particle surface spectrum (not displayed here) exhibits similar features as spectrum c. This indicates that no Si is in or on the surface of the metallic particle.

The combination of the oxygen and silicon near-edge fine structure analyses unambiguously shows that an ordered oxide layer surrounds the Pt particles. The very low intensity of the spectral changes indicates that the thickness of this layer is in fact only around a few monolayers. The changes in the energy loss spectra are so significant that a modulation because of contamination or artifacts can be excluded. This structure can be explained by a partial surface oxidation or

chemisorption of oxygen on the Pt–metal particle during the calcination at high temperatures. An adsorbed layer of oxygen after calcination would not be stable under the electron beam, hence a Pt–O surface layer seems the best explanation. The fact that bulk platinum is regarded as a noble metal and therefore very hard to oxidize does not contradict this observation, because small metal particles often exhibit a completely different behavior with decreasing particle size.<sup>[4]</sup> The second set of Pt/SiO<sub>2</sub> system was heated in air from room temperature to 250°C and kept at this temperature for 3 hr. The TEM sample was prepared in the same manner as the previous one. TEM measurements reveal that the average particle size is ~15 nm with a dispersion of ~6%.

The room temperature Z-contrast images (Fig. 3A) show a similar particle structure to the previous sample, with the bright core and the darker halo around the center. The positions where the EEL spectra are acquired are indicated in Fig. 3A and the corresponding spectra are displayed in Fig. 3B. The oxygen edges were detected only at the supporting oxide and the interface. The SiO<sub>2</sub> bulk spectrum (spectrum a) looks similar to the bulk spectrum of the amorphous support in the previous section. For the center of the interface between the support and the Pt particle (spectrum b), all the edges are still visible, and the peak intensity ratios are different because of the decreased specimen thickness. The spectra from the edge of the interface show some interesting changes in the fine structure. Here, the L<sub>1</sub> and L<sub>3</sub> edge intensities decrease and a shift in the edge onset from 105.5 to 102 eV can be measured. Spectrum e shows the energy loss spectrum from a different bulk crystalline Si sample. Because of the unavoidable surface oxidation of Si, this spectrum represents a mixture of amorphous SiO<sub>2</sub> surface layers and crystalline Si. Spectrum b as well as spectrum c show a remarkable similarity to the Si–SiO<sub>2</sub> reference spectrum. All interface spectra are

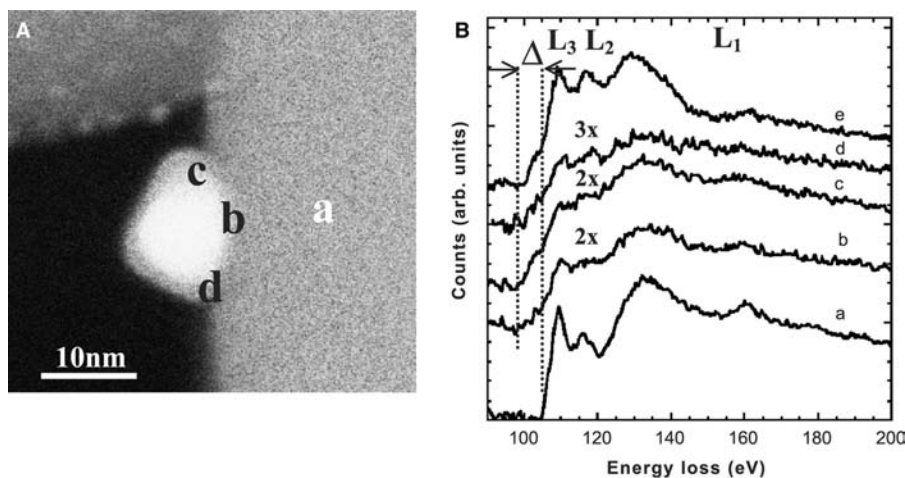


**Fig. 4** Pt/SiO<sub>2</sub> (calcined at 250°C) at 300°C in  $5 \times 10^{-8}$  Pa after 3 hr of heating. (A) Z-contrast image showing the heated metal particle and locators for EEL spectra. (B) Si L edges from the indicated positions with acquisition time  $t = 0.3$  sec. Spectrum e reflects a model spectrum of pure silicon. The interface spectra are magnified by a factor of 2–3 to observe the changes in the fine structure. The dotted lines indicated the edge onsets with an edge-onset shift of  $\Delta = 3.5$  eV.

magnified by a factor of 4 to enhance the visibility of the fine structure.

To investigate further these changes in the fine structure of the Si L edges, the sample was then heated in the microscope column to a temperature of 300°C for 3 hr. Afterward, the same set of measurements was repeated on a different particle with similar bulk and interfacial features. The structure of the particles seems to be unchanged (Fig. 4A) and the heating holder is stable enough at these temperatures to acquire even atomic resolution Z-contrast images. The SiO<sub>2</sub> bulk spectrum onset (spectrum a) is located at 105 eV, similar to the unheated bulk spectrum, but the spectra b, c, and d display an enhanced decrease in the L<sub>3</sub>, L<sub>2</sub>, and L<sub>1</sub> edge intensity than was previously observed. In addition to the nearly total disappearance of the L<sub>3</sub> and L<sub>1</sub> peaks, there is also an extra intensity below this onset of the bulk spectrum. An EEL spectrum taken from crystalline bulk Si (with SiO<sub>2</sub> surface layer) is displayed as spectrum e. Furthermore, we acquired a series of spectra under similar conditions close to the surface of Si spheres without any Pt particles attached and no change in the L<sub>3</sub>, L<sub>2</sub> intensity was observed.

The integrated Si/O ratio<sup>[40]</sup> was calculated for the bulk and interface spectra at room and elevated temperatures, and a decrease in the oxygen content toward the interface was determined. At room temperature the Si:O intensity ratio (note that this is not the chemical composition ratio, as the scattering cross sections are not taken into account) increased from  $0.9 \pm 0.1$  in the support to  $1.2 \pm 0.1$  at the heterointerface, whereas at 300°C this difference is further enhanced ( $0.9 \pm 0.1$  in the support and  $1.9 \pm 0.1$  at the interface).

The monolayer of surface oxide around the Pt clusters was not observed for the sample calcined in air at 250°C (this suggests that the oxidation of these Pt particles occurs at higher temperatures). However, the more interesting result in this sample is the change in

the fine structure of the silicon L edges, which can be attributed to the transformation of amorphous SiO<sub>2</sub> in the bulk of the spheres toward a reduced form of SiO<sub>2</sub> at the interface. Furthermore, the spectra that are observed at the interface can be reconstructed from a linear combination of SiO<sub>2</sub> and Si. In addition, the interface spectra exhibit a very similar prepeak intensity with respect to the white-line intensities as the reference Si/SiO<sub>2</sub> spectrum.

The reason for the formation of such an interface layer remains unsolved. One possible explanation might be that a thermally induced PtSi<sub>x</sub> layer, very similar to the CoSi<sub>x</sub> interface structure observed in Co/SiO<sub>2</sub>/Si<sup>[41]</sup> can build up at the heterointerface. The fact that the Si prepeak increases upon in situ reduction suggests a growing amount of Si present in the interface. Therefore, we cannot rule out this formation mechanism. Further investigations of similar systems and the correlation of these data to other conventional techniques will help to solve the origin of this effect and lead to an understanding of the influence of this interface layer on the overall performance of the catalytic system.

### Pd/Al<sub>2</sub>O<sub>3</sub>

A gamma alumina ( $\gamma$ -Al<sub>2</sub>O<sub>3</sub>) powder (BET SA 160 m<sup>2</sup>/g and Hg pore volume 2.3 mL/g) and sufficient solution of Na<sub>2</sub>PdCl<sub>4</sub> (adjusted to pH = 4) was used to prepare the catalyst, thus giving a Pd loading of 2 wt.%. The samples were dried overnight at 393 K and portions were reduced at temperatures of 250°, 500°, and 800°C with 4% H<sub>2</sub> in Ar (for more details, see Ref.<sup>[42]</sup>).

To obtain the particle size distribution for the catalyst reduced at 250°, 500°, and 800°C, 200 particles from different areas of each specimen of the catalyst were examined. At the reduction temperature of

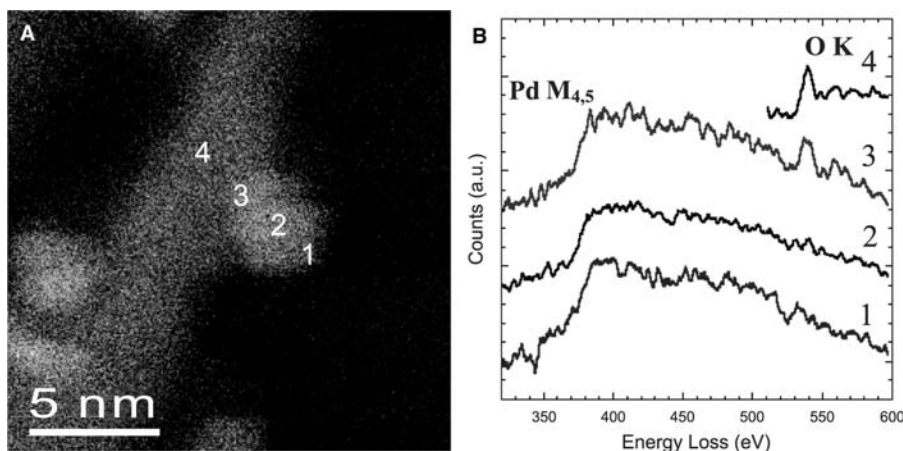


**Fig. 5** (A) Z-contrast image showing the locations of EEL spectra. (B) EEL spectra acquired from a Pd particle in the Pd/ $\gamma$ -Al<sub>2</sub>O<sub>3</sub> catalyst reduced at 250°C.

250°C, the statistical results indicate that most particles are less than 7 nm (in the size range of 2–5 nm). The overall size distribution at 500°C is increased slightly. At the reduction temperature of 800°C, the distribution of the particle sizes is dramatically altered. Most of the particles have grown into the size range of 7–30 nm with several very large particles (>30 nm) observed because of sintering at these high temperatures. Unlike the samples reduced at lower temperatures, the particle size distribution in the sample reduced at 800°C is very wide. Furthermore, most of the particles are faceted with flat surfaces, which is significantly different from those samples reduced at lower temperatures.

Fig. 5A shows a high-magnification Z-contrast image of the catalyst reduced at 250°C, in which a small particle coexisting with an alumina crystal is clearly observed. The corresponding energy-loss spectra are shown in Fig. 5B. Spectra 1 and 2 are acquired from the surface and center of the particle. The spectra consist of delayed Pd M<sub>4,5</sub> (for metallic Pd with onset at 335 eV) and the M<sub>2,3</sub> (at 532.3 eV for metallic Pd) edges, or the oxygen K edge (onset at around 532 eV). It is obvious that the Pd M<sub>2,3</sub> edges overlap with the

oxygen K edge, which makes the identification of the oxidation state of the Pd particles difficult. Nevertheless, no obvious peaks showing up at around 532 eV in the two spectra suggests that this particle is primarily composed of metallic Pd. Comparing spectrum 3, acquired from the interface with spectrum 4 from the support, we can see there is no obvious chemical shift of the oxygen K edge or Pd M<sub>2,3</sub> edges in the interface spectrum. This is the case for all interfaces studied, except for the one large particle, where a 4.8-eV negative chemical shift was observed in the M<sub>2,3</sub> interface spectrum.

Fig. 6A shows the catalyst reduced at 500°C in which a Pd particle coexists with the alumina support. Energy-loss spectra acquired from the positions marked in Fig. 6A are shown in Fig. 6B. Spectra 1 and 2 show metallic Pd features, which suggest that the small clusters formed at this temperature are metallic Pd. No obvious oxygen K edge (or Pd M<sub>2,3</sub> edges) shift for the interfacial spectrum 3 relative to the support spectrum 1 was observed. However, chemical shifts larger than 2.4 eV were observed for the spectra acquired from the interfaces between the large particles and the alumina support.

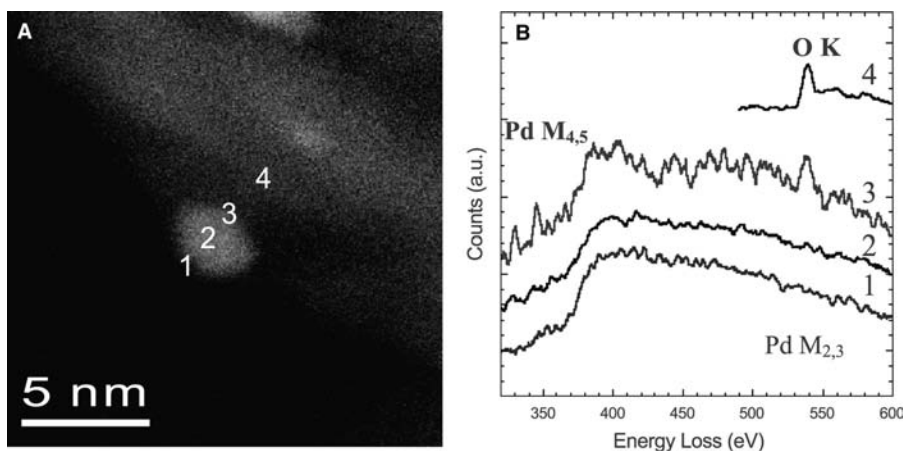


**Fig. 6** (A) Z-contrast image showing the locations of EEL spectra. (B) EEL spectra acquired from a Pd particle in the Pd/ $\gamma$ -Al<sub>2</sub>O<sub>3</sub> catalyst reduced at 500°C.

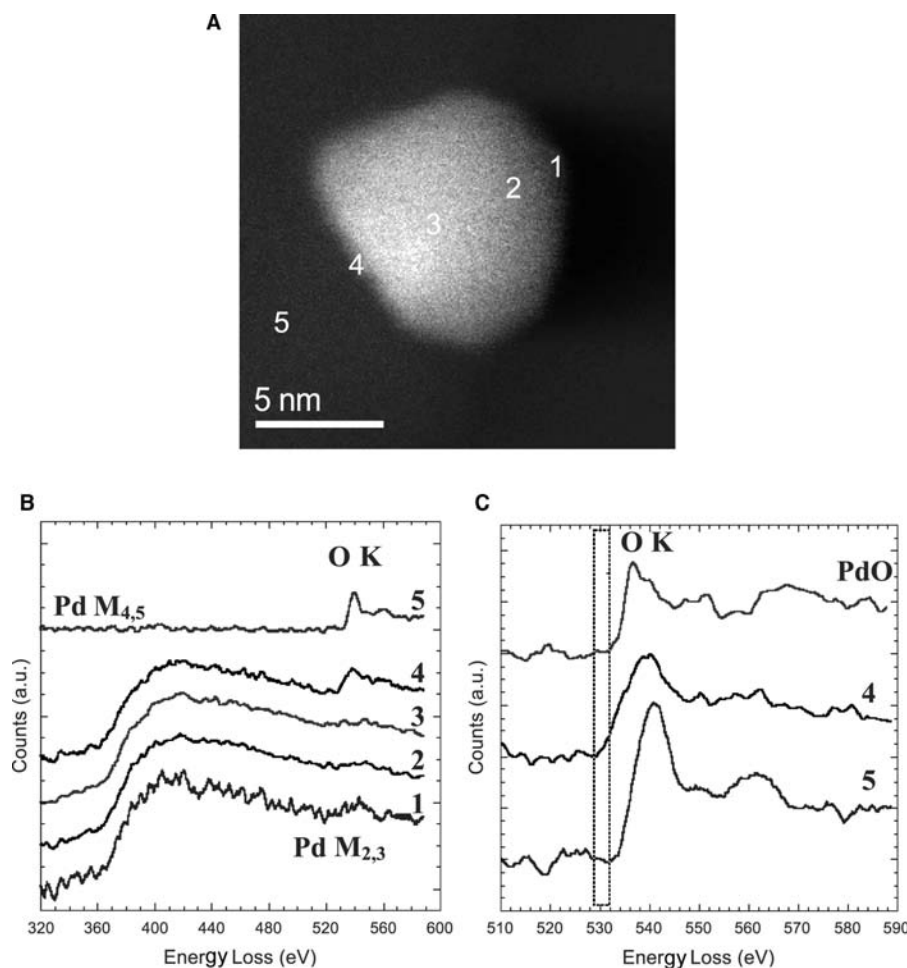


**Fig. 7** (A) Z-contrast image showing the locations of (B) EEL spectra acquired from a Pd particle in the Pd/ $\gamma$ -Al<sub>2</sub>O<sub>3</sub> catalyst reduced at 800°C, (C) oxygen K edges of the interface spectrum 4, the support spectrum 5, and a spectrum acquired from PdO.

Fig. 7A shows a high-magnification Z-contrast image of the catalyst reduced at 800°C. Here the particle sizes are much larger than in the previous two specimens. The spectra (1 to 3, Fig. 7B) acquired from the large particle indicate that it is metallic Pd. However, spectrum 4 is noticeably different from these three spectra. The onset of oxygen K edge (or Pd M<sub>2,3</sub> edges) exhibits a shift of  $3.6 \pm 0.6$  to 528.4 eV in the interface spectrum. These large chemical shifts are the same as have been observed in interfacial spectra acquired from the interfaces involving larger particles in the previous specimens. Fig. 7C shows only the oxygen K edges (Pd M<sub>2,3</sub> edges) of the interface spectrum along with reference spectra from PdO, together with  $\gamma$ -Al<sub>2</sub>O<sub>3</sub> (spectrum e) and a spectrum that is a combination of the PdO and  $\gamma$ -Al<sub>2</sub>O<sub>3</sub>. It can be seen that the full width at half maximum (FWHM) of the main peak in the spectrum 4 is larger than those of the reference spectra and it has a  $3.6 \pm 0.6$ -eV negative shift in the edge onset. The fact that the fine structure of the interface spectrum is similar to the addition of the PdO and  $\gamma$ -Al<sub>2</sub>O<sub>3</sub> spectra suggests that this shift is due to a downward shift in energy of the Pd M<sub>2,3</sub> edge.

The above results show that there exist chemical shifts in the interface spectra acquired from the interfaces between larger (>10 nm) Pd particles and the support. This may be because of an interaction between the metal clusters and support that is size dependent. The edge shifts are much larger than those in known Al–Pd alloys, which have been reported to be 1.7–1.9 eV for AlPd and 2.5 eV for Al<sub>3</sub>Pd,<sup>[18]</sup> indicating that the observed shifts are not due to the formation of an Al–Pd alloy. Furthermore, the shifts appear not to be due to the oxidation of Pd, as the Pd 3d<sub>5/2</sub> binding energy for metallic Pd is smaller than that for PdO.<sup>[19,20]</sup> This indicates that once oxidized, the Pd 3d<sub>5/2</sub> binding energy will shift to a higher energy—the reverse of what is observed. Moreover, electronic structure calculations of Pd–alumina interfaces also showed that the Pd–O interaction is relatively weak, while the Pd–Al interaction plays a more important role in metal–alumina bonding.<sup>[21]</sup>

The negative energy shift therefore suggests that the Pd particles are negatively charged. This may be because of the charge transfer from the support to the Pd particles during reduction; a mechanism that is consistent with general chemistry principles.<sup>[22]</sup>

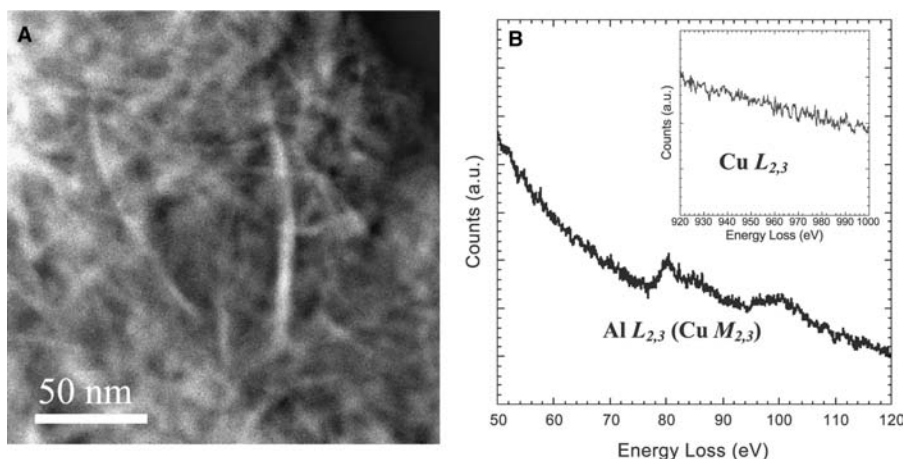


**Fig. 8** (A) Low-magnification Z-contrast image of the catalyst reduced at 250°C. (B) EEL spectra collected from different parts of the specimen.

It means that the support can act as an electron donor to the Pd particles, resulting in negatively charged Pd clusters.

### Cu/Al<sub>2</sub>O<sub>3</sub>

Gamma alumina powder with a BET surface area and pore volume of 160 m<sup>2</sup>/g, and 1.3 mL/g, respectively, was used as the catalyst support. A 10% aqueous slurry of the alumina and an aqueous solution as CuCl<sub>2</sub> · 2H<sub>2</sub>O to get 1.0 wt.% Cu loading were prepared. The slurry was heated (70°C for 30 min), filtered, and dried in an oven in air at 120°C overnight. This dried catalyst was reduced in a tube furnace by a stream of 4% H<sub>2</sub>/Ar (at a flow rate of 40 mL/min) for 2 hr at various temperatures (250°, 500°, and 800°C) (for more details, see Ref.<sup>[43]</sup>). Specimens were prepared for electron microscopy analysis by placing the powders on holey carbon-coated copper grids.

Fig. 8A shows low-magnification images taken from the Cu/γ-Al<sub>2</sub>O<sub>3</sub> catalyst reduced at 250°C. From the images we can see that the catalyst consists of mainly needlelike particles and some small irregular

particles. No separated copper species can be resolved from the Z-contrast images, although there exists a great Z difference between Cu and Al and O. Moreover EEL spectra collected from different particles do not show the expected copper L<sub>2,3</sub> edges (see the insert shown in Fig. 8B). As the Cu M<sub>2,3</sub> edges (onset: 74 eV) overlap with the Al L<sub>2,3</sub> edges (onset: 78 eV), we could not identify whether or not the EEL spectrum shown in Fig. 8B contains the copper peaks. However, energy dispersive X-ray spectroscopy (EDS) clearly shows the presence of copper in the catalyst. The fact that no obvious copper species can be directly resolved indicates that copper species is highly dispersed within the catalyst when reduced at 250°C.

Fig. 9 shows results obtained from the catalyst reduced at 500°C with two types of morphological particles, ringlike besides the needlelike particles. One interesting feature is that bulklike particles always coexist with ringlike particles, although they are not completely encapsulated by the ringlike particles. The Z-contrast image with several particles marked as “a” and “b” (ringlike), “c” (bulklike), and “d” (needlelike).

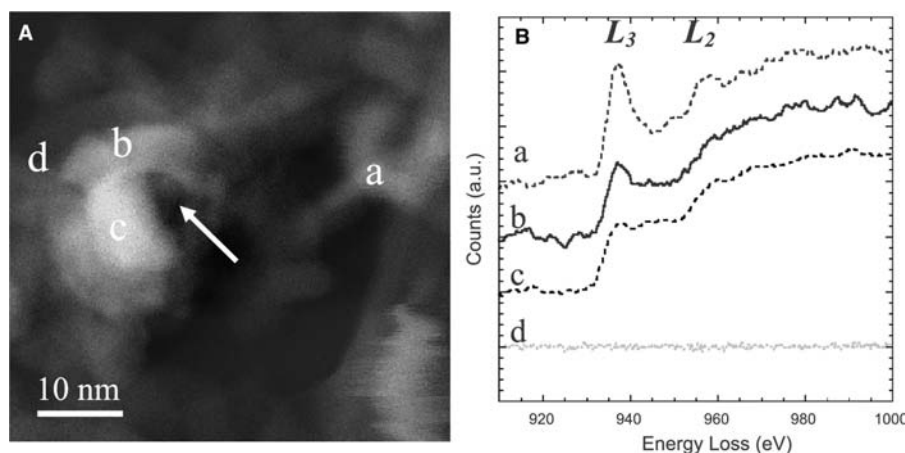


**Fig. 9** (A) Z-contrast images with ringlike feature of the catalyst reduced at 500°C, (B) corresponding EEL spectra.

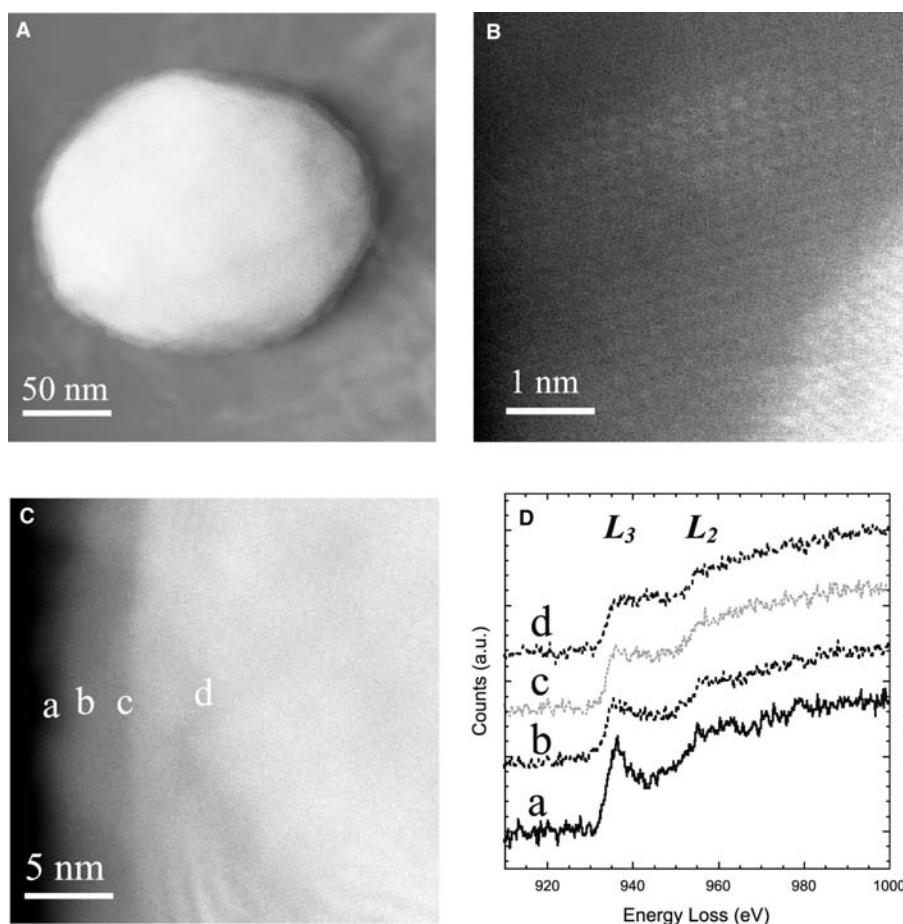


**Fig. 10** (A), (B), and (C) Z-contrast images and (D) EEL spectra from a particle having a core-shell structure formed when the catalyst was reduced at 800°C.

As the white-line intensity of the Cu  $L_{2,3}$  edges is inversely proportional to the occupancy of the Cu 3d orbitals, the intensity of the white lines gives an accurate indication of the copper valence. For metallic copper, the white lines are not present and the intensity in the spectrum corresponds to transitions to the relatively flat region of the density of states with d character. Upon oxidation, electrons are transferred from these orbits to oxygen atoms and the white-line intensity increases.<sup>[44–46]</sup> The white-line intensity can thus simply be used to fingerprint the oxidation state of the Cu atoms. Based on the  $L_3/L_2$  intensity ratios calculated from reference spectra, the CuO and Cu valence states can be obtained. Fig. 9B shows that a mixture of metallic Cu and  $\text{Cu}^{1+}$  is present in the metallic clusters. Copper species in the ringlike particles (spectra a, b) exists as  $\text{Cu}^{2+}$  state.

Several very large spherical particles were observed in the catalyst reduced at 800°C (Fig. 10A). The image clearly shows this particle has a core-shell structure (Fig. 10B). To identify the structure of this particle, an EELS profile across the particle was acquired. Fig. 10C shows the positions of the particle from which EEL spectra were collected and the corresponding EEL spectra are shown in Fig. 10D. Based on the

obtained  $L_3/L_2$  intensity ratios, spectra a and b are identified as  $\text{Cu}^{1+}$  (spectrum b may indicate a mixture between  $\text{Cu}^{1+}$  and metallic Cu) and spectrum c was acquired from an overlapped area of  $\text{Cu}^{1+}$  and metallic Cu species and spectrum d mainly metallic Cu.

For comparison, the catalyst prerduced at 250°C was also in situ heated at 550°C in the microscope and small particles are formed. These particles grow larger with increased heating times as shown in the image in Fig. 11A (which was acquired after the specimen had been kept at 550°C for about 40 min). Analysis of the EEL spectra (Fig. 11B) ( $L_3/L_2$  intensity ratios  $a = 2.44$  and  $b = 1.7$ ) indicates that the particle again contains metallic cores with a partially oxidized surface layer. This is an intriguing result as oxygen partial pressure in the microscope column is about  $5 \times 10^{-8}$  Pa during the experiment, i.e., it is a highly reducing atmosphere. This experiment clearly indicates that reduction at higher temperatures can result in partially oxidized states of copper.

The data demonstrate that no separated copper species were detected in the catalyst reduced below 250°C. Upon reduction at 500°C, the catalyst is reduced to  $\text{Cu}^{1+}$  and metallic Cu species, and the redistribution of these species occurs. At the temperatures higher



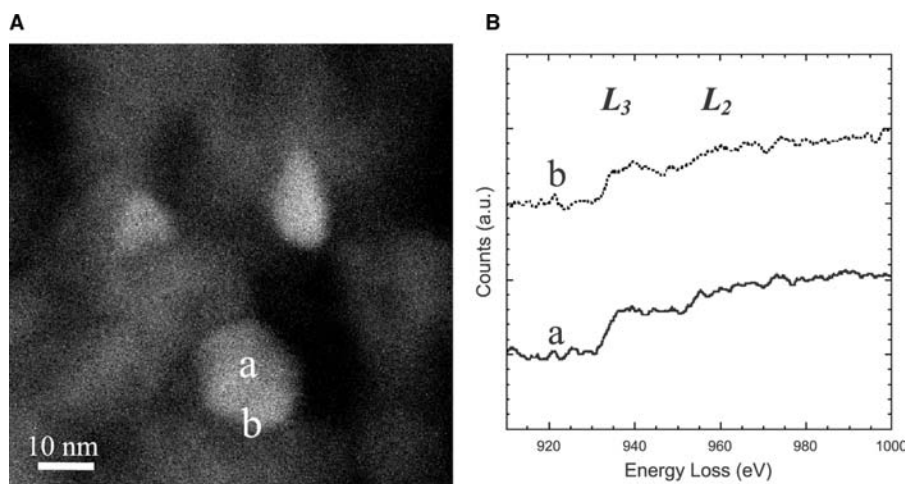


**Fig. 11** Z-contrast images taken from the prerduced copper catalyst at 250°C, (A) during in situ heating at 550°C K in the microscope for 40 min. (B) EEL spectra acquired from different parts are shown in (A).

than 800°C,  $\text{Cu}^{1+}$  species still exists in shells of some big spherical particles having core-shell structures with metallic Cu in the cores.

It should be noted that we did not avoid exposure of the catalyst to air after the catalysts had been reduced in the catalyst and specimen preparation procedures. Therefore, the possibility that the  $\text{Cu}^{1+}$  species in the reduced catalyst are formed because of the reoxidation of metallic Cu when the catalyst was exposed to air cannot be completely ruled out.<sup>[47]</sup> X-ray absorption near-edge spectroscopy (XANES) of  $\text{Cu}/\gamma\text{-Al}_2\text{O}_3$  shows that the catalyst did not change markedly on exposure to air at 21°C.<sup>[48]</sup> This means that for a similar system, the reduced metallic copper species did not react with the oxygen in air, and the in situ heating experiment indicated that upon reduction in the microscope at high temperatures, partially oxidized copper species are obtainable.

Based on these results, it is probable that the  $\text{Cu}^{1+}$  species in the reduced catalysts are formed by the interaction of copper species with the  $\gamma\text{-Al}_2\text{O}_3$  support. Such a mechanism is supported by the observations in several studies of the formation of a  $\text{Cu}_2\text{O}$  phase between metallic copper and alumina substrates.<sup>[45,49,50]</sup> It was found that the oxidation state of copper at the interface is nominally  $\text{Cu}^{1+}$ , i.e., the bonds at the interface being preferentially established between Cu–O rather than Cu–Al and the formation of  $\text{Cu}_2\text{O}$  at the interface is independent of oxygen partial pressure. Given the propensity of metallic Cu to form bonds with oxygen, it may well be that the oxide surface is formed from an interaction with the support oxide and acts as a protective skin against further oxidation when exposed to air afterward.

## PdO

PdO specimens were prepared by placing some powder (Aldrich) on holey carbon-coated molybdenum grids

directly. Fig. 12A, C, and E shows Z-contrast images of a PdO particle upon heating at the temperature of 300°C for about 15, 30, and 90 min, respectively. These images show that the morphology of the particle changed after the specimen has been kept at 300°C for 90 min. Shrinkage of the whole particle and also two dark areas, which suggests the formation of voids inside the particle, can be observed. Fig. 12B, D, and F shows corresponding EEL spectra. The features of the EEL spectra show that upon heating at the temperature of 300°C in the microscope, PdO has been reduced to metallic Pd from the surface. The whole PdO particle seems to have been reduced to metallic Pd when it has been heated for about 90 min.

The above in situ EELS studies directly indicate that PdO reduces upon being heated in the microscope via the shellwise manner as previously reported.<sup>[51,52]</sup> First, a metallic shell is formed, and then the whole particle is reduced to metallic Pd at further reduction. Moreover, it demonstrates that this atomic resolved spectroscopic technique is much suitable for the study of nanoparticles with core-shell structures.

It has been known that metal oxides may experience damage under electron beam irradiation.<sup>[53]</sup> Here, the behavior of the PdO phase under electron beam irradiation at room temperature was studied. Fig. 13A is a Z-contrast image taken from a PdO particle. A series of EEL spectra (Fig. 13B) was acquired by placing the electron probe at the position marked as 1 in Fig. 13A for different duration times of 3, 60, 180, and 240 sec, respectively. It shows that the intensity of the oxygen K ( $\text{Pd M}_{2,3}$ ) edges decreases after the sample has been irradiated by the probe for about 60 sec, which indicates that PdO started to be reduced. Once the irradiation time has reached about 240 sec, PdO has been reduced completely to metallic Pd. Fig. 13C shows the oxygen K and the Pd M edges for the corresponding irradiation times, and the changes in the near-edge fine-structure clearly show the reduction of PdO.

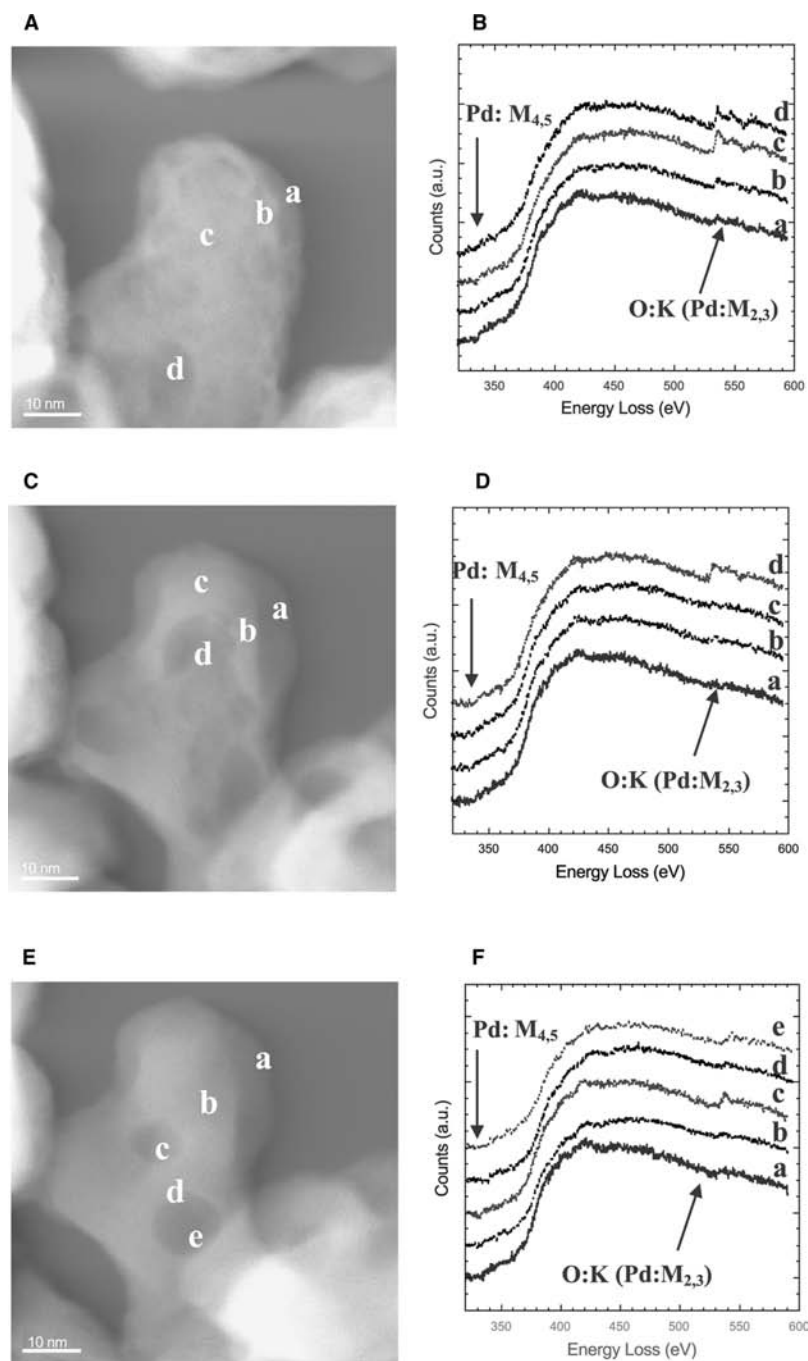


**Fig. 12** (A), (C), and (E) show Z-contrast images of a PdO particle upon heating at the temperature of 300°C for about 15, 30, and 90 min, respectively. (B), (D), and (F) are corresponding EEL spectra.

From the in situ EELS study of the PdO phase under a strong focused-beam irradiation, it is clear that if a relatively long dwelling time was used for EEL spectra collection, we could not obtain the “real” oxidation state of Pd in the PdO phase, as the oxide has been reduced. Hence, it is essential for high-resolution studies of PdO and other oxide catalyst systems to reduce the exposure of the system to the beam as much as possible.

Experimentally, imaging a particle at low magnification and acquiring a spectrum using a dwelling time

shorter than 10 sec, it is still possible to acquire an EEL spectrum characterizing Pd<sup>2+</sup>.

## CONCLUSION

In conclusion, the ability to observe the structure, characterize the composition, and map electronic structure changes at atomic resolution under various thermodynamic conditions provides an unparalleled capability to understand the effects that the interface and

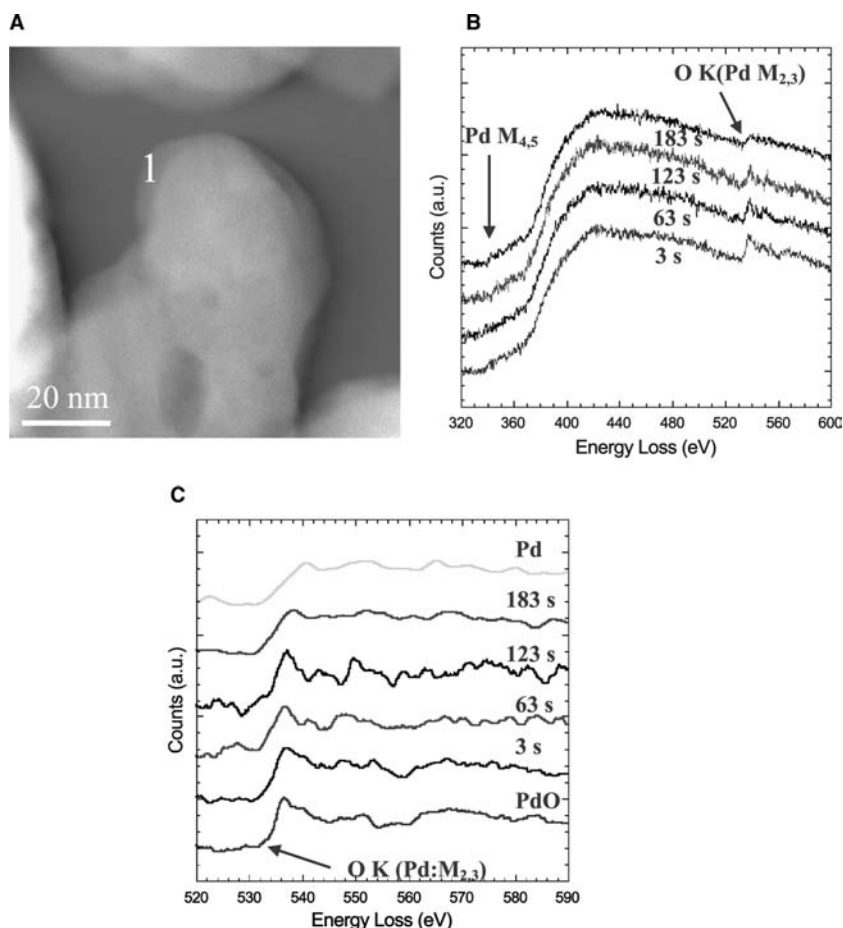


**Fig. 13** (A) Z-contrast images of a PdO particle. (B) EEL series spectra acquired from the position 1 after having been irradiated for different times. (C) Oxygen K and Pd M<sub>2,3</sub> edges of the profile spectra together with Pd and PdO spectra.

surface of metallic particles impose on the overall behavior of heterogeneous catalytic systems. We have shown that atomic resolution analysis is possible with a chemical and spatial sensitivity never achieved before.

Results from Pt/SiO<sub>2</sub> show that single layer of material on surface of the metal clusters as well as at the cluster support can be studied. Furthermore, it can be seen that the surface morphology of the Pt metal clusters and the heterointerface structure depends strongly on the catalyst preparation. Although the metal support interaction in these systems is considered weak, we could detect a few monolayers of reduced support oxide at the interface, which might indicate an even stronger reduction for higher metal-support interaction systems.

The studies of the Pd/ $\gamma$ -Al<sub>2</sub>O<sub>3</sub> catalysts, reduced at three different temperatures, show that small metallic Pd particles are formed when reduced at lower temperatures with no detectable alteration of the interfacial support oxide. With increasing reduction temperature, the Pd particles grow in size, but a strong interaction occurs only between the larger metallic Pd clusters and the alumina support, resulting in negatively charged Pd cluster. The overall interaction between the particles and the support can be correlated

with the activity of the catalyst in CO dissociation. The microstructure of a Cu/ $\gamma$ -Al<sub>2</sub>O<sub>3</sub> catalyst during its heating in H<sub>2</sub>/Ar has also been studied. Based on the results presented here, at low reduction temperatures, no detectable separated copper species are formed in the catalyst. At higher reduction temperatures, larger pure metallic Cu particles are formed in addition to smaller Cu particles that are partially covered by a Cu<sub>2</sub>O shell, which ultimately grows to form CuO<sub>2</sub> shells surrounding metallic Cu clusters. This indicates that the MSI results in an oxygen transfer from the support to the catalyst particles to fully oxidize the Cu clusters. In the future, the combination of Z-contrast imaging and EELS in correlation with conventional methods such as chemisorption or X-ray diffraction has the potential to provide an exceptional tool to investigate the new effects observed in these catalytic systems and achieve the long-term goal of explaining their origin.

## ACKNOWLEDGMENTS

This research was sponsored by ExxonMobil Research and Engineering Company, and Monsanto Company.

The experimental results were obtained on the JEOL 2010F operated by the Research Resources Center at UIC and funded by NSF under grant number DMR-9601796. The authors would like to thank S. Miseo and W. C. Horn from ExxonMobil Research and Engineering, NJ, and N. Nag from Engelhard Corporation for providing the catalyst samples.

## REFERENCES

- Bond, G.C. *Heterogeneous Catalysis: Principles and Applications*; Oxford Science Publications: Oxford, 1987.
- Datye, A.K.; Smith, D.J. The study of heterogeneous catalysts by high-resolution transmission electron-microscopy. *Catal. Rev.* **1992**, *34*, 129–178.
- Mergler, Y.J.; van Aalst, A.; van Delft, J.; Nieuwenhuys, B.E. Promoted Pt catalysts for automotive pollution control: characterization of Pt/SiO<sub>2</sub>, Pt/CoO<sub>x</sub>/SiO<sub>2</sub>, and Pt/MnO<sub>x</sub>/SiO<sub>2</sub> catalysts. *J. Catal.* **1996**, *161*, 310–318.
- Mojet, B.L.; Miller, J.T.; Ramaker, D.E.; Koningsberger, D.C. A new model describing the metal–support interaction in noble metal catalysts. *J. Catal.* **1999**, *186*, 373–386.
- Reuel, R.C.; Batholomew, C.H. Effects of support and dispersion on the CO hydrogenation activity/selectivity properties of cobalt. *J. Catal.* **1984**, *85*, 78–88.
- Vannice, M.A.; Poondi, D. The effect of metal–support interactions on the hydrogenation. *J. Catal.* **1997**, *169*, 166–175.
- Bernal, S.; Botana, F.J.; Calvino, J.J.; Cifredo, G.A.; Garcia, R.; Rodrigues-Izquierdo, J.M. HREM characterization of metal-catalysts supported on rare-earth-oxides–samarium oxide as support. *Ultramicroscopy* **1990**, *34*, 60.
- Pennycook, S.J.; Boatner, L.A. Chemically sensitive structure-imaging with a scanning-transmission electron-microscope. *Nature* **1986**, *366*, 565–566.
- Browning, N.D.; Chrisholm, M.F.; Pennycook, S.J. Atomic resolution chemical analysis using a scanning transmission electron microscope. *Nature* **1993**, *366*, 143–146.
- Nellist, P.D.; Pennycook, S.J. Direct imaging of the atomic configuration of ultradispersed catalysts. *Science* **1996**, *274*, 413–415.
- Disko, M.M.; Ahn, C.C.; Fultz, B. *Transmission Electron Energy Loss Spectrometry in Materials Science*; The Minerals, Metals & Materials Society: New York, 1992.
- Egerton, R.F. *Electron Energy Loss Spectroscopy in the Electron Microscope*; Plenum: New York, 1986.
- Taylor, K.C. Nitric-oxide catalysis in automotive exhaust systems. *Catal. Rev., Sci. Eng.* **1993**, *35* (4), 457–481.
- Poutsma, M.L.; Elek, L.F.; Ibarbia, P.A.; Risch, A.P.; Rabo, J.A. Selective formation of methanol from synthesis gas over palladium catalysts. *J. Catal.* **1978**, *52*, 157.
- Forzatti, P.; Tronconi, E.; Pasquon, I. Higher alcohol synthesis. *Catal. Rev., Sci. Eng.* **1991**, *33*, 109–123.
- Centi, G. Supported palladium catalysts in environmental catalytic technologies for gaseous emissions. *J. Mol. Catal., A* **2001**, *173* (1–2), 287–312.
- Almusaiteer, K.; Chuang, S.S.C. Dynamic behavior of adsorbed NO and CO under transient conditions on Pd/Al<sub>2</sub>O<sub>3</sub>. *J. Catal.* **1999**, *184* (1), 189–201.
- Thiemens, M.H.; Troglor, W.C. Nylon production: an unknown source of atmospheric nitrous oxide. *Science* **1999**, *251*, 932.
- Centi, G.; Perathoner, S. Nature of active species in copper-based catalysts and their chemistry of transformation of nitrogen-oxides. *Appl. Catal., A* **1995**, *132* (2), 179–259.
- Dandekar, A.; Vannice, M.A. Decomposition and reduction of N<sub>2</sub>O over copper catalysts. *Appl. Catal., B* **1999**, *22* (3), 179–200.
- Matsuoka, M.; Ju, W.; Takahashi, K.; Yamashita, H.; Anpo, M. Photocatalytic decomposition of N<sub>2</sub>O into N-2 and O-2 at 298 K on Cu(I) ion catalysts anchored onto various oxides. The effect of the coordination state of the Cu(I) ions on the photocatalytic reactivity. *J. Phys. Chem., B* **2000**, *104* (20), 4911–4915.
- Praliaud, H.; Mikhailenko, S.; Chajar, Z.; Primet, M. Surface and bulk properties of Cu–ZSM-5 and Cu/Al<sub>2</sub>O<sub>3</sub> solids during redox treatments. Correlation with the selective reduction of nitric oxide by hydrocarbons. *Appl. Catal., B* **1998**, *16* (4), 359–374.
- Radtke, F.; Koepfel, R.A.; Minardi, E.G.; Baiker, A. Catalytic reduction of nitrogen oxides by olefins in the presence of oxygen over copper/alumina: influence of copper loading and formation of byproducts. *J. Catal.* **1997**, *167* (1), 127–141.
- Chen, C.; Cheng, W.; Lin, S. Mechanism of CO formation in reverse water–gas shift reaction over Cu/Al<sub>2</sub>O<sub>3</sub> catalyst. *Catal. Letters* **2000**, *68* (1–2), 45–48.
- Choi, K.J.; Vannice, M.A. CO oxidation over Pd and Cu catalysts: IV. Prereduced Al<sub>2</sub>O<sub>3</sub>-supported copper. *J. Catal.* **1991**, *131*, 22.
- Szanyi, J.; Goodman, D.W. CO oxidation on a Cu[100] catalyst. *Catal. Letters* **1993**, *21* (1–2), 165–174.
- Trimm, D.L.; Önsan, Z.I. Onboard fuel conversion for hydrogen-fuel-cell-driven vehicles. *Catal. Rev.* **2001**, *43* (1–2), 31–84.
- Fleisch, T.H.; Hicks, R.F.; Bell, A.T. An XPS study of metal-support interactions on Pd/SiO<sub>2</sub> and Pd/La<sub>2</sub>O<sub>3</sub>. *J. Catal.* **1984**, *87*, 398.
- Haller, G.L.; Resasco, D.E. Metal-support interaction: Group VIII metals and reducible oxides. *Adv. Catal.* **1989**, *35*, 173.
- Baker, R.T.K.; Prestridge, E.B.; McVicker, G.B. The interaction of palladium with alumina and titanium oxide supports. *J. Catal.* **1984**, *89*, 422.
- Lomot, D.; Karpinski, Z. The effect of Pd/Al<sub>2</sub>O<sub>3</sub> pretreatment on catalytic activity in cyclopentane/deuterium exchange. *Catal. Letters* **2000**, *69* (1–3), 133–138.
- Browning, N.D.; James, E.M.; Kishida, K.; Arslan, I.; Buban, J.P.; Zaborac, J.A.; Pennycook, S.J.; Xin, Y.; Duscher, G. Investigating the atomic scale structure

- and chemistry of grain boundaries in high-T-c superconductors. *Rev. Adv. Mater. Sci.* **2000**, *1*, 1–26.
33. James, E.M.; Browning, N.D. Practical aspects of atomic resolution imaging and analysis in STEM. *Ultramicroscopy* **1999**, *78*, 125–139.
  34. James, E.M.; Browning, N.D.; Nicholls, A.W.; Kawasaki, M.; Xin, Y.; Stemmer, S. Demonstration of atomic resolution Z-contrast imaging by a JEOL JEM-2010F scanning transmission electron microscope. *J. Electron Microsc.* **1998**, *47* (6), 561–571.
  35. Nellist, P.D.; Pennycook, S.J. Incoherent imaging using dynamically scattered coherent electrons. *Ultramicroscopy* **1999**, *78*, 111–124.
  36. Cowley, J.M. Electron diffraction phenomena observed with a high resolution STEM instrument. *J. Electron Microsc. Tech.* **1986**, *3*, 25–44.
  37. Jesson, D.E.; Pennycook, S.J. Incoherent imaging of crystals using thermally scattered electrons. *Proc. R. Soc. Lond., A* **1995**, *449*, 273–293.
  38. Fertig, J.; Rose, H. Resolution and contrast of crystal-line objects in high-resolution scanning transmission electron microscopy. *Optik* **1981**, *59*, 407.
  39. Klie, R.F.; Ito, Y.; Stemmer, S.; Browning, N.D. Observation of oxygen vacancy ordering and segregation in perovskite oxides. *Ultramicroscopy* **2001**, *86*, 289–302.
  40. Batson, P.E. Simultaneous STEM imaging and electron energy-loss spectroscopy with atomic-column sensitivity. *Nature* **1993**, *366* (6457), 727–728.
  41. Kurmaev, E.Z.; Shamin, S.N.; Galakhov, V.R.; Kasko, I. Application of high energy resolved X-ray emission spectroscopy for monitoring of silicide formation in Co/SiO<sub>2</sub>/Si system. *Thin Solid Films* **1997**, *311*, 28–32.
  42. Sun, K.; Liu, J.; Nag, N.; Browning, N.D. Studying the metal–support interaction in Pd/ $\gamma$ -Al<sub>2</sub>O<sub>3</sub> catalysts by atomic-resolution imaging and spectroscopy. *Catal. Letters* **2002**, *84* (3–4), 193–199.
  43. Sun, K.; Liu, J.Y.; Browning, N.D. Direct atomic scale analysis of the distribution of Cu valence states in Cu/ $\gamma$ -Al<sub>2</sub>O<sub>3</sub> catalysts. *Appl. Catal., B* **2002**, *38* (4), 271–281.
  44. Leapman, R.D.; Gruncs, L.A.; Fejes, P.L. Study of the L<sub>23</sub> edges in the 3d transition metals and their oxides by electron-energy-loss spectroscopy with comparisons to theory. *Phys. Rev., B* **1982**, *26* (2), 614–635.
  45. Scheu, C.; Stein, W.; Ruhle, M. Electron energy-loss near-edge structure studies of a Cu/(1120)alpha-Al<sub>2</sub>O<sub>3</sub> interface. *Phys. Status Solidi, B* **2000**, *222* (1), 199–211.
  46. Long, N.J.; Fetford-Long, A.K. In-situ electron-beam-induced reduction of CuO: A study of phase transformations in cupric oxide. *Ultramicroscopy* **1986**, *20* (1–2), 151–159.
  47. Urban, J.; Sack-Kongehl, H.; Weiss, K. HREM studies of the structure and the oxidation process of copper clusters created by inert gas aggregation. *Z. Phys., D* **1996**, *36* (1), 73–83.
  48. Edelmann, A.; Schießer, W.; Vinek, H.; Jentys, A. Oxidation state of bimetallic PdCu catalysts during liquid phase nitrate reduction. *Catal. Letters* **2000**, *69* (1–2), 11–16.
  49. Dehm, G.; Scheu, C.; Möbus, G.; Brydson, R.; Rühle, M. Synthesis of analytical and high-resolution transmission electron microscopy to determine the interface structure of Cu/Al<sub>2</sub>O<sub>3</sub>. *Ultramicroscopy* **1997**, *67* (1–4), 207–217.
  50. Alber, U.; Müllejanm, H.; Ruhlem, M. Wetting of copper on alpha-Al<sub>2</sub>O<sub>3</sub> surfaces depending on the orientation and oxygen partial pressure. *Micron* **1999**, *30* (2), 101–108.
  51. Su, S.C.; Carstens, J.N.; Bell, A.T. A study of the dynamics of Pd oxidation and PdO reduction by H<sub>2</sub> and CH<sub>4</sub>. *J. Catal.* **1998**, *176*, 125–135.
  52. Crozier, P.A.; Sharma, R.; Datye, A.K. ASU electron microscopy workshop—in situ electron microscopy: introduction. *Microsc. Microanal.* **1998**, *4*, 278–285.
  53. Lyman, C.E.; Ferretti, A.; Long, N.J. *Analytical Electron Microscopy*; Williams, D.B., Joy, D.C., Eds.; San Francisco Press: San Francisco, 1984.

# Heterogeneous Catalytic Reactions by Mass Spectrometry

Steven M. Thornberg

Deborah E. Hunka

Sandia National Laboratories, Albuquerque, New Mexico, U.S.A.

## INTRODUCTION

One of the challenges facing chemists from a variety of disciplines (e.g., catalysis, biochemistry, materials science) is to determine the identity of unknowns, mechanisms and kinetics of reactions, and the nature and stability of intermediates. For example, understanding the mechanisms for catalytic reactions can allow for the design of custom catalysts. Powerful analytical tools (e.g., FT-IR, NMR, X-ray) are often used to study such things as surface states, adsorbed species, intermediates, and products.<sup>[1–4]</sup> Studying these reactions and chemical species in realistic chemical and physical environments representative of actual conditions is challenging.

Mass spectroscopy (MS) has been used for decades for compound identification as well as following the progress of reactions.<sup>[5–7]</sup> Commonly, mass spectral measurements are very rapid, making it ideal to provide information about intermediates while monitoring the consumption of reactants and the formation of products.

In this entry, Fourier transform ion cyclotron resonance mass spectroscopy (FT-ICR/MS) will be shown to be a powerful tool for investigating chemical reactions. FT-ICR/MS is capable of providing high-resolution mass values of molecules for compound identification. When monitoring reactions, relative abundances and mass values of reactants, intermediates, and products are recorded simultaneously as a function of time. Very good discussions on FT-ICR/MS theory are found elsewhere,<sup>[8,9]</sup> so only a brief summary will be presented here.

## FT-ICR/MS DESCRIPTION

High-resolution FT-ICR/MS provides the empirical formula of the molecule by measuring what is typically called the “exact mass.” Of course, some measurement uncertainty is associated with the measured mass but with parts-per-million resolution, very few combinations of atoms will add up to the measured mass. The number of combinations is usually further reduced

by incorporating some knowledge about the reaction to eliminate consideration of some atomic combinations when certain atoms are known to be absent in the reaction. A simple example is the identification of CO and N<sub>2</sub>. Both have a nominal mass of 28 Daltons (Da), but more precise calculations of the masses show CO to equal 27.99491 Da and nitrogen to equal 28.00615 Da (both rounded to five places past the decimal). Although the difference between the masses of CO and N<sub>2</sub> is only 0.01124 Da, the peaks are readily distinguishable at typical FT-ICR/MS resolutions.

Ions may be created in many ways including electron impact (EI) ionization, chemical ionization (CI), photoionization (PI), and others.<sup>[8,9]</sup> Each has advantages and disadvantages depending on the sample type and analysis needed. This entry will deal primarily with ionization as a result of laser ablation (discussed later).

A typical “rectangular” FT-ICR/MS trapping cell is shown in Fig. 1. In FT-ICR/MS, ions are “trapped” in a high-magnetic field between electrodes or end plates. Applying the appropriate positive or negative direct current (DC) voltage to the plate can trap either positive or negative ions. Although most FT-ICR/MS methods trap one or the other exclusively, trapping both positive and negative ions simultaneously is possible using RF trapping in a novel cell design.<sup>[10]</sup>

Trapped ions generally remain colinear with the static magnetic field and are repelled by the end electrodes. Many trap geometries have been used<sup>[10–17]</sup> including cylindrical, cylindrical with a concentric wire, segmented plates, and even an open cell using RF excitation to trap ions. Theoretical modeling of cell geometries and ion trajectories is typically performed using an ion simulation program such as SIMION.<sup>[11,15,17–26]</sup> In some instruments, two cells are connected together having a common electrode, or plate, between them. With this arrangement, ions can be trapped in either or both cells and transferred from one cell to the other. To detect the trapped ions, excitation waveforms are applied to the excitation plates causing the ions to assume orbits within the trap passing close to the detection plates (Fig. 2). As the ions pass by these plates, the oscillating potential is recorded as a function of time. The frequency of the orbit is related to



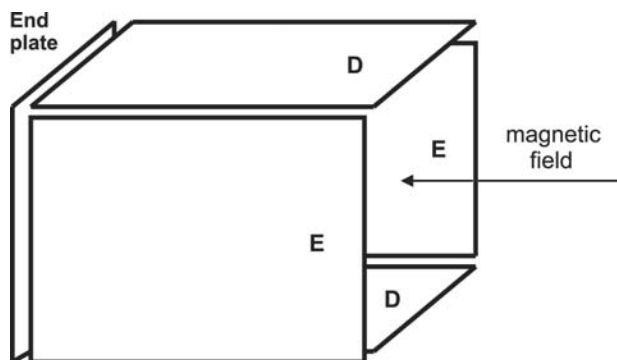


**Fig. 1** Example of an ion trap. Excitation plates (E) and detection plates (D) are shown. The right end plate is left out for clarity.

the mass-to-charge ratio of the molecular ion or fragment ion, so a Fourier transform<sup>[27]</sup> of that data set will yield data relatable to the mass-to-charge ratio.

In an FT-ICR experiment, the sequence and timing of events is programmed and executed. A sample timing diagram of an experimental sequence is shown in Fig. 3 and examples of other sequences specific to research applications are presented elsewhere.<sup>[16,28–31]</sup> Timing is very precise with submicrosecond accuracies possible with readily available data acquisition clocks. Many parameters can be varied in the experiment including event duration, timing between events, plate voltages, and excitation frequencies and magnitudes. As the parameter space is very large, learning the fundamentals of FT-ICR to understand the impact of changing the various parameters is very helpful.

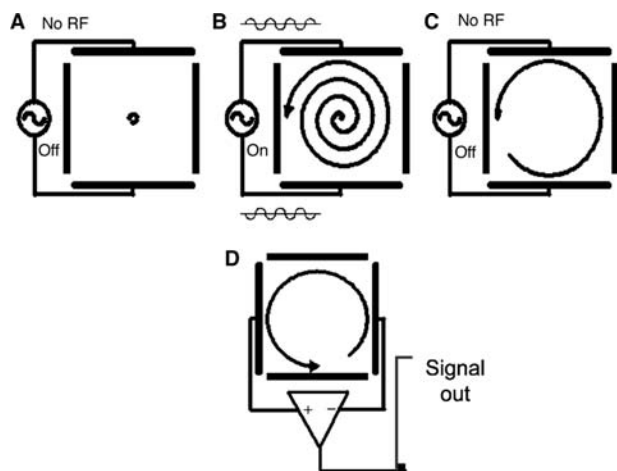


**Fig. 2** Schematic view of an ion trap looking down the direction of the magnetic field. Once ions are inside the trap and axialized to the center of the trap as in (A), the RF excitation waveform is applied to two excitation plates causing the orbital radius of the ions to increase (B). When the excitation is “off,” the ions continue to orbit near the plates (C) allowing detection (D).

Utilizing an ion-modeling program can also assist in determining desired parameters for a specific experiment.

Ions may be selectively excited and/or rejected from the trap by using a SWIFT (stored waveform inverse Fourier transform) waveform.<sup>[28,32]</sup> For SWIFT excitation, a waveform is calculated that contains the resonant frequencies of the mass-to-charge ratios of interest. If a large excitation voltage is used, the selected mass-to-charge ratio will be ejected from the trap. By careful application of this technique, the ion populations within the trap(s) can be tailored for the particular reaction being studied.

A great amount of research has been performed to optimize parameters once the ions are trapped in the cell. For example, resolution suffers greatly if ions are widely dispersed, so tightly organized “packets” of ions are desirable. When using ionization methods such as laser ablation, the ions produced exhibit a wide range of kinetic energy and spatial distributions, which is undesirable for FT-ICR/MS analyses. A wide spatial distribution makes excitation difficult because some of the coherency as well as some of the ions is lost. The ions that are detected will not be in a well-organized packet, which will decrease the resolution. Additionally, transfer of ions from one trap to another, in the case of a dual-cell instrument, is not very feasible as most of the ions are not aligned with the small conductance limit orifice between the cells. The high kinetic energies of these ablated molecules have been described as the major problem for trapping and detection.<sup>[17]</sup> In order to alleviate this problem, a process called axialization is employed to collect ions in the center of the trap before excitation starts. This process results in enhancements of both resolution and ion yield. In one example, the resolution for a peak was improved from 2400 without axialization to 144,000 with axialization.<sup>[33]</sup> Common methods for axializing ions include inserting a time delay prior to excitation to allow for the decay of excess energy as the ions orbit in the trap, adding an inert buffer gas so that collisions remove the energy, and RF axialization of the ions. Simply waiting for the energy to decay is not practical because of ion loss. Buffer gases are effective and easy to implement,<sup>[31,34,35]</sup> however, ramping the trapping plate potentials down linearly to potentials normally used for excitation has been shown to be effective, even without a buffer gas.<sup>[34]</sup> In one application, an ablation chamber impedes the spreading of the neutrals after ablation so they act as the buffer gas.<sup>[31]</sup> Radio-frequency axialization involves applying pulses of excitation voltages to various plates (depending on the trap geometry) to cause the ions to align themselves axially with the trap magnetic axis near the center of the trapping cell.<sup>[13,14,16,17,20,28,36–41]</sup> Further tests have shown that a combination of a buffer gas (e.g.,  $5 \times 10^{-7}$  Torr argon) with active RF axialization

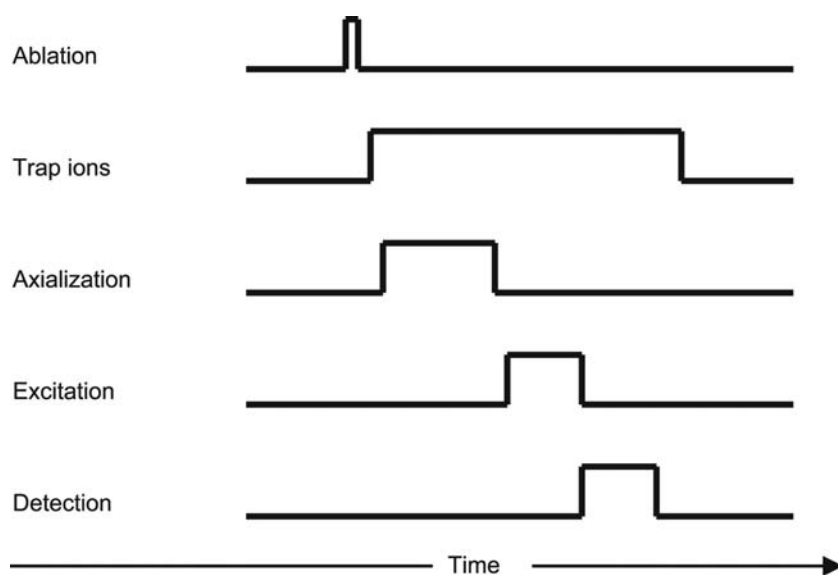


**Fig. 3** Sequence of events in a typical laser ablation FT-ICR/MS experiment.

has been shown effective.<sup>[33,42–45]</sup> Once an effective way to axialize the ions is realized, not only are better spectra obtained, but the ions can be re-excited and remeasured, provided that the ions are axialized between scans.<sup>[33]</sup>

Another way to improve peak resolution is to correct the data for the frequency drift of ions during data acquisition. By mathematically correcting the data using digital quadrature heterodyning, improvements in resolution of up to several orders of magnitude have been realized.<sup>[46,47]</sup>

Once a well-resolved peak is obtained, an accurate mass measurement is possible. Mass calibration is most accurate when known peaks exist within the spectra from which the frequency-to-mass relationship can be calculated.<sup>[48]</sup> One study compared the accuracy of two common frequency-to-mass algorithms showing calculated mass errors are very small (ppb).<sup>[49]</sup>

Accurate mass determination and ion manipulation make high-resolution FT-ICR/MS a powerful analytical tool to ascertain the empirical formula of a molecule and to study chemical reactions. In the next sections, the combination of laser ablation with FT-ICR/MS will be shown to be well suited for heterogeneous catalysis research.

## LASER ABLATION

Laser ablation is a technique commonly used to vaporize and ionize a solid sample in preparation for FT-ICR/MS analysis. A review of recent advances and applications of laser ablation shows widespread application and utility.<sup>[50]</sup> Parameters that can be varied to optimize ablation include wavelength, power density, and total energy deposited on the sample. Laser energy is focused on a sample causing the sample

to heat, bonds to be broken, and material to be ejected from the bulk via a short-lived plasma. The plume of sample vapors expands out from the surface of the solid in a shape that is proposed to be similar to a supersonic jet expansion.<sup>[51,52]</sup> Vapors produced are a combination of ions and neutrals, the distribution of which was estimated to be about 1% ions and 99% neutrals for ablated silicon carbide.<sup>[53]</sup>

Once ions have been produced, they need to get into the trap volume where they are stored for subsequent reactions and/or analyses. If the ablation occurs in<sup>[12]</sup> or close to the trap, the kinetic energies of the ions are used to transport the ions into the trap. However, if the distance to the trap is great or other barriers prevent the ions from freely entering the trap (e.g., the magnetic field), an ion guide is necessary to funnel the ions into the trap. Many schemes for ion transport have been contrived but typically potentials on electrodes are used to accelerate and decelerate ions, and RF excitation voltages are used to keep the ions traveling on a coherent path. SIMION (discussed previously) or some other ion trajectory modeling program can be used to aid in the design.<sup>[25]</sup> Theoretical and practical ion optics considerations for designing an ion guide are presented elsewhere.<sup>[54]</sup> Other developments include a ring ion guide,<sup>[55]</sup> an off-axis ion injection from a continuous ion source,<sup>[52]</sup> an RF octapole,<sup>[56]</sup> and a cylindrical ion guide with a concentric wire electrode.<sup>[21,22]</sup>

Trapping the ions is not a simple operation as ablated ions have kinetic energies ranging from less than one to hundreds of electron volts.<sup>[22,51,53,56–61]</sup> Some ablation sources are close to the trap eliminating the need for an ion guide, but that means the trap must be operated in such a mode as to effectively trap many ions. Even with ion guides to direct ions into the trap,

the timing and plate voltages must be carefully tuned. Most often, only a part of the ions ablated are ever retained in the trap because the slow, low-energy ions do not reach the trap before the trap voltages are applied, and/or the fast, high-energy ions either pass through the trap before the voltages are applied or simply cannot be trapped with the voltages used. The timing and trap voltage are set so as to maximize the number of ions of interest retained in the trap.

Varying the power density and wavelength applied to the sample can cause different fragmentation patterns. In a study using 1064-nm Nd-YAG laser excitation at powers of 200, 900, and 2000 MW/cm<sup>2</sup>, fragmentation patterns for several zeolites showed a dependence on power density.<sup>[29]</sup> These data showed that the higher energy density yielded larger fragments and clusters. By changing the wavelength of the ablating laser, the fragmenting and clustering patterns also change. Stöber silica was ablated using 193-, 248-, and 355-nm laser radiation, and the longer wavelengths generated larger fragments.<sup>[62]</sup>

Another type of laser ablation suitable for ionizing large molecules without extensive fragmentation is called matrix-assisted laser desorption ionization (MALDI).<sup>[63]</sup> In this technique, the molecules of interest are mixed with another molecule that strongly absorbs the laser energy. The strongly absorbing molecule will cause the large molecules to be ionized and released from the surface via energy transfer. This technique has been very successful in biological fields.<sup>[35,64–67]</sup>

## ZEOLITE/SILICA MASS SPECTROSCOPY RESEARCH

Mass spectroscopic studies of catalysts, in particular zeolites, commonly involve the use of gas chromatography/mass spectroscopy (GC/MS) to determine the efficiencies of various catalytic beds and reactant combinations.<sup>[68–70]</sup> In one recent application, product and reactant gases from a Parr reaction vessel were monitored in real-time using low-resolution MS.<sup>[71]</sup> However, relatively few studies of zeolites using high-resolution FT-ICR exist.<sup>[72]</sup>

Laser ablation of zeolites is difficult because the fragments ablated tend to undergo clustering and rearrangement. Clustering is not uncommon given the high-energy plasma environment during ablation and has been seen with other materials, e.g., dichlorosilane<sup>[73]</sup> and metals.<sup>[59,74,75]</sup> Several researchers have looked at the laser-ablated zeolites and silica powders and have observed SiO<sub>2</sub> clustering using time-of-flight/MS (TOF/MS)<sup>[76–79]</sup> and high-resolution FT-ICR/MS.<sup>[29,62,80]</sup> Fig. 4 shows a small portion of a typical mass spectrum showing the repeating peaks every 60 Da for laser-ablated beta zeolite. The distinctive “triplets” seen in a mass spectrum arise from the isotopic abundances of the naturally occurring isotopes of silicon<sup>[7]</sup> and provide a simple way to visually identify a silicon-containing compound.

Table 1 shows a summary of the experiments and the (SiO<sub>2</sub>)X<sup>−</sup> cluster series reported (others may have

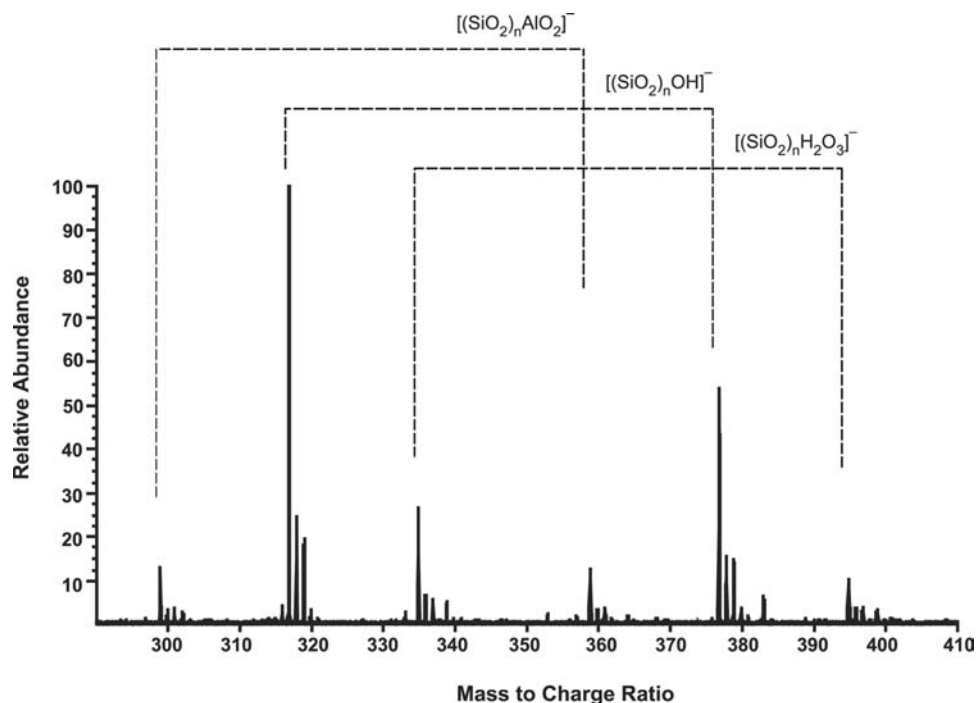


Fig. 4 Three series seen in the mass spectrum when beta zeolite is ionized using laser ablation.

**Table 1** Summary of silica and zeolite related experiments

Author (year)	Jeong (1995)	Lafargue (1996)	Lafargue (1998)	Thornberg (2002)	Xu (1997)	Xu (1998)	Zhao (1996)
Ref No.	[29]	[62]	[80]	[81]	[77]	[78]	[79]
Laser $\lambda$ (nm)	1064	193, 248, 355	355	10,600	308	308	308
Power density (MW/cm <sup>2</sup> )	1–2000	.1–10,000	6,000	625	40	15–50	15–50
MS	FT-ICR	FT-ICR	FT-ICR	FT-ICR	TOF	TOF	TOF
Sample	NaMOR, KLTL, and NaLTA zeolites	E2, Merk, and Stöber silica	Thermally treated Stöber silica	Propene, deuterated propene reacted with silica clusters from beta zeolite	Amorphous SiO <sub>2</sub> powder	MFI zeolite, MCM-41, ZSM-39, carbon-doped silica aerogel	Silica aerogel doped with carbon, Rhodamine-6G, fullerene, and carbon soot
(SiO <sub>2</sub> ) <sub>n</sub> <sup>-</sup>	Yes	Yes	Yes		Yes	Yes	Yes
(SiO <sub>2</sub> ) <sub>n</sub> H <sup>-</sup>					Yes	Yes	Yes
(SiO <sub>2</sub> ) <sub>n</sub> O <sup>-</sup>	Yes	Yes	Yes	Yes	Yes	Yes	Yes
(SiO <sub>2</sub> ) <sub>n</sub> HO <sup>-</sup>	Yes	Yes	Yes	Yes	Yes	Yes	Yes
(SiO <sub>2</sub> ) <sub>n</sub> H <sub>3</sub> O <sub>2</sub> <sup>-</sup>		Yes		Yes		Yes <sup>a</sup>	Yes <sup>a</sup>
Na(SiO <sub>2</sub> ) <sub>n</sub> O <sup>-</sup>	Yes						
K(SiO <sub>2</sub> ) <sub>n</sub> O <sup>-</sup>	Yes						
AlO(SiO <sub>2</sub> ) <sub>n</sub> O <sup>-</sup>	Yes			Yes			
(SiO <sub>2</sub> ) <sub>n</sub> Si <sup>-</sup>						Yes	
(SiO <sub>2</sub> ) <sub>n</sub> OSi <sup>-</sup>						Yes	
(SiO <sub>2</sub> ) <sub>n</sub> SiCH <sub>3</sub> <sup>-</sup>						Yes	

<sup>a</sup>A series (SiO<sub>2</sub>)<sub>n</sub> H<sub>x</sub>O<sub>2</sub><sup>-</sup> was identified but the experimental resolution was not adequate to identify *x*, the number of hydrogens.

been detected but not reported). The order of the atoms in the formula is not intended to imply any structural significance (e.g.,  $\text{HO}^-$  vs.  $\text{OH}^-$ ). Series that are in common include  $(\text{SiO}_2)_n \text{O}^-$  and  $(\text{SiO}_2)_n \text{HO}^-$ , regardless of the type of zeolite or silica, laser wavelength, and the power density used. As the formation of these series is independent of these variables, dissociation and recombination reactions in the ablation plasma must dominate their formation. Lafargue ejected ions such as  $[\text{SiO}_2]^-$  and  $[\text{OH}]^-$  from the trap that would act as building blocks for cluster formation in order to exclude the possibility of in-trap clustering. No changes in the spectra were found, implying clustering was complete prior to entering the trap.<sup>[62]</sup> Further confirmation of this is that the mass spectrum was the same for doped silica aerogels (carbon introduced through pyrolysis and Rhodamine-6G dopants) as with undoped silica aerogels.<sup>[79]</sup> However, if the silica aerogel was doped with fullerene or coke, the mass spectra showed peaks arising from the dopants only, and none from the host matrix (the silica aerogel). The table also shows a number of differences between the experiments. The  $[(\text{SiO}_2)_n \text{H}]^-$  series is only seen in the TOF/MS experiments and not in the FT-ICR/MS experiments. Zeolite ablation also yielded series containing the associated cation,  $\text{Na}^+$  and  $\text{K}^+$ , for the NaMOR (mordenite), KLTL (Linde Type L), and NaLTA (Linde Type A) zeolites. An aluminum-containing series,  $[\text{AlO}(\text{SiO}_2)_n \text{O}]^-$ , was also detected for some zeolites containing aluminum framework atoms. Additionally, the TOF/MS analysis of UV-ablated (308 nm) zeolites, silicalite-1 and MCM-41, showed series  $[(\text{SiO}_2)_n \text{Si}]^-$  and  $[(\text{SiO}_2)_n \text{OSi}]^-$  that were not reported for the IR-ablated (1064 nm) NaMOR, KLTL, and NaLTA zeolites analyzed by FT-ICR/MS.

Positive ion spectra of zeolites and silicas show no clustering with the primary cations identified as  $\text{Na}^+$ ,  $\text{Al}^+$ ,  $\text{K}^+$ ,  $\text{Si}^+$ ,  $\text{AlH}_2\text{O}^+$ , and  $\text{KAlO}_2^+$  for the NaMOR, KLTL, and NaLTL zeolites.<sup>[29]</sup> For Stöber silica, the primary cations detected were  $\text{Si}^+$  and  $[\text{SiOH}]^+$ .<sup>[62]</sup>

Negative ion mass spectra of ablated zeolites and silicas are typically very complex, having hundreds of peaks. Routinely, series of peaks can be addressed with a single descriptor (e.g.,  $[(\text{SiO}_2)_n]^-$ ) and an integer range that describes cluster sizes in the series (e.g.,  $n = 1-8$ ). However, when analyzing the mass spectrum peak-by-peak, a quick method for determining the identity of a peak's series is useful. One such method is to use the modulus equivalent, calculated using the repeating molecular mass as the base, for the experimentally measured mass of a peak.<sup>[81]</sup> For example, a peak occurring at mass 377 in a silica cluster series can be quickly categorized as part of the  $\text{OH}^-$  ligand series by computing the following:  $\text{Mod}_{60}(377) = 17$  (note: mass of  $\text{SiO}_2$  is 60 Da, and mass of  $\text{OH}$  is 17 Da). This works if each series is

separated from the other by at least 1 amu and if the ligands have a mass less than that of the cluster unit. This simple technique is readily applicable to other types of clusters (e.g., metal clusters) by simply changing the value for the base of the modulus calculation.

## CHEMISTRY INSIDE THE TRAP

Another powerful capability of FT-ICR/MS is the ability to perform chemical reactions within the ion trap between ions or between ions and neutrals. This ability has been used in many applications in many industries.<sup>[82]</sup> For example, the kinetics and mechanisms for reactions that formed explosive solid residues in dichlorosilane process exhaust stacks were identified for the semiconductor industry using FT-ICR/MS.<sup>[73]</sup> Knowing the details of the reaction made it possible to implement mitigation measures.

Few studies exist exploring the chemical reactions of zeolites, silicas, silicon dioxide, or clusters using FT-ICR/MS. In one study, hydrocarbons were desorbed from the surface of HMF1 zeolite ( $\text{Si}/\text{Al} = 55$ ) and characterized using FT-ICR/MS.<sup>[72]</sup> The zeolite was exposed to ethene for 30 min at different temperatures (298, 420, and 560 K). The ethene-treated zeolite samples were 1) introduced into the vacuum region of the trap causing the release of the hydrocarbons whereupon EI spectra were obtained; 2) laser ablated at 1064 nm but storing only positive ions, which favored hydrocarbons; and 3) chemically ionized using  $\text{Au}^+$ . Oligomerization of the ethene was evident for all three tests. In other FT-ICR/MS research, chemical reactions of  $\text{Si}_n^+$  clusters with ammonia<sup>[83]</sup> and ethylene<sup>[84]</sup> were studied.

In studies undertaken in our laboratory, alkenes (ethene, propene, 1-butene, and 2-butene) were reacted with silica clusters arising from laser ablation of beta zeolite.<sup>[81]</sup> As with the above examples of ablated zeolite and silica, dissociative and recombinative reactions in the ablation plasma are dominant for the beta zeolite as well. Fig. 5 shows the spectra obtained from the reaction of alkenes with silica clusters from beta zeolite. The attachment is seen primarily on the  $[(\text{SiO}_2)_n \text{HO}]^-$  series, but also seen to a lesser degree on the  $[\text{AlO}(\text{SiO}_2)_n \text{O}]^-$  series and not at all on the  $[(\text{SiO}_2)_n \text{H}_2\text{O}_3]^-$  series.

One criticism that must be addressed is the relevance of studying ion chemistry to bulk solution processes. A detailed comparison of gas phase vs. solution chemistry was published by Speranza.<sup>[85]</sup> One major difference is that solvation effects are not replicated in the gas phase work. Consequently, not all information obtained in the gas phase is directly applicable to solution chemistry. However, Speranza notes that gas phase chemistry provides “invaluable information

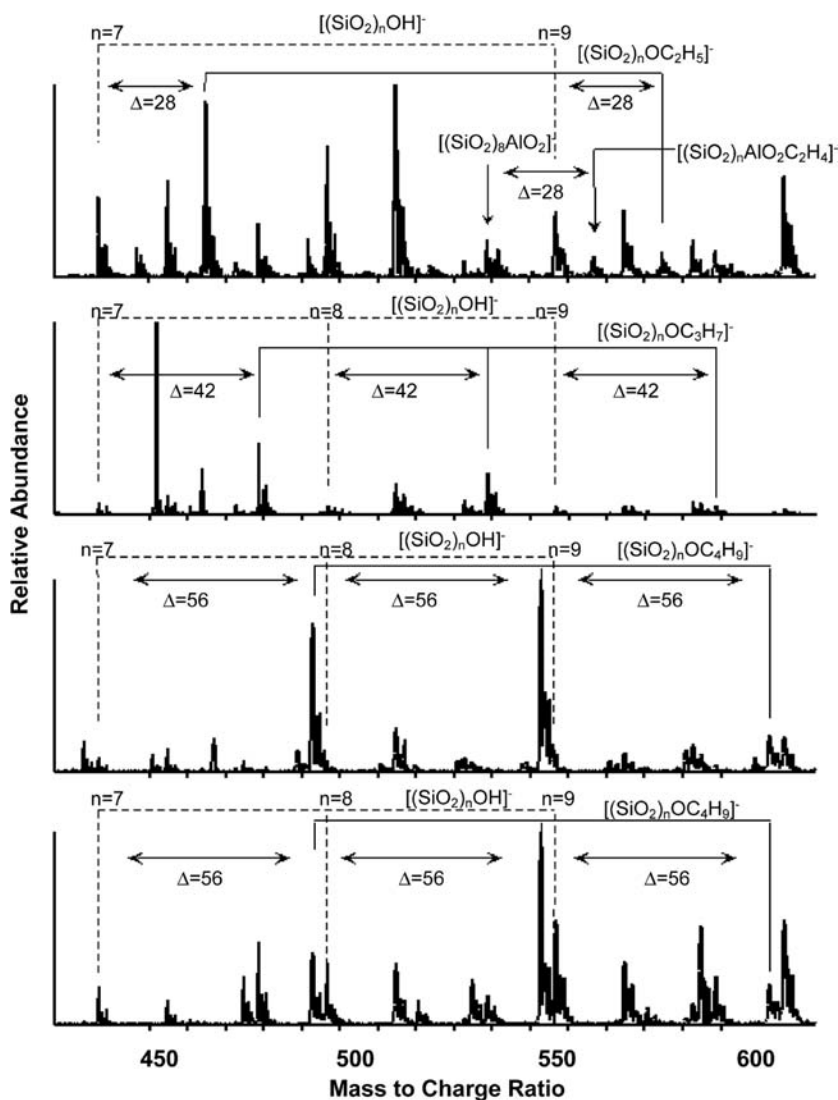


Fig. 5 Hydrocarbon attachment to zeolite fragments is shown above for (A) ethene, (B) propene, (C) 1-butene, and (D) 2-butene.

upon the nature and stability of the ionic intermediates involved in ionic reactions.” Thus FT-ICR/MS can provide very elusive information about reactions such as compound identification (reactants, intermediates, products), ion stabilities, mechanisms, etc.

## CONCLUSION

FT-ICR/MS is a powerful analytical tool capable of providing information about mechanisms, kinetics, intermediates, and compound identification in heterogeneous catalysis research. By simultaneously identifying reactants, intermediates, and products using the high-resolution mass determinations, detailed mechanisms can be determined. The ability to follow reactions as a function of time and measure all masses simultaneously provides vital information on relative abundances as reactions progress. Finally, new and

novel chemistries, e.g., cluster chemistry, can be explored easily and quickly with FT-ICR/MS.

## ACKNOWLEDGMENTS

The authors gratefully acknowledge the assistance of reviewers Russell L. Jarek and Nancy L. Jackson for their insightful comments. The authors also thank Jessica Sanders and Genoveva Buelna for their assistance in manuscript preparation.

## REFERENCES

1. van Santen, R. Theory, spectroscopy and kinetics of zeolite catalysed reactions. *Catal. Today* **1999**, *50* (3–4), 511–515.
2. Siffert, S.; Gaillard, L.; Su, B. Alkylation of benzene by propene on a series of beta zeolites: Toward a better



- understanding of the mechanisms. *J. Mol. Catal., A Chem.* **2000**, *153* (1–2), 267–279.
3. Thomas, J.M.; Thomas, W.J. *Principles and Practice of Heterogeneous Catalysis*; VCH Verlagsgesellschaft GmbH: Weinheim, 1997.
  4. Dumesic, J.A.; Rudd, D.F.; Aparicio, L.M.; Rekoske, J.E.; Trevino, A.A. *The Microkinetics of Heterogeneous Catalysis*; American Chemical Society: Washington, DC, 1993.
  5. Hill, H. *Introduction to Mass Spectrometry*; Spectroscopy in Education; Sadtler Research Laboratories: Philadelphia, 1966; 3 pp.
  6. McDowell, C.A. *Mass Spectrometry*; McGraw-Hill Series in Advanced Chemistry; McGraw-Hill: New York, 1963.
  7. McLafferty, F.W. *Interpretation of Mass Spectra*; University Science Books: Mill Valley, CA, 1980.
  8. Marshall, A.; Hendrickson, C.; Jackson, G. Fourier transform ion cyclotron resonance mass spectrometry: A primer. *Mass Spectrom. Rev.* **1998**, *17* (1), 1–35.
  9. Marshall, A.; Verdun, F. *Fourier Transforms in NMR, Optical and Mass Spectroscopy: A User's Handbook*; Elsevier: Amsterdam, 1989.
  10. Frankevich, V.; Zenobi, R. Dynamic ion trapping in a cylindrical open cell for Fourier transform ion cyclotron resonance mass spectrometry. *Int. J. Mass Spectrom.* **2001**, *207* (1–2), 57–67.
  11. Bruce, J.; Anderson, G.; Lin, C.; Gorshkov, M.; Rockwood, A.; Smith, R. A novel high-performance Fourier transform ion cyclotron resonance cell for improved biopolymer characterization. *J. Mass Spectrom.* **2000**, *35* (1), 85–94.
  12. Frankevich, V.; Zenobi, R. Flexible open-cell design for internal-source matrix-assisted laser desorption/ionization Fourier transform ion cyclotron resonance mass spectrometry. *Rapid Commun. Mass Spectrom.* **2001**, *15* (12), 979–985.
  13. Guan, S.; Marshall, A. Filar ion-cyclotron resonance ion-trap-spatially multiplexed dipolar and quadrupolar excitation for simultaneous ion axialization and detection. *Rev. Sci. Instrum.* **1995**, *66* (1), 63–66.
  14. Guan, S.; Xiang, X.; Marshall, A. Axial and radial ion cloud compression-coupling of magnetron and cyclotron motion to axial motion in a segmented cubic Fourier-transform ion-cyclotron resonance ion trap. *Int. J. Mass Spectrom. A* **1993**, *124* (1), 53–67.
  15. Jackson, G.; White, F.; Guan, S.; Marshall, A. Matrix-shimmed ion cyclotron resonance ion trap simultaneously optimized for excitation, detection, quadrupolar axialization, and trapping. *J. Am. Soc. Mass Spectrom.* **1999**, *10* (8), 759–769.
  16. Marto, J.; Guan, S.; Marshall, A. Wide-mass-range axialization for high-resolution Fourier-transform ion-cyclotron resonance mass-spectrometry of externally generated ions. *Rapid Commun. Mass Spectrom.* **1994**, *8* (8), 615–620.
  17. Solouki, T.; Gillig, K.; Russell, D. Detection of high-mass biomolecules in Fourier-transform ion-cyclotron resonance mass-spectrometry—Theoretical and experimental investigations. *Anal. Chem.* **1994**, *66* (9), 1583–1587.
  18. Danell, R.; Glish, G. A new approach for effecting surface-induced dissociation in an ion cyclotron resonance mass spectrometer: A modeling study. *J. Am. Soc. Mass Spectrom.* **2000**, *11* (12), 1107–1117.
  19. Gard, E.; Green, M.; Warren, H.; Camara, E.; He, F.; Penn, S.; Lebrilla, C. A dual vacuum chamber Fourier transform mass spectrometer with rapidly interchangeable FAB, MALDI and ESI sources: Electrospray results. *Int. J. Mass Spectrom. A* **1996**, *158*, 115–127.
  20. Jackson, G.; Canterbury, J.; Guan, S.; Marshall, A. Linearity and quadrupolarity of tetragonal and cylindrical penning traps of arbitrary length-to-width ratio. *J. Am. Soc. Mass Spectrom.* **1997**, *8* (3), 283–293.
  21. Limbach, P.; Marshall, A.; Wang, M. An electrostatic ion guide for efficient transmission of low-energy externally formed ions into a Fourier-transform ion-cyclotron resonance mass-spectrometer. *Int. J. Mass Spectrom. A* **1993**, *125* (2–3), 135–143.
  22. Marto, J.; Marshall, A.; May, M.; Limbach, P. Ion trajectories in an electrostatic ion guide for external ion-source Fourier-transform ion-cyclotron resonance mass-spectrometry. *J. Am. Soc. Mass Spectrom.* **1995**, *6* (10), 936–946.
  23. Oksman, P. A Fourier-transform time-of-flight mass-spectrometer—A SIMION calculation approach. *Int. J. Mass Spectrom. A* **1995**, *141* (1), 67–76.
  24. Pikver, R.; Past, J.; Subbi, J.; Aguraiuja, R.; Lippmaa, E. Some practical aspects of the acceleration–deceleration method for ion kinetic energy focusing in matrix-assisted laser desorption/ionization Fourier transform ion cyclotron resonance mass spectrometry. *Eur. J. Mass Spectrom.* **2000**, *6* (3), 289–297.
  25. Van Vaeck, L.; Van Espen, P.; Gijbels, R.; Baykut, G.; Laukien, F. A new electrostatic transfer line for improved transmission in Fourier transform laser microprobe mass spectrometry with external ion source. *Eur. J. Mass Spectrom.* **2000**, *6* (3), 277–287.
  26. Wilcox, B.; Hendrickson, C.; Marshall, A. Improved ion extraction from a linear octopole ion trap: SIMION analysis and experimental demonstration. *J. Am. Soc. Mass Spectrom.* **2002**, *13* (11), 1304–1312.
  27. Ramirez, R.W. *The Fft Fundamentals and Concepts*; Prentice Hall PTR: Englewood Cliffs, NJ, 1985.
  28. Guan, S.; Marshall, A. Stored waveform inverse Fourier transform (SWIFT) ion excitation in trapped-ion mass spectrometry: Theory and applications. *Int. J. Mass Spectrom. A* **1996**, *158*, 5–37.
  29. Jeong, S.; Fisher, K.; Howe, R.; Willett, G. Laser-ablation Fourier-transform mass-spectrometric study of zeolites. *Microporous Mater.* **1995**, *4* (6), 467–473.
  30. Li, G.; Kim, H.; Guan, S.; Marshall, A. Radiatively self-cooled penning-trapped electrons: A new way to make gas-phase negative ions from neutrals of low electron affinity. *J. Am. Chem. Soc.* **1997**, *119* (9), 2267–2272.
  31. Solouki, T.; Russell, D. Laser desorption studies of high mass biomolecules in Fourier-transform ion-cyclotron resonance mass-spectrometry. *Proc. Natl. Acad. Sci. U. S. A.* **1992**, *89* (13), 5701–5704.
  32. Guan, S.; Marshall, A. Stored wave-form inverse Fourier-transform axial excitation/ejection for quadrupole

- ion-trap mass-spectrometry. *Anal. Chem.* **1993**, *65* (9), 1288–1294.
33. Guan, S.; Kim, H.; Marshall, A.; Wahl, M.; Wood, T.; Xiang, X. Shrink-wrapping an ion cloud for high-performance Fourier-transform ion-cyclotron resonance mass-spectrometry. *Chem. Rev.* **1994**, *94* (8), 2161–2182.
  34. Gorshkov, M.; Masselon, C.; Anderson, G.; Udseth, H.; Harkewicz, R.; Smith, R. A dynamic ion cooling technique for FTICR mass spectrometry. *J. Am. Soc. Mass Spectrom.* **2001**, *12* (11), 1169–1173.
  35. McIver, R.; Li, Y.; Hunter, R. High-resolution laser-desorption mass-spectrometry of peptides and small proteins. *Proc. Natl. Acad. Sci. U. S. A.* **1994**, *91* (11), 4801–4805.
  36. Guan, S.; Marshall, A. Bloch equations applied to ion-cyclotron resonance spectroscopy—Broad-band interconversion between magnetron and cyclotron motion for ion axialization. *J. Chem. Phys.* **1993**, *98* (6), 4486–4493.
  37. Guan, S.; Marshall, A. Ion traps for Fourier-transform ion-cyclotron resonance mass-spectrometry—Principles and design of geometric and electric configurations. *Int. J. Mass Spectrom. A* **1995**, *146*, 261–296.
  38. Guan, S.; Marshall, A. Two-way conversation with a mass spectrometer: Non-destructive interactive mass spectrometry. *Anal. Chem.* **1997**, *69* (1), 1–4.
  39. Guan, S.; Marshall, A.; Wahl, M. Ms/Ms with high detection efficiency and mass resolving power for product ions in Fourier-transform ion-cyclotron resonance mass-spectrometry. *Anal. Chem.* **1994**, *66* (8), 1363–1367.
  40. Guan, S.; Wahl, M.; Marshall, A. Broad-band axialization in an ion-cyclotron resonance ion-trap. *J. Chem. Phys.* **1994**, *100* (9), 6137–6140.
  41. Xiang, X.; Guan, S.; Marshall, A. Simulated ion trajectory and induced signal in ion-cyclotron resonance ion traps. *J. Am. Soc. Mass Spectrom.* **1994**, *5* (4), 238–249.
  42. Guan, S.; Marshall, A. Multiply pulsed collision gas for ion axialization in Fourier-transform ion-cyclotron resonance mass-spectrometry. *Rapid Commun. Mass Spectrom.* **1993**, *7* (9), 857–860.
  43. Guan, S.; Wahl, M.; Wood, T.; Marshall, A. Enhanced mass resolving power, sensitivity, and selectivity in laser-desorption Fourier-transform ion-cyclotron resonance mass-spectrometry by ion axialization and cooling. *Anal. Chem.* **1993**, *65* (13), 1753–1757.
  44. Li, G.; Vining, V.; Guan, S.; Marshall, A. Laser-induced fluorescence of Ba<sup>+</sup> ions trapped and mass-selected in a Fourier transform ion cyclotron resonance mass spectrometer. *Rapid Commun. Mass Spectrom.* **1996**, *10* (14), 1850–1854.
  45. Schweikhard, L.; Guan, S.; Marshall, A. Quadrupolar excitation and collisional cooling for axialization and high-pressure trapping of ions in Fourier-transform ion-cyclotron resonance mass-spectrometry. *Int. J. Mass Spectrom. A* **1992**, *120* (1–2), 71–83.
  46. Guan, S.; Wahl, M.; Marshall, A. Elimination of frequency drift from Fourier-transform ion-cyclotron resonance mass-spectra by digital quadrature heterodyning—ultrahigh mass resolving power for laser-desorbed molecules. *Anal. Chem.* **1993**, *65* (24), 3647–3653.
  47. Pasatolic, L.; Huang, Y.; Guan, S.; Kim, H.; Marshall, A. Ultrahigh-resolution matrix-assisted laser-desorption ionization Fourier-transform ion-cyclotron resonance mass-spectra of peptides. *J. Mass Spectrom.* **1995**, *30* (6), 825–833.
  48. Beavis, R.; Chait, B. High-accuracy molecular mass determination of proteins using matrix-assisted laser desorption mass-spectrometry. *Anal. Chem.* **1990**, *62* (17), 1836–1840.
  49. Shi, S.; Drader, J.; Freitas, M.; Hendrickson, C.; Marshall, A. Comparison and interconversion of the two most common frequency-to-mass calibration functions for Fourier transform ion cyclotron resonance mass spectrometry. *Int. J. Mass Spectrom.* **2000**, *196*, 591–598.
  50. Russo, R.; Mao, X.; Liu, H.; Gonzalez, J.; Mao, S. Laser ablation in analytical chemistry—A review. *Talanta* **2002**, *57* (3), 425–451.
  51. Beavis, R.; Chait, B. Velocity distributions of intact high mass polypeptide molecule ions produced by matrix assisted laser desorption. *Chem. Phys. Lett.* **1991**, *181* (5), 479–484.
  52. Guan, S.; Pasatolic, L.; Marshall, A.; Xiang, X. Off-axis injection into an ICR ion-trap—A means for efficient capture of a continuous beam of externally generated ions. *Int. J. Mass Spectrom. A* **1994**, *139*, 75–86.
  53. Capano, M. Time-of-flight analysis of the plume dynamics of laser-ablated 6h-silicon carbide. *J. Appl. Phys.* **1995**, *78* (7), 4790–4792.
  54. Marshall, A.; Guan, S. Ion optics for Fourier-transform ion-cyclotron resonance mass-spectrometry. *Nucl. Instrum. A* **1995**, *363* (1–2), 397–405.
  55. Guan, S.; Marshall, A. Stacked-ring electrostatic ion guide. *J. Am. Soc. Mass Spectrom.* **1996**, *7* (1), 101–106.
  56. Huang, Y.; Guan, S.; Kim, H.; Marshall, A. Ion transport through a strong magnetic field gradient by Rf-only octapole ion guides. *Int. J. Mass Spectrom. A* **1996**, *152* (2–3), 121–133.
  57. Frankevich, V.; Zenobi, R. Deceleration of high-energy matrix-assisted laser desorption/ionization ions in an open cell for Fourier transform ion cyclotron resonance mass spectrometry. *Rapid Commun. Mass Spectrom.* **2001**, *15* (21), 2035–2040.
  58. Manson, J.; Renger, M.; Rubahn, H. Subthermal kinetic energy distributions of neutral atoms photodesorbed from Na cluster surfaces. *Phys. Lett. A* **1996**, *224* (1–2), 121–126.
  59. Dang, H.; Han, Z.; Dai, Z.; Qin, Q. Characterization of laser ablated species from a La–Ca–Mn–O target by angle- and time-resolved mass spectrometry. *Int. J. Mass Spectrom.* **1998**, *178* (3), 205–212.
  60. Tang, Y.; Qin, Q. Mass, velocity and angular distributions of the species ejected from laser ablation of LiCoO<sub>2</sub>. *Chem. Phys. Lett.* **2001**, *343* (5–6), 452–457.
  61. Varel, H.; Wahmer, M.; Rosenfeld, A.; Ashkenasi, D.; Campbell, E. Femtosecond laser ablation of sapphire: Time-of-flight analysis of ablation plume. *Appl. Surf. Sci.* **1998**, *129*, 128–133.
  62. Lafargue, P.; Gaumet, J.; Muller, J.; Labrosse, A. Laser ablation of silica: Study of induced clusters by Fourier

- transform ion cyclotron resonance mass spectrometry. *J. Mass Spectrom.* **1996**, *31* (6), 623–632.
63. Hendrickson, C.; Guan, S.; Marshall, A. Matrix-assisted laser desorption/ionization (MALDI) FT-ICR mass spectrometry in a 20 Tesla resistive. Magnet. Abs. Pap. ACS **1996**, *212*, 77-ANYL.
  64. Solouki, T.; Emmett, M.; Guan, S.; Marshall, A. Detection, number, and sequence location of sulfur-containing amino acids and disulfide bridges in peptides by ultrahigh-resolution MALDI FTICR mass spectrometry. *Anal. Chem.* **1997**, *69* (6), 1163–1168.
  65. Solouki, T.; Marto, J.; White, F.; Guan, S.; Marshall, A. Attomole biomolecule mass analysis by matrix-assisted laser-desorption ionization Fourier-transform ion-cyclotron resonance. *Anal. Chem.* **1995**, *67* (22), 4139–4144.
  66. Solouki, T.; Reinhold, B.; Costello, C.; O'Malley, M.; Guan, S.; Marshall, A. Matrix-assisted laser desorption/ionization (MALDI) FT-ICR mass spectrometry of oligosaccharides. *Biochemistry* **1996**, *35* (28), 21.
  67. Green, M.; Vestling, M.; Johnston, M.; Larsen, B. Distinguishing small molecular mass differences of proteins by mass spectrometry. *Anal. Biochem.* **1998**, *260* (2), 204–211.
  68. Wichterlova, B.; Cejka, J.; Zilkova, N. Selective synthesis of cumene and P-cymene over Al and Fe silicates with large and medium pore structures. *Microporous Mater.* **1996**, *6* (5–6), 405–414.
  69. He, Y.; Wang, R.; Liu, Y.; Chang, Y.; Wang, Y.; Xia, C.; Suo, J. Study on oxidation mechanism of cumene based on GC-MS analysis. *J. Mol. Catal., A Chem.* **2000**, *159* (1), 109–113.
  70. VanOrden, S.; Malcomson, M.; Buckner, S. Mechanistic and kinetic aspects of chemical ionization mass-spectrometry of polynuclear aromatic-hydrocarbons and their halogen-substituted analogs using oxidizing reagents—A gas-chromatographic mass-spectrometric and Fourier-transform mass-spectrometric study. *Anal. Chim. Acta* **1991**, *246* (1), 199–201.
  71. Buelna, G.; Jarek, R.; Thornberg, S.; Nenoff, T. Real-time study on cumene formation based on RGA/MS analysis. *J. Mol. Catal., A Chem.* **2003**, *198*.
  72. Jeong, S.; Fisher, K.; Howe, R.; Willett, G. A Fourier transform mass spectrometry study of ethene oligomers in HMF1 zeolite. *Microporous Mesoporous Mater.* **1998**, *22* (1–3), 369–377.
  73. Jarek, R.; Thornberg, S. Hazards of dichlorosilane exhaust deposits from the high-temperature oxide process as determined by FT-ICR mass spectrometry. *IEEE Trans. Semicond. Manuf.* **2001**, *14* (1), 20–25.
  74. Aubriet, F.; Maunit, B.; Courrier, B.; Muller, J. Studies of the chromium oxygenated cluster ions produced during the laser ablation of chromium oxides by laser ablation ionization Fourier transform ion cyclotron resonance mass spectrometry. *Rapid Commun. Mass Spectrom.* **1997**, *11* (14), 1596–1601.
  75. McCullough, S.; Gard, E.; Lebrilla, C. A 3t external source quadrupole Fourier-transform mass-spectrometer for ion molecule reactions and analysis. *Int. J. Mass Spectrom. A* **1991**, *107* (1), 91–102.
  76. Tanaka, K.; Ishigoh, K.; Nakata, R. Pulsed 266 nm laser desorption of aluminum, hydrogen, and water from H-Y zeolites studied with time-of-flight mass spectrometric analysis. *J. Phys. Chem.* **1996**, *100* (33), 14074–14080.
  77. Xu, C.; Wang, L.; Qian, S.; Zhao, L.; Wang, Z.; Li, Y. Laser-induced clustering dynamics of [(SiO<sub>2</sub>)(n)X] (–) from porous silica powders. *Chem. Phys. Lett.* **1997**, *281* (4–6), 426–430.
  78. Xu, C.; Long, Y.; Zhang, R.; Zhao, L.; Qian, S.; Li, Y. Laser ablation time-of-flight mass spectrometric probing of the surface states of SiO<sub>2</sub>-Based porous materials. *Appl. Phys. A-Mater. Sci. Process.* **1998**, *66* (1), 99–102.
  79. Zhao, L.; Zhu, L.; Liu, L.; Zhang, J.; Li, Y.; Zhang, B.; Shen, J.; Wang, J. Cluster generation from doped silica aerogels by XeCl excimer laser ablation. *Chem. Phys. Lett.* **1996**, *255* (1–3), 142–146.
  80. Lafargue, P.; Gaumet, J.; Muller, J. Analysis of thermally treated silica gel using Fourier transform ion cyclotron resonance mass spectrometry. *Chem. Phys. Lett.* **1998**, *288* (2–4), 494–498.
  81. Thornberg, S.M.; Jarek, R.L.; Abraham, I.C.; Buelna, G.; Nenoff, T.M. Energy Efficient Catalytic Reaction for Synthesis of Cumene: FT-ICR/MS. In *224th American Chemical Society Meeting, Boston, MA*; 2002.
  82. Moulijn, J.A., van Leeuwen, P.W.N.M., van Santen, R.A., Eds.; *Catalysis: An Integrated Approach to Homogeneous, Heterogeneous and Industrial Catalysis*; Elsevier Science Publishers B.V.: Amsterdam, 1993.
  83. Alford, J.; Laaksonen, R.; Smalley, R. Ammonia chemisorption studies on silicon cluster ions. *J. Chem. Phys.* **1991**, *94* (4), 2618–2630.
  84. Anderson, L.; Maruyama, S.; Smalley, R. Ethylene chemisorption on levitated silicon cluster ions—Evidence for the importance of annealing. *Chem. Phys. Lett.* **1991**, *176* (3–4), 348–354.
  85. Speranza, M. Gas-phase ion chemistry versus solution chemistry. *Int. J. Mass Spectrom. A* **1992**, *118*, 395–447.

# Heterogeneous Surfaces with Nanosized Channel Lattices

Lifeng Chi

Department of Physics, Westfälische Wilhelms-Universität Münster, Münster, Germany

Michael Gleiche

Steven Lenhart

Nan Lu

Physikalisches Institut, Westfälische Wilhelms-Universität Münster, Münster, Germany

## INTRODUCTION

Microscopically engineered surface structures allow the local control of physical properties such as adhesion, friction, and wettability. These properties are related both to molecular interactions and surface topology.<sup>[1,2]</sup> If the structure features are small enough—till nanometer scale—and well ordered, they may be applicable to electron confinement for light emission or novel electronic devices.<sup>[3]</sup> Commonly used techniques to create laterally structured surfaces are photolithography and electron beam lithography. Based on these structures, the feature size can be reduced down to 30 nm using soft lithography (microcontact printing).<sup>[4]</sup> A newly developed technique named as *Nanoimprinting* can be used to create surface features down to 5 nm over macroscopic areas.<sup>[5,6]</sup> Another way to create structured surface with nanometer-sized features is to introduce surface coating layers with defined structures, for instance, by using block copolymer lithography<sup>[7]</sup> and surface-induced patterning using polymers.<sup>[8,9]</sup>

Ultrathin organic films prepared, for example, with the *Langmuir-Blodgett* (LB) and the *self-assembly* (SA) techniques are other promising candidates for surface modification.<sup>[10]</sup> By using these techniques, organic molecules with great variability can be incorporated into organized assemblies in a well-controlled manner.<sup>[11]</sup> During the condensation procedure of molecules into densely packed states, lateral structures with adjustable shapes and arrangements may occur, which can be understood in terms of dipole-dipole interaction and line tension.<sup>[12,13]</sup> The size of structures induced in this way is usually in the range of 1–100  $\mu\text{m}$ , and many of them (especially the anisotropic structures) are randomly arranged. Less addressed are the nanoscopic structures created in these quasi two-dimensional systems, although the existence of “micelle” clusters in organic monolayers has been suggested even at the very early stage by Langmuir.<sup>[14]</sup> This was partially because of lack of high-resolution real space approach in detection methods for this size

range, until the advent of *scanning probe microscopy* (SPM) applicable on thin organic films.<sup>[15,16]</sup>

A different approach to create microscopically patterned surface is based on the wetting instability during LB transfer, as first reported by Riegler. By withdrawing a hydrophilic solid substrate (Si-wafer) through a monolayer-covered [*L*- $\alpha$ -dipalmitoyl-phosphatidylcholine (DPPC)] water surface under suitable conditions, parallel stripe patterns can be created.<sup>[17]</sup> The chemical formula of DPPC, the surface pressure/area, and the transfer position are shown in Fig. 1. The stripes are parallel to the three-phase contact line (air-substrate monolayer-covered water surface), i.e., perpendicular to the deposition direction, as shown schematically in Fig. 2. The width (several micrometers) and distance (1 to 100  $\mu\text{m}$ ) of stripes were found to be adjustable with the transfer speed, which varied from 0.5 to 4.0  $\mu\text{m sec}^{-1}$ .<sup>[18]</sup> At higher transfer speeds, the distance became smaller. Later on, Gleiche<sup>[19]</sup> observed the similar phenomena by using the same molecule but with another substrate (mica instead of Si-wafer) and at another speed range (from 83.3 to 333.3  $\mu\text{m sec}^{-1}$ ). The question of what the size (width) limitation of the stripes and the distance between them are if the monolayer is drawn further faster arises.

## REGULAR NANOCHANNEL LATTICE

To miniaturize the structure features, we first chose mica instead silicon as substrate to transfer DPPC monolayer. The freshly cleaved muscovite mica,  $\text{K}[\text{Al}_2(\text{Si}_3\text{AlO}_{10})(\text{OH})_2]$ , is negatively charged, while DPPC has a zwitterionic head group. The electrostatic interaction between DPPC and mica allows a very fast deposition of the DPPC monolayer. By increasing the transfer speed by 1–3 orders of magnitude compared with the previous works, the similar phenomenon as reported by Riegler was observed: the faster the transfer speed, the smaller the distance between the stripes. For instance, at a withdrawing speed of 33  $\mu\text{m sec}^{-1}$

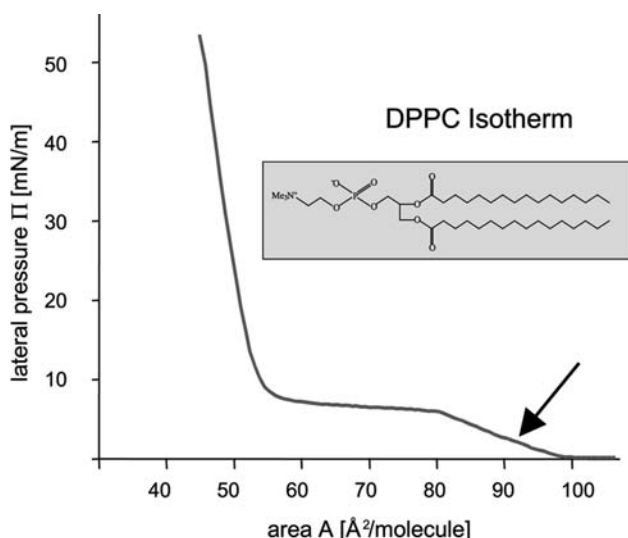


**Fig. 1** Chemical structure of *L*- $\alpha$ -dipalmitoyl-phosphatidylcholine (DPPC), surface pressure/area isotherm, and the transfer position (arrow).

(2 mm  $\text{min}^{-1}$ ), the average distance between the stripes is measured to be  $14.3 \pm 1.8 \mu\text{m}$  (as shown in Fig. 3), while it became  $4.0 \pm 0.32 \mu\text{m}$  at a withdrawing speed of  $167 \mu\text{m sec}^{-1}$  (10 mm  $\text{min}^{-1}$ ) and  $2.5 \pm 0.20 \mu\text{m}$  at a withdrawing speed of  $500 \mu\text{m sec}^{-1}$  (30 mm  $\text{min}^{-1}$ ).<sup>[19]</sup>

By further increasing the withdrawing speed till  $1000 \mu\text{m sec}^{-1}$  (60 mm  $\text{min}^{-1}$ ) and under a low surface packing density ( $85 \text{\AA}^2/\text{mol}$ ,  $3 \text{mN m}^{-1}$ ) in the pure liquid expanded (LE) phase, the stripe patterns become periodic!<sup>[20]</sup> Surface topography inspections with scanning force microscopy (SFM) reveal regular hydrophilic channels of about 200 nm in width, which are separated by hydrophobic stripes of monolayer with a latitude of about 800 nm as shown in Fig. 4. The height difference between the stripe region and the channel region is about one monolayer thick. Here the “stripe” is defined as the monolayer-covered region, and “channel” is defined as the uncovered

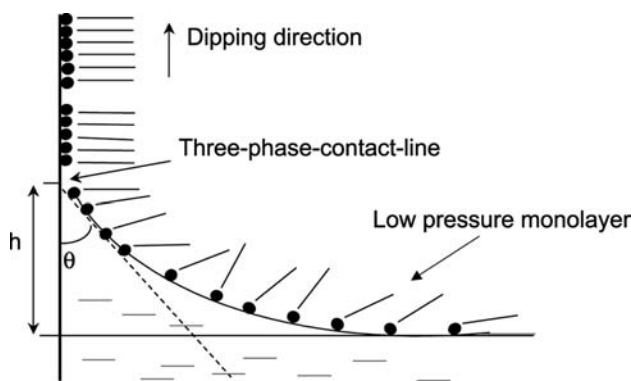


**Fig. 2** Schematic illustration of stripe formation as a result of substrate-induced condensation during Langmuir-Blodgett transfer of amphiphilic molecules in liquid-expanded phase.

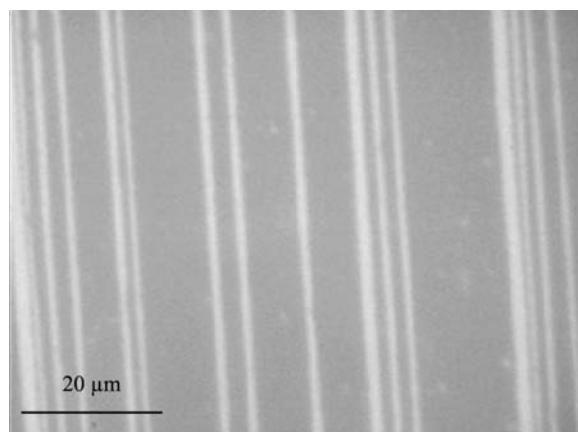


**Fig. 3** Optical micrograph of parallel stripe patterns on mica surface formed by transferring DPPC monolayer at a surface pressure of  $3.5 \text{mN m}^{-1}$  with a withdrawing speed of  $33 \mu\text{m sec}^{-1}$  (2 mm  $\text{min}^{-1}$ ). The surface was decorated with a thin silver layer to obtain optical contrast.

region. The tiniest channels obtained so far with this method exhibit a width of about 100 nm. This method is fast and reliable. For example, only 1 min is required to produce a sample of 6 cm in length fully covered with the channel lattice structure with a density of  $10,000 \text{cm}^{-1}$ . These structures can extend over the whole substrate areas, which can be easily visualized with an optical microscope by decorating the surface

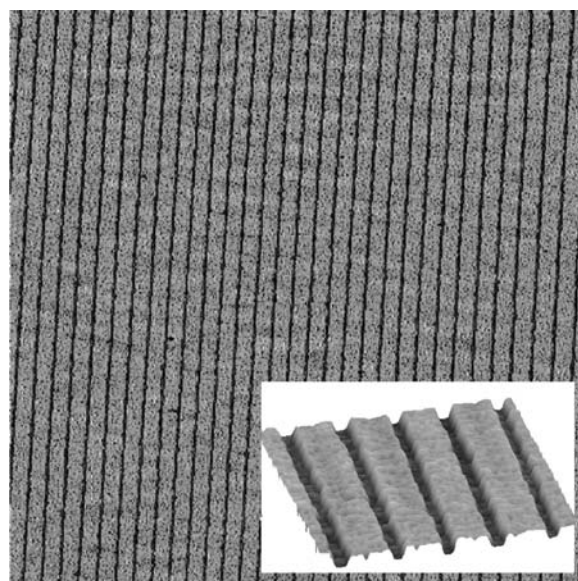


**Fig. 4** Scanning force microscopy images of the structured mica surface (image size  $30 \times 30 \mu\text{m}^2$ ). Scanning force microscopy inspections reveal channels of about 200 nm in width separated by stripes (800 nm wide) of a monomolecular DPPC film (inset,  $6 \times 6 \mu\text{m}^2$ ) imaging. The monolayer prepared on pure water was rapidly transferred with a speed of  $1000 \mu\text{m sec}^{-1}$  (60 mm  $\text{min}^{-1}$ ), at a lateral surface pressure of  $3.0 \text{mN m}^{-1}$  and constant temperature of  $22.5^\circ\text{C}$ .

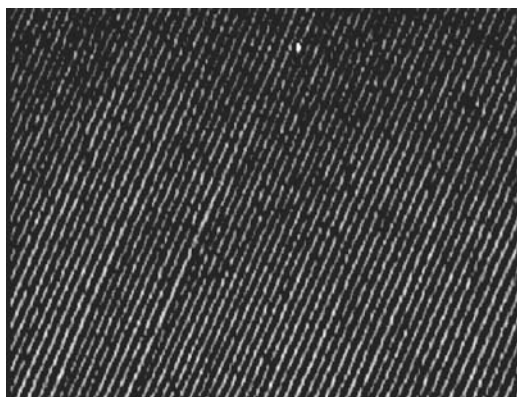


**Fig. 5** Optical micrograph representing the regular stripe structure over an area of  $80 \times 60 \mu\text{m}^2$ . The hydrophilic channels were filled with more silver coating (bright lines), whereas the DPPC monolayer depicted dark (less silver).

with a thin silver layer (2 nm). By thermal evaporation, silver atoms preferentially wetting the mica surface (channels) than the monolayer stripes results to an optical contrast,<sup>[21]</sup> as shown in Fig. 5.

The formation of the observed stripe structure can only take place during the molecular transfer of a low-pressure precursor film, which equals to a low surface packing density of molecules at the air/water interface. The transfer from such an isotropic liquid-expanded state (no predefined orientations) is normally not expected to build up close packed monolayers. In our experiments, the transfer ratio was approximately unity, but only 70–80% of the surface is actually covered. This corresponds well to the difference in the molecular packing density between the condensed phase on the mica surface and the expanded phase on the water surface. The mechanism of stripe formation differs from that which is responsible for striation in multilamellar liposomes at lower temperature (ripple phase)<sup>[22]</sup> or in simple granular mixtures<sup>[23]</sup> and in shrinking experiments.<sup>[24]</sup> Anisotropic domain growth at the air/water interface can also lead to stripe patterns, which can be understood in terms of a lowered line tension competing with dipole–dipole interactions.<sup>[25,26]</sup> There, however, the resulting structure has a random distribution of alignment. The transfer-induced regular structures differ remarkably from stripe phases of monolayers grown at the air/water interface because of their highly reproducible regularity and predefined orientation parallel to the three-phase contact line.

It turned out that slow monolayer deposition results in large distributions of channel distances and widths, whereas an improvement of the regularity is observed with increasing transfer velocity. The deposition speed always exhibits an upper limit where the molecular transfer ratio decreases, although the best quality of the stripe structure (i.e., homogeneous periodicity over the whole substrate) is obtained close to this critical

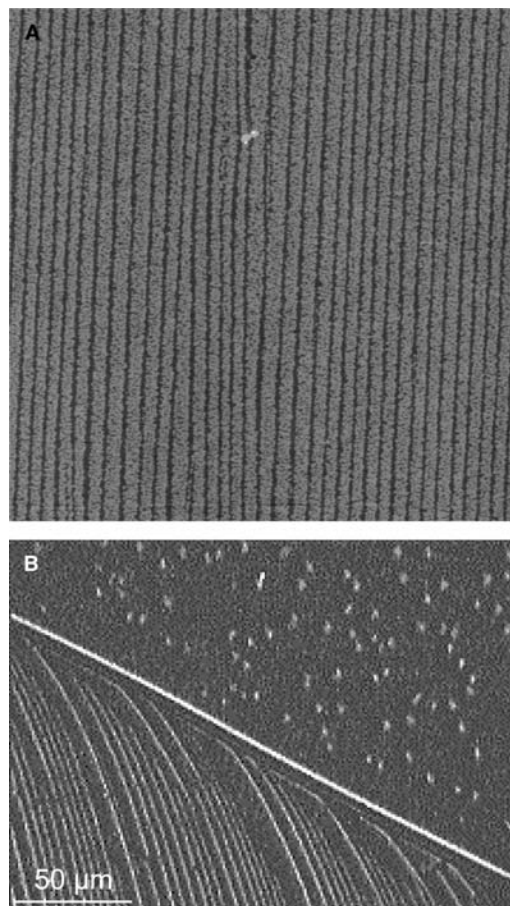


**Fig. 6** Defects which disturb the regularity of the stripe structure owing to A) contaminations and B) step edges on mica surface.

value at which the meniscus oscillation becomes self-synchronized. Besides the transfer speed, other experimental conditions such as temperature and molecular packing density (surface pressure) can also strongly influence the formation of the regular linear structure. With increased surface pressure (higher molecular packing density), even before the main phase transition, no stripe structure parallel to the contact line is observed.

Although the periodic structure can be found everywhere on the whole substrate, a variation in channel widths and distances must be taken into account, especially when contaminations at the air/water interface or defects on solid substrate exist, as shown in Fig. 6. To obtain long-range well-ordered structure, both DPPC solution and the LB trough have to be kept in clean conditions.

## MODELS OF WETTING INSTABILITY

Although the origin of the periodic structures by Langmuir wetting is not yet fully understood, there



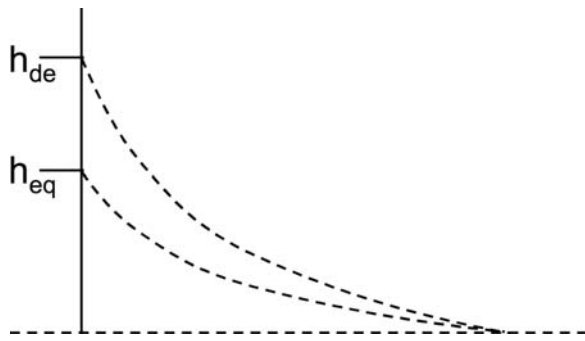


**Fig. 7** Increased water meniscus height dynamic wetting ( $h_{de}$ ) compared with static wetting ( $h_{eq}$ ).

are several possible qualitative explanations falling mainly into two categories. One is the oscillation of the meniscus height induced by the substrate-mediated condensation, and the other is the local pressure oscillation induced by the transfer.

It is well known that the contact line between the water and a hydrophilic solid substrate (three-phase contact line) normally exceeds the planar water surface up to a few millimeters by surface tension, thus defining the static equilibrium meniscus height, as shown in Fig. 7. This meniscus height  $h_{eq}$  can be expressed with liquid/vapor interfacial tension  $\gamma_{LV}$  and the contact angle  $\theta$ <sup>[27]</sup> as

$$h_{eq} = \sqrt{\frac{2\gamma_{LV}}{\rho g} (1 - \sin \theta)} \quad (1)$$

Combining with the well-known Young's equation

$$\gamma_{SV} = \gamma_{SL} + \gamma_{LV} \cos \theta \quad (2)$$

where  $\gamma_{SV}$  and  $\gamma_{SL}$  are the solid/vapor interfacial tension and solid/liquid interfacial tension, respectively, we obtain

$$h_{eq} = \sqrt{\frac{2}{\rho g} \sqrt{\gamma_{LV} - \sqrt{\gamma_{LV}^2 - (\gamma_{SV} - \gamma_{SL})^2}}} \quad (3)$$

When the water surface is covered with a monolayer of amphiphilic molecules, the molecules can condense on the substrate surface at the three-phase contact line generated as a result of the interaction between the molecules and the substrate. This is named substrate-mediated condensation (SMC).<sup>[28]</sup> Depending on experimental conditions, the condensation can either lead to a straight-line, liquid-condensed stripes and/or regular fingers. A decreased meniscus height was experimentally observed in the course of SMC. According to Eq. (3), this can be understood as a consequence of a decreased solid/vapor interfacial

tension ( $\gamma_{SV}$ ). On the other hand, the meniscus height will tend to exceed its equilibrium value by a continuous substrate motion (upstroke) building up a dynamic equilibrium height  $h_{de}$  (Fig. 4). If the water surface is covered with a monolayer, the increased meniscus height will result in an accelerated molecular adsorption on the substrate.<sup>[18]</sup> Thus the dynamic behavior of the meniscus height is governed by two counteracting processes, which lead to an oscillation of the meniscus and result in regions of transfer depletion normal to the dipping direction. It turned out in our work that the oscillation of the meniscus height may become periodic in the submicrometer size under certain controllable conditions. A similar stick-jump motion of the meniscus has been found in monolayers of dimethyldioctadecylammonium bromide, resulting in a striped surface, but on a significantly larger length scale ( $\sim 1$  mm).<sup>[29]</sup>

The second possible explanation for the generation of the periodic structures is the local surface pressure (or local surface density) oscillation instead of the meniscus oscillation. With a strong molecule–substrate interaction, molecules change their state very fast from the liquid-expanded phase to the liquid-condensed phase at the three-phase contact line. This process must result in a sudden area reduction of the molecules. Because of the viscoelasticity of monolayers, which is related to the cohesive energy of the molecules, the molecules very near the contact line will be drawn up and condensed on the substrate resulting in a low surface pressure region because of the reduced molecular density. With a very fast transfer speed, the surface pressure can even reach zero resulting in a transfer depletion. Such kind of low surface density regions were observed previously around the liquid-condensed domains, when monolayers were transferred in the two-phase coexistence region.<sup>[30]</sup> After the depletion, the surface pressure will increase because the molecules will accumulate again at the contact line by the moving barrier, thus resulting in a local surface pressure oscillation.

If the second model is correct, one should expect a temperature dependence of the periodicity because the cohesive energy of molecules depends on the temperature. At increased temperature, the cohesive energy gets reduced. Thus the periodicity should decrease with increased temperature. This is indeed observed experimentally. However, it is not possible to distinguish this mechanism from the first one solely in terms of temperature effect because the condensation will also depend on the temperature (or more precisely, the temperature gradient).

Just recently, some theoretical groups proposed models to understand such a periodic oscillation during LB deposition. One of the groups used a model for one-dimensional flow of a van der Waals fluid near

its discontinuous liquid–gas transition. They found that steady-state flow becomes unstable in the vicinity of the phase transition, and this instability can lead to complex periodic density oscillations at some suitable chosen sets of parameters.<sup>[31]</sup> It is expected that, combining theoretical and experimental works, one will be able to quantitatively understand the mechanism of the periodic pattern formation during LB transfer in the near future.

### ROBUST STRUCTURED SILICON SURFACES WITH CHEMICAL CONTRAST

Compared with other lithography methods, the Langmuir–Blodgett-based preparation for regular stripe patterns shows its advantages of low costs, fast, and an unusual ratio between the width and the length of the linear structures (the line width can be as small as 100 nm, and the length is, in principle, unlimited). However, with the combination of DPPC as the organic monolayer and mica as the substrate, the structure is not stable to be inserted into aqueous solutions and polar solvents. This restricts the application potential of such patterned surfaces as a template in many cases, especially for biological systems.

The concept was then expanded to form stable patterns on silicon surfaces based on template-directed self-assembly. First, line patterns with regular channels and stripes composed of DPPC on silicon surfaces were fabricated with the Langmuir–Blodgett technique, as previously performed on mica surfaces. By using oxygen plasma-treated silicon surface, similar periodic monolayer stripes are obtained.<sup>[32]</sup> The optimal transfer conditions of DPPC on silicon surfaces are different from that of DPPC on mica surfaces because of the different surface properties between silicon and mica. The periodicity can be as small as 410 nm, as shown in Fig. 8, and even below.

The stripe structure of DPPC on silicon is not stable when the slide is inserted into an aqueous solution as well as in the case of DPPC on mica. To obtain stable and functional structures on silicon surfaces, we used the DPPC-structured silicon surface as a mask for the pattern transfer. A general approach is based on the substitution of the stripes and channels by two different molecules (e.g., silane 1 and silane 2), which are terminated with different chemical groups, according to different purposes. Thus a robust, covalently bound, chemically active and selective patterned surface can be fabricated onto the silicon surface. Finally, a line pattern of covalently bonded molecules with selective functionality replaced the physically adsorbed DPPC structure. In Fig. 9, the basic strategy for fabricating chemically functionalized surfaces by using DPPC stripes as a template is illustrated schematically.

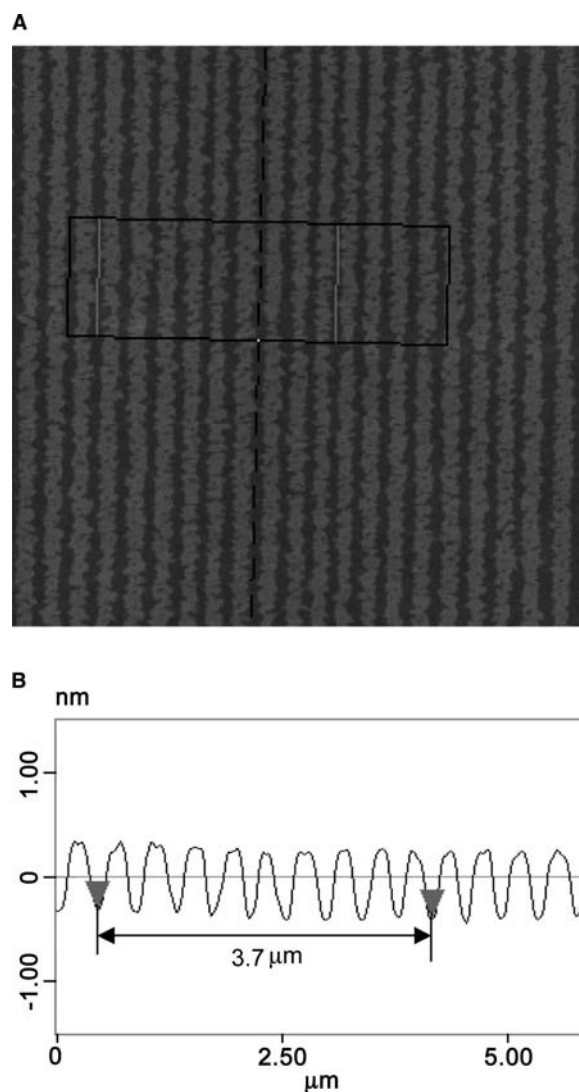


**Fig. 8** Scanning force microscopy image of DPPC stripe structure on silicon surface (left,  $9.2 \times 9.2 \mu\text{m}^2$ ). The periodicity can be as small as 410 nm, as indicated by the section analysis (right) which is taken from the black frame of the left image.

The second step of the general approach depicted in Fig. 9 is realized using 3-Aminopropyltrimethoxysilane to silanize in the channels selectively. After that, the DPPC stripes were washed away (step 3 depicted in Fig. 9). Fig. 10 shows a topographical image of the resulting surface obtained by SFM. The topography of the striped structure has been inverted. New stripes consisting of silane molecules formed in the original channel areas. The height of the new stripes is around 0.4 nm in the case of amino silane, which is smaller than the theoretical length of the chain. This kind of height anomaly is quite common when measuring soft organic films in tapping mode.<sup>[33]</sup> Furthermore, functional surfaces can be fabricated according to the schematic procedure depicted in Fig. 9. The original

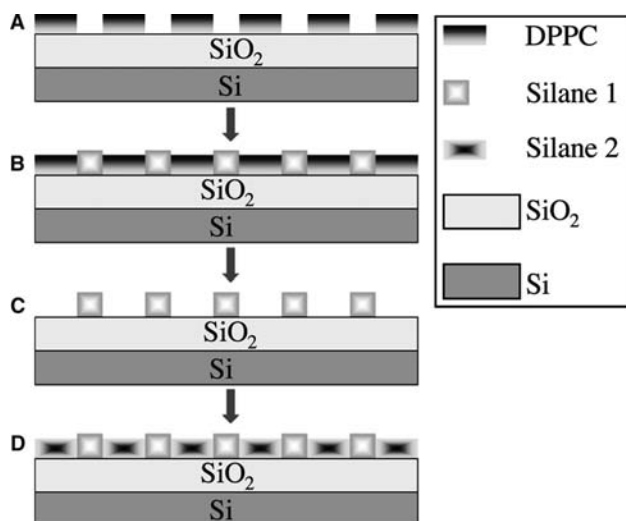


**Fig. 9** Schematic illustration for the pattern transfer based on the self-assembly on silicon surfaces. A) Step 1: DPPC stripes on the silicon surface. B) Step 2: Silane molecule 1 silanizing the channel area of the silicon surface. C) Step 3: Silane molecule 2 on the previous stripe regions after removing the DPPC stripes. D) Step 4: Structured silicon surface with silane molecules 1 and 2. Source: From Ref.<sup>[32]</sup>.

DPPC-occupied areas were silanized with octadecyltrichlorosilane (OTS) (step 4). The resulting surface structure is shown in Fig. 10B. Because of defects in the original DPPC stripes, the conversion to an OTS layer is not complete. The holes in the stripe structure are converted to the amino silane in the first step and represent imperfections in the forming OTS layer. The images were taken in the contact mode presenting the lateral force signal (friction). The contrast in lateral force is induced by the two different functional groups ( $-\text{NH}_2$  and  $-\text{CH}_3$ ).

### ANISOTROPIC WETTING AND TEMPLATE-DIRECTED SELF-ASSEMBLY

Structured surfaces of this type introduce an anisotropic wetting behavior. Thus the shape of the liquid/solid phase boundary can be strongly influenced.<sup>[34]</sup> For example, the contact line of a droplet placed on a chemically structured surface of this type may deviate from that of an ideal circle<sup>[35]</sup> and becomes orientation-dependent. This deviation depends on the ratio of the droplet radius and the lateral size of the heterogeneity and is more prominent for comparatively small droplets. In the following wetting study, we use phenyloctane as a wetting liquid. The inset of Fig. 11 shows a droplet of phenyloctane on the structured surface (diameter of about 65  $\mu\text{m}$ ). A polygonal contact line parallel to the channels can

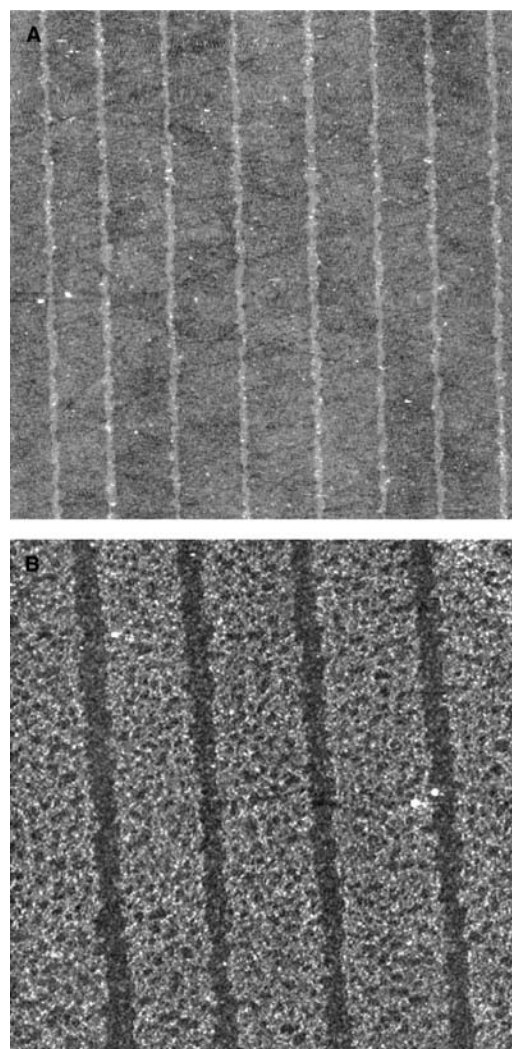


**Fig. 10** Scanning force microscopy images of the silanized silicon surfaces with two different silane molecules. A) SFM topographical image of 3-Aminopropyltrimethoxysilane assembled in the DPPC-free channels (image size  $10 \times 10 \mu\text{m}^2$ ). B) SFM lateral force image of 3-Aminopropyltrimethoxysilane and octadecyltrichlorosilane (OTS) assembled in the DPPC channels and stripes (image size  $5 \times 5 \mu\text{m}^2$ ).

be clearly observed. Furthermore, the drying process of this small droplet is found to be surface structure-dependent. Its phase boundary parallel to the stripe direction retracts discontinuously, jumping abruptly from channel to channel during the evaporation, whereas the contact line perpendicular to the stripe direction shows a smooth and continuous motion. Fig. 11 represents an optical micrograph of a temporal sequence gradually revealing the surface chemical structure periodicity. As a consequence, the droplet diameter perpendicular to the channel direction is determined by an even multitude of the lattice period. The dotted lines in Fig. 11 were drawn tangentially to



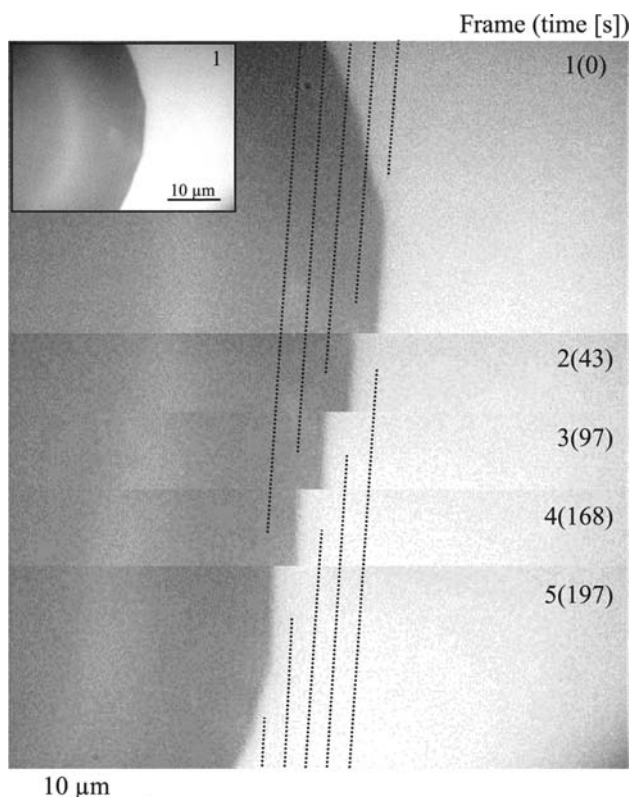


**Fig. 11** Time-dependent discontinuous dewetting observed with an optical microscope during the evaporation of a phenyloctane droplet. A superposition of five frames showing the retracting perimeter (from top to bottom, elapsed time in parenthesis). The contact line of the droplet parallel to the stripe direction shows a stick-jump behavior moving from channel to channel (periodicity  $\sim 1.6\ \mu\text{m}$ ). The dotted lines indicate the orientation of the underlying structure. The inset represents the initial state ( $32 \times 43\ \mu\text{m}^2$ ). Source: From Ref.<sup>[36]</sup>.

the droplet perimeter emphasizing the underlying structure. This discontinuous dewetting process is evoked by the regular change in the interfacial tension when moving across the surface. Considering a periodically striped surface with alternating chemical properties, an anisotropic wetting behavior is expected as discussed in Ref.<sup>[36]</sup>.

In recent years, template-directed selective deposition/self-assembly of nanosized materials and functional molecules received more and more scientific and technological interests. The structured mica or silicon surfaces reported here offer an easily prepared template with wetting or chemical selectivity. The different wetting behavior of the hydrophilic channels and the hydrophobic stripes can be used to deposit materials along the channels, for example, by an anisotropic surface structure-determined wetting/dewetting process<sup>[37,38]</sup> by using capillary (capillary filling)<sup>[39,40]</sup> and electrostatic forces.<sup>[41]</sup>

## Template-Directed Self-Assembly from Organic Solutions

Surface structure-dependent adsorption is obtained by applying a suitable solution carrying the material to deposit. Water-insoluble gold clusters ( $\text{Au}_{55}$ ) stabilized by an organic ligand shell<sup>[42]</sup> dissolved in 1-phenyloctane were dropped on the structured mica surface and investigated with SFM after the drop has been removed. Exposed to this solvent, the DPPC film remains absolutely stable. Channels filled with  $\text{Au}_{55}$  clusters are shown in Fig. 12. Cluster aggregates were lined up in the channels. Their height (almost 4 nm) corresponds to a single cluster diameter, but some of them exceed the monolayer height. In contrast, the DPPC monolayer is virtually not wetted and only a few cluster aggregates are located on the top of the stripe region resulting in a nearly perfect selective adsorption. With the same method, CdSe nanoclusters (5 nm) trapped by an organic ligand layer<sup>[43]</sup> were successfully selective-deposited in the channel region, as shown in Fig. 13. In the inset, an image of scanning near-field microscopy (SNOM) is shown which was taken with a home-designed setup and newly developed scanning tip<sup>[44]</sup> at the excitation wavelength of 488 nm (emission maximum of the 5-nm CdSe cluster is 532 nm). Thus we obtain the clear evidence that the channel regions are really filled with nanoclusters as wished.

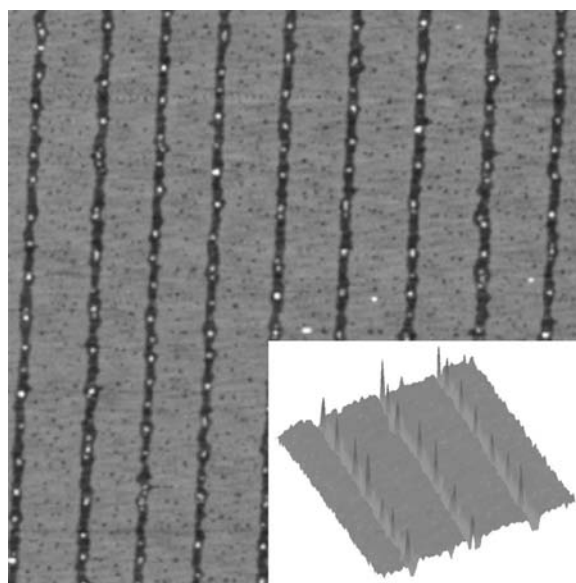


**Fig. 12** Scanning force microscopy image of selective deposited  $\text{Au}_{55}$  cluster aggregates (bright spots) aligned along the channels (image size  $11 \times 11\ \mu\text{m}^2$ ) on mica surface. The spikes depicted in the three-dimensional rendered selected area (inset) indicate that the height of many cluster aggregates is about one cluster layer thick, although lateral size of the aggregates is larger than the individual clusters (image size  $5 \times 5\ \mu\text{m}^2$ ).

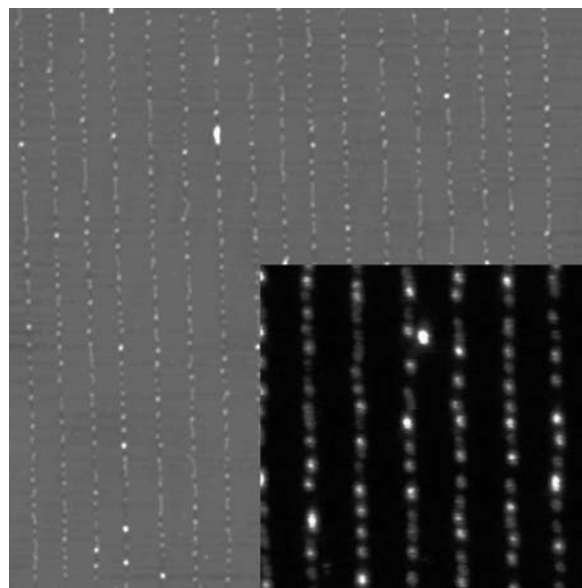


**Fig. 13** Scanning force microscopy image of selective deposited CdSe cluster aggregates (bright spots) aligned along the channels (image size  $10 \times 10 \mu\text{m}^2$ ) on silicon surface. The SNOM image (image size  $5 \times 5 \mu\text{m}^2$ ) shown in the inset indicates that the channels are filled evidently with CdSe nanoclusters.

### Template-Directed Self-Assembly from Aqueous Solutions

On the other hand, water-soluble  $\text{Au}_{55}$  cluster can be deposited selectively onto the robust structured silicon surfaces with chemical contrast. Here  $\text{Au}_{55}$  clusters were solved in water and dropped on the structured silicon surface. Experimental results indicate that  $\text{Au}_{55}$  clusters stay in separated form and assemble selectively on the stripes formed by the amino silane as shown in Fig. 14. The density of the cluster is higher than that assembled on the DPPC-structured mica surface and the clusters.

### Template-Directed Self-Assembly from Gas Phases

A small droplet of  $\text{FeCl}_3$  solution was brought onto the structured mica surface and evaporated slowly. The  $\text{FeCl}_3$  molecules condensing from the vapor phase were selectively adsorbed in the channels, whereas the monolayer stripes were not coated. In some places, three-dimensional crystals growing along the channel direction are observed, as shown in Fig. 15. The SFM images were taken at positions several centimeters away from the droplet of  $\text{FeCl}_3$ . Channels filled with paramagnetic  $\text{FeCl}_3$  molecules provide a contrast in magnetic force microscopy (MFM).<sup>[20]</sup>

Thermally evaporating silver in high-vacuum ( $1 \times 10^{-6}$  Torr) silver atoms will first selectively wet

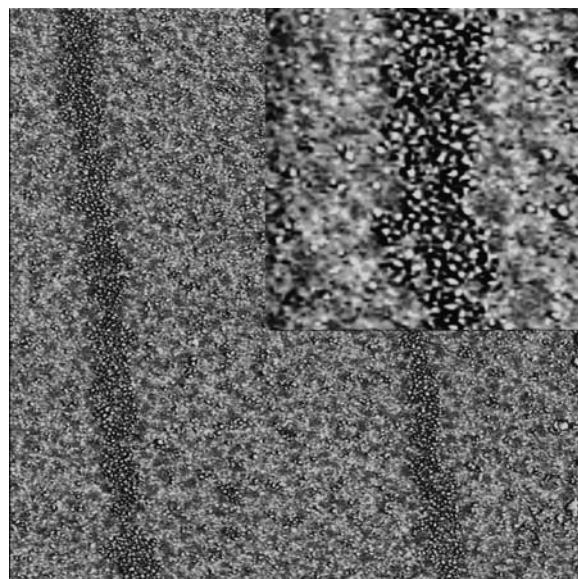


**Fig. 14** Scanning force microscopy images of water-soluble  $\text{Au}_{55}$  cluster selectively deposited on the patterned silicon surface (image size  $3.5 \times 3.5 \mu\text{m}^2$ ). The inset represents the phase image (image size  $700 \times 700 \text{nm}^2$ ), where the single clusters packing along the channel region are observed. *Source: From Ref.<sup>[32]</sup>.*

the channel regions on mica surface, as discussed previously (Fig. 5). If less silver is evaporated (not more than 2 nm), only the channel regions are fully covered with silver, as shown in Fig. 16. This offers the possibility to make one-dimensional electrodes.

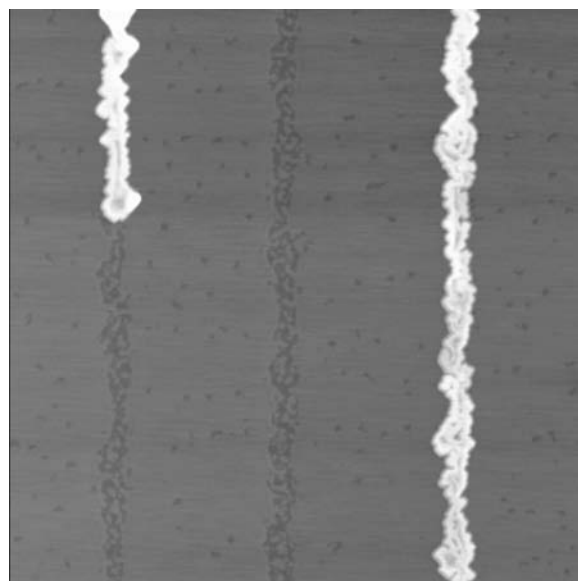


**Fig. 15** Scanning force microscopy image ( $4 \times 4 \mu\text{m}^2$ ) of the channel structure filled with paramagnetic  $\text{FeCl}_3$  molecules with gas deposition. In some locations, three-dimensional crystals were growing along the channels.

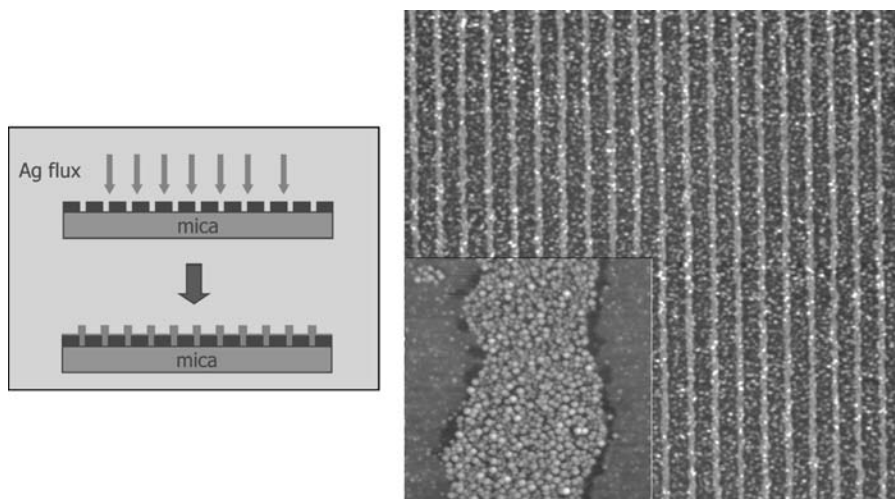


**Fig. 16** Evaporating silver on structured mica surface, silver atoms deposit preferably onto uncovered mica surface (channel regions), as schematically shown here (left). The SFM image (topography, image size  $16 \times 16 \mu\text{m}^2$ ) indicates that if a small amount of silver is evaporated (less than 2 nm), only the channel regions are fully covered, as shown in the inset.

## CONCLUSION

The original goal of the application of Langmuir–Blodgett technique was to achieve extended homogeneous monolayer/multiplayer of organic molecules, which should be highly ordered at the *molecular level*. It turns out in this work, however, that by adjusting the molecule–molecule interactions and molecule–substrate interactions, the LB transfer under appropriate experimental conditions can lead to long-range-ordered *nanoscopic structures* over macroscopic areas. Interestingly, the precursor LB monolayer has to be in a highly isotropic, disordered phase. Besides the nanoscopic feature size and characteristic long-range order, the structure may be heterogeneous. The potential applications of ordered heterogeneous surfaces with nanosized features as template structures for selective deposition of nanoclusters and molecules are demonstrated. The method presented above should not be restricted to a specific molecule–substrate pair and may be extended to other amphiphilic molecules and polymers.

## ACKNOWLEDGMENTS

The authors are grateful to Prof. Guenter Schmid, Dr. GAndrey Rogach for providing nanoclusters, Prof. Dr. Harald Fuchs for stimulating discussions, and the Deutsche Forschungsgemeinschaft (DFG), the state of North-Rhine Westphalia (NRW), for the financial support.

## REFERENCES

- Abbott, N.L.; Folkers, J.P.; Whitesides, G.M. Manipulation of the wettability of surfaces on the 0.1- to 1-micrometer scale through micromachining and molecular self-assembly. *Science* **1992**, *257*, 1380–1382.
- Barthlott, W.; Neinhuis, C. The purity of sacred lotus or escape from contamination in biological surfaces. *Planta* **1997**, *202*, 1–8.
- Kreibig, U.; Vollmer, M. Optical Properties of Metal Clusters. In *Springer Series in Material Science*; Springer: Berlin, 1995; Vol. 25.
- Harrison, D.J.; Fluri, K.; Seiler, K.; Fan, Z.; Effenhauser, C.S.; Manz, A. Micromachining a miniaturized capillary electrophoresis-based chemical analysis system on a chip. *Science* **1993**, *261*, 895–897.
- Chou, S.Y.; Krauss, P.R.; Renstrom, P.J. Nanoimprint lithography. *J. Vac. Sci. Technol.* **1996**, *B14*, 4129–4133.
- Luo, Y.; Collier, C.P.; Jeppesen, J.O.; Nielsen, K.A.; Delonno, E.; Ho, G.; Perkins, J.; Tseng, H.-R.; Yamamoto, T.; Stoddart, J.F.; Heath, J.R. Two-dimensional molecular electronics circuits. *ChemPhysChem* **2002**, *3*, 519–525.
- Park, M.; Harrison, Ch.; Chaikin, P.M.; Register, R.A.; Adamson, D.H. Blockcopolymer lithography: Periodic arrays of  $\sim 1011$  holes in 1 square centimeter. *Science* **1997**, *276*, 1401–1404.
- Spatz, J.P.; Sheiko, S.; Möller, M. Substrate induced lateral microphase separation of a diblock copolymer. *Adv. Mater.* **1996**, *8*, 513–517.
- Böltau, M.; Walheim, S.; Mlynek, J.; Krausch, G.; Steiner, U. Surface-induced structure formation of polymer blends on patterned substrates. *Nature* **1998**, *391*, 877–879.
- Fuchs, H.; Ohst, H.; Prass, W. Organic films: Molecular architectures for advanced optical, electrical and bio-related systems. *Adv. Mater.* **1991**, *3*, 10–18.
- Kuhn, H.; Möbius, D. Monolayer Assemblies. In *Investigations of Surface and Interfaces—Part B*, 2nd Ed.; Bryant, W.R., Roger, C.B., Eds.; Physical Methods of Chemistry Series, John Wiley & Sons, Inc.: New York, 1993; Vol. IXB, 375–542.
- Möhwald, H. Direct characterization of monolayers at the air–water interface. *Thin Solid Films* **1988**, *159*, 1–15.
- McConnell, H.M. Harmonic shape transitions in lipid monolayer domains. *J. Phys. Chem.* **1990**, *94*, 4728–4731.
- Langmuir, I. Oil lenses on water and the nature of monomolecular expanded films. *J. Chem. Phys.* **1933**, *1*, 756–776.



15. Chi, L.F.; Jacobi, S.; Anczykowski, B.; Overs, M.; Schäfer, H.J.; Fuchs, H. Supramolecular periodic structures in monolayers. *Adv. Mater.* **2000**, *12*, 25–30.
16. Kato, T.; Kameyama, M.; Ehara, M.; Iimura, K.I. Monodisperse two-dimensional nanometer size clusters of partially fluorinated long-chain acids. *Langmuir* **1998**, *14*, 1786–1798.
17. Riegler, H.; Spratte, K. Structural changes in lipid monolayers during the Langmuir–Blodgett transfer due to substrate/monolayer interactions. *Thin Solid Films* **1992**, *210/211*, 9–12.
18. Spratte, K.; Chi, L.F.; Riegler, H. Physisorption instabilities during dynamic Langmuir wetting. *Euro. Phys. Lett.* **1994**, *25* (3), 211–217.
19. Gleiche, M. Verfahren zur Herstellung periodischer Strukturen durch Benetzungsinstabilitäten. In *Dissertation*; Muenster University: Germany, 2001.
20. Gleiche, M.; Chi, L.F.; Fuchs, H. Nanoscopic channel lattices with controlled anisotropic wetting. *Nature* **2000**, *403*, 173–175.
21. Gleiche, M.; Chi, L.F.; Fuchs, H. Molecular property related silver decoration on fatty acid Langmuir–Blodgett monolayers. *Thin Solid Films* **1998**, *327–329*, 268–272.
22. Zasadzinski, J.A.N.; Schneider, M.B. Ripple wavelength, amplitude, and configuration in lyotropic liquid crystals as a function of effective headgroup size. *J. Phys. (France)* **2001**, *48*, 2001–2011.
23. Maske, H.A.; Havlin, S.; King, P.R.; Stanley, E. Spontaneous stratification in granular mixtures. *Nature* **1997**, *386*, 379–382.
24. Bowden, N.; Brittain, S.; Evans, A.G.; Hutchinson, J.W.; Whitesides, G.M. Spontaneous formation of ordered structures in thin films of metals supported on an elastomeric polymer. *Nature* **1998**, *393*, 146–149.
25. Weis, R.M.; McConnel, H.M. Cholesterol stabilizes the crystal–liquid interface in phospholipid monolayers. *J. Phys. Chem.* **1985**, *89*, 4453–4459.
26. Chunbo, Y.; Xinmin, L.; Desheng, D.; Bin, L.; Hongjie, Z.; Zuhong, L. Lanthanide ion induced formation of stripes domain structure in phospholipid Langmuir–Blodgett monolayers film observed by atomic force microscopy. *Surf. Sci.* **1996**, *366*, L729–L734.
27. Neumann, A.W. Contact angles and their temperature dependence: Thermodynamic status, measurement, interpretation and application. *Adv. Colloid Interface Sci.* **1974**, *4*, 105–191.
28. Riegler, H.; Spratte, K. Nucleation, Deposition and Domain Growth of Monomolecular Organic Films at the Three-Phase-Line of a Typical Langmuir–Blodgett Transfer Configuration. In *Dynamical Processes in Condensed Molecular Systems*; Blumen, Klafter, Haarer, Eds.; World Scientific Publishing: London, 1990; 105–115.
29. Erikson, L.G.T.; Cleasson, P.M.; Ohnishi, S.; Hato, M. Stability of dimethyldioctadecylammonium bromide Langmuir–Blodgett films on mica in aqueous salt solutions—Implications for surface force measurements. *Thin Solid Films* **1997**, *300*, 240–255.
30. Chi, L.F.; Fuchs, H.; Johnston, R.R.; Ringsdorf, H. Investigations of phase-separated Langmuir–Blodgett films by atomic force microscopy. *Thin Solid Films* **1994**, *242*, 151–156.
31. Loh, K.-K.; Saxena, A.; Lookman, T.; Parikh, A. Phase transition induced hydrodynamic instability. *Comput. Nanosci. Nanotechnol.* **2002**, 409–410.
32. Lu, N.; Gleiche, M.; Zheng, J.W.; Lenhart, S.; Xu, B.; Chi, L.F.; Fuchs, H. Fabrication of chemically patterned surfaces based on template directed self-assembly. *Adv. Mater.* **2002**, *14*, 1812–1815.
33. Chi, L.F. Application of scanning force microscopy operating in dynamic modes on selforganized assemblies and organic amphiphiles. *Appl. Phys., A* **1999**, *68*, 203–210.
34. Lenz, P. Wetting phenomena on structured surfaces. *Adv. Mater.* **1999**, *11* (18), 1531–1534.
35. Pompe, T.; Fery, A.; Herminghaus, S. Measurement of contact line tension by analysis of the three phase boundary with nanometer resolution. *J. Adhes. Sci. Technol.* **1999**, *13*, 1155–1164.
36. Gleiche, M.; Chi, L.F.; Gedig, E.; Fuchs, H. Anisotropic contact-angle hysteresis of chemically nanostructured surfaces. *ChemPhysChem* **2001**, *3*, 187–191.
37. Gau, H.; Herminghaus, S.; Lenz, P.; Lipowsky, R. Liquid morphologies on structured surfaces: From microchannels to microchips. *Science* **1999**, *283*, 46–49.
38. Biebuyck, H.A.; Whitesides, G.M. Self-organization of organic liquids on patterned self-assembled monolayers of alkanethiolates on gold. *Langmuir* **1994**, *10*, 2790–2793.
39. Kim, E.; Xia, Y.; Whitesides, G.M. Polymer microstructures formed by moulding in capillaries. *Nature* **1995**, *376*, 581–584.
40. Xia, Y.; Whitesides, G.M. Soft lithography. *Annu. Rev. Mater. Sci.* **1998**, *28*, 153–184.
41. Gallardo, B.S.; Gupta, V.K.; Eagerton, F.D.; Jong, L.I.; Craig, V.S.; Shah, R.R.; Abbott, N. Electrochemical principles for active control of liquids on submillimeter scales. *Science* **1999**, *283*, 57–60.
42. Schmid, G. Large clusters and colloids. Metal in the embryonic state. *Chem. Rev.* **1992**, *92*, 1709–1727.
43. Talapin, D.V.; Rogach, A.L.; Kornowski, A.; Haase, M.; Weller, H. Highly luminescent monodisperse CdSe and CdSe/ZnS nanocrystals synthesized in a hexadecylamine-triethylphosphine oxide-triethylphosphine mixture. *Nano Lett.* **2001**, *1*, 207–211.
44. Naber, A.; Molenda, D.; Fischer, U.C.; Maas, H.-J.; Höppener, C.; Lu, N.; Fuchs, H. Enhanced light confinement in a near-field optical probe with a triangular aperture. *Phys. Rev. Lett.* **2002**, *89*, 210801-(1-4).

# Hierarchically Imprinted Nanostructures for Separation

**Sheng Dai**

*Chemical Sciences Division, Oak Ridge National Laboratory, Oak Ridge, Tennessee, U.S.A.*

**Zongtao Zhang**

**Chengdu Liang**

*Oak Ridge National Laboratory, Oak Ridge, Tennessee, U.S.A.*

## INTRODUCTION

Hierarchical structures can be found in nature from the macroscopic level to the microscopic level. Biomaterials are selectively self-organized from molecular- to macrolength scales, with organized units of subassemblies that are generated to serve biological purposes.<sup>[1]</sup> Inspired by the complexity of biomaterials, research has been initiated to mimic biomineralization processes and chemically produce hierarchical structures.<sup>[1–10]</sup> This entry is focused on a new methodology to generate hierarchical materials as novel sorbents for separation of metal ions via hierarchical imprinting synthesis.

## Molecular Imprinting

The concept of molecular-imprinted polymers was originally introduced by Wulff and Sarhan in the early 1970s.<sup>[11]</sup> Imprinting synthesis (Fig. 1) is a polymerization method that creates selective adsorption cavities inside or on the surface of solid materials with functionalities spatially organized around templates. The templates interact with a complementary portion of a functional monomer, by either covalent<sup>[12]</sup> or non-covalent<sup>[13]</sup> interactions such as ionic, coordinative, hydrophobic, or hydrogen bonding. The functional monomers are fixed around the templates upon polymerization. After removal of templates, a set of recognition sites is retained in the polymer matrices or on the surface of the substrates. Recognition sites are employed to rebind the imprinting templates or some analogous molecule with similar physical/chemical characteristics. The imprinted cavities have “one-to-one” specific selectivity, which mimics enzyme. Accordingly, the imprinted sorbents are also called artificial enzyme or biomimic antibodies. Templates ranging from the smallest species (proton) to biomacromolecules (proteins) have been successfully imprinted.<sup>[12–21]</sup> Various applications have been

utilized in the areas of separation, catalysis, chemosensors, biomimic enzymes, drug delivery, etc.

## WHY HIERARCHICAL IMPRINTING SYNTHESIS?

Molecularly imprinted polymers are usually synthesized as bulk materials.<sup>[12]</sup> Templates are removed via extraction after grinding the bulk polymers into fine particles. Although imprinting synthesis has proven to be the most efficient method for tailoring binding sites, both site accessibility and site heterogeneity remain as problematic issues. The imprinted cavities located on the surface of the fine particles are fully accessible. However, those located inside the particles are only partially accessible or inaccessible, depending on the porosities of the corresponding hosts. Grinding of the imprinted polymers can be eliminated by casting thin films, making porous membranes, or producing small spherical particles via emulsion polymerization. Site accessibility is significantly improved through these synthesis techniques without increasing the template population. Porous membranes and surface imprinted substrates are the prototype of the imprinted sorbents with hierarchical structures. The original concept of hierarchically imprinted porous sorbents was coined based on the imprinting synthesis involving multiple templates over several discrete dimension scales.<sup>[23]</sup> This concept has been extended from its original metal-ion imprinting to various target chemical species.<sup>[60]</sup> Hierarchically imprinted porous sorbents have advantages of perfect binding-site integrity, fully accessibility of imprinted sites, excellent mass transport, and finely adjustable hydrodynamic properties.

Hierarchically imprinted structures can be assembled via two methodologies: 1) coassembly<sup>[22,23]</sup> and 2) stepwise assembly.<sup>[40,60]</sup> Imprinting synthesis through a coassembly method is based on the self-assembly of hierarchical structures through simultaneous uses of multiple templates. However, the stepwise assembly

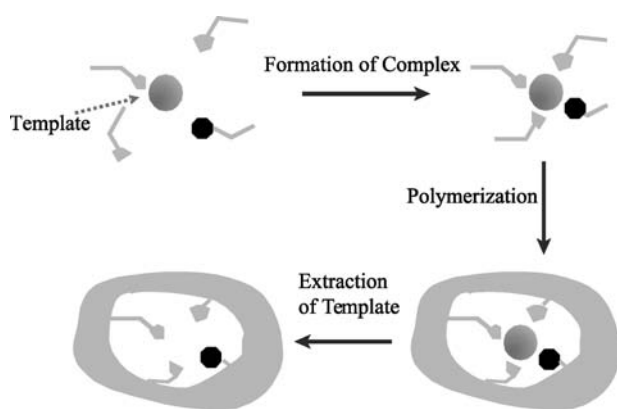


**Fig. 1** Schematic diagram of imprinting polymerization. Source: From Ref.<sup>[23]</sup>.

method involves sequential generation of hierarchical structures. Both methods have been successfully employed to synthesize hierarchically imprinted sorbents for metal separation. Hierarchically imprinted sorbents have more than one type of porosity, which takes different roles in applications. The primary porosity is the recognition cavities, which function as selective binding sites for template species. The secondary porosity can be mesopores. The mesopores open the accesses of solution to the binding sites. The uniformity of the mesopores offers homogeneous diffusion of the target analytes. Macropores are attributed to the tertiary porosity. Both the secondary and tertiary porosities substantially improve the mass transport properties of the hierarchically imprinted sorbents. Fig. 2 illustrates the topological structure of hierarchically imprinted sorbents. In the following, examples for the applications of these two hierarchical imprinting methodologies in developing novel sorbents are reviewed.

## COASSEMBLY SYNTHESIS APPROACH

### Mesoporous Silica Sorbents via Hierarchical Imprinting

The discovery of ordered mesoporous materials using a surfactant-templated approach has opened a new era in synthesis of ordered nanoscale materials.<sup>[23,24]</sup> This class of materials has attracted the attention of scientists from different fields because of their unique structural features. Firouzi et al.<sup>[25]</sup> have developed a model that makes use of the cooperative organization of inorganic and organic molecular species in three-dimensional arrays. They divided the global surfactant-directed ordered porous material synthetic process into three reaction steps: multidentate binding of silicate oligomers to the cationic surfactant and the silicate, preferential silicate polymerization in the interface region, and charge density matching between the surfactant and the silicate. This micelle-based template synthesis can be viewed as a mesoscale-imprinting process and ideal to generate uniform mesopores.

The combination of the above mesoscale-imprinting synthesis with metal ion-imprinting synthesis has resulted in novel hierarchical sorbents for metal separation.<sup>[22]</sup> The concept behind this multilevel imprinting is as follows. Surfactant micelles and metal ions both simultaneously act as templates in these hierarchically imprinted sorbents. An acidic ethanol solution leaches and extracts the metal ion and surfactant. The leaving of these templates results in two different yet associated imprints within the silica matrixes. Each imprint carries out a specific function individually. On the microporous level, removal of the metal ions from the corresponding complex leaves cavities (1–3 Å) that exhibit ionic recognition. These pores give the sorbents

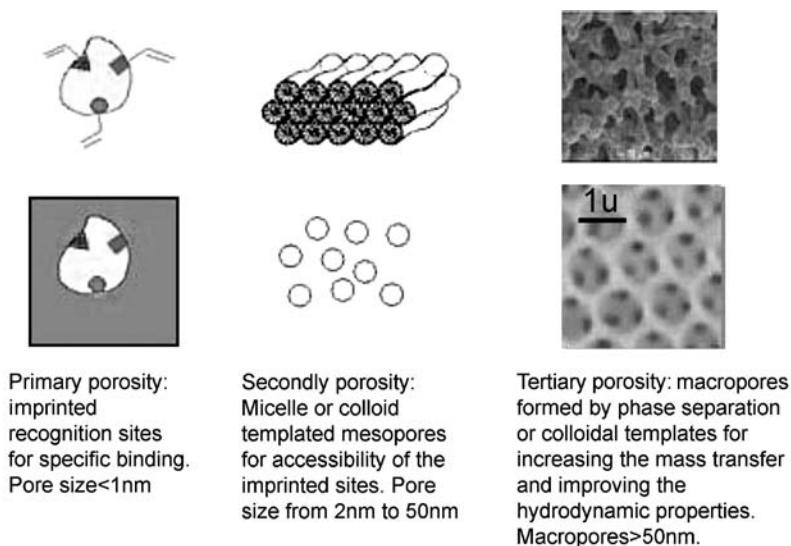


**Fig. 2** Topological structures of hierarchically imprinted porous sorbents.

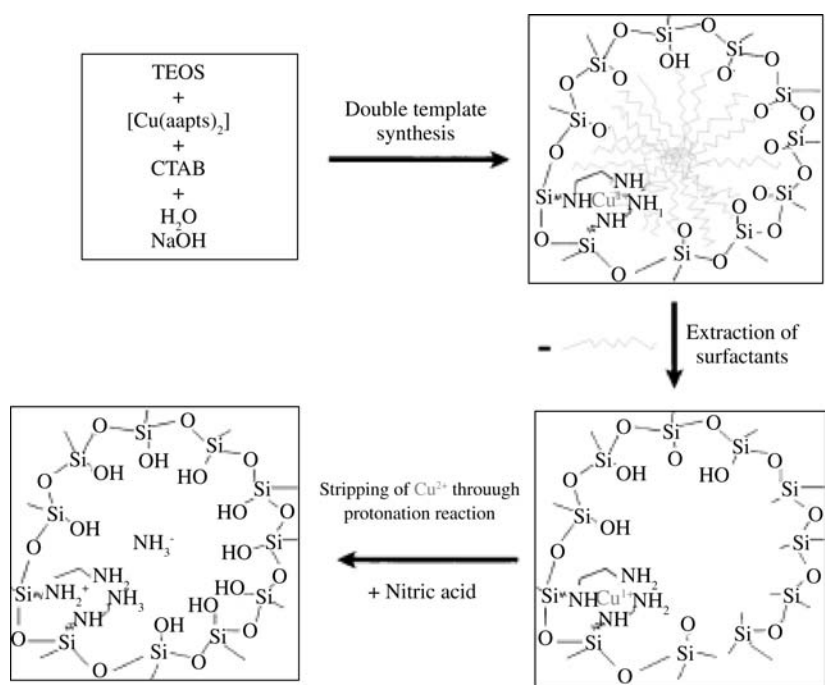


**Fig. 3** Schematic diagram showing the synthesis of a hierarchically imprinted sorbent using Cu<sup>2+</sup> and CTAB simultaneously as templates. *Source:* From Ref.<sup>[23]</sup>.

enhanced selectivity for the given ions. On the mesoporous level, removal of the surfactant micelles results in the formation of relatively large, cylindrical pores (diameters of 25–40 Å) that give the gel an overall porosity, including large surface areas and excellent metal-ion transport kinetic.<sup>[26–29]</sup> Pore sizes can be easily controlled by the chain length of the surfactant molecules.<sup>[30–35]</sup> This combination of selectivity and high capacity, coupled with fast kinetics, makes these materials ideal candidates for many separation applications.

The synthetic procedure was developed to produce hierarchically imprinted sorbents for Cu<sup>2+</sup>.<sup>[22]</sup> Briefly, the Cu<sup>2+</sup> template is coordinated with a bifunctional ligand 3-(2-aminoethylamino)propyltrimethoxysilane (aapts) via a standard literature procedure.<sup>[36]</sup> The [Cu(aapts)<sub>2</sub>]<sup>2+</sup> complex and a surfactant typically cetyltrimethylammonium bromide (CTAB) are imprinted into a silica matrix by the base-catalyzed hydrolytic condensation of tetraethylorthosilicate (TEOS). The resulting blue solid is collected by filtration. An ethanol/HCl solution effectively removes all templates. The bidental amine ligands lose the metal cations when protonated at pH 3 or below. The surfactant is extracted by the acidic ethanol. Fig. 3 gives a schematic illustration of this hierarchical imprinting methodology for the synthesis of Cu<sup>2+</sup> templated sorbents. Small-angle X-ray scatterings (Fig. 4) of the surfactant-free mesoporous sorbents show a peak around  $Q = 1.2\text{--}2.4\text{ nm}^{-1}$ . This peak indicates a long-range ordered or a wormy structure organized by the surfactant templates. Fig. 5 shows the comparison of the UV-Vis spectrum of [Cu(aapts)<sub>2</sub>]<sup>2+</sup> in a

methanol solution with the corresponding diffuse reflectance spectrum of a washed-and-dried as-synthesized mesoporous silica. The close match between the spectrum of [Cu(aapts)<sub>2</sub>]<sup>2+</sup> and that of

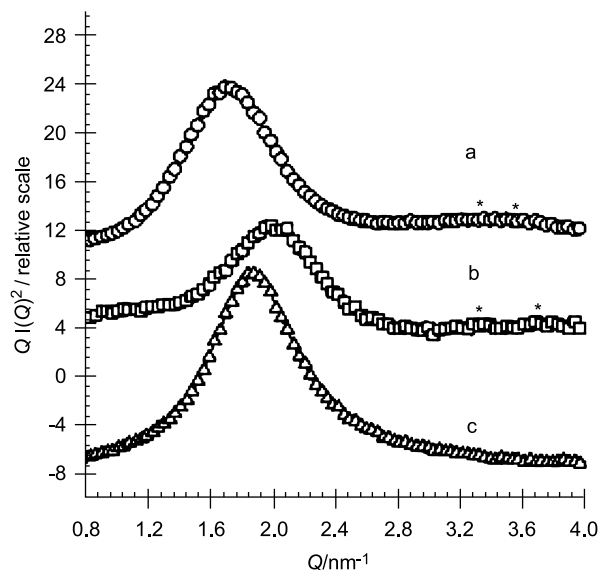


**Fig. 4** Small-angle scatterings of hierarchically imprinted sorbents using (A) CTAB, (B) sodium dodecyl sulfate (SDS), and (C) dideoxyadenosine DDA, where  $Q = (4\pi/\lambda)\sin(\theta/2)$ , where  $\lambda$  is the X-ray wavelength (0.154 nm) and  $\theta$  is the scattering angle. The asterisks in (A) and (B) indicate the other diffraction peaks from the hexagonally packed mesoporous materials. No additional diffraction peaks in (C) are consistent with the fact that the neutral surfactant template DDA gives rise to the worm-structured mesoporous materials. *Source:* From Ref.<sup>[23]</sup>.

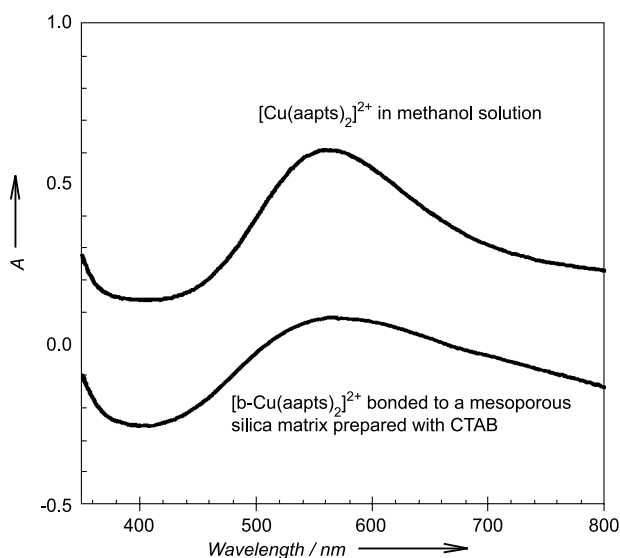
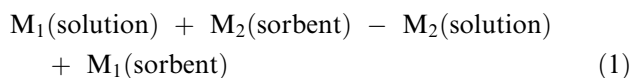


**Fig. 5** UV/Vis spectra of  $[\text{Cu}(\text{aapts})_2]^{2+}$  in methanol and immobilized in a mesoporous sorbent prepared by CTAB as a structure directing reagent. Source: From Ref.<sup>[23]</sup>.

$[\text{Cu}(\text{b-aapts})_2]^{2+}$  (b-aapts = aapts ligand covalently bonded to silica) indicates that the stereochemical environments of the copper ion in the two systems are similar. Therefore the complex is covalently doped in the bulk silica matrix. The absorption position of the peak is consistent with the fact that  $\text{Cu}^{2+}$  is coordinated with four amine ligands, because both three and two amine-coordinated copper complexes have absorption peaks at much longer wavelengths.<sup>[37]</sup> Therefore the imprint of  $\text{Cu}^{2+}$  is successfully formed in the mesoscopic composite materials.

Competitive ion-binding studies were conducted with  $\text{Cu}^{2+}$  and  $\text{Zn}^{2+}$  ions to measure the selectivity of the imprinted material. The  $\text{Zn}^{2+}$  ion was chosen as the competitor species because it has the same charge and nearly identical size, and also binds well with the diamine ligand. The selectivity coefficient,  $k$ , for the binding of a specific ion in the presence of competitor species can be obtained from equilibrium binding data<sup>[38,39]</sup> according to Eqs. (1–3):



$$k = \frac{\{[\text{M}_2]_{\text{solution}}[\text{M}_1]_{\text{sorbent}}\}}{\{[\text{M}_1]_{\text{solution}}[\text{M}_2]_{\text{sorbent}}\}} = K_d(\text{Cu})/K_d(\text{Zn}) \quad (2)$$

where  $K_d$  is the distribution coefficient, expressed as:

$$K_d = \left\{ \frac{(C_i - C_f)}{C_f} \right\} \times \left\{ \frac{\text{volume solution (mL)}}{\text{mass gel (g)}} \right\} \quad (3)$$

Here  $C_i$  is the initial solution concentration and  $C_f$  is the final solution concentration. Comparison of the  $k$

values for the imprinted and control blank gels can show the effect that imprinting exerts on the metal-ion selectivity for a given material. A measure of the increase in selectivity due to molecular imprinting can be defined by the ratio of the selectivity coefficients of the imprinted and non-imprinted materials:

$$k' = k_{\text{imprinted}}/k_{\text{nonimprinted}}$$

Significant increases in  $K_d(\text{Cu})$ ,  $k$ , and  $k'$  for  $\text{Cu}^{2+}$  through hierarchical imprinting has been observed with the largest  $k \approx 33,000$  and the largest  $k' \approx 240$ . These values are, to our knowledge, the highest  $k$  and  $k'$  values currently achieved for imprinting synthesis with metal ions.<sup>[40]</sup> The hierarchical imprinting approach gives rise to a significant improvement over imprinted organic polymer sorbents in both capacity and selectivity.<sup>[38,39]</sup> The  $K_d(\text{Cu})$  and  $k$  values of the sorbents prepared without the use of surfactant templates are only 250 and 26, respectively. Both values are significantly less than those of the hierarchically imprinted sorbents, demonstrating the synergism of different scale templating synthesis.

### Mesoporous Bridged Polysilsesquioxane Sorbents Synthesized via Hierarchical Imprinting

A new approach for the hierarchical synthesis of ion-imprinted sorbents<sup>[41]</sup> is based on the newly developed mesoporous bridged polysilsesquioxane materials.<sup>[42–46]</sup> Structural similarities between bridged silsesquioxanes and organosilanes allow a good mixing of these sol-gel precursors and a uniform incorporation of the functional ligands into the mesoporous polysilsesquioxane framework. Inagaki, et al.<sup>[44]</sup> pioneered the synthesis of ordered mesoporous bridged polysilsesquioxane materials. The bridged silsesquioxane precursor that had been explored to generate hierarchically imprinted sorbents is 1,2-bis(triethoxysilyl)ethane (BTSE). In general, the copolymerization of BTSE with metal ion complexes of aapts around supramolecular assemblies of cetyltrimethylammonium chloride (CTAC) gives a nanocomposite polymer.<sup>[41]</sup> Extraction of the surfactant and metal ions results in a porous material with a high affinity for the metal ion template. Again, both the metal ions and the surfactant micelles act simultaneously as templates in this system. Removal of the surfactant leaves a network of pore channels that give these sorbents large surface area and excellent metal ion transfer kinetics. Removal of the metal ions results in the formation of tailored binding sites made of ethylenediamine functionalities. Arranged functionalities in conformations favor the rebinding to the metal ion

template. Selective sorbents have been synthesized for Cu(II), Ni(II), and Zn(II).

The batch tests indicated that the  $K_d(\text{Ni})$  of the Ni-imprinted sorbent and  $K_d(\text{Zn})$  of the Zn-imprinted sorbent over thousands have been achieved.<sup>[41]</sup> The selectivities of the nickel and zinc-imprinted sorbents were investigated by competitive sorption. All initial solutions contained equimolar amounts of Ni(II) and Zn(II) at five different concentrations from  $10^{-4}$  to  $10^{-3}$  M (with respect to both ions) and pH 6.0. Interestingly, the nickel-imprinted sorbent adsorbed more Ni(II) than Zn(II) at all concentrations. This results in higher distribution coefficients for Ni(II) than Zn(II) with the nickel-imprinted material. This sorbent removed nearly all of both metal ion species from the highly diluted Ni(II):Zn(II) mixture ( $10^{-4}$ : $10^{-4}$  M). At low concentration, the population of binding sites is larger than the total number of metal ions. The lack of competition may cause the loss of selectivity. In direct contrast to the adsorption behavior of the nickel-imprinted material, the zinc-imprinted sorbent absorbed more Zn(II) than Ni(II) at all concentrations studied. This results in higher distribution coefficients for Zn(II) than Ni(II) with the zinc-imprinted material.

### Polymer Sorbents Prepared by Emulsion Polymerization

The surface template polymerization diverges from the bulk imprinted materials by creating microspheres with imprinted external surfaces.<sup>[48,51]</sup> The original methodology was pioneered by Uezo, Goto, and Nakashio.<sup>[48]</sup> The microspheres have a hierarchical structure of spherical surfaces and imprinted cavities

scattering on the surfaces. Such a structure is formed via a coassembly synthesis approach. In this synthesis, metal ions, amphiphilic functional molecules, surfactants, and monomers play the roles of imprinting targets, selectively binding ligands, morphology-controlling agents, and polymer matrix precursors, respectively. During emulsion polymerization, each component fulfills its role, individually. The surfactants control the shape and size of the final spherical particles with certain size distribution. The complexes of the metal ions and the amphiphilic functional molecules are imbedded on the surfaces of the spherical polymer matrix to form imprinted cavities. The amphiphilic nature of the functional molecules is the key factor for this surface template polymerization. The functional molecules play two roles in this coassembly synthesis: 1) interface between hydrophobic matrixes and hydrophilic templating ions; and 2) generation of imprinted sites. Fig. 6 illustrates the methodology of the surface template polymerization. The imprinted surface has better site accessibility than the conventional molecularly imprinted polymers (MIPs). Therefore this technique overcomes the fundamental drawbacks of conventional polymer imprinting methods.<sup>[47-54]</sup>

After many years of intensive studies by several groups, surface-imprinted polymers evolved from water-in-oil (W/O) and oil-in-water (O/W) systems to more complicated water-in-oil-in-water (W/O/W) system for the better control of imprinting effect. The imprinting effect has also been improved by using rigid polymer matrixes and strong binding ligands. Trimethylolpropane trimethacrylate (TRIM) replaced divinylbenzene (DVB) in some applications by offering improved matrix rigidity. Diphenyldodecylidiphosphonic acid (DDDDPA) has been found as an efficient

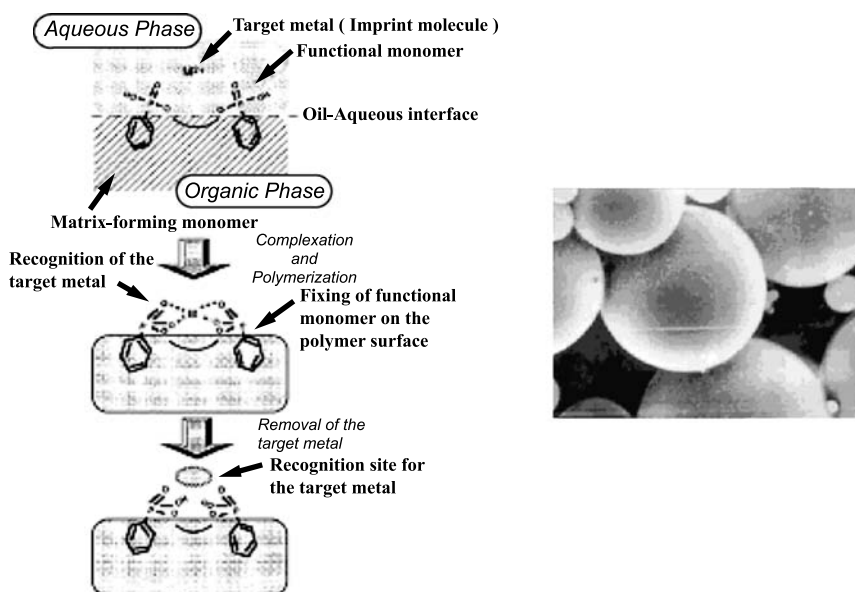


**Fig. 6** Schematic diagram of ion imprinting in microspheres. Source: From Ref.<sup>[52]</sup>.



functional molecule for metal ion imprinting.<sup>[47–51]</sup> Several applications have been made for selective binding of  $\text{Zn}^{2+}$ ,  $\text{Cu}^{2+}$ , and lanthanide ions. The pH dependence of the absorption of the imprinted polymer to metal ions has been investigated. The dissociation of the metal ion/polymer complex is suppressed by the elevated pH value. Therefore the uptake of metal ions from aqueous solution is enhanced with the increase of pH. Size exclusion effect was observed when Dy(III), Ce(III), and La(III) ions were imprinted.<sup>[55]</sup> Dy(III) ion imprinted polymer excludes the accesses of the other two ions, while La(III) ion imprinted one accepts all ions. As a result of the similarity of the affinities of the lanthanoid ions to the functional molecules, the selectivity of the imprinted polymers to lanthanoids is only contributed by the size selectivity. This result is consistent with the ion radius order of Dy(III), Ce(III), and La(III), which are 1.083, 1.196, and 1.216 Å, respectively.

## STEPWISE ASSEMBLY

### Surface-Imprinted Mesoporous Sorbents

Hierarchical imprinting can also be accomplished in mesoporous materials through stepwise assembly.<sup>[40]</sup> First, ordered mesoporous materials can be fabricated via surfactant templating synthesis. Functional groups are then introduced to the pore surface of mesoporous silica through *imprint coating*. The key to this stepwise design is to coat the mesopore surface with complexes between ligands and target metal ions rather than just the free ligands. After the removal of metal ions, the ligand imprints of the template metal ions are created on the mesopore surfaces. This organization reflects both the size and stereochemical signature of the

template ion, and should ultimately lead to future ion recognition and selective rebinding of the target ion from ion mixtures. Such functionalized ordered mesoporous materials exhibit significantly greater target ion binding selectivities than sorbents prepared by conventional coating methods. The success of this new approach is built on the unique environments of ordered, hexagonally packed mesopore surfaces for conducting surface imprinting. These include: 1) circularly curved, extremely rigid pore surfaces, and optimum pore diameters (20–100 Å), which match the stereochemical requirements for surface imprinting of 4- or 6-coordinated metal ions; 2) a very uniform pore size distribution which allows the generation of the uniform imprints and limits the possible choices of coordination environments.

Fig. 7 shows a schematic diagram for making the sorbents for  $\text{Cu}^{2+}$  via the stepwise assembly. The batch uptake tests have indicated that imprinted sorbents exhibit distinctly higher effective capacities for  $\text{Cu}^{2+}$  than their respective control blanks. Fig. 8 shows samples of imprinted and non-imprinted monolith mesoporous beads after being exposed to identical solutions containing 0.001 M  $\text{Cu}^{2+}$ . The capacity enhancement due to molecular imprinting can be easily observed via the development of blue color associated with the formation of  $\text{Cu}^{2+}$ -amine complexes only in the surface-imprinted beads. Adsorption equilibria for these coated, mesoporous sorbents are generally achieved in less than 15 min, attesting to the fact that the adsorption kinetics for these materials are also significantly faster than those for analogous microporous materials. Furthermore, their capacity does not change after repeated cycles of loading and elution. These properties make them ideal for many separation applications requiring recyclable solid phases. The selectivities of these new sorbents were investigated by using

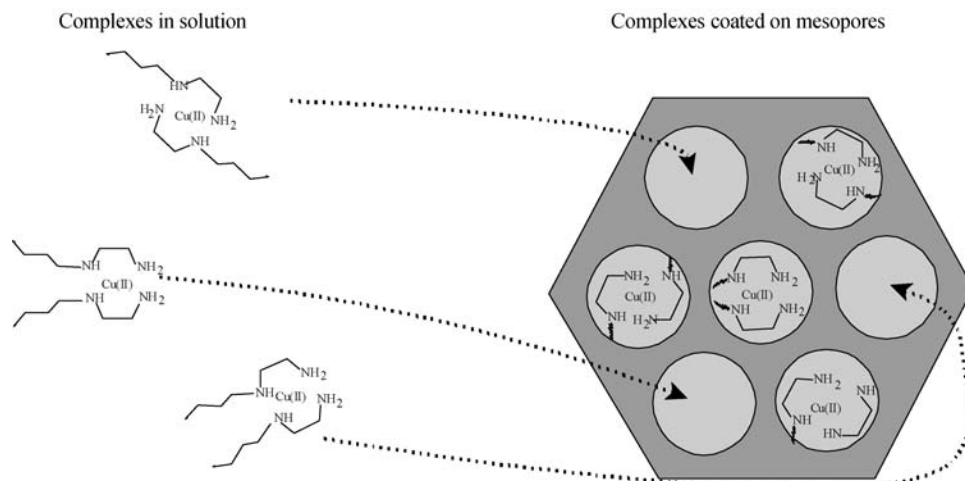


Fig. 7 Surface imprinting on mesoporous materials.



**Fig. 8** Comparison of non-imprinted (left) and imprinted (right) sorbent beads.

aqueous solutions of zinc and copper. Comparison of the  $K_d$  values for  $\text{Cu}^{2+}$  imprinted with control-blank samples for the aapts-coated sorbent system shows a sixfold increase in  $K_d$  for  $\text{Cu}^{2+}$ , while  $K_d$  for  $\text{Zn}^{2+}$  decreases by the same amount. The  $k'$  value of 40 for aapts-imprint-coated sorbent has been observed.

### Ion-Imprinted Zeolitic Sorbents

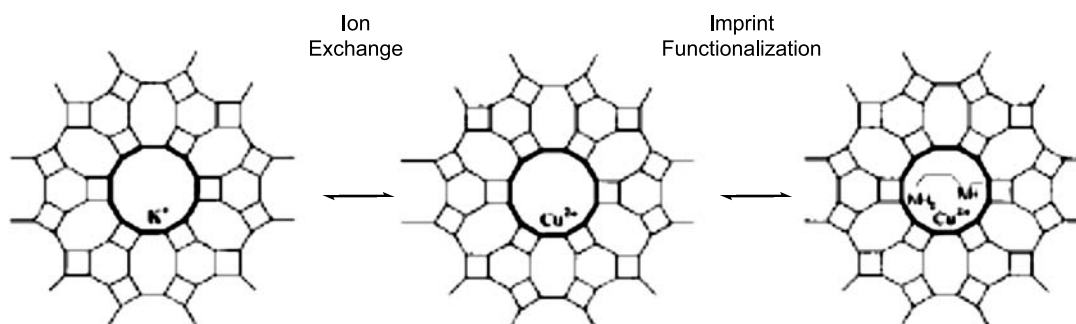
Zeolites consist of a crystal lattice having defined pores and cavities.<sup>[56]</sup> They are usually synthesized by hydrothermal methods in the presence of certain organic molecules (e.g., quarternary ammonium salts) acting as templates to control the type of lattice being formed. The harsh synthesis conditions eliminate the possibility of using the coassembly method for synthesizing hierarchically imprinted zeolitic sorbents. A “ship in bottle” imprinting technique has been developed for the assembly of cavity sites for uptakes of metal ions. The essence of this stepwise assembly method involves first introduction of metal ion via ion exchange, which is followed by a facilitated surface functionalization.

Fig. 9 shows a schematic diagram for synthesizing  $\text{Cu}^{2+}$ -imprinted zeolite-L sorbents. A comparison of the  $k$  value for the  $\text{Cu}^{2+}$ -imprinted sorbent with that

for the corresponding control sample showed an increase in  $k$  for  $\text{Cu}^{2+}$  through ion imprinting, with the  $k$  value for the imprinted zeolite near 30 and  $k'$  more than 2. For comparison, the competitive adsorption for the unfunctionalized plain zeolite has exhibited similar  $K_d$  values for both  $\text{Cu}^{2+}$  and  $\text{Zn}^{2+}$ . In this case, the mechanism of absorption is through the ion exchange reaction. This indicates that the original zeolite network has no selectivity toward a specific ion. The selectivity of the imprinted zeolite is generated through ion imprinting and surface functionalization.

### Ion-Imprinted Lamellar Sorbents

Lamellar structured silicate materials, which are composed of one or multiple negatively charged sheets of  $\text{SiO}_4$  tetrahedra with abundant silanol-terminated surfaces, provide an adjustable space with their intergaleries, whose negative charges are balanced by either  $\text{Na}^+$  or  $\text{H}^+$  in the interlayer spacing.<sup>[57]</sup> Various chemical species (charged or neutral) have been intercalated into the galleries of layered silicate such as magadiite to form the corresponding intercalation compounds for various applications. Many novel materials have been derived from layered silicate materials. For example, organic functional groups can be covalently grafted on the silanol-terminated interlayer surfaces through the use of organosilanes containing the functional ligands.<sup>[58,59]</sup> Surface imprinting synthesis of these materials as sorbents for  $\text{Cu}^{2+}$  has been successfully demonstrated via stepwise assembly. The  $^{29}\text{Si}$  cross-polarization (CP)/magic angle spinning (MAS) nuclear magnetic resonance (NMR) spectra of imprint-functionalized magadiite (A) and control blank magadiite (B) are shown in Fig. 10. The  $^{29}\text{Si}$  resonance peaks at ca.  $-103$  and  $-114$  ppm are assigned to the  $^{29}\text{Si}$  nuclei of  $\text{Q}^3$  and  $\text{Q}^4$  environments, respectively. The relative narrow peak widths indicate that the crystalline structure of the magadiite framework has been retained during the functionalization reactions. The resonance peaks at ca.  $-56.5$  and  $-67.5$  ppm arise from the  $(-\text{O})_2\text{Si}(\text{OH})\text{R}$  and  $(-\text{O})_3\text{SiR}$  species assigned



**Fig. 9** Schematic diagram of molecular imprinting in L-zeolite. *Source:* From Ref.<sup>[56]</sup>.

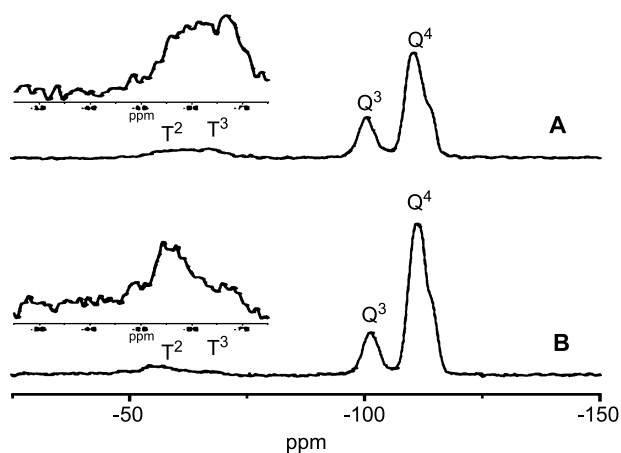


**Fig. 10**  $^{29}\text{Si}$  MAS NMR spectra of (A) imprint-functionalized magadiite and (B) control blank magadiite (inset: expansion spectrum between  $-25$  and  $-75$  ppm). *Source:* From Ref.<sup>[57]</sup>.

to T<sup>2</sup> and T<sup>3</sup>, respectively. The presence of the T<sup>2</sup> and T<sup>3</sup> bands indicates that the apts functional groups are covalently bonded to the magadiite surface. The major reactions employed in this intersurface imprinting using the magadiite host are schematically shown in Fig. 11. The enhanced uptake of Cu<sup>2+</sup> by the Cu<sup>2+</sup>-imprinted layered sorbent has been observed. The  $K_d$  value of the Cu<sup>2+</sup>-imprinted sample is threefold greater than that of the control sample. The value of the relative selectivity coefficient  $k'$  (3.24) is  $>1$ , which indicates enhanced adsorption through the ion-imprinting synthesis. The capacity did not change after several cycles of loading and stripping.

### Toward “Biomimic” and “Enzyme Mimic” Nanoporous Materials

Three-dimensional ordered nanoporous materials are widely found in nature.<sup>[60]</sup> Those materials possess hierarchically ordered structures having at least one dimension down to the nanoscale. Proteins, enzymes, and biomembranes are known as hierarchically structured materials carrying out various biological functions such as sensing, catalysis, size and shape selection, and response. The marvelous functions of biomaterials attract research interests from many fields. Material scientists simulate the bioactivity by creating artificial biomaterials through “biomimic” or “enzyme mimic.” Ion selectivity is one of the most important properties of those biomaterials. For example, the Na<sup>+</sup>/K<sup>+</sup> pump of the cell membrane maintains that the Na<sup>+</sup> concentration inside the cell is 36 times higher than that outside of the cell.

A recent report demonstrated the control of the three-dimensional architecture based on a stepwise assembly technique.<sup>[60]</sup> This approach created a novel hierarchical porous material with tunable size- and shape-selective pore structures to mimic the microchannels in biomembranes. Ordered mesoporous materials are formed by micelle templates. A monolayer of ligand is sequentially grafted to the channel surface by surface imprinting. This material consists of a rigid mesoporous oxide frame and a soft monolayer with tailored microcavities that mimics the shape and size selectivity of the biomaterials. Fig. 12 shows the scheme of the hierarchical porous materials with ordered mesoporosities and microcavities in the

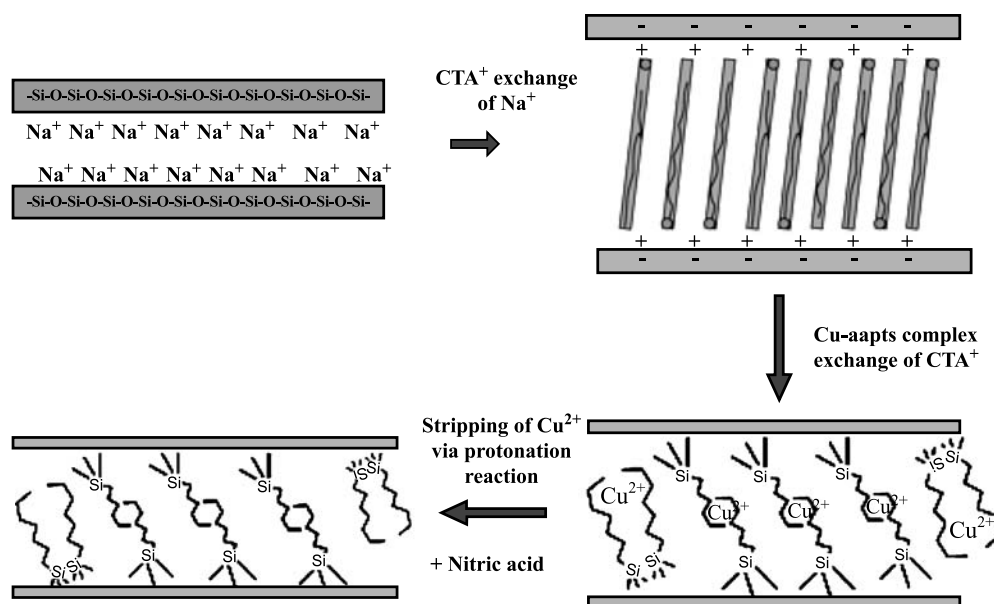


**Fig. 11** Schematic diagram of molecular imprinting in magadiite silicate. *Source:* From Ref.<sup>[57]</sup>.

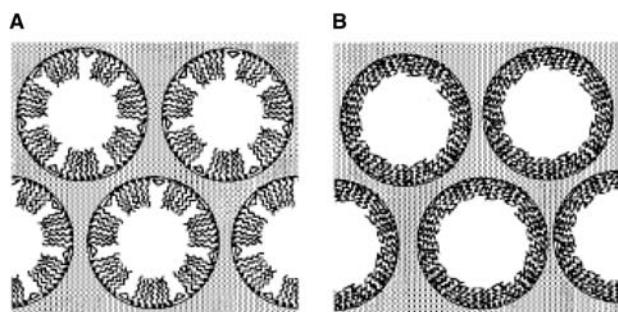


**Fig. 12** Schematic of the hierarchical porous materials with ordered mesoporosities and microcavities in the long-chain molecular monolayer coatings. The triangular shape in the cavity represents the template molecules, or the idealized shape of the cavity. (A) The porosity in an open position. (B) The porosity in a closed position. *Source:* From Ref.<sup>[60]</sup>.

long-chain molecular monolayer coatings. The triangular shape in the cavity represents the template molecules, or the idealized shape of the cavity.

## CONCLUSION

Synthesis methodologies of hierarchically structured sorbents for metal ions were reviewed. Such hierarchically structured sorbents exhibit not only fast binding kinetics and high capacities, but also molecular recognition capabilities. The simplicity of this technique should lead to a wide variety of highly selective sorbents, the properties of which can be optimized for many metal ions with the proviso that they form stable coordination complexes with suitable bifunctional ligands. Furthermore, this hierarchical imprinting methodology should not be limited to the synthesis of sorbents for the binding of metal ions. Organic molecules can be used as templates for generation of sorbents exhibiting molecular recognition of the target molecules. The general design principles illustrated by these results highlight opportunities in areas such as selective sorbents, chemical sensors, and catalysts offered by the imprinted mesoporous materials as molecular recognition devices.

## REFERENCES

- Mann, S.; Ozin, G.A. Synthesis of inorganic materials with complex form. *Nature* **1996**, *382*, 313.
- Ozin, G.A. Panoscopic materials: synthesis over 'all' length scales. *Chem. Commun.* **2000**, 419.
- Ozin, G.A. Morphogenesis of biomineral and morpho-synthesis of biomimetic forms. *Acc. Chem. Res.* **1997**, *30*, 17.
- Mann, S.; Burkett, S.L.; Davis, S.A.; Fowler, C.E.; Mendelson, N.H.; Sims, S.D.; Walsh, D.; Whilton, N.T. Sol-gel synthesis of organized matter. *Chem. Mater.* **1997**, *9*, 2300.
- Mann, S. *J. Chem. Soc. Dalton* **1997**, 3953.
- Mann, S.; Shenton, W.; Li, M.; Connolly, S.; Fitzmaurice, D. Biologically programmed nanoparticle assembly. *Adv. Mater.* **2000**, *12*, 147.
- Holland, B.T.; Abrams, L.; Stein, A. Dual templating of macroporous silicates with zeolitic microporous frameworks. *J. Am. Chem. Soc.* **1999**, *121*, 4308.
- Yang, P.D.; Deng, T.; Zhao, D.Y.; Feng, P.; Pine, D.S.; Chmelka, B.F.; Whitesides, G.M.; Stucky, G.D. Hierarchically ordered oxides. *Science* **1998**, *282*, 2244.
- Schacht, S.; Huo, Q.; Voigt-Martin, I.G.; Stucky, G.D.; Schuth, F. Oil-water interface templating of mesoporous macroscale structures. *Science* **1996**, *273*, 768.
- Fan, H.; Lu, Y.; Stump, A.; Reed, S.T.; Baer, T.; Schunk, R.; Perez-Luna, V.; Lopez, G.P.; Brinker, C.J. Rapid prototyping of patterned functional nanostructures. *Nature* **2000**, *405*, 56.
- Wulff, G.; Sarhan, A. The use of polymers with enzyme-analogous structures for the resolution of racemates. *Angew. Chem., Int. Ed. Engl.* **1972**, *11*, 341.
- Wulff, G. Molecular imprinting in cross-linked materials with the aid of molecular templates—A way towards artificial antibodies. *Angew. Chem., Int. Ed. Engl.* **1995**, *34*, 1812.
- Mosbach, K. Molecular imprinting. *Trends Biochem. Sci.* **1994**, *19*, 9.
- Shea, K.J. *Trends Polym. Sci.* **1994**, *2*, 166.
- Katz, A.; Davis, M.E. Molecular imprinting of bulk, microporous silica. *Nature* **2000**, *403*, 286.
- Bartsch, R.A.; Maeda, M.; Eds.; *Molecular and Ionic Recognition with Imprinted Polymers*; ACS: Washington, DC, 1998.
- Sellergren, B.; Shea, K.J. Origin of peak asymmetry and the effect of temperature on solute retention in enantiomer separations on imprinted chiral stationary phases. *J. Chromatogr., A* **1995**, *690*, 29.
- Cheong, S.H.; McNiven, S.; Rachkov, A.; Levi, R.; Yano, K.; Karube, I. Testosterone receptor binding mimic constructed using molecular imprinting. *Macromolecules* **1997**, *30*, 1317.
- Yu, C.; Mosbach, K. Molecular imprinting utilizing an amide functional group for hydrogen bonding leading to highly efficient polymers. *J. Org. Chem.* **1997**, *62*, 4057.
- Vidyasankar, S.; Ru, M.; Arnold, F.H. Molecularly imprinted ligand-exchange adsorbents for the chiral separation of underivatized amino acids. *J. Chromatogr., A* **1997**, *775*, 51.
- Liang, C.D.; Weaver, M.J.; Dai, S. Change of pH indicator's  $pK_a$  value via molecular imprinting. *Chem. Comm.* **2002**, 1620–1622.
- Dai, S.; Burleigh, M.C.; Ju, Y.H.; Gao, H.J.; Lin, J.S.; Pennycook, S.J.; Barnes, C.E.; Xue, Z.L. Hierarchically

- imprinted sorbents for the separation of metal ions. *J. Am. Chem. Soc.* **2000**, *122*, 992.
23. Dai, S. Hierarchically imprinted sorbents. *Chem. Eur. J.* **2001**, *7*, 763.
  24. Kresge, C.T.; Leonowicz, M.E.; Roth, W.J.; Vartuli, J.C.; Beck, J.S. Ordered mesoporous molecular sieves synthesized by a liquid-crystal template mechanism. *Nature* **1992**, *359*, 710.
  25. Firouzi, A.; Kumar, D.; Bull, L.M.; Besier, T.; Siegr, P.; Huo, Q.; Walker, S.A.; Zasadzinski, J.A.; Glinka, G.; Nicol, J.; Margolese, D.; Stucky, G.D.; Chmelka, B.F. Cooperative organization of inorganic-surfactant and biomimetic assemblies. *Science* **1995**, *267*, 1138.
  26. Feng, X.; Fryxell, G.E.; Wang, L.-Q.; Kim, A.Y.; Liu, J.; Kemner, K.M. Functionalized monolayers on ordered mesoporous supports. *Science* **1997**, *276*, 923.
  27. Liu, J.; Feng, X.; Fryxell, G.E.; Wang, L.-Q.; Kim, A.Y.; Gong, M. Hybrid mesoporous materials with functionalized monolayers. *Adv. Mater.* **1998**, *10*, 161.
  28. Mercier, L.; Pinnavaia, T.J. Access in mesoporous materials: advantage of a uniform pore structure in the design of a heavy metal ion adsorbent for environmental remediation. *Adv. Mater.* **1997**, *9*, 500.
  29. Shin, Y.S.; Burlergh, M.C.; Dai, S.; Barnes, C.E.; Xue, Z.L. Investigation of uranyl adsorption on mesoporous titanium-based sorbents. *Radiochim. Acta* **1999**, *84*, 37.
  30. Hall, S.R.; Fowler, C.E.; Lebeau, B.; Mann, S. Template-directed synthesis of bi-functionalized organo-MCM-41 and phenyl-MCM-48 silica mesophases. *Chem. Commun.* **1999**, 201.
  31. Brown, J.; Mercier, L.; Pinnavaia, T.J. Selective adsorption of  $Hg^{2+}$  by thiol-functionalized nanoporous silica. *Chem. Commun.* **1999**, 69.
  32. Fowler, C.E.; Burkett, S.L.; Mann, S. Synthesis and characterization of ordered organo-silica-surfactant mesophases with functionalized MCM-41-type architecture. *Chem. Commun.* **1997**, 1769.
  33. Macquarrie, D.J. Direct preparation of organically modified MCM-type materials. Preparation and characterisation of aminopropyl-MCM and 2-cyanoethyl-MCM. *Chem. Commun.* **1996**, 1961.
  34. Lim, M.H.; Blanford, C.F.; Stein, A. Synthesis and characterization of a reactive vinyl-functionalized MCM-41: probing the internal pore structure by a bromination reaction. *J. Am. Chem. Soc.* **1997**, *119*, 4090.
  35. Yang, H.; Kuperman, A.; Coombs, N.; Mamiche-Afara, S.; Ozin, G.A. Synthesis of oriented films of mesoporous silica on mica. *Nature* **1996**, *379*, 703.
  36. De, G.T.; Epifani, M.; Licciulli, A. Copper-ruby monoliths by the sol-gel process. *J. Non-Cryst. Solids* **1996**, *201*, 250.
  37. Baker, A.T. The ligand field spectra of copper(II) complexes. *J. Chem. Educ.* **1998**, *75*, 98.
  38. Kuchen, W.; Schram, J. *Angew. Chem.* **1998**, *100*, 1757.
  39. Metal-ion selective exchange resins by matrix with methacrylates. *Angew. Chem., Int. Ed. Engl.* **1988**, *27*, 1695.
  40. Dai, S.; Burleigh, M.C.; Shin, Y.S.; Morrow, C.C.; Barnes, C.E.; Xue, Z.L. Imprint coating: a novel synthesis of selective functionalized ordered mesoporous sorbents. *Angew. Chem., Int. Ed.* **1999**, *38*, 1235.
  41. Burleigh, M.C.; Dai, S.; Hagaman, E.W.; Lin, J.S. Imprinted polysilsesquioxanes for the enhanced recognition of metal ions. *Chem. Mater.* **2001**, *13*, 2537.
  42. Loy, D.A.; Shea, K.J. Bridged polysilsesquioxanes. Highly porous hybrid organic-inorganic materials. *Chem. Rev.* **1995**, *95*, 1431.
  43. Corriu, R.J.P. Ceramics and nanostructures from molecular precursors. *Angew. Chem., Int. Ed. Engl.* **2000**, *39*, 1376.
  44. Inagaki, S.; Guan, S.; Fukushima, Y.; Ohsuna, T.; Terasaki, O. Novel mesoporous materials with a uniform distribution of organic groups and inorganic oxide in their frameworks. *J. Am. Chem. Soc.* **1999**, *121*, 9611.
  45. Asefa, T.; MacLachlan, M.J.; Coombs, N.; Ozin, G.A. Periodic mesoporous organosilicas with organic groups inside the channel walls. *Nature* **1999**, *402*, 867.
  46. Melde, B.J.; Holland, B.T.; Blanford, C.F.; Stein, A. Mesoporous sieves with unified hybrid inorganic/organic frameworks. *Chem. Mater.* **1999**, *11*, 3302.
  47. Tsukagoshi, K.; Yu, K.Y.; Maeda, M.; Takagi, M. *Bull. Chem. Soc. Jpn.* **1993**, *66*, 114.
  48. Uezu, K.; Goto, M.; Nakashio, F. *Molecular and Ionic Recognition with Imprinted Polymers*; ACS Symposium Series; Bartsch, R.A., Maeda, M., Eds.; American Chemical Society: Washington, DC, 1998; 703, 278–289.
  49. Uezu, K.; Nakamura, H.; Goto, M.; Murata, M.; Maeda, M.; Takagi, M.; Nakashio, F. Novel metal ion-imprinted resins prepared by surface template polymerization with w/o emulsion. *J. Chem. Eng. Jpn.* **1994**, *27*, 436.
  50. Uezu, K.; Nakamura, H.; Kanno, J.; Sugo, T.; Goto, M.; Nakashio, F. Metal ion-imprinted polymer prepared by the combination of surface template polymerization with postirradiation by  $\gamma$ . *Macromolecules* **1997**, *30*, 3888.
  51. Yoshida, M.; Uezu, K.; Goto, M.; Nakashio, F. Metal ion-imprinted resins with novel bifunctional monomer by surface template polymerization. *J. Chem. Eng. Jpn.* **1996**, *29*, 174.
  52. Yoshida, M.; Uezu, K.; Goto, M.; Furusaki, S. Required properties for functional monomers to produce a metal template effect by a surface molecular imprinting technique. *Macromolecules* **1999**, *32*, 1237.
  53. Yoshida, M.; Uezu, K.; Goto, M.; Furusaki, S.M.; Takagi, M. An enantioselective polymer prepared by the surface molecular-imprinting technique. *Chem. Lett.* **1998**, 925.
  54. Toorisaka, E.; Yoshida, M.; Uezu, K.; Goto, M.; Furusaki, S. *Chem. Lett.* **1998**, 387.

55. Comba, P.; Gloc, K.; Inoue, K.; Aduger, T.; Stephan, H.; Yoshizuka, K. *Inorg. Chem.* **1998**, *37*, 3310.
56. Zhang, Z.T.; Dai, S.; Hunt, R.D.; Wei, Y.; Qiu, S.L. Ion-imprinted zeolite: a surface functionalization methodology based on the “Ship-in-Bottle” technique. *Adv. Mater.* **2001**, *13*, 493.
57. Zhang, Z.; Saengerdsu, S.; Dai, S. Intersurface ion-imprinting synthesis on layered magadiite hosts. *Chem. Mater.* **2003**, *15* (15), 2921–2925.
58. Isoda, K.; Kuroda, K.; Ogawa, M. Interlamellar grafting of  $\gamma$ -methacryloxypropylsilyl groups on magadiite and copolymerization with methyl methacrylate. *Chem. Mater.* **2000**, *12*, 1702.
59. Ogawa, M.; Okutomo, S.; Kuroda, K. Control of inter-layer microstructures of a layered silicate by surface modification with organochlorosilanes. *J. Am. Chem. Soc.* **1998**, *120*, 7361.
60. Shin, Y.; Liu, J.; Wang, L.-Q.; Nie, Z.; Samuels, W.D.; Fryxell, G.E.; Exarhos, G.J. Ordered hierarchical porous materials: towards tunable size- and shape-selective microcavities in nanoporous channels. *Angew. Chem., Int. Ed. Engl.* **2000**, *39*, 2702.



# High-Strength Alloys: Nanogranular Phases

Dmitri Valentinovich Louzguine

Akihisa Inoue

*Institute for Materials Research, Tohoku University, Sendai, Japan*

## INTRODUCTION

High-strength alloys with a nanoscale-size microstructure (nanostructured alloys and composites on their base) demonstrate superior mechanical properties in a wide range obtained because of very small grain (particle) size ranging from 1 to 100 nm. Nanoscale grains (particles) can have a crystalline, quasicrystalline, or amorphous structure. These alloys often have non-equilibrium nature, although many of them exhibit remarkable stability against structural coarsening. The classical example of strong dispersion-strengthened alloys are age-hardened Al–Cu alloys, discovered in the beginning of the 20th century,<sup>[1]</sup> with nanoscale Guinier–Preston zones,  $\theta''$  and  $\theta'$  phases,<sup>[2,3]</sup> which can be considered as one of the first examples of the use of nanogranular phases in alloys for practical purposes. Because of the very small size, observation of the Guinier–Preston zones and these nanogranular phases requires application of transmission electron microscopy.

At present, alloys with nanostructured phases exhibit mechanical properties that are superior to that of conventional polycrystalline alloys. They possess high hardness, tensile, and compressive strength values, and exhibit superplastic behavior at low reduced temperature.

## FORMATION OF A NANOSTRUCTURE

Nanostructured alloys are usually produced by inert gas condensation from vapor phase,<sup>[4]</sup> sputtering,<sup>[5]</sup> rapid solidification of the melt,<sup>[6]</sup> electrodeposition,<sup>[7]</sup> or mechanical attrition<sup>[8]</sup> severe plastic deformation<sup>[9]</sup> of the solid phase as well as by devitrification of glassy alloys,<sup>[10]</sup> and other techniques.

The processing procedure can be a single-step or double/multistep one. The same material can be produced by different techniques. However, the production technique often makes significant influence of the properties of nanomaterials.

If the process involves nucleation and growth, then high nucleation rate and low growth rate of the

precipitating phase are required in order to obtain a nanostructure. Such conditions are usually obtained under primary devitrification with long-range, diffusion-controlled growth.<sup>[11]</sup> For example, Al-rich amorphous alloys with high Al concentrations above 85 at.%, in general, suffer double or multistage devitrification in which the first-stage exothermic reaction is due to the precipitation of fcc-Al, and the other exothermic peaks result from the decomposition of the residual amorphous phase to intermetallic compounds. Another way of forming a nanostructure by devitrification of the metallic glasses is spinodal decomposition.<sup>[12,13]</sup>

Al–RE–TM (RE—rare earth metals, TM—transition metal) system glassy alloys were produced in the late 1980s in Japan<sup>[14]</sup> and the United States.<sup>[15]</sup> These alloys are usually produced in a ribbon shape by the melt spinning technique<sup>[16]</sup> or in a powder one by gas atomization.<sup>[17]</sup> Al<sub>85</sub>Ni<sub>10</sub>Ce<sub>5</sub> (here and elsewhere alloy compositions are given in nominal atomic percents, at.%) bulk amorphous samples of high relative density were obtained by warm extrusion of atomized amorphous powder.<sup>[18]</sup>

Various Al–RE–TM glasses containing about 85 at.% Al show primary precipitation of Al solid solution ( $\alpha$ -Al) nanoparticles on heating<sup>[19]</sup> with extremely high nucleation rate<sup>[20]</sup> of above  $10^{20} \text{ m}^{-3} \text{ sec}^{-1}$ . fcc  $\alpha$ -Al lattice parameter measurements and atom probe ion field microscopy investigation<sup>[21]</sup> showed very low concentration of the alloying elements in nanocrystalline Al in accordance with phase diagrams<sup>[22]</sup> of Al–RE and Al–TM. Segregation of the RE metal having low trace diffusivity in Al on the  $\alpha$ -Al/amorphous phase interface is considered to be one of the most important reasons for the low growth rate of  $\alpha$ -Al. Nearly the same effects were observed during the formation of the  $\alpha$ -Fe nanocrystals.<sup>[23]</sup>

The supercooled liquid region and the regimes of heat treatment used play an important role in the devitrification behavior of the glassy alloys. Y-, Sm-, Gd-, and Dy-bearing glassy alloys of the Al<sub>85</sub>RE<sub>8</sub>-Ni<sub>5</sub>Co<sub>2</sub> composition showed a precipitation of the  $\alpha$ -Al nanoparticles after continuous heating using DSC at high enough heating rate to prevent devitrification

below  $T_g$  (0.67 K/sec and higher) or annealing at the temperature above  $T_g$ . At the same time, Y-, Gd-, and Dy-bearing metallic glasses as well as the  $\text{Al}_{85}\text{Y}_4\text{Nd}_4\text{Ni}_5\text{Co}_2$  showed simultaneous formation of the intermetallic compound(s) and  $\alpha$ -Al nanoparticles, or primary formation of the only intermetallic compound after annealing below  $T_g$ .<sup>[24]</sup> For example, the  $\text{Al}_{85}\text{Y}_8\text{Ni}_5\text{Co}_2$  alloy shows a formation of an unknown intermetallic compound conjointly with  $\alpha$ -Al nanoparticles after annealing up to the completion of the primary phase transformation. The intermetallic compound is metastable and has a multicomponent composition. The volume fraction of the intermetallic compound is higher than that of  $\alpha$ -Al and the fraction of  $\alpha$ -Al depends upon an annealing temperature below  $T_g$ .

Devitrification of the  $\text{Ti}_{50}\text{Ni}_{20}\text{Cu}_{23}\text{Sn}_7$  alloy begins from the primary precipitation of a nanoscale equiaxed, almost spherical particles of cF96  $\text{Ti}_2\text{Ni}$  solid solution (other alloying elements are partially dissolved in this phase) (Fig. 1A,B).<sup>[25]</sup> One should mention that these particles exhibit high thermal stability against coarsening and retain their nanoscale size

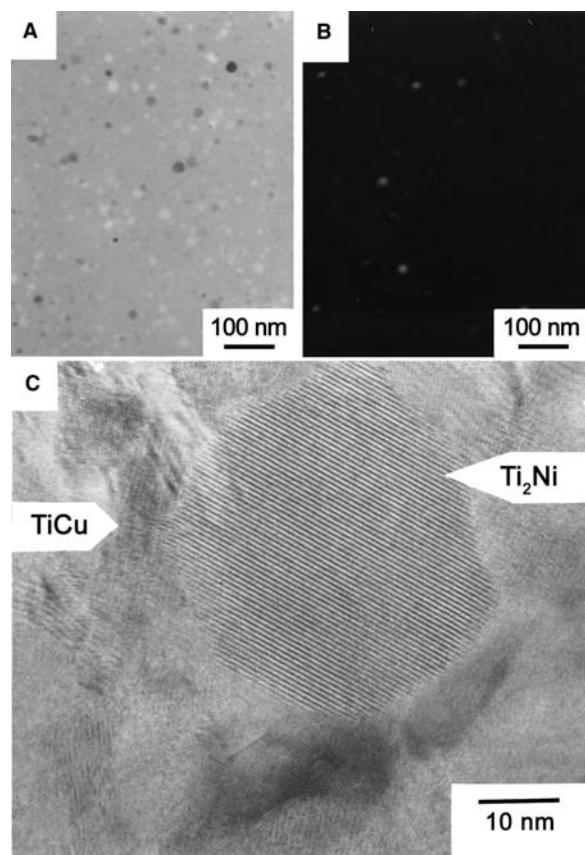


**Fig. 1** (A) Bright- and (B) dark-field TEM images of  $\text{Ti}_{50}\text{Ni}_{20}\text{Cu}_{23}\text{Sn}_7$  alloy after isothermal calorimetry at 725 K for 2200 sec. (C) HRTM after DSC at 0.67 K/sec up to 850 K. Source: From Ref.<sup>[25]</sup>.

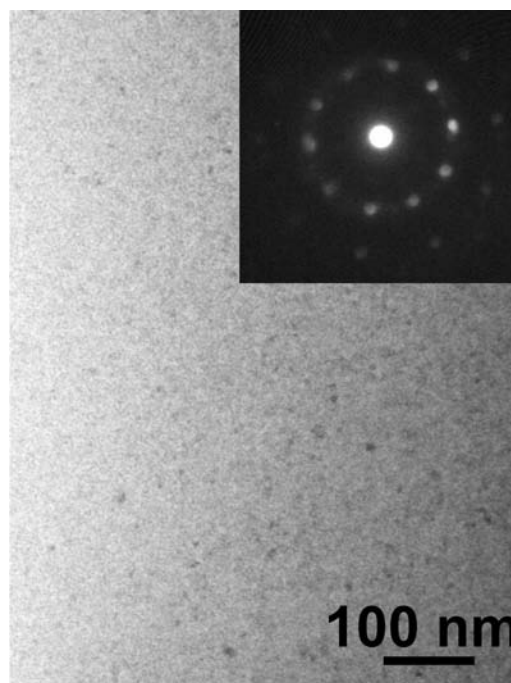


**Fig. 2** Bright-field micrograph of the  $\text{Cu}_{55}\text{Zr}_{30}\text{Ti}_{10}\text{Pd}_5$  alloy annealed for 1.2 ksec at 750 K. The insert-nanobeam electron diffraction pattern of fivefold symmetry.

even after heating up to 850 K when  $\text{TiCu}$  phase starts to precipitate from the residual glassy matrix (Fig. 1C).

Formation of the nanoscale icosahedral phase was observed in  $\text{Zr-Cu-Al}$ ,  $\text{Zr-Al-Ni-Cu}$ ,<sup>[26]</sup> and  $\text{Zr-Ti-Ni-Cu-Al}$ <sup>[27]</sup> glassy alloys containing an impurity of oxygen above about 1800 mass ppm, although no icosahedral phase is formed if oxygen content is lower than 1700 mass ppm. Later, the nanoscale icosahedral phase was obtained in Zr-based alloys containing noble metals<sup>[28]</sup> as well as a result of V, Nb, or Ta addition at much lower (typically about 800 mass ppm) oxygen content. Some  $\text{Hf-NM-(Ni,Cu)-Al}$  alloys also devitrify forming nanoicosahedral phase.<sup>[29]</sup> The study of amorphous  $\rightarrow$  icosahedral phase transformation in a  $\text{Zr}_{65}\text{Al}_{7.5}\text{Ni}_{10}\text{Cu}_{7.5}\text{Ag}_{10}$  showed that the quasilattice constant decreases with annealing time and the zirconium and silver content in the icosahedral particles differ from those in the remaining amorphous matrix<sup>[30]</sup> as it should be in the case of primary-type reaction. Recently, nanoscale icosahedral phase with a size of less than 10 nm homogeneously dispersed in the residual glassy matrix was formed in Cu-based alloy<sup>[31]</sup> (Fig. 2).

The local atomic structures around Pt as well as Zr in the amorphous and quasicrystalline  $\text{Zr-Al-Ni-Pt}$  alloys have been determined by the anomalous X-ray scattering method.<sup>[32]</sup> The existence of chemical short-range order clusters was found in the glassy state as well. Moreover, recently it was shown that the

icosahedral order exists in the liquid phase of Ti–Zr–Ni quasicrystal-forming alloy.<sup>[33]</sup>

Two very important parameters of such composite nanomaterials are grain (particle) size and its volume fraction. Primary devitrification of highly supercooled liquid or amorphous phase often has the following unique features, i.e., high nucleation frequency, low crystal growth rate, high concentration gradient of solute element at liquid/solid interface resulting from low atomic diffusivity, formation of metastable phases by the control of redistribution of solute elements, formation of a residual amorphous phase with high solute concentration, defect-free nanocrystalline particles with low residual strain, highly dense packed structure at liquid/solid interface, nanoscale interparticular spacing, and size and shape effects of nanoscale spherical particles. Relying upon the aforementioned, new nanoscale mixed-phase alloys containing a residual amorphous phase were obtained by devitrification of glassy alloys.<sup>[34]</sup>

## STRUCTURE AND MECHANICAL PROPERTIES

### Single-Phase Nanocrystalline Alloys

In general, bulk single-phase nanostructured materials were found to exhibit low ductility at room temperature, which impedes a limit on their practical applications. For example, electrodeposited nanocrystalline Ni with a mean grain size of 10 nm showed yield strength, ultimate tensile strength, and elongation to fracture of 900 MPa, 2000 MPa, and 1%, respectively, compared to 100 MPa, 400 MPa, and 50%, respectively, for polycrystalline Ni with 10- $\mu$ m grain size<sup>[35]</sup> The major reasons for the brittleness of bulk metallic nanomaterials are connected with the difficulties of dislocation generation and movement, porosity, and other artifacts as well as instability of crack nucleation and propagation. However, recent studies on nanocrystalline pure metals showed that quite high ductility values on tensile test can be obtained at definite grain size after proper treatment.<sup>[36]</sup> For example, nanocrystalline hcp Co samples with a mean grain size of 12 nm produced by pulse electroplating on Ti substrate followed by a thermomechanical treatment showed an ultimate tensile strength of 1865 MPa, yield strength of 1000 MPa at 7% elongation, which is an example of a very good combination of strength and ductility.<sup>[37]</sup>

Mechanical yield strength of conventional polycrystalline materials obeys the well-known Hall–Petch relationship that has been extrapolated to nanomaterials as well. The Hall–Petch relation states that the yield strength  $\sigma_y$  increases monotonically with

decreasing the average grain size  $d$  as:

$$\sigma_y = \sigma_0 + kd^{-1/2} \quad (1)$$

where  $\sigma_0$  is the friction stress needed to move dislocations and  $k$  is a material-dependent constant. Considerable strengthening is achieved on reducing the grain size from the macro- to the micro- and finally to the nanoscale size. However, different types of strength variation with nanoscale grain size have been reported, ranging from respecting the Hall–Petch relationship to showing a saturation of strength or even fall of strength at the finest grain sizes.<sup>[38–40]</sup>

A number of models have been proposed to interpret the inverse Hall–Petch behavior. Some calculations<sup>[41]</sup> based on the idea that very small grains cannot sustain significant dislocation activity indicate that the Hall–Petch behavior should cease when the average grain size is below 10–20 nm. Numerous models have been proposed to explain the deformation when the grain size falls below the cut-off value for significant dislocation activity. It is frequently predicted by a mechanism based on grain boundary sliding accommodated by diffusion or by the emission of dislocations into the grains.<sup>[42]</sup> The inverse Hall–Petch relation is also explained by the size-dependent line tension where the dislocation elastic strain is assumed to be screened within the distance of the grain diameter.<sup>[43]</sup> On the basis of the composite model involving a crystalline matrix and intercrystalline layers, the yield stress of nanocrystalline materials can be expressed as the sum of the matrix contribution and the intercrystalline contribution, both of which are assumed to be linearly connected with the corresponding shear module and to be functions of the grain size.<sup>[44]</sup> The attempt was also done to explain the inverse Hall–Petch relation by the change of the deformation mechanism from a dislocation glide process to the Coble creep.

### Multiphase Nanostructured Alloys

Commercial high-strength materials usually have a multiphase microstructure. For example, a new Mg<sub>97</sub>Zn<sub>1</sub>Y<sub>2</sub> low alloy with high yield strength and ductility was produced recently by compaction and extrusion of the powder produced by high-pressure gas atomization.<sup>[45]</sup> As the extrusion temperature rises, the resulting tensile yield strength changes from 600 to 420 MPa, while the percentage elongation increases from 5% to 15%. These values are extremely high for Mg-based alloys.

Mg–Zn–Y alloys show a novel long periodic hexagonal matrix phase. Fig. 3 shows the TEM image of the Mg<sub>97</sub>Zn<sub>1</sub>Y<sub>2</sub> alloy obtained by extrusion at 573 K. The alloy consists of fine grains with grain sizes ranging

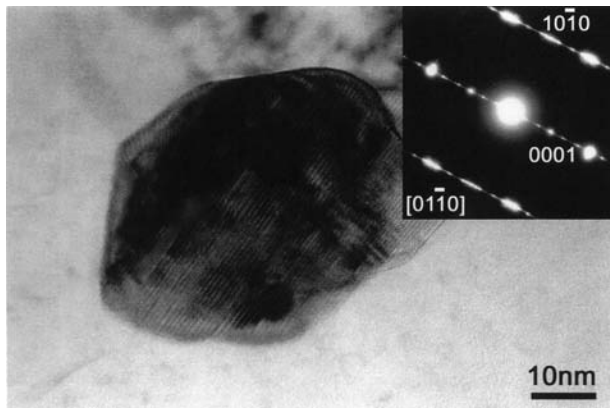


**Fig. 3** High-resolution TEM image and selected-area electron diffraction pattern of the RS/PM  $\text{Mg}_{97}\text{Zn}_1\text{Y}_2$  alloy produced at 573 K. *Source:* From Ref.<sup>[46]</sup>.

from 100 to 150 nm. In addition, each grain contains a high density of stacking fault-similar defects as well as very fine precipitates with a size of about 10 nm. In the selected-area electron diffraction pattern shown in Fig. 3,<sup>[46]</sup> one can see extra reflection spots in the direction of (0001), indicating the formation of a long-periodic structure in which the periodicity is longer than that for the ordinary hcp-Mg phase.

This long-period ordered structure has a unit cell composed of six close-packed planes of the magnesium crystal with a stacking sequence of ABCBCB', where the A and B' layers are significantly enriched in Zn and Y.<sup>[47]</sup> However, an atomic structure model of the Mg–(Zn, Y) long-period ordered structure was constructed based on a monoclinic lattice with  $\gamma = 88^\circ$ ,  $a = 0.56$ ,  $b = 0.32$ ,  $c = 1.56$  nm, by using the lattice distortion from the ideal long periodic hexagonal structure. The lattice distortion from an ideal hexagonal lattice arises from an asymmetry of the chemical order with respect to the hexagonal-type stacking order. In addition to the change in the structure of the matrix phase, homogeneous dispersion of fine precipitates of a  $\text{Mg}_{24}\text{Y}_5$  phase with cubic lattice and a size of about 7 nm was observed.

$\text{Mg}_{97}\text{Zn}_1\text{Y}_2$  alloy also exhibited high strain rate superplasticity showing tensile elongation above 700% at 623 K at a high strain rate of  $0.1 \text{ sec}^{-1}$  as well as a high strain rate sensitivity exponent of 0.4. The sample with the largest elongation at a high strain rate of  $0.1 \text{ sec}^{-1}$  was elongated through a homogeneous deformation mode. Thus the  $\text{Mg}_{97}\text{Zn}_1\text{Y}_2$  alloy has excellent mechanical properties as well as high strain rate superplasticity.

Recently, it has been shown also that a 3-mm-diameter cylindrical rod of cast  $\text{Ti}_{60}\text{Cu}_{14}\text{Ni}_{12}\text{Sn}_4\text{Nb}_{10}$  alloy consisting of a micron-size  $\beta$ -Ti dendrites and nanostructured precipitates exhibits high ultimate compressive strength of 2.4 GPa and 14.5% plastic strain.<sup>[48]</sup>

## Nanoquasicrystalline Alloys

High strength and good ductility for the icosahedral base alloys can be obtained in a nanostructured state when the icosahedral phase coexists with the fcc  $\alpha$ -Al phase and has a spherical morphology, small grain size, and homogeneous dispersion. The mixed structure consisting of icosahedral and  $\alpha$ -Al phases is formed in the Al-rich melt-spun Al–Mn–RE alloys, and the mixed phase alloys have good bending ductility and high fracture strength reaching 1320 MPa. The high-strength  $\text{Al}_{92}\text{Mn}_6\text{Ce}_2$  alloy consists of spherical icosahedral particles with a size of about 50 nm surrounded by nanoscale fcc- $\alpha$ -Al layer with a thickness of 5 to 10 nm. The similar nanoscale mixed structure is also formed in rapidly solidified Al–Cr–Ce–Co alloys<sup>[49]</sup> and the icosahedral particles with a size of 20–40 nm are homogeneously dispersed in the Al phase. For example,  $\text{Al}_{94.5}\text{Cr}_3\text{Ce}_1\text{Co}_{1.5}$  alloy exhibits high fracture strength of 1340 MPa.

The icosahedral phase-based alloys also have good cold deformability and can be cold rolled up to the significant reduction ratio in thickness above 70%.<sup>[50]</sup> The cold-rolled alloy has a much finer mixed structure consisting of an icosahedral phase with a size of 5 to 10 nm in coexistence with nanoscale fcc  $\alpha$ -Al phase.

Here it is important to point out that the high tensile strength combined with good ductility is obtained only for the mixed phase alloys prepared through the unique solidification process in which the nanoquasicrystalline phase precipitates as a primary phase, followed by the solidification of  $\alpha$ -Al from the remaining liquid. On the other hand, when the Al-based alloys have the other type of solidification processes in which an  $\alpha$ -Al solid solution is formed first, followed by the precipitation of an icosahedral phase within  $\alpha$ -Al grains and along  $\alpha$ -Al grain boundaries, the studied alloys showed low tensile strength and ductility.

In addition, the same mixed structure consisting of the nanoscale icosahedral phase surrounded by the fcc  $\alpha$ -Al phase is also formed for atomized powders in Al–Mn–RE and Al–Cr–RE–TM systems as well as in Al–Mn–TM and Al–Cr–TM systems without the RE element.<sup>[51]</sup> For the atomized powders extruded in the temperature range below 673 K, which is lower than the decomposition temperature of the icosahedral phase, one can obtain fully dense bulk icosahedral-base alloys.<sup>[52]</sup> Fig. 4 shows the relation between tensile strength and plastic elongation for the extruded bulk icosahedral base alloys in comparison with the data of conventional Al-based alloys. The bulk icosahedral-based alloys have high fracture strength values of 500 to 850 MPa combined with large elongation of 5–25%, which are much superior to those for the conventional Al-based alloys.



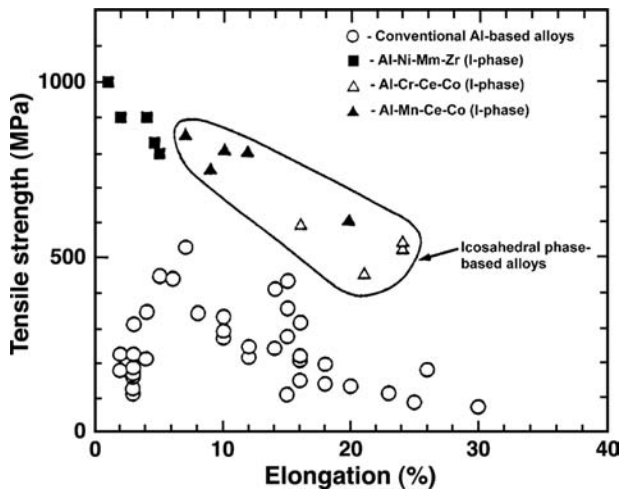


**Fig. 4** Relation between tensile strength and plastic elongation for the extruded bulk icosahedral base alloys. The data of conventional Al-based alloys are also shown for comparison. *Source:* From Ref.<sup>[18]</sup>.

A mostly single icosahedral phase was obtained for the Al-Fe-Cr-Ti alloys.<sup>[53]</sup> The new Al-Fe-Cr-Ti alloys exhibit excellent elevated temperature strength of 400 to 460 MPa at 473 K and 350 to 360 MPa at 573 K. It has further been shown that the high elevated temperature strength level of the extruded  $Al_{93}Cr_3Fe_2Ti_2$  alloy is maintained even after annealing for 1000 hr at 573 K. The annealed alloy also keeps a fine mixed structure consisting of fine icosahedral particles and fine Al grains.

Thus the icosahedral phase-based Al alloys can be classified into three groups: 1) high-strength-type alloys in Al-Mn-RE and Al-Cr-RE-TM systems; 2) high-ductility-type alloys in Al-Mn-Cu-TM and Al-Cr-Cu-TM systems; and 3) high-elevated-temperature-strength-type alloys in Al-Fe-Cr-Ti system. The present nanoquasicrystalline Al alloys exhibit good combination for almost all properties including tensile strength, elevated temperature strength, Charpy impact fracture energy, cold workability, elongation and Young's modulus except thermal expansion. Fine-grained magnesium alloys reinforced by quasicrystalline particles were developed by thermomechanical processes for as-cast  $Mg_{96}Zn_{3.4}Y_{0.6}$  and  $Mg_{94.8}Zn_{4.3}Y_{0.7}Zr_{0.2}$  alloys.<sup>[54]</sup>

### Nanostructured Alloys with Glassy Phase

Nanocomposite materials can be produced using a single-step process, e.g., on rapid solidification by controlling the cooling rate or by using a double-step one such as devitrification of the glassy matrix.

The structure types of Al-<sup>[55]</sup> and Zr-based<sup>[56]</sup> nanostructured alloys are shown in Figs. 5 and 6 together with their typical mechanical properties.

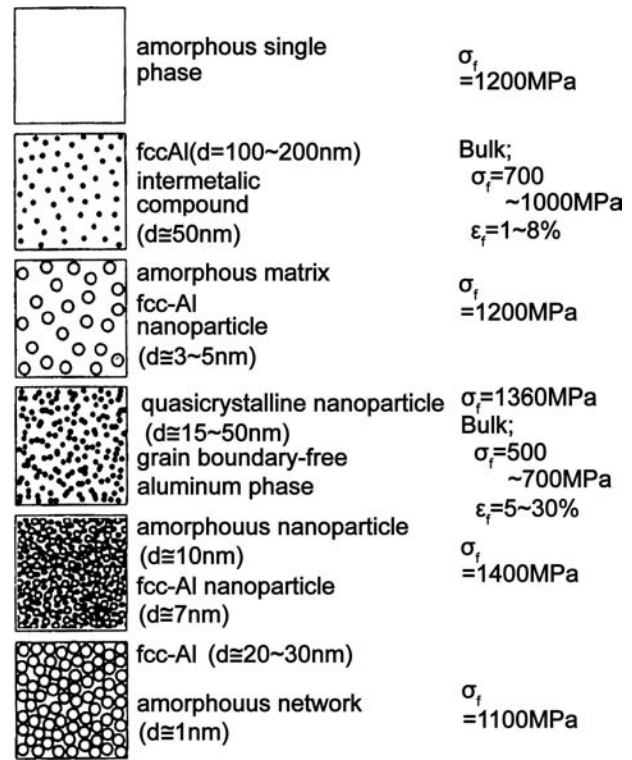


**Fig. 5** Microstructure and mechanical properties of nonequilibrium Al-based alloys. *Source:* From Ref.<sup>[55]</sup>.

One should also mention that some bulk glassy alloys contain medium-range order (MRO) zones and nanoscale particles<sup>[57,58]</sup> in as-solidified state (Fig. 7),<sup>[59]</sup> although these precipitates do not produce diffraction peaks in the XRD and selected-area electron diffraction pattern because of their low volume fraction.

Al-based amorphous alloys exhibit high tensile strength exceeding 1200 MPa.<sup>[60]</sup> It is important that amorphous alloys in the ternary Al-RE-TM system, e.g., Al-Y-Ni, in addition to their high strength, possess good bend ductility. An addition of Co partially replacing Y in the  $Al_{85}Y_{10}Ni_5$  increased the tensile fracture strength, e.g., from 920 to 1250 MPa, in the case of  $Al_{85}Y_8Ni_5Co_2$  metallic glass, without worsening of bend ductility.<sup>[61]</sup> At the same time, the addition of 2 at.% Co to  $Al_{85}Y_{10}Ni_5$  alloy also caused a drastic increment of the glass-forming ability.

Subsequently, it has been noticed that the homogeneous dispersion of nanoscale fcc  $\alpha$ -Al particles in an amorphous matrix causes a drastic increase in tensile fracture strength to 1560 MPa for the  $Al_{85}Y_8Ni_5Co_2$  without a reduction in bend ductility.<sup>[62]</sup> An optimum strength value was obtained for a crystalline phase volume fraction ranging from 5% to 25%.<sup>[63]</sup> The volume fraction of the fcc-Al phase is controlled by changing the rotation speed of the wheel and is evaluated by the change in the exothermic amount due to

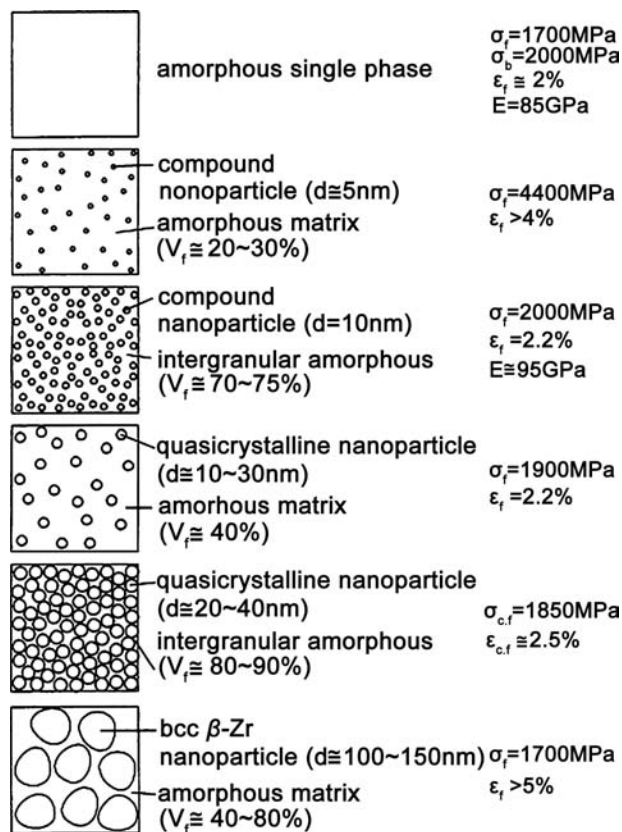


**Fig. 6** Microstructure and mechanical properties of non-equilibrium Zr-based bulk alloys in Zr–Al–Ni–Cu and Zr–Al–Ni–Cu–M (M = Ag, Pd, Au, Pt or Nb) systems. *Source:* From Ref.<sup>[56]</sup>.

crystallization. The tensile fracture strength increases from about 1100 MPa at volume fraction of fcc-Al ( $V_f$ )  $V_f = 0\%$  to 1560 MPa at  $V_f = 25\%$ , accompanying an increase in Vickers hardness from 280 to 400 and Young's modulus from 63 to 71 GPa.<sup>[51]</sup> The significant decrease in tensile fracture strength by the further increase in  $V_f$  is due to the embrittlement of the remaining amorphous phase by the progress of structural relaxation and the enrichment in the solute elements.

$\text{Al}_{88}\text{Y}_2\text{Ni}_9\text{Fe}_1$  amorphous alloy containing 7% volume fraction of the fcc-Al particles with a size of about 3–7 nm (Fig. 8) has a high tensile fracture strength of 1320 and 1260 MPa with volume fraction of 24%, respectively.<sup>[64]</sup> It is notable that the values for the former alloy are higher than the highest values of Al-based amorphous single-phase alloys. The high strength is combined with good bend ductility.

Bulk  $\text{Al}_{88.5}\text{Ni}_8\text{Mm}_{3.5}$  alloy having a mixed structure consisting of amorphous and fcc-Al phases was produced by extrusion of atomized powders at an extrusion ratio of 10 and at 633 K and was found to exhibit high tensile strength of 940 MPa at room temperature, 700 MPa at 423 K and 520 MPa at 473 K.<sup>[65]</sup>

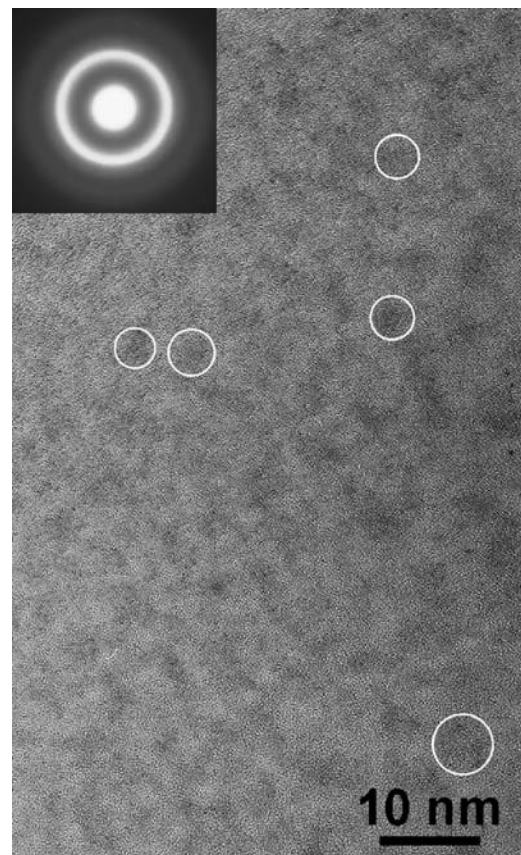


**Fig. 7** HRTEM image of rod-shaped bulk (2 mm in diameter)  $\text{Zr}_{55}\text{Co}_{20}\text{Al}_{12}\text{Cu}_5\text{Nb}_8$  glassy alloy containing MRO zones and nanoscale particles in as-solidified state. The insert represents selected-area electron diffraction pattern. *Source:* From Ref.<sup>[59]</sup>.

Similarly, the yield strength is also as high as 845 MPa at room temperature and 420 MPa at 473 K. The high values of strength remain unchanged even after annealing for 100 hr at these testing temperatures. The fatigue limit after the cycles of 10<sup>7</sup> is also as high as 330 MPa at 293 K and 220 MPa at 473 K. The fatigue limit at room temperature is also 1.2 times as high as the highest value for conventional Al-based alloys.

The deformation of amorphous materials is concentrated on the shear band of maximum shear stress, which maintains about 45° with the load (tensile or compressive) direction. The width of the shear band, e.g., in Al alloys, is about 20 nm. An  $\text{Al}_{88}\text{Ni}_{10}\text{Ce}_2$  glassy alloy primarily transforms from amorphous to amorphous plus fcc  $\alpha$ -Al state and exhibits a large elongation reaching 45% in the temperature range of 450 to 465 K. In this temperature range, primary fcc-Al particles with a size of about 12 nm precipitate homogeneously in the amorphous matrix with an interparticle spacing of about 6 nm. The appearance of the significant elongation is due to a crystallization-induced elongation phenomenon. The process occurs through inhomogeneous deformation along shear



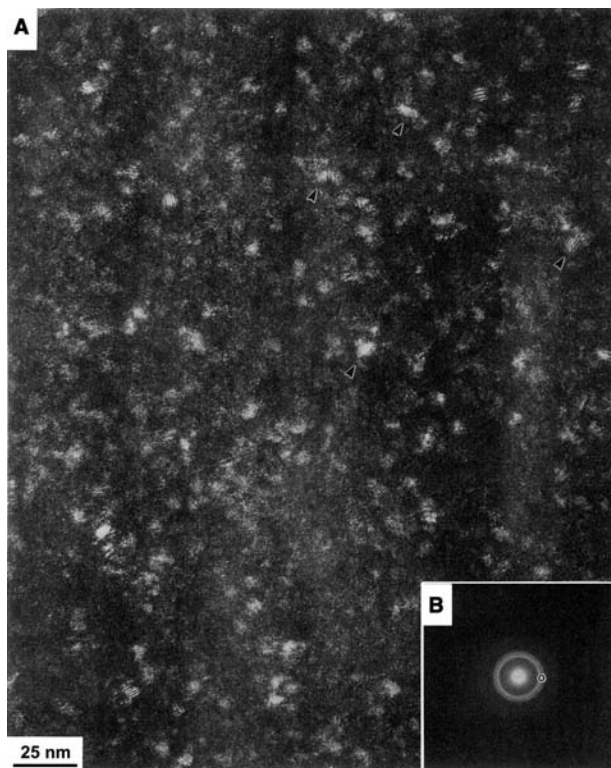


**Fig. 8** Dark-field electron micrograph (A) and electron diffraction pattern (B) of a rapidly solidified  $\text{Al}_{88}\text{Y}_2\text{Ni}_9\text{Fe}_1$  alloy. The circle in the diffraction pattern represents the position and size of the aperture used to take the dark-field electron micrograph. Source: From Ref.<sup>[64]</sup>.

plane, followed by deformation-induced preferential precipitation of Al particles on the shear plane and then propagation of the deformation site to other site resulting from the precipitation-induced strengthening in the deformed area.<sup>[60]</sup>

The increase in strength by the dispersion of nanoscale fcc-Al particles in the amorphous matrix has been thought to result from the combination of the following three effects, i.e., 1) defect-free effect of nanoscale fcc-Al particles, as the Al particles are too fine to contain dislocations; 2) interface effect, as the amorphous/Al particle interface has a highly dense packed structure without excess vacancies owing to a low interfacial energy; and 3) nanoscale effect, as the Al particle size is smaller than the width of the inhomogeneous shear deformation region and hence the nanoscale Al particles can act as an effective barrier against the shear deformation of amorphous matrix.<sup>[34]</sup> It also explains the maintenance of a good bend ductility. At the same time, it was also suggested<sup>[66]</sup> that the hardening could be attributed mainly to solute enrichment of the residual glassy matrix due to the lowering of the Al content.

A model of the ductile–brittle transition of partially crystallized amorphous Al–Ni–Y alloys was proposed

in Ref.<sup>[67]</sup>. The maximum strength of the partially crystalline Al–Ni–Y alloys was obtained when the size of Al particles is 10 nm. However, partially crystallized Al–Ni–Y alloys become brittle when the size and the volume fraction of the Al particles exceeded the optimum values. It was assumed that the Al–Ni–Y alloys become brittle when the solute content of the interface layers reached the critical value (20%). The predictions were found to be in good agreement with the published data.

However, in some cases the formation of the primary  $\alpha$ -Al particles worsens the mechanical properties of Al-based alloy. For example, partial replacement of Ni by Cu in the  $\text{Al}_{85}\text{Y}_8\text{Ni}_5\text{Co}_2$  metallic glass caused the formation of the nanoscale  $\alpha$ -Al particles that resulted in sharp decrement in tensile strength, hardness, crystallization temperature, and disappearance of the supercooled liquid prior to crystallization.<sup>[68]</sup> Cu has a much lower absolute value of heat of mixing with Al, Y, and Co than Ni that leads to decrement of the interatomic constraint force. Thus Cu may weaken the interaction needed for the stability of the glass, thus resulting in the disappearance of  $T_g$  and precipitation of  $\alpha$ -Al nanocrystals. In addition, the volume fraction of the  $\alpha$ -Al nanocrystals in  $\text{Al}_{85}\text{Y}_8\text{Ni}_3\text{Co}_2\text{Cu}_2$ , for example, is much lower than that in the primarily devitrified  $\text{Al}_{85}\text{Y}_8\text{Ni}_5\text{Co}_2$  metallic glass.  $\alpha$ -Al interparticle distances in the  $\text{Al}_{85}\text{Y}_8\text{Ni}_3\text{Co}_2\text{Cu}_2$  metallic glass significantly exceed the particle size. Thus  $\alpha$ -Al particles cannot act as an effective barrier against the shear deformation of amorphous matrix as was supposed for the  $\text{Al}_{85}\text{Y}_8\text{Ni}_5\text{Co}_2$  metallic glass.

At the same time the existence of the MRO zones and nanoscale particles in as-cast rod-shaped bulk (2 mm in diameter)  $\text{Zr}_{55}\text{Co}_{20}\text{Al}_{12}\text{Cu}_5\text{Nb}_8$  glassy alloy (Fig. 6) enhances its ductility leading to the appearance of a plastic deformation region of about 1% deformation. Moreover, nanocrystalline bulk  $\text{Zr}_{55}\text{Al}_{10}\text{Cu}_{30}\text{Ni}_5$  alloy containing nanoscale crystals embedded uniformly in a glassy matrix also has both high tensile strength of 1.7 GPa and good ductility.

It can be shown that the cylindrical bulk sample of  $\text{Zr}_{65}\text{Al}_{7.5}\text{Cu}_{7.5}\text{Ni}_{10}\text{Pd}_{10}$  alloy, the structure of which consists of an almost single icosahedral phase with nanoscale grain sizes of 20–40 nm, shows better combination of mechanical properties than the as-cast glassy sample. The Young's modulus, 0.2% proof stress, ultimate tensile strength, total percentage elongation including elastic elongation are 85 GPa, 1640 MPa, 1750 MPa, and 2.2%, respectively, for the glassy alloy and 88 GPa, 1780 MPa, 1830 MPa, and 3.1%, respectively, for the icosahedral phase-based alloy.<sup>[69]</sup> However, it is well known that stoichiometric icosahedral phase-based alloys have high hardness and are extremely brittle. Thus it is difficult to consider that the icosahedral phase itself in the present alloys has

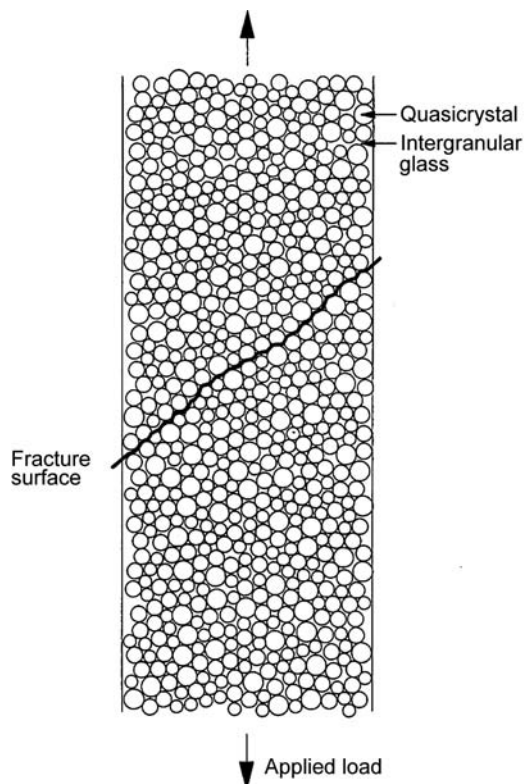


**Fig. 9** Schematic illustration of the deformation and fracture modes of the nanoquasicrystalline Zr–Al–Ni–Cu–Pd alloy. Source: From Ref.<sup>[56]</sup>.

plastic deformability.<sup>[70]</sup> The good mechanical properties are attributed to the existence of residual intergranular glassy phase, although the volume fraction of the glassy phase is estimated to be less than 5%. The deformation of the icosahedral-based alloy takes place in the intergranular glassy phase along the maximum shear plane. The existence of nanoscale icosahedral or crystalline particles can act as a resistant medium against shear deformation (Fig. 9). The good ductility of the glassy layer is also attributed to the localization effect of deformation. The localization generates the multi-axis stress condition as well as causes the increase in the temperature.

At the same time it is shown<sup>[71]</sup> that the nanoicosahedral phase can be obtained in Zr-based alloys with the addition of Ti instead of Pd and Al.

## CONCLUSION

Nanogranular phases of crystalline and quasicrystalline origin play a very important role in the strengthening of conventional polycrystalline as well as glassy alloys as an effective barrier for dislocation activity and shear bands propagation in the former and latter case, respectively. Moreover, nanogranular precipitates

enhance the ductility of bulk glassy alloys, which opens an area for their future application as structural materials. At the same time recent studies showed that even pure metals in nanocrystalline single-phase state after proper treatment can show high strength and good ductility values on tensile test. All the abovementioned promotes further studies on nanostructured alloys.

## REFERENCES

1. Wilm, A. Physikalisch-metallurgische Untersuchungen über magnesiumhaltige Aluminiumlegierungen. *Metallurgie* **1911**, *8*, 225–227.
2. Guinier, A. Structure of age-hardened aluminium-copper alloys. *Nature* **1938**, *142*, 569.
3. Preston, G.D. *Nature* **1938**, *142*, 570.
4. Gleiter, H. Nanocrystalline materials. *Prog. Mater. Sci.* **1989**, *33* (4), 223–315.
5. Comber, P.G.; Le Madan, A.; Spear, W.E. *Electronic and Structural Properties of Amorphous Semiconductors*; Comber, P.G., Le Mort, J., Eds.; Academic Press: London, 1973; Vol. 373, 273–289.
6. Elliot, S.R. *Physics of Amorphous Materials*; Longman Group: Harlow, 1990.
7. Ebrahimi, F.; Bourne, G.R.; Kelly, M.S.; Matthews, T.E. Mechanical properties of nanocrystalline nickel produced by electrodeposition. *Nanostruct. Mater.* **1999**, *11* (3), 343–350.
8. Fecht, H.J. Nanostructure formation by mechanical attrition. *Nanostruct. Mater.* **1995**, *6* (1–4), 33–42.
9. Valiev, R.Z. Structure and mechanical properties of ultrafine-grained metals. *Mater. Sci. Eng., A* **1997**, *234–236*, 59–66.
10. Greer, A.L. Metallic glasses. *Science* **1995**, *267* (5206), 1947–1953.
11. Yavari, A.R.; Negri, D. Effect of concentration gradients on nanostructure development during primary crystallization of soft-magnetic iron-based amorphous alloys and its modelling. *Nanostruct. Mater.* **1997**, *8* (8), 969–986.
12. Cahn, J.W. On spinodal decomposition. *Acta Metall.* **1961**, *9* (9), 795–801.
13. Schneider, S.; Thiyagarajah, P.; Geyer, U.; Johnson, W.L. SANS of bulk metallic ZrTiCuNiBe glasses. *Phys. Condens. Matter* **1997**, *241–243*, 918–920.
14. Inoue, A.; Ohtera, K.; Tsai, A.P.; Masumoto, T. New amorphous alloys with good ductility in Al–Y–M and Al–La–M (M = Fe, Co, Ni or Cu) systems. *Jpn. J. Appl. Phys.* **1988**, *27* (3), L280–L282.
15. He, Y.; Poon, S.J.; Shiflet, G.J. Synthesis and properties of metallic glasses that contain aluminum. *Science* **1988**, *241* (4873), 1640–1642.
16. Cantor, B. Nanocrystalline materials manufactured by advanced solidification processing methods. *Adv. Nanocryst.* **1999**, *307*, 143–151.
17. Kawamura, Y.; Mano, H.; Inoue, A. Synthesis of ZrC/Zr<sub>55</sub>Al<sub>10</sub>Ni<sub>5</sub>Cu<sub>30</sub> metallic-glass matrix composite powders by high pressure gas atomization. *Scr. Mater.* **2000**, *43* (12), 1119–1124.

18. Inoue, A.; Kimura, H.M. Fabrications and mechanical properties of bulk amorphous, nanocrystalline, nano-quasicrystalline alloys in aluminum-based system. *J. Light Metals* **2001**, *1*, 31–41.
19. Kim, Y.H.; Inoue, A.; Masumoto, T. Increase in mechanical strength of Al–Y–Ni amorphous alloys by dispersion of nanoscale fcc–Al particles. *Mater. Trans., JIM* **1991**, *32*, 331–337.
20. Foley, J.C.; Allen, D.R.; Perepezko, J.H. Analysis of nanocrystal development in Al–Y–Fe and Al–Sm glasses. *Scr. Mater.* **1996**, *35* (5), 655–660.
21. Hono, K.; Zhang, Y.; Tsai, A.P.; Inoue, A.; Sakurai, T. Solute partitioning in partially crystallized Al–Ni–Ce(–Cu) metallic glasses. *Scr. Metall. Mater.* **1995**, *32* (2), 191–196.
22. Massalski, T.B. *Binary Alloy Phase Diagrams*; ASM International: Materials Park, OH, 1990.
23. Yavari, A.R.; Drbohlav, O. Thermodynamics and Kinetics of nanostructure formation in soft-magnetic nanocrystalline alloys. *Mater. Trans., JIM* **1995**, *36* (7), 896–902.
24. Louzguine, D.V.; Inoue, A. Crystallization behaviour of Al-based metallic glasses below and above the glass-transition temperature. *J. Non-Cryst. Solids* **2002**, *311* (3), 281–293.
25. Louzguine, D.V.; Inoue, A. Nanocrystallization of Ti–Ni–Cu–Sn amorphous alloy. *Scr. Mater.* **2000**, *43* (4), 371–376.
26. Koster, U.; Meinhardt, J.; Roos, S.; Liebertz, H. Formation of quasicrystals in bulk glass forming Zr–Cu–Ni–Al alloys. *Appl. Phys. Lett.* **1996**, *69* (2), 179–181.
27. Xing, L.Q.; Eckert, J.; Loser, W.; Schultz, L. Effect of cooling rate on the precipitation of quasicrystals from the Zr–Cu–Al–Ni–Ti amorphous alloy. *Appl. Phys. Lett.* **1998**, *73* (15), 2110–2112.
28. Inoue, A.; Zhang, T.; Chen, M.W.; Sakurai, T.; Saida, J.; Matsushita, M. Formation and properties of Zr-based bulk quasicrystalline alloys with high strength and good ductility. *J. Mater. Res.* **2000**, *15* (10), 2195–2208.
29. Louzguine, D.V.; Inoue, A. Nanoscale cF96 cubic versus icosahedral phase in devitrified Hf-based metallic glasses. *Ann. Chim.* **2002**, *27* (5), 91–97.
30. Jiang, J.Z.; Rasmussen, A.R.; Jensen, C.H.; Lin, Y.; Hansen, P.L. Change of quasilattice constant during amorphous-to-quasicrystalline phase transformation in  $Zr_{65}Al_{7.5}Ni_{10}Cu_{7.5}Ag_{10}$  metallic glass. *Appl. Phys. Lett.* **2002**, *80* (12), 2090–2092.
31. Louzguine, D.V.; Inoue, A. Nanoparticles with icosahedral symmetry in Cu-based bulk glass former induced by Pd addition. *Scr. Mater.* **2003**, *48* (9), 1325–1329.
32. Matsubara, E.; Sakurai, M.; Nakamura, T.; Imafuku, M.; Sato, S.; Saida, J.; Inoue, A. Environmental structural studies in amorphous and quasicrystalline  $Zr_{70}Al_6Ni_{10}Pt_{14}$  alloys. *Scr. Mater.* **2001**, *44*, 2297–2301.
33. Kelton, K.F.; Lee, G.W.; Gangopadhyay, A.K.; Hyers, R.W.; Rathz, T.J.; Rogers, J.R.; Robinson, M.B.; Robinson, D.S. First X-ray scattering studies on electrostatically levitated metallic liquids: demonstrated influence of local icosahedral order on the nucleation barrier. **2003**, *90* (19), 195504-1–195504-4.
34. Inoue, A.; Kimura, H.M.; Kita, K. *New Horizons in Quasicrystals*; Scientific Strength Al-Based Alloys by Utilizing Nanogranular Quasicrystalline Phase; Goldman, A.I., Sordelet, D.J., Thiel, P.A., Dubois, J.M., Eds.; World Scientific: Singapore, 1997; 256–289.
35. Robertson, A.; Erb, U.; Palumbo, G. Practical applications for electrodeposited nanocrystalline materials. *Nanostruct. Mater.* **1999**, *12* (5–8), 1035–1040.
36. Koch, C.C. Ductility in nanostructured and ultra fine-grained materials: recent evidence for optimism. *J. Metastable Nanocryst. Mater.* **2003**, *18*, 9–19.
37. Karimpoor, A.A.; Erb, U.; Aust, K.T.; Wang, Z.; Palumbo, G. Tensile properties of bulk nanocrystalline hexagonal cobalt electrodeposits. *Mat. Sci. Forum* **2002**, *386-3*, 415–420.
38. Chokshi, A.H.; Rosen, A.; Karch, J.; Gleiter, H. On the validity of the Hall–Petch relationship in nanocrystalline materials. *Scr. Metall.* **1989**, *23* (10), 1679–1683.
39. Erb, U. Electrodeposited nanocrystals: synthesis, properties and industrial applications. *Nanostruct. Mater.* **1995**, *6* (5–8), 533–538.
40. Sanders, P.G.; Youngdahl, C.J.; Weertman, J.R. The strength of nanocrystalline metals with and without flaws. *Mater. Sci. Eng., A* **1997**, *234-236*, 77–82.
41. Nieh, T.G.; Wadsworth, J. Hall–Petch relation in nanocrystalline solids. *Scr. Metall. Mater.* **1991**, *25* (4), 955–958.
42. Masumura, R.A.; Hazzledine, P.M.; Pande, C.S. Yield stress of fine grained materials. *Acta Mater.* **1998**, *46* (13), 4527–4534.
43. Scattergood, R.O.; Koch, C.C. A modified model for Hall–Petch behavior in nanocrystalline materials. *Scr. Metall. Mater.* **1992**, *27* (9), 1195–1200.
44. Gryaznov, V.G.; Gutkin, M.Yu.; Romanov, A.E.; Trusov, L.I. On the yield stress of nanocrystals. *J. Mater. Sci.* **1993**, *28* (16), 4359–4365.
45. Kawamura, Y.; Hayashi, K.; Inoue, A.; Masumoto, T. Rapidly solidified powder metallurgy  $Mg_{97}Zn_1Y_2$  alloys with excellent tensile yield strength above 600 MPa. *Mater. Trans.* **2001**, *42* (7), 1172–1176.
46. Inoue, A.; Kawamura, Y.; Matsushita, M.; Hayashi, K.; Koike, J. Novel hexagonal structure and ultrahigh strength of magnesium solid solution in the Mg–Zn–Y system. *J. Mater. Res.* **2001**, *16*, 1894–1899.
47. Abe, E.; Kawamura, Y.; Hayashi, K.; Inoue, A. Long-period ordered structure in a high-strength nanocrystalline Mg-1 at% Zn-2 at% Y alloy studied by atomic-resolution Z-contrast STEM. *Acta Mater.* **2002**, *50* (15), 3845–3857.
48. He, G.; Eckert, J.; Loser, W.; Schultz, L. Novel Ti-base nanostructure-dendrite composite with enhanced plasticity. *Nat. Mater.* **2003**, *2*, 33–37.
49. Inoue, A.; Kimura, H.M.; Sasamori, K.; Masumoto, T. Ultrahigh strength of rapidly solidified  $Al_{96-x}Cr_3Ce_{1-x}Co_x$  ( $x = 1, 1.5$  and  $2\%$ ) alloys containing an icosahedral phase as a main component. *Mater. Trans., JIM* **1994**, *35* (2), 85–94.
50. Inoue, A.; Kimura, H.M.; Watanabe, M.; Kawabata, A. Work softening of aluminum base alloys containing nanoscale icosahedral phase. *Mater. Trans., JIM* **1997**, *38* (9), 756–760.

51. Inoue, A.; Kimura, H.M. High-strength Al-based alloys consisting mainly of nanoscale quasicrystalline or amorphous particles. *Mat. Sci. Forum* **1997**, *235–238*, 873–880.
52. Kita, K.; Saitoh, K.; Inoue, A.; Masumoto, T. Mechanical properties of Al based alloys containing quasicrystalline phase as a main component. *Mater. Sci. Eng., A* **1997**, *226–228*, 1004–1007.
53. Inoue, A.; Kimura, H. High elevated-temperature strength of Al-based nanoquasicrystalline alloys. *Nanostruct. Mater.* **1999**, *11* (2), 221–231.
54. Bae, D.H.; Lee, M.H.; Kim, K.T.; Kim, W.T.; Kim, D.H. Application of quasicrystalline particles as a strengthening phase in Mg–Zn–Y alloys. *J. Alloys Compd.* **2002**, *342* (1–2), 445–450.
55. Inoue, A.; Kimura, H.M. High-strength Al and Mg-based alloys with nanocrystalline or nanoquasicrystalline phase. *J. Metastable Nanocryst. Mater.* **2001**, *e-volume*, 41–56.
56. Inoue, A.; Fan, C.; Saida, J.; Zhang, T. High-strength Zr-based bulk amorphous alloys containing nanocrystalline and nanoquasicrystalline particles. *Sci. Technol. Adv. Mater.* **2000**, *1*, 73–86.
57. Chen, Y.; Zhang, T.; Zhang, W.; Ping, D.; Hono, K.; Inoue, A.; Sakurai, T. Microstructure feature of bulk glassy  $\text{Cu}_{60}\text{Zr}_{30}\text{Ti}_{10}$  alloy in as-cast and annealed states. *Mater. Trans.* **2002**, *43* (10), 2647–2650.
58. Jiang, J.Z.; Saida, J.; Kato, H.; Ohsuna, T.; Inoue, A. Is  $\text{Cu}_{60}\text{Ti}_{10}\text{Zr}_{30}$  a bulk glass-forming alloy? *Appl. Phys. Lett.* **2003**, *82* (23), 4041–4043.
59. Wada, T. *Master Thesis*; Tohoku University, 2003.
60. Inoue, A.; Kim, Y.-H.; Masumoto, T. A large tensile elongation induced by crystallization in an amorphous  $\text{Al}_{88}\text{Ni}_{10}\text{Ce}_2$  alloy. *Mater. Trans., JIM* **1992**, *33* (5), 487–490.
61. Inoue, A.; Matsumoto, N.; Masumoto, T. Al–Ni–Y–Co Amorphous alloys with high mechanical strengths, wide supercooled liquid region and large glass-forming capacity. *Mater. Trans., JIM* **1990**, *31* (6), 493–500.
62. Kim, Y.H.; Inoue, A.; Masumoto, T. Ultrahigh mechanical strengths of  $\text{Al}_{88}\text{Y}_2\text{Ni}_{10-x}\text{M}_x$  (M = Mn, Fe or Co) amorphous alloys containing nanoscale fcc-Al particles. *Mater. Trans., JIM* **1991**, *32* (7), 599
63. Inoue, A.; Kimura, H. High-strength Al-based nanostructure alloys. *Curr. Opin. Solid State Mater. Sci.* **1997**, *2* (3), 305–310.
64. Kim, Y.H.; Inoue, A.; Masumoto, T. Ultrahigh mechanical strengths of  $\text{Al}_{88}\text{Y}_2\text{Ni}_{10-x}\text{M}_x$  (M = Mn, Fe or Co) amorphous alloys containing nanoscale fcc-Al particles. *Mater. Trans., JIM* **1991**, *32*, 599–608.
65. Ohtera, K.; Inoue, A.; Terabayashi, T.; Nagahama, H.; Masumoto, T. Mechanical properties of an  $\text{Al}_{88.5}\text{Ni}_8\text{Mm}_{3.5}$  (Mm: Misch metal) alloy produced by extrusion of atomized amorphous plus fcc-Al phase powders. *Mater. Trans., JIM* **1992**, *33* (8), 775–781.
66. Greer, A.L. Partially or fully devitrified alloys for mechanical properties. *Mater. Sci. Eng., A* **2001**, *304–306*, 68–72.
67. Kim, H.S.; Hong, S.I. A model of the ductile-brittle transition of partially crystallized amorphous Al–Ni–Y alloys. *Acta Mater.* **1999**, *47* (7), 2059–2066.
68. Louzguine, D.V.; Inoue, A. Investigation of structure and properties of the Al–Y–Ni–Co–Cu metallic glasses. *J. Mater. Res.* **2002**, *17*, 1014–1018.
69. Inoue, A.; Zhang, T.; Chen, M.W.; Sakurai, T.; Saida, J.; Matsushita, M. Ductile quasicrystalline alloys. *Appl. Phys. Lett.* **2000**, *76* (8), 967–969.
70. Inoue, A.; Zhang, T.; Ishihara, S.; Saida, J.; Matsushita, M. Preparation and mechanical properties of nanoquasicrystalline base bulk alloys. *Scr. Mater.* **2001**, *44* (8–9), 1615–1619.
71. Louzguine, D.V.; Inoue, A. Formation of a nanoquasicrystalline phase in Zr–Cu–Ti–Ni metallic glass. *Appl. Phys. Lett.* **2001**, *78* (13), 1841–1843.

# Hydrogel Nanoparticles Made of Cross-Linked Polyvinylpyrrolidone

**Susmita Mitra**

*Department of Chemistry, University of Delhi, Delhi, India*

**Dhruba Jyoti Bharali**

*Institute of Laser Photonics and Biophotonics, State University of New York at Buffalo, Buffalo, New York, U.S.A.*

**Amarnath Maitra**

*Department of Chemistry, University of Delhi, Delhi, India*

## INTRODUCTION

Carrier-mediated drug delivery has witnessed a sea change in the last two decades, wherein the focus on particulate carriers has shifted from lipid-based vesicles to polymeric nanoparticles. The inadequacy of the liposomal system has led researchers to focus on carriers with properties more conducive to drug loading, in vivo controlled drug release, and storage stability. The polymeric nanoparticles have evolved as an outcome of these requirements, and innumerable reports on studies in this area can be encountered in the scientific literature.<sup>[1–3]</sup> Synthetic biomaterials that are highly biocompatible and non-immunogenic have paved the way for the development and synthesis of nanoparticles from homo/copolymeric blends that can be suitably monitored according to the type of drug that requires to be delivered. In light of this interest, poly(*N*-vinylpyrrolidone) (PVP), the water-soluble homopolymer of *N*-vinyl-2-pyrrolidone (NVP), which has long been used as a blood-plasma substitute and extender, became of interest for its application in nanoparticles. Such a highly biocompatible and biologically acceptable polymer could form ideal carriers for hydrophilic drugs. The hydrogel properties of the polymer could also provide hydrophilic surface properties that would help the nanoparticles in evading the reticuloendothelial system (RES) of the body. This entry highlights various studies incorporating the preparation of PVP nanoparticles in reverse micelles and its applications.

## BACKGROUND

It is a well-documented fact that the intravascular delivery of particulate carriers—particularly those that promote opsonization—is limited due to the

recognition and scavenging by the RES. The polymeric nanoparticles being used for drug delivery investigations were prepared primarily from hydrophobic polymers, such as polyalkylcyanoacrylate, polymethylmethacrylate, polylactate, polylactate-co-glycolate, etc.<sup>[4–6]</sup> Subsequent strategies of surface modifications that would confer stealth properties to these nanoparticles had been developed so as to evade RES uptake. Several polymers with hydrophilic groups have been used for the purpose of conferring surface hydrophilicity and steric stabilization, these include PEG, PEO, the poloxamers and poloxamines, polyacrylamide, polyvinylpyrrolidone, dextran, etc.<sup>[7–12]</sup>

Besides surface hydrophilicity, the size of the nanoparticles plays an important role in ensuring access to all sites in the body without attracting RES uptake. In keeping with the architecture of normal as well as diseased tissue, nanoparticles < 100 nm in diameter are ideal candidates for access to all cell types following extravasation from the systemic circulation. To borrow an example from nature, disease-causing microorganisms, the viruses in particular, are able to aptly evade the RES and invade target cells. An important observation is that most animal viruses are considerably less than 100 nm in size. The ultralow size of these viral particles is considered to be one of the reasons for efficient evasion of the RES. Further, a virus escapes exclusion from the kidney because its size is large enough to avoid renal excretion. As a result, they are able to circulate in blood for a long time, and as the size is less than 100 nm they can extravasate to reach the target sites, where they attach and invade the host cells. The viral architecture thus provides an ideal example to emulate.

On the other hand, with the advent of recombinant DNA technology, various types of proteins and polypeptides are being used as drugs as well as vaccines.

The pace of development in the protein and peptide drug industry has altered the course of drug delivery using polymeric nanoparticles. The hydrophobic nanoparticles were not ideal candidates for entrapment of these hydrophilic drugs. Thus nanoparticles of hydrogel materials were thought to be the most suitable for overcoming these limitations. The development of hydrophilic biomedical materials or the “hydrogels” as novel pharmaceutical formulations for delivery of drugs, primarily peptides and proteins, was necessitated. The hydrogels, which are three-dimensional hydrophilic polymeric networks, are capable of imbibing large amounts of water or biological fluids, and exhibit a thermodynamic compatibility with water, which allows them to swell in aqueous media. They resemble natural living tissue more than any other class of synthetic biomaterials, because of their high water content and soft consistency. The networks may be composed of homopolymers or copolymers, which are insoluble because of the presence of cross-links (tie-points, junctions) or physical cross-links such as entanglements or crystallites. The suitability of a hydrogel as a drug delivery device, and its performance in a particular application, depends to a large extent on its bulk structure. The network structure and the thermodynamic nature of the components of these networks play a key role in the molecular mesh size changes, their diffusion behavior, and the associated molecular stability of the incorporated bioactive agents, especially in environmentally responsive hydrogels.<sup>[13]</sup> These materials do not simply release the drug, peptide, or protein at some characteristic rate, but do so in a way that the pharmaceutical scientists and molecular designers require.

Hydrogels have attracted considerable attention as excellent candidates for controlled release devices, as well as targetable carriers of therapeutic agents.<sup>[14,15]</sup> In the present context, nanoparticulate devices composed of hydrogels have greater advantages over disk- or film-shaped macrogels hitherto developed, as they would have both extensive swelling kinetics of hydrogels, as well as a wide variety of biomedical applications because of their small size. The preparation of ultralow size hydrogel nanoparticles as drug carriers for the purpose of drug targeting is a challenging area of research. Considerable effort has been devoted to the creation of nanoparticles acceptable for general systemic use and capable of carrying a drug to its target, at the tissue or cellular level. The delivery of hydrophilic drugs through targeting of nanoparticles to sites other than the RES presents an important challenge in the present context of drug delivery. Nanoparticles of hydrogel materials can be made RES evading and long circulating, without making any surface modifications. Moreover, the presence of reactive groups on the particle surface makes

attachment of appropriate ligands possible. By adjusting the chemical composition of these hydrogel materials, smart hydrogel nanoparticles encapsulating water-soluble drugs can also be prepared.

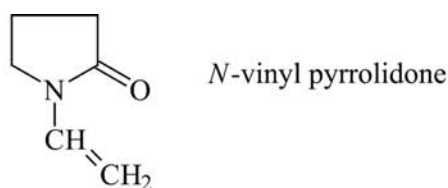
Hydrophilic polymeric nanoparticles were previously prepared by Birrenbach and Speiser<sup>[16]</sup> in 1976, using reverse micelles, but were eventually discarded due to certain inherent drawbacks. Following the basic conceptual preparative method of Birrenbach and Speiser, with the necessary modifications, nanoparticles of the hydrogel PVP have been prepared.<sup>[17]</sup> The method is suitable for any hydrophilic polymer, but the extensive biomedical usage and general acceptability of polyvinylpyrrolidone led to its use in the preparation of nanoparticles by the revised method.

### A WIDELY USED HYDROGEL— POLYVINYLPIRROLIDONE

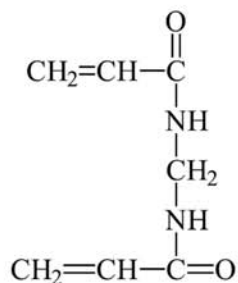
Poly(*N*-vinylpyrrolidone), the water-soluble homopolymer of *N*-vinyl-2-pyrrolidone (NVP), was first synthesized by Professor Walter Reppe and his colleagues<sup>[18]</sup> during the 1930s, and was widely used as a blood-plasma substitute and extender during World War II. Traditionally, the synthesis of NVP and the polymerization of the homopolymer have been based on the Reppe acetylene chemistry, represented by the series of reactions shown in Fig. 1. NVP is one of the various products of the acetylene chemistry discovered by Reppe.<sup>[19]</sup> Polymerization can be carried out in bulk (including solid state), in solution, or in suspension. Radical initiation in solution is the most important method for the synthesis of linear PVP with weight-average molar masses from 2500 to 1 million. The relevant techniques are described in detail by Kern and Cherdron.<sup>[20]</sup>

PVP preparations are available in different molecular weight ranges, with means varying from a few thousand to over 1 million. Molecular weights between 2500 and  $10^6$  g/mol are described. It seems quite difficult to get a trustworthy value for the molecular weight of PVP, and it is quite common to measure its viscosity in solution and to apply the “Fikentscher *k*-value–molecular weight relationship” for its calculation.<sup>[21]</sup> Kern and Cherdron<sup>[20]</sup> have developed a relationship between  $M_w$ ,  $M_n$ , and  $k$ :  $M_w = 15k^{2.3}$ ,  $M_n = 24k^2$ . The letter  $k$  and an appropriate number related to the molecular weight are used to designate the different PVPs.  $k$ -12 has an average molecular weight of around 4000 and  $k$ -90 has an average molecular weight of around 1 million. Furthermore, PVP with a specified  $k$ -value and average molecular weight consists of a range of molecular sizes with a slightly skewed bell-shaped distribution around the average.

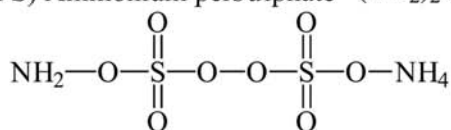




(MBA) *N,N*-Methylene bis acrylamide



(APS) Ammonium persulphate  $(\text{NH}_4)_2\text{S}_2\text{O}_8$



(FAS) Ammonium ferrous sulphate

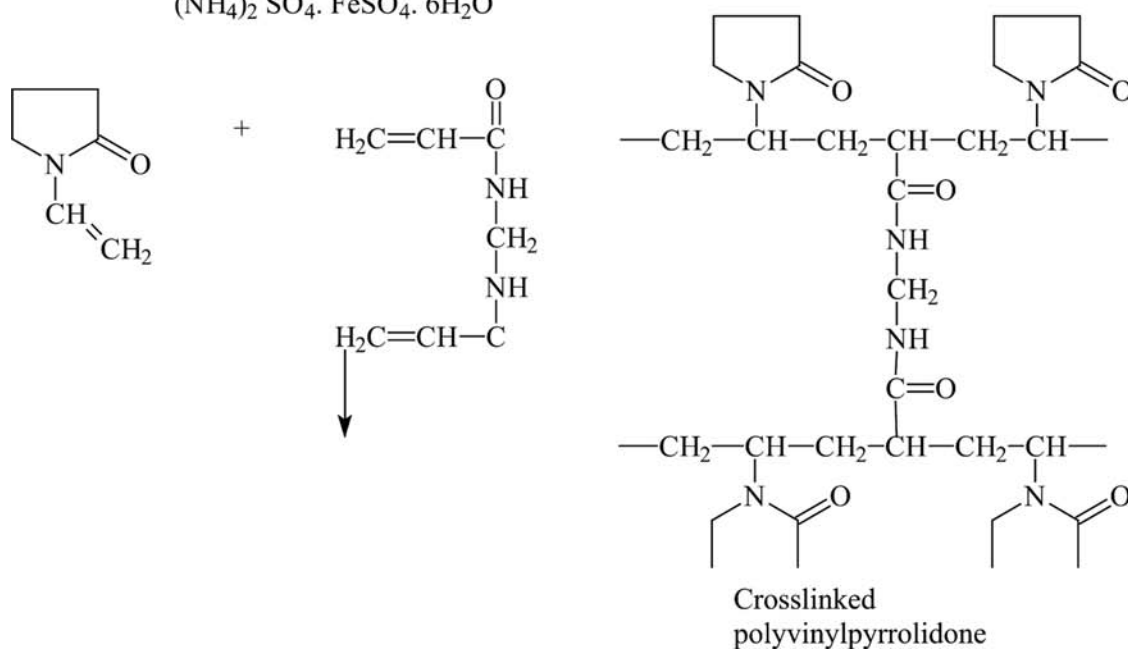
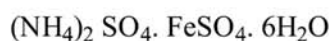


Fig. 1 Reppe reaction for the polymerization of *N*-vinylpyrrolidone.

### PROPERTIES OF POLY(*N*-VINYLPIRROLIDONE)

A special and unusual property of polyvinylpyrrolidone is its solubility in water as well as in various organic solvents. The reason for this phenomenon is that PVP has hydrophilic as well as hydrophobic functional

groups, and therefore interactions with various solvents are possible. Only the viscosity of the resulting solution limits the extent of solubility, for all practical purposes. Aqueous solution of PVP shows that the viscosity is not affected by electrolytes. In solution, PVP probably exists as a random coil. Depending on the

molecular weight, the coil dimensions in an aqueous solution of sodium chloride have an average end-to-end distance of between 10 and 1000 Å. The size of the coil is important for applications in the medical field, in particular for the ability of the human body to excrete the polymer.<sup>[22]</sup> PVP cannot be processed in the melt because of its low decomposition temperature, and the extremely poor flow properties of the melt. Films coated from solution are very brittle, clear, and glassy. The glass transition temperature ( $T_g$ ) increases with molecular weight and reaches a plateau at about 175°C, which corresponds to a molecular weight of about 1 million. At low molecular weight  $T_g$  falls to values below 100°C. The addition of small amounts of water also leads to lower  $T_g$  values.<sup>[23]</sup>

The heat of PVP solution is  $-4.81$  kJ/mol ( $-1.15$  kcal/mol); aqueous solutions are slightly acidic, pH 4–5. Under ordinary conditions PVP is stable as a solid as well as in solution. It is also relatively inert to chemical modification. Exposure of PVP solution to light in the presence of oxidizing agents or diazo compounds can cause gelation. When aqueous solutions of PVP are heated with strong bases such as lithium carbonate, trisodium phosphate, or sodium metasilicate, a precipitate results from the opening of the pyrrolidone ring and the subsequent reaction across different chains. This precipitation mostly occurs at elevated temperatures. PVP is non-antigenic, biologically compatible, has low toxicity, film forming, and adhesive characteristics, unusual complexing ability, relatively inert behavior toward salts, and is resistant to thermal degradation in solution.

### Uses of Polyvinylpyrrolidone Homopolymer

PVP has come into prominence as a biomedical polymer, because of its primary use as a blood plasma extender or substitute, and because of its low toxicity.<sup>[24]</sup> Presently, it is no longer used as a blood plasma extender, but has found extensive application in diverse areas of pharmaceuticals, biomedical sciences, biotechnology, food and beverage, cosmetic and toiletry, as well as the photographic industries.<sup>[25–27]</sup> The major use of PVP in quantitative terms has been in the manufacture of tablets. It has been widely used medically in the manufacture of tablets and for both diagnostic and therapeutic purposes since the early 1940s. Under U.S. law PVP has a number of permitted uses in foodstuff, including use as a binder for vitamin and mineral concentrate tablets, as well as a binder for synthetic sweetener tablets. It is also used as a diluent and dispersant for food colors. PVP is permitted as a coating for fresh citrus fruit and as a component in the packaging materials, which are in contact with aqueous, fatty, and dry foods.

PVP-iodine aqueous solution, Povidone-iodine, is a form of iodine commonly used for skin cleansing, as a prophylaxis or treatment for wound infection. Present literature focuses on the importance of using such “traditional” methods of combating and preventing wound infection,<sup>[28]</sup> and as a disinfectant for cold sterilization of oral cavity prior to surgery.<sup>[29,30]</sup> PVP finds use as a protectant for the cryopreservation of microorganisms and has been used widely with satisfactory results.<sup>[31]</sup> It is also added to the protective solution used for lyophilization of human red blood cells.<sup>[32]</sup> An optimum concentration of 40% PVP in DMSO renders optimum protection to RBC. The film-forming, membrane-forming, and adhesive properties of PVP have been used to improve the adhesion properties of available water-soluble pressure-sensitive adhesives.<sup>[33–35]</sup>

Many undesirable effects of protein adsorption at solid–liquid interfaces are encountered in variable situations. Surface-induced thrombosis due to adsorption of plasma proteins, fouling of membranes used in food and beverage processing, or performance degradation in analytical protein liquid chromatography, are some of such instances. Although various factors affect protein adsorption, the surface chemistry of the substrate has been studied most intensively with the goal of affecting protein adsorption via a variety of surface modification techniques. Polymer coatings designed to reduce protein adsorption have been used to modify a variety of polymeric substrates such as polycarbonate, polysulfone, polypropylene, low-density polyethylene, polystyrene latex, as well as glass and ceramic surfaces. The nonionic polymer, PVP, has proven effective in reducing adsorption of many proteins such as lactoglobulin and bovine serum albumin onto polysulfone surfaces.<sup>[36]</sup> It has been suggested that the degree of reduction in protein adsorption is determined largely by the effect of protein exclusion from the native surface due to the polymer surface chains that provide a steric barrier.<sup>[37]</sup> PVP has also been considered for modifying ceramic surfaces to reduce fouling of ceramic membranes during protein ultrafiltration, and for producing ceramic biocompatible surfaces for biomedical applications. The potential effectiveness of PVP as a zirconia surface modifier was investigated using lysozyme. The study demonstrated that a PVP brush layer is capable of reducing lysozyme adsorption up to about 76%.<sup>[38]</sup>

### ULTRAFINE POLY(N-VINYL PYRROLIDONE) NANOPARTICLES

In order to encapsulate water-soluble drugs, it is necessary to have nanoparticles with complete hydrogel behavior. That is, both the outer shell and the inner core should be hydrophilic. Preparation of nanoparticles by

chemical polymerization or cross-linking reactions within emulsion droplets invariably produces particles with high polydispersity.<sup>[39]</sup> This problem can be overcome by carrying out polymerization reaction in reverse micelles.<sup>[40]</sup> As the size of the reverse micellar droplets is in the order of a couple of tens of nanometers in diameter, and these droplets are highly monodispersed, preparations of drug-loaded nanoparticles of diameter smaller than 100 nm in the reverse micellar droplets would be possible. These particles are expected to be fairly monodispersed. Controlling the size of the aqueous core of the reverse micellar droplets could also control the size of the nanoparticles. The water-in-oil reverse microemulsions contain pools of water enclosed in surfactant reverse micelles, surrounded by oil molecules. Each of these water droplets may be used as miniature nanoreactor to produce hydrogel nanoparticles. Chemical thermodynamics governing the reverse micellar system drives the monomer molecules added to the solution right into the water droplets. The polymerization reaction occurs inside the water droplets, triggered by the addition of an appropriate initiator substance into the micellar droplets. The microscopic polymerization process inside the tiny water droplet is similar to macroscopic polymerization. It is during this polymerization process that the polymer material takes up the hydrophilic drug molecules that are intended to be encapsulated within the nanoparticles, and the nanoparticles formed assume the spherical shape of the water droplet. The size of the resulting nanoparticles is restricted by the diameter of the water droplet, and the size of the droplet in turn depends on various parameters of the reverse micellar systems.

Most previous attempts to develop hydrophilic nanoparticles through the reverse micellar route led to an uncontrolled size distribution of the nanoparticles. By the polymerization of acrylamide and *N,N'*-methylene bisacrylamide (MBA), Birrenbach and Speiser<sup>[16]</sup> succeeded in preparing nanospheres containing several tracers or active substances, such as iodine-labeled human IgG, tetanus toxoid, and urease. The method used to prepare polyacrylamide nanospheres is a polymerization in a reverse micelles. This method requires 1) large amounts of organic solvents, e.g., hexane, toluene, or chloroform, as the external phase; 2) anionic surfactants such as sodium bis(2-ethyl hexyl) sulfosuccinate, i.e., AOT, to produce the reverse micelles; and finally, 3) an induction of the polymerization by either a physical or chemical initiator. Kopf et al.<sup>[41]</sup> succeeded in entrapping 96% of norephedrine HCl in these nanospheres. But Couvreur et al.<sup>[42]</sup> and later Labhatssewar and Dorle<sup>[43]</sup> had poor results with fluorescein, metronidazole, and primaquine. High amounts of active substances have always been included in the polymerization medium rather than adsorbed afterwards. In the previously

used preparative method, purification was always necessary to eliminate the solvents, the surfactants, and if used, the chemical initiator. Based on these initial investigations, several research groups improved and modified the original processes.<sup>[44]</sup> This included reduction in the amount of solvent and polymerization initiator in the polymerization methods. But due to several lacunae in the preparation protocols, none of these methodologies could be successfully used. Eventually, they were abandoned, and scientists reverted to nanoparticle preparation in emulsion medium.

In the earlier methods of nanoparticle preparation involving reverse micelles for pharmaceutical applications,<sup>[41–43]</sup> the most important point, i.e., the control of particle size, was always overlooked. As a matter of fact, the condition of an exact micellar phase with discrete droplets dispersed in a hydrocarbon medium was not maintained, and in most cases the polymerization took place in a separate aqueous phase in which uncontrolled particle size resulted. Other limitations of the previous reverse micelle-mediated process for preparation of drug-loaded nanoparticles were the failure of complete elimination of toxic materials, such as organic solvents, surfactants, and if used, chemical initiators, from the final product. Fine-tuning of these various aspects was necessary so as to obtain a preparative procedure that would take into account the particle size as well as the toxicity of the end product.

### Preparation of Cross-Linked Polyvinylpyrrolidone Nanoparticles

The preparation of PVP nanoparticles was optimized in our laboratory, following the original method previously developed<sup>[16]</sup> by Maitra et al. in 1997.<sup>[17]</sup> AOT was selected for the formation of reverse micelles because this surfactant aggregates in oil without the help of any cosurfactant, and the reverse micellar solution can dissolve a considerable amount of water and other hydrophilic materials. Moreover, unlike other surfactants, the removal of AOT from the aqueous system through its precipitation as calcium salt is easy, quantitative, and rapid. The reverse micelles were prepared in *n*-hexane as it is easily removable by evaporation, and for this purpose a typical system was prepared by dissolving AOT in *n*-hexane (usually 0.03 to 0.1 M of AOT solution). Because the reverse micellar droplets are highly monodispersed and the droplet size can be varied, the nanoparticles prepared using reverse micelles medium are nearly monodispersed with narrow size distribution dispersions. Moreover, controlling the size of the reverse micellar droplets can modulate their size. A typical protocol for the preparation of PVP nanoparticles is as follows.

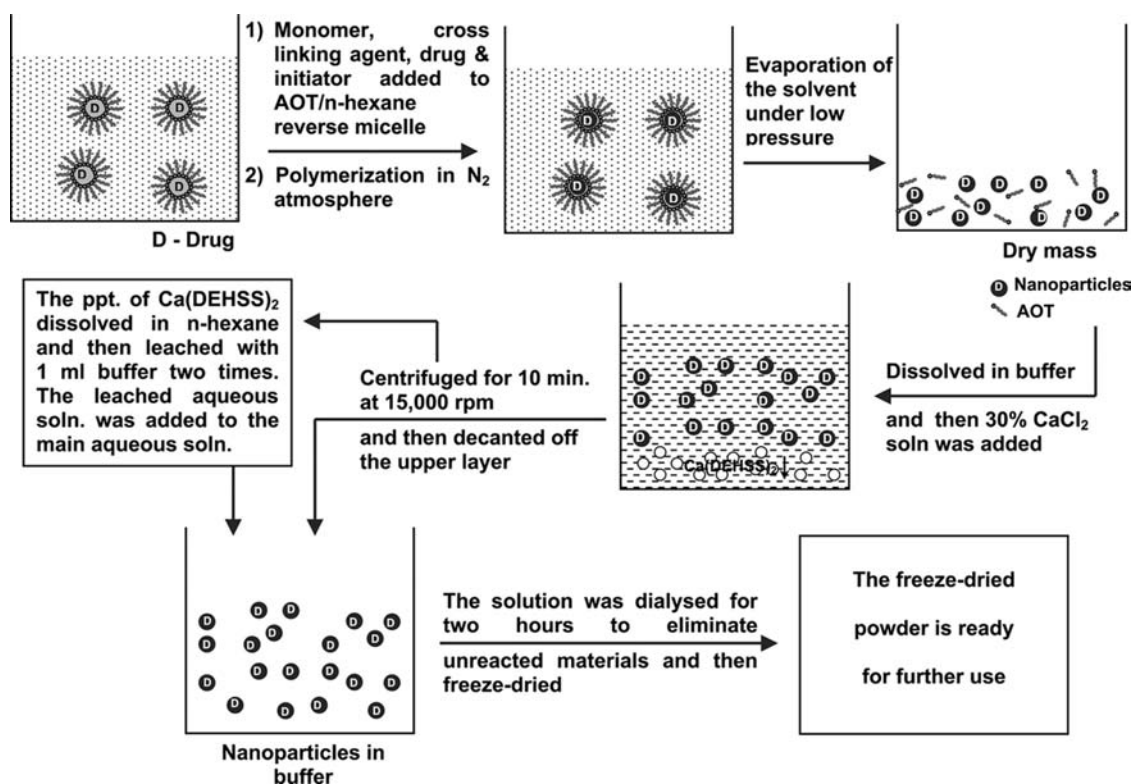


Fig. 2 Flowchart of PVP nanoparticles.

Forty milliliters of 0.03 M AOT solution in hexane was taken and to it 280  $\mu$ L of freshly distilled NVP, 100  $\mu$ L of MBA (0.049 g/mL), 20  $\mu$ L of *N,N,N,N'*-Tetramethylethylenediamine (TEMED), and aqueous solutions of 20  $\mu$ L of ammonium persulphate (20% w/v) and 50  $\mu$ L of an active compound, such as fluorescein isothiocyanate-dextran ( $M_w = 10$  kDa) (FITC-dextran) (3.2% w/v), were added. The solution was homogeneous and optically transparent. For the entrapment of a protein solution or hydrophilic drug, FITC-dextran was replaced with 50  $\mu$ L of the required substance used. Polymerization was carried out at

37°C for 8 hr in a thermostated water bath with continuous stirring. After the completion of the reaction, the excess solvent (hexane) was evaporated off in a rotary evaporator and the dry mass was resuspended in 10 mL of water by sonication. Then 1-mL aliquots of 30% w/v calcium chloride solution were added drop by drop with continuous stirring to precipitate the AOT (surfactant) as calcium salt of di-ethyl-hexylsulfosuccinate, Ca (DEHSS)<sub>2</sub>. It was then dialysed for 2 hr. Ca (DEHSS)<sub>2</sub> was separated by centrifugation at 10,000 rpm for 10 min. The centrifuged aqueous solution contained the dye/drug-loaded

% YIELD	5	10	15	20	25
PARAMETERS					
Effect of monomer concentration (mg/ml)	-	-	50,	150,	275, 300, 350,
Effect of initiator concentration (mg/ml)	50,	10, 32,	12, 25,	20,	-
Effect of polymerization temperature (°C)	25, 55,	50,	30, 45,	35, 40,	38,

Fig. 3 Relationship of some physico-chemical parameters of polymerization, on the yield (%) of cross-linked PVP nanoparticles.

PVP nanoparticles that were homogeneous and transparent. The precipitate of Ca (DEHSS)<sub>2</sub> after centrifugation contained some dye/drug-loaded PVP nanoparticles absorbed on it. The precipitated pellet was dissolved in 15 mL of hexane and the hexane solution was washed three times with 1 mL of water. The phase-separated aqueous layer was drained out and added to the previously centrifuged supernatant solution containing the PVP nanoparticles. The total aqueous dispersion of nanoparticles was lyophilized immediately to dry powder. Lyophilized nanoparticles were easily redispersible in aqueous buffer. The flow diagram for the preparation of the nanoparticles through reverse micelles is shown in Fig. 2.

### Properties of Cross-Linked Poly(*N*-Vinylpyrrolidone) Nanoparticles

PVP nanoparticles prepared in reverse micellar droplets have a particle diameter < 100 nm with a narrow size distribution. When dispersed in aqueous buffer these particles appear to be transparent and give an optically clear solution. Lyophilized powder of these nanoparticles is redispersible in aqueous buffer, without any change in size and morphology of the particles. The yield of the nanoparticles was found to be dependent on certain physicochemical parameters, such as monomer concentration, initiator concentration, and temperature of polymerization (Fig. 3). The optimum monomer concentration is 280 mg/mL, beyond which no further increase in yield is obtained. The optimum quantity of polymer is produced at a monomer concentration of 20 mg/mL and reaction temperature of 37°C. From gel permeation chromatography data, the approximate molecular weight of the polymeric nanoparticles was found to be about 3500 kDa. The entrapment efficiency of FITC-dextran by these nanoparticles is high (> 70%), and this also depends on the amount of cross-linking agent present in the polymeric material. The release of the entrapped molecules from these nanoparticles depends on the degree of polymer cross-linking, particle size, pH of the medium, extent of loading, as well as the temperature of the aqueous phase. Extensive study and detailed characterization of the cross-linked nanoparticles was reported by Bharali et al.<sup>[45]</sup>

Characterization was done on the basis of the data obtained from FT-IR, <sup>1</sup>H NMR, dynamic light scattering (DLS) measurements of particle size, and transmission electron microscopic (TEM) pictures, to establish particle morphology. As the cross-linked PVP nanoparticles were prepared by the vinyl polymerization of the monomer, vinylpyrrolidone, in the presence of cross-linking agent methylene bisacrylamide (MBA), using the initiator ammonium

persulphate (APS), the spectra of the starting material as well as the polymer were obtained for comparative assessment. According to the FT-IR spectra (Fig. 4), the strong peak at 850 cm<sup>-1</sup> corresponding to the =CH<sub>2</sub> wagging of the vinyl double bond, and the peaks at 1630 and 1426 cm<sup>-1</sup> for -C=C- and vinyl scissoring vibration present in the monomer are absent in the spectrum corresponding to the polymer spectrum. This confirms the formation of the polymer. The C-H stretching vibration of the polymer backbone is manifested through a strong peak at 2928 cm<sup>-1</sup> corresponding to >C=O stretching from pyrrolidone units. From the <sup>1</sup>H NMR (Fig. 5) analysis polymerization is

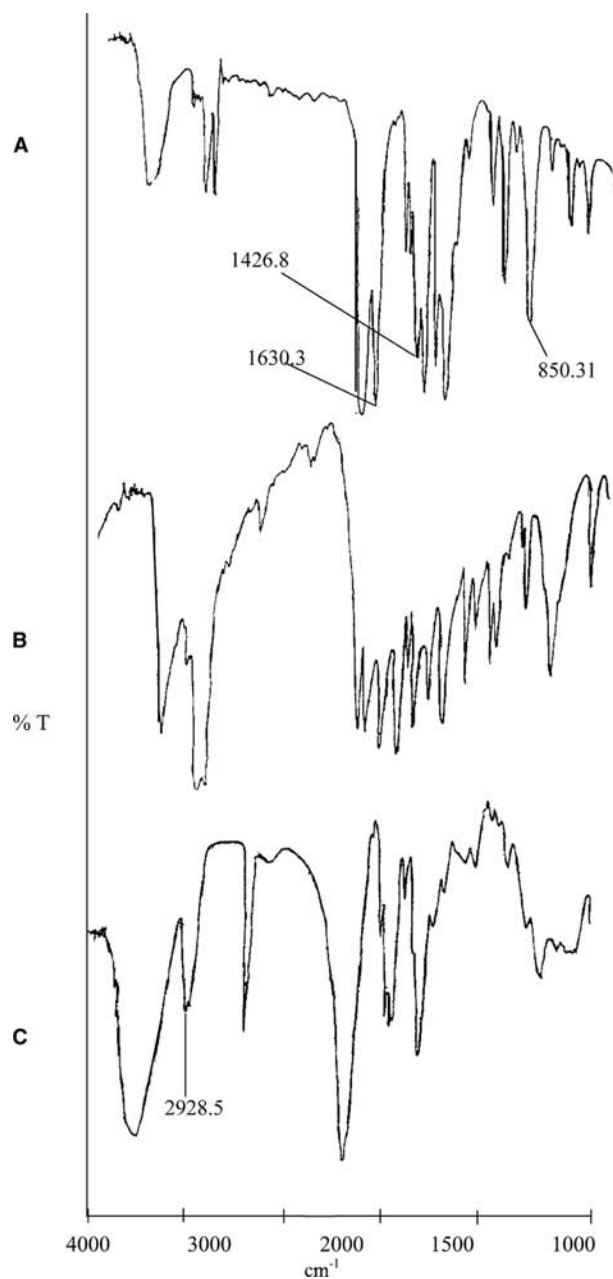


Fig. 4 FT-IR spectra of cross-linked PVP. Source: From Ref.<sup>[45]</sup>.

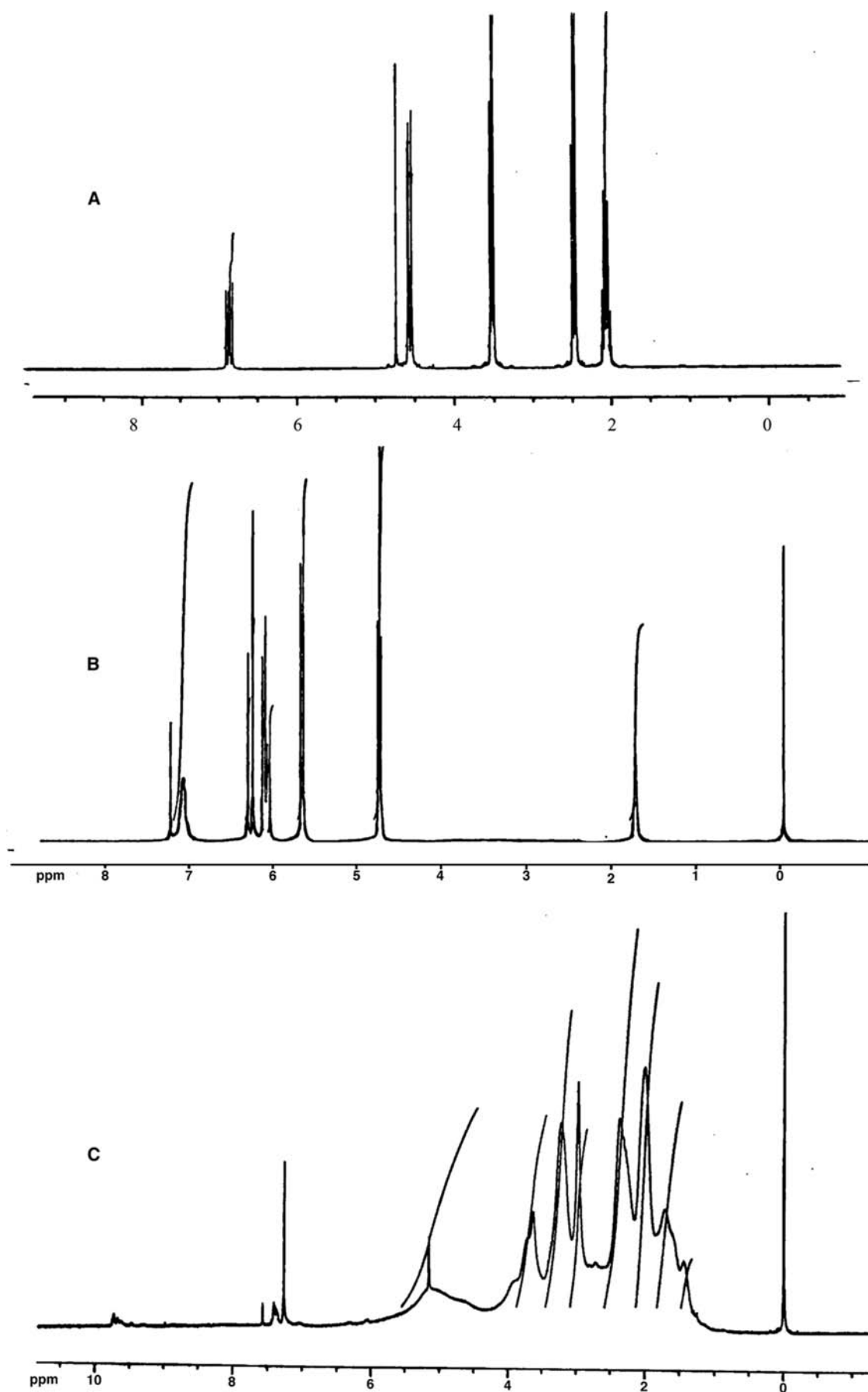
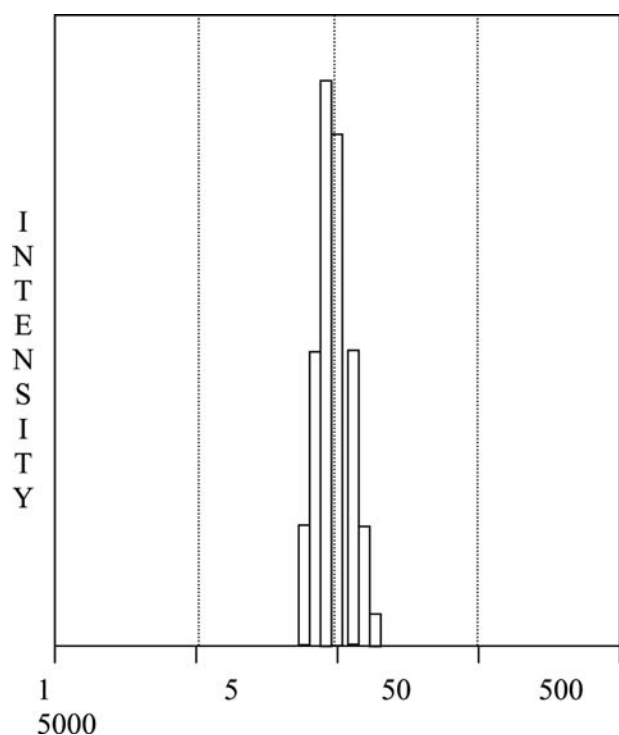


Fig. 5 NMR spectra of cross-linked PVP. Source: From Ref.<sup>[45]</sup>.





**Fig. 6** Size distribution spectra of 0.6% cross-linked PVP nanoparticles.

indicated by the absence of a double doublet for two protons at  $\delta = 4.4$  for  $\text{CH}=\text{CH}_2$  in *N*-vinylpyrrolidone, due to coupling with the neighboring proton. The absence of downfield protons in the starting compound MBA in the range  $\delta = 6.3$ – $5.7$  for unsaturation confirms cross-linking during polymerization.

The PVP nanoparticles loaded with a marker molecule, FITC-dextran, having 0.6% w/w cross-linking prepared in AOT reverse micelles of  $w_o = 15$  were found, as measured by DLS, to be around 50 nm (Fig. 6). The same particles exhibit a diameter of about

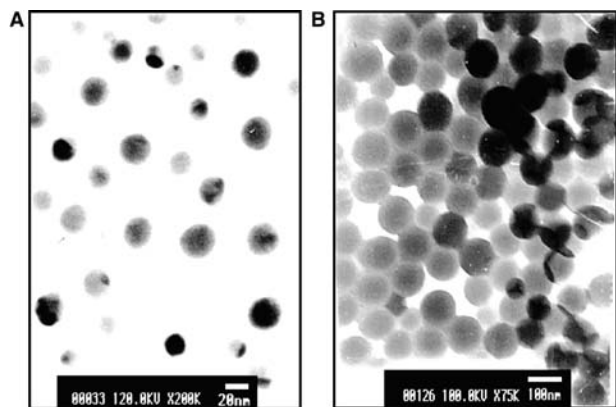


**Fig. 7** (A) TEM picture of PVP nanoparticles (cross-linking agent 0.6%). (B) TEM picture of PVP nanoparticles (cross-linking agent 1.2%).

30–35 nm in the TEM picture (Fig. 7A), while a 1.2% w/w of MBA in the polymer composition results in an increase in particle size from 35 to 80 nm (Fig. 7B). The possible difference in particle size observed for 0.6% cross-linked particles by DLS and TEM measurements could be due to the hydration and swelling of the particles in aqueous buffer. The cross-linking ratio is one of the most important factors that affect the swelling of hydrogels. It is defined as the ratio of moles of cross-linking agent to the moles of polymer repeating units. In the case of bulk gels, highly cross-linked hydrogels have a tighter structure and swell less compared to the same hydrogels with lower cross-linking ratios. Cross-linking hinders the mobility of the polymer chain, hence lowering the swelling ratio.<sup>[46]</sup> But, contrary to the observations in the bulk phase, the increase in particle size on increasing the cross-linking agent can be explained on the basis of higher interlinking of the primary polymeric particles, during interdroplet interaction in the reverse micellar phase. A detailed analysis of particle growth in reverse microemulsion may be found in the previous publications of Bharali et al.<sup>[45]</sup> and Munshi, De, and Maitra<sup>[47]</sup>

### In Vivo Applications of PVP Nanoparticles

Biodistribution of the PVP nanoparticles prepared by the optimized method<sup>[17]</sup> was studied in Balb/c mice using the hydrophilic fluorescent dye, FITC-dextran. These particles show practically negligible (< 1%) uptake by the macrophages in liver and spleen (Fig. 8), and 5–10% of these particles remain in circulation even 8 hr after intravenous injection.<sup>[48]</sup> Due to the longer residence time in blood, these PVP nanoparticles have potential therapeutic applications, particularly in cancer. The water-soluble cytotoxic agents encapsulated in these particles can be targeted to tumors while minimizing the likelihood of toxicity to the RES. PVP nanoparticles containing taxol, prepared by reverse

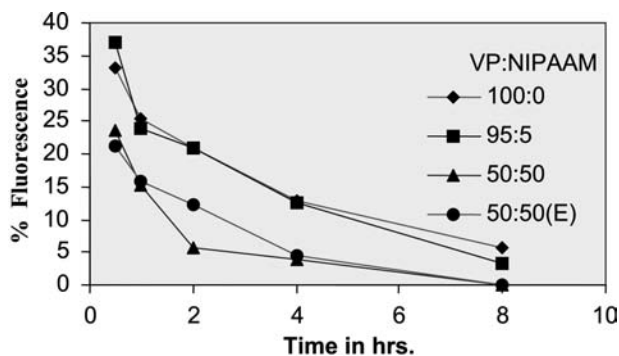


**Fig. 8** Blood clearance of cross-linked PVP nanoparticles, surface modified with hydrophobic groups.

microemulsion method, with particle size ranging between 50 and 60 nm, show antitumor effect in B16F10 murine melanoma transplanted in C57B1/6 mice. The *in vivo* efficacy of Taxol-containing nanoparticles, as measured by reduction in tumor volume and increased survival time, is significantly greater than an equivalent concentration of free Taxol.<sup>[49]</sup> PVP nanoparticles provide a promising delivery system for proteins, as they are biocompatible, conserve the integrity and biological activity of proteins, augment antibody response, and provide a sustained antibody level with single-step immunization. The formulation may also be useful for hyposensitization therapy for various allergens.<sup>[50]</sup> Targeted delivery of PVP nanoparticles encapsulating FITC-dextran was established in human hepatoblastoma cells (HepG2). Cytosolic delivery of nanoparticles was achieved by encapsulation in F-virosomes, which are capable of membrane-mediated delivery of nanoparticles to the cell cytoplasm.<sup>[51]</sup> The hybrid vector has the potential to deliver hydrophilic drugs to liver cells *in vivo*. Plasmid DNA encapsulated in PVP nanoparticles was also used successfully for *in vitro* transfection of MCF-7 cell line. Significant *in vivo* tissue expression of pSV  $\beta$ gal, delivered in PVP nanoparticles as vectors, was observed in the lung and liver tissue of Swiss albino mice.<sup>[52]</sup>

Using the reverse micellar system, pH- and temperature-sensitive hydrogel nanoparticles of copolymers of vinylpyrrolidone and acrylic acid, cross-linked with *N,N'*-methylenebisacrylamide, were prepared, with size ranging between 35 and 60 nm. Particle size increases with increasing molar ratio of acrylic acid (AA), due to the self-adhesive behavior of AA.<sup>[53]</sup> The release of FITC-dextran from these nanoparticles was highly pH- and temperature dependent. Release rate was increased with increase in temperature and pH, and decreased at acidic pH. Such copolymeric nanoparticles can be used as ideal carriers for oral delivery of hydrophilic drugs,<sup>[54]</sup> as AA provides muco-adhesivity, while the presence of a hydrophobic entity provides surface hydrophobicity for recognition and uptake by the Peyer's patches in the GI tract. Oral delivery of insulin using such copolymeric nanoparticles gradually reduces blood glucose level in alloxan/streptozotocin-induced diabetic rats.<sup>[55]</sup>

## CONCLUSION

Nanoparticles of polyvinylpyrrolidone cross-linked with methylene bis-acrylamide can be used for entrapping vaccines, peptide drugs, other hydrophilic drugs, and DNA. The ultralow size of these nanoparticles prepared in the aqueous core of reverse micelles, and their hydrogel nature which renders them inconspicuous to the RES, makes them ideal candidates for

*in vivo* drug delivery. The longer residence time of these nanoparticles in the blood circulation makes it possible to use them for several therapeutic purposes, particularly for drug delivery to solid tumors. Attachment of specific ligands can provide tissue- or cell-targeting ability to these nanoparticles. Further investigations in this front may yield many exciting possibilities related to drug and gene delivery in the future, using PVP nanoparticles as carriers.

## ACKNOWLEDGMENTS

Several scientists from this laboratory, such as U. Gaur, T.K. De, S.K. Sahoo, and N. Munshi, whom the authors gratefully acknowledge, have contributed in the works embodied in this article. Financial assistance from the Departments of Science and Technology and Biotechnology, Government of India, is also thankfully acknowledged.

## REFERENCES

1. Curt, T. *Controlled Release of Drugs: Polymers and Aggregated Systems*; Rosoff, M., Ed.; VCH Publishers: New York, 1989.
2. Kohn, J. *Biodegradable Polymers as Drug Delivery Systems*; Chasin, M., Langer, R., Eds.; Marcel Dekker: New York, 1990; 195 pp.
3. Okano, T.; Yui, N.; Yokoyama, N.; Yoshida, R. *Advances in Polymeric Systems For Drug Delivery*; Gordon and Breach Science Publishers: Switzerland, 1994; Vol. 4.
4. Kreuter, J. *Ophthalmic Drug Delivery Systems*; Mitra, A.K., Ed.; Marcel Dekker: New York, 1993.
5. Kreuter, J. *Colloidal Drug Delivery Systems*; Marcel Dekker Inc.: New York, 1994.
6. Gallardo, B.D.; Courraze, M.; Denizot, L.; Treupel, L.; Couvreur, P.; Puineux, F. Study of the mechanisms of formation of nanoparticles and nanocapsules of polyisobutyl-2-cyanoacrylate. *Int. J. Pharm.* **1993**, *100*, 55.
7. Chen, W.; Yang, X. Researches on PEG-modified copolymer nanoparticles. *Sheng Wu Yi Xue Gong Cheng Xue Za Zhi* **2003**, *20* (1), 143–147.
8. Peracchia, M.T.; Fattal, E.; Desmaele, D.; Besnard, M.; Noel, J.P.; Gomis, J.M.; Appel, M.; d'Angelo, J.; Couvreur, P. Stealth PEGylated polycyanoacrylate nanoparticles for intravenous administration and splenic targeting. *J. Control. Release* **1999**, *60*, 121–128.
9. Crommelin, D.J.A.; Storm, G. Stealth therapeutic systems: rationale and strategies. In *Targeting of Drugs: Strategies for Stealth Therapeutic Systems*; Gregoriadis, G., Ed.; Plenum Press: New York, 2000.
10. Moghimi, S.M.; Hunter, A.C.; Murray, J.C. Long-circulating and target-specific nanoparticles: theory to practise. *Pharmacol. Rev.* **2001**, *53* (2), 283–318.

11. Torchilin, V.P.; Trubetskoy, V.S. Which polymers can make nanoparticulate drug carriers long circulating? *Adv. Drug Deliv. Rev.* **1995**, *16*, 141–155.
12. Torchilin, V.P.; Shtilman, M.I.; Trubetskoy, V.S.; Whiteman, K.; Milstein, A.M. Amphiphilic vinyl polymers effectively prolong liposome circulation time in vivo. *Biochim. Biophys. Acta* **1994**, *1195*, 181–184.
13. Peppas, N.A.; Bures, P.; Leobandung, W.; Ichikawa, H. Hydrogels in pharmaceutical formulations. *Eur. J. Pharm. Biopharm.* **2000**, *50*, 27–46.
14. Mitra, S.; De, T.K.; Maitra, A.N. Hydrogel nanoparticles: their applications in drug delivery. In *The Encyclopedia of Surface and Colloid Science*; Marcel Dekker: New York, 2001.
15. Lowman, A.M.; Peppas, N.A. Hydrogels. In *Encyclopedia of Controlled Drug Delivery*; Mathiowitz, E., Ed.; Wiley: New York, 1999; 397–418.
16. Birrenbach, G.; Speiser, P.P. Polymerized micelles and their use as adjuvants in immunology. *J. Pharm. Sci.* **1976**, *65*, 1763–1766.
17. Maitra, A.N.; Ghosh, P.K.; De, T.K.; Sahoo, S.K. Process for the Preparation of Highly Monodispersed Hydrophilic Polymeric Nanoparticles of Size Less than 100 nm. . US Patent 5,874,111, 1999.
18. Reppe, W.; Herrle, K.; Fikentscher, H. German Patent, 92, 378 1955.
19. Reppe, W. P.P. Report. 18, 852-s-18. Bibliogr. Tech. Rep. **1948**, *10*, 348.
20. Kern, W.; Cherdron, H. *Houben Weyl Methoden der Organischen Chemie*, 11th Ed.; George Thieme Verlag: Stuttgart, 1961; 14 (4), 1106–1118.
21. Nuyken, O.; Billig-Peters, W. Polystyrenes and Other Poly(Vinyl Compound)s. In *Dictionary of Organic Chemistry*; 114–123.
22. Lorenz, D.H. *N-Vinyl Amide Polymers in EPST*, 1st Ed. Ed.; GAF Corporation: 11, 239–251.
23. Lorenz, D.H. *The Association for Finishing Processes of SME, Technical Paper, FC 76-526*; Dearborn: Mich, 1976.
24. Mallick, S.; Sahoo, A.; Mitra, S.S. Preparation, physico-chemical characterization and drug release studies of albendazole solid dispersions. *Boll. Chim. Farm.* **2003**, *142* (4), 180–186.
25. Risbud, M.V.; Hardikar, A.A.; Bhat, S.V.; Bhonde, R.R. pH sensitive freeze-dried chitosan-polyvinylpyrrolidone hydrogels as controlled release system for antibiotic delivery. *J. Control. Release* **2000**, *68* (1), 23–30.
26. Tsunoda, S.; Kamada, H.; Yamamoto, Y.; Ishikawa, T.; Matsui, J.; Koizumi, K.; Kaneda, Y.; Tsutsumi, Y.; Ohsugi, Y.; Hirano, T.; Mayumi, T. Molecular design of polyvinylpyrrolidone-conjugated interleukin-6 for enhancement of in vivo thrombopoietic activity in mice. *J. Control. Release* **2000**, *68*, 335–341.
27. Peppas, N.A. Hydrogels of poly (Vinyl Alcohol) and its copolymers. In *Hydrogels in Medicine and Pharmacy*; Peppas, N.A., Ed.; CRC Press: Boca Raton, FL, 1986; Vol. 2, 1–48.
28. Flynn, J. Povidone-iodine as a topical antiseptic for treating and preventing wound infection: a literature review. *Br. J. Community Nurs.* **2003**, *8*, S 36–S 42.
29. de Souza, R.E.; de Souza, E.A.; Sousa-Neto, M.D.; Pietro, R.C. In vitro evaluation of different chemical agents for the decontamination of gutta-percha cones. *Pesqui. Odontol. Bras.* **2003**, *17*, 75–77.
30. Okuda, M.; Kaneko, Y.; Ichinohe, T.; Ishihara, K.; Okuda, K. Reduction of potential respiratory pathogens by oral hygienic treatment in patients undergoing endotracheal anesthesia. *J. Anesth.* **2003**, *17*, 84–91.
31. Hubalek, Z. Protectants used in the cryopreservation of microorganisms. *Cryobiology* **2003**, *46*, 205–229.
32. Quan, G.B.; Han, Y.; Liu, A.; Jin, P.; Cao, W. Effect of vitrification state of protective solutions on recovery of red blood cells after lyophilization reservation. *Zhongguo Shi Yan Xue Ye Xue Za Zhi* **2003**, *11*, 308–311.
33. Rao, P.R.; Reddy, M.N.; Ramakrishna, S.; Diwan, P.V. Comparative in vivo evaluation of propranolol hydrochloride after oral and transdermal administration in rabbits. *Eur. J. Pharm. Biopharm.* **2003**, *56*, 81–85.
34. Cranford, R.J.; Darmstadt, H.; Yang, J.; Roy, C. Polyetherimide/polyvinylpyrrolidone vapour permeation membranes, physical and chemical characterization. *J. Membr. Sci.* **1999**, *155*, 231–240.
35. Minghetti, Y.; Cilurzo, F.; Tosi, L.; Casiraghi, A.; Montanari, L. Design of a new water-soluble pressure-sensitive adhesive for patch preparation. *AAPS Pharm. Sci. Tech.* **2003**, *4*, E8.
36. Bearinger, J.P.; Castner, D.G.; Golledge, S.L.; Rezanian, A.; Hubchak, S.; Healy, K.E. P(AAm-co-EG) interpenetrating polymer networks grafted to oxide surfaces: surface characterization, protein adsorption, and cell detachment studies. *Langmuir* **1997**, *13*, 5175.
37. Schroen, C.G.P.H.; Wijers, M.C.; Cohen-Stuart, M.A.; Van der Padt, A.; Van't Riet, K. Membrane modification to avoid wettability changes due to protein adsorption in an emulsion/membrane bioreactor. *J. Membr. Sci.* **1993**, *80*, 265.
38. Montserrat, R.-B.; Francesc, G.; Yoram, C. Protein adsorption onto zirconia modified with terminally grafted polyvinylpyrrolidone. *J. Colloid Interface Sci.* **2001**, *235*, 70–79.
39. Vauthier-Holtzscheler, C.; Benabbou, S.; Spenlehauer, G.; Veillard, M.; Couvreur, P. Methodology for the preparation of ultra-dispersed polymer systems. *S.T.P. Pharm.* **1991**, *1*, 109–116.
40. Candau, F.; Holtzscheler, C. Microlatex inverses: etude de leur formation et de leurs proprietes. *J. Chim. Phys.* **1985**, *82*, 691–694.
41. Kopf, H.; Joshi, R.K.; Soliva, M.; Speiser, P. Studium der Mizellpolymerisation in Gegenwart niedermolekularer Arzneistoffe. *Pharm. Ind.* **1977**, *39*, 993–997.
42. Couvreur, P.; Tulkens, P.; Roland, M.; Trouet, A.; Speiser, P. Nanocapsules: A new type of lysosomotropic carrier. *FEBS Lett.* **1977**, *84*, 323–326.
43. Labhatsewar, V.D.; Dorle, A.K. Nanoparticles. A colloidal drug delivery system for primaquine and metronidazole. *J. Control. Release* **1990**, *12*, 113–119.
44. Rolland, A.; Gibassier, D.; Sado, P.; Le Verge, R. Methodologie de preparation de vecteurs nanoparticulaires a base de polymeres acryliques. *J. Pharm. Belg.* **1986**, *41*, 83–93.
45. Bharali, D.J.; Sahoo, S.K.; Mozumdar, S.; Maitra, A.N. Cross-linked polyvinylpyrrolidone nanoparticles: a

- potential carrier for hydrophilic drugs. *J. Colloid Interface Sci.* **2003**, *258*, 415–423.
46. Peppas, N.A.; Colombo, P. Analysis of drug release behavior from swellable polymer carriers using the dimensionality index. *J. Control. Release* **1997**, *45*, 35–40.
  47. Munshi, N.; De, T.K.; Maitra, A.N. Size modulation of polymeric nanoparticles under controlled dynamics of microemulsion droplets. *J. Colloid Interface Sci.* **1997**, *190*, 87–391.
  48. Gaur, U.; Sahoo, S.K.; De, T.K.; Ghosh, P.C.; Maitra, A.N.; Ghosh, P.K. Biodistribution of fluoresceinated dextran using novel nanoparticles evading reticuloendothelial system. *Int. J. Pharm.* **2000**, *202*, 1–10.
  49. Sharma, D.; Chelvi, T.P.; Kaur, J.; Chakravorty, K.; De, T.K.; Maitra, A.; Ralhan, R. Novel taxol formulation: polyvinylpyrrolidone nanoparticles encapsulated taxol for drug delivery in cancer therapy. *Oncol. Res.* **1996**, *8* (7–8), 281–286.
  50. Madan, T.; Munshi, N.; De, T.K.; Maitra, A.; UshaSarma, P.; Aggarwal, S.S. Biodegradable nanoparticles as a sustained release system for the antigens/allergens of *Aspergillus fumigatus*: Preparation and characterization. *Int. J. Pharm.* **1997**, *159*, 135–147.
  51. Jana, S.S.; Bharali, D.J.; Mani, P.; Maitra, A.N.; Gupta, C.M.; Sarkar, D.P. Targeted cytosolic delivery of hydrogel nanoparticles into HepG2 cells through engineered Sendai viral envelopes. *FEBS Lett.* **2002**, *515*, 184–188.
  52. Bharali, D.J.; Chattopadhyay, D.; Mozumdar, S.; Maitra, A.N. Cross-linked polyvinylpyrrolidone nanoparticles as Non-viral vectors for in vitro and in vivo delivery of genes. Proceedings of the 30th annual meeting and exposition of the controlled release society; July 19–23, 2003; 579 pp.
  53. Sahoo, S.K.; De, T.K.; Ghosh, P.K.; Maitra, A. pH- and thermosensitive hydrogel nanoparticles. *J. Colloid Interface Sci.* **1998**, *206*, 361–368.
  54. Sahni, M. et al. Partially Surface Hydrophobic Mucoadhesive PVP Nanoparticles as Potential Oral Delivery Carrier for Hydrophilic Drugs unpublished results.
  55. Maitra, A.N. *Oral delivery Formulations of Insulin. Work Done Under NMITLI (CSIR) Project*; 2002.

# Ice Nanotubes inside Carbon Nanotubes

Kenichiro Koga

Hideki Tanaka

Department of Chemistry, Okayama University, Okayama, Japan

## INTRODUCTION

The carbon nanotube provides a well-defined quasi one-dimensional (1-D) space where one can prepare a quasi 1-D material and explore its new properties that have not been found for the corresponding bulk material. Water is one of the substances that may actually be confined to the carbon nanotube, but its properties in the quasi 1-D space had been as little studied as, or even less studied than, those of other quasi 1-D materials despite the fact that water itself has been more studied than any other substance. However, recent theoretical studies and the following experimental studies of water confined in the carbon nanotube showed that the confined water freezes into crystalline structures that were never found in the bulk water and exhibits the phase behavior of melting and freezing that no bulk system has ever shown.<sup>[1–3]</sup> This entry is a review of these theoretical studies of the confined water. There are other theoretical or experimental studies on water in the carbon nanotube, focusing on the dynamic properties of water,<sup>[4]</sup> and more studies of confined water in general.<sup>[5]</sup>

Computer simulation studies<sup>[1]</sup> show that the structure of solid water in the zigzag ( $\ell$ , 0), single-walled, carbon nanotube (SWCN) (with  $\ell = 13, 14, \dots$ , or 17) is quite different from the bulk ice structure; it is a 1-D array of  $n$ -gonal “rings” consisting of  $n$  molecules. As in ordinary ice—in fact, as in any one of the 12 bulk ice polymorphs excluding ice X—every H<sub>2</sub>O molecule in the solid water in the carbon nanotube is hydrogen bonded to its four neighboring molecules. Because it has a hollow-tube structure and its width is of the order of 1 nm ( $=10^{-9}$  m), this quasi 1-D ice is called the ice nanotube. Simulations show that liquid water confined in carbon nanotubes freezes into a square, pentagonal, hexagonal, and heptagonal form of the ice nanotube, each corresponding to  $n = 4, 5, 6$ , and 7, respectively. Which structure is selected on freezing is dependent on the diameter of the carbon nanotube and the external conditions such as pressure and temperature. It is also found from the simulations and free-energy calculations that the phase behavior of confined water is qualitatively different from the bulk counterpart. Melting and freezing in

any bulk system occur as an infinitely sharp change of the state of matter, i.e., as the first-order phase transition; however, freezing into and melting from the ice nanotube are either continuous with no well-defined melting point or discontinuous as in any bulk system.

In 2002, it was reported<sup>[3]</sup> that the structure of water inside the carbon nanotube at low temperatures determined by X-ray diffraction is consistent with that of the ice nanotube found in the computer simulation.

## STRUCTURE OF ICE NANOTUBE

In any known crystalline ice every water molecule is hydrogen bonded to its four neighboring molecules. This is because with this condition the potential energy of the system would be significantly lower than otherwise. Thus, all the 12 different forms of bulk ice have a perfect hydrogen bond network structure. If this condition were possible in a quasi 1-D space, water would freeze into a quasi 1-D ice with a perfect hydrogen bond network. The ice nanotube is one type of such a quasi 1-D ice. It refers to a set of crystalline ice forms that extend in only one direction with a constant diameter of the order of 1 nm. The structure of the ice nanotube, which will be described in the following, was speculated and was analyzed by the classical and quantum calculations of the potential energy in vacuum at 0 K<sup>[6]</sup> before the actual demonstration by the computer simulation that liquid water freezes into the ice nanotube in the carbon nanotube.<sup>[1]</sup>

The ice nanotube is a 1-D array of  $n$ -gonal rings of water molecules. Imagine a strip of the 2-D square lattice with some finite width and infinite height (Fig. 1A). There is a water molecule at each intersection of the vertical and horizontal lines. In this way, every molecule, except those along the two edges of the strip, is connected to its four neighbors by hydrogen bonds as denoted by the solid line segments in the figure. Now if one rolls up the strip and joins the two long edges such that each molecule along one edge forms the fourth bond with a molecule along the other edge at the same height, then one would obtain a hollow-tube structure of water with a perfect hydrogen bond network (Fig. 1B), which is the basic structure of the

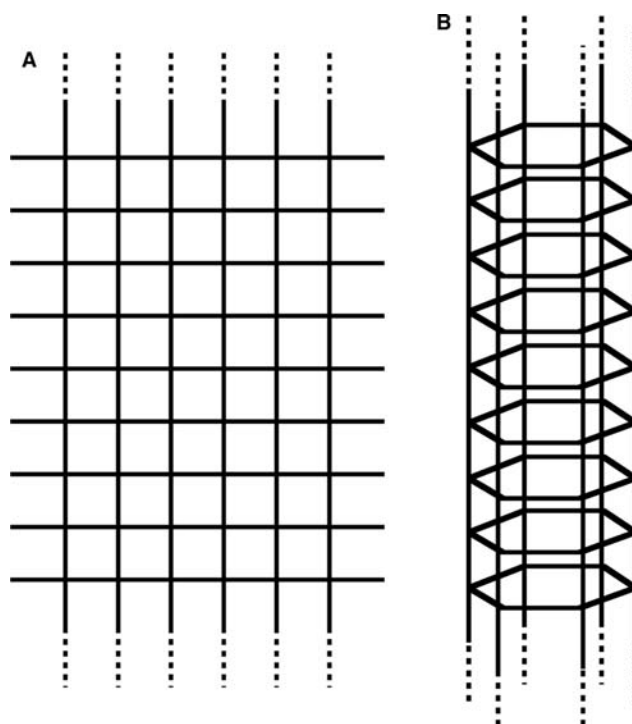


**Fig. 1** (A) Square lattice with finite width and infinite height; (B) The basic structure of a perfect hydrogen bond network in the ice nanotube.

ice nanotube. This is analogous to the SWCN, which may also be viewed as a rolled graphite sheet. The difference between this ice and the carbon nanotube is that, when unrolled, the carbon nanotube has a honeycomb lattice structure, whereas the ice nanotube has a square lattice structure. Also, while the carbon nanotube may take many different forms each being specified by the index  $(\ell, m)$ , the ice nanotube seems to have only a small number of different forms; only four forms, square ( $n = 4$ ), pentagonal ( $n = 5$ ), hexagonal ( $n = 6$ ), and heptagonal ( $n = 7$ ) ice nanotubes, were found in the computer simulation,<sup>[1]</sup> and even less structures were found in the experiment.<sup>[3]</sup> The diameter of the narrowest square ice nanotube is about 4 Å and that of the widest heptagonal ice nanotube is about 6 Å.

As in the ordinary ice, each oxygen atom is surrounded by four others, and between the central O and each one of its four neighboring O's is a hydrogen atom. These four H's are not at the midpoints between two O's, but two are closer to the central O (forming H<sub>2</sub>O with the central O) and two are closer to the neighboring O's. These conditions, which are referred to as the ice rule, are satisfied in most of the bulk ice forms. In the ordinary crystalline form of ice, i.e., ice Ih, every configuration satisfying the ice rule has nearly the same potential energy. The number of such configurations is  $(3/2)^N$ , with  $N$  being the number of water molecules as obtained by Pauling, so that the residual

entropy  $S$  per mole because of the degeneracy is, with  $R$  the gas constant,  $S = R \ln(3/2) = 0.81 \text{ cal}/(\text{mol K})$ , in essential agreement with experiment.

In the ice nanotube, however, not all the configurations satisfying the ice rule correspond to the ground state; only some of them would have nearly a same lowest potential energy and contribute to the residual entropy. This is because four neighboring molecules of any given molecule are lying in the directions significantly different from the ideal tetrahedral directions as in ice Ih (Fig. 2). Two neighbors are those in the same  $n$ -gonal ring, and thus the two directions from

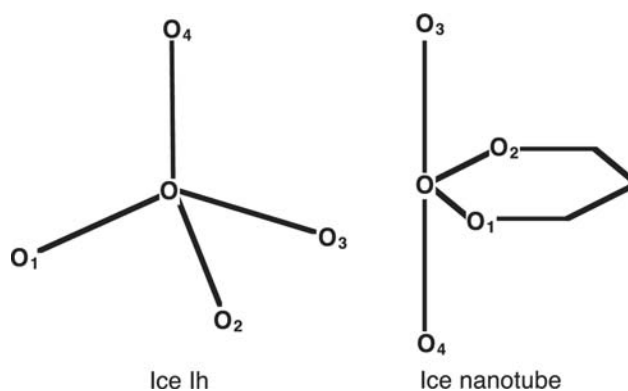


**Fig. 2** Configuration of an O atom and its four neighboring O atoms in the ordinary ice (ice Ih) and in the ice nanotube.



the central molecule to such two neighbors form an angle  $\pi(1 - \frac{2}{n})$ ; Two other neighbors are those in the two adjacent rings, and thus the two directions to such neighbors are both along an edge of the  $n$ -gonal prism and just opposite, forming an angle  $\pi$ . In ice Ih, two OH “arms” in a H<sub>2</sub>O molecule may be in any two directions, and thus each molecule has six possible orientations. But in the ice nanotube, two OH arms of one molecule would never form hydrogen bonds with two neighbors in the two opposite directions along the edge of the  $n$ -gonal prism because the angle  $\pi$  is too large. With this constraint, if the two OH arms formed hydrogen bonds with two neighbors in the same ring, then the formation of a closed loop of the hydrogen bonds along that ring would be impossible. Therefore, one OH arm of a molecule must form a hydrogen bond with one neighbor in the same ring and the other OH arm of the molecule must form a hydrogen bond with one neighbor at the same edge of the prism. This is a condition that every molecule in the ice nanotube must satisfy in addition to the ice rule. It follows from this condition that the OH arms along each ring line up either clockwise or counterclockwise and that the OH arms along each edge of the  $n$ -gonal prism are either all up or all down. That is, there are only two ways of arranging a set of all the OH arms along each ring or along each edge. Because the number of such rings is  $N/n$  and the number of such edges is  $n$ , the total number of possible configurations of OH arms, or H atoms, in the  $n$ -gonal ice nanotube of  $N$  molecules would be  $2^{n+(N/n)}$ .

However, the numerical calculation shows that configurations of an  $n$ -gonal ice nanotube would have significantly lower potential energies if they have the smallest number of two neighboring edges both with the same direction of the OH arms (up or down); the smallest number is 0 if  $n$  is even and 1 if  $n$  is odd. This is a special condition on the configuration of H atoms in the ice nanotube. The possible number of configurations would then be  $2^{(N/n)}$  for the  $n$ -gonal ice nanotube. The numerical calculation shows that the potential energy is nearly the same for these configurations. With  $R = N_A k$ , where  $N_A$  is Avogadro's number and  $k$  is Boltzmann's constant, the degeneracy  $W$  per mole is then  $2^{(N_A/n)}$  and the residual entropy  $S$  per mole is  $S = k \ln W = (R/n) \ln 2$ ; thus for  $n = 4, 5, 6,$  and  $7$ , we have  $S = 0.70, 0.56, 0.47,$  and  $0.40$  cal/(mol K), respectively, which is smaller than that of ice Ih.

## FREEZING AND MELTING BEHAVIOR

### Necessary Conditions

The computer simulation and the free-energy calculation<sup>[1]</sup> show that the following three conditions are

essential for the formation of the ice nanotube. First, water may freeze into the ice nanotube only when it is confined to a cylindrical pore; the spontaneous formation of the ice nanotube without confinement has never been observed in experiment or in computer simulation. Second, the diameter of the cylindrical pore must be in a range between 10 and 15 Å. The  $n$ -gonal ice nanotube with large  $n$ , say 10 or 20, would fit a pore with larger diameter, but then all the hydrogen bond angles would be so different from the ideal angle that such a structure becomes energetically less favorable than other possible crystalline or amorphous forms. Third, the surface of cylindrical pore should be hydrophobic in the sense that water molecules do not form hydrogen bonds to the surface atoms. This is because the closed hydrogen bond network of water molecules, i.e., the structure of ice nanotube, would be impossible if water molecules interact with the surface more strongly than with each other. The inner space of the carbon nanotube with an appropriate diameter may satisfy all the conditions described above and thus serve truly an ideal environment for the formation of the ice nanotube.

### Freezing into the Ice Nanotube

The structure of the ice nanotube was noted as a possible form that the hydrogen bond network may extend only in one dimension with perfect connectivity, i.e., with every water molecule being hydrogen bonded to each of its four neighbors, and the stability of various forms of the ice nanotube at 0 K in vacuum was studied.<sup>[6]</sup> However, whether liquid water may really freeze into that structure in the carbon nanotube had remained to be seen until the molecular dynamics simulations<sup>[1]</sup> demonstrated the spontaneous freezing of water into the ice nanotube at various conditions.

The potential functions and their parameters were chosen to simulate water molecules confined in the zigzag  $(\ell, 0)$  SWCN. The diameter  $D$  of this form of the carbon nanotube is given by  $D = \sqrt{3}a/\sin(\pi/\ell)$  with  $a = 1.423$  Å is the distance between two neighboring carbon atoms. Freezing and melting behavior of water was examined for the systems of the (13, 0), (14, 0), (15, 0), (16, 0), (17, 0), and (18, 0) carbon nanotubes with  $D = 10.3, 11.1, 11.9, 12.6, 13.4,$  and  $14.2$  Å. Equilibrium properties of each system at a given temperature  $T$  and a given pressure  $P_z$  in the direction parallel to the axis of the carbon nanotube was achieved by the constant  $NP_zT$  ensemble molecular dynamics simulation. For each system, a series of such simulation was performed along the isobaric path or along the isothermal path. Details of the simulation methods are given elsewhere.<sup>[1]</sup>

At high enough  $T$  (e.g., 350 K or 80°C) and low or moderate  $P_z$  (e.g., around or below 50 MPa), water confined in any of these carbon nanotubes is in a liquid state; it has no long-range order in its structure and has high diffusivity. The potential energy of the system because of the intermolecular interactions between water molecules at such  $T$  and  $P_z$  is much higher than that of the bulk water at the corresponding condition. This indicates that the hydrogen bonds in the liquid water are on average not strengthened but weakened by the hydrophobic inner surface of the carbon nanotube, as opposed to the hydrophobic effect on the structure of water around a hydrophobic solute molecule.

However, such a disordered structure of water at high  $T$  turns into an ordered structure at sufficiently low  $T$  in the (13, 0), (14, 0), (15, 0), (16, 0), and (17, 0)

carbon nanotube (Fig. 3). The resulting ordered structure is identical or almost identical to the anticipated structure of the ice nanotube; the only difference, if any, is that some defects may exist in the otherwise ordered structure, and such defects may in turn cause a twisted structure (Fig. 3B). It is unclear as yet whether an ordered structure with a few defects is already in equilibrium at finite  $T$  or would be ultimately replaced by a perfect defect-free structure. In any case, water molecules in the ordered phase have extremely small or nearly zero diffusivity, which is also indicative of a solid state.

The diameter of the carbon nanotube plays a crucial role in selecting a crystalline form of the ice nanotube. When  $P_z$  is fixed at 50 MPa and  $T$  is decreased stepwise, liquid water freezes into the square ice nanotube ( $n = 4$ ) in the (13, 0) and (14, 0) carbon nanotube, whereas

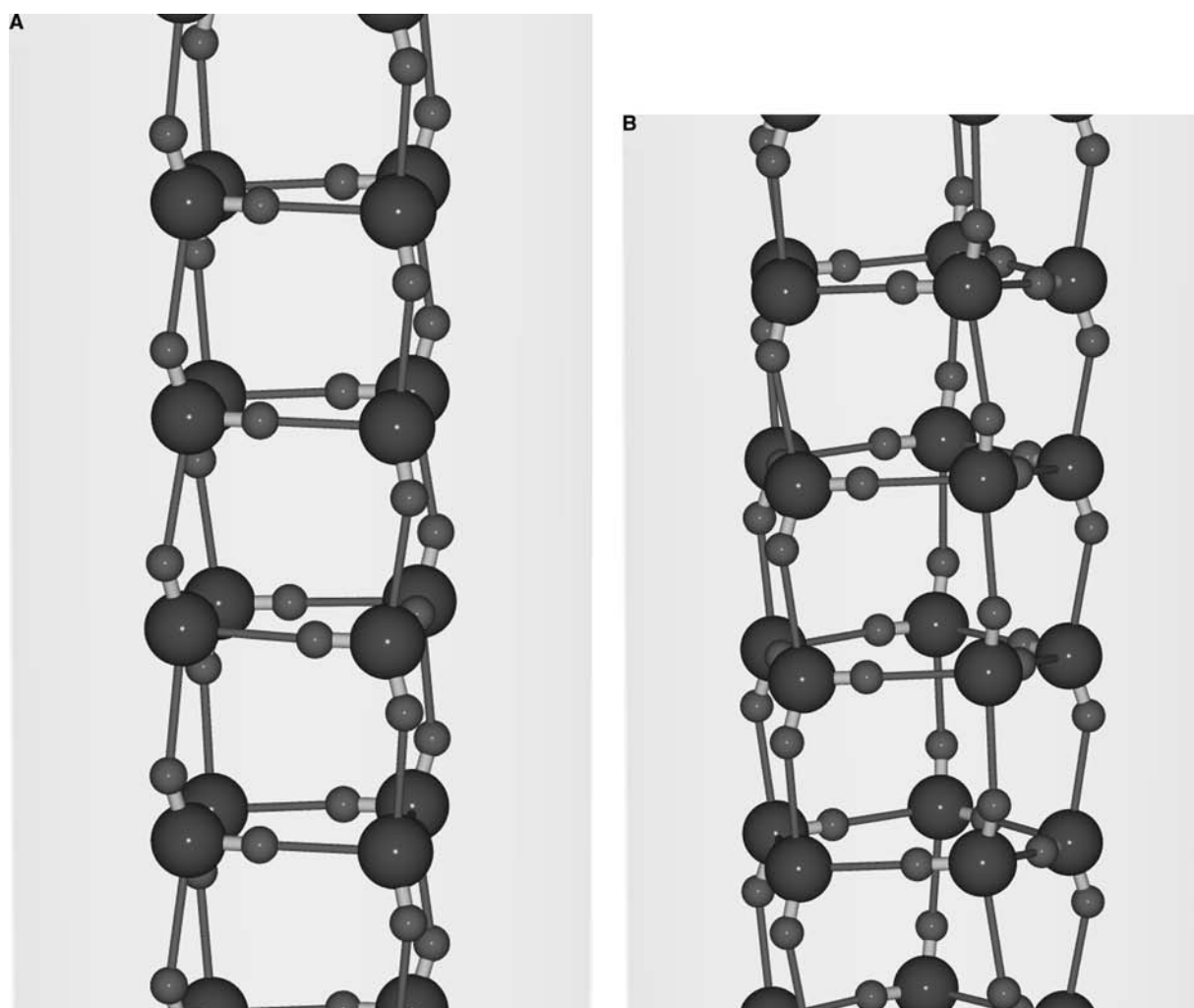


**Fig. 3** (A) Square, (B) pentagonal, (C) hexagonal, (D) heptagonal ice nanotubes at 240 K (except  $d$  at 230 K) at 50 MPa in the (14, 0), (15, 0), (16, 0), (17, 0) carbon nanotubes, and (E)–(H) the corresponding liquid phases at 320 K (except  $h$  at 300 K) at 50 MPa. Shown here for clarity are the structures at the local minima of the potential-energy surface; any instantaneous displacement from these structures because of the thermal vibrations is absent.

it freezes into the pentagonal, hexagonal, and heptagonal ice nanotubes ( $n = 5, 6,$  and  $7$ ) in the  $(15, 0)$ ,  $(16, 0)$ , and  $(17, 0)$  carbon nanotubes, respectively.

In the  $(18, 0)$  carbon nanotube, however, crystallization was not observed, at least within the timescale of simulation. As remarked earlier, the structure of the ice nanotube becomes increasingly unstable as  $n$  goes up from 6. Thus, there must be an upper limit for  $n$  for the possible forms of the ice nanotube. Then there must also be a corresponding upper limit for the index  $\ell$  or the diameter  $D$  of the carbon nanotube in which water may freeze into the ice nanotube. The results of the simulation suggest  $n = 7$  (i.e., the heptagonal ice nanotube) to be the upper limit, although it does not exclude the possibility of  $n = 8$  (i.e., the octagonal ice nanotube). However, formation of the ice nanotube with  $n > 8$  from pure water confined to a wider carbon nanotube seems unlikely.

In any ordered structure found at low  $T$  in the simulation, the orientation of water molecules indeed satisfies the special condition described in the previous section, as seen in Fig. 3; that is, the configuration of H atoms lying along the  $n$  edges parallel to the axis of the  $n$ -gonal prism is uniquely determined, and the only disorder is that in the arrangement of the

clockwise and counterclockwise configurations of H atoms along each  $n$ -gonal ring.

### Sharp and Continuous Freezing

Melting and freezing in general always occur as a discontinuous change of the state of matter, which is called the first-order transition. This is not necessarily true in a 1-D or quasi 1-D system. The simulation of water in the carbon nanotube indicates that both continuous and discontinuous freezing may occur depending on the diameter of the carbon nanotube and on the path followed in the thermodynamic  $P_z$ - $T$  plane.

Fig. 4 shows plots of the potential energy of water confined in the  $(\ell, 0)$  carbon nanotube ( $\ell = 13, \dots, 18$ ) as a function of temperature. When  $\ell = 13, 14,$  and  $15$  at  $P_z = 50$  MPa, the potential energy decreases continuously with decreasing  $T$  while when  $\ell = 16$  and  $17$  at the same pressure it makes an abrupt decrease at a certain point on cooling and exhibits a large hysteresis on heating. The molar volume of water also exhibits discontinuity or continuity just as the potential energy does. The discontinuity or continuity in the macroscopic properties of water is associated with

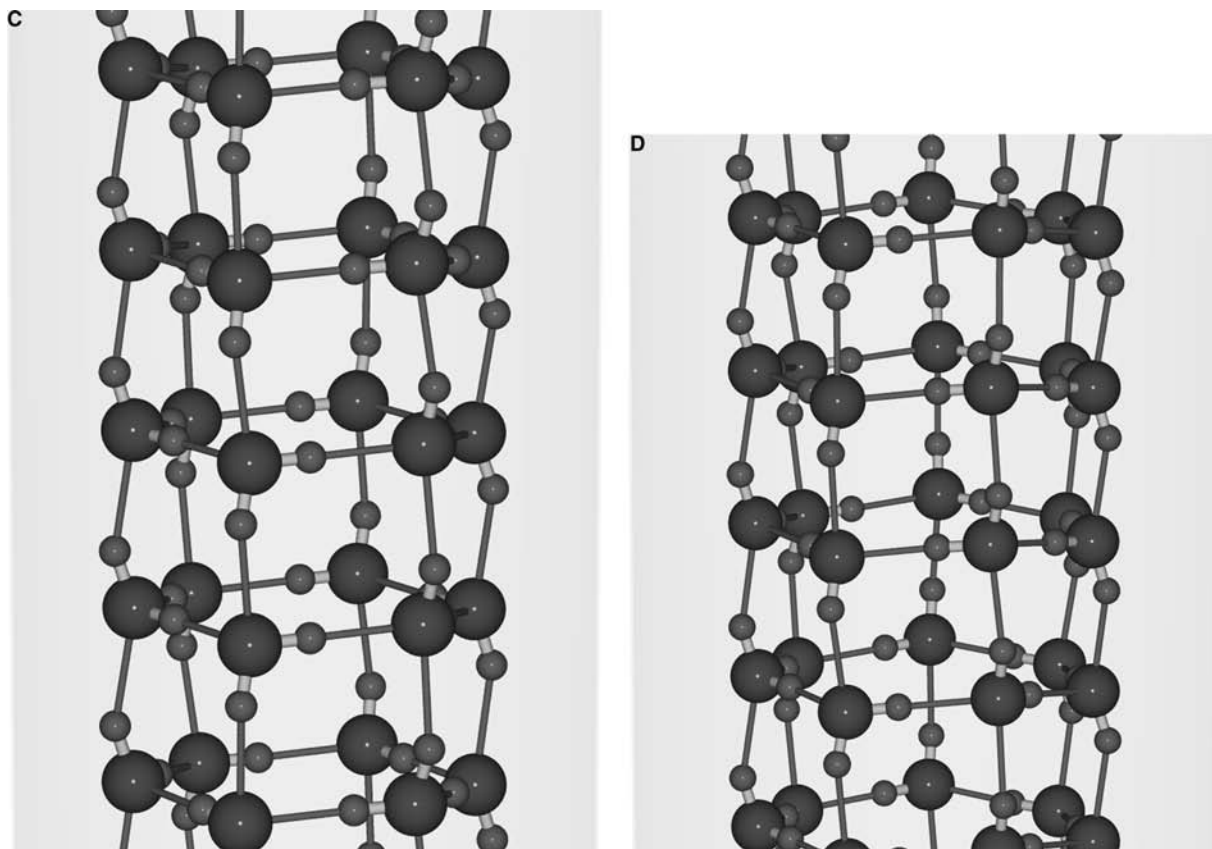


Fig. 3 (Continued).

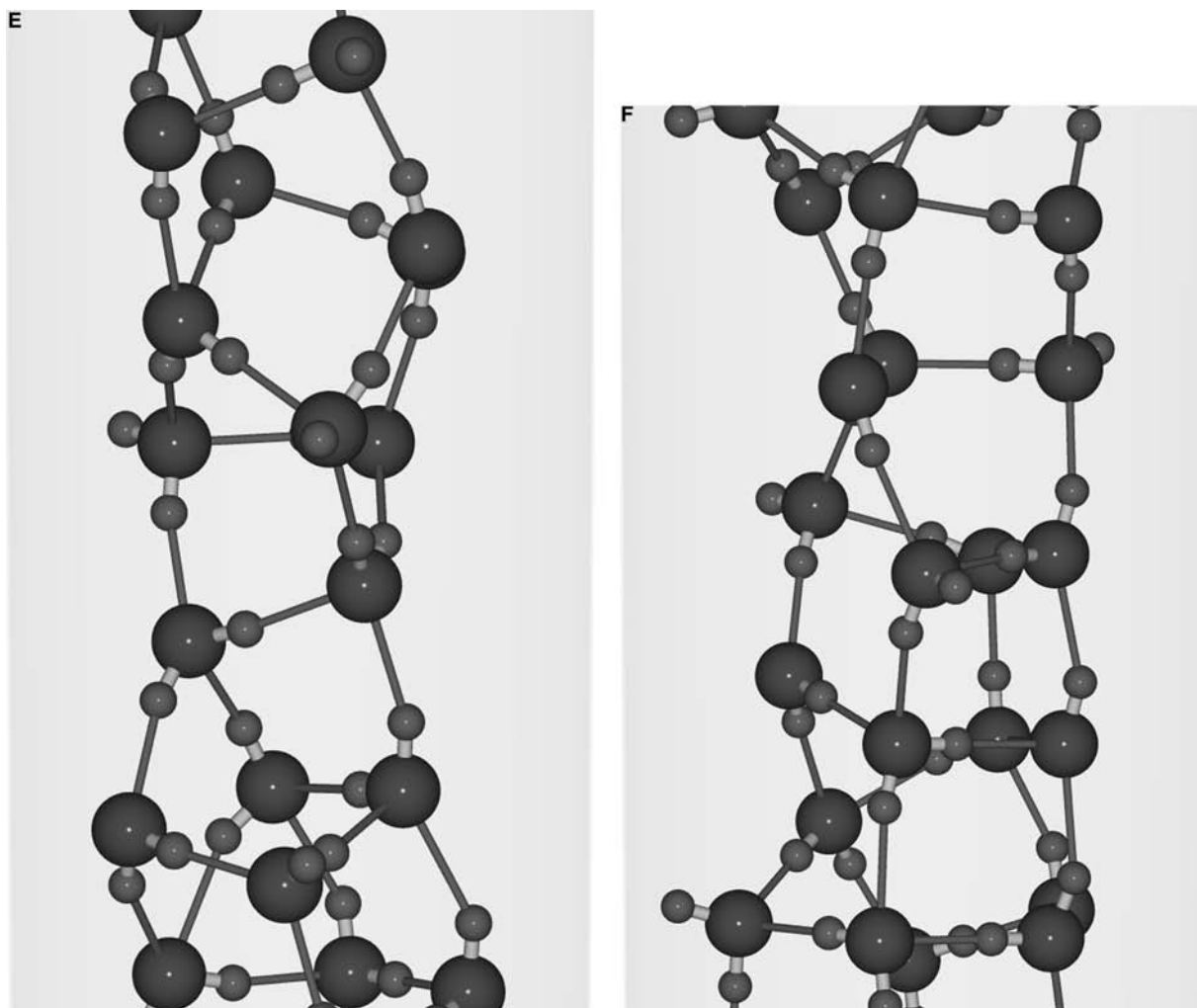


Fig. 3 (Continued).

the discontinuous or continuous change from a disordered structure (of liquid water) to an ordered structure (of the ice nanotube) or vice versa. In the (18, 0) carbon nanotube, the potential energy decreases nearly linearly with decreasing  $T$  and the disordered liquidlike structure at high  $T$  remains even at the lowest  $T$ .

Whether freezing occurs continuously or discontinuously depends not only on the index  $\ell$  or the diameter  $D$  of the carbon nanotube but also on the pressure  $P_z$ . Under a very high pressure (500 MPa), water in the (15, 0) carbon nanotube freezes *discontinuously* to the *hexagonal* form of ice nanotube; remember that it freezes *continuously* to the *pentagonal* form at 50 MPa (Fig. 4C). More complex behavior is found in the (14, 0) carbon nanotube (Fig. 4B). On cooling at 50 MPa water freezes *continuously* into the square ice nanotube; at 200 MPa, it freezes *discontinuously* into the pentagonal ice nanotube; and finally at 500 MPa it freezes *continuously* into the pentagonal ice nanotube.

A set of isotherms in the  $P_z$ - $V$  plane allows us to understand such complex phase behavior and can be a basic source to construct a phase diagram. Each isotherm is a plot of the system's volume against  $P_z$  at fixed  $T$ , which is readily obtained from the  $NP_zT$ -constant molecular dynamics simulation. Fig. 5 shows the set of isotherms for the (14, 0) carbon nanotube system. When  $T$  is fixed at 280 K,  $V$  makes a sudden drop at 200 MPa on compressing and a sudden jump at 170 MPa on decompressing; that is, the isotherm shows discontinuity and a hysteresis. The low-density phase (before the sudden drop or after the sudden jump in  $V$  is observed) has a liquidlike disordered structure, whereas the high-density phase (after the sudden drop or before the sudden jump in  $V$  is observed) is basically a pentagonal ice nanotube. The diffusion constants of the low-density phase (at 190 MPa) and the high density phase (at 200 MPa), both during compression at 280 K, are  $1 \times 10^{-6}$  and  $1 \times 10^{-10}$  cm<sup>2</sup>sec<sup>-1</sup>, respectively, which reinforces

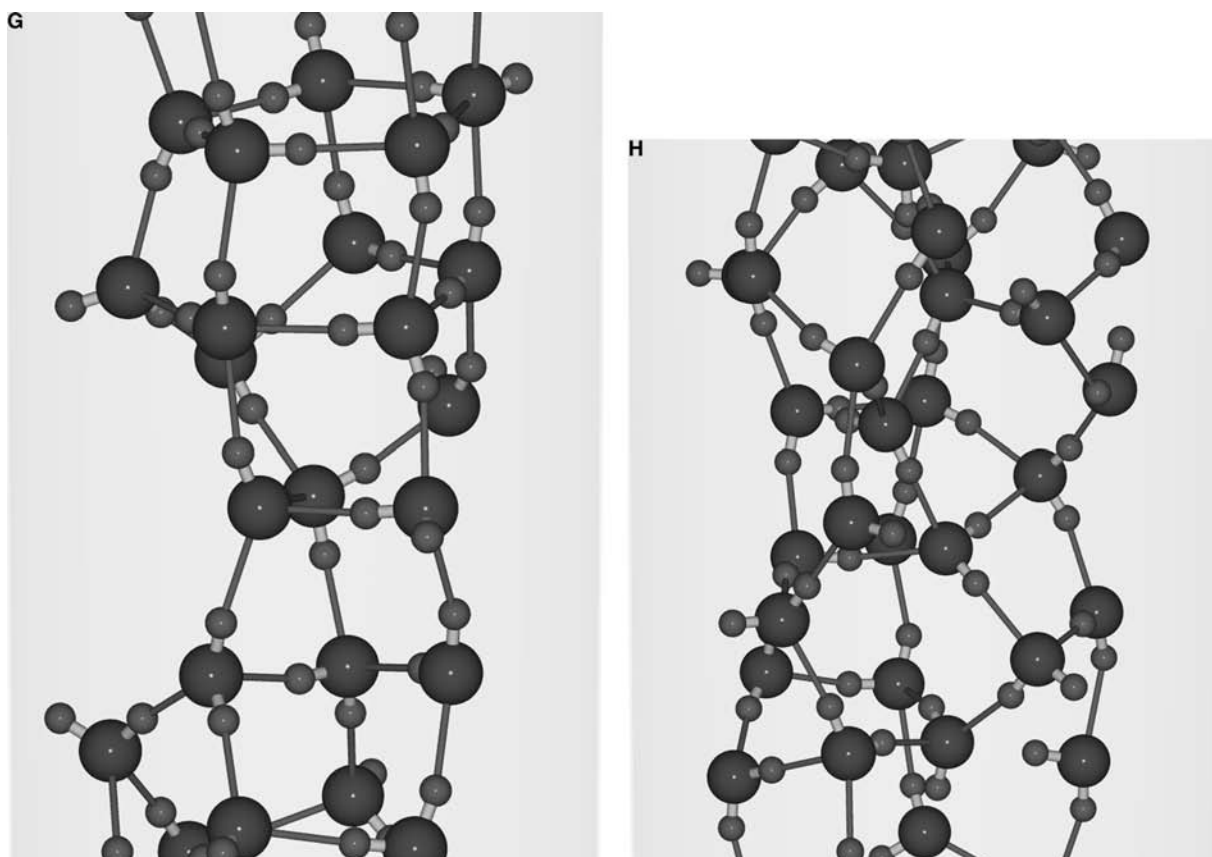


Fig. 3 (Continued).

that the low-density phase is liquidlike, whereas the high-density phase is solidlike. When  $T$  is fixed at 300 K, however,  $V$  shows a marked decline between 250 and 330 MPa but with no discontinuity, although the same liquidlike and solidlike phases are found at low and high pressures, respectively. This means the liquid–solid transformation at this temperature is *continuous*. When  $T$  is fixed at 330 K, the isotherm is much less steep, and at 350 K it slopes down even more gently. Thus, the isotherms for the (14, 0) carbon nanotube system are similar to typical isotherms around the critical point of fluids.

For the (15, 0) carbon nanotube system, all the isotherms obtained at  $T = 280, 300, 320$  K show discontinuity, and the low-density phase is always liquidlike at these temperatures whereas the high-density phase is the hexagonal ice nanotube (even at 320 K!).

## PHASE DIAGRAM

A phase diagram of water confined in the carbon nanotube is inferred from the results of the computer simulation and free-energy calculation. Before

presenting the phase diagram, however, we note that it is not obvious whether or not a quasi 1-D system would show any phase transition or phase separation, even if the corresponding bulk system does. This is because when the dimension  $d$  is less than 2, much of the theoretical models in studies of the phase transition no longer exhibit any phase transition at any finite  $T$ . We should also note that the computer simulation itself cannot prove or disprove the existence of the phase transition because it cannot treat a macroscopic number  $N \sim 10^{23}$  of molecules corresponding only to a thermodynamic limit in which the phase transition occurs. Nevertheless, the computer simulation can demonstrate discontinuous changes in microscopic and macroscopic properties of a system with changes in the temperature, pressure, or other thermodynamic field variable, and such discontinuous changes in a finite system do correspond to some abrupt, if not discontinuous, change of the state of the macroscopic system. Thus, in this sense we now use the terms “phase transition” and “phase boundary” for quasi 1-D water.

Fig. 6 shows a schematic phase diagram in the  $T$ – $P_z$  plane for the (14, 0) carbon nanotube system. The phase boundary separates the high- and low-density

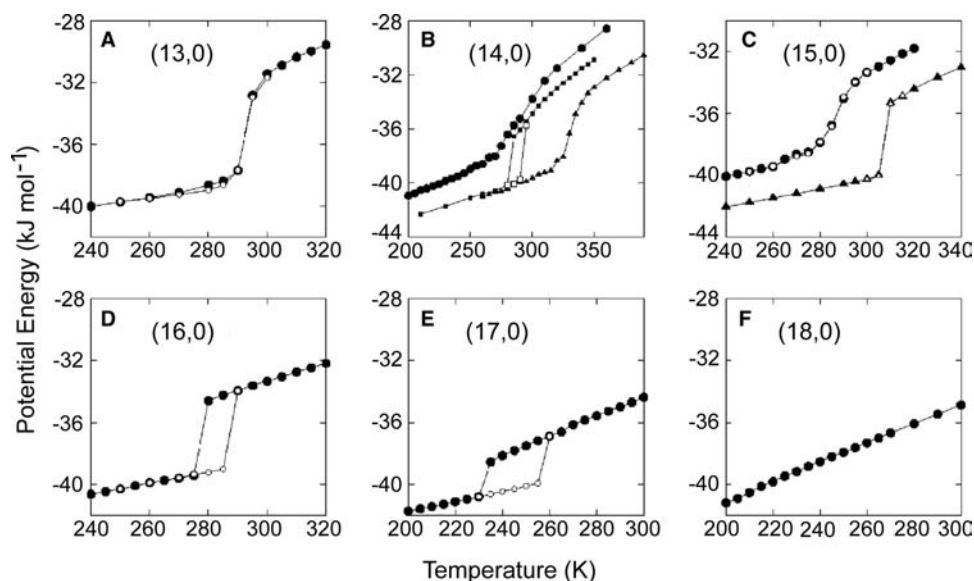


**Fig. 4** The potential energy vs. temperature for water confined to the  $(\ell, 0)$  carbon nanotube with  $\ell = 13$ –18 (A–F). The axial pressure is fixed at  $P_z = 50$  MPa ( $\bullet$  and  $\circ$  in A–F), 200 MPa ( $\blacksquare$  and  $\square$  in B), and 500 MPa ( $\blacktriangle$  and  $\triangle$  in B and C). Filled and open symbols indicate the cooling and heating process, respectively. The potential energy is the energy associated with the intermolecular interactions between water molecules.

phases, which are now referred to as pentagonal and square phases for convenience. At low temperatures (e.g., 200 K) both phases are solidlike; at higher temperatures (e.g., 270 K) the high-density phase is still solidlike, whereas the low-density phase is liquidlike. Because the phase change becomes continuous above 280 K, the phase boundary should terminate at some

point around that temperature. The point is referred to as a “critical point” in the same restricted sense as remarked above. This phase diagram explains the complex phase behavior of the  $(14, 0)$  carbon nanotube system (Fig. 4B): the isobaric path at 50 MPa does not cross the phase boundary, and thus the phase change between the liquid and the square ice

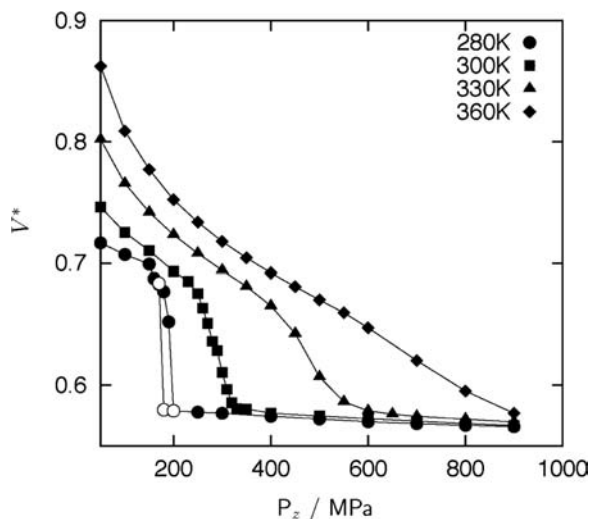


**Fig. 5** Isotherms in the  $P_z$ – $V^*$  plane for confined water in the  $(14, 0)$  carbon nanotube at temperatures 280 K ( $\bullet$  and  $\circ$ ), 300 K ( $\blacksquare$ ), 330 K ( $\blacktriangle$ ), and 360 K ( $\blacklozenge$ ).  $V^* = V/(N\pi r^2 \text{ \AA}^2)$ . Filled and open symbols indicate the compressing and decompressing process, respectively.

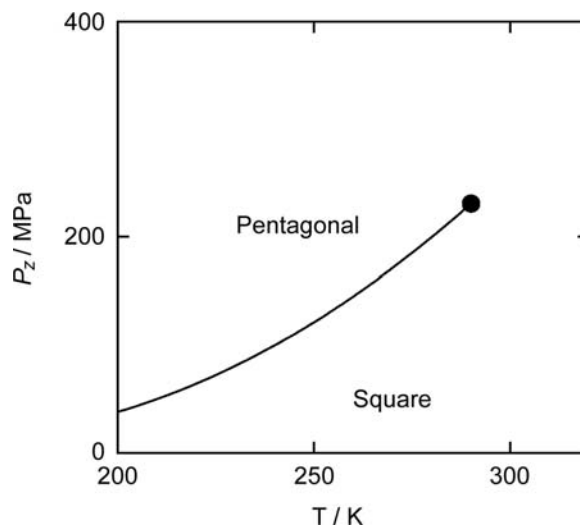


**Fig. 6** A schematic  $T$ – $P_z$  phase diagram of water confined to the  $(14, 0)$  carbon nanotube. The phase boundary (solid line) divides the low-density (square) and high-density (pentagonal) phases. The phase boundary terminates at a critical point ( $\bullet$ ) around 280 K.



nanotube phase is continuous; the isobaric path at 200 MPa, however, crosses the phase boundary, and thus the change is between the liquidlike square phase and the solid pentagonal phase and it is discontinuous; and finally, the isobaric path at 500 MPa does not cross the boundary because it is above the critical pressure, and thus the change between the square and pentagonal phases is continuous.

For the (15, 0) carbon nanotube system, the phase boundary separates the low- and high-density phases, which may be referred to as pentagonal and hexagonal phases, respectively, because at low temperatures they are the pentagonal and hexagonal ice nanotubes. Unlike in the (14, 0) carbon nanotube system, no continuous path from one phase to another has been found in the  $T$ - $P_z$  plane examined by the simulation. That is, the phase boundary may not terminate at any critical point, just as in any bulk liquid–solid phase equilibrium.

Similarly, for the (16, 0) carbon nanotube system, low-density and high-density phases are separated by a phase boundary that does not terminate at any critical point. The low-density phase is in a liquid state, whereas the high-density phase is a solid hexagonal ice nanotube.

For the (17, 0) carbon nanotube systems—the widest nanotube that allowed formation of the ice nanotube in the simulation—again the two phases, which we now call simply the solid and liquid phases, are separated by a phase boundary with no critical point. The solid phase is identified as the heptagonal ice nanotube. In this system, unlike in other systems, liquid water expands as it freezes into the ice nanotube at 50 MPa. That is, the density of the heptagonal ice nanotube is smaller than that of the liquid at the phase boundary at 50 MPa. At higher  $P_z$  this would hold even more strongly because the density of liquid increases more rapidly than that of the solid with increasing  $P_z$ . Thus, for the (17, 0) carbon nanotube system, the slope of the phase boundary in the  $T$ - $P_z$  plane should always be negative:  $dP_z/dT < 0$ .

As we have seen above in the phase diagrams, the phase behavior of water confined in the different carbon nanotubes is qualitatively different even if the index  $\ell$  of the carbon nanotube differs only by 1. However, if  $\ell$  (or  $D$ ) is taken to be continuous, rather than discrete, and is introduced as another axis in the original phase diagram, the resulting global phase diagram in the 3-D  $TP_z\ell$  (or  $TP_zD$ ) space would account for how these apparently independent phase diagrams at discrete  $\ell$  (or  $D$ ) are related to each other.<sup>[2]</sup> From the thermodynamic relations analogous to the Clapeyron equation and the simulations for several systems with noninteger values of  $\ell$ , e.g., a hypothetical (14.2, 0) carbon nanotube system, we find the following picture of the global phase diagram. First, there are at least five

phase boundaries, which are now surfaces in the  $TP_z\ell$  space and have very steep slopes with respect to the  $\ell$  axis. Two of them, a surface separating the square and pentagonal phases and a surface separating the liquid and square phases, seem to terminate at a “critical line.” The other three are the surfaces separating the pentagonal and liquid (hexagonal) phases, the hexagonal and liquid (heptagonal) phases, and the heptagonal and liquid phases, and they seem not to terminate at any critical line.

## RELATED SIMULATIONS AND EXPERIMENTS

Some computer simulations have been performed to examine the structure of an alkali halide, KI, inside the SWCNs and the mechanism of encapsulation of the molten salt into the hollow space of the carbon nanotubes.<sup>[7]</sup> The results of the simulations suggest that the salt is crystallized rather easily in the carbon nanotubes even at temperatures at which the bulk counterpart is a melt. Coulombic interaction facilitates the formation of the crystalline structures of KI inside the SWCNs. In this sense, the salt in the confined space exhibits a phase behavior similar to that of water; however, water shows the more facile transition because of its characteristic intermolecular interaction, i.e., the hydrogen bond. Those structures of the salt are either fragments of the bulk KI crystal or a twisted one, the latter of which has nothing to do with the bulk crystalline structure. Further investigation is required to discern which structure is the real entity in the SWCNs. Among other interesting topics are the structure and phase behavior of aqueous electrolyte solutions in SWCNs, which are expected to be greatly different from those of pure water in SWCNs. The hydration structure around ions and the ion-pair formation could be influenced by the quasi 1-D confinement, and they may become distinct from the bulk counterparts.<sup>[7]</sup>

Formation of the heptagonal ice nanotube in the SWCN has recently been observed experimentally,<sup>[3]</sup> which reinforces the theoretical prediction by the molecular dynamics and free energy calculations. Also observed in the experiment is that the melting point increases with decreasing the diameter of the carbon nanotube (Y. Maniwa, private communication).

## ACKNOWLEDGMENTS

The authors thank Professor X. C. Zeng, Professor G. T. Gao, and Professor R. D. Parra for the collaborations on the main subject of this article. KK and HT are supported by the Japan Society for the

Promotion of Science (JSPS), the Japan Ministry of Education, and the Institute of Molecular Science. KK acknowledges the award of the JSPS Fellowship for Research Abroad 2001.

## REFERENCES

1. Koga, K.; Gao, G.T.; Tanaka, H.; Zeng, X.C. Formation of ordered ice nanotubes inside carbon nanotubes. *Nature* **2001**, *412* (6849), 802–805.
2. Koga, K.; Gao, G.T.; Tanaka, H.; Zeng, X.C. How does water freeze inside carbon nanotubes? *Physica, A* **2002**, *314*, 462–469.
3. Maniwa, Y.; Kataura, H.; Abe, M.; Suzuki, S.; Achiba, Y.; Kira, H.; Matsuda, K. Phase transition in confined water inside carbon nanotubes. *J. Phys. Soc. Jpn.* **2002**, *71* (12), 2863–2866.
4. Hummer, G.; Rasaiah, J.C.; Noworyta, J.P. Water conduction through the hydrophobic channel of a carbon nanotube. *Nature* **2001**, *414*, 188–190.
5. Buch, V., Devlin, J.P., Eds.; *Water in Confining Geometries*; Springer-Verlag, *in press*.
6. Koga, K.; Parra, R.D.; Tanaka, H.; Zeng, X.C. Ice nanotubes: What does the unit cell look like? *J. Chem. Phys.* **2000**, *113*, 5037–5040.
7. Wilson, M. Structure and phase stability of novel ‘twisted’ crystal structures in carbon nanotubes. *Chem. Phys. Lett.* **2002**, *366*, 504–509.

# In-Situ Electron Microscopy

Charles W. Allen

Materials Science Division, Argonne National Laboratory,  
Argonne, Illinois, U.S.A.

## INTRODUCTION

For decades, electron microscopies, transmission electron microscopy especially, have been employed as an important tool in materials research studies in nanoscience and developments in nanotechnology, for their powerful analytical techniques at spatial resolution and also as a kind of microlaboratory in which dynamic studies have been conducted “in situ.” Such in situ or real-time studies have included those involving phase transformations, mechanical deformation and failure, irradiation-related phenomena, and a host of others involving changes in physical, chemical, magnetic, and electrical structure, microstructure, and properties. This entry will present a number of examples from in situ studies to illustrate how such electron microscopy-based studies may contribute, often in unique ways, to the understanding of the behavior of material systems of relevance to modern nanoscience and nanotechnology. We will also review briefly a number of analytical techniques that have been developed over the years and applied to electron microscopies and finally comment on potential impact ongoing developments, particularly the correction of electron optical aberrations, will have on in situ studies.

## OVERVIEW

The initial demonstration of an in situ experiment with photographic record is often ascribed to an English-born photographer, Eadweard Muybridge. In the 1870s and 1880s, in part under the auspices of Leland Stanford, then Governor of California, Muybridge employed a series of photographic cameras triggered sequentially as a horse trotted by. The resulting sequence of photographs clearly demonstrated that the depiction of horses in motion in paintings and in the common belief of the time had been anatomically incorrect; that, rather than the horse’s gait being side to side with one pair of legs at a time, all four legs come

off the ground at once as a horse trots or gallops (For example, see Ref.<sup>[1]</sup>).

An in situ experiment is somewhat like watching an entire football match, rather than trying to imagine what happened by checking the score occasionally. For systems of almost any complexity or with events occurring rapidly as in the trotting horse example, it is not always possible to correctly deduce the evolution of changes simply by observing the end results in relation to the initial and final or sometimes even selected intermediate conditions. Furthermore, a well-designed in situ experiment may be an extremely efficient way to perform a scientific or technological study.

For many years in situ experiments have been performed involving a host of different analytical tools including X-ray diffractometers and synchrotron radiation sources, optical microscopes, and electron microscopes and have involved techniques of observation and measurement in real time or near real time such as microscopies (i.e., imaging of events), diffraction, elemental microanalysis, and changes in various physical properties. This entry focuses mainly on the application of transmission and scanning transmission electron microscopies (TEM and STEM), and to a lesser extent on scanning electron microscopy, for in situ experiments with particular emphasis on applications related to nanoscience and nanotechnology. The topic of related instrumentation such as scanning tunneling microscopy (STM) and atomic force microscopy (AFM) is presented elsewhere in this volume.

In situ techniques are often very powerful in yielding insight into the mechanisms of real-time behavior, such as when two or more phenomena compete in producing changes or when highly localized short-term changes are superimposed on long-term trends. A further situation in which in situ observation is essential is when elevated or cryogenic temperatures, loads, or fields are employed in a materials study, and further changes in the experimental object would occur as a consequence of returning the material to room temperature, zero load, or zero field for subsequent observation and analysis. The same may be said for all types of in situ studies, X-ray, neutron, and electron.

**Table 1** Comparison of selected (approximate) characteristics of state-of-the-art neutron, x-ray, and electron sources employed for materials research

Type of radiation	Source brightness (particles/cm <sup>2</sup> /sr/eV)	Elastic mean-free path (nm)	Absorption length (nm)	Minimum probe size (nm)	Spatial resolution (nm)
Neutrons (SNS)	10 <sup>14</sup>	10 <sup>7</sup>	10 <sup>8</sup>	10 <sup>6</sup>	10 <sup>6</sup>
X-rays (APS)	10 <sup>26</sup>	10 <sup>3</sup>	10 <sup>5</sup>	10 <sup>2</sup>	10 <sup>2</sup>
Electrons (S)TEM	10 <sup>29</sup>	10 <sup>1</sup>	10 <sup>2</sup>	10 <sup>-1</sup>	10 <sup>-1</sup>

SNS, spallation neutron source at Oak Ridge National Laboratory; APS, advanced photon source at Argonne National Laboratory.

In situ electron microscopy studies should be regarded as complementary to similar synchrotron studies and, for very slowly varying phenomena, neutron scattering studies. The latter present a view of time-dependent phenomena, generally averaged over much larger volumes of observation. It is, however, sometimes difficult to convince people who have extensive experience with X-ray or neutron scattering studies of the value-added aspect of complimentary analyses by some form(s) of electron microscopy, including the application of in situ techniques. This complementarity of techniques is emphasized in Table 1 in terms of selected characteristics for each of these types of radiation sources.

The elastic mean free paths for neutrons and X-rays are large compared to that for electrons, which means that elastic scattering, for example, is relatively inefficient in the former requiring very high intensities or long data acquisition times to achieve reasonable spatial resolutions. On the other hand, small absorption lengths for electrons require very thin specimens, but because electrons are readily focused by electromagnetic and electrostatic lenses, very fine, intense probes may be formed which, coupled with the thin specimen, result in excellent spatial resolution. The bottom line is simply that these related techniques can and should be more often understood as complementary rather than competitive.

## EXAMPLES OF IN SITU ELECTRON MICROSCOPY STUDIES

It may be easier to grasp the value of applying in situ techniques in electron microscopy by considering a variety of representative examples. By no means will these form an exhaustive compilation of such studies. The examples presented are brief excerpts from in situ TEM or STEM studies. However, some of these same ideas may be adapted or have been adapted for in situ SEM studies. Furthermore, variable pressure or environmental SEMs offer other altogether unique aspects for in situ experiments.

## Magnetic Studies

The techniques for imaging and analysis of magnetic structures in TEM have been developed over many decades. These include Fresnel, Foucault, electron holographic, and differential phase contrast imaging. The Fresnel technique is an off-focus technique which, for example, images magnetic domain walls as bright or dark lines due to an excess or deficiency of local image brightness. Foucault imaging is a dark field technique (i.e., employing scattered rather than transmitted electrons) in which the objective aperture selects a segment of a split deflected beam, which is due to different local magnetization directions within the imaged area. Electron holography is a field-imaging technique which results from the interaction of bright field specimen waves with a reference wave usually from an adjacent open area of specimen. Differential phase contrast imaging is a STEM technique employing position-sensitive detection.

For an in situ TEM investigation of the effect size of elliptical disk-shaped particles of a Permalloy (Ni + 19 at.% Fe), arrays of such particles 8 nm thick were prepared employing electron beam lithography and a 30-nm Si<sub>3</sub>N<sub>4</sub> support film. Four such particles are shown in Fig. 1, whose aspect ratios (major axis dimension/minor axis dimension) are 2:1 and whose major axes vary from 3.4 to 5.0 μm. This system of particles has been magnetically saturated in the direction indicated by the large arrow and then is subjected to an increasing applied field in the opposite sense (smaller arrows) as the specimen is imaged using the Fresnel technique (also known as Lorentz microscopy), the resulting contrast of which is sensitive to local variations of a particle's magnetic induction and its gradients in the horizontal plane. The interaction of such variations with the incident electrons produces complementary image contrast when the objective lens is under- or overfocused. The series of images in Fig. 1 shows the dependence and sequential details of the reverse magnetization processes in the four particles. Image defocus is constant. While the geometrical demagnetization factor is the same for the four disks (constant aspect ratio), the observed

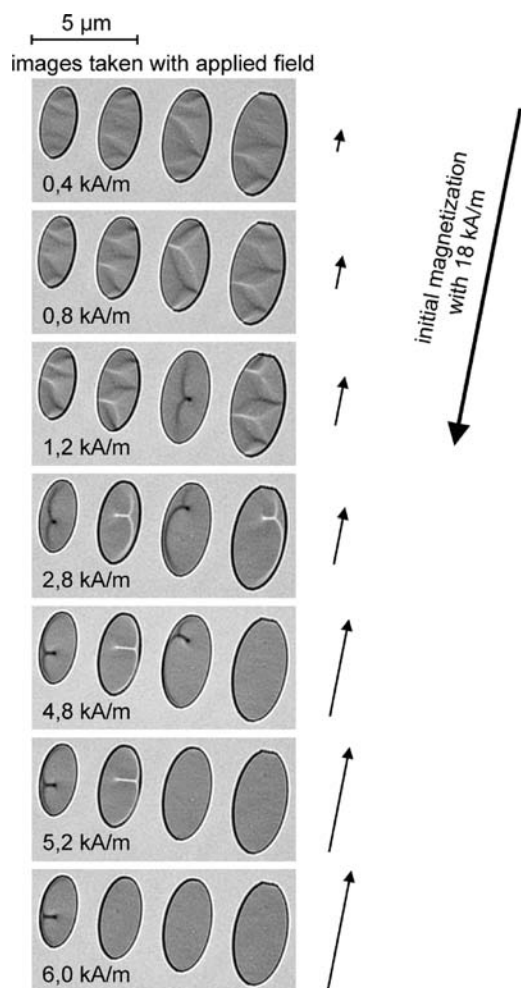


**Fig. 1** Magnetization reversal in elliptical disks 30 nm thick and major axes ranging from 3.4 to 5.0  $\mu\text{m}$ ; Ni + 19 at.% Fe and constant aspect ratios 2:1. Following saturation in one easy direction (large arrow), magnetization reversal process under oppositely directed applied field (small arrows) depends on size, the larger disks reversing at smaller fields. Lorentz TEM. (Joseph Zweck, private communication, 2003.)

differences for a given applied field are due, in part, to the role of the resulting demagnetizing fields associated with the different intrinsic distributions of magnetic moment within each particle due to size (the total energy of individual particles must be minimized). In this experiment a commercially available Lorentz objective lens is employed in which the usual field of the objective may be switched off and a pair of mini-lenses is employed in its place, whose fields can be set to cancel at the specimen position; a special specimen holder incorporates a set of miniature coils to produce the required variable magnetic field in the plane of the specimen.<sup>[2]</sup> In such a situation, image resolution is limited to several nanometers (Josef Zweck, personal communication, 2003).

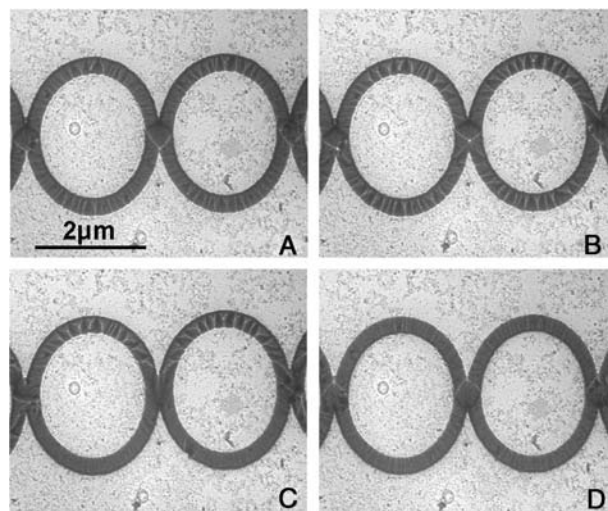


**Fig. 2** Reversal of the magnetic domain state of a row of sputter-deposited Co rings on silicon nitride. In-plane field component normal to row increases from (A) to (D), reversing magnetic state. Lorentz STEM. (Zaluzec, N.; Metlushko, V., private communication, 2003.)

There are a number of useful although sometimes less quantitative examples of in situ magnetic studies in which magnetic structure changes of a specimen are achieved by tilting the specimen in the objective lens field, which results in an increasing component of applied field in the plane of the specimen. An example of this is the following study of magnetization reversal in a series of patterned interconnected rings as shown in Fig. 2. Again the imaging technique involves a form of Lorentz microscopy but this time in a scanning transmission electron microscope (STEM). The material is sputter-deposited Co on a thin silicon nitride substrate. In the actual experiment the specimen was tilted in  $1^\circ$  increments about an axis parallel to the ring array. Fig. 2 shows Lorentz images at four stages in the magnetization reversal process. Many essential features of this process may be deduced unambiguously from the series of images; for example, the white and dark lines at the ring intersections in Figs. 2A and D are  $90^\circ$  domain walls (Nestor Zaluzec and Natali Metlushko, personal communication, 2003).

### Electrical Property Studies

Studies analogous to those for magnetic materials may also be performed in situ for ferro- and ferrielectric material systems, which are in some ways more straightforward because the applied fields are electric rather than magnetic fields. The magnetic field of the objective lens has little effect on electric polarization processes.

Another type of electrical property study with simultaneous TEM is a quantized conductance study of gold wires of nanometer and subnanometer cross section (quantum point contacts). In this instance a miniaturized STM was incorporated as part of the specimen holder of an ultrahigh vacuum high-resolution TEM. By means of the shear-type piezoelectric positioner, a sharpened gold tip was brought into contact with a gold island and slowly withdrawn at constant speed under computer control. Structural changes were observed continuously and video recorded as indicated in Fig. 3A–F, and electrical conductance was measured simultaneously as shown in Fig. 3G. In the same work a single row of four gold atoms (the ultimate wire) parallel to [100] was formed whose conductance was  $\sim 13 \text{ k}\Omega^{-1}$  corresponding to

$2e^2/h$ , the quantized conduction unit. In addition the conductance of a double row was twice this value, showing that equipartition holds for electron transport in these quantum systems. The high-resolution microscopy was clearly essential to the analysis of the conductance data.<sup>[3]</sup>

### Mechanical Property Studies

The deformation and fracture behavior of metals and alloys represents one of the most common applications for in situ microscopy studies since the 1960s, often having been performed in high-voltage TEM because of greater thickness for observation afforded by the higher energy electrons. In our context, the goal of

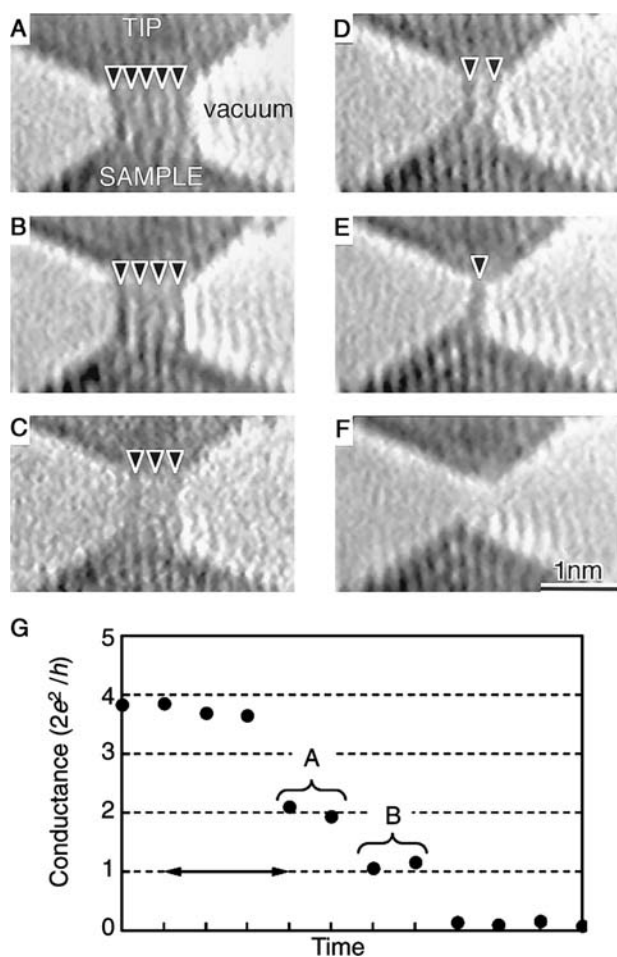


**Fig. 3** Quantum conductance of [110] rows of gold atoms. (A)–(E) Gold tip is withdrawn from gold sample, causing continuous reduction in the number of vertical gold atom rows to fracture at (F), with simultaneous conductance measurement. Note dislocation in (A). At (E) conductance is  $\sim 2 \times (13 \text{ k}\Omega)^{-1}$ , two times unit conductance (unit conductance =  $2e^2/h$ ). (G) Quantized conductance measured during withdrawal of the gold tip [as in (D)–(F)]. *Source:* From Ref.<sup>[3]</sup>.

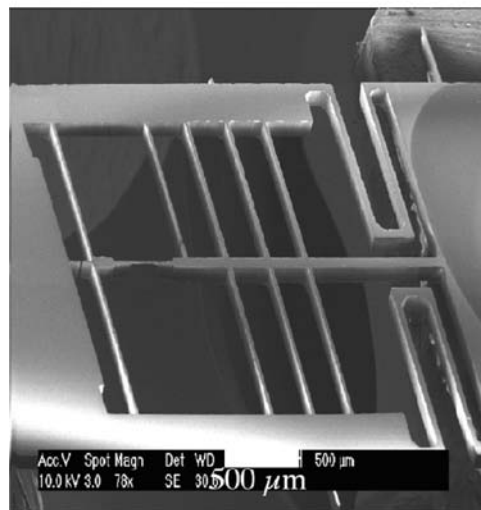
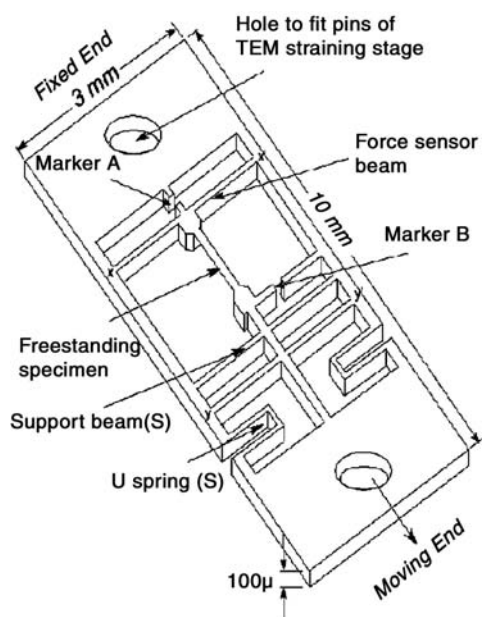


**Fig. 4** Schematic drawing and SEM micrograph of tensile testing chip. *Source:* From Ref.<sup>[4]</sup>.



such studies is to determine the fundamental mechanisms controlling the mechanical response of nanostructured systems and to correlate it with the observed mechanical behavior. For example, to achieve this goal a novel MEMS microtensile test device has been developed which allows measurement of the applied load and sample displacement with concurrent observation of the deformation mechanisms. The device is such that it can be used in a wide range of instruments, although it has been used primarily in SEM and TEM studies. The device consists of a thin dogbone-shaped test specimen that is patterned and cofabricated with microforce and displacement sensors and supports made of silicon using standard photolithographic and deep reactive ion etching techniques. The support beams ensure true uniaxial loading. Fig. 4 describes the fabricated device. The specimen is freestanding between the beams, allowing its inherent response to loading to be determined, including details of the deformation and fracture mechanisms. Because the specimen is integrally fabricated with the loading device structure, issues of attaching it to the test frame and aligning it to ensure uniaxial loading are mitigated.<sup>[4]</sup> Fig. 5 is a series of TEM micrographs showing the glide of a dislocation from the interior of a 200-nm-thick grain to a grain boundary into which it is absorbed, leaving no trace. This demonstrates in a very elementary way the need for such dynamic in situ studies (Ian Robertson, private communication, 2003).

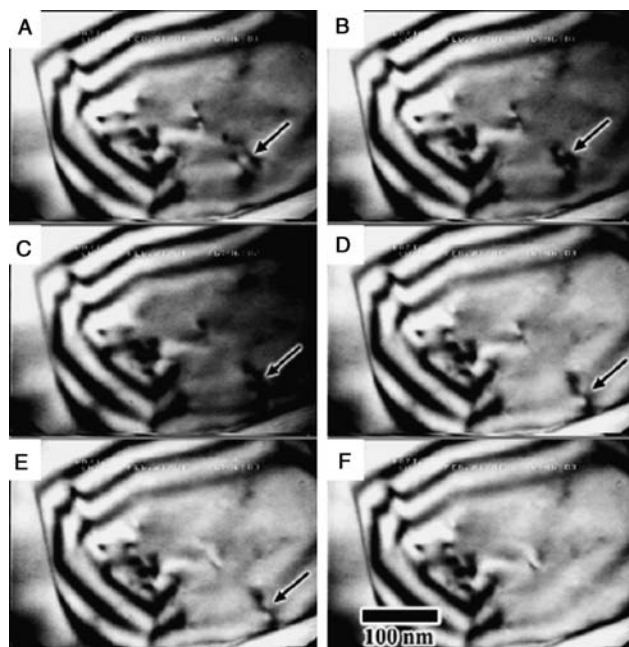


**Fig. 5** Dislocation motion and incorporation into a grain boundary in an Al crystal under increasing tension in device described in Fig. 4. (Ian Robertson, private communication, 2003.)

An example, quite different from the first, of the determination of elastic properties of carbon nanotubes by in situ TEM is represented in Fig. 6.<sup>[5]</sup> In this case the long carbon nanotube shown is excited to mechanical resonance by a high-frequency electric field imposed between it and a nearby positionable counter-electrode. The first and second harmonics are induced by tuning the frequency. The shape of the nanotube at resonance corresponds closely to that expected for a cantilevered uniform beam, which allows its bending modulus to be determined from the dimensions of the nanotube and the driving frequency at resonance. For nanotubes produced by arc-discharge, it is found that this modulus varies from about 1.2 TPa (like the value for diamond) for nanotubes smaller than 8 nm to as little as 0.2 TPa for those with diameters larger than 30 nm. Static electric fields which induce bending of carbon nanotubes in situ may also be employed for elastic modulus determination.<sup>[6]</sup>

Finally, Fig. 7A describes a TEM/STEM specimen holder for nanoindentation of a thin foil or film, which, like that employed in the vibrating carbon nanotube example and the earlier quantum contact example, involves piezoelectric positioning of a part of the experimental apparatus (the indenter, the counterelectrode, or the gold tip). Fig. 7B–E shows TEM micrographs of dislocation activity during the indentation process.<sup>[7,8]</sup>

### Catalysis and Other Reaction Studies

Catalysis is responsible for the commercial production of countless organic substances, the catalytic particles responsible by necessity being in the nanosize regime. One of the aspects of this topic relevant to in situ

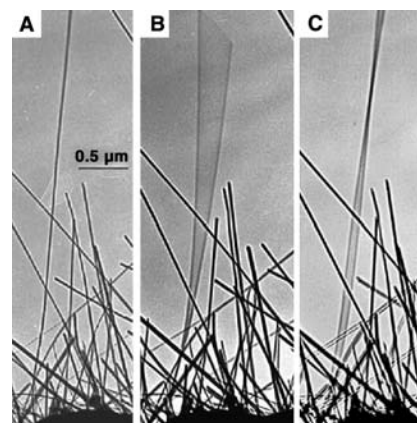


**Fig. 6** Electric-field-induced mechanical resonance in a carbon nanotube. (A) The nanotube is quasi-stationary (thermal vibration only). (B) The first and (C) second harmonic resonance is induced by high-frequency electric fields (MHz range). Source: From Ref.<sup>[5]</sup>.

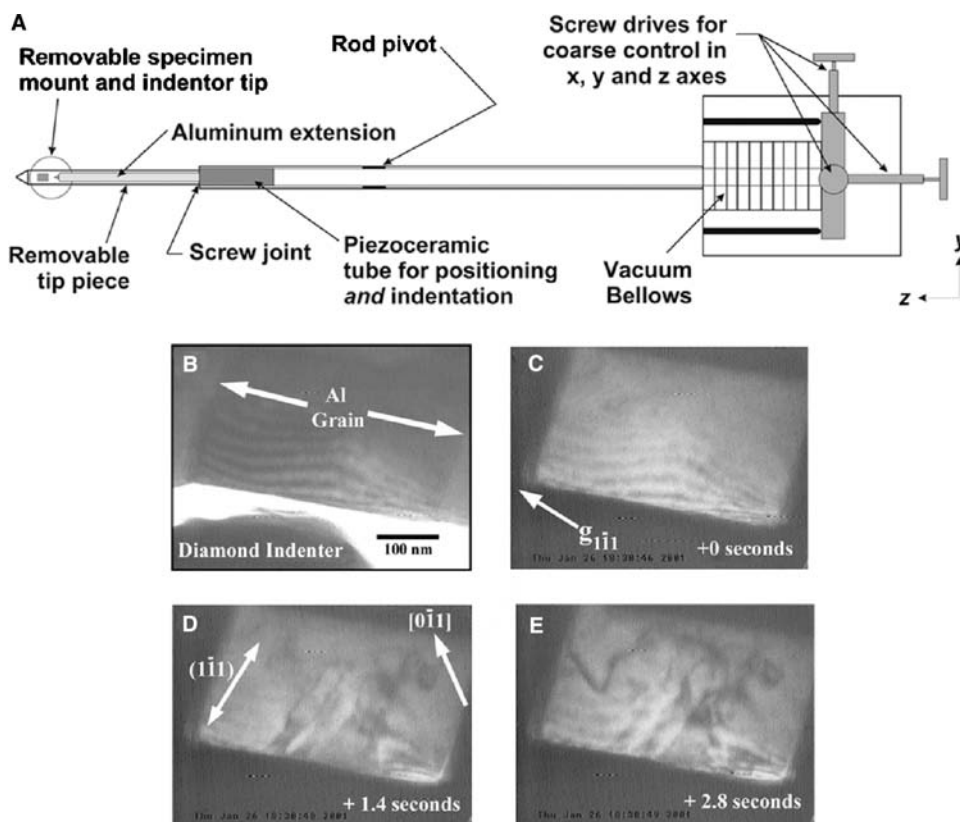


**Fig. 7** (A) Schematic drawing of dedicated in situ nanoindentation holder for TEM/STEM. (B) Bright field transmission electron micrograph showing indenter tip and single grain of aluminum thin film on silicon. (C–E) Sequence of dark field images showing introduction and glide of dislocations into the aluminum grain during indentation (indenter no longer visible in dark field). *Source:* From Refs.<sup>[7]</sup> and <sup>[8]</sup>.

microscopy studies, for example, involves ensuring that a catalyst remains in the nanosize regime under conditions simulated in the microscope for those to be encountered in production of a particular product. There have been two quite different approaches to allow such studies to be conducted in situ in TEM or STEM, one involving the design of environmental specimen holders which contain the entire experiment, environment and all, used in conjunction with an unmodified microscope, and the other, the design of a dedicated environmental microscope into which the desired chemical environment is introduced in the presence of a specimen holder which may provide independent capabilities such as heating. In the case of the environmental holder concept, windows with adequate electron transparency must be employed to isolate the experimental environment from the vacuum of the microscope, which may severely limit the pressures employed as well as instrumental spatial resolution. In an environmental microscope, as in older environmental cells that were inserted between the objective poles, usually of high-voltage electron microscopes (HVEMs), a pair of apertures, one pair before and the other after the specimen holder, serve this

isolation function, there being differential pumping within each aperture pair. Alignment of the apertures is critical. The success of the dedicated in situ microscope concept, especially since about 1995, attests to its experimental versatility and economic advantage for catalysis research in both industry and university.

The first of two short examples of its application is from a study of the stability of Ru particles in  $\text{TiO}_2$  during the hydrogenation of adiponitrile during the production of Nylon 6,6. Fig. 8 shows the catalyst (the 2–3-nm Ru particles) in hydrogen at 20°C and at 280°C after 2 hr, demonstrating no obvious reaction between the Ru particles and  $\text{TiO}_2$  support. Such reaction associated with reduction by hydrogen is known for this important commercial system above 500°C. This type of in situ finding has important implications for the utility and performance of such catalysts in the selective hydrogenation reaction.

The second example illustrates the in situ observation of catalyst-promoted polymerization and involves the same environmental TEM/STEM as the first example and a heating holder incorporating a windowless wet cell (the microscope provides the atmosphere and the wet cell, a microliter or so of fluid in

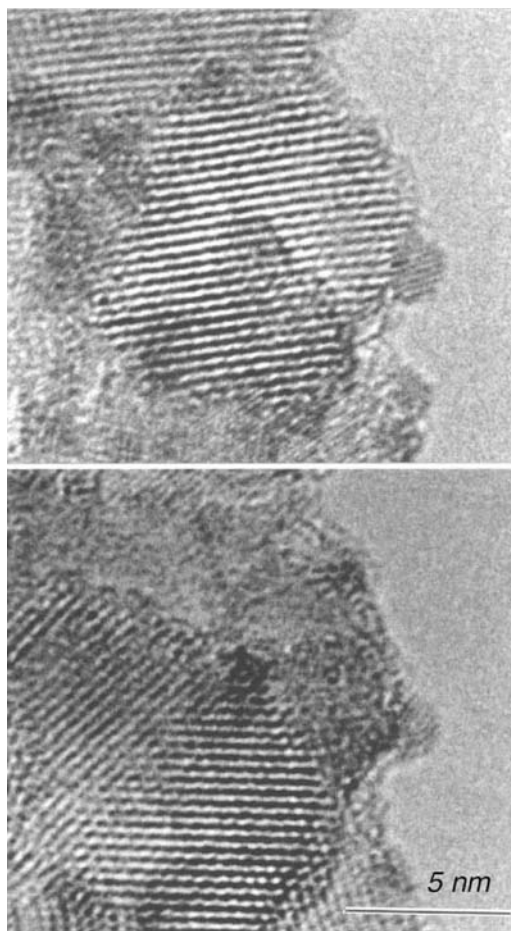


**Fig. 8** In situ real-time EHREM dynamic observations of Ru on titania xerogel catalyst in hydrogen environment recorded (A) at room temperature and subsequently during reaction at about 280°C for 2 hr. *Source:* From Ref.<sup>[9]</sup>.

contact with catalyst). In the case shown in Fig. 9 the catalyst/support particle (m), composed of a Ru–Co alloy on TiO<sub>2</sub>, is immersed in a solution of hexamethylene diamine and adipic acid, at ~188°C. The polymerization reaction to the polyamide is observed to occur at the interface with the particle seen in Fig. 9B. The observations demonstrate a stable catalyst and the formation of an essentially clean polymer structure. In this example a specialized specimen holder was employed. An example of a cell designed for studies of electrochemical reactions such as electroplating is shown in Fig. 10. The cell simply inserts in a holder for insertion in TEM or STEM (Frances Ross, private communication, 2003).

### Irradiation Effects Studies

Generally, in situ studies of irradiation effects require somewhat specialized electron microscopes. Because displacement thresholds by electrons, in terms of

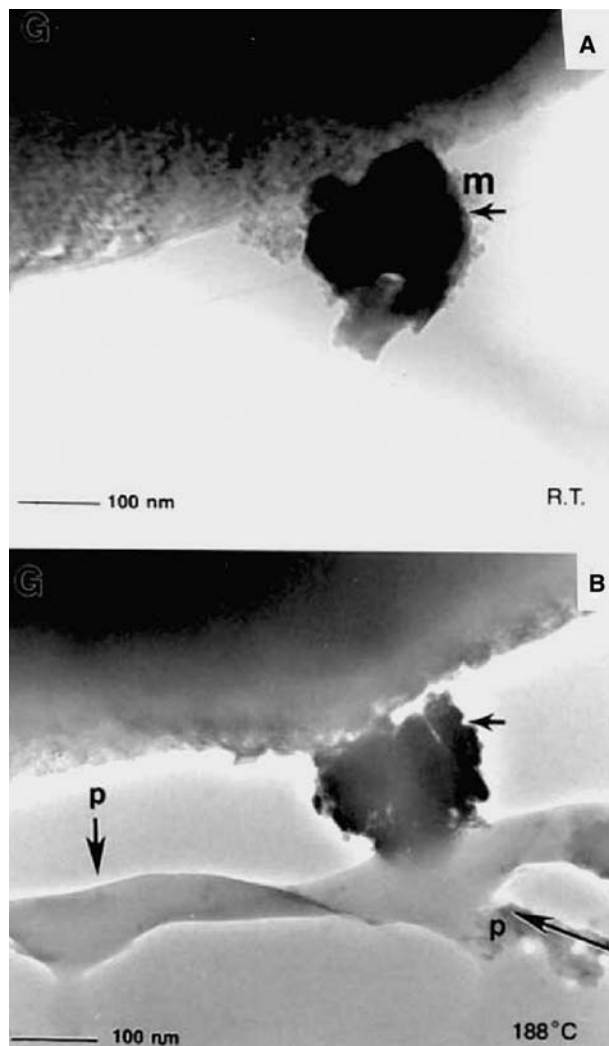


**Fig. 9** Wet-ETEM of in situ polymerization. (A) Co–Ru on titania catalyst system particle at m (supported on sample grid G) with reactant solution from which (B) polymerization over the catalyst occurs at about 188°C. *Source:* From Ref.<sup>[10]</sup>.

incident electron energies, vary from 0.1 MeV or less for oxygen in some oxides to more than 1.5 MeV for large atomic number elements, HVEM have routinely been used for such studies since their introduction in the 1960s. For electrons in this range of energies, damage consists largely of single Frenkel pairs (vacancy–interstitial pairs). Since 1961 when the first observations of unintentional in situ ion damage were reported in Au in an 80-kV TEM, due to negative ions desorbed from the microscope’s electron source, in situ TEM studies of ion irradiation effects have become well established for both fundamental and applied irradiation effects research. While the field is often associated with nuclear science and technology, it is relevant to other areas as well such as degradation of microelectronic components in radiation environments, and

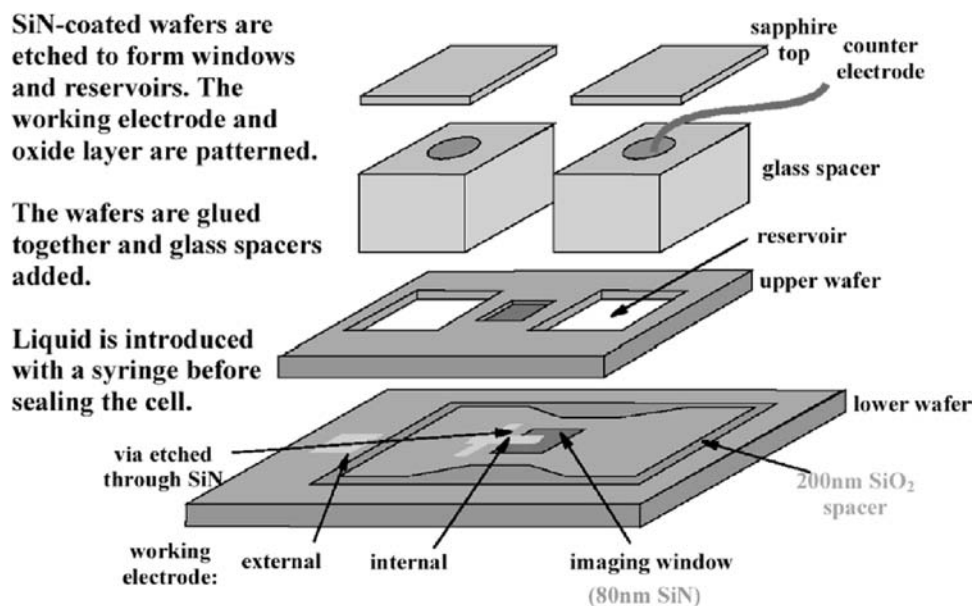


**Fig. 10** Schematic drawing of a closed system electrochemical cell for insertion in a TEM/STEM specimen holder. (Frances Ross, private communication, 2003.)

doping and creation of buried layers by ion implantation in semiconductors. Ion implantation and its associated damage consists of implanted atoms and cascades of point defect clusters which may collapse to form voids or other 3-D defects or partial dislocations which may have profound effects on physical properties. In situ ion beam-related studies require the integration of the microscope and one or more ion sources or ion accelerators, more than a dozen of which have been constructed, mostly in Japan with one in France and two in the United States, involving ion sources ranging from a focused ion beam (FIB) source to a 2-MV tandem accelerator. Two of the Japanese HVEMs employ two ion accelerators each

for simultaneous dual ion experiments. In order to do quantitative work in this area, electron and/or ion beam dosimetry, employing miniaturized Faraday cups and effectively performed at or near the specimen position, is a standard requirement.<sup>[11,12]</sup>

A simple example of a study involving high-energy electrons as the stimulus is shown in Fig. 11. The initial specimen was prepared by implantation of Xe in Al at room temperature. The Xe is very insoluble in the Al matrix and precipitates as nanocrystals, provided they are less than about 10 nm in diameter (at larger sizes the Xe precipitates are fluid). Two such Xe crystals are shown at high resolution in Fig. 11 under 1-MeV electron irradiation in an HVEM, the series of images

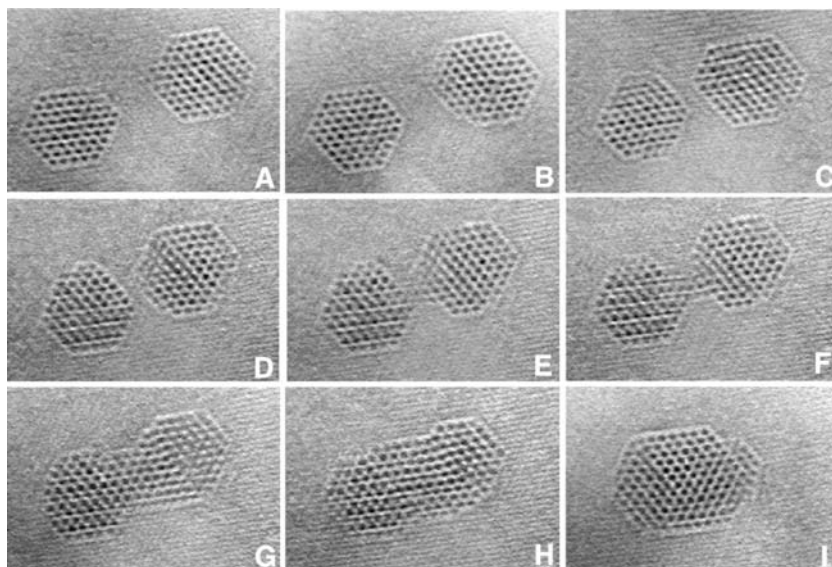


**Fig. 11** Migration and coalescence of two isolated crystalline Xe precipitates during continuous 1-MeV electron irradiation. Measured from the first image, the elapsed times at which video frames were recorded are (A) 0, (B) 101, (C) 418, (D) 549, (E) 550, (F) 551, (G) 561, (H) 584, and (I) 727 sec. Source: From Ref.<sup>[13]</sup>; © 1999 by the American Physical Society.



having been grabbed from videotape. In the sequence, the precipitates experience significant shape changes that lead to their migration. Immediately prior to their coalescence, the precipitates remain with a single plane of Al atoms separating them for several tens of seconds, indicating an absence of elastic interaction of the precipitates. Following coalescence, the resultant precipitate tends to spheroidize as one would expect. Such precipitates of gases in metals appear to grow only by migration and coalescence, as opposed to Ostwald ripening characteristic of purely metallic systems, an important fact which was not heretofore factored into simulations of life expectancies of nuclear reactor materials. In related experiments with the Xe-Al system, the absolute values of  $\{100\}$  and  $\{111\}$  Xe/Al interface tensions were determined and ordering at fluid Xe/solid Al interfaces demonstrated.<sup>[13-15]</sup>

Fig. 12 shows two TEM images from an ion irradiation-induced crystalline study of  $\text{CoSi}_2$ , a material studied extensively as a buried layer in Si. In this study Co and Si were coevaporated onto a thin silicon nitride substrate to produce non-crystalline  $\text{CoSi}_2$ , which was then heated in the TEM to partially crystallize it (the large “spheres” in Fig. 12). It was then subjected to 1.5-MeV Kr irradiation in situ at room temperature, causing additional fine nucleation and growth of crystals (the tiny spheres) during formation and recovery of the cascades of point defects produced by the ions. Fig. 12 shows the ion-stimulated crystallization process at two stages during continuous irradiation. From such in situ experiments one may determine the ion-induced nucleation and growth rates for the particular irradiation conditions and explore the dependence of these kinetic processes on ion mass and energy which result in different cascade structures.<sup>[16]</sup>

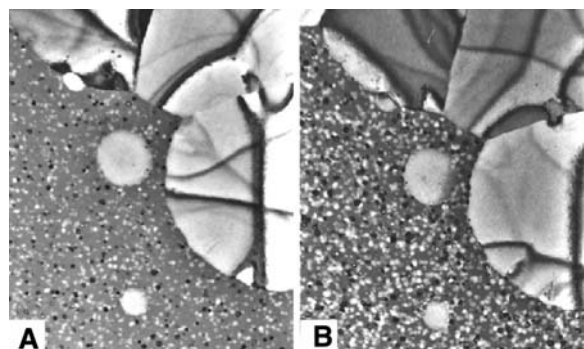


**Fig. 12** Ion-irradiation-assisted crystallization of  $\text{CoSi}_2$  thin film at 300 K (fine dispersion of crystals), following in situ partial thermal crystallization (massive crystals; the medium-sized sphere near the middle is 500 nm in diameter). Specimen has been irradiated with 1.5 MeV Kr to (A)  $3.4 \times 10^{18}$  and (B)  $8.5 \times 10^{18} \text{ m}^{-2}$  at 300 K in an HVEM. *Source:* From Ref.<sup>[16]</sup>.

## Quantum Dot and Thin Film Growth Studies

The first example is that of growth of quantum dots of Ge on Si. During lattice mismatched epitaxy a range of interesting structures can form spontaneously in order to minimize the total strain and surface energies. In many semiconductor systems having moderate lattice mismatch, greater than about 2%, a common growth mode is the formation of individual, coherently strained 3-D islands. The material at the top of the islands is partially elastically relaxed, reducing the total energy although the surface area of the system increases. For a lattice mismatch of several percent the islands formed have dimensions in the nanoscale regime (up to several tens of nanometers) and this restricted size can lead to interesting optical and electronic properties. This makes such self-assembled islands, or quantum dots, interesting for a range of applications from solid-state lasers to quantum cellular automata.

To understand the growth process, island self-assembly in Ge on Si was examined in real time in the TEM. Ge was grown in situ by CVD onto Si (001) at a specimen temperature of 650°C using digermene gas ( $\text{Ge}_2\text{H}_6$ ). A weak beam (dark field) imaging condition was chosen which revealed the strain field around each island. This allowed island positions and sizes to be determined, although the images do not show well the shapes of individual islands. The in situ observations reveal a rich evolutionary process as shown in Fig. 13. After nucleation, a bimodal distribution of sizes consisting of domes and pyramids is visible; later the smaller (pyramid) peak almost disappears.

A simple model was developed based on the existence of the two island shapes. During growth, islands can exchange Ge atoms by surface diffusion. If one

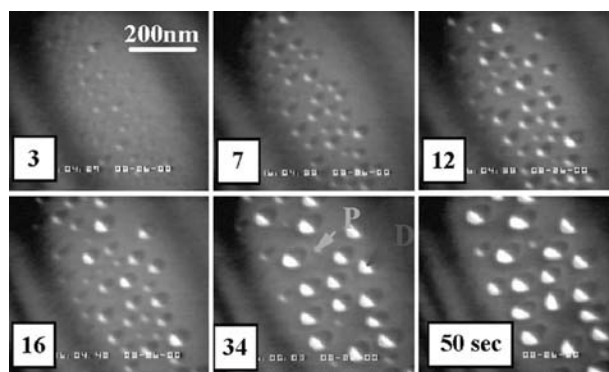


**Fig. 13** The evolution of Ge islands growing on a thin Si(001) substrate by in situ CVD at 650°C in a TEM. By 3 sec, nucleation of islands is evident, which coarsens with time; after 16 sec a transition occurs in which steep-walled domes form at the expense of shrinking shallow pyramids. *Source:* Frances Ross, private communication, 2003.

island, due to its shape or size, has a lower energy per atom than another island, Ge atoms will preferentially detach from higher energy islands and attach to the lower energy island. Islands thus shrink or grow depending on their energy per atom in comparison to other islands in the neighborhood. If all islands were the same shape, larger islands would always have a lower energy per atom than smaller ones by virtue of their lower surface energy/volume ratio. Larger islands would grow at the expense of smaller ones (Ostwald ripening). However, if two different island shapes are allowed, the process becomes much more complex and interesting. In the model, islands reaching a critical volume make the transition from pyramids to domes and rapidly grow at the expense of smaller pyramids. These real-time TEM observations, therefore, have led to a kinetic model for island growth that predicts how best to control island size and shape given the kinetic nature of the process so that uniformly sized island arrays may be grown. Island positioning now remains the greatest challenge to the use of self-assembled islands in novel devices, and in situ TEM can also be used to investigate the effects on island nucleation of chemical and topographic patterning of the substrate (Frances Ross, private communication, 2003).

By way of introduction to the second example, the relaxation of strain in semiconductor heterostructures is frequently accomplished by the deposition of misfit dislocation segments at the interface between the heteroepitaxial layer and the growth substrate when the film is sufficiently highly strained. These dislocations must first nucleate and then propagate to the interface. However, as the dislocations move through the film, they will likely interact with other, preexisting interfacial misfit dislocation segments. If the level of strain in the heterolayer is high, these interactions will not block the motion of the moving “threading” portion of the dislocations. However, when the epitaxial strain is lower, the preexisting interfacial misfit segments may block the threading dislocations. This limits the ability of the film to relax; these threading segments deleteriously affect the electronic performance of heterostructure devices.

In situ TEM techniques were used to investigate how individual dislocations interact during growth and annealing in strained layer heterostructures. SiGe films of varying composition and thickness were deposited onto clean Si substrates in situ in the modified ultrahigh vacuum TEM of the previous example. This allows the real-time observation of the nucleation, propagation, and interaction of dislocations during strain relaxation, an example of which is shown in Fig. 14. The experimental observations indicated that at very low levels of heteroepitaxial strain, all dislocations become blocked as a result of interactions,

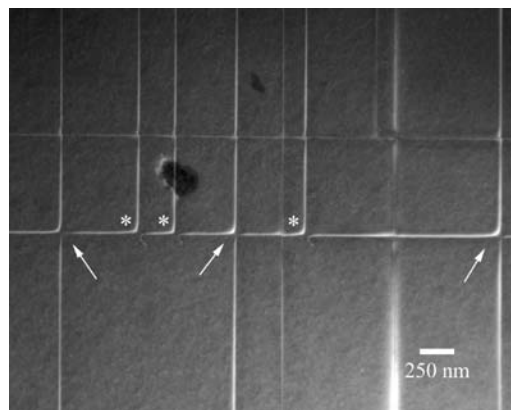


**Fig. 14** Dark field TEM micrograph from an in situ study of dislocation interactions during recovery in a strained 70-nm-thick  $\text{Si}_{80}\text{Ge}_{20}/\text{Si}$  (001) heterostructure. Dislocation pairs of identical Burgers character are indicated by an asterisk if the reaction results in blocking and by an arrow for cases in which interaction does not produce blocking. Source: From Ref.<sup>[17]</sup>.

whereas for a regime at higher levels of strain, only dislocations with parallel Burgers vectors may become blocked during interactions, as illustrated in Fig. 14 (at the arrows). Computational simulations indicated that dislocation reactions that occur between dislocations with parallel Burgers vectors result in a stable configuration, and that the stability of this configuration is a function not only of the Burgers vector combination, but also of the direction of approach of the dislocations.<sup>[17,18]</sup>

### A Comment on Specialized Apparatus for In Situ Studies

While the most common in situ studies may involve only heating or cooling of the specimen, several pieces of more specialized apparatus have already been mentioned in conjunction with the specific studies cited above. These include specimen holders which 1) allow application of a magnetic field of known strength and direction, 2) incorporate piezoelectric positioning of some component of an experiment (technology borrowed from scanning probe microscope technology), and 3) incorporate MEMS-type devices for mechanical testing of thin films, nanowires, and the like. At the other extreme of size and investment are microscopes largely dedicated to in situ studies in ultrahigh vacuum or in other environments and to studies involving irradiation effects. The latter may involve connection of an ion accelerator or other radiation source to a microscope with devices for irradiation dosimetry near the position of the specimen.<sup>[12]</sup> What sets these types of studies apart from their ex situ counterparts is the



value-added advantage afforded by the simultaneous availability of a variety of imaging, electron scattering, and chemical and elemental analytical techniques while the specimen is being stimulated in appropriate ways. The possibilities for designing and performing in situ studies are limited largely by the imagination of the investigator.

### ANALYTICAL TECHNIQUES SUITABLE FOR IN SITU STUDIES

The extent to which a particular analytical technique or material property measurement method is useful for in situ applications depends largely on the time resolution required per meaningful observation. As a simple example, imagine that one wishes to study Brownian motion of 5-nm Au particles on (0001) graphite in an SEM with field emission gun (FEG). At video scan rates the spatial resolution may be worse than the size of the objects to be observed, and at slow high-resolution rates perhaps the particles move 10 nm on average over the course of a 30-sec exposure scan, for which the effective frame rate is reduced by a factor of nearly 900. Perhaps some intermediate conditions would be suitable, of course. On the other hand, in a conventional TEM it is likely that such observations would be possible at video frame rates at a resolution of 1 nm or better. In TEM the image of the entire area of view is formed at once. Unfortunately, even in this case the recording is not instantaneous though. This example points out the first two factors that are important in conducting in situ studies: the basic instrument

in which the experiment is to be conducted and the space/time capabilities of instrumentation for recording the relevant experimental information. The third important factor is the specimen itself. In the case of the SEM experiment the single-crystal graphite substrate could be relatively thick, several micrometers for example, whereas in the TEM experiment the substrate would have to be electron transparent, several tens of nanometers, for example; the thinner the better from a resolution point of view. Finally, in general, if the experimental observations involve imaging, it is important to remember that TEM images are formed in parallel (i.e., all pixels of a given image develop at the same time as mentioned above) whereas in both SEM and STEM, images are formed serially as the area of observation is repetitively scanned. This is not to say that SEM and STEM are categorically inappropriate instruments in which to conduct in situ studies; the choice of instrument largely depends on the nature of the study and the time resolution required in relation to the spatial resolution required.

While it is common and not improper to call SEMs, TEMs, and STEMs microscopies, their several image forming modes of operation are by no means their only modes of operation. For simplicity the other modes may be lumped into two categories, namely, electron scattering and other analytical modes corresponding to various signals from a material specimen resulting from interactions of the incident electron beam with the specimen. These signals may include secondary and Auger electrons, back scattered electrons, visible light and characteristic X-rays as useful signals in the case of SEM, and transmitted electrons, elastically

**Table 2** Analytical functions for various operational modes for SEM, TEM, and STEM<sup>a</sup>

Category	Specific operational mode		
	SEM	TEM	STEM
Imaging	<b>SEI, BEI, SC, VCI, VPSEM, LM, OIM, SI, CL</b>	<b>BF, DF, HREM, LM, EFI</b>	<b>BF, DF, HAADF, LSTEM, SI, EFI, OIM, SEI, BEI</b>
Diffraction	<b>(BS)ECP</b>	<b>SAD, CBED, RHEED, EFED</b>	<b>PRD</b>
Elemental microanalysis	<b>(X)EDS, SI, AES, WDS</b>	<b>(X)EDS, SI, EELS</b>	<b>(X)EDS, SI, EELS</b>
Chemical analysis (DOS)	<b>AES</b>	<b>EELS, AES, ELNES, EXELFS</b>	<b>EELS, AES, ELNES</b>
Atom site location		<b>EXELFS, HREM</b>	<b>ALCHEMI, EXELFS, HAREXCS, HAADF</b>

ALCHEMI, atom location by channeling-enhanced microanalysis; BF, bright field imaging; AES, Auger electron spectroscopy; (BS)ECP, (back scattered) electron channeling pattern; BEI, back scattered electron imaging; CBED, convergent beam electron diffraction; CL, cathodoluminescence; DF, dark field imaging; DOS, density of states; (X)EDS, (X-ray) energy dispersive spectroscopy; EELS, electron energy loss spectroscopy; EFED, energy filtered electron diffraction; EFI, energy filtered imaging; ELNES, energy loss near edge fine structure; EXELFS, extended energy loss fine structure; HAADF, high angle annular dark field; HAREXCS, high angular resolution electron channeling X-ray spectroscopy (based on PRD); HREM, high-resolution (transmission) electron microscopy; LM, Lorentz microscopy; LSTEM, Lorentz STEM; OIM, orientation imaging microscopy (based on BSECP); PRD, position-resolved diffraction; RHEED, reflection high energy electron diffraction; SAD, selected area diffraction; SC, specimen current; SEI, secondary electron imaging; SI, spectrum imaging (or elemental mapping); VCI, voltage contrast imaging; VPSEM (or ESEM), variable pressure (or environmental) SEM; WDS, wavelength dispersive (X-ray) spectrometry.

<sup>a</sup>Specific modes that may be more suitable for in situ studies are shown in bold.

and inelastically scattered electrons, Auger electrons, visible light, and characteristic and diffuse X-rays in the cases of TEM and STEM. A host of specific analytical techniques using these signals have been developed over the past decades as the sophistication of instrumentation has evolved. A number of these are summarized in Table 2, which is not all inclusive. Acronyms for techniques that lend themselves to at least some real-time studies are emphasized in bold. Few of these have been extensively exploited for in situ studies, however.

As indicated in Table 2, in TEM and STEM the addition of (electron) energy filtering capability, in column or post column, further enhances the quantitative and aesthetic value for nearly all those analytical techniques involving electrons directly, i.e., bright and dark field imaging, electron scattering, and electron energy loss mapping and spectroscopy.

### IMPACT OF ABERRATION CORRECTION OF ELECTRON OPTICS ON IN SITU MICROSCOPIES

With the exception of electron guns and stigmators, which incorporate electrostatic elements, all electron optical lenses in commercial electron microscopes have been electromagnetic (magnetic fields) with cylindrical symmetry (“round lenses”) which unavoidably suffer from positive spherical aberration<sup>[19]</sup> as well as the other resolution-limiting aberrations familiar in light optics.<sup>[20]</sup> However, whereas in conventional light optics spatial resolution for imaging (minimum separation of two objects which are distinguishable) is diffraction or wavelength-limited to a few hundred nanometers, in electron optics for which wavelengths are very short (for 100 kV electrons, 3.7 pm) ultimate spatial resolutions are aberration-limited, usually to a few tenths of nanometers for 100 kV, for example.

For some years, several electron optical aberrations—1) defocus, 2) twofold astigmatism, and 3) axial coma—have been routinely correctable by varying 1) the objective lens current (imaging modes in TEM, STEM, and SEM) or diffraction lens current (diffraction modes in TEM); 2) a biasing field of a weak magnetic octopole within the objective lens (imaging modes in TEM, STEM, and SEM) or diffraction lens (diffraction modes in TEM) which corrects astigmatism introduced by the specimen and objective aperture as well as that of the lens; and 3) accurate correction of beam tilt with respect to the optic axis of the objective lens (especially high-resolution imaging modes in TEM or STEM).

In the past for high-resolution TEM (HREM), the effects of (third-order axial) spherical aberration

(described by the coefficient of spherical aberration  $C_s$  or  $C_3$ ) have been partially mitigated to achieve improved spatial resolution by choosing defocus of the objective to optimize phase contrast, known as Scherzer defocus,<sup>[21]</sup> or to minimize the disk of least confusion, known as focus of least confusion.<sup>[22]</sup> Successful demonstration in the 1990s of hardware correctors for  $C_s$  has spurred commercial development of a number of aberration correction systems for electron microscopes based on combinations of electrostatic and magnetostatic hexapole and octupole elements of variable strength. While the concept was introduced 40 years earlier, its realization depended on more recent development of high-speed computer capability and of CCD cameras for execution of the necessary involved, iterative alignment procedures for the corrector elements with respect to one another and with respect to the round lenses of the instrument. The other critical element is the development of current and high-voltage power supplies of significantly improved stability. By 2003, point-to-point resolution for imaging in TEM at Scherzer defocus was improved from 0.24 to  $\sim 0.13$  nm at 200 kV. The correction of  $C_s$  in TEM, STEM, and SEM is achieved with assemblies of multipole electrostatic elements, rendering  $C_s$  a free parameter of the instrument (like defocus) rather than a fixed property of the objective lens. In addition, for high-resolution imaging in a  $C_s$ -corrected TEM, it is possible to partially mitigate the next higher order spherical aberration coefficient for the instrument ( $C_5$ ) by choosing a slightly negative value for  $C_s$  for the corrected objective lens.

These continuing developments of aberration correction systems impact ultimate instrumental resolution both for imaging and microanalysis (or more appropriately nanoanalysis) and for in situ applications.<sup>[23]</sup> In the case of in situ TEM, correction of  $C_s$  allows more space around the specimen, into which experimental devices may be incorporated. Previously, increased space was achieved by employing instruments with shorter wavelength electron sources, namely, HVEM, spatial resolution being proportional to  $C_s \lambda^{4/3}$ . However, in the cases of conventional HVEM and  $C_s$ -corrected TEM, spatial resolution remains a sensitive function of the objective lens focal length (gap size in a side-entry objective) due to chromatic aberration associated with high voltage and lens current instabilities (characterized by  $C_c$ ). For example, in an uncorrected TEM, spatial resolution for imaging of magnetic structures (Lorentz microscopy) is about 2 nm. With both  $C_s$  and  $C_c$  correction, it should be possible to improve this by an order of magnitude in an experimental space several centimeters in every dimension (Bernd Kabius, private communication, 2003). Furthermore,  $C_c$  correction regains some of the advantage of greater penetrating power associated

with higher voltage TEM for thicker specimens. Inelastic scattering for thicker specimens diminishes the information limit; this can be compensated by correcting  $C_c$ . The development of correction not only for spherical but for chromatic aberration as well should provide, therefore, a strong stimulus for both superb imaging and other analytical functions and for much improved in situ capabilities, in TEM, STEM, and SEM.

## CONCLUSION

Over the past several decades, in situ techniques applied to various electron microscopies have contributed extensively to our current understanding of dynamic processes in the areas of materials science and engineering and materials physics. This trend should thrive in the environment of nanoscience and nanotechnology in the future as well, as new and improved instrumentation and experimental techniques, as well as existing analytical techniques which have not been extensively exploited yet, are conceived and brought to bear on the many materials and material systems problems ahead. Performing studies in situ can be a very efficient way to get the job done and, in addition, oftentimes provide an entirely new insight and understanding to physical processes and mechanisms. The possibilities for designing and performing such in situ studies are limited largely by our imaginations.

## ACKNOWLEDGMENTS

Special thanks are due to Joseph Zweck, Frances Ross, Kunio Takayanagi, Eric Stach, Zhong Lin Wang, Pratibha Gai, Robert Birtcher, Nestor Zaluzec, and Ian Robertson for providing the various examples of in situ TEM and STEM studies and designs of specialized experimental holders; to Bernd Kabius for many discussions and suggestions relating to aberration correction; to Robert Birtcher and Nestor Zaluzec for help with the preparation of figures, and last, but not least, to the editors of the *Encyclopedia of Nanoscience and Nanotechnology* for patiently watching my deadlines pass. The author is grateful to the Office of Science, U.S. Department of Energy, under Contract No. W-31-109-Eng-38 for support of this work.

## REFERENCES

1. <http://web.inter.nl.net/users/anima/chronoph/muybridge/index.htm>. (accessed August 2003).
2. Uhlig, T.; Heumann, M.; Hoffmann, H.; Zweck, J. Development of a specimen holder for in-situ generation of pure in-plane magnetic fields in a transmission electron microscope. *Ultramicroscopy* **2003**, *94*, 193–196.
3. Ohnishi, H.; Kondo, Y.; Takayanagi, K. Quantized conductance through individual rows of suspended gold atoms. *Nature* **1998**, *395*, 780–783.
4. Haque, M.A.; Saif, M.T.A. In-situ tensile testing of nano-scale specimens in SEM and TEM. *Exp. Mech. Exp. Mech.* **2002**, *42* (1), 123–128.
5. Wang, Z.L. Scanning probe microscopy in TEM: And in-situ approach for nano-scale property measurements. *Microsc. Microanal.* **2002**, *8* (Suppl. 2), 300–301.
6. Poncharal, P.; Wang, Z.L.; Ugarte, D.; de Heer, W.A. Electrostatic deflections and electromechanical resonances of carbon nanotubes. *Science* **1999**, *283*, 1513–1516.
7. Stach, E.A.; Freeman, J.T.; Minor, A.M.; Owen, D.K.; Cumings, J.; Wall, M.A.; Chraska, T.; Morris, J.W., Jr.; Zettl, U. Development of a nanoindenter for in situ transmission electron microscopy. *Microsc. Microanal.* **2001**, *7*, 507–517.
8. Minor, A.M.; Morris, J.W., Jr. Quantitative in situ nanoindentation in an electron microscope. *Appl. Phys. Lett.* **2001**, *79*, 1625–1627.
9. Gai, P.L.; Kourtakis, K.; Ziemecki, S. In situ real-time environmental high resolution electron microscopy of nanometer size novel xerogel catalysts for hydrogenation reactions in Nylon 6.6. *Microsc. Microanal.* **2000**, *6*, 335–342.
10. Gai, P.L. Development of wet environmental TEM (Wet-TEM) for in situ studies of liquid catalyst reactions on the nanoscale. *Microsc. Microanal.* **2002**, *8*, 21–28.
11. Allen, C.W. In situ ion- and electron-irradiation effects studies in transmission electron microscopies. *Ultramicroscopy* **1994**, *56*, 200–210.
12. Allen, C.W.; Ryan, E.A. In situ transmission electron microscopy employed for studies of effects of ion and electron irradiation on materials. *Microsc. Res. Tech.* **1998**, *42*, 255–259.
13. Birtcher, R.C.; Donnelly, S.E.; Song, M.; Furuya, K.; Mitsuishi, K.; Allen, C.W. Behavior of crystalline Xe nanoprecipitates during coalescence. *Phys. Rev. Lett.* **1999**, *83*, 1617–1620.
14. Allen, C.W.; Birtcher, R.C.; Donnelly, S.E.; Song, M.; Mitsuishi, K.; Furuya, K.; Dahmen, U. Determination of interfacial tensions for Xe nanoprecipitates in Al at 300 K. *Philos. Mag. Lett.* **2003**, *83*, 57–64.
15. Donnelly, S.E.; Birtcher, R.C.; Allen, C.W.; Morrison, I.; Furuya, K.; Song, M.; Mitsuishi, K.; Dahmen, U. Ordering in a fluid inert gas confined by flat surfaces. *Science* **2002**, *296*, 507–510.
16. Allen, C.W.; Smith, D.A. In situ study of effects of ion irradiation on solid-state crystallization of cobalt disilicide thin films. *Ultramicroscopy* **1991**, *39*, 222–230.
17. Stach, E.A.; Hull, R.; Schwarz, K.W.; Ross, F.M.; Tromp, R.M. New mechanisms for dislocation blocking

- in strained layer epitaxial growth. *Phys. Rev. Lett.* **2000**, *84* (5), 947–950.
18. Stach, E.A.; Hull, R.; Tromp, R.M.; Ross, F.M.; Reuter, M.C.; Bean, J.C. In-situ transmission electron microscopy studies of the interaction between dislocations in strained SiGe/Si(001) heterostructures. *Philos. Mag., A* **2000**, *80*, 2159–2200.
  19. Scherzer, O. Über einige fehler von elektronenlinsen. *Z. Phys.* **1936**, *101*, 593–603.
  20. Hawkes, P.W.; Kasper, E. Aberration Correction. In *Principles of Electron Optics*; Hawkes, P.W., Kasper, E., Eds.; Academic Press: New York, 1989; Vol. 2, 857–877.
  21. Scherzer, O. The theoretical resolution limit of the electron microscope. *J. Appl. Phys.* **1949**, *20*, 20–29.
  22. Lichte, H. Optimum focus for taking electron holograms. *Ultramicroscopy* **1991**, *38*, 13–22.
  23. Kabius, B.; Haider, M.; Uhlemann, S.; Schwan, E.; Urban, K.; Rose, H. Benefits of a  $C_s$  corrector for materials science. *Microsc. Microanal.* **2001**, *7* (Suppl. 2), 902–903.

# Indium Arsenide Islands on Silicon

P. C. Sharma

Kang L. Wang

*Electrical Engineering Department, University of California–Los Angeles,  
Los Angeles, California, U.S.A.*

## INTRODUCTION

Realization of nanometer-scale semiconductor quantum dot structures has become an important area of research focus in recent years primarily because of the potential of nanometer-scale systems in future device applications.<sup>[1–5]</sup> With the conventional silicon technology rapidly moving toward saturation in terms of scalability and complexity of fabrication, semiconductor quantum dot structures hold promise as future electronic devices beyond silicon electronics. Furthermore, developing nanometer-scale quantum dot devices on Si and GaAs substrates offers the possibility of advancing their mature device technologies. As a consequence, InAs/GaAs<sup>[6–8]</sup> and Ge/Si<sup>[9–11]</sup> heterostructures are currently being investigated extensively to develop nanometer-scale quantum devices. While these structures have been extensively investigated because of the availability of advanced GaAs and Si device technologies and the relative ease of growing self-assembled III–V and Si–Ge nanostructures, the InAs/Si heterostructure offers the possibility of growing direct gap InAs on indirect gap Si and holds considerable promise as a candidate for silicon-based optoelectronics as the incorporation of direct band InAs in silicon could significantly improve the radiation recombination efficiency.<sup>[12]</sup> Although there is more than 11% lattice mismatch between InAs (6.0583 Å) and silicon (5.4310 Å) making InAs/Si a highly strained system, their closely matched thermal expansion coefficients (InAs:  $4.70 \times 10^{-6} \text{ K}^{-1}$ ; Si:  $4.68 \times 10^{-6} \text{ K}^{-1}$ ) make InAs/Si a promising heterostructure to grow nanometer-scaled InAs islands. Also, this large lattice mismatch can, in fact, be exploited to grow a high density of InAs islands on silicon surface under optimized growth conditions. Laser structures emitting at 1.013 μm have already been fabricated on silicon substrates using quantum dots of compositional InGaAs alloys as active layers.<sup>[13]</sup>

## OVERVIEW

The initial stages of semiconductor heteroepitaxial growth are governed by three possible growth modes,

viz., the Frank–van der Merve mode involving layer-by-layer growth, the Volmer–Weber (VW) mode involving island growth, and the Stranski–Krastanow (SK) mode involving layer-by-layer growth followed by island growth.<sup>[14]</sup> Of these, the SK growth mode has been predominantly used to achieve nanometer island formation in lattice mismatched semiconductor heterostructures including InAs/Si. While the large lattice mismatch may seem to indicate island growth in the SK mode, VW mode has also been observed in the InAs/Si system under certain growth conditions in the growth temperature range of 300–400°C.<sup>[15,16]</sup> Although conditions favoring specific growth modes have not been extensively studied, considerable research efforts continue to focus on the dependence of InAs island morphology on the growth parameters involved. Furthermore, solid source molecular beam epitaxy (MBE) remains the growth method of choice to produce nanoscale InAs islands on Si. Mano et al.<sup>[17]</sup> first established the possibility of growing high-quality InAs nanocrystals on hydrogen-terminated Si (100) by using MBE growth technique and used cross-section transmission electron microscopy (XTEM) and field emission scanning electron microscopy (FESEM) to characterize the crystalline quality. Their evaluation of InAs/Si interface band discontinuity indicates that both holes and electrons can be confined in InAs nanocrystals. Growth conditions favorable for yielding a high density of uniform InAs islands on silicon were studied in detail by Hansen, Bensing, and Waag<sup>[18,19]</sup> by using in situ surface analytical techniques such as reflection high energy electron diffraction (RHEED) and X-ray photoelectron spectroscopy (XPS). They have also studied the growth of InAs on Si (001) and Si (111) substrates. In addition to conventional SK growth mode, they have used a dewetting method to grow InAs islands on Si (001). This method involves devolution of continuous two-dimensional (2-D) InAs film into small three-dimensional (3-D) InAs islands by cooling the substrate temperature from the growth temperature (~370°C) down to approximately 320–300°C soon after the growth of about 1 monolayer (ML) of InAs. The InAs islands thus grown, however, have been found to be dislocated as also the InAs islands grown on arsenic (As)-terminated

Si (111).<sup>[20]</sup> While their observations suggest this dewetting transition in InAs/Si (001) to be irreversible, a similar dewetting transition used recently to grow InAs islands on GaAs (100) at high substrate temperatures ( $\sim 540^\circ\text{C}$ ) has been found to be reversible.<sup>[21]</sup> Uragami et al.<sup>[22,23]</sup> investigated the structural properties of InAs quantum dots on Si (100) by comparing data obtained from generalized grazing incidence X-ray diffraction (G-GIXD) technique with the finite element method (FEM) calculations of the structural factors. G-GIXD technique enables the observation of fine changes in lattice constant both in lateral and normal directions of island growth over the substrate surface. They found that the InAs dots were dilated in the normal direction and compressed in the lateral direction because of the strain from the lattice mismatch and conclude that the introduction of misfit dislocations beneath InAs dots alone is not sufficient to relieve the strain and that shape change of dots is also a contributing factor in releasing the lateral strain. Combining Rutherford backscattering spectroscopy (RBS) and secondary-ion mass spectroscopy, Karl et al.<sup>[24]</sup> have studied the stoichiometry of MBE-grown InAs nanocrystals buried in a silicon matrix and found significant diffusion of indium (In) and As into the Si matrix and the presence of excess As on the surface in addition to a layer of stoichiometric InAs nanocrystals. Based on these observations, the authors recommend low growth temperatures and small As/In flux ratios to successfully grow InAs nanocrystals on Si (100). Although MBE remains the most convenient growth technique to study InAs/Si nanostructures, there also have been successful attempts to form InAs nanocrystals in a silicon matrix by sequential ion implantation of In and As ion species in Si (100).<sup>[25,26]</sup> Using RBS, TEM, and X-ray diffraction (XRD/XD), the authors of this study establish that it is possible to produce InAs nanocrystals in Si (100) by ion implantation at  $500^\circ\text{C}$  followed by a  $900^\circ\text{C}$  thermal annealing cycle. Their ion implantation studies further reveal that morphological changes can be effected by reversing the order of implantation between As and In as implanting either In or As first produces distinctly different morphologies. Nanocrystals of diameter 20–70 nm imbedded in silicon were produced by this method. Si-exposed GaAs substrates have also been used recently to grow self-assembled InAs quantum dots.<sup>[27]</sup> These studies indicate that the exposure of GaAs substrates to a Si-molecular beam flux prior to InAs deposition aids in achieving higher uniformity in InAs dot lateral dimensions possibly because Si atoms on GaAs surface act as nucleation centers and create preferential growth regions for InAs.

The chief motivation for the study of nanometer-scale InAs islands on Si is to exploit the interesting optical properties that arise out of integrating InAs

into well-established silicon technology. By growing InAs nanocrystals of desired dimensions, it is possible to bring about changes in the optoelectronic properties of InAs/Si system. Cirilin et al. have conducted photoluminescence (PL) studies on InAs nanocrystals grown in both SK and VW modes in a Si matrix<sup>[15,16]</sup> and also on samples deposited with various InAs ML coverages and 30–60 nm silicon cap layers.<sup>[28–30]</sup> They found a luminescence band exhibited by these samples around 1.3- $\mu\text{m}$  region that showed a shift toward higher energies with increasing excitation density. The authors determined that the origin of this luminescence band was indeed from InAs nanocrystals by eliminating the influence of silicon substrate and the cap layer on the PL signal. They also found that samples with very small InAs coverages showed no noticeable luminescence as very small InAs inclusions ( $<5\text{ nm}$ ) would produce no charge localization. Their experiments on the temperature dependence of PL showed a monotonic shift from 1.3  $\mu\text{m}$  at 10 K up to 1.6  $\mu\text{m}$  at 290 K.

We describe below our studies on the formation of nanometer-scale InAs islands on silicon including the experimental procedures, the dependence of island morphology on critical growth parameters such as the monolayer coverage, the flux ratios, and the growth temperature. Our observations and results are also compared with the results available in the published literature of other research groups working on the InAs/Si heterostructure for nanometer InAs island growth.

## EXPERIMENTAL DETAILS

Samples used for our studies were grown on (100)-oriented epitaxially silicon wafers in a solid source-integrated molecular beam epitaxy system (Perkin-Elmer) equipped with in situ reflection high energy electron diffraction (RHEED), residual gas analysis (RGA), k-space data acquisition (KSA), and pre-growth heating systems. Effusion cells of elemental Ga, In, Al, and As and dopants C and Si are typically loaded in the system. Prior to introduction into the load-lock module, the samples were cleaned using Shiraki procedure<sup>[31]</sup> and then hydrogen-terminated in dilute HF solution. While the evolution of the growth front was monitored by RHEED, a combination of pyrometer and thermocouple was used to sense and measure the substrate temperature. The samples were heated for outgassing prior to their introduction into the growth chamber and heated up to  $600\text{--}650^\circ\text{C}$  in the growth chamber to facilitate hydrogen desorption. The surface morphology of the samples was studied by atomic force microscopy (AFM) (Park Scientific Instruments) scans. Using line scan analysis of AFM, the dimensions of several individual



islands were directly measured and the image analysis was carried out by using ImagePro, an image analysis software to collect the statistical data on island distributions. The growth rate of InAs was calibrated by RHEED specular spot intensity oscillations using InAs homoepitaxy. The arsenic source in the system is coupled to a valved cracker to produce  $\text{As}_2$  which aids in better crystalline quality of the grown layers as  $\text{As}_2$  incorporates more efficiently than  $\text{As}_4$  on the growth surfaces.<sup>[32]</sup> The cracker mechanism also helps in economizing the consumption of arsenic material.

## RESULTS AND DISCUSSION

To study the evolution of growth front morphology with increasing InAs thickness, we have grown samples by depositing InAs of varying thicknesses on Si (100) using growth conditions optimized for producing InAs islands in SK mode. As mentioned earlier, InAs grows either in SK mode or VW mode depending on the growth conditions. In SK mode, 3-D islands begin to grow over an initial 2-D wetting layer when a critical thickness ( $t_c$ ) is reached. This critical thickness at which the growth transition takes place is dependent on important growth parameters such as the growth (substrate) temperature ( $T_s$ ), the flux ratios of reacting species In and As, the substrate orientation, and even the substrate cleaning method prior to growth. As a

consequence, there is considerable variation in the critical thickness reported by different groups. Using a growth temperature of  $450^\circ\text{C}$ , we have grown samples with nanometer-scale InAs islands by depositing 3.8 to 5 ML of InAs on Si (100).<sup>[33]</sup> The AFM images of four such samples are shown in Fig. 1A–D. Within a short range of approximately 1.5 ML InAs coverage, we observed the rapid formation of 3-D InAs islands on a 2-D wetting layer, right from the appearance of sparsely distributed small islands (Fig. 1A) through a dense formation of uniform islands (Fig. 1B) to the merging of several small islands to form larger islands (Fig. 1D). While InAs coverages below 3.8 ML showed no significant island formation, deposition of InAs material beyond  $\sim 6$  ML resulted in the formation of very large relaxed InAs islands with greatly reduced densities. Thus depending on As/In flux ratios, it is possible to obtain coherently strained InAs islands on silicon with a monolayer coverage of up to 6 ML by using moderate growth temperatures ( $<475^\circ\text{C}$ ). The dense formation of islands was found to be uniformly spread all across the substrate with no significant differences in island densities between any two regions on the sample surface. The mean dimensions of the islands obtained through direct AFM measurements on the samples in Fig. 1 are plotted against the InAs monolayer coverage in Fig. 2. It can be suggested from this figure that InAs coverage of about 4 ML may be optimum for obtaining closely related

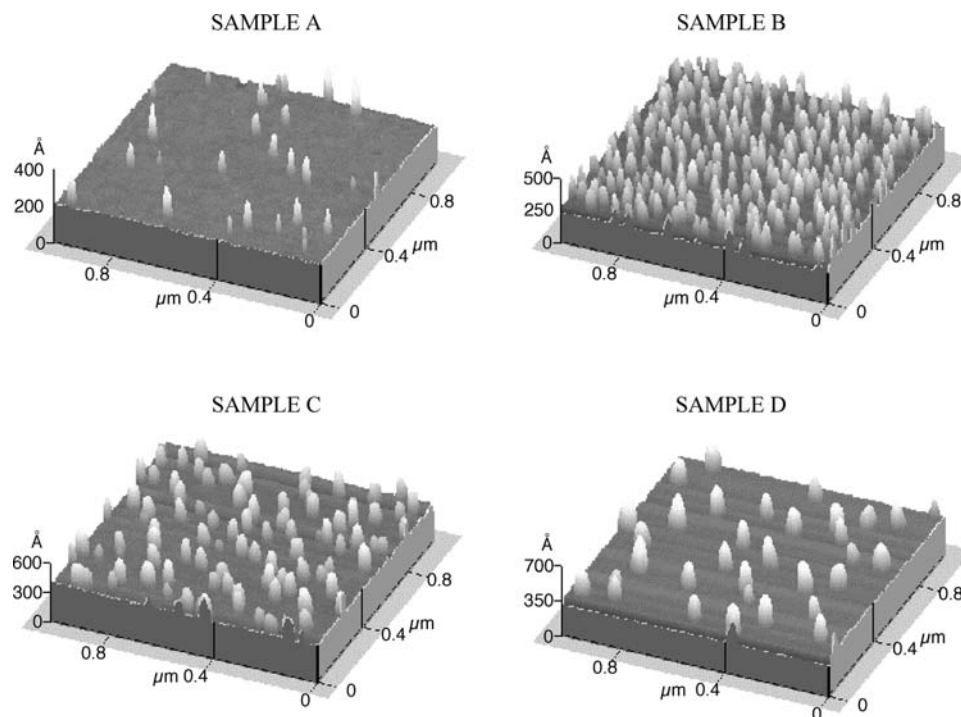


**Fig. 1** Atomic force microscopy images ( $1 \times 1 \mu\text{m}$ ) of Si (100) samples with nominal InAs coverages of (A) 3.8 ML, (B) 4.1 ML, (C) 4.6 ML, and (D) 5.0 ML. All the samples are grown at  $450^\circ\text{C}$ . Source: From Ref.<sup>[33]</sup>.

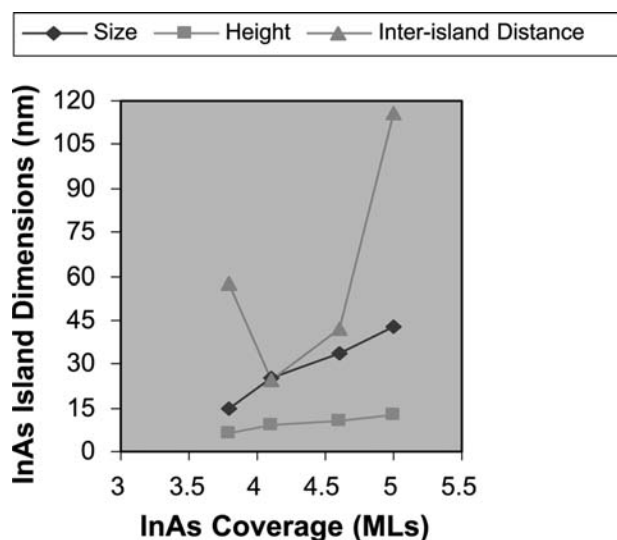


**Fig. 2** Average island dimensions for different InAs coverages of samples grown at 450°C. InAs thicknesses of 4 to 4.5 ML yield uniform island dimensions with narrow distributions. *Source:* From Ref.<sup>[33]</sup>.

island dimensions with high densities under the growth conditions used to grow these samples. Also, a monolayer coverage in the range of 3–6 ML of InAs has, in general, been found to yield uniform nanometer-scale islands on Si.<sup>[12,17,33]</sup> The statistical data collected from large ensembles of InAs islands using image analysis of AFM images for different monolayer coverages are presented in Table 1. The retention of uniform dimensions and small standard deviations even at larger island sizes (>40 nm) averaged over large ensembles is evident from this table. The initial rapid increase in island density with monolayer coverage followed by a decrease as seen in Fig. 2 is consistent with the evolution mechanism of InAs islands on Si. In InAs/Si heteroepitaxy, strain as a result of initial overlayers is relieved by the energetically favorable formation of large ensembles of 3-D islands elastically strained to the substrate (Fig. 1B). Strain as a result of further InAs deposition leads to changes in the geometry of islands as they tend to attain irregular shapes and

eventually become faceted. Fig. 1C represents such a scenario of faceted InAs islands. Strain upon further InAs growth is accommodated by the introduction of dislocations beneath large islands formed by the coalescing of several smaller InAs islands. Fig. 1D shows such large dislocated InAs islands under coalescence. The formation of such large islands is a consequence of Ostwald ripening which is characterized by the re-evaporation of material from nearby smaller islands to larger islands. Uragami et al.'s investigations also provide physical evidence<sup>[22,23]</sup> to our explanation of strain-relieving mechanisms in effect during the evolution of InAs island morphology on silicon. The very high InAs island densities observed in our experiments are essentially a result of the high strain arising out of large lattice mismatch between InAs and Si as it becomes energetically favorable to form a proportionally large number of 3-D islands all across the substrate surface. The inter-island distances in our images showed a random spatial distribution with the Fourier transform images of island spreads for various InAs coverages showing no order. Table 2 summarizes the InAs island data obtained by various groups using different growth temperatures and growth methods. It can be seen from this table that there is a close match among InAs island sizes obtained under wide-ranging growth conditions. Coherent islands with lateral dimensions in the range of 10–40 nm may find useful applications as it is possible to achieve charge localization within these islands.<sup>[12]</sup>

Another important growth parameter found to have significant influence on the island morphology and composition is the flux ratio of reacting species In and As. Attempts made to deposit InAs islands on Si using As/In ratios from 2 to 12 revealed that while very high growth temperatures produced no islanding independent of As/In flux ratios, very high flux ratios (>7) resulted in the reduction of an order of magnitude in island density.<sup>[15,16,18]</sup> Our experiments to grow InAs islands at 450°C using very low As/In flux ratios resulted in the formation of In-rich clusters all across the sample surface as shown in Fig. 3. To explain this observation, it can be argued that the depleted As levels at low flux ratios result in stoichiometric

**Table 1** Atomic force microscopy statistical data of InAs islands grown on Si (100) surface for different InAs monolayer thicknesses obtained through direct measurements on individual InAs islands

Sample code	InAs coverage (MLs)	Mean island size/S.D. (nm)	Mean island height (nm)	Aspect ratio size/height	Inter-island distance (nm)	Island density (cm <sup>-2</sup> )
A	3.8	15.04/3.60	6.30	2.39	57.89	1.0 × 10 <sup>10</sup>
B	4.1	25.58/5.35	8.90	2.87	24.67	6.6 × 10 <sup>11</sup>
C	4.6	33.67/5.50	10.65	3.16	44.23	7.7 × 10 <sup>10</sup>
D	5.0	42.77/7.80	12.80	3.34	115.48	1.1 × 10 <sup>10</sup>

*Source:* Ref.<sup>[33]</sup>.

**Table 2** Island sizes for InAs islands grown on silicon by various groups at different growth temperatures

Authors	Growth method	Growth temperature ( $T_s$ ) (°C)	Monolayer coverage (ML)	Island size range (nm)	Reference number
Cirlin et al.	MBE	400	7	10–40	[12,15]
		300		3	[28–30]
Hansen et al.	MBE	370	2.5	30	[18–20]
Mano et al.	MBE	300–500	4	30–70	[17,22,23]
Sharma et al.	MBE	450	3.8–5	15–50	[33,34]
Tchebotereva et al.	Ion implantation	500	NA	60	[25,26]
Saucedo-Zeni et al.	MBE GaAs:Si <sup>a</sup>	480	2–2.5	18–30	[27]

<sup>a</sup>GaAs (100) substrate exposed to silicon flux.

deviations as several As atoms tend to adsorb to Si and several others diffuse into the Si substrate, thereby reducing the probability of 1:1 chemical bonding between In and As atoms at high growth temperatures. Thus as a trade-off between low island density at high flux ratios and In clustering at low flux ratios, a 3–6 flux ratio of As/In maybe suitable for growing stoichiometric InAs nanoislands on Si. The crystalline orientation of substrate is also of considerable importance in the growth of InAs islands. Table 3 summarizes the InAs island sizes on Si substrates of different orientations reported in literature. We used Si (100) substrates because silicon complementary metal oxide semiconductor (CMOS) manufacturing technology is based on this surface. However, hydrogen-terminated Si (111) is also being used to develop silicon-based optoelectronic devices such as the green and blue light-emitting diodes (LEDs). As can be seen from Table 3, the island dimensions of InAs grown on Si (100) by various groups are very close to those grown

on Si (111) by Hansen et al.<sup>[20]</sup> Likewise, the island densities achieved by various groups on silicon surfaces of different orientations are uniformly high in the range of  $5 \times 10^{10}$  to  $6 \times 10^{11} \text{ cm}^{-2}$ . It is interesting to note that unlike GaAs,<sup>[35]</sup> silicon of different surface orientations is amenable to the growth of InAs nanometer islands.<sup>[20]</sup> The nature of surface termination of Si has also an effect on the morphology of InAs islands grown clearly because surface preparation influences the nature of chemical bonding between reacting In and As species impinging on silicon surface. Our choice of hydrogen termination of silicon is to saturate the dangling bonds at the surface with hydrogen to try and minimize dangling Si bonds that act as adsorption sites. Empirically, InAs growth on Si (100):H seems to result in the formation of dislocation-free islands even for higher monolayer coverages and growth temperatures<sup>[17,33]</sup> as opposed to growth on Si (001):As surfaces.<sup>[20]</sup> Likewise, surface preparation by desorption of oxide layer on silicon by a high-temperature treatment step prior to growth appears to hasten the process of defect introduction at the Si–InAs interface for smaller InAs coverages.

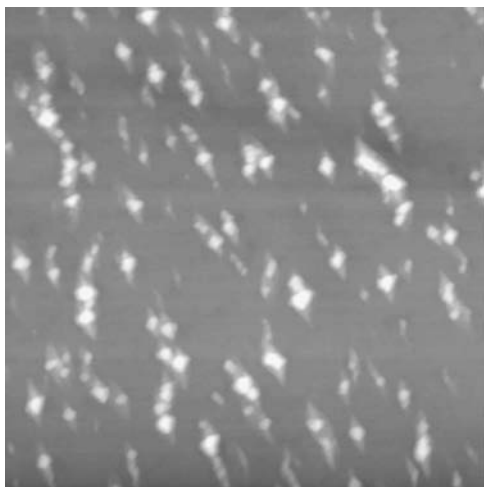


**Fig. 3** Atomic force microscopy image ( $1 \times 1 \mu\text{m}$ ) of InAs/Si (100) sample grown using a low As/In flux ratio of 2:1. The patchy spread of matter seen in this image is clustered indium.

**Table 3** Island sizes of InAs grown on silicon surfaces of different orientations by various groups

Substrate orientation	Growth temperature (°C)	Island size <sup>a</sup> (nm)	Author	Reference number
Si (100)	450	32	Sharma et al.	[33]
Si (001)	370	30	Hansen et al.	[18]
Si (111)	370	20	Hansen et al.	[20]
Si (100)	400	30	Mano et al.	[17]
Si (100)	400	37	Uragami et al.	[22]
Si (100)	250	12	Cirlin et al.	[12]
Si (100)	400	12	Egorov et al.	[30]

<sup>a</sup>Island size is generally the average value of a few base diameters of individual islands. Island size given here is the average value of the size ranges.

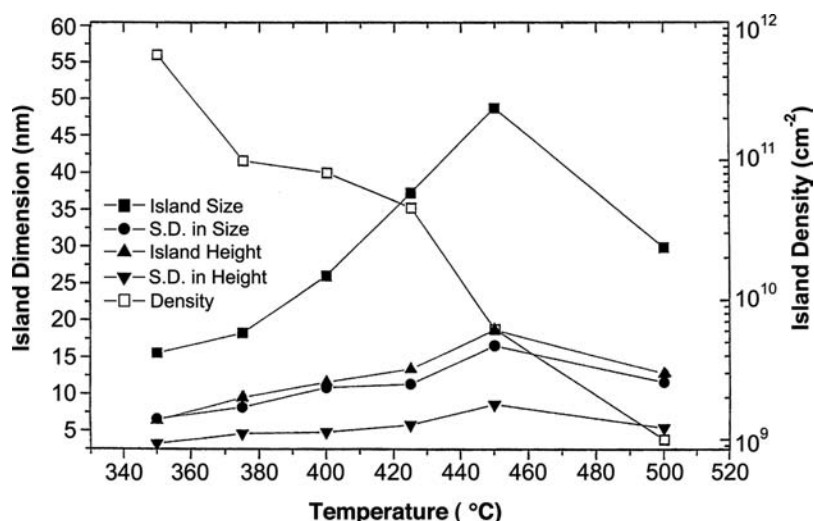


**Fig. 4** InAs island dimensions vs. growth temperature. Data on standard deviations are also presented to signify the uniformity of InAs islands, particularly those grown using temperatures in 400–425°C range. *Source:* From Ref.<sup>[34]</sup>.

We have also investigated the effects of growth temperature ( $T_s$ ) on the formation and morphology of InAs islands on Si (100). Choosing a temperature range of 350–530°C, we have obtained samples grown at the intervals of  $\sim 25^\circ\text{C}$  using optimized growth conditions and InAs monolayer coverages. Within this range of temperatures, we have observed drastic changes in the formation and morphology of islands. We notice that the island density increases with decreasing growth temperatures from near-zero island formation at a temperature of 530°C to an extremely dense ( $>5 \times 10^{11} \text{ cm}^{-2}$ ) formation of islands at a temperature of 350°C. Furthermore, we find the complete absence of 3-D SK island formation for temperatures higher than 530°C as evidenced both by in situ RHEED patterns and by postgrowth AFM observations. For higher growth temperatures ( $>530^\circ\text{C}$ ), the RHEED patterns remain streaky indicative of only 2-D InAs layer-by-layer growth. On the other hand, at low growth temperatures, the island formation is too dense to render any accurate measurements difficult. However, we find that a narrower growth temperature range of 400–425°C yields dense InAs 3-D islands of uniform dimensions with narrow distributions and small standard deviations. These observations, in general, are consistent with the observations of other groups.<sup>[15–18]</sup> The temperature dependence of island dimensions is shown in Fig. 4. It can be seen from this figure that the island dimensions exhibit an increase up to a growth temperature of around 450°C and then a decrease to nearly half their values around 500°C before 3-D island formation finally ceases at 530°C. This trend in island formation is possibly a result of the availability of greater thermal energy for strain relaxation at higher growth temperatures which limits island formation as a dominant mechanism to accommodate interfacial strain. The RHEED patterns of islands grown particularly in the 400–450°C range

showed prominent chevrons indicative of curved facets on InAs islands.

## CONCLUSION

Investigations on InAs/Si heterostructure as a candidate for nanometer-scale optoelectronic and quantum-optic devices show considerable promise as it is possible to realize coherent nanometer islands of direct gap InAs on indirect gap Si. We have investigated the dependence of InAs island morphology on various growth parameters such as growth temperature, As/In flux ratios, substrate orientation, and surface termination. Our experimental results establish the possibility of growing elastically strained InAs islands of uniform dimensions on Si surface using MBE under optimized growth conditions involving low flux ratios, low InAs coverages, and low growth temperatures. While photoluminescence studies by Cirlin et al. pave the way for device applications, the InAs island formation through a dewetting transition observed by Hansen et al. might lead to better insights into InAs island formation for smaller coverages well into the submonolayer regime. However, it is essential to address the issues of defect formation, reproducibility of morphologies, effects of capping layers, and luminescence properties in future through systematic characterization. Vertical stacking of island layers separated by spacer layers is another future research direction toward realizing InAs/Si nanodevices.

## ACKNOWLEDGMENTS

The authors wish to acknowledge the funding for this work provided by Army Research Office (ARO) and

Joint Services Electronics Program (JSEP) and thank Prof. Alexander Balandin, Department of Electrical Engineering, University of California, Riverside, for useful discussions.

## REFERENCES

- Tommy, W.B.; Mork, J. Quantum dot amplifiers with high output power and low noise. *Appl. Phys. Lett.* **2003**, *82* (18), 3083–3085.
- Cornaglia, P.S.; Balseiro, C.A. Transport through quantum dots in mesoscopic circuits. *Phys. Rev. Lett.* **2003**, *90* (21), 216801–216804.
- Song, J.F.; Ochiai, Y.; Bird, J.P. Fano resonances in open quantum dots and their application as spin filters. *Appl. Phys. Lett.* **2003**, *82* (25), 4561–4563.
- Blauwe, J.De. Nanocrystal nonvolatile memory devices. *IEEE Trans. Nanotechnol.* **2002**, *1* (1), 72–77.
- Wang, K.L.; Balandin, A.A. Quantum Dots: Physics and Applications. In *Optics of Nanostructured Materials*; Markel, V.A., George, T.F., Eds.; Wiley & Sons: New York, 2001; 515–549.
- Liu, H.Y.; Hopkinson, M. Tuning the optical and structural properties of 1.3- $\mu\text{m}$  InAs/GaAs quantum dots by a combined InAlAs and GaAs strained buffer layer. *Appl. Phys. Lett.* **2003**, *82* (21), 3644–3646.
- Yu, P.; Bhattacharya, P.; Cheng, J.-C. Enhanced spontaneous emission from InAs/GaAs self-organized quantum dots in a GaAs photonic-crystal-based microcavity. *J. Appl. Phys.* **2003**, *93* (10), 6173–6176.
- Le Ru, E.C.; Howe, P.; Jones, T.S.; Murry, R. Strain-engineered InAs/GaAs quantum dots for long wavelength emission. *Phys. Rev., B* **2003**, *67* (15 (II)), 165303–165307.
- Kim, D.-W.; Hwang, S.; Edgar, T.F.; Banerjee, S. Characterization of SiGe quantum dots on SiO<sub>2</sub> and HfO<sub>2</sub> grown by rapid thermal chemical deposition for nanoelectronic devices. *J. Electrochem. Soc.* **2003**, *150* (4), G240–G243.
- Yakimov, A.I.; Dvurechenskii, A.V.; Nikiforov, A.I.; Proskuryakov, Y.Y. Interlevel Ge/Si quantum dot infrared photodetector. *J. Appl. Phys.* **2001**, *89* (10), 5676–5681.
- Kamins, T.I.; Ohlberg, D.A.A.; Williams, S.R. Effect of phosphorous on Ge/Si island formation. *Appl. Phys. Lett.* **2001**, *78* (15), 2220–2222.
- Cirlin, G.E.; Petrov, V.N.; Dobrovskii, V.G.; Masalov, S.A.; Golubok, A.O.; Komyak, N.I.; Ledentsov, N.N.; Alferov, Zh.I.; Bimberg, D. Fabrication of InAs quantum dots on silicon. *Tech. Phys. Lett.* **1998**, *24* (4), 290–292.
- Linder, K.K.; Phillips, J.; Qasaimeh, O.; Liu, X.F.; Krishna, S.; Bhattacharya, P.; Jiang, J.C. Self-organized In<sub>0.4</sub>Ga<sub>0.6</sub>As quantum-dot lasers grown on Si substrates. *Appl. Phys. Lett.* **1999**, *74* (10), 1355–1357.
- Eaglesham, D.J.; Cerullo, M. Dislocation-free Stranski-Krastanow growth of Ge on Si(100). *Phys. Rev. Lett.* **1990**, *64* (16), 1943–1946.
- Cirlin, G.E.; Polyakov, N.K.; Petrov, V.N.; Egorov, V.A.; Denisov, D.V.; Volovik, B.V.; Ustinov, V.M.; Alferov, Zh.I.; Ledentsov, N.N.; Heitz, R.; Bimberg, D.; Zhakarov, N.D.; Werner, P.; Gosele, U. Heteroepitaxial growth of InAs on Si: The new type of quantum dots. *Mater. Phys. Mech.* **2000**, *1* (1), 15–19.
- Cirlin, G.E.; Polyakov, N.K.; Petrov, V.N.; Egorov, V.A.; Denisov, D.V.; Volovik, B.V.; Ustinov, V.M.; Alferov, Zh.I.; Ledentsov, N.N.; Heitz, R.; Bimberg, D.; Zhakarov, N.D.; Werner, P.; Gosele, U. Incorporation of InAs nanostructures in a silicon matrix: Growth, structure and optical properties. *Mater. Sci. Eng., B* **2001**, *80* (1–3), 108–111.
- Mano, T.; Fujioka, H.; Ono, K.; Watanabe, Y.; Oshima, M. InAs nanocrystal growth on Si (100). *Appl. Surf. Sci.* **1998**, *130–132*, 760–764.
- Hansen, L.; Bensing, F.; Waag, A. InAs quantum dots embedded in silicon. *Thin Solid Films* **2000**, *367* (1), 85–88.
- Hansen, L.; Bensing, F.; Waag, A. Molecular beam epitaxial growth of InAs quantum dots directly on silicon. *Jpn. J. Appl. Phys., Part I* **1999**, *38* (11), 6219–6221.
- Hansen, L.; Ankudinov, A.; Bensing, F.; Wagner, J.; Ade, G.; Hinze, P.; Wagner, V.; Geurts, J.; Waag, A. Growth and characterization of InAs quantum dots on silicon. *Phys. Status Solidi, B* **2001**, *224* (2), 515–519.
- Mirin, R.P.; Roshko, A.; van der Puijl, M.; Norman, A.G. Formation of InAs/GaAs quantum dots by dewetting during cooling. *J. Vac. Sci. Technol., B* **2002**, *20* (4), 1489–1492.
- Uragami, T.; Fujioka, H.; Waki, I.; Mano, T.; Ono, K.; Oshima, M.; Takagi, Y.; Kimura, M.; Suzuki, T. Generalized grazing incidence-angle x-ray diffraction studies on InAs quantum dots on Si (100) substrates. *Jpn. J. Appl. Phys., Part I* **2000**, *39* (7B), 4483–4485.
- Uragami, T.; Acosta, A.S.; Fujioka, H.; Mano, T.; Ohta, J.; Ofuchi, H.; Oshima, M.; Takagi, Y.; Kimura, M.; Suzuki, T. Characterization of strain distribution in quantum dots by x-ray diffraction. *J. Cryst. Growth* **2002**, *234* (1), 197–201.
- Karl, H.; Grosshans, I.; Wenzel, A.; Stritzker, B.; Claessen, R.; Strocov, V.N.; Cirlin, G.E.; Egorov, V.A.; Polyakov, N.K.; Samsenko, Yu.B.; Denisov, D.V.; Ustinov, D.V.; Alferov, Zh.I. Stoichiometry and absolute atomic concentration profiles obtained by combined Rutherford backscattering spectroscopy and secondary-ion mass spectroscopy: InAs nanocrystals in Si. *Nanotechnology* **2002**, *13* (4), 631–634.
- Tchebotareva, A.; Brebner, J.L.; Roorda, S.; Desjardins, P.; White, C.W. Structural properties of InAs nanocrystals formed by sequential implantation of In and As ions in the Si (100) matrix. *J. Appl. Phys.* **2002**, *92* (8), 4664–4671.
- Tchebotareva, A.L.; Brebner, J.L.; Roorda, S.; White, C.W. Properties of InAs nanocrystals in silicon formed by sequential ion implantation. *Nucl. Instrum. Methods Phys. Res., Sect. B* **2001**, *175–177*, 187–192.
- Saucedo-Zeni, N.; Zamora-Peredo, L.; Gorbachev, A.Yu.; Lastras-Martinez, A.; Balderas-Navarro, R.; Medel-Ruiz, C.I.; Mendez-Garcia, V.H. Growth of

- self-assembled InAs quantum dots on Si exposed GaAs substrates by molecular beam epitaxy. *J. Cryst. Growth* **2003**, *251* (1–4), 201–207.
28. Cirlin, G.E.; Petrov, V.N.; Dubrovskii, V.G.; Samsonenko, Yu.B.; Polyakov, N.K.; Golubok, A.O.; Masalov, S.A.; Komyak, N.I.; Ustinov, V.M.; Egorov, A.Yu.; Kovsh, A.R.; Maximov, M.V.; Tsatsul'nikov, A.F.; Volvik, B.V.; Zhukov, A.E.; Kop'ev, P.S.; Ledentsov, N.N.; Alferov, Zh.I.; Bimberg, D. Hetero-epitaxial growth of InAs on Si: A new type of quantum dot. *Semiconductors* **1999**, *33* (9), 972–975.
  29. Heitz, R.; Ledentsov, N.N.; Bimberg, D.; Egorov, A.Yu.; Maximov, M.V.; Ustinov, V.M.; Zhukov, A.E.; Alferov, Zh.I.; Cirlin, G.E.; Soshnikov, I.P.; Zhakarov, N.D.; Werner, P.; Gosele, U. Optical properties of InAs quantum dots in a Si matrix. *Appl. Phys. Lett.* **1999**, *74* (12), 1701–1703.
  30. Egorov, A.Yu.; Kovsh, A.R.; Ustinov, V.M.; Zhukov, A.E.; Maksimov, M.V.; Cirlin, G.E.; Ledentsov, N.N.; Bimberg, D.; Werner, P.; Alferov, Zh.I. Self-organized InAs quantum dots in a silicon matrix. *J. Cryst. Growth* **1999**, *201/202*, 1202–1204.
  31. Ishizaka, A.; Shiraki, Y. Low temperature surface cleaning of silicon and its application to silicon MBE. *J. Electrochem. Soc.* **1986**, *133* (4), 666–671.
  32. Foxon, C.T. MBE growth of GaAs and III–V alloys. *J. Vac. Sci. Technol., B* **1983**, *1* (2), 293–297.
  33. Sharma, P.C.; Alt, K.W.; Yeh, D.Y.; Wang, D.; Wang, K.L. Formation of nanometer-scale InAs islands on silicon. *J. Electron. Mater.* **1999**, *28* (5), 432–436.
  34. Sharma, P.C.; Alt, K.W.; Yeh, D.Y.; Wang, K.L. Temperature-dependent morphology of three-dimensional InAs islands grown on silicon. *Appl. Phys. Lett.* **1999**, *75* (9), 1273–1275.
  35. Joyce, B.A.; Jones, T.S.; Belk, J.G. Reflection high-energy electron diffraction/scanning tunneling microscopy study of InAs growth on the three low index orientations of GaAs: Two-dimensional versus three-dimensional growth and strain relaxation. *J. Vac. Sci. Technol., B* **1998**, *16* (4), 2373–2380.



# Infrared Spectroscopy: Biomolecular Structure at Interfaces

Curtis W. Meuse

*Biomolecular Materials Group, National Institute of Standards and Technology (NIST), Gaithersburg, Maryland, U.S.A.*

## INTRODUCTION

Cell membranes have many important biological functions such as controlling signal transduction and molecular transport between the inside and outside of cells.<sup>a</sup> A greater understanding of the structures and functions of the cell membrane components involved in signal transduction and/or molecular transport could be used to improve the delivery and specificity of pharmaceuticals.

Cell membranes are complex and dynamic structures generally described in terms of the “fluid mosaic” model.<sup>[1]</sup> Like any theory, the “fluid mosaic” theory is still being refined.<sup>[2]</sup> One way refinements are being tested is using nanotechnology to assemble biological and/or biomimetic components into membrane mimics to help clarify our understanding of cell membrane processes.

This entry describes measurements characterizing a particular mimetic called a hybrid bilayer membrane (HBM). HBMs are surface-supported bilayers composed of a monolayer of alkanethiol, which is tightly bound to the surface through a strong association between sulfur and gold, and a second non-covalently bound monolayer of phospholipid (Fig. 1).<sup>[3,4]</sup> The nanometer-size scale of the membrane components makes the construction and characterization of these mimetic membranes dependant on sophisticated measurement technologies. Hybrid bilayers are analytically addressable by a wide range of surface analytical techniques such as surface plasmon resonance, impedance analysis, electrochemistry, infrared spectroscopy, atomic force microscopy, ellipsometry, and neutron reflectivity.<sup>[5,6]</sup> While information from the spontaneously formed hybrid bilayers can be cross-referenced between different independent experiments, it is often desirable to obtain as much information as possible from a single technique. This article reviews the different types of information that can be obtained by using infrared

spectroscopy to study the interfacial structures of hybrid bilayer membranes.

## BIOMOLECULAR STRUCTURE AT INTERFACES

Interfaces are important in both nanotechnology and biology. Nanoscale entities, ranging in size from approximately 1 to 10,000 nm, have large surface-area-to-volume ratios. Molecules occupying an interfacial region are strongly linked to system properties. An example of this is a protein in/on a cell membrane dictating the membrane’s transport and signal transduction properties. The importance of membrane transport and signal transduction in medical science drives efforts to understand and control the composition and conformation of molecules in the interfacial regions of cells.

Biological membranes are complex and dynamic structures and their biological functions involve a number of different molecular species. Consequently, the details of the “fluid mosaic” model of freely diffusing proteins and lipids in a two-dimensional fluid<sup>[1]</sup> are still emerging.<sup>[2]</sup> To continue to clarify the complex nature of this model, better measurements, which determine the composition and/or the conformation of these moieties (proteins, lipids, etc.), are needed.

Direct attempts to determine structure at the atomic level of both lipid and protein components of membranes by crystallization and X-ray diffraction are difficult, and only a few membrane protein structures have been determined.<sup>[7–9]</sup> While it is assumed that a protein’s crystal structure is similar to that of the active protein in its native membrane environment, the surrounding dynamic lipid matrix may also influence it. Because the functions of membrane proteins often depend on conformational changes, for example, during transport across the lipid barrier, or during intracellular kinase activation after extracellular ligand binding, the motions of both the lipid and the protein must be taken into account, which limits the applicability of X-ray diffraction studies.

Without atomic-level structure, model membrane systems have allowed the study of isolated features of these otherwise highly complicated biological

<sup>a</sup>The specification of commercial products in this article is for clarity only and does not constitute endorsement by the National Institute of Standards and Technology.

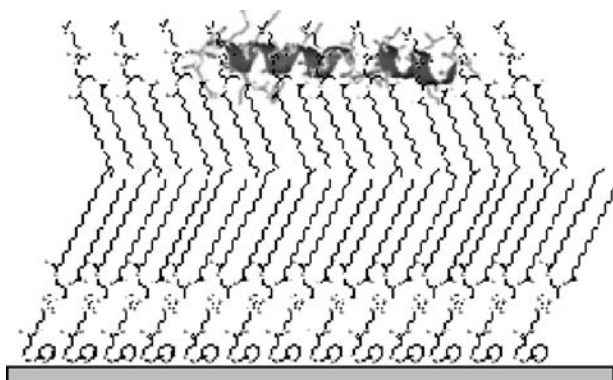


**Fig. 1** An illustration of a hybrid bilayer consisting of *N*-PDP-phosphatidylethanolamine, 1,2-diacyl-*sn*-glycero-3-phosphocholine and melittin.

nanostructures, and have been essential to the development of our understanding. Lipid vesicles or liposomes,<sup>[10]</sup> black lipid membranes,<sup>[11]</sup> multilayers of lipid for diffraction studies,<sup>[12]</sup> planar lipid bilayers on solid supports,<sup>[13,14]</sup> and more recently, bicelles<sup>[15]</sup> are all forms of model systems having advantages and disadvantages as models of membranes. The liposome or proteoliposome (incorporating membrane proteins) is probably the most popular model membrane, and has contributed greatly to our understanding of biological membranes. A related type of model membrane, supported lipid bilayers are a model membrane system on a planar support and have also been employed in many important biophysical studies.<sup>[16–20]</sup>

Recently, supported bilayer systems have been extended to include metal-tethered membranes called hybrid bilayer membranes (HBMs).<sup>[3–6]</sup> HBMs are composed of a monolayer of alkanethiol, which is tightly bound to the surface through a strong association between the thiol and the gold surface, and a second monolayer of phospholipid (Fig. 1). Hybrid bilayers on metal supports are analytically addressable by a wide range of surface analytical techniques such as infrared spectroscopy, atomic force microscopy, ellipsometry, neutron reflectivity of single bilayer membranes, and nonlinear optical spectroscopy, surface plasmon enhanced fluorescence, surface plasmon resonance, impedance analysis, and electrochemistry.<sup>[5,21,22]</sup> These techniques can be used to probe the kinetics of bilayer formation, study the kinetics of ligand binding, and provide structural information.

Surface-supported bilayers generally need to be characterized by a number of analytical techniques, or by a single technique capable of describing several cross-validating features of the layer. This is important because the use of crosscutting information can reduce ambiguity and prevent erroneous conclusions. For

example, the simultaneous use of surface plasmon resonance (SPR) and impedance analysis to measure the kinetics of bilayer formation showed differences in the density of lipid layers that added to different thiol-tethered monolayers,<sup>[23]</sup> demonstrated the hydration of a cholera toxin layer bound to an HBM containing  $G_{M1}$  ganglioside,<sup>[24]</sup> and permitted discrimination between specific and nonspecific binding of ligands to the supported membrane surface.<sup>[25]</sup>

The focus of this article will be a review of the methods to obtain crosscutting information from infrared spectroscopy about hybrid bilayer membranes. However, it is important to remember that other groups of cross-validating experiments may be more appropriate in other circumstances for the study of supported bilayer membranes.

## INFRARED SPECTROSCOPY OF HYBRID BILAYER MEMBRANES

Infrared spectroscopy has long been used to characterize the molecular structure, conformation, and orientation of lipid monolayers, bilayers and their biological additives, proteins and carbohydrates.<sup>[20,26,27]</sup> Infrared spectral signatures are used to characterize the normal modes of vibrations caused by displacements of the permanent bond dipole moments in the contributing bonds. These displacements are sensitive to differences in the configuration and conformations of the chemical bonds. Thus infrared spectroscopy can be used to characterize the number (or mass), composition, structure, and conformation of the molecules comprising an HBM. For example, in a supported bilayer system, the protein of interest, the inner, and the outer leaflets of the bilayer can be simultaneously observed, allowing their complex interactions to be characterized.

As more data analysis methods are developed, this wide variety of information serves as a method to cross-check the sample preparation and structures of the various bilayer components. Other advantages of infrared spectroscopy are: 1) it is nondestructive; 2) it operates on a short time scale ( $\sim 10^{-12}$  sec), which prevents the time averaging of molecular motions; and 3) it does not require invasive and possibly perturbing molecular tags.

## External Reflection Infrared Spectroscopy of Dry HBMs

HBMs were first characterized via infrared spectroscopy using the external reflection geometry.<sup>[28,29]</sup> The external reflection technique uses a high angle of incidence reflection ( $\sim 80^\circ$  from the sample normal)

from a sample supported on an approximately 150-nm-thick gold film. In this configuration, reflected light polarized perpendicular to the plane of incidence and parallel to the substrate undergoes a nearly 180°-phase change. With this phase change, the incident and reflected light destructively interfere with each other and leave very little of the light polarized parallel to the surface to interact with the HBM. This phenomenon increases the field strength of the perpendicular polarized light and provides a sensitive technique to observe the composition, molecular conformation, and orientation of HBMs.

When the structure of the HBM was first being characterized, external reflection data showed bands from the alkane chains and the choline head groups of the phospholipids in HBMs, and confirms the presence of the phospholipid layer.<sup>[28]</sup> A variety of HBMs with different alkanethiol (hexanethiol, decanethiol, and octadecanethiol) and phospholipid (1,2-dimyristoyl-*sn*-glycero-3-phosphocoline (DMPC), 1,2-dipalmitoyl-*sn*-glycero-3-phosphocoline (DPPC), 1,2-distearoyl-*sn*-glycero-3-phosphocoline (DSPC)) chain lengths were characterized. The study also characterized the effect the addition of phospholipid had on the structure of the underlying alkanethiol by using surface-enhanced Raman spectroscopy and external reflection spectra of alkanethiols in the presence and absence of an added layer of deuterated phospholipid. From this work, it is apparent that the addition of phospholipid generally causes small structural changes that are consistent with an ordering of the alkanethiol chains.

In another external reflection infrared study, the spectra revealed a series of CH<sub>2</sub> wagging progression bands in the 1000–1500 cm<sup>-1</sup> region for HBMs formed with hydrogenated phospholipids.<sup>[29]</sup> As wagging progressions are too weak to be observed in alkanethiol monolayers,<sup>[30]</sup> it was concluded that these progression bands were from the lipid layer. Furthermore, the progression bands suggested that the phospholipid portions of the HBMs had a high degree of intramolecular order.<sup>[29,31]</sup>

To evaluate the separation of the wagging progressions, a spectrum of DPPC-*d*<sub>62</sub> in an HBM was subtracted from the spectrum of DPPC in an HBM. After subtraction, only features due to the hydrogenated alkane chains of DPPC remain in the spectrum and support the idea that the wagging progressions are from the lipid layer. Separations between these wagging progression bands,  $\Delta\nu$ , were related to the number of *trans* bonds contributing to the wag-twist modes, *m*, by:<sup>[29,30]</sup>

$$\Delta\nu = 326/(m + 1)$$

Table 1 reports *m* values for a variety of acyl chain lengths and compares these values to those expected

**Table 1** Analysis of the wagging progression modes and the number of *trans* bonds as a function of lipid chain length

Lipid	Number of bonds	Frequency shift (cm <sup>-1</sup> )	% <i>trans</i> bonds
DSPC	17	19.8 ± 0.7	91 ± 4
DPPC	15	21.6 ± 0.9	95 ± 4
DMPC	13	26.0 ± 1.9	87 ± 6

from all *trans* chains. These values indicate that HBMs in air consist of chains averaging one gauche bond per chain. This would be expected for DPPC and DSPC with gel-to-liquid crystalline transition temperatures of 41 and 55°C, respectively. However, the gel-to-liquid crystalline transition temperature of DMPC is 23°C. Thus DMPC would be expected to be more disordered. The highly ordered structures of the lipids in the HBMs were assumed to come from either the stability of the octadecane thiol leaflet of the HBM or a lower degree of lipid hydration that could have effectively raised the transition temperatures of the HBM lipids.

### Infrared External Reflection Spectroscopy for Molecular Orientation in HBMs

Molecular orientation can be characterized using external reflection by matching experimental spectra with spectra simulated using the electromagnetic wave theory. The theory uses knowledge of the isotropic optical constants of the layer of interest and an assumed molecular conformation to scale the relative intensities of the different molecular functional groups as a function of the molecular orientation. This technique allows the degree of molecular tilt, twist, and azimuthal rotation to be determined. In addition, descriptions of the relative orientations of the constituent functional groups can be used to characterize, for example, the average *trans/gauche* conformation of the terminal methyl group of the lipid alkane chains.

There are a number of different implementations of the electromagnetic wave theory that have been developed. An early isotropic version by Hansen<sup>[32]</sup> uses a series of 2 × 2 matrices to describe an *N*-phase layer model. Hasegawa et al.<sup>[33]</sup> extended Hansen's calculations to describe uniaxially oriented layers of cadmium stearate on a GaAs substrate using a three-phase model. Parikh and Allara<sup>[34]</sup> developed a 4 × 4 matrix model for the quantitative treatment of biaxially oriented *N*-phase layered samples. More importantly, they also describe how to obtain optical constants from transmission measurements of bulk isotropic samples of the layer materials. These techniques use the entire set of information from the infrared

spectrum to determine cross-validated information about monolayer and bilayer structure.

To illustrate this technique, infrared external reflection spectroscopy was used to study the classical example of an octadecanethiol monolayer. The optical constants of isotropic octadecanethiol for the external reflection spectra calculations were modeled by using the transmission spectra calculations developed by Parikh and Allara.<sup>[34]</sup> A spectrum of isotropic octadecanethiol was obtained and decomposed into its constituent vibrational bands. For each vibration, a matrix was then constructed to determine the direction of the dynamic dipole for a chain with its carbon backbone perpendicular to the gold surface. The tilt, twist, and azimuthal orientations of the molecule were then selected relative to the surface. A rotation matrix was applied to transform the initial matrix to that of the newly oriented molecule to describe the imaginary part of the refractive index. The intensity of IR absorption is given by the square of the projection of the calculated vibration onto the  $z$  axis of the oriented molecule. Using the computed value as the imaginary part of the refractive index, a Kramers–Kronig transformation was used to determine the real part of the refractive index of the monolayer.

A three-layer model of air, octadecanethiol, and gold was then constructed by using Parikh and Allara's<sup>[34]</sup>  $4 \times 4$  matrix version of electromagnetic wave theory. At first, theory and experiment did not match well because the relative orientations of the methyl groups to the alkane chains are not the same in the monolayers as in the isotropic polycrystalline reference samples. The inclusion of gauche conformers in the structural model substantially improved the fit, especially in the region close to the symmetric and asymmetric  $\text{CH}_3$  stretching band near  $2960\text{ cm}^{-1}$ . Fig. 2 shows the juxtaposition of the external reflection experimental and calculated spectra. The spectra match with small deviations attributed to differences in conformation, and therefore band widths, between the polycrystalline transmission samples and the monolayers. The modeling procedure reveals that 21% of the methyl groups are in a gauche conformation, the acyl chains are tilted  $26^\circ$  to the surface normal, twisted by  $56^\circ$  around the chains' long axis, and that the spectra are insensitive to changes in azimuthal angle (Fig. 3). These values match well with values determined previously using similar methods.<sup>[34,35]</sup>

This method was previously used to compare the infrared external reflection spectra of HBMs with spectra calculated for different molecular orientations using electromagnetic wave theory.<sup>[29]</sup> As indicated above, the infrared spectrum of an HBM shows a well-packed lipid layer similar to the packing of a gel phase lipid bilayer. This means that the assumption of a nearly all *trans* chain conformation similar to

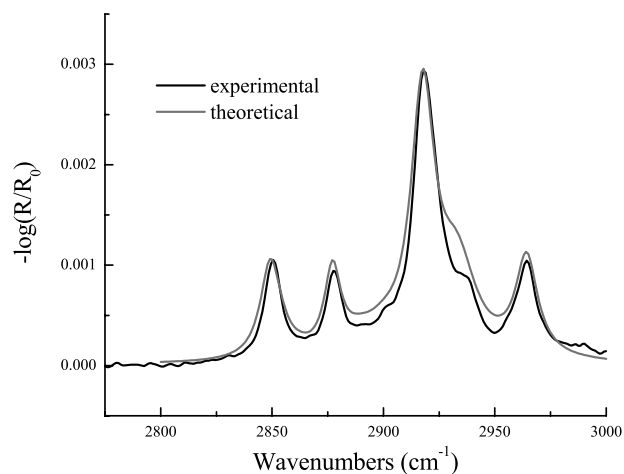


**Fig. 2** Experimental and theoretical external reflection infrared spectra at an  $80^\circ$  angle of incidence.

the alkanethiol case is appropriate for the lipid layer. Simulations of the CH stretching region of the external reflection spectra of DPPC layers reveal that the tilt and twist of the acyl chains are  $34^\circ$  and  $-38^\circ$ , respectively.<sup>[29]</sup> In fitting the simulated spectra to the measured spectra, several details are clarified. The lipid layers can be described as uniaxial with the azimuthal angle having little effect on the simulated spectra. The alignment of the methyl groups compared to the rest of the acyl chains is different than the alignment of the methyl groups in the polycrystalline reference spectra from which the optical constants for the calculation are derived. This difference can be attributed to  $26 \pm 16\%$  gauche terminal methyl conformations.<sup>[29,34]</sup>

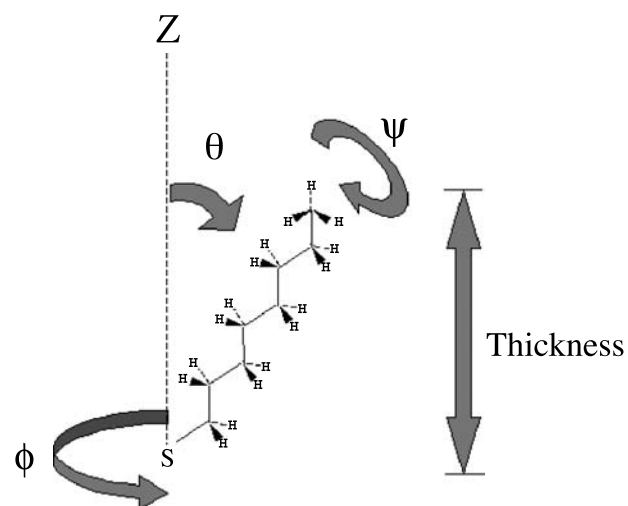


**Fig. 3** Schematic diagram of the  $z$ -axis normal to the gold surface, the monolayer thickness, the tilt ( $\theta$ ), twist ( $\psi$ ), and azimuthal ( $\phi$ ) angles describing the orientation of the molecules in the monolayer.

## Infrared Spectroscopic Ellipsometry

Using infrared spectroscopic ellipsometry (IRSE), the powerful method of fitting optical models to experimental data to extract information about the molecular structure of monolayers/bilayers can be extended to obtain the optical thickness of the layer. Self-assembled monolayers were used as reference materials to demonstrate the sensitivity of this approach.<sup>[36]</sup> Film properties such as molecular orientation and thickness were used to predict the spectra of the real and imaginary components of the complex optical density,  $D$ . The calculated  $D$  spectra are compared to the measured spectra and the model revised. This iterative process continues until changes in the model produce the best fit to the experimental results.

The graph in Fig. 4 shows a comparison of experimental data (solid line) with an electromagnetic wave theory calculations (dashed line) for a hexadecanethiol monolayer. Fig. 3 illustrates the description of the molecular orientation and thickness information determined from the ellipsometric measurements. For example, the shift in the baseline of the simulated  $\text{Im}(D)$  matches the measured  $\text{Im}(D)$  shift, which suggests a film thickness of 2.0 nm. The peak intensities

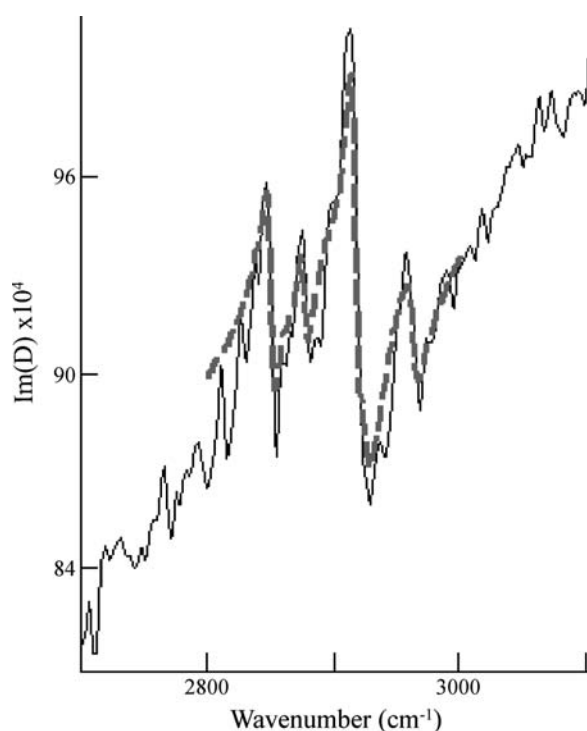


**Fig. 4** Two infrared ellipsometric spectra describing the imaginary part of the complex optical density function,  $D$ , for a hexadecanethiol monolayer. The solid line depicts experimentally measured data and the dashed line depicts data simulated using electromagnetic wave theory as described in the text.

in the simulation of  $\text{Re}(D)$  (not shown, but similar to Fig. 2) also match that of the hexadecane in the electromagnetic model. In this case, the hexadecane chain is tilted at an angle of  $26^\circ$  to the surface normal and twisted by  $48^\circ$  around its long axis, similar to the octadecanethiol monolayer.<sup>[36]</sup>

Two sources of error were analyzed: analyzer repositioning and angle of incidence changes between reference and sample measurements. Results indicated that the error resulting from the analyzer position is smaller than the error arising from differences in the angles of incidence. If a simulated  $\text{Im}(D)$  is matched to two consecutive  $\text{Im}(D)$  measurements, a difference in the thickness of only 0.05 nm is revealed. A series of four measurements of the thickness of a heptanethiol monolayer were performed to evaluate the error caused by differences in the angle of incidence between the sample and the reference. Analysis revealed a thickness of  $1.0 \pm 0.2$  nm, which is similar to the value and standard deviations previously measured using visible spectroscopic ellipsometry. However, they did not require the inclusion of an extra unknown layer to describe the interface between the gold and the alkanethiol, as required in visible ellipsometry models.<sup>[36]</sup> The error in the reproducibility of these measurements,  $\pm 0.2$  nm, is equivalent to  $\pm 0.0005$   $\text{Im}(D)$  units. This study also illustrates that IRSE can be utilized to discriminate between the hexanethiol, dodecanethiol, and hexadecanethiol self-assembled monolayers on gold on the basis of thickness, and the simulations revealed values of 0.8, 1.5, and 2.0 nm, respectively.<sup>[36]</sup>

These examples illustrate the variety of structural information that can be obtained from infrared data. Optical modeling provides a method to cross-validate the identity, amount, conformation, and molecular orientation of a supported bilayer sample. The extension of these powerful techniques to more biologically relevant samples under aqueous solution is described below.

### HBMs Characterized under Aqueous Solution Using External Reflection

Polarization-modulation infrared reflection adsorption spectroscopy has been utilized to characterize HBMs under aqueous solution.<sup>[37]</sup> HBMs consisting of DMPC and hexadecanethiol with and without gramicidin D were characterized. The data clearly show the difference between the hexadecanethiol monolayer, the hexadecanethiol/DMPC HBM and the HBM containing the gramicidin. Changes in the absorbances in the CH stretching region,  $2800\text{--}3000\text{ cm}^{-1}$ , for the spectra of the self-assembled monolayer (SAM) and the HBM, are consistent with the formation of a complete bilayer. For the HBM, the frequency of the

$\text{CH}_2$  asymmetric stretching band,  $2917\text{ cm}^{-1}$ , indicates that the lipid layer acyl chains are quite ordered compared to a frequency of  $2924\text{ cm}^{-1}$  for disordered chains. Amide A, I and II bands characteristic of proteins and peptides are observed in HBMs containing gramicidin D. Shifts in these bands to lower frequencies compared to spectra in aqueous bulk solution suggest that the environment or conformation of Gramicidin is altered by incorporation into the HBM.

### HBMs under Aqueous Solution Characterized by Multiple Internal Reflection

In contrast to external reflection, internal reflection involves coating a thin ( $< 20\text{ nm}$ ) gold layer on an internal reflection element. The light impinges on the from the back, or supporting side through the thin gold layer. Similar techniques have been described for electrochemical measurements (e.g., see Neff et al.<sup>[38]</sup> and references therein). Generally, these methods are difficult and no standard methods exist.<sup>[39]</sup> Understandably, reproducibly coating a continuous thin layer of metal on an internal reflection element can be difficult. It is also difficult to determine if the gold layer is continuous because commercially available internal reflection elements are polished to optical tolerances using polishing grit (generally  $0.1\text{--}1\text{ }\mu\text{m}$  in diameter). With this type of surface finish, it is difficult to observe roughness on the order of the thickness of the gold layers.

Recently, there have been several reports of surface-enhanced infrared spectroscopy have taken advantage of the higher plasmon density at the surface of discontinuous gold layers to increase the IR signal.<sup>[40]</sup> These discontinuous gold layers present a dilemma in terms of determining the structure of the HBM. Because the thiols only adsorb to the gold-coated portion of the surface, it is unclear whether the HBM consists of a proximal alkanethiol and a distal phospholipid, or if the proximal layer is a mixture of alkanethiol and phospholipid. In addition, the plasmon density, and therefore optical field strength of these discontinuous layers, is not uniform. The non-uniformity of the field strength makes it difficult to relate the observed spectral intensities to the molecular properties of the HBMs.

For example, Sevin-Landais et al.<sup>[41]</sup> and Liley et al.,<sup>[42]</sup> using the same type of gold coating, estimated that as much as 15–20% of the crystal surface was not coated with gold. Another example is the study by Cheng et al.,<sup>[43]</sup> which describes a 14-reflection crystal coated with 20 nm of gold leaving a total path length of at least 140 nm through gold. Because the decay length for the intensity of the light is given by  $4\pi k/\lambda = \sim 13\text{ nm}$  for the CH stretching region, a path of 140 nm would essentially leave no light. However, if the gold layer is discontinuous, the path through the

gold could be substantially less and the signal proportionally greater. The Cheng et al.<sup>[43]</sup> study used infrared spectroscopy to characterize lipid bilayers formed by vesicle fusion to surfaces containing different concentrations of immobilized cholesterol. Phospholipid adsorption from vesicles was only detected for surfaces at least 24% covered with cholesterol. Because of the signal attenuation of the gold, they report field amplitudes to be small,  $\sim 0.1$  and  $0.01$  for p and s polarizations, respectively. When these values are used to determine the orientation of the lipid acyl chains, they suggest a tilt of  $12^\circ$  compared to  $26^\circ$  for a 30 mol% cholesterol layer in bulk DMPC by nuclear magnetic resonance (NMR).<sup>[43]</sup> They suggest this discrepancy is caused by a more “rigid” bilayer on the surface. However, Huber and Mantsch<sup>[44]</sup> report a  $26^\circ$  tilt for DMPC in the gel phase on an attenuated total reflection (ATR) crystal. It is more likely that the difference can be explained by a low signal-to-noise ratio caused by low field strengths.

### HBMs under Aqueous Solution Characterized by a Single Internal Reflection

Recently, Elliott et al.<sup>[5]</sup> minimized the problem of signal attenuation by the thin gold layer in the multiple internal reflection geometry by using a single internal reflection accessory. The integrity of the gold layer was improved by using a silicon crystal, like the majority of the gold supporting substrates in monolayer work. This layer has a root-mean-square (RMS) roughness on the order of 0.3 nm, and therefore only minimally perturbs the HBMs. Fig. 5 shows the electric field strengths at the gold surface for different gold film thickness. These values are calculated by

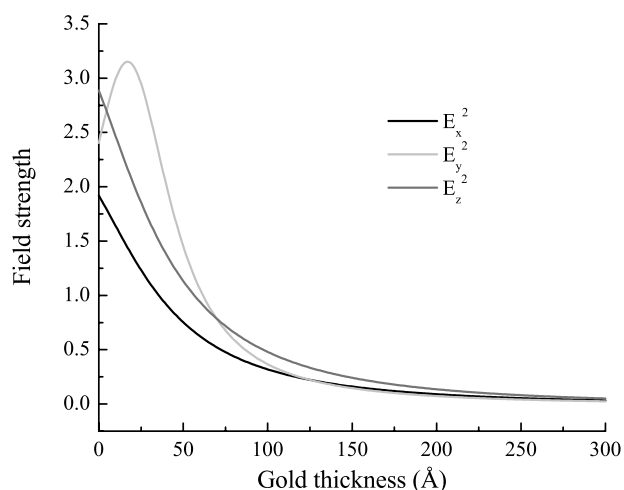


**Fig. 5** Three-layer model (silicon/gold/water) description of the field strengths in the  $x$ ,  $y$ , and  $z$  directions at the gold/water interface as a function of gold thickness.



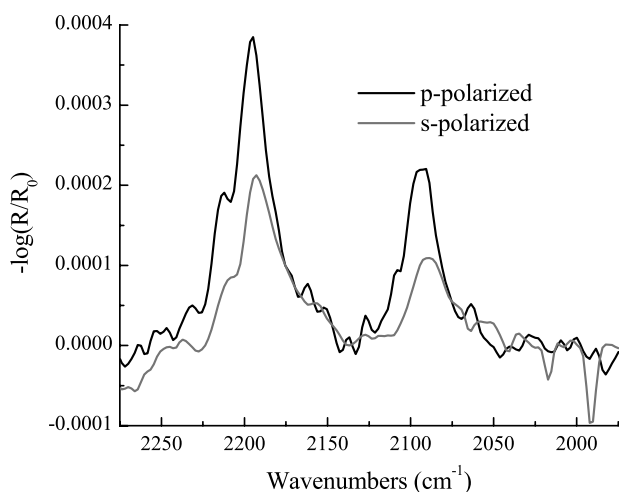


**Fig. 6** s- and p-polarized infrared internal reflection data in the C–D stretching region of a deuterated DMPC layer in a HBM measured under aqueous buffer solution.

using the method of Hansen<sup>[32]</sup> as implemented by Citra and Axelsen.<sup>[45]</sup> From these data, the effect of multiple reflections through the gold on the field strength can be approximated by the field strengths at multiples of the gold thickness values.

As an example of the information available from this type of experiment, Fig. 6 shows parallel- and perpendicularly polarized spectra of a deuterated DMPC HBM. Using this data and the three-layer model of Citra and Axelsen,<sup>[45]</sup> the average orientation of the lipid acyl chains with respect to the membrane surface normal was calculated to be  $\sim 25^\circ$ . This value is comparable with the NMR value reported by Cheng et al.,<sup>[43]</sup> and with the  $26^\circ$  tilt angle for DMPC in the gel phase on an ATR crystal reported by Huber and Mantsch.<sup>[44]</sup> Similar techniques can also be used to describe the orientation of proteins incorporated in HBMs.

## CONCLUSION

Supported bilayer membranes embody a nanotechnology that developed to determine the structure and function of cell membranes and to clarify issues in the details of the “fluid mosaic” model in the fields of biology and medicine. The current challenge for the characterization of supported bilayer membranes is to obtain information that can be cross-validated either between different measurement techniques, or by methods measuring independent information from the same technique. This article described how infrared spectroscopy is used to obtain information from bilayer membranes supported on metal surfaces. While some methods have been developed for the characterization of lipid/protein layers at the surfaces of internal reflection crystals, complications and

enhancements associated with the addition of the gold layer still need to be addressed. For example, improved models of molecular orientation may allow more about the distribution of the molecular orientation and/or the distance a functional group is from the surface. Another area in which the analysis of infrared spectroscopy of supported bilayer membranes can be improved lies in techniques to exploit improvements in isotopic editing of proteins.<sup>[46]</sup>

## ACKNOWLEDGMENT

The author like to thank J. T. Elliott for help collecting the infrared data in Figure 6.

## REFERENCES

1. Singer, S.J.; Nicolson, G.L. The fluid mosaic model of the structure of cell membrane. *Science* **1972**, *175*, 720–731.
2. Jacobson, K.; Sheets, E.D.; Simson, R. Revisiting the fluid mosaic model of membranes. *Science* **1995**, *268*, 1441.
3. Plant, A.L. Self-assembling phospholipid alkanethiol biomimetic bilayers on gold. *Langmuir* **1993**, *9*, 2764–2767.
4. Plant, A.L. Supported hybrid bilayer membranes as rugged cell membrane mimics. *Langmuir* **1999**, *15*, 128–5135.
5. Elliott, J.T.; Meuse, C.W.; Silin, V.; Krueger, S.; Woodward, J.T.; Petralli-Mallow, T.; Plant, A.L. Biomimetic Membranes on Metal Supports. In *Biomolecular Films Design, Function and Applications*; Rusling, J.F., Ed.; Marcel Dekker, Inc.: New York, 2003; 99–162.
6. Cornell, B.A.; Braach-Maksvytis, V.L.; King, L.G.; Osman, P.D.; Raguse, B.; Wiczorek, L.; Pace, R.J. A biosensor that uses ion-channel switches. *Nature* **1997**, *387*, 580–583.
7. Ostermeier, C.; Michel, H. Crystallization of membrane proteins. *Curr. Opin. Struct. Biol.* **1997**, *7*, 697.
8. Pautsch, A.; Schulz, G.E. High-resolution structure of the OmpA membrane domain. *J. Mol. Biol.* **2000**, *298*, 273.
9. Palczewski, K.; Kumasaka, T.; Hori, T.; Behnke, C.A.; Motoshima, H.; Fox, B.A.; Le, T.; Teller, D.C.; Okada, T.; Stenkamp, R.E.; Yamamoto, M.; Miyano, M. Crystal structure of rhodopsin: A G protein-coupled receptor. *Science* **2000**, *289*, 739.
10. Bangham, A.D. Liposomes—The Babraham connection. *Chem. Phys. Lipids* **1993**, *64*, 275–285.
11. Montal, M. Reconstitution of channel proteins from excitable cells in planar lipid bilayer membranes. *J. Membr. Biol.* **1987**, *98*, 101–115.
12. Levine, Y.K. X-ray diffraction studies of membranes. *Prog. Surf. Sci.* **1973**, *3*, 279.
13. Sackmann, E. Supported membranes: Scientific and practical applications. *Science* **1996**, *271*, 43–48.
14. Sackmann, E.; Tanaka, M. Supported membranes on soft polymer cushions: Fabrication, characterization and applications. *Trends Biotechnol.* **2000**, *18*, 58–64.

15. Sanders, C.R.; Prosser, R.S. Bicycles: A model membrane system for all seasons?. *Struct. Fold. Des.* **1998**, *6*, 1227–1234.
16. Tamm, L.K.; McConnell, H.M. Supported phospholipid bilayer. *Biophys. J.* **1985**, *47*, 105–113.
17. Groves, J.T.; Wulfing, C.; Boxer, S.G. Electrical manipulation of glycan phosphatidyl inositol tethered proteins in planar supported bilayers. *Biophys. J.* **1996**, *71*, 2716–2723.
18. McConnell, H.M.; Watts, T.H.; Weis, R.M.; Brian, A.A. Supported planar membranes in studies of cell–cell recognition in the immune-system. *Biochim. Biophys. Acta* **1986**, *864*, 95–106.
19. Seul, M.; Subramaniam, S.; McConnell, H.M. Monolayers and bilayers of phospholipids at interfaces interlayer coupling and phase-stability. *J. Phys. Chem.* **1985**, *89*, 3592–3595.
20. Goormaghtigh, E.; Raussens, V.; Ruyschaert, J.-M. Attenuated total reflection infrared spectroscopy of proteins and lipids in biological membranes. *Biochim. Biophys. Acta* **1999**, *1422*, 105–185.
21. Liebermann, T.; Knoll, W. Streptavidin arrays as supramolecular architectures in surface-plasmon optical sensor formats. *Colloids Surf., A* **2000**, *171*, 115–137.
22. Enderlein, J. A theoretical investigation of single-molecule fluorescence detection on thin metallic layers. *Biophys. J.* **2000**, *78*, 2151–2158.
23. Lingler, S.; Rubinstein, I.; Knoll, W.; Offenhausser, A. Fusion of small unilamellar lipid vesicles to alkanethiol and thiolipid self-assembled monolayers on gold. *Langmuir* **1997**, *13*, 7085–7091.
24. Terrettaz, S.; Stora, T.; Duschl, C.; Vogel, H. Protein-binding to supported lipid-membranes—Investigation of the cholera-toxin ganglioside interaction by simultaneous impedance spectroscopy and surface-plasmon resonance. *Langmuir* **1993**, *9*, 1361–1369.
25. Stelzle, M.; Weissmuller, G.; Sackmann, E. On the application of supported bilayers as receptive layers for biosensors with electrical detection. *Phys. Chem.* **1993**, *97*, 2974–2981.
26. Tamm, L.K.; Tatulian, S.A. Infrared spectroscopy of proteins and peptides in lipid bilayers. *Q. Rev. Biophys.* **1997**, *30*, 365–429.
27. Dluhy, R.A. Infrared spectroscopy of biophysical monomolecular films at interfaces: Theory and applications. *Appl. Spectrosc. Rev.* **2000**, *35* (4), 315–351.
28. Meuse, C.W.; Niaura, G.; Lewis, M.L.; Plant, A.L. Assessing the molecular structure of alkanethiol monolayers in hybrid bilayer membranes with vibrational spectroscopies. *Langmuir* **1998**, *14*, 1604–1611.
29. Meuse, C.W.; Krueger, S.; Majkrzak, C.F.; Dura, J.A.; Fu, J.; Conner, J.T.; Plant, A.L. Hybrid bilayer membranes in air and water: Infrared spectroscopy and neutron reflectivity studies. *Biophys. J.* **1998**, *74*, 1388–1398.
30. Parikh, A.H.; Liedberg, B.; Atre, S.V.; Ho, M.; Allara, D.L. Correlation of molecular organization and substrate wettability in the self-assembly of *n*-alkylsiloxane monolayers. *J. Phys. Chem.* **1995**, *99*, 9996–10008.
31. Snyder, R.G.; Schachtschneider, J.H. Vibrational analysis of the *n*-paraffins I assignments of infrared bands in the spectra of C<sub>3</sub>H<sub>8</sub> through *n*-C<sub>19</sub>H<sub>40</sub>. *Spectrochim. Acta, Part A* **1963**, *19*, 85.
32. Hansen, W.N. Electric fields produced by the propagation of plane coherent electromagnetic radiation in a stratified medium. *J. Opt. Soc. Am.* **1967**, *38*, 380–390.
33. Hasegawa, T.; Takeda, S.; Kawaguchi, A.; Umemura, J. Quantitative analysis of uniaxial molecular orientation in Langmuir–Blogett films by infrared reflection spectroscopy. *Langmuir* **1994**, *11*, 1236–1243.
34. Parikh, A.N.; Allara, D.L. Quantitative determination of molecular structure in multilayered thin films of biaxial and lower symmetry from photon spectroscopies. I. Reflection infrared vibrational spectroscopy. *J. Chem. Phys.* **1992**, *96*, 927–945.
35. Terrill, R.H.; Tanzer, T.A.; Bohn, P.W. Structural evolution of hexadecanethiol monolayers on gold during assembly: Substrate and concentration dependence of monolayer structure and crystallinity. *Langmuir* **1997**, *14*, 1604–1611.
36. Meuse, C.W. Infrared spectroscopic ellipsometry of self-assembled monolayers. *Langmuir* **2000**, *16*, 9483–9487.
37. Ha, J.; Henry, C.S.; Fritsch, I. Formation and characterization of supported hexadecanethiol/dimyristoyl phosphatidylcholine hybrid bilayers containing Gramicidin D. *Langmuir* **1998**, *14*, 5850–5857.
38. Neff, H.; Lange, P.; Roe, D.K.; Sass, J.K. A modulated infrared-ATR spectroscopy study of water in the electric double-layer. *J. Electroanal. Chem.* **1983**, *150*, 513–519.
39. Bauhofer, J. Electrical Applications of Internal Reflection Spectroscopy. In *Internal Reflection Spectroscopy: Theory and Applications*; Mirabella, F.M., Ed.; Marcel Dekker, Inc.: New York, 1993; 233–254.
40. Kellner, R.; Mizaikoff, B.; Jakusch, M.; Wanzenbock, H.D.; Weissenbacher, N. Surface-enhanced vibrational spectroscopy: A new tool in chemical IR sensing?. *Appl. Spectrosc.* **1997**, *51*, 495–503.
41. Sevin-Landais, A.; Rigler, P.; Tzartos, S.; Hucho, F.; Hovius, R.; Vogel, H. Functional immobilisation of the nicotinic acetylcholine receptor in tethered lipid membranes. *Biophys. Chemist.* **2000**, *85*, 141–152.
42. Liley, M.; Keller, T.A.; Duschl, C.; Vogel, H. Direct observation of self-assembled monolayers, ion complexation, and protein conformation at the gold/water interface: An FTIR spectroscopic approach. *Langmuir* **1997**, *13*, 4190–4192.
43. Cheng, Y.; Boden, N.; Bushby, R.J.; Clarkson, S.; Evan, S.D.; Knowles, P.F.; March, A.; Miles, R.E. Attenuated total reflection Fourier transform infrared spectroscopic characterization of fluid lipid bilayers tethered to solid supports. *Langmuir* **1998**, *14*, 839–844.
44. Hubner, W.; Mantsch, H.H. Orientation of specifically C-13=O labeled phosphatidylcholine multilayers from polarized attenuated total reflection FTIR spectroscopy. *Biophys. J.* **1991**, *59*, 1261–1272.
45. Citra, M.J.; Axelsen, P.H. Determination of molecular order in supported lipid membranes by internal reflection Fourier transform infrared spectroscopy. *Biophys. J.* **1996**, *71*, 1796–1805.
46. Arkin, I.T.; Adams, P.D.; Brünger, A.T.; Smith, S.O.; Engleman, D.M. Structural perspectives of phospholamban, a helical transmembrane pentamer. *Annu. Rev. Biophys. Biomol. Struct.* **1997**, *26*, 157–179.

# Inorganic Nanotubes

Reshef Tenne

Materials and Interfaces Department, Weizmann Institute of Science,  
Rehovot, Israel

## INTRODUCTION

Nanoparticles of inorganic layered compounds, such as  $WS_2$ , were shown to be unstable in the planar form and, in analogy to carbon nanoparticles, they form closed-cage structures with polyhedral or nanotubular shapes. These findings extend the paradigm of carbon fullerenes and nanotubes to the field of inorganic chemistry, where numerous examples for its validity have been documented in recent years. Templated growth of nanotubes from isotropic (3-D) compounds such as metal oxides and chalcogenides was reported as well, but these nanotubes are generally not perfectly crystalline. Various issues in the structure, synthesis, and properties of such inorganic nanotubular and fullerene-like structures are reviewed, together with some possible applications.

## CARBON FULLERENES AND NANOTUBES

When the first generation of high-resolution transmission electron microscopes (TEM) became available during the late 1960s, nanoparticles of fired soot with unique character were revealed. These multilayer polyhedra (“onions”) were essentially closed graphitic sheets with an empty core, which were thought to consist of pieces of small graphitic platelets “stitched” together by an unknown “glue.” In 1980, Iijima proposed that such structures were in fact made of graphitic sheets “glued” together by pentagonal rings. He suggested that according to the Euler rule each polyhedron in the onion consists of 12 carbon pentagons and a large number of hexagons. Each pentagon forces the flat hexagonal network of graphitic sheets to distort from the planar structure, and disposing such 12 pentagons leads to closure of the entire plane into a hollow caged structure.

The stunning discovery of the  $C_{60}$  molecule by Kroto, Smalley, and Curl<sup>[1]</sup> led to a new era in the science of nanomaterials. This molecule was shown to consist of 20 hexagons and 12 symmetrically disposed pentagons. Following this discovery, many other fullerenes and related forms of carbon were identified,

in particular multiwall and single-wall nanotubes, discovered by Iijima.<sup>[2]</sup> Carbon nanotubes are made of rolled graphene sheets capped with half a fullerene molecule of the same diameter at each of the two ends. Therefore, these structures can be viewed as an elongated form of a fullerene. Both fullerenes and nanotubes are seamless structures having threefold bonded carbon atoms only. The absence of dangling bonds renders these structures energetically very stable. Nonetheless, the deviation from planarity induces a non-negligible amount of stress into the fullerenes, which explains many of their chemical and physical properties.

## CAN THE PARADIGM OF FULLERENES AND NANOTUBES BE EXTENDED BEYOND CARBON?

The driving force for the formation of carbon fullerenes and nanotubes stems from the abundant reactive atoms on the periphery of the quasi 2-D graphitic nanostructure. These rim atoms are only twofold bonded rather than being threefold ( $sp^2$ ) bonded as in the bulk (Fig. 1). It was concluded, therefore, that in spite of the elastic strain of the folded nanoparticles, the planar topology of graphitic nanoparticles is unstable with respect to folding into the seamless fullerenes. Using similar reasoning, it has been proposed<sup>[3,4]</sup> that the formation of fullerenes is not unique to carbon and in fact is a genuine property of 2-D (layered) compounds. Inorganic layered compounds are abundant, in particular among the transition-metal chalcogenides (sulfides, selenides, and tellurides), halides (chlorides, bromides, and iodides), oxides, and numerous ternary (quaternary) compounds. However, in contrast to graphite, each molecular sheet consists of multiple layers of different atoms chemically bonded to each other.

If one considers  $MoS_2$  as an example (Fig. 1), each molecular sheet is made of a layer of molybdenum atoms sandwiched between two outer sulfur layers. The Mo atoms are sixfold bonded to sulfur atoms, forming a trigonal bipyramid. In analogy to graphite, the S–Mo–S layers are stacked together through weak van der Waals forces. Like graphite, such compounds

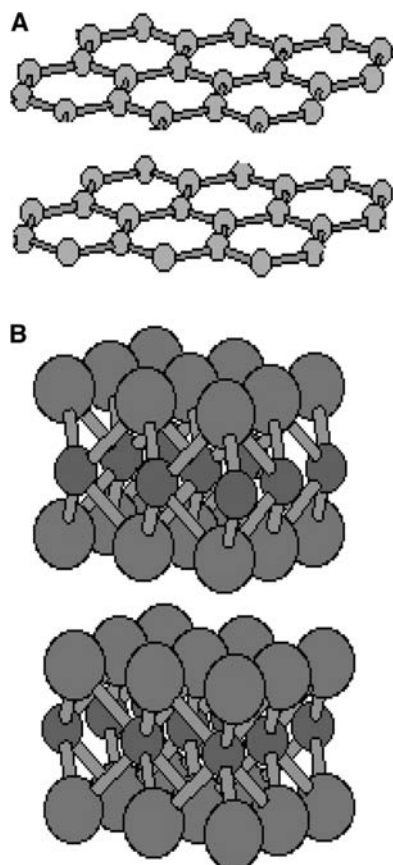


**Fig. 1** Schematic drawings of graphite (A) and MoS<sub>2</sub> (B) nanoclusters. Note that in both cases, the surface energy, which destabilizes the planar topology of the nanocluster, is concentrated in the rim atoms, which are situated on the prismatic edges parallel to the *c*-axis.

are highly anisotropic with respect to many of their physical and chemical properties. The (00.1) surfaces (van der Waals surfaces) of the crystal, which are perpendicular to the *c*-axis, consist of threefold bonded sulfur atoms, which are chemically not reactive. In contrast to the fully bonded bulk atoms, the sulfur and molybdenum atoms on the rim of the nanocluster, i.e., on the prismatic (10.0) faces (parallel to the *c*-axis), are not fully bonded and are therefore chemically very reactive. Indeed, each molybdenum atom in the (10.0) prismatic edge is bonded to only two sulfur atoms of the upper plane and two sulfur atoms of the lower plane. Therefore, each Mo atom has two dangling bonds per atom on the (10.0) face and is consequently chemically reactive. On the opposite face ( $-10.0$ ) of the MoS<sub>2</sub> nanosheet, sulfur atoms are only twofold bonded and they possess one dangling bond per atom. Therefore, the Mo atoms of the (10.0) face would tend to recombine with the S atoms of the opposite side of the platelet. Because the ratio between peripheral (partially bonded) and bulk (fully bonded) molybdenum (sulfur) atoms increases with shrinking size of the

platelet (sheet), nanoparticles of MoS<sub>2</sub> are not stable in the planar form and they fold into closed-cage nanostructures. This hypothesis has been invariably confirmed by both experiment and theory. Extensive experimental data available now tend to substantiate this initially intuitive hypothesis and show that this new curved and hollow phase of layered compounds, designated as inorganic fullerene-like (IF) material, is the thermodynamically stable form, given the constraint that the particles cannot grow beyond, say 0.2  $\mu\text{m}$ . Initially, however, energy must be provided to overcome the activation barrier ensuing from the elastic energy of bending of the otherwise planar sheet. In most cases, heating (thermal energy) was provided for this purpose, but other energy sources, such as irradiation, microwave, sonochemical, and electrical energy were found to activate the nanoparticles' folding process.

Fig. 2 shows a TEM image of typical MoS<sub>2</sub> hollow nanoparticles (onions) consisting of more than 10 molecular MoS<sub>2</sub> layers arranged in a concentric seam-less form. A few kilograms of nested (fullerene-like)

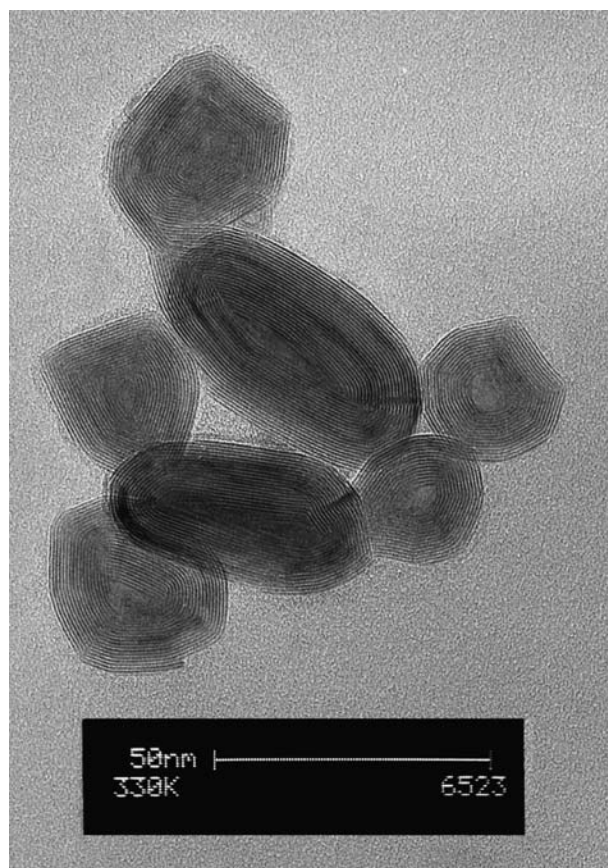


**Fig. 2** TEM image of typical MoS<sub>2</sub> nanoparticles with fullerene-like structure. Each dark line represents an atomic layer of the basal plane (00.1). The distance between each two layers is 6.18  $\text{\AA}$ . The *c*-axis is always normal to the surface of the nested fullerene-like structure.

WS<sub>2</sub> structures were synthesized by the Weizmann Institute laboratory over the last year and efforts to scale up this production are well under way. Fig. 3 shows typical TEM images of multiwall WS<sub>2</sub> nanotubes. Nanotubes of this kind are currently produced by the grams, albeit not as a pure phase, yet.

Theoretical considerations show that the bending energy of isotropic (3-D) materials such as silicon or TiO<sub>2</sub> is exceedingly higher than that of 2-D compounds. This energy cannot be fully compensated for by remediation of the dangling bonds,<sup>[5]</sup> which makes their folding into crystalline nanotubes unlikely. Furthermore, for such nanostructures to become stable, their surface must be passivated, or else they will react with the surrounding and form new entities with a different chemical composition. Therefore, isotropic (3-D) materials are not likely to form stable IF nanostructures. Recently, however, nanotubes of various 3-D (quasi-isotropic) compounds such as GaN with highly faceted (hexagonal) cross-section were reported. Synthesis of semicrystalline nanotubes from such isotropic compounds has been devised, mostly through templated growth (see, e.g. Ref.<sup>[6]</sup>). In spite of this fact, or perhaps because their surface atoms are not fully bonded, semicrystalline nanotubes can be very useful. Their large surface area, combined with their nanometer-scale pore sizes and reactive chemical moieties, may lead to the development of highly reactive and selective catalysts, sensors, and a host of other applications.

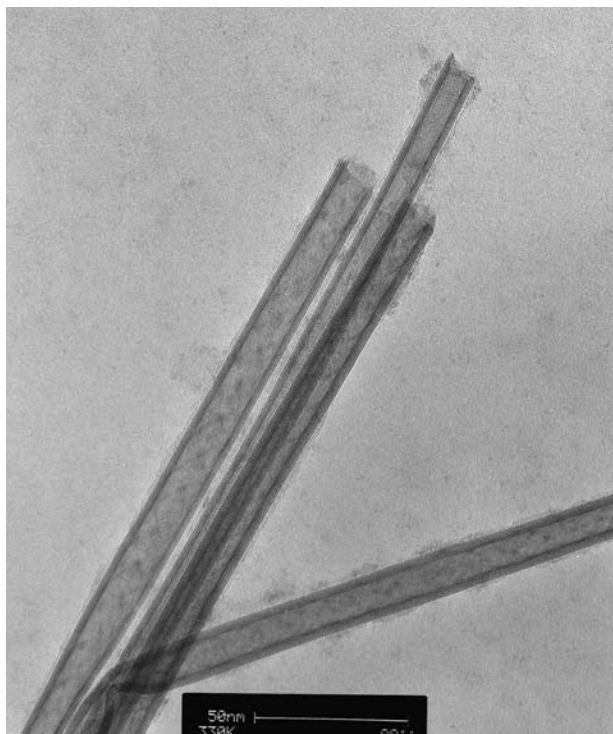


**Fig. 3** TEM micrographs of three very long WS<sub>2</sub> nanotubes.

Therefore, from the chemical perspective a question of great importance concerns the borderline between those materials that can form fully crystalline, IF nanostructures and isotropic materials that cannot afford fully crystalline, evenly folded nanostructures, or can result only in semicrystalline nanotubes. Stated differently, it is possible to ask whether IF structures are generic to all 2-D layered compounds, a group of a few thousands materials, or else only to a subset of this large canon. One way to address this issue is to try to synthesize IF nanostructures from layered compounds of completely different chemical nature. For instance, by synthesizing NiCl<sub>2</sub> nanotubes<sup>[7]</sup> it became apparent that even 2-D compounds of highly ionic character, which are very hygroscopic and are quite unstable in the ambient, are able to form stable IF nanostructures. Incidentally, the kinetics of water uptake by the seamless IF NiCl<sub>2</sub> nanostructures is appreciably slower than the water uptake by nanoplatelets of the same compound, making the former much less hygroscopic and amenable to detection by electron microscopy.

## SYNTHESIS OF INORGANIC NANOTUBES

To produce pure IF phases, and nanotubes in particular, it is imperative to prevent the nanocrystallites from growing beyond a certain size during the process (arrested growth). Numerous methods have been devised for this purpose. A few grams of IF WS<sub>2</sub> were initially synthesized from the respective oxide phase.<sup>[8]</sup> However, lately a few kilograms of this phase were synthesized using the fluidized bed reactor.<sup>[9]</sup> In the first step of this reaction, which lasts about a second, heated WO<sub>3</sub> nanoparticles react with H<sub>2</sub>S gas at 840°C and are sulfidized at the surface. This fast reaction produces one closed layer of WS<sub>2</sub>, enfolding the entire WO<sub>3</sub> nanoparticle. The sulfide-encapsulated oxide nanoparticles become surface passivated and they cannot grow further in size. Once this protective layer has been completed, a slow diffusion-controlled process leads to the conversion of the oxide core into a metal disulfide in a highly uniform and regular fashion. Notably, although the inward diffusion of the (H<sub>2</sub>S) gas is isotropic, the growth of the WS<sub>2</sub> layers occurs along one growth front only, which explains the almost perfect crystallinity of the IF nanoparticles.

In early reports, only minor amounts of WS<sub>2</sub>,<sup>[3]</sup> MoS<sub>2</sub>,<sup>[10]</sup> and BN<sup>[11]</sup> nanotubes could be produced. However, recently, different strategies were successfully developed for the synthesis of various nanotubes. Thus, using the same fluidized bed reactor that is used for the synthesis of fullerene-like WS<sub>2</sub> nanoparticles, under slightly modified operating conditions, a few grams of very long and slender WS<sub>2</sub> nanotubes are being synthesized.<sup>[12]</sup> In another study, a two-step

growth process, in which an oxide nanowhisker phase is first obtained and is subsequently converted into WS<sub>2</sub> nanotubes phase in H<sub>2</sub>S atmosphere, was demonstrated.<sup>[13]</sup> Uniform WS<sub>2</sub> nanotubes were obtained also by the chemical vapor transport (CVT) technique,<sup>[14]</sup> in which the WS<sub>2</sub> powder is transported from the hot to the cold zones of a quartz ampoule using a transporting agent, such as iodine. Extremely uniform and very long single-wall MoS<sub>2</sub> nanotubes with diameter of less than 1 nm were synthesized.<sup>[15]</sup> These nanotubes all come in the armchair (3,3) configuration. Their perfectness can be also gauged by the fact that they self-assemble into a hierarchy of higher-order structures, from the single-nanotube level to macroscopic crystallites. Interestingly, these nanotubes were obtained via a CVT process using C<sub>60</sub> as a catalyst. Nanotubes of the disulfides (and some diselenides) of the transition metals W, Mo, Nb, Ta, Zr, Hf, and Ti were synthesized by high-temperature annealing of the respective metal trisulfides (see, e.g., Ref.<sup>[16]</sup>). This effort was recently summarized in a comprehensive review entry.<sup>[17]</sup> Double-wall boron nitride (BN) nanotubes of high uniformity were produced via the arc-discharge method.<sup>[18]</sup> V<sub>2</sub>O<sub>5</sub> nanotubes were synthesized using organic amines as templating molecules in a sol-gel process followed by hydrothermal treatment.<sup>[19]</sup> Whereas some of the nanotubes are open-ended and have scroll-like shape, others were made of concentric layers and with a closed tip. The inorganic-organic superstructure, obtained from the rather ionic oxide and the aliphatic amine, leads to softening of the layers making them more amenable to folding. The use of “chimie douce” processes for the preparation of new kinds of nanotubes from a number of oxide compounds has recently gained appreciable attention. Thus, scroll-like nanotubules have been obtained from potassium hexaniobate, K<sub>4</sub>Nb<sub>6</sub>O<sub>17</sub>, by acid exchange and careful exfoliation in basic solution.<sup>[20]</sup> The exfoliation process results in monomolecular layers, which are unstable against folding even at room temperature, and consequently form the more stable scroll-like structures. Moreover, although the binary oxides of these transition metals do not possess the lamellar structure, and consequently they cannot form crystalline nanotubular structures, the reduced oxides of these phases can. A typical example belonging to this category is the compound H<sub>2</sub>Ti<sub>3</sub>O<sub>7</sub>, which is a member of the class of lamellar H<sub>2</sub>Ti<sub>n</sub>O<sub>2n+1</sub> phases. This nanotubular phase was prepared by the usual sol-gel process and subsequent treatment with a concentrated NaOH solution at 130°C.<sup>[21]</sup> Numerous other strategies were employed for the synthesis of these and other inorganic nanotubes in recent years. These works demonstrate the richness of the chemical apparatus in the context of inorganic nanotubes and fullerene-like nanostructures.

Hydrothermal synthesis has recently been used extensively for the synthesis of various nanotubes. Thus, bismuth nanotubes were obtained by hydrothermal treatment of a basic bismuth nitrate solution and hydrazine at 120°C.<sup>[22]</sup> Tellurium nanotubes were obtained by hydrothermal reduction of Na<sub>2</sub>TeO<sub>3</sub> in ammonia solution at 180°C.<sup>[23]</sup> The chiral motif of the nanotubes can be attributed to the spiral structure of the trigonal unit cell of tellurium. InS nanotubes were obtained by refluxing *tert*-butyl indium with H<sub>2</sub>S gas at 203°C.<sup>[24]</sup> Interestingly, the layered form of this compound was not known before. Obviously, therefore, the seamless nanotubular structure endows extra kinetic stability to the lamellar phase. Numerous other nanotubular and fullerene-like structures have been reported in the literature over the last few years.

### STRUCTURE OF INORGANIC FULLERENE-LIKE NANOPARTICLES

C<sub>60</sub> is made of hexagons and pentagons only, exhibiting icosahedral symmetry. Neither graphite nor MoS<sub>2</sub> have pentagonal elements within their native structure. However, the trigonal network of MoS<sub>2</sub> possesses triangles and rectangles (rhombi) as genuine elements of lower symmetry. It was therefore proposed<sup>[4]</sup> and later on experimentally verified<sup>[25]</sup> that MoS<sub>2</sub> octahedra (bucky octahedra) made of six symmetrically disposed rectangular (rhombohedral) corners can be obtained. Similarly, in one case a MoS<sub>2</sub> “bucky tetrahedron,” made of symmetrically disposed four triangles in its corners, was observed. These structures are likely to be the most stable form of IF MoS<sub>2</sub> nanoparticles, i.e., the analog of C<sub>60</sub> in MoS<sub>2</sub>. Presently, the synthesis of bucky octahedra from MoS<sub>2</sub> and other compounds remains a most challenging task. Recently, rather small IF MoS<sub>2</sub> nanoparticles have been prepared by discharging graphite and MoS<sub>2</sub> electrodes embedded in deionized water.<sup>[26]</sup> Most of the nanoparticles were found to have rectangular (rhombi)-shaped corners, alluding to the great stability of such nanoparticles.

Boron nitride nanotubes and fullerene-like nanoparticles were among the early noncarbon systems to be studied. Boron is situated to the left of carbon in the periodic table while nitrogen is to its right. In analogy to carbon, BN exists in two main phases: hexagonal (graphitelike) and cubic (diamond-like). Moreover, the stable form of BN at room temperature is the graphitic (hexagonal) polytype. Therefore, nanoparticles of this phase are expected to be unstable in the planar form and afford a fullerene-like structure. Because B–B or N–N pairs are not favorable nearest neighbors, pentagonal rings cannot form. Instead, the folding can be obtained by introducing six squares into the hexagonal network. The smallest stable fullerene-like structure



was calculated to be the  $B_{12}N_{12}$  octaheder,<sup>[27]</sup> consisting of six hexagonal rings and six squares. Indeed, BN nanooctahedra with symmetrically disposed six squares<sup>[28]</sup> and nanotubes with flat tops having three squares<sup>[29]</sup> were indeed synthesized by various methods.

Using an elastic continuum model, the topology of  $WS_2$  ( $MoS_2$ ) cage structures was studied.<sup>[5]</sup> A first-order phase transition from an evenly curved (quasi-spherical) structure into a polyhedral cage was predicted for nanoparticles with shell thickness larger than about 1/10. The same model foresaw a similar transition for nanoparticles two layers thick and with radius of curvature smaller than 10 nm. A transition of this kind was observed during the synthesis of IF  $WS_2$  particles from 50-nm  $WO_3$  nanoparticles.<sup>[8]</sup> The conversion of  $WO_3$  nanoparticles to IF  $WS_2$  proceeds from the surface of the nanoparticles inward.<sup>[8]</sup> When the number of  $WS_2$  layers is three or less, the nanoparticles appear to be evenly folded and therefore have quasi-spherical shape. However, when the conversion process continues and the thickness of the sulfide shell in the nanoparticles exceeds a few nanometers, i.e., four layers and more, the nanoparticles are transformed into a faceted structure. Further agreement with the above model was obtained in a number of other experimental studies. Fullerene-like  $MoS_2$  nanoparticles 3–4 nm in diameter and two to three layers thick, prepared by laser ablation, were found to adopt a highly faceted octahedral shape.<sup>[25]</sup> Moreover, in accordance with this theory,  $NbS_2$  nanoparticles, which have larger Young's modulus than their  $WS_2$  counterparts, are found to be appreciably more faceted.<sup>[7]</sup> In contrast to the caged fullerene-like nanoparticles,  $WS_2$  nanotubes with 20-nm diameters are rarely faceted. Obviously, the elastic strain involved in folding along one axis (nanotubes) is appreciably smaller than that of nanoparticles folded along two axes (fullerene-like nanoparticles). This idea is further vindicated by comparing the stability of phosphorous nanotubes and fullerene-like structures as predicted from ab initio density functional theory tight-binding calculations. While the 1-D nanostructures are found to be perfectly stable,<sup>[30]</sup> the phosphorous fullerenes are unstable and they decompose into  $P_4$  clusters.<sup>[31]</sup>

The ionic character of layered metal chlorides, such as  $NiCl_2$  or  $CdCl_2$ , is appreciably higher than that of the layered metal dichalcogenides. Consequently, the bending modulus of the former compounds is about twice as large as that of the latter compounds. Furthermore, the free slippage of the molecular layers on top of each other is crucial in maintaining low elastic strain during folding of the nanoparticles. However, the shearing energy in the ionic  $NiCl_2$  is sixfold larger than for  $MoS_2$ .<sup>[32]</sup> Not surprisingly therefore, whereas one-layer-thick fullerene-like nanoparticles of metal dihalides afford either quasi-spherical or faceted

polyhedral structure,<sup>[7,32,33]</sup> three-layer-thick polyhedra are invariably highly faceted. The most common motif for fullerene-like nanoparticles of this family is a hexagonal polyhedron. On the other hand,  $NiCl_2$  nanotubes are generally cylindrical.<sup>[7,32]</sup>

The topology of polyhedra made of one layer has been investigated virtually for hundreds of years. Contrarily, the mathematics of polyhedra made of a number of interconnected layers with fixed lattice points in each layer, which is commonplace in IF structures, has been barely studied. This challenging issue is clearly demonstrated in the case of IF  $CdCl_2$ , where only partial information regarding the structure of the hexagonally shaped polyhedron is available. Furthermore, realistic models of IF structures, like  $MoS_2$  octahedra consisting of some 1800 atoms, require highly developed ab initio calculations, which makes this task presently quite intractable. Some progress in this direction was discussed in Ref.<sup>[34]</sup> Future developments in handling these mammoth calculations is likely to have tremendous impact on our ability to decipher the structural details and the physical properties of IF structures. In conclusion, the synthesis and elucidation of the structure of IF nanoparticles remains a most challenging task for years to come.

## PROPERTIES

Early theoretical work was concerned with BN,  $BC_2N$ , and  $BC_3$  nanotubes.<sup>[35]</sup> More recently, nanotubes of other compounds, such as phosphorous,<sup>[30]</sup>  $GaSe$ ,<sup>[36]</sup>  $WS_2$ ,<sup>[37]</sup>  $MoS_2$ ,<sup>[34]</sup> and others, were studied. It follows that nanotubes of semiconducting compounds remain so also after folding. However, the bandgap was found to shrink with decreasing diameter of the nanotubes. Therefore, the bandgap of semiconducting nanotubes can be tuned all the way from the UV spectrum (ca. 3 eV) down to the infrared (ca. 0.2 eV) by varying the diameter of the nanotubes. This behavior stands in sharp contrast with the generic behavior of semiconductor quantum dots, where the bandgap expands with decreasing diameter of the nanoparticles because of the quantum size effect.

This opposite shift was experimentally confirmed by measuring the absorption spectrum of IF  $MoS_2$  and IF  $WS_2$  of different sizes and numbers of shells.<sup>[38]</sup> More recently, however,  $I$ - $V$  curves for single  $WS_2$  nanotube was recorded using scanning tunneling microscopy, and consequently the bandgap of the nanotubes could be determined.<sup>[39]</sup> Fig. 4 shows variation of the normalized bandgap as a function of the nanotube diameter as determined in this study. As expected, shrinkage of the energy gap with the nanotube diameter was observed. This observation was confirmed

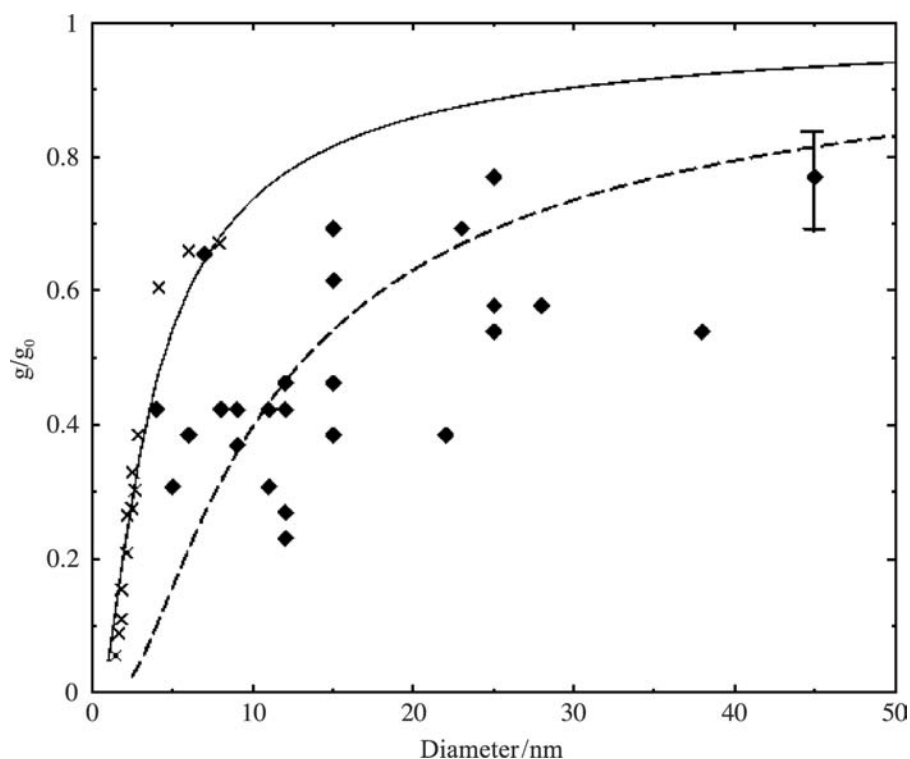


**Fig. 4** Comparison between theoretically calculated and STM measured normalized bandgap ( $g/g_0$ ) of  $WS_2$  nanotubes with varying diameters.  $g_0$  is the energy gap of the bulk materials (1.2 eV). Notwithstanding the scattering in the experimental data, the dependence of the bandgap on the nanotube diameter is clearly demonstrated. *Source:* From Ref.<sup>[33]</sup>.

by first-principle theoretical calculations.<sup>[39]</sup> The same theory shows<sup>[34,37]</sup> that armchair nanotubes possess an indirect bandgap for the lowest electronic transition, whereas zigzag nanotubes exhibit a direct transition. This surprising observation suggests that zigzag  $WS_2$  ( $MoS_2$ ) nanotubes could show strong optical absorption and luminescence, or even stimulated emission (laser action). First-principle theory also shows that independent of their diameter and chirality,  $NbS_2$  nanotubes are metallic,<sup>[40]</sup> which suggests that they will be very good field emitters. Indeed, the superconducting behavior of  $NbS_2$  and  $NbSe_2$  nanotubes was recently confirmed.<sup>[17,41]</sup>

## APPLICATIONS

2H- $MoS_2$  (2H- $WS_2$ ) are used as additives to heavy-duty tribological fluids, as tribological coatings, or as lubricating powders in ultra-high-vacuum instrumentation. The spherical shape of the fullerene-like  $WS_2$  nanoparticles and their inert sulfur-terminated surfaces offer enhanced tribological behavior for solid lubricant nanoparticles of this kind. The usefulness of IF powder as a superior solid lubricant has been worked out through a long series of experiments in the laboratory of Rapoport.<sup>[42]</sup> Further experiments show that IF  $WS_2$  and IF  $MoS_2$  powders exhibit superior tribological applications in different modalities,<sup>[43,44]</sup> suggesting almost countless number of possible applications. Fig. 5 shows the results of a

tribological test in which bronze-graphite partly prepared by powder metallurgy and impregnated with 5% IF  $WS_2$  outperforms the non-impregnated part. This work has stimulated substantial commercial interest recently.

Recently, substantial interest has been paid to metal and hydrogen intercalation in inorganic nanotubes of various kinds. Thus, Li intercalation and deintercalation in  $V_2O_5$  and  $Mn_xV_2O_{5+x}$  nanotubes were studied. Potassium and sodium intercalation in  $MoS_2$  ( $WS_2$ ) fullerene-like nanoparticles was also investigated. Reversible hydrogen<sup>[45]</sup> and lithium<sup>[46]</sup> intercalation in  $MoS_2$  nanotubes was demonstrated. The charge/discharge cycles were found to be reversible and relatively facile, which can be attributed to the high surface area and the open tips of the nanotubes. The reversibility of these systems can be attributed to the perfect crystallinity of the nanotubes, allowing one to accomplish numerous charge/discharge cycles of the rechargeable electrode without losing its loading capacity. Catalytic conversion of  $CO+H_2$  into methane and water using  $MoS_2$  nanotubes as catalyst was recently demonstrated.<sup>[47]</sup> The mechanism of the catalytic action of the nanotubes is quite a puzzle, because the fully bonded sulfur atoms in the van der Waals surfaces and in the galleries between the  $MoS_2$  layers (van der Waals gap) of the nanotubes are not expected to be chemically very reactive. This surprising result is nevertheless promising to incite a new research effort into the catalytic properties of inorganic nanotubes.

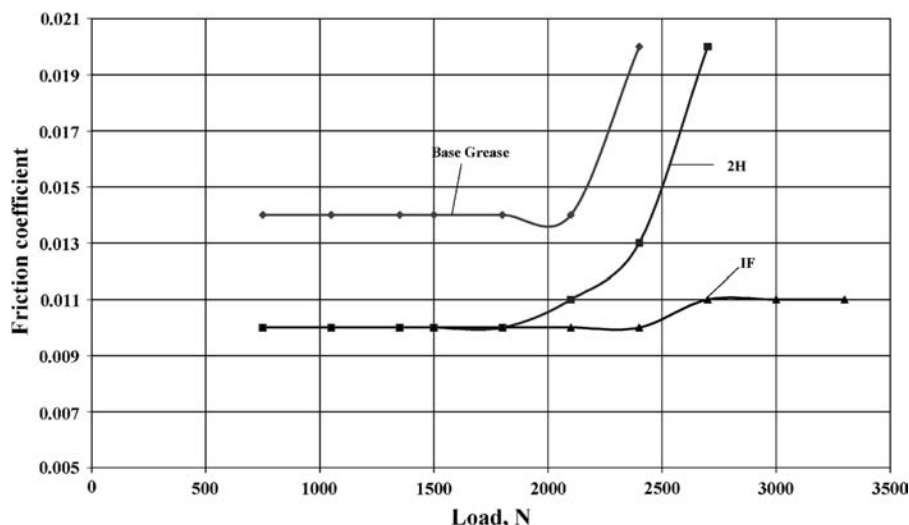


**Fig. 5** Friction coefficient as a function of load (in newtons) for a heavy-duty grease. 2H is the curve for a grease mixed with 2H-MoS<sub>2</sub> platelets, while IF is the curve for the same grease mixed with 5% fullerene-like WS<sub>2</sub> nanoparticles.

## CONCLUSION

The advent of nanotubes and fullerene-like particles from inorganic layered compounds has opened new avenues in the solid-state chemistry of inorganic compounds and new opportunities for application of such nanostructures in the emerging field of nanotechnology as well as in numerous other areas. Fundamental questions remain to be solved to permit a more judicious approach to the synthesis and study of the properties of these new nanophase materials. The elucidation of the detailed structure of IF nanoparticles, which is a most demanding and important issue in this field, is progressing by combining theory and experiment.

## ACKNOWLEDGMENTS

I am grateful to Dr. Y. Feldman, Dr. A. Zak, A. Margolin, Dr. R. Rosentsveig, Dr. Y. Rosenfeld Hacothen, and Dr. R. Popovitz-Biro, all from the Weizmann Institute of Science; Prof. L. Rapoport (Holon Academic Institute of Technology); and Prof. G. Seifert (TU Dresden). Support of the Israeli Ministry of Science (Tashtiot), Israeli Academy of Sciences (First), the Israel Science Foundation, and Minerva Foundation (Munich) are greatly acknowledged.

## REFERENCES

- Kroto, H.W.; Heath, J.R.; O'Brein, S.C.; Curl, R.F.; Smalley, R.E. C<sub>60</sub>: buckminsterfullerene. *Nature* **1985**, *318*, 162–163.
- Iijima, S. Helical microtubules of graphitic carbon. *Nature* **1991**, *354*, 56–58.
- Tenne, R.; Margulis, L.; Genut, M.; Hodes, G. Polyhedral and cylindrical structures of WS<sub>2</sub>. *Nature* **1992**, *360*, 444–445.
- Margulis, L.; Salitra, G.; Tenne, R.; Talianker, M. Nested fullerene-like structures. *Nature* **1993**, *365*, 113–114.
- Srolovitz, D.J.; Safran, S.A.; Homyonfer, M.; Tenne, R. Relaxed curvature elasticity and morphology of nested fullerenes. *Phys. Rev. Lett.* **1995**, *74*, 1779–1782.
- Satishkumar, B.C.; Govindaraj, A.; Vogl, E.M.; Baumallick, L.; Rao, C.N.R. Oxide nanotubes prepared using carbon nanotubes as templates. *J. Mater. Res.* **1997**, *12*, 604–606.
- Rosenfeld Hacothen, Y.; Grunbaum, E.; Tenne, R.; Sloan, J.; Hutchison, J.L. Cage structures and nanotubes of NiCl<sub>2</sub>. *Nature* **1998**, *395*, 336.
- Feldman, Y.; Frey, G.L.; Homyonfer, M.; Lyakhovitskaya, V.; Margulis, L.; Cohen, H.; Hodes, G.; Hutchison, J.L.; Tenne, R. Bulk synthesis of inorganic fullerene-like MS<sub>2</sub> (M = Mo, W) from the respective trioxides and the reaction mechanism. *J. Am. Chem. Soc.* **1996**, *118*, 5362–5367.
- Feldman, Y.; Zak, A.; Popovitz-Biro, R.; Tenne, R. New reactor for production of tungsten disulfide onion-like (inorganic fullerene-like) nanoparticles. *Solid State Sci.* **2000**, *2*, 663–672.
- Feldman, Y.; Wasserman, E.; Srolovitz, D.J.; Tenne, R. Nested inorganic fullerenes and nanotubes. *Science* **1995**, *267*, 222–225.
- Chopra, N.G.; Luyken, J.; Cherry, K.; Crespi, V.H.; Cohen, M.L.; Louie, S.G.; Zettl, A. Boron-nitride nanotubes. *Science* **1995**, *269*, 966–967.
- Rosentsveig, R.; Margolin, A.; Feldman, Y.; Popovitz-Biro, R.; Tenne, R. WS<sub>2</sub> nanotube bundles and foils. *Chem. Mater.* **2002**, *14*, 471–473.
- Zhu, Y.Q.; Hsu, W.K.; Grobert, N.; Chang, B.H.; Terrones, M.; Terrones, H.; Kroto, H.W.; Walton, D.R.M. Production of WS<sub>2</sub> nanotubes. *Chem. Mater.* **2000**, *12*, 1190–1194.
- Remskar, M.; Skraba, Z.; Regula, M.; Ballif, C.; Sanjinés, R.; Lévy, F. New crystal structures of

- WS<sub>2</sub>: microtubes, ribbons and ropes. *Adv. Mater.* **1998**, *10*, 246–249.
15. Remskar, M.; Mrzel, A.; Skraba, Z.; Jesih, A.; Ceh, M.; Demsar, J.; Stadelmann, P.; Lévy, F.; Mihailovic, D. Self-assembly of subnanometer-diameter single-wall MoS<sub>2</sub> nanotubes. *Science* **2001**, *292*, 479–481.
  16. Nath, M.; Rao, C.N.R. New metal disulfide nanotubes. *J. Am. Chem. Soc.* **2001**, *123*, 4841–4842.
  17. Nath, M.; Rao, C.N.R. Inorganic nanotubes. *Dalton Trans.* **2003**, *1*, 1–25.
  18. Cumings, J.; Zettl, A. Mass-production of boron nitride double-wall nanotubes and nanococoons. *Chem. Phys. Lett.* **2000**, *316*, 211–216. See also erratum in *Chem. Phys. Lett.* **2000**, *318*, 497.
  19. Spahr, M.E.; Bitterli, P.; Nesper, R. Redox-active nanotubes of vanadium oxide. *Angew. Chem., Int. Ed. Engl.* **1998**, *37*, 1263–1265.
  20. Saupe, G.B.; Waraksa, C.C.; Kim, H.-N.; Han, Y.J.; Kaschak, D.M.; Skinner, D.M.; Mallouk, T.E. Nano-scale tubules formed by exfoliation of potassium hexaneobate. *Chem. Mater.* **2000**, *12*, 1556–1562.
  21. Du, G.H.; Chen, Q.; Che, R.C.; Yuan, Z.Y.; Peng, L.-M. Preparation and structure analysis of titanium oxide nanotubes. *Appl. Phys. Lett.* **2001**, *79*, 3702–3704.
  22. Li, Y.; Wang, J.; Deng, Z.; Wu, Y.; Sun, X.; Yu, D.; Yang, P. Bismuth nanotubes: a rational low temperature synthetic route. *J. Am. Chem. Soc.* **2001**, *123*, 9904–9905.
  23. Mo, M.; Zeng, J.; Liu, X.; Yu, W.; Zhang, S.; Qian, Y. Controlled hydrothermal synthesis of thin single-crystal tellurium nanobelts and nanotubes. *Adv. Mater.* **2002**, *14*, 1658–1662.
  24. Hollingsworth, J.A.; Poojary, D.M.; Clearfield, A.; Buhro, W.E. Catalyzed growth of a metastable InS crystal structure as colloidal crystals. *J. Am. Chem. Soc.* **2000**, *122*, 3562–3563.
  25. Parilla, P.A.; Dillon, A.C.; Jones, K.M.; Riker, G.; Schulz, D.L.; Ginley, D.S.; Heben, M.J. The first inorganic fullerenes? *Nature* **1999**, *397*, 114.
  26. Sano, N.; Wang, H.; Chhowalla, M.; Alexandrou, I.; Amaratunga, G.A.J.; Naito, M.; Kanki, T. Fabrication of inorganic molybdenum disulfide fullerenes by arc in water. *Chem. Phys. Lett.* **2003**, *368*, 331–337.
  27. Jensen, F.; Toftlund, H. Structure and stability of C<sub>24</sub> and B<sub>12</sub>N<sub>12</sub> isomers. *Chem. Phys. Lett.* **1993**, *201*, 95–98.
  28. Stéphan, O.; Bando, Y.; Loiseau, A.; Willaime, F.; Shramchenko, N.; Tamiya, T.; Sato, T. Formation of small single-layer nested BN cages under electron irradiation of nanotubes and bulk materials. *Appl. Phys., A* **1998**, *67*, 107–111.
  29. Terrones, M.; Hsu, W.K.; Terrones, H.; Zhang, J.P.; Ramos, S.; Hare, J.P.; Castillo, R.; Prassides, K.; Cheetham, A.K.; Kroto, H.W.; Walton, D.R.M. Metal particle catalyzed production of nanoscale BN structures. *Chem. Phys. Lett.* **1996**, *259*, 568–573.
  30. Hernandez, G.; Seifert, G. Theoretical prediction of phosphorous nanotubes. *Chem. Phys. Lett.* **2000**, *318*, 355–360.
  31. Seifert, G.; Heine, T.; Fowler, P.W. Inorganic nanotubes and fullerenes. *Eur. Phys. J., D* **2001**, *16*, 341–343.
  32. Hacoheh, Y.R.; Popovitz-Biro, R.; Prior, Y.; Gemming, S.; Seifert, G.; Tenne, R. Synthesis of NiCl<sub>2</sub> nanotubes and fullerene-like structures by laser ablation. *Phys. Chem. Chem. Phys.* **2003**, *5*, 1644–1651.
  33. Popovitz-Biro, R.; Twersky, A.; Rosenfeld Hacoheh, Y.; Tenne, R. Nanoparticles of CdCl<sub>2</sub> with closed cage structure. *Isr. J. Chem.* **2001**, *41*, 7–14.
  34. Seifert, G.; Terrones, H.; Terrones, M.; Jungnickel, G.; Frauenheim, T. Structure and electronic properties of MoS<sub>2</sub> nanotubes. *Phys. Rev. Lett.* **2000**, *85*, 146–149.
  35. Rubio, A.; Corkill, J.L.; Cohen, M.L. Theory of graphitic boron nitride nanotubes. *Phys. Rev., B* **1994**, *49*, 5081–5084.
  36. Cote, M.; Cohen, M.L.; Chadi, D.J. Theoretical study of the structural and electronic properties of GaSe nanotubes. *Phys. Rev., B* **1998**, *58*, R4277–R4280.
  37. Seifert, G.; Terrones, H.; Terrones, M.; Jungnickel, G.; Frauenheim, T. On the electronic structure of WS<sub>2</sub> nanotubes. *Solid State Commun.* **2000**, *115*, 245–248.
  38. Frey, G.L.; Elani, S.; Homyonfer, M.; Feldman, Y.; Tenne, R. Optical absorption spectra of inorganic fullerene-like MS<sub>2</sub> (M = Mo, W). *Phys. Rev., B* **1998**, *57*, 6666–6671.
  39. Scheffer, L.; Rosentsveig, R.; Margolin, A.; Popovitz-Biro, R.; Seifert, G.; Cohen, S.R.; Tenne, T. Scanning tunneling microscopy study of WS<sub>2</sub> nanotubes. *Chem. Phys. Phys. Chem.* **2002**, *4*, 2095–2098.
  40. Seifert, G.; Terrones, H.; Terrones, M.; Frauenheim, T. Novel NbS<sub>2</sub> metallic nanotubes. *Solid State Commun.* **2000**, *115*, 635–638.
  41. Nath, M.; Kar, S.; Raychaudhuri, A.K.; Rao, C.N.R. Superconducting NbSe<sub>2</sub> nanostructures. *Chem. Phys. Lett.* **2003**, *368*, 690–695.
  42. Rapoport, L.; Bilik, Yu.; Feldman, Y.; Homyonfer, M.; Cohen, S.R.; Tenne, R. Hollow nanoparticles of WS<sub>2</sub> as potential solid-state lubricants. *Nature* **1997**, *387*, 791–793.
  43. Chhowalla, M.; Amaratunga, G.A.J. Thin films of MoS<sub>2</sub> fullerene-like nanoparticles with ultra-low friction and wear. *Nature* **2000**, *407*, 164–167.
  44. Rapoport, L.; Lvovsky, M.; Lapsker, I.; Leshchinsky, V.; Volovik, Yu.; Feldman, Y.; Margolin, A.; Rosentsveig, R.; Tenne, R. Slow release of fullerene-like WS<sub>2</sub> nanoparticles from Fe–Ni–graphite matrix: a self-lubricating nanocomposite. *Nano Lett.* **2001**, *1*, 137–140.
  45. Chen, J.; Kuriyama, N.; Yuan, H.; Takeshita, H.T.; Sakai, T. Electrochemical hydrogen storage in MoS<sub>2</sub> nanotubes. *J. Am. Chem. Soc.* **2001**, *123*, 11,813–11,814.
  46. Dominko, R.; Arcon, D.; Mrzel, A.; Zorko, A.; Cevc, P.; Venturini, P.; Gaberscek, M.; Remskar, M.; Mihailovic, D. Dichalcogenide nanotube electrodes for Li-ion batteries. *Adv. Mater.* **2002**, *14*, 1531–1534.
  47. Chen, J.; Li, S.-L.; Xu, Q.; Tanaka, K. Synthesis of open-ended MoS<sub>2</sub> nanotubes and the application as the catalyst for methanation. *Chem. Commun.* **2002**, 1722–1723.

# Inorganic Nanotubes: Synthesis by Chemical Transport Reaction

Maja Remskar

Jozef Stefan Institute, Ljubljana, Slovenia

## INTRODUCTION

Nanotubes of transition metal dichalcogenides have raised much scientific attention since the first report on the synthesis and structure of MoS<sub>2</sub> and WS<sub>2</sub> nanotubes in 1992.<sup>[1]</sup> The two most efficient methods producing tenths of grams of nanotubes consist in annealing the oxidized transition metal films or particles in a stream of H<sub>2</sub>S gas<sup>[2]</sup> or in thermal decomposition of (NH<sub>4</sub>)<sub>2</sub>MoS<sub>4</sub> or MoS<sub>3</sub> in hydrogen.<sup>[3]</sup> Other growth techniques with lower efficiencies make use of electron beam irradiation in transmission electron microscope<sup>[4]</sup> and in scanning tunneling microscope,<sup>[5]</sup> sonoelectrochemical bath reaction,<sup>[6]</sup> and electrochemical deposition from ethylene glycol solution.<sup>[7]</sup>

The nanotubes of other transition metal dichalcogenides (NbS<sub>2</sub>, TaS<sub>2</sub>) have been recently synthesized. The reduction of NbS<sub>3</sub> and TaS<sub>3</sub> powder in a stream of H<sub>2</sub> at 1000°C for 30–60 min led to the growth of thick-walled NbS<sub>2</sub> and TaS<sub>2</sub> nanotubes with inside diameters ranging from 4 to 15 nm.<sup>[8]</sup> The silver alloyed NbS<sub>2</sub> nanotubes have been grown by partial decomposition of the Ag-(NbS<sub>4</sub>)<sub>x</sub>I ( $x \approx 4$ ) precursor crystals using electron beam irradiation or microwave irradiation. They represent the first case of nanotubes grown by self-assembly of nanocrystallites.<sup>[9]</sup>

The MoS<sub>2</sub> and WS<sub>2</sub> nanotubes were also synthesized by the chemical transport reaction, which is the standard method for the growth of transition metal dichalcogenide-layered crystals.<sup>[10]</sup> In the present report, the overview of growth mechanisms, their structural properties, and self-assembly at different range scales are presented. Besides pure MoS<sub>2</sub> and WS<sub>2</sub> nanotubes, the alloyed nanotubes with silver and gold are shown, evidencing the geometrical stabilization of new compounds, which are not known in the usual plane geometry. The subnanometer-diameter MoS<sub>2-x</sub> nanotubes, which self-organize to the first case of molecular crystals composed of inorganic nanotubes, represent the extreme case of inorganic nanotubes. Because of their metallic

conductivity, we can rank them to the promising family of molecular wires.

## THE MoS<sub>2</sub> AND WS<sub>2</sub> MULTIWALL NANOTUBES

The chemical transport method enables growth of inorganic nanotubes with very slow rate from the vapor phase. The transport agent, iodine in our case, reacts with the transition metal at high temperature, forming the volatile product that decomposes at lower temperature, where transition metal reacts again with sulfur to solid transition metal disulfide. The silica ampoules containing MoS<sub>2</sub> or WS<sub>2</sub> powder and iodine in amount of 5 mg/cm<sup>3</sup> were evacuated and sealed at a pressure of 10<sup>-5</sup> Pa. The transport reaction using iodine as a transport agent ran at 1060 K with a temperature gradient of 5.6 K/cm in two-zone furnace. After 3 weeks of growth, the silica ampoules were slowly cooled to room temperature with a controlled cooling rate of 15°C/hr. Approximately a few percent of the starting material was transported by the reaction to form nanotubes, while the rest of the transported material grows as strongly undulated thin plate-like crystals. The lasting nearly equilibrium growth conditions enable the synthesis of nanotubes of different diameters, length, and wall thickness, but with extremely low density of structural defects. They grow up to several millimeters in length. The diameters in multiwall nanotubes range from several micrometers to less than 10 nm. While microtubes usually grow as single tubes, the nanotubes frequently combine ropes formed by self-assembly and syntactic coalescence of primary nanotubes (Fig. 1).

## Crystal Structure of MoS<sub>2</sub> and WS<sub>2</sub> Plate-Like Crystals

MoS<sub>2</sub> and WS<sub>2</sub> compounds belong to Group VI family of transition metal dichalcogenides.<sup>[11]</sup> They are

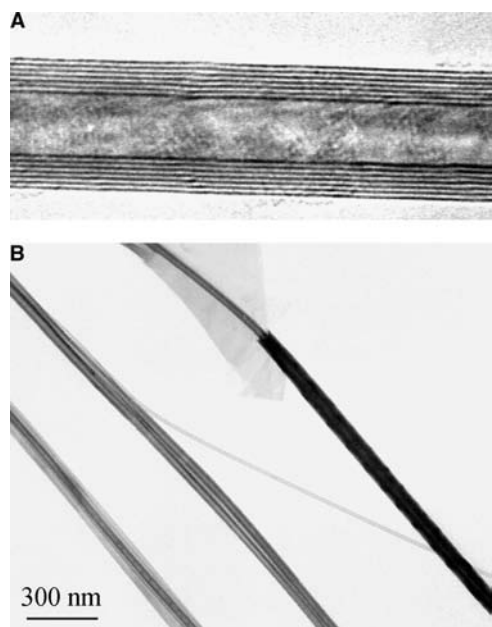


**Fig. 1** (A) The high-resolution electron micrograph of a  $\text{MoS}_2$  nanotube, 15 nm in diameter, reveals the tube walls built of seven molecular layers. The distance between the layers is expanded by 3% with respect to the corresponding parameter of the plate-like crystal. (B) A  $\text{WS}_2$  single nanotube, 12 nm in diameter, and ropes grown in coaxial or side-by-side type of self-assembly.

extremely unisotropic solids with layer-type structure. The interaction holding the layers is in great part of van der Waals (VdW) type. The molecular layer S–Mo–S or S–W–S shows a trigonal symmetry. The transition metal atom is coordinated by six sulfur atoms situated at corners of a trigonal prism.

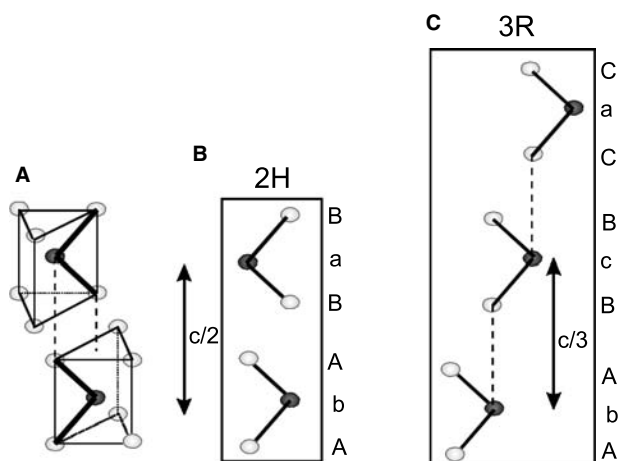


**Fig. 2** Two possible stacking of adjacent  $\text{MoS}_2$  and  $\text{WS}_2$  molecular layers: (A) three-dimensional model of the stable 2Hb stacking; (B and C) the  $[11\bar{2}0]$  sections of 2H and 3R stacking, respectively.

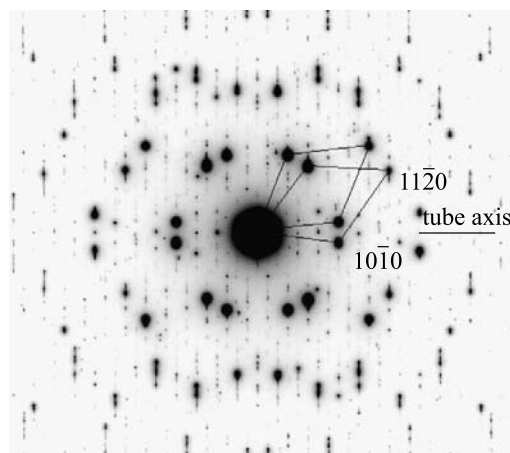


**Fig. 3** Electron diffraction pattern of  $\text{MoS}_2$  nanotube as a superposition of electron scattered by both nanotube walls revealing the chiral growth mode.

The molecular layers can be stacked in two ways (Fig. 2), as a hexagonal polytype 2Hb with two molecular layers (P63/mmc) and as rhombohedral polytype 3R with three molecular layers per unit cell (R3m). Filled  $d_{z^2}$  orbitals promoting to the space between the molecular layers prevent a stacking of molecular layers in such a manner that the positions of transition metal atoms would be one above the other perpendicular to the layers.

$\text{MoS}_2$  and  $\text{WS}_2$  plate-like crystals usually grow in the hexagonal 2H polytype, while the rhombohedral 3R polytype is metastable at room conditions. It was found that the 3R polytype of  $\text{MoS}_2$  is stable—it grows above  $1000^\circ\text{C}$  and at high pressures (40 kbar), but it transforms back to the 2H polytype when the pressure is decreased.<sup>[11]</sup> Lattice parameters of 3R polytypes, with respect to the 2H polytype, are slightly larger in basal plane (1% for  $\text{MoS}_2$  and 2% for  $\text{WS}_2$ ), while perpendicular to the layers, the c-parameters are shortened for  $\approx 0.2\%$  in both compounds<sup>[11]</sup> (Fig. 3).

### Nucleation and Lattice Structure of $\text{MoS}_2$ and $\text{WS}_2$ Microtubes and Nanotubes

The  $\text{MoS}_2$  and  $\text{WS}_2$  tubes grow by helical winding of molecular layers with the basal plane perpendicular

**Table 1** Unit cell parameters of  $\text{MoS}_2$  and  $\text{WS}_2$  plate-like crystals

Unit cell	2Hb- $\text{MoS}_2$	3R- $\text{MoS}_2$	2Hb- $\text{WS}_2$	3R- $\text{WS}_2$
a [nm]	0.316	0.3164	0.3154	0.3162
c [nm]	1.229	1.839	1.2362	1.85

Source: From Ref.<sup>[11]</sup>.



to the tube cross section. They typically exhibit the relative ratio of expansion of the distance between molecular layers of 1–3% with respect to plate-like crystals (Table 1). Nonalloyed tubes are always found in the helical forms.<sup>[10,12–14]</sup> They grow by a single molecular layer, which continuously winds around the tube. Projection of a tube axis onto the basal [0001] plane of the wall is rotated with respect to the  $\langle 10\bar{1}0 \rangle$  lattice directions for an angle of chirality  $\alpha$ .

Two growth mechanisms have been observed.<sup>[10]</sup> Thin folded flakes can directly roll up and adopt the cylindrical shape. The folds of strongly undulated layered crystals at a microlevel size can also serve as an origin of turbulent gas flow of transported molecules, which promotes a tube-like growth mode. Instability of weakly bonded molecular layers at plate-like crystal edges and at surface growth steps against bending causes the growth of very narrow nanotubes (Fig. 4). The nanotube nucleation stops the growth of the crystal flake in the basal plane.

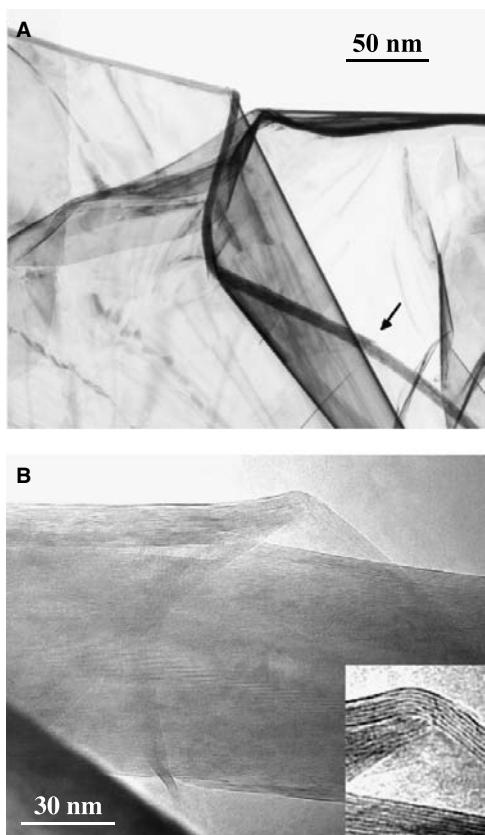


**Fig. 4** (A) The nucleation of the nanotube at the layered-crystal edge. The area of extrication of the multiwall nanotube, 78 nm in diameter, from the nucleation envelope is marked by arrow. (B) The bonds between the top tube layers and the envelope are broken deeply to the inside of the nucleation channel. The envelope wall is composed of seven molecular layers.

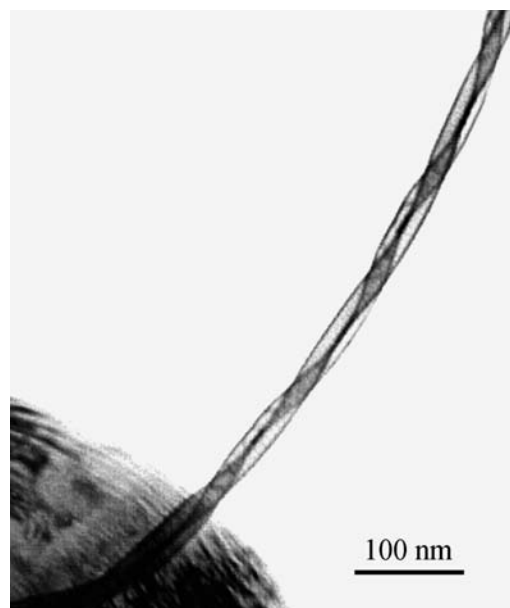


**Fig. 5** The  $\text{WS}_2$  nanorope composed of two mutually rolled-up nanotubes with diameters of 15 nm and a spiral period of 110 nm. The pair of nanotubes nucleated at the inner surface step of the nanotube, 1.2  $\mu\text{m}$  in diameter.

The nanotube extricates from the nucleation envelope at the crystal edge and continues to grow. The area of extrication of the multiwall nanotube, 78 nm in diameter, from the nucleation envelope is marked by arrow. The bonds between the top tube layers and the envelope are deeply broken to the inside of the nucleation channel. The envelope wall is composed of seven molecular layers.<sup>[15]</sup>

Several tubes can nucleate by such a way at the same crystal edge, where they combine and continue in growth like a rope. The nanotube in a rope still grows in longitudinal direction, up to a few millimeters in length, while its radius is limited by cogrown nanotubes. The second kind of the nanotube nucleation sites are the helical extremities of external and inner spirally rolled-up molecular layer building the already growing tube.<sup>[14]</sup> They are subject of bending like surface steps or edges of flat crystals. The nanotubes in so created ropes are usually rolled around or inside the central tube. They present a special case of growth by syntactic coalescence, where the wound tubes follow the crystal structure of the supporting tube. In a case where several nanotubes nucleate at the same inner extremity, they are mutually rolled up (Fig. 5).<sup>[13]</sup>

### Explanation of the Instability of Thin Crystal Flakes against Bending

The cause of the folding of thin crystal flakes or inner or outer helical extremities of supporting nanotubes is

ABCABCABCABCABCABCABCABC

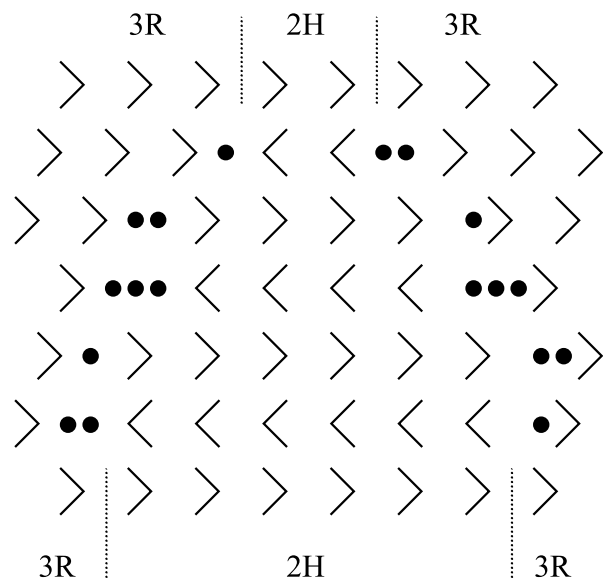


**Fig. 6** Schematically presented transition between 3R (AbA BcB CaC) and 2Hb (AcA CaC) stacking shown in the [1120] section. *Source:* From Ref.<sup>[14]</sup>.

still not known. The atomic force microscopy of the top surface of a MoS<sub>2</sub> microtube revealed superstructures that are explained as nucleation stages of rhombohedral and hexagonal stacking.<sup>[16]</sup> The subsequent nucleation of both polytypes is associated by an appearance of grain boundaries. The mismatch between both polytypes results in creation of vacancies (Fig. 6).<sup>[14]</sup> Their non-symmetrical distribution at 3R–2Hb transitions induces shearing stresses along the basal planes. The bending with shrinkage/extension effects decreases the stress caused by lattice mismatch. The perpendicular component of the strain

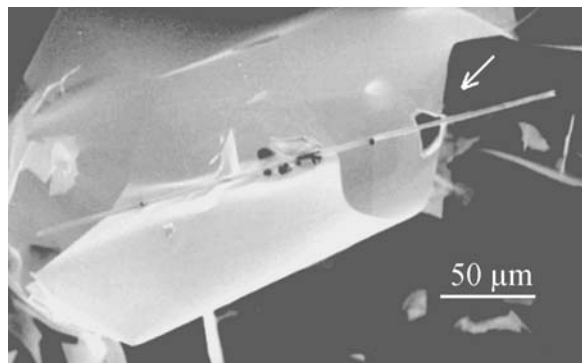


**Fig. 7** The nucleation of nanotube in microfold of undulated layered crystal.<sup>[10]</sup> The arrow marks a perforation of crystal flake caused by preferential growth of nanotube with respect to the layered crystal.

tensor is caused by slightly different unit cell parameters of both polytypes (Table 1).

When the tube nucleates, the cylindrical growth mode is dominant with respect to the plate-like geometry. For example, the 3.3- $\mu\text{m}$ -diameter tube shown in Fig. 7 nucleated in microfold of thin, undulated layered crystal. At the point where the tube was in contact with the crystal flake (marked by arrow), the perforation of the flake appeared. The tube has obviously grown on account of already grown layered crystal. This kind of recrystallization contributes to the very rigid growth mode of nanotubes. When an obstacle in the form of a plate-like crystal is met during growth, the perforation of crystal flakes, as a result of recrystallization, enables the straightforward growth of the tubes.

### Stacking-Order Dependence on a Tube Diameter

It was found that the variety of polytypic stackings does not only influence the instability of thin crystal flakes against bending, but also controls the diameter of nanotubes and wall thickness. Both known polytypes (2H and 3R) simultaneously nucleate on the surface of a nanotube, but one of them prevails during the process of growth. Besides the strain caused by different stacking, an enlarged circumference and bending of molecular layers increase the elastic energy by extension and/or contraction of the layers. Considering the transition metal layer as a reference layer without deformations due to bending, the external sulfur layer of the corresponding molecular layer is stretched, whereas the internal sulfur layer, which is closer to the tube axis, is compressed. The sum of elastic energy per primitive cell caused by enlarged circumference and

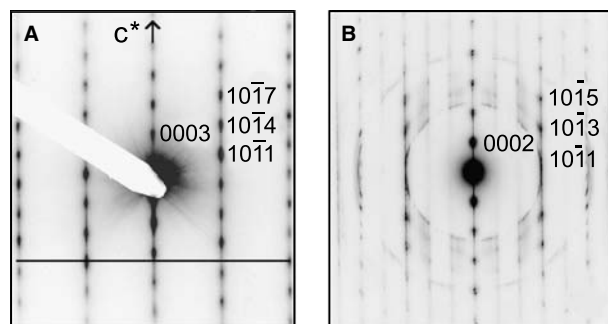


**Fig. 8** Transmission electron diffraction patterns taken at the tube edge presenting the [010] zones of a tube.<sup>[16]</sup> (A) 3.5  $\mu\text{m}$  in diameter; the position of side spots of (101 $l$ ) type reveal the rhombohedral 3R stacking in accordance with the rule  $(-h + k + l = 3n)$ ; (B) 190 nm in diameter; the side spots (101 $l$ ) satisfy the rule  $l = \pm(2n + 1)$ .

by bending is relatively larger in nanotubes than in microtubes, where the elastic energy is distributed over a larger number of atoms.

Actually, we have found that the stacking between molecular layers composing the walls of nanotubes with diameters up to 200 nm is different than in those tubes with diameters above few micrometers (Fig. 8).<sup>[16]</sup> The selected area diffraction on the microtube wall revealing the rhombohedral (3R) stacking, otherwise stable at elevated pressure,<sup>[11]</sup> indirectly evidences the presence of the strain incorporated into the microtube wall. The intensity of incorporated strain increase toward the tube axis, causing the contraction of interlayer distance and an instability of inner molecular layers at place where the incorporated strain is relaxed with the creation of edge dislocations or stacking faults. In nanotubes with diameters below 200 nm, the strain is relaxed, stabilizing the hexagonal (2H) stacking.

### The Dependence of Nanotube Chirality on Interlayer Distances

The contraction of interlayer distances caused by internal strain incorporated in the tube wall influences the chirality of the nanotubes. Each winding of the molecular layer of thickness  $t$ , i.e., 0.6147 nm for MoS<sub>2</sub>,<sup>[11]</sup> enlarges the tube circumference for  $\pi t$ . Because this value is not an integer multiple of lattice parameter  $a$  in the basal plane (0.316 nm), the molecular layers have to be strained and/or helical, assuming that a regular crystal lattice is formed at least in narrow strips parallel with the nanotube axis. Increasing strain intensity toward the nanotube central hole

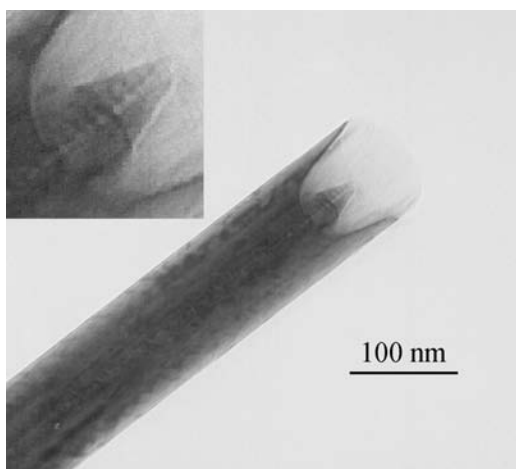


**Fig. 9** The WS<sub>2</sub> nanotube, 76 nm in diameter, terminated in geometry of a steep crater with a small truncated cone (insert) in the central part of the tube.



**Fig. 10** The tip-shape termination of the WS<sub>2</sub> nanotube associated with the change of the chirality.

causes the coexistence of several chiralities in the same nanotube. In thick-walled nanotubes, the incorporated strain causes the reduction of the interlayer distances, in some tubes even below the value typical for plate-like crystals. In such a case, the nanotubes are stopped in longitudinal growth with the typical crater-cone terminations. For example, a thick-walled nanotube, 76 nm in diameter, terminated in geometry of a steep crater with a small truncated cone in the central part of the tube (Fig. 9). The diameter of the inner hole is less than 2 nm. At the top of the truncated cone, the hole is widened because the intensity of incorporated strain is reduced as a result of the decreasing number of rolled-up molecular layers (insert).

The abrupt change of chirality in a role of the strain relaxation can change the geometry of nanotubes and stops the longitudinal growth. For example, the WS<sub>2</sub> nanotube, 20 nm in diameter, terminates in a sharp tip shape (Fig. 10). The surface steps show the increasing of the chiral angle along the direction toward the tip termination of the nanotube. The wall thickness is decreased by 50% near the area of the transition from the cylindrical to the tip shape and by an additional 30% at the conical-shaped termination. The thickness of a nanotube wall dictates its chirality and vice versa, i.e., the chirality influences the wall thickness.

### NANOTUBES ALLOYED WITH SILVER AND GOLD

Change of the nanotube crystal structure is typical also for MoS<sub>2</sub> and WS<sub>2</sub> nanotubes alloyed with gold and silver, which are found mainly non-helical.<sup>[17,18]</sup> MoS<sub>2</sub> and WS<sub>2</sub> plate-like crystals are inert materials and only few intercalated compounds are known, mainly with alkali metals.<sup>[19]</sup> Phases composed of MoS<sub>2</sub> or WS<sub>2</sub> and noble metals have not been reported up to now in usual plane geometry. On the contrary, MoS<sub>2</sub> and WS<sub>2</sub> microtubes and nanotubes have been successfully alloyed with silver and gold. The typical tubular structure stabilizes the compounds, which are not stable in the plate-like geometry. The noble metals in proportion of 0.5 at.% were added to sulfur, molybdenum,

or tungsten for the synthesis of the starting material before the transport reaction. The transport reaction ran for 22 days at 1060 K in an evacuated silica ampoule at a pressure of  $10^{-2}$  Pa and with a temperature gradient of 5.6 K/cm.

The walls of the  $\text{MoS}_2$  and  $\text{WS}_2$  nanotubes alloyed with gold and silver are composed of molecular layers grown in the form of coaxial cylinders. Two orientation relationships of the crystal lattice with respect to the tube axis are possible: The projection of the lattice can be parallel with the  $[11\bar{2}0]$  direction (A type) or with the  $[10\bar{1}0]$  direction (B type).

The coaxial growth mode of the type A is inferred from electron diffraction patterns of Au- $\text{WS}_2$  tube, 0.1  $\mu\text{m}$  in diameter (Fig. 11). The diffraction diagram is a superposition of two specific patterns belonging to  $[001]$  and  $[010]$  zones. Electrons are scattered (1) by both tube walls with the basal planes perpendicular to the electron beam— $[001]$  zone; and (2) by the tube longitudinal edge with the basal planes parallel with the beam— $[010]$  zone. The  $(10\bar{1}0)^*$  direction, perpendicular to the  $c^*$  direction, is parallel with the tube axis. The side spots  $(10\bar{1}l)$  satisfy the rule  $l = \pm(2n + 1)$  that corresponds to the 2Hb polytype.

Both types of non-chiral growth mode (A type and B type) can coexist in the same nanotube. The diffraction diagram measured with the Au- $\text{MoS}_2$  tube (Fig. 12) is a superposition of two hexagonal patterns belonging to the  $[001]$  zone rotated by  $30^\circ$  with respect to each other. The tube axis, perpendicular to the direction of the spot elongation, is aligned along the  $[11\bar{2}0]$  direction of one of both possible orientations (A type and B type).

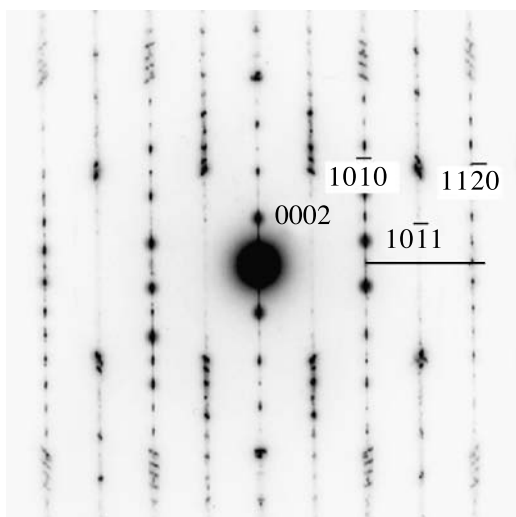


**Fig. 11** The transmission electron diffraction patterns of electrons scattered by both walls of the Au- $\text{WS}_2$  tube with the  $[11\bar{2}0]$  direction parallel with the tube axis revealing the suppression of the chirality. Source: From Ref.<sup>[17]</sup>.

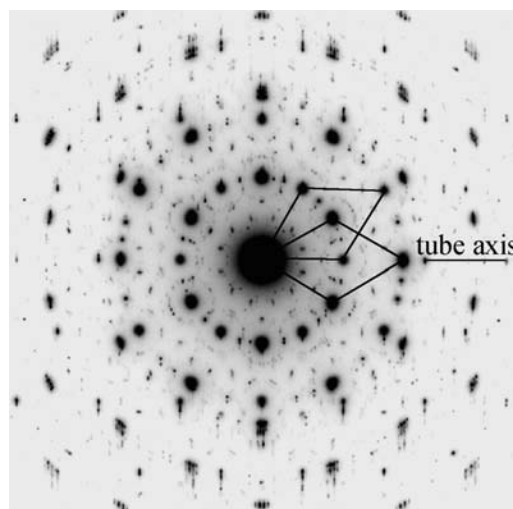


**Fig. 12** The transmission electron diffraction patterns of electrons scattered by both walls of the Au- $\text{MoS}_2$  tube as a superposition of two orientational variants with  $[11\bar{2}0]$  or  $10\bar{1}0$  direction parallel with the tube axis. Source: From Ref.<sup>[17]</sup>.

Two types of interlayer interstices exist in the 2Hb polytype, octahedral and tetrahedral ones. In the closed-packed stacking of spherical ions, the volume of octahedral and tetrahedral interstices is smaller than 0.02 and 0.005  $\text{nm}^3$ , respectively. Comparison between atomic or ionic radius of gold (0.146 nm, 0.137 nm) and

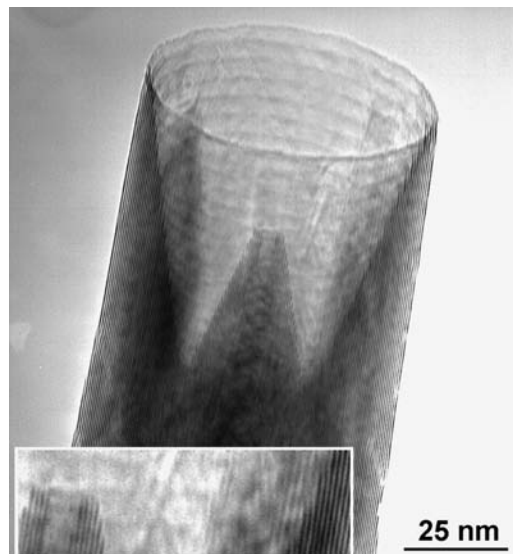


**Fig. 13** The crater-cone shape of typical extremity of the alloyed Au- $\text{WS}_2$  nanotube in the shape of a crater and a hollow truncated cone in the central part of the tube; double layer by double layer growth mode on the crater surface and layer by layer growth of the central cone of the tube (inset). The regular distribution of the circles reveals the abrupt termination in growth of double layers. Source: From Ref.<sup>[17]</sup>.

silver (0.144 nm, 0.126 nm) with the interstice sizes shows that the noble metal atoms can occupy octahedral sites only if no shear is present. Because of the size mismatch between the octahedral interstices and noble metal atoms or ions, the van der Waals gaps have to extend in any case.

The built-in noble metal species in the tube walls increase the interaction between molecular layers and cause a double layer by double layer growth mode. Consequently, the interlayer distances are expanded, causing the change in the tube morphology. The chirality is completely or partially suppressed. The tube walls are composed of molecular layers grown in the form of coaxial cylinders (Fig. 13).

The presence of chirality in non-alloyed tubes and its suppression in the MoS<sub>2</sub> and WS<sub>2</sub> nanotubes alloyed with gold and silver are geometrically explicable. A cross section of a chiral tube perpendicular to the tube axis shows a spiral shape with  $c_0$  spacing between adjacent turns of the spiral. The difference in length of adjacent turns of the spiral is the same as the difference in circumference of two adjacent coaxial cylinders, i.e.,  $2\pi c_0$ . The length of the curve between the spiral pole and the point of the  $n$ th turn ( $L_n$ ) of the spiral is in the approximation of large angles ( $\varphi = n2\pi$ ):  $L_n = [c_0/(2\pi)][n^2(2\pi)^2/2]$ , where  $c_0$  is the spacing between adjacent turns in the radial direction. The length of the  $n$ th turn, i.e.,  $c_0\pi(2n - 1)$ , differs by  $2\pi c_0$  from the length of the previous one. This difference has to be an integer multiple ( $N$ ) of the lattice parameter in a basal [0001] plane perpendicular to the tube axis. In tubes with the tube axis parallel to one [11 $\bar{2}$ 0] direction (A type), the difference in circumferences has to be an integer multiple of the parameter  $a$ , while in the tubes with the tube axis parallel to one [10 $\bar{1}$ 0] direction (B type), it has to be an

integer multiple of  $a\sqrt{3}/2$ . In chiral tubes, the tube axis is rotated with respect to the [10 $\bar{1}$ 0] direction for the chiral angle  $\alpha$ . The tube axis is close to one [10 $\bar{1}$ 0] direction (A\* type), if  $0^\circ < \alpha < 15^\circ$ , or to one [11 $\bar{2}$ 0] direction (B\* type) for  $\alpha > 15^\circ$ . Values of the multiple number  $N$  at different extensions of lattice parameter  $c_0$  are summarized in Table 2, assuming that the lattice parameters in the basal plane are not deformed, i.e.,  $a = 0.3154$  nm (WS<sub>2</sub>) and  $a = 0.316$  nm (MoS<sub>2</sub>).<sup>[11]</sup>

The 1–3% expansion ratios in non-alloyed tubes correspond to numbers  $N$  in the intervals 12.4–12.7 (A\* type) and 14.3–14.7 (B\* type). These values do not meet the requirement that  $N$  has to be an integer. The molecular layers in such a case cannot satisfy the stacking order with respect to the previous turn without a rotation with respect to the tube axis. This geometrical matching leads to the spiral growth mode. The chiral angle  $\alpha$  can be estimated from the simple geometrical equation:

$$\alpha = 30^\circ - \arccos\left(\frac{Na\sqrt{3}}{4\pi c_0}\right)$$

The typical values of the chiral angle  $7.1$ – $2.5^\circ$  ( $N = 13$ ) and  $22.7$ – $12.1^\circ$  ( $N = 14$ ) are calculated for 0–3% expansion ratios without considering the internal strain and defects incorporated into real tube walls.

Alloyed MoS<sub>2</sub> and WS<sub>2</sub> nanotubes do not show the self-assembly in any different morphology, i.e., among microtubes, nanotubes, or ribbons-collapsed tubes, in spite of the sizes similar to those of non-alloyed tubes. The absence of the assembly in alloyed tubes evidences that the self-assembly is influenced not only by the tube dimensions but also by its chemical and/or structural properties.

**Table 2** Values of the number  $N$  calculated for the hexagonal 2H<sub>b</sub> stacking of MoS<sub>2</sub> and WS<sub>2</sub> tubes

MoS <sub>2</sub>	Plate-like crystal 2H <sub>b</sub> <sup>[11]</sup>	Non-alloyed tubes		Alloyed tubes	
$a$	0.316 nm	MoS <sub>2</sub>	Au-MoS <sub>2</sub>	Ag-MoS <sub>2</sub>	
$c_0 = c/2$	0.6147 nm	0.621 nm–0.633 nm		0.652 nm	0.649 nm
Relative expansion of $c$		1%	3%	6%	5.5%
Number $N$ (A* and A types)		12.35	12.6	12.96	12.89
Number $N$ (B* and B types)		14.25	14.53	14.96	14.88
WS <sub>2</sub>	Plate-like crystal 2H <sub>b</sub> <sup>[13]</sup>	Non-alloyed tubes		Alloyed tubes	
$a$	0.3154 nm	WS <sub>2</sub>		Au-WS <sub>2</sub>	Ag-WS <sub>2</sub>
$c_0 = c/2$	0.6181 nm	0.624 nm–0.637 nm		0.655 nm	
Relative expansion of $c$		1%	3%	6%	5.5%
Number $N$ (A* and A types)		12.43	12.68	13.05	12.99
Number $N$ (B* and B types)		14.36	14.64	15.06	14.99



## SELF-ASSEMBLY OF SINGLE-WALLED $\text{MoS}_{2-x}$ NANOTUBES

The subnanometer-diameter  $\text{MoS}_{2-x}$  nanotubes were grown by a catalyzed transport method.<sup>[20]</sup> The crucial conceptual novelty in the synthesis procedure, compared to standard transport growth, is in the use of  $\text{C}_{60}$  as a growth promoter in the reaction. Thus  $\text{C}_{60}$  in proportion of 5 wt.% was added to  $\text{MoS}_2$  powder in the transport tube as a catalyst. The transport reaction was running typically for 22 days at 1010 K in an evacuated silica ampoule at a pressure of  $10^{-3}$  Pa with a temperature gradient of 6 K/cm. Iodine had been used as a transport agent. Approximately 15 wt.% of the source material was transported by the reaction to form nanotubes, with the rest remaining at the initial side in the form of layer crystals. The transported material was subsequently thoroughly washed with toluene to remove  $\text{C}_{60}$ .

The transported material grows in the form of thin furry foil composed of mutually oriented needles (Fig. 14), which are themselves bundles of  $\text{MoS}_2$  nanotubes. The bundles start to grow in “hedgehog”—needles from randomly distributed nuclei on the quartz surface. The color of the dense backside of the sample shows metallic luster while the front side is black because of the high porosity and strong light absorption. When adjacent structures touch, growth perpendicular to the quartz substrate appears to prevail. The bundles usually terminate in a sharp tip forming remarkably clean and sharp needles. Each bundle contains more than 500,000 ordered nanotubes. The secondary nucleation of the bundles on the rough top surface of the foil leads to the formation of microscopic geometrical shapes, such as spheres or rectangular forms.<sup>[20]</sup>

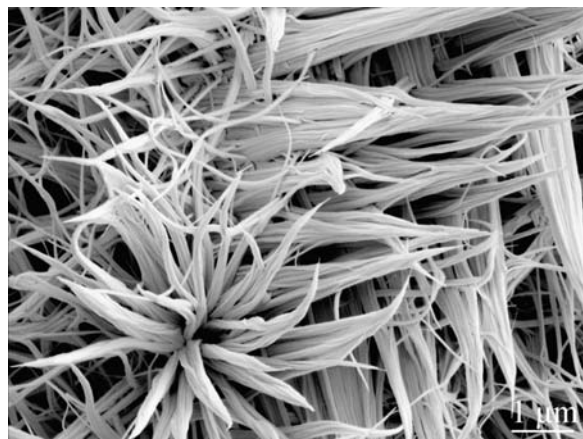


**Fig. 14** Self-arrangement of the  $\text{MoS}_{2-x}\text{I}_y$  bundles at different range scales. *Source:* Image taken by Dr. E. Klein, Weizmann Institute of Science, Rehovot.

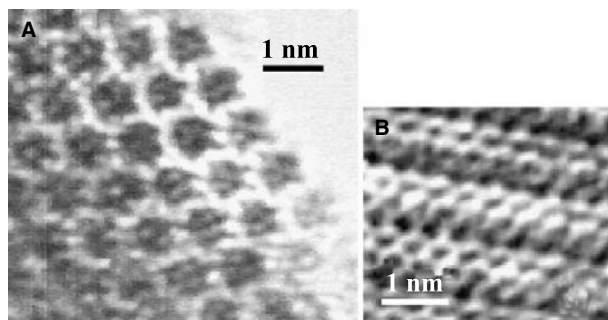


**Fig. 15** The high-resolution transmission electron images of (A) the bundle of subnanometer  $\text{MoS}_{2-x}$  nanotubes along the [001] direction, revealing the regular hexagonal close package of the nanotubes; (B) the side view of the bundle along [101] direction, evidencing the ordered stacking of the nanotubes along the bundle axis.

A high-resolution transmission electron microscopy (HRTEM) investigation of the bundles along their longitudinal direction revealed a hexagonal close package of identical nanotubes (Fig. 15), where the center-to-center distance between two tubes is 0.96(1) nm. High-resolution TEM approximately perpendicular to the nanotube axis resolved the ordered structure of individual nanotube as well as their regular stacking in the bundle (insert).

Based on transmission electron diffraction and X-ray diffraction, the proposed unit cell of the hexagonal close-packed nanotubes within a bundle is 0.40(1) nm along the bundle axis and 0.96 nm perpendicular to the bundle axis. High-resolution simulations using the symmetry operations of Group  $P6_3$ -No. 173 was

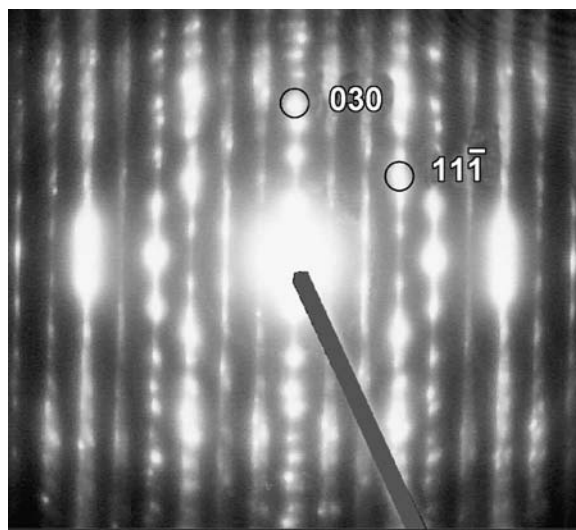


**Fig. 16** Transmission electron diffraction pattern of  $\text{MoS}_{2-x}\text{I}_z$  bundle indexed in accordance with the model structure. *Source:* From Ref.<sup>[20]</sup>.



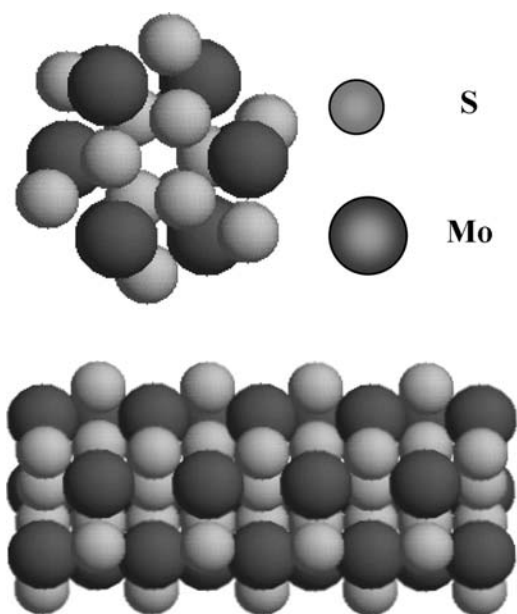


**Fig. 17** The model structure of a single-wall  $\text{MoS}_2$  nanotube in the top and the side view.<sup>[15]</sup> Considering covalent radii in the model, the diameter of the inner sulfur cylinder is 0.32 nm, the diameter of the molybdenum cylinder is 0.58 nm, and that of the outer sulfur cylinder is 0.75 nm.

found in agreement with the observed high-resolution images. The stoichiometry is still not exactly determined, especially in the case of the molybdenum–sulfur ratio. The reason is a strong overlap of the X-ray characteristic peaks, which prevents the accurate quantitative chemical analysis. Moreover, the X-ray and electron diffraction spectra are dominated by heavy molybdenum atoms, which make the determination of crystal structure difficult (Fig. 16).

The proposed model structure of a subnanometer-diameter  $\text{MoS}_2$  nanotube<sup>[20]</sup> consists of sulfur–molybdenum–sulfur cylinders (Fig. 17). Following the usual nomenclature,<sup>[21]</sup> the structure corresponds to a (3, 3) armchair nanotube. van der Waals interaction is proposed as a force that keeps the nanotubes together. The closest sulfur atoms on adjacent nanotubes in a bundle are separated by 0.35(1) nm, which approximately corresponds to their van der Waals bond length. Iodine atoms are inserted in interstitial trigonal voids between the nanotubes creating one-dimensional rows along the bundle axis. Iodine could also serve as a charge exchange reservoir between the  $\text{Mo}_3\text{S}_{6-x}$  units. It would contribute to the bonding. The periodicity of possible sites for iodine position along the bundle is 0.40 nm, which is slightly less than the van der Waals distance for iodine (0.43 nm). Iodine was only partially removed by ultrasound bathing in ethanol, which was used to decompose the bundles. The energy dispersive X-ray

analysis (EDX) evidenced the lowered concentration of iodine after the decomposition. Scanning tunneling microscopy (STM) studies show that iodine is removed from the surface of a bundle, but it might stay inserted in between the associated nanotubes. It is suggested that iodine with high density of electrons increases the stability of nanobundles on the substrate, while single nanotubes are strongly affected by the scanning STM tip.

The strong self-assembly of the single-wall nanotubes into the bundles suggests the role of  $\text{C}_{60}$  as template during the synthesis. The presence of  $\text{C}_{60}$  in the growth process was found essential, and the single-walled  $\text{MoS}_2$  nanotubes do not grow in its absence. The detailed growth mechanism is not clear at present. We remark on the fact that the (1,1,1) plane of  $\text{C}_{60}$  crystals shows a hexagonal pattern with the in-plane lattice parameter of 1.004 nm,<sup>[22]</sup> which nearly matches the nanotube crystal lattice shown in Fig. 15. In addition, it is conceivable that the mismatch between the lattice parameter of  $\text{C}_{60}$  (1.004 nm) and  $\text{MoS}_2$  nanotubes (0.96 nm) plays an active role in promoting the growth of the bundle in the typical tip shape.  $\text{C}_{60}$  is most probably situated at the extremities of the nanotubes during the growth.

## ASPECTS OF POSSIBLE APPLICATIONS OF INORGANIC NANOTUBES

As a result of their cylindrical geometry, these novel advanced nanomaterials have a low mass density, a high porosity, and an extremely large surface to weight ratio. Their potential applications range from high porous catalytic and ultralight anticorrosive materials, atomic probes, and electron field emitters to non-toxic strengthening fibers. This may lead to a more efficient use and an increase in durability of materials. Doping of these semiconducting nanostructured materials may also allow further miniaturization of electronic systems and may lead to new optoelectronic materials. The helical structure of undoped tubes with semiconductor behavior and their optical activity enable possible applications in non-linear optics and in solar cell technology. By functionalizing the nanotubes, e.g., using specific Mo containing enzymes, novel functional biomaterials could be made.

Among others,  $\text{MoS}_2$  and  $\text{WS}_2$  are also applicable for construction of photovoltaic cells in which electron-hole pairs are photoexcited and do not recombine but migrate to the edge of the crystal. Most research in this area has been concentrated on growth of large and pure layered crystals, which has been technologically very expensive and complicated. However, similar effects need to be investigated in nanotubes and

other nanostructures of the same materials, whereby acceptor molecules can be included in between the layers that will inhibit recombination and allow more efficient use in photovoltaic applications.

The  $\text{MoS}_{2-x}\text{I}_y$  subnanometer-diameter nanotubes with observed self-assembly at different scales are due to the tip geometry and the porous structure, promising candidates for applications as reversible lithium batteries,<sup>[23]</sup> in advanced electronics as molecular wires in nanodevices,<sup>[24]</sup> and as electron field emitters.<sup>[25]</sup>

## CONCLUSION

In conclusion, the chemical transport reaction enables synthesis of different transition metal dichalcogenide nanotubes. The advantage of lasting transport reaction is that the so grown nanotubes contain extremely low density of structural defects. The tubes grow up to several millimeter lengths with diameters ranging from several micrometers to less than 10 nm. The  $\text{MoS}_2$  and  $\text{WS}_2$  nanotubes have been successfully alloyed with gold and silver. The chirality, otherwise typical for the pure  $\text{MoS}_2$  and  $\text{WS}_2$  nanotubes, was partially or completely removed in the alloyed nanotubes and the electrical properties were changed. The existence of noble metal– $\text{MoS}_2$  ternary compounds gives evidence that the cylindrical geometry of crystals can stabilize new compounds otherwise unknown in a plane geometry.

The subnanometer  $\text{MoS}_{2-x}\text{I}_y$  nanotubes have been synthesized using  $\text{C}_{60}$  as a growth promoter. The nanotubes display a self-assembly on different length scales. They group to the first case of molecular crystals composed of inorganic nanotubes. Scanning tunneling microscopy investigations of individual nanotubes and nanotube bundles reveal metallic behavior in two dimensions, along the tubes and along its circumference, while the conductivity among nanotubes is hindered revealing the semiconductivity. As a result of the metallic behavior, these smallest known inorganic nanotubes belong to the family of promising molecular wires.

## ACKNOWLEDGMENTS

The author thanks Dr. Ales Mrzel, JSI, and Prof. Francis Levy, EPFL, for their cooperation, Mrs. Zora Skraba, JSI, for the technical assistance in crystal growth, and Prof. Pierre Stadelmann, EPFL, for supporting the access to the electron microscopes. The work was in main part financed by the Ministry for Education, Science, and Sports of Slovenia.

## REFERENCES

1. Tenne, R.; Margulis, L.; Genut, M.; Hodes, G. Polyhedral and cylindrical structures of tungsten disulphide. *Nature* **1992**, *360*, 444.
2. Rothschild, A.; Sloan, J.; Tenne, R. Growth of  $\text{WS}_2$  nanotubes phases. *J. Am. Chem. Soc.* **2000**, *122*, 5169.
3. Nath, M.; Govindaray, A.; Rao, C.N.R. Simple synthesis of  $\text{MoS}_2$  and  $\text{WS}_2$  nanotubes. *Adv. Mater.* **2001**, *13*, 283.
4. José-Yacamán, M.; Lopez, H.; Santiago, P.; Galvan, D.H.; Garzón, I.L.; Reyes, A. Studies of  $\text{MoS}_2$  structures produced by electron irradiation. *Appl. Phys. Lett.* **1996**, *69*, 1065.
5. Homyonfer, M.; Mastai, Y.; Hershinkel, M.; Volterra, V.; Hutchison, J.-L.; Tenne, R. Scanning tunnelling microscope induced crystallization of fullerene-like  $\text{MoS}_2$ . *J. Am. Chem. Soc.* **1996**, *118*, 7804.
6. Mastai, Y.; Homyonfer, M.; Gedanken, A.; Hodes, G. Room temperature sonoelectrochemical syntheses of molybdenum sulfide fullerene-like nanoparticles. *Adv. Mater.* **1999**, *11*, 1010.
7. Albu-Yaron, A.; Lévy-Clément, C.; Hutchison, J.L. A study on  $\text{MoS}_2$  thin films electrochemically deposited in ethylene glycol at 165°C. *Electrochem. Solid-State Lett.* **1999**, *2*, 627.
8. Nath, M.; Rao, C.N.R. New metal disulfide nanotubes. *J. Am. Chem. Soc.* **2001**, *123*, 4841.
9. Remskar, M.; Mrzel, A.; Jesih, A.; Levy, F. Metal-alloyed  $\text{NbS}_2$  nanotubes synthesized by the self-assembly of nanoparticles. *Adv. Mater.* **2002**, *14*, 680.
10. Remskar, M.; Skraba, Z.; Cleton, F.; Sanjines, R.; Levy, F.  $\text{MoS}_2$  as microtubes. *Appl. Phys. Lett.* **1996**, *69*, 351.
11. Wilson, J.A.; Yoffe, A.D. The transition metal dichalcogenides. *Adv. Phys.* **1969**, *18*, 193.
12. Remskar, M.; Skraba, Z.; Cleton, F.; Sanjines, R.; Levy, F.  $\text{MoS}_2$  microtubes: An electron microscopy study. *Surf. Rev. Lett.* **1998**, *5*, 423.
13. Remskar, M.; Skraba, Z.; Ballif, C.; Regula, M.; Sanjinés, R.; Lévy, F. New crystal structures of  $\text{WS}_2$ : microtubes, ribbons and ropes. *Adv. Mater.* **1998**, *10*, 246.
14. Remskar, M.; Skraba, Z.; Sanjinés, R.; Lévy, F. Syntactic coalescence of  $\text{WS}_2$  nanotubes. *Appl. Phys. Lett.* **1999**, *74*, 633.
15. Remskar, M.; Mrzel, A.; Levy, F. Self-assembly of inorganic nanotubes synthesised by the chemical transport reaction. In *Perspectives of Fullerene Nanotechnology*; Osawa, E., Ed.; Kluwer: Dordrecht, 2001; 113–124.
16. Remskar, M.; Skraba, Z.; Ballif, C.; Sanjines, R.; Levy, F. Stabilization of the rhombohedral polytype in  $\text{MoS}_2$  and  $\text{WS}_2$  microtubes: TEM and AFM study. *Surf. Sci.* **1999**, *433–435*, 637.
17. Remskar, M.; Skraba, Z.; Stadelmann, P.; Levy, F. Structural stabilization of new compounds:  $\text{MoS}_2$  and  $\text{WS}_2$  micro- and nanotubes alloyed with gold and silver. *Adv. Mater.* **2000**, *12*, 814.
18. Remskar, M.; Skraba, Z.; Sanjines, R.; Levy, F.  $\text{MoS}_2$  and  $\text{WS}_2$  nanotubes alloyed with gold and silver. *Surf. Rev. Lett.* **1999**, *6*, 1283.
19. Bronger, W. *Crystallography and Crystal Chemistry of Materials with Layered Structures*; Levy, F., Ed.;

- D. Reidel Publishing Company: Dordrecht, Holland, 1976.
20. Remskar, M.; Mrzel, A.; Skraba, Z.; Jesih, A.; Ceh, M.; Demsar, J.; Stadelmann, P.; Lévy, F.; Mihailovic, D. Self-assembly of subnanometer-diameter single-wall MoS<sub>2</sub> nanotubes. *Science* **2001**, *292*, 479.
  21. Dresselhaus, M.S.; Dresselhaus, G.; Ecklund, P.C. *Science of Fullerenes and Carbon Nanotubes*; Academic Press: New York, 1996.
  22. Kratschmer, W.; Lamb, L.D.; Fostiropoulos, K.; Huffman, D.R. Solid C<sub>60</sub>: A new form of carbon. *Nature* **1990**, *347*, 354.
  23. Dominko, R.; Arcon, D.; Mrzel, A.; Zorko, A.; Cevc, P.; Venturini, P.; Gaberscek, M.; Remskar, M.; Mihailovic, D. Dichalcogenide nanotube electrodes for Li-ion batteries. *Adv. Mater.* **2002**, *14*, 1531.
  24. Remskar, M.; Mrzel, A.; Sanjines, R.; Cohen, H.; Lévy, F. Metallic sub-nanometer MoS<sub>2-x</sub>I<sub>y</sub> nanotubes. *Adv. Mater.* **2003**, *15*, 237.
  25. Nemanic, V.; Zumer, M.; Zajec, B.; Pahor, J.; Remskar, M.; Mrzel, A.; Panjan, P.; Mihailovic, D. Field-emission properties of molybdenum disulfide nanotubes. *Appl. Phys. Lett.* **2003**, *82*, 4573.

# Inorganic Sulfide Nanotubes: Mechanical Behavior

Ifat Kaplan-Ashiri  
H. Daniel Wagner

*Materials and Interfaces Department, Weizmann Institute of Science, Rehovot, Israel*

Gotthard Seifert

*Institut für Physikalische Chemie, Technische Universität Dresden, Dresden, Germany*

Reshef Tenne

*Materials and Interfaces Department, Weizmann Institute of Science, Rehovot, Israel*

## Abstract

The combination of nanometric (the diameter) and micrometric (the length) scales make nanotubes a unique and attractive object of research, including the study of mechanical properties and fracture in particular. However, it is precisely this small size that makes the study of the mechanical properties of nanotubes difficult. Atomic force microscopy (AFM) and high-resolution scanning electron microscopy (HRSEM) are very efficient techniques to overcome this challenge.

WS<sub>2</sub> and MoS<sub>2</sub> form nanotubes with a similar crystalline structure, hence they are quite likely to show comparable mechanical behavior. Also, these materials are expected to have superior mechanical properties when compared with the bulk material, which was shown earlier for carbon nanotubes.

The investigation of the mechanical properties of WS<sub>2</sub> and MoS<sub>2</sub> nanotubes included both an experimental and a theoretical part. Young's modulus was studied by various techniques, including atomic force microscope (AFM) and scanning electron microscope (SEM); it was also calculated by using the density-functional-based tight-binding (DFTB) method. Tensile tests of individual WS<sub>2</sub> nanotubes and bending tests of MoS<sub>2</sub> nanotubes were performed as well.

Young's modulus of WS<sub>2</sub> nanotubes was found to be in the range of 150–170 GPa, which is in good agreement with DFTB calculations. As for MoS<sub>2</sub> nanotubes, Young's modulus of 120 GPa was measured while the calculated value was 238 GPa. WS<sub>2</sub> nanotubes also showed tensile strength as high as 16 GPa and fracture strain of 14%. These results indicate the high quality of these nanotubes, which reach their theoretical strength. The maximal strain of MoS<sub>2</sub> nanotubes according to molecular dynamics simulations was found to be 17–19%. Bending tests of WS<sub>2</sub> nanotubes resulted in interlayer shear modulus of 2 GPa, while similar tests of MoS<sub>2</sub> ropes of nanotubes resulted in modulus of 160 MP.

## INTRODUCTION

The mechanical properties of nanomaterials are of great interest both from theoretical and application point of view. Among the nanomaterials, the nanotubes are a very important group since it has almost perfect crystalline shape. Over the last few years, numerous theoretical and experimental studies were dedicated to the mechanical properties of carbon nanotubes.<sup>[1–6]</sup> These works revealed the unique properties of carbon nanotubes, which are high strength materials and deform elastically both in tension and under compression. The superior mechanical properties of carbon nanotubes can be attributed to their layered structure, which can be made almost defect-free. Since other layered materials like WS<sub>2</sub>, MoS<sub>2</sub>, BN, etc. can also form nanotubes, they are expected to have unique mechanical properties as well.

Studying the mechanical properties of the nanotubes is challenged by their small size. Atomic force microscopy (AFM) and high-resolution scanning electron microscopy (HRSEM) are efficient techniques to overcome this challenge. AFM is used to measure forces in the nano-Newton range and the scanning electron microscope (SEM) is used for imaging and controlled movement of nano-objects (by using an in situ nanomanipulator). The mechanical properties of individual nanotubes can be directly measured using AFM by attaching a nanotube to a silicon cantilever.<sup>[7,8]</sup> The cantilever is functioning as a force sensor (like a spring). When force is applied on the nanotube, the silicon cantilever deflects in response. The deflection can be tracked either by AFM (the deflection is tracked by a laser signal from the cantilever to the photodiode) or by SEM (the cantilever's movement is imaged).

## BACKGROUND

Significant progress has been made in the area of nanoscale science and technology in the past decade. Since the discovery of inorganic fullerene-like nanostructures and nanotubes (IF) of WS<sub>2</sub> in 1992,<sup>[9]</sup> many more IF nanoparticles were reported, including MoS<sub>2</sub>,<sup>[10]</sup> BN,<sup>[11]</sup> VO<sub>x</sub>,<sup>[12]</sup> NiCl<sub>2</sub>,<sup>[13]</sup> and CdS.<sup>[14]</sup> The nanotubes (especially carbon) have received significant attention in terms of fundamental property measurements and potential applications. This is largely due to the impressive physical behavior as revealed from both theoretical and experimental studies. It was realized that this brand of new nanomaterials possesses a wide range of electrical and optical properties, which can be tuned with the diameter of the nanotubes.<sup>[15]</sup> Furthermore, the electrical properties of nanotubes may be tuned by mechanical deformation as well.<sup>[16–19]</sup> Such properties are of great interest for applications such as sensors or smart materials. The utility of nanotubes as the strongest or stiffest elements in nanoscale devices or composite materials remains a powerful motivation for the research in this area.

The combination of nanometric (the diameter) and micrometric (the length) scales make nanotubes a unique and attractive object of research, including the study of mechanical properties and fracture in particular. However, it is precisely this small size that makes the study of the mechanical properties of nanotubes difficult. Atomic force microscopy HRSEM are very efficient techniques to overcome this challenge. Atomic force microscopy is used to measure forces in the nano-Newton range and the SEM is used to manipulate and image nano-objects. The mechanical properties of individual nanotubes can be directly measured using AFM by attaching a nanotube to a silicon cantilever.<sup>[1,7,20]</sup> The cantilever is functioning as a force sensor (like a spring). When force is applied on a nanotube, the silicon cantilever deflects and this deflection can be tracked either by AFM (the deflection is tracked by a laser signal from the cantilever to the photodiode) or by SEM (the cantilever's movement is imaged).

## WS<sub>2</sub> NANOTUBES

The mechanical properties of WS<sub>2</sub> nanotubes including Young's modulus, tensile strength, elongation, shock wave resistance, and their mechanical behavior under different conditions were studied lately. The synthesis of WS<sub>2</sub> IF nanoparticles and nanotubes was first reported in 1992.<sup>[9]</sup> A number of methods have been developed for synthesis of WS<sub>2</sub> multiwall nanotubes, for instance sulfidization of the metal oxide<sup>[9,21]</sup> or direct synthesis from vapor phase by chemical transport reaction.<sup>[22]</sup> At present, WS<sub>2</sub> nanoparticles with fullerene-like

structure enriched by 5% chiral multiwall nanotubes can be obtained<sup>[21]</sup> by using the fluidized bed reactor (FBR) with somewhat modified conditions. The length of these nanotubes varied from several hundred nanometers to several micrometers. Along with these, much longer (up to 0.3 mm) nanotubes were also observed. The nanotubes are quite uniform in shape and open-ended. Their outer diameter varies from 10 to 30 nm, with the main size distribution centered between 15 and 20 nm. The typical number of layers in a nanotube is between 5 and 8. Thus, the hollow core of such nanotubes occupies up to 70% of their total volume. According to transmission electron microscopy (TEM) analysis, the nanotubes were found to be quite perfectly crystalline and almost defect-free. These nanotubes exhibit an average chirality angle of 7–12°. First-principles calculations confirmed that such nanotubes are indeed energetically stable.<sup>[23]</sup>

## YOUNG'S MODULUS

Young's modulus of the nanotubes is of great interest for many applications. Several techniques, including axial compression and tension, were applied to measure Young's modulus of WS<sub>2</sub> nanotubes.

An axial compression force can be applied on a nanotube until Euler's buckling point and beyond. It is possible to calculate Young's modulus either from Euler's buckling equation<sup>[24]</sup> or by using the Elastica theory.<sup>[25]</sup> An individual WS<sub>2</sub> nanotube can be attached to the AFM cantilever, and axial compression force can then be applied either by using an AFM or in a SEM chamber, as desired. Young's modulus is calculated according to Euler's buckling equation from the force vs. displacement trace for each nanotube measured by AFM<sup>[24]</sup> (Fig. 1):

$$F_{\text{Euler}} = \frac{\pi^2 EI}{L^2} \quad (1)$$

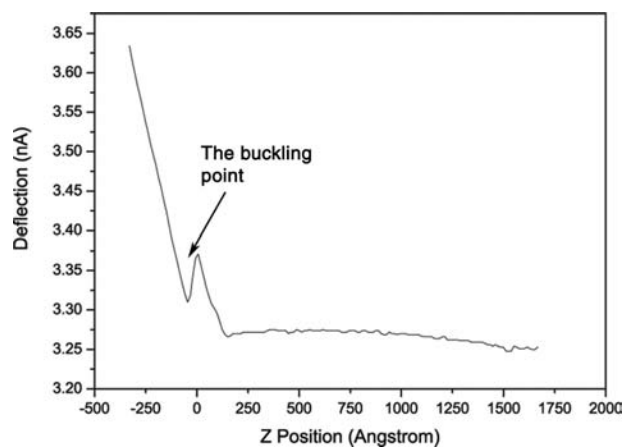


**Fig. 1** Deflection of the silicon cantilever vs. its Z position as recorded by AFM. Source: Adapted from Ref.<sup>[24]</sup>.

where  $F_{\text{Euler}}$  is Euler's buckling force (which can be seen clearly as the discontinuity point in the force trace),  $E$  is Young's modulus,  $I$  is the second (or geometrical) moment of inertia (applied here to a hollow cylinder geometry), and  $L$  is the nanotube's length. The average Young's modulus obtained from these measurements was 171 GPa. The scatter of the results is quite large, apparently because not all the nanotubes were perpendicular to the surface (it is quite difficult to control the position of the nanotube relative to the surface during AFM investigations). Notwithstanding the large scattering, the measured value of Young's modulus of WS<sub>2</sub> tubes was quite close to the theoretical value, which is 150 GPa. A similar experiment using SEM<sup>[25]</sup> was conducted and the post-buckling behavior was studied (Fig. 2). Here, using the SEM images, force vs. deflection curves were constructed in which the AFM cantilever movement and the position of the nanotube were observed. The SEM-based results were analyzed using the Elastica theory. According to this theory, the running coordinates of the (large) displacement of a very thin, flexible rod with a stiffness  $EI$  can be expressed at any point  $(x,y)$  along its length  $(s)$  as a function of an axial force  $P$  applied at the free end, see Fig. 3. Here, only the expression for the  $y$  coordinate was used:

$$y = \sqrt{\frac{EI}{4P}} \int_0^\alpha \frac{\sin \theta d\theta}{\sqrt{\sin^2 \alpha/2 - \sin^2 \theta/2}} \quad (2)$$

The Young's modulus values evaluated using the above principle varied, and were close to 150 GPa only when  $\theta$  was almost identical to  $\alpha$  (edge of the nanotube). These results suggest that the assumption that the geometrical moment of inertia  $I$  (and thus the geometry of the cross-section) is constant along the buckled nanotube is in fact incorrect. A TEM image (Fig. 4) of a highly bent nanotube shows an obvious distortion of the cross-section at the locus of maximal

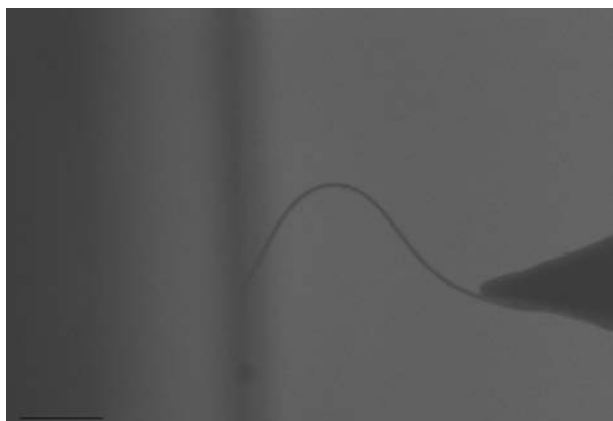


**Fig. 2** The large deformation of the nanotubes in the post-buckling stage is described by the SEM image (bar 1  $\mu\text{m}$ ). *Source:* Adapted from Ref.<sup>[25]</sup>.

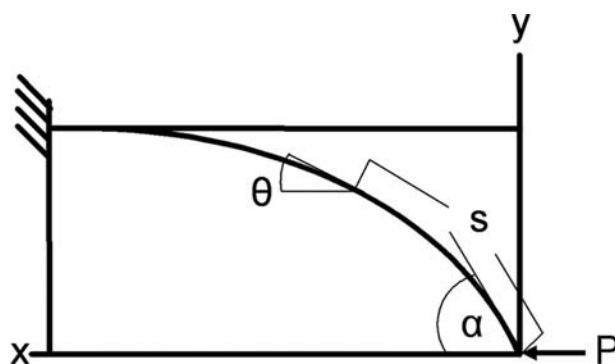


**Fig. 3** Scheme of the post-buckling shape of a beam, which is used for the Elastica analysis. The parameters used for the Elastica equations are presented in this scheme. *Source:* Adapted from Ref.<sup>[25]</sup>.

curvature and the local geometry, therefore, strongly deviates from the assumed cylindrical shape.

A tension force can be axially applied to a nanotube<sup>[5,6]</sup> in a way similar to macroscopic tensile tests, but with some technical differences. Indeed, here the nanotubes are attached to two silicon cantilevers with different spring constants, and the nanotube is then pulled to fracture (Fig. 5). By analyzing the SEM images, the applied force and the nanotube's length are obtained.<sup>[25]</sup> The stress is calculated as the applied force divided by the cross-sectional area (of the outer shell only, since it is generally accepted that it is the only layer that bears significant load); the strain is simply the measured elongation divided by the original nanotube length. Plotting the stress against the strain



**Fig. 4** TEM image of a naturally buckled nanotube. This image demonstrates clearly that the cross-section of the nanotube is not constant (bar 20 nm). *Source:* Adapted from Ref.<sup>[25]</sup>.



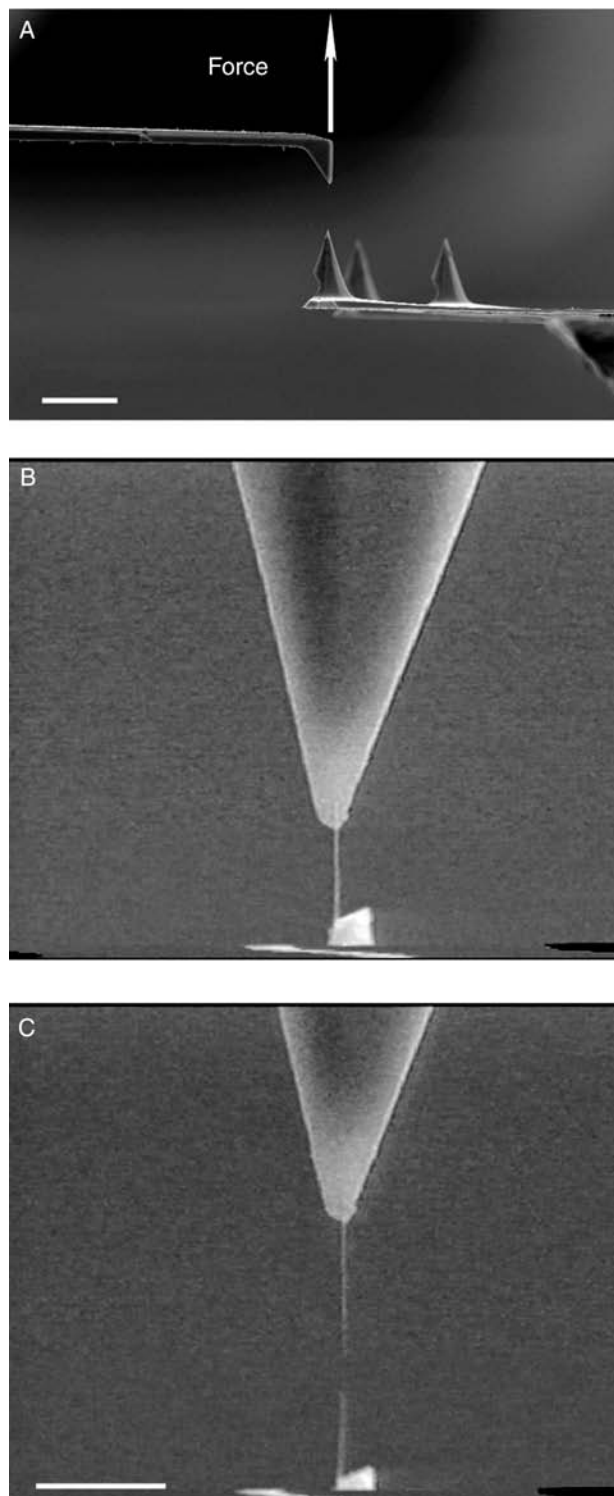


**Fig. 5** SEM images of tensile test of an individual  $\text{WS}_2$  nanotube: (A) The tensile test set-up—the nanotube (ca. 20 nm in diameter) is attached to two AFM cantilevers (amorphous carbon serves as a glue); the force is applied through the upper cantilever, which has higher force constant when compared with the lower one (bar is 20  $\mu\text{m}$ ). (B) A loaded nanotube, before fracture. (C) Two pieces of the nanotube after fracture occurred (bar is 2  $\mu\text{m}$ ). Source: Adapted from Ref. [25].

yields the nanotube Young's modulus according to Hooke's law. The average Young's modulus from such measurements is 152 GPa ( $\pm 68$ ).

Regardless of the experimental setup or model used, Young's modulus of  $\text{WS}_2$  nanotubes fell in the 150–170 GPa range. The good agreement between the results from different measurements and the theoretically expected value of 150 GPa reflects the relatively uniform and defect-free structure of  $\text{WS}_2$  nanotubes synthesized in our laboratory.

## TENSILE STRENGTH AND ELONGATION

The strength of macroscopic objects can generally be determined by either their intrinsic molecular structure or by such extrinsic factors as grain boundaries, dislocations, vacancies, and other defects.<sup>[26,27]</sup> The extrinsic factors are affected by the manufacturing processes used for the preparation of a specific specimen. Thus, the strength of macroscopic objects is generally much smaller than the theoretical value (of the order of one-tenth of Young's modulus). This apparent discrepancy highlights the fact that the strength of materials is only partially determined by their intrinsic mechanical properties,<sup>[26,27]</sup> i.e. the strength of their chemical bonds.

In contrast to macroscopic models, which deal with a statistically large number of defects within a body or a continuum of matter, nanomaterials and nanotubes, in particular, must be studied and modeled on a microscopic (atomistic) level.<sup>[28,29]</sup> Only a discrete number of atomistic defects are present in the nanotube; therefore, the effect of individual defects must be examined theoretically and, if at all possible, experimentally. By isolating and studying individual nanostructures, which contain practically no defects, one may hope to achieve strengths much larger than the macroscopic analogues. Also, below a certain size, the size (diameter) of a nanospecimen has been claimed to be irrelevant with respect to mechanical strength,<sup>[30]</sup> although this remains a deeply controversial issue. Rather, the control of the synthesis of the nanotubes determines their perfectness and consequently their strength. Indeed, long and defect-free nanotubes can be stronger than shorter nanotubes, which contain even a very small number of point defects.

The ultimate strength of the  $\text{WS}_2$  nanotubes as well as the maximal elongation under axial tension was studied as described here.<sup>[25]</sup> The maximal load and length of the nanotube was obtained from SEM images. To calculate the applied stress, it was assumed that the load was applied only to the outer layer of the nanotube since the bond to the force transducer covered only the outer surface of the nanotube. Hence, rupture of the nanotube occurred only at the outer shell, and inner

shell movement followed it in a telescopic manner. This hypothesis was confirmed by observing that the total length of the fragments was significantly larger than the initial nanotube length (see Fig. 5). The ultimate strength and the maximal elongation of the WS<sub>2</sub> nanotubes are 3.7–16.3 GPa ( $\pm 11\%$ ) and 5–14% ( $\pm 0.1\%$ ), respectively. The high tensile strength of these nanotubes seems to be very promising when compared with other known (bulk) high strength materials as presented in Table 1.<sup>[5,6,27]</sup> The combination of high tensile strength and ca. 14% elongation is a unique property of all the nanotubes measured so far.<sup>[5,6]</sup> Furthermore, the strength of the strongest nanotubes is about 11% of their Young's modulus, corresponding approximately to the theoretical value of the material's strength. This value is appreciably larger than typical high-strength engineering materials. Such findings indicate that the WS<sub>2</sub> nanotubes seem to be remarkably free of critical defects.

The stress-strain plots (Fig. 6) show that the nanotubes deformed elastically, almost until failure. Weibull statistics<sup>[31,32]</sup>, which is used to predict the probability of failure of bulk materials, was found to be valid for the WS<sub>2</sub> nanotubes. This implies that either the WS<sub>2</sub> nanotubes are defect-free or that the role of defects in the nanotubes is completely different and should be estimated using another approach. Recently, a new approach to nanomaterials fracture mechanics, quantized fracture mechanics (QFM), was proposed.<sup>[33]</sup> The QFM model attempts to predict the strength of nanotubes as a function of the number of discrete critical defects. Based on the QFM model, it was found out that some of the nanotubes appear to be defect-free, while others contain 1–21 critical defects leading to fracture.

It was demonstrated that WS<sub>2</sub> nanotubes are both ultra-strong and extensible, distinguishing them from other known materials. Furthermore, the tensile strength results were found to be in good agreement with the QFM model, suggesting that the mechanical properties

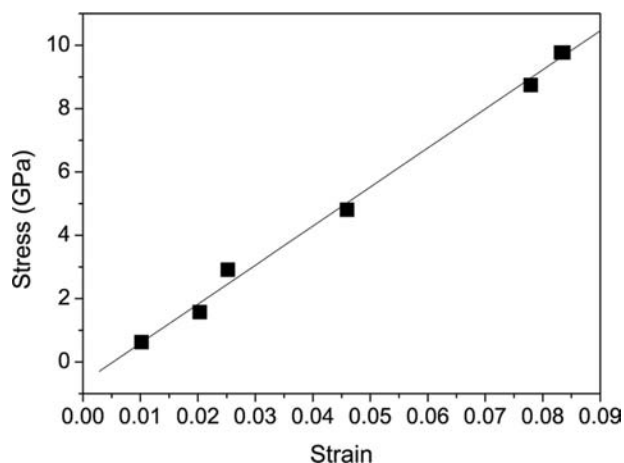


**Fig. 6** Stress-strain plot of an individual WS<sub>2</sub> nanotube. The linear behavior of the plot indicates that the nanotubes deformed elastically until failure. *Source:* Adapted from Ref.<sup>[25]</sup>.

of WS<sub>2</sub> nanotubes are dictated by a discrete number of critical defects and the intrinsic strength of the W-S chemical bond. Thus, individual nanotubes have been shown to demonstrate quasi-ideal strength, providing strong evidence for defect-free structures.

## INTERLAYER SHEAR MODULUS

The cylindrical geometry of nanotubes dictates a strong anisotropy of their physical properties. In practice, the difficulty in extracting individual components of the elastic tensor has limited the available information to only very partial and indirect experimental data. By performing bending tests, the interlayer shear (sliding) modulus ( $C_{44}$ ) of single WS<sub>2</sub> nanotubes was studied.<sup>[34]</sup>

Clamped nanotubes were loaded laterally at the center of their suspended length by means of an AFM tip, and force-deflection ( $F-d$ ) curves were recorded.<sup>[28,35]</sup> According to the  $F-d$  curves, the nanotubes exhibit a linear elastic behavior at small deflections, non-linear deflection is evident when the deflection exceeded 20 nm.

A clamped beam, which is subjected to a point load, can be described by Timoshenko's bending equation.<sup>[36]</sup> The total flexural deformation is composed of tension, compression, and shearing. Hence, the total bending is composed of the bending deflection and the shear deflection, which are linked to the bending stiffness ( $EI$ ) and to the shear stiffness ( $GA$ ), respectively. To calculate the Young's modulus from the  $F-d$  curve, the shear modulus is required and vice versa.<sup>[37,38]</sup> The bending equation is:<sup>[39]</sup>

$$\delta = \delta_b + \delta_s = \frac{FL^3}{192EI} + \frac{f_s FL}{4GA} \quad (3)$$

**Table 1** Mechanical properties of strong materials

Material	Modulus of Elasticity (GPa)	Tensile Strength (GPa)	Elongation (%)
Steel alloy 4340	207	1.76	12
Stainless alloy 440A	200	1.79	3.5
Tungsten	400	0.76	2
Diamond	700–1200	1.05	
Silicon nitride	304	0.7–1	
Zirconia	205	0.8–1.5	
Aramid fiber	60–150	3.6–4.1	2.8
Carbon fiber	200–750	4.65–7.1	1.8
E-Glass	72	3.45	4.3

where  $\delta$  is the nanotube's deflection,  $F$  is the applied lateral force,  $L$  is the suspended nanotube length,  $E$  is the Young's modulus.  $I$  is the second moment of area (for a cylinder:  $I = \pi/4(r_{\text{out}}^4 - r_{\text{in}}^4)$ ) where  $r_{\text{out}}$  and  $r_{\text{in}}$  are the outer and inner radii of the nanotube, respectively.  $f_s$  is the shape factor (10/9 for a cylinder),  $G$  is the shear modulus,  $A$  the cross-sectional area of the beam. The previously determined Young's modulus value of 150 GPa<sup>[24,25]</sup> was introduced into the equation and an average shear modulus of 2.0 GPa ( $\pm 1.1$ ) was extracted.

Different models can be used to describe the shear process. The mechanism for shear deformation of a beam in a point load-bending test can be evaluated by considering thin cross-sectional elements, which can slide relative to the adjacent ones.<sup>[39]</sup> This corresponds to "in-plane" ( $C_{12}$ ) shear forces. Furthermore, in analogy to the case of the nanotubes, bending tests of sandwich materials made of alternating layers of hard and soft matter, result in a deformation, which can be characterized by shearing of the soft layers.<sup>[40]</sup> In analogy to sandwich materials, the nanotubes can be regarded as being made of a superstructure of alternating hard (chemically bonded) WS<sub>2</sub> layers and soft interlayer spacing where weak van der Waals forces predominate. Hence, it is believed that the shear deformation of the nanotubes is obtained by slip between adjacent WS<sub>2</sub> layers.

The observed value of 2 GPa agrees well with the value of 4 GPa obtained by first principle density functional tight-binding calculations for 2H-MoS<sub>2</sub>. This value of the shear modulus represents a much higher degree of anisotropy than for carbon nanotubes, and enables assignment of the mode of shear deformation.

## SHOCK WAVE RESISTANCE

Inorganic nanotubes possess some mixed covalent-ionic nature. In fact, some like WS<sub>2</sub> and MoS<sub>2</sub> are more covalent in nature, while metal-halide nanotubes, like those of NiCl<sub>2</sub>, are much more ionic, and are expected to be chemically much more reactive. The known phase diagram of Mo-S and W-S does not contain any specific high-pressure phase and consequently these materials are not expected to yield under load.<sup>[17]</sup> Indeed, diamond anvil cell experiments showed that both materials are stable under a pressure of 21–25 GPa,<sup>[41,42]</sup> Recently, the shock wave resistance of both fullerene-like nanotubes of WS<sub>2</sub> and MoS<sub>2</sub>, respectively, was studied. Shock waves generate concurrently extremely high dynamic pressures and temperatures. Pressure propagation in samples causes very high shear stresses, thereby differing from stresses produced by static pressure. According to TEM analysis of the nanotubes (Fig. 7), some of the WS<sub>2</sub> nanotubes were strong enough to withstand a pressure of

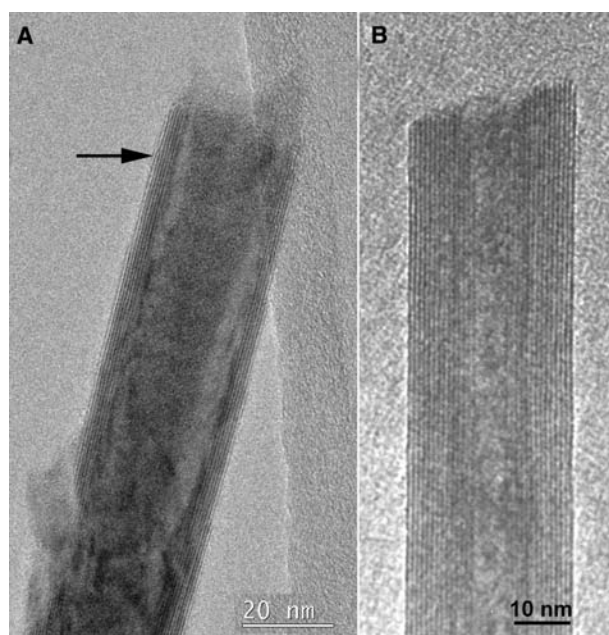


**Fig. 7** HRTEM images of WS<sub>2</sub> nanotubes with 0.62 nm layer separation: (A) post-shock sample, layer-mismatch arrowed; (B) prior to shock waves. *Source:* Adapted from Ref.<sup>[41]</sup>.

21 GPa. Sometimes, defects like layer mismatches were present but did not lead to degradation of the mechanical properties, and structures were fairly well preserved. It was shown that the nanotubes were more resistant to shear stresses when compared with the fullerene-like nanoparticles. Nanotubes, which are folded only along one axis, are less strained and chemically more stable than the fullerene-like nanoparticles of WS<sub>2</sub>. Furthermore, nanotubes are structurally perfect when compared with the IF nanoparticles, which always has defects owing to their faceted structure. Therefore, nanotubes appear to be able to survive much higher shock-waves pressure and shear stresses. X-ray diffraction (XRD) and Raman studies of the IF nanoparticles and nanotubes show that the materials are strong enough to withstand 21 GPa shock waves. When compared with carbon nanotubes, in which going through a phase transition to diamond at this pressure, the IF nanoparticles and nanotubes seem to be significantly more stable.

## MoS<sub>2</sub> NANOTUBES

The mechanical properties of MoS<sub>2</sub> nanotubes were studied both experimentally and theoretically. The synthesis of fullerene-like MoS<sub>2</sub> nanoparticles and nanotubes was first reported in 1993,<sup>[43]</sup> and subsequently MoS<sub>2</sub> nanotubes were reported.<sup>[10,44]</sup> Several methods can be used to prepare the MoS<sub>2</sub> nanotubes and fullerene-like nanoparticles.<sup>[44]</sup> The MoS<sub>2</sub>

nanotubes, which were used for the mechanical studies, were produced by a catalyzed transport reaction involving  $C_{60}$ .<sup>[45]</sup> Single-wall nanotubes were grown by a catalyzed chemical vapor transport method using iodine as a transport agent and the reaction was run for 22 days at 1010 K in an evacuated silica ampoule at a pressure of  $10^{-3}$  Pa. The material grows in the form of bundles, consisting of individual nanotubes 0.961 nm in diameter. It should be emphasized that the dihedral angle of the single-wall  $MoS_2$  reported in this work ( $70^\circ$ ) is appreciably smaller than the one observed in the bulk material ( $94^\circ$ ), indicating that the reported nanotubes are highly strained.

The bundles containing  $> 500,000$  nanotubes usually terminated in a sharp tip. They can be disassembled into thinner ones and even individual tubes by dispersion in ethanol using ultrasonic bath. Nanotubes as long as a few hundreds of micrometers in length were obtained.

## YOUNG'S MODULUS

Young's modulus of  $MoS_2$  ropes (bundles) was studied experimentally.<sup>[35]</sup> Suspended ropes were deposited on a surface of  $Al_2O_3$  membrane with average pore size of 200 nm (Fig. 8). The ropes were elastically deflected by applying a normal force with AFM. Young's and shear moduli can be calculated from the deflection vs. force data sets by using the unit load method. Here, the total deformation is considered as the sum of  $\delta_b$ -(bending) and  $\delta_s$ -(shearing) deformations as described in Eq. (3). According to these measurements, the lowest

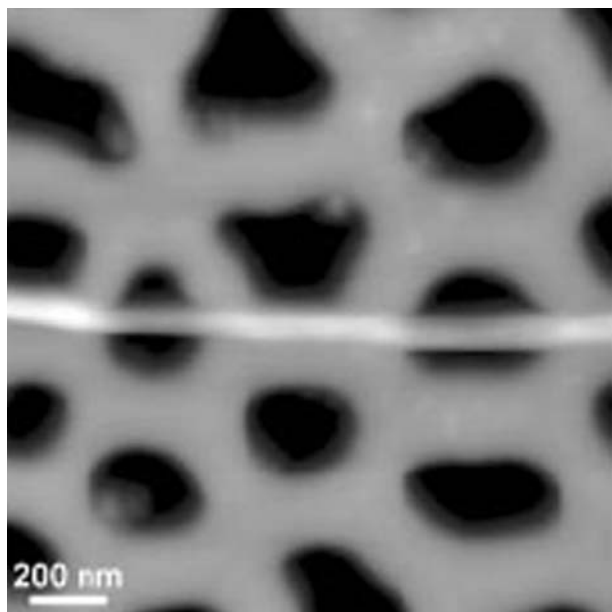


**Fig. 8** AFM image of  $MoS_2$  rope lying over two pores. The rope's diameter is 17 nm. *Source:* Adapted from Ref.<sup>[35]</sup>.

limit for Young's modulus was estimated to be 120 GPa.

Young's modulus of single-wall  $MoS_2$  nanotubes was calculated by using a DFTB method and periodic boundary conditions.<sup>[36]</sup> Young's modulus was calculated using the conventional definition:

$$Y = \frac{1}{V_0} \left. \frac{\partial^2 E}{\partial \epsilon^2} \right|_{\epsilon_0} \quad (4)$$

where  $V_0 = 2\pi L_0 R_0 \delta R$  is the equilibrium volume of the nanotube, with  $L_0$  and  $R_0$  the calculated unit length and the average radius of the nanotubes, respectively. As in the case of carbon nanotubes,  $\delta R$  was chosen as the interlayer separation in the corresponding layered bulk material ( $\delta R$  is equal 0.62 nm for  $MoS_2$ ). Young's modulus for a series of armchair ( $n,n$ ) and zigzag ( $n,0$ )  $MoS_2$  single-wall nanotubes that were calculated from first principles are shown as a function of the tube radius in Fig. 9. As one can see from the figure, the zigzag ( $n,0$ ) nanotubes have a considerably larger Young's modulus than armchair ( $n,n$ ) nanotubes with similar radius. Whereas Young's modulus of ( $n,0$ ) nanotubes remains essentially invariant with the tube's radius, the value of  $E$  increases with the radius for ( $n,n$ ) nanotubes. Also, the value of Young's modulus of the ( $n,0$ ) nanotubes is very close to that of bulk  $MoS_2$  (238 GPa). Extrapolating the calculated Young's modulus of the ( $n,n$ ) nanotubes to radii of approximately 10 nm will lead to values for Young's modulus around those of a bulk  $MoS_2$ , too. Young's modulus of  $MoS_2$  single-wall nanotubes is very similar to that of the bulk material; i.e., the tube formation does not alter the interaction within the single layers.

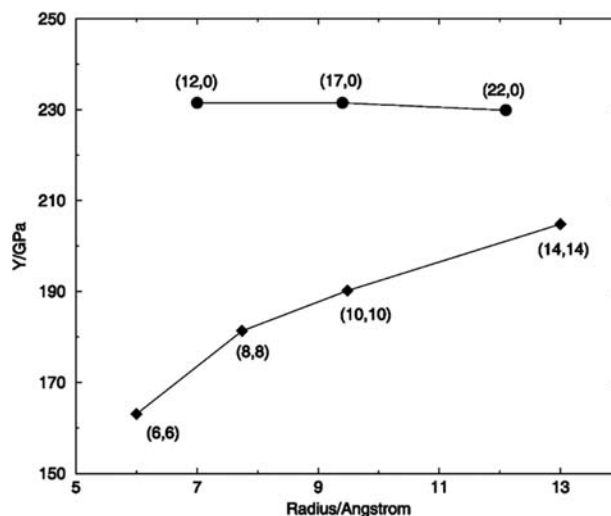


**Fig. 9** Calculated Young's modulus of ( $n,m$ )  $MoS_2$  nanotubes. *Source:* Adapted from Ref.<sup>[24]</sup>.

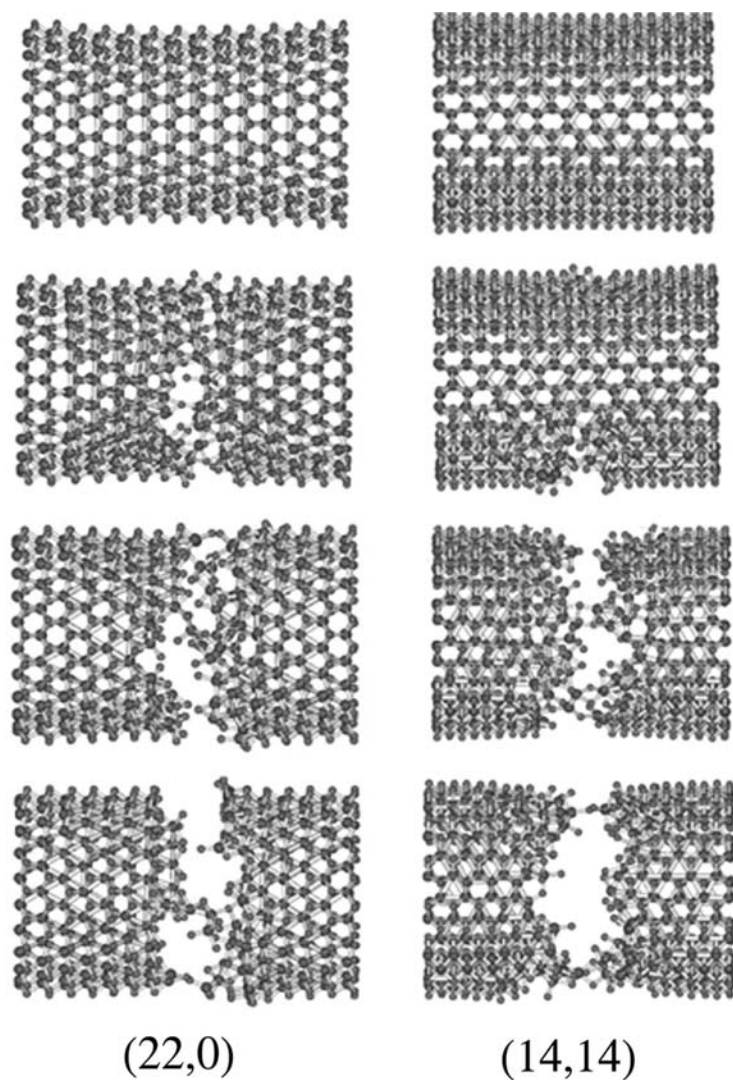


**Fig. 10** Simulated tensile tests of single-wall MoS<sub>2</sub> nanotubes: The rupture progress is described by DFTB-MD simulation for zigzag (22,0) and armchair (14,14) nanotubes. Elongation values are 17% and 19%, respectively, for the zigzag and armchair nanotubes. *Source:* Adapted from Ref.<sup>[25]</sup>.

The calculated Young's modulus is ca. double of the one measured for single-wall MoS<sub>2</sub>.<sup>[35]</sup> The difference can be attributed to experimental errors (ca 50%) and to the difference between bundles and individual nanotubes. As indicated above, the smaller dihedral angles observed for the nanotubes when compared with the bulk material is most likely to weaken their chemical bonds, adversely affecting their mechanical properties. Also, the experimental measurements are influenced by the presence of defects in the structure, which affect their mechanical properties.

### SHEAR MODULUS

As described above,<sup>[35]</sup> the shear and Young's moduli can be calculated from bending experiments of a nanotube or a rope. In the case of ropes (bundle), the shear modulus ( $G$ ) describes the sliding between individual tubes comprising the rope and not the shear of the layers. The shear modulus is expected to be

appreciably smaller when compared with Young's modulus due to the low friction between the MoS<sub>2</sub> nanotubes within the bundle. The shear modulus determined in this way is 160 MPa ( $\pm 30$ ). This value is quite low when compared with ropes of single-wall carbon nanotubes (1–10 GPa). This may be explained by the weak interaction of sulfur atoms on the outer surface of the nanotube.

### TENSILE STRENGTH AND ELONGATION

A combined molecular dynamics-density functional-tight-binding (MD-DFTB) simulation of the stretching process was performed for single-wall MoS<sub>2</sub> nanotubes.<sup>[25]</sup> According to these simulations, the failure of the nanotube is abrupt starting at a single atomic defect and propagating very quickly across its entire circumference. The calculated stress and strain are: 40 GPa and 18% for the zigzag (22,0) tube, 34 GPa and 17% for the armchair (14,14) tube. Fig. 10

presents the simulated rupture process. No experimental study of the tensile tests of MoS<sub>2</sub> nanotubes is available in the literature, but the strain results can be compared with those of WS<sub>2</sub> nanotubes. The values of the tensile strength obtained in the simulation compare favorably with the experimental strength (11% of their Young's modulus) and elongation (14% values) of WS<sub>2</sub> nanotubes. The small differences between theory and experimental data can be attributed to the fact that under the present experimental conditions, equilibrium may not be established. Furthermore, thermal fluctuations, which can lead to "early" failure, could not be fully accounted for in the calculations. Finally, the experimental elongation is a lower bound, since for technical reasons, the series of SEM micrographs, which are taken during the experiments and serve for the analysis, do not cover the entire process until the failure point is reached.

## SUMMARY

The mechanical properties of WS<sub>2</sub> and MoS<sub>2</sub> nanotubes were studied using various techniques, by both experimental and theoretical calculations. The multiwall WS<sub>2</sub> nanotubes were studied by a variety of techniques, and showed superior mechanical behavior and properties. These nanotubes have Young's modulus of ca. 150 GPa and tensile strength above 16 GPa. They deform elastically to a large extent both under compression and in tension. Furthermore, they seem to be almost defect-free, since they reach the theoretical strength. As for MoS<sub>2</sub> nanotubes, only a limited set of experiments were reported. Young's modulus of these nanotubes was found to be 120 GPa according to bending tests and 238 GPa according to calculations. This discrepancy was attributed to the fact that ropes (bundles) of single-wall nanotubes and not individual nanotubes were measured and they are suspected to have defects, while the calculation took into account individual single-wall nanotubes, which are free of defects. The low shear modulus of these ropes (160 MPa) is indicative of the low shear between the nanotubes in the ropes, hence pointing out the low friction between them. The theoretical simulation of tensile tests shows a similar mechanical behavior for both MoS<sub>2</sub> and WS<sub>2</sub> nanotubes.

## REFERENCES

- Barber, A.H.; Cohen, S.R.; Wagner, H.D. *Appl. Phys. Lett.* **2003**, *82* (23), 4140–4142.
- Demczyk, B.G.; Wang, Y.M.; Cumings, J.; Hetman, M.; Han, W.; Zettl, A.; Ritchie, R.O. *Mater. Sci. Eng. A—Struct. Mater. Properties Microstruct. Process.* **2002**, *334* (1–2), 173–178.
- Lourie, O.; Cox, D.M.; Wagner, H.D. *Phys. Rev. Lett.* **1998**, *81* (8), 1638–1641.
- Williams, P.A.; Papadakis, S.J.; Patel, A.M.; Falvo, M.R.; Washburn, S.; Superfine, R. *Phys. Rev. Lett.* **2002**, *89* (25), 255–502.
- Yu, M.F.; Files, B.S.; Arepalli, S.; Ruoff, R.S. *Phys. Rev. Lett.* **2000**, *84* (24), 5552–5555.
- Yu, M.F.; Lourie, O.; Dyer, M.J.; Moloni, K.; Kelly, T.F.; Ruoff, R.S. *Science* **2000**, *287* (5453), 637–640.
- Dai, H.J.; Hafner, J.H.; Rinzler, A.G.; Colbert, D.T.; Smalley, R.E. *Nature* **1996**, *384* (6605), 147–150.
- Nishijima, H.; Akita, S.; Nakayama, Y. *Japan. J. Appl. Phys. Part 1—Regular Papers Short Notes & Review Papers* **1999**, *38* (12B), 7247–7252.
- Tenne, R.; Margulis, L.; Genut, M.; Hodes, G. *Nature (London)* **1992**, *360* (6403), 444–446.
- Feldman, Y.; Wasserman, E.; Srolovitz, D.J.; Tenne, R. *Science (Washington)* **1995**, *267* (5195), 222–225.
- Chopra, N.G.; Luyken, R.J.; Cherrey, K.; Crespi, V.H.; Cohen, M.L.; Louie, S.G.; Zettl, A. *Science* **1995**, *269* (5226), 966–967.
- Spahr, M.E.; Bitterli, P.; Nesper, R.; Muller, M.; Krumeich, F.; Nissen, H.U. *Angewandte Chemie—International Edition* **1998**, *37* (9), 1263–1265.
- Rosenfeld Hacohe, Y.; Popovitz-Biro, R.; Prior, Y.; Gemming, S.; Seifert, G.; Tenne, R. *Phys. Chem. Chem. Phys.* **2003**, *5* (8), 1644–1651.
- Rao, C.N.R.; Govindaraj, A.; Deepak, F.L.; Gunari, N.A.; Nath, M. *Appl. Phys. Lett.* **2001**, *78* (13), 1853–1855.
- Tenne, R. *Angewandte Chemie, International Edition* **2003**, *42* (42), 5124–5132.
- Bezryadin, A.; Verschueren, A.R.M.; Tans, S.J.; Dekker, C. *Phys. Rev. Lett.* **1998**, *80* (18), 4036–4039.
- Cao, J.; Wang, Q.; Dai, H.J. *Phys. Rev. Lett.* **2003**, *90* (15), 157–601.
- Paulson, S.; Falvo, M.R.; Snider, N.; Helsen, A.; Hudson, T.; Seeger, A.; Taylor, R.M.; Superfine, R.; Washburn, S. *Appl. Phys. Lett.* **1999**, *75* (19), 2936–2938.
- Tombler, T.W.; Zhou, C.W.; Alexseyev, L.; Kong, J.; Dai, H.J.; Lei, L.; Jayanthi, C.S.; Tang, M.J.; Wu, S.Y. *Nature* **2000**, *405* (6788), 769–772.
- Barber, A.H.; Andrews, R.; Schadler, L.S.; Wagner, H.D. *Appl. Phys. Lett.* **2005**, *87* (20), 203106.
- Rosentsveig, R.; Margolin, A.; Feldman, Y.; Popovitz-Biro, R.; Tenne, R. *Chem. Mater.* **2002**, *14* (2), 471–473.
- Remskar, M.; Skraba, Z.; Regula, M.; Ballif, C.; Sanjines, R.; Levy, F. *Adv. Mater.* **1998**, *10* (3), 246.
- Seifert, G.; Kohler, T.; Tenne, R. *J. Phys. Chem. B* **2002**, *106* (10), 2497–2501.
- Kaplan-Ashiri, I.; Cohen, S.R.; Gartsman, K.; Rosentsveig, R.; Seifert, G.; Tenne, R. *J. Mater. Res.* **2004**, *19* (2), 454–459.
- Kaplan-Ashiri, I.; Cohen, S.R.; Gartsman, K.; Ivanovskaya, V.; Heine, T.; Seifert, G.; Wiesel, I.



- Wagner, H.D.; Tenne, R. Proc. Natl. Acad. Sci. USA **2006**, *103* (3), 523–528.
26. Ashby, M.F. Acta Metallurgica **1989**, *37* (5), 1273–1293.
  27. Callister, W.D. *Materials Science and Engineering: An Introduction*, 5th Ed.; Wiley: New York, 2000; p. xxi, 871.
  28. Wu, B.; Heidelberg, A.; Boland, J.J. Nat. Mater. **2005**, *4* (7), 525–529.
  29. Yakobson, B.I.; Avouris, P. Carbon Nanotubes **2001**, *80*, 287–327.
  30. Gao, H.J.; Ji, B.H.; Jager, I.L.; Arzt, E.; Fratzl, P. Proc. Natl. Acad. Sci. USA **2003**, *100* (10), 5597–5600.
  31. Mann, N.R.; Schafer, R.E.; Singpurwalla, N.D. *Methods for Statistical Analysis of Reliability and Life Data*, Wiley: New York, 1974; p. ix, 564.
  32. Wagner, H.D. J. Polym. Sci. Part B–Polym. Phys. **1989**, *27* (1), 115–149.
  33. Pugno, N.M.; Ruoff, R.S. Philos. Mag. **2004**, *84* (27), 2829–2845.
  34. Kaplan-Ashiri, I.; Cohen, S.R.; Apter, N.; Wang, Y.K.; Seifert, G.; Wagner, H.D.; Tenne, R. J. Phys. Chem. C **2007**, *111* (24), 8432–8436.
  35. Kis, A.; Mihailovic, D.; Remskar, M.; Mrzel, A.; Jesih, A.; Piwonski, I.; Kulik, A.J.; Benoit, W.; Forro, L. Adv. Mater. **2003**, *15* (9), 733–736.
  36. Timoshenko, S. *Theory of Elastic Stability*, 2nd Ed.; McGraw-Hill: New York, 1961; 541 pp.
  37. Wagner, H.D.; Fischer, S.; Roman, I.; Marom, G. Composites **1981**, *12* (4), 257–259.
  38. Wagner, H.D.; Marom, G.; Roman, I. Fibre Sci. Technol. **1982**, *16* (1), 61–65.
  39. Timoshenko, S. *Strength of Materials*, 3rd Ed.; Van Nostrand: New York, 1955; 2v.
  40. Vinson, J.R.; NetLibrary Inc. *The Behavior of Sandwich Structures of Isotropic and Composite Materials*, Technomic Pub. Co.: Lancaster, PA, 1999; xvi, 378.
  41. Zhu, Y.Q.; Sekine, T.; Brigatti, K.S.; Firth, S.; Tenne, R.; Rosentsveig, R.; Kroto, H.W.; Walton, D.R.M. J. Am. Chem. Soc. **2003**, *125* (5), 1329–1333.
  42. Zhu, Y.Q.; Sekine, T.; Li, Y.H.; Fay, M.W.; Zhao, Y.M.; Poa, C.H.P.; Wang, W.X.; Roe, M.J.; Brown, P.D.; Fleischer, N.; Tenne, R. J. Am. Chem. Soc. **2005**, *127* (46), 16,263–16,272.
  43. Margulis, L.; Salitra, G.; Tenne, R.; Talianker, M. Nature **1993**, *365* (6442), 113–114.
  44. Remskar, M. Adv. Mater. **2004**, *16* (17), 1497–1504.
  45. Remskar, M.; Mrzel, A.; Skraba, Z.; Jesih, A.; Ceh, M.; Demsar, J.; Stadelmann, P.; Levy, F.; Mihailovic, D. Science **2001**, *292* (5516), 479–481.

# Integrated Methods in Quantum Chemistry

Stephan Irle  
Keiji Morokuma

Department of Chemistry, Emory University, Atlanta, Georgia, U.S.A.

## INTRODUCTION

Coinciding with the discovery of the C<sub>60</sub> buckminsterfullerene molecule,<sup>[1]</sup> nanotechnology was envisioned in the mid-1980s<sup>[2]</sup> as the art of manipulating matter at the atomic level. Since then, nanotechnology rapidly became a growing interdisciplinary research area, driven by one promise: Regardless of the rate at which nanotechnology will be implemented, it holds the potential to change *everything*. Unfortunately, it has proven to be very difficult to obtain reliable structural data on nanostructures, and their chemical reaction mechanisms are still largely unknown, making it extremely difficult to create commercially successful applications. In addition to these difficulties, the quantum effects responsible for the properties and reactivity of nanoscale chemical systems are very often qualitatively different from those of either bulk material or atoms and molecules, thereby preventing us to make use of our knowledge of their electronic structures. We find ourselves today forced to study nanoscale electronic structures from the very beginning with the focus on a size domain where quantum mechanics and classical mechanics meet to create new fascinating phenomena and structural wonders. Unfortunately, the computational cost of traditional electronic structure methods remains by far too large even today at the age of ultrafast computers to permit direct investigation of realistic models relevant to the nanoscale at the quantum chemical level. The problem is the vast number of atoms involved in these structures. For instance, when one assumes an interatomic distance of ~0.2 nm in the solid state, a 3-D system only 10 nm in size involves ~125,000 atoms. Although advances in massively parallel processing, linear scaling techniques, localized orbital methods, and sophisticated integral approximation methods have in recent years extended the applicability of ab initio molecular orbital (MO) and density functional theory (DFT) methods to larger and larger systems, calculations on the nanometer scale remains far beyond their reach. Atomic level modeling of systems of this size is only theoretically achievable by means of molecular mechanics force fields. Unfortunately, classical mechanical force field approaches are incapable of

describing fundamental chemical processes such as oxidation, reduction, electronic excitation, and bond breaking. Band gaps, relative position of conduction and valence bands, lifetimes of electron/hole pairs, magnetic response, optical response, charge transfer rates, (photo)oxidation/reduction rates, and bond breaking/formation rates are important properties of quantum character that require a rigorous quantum chemical treatment where conventional molecular mechanics force field approaches naturally fail.

Clearly, describing electronic structure at the nanoscale is a great challenge, which has been taken on by many research groups worldwide using a variety of different approaches. As a zero-order approximation, computationally inexpensive and not very accurate semiempirical or tight-binding methods have been used to compute the electronic structures of large clusters and nanostructures, and in some cases DFT methods in combination with small basis sets were employed, unwillingly accepting a low level of accuracy. In very few cases, higher-accuracy methods such as second-order Møller–Plesset perturbation theory (MP2) with reasonably sized basis sets were used to predict equilibrium geometries for highly symmetrical structures.<sup>[3,4]</sup> In general, however, chemically accurate (within ~3 kcal/mol) calculations for nanoscale systems cannot be performed using straightforward, high-accuracy quantum chemical methods. As a possible solution to this dilemma, so-called “integrated” or “hybrid” methods have recently become an attractive alternative for large-scale quantum chemistry, by combining high-accuracy calculations for small parts of the nanostructures and less accurate lower levels of theory for the entire system. In fact, if applied carefully, these methods are capable of delivering chemical accuracy in the prediction of electronic structures and reactivities in the chemistry on the nanoscale. Their recent contributions toward a deeper and more accurate understanding of nanoscale quantum chemistry are subject of this review.

At first we will introduce quantum chemical methods applicable to extended molecular systems or parts of them, describe in short the theory behind integrated methods, and in the second part discuss their applications to the most recognizable areas of

nanochemistry, namely, the chemistry of fullerenes, nanotubes, and silica-based nanosystems. Finally, we will give an outlook into the future development of integrated methods and their tremendous potential in the theoretical investigation of quantum chemistry on the nanoscale.

## QUANTUM CHEMICAL METHODS FOR EXTENDED SYSTEMS

### Semiempirical Methods

Similar to ab initio Hartree–Fock (HF) theory, semiempirical methods are based on the Roothaan–Hall equations:<sup>[5,6]</sup>

$$\mathbf{FC} = \mathbf{SCE} \quad (1)$$

Here,  $\mathbf{F}$  is the Fock matrix and  $\mathbf{S}$  is the overlap integral matrix between atomic basis functions,  $\mathbf{C}$  is the matrix of molecular orbitals in an atom-centered orbital basis following the linear combination of atomic orbitals (LCAO) approach of Hund and Mulliken,<sup>[7–9]</sup> and  $\mathbf{E}$  is diagonal and its elements are eigenvalues (orbital energies) of the Fock matrix  $\mathbf{F}$ . While ab initio HF requires that all elements of  $\mathbf{F}$  have to be calculated fully without approximation, in semiempirical calculations several simplifications to the evaluation of the elements of  $\mathbf{F}$  are made.

The main effect regarding a reduction of computer time is achieved by elimination or approximation of some of the integrals needed for the evaluation of the Fock matrix elements. Furthermore, only valence electrons are considered in semiempirical methods, all other electrons are included in the “core.” Usually, Slater type (*s*-, *p*-, and *d*-type) functions are used as atom-centered basis functions. With the noticeable exception of extended Hückel theory<sup>[10,11]</sup> most semiempirical methods make use of the zero differential overlap (ZDO) approximation, which defines the overlap integral between different basis functions as zero. The overlap matrix  $\mathbf{S}$  in the Roothaan–Hall equations thus becomes a unit matrix:

$$\mathbf{FC} = \mathbf{CE} \quad (2)$$

The various ZDO models can be grouped according to their approximations for the one- and two-electron integrals and their different approaches to parameterization:

- CNDO: complete neglect of differential overlap,<sup>[12]</sup>
- NDDO: neglect of diatomic differential overlap<sup>[13]</sup>
- INDO: intermediate neglect of differential overlap<sup>[14]</sup>
- MINDO/3: modified INDO<sup>[15]</sup>
- MNDO: modified neglect of diatomic overlap<sup>[16]</sup>
- AM1: Austin Model 1<sup>[17]</sup> analogue of MNDO

- SAM1: improved AM1,<sup>[18]</sup>
- PM3 and PM5: third (fifth) parametrization of MNDO<sup>[19,20]</sup> analogue of MNDO

Most of the integrals of these methods are estimated from experimental values. Hence outside the class of chemical compounds for which these estimations are parameterized, results may be doubtful. This is especially a problem in the case of nanotechnological systems, where experimental values for quantum chemical integrals are almost impossible to obtain.

The extended Hückel theory (also sometimes called “tight-binding” method) and its charge iterative cousins neglect the two-electron integrals altogether or retain only the most important two-center repulsion integrals.<sup>[10,11]</sup> Their simplicity and resulting tremendous computational speed make them potent candidates for a qualitative treatment of electronic effects in large, extended systems. In particular, molecular dynamics (MD) calculations for systems at finite temperature have been carried out using semiempirical methods in the context of nanometer-sized systems.<sup>[21–24]</sup>

### Linear Scaling, Resolution of Identity, and Localized MO Methods

In the quest to make conventional quantum chemical methods computationally more economical, efforts toward low-order scaling have been made in recent years by taking advantage of the fact that long-range interactions can be evaluated approximately by power series expansion or by mathematical projection techniques (resolution of identity, or RI).<sup>[25,26]</sup> For instance, in DFT, the long-range Coulomb potential has been successfully approximated using a variety of linear scaling versions of the fast multipole method (FMM), and the scaling of exchange and correlation functionals has been linearized using quadrature techniques, allowing the implementation of purely  $O(N)$  DFT. The RI method is an alternative to FMM, where four-center coulombic integrals are approximated by three-center integrals, using fitting functions for the electron density in the spirit of Baerends, Ellis, and Ros.<sup>[27]</sup> An efficient implementation of RI-DFT can be found, e.g., in the TURBOMOLE program package.<sup>[28]</sup>

More accurate methods such as MP2 are based on the evaluation of orbital–orbital interactions and are very expensive because of their large number and the delocalized nature of HF orbitals. The RI method has found its application in MP2 calculations as well,<sup>[29]</sup> and analytical gradients are available. In another approach to simplify MP2, several groups found that replacing delocalized canonical HF MOs by localized molecular orbitals (LMOs) leads to a tremendous speedup for localized MP2 (LMP2)

calculations at a small loss of accuracy.<sup>[30–32]</sup> However, LMP2 analytical gradients desperately required for geometry optimizations of large molecular systems are not generally available until now. While electron correlation methods based on LMOs are still not applicable to systems beyond the size of about 100 atoms today, they certainly will provide a way to significantly extend the range of applicability for these methods.

### Hybrid Quantum Mechanics/Molecular Mechanics Methods

Hybrid methods use different levels of theory for different parts of the molecular system under investigation. The earliest practical implementation of such a technique by Warshel and Karplus combined a semiempirical MO method with a classical molecular mechanics method,<sup>[33]</sup> a methodology commonly called the “QM/MM” method.<sup>[34,35]</sup> In most QM/MM implementations, “link atoms” are introduced to satisfy the valencies of the QM atoms that are connected to any MM atoms. The Hamiltonian describing the entire system is typically partitioned as

$$H = H^{\text{QM}} + H^{\text{MM}} + H^{\text{QM-MM}} \quad (3)$$

where  $H^{\text{QM}}$  is the QM part of the Hamiltonian,  $H^{\text{MM}}$  is the energy of the MM part, and  $H^{\text{QM-MM}}$  represents the interaction between the QM part and the MM part, treated either by molecular mechanics or by quantum mechanical calculations. More recently, ab initio or DFT QM/MM methods have gained considerable popularity (see, e.g., Refs.<sup>[36,37]</sup>, and<sup>[38]</sup>). While QM/MM methods are being successfully applied in bioorganic and bioinorganic systems such as enzymes consisting of proteins the size of hundreds of thousands of atoms with a local reactivity center, their usefulness in the context of nanoscale chemistry is somewhat limited because of the extended delocalized electronic structures encountered here. For instance, carbon nanosystems typically possess almost infinitely extended  $\pi$ -conjugated systems, and the electronic structures of metallic nanoclusters closely resemble electronic bands in dependence of the system size. Because MM is not capable of incorporating these electronic effects, their influence on the QM part is missing in a QM/MM treatment of nanochemistry systems. Nevertheless, the QM/MM approach finds its use in the theoretical investigation of nanostructures because of the ability of MM to impose structural constraints, such as, e.g., ring strain and steric repulsion.

### Integrated Methods

The ONIOM (our N-layered integrated molecular orbital and molecular mechanics) method can also be

considered as a hybrid method. It has the advantage of greater conceptual simplicity than QM/MM, is well defined, can make use of all of the methods described above, and is exact in the case when identical methods are used for different layers of the system. The author and his coworkers developed ONIOM as an onion-skin-like extrapolation method (Fig. 1) that allows the combination of a variety of QM methods and optionally an MM method in a hypothetically unlimited number of layers.<sup>[39–44]</sup> Practically, two and three layers are being used, usually denoted as ONIOM2 and ONIOM3, respectively. The system can additionally be solvated by applying a well-defined integrated solvation scheme, commonly called ONIOM-PCM.<sup>[45]</sup> The ONIOM implementation of the GAUSSIAN03 program package<sup>[46]</sup> provides the flexibility to call external QM or MM program codes for individual layers, making ONIOM independent from the methods offered by GAUSSIAN itself.

The goal of ONIOM is to describe a large *real* system at a *high* level of theory, which is usually prohibitively expensive,  $E(\text{high, real})$ . In ONIOM, this target calculation is extrapolated from a computationally more feasible, *lower*-level calculation for the *real* system,  $E(\text{low, real})$ , and an accurate *high*-level calculation for a *model* system,  $E(\text{high, model})$ , together with a “correction” term  $E(\text{low, model})$ :

$$\begin{aligned} E(\text{ONIOM, real}) &= E(\text{low, real}) \\ &+ E(\text{high, model}) \\ &- E(\text{low, model}) \quad (4) \end{aligned}$$

These are three calculations that can be carried out independently from each other, and the scheme can easily be extended to three or more layers of any theoretical method, as shown in Fig. 1. Unique to ONIOM and in contrast to the QM/MM hybrid method, it is possible to combine different theoretical levels of MO-based methods, making ONIOM more useful for extended quantum systems. Furthermore, energy gradients with respect to nuclear coordinates  $\partial E(\text{ONIOM,real})/\partial E(\mathbf{R}_{\text{real}})$  as well as various properties, such as electron densities, dipole moments, nuclear magnetic shielding, etc., are well defined and can be calculated in the same spirit as ONIOM expectation values of the corresponding operator  $o$  as

$$\begin{aligned} \langle o(\text{ONIOM, real}) \rangle &= \langle o(\text{low, real}) \rangle \\ &+ \langle o(\text{high, model}) \rangle \\ &- \langle o(\text{low, model}) \rangle \quad (5) \end{aligned}$$

Specific ONIOM combinations are uniquely denoted as ONIOM(high-level method: low-level method) with a “:” (colon) separating individual layer methods.

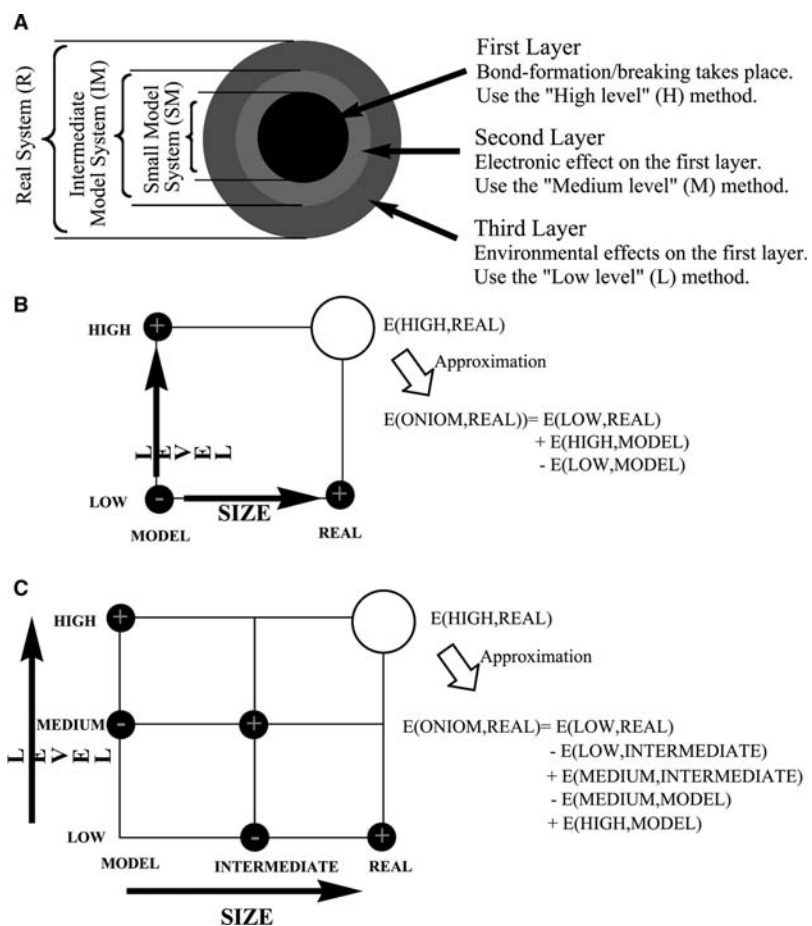


**Fig. 1** The ONIOM method. (A) The onion skin-like layers and models. (B) The two-layer ONIOM method. (C) Three-layer ONIOM method.

Although ONIOM(MO:MO)-type calculations include the extended electronic structure of the real system in the low layer, the user is not released from the duty of paying attention if the system under investigation can be soundly partitioned into a high-level and a low-level layer. ONIOM works well only if the "major players," i.e., the area of chemical transformation, are fairly localized in a specific region of the system, with the outer environment playing the role of "minor players" or "spectators." An arbitrary choice of partitioning scheme and method combination may not work, and therefore a systematic procedure to test the reliability of the level/method combination has been devised.<sup>[44]</sup> This test is based on the so-called

$S$ -value (substituent value), which is defined at a given level as

$$S(\text{level}) = E(\text{level, real}) - E(\text{level, model}) \quad (6)$$

and represents the influence of the environment on the model system. ONIOM becomes exact when  $S(\text{low})$  is identical to  $S(\text{high})$ . The test requires knowledge of  $S(\text{high})$ , and in practice one performs an expensive target calculation for a few compounds out of a series of related systems to which ONIOM is to be applied in order to calibrate the accuracy of ONIOM for the chosen layer/method combination. To illustrate the  $S$ -value test, Table 1 shows an example for the

**Table 1**  $S$ -values (in kcal/mol) and their differences (in parenthesis) for  $C_{sp^3}$ -H bond dissociation for *Iso*-Butane and Toluene, employing a minimal (methane) model and B3LYP/6-31G geometries

Level	<i>iso</i> -Butane		Toluene		
G2MS(R)	-7.75	(0.00)	-16.21	(0.00)	target (high) level
UHF/6-31G(d)	-7.29	(+0.46)	-26.12	(-9.91)	poor low level
RHF/6-31G(d)	-6.73	(+1.02)	-10.28	(+5.93)	poor low level
UMP2/6-31G(d)	-7.72	(+0.03)	6.93	(+23.14)	poor low level
RMP2/6-31G(d)	-8.10	(-0.35)	-15.04	(+1.17)	excellent low level

C<sub>sp3</sub>-H bond-dissociation energy of a series of hydrocarbons and derivatives. Test molecules are *iso*-butane and toluene, with a minimal CH<sub>3</sub>-H as the model system for the bond dissociation process. Here the RMP2/6-31G(d) *S*-value is very close to that of the target high-level G2MS calculation, which is itself an extrapolation method based on CCSD(T) and MP2 energetics<sup>a</sup>, making RMP2/6-31G(d) an ideal low-level method in conjunction with the high-level G2MS method in this example. Other methods in Table 1 are, however, off by as much as 20 kcal/mol, indicating that these are very poor level methods in combination with the G2MS high-level method. Tests such as these are necessary in order to assess the reliability of ONIOM calculations. Keeping this in mind, however, ONIOM is potentially a very powerful, and to date in fact the only large-scale, electronic structure method delivering high accuracy.

## APPLICATION OF HYBRID AND INTEGRATED METHODS IN NANOCHEMISTRY

### Fullerene Chemistry

Following their first appearance in mass spectra, C<sub>60</sub>, larger and smaller fullerenes, as well as their derivatives and chemical reactions, have become some of the most popular objects for research in theoretical and computational chemistry worldwide. Almost any theoretical method available to the computational chemist has been applied in the calculation of their properties and reactivities, with the only exception of expensive correlation methods based on multireference wave functions.<sup>[47–49]</sup> Here we will concentrate on the application of integrated methods that have been employed in the theoretical study of fullerene chemistry.

### Bond-breaking energies in C<sub>60</sub> fullerene

The first documented work on C<sub>60</sub> using an integrated method was published in 1999 and presented ONIOM3 results for adiabatic S<sub>0</sub> → T<sub>1</sub> and S<sub>0</sub> → Q energy splittings as models for bond-breaking processes in fullerene molecules.<sup>[50]</sup> The target method in this case was the highly accurate, single-reference G2MS level of theory, and a three-layer ONIOM3 approach was chosen to extrapolate G2MS single-point energetics for the singlet ground state and first triplet and quintet states of C<sub>60</sub> for AM1-optimized geometries. This way, single- and double-bond-breaking processes for the hexagon/hexagon C–C bond in C<sub>60</sub> were studied, using

ethylene as the high-level model and naphthalene as the intermediate-level model. For this system size with G2MS as target method, performing an *S*-value test is clearly impossible, and therefore the accuracy of different ONIOM3 energetics was determined by comparison with the experimental adiabatic S<sub>0</sub> → T<sub>1</sub> splitting of 36.1 kcal/mol. At the time this work was done, it was found that the best ONIOM3 methodology applicable to this problem was a G2MS:MP2:HF (H)igh:(I)ntermediate:(L)ow-level combination with naphthalene and ethylene as intermediate and small model, respectively, specifically the ONIOM(G2MS(R):ROMP2/6-31G(d):RHF/6-31G) methodology with a computed S<sub>0</sub> → T<sub>1</sub> splitting of 35.1 kcal/mol in almost perfect agreement with experiment. This was an indication that the G2:MP2:HF combination generally seems to work very well. In a later study it was observed that, if the target level is CCSD(T) or a G2-like method, the best choice of lower level is MP2, and that HF is a good lower-level choice for MP2.<sup>[44]</sup> No practicable single-level quantum chemical methods can even give qualitatively similar results for the bond-breaking processes of C<sub>60</sub>, as HF/6-31G for the real system lacks important dynamic electron correlation, and correlated calculations on model systems alone lack sufficient  $\pi$ -conjugation and the strain of the carbon cage.

### Insertion of a small atom or ion into the C<sub>60</sub> cage

Encouraged by the success of the previously described G2:MP2:HF ONIOM3 study, a similar ONIOM scheme was applied for the study of Li<sup>+</sup> insertion into the orifice of a chemically modified C<sub>60</sub>,<sup>[51]</sup> created by a concerted ring-opening retro [2 + 2 + 2] cycloaddition reaction as proposed by Rubin et al.<sup>[52]</sup> Precursors to the opened species are hypothetical hexahydro and hexamethyl derivatives, as well as the experimentally studied bistriazoline and bislactam derivatives. Common to these modified fullerene molecules are six substituent bonds attached to a single hexagon of C<sub>60</sub>, leading to six single C–C bonds, thereby interrupting  $\pi$ -conjugation in this region. As can be seen in Fig. 2 (which also shows the three different ONIOM layers), this hexagon can easily break open in two ways to reduce ring strain and reestablish  $\pi$ -conjugation by cutting bonds of either adjacent five-membered (5-open) or six-membered (6-open) rings. Aromatic stabilization arguments already suggest that leaving six-membered  $\pi$ -conjugated rings intact (5-open species) would be preferable, and previous AM1 and PM3 semiempirical methods already indicated this preference. The *S*-value of ONIOM is very helpful in quantifying these effects. Here particularly interesting is the *S*(I–M)-value between the (M)odel and (I)ntermediate systems, which is calculated to be about 28 kcal/mol more

<sup>a</sup>The G2MS energy is a simplified version of the G2 method and is defined as G2MS = CCSD(T)/6-31G(d) + MP2/6-311 + G(2df,2p)-MP2/6-31G(d), which extrapolates the CCSD(T)/6-311 + G(2df,2p) result.



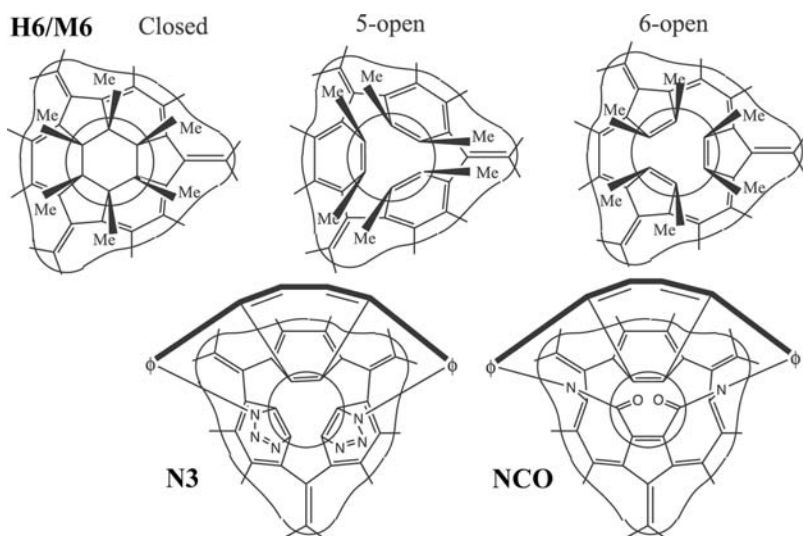


**Fig. 2** Schematic drawings of the structures and ONIOM models for **H6**, **H6-5o**, **H6-6o**, **M6**, **M6-5o**, **M66o**, **N3**, and **NCO**. The atoms inside the smaller circle (plus link H atoms) constitute the small model system **M** and the larger circular curve (plus link H atoms) the intermediate model system **I**. *Source:* From Ref.<sup>[51]</sup>.

stabilizing for 5-open species as opposed to the 6-open species. Subsequent  $\text{Li}^+$  insertion barriers were optimized using an ONIOM2 approach with MP2/6-31G(d) and RHF/3-21G for the intermediate model and the real system, respectively, and the transition states characterized by performing vibrational frequency analysis at the same level of theory. The lithium cation, as the smallest representative of a metal, experiences still a relatively high barrier for the hypothetical hexahydro and hexamethyl open derivatives between 45 and 62 kcal/mol, its value closely related to the size of the opening diameter. The bistriazoline and bislactam systems, however, exhibit slightly larger orifices, causing the barrier to drop down to 20 and 16 kcal/mol. In recent experiments, He atoms with a comparable atomic radius to  $\text{Li}^+$  have indeed been successfully inserted into the bislactam species,<sup>[53]</sup> confirming the predictions of this ONIOM3 work.

### Dynamics of endohedral fullerene complexes

Besides the formation mechanism and/or synthetic routes for endohedral and exohedral metal fullerene complexes, the dynamics of metal atoms in these systems is of great interest to theoreticians, because experimentally only very limited information can be obtained on their dynamics within or on the surface of the carbon cage. However, because strong charge transfer typically characterizes most endohedral and exohedral fullerene complexes, reasonable quantum chemical molecular dynamics simulations have to be performed for this purpose. Only recently, semiempirical QM/MM MD studies on the dynamical change of Be effective charges in  $(\text{Be} + n\text{H}_2)\text{-C}_{60}$  endohedral fullerene complexes ( $n = 0, 1, \text{ and } 2$ ) in the bulk were published by Shigeta and Saito<sup>[54]</sup> in order to elucidate the controversial question<sup>[55]</sup> as to whether the Be

atom could become negatively charged for  $n = 0$  at finite temperatures. In this study, spin-restricted AM1 dynamics are performed on singlet and triplet electronic states for a single complex, surrounded by periodic replicant MM images to simulate NVT ensembles. While MM2 parameter sets were used for MM interactions, the NDDO approximation was selected for QM/MM electrostatic interactions, with effective charges on MM atoms being replaced by the single molecule AM1 Mulliken charges. Total simulation time was 8 psec with time steps of 0.2 fsec under constant temperatures at 0, 100, 200, 300, and 400 K. In these simulations it is found that the endohedral Be atoms are indeed negatively charged in the  $n = 0$  and 1 cases, with charge fluctuation reaching  $0.1 e^-$  at higher temperatures, and that even for the  $n = 2$  case Be becomes occasionally slightly negatively charged during 10 psec of simulations at 400 K. This study revealed that dynamic charge fluctuations are potentially problematic for the design of molecular memory cells based on endohedral fullerene charge transfer complexes.

### Van der Waals interactions with fullerene

Van der Waals complexes represent a challenge for computational chemistry methods because at least the MP2 level with a polarized basis set is required for a qualitatively reasonable treatment of dispersion forces. Although fullerene molecules themselves have been treated before at the MP2 level of theory, these calculations were made possible by taking advantage of the high molecular symmetry characteristic for fullerenes.<sup>[3]</sup> Under chemical transformations, however, the high symmetry is lost, and pure MP2 calculations become beyond the reach of computational practicality. Fomine et al. investigated chemical reactions

of  $C_{60}$  with exactly these requirements, namely, complex formation with the donor molecules dimethyl ether, dimethylamine, dimethylsulfide, furan, pyrrole, and thiophene, choosing a two-layer ONIOM(MP2/6-31G(d):PM3) approach for geometry optimizations.<sup>[56]</sup> Their high-level model system included donor molecule as well as a naphthalene unit (two hexagons plus one adjacent pentagon) of the fullerene. Binding energies were then evaluated using pure LMP2 single-point energies in combination with the 6-31G(d) and 6-311G(d,p) basis sets. Tests on the reliability of the applied methods were carried out only for LMP2 benzene dimer interactions. As LMP2 analytical gradients have not yet been developed for this particular approach, ONIOM2 provided a valuable alternative for the calculation of these fullerene van der Waals complexes.

## Carbon Nanotube Chemistry

The electronic structures of carbon nanotubes (CNTs) have been studied extensively using semiempirical extended Hückel and tight-binding methods, and periodic DFT functionals have been employed as well.<sup>[57,58]</sup> In particular, band gaps and the associated electrical conducting properties for pristine nanotubes with different helical indices and diameters can be explained by using the simple Hückel theory.<sup>[59]</sup> This circumstance is particularly fortunate for theoretical investigations of carbon nanotubes using integrated MO:MO approaches, as the extended tube  $\pi$ -system can be included qualitatively at the low level using low computational cost semiempirical methods. Yet, MO:MM methods have also found application in the theoretical study of CNT chemistry, because they allow the introduction of curvature in these rolled graphitic sheets by means of a “shape restraint” at the low level.

### Functionalization of CNTs

Recent studies by Basiuk et al.<sup>[60–62]</sup> examined the suitability of either AM1 or universal force field (UFF)<sup>[63]</sup> for the lower theoretical level in ONIOM on nanotube chemistry by systematically comparing ONIOM2(B3LYP/6-31G(d):AM1) and ONIOM2(B3LYP/6-31G(d):UFF) approaches for the study of aliphatic amine interaction with carboxylated achiral, hydrogenated open SWCNTs. The model system for the carboxylated armchair or zigzag nanotubes employed in this study included just one hexagon plus two nearest neighbored carbon atoms at the opening with the  $-COOH$  group pointing outside the tube. Also included in the B3LYP/6-31G(d) layer were amines as large as nonylamine, interacting with the carboxylate via a

hydrogen bond. Reactant complexes, transition states, and hydrogen-bonded as well as separated products were computed at both levels, as well as single-level AM1 and UFF. It was found throughout their studies that armchair nanotubes are more reactive than the zigzag type, a conclusion that correlates very well with the fact that the Hückel HOMO–LUMO band gap is zero for infinite armchair nanotubes.<sup>[59]</sup> Because a target B3LYP/6-31G(d) calculation was not performed, the authors could not give a definitive answer as to which method would be more suitable for the lower level, except for the obvious advantage that UFF requires much less computer time than AM1.

Cycloaddition reactions are a natural choice for the functionalization of CNTs, and several types have been studied using integrated methods. Experimentally, the first CNT functionalization was carried out using dichlorocarbene,<sup>[64]</sup> and [2 + 1] cycloaddition reactions investigated using an ONIOM2(B3LYP/6-31G(d):AM1) scheme include dichlorocarbene, silylene, germylene, and also experimentally used oxycarbonylnitrene.<sup>[65]</sup> A pyrene-like, high-level model was chosen for a hydrogenated, open (5,5) armchair nanotube  $C_{130}H_{20}$ , and two reaction sites were investigated: the central, biphenyl-like 1,2-bond, and an adjacent 2,3-bond. The calculations revealed a strong preference for the 1,2-pair site, with thermal stabilities in the order oxycarbonylnitrene  $\gg$  dichlorocarbene  $>$  silylene  $>$  germylene, and suggest that silylene is a favorable [2 + 1] cycloaddition partner which could be employed in future CNT functionalizations.

The same group studied 1,3-dipolar cycloaddition reactions with a series of 1,3-dipolar molecules<sup>[66]</sup> as well as ozone<sup>[67]</sup> and Diels–Alder reactions with 1,3-butadiene and quinodimethane<sup>[68]</sup> on the sidewalls of differently sized armchair nanotubes, using again a pyrene-like part of the sidewall as high-level model in ONIOM2(B3LYP/6-31G(d):AM1) studies. In these studies it is found that both 1,3-dipolar cycloaddition and retro-cycloadditions are moderately dependent on the diameters of the SWCNT, implying the feasibility of making use of such addition reactions to purify and separate SWCNTs diameter specifically.

In a study by a different group, a pyrene-like, high-level model for a (5,5) armchair SWCNT was also selected in an ONIOM2(B3LYP/LANL2DZ:UFF) study on the problem of sidewall oxidation and complexation by  $NH_3$ -catalyzed, synchronized [3 + 2] cycloaddition of transition osmium tetroxide. Reactants, transition states, and cycloaddition products were investigated in the presence of  $NH_3$  and without, and the prediction of this study was that base-catalyzed osmylation should be a very feasible new way to provide a starting point to further functionalize SWCNTs.

## Binding energies of atoms and molecules with CNTs

In 2000, Bauschlicher published the first theoretical binding energies of fluorine and hydrogen atoms to the side walls of a (10,0) open-ended, hydrogen-saturated  $C_{200}H_{20}$  carbon nanotube, using the ONIOM2 (B3LYP/4-31G:UFF) approach.<sup>[69]</sup> These calculations served as an alternative for the high-level *ab initio* calculations of Jaffe on small polyaromatic hydrocarbon molecules, where curvature was artificially introduced by constraining the distance between carbon edge bonds on one hand,<sup>[70]</sup> and the semiempirical AM1 calculations of Kelly et al. on a (10,10) tube<sup>[71]</sup> on the other. Bauschlicher's high-level model was composed of six hexagons surrounding a central hexagon and included 24 carbon atoms, 12 hydrogen link atoms, as well as one hydrogen or fluorine probe atom. Attempts to use semiempirical methods for the low level reportedly failed due to SCF convergence problems that can be attributed to the high density of states near the HOMO–LUMO gap for nanotubes, and the UFF was used instead. It was found that the sum of the first two F atom binding energies of 78 kcal/mol in a 1,2-type addition is significantly larger than the  $F_2$  bond energy, which is only 34 kcal/mol at the B3LYP/4-31G level of theory, whereas calculated binding energies suggest that covalent bonding of hydrogens to the (10,0) tube would be only slightly exothermic. Most noticeably, the first addition of F as well as H yields much smaller binding energies as compared to the second addition. In the quest to investigate the addition of hydrogen to CNT side walls in more detail, ONIOM2 studies on so-called “high coverages” of hydrogen on (10,0) and (9,0) zigzag, and (5,5) armchair achiral, capped tubes have been performed.<sup>[72,73]</sup> These studies with CNT coverage rates between 24% and 100% employ also B3LYP/4-31G and B3LYP/6-31G methods in the high level and use either UFF molecular mechanics or AM1 semiempirical methods in the low level. Twenty-four carbon atoms at the center of the tubes are treated at the high level. It was found that the average C–H binding energies for similar patterns are similar for all three tubes. The 100% coverage on the outside appears to be unfavorable, while 50% hydrogen on the inside and 50% on the outside seem to be a very favorable bonding situation, thus making hydrogen storage in carbon nanotubes a strong, realistic proposition. Similar conclusions were also reached by Froudakis in ONIOM2(B3LYP/6-31G(d):UFF) studies on hydrogen-terminated, open-ended SWCNTs with smaller diameters doped with alkali metal dopants and without.<sup>[74,75]</sup>

CNTs are easy to oxidize and exhibit different electrical conductivities in their oxidized states. There are indications that oxidation might be a reversible pro-

cess, possibly allowing the manufacturing of switches in molecular wires based on oxidized CNTs. The experimental binding energies of  $O_2$  to CNTs remain unknown to date. ONIOM2(MP2:UFF) calculations were carried out both on the physisorption and on the chemisorption of  $O_2$  on the inner and outer walls of a (9,0) CNT to elucidate the binding nature between molecule and tube.<sup>[76]</sup> The basis set for geometry optimizations was 6-31 + G(d,p), whereas larger, augmented, and polarized triple zeta basis sets were used for single-point energetics. Several models were examined, ranging from four to seven fused carbon hexagons plus one  $O_2$  molecule. Similar to the case of fullerenes described above, the MP2 method was used to describe van der Waals interactions between the tube and the  $O_2$  molecule. Physisorption was found to be favorable inside and outside over a single hexagon, with a small binding energy of about 2.5 kcal/mol for triplet  $O_2$  being aligned parallel to the hexagon plane. Little charge transfer was found with Mulliken population analysis, suggesting that the band gap of the CNT would only be insignificantly modified. Chemisorption in a [2 + 2] cycloaddition reaction was computed to be favorable by 20 kcal/mol, but associated with a large barrier of 65 kcal/mol, making this process very unlikely. The nature of defects of significantly modified oxidized CNTs remains therefore unclear and subject to future studies.

Very similar in spirit, however, with a much smaller high-level model system, an ONIOM2(MP2:UFF) study was carried out for the interaction of a (9,0) capped tube with the  $N_2$  molecule, where the experimental binding energy is known to be 2 kcal/mol, suggesting physisorption in this case.<sup>[77]</sup> Similar to the previously described studies, large basis sets were used for single-point MP2 energetics, while 6-31G(d) was used for geometry optimizations. However, as high-level model, only ethylene plus  $N_2$  was considered, and no *S*-value test was performed. Their good agreement of the computed binding energy of 1.88 kcal/mol with experiment was explained to be related to error compensation. The same group published also interaction energies of N and O atoms with CNTs using ONIOM2(B3LYP/6-31G(d):UFF) and ONIOM2(B3LYP/6-31G(d):B3LYP/STO-3G) approaches.<sup>[78]</sup> Once again, ethylene was used as the high-level model part for the CNT, and both the doublet and quartet states for the N-bridged structure are found to be bound. The author says that in case of O the present ONIOM calculation fails “miserably.” As no *S*-value test was performed, it is not clear whether the poor model or the poor low-level method is responsible for this failure.

## Vibrational spectroscopy

While there have been many calculations on the vibrational spectra of various types of pristine carbon

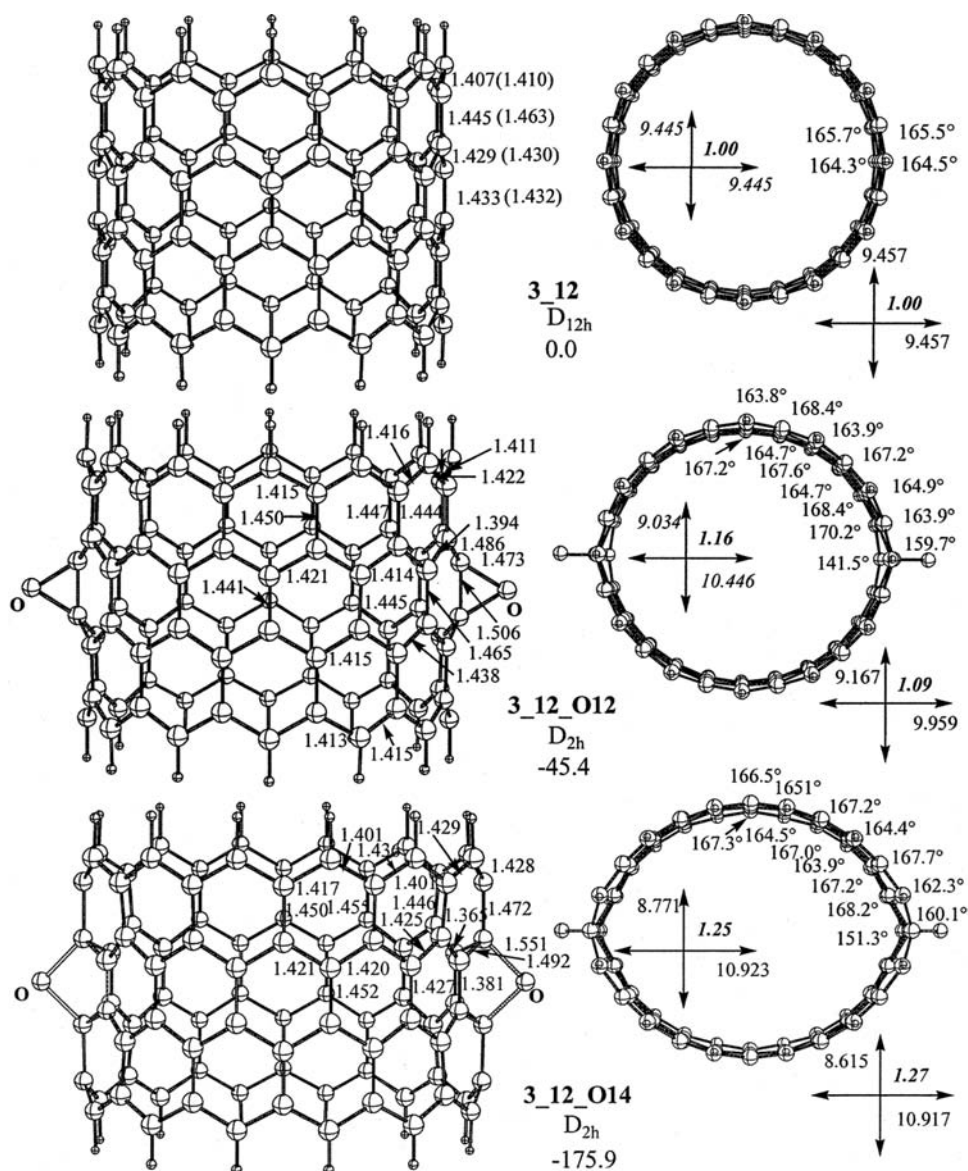


**Fig. 3** Side and top views of the ONIOM(B3LYP/6-31 G(Od):B3LYP/STO-3G)- optimized geometries of three-layered belt of [12]-cyclacene **3\_12** and its doubly oxidized 1,2-(**3\_12\_012**) and 1,4-forms (**3\_12\_014**). Bond lengths are given in angstrom. For **3\_12**, numbers in parentheses correspond to a pure B3LYP/6-31 optimization. For **3\_12\_012** and **3\_12\_014**, numbers inside the ring correspond to the inner ring, whereas the numbers outside correspond to the outer rings. Source: From Ref.<sup>[79]</sup>.

nanotubes using periodic semiempirical extended Hückel or simple molecular mechanics calculations, only one work appeared in the literature predicting the change in Raman spectra for models of SWCNTs upon oxidation.<sup>[79]</sup> In this study, geometry optimizations and frequency calculations were performed using pure B3LYP/6-31G(Od)<sup>b</sup> density functional theory for small cyclacene rings, and the ONIOM2 (B3LYP/6-31G(Od):B3LYP/STO-3G) method for a larger

<sup>b</sup>The simple 6-31G basis set was used for carbons and *d*-polarization functions were used only on oxygen.

SWCNT model. Macrocycles consisting of 6 and 12 fused C<sub>6</sub> hexagon units, C<sub>24</sub>H<sub>12</sub> and C<sub>48</sub>H<sub>24</sub> or [6]- and [12]-cyclacene, respectively, were chosen as models for the pure B3LYP/6-31G(Od) calculations, whereas a vertically extended belt model with three fused [12]-cyclacenes, C<sub>96</sub>H<sub>24</sub>, was studied at the ONIOM level. The oxidation was modeled by 1,2- or 1,4-cycloaddition products of two oxygen atoms at the furthest ends of each macrocycle; 1,4-adducts are found to be much more stable than 1,2-adducts and are possibly the actual oxidation products. It was found for all these cases that, when oxygen atoms react, the macrocycles undergo large deformation from the totally symmetric

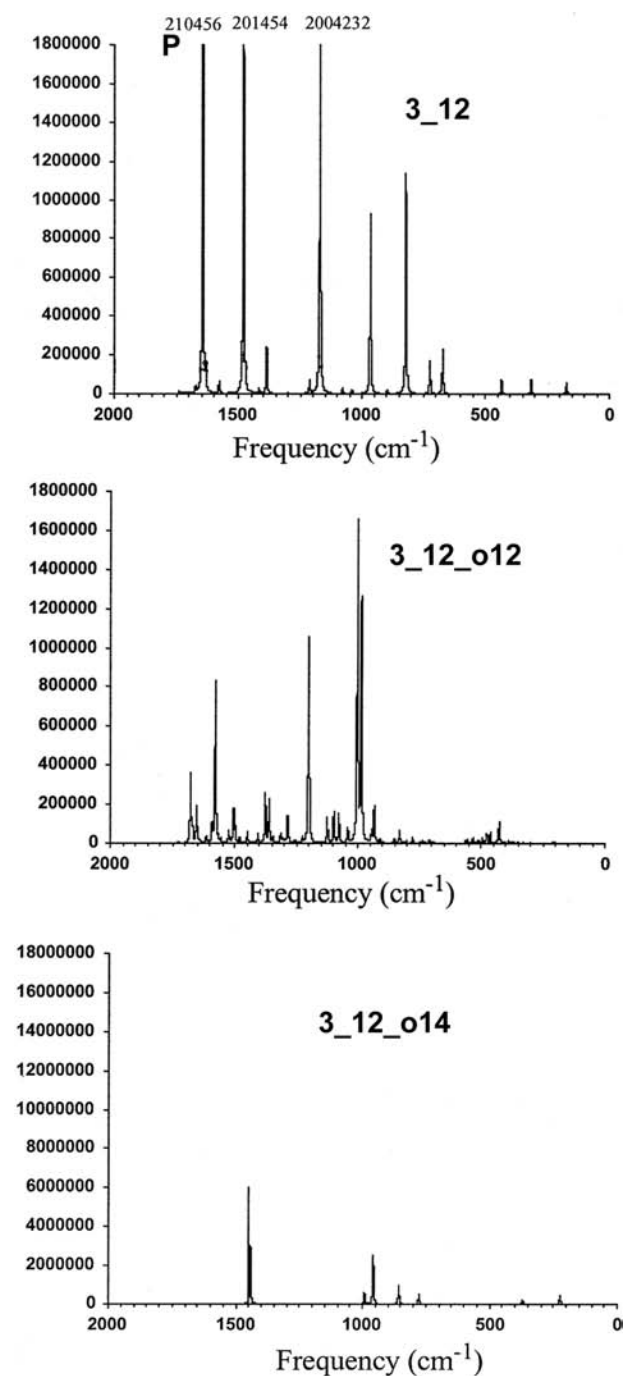


**Fig. 4** Calculated Raman spectra for the three-layered belt of [12]-cyclacene **3\_12** and its oxidized forms **3\_12\_012** and **3\_12\_014**. Source: From Ref.<sup>[79]</sup>.

cyclic structure toward an oval shape (Fig. 3). This is due to the introduction of  $sp^3$  centers on the ring and subsequent relaxation of the adjacent  $C_6$  hexagon units. Upon oxidation, the calculated Raman spectra show a large reduction in peak intensities (Fig. 4), which can be ascribed to the loss of cylindrical symmetry due to structural deformation. Thus this study suggested a novel explanation for the experimental

observation that the Raman spectra of individual CNTs are highly sensitive to oxidization.

### Photoluminescence of Silica-Based Nanoscale Materials

The study of silica-based nanoscale materials is an important issue because of their potential broad applications in the design of combined Si/SiO<sub>2</sub> systems such as metal-oxide-semiconductor (MOS) and nanoscale silicon optoelectronic devices and Si/SiO<sub>2</sub> superlattices.<sup>[80,81]</sup> However, the origin of the photoluminescence (PL) properties of Si/SiO<sub>2</sub> systems is still a subject of speculation and theoretically very difficult to tackle as electronically excited state calculations have to be carried out which are usually very expensive and prohibitive for nanometer-sized systems. However, Mebel et al. recently performed a combined experimental and theoretical study using a two-layer ONIOM2(B3LYP/6-31G(d):PM3) approach for geometry optimizations with subsequent time-dependent density functional theory (TDDFT) single-point calculations for excited state energies,<sup>[82]</sup> and showed that combined defects including nonbridging oxygens (NBO) and an oxygen vacancy (OV) in various positions exhibit suitable properties both for energies and oscillator strengths, which are responsible for the observed PL bands. These combined defects are proposed to occur in extremely thin (~1 nm) nonequilibrium substoichiometric silicon oxide (SiO<sub>x</sub>,  $x < 2$ ) layers. The combined ONIOM2 and TDDFT calculations clearly indicate that the PL band shift can be induced by one, two, and three OVs in the nearest vicinity of NBO, and that Si-Si bond relaxation in OVs as well as the orientation of NBOs and distances between them and OVs influences transition energies and oscillator strengths. In order to compute equilibrium geometries for these defect sites, a high-level layer containing 5 Si and 12–15 O atoms was introduced, surrounded by a low-level SiO<sub>2</sub> cluster treated with the semiempirical PM3 method. The combination of ONIOM ground state equilibrium geometry optimization with single-point TDDFT results leads to excitation energies that closely match the PL peaks observed.

### Data Storage on an Atomic Scale

Bauschlicher et al. have suggested in a series of papers<sup>[83–86]</sup> that it could be possible to store one bit of data on a surface using one atom, leading to a hypothetical data density that is about 1 million times higher than today's storage technique using magnetic disks. Their idea is based on the experiments of Avouris et al. who demonstrated that specific hydrogen

atoms can be removed from a hydrogen passivated silicon surface using an atomic force microscopy (AFM) by applying an electric field.<sup>[87]</sup> According to Bauschlicher et al., data could be stored by depositing heteroatoms X on the missing hydrogen positions and be read using a functionalized CNT. For this purpose it is extremely important that a clear difference can be found between the presence of data atoms X and hydrogen on the surface, and highly accurate calculations for the tip/H and tip/X interactions are required. Pure B3LYP/6-31G quantum chemical calculations were performed on a surface model featuring 13 Si atoms, and the AFM tip was modeled using a pyridine molecule. These calculations were applied to the study of four scenarios: the interaction of pyridine with X surrounded by six X or H atoms, or H surrounded by six X or H atoms. It was found that the choice of chlorine as data atom X is preferable over fluorine or cyanide, as the pyridine/Cl interactions were distinguishable from pyridine/H interactions by more than 1 kcal/mol in the worst-case scenario. In order to make their system more realistic, the ONIOM3-(B3LYP/6-31G:AM1:UFF) three-layer approach was employed for a Si<sub>74</sub>H<sub>61</sub>X<sub>7</sub> (X = H or Cl) two-slab model for the silicon surface, with the pyridine molecule being attached to an approximately 17-Å-long (5,5) SWCNT.<sup>[88]</sup> In order to include the effect of the CNT electronic structure, the nanotube was always treated at the AM1 semiempirical level, while the pyridine and all seven data atoms are chosen to be members of the B3LYP/6-31G high level. The silicon surface was treated using AM1 for the first slab consisting of 37 silicon atoms, allowing the electronic structure of silicon to influence the electronic charges on data atoms, while the UFF force field was applied to the second slab in order to prevent the silicon surface from deforming too much due to the different Si-Cl and Si-H interactions. Full geometry optimizations on all four scenarios were carried out, and it was found that in particular the addition of the second silicon slab improves the stability of the surface model greatly while interaction energies and N-surface distances were quite similar to those obtained with the smaller models at the pure B3LYP/6-31G(d) models. The electronic structure of the CNT did not significantly affect the interaction energies, and the conclusion of Bauschlicher et al. is that the Si (111) surface with H and Cl data atoms should be seriously considered as a possible method for data storage at the atomic level.

## CONCLUSION

Without doubt, hybrid QM/MM and even more so integrated ONIOM (MO:MO) methods have found

widespread application in a variety of nanochemical problems. They have served to accurately predict carbon-carbon bond energies in fullerene and the insertion barriers of metal atoms into their chemically modified derivatives, to study cycloaddition functionalization reactions of carbon nanotubes, to describe van der Waals complexes between adsorbent molecules and carbon nanostructures, and to predict vibrational and excitation spectra of systems with as large as 100 atoms. While these investigations mark already remarkable achievements on the way toward better understanding of the chemistry on the nanoscale, we would like to emphasize that the potential of integrated methods is actually far greater and predict that they will play an even more important role for the study of nanoscale electronic structures.

A major obstacle in their current applications is the fact that *S*-value tests cannot be performed simply in the context of nanochemistry using conventional high-level methods. Yet, linear scaling and RI-DFT methods are becoming more and more available<sup>c</sup> and popular, pushing the limits of DFT applicability to systems with up to approximately 1000 atoms. *S*-value testing thus becomes much more realistic, e.g., in an RI-DFT:AM1 approach, and knowledge obtained in these tests can be transferred to similar combinations such as B3LYP:AM1, where no *S*-value test can be performed.

Another benefit of these and LMP2 and RI-MP2 methods is that the size of the high or intermediate model systems can be increased to several hundred atoms as well, allowing calculations of systems with several thousands of atoms with semiempirical methods in the low layer. A very promising, yet never attempted low-level method is the self-charge consistent density functional tight-binding (SCC-DFTB) method, which will give more consistent results in combination with DFT high-level methods than more traditional semiempirical methods such as AM1 and PM3. Extension of DFTB in a massively parallel scheme toward the treatment of perhaps 100,000 atom systems is within current reach, expanding the size of future ONIOM calculations dramatically.

In addition, RI-MP2 analytical gradients are available and proved to be very accurate and reliable approximations for true MP2 gradients, thus allowing van der Waals complexes to be fully optimized in an ONIOM scheme with an approximated MP2 quality for the interaction region, electronically embedded in the remainder of the nanostructure-treated DFT or semiempirical methods. Three-layer ONIOM schemes,

<sup>c</sup>For instance, RI-DFT as implemented in the TURBOMOLE program package<sup>[28]</sup> can be easily facilitated in the GAUSSIAN external ONIOM scheme.<sup>[46]</sup>



although not popularly practiced yet, have impressively proven their predictive powers and should play a much more pronounced role in the future, e.g., in a G2MS:RI-MP2:HF hierarchy. For electronic excited states, computationally efficient TDDFT and RI-CC<sup>[89]</sup> methods will play an important role to extend the size of the low level in ONIOM calculations, where the model system is described using multireference wavefunction methods.

While all of the above schematics explore chemistry in a static manner, quantum chemical molecular dynamics have become an indispensable tool for the study of phenomena at the nanoscale. A spectacular success was recently presented where single-level DFTB MD has been used to elucidate the formation mechanism of fullerenes.<sup>[23,24]</sup> ONIOM MD has recently been performed on the solvation problem of simple metal cations,<sup>[90,91]</sup> and we expect even greater and more accurate insight into the dynamics of nanostructures on the atomic level using high-level quantum chemical methods.

## ACKNOWLEDGMENTS

This work was partially supported by a grant from the Petroleum Research Fund, the American Chemical Society.

## REFERENCES

- Kroto, H.W.; Heath, J.R.; O'Brien, S.C.; Curl, R.F.; Smalley, R.E. C<sub>60</sub>: Buckminsterfullerene. *Nature* **1985**, *318*, 162–163.
- Drexler, K.E. *Engines of Creation. The Coming Era of Nanotechnology*; Anchor Press: Garden City, NY, 1986.
- Haeser, M.; Almlof, J.; Scuseria, G.E. The equilibrium geometry of the carbon sixty-atom molecule as predicted by second-order (MP2) perturbation theory. *Chem. Phys. Lett.* **1991**, *181* (6), 497–500.
- Boese, A.D.; Scuseria, G.E. C<sub>2</sub> fragmentation energy of C<sub>60</sub> revisited: Theory disagrees with most experiments. *Chem. Phys. Lett.* **1998**, *294* (1–3), 233–236.
- Roothaan, C.C.J. New developments in molecular orbital theory. *Rev. Mod. Phys.* **1951**, *23*, 69–89.
- Hall, G.G. The molecular-orbital theory of chemical valency: VIII. A method of calculating ionization potentials. *Proc. R. Soc.* **1951**, *A205*, 541–552.
- Hund, F. Molecular spectra. *Z. Phys.* **1928**, *51*, 759–796.
- Mulliken, R.S. The assignment of quantum numbers for electrons in molecules: I. *Phys. Rev.* **1928**, *32*, 186–222.
- Mulliken, R.S. The assignment of quantum numbers for electrons in molecules: II. Correlation of molecular and atomic electron states. *Phys. Rev.* **1928**, *32*, 761–772.
- Mulliken, R.S. Magic formula, structure of bond energies, and isovalent hybridization. *J. Phys. Chem.* **1952**, *56*, 295–311.
- Wolfsberg, M.; Helmholz, L. The spectra and electronic structure of the tetrahedral ions MnO<sub>4</sub><sup>-</sup>, CrO<sub>4</sub><sup>-</sup>, and ClO<sub>4</sub><sup>-</sup>. *J. Chem. Phys.* **1952**, *20*, 837–843.
- Pople, J.A.; Segal, G.A. Approximate self-consistent molecular orbital theory: II. Calculations with complete neglect of differential overlap. *J. Chem. Phys.* **1965**, *43* (10), S136–S151.
- Pople, J.A.; Santry, D.P.; Segal, G.A. Approximate self-consistent molecular orbital theory: I. Invariant procedures. *J. Chem. Phys.* **1965**, *43* (10), S129–S135.
- Pople, J.A.; Beveridge, D.L.; Dobosh, P.A. Approximate self-consistent molecular-orbital theory: V. Intermediate neglect of differential overlap. *J. Chem. Phys.* **1967**, *47* (6), 2026–2033.
- Bingham, R.C.; Dewar, M.J.S.; Lo, D.H. Ground states of molecules: XXV. MINDO/3. Improved version of the MINDO semiempirical SCF-MO method. *J. Am. Chem. Soc.* **1975**, *97* (6), 1285–1293.
- Dewar, M.J.S.; Thiel, W. A semiempirical model for the two-center repulsion integrals in the NDDO approximation. *Theor. Chim. Acta* **1977**, *46* (2), 89–104.
- Dewar, M.J.S.; Zoebisch, E.G.; Healy, E.F.; Stewart, J.J.P. Development and use of quantum mechanical molecular models: 76. AM1: A new general purpose quantum mechanical molecular model. *J. Am. Chem. Soc.* **1985**, *107* (13), 3902–3909.
- Dewar, M.J.S.; Jie, C.; Yu, J. SAM1 the first of a new series of general purpose quantum mechanical molecular models. *Tetrahedron* **1993**, *49* (23), 5003–5038.
- Stewart, J.J.P. Optimization of parameters for semiempirical methods: I. Method. *J. Comp. Chem.* **1989**, *10* (2), 209–220.
- MOPAC2002; Fujitsu Limited: Tokyo, Japan.
- Galli, G. Tight-binding molecular dynamics for carbon systems: Fullerenes on surfaces. *Comput. Mater. Sci.* **1998**, *12* (3), 242–258.
- Masuda-Jindo, K.; Menon, M.; Subbaswamy, K.R.; Aoki, M. Atomistic simulation of lattice defects in nano-scale semiconductors: Minimal-basis TBMD method. *Comput. Mater. Sci.* **1999**, *14* (1–4), 203–208.
- Irle, S.; Zheng, G.; Elstner, M.; Morokuma, K. Formation of fullerene molecules from carbon nanotubes: A quantum chemical molecular dynamics study. *Nano Lett.* **2003**, *3* (4), 465–470.
- Irle, S.; Zheng, G.; Elstner, M.; Morokuma, K. From C<sub>2</sub> molecules to fullerenes in quantum chemical self-assembly dynamics. *Nature*. Submitted.
- Eichkorn, K.; Treutler, O.; Oehm, H.; Haeser, M.; Ahlrichs, R. Auxiliary basis sets to approximate Coulomb potentials. *Chem. Phys. Lett.* **1995**, *240* (4), 283–290.
- Skylaris, C.-K.; Gagliardi, L.; Handy, N.C.; Ioannou, A.G.; Spencer, S.; Willetts, A. On the resolution of identity Coulomb energy approximation in density functional theory. *J. Mol. Struct., Theochem.* **2000**, *501–502*, 229–239.
- Baerends, E.J.; Ellis, D.E.; Ros, P. Self-consistent molecular Hartree-Fock-Slater calculations: I. Computational procedure. *Chem. Phys.* **1973**, *2* (1), 41–51.
- Ahlrichs, R.; Baer, M.; Haeser, M.; Horn, H.; Koelmel, Ch. Electronic structure calculations on workstation

- computers: The program system TURBOMOLE. *Chem. Phys. Lett.* **1989**, *162* (3), 165–169.
29. Weigend, F.; Koehn, A.; Haettig, S. Efficient use of the correlation consistent basis sets in resolution of the identity MP2 calculations. *J. Chem. Phys.* **116** (8), 3175–3813.
  30. Saebo, S.; Pulay, P. Local treatment of electron correlation. *Ann. Rev. Phys. Chem.* **1993**, *44*, 213–236.
  31. Murphy, R.B.; Beachy, M.D.; Friesner, R.A.; Ringnalda, M.N. Pseudospectral localized Moeller–Plesset methods: Theory and calculation of conformational energies. *J. Chem. Phys.* **1995**, *103* (4), 1481–1490.
  32. Hetzer, G.; Pulay, P.; Werner, H.-J. Multipole approximation of distant pair energies in local MP2 calculations. *Chem. Phys. Lett.* **1998**, *290*, 143–149.
  33. Warshell, A.; Karplus, M. Calculation of ground and excited state potential surfaces of conjugated molecules: I. Formulation and parametrization. *J. Am. Chem. Soc.* **1972**, *94* (16), 5612–5625.
  34. Field, M.J.; Bash, P.A.; Karplus, M. A combined quantum mechanical and molecular mechanical potential for molecular dynamics simulations. *J. Comput. Chem.* **1990**, *11* (6), 700–733.
  35. Jiali, G. Absolute free energy of solvation from Monte Carlo simulations using combined quantum and molecular mechanical potentials. *J. Phys. Chem.* **1992**, *96* (2), 537–540.
  36. Deng, L.; Woo, T.K.; Cavallo, L.; Margl, P.M.; Ziegler, T. The role of bulky substituents in brookhart-type Ni(II) diimine catalyzed olefin polymerization: A combined density functional theory and molecular mechanics study. *J. Am. Chem. Soc.* **1997**, *119* (26), 6177–6186.
  37. Lyne, P.D.; Hodoscek, M.; Karplus, M. A hybrid QM-MM potential employing Hartree–Fock or density functional methods in the quantum region. *J. Phys. Chem., A* **1999**, *103* (18), 3462–3471.
  38. Loferer, M.J.; Loeffler, H.H.; Liedl, K.I.R. A QM-MM interface between CHARMM and TURBOMOLE: Implementation and application to systems in bulk phase and biologically active systems. *J. Comput. Chem.* **2003**, *24* (10), 1240–1249.
  39. Humbel, S.; Sieber, S.; Morokuma, K. The IMOMO method: Integration of different levels of molecular orbital approximations for geometry optimization of large systems. Test for *n*-butane conformation and  $S_N2$  reaction:  $\text{RCl} + \text{Cl}^-$ . *J. Chem. Phys.* **1996**, *105*, 1959–1967.
  40. Svensson, M.; Humbel, S.; Froese, R.D.J.; Matsubara, T.; Sieber, S.; Morokuma, K. ONIOM: A multilayered integrated MO + MM method for geometry optimizations and single point energy predictions. A test for Diels–Alder reactions and  $\text{Pt}(\text{t-Bu})_3)_2 + \text{H}_2$  oxidative addition. *J. Phys. Chem.* **1996**, *100*, 19357–19363.
  41. Froese, R.D.J.; Morokuma, K. Hybrid Method. The ONIOM Method. Integration of Different Levels of Molecular Orbital Methods and/or Molecular Mechanics Methods for Large Molecular Systems and Its Applications to Structures, Energies and Chemical Reactions. In *The Encyclopedia of Computational Chemistry*; Schleyer, P.v.R., Allinger, N.L., Clark, T., Gasteiger, J., Kollman, P.A., Schaefer, H.F., III, Schreiner, P.R., Eds.; John Wiley: Chichester, 1998; 1245–1257.
  42. Dapprich, S.; Komaromi, I.; Byun, K.S.; Morokuma, K.; Frisch, M.J. A New ONIOM implementation in Gaussian 98: Part I. The calculation of energies, gradients, vibrational frequencies and electric field derivatives. *J. Mol. Struct., Theochem* **1999**, *461–462*, 1–21.
  43. Maseras, F. Hybrid quantum mechanics/molecular mechanics methods in transition metal chemistry. *Top. Organomet. Chem.* **1999**, *4*, 165–191.
  44. Vreven, T.; Morokuma, K. On the application of the IMOMO (Integrated Molecular Orbital + Molecular Orbital) method. *J. Comp. Chem.* **2000**, *21*, 1419–1432.
  45. Vreven, T.; Mennucci, B.; da Silva, C.O.; Morokuma, K.; Tomasi, J. The ONIOM-PCM method: Combining the hybrid molecular orbital method and the polarizable continuum model for solvation. Application to the geometry and properties of a merocyanine in solution. *J. Chem. Phys.* **2001**, *115*, 62–72.
  46. Frisch, M.J.; Trucks, G.W.; Schlegel, H.B.; Scuseria, G.E.; Robb, M.A.; Cheeseman, J.R.; Montgomery, J.A., Jr.; Vreven, T.; Kudin, K.N.; Burant, J.C.; Millam, J.M.; Iyengar, S.S.; Tomasi, J.; Barone, V.; Mennucci, B.; Cossi, M.; Scalmani, G.; Rega, N.; Petersson, G.A.; Nakatsuji, H.; Hada, M.; Ehara, M.; Toyota, K.; Fukuda, R.; Hasegawa, J.; Ishida, M.; Nakajima, T.; Honda, Y.; Kitao, O.; Nakai, H.; Klene, M.; Li, X.; Knox, J.E.; Hratchian, H.P.; Cross, J.B.; Adamo, C.; Jaramillo, J.; Gomperts, R.; Stratmann, R.E.; Yazyev, O.; Austin, A.J.; Cammi, R.; Pomelli, C.; Ochterski, J.W.; Ayala, P.Y.; Morokuma, K.; Voth, G.A.; Salvador, P.; Dannenberg, J.J.; Zakrzewski, V.G.; Dapprich, S.; Daniels, A.D.; Strain, M.C.; Farkas, O.; Malick, D.K.; Rabuck, A.D.; Raghavachari, K.; Foresman, J.; Ortiz, J.V.; Cui, Q.; Baboul, A.G.; Clifford, S.; Cioslowski, J.; Stefanov, B.B.; Liu, G.; Liashenko, A.; Piskorz, P.; Komaromi, I.; Martin, R.L.; Fox, D.J.; Keith, T.; Al-Laham, M.A.; Peng, C.Y.; Nanayakkara, A.; Challacombe, M.; Gill, P.M.W.; Johnson, B.; Chen, W.; Wong, M.W.; Gonzalez, C.; Pople, J.A. Gaussian 03, Revision B.01. Gaussian, Inc.: Pittsburgh, PA, 2003.
  47. Andreoni, W. Computational approach to the physical chemistry of fullerenes and their derivatives. *Annu. Rev. Phys. Chem.* **1998**, *49*, 405–439.
  48. Ahlrichs, R.; Elliott, S.D.; Huniar, U. Quantum chemistry. Large molecules—Small computers. *Ber. Bunsen-Ges.* **1998**, *102* (6), 795–804.
  49. Srivastava, D.; Menon, M.; Cho, K. Computational nanotechnology with carbon nanotubes and fullerenes. *Comput. Sci. Eng.* **2001**, *3* (4), 42–55.
  50. Froese, R.D.J.; Morokuma, K. Accurate calculations of bond breaking energies in  $\text{C}_{60}$  using the three-layered ONIOM method. *Chem. Phys. Lett.* **1999**, *305*, 419–424.
  51. Irle, S.; Rubin, Y.; Morokuma, K. An ONIOM study of ring opening and metal insertion reactions with derivatives of  $\text{C}_{60}$ : Role of aromaticity in the opening process. *J. Phys. Chem., A* **2002**, *106*, 680–688.
  52. Rubin, Y. Organic approaches to endohedral metallofullerenes: Cracking open or zipping up carbon shells? *Chem. Eur. J.* **1997**, *3* (7), 1009–1016.

53. Rubin, Y.; Jarrosson, Th.; Wang, G.-W.; Bartberger, M.D.; Houk, K.N.; Schick, G.; Saunders, M.; Cross, R.J. Insertion of helium and molecular hydrogen through the orifice of an open fullerene. *Angew. Chem., Int. Ed.* **2001**, *40* (8), 1543–1546.
54. Shigeta, Y.; Saito, H. A QM/MM molecular dynamics study of a dynamical change in effective charge on Be atom in  $(\text{Be} + n\text{H}_2)\text{-C}_{60}$ . *Synth. Met.* **2003**, *135–136*, 765–766.
55. Turker, L. Certain endohedrally hydrogen doped Be-C<sub>60</sub> systems—A theoretical study. *Theochem* **2002**, *577* (2–3), 205–211.
56. Fomina, L.; Reyes, A.; Fomine, S. Complexes of C<sub>60</sub> fullerenes with simple donor molecules: Theoretical study. *Int. J. Quant. Chem.* **2002**, *89*, 477–483.
57. White, C.T.; Robertson, D.H.; Mintmire, J.W. Helical and rotational symmetries of nanoscale graphitic tubules. *Phys. Rev., B* **1993**, *47* (9), 5485–5488.
58. Saito, R.; Fujita, M.; Dresselhaus, G.; Dresselhaus, M.S. Electronic structure of graphene tubules based on C<sub>60</sub> fullerene. *Phys. Rev., B* **1992**, *46* (3), 1804–1811.
59. Tanaka, K.; Okahara, K.; Okada, M.; Yamabe, T. Electronic properties of bucky-tube model. *Chem. Phys. Lett.* **1992**, *191* (5), 469–472.
60. Basiuk, V.A. ONIOM studies of chemical reactions on carbon nanotube tips: Effects of lower theoretical level and mutual orientation of the reactants. *J. Phys. Chem., B* **2003**, *107* (34), 8890–8897.
61. Basiuk, V.A. Reactivity of carboxylic groups on armchair and zigzag carbon nanotube tips: A theoretical study of esterification with methanol. *Nano Lett.* **2002**, *2* (8), 835–839.
62. Basiuk, V.A.; Basiuk, E.V.; Saniger-Blesa, J.-M. Direct amidation of terminal carboxylic groups of armchair and zigzag carbon nanotube tips: A theoretical study of esterification with methanol. *Nano Lett.* **2001**, *1* (11), 657–661.
63. Rappe, A.K.; Casewit, C.J.; Colwell, K.S.; Goddard, W.A., III; Skiff, W.M. UFF, a full periodic table force field for molecular mechanics and molecular dynamics simulations. *J. Am. Chem. Soc.* **1992**, *114* (25), 10024–10035.
64. Chen, Y.; Haddon, R.C.; Fang, S.; Rao, A.M.; Eklund, P.C.; Lee, W.H.; Dickey, E.C.; Grulke, E.A.; Pendergrass, J.C.; Chavan, A.; Haley, B.E.; Smalley, R.E. Chemical attachment of organic functional groups to single-walled carbon nanotube material. *J. Mater. Res.* **1998**, *13* (9), 2423–2431.
65. Lu, X.; Tian, F.; Zhang, Q. The [2 + 1] cycloadditions of dichlorocarbene, silylene, germylene, and oxycarbonylnitrene onto the sidewall of armchair (5,5) single-wall carbon nanotube. *J. Phys. Chem., B* **2003**, *107* (33), 8388–8391.
66. Lu, X.; Tian, F.; Wang, X.X.; Zhang, Q. A theoretical exploration of the 1,3-dipolar cycloadditions onto the sidewalls of (n,n) armchair single-wall carbon nanotubes. *J. Am. Chem. Soc.* **2003**, *125* (34), 10459–10464.
67. Lu, X.; Zhang, L.; Xu, X.; Wang, N.; Zhang, Q. Can the sidewalls of single-wall carbon nanotubes be ozonized? *J. Phys. Chem., B* **2002**, *106*, 2136–2139.
68. Lu, X.; Tian, F.; Wang, N.; Zhang, Q. Organic functionalization of the sidewalls of carbon nanotubes by Diels–Alder reactions: A theoretical prediction. *Org. Lett.* **2003**, *4* (24), 4313–4315.
69. Bauschlicher, C.W., Jr. Hydrogen and fluorine binding to the sidewalls of a (10,0) carbon nanotube. *Chem. Phys. Lett.* **2000**, *322*, 237–241.
70. Jaffe, R. unpublished.
71. Kelly, K.F.; Chiang, I.W.; Mickelson, E.T.; Hauge, R.H.; Margrave, J.L.; Wang, X.; Scuseria, G.E.; Radloff, C.; Halas, N.J. Insight into the mechanism of sidewall functionalization of single-walled nanotubes: An STM study. *Chem. Phys. Lett.* **1999**, *313* (3,4), 445–450.
72. Bauschlicher, C.W., Jr. High coverages of hydrogen on a (10,0) carbon nanotube. *Nano Lett.* **2001**, *1* (5), 223–226.
73. Bauschlicher, C.W., Jr.; So, C.R. High coverages of hydrogen on (10,0), (9,0), and (5,5) carbon nanotubes. *Nano Lett.* **2002**, *2* (4), 337–341.
74. Froudakis, G.E. Hydrogen interactions with single walled carbon nanotubes: A combined quantum chemical/molecular mechanics study. *Nano Lett.* **2001**, *1* (4), 179–182.
75. Froudakis, G.E. Why alkali-metal-doped carbon nanotubes possess high hydrogen uptake. *Nano Lett.* **2001**, *4* (10), 531–533.
76. Ricca, A.; Drocco, J.A. Interaction of O<sub>2</sub> with a (9,0) carbon nanotube. *Chem. Phys. Lett.* **2002**, *362*, 217–223.
77. Walch, S.P. The bonding of N<sub>2</sub> to models of a (9,0) carbon nanotube and graphite. *Chem. Phys. Lett.* **2003**, *373*, 422–425.
78. Walch, S.P. On the reaction of N and O atoms with carbon nanotubes. *Chem. Phys. Lett.* **2003**, *374*, 501–505.
79. Irle, S.; Mews, A.; Morokuma, K. Theoretical study of structure and Raman spectra for models of carbon nanotubes in their pristine and oxidized forms. *J. Phys. Chem., A* **2002**, *106*, 11973–11980.
80. Conley, J.F.; Lenahan, P.M. Room temperature reactions involving silicon dangling bond centers and molecular hydrogen in amorphous silicon dioxide thin films on silicon. *Appl. Phys. Lett.* **1993**, *62* (1), 40–42.
81. Hess, K.; Tuttle, B.; Register, F.; Ferry, D.K. Magnitude of the threshold energy for hot electron damage in metal-oxide-semiconductor field effect transistors by hydrogen desorption. *Appl. Phys. Lett.* **1999**, *75* (20), 3147–3149.
82. Zyubin, A.S.; Glinka, Yu.D.; Mebel, A.M.; Lin, S.H.; Hwang, L.P.; Chen, Y.T. Red and near-infrared photoluminescence from silica-based nanoscale materials: Experimental investigation and quantum-chemical modeling. *J. Chem. Phys.* **2002**, *116* (1), 281–294.
83. Bauschlicher, C.W., Jr.; Ricca, A.; Merkle, R. Chemical storage of data. *Nanotechnology* **1997**, *8* (1), 1–5.
84. Bauschlicher, C.W., Jr.; Rosi, M. Differentiating between hydrogen and fluorine on a diamond surface. *Theor. Chem. Acc.* **1997**, *96*, 213–216.

85. Bauschlicher, C.W., Jr.; Rosi, M. Differentiating between H and F or H and CN on C(111) or Si(111) surfaces. *J. Phys. Chem., B* **1998**, *102*, 2403–2405.
86. Bauschlicher, C.W., Jr.; So, C.R. Using hydrogen and chlorine on Si(111) to store data. *Chem. Phys. Lett.* **2001**, *333* (1–2), 1–5.
87. Avouris, Ph.; Walkup, R.E.; Rossi, A.R.; Shen, T.-C.; Abeln, G.C.; Tucker, J.R.; Lyding, J.W. STM-induced H atom desorption from Si(100): Isotope effects and site selectivity. *Chem. Phys. Lett.* **1996**, *257*(1,2), 148–154.
88. Rosi, M.; Bauschlicher, C.W., Jr. Using hydrogen and chlorine on Si(111) to store data, an improved model. *Chem. Phys. Lett.* **2001**, *347*, 291–296.
89. Hättig, C.; Weigend, F. CC2 excitation energy calculations on large molecules using the resolution of the identity approximation. *J. Chem. Phys.* **2000**, *113*, 5154–5163.
90. Kerdcharoen, T.; Morokuma, K. ONIOM-XS: An extension of ONIOM method for molecular simulation in condensed phase. *Chem. Phys. Lett.* **2002**, *355*, 257–262.
91. Kerdcharoen, T.; Morokuma, K. Combined QM/MM simulation of Ca<sup>2+</sup>/ammonia solution based on the ONIOM-XS method: Octahedral coordination and implication to biology. *J. Chem. Phys.* **2003**, *118*, 8856–8862.

# Intercalated Polypropylene Nanocomposites

**Michael J. Solomon**

*Chemical Engineering, University of Michigan, Ann Arbor, Michigan, U.S.A.*

**Anongnat Somwangthanaroj**

*Macromolecular Science and Engineering Program, University of Michigan, Ann Arbor, Michigan, U.S.A.*

## INTRODUCTION

Polypropylene (PP) is a versatile material whose use has significantly penetrated numerous sectors of the manufacturing, medical, and packaging industries. Polymer clay nanocomposites are multiphase organic/inorganic hybrid materials pioneered by researchers at Toyota,<sup>[1–3]</sup> which may exhibit significantly improved mechanical, flammability, and permeability properties relative to the base polymer matrix at very low clay loading. Although first demonstrated for nylon, polymer clay nanocomposites have since been prepared for a range of thermoplastic and thermoset polymers. However, the development of PP clay nanocomposites poses special challenges because of polypropylene's hydrophobicity. Nevertheless, possible commercial applications have motivated substantial research into strategies for the dispersion of clays in this technologically important polymer. This entry reviews recent progress in the synthesis, preparation, and characterization of polypropylene nanocomposites. The resulting clay intercalation structure receives particular attention because most polypropylene nanocomposites prepared to date have yielded significant structures of this kind. After reviewing the state-of-the-art in polypropylene nanocomposite synthesis, characterization of clay and polymer morphology, and measurement of rheological and mechanical properties, we identify future research challenges that should be addressed to continue improving the possibility for commercial applications of these materials.

## OVERVIEW

Mixtures of clay platelets and polymer chains compose a colloidal system. Thus in the melt state, the propensity for the clay to be stably dispersed at the level of individual disks (an exfoliated clay dispersion) is dictated by clay, polymer, stabilizer, and compatibilizer potential interactions and the entropic effects of orientational disorder and confinement. Anisometric dimensions of clay platelets also have implications for stability

because liquid crystalline phases may form. In addition, the very high melt viscosity of polypropylene and the colloidal size of clay imply slow particulate dynamics, thus equilibrium structures may be attained only very gradually. Agglomerated and networked clay structures may also lead to non-equilibrium behavior such as trapped states, aging, and glassy dynamics.

Clay structure in polymer nanocomposites can be characterized as a combination of exfoliated platelets and intercalated tactoids. Clays themselves are layered silicate minerals with charged surfaces neutralized by interlayer counterions. Unless a liquid crystalline order disorder transition occurs, the exfoliated structure is spatially and orientationally disordered and the clay is dispersed at the level of individual disks. Intercalated clay retains interlayer ordering, at least within a particular tactoid; however, intergallery spacing is increased relative to natural clay because stabilizing surfactants, compatibilizers, and/or matrix polymers are infiltrated within the clay galleries. In the extreme case of clay/polymer matrix immiscibility, intercalation spacing not much greater than the clay and its counterion indicates negligible penetration of polymeric or compatibilizing species between clay layers. Clay platelets or tactoids themselves comprise the mesoscale structure of nanocomposites. Possible structures include that of a dispersed suspension, a percolated network, or a liquid crystal with orientational order. The hierarchy of possible states is depicted in Fig. 1.

The reinforcement of polypropylene and other thermoplastics with inorganic particles such as talc and glass is a common method of material property enhancement. Polymer clay nanocomposites extend this strategy to the nanoscale. The anisometric shape and approximately 1 nm width of the clay platelets dramatically increase the amount of interfacial contact between the clay and the polymer matrix. Thus the clay surface can mediate changes in matrix polymer conformation, crystal structure, and crystal morphology through interfacial mechanisms that are absent in classical polymer composite materials.

For these reasons, it is believed that nanocomposite materials with the clay platelets dispersed as isolated,

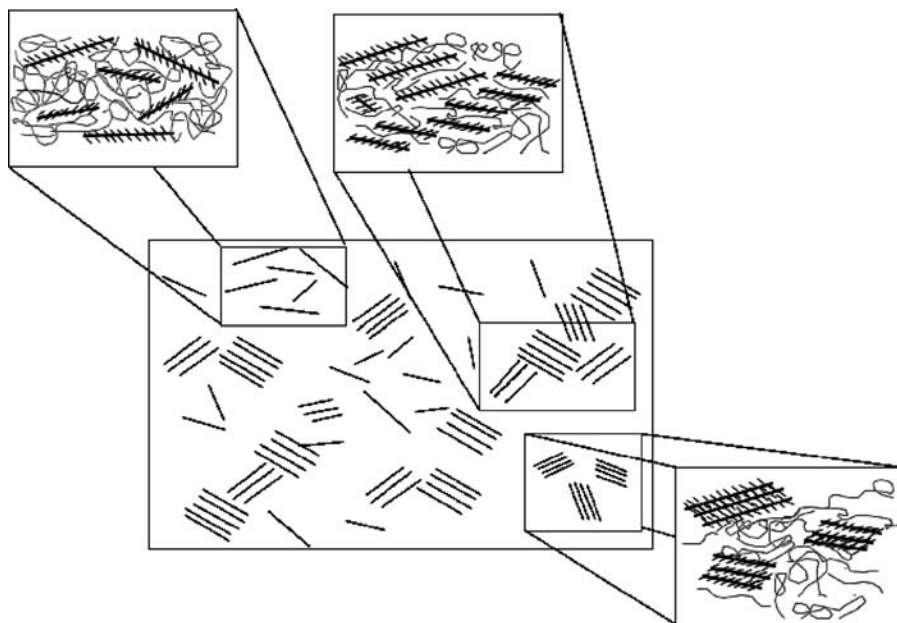


**Fig. 1** Schematic of the hierarchy of clay structures in polypropylene nanocomposites of mixed morphology. Clay tactoids and exfoliated platelets comprise the mesoscale morphology. The internal intercalation structure of clay tactoids is determined by the compatibilizer and compounding conditions.

exfoliated platelets are optimal for end-use properties. For example, the high aspect ratio of the exfoliated disk and their nanoscale width provide the greatest potential for solid-state mechanical property enhancement. Furthermore, the probability of defects and inclusions that can compromise the impact strength of composite materials is reduced by homogeneous dispersion at the nanoscale. However, even intercalated clay nanocomposites yield valuable mechanical property enhancement and other useful end-use properties.

This entry focuses on polypropylene–clay hybrid materials. Recent general reviews of polymer clay nanocomposites and their properties are available elsewhere.<sup>[4–6]</sup>

## SYNTHESIS AND PREPARATION

Organophilic smectite clays can be introduced into a polymer matrix by methods involving in situ polymerization or melt mixing. Commonly used layered silicates of this kind include montmorillonite or synthetic sodium fluoromica. These clays typically have submicron disk radii and a width of about 1 nm. Before introducing them into the polymer host, the clays are rendered organophilic by the exchange of natural counterions for more hydrophobic species such as amine surfactants. The ion exchange treatment increases clay intergallery spacing because of the increased excluded volume of the hydrophobic surfactant. Amines with alkyl chain length in the range  $C_{12}$ – $C_{18}$  are most effective in increasing the intercalation spacing of a fluoromica clay.<sup>[7]</sup> However, for polypropylene, these steps alone are insufficient to

generate significant polypropylene intercalation or clay exfoliation.<sup>[8]</sup> The additional step of introducing a compatibilizer consisting of short-chain polypropylene with grafted maleic anhydride (PP-MA) functionality leads to enhanced intercalation and some exfoliation.<sup>[8–12]</sup> The blending has been accomplished by using a molecular diluent, such as toluene or trichlorobenzene, but this requires an additional step to remove the solvent.<sup>[13–15]</sup> Direct melt preparation by twin-screw extrusion or Braebender mixing is more consistent with potential commercial applications. Although the detailed mechanism of intercalation has yet to be elucidated, a qualitative explanation is that the polarity of the maleic anhydride yields more favorable interactions with organophilic clay. These interactions offset the entropic penalty for confinement of intercalated chains. There also exists the possibility of acid–base equilibrium reactions of the amine surfactant and maleic anhydride.

In efforts to manipulate the degree of dispersion and mechanical properties of polypropylene nanocomposites, researchers have varied clay surface treatment, compatibilizer molar mass, and compatibilizer acid content. The miscibility of the compatibilizer with neat polypropylene at melt temperatures,<sup>[10]</sup> higher compatibilizer acid content,<sup>[11]</sup> and larger compatibilizer loading<sup>[16]</sup> have been reported to be conducive to improved intercalation spacing and dispersion. However, the molar ratio of MA to PP-MA has also been proposed as an indicator of intercalation capability.<sup>[17]</sup> Kim, Kim, and Lee<sup>[18]</sup> found that maleic anhydride content above about 1.0% is undesirable because it leads to the reordering of clay layers. Other intercalation and compatibilization agents, such as diethyl maleate graft polypropylene, semifluorinated



alkyltrichlorosilane, and epoxypropyl methacrylate, have also been used to prepare polypropylene nanocomposites.<sup>[15,19,20]</sup> Recently, novel methods to promote dispersion by supercritical processing have been disclosed.<sup>[21]</sup>

The effect of melt compounding fluid dynamics on dispersion and end-use properties has, to date, received limited attention for the specific case of polypropylene nanocomposites. Lack of control of these parameters is likely a significant source of the substantial variation among literature reports of intercalation spacing and materials property characterization. A possible mechanism for the interaction of flow and clay dispersion has been provided by Fornes et al.<sup>[22]</sup> Their schematic, reproduced in Fig. 2, shows that when clay is dispersed by non-equilibrium mechanisms such as melt compounding, applied flow fields can act to rupture initially large clay aggregates, to refine tactoid dimensions, and to promote exfoliation by contacting the compatibilizer, clay, and matrix polymer.

Although melt compounding is currently the principal method of polypropylene nanocomposite preparation, metallocene catalysis yields nanocomposites with high polymer isotacticity by in situ polymerization.<sup>[23]</sup> In situ polymerization to prepare polypropylene nanocomposites is potentially attractive because of the reduced need for compatibilizer treatments that are

required in melt compounding. Although exfoliation and mechanical property enhancement are achieved by in situ polymerization, current reports indicate that the dispersion is not entirely homogeneous because micrometer-size, clay-rich particles persist after polymerization.<sup>[23]</sup>

## CHARACTERIZATION OF CLAY INTERCALATION AND EXFOLIATION STRUCTURE

X-ray diffraction (XRD) and transmission electron microscopy (TEM) are principal methods for the interrogation of the intercalation structure of polymer clay nanocomposites. The ordered clay layers yield peaks in XRD intensity at scattering angles specified by the Bragg condition. For example, the spacing for naturally occurring Na-montmorillonite is about 1.1 nm. For one preparation,<sup>[24]</sup> when natural counterions were exchanged for stearylamine, the interlayer spacing increased to 2.1 nm, and melt compounding in polypropylene with a PP-MA compatibilizer further increased the intercalation spacing to 2.9 nm. In comparison, melt compounding of organophilic montmorillonite in neat polypropylene yields little increase in spacing,<sup>[10]</sup> thereby demonstrating the role of the PP-MA compatibilizer in promoting intercalation.

A major challenge in polymer nanocomposite characterization is to quantify dispersion in mixed systems comprised of both intercalated tactoids and exfoliated clay sheets, such as that depicted in Fig. 1. XRD alone offers little scope for such quantification,<sup>[25]</sup> however, quantitative analysis of sufficiently large regions of TEM micrographs is a promising way forward. Techniques for the quantification of the degree of exfoliation in polypropylene nanocomposites with mixed clay morphology have recently been discussed.<sup>[15,17]</sup> These methods should be more routinely employed to better permit the assessment of the relative performance of available synthetic and compounding strategies.

## CRYSTALLIZATION STRUCTURE AND KINETICS

The mechanical properties of semicrystalline isotactic polypropylene materials that are formed by injection molding are inferior to theoretical upper limits based on the polypropylene unit cell. Processing modifications designed to enhance the orientation of PP, such as low injection temperature or dynamic packing operation, can generate modest improvements in tensile modulus, even without the addition of conventional or nanoscopic filler. However, the traditional avenue

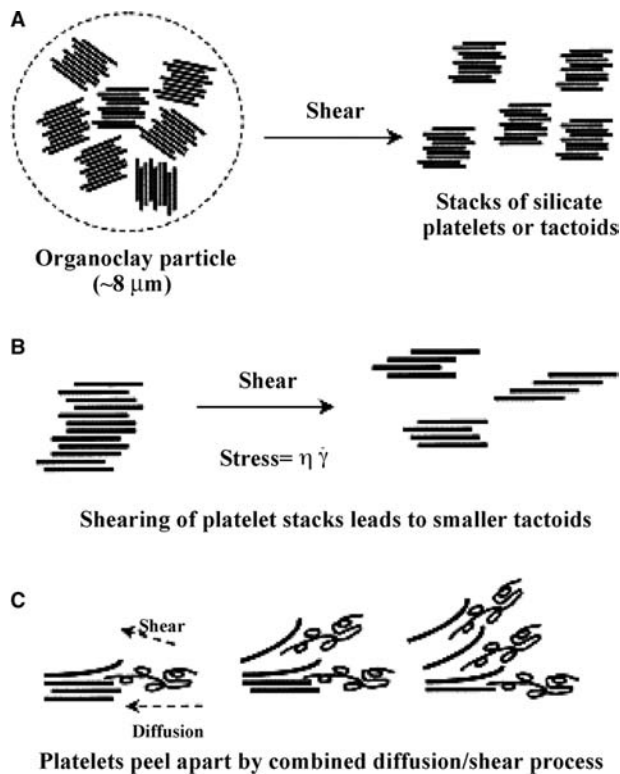


**Fig. 2** The mechanisms by which the fluid dynamics of compounding may affect clay dispersion in polymer/clay nanocomposites. *Source:* From Ref.<sup>[22]</sup>. ©Elsevier Science Ltd., 2001.

to manipulate polypropylene properties is to reinforce the polymer with anisometric, high-modulus inorganic particles, such as talc. Another more promising possibility is to tailor the filler so as to induce morphological changes in the crystalline structure of polypropylene itself. These morphological changes will in turn have implications for mechanical properties such as modulus, strength, and toughness. In this scenario, the nanoscopic scale of the filler becomes relevant because smaller fillers, with their larger surface area-to-volume ratio, reside in close proximity to a greater percentage of the bulk PP than conventional fillers. There are a number of ways in which nanoscopic fillers, such as exfoliated or intercalated layered silicate, may influence the crystalline morphology of PP.

First, the crystalline unit cell may change. This effect has been observed in, for example, nylon 6 nanocomposites where addition of clay induces a change from  $\alpha$  to  $\gamma$  crystalline form.<sup>[26]</sup> Three crystalline lattices for isotactic PP are known and there is evidence for preferential formation of the  $\gamma$ -phase in PP nanocomposites.<sup>[27,28]</sup>

Second, the crystalline morphology may be affected. For example, a transformation from spherulitic to oriented structure may occur. When crystallized at high shear rates, PP forms oriented structures that can hypothetically be modified by the presence of dispersed clay.<sup>[29]</sup> Fibrous crystalline morphology has also been reported in PP nanocomposites.<sup>[30]</sup>

Third, the degree of crystallization may change. As quantified by differential scanning calorimetry, it has been reported that the crystallinity of PP nanocomposites decreases modestly with increased clay content.<sup>[31]</sup>

Fourth, the characteristic size of crystalline morphology may be affected. Svoboda et al.<sup>[31]</sup> found that for nanocomposites with spherulitic structure, the average crystallite size decreases significantly with increasing clay content, possibly because of a role of clay in nucleation. Time-resolved light scattering and optical microscopy at the early stages of crystallization have also identified differences in the number of point nuclei in PP and PP nanocomposites.<sup>[32]</sup>

Fifth, the kinetics of crystallization may be modified. Time-resolved light scattering and differential scanning calorimetry studies have found that added intercalated clay can either increase or decrease characteristic crystallization times for polypropylene.<sup>[30–34]</sup> Interactions between an initially present nucleating agent, a PP-MA compatibilizer, and the dispersed clay generate complex crystallization kinetics, even in isothermal crystallization studies.<sup>[32]</sup> The data suggest that nanocomposite crystallization is dominated by the presence of a compatibilizer because nanocomposite data overlay PP/PP-MA blend measurements and crystallization times are not significantly affected by changes in clay loading.<sup>[32]</sup>

Interestingly, there have been preliminary reports of segregation of clay particles at the spherulitic boundary of maleated PP nanocomposites.<sup>[34]</sup> The possibility of polymer crystallization-induced changes in meso-scale clay morphology warrants further investigation because of the implications of such segregation for nanocomposite mechanical properties.

## RHEOLOGY

The flow properties of polypropylene nanocomposites are relevant to processing operations such as injection molding. In addition, the viscoelastic response to linear and non-linear deformation is a sensitive indicator of clay dispersion and interaction. Thus rheology can be used to evaluate the performance of various strategies for synthesizing and compounding polypropylene nanocomposites.

The compounding of organophilic clay and compatibilizer with polypropylene dramatically changes the linear viscoelastic response to shear deformation as quantified by the storage modulus  $G'$  and the loss modulus  $G''$ . Fig. 3 compares the  $G'$  and  $G''$  of polypropylene and an intercalated nanocomposite with 4.8% inorganic clay. The curves differ significantly, particularly at low frequencies. The apparent plateau in the nanocomposite data at low frequencies is consistent either with the response of a viscoelastic solid, or a viscoelastic liquid with a long relaxation time. The abrupt transition from liquidlike to solidlike linear viscoelasticity as clay loading is increased is suggestive of the generation of a gel or a network structure at a critical clay volume fraction. Because it is thought that such clay clustering is not likely to lead to optimal

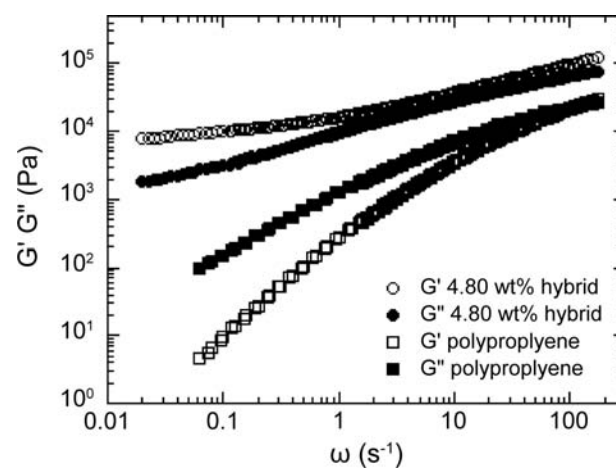


**Fig. 3** The melt state linear viscoelastic moduli of 4.8 wt.% intercalated polypropylene nanocomposites. *Source:* From Ref.<sup>[24]</sup>. © 2001 American Chemical Society.

end-use properties such as modulus and toughness, measurement of melt state linear viscoelasticity is a useful tool to indirectly characterize the nanocomposite clay structure. Toward this end, qualitative effects of alkyl amine clay treatment and PP-MA compatibilizer acid content on clay structure have been assessed by rheological characterization.<sup>[17,24]</sup> Intercalation kinetics has also been estimated.<sup>[35]</sup> Koo et al.<sup>[36]</sup> generated maleated polypropylene nanocomposites with different intercalated and exfoliated clay morphologies by varying the matrix polymer molecular weight and found that the linear viscoelastic modulus  $G'$  was sensitive to morphological changes.

Non-linear rheological characterization is predictive of nanocomposite behavior in typical processing operations such as injection molding. The presence of intercalated clay even at a clay loading of less than 5.0 wt.% can increase the viscosity by many orders of magnitude at low shear rates; however, at higher shear rates, which are more characteristic of processing conditions, viscosity enhancement is much more modest. This strong shear thinning behavior may have two origins: 1) anisometric particles such as rods and disks display shear thinning even at low concentrations because flow preferentially orients the particles in the flow direction; and 2) deformation applied to a gel cluster network can induce rupture of mechanical contacts and, consequently, shear thinning.<sup>[24]</sup>

Furthermore, non-linear rheological measurements indicate that intercalated polypropylene nanocomposites possess fragile structures that are easily manipulated by flow. For example, the onset of strain dependence of the storage modulus occurs at an applied strain  $\gamma_0 \sim 0.3$  for neat polypropylene; however, the transition for a 4.8 wt.% nanocomposite occurs at  $\gamma_0 \sim 0.007$ .<sup>[24]</sup> The startup of steady shear experiments after samples were presheared and then allowed to rest quiescently demonstrates that structures deformed during flow reestablish themselves on time scales longer than hundreds of seconds.<sup>[24]</sup> Linear viscoelasticity and XRD of intercalated polypropylene nanocomposites annealed for various periods provide additional evidence that structural evolution persists even longer—at least for many hours.<sup>[37,38]</sup> This evolution in linear and non-linear rheology is likely related to strong attractive interactions, aging, and glassy dynamics in polymer nanocomposites that are not stably dispersed.<sup>[24,39,40]</sup>

Although shear rheology has been the focus of most studies to date, a report on the effect of uniaxial elongational flow on maleic anhydride-modified polypropylene nanocomposites has recently appeared.<sup>[41]</sup> Post facto TEM images indicate that at an elongational rate of  $1.0 \text{ sec}^{-1}$  and a Hencky strain of 1.3, clay platelets align perpendicular to the flow direction. Because flow in injection molding is comprised

of a significant extensional component, these results point to the possibility of direction-dependent material properties in components molded by this method.

## MECHANICAL PROPERTIES

Modulus, yield stress, toughness, and heat deflection temperature (HDT) are measures that characterize the potential for improved end-use performance of a polymer nanocomposite relative to the neat polymer or a traditional composite. Dispersed clay can affect the mechanical properties of a semicrystalline thermoplastic such as polypropylene in a number of ways. First, the high-modulus clay inclusions of anisotropic shape can reinforce the thermoplastic. This mechanism differs little from the classical picture of composite reinforcement. Thus in this view, the anisotropic shape of the discotic clay is important to mechanical property enhancement; however, the nanoscopic dimension of the clay plays no direct role. Second, inhomogeneous dispersion that results when even a small amount of micron-scale clay aggregates is present can seriously compromise the material's impact strength. Thus homogeneous dispersion at the submicron scale is desirable for successful practical application of polymer nanocomposites. Third, the nanoscale dimension of the clay filler leads to a large interfacial region at the clay surface. Thus even small amounts of clay can possibly mediate large changes in polymer matrix conformation, crystal structure, or crystal morphology. There is indirect evidence for a role of each of these conditions in mediating polypropylene nanocomposite mechanical properties.

The first reports of the successful preparation of polypropylene nanocomposites showed that the materials demonstrated only modest mechanical property enhancement relative to neat polypropylene or blends of polypropylene and PP-MA. At 7.2 wt.% inorganic clay content, 29% enhancement in tensile modulus was observed for the highest concentration of PP-MA studied.<sup>[12]</sup> Later work has generated improved tensile modulus enhancement. By varying the amine surfactant treatment and anhydride content of the compatibilizer, Reichert et al.<sup>[7]</sup> generated an increase in tensile modulus at 5 wt.% organophilic clay loading, which was as large as 74%. If nanocomposites are prepared in a matrix of pure PP-MA, the relative material property enhancement is slightly greater. For example, at approximately 5 wt.% inorganic clay content, the tensile modulus increased by 86% relative to PP-MA; however, the nanocomposite modulus is still inferior to that typical of neat polypropylene.<sup>[42]</sup> Polypropylene nanocomposites prepared by in situ polymerization

using metallocene catalysis have generated a >100% enhancement in tensile modulus at 10.5 wt.% clay loading.<sup>[23]</sup> A similar performance has been obtained for in situ polymerized PP synthesized by the Ziegler–Natta catalysis.<sup>[43]</sup> These improvements exceed results for other anisometric fillers, such as talc, which are not nanoscopic. For example, Walter et al.<sup>[44]</sup> found that more than 30 wt.% talc was required to yield modulus enhancement comparable to clay nanocomposites with less than 7 wt.% inorganic content.

Although significant progress in enhancing polypropylene nanocomposite tensile moduli has been achieved, this improvement is offset by the reduced elongation at break and impact strength of these materials. Elongation at break, which is a determinant of toughness, has been reported to fall by more than an order of magnitude relative to neat PP on melt mixing with organophilic clays and compatibilizers.<sup>[7,12]</sup> The changes have a number of possible origins: 1) the reduced toughness of PP-MA relative to PP because of its low molar mass; 2) the improved adhesion between the polymer matrix and the intercalated clay induced by the compatibilizer, which contributes to yielding a more brittle material; and 3) immiscible aggregates of clay acting as defects and stress concentrators, which contribute to failure even if they are present only at low concentrations.

A limitation to the penetration of polypropylene into various component and market categories is its low upper use temperature. One measure of this property is the HDT. At 8 wt.% clay, the HDT of polypropylene nanocomposites synthesized by in situ Ziegler–Natta catalysis is 40°C greater than for pure PP.<sup>[43]</sup>

## CONCLUSION

Recent research has generated advances in polypropylene nanocomposites that are sufficient to motivate new technological applications. For example, PP-based nanocomposites have been developed for application as exterior automotive components.<sup>[45]</sup> Cone calorimetry measurements of peak heat release rate from maleated PP nanocomposites with 4% loading are reduced by 75% relative to the pure polymer.<sup>[46]</sup> These improvements are relevant to applications requiring reduced flammability.

Yet, relative to other thermoplastic nanocomposites, such as nylon 6, the improvement in end-use properties for polypropylene nanocomposites has been modest. Thus research in the areas of synthesis and, especially, compounding, which are aimed at closing this performance gap, is necessary. Alternatively, improved fundamental understanding of the

detailed interactions and chemistry between clays, amine surfactants, and maleic anhydride compatibilizers can help elucidate the complex thermodynamics of clay dispersion. In addition, noting that many synthesized PP nanocomposites are likely to exist as non-equilibrium structures, research into the aging and rejuvenation of these mesoscale structures is warranted. Furthermore, better methods to characterize the full distribution and hierarchy of structural states present in PP nanocomposites are required because, for example, rare aggregates can seriously compromise non-linear mechanical properties such as toughness, yield stress, and elongation at break. Finally, the interaction between clay platelets and polymer crystallization requires further attention because these interactions are likely a significant determinant of the end-use properties of polypropylene nanocomposites.

## REFERENCES

1. Kojima, Y.; Usuki, A.; Kawasumi, M.; Okada, A.; Fukushima, Y.; Kurauchi, T.; Kamigaito, O. Mechanical properties of nylon 6–clay hybrid. *J. Mater. Res.* **1993**, *8* (5), 1185–1189.
2. Usuki, A.; Kawasumi, M.; Kojima, Y.; Okada, A.; Kurauchi, T.; Kamigaito, O. Swelling behavior of montmorillonite cation exchanged for  $\omega$ -amino acids by  $\epsilon$ -caprolactam. *J. Mater. Sci.* **1993**, *8* (5), 1174–1178.
3. Usuki, A.; Kojima, Y.; Kawasumi, M.; Okada, A.; Fukushima, Y.; Kurauchi, T.; Kamigaito, O. Synthesis of nylon 6–clay hybrid. *J. Mater. Res.* **1993**, *8* (5), 1179–1184.
4. Vaia, R.; Giannelis, E.P. Polymer nanocomposites: status and opportunities. *MRS Bull.* **2001**, *26* (5), 394–401.
5. Alexandre, M.; Dubois, P. Polymer-layered silicate nanocomposites: preparation, properties and uses of a new class of materials. *Mater. Sci. Eng., R Rep.* **2000**, *28* (1–2), 1–63.
6. Krishnamoorti, R.; Yurekli, K. Rheology of polymer layered silicate nanocomposites. *Curr. Opin. Colloid Interface Sci.* **2001**, *6* (5–6), 464–470.
7. Reichert, P.; Nitz, H.; Klinke, S.; Brandsch, R.; Thomann, R.; Mulhaupt, R. Poly(propylene)/organoclay nanocomposite formation: influence of compatibilizer functionality and organoclay modification. *Macromol. Mater. Eng.* **2000**, *275*, 8–17.
8. Hasegawa, N.; Okamoto, H.; Kawasumi, M.; Kato, M.; Tsukigase, A.; Usuki, A. Polyolefin–clay hybrids based on modified polyolefins and organophilic clay. *Macromol. Mater. Eng.* **2000**, *280* (7–8), 76–79.
9. Usuki, A.; Kato, M.; Okada, A.; Kurauchi, T. Synthesis of polypropylene–clay hybrid. *J. Appl. Polym. Sci.* **1997**, *63* (1), 137–139.

10. Kawasumi, M.; Hasegawa, N.; Kato, M.; Usuki, A.; Okada, A. Preparation and mechanical properties of polypropylene–clay hybrids. *Macromolecules* **1997**, *30* (20), 6333–6338.
11. Kato, M.; Usuki, A.; Okada, A. Synthesis of polypropylene oligomer–clay intercalation compounds. *J. Appl. Polym. Sci.* **1997**, *66* (9), 1781–1785.
12. Hasegawa, N.; Kawasumi, M.; Kato, M.; Usuki, A.; Okada, A. Preparation and mechanical properties of polypropylene–clay hybrids using a maleic anhydride-modified polypropylene oligomer. *J. Appl. Polym. Sci.* **1998**, *67* (1), 87–92.
13. Kurokawa, Y.; Yasuda, H.; Oya, A. Preparation of a nanocomposite of polypropylene and smectite. *J. Mater. Sci. Lett.* **1996**, *15* (17), 1481–1483.
14. Kurokawa, Y.; Yasuda, H.; Kashiwagi, M.; Oyo, A. Structure and properties of a montmorillonite/polypropylene nanocomposite. *J. Mater. Sci. Lett.* **1997**, *16* (20), 1670–1672.
15. Manias, E.; Touny, A.; Wu, L.; Strawhecker, K.; Lu, B.; Chung, T.C. Polypropylene/montmorillonite nanocomposites. Review of the synthetic routes and materials properties. *Chem. Mater.* **2001**, *13* (10), 3516–3523.
16. Xu, W.B.; Liang, G.D.; Wang, W.; Tang, S.P.; He, P.S.; Pan, W.P. PP-PP-g-MA-Org-MMT nanocomposites: 1. Intercalation behavior and microstructure. *J. Appl. Polym. Sci.* **2003**, *88* (14), 3225–3231.
17. Marchant, D.; Jayaraman, K. Strategies for optimizing polypropylene–clay nanocomposite structure. *Ind. Eng. Chem. Res.* **2002**, *41* (25), 6402–6408.
18. Kim, K.N.; Kim, H.; Lee, J.W. Effect of interlayer structure, matrix viscosity and composition of a functionalized polymer on the phase structure of polypropylene–montmorillonite nanocomposites. *Polym. Eng. Sci.* **2001**, *41* (11), 1963–1969.
19. Garcia-Lopez, D.; Picazo, O.; Merino, J.C.; Pastor, J.M. Polypropylene–clay nanocomposites: effect of compatibilizing agents on clay dispersion. *Eur. Polym. J.* **2003**, *39* (5), 945–950.
20. Liu, X.H.; Wu, Q.J. PP/clay nanocomposites prepared by grafting–melt intercalation. *Polymer* **2001**, *42* (25), 10,013–10,019.
21. Manke, C.W.; Gulari, E.; Mielewski, D.F.; Lee, E.C. System and Method of Delaminating a Layered Silicate Material by Supercritical Fluid Treatment. US Patent 6,469,073, October 22, 2002.
22. Fornes, T.D.; Yoon, P.J.; Keskkula, H.; Paul, D.R. Nylon 6 nanocomposites: the effect of matrix molecular weight. *Polymer* **2001**, *42*, 9929–9940.
23. Sun, T.; Garces, J.M. High-performance polypropylene–clay nanocomposites by in-situ polymerization with metallocene/clay catalysts. *Adv. Mater.* **2002**, *14* (2), 128+.
24. Solomon, M.J.; Almusallam, A.S.; Seefeldt, K.F.; Somwangthanoj, A.; Varadan, P. Rheology of polypropylene/clay hybrid materials. *Macromolecules* **2001**, *34* (6), 1864–1872.
25. Morgan, A.B.; Gilman, J.W. Characterization of polymer-layered silicate (clay) nanocomposites by transmission electron microscopy and X-ray diffraction: a comparative study. *J. Appl. Polym. Sci.* **2003**, *87* (8), 1329–1338.
26. Lincoln, D.M.; Vaia, R.A.; Wang, Z.-G.; Hsiao, B.S.; Krishnamoorti, R. Temperature dependence of polymer crystalline morphology in nylon 6/montmorillonite nanocomposites. *Polymer* **2001**, *42*, 9975–9985.
27. Maiti, P.; Nam, P.H.; Okamoto, M.; Kotaka, T.; Hasegawa, N.; Usuki, A. The effect of crystallization on the structure and morphology of polypropylene/clay nanocomposites. *Polym. Eng. Sci.* **2002**, *42* (9), 1864–1871.
28. Nam, P.H.; Maiti, P.; Okamoto, M.; Kotaka, T.; Hasegawa, N.; Usuki, A. A hierarchical structure and properties of intercalated polypropylene/clay nanocomposites. *Polymer* **2001**, *42* (23), 9633–9640.
29. Liedauer, S.; Eder, G.; Janeschitz-Kriegl, H. On the limitations of shear induced crystallization in polypropylene melts. *Int. Polym. Process.* **1995**, *X*, 243–250.
30. Hambir, S.; Bulakh, N.; Kodgire, P.; Kalgaonkar, R.; Jog, J.P. PP/clay nanocomposites: a study of crystallization and dynamic mechanical behavior. *J. Polym. Sci. B. Polym. Phys.* **2001**, *39* (4), 446–450.
31. Svoboda, P.; Zeng, C.; Wang, H.; Lee, J.; Tomasko, D.L. Morphology and mechanical properties of polypropylene/organoclay nanocomposites. *J. Appl. Polym. Sci.* **2002**, *85*, 1562–1570.
32. Somwangthanoj, A.; Lee, E.C.; Solomon, M.J. Early stage quiescent and flow-induced crystallization of intercalated polypropylene nanocomposites by time-resolved light scattering. *Macromolecules* **2003**, *36* (7), 2333–2342.
33. Ma, J.; Zhang, S.; Qi, A.; Li, G.; Hu, Y. Crystallization behaviors of polypropylene/montmorillonite nanocomposites. *J. Appl. Polym. Sci.* **2002**, *83*, 1978–1985.
34. Maiti, P.; Nam, P.H.; Okamoto, M.; Hasegawa, N.; Usuki, A. Influence of crystallization on intercalation, morphology, and mechanical properties of polypropylene/clay nanocomposites. *Macromolecules* **2002**, *35* (6), 2042–2049.
35. Li, J.; Zhou, C.X.; Wang, G.; Zhao, D.L. Study on kinetics of polymer melt intercalation by a rheological approach. *J. Appl. Polym. Sci.* **2003**, *89* (2), 318–323.
36. Koo, C.M.; Kim, M.J.; Choi, M.H.; Kim, S.O.; Chung, I.J. Mechanical and rheological properties of the maleated polypropylene-layered silicate nanocomposites with different morphology. *J. Appl. Polym. Sci.* **2003**, *88* (6), 1526–1535.
37. Galgali, G.; Ramesh, C.; Lele, A. A rheological study on the kinetics of hybrid formation in polypropylene nanocomposites. *Macromolecules* **2001**, *34* (4), 852–858.
38. Lele, A.; Mackley, M.; Galgali, G.; Ramesh, C. In situ rheo-x-ray investigation of flow-induced orientation in layered silicate-syndiotactic polypropylene

- nanocomposite melt. *J. Rheol.* **2002**, *46* (5), 1091–1110.
39. Fielding, S.M.; Sollich, P.; Cates, M.E. Aging and rheology in soft materials. *J. Rheol.* **2000**, *44* (2), 323–369.
40. Ren, J.; Casanueva, B.; Mitchell, C.; Krishnamoorti, R. Disorientation kinetics of aligned polymer layered silicate nanocomposites. *Macromolecules* **2003**, *36* (11), 4188–4194.
41. Okamoto, M.; Nam, P.H.; Maiti, P.; Kotaka, T.; Hasegawa, N.; Usuki, A. A house of cards structure in polypropylene/clay nanocomposites under elongational flow. *Nano Lett.* **2001**, *1* (6), 295–298.
42. Hasegawa, N.; Okamoto, H.; Kato, M.; Usuki, A. Preparation and mechanical properties of polypropylene–clay hybrids based on modified polypropylene and organophilic clay. *J. Appl. Polym. Sci.* **2000**, *78* (11), 1918–1922.
43. Ma, J.S.; Qi, Z.N.; Hu, Y.L. Synthesis and characterization of polypropylene/clay nanocomposites. *J. Appl. Polym. Sci.* **2001**, *82* (14), 3611–3617.
44. Walter, P.; Mader, D.; Reichert, P.; Mulhaupt, R. Novel polypropylene materials. *J. Macromol. Sci., Pure Appl. Chem., A* **1999**, *36* (11), 1613–1639.
45. Sherman, L.M. Nanocomposites: a little goes a long way. *Plast. Technol.* **1999**, *45* (6), 52–57.
46. Gilman, J.W.; Jackson, C.L.; Morgan, A.B.; Harris, R.; Manias, E.; Giannelis, E.P.; Wuthenow, M.; Hilton, D.; Phillips, S.H. Flammability properties of polymer–layered-silicate nanocomposites. Polypropylene and polystyrene nanocomposites. *Chem. Mater.* **2000**, *12* (7), 1866–1873.



# Interfacial Forces: Colloidal Particle–Liquid

Sarah A. Nespolo  
Geoffrey W. Stevens

*Department of Chemical and Biomolecular Engineering, University of Melbourne,  
Melbourne, Victoria, Australia*

## INTRODUCTION

Coalescence phenomena, emulsion stability, and the role of colloids in stabilizing liquid–liquid emulsions have been the subject of intensive study, yet there is still no satisfactory quantitative theory for the prediction of the rate of coalescence of drops at an interface or in an emulsion. Direct measurement of the forces between a liquid interface and another liquid interface or a colloid particle has been a key piece of information that has been missing. This entry describes recent advances in the theory and experimental techniques in colloid chemistry that enable the direct measurement of these forces.

This is an important step in the understanding of coalescence and emulsion stability phenomena.

## BACKGROUND OF THE MEASUREMENT OF SURFACE FORCES

The measurement of surface forces has, for many years, been the focus of much interest in the field of colloid and surface science.<sup>[1]</sup> This is principally because the long-range interactions between particles frequently control the ability of a dispersion to resist coagulation/flocculation. In addition, the rheology of dispersions can also be determined to a large degree by interparticle forces.

The interaction of solid colloidal particles with deformable liquid interfaces is of fundamental interest in many technologically important areas. Understanding the behavior of the forces acting at a liquid interface and, hence, the interactions that occur in solid/fluid particulate dispersions, is motivated by the myriad of problems encountered in many chemical engineering and processing applications within the pharmaceutical, cosmetic, and mineral processing industries, in the preparation and processing of foods, and in a vast range of biomedical technologies. For example, the interactions between solid and deformable fluid interfaces are important in determining the wetting characteristics of surfaces by liquids.<sup>[2]</sup> The

quantitative understanding of the forces acting at a liquid interface and how they are influenced by various additives is important to understanding the behavior and properties of fluid and solid particulate dispersions. The need to understand the interactions present in these systems is evident, in view of their ubiquitous presence and importance.

Interaction forces involving such interfaces have been deduced previously from measurements of related properties, such as contact angle, interfacial tension, and electrophoretic mobility. These measurements, while invaluable, provide only a qualitative assessment of long-range forces, and are unable to describe the response of a deformable interface to an approaching particle or surface.<sup>[2]</sup> Hence, the direct measurement of surface forces involving a deformable surface is important. The measurement of surface forces involving liquid interfaces is complex due to interfacial fluidity and deformability. These two features can have a great impact on hydrodynamic interactions and the resulting dynamic properties of such systems,<sup>[3–9]</sup> which are particularly important for the kinetic stability of emulsions.<sup>[3–5,10,11]</sup> With the exception of thin film measurements<sup>[12–19]</sup> (discussed later), the experimental complexities associated with direct force measurements between deformable interfaces have restricted their study. Until recently, there has not been any equilibrium study of surface forces, either experimentally or theoretically, which provides a description of the influence of surface interaction on these deformable systems. Attempts to obtain direct force measurements experimentally have been performed recently on solid–oil droplet systems and are described in the following paragraphs.

## INTERFACIAL (DLVO AND NON-DLVO) FORCES

The methodologies for the study of interactions between non-deformable surfaces are well established, and for well-characterized systems, experimental results are in good agreement with theoretical

predictions.<sup>[20–22]</sup> In the literature there is much data describing the interaction between two solid surfaces or particles dispersed in an aqueous solution. Most of these results have for their fundamental origin the mean-field theory of colloidal interaction published over 50 years ago by Derjaguin et al.<sup>[20,21]</sup> In recent years, Chan et al.<sup>[23–27]</sup> have, as a result of systematic studies covered many possible configurations of particle charge and shape, produced abundant data useful to the colloid chemist or physicist.

The stability of a colloid depends on the relative magnitude of the potential energies of attraction and repulsion with separation between a pair of particles.<sup>[28]</sup> The two most important forces acting in colloidal dispersions are the electrical double-layer (EDL) force and the van der Waals (vdW) force. The Derjaguin–Landau–Verwey–Overbeek (DLVO) theory, which includes only the combined effects of these two forces, is widely used to explain properties of colloids. The interaction free energy between two surfaces,  $V_T$ , is calculated by summing the repulsive EDL interaction energy,  $V_R$ , and attractive vdW interaction energy,  $V_A$ , thus:

$$V_T = V_A + V_R \quad (1)$$

According to DLVO theory, the stability of a lyophobic colloidal sol is determined by the shape of the total potential energy curve, which is the balance between the repulsive and attractive forces that the particles experience as they approach each other. The shape of the total potential energy curve for a sol is very important in understanding its behavior (Fig. 1).

At a fundamental level, van der Waals interactions are of importance in colloid and polymer science. The force of attraction between colloidal particles occurs between all particles in any suspension medium.<sup>[29]</sup> In many cases, these forces alone determine the stability of colloidal suspensions. A repulsive force can be introduced by adding an electrical charge to the particles. This results in an electrostatic force between the particles. Altering the magnitude of the repulsion, either by increasing the ionic strength of the solution or by changing the surface potential on the particles alters the total potential energy of interaction,  $V_T$ .

Although DLVO theory provides an excellent approximation of the interaction forces between many colloidal particles, it has become clear that it does not account for all of the phenomena observed in colloidal dispersions. There are many systems where the simple interplay between electrostatic repulsion and van der Waals attraction is neither a complete nor an accurate description of interfacial interactions. This is because beyond their simple definition as a dielectric

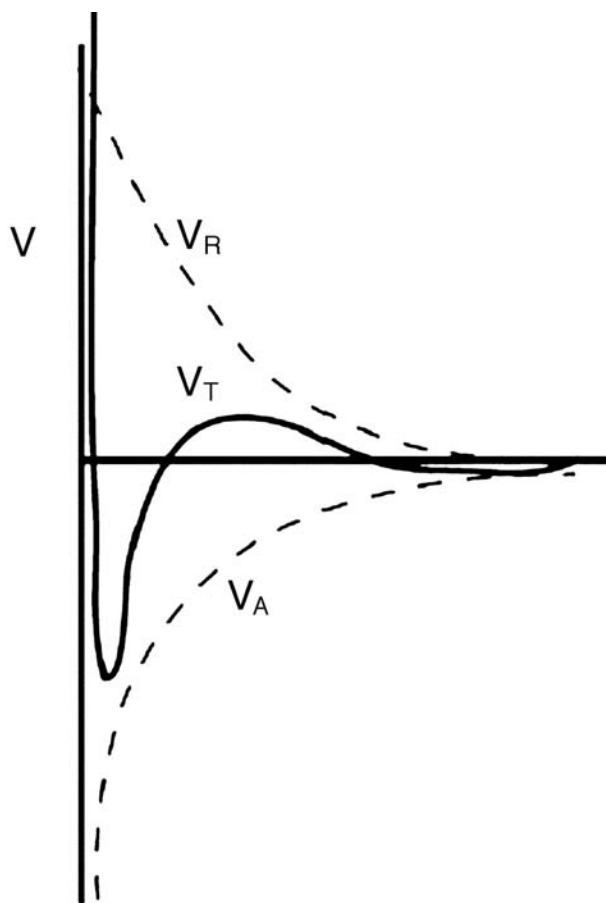


**Fig. 1** Total potential energy of interaction,  $V_T = V_A + V_R$  for two interacting surfaces. The broken curves show the potential energy of repulsion,  $V_R$ , due to the electrical force whereas  $V_A$  is the van der Waals attraction. The full curve,  $V_T$ , is obtained by summing  $V_R$  and  $V_A$ .

continuum containing point charges, the solvent and solutes surrounding a surface are not intrinsically considered in DLVO theory. In reality, the most “real” technological and biological interactions occur in systems where the relationship between the surface and solvent/solute mixtures is more complex. In the past few decades, other types of interparticle forces have been shown to play an important role in the stability of dispersions. These include hydrodynamic, hydration, steric, hydrophobic, and depletion interactions. In general, the net interaction energy profile resulting from all such forces governs the behavior of a suspension.<sup>[28,30]</sup>

An important non-equilibrium force when considering the forces between solid and liquid particles is the hydrodynamic force. Hydrodynamic forces include effects due to viscosity, density difference between the phases, film area, and mobility of the interfaces. The drainage of fluid from between two approaching

surfaces is not only dependent on surface forces acting between the surfaces, but also on the hydrodynamics of the system and, in particular, the speed at which the interacting surfaces approach each other. Increasing the viscosity of the intervening fluid, the film area, and the immobility of the surfaces acts to hinder film drainage and results in a decrease in the rate of fluid flow from between the plates.

An immobile surface is a surface for which the tangential components of the velocity are equal to zero. Surfaces can be rendered immobile by increasing the concentration of surfactant adsorbed to the surfaces. This is achieved by surfactant molecules adsorbed at the surfaces confining the film that are carried in the direction of fluid flow, resulting in the accumulation of surfactant molecules at the film periphery.<sup>[4,31,32]</sup> This results in the formation of interfacial tension gradients along the interfaces, which in turn induces stresses in the system and acts to restore the equilibrium distribution of adsorbed surfactant molecules. These stresses are commonly known as Marangoni stresses and act to inhibit further drainage of the film. Recent work in measuring film drainage has shown this phenomenon is important in many cases where liquid interfaces are involved.<sup>[33]</sup>

## INTERACTIONS INVOLVING DEFORMABLE INTERFACES

### Indirect Measurements of the Physicochemical Properties of Deformable Interfaces

Techniques such as electrokinetic, light scattering, and surface tension studies can be used to investigate the effect of additives on the interactions between colloids in dispersions indirectly. Measurements of isolated properties, such as contact angle, interfacial tension, and electrophoretic mobility have been used in the past to estimate the interaction forces between deformable interfaces.

#### Electrophoretic measurements

Electrophoresis is the study of the movement of particles in response to an electric field. The electrophoretic velocity of the particles can be used to calculate the  $\zeta$ -potential of the particle. Interfaces acquire surface charge in aqueous environments through the dissociation of surface groups and/or adsorption of ions from solution. Electrostatic repulsive forces resulting from the interaction between such charged surfaces are frequently responsible for the stability of colloidal suspensions or emulsions as they approach coagulation or coalescence.<sup>[34]</sup> It has long been recognized that the

$\zeta$ -potential, i.e., the electrostatic potential measured at the shear plane of isolated surfaces or particles, is a good indicator of the magnitude of the electrostatic potential present at the interface.

Many attempts have been made over the last 100 years to measure the electrical potential and charge at bubble and emulsion interfaces under different conditions using electrophoretic measurements. These involve measurements of bubble and emulsion mobility using conventional electrophoresis<sup>[2,34–46]</sup> and, more recently, electroacoustic techniques.<sup>[47–50]</sup>

It has been widely reported that negative potentials exist at the hydrocarbon–aqueous and air–aqueous interfaces in simple salt solutions or distilled water.<sup>[51–53]</sup> It has been postulated for the case of electrolytes that negative adsorption of cations occurs, giving rise to a charge separation. Preferential adsorption of  $\text{OH}^-$  ions at such interfaces has also been proposed as a mechanism for the acquisition of a net negative surface charge.<sup>[54]</sup>

A major problem with these measurements on non-rigid particles is that results are often affected by incidental contamination by surface-active materials adsorbed at the surface–aqueous solution interface.<sup>[35]</sup> Rigorously clean conditions are required for electrophoretic experiments.<sup>[2]</sup> Another problem arises in data interpretation. Classical electrophoretic mobility theories require a well defined slip boundary condition at the surface of a particle, prohibiting both the two-dimensional motion of charge at the interface and material circulation within the particle of interest, all of which cannot be assumed to be true for liquid particles. Most droplet electrophoresis studies in the literature assume solid particle hydrodynamic properties and use the theory of Smoluchowski to interpret the droplet shear surface potential, or  $\zeta$ -potential. The Smoluchowski result is reasonable in the limit of thin double layers, but for oil droplets the assumption of solid particle hydrodynamic behavior has not been justified by independent measurements.<sup>[34,41–46]</sup> The O'Brien and White theory is the accepted standard for relating measured electrophoretic mobilities to the  $\zeta$ -potentials for solid particles up to 250 mV.<sup>[55]</sup> An extension of O'Brien and White's theory was made by Ohshima, Healy, and White<sup>[42]</sup> to include the effects of internal hydrodynamic circulation in a liquid particle. Baygents and Saville<sup>[44]</sup> have also extended the Ohshima, Healy, and White theory for the analysis of bubbles and droplets. Electrophoretic studies of immiscible oil droplets therefore involve an added complexity associated with droplet hydrodynamics. Recently, using both the O'Brien and White<sup>[55]</sup> and Ohshima, Healy, and White<sup>[42]</sup> theories, an independent determination of the surface potential of the liquid interface was achieved, using a combination of light scattering and surface tension experiments, which

permitted the unambiguous determination of the  $\zeta$ -potential of liquid droplets in the presence of surfactant.<sup>[53]</sup> It was found for the system characterized that the  $\zeta$ -potentials had no obvious dependence on bulk surfactant concentrations and that the surfactant-coated oil droplets were also shown to behave like solid particles in terms of their hydrodynamic mobility for all surfactant concentrations studied.

Several other approaches including laser Doppler anemometry and the spinning cylinder technique have also been used for measuring the  $\zeta$ -potential of a gas–liquid interface.<sup>[37]</sup>

### Contact angle measurements

Contact angle measurement remains a favored methodology for assessing the interactions between liquid and solid media.<sup>[56]</sup> From the contact angle between two droplets, information about the relative depth of the interaction potential can also be obtained.

Using calculations of surface free energies derived from the Young–Dupré equation, various researchers have also attempted to develop theoretical techniques for describing the macroscopic contact angle in terms of the long-range electrostatic and van der Waals interactions implicit in DLVO theory. Klahn et al.<sup>[57]</sup> have extended this by developing analytical expressions for the nonretarded London-van der Waals potential of two identical flattened spheres and the existing force between them. The results obtained extend the applicability of the “classical” Hamaker-type equations.

Chatelier et al.<sup>[58]</sup> presented a theoretical description for the macroscopic contact angle of a solid/vapor/aqueous solution interface when the solid surface is ionizable and relatively hydrophobic. The contact angle is related to the free energy of formation of the ionizable surface in aqueous solution. Therefore, the theoretical approach takes into account the electrostatic free energy of charging the surface and the change in the free energy associated with the acid–base reactions of the surface sites.

### Scattering techniques

Colloidal particles and aggregates in a fluid can diffract light under conditions where the wavelength of the light is comparable to the size of the particles. Hence, optical techniques such as light scattering, neutron scattering, and X-ray diffraction can be used to characterize the size and structure of colloidal dispersions. Several studies have probed emulsions using static and dynamic light scattering.<sup>[59–72]</sup> Theoretical studies have also been conducted.<sup>[73–75]</sup>

## Direct Measurements of the Interactions of Liquid/Deformable Interfaces

### Thin film techniques

Thin liquid films are considered to be the basic structural elements of foam and emulsion systems. The surface forces that operate within them control the structure and stability of emulsions and foams.<sup>[76]</sup> Consequently, considerable effort has been invested in the study of thin liquid films, with a view to elucidating the interactions between the confining surfaces.<sup>[3]</sup> Thin film balance techniques have been used to measure the forces for single foam, emulsion, and solid–fluid films.<sup>[16,17,59,77–82]</sup> Investigations have focused primarily on the collapse of a drop at a flat interface or the coalescence of two drops, because results from single-drop experiments may be related to emulsion stability in a qualitative fashion. Although many theoretical and experimental investigations have been carried out to recognize the factors that affect coalescence, the phenomenon is not yet fully understood.<sup>[60,61]</sup> One of the main reasons for this is that coalescence occurs at the interfacial region, which often contains surface-active agents. Surfactants and trace impurities have been shown to have a significant effect on interfacial mobility and film flow behavior.<sup>[3–8,19,62]</sup>

The simplest thin film experiment uses an apparatus that allows a bubble or oil droplet to be manipulated near a solid surface, such as that of a plane parallel film of an aqueous solution confined between a solid and a deformable surface. The thickness of this film is monitored using an interferometric technique.<sup>[33,63]</sup> The pressure inside the bubble may be calculated from its dimensions. By controlling bubble dimensions and/or the radius of the plane parallel film, the pressure applied across the plane parallel film (which balances the disjoining pressure between the solid–liquid and air–liquid interface) is varied. In this way, a disjoining pressure–film thickness isotherm is defined.

Other refinements have been made to the thin film apparatus.<sup>[64,65]</sup> In particular, the design of the liquid surface forces apparatus (LSFA) is that of a thin capillary in which a small oil droplet in an aqueous phase can be moved in a controlled manner toward an oil–water interface.<sup>[66,67]</sup> A feature of the LSFA is that disjoining pressure isotherms may be determined for emulsion films of a few micrometers radius (i.e., of similar dimensions to the films formed by contact of two emulsion drops in a bulk emulsion).<sup>[67]</sup> Theoretical models have been produced with the aim to account for the observations of film stability and structure formation inside a liquid film containing colloidal particles.<sup>[68–71]</sup>

## DIRECT MEASUREMENT TECHNIQUES

### Surface Force Measurement Techniques

The direct measurement of surface forces between solid surfaces has been undertaken by measuring the force between macroscopic solid interfaces as a function of their separation. A large amount of data can be found in the literature that describes the interaction between two solid surfaces or particles dispersed in aqueous solution. These data have generally been obtained using devices such as the surface force apparatus (SFA) and the atomic force microscope (AFM). The AFM has one significant advantage over the SFA. It is not confined to studying optically transparent surfaces that are molecularly smooth over a large surface area. This application has enabled experimentation on systems that are not accessible using the SFA. Continuing development in atomic force microscopy has subsequently allowed progression to solid-liquid and solid-gas systems. The AFM is a useful tool for studying surface interactions because of the ease by which force-separation information may be extracted.<sup>[72]</sup> AFM force-distance curves are routinely used in several kinds of measurements for the determination of elasticity, Hamaker constants, surface charge densities, and degrees of hydrophobicity. It is also possible to extract some information about the adhesion between

the tip and the surface and the elasticity of the surface being probed. Surfaces that are not rigid can easily be deformed by the AFM tip and, consequently, the material properties of such surfaces can be studied. In Fig. 2 a schematic of the AFM is given and it demonstrates how the AFM is used to determine forces of solid surfaces.

The core of the AFM is a cantilever with a micro-fabricated tip that deflects when interacting with the sample surface. As long as the sample can be mounted on a piezoelectric scanning stage, the cantilever deflection will reproduce the sample topography. A controller regulates, collects, and processes the data and drives the piezoelectric scanner. Because the AFM measures forces between a tip and a sample surface it can be used to study interactions between the tip (or a colloidal probe attached to the tip, called the colloidal probe technique) and the sample as a function of separation. Although the colloidal probe technique of atomic force microscopy is now a routine method for exploring interfacial phenomena between two solid surfaces,<sup>[83,84]</sup> precise measurement of such forces when one or both of the particles is deformable, such as a liquid droplet, is more complex because of interfacial fluidity and deformability.

Another technique that is becoming more commonly used is total internal reflection microscopy (TIRM). TIRM monitors Brownian fluctuations in

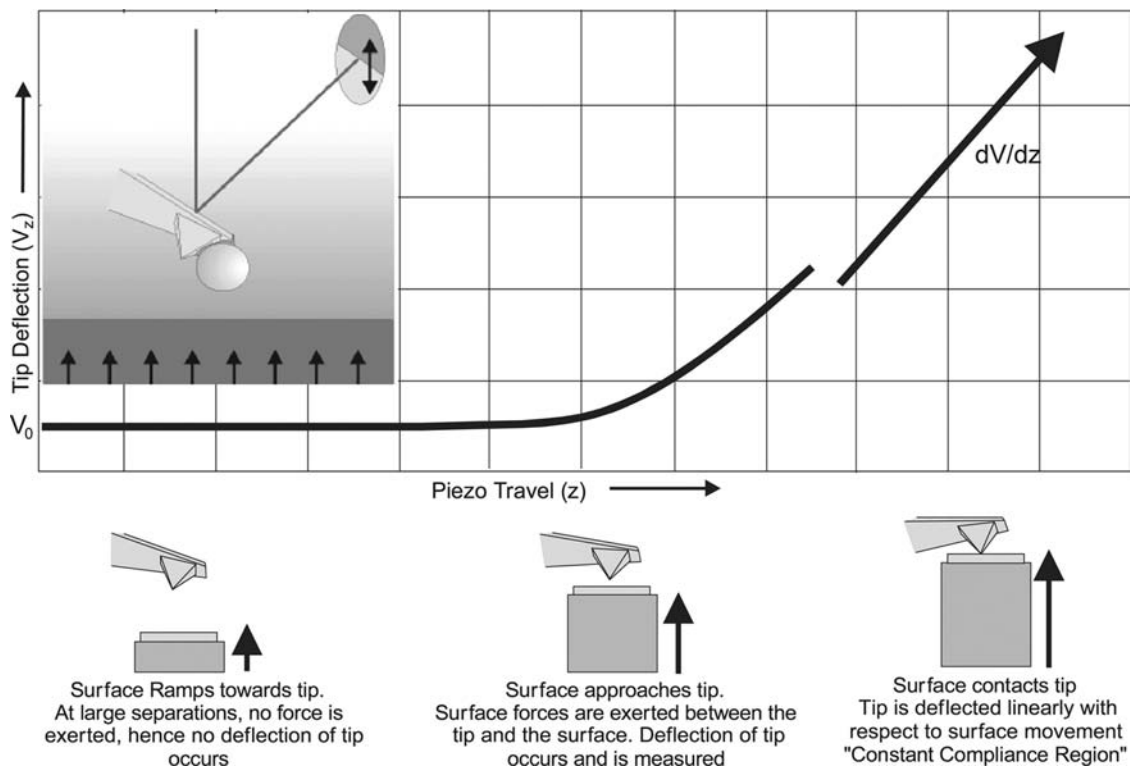


Fig. 2 Use of the atomic force microscope on solid surfaces. Source: From Ref.<sup>[30]</sup>.

elevations as small as 1 nm by measuring the scattering created from a single sphere illuminated by an evanescent wave when the sphere is levitated by colloidal forces such as electrostatic double-layer repulsion near an interface.<sup>[85]</sup> TIRM<sup>[85,86]</sup> can measure much smaller interactions than either the SFA or the AFM. Forces as small as  $10^{-13}$  N have been measured to within a few percent of known values with TIRM,<sup>[87]</sup> compared with  $10^{-9}$  N with SFA<sup>[88]</sup> or  $10^{-11}$  N with AFM.<sup>[89]</sup> TIRM has no control over separation, unlike the SFA and AFM.

Leal-Calderon et al.<sup>[90]</sup> developed a force measurement technique that allows the determination of force vs. distance between minute colloidal droplets. This technique requires the use of monodisperse oil-in-water ferrofluid emulsions whose resultant droplets are paramagnetic.<sup>[91]</sup> This technique uses the anisotropy of the forces between magnetic dipoles, which causes particles to form linear chains. At low particle volume fraction, well-separated linear chains with a thickness of one particle and oriented parallel to the field direction are produced. The repulsive forces between droplet interfaces can be deduced once the dipolar magnetic interaction is known. Variation of the intensity of the applied magnetic field allows the full force–distance profile to be determined.<sup>[92]</sup>

### Deformable interactions

Ducker, Senden, and Dashley<sup>[83]</sup> and Butt<sup>[89]</sup> were the first to report the attachment of a colloidal probe to a cantilever for probing colloidal forces. The attachment of a colloidal probe to a cantilever has meant that virtually any colloidal particle of interest can be used with the benefit of measurements being relatively fast and easy to perform. The first direct measurements of particle–deformable interface interactions were made subsequently by Butt.<sup>[93]</sup> He measured forces between a silica particle attached to the AFM cantilever and an air bubble anchored to the piezo-driven stage in an aqueous environment. Similar experiments with air bubbles have been reported.<sup>[94–100]</sup>

Preuss and Butt<sup>[96]</sup> determined the influence of an anionic and a cationic surfactant on the force between hydrophilic and hydrophobized 5- $\mu\text{m}$ -diameter silica particles and an air bubble. It was found that the force between a hydrophobic particle and an air–water interface becomes repulsive when surfactants are added to the aqueous solution. The bubble repelled hydrophilic particles, although different behavior was observed depending on the adsorption of the surfactant to the particle surface. The measured forces were interpreted in terms of simple surface forces, which, as discussed, is clearly not the case.

The first measurements of forces between a probe particle and sessile oil drops submerged in water have

been reported by Mulvaney et al.<sup>[101]</sup> followed by Synder, Aston, and Berg<sup>[102]</sup> Hartley et al.<sup>[103]</sup> Basu and Sharma,<sup>[104]</sup> and Aston and Berg.<sup>[105,106]</sup>

Recently, however, new developments in micropositioning and displacement detection have stimulated renewed interest in the measurement of surface forces operating between deformable interfaces, and have allowed the first steps to be taken toward a comprehensive understanding of the interactions responsible for their equilibrium behavior.

### Theoretical Analysis of Deformable Surfaces

In the case of identically charged materials interacting, DLVO theory separates the total interaction into two contributions: an attractive van der Waals interaction and electrical double-layer repulsion. Importantly, the total interaction free energy can be taken as the sum of these two contributions. If the interacting surfaces have dissimilar charges, the electrical double-layer contribution can be either attractive or repulsive or can even change from one to the other through charge regulation with changes in separation. For force measurements made between a sphere and a flat plate, the Derjaguin approximation is used to relate the interaction energy per unit area between parallel plates to the force between a sphere and flat plate.

Traditionally the deformation of elastic particles has been described by the Hertz<sup>[107]</sup> and the Johnson, Kendall, and Roberts (JKR)<sup>[108]</sup> theories. The Hertz theory assumes only normal stresses and is used to predict the contact area as a function of the applied load. The JKR theory has been extended to include the effect of surface forces on contact deformation, which results in the surfaces adhering when in contact. It was predicted that the solids would separate abruptly once a critical finite tensile load (the pull-off force) was reached. Both approaches assume particles interact only when in contact and ignore the extended range of the interactions in real systems.

The Derjaguin, Muller, and Toporov (DMT)<sup>[109]</sup> model, in contrast, assumes a Hertzian pressure distribution in the contact area and that the attractive forces between the surfaces act over a finite range in a region just outside the contact zone. It was predicted that the solids would separate only when the contact area was reduced to zero and the estimated pull-off force was larger than that estimated by the JKR model.

Beyond these contact theories are the soft contact approaches,<sup>[110–112]</sup> that take into account these extended interactions, although they are also based on linear elasticity. Recently, work has been conducted on developing theoretical models.<sup>[113–118]</sup> Experiments have been performed to measure surface profiles at small separations using both the SFA and AFM and



comparing these results with the classical models<sup>[119,120]</sup> and newer, more complex models.<sup>[121]</sup> More recently, viscoelastic response interaction forces between a spherical silica probe and a cross-linked polydimethylsiloxane colloidal droplet have been performed.<sup>[122–124]</sup>

The asymmetric nature of the interaction operating between an air bubble and a particle is an added complication of a deformable surface. Miklavcic et al.<sup>[125–128]</sup> addressed the mathematical complexities associated with such systems. The development of this theory has been assisted by the work of Horn et al.<sup>[129]</sup> which involves the measurement of surface and hydrodynamic forces between a flat mica surface and a mercury drop emerging from a thin capillary. Surface forces can be detected due to very small deformations of the drop (~1 nm). By measuring the shape of the mercury drop, they were able to deduce the force between the mica surface and the drop, using a modification of the SFA, while the separation between the surface and the drop was measured using an optical interference technique. Miklavcic, Horn, and Bachmann<sup>[125]</sup> found that deformation even at a microscopic scale enhances the effective area of interaction and results in a large difference in the measured force arising from deformations.

### Force Curve Analysis of AFM Experiments

The methodologies for the study of interactions between non-deformable surfaces by AFM are well established, and for well characterized systems, experimental results are in good agreement with theoretical predictions.<sup>[20–22]</sup> Unfortunately, interpretation of AFM interparticle force experiments is not straightforward when the surfaces deform during interaction. This is because a liquid surface is much more deformable than a solid surface and can change shape dramatically in response to a surface force. Because of such deformations, the surface shapes and hence the effective interaction areas are not known a priori, but will vary with surface separation. To fully interpret the surface force measurements, knowledge of the true separation between the solid–liquid interface is required. This is a critical ingredient for developing an understanding of the apparent interplay between interfacial deformation and double-layer interactions observed in these experiments.

Until recently, the interpretation of these measurements required the additional assumption that the bubble or droplet be treated as either elastic or a non-deformable solid. For instance, the work of Ducker, Xu, and Israelachvili<sup>[94]</sup> assumed that the air bubble deforms in a linear manner in order to estimate the separation between the two interfaces in AFM force measurements. They treated the deformable

interface and cantilever as two springs in series, where the measured stiffness  $K_m$  is given by

$$\frac{1}{K_m} = \frac{1}{K_s} + \frac{1}{K_{\text{int}}} \quad (2)$$

where  $K_s$  is the spring constant of the AFM cantilever and the stiffness of the interface,  $K_{\text{int}}$  can be calculated, from the slope of the measured force in the pseudo-linear regime [Eq. (3)].  $K_{\text{int}}$  has been referred to as an effective spring constant:

$$K_{\text{int}} = K_s \left( \frac{\Delta h}{\Delta c} - 1 \right)^{-1} \quad (3)$$

The disadvantage of this method is that the bubble or droplet is treated as either an elastic or a non-deformable solid. A disadvantage with the AFM is that because of surfaces deforming during interaction, it does not provide an absolute measure of separation between the surfaces. Upon interaction of a deformable colloid with either another colloidal particle or a surface, deformation results in additional variation of the surface separation and/or the contact area, and it is inappropriate to describe the interaction behavior in the same way as for rigid colloids.<sup>[83,89,130,131]</sup>

The AFM measures force and separation, but not the absolute separation between the colloidal probe and sample. Instead, separations are calculated relative to a hard wall contact. The accurate evaluation of the data requires that a hard wall, referred to as the “constant compliance” region, be reached. In this region, it is assumed that the expansion of the piezo leads only to a corresponding deflection of the cantilever, i.e., the surfaces are in hard contact but are incompressible. However, a problem, commonly referred to as “the zero separation problem,” arises when either of the surfaces under investigation are not rigid, as is true for surfaces bearing polymers, surfactants, or biomolecules, or deformable surfaces such as air bubbles or oil droplets. Hence, an absolute separation cannot be determined with this type of analysis. Previously, the deformable system has been analyzed by defining a zero “relative separation” at the point at which a deflection of the cantilever was first observable. Hartley et al. defined zero to be when the force divided by the radius ( $F/R$ ) was equal to 0.01 mN/m.<sup>[103]</sup> Although this type of analysis allows comparison between experiments, no information about absolute separation can be obtained. A theoretical model was developed by Bhatt, Newman, and Radke.<sup>[132]</sup> Although, they developed a way of comparing experiments to theoretical predictions, they did not give a direct comparison between theory and experimental data.

The true surface separation between the solid and the deformable liquid interface needs to be determined, so that the surface forces operating at liquid–liquid interfaces can be quantitatively determined. Because this information cannot be obtained from direct measurements, a model is needed, which provides the determination of the true separation between the solid–liquid interface as well as provides an understanding of the interplay between interfacial deformation and surface forces in the system. A number of theoretical models have been recently published.<sup>[118,125–128,132,133]</sup> A theoretical model that allows the determination of the true separation between the solid–liquid interface has been developed.<sup>[118,133]</sup> Chan, Dagastine, and White<sup>[118]</sup> modeled the AFM measurement of forces between a solid colloidal particle probe and a deformable liquid sessile drop on the piezo-driven stage. Independent measurements of droplet surface potential, colloidal probe surface potential, contact angle, interfacial tension, and probe radius are needed as inputs into the interpretive theory to provide a quantitative understanding of the measured forces operating at liquid–liquid interfaces. This theory provides the possible determination of the true separation between the solid and the deformable liquid interface. It provides the link between interfacial deformation and disjoining pressure due to electrical double-layer and van der Waals interactions in contributing to the observed force in these experiments. From this theory, it is possible to deduce a quantitative picture of the deformation of the liquid interface as a function of separation.

Recent results for SDS solutions have shown an unambiguous determination of the absolute separation between the particle probe and the droplet interface was achieved if all physical parameters of the system were known. The adsorption of SDS provides the droplet interface with a surface potential of sufficiently high magnitude to stabilize the particle–droplet system against engulfment because of the ever-present attractive van der Waals interactions. Under these circumstances, deformation of the droplet interface provides a mechanism to increase the effective areas of repulsive interaction between the particle and the droplet, which stabilizes the system against engulfment even at the highest forces that can be applied in the AFM.<sup>[134]</sup> Fig. 3 shows a typical result for the force vs. separation distance between a colloid particle and a decane drop compared with the theory of Chan, Dagastine, and White.<sup>[118]</sup>

For electrolyte solutions, the surface potential of the droplet interface was not known with precision. In these cases, the model could not fully account for the interactions observed. Factors such as hydrodynamics, roughness, and Marangoni effects were considered, but did not resolve the inconsistencies seen between

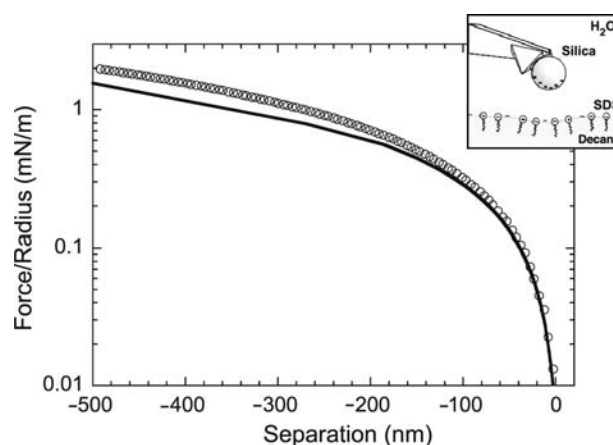


**Fig. 3** Use of the atomic force microscope to measure forces between a liquid interface and a silica probe in the presence of 10 mM SDS and 1 mM NaNO<sub>3</sub>. Open circles are experimental data, the solid line is the theoretical prediction from the theory of Chan, Dagastine, and White.<sup>[118]</sup> The gray area is the estimated error in the data.

the experimental and theoretical data. A definitive resolution of this issue will require accurate determinations of the surface potentials of the decane–electrolyte interface in the absence of added surfactant.<sup>[135]</sup> This theory allows the determination of the true separation between the solid–liquid interface and provides an understanding of the interplay between interfacial deformation and surface forces in this system and known material properties needed to calculate the electrical double-layer and van der Waals interactions with retardation and salt screening effects. The picture that emerges has important implications in understanding both emulsion stability and wetting phenomena.

## CONCLUSION

Recent theoretical and experimental developments have led to the first direct force measurements between a solid colloidal particle and a deformable interface using the atomic force microscope. This development is crucial to the understanding of a range of phenomena associated with emulsion stability, coalescence of drops, etc. This entry reviews developments in this area and describes how developments in the interpretation of signals from the atomic forces microscope can be interpreted as forces and how this compares with other methods for determining these forces.

## REFERENCES

1. Israelachvili, J.N. *Intermolecular and Surface Forces*, 2nd Ed.; Academic Press: London, 1991.

2. Kelsall, G.H.; Tang, S.; Yurdakul, S.; Smith, A.L. Electrophoretic behaviour of bubbles in aqueous electrolytes. *J. Chem. Soc., Faraday Trans.* **1996**, *92* (20), 3887.
3. Ivanov, I.B.; Kralchevsky, P.A. *Thin Liquid Films. Fundamentals and Applications*; Surfactant Science Series, Ivanov, I.B., Ed.; Marcel Dekker: New York, 1988; Vol. 29.
4. Ivanov, I.B. Dynamic behaviour of liquid films. *Pure Appl. Chem.* **1980**, *52*, 1241.
5. Ivanov, I.B.; Dimitrov, D.S.; Somasundaran, P.; Jain, R.K. Thinning of films with deformable surfaces: diffusion-controlled surfactant transfer. *Chem. Eng. Sci.* **1985**, *44*, 137.
6. Traykov, T.T.; Ivanov, I.B. Hydrodynamics of thin liquid films. Effect of surfactants on the velocity of thinning of emulsion films. *Int. J. Multiph. Flow* **1977**, *3* (5), 471.
7. Zhang, X.; Davis, R.H. The rate of collisions due to Brownian or gravitational motion of small drops. *J. Fluid Mech.* **1991**, *230*, 479.
8. Yiantsios, S.G.; Davis, R.H. Close approach and deformation of two viscous drops due to gravity and van der Waals forces. *J. Colloid Interface Sci.* **1991**, *144*, 421.
9. Miller, C.A.; Neogi, P. *Interfacial Phenomena*; Surfactant Series; Marcel Dekker: New York, 1985; Vol. 17.
10. Chen, J.D.; Slattery, J.C. Effects of London-van der Waals forces on the thinning of a dimpled liquid-film as a small drop or bubble approaches a horizontal solid plane. *AIChE J.* **1982**, *28* (6), 955.
11. Joye, J.-L.; Miller, C.A.; Hirasaki, G.J. Dimple formation and behavior during axisymmetrical foam film drainage. *Langmuir* **1992**, *8* (12), 3083.
12. Mysels, K.J.; Jones, M.N. Direct measurement of variation of double-layer repulsion with distance. *Discuss. Faraday Soc.* **1966**, *42*, 42.
13. Sonntag, H.; Netzel, J.; Klare, H. Untersuchungen über die Stabilität von Emulsionen in Gegenwart grenzflächenaktiver Stoffe. *Kolloid-Z. Z. Polym.* **1966**, *211* (1-2), 121.
14. Herrington, T.M.; Midmore, B.R.; Sahi, S.S. Influence of non-ionic surfactants on the equilibrium distance of approach of emulsion droplets. *J. Chem. Soc., Faraday Trans. 1* **1982**, *78*, 2711.
15. Fisher, L.R.; Parker, N.S. Interferometric studies of lipid bilayer interactions. *Faraday Discuss. Chem. Soc.* **1986**, *81*, 249.
16. Ivanov, I.B.; Chakarova, S.K.; Dimitrova, B.I. Instability of emulsion liquid-films induced by the transfer of acetic acid. *Colloids Surf.* **1987**, *22* (2-4), 311.
17. Velev, O.D.; Gurkov, T.D.; Borwankar, R.P. Spontaneous cyclic dimpling in emulsion films due to surfactant mass-transfer between the phases. *J. Colloid Interface Sci.* **1993**, *159* (2), 497.
18. Velev, O.D.; Gzurkov, T.D.; Chakarova, S.K.; Dimitrova, B.I.; Ivanov, I.B.; Borwankar, R.P. Experimental investigations on model emulsion systems stabilized with nonionic surfactant blends. *Colloids Surf., A* **1994**, *83* (1), 43.
19. Nikolov, A.D.; Wasan, D.T. Effects of surfactant on multiple stepwise coalescence of single drops at liquid-liquid interfaces. *Ind. Eng. Chem. Res.* **1995**, *34*, 3653.
20. Derjaguin, B.V.; Landau, L. Theory of the stability of strongly charged lyophobic sols and of the adhesion of strongly charged particles in solutions of electrolytes. *Acta Physicochem.* **1941**, *14*, 633.
21. Verwey, E.J.W.; Overbeek, J.T.G. *Theory and Stability of Lyophobic Colloids*; Elsevier: Amsterdam, 1948.
22. Hunter, R.J. *Foundations of Colloid Science*; Oxford Science Publishers: Oxford, 1989; Vol. 1.
23. Carnie, S.L.; Chan, D.Y.C.; Gunning, J.S. Electrical double layer interaction between dissimilar spherical colloidal particles and between a sphere and a plate—The linearized Poisson-Boltzmann theory. *Langmuir* **1994**, *10* (9), 2993.
24. Carnie, S.L.; Chan, D.Y.C.; Stankovich, J. Computation of forces between spherical colloidal particles—nonlinear Poisson-Boltzmann theory. *J. Colloid Interface Sci.* **1994**, *165* (1), 116.
25. Carnie, S.L.; Chan, D.Y.C. Interaction free energy between plates with charge regulation—a linearized model. *J. Colloid Interface Sci.* **1993**, *161* (1), 260.
26. Carnie, S.L.; Chan, D.Y.C. Interaction free-energy between identical spherical colloidal particles—the linearized Poisson-Boltzmann theory. *J. Colloid Interface Sci.* **1993**, *155* (2), 297.
27. McCormack, D.; Carnie, S.L.; Chan, D.Y.C. Calculations of electric double-layer force and interaction free-energy between dissimilar surfaces. *J. Colloid Interface Sci.* **1995**, *169* (1), 177.
28. Hiemenz, P.C.; Rajagopalan, R. *Principles of Colloid and Surface Chemistry*, 3rd Ed.; Marcel Dekker, 1997.
29. Hunter, R.J. *Introduction to Modern Colloid Science*; Oxford Science Publications, Oxford University Press, 1993.
30. Hartley, P.G. Measurement of colloidal interactions using the atomic force microscope. In *Colloid and Polymer Interactions: Techniques and Applications*; Farinato, R., Dubin, P., Eds.; John Wiley & Sons, Inc.: New York, 1999.
31. Nierstrasz, V.A.; Frens, G. Marginal regeneration and the Marangoni effect. *J. Colloid Interface Sci.* **1999**, *215* (1), 28.
32. Stebe, K.J.; Maldarelli, C. Remobilizing surfactant retarded fluid particle interfaces. 2. Controlling the surface mobility at interfaces of solutions containing surface active components. *J. Colloid Interface Sci.* **1994**, *163* (1), 177.
33. Goodall, D.G.; Gee, M.L.; Stevens, G.W.; Perera, J.M.; Beaglehole, D. An investigation of the critical thickness of film rupture and drainage phenomena using dual wavelength ellipsometry. *Colloids Surf., A* **1998**, *143* (1), 41.
34. Hunter, R.J. *Zeta Potential in Colloid Science*; Academic Press Inc.: London, 1981.
35. Kelsall, G.H.; Tang, S.; Yurdakul, S.; Smith, A.L. Measurement of rise and electrophoretic velocities of

- gas bubbles. *J. Chem. Soc., Faraday Trans.* **1996**, *92* (20), 3879.
36. Yoon, R.H.; Yordan, J.L. Zeta-potential measurements on microbubbles generated using various surfactants. *J. Colloid Interface Sci.* **1986**, *113* (2), 430.
  37. Collins, G.L.; Mortarjemi, M.; Jameson, G.J. Method for measuring charge on small gas-bubbles. *J. Colloid Interface Sci.* **1978**, *63* (1), 69.
  38. Fukui, Y.; Yuu, S. Measurement of the charge on small gas bubble. *AIChE J.* **1982**, *28* (5), 866.
  39. Okada, K.; Akagi, Y. Method and apparatus to measure the zeta-potential of bubbles. *J. Chem. Eng. Jpn.* **1987**, *20* (1), 11.
  40. Booth, F. The cataphoresis of spherical fluid droplets in electrolytes. *J. Chem. Phys.* **1951**, *19* (11), 1331.
  41. Levich, V.G. *Physicochemical Hydrodynamics*; Prentice-Hall: Englewood Cliffs, NJ, 1962.
  42. Ohshima, H.; Healy, T.W.; White, L.R. Electrokinetic phenomena in a dilute suspension of charged mercury drops. *J. Chem. Soc., Faraday Trans. 2* **1984**, *80*, 1643.
  43. Levine, S.; O'Brien, R.N. A theory of electrophoresis of charged mercury drops in aqueous electrolyte solution. *J. Colloid Interface Sci.* **1973**, *43* (3), 616.
  44. Baygents, J.C.; Saville, D.A. Electrophoresis of drops and bubbles. *J. Chem. Soc., Faraday Trans.* **1991**, *87* (12), 1883.
  45. Baygents, J.C.; Saville, D.A. Electrophoresis of small particles and fluid globules in weak electrolytes. *J. Colloid Interface Sci.* **1991**, *146* (1), 9.
  46. Ohshima, H. A simple expression for the electrophoretic mobility of charged mercury drops. *J. Colloid Interface Sci.* **1997**, *189* (2), 376.
  47. Hunter, R.J.; O'Brien, R.W. Electroacoustic characterization of colloids with unusual particle properties. *Colloids Surf., A* **1997**, *126* (2-3), 123.
  48. O'Brien, R.W. The dielectric response of a dilute suspension of semiconducting particles. *J. Colloid Interface Sci.* **1996**, *177* (1), 280.
  49. Hunter, R.J. Recent developments in the electroacoustic characterisation of colloidal suspensions and emulsions [review]. *Colloids Surf., A* **1998**, *141* (1), 37.
  50. Carasso, M.L.; Rowlands, W.N.; Kennedy, R.A. Electroacoustic determination of droplet size and zeta potential in concentrated intravenous fat emulsions. *J. Colloid Interface Sci.* **1995**, *174* (2), 405.
  51. Huddleston, R.W. *Int. Foams Conference*; Brunel University, 1975.
  52. Dunstan, D.E.; Saville, D.A. Electrophoretic mobility of colloidal alkane particles in electrolyte solutions. *J. Chem. Soc., Faraday Trans.* **1992**, *88* (14), 2031.
  53. Nespolo, S.A.; Bevan, M.A.; Chan, D.Y.C.; Grieser, F.; Stevens, G.W. Hydrodynamic and electrokinetic properties of decane droplets in aqueous SDS solutions. *Langmuir* **2001**, *17*, 7210.
  54. McShea, J.A.; Callaghan, I.C. Electrokinetic potentials at the gas-aqueous interface by spinning cylinder electrophoresis. *Colloid Polym. Sci.* **1983**, *261* (9), 757.
  55. O'Brien, R.; White, L.R. Electrophoretic mobility of a spherical colloidal particle. *J. Chem. Soc., Faraday Trans. 2* **1978**, *74*, 1607.
  56. van Oss, C.J. *Interfacial Forces in Aqueous Media*; Marcel Dekker: New York, 1994.
  57. Klahn, J.K.; Ageterof, W.G.M.; Agterof, F.; van Voorst Vader, F.; Groot, R.D.; Groeneweg, F. The London-van der Waals force between two approaching droplets: The consequences of flattening of the spherical bodies. *Colloids Surf.* **1992**, *65*, 151.
  58. Chatelier, R.C.; Hodges, A.M.; Drummond, C.J.; Chan, D.Y.C.; Griesser, H.J. Determination of the intrinsic acid-base dissociation constant and site density of ionizable surface groups by capillary rise measurements. *Langmuir* **1997**, *13* (11), 3043.
  59. Gillespie, T.; Rideal, E.K. The coalescence of drops at an oil-water interface. *Trans. Faraday Soc.* **1956**, *52*, 173.
  60. Petsev, D.N.; Denkov, N.D.; Kralchevsky, P.A. Flocculation of deformable emulsion droplets. *J. Colloid Interface Sci.* **1995**, *176*, 201.
  61. Denkov, N.D.; Petsev, D.N.; Danov, K.D. Flocculation of deformable emulsion droplets. *J. Colloid Interface Sci.* **1995**, *176*, 189.
  62. Churaev, N.V.; Ershov, A.P.; Esipova, N.E.; Iskandarjan, G.A.; Madjarova, E.A.; Sergeeva, I.P.; Sobolev, V.D.; Svitova, T.F.; Zakharova, M.A.; Zorin, Z.M.; Poirier, J.E. Interaction of oil droplets with silica surfaces. *Colloids Surf., A* **1994**, *91*, 97.
  63. Goodall, D.G.; Stevens, G.W.; Beaglehole, D.; Gee, M.L. Imaging ellipsometry/reflectometry for profiling the shape of a deformable droplet as it approaches an interface. *Langmuir* **1999**, *15*, 4579.
  64. Blake, T.D.; Kitchener, J.A. Stability of aqueous films on hydrophobic methylated silica. *J. Chem. Soc., Faraday Trans.* **1972**, *68* (8), 1435.
  65. Aronson, M.P.; Petko, M.F.; Princen, H.M. On the stability of aqueous films between oil and silica. *J. Colloid Interface Sci.* **1978**, *65* (2), 296.
  66. Aveyard, R.; Binks, B.P.; Cho, W.-G.; Fisher, L.R.; Fletcher, P.D.I.; Flinkhammer, F. Investigation of the force-distance relationship for a small liquid drop approaching a liquid-liquid interface. *Langmuir* **1996**, *12* (26), 6561.
  67. Binks, B.P.; Cho, W.-G.; Fletcher, P.D.I. Disjoining pressure isotherms for oil-water-oil emulsion films. *Langmuir* **1997**, *13* (26), 7180.
  68. Zapryanov, Z.; Malhotra, A.K.; Aderangi, N.; Wasan, D.T. Emulsion stability—an analysis of the effects of bulk and interfacial properties on film mobility and drainage rate. *Int. J. Multiph. Flow* **1983**, *9* (2), 105.
  69. Chu, X.L.; Nikolov, A.D.; Wasan, D.T. Thin liquid film structure and stability: the role of depletion and surface-induced structural forces. *J. Chem. Phys.* **1995**, *103* (15), 6653.
  70. Vrij, A.; Hesselink, F.T.; Lucassen, J.; van den Tempel, M. Waves in thin films. 2. Symmetrical modes in very thin films and film rupture. *Proc. K. Ned. Akad. Wet., B* **1970**, *73* (2), 124.
  71. Lucassen, J.; van den Tempel, M.; Vrij, A.; Hesselink, F.T. Waves in thin liquid films. 1. Different modes of vibration. *Proc. K. Ned. Akad. Wet., B* **1970**, *73* (2), 109.

72. Cappella, B.; Dietler, G. Force-distance curves by atomic force microscopy. *Surf. Sci. Rep.* **1999**, *34*, 1.
73. Lisy, V.; Brutovsky, B. Interpretation of static and dynamic neutron and light scattering from microemulsion droplets: effects of shape fluctuations. *Phys. Rev., E Stat. Phys. Plasmas Fluids* **2000**, *61* (4 Part B), 4045.
74. Evilevitch, A.; Lobaskin, V.; Olsson, U.; Linse, P.; Schurtenberger, P. Structure and transport properties of a charged spherical microemulsion system. *Langmuir* **2001**, *17* (4), 1043.
75. Kaler, E.W.; Prager, S. A model of dynamic scattering by micro-emulsions. *J. Colloid Interface Sci.* **1982**, *86* (2), 359.
76. Nikolov, A.D.; Wasan, D.T. Effect of film size and micellar polydispersity on film stratification. *Colloids Surf., A* **1997**, *128*, 243.
77. Bergeron, V.; Radke, C.J. Equilibrium measurements of oscillatory disjoining pressure in aqueous foam films. *Langmuir* **1992**, *8* (12), 3020.
78. Manev, E.D.; Pugh, R.J. Diffuse layer electrostatic potential and stability of thin aqueous films containing a nonionic surfactant. *Langmuir* **1991**, *7* (10), 2253.
79. Zorin, Z.M.; Churaev, N.V.; Esipova, N.E.; Sergeeva, I.P.; Sobolev, V.D.; Gasanov, E.K. Influence of cationic surfactant on the surface-charge of silica and on the stability of aqueous wetting films. *J. Colloid Interface Sci.* **1992**, *152* (1), 170.
80. Tchaliiovskia, S.; Herder, P.; Pugh, R.J.; Stenius, P.; Eriksson, J.C. Studies of the contact interaction between an air bubble and a mica surface submerged in dodecylammonium chloride solution. *Langmuir* **1990**, *6* (10), 1535.
81. Fisher, L.R.; Mitchell, E.E.; Parker, N.S. The effect of adsorbed lysozyme on interaction forces and coalescence of triglyceride droplets in aqueous salt-solutions. *J. Colloid Interface Sci.* **1989**, *128* (1), 35.
82. Koczo, K.; Nikolov, A.D.; Wasan, D.T.; Borwankar, R.P.; Gonsalves, A. Layering of sodium caseinate submicelles in thin liquid films—a new stability mechanism for food dispersions. *J. Colloid Interface Sci.* **1996**, *178*, 694.
83. Ducker, W.A.; Senden, T.J.; Pashley, R.M. Direct measurement of colloidal forces using an atomic force microscope. *Nature* **1991**, *353*, 239.
84. Ducker, W.A.; Senden, T.J.; Pashley, R.M. Measurement of forces in liquids using a force microscope. *Langmuir* **1992**, *8* (7), 1831.
85. Liebert, R.B.; Prieve, D.C. Species-specific long range interactions between receptor/ligand pairs. *Biophys. J.* **1995**, *69*, 66.
86. Prieve, D.C.; Luo, F.; Lanni, F. Brownian-motion of a hydrosol particle in a colloidal force-field. *Faraday Discuss.* **1987**, *83*, 22.
87. Prieve, D.C.; Frej, N.A. Total internal reflection microscopy: a quantitative tool for the measurement of colloidal forces. *Langmuir* **1990**, *6* (2), 396.
88. Parker, J.L.; Claesson, P.M. Direct measurements of the attraction between solvophobic surfaces in ethylene-glycol and mixtures with water. *Langmuir* **1992**, *8* (3), 757.
89. Butt, H.-J. Measuring electrostatic, van der Waals, and hydration forces in electrolyte solutions with an atomic force microscope. *Biophys. J.* **1991**, *60*, 1438.
90. Leal-Calderon, F.; Stora, T.; Mondain-Monval, O.; Poulin, P.; Bibette, J. Direct measurement of colloidal forces. *Phys. Rev. Lett.* **1994**, *72* (18), 2959.
91. Bibette, J. Monodisperse ferrofluid emulsions. *J. Magn. Magn. Mater.* **1993**, *122* (1–3), 37.
92. Mondain-Monval, O.; Leal-Calderon, F.; Bibette, J. Forces between emulsion droplets: Role of surface charges and excess surfactant. *J. Phys., II* **1996**, *6* (9), 1313.
93. Butt, H.-J. A technique for measuring the force between a colloidal particle in water and a bubble. *J. Colloid Interface Sci.* **1994**, *166*, 109.
94. Ducker, W.A.; Xu, Z.; Israelachvili, J.N. Measurements of hydrophobic and DLVO forces in bubble-surface interactions in aqueous solutions. *Langmuir* **1994**, *10* (9), 3279.
95. Fielden, M.L.; Hayes, R.A.; Ralston, J. Surface and capillary forces affecting air bubble-particle interactions in aqueous electrolyte. *Langmuir* **1996**, *12* (15), 3721.
96. Preuss, M.; Butt, H.-J. Direct measurement of particle-bubble interactions in aqueous electrolyte: dependence on surfactant. *Langmuir* **1998**, *14* (12), 3164.
97. Preuss, M.; Butt, H.J. Direct measurement of forces between particles and bubbles. *Int. J. Miner. Process.* **1999**, *56* (1–4), 99.
98. Ralston, J.; Fornasiero, D.; Hayes, R. Bubble-particle attachment and detachment in flotation. *Int. J. Miner. Process.* **1999**, *56* (1–4), 133.
99. Ecke, S.; Preuss, M.; Butt, H.J. Microsphere tensiometry to measure advancing and receding contact angles on individual particles. *J. Adhes. Sci. Technol.* **1999**, *13* (10), 1181.
100. Carambassis, A.; Jonker, L.C.; Attard, P.; Rutland, M.W. Forces measured between hydrophobic surfaces due to a submicroscopic bridging bubble. *Phys. Rev. Lett.* **1998**, *80* (24), 5357.
101. Mulvaney, P.; Perera, J.M.; Biggs, S.; Grieser, F.; Stevens, G.W. The direct measurement of the forces of interaction between a colloid particle and an oil droplet. *J. Colloid Interface Sci.* **1996**, *183*, 614.
102. Synder, B.A.; Aston, D.E.; Berg, J.C. Particle-drop interactions examined with an atomic force microscope. *Langmuir* **1997**, *13* (3), 590.
103. Hartley, P.G.; Grieser, F.; Mulvaney, P.; Stevens, G.W. Surface forces and deformation at the oil-water interface probed using AFM force measurement. *Langmuir* **1999**, *15* (21), 7282.
104. Basu, S.; Sharma, M.M. Measurement of critical disjoining pressure for dewetting of solid surfaces. *J. Colloid Interface Sci.* **1996**, *181* (2), 443.
105. Aston, D.E.; Berg, J.C. Fluid interfacial separations for secondary fibre recovery as probed with atomic force microscopy. *J. Pulp Pap. Sci.* **1998**, *24* (4), 121.
106. Aston, D.E.; Berg, J.C. Quantitative analysis of fluid interface-atomic force microscopy. *J. Colloid Interface Sci.* **2001**, *235* (1), 162.

107. Hertz, H. Über den Kontakt elastischer Körper. *Reine Angew. Math.* **1881**, 92, 156.
108. Johnson, K.L.; Kendall, K.; Roberts, A.D. Surface energy and contact of elastic solids. *Proc. R. Soc. Lond., A* **1971**, 324, 301.
109. Derjaguin, B.V.; Muller, V.M.; Toporov, Y.P. Effect of contact deformations on adhesion of particles. *J. Colloid Interface Sci.* **1975**, 53 (2), 314.
110. Hughes, B.D.; White, L.R. Soft contact problems in linear elasticity. *Q. J. Mech. Appl. Math.* **1979**, 32, 445.
111. Muller, V.M.; Yushchenko, V.S. On the influence of molecular forces on the deformation of an elastic sphere and its sticking to a rigid plane. *J. Colloid Interface Sci.* **1980**, 77 (1), 91.
112. Attard, P.; Parker, J.L. Deformation and adhesion of elastic bodies in contact. *Phys. Rev., A* **1992**, 46 (12), 7959.
113. Attard, P. Interaction and deformation of elastic bodies: origin of adhesion hysteresis. *J. Phys. Chem., B* **2000**, 104 (45), 10,635.
114. Attard, P. Interaction and deformation of viscoelastic particles: nonadhesive particles. *Phys. Rev., E* **2001**, 6306 (6 Part 1), 1604.
115. Attard, P. Interaction and deformation of viscoelastic particles. 2. Adhesive particles. *Langmuir* **2001**, 17 (14), 4322.
116. Attard, P. Contact-angle hysteresis in solid-on-solid wetting. *Phys. Rev., E* **2001**, 6301 (1 Part 1), 1601.
117. Attard, P.; Miklavcic, S.J. Effective spring description of a bubble or a droplet interacting with a particle. *J. Colloid Interface Sci.* **2002**, 247 (1), 255.
118. Chan, D.Y.C.; Dagastine, R.R.; White, L.R. Forces between a rigid probe particle and a liquid interface. I. The repulsive case. *J. Colloid Interface Sci.* **2001**, 236 (1), 141.
119. Horn, R.G.; Israelachvili, J.N.; Pribac, F. Measurement of the deformation and adhesion of solids in contact. *J. Colloid Interface Sci.* **1987**, 115 (2), 480.
120. Vakarelski, I.U.; Toritani, A.; Nakayama, M.; Higashitani, K. Deformation and adhesion of elastomer microparticles evaluated by AFM. *Langmuir* **2001**, 17 (16), 4739.
121. Parker, J.L.; Attard, P. Deformation of surfaces due to surface forces. *J. Phys. Chem.* **1992**, 96 (25), 10,398.
122. Gillies, G.; Prestidge, C.A.; Attard, P. Determination of the separation in colloid probe atomic force microscopy of deformable bodies. *Langmuir* **2001**, 17 (25), 7955.
123. Gillies, G.; Prestidge, C.A.; Attard, P. An AFM study of the deformation and nanorheology of cross-linked PDMS droplets. *Langmuir* **2002**, 18 (5), 1674.
124. Attard, P.; Gillies, G. Deformation and adhesion of viscoelastic particles: theory and experiment. *Aust. J. Chem.* **2001**, 54 (8), 477.
125. Miklavcic, S.J.; Horn, R.G.; Bachmann, D.J. Colloidal interaction between a rigid solid and a fluid drop. *J. Phys. Chem.* **1995**, 99 (44), 16,357.
126. Bachmann, D.J.; Miklavcic, S.J. Deformation of fluid interfaces induced by electrical double-layer forces and its effect on fluid-solid interactions. *Langmuir* **1996**, 12, 4197.
127. Miklavcic, S.J. Deformation of fluid interfaces under double-layer forces stabilizes bubble dispersions. *Phys. Rev., E Stat. Phys. Plasmas* **1996**, 54 (6).
128. Miklavcic, S.J.; Attard, P. The equilibrium shape of an axisymmetric sessile drop subject to local stresses. *J. Phys., A, Math. Gen.* **2001**, 34 (38), 7849.
129. Horn, R.G.; Bachmann, D.J.; Connor, J.N.; Miklavcic, S.J. The effect of surface and hydrodynamic forces on the shape of a fluid drop. *J. Phys., Condens. Matter* **1996**, 8 (47), 9483.
130. Hartmann, U. Van der Waals interactions between sharp probes and flat sample surfaces. *Phys. Rev., B* **1991**, 43 (3), 2404.
131. Butt, H.J.; Kappl, M.; Mueller, H.; Raiteri, R.; Meyer, W.; Ruhe, J. Steric forces measured with the atomic force microscope at various temperatures. *Langmuir* **1999**, 15 (7), 2559.
132. Bhatt, D.; Newman, J.; Radke, C.J. Equilibrium force isotherms of a deformable bubble/drop interacting with a solid particle across a thin liquid film. *Langmuir* **2001**, 17 (1), 116.
133. Dagastine, R.R.; White, L.R. Forces between a rigid probe particle and a liquid interface. II. The general case. *J. Colloid interface Sci.* **2002**, 247 (2), 310.
134. Nespolo, S.; Chan, D.; Grieser, F.; Hartley, P.; Stevens, G. Forces between a rigid probe particle and a liquid interface: Comparison between experiment and theory. *Langmuir* **2003**, 19 (6), 2124.
135. Nespolo, S.A. *Direct Measurement of Forces at Deformable Interfaces and in Complex Fluids*; Department of Chemical and Biomolecular Engineering, The University of Melbourne: Melbourne, 2002.



# Interfacial Phenomena: Chemical Selectivity

Vinay K. Gupta

Department of Chemical Engineering, University of Illinois at Urbana–Champaign,  
Urbana, Illinois, U.S.A.

## INTRODUCTION

The capability to control and manipulate structure and properties of chemical, biological, and physical systems at nanometer dimensions holds immense potential for technological advancement. This promise of nanotechnology has spurred increasing investment into research at the nanometer length scale in virtually every scientific discipline. One of the hallmarks of nanoscience and engineering research is the predominance of interfacial phenomena, which occurs as a natural consequence of the shrinking length scale. Examples of these phenomena include molecular interactions at interfaces within chemical or biological systems, behavior of complex fluids such as polymers confined to an interface or between surfaces, synthesis of tailored nanoparticles, and two-dimensional nanostructures built by assembling nanoscale building blocks. One of the central questions faced in the studies of interfacial phenomena at the nanoscale is the impact of the interplay between molecular structure, forces, and organization. Here we discuss how this interplay can result in an exquisite molecular selectivity at a self-assembled surface, which in turn can form the basis of innovative applications in separations, analysis, and diagnostics.

## MOLECULAR RECOGNITION AT INTERFACES

In the last few years, molecular assemblies such as self-assembled monolayers (SAMs) and Langmuir–Blodgett (LB) films have become a popular vehicle for the investigation of interfacial interactions. The phenomenon of molecular recognition and association, in particular, has been actively studied because of its relevance in immunoassays, sensing, and other applications based on selective affinity of molecules to surfaces as well as its significance to fundamental studies of supramolecular interactions in well-defined geometries.<sup>[1–10]</sup> A number of investigations have relied on SAMs of organosulfides on gold because of the ease of preparation and the flexibility in design of the chemical interface.<sup>[11,12]</sup> It has been demonstrated that

SAMs formed from alkanethiols and thiolated ligands can bind metal ions, surfactants, and volatile organic compounds.<sup>[8,13,14]</sup> Recent attention has focused on SAMs formed from complex synthetic “host” receptors such as cyclodextrins<sup>[15–17]</sup> and calix[*n*]resorcinarenes.<sup>[18–25]</sup> These hosts contain a molecular cavity for targeted recognition of “guest” molecules. A primary challenge here has been to understand the role of molecular organization, structure, and forces in the guest–host recognition process and thereby to improve the selectivity of surfaces for binding metal ions, sugars, organic vapors, steroids, and apolar molecules.

Calix[4]resorcinarenes are macrocyclic host molecules that possess a bowl-shaped molecular cavity formed by four resorcinol units (Fig. 1). These cyclic tetramers are prepared by acid-catalyzed condensation of resorcinol and aldehydes.<sup>[26,27]</sup> In pioneering work, Aoyama et al. demonstrated that calix[4]resorcinarenes could trap various guest molecules such as sugars in aqueous solutions within the bowl-shaped cavity.<sup>[28–35]</sup> The trapping was driven by either  $\pi$ -acid/base interactions or by cooperative hydrogen-bonding interactions between the guest and the host molecules.

Thoden van Velzen, Engbersen, and Reinhoudt<sup>[36]</sup> extended the strategy to self-assembled surfaces. Calix[4]resorcinarenes were modified with dialkyl sulfides that undergo physisorption on gold surfaces.<sup>[37,38]</sup> The tetrasulfide calix[4]resorcinarene host had a cavity that was made rigid by bridging the oxygen atoms of neighboring aromatic rings (Fig. 1A). One of the first studies reported selective recognition of tetrachloroethylene from the gas phase.<sup>[39]</sup> However, similar selectivity of organic vapors by amorphous polymer films demonstrated that general dispersion interactions rather than specific interactions heavily influence recognition from vapor phase.<sup>[40]</sup> In contrast, more recent studies have shown that specific recognition of steroids or other neutral molecules occurs readily from aqueous solutions on SAMs of oxygen-bridged tetrasulfide calix[4]resorcinarene.<sup>[22,41]</sup>

We and others have also reported recognition by self-assembled surfaces wherein calix[4]resorcinarenes were modified with alkylthiols (Fig. 1B) that strongly chemisorb onto gold.<sup>[18–21]</sup> Recent studies have demonstrated that self-assembled surfaces of tetrathiol

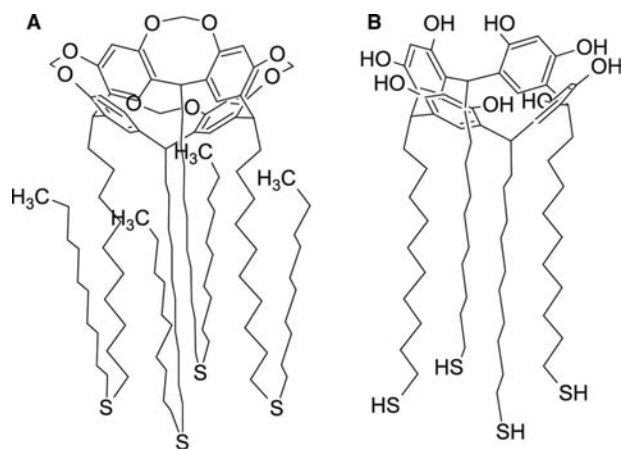


**Fig. 1** Chemical structures of calix[4]resorcinarene host molecules. (A) Tetrasulfide host where the aromatic rings are covalently bound by oxygen bridges and the dialkyl sulfide chains are similar in length; (B) tetrathiol host where the macrocyclic cavity is not oxygen-bridged.

calix[4]resorcinarene (Fig. 1B) discriminate between guest molecules that differ slightly in their molecular structure as well as between structural isomers.<sup>[18,42]</sup> These studies have established that small differences in the chemical structure of the guest molecules are important and that recognition of the guest is driven by a combination of factors such as hydrogen-bonding, hydrophobic interactions, and steric match. Furthermore, the structure of the host molecule and the organization of the self-assembled monolayer strongly influence the association of neutral molecules in aqueous solutions.<sup>[19]</sup> Results from these studies illustrate the critical relationships between molecular organization of the monolayer, the forces that drive molecular recognition, and the structure of the guest and the host molecules.

## CHEMICAL SELECTIVITY OF SURFACES: SOME REPRESENTATIVE RESULTS

### Role of Molecular Structure and Molecular Interactions

In Fig. 2, we show the experimental results from Faull and Gupta<sup>[18]</sup> that illustrate the role of molecular structure and the forces in guest–host association properties of SAMs formed from tetrathiol calix[4]resorcinarene. The three guest molecules possess slight differences in the pendant group—butyrolactone (BL), hydroxy- $\gamma$ -butyrolactone (HBL), and pantooylactone (PL) (Fig. 2A). Surface plasmon resonance (SPR) and polarization-modulation infrared reflection absorption spectroscopy (PM-IRRAS) were used to investigate

the recognition of guest molecules from aqueous solutions by the SAMs. In SPR (Fig. 2B), total internal reflection of an incident beam of light occurs. An exponentially decaying evanescent optical field probes the solid–liquid interface and resonates with the plasmon surface polariton on the metallic at the SPR angle ( $\theta_p$ ). The association at the surface was monitored by measuring the change in the SPR angle ( $\Delta\theta$ ) as the solution of the guest molecule was pumped over a gold film supporting the self-assembled monolayer.

The typical evolution of the SPR angle [ $\Delta\theta(t)$ ] when a SAM formed from the tetrathiol calix[4]resorcinarene host was placed in contact with an aqueous solution of  $\alpha$ -HBL and BL is shown in Fig. 2C. A rapid rise was observed for  $\Delta\theta$  in the case of  $\alpha$ -HBL indicating fast association with the surface, but no recognition of BL was observed. Thus the surface selectively interacts with HBL. Fig. 2C shows that for  $\alpha$ -HBL, the maximum change in  $\Delta\theta$  is reached within 1000 sec. Experiments with multiple sample surfaces reveal that typically,  $\Delta\theta_{\max}$  lies between  $0.06^\circ$  and  $0.08^\circ$ . In Fig. 2C, it is observed that upon switching the flow to pure water,  $\Delta\theta_{\max}$  dropped by approximately  $0.02^\circ$  and then stabilized, indicating that only some of the  $\alpha$ -HBL is washed away with pure water. Rinsing the surface with a few milliliters of pure ethanol, on the other hand, readily removes all of the HBL. When the rinsed surface is again placed in contact with a solution of HBL, the shift in the SPR angle is reproduced indicating that a self-assembled surface with the host receptor can be used for multiple recognition steps. Fitting of the reflectivity curve using the optical model gives a thickness of  $\sim 4 \text{ \AA}$  for the HBL layer and indicates that multilayering of the guest adsorbate is largely absent.

The SPR results in Fig. 2C show an interesting contrast with the reports on guest–host association on the more rigid, tetrasulfide calix[4]resorcinarene with O-bridged aromatic cavity (Fig. 1A). Friggeri et al.<sup>[22,41]</sup> and Schierbaum et al.<sup>[39]</sup> have reported that association of guest molecules such as benzoic acid and its derivatives occurs in a few seconds, which is significantly faster than the results on the tetrathiol calix[4]resorcinarene. Furthermore,  $\alpha$ -HBL associated with a SAM formed from the tetrathiol calix[4]resorcinarene cannot be completely rinsed using water, but the association of benzoic acid derivatives with the tetrasulfide calix[4]resorcinarene was reported to be reversed by washing with water. The absence of measurable association between BL and surfaces formed from tetrathiol calix[4]resorcinarene suggests that hydrogen-bonding interactions as a result of the hydroxyl (OH) pendant group on the  $\alpha$ -HBL play an important role in guest–host recognition at these surfaces. The importance of hydrogen bonding agrees with conclusions by Friggeri et al. based on the association of benzoic acid derivatives with various tetrasulfide

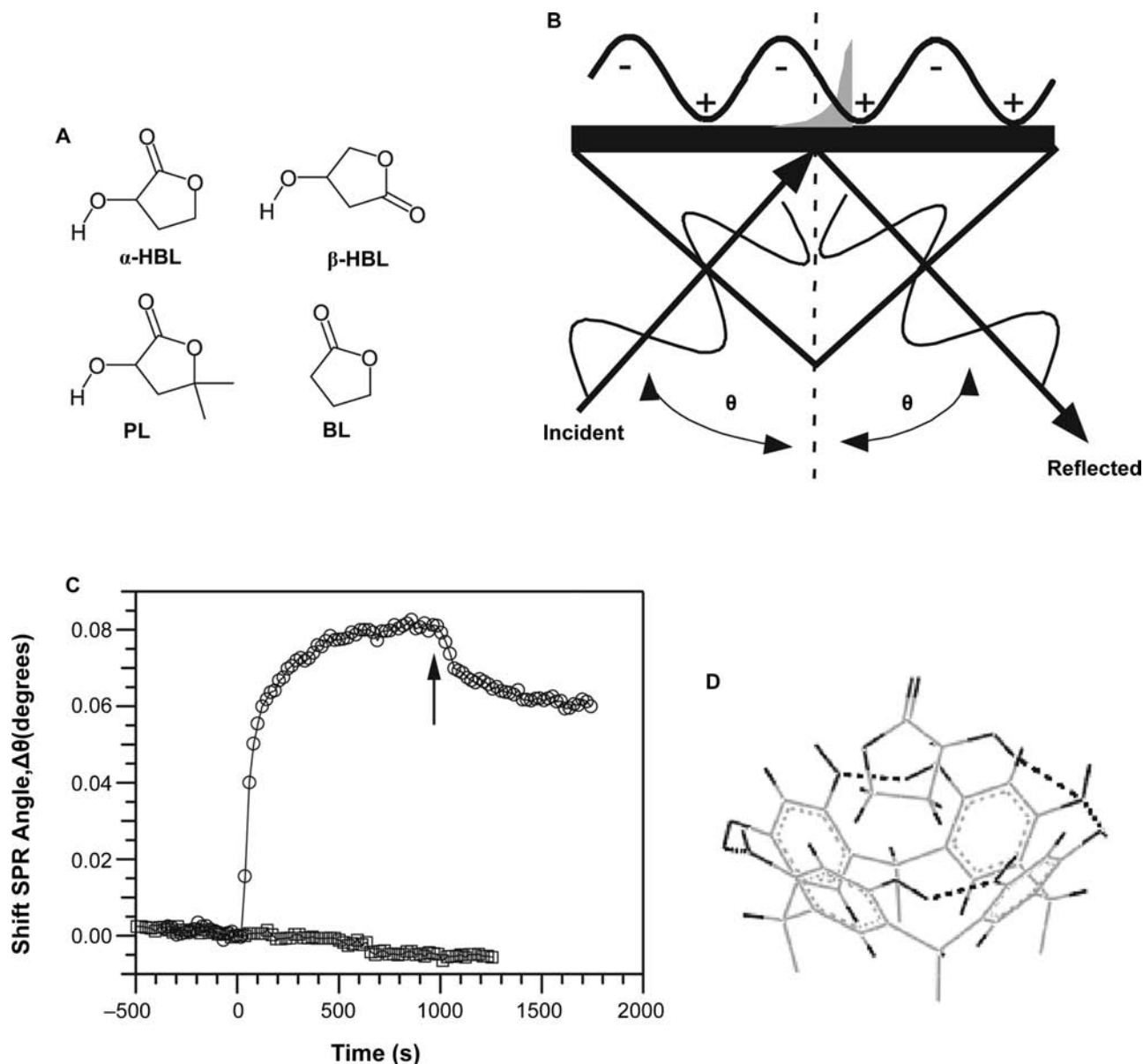


**Fig. 2** (A) Chemical structures of the guest molecules BL,  $\alpha$ -HBL and  $\beta$ -HBL, and PL. (B) Schematic of the SPR arrangement. (C) Shift in SPR angle caused by adsorption from 1 mM  $\alpha$ -HBL (circles) and BL (squares) solutions on a monolayer formed from tetrathiol calix[4]resorcinarene. Pure water flows through at  $t < 0$  and the adsorbate solution is injected at  $t = 0$ . The arrow indicates a rinse with pure water. (D) Schematic of the complex formed between  $\alpha$ -HBL and the macrocyclic cavity. For clarity, only the macrocyclic cavity is shown. Dashed lines indicate hydrogen bonds.

calix[4]resorcinarene. The association of  $\alpha$ -HBL reported here with tetrathiol calix[4]resorcinarene is plausibly enhanced by the presence of hydroxyl groups on the rim of the macrocyclic cavity.

To gain insight into the orientation of the  $\alpha$ -HBL associated with the surface, PM-IRRAS was used to characterize the surface before and after association. After 1200 sec of contact with an aqueous 1-mM solution of  $\alpha$ -HBL, a large positive peak at  $\sim 1744\text{ cm}^{-1}$  and a weaker peak at  $1125\text{ cm}^{-1}$  were observed. The peak at  $\sim 1744\text{ cm}^{-1}$  can be assigned to the carbonyl,

C=O, bond in  $\alpha$ -HBL. Comparison with a spectrum of a cast film of  $\alpha$ -HBL on gold shows that the peak at  $1125\text{ cm}^{-1}$  in the surface may be a result of the C-C(=O)-O- bond stretch in  $\alpha$ -HBL.<sup>[43]</sup> Because the frequencies corresponding to both the C=O bond and the C-C(=O)-O- bond can be discerned in the IR spectra, it can be inferred that the HBL molecule is oriented such that the transition moments of these two bonds have components along the normal to the surface. The lack of a peak in the  $1100\text{--}1300\text{ cm}^{-1}$  region, where typically the -C-O-H bend vibration

would be observed, indicates that  $-C-O-H$  absorption is either quite weak or has a large component parallel to the surface. Fig. 2D shows the associated complex that conforms with the IR results and shows the potential hydrogen bond between the OH group of  $\alpha$ -HBL and the tetrathiol calix[4]resorcinarene. A Corey-Pauling-Koltun (CPK) model of Fig. 2D shows that there is a close steric match between the guest and the host. Interestingly, this model of the association predicts that the  $\alpha$ -HBL projects out by a distance of approximately 3.5 Å, which matches quite well with the estimated thickness from SPR.

As a control experiment, a surface formed by the self-assembly of  $HO(CH_2)_{11}SH$  was used to test the interaction of  $\alpha$ -HBL with a hydrophilic surface. No measurable shift is observed in the SPR angle suggesting that the hydrophobic interactions contribute to the guest–host recognition by tetrathiol calix[4]resorcinarene. To further test the recognition capability of the SAMs formed from host surface, pantooylactone (PL) was used as a guest molecule. The guest molecule PL possesses a pendant hydroxyl (OH) group and two pendant methyl ( $CH_3$ ) groups (Fig. 2A). No measurable shift in the SPR angle was observed when an aqueous solution of PL was brought in contact with the tetrathiol calix[4]resorcinarene surface. The absence of interaction of PL with the surface formed from tetrathiol calix[4]resorcinarene surface can be interpreted in light of the schematic illustrated in Fig. 2D. Unlike  $\alpha$ -HBL, hydrogen-bonding interaction between tetrathiol calix[4]resorcinarene and the hydroxyl moiety in PL is not possible as the pendant methyl groups pose a large steric hindrance.

It has been demonstrated recently that the balance between various forces contributing to the recognition of guest molecules by SAMs formed from tetrathiol calix[4]resorcinarene can be exploited to selectively discriminate between two structural isomers.<sup>[18,42]</sup> Fig. 3 shows that in contrast to the positive  $\Delta\theta$  observed with  $\alpha$ -HBL, no shift in the SPR angle is observed when a solution of  $\beta$ -HBL is placed in contact with the surface formed from tetrathiol calix[4]resorcinarene. Like pantooylactone, hydrogen-bonding interactions between the hydroxyl group of  $\beta$ -HBL with the tetrathiol-calix are hindered, plausibly, because the oxygen atom in the  $C=O$  group precludes a steric match with the macrocyclic cavity.

Faull and Gupta<sup>[42]</sup> have also demonstrated that the chemical selectivity of SAMs of host molecules such as calix[4]resorcinarenes extends to isomers of several different guest molecules besides those discussed above. By using structural isomers of guest molecules such as bipyridine and nitrophenol that are multidentate hydrogen bond acceptors, it has been shown that geometric match between guest and host molecules is an integral aspect of the recognition phenomena.

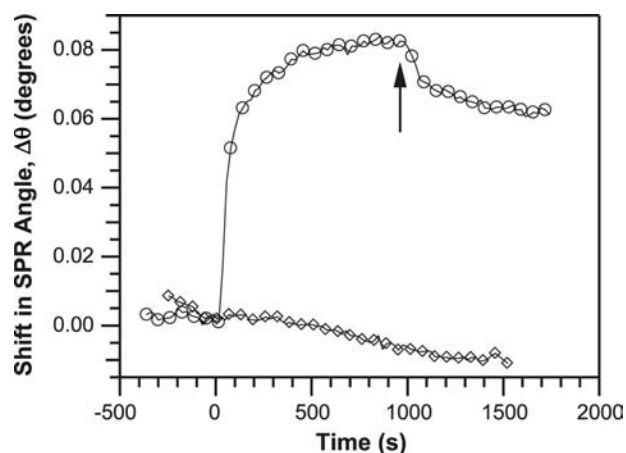


**Fig. 3** Shift in SPR angle during adsorption of  $\alpha$ -HBL and  $\beta$ -HBL on a monolayer formed from tetrathiol calix[4]resorcinarene. The curves are offset such that pure water is flowing through the cell at  $t < 0$  and the solution of adsorbate is injected at  $t = 0$ . The arrow indicates the time at which the surface was rinsed with pure water after HBL adsorption. Sparse markers have been used for clarity (every third point is shown).

Results from SPR and PM-IRRAS experiments highlight the interplay between steric size and forces such as hydrogen-bonding and hydrophobic interactions. These experimental studies also highlight the value of molecular modeling studies of the interaction between groups such as hydroxyl (OH), nitro ( $NO_2$ ), and pyridine nitrogen of guest molecules and hydroxyl groups of host surfaces and the molecular orientations of the guest that favor these interactions. In other experiments<sup>[42]</sup> on competitive and sequential adsorption of guest molecules such as  $\alpha$ -HBL and 4,4'-bipyridine, it has been shown that the guests compete for the same binding sites on the surface and the interplay between steric size and molecular forces underlies the preferential selectivity of one guest molecule over another. Such studies promise valuable insights into the fundamentals of the interfacial recognition phenomena and tailoring of surfaces to exploit the phenomena in novel applications.

### Interplay between Molecular Organization and Molecular Interactions

While the discussion in the previous section points to the impact of guest structure and molecular forces in the interfacial recognition process at nanometer length scales, the molecular organization of a monolayer is known to be a sensitive function of the chemical and physical structure of the molecules that form the monolayers and therefore can be expected to play an important role in the molecular association. This has



been illustrated recently in studies<sup>[19]</sup> on comparative studies of guest–host recognition on SAMs formed by two different host molecules—thiol-derivatized and dialkyl-sulfide-derivatized calix[4]resorcinarene molecules that possess similar head groups (Fig. 4A).

The impact of the host structure on the monolayer structure is clearly observed in Fig. 4B, which shows PM-IRRAS spectra of self-assembled monolayers formed from the two host molecules. For comparison, SAMs formed from hexadecanethiol [ $\text{CH}_3(\text{CH}_2)_{15}\text{SH}$ ] and octanethiol [ $\text{CH}_3(\text{CH}_2)_7\text{SH}$ ] are also shown. Both tetrathiol calix[4]resorcinarene and tetrasulfide calix[4]resorcinarene show peaks corresponding to the stretching modes of methylene ( $-\text{CH}_2$ ) groups at  $\nu_{\text{as}} = 2929\text{--}2930\text{ cm}^{-1}$  and at  $\nu_{\text{s}} = 2856\text{ cm}^{-1}$ . For the tetrathiol derivative, no peaks are observed at

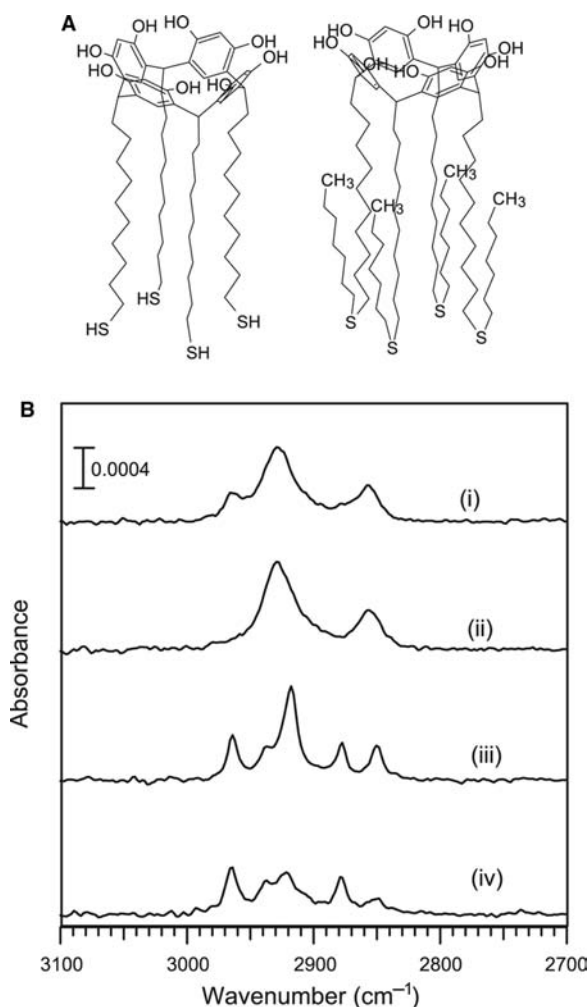


**Fig. 4** (A) Chemical structures of calix[4]resorcinarene host molecules modified with 4 alkylthiol or dialkyl sulfide anchors. (B) PM-IRRAS spectra of monolayers formed from (i) tetrasulfide calix[4]resorcinarene, (ii) tetrathiol calix[4]resorcinarene, (iii)  $\text{CH}_3(\text{CH}_2)_{15}\text{SH}$ , and (iv)  $\text{CH}_3(\text{CH}_2)_7\text{SH}$  on gold in the spectral region  $3100\text{--}2700\text{ cm}^{-1}$ .

frequencies corresponding to the methyl stretch (near  $2936$ ,  $2964$ , and  $2877\text{ cm}^{-1}$ ) because the molecule does not contain methyl groups (Fig. 4A). In comparison, the spectrum of tetrasulfide shows a broad shoulder at  $\nu_{\text{as}} = 2962\text{ cm}^{-1}$ , which corresponds to the asymmetric stretch of the methyl ( $-\text{CH}_3$ ) group. This is consistent with the presence of the methyl on the dialkyl sulfide tether (Fig. 4B).

Comparison of the PM-IRRAS spectra of the calix[4]resorcinarene hosts and the reference spectra of monolayer formed from  $\text{CH}_3(\text{CH}_2)_{15}\text{SH}$  highlights the differences in molecular organization of these monolayers. In the two SAMs formed from the calix[4]resorcinarene hosts, the asymmetric stretch of the  $-\text{CH}_2$  groups is observed at a higher wave number than in a monolayer of  $\text{CH}_3(\text{CH}_2)_{15}\text{SH}$  ( $2929\text{--}2930\text{ cm}^{-1}$  vs.  $2918\text{ cm}^{-1}$ ). A similar shift toward higher wave numbers is also observed in the symmetric  $-\text{CH}_2$  peak ( $2856\text{ cm}^{-1}$  vs.  $2850\text{ cm}^{-1}$ ). These shifts indicate that the alkyl chains in the SAMs formed from both macrocyclic hosts possess more gauche conformations and less order. Previous reports by Reinhoudt et al. on O-bridged, dialkyl sulfide SAMs of calix[4]resorcinarene have also shown that SAMs formed from these bulky macrocyclic hosts lack the well-ordered nature of simple, long-chain alkanethiols.

Fig. 4B shows that the peak positions for  $-\text{CH}_2$  absorption occur at comparable frequencies for the tetrathiol calix[4]resorcinarene and tetrasulfide calix[4]resorcinarene, which indicates that the degree of conformational ordering within these two types of monolayers is similar. In previous studies, Thoden van Velzen et al.<sup>[24]</sup> reported an asymmetric  $-\text{CH}_2$  peak absorption near  $2925\text{--}2927\text{ cm}^{-1}$  for monolayers formed from O-bridged, calix[4]resorcinarene molecules with dialkyl sulfide tethers (Fig. 1A). Thoden van Velzen et al. estimated the cross-sectional area of a calix[4]resorcinarene head group as  $\sim 140\text{ \AA}^2$  and speculated that because four alkylthiol chains with an area  $\sim 4 \times 20\text{ \AA}^2$  do not fill the void space beneath the macrocyclic cavity, a host with eight dialkyl sulfide is necessary to form monolayers with higher order. In later studies, Schoenherr et al.<sup>[44]</sup> used a computational model to correct the head group cross-sectional area of the host shown in Fig. 1A to  $\sim 117\text{ \AA}^2$ . Results in Fig. 4B indicate that increasing the number of alkyl tethers from tetrathiol to tetrasulfide does not necessarily enhance the order. Molecular modeling results show that the cross-sectional area of the calix[4]resorcinarene head group in Fig. 4A is  $\sim 85\text{--}95\text{ \AA}^2$ , which suggests that the four alkylthiol chains instead of the dialkyl sulfide chains provide a better fit to the head group size.<sup>[19]</sup> These simple geometric arguments alone indicate that the tetrasulfide host should occupy a larger area per molecule and will consequently have a lower density than tetrathiol derivative. The IR spectra

support the impact of host structure on the organization of the monolayers as they show comparable intensity for the asymmetric  $-\text{CH}_2$  ( $2929\text{--}2930\text{ cm}^{-1}$ ) peak in both hosts. Because the absorption as a result of  $-\text{CH}_2$  groups remains the same despite the increase in the number of methylene moieties, the spectra indicate that the density of tetrasulfide calix[4]resorcinarene within the monolayers is smaller than tetrathiol calix[4]resorcinarene. A schematic illustration of the monolayers is shown in Fig. 5A.

The changes in the monolayer structure illustrated in Fig. 5A are manifested in interfacial wettability and film thickness measurements. The thickness of the monolayer of tetrathiol calix[4]resorcinarene was found to be  $21\text{ \AA}$  ( $\pm 1\text{ \AA}$ ), while self-assembled monolayers formed from tetrasulfide calix[4]resorcinarene were determined to be  $13\text{ \AA}$  ( $\pm 1\text{ \AA}$ ) by SPR, which indicates that the dialkyl sulfide chains do not fold neatly beneath the calix[4]resorcinarene head group. The SAMs formed from tetrasulfide calix[4]resorcinarene also show a slightly greater hydrophobic nature (larger advancing contact angles) as well as a higher receding angle. This difference in hydrophobic nature can, in turn, be expected to impact the molecular forces at play in the guest–host recognition.

A typical temporal evolution of the SPR angle [ $\Delta\theta_p(t)$ ], when SAMs formed from the two hosts were placed in contact with an aqueous solution of  $\alpha$ -HBL, is shown in Fig. 5B. Both surfaces show a rapid rise in  $\Delta\theta_p$  indicating fast association of  $\alpha$ -HBL with the self-assembled surfaces. The magnitude of the maximum shift ( $\Delta\theta_{\text{max}}$ ) is  $\sim 0.1\text{--}0.12^\circ$ , which indicates the molecular dimension of the adsorbed layer ( $\sim 3\text{--}5\text{ \AA}$ ). Subsequent water rinse causes a slight decrease in  $\Delta\theta_{\text{max}}$  but does not wash out the  $\alpha$ -HBL. Interestingly, the interaction of  $\alpha$ -HBL with a SAM formed from tetrasulfide calix[4]resorcinarene shows that the time scale of the rise in  $\Delta\theta_p$  and the magnitude of the angular shift are comparable to tetrathiol calix[4]resorcinarene. The orientation of the  $\alpha$ -HBL associated with the two surfaces can be probed by using PM-IRRAS to characterize each surface before and after association. The spectra of both surfaces show a large positive peak at  $\sim 1744\text{ cm}^{-1}$  as a result of the carbonyl,  $\text{C}=\text{O}$ , bond in HBL and weaker peaks at  $1260$  and  $1125\text{ cm}^{-1}$  as a result of the  $\text{C}\text{--}\text{C}(=\text{O})\text{--}\text{O}$  bond stretch in HBL. The orientation of the HBL molecule and its association with the calix[4]resorcinarene cavity follows the schematic shown in Fig. 2D.

Differences in the structure and monolayer organization between the tetrasulfide and tetrathiol hosts do not show significant effects in SPR and IR measurements on the molecular association with  $\alpha$ -HBL. Because the thermodynamic affinity of  $\alpha$ -HBL to the surface is a sensitive function of the forces driving the interaction, and because the SAMs formed from

the two hosts differ in their hydrophobic nature and molecular organization, the association of  $\alpha$ -HBL was measured as a function of its bulk concentration in solution. Fig. 6 shows a plot of the shift in  $\Delta\theta_p$  observed for  $\alpha$ -HBL concentration varying between  $0.01$  and  $10\text{ mM}$ . Both surfaces show a Langmuir-type behavior with saturation of the response at high concentration. This behavior is in stark contrast to the measurements reported by Friggeri et al.<sup>[22]</sup> for SAMs formed from the O-bridged calix[4]resorcinarene host (Fig. 1A). Friggeri et al. reported that  $\Delta\theta_p$  for a guest molecule such as benzoic acid increased linearly with bulk concentration, which was interpreted to result from physisorption and formation of multilayers of the guest.

The experimental data in Fig. 6 were fit to the equation derived from a Langmuir isotherm, and regression analysis gives  $\Delta\theta_{\text{sat}} = 0.166 \pm 0.006$  and  $\Delta G^\circ_{\text{ads}} = -4.6 \pm 0.5\text{ kcal/mol}$  for the association with the tetrasulfide calix[4]resorcinarene surface and  $\Delta\theta_{\text{sat}} = 0.1 \pm 0.002$  and  $\Delta G^\circ_{\text{ads}} = -5.2 \pm 0.6\text{ kcal/mol}$  for the tetrathiol calix[4]resorcinarene surface. Comparison of this complexation energy with measurements in bulk solution will be important to understand how preorganization of host molecules on a surface and conformational mobility influence the phenomena of guest–host recognition. The estimates suggest that the difference in the energy of association is comparable to thermal energy and the saturation capacity of the surface formed from tetrasulfide calix[4]resorcinarene surface is larger than tetrathiol calix[4]resorcinarene surface.

Because the structural characterization strongly indicated that there are fewer tetrasulfide calix[4]resorcinarene surface molecules per unit area compared with tetrathiol derivative, the above result suggests that the guest  $\alpha$ -HBL molecules come in contact with binding sites other than the macrocyclic cavity on self-assembled surfaces of tetrasulfide calix[4]resorcinarene. The schematic structure shown in Fig. 5A indicates that interstitial cavities can exist within the monolayers because of the incommensurate packing of dialkyl sulfide chains below the calix[4]resorcinarene head group. The interstitial cavities are similar to the macrocyclic cavity of the calix[4]resorcinarene head group with, plausibly, some difference in the steric structure as well as the hydrophobic character. Previous studies on both self-assembled monolayers and Langmuir films have demonstrated that steric traps (similar to the interstitial cavities in SAMs of tetrasulfide calix[4]resorcinarene) can cause molecular recognition.<sup>[8,45,46]</sup> It is therefore reasonable to expect that intercalation of HBL is possible within these interstitial cavities. Faull and Gupta<sup>[19]</sup> have shown that the intercalation of guest molecules has important consequences when multiple



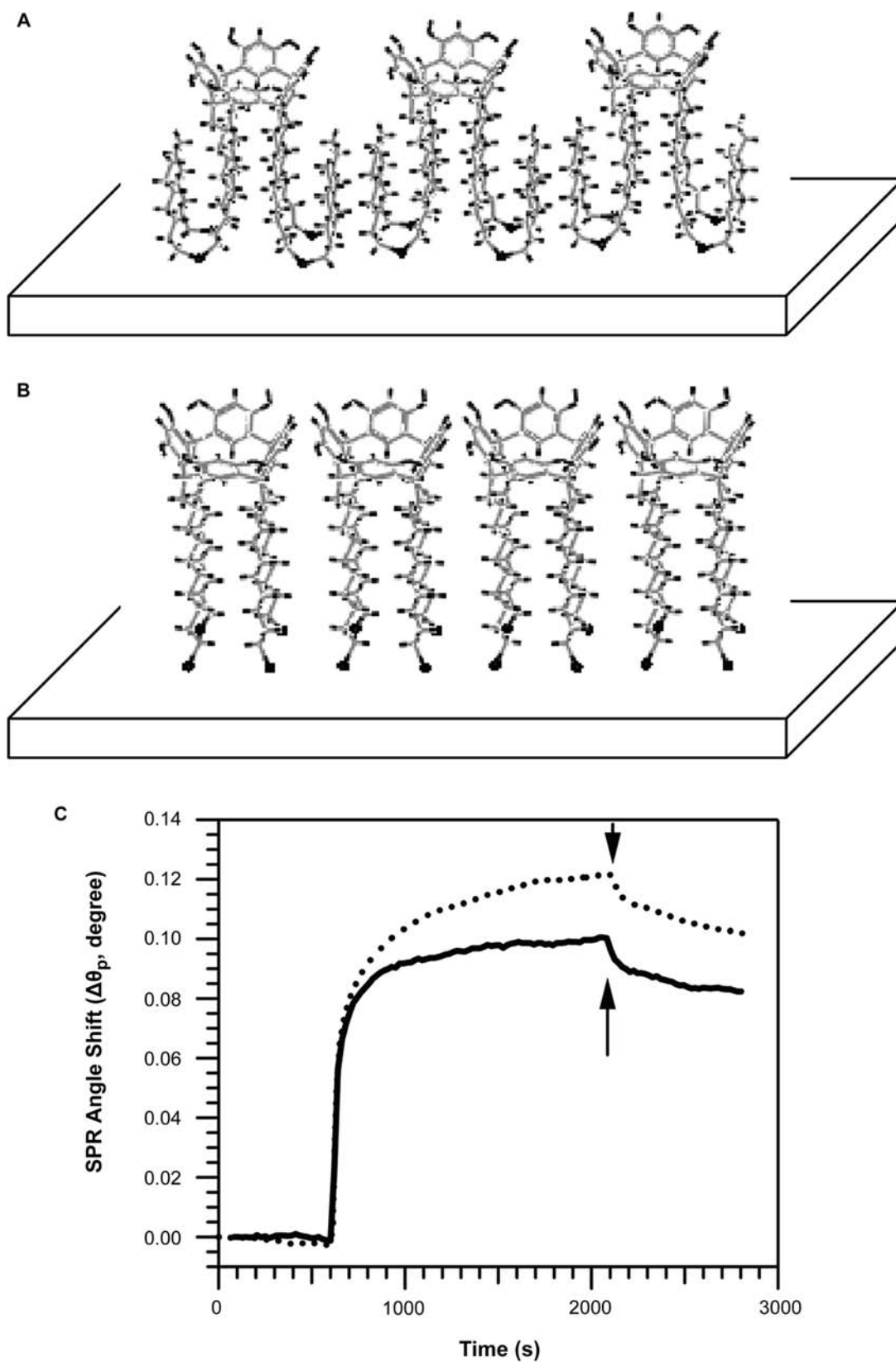


**Fig. 5** Schematic illustration of monolayers formed from tetrasulfide (A) and tetrathiol (B) calix[4]resorcinarene hosts. (C) Shift in SPR angle ( $\Delta\theta_p$ ) caused by adsorption from a 1-mM aqueous solution of HBL on monolayers formed from tetrasulfide calix[4]resorcinarene (dotted curve) and tetrathiol calix[4]resorcinarene (solid curve). The arrow indicates the time at which the surface was rinsed with pure water.

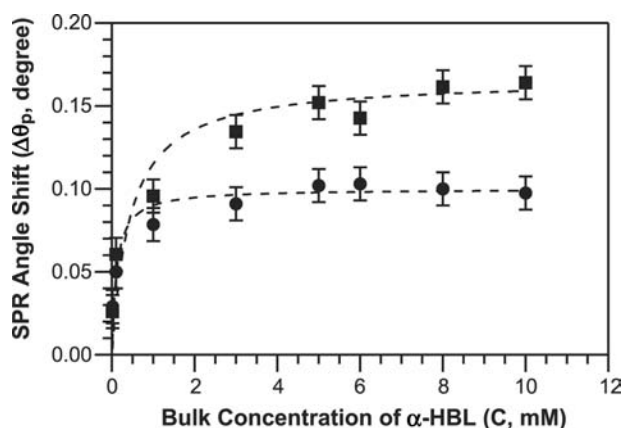


**Fig. 6** Magnitude of the shift in SPR angle ( $\Delta\theta_p$ ) for adsorption of HBL from aqueous solutions of different bulk concentration ( $C$ ) onto self-assembled surfaces of tetrasulfide calix[4]resorcinarene (squares) and tetrathiol calix[4]resorcinarene (circles). Dashed lines are drawn as a guide to the eye.

adsorption–desorption is performed using the self-assembled surfaces. Whereas HBL bound to the SAMs formed from tetrathiol derivative could be almost completely desorbed into an organic solvent, the binding to the tetrasulfide surface was largely irreversible. Multiple adsorption cycles revealed that the ratio of reversibly associating HBL molecules is 25–30% for SAMs formed from tetrasulfide calix[4]resorcinarene relative to over 95% for tetrathiol calix[4]resorcinarene. Thus the interstitial trapping on the SAMs of the tetrasulfide host results in complexation that is relatively strong in comparison to the host–guest complexation within the macrocyclic cavity.

## CONCLUSION

Incorporation of synthetic receptors such as calix[4]resorcinarene within molecular assemblies of Langmuir or Langmuir–Blodgett films, self-assembled monolayers, and lipid bilayers is a useful route to promote selective molecular association in a manner that is analogous to enzymatic recognition. The phenomenon of molecular recognition and association plays a critical role in immunoassays, sensing, and other applications based on selective affinity of molecules to surfaces. The results reviewed here demonstrate that the SAMs formed from hosts such as calix[4]resorcinarene provide a unique environment to study the relationships between molecular structure, organization, and forces that drive intermolecular association at the solid–liquid interface.

The experiment highlights several promising directions for future studies on the interfacial phenomenon of molecular recognition. The interplay between the

host structure and the molecular organization of the self-assembled surface and its impact on the trapping of molecules suggests that tailoring of the terminal functionality of the dialkyl sulfide derivatives can be used to manipulate the molecular forces at play in the interstitial trapping. It is also clear that the capability to prepare surfaces of these complex synthetic hosts and their use in targeted recognition of organic molecules can now be greatly expanded to systems such as chiral calix[4]resorcinarene hosts for enantioselective recognition and ionized calix[4]resorcinarene assemblies for recognition of cationic analytes. Concurrently, the experimental results indicate that more definitive insights into the molecular association process also require direct measurement of the monolayer structure and the binding of the guest molecule to the surface. Future studies that employ methods such as scanning probe microscopy (STM and AFM) for molecular imaging of the self-assembled surfaces and the guest–host interactions will be highly instructive. Finally, an inevitable consequence of the nanometer length scale of guest–host recognition at interfaces is that the experiments need to be supplemented by computational modeling and visualization to fully elucidate the complex molecular interactions.

## ACKNOWLEDGMENTS

The author acknowledges financial support for the research from the University of Illinois, National Science Foundation, and the American Chemical Society—Petroleum Research Fund. The contributions of John Faull and Jonathan Galownia toward the research are also acknowledged.

## REFERENCES

1. Weiss, T.; Schierbaum, K.D.; Thoden van Velzen, U.; Reinhoudt, D.N.; Goepel, W. Self-assembled monolayers of supramolecular compounds for chemical sensors. *Sens. Actuators*, **B** **1995**, *B26* (1–3), 203–207.
2. Allara, D.L. Critical issues in applications of self-assembled monolayers. *Biosens. Bioelectron.* **1995**, *10* (9/10), 771–783.
3. Tidwell, C.D.; Ertel, S.I.; Ratner, B.D.; Tarasevich, B.; Atre, S.; Allara, D.L. Endothelial cell growth and protein adsorption on terminally functionalized, self-assembled monolayers of alkanethiolates on gold. *Langmuir* **1997**, *13* (13), 3404–3413.
4. Rubinstein, I.; Steinberg, S.; Tor, Y.; Shanzer, A.; Sagiv, J. Ionic recognition and selective response in self-assembling monolayer membranes on electrodes. *Nature* **1988**, *332* (6163), 426–429.
5. Dawson, S.L.; Elman, J.; Margevich, D.E.; McKenna, W.; Tirrell, D.A.; Ulman, A. Molecular Recognition at

- a Monolayer Interface. 2,4-Diaminopyrimidine-Succinimide Host-Guest Partners. In *Hydrogels and Biodegradable Polymers for Bioapplications*; ACS Symposium Series; American Chemical Society: Washington, DC, 1996; Vol. 627, 187–196.
- Kooyman, R.P.H.; van den Heuvel, D.J.; Drijfhout, J.W.; Welling, G.W. The use of self-assembled receptor layers in immunosensors. *Thin Solid Films* **1994**, *244* (1–2), 913–916.
  - Spinke, J.; Liley, M.; Schmitt, F.J.; Guder, H.J.; Angermaier, L.; Knoll, W. Molecular recognition at self-assembled monolayers: Optimization of surface functionalization. *J. Chem. Phys.* **1993**, *99* (9), 7012–7019.
  - Chailapakul, O.; Crooks, R.M. Interactions between organized, surface-confined monolayers and liquid-phase probe molecules. 4. Synthesis and characterization of nanoporous molecular assemblies: Mechanism of probe penetration. *Langmuir* **1995**, *11* (4), 1329–1340.
  - Prime, K.L.; Chu, Y.H.; Schmid, W.; Seto, C.T.; Chen, J.K.; Spaltenstein, A.; Zerkowski, J.A.; Whitesides, G.M. Molecular Recognition in Gels, Monolayers, and Solids. In *Macromolecular Assemblies and Polymeric Systems*; ACS Symposium Series; American Chemical Society: Washington, DC, 1992; Vol. 493, 227–239.
  - Spinke, J.; Liley, M.; Guder, H.J.; Angermaier, L.; Knoll, W. Molecular recognition at self-assembled monolayers: The construction of multicomponent multilayers. *Langmuir* **1993**, *9* (7), 1821–1825.
  - Bain, C.D.; Troughton, E.B.; Tao, Y.-T.; Evall, J.; Whitesides, G.M.; Nuzzo, R.G. Formation of monolayer films by the spontaneous assembly of organic thiols from solution onto gold. *J. Am. Chem. Soc.* **1989**, *111*, 321–335.
  - Ullman, A. *Ultrathin Organic Films*; Academic Press: Boston, 1991.
  - Sigal, G.B.; Mrksich, M.; Whitesides, G.M. Using surface plasmon resonance spectroscopy to measure the association of detergents with self-assembled monolayers of hexadecanethiolate on gold. *Langmuir* **1997**, *13* (10), 2749–2755.
  - Sun, L.; Kepley, L.J.; Crooks, R.M. Molecular interactions between organized, surface-confined monolayers and vapor-phase probe molecules: Hydrogen-bonding interactions. *Langmuir* **1992**, *8* (9), 2101–2103.
  - Maeda, Y.; Fukuda, T.; Yamamoto, H.; Kitano, H. Regio- and stereoselective complexation by a self-assembled monolayer of thiolated cyclodextrin on a gold electrode. *Langmuir* **1997**, *13* (16), 4187–4189.
  - Rojas, M.T.; Koeniger, R.; Stoddart, J.F.; Kaifer, A.E. Supported monolayers containing preformed binding sites. Synthesis and interfacial binding properties of a thiolated *b*-cyclodextrin derivative. *J. Am. Chem. Soc.* **1995**, *117* (1), 336–343.
  - Weisser, M.; Nelles, G.; Wenz, G.; Mittler-Neher, S. Guest-host interactions with immobilized cyclodextrins. *Sens. Actuators, B* **1997**, *B38* (1–3), 58–67.
  - Faull, J.D.; Gupta, V.K. Selective guest-host association on self-assembled monolayers of calix[4]-resorcinarene. *Langmuir* **2001**, *17* (5), 1470–1476.
  - Faull, J.D.; Gupta, V.K. Impact of host structure on guest-host recognition at self-assembled surfaces of tetrathiol and tetrasulfide derivatives of calix[4]-resorcinarene. *Langmuir* **2002**, *18* (17), 6584–6592.
  - Adams, H.; Davis, F.; Stirling, C.J.M. Selective adsorption in gold-thiol monolayers of calix-4-resorcinarenes. *J. Chem. Soc., Chem. Commun.* **1994**, *21*, 2527–2529.
  - Davis, F.; Stirling, C.J.M. Calix-4-resorcinarene monolayers and multilayers: Formation, structure, and differential adsorption I. *Langmuir* **1996**, *12* (22), 5365–5374.
  - Friggeri, A.; Van Veggel, F.C.J.M.; Reinhoudt, D.N.; Kooyman, R.P.H. Self-assembled monolayers of cavitand receptors for the binding of neutral molecules in water. *Langmuir* **1998**, *14* (19), 5457–5463.
  - Huisman, B.H.; Kooyman, R.P.H.; Van Veggel, F.C.J.M.; Reinhoudt, D.N. Molecular recognition by self-assembled monolayers detected with surface plasmon resonance. *Adv. Mater.* **1996**, *8* (7), 561–564.
  - Thoden van Velzen, E.U.; Engbersen, J.F.J.; de Lange, P.J.; Mahy, J.W.G.; Reinhoudt, D.N. Self-assembled monolayers of resorcin[4]arene tetrasulfides on gold. *J. Am. Chem. Soc.* **1995**, *117* (26), 6853–6862.
  - Cygan, M.T.; Collins, G.E.; Dunbar, T.D.; Allara, D.L.; Gibbs, C.G.; Gutsche, C.D. Calixarene monolayers as quartz crystal microbalance sensing elements in aqueous solution. *Anal. Chem.* **1999**, *71* (1), 142–148.
  - Gutsche, C.D. *Calixarenes*; Royal Society of Chemistry: Cambridge, 1989.
  - Gutsche, C.D. *Calixarenes Revisited*; Royal Society of Chemistry: Cambridge, 1998.
  - Aoyama, Y.; Tanaka, Y.; Toi, H.; Ogoshi, H. Polar host-guest interaction. Binding of nonionic polar compounds with a resorcinol-aldehyde cyclooligomer as a lipophilic polar host. *J. Am. Chem. Soc.* **1988**, *110* (2), 634–635.
  - Aoyama, Y.; Tanaka, Y.; Sugahara, S. Molecular recognition. 5. Molecular recognition of sugars via hydrogen-bonding interaction with a synthetic polyhydroxy macrocycle. *J. Am. Chem. Soc.* **1989**, *111* (14), 5397–5404.
  - Tanaka, Y.; Ubukata, Y.; Aoyama, Y. Molecular recognition. 7. Selective sugar binding with a synthetic polyhydroxy macrocycle. A remarkable selectivity for fructose over glucose. *Chem. Lett.* **1989**, *11*, 1905–1908.
  - Kikuchi, Y.; Kobayashi, K.; Aoyama, Y. Molecular recognition. 18. Complexation of chiral glycols, steroidal polyols, and sugars with a multibenzenoid, achiral host as studied by induced circular dichroism spectroscopy: Exciton chirality induction in resorcinol-aldehyde cyclo-tetramer and its use as a supramolecular probe for the assignments of stereochemistry of chiral guests. *J. Am. Chem. Soc.* **1992**, *114* (4), 1351–1358.
  - Fujimoto, T.; Yanagihara, R.; Kobayashi, K.; Aoyama, Y. C–H  $\pi$  hydrogen bonding between electron-rich benzene rings and polarized C–H bonds: Selectivity in the complexation of highly hydrophilic guest molecules with calix[4]resorcinarene hosts in water. *Bull. Chem. Soc. Jpn.* **1995**, *68* (8), 2113–2124.
  - Tanaka, Y.; Kato, Y.; Aoyama, Y. Molecular recognition. 8. Two-point hydrogen-bonding interaction: A

- remarkable chain-length selectivity in the binding of dicarboxylic acids with resorcinol-aldehyde cyclotetramer as a multidentate host. *J. Am. Chem. Soc.* **1990**, *112* (7), 2807–2808.
34. Yanagihara, R.; Aoyama, Y. Enhanced sugar-binding ability of deprotonated calix[4]resorcinarene in water: Balance of CH– $\pi$  interaction and hydrophobic effect. *Tetrahedron Lett.* **1994**, *35* (52), 9725–9728.
  35. Pietraszkiewicz, O.; Kozbial, M.; Pietraszkiewicz, M. Charge transfer complexes involving calix[4]resorcinarenes: Potential candidates for non-linear optics. *Adv. Mater. Opt. Electron.* **1998**, *8* (5), 277–284.
  36. Thoden van Velzen, E.U.; Engbersen, J.F.J.; Reinhoudt, D.N. Synthesis of self-assembling resorcin[4]arene tetrasulfide adsorbates. *Synthesis* **1995**, *8*, 989–997.
  37. Lavrich, D.J.; Wetterer, S.M.; Bernasek, S.L.; Scoles, G. Physisorption and chemisorption of alkanethiols and alkyl sulfides on Au(111). *J. Phys. Chem., B* **1998**, *102* (18), 3456–3465.
  38. Troughton, E.B.; Bain, C.D.; Whitesides, G.M.; Nuzzo, R.G.; Allara, D.L.; Porter, M.D. Monolayer films prepared by the spontaneous self-assembly of symmetrical and unsymmetrical dialkyl sulfides from solution onto gold substrates: Structure, properties, and reactivity of constituent functional groups. *Langmuir* **1988**, *4* (2), 365–385.
  39. Schierbaum, K.D.; Weiss, T.; Thoden van Velzen, E.U.; Engbersen, J.F.J.; Reinhoudt, D.N.; Goepel, W. Molecular recognition by self-assembled monolayers of cavitand receptors. *Science* **1994**, *265* (5177), 1413–1415.
  40. Grate, J.W.; Patrash, S.J.; Abraham, M.H.; Du, C.M. Selective vapor sorption by polymers and cavitands on acoustic wave sensors: Is this molecular recognition? *Anal. Chem.* **1996**, *68* (5), 913–917.
  41. Friggeri, A.; Van Veggel, F.C.J.M.; Reinhoudt, D.N. Recognition of steroids by self-assembled monolayers of calix[4]arene—resorcin[4]arene receptors. *Chem. Eur. J.* **1999**, *5* (12), 3595–3602.
  42. Faull, J.D.; Gupta, V.K. Chemical selectivity of self-assembled monolayers of calix[4]resorcinarene. *Thin Solid Films* **2003**, *440* (1-2), 129–137.
  43. Silverstein, R.M.; Bassler, G.C.; Morill, T.C. *Spectrometric Identification of Organic Compounds*, Fourth Ed.; John Wiley & Sons: New York, 1981.
  44. Schoenherr, H.; Vancso, G.J.; Huisman, B.-H.; van Veggel, F.C.J.M.; Reinhoudt, D.N. An atomic force microscopy study of self-assembled monolayers of calix[4]resorcinarene adsorbates on au(111). *Langmuir* **1997**, *13* (6), 1567–1570.
  45. Chailapakul, O.; Crooks, R.M. Synthesis and characterization of simple self-assembling, nanoporous monolayer assemblies: A new strategy for molecular recognition. *Langmuir* **1993**, *9* (4), 884–888.
  46. Cha, X.; Ariga, K.; Kunitake, T. Molecular recognition of aqueous dipeptides at multiple hydrogen-bonding sites of mixed peptide monolayers. *J. Am. Chem. Soc.* **1996**, *118* (40), 9545–9551.

# Ionic Strength Effects: Tunable Nanocrystal Distribution in Colloidal Gold Films

**E. Stefan Kooij**

*Faculty of Science and Technology, Department of Solid State Physics, University of Twente, Enschede, The Netherlands*

**E.A. Martijn Brouwer**

*Solid State Physics, University of Twente, Enschede, The Netherlands*

**Herbert Wormeester**

*Faculty of Science and Technology, University of Twente, Enschede, The Netherlands*

**Bene Poelsema**

*Faculty of Applied Physics, University of Twente, Enschede, The Netherlands*

## INTRODUCTION

The self-assembly of colloidal particles into disordered structures or highly ordered superlattices can be achieved in different ways. Hydrodynamic forces during controlled drying allow control over the deposition process<sup>[1,2]</sup> by varying the solvent vapor pressure<sup>[3]</sup> and temperature, or, more physically, by structuring the substrate.<sup>[4]</sup> Impressive results have been obtained, for example, with nanocolloidal magnetic particles.<sup>[5,6]</sup> In addition, the application of electric and magnetic fields during drying leads to modifications of the deposited structures.<sup>[7–12]</sup>

To study deposition processes without the influence of hydrodynamic interactions, colloidal superstructures need to be formed prior to evaporation of the solvent. One way to achieve this is by chemical modification of the substrate to induce a specific affinity for the colloidal particles. For a number of different particles, chemical modifications by using either polymers, amino-functionalized and thiol-functionalized monolayers, or even DNA have been described.<sup>[13–21]</sup> For example, for gold nanocrystals, there is a strong attractive electrostatic interaction between positively charged  $\text{NH}_2$  groups on the derivatized substrate and negatively charged citrate groups on the surface of the suspended gold particles.<sup>[2,13,15,19,22,23]</sup>

The high surface affinity and the resulting strong bonding of the deposited gold particles to the surface give rise to negligible surface mobility and sticking probability of one. Deposition processes governed by these characteristics can be adequately described as a

random sequential adsorption (RSA) process.<sup>[24–33]</sup> In RSA simulations, the adsorbing particles are treated as “hard” disks, which are randomly placed on a planar surface. Placement of such a disk is only successful when it does not overlap with any other previously deposited disks. The maximum particle density after an RSA event is markedly lower than that of a hexagonal close-packed monolayer of spherical particles. The saturation coverage has been determined from extensive numerical calculations and is equal to the jamming limit  $\theta_{\text{jam}} = 54.7\%$ .<sup>[24,26–30,32]</sup> However, strong repulsive interactions, for example, because of electrostatic forces, can lead to a considerably lower maximum attainable coverage,<sup>[24,25,28–32]</sup> in agreement with the Derjaguin-Landau-Verwey-Overbeek (DLVO) theory.<sup>[34,35]</sup> This will be described in more detail in “Electrostatic Interactions in Particle Deposition.”

In previous work, many investigations into the importance of electrostatic interactions in colloid deposition processes have been described based on results using large particles (diameter  $> 100$  nm). In this entry, we use scanning electron microscopy (SEM) to study *ex situ* the deposition of colloidal gold nanocrystals ( $\approx 13$  nm) on Si/SiO<sub>2</sub> substrates, derivatized with aminopropyltriethoxysilane (APTES). Spatial distributions after saturation of the deposition experiments are analyzed in terms of radial distribution functions, and indicate that the interparticle distance is tunable by varying the ionic strength. The results are shown to be in good quantitative agreement with other experiments on markedly larger particles.

## ELECTROSTATIC INTERACTIONS IN PARTICLE DEPOSITION

Electrostatic interactions play a dominant role in the field of colloid science.<sup>[35,36]</sup> One of the most prominent examples is that of charge-stabilized colloidal systems.<sup>[34]</sup> Generally, the surface charge of particles suspended in a liquid gives rise to a double layer of countercharge surrounding the particle. This is schematically illustrated in Fig. 1. Overlap of the double layers of neighboring particles is energetically unfavorable, leading to a repulsion of the suspended colloids and thus to a stable suspension. Variation of the ionic strength allows tuning of this double-layer interaction; a higher ionic strength is accompanied by a more effective screening of the surface charge and thus a thinner double layer. The spatial extent of the repulsive interaction, as described by the DLVO theory, is related to the Debye screening length  $\kappa^{-1}$ . The Debye screening parameter  $\kappa$  is given by:<sup>[34–36]</sup>

$$\kappa^2 = \frac{e^2 \sum_i n_i z_i^2}{\epsilon \epsilon_0 k T} \quad (1)$$

where  $n_i$  and  $z_i$  are the number density and valence of ions  $i$ , respectively; and  $e$ ,  $k$ ,  $T$ , and  $\epsilon \epsilon_0$  are the elementary charge, Boltzmann constant, absolute

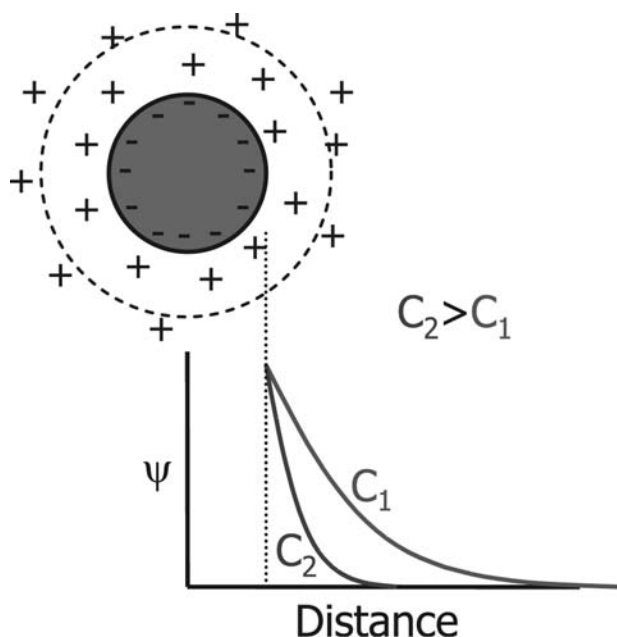


**Fig. 1** Schematic representation of the double layer formed near the surface of a charged (colloidal) particle because of accumulation of countercharge. Assuming a constant surface potential, the spatial extent of the double layer is smaller for higher ionic strengths. This is indicated by the schematic graph of the potential  $\psi$  as a function of distance from the particle surface, for two concentrations with  $C_2 > C_1$ .

temperature, and dielectric permittivity of the electrolyte, respectively. Recently, the tunability of the repulsive interaction because of double-layer overlap, in combination with an externally applied potential, has been elegantly used to control the crystallographic structure of colloidal superstructures.<sup>[37]</sup>

The stabilization of colloidal suspensions is often governed by electrostatic repulsive interactions, whereas attractive electrostatic forces between colloids and the substrate can be employed to control the deposition of particles.<sup>[2,14,16,22,25,32,33]</sup> In this work, we investigate the adsorption of negatively charged nanocolloidal gold particles on positively charged APTES-derivatized silicon surfaces.<sup>[38]</sup> However, attractive interactions have been used in systems of a very different nature to control the deposition and the resulting morphology. Examples including proteins<sup>[30,39]</sup> and bacteria,<sup>[40]</sup> and the self-organization of charge-bidisperse mixtures of colloidal particles have been studied.<sup>[41–43]</sup> Furthermore, the adsorption of polyelectrolytes onto surfaces,<sup>[16,44–46]</sup> both in a single layer and layer-by-layer self-assembly, is also governed by electrostatic interactions arising from negatively charged polyanions and positively charged polycations. Similarly, combinations of colloidal particles and polyelectrolytes have been used to controllably grow polymer/nanoparticle multilayer films.<sup>[15,16,20,21,23]</sup> In addition, the roughness of polyelectrolyte films has been shown to depend on the ionic strength.<sup>[45]</sup> With increasing salt concentration, the polymers go through a transition from an extended conformation, because of repulsive interactions between charged groups on the chain, to a more compact form.

As mentioned in the “Introduction,” deposition processes governed by strong attractive interactions between particles and substrates are generally characterized by large sticking probability and low lateral surface mobility. These systems have been adequately described in terms of RSA,<sup>[25–33]</sup> in which the adsorbing particles are treated as “hard” disks. The maximum saturation coverage in the RSA model amounts to  $\theta_{\text{jam}} = 54.7\%$ .<sup>[24,26–30,32]</sup> Markedly different results have been obtained in experimental studies on the deposition of charge-stabilized colloidal particles. The maximum attainable coverage is considerably lower than the aforementioned jamming limit,<sup>[2,14,16,19,25–32,38]</sup> which can be understood by considering the interparticle repulsion in suspension. This is schematically illustrated in Fig. 2, where universal coverage curves are plotted as a function of the effective screening parameter  $\kappa a$ , where  $\kappa$  is the Debye screening parameter as given by Eq. (1) and  $a$  is the particle radius. On the right in Fig. 2, the coverage approaches the jamming limit  $\theta_{\text{jam}}$  at  $\kappa a \gg 1$ , which corresponds to “hard,” non-interacting spheres with a Debye screening length much smaller than the particle radius  $a$ . For low ionic strengths and/or relatively



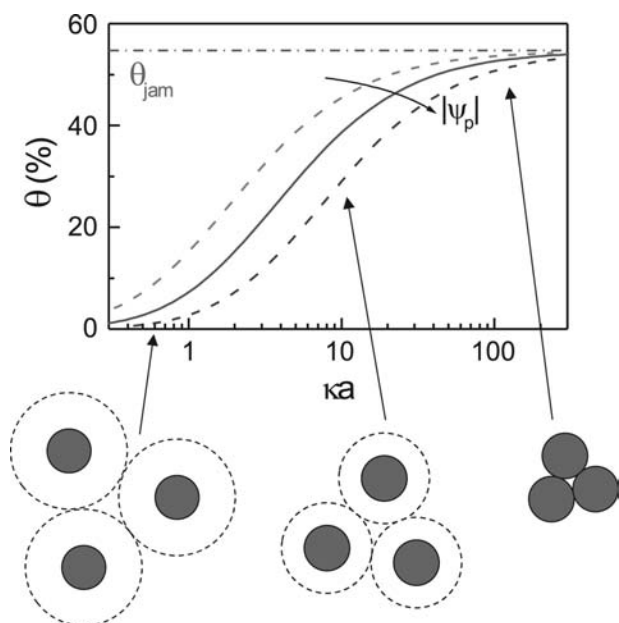


**Fig. 2** Schematic representation of the coverage as a function of the screening parameter  $\kappa a$ . The dash-dotted line represents the jamming limit for random sequential adsorption. The solid and dashed lines show the variation of the coverage with varying double-layer thickness and surface potential.

small particles (small  $\kappa a$ ; left in Fig. 2), the interparticle repulsion in suspension dominates and the maximum coverage is well below the jamming limit. The concept of RSA is still applicable, but the colloidal particles, with their electric double layer, are best treated as spheres with an effective radius  $a_{\text{eff}}$  markedly larger than their actual size  $a$ . The maximum attainable surface coverage  $\theta_{\text{max}}$ , in relation to the jamming limit  $\theta_{\text{jam}}$ , is described by:

$$\theta_{\text{sat}} = \theta_{\text{jam}} \left( \frac{a}{a_{\text{eff}}} \right)^2 \quad (2)$$

The effective radius  $a_{\text{eff}} = a + \Delta a$  not only depends on the ionic strength, but also on the particle surface potential  $\psi_p$ . For low surface potentials, the effective enlargement  $\Delta a$  of the radius is much smaller than for high surface potentials. This results in a shift of the saturation coverage curve to larger  $\kappa a$  values, as indicated in Fig. 2. In fact, a comparison of calculations to the measured saturation coverage values allows a rough determination of the particle surface potential.

## SYNTHESIS AND IRREVERSIBLE ADSORPTION OF GOLD NANOCRYSTALS

### Synthesis of Nanocolloidal Gold Suspension

Colloidal suspensions of gold nanocrystals are prepared by standard citrate reduction.<sup>[22,47]</sup> In a

typical synthesis, 250 mL of a 1-mM  $\text{HAuCl}_4$  aqueous solution is heated to 100°C under refluxing conditions. Under vigorous stirring, 25 mL of a 38.8-mM sodium citrate solution is rapidly added. This results in color changes of the originally yellow solution to transparent, to dark blue/gray, and, finally, after approximately 2 min, to burgundy red, which marks the end of the reaction. For 15–20 min, the reaction vessel is kept at 100°C. Subsequently, it is cooled to room temperature, still stirring continuously.

Based on their size and the initial gold concentration, the nanocrystal density in the as-prepared suspension is estimated to be  $7.70 \times 10^{18} \text{ m}^{-3}$ . The ionic strength of the as-prepared colloidal solution is estimated based on the composition of the initial reactants, and by taking into account the pH ( $\approx 5$ ) of the solution. In this way, we obtain an ionic strength  $I = 0.5 \sum_i z_i^2 c_i = 15.8 \text{ mM}$ , where the summation is over all ions  $i$  in solution, with  $z_i$  and  $c_i$  as their valence and concentration, respectively. The ionic strength is varied by adding NaCl to the suspension.

All chemicals are used as-received, without any further purification. Sodium citrate ( $\text{Na}_3\text{C}_6\text{H}_5\text{O}_7$ , 99%) and hydrogen tetrachloroaurate ( $\text{HAuCl}_4$ , 99.999%) are from Aldrich; all other chemicals are “for-analysis” grade from Merck. Aqueous solutions are prepared with water purified in a Milli-Q system (18.2 MΩ cm).

### Gold Nanocrystal Size Distribution

Several methods have been employed to characterize the size distribution of the gold nanocrystals. The diameter distribution, as determined by transmission electron microscopy (TEM) measurements, is shown in Fig. 3.

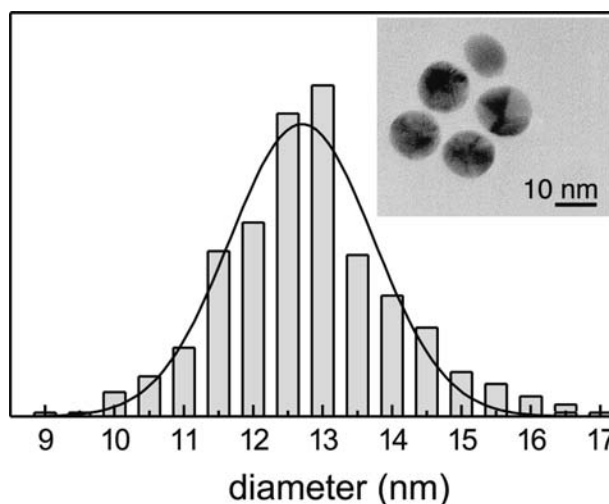


**Fig. 3** Distribution of particle sizes determined from TEM images, such as that shown in the insert. The solid line represents a Gaussian fit to the data, which yields an average radius  $a = 6.4 \text{ nm}$  and a standard deviation  $\sigma = 1.05 \text{ nm}$ .

The distribution exhibits a peak at diameters of  $2a = 12.5\text{--}13.0$  nm. In agreement with this, a Gaussian fit yields an average particle size of 12.7 nm (i.e., a radius  $a = 6.4$  nm), with a standard deviation  $\sigma = 1.05$  nm, which corresponds to a polydispersity of approximately 8%. The TEM results also show that nearly all particles are spherical; the number of particles with a measurable shape anisotropy is less than 0.5%.

Atomic force microscopy (AFM) measurements on colloidal films<sup>[38,48]</sup> also provide an indication of the particle size. From the pixel height diagram, the difference between the substrate level and the top of the particles amounts to 13.2 nm, thus an average particle radius  $a = 6.6$  nm. In addition, the coverage as obtained from counting the particles in AFM images of known size has been compared with the total amount of gold atoms determined by X-ray fluorescence (XRF) measurements.<sup>[48]</sup> A linear relationship is obtained, which yields an average total of  $7.6 \times 10^4$  gold atoms per colloidal nanocrystal. Based on TEM images, such as the insert in Fig. 3, we conclude that the particles consist of a number of crystalline domains. Therefore we use the bulk density of gold to deduce from the XRF measurements an average particle radius of 6.7 nm, slightly larger than what is found by the other two methods. In the following sections of this contribution, we use the average radius of the aforementioned values (i.e.,  $a = 6.6$  nm).

### Substrate Treatment and Particle Deposition

We use polished silicon (100) wafers, with typically a 1.5-nm native oxide layer. For reflectometry measurements, a thicker oxide of 45 nm provides higher accuracy. The wafers are cleaved into  $12 \times 12\text{-mm}^2$  pieces. The substrates are cleaned ultrasonically in methanol for at least 15 min prior to further handling. High surface affinity for the colloidal gold particles is achieved by derivatization<sup>[23]</sup> of the silicon substrates in a 10% APTES solution in methanol for 60 min, followed by thorough rinsing in methanol. After drying in nitrogen flow, the samples are immersed in water for 15 min.

Deposition of the gold particles is done by immersing the derivatized substrates in the colloidal suspension for at least 12 hr. The suspension is diluted five times, which leads to an effective particle concentration

of  $1.54 \times 10^{18} \text{ m}^{-3}$  for all experiments. Samples that have not been treated with APTES do not show any deposition of gold on the surface. All of these procedures are performed at room temperature.

### SPATIAL DISTRIBUTION AND SATURATION COVERAGES

In a recent publication, we presented a study of the tunable spatial distribution of colloidal gold nanocrystals based on AFM images.<sup>[48]</sup> Because the particles and the AFM tip have radii of the same order of magnitude, adsorbed nanocrystals appear markedly larger than they actually are. This hinders accurate determination of particle positions, especially within clusters consisting of a number of touching particles. Consequently, this limits the accuracy of the spatial distribution obtained from the analysis. Here we present similar images, but in this case, they were obtained using low-voltage SEM. The SEM measurements are performed with a LEO Gemini 1550 FEG-SEM, equipped with a field emission gun plus Thermo Noran Vantage EDX system and Thermo Noran MAXray parallel beam spectrometer. The electron acceleration voltage can be set between 200 V and 30 kV; because of the low voltage, the deposition of a thin metal (gold) film is not required to ensure electric conduction. The lateral resolution is approximately 2 nm, which enables accurate determination of particle positions.

In Fig. 4, three typical SEM images are shown for colloidal gold assemblies at maximum coverage. Saturation of the coverage is obtained after 5–6 hr, which is primarily determined by diffusion of nanocrystals to the surface. However, generally, deposition is performed overnight, ensuring that, indeed, the surface particle density has reached its maximum value. The ionic strength in Fig. 4 increases from left to right. In agreement with the DLVO theory,<sup>[34,35]</sup> the average distance between particles decreases with increasing ionic strength, leading to an increase of the overall coverage. The SEM measurements in Fig. 4 were obtained after removal of the samples from the colloidal suspension, thorough rinsing with water and, finally, drying. The adherence of the nanocrystals

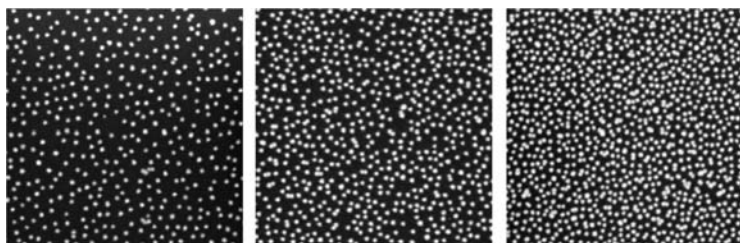


**Fig. 4** Typical SEM images of colloidal gold particles irreversibly adsorbed at silicon/silicon oxide substrates, derivatized with APTES. The image size amounts to  $750 \times 750 \text{ nm}^2$ . The ionic strength was varied to tune the average interparticle distance. Coverages are obtained by manual counting and amount to 10% (left), 18% (middle), and 28% (right) for the three images.

to the substrate is good, as multiple reimmersion, rinsing, and drying steps do not lead to a measurable change in the particle distribution and/or coverage.

More quantitative information is obtained from radial distribution functions, calculated from SEM images such as those presented in Fig. 4. Positions of all particles in these images are determined using Scion Image (Beta 4.0.2; Scion Corporation). The radial distribution function (also referred to as the pair correlation function) is obtained from these positions by calculating:

$$g'_i(r) = \frac{\delta N(r)}{n2\pi r\delta r} \quad (3)$$

for every particle  $i$ , where  $\delta N(r)$  represents the number of particles within a ring of width  $\delta r$  at a distance  $r$ . The overall surface density of particles is represented by  $n$ . The total radial distribution function  $g(r) = N^{-1}\sum_i g'_i(r)$  is found by averaging over all  $N = nA$  particles, with  $A = 0.56\mu\text{m}^2$  as the surface area in the image. In Fig. 5, the radial distribution functions obtained from the images in Fig. 4 are shown. As mentioned above, we have recently shown<sup>[48]</sup> that all  $g(r)$  curves in the coverage range considered in this work scale onto a single radial distribution function  $g(r/r_0)$  when the distance  $r$  is normalized by  $r_0 = n^{-1/2}$ . This scaling behavior is also exhibited in the coverage

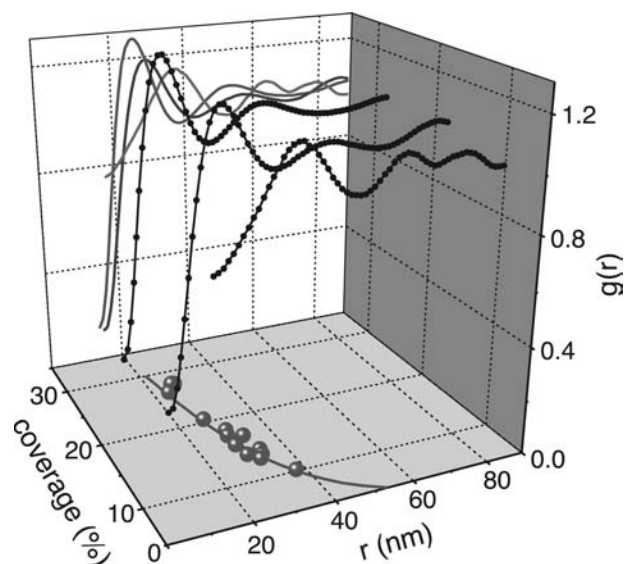


**Fig. 5** Three-dimensional representation of the coverage-dependent radial distribution functions  $g(r)$ , calculated from the three images in Fig. 4. The projected curves on the back panel clearly show the increase of the peak height and its shift to smaller distances for higher coverage. In the bottom plane, the coverage-dependent shift of the peak maxima for a larger number of radial distribution functions is shown; the solid line is a guide to the eye.

dependence of the peak positions in the bottom plane of Fig. 5; the solid line is given by  $r = (\pi a^2/\theta)^{-1/2}$ . Surprisingly, this scaling implies an approximately cubic distribution of nanocrystals over large ranges on the surface. For a close-packed distribution, hexagonal distribution is expected, which is not the case as can clearly be seen in Fig. 4. Nevertheless, the cubic distribution is also not evident from the SEM images.

The fact that the curves can be scaled indicates that, in the range of ionic strengths considered in this work, the spatial distribution of nanocrystals is universal. Apparently, a single mechanism dominates the nanocrystal organization on the surface, irrespective of the ionic strength. Obviously, for considerably lower coverages, at which the interparticle interactions can be neglected, this is no longer valid. In that case, the statistical distribution of nanocrystals results in a Boltzmann distribution. Careful examination of the heights of the maxima in the radial distribution functions (see back panel in Fig. 5) indeed exhibits a decrease with lower coverages (i.e., for lower ionic strengths).

The radial distributions exhibit features such as the maximum at  $r_0$ , followed by the shallow minimum near  $1.5r_0$ , which are in good agreement with results of RSA simulations assuming effectively enlarged colloidal particles<sup>[24–26,29–32]</sup> (i.e., with an electric double layer on the order of, or larger than, the particle radius). For ideally distributed highly monodisperse nanoparticles, a considerably higher and narrower peak is expected, followed by a larger number of minima at larger distances. However, polydispersity of the colloidal suspension gives rise to a lower maximum and widening of the peak; this phenomenon is even more pronounced for particles in the low-nanometer range, compared with much larger particles.<sup>[29,49]</sup> Moreover, for ideal distribution, the polydispersity must be below 5%, which is obviously not the case in our suspensions.

Unfortunately, with the citrate-stabilized nanocolloidal gold system, only a limited range of ionic strengths is available. At high ionic strength, the repulsive interaction between particles is reduced and the van der Waals attraction begins to dominate. Eventually, this leads to irreversible coagulation of the particles in suspension, which gives rise to the deposition of larger clusters on the substrates. For gold suspensions, an upper limit for the ionic strength of  $I = 24\text{mM}$  has been reported.<sup>[34]</sup> This corresponds to a maximum coverage of approximately 35%, which is also the upper limit of the data in Fig. 5. Low ionic strengths can only be achieved by dialysis or ultracentrifugation. In both cases, the citrate concentration in the solution becomes so low that citrate groups on the particles (the stabilizing mechanism) start to desorb. This then leads to instability of the colloidal suspension.

## KINETICS OF NANOCOLLOIDAL GOLD ADSORPTION

In addition to the aforementioned study of spatial distributions after saturation of the coverage, we have also investigated the ionic strength-dependent kinetics of nanocolloidal gold adsorption at APTES-derivatized surface. For this in situ study, we used single wavelength reflectometry, in combination with a radial impinging jet cell<sup>[14,24]</sup> geometry to provide a controlled supply of colloidal particles to the substrate surface. This setup is often combined with an optical microscope to visualize the adsorbed particles,<sup>[7,9,10,24,32]</sup> but as the gold nanocrystals are markedly smaller than the wavelength of the probing light (HeNe laser, 632 nm), we use a non-imaging polarized optical reflection technique. The coverage is calculated from the reflectometry signal using the thin island film theory, similar to what was described previously.<sup>[38]</sup>

In Fig. 6, typical reflectometry transients, obtained at various ionic strengths, are shown. The intrinsic ionic strength of the diluted suspension amounts to 3.6 mM. The ionic strength of the solution is varied by adding 0–15 mM NaCl, which corresponds to Debye screening lengths from 5.1 to 2.2 nm. Two distinct regimes are observed in the curves in Fig. 6. For short times, the deposition rate is constant and independent of the ionic strengths, which implies that, initially, the deposition process is limited by the supply of colloidal particles to the surface. The hydrodynamics of colloid deposition in a radial impinging jet

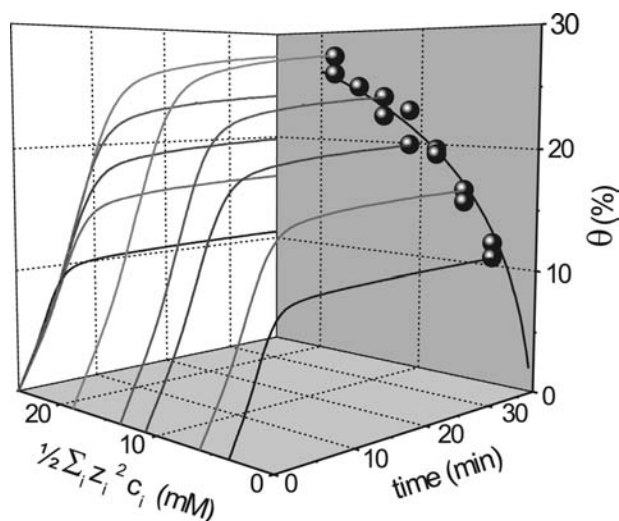


**Fig. 6** Three-dimensional representation of the ionic strength-dependent adsorption kinetics of gold nanocolloidal particles in stagnation point flow geometry. The coverage is obtained by polarized reflectometry. The data on the back panel indicate the evolution of the saturation coverage with increasing ionic strength for a number of reflectometry experiments; the solid line is a guide to the eye.

cell has been discussed by Dabros and Van de Ven.<sup>[50]</sup> The particle flux toward the surface is, in principle, constant and is merely determined by the cell geometry, the fluid viscosity, the diffusion constant of the particles, and the colloid density in the suspension. Assuming a sticking probability of one in the initial stage of the deposition process, a constant deposition rate  $d\theta/dt$  is expected because the particle concentration and the nanoparticle diffusion constant are constant for all reflectometry measurements. This is indeed observed in the transients for the first few minutes.

The initial linear deposition region is followed by a transition to a region where the deposition rate decreases and the adsorption saturates. A quantitative analysis of this transition range lies outside the scope of this work, and will be described in a forthcoming publication. We now turn to the saturation regime of the deposition curves in Fig. 6. With increasing ionic strengths, the maximum attainable coverage becomes larger, as it is also indicated by the solid line in the back panel. As we already discussed above, this is in agreement with the DLVO theory, considering that the double layer surrounding every particle gives rise to an enlarged effective nanocrystal radius  $a_{\text{eff}} = a + \Delta a$ , with  $\Delta a \sim 1/\kappa$ . This in turn gives rise to saturation coverages below the RSA jamming limit of 54.7%, in agreement with Eqs. (1) and (2). In “Quantitative Analysis,” the results presented in Figs. 5 and 6 will be discussed quantitatively, also in comparison to literature data.

## QUANTITATIVE ANALYSIS

The results described in “Kinetics of Nanocolloidal Gold Adsorption” can be compared with calculations using a relatively simple model for the repulsive interaction between particles. Many experiments dealing with the influence of the ionic strength on the deposition of large particles in the 100–1000 nm range have been published. Different techniques were employed, including optical microscopy, AFM, and SEM. To quantitatively compare results for varying ionic strengths and particle radii, and to obtain a universal curve, the coverage is often plotted as a function of the screening parameter  $\kappa a$ .<sup>[24–30,32,49]</sup> For deposition processes with “hard,” non-interacting spheres, with a Debye screening length considerably shorter than the particle diameter, which are governed by RSA, the saturation coverage approaches the aforementioned jamming limit  $\theta_{\text{jam}} = 54.7\%$ . For small values of the screening parameter  $\kappa a$  (i.e., for low ionic strengths and/or small particles), the repulsive interaction between particles in the solution limits the coverage to values well below the jamming limit.

In Fig. 7, the data from Figs. 5 and 6, together with our previous results using AFM,<sup>[48]</sup> are plotted as a



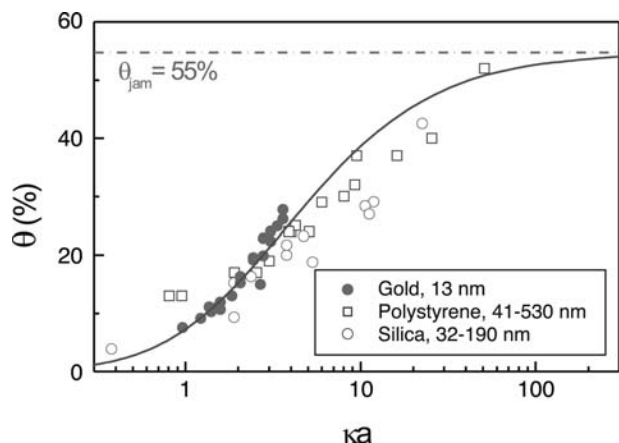


**Fig. 7** Experimental coverage, obtained from the data in Figs. 5 and 6, as a function of the screening parameter  $\kappa a$ , compared with the calculated curves as shown in Fig. 2. Also shown are the data for polystyrene particles with sizes in the 40–530 nm range and for silica particles with sizes in the 32–190 nm range. *Source:* From Refs.<sup>[14,31,51]</sup>

function of the screening parameter. Also shown are the results calculated from experiments on polystyrene<sup>[31]</sup> and silica<sup>[14,51]</sup> particles. The results are compared with a calculation for ionic strength-dependent coverage, represented by the solid line. Generally, the repulsive interaction between neighboring colloidal spheres, owing to the overlap of their double layers, can be obtained by solving the Poisson–Boltzmann equation. For a system of two spherical particles, the Poisson–Boltzmann equation cannot be solved analytically, and an approximation has to be used. The frequently employed low surface potential approximations<sup>[34–36]</sup> are not valid for our citrate-stabilized colloidal gold system because the particles have a surface potential on the order of 80–100 meV.<sup>[52,53]</sup> However, because of the limited available range of ionic strengths, the distance between neighboring particles is, in all cases, relatively large, which enables a description in terms of a far field effective potential. Sader<sup>[54]</sup> formulated an accurate analytical expression for the particle–particle repulsive interaction  $U_{pp}(r/a)$ , which is valid for all values of the screening parameter:

$$U_{pp}\left(\frac{r}{a}\right) = kTB_{pp} \frac{a}{r} e^{-\kappa(r-2a)} \quad (4)$$

where  $r$  is the center-to-center distance between particles. The characteristic particle–particle repulsion is given by:<sup>[30]</sup>

$$B_{pp} = \left(\frac{4\pi\epsilon\epsilon_0 kTa}{e^2}\right) \left(\frac{y_p + 4\gamma\Omega\kappa a}{1 + \Omega\kappa a}\right)^2 \quad (5)$$

where  $y_p = \psi_p(e/kT)$  is the dimensionless particle

surface potential. The quantities  $\gamma$  and  $\Omega$  are defined as:

$$\gamma = \tanh(y_p) \quad (6a)$$

$$\Omega = \frac{y_p - 4\gamma}{2\gamma^3} \quad (6b)$$

If we assume a constant surface potential  $\psi_p$ , the interparticle distance  $r_{kT}$  at which  $U_{pp}$  drops below  $kT$  can be obtained numerically as a function of the screening parameter  $\kappa a$  from Eqs. (456b). From Eq. (2), with  $a_{\text{eff}} = 0.5r_{kT}$ , the corresponding coverage is obtained. The choice of  $kT$  is, in principle, arbitrary, but it originates from the fact that the repulsive interaction is competing with the Brownian motion of the nanocrystals in suspension; the energy involved in the latter process is on the order of  $kT$ . The solid line in Fig. 7 represents a fit to our data for nanocolloidal gold particles with an average diameter of 13 nm. From the fit, we find a surface potential  $|\psi_p| = 129$  meV, which is considerably larger than the absolute value of the  $\zeta$ -potential found by Chow and Zukoski<sup>[52]</sup> and Van der Zander et al.<sup>[53]</sup> from electrokinetic measurements at comparable ionic strengths. This discrepancy is very common and is extensively described in standard colloid chemistry textbooks.<sup>[35]</sup>

When we compare our results and the corresponding fit curve in Fig. 7 to results obtained for silica and polystyrene particles,<sup>[14,31,51]</sup> qualitative agreement between the different experiments is found. In the region  $\kappa a = 1$  and  $\kappa a = 5$ , the coverage for all types of particles and sizes is comparable to what we find for gold nanocolloids. The data for polystyrene and silica particles for values of the screening parameter  $\kappa a > 5$  deviate from the fitted curve. This can be understood by considering that the far field potential approximation we employed in Eqs. (4) and (5) is only valid at relatively large particle separations. For higher coverage at larger values of the screening parameter, this approximation no longer provides an accurate description of the interparticle repulsive interaction. Furthermore, polydispersity may also give rise to deviations from ideal behavior, but in that case, a higher coverage is to be expected, compared with model calculations. Finally, the surface potential of the polystyrene and silica particles probably differs from the value of citrate-stabilized gold colloids. As indicated schematically in Fig. 7, this also gives rise to deviations from the calculated curve.

## CONCLUSION

Using SEM, we present an investigation into the influence of ionic strength on the spatial distribution of nanocolloidal gold particles irreversibly deposited at APTES-derivatized substrates. Radial distribution

functions are used to analyze the SEM images, and indicate that the deposition process is governed by RSA. This is in agreement with the large sticking probability and the low lateral mobility of gold nanocrystals on the surface after adsorption.

The radial distribution functions exhibit a maximum, which corresponds to the minimum interparticle separation of the adsorbed nanocrystals. This distance, and thus the overall surface coverage, can be tuned by varying the ionic strength, in agreement with DLVO theory. Scaling indicates an approximately cubic long-range distribution of particles. The results are in agreement with calculations, in which the repulsive particle-particle interactions are described using a far field potential approximation. Furthermore, our results for nanocolloidal gold films are in qualitative agreement with similar results deduced from literature for silica and polystyrene particles with sizes in the range of 332–530 nm.

## ACKNOWLEDGMENTS

This work is part of the research program of the Stichting voor Fundamenteel Onderzoek der Materie (FOM), financially supported by the Nederlandse Organisatie voor Wetenschappelijk Onderzoek (NWO) and Philips Research.

## REFERENCES

1. Salamanca, J.M.; Ciampi, E.; Faux, D.A.; Glover, P.M.; McDonald, P.J.; Routh, A.F.; Peters, A.C.I.A.; Satguru, R.; Keddie, J.L. Lateral drying in thick films of waterborne colloidal particles. *Langmuir* **2001**, *17* (11), 3202–3207.
2. Liu, S.; Zhu, T.; Hu, R.; Liu, Z. Evaporation-induced self-assembly of gold nanoparticles into a highly organized two-dimensional array. *Phys. Chem. Chem. Phys.* **2002**, *4*, 6059–6062.
3. Jiang, P.; Bertone, J.F.; Hwang, K.S.; Colvin, V.L. Single-crystal colloidal multilayers of controlled thickness. *Chem. Mater.* **1999**, *11* (8), 2132–2140.
4. Yin, Y.; Xia, Y. Self-assembly of monodispersed spherical colloids into complex aggregates with well-defined sizes, shapes, and structures. *Adv. Mater.* **2001**, *13* (4), 267–271.
5. Sun, S.; Murray, C.B.; Weller, D.; Folks, L.; Moser, A. Monodisperse FePt nanoparticles and ferromagnetic FePt nanocrystal superlattices. *Science* **2000**, *287*, 1989–1992.
6. Puentes, V.F.; Krishnan, K.M.; Alivisatos, P. Synthesis, self-assembly, and magnetic behavior of a two-dimensional superlattice of single-crystal  $\epsilon$ -Co nanoparticles. *Appl. Phys. Lett.* **2001**, *78* (15), 2187–2189.
7. Böhmer, M.R. In situ observation of 2-dimensional clustering during electrophoretic deposition. *Langmuir* **1996**, *12* (24), 5480–5747.
8. Giersig, M.; Mulvaney, P. Preparation of ordered colloid monolayers by electrophoretic deposition. *Langmuir* **1993**, *9* (12), 3408–3413.
9. Trau, M.; Daville, D.A.; Aksay, I.A. Assembly of colloidal crystals at electrode interfaces. *Langmuir* **1997**, *13* (24), 6375–6381.
10. Hayward, R.C.; Saville, D.A.; Aksay, I.A. Electrophoretic assembly of colloidal crystals with optically tunable micropatterns. *Nature* **2000**, *404*, 56–59.
11. Legrand, J.; Petit, C.; Pileni, M.P. Domain shapes and superlattices made of 8 nm cobalt nanocrystals: fabrication and magnetic properties. *J. Phys. Chem., B* **2001**, *105* (24), 5643–5646.
12. Giersig, M.; Hilgendorff, M. The preparation of ordered colloidal magnetic particles by magnetophoretic deposition. *J. Phys., D. Appl. Phys.* **1999**, *32* (22), L111–L113.
13. Zhu, T.; Fu, X.; Mu, T.; Wang, J.; Liu, Z. pH-dependent adsorption of gold nanoparticles on *p*-aminothiophenol-modified gold substrates. *Langmuir* **1999**, *15* (16), 5197–5199.
14. Böhmer, M.R.; van der Zeeuw, E.A.; Koper, G.J.M. Kinetics of particle adsorption in stagnation point flow studied by optical reflectometry. *J. Colloid Interface Sci.* **1998**, *197* (2), 242–250.
15. Böhmer, M.R. Effects of polymers on particle adsorption on macroscopic surfaces studied by optical reflectometry. *J. Colloid Interface Sci.* **1998**, *197* (2), 251–256.
16. Schmitt, J.; Mächtle, P.; Eck, D.; Möhwald, H.; Helm, C.A. Preparation and optical properties of colloidal gold monolayers. *Langmuir* **1999**, *15* (9), 3256–3266.
17. Aizenberg, J.; Braun, P.V.; Wiltzius, P. Patterned colloidal deposition controlled by electrostatic and capillary forces. *Phys. Rev. Lett.* **2000**, *84* (13), 2997–3000.
18. Kumar, A.; Pattarkine, M.; Bhadbhade, M.; Mandale, A.B.; Ganesh, K.N.; Datar, S.S.; Dharmadhikari, C.V.; Sastry, M. Linear superclusters of colloidal particles by electrostatic assembly on DNA templates. *Adv. Mater.* **2001**, *13* (2), 341–344.
19. Reincke, F.; Hickey, S.G.; Kelly, J.J.; Braam, T.W.; Jenneskens, L.W.; Vanmaekelbergh, D. Electrochemical and topological characterization of gold(111)/oligo(cyclohexylidene) / gold nanocrystal interfaces. *J. Electrochim. Acta* **2002**, *522*, 2–10.
20. Hicks, J.F.; Seok-Shon, Y.; Murray, R.W. Layer-by-layer growth of polymer/nanoparticle films containing monolayer-protected gold clusters. *Langmuir* **2002**, *18* (6), 2288–2294.
21. Zheng, H.; Rubner, M.F.; Hammond, P.T. Particle assembly on patterned plus/minus polyelectrolyte surfaces via polymer-on-polymer stamping. *Langmuir* **2002**, *18* (11), 4505–4510.
22. Grabar, K.C.; Freeman, R.G.; Hommer, M.B.; Natan, M.J. Preparation and characterization of Au colloid monolayers. *Anal. Chem.* **1995**, *67* (4), 735–743.
23. Cant, N.E.; Critchley, K.; Zhang, H.-L.; Evans, S.D. Surface functionalisation for the self-assembly of



- nanoparticle/polymer multilayer films. *Thin Solid Films* **2003**, *426*, 31–39.
24. Adamczyk, Z.; Zembala, M.; Siwek, B.; Warszyński, P. Structure and ordering in localized adsorption of particles. *J. Colloid Interface Sci.* **1990**, *140* (1), 123–137.
  25. Johnson, C.A.; Lenhoff, A.M. Adsorption of charged latex particles on mica studied by atomic force microscopy. *J. Colloid Interface Sci.* **1996**, *179* (2), 587–599.
  26. Oberholzer, M.R.; Stankovich, J.M.; Varnie, S.L.; Chan, D.Y.C.; Lenhoff, A.M. 2-D and 3-D interactions in random sequential adsorption. *J. Colloid Interface Sci.* **1997**, *194* (1), 138–153.
  27. Semmler, M.; Mann, E.K.; Rička, J.; Borkovec, M. Diffusional deposition of charged latex particles on water–solid interfaces at low ionic strength. *Langmuir* **1998**, *14* (18), 5127–5132.
  28. Adamczyk, Z.; Weroński, P. Applications of the DLVO theory for particle deposition problems. *Adv. Colloid Interface Sci.* **1999**, *83* (1–3), 137–226.
  29. Semmler, M.; Rička, J.; Borkovec, M. Diffusional deposition of colloidal particles: electrostatic interaction and size polydispersity effects. *Colloids Surf., A* **2000**, *165* (1–3), 79–93.
  30. Yuan, Y.; Oberholzer, M.R.; Lenhoff, A.M. Size does matter: electrostatically determined surface coverage trends in protein and colloid adsorption. *Colloids Surf., A* **2000**, *165* (1–3), 125–141.
  31. Hanarp, P.; Sutherland, D.S.; Gold, J.; Kasemo, B. Control of nanoparticle film structure for colloidal lithography. *Colloids Surf., A* **2003**, *214* (1–3), 23–36.
  32. Adamczyk, Z. Particle adsorption and deposition: role of electrostatic interactions. *Adv. Colloid Interface Sci.* **2003**, *100–102*, 267–347.
  33. Onoda, G.Y.; Liniger, E.G. Experimental determination of the random-parking limit in two dimensions. *Phys. Rev., A* **1986**, *33* (1), 715–716.
  34. Verwey, E.J.W.; Overbeek, J.Th.G. *Theory of the Stability of Lyophobic Colloids*; Elsevier: New York, 1948.
  35. Lyklema, J. *Fundamentals of Interface and Colloid Science*; Academic Press: London, 1995.
  36. Hunter, R.J. *Foundations of Colloid Science*; Oxford University Press: Oxford, 2001.
  37. Yethiraj, A.; van Blaaderen, A. A colloidal model system with an interaction tunable from hard sphere to soft and dipolar. *Nature* **2003**, *432*, 513–517.
  38. Kooij, E.S.; Wormeester, H.; Brouwer, E.A.M.; van Vroonhoven, E.; van Silfhout, A.; Poelsema, B. Optical characterization of thin colloidal gold films by spectroscopic ellipsometry. *Langmuir* **2002**, *18* (11), 4401–4413.
  39. Adamczyk, Z. Kinetics of diffusion-controlled adsorption of colloid particles and proteins. *J. Colloid Interface Sci.* **2000**, *229* (2), 477–489.
  40. Poortinga, A.T.; Bos, R.; Norde, W.; Busscher, H.J. Electric double layer interactions in bacterial adhesion to surfaces. *Surf. Sci. Rep.* **2002**, *47* (1), 1–32.
  41. Kumar, A.; Mandale, A.B.; Sastry, M. Sequential electrostatic assembly of amine-derivatized gold and carboxylic acid-derivatized silver colloidal particles on glass substrates. *Langmuir* **2000**, *16* (17), 6921–6926.
  42. Gray, J.J.; Bonnecaze, R.T. Adsorption of charge-bidisperse mixtures of colloidal particles. *Langmuir* **2001**, *17* (25), 7935–7947.
  43. Kolny, J.; Kornowski, A.; Weller, H. Self-organization of cadmium sulfide and gold nanoparticles by electrostatic interaction. *Nanoletters* **2002**, *2* (4), 361–364.
  44. Decher, G. Fuzzy nanoassemblies: toward layered polymeric multicomposites. *Science* **1997**, *277*, 1232–1237.
  45. McAloney, R.A.; Sinyor, M.; Dudnik, V.; Goh, M.C. Atomic force microscopy studies of salt effects on polyelectrolyte multilayer film morphology. *Langmuir* **2001**, *17* (21), 6655–6663.
  46. Hempenius, M.A.; Péter, M.; Robins, N.S.; Kooij, E.S.; Vancso, G.J. Water-soluble poly(ferrocenylsilanes) for supramolecular assemblies by layer-by-layer deposition. *Langmuir* **2002**, *18* (20), 7629–7634.
  47. Frens, G. Controlled nucleation for the regulation of particle size in monodisperse gold solutions. *Nat. Phys. Sci.* **1973**, *241* (105), 20–22.
  48. Kooij, E.S.; Brouwer, E.A.M.; Wormeester, H.; Poelsema, B. Ionic strength mediated self-organization of gold nanocrystals: An AFM study. *Langmuir* **2002**, *18* (20), 7677–7682.
  49. Hanarp, P.; Sutherland, D.S.; Gold, J.; Kasemo, B. Influence of polydispersity on adsorption of nanoparticles. *J. Colloid Interface Sci.* **2001**, *241* (1), 26–31.
  50. Dabros, T.; Van de Ven, T.G.M. A direct method for studying particle deposition onto solid surfaces. *Colloid Polym. Sci.* **1983**, *261*, 694–707.
  51. Hayes, R.A.; Böhmer, M.R.; Fokkink, L.G.J. A study of silica nanoparticle adsorption using optical reflectometry and streaming potential techniques. *Langmuir* **1999**, *15* (8), 2865–2870.
  52. Chow, M.K.; Zukoski, C.F. Gold sol formation mechanisms: Role of colloidal stability. *J. Colloid Interface Sci.* **1994**, *165* (1), 97–109.
  53. Van der Zande, B.M.I.; Dhont, J.G.K.; Böhmer, M.R.; Philipse, A.P. Colloidal dispersions of gold rods characterized by dynamic light scattering and electrophoresis. *Langmuir* **2000**, *16* (2), 459–464.
  54. Sader, J.E. Accurate analytic formulae for the far field effective potential and surface charge density of a uniform charged sphere. *J. Colloid Interface Sci.* **1997**, *188* (2), 508–510.

# Iron Nanoparticles

**Dale L. Huber**

*Nanostructures and Advanced Materials Chemistry Department,  
Sandia National Laboratories, Albuquerque, New Mexico, U.S.A.*

## Abstract

Iron has a number of properties that make it particularly useful as a nanoparticle. Iron is cheap and plentiful, it is environmentally benign, and has no human toxicity except in extreme doses. Its magnetic properties are also very useful. Iron has the highest room temperature saturation magnetization of any element, and its cubic crystalline structure helps make it a soft magnetic material. The high saturation magnetization means that an iron nanoparticle can possess a very large magnetic moment, while the fact that it is a soft magnet means that a fairly large nanoparticle (with a correspondingly large moment) can still have a superparamagnetic blocking temperature at a relatively low temperature. The magnetic softness of iron nanoparticles can, however, be overcome if necessary. For magnetic storage applications, where a hard magnet is desirable, iron rods can be used. The shape anisotropy of the nanorods makes them extremely hard. In either case, the high magnetic moment of iron is a huge advantage.

Iron has one major weakness that impacts its usefulness in nanoparticle form, its reactivity. Iron is very reactive towards both water and the oxygen in air. This reactivity manifests itself slowly in large iron structures as rusting, but in nanoparticles it can occur rapidly and spectacularly. This has effectively limited the use of iron nanoparticles to inert or reducing environments unless they are pretreated to passivate them towards oxidation. This entry highlights the various methods of preparing iron nanoparticles, the existing and potential applications, and some of the fundamental properties of iron nanoparticles.

## PROPERTIES

### Magnetic Properties

Probably, the most interesting property that magnetic nanoparticles can possess is superparamagnetism. It is by no means unique to iron, but it is commonly seen in iron nanoparticles. For a particle to be superparamagnetic, it must not only be strongly magnetic (with ferromagnetic or ferrimagnetic ordering of its atoms' spins), but also consist of a single magnetic domain. This occurs when the particle is smaller than the characteristic magnetic domain in the material. For iron, the single domain size is about 20 nm, and particles below this size tend to be single domain. The result of the particle being a single domain is that we can think of it as possessing a single giant spin whose magnitude is the sum of the individual atoms' spins for a ferromagnetic material like iron.

In addition to being single domain particles, superparamagnetic particles must have enough thermal energy that the spins of the single domain particles can freely reorient. The energy required for the reorientation of a particle's spin is proportional to the volume of the particle. As a practical matter, this generally places a greater limitation on the size of particles that exhibit superparamagnetism than the requirement that they be single domain.

As an illustrative example, we can imagine beginning with a lone iron atom (or ion) and growing an

iron nanoparticle around it and see how its magnetic properties change. A lone iron atom, owing to its unpaired electrons, will exhibit paramagnetism. Once we have a small cluster of iron atoms, due to the strong magnetic exchange coupling, the spins will align and exhibit superparamagnetism. As the nanoparticle grows in size, though the spins remain fully aligned, the energy barrier to spin reorientation grows to the point that it cannot occur in a certain timeframe (by convention 100 sec), and coercivity appears. Coercivity is a measure of how difficult it is to magnetize or demagnetize a sample, where materials with low coercivity are termed soft and highly coercive materials are hard magnets. At this point, the nanoparticles are magnetically soft ferromagnets. As this particle grows, the energy barrier to spin reorientation grows with it, and the particles become a highly coercive, hard magnet. Finally, at some size above 20 nm, it becomes energetically favorable for the particle to break into multiple magnetic domains. The size where this occurs represents the tipping point between two features that increase the energy of the system. Single magnetic domains have a higher flux leakage, a term used to describe the energy stored in an external magnetic field, than multiple domain particles. Lines of flux emanate from the north pole of a magnet and return to the south pole, and having multiple poles in a single particle decreases the energy by having shorter paths from north to south poles. Breaking into multiple magnetic domains increases energy through a different

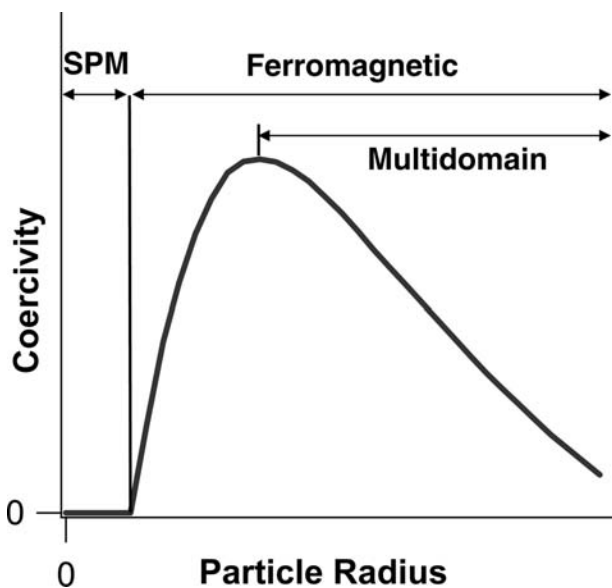


**Fig. 1** The progression of the coercivity of a magnetic nanoparticle as its size is increased. Very small nanoparticles have no coercivity and are superparamagnetic. When coercivity appears, they become superparamagnetic, and somewhere near the maximum coercivity, the particle breaks into multiple magnetic domains. From here, the particle coercivity begins an approach to bulk coercivity. *Source:* Adapted from Refs.<sup>[1,2]</sup>.

mechanism, the energy stored in the interfaces between domains. The point where the energy decrease from lowered flux leakage is greater than the energy increase from the new domain walls is where the particle becomes multidomain. At this point, the coercivity along with its other magnetic properties begin to move towards bulk values. This progression is illustrated in Fig. 1.

Now, we will discuss a superparamagnetic sample as discussed earlier, and look at its magnetic properties as a function of temperature. At very low temperatures, there is insufficient thermal energy to allow the free reorientation of magnetic spins, and the particles are ferromagnetic. If we begin with an unmagnetized sample and slowly increase the temperature under a constant field, the magnetization of the sample increases as more reorientation is allowed. If we stopped at temperatures along the way to measure hysteresis loops, we would also notice the hysteresis decreasing with increasing temperatures. At some temperature, a maximum in magnetization at a constant field is reached, and the magnetization begins to decrease as  $T^{-1}$ . The maximum in magnetization coincides with a total loss in coercivity, and is termed the blocking temperature, as below this temperature spin reorientation is blocked. Above the blocking temperature, the sample is superparamagnetic and has no hysteresis but can have a very high susceptibility. The magnetization falls off as  $T^{-1}$ , as temperature is increased above the blocking temperature. This

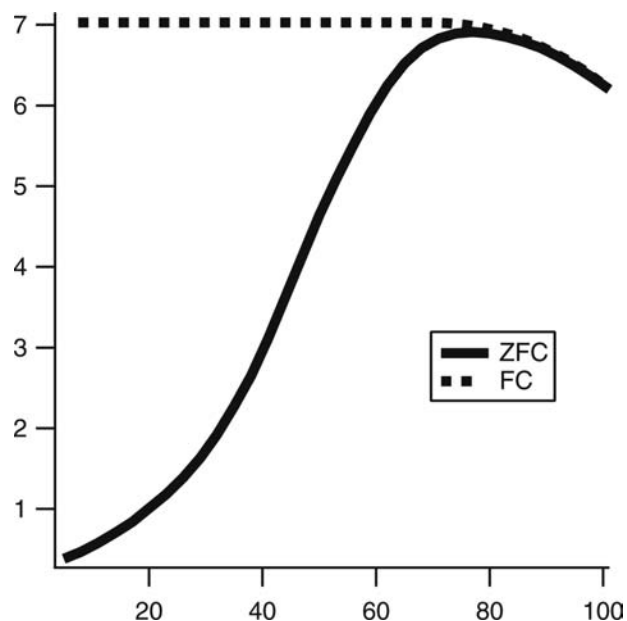


**Fig. 2** A typical magnetometry experiment on iron nanoparticles. The particles are cooled in the absence of a magnetic field, a weak field is applied (here 1 mT), then the particle sample is slowly heated and the moment measured as a function of temperature. This progression produces the ZFC (zero-field cooled) curve shown earlier. The ZC (field cooled) curve is produced by stopping the warming, and recooling the sample.

progression describes a ZFC (zero-field cooled) plot in magnetometry, and is shown graphically in Fig. 2. The field-cooled curve (FC) is produced after the ZFC curve by subsequent cooling in the presence of the magnetic field used in the ZFC curve. The two curves are coincident where the sample is superparamagnetic (there is no hysteresis), but separate at the blocking temperature, as the FC curve remains fully magnetized.

An interesting result of all of this is that nanoparticles can represent the lowest coercivity possible (zero for superparamagnetic particles) or very highly coercive for somewhat larger nanoparticles. These high coercivities can in fact be increased further through shape anisotropy by, for example, producing high aspect ratio particles. This has led to the use of iron nanorods in high-density magnetic recording.

Surface effects are very important in nanoparticles, and the effects of the surface are extremely important in the magnetism of iron nanoparticles. The reactivity of iron nanoparticles makes it difficult to keep the surface in its fully reduced form. Even when fully protected from oxygen and water, the surface of iron nanoparticles can be effectively oxidized by the surfactant used to stabilize them. In some cases, a detectable oxide can be formed by the action of a surfactant such as a carboxylic acid.<sup>[3]</sup> Surface oxides tend to add little or nothing to the overall magnetism of the particle, and

may even decrease the magnetic response of the underlying, unoxidized iron. The reason for the lack of magnetic response of the oxide is the pinning of the spins in the oxide. These pinned spins do not reorient with the particle spin, and contribute nothing to particle moment.<sup>[4]</sup> While in the case of larger particles, this may not be a serious issue, for particles below about 5 nm, a surface oxide can essentially destroy the magnetic properties of an iron particle.

Even in the absence of an oxide layer, a strongly interacting surfactant can disturb the electronic structure of iron enough to seriously impact the magnetic properties of the nanoparticle. This effect was well demonstrated by a series of experiments by Gedanken and coworkers.<sup>[5]</sup> Iron nanoparticles were synthesized with no stabilizing surfactant, and these particles were then coated with a series of surfactants. The surfactants decreased the saturation magnetization of the particles depending on the strength of their interactions, with surfactants such as a sulfonic acid or phosphonic acid causing a huge reduction, while much milder alcoholic surfactants had a less dramatic effect. Nearly all of the saturation magnetization of an iron nanoparticle can be maintained by selecting a sufficiently weakly interacting surfactant, such as a  $\beta$ -diketone.<sup>[6]</sup>

### Chemical Properties

Iron nanoparticles are extraordinarily reactive, most notably being pyrophoric. It is important to keep this in mind whenever handling iron nanoparticles both for safety reasons and to maintain the nanoparticles' integrity. There are a number of ways to mitigate the extreme reactivity that iron nanoparticles have towards oxidizing agents, including gently oxidizing the surface. By exposing the surface of the particles to a weak oxidizer, or a very dilute strong oxidizer, the particles can be passivated. At ambient temperatures, the oxidation of iron nanoparticles typically produces magnetite, which is a strongly adherent layer that can passivate the particles towards further oxidation. While rapid oxidation produces heat that can lead to delamination of the oxide and wholesale oxidation in a potentially spectacular reaction, the slow, gentle oxidation of the surface only can protect the core and maintain it as iron. An example of this is shown in Fig. 3. Species that have been used successfully for this passivation include: low partial pressures of oxygen,<sup>[7]</sup> carboxylic acids,<sup>[3]</sup> and alcohols.<sup>[8]</sup> This gentle passivation can be of particular use to particles destined for catalytic application as they can later be reduced back to elemental iron. Early work by Selwood<sup>[9]</sup> not only demonstrated that this conversion could be performed on nanoscale iron, but also showed that the reduction and oxidation could be followed by measuring the

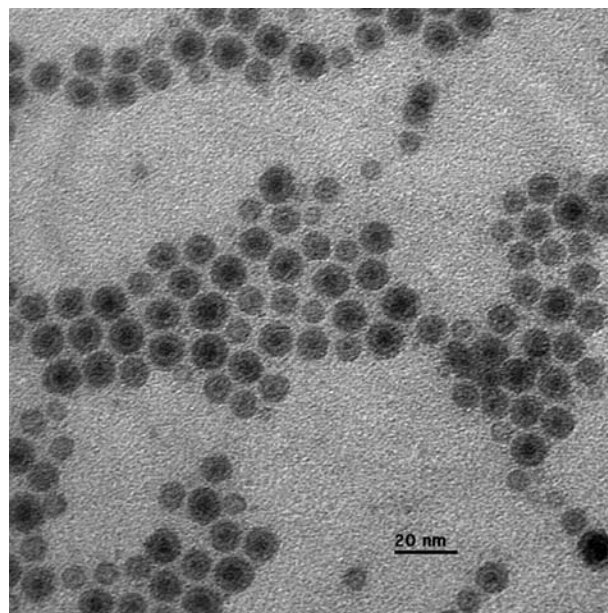


**Fig. 3** Iron nanoparticles whose shells have been gently oxidized by oleic acid. These particles can be handled in dry air without further damage to their iron cores.

magnetic moment of the catalyst material. While oxidizing the surface may leave the core unchanged, it will still enormously change the properties of the nanoparticle. The chemical properties are obviously greatly altered as are magnetic properties due to the very large fraction of the volume that is contained in the outer layers of the particle. These are also issues for the other methods of preventing oxidation: coating with oxidation-resistant coatings, and alloying. Alloying will naturally make an entirely different material, such as iron platinum alloys that are still highly magnetic, but are indefinitely stable in air. Even coating particles has a surprisingly strong effect on the magnetic properties of the particles, generally greatly weakening them. This has been shown by a number of researchers to occur when gold coating iron nanoparticles.

The extreme reactivity of iron nanoparticles can be of use in catalytic applications, however. The tendency to oxidize in air does limit the application to carefully controlled systems that contain either inert atmospheres, or even reducing atmospheres. There is one important industrial application for iron nanoparticles as catalyst, and that is the Fischer–Tropsch conversion of carbon monoxide and hydrogen gas into alkanes. This process is conducted in a reducing atmosphere, so iron's tendency to oxidize is not detrimental to the reaction, and in fact the easy oxidation of iron may be a crucial part of its catalytic activity in this reaction. Iron nanocatalysts have a number of advantages in Fischer–Tropsch reactions, including the abundance and low cost of iron, the high catalytic activity,<sup>[10]</sup>

and ability to maintain its high catalytic activity in this reaction. In contrast, applications of iron nanoparticles for the liquefaction of coal have been continuously hampered by the presence of sulfur-containing species that very quickly poison iron nanoparticle-based catalysts. Iron nanoparticles have been shown to catalyze numerous other reactions including the growth of carbon nanotubes,<sup>[11]</sup> hydrogenation of naphthalene,<sup>[12]</sup> and degradation of trichloroethylene.<sup>[13]</sup>

## PREPARATION

Mechanical grinding of iron nanoparticles,<sup>[14,15]</sup> while certainly the most intuitively simple approach to nanoparticle formation, is in fact a difficult to produce and well-defined product. The product of high-energy milling tends to be irregularly shaped and polydisperse. The advantage of this process is the ease with which it can be scaled up to produce large quantities.

Iron nanoparticles can also be produced by vapor deposition onto a non-wetting surface. If an appropriate amount of iron is deposited onto the surface, the iron forms discrete nanoparticles, while if too much is applied, the iron will form a continuous film. Obviously, this process is surface area limited, making it difficult to produce appreciable quantities of nanoparticles. Several clever methods have been used to increase the yield of this type of procedure by constantly refreshing the surface. For example, by codepositing a metal and frozen solvent, Klabunde and coworkers were able to produce finely divided magnesium.<sup>[16]</sup> When applying this process to iron, they codeposited iron with other metals and inorganic compounds to form iron nanoparticles protected from oxidation by being embedded in micron-scale particles of the other chemical species (i.e., barium fluoride,<sup>[17]</sup> indium,<sup>[18]</sup> magnesium,<sup>[19]</sup> magnesium fluoride,<sup>[17,19]</sup> and neodymium<sup>[18]</sup>).

Another approach is shown in Fig. 4.<sup>[20]</sup> In this process, a drum is rotated around the evaporation source, with the bottom submerged in a viscous liquid. This viscous liquid forms a film over the drum, and the particles collect in this liquid, directly forming a ferrofluid.

By far, the most common method of forming iron nanoparticles to be found in the literature is the use of wet chemical synthesis. There are two primary methods of chemical synthesis of iron nanoparticles: decomposition of iron compounds and reduction of iron salts or oxides. I will discuss each of these methods in the following paragraphs.

The most popular chemical decomposition method is the thermal decomposition of iron pentacarbonyl. This method has long been used to make micron-scale iron particles, often called carbonyl iron. The advantage of the decomposition of this species is that its

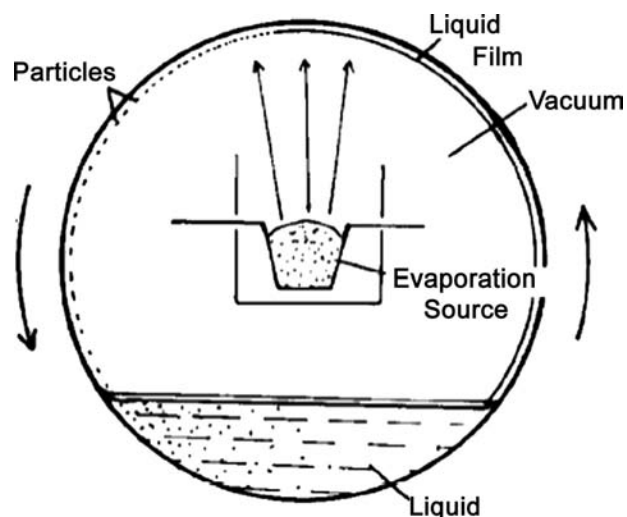


**Fig. 4** Formation of a ferrofluid by evaporating iron into a continuously refreshed thin film of liquid. *Source:* Reproduced with permission from Ref.<sup>[20]</sup>.

decomposition yields only iron and carbon monoxide, which leaves as a gas. There are no ions or other impurities to contaminate the product (if the iron pentacarbonyl was pure). Iron pentacarbonyl is also very soluble in organic solvents, which is useful as one will not easily yield metallic iron nanoparticles in an aqueous environment. Iron pentacarbonyl also decomposes at modest temperatures, with the rate becoming appreciable around 100°C and being quite fast around 200°C (at this temperature, a typical decomposition reaction can be complete in under an hour). Precise control of particle size is rather difficult in these types of systems, owing to the extraordinarily complex kinetics of the decomposition of iron pentacarbonyl. The decomposition rate, and even the mechanism and kinetic order of the decomposition, are highly dependent on the reaction conditions. The decomposition is self-catalyzed, as well as being catalyzed by numerous other species,<sup>[21]</sup> so that as concentrations change through the course of the reaction, the reaction rate can change greatly. The first literature reports of the formation of iron nanoparticles through iron pentacarbonyl used a variety of polymers as both catalyst and surfactant.<sup>[21,22]</sup> A number of other surfactants have been used for this type of reaction, but the essence of the reaction has changed a little. The iron carbonyl, an appropriate high boiling point solvent, and the surfactant are placed in a vessel under an inert atmosphere and heated. The carbon monoxide must be allowed to vent for the reaction to continue to completion, so an oil bubbler is often used as a one-way valve.

Sonochemical decomposition of iron pentacarbonyl to form nanoscopic iron powders,<sup>[23]</sup> then well-dispersed

nanoparticles<sup>[24]</sup> was demonstrated by Suslick et al. In this approach, the decomposition of iron pentacarbonyl proceeds at a globally low temperature, with highly localized energy provided through acoustic cavitation. This method suffers from the same difficulty as the thermal decomposition, in that the reaction is kinetically complex, and precise size control is difficult.

On the whole, decomposition of iron pentacarbonyl to form iron nanoparticles has been shown to be an extremely versatile approach. A large number of surfactants with varying functionalities can be used to produce iron nanoparticles, including alcohols,<sup>[25,26]</sup> carboxylic acids,<sup>[3,24,27,28]</sup> amines,<sup>[3]</sup> amides,<sup>[3]</sup>  $\beta$ -diketones,<sup>[6]</sup> polyvinylpyrrolidone,<sup>[24]</sup> polybutadiene,<sup>[21]</sup> poly(styrene-*co*-butadiene),<sup>[21]</sup> poly(styrene-*co*-4-vinylpyridine),<sup>[21]</sup> alkanethiols,<sup>[27,29]</sup> alkyl sulfates,<sup>[30]</sup> chlorosilanes,<sup>[30]</sup> and alkyl sulfonic acids.<sup>[31]</sup>

Chemical reduction of metal salts has long been the most common method for the formation of metallic nanoparticles. This procedure is not as common in iron as in other metals, primarily due to iron's chemical reactivity. Many of the most popular methods of nanoparticle production are done in aqueous environments (either purely aqueous, or in a two-phase aqueous/organic system). The presence of water can make it very difficult to keep iron in its zero-valent state, as it has a strong tendency to re-oxidize the iron. Even some of the most popular reducing agents can contaminate iron nanoparticles, in particular the borohydrides, which are known to lead to formation of iron borides.<sup>[32,33]</sup>

There are, however, a number of reports of iron nanoparticles synthesized through the reduction of salts. The synthesis is a fairly simple one, requiring only the mixing of a reducing agent into a solution of iron salt and a surfactant to prevent wholesale agglomeration. The choice of a surfactant is a critical one, as it limits the choice of solvents and reducing agents, as well as altering the properties of the finished nanoparticles. Particular attention must be paid to the surfactant-reducing agent compatibility, because, for example, oleic acid and lithium aluminum hydride are incompatible (the acid will be reduced). To avoid incompatibilities with reducing agents, it is common to use reduction-resistant surfactants such as quaternary ammonium salt<sup>[13,33,34]</sup> or poly-ether<sup>[33]</sup> based surfactants for syntheses involving the reduction of iron salts.

The reduction of iron oxides has also been used to synthesize iron nanoparticles, but the approach is generally quite different. Iron oxides are not very soluble and their reduction to form iron nanoparticles, therefore, generally takes place in the solid state. The typical approach is heating the iron oxide particles in a reducing atmosphere, generally containing hydrogen.<sup>[8,35]</sup> The particle dimensions and shape are determined by the oxide precursor particles, and are largely

maintained during reduction.<sup>[8]</sup> Since iron oxide particles are generally easy to make, can be made in large quantities, and can be made with good control of shape and size, this is a major industrial process used to make iron needles for high-density magnetic data storage.

## APPLICATIONS AND POTENTIAL APPLICATIONS

The largest current application of iron nanoparticles is without a doubt the use of iron nanorods in magnetic recording media. This is the current state-of-the-art material for removable drive material. While this may be the only large-scale industrial application of iron nanoparticles at the moment, there are a number of other applications under investigation. The unique magnetic properties of iron nanoparticles underlie many of them. Potential applications based on the iron nanoparticles' high magnetic saturation and low hysteresis include transformer cores, motors, magnetic record heads, and other small electromagnets. The magnetic properties may also be useful in biomedical applications, including magnetic resonance imaging (MRI) contrast enhancers, and the destruction of tumors through magnetic heating of nanoparticles by oscillating magnetic fields (hyperthermia). Detailed discussions of these and other potential applications are beyond the scope of this entry, but can be found in a number of other references.<sup>[2,36,37]</sup>

## CONCLUSION

Iron nanoparticles are a fascinating material with a few current uses and a great deal of untapped potential. Their two most promising properties are their extreme reactivity, with possible applications in catalysis, and their magnetic properties, with applications in information storage, electromagnetic applications, and biomedical imaging.

The preparation of iron nanoparticles has progressed greatly in the past decade or two, and in the cases of the non-catalytic applications, the only thing standing between the use of this material is a convenient method of treating the particles to mitigate their extreme reactivity. Iron is an outstanding magnetic material and it is here where iron nanoparticles may have the greatest impact.

## ACKNOWLEDGMENTS

The author thanks Paula Provencio for TEM analysis. Funding for research presented here was provided by



the Office of Basic Energy Sciences, United States Department of Energy, and by Sandia's Laboratory Directed Research and Development program. Sandia is a multiprogram laboratory operated by Sandia Corporation, a Lockheed Martin Company, for the United States Department of Energy's National Nuclear Security Administration under contract DE-AC04-94AL85000.

## REFERENCES

- Jacobs, I.; Bean, C. Fine particles, thin films and exchange anisotropy. In *Magnetism (vol 3)*; Rado, G.T., Suhl, H., Eds.; Academic Press: New York and London, 1963; 271–350.
- Huber, D.L. Synthesis, properties, and applications of iron nanoparticles. *Small* **2005**, *1* (5), 482–501.
- Farrell, D.; Majetich, S.; Wilcoxon, J. Preparation and characterization of monodisperse Fe nanoparticles. *J. Phys. Chem. B* **2003**, *107* (40), 11,022–11,030.
- Huang, R.; Xiong, H.; Lu, Q.; Hsia, Y.; Liu, R.; Ji, R.; Lu, H.; Wang, L.; Xu, Y.; Fang, G. Investigation of the oxide surface layer on fine iron particles. *J. Appl. Phys.* **1993**, *74* (6), 4102–4104.
- Kataby, G.; Koltypin, Y.; Ulman, A.; Felner, I.; Gedanken, A. Blocking temperatures of amorphous iron nanoparticles coated by various surfactants. *Appl. Surf. Sci.* **2002**, *201* (1–4), 191–195.
- Huber, D.L.; Martin, J.E.; Venturini, E.I.; Provencio, P.P.; Patel, R.J. Synthesis of highly magnetic iron nanoparticles suitable for field-structuring using a beta-diketone surfactant. *J. Magn. Magn. Mater.* **2004**, *278*, 311–316.
- Kuhn, L.T.; Bojesen, A.; Timmermann, L.; Nielsen, M.M.; Morup, S. Structural and magnetic properties of core-shell iron-iron oxide nanoparticles. *J. Phys. Cond. Matter* **2002**, *14* (49), 13,551–13,567.
- Varanda, L.C.; Jafelicci, M.; Tartaj, P.; O'Grady, K.; Gonzalez-Carreno, T.; Morales, M.P.; Munoz, T.; Serna, C.J. Structural and magnetic transformation of monodispersed iron oxide particles in a reducing atmosphere. *J. Appl. Phys.* **2002**, *92* (4), 2079–2085.
- Selwood, P.W.; Ellis, M.; Wethington, K. Supported oxides of iron. *J. Amer. Chem. Soc.* **1949**, *71* (6), 2181–2184.
- Marchetti, S.G.; Cagnoli, M.V.; Alvarez, A.M.; Bengoa, J.F.; Gallegos, N.G.; Yeramian, A.A.; Mercader, R.C. Iron uniform-size nanoparticles dispersed on MCM-41 used as hydrocarbon synthesis catalyst. *Hyperfine Interactions* **2002**, *139* (1/4), 33–40.
- Vander Wal, R. Fe-catalyzed single-walled carbon nanotube synthesis within a flame environment. *Combust. Flame* **2002**, *130* (1–2), 37–47.
- Zhan, X.D.; Guin, J.A. High-pressure hydrogenation of naphthalene using a reduced iron catalyst. *Energy Fuels* **1994**, *8* (6), 1384–1393.
- Li, F.; Vipulanandan, C.; Mohanty, K. Microemulsion and solution approaches to nanoparticle iron production for degradation of trichloroethylene. *Colloids Surf. A-Physicochem. Eng. Aspects* **2003**, *223* (1–3), 103–112.
- Kerekes, L.; Hakl, J.; Meszaros, S.; Vad, K.; Gurin, P.; Kis-Varga, I.; Uzonyi, I.; Szabo, S.; Beke, D. Study of magnetic relaxation in partially oxidized nanocrystalline iron. *Czech. J. Phys.* **2002**, *52*, A89–A92.
- PardaviHorvath, M.; Takacs, L. Magnetic nanocomposites by reaction milling. *Scripta Metallurgica et Materialia* **1995**, *33* (10/11), 1731–1740.
- Klabunde, K.J.; Efner, H.F.; Satek, L.; Donley, W. Preparation of an extremely active magnesium slurry for Grignard-reagent preparations by metal atom-solvent cocondensations. *J. Organometallic Chem.* **1974**, *71* (3), 309–313.
- Zhang, D.J.; Klabunde, K.J.; Sorensen, C.M.; Hadjipanayis, G.C. Synthesis of nanoscale magnetic metal particles encapsulated in magnesium fluoride and the properties of these materials. *High Temp. Mater. Sci.* **1996**, *36* (2–3), 135–154.
- Zhang, D.; Glavee, G.; Klabunde, K.J.; Hadjipanayis, G.C.; Sorensen, C.M. Nanoscale iron crystallites encapsulated in nonmagnetic metal shells. *High Temperature Mater. Sci.* **1996**, *36* (2/3), 93–115.
- Zhang, D.J.; Klabunde, K.J.; Sorensen, C.M.; Hadjipanayis, G.C. Encapsulated iron, cobalt and nickel nanocrystals: effect of coating material (Mg, MgF<sub>2</sub>) on magnetic properties. *Nanostructured Mater.* **1999**, *12* (5–8), 1053–1058.
- Nakatani, I.; Furubayashi, T.; Takahashi, T.; Hanaoka, H. Preparation and magnetic properties of colloidal ferromagnetic metals. *J. Magn. Magn. Mater.* **1987**, *65* (2/3), 261–264.
- Smith, T. Preparation of colloidal iron dispersions by the polymer-catalyzed decomposition of iron carbonyl and iron organocarbonyl compounds. Xerox Corporation: USA, 1979.
- Smith, T.; Wychick, D. Colloidal iron dispersions prepared via the polymer-catalyzed decomposition of iron pentacarbonyl. *J. Phys. Chem.* **1980**, *84* (12), 1621–1629.
- Suslick, K.S.; Choe, S.B.; Cichowlas, A.A.; Grinstaff, M.W. Sonochemical synthesis of amorphous iron. *Nature* **1991**, *353* (6343), 414–416.
- Suslick, K.; Fang, M.; Hyeon, T. Sonochemical synthesis of iron colloids. *J. Amer. Chem. Soc.* **1996**, *118* (47), 11,960–11,961.
- Kataby, G.; Prozorov, R.; Gedanken, A. Characterization of self-assembled alcohol coatings on amorphous iron. *Nanostructured Mater.* **1999**, *12* (1–4), 421–424.
- Kataby, G.; Ulman, A.; Prozorov, R.; Gedanken, A. Coating of amorphous iron nanoparticles by long-chain alcohols. *Langmuir* **1998**, *14* (7), 1512–1515.
- Kataby, G.; Ulman, A.; Cojocar, M.; Gedanken, A. Coating a bola-amphiphile on amorphous iron nanoparticles. *J. Mater. Chem.* **1999**, *9* (7), 1501–1506.
- Kataby, G.; Cojocar, M.; Prozorov, R.; Gedanken, A. Coating carboxylic acids on amorphous iron nanoparticles. *Langmuir* **1999**, *15* (5), 1703–1708.
- Katabi, G.; Koltypin, Y.; Cao, X.; Gedanken, A. Self-assembled monolayer coatings of iron nanoparticles with thiol derivatives. *J. Crystal Growth* **1996**, *166* (1–4), 760–762.

30. Rozenfeld, O.; Kolytyn, Y.; Bamnolker, H.; Margel, S.; Gedanken, A. Self-assembled monolayer coatings on amorphous iron. *Langmuir* **1994**, *10* (11), 3919–3921.
31. Yee, C.; Kataby, G.; Ulman, A.; Prozorov, T.; White, H.; King, A.; Rafailovich, M.; Sokolov, J.; Gedanken, A. Self-assembled monolayers of alkanesulfonic and -phosphonic acids on amorphous iron oxide nanoparticles. *Langmuir* **1999**, *15* (21), 7111–7115.
32. Glavee, G.N.; Klabunde, K.J.; Sorensen, C.M.; Hadjipanayis, G.C. Chemistry of borohydride reduction of iron(II) and iron(III) ions in aqueous and nonaqueous media - formation of nanoscale Fe, Fe<sub>2</sub>O<sub>3</sub>, and Fe<sub>2</sub>S<sub>3</sub> powders. *Inorg. Chem.* **1995**, *34* (1), 28–35.
33. Martino, A.; Stoker, M.; Hicks, M.; Bartholomew, C.; Sault, A.; Kawola, J. The synthesis and characterization of iron colloid catalysts in inverse micelle solutions. *Appl. Catal. A-General* **1997**, *161* (1–2), 235–248.
34. Seip, C.; O' Connor, C. The fabrication and organization of self-assembled metallic nanoparticles formed in reverse micelles. *Nanostruct. Mater.* **1999**, *12*, 183–186.
35. Hisano, S.; Saito, K. Research and development of metal powder for magnetic recording. *J. Magn. Magn. Mater.* **1998**, *190* (3), 371–381.
36. McCurrie, R.A. *Ferromagnetic Materials Structure and Properties*; Academic Press: London, 1994; 297 pp.
37. Klabunde, K. Introduction to nanotechnology. In *Nanoscale Materials in Chemistry*; Klabunde, K., Ed.; Wiley Interscience: New York, 2001; 1–13.

# Iron Oxide Nanoparticles

Mamoru Senna

Department of Applied Chemistry, Keio University, Yokohama, Japan

## INTRODUCTION

Iron oxide is one of the oldest materials used even in archeological finds, e.g., in Ajanta or in Altamira, as red pigments. Even today, its significance in the pigmental materials is not lost. Since the advent of magnetic recording systems, however, ferromagnetic iron oxides gained its importance quite rapidly. These two important application fields are coupled to gain magnetic or intelligent inks.

There are many chemical species categorized as iron oxides. While hematite ( $\alpha$ -Fe<sub>2</sub>O<sub>3</sub>), maghemite ( $\gamma$ -Fe<sub>2</sub>O<sub>3</sub>), and magnetite (Fe<sub>3</sub>O<sub>4</sub>) are, by far, the most important species of pure iron oxides, many hydroxides, such as ferric hydroxide (Fe(OH)<sub>3</sub>), and oxyhydroxides, such as goethite ( $\alpha$ -Fe(O)OH), are also of industrial significance, particularly as precursors of pure or complex oxides. As for the complex iron oxides, ferrites are of particular importance as ferromagnetic materials.

Like many other nanoparticles, those of iron oxides and ferrites are prepared either via wet chemical routes such as colloid chemical or sol-gel methods or by dry processes such as vapor deposition techniques. Usually, nanoparticles are not shaped by conventional granulometrical methods. Instead, they are most frequently arranged to films, so that many preparation methods of thin films are regarded as those for nanoparticles as well. It is often desired to assemble or pattern iron oxide nanoparticles to give magnetic or optomagnetic functions.

This review summarizes the preparation, magnetic properties, and some representative examples for application of the pure and complex iron oxides.

## PREPARATION OF PARTICULATES

### Concepts

Morphological states of nanoparticles are generally divided into two, i.e., matrix-supported and self-supported. It is also important to select whether the produced primary particles should be well dispersed or aligned. While self-supported or free particles are prepared either by wet chemical or by vaporization-condensation processes, supported particles are

prepared by the methods usually used for making thin films, as mentioned in "Introduction."

### Preparation of Pure Oxides via Colloid Chemical Routes

Preparation of iron oxide ultrafine particles has been developed in view of obtaining magnetic fluids, whereby iron oxide nanoparticles are usually produced via a surface modification after the formation of magnetic nanoparticles.<sup>[1,2]</sup> A typical preparation method of magnetite nanosol is to wash magnetite precipitates by very diluted HCl and put into a soap solution, e.g., 1% aqueous solution of sodium oleate.<sup>[3]</sup> It is possible, however, to peptize a nanosol without using any organic species. The method is quite simple: A mixed aqueous solution of ferric and ferrous chlorides (e.g., 40 ml of 1 M FeCl<sub>2</sub> and 10 ml of 2 M FeCl<sub>3</sub> in 2 M HCl) was added to an ammonia solution (e.g., 500 ml 0.7 M). When the precipitate was stirred with 2 M aqueous solution of 2 M perchloric acid, peptization was achieved by merely diluting with water.<sup>[3]</sup>

On the other hand, we have wonderful models of preparing iron oxide nanoparticles in nature. Many wandering animals have inborn abilities to orient themselves by magnetic particles, mostly magnetite. They are formed generally from soluble precursors within a soft-tissue matrix.<sup>[4]</sup> The difference from common preparation methods of magnetic fluids by using soaps or similar surfactants and biological formation is the growth of the magnetite nanoparticles in the presence of polymers in the latter. It is therefore reasonable to prepare magnetic nanoparticles in some aqueous polymer dispersion. One of the examples is to precipitate magnetite particles by adding ferrous and ferric chlorides in an aqueous solution of poly(vinyl chloride) containing NaOH to set the initial pH value as high as 13.8. Well-dispersed, phase pure magnetite particles of ca. 8 nm were obtained.<sup>[5,6]</sup>

When 0.1% of OH groups of poly(vinyl alcohol) (PVA) were converted to COOH groups, a polymer layer was observed on the particles; forming a cluster, they are similar to magnetotactic bacteria, which contain chains of magnetic nanoparticles.<sup>[7]</sup>

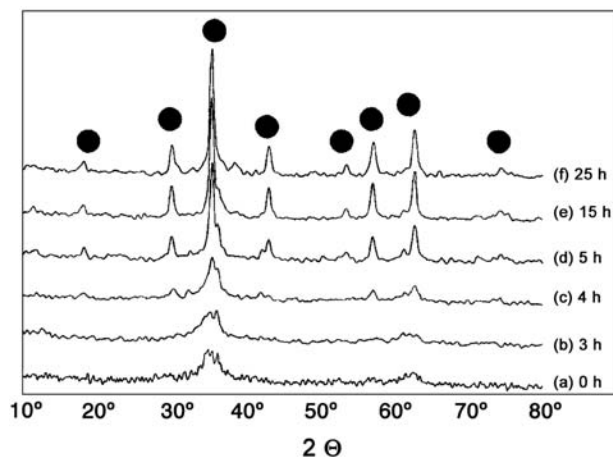


**Fig. 1** XRD patterns of the prepared powder for various ultrasonic irradiation times; ●:  $\text{NiFe}_2\text{O}_4$ . Source: From Ref.<sup>[8]</sup>.

### Ferrites and Composites

Usually, ferrite nanocrystals are available only after heating at elevated temperatures. Immediate products from colloid chemical processing, most commonly by coprecipitation, are quite often either amorphous or poorly crystallized, so that they are regarded as precursors and subject to subsequent heating. It is therefore important to promote nucleation in the precursor and decrease the temperature needed for crystallization. Ultrasonication, for instance, was revealed to promote crystallization. Shin et al.<sup>[8]</sup> obtained fairly well crystallized Ni–Cu ferrite nanoparticles by ultrasonication. After ultrasonication for 5 hr, distinct crystalline ferrite powders were obtained, as shown in Fig. 1. By prolonged irradiation (for 25 hr), its crystallinity became higher than those heated at 500°C for 2 hr.

Reactant solutions are often confined into a micro-space to guarantee limited growth of the particles to obtain well-dispersed nanoparticles. Inverse micelle or microemulsion methods are typical examples under these concepts. Barium ferrite nanoparticles were prepared in a

microemulsion dispersed in *n*-octane by using cetyl trimethyl ammonium bromide (CTAB) as a surfactant and 1-butanol as a cosurfactant.<sup>[9]</sup> Two identical emulsions were prepared containing a mixed aqueous solution of barium and ferric nitrates in the first one and an aqueous solution of ammonium carbonate in the second. Well-dispersed precipitates of the precursor comprising particles between 3 and 8 nm were calcined at 950°C for 12 hr to obtain phase pure magnetoplumbite. Particle size did not exceed 100 nm despite fairly severe heating condition.

An alternative preparation of ferrite nanoparticles is autocombustion. Mg–Zn ferrites doped with Cu were prepared from a mixed solution comprising nitrates of respective metallic species and citric acid.<sup>[10]</sup> Dried gel obtained by heating the solution at 135°C under constant stirring was subsequently ignited to commence self-propagating combustion, which ended up with the formation of fairly well crystallized loose powder. Average particle size was 56 nm determined from a XRD profile by Scherrer method.<sup>[11]</sup>

Iron oxide–metal nanocomposites were obtained from ethanolic solution of ferric nitrate by slow addition of propylene oxide to occur rapid gelation.<sup>[12]</sup> When other fine-grained metal powders (e.g., Al) were added to the stirred Fe(III)/epoxide solution just before gelation, rigid composite gel was obtained. Slow evaporation or supercritical extraction with  $\text{CO}_2$  brought about xerogel. As shown in Fig. 2, the microstructure of the monolithic xerogel comprises interconnected clusters of hematite (3–10 nm) with well-dispersed Al powers of ca. 30 nm.

### ORIENTATION AND PATTERNING

#### Concepts

One of the most important properties of the ensemble of magnetic particles is their coherency or chain-like

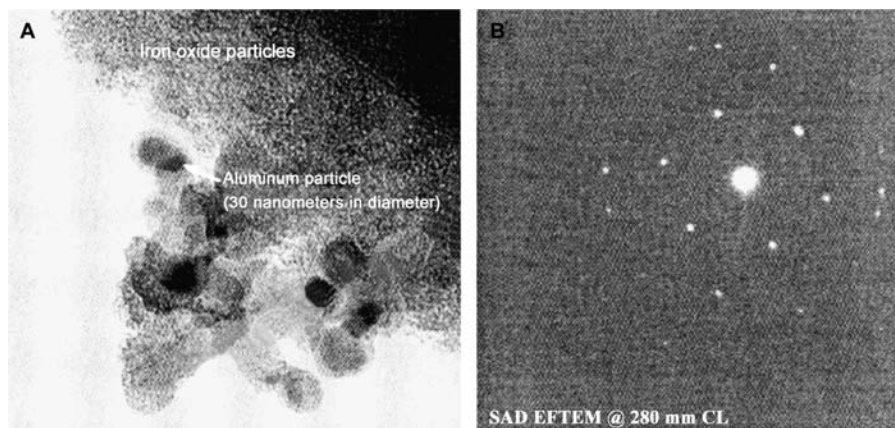


**Fig. 2** (A) HRTEM of  $\text{Fe}_2\text{O}_3$ /ultra-fine-grained Al powers xerogel nanocomposite and (B) SAED pattern of the labeled Al particle in (A). Source: From Ref.<sup>[12]</sup>.

clustering. Anisotropic aggregation, in turn, inevitably results in the anisotropy of the magnetic properties. Patterning and two-dimensional assemblage, on the other hand, are not exclusive for magnetic particles. Many functional materials could be prepared, however, from these techniques on iron oxides as well. Some typical examples are given below.

### Thin Films with Aligned Magnetic Nanoparticles

Starting from a commercially available water-based magnetic fluid comprising  $\text{Fe}_3\text{O}_4$  particles of ca. 10 nm, PVA was added and the viscosity was adjusted by water evaporation.<sup>[13]</sup> Spin-coated films were then formed in the magnetic field up to 5 kOe. Orientation of the chain clusters with increasing the magnetic field is visible in Fig. 3. The separation of the chain cluster was estimated to be  $0.27\ \mu\text{m}$  regardless of the magnetic field.

Magnetic susceptibility was measured in the field parallel ( $\parallel$ ) and perpendicular ( $\perp$ ) to that during the film preparation. As shown in Fig. 4, their deviation becomes larger with increasing the applied field during film formation.

The film serves as an optical grating because of the angle dependence of the transmittance measured by using 628 nm linearly polarized light. Optical anisotropy was revealed to be proportional to the magnetic anisotropy. This kind of materials can serve as a

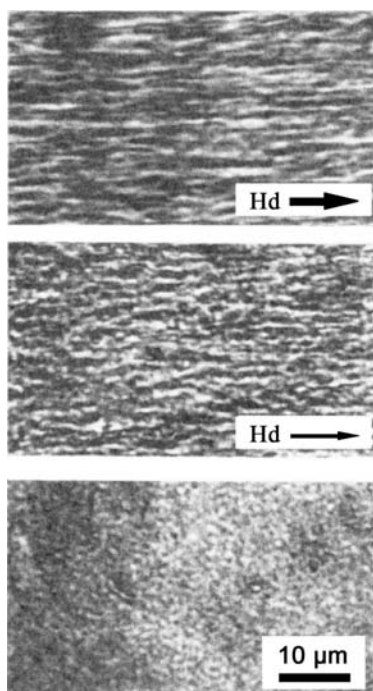


**Fig. 3** Photographs of films for three different alignment field strengths  $H_d$ : (A) 5.0 kOe; (B) 0.1 kOe; and (C) 0 kOe. Source: From Ref.<sup>[13]</sup>.

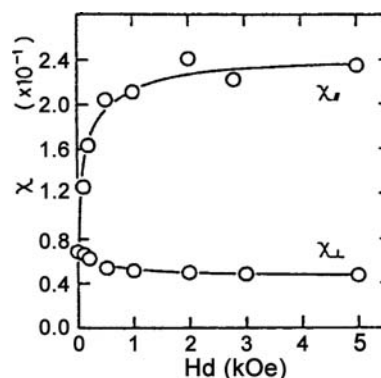


**Fig. 4** Change in the susceptibility,  $\chi$ , of films with  $H_d$ . Source: From Ref.<sup>[13]</sup>.

light-controlling device utilizing magneto-optical effects.

### Two-Dimensional Array

Not only one-dimensional assembly, as mentioned in the previous section, but also two-dimensional array of nanoparticles gives rise to many new functions. Use of self-organizing properties of organic molecules is a rational method to realize such an assemblage. Ferritin, being a popular iron-containing protein, is appropriate for such a purpose.<sup>[14]</sup> Ferritin was obtained from a horse spleen by adding  $\text{CdSO}_4$ . On the surface of dilute ferritin solution containing NaCl and phosphate buffer, poly-1-benzyl-L-histidine was spread after solubilization in chloroform. After a heat treatment, well-ordered two-dimensional array of ferritin molecules was obtained at the air-water interface. The array was easily transferred to different substrates, i.e., Si single crystals. By subsequent heat treatment up to  $700^\circ\text{C}$  in nitrogen, protein shell of the ferritin molecules was eliminated to obtain FeO nanoparticles.<sup>[14]</sup> Closer examination by FT-IR and thermogravimetry, it turned out that FeO was obtained after heating at above  $450^\circ\text{C}$ . Heating at higher temperatures tends to break assemblage, as shown in Fig. 5.

The array of iron oxide cores can be observed after heating up to  $500^\circ\text{C}$ . As SEM cannot visualize the protein shell of the ferritin molecule, AFM study in contact mode is necessary to examine the existence of the shell and subunits of the ferritin molecule.<sup>[14]</sup>

### In Situ Patterning

Microscopic patterning by iron oxides was made by using the hydrophilic self-assembled organic monolayers and subsequent microcontact printing ( $\mu\text{CP}$ ).<sup>[15]</sup> Stamps with patterned relief structure were prepared by mixing poly(dimethyl siloxane) (PDMS) with a curing agent at room temperature and

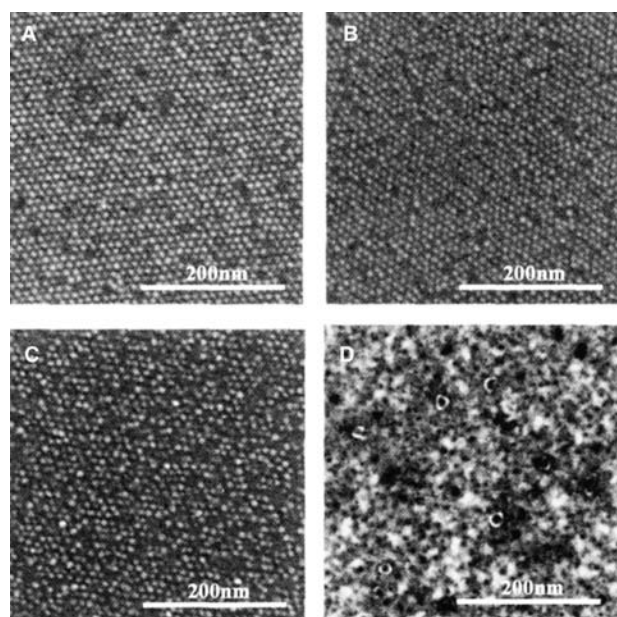


**Fig. 5** H-SEM images of arrays of the ferritin molecules (A) before and (B–D) after heat treatment under nitrogen at 300°C, 500°C, and 700°C for 1 h, respectively. *Source:* From Ref.<sup>[14]</sup>.

subsequently cured at 100°C. Chrome and gold layers were sputtered. For inking, the stamps were dipped into a dilute ethanolic solution of hexadecanethiol. After curing the inked stamps, they were conformably contacted to the gold surface to create hydrophobic self-assembled monolayers (SAMs). The samples were dipped into hydrophilic SAMs solutions to deposit dithiothreitol SAMs for the area, where hexadecanethiol was not stamped. Selective deposition of iron oxide films was then carried out from an iron nitrate aqueous solution. By annealing under different conditions, patterned  $\alpha$ - or  $\gamma$ - $\text{Fe}_2\text{O}_3$  or  $\text{Fe}_3\text{O}_4$  nanoparticles were obtained with a line width as narrow as 1  $\mu\text{m}$ .<sup>[15]</sup>

## MAGNETIC PROPERTIES

### Concepts

Downsizing of magnetic particles is accompanied by the decrease in the saturation magnetization. The mechanisms of such magnetic degradation are manifold but are somehow associated with increases in the specific surface and lattice defects. Some data with this context are given with possible strategy of preventing size-dependent degradation.

Mössbauer spectroscopy is a versatile tool for iron-containing materials. The second half of this article deals with the use of Mössbauer spectra in the analyses of iron oxide nanoparticles.

## Saturation Magnetization and Coercive Force

Ferrite particles with their average particle size smaller than 20 nm were primarily applied to magnetic fluids, so that their magnetic properties, among others, saturation magnetization, have been studied in detail. Saturation magnetization of most of those particles decreases drastically when their particle size becomes below 20–30 nm. In the case of ultrafine magnetite, for instance, saturation magnetization amounts between 30 and 60 emu/g as compared with that of bulk material, 92 emu/g.<sup>[16]</sup> Variation of the saturation magnetization is illustrated in Fig. 6 for some representative ferrites.<sup>[16]</sup>

Crystalline magnetic anisotropy constant,  $K_1$ , also plays an important role on the relative saturation magnetization. As shown in Fig. 7, the relative saturation magnetization is smaller for materials with a larger value of  $K_1$ .

It is well known that saturation magnetization decreases with the decrease of the crystallinity. However, even when the particles are well crystallized as confirmed by high-resolution electron micrographs, decrease in the magnetization is unavoidable. One of the main reasons for the decrease is then the existence of the magnetically inactive surface layer. The relationship between the crystalline magnetic anisotropy constant and the thickness of the inactive layer is displayed in Fig. 8.

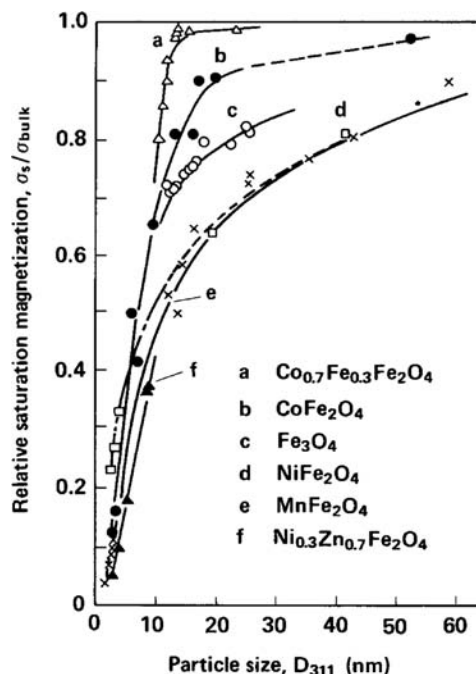


**Fig. 6** Dependence of the relative saturation magnetization,  $\sigma_s/\sigma_{\text{bulk}}$ , on average particle size  $D_{311}$ . Solid line: particles by coprecipitation; broken line: grown particles by heat treatment. *Source:* From Ref.<sup>[16]</sup>.



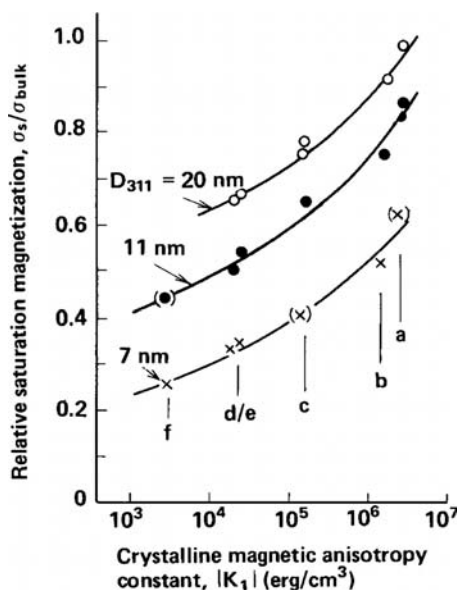


**Fig. 7** Relationship between  $\sigma_s/\sigma_{\text{bulk}}$  and  $K_1$  at constant particle size for several different ferrites. Points of a to f indicate materials corresponding to those of Fig. 6 and the symbols with parentheses indicate estimated values. Source: From Ref.<sup>[16]</sup>.

Crystalline magnetic anisotropy is closely related with the coercive force. Many attempts were therefore made to control large  $K_1$  by varying preparation methods without great success hitherto. It is to be noted, however, that coexistence of  $\alpha\text{-Fe}_2\text{O}_3$  in  $\gamma\text{-Fe}_2\text{O}_3$  brings about substantial increase in the coercivity.<sup>[17]</sup> This kind of materials is prepared by careful annealing of conventionally precipitated hydrous oxide.<sup>[17]</sup>

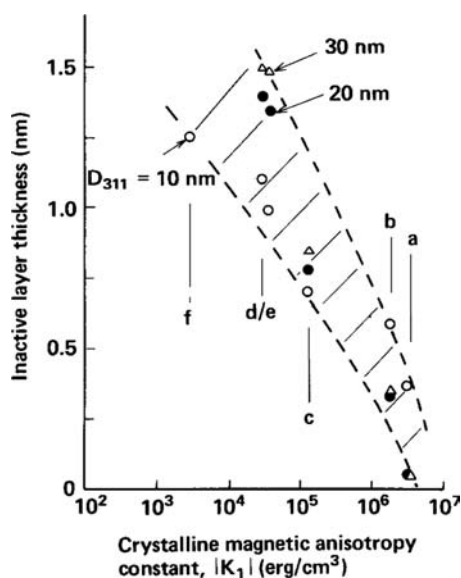


**Fig. 8** Relation between magnetically inactive layer thickness and  $K_1$ . Source: From Ref.<sup>[16]</sup>.

## Mössbauer Spectra

Characterization of detailed structure of nanoparticles is not particularly easy. In case of iron-containing compounds, however, Mössbauer spectroscopy serves as a versatile tool for characterization. A typical Mössbauer study was made on Mn-Zn ferrite nanoparticles embedded in silica matrix.<sup>[18]</sup> The spectrum comprises two components superimposing with each other, i.e., one sextet as a result of ferromagnetic particles and a doublet as a result of superparamagnetic behavior of nanosized ferrite at the center. Quadrupole splitting of the nanoparticles is larger than that of bulk ferrite presumably because of the loss of cubic symmetry in the finer particles.

A more detailed study on the Mössbauer spectra is given on the pressed sample of 3 nm  $\alpha\text{-FeOOH}$ .<sup>[19]</sup>

When nanoparticles are compressed together, significant Mössbauer absorption is observed even at room temperature, with a quadrupole doublet typical for superparamagnetic materials as shown in Fig. 9. This is not the case on the loose power. The difference is attributed to the suppression of the particle motion, which is significant for such nanoparticles because of the loss of recoilless fraction by the particle motion, overlapped with the lattice vibration. At temperatures

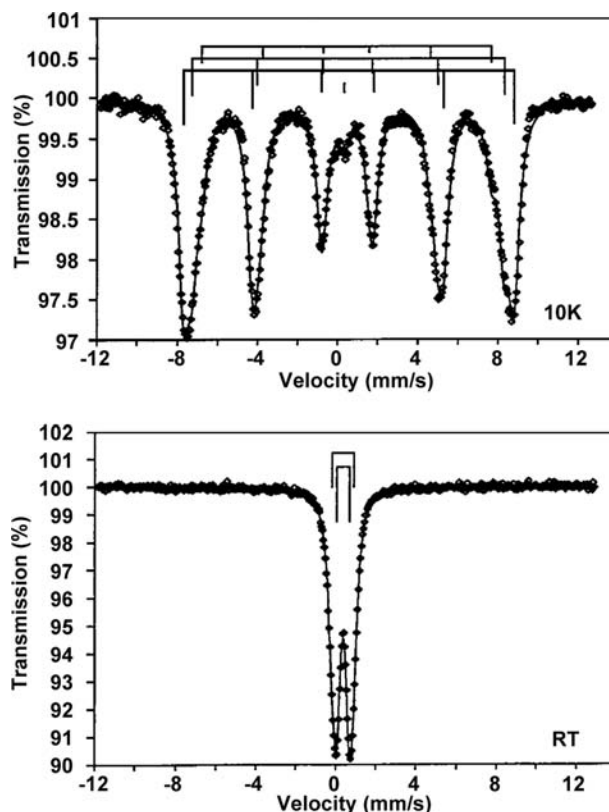


**Fig. 9** Mössbauer spectra of compressed 3 nm  $\alpha\text{-FeOOH}$  at 10 K and room temperature. Source: From Ref.<sup>[19]</sup>.

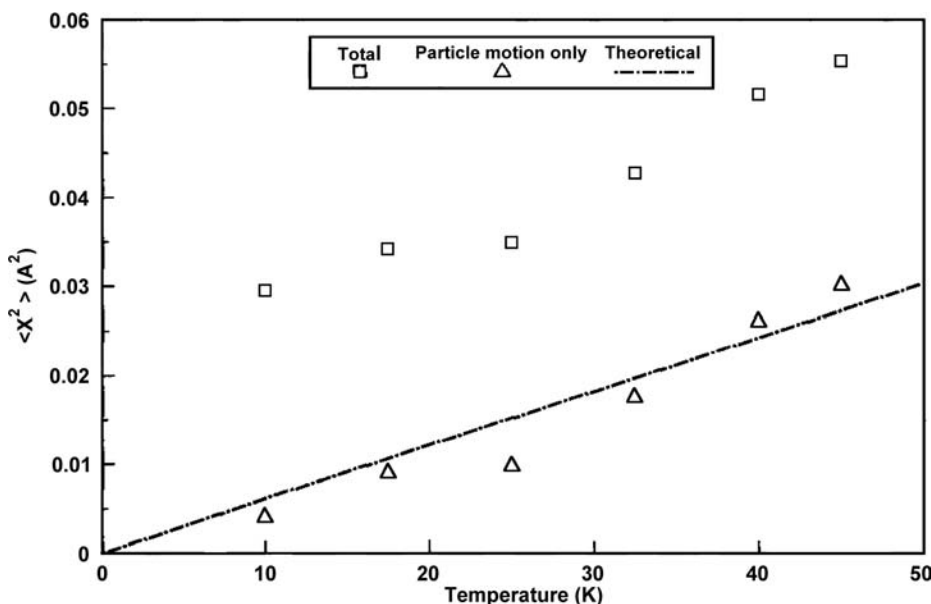


**Fig. 10** Plot of  $\langle x^2 \rangle$  as a function of temperature for the as-prepared sample. Theoretical line is also plotted with  $\omega = 2 \times 10^{11}$ . Source: From Ref.<sup>[19]</sup>.

as low as 10 K, we observe well-known hyperfine structure.

By detailed analysis of the spectra, the amount of the mean-square amplitude of the vibration in the direction of  $\gamma$ -ray emission,  $\langle x^2 \rangle$ , was calculated and plotted as a function of temperature, as shown in Fig. 10.

## FUNCTIONS AND APPLICATION

### Concepts

Functions and application of iron oxide nanoparticles, mostly with their assembly, are quite diverse in nature and large in quantity, if not of industrial significance for the time being. Some interesting case studies are given below.

### Catalysis

Catalytic activity depends largely on the specific surface so that downsizing of the particles is always

favorable for catalysis. Milling products are generally considered to have drawbacks for any characteristics attractive for modern industrial application just because of lower crystallinity. Milling zinc ferrites, for instance, were, nevertheless, revealed to be very effective for adsorption of gaseous species such as  $\text{H}_2\text{S}$ .<sup>[20]</sup> Mechanical activation leads to the substantial increase of its sulfur absorption capacity. Increased mobility of cations at sulfurization temperature, connected with their thermally stimulated return from the inversion into equilibrium sites, is the main reason for the increase in the absorption capacity.

### Magnetic Inks

A product of extended traditional technology of magnetic fluids is an intelligent ink, i.e., a colored water-based magnetic fluid. This is appropriate for an ink-jet-type printer<sup>[21]</sup> and is extended to magneto-fluidgraphy.<sup>[22]</sup> By combining Mg-Zn and Mn-Zn ferrites with appropriate dyes, the concept for intelligent ink could be furnished by red and yellow azo dyes

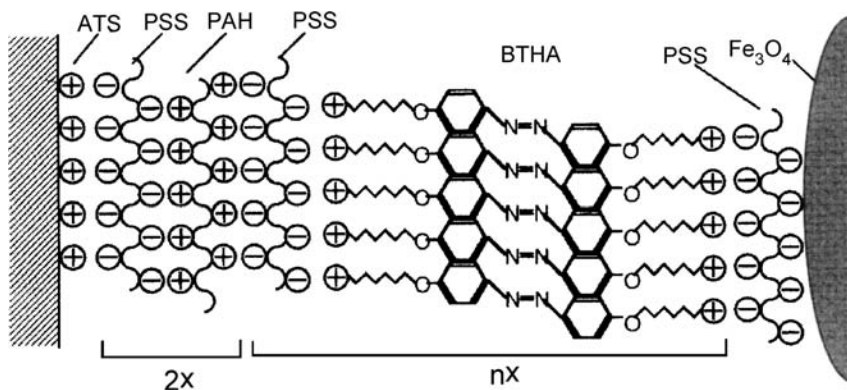


**Fig. 11** Proposed structure of the self-assembled films consisting of the BTHA dication, anionic polyelectrolytes, and  $\text{Fe}_3\text{O}_4$  particles. Abbreviations: ATS (3-aminopropyltrimethoxysilane); PSS (sodium polystyrenesulfonate); PAH (polyallylaminehydrochloride); and BTHA [4,4'-bis(trimethyl ammonium hexyloxy) azobenzene bromide]. Source: From Ref.<sup>[24]</sup>.

or mixed with copper phthalocyanine for blue magnetic inks.<sup>[23]</sup> Viscosity of these magnetic inks ranges between 1.5 and 2.0 mPa · S, being fluid enough for practical rapid printing.

## Electromagnetic Functions

When ferromagnetic iron oxide particles are well assembled in a thin film together with photoisomerizable molecules such as azobenzene-containing layers, the magnetic properties of the film can be controlled by photoillumination at room temperature.<sup>[24]</sup> Self-assembled films were prepared by dipping a substrate, e.g., silanized quartz, into an aqueous solution of cationic and anionic polyelectrolytes alternatively. Cationic colloidal magnetite was subsequently adsorbed on the precoated substrate to obtain the final organized layer. A corresponding surface chemical structure is schematically illustrated in Fig. 11.

Photoisomerization of the film was examined by UV-vis spectra. The initial *trans* state was illuminated with 360-nm UV light to transform to the *cis* state. The latter, in turn, reversibly transformed to the *trans* state by illuminating visible light (400–700 nm). The photoisomerization was accompanied by the reversible change in the magnetization of the film to exhibit photoswitching properties at room temperature.<sup>[24]</sup>

Similar photoswitching properties were observed in conjunction with the light-induced excited spin state trapping (LIESST).<sup>[25]</sup> Some ferric coordination compounds were found to be sensitive to LIESST so that their application toward molecular devices is expected.<sup>[26]</sup>

Fine particulate ferrites prepared by self-combustion method are quite appropriate for multilayer chip ferrite inductor (MLCI).<sup>[10,11]</sup> Because of the low temperature necessary for sintering (<950°C), fineness of the grain is maintained without disturbing thermal stability.

## CONCLUSION

Preparation, properties, and application of pure and complex iron oxides were presented with special emphasis on the particularity of downsizing as well as particles organization. Intrinsic properties of nanoparticles are symbolized by the increased significance of magnetically inert near-surface region and superparamagnetism. While unsupported, unorganized nanoparticles are not particularly attractive from application viewpoints; alignment and assemblage of nanoparticles look quite promising for various functional devices. Experimental characterization, particularly its topochemical aspect, is quite insufficient just because of the resolution limit of the existing analytical tools. Simulation studies with

emphasis on the near-surface region might compliment these experimental difficulties.

## REFERENCES

1. Kaiser, R.; Miskolczy, G. Magnetic properties of stable dispersions of subdomain magnetite particles. *J. Appl. Phys.* **1970**, *41*, 1064–1071.
2. Berkowitz, A.E.; Lahut, J.A.; Vanburen, C.E. Properties of magnetic fluid particles. *IEEE Trans. Magn.* **1980**, *16*, 184–190.
3. Massart, R. Preparation of aqueous magnetic liquids in alkaline and acidic media. *IEEE Trans. Magn.* **1981**, *MAG-17*, 1247–1248.
4. Sobon, C.A.; Bowen, H.K.; Broad, A.; Calvert, P.D. Precipitation of magnetic oxides in polymers. *J. Mater. Sci. Lett.* **1987**, *6*, 901–904.
5. Lee, J.-W.; Isobe, T.; Senna, M. Preparation of ultrafine Fe<sub>3</sub>O<sub>4</sub> particles by precipitation in the presence of PVA at high pH. *J. Colloid Interface Sci.* **1996**, *177*, 490–494.
6. Lee, J.-W.; Isobe, T.; Senna, M. Magnetic properties of ultrafine magnetite particles and their slurries prepared via in situ precipitation. *Colloids Surf., A Physicochem. Eng. Asp.* **1996**, *109*, 121–127.
7. Matsunaga, T.; Kamiya, S. Use of magnetic particles isolated from magnetotactic bacteria for enzyme immobilization. *Appl. Microbiol. Biotechnol.* **1987**, *26*, 328–332.
8. Shin, H.-C.; Oh, J.-H.; Lee, J.-C. Ultrasonically accelerated crystallization processing for the nano-size ferrite powder. *Phys. Status Solidi* **2002**, *189*, 735–739.
9. Pillai, V.; Kumar, P.; Shah, D.O. Magnetic properties of barium ferrite synthesized using a microemulsion mediated process. *J. Magn. Magn. Mater.* **1992**, *116*, L299–L304.
10. Yue, Z.; Zhou, J.I.; Li, L.Y.; Wang, X.H.; Gui, Z.L. Effect of copper on the electromagnetic properties of Mg–Zn–Cu ferrites prepared by sol-gel auto-combustion method. *Mater. Sci. Eng.* **2001**, *B86*, 64–69.
11. Yue, Z.; Zhou, J.I.; Wang, X.H.; Gui, Z.L.; Li, L.Y. Low-temperature sintered Mg–Zn–Cu ferrite prepared by auto-combustion of nitrate–citrate gel. *J. Mater. Sci. Lett.* **2001**, *20*, 1327–1329.
12. Tillotson, T.M.; Gash, A.E.; Simpson, R.L.; Hrubesh, L.W.; Satcger, J.H., Jr.; Poco, J.F. Nanostructured energetic materials using sol-gel methodologies. *J. Non-Cryst. Solids* **2001**, *285*, 338–345.
13. Yamaguchi, K.; Matsumoto, K.; Fujii, T. Magnetic anisotropy by ferromagnetic particles alignment in a magnetic field. *J. Appl. Phys.* **1990**, *67*, 4493–4495.
14. Yamashita, I. Fabrication of a two-dimensional array of nano-particles using ferritin molecule. *Thin Solid Films* **2001**, *393*, 12–18.
15. Shin, H.; Jeon, J.-U.; Pak, Y.E.; Im, H.; Kim, E.-S. Formation and characterization of crystalline iron oxide films on self-assembled organic monolayers and their in situ patterning. *J. Mater. Res.* **2001**, *16*, 564–569.
16. Sato, T.; Iijima, T.; Seki, M.; Inagaki, N. Magnetic properties of ultrafine ferrite particles. *J. Magn. Magn. Mater.* **1987**, *65*, 252–256.

17. Ichiyanagi, Y.; Uozumi, T.; Kimishima, Y. Magnetic properties of Fe<sub>2</sub>O<sub>3</sub> nanoparticles. *Trans. Mater. Res. Soc. Jpn.* **2001**, *26*, 1097–1100.
18. Mandal, K.; Mandal, S.P.; Agudo, P.; Pal, M. A study of nanocrystalline (Mn–Zn) ferrite in SiO<sub>2</sub> matrix. *Appl. Surf. Sci.* **2001**, *182*, 36–389.
19. Ganguly, B.; Huggins, F.E.; Feng, Z.; Huffman, G.P. Anomalous recoilless fraction of 30-Å-diameter FeOOH particles. *Phys. Rev., B* **1994**, *49*, 3036–3042.
20. Sepelak, V.; Rogachev, A.Yu.; Steinike, U.; Uecker, D.Ch.; Krumeich, F.; Wißmann, S.; Becker, K.D. The synthesis and structure of nanocrystalline spinel-ferrite produced by high-energy ball-milling method. *Mat. Sci. Forum* **1997**, 235–238, 139–144.
21. Sambucetti, C.J. Magnetic ink for jet printing. *IEEE Trans. Magn.* **1980**, *MAG-16*, 363–367.
22. Maruno, S.; Yubakami, K.; Soga, M. Plain paper recording process using magnetic fluids magneto-fluid-graphy. *J. Magn. Magn. Mater.* **1983**, *39*, 187–189.
23. Atarashi, T.; Imai, T.; Shimoizaka, J. On the preparation of the colored water-based magnetic fluids (Red, yellow, blue and black). *J. Magn. Magn. Mater.* **1990**, *85*, 3–6.
24. Einaga, Y.; Gu, Z.-Z.; Hayami, S.; Fujishima, A.; Sato, O. Reversible photoinduced switching of magnetic properties at room temperature of iron oxide particles in self-assembled films containing azobenzene. *Thin Solid Films* **2000**, *374*, 109–113.
25. Gütlich, P.; Hauser, A.; Spiering, H. Thermal and optical switching of iron(II) complexes. *Angew. Chem., Int. Ed. Engl.* **1994**, *33*, 2024–2054.
26. Hayami, S.; Gu, Z.-Z.; Shiro, M.; Einaga, Y.; Fujishima, A.; Sato, O. First observation of light-induced excited spin state trapping for an iron(III) complex. *J. Am. Chem. Soc.* **2000**, *122* (71), 7126–7127.

# Island Nucleation: Predictions

Maria C. Bartelt

Lawrence Livermore National Laboratory, Livermore, California, U.S.A.

## INTRODUCTION

Under a range of technologically interesting conditions, films of metals, certain oxides, and semiconductors grow or etch via two-dimensional island formation. Atomic-scale control of the resulting island distribution and final morphology of these films depends on a detailed understanding of these early stages of island formation. This, in turn, requires a precise treatment of the environment dependence of adatom or ad-vacancy capture by other adatoms or ad-vacancies and by growing islands. In particular, the evolution of the densities of islands of different sizes (i.e., of the island size distribution) reflects the form of the “capture numbers” and specifically their dependence on island size, which measures the propensity for islands of different sizes (in a variety of environments) to capture diffusing ad-species.<sup>[1–3]</sup> One current challenge is the formulation of both an analytic treatment of the observed form of the “capture numbers” and new simulation strategies for analysis of the asymptotic behavior of models of island formation, in the regime of large characteristic lengths, which is still expensive to simulate with conventional algorithms.

Traditional mean-field rate-equation treatments,<sup>[4]</sup> in which the typical environment of an island is assumed independent of its shape and size, fail to reproduce the form and scaling properties of the island size distributions observed in experimental and simulation studies.<sup>[5–10]</sup> This has been a half-century-old challenge. Recent simulation studies revealed not only the well-known spatial correlation of island positions associated with depletion of the population of nearby islands (as a result of competition by islands for diffusing ad-species),<sup>[11]</sup> which has been incorporated into mean-field approaches,<sup>[4]</sup> but also a more subtle correlation between the size and separation of islands, which is still missing and is hard to fold into traditional mean-field approaches. It is the latter correlation that controls the individual island growth rates and the island size dependence of the “capture numbers” and thus the selection of the shape of the island size distribution.

## OVERVIEW

Key to quantifying and elucidating the development of this island size-spatial correlation is a precise characterization of island nucleation,<sup>[8–10]</sup> especially when nucleation is irreversible. A basic observation is that when only a few islands exist, nucleation occurs quasi-deterministically, not surprisingly near the dominant maximum in the density of the diffusing ad-species. However, once a more complex landscape of islands develops, nucleation occurs more randomly, often near secondary maxima. Very importantly, these deviations from the dominant maxima allow for stronger correlations in the growth rates of neighboring islands.<sup>[10]</sup> They have not been characterized in detail in the literature.

Some of these basic features are best illustrated for a few-island system. A system of two-dimensional vacancy islands or pits, obtained by exposure of a Si(001) terrace to molecular oxygen,<sup>[7]</sup> is chosen below for this purpose. However, only results for larger simulation systems allow a statistically relevant characterization of the island nucleation process, i.e., the typical behavior and fluctuations. In particular, one is interested in assessing the generally expected tendency for islands to nucleate near the boundaries of a suitable tessellation of the surface (into so-called “capture areas or cells”) based on the island positions. This information is essential to guide the development of simpler, geometric-like, and computationally less-expensive models of island formation.<sup>[12]</sup>

The main goal of this work is then to provide exact predictions of island nucleation obtained from kinetic Monte Carlo (KMC) simulations of a realistic model of island formation during deposition or etching. The focus is entirely on the simplest case of irreversible two-dimensional island formation, via homogeneous nucleation, mediated by isotropic diffusion of ad-species. Work on the reversible case has just begun. Several quantities describing spatial features of the nucleation process are monitored in the simulations. The results show that they are generally characterized by broad probability distributions, implying a broad spread of environments for islands of each size. This feature underlies observed scaling properties.

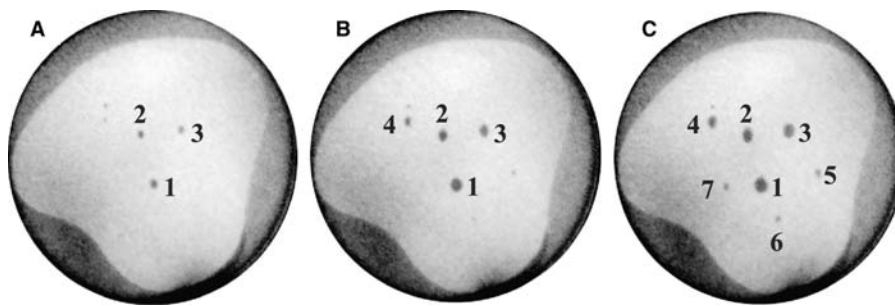


**Fig. 1** Dark-field LEEM images, a few seconds apart, recorded during the etching of a 10- $\mu\text{m}$ -wide terrace at 1235 K, in an oxygen pressure in the  $10^{-7}$  Torr range. Darker gray regions have lower height. The islands are labeled in the order in which they nucleated. *Source:* Courtesy of J.B. Hannon and G.L. Kellogg, Sandia National Laboratories, New Mexico.

## OUTLINE

The remainder of this work is organized as follows. The next section describes the experimental and simulation study of the system of a few islands formed irreversibly during the etching of a large Si(001) terrace at high temperatures and oxygen pressures. This example illustrates perfectly the failure of purely deterministic models of island formation to even qualitatively predict basic aspects of island nucleation, such as the sequence of nucleation events, the resulting spatial arrangement of the islands, and, ultimately, their individual growth rates. For quantitative predictions for irreversible island formation, a general model and simulations are then developed, which also serve to illustrate the unique power of simulations to address these nucleation issues. The goal is to describe in detail the exact nature of the non-equilibrium spatial correlations that develop during the nucleation process and thereby predict, using suitable measures, the expected impact of a nucleation event on the evolution of a large system of islands.

### A FIRST VIEW OF ISLAND NUCLEATION: ETCH PITS ON Si(100)

As mentioned above, a small system of islands can provide a direct view into basic aspects of the island nucleation process and motivate and guide specific studies on larger systems. In fact, the etching study described here is one of the existing few that have provided a real time, in situ view of island nucleation. The actual nucleation positions of the etch pits, recorded with low-energy electron microscopy (LEEM), were compared with predictions from solving the diffusion equation for the ad-vacancy species density, with appropriate boundary conditions, and from kinetic Monte Carlo (KMC) simulations. The solution of the diffusion equation was used to study simplified, deterministic rules of island formation, which fail to describe the exact behavior observed in the KMC simulations.

### Basic Experimental Observations

At elevated temperatures ( $>1000$  K), exposure of a clean Si(001) surface to molecular oxygen leads to

the production of volatile SiO and a net removal of Si from the surface. No oxide layer develops. On large, step-free surfaces, this active etching process begins with the nucleation of two-dimensional vacancy islands or pits, as illustrated in the sequence of LEEM images in Fig. 1. The LEEM images were formed using the (1/2,0) beam associated with one of the  $(2 \times 1)$  reconstruction domains of the Si(001) surface, resulting in contrast across adjacent terraces. Islands are the darker gray regions in Fig. 1. Under continued oxygen exposure, these islands grow, each at a rate that directly reflects the local distribution of neighboring islands.<sup>[7]</sup> Islands with large “capture areas” (like island no. 3 in Fig. 1) grow much faster than those with many close neighbors, indicative of a diffusion-mediated island formation process. The observed island growth rates have been reproduced quantitatively<sup>[7,13]</sup> in simulations of a model that assumes irreversible incorporation of ad-vacancies at the edge of near-elliptical islands and at the terrace outer step. The model has no free parameters because the ad-vacancy diffusion coefficient and (weak) anisotropy have been estimated from experimental data<sup>[14]</sup> and from first-principles calculations,<sup>[15]</sup> and an estimate of the vacancy flux was obtained from a combination of etching experiments.<sup>[7]</sup>

### Purely Deterministic vs. Stochastic Rules for Nucleation

The issue of the island nucleation positions was not addressed in the work mentioned above. Fig. 2 shows clearly that a purely deterministic rule for nucleation, by which islands nucleate at the instantaneous global maximum of the ad-vacancy species density, produces a different “time” sequence of nucleation events and a different final island spatial configuration (reflecting the near sixfold symmetry of the terrace) than experiment.<sup>[16]</sup> The maxima were obtained by solving the steady-state diffusion equation,  $D\nabla^2 n + F = 0$ , with absorbing boundary conditions ( $n = 0$ ) at the edges of previously nucleated islands and at the outer terrace step. Here  $D$  is the diffusion coefficient of the ad-vacancy species,  $n$  is the ad-vacancy species density,



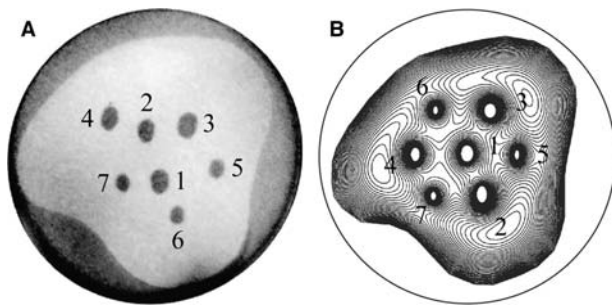


**Fig. 2** Comparison between (A) the actual island nucleation positions observed with LEEM and (B) the predictions of a purely deterministic nucleation rule based on the location of the instantaneous global maximum of the ad-vacancy species density.

and  $F$  is the net flux (chosen as estimated from experiment<sup>[7]</sup>). Even if the actual positions of previously nucleated islands are assumed, deviations in the location of the next nucleation event from the instantaneous global maximum, toward a secondary maximum, are typical (Fig. 3). Kinetic Monte Carlo simulations confirm that, indeed, nucleation is a stochastic process. In Fig. 4, island nucleation positions were marked for several millions of nucleation events obtained during irreversible island formation (consistent with the model that matched the island growth rates at a lower oxygen pressure or lower flux.<sup>[7,13]</sup>) The nucleation conditions and initial island configurations are the same as for Fig. 3 (except that the steady-state condition was not assumed a priori). These simulation results show a considerable spread in the regions of significant nucleation probability, well beyond the neighborhood of the global and secondary maxima.

### Pit Positions Relative to Diffusion Cell Boundaries

Finally, it is interesting to compare the actual island nucleation positions for the Si(001) system with the

location of the boundaries of a tessellation of the terrace based on the numerical solution of the steady-state diffusion equation for the ad-vacancy species density. The net flux of diffusing ad-vacancies is zero across the boundaries of the tessellation cells (“diffusion cells” or DCs). Inside each DC associated with an island, the lines of flux converge to that island. It is thus easy to show that the free area inside a DC is exactly proportional to the rate of diffusion-mediated ad-vacancy capture by the associated island.<sup>[5,6]</sup> For this small system of islands, the nucleation positions appear all near the DC boundaries (Fig. 5). However, for larger, statistically more relevant systems of islands, the results are more complex. In fact, the probability of island nucleation is non-zero and fairly high in wide regions around the DC boundaries, extending well inside the cells. This feature is revisited below.

## GENERAL BEHAVIOR OF MODELS OF IRREVERSIBLE ISLAND FORMATION

### Basic Model Prescription

During irreversible island formation on a single-crystal surface, represented by a regular array of adsorption sites, ad-species are created randomly at rate  $F$  per adsorption site, they hop between adjacent sites at total rate  $h$ , irreversibly nucleate new islands upon meeting, and irreversibly incorporate into existing islands upon aggregation. Compact, near-equilibrium island shapes are chosen whenever island-shape restructuring upon capture of ad-species by islands is efficient on the timescale of aggregation. To describe behavior at very low coverages, when islands cover only a small fraction of the surface, one can consider simpler “point-island” models,<sup>[17]</sup> in which islands occupy a single site, but carry a label indicating their size. Point-island models are especially useful to separate correlations that develop during the island formation process from

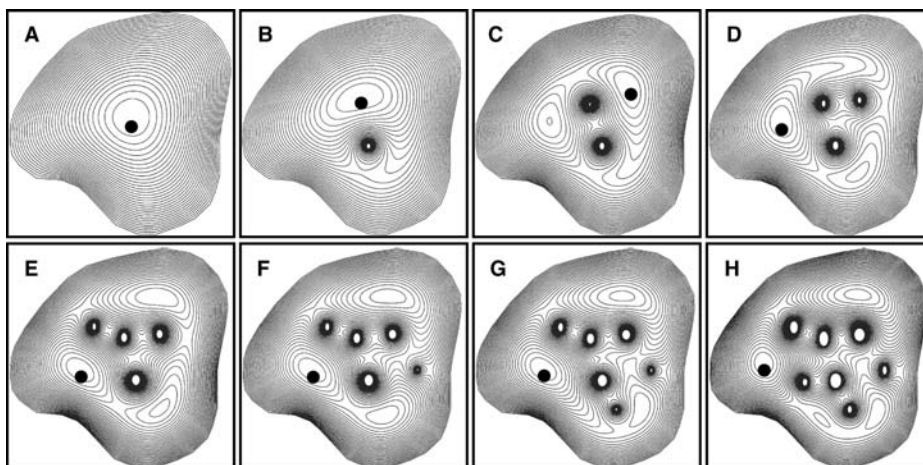


**Fig. 3** Contours of the ad-vacancy species density from the numerical solution of the steady-state diffusion equation with absorbing boundary conditions at island and step edges, for each partial set of islands observed in the experimental sequence of Fig. 1. The position of the instantaneous global maximum is marked with a dot. Only the 1st, 2nd, and 3rd islands nucleate near the global maximum.

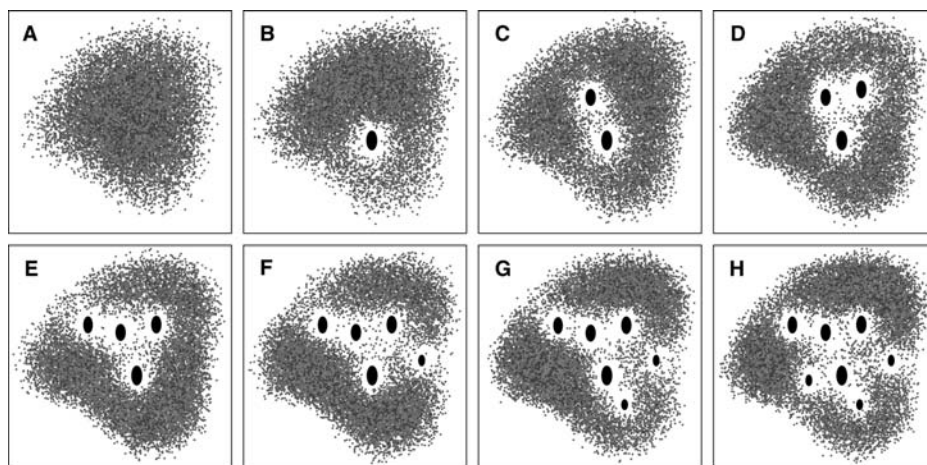


**Fig. 4** Simulation results for the spatial distribution of nucleation events during the etching of the Si(001) terrace of Fig. 1. Each dot marks the location of a nucleation event for the partial island configuration shown in each panel. The color of the dots is chosen according to the probability for nucleation, which increases from red to blue to green to yellow.

other subtle effects because of the island finite extent. Fig. 6 compares island configurations for point- and near-square islands. Measured two-point correlation functions for the positions of the island centers show similar results for the two models at submonolayer coverages. The basic shape of the island size distribution is also similar.

### Basic Algorithm for Simulation

To characterize the general behavior of the model, an  $L \times L$  square lattice (typically with  $L > 1000$ ) is used, with periodic boundary conditions. Ratios  $h/F$  typical for many systems are larger than  $10^7$ , requiring for efficiency that one keep a compact list of the positions of all hopping ad-species. With probabilities

proportional to total rates, one randomly chooses between creation (total rate  $L^2F$ ) and hopping (total rate  $h$  times the number of hopping ad-species). For the former, one randomly chooses a site. For the latter, one randomly chooses an entry from the list, which is updated after each hopping, creation, or aggregation event.

### Analyses

For understanding various spatial features of island nucleation and the detailed shape of the island size distribution, a central concept already introduced above is that of “capture zones” (CZs) associated with each island. Because construction of “exact” CZs based on the solution of the diffusion equation for the ad-species density is non-trivial and computationally

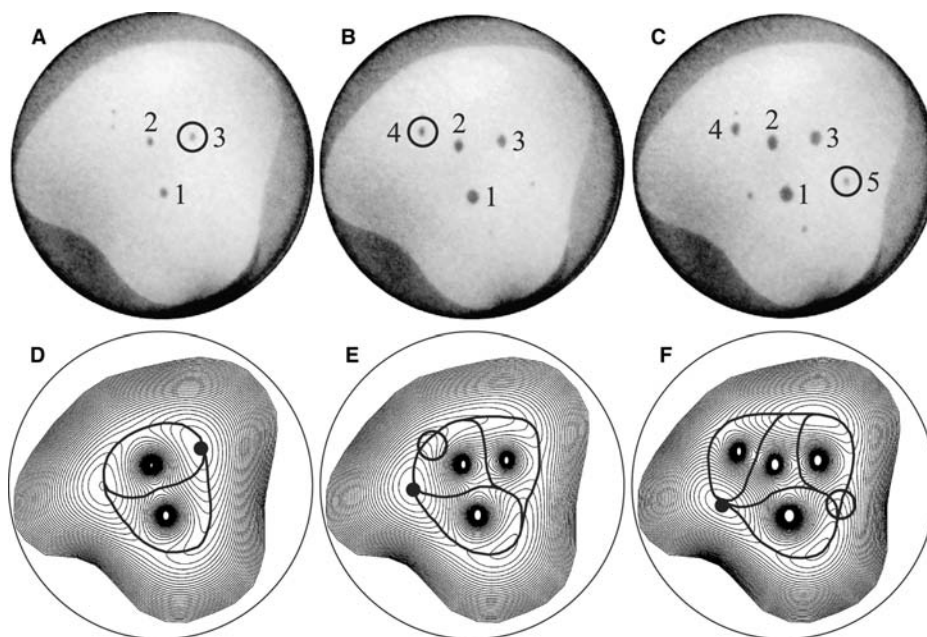


**Fig. 5** Comparison between (A)–(C) the actual nucleation position of the 3rd, 4th, and 5th island and (D)–(F) the location of the DC boundaries for the configuration of islands that exist prior to nucleation. As in Fig. 3, the dot in each panel marks the location of the global maximum of the ad-vacancy species density.

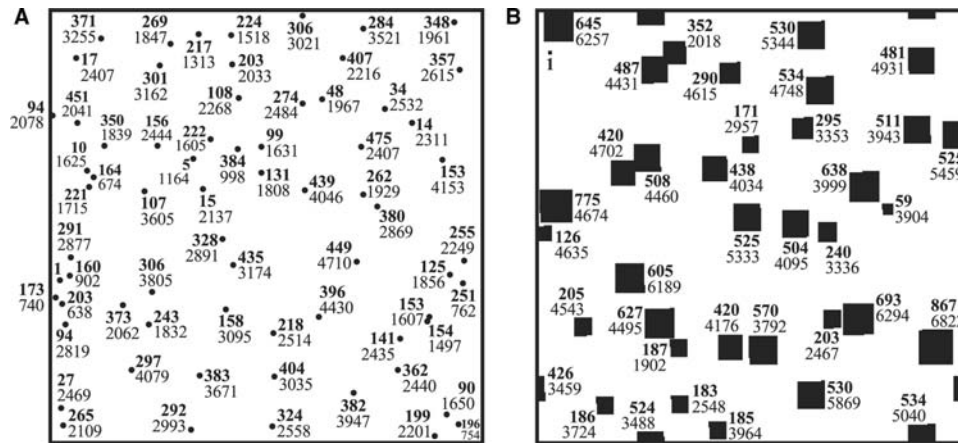


**Fig. 6** Simulation snapshots ( $400 \times 400$  sites) of typical configurations of (A) point-islands ( $s_{av} = 255$ ,  $A_{av} = 2550$ ) and (B) near-square islands ( $s_{av} = 459$ ,  $A_{av} = 4590$ ), for  $h/F = 10^{10}$ ,  $\theta = 0.1$  ML. The labels are the island size (in bold, in units of atoms) and the area of the EC of the island (in units of sites), which includes the island “footprint.”

expensive, it is convenient (and often a reasonable approximation) to construct CZs based on geometric tessellations of the surface that reflect the island spatial arrangement. The simplest possibility is to use Voronoi cells (VCs), which are based on the distance between the island centers. Sites within a VC are closer to the center of the associated island than to that of any other island. A more realistic alternative for islands of finite extent is to use “edge cells” (ECs), which are based on the distance to the island edges.<sup>[6]</sup> The tessellations of VCs and ECs coincide for point-islands.

In the simulations, one can readily monitor several quantities of interest. In particular, from  $N_{s,A}$ , the density of islands of size  $s$  and CZ area  $A$  ( $s$  and  $A$  measured in lattice sites), one gets 1) the density,  $N_s = \sum_A N_{s,A}$ , of islands of size  $s$  (averaged over CZ areas), 2) the density,  $N_A = \sum_s N_{s,A}$ , of islands of CZ area  $A$ , 3) the average island density  $N_{av} = \sum_{s>1} N_s$ , 4) the average CZ area for islands of size  $s$ ,  $A_s = \sum_A A N_{s,A} / N_s$ , 5) the average CZ area for all islands (note that the partition fills the surface),  $A_{av} = \sum_{s>1} A_s N_s / N_{av} = 1 / N_{av}$ , 6) the coverage (or fraction of the surface covered by islands and diffusing ad-species),  $\theta = Ft = \sum_{s>1} s N_s$ , where  $t$  is the duration time of deposition or etching, and 7) the average island size,  $s_{av} = \sum_{s>1} s N_s / N_{av} = (\theta - N_1) / N_{av}$ . In the scaling regime of large  $s_{av} \approx \theta / N_{av}$  and  $N_1 \ll N_{av}$ , one introduces continuous scaled variables  $x = s / s_{av}$  and  $\alpha = A / A_{av}$  and defines scaling functions  $H(x, \alpha)$ ,  $f(x)$ , and  $g(\alpha)$  such that

$$\begin{aligned} N_{s,A} &\approx N_{av} (s_{av} A_{av})^{-1} H(x, \alpha), \\ N_s &\approx N_{av} (s_{av})^{-1} f(x), \text{ and} \\ N_A &\approx N_{av} (A_{av})^{-1} g(\alpha) \end{aligned} \quad (1)$$

with

$$\begin{aligned} f(x) &= \int_{0 \leq x \leq \infty} d\alpha H(x, \alpha), \\ g(\alpha) &= \int_{0 \leq x \leq \infty} dx H(x, \alpha), \text{ and } \int_{0 \leq x \leq \infty} dx \\ &\quad \times \int_{0 \leq \alpha \leq \infty} d\alpha H(x, \alpha) x^i \alpha^j = 1 \end{aligned} \quad (2)$$

for  $i$  or  $j = 0$  or  $1$

As indicated above, the focus here is on quantities that characterize basic aspects of the island nucleation process, motivated by the realization that they influence the selection of the shape of the scaling functions  $H$ ,  $f$ , and  $g$ .<sup>[2,8–10]</sup> Such quantities include the distribution of CZ areas for just-nucleated islands, the distribution of the number of existing islands whose CZ’s are reduced by each nucleation event, the fraction of area that each contributes to the CZ of a just-nucleated island, and some measure of the tendency for nucleation to occur near the boundaries of the CZs. Whenever significant, behavior for point-islands is compared with that of near-square islands.

## CHARACTERIZATION OF THE ISLAND NUCLEATION PROCESS

### The Nucleation Rate

In the initial stages of irreversible island formation, on an initially empty substrate, one expects a transient regime where the ad-species concentration increases linearly with time, in proportion to the flux,  $F$ , followed by a steady-state regime where gain of

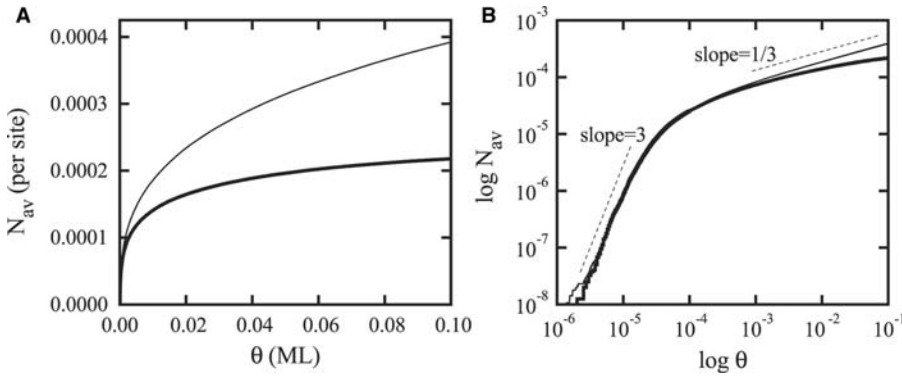


**Fig. 7** Simulation results for the evolution of the average island density,  $N_{av}$ , for point-islands (thin solid line) and near-square islands (thick solid line), for  $h/F = 10^{10}$ ,  $\theta \leq 0.1$  ML. Statistics were obtained for nearly 200,000 point-islands and 100,000 near-square islands.

ad-species is roughly balanced by loss as a result of aggregation with existing islands. For small  $\theta$ , one can write simple rate equations for the diffusing ad-species density,  $N_1$ , and for  $N_{av}$ , that can capture this behavior. Keeping only the dominant terms (for large  $h/F$ ), one has for isotropic diffusion

where  $\sigma_1$  and  $\sigma_{av} = \sum_{s>1} \sigma_s N_s / (\sum_{s>1} N_s)$  measure the propensity for diffusing ad-species to be captured by other diffusing ad-species or by islands, respectively. Logarithmic corrections are discussed in Ref.<sup>[17]</sup>. It follows that

$$\begin{aligned} dN_1/dt &\sim F - \sigma_{av} h N_1 N_{av} \text{ and } dN_{av}/dt \\ &\sim \sigma_1 h (N_1)^2 \end{aligned} \quad (3)$$

$$N_1 \sim \theta \text{ and } N_{av} \sim (h/F) \int d\theta \sigma_1 \theta^2 \quad (4)$$

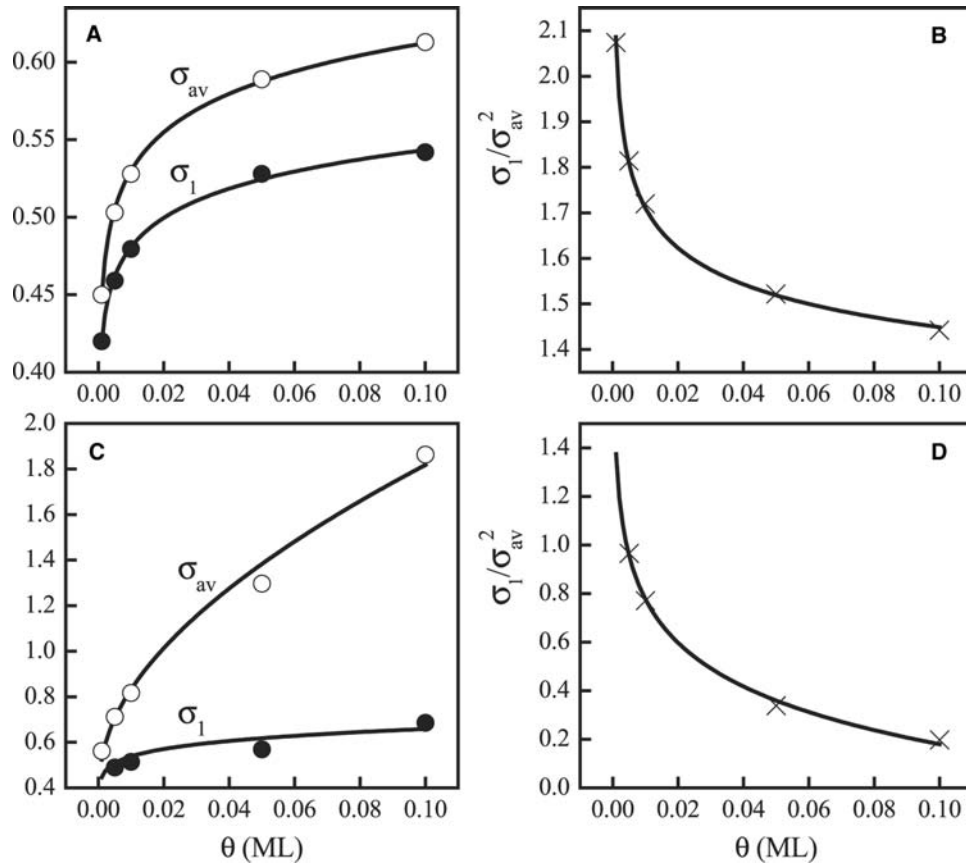


**Fig. 8** Simulation results for the dependence of  $\sigma_1$  (solid circles) and  $\sigma_{av}$  (open circles) on  $\theta$  for (A) point-islands and (C) near-square islands, for  $h/F = 10^8$ ,  $0.001$  ML  $\leq \theta \leq 0.1$  ML. In (A), the lines are the fits  $\sigma_1 = 0.606 + 0.0272\ln(\theta)$  and  $\sigma_{av} = 0.695 + 0.0358\ln(\theta)$ . The fits in (C) are not as simple. Simulation data (symbols) for the fraction  $\sigma_1/\sigma_{av}^2$  are shown in (B) for point-islands and in (D) for near-square islands. Nearly perfect fits (lines) are obtained with  $\sigma_1/\sigma_{av}^2 = 1.11 - 0.136\ln(\theta)$  in (B) and  $\sigma_1/\sigma_{av}^2 = -0.417 - 0.259\ln(\theta)$  in (D). In (D), but not in (B), the logarithmic term dominates in the range of  $\theta$  considered.



in the transient regime, where  $\theta \ll \theta^* \sim (h/F)^{-1/2}$ ,<sup>[17]</sup> and

$$N_1 \sim F/(\sigma_{av}hN_{av}) \text{ and} \\ N_{av} \sim (h/F)^{-1/3} \left( \int d\theta \sigma_1/\sigma_{av}^2 \right)^{1/3} \quad (5)$$

in the steady-state regime ( $dN_1/dt \sim 0$ ), where  $\theta \gg \theta^*$ . Simulation data for point-islands shown in Fig. 7 are consistent with  $\sigma_1$  and  $\sigma_1/\sigma_{av}^2$  weakly dependent on  $\theta$ . In fact, simulation data shown in Fig. 8 suggest the relation  $\sigma_1/\sigma_{av}^2 \approx 0.606/0.695^2 \approx 1.25$ , for not too small  $\theta \geq 0.01$ . For sufficiently large  $h/F$  values, one also finds from the simulation data that

$$N_{av} \sim (h/F)\theta^3 \quad (6)$$

in the transient regime and

$$N_1 \sim (h/F)^{-2/3}\theta^{-1/3} \text{ and } N_{av} \sim (h/F)^{-1/3}\theta^{1/3} \quad (7)$$

in the steady-state regime, again consistent with  $\sigma_1$  and  $\sigma_1/\sigma_{av}^2$  weakly dependent on  $\theta$ . At fixed  $\theta$ , Eqs. (6) and (7) give also the  $h/F$  dependence of the densities for finite-extent, compact islands (near-square islands are used here). However, the steady-state  $\theta$  dependence (at fixed  $h/F$ ) is significantly modified from point-island

scaling, even for small  $\theta \ll 1$ . For example, for  $h/F = 10^{10}$ , the deviation between point-island and near-square island behavior, i.e., the difference in the actual values of  $N_{av}$  in Fig. 7(A) and in the scaling with  $\theta$  in Fig. 7B, is significant already for coverages on the order of  $10^{-3}$  ML. These differences reflect stronger  $\theta$  dependence (in the form of logarithmic corrections) of  $\sigma_1/\sigma_{av}^2$  for near-square than for point-islands. This is because of more efficient capture of random walkers by finite-extent islands than by point-islands. More details are shown in Fig. 8. For near-square islands, one finds  $\sigma_1/\sigma_{av}^2 \propto -\ln(\theta)$ , in the range of  $\theta$  considered here, so, from Eq. (5), one gets  $N_{av} \propto \theta^{1/3} [-\ln(\theta)]^{1/3}$ , the  $\ln(\theta)$  factor producing the observed saturation of  $N_{av}$  with  $\theta$  shown in Fig. 7. If one assumes the form  $N_{av} = \gamma(h/F)^{-\chi}$ , at each fixed  $\theta$ , then one finds for the effective exponent  $\chi$  and prefactor  $\gamma$  the values  $\chi = 0.24, 0.29, 0.30, 0.31$ , and  $0.31$  and  $\gamma = 0.022, 0.12, 0.19, 0.38$ , and  $0.49$  (consistent with the relation  $\gamma \approx 1.08\theta^{1/3}$ ; Fig. 8) for point-islands and  $\chi = 0.26, 0.31, 0.32, 0.33$ , and  $0.33$  and  $\gamma = 0.028, 0.15, 0.23, 0.42$ , and  $0.49$  for near-square islands, at fixed  $\theta = 0.001, 0.005, 0.01, 0.05$ , and  $0.1$  ML, respectively, for  $10^8 \leq h/F \leq 10^{10}$ .

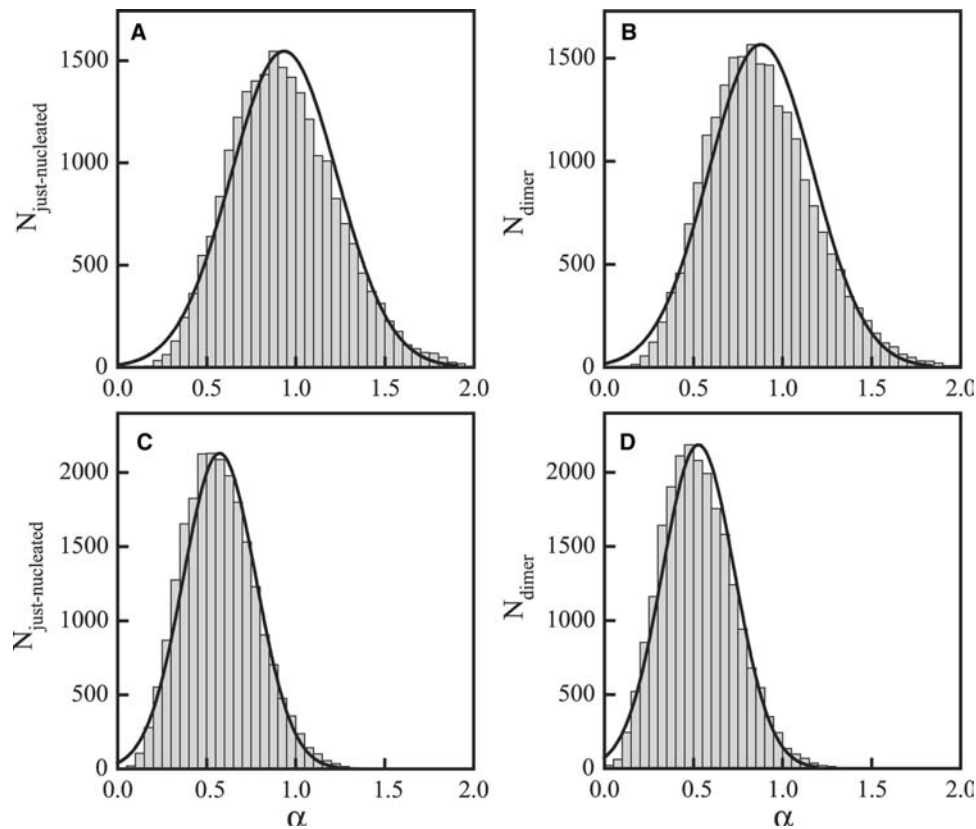


**Fig. 9** Scaled area distributions ( $\alpha = A/A_{av}$ ) for (A)–(B) VCs of point-islands ( $A_{av} = 612.7$  sites) and (C)–(D) ECs of near-square islands ( $A_{av} = 979.4$  sites) of size  $s = 2$ , obtained with  $h/F = 10^8$ ,  $\theta = 0.1$  ML. In (A) and (C), data are for just-nucleated dimers only, and in (B) and (D), data are for all dimers. The average dimer areas are  $A_{\text{just-nucleated}} \approx 0.93A_{av}$  ( $0.57A_{av}$ ) and  $A_2 \approx 0.88A_{av}$  ( $0.53A_{av}$ ) for point-islands (near-square islands). The distributions are slightly skewed relative to a Gaussian (line fits).

**Table 1** Statistical properties of the area distributions for VCs of point-islands (PI) and ECs of near-square islands (NSI) of size  $s = 2$  (just-nucleated dimers and all dimers) at  $\theta = 0.1$  ml

System	$h/F$	$A_{\text{just-nucleated}}$	$A_2$	$\nu_{\text{just-nucleated}}$	$\nu_2$	$\kappa_{\text{just-nucleated}}$	$\kappa_2$
PI	$10^7$	284.7	268.3	88.6	87.7	0.40	0.45
	$10^8$	572.7	537.5	182.8	179.2	0.42	0.45
	$10^9$	1165.0	1098.1	381.3	374.2	0.42	0.45
NSI	$10^7$	268.7	251.8	93.9	94.8	0.39	0.40
	$10^8$	560.6	515.9	198.7	199.5	0.37	0.43
	$10^9$	1125.0	1076.1	455.5	427.8	0.40	0.42

The  $A$ 's denote the average area, the  $\nu$ 's denote the standard deviation, and the  $\kappa$ 's denote the skewness. Average areas for all islands are  $A_{\text{av}} = 307.0, 612.7,$  and  $1243.9$  for point-islands, and  $A_{\text{av}} = 461.9, 979.4,$  and  $2110.0$  for  $h/F = 10^7, 10^8,$  and  $10^9,$  respectively. Areas and standard deviations are in units of surface sites. The skewness is dimensionless.

Finally, for both point-islands and near-square islands, note that the island density  $N_{\text{av}} \sim (h/F)^{-1/2}$  at the onset of the steady-state regime,  $\theta \sim \theta^*$ , is well below the steady-state value of  $N_{\text{av}} \sim (h/F)^{-1/3}$ . Thus most nucleation occurs in the steady-state regime, in which the next sections focus.

### Distribution of Capture Zone Areas of Just-Nucleated Islands

Once a nucleation event occurs, the distribution of CZs (and the growth rates) of the islands neighboring the nucleation site is modified. The typical area assigned to the new island is an essential quantity in rate-equation formulations of the evolution of the CZ area distribution during island formation.<sup>[2,8,9,18]</sup> Typical distributions of CZ areas for a new island, for tessellations of ECs, are shown in Fig. 9, for a selected set of simulation parameters. It is interesting to compare these distributions with those of the CZ areas for all dimers. First, note that the average CZ area of a dimer must be strictly smaller than the average CZ area of a just-nucleated dimer (and both of these smaller than the average CZ area for all islands) because areas of just-nucleated dimers can only decrease with continued island nucleation. However, the basic statistical properties of the two distributions, including the area fluctuations, are similar

(Fig. 9 and Table 1). Second, there is a noticeable difference for point-islands and near-square islands in the average CZ areas of dimers or just-nucleated islands relative to the total average CZ area (for all islands). For near-square islands, the ratio is smaller than 0.6 (and only slightly higher, if taking the ratio to the average free area, defined as  $A_{\text{av}} - s_{\text{av}}$ , instead) compared with 0.9 for point-islands. Finally, for contrast, Fig. 10 shows the CZ area distribution for all islands. Note that the (normalized) envelope of this distribution is the function  $g(\alpha)$ .

### The Impact of Nucleation on the Capture Zones of Existing Islands

Some of the natural measures of the impact of nucleation on a configuration of islands, and in particular on its CZ area distribution, are 1) the probability that the CZ of a given island will be overlapped (and thus reduced) by the CZ of the just-nucleated island, 2) the typical number of such overlapped islands, per nucleation event, sorted by island size or CZ area, and 3) the typical fraction of the area that each overlapped island contributes to the CZ area of the just-nucleated island (see the schematic in Fig. 11). Simulation results for each of these measures are presented below.

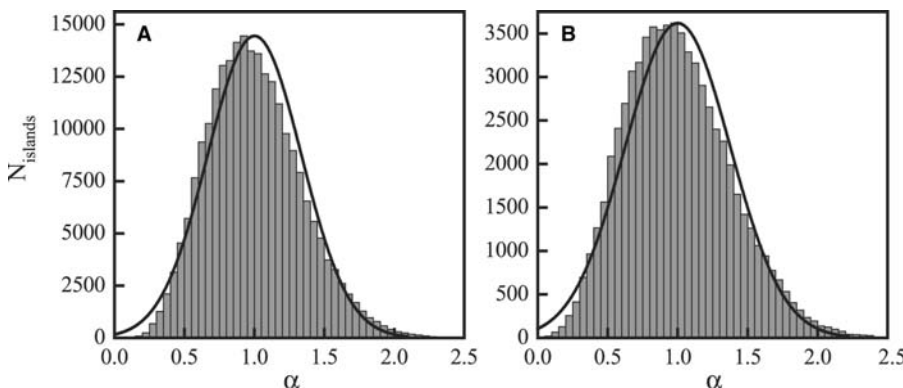


**Fig. 10** Scaled area distributions ( $\alpha = A/A_{\text{av}}$ ) for (A) VCs of point-islands and (B) ECs of near-square islands of all sizes ( $h/F = 10^8,$   $\theta = 0.1$  ML). The lines are Gaussian fits. The standard deviation and skewness of the data are  $\nu \approx 0.33A_{\text{av}}, \kappa \approx 0.46$  for point-islands, and  $\nu \approx 0.38A_{\text{av}}, \kappa \approx 0.46$  for near-square islands. The skewness for a random Voronoi tessellation in two dimensions is significantly higher ( $\approx 0.66$ ). Source: From Ref.<sup>[19]</sup>.



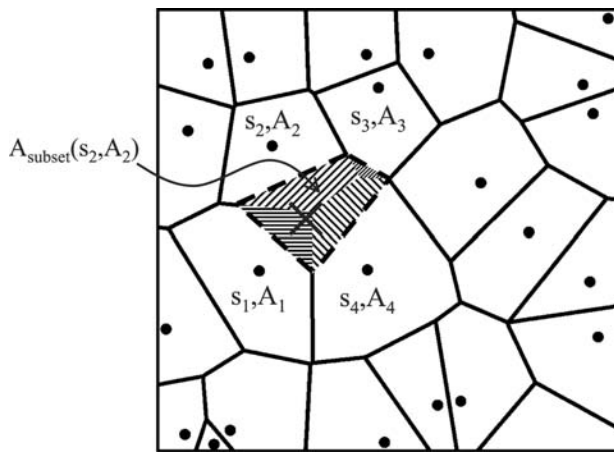


**Fig. 11** Schematic showing the rearrangement of VC boundaries for a point-island distribution ( $h/F = 10^{10}$ ,  $\theta = 0.001$  ML) following a  $M_0 = 4$  nucleation event. The new island is marked with a  $\times$ , and existing islands are marked with dots. The shifted boundaries (dashed lines) enclose the CZ of the new island. Little or no rearrangement occurs for cells beyond the nearest neighbors of the new island. The four area portions contributed to the cell of the new island are highlighted with a pattern.

These three measures are not independent. If  $P_{s,A}$  denotes the probability that a nucleation event reduces the CZ of area  $A$  belonging to an island of size  $s$  and  $\langle M_0 \rangle$  denotes the average number of existing CZs overlapped by the CZ of a just-nucleated island, then one has the normalization condition

$$\sum_s \sum_A P_{s,A} = \langle M_0 \rangle \tag{8}$$

In addition, if  $A_{\text{subset}}(s,A)$  denotes the average area of the portion of the CZ of the just-nucleated island that overlaps the existing CZ of area  $A$  belonging to an

island of size  $s$  and  $\langle A_{\text{subset}} \rangle$  denotes the average area of such individual portions, then one also has the constraint

$$\begin{aligned} \sum_s \sum_A A_{\text{subset}}(s,A) P_{s,A} &= \langle A_{\text{subset}} \rangle \langle M_0 \rangle \\ &= A_{\text{just-nucleated}} \end{aligned} \tag{9}$$

where  $A_{\text{just-nucleated}}$  is the average area of a just-nucleated island (Fig. 9 and Table 1).

The probability that a nucleation event reduces the capture zone of an existing island

Although the probability  $P_{s,A}$  that a nucleation event impacts (i.e., reduces) a CZ of area  $A$  belonging to an island of size  $s$  includes contributions from nucleation events occurring inside that area- $A$  cell and inside neighboring cells, generally of different area, one anticipates that  $P_{s,A}$  scales directly with the fraction of islands of size  $s$  and CZ area  $A$ ,  $N_{s,A}/N_{\text{av}}$ . One can then write

$$P_{s,A} \approx (N_{s,A}/N_{\text{av}})q(s,A) \tag{10}$$

where the scaling factor  $q(s,A)$  reflects the actual propensity for overlap. The simulation data shown in Fig. 12 for the reduced probabilities  $P_s = \sum_A P_{s,A}$  that a nucleation event impacts the CZ of some island of size  $s$  and  $P_A = \sum_s P_{s,A}$  that a nucleation event reduces the CZ of some island of CZ area  $A$  indeed have a shape similar to  $N_s$  and  $N_A$ , respectively. If the above factorization holds, this behavior of the reduced probabilities implies that the factor  $q(s,A)$  is a weak function of both  $s$  and  $A$ , in the range where  $N_{s,A}$  is significant. In fact,  $q(s,A)$  is probably a stronger function of  $A$  than of  $s$  because the likelihood of overlap should depend primarily on the area  $A$ .<sup>[9]</sup>

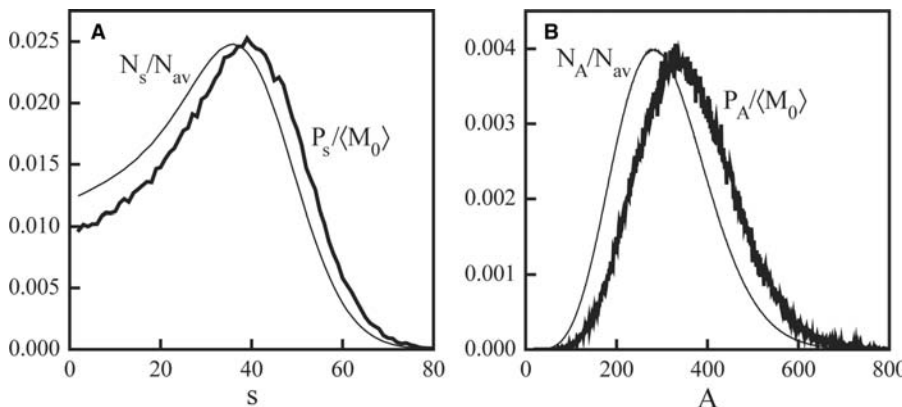


**Fig. 12** Simulation results for (A)  $P_s$  and (B)  $P_A$ . Data are for point-islands,  $h/F = 10^7$ ,  $\theta = 0.1$  ML ( $A_{\text{av}} \approx 307$ ,  $s_{\text{av}} \approx 30.7$ ). The thinner lines are the average density of islands of size  $s$ , in (A), and the average density of islands of CZ area  $A$ , in (B). The data were normalized so that the area under all the curves is unity.

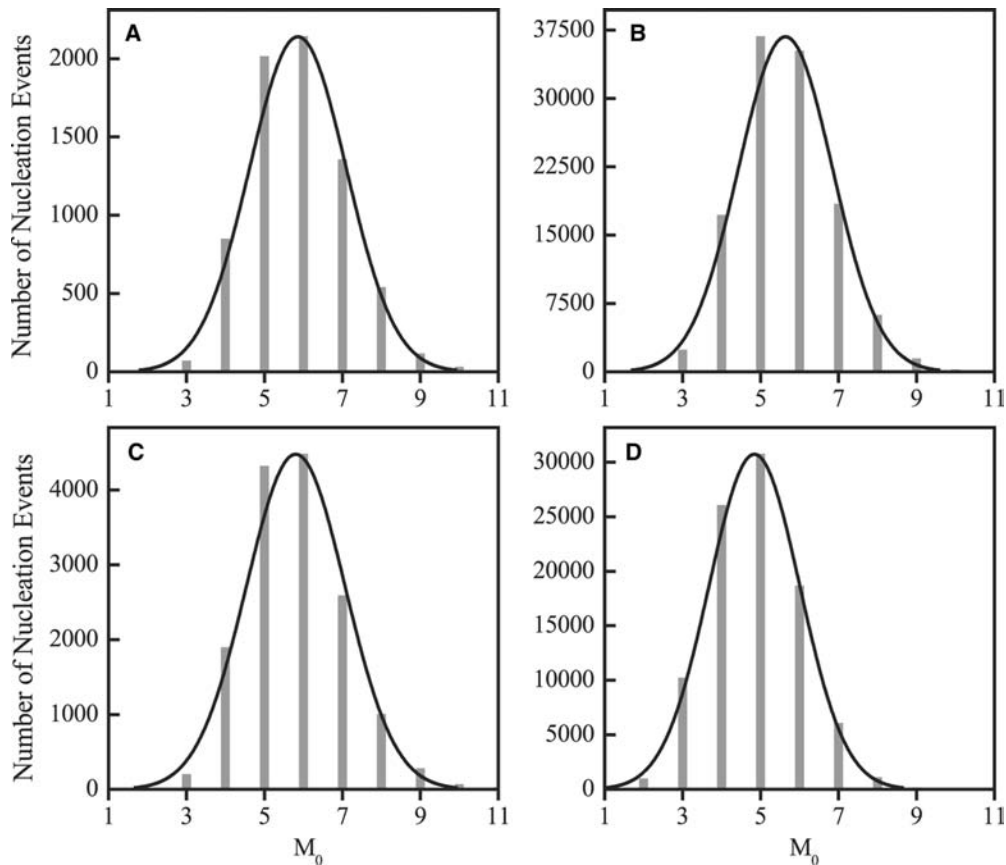


**Fig. 13** The distribution of  $M_0$  values for (A)–(B) point-islands and (C)–(D) near-square islands, for  $h/F = 10^8$ . In (A) and (C),  $\theta = 10^{-3}$  ML; in (B) and (D),  $\theta = 0.1$  ML. The lines are Gaussian fits. The average,  $\langle M_0 \rangle$ , and the standard deviation,  $\nu_{M_0}$ , are (A)  $\langle M_0 \rangle = 5.9$ ,  $\nu_{M_0} = 1.2$ , (B)  $\langle M_0 \rangle = 5.6$ ,  $\nu_{M_0} = 1.2$ , (C)  $\langle M_0 \rangle = 5.8$ ,  $\nu_{M_0} = 1.3$ , (D)  $\langle M_0 \rangle = 4.8$ ,  $\nu_{M_0} = 1.2$ . Statistics were obtained for 10,000–100,000 nucleation events.

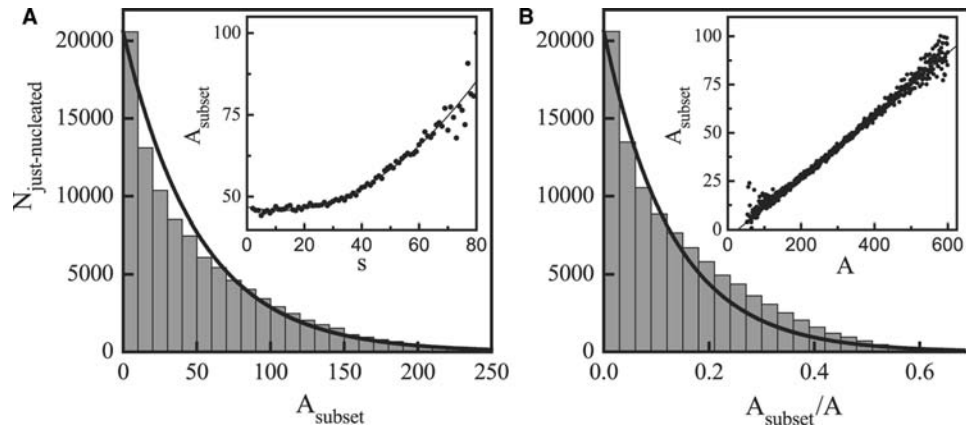


**Fig. 14** Simulation data for  $A_{\text{subset}}$ ; in (A), scaled by the total area,  $A$ , of the overlapped CZs, in (B). Data are for 100,000 point-island nucleation events, with  $h/F = 10^7$ ,  $\theta = 0.1$  ML ( $A_{\text{av}} \approx 307$ ,  $s_{\text{av}} \approx 30.7$ ):  $\langle A_{\text{subset}} \rangle \approx 52$ ,  $\nu_{\text{subset}} \approx 51$ ,  $\kappa_{\text{subset}} \approx 1.5$ ,  $\langle A_{\text{subset}}/A \rangle \approx 0.14$ ,  $\nu_{\text{subset}/A} \approx 0.13$ ,  $\kappa_{\text{subset}/A} \approx 1.1$ . The lines are fits with an exponential distribution. The insets show  $A_{\text{subset}}(s)$ , averaged over  $A$ , in (A), and  $A_{\text{subset}}(A)$ , averaged over  $s$ , in (B). Here, statistics were obtained from nearly 500,000 nucleation events. The lines in the insets are guides to the eye only.

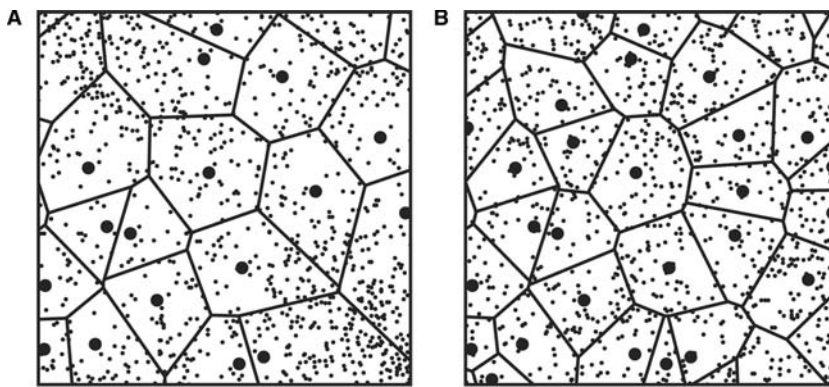


**Fig. 15** One thousand nucleation events (small dots) for a fixed configuration of point-islands (large dots) obtained at (A) 0.001 ML ( $s_{av} = 12.0$ ) and (B) 0.01 ML ( $s_{av} = 53.8$ ), for  $h/F = 10^{10}$ . The tessellation of VCs is also shown. The average VC area is (A) 12,100 and (B) 5375 lattice sites. Both panels are a  $380 \times 380$  site zoom of a larger simulation lattice.

### The distribution of $M_0$ values

Fig. 13 shows distributions of  $M_0$  values for two distinct coverages, one near the onset of the steady state, where point-islands and near-square islands behave similarly, and the other within the steady state. In either case, note that no nucleation events with  $M_0 = 1$  were recorded in the simulations; that is, the CZ of a just-nucleated island never overlapped just one existing CZ. Thus despite the dramatic simplification of theory that this scenario brings,<sup>[2,8]</sup> such an assumption is not well justified. Other features are interesting to note. With increasing coverage, there is a large shift in the distribution for near-square islands toward smaller  $M_0$ . For example, far fewer nucleation events with  $M_0 \geq 7$  and many more events with  $M_0 = 3$  occur at 0.1 ML than at  $10^{-3}$  ML. Such shift would be consistent with an increasing preference to nucleate closer to triple points (assuming the average number of neighboring cells of a CZ, which is about 6,<sup>[13]</sup> and other topological properties of the tessellation do not change significantly with increasing coverage).

### The portions, $A_{\text{subset}}$ , of existing capture zone areas overlapped by the capture zone of a New Island

The distribution of  $A_{\text{subset}}$  values, distinguished by size and area ( $A$ ) of the overlapped CZs, is well described by an exponential distribution, as shown in Fig. 14. (Note that for an exponential distribution, the mean and variance are equal, and the skewness is equal to 2.) It exhibits a significant population at small area portions and exponentially small populations for  $A_{\text{subset}}$  above  $A_{av}$ . In fact,  $A_{\text{subset}}$  is, on average, only  $0.14A$  and only  $0.17A_{av}$ . However, it does follow, as anticipated, that  $A_{\text{subset}}(s,A)$  is mainly determined by  $A$  (that is, it is a weaker function of  $s$ ) (see the insets in Fig. 14 and Ref.<sup>[9]</sup> for more details). Note that the relation  $A_{\text{just-nucleated}} = \langle A_{\text{subset}} \rangle \langle M_0 \rangle$  holds, e.g., for  $h/F = 10^7$ ,  $\theta = 0.1$  ML, one finds  $A_{\text{just-nucleated}} \approx 285$  (Table 1),  $\langle A_{\text{subset}} \rangle \approx 52$  (Fig. 14), and  $\langle M_0 \rangle \approx 5.5$  (Ref.<sup>[9]</sup>).

### The Island Nucleation Positions

A natural expectation is that most nucleation events that occur in the steady-state regime must occur near the boundaries of CZs where the diffusing ad-species density (and thus the nucleation rate) is relatively high. (Some caution is justified when using geometric tessellations, as these do not exactly reflect the spatial profile of the ad-species density.) Small sets of nucleation events do show such bias.<sup>[20]</sup> However, for statistically more relevant sets of nucleation events, this feature is less obvious (Figs. 4 and 15). Fig. 15 shows not only some clustering of nucleation events near boundaries and triple points, but also many nucleation events occurring inside the larger cells. This, no doubt, reflects the feature that the ad-species density does not vary sharply across the CZ boundaries, as is often assumed.

### CONCLUSION

The selection of simulation results discussed above underscores two important features of the behavior of canonical lattice-gas models of thin film epitaxy. First, the exact behavior of even simple quantities, including those describing spatial aspects of island nucleation, is highly non-intuitive, making phenomenological approximations of their behavior often unreliable. Second, most quantities are better described by broad probability distributions, reflecting strong fluctuations about the average environment of an island, and the stochastic nature of the island nucleation process. Moments of these distributions are key input to refined rate-equation formulations.<sup>[8,9]</sup>

### ACKNOWLEDGMENTS

I thank Jim Evans (Department of Mathematics and Ames Laboratory-USDOE, Iowa State University) for help with Figs. 2, 3, and 5. This work was performed under the auspices of the U.S. Department of Energy by the University of California, Lawrence

Livermore National Laboratory under contract No. W-7405-Eng-48.

## REFERENCES

- Bartelt, M.C.; Evans, J.W. Exact island-size distributions for submonolayer deposition: Influence of correlations between island size and separation. *Phys. Rev., B* **1996**, *54* (24), R17359–R17362.
- Mulheran, P.A.; Robbie, D.A. Theory of the island and capture zone size distributions in thin film growth. *Europhys. Lett.* **2000**, *49* (5), 617–623.
- Vvedensky, D.D. Scaling functions for island-size distributions. *Phys. Rev., B* **2000**, *62* (23), 15435–15438.
- Bales, G.S.; Chrzan, D.C. Dynamics of irreversible island growth during submonolayer epitaxy. *Phys. Rev., B* **1994**, *50* (9), 6057–6067.
- Bartelt, M.C.; Schmid, A.K.; Evans, J.W.; Hwang, R.Q. Island size and environment dependence of adatom capture: Cu/Co islands on Ru(0001). *Phys. Rev. Lett.* **1998**, *81* (9), 1901–1904.
- Bartelt, M.C.; Stoldt, C.R.; Jenks, C.J.; Thiel, P.A.; Evans, J.W. Adatom capture by arrays of two-dimensional Ag islands on Ag(100). *Phys. Rev., B* **1999**, *59* (4), 3125–3134.
- Hannon, J.B.; Bartelt, M.C.; Bartelt, N.C.; Kellogg, G.L. Etching of the Si(001) surface with molecular oxygen. *Phys. Rev. Lett.* **1998**, *81* (21), 4676–4679.
- Evans, J.W.; Bartelt, M.C. Nucleation, adatom capture, and island size distributions: Unified scaling analysis for submonolayer deposition. *Phys. Rev., B* **2001**, *63* (23), 235408–235422.
- Evans, J.W.; Bartelt, M.C. Island size and capture zone areas in submonolayer deposition: Scaling and factorization of the joint probability distribution. *Phys. Rev., B* **2002**, *66* (23), 235410–235421.
- Ratsch, C.; Gyure, M.F.; Chen, S.; Kang, M.; Vvedensky, D.D. Fluctuations and scaling in aggregation phenomena. *Phys. Rev., B* **2000**, *61* (16), R10598–R105601.
- Evans, J.W.; Bartelt, M.C. Irreversible island formation during deposition: Separation distributions and diffraction profiles. *Surf. Sci.* **1993**, *284* (3), L437–L443.
- Li, M.; Bartelt, M.C.; Evans, J.W. Efficient geometry-based modeling of submonolayer film growth. *Phys. Rev. Lett.*, **2003**, 3.
- Bartelt, M.C.; Hannon, J.B.; Schmid, A.K.; Stoldt, C.R.; Evans, J.W. Island formation during deposition or etching. *Colloids Surf., A* **2000**, *165* (1–3), 373–403.
- Watanabe, H.; Ichikawa, M. Anisotropic kinetics of vacancy diffusion and annihilation on Si(001) surfaces studied by scanning reflection electron microscopy. *Phys. Rev., B* **1997**, *55* (15), 9699–9705.
- Jeong, M.S.; Lee, Y.H.; Hwang, Y.G. Equilibrium structure and migration of a single dimer vacancy on the Si(001) surface. *Phys. Rev., B* **1995**, *51* (23), 17151–17157.
- Evans, J.W.; Thiel, P.A.; Bartelt, M.C. Nanostructure evolution during deposition of commensurate adlayers and epitaxial films. *Surf. Sci. Rep.* **2003**, in preparation.
- Bartelt, M.C.; Evans, J.W. Scaling analysis of diffusion-mediated island growth in surface adsorption processes. *Phys. Rev., B* **1992**, *46* (19), 12675–12687.
- Amar, J.G.; Popescu, M.N.; Family, F. Rate-equation approach to island capture zones and size distributions in epitaxial growth. *Phys. Rev. Lett.* **2001**, *86* (14), 3092–3095.
- Hinde, A.L.; Miles, R.E. Monte Carlo estimates of the distributions of the random polygons of the Voronoi tessellation with respect to a Poisson process. *J. Stat. Comput. Simul.* **1980**, *10* (3–4), 205–223.
- Bartelt, M.C. In *Spatial Correlations in Growing Films. Recent Developments in Oxide and Metal Epitaxy—Theory and Experiment*, Materials Research Society Symposium Proceedings Vol. 619, San Francisco, CA, April, 23–26, 2000; Yeadon, M., Chiang, S., Farrow, R.F.C., Evans, J.W., Auciello, O., Eds.; Materials Research Society: Warrendale, PA, 2000, 35–48.

# Island Surfaces: Fabrication on Self-Assembled Monolayers

## Hongjie Liu

*Department of Chemical Engineering, City College of New York,  
New York, New York, U.S.A.*

## Charles Maldarelli

*Department of Chemical Engineering and the New York Center for Biomedical Engineering,  
City College of New York, New York, New York, U.S.A.*

## M. Lane Gilchrist

*New York Center for Biomedical Engineering, City College of New York,  
New York, New York, U.S.A.*

## Alexander Couzis

*Department of Chemical Engineering, City College of City University of New York,  
New York, New York, U.S.A.*

## INTRODUCTION

Nanoisland patterned surfaces, in which functionalized nanodomains are surrounded by a matrix of secondary functionality, are scientifically and technologically important for their wide variety of applications in biomimetic materials, templated nanocrystallization, induced reactions (as surface catalysts), etc. Islands terminated with particular groups can serve as direct sites for molecular recognition and can therefore be used in separations (e.g., as chromatographic supports). Designing the matrix to be nonadsorbing reduces the fouling of the surface and enhances the island activity for molecular arraying. For example, polyethylene glycol (PEG) terminations are particularly important for their resistance to nonspecific protein adsorption and thus are valuable in bioassaying, in which the receptors are often large molecules (ranging from a few nanometers in cross section for DNA to several nanometers for proteins). Corralling of these receptors into domains is not always effective because steric interaction limits the number of targets that can bind to the receptors. In this case, it is more advantageous to individually isolate the receptors onto nanoscale island sites, where only one receptor is anchored by the terminal group in the island. In addition, by anchoring the terminal group in recessed islands (pockets), the conformation of the binding site can be arranged for optimum accessibility of the target. For example, thiol functionalization of the island self-assembled monolayer (SAM) can be used to link a protein through disulfide linkages to cysteine residues. Another important potential application of nanoislands is for nanocrystallization. Due to their small size and unique electrical, photonic, and transport properties, nanoparticles have been the focus of much research intended to

take advantage of their unique properties. The nanoparticulate form is a preferred route of delivery because of the ready passage of the particles through the circulatory system, and unimpeded transport across cell membranes. The ability to tailor the band gap structure of a semiconductor nanoparticle by controlling the particle size<sup>[1]</sup> leads to useful technological applications.<sup>[2]</sup> Recessed nanoislands can serve as vestibules for the crystallization of nanocrystals or the sequestering of nanosized particles such as liposomes. It is well recognized that chemically functionalized surfaces at the interface of a crystallizing solution can heterogeneously nucleate crystallites, sometimes with polymorph selectivity. Charged functionalizations are effective nucleators of ionic crystals as they attract oppositely charged counterions in the solution to the surface, which leads to the assembly of the incipient nucleus. Island patterned surfaces consisting of recessed nanodomains that have floors that are functionalized with active templates and that are surrounded by a matrix inert to crystallization can nucleate individual, nonagglomerating nanoparticles of controlled size. Particles covered with island cavities on their surfaces sequestering grown nanoparticles can subsequently be dispersed in an appropriate matrix (e.g., glass or polymers) to achieve a substantial collective response, avoiding the usual problems associated with nanoparticle agglomeration.

In order to fabricate nanoisland surfaces, some approaches with SAMs have been developed to chemically pattern surfaces in the nanoscale. For example, the tip of a scanning probe microscope [atomic force microscope (AFM) or scanning tunneling microscope (STM)] has been used to pattern the surface,<sup>[3,4]</sup> with the tip being used to displace molecules of an already deposited SAM either physically (AFM, nanoshaving) or electrically (STM, electrochemical etching) to create

a pattern. Alternatively, in dipped pen nanolithography, the tip is used to transfer a self-assembled surfactant onto the surface, creating the pattern. While these techniques can be used to create intricate patterns, as well as the island domains of interest here, they do suffer from certain drawbacks compared to the backfilling and mixed adsorption techniques we have developed here. First, the backfilling and mixed adsorption methods are easier to employ than the scanning probe methods, and while intricate patterns cannot be created, island patterns are all that are required in many applications. Second, the scanning probe methods allow only patterning over square micrometer-sized planar areas. While this may be acceptable for some applications (e.g., miniaturized sensors), other technologies that require a high surface area per volume may require patterning onto the curved surface of a particulate (e.g., particulate patterned with island receptors for chromatographic support, and beads patterned with recessed island templates to produce nanocrystals on a large scale). Such patterning cannot be undertaken with scanning probe lithography, but can easily be undertaken by the backfilling and mixed adsorption methods to be developed here. In this paper, we review the literature on using SAMs for the preparation of island surfaces and then explore newly developed approaches.

## BACKGROUND

The most widely used SAMs are generally classified into thiol and silane SAMs.<sup>[4–8]</sup> In the case of alkylthiols  $[X-(CH_2)_n-SH]$  adsorbed on gold (1 1 1), the  $-SH$  head group covalently bonds to the hollow sites of the hexagonally arrayed Au atoms of the (1 1 1) surface. For methyl terminated alkylthiol SAMs  $[CH_3-(CH_2)_{n-1}-SH]$  at room temperature, when  $n$  is approximately six or more, the van der Waals cohesion between the chains is large enough to drive the amphiphiles into a dense crystalline array at full coverage, whereas for smaller hydrophobic chain lengths ( $n < 6$ ), the SAM at complete coverage has a mottled appearance.<sup>[9,10]</sup> The adsorption of alkyl trifunctional silanes  $[X-(CH_2)_n-SiY_3]$ ;  $Y = Cl, OMe, \text{ or } OEt]$  to hydroxylated surfaces does not initially involve covalent linking to the surface<sup>[11–13]</sup> but involves a three step adsorption process,<sup>[14,15]</sup> in which the chloro or trifunctional silane groups are first hydrolyzed to form silanols  $[X-(CH_2)_n-Si(OH)_3]$ ; the alkylsilanols then hydrogen bond to the physisorbed water layer on the surface, and gradually siloxane crosslinking bridges form between adjacent amphiphiles and a few surface hydroxyl groups. At full coverage at room temperature, SAMs of the methyl terminated long chain octadecyltrichlorosilane [OTS:  $CH_3(CH_2)_{17}SiCl_3$ ], the

most well-studied alkylchlorosilane, form a well-ordered SAM with the hydrophobic chains trans extended canted approximately  $10^\circ$  from the normal and an area per molecule of approximately  $21 \text{ \AA}^2$ , equivalent to the alkylthiols. As the chain length decreases, gauche defects appear in the chain because of the reduced van der Waals cohesion; the chains begin to become disordered, and their tilt from the normal and the area per molecule increases. For alkylchlorosilanes with only a few methylene groups the monolayers are completely disordered.<sup>[16–18]</sup>

With regard to using the alkylthiol and alkylsilane amphiphiles to form nanoisland surfaces by backfilling, both exhibit the prerequisite clustering into nanoislands for adsorption times less than those required for full coverage. Methyl terminated alkylthiols of  $n > 6$  adsorb at room temperature on a clean gold surface at first randomly as a lattice gas, and then form the stripped lying down phase in which the head groups pair and the chains lie along the surface. Upon further adsorption, the stripped phase undergoes a series of transitional states from which emerge nanoisland domains of upright, densely packed,  $c(4 \times 2)$  ordered phase, which grow and form the complete monolayer.<sup>[19–22]</sup> The fact that the condensed islands arise from the stripped and intermediate phases makes it difficult to fill around them using a second functional phase.<sup>[23,24]</sup>

Rondelez and coworkers<sup>[25,26]</sup> studied the adsorption of the alkyltrichlorosilanes on hydrated silicon oxide surfaces. For sufficiently hydrated surfaces, they measured OTS as a function of temperature (in the range of  $5\text{--}60^\circ\text{C}$ ) and found that below a critical temperature  $T_c (= 28 \pm 4^\circ\text{C})$  the prepared monolayers exist in the condensed well-ordered state. In contrast, in those prepared above the critical temperature, the infrared (IR) peak shifted, signifying reduction of the trans conformers and the rise of gauche defect populations. Simulations of the IR adsorption data indicated that the disordered regions existed as islands rather than being uniformly mixed. This suggested, in analogy with the Langmuir monolayers, that below the critical temperature, the SAM forms by direct condensation of a gaseous phase to a condensed phase, while above  $T_c$  an intermediate liquid phase forms; the condensed phase nucleates from the liquid and complete monolayers retain some liquid domains. Atomic force microscopy studies have directly confirmed this picture and provided details of the assembly process: Height AFM images of partially complete OTS monolayers prepared at room temperature show, after a few seconds of immersion, condensed island domains with heights of the order of the fully extended chain and island sizes in the hundreds of nanometers size range.<sup>[27–29]</sup> With time, these islands grow to micrometer sizes and eventually become surrounded



by a matrix liquid phase whose height begins to grow with time and arrests the growth of the island phase. For deposition conditions below 16°C, Maboudian et al.<sup>[29]</sup> found that the micrometer-sized islands with fully extended chain heights are once again observed after a few seconds, but grow continuously, with the surrounding area remaining bare (or with a gaseous monolayer) during the growth. These low temperatures are below the critical temperature for the existence of a liquid phase, and the monolayer develops directly by condensation from the gaseous state. Whether this state is gaseous cannot be established conclusively from scanning probe topography images and it could also be a liquid phase of low density in equilibrium with the condensed phase.<sup>[28]</sup>

While the clustering of condensed domains in a sparse background for alkylsilanes is now well recognized, there have been only a few studies that have considered using backfilling to produce nanoisland topography. Mathauer and Frank<sup>[30]</sup> studied the system of OTS and a naphthalene terminated silane with an 11-carbon hydrophobic spacer, alternatively backfilling either with OTS or the naphthalene silane. Examination of the ratio of the intensities of the excimer to monomer fluorescence of the naphthalene terminal group gave no indication of macroscale phase separation because the ratio increased uniformly with increase in the amount of the naphthalene amphiphile. These observations did not provide clear insight into the existence of nanoscale separation in the monolayer. In a related effort, Knobler et al.<sup>[31]</sup> spread Langmuir monolayers of alkyl trichlorosilanes, transferred them by the Langmuir–Blodgett technique onto hydrophilic surfaces, and then heated the surface to create condensed micrometer-sized domains that were then backfilled by deposition of a second silane.

Phase separation in mixed SAMs of alkylthiols due to mixed adsorption was first studied by Whitesides et al.<sup>[32,33]</sup> in the course of their investigations on the relationship between wetting and the composition of the mixed SAMs. In order for phase separation to take place, two conditions must be met. First, preferential interactions between the amphiphiles of one component in the binary mixture must be able to counter the entropic energy gain that is realized through random mixing of the two components in the monolayer. Second, the adsorbed amphiphiles should be laterally mobile so that molecules of one kind can take advantage of the preferential interaction. Whitesides et al. studied two examples of preferential interaction in their wetting studies. The first was a significant difference in the length of the hydrocarbon spacer, and the second was hydrogen bonding interactions of the terminal group. When the hydrophobic chains of one amphiphile are much larger than those of the other, there is an increased van der Waals dispersive cohesion

that is especially important when the chains pack in the lengthwise fashion of assembled alkylthiols. Monte Carlo and molecular dynamic simulations of laterally mobile alkylthiols have shown phase separation for methyl terminated thiols when the difference between the chain lengths is larger than approximately 7–10 methylene units.<sup>[34]</sup> Laibinis, Nuzzo, and Whitesides<sup>[33]</sup> measured the contact angles of binary alkylthiol SAMs in which the thiols differed by 10 methylene units and were terminated by methyl groups. The contact angles of the pure components were almost identical, while the mixed SAMs showed a pronounced minimum in contact angle. If macroscopic islands (domains micrometers in size, which would be the only ones expected to affect the contact angles) were present, then, since the methyl groups in the islands would be ordered and well packed, the mixed monolayer should have contact angles the same as those of the pure component surfaces. However, nanoscale separation was not ruled out, and IR spectroscopy provided some evidence of islands of the longer chain thiolate.<sup>[33]</sup> Recently, a few scanning probe microscopy studies have provided definitive evidence for nanoscale separation. Tamada et al.<sup>[35]</sup> have shown nanometer scale phase separation of mixtures of the alkylthiols  $\text{CH}_3(\text{CH}_2)_3\text{SH}$  and  $\text{CH}_3(\text{CH}_2)_{11}\text{SH}$ . The second preferential interaction studied by Whitesides et al. is hydrogen bonding interactions at the terminal group of one of the components.<sup>[32]</sup> Contact angles of water on a binary SAM in which both amphiphiles have the same hydrophobic length but one is capable of hydrogen bonding [ $\text{HS}(\text{CH}_2)_{10}\text{CH}_2\text{OH}$  and  $\text{HS}(\text{CH}_2)_{10}\text{CH}_3$ ] decreased in a convex monotonic form with constant hysteresis as a function of the fraction of the polar component, indicating no microscopic separation. The nanoscale features of this system remain unclear and related studies using scanning probe microscopy are contradictory as to whether phase nanoscale separation occurs.<sup>[36]</sup> However, nanoscale phase separation has been consistently observed in the case in which the terminal groups of short chain hydrogen bonds as shown in the systems  $\text{HO}(\text{CH}_2)_4\text{SH}/\text{CH}_3(\text{CH}_2)_{16}\text{SH}$  by Allara, Liedberg, and Allara,<sup>[37]</sup>  $\text{HOOC}(\text{CH}_2)_2\text{SH}/\text{CH}_3(\text{CH}_2)_{16}\text{SH}$  by Imabayashi et al.,<sup>[36]</sup> and 4-aminothiophenyl/ $\text{CH}_3(\text{CH}_2)_{16}\text{SH}$  by Hayes et al.<sup>[38]</sup> Evidently the extra attraction between the shorter chain hydrogen bonding amphiphile insures its exclusion from the condensed domain forming from the longer chain amphiphile.

There have been several studies of two component SAMs deposited from binary alkyltrichlorosilane solutions, but not many researchers have investigated the formation of nanoislands. Mixed methyl terminated SAMs with two different alkyl chain lengths have been studied by a few authors,<sup>[39]</sup> but for the most part they have focused more on the determination of

composition in the monolayer and not on phase separation. Offord and Griffin noted from measurements of the surface energies of mixed monolayers of methyl terminated short (*n*-butyl and *tert*-butyl) and long chains (dodecyl, hexadecyl, octadecyl) that because the surface free energies of the mixed SAMs were higher than the energies of the single components, it was doubtful whether there was macroscopic phase separation, since the surface energy of the mixed SAM would be a weighted average of the two contact angles. Mixed SAMs of an aryl and methyl terminated SAMs have also been studied, but only the study of Mathauer and Frank,<sup>[40]</sup> who observed no macroscopic separation, addressed the issue of phase segregation. Silane amphiphiles with hydrophobic spacers consisting of  $-\text{CF}_2$  rather than  $-\text{CH}_2$  groups, which make the hydrophobic spacers less flexible, are plausible candidates for phase separation when mixed with amphiphiles with methylene spacers, because analogous Langmuir monolayers phase segregate. Studies of mixed monolayers of octyltrichlorosilane and  $\text{CF}_3(\text{CF}_2)_5(\text{CH}_2)_2\text{SiCl}_3$  by Chuang et al.<sup>[41,42]</sup> demonstrated preferential adsorption of the fluorosilane and showed that macroscopic phase separation was unlikely; however, no conclusions could be reached on whether the fluorosilanes altered the structure by being well mixed in the monolayer or in nano-sized islands. Finally, a few other studies focusing on the composition of mixed monolayers of methyl terminated and, among others, either carboxyl,<sup>[43]</sup> halogen, ester,<sup>[44]</sup> or cyano terminated silanes have been undertaken.

The above discussion makes it clear that alkyltrichlorosilanes are preferable to alkylthiols for use in the backfilling method. With regard to binary mixed adsorption, while it is clear from the few scanning probe microscopy studies mentioned above that alkylthiols can phase separate into nanodomains under the right conditions (e.g., if the amphiphiles differ sufficiently in chain length), none of these studies demonstrate an ability to manipulate the size of the islands. Due to the covalent linking of the thiol group to the gold, lateral diffusion is limited, and it is doubtful that the size can be easily manipulated. On the other hand, while there have been no studies identifying nanoislands in mixed alkylchlorosilanes, their lateral mobility and analogous behavior to Langmuir and Langmuir–Blodgett monolayers makes them better candidates for use in sequential adsorption, and hence we use the alkylsilanes for both the sequential and mixed adsorption studies.

## APPROACHES TO PREPARING ISLAND SURFACE

Self-assembled monolayers of trichlorosilane or trialkylsilane amphiphiles,  $\text{X-R-SiY}_3$  (where X is the terminal

group and R the hydrophobic spacer; Y is a chloro or alkyl group), have been used here to fabricate functionalized nanoisland surfaces. Since the surface property of SAMs is primarily determined by the terminal functional groups ( $-\text{X}$ ) of the assembled molecules, the functionalization of nanodomains could be simply tethering the desired functional group moiety to the hydrophobic assembled silane. But if the moiety is reactive to the silane group or has an affinity for the surface (which competes with the attachment of the silane group to the surface and compromises chain packing and ordering), an unreactive precursor has to be assembled with the SAMs first and then subsequently the desired moiety has to be derivatized. Because of space constraints, details of precursor synthesis are omitted here.

## Backfilling (Sequential Adsorption)

In the backfilling technique, the nanoisland domains are created first. They are assembled by using silanes that when adsorbed (for periods of deposition shorter than those necessary to achieve complete coverage) could phase separate into condensed islands and a background gaseous phase. To insure this phase separation, the deposition is carried out for relatively short deposition times, so that the condensed phase does not entirely cover the surface, at temperatures below room temperature, and using the longer chain silanes: OTS ( $n = 17$ ) for methyl termination, aminophenyltrimethoxysilane [APhMS:  $\text{NH}_2\text{C}_6\text{H}_4\text{-Si}(\text{OMe})_3$ ] for amine termination,  $\text{CF}_3\text{CH}_2\text{O}(\text{CO})(\text{CH}_2)_{17}\text{SiCl}_3$  for carboxylate termination, and  $\text{CH}_3(\text{CO})\text{S}(\text{CH}_2)_{17}\text{SiCl}_3$  for thiol termination (in situ reactions can change these precursor functionalities to the desired ones). Phase separation of the long chain cyano, trifluoroester, and acetothiol silanes has not been studied; however, their long chains should provide enough cohesive energy to drive the condensation phase transition despite the opposing effect of the bulkiness of the terminal groups.

Another case that we observed in our experiments is that, instead of nanoisland formation, long chain amphiphile deposition on the surface for a relatively long time (not long enough to completely cover the whole surface) led to the formation of a continuous phase with nanoscale holes (nanowells). Fig. 1 is a typical AFM image of a 2-[methoxy(polyethylenoxy) propyl]trimethoxysilane [mPEG:  $\text{CH}_3\text{O}(\text{CH}_2\text{CH}_2\text{O})_n\text{C}_3\text{H}_6\text{Si}(\text{OMe})_3$ ;  $n = 6\text{--}9$ ] nanoisland surface formed by this approach (for convenience, the term nanoisland is used for both nanoscale pillars and holes). After an mPEG nanoisland surface of desired size is obtained, the nanoisland can also be modified by a secondary chemical functionality, like amino, cyano, ester, or thioacetyl terminated silane.

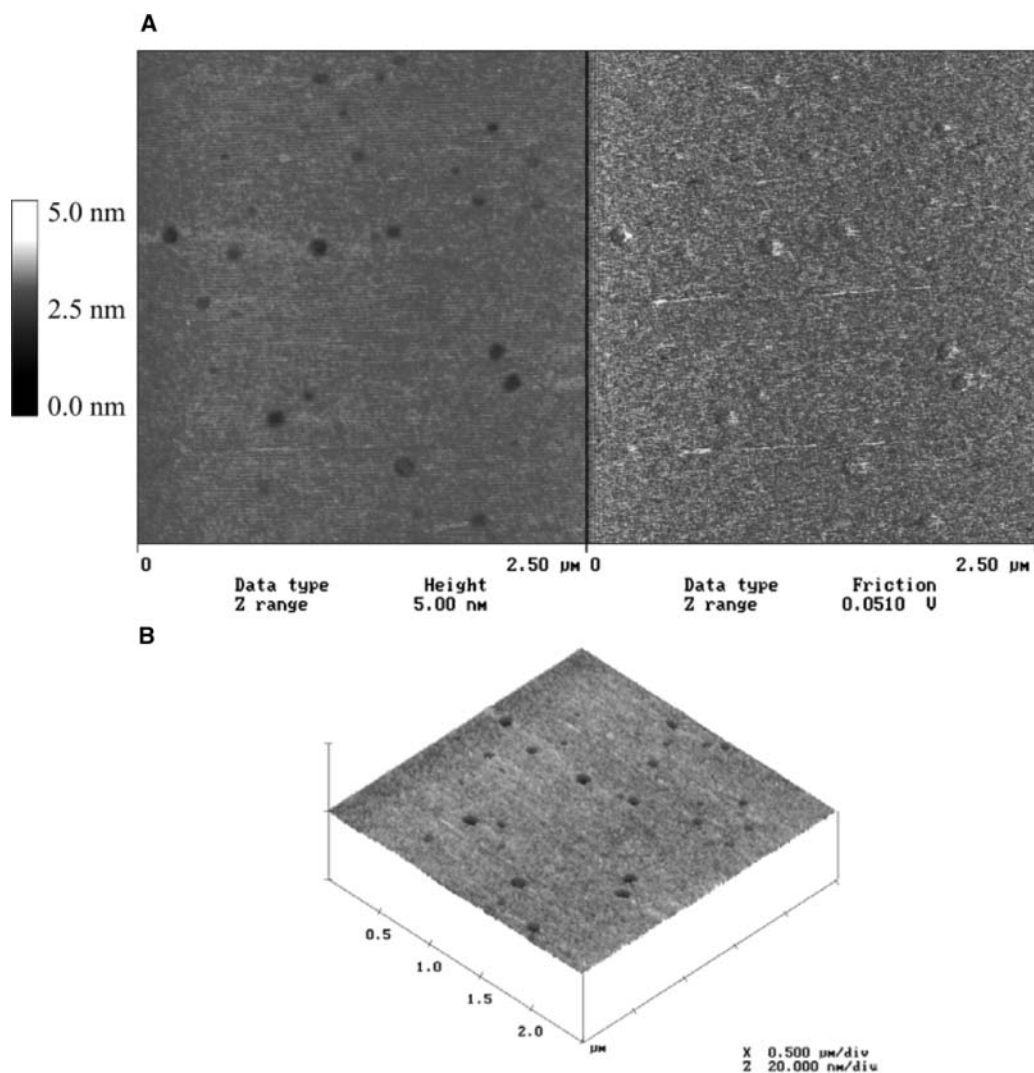


**Fig. 1** (A) AFM image of partially packed mPEG surface with nanoisland defects. Cross-section analysis gives average diameter of island to be about 100–300 nm and depth approximately 2.5 nm. (B) In situ three-dimensional image.

The major issue in the backfilling technique—once self-condensation has been established in the first step—is how to control the size of the islands (“pillar” or “holes”) and their density. These features are controlled in the first step by controlling the size and density of the condensed islands, and it is clear that the deposition time, the concentration of the silane, and the amount of water in the solvent (determined by the polarity of the solvent and its state of hydration) are the parameters that control how much silane adsorbs onto the surface, and therefore the area occupied by the condensed phase. Hence, these parameters can be used to determine the rough island sizes and densities. But given a certain condensed phase area, how can the island size be fine-tuned? During the first deposition, the line tension created at the island perimeter between the silane’s methylene chain and the depositing solvent plays a central role: Large

tensions favor large and less numerous islands, and lower tensions smaller and more islands, each within the constraint of how much condensed phase has adsorbed. As the spacer is hydrophobic, the more polar the solvent the larger the tension and the coarser the island structure—for the same amount of condensed silane adsorbed. Therefore, our strategy is to first obtain a reference “rough scale” island structure for a given concentration, deposition time, and solvent, and then fine-tune the island size by changing the solvent while adjusting the concentration and deposition time to keep constant the amount of silane adsorbed. Thus, if the adsorption is from a polar solvent yielding large islands, we could fine-tune to smaller islands by reducing the polarity of the solvent. To compensate for the probable reduction in available water necessary for chlorosilane hydrolysis, the concentration of silane can be increased or the deposition

time lengthened so as to keep constant the total amount adsorbed.

### Mixed Adsorption

In the mixed adsorption technique, the silicon wafer is dipped into a solution containing the silanes that make up both the island and matrix phases, and these, upon adsorption, phase separate to form the desired pattern. The central challenge is to insure that the segregation takes place, and this requires an understanding of the factors that control the phase separation as opposed to those that promote uniform mixing. As discussed before, most of our insight into phase separation in mixed systems derives from alkylthiol studies, which showed that mixtures with disparate chain lengths (i.e.,  $n < 5$  and  $n > 16$ ) segregate due to the increased cohesion of the longer chains, which drives their mutual aggregation into condensed domains, excluding the lower chain amphiphiles, which organize themselves into a more disordered phase. Chain length induced phase separation has also been verified by computer simulations of the adsorption of two alkylthiols with differing chain length on Au (1 1 1); these demonstrate phase separation when the chain length differs by more than seven or eight methylene units. Another crucial factor that needs to be taken into account is the interactions of functionalities embedded in the hydrophobic spacer or at the terminus. In principle, if one of the amphiphiles in the binary mixture contains a terminal group (or a group embedded in the hydrocarbon spacer) that is strongly attractive to itself (as for example hydrogen bonding moieties), this extra interaction could promote phase separation. This kind of phase separation has been observed in mixed monolayers spread at the air/water interface and subsequently transferred to a hydrophilic surface by the Langmuir–Blodgett technique. For example, two amphiphiles, each with the same chain length but one containing an amide head group [ $-C(O)NH_2$ ] and the other an amide and carboxylic head group [ $-C(O)NH(CH_2)_2COOH$ ], phase separate due to the extra hydrogen bonding of the carboxylic group. Analogous experiments by Allara et al. on mixed SAM formation via the coadsorption of two thiols of approximately the same chain length with one capable of hydrogen bonding [ $CH_2O_2(CH_2)_{15}SH$ ] while the other is unable to hydrogen bond [ $CH_3(CH_2)_{16}SH$ ] show nanoisland phase separation. However, contradictory results have been obtained with similar systems by Bo and Lieberg using  $HOC(CH_2)_{10}SH/CH_3(CH_2)_{10}SH$  and Kakiuchi et al. using  $HOOC(CH_2)_{10}SH/CH_3(CH_2)_{10}SH$ , each of which showed no evidence of phase separation. If the chain length of the methyl terminated amphiphile is

much longer than the length of the amphiphile with the hydrogen bonding terminus, phase separation is observed consistently, as shown in the systems  $HO(CH_2)_4SH/CH_3(CH_2)_{16}SH$  by Allara et al.,  $HOOC(CH_2)_2SH/CH_3(CH_2)_{16}SH$  by Imabayashi, and 4-aminothiophenyl/ $CH_3(CH_2)_{16}SH$  by Hayes et al. Evidently the extra attraction between the shorter chain hydrogen bonding amphiphile insures its exclusion from the condensed domain forming from the longer chain amphiphile.

We use different chain lengths as our primary tool to insure segregation. Because of the flexibility of the ethylene oxide chain for oligomeric and polymeric PEG silanes, we take advantage of this to use PEG-grated silane to form the long chain phase. Once phase separation is assured, the amphiphile that constitutes the matrix phase and the size of the islands is governed primarily by which amphiphile adsorbs more quickly to the surface, as this is the one that usually forms the continuous matrix phase, with the slower adsorbing species forming the island phase. The factors that govern the relative rates of adsorption of the silanes are principally: 1) the composition ratio in the bulk; 2) the affinity of the terminal groups for the surface; 3) the affinity of the amphiphile for the solvent; and 4) any cooperative effects that enhance the adsorption of one amphiphile once some adsorbed molecules of that amphiphile are already down on the surface. The latter effect is particularly important for the mixed adsorption of short and long chain thiols, where the greater cohesive force of larger chains may be expected to accelerate their adsorption and leads to a surface enrichment relative to the solution phase. In the design of our systems, we begin by using the composition ratio of the bulk solution to set principally which phase is the island phase and which is the matrix, and the size and density of island. Total concentration of amphiphiles in the depositing solution and the time of deposition are adjusted to allow for full coverage. Once a rough scale for the size and density is achieved with a given composition ratio, we again use the solvent polarity to tune the island size and density on the surfaces.

### EXAMPLES

In the following, we give some examples of nanoisland surfaces prepared by the backfilling and mixed adsorption methods discussed above. Usually, we use single crystal silicon wafers (double side polished, n-type, (1 1 1)) with a native oxide layer to assemble silane monolayers. These substrates were cleaned, stored in deionized water, and dried in a stream of nitrogen prior to use; treated in this way, the substrates retain a physisorbed water layer upon immersion into the nonpolar solvent. All chemicals, including silanes and organic

solvents with different polarities (chloroform, carbon tetrachloride, toluene, etc.), were used as received without further purification. The bulk solutions of different silanes were prepared by adding OTS, 3-aminopropyltrimethoxysilane [APS:  $\text{NH}_2\text{C}_3\text{H}_6\text{Si}(\text{OMe})_3$ ], APhMS, or mPEG in the required quantities to the organic solvent. The silane amphiphiles were assembled onto the silicon oxidized substrates by adsorption from solutions of varying polarity. The cleaned silicon substrates were immersed into the bulk solution with different compositions for a certain amount of time so that the silanes could be hydrolyzed by the water present in the solution. The deposition was terminated by rinsing the substrates in organic solvent for 5 min or sonicating for 1 min if necessary. The excess solvent was blown off with a dry nitrogen beam. The substrates could also be baked on a hot plate at  $120^\circ\text{C}$  to complete the chemisorption of the silane to the hydroxylated surface by promoting siloxane bridging linkages between silanes and the surface.

We used the solvent polarity to tune the island size and density. After deposition for a prescribed time in the assembled silane solution, the wafers were rinsed (or sonicated) to remove excess silane or siloxane oligomers from the surface, and dried by nitrogen stream. In situ modifications (i.e., CN reduction to amines, ester hydrolysis to carboxylates, thioacetyl hydrolysis to thiols), if required, followed. For mixed adsorption, the process was then complete. In the case of sequential adsorption, the dried and possibly modified substrates were then redipped in a second silane solution, sonicated, dried, and (if necessary) in situ modified once again.

The primary tool to visualize the surface morphology is atomic force microscopy, which allows direct in situ scanning of the surfaces. Atomic force microscopy images were obtained by using a Nanoscope III instrument (Digital Instruments, Inc.). Silicon nitride sharpened tips with a force constant of  $0.58\text{ N/m}$  were used for height and friction images in contact mode. A normal force of approximately  $10\text{ nN}$  was used in the contact mode experiments. For every sample, at least three different locations were acquired. Height and friction data for various phases on the samples were obtained by taking cross sections at random locations. All the friction images acquired were from the same area as that from which the height images were acquired.

Long chain methyl terminated silane OTS and short chain amine terminated APS were mixed adsorbed on the surface to form a pattern in which the recessed islands with charged functionality were surrounded by a hydrophobic methyl terminated matrix. The total concentration of amphiphiles in the depositing solution and the time of deposition were adjusted to allow for full coverage. The use of the short chains of APS

relative to the long chain OTS insures phase separation, and the matrix is elevated  $1.5\text{--}2.0\text{ nm}$  relative to the islands. The significant hydrogen bond of amine strengthens the later chain interaction and thus enhances the segregation. The islands of the polar terminated silanes are formed because the composition ratio favors the methyl terminated silanes. As Fig. 2 shows, the binary OTS/APS system phase separates on the surface to form the nanoisland surface when the OTS/APS ratio in the bulk solution is 3:1 and total concentration is  $2.0\text{ mM}$  in anhydrous chloroform with  $0.02\%$  (v/v) water added. The water contact angle equals  $98^\circ$ , implying that the majority phase is hydrophobic OTS (pure OTS has a contact angle of  $110^\circ$ ). The friction image (right) with the same pattern also confirms this result, since the amino group of APS has relatively higher friction compared with the alkyl group of OTS, so that the lower islands of APS (“dark dots”) on the height image appear to be bright spots on the friction image (right). Cross-section analysis gives an island size of  $\sim 50\text{ nm}$  and a depth of  $\sim 1.5\text{ nm}$ , consistent with the former thickness prediction.

Phase separation on solid-liquid interface from a binary mixture of amphiphiles in which one component terminates in a PEG chain has not been studied, either for the thiol or the silane case. The steric repulsion between the ethoxylated head groups of the oligomeric (6–9 units) PEG terminated silanes acts to form a disordered SAM relative to the ordering we might expect from the long alkyl chain silanes. Therefore, we use amino terminated silanes (APhMS) and coadsorb these with oligomeric mPEG terminated silanes. Following the same protocol and using APhMS and long chain mPEG to replace OTS and APS, respectively, we also obtained a similar nanoisland pattern on the surface (Fig. 3). Cross-section analysis shows that the approximate size of the recessed island is about  $300\text{ nm}$  and the depth is about  $3.0\text{ nm}$  from matrix. The height image and friction image of the surface tell us that the island is APhMS and the matrix is mPEG. The depth of the island is also consistent with the height difference between the two amphiphiles.

As discussed before, the deposition conditions are essential for the phase separation behavior on the surface. For the same system and experimental conditions, when the composition of the bulk solution is changed, phase separation still occurs, but the pattern of each phase domain is totally different. Fig. 4 shows the same system of APhMS/mPEG with the same bulk composition ratio of 1:1 for an immersion time of 3 hr. Instead of APhMS holes forming, the long chain mPEG forms pillars and the APhMS forms a continuous matrix. The mPEG pillars appeared to be bright patches on the height image (left) and dark patches on the friction image (right). The size of the mPEG

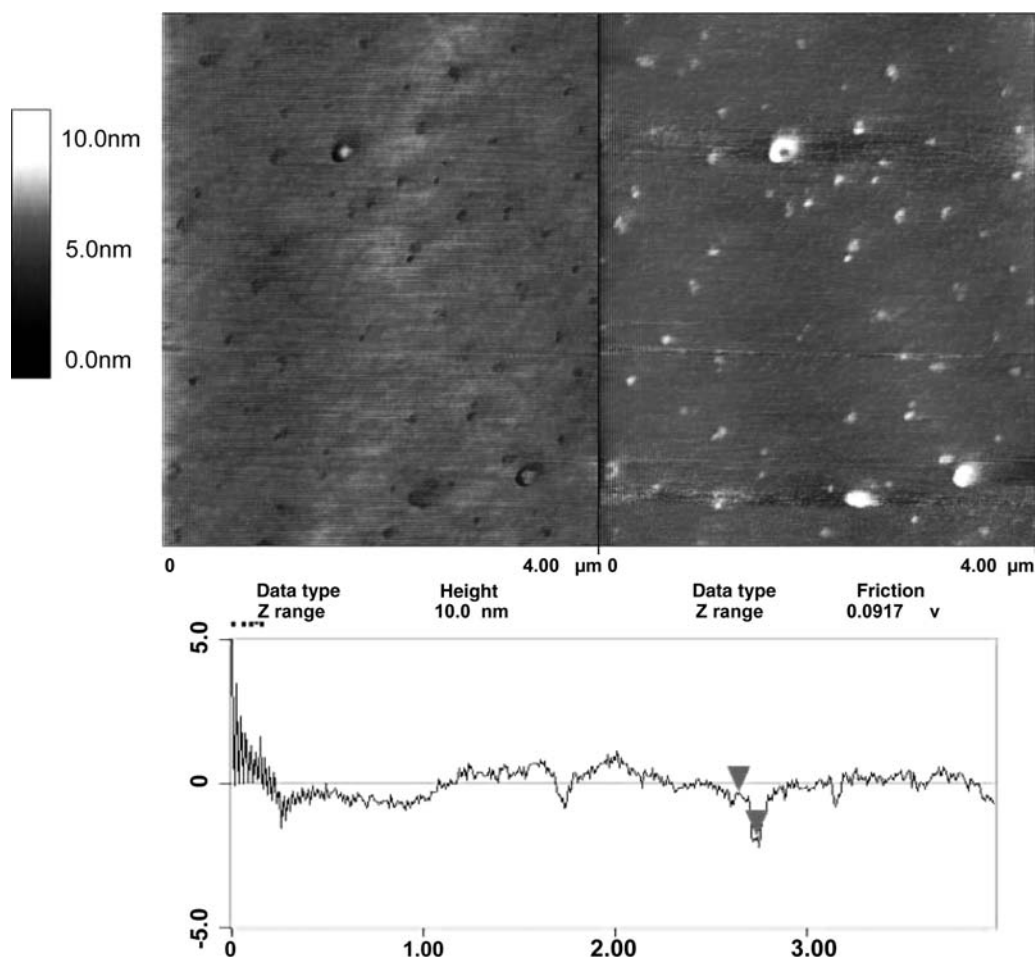


**Fig. 2** AFM image of nanoisland surface formed by OTS/APS mixed monolayer (2 mM; bulk ratio 3 : 1) in anhydrous chloroform and 0.02% (v/v) water for 2 hr; contact angle = 98°. Cross-section analysis shows it to be 50 nm in diameter and 1.5 nm recessed from matrix. Bright spots on friction image correspond to higher friction of amino group of APS.

pillars is about 150 nm and the height from the surrounding APhMS matrix, 1.5 nm. The simple explanation for these different results is that because of the strong intermolecular interaction between the long alkyl chains, for the mPEG-rich sample (Fig. 3), the short chain APhMS tends to form islands, whereas when the composition ratio is changed to 1 : 1, mPEG becomes the minority phase and forms pillars within an amine terminated matrix. The discrepancy in the island depth and pillar height in Figs. 3 and 4 is also due to the different phase coverage on the surface. In Fig. 3, the long chain mPEG on the surface is the majority phase, so that the chains are densely packed and do not have much space to sway but extend perpendicularly, while in Fig. 4, the mPEG is the minority phase on the surface, so that the extruded chains have more spatial freedom to sway around, thus leading to the lower height value measured when scanned with an AFM tip.

The steric repulsion between the ethoxylated head groups of the oligomeric PEG terminated silanes

makes it difficult to form a condensed SAM. For most situations this is undesirable for nanopattern formation because of the loose structure. However, if we can control the formation conditions and manipulate the deposition parameters, like the deposition time, solvent polarity, etc., the defective structure with well-distributed holes on the surface can serve as the first step of the backfilling process. Fig. 1 is the AFM image of an mPEG surface with defect nanowells. With short deposition time, the mPEG silanes did not have enough time to fully cover the surface and formed the partially packed monolayer with nanoscale defects. The AFM height image and friction image both give good distribution and the correct friction pattern, in which the lower holes on the height image appear to be bright (because of the partially negatively charged hydroxylated silicon bare surface). Cross-section analysis gives the size of the spherical defect to be about 100–300 nm and the depth, 2.5 nm. Also due to the loose structure and disordered packing, this length is understandably a little lower than the fully extended



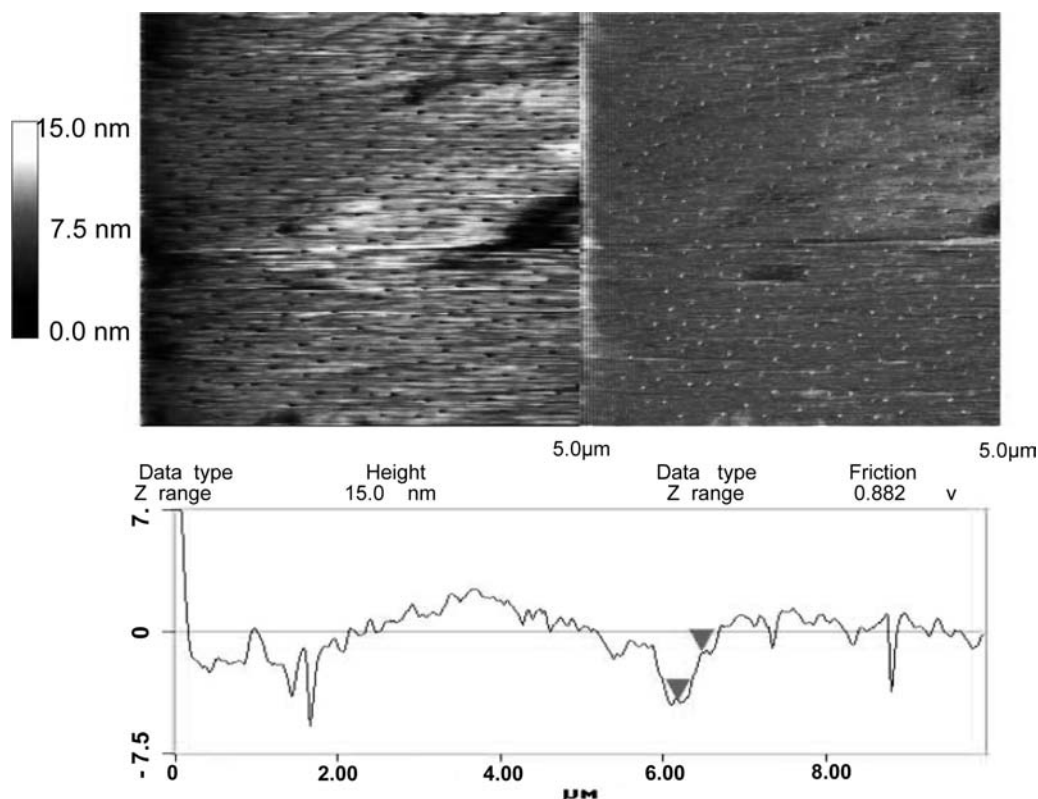
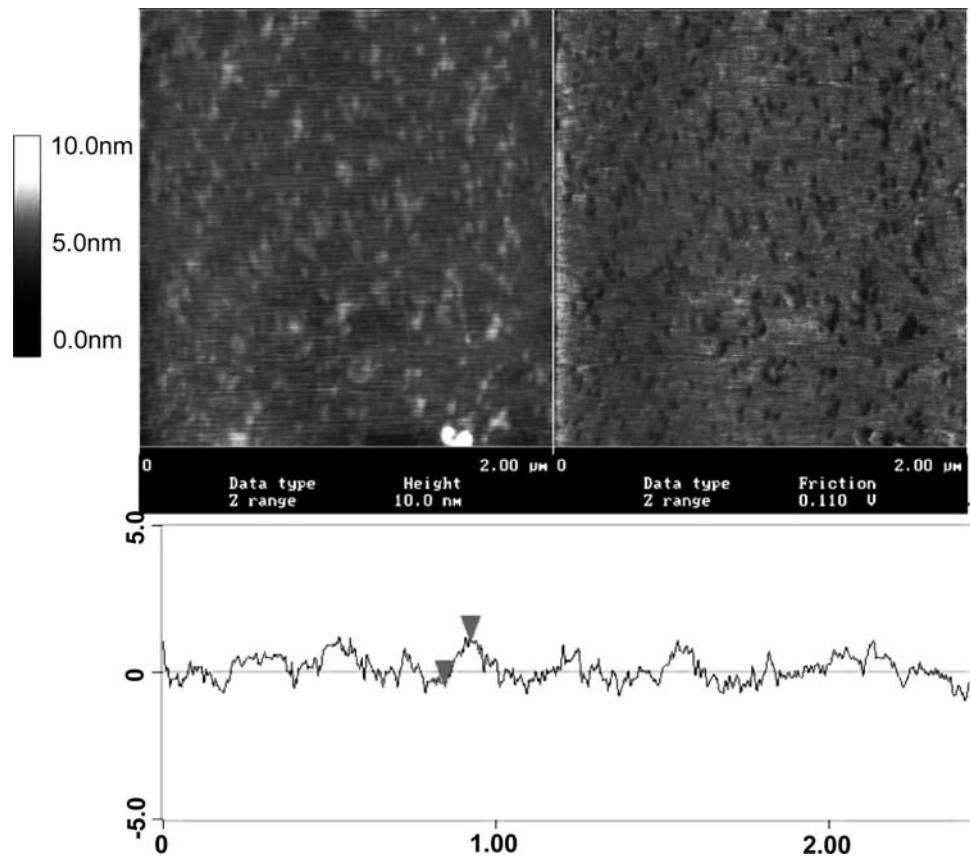


**Fig. 3** AFM image of nanoisland surface from mPEG/APhMS mixed monolayer (1 mM; bulk ratio 3 : 1) in anhydrous chloroform for 3 hr and toluene rinsed for 1 min. Cross-section analysis gives size of 300 nm and depth of 3.0 nm (average).

length of 3.0 nm. The in situ three-dimensional image gives the direct visualization of the distribution of holes on the surface. After the mPEG surface with the defects is prepared, further backfilling with other desired functional groups can be undertaken, since the bottom surface of the defect holes is still bare hydrated surface, so that further hydrolysis can take place. Fig. 5 is the mPEG nanoisland surface after APhMS monolayer backfilling. Compared to the pure mPEG nanoisland pattern in Fig. 1, the most distinct change is that the bright spots on the friction image (right) have disappeared after amino group modification. The possible explanation is that the frictions of the amino terminal groups and methoxy terminal groups of mPEG are very similar in aqueous buffer solution, so that they are hardly to be detected by AFM imaging.

Oligo(ethylene glycol) (OEG) spacer is recognized as a resistant material that prevents non-specific adsorption of proteins, so that it has been incorporated into SAMs to form nanoisland surfaces because of its ability to render surfaces biocompatible.<sup>[45]</sup> As one of the important applications of nanoisland surfaces, we immobilized intact small unilamellar liposome vesicles (SUV) onto the abovementioned nanoisland for future biosensing application. In general, the liposome

vesicles tend to unravel and spread on the solid surface and eventually form multiple layers when exposed to either hydrophobic or hydrophilic solid supports. This is undesirable for many special situations, for example when the conformation and fluidity of lipid membrane are necessary for the embedded protein receptors to function in biosensor and molecular-recognition applications. The nanoisland surfaces in our research provide an alternative mechanism to circumvent this problem and maintain the liposome vesicle intact. Fig. 6 is the AFM image (under fluid cell) of a nanoisland surface after liposome exposure. The negatively charged liposome (SUV) was prepared from pre-liposome formulation-4 [L- $\alpha$ -phosphatidylcholine- $\beta$ -oleoyl- $\gamma$ -palmitoyl (POPC), L- $\alpha$ -phosphatidyl-DL-glycerol (PGDO), dioleoyl, and cholesterol from Sigma-Aldrich Co.] by standard extrusion through 0.2  $\mu$ m filter and has  $\sim$ 200 nm size distribution in solution (by light scattering measurement). Unlike the usual case of unraveling on the surface, most of the liposome vesicles under buffer solution maintained their intact structure, with a height of 40 nm and diameter of 400 nm (from cross-section analysis of the zoom-in image of Fig. 6B). The flattening deformation of the liposome shape was attributed to the gravity of the interior buffer liquid and the electronic attraction



Integrated - Island

**Fig. 4** AFM image of mPEG island from mPEG/APhMS mixed monolayer (1 mM; bulk ratio 1 : 1) in dry chloroform and 0.02% water (v/v) for 3 hr. Contact angle = 35°. Cross-section analysis gives approximately 150–200 nm diameter and 1.5 nm recessed from matrix. Lower friction of mPEG (methoxy terminal group) shows dark patches in friction image (right) corresponding to bright (higher) patches on height image (left).

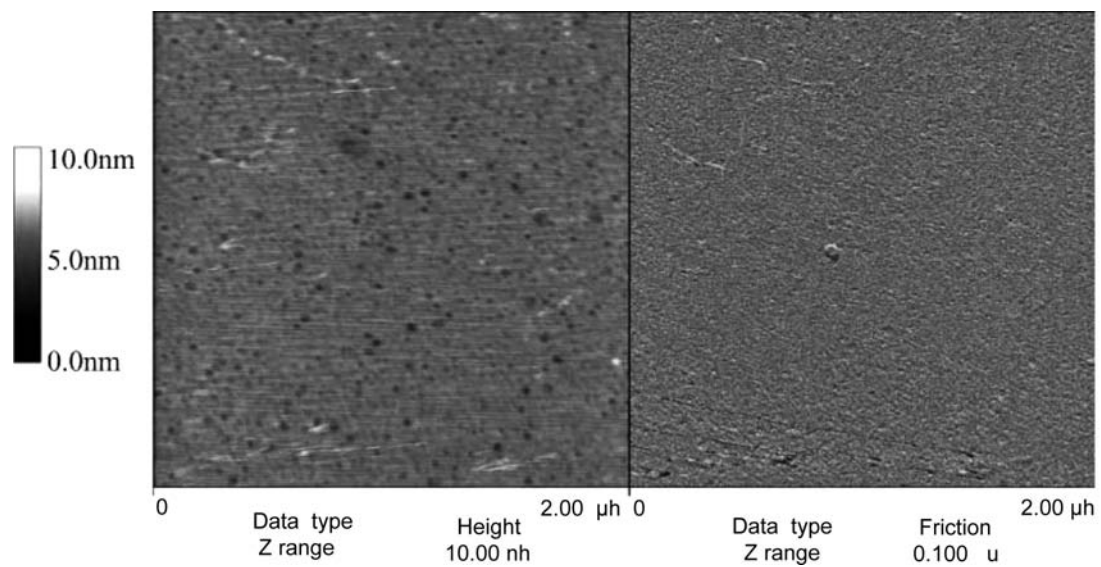


**Fig. 5** AFM image of nanoisland surface of mPEG monolayer after APhMS backfilling. Bright spots on friction image (right) disappeared after amino group modification.

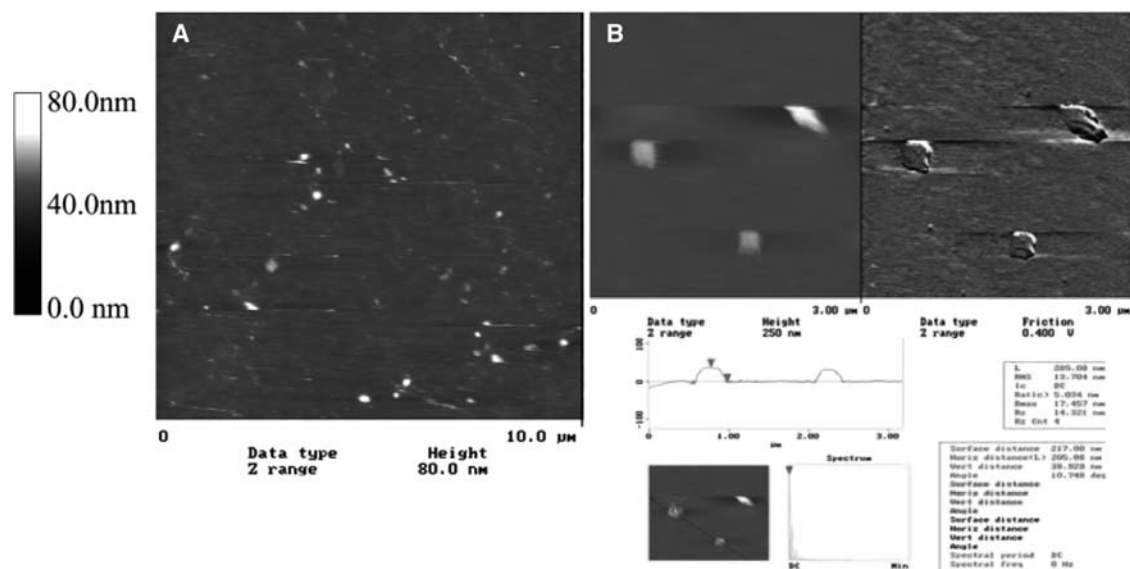


**Fig. 6** (A) AFM image (under fluid cell with buffer solution) of liposome ( $\varnothing = 0.2 \mu\text{m}$ ) exposed to nanoisland surface after buffer rinsing. (B) Cross-section analysis of zoom-in image shows height of 40 nm and size of 400 nm approximately.

of the island surface. The deformation of the spherical shape to square shape in the zoom-in image is the result of AFM tip scratch (especially in contact mode). The mechanism of intact liposome immobilization on the nanoisland surface is as follows: The nanoislands on the nanopattern surface have the same order of size range (100–300 nm) as the liposomes ( $\sim 200$  nm) so that a complete bilayer cannot be accommodated; the oppositely charged terminal groups (positively charged amino groups) of the island bind the liposome via electrostatic force; the inert surrounding mPEG matrix resists the liposome adsorption. In addition, because of recessing of the islands relative to the matrix so that liposomes are physically removed from the matrix, the nanoisland surface with specially tethered functionality is a good model to prevent the spreading and unraveling of the liposome bilayer on the surface and to maintain the intact conformation of liposome vesicles.

## CONCLUSIONS

Self-assembled monolayers provide a route for tailoring functionalities and submicrometer patterns on surfaces. The phase separation of SAMs has been explored to fabricate heterogeneous, robust arrays of nanodomains with variable functionalities. Uniformly arranged nanoisland (nanowell) domains with specific functionality have been patterned on solid surfaces through mixed adsorption and backfilling approaches. Given a well-defined binary system with specific molecular structure, functionalities and preparation approaches, the morphology of phase separation, to a certain extent, could be controlled by manipulating

the deposition conditions. Compared to other nanopattern techniques, these approaches provide a convenient alternative to pattern large surface areas and curved surfaces with nanoscale domains. As a future application of this work, intact liposome vesicles could be incorporated or loaded with desired reagents, drug molecules, or membrane protein receptors and arrayed onto our nanoisland surfaces for further bioassay, biosensor, or drug delivery studies.

## REFERENCES

- Banerjee, R.; Jayakrishnan, R.; Banerjee, R.; Ayyub, P. Effect of the size-induced structural transformation on the band gap in CdS nanoparticles. *J. Phys. Condens. Matter* **2000**, *12* (18), 10,647.
- Rajalakshmi, M.; Arora, A.K. Optical properties of selenium nanoparticles dispersed in polymer. *Solid State Commun.* **1999**, *110* (2), 75.
- Song Xu, S.M.; Laibinis, P.E.; Liu, G.-y. Fabrication of nanometer scale patterns within self-assembled monolayers by nanografting. *Langmuir* **1999**, *15*, 7244.
- Whitesides, G.M.; Laibinis, P.E. Wet chemical approaches to the characterization of organic surfaces: self-assembled monolayers, wetting, and the physical-organic chemistry of the solid-liquid interface. *Langmuir* **1990**, *6*, 87.
- Dubois, L.H.; Nuzzo, R.G. Synthesis, structure, and properties of model organic surfaces. *Ann. Rev. Phys. Chem.* **1992**, *43*, 437.
- Ulman, A. Formation and structure of self-assembled monolayers. *Chem. Rev.* **1996**, *96*, 1533.
- Poirier, G.E. Characterization of organosulfur molecular monolayers on Au(1 1 1) using scanning tunneling microscopy. *Chem. Rev.* **1997**, *97* (4), 1117.

8. Schreiber, F. Structure and growth of self-assembling monolayers. *Prog. Surf. Sci.* **2000**, *65* (5–8), 151.
9. Porter, M.D.; Bright, T.B.; Allara, D.L.; Chidsey, C.E.D. Spontaneously organized molecular assemblies. 4. Structural characterization of *n*-alkyl thiol monolayers on gold by optical ellipsometry, infrared spectroscopy, and electrochemistry. *J. Am. Chem. Soc.* **1987**, *109* (12), 3559.
10. Chailapakul, O.; Sun, L.; Xu, C.; Crooks, R.M. Interactions between organized, surface-confined monolayers and vapor-phase probe molecules. 7. Comparison of self-assembling *n*-alkanethiol monolayers deposited on gold from liquid and vapor phases. *J. Am. Chem. Soc.* **1993**, *115* (26), 12459.
11. Sagiv, J. Organized monolayers by adsorption. 1. Formation and structure of oleophobic mixed monolayers on solid surfaces. *J. Am. Chem. Soc.* **1980**, *102*, 92.
12. Maoz, R.; Sagiv, J. Penetration controlled reactions in organized monolayer assemblies III. Organic permanganate interaction with self-assembling monolayers of long chain surfactants. *Thin Solid Films* **1985**, *132*, 135.
13. Cohen, S.R.; Naaman, R.; Sagiv, J. Thermally induced disorder in organized organic monolayers on solid substrates. *J. Phys. Chem.* **1986**, *90*, 3054.
14. Silberzan, P.; Leger, L.; Auserre, D.; Benattar, J.J. Silanation of silica surfaces. A new method of constructing pure or mixed monolayers. *Langmuir* **1991**, *7*, 1647.
15. Tripp, C.P.; Hair, M.L. Direct observation of the surface bonds between self-assembled monolayers of octadecyltrichlorosilane and silica surfaces: a low-frequency IR study at the solid/liquid interface. *Langmuir* **1995**, *11*, 1215.
16. Wasserman, S.R.; Whitesides, G.M.; Tidswell, I.M.; Ocko, B.M.; Pershan, P.S.; Axe, J.D. The structure of self-assembled monolayers of alkylsiloxanes on silicon: a comparison of results from ellipsometry and low-angle X-ray reflectivity. *J. Am. Chem. Soc.* **1989**, *111* (15), 5852.
17. Tillman, N.; Ulman, A.; Schildkraut, J.S.; Penner, T.L. Incorporation of phenoxy groups in self-assembled monolayers of trichlorosilane derivatives. Effects on film thickness, wettability, and molecular orientation. *J. Am. Chem. Soc.* **1988**, *110* (18), 6136.
18. Vallant, T.; Kattner, J.; Brunner, H.; Mayer, U.; Hoffmann, H. Investigation of the formation and structure of self-assembled alkylsiloxane monolayers on silicon using in situ attenuated total reflection infrared spectroscopy. *Langmuir* **1999**, *15*, 5339.
19. Poirier, G.E.; Pylant, E.D. The self-assembly mechanism of alkanethiols on Au(1 1 1). *Science* **1996**, *24* (272), 1145.
20. Xu, S.; Cruchon-Dupeyrat, S.J.N.; Garno, J.C.; Liu, G.-Y.; Jennings, G.K.; Yong, T.-H.; Laibinis, P.E. In situ studies of thiol self-assembly on gold from solution using atomic force microscopy. *J. Chem. Phys.* **1998**, *108* (12), 5002.
21. Poirier, G.E. Coverage-dependent phases and phase stability of decanethiol on Au(1 1 1). *Langmuir* **1999**, *15*, 1167.
22. Schreiber, F.; Eberhardt, A. Adsorption mechanisms, structures, and growth regimes of an archetypal self-assembling system: decanethiol on Au(1 1 1). *Phys. Rev. B* **1998**, *57*, 12476.
23. Poirier, G.E.; Tarlov, M.J.; Rushmeier, H.E. Two-dimensional liquid phase and the  $\bar{p} \times \sqrt{3}$  phase of alkanethiol self-assembled monolayers on Au(1 1 1). *Langmuir* **1994**, *10* (10), 3383.
24. Mirkin, C.A. Programming the assembly of two- and three-dimensional architectures with DNA and nanoscale inorganic building blocks. *Inorg. Chem.* **2000**, *39*, 2258.
25. Brzoska, J.B.; Shahidzadeh, N.; Rondelez, F. Evidence of a transition temperature for the optimum deposition of grafted monolayer coatings. *Nature* **1992**, *360*, 719.
26. Brzoska, J.B.; Ben Azouz, I.; Rondelez, F. Silanization of solid substrates: a step toward reproducibility. *Langmuir* **1994**, *10* (11), 4367.
27. Schwartz, D.K.; Steinberg, S.; Israelachvili, J.; Zasadzinski, J.A. Growth of a self-assembled monolayer by fractal aggregation. *Phys. Rev. Lett.* **1992**, *69* (23), 3354.
28. Goldmann, M.; Davidovits, J.V.; Pho, V.; Silberzan, P. Temperature influence on the formation of silanized monolayers on silica: an atomic force microscopy study. *Surf. Sci.* **1996**, *352–354*, 369.
29. Sung, M.M.; Carraro, C.; Yauw, O.W.; Kim, Y.; Maboudian, R. Reversible liquid–liquid transitions in the early stages of monolayer self-assembly. *J. Phys. Chem. B* **2000**, *104*, 1556.
30. Mathauer, K.; Frank, C.W. Binary self-assembled monolayers as prepared by successive adsorption of alkyltrichlorosilanes. *Langmuir* **1993**, *9*, 3446.
31. Fang, J.; Knobler, C.M.; Gingery, M.; Eiserling, F.A. Imaging bacteriophage T4 on patterned organosilane monolayers by scanning force microscopy. *J. Phys. Chem. B* **1997**, *101*, 8692.
32. Folkers, J.P.; Laibinis, P.E.; Whitesides, G.M. Self-assembled monolayers of alkanethiols on gold: comparisons of monolayers containing mixtures of short- and long-chain constituents with methyl and hydroxymethyl terminal groups. *Langmuir* **1992**, *8*, 1330.
33. Laibinis, P.E.; Nuzzo, R.G.; Whitesides, G.M. Structure of monolayers formed by coadsorption of two *n*-alkanethiols of different chain lengths on gold and its relation to wetting. *J. Phys. Chem.* **1992**, *96*, 5097.
34. Mizutani, W.; Ishida, T.; Tokumoto, H. Monte Carlo simulation of phase-separated self-assembled films. *Appl. Surf. Sci.* **1998**, *130–132*, 792.
35. Tamada, K.; Hara, M.; Sasabe, H.; Knoll, W. Surface phase behavior of *n*-alkanethiol self-assembled monolayers adsorbed on Au(1 1 1): an atomic force microscope study. *Langmuir* **1997**, *13*, 1558.
36. Imabayashi, S.-I.; Gon, N.; Sasaki, T.; Hobara, D.; Kakiuchi, T. Effect of nanometer-scale phase separation on wetting of binary self-assembled thiol monolayers on Au(1 1 1). *Langmuir* **1998**, *14*, 2348.
37. Atre, S.V.; Liedberg, B.; Allara, D.L. Chain length dependence of the structure and wetting properties in binary composition monolayers of OH- and CH<sub>3</sub>-terminated alkanethiolates on gold. *Langmuir* **1995**, *11*, 3882.

38. Hayes, W.A.; Kim, H.; Yue, X.; Perry, S.S.; Shannon, C. Nanometer-scale patterning of surfaces using self-assembly chemistry. 2. Preparation, characterization, and electrochemical behavior of two-component organothiols monolayers on gold surfaces. *Langmuir* **1997**, *13*, 2511.
39. Offord, D.A.; Griffin, J.H. Kinetic control in the formation of self-assembled mixed monolayers on planar silica substrates. *Langmuir* **1993**, *9*, 3015.
40. Mathauer, K.; Frank, C.W. Naphthalene chromophore tethered in the constrained environment of a self-assembled monolayer. *Langmuir* **1993**, *9*, 3002.
41. Song, K.J.; Lagutchev, A.S.; Chuang, T.J.; Huang, J.Y.; Yang, P.K. Sum-frequency vibrational spectroscopic study of mixed alkylsiloxane monolayers self-assembled on fused silica surface. *Surf. Coatings Technol.* **1997**, *94*, 383.
42. Huang, J.Y.; Song, K.J.; Lagoutchev, A.; Yang, P.K.; Chuang, T.J. Molecular conformation and nanomechanics of self-assembled alkylsiloxane monolayers. *Langmuir* **1997**, *13*, 58.
43. Wasserman, S.R.; Tao, Y.T.; Whitesides, G.M. Structure and reactivity of alkylsiloxane monolayers formed by reaction of alkyltrichlorosilanes on silicon substrates. *Langmuir* **1989**, *5*, 1074.
44. Kitaev, V.; Seo, M.; McGovern, M.E.; Huang, Y.-J.; Kumacheva, E. Mixed monolayers self-assembled on mica surface. *Langmuir* **2001**, *17* (14), 4274.
45. Chapman, R.G.; Ostuni, E.; Yan, L.; Whitesides, G.M. Preparation of mixed self-assembled monolayers (SAMs) that resist adsorption of proteins using the reaction of amines with a SAM that presents interchain carboxylic anhydride groups. *Langmuir* **2000**, *16* (17), 6927.

# Lab-on-a-Chip Microreactors

Paul D.I. Fletcher  
Stephen J. Haswell  
Paul Watts  
Xunli Zhang

*Department of Chemistry, University of Hull, Hull, U.K.*

## INTRODUCTION

Micro reactors, in their simplest form, consist of a network of micron-sized channels (typical dimensions are in the range 10–300  $\mu\text{m}$ ) etched into a solid substrate (see Refs.<sup>[1–9]</sup> for introductory overviews). The ability to move chemical reagents around the channel network enables spatial control of reactions, which can be exploited to alter yield and product selectivity in synthetic chemical processes. This extra dimension of reaction control, not achievable in bulk reactors where concentrations are uniform, is comparable with compartmentalized biosynthetic processes in biological cells. Hence, in addition to their applications in analysis, micro reactors open up new horizons for the controlled synthesis of fine chemicals. This entry discusses the current and future applications of micro reactors in the fields of chemical synthesis and drug discovery. The fabrication and physical characterization of micro reactors, together with details of their use and operation, is described. Examples of liquid and gas phase reactions are used to illustrate some key advantages of performing chemical reactions in micro reactors.

## BACKGROUND

For solution-based chemistry, the channel networks of the micro reactors are connected to a series of reservoirs containing chemical reagents to form the complete device or “chip” with overall dimensions of a few centimeters, a simple example of which is illustrated in Fig. 1. In the micro reactor, reagents can be brought together in a specific sequence, mixed and allowed to react for a specified time in a controlled region of the channel network using electrokinetic or hydrodynamic pumping. For electrokinetically driven systems, electrodes are located in the appropriate reservoirs to which specific voltage sequences can be delivered under automated computer control. This control offers a simple but effective method of moving

and separating reactants and products within a micro reactor, without the need for moving parts. Hydrodynamic pumping exploits conventional or microscale pumps, notably syringe-type pumps, to maneuver solutions around the channel network. However, for hydrodynamic pumping, either an interface between large external pumps and the chip is required or it is necessary to fabricate complex small moving parts within the device itself.

Alongside the continuing development of miniaturized total analytical systems ( $\mu\text{-TAS}$ ) and related analytical applications,<sup>[10–17]</sup> a concerted effort is now underway to establish the benefits that micro reactors can bring to the field of reaction chemistry. The ability to manipulate reagent concentrations in space and time by electrokinetic control within a micro reactor provides a level of reaction control that is not possible in traditional batch reactors where concentrations are generally uniform. Interestingly, the spatial and temporal control of chemical reactions in micro reactors, coupled with the features of very small reaction volumes and high surface interactions, makes this technology akin to the conditions under which reactions occur within biological cells. Nature has become very effective at exploiting the organized distribution of reagents within the micron-sized domains of cells to control the chemical selectivity of compound production, relative to the situation of large-scale synthetic methodology. Based on this notion, it has now been demonstrated that many chemical reactions show improved reactivity, product yield, and selectivity when performed in micro reactors compared with the same reaction performed using conventional laboratory procedures with macroscale reactors. Reported research confirms that micro reactor methodology is applicable to performing both gas and liquid phase reaction chemistry. From the work cited in this entry, the evidence is that the unique modus operandi of micro reactors (namely, the low-volume spatial and temporal control of reactants and products in a diffusive, laminar flow mixing environment) offers a novel method for chemical manipulation and product



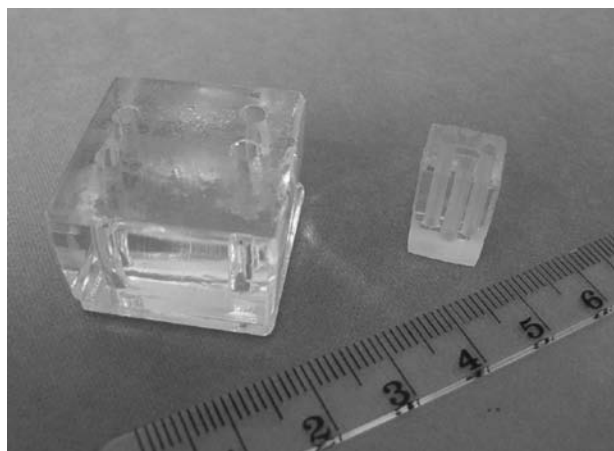


Fig. 1 Borosilicate glass micro reactors.

generation. In short, micro reactors are new tools with which to generate molecules and increase our knowledge of complex chemical processes.

In the authors' experience, a reaction performed within a micro reactor can commonly be speedily optimized to generate relatively pure products in higher yield and in shorter time, when compared with the equivalent bulk reaction. Product amounts, although relatively small, are generally sufficient to perform full instrumental characterization. One of the immediate and obvious applications is therefore in drug and process discovery, where the generation of compounds either with different reagents or under variable conditions is an essential factor. An interesting twist to the micro reactor chemistry carried out in the authors' laboratories is not just the opportunity to separate reactants and products in real time, but also the capability to manufacture and use reagents in situ.

## MICROREACTOR FABRICATION

Materials such as silicon, quartz, glass, metals, and polymers have all been used to fabricate micro reactors.<sup>[9,11]</sup> Important considerations in material choice include chemical resistance, ease and reproducibility of fabrication, compatibility with detection methods, and, if relevant, whether the material supports electro-osmotic flow (EOF) with the solvents of interest. Glass is a popular choice because it allows EOF with many common solvents, is chemically inert, enables the use of a range of visible light detection methods, and fabrication techniques are well established.

Depending on the material used, a range of channel microfabrication methods such as photolithography, hot embossing, powder blasting, injection molding, and laser microforming are available.<sup>[18]</sup> For glass micro reactors, photolithographic fabrication of

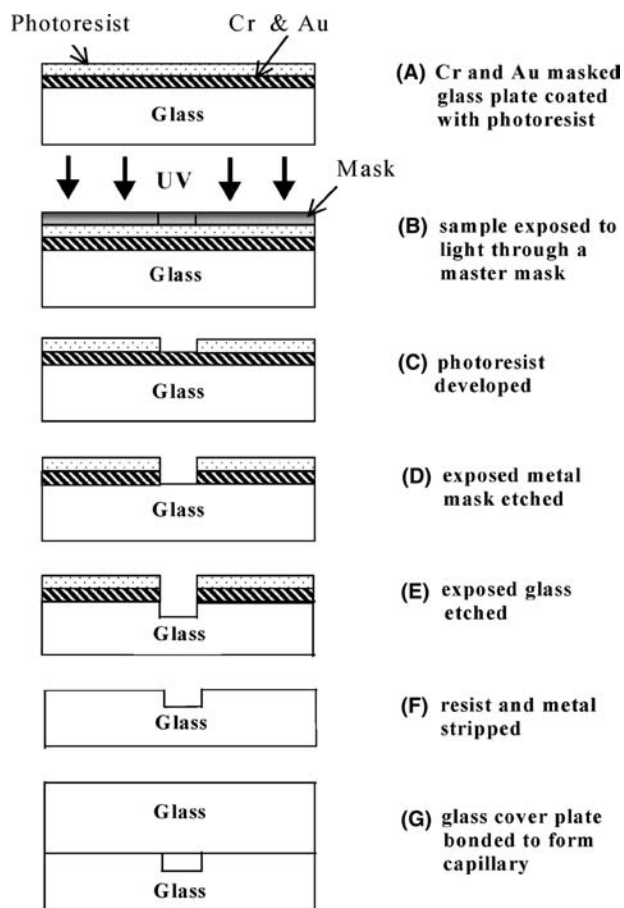
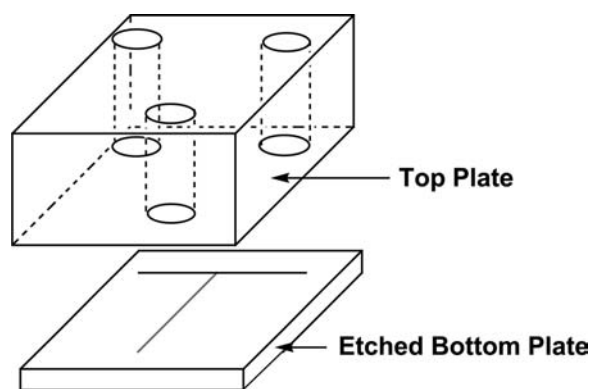


Fig. 2 Photolithographic fabrication of channel networks in glass.

channel networks is performed as shown schematically in Fig. 2.<sup>[19,20]</sup> First, the channel network is designed and printed using suitable computer drawing software and a film negative of the desired final size is then prepared by photoreduction to form the optical mask. Commercially available borosilicate glass photolithographic plates (thickness of 3 mm) coated with a thin metal etch mask layer (normally chromium) plus an upper layer of positive photoresist (0.5–2.0  $\mu\text{m}$  depth) are used for channel network fabrication. The pattern of interconnecting channels is transferred from the optical mask to the photoresist layer. After light exposure, the photoresist is developed and removed, together with the chromium layer, to reveal the areas of glass to be etched. The patterned plate is then heated to allow the volatiles to evaporate before performing the chemical etch. The channels may be etched, for example, using a mixture of 1% HF and 5%  $\text{NH}_4\text{F}$  in water at 65°C, resulting in an etch rate of typically 0.3 to 0.5  $\mu\text{m min}^{-1}$ . During the etch process, the system must be well agitated to ensure a consistent supply of etchant to the surface and the efficient removal of etch debris. In our laboratories, we have found that



**Fig. 3** Exploded view of a micro reactor constructed from a base plate containing the etched channel network and thermally bonded to a thick upper plate containing reagent reservoirs.

ultrasound irradiation during the etch process is effective.<sup>[20]</sup>

The base plate containing the etched channel network must next be sealed by bonding to an upper plate (17 mm thick) containing predrilled holes to act as reservoirs for reagents and products. In our laboratories, the upper plate is aligned with the channel geometry and thermally bonded to the base plate (typically at 575°C for 3 hr).<sup>[19,20]</sup> Thermal bonding is aided by placing a weighting block of non-adhering quartz of high softening temperature on the upper plate. A schematic of the device produced by this method is illustrated in Fig. 3, and a photograph of such a micro reactor is shown in Fig. 1. For good thermal bonding, it is important to ensure that both pieces of glass have the correct thermal softening and expansion properties. In addition, the surfaces to be bonded must be clean and flat. More recently, the thermal bonding of ceramic adaptors to glass has enabled hydrodynamic pumping to be more effectively realized. Fig. 4 shows a glass

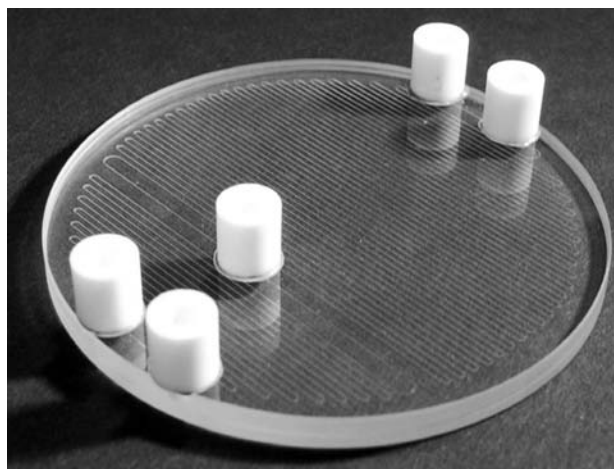


**Fig. 4** Micro reactor with ceramic fittings. *Source:* Micro Chemical Systems Ltd.

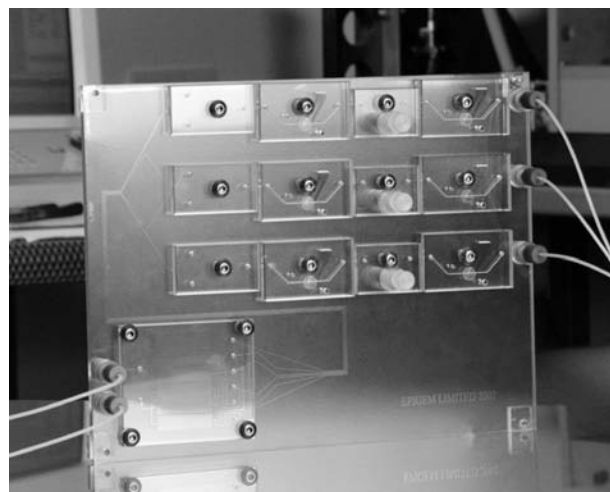


**Fig. 5** Micro reactors fabricated from polymers. *Source:* Epigem Ltd.

micro reactor with ceramic adaptors, enabling high-performance liquid chromatography (HPLC)-type fittings to be connected directly to the chip.

Fabrication in polymeric materials, while attractive from an engineering and cost perspective, poses a number of reagent compatibility issues. However, the U.K. Lab-on-a-Chip consortium project has demonstrated that devices containing channels fabricated from an epoxy resin (SU-8) coated onto a polymer support, such as methacrylate, are relatively robust to chemical attack (Fig. 5). This methodology has the advantage that the non-wetted bulk of the chip can be fabricated from low-cost commodity polymers.

Of all the fabrication media, perhaps metal is the most robust in terms of engineering requirements and, more specifically, micromixers have been constructed and applied in chemical processing.<sup>[9]</sup> A number of alternative methods for producing channels in glass have also been reported, such as deep reactive ion etching, powder blasting, and laser ablation.<sup>[9]</sup>

## PRINCIPLES OF REACTION CONTROL IN MICROREACTORS

Pumping of solutions around a channel network by EOF, using voltages applied via electrodes placed in the reservoirs, has several significant advantages over alternative pumping methods. It can be easily miniaturized because no mechanical moving parts are involved and the required voltage sequences can be readily applied under automated computer control. For a glass micro reactor, the channel wall-solution interface normally has a negative charge, arising from ionization of immobile surface silanol groups. This immobile surface charge attracts a diffuse layer

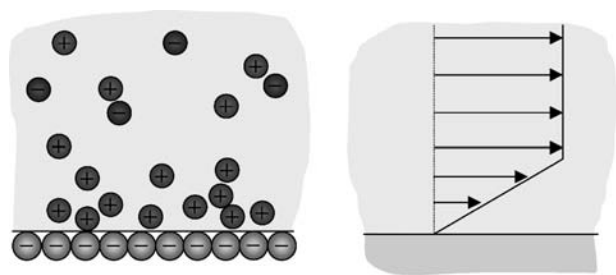


**Fig. 6** Voltage-driven movement of the diffuse layer of cations adsorbed at the negatively charged channel wall (left-hand figure) produces a flat EOF velocity profile across the channel except within the nanometer-thick diffuse counterion layer (right-hand figure).

(of thickness of the order of nanometers) of mobile, oppositely charged counterions in the solution adjacent to the channel wall (cations for a negatively charged glass channel wall). As shown schematically in Fig. 6, application of an electric field along the channel length causes the nanometer-thick “skin” of mobile cations to move toward the more negative electrode and drags all the intervening solution in the bulk of the channel with it.<sup>[21–23]</sup> An important feature of EOF is that the liquid EOF velocity is constant across the channel except in the nanometer-thick regions of the diffuse layer of counterions very close to the wall. Unlike EOF, pressure-driven flow produces a parabolic velocity profile with high velocities in the channel center and slow velocities near to the wall, giving rise to increased “blurring” of reagent zones along a channel length. The imaging of velocity profiles induced by EOF and pressure-driven flow has been described by Paul et al.<sup>[24]</sup>

The EOF fluid velocity  $v_{\text{eof}}$  is given by Eq. (1)

$$v_{\text{eof}} = \frac{E\epsilon\epsilon_0\zeta}{\eta} \quad (1)$$

where  $E$  is the electric field (voltage divided by electrode separation),  $\epsilon$  is the relative dielectric constant of the liquid,  $\epsilon_0$  is the permittivity of free space,  $\zeta$  is the zeta potential of the channel wall–solution interface, and  $\eta$  is the liquid viscosity.<sup>[21–23]</sup> For the glass–aqueous solution interface, the value of  $\zeta$  varies from  $-50$  to  $-150$  mV at pH 7 (dependent on ionic strength), but decreases in magnitude to 0 at pH around 2.5.<sup>[25]</sup> The magnitude of the electric field applied in micro reactors (typically some hundreds of volts per centimeter) gives EOF velocities in the range  $0.1$  to  $1$  mm  $\text{sec}^{-1}$  for aqueous solutions at pH 7.

From Eq. (1), it can be seen that  $v_{\text{eof}}$  is proportional to the applied voltage and depends on the properties of both the liquid and the channel material. Electroosmotic flow does not occur with low polarity solvents such

as alkanes where no diffuse layer of surface counterions exists. The EOF velocity  $v_{\text{eof}}$  is independent of the channel cross-sectional dimensions, whereas the EOF volumetric flow rate (given by the product of  $v_{\text{eof}}$  multiplied by the channel cross-sectional area) depends on the channel dimensions.

Under EOF voltage control, the solvent and any uncharged solutes move with a velocity  $v_{\text{eof}}$ . Within the electric field, charged solutes have an additional electrophoretic velocity  $v_{\text{ph}}$  which is given by Eq. (2)

$$v_{\text{ph}} = \frac{zeED}{kT} \quad (2)$$

where  $z$  is the charge number on the species,  $e$  is the electronic charge,  $D$  is the diffusion coefficient of the species,  $k$  is the Boltzmann constant, and  $T$  is the absolute temperature.<sup>[21,23]</sup> The magnitude of  $v_{\text{ph}}$  for typical micro reactor operating voltages is commonly comparable with  $v_{\text{eof}}$ . The total velocity of a charged species is given by the vector sum of  $v_{\text{eof}}$  and  $v_{\text{ph}}$ . The direction of EOF for aqueous solutions in a glass micro reactor is normally toward the more negative electrode, whereas for a cationic solute species,  $v_{\text{ph}}$  will be in the same direction as the EOF (i.e., toward the more negative electrode) and will move faster down the channel than the solvent and neutral species. Anionic solutes will be retarded and may, if the magnitude of  $v_{\text{ph}}$  is greater than  $v_{\text{eof}}$ , move in the opposite direction. In this way, electrophoretic separation of solutes occurs along with EOF in the micro reactor channels when operated under electrokinetic control. The ability to use electrophoretic mobility to spatially locate charged reagents and products within a micro reactor independently of the solvent forms a useful aspect of reaction control. Differential electrophoretic mobilities have been exploited to selectively control product detection times in the capillary electrophoresis technique of electrophoretically mediated microanalysis (EMMA).<sup>[26–29]</sup>

The strategy of using micro reactors to electrokinetically control the spatial and temporal evolution of chemical reactions relies on the ability to use voltage sequences to direct reagents to selected points at specified times within a channel network. For an intricate channel network with many reservoirs and electrodes, the relationships between the applied voltages and the liquid flow rates and solute mobilities in the different sections of the network can be very complex. The basic approach is to analyze the channel network in terms of an equivalent d.c. circuit where the different channel sections correspond to resistance elements and, as will be shown, the electrical currents are proportional to the volumetric liquid flow rates within the corresponding channel sections.<sup>[30–32]</sup> As an illustrative example, we discuss the channel network

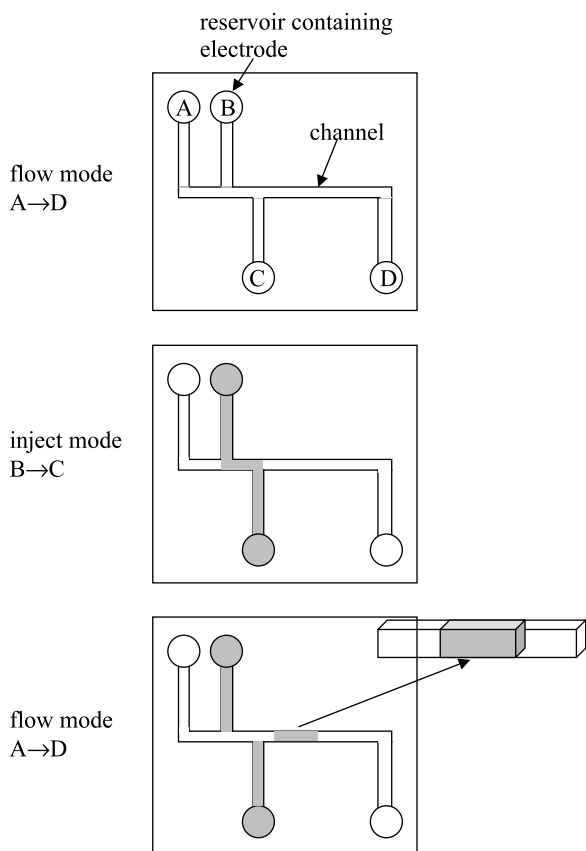


**Fig. 7** Double T-junction channel network and flow-inject-flow required to achieve a “slug” of one reagent within a flowing stream of a second reagent.

shown in Fig. 7 where we wish to achieve a flow-inject-flow sequence to obtain a “slug” of one reagent in a flowing stream of a second reagent. In the “flow” mode, we require flow from reservoir A to D with zero flow from both B and C to D. In the “inject” mode, we require flow from B to C with zero flow from A to D. To obtain both modes, a multichannel voltage supply operating under computer control using LabVIEW software is used to deliver the correct voltage sequences to the electrodes in reservoirs A, B, and C (voltages  $V_A$ ,  $V_B$ , and  $V_C$ ) relative to reservoir D, set to ground voltage. The following analysis shows how the voltages are related to the electrical currents ( $I_A$ ,  $I_B$ , and  $I_C$ ) which, in turn, are related to the volumetric flow rates in the corresponding channel sections  $F_A$ ,  $F_B$ , and  $F_C$ .

We consider the simplest possible situation in which the channel network of Fig. 7 is filled with a liquid of uniform electrical conductivity  $\kappa$  and the zeta potential of the channel wall is equal in all channel sections. Experimentally, this situation can be achieved even when mixing different reactant solutions by ensuring a high background concentration of an inert electrolyte. For the sake of simplicity, we ignore the (normally

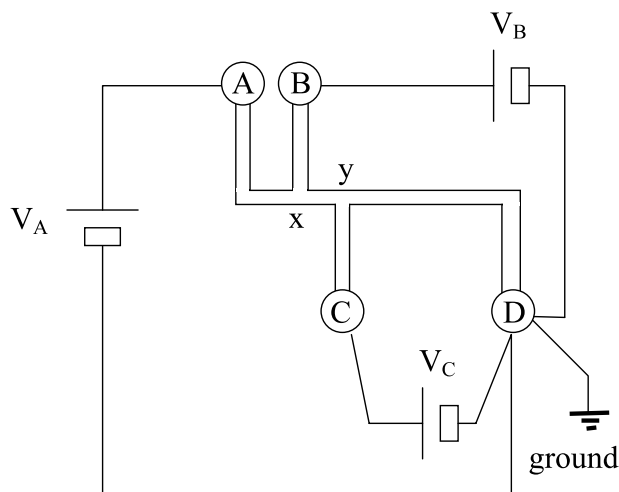


**Fig. 8** Direct current circuit used to drive the channel network of Fig. 6. Reservoir voltages (relative to ground in D) are  $V_A$ ,  $V_B$ , and  $V_C$  and  $x$  and  $y$  denote the channel junctions. The electrical current in channel section Ax is  $I_A$ , section Bx is  $I_B$ , section Cy is  $I_C$ , section xy is  $(I_A + I_B)$ , and section yD is  $(I_A + I_B + I_C)$ .

small) contribution to the overall conductivity of a channel section, which arises from surface conduction.<sup>[21–23,31]</sup> With these approximations, the electrical resistance of the  $i$ th channel section  $R_i$  is given by Eq. (3)

$$R_i = \frac{L_i}{\kappa A_i} \tag{3}$$

where  $L_i$  and  $A_i$  are the length and cross-sectional area of the  $i$ th channel section, respectively. The d.c. circuit used to drive flow in the channel network of Fig. 7 is shown in Fig. 8 and serves to define the current values in the different channel sections. In each of the loops of the coupled circuit, the applied voltages equal the sums of the products of the resistances and currents. Writing these gives a series of  $(n - 1)$  simultaneous equations, where  $n$  is the number of reservoirs containing electrodes (it is  $n - 1$  because one electrode is set to ground). For the channel network considered here, we have the set of three equations shown below.

$$\begin{aligned} V_A &= R_{Ax}I_A + R_{xy}(I_A + I_B) + R_{yD}(I_A + I_B + I_C) \\ V_B &= R_{Bx}I_B + R_{xy}(I_A + I_B) + R_{yD}(I_A + I_B + I_C) \\ V_C &= R_{Cy}I_C + R_{yD}(I_A + I_B + I_C) \end{aligned} \tag{4}$$

Solving these simultaneous equations (using a software package such as MathCAD) yields the corresponding expressions for the electrical currents shown in Eq. (5). The volumetric liquid flow rate in the  $i$ th channel section  $F_i$  is proportional to the corresponding

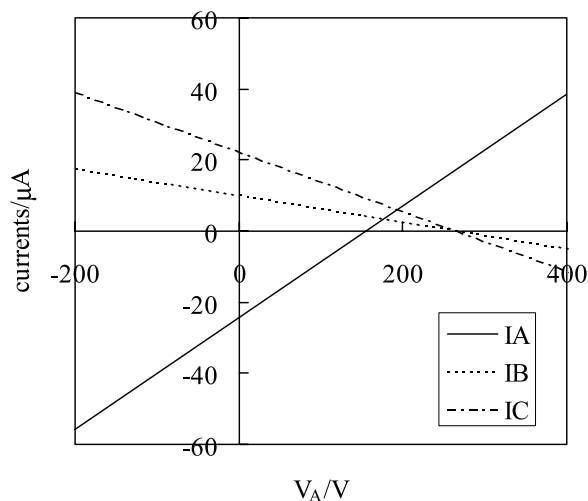


**Fig. 9** Illustrative plots of electrical currents versus  $V_A$  for  $V_B$  and  $V_C$  both set to 200 V. The data refer to the channel network of Fig. 6 filled with 50 vol.% ethanol/water containing 35 mM phosphate buffer at pH 7.5.

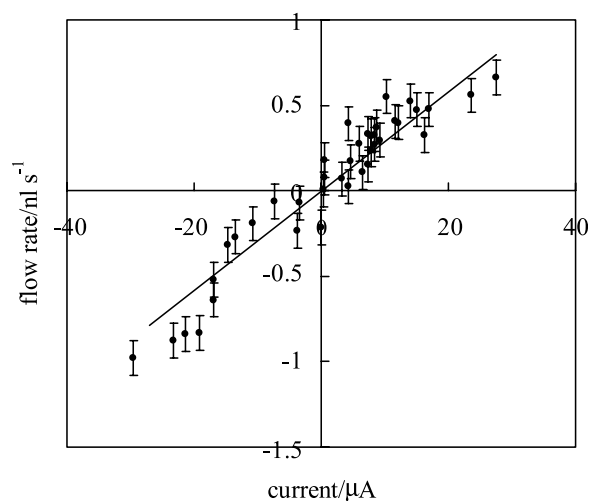


**Fig. 10** Correlation between measured volumetric liquid flow rates and the corresponding electrical currents for the channel network of Fig. 6 filled with 50 vol.% ethanol/water containing 35 mM phosphate buffer at pH 7.5.

electrical current  $I_i$  according to Eq. (6).<sup>[21,23]</sup>

$$F_i = -I_i \left( \frac{\varepsilon \varepsilon_0 \zeta}{\eta \kappa} \right) \quad (6)$$

To determine the voltages required to achieve a particular pattern of flow rates (e.g., “flow” or “inject” modes described above), all the resistance values of the different channel sections, filled with the liquid of interest, must be known. This can be performed by measuring the currents as a function of the various voltages within the micro reactor and computer fitting the resistance values. Alternatively, one can measure the liquid conductivity (using a conventional conductivity meter) and all the channel dimensions and calculate the required resistances according to Eq. (3). Calibration measurements of liquid flow rates within the micro reactor as a function of different set currents yield the value of  $\zeta$ , which then enables the conversion of measured currents (logged during a run) to liquid flow rates from Eq. (6).

Representative plots of electrical currents vs. one of the voltages (with the remaining voltages being fixed) are shown in Fig. 9. The current values are typically

in the microampere range, and, as expected from Ohm’s law, they are proportional to the voltage. However, because of the linking together of the different limbs of the overall circuit, the voltages required to produce zero current in a particular channel section are determined by a complex function of all resistance and voltage values. An example of the linear correlation between the electrical current and liquid flow rates in corresponding channel sections is shown in Fig. 10. Applying this type of information, Table 1 lists the calculated voltage settings required to achieve flow and injection modes with set flow rates for the system shown in Fig. 10.

Full details have been published<sup>[31]</sup> where it is demonstrated that measurement of the liquid conductivity  $\kappa$ , zeta potential  $\zeta$ , and all channel dimensions enables the correct calculation of the voltages needed to achieve any set of flow rates. However, several notes of caution should be emphasized. First, the results reported indicate that correction of the overall electrical current for surface conduction along the channel walls is sometimes required. The surface conduction may become non-negligible when the bulk conductivity of the liquid is relatively low. Second, the analysis

$$\begin{aligned}
 I_A &= \frac{(R_{Cy}R_{xy} + R_{Cy}R_{yD} + R_{Bx}R_{yD} + R_{xy}R_{yD} + R_{Cy}R_{Bx})V_A - (R_{Cy}R_{yD} + R_{Cy}R_{xy} + R_{xy}R_{yD})V_B - R_{Bx}R_{yD}V_C}{R_{Cy}R_{Bx}R_{Ax} + R_{Cy}R_{xy}R_{Bx} + R_{Cy}R_{xy}R_{Ax} + R_{Cy}R_{yD}R_{Bx} + R_{Cy}R_{yD}R_{Ax} + R_{Bx}R_{yD}R_{Ax} + R_{xy}R_{yD}R_{Bx} + R_{xy}R_{yD}R_{Ax}} \\
 I_B &= \frac{-(R_{Cy}R_{xy} + R_{Cy}R_{yD} + R_{Bx}R_{yD})V_A - (R_{Cy}R_{xy} + R_{Cy}R_{yD} + R_{Cy}R_{Ax} + R_{xy}R_{yD} + R_{yD}R_{Ax})V_B - R_{Ax}R_{yD}V_C}{R_{Cy}R_{Bx}R_{Ax} + R_{Cy}R_{xy}R_{Bx} + R_{Cy}R_{xy}R_{Ax} + R_{Cy}R_{yD}R_{Bx} + R_{Cy}R_{yD}R_{Ax} + R_{Bx}R_{yD}R_{Ax} + R_{xy}R_{yD}R_{Bx} + R_{xy}R_{yD}R_{Ax}} \\
 I_C &= \frac{-(R_{Bx}R_{yD})V_A - (R_{yD}R_{Ax})V_B - (R_{Bx}R_{Ax} + R_{yD}R_{Ax} + R_{xy}R_{Ax} + R_{xy}R_{Bx} + R_{Bx}R_{yD})V_C}{R_{Cy}R_{Bx}R_{Ax} + R_{Cy}R_{xy}R_{Bx} + R_{Cy}R_{xy}R_{Ax} + R_{Cy}R_{yD}R_{Bx} + R_{Cy}R_{yD}R_{Ax} + R_{Bx}R_{yD}R_{Ax} + R_{xy}R_{yD}R_{Bx} + R_{xy}R_{yD}R_{Ax}} \quad (5)
 \end{aligned}$$



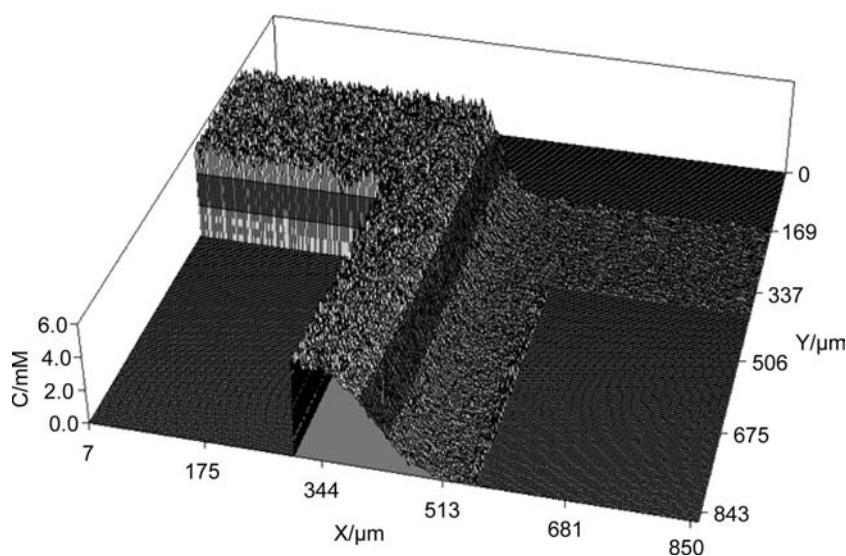
**Table 1** Voltages, electrical currents, volumetric flow rates, and liquid EOF velocities for flow and injection modes in the system of Fig. 10

Variable	Flow mode (A→D)	Inject mode (B→C)
$V_A$ (V)	225	1
$V_B$ (V)	169	86
$V_C$ (V)	169	-38
$I_A$ ( $\mu$ A)	15 (set)	0 (set)
$I_B$ ( $\mu$ A)	0 (set)	8 (set)
$I_C$ ( $\mu$ A)	0 (set)	-8 (set)
$F_A$ (nL sec <sup>-1</sup> )	0.45	0
$F_B$ (nL sec <sup>-1</sup> )	0	0.24
$F_C$ (nL sec <sup>-1</sup> )	0	-0.24
$v_{eof}$ (A) (mm sec <sup>-1</sup> )	0.05	0
$v_{eof}$ (B) (mm sec <sup>-1</sup> )	0	0.03
$v_{eof}$ (C) (mm sec <sup>-1</sup> )	0	-0.03

given here applies to the situation in which the liquid conductivity and the zeta potential are both uniform throughout the channel network. Mixing of reagent solutions, which possess different conductivities and/or different zeta potentials, with the channel walls will produce moving channel zones with non-uniform properties and EOF mobilities. Obviously, this situation requires a considerably more complex analysis. Last, the simplified analysis presented here, although sufficient to illustrate the main features of flow control, takes no account of flow inertial effects and the non-uniformity of the electrical field around channel junctions. At a microscopic level, the effects cause complex local flow patterns in these regions, which can be modeled using sophisticated fluid dynamics software.<sup>[33–38]</sup>

In addition to its use in determining the required electrokinetic flow control parameters, in situ monitoring of electrical currents in channel networks provides useful diagnostic information on micro reactor operation. First, the observation of a current dropping to zero in a branch of the channel network can indicate the position of a channel blockage. Second, application of an excessive voltage across a channel network can cause electrochemical reactions, which may result in the release of gas bubbles. Electrolysis occurs in micro reactors when the overall voltage difference between an electrode pair (typically several hundred volts) is sufficiently high or the electrical resistance of the relevant channel section is low such that the voltage change across an electrode / solution interface (typically a fraction of a volt) exceeds the redox potential required for an electrochemical reaction. Last, for chemical reactions, which result in a change of conductivity of the solution, in situ current monitoring can, in principle, be exploited to monitor the extent of a reaction within the channel network.

Except for unimolecular reactions, two or more reactant solutions must be mixed as a necessary first step to achieving reaction. Two main modes of mixing are possible which have very different characteristics. The first mode, denoted “diffusive mixing,” is illustrated in Fig. 11 which shows the 3-D concentration profile resulting when a dye solution (entering from the left channel) is combined with solvent entering from the right-hand channel of a T-junction. The two solutions flow together down the leg of the T. For typical EOF conditions, the linear fluid velocities are of the order of 0.1–1 mm sec<sup>-1</sup>. The Reynolds number  $R_e$  (equal to  $D_e v \rho / \eta$  where  $D_e$  is the effective channel diameter,  $v$  is the velocity,  $\rho$  is the liquid density, and  $\eta$  is the liquid viscosity) for such flow is  $< 10$ , well below the transition from laminar to turbulent flow,

**Fig. 11** 3-D plot of dye concentration vs. position within a T-junction. The dye solution enters from the left and is combined with solvent entering from the right. The flow velocity down the “leg” of the T is 0.48 mm sec<sup>-1</sup>. Detailed analysis of the diffusional broadening of the dye–solvent interface seen as the laminar streams move down the channel (corresponding to different times after contact) yields the diffusion coefficient of the dye ( $4.0 \times 10^{-10}$  m<sup>2</sup> sec<sup>-1</sup> in this example).



which occurs at  $R_e$  values of around 2500. The co-flowing reagent streams therefore retain their laminar flow pattern and mixing occurs only by interdiffusion. From the 3-D concentration plot of the dye, it can be seen that only a small extent of diffusional mixing occurs in the time between the first contact of the solution streams flow to a position corresponding to the bottom edge of the image. For the flow velocity used ( $0.48 \text{ mm sec}^{-1}$ ), this time corresponds to approximately 2 sec. In this mode of mixing, at very long times, the reagent concentrations are diluted by a ratio equal to the ratio of the flow rates of the incoming streams. A crude estimate of the time required for mixing across the complete width of the channel ( $w$ ) is given by  $t \approx 5w^2/D$ , where  $D$  is the diffusion coefficient of the solute species. For a typical channel width of  $100 \mu\text{m}$  and a value of  $D$  of  $5 \times 10^{-10} \text{ m}^2 \text{ sec}^{-1}$ , this time is of the order of 100 sec. It can be seen that the mixing of two streams flowing at  $1 \text{ mm sec}^{-1}$  in a typical channel length of a few centimeters will normally be very incomplete. Imaging of the diffusive broadening of the concentration gradient perpendicular to the laminar-flowing streams at different times has, in fact, been used to determine diffusion coefficients of absorbing or fluorescent species.<sup>[32,39]</sup>

Complete mixing by diffusion can be achieved by using slow (or stopped) flow to increase the contact time. Alternatively, faster flow or smaller channel cross sections, within long channels (generally folded to reduce overall device size), will achieve the same result. Elegant designs of networks containing cascades of T-junctions connected by suitably long, tortuous channels have produced output channels giving simultaneously a series of fully mixed dilutions of the original input solution<sup>[40,41]</sup> or concentration gradients of complex shapes.<sup>[42]</sup> This type of multiple outputs is useful when using a micro reactor to determine, for example, a calibration plot of detector signal vs. the concentration of an analyte species. The fact that the laminar flows of reagent streams interdiffuse only relatively slowly has been exploited by using chemically reactive reagent streams. Reactions between appropriate reagents at the interface between laminar, co-flowing streams of the reactants have been used, for example, to deposit very thin lines of metals (plus a range of other species) at the channel base as a novel means of fabricating “nanowires” in specified locations.<sup>[43]</sup>

The second mode of mixing, “slug injection,” is illustrated in Fig. 7. Using a pair of offset T-junctions and the “flow–inject–flow” sequence described earlier, a slug of one reagent is produced within a flowing stream of a second reagent. We illustrate the main features of this mode by considering the behavior of a slug of a reagent X in a flowing stream of a reagent Y where X and Y can chemically react to give product Z. We consider the situation where the reactant concentrations and the reaction rate constant are such that chemical

reaction occurs fast; that is, virtually immediately, the reagents are locally mixed in a particular channel section. Using the simulation procedure described in Ref.<sup>[30]</sup>, we are able to calculate the concentrations of all the species X, Y, and Z as a function of the distance along the flow channel length for different times after the production of the initial rectangular slug of X in the stream of Y. Input variables include the initial concentrations of X, Y, and Z, the forward and reverse rate constants for the reaction  $X + Y \rightleftharpoons Z$ , the EOF velocity, and the electrophoretic velocities of X, Y, and Z. The first simulation (Fig. 12) shows a series of time snapshots for the situation in which the electrophoretic velocities of X, Y, and Z are all zero (corresponding to these species all being uncharged). In this case, all species move with velocities equal to  $v_{\text{eof}}$  and mixing (and hence reaction) occurs only by interdiffusion at the leading and trailing edges of the slug of X. For the wide slug and the short time shown, the interdiffusion and therefore

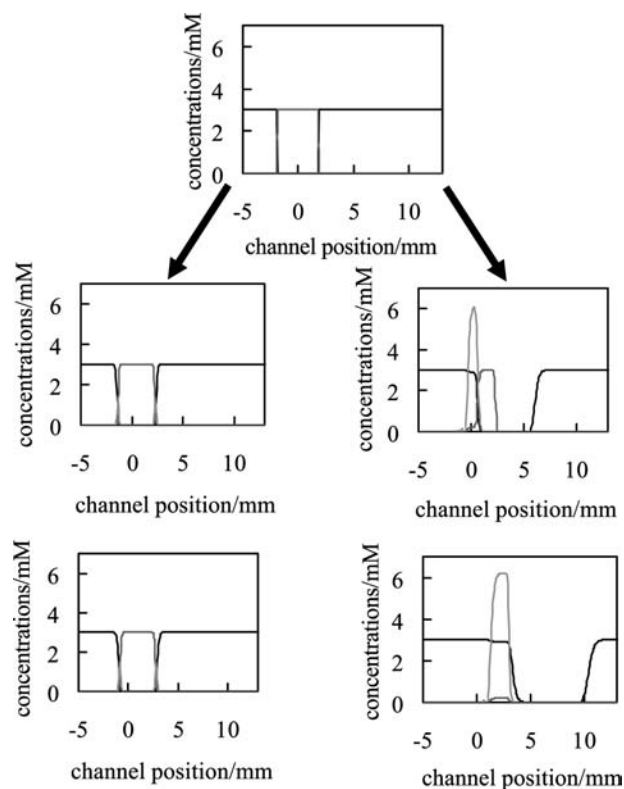


**Fig. 12** Time snapshots at 0, 10, and 20 sec of the concentration profiles of reactants X (red) and Y (black) and product Z (blue). The top plot shows the initial configuration of a rectangular slug of X in a stream of Y, centered at channel position = 0. The left-hand plots correspond to  $v_{\text{eof}} = 0.05 \text{ mm sec}^{-1}$  with  $v_{\text{ph}}$  of all species = 0 (diffusive mixing only). The right-hand plots correspond to  $v_{\text{eof}} = 0.05 \text{ mm sec}^{-1}$  and  $v_{\text{ph}}$  (X) = 0,  $v_{\text{ph}}$  (Y) =  $0.76 \text{ mm sec}^{-1}$ , and  $v_{\text{ph}}$  (Z) =  $0.23 \text{ mm sec}^{-1}$ . In this case, mixing of X and Y occurs mainly as a result of the different electrophoretic velocities.

the extent of the reaction are low. The time for diffusive mixing across the slug (approximately  $5w_s^2/D$ , where  $w_s$  is the slug width) can be made shorter by reducing the slug width. To maximize the conversion to products in this mixing mode, a series of many narrow slugs are therefore more effective than a single, broad slug. Elegant methods to achieve very narrow slug widths have been described.<sup>[35]</sup>

In the second simulation shown in Fig. 12,  $v_{ph}$  for X is set to zero, but  $v_{ph}$  for Y and Z are set to positive values corresponding to these species bearing positive charges. Y now moves slowly with a velocity  $v_{eof}$ , whereas X moves faster with a velocity  $v_{eof} + v_{ph}$ . In this situation, the slug of X becomes displaced relative to the concentration “gap” in Y and mixing of X and Y therefore occurs relatively rapidly as a result of the different electrophoretic mobilities of the two species and results in reaction at the trailing edge of the slug of X. It should be noted that, in contrast to the “diffusive mixing” mode discussed above, mixing by differential electrophoretic mobilities does not result in dilution of the localized reagent concentrations. Fig. 13 shows the experimental realization of this type of mixing and reaction. A slug of the uncharged ligand,

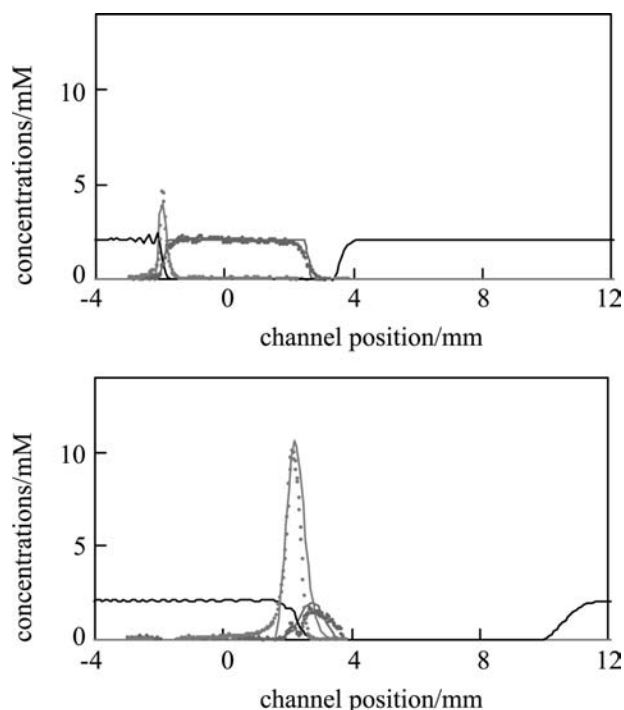


**Fig. 13** Comparison of simulated (solid lines) and measured (data points) concentration profiles for the reaction between  $Ni^{2+}$  ions (black) and a slug of the ligand PADA (red) to form the  $NiPADA^{2+}$  complex (blue) at the trailing edge of the PADA slug. Concentration profiles of the coloured PADA and complex species were determined by analysis of digitized video images. The concentration profiles correspond to 10 sec (upper plot) and 70 sec (lower plot) after PADA slug injection.

pyridine-azo-dimethylaniline (PADA), is injected into a flowing stream of  $Ni^{2+}$  ions. As seen in the measured concentration profiles along the channel length, fast complexation to form the  $NiPADA^{2+}$  complex occurs at the trailing edge of the PADA slug and can be successfully modeled using the kinetic rate parameters measured for the forward (complexation) and reverse (complex dissociation) reactions.<sup>[32]</sup>

Following the time sequence shown in Fig. 13, it is possible to reverse the flow, which moves the  $NiPADA^{2+}$  complex product peak back into the concentration “gap” of  $Ni^{2+}$ . Because the complex formation reaction is reversible, the complex dissociates via the back reaction into PADA and  $Ni^{2+}$ . This example, using a mechanistically very simple reaction, demonstrates how micro reactors can be used to realize an extra dimension of spatial and temporal control of reactions, which is unachievable in bulk solution reactors where all concentrations are uniform.

## REACTIONS PERFORMED IN MICRO REACTORS

To date, most reactions that have been performed in micro reactors have been conducted simply to demonstrate that it is possible to perform reactions within such devices. A summary of the reactions that have been performed in micro reactors is presented in Table 2, and many of these are reviewed in detail in Refs.<sup>[44]</sup> and <sup>[45]</sup>. The following section reviews some reactions that have been performed within micro reactor systems that have demonstrated interesting results.

Skelton et al. have reported the application of micro reactors for the Wittig reaction<sup>[66,67]</sup> where they prepared *cis*- and *trans*-nitrostilbene esters **1** and **2** (Scheme 1). A number of features such as stoichiometry and stereochemistry were investigated in the micro reactor environment. When two equivalents of the aldehyde **3** to the phosphonium salt **4** were used in the reaction, a conversion of 70% was achieved. The micro reactor demonstrated an increase in reaction efficiency of 10% over the traditional batch synthesis. The reaction stoichiometry was subsequently reduced to 1:1, but using continuous flow of reagents, as above, the conversion was poor (39%). The conversion was increased to 59% using an injection technique, where slugs of the phosphonium salt **4** were injected into a continuous flow of the aldehyde **3**.

The research was extended to investigate the stereochemistry of the reaction. The ratio of isomers **1** and **2** was controlled by altering the voltages applied to the reagent reservoirs within the device, which, in turn, affected the EOF and electrophoretic velocities of the reagents. The variation in the external voltage subsequently altered the relative reagent concentrations within the device, producing *Z/E* ratios in the region

**Table 2** Reactions conducted in a micro reactor

Reaction	Ref.
Kumada coupling	[46]
Aldol	[47]
Enamine	[48]
Diazo coupling	[49]
Diazotization	[50]
Nitration	[51]
Cycloaddition	[52]
Photochemical generation of singlet oxygen	[53]
Phase transfer	[54]
Dehydration	[55]
Esterification	[56]
Hydrogenation	[57]
Free radical fluorination	[58]
Fluorination	[59]
Partial oxidation of ammonia	[60]
Generation of hydrogen cyanide	[61]
Synthesis of amides	[62]
	[63]
Photocyanation	[64]
Pyrrazole synthesis	[65]

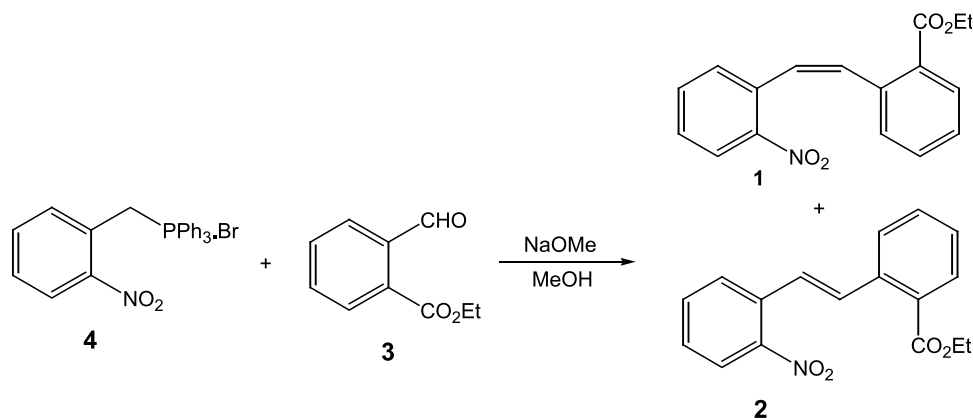
0.57 to 5.21. In comparison, the authors report that when a traditional batch synthesis was performed based on the same reaction time, concentration, solvent, and stoichiometry, a *Z/E* ratio of approximately 3:1 was observed. This demonstrated that significant control was possible in a micro reactor compared with batch reactions. The authors also demonstrated that micro reactors could be used for the rapid reaction development and optimization, based on analog chemistry, by using other aldehydes in the reaction.<sup>[66,67]</sup>

Carbanion chemistry is one of the most common methods of C–C bond formation used in the pharmaceutical

industry. Wiles et al.<sup>[68]</sup> reported the preparation of the enolates from a series of 1,3-diketones using an organic base and their subsequent reaction with a variety of Michael acceptors such as **5** to afford 1,4-addition products within a micro reactor (Scheme 2).

When using a continuous flow of the reagents **5** and **6**, 15% conversion to the adduct **8** was observed, compared with 56% when the diketone **7** was reacted with **5** forming the Michael adduct **9**. The authors, however, demonstrated enhancements in conversions through the application of the stopped flow technique. This procedure involved the mobilization of reagents through the device for a designated period of time, using an applied field, and the flow was subsequently paused by the removal of the applied field, prior to reapplying the field. Using the regime of 2.5 sec on and 5 sec off, the conversion to the product **8** was improved to 34%, while lengthening the stopped flow period to 10 sec resulted in a further increase to 100%. This was compared with the preparation of **9**, in which the regime of 2.5 sec on and 5 sec off resulted in an increase in conversion to 95%. This demonstrated that the enolate of 2,4-pentanedione **7** was more reactive than the corresponding enolate of benzoyl acetone **6**. The authors propose that the observed increase in conversion, when using the technique of stopped flow, was a result of an effective increase in residence time within the device corresponding to the different kinetics associated with these reactions. This approach is clearly relevant to those wishing to study the kinetics of such reactions, and the results demonstrate the ease with which reactions may be optimized in micro reactors when conducting combinatorial synthesis.

Although the previous result demonstrates the ease with which reaction conditions may be optimized, it is still sometimes necessary to heat reactions to achieve high yields of products. Industrially, special equipment is required when performing large-scale reactions at elevated temperature. However, Fernandez-Suarez, Wong,

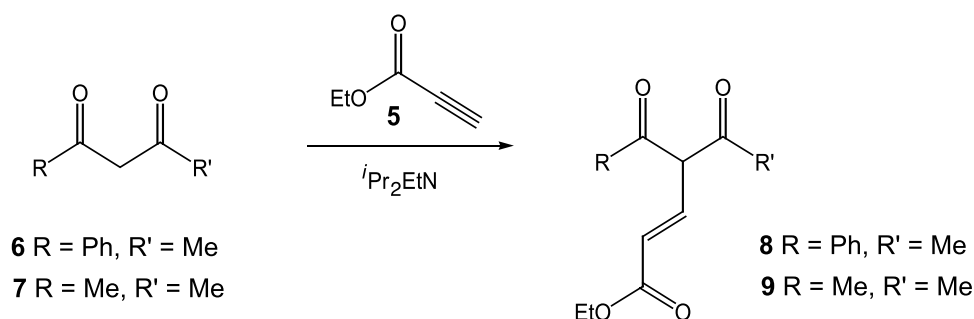
**Scheme 1**

Warrington<sup>[69]</sup> have demonstrated the synthesis of a series of 2-aminothiazoles using a Hantzsch synthesis within a micro reactor. During the experiments, the T-shaped micro reactor was heated to 70°C using a Peltier heater, which was aligned with the channels, and the heat generated by the device was applied to the base of the micro reactor. Reaction of  $\alpha$ -bromoketones such as **10** with a thiourea derivative such as **11**, using NMP as solvent, resulted in the preparation of the aminothiazoles **12** in up to 85% conversion (Scheme 3).

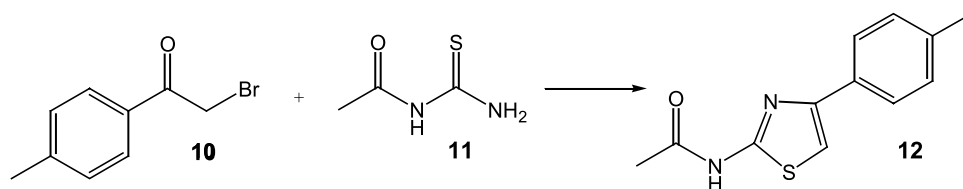
Nitration reactions in organic synthesis are problematic because of the use of excess quantities of concentrated nitric and sulfuric acids. The reactions are extremely exothermic and it is hence difficult to control the temperature of such reactions when performed on a large scale. As a result, micro reactors have a considerable attraction for these reactions because the reactor enables excellent temperature control of the reaction. Doku et al.<sup>[70]</sup> have reported the nitration of benzene **13** in a borosilicate glass micro reactor. The benzene was mobilized by electroosmotic flow as a microemulsion using the surfactant sodium dodecyl sulfate (SDS). The nitronium ions, which were produced in

situ by mixing sulfuric and nitric acids, underwent electrophoretic-induced mobility. A co-solvent, butan-1-ol, was used to enhance the solubility of the benzene in the aqueous system. The authors report that mononitration occurs in 65% conversion to give nitrobenzene **14** (Scheme 4) and that approximately 8% of 1,3-dinitrobenzene **15** and 5% of 1,3,5-trinitrobenzene **16** were obtained. Importantly, Doku et al. demonstrated that it is possible to mobilize a nonpolar liquid, such as benzene, using EOF by dissolving it in a microemulsion.

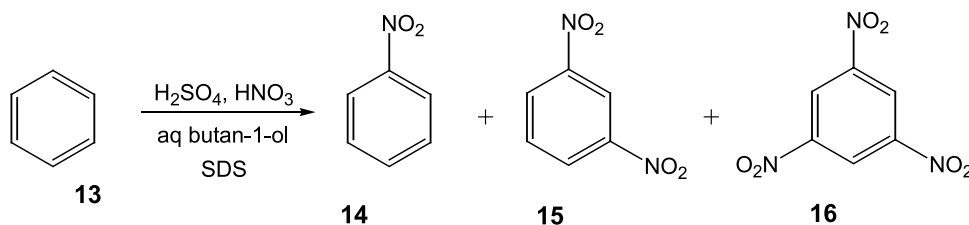
Lu, Schmidt, and Jenson<sup>[71]</sup> have reported a photochemical reaction within a micro reactor. The reactor was fabricated by bonding a patterned silicon wafer to a quartz wafer, the advantage of this fabrication technique being that the quartz substrate allows reaction and detection using UV light of lower wavelengths than permitted by Pyrex substrates. The authors investigated the pinacol formation reaction of benzophenone **17** in propan-2-ol (Scheme 5). The reaction is known to follow a radical reaction pathway, and it is reported that the longer the residence time of the reaction, the greater the conversion to benzopinacol **18**. The authors report that there



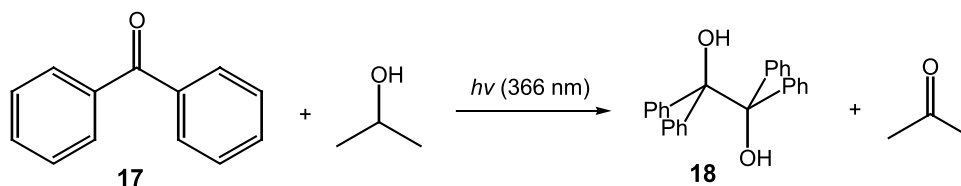
Scheme 2



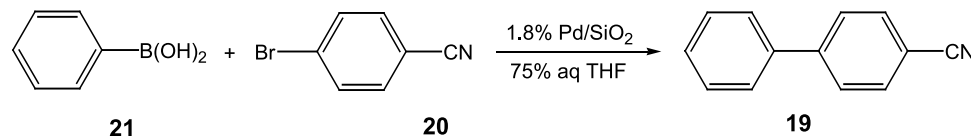
Scheme 3



Scheme 4



Scheme 5



Scheme 6

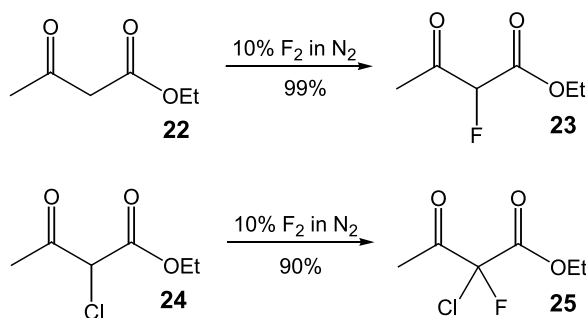
was no detectable product formation for flow rates  $> 10 \mu\text{l min}^{-1}$ . With reduced flow rates, having larger residence times, the conversion improves because the amount of light absorbed increases, and there is therefore sufficient time for the excited species to diffuse and react with the benzophenone. The authors report conversions of up to 60% when using flow rates of  $4 \mu\text{l min}^{-1}$ .

Greenway et al.<sup>[72]</sup> have demonstrated the Suzuki reaction within a micro reactor device using an immobilized heterogeneous catalysis where 1.8% palladium on silica was placed in the central channel of the micro reactor. The catalyst was immobilized between microporous silica frits prepared from potassium silicate and formamide. The micro reactor was optimized using flow injection analysis principles, producing a conversion of 67% of cyanobiphenyl **19** at room temperature. The flow injection method adopted allowed the periodic injection of the aryl halide **20** into a continuous flow of the phenylboronic acid **21** (Scheme 6). Traditionally, tetrahydrofuran (THF) is used as the solvent in this reaction. As has been found with many organic solvents, however, THF has very low natural EOF properties, and for this reason, it was mixed with water (75:25). The conversions obtained were comparable with Suzuki reactions carried out on a batch scale using homogeneous catalysis. Importantly, there were negligible levels of the palladium catalyst in the product, which was demonstrated using inductively coupled-mass spectrometry (ICP-MS), thus illustrating that the catalyst was not leaching from the reactor.

One of the interesting observations of the reaction was that, unlike conventional Suzuki reactions, an additional base was not required. Although the exact reason for this is not clear, it is postulated that the electric field may be sufficient to cause ionization of the water at the metal surface. Possibly the hydroxide formed in this way may be sufficient to perform the function of the conventional organic or inorganic base. Alternatively, a more basic environment may be formed at the surface of the micro reactor.

The use of elemental fluorine in organic synthesis is problematic because of the difficulties associated with the safe handling of gaseous fluorine.<sup>[73,74]</sup> In addition, fluorination reactions are generally extremely exothermic and it is difficult to control the temperature of such reactions when performed on a large scale. Microreactors have a considerable attraction for direct fluorination processes because there is only a small amount of fluorine in the reactor at any given time. In addition, the micro reactor enables excellent thermal dissipation and temperature control of the reaction as well as an opportunity for scale up by the simultaneous use of many such reactors.

Chambers and Spink<sup>[75]</sup> and Chambers et al.<sup>[76]</sup> have reported the use of micro reactors for the fluorination and perfluorination of organic compounds using elemental fluorine. A nickel or copper micro reactor was used for the investigation, and the liquid reactants and solvents were introduced into the reaction chamber via a syringe using a syringe pump. Fluorine, in a nitrogen carrier gas, was introduced from a cylinder using a mass-flow controller. The liquid-gas mixing proceeded via "cylindrical flow," where the liquid forms an outer cylinder coating the reactor surface with the gas flowing through the center. This flow regime has enormous benefits in that it provides very large surface-to-volume ratios for the liquid phase, producing a very efficient reaction over a short distance. The products were trapped in a tube, which was cooled with either a salt/ice bath ( $0^\circ\text{C}$ ) or an acetone/carbon dioxide bath ( $-78^\circ\text{C}$ ). The fluorination of  $\beta$ -dicarbonyl compounds proceeded with a high efficiency using 10% fluorine in nitrogen at  $5^\circ\text{C}$  and with formic acid as the solvent. Ethyl acetoacetate **22** was fluorinated in 99% conversion to give ethyl 2-fluoroacetoacetate **23**, while ethyl 2-chloroacetoacetate **24** was fluorinated in 90% conversion, yielding ethyl 2-chloro-2-fluoroacetoacetate **25** (Scheme 7). Importantly, under these conditions, no perfluorination of the substrates was observed, with only the

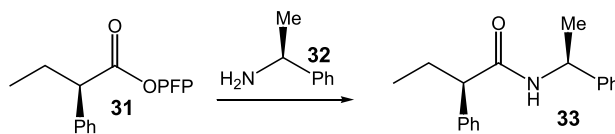


Scheme 7

monofluorinated derivatives being isolated. The authors report that the bulk fluorination of ethyl 2-chloroacetate **24** gives only a low conversion to **25**,<sup>[77]</sup> illustrating that the flow system is more efficient. This illustrates the catalytic effect of the fluorinated metal surface.

Watts et al.<sup>[78,79]</sup> have recently demonstrated the first example of a multistep synthesis in a micro reactor where they have used their devices in peptide synthesis. Reaction of pentafluorophenyl ester **26** with amine **27** formed dipeptide **28**, which was reacted with 1,8-diazabicyclo[5.4.0]undec-7-ene (DBU) to effect Fmoc deprotection. The amine **29** was then reacted in situ with another equivalent of pentafluorophenyl ester **26** to prepare tripeptide **30** in 30% overall conversion (Scheme 8). The approach clearly demonstrates that intermediates may be generated in situ and used in subsequent reactions enabling the combinatorial synthesis of peptides, which are of biological and pharmaceutical interest.

Having demonstrated that peptide bonds could be successfully formed when using a micro reactor, the authors then investigated racemization in peptides derived from  $\alpha$ -amino acids.<sup>[80]</sup> Reaction of the pentafluorophenyl ester of *R*-2-phenylbutyric acid **31**, at 0.1 M concentration, with  $\alpha$ -methylbenzylamine **32**, gave the product **33** in quantitative conversion with

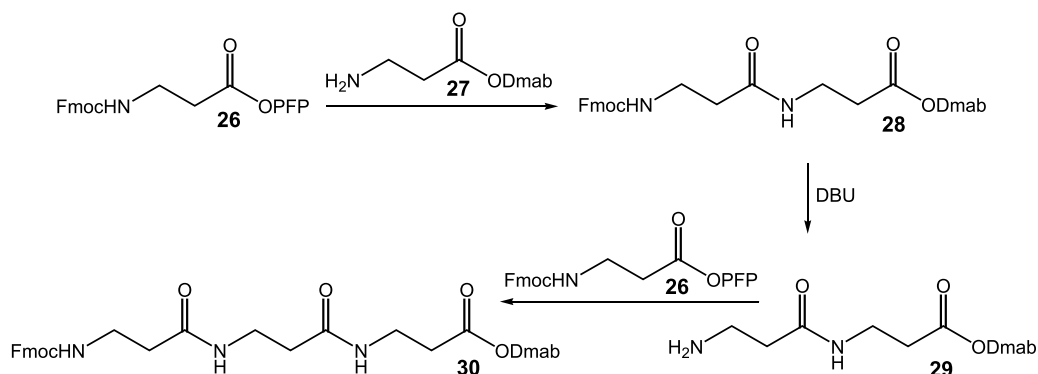


Scheme 9

4.2% racemization (Scheme 9). Importantly, there was less racemization than observed in the batch reaction at the same concentration and temperature. The reduced level of racemization was attributed to the reduced reaction times observed within the micro reactors. This demonstrates that there would be real advantages to performing the combinatorial chemistry in microfluidic reactors compared with traditional batch systems.

## CONCLUSION

Micro reactor chemistry currently shows great promise as a novel method on which to build new chemical technology and processes in which the reactions generally produce the desired product in higher yield and purity in shorter periods of time. The technology is still in its early development, but some early trends are clear. One of the immediate and obvious applications is in combinatorial chemistry and drug discovery, where the generation of compounds with different reagents or under variable conditions is an essential factor. Perhaps more intriguing, micro reactors may bring new approaches to reaction chemistry and these possibilities are only now emerging. For example, extending the heterogeneous catalyst work already described, one can see how immobilized or supported reagents could be placed within a device to impart functionality to a reaction while maintaining spatial and temporal control. A microchannel system may provide a potential separation column and integration of a micro reactor device to one of the many highly sensitive microchannel-based biological assay systems and may also address some of the pharmaceutical



Scheme 8



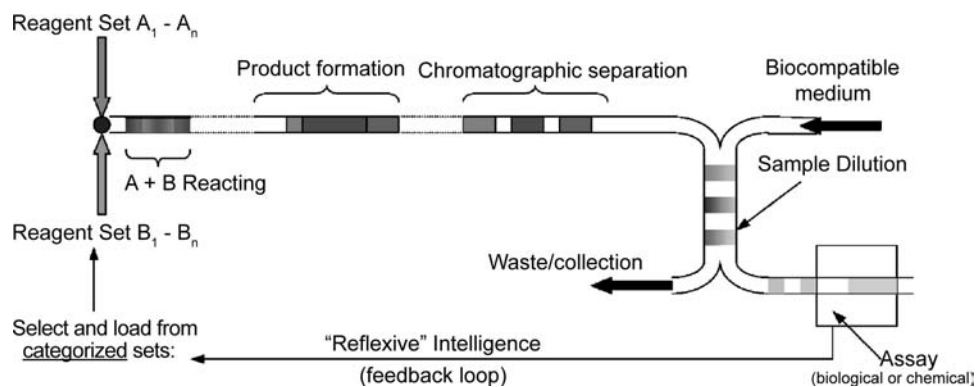


Fig. 14 Integration of a micro reactor with a bioassay system.

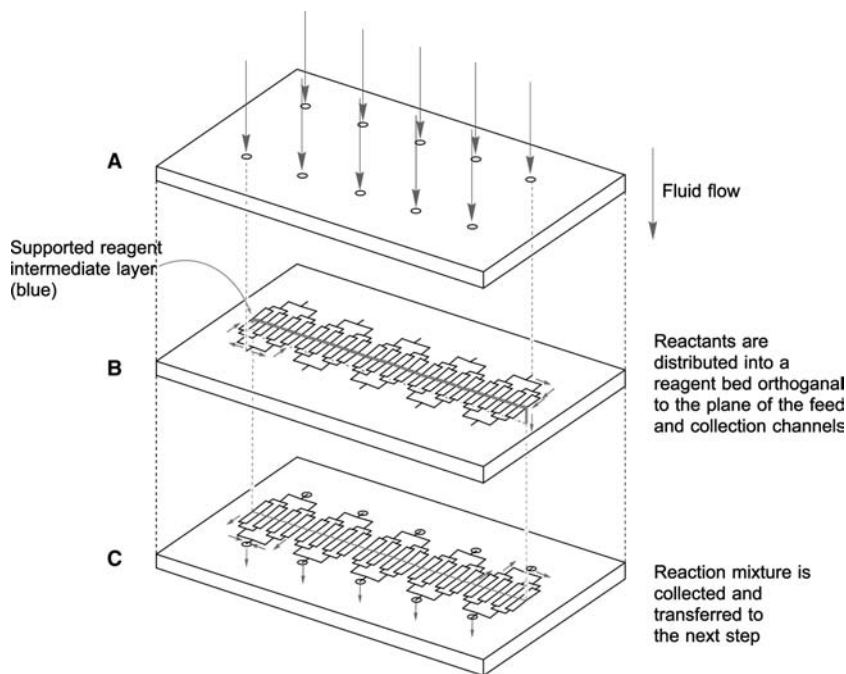
industries' potential requirements. Apart from the greatly reduced reaction times demonstrated for the micro reactors, handling times to assay and chemical reagent costs may be virtually eliminated. This paradigm is shown diagrammatically in Fig. 14.

Reactions within the micro reactors are found to be more atom-efficient, which is of significant environmental importance as this reduces the quantities of raw materials required and minimizes waste. Furthermore, the technology allows the temperature of reactions to be controlled, enabling reactions to be conducted safely, where explosion may be observed if the reaction was conducted on a batch scale.

The use of solvent for purification of products is often the largest contributor to waste in a chemical

process. Research is currently underway to investigate the purification of chemicals within the micro reactors by exploiting the electrophoretic mobility of the chemical species, which would not require any solvent to be moved within the reactor.

In terms of Green Chemistry, micro reactors offer considerable potential in performing safer and more efficient chemical reactions by the use of novel methodologies such as solvent-free mixing, in situ reagent generation, and integrated separation techniques. The capability of producing a parallel network of micro reactors, the so called "scaling out" of the process, offers a clear route to generating product volume, as shown schematically in Fig. 15. Furthermore, this methodology would enable chemicals to be prepared



Device shown exploded for clarity, can be operated in any orientation  
3 layers A,B & C constitute a system for one step of reaction:  
Further steps could be added by stacking ABC modules together

Fig. 15 A micro reactor system, in parallel mode of operation for scale out.

on demand, at the point of use, so reducing the need to store and transport hazardous or reactive chemicals.

## REFERENCES

- Bradley, D. Chemical reduction. *Eur. Chem.* **1999**, *1*, 17–20.
- Fletcher, P.D.I.; Haswell, S.J. Downsizing synthesis. *Chem. Br.* **1999**, *35*, 38–41.
- Cowen, S. Chip service. *Chem. Ind.* **1999**, *2 August*, *15*, 584–586.
- McCreeady, T. Reducing the risks of synthesis. *Chem. Ind.* **1999**, *2 August*, *15*, 588–590.
- Barrow, D.; Cefai, J.; Taylor, S. Shrinking to fit. *Chem. Ind.* **1999**, *2 August*, *15*, 591–594.
- Cooper, J.; Disley, D.; Cass, T. Lab-on-a-chip and microarrays. *Chem. Ind.* **2001**, *15 Oct.*, *20*, 653–655.
- Haswell, S.J.; Middleton, R.J.; O'Sullivan, B.; Skelton, V.; Watts, P.; Styring, P. The application of micro reactors to synthetic chemistry. *Chem. Commun.* **2001**, 391–398.
- Matlosz, M.; Ehrfeld, W.; Baselt, J.P.; Eds.; *IMRET 5: Proceedings of the Fifth International Conference on Microreaction Technology*; Springer: Berlin, 2002.
- Ehrfeld, W.; Hessel, V.; Löwe, H. *Microreactors: New Technology for Modern Chemistry*; Wiley-VCH, 2000.
- Haswell, S.J. Development and operating characteristics of micro flow injection analysis systems based on electroosmotic flow. *Analyst* **1997**, *122*, 1R–10R.
- Manz, A.; Harrison, D.J.; Verpoorte, E.; Fettingner, J.C.; Ludi, H.; Widmer, H.M. Miniaturization of chemical analysis systems—a look into next century technology or just a fashionable craze. *Chimia* **1991**, *45*, 103–105.
- Manz, A.; Harrison, D.J.; Verpoorte, E.; Widmer, H.M. Planar chip technology for miniaturization of separating systems—a developing perspective in chemical monitoring. *Adv. Chromatogr.* **1993**, *33*, 1–66.
- Freemantle, M. Downsizing chemistry. *CEN* **1999**, *22 February*, *77* (8), 27–36.
- Harrison, D.J.; van den Berg, A.; Eds.; *Proceedings of the Micro Total Analytical Systems '98 Workshop*; Kluwer Academic Press: Dordrecht, 1998.
- van den Berg, A.; Lammerink, T.S.J. Micro total analysis systems: microfluidic aspects, integration concept and applications. *Top. Curr. Chem.* **1998**, *194*, 21–49.
- Harrison, D.J.; Fluri, K.; Seiler, K.; Fan, Z.H.; Effenhauser, C.S.; Manz, A. Micromachining a miniaturized capillary electrophoresis-based chemical-analysis system on a chip. *Science* **1993**, *261*, 895–897.
- Jacobson, S.C.; Hergenroder, R.; Koutny, L.B.; Ramsey, J.M. High-speed separations on a microchip. *Anal. Chem.* **1994**, *66*, 1114–1118.
- Madou, M. *Fundamentals of Microfabrication*; CRC Press: Boca Raton, 1997.
- McCreeady, T. Fabrication techniques and materials commonly used for the production of micro reactors and micro total analytical systems. *TrAC* **2000**, *19*, 396–401.
- McCreeady, T. Rapid prototyping of glass and PDMS microstructures for micro total analytical systems and micro chemical reactors by microfabrication in the general laboratory. *Anal. Chim. Acta* **2001**, *427*, 39–43.
- Overbeek, J.Th.G. *Colloid Science*; Kruyt, H.R., Ed.; Elsevier: Amsterdam, 1952; vol. 1, 195–244. Chap. V.
- Rice, C.L.; Whitehead, R. Electrokinetic flow in a narrow cylindrical capillary. *J. Phys. Chem.* **1965**, *69*, 4017–4024.
- Hunter, R.J. *Zeta Potential in Colloid Science*; Academic Press: London, 1981.
- Paul, P.H.; Garguilo, M.G.; Rakestraw, D.J. Imaging of pressure and electrokinetically driven flows through open capillaries. *Anal. Chem.* **1998**, *70*, 2459–2467.
- Jednacak, J.; Pravdic, V.; Haller, W. The electrokinetic potential of glasses in aqueous electrolyte solutions. *J. Colloid Interface Sci.* **1974**, *49*, 16–23.
- Harmon, B.J.; Patterson, D.H.; Regnier, F.E. Mathematical treatment of electrophoretically mediated microanalysis. *Anal. Chem.* **1993**, *65*, 2655–2662.
- Harmon, B.J.; Leesong, I.; Regnier, F.E. Selectivity in electrophoretically mediated microanalysis by control of product detection time. *Anal. Chem.* **1994**, *66*, 3797–3805.
- Regnier, F.E.; Patterson, D.H.; Harmon, B.J. Electrophoretically mediated microanalysis (EMMA). *TrAC* **1995**, *14*, 177–181.
- Patterson, D.H.; Harmon, B.J.; Regnier, F.E. Dynamic modelling of electrophoretically mediated microanalysis. *J. Chromatogr., A* **1996**, *732*, 119–132.
- Fletcher, P.D.I.; Haswell, S.J.; Paunov, V.N. Theoretical considerations of chemical reactions in micro reactors operating under electroosmotic and electrophoretic control. *Analyst* **1999**, *124*, 1273–1282.
- Fletcher, P.D.I.; Haswell, S.J.; Zhang, X. Electrical current and liquid flow rates in micro reactors. *Lab Chip* **2001**, *1*, 115–121.
- Fletcher, P.D.I.; Haswell, S.J.; Zhang, X. Electrokinetic control of a chemical reaction in a Lab on a Chip micro reactor. *Lab Chip* **2002**, *2*, 102–112.
- Jacobson, S.C.; Hergenroder, R.; Koutny, L.B.; Warmack, R.J.; Ramsey, J.M. Effects of injection schemes and column geometry on the performance of microchip electrophoresis devices. *Anal. Chem.* **1994**, *66*, 1107–1113.
- Ermakov, S.V.; Jacobson, S.C.; Ramsey, J.M. Computer simulations for microchip electrophoresis. In *Micro Total Analysis Systems '98*; Harrison, D.J., van den Berg, A., Eds.; Kluwer: Dordrecht, 1998; 149 pp.
- Knight, J.B.; Vishwanath, A.; Brody, J.P.; Austin, R.H. Hydrodynamic focusing on a silicon chip. *Phys. Rev. Lett.* **1998**, *80*, 3863–3866.
- Patankar, N.A.; Hu, H.H. Numerical simulation of electroosmotic flow. *Anal. Chem.* **1998**, *70*, 1870–1881.
- Ermakov, S.V.; Jacobson, S.C.; Ramsey, J.M. Computer simulations of electrokinetic injection techniques in microfluidic devices. *Anal. Chem.* **2000**, *72*, 3512–3517.
- MacInnes, J.M. Computation of reacting electrokinetic flow in microchannel geometries. *Chem. Eng. Sci.* **2002**, *57*, 4539–4558.
- Kamholz, A.E.; Weigl, B.H.; Finlayson, B.A.; Yager, P. Quantitative analysis of molecular interaction in a microfluidic channel. *Anal. Chem.* **1999**, *71*, 5340–5347.

40. Jacobson, S.C.; McKnight, T.E.; Ramsey, J.M. Microfluidic devices for electrokinetically driven parallel and serial mixing. *Anal. Chem.* **1999**, *71*, 4455–4459.
41. Polson, N.A.; Hayes, M.A. Microfluidics—controlling fluids in small spaces. *Anal. Chem.* **2001**, *73*, 312A–319A.
42. Dertinger, S.K.W.; Chui, D.T.; Jeon, N.L.; Whitesides, G.M. Generation of gradients having complex shapes using microfluidic networks. *Anal. Chem.* **2001**, *73*, 1240–1246.
43. Kenis, P.J.A.; Ismagilov, R.F.; Whitesides, G.M. Microfabrication inside capillaries using multiphase laminar flow patterning. *Science* **1999**, *285*, 83–85.
44. Fletcher, P.D.I.; Haswell, S.J.; Pombo-Villar, E.; Warrington, B.H.; Watts, P.; Wong, S.Y.F.; Zhang, X. Micro reactors: principles and applications in organic synthesis. *Tetrahedron* **2002**, *58*, 4735–4757.
45. Schwalbe, T.; Autze, V.; Wille, W. Chemical synthesis in micro reactors. *Chimia* **2002**, *56*, 636–646.
46. Haswell, S.J.; O'Sullivan, B.; Styring, P. Kumada–Corriu reactions in a pressure-driven microflow reactor. *Lab Chip* **2001**, *1*, 164–166.
47. Wiles, C.; Watts, P.; Haswell, S.J.; Pombo-Villar, E. The aldol reaction of silyl enol ethers within a micro reactor. *Lab Chip* **2001**, *1*, 100–101.
48. Sands, M.; Haswell, S.J.; Kelly, S.M.; Skelton, V.; Morgan, D.O.; Styring, P.; Warrington, B.H. The investigation of an equilibrium dependent reaction for the formation of enamines in a microchemical system. *Lab Chip* **2001**, *1*, 64–65.
49. Salimi-Moosavi, H.; Tang, T.; Harrison, D.J. Electroosmotic pumping of organic solvents and reagents in microfabricated reactor chips. *J. Am. Chem. Soc.* **1997**, *119*, 8716–8717.
50. Wootton, R.C.R.; Fortt, R.; de Mello, A.J. On-chip generation and reaction of unstable intermediates—monolithic nanoreactors for diazonium chemistry: Azo dyes. *Lab Chip* **2002**, *2*, 5–7.
51. Burns, J.R.; Ramshaw, C.G. IMRET 4: 4th International Conference of Micro Reaction Technology Topical Conference Proceedings, AIChE Spring National Meeting, Atlanta, GA, USA, March, 5–9, 2000, 133 pp.
52. Garcia-Egido, E.; Wong, S.Y.F.; Warrington, B.H. Synthesis of a three-member array of cycloadducts in a glass microchip under pressure driven flow. *Lab Chip* **2002**, *2*, 170–174.
53. Wootton, R.C.R.; Fortt, R.; de Mello, A.J. A microfabricated nanoreactor for safe, continuous generation and use of singlet oxygen. *Org. Process Res. Dev.* **2002**, *6*, 187–189.
54. Hisamoto, H.; Saito, T.; Tokeshi, M.; Hibara, A.; Kitamori, T. Fast and high conversion phase-transfer synthesis exploiting the liquid–liquid interface formed in a microchannel chip. *Chem. Commun.* **2001**, *24*, 2662–2663.
55. Wilson, N.G.; McCreedy, T. On-chip catalysis using a lithographically fabricated glass micro reactor—the dehydration of alcohols using sulfated zirconia. *Chem. Commun.* **2000**, *9*, 733–734.
56. McCreedy, T.; Wilson, N.G. Microfabricated reactors for on-chip heterogeneous catalysis. *Analyst* **2001**, *126*, 21–23.
57. Dietzsch, E.; Hönicke, D.; Fichtner, M.; Schubert, K.; Weißmeier, G. IMRET 4: 4th International Conference of Micro Reaction Technology Topical Conference Proceedings, AIChE Spring National Meeting, Atlanta, GA, USA, March, 5–9, 2000, 89 pp.
58. Chambers, R.D.; Grievson, B.; Drakesmith, F.G.; Powell, R.L. Free radical chemistry. Part 5. [1] A new approach to the synthesis of perfluorinated ethers. *J. Fluorine Chem.* **1985**, *29*, 323–339.
59. de Mas, N.; Jackman, R.J.; Schmidt, M.A.; Jenson, K.F. *IMRET 5: Proceedings of the Fifth International Conference on Microreaction Technology*; Springer: Berlin, 2002; 60 pp.
60. Srinivasan, R.; Hsing, I.-M.; Berger, P.E.; Jensen, K.F.; Firebaugh, S.L.; Schmidt, M.A.; Harold, M.P.; Lerou, J.J.; Ryley, J.F. Micromachined reactors for catalytic partial oxidation reactions. *AIChE J.* **1997**, *43*, 3059–3069.
61. Hessel, V.; Ehrfeld, W.; Golbig, K.; Hofman, C.; Jungwirth, S.; Löwe, H.; Richter, T.; Storz, M.; Wolf, A. *IMRET 3: Proceedings of the Third Conference on Microtechnology*; 2000; 151 pp.
62. Kikutani, Y.; Horiuchi, T.; Uchiyama, K.; Hisamoto, H.; Tokeshi, M.; Kitamori, T. Glass microchip with three-dimensional microchannel network for  $2 \times 2$  synthesis. *Lab Chip* **2002**, *2*, 188–192.
63. Kikutani, Y.; Hibara, A.; Uchiyama, K.; Hisamoto, H.; Tokeshi, M.; Kitamori, T. Pile-up glass micro reactor. *Lab Chip* **2002**, *2*, 193–196.
64. Ueno, K.; Kitagawa, F.; Kitamura, N. Photocyanation of pyrene across an oil water interface in a polymer microchannel chip. *Lab Chip* **2002**, *2*, 231–234.
65. Garcia-Egido, E.; Spikmans, V.; Wong, S.Y.F.; Warrington, B.H. Synthesis and analysis of combinatorial libraries performed in an automated micro reactor system. *Lab Chip* **2003**, *3*, 73–76.
66. Skelton, V.; Greenway, G.M.; Haswell, S.J.; Styring, P.; Morgan, D.O.; Warrington, B.; Wong, S.Y.F. The preparation of a series of nitrostilbene ester compounds using micro reactor technology. *Analyst* **2001**, *126*, 7–10.
67. Skelton, V.; Greenway, G.M.; Haswell, S.J.; Styring, P.; Morgan, D.O.; Warrington, B.; Wong, S.Y.F. The generation of concentration gradients using electroosmotic flow in micro reactors allowing stereoselective chemical synthesis. *Analyst* **2001**, *126*, 11–13.
68. Wiles, C.; Watts, P.; Haswell, S.J.; Pombo-Villar, E. 1,4-Addition of enolates to  $\alpha,\beta$ -unsaturated ketones within a micro reactor. *Lab Chip* **2002**, *2*, 62–64.
69. Fernandez-Suarez, M.; Wong, S.Y.F.; Warrington, B.H. A Hantzsch synthesis of 2-aminothiazoles performed in a heated micro reactor system. *Lab Chip* **2002**, *2*, 31–33.
70. Doku, G.N.; Haswell, S.J.; McCreedy, T.; Greenway, G.M. Electric field-induced mobilisation of multiphase solution systems based on the nitration of benzene in a micro reactor. *Analyst* **2001**, *126*, 14–20.
71. Lu, H.; Schmidt, M.A.; Jenson, K.F. Photochemical reactions and on-line UV detection in microfabricated reactors. *Lab Chip* **2001**, *1*, 22–28.

72. Greenway, G.M.; Haswell, S.J.; Morgan, D.O.; Skelton, V.; Styring, P. The use of a novel micro reactor for high throughput continuous flow organic synthesis. *Sens. Actuators, B* **2000**, *63*, 153–158.
73. Rozen, S. Elemental fluorine: not only for fluoroorganic chemistry. *Acc. Chem. Res.* **1996**, *21*, 243–248.
74. Purrington, S.T.; Kagen, B.S.; Patrick, T.B. The application of elemental fluorine in organic synthesis. *Chem. Rev.* **1986**, *86*, 997–1018.
75. Chambers, R.D.; Spink, R.C.H. Microreactors for elemental fluorine. *Chem. Commun.* **1999**, (10), 883–884.
76. Chambers, R.D.; Holling, D.; Spink, R.C.H.; Sandford, G. Elemental fluorine. Part 13. Gas–liquid thin film micro reactors for selective direct fluorination. *Lab Chip* **2001**, *1*, 132–137.
77. Chambers, R.D.; Greenhall, M.P.; Hutchinson, J. Direct fluorination of 1,3-dicarbonyl compounds. *Tetrahedron* **1996**, *52*, 1–8.
78. Watts, P.; Wiles, C.; Haswell, S.J.; Pombo-Villar, E.; Styring, P. The synthesis of peptides using micro reactors. *Chem. Commun.* **2001**, (11), 990–991.
79. Watts, P.; Wiles, C.; Haswell, S.J.; Pombo-Villar, E. Solution phase synthesis of  $\beta$ -peptides using micro reactors. *Tetrahedron* **2002**, *58*, 5427–5439.
80. Watts, P.; Wiles, C.; Haswell, S.J.; Pombo-Villar, E. Investigation of racemisation in peptide synthesis within a micro reactor. *Lab Chip* **2002**, *2*, 141–144.

# Langmuir-Blodgett Films

Ursula Mazur

*Department of Chemistry and Materials Science, Washington State University,  
Pullman, Washington, U.S.A.*

## INTRODUCTION

Very often thin organic films, such as Langmuir-Blodgett (LB) films, are designed for chemical, optical, electrical, or magnetic applications. The Langmuir-Blodgett technique is a unique methodology for building up nanoscale supermolecular assemblies from designed organic molecules under fully controlled processes involving intermolecular interactions at the air-liquid interface. With three different vertical film withdrawing protocols (X, Y, and Z), a horizontal film lift option, and an alternating layer buildup capability, a great variety of supermolecular structures can be assembled.<sup>[1-3]</sup> These diverse architectural strategies provide an elegant and efficient way to fabricate molecular electronic devices. It has been well demonstrated that the optical, electronic, and magnetic properties of LB based nanoscale devices are highly dependent on the relative orientation and distance of the molecules from each other.<sup>[4-6]</sup> Furthermore, reliable operation of these devices requires quantitative control over the nanomechanical and nanotribological properties of the molecular structures that comprise them. Structural and chemical characterization can be carried out using established techniques (AFM, STM, XPS, Surface Enhanced Raman, and FTIR), and processing conditions can be well characterized. Commercial indentation instrumentation and scanning probe microscopy techniques have been shown to be an effective means for nanomechanical characterization of submicron thick organic films. One critical component of testing the mechanical properties of thin film systems is the relationship between the structure and the chemistry of the film. Measuring and quantifying the mechanical properties to close the feedback loop in the ability to tailor nanoscale supermolecular organic LB assemblies with specific properties has been an active area of research within during the last few years. The systems of interest include those with highly ordered films with non-covalent  $\pi$ - $\pi$  interaction (e.g., phthalocyanines and thiophenes), those with van der Waals interactions between paraffinic chains, and systems driven primarily by H-bonding and polar interaction.<sup>[7-10]</sup> These all have potential use in molecular electronics.<sup>[11,12]</sup> This report summarizes some of the

recent work on the surface properties and nanomechanical behavior of well-organized Langmuir-Blodgett layers. The nanomechanical properties of well-organized LB systems will be discussed in terms of their relationship to the physical structure and the chemistry of monolayer and multilayer films.

## FABRICATION OF LANGMUIR-BLODGETT FILMS

Langmuir films are (most often) mechanically assembled 2-D arrays of molecules upon the surface of a liquid. Once the molecules are compressed to the desired organization, the monolayer film can be transferred on to a solid support. Film characteristics, such as thickness and molecular arrangement can be controlled at the molecular level with the LB deposition method. There are numerous excellent review articles as well as books that provide comprehensive information about the field of LB monolayers and multilayers.<sup>[1-3,13-16]</sup>

Langmuir and LB films are generally composed of amphiphilic molecules containing both hydrophobic and hydrophilic moieties, as in the fatty acids. A monolayer of insoluble amphiphiles at the air/liquid interface is referred to as a Langmuir monolayer. Films of Langmuir monolayers transferred onto a solid substrate are known as Langmuir-Blodgett films; they can be single or multiple layers.

To fabricate a Langmuir monolayer one needs a trough with movable barriers that can glide over the surface of the subphase (water, mercury, hydrocarbons, and alcohols) and an electrobalance (Wilhelmy balance) that measures surface tension. In addition to temperature control, the aqueous subphase can be monitored for pH and ionic content. Molecules of interest are dissolved in a volatile organic solvent (chloroform, benzene, or hexane) and placed on the surface of the subphase. Since the number of molecules spread on the surface is a known quantity the monolayer area can and is generally expressed as area per molecule. The physical state of the monolayer on the water is monitored by measuring the surface pressure,  $\Pi$ , defined as the difference between the surface tension

of the monolayer and that of the bare subphase. A measurement of the surface pressure as a function of molecular area at constant temperature is the standard thermodynamic measurement made on Langmuir monolayers known as a  $\Pi$ - $A$  isotherm. As an example of such an isotherm for a long-chain fatty acid is depicted in Fig. 1.<sup>[17]</sup> Thermodynamic phase transitions of the 2-D monolayer system are signaled by changes in the slope of the curve which correspond to the gas, liquid, and solid phases analogous to phase changes in 3-D systems. With increasing surface pressure the 2-D crystalline film will eventually collapse, either sliding over upon itself or folding under into the subphase. By extrapolating the steepest part of the curve to zero pressure, just prior to film collapse, one can estimate of the cross sectional area per molecule. This is known as the Pockel's point.

The processing of the Langmuir monolayers involves the judicious selection of a solid support. Typical solid supports include mica, glass, silicon, and quartz. The choice of substrate is expected to play at least three significant roles in the overall film properties. It will affect the electrical and optical properties (e.g., the surface plasmons of a conducting substrate can have a pronounced effect on the lifetime of excited states). It will strongly influence the overall uniformity and quality of the LB film (through differences in adsorption energy and the presence of specific interactions with the substrate surface). The choice of substrate can significantly affect the nanomechanical properties of the films.<sup>[18-20]</sup>

Transferring the Langmuir monolayers from the water-air interface onto a solid substrate to form Langmuir-Blodgett layers can be accomplished with

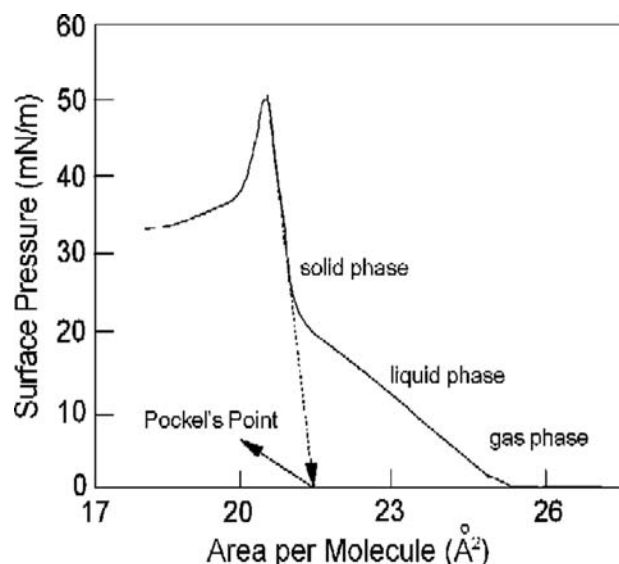


**Fig. 1** Spreading pressure vs. area of cadmium stearate acquired on a water subphase at pH 3.5 and 20°C.

two different trough set-ups: the Langmuir-Blodgett and the Langmuir-Schaefer methods, Fig. 2. The Langmuir-Blodgett trough facilitates three different vertical film withdrawing procedures. These protocols in turn yield different film architectures. Y-type multilayers (alternating upstroke and down stroke) are commonly prepared from long carbon chain amphiphiles. The head-head and tail-tail interactions lead to the stability and strength of the film. X-type (down stroke only) and Z-type (upstroke only) deposition can be applied to the build up of films composed of molecules that are weakly hydrophilic or non-polar. Both X and Z category films are non-centrosymmetric and, therefore, important for non-linear optical and pyroelectric applications.

Another way of building LB structures is to horizontally lift the Langmuir layers onto a substrate; this is the Langmuir-Schaefer method. In this method, a flat substrate is placed horizontally on a compressed Langmuir layer at the air-water interface. When the substrate is lifted the monolayer is transferred onto the solid support. The Langmuir-Schaefer method is especially useful for depositing very rigid high viscosity films.

The molecular building blocks used for fabricating LB monolayers and multilayers range from simple paraffinic amphiphiles,<sup>[1,21]</sup> to complex aromatics,<sup>[4,5]</sup> biomolecules,<sup>[4,22]</sup> transition metal complexes,<sup>[23,24]</sup> and hybrid organic-inorganic systems.<sup>[23,25-27]</sup> The intra and interlayer architecture of the films can be further diversified by combining different classes of molecules together during the processing of a Langmuir layer or by altering layer by layer film composition. The LB structural designs rely for the

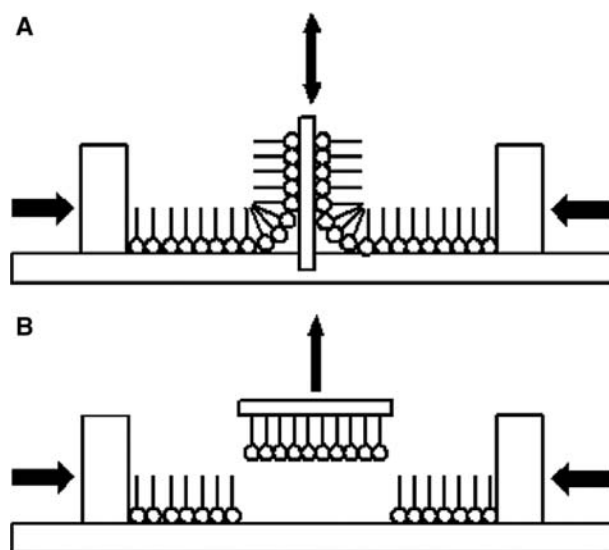


**Fig. 2** Langmuir-Blodgett (A) and Langmuir-Schaefer and (B) film withdrawal methods.



most part on intermolecular forces, such as van der Waals attraction, ionic and hydrogen bonding,  $\pi$ - $\pi$  interaction, and entropic effects. It is also possible to change the nature of the LB molecular interactions by post deposition treatments of the layers such as annealing or irradiation.<sup>[28]</sup> Thus, the LB platform with its exceptional and varied capabilities of controlling the orientation and placement of molecules in monolayers has allowed researchers to engineer supermolecular condensed phases with unique optical, electronic, and magnetic properties. There exists an enormous body of literature on the fabrication of these types of materials. Several excellent general reviews are recommended.<sup>[1-5,7,13-16]</sup>

## STRUCTURAL CHARACTERIZATION OF LANGMUIR-BLODGETT FILMS

Nanomechanical properties of molecular films depend on their chemical and physical characteristics. Properties, such as chemical composition, molecular orientation and packing, film thickness and coverage, interlayer spacing, and surface morphology play critical roles in measuring and quantifying the elastic modulus, hardness, and adhesive strength of the molecular layers. Consequently, it is useful to first characterize the fabricated LB film as completely as possible prior to its mechanical testing. The ultimate goal of such an approach is of course to facilitate chemical tuning of the film's structure in order to optimize its mechanical properties. The chemical and structural characterization can be carried out using established techniques, such as X-ray diffraction, XPS, FTIR, Raman, solid state NMR, AFM, and STM. The application of all these and other spectroscopic and microscopic tools to the study of LB films is extensively described elsewhere.<sup>[1-5,7,13-16]</sup> What follows is a brief synopsis of the capabilities of some of the more routine methods for analyzing the molecular composition and structure of the films.

One of the earliest techniques employed in characterizing LB films was x-ray diffraction. This is a reliable technique for investigating concentration profiles, molecular organization, interlayer spacing, and film thickness.<sup>[13,29]</sup> Depths of micrometers can be probed depending on the material. Monolayer sensitivity can be obtained with synchrotron radiation. Grazing-incidence x-ray diffraction (GIXD) is a method for determining the arrangement of molecules within a floating Langmuir monolayer. This method can be applied to films transferred onto solid support, but this is more problematical because the substrates may not be as flat as the surface of water subphase.<sup>[13,29]</sup>

X-ray photoelectron spectroscopy, XPS, is an ultra high vacuum surface analytical technique that can

probe up to a few nanometers of depth and determine the elemental composition and homogeneity of the deposited LB films. In addition to distinguishing the elements in the sample, it is also possible to identify the chemical state of the elements present and their bonding environments.<sup>[30]</sup> The relative concentrations of the elements can be determined from the measured photoelectron intensities.<sup>[31]</sup>

Fourier Transform Infrared Spectroscopy, FTIR, is an essential tool for characterizing the chemical makeup of LB films: transmission, reflection absorption (RAIR), and attenuated total reflectance (ATR) spectroscopy are the most suitable sampling techniques. These methods are sensitive enough to study monolayer films and can also probe substrate adsorbate interfaces. In transmission mode the measured vibrational transitions and their intensities provide quantitative information about the chemical composition of the film.<sup>[1,2]</sup> In the RAIR and ATR modes quantitative estimates of the orientation of molecules within the LB layers relative to the substrate can also be obtained.<sup>[32-34]</sup> Raman spectroscopy is a complementary vibrational technique to infrared spectroscopy. This technique is not only used to identify chemical species, but can also be employed for characterizing the structural order, phase transitions, and strain states in both thin and thick films. Because Raman scattering is an intrinsically weak process, some enhancement mechanism is usually needed to study LB layers. An increase in the signal can usually be achieved by depositing films onto the surfaces of noble metals or by the interaction with surface plasmons (Surface Enhanced Raman Spectroscopy).<sup>[35,36]</sup> For materials with electronic transition in the visible light region, the resonance Raman effect can be used to enhance certain vibrational bands.<sup>[37,38]</sup>

Magic angle spinning (MAS) solid state NMR can yield both qualitative and quantitative identification of chemical species well as characterization of the local chemical bonding environments and conformations in ordered and disordered surface bound molecules.<sup>[39]</sup> This technique has not been extensively applied to the study of LB films largely because of sampling limitations.<sup>[40,41]</sup> LB films are typically deposited on low surface area substrates and consequently the number of nuclei per monolayer is not very high unless isotopic enrichment is employed.<sup>[39]</sup>

The use of Scanning Probe Microscopy, SPM, has become a routine surface analysis tool in LB research. The SPM techniques are unsurpassed as high resolution, 3-D profilometers. They can provide information about surface structure ranging from atomic resolution to surface morphology of about 100  $\mu\text{m}$ . Scanning Tunneling Microscopy, STM, records the overlap of the local electron density of states between the probe and the adsorbate molecules on a conducting

substrate. Consequently, STM can provide not only morphological information, but also spectroscopic data about HOMO and LUMO states of molecular systems.<sup>[42]</sup> Atomic Force Microscopy, AFM, and its variants (frictional force microscopy and magnetic force microscopy) do not require conducting substrates and can be used to image both soft and stiff samples. AFM measures the elastic response of the molecules to the force exerted by the scanning probe. Thus, it can provide direct images of surfaces and also be employed in measuring mechanical properties of molecular assemblies.<sup>[10,43,44]</sup>

### NANOMECHANICAL MEASUREMENTS OF LANGMUIR-BLODGETT FILMS

The most common quantitative method of measuring the mechanical properties of thin films is nanoindentation, followed closely by scanning probe microscopy techniques. Nanoindentation, also known as instrumented indentation, is depth-sensing indentation testing of materials in the submicron range. When used in conjunction with an atomic force microscope, in situ imaging of the nanoindentation deformation and cracking can be obtained. A dynamic indentation system (commonly referred to as continuous or dynamic stiffness testing, CSM), allows one to determine the properties of materials as a function of time and depth during a given indentation (Fig. 3). There are significant advantages to this type of test for studying organic systems.<sup>[45–47]</sup> The CSM technique makes the continuous measurement of mechanical properties of materials possible in one sample experiment without the need for discrete unloading cycles. The measurements of contact stiffness, elastic modulus, hardness, creep resistance, and fatigue properties can be made on nanometer thick films. Furthermore, CSM has a relatively small time constant that makes it especially useful for measuring the properties of polymeric materials, non-homogeneous materials, and layered films, where the microstructure and mechanical properties change with indentation depth.<sup>[45,47]</sup>

For organic films indented by a diamond tip the elastic modulus of the tip is much greater than the film being indented and the reduced modulus is considered to be a function of the elastic properties of the surface. The material hardness  $H$  is defined as the maximum load  $P_{\max}$  divided by the corresponding projected indentation area  $A_{\max}$ . The hardness values of the LB molecular layers are not expected to be the same as those of the corresponding bulk compounds. Further, the hardness of the multilayers will depend on the loading rate, the temperature of the material, and the substrate material.<sup>[18–20]</sup> Therefore, the hardness values

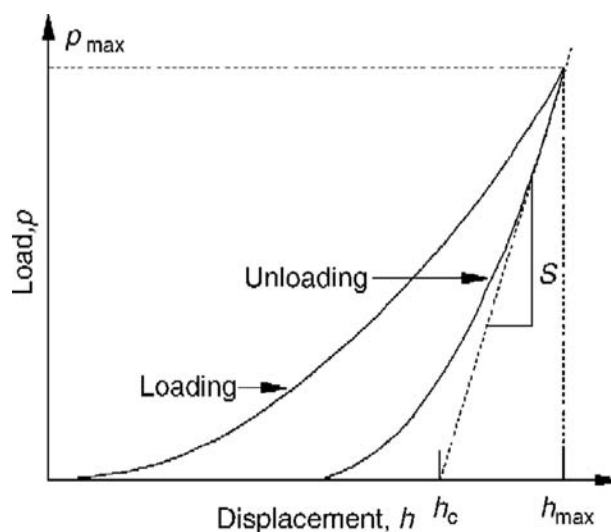


**Fig. 3** A typical load–displacement curve and the deformation pattern of an elastic–plastic sample during and after indentation:  $h_{\max}$  represents the displacement at the peak load,  $P_{\max}$ . The contact depth  $h_c$  is defined as the depth of the indenter in contact with the sample under load.  $S$  is the initial unloading contact stiffness. The elastic modulus of the indented sample can be inferred from the initial unloading contact stiffness,  $S = dP/dh$ , i.e., the slope of the initial portion of the unloading curve.

are usually considered to be “effective hardness” values that are related to the particular testing conditions. Elastic modulus and hardness values are estimated for indentation depths of less than 30% of the total film thickness in order to minimize the contributions from the substrate. Although nanoindentation testing has been performed on thick organic layers,<sup>[48–55]</sup> it has only recently been applied to LB films.<sup>[2]</sup> The application of frictional force mode in Scanning Force Microscopy (SFM) allows estimation and quantitative description of elasticity (or stiffness), hardness, adhesion, viscosity, and other properties of monolayer films.<sup>[11,56]</sup> Acquisition of data relating to these properties can often be performed simultaneously with topography imaging. The mechanical response of the sample is typically modeled using Hertzian mechanics, for the case of a spherical contact on a flat, infinitely thick plane. There are numerous reports of mechanical properties of LB monolayers studied by SFM.

LB films of derivitized metal phthalocyanines (MPc) are of interest because they exhibit the strong tendency to aggregate in columnar assemblies (through Pc–Pc ring  $\pi$ – $\pi$  interaction), many with discotic liquid crystalline properties. These systems are extremely likely candidates for molecular electronic and photonic applications.<sup>[57,58]</sup> Symmetrically substituted copper phthalocyanine complexes,  $\text{CuPc}(\text{OCH}_2\text{CH}_2\text{OBz})_8$ ,

CuPc(OCH<sub>2</sub>CH<sub>2</sub>OCH<sub>2</sub>CH=CHPh)<sub>8</sub>, and CuPc(OCH<sub>2</sub>-CH<sub>2</sub>CH=CHPh)<sub>8</sub> reported by Armstrong<sup>[8,32,59]</sup> and peripheral and non-peripheral, butoxy and octyloxy copper phthalocyanine, CuPc(OBu)<sub>8</sub>, and CuPc(OOC)<sub>8</sub>, studied by Mazur<sup>[10,43,44]</sup> make beautifully stable, stiff, and highly organized monolayer and bilayer LB films. All these molecules formed coherent and rigid Pc columns with the expected Pc-Pc macrocycle interactions and the added interactions between the terminal R groups (Fig. 4). RAIRS provided important insights into film order and the orientation of chromophores relative to the substrate.<sup>[8,10]</sup> The measured angle of incline relative to the substrate ranged from 15° to 30° and a twist angle from 30° to 40° was reported for pCuPc(OR)<sub>8</sub> LB discotic assemblies. Mazur et al. found that the mechanical properties of CuPc(OR)<sub>8</sub> LB films depended strongly on the level of organization of the phthalocyanine molecules within the layered structures.<sup>[10]</sup> Small tilt angles of the Pc rings optimized the  $\pi$ - $\pi$  interaction between the CuPc chromophores which formed highly stable rigid columns. With the increase in tilt angle associated with the introduction of non-peripheral substituents, the  $\pi$ - $\pi$  overlap was reduced and the rings began to twist to recover electronic stability. This molecular motion

produced strain in the cofacial arrangement, which lead to disorder within the columnar aggregates. Thus, significant softening and reduction in stiffness occurred in the LB layers (low values of modulus of elasticity), Fig. 5. The long C-8 paraffinic chains, also play a significant role in reinforcing the interlayer structure of the LB layers through interdigitation.<sup>[41]</sup> This interdigitation is indicated by solid state <sup>13</sup>C NMR of the multilayer CuPc(OR)<sub>8</sub> assemblies. The measured Young's modulus of the LB multilayers is between 83 and 63 GPa, with the greatest value for pCuPc(OBu)<sub>8</sub>, and the smallest for nCuPc(OOC)<sub>8</sub>. The hardness values for the three best elastomers are similar, averaging to approximately 0.57 GPa (Table 1). Both elasticity and hardness of CuPc(OR)<sub>8</sub> multilayers were comparable to those of metal surfaces such as Al, Mg, and Cu and were greater than for organic polymers such as polyethylene. This is a remarkable result because CuPc(OR)<sub>8</sub> films are molecular films that possess no intermolecular covalent bonds as in the case of polymers. An AFM topograph in Fig. 6 shows indented regions of a pCuPc(OBu)<sub>8</sub> 10 LB layers film on mica. This film actually fractures sequentially, monolayer by monolayer, without causing discontinuities in the underlying layers and illustrates the incredible

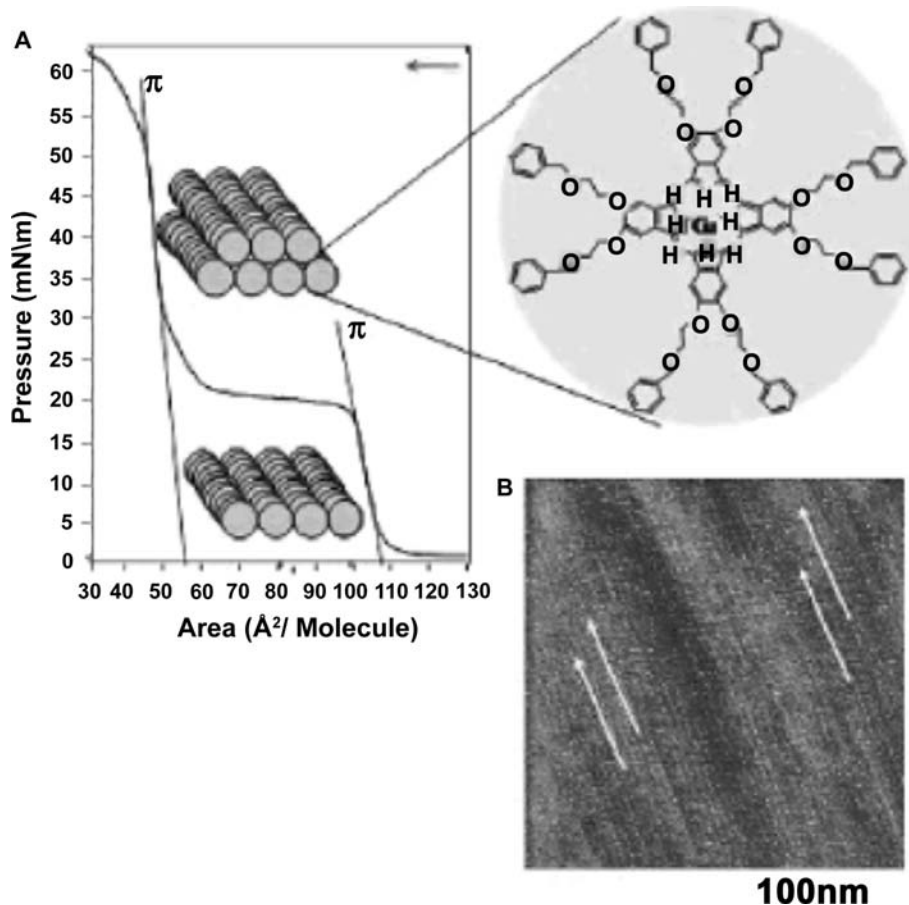


**Fig. 4** (A) A Langmuir-Blodgett pressure-area isotherm of CuPc(OCH<sub>2</sub>CH<sub>2</sub>OBz)<sub>8</sub> and a schematic of its structure; (B) 100 nm × 100 nm AFM (friction) image of a single bilayer the complex on Si(100) modified with silazanes showing an average column-column separation distance of  $d = \sim 27$  Å and a rms roughness along the top of each Pc column of  $\sim 6$  Å. Source: Reprinted with permission from American Chemical Society, © 2004 (see Ref.<sup>[8]</sup>).

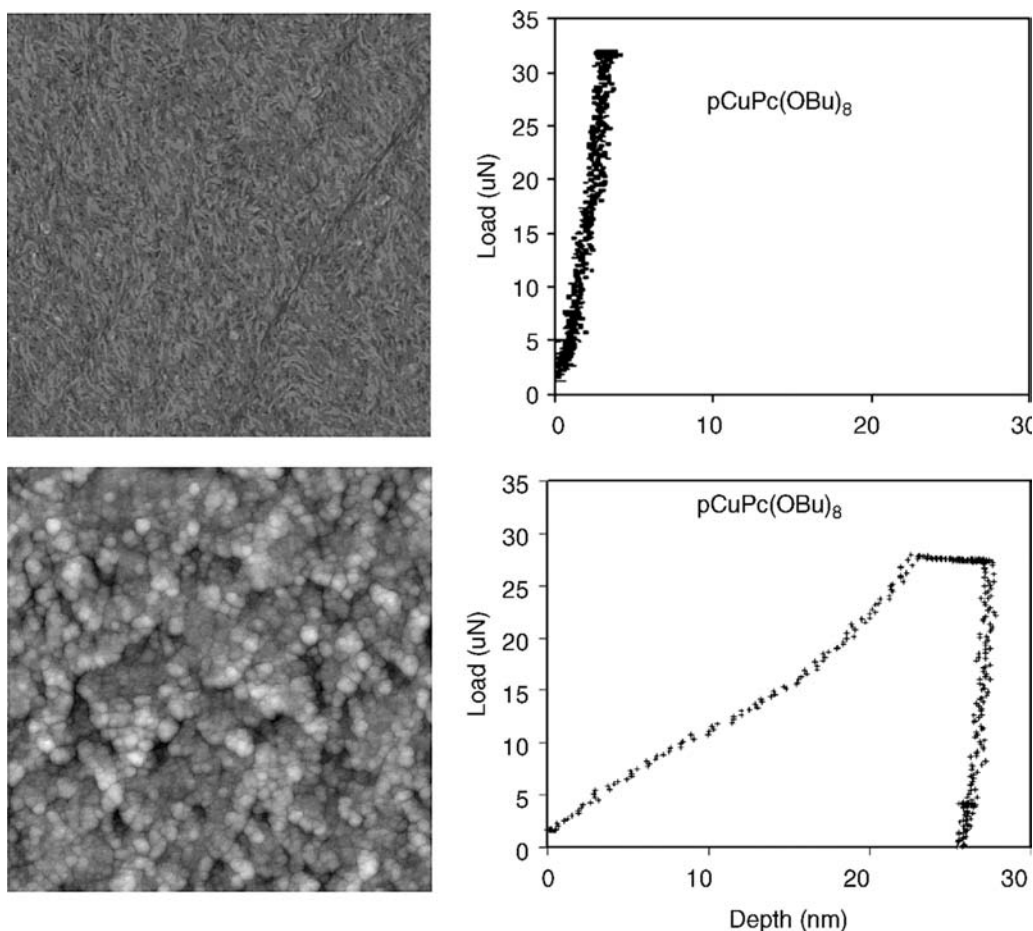


**Fig. 5** AFM tapping mode  $5\ \mu\text{m} \times 5\ \mu\text{m}$  area images of 10 LB monolayers of (A) peripheral CuPc(OBu)<sub>8</sub> and (B) non-peripheral CuPc(OBu)<sub>8</sub> multilayers on hydrophilic mica substrate acquired in air. To the right of each AFM image is a corresponding load vs. depth curve for each of the films. The 10 LB layers of the peripherally substituted CuPc(OBu)<sub>8</sub> the indentation response is reversible with virtually no hysteresis at loads of  $30\ \mu\text{N}$  or less. This means that the film deforms elastically; this involves stretching, rather than breaking of the coherent columnar assemblies. Consequently, when the applied load is removed, the material reverts to its original undeformed condition cycle due to creep. The nanoindentation profile of the non-peripherally substituted CuPc(OBu)<sub>8</sub> multilayer indicates the indent probe has penetrated this material substantially deeper than the total film thickness of 10 LB layers ( $\sim 15\ \text{nm}$ ). The permanent deformation in this multilayer is likely due to contributions from plastic deformation involving permanent breaking of cofacial stacks, sample roughness, and variation in film stiffness near or at the surface. Localized deformation is less than the total thickness of the compliant coating ( $<30\%$ ) in order to eliminate the effects of the solid support.

rigidity of the pCuPc(OBu)<sub>8</sub> material which is an excellent candidate for deposition strategies such as mechanical stamping, allowing the rapid transfer of film sections to various substrates without the loss of order.<sup>[10]</sup>

Poly(3-alkylthiophene)s are excellent candidates for field-effect transistors (FET) because they exhibit good electrical and optical properties as well as good chemical stability. These molecules aggregate through a variety of modes including  $\pi$ - $\pi$  interaction between thiophene units that favors parallel stacking, van der Waals interactions between alkyl chains, and H-bonding and polar interactions.<sup>[11,60]</sup> Salmeron and coworkers studied the structural and mechanical

properties of Langmuir-Blodgett monolayer and multilayer films of heptathiophene-acetic acid on mica by atomic force microscopy (AFM) as a function of humidity, temperature, and applied force.<sup>[11,60]</sup> In the presence of coadsorbed water the film height was 2 nm when imaged at loads of a few nanonewtons (Fig. 7). This height was a fully stretched molecular conformation (2.1 nm tall), likely helped by hydrophobic interactions of the alkyl chains with the water sitting in the vicinity near the carboxyl and polar thiophene units. In the presence of coadsorbed water the molecules were oriented with the carboxylic acid group pointing toward the mica surface and the alkyl side chains exposed to the air interface. With increased

**Table 1** Young's modulus (as measured by indentation) and effective hardness for different thin film materials obtained from nanoindentation experiments

Molecule	Indentation based Young's modulus (GPa)	Hardness (GPa)
pCuPc(OBu) <sub>8</sub> (by AFM)	110 ± 15 (on mica)	
pCuPc(OBu) <sub>8</sub>	83 ± 5.0 (on W)	0.60 ± 0.03
pCuPc(OOc) <sub>8</sub>	71 ± 4.2 (on W)	0.60 ± 0.03
nCuPc(OOc) <sub>8</sub>	63 ± 5.7 (on W)	0.52 ± 0.02
W	411 (on glass)	3.4
Copper	130	0.6
Aluminum	70 (on Si)	0.4
Polyfluoroethylene	7.5	0.1
Magnesium	45	0.3
Polyethylene	3.0 ± 0.8	0.10 ± 0.03
Alpha-keratin fiber	3.0 ± 0.6	0.048 ± 0.01
Polyformaldehyde	2.9	0.21

All CuPc(OR)<sub>8</sub> films measured were ten monolayers thick. *Source:* Reprinted with permission from American Chemical Society, © 2004 (see Ref.<sup>[8]</sup>).

load, the film is compressed easily from an initial height of 2 to 1.2 nm (Fig. 6). After compression the films supported higher loads without loss of height due to the tilting of the alkyl segments. Annealing monolayers or multilayers resulted in film breakdown, which was irreversible above 100°C.

LB films of long chain paraffinic amphiphiles, their fluorinated derivatives, and polymer composites have potential applications as no-wear and low-friction

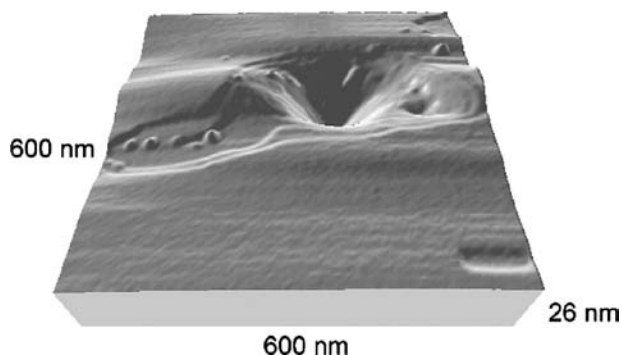


**Fig. 6** AFM tapping mode image of a surface following an AFM based indentation. The film is 10 LB layers of pCuPc(OBu)<sub>8</sub> on mica. The surface of the sample appears very smooth except for the defects induced by the silicon tip with a nominal load of 50 nN. The induced defect in the center has a depth of 14 nm with material expelled by the penetrating tip appearing as a pileup on the sides of the indent. Monolayers detach sequentially with increasing probe penetration.

lubricants. The alkyl chains in paraffinic acids tend to arrange themselves in a trans-trans fashion in LB layers resulting in highly homogeneous films. Tsukruk used SPM to study the dynamics of wear and reconstruction of LB monolayers of stearic acid under the shear forces.<sup>[61]</sup> Significant compression of the stearic acid monolayers was observed under the tip reaching 35% of initial thickness before producing fatal film damage. Film compression was related to the cooperative tilting of the alkyl chains due to formation of gauche conformers. The estimated Young's modulus ranged from 0.2 to 0.7 GPa for very small deformations (<3% of thickness). The elastic modulus decreased sharply to tens of megapascal with higher deformations.

Oishi performed AFM based mechanical studies of behenic acid, CH<sub>3</sub>(CH<sub>2</sub>)<sub>20</sub>COOH, monolayers on mica prepared at different temperatures.<sup>[43,44]</sup> The elastic modulus of the behenic acid monolayer fabricated at room temperature was 5.2 GPa. This value is close to that for the monolayers of stearic acid and cadmium stearate, 1–5 GPa, or for the LB film of cadmium arachidate, 21 GPa.<sup>[43,44]</sup> A monolayer of behenic acid fabricated at a lower subphase temperature deformed to either an elastic or a plastic state depending on the normal force, whereas at higher temperatures the monolayer is in a plastic state irrespective of normal force. This difference was attributed to the introduction of gauche conformation units into the alkyl chain. The normal force acting on the films was within the range of the activation energy (15–26 kJ/mol) required to create trans-gauche transformation of surface bound alkanes.

Salmeron investigated the structural, mechanical, and spectroscopic properties of highly ordered alkane thiol SAM and LB monolayers on quartz, mica and gold by SFG (sum frequency generation) and AFM.<sup>[62]</sup> He found that that under moderate pressures of a few tens of megapascal, the methyl end group of the alkane chains rotated to accommodate a terminal gauche distortion. The alkane chain, however, retained its upright close-packed structure with a lattice periodicity in registry with the substrate when ordered. At pressures above 0.1 GPa, changes in the form of collective molecular tilts take place that lower the height of the monolayer. Only certain angles of tilt are allowed because of the interlocking of methylene units in neighboring chains. The discrete angular tilts are accompanied by increases in friction. Upon removal of the load the molecules recovered to their original steric configuration. The author developed a model based on the van der Waals attractive energy between chains to explain the stability of the films and to estimate the cohesive energy changes during tilt for various paraffinic chain lengths. Their calculations indicated that stabilization effect of the van der Waal

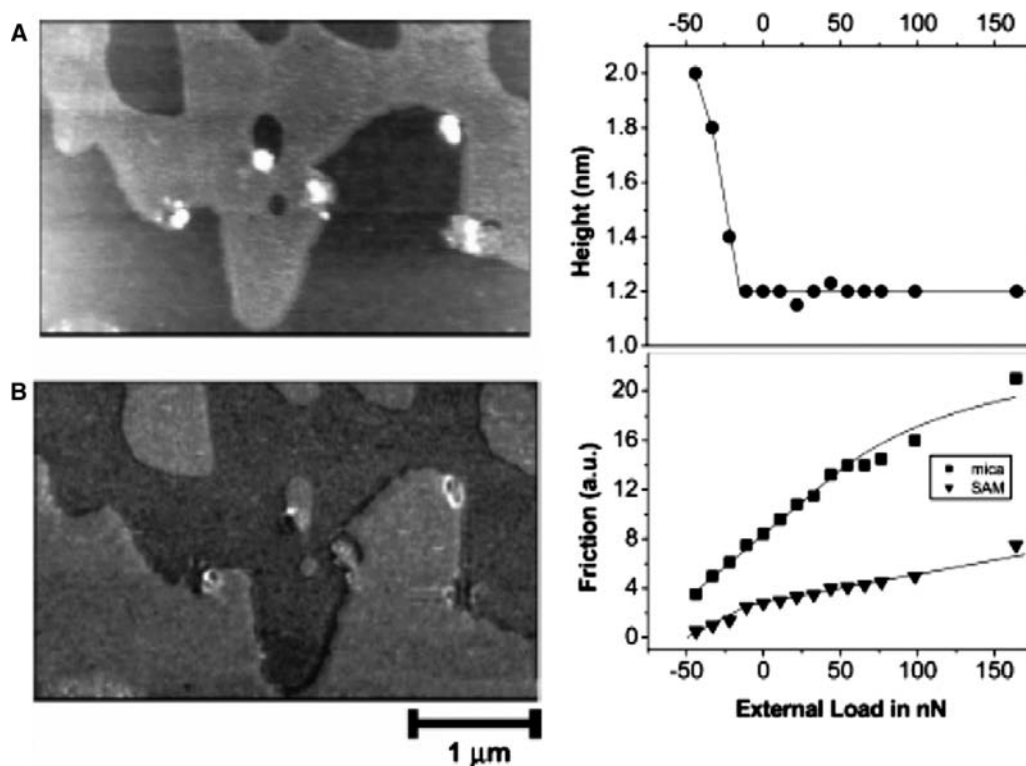


**Fig. 7** AFM images of a freshly drawn LB film of  $\beta$ -substituted-T7 oligothiophene acquired at a 0-nN external load. (A) topographic image and (B) simultaneous acquired friction force image showing low friction over the film relative to the surrounding mica. To the right are graphs of height and friction vs. load of  $\beta$ -substituted-T7 islands. The height is  $2.0 \pm 0.1$  nm at small loads and decreases to a value around 1.2 nm when the load is above  $-15$  nN. This height decrease suggests a large tilt of the alkyl chains due to gauche distortions generated near the thiophene units. In the bottom graph the friction force on the  $\beta$ -substituted-T7 islands increases rapidly first and more slowly after the decrease in film height. The friction force curve obtained in the surrounding mica is shown for comparison. *Source:* Reprinted with permission from American Chemical Society, © 2005 (see Ref.<sup>[61]</sup>).

forces on the individual methylene chains saturates at about eight to ten carbon atoms.

Swalen measured dynamic friction and wear of tribological pairs of silicon substrates and ceramic sliders, both with oxidized surfaces coated with Langmuir-Blodgett (LB) monolayers and multilayers of cadmium arachidate. He showed that the most stable couple had one LB film on each surface and had wear rates up to five orders of magnitude lower than those of uncoated surfaces at contact pressures up to  $10^8$  N/m<sup>2</sup>.<sup>[55]</sup> In comparison with physisorbed, fully fluorinated lubricants of the same thickness, mechanical durability of orders of magnitude higher was observed with LB layers. Cong et al. used thermodynamic analysis of the LB  $\Pi$ -A isotherms combined with contact angle and pin-on-plate friction measurements to study partially fluorinated acid ethyl ester LB films.<sup>[63]</sup> It was found that the coefficient of friction for a single monolayer correlated well with film energy and modulus of elasticity. The frictional properties depended on film strength. They suggested that enhancing intermolecular forces may be an

effective way to improve lubricating properties of ultra-thin films.<sup>[63]</sup>

Overney et al. studied LB films with mixtures of fluorocarbons and hydrocarbons on the nanometer scale by AFM.<sup>[64]</sup> Local elastic compliance was measured simultaneously with topography and friction. On phase separated fluorocarbon domains, higher friction and lower Young's modulus was found than on isolated hydrocarbon domains. The authors used changes in cohesion of the LB film molecules to probe the effects of cohesion on the adhesive wear. It also has been demonstrated that variations in pH during LB film formation of these mixed fluorocarbon/hydrocarbon systems leads to variations in topography, elasticity, and friction (as measured by AFM).<sup>[18-20]</sup> On increasing pH, both the Young's modulus and the friction force are found to decrease. For films prepared at pH 4.5, the Young's modulus was measured as 0.4 GPa; at basic pH the elastic compliance of the monolayers was lowered to 0.2 GPa. The simultaneous influence of pH on morphology and density was directly observed. At low pH, both friction and



in-plane molecular density increased. This was attributed to molecular “roughness” resulting from incorporation of extraneous free acid molecules into the film. Interest in these mixed LB films continues, with recent efforts directed at determining the compression moduli.<sup>[65]</sup>

## CONCLUSION

Highly ordered LB films show great promise as supermolecular assemblies for molecular electronics applications. As the dimensions of molecular based devices shrink toward the nanometer scale a new approach is required for designing Langmuir-Blodgett films with predictable performance characteristics. In this approach, the mechanical properties of thin film systems need to be systematically evaluated in terms of their relationship to the physical structure and the chemistry of the film. Furthermore, generalized models for the interplay of structural, mechanical, and optical and electronic properties have to be developed. With these models, new LB thin film structures can be designed and fabricated with optimized optical, electronic, and magnetic properties and great strength and durability.

## ACKNOWLEDGMENTS

I would like to thank my students and collaborators, T. Oshiro, K. Stevenson, N. Miyashita, K. W. Hipps, D. F. Bahr, and J. Smieja for contribution to the research reported in this article. This work was supported in part by the National Sciences Foundation under grants CHE 0138409 and CHE 0234726.

## REFERENCES

1. Ulman, A. *An Introduction to Ultrathin Organic Films From Langmuir-Blodgett to Self-Assembly*; Academic Press: CA, 1991.
2. Petty, M.C. *Langmuir-Blodgett: An Introduction*; Cambridge University Press: Cambridge, 1996.
3. Roberts, G. *Langmuir-Blodgett Films*; Plenum Press: NY, 1990.
4. Flood, A.H.; Ramirez, J.A.; Deng, W.Q.; Muller, R.P.; Goddard, W.A., III; Stoddart, J.F. Meccano on the nanoscale—a blueprint for making some of the world’s tiniest machines. *Aust. J. Chem.* **2004**, *57*, 301–322.
5. Talham, D.R. Conducting and magnetic Langmuir-Blodgett films. *Chem. Rev.* **2004**, *104*, 5479–5501.
6. Flora, W.H.; Hank, K.; Hall, H.K.; Neal, R.; Armstrong, N.R. Guest emission processes in doped organic light-emitting diodes: use of phthalocyanine and naphthalocyanine near-IR dopants. *J. Phys. Chem. B* **2003**, *107*, 1142–1150.
7. Ashwell, G.J. Langmuir-Blodgett films: molecular engineering of non-centrosymmetric structures for second-order nonlinear optical applications. *J. Mater. Chem.* **1999**, *9*, 1991–2003.
8. Xia, W.; Minch, B.A.; Carducci, D.; Armstrong, N.R. LB Films of rodlike phthalocyanine aggregates: specular x-ray reflectivity studies of the effect of interface modification on coherence and microstructure. *Langmuir* **2004**, *20*, 7998–8005.
9. Bjørnholm, T.; Tue Hassenkam, T.; Reitzel, N. Supramolecular organization of highly conducting organic thin films by the Langmuir-Blodgett technique. *J. Mater. Chem.* **1999**, *9*, 1975–1990.
10. Oshiro, T.; Backstrom, A.; Cumberlidge, A. et al. Nanomechanical properties of ordered phthalocyanine Langmuir-Blodgett layers. *J. Mater. Res.* **2004**, *19*, 1461–1470.
11. Chen, J.; Ratera, I.; Ogletree, D.F. et al. Atomic force microscopy study of  $\beta$ -substituted-T7 oligothiophene films on mica: mechanical properties and humidity-dependent phases. *Langmuir* **2005**, *21*, 1080–1085.
12. Davis, F.; Higson, S.P.J. Structured thin films as functional components within biosensors. *Biosens. Bioelectron.* **2005**, *21*, 1–20.
13. Schwartz, D.K. Langmuir-Blodgett film structure. *Surf. Sci. Rep.* **1997**, *27*, 241–334.
14. Hann, R.A. Molecules for Langmuir-Blodgett film formation. *Phil. Trans. R. Soc. Lond. A* **1990**, *330*, 141–152.
15. Kakkar, A.K. Nano-organometallics: heterogenizing homogeneous catalysts via thin film methodology. *Chem. Rev.* **2002**, *102*, 3579–3588.
16. McCullough, D.H., III; Regen, S.L. Don’t forget Langmuir-Blodgett films. *Chem. Commun.* **2004**, *278*, 7–2791.
17. Schmidt, T.J. Fabrications and characterization of stearic acid Langmuir-Blodgett films, MS Thesis, Washington State University: U.S.A.; 1999; 49 pp.
18. Usually, researchers limit localized deformation (indentations) to depths much smaller than the total thickness of the compliant coating (<20%) to eliminate contributions from the support. Unfortunately, for molecular layers with thickness of 2–10 nm, probing at these depths (1–2 nm) is frequently very difficult. Tsukruk, V.V.; Sidorenko, A.; Gorbunov, V.V.; Chizhik, S.A. Surface nanomechanical properties of polymer nanomechanical properties of polymer nanocomposite layers. *Langmuir* **2001**, *17*, 6715–6719.
19. Shi, B.; Lu, X.; Zou, R. et al. Observations of the topography and friction properties of macromolecular thin films at the nanometer scale. *Wear* **2001**, *73*, 1177–1182.
20. Overney, R.M.; Meyer, E.; Frommer, J. et al. Force microscopy study of friction and elastic compliance of phase-separated organic thin Films. *Langmuir* **1994**, *10*, 1281–1286.
21. Peng, J.B.; Barnes, G.T.; Gentle, I.R. The structures of Langmuir-Blodgett films of fatty acids and their salts. *Adv. Colloid Interface Sci.* **2001**, *91*, 163–219.

22. Ve'lez, M.; Vieira, S.; Chambrier, I.; Cook, M.J. Molecular order within Langmuir-Blodgett films of two amphiphilic octasubstituted phthalocyanines studied by atomic force microscopy. *Langmuir* **1998**, *14*, 4227-4231.
23. DeArmond, M.K.; Fried, G.A. Langmuir-Blodgett films of transition metal complexes. *Prog. Inorg. Chem.* **1997**, *44*, 97-141.
24. Mitzi, D.B. Thin-film deposition of organic-inorganic hybrid materials. *Chem. Mater.* **2001**, *13*, 3283-3298.
25. Xu, H.; Li, H.; Liu, K. Synthesis of novel amphiphilic zinc phthalocyanines and fabrication of zinc phthalocyanine-titanium oxide multilayers. *Dyes Pigments* **2001**, *49*, 9-14.
26. Antipina, T.M.N.; Gainutdinov, R.V.; Golubeva, I.V. et al. The design, fabrication and characterization of rare-earth containing multilayer supramolecular films with nanometer-scale controlled composition, structure and properties. *Surf. Sci.* **2003**, *35*, 1017-1024.
27. Huo, L.; Gao, S.; Zhao, J.; Wang, H.; Xib, S. An organic-inorganic hybrid ultrathin film: preparation and characterization of copper phthalocyanine derivative-ferric oxide nanoparticles. *J. Mater. Chem.* **2002**, *12*, 392-395.
28. Donley, C.L.; Xia, W.; Minch, B.A. et al. Thin films of polymerized rodlike phthalocyanine aggregates. *Langmuir* **2003**, *19*, 6512-6522.
29. Basu, J.K.; M, K.; Sanyal, M.K. Ordering and growth of Langmuir-Blodgett films: x-ray scattering studies. *Phys. Rep.* **2002**, *363*, 1-84.
30. Mazur, U.; Leonetti, M.; English, W.W.; Hipps, K.W. Spontaneous solution-phase redox deposition of a dense cobalt(II) phthalocyanine monolayer on gold. *J. Phys. Chem. B.* **2004**, *108*, 17,003-17,006.
31. Raynala, F.; Etcheberry, A.; Reynaudb, C.; Perezb, H. Quantitative analysis and thickness dependence study of Langmuir-Blodgett films of functionalized platinum nanoparticles by x-ray photoelectron spectroscopy. *Appl. Surf. Sci.* **2004**, *236*, 198-207.
32. Smolenyak, P.; Peterson, R.; Nebesny, K.; Tolrker, M.; O'Brien, D.F.; Armstrong, N.R. Highly ordered thin films of octasubstituted phthalocyanines. *J. Am. Chem. Soc.* **1999**, *121*, 8628-8636.
33. Sato, T.; Ozaki, Y.; Iriyama, K. Molecular aggregation and photoisomerization of Langmuir-Blodgett films of azobenzene-containing long-chain fatty acids and their salts studied by ultraviolet-visible and infrared spectroscopies. *Langmuir* **1994**, *10*, 2363-2369.
34. Faucher, K.M.; Dluhy, R.A. Thermally induced microdomain formation in fatty acid Langmuir-Blodgett films observed by attenuated total reflectance infrared spectroscopy. *Colloids Surfaces, A: Physicochem. Eng. Aspects* **2003**, *219*, 125-145.
35. Itoh, K.; Kudryashov, I.; Yamagata, J.; Nishizawa, T.; Fujii, M.; Osaka, N. Raman microspectroscopic study on polymerization and degradation processes of a diacetylene derivative at surface enhanced Raman scattering active substrates 2. Confocal Raman microscopic observation of polydiacetylene adsorbed on active sites. *J. Phys. Chem. B* **2005**, *109*, 271-276.
36. Goulet, P.J.G.; Pieczonka, N.P.W.; Aroca, R.F. Mapping single-molecule SERRS from Langmuir-Blodgett monolayers on nanostructured silver island films. *J. Raman Spectrosc.* **2005**, *36*, 574-580.
37. del Cano, T.; Goulet, P.J.G.; Pieczonka, N.P.W.; Aroca, R.F.; De Saja, J.A. Nano-structured Langmuir-Blodgett mixed films of titanyl(IV) phthalocyanine and bis (neopentylimido)perylene. *Synth. Met.* **2005**, *148*, 31-35.
38. Constantino, C.J.L.; Lemma, T.; Antunes, P.A.; Goulet, P.; Aroca, R. Surface-enhanced resonance Raman scattering Single-molecule detection in a Langmuir-Blodgett monolayer. *Appl. Spectrosc.* **2003**, *57*, 649-654.
39. Pawsey, S.; McCormick, M.; De Paul, S. et al. <sup>1</sup>H Fast MAS NMR Studies of hydrogen-bonding Interactions in self-assembled monolayers. *J. Am. Chem. Soc.* **2003**, *125*, 4174-4184.
40. Fanucci, G.E.; Bowers, C.R.; Talham, D.R. Application of solid-state <sup>31</sup>P NMR to the study of Langmuir-Blodgett Films. *J. Am. Chem. Soc.* **1999**, *121*, 1088-1089.
41. Rude, E.; Mitchell, D.J.; Mazur, U. Solid state NMR studies of copper phthalocyanine Langmuir-Blodgett multilayers. In *Langmuir to be published*.
42. Hipps, K.W.; Barlow, D.E.; Mazur, U. Orbital mediated tunneling in vanadyl phthalocyanine observed in both tunnel diode and STM environments. *J. Phys. Chem. B.* **2000**, *104*, 2444-2447.
43. Oishi, Y.; Umeda, T.; Kuramori, M.; Suehiro, K. Mechanical properties of a Langmuir-Blodgett film measured by atomic force microscopy. *Langmuir* **2002**, *18* (3), 945-947.
44. Stevenson, K.; Miyashita, N.; Smieja, J.; Mazur, U. Highly ordered thin films prepared with octabutoxy copper phthalocyanine complexes. *Ultramicroscopy* **2003**, *97*, 271-278.
45. Oliver, W.C.; Pharr, G.M. Improved technique for determining hardness and elastic modulus using load and displacement sensing indentation experiments. *J. Mater. Res.* **1992**, *7*, 1564-1580.
46. Asif, S.A.S.; Pethica, J.B. Nano-scale indentation creep testing at non-ambient temperature. *J. Adhes.* **1998**, *67*, 153-165.
47. Li, X.; Bhushan, B. A review of nanoindentation continuous stiffness measurement technique and its applications. *Mater. Charact.* **2002**, *48*, 11-36.
48. deBoer, M.P.; Kriese, M.D.; Gerberich, W.W. Investigation of a new fracture mechanics specimen for thin film adhesion measurement. *J. Mater. Res.* **1997**, *12*, 2673-2685.
49. Bahr, D.F.; Hoehn, J.W.; Moody, N.R.; Gerberich, W.W. Adhesion and acoustic emission analysis of failures in nitride films with a metal interlayer. *Acta Mater.* **1997**, *45*, 5163-5175.
50. Kriese, M.D.; Moody, N.R.; Gerberich, W.W. Adhesion measurements of ductile copper films by nanoindentation. *Proc. Mater. Res. Soc.* **1998**, *505*, 363-369. Thin Films-Stresses and Mechanical Properties VII.
51. Marshall, D.B.; Evans, A.G. Measurement of adherence of residually stressed thin films by indentation. *J. Appl. Phys.* **1994**, *56*, 2632-2638.
52. Thouless, M.D.; Hutchinson, J.W.; Liniger, E.G. Plane strain, buckling driven delaminations of thin

- films: model experiments and mode II fracture. *Acta Metall. Mater.* **1992**, *40*, 2639–2649.
53. Weppelmann, E.R.; Hu, X.Z.; Swain, M.V. Observations and simple fracture mechanics analysis of indentation fracture delamination of TiN films on silicon. *J. Adhes. Sci. Tech.* **1994**, *8*, 611–624.
  54. Hutchinson, J.W.; Suo, Z. Mixed mode cracking in layered materials. *Adv. Appl. Mech.* **1992**, *29*, 63–191.
  55. Novotny, V.; Swalen, J.D. Tribology of Langmuir-Blodgett layers. *Langmuir* **1989**, *5*, 485–489.
  56. Moraille, P.; Badia, A. Highly parallel, nanoscale stripe morphology in mixed phospholipid monolayers formed by Langmuir-Blodgett transfer. *Langmuir* **2002**, *18* (11), 4414–4419.
  57. McKeown, N.B. *Phthalocyanine Materials: Synthesis Structure, and Function*; Cambridge University Press: Cambridge, U.K., 1998.
  58. Cook, M.J. Phthalocyanine thin films. *Pure Appl. Chem.* **1999**, *71*, 2145–2151.
  59. Zangmeister, R.A.P.; O'Brien, D.F.; Armstrong, N.R. Deposition of rod-like phthalocyanine aggregates on Au surfaces patterned with a combination of microcontact printing and electropolymerization. *Adv. Funct. Mater.* **2002**, *12*, 179–186.
  60. Wu, Z.i.; Wu, S.e.; Lu, Z.; Liang, Y. Organization and properties of a conjugated poly (heteroarylene methines) at the air-water interface and in the Langmuir-Blodgett films. *J. Colloid Interface Sci.* **2002**, *25*, 125–130.
  61. Tsukruk, V.V.; Bliznyuk, V.N.; Hazel, J.; Visser, D.; Everson, M.P. Organic molecular films under shear forces: fluid and solid Langmuir-Monolayer. *Langmuir* **1996**, *12*, 4840–4849.
  62. Salmeron, M. Generation of defects in model lubricant monolayers and their contribution to energy dissipation in friction. *Tribol. Lett.* **2001**, *10*, 69–79.
  63. Cong, P.; Igari, T.; Nanao, H.; Mori, S. Film structures and frictional properties of monolayers of partially fluorinated carboxylic acid ethyl esters. *Sekiyu Gakkaishi* **2000**, *43*, 241–247.
  64. Overney, R.M.; Bonner, T.; Meyer, E. et al. Elasticity, wear, and friction properties of thin organic films observed with atomic force microscopy. *J. Vac. Sci. Tech. B* **1994**, *12*, 1973–1976.
  65. Dhathathreyan, A.; Baskar, G.; Ramasami, T.; Juhue, D. Interfacial organization of fluoropolymers in Langmuir films: role of additives. *Langmuir* **2002**, *18*, 4704–4708.

# Laser-Based Deposition: Patterning

**Edward M. Nadgorny**

*Department of Physics, Michigan Technological University,  
Houghton, Michigan, U.S.A.*

**Jaroslav Drelich**

*Department of Metallurgical and Materials Engineering, Michigan Technological University,  
Houghton, Michigan, U.S.A.*

## INTRODUCTION

The laser-based particle deposition (LBPD) technique is one of “direct-write” techniques that can be used for patterning nanoparticles into a variety of microstructures. If properly developed, LBPD may have wide application in manufacturing novel electronic, sensing, catalytic, and other devices that require specific structures, combinations of unlike materials, and unconventional substrates. The technique makes use of laser-induced optical forces to guide particles by a narrow laser beam from an atomizer source until depositing them on a substrate. One of the LBPD versions based on aperture guidance is reviewed in this entry.

The discussion covers both the fundamentals of both laser guidance and solid–liquid interactions during patterning, including recommendations for the best setups, as well as a more detailed description of optical and other forces exerted on particles inside the LBPD apparatus. Some examples of nanoparticle deposition and patterning are also presented.

## LASER-BASED PARTICLE DEPOSITION TECHNOLOGY

A wide range of techniques generally referred to as “direct-write technologies” have recently emerged in response to the needs for rapid prototyping of micro-patterns made of continuous phase or fine particles.<sup>[1]</sup> Technologies such as inkjet printing, micropen writing, plasma spray, laser particle guidance, and matrix-assisted pulsed-laser evaporation are capable of direct fabrication of microstructures on a variety of substrates using a wide range of materials. All of these approaches have the advantage of avoiding the need for masks and complicated lithographic technologies associated with microscale electronic device fabrication. These rapid prototyping techniques are often able to consolidate powder materials into three-dimensional structures.

Laser-based particle deposition technique is one of many such techniques under recent development that has a promising potential for the fabrication of electronics and sensors based on microvolume materials. The LBPD technique makes use of laser-induced optical forces to guide particles by a narrow laser beam until depositing them on a substrate. As described in Ref.<sup>[2]</sup>, LBPD has many advantages over existing patterning techniques. “...In contrast to photolithography, the process adds material to the surface (as opposed to etching material) and does not require harsh or corrosive chemicals. In contrast to robotic microspotting, deposition, inkjetting, and screenprinting, particles are strongly localized within the laser beam and the deposition accuracy can be below one micrometer. Most importantly, nearly any material in either liquid or aerosol suspension can be captured and deposited as long as convection and gravity are weaker than the guidance forces (typically in the nanonewton range).”

Additionally, LBPD allows one the fabrication of various porous structures of nanoparticles, which can serve, for example, as microsensors.<sup>[3]</sup> Although perfection in nanoparticle arrays is not required in such applications, achieving sufficient control over deposited micropatterns to manufacture porous microstructure is not a trivial task. There are only two promising techniques for such applications at present, inkjet writing and LBPD. Each of them has different merits and demerits, so that they rather complement each other being suitable for a different range of applications. Although both techniques can produce similar structures, the resolution of inkjet writing at present reaches only 10–20 μm; LBPD is not restricted either by solvent viscosity to the degree required by inkjet techniques. More importantly, LBPD is also temperature-flexible: When the transporting particles absorb laser light, the resulting heat, if required, can activate chemical reactions and/or phase transformations during and after deposition. At the same time, the laser-induced heat can also be rather low: Because of

high transporting velocities and such option as cooling carrier gas, both the droplet and substrate temperatures can be controlled allowing only moderate short-duration temperature increases. Because the LRPD-transported material is in the form of either liquid precursor or colloidal suspension atomized to micrometer-size droplets, the deposited particles can be of any size between several nanometers to about a micron. Finally, LRPD is capable of codepositing dissimilar materials offering a potential to fabricate both heterostructured and porous patterns that combine distinct electronic, organic, and biological materials using the same basic fabrication technology.

The LRPD technique, although still in its early stages of development, has been used to fabricate micron-scale structures from a wide variety of materials, such as metals (Au, Ag, In, Cu, Pt), semiconductors (Si), oxides (CuO, RuO<sub>2</sub>, Al<sub>2</sub>O<sub>3</sub>), ferroelectrics (BaTiO<sub>3</sub>), ionic crystals (NaCl, KI), biological cells (neurons, others) on such various substrates as glass, alumina, silicon, sapphire, and various polymers.<sup>[2–8]</sup> In principle, LRPD allows depositing virtually any material that can be suspended in a liquid or formed by decomposition of a precursor. The primary restrictions on the LRPD technique are that the substrate is transparent to light at the laser frequency (to avoid substrate heating) and that the particles being deposited should not undergo unwanted reactions (e.g., decomposition) during transport in the laser beam.

Historically, it was Ashkin<sup>[9]</sup> who was the first to demonstrate the optical “levitation” that moved and

suspended micrometer-sized particles against gravity in a focused laser beam. Stable three-dimensional trapping of such particles in the minimum-waist region of a highly focused laser beam was demonstrated later.<sup>[10]</sup> These and other findings formed the basis of the so-called optical tweezers used in many applications.<sup>[11]</sup> Renn and Pastel<sup>[4,5]</sup> were the first to demonstrate laser guidance and trapping of mesoscale particles from suspensions and liquid droplets in hollow-core optical fibers. The obtained data gave rise to industrial applications of a laser-guided direct write of electronic and biological components.<sup>[2]</sup> Finally, LRPD technique with aperture guidance was demonstrated recently.<sup>[12]</sup> Unlike optical trapping techniques,<sup>[9–11]</sup> LRPD utilizes optical transverse gradient forces to confine particles inside weakly focused laser beams and take advantage of the radiation pressure to move particles axially along through an aperture onto a substrate within the near-field region. This version of the LRPD technique as developed at Michigan Technological University is described in this review.

The principal LRPD setup is shown schematically in Fig. 1. It includes a mist chamber (MC), source chamber (SC), process chamber (PC), and a laser system. The mist chamber includes an atomizer and delivery system to make a mist of micron-sized liquid droplets (or particles) that are precursors for the deposited material. The droplets are delivered from the atomizer to the source chamber by a carrier gas, and a mass flow meter measures and controls the gas flow. The source chamber is connected to a process chamber by a micron-sized aperture, with a typical size in the range

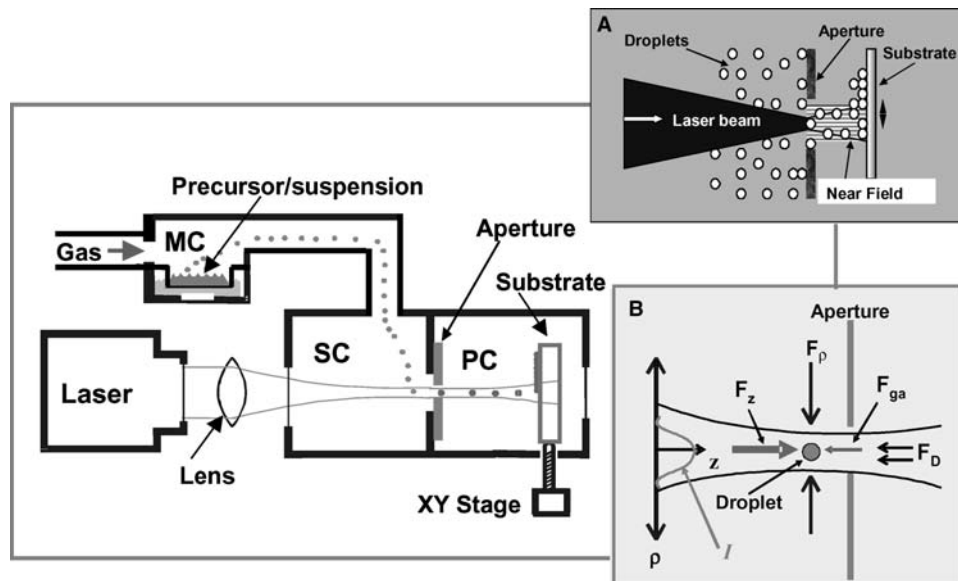


**Fig. 1** Schematic of the MTU LRPD system: source of deposited material (carrier gas supply and atomizer inside mist chamber MC); supply (SC) and process (PC) chambers linked by a high-power laser aperture (details shown in the insets); laser system (laser and focusing lenses); movable substrate on a translational stage.

from 15 to 35  $\mu\text{m}$ . The droplets are usually much smaller, of the order of a micron or less. The laser beam is coupled into the aperture by an optical lens of low numerical aperture to allow particle guidance to a substrate that is mounted on a translational stage. The supply chamber both provides an environment suitable for the deposition process and shields the particles from convection currents that can deflect particles out of a laser's confinement.

As shown in Fig. 1, in contrast to optical tweezers,<sup>[9–11]</sup> LBPD allows droplets to be captured continuously from the supply chamber and transport them onto the substrate to “write” on it. Guidance in the LBPD aperture-based system is achieved by a weakly focused laser beam and diffracted laser radiation within near-field limits at the front and the rear of the aperture, respectively.<sup>[12]</sup> Also shown in Fig. 1 (inset b) are the main forces exerted on a particle in the apparatus. Three of them, the optical radiation force  $F_z$ , the optical transverse gradient force  $F_\rho$ , and optical axial gradient force  $F_{\text{ga}}$ , are resulted from the interaction of the particle with incident laser beam, and the drag force  $F_D$  is due to the interaction of a moving particle with the ambient. They and other forces will be discussed in detail below.

Examples of different materials deposited by the LBPD apparatus can be found elsewhere.<sup>[2,3,7,8,13]</sup> Several additional examples are shown in Fig. 2.

## LBPD BASICS

### Optical Field Inside the LBPD System

It is important to discuss the spatial distribution of laser optical field near an aperture as the light intensity provides both axial and transverse guidance of particles. In particular, it is the optical axial force  $F_z$  and the optical transverse gradient force  $F_\rho$  that determine the guidance efficiency, the particle velocity, and the throughput rate of an LBPD apparatus.

We will consider the laser beam with a TEM<sub>00</sub> (or fundamental) mode that can be represented by an ideal Gaussian intensity profile. Such a beam with the total power  $P$  propagates in free space along the  $z$  direction toward a centered circular aperture with radius  $a$  (Fig. 1B). The intensity (or irradiance)  $I(z, \rho)$  of such a beam is then.<sup>[14]</sup>

$$I(z, \rho) = I_0 e^{-2\rho^2/w^2} \quad (1)$$

where  $I_0(z) = 2P/\pi w^2$  is the axial (peak) intensity at  $\rho = 0$ ,  $w(z)$  is the spot radius diverging with the distance as  $w(z) = w_0 \sqrt{1 + (z/z_R)^2}$ , and the smallest spot radius  $w_0$  (at the beam waist) is at  $z = 0$ . For such a beam, the distance  $z_R$ , the waist spot radius  $w_0$ , and the beam full-angle divergence  $\theta$  are beam parameters

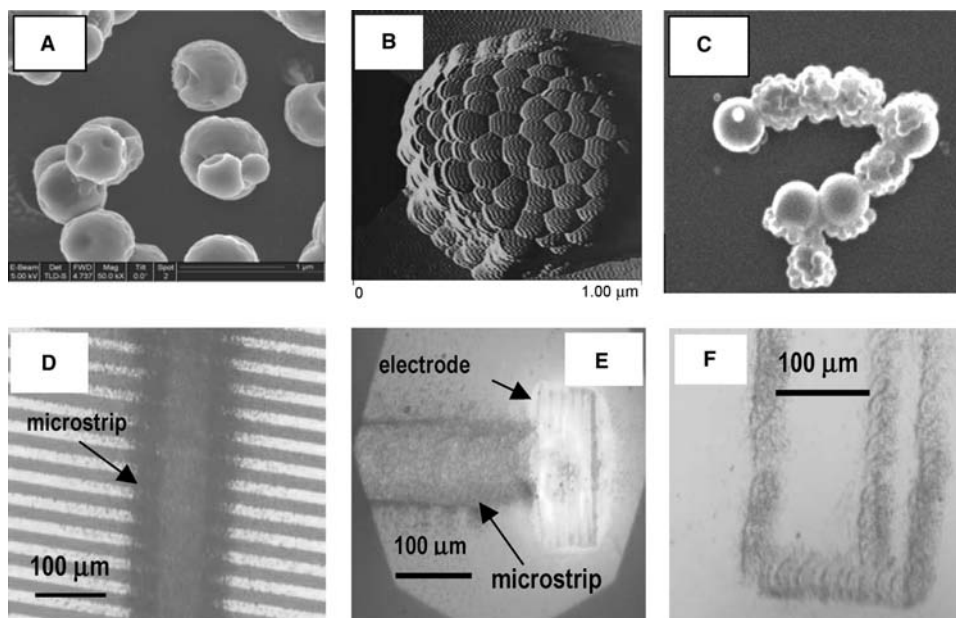


**Fig. 2** Examples of materials deposited by the LBPD apparatus: (A) SEM micrograph of microspheres formed by 7-nm Au-S(CH<sub>2</sub>)<sub>7</sub>CH<sub>3</sub> particles deposited by a 200-mW laser; (B) AFM image of a cluster of 100-nm polystyrene particles; (C) SEM micrograph of an array of 400-nm polystyrene spheres partially coated with 100-nm polystyrene spheres; (D) optical image of the 7-nm Au-S(CH<sub>2</sub>)<sub>7</sub>CH<sub>3</sub> particles deposited on an array of gold microelectrodes by a 200-mW laser; (E) similar to (D), after an electrode was produced by in situ melting by a 500-mW laser beam. (F) Structure made of ~20-nm Au-S(CH<sub>2</sub>)<sub>7</sub>CH<sub>3</sub> particles deposited after atomization of 2–4 g/L suspension of nanoparticles in toluene.



defined as<sup>a</sup>

$$z_R = \pi w_0^2 / \lambda, \quad \theta = 2\lambda M^2 / \pi w_0 \quad (2)$$

where  $M^2 \geq 1$  is a factor representing the beam quality (for an ideal Gaussian beam,  $M^2 = 1$ ), and for a beam behind a circular aperture with radius  $a$ ,  $z_R = \pi a^2 / \lambda$ . The parameter  $z_R$  is referred to as the Rayleigh range indicating an approximate border between the near-field diffraction region (at  $z < z_R$ ) and the far-field diffraction region (at  $z > z_R$ ). The extent along the beam between  $\pm z_R$  points relative to the beam waist is commonly considered as the collimated waist region. The diffraction angle  $\theta$  of a beam spreads in the far field, where  $w(z) \approx w_0 z / z_R = \lambda z / \pi w_0$  at  $z \gg z_R$ . The angle  $\theta$  is often considered as a laser primary parameter because divergence is of fundamental importance for many laser applications. However, any one of the beam parameters completely characterizes the optical field along the entire Gaussian beam because only one is independent at a particular wavelength  $\lambda$ . Therefore the axial intensity  $I_0$  of a laser cannot be increased by reducing  $w_0$  without also increasing its divergence. As we will see, this is especially important for the LRPD systems. The beam intensity falls off very fast with radius  $\rho$  beyond the spot size  $w$ : at  $\rho = w$  the intensity decreases to  $0.135I_0$  ( $1/e^2$  criterion) and to about  $0.01I_0$  (often called 99% criterion) at  $\rho = \pi w / 2$ .

The circular aperture, which links the supply and process chambers of the LRPD apparatus (Fig. 1), changes the beam optical field by two different ways. First, due to aperture truncation, the power transmission of the passing beam can be cut off considerably depending on the ratio  $a/w_0$ , especially at  $a/w_0 \leq 1$ . Even an aperture with radius  $a = w_0$  transmits only  $\approx 86\%$  of the total beam power  $P$ . However, this effect can be avoided by increasing the ratio: An aperture transmits as much as 99% after the ratio increase to  $a/w_0 \geq \pi/2 = 1.6$ . Secondly, diffraction of the beam on an aperture produces more complex intensity patterns in both the near-field and far-field regions.<sup>[14,15]a</sup> In the far field, the axial intensity decreases due to standard Gaussian beam divergence: According to Eq. (1), the axial intensity changes with distance as  $I_0(z) = (z_R/z)^2 I_{00}$ , where  $I_{00}$  is the axial intensity at the beam waist. Additionally, a diffracting aperture perturbs the beam creating well-known diffraction effects that significantly change the optical field distribution including the central far-field lobe intensity. In the near field, the changes in the

characteristics of the diffracted beam are the most essential. The intensity ‘‘Fresnel’’ ripples appear and become more and more distinguished as the ratio  $a/w_0$  decreases. The intensity variation  $\Delta I/I$  can be as large as  $\pm 20\%$  even for a 99% aperture. (The far-field central intensity will also be decreased by 20% by such an aperture.) As a result, rings of a higher and lower intensity are typical in the near-field region, their location, amplitude, and number changing with distance and with the ratio  $a/w_0$  (Fig. 3). On the other hand, the average intensity is practically a constant or even increasing with distance in the near-field region at  $z < z_R$ . Finally, there is a peak at or near the beam axis that might be rather spiky closer to the aperture.

For a typical double-frequency YAG-laser ( $\lambda = 532$  nm,  $\theta = 0.5$  mrad and  $M^2 = 1$ ), Eq. (2) then gives  $w_0 \approx 0.7$  mm and a long collimated waist region of  $2z_R \approx 5.4$  m. Focusing such a collimated beam with a lens of the focal length  $f = 35$  mm decreases the original waist spot diameter  $2w_0$  to  $2w_0' = 2\theta f = 35$   $\mu$ m. At the same time, the divergence increases to  $\theta' = w_0\theta/w_0' \approx 20$  mrad and the beam Rayleigh range  $z_R$  diminishes to 1.8 mm. Obviously, the same  $z_R = 1.8$  mm is for the beam after passing an aperture with the diameter  $2a = 2w_0' = 35$   $\mu$ m.

The intensity of a real laser beam can be different than that of an ideal Gaussian beam because of both a possible mixture with higher-order modes and effects of nonideal optics. Although the Rayleigh range is still the same in such cases, the waist spot size and divergence are larger, as can be seen from Eq. (2) for  $M^2 > 1$ . The most distinguished feature, however, is the more complex intensity profile of such laser beams: Instead of Eq. (1), the intensity distribution exhibits local maxima and minima inside the collimated region or focus.

## Setup Optimization of the LRPD System

The discussion above and computational results based on the paraxial approximation of a Gaussian beam diffracted by a circular aperture<sup>[15–17]</sup> suggest several factors important for the optimal setup of LRPD. The calculations and experimental comparison of the diffraction patterns with the best particle flux through the 25- and 35- $\mu$ m apertures have shown that one of the most important factors is the ratio  $a/w_0$ . The ratio affects the far-field diffraction pattern as can be seen in Fig. 3 for seven ratios  $a/w_0$ . The calculations are performed for conditions close to real experimental setups: Gaussian beams with  $w_0 = 3$ –20  $\mu$ m and circular apertures with diameters from 35 to 5  $\mu$ m. Only three pairs of maxima and minima without a

<sup>a</sup>Eq. 2 is analogous to the optical (the Smith–Helmholtz) invariant in an optical system comprising only lenses. In practice, lasers as a rule are characterized not only by the beam-waist spot  $w_0$  but also by the beam divergence  $\theta$ .

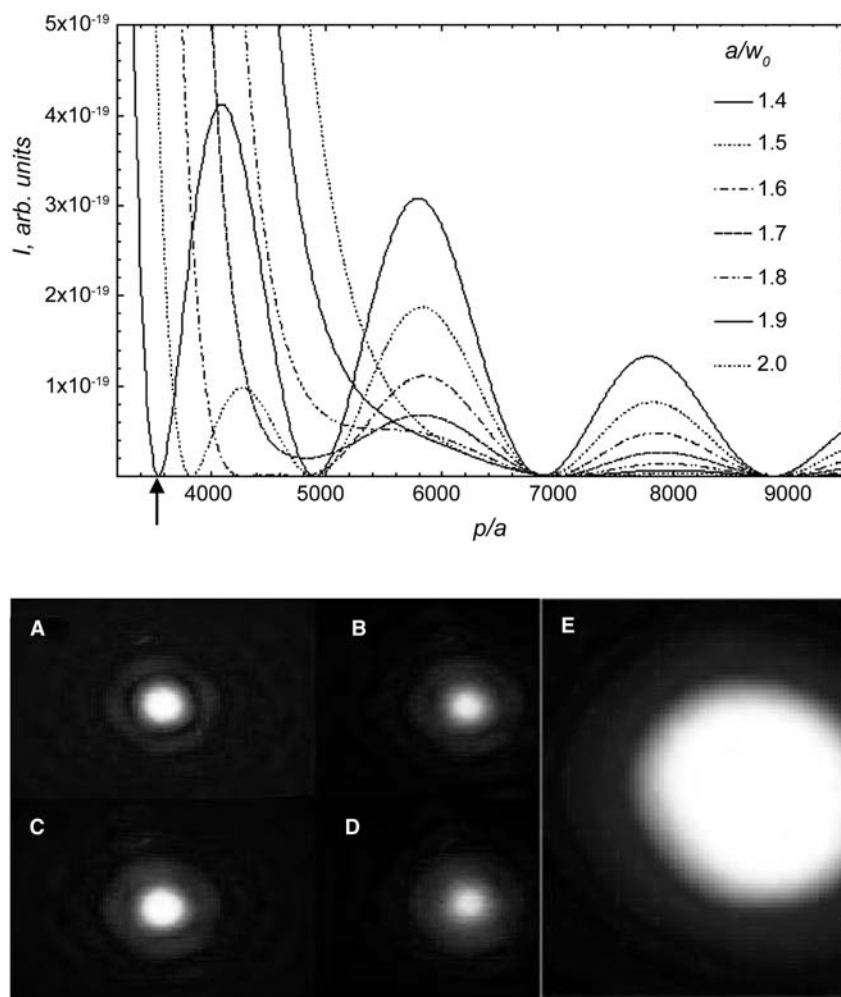


**Fig. 3** The transverse diffracted intensity  $I$  calculated for different ratios  $a/w_0$  as a function of the transverse distance  $\rho$  from the beam axis normalized by the aperture radius  $a$ , and corresponding diffraction images. The arrow in the plot marks the first minimum for the ratio  $a/w_0 = 1.4$ . The ratio  $a/w_0$  increases from (A) to (E); the latter corresponds to a typical working setup with  $a/w_0 \approx 1.8$ . In (A), the size of the first ring is about 70 mm. The images were obtained with a digital camera in the far-field diffraction region of the 35- $\mu\text{m}$  aperture.

much higher central maximum are displayed. As seen, both the positions of the first minima and the diffraction contrast (determined as the intensity difference between the first maximum and minimum) depend on the ratio  $a/w_0$ . The contrast decreases as the ratio increases, and the first minimum completely vanishes at  $a/w_0 \geq 1.8$ .

Experimentally, the ratio  $a/w_0$  can be changed by either displacing different focusing lenses relative to the laser (changing the waist radius  $w_0$  only), or changing the aperture size, or both. The experimental data confirm the calculation results (Fig. 3). The images are obtained by axially displacing a 35- $\mu\text{m}$  aperture closer and closer to the beam waist, until the first minimum cannot be seen anymore in Fig. 3(E). Using such images, one can find the best alignment of the laser-lens-aperture system. Numerous deposition experiments with apertures and laser beam waists of various

sizes confirmed that deposition is impossible when the contrast between the first minimum and the first maximum is high, such as in Fig. 3(A) through (D). As the contrast decreases, deposition is finally made possible near  $a/w_0 \approx 1.7$ . This number is larger than the ratio of 1.125 required for a maximum axial intensity in the far-field range but closer to  $\pi/2$  that corresponds to  $\geq 99\%$  power transmission.<sup>[14]</sup> The other important factor is the divergence of the beam ahead of the aperture. A large divergence in the region near the beam waist (as utilized in optical tweezers)<sup>[11]</sup> can lead to reverse radiation pressure, especially for small  $w_0 \leq \lambda$ .<sup>[18]</sup> Our experiments with 100-nm polystyrene spheres, 25- $\mu\text{m}$  circular aperture, and 30-mm focusing lens have shown that the setup can be optimized to provide guidance at as low laser power as  $P \approx 100 \text{ mW}$ .<sup>[17]</sup>

High accuracy is essential for direct-write applications. Because it is determined by many factors,

systematic studies are required to estimate their contributions. Preliminary experiments with five different materials<sup>[19]</sup> have shown that the deposition accuracy is inversely proportional to the transport distance. The accuracy also strongly depends on the material properties of the transported particles, such as the refractive index and absorption, and relatively weakly on the laser power when measured inside a relatively low-power range. To increase deposition precision and utilize the features of the near-field intensity pattern, the substrates during LRPD operations are usually located at  $z < z_R$ , i.e., closer to the aperture.

### Particle Dynamics and Forces in the LRPD System

Two special features critically influencing the forces exerted on droplets inside a LRPD apparatus are a nonuniform optical field with on-axis maximum intensity and a droplet small size of  $R \leq \lambda$ . There are three types of forces important for LRPD: optical forces, radiometric forces, and the drag force. The optical forces arise from scattering and absorption of light by the particle; the radiometric forces result from the temperature gradients either inside the particle or in the medium; and the drag force develops due to the resistance of the medium to a moving particle. Additionally, the force of gravity and hydrodynamic interaction forces between particles are also present. However, a characteristic feature of the dynamics of droplets inside the LRPD system is that the interaction forces between particles and the force of gravity are, in most cases, considerably less than the other three. For submicron particles typical of the LRPD technique, the force of gravity is below the  $10^{-14}$ -N range and decreases significantly with the particle size, so that we can safely ignore the gravity force. The droplets can also be considered independent of one another inside the supply chamber because of their relatively low concentration so that we can neglect hydrodynamic forces as well. On the other hand, the particle interaction might be important during delivery from the atomizer to the supply chamber, as the clouds of particles not only move faster than the individual particles<sup>[20]</sup> but also the particles can coagulate forming larger droplets or clustered particles.

When a particle is illuminated by an incident beam, its electromagnetic energy and momentum are lost because of absorption and scattering processes. The use of conservation of energy and momentum allows calculating the beam-induced stress tensor on the surface of the particle and the corresponding optical force field; such forces are collectively called the radiation forces. They depend on the size, shape and material of the particle, the beam polarization and intensity

distribution, and the position of the particle inside the beam.<sup>[21–23]</sup> Then the forward force exerted on a spherical particle of radius  $R$  inside a gaseous medium with the refractive index  $n_b \approx 1$  by a beam with the axial intensity  $I_0$  and the waist spot  $w_0 \gg R$  is given by<sup>[21]</sup>

$$F_z = \frac{\pi R^2 I_0}{c} Q_{pr} = \frac{\pi R^2 I_0}{c} (Q_{ext} - Q_{sca} \overline{\cos \theta}) \quad (3)$$

where  $Q_{pr}$ ,  $Q_{ext}$ , and  $Q_{sca}$  are the so-called efficiencies for radiation pressure, extinction, and scattering, respectively,  $Q_{ext} = Q_{sca} + Q_{abs}$  (where  $Q_{abs}$  is the efficiency for absorption),  $c$  is the velocity of light in free space, and the average cosine of the scattering angle  $\overline{\cos \theta}$  is the scattering asymmetry parameter. Because the refractive index of gases is very close to 1, we can use  $c$  instead of the velocity of light in the medium in Eq. (3). For low-absorbing particles (such as liquid droplets of water-based dilute solutions),  $Q_{pr} \approx (1 - \overline{\cos \theta}) Q_{sca}$ ; in the opposite limit of particles with no scattering (ideal “black” particles),  $Q_{pr} \approx Q_{abs}$ . Eq. (3) allows calculating the forward axial force  $F_z$  based on various approximations of light scattering models.<sup>[21–23]</sup> To include both absorption and scattering processes into the calculations, the refractive index  $m$  of the particle is represented by a complex number,  $m = n + i\kappa$ , where the real part  $n$  is responsible for scattering and the imaginary part  $\kappa$  (or the extinction coefficient) is responsible for absorption. The extinction coefficient  $\kappa$  is related to the absorption coefficient  $\alpha$  (sometimes also called the turbidity or attenuation coefficient) of the Beer–Lambert law,  $I_t = I_i \exp(-\alpha l)$ , as  $\kappa = \lambda \alpha / 4\pi$ , where the incident intensity  $I_i$  decreases to  $I_t$  over the path length  $l$ . The refractive index  $m$  can vary over a wide range of  $1 \leq m < \infty$ , where the lower limit corresponds to translucent liquids and solids, and the upper limit, typical of metals in the infrared region, corresponds to total reflection. The other way to characterize particles is through the relative dielectric constant  $\epsilon_r = \epsilon_1 + i\epsilon_2 = m^2$ , so that  $\epsilon_1 = n^2 - \kappa^2$  and  $\epsilon_2 = 2n\kappa$ .

In the calculation, the particle size is represented by the normalized size parameter  $x = 2\pi R/\lambda$ , which for particle sizes typical for LRPD,  $50 \leq R \leq 500$  nm, is approximately within a range of  $0.6 \leq x \leq 6$ .<sup>b</sup> Such a range requires a rigorous calculation to find  $F_z$ , and it can be performed using the generalized Lorenz–Mie theory (GLMT).<sup>[21]</sup> If the particle is spherical, scattering can be simulated with the GLMT independently of the spheres’ diameter and refractive

<sup>b</sup>Note that although we have propelled and deposited as small solid particles as 7 nm,<sup>[3,7,8]</sup> they were in suspensions.

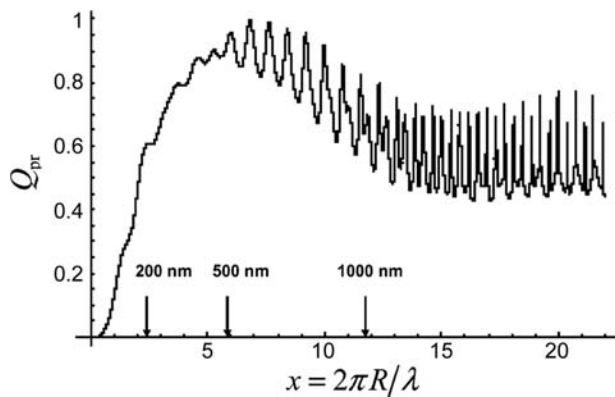


**Fig. 4** Typical size dependence of the efficiency factor  $Q_{pr}$  for a polystyrene sphere (the refractive index  $m = 1.431$ ) obtained by numerical calculation based on a generalized Lorentz–Mie theory with no absorption. The arrows show the corresponding radii  $R$  for  $\lambda = 532$  nm. Source: From Ref.<sup>[19]</sup>.

index. An example of such a calculation is shown in Fig. 4;<sup>[19]</sup> similar calculations were performed for weakly absorbing spheres.<sup>[21–23]</sup> As seen, the average envelope of the  $Q_{pr}-x$  curve shows a relatively small change as  $x$  decreases from 20 to 3 remaining at  $Q_{pr} \approx 0.5$ , with a flat maximum near  $x = 6$ . Taking LRPD typical conditions for a collimated beam of  $w_0 \approx 10 \mu\text{m}$  and  $P = 1$  W yields  $F_z \approx 6 \times 10^{-12}$  and  $1 \times 10^{-12}$  N for the particles of  $R = 500$  and  $200$  nm, respectively.<sup>c</sup> The other feature is a superposition of ripple structures with maxima and sharp spikes that originate in resonant electromagnetic normal modes of a sphere.<sup>[22]</sup> Such structures are typical of the morphology-dependent resonances (MDRs); they were both predicted by the Mie theory and observed in experiments involving several different techniques.<sup>[25]</sup> During the deposition process, laser-induced evaporation of the moving droplets changes the particle size so that the forward force experiences the corresponding fluctuations of MDRs. However, the droplet motion in gaseous medium is normally overdamped because of the drag force (see below) so that such short peaks should not affect the particle motion.

The classical Mie–Lorentz theory assumes only planar waves in the incident optical field,<sup>[24]</sup> but it can also be applied to a real laser beam provided that the waist spot  $w_0 \gg R$ . To include into consideration also gradient forces, important for both LRPD and optical trapping, other approach is required. A gradient force arising from electrical forces on a polarizable particle

can be calculated directly from a standard expression,

$$F_g = (\alpha/2) \nabla E^2 \quad (4)$$

where  $\nabla E$  is the gradient of laser electric field  $E$  and  $\alpha = 4\pi R^3(\epsilon_r - 1)/(\epsilon_r + 2)$  is the particle polarizability for small particles when  $x \ll 1/\kappa$ .<sup>[23]</sup> For larger particles, the expression for  $\alpha$  can be corrected.<sup>[26]</sup> Alternative models have also been proposed to calculate both gradient and forward forces for small particles of  $2R \leq \lambda$ . The models use either an extended GLMT<sup>[18]</sup> or a two-component approach,<sup>[27]</sup> and in all cases the transverse gradient force  $F_\rho$  is larger than the axial force  $F_z$ . Such gradient force  $F_g$  is large enough to confine the particles to the laser beam: The force is attracted toward high intensity for positive  $\alpha$  and thus provides the necessary guidance along the laser-beam axis. Estimates also demonstrate<sup>[4]</sup> that the potential created by such gradient forces is several orders of magnitude larger than the thermal energy of the ambient molecules, which ensure particle guidance under ambient conditions. The models also revealed that an additional, axial gradient force  $F_{ga}$  can exist in tight-focused systems that can produce trapping in the diverging part of the beam (the inverse radiation pressure). To avoid this, a better optical design with focusing lenses of low numerical aperture is required.

The drag force  $F_D$  is given by the well-known Stokes' formula

$$F_D = 6\pi\eta Rv \quad (5)$$

where  $\eta$  is the ambient shear viscosity ( $R/l \gg 1$ ,  $l$  is the mean free path of the ambient molecules), and  $v$  is the particle velocity. Depending on the particle radius  $R$ , the force  $F_D$  diminishes either linearly or steeper with  $R$ . As  $l \sim 10$  nm in air at atmospheric pressure,  $F_D$  decreases linearly as far as  $R$  is less than several hundreds of nanometers, and approximately quadratically at  $R \leq 20$  nm (molecular kinetics regime). A transition region exists at intermediate particle sizes where one of the two dependencies trends to the other. The drag force  $F_D$  can be reduced substantially, practically almost to zero, by decreasing the ambient pressure.

Absorption not only directly increases the forward force but also determines the guided particle temperature and therefore creates two additional effects: the appearance of the radiometric force  $F_T$  and initiation of such thermal processes as evaporation, in-flight chemical reactions inside transported droplets, and even melting of strongly absorbing particles. Estimates show that the absorption becomes especially important for the particles with  $R \leq 50$  nm as the scattering contribution into the forward force decreases as  $R^6$  in

<sup>c</sup>Note that the force on particles with stronger absorption might be significantly higher; we deposited metallic particles in suspension at as low laser power as less than 100 mW.

this size range, while the absorption contribution only as  $R^3$ . The radiometric force  $F_T$  arises from a temperature gradient  $\Delta T$  inside the particle illuminated from one side and points against the gradient, i.e., in the forward axial direction. Because in LBD systems  $R/l \gg 1$ ,  $F_T$  provides an additional axial forward force due to a rather complicated and different than normal viscous flow process, often called radiometric flow or thermal creep. Under a simplified assumption that  $\Delta T$  is constant over a spherical particle (which is rarely the case for dielectric particles<sup>[6]</sup> but provides a reasonable estimate) with the thermal conductivity  $\chi$ , the radiometric force is given as.<sup>[20]</sup>

$$F_T = \frac{3\pi\eta^2 R_g}{pM} R \Delta T \approx \frac{3\pi\eta^2 R_g \alpha_b}{2pM\chi} R I_0 \quad (6)$$

where  $R_g$  is the molar gas constant,  $p$  the pressure,  $M$  the molecular weight of the gas, and  $\alpha_b$  the absorption factor (for the absolutely black particle,  $\alpha_b = 1$ ). Estimates show that proper illumination can create  $F_T$  that is comparable with  $F_z$  in strongly absorbing particles; an effect of such a radiometric force was also observed experimentally.<sup>[28]</sup>

## SOLID-LIQUID INTERACTIONS DURING PATTERNING

The LBDP technique relies on precise and controlled deposition of liquid droplets, suspensions, and wet formulations. The capillary forces operating in these multiphase systems govern the dimensions and morphology of the deposited clusters as well as the extent of fusion among deposited clusters. An understanding of the solid-liquid interactions is crucial in achieving three major objectives in laser-deposition technology: 1) to prepare suspensions that remain stable during the time of deposition; 2) to control phase separation (promote or avoid, depending on the need) in solid particle-in-liquid droplets transported by a beam; and 3) to manipulate the spread of deposited droplets and formation of pattern over a substrate. Fulfillment of these tasks requires an understanding and the manipulation of the surface properties of solids, both dispersed in liquid and used as substrates for patterning. If surface properties of particles or substrates cannot be manipulated, selection of the appropriate solvent or solution is needed.

The solid-liquid interactions specific for the processes important for laser-deposition systems have not been considered in depth so far. The discussion presented below relies rather on fragmentary experimentation and observations during the laser deposition process combined with the knowledge of solid-liquid interactions

extracted from broad surface chemistry research activities. A unified (but simplified) theory on solid-liquid interactions is reviewed in the first part of this section and then the applicability of this theory to laser-deposition systems is discussed in subsequent parts.

## Solid-Liquid Interfacial Energy

The interfacial interactions are analyzed in this paper using the Lifshitz-van der Waals Lewis acid-base interaction theory developed by van Oss, Good, and Chaudhury at the end of 20th century.<sup>[24,29,30]</sup> According to this theory, the total free energy of interaction between two surfaces, e.g., liquid and solid, is given by

$$\Delta G_{SL} = \Delta G_{SL}^{LW} + \Delta G_{SL}^{AB} \quad (7)$$

where  $\Delta G_{SL}^{LW}$  and  $\Delta G_{SL}^{AB}$  are the Lifshitz-van der Waals component and Lewis acid-base component, respectively, of the free energy of interaction between a solid (S) and a liquid (L). The  $\Delta G_{SL}^{LW}$  component refers to interfacial apolar interactions caused by orientation, induction, and dispersion forces, whereas the  $\Delta G_{SL}^{AB}$  component reflects the contribution from the (Lewis) acid-base (polar) interfacial interactions. Both components, as well as their combination, are assumed in this theory to follow the Dupre equations,<sup>[24,30]</sup>

$$\Delta G_{SL}^{LW} = \gamma_{SL}^{LW} - \gamma_S^{LW} - \gamma_L^{LW} \quad (8)$$

$$\Delta G_{SL}^{AB} = \gamma_{SL}^{AB} - \gamma_S^{AB} - \gamma_L^{AB} \quad (9)$$

$$\Delta G_{SL} = \gamma_{SL} - \gamma_S - \gamma_L \quad (10)$$

where  $\gamma$  is the surface or interfacial free energy; the subscripts S, L, and SL refer to solid and liquid surfaces, and solid-liquid interface, respectively; and the superscripts LW and AB denote the Lifshitz-van der Waals and acid-base interactions, respectively.

Because of the symmetrical nature of the LW interactions, both the total LW interaction energy and the LW surface free energy components follow a combining rule,<sup>[24,29,30]</sup>

$$\Delta G_{SL}^{LW} = -2\sqrt{\gamma_S^{LW}\gamma_L^{LW}} \quad (11)$$

$$\gamma_{SL}^{LW} = \left( \sqrt{\gamma_S^{LW}} - \sqrt{\gamma_L^{LW}} \right)^2 \quad (12)$$

The combining rule does not apply to asymmetrical AB interactions; instead, they have been defined

(a priori) by the following two equations,

$$\Delta G_{SL}^{AB} = -2\left(\sqrt{\gamma_S^- \gamma_L^+} + \sqrt{\gamma_S^+ \gamma_L^-}\right) \quad (13)$$

$$\gamma_i^{AB} = 2\sqrt{\gamma_i^+ \gamma_i^-} \quad (14)$$

where the superscripts  $-$  and  $+$  refer to the electron donor (Lewis base) parameter and electron acceptor (Lewis acid) parameter, respectively. Combining Eqs. (11) and (13) with Eq. (7) then yields

$$\Delta G_{SL} = -2\left(\sqrt{\gamma_S^{LW} \gamma_L^{LW}} + \sqrt{\gamma_S^+ \gamma_L^-} + \sqrt{\gamma_S^- \gamma_L^+}\right) \quad (15)$$

Another expression for the total free energy of interaction between two surfaces  $\Delta G_{SL}$  can be obtained by substituting the Young's equation,

$$\gamma_S - \gamma_{SL} = \gamma_L \cos \theta \quad (16)$$

into Eq. (10), in the form

$$\Delta G_{SL} = -\gamma_L(1 + \cos \theta) \quad (17)$$

where  $\gamma_L$  is the surface tension of liquid and  $\theta > 0$  is the contact angle for liquid on the solid surface.

The two equations (15 and 17) are commonly used for the calculations of the surface free energy and surface free energy components of a solid surface and a liquid from contact angle measurements. Because Eq. (15) contains three unknowns ( $\gamma_S^{LW}$ ,  $\gamma_S^-$ ,  $\gamma_S^+$ ), the contact angles of three liquids with known surface tension must first be measured, so that three simultaneous equations can then be solved.<sup>[24,29,30]</sup>

The  $\gamma^{LW}$ ,  $\gamma^+$ , and  $\gamma^-$  components of surface free energy were determined for a number of liquids and solids and several examples are shown in Tables 1 and 2; the values for  $\gamma^+$  and  $\gamma^-$  are relative, as they refer to a standard value assumed for water,  $\gamma^+ = \gamma^- = 25.5 \text{ mJ/m}^2$ .<sup>[24,30]</sup>

## Preparation of Suspensions

The stability and homogeneity of the suspension used for the generation of a mist in laser-based deposition technology is crucial for maintaining a constant concentration of solid particles carried by droplets. The quality and reproducibility of patterned structures strongly depend on the concentration of particles and reproducibility of this concentration in the droplets. The stability of suspensions is controlled by particle-particle forces, which include the van der Waals (apolar) interactions, Lewis acid-base (polar)

**Table 1** Surface tension (surface free energy) components for selected liquids<sup>a</sup>

Liquid	$\gamma_L$ [mJ/m <sup>2</sup> ]	$\gamma_L^{LW}$ [mJ/m <sup>2</sup> ]	$\gamma_L^-$ [mJ/m <sup>2</sup> ]	$\gamma_L^+$ [mJ/m <sup>2</sup> ]
Benzaldehyde	38.5	38.5	14.0	0
Benzene	28.85	28.85	2.7	0
Chloroform	27.15	27.15	0	3.8
Diiodomethane	50.8	50.8	~0	0
Dodecane	25.35	25.35	0	0
Ethanol	22.4	18.8	~68	~0.02
Ethyl acetate	25.2	25.2	13.1	0
Ethylene glycol	48	29.0	47.0	1.9
Formamide	58	39	39.6	2.28
Glycerol	64	34	57.4	3.92
Heptane	20.14	20.14	0	0
Methanol	22.5	18.2	~77	~0.06
<i>N</i> -Octanol	27.5	27.5	18.0	0
Toluene	28.5	28.5	2.3	0
Water	72.8	21.8	25.5 <sup>b</sup>	25.5 <sup>b</sup>

<sup>a</sup>See footnote h.

<sup>b</sup>Assumed standard values.

Source: From Ref.<sup>[33]</sup>.

**Table 2** Surface free energy components for selected solids<sup>a</sup>

Solid	$\gamma_S$ [mJ/m <sup>2</sup> ]	$\gamma_S^{LW}$ [mJ/m <sup>2</sup> ]	$\gamma_S^-$ [mJ/m <sup>2</sup> ]	$\gamma_S^+$ [mJ/m <sup>2</sup> ]
Alumina	39.7	31.6	27.2	0.6
Apatite	35.4	35.4	20.5	0
Calcite	57	40.2	54.4	1.3
Cellulose	54.5	44	17.2	1.6
Cellulose nitrate	45.1	44.7	13.9	0.003
Dolomite	42.5	37.6	30.5	0.2
Glucose	42.2	42.2	34.4	0
Hematite	53.4	45.6	50.4	0.3
Human fibronectin (dry)	59.3	29.5	51.6	4.3
Lactose	41.1	41.1	26.8	0
Maltose	44.9	41.3	63.7	0.05
Polyethylene	33	33	0	0
Polyisobutylene	25	25	0	0
Polymethyl methacrylate	40	40	14.6	0
Polystyrene	42	42	1.1	0
Polyvinyl alcohol	42	42	17–57	0
Polyvinyl chloride	43.8	43	3.5	0.04
Rutile	47.1	40.8	32.8	0.3

<sup>a</sup>See footnote h.

Source: From Ref.<sup>[33]</sup>.



interactions, electrostatic interactions, and Brownian movement forces.<sup>[24,30,31]</sup> As intense mixing results in dynamic conditions of suspension, the effect of Brownian movement forces on the stability of suspensions used in the formulation of mist can be ignored. For the same reason, any flocculation effects caused by long-range forces and by the presence of a secondary minimum in attraction<sup>[24,30,31]</sup> can also be neglected in this simple analysis. A more accurate analysis of the interactions between surfaces as a function of distance is beyond the scope of this paper and therefore is excluded from further discussion. Finally, although the electrostatic forces originating from the Coulomb interaction between surface charges are important to many aqueous suspensions and some other organic solvent-based suspensions (and can be used in stabilization of suspensions), they are also ignored to simplify our analysis; the electrostatic interactions in apolar and weakly polar solvents have often only negligible effect on the stability of suspensions.

Keeping the abovementioned simplifications in mind, it can be said that suspensions of particles remain stable if solid-liquid adhesion exceeds the cohesion forces for liquid molecules and particles. As a result, the interaction energy between two solid surfaces immersed in a liquid can be estimated from the Lifshitz-van der Waals Lewis acid-base interaction theory using the following equation:<sup>[24,30]</sup>

$$\begin{aligned} \Delta G_{\text{SLS}} = & -2\left(\gamma_{\text{S}}^{\text{LW}} + \gamma_{\text{L}}^{\text{LW}} - 2\sqrt{\gamma_{\text{S}}^{\text{LW}}\gamma_{\text{L}}^{\text{LW}}}\right) \\ & + 4\left(\sqrt{\gamma_{\text{S}}^+ \gamma_{\text{L}}^-} + \sqrt{\gamma_{\text{S}}^- \gamma_{\text{L}}^+}\right) \\ & - \sqrt{\gamma_{\text{S}}^+ \gamma_{\text{S}}^-} - \sqrt{\gamma_{\text{L}}^+ \gamma_{\text{L}}^-} \end{aligned} \quad (18)$$

Spontaneous dispersion and complete stability of the suspension can only be accomplished when the  $\Delta G_{\text{SLS}}$  value is positive.<sup>[24,30]</sup> However, such a strong stability of suspension is not always necessary in the formulation of the mist for laser deposition. In our research, different suspensions with small negative  $\Delta G_{\text{SLS}}$  values were successfully used in making the mist and used for patterning.<sup>d</sup> For example, 8–20-nm gold nanoparticles modified with self-assembled monolayers of thiols terminated with either methyl or benzyl functionality have been used for patterning of porous chemiresistor sensors.<sup>[3,13]</sup> The gold-thiolate particles functionalized with  $\text{CH}_3$ - groups disperse well in many apolar or weakly polar solvents such as saturated hydrocarbons,

chloroform, and toluene, but because of the hydrophobic nature of these particles they flocculate in polar solvents such as water and, to a lesser extent, in ethanol and methanol. The behavior of  $\text{Au-S}(\text{CH}_2)_n\text{CH}_3$  particles, or other particles, in solvents can be predicted from the calculated  $\Delta G_{\text{SLS}}$  value.<sup>e</sup> Examples of calculation of the  $\Delta G_{\text{SLS}}$  value for  $\text{Au-S}(\text{CH}_2)_n\text{CH}_3$  dispersed in different solvents are shown in Table 3. It can be seen that the  $\Delta G_{\text{SLS}}$  value for  $\text{Au-S}(\text{CH}_2)_n\text{CH}_3$  particles is close to zero for such good solvents as chloroform, toluene, or dodecane but increases for polar solvents from  $-5.4 \text{ mJ/m}^2$  for ethanol to over  $-102 \text{ mJ/m}^2$  for water.<sup>f</sup>

The surface free energy characteristics for gold-thiolate particles change drastically if the self-assembled monolayer of a “long-chain” thiol with  $\text{CH}_3$ - functionality is replaced with a monolayer of a short-chain thiol ended with the benzyl group (Table 3). The  $\text{Au-S}(\text{CH}_2)_2\text{C}_6\text{H}_5$  particles disperse spontaneously in chloroform, ethylene glycol, and water but have a tendency to flocculate in toluene, dodecane, ethanol, and methanol. As water is a convenient liquid carrier in the laser-based deposition technique because of its high surface tension and limited evaporation, the formulation of stable suspensions of  $\text{Au-S}(\text{CH}_2)_2\text{C}_6\text{H}_5$  nanoparticles in water without stabilizing chemicals is advantageous.

The selection of a carrier liquid for polymeric particles is often more difficult. For example, Table 3 shows the calculated  $\Delta G_{\text{SLS}}$  values for polystyrene dispersed in different apolar and polar liquids. Positive or close-to-zero negative value is predicted for chloroform and toluene. These two solvents, unfortunately, dissolve polystyrene.<sup>g</sup> In such cases more polar solvents are required for use in the formulation of suspension.

<sup>e</sup>Long-range colloidal forces should be included in detailed analysis of the system; see Ref.<sup>[33]</sup> and footnote 8 for more details.

<sup>f</sup>The drawback of the Lifshitz-van der Waals Lewis acid-base theory is that small  $\Delta G_{\text{SLS}}$  values are not very reliable. The values of electron-acceptor and electron-donor parameters for both solids and liquids can change significantly with only a small variation in measured contact angles. For example, it should be recognized that the  $\Delta G_{\text{SLS}}$  values in Table 3 were calculated based on not always precise surface free energy components of solids and liquids and therefore the values shown in Table 3 should be treated as estimates. This is particularly true for methanol and ethanol, for which electron-donor and electron-acceptor parameters need to be determined with better accuracy. Additionally, ethanol can carry a trace amount of water as a contaminant or pick it up from the laboratory humid environment. Such a contamination might affect the suspension stability if water separates or adsorbs on the particle surface. The other concern is that gold nanoparticles might carry less perfect self-assembled monolayers of thiols as those commonly formed on flat macroscopic surfaces of gold. Any uncoated areas of gold particles will enhance the attractive interactions between suspended nanoparticles.

<sup>g</sup>Entropic term must be added to the equation on  $\Delta G_{\text{SLS}}$  to calculate the interaction energy of dissolution and predict the behavior of the polymer in a solvent (Ref.<sup>[33]</sup>).

<sup>d</sup>Spherical and relatively large particles, 100 nm and larger, are easier to disperse in liquids than nanoparticles having a diameter of a few nanometers and crystalline shape due to increasing adhesion expressed per volume of the particle with decreasing particle size.

**Table 3** The interaction energy for selected apolar and polar liquids with polystyrene and gold-hexadecanethiol

Liquid	Polystyrene ( $\gamma_S^{LW} = 42$ , $\gamma_S^- = 1.1$ , $\gamma_S^+ = 0 \text{ mJ/m}^2$ )		Gold-thiolate			
	$\Delta G_{SLS} [\text{mJ/m}^2]$	$\Delta G_{SLV} [\text{mJ/m}^2]$	Au-S(CH <sub>2</sub> ) <sub>n</sub> CH <sub>3</sub> ; $n > 7$ ( $\gamma_S^{LW} = 24.6$ , $\gamma_S^- = \gamma_S^+ \cong 0 \text{ mJ/m}^2$ ) <sup>a</sup>		Au-S(CH <sub>2</sub> ) <sub>2</sub> C <sub>6</sub> H <sub>5</sub> ( $\gamma_S^{LW} = 37.0$ , $\gamma_S^- = 52.7$ $\gamma_S^+ = 0.46 \text{ mJ/m}^2$ ) <sup>***</sup>	
	$\Delta G_{SLS} [\text{mJ/m}^2]$	$\Delta G_{SLV} [\text{mJ/m}^2]$	$\Delta G_{SLS} [\text{mJ/m}^2]$	$\Delta G_{SLV} [\text{mJ/m}^2]$	$\Delta G_{SLS} [\text{mJ/m}^2]$	$\Delta G_{SLV} [\text{mJ/m}^2]$
Chloroform	+4.7 (dissolves)	+10.7	-0.1	-1.3	+35.4	+32.8
Toluene	-2.6 (dissolves)	+6.1	-0.3	-2.0	-16.7	+6.0
Dodecane	-4.2	+7.3	~0	-0.4	-21.9	+5.3
Ethanol	(-13.3) <sup>b</sup>	(+4.9) <sup>b</sup>	(-5.4) <sup>b</sup>	(-2.0) <sup>b</sup>	(-4.0) <sup>b</sup>	(+16.1) <sup>b</sup>
Methanol	(-18.6) <sup>b</sup>	(+1.4) <sup>b</sup>	(-9.6) <sup>b</sup>	(-5.6) <sup>b</sup>	(-4.0) <sup>b</sup>	(+14.6) <sup>b</sup>
Ethylene glycol	-34.6	-29.0	-38.4	-40.1	+0.2	-4.8
Water	-87.4	-82.9	-102.2	-100.6	+34.6	-15.2

<sup>a</sup>Arbitrarily chosen values based on the data from Ref.<sup>[49]</sup>

<sup>b</sup>Estimate due to uncertain values for the electron-donor and electron-acceptor parameters for ethanol and methanol<sup>h</sup>.

Because of the poor compatibility between polystyrene and polar solvents such as ethanol, ethylene glycol, or water, the suspensions formulated without stabilizing agents will flocculate even under intense mixing conditions. A modification of the surface properties of polystyrene particles is required and it can be accomplished by using surfactants that reduce the hydrophobicity of the polymer and improve the polar interaction with liquid and enhance the repulsive interactions between surfactant-coated particles.

### Nanoparticles in Transported Droplets

Suspensions with a reduced solid-liquid interaction favor the formation of aggregates, as discussed in the previous section, and also often promote accumulation of particles at the liquid/droplet surface. A film of particles formed at a liquid surface increases the droplet's surface rigidity and influences the structure of deposited clusters. The particles carried on the surface of a droplet form more-or-less regular monolayer structures that often promote the formation of spherical clusters with a well-organized assembly of particles. Also, due to reduced liquid-air area, the rate of liquid evaporation is reduced during transportation by the laser beam.

The tendency for particles to attach to the liquid droplet surface can be predicted by the Lifshitz-van der Waals Lewis acid-base interaction theory by calculating the interaction energy between a particle and a liquid-gas interface:<sup>[24,30]</sup>

$$\Delta G_{SLV} = -\gamma_L^{LW} + \sqrt{\gamma_S^{LW}\gamma_L^{LW}} + 2\left(\sqrt{\gamma_S^-\gamma_L^+} + \sqrt{\gamma_S^+\gamma_L^-} - 2\sqrt{\gamma_L^-\gamma_L^+}\right) \quad (19)$$

The positive  $\Delta G_{SLV}$  value indicates that the particle will avoid the liquid-gas interface, whereas the negative value indicates the preferential adhesion of particles to this interface. More negative  $\Delta G_{SLV}$  values point toward stronger adhesion of the particle to the liquid-air interface, which ultimately leads to a larger portion of the particle that is exposed to a gas phase after attachment. The position of the particle at the liquid-gas interface is determined by the wetting characteristics of the solid expressed in contact angle values.<sup>[33]h</sup> Table 3 shows examples of calculated  $\Delta G_{SLV}$  values for polystyrene and gold-thiolate particles. Because of the positive  $\Delta G_{SLV}$  values, polystyrene does not adhere to the surface of ethanol, methanol, and dodecane, although because of negative  $\Delta G_{SLS}$  values the polystyrene particles will likely flocculate inside the bulk of these liquids. Therefore the structure and, to a lesser extent, shape of the deposited clusters might become unpredictable.

It can be seen from the data in Table 3 that it requires the use of liquids with relatively high surface tension value such as ethylene glycol or water to generate droplets coated with films of polystyrene particles. Unfortunately, as also discussed in the previous section, the formulation of suspensions of polystyrene in water (or ethylene glycol) that are stable for at least a few seconds (time required to prepare a mist and transport the droplets to a substrate) is a challenge. In such systems the use of surface-active compounds or additional particulates that adsorb on the surface

<sup>h</sup>The contact angle measured for a liquid in contact with a nanoparticle is usually different from the contact angle measured on large (millimeter-sized) particles as a result of a contribution of the linear free energy at the highly curved three-phase line (Ref.<sup>[34]</sup>).

of polystyrene and strengthen the interactions of the particles with liquid is usually a need.

The surface free energy of self-assembled monolayers of  $\text{HS}(\text{CH}_2)_n\text{CH}_3$  ( $n > 7$ ) on a gold surface is much smaller than the surface free energy of polystyrene, and, therefore, the gold-thiolate particles can coat almost any liquid listed in Table 3. However, small negative  $\Delta G_{\text{SLV}}$  values for chloroform, dodecane, and toluene indicate that adhesion of  $\text{Au-S}(\text{CH}_2)_n\text{CH}_3$  particles to these liquids is weak and the particles can easily detach from the liquid-air interface. As a result, irregular and irreproducible clusters usually result from deposited suspensions formulated using one of these three solvents. The use of polar solvents such as ethanol, methanol, water, and ethylene glycol promotes the accumulation and alignment of  $\text{Au-S}(\text{CH}_2)_n\text{CH}_3$  particles at the droplet surface. Again, due to strong particle-particle interactions in these liquids, good stability of  $\text{Au-S}(\text{CH}_2)_n\text{CH}_3$  suspension is difficult to maintain.

The scenario is completely different for  $\text{Au-S}(\text{CH}_2)_2\text{C}_6\text{H}_5$  particles. As the  $\Delta G_{\text{SLV}}$  values shown in Table 3 indicate these particles will avoid the liquid-air interface when suspended in chloroform, toluene, dodecane, ethanol, and methanol. Although the  $\text{Au-S}(\text{CH}_2)_2\text{C}_6\text{H}_5$  particles disperse extremely well in chloroform, they tend to flocculate in toluene, dodecane, ethanol, and methanol. The  $\Delta G_{\text{SLV}}$  values are also negative for the  $\text{Au-S}(\text{CH}_2)_2\text{C}_6\text{H}_5$  particles dispersed in ethylene glycol and water. These two systems, with positive  $\Delta G_{\text{SLS}}$  values and negative  $\Delta G_{\text{SLV}}$  values, seem to be exceptionally suitable for the deposition of uniformly shaped clusters of particles. Particles with negative  $\Delta G_{\text{SLV}}$  values tend to form well-organized films on the surface of a liquid droplet during transportation and at the same time particle-particle repulsive forces (positive value of  $\Delta G_{\text{SLS}}$ ) are responsible for a good dispersion of the remaining particles in the liquid bulk, protecting them against aggregation.

As discussed above, the control of adhesion of particles to the droplet surface promotes the structuring of deposited clusters. Fig. 5 shows two extreme cases. Irregular clusters made of  $\text{Au-S}(\text{CH}_2)_7\text{CH}_3$  particles that were deposited on a hydrophobized glass slide from particle-in-toluene suspensions are shown in Fig. 5A:  $\Delta G_{\text{SLS}} = -0.3 \text{ mJ/m}^2$  and  $\Delta G_{\text{SLV}} = -2.0 \text{ mJ/m}^2$ . The negative value of  $\Delta G_{\text{SLS}}$  is disadvantageous for uniform alignment and tight packing of the particles in a cluster. On the contrary, the negative value of  $\Delta G_{\text{SLV}}$  is advantageous, although  $\Delta G_{\text{SLV}} = -2.0 \text{ mJ/m}^2$  indicates a weak adhesion of particles to the interface and easy disturbance of particle-at-interface organization process. Spherical clusters made of regularly aligned polystyrene particles were deposited from suspension formulated in

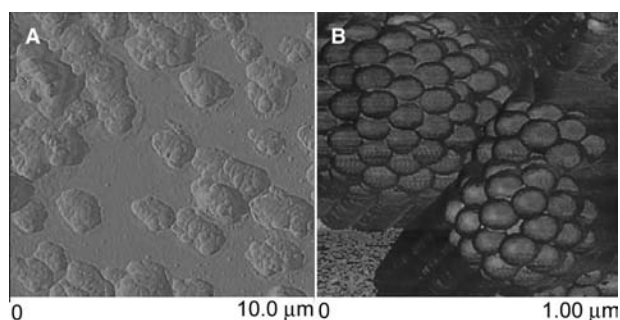


**Fig. 5** AFM phase images of clusters made of (A)  $\sim 20$ -nm  $\text{Au-S}(\text{CH}_2)_7\text{CH}_3$  particles and (B) 100-nm polystyrene particles. Gold nanoparticles were deposited from toluene suspensions whereas polystyrene particles were deposited from aqueous suspensions stabilized with surfactants and addition of avidin.

phosphate buffer solution with the addition of proteins and are shown in Fig. 5B;  $\Delta G_{\text{SLS}} \cong 0 \text{ mJ/m}^2$  and  $\Delta G_{\text{SLV}} \ll 0 \text{ mJ/m}^2$  (exact values have not been determined).

Packing density and alignment of nanoparticles in the film formed over the droplet surface are controlled by the size and shape of particles and interparticle interactions operating through both liquid and gas phases.<sup>[33,35]</sup> Capillary forces are negligible in these systems because of the small dimensions of particles and resulting flat menisci formed by the liquid between particles.<sup>[33]</sup> This is not necessarily true for the transported and deposited droplets if the laser beam strongly interacts with the droplet content. The resulting increase in temperature of the transported droplet causes the liquid to evaporate at a higher rate. Consequently, depletion of the liquid volume in the droplet that carries a high concentration of particles forces the liquid to shrink into interparticle space, and capillary forces start to operate among newly formed menisci aligning particles into regular spherical clusters with particles tightly bound to each other.<sup>1</sup>

### Capillarity Phenomena for Droplet-on-Substrate Deposits

The laser beam guides droplets or clusters (wet or dry) and deposits them on a substrate. Dry clusters and clusters carrying inside a small volume of liquid practically remain intact after deposition on a substrate. It is well documented that large droplets and wet clusters

<sup>1</sup>On the contrary, fast evaporation of a liquid carrying a small quantity of particles leads to droplets of such small sizes that the laser beam cannot guide them effectively so that the droplets spread in almost every direction instead of following the path of the beam.

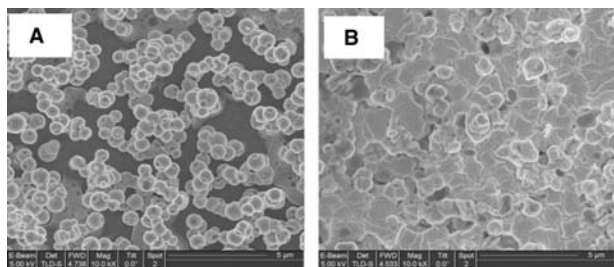


**Fig. 6** Scanning electron micrographs of intact clusters made of (A) 7-nm Au-S(CH<sub>2</sub>)<sub>7</sub>CH<sub>3</sub> deposited from toluene suspension and (B) plate-like structure made of the same particles but formed from wet clusters that fused to each other.

might deform during impact with the substrate, particularly if they travel at high velocity.<sup>[36,37]</sup> However, because of very small Reynolds number,  $Re = (1.5 \text{ to } 6.0) \times 10^{-4}$ , and Weber number,  $We = 10^{-15}$  to  $10^{-8}$  for the micron-sized droplets impacting substrates during the deposition with a laser beam,<sup>j</sup> droplet deformation is negligible and has no practical consequences in patterning process.

The deposited droplets with no particles or particles weakly adhered to the liquid–gas surface will spread over the substrate and the extent of spreading is governed by the substrate–suspension interactions. Droplets and wet clusters will also fuse into each other and spread to form larger clusters if one is deposited on top or at very close proximity of another droplet or cluster. Fig. 6 shows two examples of gold-thiolate nanoparticle clusters deposited over a silanized glass slide in either dry (or almost dry) (a) or wet (b) form. Dry spherical clusters with a diameter of about 0.2 to 1  $\mu\text{m}$  remain intact after deposition, although they have a tendency to form chains and aggregates of clusters—likely as a result of attractive interactions among clusters stronger than interactions between clusters and substrate (Fig. 6A). Fig. 6B shows, on the other hand, that wet clusters formed plate-like structures as a result of liquid spreading and evaporation. Partially fused (disintegrated) clusters are also visible on top of the plate-like structure in Fig. 6B. Cracks between “plates” reflect boundaries between fused clusters and also some of them result from contraction of the volume of the deposited material during drying.

Spreading of deposited liquid drops (or wet clusters) over a substrate surface is controlled by the competition between the substrate–liquid adhesion and

cohesion forces of liquid. This can be analyzed through the spreading coefficient  $S_{SLV}$ ,<sup>[38]</sup>

$$S_{SLV} = \gamma_S - \gamma_{SL} - \gamma_L \quad (20)$$

which for finite contact angles ( $\theta > 0$ ) becomes

$$S_{SLV} = \gamma_L(\cos \theta - 1) \quad (21)$$

where  $\gamma_S$ ,  $\gamma_L$ , and  $\gamma_{SL}$  are the surface free energy of solid, liquid, and solid–liquid interfacial free energy; and  $\theta$  is the contact angle.

Using the Lifshitz–van der Waals Lewis acid–base model, the spreading coefficient can also be calculated from the following equation:

$$S_{SLV} = 2 \left( \sqrt{\gamma_S^{LW} \gamma_L^{LW}} + \sqrt{\gamma_S^+ \gamma_L^-} + \sqrt{\gamma_S^- \gamma_L^+} \right) - 2\gamma_L \quad (22)$$

A spontaneous and complete spreading of liquid to form a thin film occurs when the  $S_{SLV}$  value is positive or zero, which corresponds to zero contact angle. This situation is very undesirable in patterning technology because of lack of control of the size and shape of the deposited droplets/wet clusters, and the resulting structures. It is therefore necessary to select the substrate on deposition of liquid droplets and wet clusters with such a wetting characteristic that  $\theta \gg 0$ . The contact angle from about  $\theta = 60$  to  $110^\circ$  is usually preferable if control of the size of deposited individual clusters is desired.

The base diameter of the deposited liquid droplet or wet cluster ( $d_b$ ) is an important parameter if the size of the deposited clusters must be controlled. This parameter can be predicted from the volume of the droplet delivered by a nebulizer to a deposition chamber and the geometry of formed spherical cap using the following equation,

$$d_b = \left( \frac{4}{2 - 3 \cos \theta + \cos^3 \theta} \right)^{1/3} 2R \sin \theta \quad (23)$$

## CONCLUSION

It has been demonstrated that the LBPD technique makes it possible to deposit a variety of materials at the micron scale in the form of individual particles or clusters, with the particle size ranging from tens of nanometers to less than a micron. A weakly focused, relatively low-power laser beam guides micron-sized droplets through a micron-sized aperture toward a substrate after the droplets are generated by an

<sup>j</sup>Reynolds number  $Re$  describes a balance between inertial and viscous forces,  $Re = Dv\rho/\eta$ , and Weber number  $We$  expresses a ratio of inertial to capillary forces,  $We = \rho v^2 D/\gamma$ , where  $D$  is the diameter of the droplet [ $\sim 1$  (m)],  $v$  the droplet velocity at impact [200–600 (m/sec)],  $\rho$  the density of liquid or suspension [ $\sim 1000$  (kg/m<sup>3</sup>)], and  $\eta$  the liquid viscosity [ $\sim 10^{-3}$  (kg/msec)].

atomizer from a liquid precursor or a suspension of particles. The technique allows depositing, codepositing, and patterning materials of different classes making use of the same basic fabrication technology. Another essential asset of the technique is that the light-matter interaction inside the LBDP apparatus allows controllable activation of the chemical reactions and/or phase transformations inside the droplets making the technique even more flexible. Due to such distinct features, LBDP differs from the other direct-write techniques. At the same time, as the technique is still at the early stages of its development, many material aspects of the technique are not yet well understood, so that further research is required for successful development of LBDP.

## ACKNOWLEDGMENTS

We thank our students, Changgong Zhou and Juntao Xu, for their help in the development of the LBDP technique.

## REFERENCES

- Pique, A., Chrisey, D.B., Eds.; *Direct-Write Technologies for Rapid Prototyping Applications: Sensors, Electronics, and Integrated Power Sources*; Academic Press: San Diego, CA, 2002.
- Renn, M.J.; Marquez, G.; King, B.H.; Essien, M.; Miller, W.D. Flow- and Laser-Guided Direct write of electronic and biological components. In *Direct-Write Technologies for Rapid Prototyping Applications*; Pique, A., Chrisey, D.B., Eds.; Academic Press: San Diego, CA, 2002; 475–492.
- Drelich, J.; Nadgorny, E.M.; Zellers, E.T.; Xu, J.; Zhou, Ch.; White, C.L.; Cross, W.M. Patterning of gold and polystyrene nanoparticles into mesostructures using a laser-based particle deposition. In *Functional Fillers and Nanoscale Minerals*; Kellar, J.J., Herpfer, M.A., Moudgil, B.M., Eds.; Society for Mining, Metallurgy, and Exploration, Inc.: Littleton, 2003; 85–94.
- Renn, M.J.; Pastel, R. Particle manipulation and surface patterning by laser guidance. *J. Vac. Sci. Technol.*, (B) **1998**, *16*, 3859–3863.
- Renn, M.J.; Pastel, R.; Lewandowski, H.J. Laser guidance and trapping of mesoscale particles in hollow-core optical fibers. *Phys. Rev. Lett.* **1999**, *82* (7), 1574–1577.
- Nadgorny, E.M.; Pastel, R.L.; Struthers, A.A.; Miner, A. Materials aspects of laser guided direct writing. In *Mass and Charge Transport in Inorganic Materials—Fundamentals to Devices, Part B*, Intl. Conf. Proceedings; Vincenzini, P., Buscaglia, V., Eds.; Techna: Faenza, Italy, 2000, 1107–1114.
- Xu, J.; Zhou, Ch.; Grant, S.; Nadgorny, E.; Drelich, J. Laser guidance deposition technique for patterning microstructures made of nanoparticles with varying surface functionality. In *Functional Nanostructured Materials Through Multiscale Assembly and Novel Patterning Techniques*, MRS Symposium Proceedings, Warrendale, PA; Moss, S., Ed.; 2002, S7.6.1–6.6.
- Nadgorny, E.; Zhou, Ch.; Drelich, J.; Zahn, R. MTU laser-based direct-write techniques: recent development and nanoparticles patterning results. In *Rapid Prototyping Technologies*, MRS Symposium Proceedings, Warrendale, PA; Holmes, A.S., Pique, A., Dimos, D.B., Eds.; 2003, LL4.4.1–LL4.4.6.
- Ashkin, A. Accelerating and trapping of particles by radiation pressure. *Phys. Rev. Lett.* **1970**, *24* (4), 156–159.
- Ashkin, A.; Dziedzic, J.M.; Bjorkholm, J.E.; Chu, S. Observation of a single-beam gradient force optical trap for dielectric particles. *Opt. Lett.* **1986**, *11* (5), 288–290.
- Block, S.M. *Noninvasive Techniques in Cell Biology*; Wiley: New York, 1990; 375–602.
- Drelich, J.; Nadgorny, E.; Xu, J.; Zellers, E.T.; Zhou, Ch. *MTU Invention Disclosure #200209.00*; 2002.
- Xu, J.; Drelich, J.; Nadgorny, E.M. A laser-based patterning of gold nanoparticles into porous microstructures. *Langmuir* **2003**, submitted.
- Siegman, A. *Lasers*; University Science Books: Sausalito, CA, 1986.
- Belland, P.; Crenn, J.P. Changes in the characteristics of a Gaussian beam weakly diffracted by a circular aperture. *Appl. Opt.* **1982**, *21* (2), 522–527.
- Overfelt, P.L.; Kenney, C.S. Comparison of the propagation characteristics of Bessel, Bessel-Gauss, and Gaussian beam diffracted by a circular aperture. *J. Opt. Soc. Am., A* **1991**, *8* (5), 732–745.
- Zhou, Ch.; Nadgorny, E. (unpublished results).
- Polaert, H.; Grehan, G.; Gouesbet, G. Improved standard beams with application to reverse radiation pressure. *Appl. Opt.* **1998**, *37* (12), 2435–2440.
- Pastel, R.; Geiser, P.; Struthers, A.; Nadgorny, E. (unpublished results).
- Fucks, N.A. *The Mechanics of Aerosols*; Dover Publications: New York, 1989.
- van de Hulst, H.C. *Light Scattering by Small Particles*; John Wiley & Sons, Inc.: New York, 1957.
- Kerker, M. *The Scattering of Light*; Academic Press: New York, 1969.
- Bohren, C.F.; Huffman, D.R. *Absorption and Scattering of Light by Small Particles*; John Wiley & Sons, Inc.: New York, 1983.
- van Oss, C.J. *Interfacial Forces in Aqueous Media*; Marcel Dekker, Inc.: New York, 1994.
- Pastel, R.; Struthers, A. Measuring evaporation rates of laser-trapped droplets by use of fluorescent morphology-dependent resonances. *Appl. Opt.* **2001**, *40* (15), 2510–2514.
- Svoboda, K.; Block, S.M. Optical trapping of metallic Rayleigh particles. *Opt. Lett.* **1994**, *19* (13), 930–932.
- Rohrbach, A.; Stelzer, H.K. Optical trapping of dielectric particles in arbitrary fields. *J. Opt. Soc. Am., A* **2001**, *19* (4), 839–853.
- Lewittes, M.; Arnold, S.; Oster, G. Radiometric levitation of micron sized spheres. *Appl. Phys. Lett.* **1982**, *40* (6), 455–457.

29. van Oss, C.J.; Good, R.J.; Chaudhury, M.K. The role of van der Waals forces and hydrogen bonds in hydrophobic interactions between biopolymers and low energy surfaces. *J. Colloid Interface Sci.* **1986**, *111*, 378–390.
30. Giese, F.G.; van Oss, C.J. *Colloid and Surface Properties of Clays and Related Minerals*; Marcel Dekker, Inc.: New York, 2002.
31. Israelachvili, J. *Intermolecular and Surface Forces*, 2nd Ed.; Academic Press: London, 1992.
32. Beach, E.R.; Tormoen, G.W.; Drelich, J. Pull-off forces measured between hexadecanethiol self-assembled monolayers in air using an atomic force microscope: Analysis of surface free energy. *J. Adhesion Sci. Technol.* **2002**, *16* (7), 845–868.
33. Martinez-Lopez, F.; Cabrerizo-Vilchez, M.A.; Hidalgo-Alvarez, R. Colloidal interaction at the air–liquid interface. *J. Colloid Interface Sci.* **2000**, *232*, 303–310.
34. Drelich, J. The significance and magnitude of the line tension in three-phase (solid–liquid–fluid) systems. *Colloids Surf., A Physicochem. Eng. Asp.* **1996**, *116*, 43–54.
35. Horozov, T.S.; Aveyard, R.; Clint, J.H.; Binks, B.P. Order–disorder transition in monolayers of modified monodisperse silica particles at the octane–water interface. *Langmuir* **2003**, *19*, 2822–2829.
36. Fukai, J.; Shiiba, Y.; Yamamoto, T.; Miyatake, O.; Poulikakos, D.; Megaridis, C.M.; Zhao, Z. Wetting effects on the spreading of a liquid droplet colliding with a flat surface: Experiment and modeling. *Phys. Fluids* **1995**, *7* (2), 236–247.
37. Bergeron, V.; Bonn, D.; Martin, J.Y.; Vovelle, L. Controlling droplet deposition with polymer additives. *Nature* **2000**, *405*, 772–775.
38. Hiemenz, P.C.; Rajagopalan, R. *Principles of Colloid and Surface Chemistry*, 3rd Ed.; Marcel Dekker, Inc.: New York, 1997.



# Layer-by-Layer Assembly of Electroactive Thin Films to Layered Carbon Electrodes

Tarek R. Farhat

Department of Chemical Engineering, Massachusetts Institute of Technology,  
Cambridge, Massachusetts, U.S.A.

## INTRODUCTION

The science of depositing thin polymer films over the surface of electrodes is widely used by electrochemists for sensor technology.<sup>[1–3]</sup> Applications include studying mass transport of molecules across these films, thin-film electrochemical detection, and electroactive sites or species embedded within the polymer backbone.<sup>[4,5]</sup> Electroactivity of thin polymer films on the surface of inert electrodes is the major topic covered in this article with emphasis on polyelectrolytes, ion complexes, and colloids. Thin films discussed here are not of the classical ion-exchange type,<sup>[6]</sup> nor their composites or complexes.<sup>[7,8]</sup> It focuses on layer-by-layer (LBL) thin films introduced by Decher, Hong, and Schmitt,<sup>[9]</sup> where many different types of polyelectrolytes, ion complexes, and colloids are alternately deposited to assemble multilayer thin films.<sup>[10,11]</sup> Even at this juncture research has diversified and segregating electroactive LBL thin films into separate families or categories would be helpful to scientists browsing this field. Because of the intensive work done on electroactive LBLs, the entry discusses briefly each citation with emphasis on the newly fabricated “carbon-polymer electrodes.” It includes as many references as possible starting from the early 1990s when the LBL field was born. In all the topics discussed, emphasis is made on the chemicals involved in making the LBL thin film, the type of the electrode used and the functionalization needed for thin film deposition, the application of cyclic voltammetry, and the type of electroactive or electrocatalytic center involved.

Topics that are covered in this entry comprise LBL thin films containing:

1. Phthalocyanin, porphyrins, and dendrimers
2. Electroactive complex salts
3. Polyoxometallates
4. Redox polymers
5. Metallic, semiconductor, and metal-oxide colloids
6. Conducting polymers
7. Graphite oxide and graphite carbon colloids

In each case a brief introduction is given about the mechanism of assembly and the electrochemical activity of the chemical species involved.

## PHTHALOCYANIN, PORPHYRINS, AND DENDRIMERS

The molecules of the phthalocyanin and porphyrin family possess a potential electroanalytical capability to detect soluble ions and molecules. Using LBL technique these molecules can be assembled with bipolar pyridine salts, polyelectrolytes, diazo resins, metalloporphyrins, and polyoxometallates.

**Assembly with bipolar pyridine salts.** Layer-by-layer ultrathin films containing water-soluble copper(II) phthalocyanine-3,4',4'',4'''-tetrasulfonic acid (CuPcTs) and bipolar pyridine salt  $\text{Py}^+-\text{C}_6\text{H}_{12}-\text{Ph}-\text{Ph}-\text{C}_6\text{H}_{12}-\text{Py}^+$  where ( $\text{Py}^+ = \text{C}_6\text{H}_5\text{N}^{\oplus}$ ) were assembled on gold electrodes. Six bilayers yielded a cyclic voltammogram of two redox peaks within a potential range +0.8 to -0.5 V using an acetate buffer of pH 4.5. The detection limit of the modified electrode toward Cu(II) ions is  $7 \times 10^{-6}$  M, yielded an acceptable selectivity, and a response time of 15–30 sec.<sup>[3,12]</sup> The copper center can be replaced by cobalt for carbohydrate and hydrazine detection.<sup>[1]</sup>

**Assembly with polyelectrolytes.** Layer-by-layer ultrathin films containing water-soluble copper(II) phthalocyanine CuPcTs and the polycation poly(diallyldimethylammonium chloride) (PDAC) were assembled on inert electrodes. The cyclic voltammogram of the fabricated films in 0.1 M KCl aqueous solution showed redox peaks of the CuPcTs at approximately +0.9 and +0.05 V vs. Ag/AgCl.<sup>[13]</sup> Layer-by-layer electroactive films of iron tetrasulfonated phthalocyanine (FeTsPc) and polycationic poly(allylamine hydrochloride) PAH showed reproducible pairs of oxidation–reduction peaks at 0.92 V and 0.70 V for a 50-bilayer PAH/FeTsPc film at a sweep rate of 50 mV/sec vs Ag/AgNO<sub>3</sub>.<sup>[14,15]</sup>

**Assembly with diazo resins.** A covalently attached multilayer film of a diazo-resin<sup>[16]</sup> and cobalt phthalocyanine tetrasulfonic acid tetrasodium salt (CoTsPc) was fabricated on the surface of a glassy carbon electrode by UV irradiation. Cyclic voltammetry showed the modified electrode had an excellent electrocatalytic response to the oxidation of hydrazine at a lower potential. The modified electrode also exhibited fast response, good stability, and repeatability.<sup>[17]</sup> Layer-by-layer film of a diazo-resin and CoTsPc on glassy carbon electrode induced a potentiometric response to iodide ions.<sup>[18]</sup>

**Other selected examples.** Layer-by-layer films of [tetrakis(*N*-methylpyridyl) porphyrinato] cobalt and polyoxometallate  $[M(H_2O)_n P_2 W_{18} O_{62}]^{6-}$  where  $M = Co$  or  $Eu$  were assembled on 4-aminobenzoic acid (4-ABA) modified glassy carbon electrode. Cyclic voltammetry showed remarkable electrocatalytic activity for the four-electron reduction of the oxide ion to water and the two-electron reduction of  $O^{2-}$  ion to  $H_2O_2$  in pH 1–6 buffer solutions.<sup>[19]</sup> Electrochemical and photoelectrochemical measurements on LBL ordered substituted phthalocyanine or conducting poly(thiophene-3-acetic acid)-sensitized  $TiO_2$  multilayers were used to study Gratzel-type photo-voltaic cells.<sup>[20]</sup> Layer-by-layer films of polycationic *meso*-tetra(4-pyridyl)porphyrin-4-[Ru-II(bipy)<sub>2</sub>Cl]<sup>4+</sup> and anionic porphyrins was capable of displaying electrochemical, electrocatalytic, and photochemical interactions.<sup>[21]</sup> Multilayer films of polycationic tetraruthenated zinc porphyrin, Zn[*meso*-tetra(4-pyridyl)porphyrin-4-(Ru-II(bipy))]<sup>4+</sup> and anionic *meso*-tetraphenyl porphyrin sulfonate, deposited on inert electrodes exhibited a reversible wave at 0.94 V and were photocatalytically active toward the reduction of the oxide ion.<sup>[22]</sup> Layer-by-layer films of the positively charged pentaerythritol-based metallodendrimer with ruthenium(II) terpyridine units and Poly(styrene sulfonate) (PSS) were assembled on a glassy carbon electrode to catalyze the oxidation of L-methionine and insulin at neutral pH.<sup>[23,24]</sup>

## ELECTROACTIVE COMPLEX SALTS

Complex salts such as Prussian blue can be assembled layer by layer either in combination with each other or with polyelectrolytes. The electrochromic and electrocatalytic activity is a major lure to scientists in this field.

**Layer-by-layer electroactive (salt-on-salt) deposition.** Layer-by-layer ultrathin films of metal hexacyanometallates were prepared by alternate electrostatic assembly between metal cations  $M^{m+}$  (i.e.,  $Fe^{3+}$ ,  $Fe^{2+}$ ,  $Co^{2+}$ , and  $Ni^{2+}$ ) and hexacyanometallate anions

$[M(CN)_6]^{n-}$  such as  $Fe(CN)_6^{3-}$ ,  $Fe(CN)_6^{4-}$ , and  $Co(CN)_6^{3-}$  on solid supports with typical electrochemical activity on top of their separation properties.<sup>[25–27]</sup>

Layer-by-layer films of Dawson-type tungstodiphosphate anion,  $P_2W_{18}O_{62}^{6-}$ , and cationic  $Ru(NH_3)_6^{3+}$  were alternately assembled on a 1,7-diaminoheptane functionalized glassy carbon electrode. The  $P_2W_{18}O_{62}^{6-}$  multilayers exhibited high electrocatalytic response and sensitivity toward the reduction of  $IO_3^-$  and the catalytic potential shifted positively with layer number.<sup>[28]</sup> Electrochemically assembled LBL films of Pt(IV/II) and Pd(IV/II) complexes displayed interesting electrocatalytic and electrochromic properties.<sup>[29]</sup> Layer-by-layer multilayer films of *tris*(2,2'-bipyridyl) ruthenium(II) and sodium decatungstate ( $W_{10}O_{32}^{4-}$ ) deposited on indium-tin oxide (ITO) electrode showed electrocatalytic activities manifested by the reduction of  $IO_3^-$  and the oxidation of oxalate ions.<sup>[30]</sup>

**Layer-by-layer polyelectrolyte with electroactive salts deposition.** Layer-by-layer films of Prussian blue nanoparticles and novel polyelectrolytes have been carefully monitored by cyclic voltammetry.<sup>[31]</sup> These ranged from Prussian blue nanoparticles and linear poly(ethylene imine) assembled on ITO and gold electrodes that were characterized spectroelectrochemically to silicotungstate and cationic redox polymers on cysteamine-coated Au electrodes studied by cyclic voltammetry.<sup>[32,33]</sup> Layer-by-layer films of PDAC and anionic sodium decatungstate ( $W_{10}O_{32}^{4-}$ ) were assembled onto quartz, mica, and ITO-electrode substrates. The electrochemical properties of the S-(PDAC/( $W_{10}O_{32}^{4-}$ ))<sub>n</sub> films were found to differ from those in which the polyelectrolyte remained at the outermost layer, i.e., S-(PDAC/( $W_{10}O_{32}^{4-}$ ))<sub>n</sub>/P.<sup>[34]</sup>

## POLYOXOMETALLATES

The polyoxometallates (POMs) are large crystals with multiple negative charges that can reach 42<sup>-</sup>. Most common are the molybdates, usually abbreviated as  $Mo_N$  where  $N$  is the number of the molybdenum atoms within the cluster (e.g.,  $Mo_{132}O_{372}(CH_3COO)_{30}(H_2O)_{72}^{42-}$ ). There are the metallo POMs abbreviated as M-POM where “M” symbolizes a certain metallic atom (e.g., Eu-POM =  $[Eu^{III}(H_2O)P_5W_{30}O_{110}]^{12-}$ ). The POMs have been successfully assembled with positively charged polyelectrolytes such as PDAC, PAH, and polyethyleneimine.

Using electrostatic LBL self-assembly, the formation of multilayers with polyelectrolytes and nanoscopic POM clusters of different sizes and charges is extensive.<sup>[12]</sup> Cyclic voltammetry indicates that the electrochemical properties of the POM clusters are fully maintained in the polyelectrolyte matrix, which

opens a route toward practical applications such as sensors or heterogenous catalysis.<sup>[35]</sup>

Cyclic voltammograms of (Co-POMs/PAH)<sub>10</sub> LBL film on modified ITO electrode using a 0.5 M NaCl solution produced multiple redox peaks at a potential range of -0.8 V to -0.2 V vs. Ag/AgCl.<sup>[12,36]</sup> Under similar conditions (Eu-POMs/PAH)<sub>20</sub>, LBL film yielded multiredox cyclic voltammograms.<sup>[37]</sup> Layer-by-layer electrostatic assembly was used to prepare films comprising generation-4 polyamidoamine dendrimers and dirhodium polyoxometallates on glassy carbon electrodes pretreated with a monolayer of 4-ABA. Electrocatalytic activity showed the reduction of nitrites and the oxidation of arsenites.<sup>[38]</sup> The electrochemical behavior of ultrathin multilayer films of sphere-shaped polyoxomolybdate Mo<sub>8</sub>V<sub>2</sub>O<sub>28</sub>·7H<sub>2</sub>O/PAH and wheel-shaped molybdenum POM clusters (Mo-38)<sub>n</sub>, (Mo-36)<sub>n</sub>/PAH was investigated at room temperature.<sup>[39-41]</sup> Through LBL assembly, a series of undecatungsto-zincates substituted by transition metals, ZnW<sub>11</sub>M(H<sub>2</sub>O)O<sub>39</sub><sup>n-</sup> (M = Cr, Mn, Fe, Co, Ni, Cu, or Zn) were successfully immobilized on a 4-ABA modified glassy carbon electrode surface. The electrochemical and electrocatalytic response of such LBL films toward the reduction of H<sub>2</sub>O<sub>2</sub> and BrO<sub>3</sub><sup>-</sup> was analyzed.<sup>[42]</sup> Layer-pairs of oppositely charged cationic PDAC and silicotungstate, SiW<sub>12</sub>O<sub>4</sub><sup>4-</sup>, were grown on grafted carbon substrates. The multilayer films electrocatalytically reduced NO<sub>2</sub><sup>-</sup> in acidic solution while the catalytic currents increased as more SiW<sub>12</sub>O<sub>4</sub><sup>4-</sup> layers were deposited.<sup>[43]</sup>

## REDOX POLYMERS

Most famous of these are the quaternized poly(4-vinylpyridine)-osmium complex [(Os(bpy)<sub>2</sub>Cl)<sup>2+</sup>] and the polyviologens. The redox polymers were assembled with biological molecules, polyelectrolytes, and heteropolytungstates.<sup>[44]</sup> The metallopolymer provides an LBL film with electrocatalytic and light-emitting effects.

**Redox polymer with polyelectrolytes.** Layer-by-layer films of [(Os(bpy)<sub>2</sub>Cl)<sup>2+</sup>] with two kinds of polyanions, PSS and poly[aniline-co-N-(3-sulfopropyl) aniline] assembled on gold electrodes showed different electrocatalytic response for the reduction of nitrites. High-efficiency LBL solid-state light-emitting devices have been fabricated from polymeric ruthenium (II) complex, Ru(bpy)<sub>3</sub><sup>2+</sup>, polyester and poly(acrylic acid) (PAA).<sup>[45]</sup> Redox polyelectrolytes characterized by the electrocatalysis of viologen polyelectrolyte films on platinum electrodes showed higher currents with layer number.<sup>[46,47]</sup> Layer-by-layer films of ditopic ligand 1,4-bis(2,2':6',2''-terpyridine-4'-yl) benzene and

Co(II) metallo-supramolecular coordination polyelectrolyte and PSS assembled on inert electrodes showed a reversible one-electron redox transition in the potential range of -0.15 to 0.35 V. The iron ions showed strong ion-exchange properties within the multilayer by forcing a removal of the cobalt ions. Charge transport through the multilayer was induced by electron hopping and self-exchange reactions.<sup>[46,48]</sup>

**Redox polymer with biological molecules.** Multilayers of glucose oxidase (GOD) and poly(4-vinylpyridine) complex of osmium [(Os(bpy)<sub>2</sub>Cl)<sup>2+</sup>] on gold electrodes showed that osmium exchanged electrons effectively between the immobilized GOD and the electrode surface.<sup>[2,49]</sup> Electrochemical behavior of LBL films of negatively charged horseradish peroxidase and [(Os(bpy)<sub>2</sub>Cl)<sup>2+</sup>] assembled on gold electrodes showed that multilayer films containing the enzyme and the redox polymer were highly stable. The enzyme-multilayer electrode was sensitive to the electrocatalytic reduction of hydrogen peroxide.<sup>[50]</sup> Multilayer immobilization of antibody IgG on [Os(bpy)<sub>2</sub>ClPyCH<sub>2</sub>NH poly(allylamine)] redox polymer adsorbed on thiolated gold electrodes was harnessed for molecular recognition of horseradish peroxidase-biotin conjugate as the enzyme was a part in the electrocatalytic reduction of H<sub>2</sub>O<sub>2</sub>.<sup>[51]</sup>

**Redox polymer with heteropolytungstates.** Layer-by-layer ultrathin multilayer films have been prepared by means of alternate adsorption of iron(III)-substituted heteropolytungstate anions and osmium-based cationic redox polymers on 4-ABA modified glassy carbon electrode.<sup>[52]</sup> The resulting multilayer films can effectively catalyze the reduction of H<sub>2</sub>O<sub>2</sub>, NO<sub>2</sub><sup>-</sup>, and BrO<sub>3</sub><sup>-</sup>. Layer-by-layer films were also assembled from tri-vanadium-substituted heteropolytungstate V<sub>3</sub>(P<sub>2</sub>W<sub>15</sub>O<sub>53</sub>) and a cationic polymer of [(Os(bpy)<sub>2</sub>Cl)<sup>2+</sup>] on a 4-ABA modified glassy carbon electrode. The vanadium-centered redox reaction of V<sub>3</sub>(P<sub>2</sub>W<sub>15</sub>O<sub>53</sub>) in the multilayer films effectively catalyzed the reduction of NO<sub>2</sub><sup>-</sup>, BrO<sub>3</sub><sup>-</sup> and induced the catalytic oxidation of ascorbic acid.<sup>[53]</sup> Layer by layers of silicotungstic heteropolyanion (SiW<sub>12</sub>O<sub>4</sub>)<sup>4-</sup> and [(Os(bpy)<sub>2</sub>Cl)<sup>2+</sup>] assembled on a 4-ABA modified glassy carbon electrode showed electrocatalytic reduction activities of four probes HNO<sub>2</sub>, H<sub>2</sub>O<sub>2</sub>, NO<sub>2</sub><sup>-</sup>, and BrO<sub>3</sub><sup>-</sup>.<sup>[54,55]</sup>

## METALLIC, SEMICONDUCTOR, AND METAL-OXIDE COLLOIDS

Colloidal nanoparticles have been prepared as stable suspensions in aqueous solution using a variety of methods. Therefore, many scientists utilized these

colloidal solutions to assemble LBL films that showed interesting electrochemical activity.

**Layer-by-layer films containing metallic nanoparticles.** Layer-by-layer films of Pt nanoparticles assembled by  $\text{PtCl}_6^{2-}$  and [tetrakis-(*N*-methylpyridyl)porphyrinato] cobalt on a 4-ABA modified glassy carbon electrode possessed catalytic activity for the reduction of the oxide ion to water in 0.5 M  $\text{H}_2\text{SO}_4$  solution.<sup>[56]</sup> Following LBL assembly of  $\text{PdCl}_4^{2-}$  and polycation  $[(\text{Os}(\text{bpy})_2\text{Cl})^{2+}]$  on 4-ABA modified glassy carbon electrodes, Pd nanoparticles were embedded in LBL films by electrochemical reduction of  $\text{PdCl}_4^{2-}$ . The resulting Pd nanoparticle multilayer-modified electrode possessed electrocatalytic activity for the reduction of dissolved oxygen and oxidation of hydrazine compounds in aqueous solution.<sup>[57]</sup> Layer-by-layer gold colloidal nanoparticles assembled with 1,6-hexanedithiol as cross-linker yielded a gold-multilayer electrode with electrochemical properties similar to metallic Au.<sup>[58]</sup> Gold nanoparticles functionalized with a monolayer of mercapto-decanoic acid were suitably assembled with PAH/PSS on inert electrodes. These LBL films were probed electrochemically using ferrocene as the active probe vs. Ag/AgNO<sub>3</sub>.<sup>[59]</sup>

**Layer-by-layer films containing semiconductor and/or metal oxide colloids.** Layer-by-layer films were assembled using trioctylphosphine oxidecapped *n*-type CdSe nanoparticles, 1,6-hexadecanethiol, onto *p*-doped semiconducting polymers [for example, either chemically deposited poly(3-methylthiophene) or electrochemically deposited poly(pyrrole)]. Dissymmetrical junctions showed rectification in the forward bias and a Zener breakdown in the reverse.<sup>[60]</sup> Micrometer-size gold nanowires were coated with nanoparticles of TiO<sub>2</sub> or ZnO in combination with polymer multilayer LBL film inside porous membranes to give concentric structures of TiO<sub>2</sub>/PSS, ZnO/PSS, and ZnO/polyaniline (PANI). The current–voltage characteristics of the nanowires/semiconductor nanoparticles showed some current rectification.<sup>[61]</sup> Layer-by-layer films of vanadium oxide V<sub>2</sub>O<sub>5</sub>/PANI nanocomposites were assembled to utilize the electrochemical behavior of V<sub>2</sub>O<sub>5</sub> and the chromogenic properties of PANI.<sup>[62]</sup> For example, LBL films of V<sub>2</sub>O<sub>5</sub>/PANI nanocomposites built for charge storage devices showed a charge storage capability of 2.25 mC/cm<sup>2</sup> in comparison with 1.86 mC/cm<sup>2</sup> for PANI and V<sub>2</sub>O<sub>5</sub> combined storage.<sup>[63]</sup> Positively charged tris(2,2'-bipyridyl)ruthenium (II)  $[\text{Ru}(\text{bpy})_3^{2+}]$  and negatively charged SiO<sub>2</sub> nanoparticles were assembled on ITO electrodes by LBL method. Electrochemical and electrogenerated chemiluminescence of the SiO<sub>2</sub>/[Ru(bpy)<sub>3</sub><sup>2+</sup>]<sub>*n*</sub> multilayer film-modified electrodes were studied by cyclic voltammetry.<sup>[64]</sup>

## CONDUCTING POLYMERS

Conducting polymers such as PANI, polypyrrole, PANI-sulfonate, and 3,4-polyethylenedioxythiophene–PSS can be suspended in aqueous solution in their colloidal form. In LBL films conducting polymers can be rendered electronically conductive by doping with strong acidic solutions or dopants such as anthraquinone.<sup>[65–67]</sup>

Layer-by-layer films of PANI and PSS multilayers deposited onto polystyrene colloidal particles showed that PSS/PANI multilayers maintained their chemical stability and electrochemical properties after removal of the core.<sup>[68]</sup> Layer-by-layer nanostructured films of two conducting polymers, poly(*o*-methoxyaniline) (POMA) and poly(3-thiopheneacetic acid), showed a different electrochemical response from a pure POMA cast film.<sup>[69]</sup> Layer-by-layer films of polycation, PDAC and polyanion, sulfonated polyaniline (SPANI) on ITO plates showed that PDAC/SPANI LBL films were electrically active.<sup>[70]</sup>

Layer-by-layer film of polycationic PANI and poly(anions), such as SPANI, PAA, poly(vinyl sulfonate), and PSS were successful in electrocatalyzing the oxidation of beta-nicotinamide adenine dinucleotide in neutral solution where the catalytic activity of the PANI/SPANI system showed the best performance.<sup>[71]</sup> Ultrathin multilayer films of polypyrrole and PSS deposited on various substrates (glass, mica, ITO coated glass plates) were embedded with glucose oxidase to study multielectron transfer processes.<sup>[72]</sup> Layer-by-layer stable electroactive films of myoglobin or horseradish peroxidase and PSS were grown on SPANI functionalized rough pyrolytic graphite electrodes. A highly efficient coupling between the enzymes and electrode, PDAC/SPANI/(enzyme/PSS)<sub>3</sub> films exhibited a higher sensitivity for the electrochemical catalytic reduction of hydrogen peroxide and a sensitivity for up to 14 μA/μM/cm<sup>2</sup> and a detection limit of 3 nM.<sup>[73]</sup>

## GRAPHITE OXIDE AND GRAPHITE CARBON COLLOIDS

Unfortunately, LBL conducting polymer films are weak ionic conductors and unstable in the long term. A more resilient combination is a polyelectrolyte–colloid composite such that the colloid is electronically conducting and ready to assemble. Many colloids can assemble with polyelectrolytes, but in most cases the LBL films are nonconducting. Only one original approach used exfoliated graphite oxide (GO) that is not conducting to assemble polyethyleneoxide/PDAC/GO LBL films. The problem with graphite is that it is difficult to disperse in water and it “forms

micrometer-sized irregular aggregates in organic solvents.” After assembly the GO can be converted to graphite under severe reduction conditions with H<sub>2</sub> gas.<sup>[74,75]</sup>

Recently, a new method, devised at Massachusetts Institute of Technology, directly employs polyelectrolyte graphite mixtures to assemble LBL electrodes<sup>[76,77]</sup> without having to convert the graphite powder to exfoliated GO and then back to graphite, where in both processes severe chemical, electrochemical, and thermal conditioning was applied. The LBL polyelectrolyte-carbon electrodes (LPCE) have major advantages over LBL conducting polymers. The electronic conductance of LPCE is pH independent and its structure showed good stability because it did not degrade as conducting-polymer based LBLs do. The graphite powder can be assembled as catalyzed carbon or pure carbon loaded with a suitable catalyst. In electrochemical systems, especially fuel cells, the LPCE is expected to perform multiple tasks due to their complexity. The LPCE should be ionically conducting ( $>10^{-4}$  S/cm); electrically conducting ( $>1.0$  S/cm); deposit as micrometer-thin film; hydrophobic to expel water; stable to chemical and mechanical degradation; loaded with catalysts and intimately adhere to the proton-exchange membrane and the gas-diffusion layer. Finally, its open-circuit potential should be similar to a pure metal.

Layer-by-layer polyelectrolyte-carbon electrodes assembled using the 20% Pt-Hispec3000 fuel cell carbon black catalyst showed good dispersion of platinum particles as in the powder form, with a catalyst loading that approached half that of a commercial electrode (i.e., 0.5 mg/cm<sup>2</sup>) verified by scanning electron microscopy (SEM) x-ray analysis. Depositing LPCEs on LBL membrane of PDAC and poly(2-acrylamido-2-methyl-1-propane sulfonic acid) (PAMPS) resulted in a “soft” membrane-electrode assembly (MEA) with no hot pressing applied (Fig. 1A). A cross-sectional view of a linear poly(ethyleneimine)/PAA/Pt/carbon flake LPCE using SEM revealed an electrode thickness of 5–6.0 μm with a surface roughness of less than 400 nm (Fig. 1C).

Scanning electron microscopy revealed that the graphite particulates are held in intimate contact and an electronic conductivity up to 2.0 S/cm was recorded. The electronic conductance of the LPCE decreased as humidity increased but even when soaked in water the electronic conductivity remained higher than 0.5 S/m. Unlike LBL conducting films that use conducting polymers such as poly(aniline) or poly(pyrrole), the LPCE required no dopants and was remarkably stable. It is crucial that the LPCE should maintain integrity after prolonged use in the severe environment of electrochemical devices such as fuel cells. The open circuit potential (OCP) of a solid platinum electrode

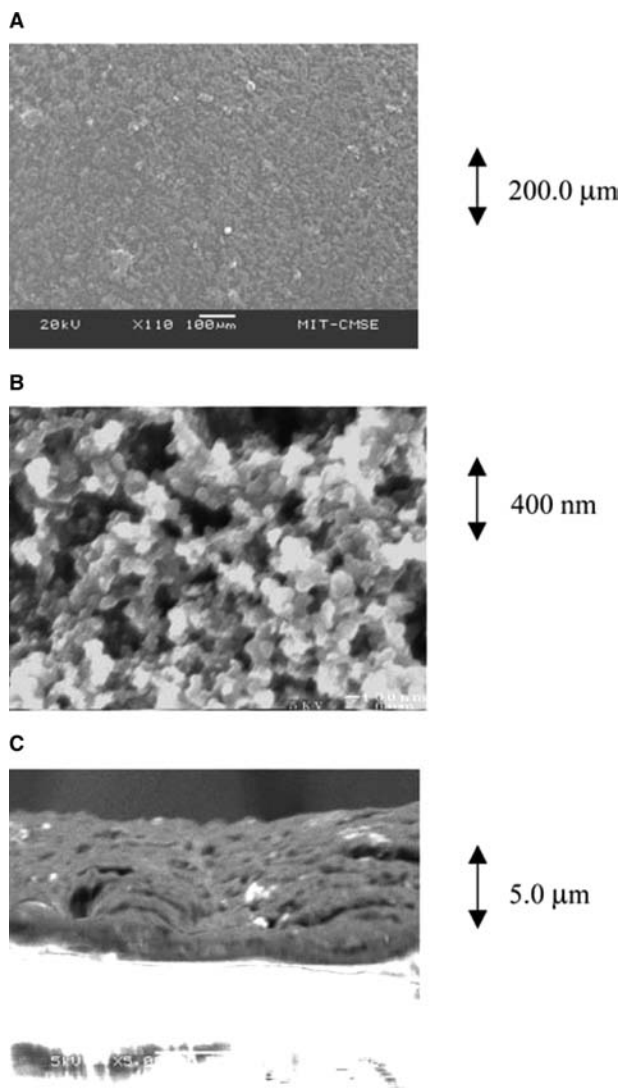


**Fig. 1** Scanning electron microscopy pictures of (A) [poly-(diallyldimethylammonium chloride)/poly(2-acrylamido-2-methyl-1-propane sulfonic acid)/20% Pt-Hispec3000 fuel cell carbon black catalyst] (i.e., PDAC/PAMPS/Hispec3000) LPCE, resolution = 100 μm;  $E_e = 5$  kV; (B) a PDAC/PAMPS/Hispec 3000 LPCE, resolution = 100 nm;  $E_e = 5$  kV; and (C) a cross sectional view of a linear poly(ethyleneimine) /PAA/Pt/carbon flake LPCE with a thickness of 4–5.0 μm and a surface roughness ~500 nm,  $E_e = 5$  kV.

vs. saturated calomel electrode (SCE) in 0.02 M·H<sub>2</sub>SO<sub>4</sub> purged in hydrogen [Pt/0.02M·H<sub>2</sub>SO<sub>4</sub>/H<sub>2</sub>(g)//SCE] measured +0.32 to +0.359 V. For Au/0.02 M·H<sub>2</sub>SO<sub>4</sub>/H<sub>2</sub>(g)//SCE the OCP = 0.005 to +0.02 V; and for a carbon coated gold electrode: [C/Au]/0.02 M·H<sub>2</sub>SO<sub>4</sub>/H<sub>2</sub>(g)//SCE the OCP = +0.005 to +0.03 V; while for LPCE coated gold electrode: [Pt-C/Au]/0.02M·H<sub>2</sub>SO<sub>4</sub>/H<sub>2</sub>(g)//SCE the OCP = +0.345 to +0.347 V. In a galvanic cell of acidified dichromate and basic borohydride solutions the OCP

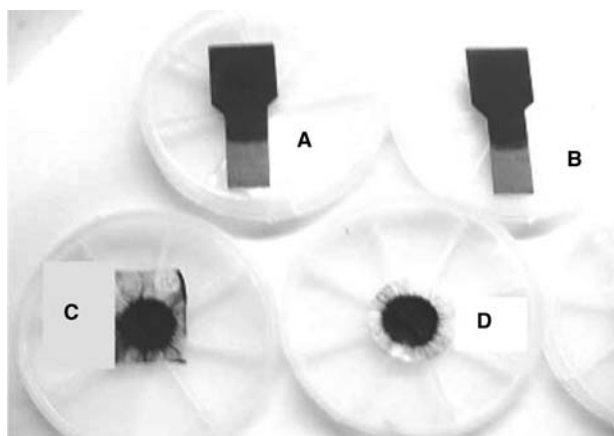


**Fig. 2** (A, B) [Poly(diallyldimethylammonium chloride)/poly(2-acrylamido-2-methyl-1-propane sulfonic acid)/20% Pt-Hispec3000 fuel cell carbon black catalyst] (i.e., PDAC/PAMPS/Hispec3000) LPCE deposited on porous stainless steel. (C) MEA of a PDAC/PAMPS/Hispec3000 LPCE deposited on Nafion112® membrane. (D) MEA of a PDAC/PAMPS/Hispec3000 LPCE deposited on LBL PDAC/PAMPS/Nucleopore® composite membrane.

of LPCE deposited on stainless steel electrode measured +1.63 V (Figs. 2 and 2B), while pure platinum electrodes yielded an OCP = +1.58 V, and an uncoated stainless steel SS316L electrode yielded an OCP = +0.89 V. The difference in the power generated is 2.0 mW/cm<sup>2</sup> by the LPCE-Hispec3000 coated SS316L, 0.088 mW/cm<sup>2</sup> by the uncoated SS316L electrodes, and 0.6 mW/cm<sup>2</sup> by the pure platinum electrodes. Results from the power generated signify effective platinum loading in the matrix of the LPCE and resiliency to acidic/basic and reductive/oxidative aqueous solutions.

The ionic conductivity  $\sigma_i$  of the LPCE reached a maximum of  $2.0 \times 10^{-4}$  S/cm in 0.02 M-H<sub>2</sub>SO<sub>4</sub> indicating the porous nature of the LPCE and efforts under way to measure  $\sigma_i$  around the catalyst. The LPCE was successfully deposited on membranes such as Nafion112® and LBL PDAC/PAMPS composite membrane (Figs. 2C and 2D), to fabricate the MEA.<sup>[76]</sup> The LPCE was found to adhere intimately to the ion conducting membrane eliminating the need to apply extreme hot pressing methods to fabricate the MEA. When properly mounted, a soft MEA, running on H<sub>2</sub> and air produced a stable OCP up to +0.9 V, similar to any commercial MEAs; however, the power delivered was only a few milliwatts per square centimeter, which should be attributed to the low ionic conduction that affects the catalyst performance.

## CONCLUSIONS

A brief review on nonbiological electroactive LBL thin films was provided to illustrate the versatility of the

LBL technique in thin film assembly. Multilayers of the phthalocyanin and porphyrin family possess a potential electroanalytical capability to detect soluble ions and molecules. The electrochromic and electrocatalytic activity of multilayer complex salts and the complexity of the polyoxometallate clusters made them potentially adaptable toward practical applications such as sensors and heterogenous catalysts. Metallo-polymer based LBL films possessed electrocatalytic and light-emitting effects. Layer-by-layer films assembled from metallic, semiconductor, and metal-oxide colloids showed interesting electrochemical activity, while those containing conducting polymers and doped with strong acids become electronically conductive. More resilient electronically conductive films can be assembled from polyelectrolyte-graphite oxide LBLs. One new method of direct assembly of carbon-polymer electrodes can combine the electrochemical activity of all the systems mentioned earlier to produce highly adaptable electrodes. The porous graphitic nature of the LBL carbon-polymer electrodes opens a wide range of application such as fuel and galvanic cells, batteries, supercapacitors, electrolyzers, and catalytic converters.

## ACKNOWLEDGMENTS

The author would like to thank Professor Paula Hammond, the Center of Material Science and Engineering at the Massachusetts Institute of Technology, and the National Science Foundation for the financial support of this project.

## REFERENCES

1. Sun, J.Q.; Sun, Y.P.; Jiang, D.; Sun, C.Q.; Gao, Q.; Zhang, X.; Shen, J.C.; Xu, H.D. Electrocatalytic oxidation of carbohydrates at a molecular deposition film electrode based on water-soluble cobalt phthalocyanine and its application to flow-through detection. *J. Electroanal. Chem.* **1996**, *411*, 73–78.
2. Sun, Y.P.; Sun, J.Q.; Zhang, X.; Sun, C.Q.; Wang, Y.; Shen, J.C. Chemically modified electrode via layer-by-layer deposition of glucose oxidase (GOD) and polycation-bearing Os complex. *Thin Solid Films* **1998**, *329*, 730–733.
3. Sun, Y.P.; Xu, H.D.; Sun, C.Q.; Zhang, X.; Shen, J.C. Selective potentiometric determination of copper(II) ions by use of a molecular deposition film electrode based on water-soluble copper phthalocyanine. *Anal. Chim. Acta* **1995**, *312*, 207–212.
4. Surridge, N.A.; Jernigan, J.C.; Dalton, E.F.; Buck, R.P.; Watanabe, M.; Zhang, H.; Pinkerton, M.; Wooster, T.T.; Longmire, M.L.; Facci, J.S.; Murray, R.W. Electron self-exchange dynamics between redox sites



- in polymers. *Faraday Discuss. Chem. Soc.* **1989**, *88*, 1–17.
5. Faulkner, L.R.; He, P.; Chen, X. Electron transport dynamics in thin polymer films containing tris(2,2'-bipyridine)osmium(III/II) complexes. *J. Electroanal. Chem.* **1987**, *222*, 223–242.
  6. Helfferich, F. *Ion Exchange*; McGraw-Hill: New York, 1962; Chapter 8.
  7. Michaels, A.S. Polyelectrolyte complexes. *Ind. Eng. Chem.* **1965**, *57*, 32–40.
  8. Rembaum, A.; Selegny, E. *Charge and Reactive Polymers—Polyelectrolytes and Their Applications*; Reidel: Boston, MA, 1975; 343pp.
  9. Decher, G.; Hong, J.D.; Schmitt, J. Buildup of ultrathin multilayer films by a self-assembly process. 3. Consecutively alternating adsorption of anionic and cationic polyelectrolytes on charged surfaces. *Thin Solid Films* **1992**, *210/211*, 831–835.
  10. Arys, X.; Jonas, A.M.; Laschewsky, A.; Lagras, R. Supramolecular polyelectrolyte assemblies. In *Supramolecular Polymers*; Ciferri, A., Ed.; Marcel Dekker: New York, 2000; 505–564.
  11. Bertrand, P.; Jonas, A.M.; Laschewsky, A.; Lagras, R. Ultrathin polymer coatings by complexation of polyelectrolytes at interfaces: suitable materials, structure and properties. *Macromol. Rapid Commun.* **2000**, *21*, 319–348.
  12. Decher, G.; Schlenoff, J. *Multilayer Thin Films—Sequential Assembly of Nanocomposite Materials*; Wiley-VCH Verlag GmbH & Co.: Weinheim, 2003.
  13. Shinbo, K.; Onishi, K.; Miyabayashi, S.; Takahashi, K.; Kato, K.; Kaneko, F.; Advincula, R.C. Fabrication and electrochemical properties of layer-by-layer deposited films containing phthalocyanine dyes. *Thin Solid Films* **2003**, *438*, 177–181.
  14. Zucolotto, V.; Ferreira, M.; Cordeiro, M.R.; Constantino, C.J.L.; Moreira, W.C.; Oliveira, O.N. Electroactive layer-by-layer films of iron tetrasulfonated phthalocyanine. *Synth. Met.* **2003**, *137* (1–3), 945–946.
  15. Zucolotto, V.; Ferreira, M.; Cordeiro, M.R.; Constantino, C.J.L.; Balogh, D.T.; Zanatta, A.R.; Moreira, W.C.; Oliveira, O.N. Unusual interactions binding iron tetrasulfonated phthalocyanine and poly(allylamine hydrochloride) in layer-by-layer films. *J. Phys. Chem. B* **2003**, *107* (16), 3733–3737.
  16. Sun, J.Q.; Wu, T.; Sun, Y.P.; Wang, Z.Q.; Zhang, X.; Shen, J.C.; Cao, W.X. Fabrication of a covalently attached multilayer via photolysis of layer-by-layer self-assembled films containing diazo-resins. *Chem. Commun.* **1998**, 1853–1854.
  17. Li, X.F.; Zhang, S.X.; Sun, C.Q. Fabrication of a covalently attached multilayer film electrode containing cobalt phthalocyanine and its electrocatalytic oxidation of hydrazine. *J. Electroanal. Chem.* **2003**, *553*, 139–145.
  18. Fu, Y.Q.; Wu, T.; Li, B.S.; Sun, C.Q. Fabrication of a covalently attached multilayer film electrode containing cobalt phthalocyanine and its application as a potentiometric sensor of iodide ion. *Anal. Chim. Acta* **2002**, *455* (1), 61–68.
  19. Shen, Y.; Liu, J.Y.; Jiang, J.G.; Liu, B.F.; Dong, S.J. Fabrication of metalloporphyrin-polyoxometalate hybrid film by layer-by-layer method and its catalysis for dioxygen reduction. *Electroanalysis* **2002**, *14* (22), 1557–1563.
  20. Ding, H.M.; Ram, M.K.; Nicolini, C. Nanofabrication of organic/inorganic hybrids of TiO<sub>2</sub> with substituted phthalocyanine or polythiophene. *J. Nanosci. Nanotechnol.* **2001**, *1* (2), 207–213.
  21. Toma, H.E.; Araki, K. Supramolecular assemblies of ruthenium complexes and porphyrins. *Coord. Chem. Rev.* **2000**, *196*, 307–329.
  22. Araki, K.; Wagner, M.J.; Wrighton, M.S. Layer-by-layer growth of electrostatically assembled multilayer porphyrin films. *Langmuir* **1996**, *12* (22), 5393–5398.
  23. Cheng, L.; Pacey, G.E.; Cox, J.A. Carbon electrodes modified with ruthenium metallodendrimer multilayers for the mediated oxidation of methionine and insulin at physiological pH. *Anal. Chem.* **2001**, *73* (22), 5607–5610.
  24. Cheng, L.; Cox, J.A. Preparation of multilayered nanocomposites of polyoxometalates and poly(amidoamine) dendrimers. *Electrochem. Commun.* **2001**, *3* (6), 285–289.
  25. Pyrasch, M.; Toutianoush, A.; Jin, W.Q.; Schnepf, J.; Tieke, B. Self-assembled films of Prussian blue and analogues: optical and electrochemical properties and application as ion-sieving membranes. *Chem. Mater.* **2003**, *15* (1), 245–254.
  26. Jin, W.Q.; Toutianoush, A.; Pyrasch, M.; Schnepf, J.; Gottschalk, H.; Rammensee, W.; Tieke, B. Self-assembled films of Prussian blue and analogues: structure and morphology, elemental composition, film growth, and nanosieving of ions. *J. Phys. Chem. B* **2003**, *107* (44), 12,062–12,070.
  27. Jaiswal, A.; Collins, J.; Agricole, B.; Ravaine, S.; Delhaes, P. Layer-by-layer self assembly of Prussian blue colloids. *Abstr. Pap. Am. Chem. Soc.* **2002**, *223*, U436–U436.
  28. Liu, J.Y.; Cheng, L.; Liu, B.F.; Dong, S.J. Multilayer assemblies of tungstodiphosphate anions on 1,7-diaminoheptane modified glassy carbon electrode and the electrocatalytic reduction to iodate. *Electroanalysis* **2001**, *13* (12), 993–998.
  29. Li, X.Y.; Pei, J.H. Layer-by-layer assembled molecular films—III: electrochemical assembly and electropolymerization of noble metal complexes. *Mol. Cryst. Liq. Cryst.* **2001**, *371*, 103–106.
  30. Bi, L.H.; Wang, H.Y.; Shen, Y.; Wang, E.K.; Dong, S.J. Multifunctional organic-inorganic multilayer films of tris(2,2'-bipyridine)ruthenium and decatungstate. *Electrochem. Commun.* **2003**, *5* (11), 913–918.
  31. Jaiswal, A.; Collins, J.; Agricole, B.; Delhaes, P.; Ravaine, S. Layer-by-layer self-assembly of Prussian blue colloids. *J. Coll. Interface Sci.* **2003**, *261* (2), 330–335.
  32. DeLongchamp, D.M.; Hammond, P.T. High-contrast electrochromism and controllable dissolution of assembled Prussian blue/polymer nanocomposites. *Adv. Funct. Mater.* **2004**, *14* (3), 224–232.
  33. Cheng, Z.L.; Cheng, L.; Gao, Q.; Dong, S.J.; Yang, X.R. Characterization of organic-inorganic multilayer films by cyclic voltammetry, UV-Vis spectrometry,

- x-ray photoelectron spectroscopy, small-angle x-ray diffraction and electrochemical impedance spectroscopy. *J. Mater. Chem.* **2002**, *12* (6), 1724–1729.
34. Moriguchi, I.; Fendler, J.H. Characterization and electrochromic properties of ultrathin films self-assembled from poly(diallyldimethylammonium) chloride and sodium decatungstate. *Chem. Mater.* **1998**, *10* (8), 2205–2211.
  35. Liu, S.Q.; Kurth, D.G.; Bredenkotter, B.; Volkmer, D. The structure of self-assembled multilayers with polyoxometalate nanoclusters. *J. Am. Chem. Soc.* **2002**, *124* (41), 12,279–12,287.
  36. Mahmoud, A.; Kieta, B.; Nadjo, L.; Oung, O.; Contant, R.; Brown, S.; DEKouchkovsky, Y. Coupled electron and proton transfers: compared behaviour of oxometalates in aqueous solution or after entrapment in polymer matrices. *J. Electroanal. Chem.* **1999**, *463*, 129.
  37. Liu, S.Q.; Kurth, D.G.; Mohwald, H.; Volkmer, D. A thin-film electrochromic device based on a polyoxometalate cluster. *Adv. Mater.* **2002**, *14*, 225.
  38. Kijak, A.M.; Perdue, R.K.; Cox, J.A. Modification of electrodes with nanostructured films containing dirhodium-substituted polyoxometalates. *J. Solid State Electrochem.* **2004**, *8* (6), 376–380.
  39. Wang, L.; Jiang, M.; Wang, E.B.; Duan, L.Y.; Hao, N.; Lan, Y.; Xu, L.; Li, Z. Preparation and characterization of the nanoporous ultrathin multilayer films based on molybdenum polyoxometalate (Mo-38)<sub>n</sub>. *J. Solid State Chem.* **2003**, *176* (1), 13–17.
  40. Wang, L.; Li, J.; Wang, E.B.; Xu, L.; Peng, J.; Li, Z. Preparation and characterization of ultrathin multilayer films based on polyoxometalate Mo<sub>8</sub>V<sub>2</sub>O<sub>28</sub> center dot 7H<sub>2</sub>O. *Mater. Lett.* **2004**, *58* (14), 2027–2031.
  41. Wang, L.; Jiang, M.; Wang, E.B.; Lian, S.Y.; Xu, L.; Li, Z. Synthesis and characterization of the nanoporous ultrathin multilayer films based on molybdenum polyoxometalate (Mo-36)<sub>n</sub>. *Mater. Lett.* **2004**, *58* (5), 683–687.
  42. Liu, J.Y.; Cheng, L.; Dong, S.J. Assembly of the transition metal substituted polyoxometalates ZnW<sub>11</sub>M(H<sub>2</sub>O)O<sup>39-</sup> (M = Mn, Cu, Fe, Co, Cr, Ni, Zn) on 4-aminobenzoic acid modified glassy carbon electrode and their electrochemical study. *Electroanalysis* **2002**, *14* (9), 569–574.
  43. Liu, S.Q.; Tang, Z.; Wang, Z.X.; Peng, Z.Q.; Wang, E.K.; Dong, S.J. Oriented polyoxometalate-polycation multilayers on a carbon substrate. *J. Mater. Chem.* **2000**, *10* (12), 2727–2733.
  44. Sun, J.Q.; Sun, Y.P.; Zou, S.; Zhang, X.; Sun, C.Q.; Wang, Y.; Sen, J.C. Layer-by-layer assemblies of polycation bearing Os complex with electroactive and electroinactive polyanions and their electrocatalytic reduction of nitrite. *Macromol. Chem. Phys.* **1999**, *200* (4), 840–844.
  45. Wu, A.; Yoo, D.; Lee, J.K.; Rubner, M.F. Solid-state light-emitting devices based on the tris-chelated ruthenium(II) complex: 3. High efficiency devices via a layer-by-layer molecular-level blending approach. *J. Am. Chem. Soc.* **1999**, *121* (20), 4883–4891.
  46. Stepp, J.; Schlenoff, J.B. Electrochromism and electrocatalysis in viologen polyelectrolyte multilayers. *J. Electrochem. Soc.* **1997**, *144*, L155–L157.
  47. Laurent, D.; Schlenoff, J.B. Multilayer assemblies of redox polyelectrolytes. *Langmuir* **1997**, *13*, 1552.
  48. Kurth, D.G.; Schutte, M.; Wen, J. Metallo-supramolecular polyelectrolyte multilayers with cobalt(II): preparation and properties. *Coll. Surf. Physicochem. Eng. Asp.* **2002**, *198*, 633–643.
  49. Calvo, E.J.; Forzani, E.; Otero, M. Gravimetric and viscoelastic changes during the oxidation–reduction of layer-by-layer self assembled enzyme multilayers wired by an Os-containing poly(allylamine) polymer. *J. Electroanal. Chem.* **2002**, *538*, 231–241.
  50. Li, W.J.; Wang, Z.; Sun, C.Q.; Xian, M.; Zhao, M.Y. Fabrication of multilayer films containing horseradish peroxidase and polycation-bearing Os complex by means of electrostatic layer-by-layer adsorption and its application as a hydrogen peroxide sensor. *Anal. Chim. Acta* **2000**, *418* (2), 225–232.
  51. Calvo, E.J.; Danilowicz, C.; Lagier, C.M.; Manrique, J.; Otero, M. Characterization of self-assembled redox polymer and antibody molecules on thiolated gold electrodes. *Biosens. Bioelectron.* **2004**, *19* (10), 1219–1228.
  52. Zhai, S.Y.; Gong, S.Y.; Jiang, J.U.; Dong, S.J.; Li, J.H. Assembly of multilayer films containing iron(III)-substituted Dawson-type heteropolyanions and its electrocatalytic properties: cyclic voltammetry, electrochemical impedance spectroscopy and UV-vis spectrometry. *Anal. Chim. Acta* **2003**, *486* (1), 85–92.
  53. Zhai, S.Y.; Liu, J.Y.; Jiang, J.G.; Dong, S.J. Multilayer assemblies consisting of tri-vanadium-substituted heteropolyanions and its electrocatalytic properties. *Electroanalysis* **2003**, *15* (14), 1165–1170.
  54. Cheng, L.; Liu, J.Y.; Dong, S.J. Layer-by-layer assembly of multilayer films consisting of silicotungstate and a cationic redox polymer on 4-aminobenzoic acid modified glassy carbon electrode and their electrocatalytic effects. *Anal. Chim. Acta* **2000**, *417* (2), 133–142.
  55. Cheng, L.; Dong, S.J. Electrochemical behavior and electrocatalytic properties of ultrathin films containing silicotungstic heteropolyanion SiW<sub>12</sub>O<sub>40</sub><sup>4-</sup>. *J. Electrochem. Soc.* **2000**, *147* (2), 606–612.
  56. Shen, Y.; Liu, J.Y.; Wu, A.G.; Jiang, J.G.; Bi, L.H.; Liu, B.F.; Li, Z.; Dong, S.J. Preparation of multilayer films containing Pt nanoparticles on a glassy carbon electrode and application as an electrocatalyst for dioxygen reduction. *Langmuir* **2003**, *19* (13), 5397–5401.
  57. Liu, J.Y.; Cheng, L.; Song, Y.H.; Liu, B.F.; Dong, S.J. Simple preparation method of multilayer polymer films containing Pd nanoparticles. *Langmuir* **2001**, *17* (22), 6747–6750.
  58. Lu, M.; Li, X.H.; Yu, B.Z.; Li, H.L. Electrochemical behavior of Au colloidal electrode through layer-by-layer self-assembly. *J. Coll. Interface Sci.* **2002**, *248* (2), 376–382.
  59. Murray, R.W.; Hicks, J.F.; Seok-Shon, Y. Layer-by-layer growth of polymer/nanoparticles films containing monolayer protected gold clusters. *Langmuir* **2002**, *18*, 2288–2294.
  60. Cassagneau, T.; Mallouk, T.E.; Fendler, J.H. Layer-by-layer assembly of thin film zener diodes from conducting polymers and CdSe nanoparticles. *J. Am. Chem. Soc.* **1998**, *120* (31), 7848–7859.

61. Kovtyukhova, N.I.; Martin, B.R.; Mbindyo, J.K.N.; Mallouk, T.E.; Cabassi, M.; Mayer, T.S. Layer-by-layer self-assembly strategy for template synthesis of nano-scale devices. *Mater. Sci. Eng. C-Biomimetic Supramol. Syst.* **2002**, *19* (1–2), 255–262.
62. Huguenin, F.; Ferreira, M.; Zucolotto, V.; Nart, F.C.; Torresi, R.M.; Oliveira, O.N. Molecular-level manipulation of V2O5/polyaniline layer-by-layer films to control electrochromogenic and electrochemical properties. *Chem. Mater.* **2004**, *16* (11), 2293–2299.
63. Ferreira, M.; Huguenin, F.; Zucolotto, V.; da Silva, J.E.P.; de Torresi, S.I.C.; Temperini, M.L.A.; Torresi, R.M.; Oliveira, O.N. Electroactive multilayer films of polyaniline and vanadium pentoxide. *J. Phys. Chem. B* **2003**, *107* (33), 8351–8354.
64. Guo, Z.H.; Shen, Y.; Wang, M.K.; Zhao, F.; Dong, S.J. Electrochemistry and electrogenerated chemiluminescence of SiO<sub>2</sub> nanoparticles/tris(2,2'-bipyridyl)ruthenium(II) multilayer films on indium tin oxide electrodes. *Anal. Chem.* **2004**, *76* (1), 184–191.
65. Rubner, M.F.; Stockton, W.B. Molecular-level processing of conjugated polymers. 4. Layer-by-layer manipulation of polyaniline via hydrogen-bonding interactions. *Macromolecules* **1997**, *30*, 2717–2725.
66. Rubner, M.F.; Fou, A.C. Molecular-level processing of conjugated polymers. 2. Layer-by-layer manipulation of in-situ polymerized P-type doped conducting polymers. *Macromolecules* **1995**, *21* (21), 7115.
67. Rubner, M.F.; Cheung, J.H.; Fou, A.F. Molecular self-assembly of conducting polymers. *Thin Solid Films* **1994**, *244*, 985.
68. Park, M.K.; Onishi, K.; Locklin, J.; Caruso, F.; Advincula, R.C. Self-assembly and characterization of polyaniline and sulfonated polystyrene multilayer-coated colloidal particles and hollow shells. *Langmuir* **2003**, *19* (20), 8550–8554.
69. Trivinho-Strixino, F.; Pereira, E.C.; Mello, S.V.; Oliveira, O.N. Self-doping effect in poly(o-methoxyaniline)/poly(3-thiopheneacetic acid) layer-by-layer films. *Langmuir* **2004**, *20* (9), 3740–3745.
70. Sarkar, N.; Ram, M.K.; Sarkar, A.; Narizzano, R.; Paddeu, S.; Nicolini, C. Nanoassemblies of sulfonated polyaniline multilayers. *Nanotechnology* **2000**, *11* (1), 30–36.
71. Tian, S.J.; Baba, A.; Liu, J.Y.; Wang, Z.H.; Knoll, W.; Park, M.K.; Advincula, R. Electroactivity of polyaniline multilayer films in neutral solution and their electrocatalyzed oxidation of beta-nicotinamide adenine dinucleotide. *Adv. Funct. Mater.* **2003**, *13* (6), 473–479.
72. Ram, M.K.; Adami, M.; Paddeu, S.; Nicolini, C. Nanoassembly of glucose oxidase on the in situ self-assembled films of polypyrrole and its optical, surface and electrochemical characterizations. *Biomimetic Nanotechnol.* **2000**, *11* (2), 112–119.
73. Yu, X.; Sotzing, G.A.; Papadimitrakopoulos, F.; Rusling, J.F. Wiring of enzymes to electrodes by ultrathin conductive polyion underlayers: enhanced catalytic response to hydrogen peroxide. *Anal. Chem.* **2003**, *75* (17), 4565–4571.
74. Fendler, J.H.; Cassagneau, T. High density rechargeable lithium-ion batteries self-assembled from graphite oxide nanoplatelets and polyelectrolytes. *Adv. Mater.* **1998**, *10* (11), 877–881.
75. Kotov, N.A.; Dekany, I.; Fendler, J.H. Ultrathin graphite oxide-polyelectrolyte composites prepared by self-assembly: *Adv. Mater.* **1996**, *8*, 637.
76. Farhat, T.R.; Hammond, P.T. Fabrication of Carbon-Polymer Electrochemical Systems Using Layer-By-Layer Technology. Patent 10/944,455, 2004.
77. Farhat, T.R.; Hammond, P.T. Designing a new generation of proton-exchange membranes using layer-by-layer deposition of polyelectrolytes. *Adv. Funct. Mater.* **2005**, *in press*.

# Layer-by-Layer Assembly of Gold Nanoclusters with Self-Assembled Monolayers

**Kohei Uosaki**

*Physical Chemistry Laboratory, Hokkaido University, Sapporo, Japan*

**Wenbo Song**

*Hokkaido University, Sapporo, Japan*

**Masayuki Okamura**

*Physical Chemistry Laboratory, Hokkaido University, Sapporo, Japan*

**Toshihiro Kondo**

*Hokkaido University, Sapporo, Japan*

## INTRODUCTION

The formation of ordered monolayers and multilayers of both organic and inorganic materials on solid substrates with various functionalities has been a subject of intensive research in view of the possible applications in a wide variety of fields in nanotechnology and nanoscience.

Metal and semiconductor nanoclusters are the good candidates as building blocks for the multilayer formation because they have various interesting characteristics, which are different from those of the bulk materials. Since the report by Brust et al.,<sup>[1]</sup> gold nanoclusters (GNCs) covered by self-assembled monolayers (SAMs) of alkanethiols have attracted many research groups<sup>[2–17]</sup> because SAM-covered GNCs have a high stability and those of a certain size with a narrow size distribution can be prepared relatively easily. Gold nanocluster with special functionalities can be constructed by using thiol molecules with special functional groups. One can utilize the rich references on alkanethiol SAMs with various functionalities<sup>[18,19]</sup> including ours.<sup>[20–27]</sup>

Structurally organized GNC multilayers have been constructed on solid substrates by various wet processes, including bond formation between a sulfur atom of an alkanedithiol, a linker, and metal atoms of a substrate as well as of a nanocluster<sup>[8,28–31]</sup> and the Langmuir–Blodgett (LB) method.<sup>[32]</sup> The electrostatic layer-by-layer (LBL) assembly method, which was initially developed for thin film fabrication of pure polymeric materials of oppositely charged polyelectrolytes,<sup>[33]</sup> has been extended to the construction of alternate multilayer assemblies composed of oppositely charged nanoparticles and polyions.<sup>[10–12,14,34,35]</sup> The simplicity and versatility of the LBL technique as well as the resulting high-quality films provide broad perspectives in both fundamental and applied research in nanostructure systems.

## OVERVIEW

In this study, multilayers composed of two types of GNC, one covered by mixed SAMs of mercaptoundecanoic acid (MUA), hexanethiol (C<sub>6</sub>SH), and ferrocenylhexanethiol (FcC<sub>6</sub>SH), MHF-GNC, and the other covered with MUA and C<sub>6</sub>SH, MH-GNC, are constructed on Au(111) and ITO surfaces using a cationic polymer, poly(allylamine hydrochloride) (PAH), as the binding layer based on the carboxylate/PAH/carboxylate electrostatic interaction. The electrochemical characteristics of these multilayers are investigated and the effects of the substrates are examined. The charge transfer mechanism within the GNC multilayers is also discussed.

## EXPERIMENTAL

### Materials

Poly(allylamine hydrochloride) (average Mw = 70,000) was purchased from Aldrich. Perchloric acid (ultrapure grade), sodium chloride, and sulfuric acid (ultrapure grade) were obtained from Wako Pure Chemicals. All chemicals were used as received. Indium–tin-oxide (ITO)-coated glass was obtained from Tokyo Kinoene Optics. Ultrapure water was obtained using a Milli-Q water purification system (Millipore), and ultrapure N<sub>2</sub> (99.999%) was obtained from Air Water.

### Substrates

A gold single crystal was prepared from a gold wire (99.999%,  $\phi = 1$  mm, Tanaka Precious Metals) by Clavilier's method.<sup>[36,37]</sup> It was cut to expose the

(111) face, mechanically polished, and then annealed at 800°C for 8 hr in an electric furnace (Denken, KDF S-70) under an ultrapure N<sub>2</sub> atmosphere. Gold substrates used for the electrochemical quartz crystal microbalance (EQCM) measurements were prepared by the vacuum evaporation of 10-nm-thick titanium followed by 100-nm-thick gold onto a 5-MHz quartz crystal plate (double-side polished) kept at 300°C with an evaporation rate of less than 0.01 nm sec<sup>-1</sup>. This procedure is known to provide a highly ordered Au(111) phase with wide terraces.<sup>[38]</sup> For the X-ray photoelectron spectroscopy (XPS) measurements, a gold disk (99.99%,  $\phi = 8$  mm, thickness = 3 mm, Tanaka Precious Metals) was used as the substrate after mechanical polishing and electrochemical treatment by cycling the potential between -0.2 and +1.5 V vs. Ag|AgCl in 0.1 M H<sub>2</sub>SO<sub>4</sub>. The ITO substrate was cleaned by immersing it in a 1:3 H<sub>2</sub>O<sub>2</sub> (30%)–H<sub>2</sub>SO<sub>4</sub> (conc.) solution for 5 sec, then thoroughly rinsing it with Milli-Q water, and finally drying it with ultrapure nitrogen.

### Preparation of Gold Nanoclusters

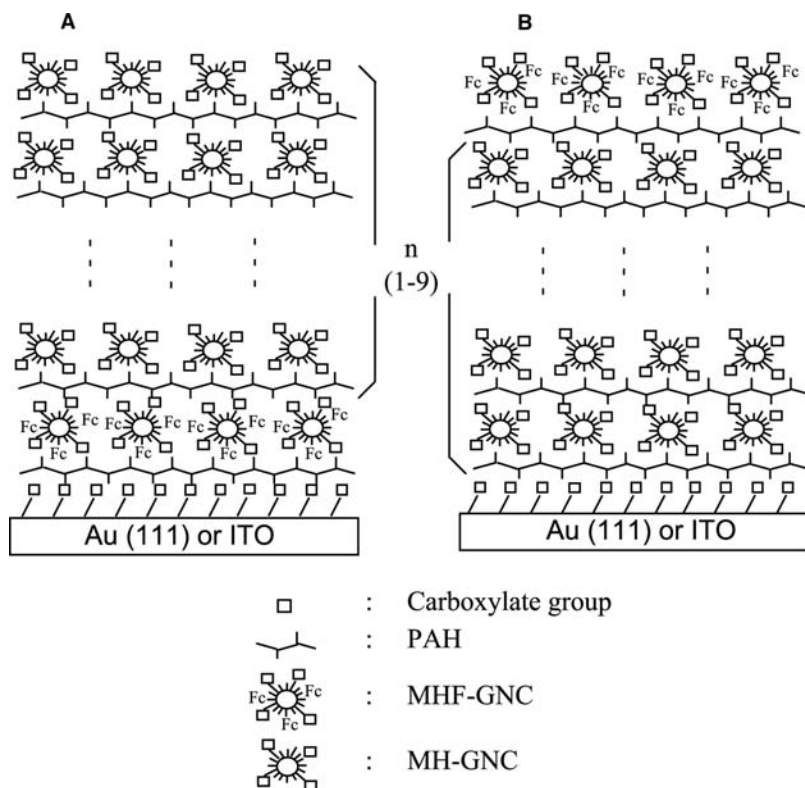
Two types of GNC protected by mixed alkanethiol SAMs, one covered by mixed SAMs of C<sub>6</sub>SH, FcC<sub>6</sub>SH, and MUA (MHF-GNC), and the other covered by C<sub>6</sub>SH and MUA (MH-GNC), were prepared by the procedures reported previously.<sup>[39–41]</sup>

Transmission electron microscopy (TEM, JEOL-2000EX, 200 kV) proved that the core diameter of the GNCs was 1.8 ± 0.4 nm in both cases. The molar ratios of C<sub>6</sub>SH:FcC<sub>6</sub>SH:MUA on the MHF-GNC surface and C<sub>6</sub>SH:MUA on the MH-GNC surface estimated by <sup>1</sup>H-NMR (Hitachi, R-1900, 90 MHz) were 47:19:34 and 26:74, respectively. Based on these results, the number of FcC<sub>6</sub>SH molecules adsorbed on one GNC is calculated to be 10 because 53 thiol molecules adsorb on a GNC with a core size of 1.8 nm.<sup>[9]</sup>

### Preparation of Multilayers of Gold Nanoclusters

Multilayers of MHF-GNC were constructed on Au(111) and ITO substrates based on the carboxylate/polycation electrostatic interaction. All the gold substrates were annealed by a hydrogen flame and cooled in air just before dipping in the thiol solution. The cleaned ITO substrate was immediately transferred to an ethanol solution containing 1 mM MUA and kept in the solution for at least 36 h.

Gold nanocluster multilayers with the following three different arrangements as described in Scheme 1 were formed on the carboxylate-terminated (MUA) SAM-modified gold substrates based on the carboxylate/PAH/carboxylate electrostatic interaction. 1) A multilayer containing only MHF-GNC/PAH [Au(111)/MUA/(PAH/MHF-GNC)<sub>n</sub>] was prepared on a gold surface by repeating the two-dip and rinse cycle as



**Scheme 1** Schematic view of the idealized layer structure of (A) Au(111) or ITO/MUA/(PAH/MHF-GNC)<sub>n</sub>, (B) Au(111) or ITO/MUA/PAH/MHF-GNC/(PAH/MH-GNC)<sub>n</sub>, and (C) Au(111) or ITO/MUA/(PAH/MH-GNC)<sub>n</sub>/PAH/MHF-GNC electrodes.

reported before.<sup>[40]</sup> 2) A multilayer of MH-GNC and MHF-GNC with only one layer of MHF-GNC existed in the layer closest to the gold electrode, i.e., the first layer, and MH-GNC in the other layers [Scheme 1a: Au(111)/MUA/PAH/MHF-GNC/(PAH/MH-GNC)<sub>n</sub>]. 3) A multilayer of MH-GNC and MHF-GNC with only one layer of MHF-GNC existed only in the outermost layer and MH-GNC in the other layers [Scheme 1b: Au(111)/MUA/(PAH/MH-GNC)<sub>n</sub>/PAH/MHF-GNC].

The gold substrate precoated with MUA SAM was dipped in a 2 wt.% PAH aqueous solution (pH = 6) containing 1 M NaCl for 30 min followed by a Milli-Q water rinse and then dipped in a 0.75 wt.% GNC ethanol solution for 30 min followed by a rinse with ethanol. This two-dip and rinse cycle was repeated to construct the multilayers.

After the MUA SAM-coated ITO substrate had been thoroughly rinsed with ethanol and dried with ultrapure nitrogen, the MHF-GNC multilayer was constructed by alternately dipping the ITO substrate in a 2.0 mg/mL PAH solution containing 1 M NaCl for 10 min and 1.0 mg/mL MHF-GNC solution for 10 min.

### Structural Characterization of the Gold Nanocluster/Poly(Allylamine Hydrochloride) Multilayers

Atomic force microscopy (AFM) was carried out using a PicoSPM (Molecular Imaging) in a contact mode. Atomic force microscopy tips were made of Pt/Si<sub>3</sub>N<sub>4</sub> with a typical spring constant of 0.12 N/m. Measurements were carried out at room temperature (ca. 20°C) and ambient humidity (ca. 38 ± 2%). X-ray photoelectron spectroscopy measurements were performed using a Rigaku XPS-7000 spectrometer with an MgK $\alpha$  X-ray source (1253.6 eV). The takeoff angle between the sample surface and the analyzer was fixed at 90° in all cases. The narrow-scan spectra of the Fe2p region were taken with a resolution of 0.1 eV and the signals of 64 scans were averaged. Cross-sectional transmission electron microscopy of a GNC multilayer was carried out using a JEOL electron microscope JEM-2010F with 200-kV acceleration voltage. A multilayer with 10 MHF-GNC/PAH deposition cycles was prepared on a silicon wafer with a pre-evaporated Au film of 150 nm. After the multilayer formation, the multilayer was further covered with the evaporated Au and epoxy resin to protect the multilayer for the preparation of a sliced sample.

### Electrochemical and Electrochemical Quartz Crystal Microbalance Measurements

Cyclic voltammograms (CVs) were recorded with an automatic polarization system (Hokuto Denko,

HSV-100). A potentiostat/galvanostat (Hokuto Denko, HA-151) and a function generator (Hokuto Denko, HB-111) were used for the EQCM measurements, which were carried out in a three-compartment cell. The resonant frequency of the quartz crystal electrode, which was oscillated using a homemade oscillation circuit, was simultaneously monitored with the electrode potential and current by a frequency counter (Hewlett-Packard, HP53131A) controlled by a personal computer (NEC, PC9821cb2) through a general purpose interface bus (GPIB) interface. The frequency stability of the EQCM system was better than 0.1 Hz for a sampling gate time of 0.1 sec. Pt wire and Ag|AgCl|NaCl(sat) were used as the counter and reference electrodes, respectively. The measurements were carried out in a 0.1 M HClO<sub>4</sub> aqueous solution, which was deaerated by passing ultrapure N<sub>2</sub> gas through it for more than 30 min before each measurement.

## RESULTS AND DISCUSSION

### Structure and Electrochemical Characteristics of the MHF-Gold Nanocluster/Poly(Allylamine Hydrochloride) Multilayers

Fig. 1 shows the cross-sectional micrograph of a multilayer with 10 MHF-GNC/PAH deposition cycles on an evaporated gold film. The substrate, GNC/PAH multilayers, and the protecting layers, i.e., the evaporated Au and epoxy resin, are clearly visible in Fig. 1A. From this image, the total thickness of the GNC multilayer with 10 GNC/PAH cycles was estimated to be about 58 nm, which is in good agreement with the previously reported value of 51 nm determined by ellipsometry for the same system.<sup>[40]</sup> This and the higher resolution image [Fig. 1B] reveal that the GNCs

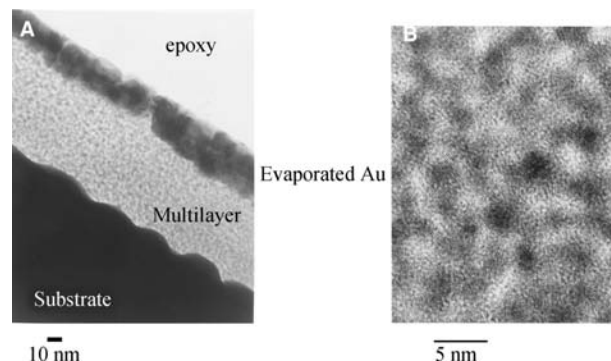


**Fig. 1** Cross-sectional TEMs of (A) a MHF-GNC multilayer film with 10 deposition cycles on an evaporated Au film on the silicon wafer and (B) a higher-resolution image of the GNC/PAH multilayer region. *Source:* From Ref.<sup>[41]</sup>.



are dispersed within the polymeric matrix rather uniformly and the well-defined layered structure as illustrated in Scheme 1 is not observed, suggesting a homogenous mixture of the GNCs and PAH in the LBL film rather than the expected vertically ordered structure with sharp interfaces between the two components. This is reasonable because the layered LBL assembly might be obscured in the case of globular nanoparticles alternatively assembled with flexible linear polymeric chains because of the interpenetration between the adjacent layers and high interlayer roughness or by embedding of the GNCs on the polymeric chains. The spherical nanoparticles are separated from each other by the organic shells and the mean size of the immobilized GNC core is about  $1.8 \pm 0.3$  nm, which is almost the same as that of the GNC in solution, revealing the absence of aggregation or reshaping of the linked GNC particles to those of larger core size in the LBL multilayers. The average separation distance of the immobilized GNCs was estimated by measuring the edge-to-edge distances of the particles in the cluster regions in Fig. 1B. The result yields an almost uniform spacing close to the cluster core size. Similar features are expected for the multilayers with the ferrocene group either existing in the innermost and or outermost layers because both types of GNCs used for the fabrication of LBL multilayers with PAH spacing layers have same core size and similar activity.

### Redox Properties of the MHF-Gold Nanocluster/Poly(Allylamine Hydrochloride) Multilayers

Fig. 2A shows the CVs of the gold electrode modified with MHF-GNC/PAH multilayers of 1–10 deposition cycles measured in a 0.1 M  $\text{HClO}_4$  aqueous solution at a scan rate of  $100 \text{ mV sec}^{-1}$ . The oxidation and reduction peaks due to the redox of  $\text{Fc}/\text{Fc}^+$  are observed around +360 mV (vs.  $\text{Ag}|\text{AgCl}$ ) in all cases. The full width at half maximum (fwhm) of the MHF-GNC multilayer-modified electrode was constant at around 90 mV regardless of the GNC deposition cycles, suggesting a simple Langmuir-type redox process of the ferrocene moieties. The peak-to-peak separation was less than 60 mV in all cases, suggesting a facile charge transfer within the MHF-GNC multilayers.

Fig. 2B shows CVs of ITO electrodes modified with MHF-GNC multilayers of various layer thickness [ITO/MUA/(PAH/GNC) $_n$ ,  $n = 1, 2, 3, 4, 5, 8$  and 10] measured in a 0.1 M  $\text{HClO}_4$  aqueous solution at the scan rate of  $100 \text{ mV sec}^{-1}$ . For all cases, quasi-reversible peaks due to the redox of the ferrocene moiety were observed around +350 mV (vs.  $\text{Ag}/\text{AgCl}$ ).

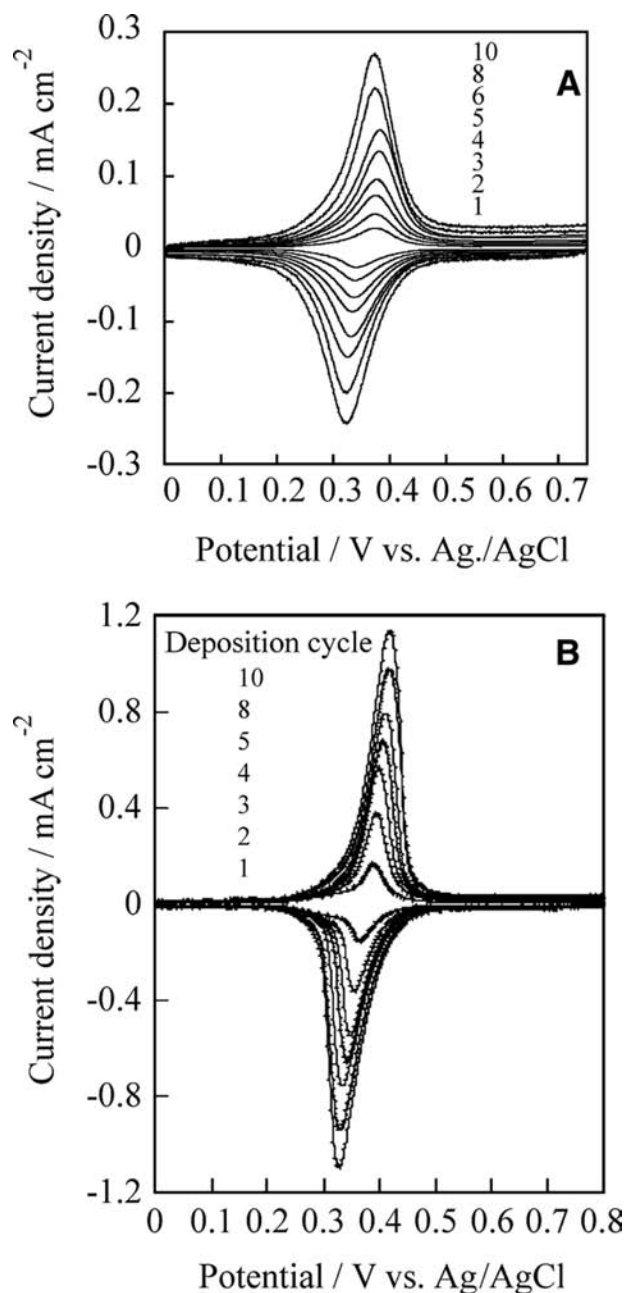


**Fig. 2** Cyclic voltammograms of Au(111)/MUA/(PAH/MHF-GNC) $_n$  for  $n = 1$ –10 (A) and an MUA SAM-precoated ITO electrode modified with MHF-GNC multilayers of various thickness (B) measured in 0.1 M  $\text{HClO}_4$  aqueous solution at a scan rate of  $100 \text{ mV sec}^{-1}$ . Number of deposition cycles is shown in the figure. *Source:* From Ref.<sup>[41]</sup> and Song et al., *Phys. Chem. Chem. Phys.* **2003**, *5*, 5279–5284.

These redox peaks were sharp in all cases with full width at half maximum (fwhm) of 45 mV ( $n = 1$ ), 47 mV ( $n = 2$ ), 52 mV ( $n = 5$ ), and 60 mV ( $n = 10$ ), which are much narrower than that expected for a simple Langmuir-type redox process observed at

**Table 1** Redox potential and peak separation of Fc/Fc<sup>+</sup> couple of an MHF-GNC/PAH multilayer-modified ITO electrode in aqueous solutions containing 0.1 M of various anions at two pH values

Anions	PH 1			PH 7		
	E <sub>pa</sub> (mV)	E <sub>pc</sub> (mV)	ΔE <sub>p</sub> (mV)	E <sub>pa</sub> (mV)	E <sub>pc</sub> (mV)	ΔE <sub>p</sub> (mV)
ClO <sub>4</sub> <sup>-</sup>	420	320	100	450	345	105
NO <sub>3</sub> <sup>-</sup>	470	370	100	490	380	110
SO <sub>4</sub> <sup>2-</sup>	625	500	125	630	500	130

the gold electrode. The peak separation increased as the MHF-GNC layers increased from 23 mV ( $n = 1$ ) to 39 mV ( $n = 2$ ), 75 mV ( $n = 5$ ), and 100 mV ( $n = 10$ ).

The electrochemical responses of the MHF-GNC multilayer film-modified ITO electrode were also investigated in acidic (pH = 1) and neutral (pH = 7) solutions containing ClO<sub>4</sub><sup>-</sup>, NO<sub>3</sub><sup>-</sup>, or SO<sub>4</sub><sup>2-</sup>. The peak potentials of the wave due to the redox of the ferrocene/ferrocenium cation (Fc/Fc<sup>+</sup>) couple were almost independent of the pH but strongly dependent on the nature of the electrolyte as shown in Table 1. The results are in good agreement with those reported for ferrocene thiol SAMs-modified gold electrodes,<sup>[42–44]</sup> indicating that the ferrocene molecules adsorbed on the GNCs behaved essentially in the same manner as those of the SAMs on planar electrodes.

The amounts of redox-active ferrocene groups of the multilayer-modified gold and ITO electrodes estimated from the anodic charge of the redox peak are plotted as a function of the number of deposition cycles in Fig. 3. Although the amount of the

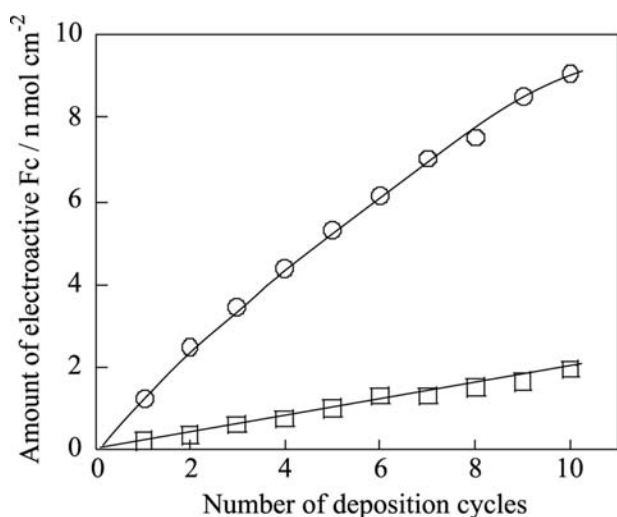


**Fig. 3** Amount of electroactive Fc groups as a function of number of MHF-GNC deposition cycles on ITO (○) and Au (□) electrodes. *Source:* From Song et al., Phys. Chem. Chem. Phys. **2003**, 5, 5279–5284.

electroactive Fc moiety increased with increase in the number of deposition cycles in both cases, the manner and the magnitude of increase in the amount of the electroactive ferrocene moiety with increase in the number of deposition cycles depended on the substrate. While the amount of the redox-active Fc group on the gold substrate increased almost linearly with increase in deposition cycles, the increment of that on the ITO substrate at each deposition cycle became smaller at higher deposition cycle. The increment of the adsorbed Fc groups at each deposition cycle on gold was  $1.8 \times 10^{-10}$  mol/cm<sup>2</sup> in average and that on ITO was  $12.5 \times 10^{-10}$  mol/cm<sup>2</sup> initially and decreased to  $5.5 \times 10^{-10}$  mol/cm<sup>2</sup> as the number of deposition cycles increased. Because one GNC contained 10 FcC<sub>6</sub>SH molecules on the surface as mentioned above, the numbers of adsorbed GNCs per deposition cycle on ITO and Au substrates were estimated to be  $7.6\text{--}3.4 \times 10^{13}$ /cm<sup>2</sup> and  $1.1 \times 10^{13}$ /cm<sup>2</sup>, respectively. Both values are greater than that calculated for a hexagonally packed monolayer of thiol-covered GNCs,  $(3.8\text{--}8.8) \times 10^{12}$ /cm<sup>2</sup>,<sup>[40]</sup> as well as that of a previously reported GNC assembly with a comparable core size.<sup>[14]</sup> One possible reason for this discrepancy is that not the monolayers but the relatively thick GNC/PAH layers were adsorbed on both surfaces at each deposition cycle under the present preparation conditions. We used a rather high concentration of salt in the PAH adsorbing solution (1 M NaCl), and it is known that the use of an adsorbing solution of high ionic strength usually results in the thicker adsorbed layers.<sup>[33]</sup> The reason for the larger amount of deposited GNC and the decrease in the deposited amount as the number of deposition cycles increased on the ITO substrate will be discussed later.

#### Differential Capacitance of MHF-Gold Nanocluster/Poly(Allylamine Hydrochloride) Multilayers

Figure 4 shows the deposition cycle dependencies of the apparent differential capacitances of GNC multilayers on ITO and gold electrodes calculated by dividing the charging currents observed before and after the

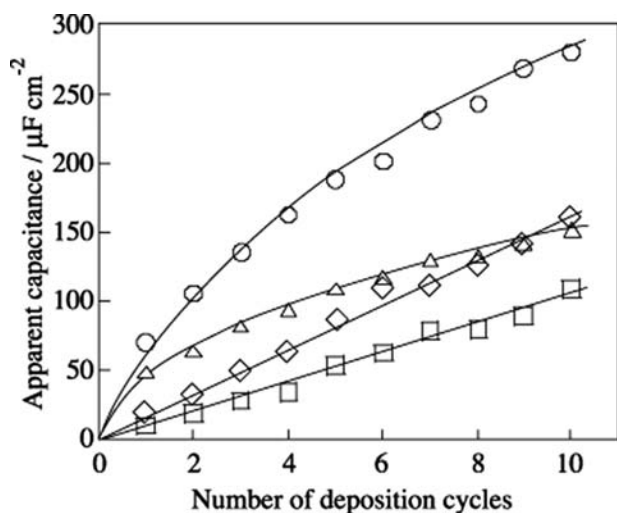


**Fig. 4** Apparent differential capacitances before ( $\Delta$  and  $\square$ ) and after ( $\circ$  and  $\diamond$ ) oxidation of ferrocene moiety as a function of MHF-GNC deposition cycles on the ITO ( $\Delta$  and  $\circ$ ) and Au ( $\square$  and  $\diamond$ ) electrodes. *Source:* From Song et al., *Phys. Chem. Chem. Phys.* **2003**, 5, 5279–5284.

redox peak by the scan rate.<sup>a</sup> For all cases, the apparent differential capacitances after the ferrocene oxidation were greater than those before the oxidation and increased with increase in the number of deposition cycles. Increase in capacitance upon oxidation of the ferrocene moiety has been observed at a ferrocene SAM-modified electrode and is known to be a result of an increase in hydrophilicity.<sup>[45]</sup>

The capacitance increased with increase in the number of deposition cycles in both cases, suggesting that the immobilized GNCs act as an ensemble of numerous nanosized electrodes. It is notable that the capacitance increased linearly with increase in the number of deposition cycles at the GNC-modified gold electrode, but the capacitance increment per deposition cycle became smaller as the number of deposition cycles increased at the GNC-modified ITO electrode. This observation is in accordance with the observation for the deposition cycle dependencies of the amount of redox-active Fc groups. The surface area of one GNC with a core size of 1.8 nm is ca.  $1.02 \times 10^{-13} \text{ cm}^2$ . Using the number of GNCs adsorbed on the ITO surface estimated from Fig. 3, the total electrode surface area of the GNCs assembled on an ITO surface of  $1 \text{ cm}^2$  can be calculated to be ca. 7.5 (1 cycle)–54 (10 cycles)  $\text{cm}^2$ . Because the capacitances of the

GNC-modified ITO electrode before and after the redox peak were ca. 50 (1 cycle)–140 (10 cycles)  $\mu\text{F}/\text{cm}^2$  and 73 (1 cycle)–280 (10 cycles)  $\mu\text{F}/\text{cm}^2$  based on the apparent surface area of the ITO electrode, the capacitances of the GNC assembly on the ITO surface in reduced and oxidized states of the ferrocene moiety based on the *real* electrode surface area were ca. 6.7–2.6 and 9.7–5.2  $\mu\text{F}/\text{cm}^2$ , respectively. Similarly, the capacitances of the GNC assembly on the Au electrode surface based on the real electrode surface area were estimated to be ca. 7.0 and 13.0  $\mu\text{F}/\text{cm}^2$  in reduced and oxidized states of the ferrocene moiety, respectively. Thus although the apparent capacitances of the GNC/PAH-modified ITO electrode were much greater than those of the GNC/PAH-modified gold electrode, the capacitances of the GNC/PAH-modified ITO electrode based on the real surface area were smaller than those of the GNC/PAH-modified gold electrode. The difference between the capacitances of the GNCs on the ITO electrode and those on the gold electrode may reflect the higher conformational order of the SAMs on the GNCs assembled on the ITO electrode than those on the gold electrode. Actually, the redox peaks at the GNC-modified ITO electrode were sharper than those at the gold electrode as mentioned before, indicating a stronger interaction between the ferrocene groups on the GNCs assembled on the ITO electrode than on the gold electrode. Thus the difference is essentially because of the difference in the amount of deposited GNCs on these surfaces, and the GNC/PAH layer on the ITO electrode is more compact than that on the gold electrode.

These capacitance values are comparable to those of ferrocene SAMs on a planar Au surface,<sup>[42]</sup> confirming that the order of ferrocene SAMs formed on a GNC surface is essentially the same to that of ferrocene SAMs formed on a planar Au surface.<sup>[7]</sup>

### Effect of the Underlying Substrate on the Formation of Gold Nanocluster/Poly(Allylamine Hydrochloride) Multilayers

The amounts of adsorbed GNC multilayers on the ITO electrode were always greater than those on the Au electrode of the same deposition cycle, suggesting that the underlying substrate plays an important role in GNC multilayer formation. Atomic force microscopy measurements of the two substrates showed that while the Au surface consisted of very large and almost atomically flat terraces, a number of hemispherical islands of ca. 100 nm in diameter and several tens of nanometers in height were observed on the ITO surface. An ordered and closely packed MUA SAM is expected to form on a gold surface as it has been well documented for the formation of

<sup>a</sup>For more accurate determination of capacitance, it needs to carry out impedance measurements using wide range of a.c. frequencies, but the values obtained in this work are still accurate enough for the purpose of this paper.

various alkanethiol SAMs, and both the adsorbed PAH and the GNC layers are expected to be well organized and closely packed when the gold surface with uniformly distributed charged sites of the carboxylate group was alternately immersed in PAH and GNC solutions.<sup>[33]</sup>

The amount of adsorbed GNC of the multilayer-modified ITO electrode was 3–7 times greater than that of the Au electrode, although the surface roughness of the ITO electrode was only ca. 2.5 times greater than that of the Au electrode, as determined from the AFM images. These findings suggest that the multilayer formation of GNC on an ITO surface and therefore the electrochemical behavior were related to but not solely determined by surface roughness. The nature of the underlying metal oxide layers on the ITO electrode as well as the adsorbed MUA molecules should play important roles in the GNC packing arrangement and therefore its electrochemical behavior. We have already demonstrated that alkanethiol molecules tend to form an island structure on the ITO surface with surface coverage of only 1/3–1/4 of that on the gold surface, although the formed SAM was well organized.<sup>[46]</sup> A nonuniform MUA SAM layer on the ITO surface and/or intrinsically dangling Sn–O<sup>−</sup> bonds resulted in disordered polymer layer adsorption. The GNCs can both adsorb on top of the polymer surface and diffuse into the layers, binding to internal sites of PAH through ion exchange of uncompensated anions. This is one possible reason for the large amount of adsorbed GNC on the ITO. The deviations from linear relations of both the adsorption amount and the capacitance of the ITO-modified electrode with the number of deposition cycles shown in Figs. 3 and 4, respectively, may be the result of the less-ordered multilayer structure on ITO than that on Au.

The decreases in the deposited amount of GNC per deposition cycle and the capacitance per unit real area with increase in the number of deposition cycles can also be explained by considering that the surface became smoother as more GNC/PHC layers were deposited.

### Electrochemical Characteristics of the Multilayers Consisting of Only One MHF-Gold Nanocluster Layer and MH-Gold Nanocluster as the Other Layers with Two Different Sequences

The electrochemical characteristics of multilayers of MHF-GNC and MH-GNC with two different sequences containing only one layer of MHF-GNC, as described in Scheme 1A and 1B, were investigated. In the first system, MHF-GNC existed in the layer

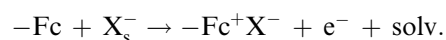
closest to the electrode surface, i.e., the first layer, and MH-GNC existed in the other layers [Scheme 1A: Au or ITO/MUA/PAH/MHF-GNC/(PAH/MH-GNC)<sub>n</sub>, *n* = 1–9]. In the other system, MHF-GNC existed only in the outermost layer and MH-GNC existed in the other layers [Scheme 1B: (Au or ITO/MUA/(PAH/MH-GNC)<sub>n</sub>/PAH/MHF-GNC, *n* = 1–9)].

The X-ray photoelectron spectra of the multilayer assemblies (A) Au(111)/MUA/PAH/MHF-GNC/(PAH/MH-GNC)<sub>n</sub> for *n* = 1, 3, and 5 and (B) Au(111)/MUA/(PAH/MH-GNC)<sub>n</sub>/PAH/MHF-GNC for *n* = 1, 3, 5, and 9 in the Fe2p region showed that while the Fe peak was observed only for *n* = 1 and no peak was observed even at *n* = 3 in the former, the peak intensity did not change with *n* in the latter, confirming that the ferrocene group definitely existed at the innermost and outermost layers in the former and the latter systems, respectively, as suggested in Scheme 1A and 1B.

The redox peaks of the ferrocene group were observed in the CVs of the former and the latter multilayer-modified gold and ITO electrodes measured in a 0.1 M HClO<sub>4</sub> aqueous solution. Although the double-layer charging currents increased with increase in the number of MH-GNC deposition cycles, suggesting sequential LBL deposition of MH-GNC on the ITO surface, the charges in the Fc redox peaks did not depend on the number of MH-GNC deposition cycles and are in good agreement with that of the electrodes modified with only one MHF-GNC layer, implying that all of the Fc groups in the innermost or outermost layer were electrochemically active regardless of the number of MH-GNC layers, showing that the transport of both electrons and anions through these two types of multilayers was rather facile.

### Charge Transfer through the Gold Nanocluster Multilayers

Because the redox process of the surface-attached ferrocene group is known to be represented by<sup>[42,47]</sup>:



where  $-\text{Fc}$  and  $-\text{Fc}^+$  are the neutral and oxidized states of the ferrocene group, respectively,  $\text{X}_s^-$  is the solvated anion in solution,  $-\text{Fc}^+\text{X}^-$  is an ion pair between the ferricenium cation and the anion, and solv. is a solvent molecule; the electron and anion should be transferred between the ferrocene moiety and the electrode, and between the electrolyte solution and the ferrocene moiety, respectively, upon the redox reaction of the ferrocene group. Thus the results shown in



Figs. 2 and 4 strongly suggest that perchlorate anion, which forms an ion pair with  $\text{Fc}^+$ , is transferred between the electrolyte solution and the ferrocene group at the innermost layer through the 1–9 PAH/MH-GNC layers at the Au/MUA/PAH/MHF-GNC/(PAH/MH-GNC) $_n$  ( $n = 1, 3, 5,$  and  $9$ ) electrodes, and an electron is transferred between the ferrocene group at the outermost layer and the gold electrode through the 1–9 PAH/MH-GNC layers at the Au/MUA/(PAH/MH-GNC) $_n$ /PAH/MHF-GNC ( $n = 1, 3, 7,$  and  $9$ ) electrodes.

Fig. 5 shows the potential dependencies of current and EQCM frequency shift at the Au/MUA/PAH/MHF-GNC/(PAH/MH-GNC) $_9$  electrode obtained simultaneously in 0.1 M  $\text{HClO}_4$  aqueous solution at a scan rate of  $10 \text{ mV sec}^{-1}$ . A significant frequency decrease and increase, i.e., weight increase and decrease, were observed when the current due to the oxidation and reduction of the ferrocene moiety, respectively, flowed. A linear relation was observed between the mass change calculated from the frequency change by using Sauerbrey's equation and the charge in the region of the ferrocene oxidation (250–550 mV) with a slope of  $216 \text{ g/mol electron}$ . A similar EQCM response was observed for the Au/MUA/PAH/MHF-GNC/(PAH/MH-GNC) $_3$  and Au/MUA/PAH/MHF-GNC/(PAH/MH-GNC) $_6$  electrodes. The slopes for the mass change–charge relations, i.e., mass per electron (mpe), for the former and the latter were 233 and 177, respectively. Furthermore, essentially the same EQCM response was obtained at the Au/MUA/(PAH/MH-GNC) $_9$ /PAH/MHF-GNC. These results clearly show that the EQCM response was not

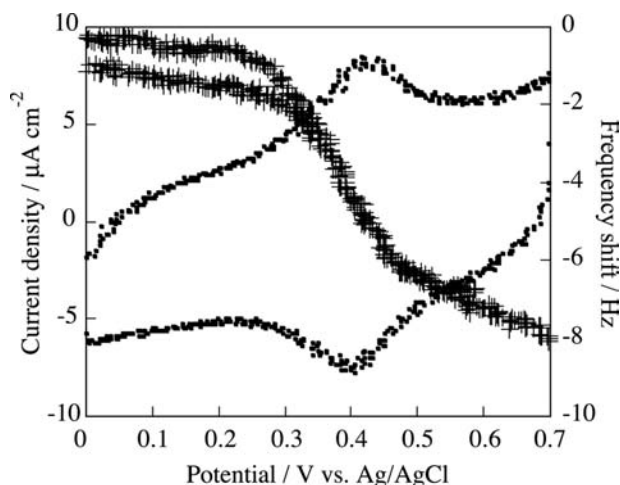
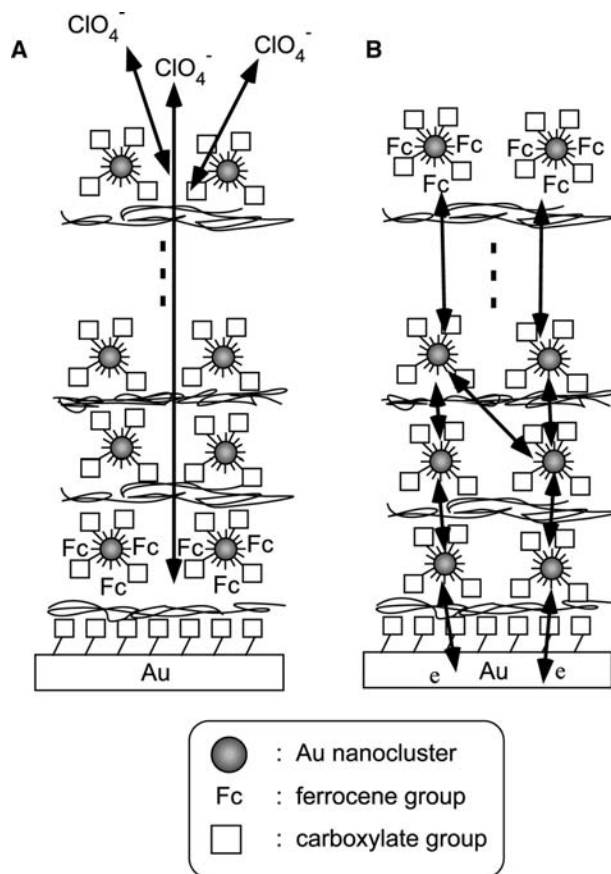


**Fig. 5** EQCM response of the Au(111)/MUA/PAH/MHF-GNC/(PAH/MH-GNC) $_9$  electrode measured in 0.1 M  $\text{HClO}_4$  aqueous solution at a scan rate of  $10 \text{ mV sec}^{-1}$ . Source: From Ref.<sup>[41]</sup>.

affected by the number of the PAH/MH-GNC overlayers, confirming that perchlorate ions are transferred between the electrolyte solution and the ferrocene group at the innermost layer through the PAH/MH-GNC. The mpe values obtained for Au/MUA/PAH/MHF-GNC/(PAH/MH-GNC) $_n$  ( $n = 3, 6,$  and  $9$ ) are in good agreement with the value observed at the gold electrode modified with PAH/MHF-GNC multilayers ( $245 \text{ g/mol electron}$ ) and are much larger than the molar mass of perchlorate ion ( $99.5 \text{ g/mol}$ ), suggesting that each perchlorate ion moves into and is released from the modified layer accompanied by 5–7 water molecules upon the oxidation and reduction of the ferrocene moiety, respectively.

Because the distance between the ferrocene group in the outermost layer and the gold electrode in the GNC multilayers with 10 deposition cycles is far too long for an electron to tunnel, i.e., more than 50 nm as evidenced from both cross-sectional transmission electron microscopy and ellipsometry, electron should be transferred between the ferrocene group and the gold electrode not by direct tunneling, but through the GNCs by hopping.



**Scheme 2** Schematically idealized model for the charge transfer during the redox of the ferrocene moiety.

## CONCLUSION

Two types of GNCs, one covered by SAMs of MUA, C<sub>6</sub>SH, and FcC<sub>6</sub>SH, MHF-GNC, and the other with MUA and C<sub>6</sub>SH, MH-GNC, were used for the construction of GNC multilayers on the MUA-modified Au(111) and ITO surfaces based on the carboxylate/polycation (PAH)/carboxylate electrostatic interaction. Electrochemical measurements at the GNC/PAH multilayer-modified gold and ITO electrodes showed that the amount of GNC adsorbed on the ITO surface was larger than that of the Au electrode, indicating the different packing arrangements of GNC on the two surfaces. Both the underlying substrate and the adsorbed MUA molecules seem to play important roles in the GNC/polymer multilayer organization. Results of electrochemical studies on the two series of multilayers of MHF-GNC and MH-GNC layers of different sequences on Au and ITO surfaces by placing MHF-GNC either as the layer closest to the gold electrode, i.e., the first layer, or as the outermost layer with MH-GNC in the other showed that both electrons and anions transferred readily through these multilayers. The results of the present study imply that 1) stable GNC multilayers can be constructed on gold and ITO surfaces through LBL assembling processes, 2) the amount of GNCs and their packing arrangement in the multilayers can be tuned by the number of deposition cycles and selection of underlying substrate, and 3) the charges, i.e., electron and anion, are transported through these multilayers as shown in Scheme 2 and the charge transport is facile.

## ACKNOWLEDGMENTS

WS acknowledges the Japan Society for the Promotion of Science for a Postdoctoral Fellowship for foreign researchers. Part of this work was supported by Grants-in-Aid for Scientific Research from the Ministry of Education, Culture, Sports, Science, and Technology, Japan (Nos. 13304047, 13554026, and 13874085). We would like to thank Prof. Shimazu and Dr. Sugawara for their help with the XPS and TEM measurements, respectively.

## REFERENCES

1. Brust, M.; Walker, M.; Bethell, D.; Schiffrin, D.J.; Whyman, R. Synthesis of thiol derivatised gold nanoparticles in a two-phase liquid/liquid system. *J. Chem. Soc., Chem. Commun.* **1994**, 801–802.
2. Freeman, R.G.; Graber, K.C.; Allison, K.J.; Bright, R.M.; Davis, J.A.; Guthrie, A.P.; Hommer, M.B.; Jackson, M.A.; Smith, P.C.; Walter, D.G.; Natan, M.J. Self-assembled metal colloid monolayers: an approach to SERS substrate. *Science* **1995**, *267*, 1629–1632.
3. Mirkin, C.A.; Letsinger, R.L.; Mucic, R.C.; Storhoff, J.J. A DNA-based method for rationally assembling nanoparticles into macroscopic materials. *Nature* **1996**, *382*, 607–611.
4. Reynolds, R.A., III; Mirkin, C.A.; Letsinger, R.L. A gold nanoparticle/latex microsphere-based colorimetric oligonucleotide detection method. *Pure Appl. Chem.* **2000**, *72* (1–2), 229–235.
5. Schaaff, T.G.; Shafiqullin, M.N.; Khoury, J.T.; Vezmar, I.; Whetten, R.L.; Cullen, W.G.; First, P.N. Isolation of smaller nanocrystal Au molecules: Robust quantum effects in optical spectra. *J. Phys. Chem., B* **1997**, *101* (40), 7885–7891.
6. Gittins, D.I.; Bethell, D.; Shiffrin, D.J.; Nichols, R.J. A nanometre-scale electronic switch consisting of a metal cluster and redox-addressable groups. *Nature* **2000**, *408*, 67–69.
7. Green, S.J.; Stokes, J.J.; Hostetler, M.J.; Pietron, J.J.; Murray, R.W. Three-dimensional monolayers: nanometer-sized electrodes of alkanethiolate-stabilized gold cluster molecules. *J. Phys. Chem., B* **1997**, *101* (14), 2663–2668.
8. Chen, S.; Murray, R.W.; Feldberg, S.W. Quantized capacitance charging of monolayer-protected Au clusters. *J. Phys. Chem., B* **1998**, *102* (49), 9898–9907.
9. Hostetler, M.J.; Templeton, A.C.; Murray, R.W. Dynamics of place-exchange reactions on monolayer-protected gold cluster molecules. *Langmuir* **1999**, *15* (11), 3782–3789.
10. Templeton, A.C.; Zamborini, F.P.; Wuelfing, W.P.; Murray, R.W. Controlled and reversible formation of nanoparticle aggregates and films using Cu<sup>2+</sup>-carboxylate chemistry. *Langmuir* **2000**, *16* (16), 6682–6688.
11. Zamborini, F.P.; Hicks, J.F.; Murray, R.W. Quantized double layer charging of nanoparticle films assembled using carboxylate/(Cu<sup>2+</sup> or Zn<sup>2+</sup>)/carboxylate bridges. *J. Am. Chem. Soc.* **2000**, *122* (18), 4514–4515.
12. Hicks, J.F.; Zamborini, F.P.; Osisek, A.J.; Murray, R.W. The dynamics of electron self-exchange between nanoparticles. *J. Am. Chem. Soc.* **2001**, *123* (29), 7048–7053.
13. Wuelfing, W.P.; Murray, R.W. Electron hopping through films of arenethiolate monolayer-protected gold clusters. *J. Phys. Chem., B* **2002**, *106* (12), 3139–3145.
14. Hicks, J.F.; Seok-Shon, Y.; Murray, R.W. Layer-by-layer growth of polymer/nanoparticle films containing monolayer-protected gold clusters. *Langmuir* **2002**, *18* (6), 2288–2294.
15. Wuelfing, W.P.; Green, S.J.; Pietron, J.J.; Cliffel, D.E.; Murray, R.W. Electronic conductivity of solid-state, mixed-valent, monolayer-protected Au clusters. *J. Am. Chem. Soc.* **2000**, *122* (46), 11465–11472.
16. Horikoshi, T.; Itoh, M.; Kurihara, M.; Kubo, K.; Nishihara, H. Synthesis, redox behavior and electrode position of biferrocene-modified gold clusters. *J. Electroanal. Chem.* **1999**, *473* (1–2), 113–116.



17. Men, Y.; Kubo, K.; Kurihara, M.; Nishihara, H. Redox behavior of biferrocene dithiol and disulfide derivatives in SAMs with and without gold clusters on the gold substrate. *Phys. Chem. Chem. Phys.* **2001**, *3* (16), 3427–3430.
18. Ulman, A. *An Introduction to Ultrathin Organic Films from Langmuir–Blodgett to Self-Assembly*; Academic Press: San Diego, CA, 1991.
19. Finklea, H.O. Electrochemistry of Organized Monolayers of Thiols and Related Monolayers on Electrodes. In *Electroanalytical Chemistry*; Bard, A.J., Rubinstein, I., Eds.; Marcel Dekker, Inc.: New York, 1996; 19, 110–333.
20. Kondo, T.; Ito, T.; Nomura, S.; Uosaki, K. Photoelectrochemical characteristics of a self-assembled monolayer of porphyrin-mercaptoquinone coupling molecules. *Thin Solid Films* **1996**, *284–285*, 652–655.
21. Kondo, T.; Yanagida, M.; Nomura, S.; Ito, T.; Uosaki, K. pH dependent photoinduced electron transfer at the gold electrode modified with self-assembled monolayers of porphyrin-mercaptoquinone coupling molecule. *J. Electroanal. Chem.* **1997**, *438* (1–2), 121–126.
22. Kondo, T.; Iso-o, K.; Kanai, T.; Uosaki, K. Effects of alkylchain length on the efficiency of photoinduced electron transfer at gold electrodes modified with self-assembled monolayers of molecules containing porphyrin, ferrocene and thiol separated each other by alkylthiols. *Z. Phys. Chem.* **1999**, *212* (1), 23–30.
23. Kondo, T.; Yanagida, M.; Zhang, X.-Q.; Uosaki, K. Effect of surface morphology of a gold substrate on photocurrent efficiency at a gold electrode modified with a self-assembled monolayer of a porphyrin-ferrocene-thiol linked molecule. *Chem. Lett.* **2000**, *29* (8), 964–965.
24. Uosaki, K.; Kondo, T.; Zhang, X.-Q.; Yanagida, M. Very efficient visible-light-induced uphill electron transfer at a self-assembled monolayer with a porphyrin-ferrocene-thiol linked molecule. *J. Am. Chem. Soc.* **1997**, *119* (35), 8367–8368.
25. Kondo, T.; Horiuchi, S.; Yagi, I.; Ye, S.; Uosaki, K. Electrochemical control of the second harmonic generation property of self-assembled monolayers containing a *trans*-ferrocenyl-nitrophenyl ethylene group on gold. *J. Am. Chem. Soc.* **1999**, *121* (2), 391–398.
26. Yanagida, M.; Kanai, T.; Zhang, X.Q.; Kondo, T.; Uosaki, K. Angle resolved X-ray photoelectron spectroscopic study on a self-assembled monolayer of a porphyrin-ferrocene-thiol linked molecule on gold: Evidence for a highly ordered arrangement for efficient photoinduced electron transfer. *Bull. Chem. Soc. Jpn.* **1998**, *71* (11), 2555–2559.
27. Kondo, T.; Kanai, T.; Uosaki, K. Control of the charge-transfer rate at a gold electrode modified with a self-assembled monolayer containing ferrocene and azobenzene by electro- and photochemical structural conversion of *cis* and *trans* forms of the azobenzene moiety. *Langmuir* **2001**, *17* (20), 6317–6324.
28. Colvin, V.L.; Goldstain, A.N.; Alivisatos, A.P. Semiconductor nanocrystals covalently bound to metal surfaces with self-assembled monolayers. *J. Am. Chem. Soc.* **1992**, *114* (13), 5221–5230.
29. Ogawa, S.; Fan, F.R.F.; Bard, A.J. Scanning tunneling microscopy, tunneling spectroscopy, and photoelectrochemistry of a film of Q-CdS particles incorporated in a self-assembled monolayer on a gold surface. *J. Phys. Chem.* **1995**, *99* (28), 11,182–11,189.
30. Nakanishi, T.; Ohtani, B.; Uosaki, K. Fabrication and characterization of CdS-nanoparticle mono- and multilayers on a self-assembled monolayer of alkanedithiols on gold. *J. Phys. Chem., B* **1998**, *102* (9), 1571–1577.
31. Inoue, H.; Ichiroku, N.; Torimoto, T.; Sakata, T.; Mori, H.; Yoneyama, H. Photoinduced electron transfer from Zinc sulfide microcrystals modified with various alkanethiols to methyl viologen. *Langmuir* **1994**, *10* (12), 4517–4522.
32. Torimoto, T.; Tsumura, N.; Miyake, M.; Nishizawa, M.; Sakata, T.; Mori, H.; Yoneyama, H. Preparation and photoelectrochemical properties of two-dimensionally organized CdS nanoparticle thin films. *Langmuir* **1999**, *15* (5), 1853–1858.
33. Decher, G. Fuzzy nanoassemblies: Toward layered polymeric multicomposites. *Science* **1997**, *277*, 1232–1237.
34. Templeton, A.C.; Wuelfing, W.P.; Murray, R.W. Monolayer-protected cluster molecules. *Acc. Chem. Res.* **2000**, *33* (1), 27–36.
35. Ostrander, J.W.; Mamedov, A.A.; Kotov, N.A. Two modes of linear layer-by-layer growth of nanoparticle-polyelectrolyte multilayers and different interactions in the layer-by-layer deposition. *J. Am. Chem. Soc.* **2001**, *123* (6), 1101–1110.
36. Clavilier, J.; Faure, R.; Guinet, G.; Durand, R. Preparation of monocrystalline Pt microelectrodes and electrochemical study of the plane surfaces cut in the direction of the 111 and 110 planes. *J. Electroanal. Chem.* **1980**, *107* (1), 205–209.
37. Clavilier, J. The role of anion on the electrochemical behaviour of a 111 platinum surface an unusual splitting of the voltammogram in the hydrogen region. *J. Electroanal. Chem.* **1980**, *107* (1), 211–216.
38. Uosaki, K.; Ye, S.; Kondo, T. Preparation of a highly ordered Au (111) phase on a polycrystalline gold substrate by vacuum deposition and its characterization by XRD, GISXRD, STM/AFM, and electrochemical measurements. *J. Phys. Chem.* **1995**, *99* (38), 14,117–14,122.
39. Kondo, T.; Okamura, M.; Uosaki, K. Formation and electrochemical characteristics of multilayers of Au nanoclusters covered by mixed self-assembled monolayers of three kinds of alkanethiols with methyl, ferrocene, or carboxylate terminal group on Au(111) surface. *Chem. Lett.* **2001**, *30* (9), 930–931.
40. Uosaki, K.; Kondo, T.; Okamura, M.; Song, W. Electron and ion transfer through multilayers of gold nanoclusters covered by self-assembled monolayers of alkylthiols with various functional groups. *Faraday Discuss.* **2002**, *121*, 373–389.
41. Song, W.; Okamura, M.; Kondo, T.; Uosaki, K. Electron and ion transport through multilayers of Au

- nanoclusters covered by self-assembled monolayers. *J. Electroanal. Chem.* **2003**, *554–555*, 385–393.
42. Uosaki, K.; Sato, Y.; Kita, H. Electrochemical characteristics of a gold electrode modified with a self-assembled monolayer of ferrocenylalkanethiols. *Langmuir* **1991**, *7* (7), 1510–1514.
  43. Rowe, G.K.; Creager, S.E. Redox and ion-pairing thermodynamics in self-assembled monolayers. *Langmuir* **1991**, *7* (10), 2307–2312.
  44. Kondo, T.; Okamura, M.; Uosaki, K. Anion effect on the electrochemical characteristics of a gold electrode modified with a self-assembled monolayer of ferrocenylhexanethiol in aqueous and dichloromethane solutions. *J. Organomet. Chem.* **2001**, *637–639*, 841–844.
  45. Delahay, P. *Double Layer and Electrode Kinetics*; Interscience: New York, 1965.
  46. Sato, Y.; Uosaki, K. Formation and electrochemical characteristics of self-assembled monolayer of 11-ferrocenylundecanethiol on indium–tin-oxide. *Denki Kagaku* **1994**, *62* (12), 1269–1275.
  47. Uosaki, K.; Sato, Y.; Kita, H. A self-assembled monolayer of ferrocenylalkene thiols on gold as an electron mediator for the reduction of Fe(III)–EDTA in solution. *Electrochim. Acta* **1991**, *36* (11–12), 1799–1801.

# Layer-by-Layer Assembly of Polyelectrolyte Films: Membranes and Catalysts

**Bernd Tieke**

*Institut für Physikalische Chemie, Universität zu Köln, Köln, Germany*

**Ali Toutianoush**

*Universität zu Köln, Köln, Germany*

## INTRODUCTION

Polyelectrolyte multilayers prepared upon alternate electrostatic adsorption of positively and negatively charged polymers have recently shown promise as membranes and catalysts. Recent progress in the preparation of membranes for gas separation, separation of liquid mixtures under pervaporation conditions, ion separation under dialysis conditions, salt transport under nanofiltration (NF) and reverse osmosis conditions, separation of enantiomers, and others have been reported. The purpose of this article is to summarize recent activities in the field of membrane<sup>[30–50]</sup> and catalyst applications<sup>[51–78]</sup> of polyelectrolyte multilayer assemblies. It describes the use of polyelectrolyte multilayers as carriers for catalysts and biocatalysts, and then covers examples of catalyzed reactions such as enzyme reactions, photocatalytic reactions, and metal-catalyzed processes.

## BACKGROUND OF MULTILAYER FILMS

About a decade ago, Decher and coworkers<sup>[1–4]</sup> reported on a new method to prepare ultrathin polymer films, based on the alternate electrostatic adsorption of cationic and anionic polyelectrolytes on solid substrates. Meanwhile, the layer-by-layer deposition technique developed into a standard method for preparation of polymer films with controlled structure and thickness in the nanometer range. Numerous studies appeared, which were either concerned with fundamental aspects of film growth, structure, and morphology,<sup>[5–22]</sup> or with the preparation and characterization of functional polyelectrolyte multilayers with photo- and electroactive properties applicable in micro- and optoelectronic devices. The state of the art has recently been reviewed in books<sup>[23,24]</sup> and articles.<sup>[25–29]</sup>

Probably one of the most interesting properties of polyelectrolyte multilayer assemblies is their selectivity in the transport of gases,<sup>[30–34]</sup> solvent mixtures,<sup>[35–42]</sup>

ions,<sup>[43–47]</sup> and enantiomers.<sup>[48]</sup> In several studies, the use of polyelectrolyte multilayers as membranes was demonstrated, e.g., for dehydration of organic solvents under pervaporation conditions,<sup>[35–42]</sup> for water softening and desalination under nanofiltration<sup>[49,50]</sup> and reverse osmosis<sup>[49]</sup> conditions, respectively. Furthermore, the incorporation of biocatalysts<sup>[51–68]</sup> and inorganic catalysts<sup>[69–78]</sup> opened a new area for the formation of membrane reactors and catalytic membranes. Early studies demonstrate the utility of the polyelectrolyte multilayers as reactors and catalysts.<sup>[51–78]</sup>

## PREPARATION OF MEMBRANES

Soon after the method of layer-by-layer assembly of polyelectrolytes was reported, ultrathin polyelectrolyte multilayers were studied as permselective membranes. In a typical process of membrane preparation, a negatively charged porous or nonporous supporting membrane is dipped into a dilute aqueous solution of a positively charged polyelectrolyte so that the polymer is adsorbed at the substrate surface as a molecularly thin film and the surface charge is reverted (Fig. 1). After careful washing, the coated substrate is dipped into the aqueous solution of a negatively charged polyelectrolyte so that this polymer is adsorbed on top of the previous one and the surface charge is reverted again. By repeating the adsorption steps several times, a polyelectrolyte multilayer is obtained, whose thickness is adjustable between a few nanometers and about half a micrometer by varying the number of dipping cycles. Scanning electron micrographs<sup>[44,79]</sup> indicate that the polyelectrolytes do not enter and block the pores of the support, but a smooth coating of the substructure with a dense and defect-free polyelectrolyte skin layer is obtained. Previous studies of materials transport across polyelectrolyte multilayer membranes have recently been reviewed.<sup>[79–87]</sup> Here an updated summary of the research activities is presented.

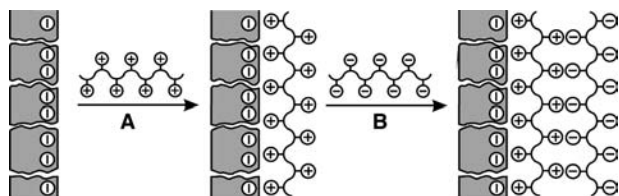


**Fig. 1** Scheme of layer-by-layer assembly of polyelectrolytes on activated porous supporting membrane. The separating membrane is obtained upon multiple repetition of steps A and B. In reality, pore diameters are 20–200 nm, while polymer chains are less ordered and partially overlapping. *Source:* From Ref.<sup>[38]</sup>.

## STUDIES OF MATERIALS TRANSPORT ACROSS POLYELECTROLYTE MULTILAYERS

### Gas Permeation

At first, studies on the transport behavior across polyelectrolyte multilayers were concerned with gas permeation.<sup>[30–33]</sup> Membranes were prepared from porous supports (Celgard,<sup>[30,32]</sup> Isopore,<sup>[32]</sup> and polyacrylonitrile/polyethylene terephthalate PAN/PET<sup>[32]</sup>), as well as nonporous supports (silicone,<sup>[30]</sup> polymethylpentene,<sup>[31]</sup> and Nafion<sup>[33]</sup>). Poly(allylamine hydrochloride) (PAH) and poly(styrenesulfonate sodium salt) (PSS) were mostly used as the polyelectrolytes. Up to a hundred layer pairs were deposited, which caused a reduction of the membrane permeability by more than a factor of  $10^3$ . Theoretical selectivities in gas permeation were generally low. For  $\text{CO}_2/\text{N}_2$  separation, a selectivity of 2.4 was reported,<sup>[32]</sup> for oxygen/nitrogen permeation the highest selectivity was 3.5.<sup>[33]</sup> This value was obtained by using a polyelectrolyte couple of PSS and poly(*N*-octadecyl-2-ethynylpyridinium bromide), a substituted polyacetylene derivative. The selectivity was ascribed to the high affinity of the unsaturated  $\text{C}=\text{C}$  bonds to oxygen.

Only recently, better results were obtained, when PAH and polyamic acids were alternately deposited followed by heat-induced imidization at  $250^\circ\text{C}$  for 2 hr.<sup>[34]</sup> The resulting polyimide multilayer membranes showed  $\text{O}_2/\text{N}_2$  selectivities of up to 6.9 and  $\text{CO}_2/\text{CH}_4$  selectivities of up to 68.

### Pervaporation of Alcohol/Water Mixtures

Polyelectrolyte multilayer assemblies were also tested as pervaporation membranes. An initial study was reported by van Ackern et al.<sup>[32]</sup> Using PAH/PSS separating membranes on a PAN/PET support, they tried to separate ethanol/water and benzene/cyclohexane mixtures. The separation was only modest, but

after a careful adjustment of several parameters the ethanol–water separation could be considerably improved.<sup>[35–40]</sup> It was found that membranes with high efficiency in alcohol/water pervaporation separation require the following.

- The use of polyelectrolytes of high charge density such as polyethyleneimine (PEI),<sup>[37,38]</sup> polyvinylamine (PVA),<sup>[38–40]</sup> polyvinylsulfate (PVS),<sup>[38–40]</sup> polyacrylic acid (PAA),<sup>[40]</sup> or polyvinylsulfonate (PVSu).<sup>[40]</sup> These polyelectrolytes form complexes with small pore size and large hydrophilicity, which favors the transport of water across the membrane.
- The use of polyelectrolyte solutions of either low pH (1.7) with a high concentration of supporting electrolyte (e.g., 1 M NaCl),<sup>[38,40]</sup> or neutral pH without supporting electrolyte for preparation of the membranes.<sup>[40]</sup> In the former case, very thick polyelectrolyte layers are adsorbed,<sup>[2,3]</sup> a thick membrane with low flux and good separation is obtained. In the latter case, very thin and smooth layers are adsorbed.<sup>[16]</sup> A thin but very dense membrane with good separation efficiency is obtained.
- Deposition of a large number of layer pairs (approximately 60) to avoid voids and defects in the membrane.<sup>[35,40]</sup>
- Annealing<sup>[35–38]</sup> of the membrane for 1 hr at  $90^\circ\text{C}$  to smoothen the surface and to heal defects in the

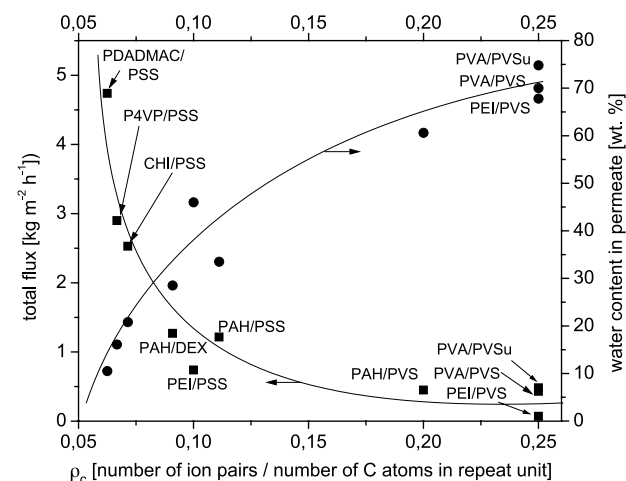
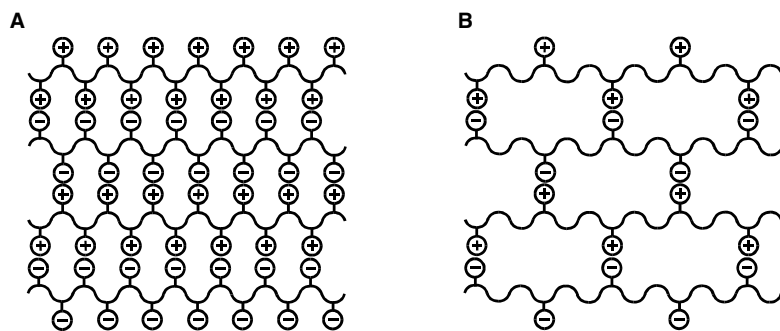


**Fig. 2** Separation characteristics of polyelectrolyte multilayer membranes (60 layer pairs) as a function of the charge density  $\rho$  of the polyelectrolyte complex. Feed solution, ethanol/water (93.8:6.2) (w/w); pervaporation temperature,  $58.5^\circ\text{C}$ . PAH: poly(allylamine); P4VP: poly(4-vinylpyridine); CHI: chitosan; PVA: poly(vinylamine); PDADMA: poly(diallyldimethylammonium bromide); PEI: branched poly(ethyleneimine); PSS: poly(styrenesulfonate); DEX: dextrane; PVS: poly(vinylsulfate); PAA: poly(acrylic acid). *Source:* From Ref.<sup>[38]</sup>.



$$\text{Charge density } \rho_c = \left[ \frac{\text{number of ion pairs per repeat unit of polyion complex}}{\text{number of carbon atoms per repeat unit of polyion complex}} \right]$$

**Fig. 3** Simplified structure model of polyelectrolyte multilayer membrane of high (A) and low (B) charge density  $\rho$ . Note that the nanopores become larger and less hydrophilic if  $\rho$  decreases. The model does not take into account possible chain interdigitation and incomplete ionization. *Source:* From Ref.<sup>[38]</sup>.

polyelectrolyte multilayer, which was especially useful in case of PEI/PVS membranes.<sup>[37]</sup>

- A pervaporation temperature of about 60°C or higher.<sup>[35,37]</sup>

The use of polyelectrolytes of high charge density<sup>[37–40,42]</sup> is especially crucial for obtaining high selectivities. This is demonstrated in Fig. 2, which shows a plot of the total flux and water content in the permeate vs. the charge density  $\rho_c$  of the polyelectrolyte complex. It can be seen that the lowest flux and the highest water content in the permeate are obtained for the membranes made from polyelectrolytes of the highest  $\rho_c$  values. The separation behavior was explained in terms of the nanopores model<sup>[86,87]</sup> shown in Fig. 3. The alternately adsorbed polycations and polyanions form a network structure, in which the polymer-bound ion pairs represent the cross-linking units. For polyelectrolytes of high charge density, a much closer network is obtained as for polyelectrolytes of low charge density. Because each pore of the network contains an ion pair, a network with narrow pores will be more hydrophilic and preferentially permeable for the small and polar water molecules, while a network with larger pore size will be less hydrophilic and more permeable for the bigger, more hydrophobic alcohol molecules. The correlation between  $\rho_c$  and the membrane selectivity holds for most of the polyelectrolytes and can even be used to predict the separation capability of unknown polyelectrolyte couples. This is surprising, because specific structural elements, such as the presence of aromatic rings, chain branching, or nature of the ionic groups, have not been taken into account yet. More detailed studies on structure/property relationships were undertaken by Toutianoush and Tieke,<sup>[40]</sup> when they studied influences of the nature of the anionic polyelectrolyte groups on the separation behavior. For this purpose, three multilayer membranes with same high charge density, but different anionic substituent groups were investigated. The polycation was always

PVA, the polyanion was either PVSu, PVS, or PAA. With increasing acidity of the polyanion, i.e., from PAA to PVSu, the membranes became increasingly hydrophilic. Therefore PVA/PVSu membranes were especially suited to remove small amounts of water from organic solvents, while the less hydrophilic PVA/PAA membranes showed the best performance at high water content of the mixture.

Using the PVA/PVSu membrane, a series of alcohol/water mixtures with alcohols of different hydrophobicity were studied.<sup>[40]</sup> As can be derived from Fig. 4, the flux and separation increased, if the hydrophilicity of the alcohols decreased. For a *t*-butanol/water (9:1) mixture, for example, a total flux  $J$  of about 2.18 kg<sup>-2</sup> h<sup>-1</sup>, a water content in the permeate of 99.9%, a separation factor  $\alpha$  of about 9000, and a separation efficiency (pervaporation separation index, PSI)  $\alpha J$  of  $1.96 \times 10^7$  were found, the pervaporation temperature being 58.5°C. The PVA/PVS membrane showed similar behavior.<sup>[39]</sup> The excellent separation is primarily a result of the lower solubility of the more hydrophobic alcohols in the multilayer membrane, and secondly, a weaker hydrogen bonding between the more hydrophobic alcohol and water molecules.

### Ion Permeation

From earlier studies,<sup>[88,89]</sup> it is known that the sequential solution casting of a cationic and an anionic polyelectrolyte leads to a so-called bipolar membrane. In such a membrane, permeating ions receive strong repulsive forces from the equally charged parts (Donnan rejection) and attractive forces from the oppositely charged parts (Donnan attraction) of the membrane. For divalent permeating ions, the interactions are much stronger than for monovalent ones and thus, a high selectivity in ion transport occurs. Polyelectrolyte multilayers resemble in their architecture the bipolar membranes except that the multilayer structure causes

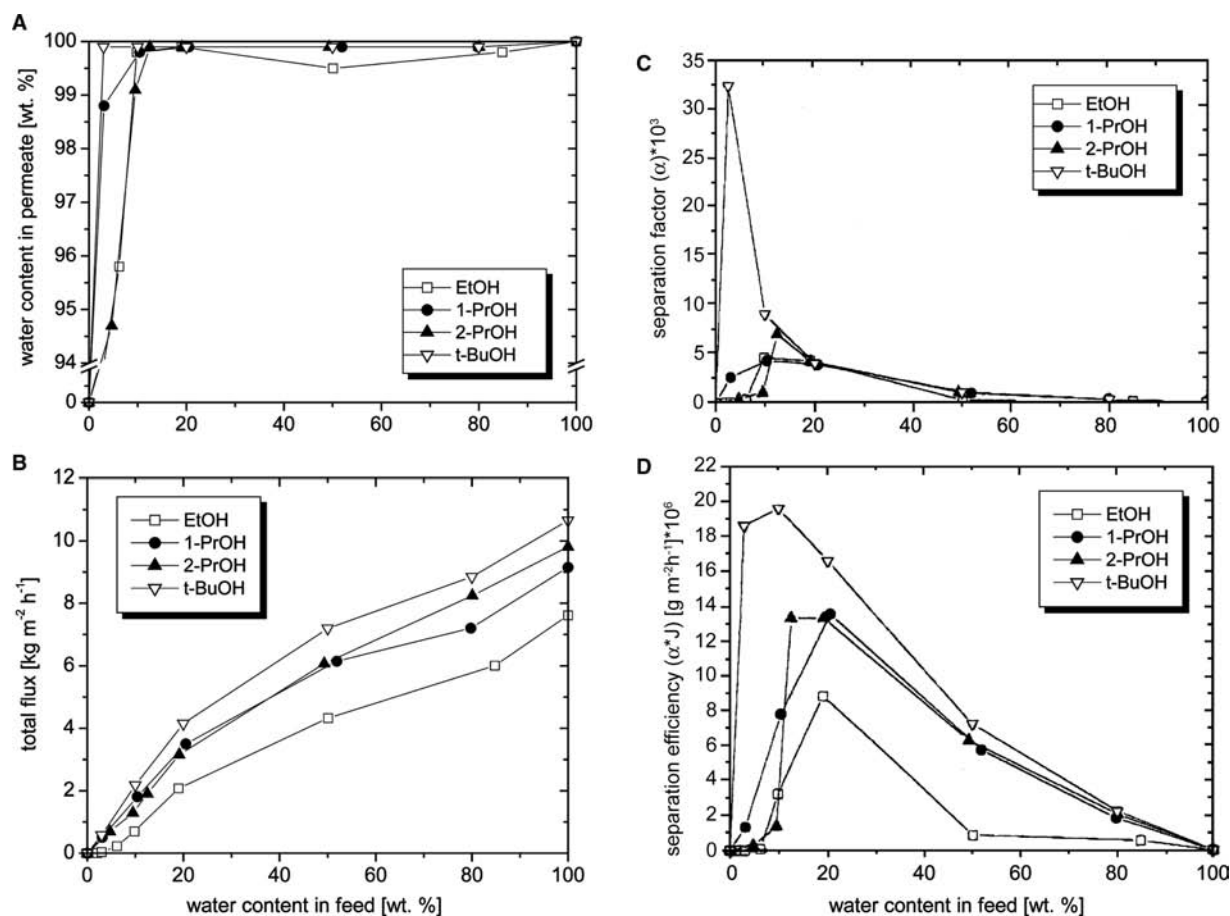


**Fig. 4** Separation characteristics of a PVA/PVSV membrane (60 bilayers) for various alcohol/water feed mixtures. Plot of water content in permeate (A), total flux (B), separation factor  $\alpha$  (C), and separation efficiency (D) vs. water content in feed mixture. Pervaporation temperature, 58.5°C. Source: From Ref.<sup>[79]</sup>.

a multipolar character of the membrane. A corresponding structure model<sup>[43]</sup> is shown in Fig. 5 and indicates that divalent ions will receive much stronger repulsive forces than monovalent ones. The model agrees with experimental results showing that the

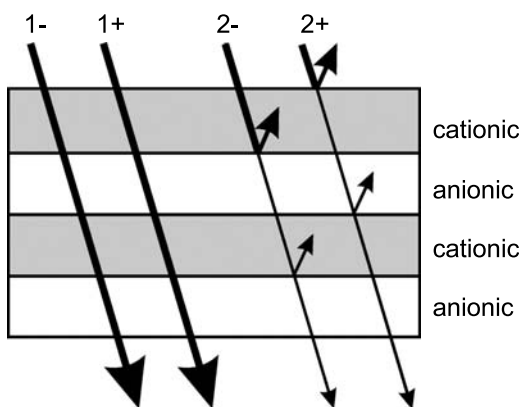


**Fig. 5** Rejection model of the multipolar polyelectrolyte multilayer membrane. Source: From Ref.<sup>[45]</sup>.

permeation rate of sodium chloride across a PAH/PSS membrane is at least 15 times higher than for magnesium chloride.<sup>[36]</sup> After careful adjustment of several parameters, Krasemann and Tieke<sup>[43]</sup> reported theoretical selectivities  $\alpha(\text{Na}^+/\text{Mg}^{2+})$  of up to 112.5 and  $\alpha(\text{Cl}^-/\text{SO}_4^{2-})$  of up to 45. The  $P_R$  values were dependent on the number of deposited layers, the charge density of the polyelectrolytes, pH, and ionic strength of the polyelectrolyte solutions used for membrane preparation. The high transport selectivity was confirmed by the study of Harris et al.<sup>[44]</sup> on anion permeation. The authors used porous aluminum oxide as support, the pore size in the skin layer was about 20 nm. The inorganic substrate was coated with several PAH/PSS layers, the  $\alpha(\text{Cl}^-/\text{SO}_4^{2-})$  and  $\alpha(\text{Cl}^-/\text{Fe}(\text{CN})_6^{3-})$  values being 7 and 310, respectively. For PAH/PAA membranes, the selectivity was comparable, but the anion flux was three times smaller.

In a more recent study, Toutianoush and Tieke<sup>[45]</sup> investigated the ion transport across highly charged PVA/PVSV membranes. In agreement with the transport model based on Donnan exclusion/inclusion, it



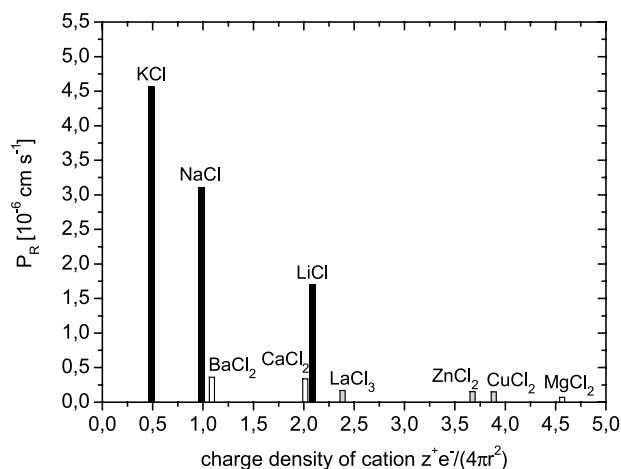
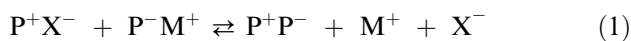


**Fig. 6** Plot of the permeation rates of various chloride salts against the charge density  $z^+e^-/4\pi r^2$  of the nonhydrated metal cations ( $z^+$ : charge number of ion;  $r$ : radius of metal cation). Membrane: 60 layer pairs PVA/PVS. Electrolyte concentration of aqueous feed solution: 0.1 M. Source: From Ref.<sup>[79]</sup>.

could be shown that the permeation rates of alkali and earth alkaline metal cations increase from Li to K, and from Mg to Ba, that is in the direction of decreasing charge density of the naked ions (Fig. 6). In the study of the permeation of NaCl, MgCl<sub>2</sub>, Na<sub>2</sub>SO<sub>4</sub>, and MgSO<sub>4</sub>, it was found that  $P_R$  values increased in the sequence 2.2-electrolyte < 2.1-electrolyte  $\cong$  1.2-electrolyte < 1.1-electrolyte, again in the direction of decreasing charge density of the ions. Furthermore, it was found that the influence of the surface charge on the permeation rates was negligible for thick membranes consisting of more than 50 bilayers. The effect of salt concentration on  $P_R$  was also studied. Up to a concentration of 0.3 mol L<sup>-1</sup>, the  $P_R$  values of NaCl or MgCl<sub>2</sub> changed only slightly, and the selectivity of the membrane was essentially maintained. However, at higher electrolyte concentration, a significant increase in ion flux was found and the selectivity dropped strongly. The effect can be explained by considering the equilibrium (1) of polyelectrolyte complex formation<sup>[46,80,83]</sup>



with  $P^+$  and  $P^-$  being charged segments of the cationic and anionic polyelectrolytes. At high concentration of permeating  $M^+$  and  $X^-$  ions, the equilibrium begins to shift to the left side. Dissociation of the polymer-bound  $P^+P^-$  pairs sets in, the pore size of the membrane increases and the flow of the electrolyte solution becomes progressively higher and less selective.

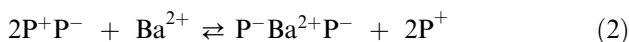
Lebedev et al.<sup>[90]</sup> modeled the salt permeability of a fixed-charge multilayer membrane taking into account the charge number of the salt ions, the diffusion

boundary layers flanking the membrane, and the different values of the ion diffusion coefficients in these layers and the membrane. The theoretical model was used in the Nernst–Planck equations together with the Donnan theory for the ionic equilibria at the membrane boundaries. Their calculations qualitatively reproduced the experimental results, but the theoretical permeabilities were considerably higher, if the experimental layer thickness was introduced.

The model of Donnan exclusion/attraction is based on the assumption that some of the polymer-bound charges within the polyelectrolyte multilayer are not balanced by polymer repeat units of opposite charge, but by small, exchangeable counterions. The excess polymer-bound charges act as ion-exchanger sites and are responsible for the high transport selectivity. The extent of polymer charge compensation in polyelectrolyte multilayers is still a matter of debate. In some studies,<sup>[91,92]</sup> evidence for incomplete polymer charge compensation and presence of small ions within the multilayers was found, while in other studies,<sup>[11,12]</sup> especially on polydiallyldimethylammonium bromide (PDADMA)/PSS multilayers, the polymer charge compensation was found to be essentially complete, the charge stoichiometry being 1:1. In that case, no selectivity in ion transport can be found, as was demonstrated by Krasemann and Tieke<sup>[43]</sup> studying PDADMA/PSS multilayers. Riegler and Essler<sup>[93]</sup> suggested that polymer charge stoichiometry depends on the charge density of the polyelectrolytes. If the distance between the charges is less than the Bjerrum length, the strong binding of the counterions (Manning condensation) prevents their release during multilayer formation, and the ion exchanger sites are permanently included in the film. This applies to the PAH/PSS multilayers, while in PDADMA/PSS membranes, the charge density is low enough to cause a complete complexation.

However, Farhat and Schlenoff<sup>[46]</sup> pointed out that small ion exchanger sites can be forced into these membranes if salt is added to the external bathing solution. Under these conditions, equilibrium (1) is partially shifted to the left because some of the polymer ion pairs dissociate. The authors demonstrated that the ion exchanger sites created in this way have a strongly nonlinear effect on the transport of redox-active ferro- and ferricyanide ions across the membrane.<sup>[46]</sup> The authors also developed<sup>[94]</sup> a theoretical base for their observations by introducing a model of ion hopping between discrete sites of polymer-bound exchanger sites. However, the model does not take into account that several kinds of permeating ions, especially multivalent ions, may also receive other than electrostatic forces within the membrane. As reported by Toutianoush and Tieke,<sup>[95]</sup> di- and multivalent Cu<sup>2+</sup>, La<sup>3+</sup>, Ba<sup>2+</sup>, and hexacyanoferrate(II) ions become permanently fixed in PVA/PVS membranes, either because of a complex

formation with the polymer-bound charged sites, as in the case of copper and hexacyanoferrate ions, or to a replacement of polymer-bound charged sites by the permeating barium ions, as indicated in Eq. 2:



### Salt Transport Under Nanofiltration and Reverse Osmosis Conditions

Very recent studies<sup>[49,50]</sup> were concerned with pressure-driven transport of aqueous inorganic salt solutions across polyelectrolyte multilayer membranes. Using either a dead-end<sup>[49]</sup> or a cross-flow apparatus,<sup>[50]</sup> ion permeation was investigated under nanofiltration (NF) (5–20 bar) and reverse osmosis conditions (more than 30 bar). In a first comprehensive study, Jin et al.<sup>[49]</sup> investigated the transport of aqueous electrolyte solutions containing NaCl, Na<sub>2</sub>SO<sub>4</sub>, MgCl<sub>2</sub>, and MgSO<sub>4</sub> across multilayer membranes consisting of 60

bilayers PVA/PVS. For the two magnesium salts, a complete rejection was found independently from the concentration of the feed solution and the pressure applied (Fig. 7). For sodium chloride and sulfate, the rejections were 84% and 96% at 5 bar, and 93.5% and 98.5% at 40 bar, respectively. The ion rejection was comparable with those of commercial membranes, but the flux was lower because the less permeable PAN/PET membrane was used as the support. Nevertheless, the study demonstrated that at low pressure, polyelectrolyte multilayers are suitable for NF applications such as water softening, while at high pressure, they can be used for water desalination. In a subsequent study, Stanton et al.<sup>[50]</sup> reported NF measurements across PAH/PSS membranes consisting of only five bilayers on porous alumina. Because of the ultra-thin polyelectrolyte membrane, water flux was higher, but the ion rejection was lower than in the previous study. Again, the authors point out that the membranes are potentially attractive for NF applications such as water and salt purification.

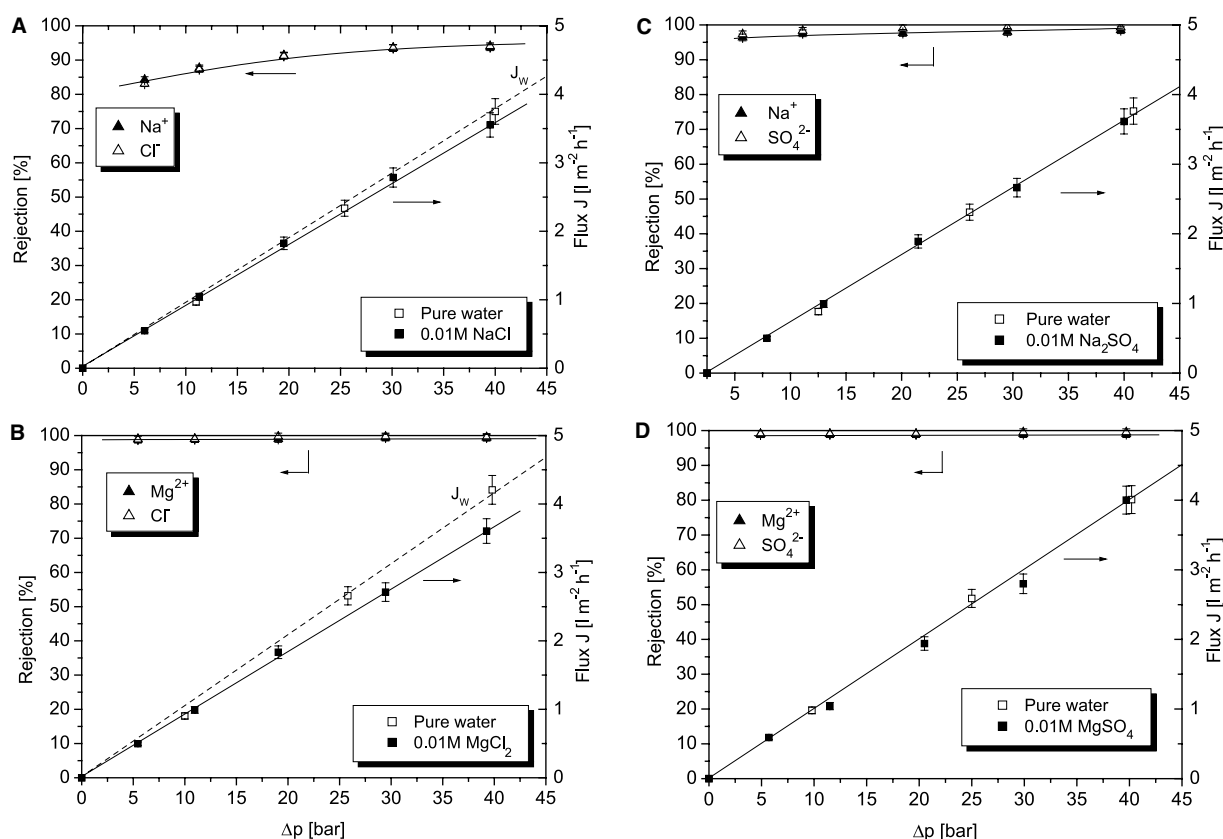


**Fig. 7** Plot of salt rejection and permeation flux  $J$  of  $10^{-2}M$  aqueous solutions of sodium chloride (A), magnesium chloride (B), sodium sulfate (C), and magnesium sulfate (D) as a function of the operative pressure  $\Delta p$ . Experiments carried out at  $20^\circ C$ ; feed solution stirred at 700 rpm.  $J_w$  indicates pure water flux. Membrane: 60 layer pairs PVA/PVS. Permeate solution was analyzed by measuring cation and anion concentration using high-performance liquid chromatography. Source: Some data were taken from Ref.<sup>[49]</sup>.

**Table 1** Percent selectivities for different membranes and chiral probes

Membrane	Percent selectivity for AA enantiomer	Percent selectivity for DOPA enantiomer
PLGA/PLL	28.1 D/L	14.1 L/D
PdGA/PdL	28.9 D/L	13.8 D/L
PdGA/PLL	0.4 D/L	0.3 D/L
PLGA/PdL	0.3 D/L	0.1 D/L

AA = ascorbic acid; DOPA = dihydroxyphenylalanine.  
Source: From Ref.<sup>[48]</sup>.

### Separation of Organic Compounds and Enantiomers

Besides small gas and solvent molecules or inorganic ions, polyelectrolyte multilayer membranes are also permeable for organic neutral molecules and ions provided they are small enough to pass the nanoporous structure of the membrane (Fig. 2). This allows the membrane to separate organic monoanions from dianions, for example, or naphthalene from the much larger pyrene or triphenylene, or phenol from hydroquinone.<sup>[96]</sup> If chiral polyelectrolytes are used for preparation of the membranes, even mixtures of enantiomeric compounds can be separated. In a recent study,<sup>[48]</sup> polyelectrolyte multilayers were prepared from polypeptides such as L- and D-poly(lysine) (PLD; PdD), L- and D-polyglutamic acid (PLGA; PdGA), and an optically active, quaternized polyvinylpyridine. As chiral probes, L- or D-ascorbic acid and 3,4-dihydroxyphenyl-L/D-alanine were used. Selectivities of up to nearly 29% were found for D/L-ascorbic acid, if PdGA/PdL membranes were used, the flux was very high (Table 1). Multilayers made from two optically active polyelectrolytes were always more selective than multilayers containing only one optically active polyelectrolyte.

### Separation of Proteins and Fouling Behavior

Polyelectrolyte multilayers were also deposited on substrates used for protein separation and filtration.<sup>[97]</sup> Celgard membranes were first treated with CO<sub>2</sub> plasma, followed by grafting of polyacrylic acid to the surface. Then a bilayer of PDADMA/PAA was adsorbed. The bilayer-modified membrane showed a much lower tendency for protein adsorption and fouling than the unmodified membrane. The flux of an aqueous solution of human serum albumin (HSA) through the modified membrane was twice as high as the flux across the merely grafted membrane.

Müller et al.<sup>[98]</sup> studied the fouling behavior of CO<sub>2</sub> plasma-treated polypropylene films modified with PEI/PAA multilayers. For the modified films,

the fouling was much lower than for the unmodified samples. Interaction of various charged model proteins such as HSA and lysozyme immunoglobulin G, and the polyelectrolyte multilayer were also investigated. Using infrared spectroscopy, small amounts of adsorbed protein were found, if the top polyelectrolyte layer and the protein were equally charged, whereas enhanced adsorption occurred for electrostatic attraction between the protein and the polyelectrolyte layer.

Graul and Schlenoff<sup>[99]</sup> also reported on the resistance of polyelectrolyte multilayers to irreversible protein adsorption. Fused silica capillaries were coated with polyelectrolyte multilayers and used for capillary zone electrophoretic separations. Basic proteins could be separated with good efficiency, and the columns were resistant to irreversible protein adsorption.

### Other Work

In a number of studies, the transport behavior of polyelectrolyte multilayers was investigated on a more fundamental, less application-oriented base. In the following, some of the papers are briefly reviewed. von Klitzing and Möhwald<sup>[100]</sup> were the first to study proton and molecular transport through polyelectrolyte multilayers. Proton transport was investigated by using PAH/PSS multilayers on glass. A fluorescent, pH-sensitive dye was embedded in the multilayers at different distances from the glass surface and the pH dependence of the fluorescence emission was studied as a function of film thickness, surface charge, and ion concentration. The data showed that the films were permeable for protons. In subsequent work,<sup>[101]</sup> the time dependence of the fluorescence of a fluorescein-labeled PAH embedded at different depth in PAH/PSS multilayer films on glass substrates was studied. Adding rhodamine to the outer phase, a quenching of the fluorescence was observed as a result of energy transfer to the permeating rhodamine molecules. Paramagnetic quenching using a spin-labeled amine-N-oxide-based compound was also studied. Because this molecule was smaller than rhodamine, the diffusion coefficient was found to be at least 2 orders-of-magnitude larger.

Harris and Bruening<sup>[102]</sup> investigated the transport of hexacyanoferrate(III) and hexaammineruthenium(III) ions across PAH/PSS and PAH/PAA films on gold electrodes using electrochemical and ellipsometric measurements. The permeability of these ions was found to depend on solution pH, number of layer pairs in the film, presence or absence of a supporting electrolyte during film deposition, and the nature of the constituent polyelectrolytes. pH-dependent measurements of ion permeation were also carried out.

In other studies, polyelectrolyte multilayer membranes were subsequently cross-linked to reduce the permeability. Upon heating, it was possible to replace the polymer-bound ion pairs of PAH/PAA multilayers by amide linkages.<sup>[103]</sup> Cross-linking of the multilayers at 130°C was found to reduce the permeability of hexacyanoferrate(III) ions to 1% of its original value. In another approach,<sup>[104]</sup> multilayer films were prepared from PAH and a maleate-based copolymer with carboxylic acid and monomethylester groups. Heating in vacuum caused more than one-half of the amino groups to be converted into imide linkages with the substituent groups of the copolymer. After cross-linking, the films displayed selective permeation of methylorange against myoglobin (Mb).

Permeability studies were also reported from polyelectrolyte multilayer capsules. Transport of small molecules such as fluorescein, 6-carboxyfluorescein, pyrene, rhodamine 6G, or ibuprofen through the multilayer wall was investigated, either from the outside to the interior of the capsules, or in the opposite direction.<sup>[105–110]</sup> The capsules were usually prepared from PAH and PSS. Capsules were found to be permeable in either direction, and the permeability could be controlled by a lipid coating of their surface,<sup>[111]</sup> by varying pH<sup>[108]</sup> or salt<sup>[109]</sup> concentration of the outside solution, or by annealing.<sup>[112]</sup> Effects of these parameters on the permeability were similar to flat multilayer membranes discussed above and thus are not further treated here.

## CATALYST APPLICATIONS

The use of polyelectrolyte multilayers as catalytic surfaces is a rather new, but interesting topic, and comparatively few publications regarding this subject are available yet. Biocatalytic films may be obtained by incorporating enzymes into the films or binding them physically or chemically to the surface; inorganic catalytic films might be obtained by incorporation of inorganic nanoparticles in the films or binding catalytically active sites to the surface. A review on biocatalytic polyelectrolyte multilayers appeared recently.<sup>[113]</sup> In the next section, the research activities on biocatalytic multilayer assemblies are compiled; then, the multilayers containing inorganic catalysts are reviewed.

### Biocatalytic Multilayer Assemblies

In an early study by Kong et al.,<sup>[51]</sup> negatively charged glucose oxidase (GOD) and bolaamphiphiles with bipyridine head groups were alternately built up on quartz slides and porous beads. For the assemblies, a high enzyme activity was reported. In a subsequent

paper,<sup>[52]</sup> the same group prepared a bolaamphiphile-based multienzyme reactor by using a 3-mercaptopropionic acid-modified gold electrode as support. The authors alternately adsorbed the cationic bolaamphiphile and anionic GOD or glucoamylase (GA). The multilayer assemblies catalyzed both the hydrolysis of maltose and the oxidation of glucose. The enzymatic activity increased with the number of GOD and GA layers, but the activity per layer decreased. The reason for this might be a limited diffusion of substrates in such condensed films.

In the following years, Kunitake et al.<sup>[53–57]</sup> prepared alternate assemblies of polyelectrolytes and enzymes and studied their catalytic activity. For example, PEI/GOD films were assembled on a quartz plate, and the reaction catalyzed by GOD was analyzed. GOD converts glucose and oxygen into gluconolactone and hydrogen peroxide, and H<sub>2</sub>O<sub>2</sub> oxidizes an indicator dye in the presence of peroxidase (POD) in aqueous solution. Finally, the blue oxidation product of the dye is monitored by ultraviolet (UV) spectroscopy. The study<sup>[55]</sup> clearly demonstrated that the activity of the enzyme was not lost in the multilayer assembly. In another study,<sup>[56]</sup> a multienzyme reactor containing PEI/GOD and PEI/GA bilayers was constructed on an ultrafiltration membrane. For the study of enzymatic activity, an aqueous starch solution was employed. When flowing across the membrane, GA decomposed starch to glucose, and GOD converted glucose to gluconolactone, thereby producing hydrogen peroxide as the product. The H<sub>2</sub>O<sub>2</sub> concentration was analyzed as described above. A high catalytic activity was found, and the efficiency of the glucose oxidation was observed to be affected by PEI/PSS intermediate layers, flow rate, and starch concentration. In another study,<sup>[57]</sup> it was found that premixing of GOD and PEI followed by alternate adsorption with PSS showed a significant increase in enzymatic activity.

Coating electrodes with enzyme/polyelectrolyte multilayers provides the basis of a biocatalytic device including an enzymatic bioreactor. Lvov et al.<sup>[58]</sup> prepared myoglobin (Mb) containing alternately assembled films at an electrode. Electrochemical reduction of the Fe<sup>III</sup> in Mb to Fe<sup>II</sup> is accompanied by H<sub>2</sub>O<sub>2</sub> formation from oxygen. H<sub>2</sub>O<sub>2</sub> is able to oxidize Fe<sup>III</sup> in the Mb into the active oxidant form ferrylmyoglobin (MbFe<sup>IV</sup>), and is thereby reduced to water. In the paper, it is demonstrated that MbFe<sup>IV</sup> is able to epoxidize styrene at the multilayer surface. Calvo et al.<sup>[59]</sup> demonstrated that GOD, lactate oxidase, and soybean peroxidase can be electrically wired to an underlying electrode through PAH with a covalently attached osmium complex. This multilayer system was able to indirectly drive lactate oxidation by the electrode via the corresponding enzyme. Earlier,

Hodak et al.<sup>[60]</sup> assembled GOD with a redoxactive poly(allylamine)ferrocene mediator on alkanethiol modified gold electrodes. GOD was found to be catalytically active in glucose oxidation, but only a small fraction of the active enzyme was electrically wired by the ferrocene polymer. Ma et al.<sup>[61]</sup> reported on electroactive Mb films grown layer-by-layer with PSS on pyrolytic graphite electrodes. Cyclic voltammetry showed the expected reversible peaks of the Mb  $\text{Fe}^{\text{III}}/\text{Fe}^{\text{II}}$  redox couple. Oxygen and trichloroacetic acid could be catalytically reduced by the Mb in the multilayer assemblies. He et al.<sup>[62]</sup> reported on multilayer devices consisting of PDADMA and the anionic bacteriorhodopsin (BR). The biological activity of BR in these assemblies could be confirmed by measuring the generation of a photocurrent.

Use of spherical particles as substrates for the enzyme-containing multilayer assemblies is advantageous because these particles offer a high surface area and a large amount of enzyme can be incorporated. Schüler and Caruso<sup>[63]</sup> reported on the construction of enzyme/polyelectrolyte multilayer films on submicrometer-sized polystyrene (PS) spheres using the layer-by-layer approach: PEI and glucose oxidase (GOD) were alternately adsorbed. Up to three layer pairs were deposited. The enzymatic activity was measured by following the coupled enzymatic reaction of GOD and horseradish peroxidase. The activity increased regularly with increasing number of GOD layers immobilized, indicating that the multilayer films were sufficiently permeable for substrate diffusion. In another study,<sup>[64]</sup> GOD, POD, or preformed enzyme-polyelectrolyte complexes were assembled in alternation with oppositely charged polyelectrolytes onto PS particles. Particles coated with the preformed enzyme-polyelectrolyte complexes displayed a significantly lower enzymatic activity (by up to 70%) than those fabricated by direct adsorption of the free enzyme. Furthermore, experiments were conducted with particles exhibiting both magnetic and catalytic functions. Magnetic support materials are widely used in biotechnology because they can easily be separated. For this purpose, 200 nm PS particles that were pre-coated with four layers of  $\text{Fe}_3\text{O}_4$  nanoparticles and PDADMA, followed by two PAH/PSS additional polyelectrolyte layers and an outer GOD layer were prepared by using the layer-by-layer approach. Then, the particles were repeatedly used as catalysts following their rapid and easy separation with a magnet.<sup>[64]</sup> Santos et al.<sup>[65]</sup> constructed biocatalytic thin films by incorporating enzymes, specifically alkaline phosphatase (AP) and GOD into multilayers of PEI and PSS supported on a glass substrate. For both enzymes, the reactive films demonstrated increased activity with the successive number of deposited enzyme layers. In hybrid films consisting of alternating layers of AP

and GOD, both enzymes retained their activities similar to those of their corresponding films of either enzyme alone.

Biocatalytic and magnetic particles prepared upon the layer-by-layer approach were also reported by Fang et al.<sup>[66]</sup> The authors started from 420-nm latex particles, onto which they alternately assembled silica or magnetite nanoparticles, GOD, and oppositely charged polyelectrolytes. The inclusion of silica layers on latex yields a higher surface area resulting in greater GOD adsorption, thereby increasing the catalytic activity. The enzymatic activity was proportional to the core surface area and also to the number of GOD layers in the shell. The presence of magnetic nanoparticles allowed the self-stirring of the nanoreactor with a rotating magnetic field and enhanced the productivity.

In a very recent study,<sup>[67]</sup> enzyme activity of organophosphorus hydrolase (OPH) in polyelectrolyte-encased multilayer assemblies coated on glass beads was reported. The stability of the multilayer systems (e.g., against exposure to high salt concentration) could be strongly enhanced by anchoring monomers, such as 1,2-dihydroxypropyl-4-vinyl-benzylether, to the outer PAA layer and subsequently polymerizing the systems by UV irradiation. The OPH activity was not affected. Preparation of high-activity, enzyme-containing multilayer films on planar substrates was reported by Jin et al.<sup>[68]</sup> Catalase microcrystals were first encapsulated by the alternate adsorption of PSS and PAH on their surface yielding extremely high enzyme loading in the polyelectrolyte multilayer capsules. Subsequently, layer-by-layer deposition of the polyelectrolyte-coated catalase microcrystals and oppositely charged polyelectrolytes was used to construct multilayer films on glass supports. The catalyze achievement of these high enzyme content films was up to 50 times higher than of those prepared by conventional layer-by-layer deposition of the enzymes.

### Multilayer Assemblies Bearing Inorganic Catalysts

Polyelectrolyte multilayers are not only able to bind bioactive compounds, such as enzymes to produce highly efficient biocatalytic surfaces, but also inorganic compounds with high catalytic activity was reported. There are many studies on the incorporation of small inorganic particles in polyelectrolyte multilayer assemblies, but applications of these systems as catalysts are only scarcely demonstrated. Mecking and Thomann<sup>[69]</sup> reported on the adsorption of a catalytically active rhodium complex on anionic latex particles, which were previously coated with a PDADMA layer. The rhodium complex was bound

to the PDADMA layer via electrostatic interactions of its sulfonated phosphine ligands. The structurally well-defined core-shell particles were able to catalyze hydroformylation reactions such as the conversion of methyl acrylate into methyl 2-formylpropionate. Wang et al.<sup>[70]</sup> fabricated PAH/PAA multilayers by using the layer-by-layer approach and selectivity bound palladium catalysts for electroless nickel plating to the surface. Depending on whether the surface was cationic or anionic, either the negatively charged tetrachloropalladate or the positively charged tetraamine palladium ion was bound to the surface. Upon immersion into an electroless nickel plating bath, the palladium-coated parts of the surface were selectively plated. Using inkjet printing, the facile patternability of the polyelectrolyte multilayers was demonstrated. Wang et al.<sup>[71]</sup> also prepared palladium nanoparticles within PAH/PAA multilayers as seeds for binding tetraamine palladium from aqueous solution to PAA carboxylic acid functionalities in the polymer film and subsequent reduction. Two-nanometer catalytic palladium particles were obtained, onto which a nickel shell of arbitrary thickness could be grown. Up to 14-nm particles were obtained. Liu et al.<sup>[72]</sup> described a similar route to the fabrication of polyelectrolyte multilayers containing catalytically active palladium nanoparticles. A 4-aminobenzoic acid-modified glassy carbon electrode was alternately coated with tetrachloropalladate dianions and a quaternized poly(4-vinylpyridine) complexed with osmium. Three-dimensional palladium particle multilayers were subsequently formed upon electrochemical reduction of the tetrachloropalladate anions. The palladium nanoparticles in the film effectively catalyzed the reduction of dissolved oxygen and the oxidation of hydrazine compounds in aqueous solution. Antipov et al.<sup>[73]</sup> prepared PAH/PSS multilayer capsules containing silver ions. Subsequently, the silver ions were reduced via photoirradiation, or by chemical methods. The potential of the prepared silver-containing capsules to serve as catalysts was checked by the reduction of 4-nitrophenol into 4-aminophenol in the presence of sodium borohydride. The system under investigation was found to possess higher activity than the pure silver solution.

In some studies, multilayers of redoxactive compounds and polymers were assembled on electrodes to obtain electrocatalytic surfaces. Sun et al.<sup>[74]</sup> prepared layer-by-layer assemblies of polycations bearing an osmium complex and PSS or poly(aniline-co-*N*-(3-sulfopropyl)aniline) on gold electrodes. The chemically modified electrodes showed electrocatalytic response for the reduction of nitrite. Cheng and Cox<sup>[75]</sup> used the layer-by-layer approach to prepare nanocomposite multilayer films of a ruthenium metallodendrimer and a Dawson-type polyoxometalate. These multilayers

were used as bifunctional electrocatalysts, able to catalyze both reductions and oxidation. Using cyclovoltammetric studies, the mediated reduction of iodate by the polyoxometalate (phosphotungstate) and the oxidation of arsenite by the ruthenium dendrimer were demonstrated. Photocatalytic porphyrin multilayer assemblies were reported by Araki et al.<sup>[76]</sup> Electrodes modified with these films were photocatalytically active toward the reduction of O<sub>2</sub>.

Finally, Sasaki et al. prepared multilayer films of PDADMA and titania nanosheet crystallites,<sup>[77]</sup> and of titania nanoparticles and PSS.<sup>[78]</sup> UV irradiation of both types of films did not cause the expected photocatalytic decomposition of pollutants or water, but instead, the entire organic polyelectrolyte inside the multilayers was decomposed, and a polymer-free inorganic film was obtained. The photocatalytic reaction was monitored via infrared and X-ray photon spectroscopy.

## CONCLUSION

In the last decade, a variety of studies demonstrated that the alternate layer-by-layer assembly of cationic and anionic polyelectrolytes is a suitable method to prepare ultrathin, dense separation membranes on solid porous or pore-free supports. The main advantages are the simple, yet elegant preparation method; the environmentally sound, purely water-based chemistry; the use of low-cost, easily available compounds; the potential to precisely control structure and thickness of the membrane in the nanometer range; and the wide variety of compounds that can be chosen for the construction of the membranes. Previous studies also demonstrated that polyelectrolyte multilayers represent multipurpose membranes, which are well suited for dehydration of organic solvents under pervaporation conditions, for separation of mono- from multivalent ions under dialysis conditions, for water softening and desalination under nanofiltration and reverse osmosis conditions, as antifouling coatings for protein separation. Although the thickness of the multilayer membranes is usually below 100 nm, the efficiency of the membranes is comparable to commercial membranes of macroscopic thickness applied in modules.

The nanoporous, physically cross-linked structure of the membrane favors the permeation of small, hydrophilic molecules and ions of low charge density. In general, the selective transport behavior and the possibility to control the transport by adjusting pH and ionic strength of the feed solution, or by a chemical modification of the membrane, are two of the most interesting properties of polyelectrolyte multilayers. Future studies will be concerned with further



improvement of the efficiency of the membranes, either by modifying hydrophilicity or cross-linking density, or by incorporating permselective compounds such as calixarenes, cyclodextrines, zeolithes, or inorganic complex salts acting as molecular filters and ion sieves. Furthermore, studies will be concerned with a better theoretical understanding of the transport behavior.

For catalyst applications, the electrostatic buildup of polyelectrolyte multilayers with catalytic sites either embedded in the films or physically attached at the surface offers great advantage over covalent coupling and chemisorption methods. As recently demonstrated, the adsorbed or embedded enzymes and inorganic nanoparticles retain, at least partially, their catalytic activity rendering the multilayer assemblies attractive as new bioactive and catalytic materials. Although this review may be incomplete, the examples presented indicate a high potential of the polyelectrolyte multilayers to serve as carriers for catalytic substances. The experiments indicate that a binding of the catalyst to the surface leads to higher efficiencies than the dispersion of the catalyst within the multilayer. Furthermore, the use of spherical particles or capsules as a substrate is superior to a binding of the catalysts to flat multilayers. The reason is the much larger surface area providing a higher catalytic activity. Future work will be concerned with more systematic studies on incorporation, mobility, and activity of catalytic compounds in polyelectrolyte multilayers. Further systems demonstrating the suitability of polyelectrolyte multilayers as bioreactors and chemical nanoreactors need to be developed.

## REFERENCES

1. Decher, G.; Hong, J.-D.; Schmitt, J. Buildup of ultrathin multilayer films by a self-assembly process: III. Consecutively alternating adsorption of anionic and cationic polyelectrolytes on charged surfaces. *Thin Solid Films* **1992**, *210–211*, 831–835.
2. Decher, G.; Schmitt, J. Fine-tuning of the film thickness of ultrathin multilayer films composed of consecutively alternating layers of anionic and cationic polyelectrolytes. *Prog. Colloid Polym. Sci.* **1992**, *89*, 160–164.
3. Lvov, Y.; Decher, G.; Möhwald, H. Assembly, structural characterization, and thermal behaviour of layer-by-layer deposited ultrathin films of poly(vinyl sulfate) and poly(allylamine). *Langmuir* **1993**, *9*, 481–486.
4. Lvov, Y.; Decher, G.; Sukhorukov, G. Assembly of thin films by means of successive deposition of alternate layers of DNA and poly(allylamine). *Macromolecules* **1993**, *26*, 5396–5399.
5. Schmitt, J.; Grünewald, T.; Decher, G.; Pershan, P.S.; Kjær, K.; Lösche, M. Internal structure of layer-by-layer adsorbed polyelectrolyte films: A neutron and

- x-ray reflectivity study. *Macromolecules* **1993**, *26*, 7058–7063.
6. Delcorte, A.; Bertrand, P.; Arys, X.; Jonas, A.; Wischerhoff, E.; Mayer, B.; Laschewsky, A. ToF-SIMS study of alternate polyelectrolyte thin films: Chemical surface characterization and molecular secondary ions sampling depth. *Surf. Sci.* **1996**, *366*, 149–165.
7. Hong, H.; Steitz, R.; Kirstein, S.; Davidov, D. Superlattice structures in poly(phenylenevinylene)-based self-assembled films. *Adv. Mater.* **1998**, *10*, 1104–1108.
8. Lowack, K.; Helm, C.A. Molecular mechanisms controlling the self-assembly process of polyelectrolyte multilayers. *Macromolecules* **1998**, *31*, 823–833.
9. Yoo, D.; Shiratori, S.S.; Rubner, M.F. Controlling bilayer composition and surface wettability of sequentially adsorbed multilayers of weak polyelectrolytes. *Macromolecules* **1998**, *31*, 4309–4318.
10. Lösche, M.; Schmitt, J.; Decher, G.; Bouwman, W.G.; Kjær, K. Detailed structure of molecularly thin polyelectrolyte multilayer films on solid substrates as revealed by neutron reflectometry. *Macromolecules* **1998**, *31*, 8893–8906.
11. Schlenoff, J.B.; Ly, H.; Li, M. Charge and mass balance in polyelectrolyte multilayers. *J. Am. Chem. Soc.* **1998**, *120*, 7626–7634.
12. Dubas, S.T.; Schlenoff, J.B. Factors controlling the growth of polyelectrolyte multilayers. *Macromolecules* **1999**, *32*, 8153–8160.
13. Farhat, T.; Yassin, G.; Dubas, S.T.; Schlenoff, J.B. Water and ion pairing in polyelectrolyte multilayers. *Langmuir* **1999**, *15*, 6621–6623.
14. Rodriguez, L.N.J.; De Paul, S.M.; Barrett, C.J.; Reven, L.; Spiess, H. Fast magic-angle spinning and double-quantum  $^1\text{H}$  solid-state NMR spectroscopy of polyelectrolyte multilayers. *Adv. Mater.* **2000**, *12*, 1934–1938.
15. Ladam, G.; Schaad, P.; Voegel, J.C.; Schaaf, P.; Decher, G.; Cuisinier, F. In situ determination of the structural properties of initially deposited polyelectrolyte multilayers. *Langmuir* **2000**, *16*, 1249–1255.
16. Shiratori, S.S.; Rubner, M.F. pH-dependent thickness behaviour of sequentially adsorbed layers of weak polyelectrolytes. *Macromolecules* **2000**, *33*, 4213–4219.
17. Castelnovo, M.; Joanny, J.-F. Formation of polyelectrolyte multilayers. *Langmuir* **2000**, *16*, 7524–7532.
18. Schlenoff, J.B.; Dubas, S.T. Mechanism of polyelectrolyte multilayer growth: Charge overcompensation and distribution. *Macromolecules* **2001**, *34*, 592–598.
19. Steitz, R.; Jaeger, W.; von Klitzing, R. Influence of charge density and ionic strength on the multilayer formation of strong polyelectrolytes. *Langmuir* **2001**, *17*, 4471–4474.
20. McAloney, R.A.; Sinyor, M.; Dudnik, V.; Goh, M.C. Atomic force microscopy studies of salt effects on polyelectrolyte multilayer film morphology. *Langmuir* **2001**, *17*, 6655–6663.
21. Schoeler, B.; Kumaraswamy, G.; Caruso, F. Investigation of the influence of polyelectrolyte charge density on the growth of multilayer thin films prepared by the

- layer-by-layer technique. *Macromolecules* **2002**, *35*, 889–897.
22. Xie, A.F.; Granick, S. Local electrostatics within a polyelectrolyte multilayer with embedded weak polyelectrolyte. *Macromolecules* **2002**, *35*, 1805–1813.
  23. Decher, G., Schlenoff, J.B., Eds.; *Multilayer Thin Films*; Wiley-VCH: Weinheim, 2003.
  24. Tripathy, S.K., Kumar, J., Nalwa, H.S., Eds.; *Handbook of Polyelectrolytes and Their Applications*; Am. Scientific Publ.: Stevenson Ranch, 2002; Vols. 1–3.
  25. Decher, G. Fuzzy nanoassemblies: Toward layered polymeric multicomposites. *Science* **1997**, *277*, 1232–1237.
  26. Decher, G.; Eckle, M.; Schmitt, J.; Struth, B. Layer-by-layer assembled multicomposite films. *Curr. Opin. Colloid Interface Sci.* **1998**, *3*, 32–39.
  27. Bertrand, P.; Jonas, A.; Laschewsky, A.; Legras, R. Ultrathin polymer coatings by complexation of polyelectrolytes at interfaces: Suitable materials, structure and properties. *Macromol. Rapid Commun.* **2000**, *21*, 319–348.
  28. Hammond, P.T. Recent explorations in electrostatic multilayer thin film assembly. *Curr. Opin. Colloid Interface Sci.* **2000**, *4*, 430–442.
  29. Schönhoff, M. Self-assembled polyelectrolyte multilayers. *Curr. Opin. Colloid Interface Sci.* **2003**, *8*, 86–95.
  30. Stroeve, P.; Vasquez, V.; Coelho, M.A.N.; Rabolt, J.F. Gas transfer in supported films made by molecular self-assembly of ionic polymers. *Thin Solid Films* **1996**, *284–285*, 708–712.
  31. Leväsalmi, J.-M.; McCarthy, T.J. Poly(4-methyl-1-pentene)-supported polyelectrolyte multilayer films: Preparation and gas permeability. *Macromolecules* **1997**, *30*, 1752–1757.
  32. Van Ackern, F.; Krasemann, L.; Tieke, B. Ultrathin membranes for gas separation and pervaporation prepared upon electrostatic self-assembly of polyelectrolytes. *Thin Solid Films* **1998**, *327–329*, 762–766.
  33. Zhou, P.; Samuelson, L.; Shridhara Alva, K.; Chen, C.-C.; Blumstein, R.B.; Blumstein, A. Ultrathin films of amphiphilic ionic polyacetylenes. *Macromolecules* **1997**, *30*, 1577–1581.
  34. Sullivan, D.M.; Bruening, M.L. Ultrathin, gas-selective polyimide membranes prepared from multilayer polyelectrolyte films. *Chem. Mater.* **2003**, *15*, 281–287.
  35. Krasemann, L.; Tieke, B. Ultrathin self-assembled polyelectrolyte membranes for pervaporation. *J. Membr. Sci.* **1998**, *150*, 23–30.
  36. Krasemann, L.; Tieke, B. Composite membranes with ultrathin separation layer prepared by self-assembly of polyelectrolytes. *Mater. Sci. Eng., C* **1999**, *8–9*, 513–518.
  37. Krasemann, L.; Tieke, B. Highly efficient composite membranes for ethanol–water pervaporation. *Chem. Eng. Technol.* **2000**, *23*, 211–213.
  38. Krasemann, L.; Toutianoush, A.; Tieke, B. Self-assembled polyelectrolyte multilayer membranes with highly improved pervaporation separation of ethanol/water mixtures. *J. Membr. Sci.* **2001**, *181*, 221–228.
  39. Toutianoush, A.; Krasemann, L.; Tieke, B. Polyelectrolyte multilayer membranes for pervaporation separation of alcohol/water mixtures. *Colloids Surf., A* **2002**, *198–200*, 881–889.
  40. Toutianoush, A.; Tieke, B. Pervaporation separation of alcohol/water mixtures using self-assembled polyelectrolyte multilayer membranes of high charge density. *Mater. Sci. Eng., C* **2002**, *22*, 459–463.
  41. Meier-Haack, J.; Rieser, T.; Lenk, W.; Lehmann, D.; Berwald, S.; Schwarz, S. Effect of polyelectrolyte complex layers on the separation properties and the fouling behaviour of surface and bulk modified membranes. *Chem. Eng. Technol.* **2000**, *23*, 114–119.
  42. Meier-Haack, J.; Lenk, W.; Lehmann, D.; Lunkwitz, K. Pervaporation separation of water/alcohol mixtures using composite membranes based on polyelectrolyte multilayer assemblies. *J. Membr. Sci.* **2001**, *184*, 233–243.
  43. Krasemann, L.; Tieke, B. Selective ion transport across self-assembled alternating multilayers of cationic and anionic polyelectrolytes. *Langmuir* **2000**, *16*, 287–290.
  44. Harris, J.J.; Stair, J.L.; Bruening, M.L. Layered polyelectrolyte films as selective ultrathin barriers for anion transport. *Chem. Mater.* **2000**, *12*, 1941–1946.
  45. Toutianoush, A.; Tieke, B. Ultrathin Self-assembled Polyvinylamine/polyvinylsulfate Membranes for Separation of Ions. In *Novel Methods to Study Interfacial Layers*; Studies in Surface Science Series; Moebius, D., Miller, R., Eds.; Elsevier: Amsterdam, 2001; *11*, 415–425.
  46. Farhat, T.R.; Schlenoff, J.B. Ion transport and equilibria in polyelectrolyte multilayers. *Langmuir* **2001**, *17*, 1184–1192.
  47. Toutianoush, A.; Tieke, B. Selective transport and incorporation of highly charged metal and metal complex ions in self-assembled polyelectrolyte multilayer membranes. *Mater. Sci. Eng., C* **2002**, *22*, 135–139.
  48. Rmaile, H.R.; Schlenoff, J.B. Optically active polyelectrolyte multilayers as membranes for chiral separations. *J. Am. Chem. Soc.* **2003**, *125*, 6602–6603.
  49. Jin, W.; Toutianoush, A.; Tieke, B. Use of polyelectrolyte layer-by-layer assemblies as nanofiltration and reverse osmosis membranes. *Langmuir* **2003**, *19*, 2550–2553.
  50. Stanton, B.W.; Harris, J.J.; Miller, M.D.; Bruening, M.L. Ultrathin, multilayered polyelectrolyte films as nanofiltration membranes. *Langmuir* **2003**, *19*, 7038–7042.
  51. Kong, W.; Zhang, X.; Gao, M.L.; Zhou, H.; Li, W.; Shen, J.C. A new kind of immobilized enzyme multilayer based on cationic and anionic interaction. *Macromol. Rapid Commun.* **1994**, *15*, 405–409.
  52. Kong, W.; Wang, L.P.; Gao, M.L.; Zhou, H.; Zhang, X.; Li, W.; Shen, J.C. Immobilized bilayer glucose isomerase in porous trimethylamine polystyrene-based on molecular deposition. *Chem. Commun.* **1994**, *1297–1298*.
  53. Lvov, Y.; Ariga, K.; Kunitake, T. Layer-by-layer assembly of alternate protein/polyion ultrathin films. *Chem. Lett.* **1994**, 2323–2326.
  54. Lvov, Y.; Ariga, K.; Ichinose, I.; Kunitake, T. Assembly of multicomponent protein films by means

- of electrostatic layer-by-layer adsorption. *J. Am. Chem. Soc.* **1995**, *117*, 6117–6123.
55. Onda, M.; Lvov, Y.; Ariga, K.; Kunitake, T. Sequential actions of glucose oxidase and peroxidase in molecular films assembled by layer-by-layer alternate adsorption. *Biotechnol. Bioeng.* **1996**, *51*, 163–167.
  56. Onda, M.; Lvov, Y.; Ariga, K.; Kunitake, T. Sequential reaction and product separation on molecular films of glucoamylase and glucose oxidase assembled on an ultrafilter. *J. Ferment. Bioeng.* **1996**, *82*, 502–506.
  57. Onda, M.; Ariga, K.; Kunitake, T. Activity and stability of glucose oxidase in molecular films assembled alternately with polyions. *J. Biosci. Bioeng.* **1999**, *87*, 69–75.
  58. Lvov, Y.M.; Lu, Z.; Schenkman, J.B.; Zu, X.; Rusling, J.F. Direct electrochemistry of myoglobin and cytochrome P450<sub>cam</sub> in alternate layer-by-layer films with DNA and other polyions. *J. Am. Chem. Soc.* **1998**, *120*, 4073–4080.
  59. Calvo, E.J.; Battaglini, F.; Danilowicz, C.; Wolosink, A.; Otero, M. Layer-by-layer electrostatic deposition of biomolecules on surfaces for molecular recognition, redox mediation and signal generation. *Faraday Discuss.* **2000**, *116*, 47–65.
  60. Hodak, J.; Etchenique, R.; Calvo, E.J.; Singhal, K.; Bartlett, P.N. Layer-by-layer self-assembly of glucose oxidase with a poly(allylamine)ferrocene redox mediator. *Langmuir* **1997**, *13*, 2708–2716.
  61. Ma, H.; Hu, N.; Rusling, J.F. Electroactive myoglobin films grown layer-by-layer with poly(styrenesulfonate) on pyrolytic graphite electrodes. *Langmuir* **2000**, *16*, 4969–4975.
  62. He, J.-A.; Samuelson, L.; Li, L.; Kumar, J.; Tripathy, S.K. Bacteriorhodopsin thin film assemblies immobilization, properties, and applications. *Adv. Mater.* **1999**, *11*, 435–446.
  63. Schüler, C.; Caruso, F. Preparation of enzyme multilayers on colloids for biocatalysis. *Macromol. Rapid Commun.* **2000**, *21*, 750–753.
  64. Caruso, F.; Schüler, C. Enzyme multilayers on colloid particles: Assembly, stability, and enzymatic activity. *Langmuir* **2000**, *16*, 9595–9603.
  65. Santos, J.P.; Welsh, E.R.; Gaber, B.P.; Singh, A. Polyelectrolyte-assisted immobilization of active enzymes on glass beads. *Langmuir* **2001**, *17*, 5361–5367.
  66. Fang, M.; Grant, P.S.; McShane, M.J.; Sukhorukov, G.B.; Golub, V.O.; Lvov, Y.M. Magnetic bio/nanoreactor with multilayer shells of glucose oxidase and inorganic nanoparticles. *Langmuir* **2002**, *18*, 6338–6344.
  67. Lee, Y.; Stanish, I.; Rastogi, V.; Cheng, T.-C.; Singh, A. Sustained enzyme activity of organophosphorus hydrolase in polymer encased multilayer assemblies. *Langmuir* **2003**, *19*, 1330–1336.
  68. Jin, W.; Shi, X.; Caruso, F. High activity enzyme microcrystal multilayer films. *J. Am. Chem. Soc.* **2001**, *123*, 8121–8122.
  69. Mecking, S.; Thomann, R. Core-shell microspheres of a catalytically active rhodium complex bound to a polyelectrolyte-coated latex. *Adv. Mater.* **2000**, *12*, 953–956.
  70. Wang, T.C.; Chen, B.; Rubner, M.F.; Cohen, R.E. Selective electroless nickel plating on polyelectrolyte multilayer platforms. *Langmuir* **2001**, *17*, 6610–6615.
  71. Wang, T.C.; Rubner, M.F.; Cohen, R.E. Manipulating nanoparticles size within polyelectrolyte multilayers via electroless nickel deposition. *Chem. Mater.* **2003**, *15*, 299–304.
  72. Liu, J.; Cheng, L.; Song, Y.; Liu, B.; Dong, S. Simple preparation method of multilayer polymer films containing Pd nanoparticles. *Langmuir* **2001**, *17*, 6747–6750.
  73. Antipov, A.A.; Sukhorukov, G.B.; Fedutik, Y.A.; Hartmann, J.; Giersig, M.; Möhwald, H. Fabrication of a novel type of metallized colloids and hollow capsules. *Langmuir* **2002**, *18*, 6687–6693.
  74. Sun, J.; Sun, Y.; Zou, S.; Zhang, X.; Sun, C.; Wang, Y.; Shen, J. Layer-by-layer assemblies of polycation bearing Os complex with electroactive and electroinactive polyanions and their electrocatalytic reduction of nitrite. *Macromol. Chem. Phys.* **1999**, *200*, 840–844.
  75. Cheng, L.; Cox, J.A. Nanocomposite multilayer film of a ruthenium metallodendrimer and a Dawson-type polyoxometalate as a bifunctional electrocatalyst. *Chem. Mater.* **2002**, *14*, 6–8.
  76. Araki, K.; Wagner, M.J.; Wrighton, M.S. Layer-by-layer growth of electrostatically assembled multilayer porphyrin films. *Langmuir* **1996**, *12*, 5393–5398.
  77. Sasaki, T.; Ebina, Y.; Fukuda, K.; Tanaka, T.; Harada, M.; Watanabe, M. Titania nanostructured films derived from a titania nanosheet/polycation multilayer assembly via heat treatment and UV-irradiation. *Chem. Mater.* **2002**, *14*, 3524–3530.
  78. Wang, Z.-S.; Sasaki, T.; Muramatsu, M.; Ebina, Y.; Tanaka, T.; Wang, L.; Watanabe, M. Self-assembled multilayers of titania nanoparticles and nanosheets with polyelectrolytes. *Chem. Mater.* **2003**, *15*, 807–812.
  79. v. Klitzing, R.; Tieke, B. Polyelectrolyte membranes. *Adv. Polym. Sci.* **2003**, in press.
  80. Tieke, B.; Pyrasch, M.; Toutianoush, A. Functional Layer-by-layer Assemblies with Photo- and Electrochemical Response and Selective Transport of Small Molecules and Ions. In *Multilayer Thin Films*; Decher, G., Schlenoff, J.B., Eds.; Wiley-VCH: Weinheim, 2003; 427–460.
  81. Bruening, M. Controlling the Ion-permeability of Layered Polyelectrolyte Films and Membranes. In *Multilayer Thin Films*; Decher, G., Schlenoff, J.B., Eds.; Wiley-VCH: Weinheim, 2003; 487–510.
  82. Schlenoff, J.B. Charge Balance and Transport in Polyelectrolyte Multilayers. In *Multilayer Thin Films*; Decher, G., Schlenoff, J.B., Eds.; Wiley-VCH: Weinheim, 2003; 99–132.
  83. Tieke, B. Polyelectrolyte Multilayer Membranes for Materials Separation. In *Handbook of Polyelectrolytes and Their Applications*; Tripathy, S.K., Kumar, J., Nalwa, H.S., Eds.; Am. Scientific Publ.: Stevenson Ranch, 2002; 3, 115–124.
  84. Berwald, S.; Meier-Haack, J. Polyelectrolyte Multilayer Systems in Membrane Applications. In *Handbook of Polyelectrolytes and Their Applications*;

- Tripathy, S.K., Kumar, J., Nalwa, H.S., Eds.; Am. Scientific Publ.: Stevenson Ranch, 2002; 3, 99–114.
85. Bruening, M.L.; Sullivan, D.M. Enhancing the ion-transport selectivity of multilayer polyelectrolyte membranes. *Chem. Eur. J.* **2002**, *8*, 3833–3837.
86. Tieke, B.; van Ackern, F.; Krasemann, L.; Toutianoush, A. Ultrathin self-assembled polyelectrolyte multilayer membranes. *Eur. Phys. J., E* **2001**, *5*, 29–39.
87. Tieke, B.; Krasemann, L.; Toutianoush, A. Tailor-made membranes for alcohol/water pervaporation and ion separation prepared upon layer-by-layer adsorption of polyelectrolytes. *Macromol. Symp.* **2001**, *163*, 97–111.
88. Urairi, M.; Tsuru, T.; Nakao, S.; Kimura, S. Bipolar reverse osmosis membrane for separating mono- and divalent ions. *J. Membr. Sci.* **1992**, *70*, 153–162.
89. Tsuru, T.; Nakao, S.; Kimura, S. Ion separation by bipolar membranes in reverse osmosis. *J. Membr. Sci.* **1995**, *108*, 269–278.
90. Lebedev, K.; Ramirez, D.; Mafé, S.; Pellicer, J. Modeling of the salt permeability in fixed charge multilayer membranes. *Langmuir* **2000**, *16*, 9941–9943.
91. Caruso, F.; Lichtenfeld, H.; Donath, E.; Möhwald, H. Investigation of electrostatic interactions in polyelectrolyte multilayer films: Binding of anionic fluorescent probes to layers assembled onto colloids. *Macromolecules* **1999**, *32*, 2317–2328.
92. Hoogveen, N.G.; Cohen Stuart, M.A.; Fleer, G.J.; Böhmer, M.R. Formation and stability of multilayers of polyelectrolytes. *Langmuir* **1996**, *12*, 3675–3681.
93. Riegler, H.; Essler, F. Polyelectrolytes. 2. Intrinsic or extrinsic charge compensation? Quantitative charge analysis of PAH/PSS multilayers. *Langmuir* **2002**, *18*, 6694–6698.
94. Farhat, T.R.; Schlenoff, J.B. Doping controlled ion diffusion in polyelectrolyte multilayers: Mass transport in reluctant exchangers. *J. Am. Chem. Soc.* **2003**, *125*, 4627–4636.
95. Toutianoush, A.; Tieke, B. Selective transport and incorporation of highly charged metal and metal complex ions in self-assembled polyelectrolyte multilayer membranes. *Mater. Sci. Eng., C* **2002**, *22*, 135–139.
96. Jin, W.; Tieke, B. In preparation.
97. Müller, M.; Rieser, T.; Lunkwitz, K.; Berwald, S.; Meier-Haack, J.; Jenichen, D. An in-situ ATR-FTIR study on polyelectrolyte multilayer assemblies on solid surfaces and their susceptibility to fouling. *Macromol. Rapid Commun.* **1998**, *19*, 333–336.
98. Müller, M.; Rieser, T.; Lunkwitz, K.; Meier-Haack, J. Polyelectrolyte complex layers: A promising concept for antifouling coatings verified by in-situ ATR-FTIR spectroscopy. *Macromol. Rapid Commun.* **1999**, *20*, 607–611.
99. Graul, T.W.; Schlenoff, J.B. Capillaries modified by polyelectrolyte multilayers for electrophoretic separations. *Anal. Chem.* **1999**, *71*, 4007–4013.
100. v. Klitzing, R.; Möhwald, H. Proton concentration profile in ultrathin polyelectrolyte films. *Langmuir* **1995**, *11*, 3554–3559.
101. v. Klitzing, R.; Möhwald, H. Transport through ultrathin polymer films. *Thin Solid Films* **1996**, *284–285*, 352–356.
102. Harris, J.J.; Bruening, M.L. Electrochemical and in situ ellipsometric investigation of the permeability and stability of layered polyelectrolyte films. *Langmuir* **2000**, *16*, 2006–2013.
103. Harris, J.J.; DeRose, P.M.; Bruening, M.L. Synthesis of passivating, nylon-like coatings through cross-linking of ultrathin polyelectrolyte films. *J. Am. Chem. Soc.* **1999**, *121*, 1978–1979.
104. Ichinose, I.; Mizuki, S.; Ohno, S.; Shiraishi, H.; Kunitake, T. Preparation of cross-linked ultrathin films based on layer-by-layer assembly of polymers. *Polym. J.* **1999**, *31*, 1065–1070.
105. Sukhorukov, G.; Dähne, L.; Hartmann, J.; Donath, E.; Möhwald, H. Controlled precipitation of dyes into hollow polyelectrolyte capsules based on colloids and biocolloids. *Adv. Mater.* **2000**, *12*, 112–115.
106. Caruso, F.; Yang, W.; Trau, D.; Renneberg, R. Microencapsulation of uncharged low molecular weight organic materials by polyelectrolyte multilayer self-assembly. *Langmuir* **2000**, *16*, 8932–8936.
107. Shi, X.; Caruso, F. Release behaviour of thin-walled microcapsules composed of polyelectrolyte multilayers. *Langmuir* **2001**, *17*, 2036–2042.
108. Antipov, A.A.; Sukhorukov, G.B.; Donath, E.; Möhwald, H. Sustained release properties of polyelectrolyte multilayer capsules. *J. Phys. Chem., B* **2001**, *105*, 2281–2284.
109. Ibarz, G.; Dähne, L.; Donath, E.; Möhwald, H. Smart micro- and nanocontainers for storage, transport, and release. *Adv. Mater.* **2001**, *13*, 1324–1327.
110. Qiu, X.; Leporatti, S.; Donath, E.; Möhwald, H. Studies on the drug release properties of polysaccharide multilayers encapsulated ibuprofen microparticles. *Langmuir* **2001**, *17*, 5375–5380.
111. Moya, S.; Donath, E.; Sukhorukov, G.B.; Auch, M.; Bäuml, H.; Lichtenfeld, H.; Möhwald, H. Lipid coating on polyelectrolyte surface modified colloidal particles and polyelectrolyte capsules. *Macromolecules* **2000**, *33*, 4538–4544.
112. Ibarz, G.; Dähne, L.; Donath, E.; Möhwald, H. Controlled permeability of polyelectrolyte capsules via defined annealing. *Chem. Mater.* **2002**, *14*, 4059–4062.
113. Ariga, K. Nanostructured Hybrid Ultrathin Films of Polyelectrolytes, Lipids, and Enzymes Prepared by Alternate Layer-by-layer Adsorption. In *Handbook of Polyelectrolytes and Their Applications*; Tripathy, S.K., Kumar, J., Nalwa, H.S., Eds.; Am. Scientific Publ.: Stevenson Ranch, 2002; 1, 99–126.

# Layer-by-Layer Assembly of Semiconducting and Photoreactive Bolaform Amphiphiles

Jason Locklin  
Derek Patton

*Department of Chemistry, University of Houston, Houston, Texas, U.S.A.*

Chuanjun Xia  
Xiaowu Fan

*Department of Chemistry, University of Alabama at Birmingham, Birmingham, Alabama, U.S.A.*

Rigoberto C. Advincula

*Department of Chemistry, University of Alabama at Birmingham, Birmingham, Alabama, U.S.A., and Department of Chemistry, University of Houston, Houston, Texas, U.S.A.*

## INTRODUCTION

In the early 1990s, Decher and Hong extended the pioneering work of Iler,<sup>[1]</sup> and introduced the layer-by-layer method of constructing multilayers on surfaces.<sup>[2-4]</sup> They demonstrated that multilayers could be prepared simply by dipping a charged substrate sequentially into solutions containing a negatively and positively charged polyelectrolyte. Because of the ease of processability and wide array of molecules that can be incorporated into these multilayers, the layer-by-layer method has become one of the most useful and widespread techniques for fabricating ultrathin films. Successful assembly has been demonstrated for a variety of materials, some of which include DNA,<sup>[5]</sup> latex particles,<sup>[6]</sup> clay,<sup>[7-10]</sup> proteins,<sup>[11,12]</sup> nanoparticles,<sup>[13-18]</sup> dyes,<sup>[19-26]</sup> semiconducting oligomers,<sup>[27,28]</sup> conjugated polymers,<sup>[29-32]</sup> and bolaform amphiphiles.<sup>[33-37]</sup>

Amphiphiles are interesting molecules that contain both hydrophilic and hydrophobic parts. A conventional water-soluble amphiphile usually consists of a long hydrocarbon chain tail and a hydrophilic head group, which is either highly polar or ionically charged, to impart some water solubility to the molecule. If the molecule bears a positive charge, such as a quaternary ammonium group, or a negative charge, such as a sulfate group, the amphiphile is categorized as a cationic or anionic amphiphile, respectively.<sup>[38]</sup> Bolaform amphiphiles, or bolaamphiphiles, are described as molecules containing two hydrophilic moieties connected by a hydrophobic chain. It has been shown that bolaform amphiphiles have unusual aggregation behavior at the air-water interface and in lyotropic<sup>[39,40]</sup>

and thermotropic phases.<sup>[41]</sup> Their self-assembly via physical adsorption on charged surfaces has been demonstrated and characterized using a variety of methods.

Bolaform amphiphiles with ionic end groups can form layers that produce charged surfaces upon their adsorption. These charged surfaces can be used to electrostatically assemble multilayer structures. The first account of the layer-by-layer assembly of bolaform amphiphiles was reported by Decher et al., where ordered multilayers of more than 70 layers were fabricated.<sup>[2-4]</sup> Electrostatically attractive interactions of the hydrophilic head groups and appropriately charged substrates (such as mica, quartz, glass, Si/SiO<sub>2</sub>, gold, etc.) force molecules to pack closely on the substrate. Short-range van der Waals forces affect the packing density and orientation of the molecules within the layered structure.

The synthetic design of the bolaamphiphile must take into account these intermolecular forces to achieve a buildup of multiple layers. End-on adsorption of the molecules would maintain a maximum charge density on the surface and is crucial to make well-ordered films. The flexible alkyl spacer in the amphiphile must be of a certain length for end-on adsorption to occur.<sup>[2]</sup> When the molecule is too short, the charges are separated by a small distance and adsorption occurs flat on the surface. At short chain length, electrostatic effects are dominant and the bolaform amphiphiles lie down on the substrate. If the length of the alkyl spacer is too long, a loop-type adsorption may occur. Either type of adsorption would lead to a reduction of charged groups on the surface making it difficult to build the consecutive adsorption of layers.

The aim of this article is to provide an overview of the layer-by-layer electrostatic adsorption and characterization of bolaform amphiphile multilayers. The rest of the entry will be divided into three parts: (1) semiconducting bolaform amphiphiles, (2) photoreactive bolaform amphiphiles, and (3) photochemical isomerization of bolaform amphiphiles. Factors such as the aggregation behavior of the molecules in solution and as ultrathin films will be discussed.

## SEMICONDUCTING BOLAFORM AMPHIPHILES

Conjugated oligomers have recently gained interest not only as model compound polymers but as active organic semiconducting materials. Thiophene oligomers, especially sexithiophene (6T), have been utilized for their potential application in organic molecular electronics. This includes field effect transistors (FETs), organic light-emitting diodes (OLEDs), and photoconductive and photovoltaic devices.<sup>[42–46]</sup> In the oligothiophenes, as with other conjugated oligomers, an increase in conjugation length typically leads to a dramatic increase in charge transport properties but also brings about a decrease in their solubility. This makes purification and device fabrication very difficult, especially by solution casting methods.

Recently, we have synthesized a bolaform amphiphile (6TN) by introducing pendant cationic alkyl end groups at the  $\alpha$  and  $\omega$  positions of 6T, preserving the conjugation of the backbone and affording water

solubility to the molecule. This molecule showed unique aggregation behavior in solution and multilayers were successfully fabricated using the layer-by-layer technique. This approach may provide for a new fabrication method for FETs.

## Solution Studies of the 6TN Bolaform Amphiphile

As stated above, bolaamphiphiles show very interesting aggregation behavior in solutions of varying composition. The absorption spectrum of 6TN in water (Fig. 1) exhibits fine structure probably due to coupling of the fundamental  $\pi-\pi^*$  electronic transition with vibrational levels of the excited state<sup>[47]</sup> or Davydov splitting of the exciton levels,<sup>[48]</sup> or both. The origin is primarily due to the  $\pi-\pi$  stacking of the sexithiophene central core. The fine structure disappears at elevated temperature (80°C) indicating that the aggregates formed in solution are tight and dominated by the hydrophobic sexithiophene part of the bolaform amphiphile.

Adding tetrahydrofuran (THF) to the aqueous solution results in red shift of the peak maximum and disaggregation of the  $\pi-\pi$  stacks, which is a reasonable observation because THF is a better solvent for the hydrophobic part of the amphiphile. When the THF concentration is higher than 80%, the absorption maximum shifts back to the blue and the fine structure begins to appear again, similar to that found in the aqueous solution. The charged ends of the bolaform

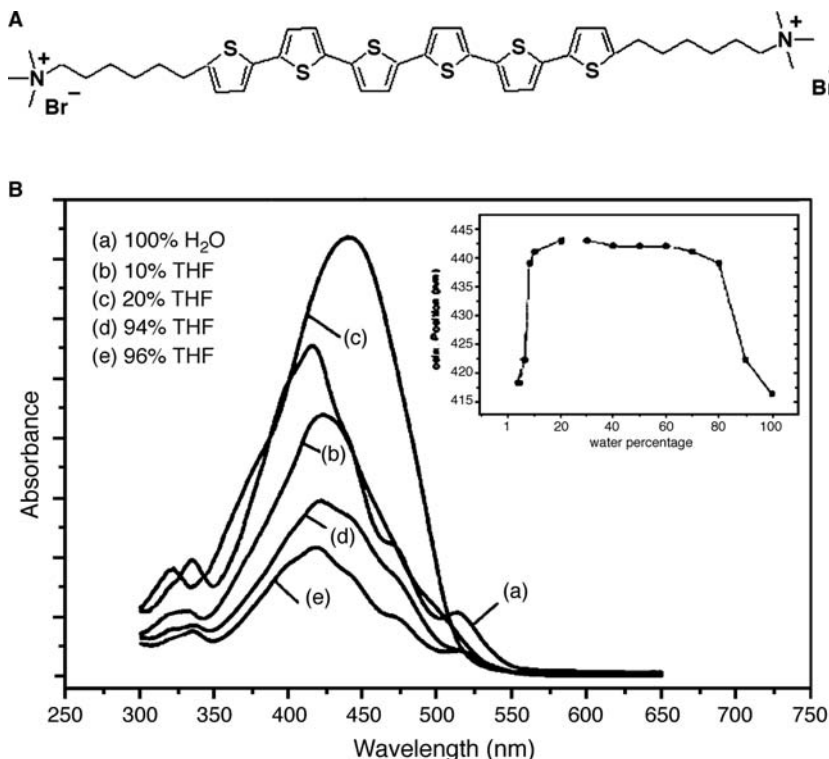


**Fig. 1** (A) Structure of the bolaform amphiphile 6TN. (B) UV-vis absorption spectra and plot of absorption maxima (inset) of 6TN in water/THF mixtures. The absorbance has been adjusted for clarity. *Source:* Reproduced with permission from *Langmuir* **2002**, *18*, 955–957. © 2002, American Chemical Society.



amphiphile are not soluble in THF and can be dissolved only in an aqueous environment. At high THF concentrations, another type of aggregate is formed, where the aggregation is dominated by the ionic interactions of the quaternary amine groups. By varying the composition of the solvent (water/THF), adsorption of the molecules onto charged surfaces can be studied in an aggregated and disaggregated state.

### Adsorption of 6TN with Polyelectrolytes

Multilayers of the 6TN bolaform amphiphile and poly(styrene sulfonate) (PSS) were fabricated from solutions of different compositions (water and water/THF, 30/70) where the molecules were in an aggregated and disaggregated state. In both cases, adsorption occurred end-on and proceeded in a stepwise, linear fashion as shown in Fig. 2.

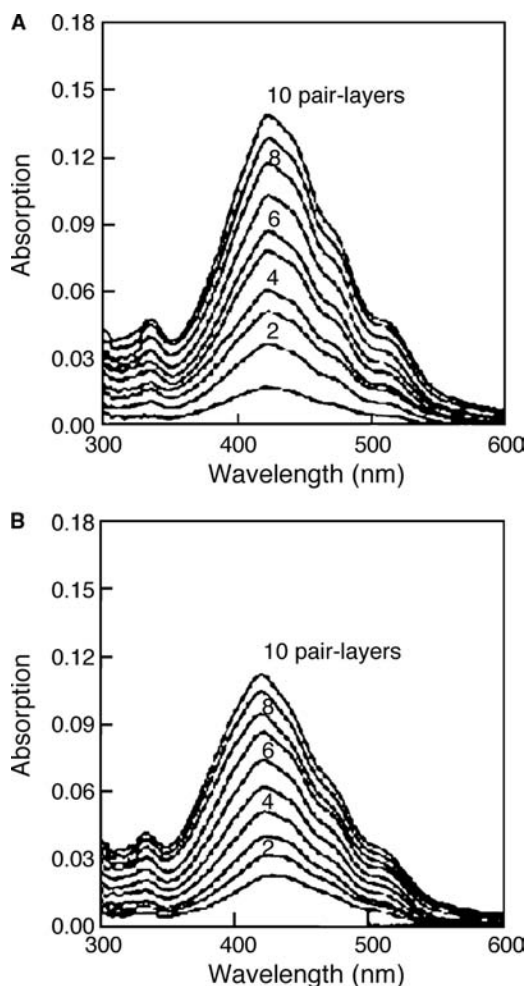


**Fig. 2** UV-vis spectra of 6TN/PSS multilayers (1–10 pair layers) prepared from 6TN in (A) water and (B) water/THF (70/30) on glass. *Source:* Reproduced with permission from<sup>[27]</sup>. © 2002, American Chemical Society.

From the fine structure at the lower-energy end in the ultraviolet (UV)-vis absorption plots, it can be seen that the films have a highly aggregated structure with considerable  $\pi$ - $\pi$  stacking. The difference in the two deposition processes can be seen in the absorption intensity of the two graphs. The deposition from pure water has a larger amount of material deposited per dipping cycle indicating that more material is deposited with molecules in a preformed aggregate state than from single molecules in the solution. This was verified using a variety of supporting techniques including X-ray photoelectron spectroscopy (XPS) and atomic force microscopy (AFM).

### Adsorption of 6TN with Inorganic Platelets

Several research groups have found interesting effects by using clays and a semiconducting material to fabricate hybrid nanocomposites. Some types of silicate clay have a unique layered structure and are negatively charged upon hydration. Anisotropic conductivity has been seen in a polyphosphazene-montmorillonite (MONT) composite material prepared by a bulk mixing process.<sup>[49]</sup> Oligothiophenes have been intercalated into vermiculite clay and the orientation of the confined oligothiophenes was studied.<sup>[50]</sup> Also, Eckel and Decher have fabricated OLEDs that included an isolated montmorillonite layer at different cycles of the layer-by-layer process.<sup>[51]</sup> The authors found that the clay sheets increased the efficiency of the device by a factor of 14 or greater when compared to that of the pure polymer system.

We have recently investigated the role of MONT clay layers in the preparation of nanostructured multilayer films of 6TN using the layer-by-layer approach. Alternating multilayers were prepared from pure aqueous and salt solution. Distinct surface morphologies of samples prepared from the two types of solution were found. The presence of salts affected the aggregation behavior and deposition of these films.

Fig. 3 shows the UV-vis spectra of 6TN/MONT multilayer samples prepared from pure water and 0.1 M NaCl. The absorbance intensity for the 0.1 M NaCl system is 5 times as large as that of pure water for the same dipping cycle. As with the 6TN/PSS multilayers fabricated from pure water and 30% THF above, this means that more 6TN is deposited from saline solution. This result was further confirmed with X-ray diffraction (XRD) measurements. One big difference in the adsorption of 6TN with polyelectrolytes and MONT sheets was that the composition and conformation of the aggregates changes upon adsorption at the surface. The interaction between the 6TN molecules and the underlying clay sheets leads to a reordering of the aggregates on the surface.

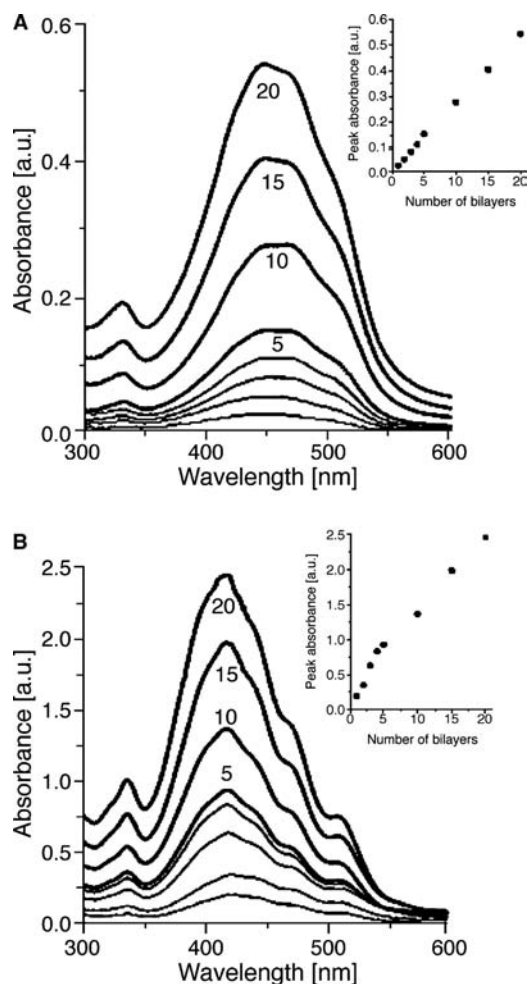


**Fig. 3** (A) UV-vis spectra of 6TN/MONT multilayer films (1–20 layers) prepared from pure water. Peak absorbance vs. number of bilayers is plotted in the inset. (B) UV-vis spectra of 6TN/MONT multilayer films (1–20 layers) prepared from 0.1 M NaCl solution. Peak absorbance vs. number of bilayers is plotted in the inset. *Source:* Reproduced with permission from Ref.<sup>[28]</sup>. © 2002, American Chemical Society.

A study of the film morphology was also done using AFM. Fig. 4 shows the deposition of one 6TN layer from pure water and 0.1 M NaCl. The figure shows that the larger average aggregate size is shown from the saline system and that better surface coverage is achieved from this solution. Fig. 5 shows the AFM images of (A) 2.5, (B) 5, and (C) 10 bilayers of 6TN/MONT on glass. From the figure, it can be seen that the RMS roughness data for the saline deposition process does not increase dramatically when moving from 2.5 to 10 bilayers. However, with the pure water system, the RMS roughness increased from 22 to 27 to 40 nm for the three multilayer samples. The reason for the dramatic increase in roughness is probably because the clay sheets are unable to cover the sublayer defects since the 6TN aggregate size is on a comparable scale to the clay particle lateral dimensions. Moreover,

isolated and unevenly distributed aggregates make it harder for the subsequent layer of MONT plates to cover the empty spaces among them, leaving many holes or defects on the surface. The roughness of these defects is further magnified as the deposition process is continued.

In conclusion, a series of experiments on a bolaform amphiphile sexithiophene were done both in solution and as ultrathin films. The aggregation size and properties were studied under various conditions in solutions of different compositions. Ultrathin films were prepared using the layer-by-layer technique with polyelectrolytes and inorganic clay platelets and the morphology and film structure were characterized with a variety of surface-sensitive techniques. These results provide useful insight into many factors that affect the adsorption process and properties of ultrathin films.

## PHOTOREACTIVE BOLAFORM AMPHIPHILES

### Phenylenediacyrylic Acid Amphiphile Derivatives

In the last few years, one area that has required a large amount of attention concerning ultrathin film applications is the improvement of film stability against mechanical, chemical, and thermal degradation. One popular concept to increase film stability has been to incorporate cross-linkable molecules or polymers into the multilayer structure. Mao et al. used a phenylenediacyrylic acid bolaform amphiphile with two pyridinium headgroups in the  $\alpha$  and  $\omega$  positions (DIPY08) along with poly(sulfonic acid) on mica to fabricate multilayer films. The bolaform amphiphile was photopolymerizable on irradiation with UV light and formed 1,3-transcyclobutane rings in the polymer main chain as can be seen in Fig. 6.

The deposition process of the bolaform amphiphile multilayers proceeded in a linear fashion. This indicated that an equal amount of amphiphile molecules was adsorbed onto the substrate with each cycle. The photopolymerization was measured by monitoring the reduction of the monomeric  $\pi$ - $\pi^*$  absorption. Fig. 7 shows the UV spectra of eight bilayers on mica UV irradiated at different times. From the rapid reduction of the peak at 310 nm after the first 5 min of irradiation, it can be concluded that most of the monomeric C=C bonds were reacted. After 1 hr, the absorbance band did not change and the photopolymerization was said to be complete.

It was also found that the photopolymerization changes the apparent electrostatic properties of the layer interface through the use of surface force measurements. Also, the photopolymerization undoubtedly increases the lateral strength of the film while maintaining and increasing its uniformity.

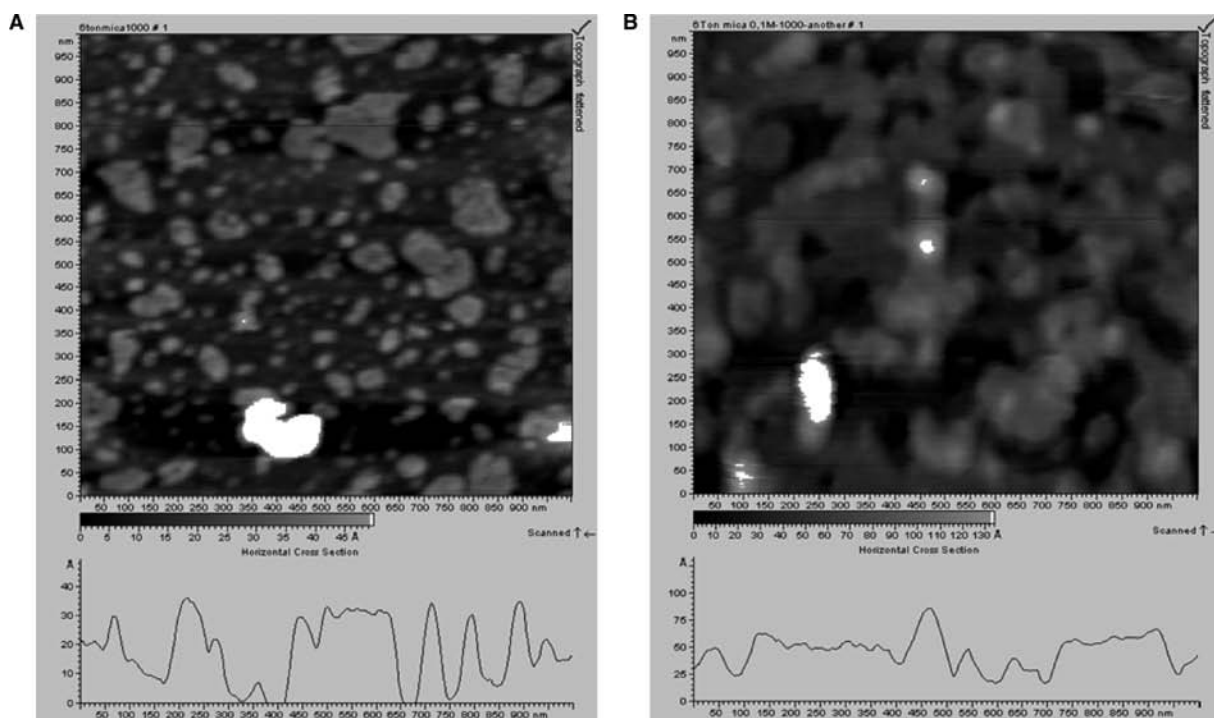


**Fig. 4** AFM morphology of 6TN aggregates on mica (A) from pure water (left) and (B) from 0.1 M NaCl (right). *Source:* Reproduced with permission from Ref.<sup>[28]</sup>. © 2002, American Chemical Society.

## Diacetylene Derivatives

Ultrathin films of polydiacetylenes have attracted great interest because of their unusual non-linear optical and photophysical properties.<sup>[52,53]</sup> If the molecules are present in a crystal-like arrangement, typical solid-state reactions such as topochemical diacetylene polymerization can occur. Before 1993, work was almost exclusively concerned with Langmuir–Blodgett (LB) films of amphiphilic diacetylene derivatives, which were then polymerized upon irradiation with UV light or high-energy radiation on the substrate.<sup>[54]</sup> The LB technique provided advantages in ultrathin film formation such as controlled thickness and orientation of the monomers before polymerization. One problem with this technique was in the difficulty to reproduce results because of preparation parameters such as temperature, pH and concentration of the subphase, surface pressure of the monolayer, and purity of the spreading solvent and starting materials. Some of these problems were addressed and overcome by the Tieke group who used bolaform amphiphiles based on diacetylene derivatives along with polyelectrolytes in the layer-by-layer deposition technique [10e,<sup>[32,55]</sup>].

Saremi et al. published a series of papers where the authors synthesized diacetylene bolaform amphiphiles with different alkyl chain lengths and different end groups to be used in fabricating multilayer assemblies along with poly(allylamine hydrochloride) (PAH).

The general structure of the bolaform amphiphiles is shown in Fig. 8.

The compounds used to fabricate multilayers with PAH are the disodium salts of 2,4-hexadiyne 1,6-disulfate (HDDS), 5,7-dodecadiyne 1,12-disulfate (DDDS) and 10,12-docosadiyne 1,22-disulfate (DCDS).

Fig. 9 shows a schematic of the film structure before and after polymerization.

The polymerization properties of the films were studied using UV–vis spectroscopy and structure and morphology investigated by XRD and AFM.

The results of the multilayer fabrication indicate that ultrathin diacetylene multilayers can be built up on charged surfaces but photopolymerization was successful only for DCDS/PAH multilayer films. The different reactivities were explained by the different packing arrangements of each amphiphile. The packing of the short-chain HDDS and DDDS was determined by the pendant sulfate end groups, preventing a dense packing arrangement necessary for the photopolymerization to occur. In the case of the DCDS bolaform, van der Waals forces between the longer alkyl chains determined the packing density, creating aggregates similar to that found in the crystal structure of DCDS verified by X-ray diffraction. Fig. 10 shows the absorption spectra of self-assembled DCDS/PAH after 8 min of UV irradiation.  $n$  corresponds to the number of dipping cycles for each film.

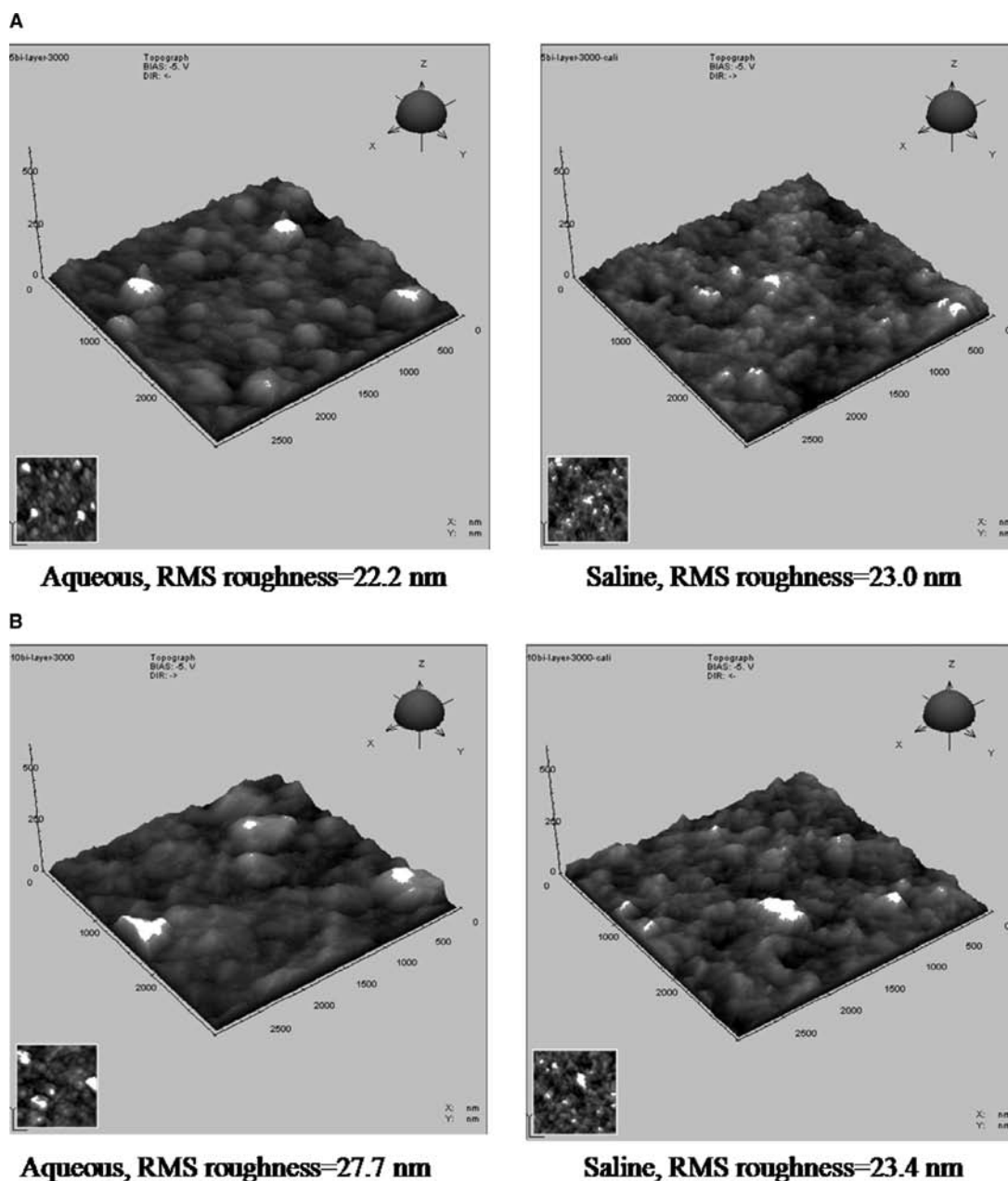


**Fig. 5** (A)–(C) Comparison of AFM images of multilayer samples with 6TN on the surface prepared from two systems. (A) Comparison of 5-layer surface morphology and roughness. (B) Comparison of 10-layer surface morphology and roughness. (C) Comparison of 20-layer surface morphology and roughness. *Source:* Reproduced with permission from Ref.<sup>[28]</sup>. © 2002, American Chemical Society.

The molecular orientation was also investigated for DCDS/PAH multilayers by X-ray diffraction and the DCDS amphiphiles were found to be in a highly tilted arrangement (tilt angle =  $38 \pm 4^\circ$ ). Morphological studies were also performed on the ultrathin films using AFM, which indicated an aggregate domain size between 100 and 300 nm with the average distance between domains between 100 and 200 nm. This is considerably smaller than that found in LB films.<sup>[56]</sup> The domains are usually not in contact with each

other, so that the multilayers do not represent a homogenous film but a fairly regular coverage of the substrate with small islands of layered structure.

As an extension of the initial work, Saremi et al. used an all-bolaform-amphiphile system to fabricate polymerizable multilayers.<sup>[57]</sup> Along with the DCDS bolaform above, the authors synthesized a positively charged 10,12-docosadiyne 1,22-dipyridinium bolaamphiphile, DCDP. It was found that these multilayers were much more photoreactive than the diacetylene/

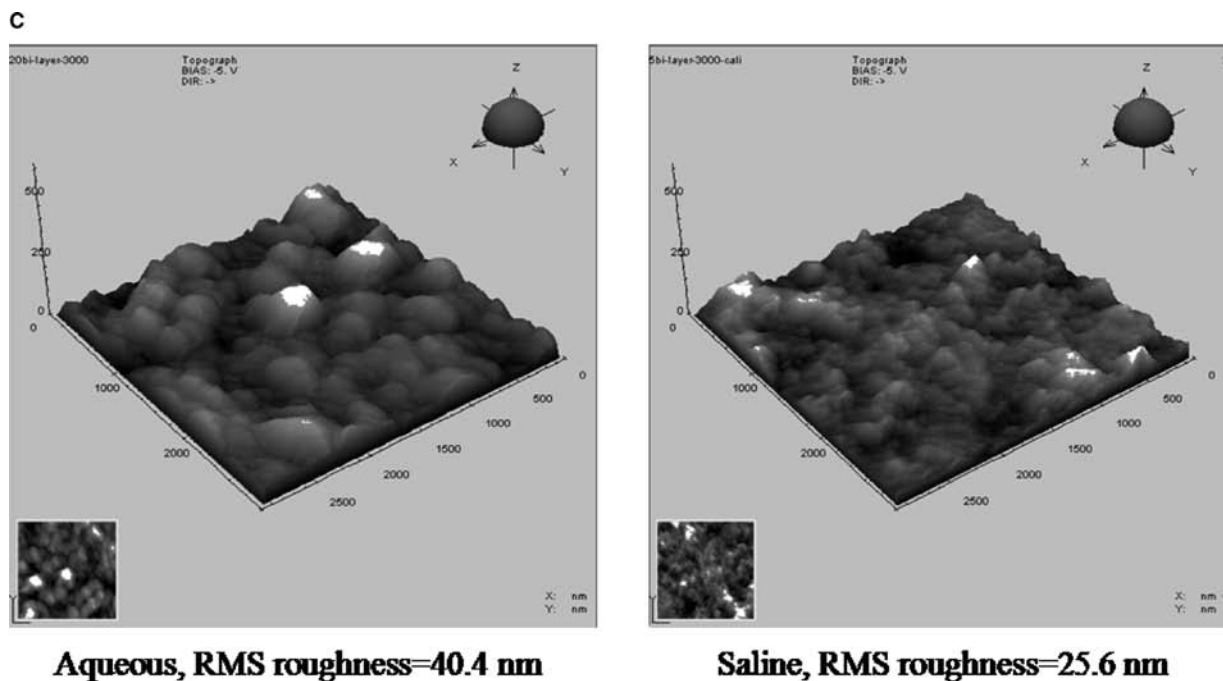
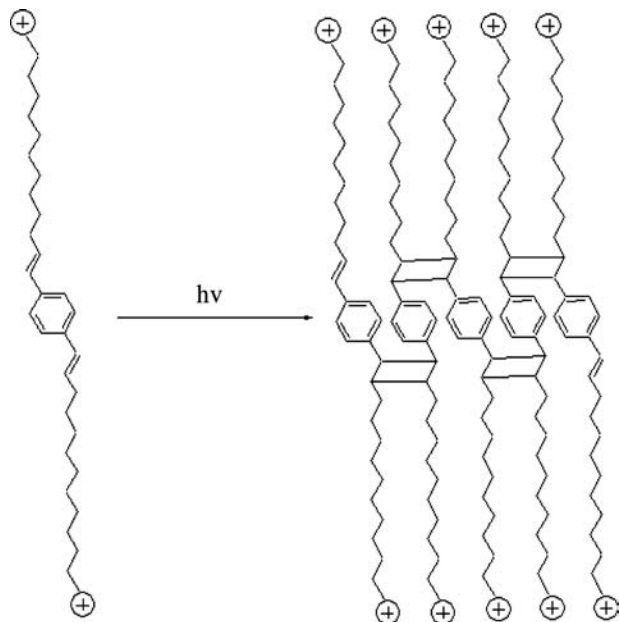


Fig. 5 (Continued).

polyelectrolyte films. The authors attributed this enhanced reactivity to a reordering of the multilayered structure into three-dimensional crystallites with a different packing geometry than either of the monomers



**Fig. 6** Idealized schematic structure of stepwise [2 + 2]-cycloaddition of the bolaform amphiphile DIPY08. Source: Reproduced with permission from *Langmuir* **1993**, *14*, 2184–2191. © 1993, American Chemical Society.

that provided for the enhanced photoreactivity. It was also shown that the reorganization of the multilayers produced reproducible surface inhomogeneities that are inherently typical of all bolaform amphiphile layer-by-layer systems. The tilt angle of the diacetylene bolaform amphiphiles in this system was calculated to be  $60.8^\circ$ .

Also, for reasons of comparison to the bolaform amphiphile systems, DCDS was polymerized in the solid state and a water-soluble polydiacetylene derivative was used to fabricate multilayers with PAH. The results were significantly different than the bolaform amphiphile system. From the UV-vis absorption spectrum, it was deduced that the polydiacetylene was adsorbed as a random coil rather than as a fully extended chain. This shows that order within the bolaform amphiphile multilayers is clearly much higher than that in the polyelectrolyte layers.

The works by the Tirrell, Ringsdorf, and Tiede groups have paved the way for the study of bolaform amphiphile molecules as useful candidates for the generation of photopolymerizable ultrathin films. The groups successfully demonstrated improved film stabilities using layer-by-layer deposition, which has many advantages over LB technique such as being independent of the substrate size and topology. It was also shown that a photopolymerizable, all-bolaform-amphiphile system can be superior to the deposition of an all-polyelectrolyte system in terms of the order within the bolaform amphiphile layers.



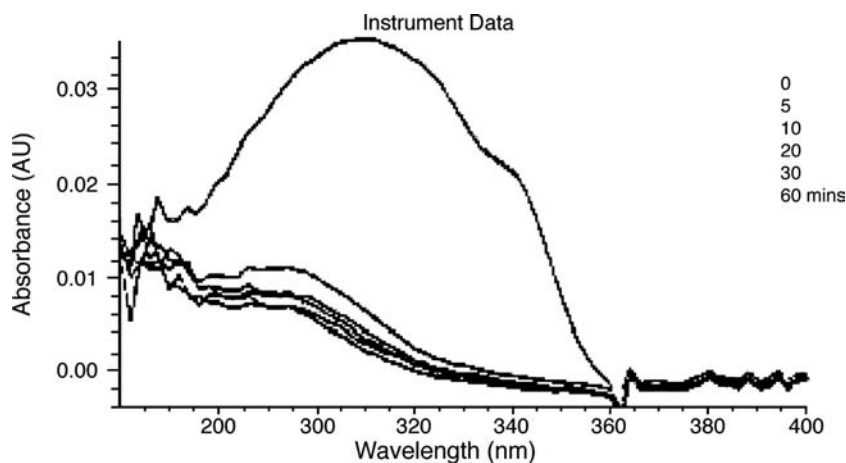


**Fig. 7** UV spectra of eight DIPY08/poly(sulfonic acid) bilayers self-assembled on mica UV irradiated at different times. *Source:* Reproduced with permission from *Langmuir* **1993**, *14*, 2184–2191. © 1993, American Chemical Society.

## PHOTOCHEMICAL ISOMERIZATION OF BOLAFORM AMPHIPHILES

### Azobenzene Containing Chromophores

Photochromic materials, whose optical properties can be reversibly varied upon exposure to light, are of great interest for potential electro-optical and optical applications.<sup>[58]</sup> Some promising applications include liquid crystal displays, holographic surface relief grating, and optical data storage media. Of particular interest in this area are those materials that contain azobenzene chromophores. Azobenzene derivatives, for instance, have been widely studied and are known to undergo photoisomerization from the thermodynamically more stable trans isomer (*E*) to the cis isomer (*Z*) upon irradiation with ultraviolet light ( $\lambda < 370$  nm), while the reverse reaction occurs either thermally or upon irradiation with visible light ( $\lambda > 450$  nm). Although this phenomenon has been observed in several different media, much of the earlier research effort was focused on photoisomerization of azobenzene in condensed phases such as LB films and self-assembled monolayers.

The first example of photoisomerization of an azobenzene-containing self-assembled multilayer came in 1998 when Saremi and Tieke<sup>[59]</sup> used layer by layer

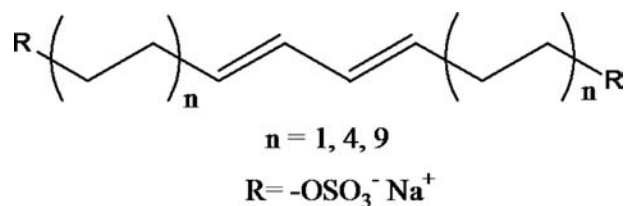


**Fig. 8** General structure of the diacetylene bolaform amphiphiles used for layer-by-layer assembly. R is the pendant ionic end group, which is either sulfate or pyridinium as depicted in the text.

to assemble multilayers composed of anionic azobenzene bolaform amphiphiles and cationic polyelectrolytes. This study presented the first comparative study of photoresponsive multilayers assembled in which the thickness of the layers could be controlled with a high degree of precision. In their experiments, they synthesized a water-soluble disodium salt of 4,4'-di(6-sulfatohexyloxy)azobenzene (DSHA) to be used in the fabrication of multilayer assemblies. For the corresponding cationic polyelectrolytes, poly(allylamine hydrochloride) (PAH), poly(ethyleneimine) (PEI), poly(dimethyldiallylammonium chloride) (PDDA), and chitosan (CHI), were used. UV-vis absorption spectroscopy was used to follow the photoisomerization process. Results showed all four cationic polyelectrolytes were suitable for preparing multilayer assemblies with the azobenzene bolaamphiphile, although the resulting multilayers showed interesting differences in their UV-vis absorption spectra. In particular, two types of spectra were observed as shown in Fig. 11.

The first type of spectra obtained showed a strong and narrow absorption band with  $\lambda_{\text{max}}$  located at 314 nm. This type of spectrum was observed from samples containing DSHA in combination with PAH or PEI, two polyelectrolytes that exhibit a high degree of charged species along the backbone of the polymer. Alternately, when a polymer with a less densely charged backbone such as PDDA or CHI was used as the polyelectrolyte layer, the UV-vis spectra showed a broad absorption with  $\lambda_{\text{max}}$  located at 340 nm. The differences in these two types of spectra were attributed to the optical absorption behavior of the azobenzene chromophore, which is sensitive to electronic interactions with neighboring chromophores in different molecular arrangements.<sup>[60]</sup> With this in mind, spectra obtained from DSHA/PAH or DSHA/PEI multilayers are indicative of a highly crystalline parallel alignment of H-aggregated chromophores, whereas



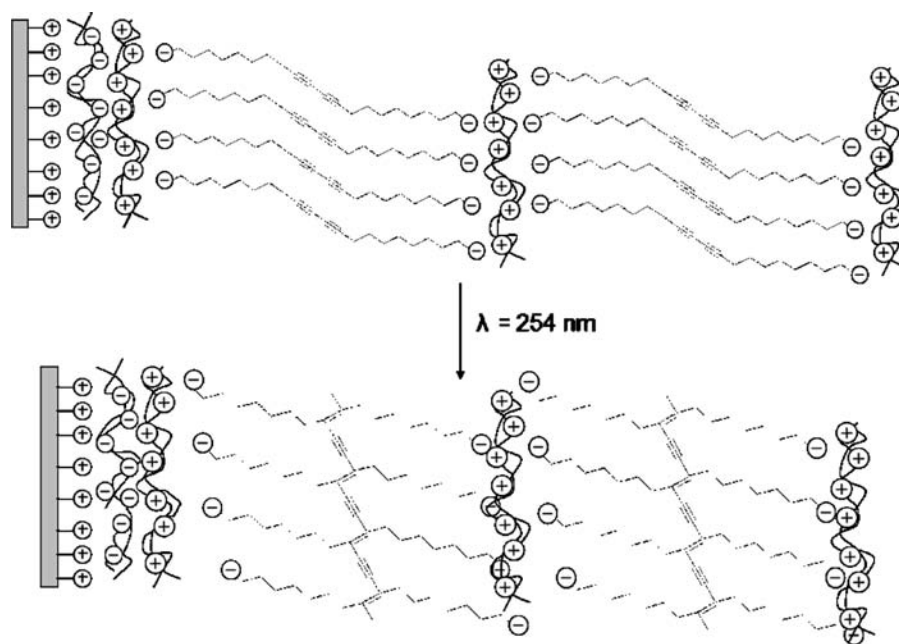


**Fig. 9** Schematic of the UV polymerization of DCDS in the electrostatically assembled multilayer. The tilt angles of the dianions are arbitrary. *Source:* Reproduced with permission from Ref.<sup>[36]</sup>. © 1993, American Chemical Society.

spectra obtained from DSHA/PDDA or DSHA/CHI are indicative of dimeric chromophores in smectic layers above the phase transition  $T_c$ .

Photoisomerization studies also reflected a dependence on the choice of polyelectrolyte. For the H-aggregated systems (DSHA/PEI and DSHA/PAH), irradiation with UV light ( $<370$  nm) produced a negligible change in the UV-vis spectrum indicating the absence of any photoisomerization of the azobenzene chromophores. This is attributed to a reduction in free volume within the H-aggregated phase. Since the isomerization of the azobenzene unit involves a

change in cross-sectional area, sufficient free volume is necessary for the photochemical reaction to occur. However, changes in the absorption spectra were observed for the DSHA/PDDA and DSHA/CHI multilayers in which the chromophores have sufficient free volume because of the less organized packing of azobenzene units in the smectic phase. A reduction in  $\lambda_{max}$  observed as a function of irradiation time indicating the photochemical conversion of *trans*-azobenzene to *cis*-azobenzene. The author's proposed orientation of DSHA dianions in both nonphotoresponsive multilayers and photoresponsive multilayers is depicted in Fig. 12. Although the effect of polyelectrolytes on the photochemical behavior of azobenzene has previously been demonstrated, the described work is unique to the application and characterization of azobenzene containing bolaform amphiphiles.

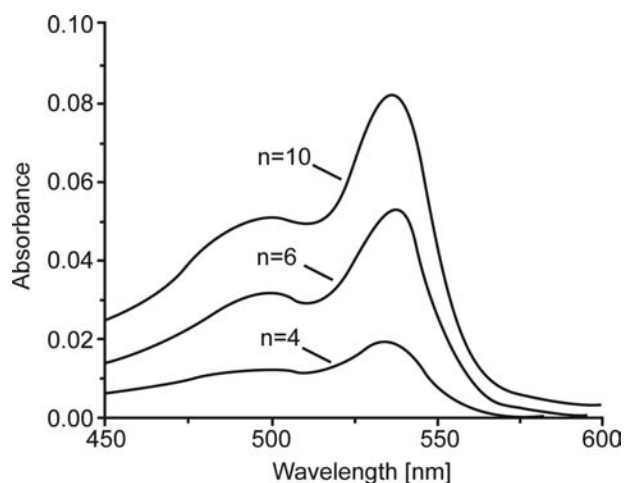


**Fig. 10** UV-vis absorption spectra of electrostatically assembled DCDS/PAH multilayers monitored after 8 min of UV irradiation.  $n$  depicts the number of dipping cycles applied. *Source:* Reproduced with permission from Ref.<sup>[36]</sup>. © 1995, American Chemical Society.

### Effect of Ionic Strength on Photochemical Isomerization

Similarly, Hong, Park, and Park studied the effects of added salts on the photoisomerization of azobenzene bolaform amphiphiles deposited with polyelectrolytes in multilayer assemblies.<sup>[61]</sup> With this study, Hong, Park, and Park described how bolaamphiphile aggregates formed in solution affect the structure of the resulting self-assembled multilayers and how the aggregate state affects the photoisomerization of the incorporated azobenzene chromophores. It is known that salt affects the conformation of the absorbing polyelectrolytes by shielding the charge on the polymer backbone,<sup>[62]</sup> thus dictating the amount of material

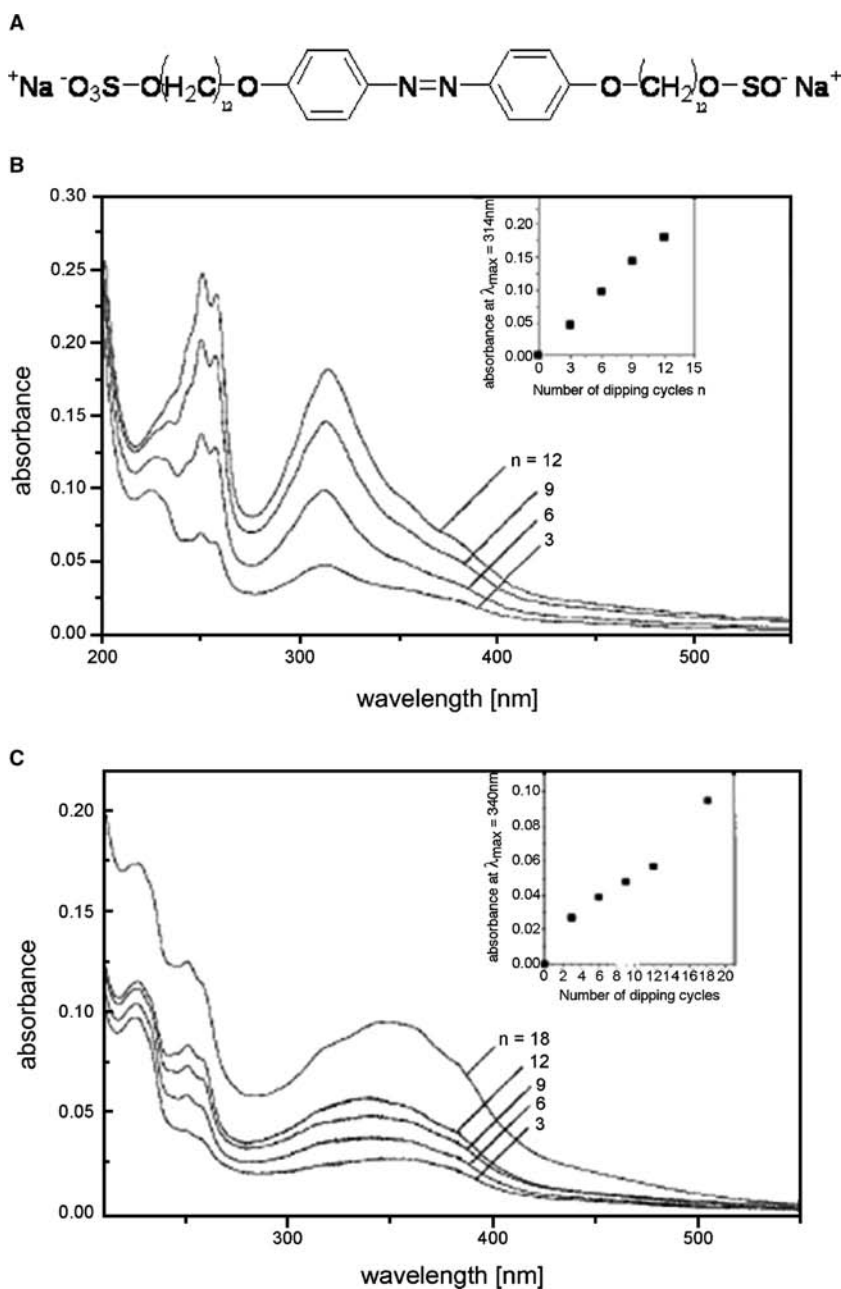


**Fig. 11** (A) Structure of bolaform amphiphile DSHA. (B) UV-vis absorption spectra of electrostatically assembled multilayers built up from alternated adsorption of DSHA and PAH, (C) DSHA and PDDA. Samples differ in the number of dipping cycles applied. The insets show the maximum absorbance of DSHA in the respective multilayer vs. number of dipping cycles applied. *Source:* Reproduced with permission from Ref.<sup>[59]</sup>. © 1995, John Wiley & Sons, Inc.

absorbed on the underlying substrate [1c]. A similar effect was observed in these bolaamphiphile systems.

Bolaform amphiphiles have previously been shown to exhibit unusual aggregation properties in dilute aqueous solution.<sup>[63]</sup> Building on these works, the authors used UV-vis absorption spectroscopy to investigate the formation of aggregates of their BA-12 azobenzene bolaamphiphile depending on both temperature and ionic strength. Fig. 13A shows the temperature dependence on the UV-vis spectra of dilute aqueous solutions of BA-12. Results show a blue shift in the  $\lambda_{\text{max}}$  of the absorption spectra from 357 nm at 58°C to 340 nm at 20°C. A strong decrease in absorption intensity was also observed with a decrease

in temperature. These results indicate the formation of H-aggregates of the azobenzene chromophores at lower temperatures. As the temperature is increased, the chromophores are then molecularly dispersed resulting in spectra corresponding to a single chromophore. Fig. 13B shows the plot of absorption maxima vs. temperature. These data indicate the existence of three phase transitions at 34°, 48°, and 58°C corresponding to a lyotropic mesophase, a biphasic lyotropic/isotropic, and an isotropic phase, respectively. The data presented is in good agreement with results published for other bolaamphiphile systems.<sup>[29]</sup>

The effect of ionic strength on the aggregation state of BA-12 at different salt (NaCl) concentrations was

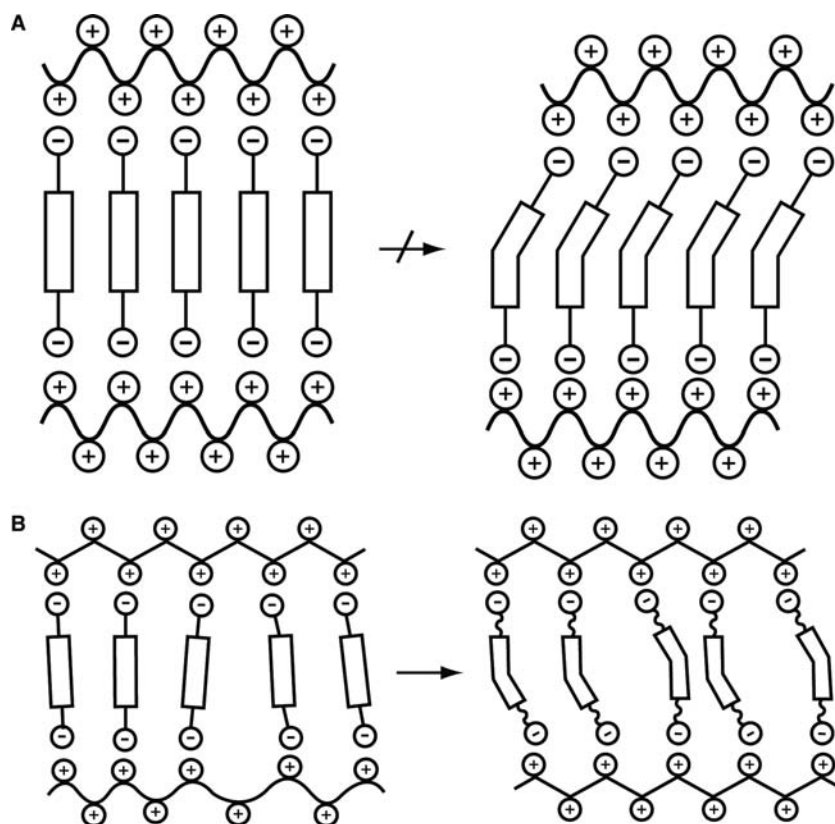


**Fig. 12** Proposed orientation of DSHA bolaform amphiphiles in non-photoreactive samples of type (A) (top), and in photoreactive samples of type (B) (bottom). *Source:* Reproduced with permission from Ref.<sup>[59]</sup>. © 1995, John Wiley & Sons, Inc.

observed by UV-vis spectroscopy. The  $\lambda_{\max}$  of BA-12 in solution with no salt present was blue shifted from 341 to 335 nm by increasing ionic strength to 1.0 M indicating the aggregation of the BA-12 molecules. Similar results were observed on film formation and multilayer growth as a function of ionic strength. Fig. 14 shows the UV-vis spectra of a 10-bilayer self-assembled film of BA-12/poly(vinyl sulfate) (PVS) on fused silica. The authors prepared films BA-12 solution at four ionic strengths (0, 0.1, 0.5, and 1.0 M). UV-vis spectra of the multilayer films closely resemble the spectra of BA-12 in solution at corresponding ionic strengths. The absorption maximum was observed at 341 nm for no salt and was blue shifted to 335 nm for 1.0 M NaCl. This suggests that BA-12 molecules are deposited from solution as preformed aggregates. This is supported by the increase in absorption intensity with increased ionic strength.

Hong, Park, and Park<sup>[61]</sup> studied the structural dependence of azobenzene photoisomerization using polarized UV-vis absorption spectroscopy. Fig. 15 shows the birefringence observed from a BA-12/PVS multilayer film. The film is irradiated with linearly polarized light, which generates a reorientation of the azobenzene chromophores perpendicular to the direction of the electric field vector of the incident light. The spectra were recorded in parallel and perpendicular

directions with respect to the initial UV polarization. From Fig. 15, it can be seen that the absorbance ( $\parallel$ ) is much less than the absorbance ( $\perp$ ). This is indicative of the photoisomerization from trans to cis of those azobenzene chromophores with an electric field vector parallel to the electric field vector of the incident light. There is also a strong time dependence on the in-plane photoisomerization of the azobenzene chromophores at different salt concentrations. In the absence of salt, in-plane photoisomerization of the azobenzene chromophores reached a steady state within 5 min. This is in contrast to 15 min for the films deposited at higher ionic strengths. These observations are consistent with the idea that the BA-12 molecules are deposited as H-aggregated domains with increased ionic strength previously discussed. These results also support the numerous reports in literature on the effects of aggregation state on the photoisomerization and photoalignment process.<sup>[64-66]</sup>

## CONCLUSION

Bolaform amphiphiles are molecules that have interesting properties both in solution and as ultrathin films. The work covered in this paper has shown how molecular design can be used to explore the diversity of

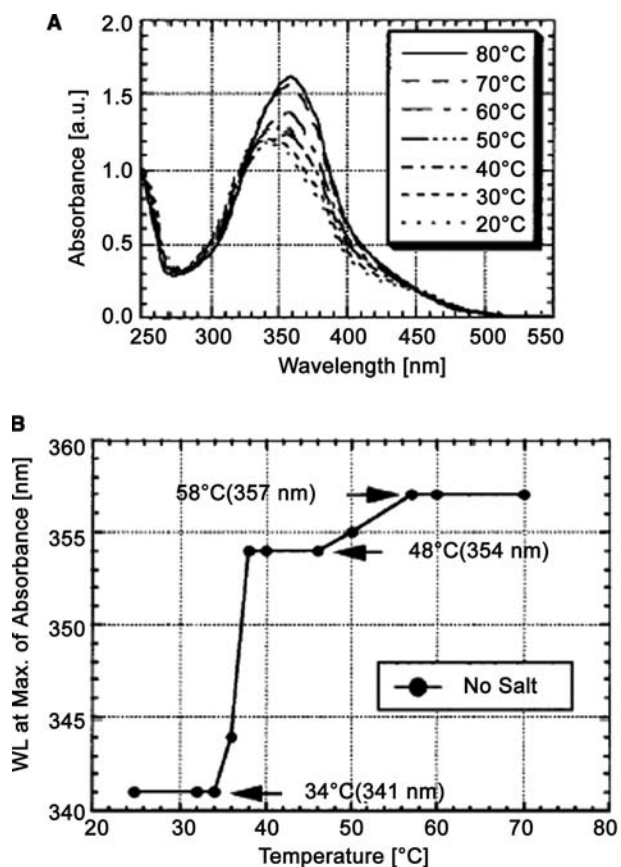


**Fig. 13** (A) UV-vis absorption spectra of BA-12 in aqueous solution (0.1 mM) depending on temperature. (B). Wavelength of the maximum absorbance vs. temperature plot of 0.1 mM aqueous BA-12 solution (from data in part A). *Source:* Reproduced with permission from Ref.<sup>[61]</sup>. © 1999, American Chemical Society.

bolaamphiphiles in various ultrathin film applications. There are critical factors such as the chain length and choice of end group that must be considered when creating bolaamphiphiles for electrostatic adsorption.

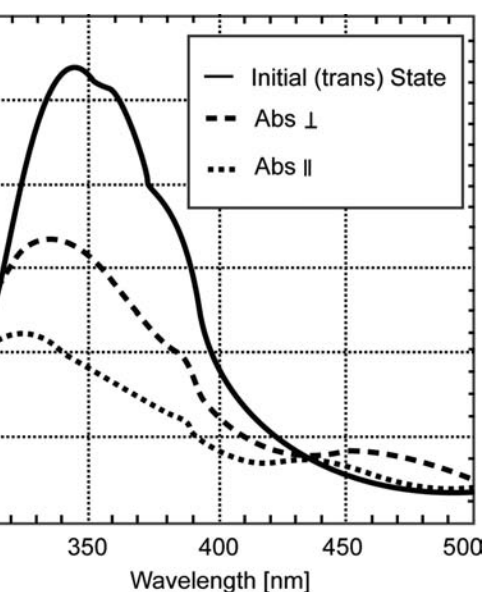
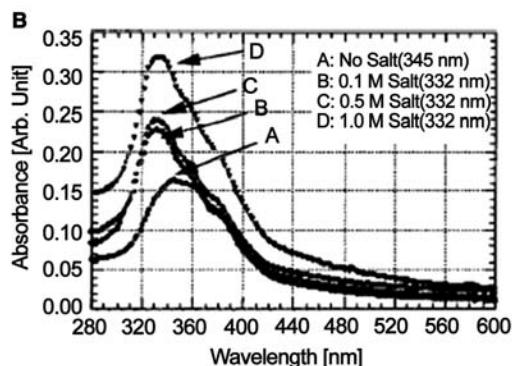
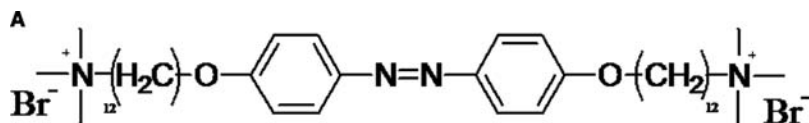


**Fig. 15** Polarized UV-vis absorption spectra of the self-assembled 10-bilayer BA-12/PVS ( $S_{0.1 M}$ ) on fused silica before (●) and after 5 min (▲, ▼) of linearly polarized UV (360 nm) irradiation. Spectra are obtained for both parallel (▼) and perpendicular (▲) to the initial UV light polarization. For reasons of clarity, only absorbance (●) of the initial *trans*-azobenzene in the multilayer assemblies is shown. *Source:* Reproduced with permission from Ref.<sup>[61]</sup>. © 1999, American Chemical Society.

The works have demonstrated the versatility of the layer-by-layer method by fabricating multilayers with polyelectrolytes, inorganic clay platelets, and other bolaform amphiphiles for specific applications. On a more general scale, bolaform amphiphiles have provided insight into aggregation behavior in solution and the effect that aggregate size may have on adsorption and multilayer structure. It was demonstrated that factors such as ionic strength and temperature

**Fig. 14** (A) Structure of the bolaform amphiphile BA-12. (B) UV-vis absorption spectra of the self-assembled 10-bilayer BA-12/PVS on fused silica. The dipping solution of BA-12 is adjusted to different ionic strengths by addition of NaCl: no salt (A); 0.1 M (B); 0.5 M (C); 1.0 M (D). *Source:* Reproduced with permission from Ref.<sup>[61]</sup>. © 1999, American Chemical Society.

drastically affect the crystallinity and film morphology of electrostatically assembled films. These works have opened the door not only to the future design and characterization of new bolaform amphiphiles, but also on the surface dynamics of layer-by-layer ultrathin films.

## REFERENCES

- Iler, R.K. Multilayers of colloidal particles. *J. Colloid Interface Sci.* **1966**, *21*, 569–594.
- Decher, G.; Hong, J.-D. Buildup of ultrathin multilayer films by a self-assembly process: I. Consecutive adsorption of anionic and cationic bipolar amphiphiles. *Makromol. Chem., Macromol. Symp.* **1991**, *46*, 321–327.
- Decher, G.; Hong, J.-D. Buildup of ultrathin multilayer films by a self-assembly process: II. Consecutive adsorption of anionic and cationic bipolar amphiphiles and polyelectrolytes on charged surfaces. *Ber. Bunsenges. Phys. Chem.* **1991**, *95*, 1430–1434.
- Decher, G.; Hong, J.-D.; Schmitt, J. Buildup of ultrathin multilayer films by a self-assembly process: III. Consecutively alternating adsorption of anionic and cationic polyelectrolytes on charged surfaces. *Thin Solid Films* **1992**, *210/211*, 831–835.
- Lvov, Y.; Decher, G.; Sukhorukov, G. Assembly of thin films by means of successive deposition of alternate layers of DNA and poly(allylamine). *Macromolecules* **1993**, *26*, 5396–5399.
- Donth, E.; Walther, D.; Shilov, V.N.; Knippel, E.; Budde, A.; Lowack, K.; Helm, C.A.; Mohwald, H. Nonlinear hairy layer theory of electrophoretic fingerprinting applied to consecutive layer by layer polyelectrolyte adsorption onto charged polystyrene latex particles. *Langmuir* **1997**, *13*, 5294–5305.
- Kleinfeld, E.R.; Ferguson, G.S. Stepwise formation of multilayered nanostructural films from macromolecular precursors. *Science* **1994**, *265*, 370–373.
- Keller, S.W.; Kim, H.N.; Mollouk, T.E. Layer-by-layer assembly of intercalation compounds and heterostructures on surfaces: towards molecular “beaker” epitaxy. *J. Am. Chem. Soc.* **1994**, *116*, 8817–8818.
- Kotov, N.A.; Dekany, I.; Fendler, J.H. Layer-by-layer self-assembly of polyelectrolyte–semiconductor nanoparticle composite films. *J. Phys. Chem.* **1995**, *99*, 13,065–13,069.
- Lvov, Y.; Ariga, K.; Ichinose, I.; Kunitake, T. Formation of ultrathin multilayers and hydrated gel from montmorillonite and linear polycations. *Langmuir* **1996**, *12*, 3038–3044.
- Lvov, Y.; Ariga, K.; Ichinose, I.; Kunitake, T. Assembly of multicomponent protein films by means of electrostatic layer-by-layer adsorption. *J. Am. Chem. Soc.* **1995**, *117*, 6117–6123.
- Caruso, F.; Mohwald, H. Protein multilayer formation through a stepwise self-assembly technique. *J. Am. Chem. Soc.* **1999**, *121*, 6039–6046.
- Gao, M.Y.; Richter, B.; Kirstein, S.; Mohwald, H. Electroluminescence studies on self-assembled films of PPV and CdSe nanoparticles. *J. Phys. Chem., B* **1998**, *102*, 4096–4103.
- Tang, Z.; Wang, Y.; Kotov, N.A. Semiconductor nanoparticles on solid substrates: Film structure, intermolecular interactions, and polyelectrolyte effects. *Langmuir* **2002**, *18*, 7035–7040.
- Malikova, N.; Pastoriza-Santos, I.; Schierhorn, M.; Kotov, N.A.; Liz-Marzan, L.M. Layer-by-layer assembled mixed spherical and planar gold nanoparticles: control of interparticle interactions. *Langmuir* **2002**, *18*, 3694–3697.
- Mamedov, A.A.; Belov, A.; Giersig, M.; Mamedova, N.N.; Kotov, N.A. Nanorainbows: Graded semiconductor films from quantum dots. *J. Am. Chem. Soc.* **2001**, *123*, 7738–7739.
- Ostrander, J.W.; Mamedov, A.A.; Kotov, N.A. Two modes of linear layer-by-layer growth of nanoparticle–polyelectrolyte multilayers and different interactions in the layer-by-layer deposition. *J. Am. Chem. Soc.* **2001**, *123*, 1101–1110.
- Pastoriza-Santos, I.; Koktysh, D.S.; Mamedov, A.A.; Giersig, M.; Kotov, N.A.; Liz-Marzan, L.M. One-pot synthesis of Ag@TiO<sub>2</sub> core-shell nanoparticles and their layer-by-layer assembly. *Langmuir* **2000**, *16*, 2731–2735.
- Cooper, T.; Campbell, A.; Crane, R. Formation of polypeptide-dye multilayers by electrostatic self-assembly technique. *Langmuir* **1995**, *11*, 2713–2718.
- Yoo, D.; Lee, J.K.; Rubner, M.F. Investigations of new self-assembled multilayer thin films based on alternately adsorbed layers of polyelectrolytes and functional dye molecules. *Mater. Res. Soc. Symp. Proc.* **1996**, *413*, 395–400.
- Zhang, X.; Gao, M.; Kong, X.; Sun, Y.; Shen, J. Build-up of a new type of ultrathin film of porphyrin and phthalocyanine based on cationic and anionic electrostatic attraction. *J. Chem. Soc., Chem. Commun.* **1994**, 1055–1056.
- Araki, K.; Wagner, M.J.; Wrighton, M.S. Layer-by-layer growth of electrostatically assembled multilayer porphyrin films. *Langmuir* **1996**, *12*, 5393–5398.
- Sellergren, B.; Swietlov, A.; Amebrant, T.; Unger, K. Consecutive selective absorption of pentamidine and phosphate biomolecules on a self-assembled layer reversible formation of a chemically selective coating. *Anal. Chem.* **1996**, *68*, 402–407.
- Ariga, K.; Lvov, Y.; Kunitake, T. Assembling alternate dye–polyion molecular films by electrostatic layer-by-layer adsorption. *J. Am. Chem. Soc.* **1997**, *119*, 2224–2231.
- Advincula, R.; Park, M.-K.; Baba, A.; Kaneko, F. Photoalignment in ultrathin films of a layer-by-layer deposited water-soluble azobenzene dye. *Langmuir* **2003**, *19*, 654–665.
- Advincula, R.C.; Fells, E.; Park, M.-K. Molecularly ordered low molecular weight azobenzene dyes and polycation alternate multilayer films: Aggregation, layer order, and photoalignments. *Chem. Mater.* **2001**, *13*, 2870–2878.
- Locklin, J.; Youk, J.H.; Xia, C.; Park, M.-K.; Fan, X.; Advincula, R.C. Nanostructured ultrathin films of water-soluble sexithiophene bolaform amphiphiles

- prepared by layer-by-layer self-assembly. *Langmuir* **2002**, *18*, 877–883.
28. Fan, X.; Locklin, J.; Youk, J.H.; Blanton, W.; Xia, C.; Advincula, R. Nanostructured sexithiophene/clay hybrid multilayers: A comparative structural and morphological characterization. *Chem. Mater.* **2002**, *14*, 2184–2191.
  29. Cheung, J.H.; Fou, A.F.; Rubner, M.F. Molecular self-assembly of conducting polymers. *Thin Solid Films* **1994**, *244*, 985–989.
  30. Ferreira, F.; Rubner, M.F. Molecular level processing of conjugated polymers. 1. Layer-by-layer manipulation of conjugated polyions. *Macromolecules* **1995**, *28*, 7107–7114.
  31. Fou, A.C.; Rubner, M.F. Molecular level processing of conjugated polymers. 2. Layer-by-layer manipulation of in-situ polymerized p-type doped conducting polymers. *Macromolecules* **1995**, *28*, 7115–7120.
  32. Cheung, J.H.; Stockton, W.B.; Rubner, M.F. Molecular-level processing of conjugated polymers. 3. Layer-by-layer manipulation of polyaniline via electrostatic interactions. *Macromolecules* **1997**, *30*, 2712–2716.
  33. Mao, G.; Tsao, Y.; Tirrell, M.; Davis, H.T.; Hessel, V.; Ringsdorf, H. Self-assembly of photopolymerizable bolaform amphiphile mono- and multilayers. *Langmuir* **1993**, *9*, 3461–3470.
  34. Mao, G.; Tsao, Y.-H.; Tirrell, M.; Davis, H.T.; Hessel, V.; Esch, J.; Ringsdorf, H. Monolayers of bolaform amphiphiles: Influence of alkyl chain length and counterions. *Langmuir* **1994**, *10*, 4174–4184.
  35. Mao, G.; Tsao, Y.-H.; Tirrell, M.; Davis, H.T.; Hessel, V.; Ringsdorf, H. Interactions, structure, and stability of photoreactive bolaform amphiphile multilayers. *Langmuir* **1995**, *11*, 942–952.
  36. Saremi, F.; Maassen, E.; Tieke, B. Self-assembled alternating multilayers built-up from diacetylene bolaamphiphiles and poly(allylamine hydrochloride): Polymerization properties, structure, and morphology. *Langmuir* **1995**, *11*, 1068–1071.
  37. Saremi, F.; Lange, G.; Tieke, B. Deeply colored self-assembled multilayers of anionic DPP bolamphiphiles and cationic polyelectrolytes. *Adv. Mater.* **1996**, *8*, 923–926.
  38. Rubingh, D.N.; Holland, P.M. *Cationic Surfactants: Physical Chemistry*; Surfactant Science Series; Marcel Dekker, Inc.: New York, 1991; Vol. 37.
  39. Abid, S.K.; Hamid, S.M.; Sherrington, D.C. *J. Colloid Interface Sci.* **1987**, *120*, 245.
  40. Alami, E.; Beinert, P.; Marie, P.; Zana, R. Alkanediyl-alpha,omega-bis(dimethylalkylammonium bromide) surfactants. 3. Behavior at the air–water interface. *Langmuir* **1993**, *9*, 1465–1467.
  41. Hessel, V.; Ringsdorf, H.; Festag, R.; Wendorff, J.H. Ionic thermotropic liquid-crystals formed by monomeric dipolar and polymeric multipolar amphiphiles with pyridinium head groups. *Makromol. Chem., Rapid Commun.* **1993**, *14*, 707.
  42. Horowitz, G.; Fichou, D.; Peng, X.; Garnier, F. Thin-film transistors based on alpha conjugated oligomers. *Synth. Met.* **1991**, *41–43*, 1127–1130.
  43. Katz, H.E.; Dodabalapur, A.; Torsi, L.; Elder, D. Precursor synthesis, coupling, and TFT evaluation of end-substituted thiophene hexamers. *Chem. Mater.* **1995**, *7*, 2238–2240.
  44. Geiger, F.; Stoldt, M.; Schweizer, H.; Bauerle, P.; Umbach, E. Electroluminescence from oligothiophene-based light-emitting devices. *Adv. Mater.* **1993**, *5*, 922.
  45. Hosokawa, G.; Higashi, H.; Kusumoto, T. Novel structure of organic electroluminescent cells with conjugated oligomers. *Appl. Phys. Lett.* **1993**, *62*, 3238–3240.
  46. Noma, N.; Tsuzuki, T.; Shirota, Y. Alpha-thiophene octamer as a new class of photoactive material for photoelectrical conversion. *Adv. Mater.* **1995**, *7*, 647–648.
  47. Hotta, S.; Rughooputh, S.D.D.V.; Heeger, A.; Wudl, F. Spectroscopic studies of soluble poly(3-alkylthienyls). *Macromolecules* **1987**, *20*, 212–215.
  48. Koren, A.B.; Curtis, M.D.; Kampf, J.W. Crystal engineering of conjugated oligomers and the spectral signature of  $\pi$  stacking in conjugated oligomers and polymers. *Chem. Mater.* **2000**, *12*, 1519–1522.
  49. Hutchison, C.J.; Bissessur, R.; Shriver, F.D. Conductivity anisotropy of polyphosphazene–montmorillonite composite electrolytes. *Chem. Mater.* **1996**, *8*, 1597–1599.
  50. Ibrahim, M.A.; Lee, B.-G.; Park, N.-G.; Rugh, J.R.; Eberl, D.D.; Frank, A.J. Synthesis of new oligothiophene derivatives and their intercalation compounds: Orientation effects. *Synth. Met.* **1999**, *105*, 35–42.
  51. Eckle, M.; Decher, G. Tuning the performance of layer-by-layer assembled organic light emitting diodes by controlling the position of isolating clay barrier sheets. *Nano Lett.* **2001**, *1*, 45–49.
  52. Kajzar, F.; Messier, J. Solid state polymerization and optical properties of diacetylene Langmuir–Blodgett multilayers. *Thin Solid Films* **1983**, *99*, 109–116.
  53. Pasquier, C.; Tieke, B.; Zahir, S.; Bosshard, C.; Guenter, P. 2-(Pentacosyl-10,12-diynylamino)-5-nitropyridine: a new polymerizable amphiphile for non-linear optical Langmuir–Blodgett films. *Chem. Mater.* **1991**, *3*, 211.
  54. Tieke, B.; Wegner, G.; Naegel, D.; Ringsdorf, H. *Angew. Chem., Int. Ed. Engl.* **1976**, *15*, 764.
  55. Saremi, F.; Tieke, B. Polymerization of 10,12-docosadiyne-1,22-disulfate in self-assembled multilayers. *Adv. Mater.* **1995**, *7* (4), 378–380.
  56. Tieke, B.; Lieser, G.; Weiss, K. Parameters influencing the polymerization and structure of long-chain diynoic acids in multilayers. *Thin Solid Films* **1983**, *99*, 95–102.
  57. Saremi, F.; Tieke, B.; Jordan, G.; Rammensee, W. Organized multilayers of polydiacetylenes prepared by electrostatic self assembly. *Supramol. Sci.* **1997**, *4*, 471–477.
  58. Ichimura, K. *Polymers as Electrooptical and Photooptical Active Media*; Shibaev, V., Ed.; Springer: Berlin, 1996.



59. Saremi, F.; Tieke, B. Photoinduced switching in self-assembled multilayers of an azobenzene bolaamphiphile and polyelectrolytes. *Adv. Mater.* **1998**, *10* (5), 388–391.
60. Shimomura, M.; Okahata, Y.; Kunitake, T. Ber. Bunsenges. Phys. Chem. **1983**, *87*, 1134.
61. Hong, J.-D.; Park, E.; Park, A. Effects of added salt on photochemical isomerization of azobenzene in alternate multilayer assemblies: bipolar amphiphile–polyelectrolyte. *Langmuir* **1999**, *15*, 6515–6521.
62. Cohen Stuart, M.A. *J. Phys.* **1988**, *49*, 1001.
63. Okahata, Y.; Kunitake, T. Formation of stable monolayer membranes and related structures in dilute aqueous solution from two-headed ammonium amphiphiles. *J. Am. Chem. Soc.* **1979**, *101*, 5231–5234.
64. Siewierski, L.M.; Brittain, W.J.; Petrash, S.; Foster, M.D. Photoresponsive monolayers containing in-chain azobenzene. *Langmuir* **1996**, *12*, 5838–5844.
65. Geue, Th.; Ziegler, A.; Stumpe, J. Light-induced orientation phenomena in Langmuir–Blodgett multilayers. *Macromolecules* **1997**, *30*, 5729–5738.
66. Stumpe, J.; Geue, Th.; Fischer, Th.; Menzel, H. Photo-orientation in LB multilayers of amphotropic polymers. *Thin Solid Films* **1996**, *284–285*, 606–611.

# Layer-by-Layer Assembly of Thin Films of Mixed Nanoparticles

**Jianchang Guo**

*Department of Chemistry, Emory University, Atlanta, Georgia, U.S.A.*

**Encai Hao**

*Department of Chemistry, Northwestern University, Evanston, Illinois, U.S.A.*

**Tianquan Lian**

*Department of Chemistry, Emory University, Atlanta, Georgia, U.S.A.*

## INTRODUCTION

In recent years, thin films of semiconductor nanoparticles have found an increasing number of applications in solar energy conversion, electronics, and light-emitting diodes (LEDs).<sup>[1–13]</sup> Different approaches, such as Langmuir–Blodgett (LB), self-assembly (SA), and layer-by-layer assembly (LBL), were developed to fabricate thin films.<sup>[4,11,14]</sup> Among these approaches, layer-by-layer assembly offers a simple scheme to fabricate films consisting of different layers. This may be potentially used to construct films with advanced functions, such as electron and energy transfer between component layers. Layer-by-layer assembly techniques which are based on electrostatic attraction between oppositely charged molecules in adjacent layers were successfully applied to the construction of multilayer films of molecules,<sup>[15]</sup> nanoparticle/polymer mixtures,<sup>[16–18]</sup> and other inorganic materials.<sup>[19]</sup> This LBL assembly method is quite simple and versatile.<sup>[11]</sup> In the preparation process, the substrate, functionalized with a charged layer, is first immersed in a solution containing materials of opposite charge to allow the deposition of the first layer. The resultant film is then rinsed and dried. To deposit the second layer, the same procedure is repeated for materials of opposite charges to the first layer. The deposition cycle can be repeated until the desired number of bilayers is reached. Because of the strong interactions between the oppositely charged layers, the LBL films have shown long-term mechanical stability in air, water, and other polar solvents.<sup>[20]</sup> Many nanoparticles, such as TiO<sub>2</sub>, CdSe, and Au, were successfully assembled into films, for which a number of advanced electronic and photonic applications were demonstrated.<sup>[16,17,19]</sup>

As an alternative method to electrostatic interaction-based LBL assembly, multilayer films based on hydrogen bonding have been reported by Stockton and Rubner<sup>[21]</sup> using polyaniline, and by Wang et al.<sup>[22,23]</sup>

using poly(vinyl pyridine)/poly(acrylic acid) (PVP/PAA). Recently, we extended this hydrogen bonding-based LBL approach to assemble inorganic nanoparticles.<sup>[24,25]</sup> In this report, we review our group's work on layer-by-layer assembly of metal and semiconductor nanoparticles. Both films of single- and multiple-particle types (size or chemical nature) have been fabricated. We will describe two approaches of LBL assembly based on hydrogen bonding interaction between adjacent layers. We will discuss the use of UV–visible absorption spectrum to monitor the buildup of the multilayers and Fourier transform infrared (FTIR) spectroscopy to investigate the hydrogen-bonding interaction between the layers.

## EXPERIMENTAL SECTION

### Materials

Poly(4-vinylpyridine) (PVP) ( $M_w = 6.0 \times 10^4$ ), poly(acrylic acid) (PAA) ( $M_w = 2.4 \times 10^5$ ), polyethylenimine (PEI) ( $M_w = 7.5 \times 10^5$ ), 4-mercaptobenzoic acid (4-MBA), selenium power (99.99%), sulfur powders, tellurium powders, hydrogen tetrachloroaurate(III) trihydrate, cadmium acetate dihydrate (98%), and sodium borohydride were purchased from Aldrich. Methanol and dimethylformide were used as they were found.

### Synthesis of Au Nanoparticles with Carboxyl Group Tailored Surfaces (4-MBA-Au)

4-Mercaptobenzoic acid (4-MBA, HS–C<sub>6</sub>H<sub>4</sub>–COOH)-capped Au nanoparticles were synthesized in methanol/acetic acid solution following a published procedure with a slight modification.<sup>[26]</sup> Briefly, 0.40 mmol of tetrachloroauric acid and 1.2 mmol of 4-mercaptobenzoic acid were codissolved in 35 mL of 6:1 methanol/acetic acid, producing a yellow solution. NaBH<sub>4</sub> (0.3 g,

8 mmol) in 15 mL of methanol was added with rapid stirring. The solution immediately changed to a black suspension. The suspension was stirred for an additional 30 min. The solvent was then removed under vacuum. The black product was washed several times with diethyl ether and dried under an N<sub>2</sub> stream. The sample was soluble in polar solvents such as water and methanol.

### Synthesis of Au Nanoparticles with Pyridine Group Tailored Surfaces (Py–Au)

A total of 55.8 mg of PVP was dissolved in 150 mL of methanol, into which 70.8 mg of HAuCl<sub>4</sub> dissolved in 10 mL of methanol was added under rapid stirring.<sup>[24]</sup> The molar ratio of metal salts to pyridine units was about 1:2. Ten minutes later, 27 mg of NaBH<sub>4</sub> in 10 mL of methanol was quickly added. A change of color from yellow to pink was immediately observed, indicating the formation of Au nanoparticles. After 30 min of further stirring, the solution was maintained at 278 K for further use.

### Synthesis of CdS (CdSe) Nanoparticles in N, N Dimethylformide (DMF)

Cadmium acetate dihydrate powder was suspended in ethanol and refluxed for 3–6 h, yielding a 0.1 M Cd precursor. NaHS (NaHSe) ethanolic solution (0.56 M) was prepared from the reaction between selenium and sodium borohydride in absolute ethanol.<sup>[27]</sup> For CdS (CdSe) nanoparticle preparation, 10 mL (1 mmol) of the Cd precursor was evaporated under reduced pressure. The resulting dry residue was dissolved in 100 mL DMF, into which 4-mercaptobenzoic acid (2.5 mmol) was added. The colorless solution was then reacted with 1.0 mL of NaHS (NaHSe) ethanolic solution under argon atmosphere, producing an orange CdS (brown CdSe) colloidal solution. After further stirring for 30 min, the solution was kept at 278 K for future use.

### Synthesis of 4-MBA-Capped CdTe Nanoparticles

4-MBA-capped CdTe nanoparticles were synthesized in two steps: first, we prepared TOPO-capped CdTe nanoparticles according to a published procedure,<sup>[28,29]</sup> then, the TOPO capping groups on CdTe nanoparticles were substituted by 4-MBA in DMF solutions, following literature procedures.<sup>[30]</sup>

### Fabrication of Polymer/Metal (Semiconductor) Nanoparticle Multilayer Films

To fabricate LBL films of polymer/metal (semiconductor)-nanoparticles, it was first necessary to pretreat the

substrates. In this step, we functionalized the substrate (e.g., quartz, CaF<sub>2</sub> plates, cover glass, and carbon-coated copper grids) with an NH<sub>2</sub>-tailored surface by immersing into a branched polymer (PEI, 0.5 wt.%) solution. Polyethylenimine is an attractive choice because it can adhere to a variety of substrate surfaces. Au nanoparticles with carboxyl group and pyridine group tailored surfaces were assembled according to the following two routes.

#### LBL assembly of PVP and 4-MBA-Au nanoparticles

The PEI-pretreated substrates were transferred to a PAA (0.252 g/L) methanol solution for 10 min, resulting in a COOH-tailored surface. The substrates were then immersed in a PVP (0.256 g/L) methanol solution for 5 min to add a layer of PVP. After rinsing with methanol, the substrates were then transferred to a methanol/acetic acid (10:1) solution of Au nanoparticles for 10 min to deposit one layer of Au nanoparticles. The procedure was repeated until the desired number of bilayers of PVP/4-MBA-Au was reached as shown in Fig. 1.

#### LBL assembly of PAA and Py–Au nanoparticles

As schematically shown in Fig. 2, the PEI-pretreated substrates were first immersed in a PAA (0.252 g/L) methanol solution for 10 min, resulting in a COOH-tailored surface. After washing with methanol, the substrates were transferred to a methanol solution of PVP-capped Au nanoparticles for another 10 min, adding one layer of Au nanoparticles. Multilayer films can be obtained by repeating the last two steps.

### LBL Assembly of PVP/CdSe and PVP/CdS Multiplayer Films

Briefly, the substrates treated with PEI solutions were transferred to a PAA methanol solution (0.252 g/L) to form a carboxylic acid terminated surface. The resulting substrates were immersed in PVP methanol solution (0.256 g/L) for 10 min to add a PVP layer. After being rinsed with methanol, the substrates were immersed into a dilute CdS (CdSe) colloid (DMF/methanol = 1:1) for 10 min to form a CdS (CdSe) layer. Multilayer films can be obtained by repeating the last two steps, as shown schematically in Fig. 1.

### LBL Assembly of CdSe/CdTe Mixed Multilayer Films

Cover glasses were first treated with PEI as described previously. The pretreated substrates were immersed into a CdSe colloid in DMF for 10 min to form a CdSe layer. The resulting substrates were rinsed with

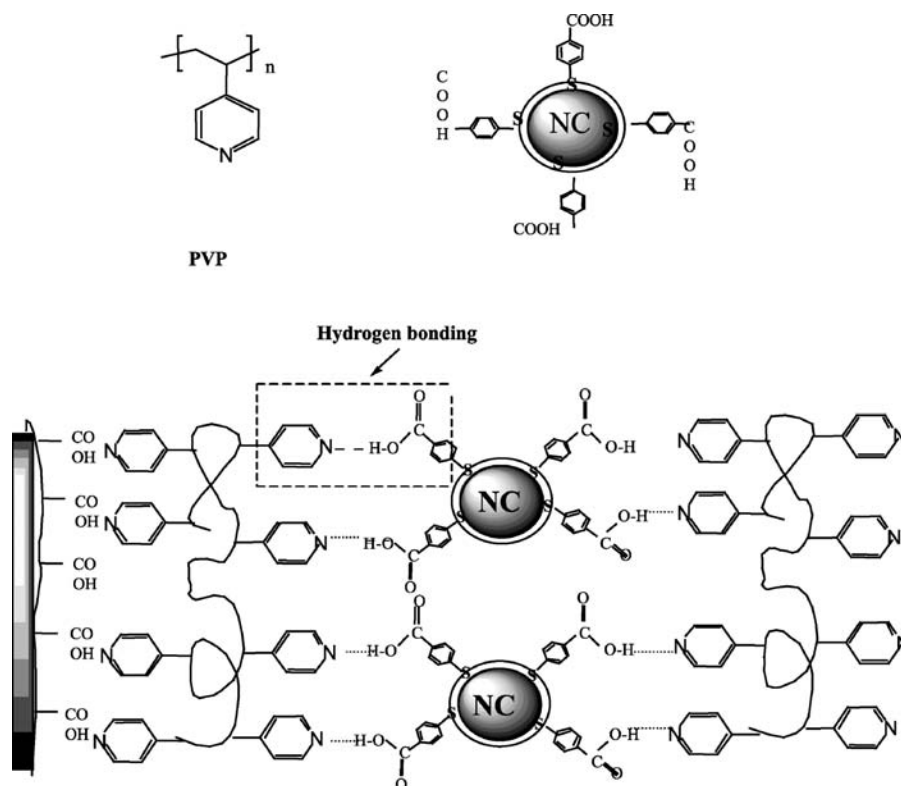


**Fig. 1** Schematic representation of the buildup of multilayer assembly by consecutive adsorption of PVP and metal or semiconductor nanocrystals (NC).

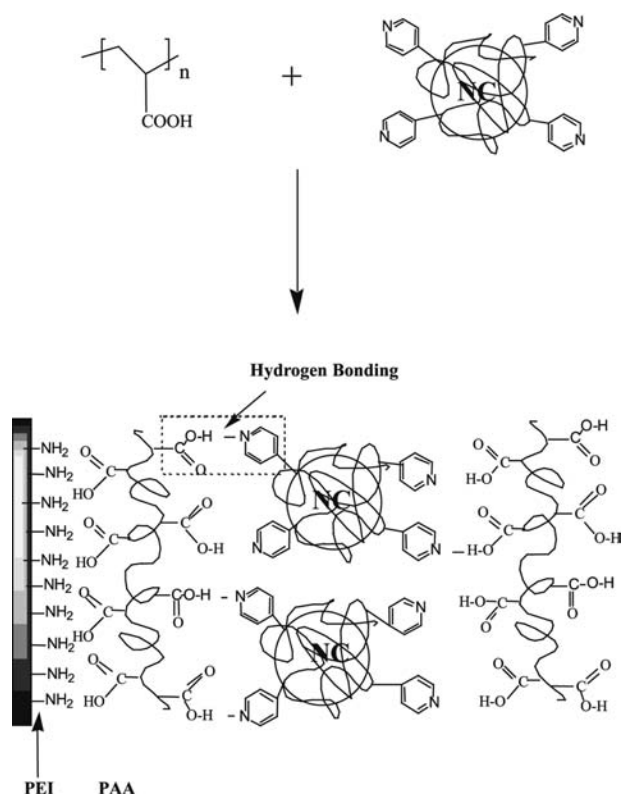


**Fig. 2** Schematic representation of the buildup of multilayer assembly by consecutive adsorption of PAA and PVP capped metal or semiconductor nanocrystals.

methanol and then immersed in PVP methanol solution (0.256 g/L) for 10 min to add a PVP layer. The substrates, after rinsed by methanol, were immersed in a CdTe colloid in DMF for another 10 min to deposit a layer of CdTe. Multilayer films could be fabricated by depositing PVP/CdSe/PVP/CdTe layers alternately.

### LBL Assembly of CdS/Py–Au Multilayer Films

The CdS/Py–Au multilayer films were assembled according to the following procedure: CaF<sub>2</sub> plates were sequentially treated in PEI, PAA, and PVP solutions. The substrates were then immersed in a dilute CdS colloid solution (DMF/methanol = 1:1) for 10 min to form a CdS layer. The substrates were then rinsed in methanol and dried. After that, the substrates were immersed into the Py–Au solution for 10 min. Multilayer films could be fabricated by depositing CdS and Py–Au layers alternately.

## RESULTS AND DISCUSSION

### Layer-by-Layer Assembly of Single-Composite Nanoparticles

LBL assembly of gold nanoparticles

Poly(vinyl pyridine) (PVP) is known to be a strong metal-chelating agent.<sup>[31,32]</sup> We synthesized stable Au

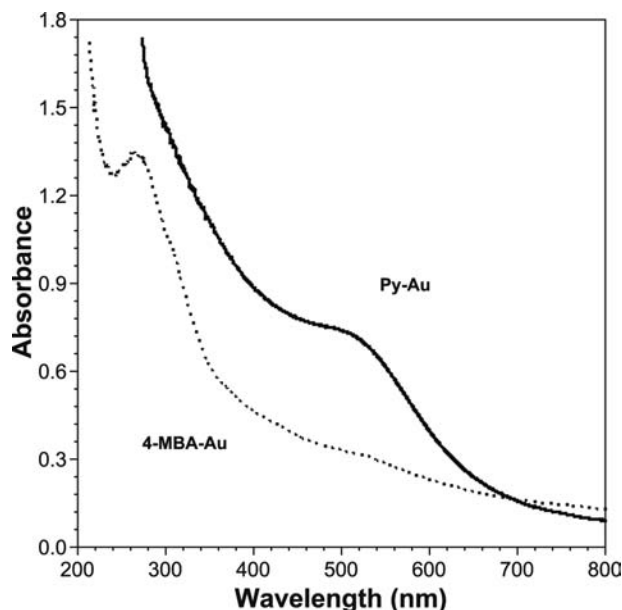


**Fig. 3** UV-visible spectra of 4-MBA capped Au nanoparticles and Py-Au nanoparticles in methanol. *Source:* From Ref.<sup>[24]</sup>. © 2000 American Chemical Society.

nanoparticles in the presence of pure PVP, producing pyridine group tailored surfaces (hydrogen-bonding acceptors). The UV-vis spectrum of Py-Au methanol solution (Fig. 3, upper curve) showed a pronounced surface plasmon (SP) band around 530 nm. Although the UV-vis spectrum of 4-MBA-capped Au nanoparticles in methanol solution (Fig. 3, bottom curve) showed only a weak SP band, transmission electron microscopy (TEM) images indicate that the Au

nanoparticles were round in shape and had an average diameter of about  $2.6 \pm 0.9$  nm.

Multilayer film buildup of Au nanoparticles was monitored by using UV-vis spectroscopy. The observed absorption could be attributed to 4-MBA and Au particles because polymer absorption in the visible region was found to be negligible. Fig. 4A shows the UV-vis absorption spectra of the multilayer film of PVP/(4-MBA-Au) with different number of bilayers on a quartz slide. The absorption spectra of PVP/(4-MBA-Au) nanoparticle multilayer films were in agreement with that of the Au nanoparticle solution (Fig. 3), indicating the successful assembly of 4-MBA-Au nanoparticles into the film. In addition, a linear increase of the absorbance with the number of bilayers (Fig. 4A) was observed, suggesting that approximately the same amount of Au nanoparticles was adsorbed in every deposition cycle.

A similar linear increase of absorbance with the number of bilayers (Fig. 4B) was observed for the PAA/(Py-Au) LBL film, again indicating a stepwise and uniform assembly process. Such behavior has been observed in many layer-by-layer deposition systems based on electrostatic interaction.<sup>[16-18,33,34]</sup> Our result demonstrated that layer-by-layer assembly based on hydrogen bonding provided an alternative way to fabricate homogeneous organic/inorganic multilayer films.

The PVP/(4-MBA-Au) LBL film was also studied by small-angle X-ray diffraction (SAXD), which is a convenient and direct method for determining film thickness.<sup>[35,36]</sup> Fig. 5 shows the SAXD pattern of a 12-bilayer film of PVP/(4-MBA-Au) on a quartz substrate. The X-ray curve revealed well-defined Kiessig

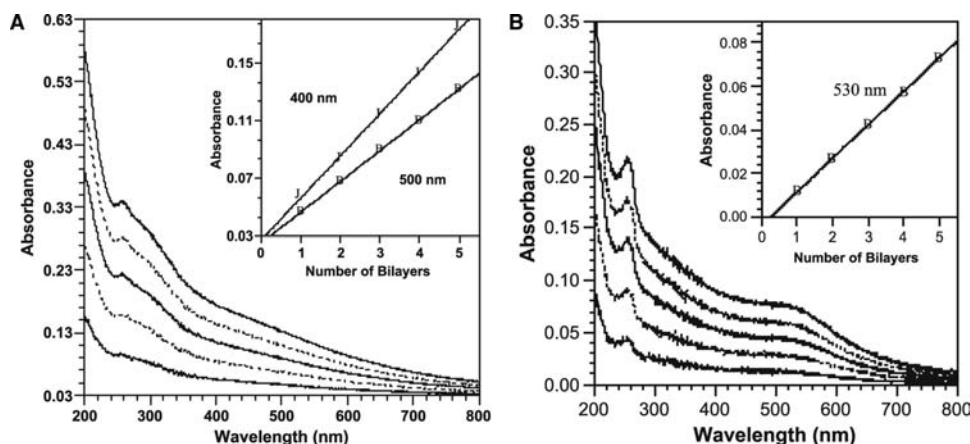


**Fig. 4** (A) UV-visible absorption spectra of the PVP/(4-MBA-Au) nanoparticle multilayer film with different numbers of bilayers. From the lower to upper curves, the number of PVP/(4-MBA-Au) bilayers is 1, 2, 3, 4, and 5. Shown in the inset is a plot of the absorbance at 400 and 500 nm vs. the number of PVP/(4-MBA-Au) bilayers. (B) UV-visible absorption spectra of PAA/(Py-Au) nanoparticle multilayer thin film with different numbers of bilayers. From the lower to upper curves, the number of PAA/(Py-Au) bilayers is 1, 2, 3, 4, and 5. The inset is a plot of the absorbance at 530 nm vs. the number of PAA/(Py-Au) bilayers. *Source:* From Ref.<sup>[24]</sup>. © 2000, American Chemical Society.

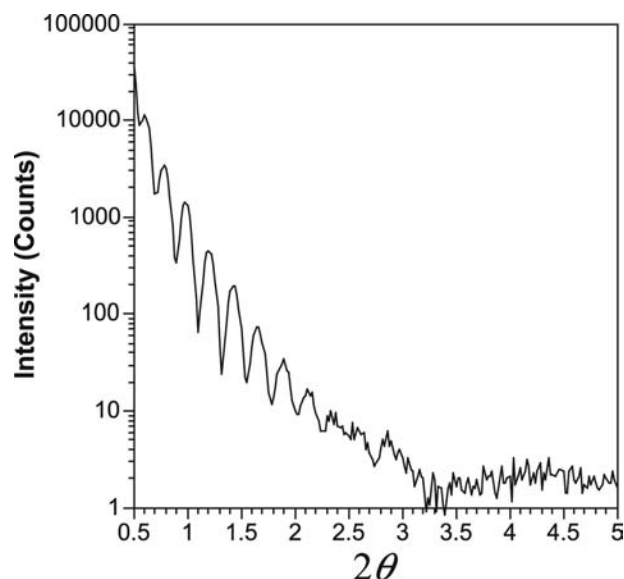


**Fig. 5** Small-angle X-ray diffraction patterns of a 12-bilayer film of PVP/Au on a quartz substrate. *Source:* From Ref.<sup>[24]</sup>. © 2000 American Chemical Society.

fringes, which indicated that the PVP/(4-MBA-Au) LBL film was uniform and flat. The total thickness of the film was estimated to be about 39.6 nm from the oscillation period. Because the UV-vis results demonstrated a stepwise and uniform assembly process, the thickness of one PVP/Au bilayer was calculated to be about 3.3 nm.

The direct evidence for hydrogen bonding between PVP and 4-MBA on the surface of Au nanoparticles was obtained by using FTIR spectroscopy. Hydrogen bonding between pyridine groups and carboxyl groups resulted in a splitting pattern of the OH stretching bands.<sup>[37–40]</sup> Fig. 6 shows the IR spectra of a cast film of 4-MBA-Au nanoparticles, a cast film of PVP, and a 10-bilayer PVP/(4-MBA-Au) film on CaF<sub>2</sub> plates. The spectrum of the 4-MBA-Au nanoparticles shows a pronounced C=O band at 1678 cm<sup>-1</sup>, which is consistent with that of 4-MBA in KBr glass.<sup>[41,42]</sup> This band, as well as the broad OH stretch (~3450 cm<sup>-1</sup>), indicates hydrogen-bonding interaction between terminal carboxyl groups of 4-MBA on the surface of Au nanoparticles.<sup>[41–43]</sup> The absorption peaks at 1595.8, 1556.6, and 1414.2 cm<sup>-1</sup> in the spectrum of the cast film of PVP are assigned to ring vibrations of pyridine groups of PVP.<sup>[22]</sup>

After Au nanoparticles were assembled into multilayer film, the C=O stretching vibration was shifted to 1710 cm<sup>-1</sup>. Another striking feature is the appearance of new bands at 1937 and 2520 cm<sup>-1</sup>. These bands were assigned to the stretching bands of hydrogen-bonded OH groups based on a similar splitting pattern of OH groups observed in polymer blends containing carboxyl and vinylpyridine groups.<sup>[37–40]</sup> The presence of these bands in the multilayer thin films indicated strong

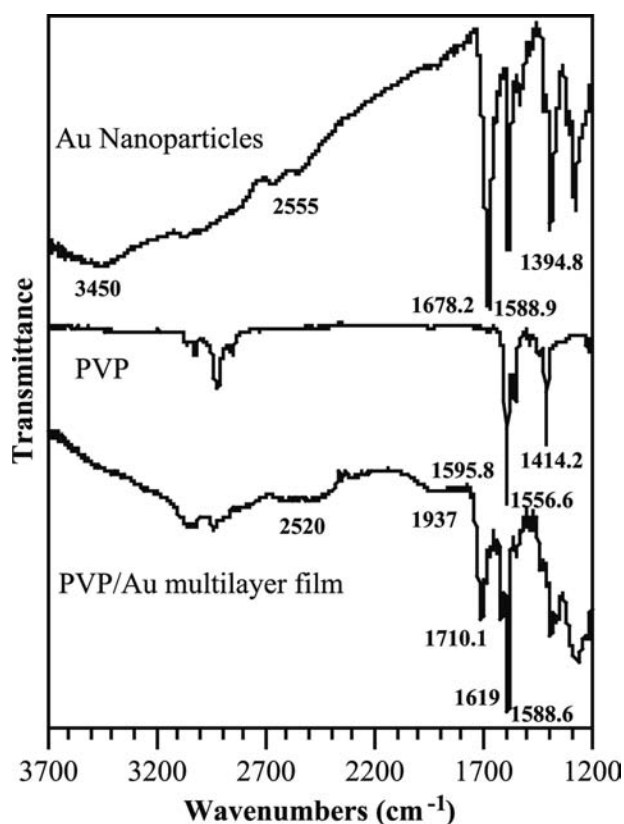


**Fig. 6** FTIR spectra of a cast film of PVP, a cast film of 4-MBA-Au nanoparticles, and a 10-bilayer PVP/Au film on CaF<sub>2</sub> plates. *Source:* From Ref.<sup>[24]</sup>. © 2000 American Chemical Society.

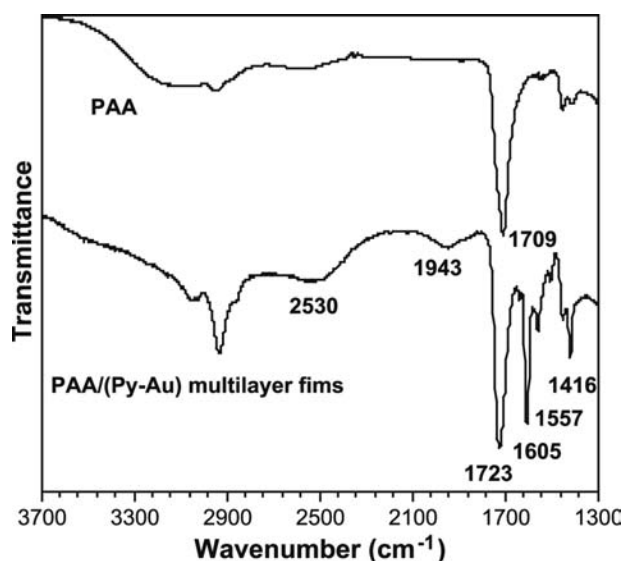
hydrogen bonding between the carboxyl groups (donors) on the surface of Au nanoparticles and pyridine groups (acceptors) of PVP. The peaks in the spectral region from 1650 to 1400 cm<sup>-1</sup> were difficult to assign because of overlapping absorption bands, although they arose mainly from the ring vibration of both 4-MBA and pyridine groups.

Fig. 7 shows the FTIR spectra of a cast film of PAA and a 10-bilayer PAA/(Py-Au) film on CaF<sub>2</sub> slides. The IR spectrum of pure PAA shows a broad absorption band around 3000 cm<sup>-1</sup> and the C=O stretching vibration at 1709 cm<sup>-1</sup>, indicating that the polymer was in an associated state.<sup>[22]</sup> For the PAA/Py-Au films, in addition to a shift of C=O stretching band to 1723 cm<sup>-1</sup>, O-H stretching vibrations at 2530 and 1943 cm<sup>-1</sup> were also observed. These spectral features indicated strong hydrogen bonding between the carboxyl groups of PAA and pyridine groups on the surface of Au nanoparticles.<sup>[37–40]</sup> Ring vibrations of pyridine groups at 1605, 1557, and 1416 cm<sup>-1</sup> were also observed.

#### LBL assembly of semiconductor nanoparticles

The PVP/4-MBA hydrogen bonding pair was also used to assemble semiconductor nanoparticles in





**Fig. 7** FTIR spectra of a cast film of pure PAA and a 10-bilayer PVP/Au film on  $\text{CaF}_2$  plates. *Source:* From Ref.<sup>[24]</sup>. © 2000 American Chemical Society.

nonhydrolytic solution. UV-visible spectroscopy was used to monitor the assembling process of PVP and CdS LBL films. Fig. 8A shows the UV-vis absorption spectra of a PVP/CdS multilayer film prepared on a quartz slide with different numbers of bilayers. The band at 370 nm was in agreement with the first exciton band of CdS colloidal particles as shown in Fig. 8A.

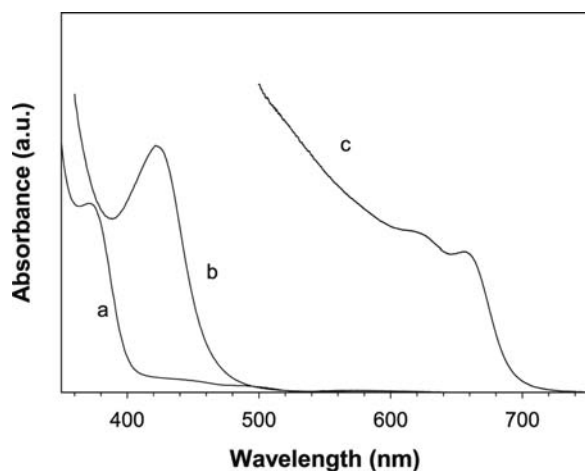


**Fig. 8** UV-visible absorption spectra of (A) the PVP/CdS multilayer film with different numbers of bilayers. From the lower to upper curves, the number of PVP/CdS bilayers is 1, 2, 3, 4, and 5, respectively. Inset: the absorbance at 370 and 300 nm vs. the number of PVP/CdS bilayers; (B) the PVP/CdSe multilayer film with different numbers of bilayers. From the lower to upper curves, the number of PVP/CdSe bilayers is 1, 2, 3, 4, and 5, respectively. Inset: the absorbance at 430 and 300 nm vs. the number of PVP/CdSe bilayers. *Source:* (B) From Ref.<sup>[25]</sup>. © 2000 American Chemical Society.

This illustrated that the CdS nanoparticles were successfully assembled into thin films. In addition, the observed linear increase of CdS absorbance vs. the number of bilayers (Fig. 8A) indicated a stepwise and uniform assembling process.

Similar results can be found for PVP/CdSe (Fig. 8B). UV-visible results for LBL assembly exhibits a well-resolved peak at 430 nm, which agrees very well with the first exciton band of CdSe colloid solution (Fig. 8A). Moreover, a linear increase of the absorbance with the number of PVP/CdSe bilayers (Fig. 8B) was observed, indicating that approximately the same amount of CdSe nanoparticles was absorbed in every deposition cycle. The flatness of PVP/CdSe film was also monitored by small-angle X-ray diffraction, as shown in Fig. 9. It revealed well-defined Kiessig fringes, which suggested that the PVP/CdSe LBL film was uniform and flat. The thickness of one PVP/CdSe bilayer was calculated to be about 24.7 Å. This is consistent with the average diameter of the CdSe particles of 17–20 Å determined by light scattering measurement.

The driving force for the construction of PVP/CdSe multilayer film was identified by infrared spectroscopy. For this study, we prepared a film without the step involving poly(acrylic acid) to avoid its strong infrared absorption. The multilayer film was fabricated by directly immersing PEI-coated  $\text{CaF}_2$  plates into CdSe and PVP solution alternately. Fig. 10 shows the IR spectra of a cast film of 4-mercaptobenzoic acid stabilized CdSe nanoparticles, a cast film of PVP, and a 10-bilayer PVP/CdSe film on  $\text{CaF}_2$  plates. The C=O band of 4-MBA-capped CdSe appeared at  $1670\text{ cm}^{-1}$  and the ring vibration of 4-MBA was observed at  $1589.7\text{ cm}^{-1}$ . The absorption peak at  $1541\text{ cm}^{-1}$  was assigned to the vibration of carboxylate salts of cadmium acetate (present in the CdSe nanoparticle solution). For the cast film of PVP, the absorption peaks at  $1595.8$ ,  $1556.6$ , and  $1414.2\text{ cm}^{-1}$  were assigned to the ring vibration of the pyridine groups of PVP. After CdSe nanoparticles were assembled into a multilayer film, a C=O stretching vibration appeared at  $1710\text{ cm}^{-1}$ , which suggested that carboxylic acid groups on the surface of CdSe were not ionized in the assembling process. In addition, broad O-H bands appeared at  $1930$  and  $2520\text{ cm}^{-1}$ , indicating the formation of hydrogen bonding between the carboxylic acid on the surface of CdSe nanoparticles and pyridine groups of PVP. These results provided the evidence that the multilayer film was assembled based on hydrogen bonding.

### LBL Assembly of Multicomposite Multilayer Films of Different Nanoparticles

As indicated above, we have successfully fabricated multiplayer films consisting of one type of nanoparticles

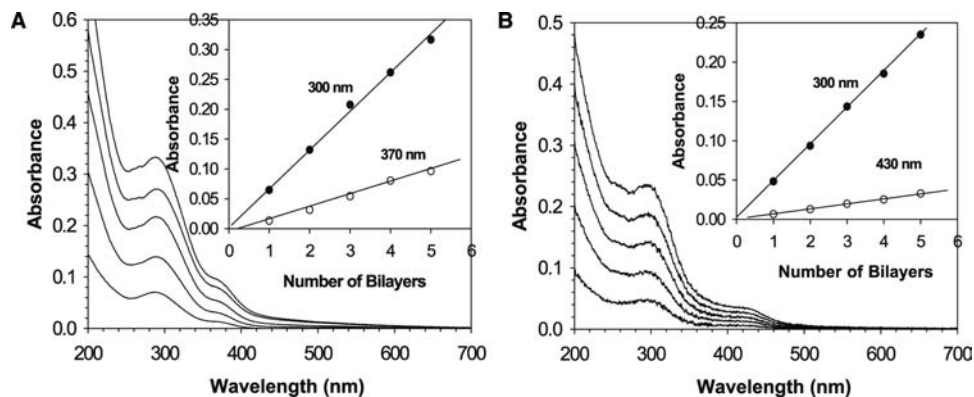


**Fig. 9** Small-angle X-ray diffraction patterns of a 12-bilayer film of PVP/CdSe on a quartz substrate. *Source:* From Ref.<sup>[25]</sup>. © 2000 American Chemical Society.

(metal or semiconductor) by using hydrogen bonding-based layer-by-layer assembly. We have demonstrated that two different approaches, as indicated in Figs. 1 and 2, can be used. More recently, we showed that the same strategies could be used to assemble thin films containing multiple types of nanoparticles. This will potentially enable the design of films with properties (such as spectral response and functionality) that cannot be easily achieved by using only one type of particles. Next, we will review our results in CdSe/CdTe and CdS/Py–Au LBL assembly.

TOPO-capped CdTe nanoparticles were prepared according the method of Peng et al.<sup>[28,29]</sup> To produce 4-MBA-capped CdTe nanoparticles, the TOPO ligands were replaced by 4-MBA, following the procedure of Mattoussi et al.<sup>[30]</sup> The 4-MBA-capped CdTe particles

were stable for over 1 month in the refrigerator. UV–visible spectrum shows a very clear first exciton peak at 660 nm, as indicated in Fig. 11C. The assembly process of a 12-bilayer LBL film of CdSe and CdTe was monitored by UV–visible spectroscopy, as indicated in Fig. 10. CdSe and CdTe nanoparticles were alternately assembled to form a film consisting of layers of CdSe /PVP/CdTe/PVP. The process is similar to the method indicated in Fig. 1. Two strong peaks

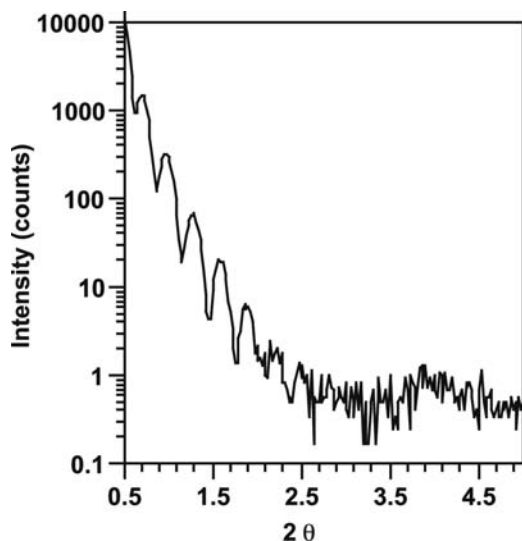


**Fig. 10** FTIR spectra of a cast film of 4-mercaptobenzoic acid stabilized CdSe nanoparticles, a cast film of PVP, and 10 bilayers of PVP/CdSe thin film on CaF<sub>2</sub> plates. *Source:* From Ref.<sup>[25]</sup>. © 2000 American Chemical Society.

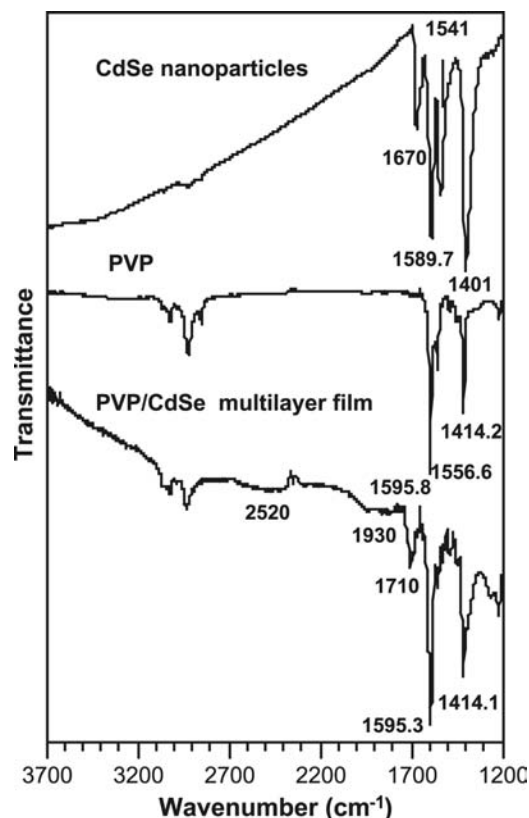


**Fig. 11** UV–visible spectrum of (A) CdS; (B) CdSe; (C) CdTe nanoparticles in DMF.

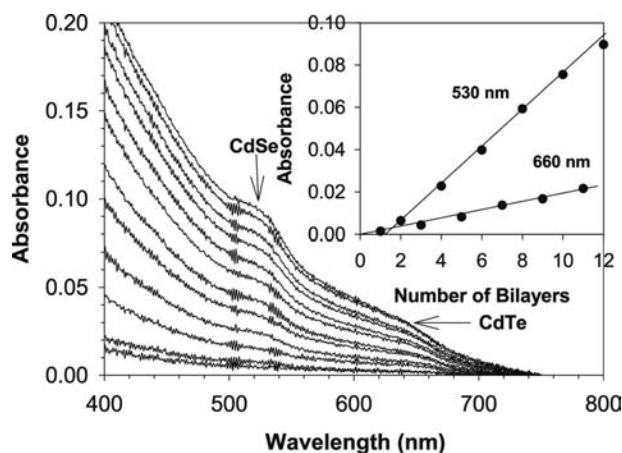


**Fig. 12** UV-vis absorption spectra of CdSe/CdTe multicomposite film with different numbers of bilayers. From the lower to upper curves, the number of CdSe and CdTe bilayers is 1, 2, 3, 4, 5, 6, 7, 8, 9, 10, 11, and 12 alternatively. Inset: the absorbance at 530 nm vs. the number of CdSe layers and the absorbance at 660 nm vs. the number of CdTe bilayers.

at 530 and 660 nm, attributed to CdSe and CdTe, respectively, were observed, indicating that CdSe and CdTe were successfully assembled into the film. A linear increase of both CdSe and CdTe absorbance as a function of layer number is also observed (Fig. 12, inset).

Multilayer CdS/Py-Au film was assembled by using the method shown in Fig. 2. The buildup was also monitored by using UV-visible spectroscopy as indicated in Fig. 13. In addition to the strong SP band of Au nanoparticles around 530 nm, a weak peak at 370 nm is also observed, which is attributed to CdS

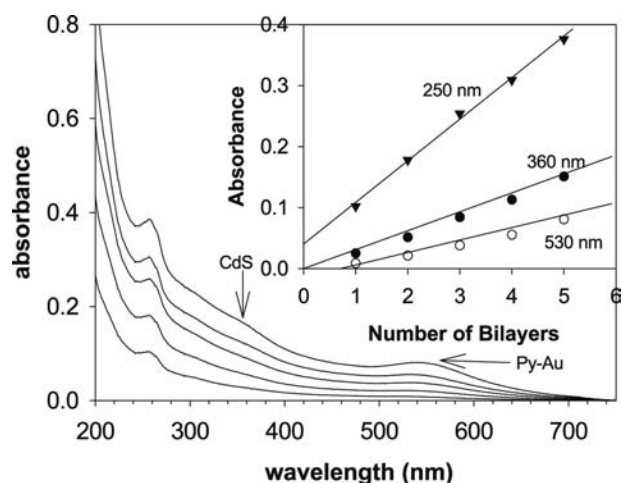


**Fig. 13** UV-vis absorption spectra of the CdS/Py-Au multilayer film with different numbers of bilayers. From the lower to upper curves, the number of CdS/Py-Au bilayers is 1, 2, 3, 4, and 5, respectively. Inset: absorbance at 530, 360, and 250 nm vs. the number of PVP/CdS bilayers.

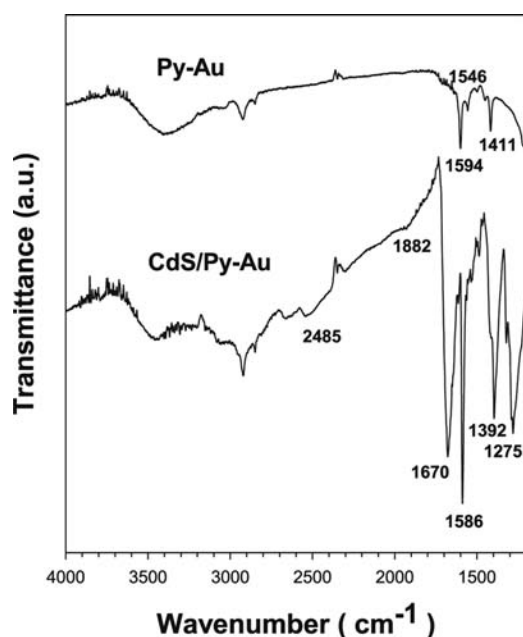


**Fig. 14** FTIR spectra of a cast film of Py-Au, and six bilayers of CdS/Py-Au thin film on CaF<sub>2</sub> plates.

on the basis of the UV-visible spectra of CdS solution (Fig. 11B). These absorption peaks suggest that both CdS and Au nanoparticles were successfully assembled into the film. In addition, a linear increase of CdS and Py-Au absorbance vs. the number of bilayers was also observed, as shown in the inset of Fig. 13. This illustrates a stepwise and uniform assembling of both CdS and Au layers.

The direct evidence for hydrogen bonding between 4-MBA-capped CdS nanoparticles and Au nanoparticles with poly (4-vinylpyridine) tailored surface was obtained via FTIR spectroscopy. Fig. 14 shows the FTIR spectra of a cast film of Py-Au and a cast film of six bilayers of CdS/Py-Au thin film on CaF<sub>2</sub> plates. For the Py-Au film, the peaks at 1594, 1546, and 1411 cm<sup>-1</sup> can be assigned to ring vibrations of the pyridine group. After the CdS and Au nanoparticles were assembled into multicomposite films, two broad peaks at 1882 and 2485 cm<sup>-1</sup> were observed, indicating hydrogen bonding between carboxylic acid on the surface of CdS and pyridine group on the surface of Au nanoparticles.

## CONCLUSION

We have presented two strategies for assembling single-composite and multicomposite multilayer thin films of inorganic nanoparticles based on hydrogen bonding. The multilayer buildups were monitored by UV-vis spectroscopy. Uniform layer deposition was achieved with this assembly technique, as indicated

by the linear increase of the film absorbance with the number of bilayers. Hydrogen bonding interaction is believed to be the driving force for the formation of multilayer films.

We demonstrated that both films of one and two types of nanoparticles could be assembled. In principle, many different nanoparticles (sizes and composition) can be assembled into different layers. Thus this technique may be potentially used to fabricate films with more complicated composition and advanced functionalities. For example, layers consisting of particles of different band gap and band edge position can be included in the film to allow directed energy and/or electron transfer. These films may find applications in LED and solar cells. Ongoing works are devoted to the understanding of interaction between different nanoparticles in the multicomposite films. Fabrication of LED or solar cells that are based on LBL assembly of highly luminescent quantum dots will also be explored.

## ACKNOWLEDGMENTS

This work is supported by the National Science Foundation grant CHE-9733796 and CHE-0135427. We would like to thank Dr. Angus Wilkinson (School of Chemistry and Biochemistry, Georgia Institute of Technology, Atlanta, GA 30332-0400) for performing the SAXD measurements and Dr. Karl Hagen for his help in synthesizing nanoparticles.

## REFERENCES

- Murray, C.B.; Norris, D.J.; Bawendi, M.G. Synthesis and characterization of nearly monodisperse CdE (E = sulfur, selenium, tellurium) semiconductor nanocrystallites. *J. Am. Chem. Soc.* **1993**, *115*, 8706–8715.
- Green, M.; O'Brien, P. Recent advances in the preparation of semiconductors as isolated nanometric particles: new routes to quantum dots. *Chem. Commun. (Cambridge)* **1999**, 2235–2241.
- Jacak, L. Semiconductor quantum dots—towards a new generation of semiconductor devices. *Eur. J. Phys.* **2000**, *21*, 487–497.
- Fendler, J.H.; Meldrum, F.C. The colloid chemical approach to nanostructured materials. *Adv. Mater. (Weinh., Germany)* **1995**, *7*, 607–632.
- Nirmal, M.; Brus, L. Luminescence photophysics in semiconductor nanocrystals. *Acc. Chem. Res.* **1999**, *32*, 407–414.
- Bruchez, M., Jr.; Moronne, M.; Gin, P.; Weiss, S.; Alivisatos, A.P. Semiconductor nanocrystals as fluorescent biological labels. *Science (Wash. D.C.)* **1998**, *281*, 2013–2016.
- Colvin, V.L.; Schlamp, M.C.; Alivisatos, A.P. Light-emitting diodes made from cadmium selenide nanocrystals and a semiconducting polymer. *Nature (Lond.)* **1994**, *370*, 354–357.
- Shipway, A.N.; Katz, E.; Willner, I. Nanoparticle arrays on surfaces for electronic, optical, and sensor applications. *ChemPhysChem* **2000**, *1*, 18–52.
- Alivisatos, A.P. Semiconductor clusters, nanocrystals, and quantum dots. *Science (Wash. D.C.)* **1996**, *271*, 933–937.
- Fendler, J.H. *Editor Nanoparticles and Nanostructured Films: Preparation, Characterization and Applications*; 1998.
- Decher, G. Fuzzy nanoassemblies: toward layered polymeric multicomposites. *Science (Wash. D.C.)* **1997**, *277*, 1232–1237.
- Fendler, J.H. Chemical self-assembly for electronic applications. *Chem. Mater.* **2001**, *13*, 3196–3210.
- Alivisatos, A.P. Perspectives on the physical chemistry of semiconductor nanocrystals. *J. Phys. Chem.* **1996**, *100*, 13,226–13,239.
- Colvin, V.L.; Goldstein, A.N.; Alivisatos, A.P. Semiconductor nanocrystals covalently bound to metal surfaces with self-assembled monolayers. *J. Am. Chem. Soc.* **1992**, *114*, 5221–5230.
- Decher, G.; MacLennan, J.; Reibel, J.; Soehling, U. Highly ordered ultrathin LC multilayer films on solid substrates. *Adv. Mater. (Weinh., Germany)* **1991**, *3*, 617–619.
- Kotov, N.A.; Dekany, I.; Fendler, J.H. Layer-by-layer self-assembly of polyelectrolyte–semiconductor nanoparticle composite films. *J. Phys. Chem.* **1995**, *99*, 13,065–13,069.
- Sun, Y.; Hao, E.; Zhang, X.; Yang, B.; Shen, J.; Chi, L.; Fuchs, H. Buildup of composite films containing TiO<sub>2</sub>/PbS nanoparticles and polyelectrolytes based on electrostatic interaction. *Langmuir* **1997**, *13*, 5168–5174.
- Cassagneau, T.; Mallouk, T.E.; Fendler, J.H. Layer-by-layer assembly of thin-film Zener diodes from conducting polymers and CdSe nanoparticles. *J. Am. Chem. Soc.* **1998**, *120*, 7848–7859.
- Gao, M.; Richter, B.; Kirstein, S.; Moehwald, H. Electroluminescence studies on self-assembled films of PPV and CdSe nanoparticles. *J. Phys. Chem., B* **1998**, *102*, 4096–4103.
- Fendler, J.H. Self-assembled nanostructured materials. *Chem. Mater.* **1996**, *8*, 1616–1624.
- Stockton, W.B.; Rubner, M.F. Molecular-level processing of conjugated polymers: 4. Layer-by-layer manipulation of polyaniline via hydrogen-bonding interactions. *Macromolecules* **1997**, *30*, 2717–2725.
- Wang, L.; Fu, Y.; Wang, Z.; Fan, Y.; Zhang, X. Investigation into an alternating multilayer film of poly(4-vinylpyridine) and poly(acrylic acid) based on hydrogen bonding. *Langmuir* **1999**, *15*, 1360–1363.
- Wang, L.; Cui, S.; Wang, Z.; Zhang, X.; Jiang, M.; Chi, L.; Fuchs, H. Multilayer assemblies of copolymer PSOH and PVP on the basis of hydrogen bonding. *Langmuir* **2000**, *16*, 10,490–10,494.
- Hao, E.; Lian, T. Buildup of polymer/Au nanoparticle multilayer thin films based on hydrogen bonding. *Chem. Mater.* **2000**, *12*, 3392–3396.

25. Hao, E.; Lian, T. Layer-by-layer assembly of CdSe nanoparticles based on hydrogen bonding. *Langmuir* **2000**, *16*, 7879–7881.
26. Brust, M.; Fink, J.; Bethell, D.; Schiffrin, D.J.; Kiely, C. Synthesis and reactions of functionalized gold nanoparticles. *J. Chem. Soc., Chem. Commun.* **1995**, 1655–1656.
27. Klayman, D.L.; Griffin, T.S. Reaction of selenium with sodium borohydride in protic solvents. Method for the introduction of selenium into organic molecules. *J. Am. Chem. Soc.* **1973**, *95*, 197–199.
28. Qu, L.; Peng, Z.A.; Peng, X. Alternative routes toward high quality CdSe nanocrystals. *Nano Lett.* **2001**, *1*, 333–337.
29. Aldana, J.; Wang, Y.A.; Peng, X. Photochemical instability of CdSe nanocrystals coated by hydrophilic thiols. *J. Am. Chem. Soc.* **2001**, *123*, 8844–8850.
30. Mattoussi, H.; Mauro, J.M.; Goldman, E.R.; Anderson, G.P.; Sundar, V.C.; Mikulec, F.V.; Bawendi, M.G. Self-assembly of CdSe–ZnS quantum dot bioconjugates using an engineered recombinant protein. *J. Am. Chem. Soc.* **2000**, *122*, 12,142–12,150.
31. Templeton, A.C.; Wueling, W.P.; Murray, R.W. Monolayer-protected cluster molecules. *Acc. Chem. Res.* **2000**, *33*, 27–36.
32. Spatz, J.P.; Roescher, A.; Moeller, M. Gold nanoparticles in micellar poly(styrene)-*b*-poly(ethylene oxide) films. Size and interparticle distance control in monoparticulate films. *Adv. Mater. (Weinh., Germany)* **1996**, *8*, 337–340.
33. Gao, M.; Zhang, X.; Yang, B.; Li, F.; Shen, J. Assembly of modified CdS particles/cationic polymer based on electrostatic interactions. *Thin Solid Films* **1996**, *284–285*, 242–245.
34. Gao, M.; Richter, B.; Kirstein, S. White-light electroluminescence from self-assembled Q-CdSe/PPV multilayer structures. *Adv. Mater. (Weinh., Germany)* **1997**, *9*, 802–805.
35. Tippmann-Krayer, P.; Moehwald, H.; L'Vov, Y.M. Structural changes before and during desorption of Langmuir–Blodgett films. *Langmuir* **1991**, *7*, 2298–2302.
36. Lvov, Y.; Decher, G.; Moehwald, H. Assembly, structural characterization, and thermal behavior of layer-by-layer deposited ultrathin films of poly(vinyl sulfate) and poly(allylamine). *Langmuir* **1993**, *9*, 481–486.
37. Lee, J.Y.; Painter, P.C.; Coleman, M.M. Hydrogen bonding in polymer blends: 4. Blends involving polymers containing methacrylic acid and vinylpyridine groups. *Macromolecules* **1988**, *21*, 954–960.
38. Lee, J.Y.; Painter, P.C.; Coleman, M.M. Hydrogen bonding in polymer blends: 3. Blends involving polymers containing methacrylic acid and ether groups. *Macromolecules* **1988**, *21*, 346–354.
39. Kato, T.; Kihara, H.; Uryu, T.; Fujishima, A.; Frechet, J.M.J. Molecular self-assembly of liquid crystalline side-chain polymers through intermolecular hydrogen bonding. Polymeric complexes built from a polyacrylate and stilbazoles. *Macromolecules* **1992**, *25*, 6836–6841.
40. Kumar, U.; Kato, T.; Frechet, J.M.J. Use of intermolecular hydrogen bonding for the induction of liquid crystallinity in the side chain of polysiloxanes. *J. Am. Chem. Soc.* **1992**, *114*, 6630–6639.
41. Creager, S.E.; Steiger, C.M. Conformational rigidity in a self-assembled monolayer of 4-mercaptobenzoic acid on gold. *Langmuir* **1995**, *11*, 1852–1854.
42. Nuzzo, R.G.; Dubois, L.H.; Allara, D.L. Fundamental studies of microscopic wetting on organic surfaces: 1. Formation and structural characterization of a self-consistent series of polyfunctional organic monolayers. *J. Am. Chem. Soc.* **1990**, *112*, 558–569.
43. Johnson, S.R.; Evans, S.D.; Brydson, R. Influence of a terminal functionality on the physical properties of surfactant-stabilized gold nanoparticles. *Langmuir* **1998**, *14*, 6639–6647.

# Layer-by-Layer Electrostatic Self-Assembly

**Michael J. McShane**

Biomedical Engineering Program, Louisiana Tech University,  
Ruston, Louisiana, U.S.A.

**Yuri M. Lvov**

Institute for Micromanufacturing, Louisiana Tech University,  
Ruston, Louisiana, U.S.A.

## INTRODUCTION

Layer-by-layer (LbL) self-assembly of multilayer films involves the construction of complex composite materials with nanoscale precision in film thickness, one layer at a time, enabling the development of novel structures and devices with properties tailored by controlling the molecular makeup and arrangement. Early fundamental studies of multilayer assemblies on planar substrates demonstrated the practicality and versatility of the approach, and work over the past decade has included further investigation into the internal structure and composition of LbL films, including dynamic and long-term interactions between film components, solvents, and solute, especially transport properties. Beyond assembly onto flat planar surfaces, the multilayer deposition via LbL has been extended to colloidal templates, leading to elaborate modification of micro/nanoparticles and even to hollow capsules, both of which are exciting and attractive for many applications. While the bulk of work in LbL has been in experimental investigations, some efforts to generate theoretical descriptions for the multilayer assembly have also been undertaken, although much more work is needed in this area to establish useful models for design of devices based on this approach. Finally, applications for LbL films abound and are now being pursued at the academic level, with some examples of industrial success. Examples given here particularly focus on the biomedical arena, where sensor technology and drug release are prime candidates to benefit from use of multilayer films.

## MOTIVATION AND BASIC CONCEPTS

“What could we do with layered structures with just the right layers?” was one of the questions asked by Richard Feynman in his now-famous speech to the American Physical Society in December 1959. Feynman, considered by many to be the “father of

nanotechnology,” because of his prophetic comments given in the lecture entitled “There’s plenty of room at the bottom,” continued: “I can’t see exactly what would happen, but I can hardly doubt that when we have some *control* of the arrangement of things on a small scale we will get an enormously greater range of possible properties that substances can have, and of different things that we can do.” Since that time, scientists have begun to provide answers to this marvelously insightful question by developing practical ways to deposit materials with dimensional control on the order of single molecules. One of the most promising methods for building functional nanostructures (i.e., nanodevices) using a sequential approach to defining multilayer thin (truly *ultrathin*) films is the electrostatic LbL assembly process, which has been developed and extensively studied over the last decade.<sup>[1–8]</sup>

## Fundamentals of Electrostatic Layer-by-Layer Self-Assembly

First proposed by Iler<sup>[9]</sup> in 1966, and then rediscovered by Decher et al.<sup>[1–3]</sup> in the early 1990s, the LbL electrostatic adsorption process has only recently been reduced to practice as a general method for alternately depositing dense monolayers of charged molecules onto oppositely charged surfaces.<sup>[1]</sup> The power of the approach is evident from the generality of the process, which relies mainly on the attractive force between oppositely charged molecules; materials employed in the assembly process range from charged polymers (“polyelectrolytes” or “polyions”) to proteins, dyes, and semiconductor nanoparticles.<sup>[4–8]</sup> Each layer has a thickness on the order of a few nanometers, and this thickness is controllable through careful selection of materials and reaction parameters.<sup>[6]</sup> Furthermore, the composition of films can be engineered through the sequential deposition of different materials; thus, complex film architecture may be achieved through a common process without need for complicated chemistry. Thus the LbL method provides a practical



procedure for building precisely engineered nanocomposite films, a basis for considering the question posed by Feynman.

The principal idea of the method consists of the resaturation of polyion adsorption, resulting in the alternation of the terminal charge after every subsequent layer deposition (Fig. 1).

This idea is general, implying that there is no fundamental restriction to the choice of polyelectrolytes. The technique suggests the possibility of designing ultrathin ordered films in the range of 5–1000 nm, with a precision better than 1 nm and a definite knowledge of their molecular composition (Fig. 2).

### From Planar Substrates to Micro- and Nano-Templates

The initial fundamental research on LbL assembly was performed on planar bulk templates: Layers defined by the electrostatic adsorption process were formed on the surface of relatively large, flat, smooth, charged substrates as they were dipped in solutions of charged materials. The LbL process, however, is in no way limited to such situations; that is, the films may just as well be deposited on charged roughened surfaces or small (micro/nano)templates, given that the dimensions and materials are sufficient for the necessary interactions. Thus the procedure has also been elaborated to demonstrate the fabrication of three-dimensional (3-D) layered structures by using charged substrates with micrometer and nanometer dimensions.<sup>[10–12]</sup> Specifically, microspheres and nanoparticles have been extensively studied because of the wide availability and

attractive surface properties of spherical particles. Functional nanocomposite films can be deposited on these carriers, which are attractive for controlling catalytic reactions and other interfacial phenomena because of the high surface-to-volume ratio.<sup>[13]</sup> The key to this process is the separation of the templates from the layering materials following adsorption, which is achieved via centrifugation or filtration (Fig. 3).<sup>[14]</sup>

### From Layered Colloids to Nanocapsules

In the past several years, a technique for fabrication of hollow micro/nanocapsules has been developed using an extension of the polyelectrolyte layering process applied to colloids. Subsequent to deposition of coatings comprising charged molecules around the templates, the core material is removed using chemical etching to achieve hollow shells (Fig. 4).<sup>[10,15–20]</sup> Dimensions and shape of the capsules is dependent on the chosen nano/microtemplates: These may be latex, silica, or lipid tubules ranging from 20 to hundreds of nanometers. Methods for “replication” of more complex particles such as viruses and cells are also under development. The method is very versatile, and shell properties can be controlled: Inner diameters are dependent upon the size of templates used for assembly, wall thicknesses can be controlled precisely to within a few nanometers, and walls may be constructed using a diverse selection of charged molecules (polyelectrolytes, proteins, dyes, inorganic particles, copolymers, etc.).<sup>[10,19]</sup> The versatility in construction of these tiny capsules and control over their properties makes them attractive for use in sensor applications.

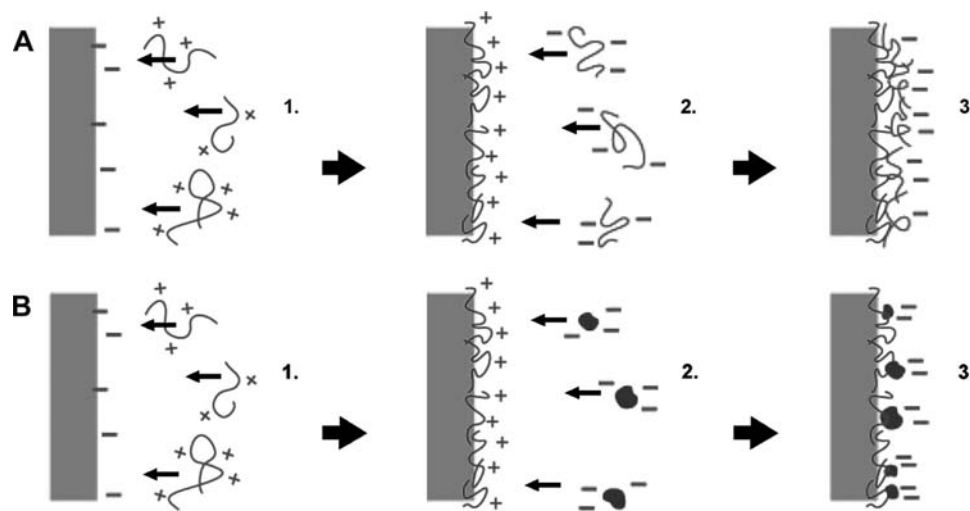


**Fig. 1** Illustration of layer-by-layer nanofabrication approach, showing adsorption of charged materials to oppositely charged surfaces. Assembly on the surface results in stable immobilization via multiple electrostatic bonds, and surface charge reversal. Materials may be (A) charged molecules, (B) particles, or combinations thereof.

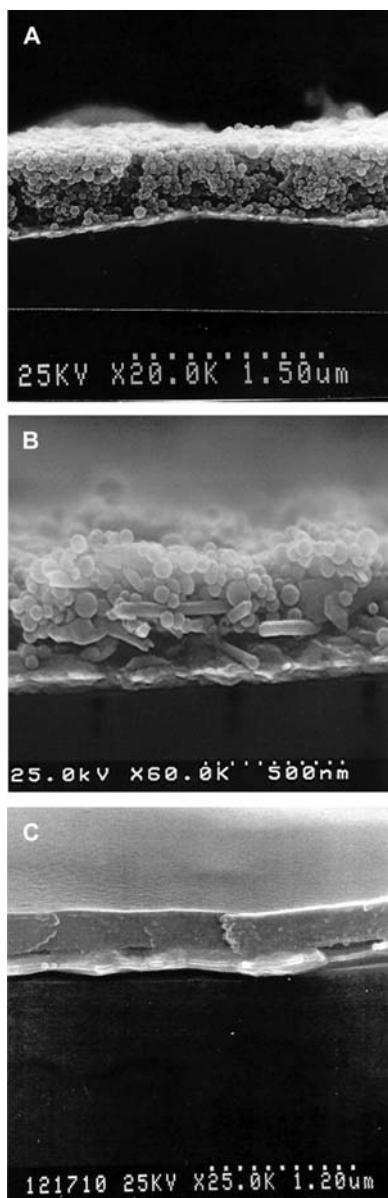


**Fig. 2** SEM cross-section view of multilayer films with different structural properties based on the varying components: (A) (PEI/40-nm silica)<sub>25</sub> multilayers; (B) (PEI/40-nm silica/PEI/50-nm diameter halloysite tubules)<sub>4</sub> multilayer; (C) (PAH/glucose oxidase)<sub>18</sub> multilayer on a silver electrode. The samples were coated with 2-nm Pt for imaging.

Polyelectrolyte capsules have been demonstrated to partition between solvents<sup>[18]</sup> as well as encapsulate small molecules such as dyes<sup>[20]</sup> and active materials such as enzymes.<sup>[19]</sup> Encapsulation depends on membrane permeability of polycation–polyanion complexes, which is strongly influenced by solution pH.<sup>[21]</sup> Opening of relatively large (~10–20 nm) pores in multilayer films is possible by varying solvent pH, which can then be used to modulate the diffusion rate

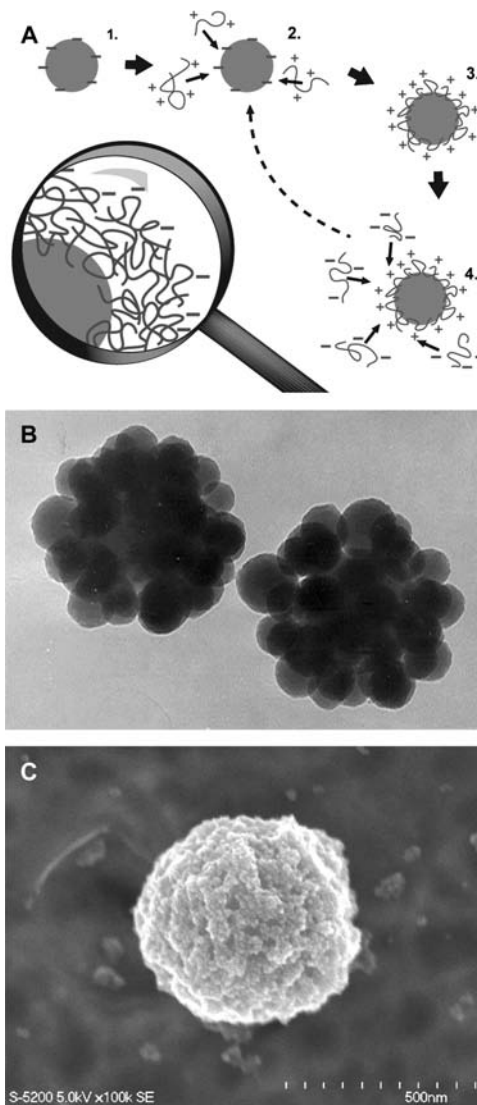


**Fig. 3** (A) Schematic of LbL assembly on colloids. Examples of nanoassembled films of nanoparticles deposited on slightly larger colloidal templates. (B) TEM image of 70-nm silica nanoparticles surrounding a negatively charged 250-nm diameter latex core, attached through interaction with PEI (polycation) interlayers; (C) SEM image of 400-nm latex covered with two monolayers of 12-nm magnetite particles in alternation with polycation. *Source:* From Ref.<sup>[14]</sup>.

of molecules through capsule walls. This concept has recently been demonstrated for encapsulation of dextran and albumin<sup>[22]</sup> and the process appears to be completely reversible. A similar effect has been noted when solution dielectric constant is changed by the addition of ethanol to aqueous solutions; however, the underlying mechanism is not yet understood<sup>[19]</sup> (Fig. 5).

Thus a prospective technology which may arise from these novel nanostructured materials is polymer

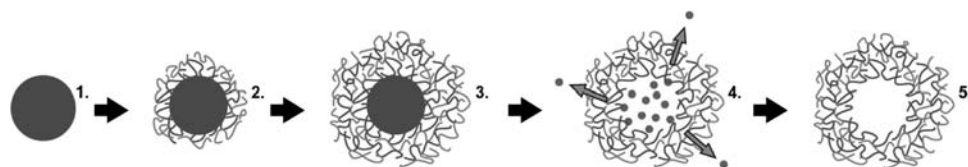


**Fig. 4** Scheme of capsule formation using adsorption of charged species to micro/nanotemplates, followed by removal of the core.

capsules with dynamically varying permeability, opening up possibilities for encapsulation and controlled release and possibly impacting environmental and medical areas such as remediation and drug delivery. With this overview of the present state and brief

suggestion of what may come from LbL multilayer films, the following sections will review candidate materials for substrates and adsorbates, the properties of LbL films and will conclude with a look at current and future applications.

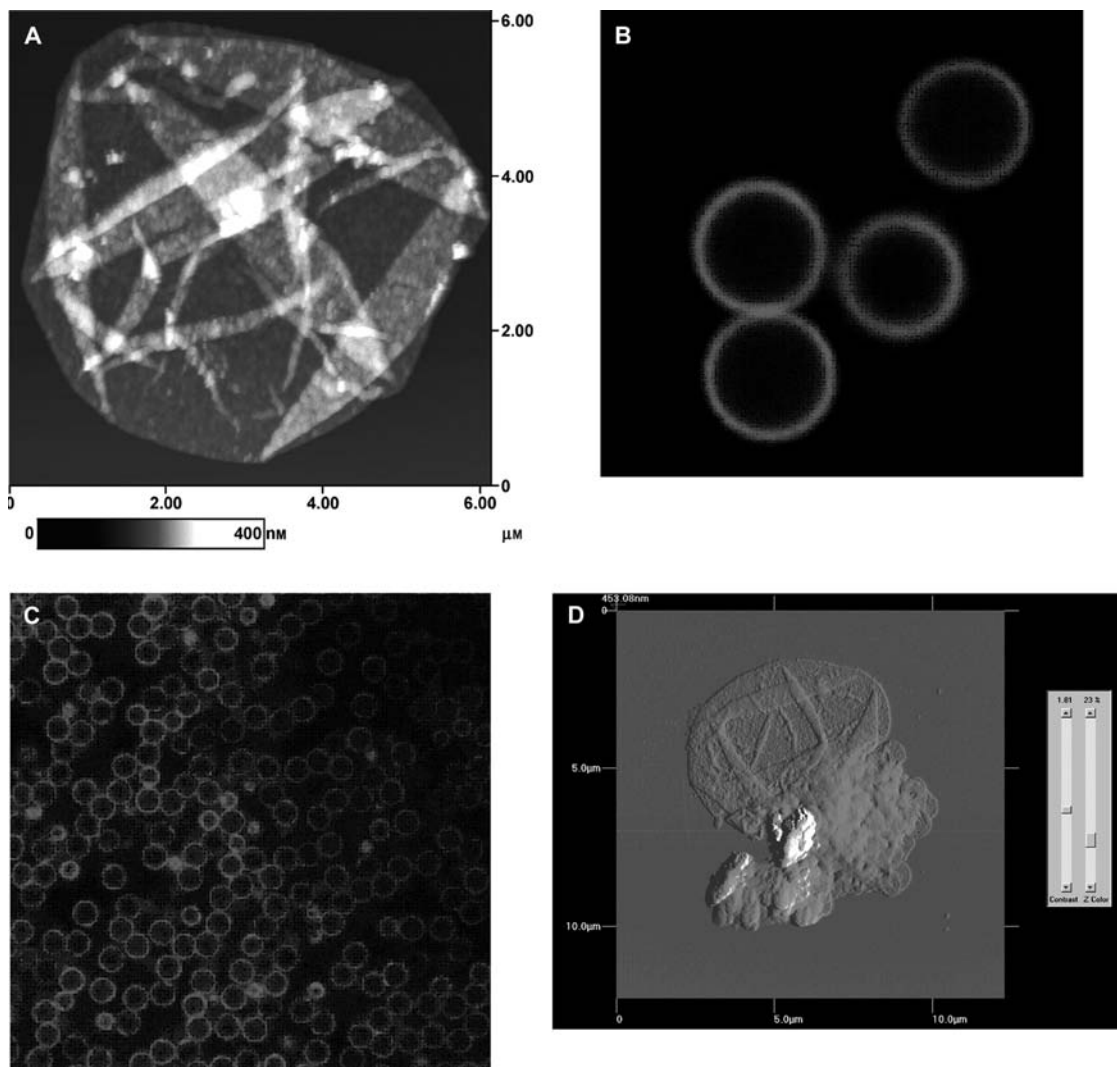


**Fig. 5** Examples of microcapsules formed via nanoassembly on dissolvable materials. In this case, 4-μm capsules with 20-nm-thick walls of (PSS/PAH)<sub>4</sub> composition were produced on MnCO<sub>3</sub> cores. (A) AFM image of dried capsule; (B) confocal scanning laser fluorescence images of hydrated capsules (PAH labeled with rhodamine); (C) zoom out of same capsules, illustrating the efficiency of the fabrication approach; (D) AFM tapping-mode image of a dry, broken capsule loaded with glucose oxidase.

## MATERIALS AND METHODS FOR LAYER-BY-LAYER ASSEMBLY

### Adsorbate Materials

Because of the general nature of the interactions dominating the LbL self-assembly process, primarily electrostatics, a large palette of materials is available for building multilayer assemblies—keeping in mind that the order and conditions of assembly also influence the properties of the assemblies, the possibilities to concoct novel nanocomposite materials from simple recipes are nearly limitless. Potential ingredients range from highly charged polymers, organic or inorganic nanoparticles, functional polymers, orientable chromophores, charged lipid micelles, and biopolymers such as short-chain polypeptides, proteins, and DNA.<sup>[2,23–26]</sup> The versatility of the multilayer formation process with respect to the variety of materials which can be used as building blocks, and the additional possibility of combination with other assembly procedures, results in a high application potential in a broad range of different areas of materials development.

The polyions predominately used in the electrostatic self-assembly process include: polycations—poly(ethylenimine) (PEI), poly(dimethyldiallyl ammonium chloride) (PDDA), poly(allylamine) (PAH), poly(lysine), and chitosan; and polyanions—poly(styrenesulfonate) (PSS), poly(vinylsulfate) (PVS), poly(acrylic acid) (PAA), and dextran sulfate. The dominant polyanion/polycation pair that has been used in published studies of LbL films to date, including microcapsules, is PSS/PAH. The specific properties of films assembled from various combinations are discussed below. In addition, multilayer assemblies of natural polyions, such as charged polypeptides, protamine sulfate, sodium alginate, and polysaccharides (e.g., heparin, chondroitin, and chitosan), are particularly interesting for biological and medical applications. DNA and polynucleotides (polyuridylic and polyadenylic acids) can be readily assembled in alternation with polycations (PEI, PAH, polylysine). Assembly of polysaccharides, such as dextran, is also possible as a means of biocompatible surface preparation.

Many proteins have been assembled in organized multilayers by alternation with oppositely charged linear polyions. Typical concentrations for assembly solutions fall within the range of 0.1–2 mg/mL, and adsorption saturation occurs within 20 min as long as the pH of the protein solutions is adjusted away from the isoelectric point so that proteins are sufficiently charged under the experimental conditions. Water-soluble proteins, including cytochrome *c* and P450, lysozyme, histones, myoglobin, pepsin, different peroxidases, hemoglobin, glucoamylase, concanavalin A, albumin, glucose oxidase, lactate oxidase, catalase,

invertase, diaphorase, bacteriorhodopsin, and immunoglobulin IgG, have been used successfully for LbL assembly.<sup>[26]</sup> A book on protein architectures reviews the materials, methods, and film characteristics of nanoassembled proteins.<sup>[26]</sup>

Advanced materials comprising nanocomposite multilayer assemblies of polymers and nanoparticles have been demonstrated using a variety of metal, semiconductor, and dielectric materials.<sup>[27–30]</sup> Ordered nanostructured films with desired periodicity have been created to tune mechanical, magnetic, electrical, optical, and optoelectronic properties.<sup>[27,30]</sup> Densely packed, conformable sheets of rigid crystals form in the adsorption process when alternated with flexible polyion “glue.”<sup>[28]</sup> Growth of nanoparticle–polyelectrolyte multilayers may occur in both normal (vertical) and in-plane (lateral) directions, depending upon assembly conditions and particle properties.<sup>[29]</sup> Nanoparticles also assemble into ordered films when alternated with globular proteins.<sup>[31]</sup> A review of nanoparticle assembly via LbL provides an excellent overview of the current state of knowledge and applications in this area.<sup>[30]</sup>

### Substrate Materials

The basic substrate for LbL assembly is a flat, charged surface, typically a slab of glass (e.g., microscope slide or cover slip) or quartz. There is essentially no limit to the template used—examples of practical cases include slides of optical materials (glass, quartz, etc.), gold-coated glass, silicon, metals, porous ceramics, plastics, filters, optical fibers—and, in reality, depend only upon the intended application. In addition to macroscale, largely planar substrates, colloidal particles have also been used as LbL templates. Typical materials used for this purpose range from dielectric nanoparticles, quantum dots, metal nanoparticles, core-shell structures, biological cells, carbon nanotubes, lipid tubules, and polymer microspheres. Methods have also been elaborated to allow coating of drug or dye crystals.

Capsules are formed by colloidal coating followed by dissolution or etching of the template core. Following core removal, hollow and closed structures are formed. These have exactly the same shape of the template, but now with walls comprising the ultrathin multilayer films deposited on the template surface; thus, it is a way to replicate structures with new materials, in effect a nanoscale version of molding. The initial demonstrations of capsules formed from core removal of LbL-coated templates used weakly cross-linked polymeric particles, e.g., melamine formaldehyde (MF), which dissolve at low pH.<sup>[32]</sup> A drawback to the use of MF is the residual polymer left in the capsule after exposure to acid, resulting in “contaminated” capsule interiors. Thus alternative templates that allow

more efficient removal of core material have been sought, such as organic particles,<sup>[33–35]</sup> inorganic microcrystals,<sup>[36]</sup> and even biological cells.<sup>[37]</sup> Examples of materials used in creation of micro/nanocapsules are melamine formaldehyde (acid removal), silica (acid etch), gold (acid etch), cadmium carbonate (acid removal),<sup>[38]</sup> manganese carbonate (acid removal), platelets,<sup>[39]</sup> and human erythrocytes (red blood cells) (oxidation removal).<sup>[40]</sup>

## Multilayer Coating Methods

### Multilayer film formation by alternate immersion

Nanoassembly by immersion of charged substrates into solutions of adsorbate is the typical procedure. Uncharged or weakly charged surfaces may be suitably modified with a layer of charged material using other interactions (e.g., SAMs) to provide the initial charged interface. For example, gold surfaces may be modified with molecules containing thiol groups [e.g., HS-(CH<sub>2</sub>)<sub>8</sub>-COOH],<sup>[41]</sup> and oxide surfaces can be similarly coated with silanes.<sup>[42]</sup> Once a suitable surface is available, LbL assembly proceeds by alternate dipping in solutions containing molecules of opposite charge from the current surface, and washing steps are used in between adsorption steps to remove weakly bound material. Typically, solutions are aqueous and adjusted to a pH at which the molecules of interest have sufficient and appropriate charge. Drying of films during assembly is optional and has been shown to affect the final film structure and properties.<sup>[43]</sup> Generally speaking, this process is inexpensive to perform and requires a minimum of specialized equipment and supplies; development work can be done under normal conditions in any reasonably clean lab. However, the dipping technique typically requires 10–30 min per adsorption step, making the assembly somewhat time-consuming.

In the case where colloids are to be coated, a method of alternate exposure of colloids to polycations and polyanions is still used, with intermediate rinse and separation cycles. The separation step is the key to this procedure, and centrifugation<sup>[44,32]</sup> and ultrafiltration<sup>[45]</sup> have been demonstrated as useful techniques for this purpose. Such methods allow multilayer assemblies to be deposited on curved surfaces in the size range of a few nanometers to several micrometers, with proof of film growth shown by microelectrophoresis and single-particle light-scattering measurements.<sup>[44,46,47]</sup>

### Spray and spin assembly of multilayer films

A disadvantage of the alternate immersion process for multilayer formation is the long time required to

assemble a single film (1 min to 1 hr, depending on adsorbing systems; typically 10–20 min). Another disadvantage is the difficulty in application of multilayers to large surface areas. In an attempt to overcome some of these problems, alternative methods for the application of multilayers using spraying and spinning approaches have been developed.<sup>[48–51]</sup>

Polyelectrolyte multilayers deposited by sequential spraying provides the advantage of rapidly obtaining a highly uniform thin film over a large area. Spray application over a large area is advantageous for rapid, high-throughput fabrication of devices bearing active or passive multilayers, for large-area membranes, and for external coatings as corrosion protection or adhesion modification. The morphology, uniformity, and chemical composition of films prepared by spraying were found to be identical to those from dipping. Disadvantages of spraying, however, include several minutes of contact time for maximum (steady-state) coverage and the inefficient use of polymer solution because it cannot be reused.<sup>[48]</sup>

Polyelectrolyte multilayers deposited by sequential spin coating (“spin-assisted” assembly) provides the advantage of drastic reduction in the preparation time per layer, i.e., from 20 min to 20 sec.<sup>[50]</sup> In spin coating using polyelectrolytes with the same molar concentrations used in alternate immersion, film thicknesses are thicker than those obtained in dipping methods.<sup>[49,52]</sup> The centrifugal force and hydrodynamic air drag, generated by a high spinning rate and short spinning time, act together to remove both water (accelerating drying) and loosely bound polymer chains from the substrate. The fast elimination of water significantly increases the local molar concentration of the polyelectrolyte solution during the short deposition time and hence the thicker films result.

A critical aspect of spun films is the lesser dependence upon charge densities; in fact, multilayer films have been successfully demonstrated using sequential adsorption of uncharged and even same-charge layers. Recently, water-soluble, cationic, anionic, and neutral polymers were used to form repeat trilayer (polycation/polyanion/uncharged polymer or polycation/polyanion/polyanion) films using spin assembly. These multilayer films assemble through physical entanglement, electrostatic, and/or H-bonding interactions.<sup>[53]</sup> Moreover, multiple deposition cycles of a single polyelectrolyte resulted in the formation of a film whose thickness grew linearly with each deposition.<sup>[53,54]</sup>

One must keep in mind a critical feature for the assembly of well-charged species: Electrostatic interactions not only drives binding between neighboring molecular layers but also recharges the surface to prevent additional adsorption of similarly charged polyions. Therefore the binding force is complemented by a force preventing uncontrollable increase in thickness that

would result from continuous deposition. From our experience, electrostatic LbL assembly of highly charged components results in more organized multilayer nanocomposites compared with multilayers assembled via biospecific or hydrogen-bonding interactions, where repulsion preventing nonspecific adsorption is absent.

Film thickness increases with increasing concentrations of the solution and decreases with spin speed due to shorter contact time.<sup>[50,51,53,54]</sup> The thickness may also be controlled by changing factors known to influence film thickness in immersion assembly, including ionic strength, pH,<sup>[50]</sup> hydrophobicity, and charge density.<sup>[53]</sup> The amount of material deposited on a substrate is inversely proportional to the logarithm of the molecular weight of polymers at low concentrations.<sup>[55]</sup> The air drag is believed to strengthen the electrostatic attraction between oppositely charged polymers.<sup>[49,52,55]</sup> In addition, spin assembly induces deposition through polymer chain entanglement between the deposited layer and the film's outer layer; as a result, spin assembly is controlled by mechanical rather than thermodynamic factors.<sup>[50,53,54]</sup>

An interesting and important difference in structure between films prepared by spinning compared to dipping lies at the interface between neighboring layers. The air shear force driven by the spinning process significantly enhances the surface planarization of the multilayer films, making them smoother compared to dip assembled films.<sup>[49,50,52]</sup> In contrast to the interpenetration of neighboring layers that is characteristic for adsorption during immersion, films prepared with the spin process possess distinct interfaces between respective layers, providing a well-ordered internal structure.<sup>[49,52]</sup>

### Nanofilm patterning

Micropatterning of LbL multilayers, an attractive extension beyond nondiscriminatory surface coverage, was initiated in the works of Hammond et al.<sup>[56–60]</sup> The interest in these systems arises from the potential for lateral definition of nanofilm features, providing further versatility in structures that may be realized. The ability to produce structures of composite materials with nanometer resolution in vertical and (ultimately, with advances in nanolithography) lateral dimensions in a simple, fast, and cost-effective process would enable manufacture of devices at increasingly smaller size and lower cost. The foundation for this has been laid using a combination of self-assembled monolayers and LbL films. For this, charged patterns are first created on gold surfaces by microstamping of thiol compounds terminated with negatively or positively charged groups. The remaining unstamped surface is then backfilled with additional hydrophobic-terminated thiols to define adsorption-resistant regions. Then, by alternate

dipping of the patterned substrates with short periods of sonication in between to remove nonspecific adsorption, multilayers of different materials following the template patterns were assembled.<sup>[56–59]</sup> Furthermore, with some additional efforts, filling of empty areas (between initially patterned strips) was achieved via hydrogen bonding with secondary materials.<sup>[60]</sup>

In another approach, traditional microlithography was combined with electrostatic LbL nanoassembly to produce 3-D structures. In contrast to the microstamping method described above, this technique integrates directly with standard silicon-processing lithographic procedures and allows for easy alignment of structures deposited in multiple steps. The process follows the typical lift-off procedure for metallization with aluminum via thermal evaporation. A layer of photoresist ( $\sim 1 \mu\text{m}$ ) is first applied to a substrate, then patterned through a mask by standard UV irradiation and photoresist development. Multilayers may then be deposited onto the substrate with patterned resist via the electrostatic LbL self-assembly technique. This step results in deposition on the exposed substrate regions as well as on top of the remaining photoresist. Finally, the photoresist with polyions on top of it is exposed to acetone, accompanied with sonication, leaving the nanofilm patterns on the substrate with intervening regions of bare substrate. As demonstrations of this process, cationic polymers (PEI or PDDA) alternated with anionic nanoparticles (silica or 40-nm fluorescent latex) were assembled into 5- $\mu\text{m}$  strips of ordered nanoparticle layers, as shown in Fig. 6.<sup>[61,62]</sup> In these patterns, the edge roughness was better than 0.2  $\mu\text{m}$ , as evident from SEM micrographs (Fig. 6A,B). In addition, the lithographic approach was used to generate clean patterns of multiple types of nanoparticles on a single 4-in. silicon wafer.<sup>[63]</sup> Metal oxide semiconductor capacitor arrays were fabricated on silicon wafers using LbL self-assembled insulator layers.<sup>[64]</sup> Recently, more complex field effect transistors based on LbL nanoassembly of tin oxide and silica nanoparticles were also demonstrated.<sup>[65]</sup>

Because of the conformal nature of LbL nanoassemblies, organized multilayers may also be used to functionalize existing microstructures. That is, substrates with preformed features may be completely modified with an overlying multilayer. As an example, multilayers of nanoparticle catalysts have been assembled in microchannels for miniature reactors (Fig. 6C).

## PROPERTIES OF LAYER-BY-LAYER FILMS

### Electrostatic and Secondary Interactions

The principal requirement for multilayer film deposition is the availability of charged species of



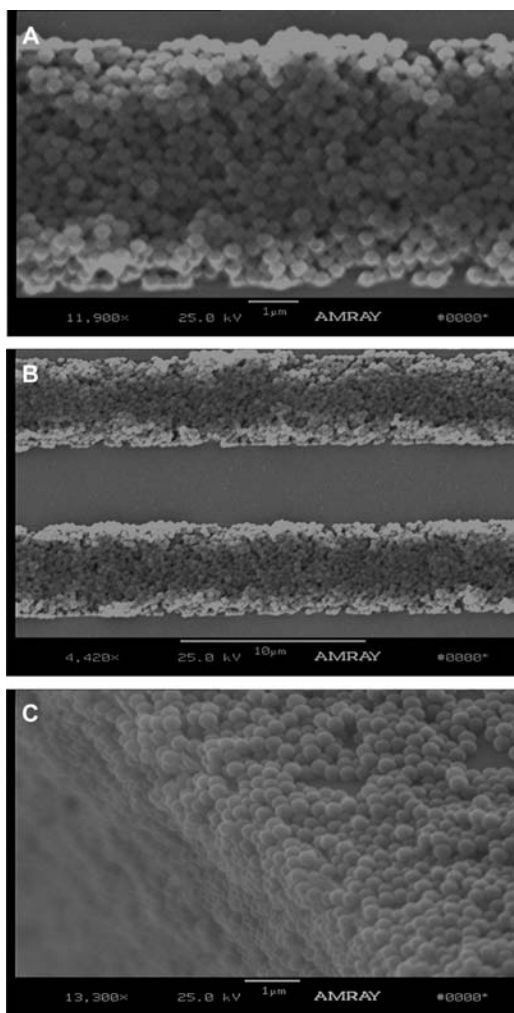


**Fig. 6** Examples of patterned LbL films—SEM images of: (A and B) (200-nm SiO<sub>2</sub> particles/PDDA)<sub>4</sub>, with 5- $\mu$ m lines; (C) (78-nm silica/PDDA)<sub>4</sub> multilayers deposited in 100- $\mu$ m channel.

sufficient charge density and molecular weight. It is clear that while small molecules are attracted and stick to oppositely charged surfaces, these do not provide a stable layer for adsorption of other molecules; generally speaking, a molecular weight greater than 10 kDa is preferable for efficient and stable film formation.<sup>[66]</sup> A number of attempts to form multilayers through alternation of linear polyanions with smaller molecules have been reported, such as boladications and Yt<sup>3+</sup> ions,<sup>[67]</sup> polycations and citric acid,<sup>[68]</sup> and via sequential deposition of Zr<sup>4+</sup> ions and diphosphonic acid.<sup>[69]</sup> Besides, in these cases, the main idea was to create an excessive charge (due to special steric structure of these ions) at every stage of assembly that leads to recharging of the outermost surface at every step of film formation.

Although the formation of LbL multilayers is typically attributed to the strong attraction arising from

multiple electrostatic bonds, other forces may also play significant roles in formation, stabilization, or rearrangement of the resulting assemblies. Other important influences include hydrophobic interactions between polymer segments<sup>[70]</sup> and specific binding based on molecular recognition. As an example of the potential importance of these interactions, the thickness of multilayers was found to depend directly on temperature and ionic strength, reflecting the increasing contribution of hydrophobic interactions, especially when charges are screened.<sup>[71]</sup> Thus the choice of adsorption species and control of assembly conditions can be critical in determining the structure of the resulting assemblies.

It is interesting to note that the adsorption of a polyion layer to preformed multilayers differs largely from adsorption to rigid, charged surfaces. An important characteristic of the films structure is the entanglement of molecules in outer multilayers. Studies have shown that about one-third of the charges of the superficial layer are complexing with exposed charges from the underlying layer (“intrinsic” compensation), whereas the remaining charges on the molecules in the outer layer are compensated by counterions (“extrinsic” compensation).<sup>[72]</sup> Some or all of the counterions are then released upon adsorption of an additional layer. The first layer, close to the surface, and the exposed “loops” of the superficial layer are less dense than the complexation region, resulting in a periodicity in film density for multilayer films.<sup>[73]</sup>

The strong interpenetration of components between neighboring film layers has been demonstrated, resulting in the concept of “fuzzy nanoassemblies,”<sup>[2]</sup> due to these blurred boundaries. This property contrasts sharply with the two-dimensional (2-D) stratification observed in Langmuir–Blodgett multilayers. The interpenetration, or overlap, of neighboring layers has been measured to be approximately 1–2 layers,<sup>[74–76]</sup> therefore, the physically separated segments of ultrathin films are not the neighboring layers, but rather the first and the third or fourth layers.

Finally, it is interesting to discuss dissolution of LbL multilayers. Generally, these ultrathin films are amazingly stable, and it is difficult to remove them from a solid substrate. There are two possibilities to remove LbL films. First, high pH ( $\sim 12$ ) can be used, which will discharge the first polycation layer and destroy the ionic bonds that stabilize the films. A second method is to expose the LbL multilayers to solution with very high ionic strength, such as 3 M NaCl, under sonication for approximately 2–3 hr. In this second method, the combination of ultrasonic energy and high concentration of free ions in solution can disrupt polycation/polyanion bridging and neutralize exposed charges with Na<sup>+</sup> and

$\text{Cl}^-$  ions. This process is well established for interpolyelectrolyte complexes and for multilayer films which never were dried. However, LbL multilayers that are dried are much more difficult to dissolve, probably as a result of additional hydrophobic interactions between polymer chains incurred during dehydration.

### Ionic Strength and pH Dependence

As noted above, the condition of electrical neutrality is met by intrinsic or extrinsic charge compensation. In the latter, complexation of polymers with exact 1:1 stoichiometry may leave uncompensated regions because of the inability of the adsorbing species to rearrange and match the exposed surface charges exactly. In this case, neutrality is maintained by counterions associated with exposed uncompensated charged groups on the polymers. Again, this situation is not completely understood, and remains an intriguing question that is still under intense investigation: While it is believed that about one-third of charges on polymers are free for binding of ions (as demonstrated by dyes adsorption into preformed layers), small counterions also appear to be removed during washing, which demands local film rearrangement to achieve neutrality or leaves a nonneutral situation.<sup>[2,24,25,71,77–80]</sup>

From a practical standpoint, it is desirable to control the thickness of film layers during deposition. Using salt solutions of varying ionic strength was the first approach to control layer thickness over a wide range.<sup>[1]</sup> The solution salt ions screen neighboring charges on the polymer, allowing linear chains stretched by electrostatic repulsion to collapse and adopting a more compact, coiled 3-D conformation. While the dependence of thickness on salt concentrations is recognized, reliable models for this behavior have been elusive. For different polyanion/polycation pairs, findings range from linear dependence of thickness on salt concentration to power-law scaling with  $[\text{salt}]^\alpha$ , where  $\alpha$  ranges from 0.05 to 0.5.<sup>[81–84]</sup> There appears to be a minimum requirement in which approximately half of monomers are ionized to achieve saturation and charge reversal as a result of overcompensation.<sup>[86,89]</sup> Above this threshold, film growth is reliable and thickness is proportional to solution ionic strength; at lower ionization levels are flat layers with minimal looping and few uncompensated charged form, resulting in neutral or weakly charged surfaces that are poor substrates for further electrostatic adsorption. For very high charge densities, the effective charge density is controlled by counterions, and the adsorption is essentially independent of

charge density in this range.<sup>[88]</sup> However, for lower charged fractions still above the threshold, thicker layers form because of the increased ability of polymer chains to adopt more highly coiled conformations in solution.<sup>[89]</sup>

Multilayers comprising weak polyelectrolytes have drawn great attention recently because the molecular charge density can be adjusted by changing solution pH value, thereby controlling the resulting film properties. For multilayers wherein both components are weak polyions, the pH of both adsorption solutions influences the thickness of layers formed.<sup>[90]</sup> Combining two fully ionized chains results in very thin layers, whereas when one of the species is kept close to full dissociation, large thicknesses are obtained.<sup>[91]</sup> Moving from one extreme to another, thickness may change over more than an order of magnitude. For weak polyelectrolyte combinations, the thickness of the adsorbing layer is determined primarily by the surface charge of the previous layer or by the charge of the adsorbing polyion chain.<sup>[90,91]</sup>

In addition, the dissociation of weak polyelectrolytes in preformed multilayers, resulting in film decomposition, can be varied by controlling external conditions. Small charged molecules can be absorbed into and released from weak polyion films, by modulating ambient pH to control dissociation within the films.<sup>[92]</sup> The local  $\text{p}K_a$  of a weak polyion assembled in a multilayer is decreased relative to the solution value and is dependent on the salt concentration.<sup>[93]</sup> The superficial layer of preformed multilayer films also influences the internal film properties; for example, the dissociation of carboxylic groups within multilayers increases when the outer layer is polycationic and decreased for a polyanionic terminal layer.<sup>[94]</sup> This behavior, in turn, affects the amount of material adsorbed in the terminating layer.<sup>[78,95]</sup> The surface potential directly determines water mobility in multilayer films as a result of changes in dissociation, swelling, or water structuring.<sup>[96]</sup>

The swelling properties of LbL multilayers have also been investigated. Films prepared from salt solutions take up water in humid air and aqueous environments, and multilayers prepared in the absence of additional salt swell when exposed to salt solutions.<sup>[81,84]</sup> In all cases, the film thickness and total volume increase as a consequence of swelling. The interaction of multilayers with water molecules is similar to that of hydrophobic polymers.<sup>[81,97–99]</sup> The swelling behavior of LbL nanoassemblies is dependent upon salt concentration and is apparently correlated with the internal hydrophobicity for a given polyion pair.<sup>[100,101]</sup> Environmental salt and pH conditions have also been shown to affect film roughness and porosity,<sup>[100,102]</sup> as has solvent.<sup>[103]</sup>

## Permeability

Because of short path lengths and tunable properties, one of the most promising uses of multilayers, in either planar or capsule form, is as a selective transport barrier, which may find application in many fields requiring filtration, controlled uptake or release, or immunoisolation. The key design goal, in most cases, is to produce materials with high transport rates, which are guaranteed by the nanometer thickness of LbL nanoassemblies and are controlled by the number of layers, layer thickness, and layer composition. A second property that is critical to many applications is a high selectivity for a target molecule or a class of molecules, which can be controlled by the chemical composition of the films.<sup>[104,105]</sup> For example, high selectivity for different ions has been reported based on film composition.<sup>[106–109]</sup> A third feature, desirable in some cases, is the ability to dynamically control the transport properties, i.e., change the permeability over time in response to a stimulus (e.g., solvent properties,<sup>[33]</sup> pH,<sup>[34,110]</sup> ionic strength,<sup>[111]</sup> temperature,<sup>[109]</sup> etc.).

While multilayer films offer the promise of fulfilling all of the needs of systems with controlled transport properties, a great deal of effort is still required to reduce these concepts to practice. Some progress has been made toward a general understanding of permeability properties of LbL nanoassemblies, but the complex, dynamic interactions between molecular components and external conditions that determine transport rates make this a difficult task. It has been noted that changes in pH or salt concentration during or after film deposition result in increased porosity, and it is still unclear whether these effects are reversible or permanent.<sup>[102,112,113]</sup>

This complex interplay between films composition, fabrication conditions, and environmental variables becomes especially important when attempting to design and prepare multilayer capsules with specific permeability. This is because the dissolution process of the template, typically involving large pH changes and high osmotic pressures, adds an additional degree of complexity that must also be considered to impact the final form and function of the multilayers. It has been shown that hollow capsules are semipermeable, although this is clearly dependent upon film composition and assembly conditions.<sup>[44]</sup>

A remarkable property of polyelectrolyte microcapsules is that the capsule interior can provide chemical conditions different from the surrounding medium. Thus the capsules act as membranes to provide a specialized, partially isolated microenvironment with internal volumes on the order of femtoliters, even attoliters, with phenomenal surface-to-volume ratios. For example, using a typical 5- $\mu\text{m}$ -diameter MF or  $\text{MnCO}_3$

template, a resulting capsule, would have an internal volume of  $\sim 65$  fL and a surface area of  $\sim 8 \times 10^{-7}$   $\text{cm}^2$ ; scaling the template down to a 50 nm silica particle would result in a volume and a surface area of  $\sim 0.065$  aL and  $\sim 8 \times 10^{-11}$   $\text{cm}^2$ , respectively. The corresponding change in surface-to-volume ratio scales directly with the change in diameter: approximately 12,000  $\text{cm}^2/\text{cm}^3$  for 5  $\mu\text{m}$  capsules and 1,200,000  $\text{cm}^2/\text{cm}^3$  for capsules with 50-nm diameter. These features form the basis for interest in performing chemical reactions within the unique volumes defined by the capsules. Several demonstrations of exploiting the partitioned environment within microcapsules have been given. Capsules have been used to selectively partition organic solvents<sup>[114]</sup> and for controlled precipitation of organic and inorganic materials.<sup>[115]</sup> Additionally, polymer synthesis within microcapsules has been performed.<sup>[116]</sup>

## Electrical Properties

In spite of efforts to use in LbL assembly of water-soluble derivatives of polypyrrole or polythiophene, no stable conductive LbL multilayers of these materials have been produced to date. Most interesting works in this direction were performed by Ferreira et al.,<sup>[117]</sup> wherein electrical conductivity of up to 100 S/cm in 50-nm-thick polypyrrole/poly(styrenesulfonate) film was achieved. More promising results were reached in semiconducting LbL films based on water-soluble derivative of well-known polyphenylene vinylene [PPV, e.g., poly(*p*-phenylene(1-tetrahydrothiophene)-ethylene chloride)].<sup>[118]</sup> Light-emitting diodes based on multilayer heterostructure of alternate poly(phenylene vinylene) and sulfonated polyaniline have also been demonstrated. A 20-nm-thick light-emitting diode device had a turn-on voltage of about 1 V, and green light was clearly observed under normal room illumination.<sup>[119]</sup> Light-emitting diodes and display devices of large area and low operating voltage is one interesting application of LbL multilayers, although such ultrathin conducting systems could also find application in biomedical devices for neuroprosthetics, e.g., retinal implants or functional electrical stimulation devices. Furthermore, neural networks may benefit from the ability to integrate living tissue by controlled cell adhesion and direction (see below) with functional electrical systems.

## THEORIES REGARDING ASSEMBLY

A number of theories have been developed to describe LbL nanoassemblies. These deal primarily with the

adsorption process and multilayer formation as well as the properties of preformed films. Models range from mathematical descriptions derived from fundamental physical theory to those that deal directly with experimental data. An initial theoretical model for adsorption and surface charge inversion was derived from first principles including the effect of solution ionic strength.<sup>[120]</sup> A theoretical phase diagram has been constructed to describe charge-reversal mechanisms with dependence on screening length and charge density,<sup>[121,122]</sup> in which model applies directly to semiflexible chains with increased rigidity, where adsorbing layers are thin and flat, and a mean field description does not apply. A Debye–Huckel model for multilayer formation was also derived, concentrating on flexible chains.<sup>[123]</sup> A phenomenological approach has also been developed to describe the excess charge of the outer layer as distributed over several underlying layers using charge overcompensation level and the charge decay length into the multilayer.<sup>[124]</sup>

Attempts to describe the kinetics of multilayer formation have also been made. The typical approach involves a two-step model, i.e., a fast adsorption phase involving the transport of chains to the surface by diffusion, followed by slow rearrangements at the surface where ionic bonds are formed because of electrostatic force.<sup>[25,73]</sup> Subsequent slow rearrangements enable segments of the adsorbing molecules to move into the inner regions of the previously deposited layer, resulting in a final irreversible complexation within deeper regions while the outer region maintains some flexibility.<sup>[82,125,126]</sup> The interaction of an adsorbing polyelectrolyte layer with a previously immobilized layer can be sufficiently strong to result in desorption of a soluble complex. In this situation, an initial increase in adsorbed mass is observed, then over time (a few minutes), the adsorbed amount decreases again, suggesting desorption of material complex from the surface.<sup>[127]</sup> This behavior has been described as the equilibrium between a solid complex phase and soluble complexes in solution as viewed by a phase diagram, including liquid and glassy states, with dependence upon ionic strength.<sup>[127]</sup>

Preformed LbL nanoassemblies are most commonly viewed as soft materials, essentially hydrogels with a cross-linking density dependent upon the charge distribution along the polymer chain.<sup>[104,108]</sup> However, multilayer films have also been described as being in a glassy, quasifrozen state<sup>[123]</sup> and as “layered complexes” which exhibit the same local interactions as identical soluble complexes, only possessing great density and a defined 2-D molecular architecture. The internal dynamics of multilayers have been probed, from which it appears that multilayers are in fact structurally similar to polyelectrolyte complexes in solution, as swelling and temperature changes result

in rearrangement processes that occur on the order of hours.<sup>[97,98,126]</sup>

## BIOMEDICAL APPLICATIONS OF LAYER-BY-LAYER FILMS

Primary biomaterial applications of planar layers involve the use as matrix materials for functional or biological molecular entities, e.g., sensors, tissue engineering scaffolds, membranes, or for surface modification of other materials. The range of potential applications is even broader when considering uses of multilayer-coated functional colloidal particles including novel sensors and reactor systems. Further expansion of applicability is given by removal of the solid colloidal core to produce stable, hollow polymeric shell structures. Such hollow, thin-walled microcapsules have attracted particular interest from the viewpoint of applications in encapsulation, for example, as drug carrier systems or microreactors.

### Surface Modification

Recent examples of how LbL is being used to modify surfaces of real systems for improving properties are found in both industrial use and envisioned potential in the scientific literature. To begin with, Ciba-Vision has patented use of the LbL process to modify contact lenses,<sup>[128]</sup> and this method continues to be studied as an approach for applying several novel, multifunctional coatings. This is believed to be the first commercial use of the process. A second example is found in functionalized food wrapping, recently released by the Japanese company Shiratori NanoTechnology in Kawasaki. Its “Yasa-sheet” coating is a multilayer coating comprising chitosan, a major sugar-based ingredient of crab shells, and an enzyme-containing liquid extracted from bamboo. The protective wrapper designed to preserve fruit and vegetables works by suppressing the food’s emission of ethylene gas, a naturally produced ripening agent that eventually makes fruits and vegetables rot.<sup>[129]</sup>

Several additional useful applications of coatings are envisioned based on solid laboratory demonstrations recently reported in the scientific literature. Corrosion control is particularly promising, as suggested by recent experiments using ultrathin (70 nm) polymer coatings deposited on stainless steel wires. When the coated wires were immersed in saltwater and biased with an electrical potential, they exhibited considerably less corrosion for all potentials when compared to untreated wires.<sup>[130]</sup> These coatings could improve the longevity of implanted devices as well as enhance environmental stability of pipes and other metal-based

systems. Optical coatings have also been proposed, including antireflection coatings, demonstrated to enhance the throughput of optical elements, offering a cost-effective alternative to current coating methods,<sup>[131]</sup> and designed profiles of silver nanoparticles and organic layers generate ideal reflection because of the refractive index gradient.<sup>[132]</sup>

As a complement to surface coatings designed to impart specific chemical or optical properties, transport barriers have been assembled on porous surfaces to assess the potential for depositing selectively permeable films for separation via controlled diffusion or filtration. Control over charge and composition in polyelectrolyte “skin” has been shown to allow highly selective separation of ions according to charge, size, or hydration energy.<sup>[133]</sup> Additionally, using “template” ions to control fixed charge density has been shown to further enhance anion-transport selectivity.<sup>[105]</sup> Deposition of polyelectrolyte nanofilms on porous supports can also yield nanofiltration membranes that allow high selectivities, water fluxes, and ion rejections, making them potentially attractive for applications in water and salt purification.

### Cell/Tissue Scaffolds

Nanostructured polyelectrolyte multilayer thin films has recently been applied as novel substrates for growth of cells in culture. This new class of biomaterial allows precise control over the cellular microenvironment, which dynamically interacts with cells to determine *in vitro* behavior, and may lead to biological test beds that more exactly match *in vivo* conditions. Fibroblasts have been shown to attach to multilayer combinations in which strong interactions dominate, whereas weakly ionically cross-linked multilayers which present hydrated surfaces resisted fibroblast attachment.<sup>[134]</sup> By controlling the multilayer assembly conditions (pH, ionic strength), a single multilayer combination may be either cell-adhesive or cell-resistant. Hydrogen-bonded multilayers were also found to exhibit high resistance to the fibroblast adhesion, even with only a single bilayer coating.<sup>[135]</sup> More recent work with protein-coated patterned polymer multilayers has shown the ability to deposit precise micropatterns of nanofilms, and the underlying architecture of these profoundly influences cell morphology.<sup>[136,137]</sup> These recent findings are likely to lay the foundation for a large effort to investigate biomaterial interactions with LbL nanoassemblies. Examples of the exciting potential of these systems are given in Fig. 7. These microscopic images of patterned LbL nanofilms demonstrate the feasibility of using especially designed multilayer structures to control and manipulate cell adhesion.<sup>[136]</sup>

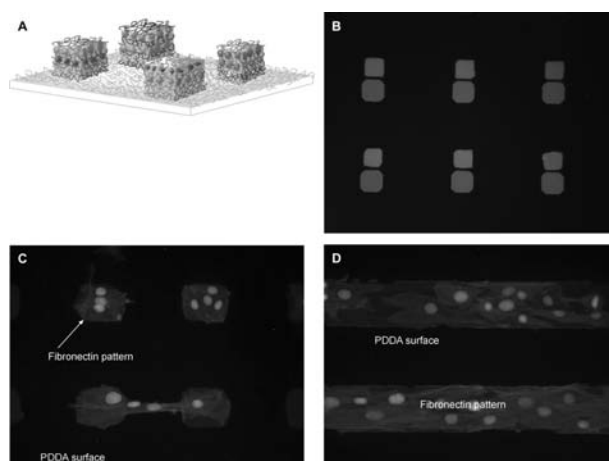


**Fig. 7** Examples of controlled cell–material interactions enabled by LbL nanofilm assembly and patterning. (A) Conceptual rendering of multifunctional substrate with four regions of different composition and structure; (B) Fluorescence micrographs for experimental demonstration of two-region pattern comprising PSS {PAH/PSS}<sub>5</sub> {PAH/FITC-secreted phospholipase A<sub>2</sub>}<sub>5</sub> (green) and PSS {PAH/PSS}<sub>5</sub> {TRITC-poly(lysine)/PSS}<sub>5</sub> {TRITC-poly(lysine)} (red) patterned on a background of PDDA on glass; (C) and (D) examples of spatially controlled cell–material interactions using rat aortic smooth muscle cells (RSMCs) grown on fibronectin-coated LbL films of PDDA/PSS patterned against a cytophobic PDDA background.

### Building Living Tissues/Organs

It may be possible to employ the exquisitely simple LbL approach to nanoassembly as an aid in wound healing and repair of damaged tissue using films containing natural materials with specific bioactivity. A tremendous possibility proposed recently is to directly deposit multilayers onto arterial walls to provide protection for the damaged blood vessels and to avoid restenosis.<sup>[138]</sup> LbL self-assembly of two polysaccharides, hyaluronan (HA) and chitosan (CH), known to have anti-inflammatory properties, was recently reported for modifying the arterial wall in *ex vivo* models. The polyanionic chitosan apparently adheres strongly to the negatively charged surfaces presented by damaged blood vessels, providing a surface for HA deposition, which can be immobilized within the films at concentrations much higher than is possible by infusion. In addition, doping of multilayers with L-arginine showed increased thromboresistance.

A second example, less remarkable yet still significant, was used to show the potential for LbL to modify implantable materials for improved biocompatibility and controlled release of substances to facilitate healing. In this case, assembly of HA and CH was used to modify endovascular stents.<sup>[139]</sup> Multilayer-coated

NiTi disks presented enhanced antifouling properties, compared to unmodified NiTi disks, as evidenced by decreased platelet adhesion in an *in vitro* assay, although *ex vivo* assay on a porcine model indicated that the coating did not prevent fouling by neutrophils. The multilayers were also used as *in situ* drug delivery systems by incorporating the nitric oxide donor sodium nitroprusside (SNP), which further reduced platelet adhesion.

### Enzyme Assemblies—Nanoreactors

The LbL deposition of organized enzyme multilayered shells on nanoscale cores is a promising approach for creating tiny reactors for biocatalysts applications, as has recently been demonstrated for glucose oxidase, peroxidase, urease, luciferase, and  $\beta$ -glucosidase.<sup>[13,14,140]</sup> Such organized enzyme/polyion multilayers, with enzymes arranged in a predetermined order within semipermeable polymeric shells, present a new class of bio/nanoreactors. The degree of order and complexity that can be imparted to these systems via the flexible LbL technique makes them distinct from the more traditional liposome- or copolymer-shelled enzymatic reactors. Additionally, an expansion of capabilities for bio/nanoreactors through inclusion of inorganic and magnetic nanoparticles within multilayer polymer/enzyme films was demonstrated. Enhanced functionality, such as catalytic activity and manipulation, may be produced by higher surface area and magnetic shells.<sup>[14]</sup> This is part of an overall strategy to create unique and complex biocolloids, with emphasis on tailored enzyme self-assembly using nanoparticle layers on latex microcores. Examples of potential applications of these general technologies include therapeutic devices, reactors for efficient catalysis, and biosensors.

### Sensors

Building upon the possibilities afforded by coating micro/nanoscale templates with functional materials such as enzymes and dyes, sensors for chemicals and biochemicals are being developed as tools for biological research, medical diagnostics and monitoring, and biodefense applications. Using nanoparticles coated with fluorescent materials that respond selectively to specific species by binding or other interactions, ratiometric nanoscale probes have been developed for intracellular and extracellular measurements of ions and oxygen.<sup>[141–145]</sup> These nanodevices have advantages over standard liquid-phase small-molecule indicators in that they provide a protective package for the chemistry, separating the dyes from the biological environment and, in doing so, reducing nonspecific

responses, dye–protein binding, and toxic effects. In addition, the immobilization of the indicators within the nanofilms provides physical linkage with reference fluorophores, allowing constant ratiometric monitoring without large shifts in calibrations otherwise seen. By coupling the chemical nanosensors with an enzyme nanoreactor, a second class of sensors may be realized, using direct monitoring of coreactants or products as an indirect means of determining the concentration of other substrates.<sup>[14,146,147]</sup>

### Therapeutic Agents

A promising use for microcapsules and therapeutic agents modified directly with multilayer coatings is in controlled release. A variety of demonstrations for protein and drug encapsulation suggest a bright future for applications in controlled delivery of therapeutic agents.<sup>[19,148–150]</sup> In an effort to exploit these possibilities toward commercial use, Capsulation GmbH (Berlin, Germany) is offering several products based on LbL coatings for drug delivery (LBL-Flash<sup>®</sup>—enhanced dissolution for poorly soluble drugs; LBL-Solv<sup>®</sup>—enhanced bioavailability for drug candidates; LBL-Intra<sup>®</sup>—prolonged circulation and enhanced intracellular uptake) and a variety of diagnostic products for improving fluorescence-based assays.<sup>[151]</sup>

### CONCLUSION

Layer-by-layer nanofabrication is a simple yet versatile means of precisely modifying any charge substrate by sequential deposition of complementary materials. The choice of molecules available is wide, the dimensional precision is high, and the potential application areas are broad. Over the past 10 years, significant progress has been made toward understanding fundamental structural, chemical, and physical properties of multilayer ultrathin films, and this work is beginning to enable creation of novel coatings tailored to realize desired properties. As a result, nanoassembly is now finding some commercial applications, and many more are expected to arise in the near future. Because of the amazing flexibility and precision allowed, this technique of self-assembly will lead to useful nanoscale devices, and the impact will likely be large.

### ACKNOWLEDGMENTS

This work is partially supported by the National Science Foundation NIRT (Grant #0210298), the Whitaker Foundation (RG-00-0388), the Louisiana Board of Regents [LEQSF(2001-04)-RD-A-18 and



LEQSF(2002-05)-RD-A-19], and the National Institutes of Health (R01 EB000739-02). Any opinions, findings, and conclusions or recommendations expressed in this material are those of the authors and do not necessarily reflect the view of the funding agencies. The authors gratefully acknowledge Melanie Baecht for the original artwork in Figs. 1, 4 and 6).

## REFERENCES

- Decher, G.; Hong, J.D.; Schmitt, J. Buildup of ultrathin multilayer films by a self-assembly process: III. Consecutively alternating adsorption of anionic and cationic polyelectrolytes on charged surfaces. *Thin Solid Films* **1992**, *210*, 831–835.
- Decher, G. Fuzzy nanoassemblies: Toward layered polymeric multicomposites. *Science* **1997**, *227*, 1232–1237.
- Lvov, Y.; Decher, G.; Möhwald, H. Assembly, structural characterization and thermal behavior of layer-by-layer deposited ultrathin films of poly(vinylsulfate) and poly(allylamine). *Langmuir* **1993**, *9*, 481–486.
- Keller, S.; Kim, H.; Mallouk, T. Layer-by-layer assembly of intercalation compounds and heterostructures on surfaces: Towards molecular “beaker” epitaxy. *J. Am. Chem. Soc.* **1994**, *116*, 8817–8818.
- Lvov, Y.; Ariga, K.; Ichinose, I.; Kunitake, T. Assembly of multicomponent protein films by means of electrostatic layer-by-layer adsorption. *J. Am. Chem. Soc.* **1995**, *117*, 6117–6123.
- Yoo, D.; Shiratori, S.; Rubner, M. Controlling bilayer composition and surface wettability of sequentially adsorbed multilayers of weak polyelectrolytes. *Macromolecules* **1998**, *31*, 4309–4318.
- Cassagneau, T.; Mallouk, T.; Fendler, J. Layer-by-layer assembly of thin film Zener diodes from conducting polymers and CdSe nanoparticles. *J. Am. Chem. Soc.* **1998**, *120* (31), 7848–7859.
- Mamedov, A.; Kotov, N. Free-standing layer-by-layer assembled films of magnetite nanoparticles. *Langmuir* **2000**, *16*, 5530–5533.
- Iler, R. Multilayers of colloidal particles. *J. Colloid Interface Sci.* **1966**, *21*, 569–594.
- Sukhorukov, G.B.; Donath, E.; Davis, S.; Lichtenfeld, H.; Caruso, F.; Popov, V.I.; Möhwald, H. Step-wise polyelectrolyte assembly on particle surfaces—A novel approach to colloid design. *Polym. Adv. Technol.* **1998**, *9*, 759.
- Caruso, F.; Caruso, R.A.; Möhwald, H. Nanoengineering of inorganic and hybrid hollow spheres by colloidal templating. *Science* **1998**, *262*, 1111–1114.
- Lvov, Y.; Price, R.; Singh, A.; Selinger, J.; Spector, M.; Schnur, J. Imaging nanoscale patterns on biologically derived microstructures. *Langmuir* **2000**, *16*, 5932–5935.
- Lvov, Y.; Caruso, F. Biocolloids with ordered urease multilayer shells as enzymatic reactors. *Anal. Chem.* **2001**, *73*, 4212–4217.
- Fang, M.; Grant, P.; McShane, M.; Sukhorukov, G.; Golub, V.; Lvov, Y. Magnetic bio/nanoreactor with multilayer shells of glucose oxidase and inorganic nanoparticles. *Langmuir* **2002**, *18*, 6338–6344.
- Sukhorukov, G.B.; Brumen, M.; Donath, E.; Möhwald, H. Hollow polyelectrolyte shells: Exclusion of polymers and Donnan equilibrium. *J. Phys. Chem., B* **1999**, *103* (31), 6434–6440.
- Donath, E.; Sukhorukov, G.B.; Caruso, F.; Davis, S.A.; Möhwald, H. Novel polymer shells via colloid-templated assembly of polyelectrolytes. *Angew. Chem., Int. Ed.* **1998**, *37*, 2201–2205.
- Voigt, A.; Lichtenfeld, H.; Sukhorukov, G.B.; Zastrow, H.; Donath, E.; Bäuml, H.; Möhwald, H. Membrane filtration for microencapsulation and microcapsules fabrication by layer-by-layer polyelectrolyte adsorption. *Ind. Eng. Chem. Res.* **1999**, *38*, 4037–4043.
- Moya, S.; Sukhorukov, G.B.; Auch, M.; Donath, E.; Möhwald, H. Microencapsulation of organic solvents in polyelectrolyte multilayer micrometer-sized shells. *J. Colloid Interface Sci.* **1999**, *216*, 297–302.
- Lvov, Y.; Antipov, A.; Mamedov, A.; Möhwald, H.; Sukhorukov, G. Urease encapsulation in nanoorganized microshells. *Nano Lett.* **2001**, *1*, 125–128.
- Sukhorukov, G.; Dähne, L.; Hartman, J.; Donath, E.; Möhwald, H. Controlled precipitation of dyes into hollow polyelectrolyte capsules based on colloids and biocolloids. *Adv. Mater.* **2000**, *12*, 112–115.
- Mendelsohn, J.; Barrett, C.; Chan, V.; Pal, A.; Mayes, A.; Rubner, M. Fabrication of microporous thin films from polyelectrolyte multilayers. *Langmuir* **2000**, *16*, 5017–5023.
- Sukhorukov, G.; Antipov, A.; Voigt, A.; Donath, E.; Möhwald, H. pH-controlled macromolecule encapsulation in and release from polyelectrolyte multilayer capsules. *Macromol. Rapid Commun.* **2000**, *22*, 44–46.
- Decher, G.; Ecker, M.; Schmitt, J.; Struth, B. Layer-by-layer assembled multicomposite films. *Curr. Opin. Colloid Interface Sci.* **1998**, *3*, 32–39.
- Hammond, P.T. Recent explorations in electrostatic multilayer thin film assembly. *Curr. Opin. Colloid Interface Sci.* **1999**, *4*, 430–442.
- Bertrand, P.; Jonas, A.; Laschewsky, A.; Legras, R. Ultrathin polymer coatings by complexation of polyelectrolytes at interfaces: Suitable materials, structure and properties. *Macromol. Rapid Commun.* **2000**, *21*, 319–348.
- Lvov, Y., Möhwald, H., Eds.; *Protein Architecture: Interfacial Molecular Assembly and Immobilization Biotechnology*; Marcel Dekker Publ.: New York, 2000; 1–394.
- Kotov, N.A.; Dékány, I.; Fendler, J.H. Layer-by-layer self-assembly of polyelectrolyte–semiconductor nanoparticle composite films. *J. Phys. Chem.* **1995**, *99*, 13065–13069.
- Kerimo, J.; Adams, D.M.; Barbara, P.F.; Kaschak, D.M.; Mallouk, T.E. NSOM investigations of the spectroscopy and morphology of self-assembled multilayered thin films. *J. Phys. Chem., B* **1998**, *102*, 9451–9460.

29. Ostrander, J.W.; Mamedov, A.A.; Kotov, N.A. Two modes of linear layer-by-layer growth of nanoparticles–polyelectrolyte multilayers and different interactions in the layer-by-layer deposition. *JACS* **2001**, *123*, 1101–1110.
30. Kotov, N.A. Ordered layered assemblies of nanoparticles. *MRS Bull.* **2001**, *26*, 992–997.
31. Lvov, Y.; Munge, B.; Giraldo, O.; Ichinose, I.; Suib, S.L.; Rusling, J.F. Films of manganese oxide nanoparticles with polycations or myoglobin from alternate-layer adsorption. *Langmuir* **2000**, *16*, 8850–8857.
32. Donath, E.; Sukhorukov, G.B.; Caruso, F.; Davis, S.A.; Möhwald, H. Novel hollow polymer shells by colloid-templated assembly of polyelectrolytes. *Angew. Chem., Int. Ed.* **1998**, *37*, 2202–2205.
33. Shi, X.Y.; Caruso, F. Release behavior of thin-walled microcapsules composed of polyelectrolyte multilayers. *Langmuir* **2001**, *17*, 2036–2042.
34. Antipov, A.A.; Sukhorukov, G.B.; Donath, E.; Mohwald, H. Sustained release properties of polyelectrolyte multilayer capsules. *J. Phys. Chem., B* **2001**, *105*, 2281–2284.
35. Qiu, X.P.; Leporatti, S.; Donath, E.; Mohwald, H. Studies on the drug release properties of polysaccharide multilayers encapsulated ibuprofen microparticles. *Langmuir* **2001**, *17*, 5375–5380.
36. Caruso, F.; Mohwald, H. Preparation and characterization of ordered nanoparticle and polymer composite multilayers on colloids. *Langmuir* **1999**, *15*, 8276–8281.
37. Moya, S.; Dahne, L.; Voigt, A.; Leporatti, S.; Donath, E.; Mohwald, H. Polyelectrolyte multilayer capsules templated on biological cells: Core oxidation influences layer chemistry. *Colloids Surf., A Physicochem. Eng. Asp.* **2001**, *183*, 27–40.
38. Antipov, A.A.; Sukhorukov, G.B.; Leporatti, S.; Radtchenko, I.L.; Donath, E.; Mohwald, H. Polyelectrolyte multilayer capsule permeability control. *Colloids Surf., A Physicochem. Eng. Asp.* **2002**, *198–200*, 535–541.
39. Ai, H.; Fang, M.; Jones, S.; Lvov, Y. Electrostatic layer-by-layer nano-assembly on biological microtemplates: Platelets. *Biomacromolecules* **2002**, *3*, 560–564.
40. Moya, S.; Dahne, L.; Voigt, A.; Leporatti, S.; Donath, E.; Mohwald, H. Polyelectrolyte multilayer capsules templated on biological cells: Core oxidation influences layer chemistry. *Colloids Surf., A Physicochem. Eng. Asp.* **2001**, *183–185*, 27–40.
41. Lvov, Y.; Lu, Z.; Schenkman, J.; Rusling, J. Direct electrochemistry of myoglobin and cytochrome P450 in alternate layer-by-layer films with DNA and other polyions. *J. Am. Chem. Soc.* **1998**, *120*, 4073–4080.
42. Whitesides, G.S. Self-Assembled Monolayers. In *Nanotechnology*; Timp, G., Ed.; Springer-Verlag: New York, 1999.
43. Decher, G.; Lvov, Y.; Schmitt, J. Proof of multilayer structural organization of polycation/polyanion self-assembled films. *Thin Solid Films* **1994**, *244*, 772–777.
44. Sukhorukov, G.B.; Donath, E.; Lichtenfeld, H.; Knippel, H.; Knippel, M.; Budde, A.; Möhwald, H. Layer-by-layer self assembly of polyelectrolytes on colloidal particles. *Colloids Surf., A Physicochem. Eng. Asp.* **1998**, *137*, 253–266.
45. Voigt, A.; Lichtenfeld, H.; Sukhorukov, G.B.; Zastrow, H.; Donath, E.; Bäuml, H.; Möhwald, H. Membrane filtration for microencapsulation and microcapsules fabrication by layer-by-layer polyelectrolyte adsorption. *Ind. Eng. Chem. Res.* **1999**, *38*, 4037–4043.
46. Sukhorukov, G.B.; Donath, E.; Davis, S.; Lichtenfeld, H.; Caruso, F.; Popov, V.I.; Möhwald, H. Stepwise polyelectrolyte assembly on particle surfaces: A novel approach to colloid design. *Polym. Adv. Technol.* **1998**, *9*, 759–767.
47. Radtchenko, I.L.; Sukhorukov, G.B.; Leporatti, S.; Khomutov, G.B.; Donath, E.; Möhwald, H. Assembly of alternated multivalent ion/polyelectrolyte layers on colloidal particles. Stability of the multilayers and encapsulation of macromolecules into polyelectrolyte capsules. *J. Colloid Interface Sci.* **2000**, *230*, 272–280.
48. Schlenoff, J.B.; Dubas, S.T.; Farhat, T. Sprayed polyelectrolyte multilayers. *Langmuir* **2000**, *16*, 9968–9969.
49. Cho, J.; Char, K.; Hong, J.D.; Lee, K.B. Fabrication of highly ordered multilayer films using a spin self-assembly method. *Adv. Mater.* **2001**, *13*, 1076–1078.
50. Lee, S.S.; Hong, J.D.; Kim, C.H.; Kim, K.; Koo, J.P.; Lee, K.B. Layer-by-layer deposited multilayer assemblies of ionene-type polyelectrolytes based on the spin-coating method. *Macromolecules* **2001**, *34*, 5358–5360.
51. Chiarelli, P.A.; Johal, M.S.; Casson, J.L.; Roberts, J.B.; Robinson, J.M.; Wang, H.L. Controlled fabrication of polyelectrolyte multilayer thin films using spin-assembly. *Adv. Mater.* **2001**, *13*, 1167–1171.
52. Lefaux, C.J.; Zimmerlin, J.A.; Mather, P.T. Influence of ionic strength on build-up of multilayer thin films using spin self-assembly. *Polym. Prepr. (Am. Chem. Soc., Div. Polym. Chem.)* **2002**, *43* (2), 356–357.
53. Johal, M.S.; Casson, J.L.; Chiarelli, P.A.; Liu, D.G.; Shaw, J.A.; Robinson, J.M.; Wang, H.L. Polyelectrolyte trilayer combinations using spin-assembly and ionic self-assembly. *Langmuir* **2003**, *19*, 8876–8881.
54. Chiarelli, P.A.; Johal, M.S.; Holmes, D.J.; Casson, J.L.; Robinson, J.M.; Wang, H.L. Polyelectrolyte spin-assembly. *Langmuir* **2002**, *18*, 168–173.
55. Lee, S.S.; Lee, K.B.; Hong, J.D. Evidence for spin coating electrostatic self-assembly of polyelectrolytes. *Langmuir* **2003**, *19*, 7592–7596.
56. Hammond, P.; Whitesides, G. Formation of polymer microstructures by selective deposition of polyion multilayers using patterned self-assembled monolayers as a template. *Macromolecules* **1995**, *28*, 7569–7571.
57. Chen, K.M.; Jiang, X.P.; Kimerling, L.C.; Hammond, P.T. Selective self-organization of colloids on patterned polyelectrolyte templates. *Langmuir* **2000**, *16*, 7825–7834.
58. Jiang, X.; Hammond, P. Selective deposition in layer-by-layer assembly: Functional graft copolymers as molecular templates. *Langmuir* **2000**, *16*, 8501–8509.
59. Jiang, X.; Zheng, H.; Gourdin, S.; Hammond, P. Polymer-on-polymer stamping: Universal approaches

- to chemically patterned surfaces. *Langmuir* **2002**, *18*, 2607–2615.
60. Zheng, H.; Lee, I.; Rubner, M.; Hammond, P. Two component particle arrays on patterned polyelectrolyte multilayer templates. *Adv. Mater.* **2002**, *14*, 569–572.
  61. Hua, F.; Lvov, Y.; Cui, T. Spatial patterning of colloidal nanoparticle-based thin film by a combinative technique of layer-by-layer self-assembly and lithography. *J. Nanosci. Nanotechnol.* **2002**, *2*, 357–361.
  62. Hua, F.; Cui, T.; Lvov, Y. Lithographic approach to pattern self-assembled nanoparticle multilayers. *Langmuir* **2002**, *18*, 6712–6715.
  63. Hua, F.; Shi, J.; Lvov, Y.; Cui, T. Patterning of layer-by-layer self-assembled multiple types of nanoparticle thin films by lithographic technique. *Nano Lett.* **2002**, *2*, 1119–1222.
  64. Hua, F.; Lvov, Y.; Cui, T. Fabrication and characterization of capacitor based on layer-by-layer self-assembled thin films. *Nanotechnology* **2003**, *14*, 453–457.
  65. Cui, T.; Hua, F.; Lvov, Y. Field effect transistor fabricated by electrostatic layer-by-layer nanoassembly. *IEEE Electron Device Lett.* **2004**, *51*, 503–507.
  66. Sui, Z.; Salloum, D.; Schlenoff, J.B. Effect of molecular weight on the construction of polyelectrolyte multilayers: Stripping versus sticking. *Langmuir* **2003**, *19*, 2491–2495.
  67. Mao, G.; Tsao, Y.; Tirrell, M.; Davis, H.; Hessel, V.; Ringsdorf, H. Self-assembly of photopolymerizable bolaform amphiphile mono and multilayers. *Langmuir* **1993**, *9*, 3461.
  68. Shchukin, D.; Sukhorukov, G.; Moehwald, H. Biomimetic fabrication of nanoengineered composite shells. *Chem. Mater.* **2003**, *15*, 3947–3950.
  69. Lee, H.; Kepley, L.; Hong, H.; Mallouk, T. Inorganic analogues of Langmuir–Blodgett films: Adsorption of ordered zirconium 1,10-decanebisphosphonate multilayers on silicon surfaces. *J. Am. Chem. Soc.* **1988**, *110*, 618.
  70. Kotov, N.A. Layer-by-layer self-assembly: The contribution of hydrophobic interactions. *Nanostruct. Mater.* **1999**, *12*, 789–796.
  71. Buscher, K.; Graf, K.; Ahrens, H.; Helm, C.A. Influence of adsorption conditions on the structure of polyelectrolyte multilayers. *Langmuir* **2002**, *18*, 3585–3591.
  72. Donath, E.; Walther, D.; Shilov, V.N.; Knippel, E.; Budde, A.; Lowack, K.; Helm, C.A.; Möhwald, H. Nonlinear hairy layer theory of electrophoretic fingerprinting applied to consecutive layer by layer polyelectrolyte adsorption onto charged polystyrene latex particles. *Langmuir* **1997**, *13*, 5294–5305.
  73. Plech, A.; Salditt, T.; Munster, C.; Peisl, J. Investigation of structure and growth of self-assembled polyelectrolyte layers by X-ray and neutron scattering under grazing angles. *J. Colloid Interface Sci.* **2000**, *223*, 74–82.
  74. Baur, J.W.; Rubner, M.F.; Reynolds, J.R.; Kim, S. Förster energy transfer studies of polyelectrolyte heterostructures containing conjugated polymers: A means to estimate layer interpenetration. *Langmuir* **1999**, *15*, 6460–6469.
  75. Lowack, K.; Helm, C.A. Molecular mechanisms controlling the self-assembly process of polyelectrolyte multilayers. *Macromolecules* **1998**, *31*, 823–833.
  76. Laurent, D.; Schlenoff, J.B. Multilayer assemblies of redox polyelectrolytes. *Langmuir* **1997**, *13*, 1552–1557.
  77. Schlenoff, J.B.; Ly, H.; Li, M. Charge and mass balance in polyelectrolyte multilayers. *J. Am. Chem. Soc.* **1998**, *120*, 7626–7634.
  78. Xie, A.F.; Granick, S. Local electrostatics within a polyelectrolyte multilayer with embedded weak polyelectrolyte. *Macromolecules* **2002**, *35*, 1805–1813.
  79. Caruso, F.; Lichtenfeld, H.; Donath, E.; Möhwald, H. Investigation of electrostatic interactions in polyelectrolyte multilayer films: Binding of anionic fluorescent probes to layers assembled onto colloids. *Macromolecules* **1999**, *32*, 2317–2328.
  80. Tedeschi, C.; Caruso, F.; Möhwald, H.; Kirstein, S. Adsorption and desorption behavior of an anionic pyrene chromophore in sequentially deposited polyelectrolyte–dye thin films. *J. Am. Chem. Soc.* **2000**, *122*, 5841–5848.
  81. Losche, M.; Schmitt, J.; Decher, G.; Bouwman, W.G.; Kjaer, K. Detailed structure of molecularly thin polyelectrolyte multilayer films on solid substrates as revealed by neutron reflectometry. *Macromolecules* **1998**, *31*, 8893–8906.
  82. Dubas, S.T.; Schlenoff, J.B. Factors controlling the growth of polyelectrolyte multilayers. *Macromolecules* **1999**, *32*, 8153–8160.
  83. Ladam, G.; Schaad, P.; Voegel, J.C.; Schaaf, P.; Decher, G.; Cuisinier, F. In situ determination of the structural properties of initially deposited polyelectrolyte multilayers. *Langmuir* **2000**, *16*, 1249–1255.
  84. Ruths, J.; Essler, F.; Decher, G.; Riegler, H. Polyelectrolytes I: Polyanion/polycation multilayers at the air/monolayer/water interface as elements for quantitative polymer adsorption studies and preparation of hetero-superlattices on solid surfaces. *Langmuir* **2000**, *16*, 8871–8878.
  85. Hoogeveen, N.; Stuart, M.; Fleer, G.; Bohmer, M. Formation and stability of multilayers of polyelectrolytes. *Langmuir* **1996**, *12*, 3675–3681.
  86. Kolarik, L.; Furlong, D.N.; Joy, H.; Struijk, C.; Rowe, R. Building assemblies from high molecular weight polyelectrolytes. *Langmuir* **1999**, *15*, 8265–8275.
  87. Steitz, R.; Jaeger, W.; von Klitzing, R. Influence of charge density and ionic strength on the multilayer formation of strong polyelectrolytes. *Langmuir* **2001**, *17*, 4471–4474.
  88. Glinel, K.; Moussa, A.; Jonas, A.M.; Laschewsky, A. Influence of polyelectrolyte charge density on the formation of multilayers of strong polyelectrolytes at low ionic strength. *Langmuir* **2002**, *18*, 1408–1412.
  89. Schoeler, B.; Kumaraswamy, G.; Caruso, F. Investigation of the influence of polyelectrolyte charge density on the growth of multilayer thin films prepared by the layer-by-layer technique. *Macromolecules* **2002**, *35*, 889–897.
  90. Yoo, D.; Shiratori, S.S.; Rubner, M.F. Controlling bilayer composition and surface wettability of

- sequentially adsorbed multilayers of weak polyelectrolytes. *Macromolecules* **1998**, *31*, 4309–4318.
91. Shiratori, S.S.; Rubner, M.F. pH-dependent thickness behavior of sequentially adsorbed layers of weak polyelectrolytes. *Macromolecules* **2000**, *33*, 4213–4219.
  92. Chung, A.J.; Rubner, M.F. Methods of loading and releasing low molecular weight cationic molecules in weak polyelectrolyte multilayer films. *Langmuir* **2002**, *18*, 1176–1183.
  93. Rmaile, H.H.; Schlenoff, J.B. Internal  $pK(a)$ 's in polyelectrolyte multilayers: Coupling protons and salt. *Langmuir* **2002**, *18*, 8263–8265.
  94. Muller, M.; Brissova, M.; Rieser, T.; Powers, A.C.; Lunkwitz, K. Deposition and properties of polyelectrolyte multilayers studied by ATR-FTIR spectroscopy. *Mater. Sci. Eng., C, Biomim. Supramol. Syst.* **1999**, *8–9*, 163–169.
  95. Xie, A.F.; Granick, S. Weak versus strong: A weak polyacid embedded within a multilayer of strong polyelectrolytes. *J. Am. Chem. Soc.* **2001**, *123*, 3175–3176.
  96. Breit, M.; Gao, M.; von Plessen, G.; Lemmer, U.; Feldmann, J.; Cundiff, S.T. Formation dynamics of layer-by-layer self-assembled films probed by second harmonic generation. *J. Chem. Phys.* **2002**, *117*, 3956–3960.
  97. Kugler, R.; Schmitt, J.; Knoll, W. The swelling behavior of polyelectrolyte multilayers in air of different relative humidity and in water. *Macromol. Chem. Phys.* **2002**, *203*, 413–419.
  98. Sukhorukov, G.B.; Schmitt, J.; Decher, G. Reversible swelling of polyanion/polycation multilayer films in solutions of different ionic strength. *Ber. Bunsenges. Phys. Chem.* **1996**, *100*, 948–953.
  99. Farhat, T.; Yassin, G.; Dubas, S.T.; Schlenoff, J.B. Water and ion pairing in polyelectrolyte multilayers. *Langmuir* **1999**, *15*, 6621–6623.
  100. Dubas, S.T.; Schlenoff, J.B. Swelling and smoothing of polyelectrolyte multilayers by salt. *Langmuir* **2001**, *17*, 7725–7727.
  101. Tedeschi, C.; Möhwald, H.; Kirstein, S. Polarity of layer-by-layer deposited polyelectrolyte films as determined by pyrene fluorescence. *J. Am. Chem. Soc.* **2001**, *123*, 954–960.
  102. Mendelsohn, J.D.; Barrett, C.J.; Chan, V.V.; Pal, A.J.; Mayes, A.M.; Rubner, M.F. Fabrication of microporous thin films from polyelectrolyte multilayers. *Langmuir* **2000**, *16*, 5017–5023.
  103. Muller, M.; Heinen, S.; Oertel, U.; Lunkwitz, K. Stimulation and binding properties of polyelectrolyte multilayers verified by ATR-FTIR spectroscopy. *Macromol. Symp.* **2001**, *164*, 197–210.
  104. Tieke, B.; van Ackern, F.; Krasemann, L.; Toutianoush, A. Ultrathin self-assembled polyelectrolyte multilayer membranes. *Eur. Phys. J., E* **2001**, *5*, 29–39.
  105. Balachandra, A.M.; Dai, J.; Bruening, M.L. Enhancing the anion-transport selectivity of multilayer polyelectrolyte membranes by templating with  $Cu^{2+}$ . *Macromolecules* **2002**, *35*, 3171–3178.
  106. Farhat, T.R.; Schlenoff, J.B. Ion transport and equilibria in polyelectrolyte multilayers. *Langmuir* **2001**, *17*, 1184–1192.
  107. Harris, J.J.; Stair, J.L.; Bruening, M.L. Layered polyelectrolyte films as selective, ultrathin barriers for anion transport. *Chem. Mater.* **2000**, *12*, 1941–1946.
  108. Krasemann, L.; Tieke, B. Selective ion transport across self-assembled alternating multilayers of cationic and anionic polyelectrolytes. *Langmuir* **2000**, *16*, 287–290.
  109. Dai, J.H.; Jensen, A.W.; Mohanty, D.K.; Erndt, J.; Bruening, M.L. Controlling the permeability of multilayered polyelectrolyte films through derivatization, cross-linking, and hydrolysis. *Langmuir* **2001**, *17*, 931–937.
  110. Harris, J.J.; Bruening, M.L. Electrochemical and in situ ellipsometric investigation of the permeability and stability of layered polyelectrolyte films. *Langmuir* **2000**, *16*, 2006–2013.
  111. Ibarz, G.; Dahne, L.; Donath, E.; Möhwald, H. Smart micro- and nanocontainers for storage, transport, and release. *Adv. Mater.* **2001**, *13*, 1324–1327.
  112. Fery, A.; Scholer, B.; Cassagneau, T.; Caruso, F. Nanoporous thin films formed by salt-induced structural changes in multilayers of poly(acrylic acid) and poly(allylamine). *Langmuir* **2001**, *17*, 3779–3783.
  113. Sukhorukov, G.B.; Antipov, A.A.; Voigt, A.; Donath, E.; Möhwald, H. pH-controlled macromolecule encapsulation in and release from polyelectrolyte multilayer nanocapsules. *Macromol. Rapid Commun.* **2001**, *22*, 44–46.
  114. Moya, S.; Sukhorukov, G.B.; Auch, M.; Donath, E.; Möhwald, H. Microencapsulation of organic solvents in polyelectrolyte multilayer micrometer-sized shells. *J. Colloid Interface Sci.* **1999**, *216*, 297–302.
  115. Sukhorukov, G.; Dahne, L.; Hartmann, J.; Donath, E.; Möhwald, H. Controlled precipitation of dyes into hollow polyelectrolyte capsules based on colloids and biocolloids. *Adv. Mater.* **2000**, *12*, 112–115.
  116. Dahne, L.; Leporatti, S.; Donath, E.; Möhwald, H. Fabrication of micro reaction cages with tailored properties. *J. Am. Chem. Soc.* **2001**, *123*, 5431–5436.
  117. Ferreira, M.; Cheung, J.; Rubner, M. Molecular self-assembly of conjugated polyions: A new process for fabricating multilayer thin film heterostructures. *Thin Solid Films* **1994**, *244*, 806–809.
  118. Onoda, M.; Yoshino, K. Heterostructure electroluminescent diodes prepared from self-assembled multilayers of poly(*p*-phenylene vinylene) and sulfonated polyaniline. *Jpn. Appl. Phys.* **1995**, *34*, L260–L263.
  119. Lee, J.; Yoo, D.; Handy, E.; Rubner, M. Thin film light emitting devices from an electroluminescent ruthenium complex. *Appl. Phys. Lett.* **1996**, *69*, 1686–1688.
  120. Joanny, J.F. Polyelectrolyte adsorption and charge inversion. *Eur. Phys. J., B* **1999**, *9*, 117–122.
  121. Netz, R.R.; Joanny, J.F. Complexation between a semiflexible polyelectrolyte and an oppositely charged sphere. *Macromolecules* **1999**, *32*, 9026–9040.
  122. Netz, R.R.; Joanny, J.F. Adsorption of semiflexible polyelectrolytes on charged planar surfaces: Charge compensation, charge reversal, and multilayer formation. *Macromolecules* **1999**, *32*, 9013–9025.
  123. Castelnovo, M.; Joanny, J.F. Formation of polyelectrolyte multilayers. *Langmuir* **2000**, *16*, 7524–7532.

124. Schlenoff, J.B.; Dubas, S.T. Mechanism of polyelectrolyte multilayer growth: Charge overcompensation and distribution. *Macromolecules* **2001**, *34*, 592–598.
125. Arys, X.; Laschewsky, A.; Jonas, A.M. Ordered polyelectrolyte ‘multilayers’: 1. Mechanisms of growth and structure formation: A comparison with classical fuzzy ‘multilayers’. *Macromolecules* **2001**, *34*, 3318–3330.
126. Wang, L.; Schonhoff, M.; Möhwald, H. Lipids coupled to polyelectrolyte multilayers: Ultraslow diffusion and the dynamics of electrostatic interactions. *J. Phys. Chem., B* **2002**, *106*, 9135–9142.
127. Kovacevic, D.; van der Burgh, S.; de Keizer, A.; Stuart, M.A.C. Kinetics of formation and dissolution of weak polyelectrolyte multilayers: Role of salt and free polyions. *Langmuir* **2002**, *18*, 5607–5612.
128. Wynterton, L.C.; Lally, J.M.; Rubner, M.; Qiu, Y. Single-Dip Process for Achieving a Layer-by-Layer Coating. USA Patent 20010048975, 2001.
129. Gorman, J. Layered approach: A simple technique for making thin coatings is poised to shift from curiosity to commodity. *Sci. News* **2003**, *164*, 91.
130. Farhat, T.R.; Schlenoff, J.B. Corrosion control using polyelectrolyte multilayers. *Electrochem. Solid-State Lett.* **2002**, *5*, B13–B15.
131. Hiller, J.; Mendelson, J.; Rubner, M. Reversibly erasable nanoporous anti-reflection coatings from polyelectrolyte multilayers. *Nat. Mater.* **2002**, *1*, 59–63.
132. Nolte, A.; Rubner, M.; Cohen, R. Creating efficient refractive index gradient within polyelectrolyte multilayer films: Molecularly assembled rugate filters. *Langmuir* **2004**, *20*.
133. Bruening, M.L.; Sullivan, D.M. Enhancing the ion-transport selectivity of multilayer polyelectrolyte membranes. *Chem. -A Eur. J.* **2002**, *8*, 3832–3837.
134. Mendelsohn, J.D.; Yang, S.Y.; Hiller, J.; Hochbaum, A.I.; Rubner, M.F. Rational design of cytophilic and cytophobic polyelectrolyte multilayer thin films. *Biomacromolecules* **2003**, *4*, 96–106.
135. Yang, S.Y.; Mendelsohn, J.D.; Rubner, M.F. New class of ultrathin, highly cell-adhesion-resistant polyelectrolyte multilayers with micropatterning capabilities. *Biomacromolecules* **2003**, *4*, 987–994.
136. Li, M.; Kondabatni, K.K.; Cui, T.; McShane, M.J. Fabrication of 3-D gelatin-patterned glass substrates with layer-by-layer and lift-off (LbL–LO) technology. *IEEE Nanotechnol. J.* **2004**, *3*, 1–8.
137. Berg, M.; Yang, S.; Hammond, P.; Rubner, M. Controlling mammalian cell interactions on patterned polyelectrolyte multilayer surface. *Langmuir* **2004**, *20*, 1362.
138. Thierry, B.; Winnik, F.; Merhi, Y.; Tabrizian, M. Nanocoatings onto arteries via layer-by layer deposition: Towards the in-vivo repair of damaged blood vessels. *JACS* **2003**, *125*, 7494–7495.
139. Thierry, B.; Winnik, F.; Merhi, Y.; Silver, J.; Tabrizian, M. Bioactive coatings of endovascular stents based on polyelectrolyte multilayers. *Biomacromolecules* **2003**, *4*, 1564–1571.
140. Pastorino, L.; Disawal, S.; Lvov, Y.; Erokhin, V. Complex catalytic colloids on the basis of firefly luciferase as optical nanosensor platform. *Biotechnol. Bioeng.* **2003**, *84*, 286–291.
141. Grant, P.S.; McShane, M.J. Development of multilayer fluorescent thin film chemical sensors using electrostatic self assembly. *IEEE Sens. J.* **2003**, *3*, 139–146.
142. Brown, J.Q.; McShane, M.J. Nanoengineered polyelectrolyte micro- and nano-capsules as fluorescent potassium ion sensors. *IEEE-EMBS Mag.* **2003**, *22*, 118–123.
143. Duchesne, T.A.; Brown, J.Q.; Guice, K.B.; Lvov, Y.M.; McShane, M.J. Encapsulation and stability properties of nanoengineered polyelectrolyte capsules for use as fluorescent sensors. *Sens. Mater.* **2002**, *14*, 293–308.
144. McShane, M.J.; Brown, J.Q.; Guice, K.B.; Lvov, Y.M. Polyelectrolyte microshells as carriers for fluorescent sensors: Loading and sensing properties of a ruthenium-based oxygen indicator. *J. Nanosci. Nanotechnol.* **2002**, *2*, 411–416.
145. McShane, M.J. Potential for glucose monitoring with nanoengineered fluorescent biosensors. *Diabetes Technol. Ther.* **2002**, *4*, 533–538.
146. Stein, E.W.; McShane, M.J. Multilayer lactate oxidase shells on colloidal carriers as engines for nanosensors. *IEEE Trans. Nanobiosci.* **2003**, *3*, 133–137.
147. Brown, J.Q.; McShane, M.J. Core-referenced ratio-metric potassium ion sensors made with layer-by-layer self assembly on europium nanoparticles. *IEEE Sens. J.* **2004**, accepted for publication.
148. Tiourina, O.; Antipov, A.; Sukhorukov, G.; Lvov, Y.; Möhwald, H. Encapsulation of  $\alpha$ -chymotrypsin into the hollow polyelectrolyte microparticles. *Macromol. Biosci.* **2001**, *1*, 209–214.
149. Ai, H.; Jones, S.; de Villiers, M.; Lvov, Y. Nanoencapsulation of furosemide microcrystals for controlled drug release. *J. Control. Release* **2003**, *86*, 59–66.
150. Qiu, X.; Leporatti, S.; Donath, E.; Möhwald, H. Studies on the drug release properties of polysaccharide multilayers encapsulated ibuprofen microparticles. *Langmuir* **2001**, *17*, 5375–5380.
151. [www.capsulation.com](http://www.capsulation.com).

# Layered Double Hydroxides: Self-Assembly and Multiple Phases

Zhi Ping Xu

Paul S. Braterman

Department of Chemistry, University of North Texas, Denton, Texas, U.S.A.

## INTRODUCTION

As an important class of clay-like materials, layered double hydroxides (LDHs) possess the promising ability to combine organic anions and metal hydroxide layers, and form variable nanometer-scale precursors that could be readily developed into porous multi-metal mixed oxide catalysts or supports.<sup>[1–3]</sup> Organic–inorganic hybrid assemblies have recently received much attention because of their abundant variations in the structures and molecular interactions.<sup>[4–6]</sup> In this entry, we briefly discuss some basic issues in LDH structural chemistry, such as the underlying sandwich structure, the natures of layer cations and interlayer anions, polytypes, superlattice, crystallite growth, and morphological features. Then we focus on LDH–surfactant hybrids, including formation of various LDH phases and the corresponding anion packing, chemical convertibility between the phases and their stability, flexible morphological features and growth habits, new perspective applications with particular emphasis on our recent work.

## LAYERED DOUBLE HYDROXIDES IN GENERAL

### Basic Structure

The layered structure of LDH is closely related to that of brucite,  $\text{Mg}(\text{OH})_2$ . In a brucite layer, each  $\text{Mg}^{2+}$  ion is octahedrally surrounded by six  $\text{OH}^-$  ions, and the different octahedra share edges to form an infinite two-dimensional layer. Partial replacement of  $\text{Mg}^{2+}$  ions by  $\text{Al}^{3+}$  gives the brucite-like layers a positive charge, which in hydrotalcite ( $\text{Mg}_6\text{Al}_2(\text{OH})_{16}\text{CO}_3 \cdot 4\text{H}_2\text{O}$ ) itself is balanced by carbonate anions, located in the interlayer region (gallery) between the two brucite-like layers (Fig. 1). This gallery also contains water molecules, hydrogen bonded to layer OH and/or to the interlayer anions. Through electrostatic interactions and hydrogen bonds, the layers are held together to form the three-dimensional structure,

as shown in Fig. 1. For hydrotalcite, the repeated interlayer spacing is 0.760 nm. In general, the thickness for the brucite-like layer is taken to be 0.480 nm (0.477 nm for brucite); thus the spacing occupied by the anion (gallery height) is ca. 0.280 nm.<sup>[1–3]</sup>

### Brucite-like Layers

Besides  $\text{Mg}^{2+}$  and  $\text{Al}^{3+}$ , there are a number of divalent and trivalent cations that can form LDHs, as listed in Table 1.<sup>[11]</sup> For these ions, the only requirement is that their radii are not too different from those of  $\text{Mg}^{2+}$  and  $\text{Al}^{3+}$ . Larger ions, such as  $\text{Mn}^{2+}$ ,  $\text{Pd}^{2+}$ ,  $\text{Cd}^{2+}$ ,  $\text{Ca}^{2+}$ ,  $\text{Y}^{3+}$ , and  $\text{La}^{3+}$ , are incorporated into the brucite-like layer by puckering or combining with other divalent or trivalent cations.<sup>[3]</sup> An extreme case is  $\text{Ca}_2\text{Al}$ -LDHs, in which Ca is distorted to be 7-coordinated while Al is still kept 6-coordinated.<sup>[8]</sup>

Although not as common as trivalent cations, some tetravalent cations, such as  $\text{V}^{4+}$ ,  $\text{Ti}^{4+}$ ,  $\text{Zr}^{4+}$ , and  $\text{Sn}^{4+}$ , have been introduced into the brucite-like layers to replace part of the trivalent cations in LDH compounds.<sup>[9–11]</sup> Similarly, monovalent cations, Li or  $\text{Li}_{1-x}\text{Na}_x$ , together with Al, can form a similar series of LDH compounds with atomic ratio Al/Li or Al/(Li + Na) fixed only at 2.<sup>[3]</sup> In addition, it is possible to incorporate multiple different ions into the layers to prepare an LDH as the precursor of mixed oxides with versatile functionalities and tunable physicochemical properties.<sup>[3]</sup>

The value of  $x$  in pure  $\text{M}_{1-x}^{2+}\text{M}_x^{3+}$ -LDHs is normally in the range of 0.2–0.33. Larger or smaller values may cause formation of hydroxide or hydrous oxides containing a single metal. As a result of the electrostatic repulsion between positive charges,  $\text{M}^{3+}$  ions should ideally not be adjacent in the brucite-like layer, but remain apart, which requires  $x$  to be no more than 1/3. Claims of values of  $x$  outside this range need careful substantiation because highly dispersed simple hydroxide phases can readily escape detection by powder X-ray diffraction (XRD).



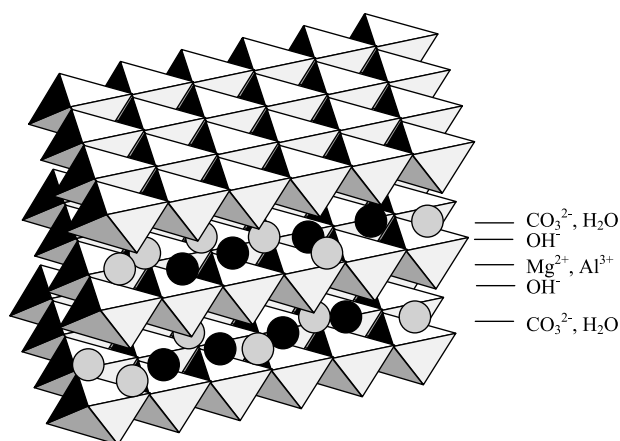


**Fig. 1** Schematic representation of the hydrotalcite three-dimensional structure.

### Interlayer Anions

As for the anions located in the interlayer gallery, the choice is much more versatile. There is almost no limitation to the nature of anions in the LDHs as long as the anions do not abstract the metal ions from the hydroxide layer and have a sufficient charge density in one cross section. Anions that have been successfully incorporated include 1) common inorganic anions; 2) various organic carboxylates, sulfates, sulfonates, and oxygenates; 3) polymeric anions; 4) complex anions; 5) isopolyoxometalates and heteropolyoxometalates; and 6) some biochemical anions.<sup>[3]</sup>

**Table 1** Ionic radii of some cations with coordinate number of 6

M <sup>2+</sup>	Radius (nm)	M <sup>3+</sup>	Radius (nm)
Fe	0.061	Al	0.054
Co	0.065	Co	0.055
Ni	0.069	Fe	0.055
Mg	0.072	Mn	0.058
Cu	0.073	Ga	0.062
Zn	0.074	Rh	0.067
Mn	0.083	Ru	0.068
Pd	0.086	Cr	0.069
Ti	0.086	V	0.074
Cd	0.095	In	0.080
Ca	0.100	Y	0.090
		La	0.103
V <sup>4+</sup>	0.058		
Ti <sup>4+</sup>	0.061	Li <sup>+</sup>	0.076
Sn <sup>4+</sup>	0.069	Na <sup>+</sup>	0.102
Zr <sup>4+</sup>	0.072		

Source: From Ref.<sup>[7]</sup>.

The various anions are very different in their structure, dimensions, and charges; however, they are all located between the brucite-like layers. Therefore their size and orientation determine the interlayer spacing. In general, the anions are oriented in such a way as to maximize the interaction with their surroundings under certain conditions. For example, planar  $\text{CO}_3^{2-}$  and  $\text{NO}_3^-$  anions are usually positioned parallel to the brucite-like layer at low  $x$  values, while at high  $x$  value, they change to tilting or alternating upper-lower orientation as a result of crowding of anions in the gallery.<sup>[3,12,13]</sup> For tetrahedral anions, such as  $\text{SO}_4^{2-}$ ,  $\text{MoO}_4^{2-}$ ,  $\text{CrO}_4^{2-}$ ,  $\text{PO}_4^{3-}$ ,  $\text{ClO}_4^-$ , and  $\text{CoCl}_4^{2-}$ , there are two possible ideal configurations: the pyramidal configuration (with its one  $C_3$  axis perpendicular to the hydroxide layer) and the edge configuration (with its one  $C_2$  axis perpendicular to the hydroxide layer). It has been found that  $\text{ClO}_4^-$  anions adopt the former configuration while  $\text{SO}_4^{2-}$  anions employ the latter.<sup>[1,3]</sup> Octahedral complexes, such as  $\text{Fe}(\text{CN})_6^{3-}$ , hydrogen bond through opposite triangles to upper and lower hydroxide layer sides, as proposed by Kikkawa and Koizumi<sup>[14]</sup> and used by Braterman, Tan, and Zhao<sup>[15]</sup> to explain the perturbation of the vibrational spectrum of cyanide groups from the ideal octahedral symmetry.

For polyoxometalates (POMs), the arrangement is highly dependent on the solution pH because the anion oligomerization degree varies from 1 to 10 with pH change from 12 to 3, as shown by Twu and Dutta.<sup>[16]</sup> In particular, polyvalent POMs and Keggin-type anions  $\alpha\text{-(XM}_{12}\text{O}_{40})^{n-}$  in LDHs act as pillars in the interlayer, giving rise to the so-called pillared LDH, and usually resulting in micropores in the gallery.<sup>[17]</sup> These may provide suitable places for some catalytic reactions to occur.

The orientations of organic anions, especially monovalent surfactant anions, lead to a range of distinct types of phases, as discussed below.

### Stacking and Polytype

We can propose many different ways for brucite-like layers to stack on top of one another; however, there are three highly symmetrical ways for the OH groups of one layer to relate to those of an adjacent layer.<sup>[18]</sup> They may be in register (giving a trigonal prism) or out of register (giving an octahedron). If out of register, the OH groups of the upper layer can be in either of two positions relating to the lower: on top of the octahedral triangle (with a cation) or the vacant triangle (without a cation), as shown in Fig. 1. It can be shown that for a two-layer repeat, there are three polytypes, all hexagonal (2H), while a three-layer repeat gives in all nine polytypes, of which only two (known as 3R<sub>1</sub> and 3R<sub>2</sub>) are rhombohedral.<sup>[18]</sup> Layered

double hydroxide minerals are known in both 2H and 3R forms, and synthetic LDHs are usually assigned to 3R<sub>1</sub>, although recently a 3R<sub>2</sub> form of synthetic hydrotalcite has been described.<sup>[19]</sup> The coexistence of two anions in the interlayer may give rise to intermediate interstratified phases. For example, the coexistence of SO<sub>4</sub><sup>2-</sup> and CO<sub>3</sub><sup>2-</sup> in the MgAl-LDH results in an alternating sequence of (brucite-CO<sub>3</sub><sup>2-</sup>)-(brucite-SO<sub>4</sub><sup>2-</sup>).<sup>[20]</sup> In the case of dicarboxylate and Cl<sup>-</sup>, the sequence is a brucite-dicarboxylate-brucite-chloride repeat unit.<sup>[21]</sup>

Long-chain organic anions will impose their own packing requirements, and, generally speaking, the OH groups of the adjacent hydroxide layers will no longer be in or out of register for close packing. The structure will then be determined by the tilting angle of the chain, and the degree of overlap between chains attached to adjacent layers, as discussed below. The incorporation of two different dicarboxylates in comparable amounts gives only the interlayer spacing expected for the larger anion despite the presence of the smaller anion in the same interlayer.<sup>[21]</sup>

### Superlattice Formation

The ideal distribution of cations within the brucite-like layer and anion in the interlayer will result in formation of superlattice. By obeying a rule analogous to Lowenstein's rule for aluminosilicates, a hexagonal superlattice (or supercell) with  $a' = 2a \sin 60^\circ = a \sqrt{3}$  ( $a'$  is the separation distance of adjacent trivalent cations, as shown in Fig. 2A) will be expected for an LDH with M(II)/M(III) = 2:1.

Complete ordering of cations has been reported for Ca<sub>4</sub>Al<sub>2</sub>(OH)<sub>12</sub>SO<sub>4</sub> · 6H<sub>2</sub>O,<sup>[22]</sup> implying such regularity in the hydroxide layers. Solin et al.<sup>[23]</sup> found a similar superlattice ordering in Ni<sub>1-x</sub>Al<sub>x</sub>-CO<sub>3</sub>-LDH ( $x = 0.33$ , i.e., Ni/Al = 2:1) from XRD patterns. There is a similar superlattice in LiAl<sub>2</sub>-CO<sub>3</sub>-LDH.<sup>[24]</sup>

In Mg<sub>2</sub>Al-benzoate-LDH, an extra reflection in XRD has been observed with diffraction distance

0.454 nm, presumably attributable to the scattering by the anions, because the difference in X-ray scattering power between Mg and Al is small. A superlattice in Ni<sub>1-x</sub>Al<sub>x</sub>-CO<sub>3</sub> and Mg<sub>1-x</sub>Fe<sub>x</sub>-CO<sub>3</sub>-LDH ( $x = 0.30$ ) has been also explained as arising from diffraction of carbonate anions.<sup>[23]</sup> It should be mentioned that the repulsion between the anions will promote such an order.

It seems reasonable to expect a related superlattice for M(II)<sub>3</sub>M(III)-LDH, as shown in Fig. 2B, with  $a' = 2a$ ; but, to the best of our knowledge, this has not yet been observed by XRD. However, this superlattice structure in a short range has been seen in the outermost layers by atomic force microscopy (AFM) and scanning tunnel microscopy (STM). Using these techniques, Cai et al.<sup>[25]</sup> and Yao et al.<sup>[26]</sup> have reported such periodicity on the surface of Mg<sub>6</sub>Al<sub>2</sub>(OH)<sub>16</sub>CO<sub>3</sub> in contact with sulfate, ferrocyanide, or ferricyanide solutions.

Even in the absence of the long-range order required for a diffraction signal, extended X-ray absorption fine structure (EXAFS) spectroscopy can detect the local (up to a few nanometers) order of the cation distribution in the hydroxide layers. Such high local ordering of the cation distribution in many LDHs, including Zn<sub>2</sub>Cr,<sup>[27]</sup> Cu<sub>2</sub>Cr,<sup>[28]</sup> Mg<sub>3</sub>Fe,<sup>[29]</sup> Co<sub>2-y</sub>Cu<sub>y</sub>Al,<sup>[30]</sup> and Co<sub>2</sub>Fe<sub>y</sub>Al<sub>1-y</sub>-LDHs,<sup>[31]</sup> has been unambiguously shown by EXAFS.

### Crystallization and Morphology

Morphology is strongly affected by the crystallization process, which depends not only on the nature of the incorporated cations and intercalated anions, but also on the details of the preparation procedure, such as reaction temperature, time, and post-treatment.

In general, as we have shown directly by pH titration,<sup>[32,33]</sup> LDH forms at a pH well below that necessary to form the most soluble hydroxide, a fact that led to the initial recognition of LDH as a distinct phase.

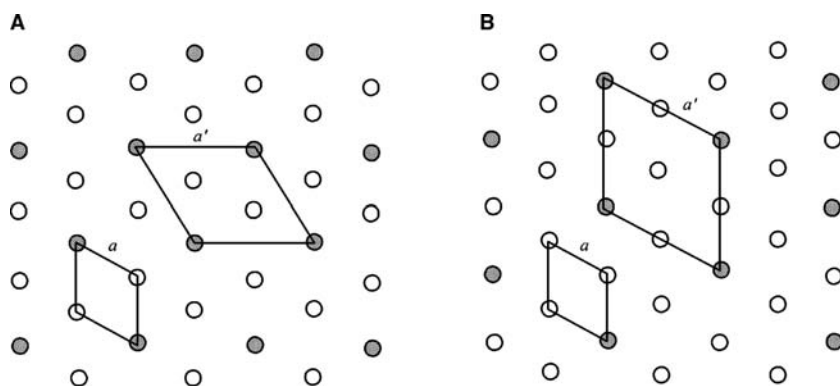


**Fig. 2** Hexagonal superlattices resulting from ideal cation ordering within a brucite-like layer in LDH with M(II)/M(III) = 2:1 ( $a, a' = 2a \sin 60^\circ = a \sqrt{3}$ ) and 3:1 ( $b, a' = 2a$ ). Open circles stand for M(II) and shaded circles for M(III).

We have observed two primary types of pH curves during LDH formation. One, observed with Cr(III)-containing LDH, consists of a single plateau at a pH lower than that necessary to precipitate either  $\text{Cr}(\text{OH})_3$  or  $\text{M}(\text{II})(\text{OH})_2$ ,<sup>[32,33]</sup> indicating direct formation of the LDH from solution. The more common form of pH curve, found for almost all Al-containing and Fe(III)-containing LDHs, exhibits two distinct plateaus.<sup>[32,33]</sup> The first plateau (pH  $\sim 4$  for Al and  $\sim 2$  for Fe) is associated with the formation of aluminum hydroxide or ferric hydrous oxide, while the second corresponds to conversion of this material to LDH.

In general, LDH materials initially form as aggregates of poor crystallinity and irregular shape, but these can be converted into euhedral hexagonal platelets through aging, often accelerated by hydrothermal or microwave treatments.<sup>[1,3,34,35]</sup> These treatments cause smaller and imperfect crystallites to evolve to larger and more perfect LDH particles through Ostwald ripening by a dissolution/recrystallization process. For example,  $\text{Mg}_3\text{Al-CO}_3$ -LDH, prepared by precipitating  $\text{Al}^{3+}$  and  $\text{Mg}^{2+}$  through hydrolyzing urea in a sealed vessel at 75–80°C for a month,<sup>[25]</sup> crystallized as perfect hexagons. Such hexagons normally have an aspect ratio of 10–20 with the in-plate dimension measured in micrometers (Fig. 3), indicating that growth along the *a* and *b* axes is preferred. We explain this growth habit in terms of intermolecular interactions. In LDH carbonate (*a* = 0.305 nm and interlayer spacing = 0.760 nm), there are 12.4 OH groups per square nanometer in the (*ab*) plane but only 5.0 OH groups per square nanometer in the (*ac*) or (*bc*) plane. Therefore to maximize the exposure of OH groups to the aqueous phase, i.e., more hydrogen bonds between water and OH in LDH or less surface tension, crystallite growth along the *a* and *b* axes is more favorable in energy. Moreover, the equal growth along these two

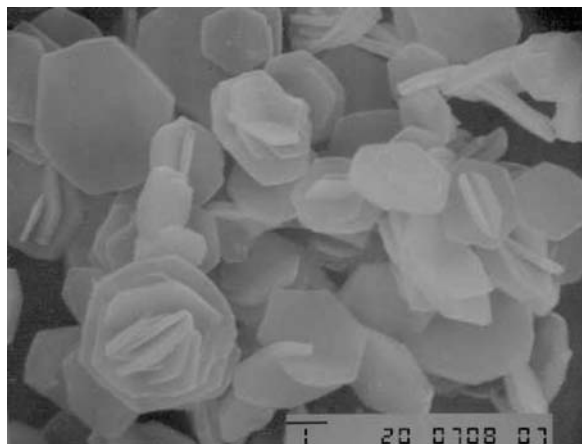


**Fig. 3** Scanning electron microscopy image of  $\text{Mg}_6\text{Al}_2(\text{OH})_{16}\text{CO}_3 \cdot 4\text{H}_2\text{O}$  with bar scale 1  $\mu\text{m}$ .

axes is the most favorable, and thus leads to the formation of hexagonal morphology. In addition, nucleation of a new layer will be less facile than growth at the edge of one that already exists.

The introduction of surfactant anions greatly changes the properties of LDH. For example, the surface hydrophilicity in LDH carbonate is totally converted to hydrophobicity. We have described this effect for LDH dodecylbenzene sulfonate,<sup>[36]</sup> but believe it to be a much more general phenomenon. These changes, related to the surfactant and its arrangement in the interlayer, remarkably affect the structure, growth habit, and morphology, as presented in the following section.

## LAYERED DOUBLE HYDROXIDE–SURFACTANT INTERACTIONS AND NANOCOMPOSITE FORMATION

### Layered Double Hydroxide Phases

We have extensively examined surfactant–LDH nanocomposite materials prepared by the anion exchange method. It is generally agreed that there are three distinct types of LDH phases. As shown in Fig. 4,  $\text{Zn}_2\text{Al}$ -stearate-LDHs show three obvious series of basal reflections, with average interlayer spacings of 3.19 (Phase I), 4.29 (Phase II), and 4.94 nm (Phase III), respectively. Very interestingly, the nominal particle thickness in all samples is nearly the same for

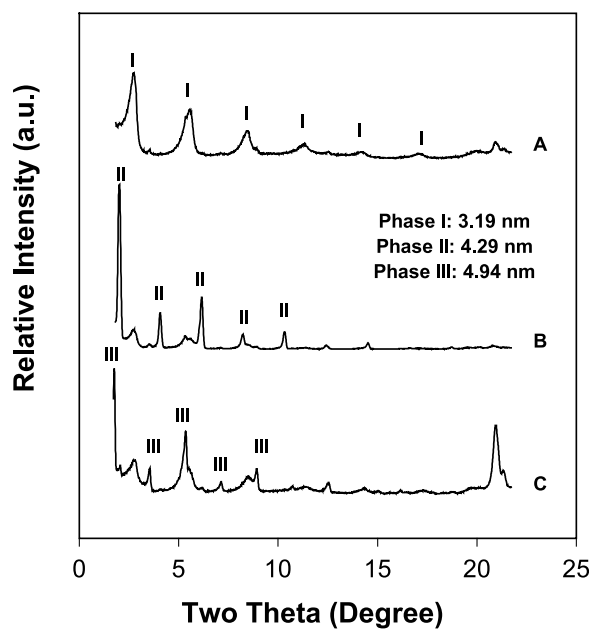


**Fig. 4** X-ray diffraction patterns of three  $\text{Zn}_2\text{Al}$ -stearate-LDH samples. (A) mainly Phase I; (B) mainly Phase II; and (C) mainly Phase III.

Phases I, II, and III, being 20–25, 50–60, and 50–60 nm, respectively, as inferred from the measured widths of diffraction peaks using the Debye–Scherrer equation.<sup>[37]</sup>

These three LDH phases give rise to distinct characteristic Fourier-transform infrared (FTIR) spectra. As shown in Fig. 5, each LDH phase is strongly related to the characteristic vibrations from carboxylate/carboxylic acid groups at 1350–1700  $\text{cm}^{-1}$ , summarized as follows:<sup>[38]</sup>

- Phase I: 1548 (broad, asymmetric  $\nu_{\text{COO}}$ ) and 1413 (broad, symmetric  $\nu_{\text{COO}}$ )  $\text{cm}^{-1}$ .
- Phase II: 1540 (sharp, asymmetric  $\nu_{\text{COO}}$ ) and 1398 (sharp, symmetric  $\nu_{\text{COO}}$ )  $\text{cm}^{-1}$ .
- Phase III: 1597 (sharp) with shoulders at 1610 and 1623 (asymmetric  $\nu_{\text{COO}}$ ), 1440 (weak), and 1413 (sharp, symmetric  $\nu_{\text{COO}}$ )  $\text{cm}^{-1}$ .

In addition, there is a common sharp peak at 1468  $\text{cm}^{-1}$  ( $\text{CH}_2$  scissoring).

We have titrated the LDH samples and found that Phases II and III contain neutral carboxylic acid in addition to carboxylate anions. The acid group is hydrogen bonded, and is characterized by a strong peak at 1597  $\text{cm}^{-1}$  and two associated shoulders at 1610 and 1623  $\text{cm}^{-1}$ .<sup>[39]</sup> This, together with the characteristic vibration peaks, can be understood in terms of the following packing modes.

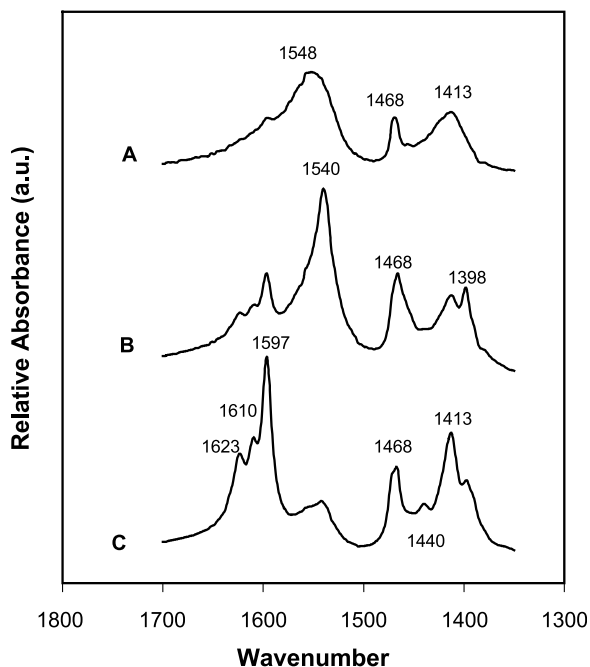


**Fig. 5** Characteristic vibration bands of  $-\text{COO}^-/\text{COOH}$  in the  $\text{Zn}_2\text{Al}$ -stearate-LDH samples of Fig. 4. (A) Phase I; (B) Phase II; (C) Phase III.

## Packing Modes

The different phases in the organo-LDH materials are supposed to be brought about by the different packing of the hydrocarbon chain in the LDH interlayer.<sup>[40]</sup> As shown in Fig. 6A for the monolayer packing (more precisely, interpenetrating packing), the two oxygen atoms in the carboxylate group are equally anchored on the hydroxide layer, which will cause the idealized extended hydrocarbon chain to be tilted at a slant angle of  $55^\circ$  (half the C–C bond angle) with an all-*trans* form.<sup>[41]</sup> The all-*trans* assignment is supported by a series of  $\text{CH}_2$  wagging bands in the range of 1150–1350  $\text{cm}^{-1}$  with an interval of 19–21  $\text{cm}^{-1}$  (Fig. 7).<sup>[39]</sup> This mode leads to a predicted interlayer spacing of 3.07 nm, unambiguously corresponding to Phase I. The actual distance, 3.19 nm, matches a tilting angle of  $61^\circ$ .<sup>[42]</sup> Based on our observations and other reports, most organic anions, including carboxylates, sulfates, sulfonates, etc. are often packed at such an angle.

The bilayer mode of Fig. 6B gives an estimated interlayer spacing of 5.00 nm, exactly the same as that found for Phase III. It also suggests hydrogen bonding of neutral COOH groups with adjacent  $\text{COO}^-$ , which is manifested in the characteristic IR spectrum of COOH/ $\text{COO}^-$  in phase III, with the asymmetrical  $\nu_{\text{COO}}$  frequency shifted from 1703  $\text{cm}^{-1}$  in the free acid to 1597  $\text{cm}^{-1}$  in the LDH gallery.<sup>[39]</sup> Most carboxylates and some secondary sulfonates use this packing, as reported elsewhere.<sup>[39–41]</sup>

However, the chain arrangement in Phase II is not as obvious as in Phases I and III. In view of the interlayer spacing, it seems to lie in between the monolayer and bilayer packing. Our experiments and other reports have shown that Phase II is formed in organo-LDH only with hydrocarbon chains longer than  $n\text{-C}_{10}\text{H}_{21}$ . Therefore we have proposed two possible packing modes in Fig. 6C, D. In the interlocking mode (Fig. 6C), the long straight chains employ a gauche configuration in the middle and are interlocked with each other. We have imposed a similar chain geometry by introducing *cis*- $\text{CH}_3(\text{CH}_2)_7\text{CH}=\text{CH}(\text{CH}_2)_7\text{COO}^-$  (oleate) into LDH, and found that the interlocking mode is the most suitable one to explain the interlayer spacing.<sup>[43]</sup> In  $\text{Mg}_2\text{Al}$ -LDH tetradecyl sulfonate ( $\text{C}_{14}\text{H}_{29}\text{SO}_3^-$ ), we have also noted this phenomenon.<sup>[44]</sup> However, this mode leaves little room for the neutral acid found to be present for saturated carboxylated/LDH materials. On the other hand, the bent chain arrangement (Fig. 6D) contains some H-bonded neutral stearic acid, in accordance with the observed results in the present case. However, it is not clear why the bending or gauche configuration occurs just in the middle part of the chain in these two modes. The nature and rigidity of packing in this

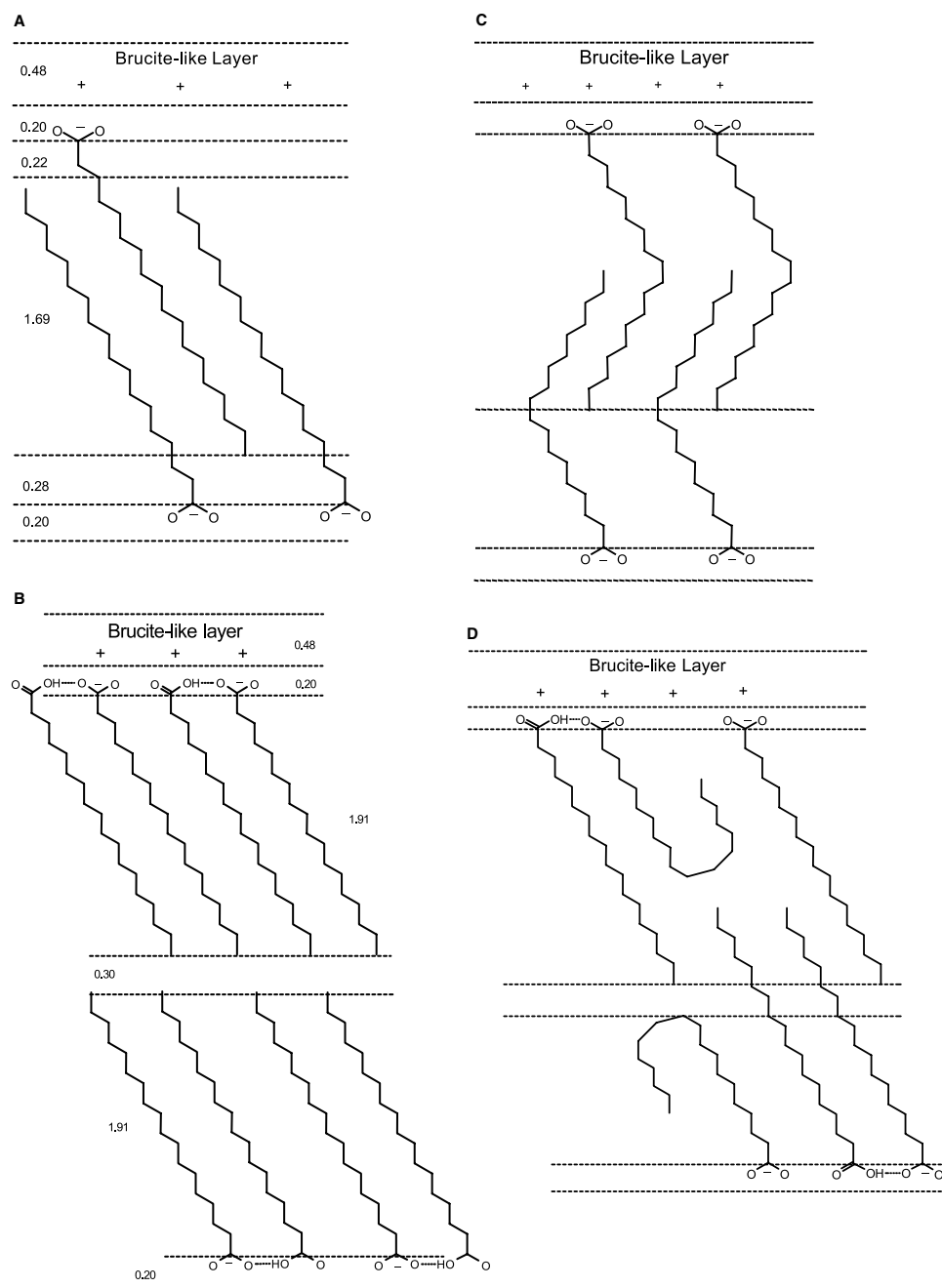


**Fig. 6** Packing modes of hydrocarbon chain: (A) monolayer; (B) bilayer; (C) interlocking; and (D) bent.

system could repay investigation by  $^{13}\text{C}$  NMR, similar to that performed by Wang et al.<sup>[45]</sup> for alkylammonium ions in montmorillonite.

It should be mentioned that Clearfield et al.<sup>[46]</sup> reported three distinct LDH phases in dodecylsulfate NiAl-, MgAl-, and ZnCr-LDHs, with different charge density in hydroxide layers. Through computer simulation, they proposed perpendicular monolayer, interdigitated, and bilayer packing modes to interpret the interlayer spacing and chain-chain hydrophobic interactions. Meyn, Beneke, and Lagaly<sup>[41]</sup> and

Carlino<sup>[40]</sup> put forward the similar perpendicular mode for packing of sulfonates and carboxylates as well.

Ideally, the packing in monolayer and bilayer has a cross section of  $0.25\text{--}0.20\text{ nm}^2$  ( $a = 0.306\text{ nm}$ , Zn/Al = 2:1), very close to that of the alkyl chains in a closely packed monolayer ( $0.20\text{ nm}^2$ ).<sup>[47]</sup> This results in very efficient hydrophobic interactions between the chains, and make the surfactant anion affinity for LDH superior to sulfate and comparable to carbonate.<sup>[36]</sup> In addition, among the three proposed modes, the packing in Phase III has full overlap between chains,

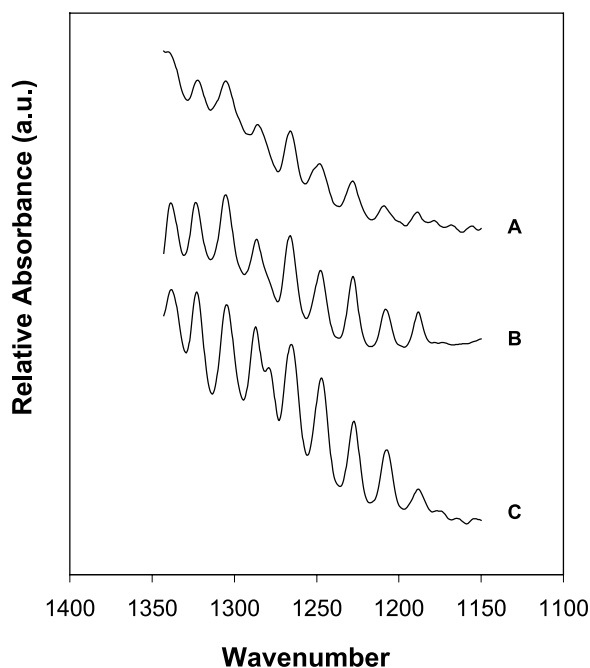


Fig. 7  $\text{CH}_2$  wagging in the range of  $1150\text{--}1350\text{ cm}^{-1}$  in the  $\text{Zn}_2\text{Al}$ -stearate-LDH samples of Fig. 4.

presumably being responsible for the strong diffraction peak at  $21^\circ$  ( $d = 0.42\text{ nm}$ ),<sup>[36]</sup> while the other two show only a weak diffraction in this region.

### Chemical Interconversion and Stability

In our experiments, we have further observed that Phase I (monolayer) can be partially converted to Phase III (bilayer) under reflux in a stearic acid solution. The appearance of new diffraction peaks in the XRD pattern (Fig. 8) after overnight reaction indicates the intercalation of neutral stearic acid. This intercalation into  $\text{Zn}_2\text{Al}$ -stearate-LDH (monolayer packing) is similar to that reported by Boehm, Steinle, and Vieweger<sup>[48]</sup> who also observed swelling of interlayer spacing of  $\text{Zn}_2\text{Cr}$ -LDH alkyl sulfate from monolayer to bilayer by intercalating *n*-alkyl alcohols or amines. The driving force for the conversion may come from the strong hydrophobic interactions because of the full overlapping and the tail-tail hydrophobic connection in the bilayer packing mode (Fig. 6). Note here that a neutral species (carboxylic acid, alcohol, or amine) is necessary to form a bilayer structure. Kanoh, Shichi, and Tagaki<sup>[49]</sup> noted the transformation of the monolayer to bilayer materials dependent on the temperature and initial stearate concentration.

In contrast, Phase III cannot be converted to Phase I by removal of acid, even in strongly alkaline solution ( $\text{pH} = 11\text{--}12$ ). This could be attributed to several

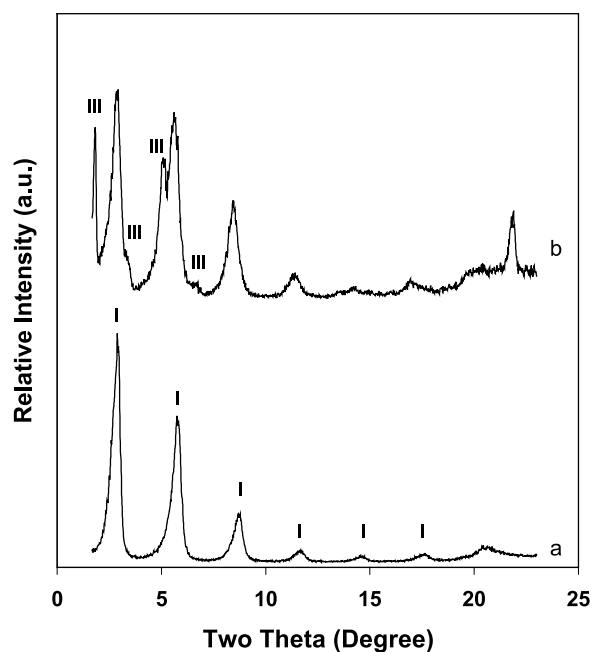


Fig. 8 X-ray diffraction pattern of  $\text{Mg}_2\text{Al}$ -stearate-LDH (initially monolayer) (a) before and (b) after reaction with stearic acid solution.

factors. It is presumably very difficult for  $\text{OH}^-$  anions to approach the gallery because the inside and outside surface of LDH particles are highly hydrophobic and repulsive to the entrance of hydrophilic  $\text{OH}^-$  groups. More seriously, the  $\text{OH}^-$  will encounter electrostatic repulsion from interlayer stearate anions when it is approaching the surface and moving into the gallery. Even if neutral  $\text{C}_{17}\text{H}_{35}\text{COOH}$  reacts with the coming  $\text{OH}^-$  to become  $\text{C}_{17}\text{H}_{35}\text{COO}^-$ , the extra anion must find its way out of the particles to maintain charge neutrality. However, its removal will break strong hydrophobic interactions as indicated above, which further limits the acid-base reaction.

As mentioned above, the bilayer packing LDH samples have neutral stearic acid inserted in the interlayer under reflux conditions. Furthermore, heating at  $150^\circ\text{C}$  in air does not lead to any noticeable change in the XRD pattern and IR spectrum. The chemical stability of these samples is in sharp contrast to phenylphosphonate LDH. As reported by Nijs, Clearfield, and Vansant<sup>[50]</sup> monovalent phenylphosphate anion ( $\text{PhP}(=\text{O})\text{O}_2\text{H}^-$ ,  $\text{p}K_a = 7.43$ )<sup>[51]</sup> can be introduced into LDH with a proper metal ratio at room temperature, but refluxing gave as the main product a layered metal phenylphosphonate compound. In addition, heating at  $115\text{--}200^\circ\text{C}$  caused the collapse of the LDH structure frame, releasing a water molecule and directly linking phosphonate and metal ion.

In general, the carboxylic acid group has a  $\text{p}K_a$  of around 5, is more acidic than monovalent



phosphonate, and should react with the hydroxide layer in a similar way. For example,  $\text{Zn}_2\text{Al}$ -stearate-LDH (bilayer packing) completely dissolves in excess acetic acid solution ( $\text{pH} = 3.2\text{--}3.6$ ) at  $90^\circ\text{C}$ . However, this material is stable in water at  $100^\circ\text{C}$  or when heated on its own to  $150^\circ\text{C}$  despite the presence of unionized carboxylic acid within the structure. Thus the hydrogen bond between  $\text{COOH}$  and  $\text{COO}^-$  (Fig. 6B) has seriously depressed the acidity of the carboxylic acid group and frozen the reaction ability of  $\text{COOH}$  toward the layer hydroxide group.

### Morphological Features and Crystallization

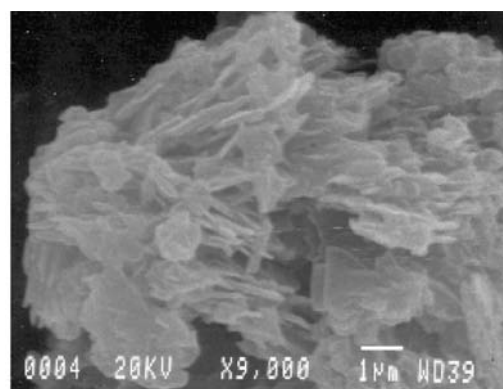
Because of the hydrophobic interactions and multiple packing modes of organic anions, the organo-LDHs show versatile morphological features. In general, as we had observed and as other researchers had reported, the organo-LDHs have bar-like, sheet-like, or ribbon-like particles with micrometer or sub-micrometer dimensions, with or without regular shapes.<sup>[36,43,44,52–55]</sup>

In particular, the particles in Phase I are normally not regularly shaped, as shown in Fig. 9A for a monolayer  $\text{Zn}_2\text{Al}$ -stearate-LDH prepared by exchange method. However, there are some exceptions. For example, in rare cases, the particles in  $\text{Mg}_2\text{Al}$ -LDH dodecylbenzene sulfonate develop a bar-like shape, although irregular shapes predominate.

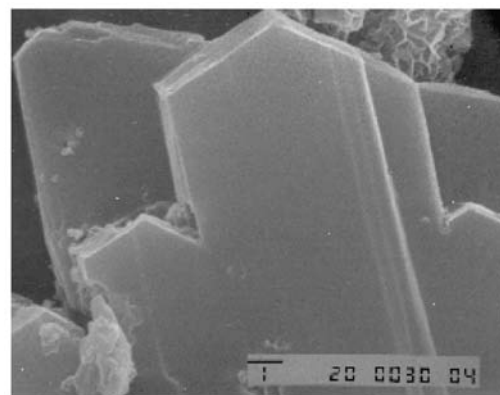
In the scanning electron micrograph (Fig. 9C), the featured sheets for Phase III (bilayer) are rectangle-shaped, but some are curved or broken. We have also observed very long rectangle-shaped ribbons for  $\text{Zn}_2\text{Al}$ -LDH elaidate although there were some irregular sheets and/or amorphous aggregates.

Phase II of  $\text{Zn}_2\text{Al}$ -stearate-LDH has also been featured with sharply edged rectangle sheets (Fig. 9B). However, we observed different particle shapes in  $\text{Zn}_2\text{Al}$ -LDH oleate<sup>[43]</sup> and  $\text{Mg}_2\text{Al}$ -LDH tetradecyl sulfonate.<sup>[44]</sup> The former has irregular shape while the latter has well-shaped hexagons elongated along the  $a$  axis.

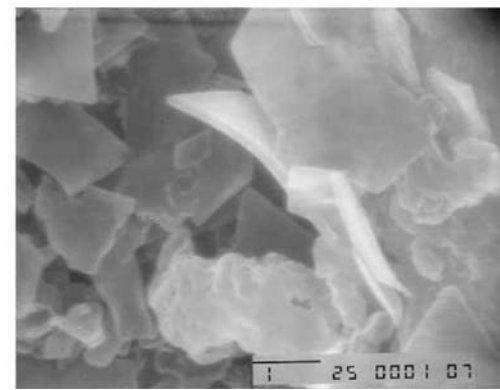
Thus it is seen that the morphology of organo-LDHs is much more complicated than the inorganic LDHs. The complexity can be attributed to the introduction of hydrophobic interactions. As previously mentioned, the LDH particle surface is hydrophobic, and thus there is no preferred growth along axis  $c$  or  $a$  or  $b$ . Growth along each axis has some advantages and disadvantages. As we know, the surfactant anions on the  $(ab)$  plane are held in plane through electrostatic interaction and must direct their hydrophobic tails toward the aqueous phase. This hydrophobic layer can now attract additional surfactants to form an antiparallel second layer, which



A monolayer



B bent



C bilayer

**Fig. 9** Scanning electron microscopy images of  $\text{Zn}_2\text{Al}$ -stearate-LDHs with predominant (A) monolayer, (B) bent, and (C) bilayer LDH phases. Scale bar  $1\ \mu\text{m}$ .

will facilitate nucleation of new sheets and self-promoted assembly for crystallite growth. Therefore growth along the  $c$  axis is kinetically more accessible in LDH–surfactant materials than in inorganic LDH, probably giving bar-like and ribbon-like particles.<sup>[36,43,44]</sup> As shown in Fig. 10, alternating and broadly parallel dark (hydroxide layer) and pale (organic layer) stripes are recorded by high-resolution transmission electron microscopy (HRTEM).<sup>[56,57]</sup>

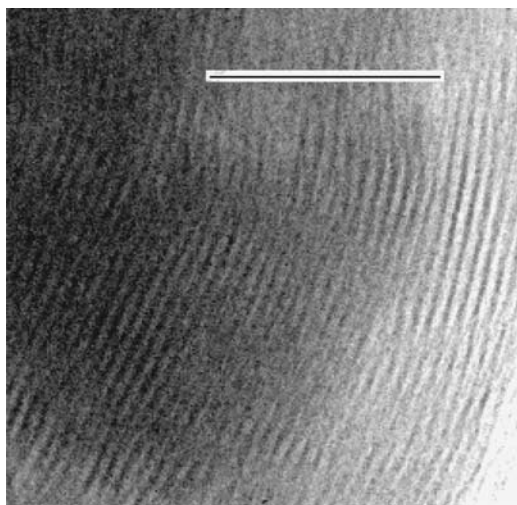


**Fig. 10** Transmission electron microscopy image of  $\text{Zn}_2\text{Al-H240-LDH}$ . Scale bar 50 nm (data supplied by Dr. K. Yu).

The measured repeat distance between similar stripes is 3.3 nm, in good agreement with the interlayer spacing (3.57 nm) given by XRD. This transmission electron microscopy (TEM) image confirms a *c*-directed growth habit, in contrast to the *a*, *b* growth of the inorganic LDHs.

However, the (*ac*) and (*bc*) planes are also hydrophobic albeit less than the (*ab*) plane. Thus the final shapes depend on the balance between several factors, such as the nature of organic anions (type, chain length, chain structure, etc.) and preparative conditions (temperature, concentration, aging). Indeed, we find large varieties in morphologies between different organic LDH materials, as previously mentioned.

Because the surface of LDH surfactant crystallites is hydrophobic, it is easier for crystallites to aggregate or self-assemble through hydrophobic forces. The intermolecular hydrophobic interactions can bring about curvature to the sheets, as we have often observed in scanning electron microscopy (SEM) images. In the particular case of the dicarboxylate surfactant anion H240 [formed from the Diels–Alder addition product of acrylic acid to conjugated (9,11 and 10,12) linoleic acids], we find that the LDH derivatives can be prepared in water as spherical aggregates with diameters of 0.5–3 μm under controlled conditions of heating and stirring. This self-assembly on the millimeter scale may possibly be connected with the double-headed nature of the surfactant.<sup>[55]</sup>

### Applications of Layered Double Hydroxide–Surfactant Hybrid Materials

Layered double hydroxides are often used as polymer additives especially for polyvinylchloride (PVC).

Miyata<sup>[58]</sup> has shown that as little as 0.05–1% well-crystallized LDH improves the thermal stability and weather resistance of thermoplastic resins containing halogen and/or acidic components from the manufacturing process. In addition, chlorine-containing polymers commonly undergo degradation under heat and UV light, giving off gaseous HCl. This corrodes molding machines and may catalyze further degradation, leading to brittleness and discoloration. Layered double hydroxides are added as environmentally benign neutralizers for this acid. It has been found<sup>[59]</sup> that  $\text{MgZnAl-LDH}$  can be a very good acid absorbent. However, inorganic LDH is immiscible with polymer because of the surface tension. Fortunately, coating or intercalating surfactant anions bring about a hydrophobic surface that can well combine the hydrophilic inorganic LDH and hydrophobic polymer to make full use of LDH in polymer reinforcement. Fisher and Gielgens<sup>[60]</sup> partially exchanged LDH with anion surfactants and then mixed with monomeric materials, e.g., caprolactam, to make well-blended polymer–LDH composites.

A newly emerging technique is to incorporate delaminated LDH surfactant sheets into polymer matrix. The nanometer-scale interaction between polymer and LDH hydroxide sheets, and the tortuosity of diffusion through such a composite, may prove to exert a tremendous influence on such properties as mechanical strength and hardness, thermal stability, flexibility and durability, and impermeability.

By incorporating surfactant anions, LDH was reported by Leroux et al.<sup>[61]</sup> to exfoliate in hexanol on heating. In elegant work, Hibino and Jones<sup>[62]</sup> prepared the glycine anion derivative of  $\text{MgAl-LDH}$  and observed its complete delamination in formamide, presumably strongly assisted by glycine–solvent hydrogen bonding. We ourselves have exfoliated  $\text{Mg}_3\text{Al-stearate-LDH}$  in hexadecane, which was removed by washing with hexane and drying in vacuum. The resultant white powder was dispersed into styrene, followed by in situ polymerization. High-resolution TEM (transmission electron microscopy) images of microtomed sections showed the presence of individually dispersed  $\text{Mg}_3\text{Al-stearate-LDH}$  single layers. O’Leary, O’Hare, and Seeley<sup>[63]</sup> also found the almost complete delamination of  $\text{Mg}_2\text{Al-dodecylsulfate}$  in polar acrylate monomer solution, leading to incorporation of the delaminated sheets into the polymer matrix after polymerization in situ. This polymer/LDH nanocomposite showed a much higher thermal stability than the pure polymer itself.

The delamination of LDH surfactant and its subsequent incorporation into polymeric matrix are still under active investigation in our laboratories.<sup>[64]</sup> We are also investigating the mesoporous and/or microporous mixed oxides and carbon/oxide composites

formed by calcination of LDH surfactant derivatives, which appear to be efficient absorbents for various heavy metal ions.

## CONCLUSION

In conclusion, LDHs vary in structures and compositions. As discussed, many cations and anions are candidates for incorporation into LDH compounds. By optimizing and carefully controlling the compositions, we can make various LDHs with particular structure and properties. For example, in the case of LDH-surfactant systems, there are in some cases at least three distinct LDH phases with the same cations and anions. The delamination of LDHs using amino acids or surfactant holds promise for the production of useful polymer-LDH nanocomposites in the near future.

## ACKNOWLEDGMENTS

We thank the Robert A. Welch Foundation (Grant B-1445), the LDRD program of Sandia National Laboratories, and the University of North Texas Faculty Research Funds.

## REFERENCES

- Cavani, F.; Trifiro, F.; Vaccari, A. Hydrotalcite-type anionic clays: preparation, properties and application. *Catal. Today* **1991**, *11*, 173–301.
- Rives, V. *Layered Double Hydroxides: Present and Future*; Nova Science Publishers, Inc.: New York, 2001.
- Braterman, P.S.; Xu, Z.P.; Yarberry, F. Chemistry of layered double hydroxides. In *Handbook of Layered Materials*; Auerbach, Carrado, K.A., Dutta, P.K., Eds.; Marcel Dekker, Inc.: New York, 2003.
- Rolandi, M.; Scott, K.; Wilson, E.G.; Meldrum, F.C. Manipulation and immobilization of alkane-coated gold nanocrystals using scanning tunneling microscopy. *J. Appl. Phys.* **2001**, *89* (3), 1588–1595.
- Huo, G.; Margolese, D.L.; Ciesla, U.; Feng, P.; Gier, T.E.; Sieger, P.; Leon, R.; Petroff, P.M.; Schuth, F.; Stucky, G.D. Generalized synthesis of periodic surfactant inorganic composite-materials. *Nature* **1994**, *368*, 317–321.
- Holland, B.T.; Blanford, C.F.; Stein, A. Synthesis of macroporous minerals with highly ordered 3-dimensional arrays of spheroidal. *Science* **1998**, *281*, 538–540.
- Lide, D.R. *Handbook of Chemistry and Physics*; Chapman & Hall: New York, 1999; 14–16.
- Rapin, J.P.; Walcarius, A.; Lefevre, G.; Francois, M. A double-layered hydroxide,  $3\text{CaO} \cdot \text{Al}_2\text{O}_3 \cdot \text{CaI}_2 \cdot 10\text{H}_2\text{O}$ . *Acta Crystallogr., C* **1999**, *55*, 1957–1959.
- Taylor, R.M. The rapid formation of crystalline double hydroxy salts and other compounds by controlled hydrolysis. *Clay Miner.* **1984**, *19*, 591–603.
- Velu, S.; Sabde, D.P.; Shah, N.; Sivasanker, S. New hydrotalcite-like anionic clays containing  $\text{Zr}^{4+}$  in the layers: Synthesis and physicochemical properties. *Chem. Mater.* **1998**, *10* (11), 3451–3458.
- Velu, S.; Suzuki, K.; Okazaki, M.; Osaki, T.; Tomura, S.; Ohashi, F. Synthesis of new Sn-incorporated layered double hydroxides and their thermal evolution to mixed oxides. *Chem. Mater.* **1999**, *11* (8), 2163–2172.
- Labajos, F.M.; Rives, V.; Ulibarri, M.A. A FT-IR and V-UV spectroscopic study of nickel-containing hydrotalcite-like compounds,  $[\text{Ni}_{1-x}\text{Al}_x(\text{OH})_2](\text{CO}_3)_{x/2} \cdot n\text{H}_2\text{O}$ . *Spectrosc. Lett.* **1991**, *24*, 499–508.
- Xu, Z.P.; Zeng, H.C. Abrupt structural transformation in hydrotalcite-like compounds  $\text{Mg}_{1-x}\text{Al}_x(\text{OH})_2(\text{NO}_3)_x \cdot n\text{H}_2\text{O}$  as a continuous function of nitrate anions. *J. Phys. Chem., B* **2001**, *105*, 1743–1749.
- Kikkawa, S.; Koizumi, M. Ferrocyanide anion bearing magnesium, aluminum hydroxide. *Mater. Res. Bull.* **1982**, *17*, 191–198.
- Braterman, P.S.; Tan, C.Q.; Zhao, J.X. Orientational effects in the infrared spectrum of the double layer material, magnesium aluminum hydroxide ferrocyanide. *Mater. Res. Bull.* **1994**, *29*, 1217–1221.
- Twu, J.; Dutta, P.K. Structure and reactivity of oxovanadate anions in layered lithium aluminate materials. *J. Phys. Chem.* **1989**, *93*, 7863–7868.
- Rives, V.; Ulibarri, M.A. Layered double hydroxides (LDH) intercalated with metal coordination compounds and oxometalates. *Coord. Chem. Rev.* **1999**, *181*, 61–120.
- Bookin, A.S.; Drits, V.A. Polytype diversity of the hydrotalcite-like minerals. I. Possible polytypes and their diffraction features. *Clays Clay Miner.* **1993**, *41*, 551–557.
- Newman, S.P.; Jones, W.; O'Conner, P.; Stamires, E.N. Synthesis of the  $3R_2$  polytype of a hydrotalcite-like mineral. *J. Mater. Chem.* **2002**, *12*, 153–155.
- Drits, V.A.; Sokolova, T.N.; Sokolova, G.V.; Cherkashin, V.I. New members of the hydrotalcite-manasseite group. *Clays Clay Miner.* **1987**, *35*, 401–417.
- Fogg, A.M.; Dunn, J.S.; O'hare, D. Formation of second-stage intermediates in anion-exchange intercalation reactions of the layered double hydroxide  $[\text{LiAl}_2(\text{OH})_6]\text{Cl} \cdot \text{H}_2\text{O}$  as observed by time-resolved, in situ x-ray diffraction. *Chem. Mater.* **1998**, *10* (1), 356–360.
- Allmann, R. Refinement of the hybrid layer structure hexahydroxoaluminum-dicalcium hemisulfate trihydrate  $[\text{Ca}_2\text{Al}(\text{OH})_6]^+[\text{SO}_4^{2-}]_{0.5} \cdot 3\text{H}_2\text{O}$ . *Neues Jahrb. Mineral., Monatsh.* **1977**, *3*, 136–144.
- Solin, S.A.; Hines, D.R.; Seidler, G.T.; Treacy, M.M.J. Novel structural properties of  $\text{Ni}_{1-x}\text{Al}_x$  layer double hydroxides. *J. Phys. Chem. Solids* **1996**, *57*, 1043–1048.
- Serna, C.J.; Rendon, J.L.; Iglesias, J.E. Crystal-chemical study of layered  $[\text{Al}_2\text{Li}(\text{OH})_6]^+\text{X}^- \cdot n\text{H}_2\text{O}$ . *Clays Clay Miner.* **1982**, *30*, 180–182.
- Cai, H.; Hillier, A.C.; Franklin, K.R.; Nunn, C.C.; Ward, M.D. Nanoscale imaging of molecular adsorption. *Science* **1994**, *266*, 1551–1555.

26. Yao, K.; Taniguchi, M.; Nakata, M.; Takahashi, M.; Yamagishi, A. Electrochemical STM observation of  $[\text{Fe}(\text{CN})_6]^{3-}$  ions adsorbed on a hydrotalcite crystal surface. *Langmuir* **1998**, *14*, 2410–2414.
27. Evans, J.; Pillinger, M.; Zhang, J.J. Structural studies of polyoxometalate-anion-pillared layered double hydroxides. *J. Chem. Soc., Dalton Trans.* **1996**, *14*, 2963–2974.
28. Roussel, H.; Briois, V.; Elkaim, E.; de Roy, A.; Besse, J.P.; Jolivet, J.P. Cationic order and structure of  $[\text{Zn}-\text{Cr}-\text{Cl}]$  and  $[\text{Cu}-\text{Cr}-\text{Cl}]$  layered double hydroxides: A XRD and EXAFS study. *J. Phys. Chem., B* **2000**, *104* (25), 5915–5923.
29. Uvelic, M.; Jones, W.; Moggridge, G.D. Cation ordering in synthetic layered double hydroxides. *Clays Clay Miner.* **1997**, *45*, 803–813.
30. Leroux, F.; Moujahid, E.M.; Roussel, H.; Flank, A.M.; Briois, V.; Besse, J.P. Local order of the transition metals for the substitution  $(\text{Co}_{1-y}\text{Cu}_y)_2\text{Al}(\text{OH})_6\text{Cl} \cdot n\text{H}_2\text{O}$  ( $0 < y < 1$ ) in a copper–aluminum-layered double hydroxide-like phase. *Clays Clay Miner.* **2002**, *50*, 254–264.
31. Intissar, M.; Segni, R.; Payen, C.; Besse, J.P.; Leroux, F. Trivalent cation substitution effect into layered double hydroxides  $\text{Co}_2\text{Fe}_y\text{Al}_{1-y}(\text{OH})\text{Cl} \cdot n\text{H}_2\text{O}$ : Study of the local order. *J. Solid State Chem.* **2002**, *167*, 508–516.
32. Bocclair, J.W.; Braterman, P.S. Layered double hydroxide stability. 1. Relative stabilities of layered double hydroxides and their simple counterparts. *Chem. Mater.* **1999**, *11*, 298–302.
33. Bocclair, J.W.; Braterman, P.S.; Jiang, J.; Lou, S.; Yarberr, F. Layered double hydroxide stability. 2. Formation of Cr(III)-containing layered double hydroxides directly from solution. *Chem. Mater.* **1999**, *11*, 303–308.
34. Kannan, S.; Jasra, R.V. Microwave-assisted rapid crystallization of Mg–M(III) hydrotalcite where M(III) = Al, Fe or Cr. *J. Mater. Chem.* **2000**, *10*, 2311–2314.
35. Ulibarri, M.A.; Pavlovic, I.; Barriga, C.; Hermosin, M.C.; Cornejo, J. Adsorption of anionic species on hydrotalcite-like compounds: Effect of interlayer anion and crystallinity. *Appl. Clay Sci.* **2001**, *18*, 17–27.
36. Xu, Z.P.; Braterman, P.S. High affinity of dodecylbenzene sulfonate for layered double hydroxides (LDH) and the resulting morphologies. *J. Mater. Chem.* **2003**, *13*, 268–273.
37. Cullity, B.D. *Elements of X-Ray Diffraction*, 2nd Ed.; Addison-Wesley: Massachusetts, 1978; 278 pp.
38. Simons, W.W. *The Sadtler Handbook of Infrared Spectra*; Sadtler Research Laboratories, Inc.: Pennsylvania, 1978; pp. 695 and 741.
39. Borja, M.; Dutta, P.K. Fatty acids in layered metal hydroxides: membrane-like structure and dynamics. *J. Phys. Chem.* **1992**, *96*, 5434–5444.
40. Carlino, S. The intercalation of carboxylic acids into layered double hydroxides: a critical evaluation and review of the different methods. *Solid State Ionics* **1997**, *98*, 73–84.
41. Meyn, M.; Beneke, K.; Lagaly, G. Anion-exchange reactions of layered double hydroxides. *Inorg. Chem.* **1990**, *29* (26), 5201–5207.
42. Meyn, M.; Beneke, K.; Lagaly, G. Anion-exchange reactions of hydroxy double salts. *Inorg. Chem.* **1993**, *32* (7), 1209–1215.
43. Xu, Z.P.; Braterman, P.S. New packing mode of unsaturated carboxylate in  $\text{Zn}_2\text{Al}$ -layered double hydroxide (LDH). In preparation.
44. Xu, Z.P.; Braterman, P.S. Multiple phases  $\text{MgAl}-\text{C}_{14}\text{H}_{29}\text{SO}_3$ -LDHs depending on the concentration and temperature. In preparation.
45. Wang, L.; Liu, J.; Exarhos, G.J.; Flanigan, K.Y.; Bordia, R. Conformation heterogeneity and mobility of surfactant molecules in intercalated clay minerals studies by solid state NMR. *J. Phys. Chem., B* **2000**, *104* (13), 2810–2816.
46. Clearfield, A.; Kieke, M.; Kwan, J.; Colon, J.L.; Wang, R.C. Intercalation of dodecyl-sulfate into layered double hydroxides. *J. Incl. Phenom. Mol. Recognit. Chem.* **1991**, *11*, 361–378.
47. Foti, G.; Belvito, M.L.; Kovats, E.S. Packing density of organyldimethylsiloxy-covered silica gel and hydrolytic stability of the coating. *J. Chromatogr.* **1988**, *440*, 315–322.
48. Boehm, H.P.; Steinle, J.; Vieweger, C.  $\text{Zn}_2\text{Cr}(\text{OH})_6\text{X} \cdot 2\text{H}_2\text{O}$ , New layer compounds capable of anion exchange and intracrystalline swelling. *Angew. Chem.* **1977**, *89*, 265–266.
49. Kanoh, T.; Shichi, T.; Tagaki, K. Mono- and bilayer equilibria of stearate self-assembly formed in hydrotalcite interlayers by changing the intercalation temperature. *Chem. Lett.* **1999**, 117–118.
50. Nijs, H.; Clearfield, A.; Vansant, E.F. The intercalation of phenylphosphonic acid in layered double hydroxides. *Microporous Mesoporous Mater.* **1998**, *23*, 97–108.
51. Buckingham, J. *Dictionary of Organic Compounds*, 5th Ed.; Chapman and Hall: New York, 1982; Vol. 5, 4658.
52. Ogawa, M.; Asai, S. Hydrothermal synthesis of layered double hydroxide–deoxycholate intercalation compounds. *Chem. Mater.* **2000**, *12* (11), 3253–3255.
53. Labajos, F.M.; Rives, V.; Ulibarri, M.A. Effect of hydrothermal and thermal treatments on the physicochemical properties of Mg–Al hydrotalcite-like materials. *J. Mater. Sci.* **1992**, *27*, 1546–1552.
54. Pavan, P.C.; Crepaldi, E.L.; Gomes, G.A.; Valim, J.B. Adsorption of sodium dodecylsulfate on a hydrotalcite-like compound. Effect of temperature, pH and ionic strength. *Colloids Surf., A* **1999**, *154*, 399–410.
55. Xu, Z.P.; Yu, K.; Braterman, P.S.; Xu, H.; Wang, Y.; Brinker, C.J.; Seifollah, N. Control of growth habit by surfactant in organic–inorganic nanocomposite materials of the layered double hydroxide family. In preparation.
56. Drezdson, M.A. Synthesis of isopolymetalate-pillared hydrotalcite via organic-anion-pillared precursors. *Inorg. Chem.* **1988**, *27*, 4628–4632.
57. Whilton, N.T.; Vickers, P.J.; Mann, S. Bioinorganic clays: synthesis and characterization of amino- and polyamino acid intercalated layered double hydroxides. *J. Mater. Chem.* **1997**, *7*, 1623–1629.

58. Miyata, S. Method for Inhibiting the Thermal or Ultraviolet Degradation of Thermoplastic Resin and Thermoplastic Resin Composition Having Stability to Thermal or Ultraviolet Degradation. U.S. Patent 4, 299, 759, November 10, 1981.
59. Ven, L.; Gemert, M.L.M.; Batenburg, L.F.; Keern, J.J.; Gielgens, L.H.; Koster, T.P.M.; Fischer, H.R. On the action of hydrotalcite-like clay materials as stabilizers in polyvinylchloride. *Appl. Clay Sci.* **2000**, *17*, 25–34.
60. Fisher, H.R.; Gielgens, L.H. Nanocomposite Material. U.S. Patent 6, 372, 837, April 16, 2002.
61. Leroux, F.; Adachi-Pagano, M.; Intissar, M.; Chauviere, S.; Forano, C.; Besse, J.P. Delamination and restacking of layered double hydroxides. *J. Mater. Chem.* **2001**, *11*, 105–112.
62. Hibino, T.; Jones, W. New approach to the delamination of layered double hydroxides. *J. Mater. Chem.* **2001**, *11*, 1321–1323.
63. O'Leary, S.; O'Hare, D.; Seeley, G. Delamination of layered double hydroxides in polar monomers: new LDH-acrylate nanocomposites. *Chem. Commun.* **2002**, (14), 1506–1507.
64. Braterman, P.S.; D'Souza, N.A.; Ranade, A.; Xu, Z.P. Delamination of a layered double hydroxide-surfactant nanocomposite and subsequent incorporation into polystyrene. In preparation.

# Ligand–Receptor Systems with Infinite Binding Affinity

Claude F. Meares

Department of Chemistry, University of California–Davis,  
Davis, California, U.S.A.

## INTRODUCTION

Biological molecules such as antibodies show exquisite specificity in binding to target molecules. This binding is naturally reversible, and the stability of the antibody–target complex is often a matter of concern because experiments can be compromised if it dissociates or exchanges with other molecules. Here we describe the current state of molecular technology for making specific complexes irreversible, so that target specificity is preserved while dissociation is effectively prevented. The emphasis is on antibody applications, but the same concepts apply to other binding systems.

## Statement of the Problem

One of the most important elementary phenomena in biochemistry and biology is the reversible binding of one molecule to another:



If  $A$  is an antibody and  $B$  is its target, this can be the first step in resistance to infection; if  $A$  is a drug molecule and  $B$  is its receptor, this can be the basis for pharmacological action; there are many other fitting examples. An important feature of this process is that binding is *specific*: sites on molecules  $A$  and  $B$  fit together to form a complex, but  $A$  and  $B$  do not bind indiscriminately to other molecules. Specific binding is generally achieved by complementary noncovalent interactions between  $A$  and  $B$ , such as hydrophobic bonding, hydrogen bonding, ion pairing, and pi-stacking. In biological systems, binding of  $A$  and  $B$  is usually accompanied by the release of several water molecules from the surface of each. This provides an entropy change in favor of complex formation.

Reversible binding (Eq. (1)) is quantitatively characterized by rate constants  $k_1$  and  $k_2$ , and an equilibrium constant  $K_d$ :

At equilibrium,  $k_1 [C] = k_2 [A][B]$  and

$$K_d = \frac{k_1}{k_2} = \frac{[A][B]}{[C]} \quad (2)$$

The brackets  $[\ ]$  denote concentrations, in units of mol/L, M. Rate constants  $k_1$  and  $k_2$  have different units: typically,  $k_1$  is expressed in units of  $\text{sec}^{-1}$  for the first-order dissociation process, while  $k_2$  is expressed in units of  $\text{M}^{-1} \text{sec}^{-1}$  for the second-order (bimolecular) association process. The units of  $K_d = k_1/k_2$  are then mol/L, M. A common rule of thumb is that useful pharmaceuticals should bind to their targets with dissociation constants  $K_d \leq 10^{-9} \text{M}$ . Note that when  $[A]$  equals  $K_d$ , then  $[B] = [C]$  and the target  $B$  is half-saturated (the complex  $C$  is formed with 50% yield).

The rate of the association reaction can be no faster than the rate at which  $A$  and  $B$  diffuse together, and it is usually found that  $k_2 \leq 10^9 \text{M}^{-1} \text{sec}^{-1}$ . We can use this to estimate the minimum bound lifetime of the complex. For the case  $K_d = 10^{-9} \text{M}$ , at maximum  $k_2 = 10^9 \text{M}^{-1} \text{sec}^{-1}$ , and the maximum value of  $k_1 = 1 \text{sec}^{-1}$ . From fundamental mathematics, the lifetime  $\tau$  of the average complex in Eq. (2) is  $\tau = 1/k_1$ , which in this case would be 1 sec. A bound lifetime of 1 sec would be too short for many practical applications. (Because we used a maximum value for  $k_1$ , we have calculated a minimum value for  $\tau$ . Few experimental on-rates are as large as  $10^9 \text{M}^{-1} \text{sec}^{-1}$ ; for a given  $K_d$ , if the on-rate  $k_2$  is smaller, then the off-rate  $k_1$  is also smaller, and the bound lifetime of the complex is longer.)

Biological molecules can exhibit more complicated properties than those described above. One common variation is that macromolecules may incorporate more than one binding site for target molecules, and undergo multivalent binding.

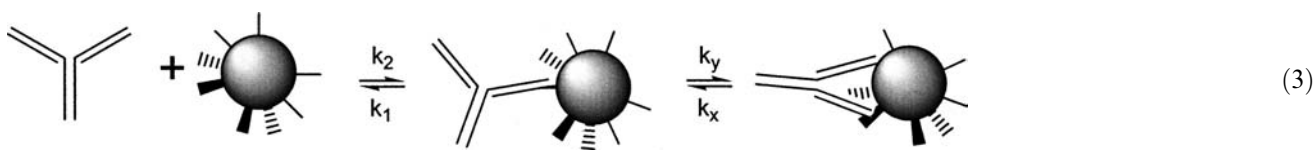
## ADDED COMPLICATIONS OF MULTIVALENT BINDING

### Elementary Kinetic Scheme has System-Dependent Terms

A ligand–receptor system in which the binding equilibrium can be more than monovalent is illustrated by the divalent antibody molecule binding to the polyvalent



target in Eq. (3). Association of the antibody to its target occurs in two distinct steps: first, the familiar association from two separate molecules with rate constant  $k_2$ , and second, a unimolecular ring-closing reaction with rate constant  $k_y \text{sec}^{-1}$ . The latter reaction involves the same ligand–receptor interaction chemistry as the bimolecular association, but here the process does not require two separate molecules to diffuse together.



It should be noted that the equilibrium constant for bivalent association is not calculated simply by squaring the equilibrium constant for monovalent association. It is commonly found for antibody binding to multivalent targets that bivalent association decreases the overall dissociation constant by a factor of 100–1000 relative to monovalent association, making binding more stable but not vastly so. However, in some cases, such as cancer cells that overexpress a particular cell-surface protein, a bivalent antibody can associate with an antigen-rich surface practically irreversibly. This has inspired considerable effort in developing systems that bind multivalently to enhance the strength of the binding interaction in practical situations. A common example is the engineering of antibodies and other proteins for multivalent binding to carbohydrates, for which monovalent binding tends to be weak.

### Effective Local Concentration

With reference to Eq. (3), it is possible to take the ratio of  $k_y/k_2$ , which is expressed in mol/L, as indicating the effective local concentration of the target in the vicinity of the monovalently bound antibody molecule. When experimental results are available, this provides an index of the density of targets on the particle in Eq. (3) and their accessibility to the second arm of the antibody molecule—a composite quantity that is difficult to calculate. The effective local concentration is sometimes a nonphysically large quantity, indicating favorable geometric and entropic properties for forming the second association.

Multivalent binding can have unwanted consequences: for example, when an antibody binds two targets on a cell surface, it can trigger the internalization of the complex and subsequent changes in the cell's behavior. Of course, if the targets are not linked

together, binding of an antibody to two targets involves two independent bimolecular association events as in Eq. (1), which does not increase binding strength. For these reasons, it is frequently desirable to enhance the strength of monovalent binding.

From the protein engineering viewpoint, reversible binding may be strengthened by combinatorially varying the amino-acid residues in the binding site, to seek mutant proteins that exhibit thermodynamically

more favorable binding.<sup>[1]</sup> There is considerable activity in developing new experimental approaches to combinatorial selection, and remarkably high binding affinities have been achieved in some cases.<sup>[2]</sup> Extrapolating this to its logical extreme leads to binding that is so strong it is not reversible.

Fig. 1 illustrates the progressive effects of increasing binding affinity (decreasing  $K_d$ ). With reference to Eqs. (1) and (2) above, this shows a semilogarithmic plot of  $[B]/[B] + [C] = K_d/K_d + [A]$  as a function of  $[A]$  for various values of  $K_d$ . Moving from right to left, we see the curves for progressively stronger binding, with their half-saturation points at  $[A] = K_d$ . The system with  $K_d = 1 \times 10^{-7} \text{M}$  has the lowest affinity, comparable to a weakly binding antibody; the system with the highest affinity,  $K_d = 1 \times 10^{-15} \text{M}$ , is comparable to the strongest-binding systems found in nature. Reducing the concentration of free target to 50% requires an amount of free antibody  $[A] = K_d$ ; reducing the concentration of free target to 1% requires an amount of free antibody  $[A] = 99K_d$ ; reducing the concentration of free target to 0.1% requires an amount of free antibody  $[A] = 999K_d$ ; and so on.

Infinite binding affinity corresponds to  $K_d = 0$ , which is the horizontal line at the bottom of Fig. 1. Here binding is irreversible and a 1:1 ratio of antibody to target is sufficient to reduce the concentration of free target to zero at equilibrium; no excess is required. Obviously, there will be practical limitations on literally achieving a zero concentration of free target with a precisely 1:1 ratio of antibody to target, because as the concentrations of antibody and target become increasingly small, the rate of the second-order association reaction ( $=k_2[A][B]$ ) tends to zero. However, a small excess of antibody can make a difference at this stage: as target  $B$  becomes depleted, the concentration  $[A]$  of antibody becomes much larger than  $[B]$  and, as a consequence, ceases to decline significantly.

## Free Ligand vs Antibody concentration

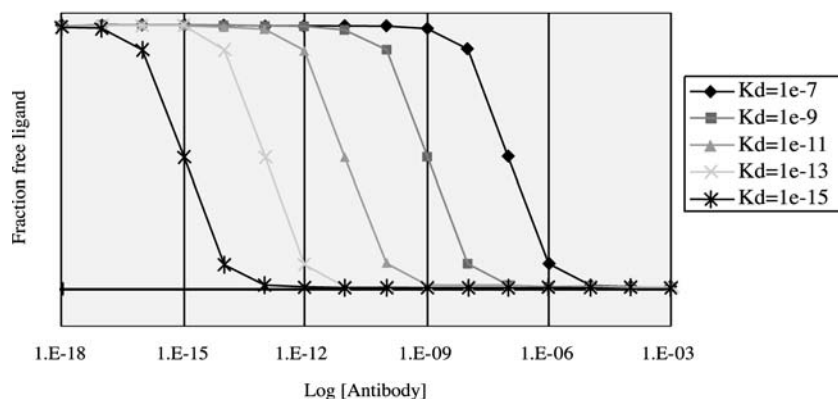


**Fig. 1** Binding curves for ligand–receptor systems with different affinities. The horizontal line at the bottom of the graph corresponds to infinite affinity.

The experimenter can control the rate of the association reaction (still  $= k_2[A][B]$ ) by choosing the amount of  $A$  to add to the system.

### PRINCIPLES OF IRREVERSIBLE BINDING

Consider an engineered monovalent antibody (fragment) that can bind irreversibly to its target. The molecular mechanism of this process is illustrated in Eq. (4), consisting of a reversible binding step followed by an irreversible locking step. The mathematics describing irreversible binding are not unlike those for bivalent binding (Eq. (3)). Conceptually, molecular recognition of the target and reversible binding is the first step in both; it is followed by an intramolecular ring closure that involves either a second binding site (Eq. (3)) or a reactive moiety in or near the first binding site (Eq. (4)).

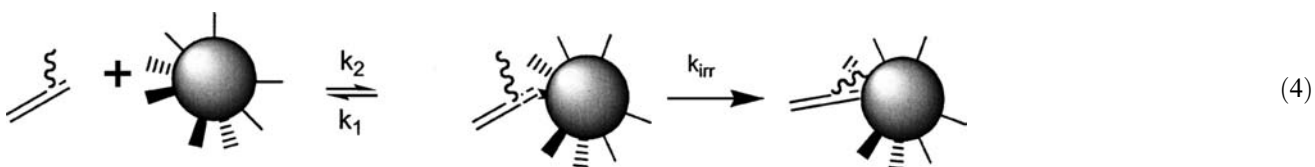
The difference is that we replace  $k_y$  with  $k_{\text{irr}}$  and  $k_x = 0$  for Eq. (4). The most valuable situation for irreversible pharmacological targeting is when  $k_{\text{irr}} \gg k_1$ , so that the complex is formed irreversibly upon binding, without dissociation. Irreversible binding with little or no dissociation has been achieved for an antibody that binds a small molecule, using synthetic chemistry to engineer the small molecule and site-directed mutagenesis to engineer the antibody.<sup>[3]</sup> This is referred to as infinite affinity, because the off-rate is effectively zero. Because the locking reaction must occur within the lifetime of the

complex  $\tau = 1/k_1$ , infinite affinity is easier to achieve when  $k_1$  is small.

### EXPERIMENTAL BACKGROUND

In the past, enzymologists, immunologists, and other professionals prepared reactive organic molecules that resembled known enzyme inhibitors or antibody haptens, and identified important residues in the respective protein binding sites by forming stable covalent bonds and analyzing the products. The reagents have employed relatively reactive electrophiles such as isothiocyanates, sulfonyl fluorides, mustards, or nitroaryl halides.<sup>[4–7]</sup> Under appropriate conditions, these electrophiles exist for a useful period of time in aqueous solution, although they are quite reactive. When the electrophilic inhibitors are bound to their targets, the effective local concentration of protein nucleophiles (particularly thiols, but also amino groups, etc.) near the bound electrophile can lead to specific attachment to one or a few amino acid side chains.

The concepts underlying these *in vitro* experiments can be extended to developing molecules for use *in vivo*, by developing ligands that are unreactive to the many nucleophiles that occur in living systems but nonetheless react efficiently with their specific protein molecules. When the protein has a conveniently located cysteine sidechain, this can be accomplished by judicious chemical synthesis of the ligand. In some



other circumstances, a cysteine can be engineered into the protein.

The favorable situation of a uniquely reactive group advantageously placed in a binding site is not often found in nature. An exceptional example from the pharmaceutical literature is given by Fry et al.<sup>[8]</sup> who synthesized 4-anilinoquinazolines carrying mildly electrophilic acryl groups, which proved to bind irreversibly to one of the cysteine residues in the catalytic domain of the epidermal growth factor receptor (EGFR). Another work with  $\alpha,\beta$ -unsaturated carbonyl compounds as enzyme inhibitors further supports this approach to irreversibly blocking an important binding site by Michael addition to a cysteine side chain.<sup>[9]</sup> When it is part of a rapidly cleared small molecule, the  $\alpha,\beta$ -unsaturated carbonyl compound does not detectably react with nucleophiles normally present in the blood because the contact time is short and they are present in low concentration.<sup>[10]</sup> The most important nucleophiles in circulation are thiols on glutathione and other small molecules, and the free cysteine side chain in albumin.

## ENGINEERING INFINITE AFFINITY

Converting a natural protein to irreversible binding has been achieved in a few instances, by engineering a cysteine residue into a chosen position in the binding site.<sup>[3,11,12]</sup> Here the aim is to exploit the exceptional nucleophilicity of a well-placed sulfur atom to form a stable covalent bond. In applications reported so far, the other binding partner has been a small organic molecule. Thus a double engineering approach is used, relying on the tools of modern molecular biology to design and produce a mutant protein, and synthetic chemistry to produce the small molecules that target the engineered binding site on the protein.

Planning the experimental strategy is made easier if a crystal structure of a natural complex is available. Chmura, Orton, and Heares<sup>[3]</sup> referred to the crystal structure of the antibody CHA255 bound to its indium-chelate haptin.<sup>[13]</sup> Levitsky, Ciolli, and Belshaw<sup>[11]</sup> used the structure of the cyclophilin A–cyclosporin A complex.<sup>[14]</sup> In each case, amino-acid residues that were near, but not in contact with, the bound organic ligand were identified.

Chmura chose residues within the binding site of the antibody (Fig. 2). These residues, which are in complementarity determining region 3 of the light chain, were chosen because their side chains: 1) are not exposed on the outer surface of the antibody; 2) do not have any direct contacts with the bound ligand; and 3) lie within a few angstroms of the para substituent on a benzene ring in the ligand. The latter criterion allowed for ease

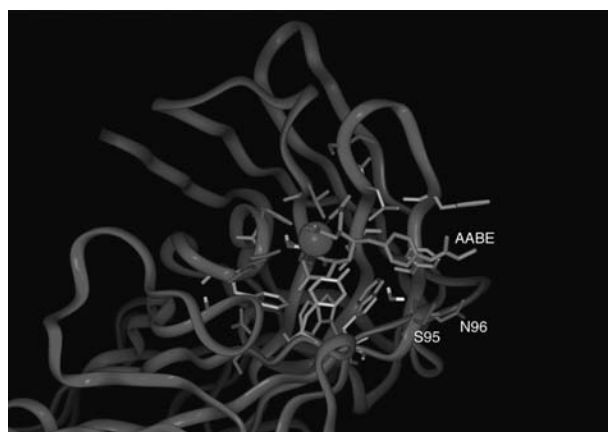


**Fig. 2** Crystal structure of antibody CHA255–indium chelate complex. Source: From Ref.<sup>[13]</sup>. Two residues in the wild-type antibody that are not directly involved in ligand binding but are favorably located close to the *para*-substituent of the ligand (yellow) are light-chain residues S95 and N96 (Kabat positions 93 and 94). Source: From Ref.<sup>[3]</sup>. © 2001, The National Academy of Sciences of the United States of America.

of synthesis of a library of candidate ligands for irreversible binding. On the other hand, Levitsky chose protein residues that: 1) are exposed on the outer surface of the protein; 2) do not have any direct contacts with the bound ligand; and 3) lie within a few angstroms of a suitable site for synthetic modification of the ligand. In each case, site-directed mutagenesis was used to prepare cysteine mutants in the chosen positions. The proteins were expressed by using appropriate cell lines, and characterized by standard methods.

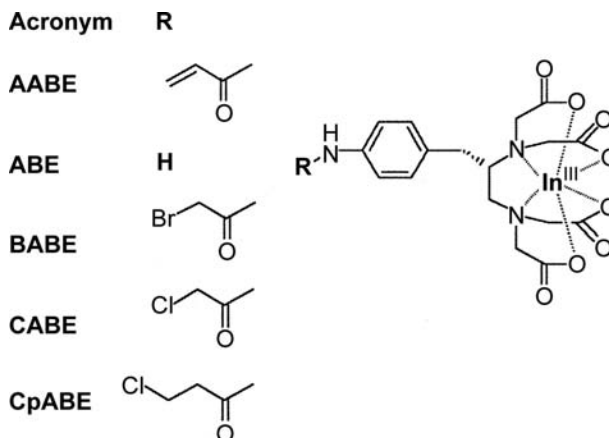


**Fig. 3** Electrophiles tested for: 1) lack of reactivity in complex physiological media; and 2) specific reaction with engineered antibody S95C (Fig. 2). Source: From Ref.<sup>[3]</sup>. © 2001, The National Academy of Sciences of the United States of America.

Chmura compared a set of electrophilic substituents (Fig. 3), not only for specific reaction with the engineered cysteine side chain but also for physiological clearance in animal models, settling on the acryl group.<sup>[10]</sup> This agrees with the experience of other researchers who have sought to use the Michael addition to cysteine sulfur for permanent binding under physiological conditions. The attack of a sulfhydryl group on the double bond of a nearby  $\alpha,\beta$  unsaturated carbonyl compound appears to have favorable properties for use in site-directed protein targeting under physiological conditions in vitro and in vivo. Under these conditions, the reaction is irreversible. The attachment is stable even to the conditions of boiling and reduction that accompany preparation of a sample for gel electrophoresis.

## CONCLUSION

Infinite affinity binding systems are at a very early stage. However, it seems clear that they offer unique advantages in practical applications where irreversible association is needed. A potentially fertile area is in pharmaceutical applications where elimination of a specific molecule is required. For example, antibodies against growth factors are under development as cancer therapies.<sup>[15]</sup> It may prove worthwhile to completely eliminate a particular growth factor by irreversible binding. In the area of in vitro assays, the avidin–biotin binding pair is widely used in circumstances where practically irreversible binding, e.g., of a biotinylated protein to a surface, is required. Avidin only binds biotin, and the binding is not actually irreversible. Many systems with infinite affinity are possible, offering the possibility of multiplexed sets of orthogonal binding pairs to localize different ligands permanently and specifically on the same surface. On the other hand, for those applications that require buffering the concentration of a ligand within a particular concentration range, reversible binding is intrinsically superior as long as a binding partner with an appropriate  $K_d$  is available.

## ACKNOWLEDGMENTS

I thank A.J. Chmura and Molly Orton, who started this field with their work in my laboratory. Other students and colleagues who made useful suggestions on various aspects include Brian D. Schmidt, Donald T. Corson, Stacey L. Traviglia, Todd M. Corneillie, Chung Song, and David A. Goodwin. Our research was supported by Research Grant CA16861

from the National Cancer Institute, National Institutes of Health.

## REFERENCES

1. Gao, C.; Mao, S.; Kaufmann, G.; Wirsching, P.; Lerner, R.A.; Janda, K.D. A method for the generation of combinatorial antibody libraries using pIX phage display. *Proc. Natl. Acad. Sci. U. S. A.* **2002**, *99* (20), 12612–12616.
2. Boder, E.T.; Wittrup, K.D. Yeast surface display for directed evolution of protein expression, affinity, and stability. *Methods Enzymol.* **2000**, *328*, 430–444.
3. Chmura, A.J.; Orton, M.S.; Meares, C.F. Antibodies with infinite affinity. *Proc. Natl. Acad. Sci. U. S. A.* **2001**, *98* (15), 8480–8484.
4. Tyacke, R.J.; Robinson, E.S.J.; Nutt, D.J.; Hudson, A.L. 5-Isothiocyanato-2-benzofuranyl-2-imidazoline (BU99006) an irreversible imidazoline2 binding site ligand: In vitro and in vivo characterisation in rat brain. *Neuropharmacology* **2002**, *43*, 75–83.
5. Beaglehole, A.R.; Baker, S.P.; Scammells, P.J. New irreversible adenosine A1 antagonists based on FSCPX. *Bioorg. Med. Chem. Lett.* **2002**, *12*, 3179–3182.
6. Frang, H.; Cockcroft, V.; Karskela, T.; Scheinin, M.; Marjamaki, A. Phenoxybenzamine binding reveals the helical orientation of the third transmembrane domain of adrenergic receptors. *J. Biol. Chem.* **2001**, *276* (33), 31279–31284.
7. Leesnitzer, L.M.; Parks, D.J.; Bledsoe, R.K.; Cobb, J.E.; Collins, J.L.; Consler, T.G.; Davis, R.G.; Hull-Ryde, E.A.; Lenhard, J.M.; Patel, L.; Plunket, K.D.; Shenk, J.L.; Stimmel, J.B.; Therapontos, C.; Willson, T.M.; Blanchard, S.G. Functional consequences of cysteine modification in the ligand binding sites of peroxisome proliferator activated receptors by GW9662. *Biochemistry* **2002**, *41* (21), 6640–6650.
8. Fry, D.W.; Bridges, A.J.; Denny, W.A.; Doherty, A.; Greis, K.D.; Hicks, J.L.; Hook, K.E.; Keller, P.R.; Leopold, W.R.; Loo, J.A.; McNamara, D.J.; Nelson, J.M.; Sherwood, V.; Smaill, J.B.; Trumpp-Kallmeyer, S.; Dobrusin, E.M. Specific, irreversible inactivation of the epidermal growth factor receptor and erbB2, by a new class of tyrosine kinase inhibitor. *Proc. Natl. Acad. Sci. U. S. A.* **1998**, *95*, 12022–12027.
9. Dragovich, P.S.; Prins, T.J.; Zhou, R.; Brown, E.L.; Maldonado, F.C.; Fuhrman, S.A.; Zalman, L.S.; Tuntland, T.; Lee, C.A.; Patick, A.K.; Matthews, D.A.; Hendrickson, T.F.; Kosa, M.B.; Liu, B.; Batugo, M.R.; Gleeson, J.P.; Sakata, S.K.; Chen, L.; Guzman, M.C.; Meador, J.W., 3rd; Ferre, R.A.; Worland, S.T. Structure-based design, synthesis, and biological evaluation of irreversible human rhinovirus 3C protease inhibitors. 6. Structure–activity studies of orally bioavailable, 2-pyridone-containing peptidomimetics. *J. Med. Chem.* **2002**, *45* (8), 1607–1623.
10. Chmura, A.J.; Schmidt, B.D.; Corson, D.T.; Traviglia, S.T.; Meares, C.F. Electrophilic chelating agents for

- binding of metal chelates to engineered antibodies. *J. Control. Release* **2002**, *78*, 249–258.
11. Levitsky, K.; Ciolli, C.J.; Belshaw, P.J. Selective inhibition of engineered receptors via proximity-accelerated alkylation. *Org. Lett.* **2003**, *5* (5), 693–696.
  12. Erlanson, D.A.; Braisted, A.C.; Raphael, D.R.; Randal, M.; Stroud, R.M.; Gordon, E.M.; Wells, J.A. Site-directed ligand discovery. *Proc. Natl. Acad. Sci. U. S. A.* **2000**, *97* (17), 9367–9372.
  13. Love, R.; Villafranca, J.E.; Aust, R.; Nakamura, K.; Jue, R.A.; Major, J.G., Jr.; Radhakrishnan, R.; Butler, W. How the anti-(metal chelate) antibody  
CHA255 is specific for the metal ion of its antigen: X-ray structures for two Fab'/hapten complexes with different metals in the chelate. *Biochemistry* **1993**, *32*, 10950–10959.
  14. Pflugl, G.; Kallen, J.; Schirmer, T.; Jansonius, J.N.; Zurini, M.G.; Walkinshaw, M.D. X-ray structure of a decameric cyclophilin–cyclosporin crystal complex. *Nature* **1993**, *361*, 91–94.
  15. Ferrara, N. Role of vascular endothelial growth factor in physiologic and pathologic angiogenesis: Therapeutic implications. *Semin. Oncol.* **2002**, *29* (6 Suppl 16), 10–14.

# Lipid Membranes: Nanostructure and Dynamic Organization

**J. Gaudio**

*Sandia National Laboratories, Albuquerque, New Mexico, U.S.A.*

**D. Y. Sasaki**

*Biomolecular Materials and Interfaces, Sandia National Laboratories, Albuquerque, New Mexico, U.S.A.*

## INTRODUCTION

Cell membranes define the size and shape of the cell. In addition to this structural role, the membrane has a crucial regulatory role determining what information, nutrients, and waste can permeate this barrier. The cell membrane consists of a lipid bilayer and proteins, which can be either transmembrane or associated with one leaflet of the bilayer. The dynamic organization of proteins and lipids into domains (e.g., rafts) within the bilayer is important for multiple cellular processes, such as recognition and signaling events.

The chemical recognition process occurring on the surface of membranes is the basis of a versatile and specific sensor system for the cell. Lipid bilayer systems that mimic certain aspects of cell membrane function have been employed in biosensor schemes and continue to generate great interest in the nanotechnology field. Chemical recognition events can also cause structures to form, providing a mechanism for creating controllable, dynamic nanoscale architectures. The two main platforms for studying the dynamic properties of membranes for both nanotechnology and nanoscience applications are vesicular structures, called liposomes, and supported lipid bilayers.

This entry aims to illustrate the importance of dynamic nanoscale structures in biological and model biological membranes. Applications of such structures for drug screening, biosensors, and microanalysis will be discussed. The emphasis will be on understanding what triggers structural reorganization on the nanoscale and how the temporal and spatial aspects of such reorganization can be controlled. The sophistication of the nanoscale machinery of the cell membrane offers many lessons that can be applied to the emerging field of nanotechnology.

## LIPIDS, LIPOSOMES, AND SUPPORTED BILAYERS

Lipids are amphiphilic molecules, having a hydrophobic tail and a polar head group (Fig. 1A). Most

commonly the tail consists of two fatty acid chains with an even number of carbon atoms (14–18 atoms long) and with various degrees of unsaturation.<sup>[1]</sup> In biological membranes, the key components are phospholipids, which have a phosphate at the head group position that is connected to the hydrophobic tails through a glycerol backbone. Often, another moiety, such as choline, serine, or inositol, is attached to the phosphate to form PC, PS, or PI-type lipids, respectively.<sup>[2]</sup>

In an aqueous solution, these amphiphilic lipids self-assemble into liposomes (Fig. 1B).<sup>[2]</sup> The spherical bilayer structure minimizes unfavorable interactions of the hydrophobic tail region with the water. The head group and tails determine the properties of the bilayer membrane, such as fluidity, charge density, and permeability. As recognized by Singer and Nicolson,<sup>[3]</sup> the membrane is a fluid mosaic of lipids and proteins. This fluid-mosaic model does not, however, preclude the existence of structured regions (domains or rafts) within the lipid bilayer. In fact, it is the membrane's fluidity that enables the creation of dynamic nanoscale structures. The lipids can exist in three distinct phases: a tightly packed, ordered gel phase, an intermediate liquid ordered phase, and a disordered liquid phase. The transition temperature for gel to liquid phase transitions ( $T_g$ ) decreases with decreasing chain length and degree of unsaturation. The steric hindrances, electrostatic charge, and hydrogen bonding of the head groups can also affect the transition temperature as well as the phase separation within the membrane. Such phase-separated domains (e.g., rafts) can undergo compositional fluctuations.<sup>[4]</sup> It is key to recognize that under physiological conditions, the membrane is a heterogeneous,<sup>[4]</sup> non-equilibrium<sup>[5]</sup> system.

As previously mentioned, liposomes and supported bilayers are the two main systems of interest. Supported lipid bilayers can be prepared by the classic Langmuir–Blodgett method. Alternately, liposomes can be fused with surfaces to form supported bilayers.<sup>[6]</sup> The fusion schemes for hydrophilic surfaces outlined in Fig. 2A and C result in opposite orientations of



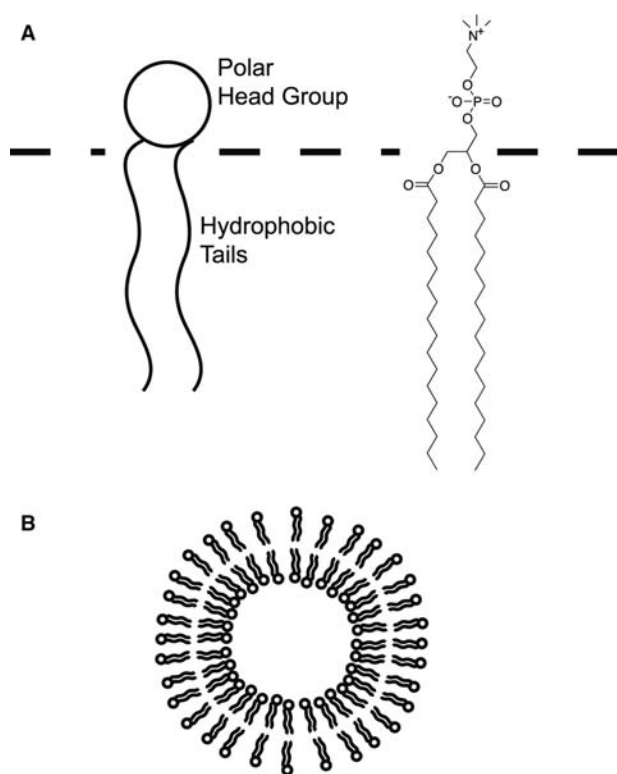


**Fig. 1** (A) Illustration of a lipid molecule showing the hydrophobic tail region and polar head group and the chemical structure for a typical lipid (1,2-distearoyl-*sn*-glycero-3-phosphocholine, DSPC). (B) The liposome (or vesicle) that spontaneously forms when lipids are placed in aqueous solutions.

membrane faces and any incorporated proteins. In Fig. 2C, the orientation of the leaflets toward the bulk aqueous solution is preserved upon fusion. In the mechanism detailed in Fig. 2A, however, the orientation of the leaflets is reversed; that is, the inside leaflet of the liposome becomes the top leaflet of the supported bilayer. Vesicle fusion to hydrophobic surfaces (Fig. 2B) can also be accomplished but the liposomes must rupture resulting in attachment and spreading of the two leaflets of the lipid bilayer. Liposome composition, surface chemistry, vesicle size, temperature, osmotic pressure, and the presence of calcium ions are all factors that influence vesicle fusion.<sup>[7,8]</sup> Typically, supported bilayers formed by vesicle fusion maintain a thin layer of water (~10 Å) between the substrate and the adjacent membrane surface.<sup>[9–11]</sup> This supported bilayer structure is very stable (days to months) in an aqueous environment, but unstable in the presence of detergents or in air. The lateral mobility of lipids within the bilayer is maintained enabling the molecules in the membrane to diffuse over long distances.

There is a suite of tools available for the characterization of nanoscale structures in lipid bilayers. For a

description of standard methods for general liposome characterization, the reader is referred to the relevant chapters in the book by D.D. Lasic<sup>[1]</sup> and the book edited by R.R.C. New.<sup>[2]</sup> Fluorescence microscopy provides a means to attain real-time data on the dynamical structures occurring in lipid bilayer systems. Single-molecule sensitivity is achievable. Fluorescence resonance energy transfer (FRET) between a fluorescently tagged donor component and a fluorescently tagged acceptor component yields accurate distance information for short length scales. In fluorescence recovery after photobleaching (FRAP), an area on the bilayer surface is photobleached and then monitored for recovery of fluorescence intensity. The fluorescence recovery is due to fluorescently labeled molecules diffusing into the bleached area and can thus be used to measure diffusion rates to evaluate lateral fluidity.

Spatial resolution of fluorescence techniques are, however, diffraction limited to a few hundred nanometers. Unfortunately, this length is often the same size as the dynamic structures. The atomic force microscope (AFM), on the other hand, can be used to characterize features in supported bilayers with sub-nanometer resolution.<sup>[12]</sup> The AFM typically requires about a minute to capture an image. Thus it is suitable for imaging relatively static systems, or slow dynamics. Fluorescence and AFM imaging are the two techniques most relevant to the work discussed in this entry, but other methods, including neutron scattering and nuclear magnetic resonance (NMR) spectroscopy,<sup>[13]</sup> have also been applied toward dynamic nanostructures in bilayer systems.

Computer simulations are also an effective tool for understanding dynamic nanostructures in bilayer membranes.<sup>[14]</sup> Nielsen and coworkers simulated binary mixtures of lipid bilayers revealing dynamic microphase separations with length scales of tens of nanometers.<sup>[4]</sup> They further showed that this nanoscale structure affects the functional properties of the membrane. Through simulations and theoretical modeling, Gil et al. analyzed protein organization in lipid bilayers.<sup>[5]</sup> The lateral organization of transmembrane proteins can be explained by the properties of the lipid bilayer. Hydrophobic matching between lipids and the hydrophobic region of proteins can lead to an enrichment of one lipid species near the protein. As such, the lipids can mediate protein attraction or repulsion. Also, the wetting of a protein by one lipid component can lead to larger protein organization patterns.

## DYNAMIC NANOSTRUCTURES IN BIOLOGICAL AND MODEL BIOLOGICAL MEMBRANES

In this section, a few examples will be given to illustrate the importance of dynamic nanostructures

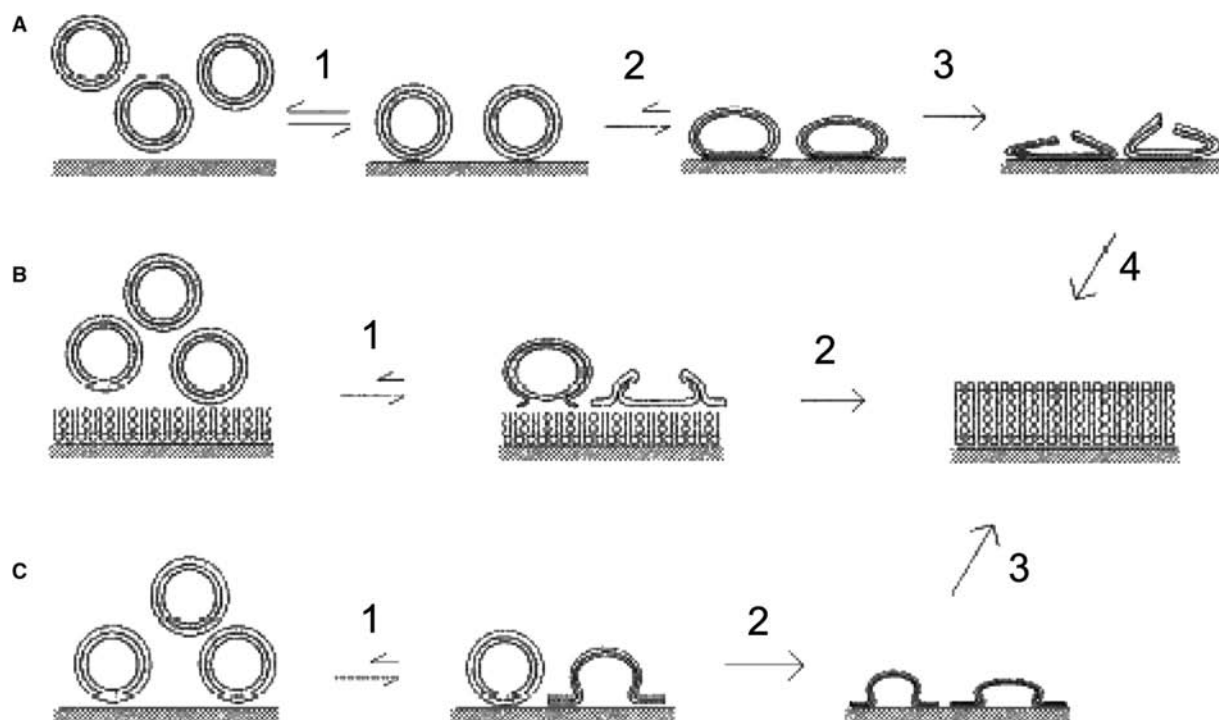


**Fig. 2** Schematic representation of the possible mechanisms for planar bilayer formation from liposomes on hydrophilic and hydrophobic surfaces. The drawings are not drawn to scale. Lipid molecules on the support are enlarged approximately 50-fold compared to a liposome. (A) Vesicle fusion on a hydrophilic surface with the leaflet orientation reversed. (B) Vesicle fusion on a hydrophobic surface. (C) Vesicle fusion on a hydrophilic surface with the leaflet orientation preserved. *Source:* From Ref.<sup>[7]</sup>. © 1997 Elsevier Science B.V.

in biological systems. Rafts, domains, and hierarchical structures are prevalent in the cell membrane and are the predominant sites of biological activity. Subczynski and Kusumi<sup>[15]</sup> reviewed the three types of rafts (Fig. 3) found, to date, in plasma membranes. In unstimulated cells there are small, unstable (lifetimes of less than 1 msec) lipid rafts (A, A', and A'' in Fig. 3) that may have associated proteins. When receptor molecules in these unstable rafts react with ligands, they can create stabilized rafts (Fig. 3B) with lifetimes of minutes. The coalescence of these two types of rafts creates transient confinement zones (TCZs), which serve as signaling rafts (Fig. 3C) by assembling the necessary constituents to switch on a downstream signaling pathway.

Such dynamic nanostructures have been shown to be important in a variety of biological systems. Sheets, Holowka, and Baird explain how the organization of the plasma membrane likely exerts spatio-temporal control on immunoglobulin E receptor-mediated signal transduction.<sup>[16]</sup> Lipid rafts also play a key role in the immunological synapse.<sup>[17–19]</sup> The T-cell antigen receptors (TCR) are located in rafts and they become cross-linked by ligand binding. The cross-linking induces raft aggregation, causing colocalization of signaling proteins. This activates the phosphorylation of tyrosine

residues on membrane-associated proteins and starts downstream signaling.

Because the biological membrane is a complex entity, most structure and function studies are performed on simpler, well-defined model membrane systems of liposomes and supported bilayers. For example, in studies of lipid raft formation, ternary mixtures of saturated lipids, unsaturated lipids, and cholesterol have been found to spontaneously form rafts over a wide range of specific lipid species and concentrations.<sup>[20–22]</sup> In these studies, micron-sized domains were imaged via fluorescence microscopy techniques. Nanostructural features in lipid bilayers can also be revealed with AFM, although the domain shape and size have been shown to be somewhat dependent on the substrate and bottom leaflet of the supported bilayer.<sup>[23,24]</sup>

Not only do lipid–lipid interactions cause domain formation but lipid–protein interactions can also induce nanoscale structures to form. Rinia et al. reported that transmembrane WALP proteins perturb the bilayer, creating striated domains of 25 nm to 10 μm with the nanoscale striations spaced at 7.5-nm intervals.<sup>[25]</sup> Furthermore, the specific physical properties of the bilayer components can modulate enzyme activity. Honger and coworkers demonstrated that

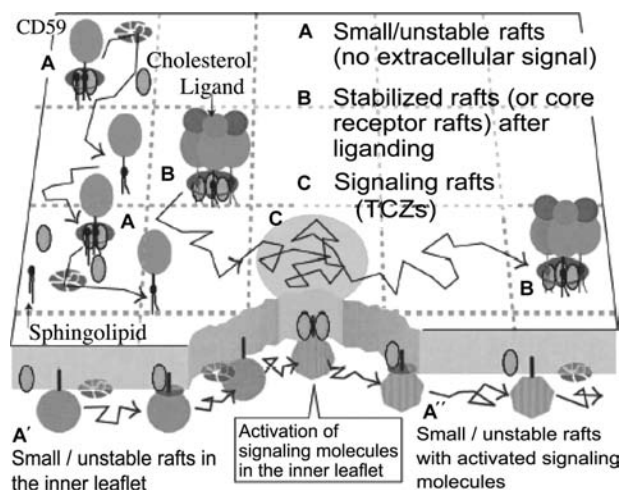


**Fig. 3** Three types of rafts found thus far in the plasma membrane. The first type (A) is prevalent in the absence of extracellular stimulation. They are small (perhaps consisting of several molecules) and unstable (the lifetimes may be less than 1 msec) and may be the kind of raft that monomeric GPI-anchored proteins associate with. The second type of raft (B) may appear when receptor molecules form oligomers upon liganding or cross-linking. The receptors may be GPI-anchored receptors or transmembrane receptors with some affinity to cholesterol and saturated alkyl chains. Oligomerized receptors may then induce small but stable rafts around them, perhaps due to the slight reduction in the thermal motion around the cluster and the subsequent assembly of cholesterol. Given the rather stable oligomerization of the receptor molecules, the second type of raft may be stable for minutes, although the associated raft-constituent molecules may be exchanged frequently between the raft and the bulk domains. Such receptor-associated rafts are called “core-receptor rafts.” The third type of raft (C) may be formed around these core receptor rafts (although the core receptor rafts may be undergoing diffusion). Here they are called “signaling rafts,” because they are likely to be directly involved in downstream signaling from the receptor molecules, by assembling signaling molecules through the (transient and/or more stable) coalescence of rafts that may contain one or two signaling molecules. Small/unstable rafts are also likely to exist in the inner leaflet of the membrane (A') and could coalesce with the core receptor rafts (B and C), where the signaling molecule in the inner leaflet is activated, which might also leave from the signaling rafts (C and A''). *Source:* From Ref.<sup>[15]</sup>. © 2003 Elsevier Science B.V.

phospholipase A<sub>2</sub> enzyme activity correlates with the degree of microheterogeneity within the bilayer.<sup>[26]</sup>

Protein binding to receptor lipids in model membranes can also induce a membrane reorganizational process.<sup>[27]</sup> Concanavalin A (Con A) protein was found to bind to bilayers composed of the mannosamine-functionalized lipid PSMU and distearylphosphatidylcholine (DSPC). Initially, PSMU forms aggregates in DSPC, but slowly disperses following Con A adsorption to the membrane surface and binding to the

mannosamine head groups. Dispersal is attributed to Con A–Con A steric interactions, distance between receptor sites, and possible protein insertion events.

Another example of a molecular recognition-induced lipid reorganization was developed by Song, Nolan, and Swanson to detect biotoxins.<sup>[28,29]</sup> Fluorescently tagged receptors are dispersed in a fluid lipid matrix of palmitoyl, 9-octadecenenoyl phosphatidylcholine (POPC). The dispersed receptors exhibit strong fluorescence. Specific, multivalent binding of the toxin to its receptors brings the fluorophores in close proximity, causing a strong decrease in fluorescence intensity due to self-quenching. Nonspecific binding of toxins to lipid bilayers can also be used in a biosensing scheme that employs optical evanescence.<sup>[30]</sup> Pattern analysis and comparison to standards are required to assign the identity of the bound toxin, but the method is rapid and can be used for multiple toxins. The original work analyzed the binding of six different protein toxins.

## DYNAMIC NANOSTRUCTURES AS NANOTECHNOLOGY BUILDING BLOCKS

The same specificity of chemical recognition events that alter the nanostructures of biological membrane systems can be utilized to make rapid and sensitive chemical sensors. In a manner similar to the Con A-induced dispersion, the Sasaki lab has developed several synthetic receptor systems for metal ions, Hg<sup>2+</sup>,<sup>[31]</sup> Cu<sup>2+</sup>,<sup>[32]</sup> and Pb<sup>2+</sup>,<sup>[33]</sup> that are sensitive to parts per billion (ppb) levels of the analyte. In all of these cases, a receptor is synthesized with a head group specific for the metal ion of interest and with a pyrene label in the lipid tail. The receptor naturally aggregates in the DSPC lipid matrix, yielding a large pyrene excimer fluorescence peak. Once the receptors chelate the metal ions they disperse, and the monomer fluorescence peak grows in intensity while the excimer diminishes. Binding of the metal ions gives the receptor head groups a net charge; electrostatic repulsion causes their dispersal into the matrix. The AFM can capture before and after images showcasing these controllable dynamic nanostructures. **Figure 4A** shows an AFM image of a supported bilayer consisting of a receptor lipid (18-crown-6 ether functionalized lipid, PS18C6) embedded in a matrix lipid (DSPC). Islands and filaments of PS18C6-rich regions are clearly visible. These nanostructures decrease in size and intensity upon the addition of Pb<sup>2+</sup> ions (**Fig. 4B**) and removal of the ions leads to a reaggregation of the PS18C6 lipids. Fluorescence measurements indicate this reorganization occurs within seconds. The undefined dynamic nanostructures provide a starting point for the development

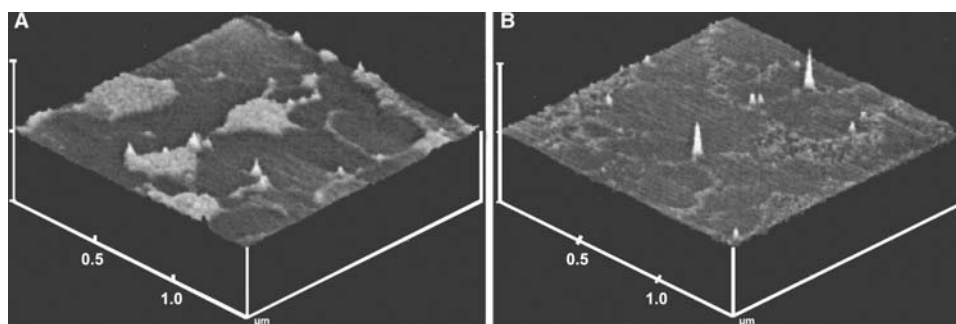


**Fig. 4** AFM topographic images of a 20% PS18C6/DSPC bilayer supported on a mica surface demonstrating the actuation of the film from aggregated to dispersed states with  $\text{Pb}^{2+}$  ions. The membrane in the (A) initial state, then (B) after addition of 0.1 mM  $\text{Pb}(\text{NO}_3)_2$ . All solutions were aqueous saline (0.1 M NaCl). *Source:* From Ref.<sup>[33]</sup>. © 2002 American Chemical Society.

of reversible nanoscale architectures controlled by chemical recognition events.

The Boxer laboratory has pioneered the field of micropatterning supported lipid bilayers. Because this work has been the subject of several excellent reviews,<sup>[34–36]</sup> it will only be briefly described here.

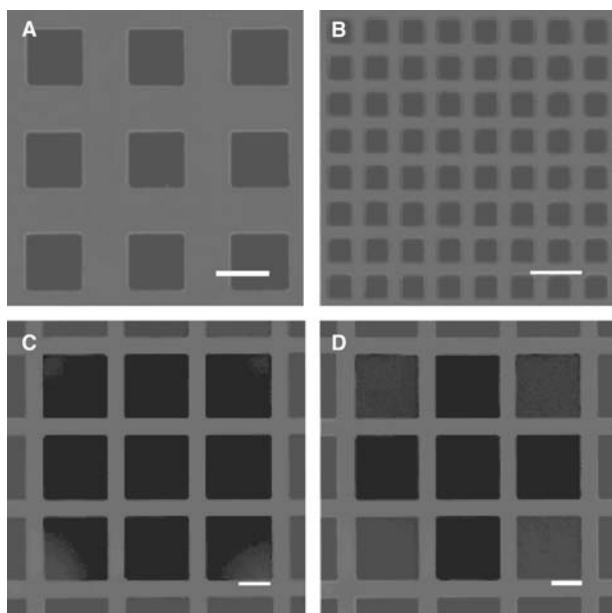


**Fig. 5** Epifluorescence images of supported membranes patterned by printing proteins. In each panel the protein is TR-BSA and is colored red, while the supported membrane regions are 2% NBD-PE-doped egg PC and are colored green. The scale bars are each 20  $\mu\text{m}$  across. (A) 20- $\mu\text{m}$  bilayer regions separated by 15- $\mu\text{m}$  protein; (B) 10- $\mu\text{m}$  bilayer regions separated by 5- $\mu\text{m}$  protein grids; (C,D) 40- $\mu\text{m}$  bilayer regions separated by 10- $\mu\text{m}$  protein grids. In panel C an octagonal spot was photobleached for 30 sec centered on the middle corral. After irradiation ceased, the lipids mix freely within each corral, creating corrals of uniform but intermediate fluorescence intensity, as seen in (D) after 360 sec of recovery. *Source:* From Ref.<sup>[40]</sup>. © 2000 American Chemical Society.

The fluid bilayers are patterned into micron-sized features by creating barriers to lateral diffusion through methods as diverse as scratching,<sup>[37]</sup> using polymer stamps to blot away lipids<sup>[38]</sup> or to microcontact print barriers,<sup>[38]</sup> and microfluidic manipulation of the lipid bilayer.<sup>[39]</sup> The supported bilayers in Fig. 5 were patterned by microcontact printing of protein (TR-BSA) barriers. After printing the proteins, vesicle fusion was used to form the supported bilayers of fluorescently doped egg-PC lipids. The bilayers only fuse to and occupy regions free of adsorbed proteins. The patterned surfaces contain the lipids within their micron-sized corrals as demonstrated by FRAP measurements (Fig. 5C and D). Although the development of these tools for patterning supported lipid bilayers has been focused on the micron scale, the tools can be scaled down into the nanoscale arena. The polymer stamps used for blotting or microcontact printing can be created with nanoscale features by using advanced photolithography or electron beam lithography and, likewise, microfluidics can be scaled to nanofluidics.

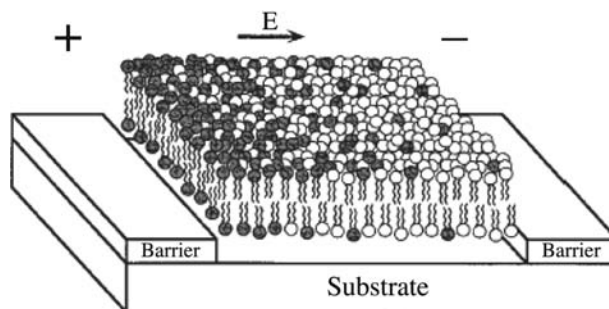


**Fig. 6** Schematic diagram of an electric field-induced reorganization of lipids in a confined patch of supported bilayer membrane. A two-component system is shown in which the negatively charged lipid (shaded) builds up a concentration gradient toward the anode side of the corral. This represents an equilibrium distribution where the field-induced drift is balanced by diffusion. *Source:* From Ref.<sup>[42]</sup>. © 1998 National Academy of Sciences, U.S.A.



The lipids within the patterned supported bilayers can be dynamically controlled on a submicron scale. The application of an electric field tangentially to the plane of the supported bilayer induces a reorganization of the charged components in a confined patch of membrane<sup>[40,41]</sup> as illustrated schematically in Fig. 6. The equilibrium concentration profile is a balance of the field-induced reorganization and Brownian diffusion. The concentration profile will be steeper for larger species, such as dimers and larger molecular aggregates, as these species will be slower diffusing.<sup>[40]</sup> Electric field manipulation takes an initially uniform membrane patch (Fig. 7A) and induces a concentration

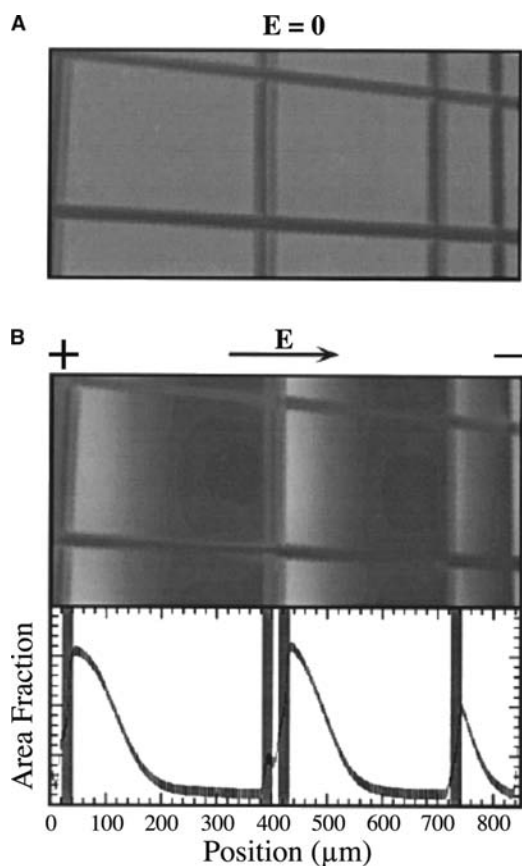


**Fig. 7** (A) Epifluorescence image of several corrals of fluid membrane separated by scratch boundaries. The membrane is of uniform composition in the absence of an electric field. Fluorescence is from 1 mol% of *N*-(Texas Red sulfonyl)-1,2-dihexadecanoyl-*sn*-glycero-3-phosphoethanolamine, triethylammonium salt doped into this egg-PC (90%) and DOPS (9%) membrane. (B) Epifluorescence image of a steady-state molecular reorganization induced by an applied field of 25 V/cm. The negatively charged components have built up concentration gradients toward the anode. A trace of the fluorescence intensity across the image is depicted below with the scratch boundaries marked with gray bars. The concentration profiles can be observed to a greater extent in the larger corrals. *Source:* From Ref.<sup>[41]</sup>. © 1997 National Academy of Sciences, U.S.A.

gradient (Fig. 7B) that can be dynamically reversed by switching the applied electric field. The behavior of charged species in the bilayer in response to an applied field can also be exploited to separate mixtures of membrane-associated molecules. Boxer and van Oudenaarden designed a geometrical Brownian ratchet that consists of an array of asymmetric patterned

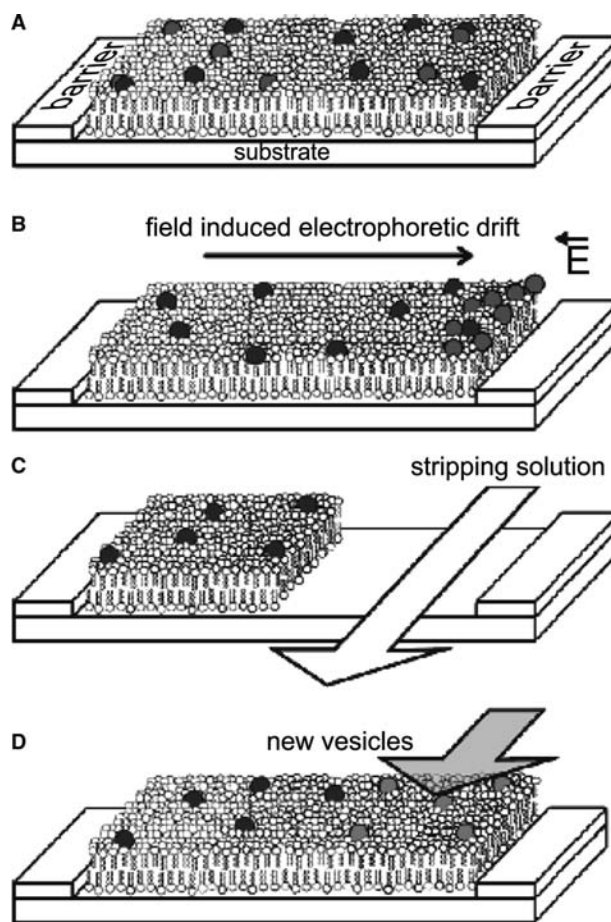


**Fig. 8** Micropatterning, electrophoresis, and stripping of lipid bilayers. (A) Schematic diagram of a supported lipid bilayer confined or corralled by microfabricated barriers. Mobile species, illustrated by lipids with red and green head groups, freely diffuse and mix, approaching a uniform concentration across the extent of the lipid bilayer. (B) Application of an electric field induces manipulation of charged membrane components (the red lipids) and represents one method of manipulating a lipid bilayer after formation; the neutral lipids (green) do not respond to this applied field and remain homogeneous in the corral. (C) A stream of stripping solution is flowed over part of the surface under laminar flow conditions, leaving an open region on the substrate. (D) A new lipid bilayer, which could contain new biomolecular species, indicated by the lipid with blue head groups is introduced. The relative sizes and organizations of the components in these drawings are for illustrative purposes only and are not to scale. *Source:* From Ref.<sup>[39]</sup>. © 2003 American Chemical Society.

barriers on a solid support.<sup>[42]</sup> The barriers rectify the lateral Brownian motion of the molecules within the membrane inducing the various molecular species (with different diffusion coefficients) to follow distinct trajectories through the device. This application of Brownian ratchets to bilayers offers a promising way to separate membrane proteins in their native conformations.

The composition of the patterned bilayer corrals can be changed after preparation. Figure 8 details a process of applying a field to concentrate a charged species near one of the barriers (field-induced reorganization; Fig. 8B). The charged species is then selectively removed with the microfluidic flow of a stripping solution (Fig. 8C);<sup>[39]</sup> thus a new bilayer species can now be introduced (Fig. 8D). Laminar flow could be used to strip sections of the patterned bilayer, carrying the species downstream to compartments on the microfluidic chip for compositional analysis. An alternate method for changing the lipid composition after patterning uses membrane-coated beads

to deliver the new species to areas of opposite charge.<sup>[43]</sup> The beads adhere to the patterned corral through an electrostatic attraction and some lipid exchange between the beads and the patterned supported bilayer occurs. This may provide a novel mechanism for incorporating membrane proteins or glycolipids into prepatterned bilayer arrays.

These micropatterned supported bilayers have multiple applications for cell culturing and drug discovery. For example, fibronectin protein barriers for the lipid bilayers create well-defined surfaces for studying cell adhesion.<sup>[44]</sup> In addition, cell spreading can be controlled and, conceivably, directed by tuning the dimensions and geometries of the patterned bilayer. Proteins can also be included in the patterned bilayer. The incorporation of antigens creates an anisotropic environment for the study of localized stimulation of rat basophilic leukemia (RBL) mast cells.<sup>[45]</sup> Scanning electron microscopy (SEM) images (Fig. 9) clearly show that RBL cell adhesion and spreading is directed by the underlying patterned supported bilayer. This

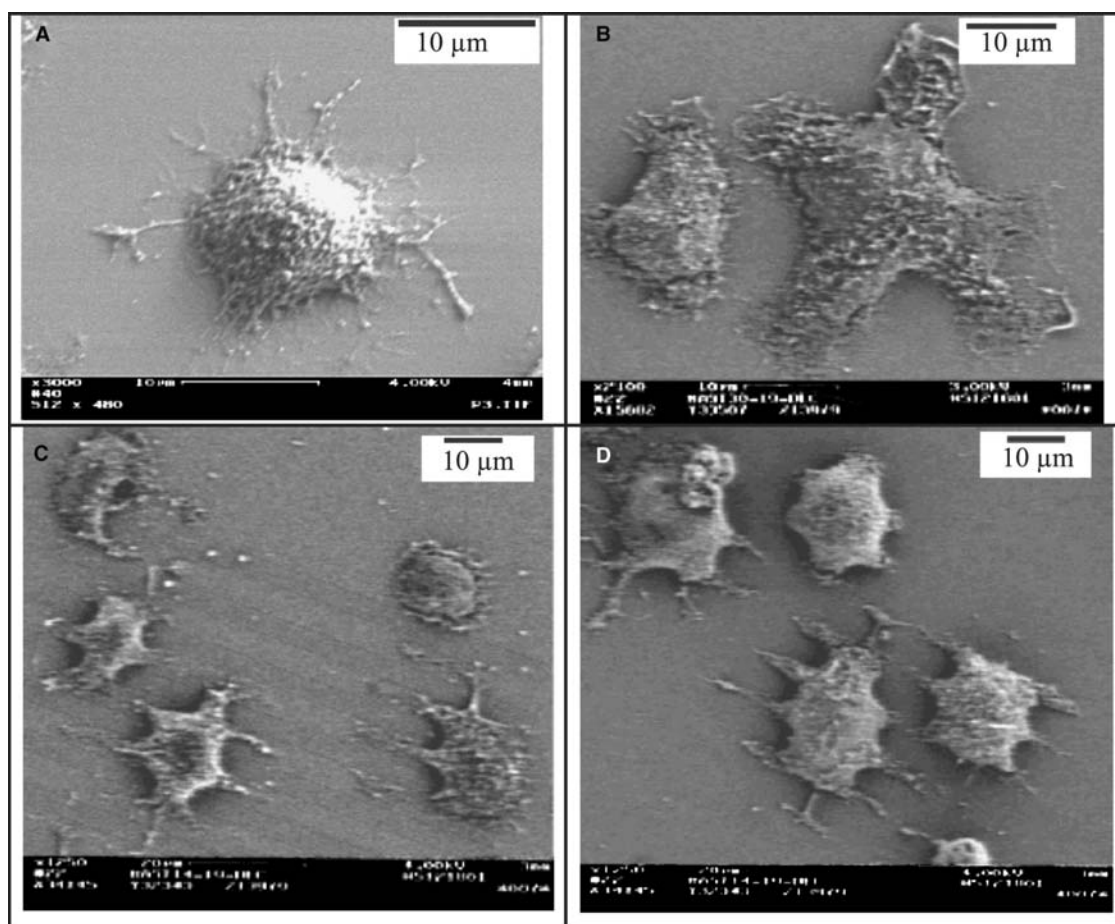


**Fig. 9** SEM images of RBL cells. (A) Resting RBL on a plain silicon surface with lamellipodia randomly spreading on the oxidized silicon substrate. Magnification:  $\times 3000$ . (B) Stimulated RBL at the corner of four patterned squares of lipids. Magnification:  $\times 2100$ . (C,D) Stimulated RBL over patterned lines of lipids. Magnification:  $\times 1250$ ,  $\times 1250$ . (C) shows gray lines where the haptened lipids were patterned. *Source:* From Ref.<sup>[46]</sup>. © 2003 American Chemical Society.



method of incorporating components in the membrane should extend to the localized confinement of other cellular receptors and provide a means to study their induced cellular responses.

Today, membrane-bound proteins account for 50% of current drug targets.<sup>[46]</sup> Yet, membrane proteins are among the most difficult to study because the protein usually requires the membrane for it to remain in its native, active conformation. Patterned membrane microarrays provide a method for studying protein–protein or protein–small molecule (e.g., drug) interactions.<sup>[47]</sup> Membrane microarrays maintain the functionality of living cell membranes while providing the simplicity and controllability of an array. The array of membrane patches can be patterned with any of the techniques mentioned above. The patches can also be printed with a quill-pin printer. This technique has

been successfully demonstrated for G-protein coupled receptor (GPCR) proteins.<sup>[46,48]</sup> GPCRs consist of seven transmembrane helices. The binding of a ligand to the extracellular side of the transmembrane helices activates a G protein on the intracellular side. The affinity of the GPCR for its ligand depends on the presence of a G protein complexed to the intracellular side. Thus it is important for G proteins to be in the membrane microarray, which is achieved with the quill-pin method. Fig. 10 shows GPCR microarray results for the determination of the affinity of a series of compounds for  $\beta_1$ ,  $\beta_2$ , and  $\alpha_2A$  subtypes of the adrenergic receptor. The BT-CGP ligand is known to be specific for  $\beta$ -subtypes and the GPCR microarray clearly shows this specificity (Fig. 10Ai) as only the  $\beta_1$  and  $\beta_2$  receptor spots show fluorescence. When the BT-CGP ligand is incubated with a microarray in

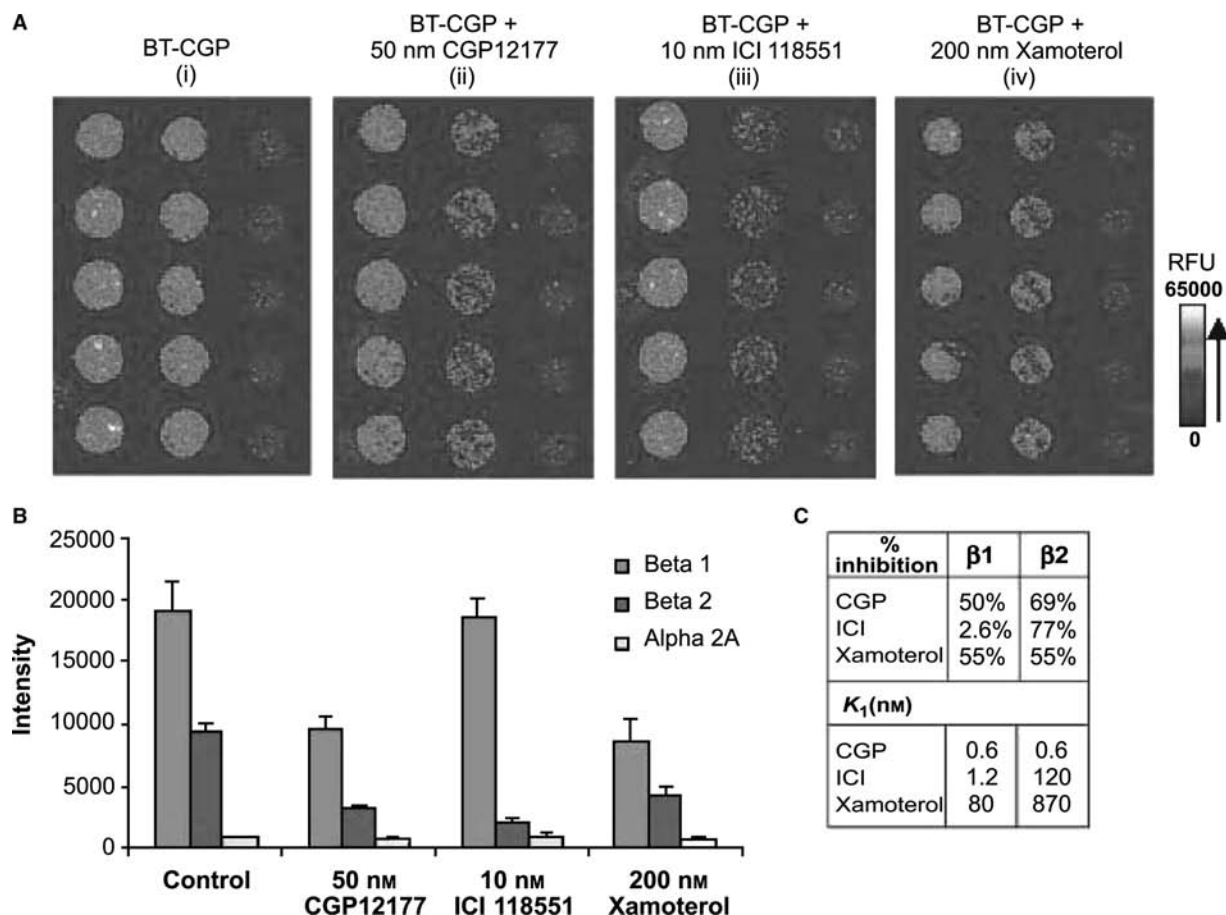


**Fig. 10** Demonstration of the use of GPCR microarrays for determining the selectivity of compounds among the different subtypes of a receptor. Each microarray consists of three columns; each column contains, from left to right, five replicate microspots of the  $\beta_1$ ,  $\beta_2$ , and  $\alpha_2A$  adrenergic receptors, respectively. (A) Fluorescence false-color images (from left to right) of the array incubated with solutions containing BT-CGP (5 nM) and mixtures of BT-CGP (5 nM) with CGP 12177 (50 nM), ICI118551 (10 nM), and xamoterol (200 nM) to the array. (B) Histogram analysis of the images in (A) showing the relative fluorescence intensities (RFU) of the arrays incubated with BT-CGP or mixtures of BT-CGP and inhibitors. (C) Table showing the amounts of inhibition and the  $K_1$  values for the inhibitors used in the experiment. *Source:* From Ref.<sup>[49]</sup>. © 2002 Wiley-VCH.

the presence of an inhibitor (e.g., CGP 12177, ICI 118551, or Xamoterol), the percent binding inhibition can be determined.

## CONCLUSION

In recent years, it has become clear that nature takes advantage of dynamic nanoscale structures in many cellular signaling pathways. As mentioned, this serves as a sensitive sensor system for the cell. The ability to monitor nanoscale features in biological systems has provided new insights into the mechanisms of this membrane activity. This article has described progress that the field of nanotechnology has made in mimicking this complex yet robust cellular component. Dynamic aggregates can be used as the basis for chemical and biosensing elements with very high sensitivity and selectivity. Spatial and temporal control of dynamic nanoscale structures in lipid membranes may serve as unique nanobuilding blocks and template scaffolds in bottom-up architectures. Advances in fabrication technology should soon enable supported lipid bilayers to be patterned at the nanoscale and, as discussed, physical methods (electric fields and fluid flows) are already in place for dynamically controlling the lipids in a patterned corral. The near future should bring efforts to combine physical control with chemical control to create more complex dynamic nanoscale structures with lipid membranes for nanotechnology applications.

## ACKNOWLEDGMENTS

Sandia is a multiprogram laboratory operated by Sandia Corporation, a Lockheed Martin Company, for the U.S. Department of Energy under contract DE-AC04-94AL85000 and supported by the Office of Basic Energy Sciences.

## REFERENCES

- Lasic, D.D. *Liposomes: From Physics to Applications*; Elsevier Science: New York, 1993; 575pp.
- New, R.R.C. *Liposomes—A Practical Approach*; IRL Press: New York, 1990; 301pp.
- Singer, S.J.; Nicolson, G.L. The fluid mosaic model of the structure of cell membranes. *Science* **1972**, *175*, 720–731.
- Nielsen, L.; Vishnyakov, A.; Jorgensen, K.; Bjornholm, T.; Mouritsen, O. Nanometre-scale structure of fluid lipid membranes. *J. Phys., Condens. Matter* **2000**, *12* (8A), A309–A314.
- Gil, T.; Ipsen, J.; Mouritsen, O.; Sabra, M.; Sperotto, M.; Zuckermann, M. Theoretical analysis of protein organization in lipid membranes. *Biochim. Biophys. Acta, Rev. Biomembr.* **1998**, *1376* (3), 245–266.
- McConnell, H.M.; Watts, T.H.; Weis, R.M.; Brian, A.A. Supported planer membranes in studies of cell–cell recognition in the immune system. *Biochim. Biophys. Acta* **1986**, *864* (1), 95–106.
- Puu, G.; Gustafson, I. Planar lipid bilayers on solid supports from liposomes—factors of importance for kinetics and stability. *Biochim. Biophys. Acta, Biomembr.* **1997**, *1327* (2), 149–161.
- Reimhult, E.; Hook, F.; Kasemo, B. Intact vesicle adsorption and supported biomembrane formation from vesicles in solution: influence of surface chemistry, vesicle size, temperature, and osmotic pressure. *Langmuir* **2003**, *19* (5), 1681–1691.
- Bayerl, T.M.; Bloom, M. Physical-properties of single phospholipid-bilayers adsorbed to micro glass beads—a new vesicular model system studied by H2 nuclear magnetic resonance. *Biophys. J.* **1990**, *58* (2), 357–362.
- Johnson, S.J.; Bayerl, T.M.; McDermott, D.C.; Adam, G.W.; Rennie, A.R.; Thomas, R.K.; Sackmann, E. Structure of an adsorbed dimyristoylphosphatidylcholine bilayer measured with specular reflection of neutrons. *Biophys. J.* **1991**, *59* (2), 289–294.
- Koenig, B.; Kruger, S.; Orts, W.; Majkrzak, C.; Berk, N.; Silverton, J.; Gawrisch, K. Neutron reflectivity and atomic force microscopy studies of a lipid bilayer in water adsorbed to the surface of a silicon single crystal. *Langmuir* **1996**, *12* (5), 1343–1350.
- Muller, D.J.; Schoenenberger, C.A.; Schabert, F.; Engel, A. Structural changes in native membrane proteins monitored at subnanometer resolution with the atomic force microscope: a review. *J. Struct. Biol.* **1997**, *119* (2), 149–157.
- Bloom, M.; Bayerl, T.M. Membranes studied using neutron scattering and NMR. *Can. J. Phys.* **1995**, *73* (11–12), 687–696.
- Scott, H. Modeling the lipid component of membranes. *Curr. Opin. Struct. Biol.* **2002**, *12* (4), 495–502.
- Subczynski, W.; Kusumi, A. Dynamics of raft molecules in the cell and artificial membranes: approaches by pulse EPR spin labeling and single molecule optical microscopy. *Biochim. Biophys. Acta, Biomembr.* **2003**, *1610* (2), 231–243.
- Sheets, E.; Holowka, D.; Baird, B. Membrane organization in immunoglobulin E receptor signaling. *Curr. Opin. Chem. Biol.* **1999**, *3* (1), 95–99.
- Grakoui, A.; Bromley, S.; Sumen, C.; Davis, M.; Shaw, A.; Allen, P.; Dustin, M. The immunological synapse: a molecular machine controlling T cell activation. *Science* **1999**, *285* (5425), 221–227.
- Blanchard, N.; Hivroz, C. The immunological synapse: the more you look the less you know.... *Biol. Cell* **2002**, *94* (6), 345–354.
- Magee, T.; Pirinen, N.; Adler, J.; Pagakis, S.; Parmryd, I. Lipid rafts: cell surface platforms for T cell signaling. *Biol. Res.* **2002**, *35* (2), 127–131.
- Veatch, S.L.; Keller, S.L. Organization in lipid membranes containing cholesterol. *Phys. Rev. Lett.* **2002**, *89* (26), 268101–268104.

21. London, E. Insights into lipid raft structure and formation from experiments in model membranes. *Curr. Opin. Struct. Biol.* **2002**, *12* (4), 480–486.
22. Silvius, J. Role of cholesterol in lipid raft formation: lessons from lipid model systems. *Biochim. Biophys. Acta, Biomembr.* **2003**, *1610* (2), 174–183.
23. Tamm, L.; Bohm, C.; Yang, J.; Shao, Z.; Hwang, J.; Edidin, M.; Betzig, E. Nanostructure of supported phospholipid monolayers and bilayers by scanning probe microscopy. *Thin Solid Films* **1996**, *285*, 813–816.
24. Tokumasu, F.; Jin, A.; Feigenson, G.; Dvorak, J. Nanoscopic lipid domain dynamics revealed by atomic force microscopy. *Biophys. J.* **2003**, *84* (4), 2609–2618.
25. Rinia, H.; Kik, R.; Demel, R.; Snel, M.; Killian, J.; van der Eerden, J.; de Kruijff, B. Visualization of highly ordered striated domains induced by transmembrane peptides in supported phosphatidylcholine bilayers. *Biochemistry* **2000**, *39* (19), 5852–5858.
26. Honger, T.; Jorgensen, K.; Biltonen, R.; Mouritsen, O. Systematic relationship between phospholipase A(2) activity and dynamic lipid bilayer microheterogeneity. *Biochemistry* **1996**, *35* (28), 9003–9006.
27. Bondurant, B.; Last, J.; Waggoner, T.; Slade, A.; Sasaki, D. Optical and scanning probe analysis of glycolipid reorganization upon Concanavalin A binding to mannose-coated lipid bilayers. *Langmuir* **2003**, *19* (5), 1829–1837.
28. Song, X.; Nolan, J.; Swanson, B. Optical signal transduction triggered by protein–ligand binding: detection of toxins using multivalent binding. *J. Am. Chem. Soc.* **1998**, *120* (19), 4873–4874.
29. Song, X.; Nolan, J.; Swanson, B. Optical biosensor based on fluorescence resonance energy transfer: ultrasensitive and specific detection of protein toxins. *J. Am. Chem. Soc.* **1998**, *120* (44), 11,514–11,515.
30. Puu, G. An approach for analysis of protein toxins based on thin films of lipid mixtures in an optical biosensor. *Anal. Chem.* **2001**, *73* (1), 72–79.
31. Sasaki, D.; Padilla, B. Dithioamide metal ion receptors on fluorescent lipid bilayers for the selective optical detection of mercuric ion. *Chem. Commun.* **1998**, (15), 1581–1582.
32. Last, J.; Waggoner, T.; Sasaki, D. Lipid membrane reorganization induced by chemical recognition. *Biophys. J.* **2001**, *81* (5), 2737–2742.
33. Sasaki, D.; Waggoner, T.; Last, J.; Alam, T. Crown ether functionalized lipid membranes: Lead ion recognition and molecular reorganization. *Langmuir* **2002**, *18* (9), 3714–3721.
34. Boxer, S. Molecular transport and organization in supported lipid membranes. *Curr. Opin. Chem. Biol.* **2000**, *4* (6), 704–709.
35. Groves, J.; Ulman, N.; Boxer, S. Micropatterning fluid lipid bilayers on solid supports. *Science* **1997**, *275* (5300), 651–653.
36. Groves, J.T.; Boxer, S.G. Micropattern formation in supported lipid membranes. *Acc. Chem. Res.* **2002**, *35* (3), 149–157.
37. Cremer, P.; Groves, J.; Kung, L.; Boxer, S. Writing and erasing barriers to lateral mobility into fluid phospholipid bilayers. *Langmuir* **1999**, *15* (11), 3893–3896.
38. Hovis, J.; Boxer, S. Patterning barriers to lateral diffusion in supported lipid bilayer membranes by blotting and stamping. *Langmuir* **2000**, *16* (3), 894–897.
39. Kam, L.; Boxer, S. Spatially selective manipulation of supported lipid bilayers by laminar flow: Steps toward biomembrane microfluidics. *Langmuir* **2003**, *19* (5), 1624–1631.
40. Kung, L.; Kam, L.; Hovis, J.; Boxer, S. Patterning hybrid surfaces of proteins and supported lipid bilayers. *Langmuir* **2000**, *16* (17), 6773–6776.
41. Groves, J.; Boxer, S.; McConnel, H. Electric field-induced reorganization of two-component supported bilayer membranes. *Proc. Natl. Acad. Sci. U. S. A.* **1997**, *94* (25), 13,390–13,395.
42. Groves, J.; Boxer, S.; McConnell, H. Electric field-induced critical demixing in lipid bilayer membranes. *Proc. Natl. Acad. Sci. U. S. A.* **1998**, *95* (3), 935–938.
43. van Oudenaarden, A.; Boxer, S.G. Brownian ratchets: molecular separations in lipid bilayers supported on patterned arrays. *Science* **1999**, *285* (5430), 1046–1048.
44. Sapuri, A.; Baksh, M.; Groves, J. Electrostatically targeted intermembrane lipid exchange with micropatterned supported membranes. *Langmuir* **2003**, *19* (5), 1606–1610.
45. Kam, L.; Boxer, S. Cell adhesion to protein-micropatterned-supported lipid bilayer membranes. *J. Biomed. Mater. Res.* **2001**, *55* (4), 487–495.
46. Orth, R.; Wu, M.; Holowka, D.; Craighead, H.; Baird, B. Mast cell activation on patterned lipid bilayers of subcellular dimensions. *Langmuir* **2003**, *19* (5), 1599–1605.
47. Fang, Y.; Frutos, A.; Webb, B.; Hong, Y.; Ferrie, A.; Lai, F.; Lahiri, J. Membrane biochips. *BioTechniques* **2002**, *33*, 62–65.
48. Groves, J. Membrane array technology for drug discovery. *Curr. Opin. Drug Discov. Dev.* **2002**, *5* (4), 606–612.
49. Fang, Y.; Frutos, A.; Lahiri, J. G-protein-coupled receptor microarrays. *ChemBioChem* **2002**, *3* (10), 987–991.

# Liposomes: Direct Force Measurement by AFM

Guangzhao Mao

Xuemei Liang

K.Y. Simon Ng

Department of Chemical Engineering and Materials Science, Wayne State University,  
Detroit, Michigan, U.S.A.

## INTRODUCTION

Liposomes serve as models for cells<sup>[1]</sup> and show increasing applications in medical and nonmedical fields.<sup>[2,3]</sup> Unilamellar vesicles are prepared from multilamellar vesicle (MLV) dispersions either by sonication<sup>[4]</sup> or extrusion.<sup>[5]</sup> The shape stability of liposomes is important in the understanding of membrane fusion, as well as in drug delivery and gene therapy. Therefore it has been the subject of numerous theoretical<sup>[6–9]</sup> and experimental studies.<sup>[10–15]</sup> Atomic force microscopy (AFM) images a surface by scanning a sharp tip attached to a cantilever at a close distance to the surface.<sup>[16]</sup> AFM is the newest tool for liposome study because it provides nano-scale analysis of liposome shape and mechanical properties simultaneously. AFM provides surface topographical images with spatial resolution close to 1 Å and force-vs.-distance curves with detection limit close to  $10^{-12}$  N. AFM has become the preferred method for imaging soft materials such as molecular crystals, proteins, and living cells.<sup>[17]</sup> This entry describes new features of adsorbed vesicles by AFM investigation. AFM imaging and force measurement were conducted simultaneously in liquid on adsorbed but intact unilamellar vesicles with sizes less than 50 nm. The unilamellar vesicles were made by sonication from egg yolk phosphatidylcholine (EggPC) dispersion. The AFM tip can be moved on top of individual vesicles so that mechanical properties of the smallest vesicles can be measured at the nanometer scale. The EggPC vesicle undergoes reversible shape changes from convex to flattened and concave shape with increasing image force. In addition to the monotonic repulsion because of vesicle resistance to the AFM tip advancement and compression, there exist several characteristic breaks in the force-vs.-distance curves. Hertz analysis of the slope of repulsion gives a measure of vesicle elastic properties. The Young's modulus ( $E$ ) and the bending modulus ( $k_c$ ) of the adsorbed EggPC vesicles were measured to be  $(1.97 \pm 0.75) \times 10^6$  Pa and  $(0.21 \pm 0.08) \times 10^{-19}$  J, respectively. The breaks in the

force curve are interpreted as the tip jumping across the bilayer.

## AFM STUDIES OF ADSORBED VESICLES—LITERATURE REVIEW

Most AFM studies of adsorbed vesicles involve supported phospholipid bilayers (SPBs), with or without proteins, from ruptured and fused vesicles. Only a few articles addressed the structure of adsorbed yet unruptured vesicles. Shape instability, size, and softness of vesicles often prevent unambiguous AFM imaging. Perhaps the earliest images of intact liposomes were obtained by Shibata-Seki et al.<sup>[18]</sup> from dipalmitoyl phosphatidylcholine (DPPC) and cholesterol mixture. Others subsequently confirmed the characteristic features of adsorbed vesicles as first reported. The features include the following:

1. Flattened spheres with length/width ratio less than 1 (about 0.4 in their case); and
2. Image quality dependence on contact pressure either by changing image force or by using tips of different curvatures.

Egawa and Furusawa reported a conical relief image of sonicated phosphatidylethanolamine (PE) vesicles with a diameter around 100 nm adsorbed on its own bilayer.<sup>[19]</sup> The conical image was attributed to unruptured yet flattened vesicles with a height/diameter ratio of 0.175. Thomson et al.<sup>[20]</sup> imaged liposomes 70 nm in diameter made from *p*-ethylmyristoyl phosphatidylcholine (EDMPC) and cholesterol mixture on aminopropylsilane-modified mica. Closely packed liposomes were imaged but can be easily disturbed by the scanning process. The paper by Reviakine and Brisson<sup>[21]</sup> provided many details about vesicle adsorption and fusion by AFM imaging. In the entry, supported vesicular layer (SVL) was used to differentiate adsorbed and intact vesicles from adsorbed and single-bilayer disks as in SPBs. It was found that vesicles of all sizes adsorbed on mica, but only vesicles

with sizes below a critical rupture radius remained intact. The bilayer disks exhibited a constant height of 5 nm, whereas the intact vesicles exhibited a height variation from 10 to 40 nm. The shape of liposomes was found to change both with applied image force and adhesion between biotin and streptavidin, which were incorporated into the vesicle and substrate layer, respectively.<sup>[22]</sup> Kumar and Hoh<sup>[23]</sup> reported intact vesicles of phospholipid and cholesterol mixture that exhibited a saucerlike structure in addition to the usual rounded protrusion (domelike structure). The saucerlike structure was attributed to wetting and fusion near the edge of the vesicle. A force curve was obtained on the intact vesicle, which showed monotonic repulsion with onset at 15 nm. The flattening from the outer edges toward the center was studied as a function of time by Jass et al.<sup>[24]</sup> and was described as the first step in a multistep processes leading toward the formation of SPBs.

In addition to nanoscale imaging, AFM enables direct force measurements between the tip and the surface by moving an AFM tip up and down over one point on the sample surface. The force-vs.-distance curves on soft materials consist of not only surface interactions such as van der Waals, electrostatic, hydration, and steric forces before contact but also bulk mechanical properties of soft materials after contact.<sup>[25–27]</sup> By collecting force curves over the scanned area (the so-called force volume), a map of mechanical property variation can be generated in force volume imaging.<sup>[28]</sup> The Young's modulus of the Torpedo synaptic vesicles was calculated to be in the range of  $2\text{--}13 \times 10^5$  Pa by fitting the indentation part of the AFM force curve to the Hertz model.<sup>[25]</sup>

AFM studies offer new insights into the adsorption, spreading, fusion, and self-healing of liposomes. Compared with other micromechanical methods such as shape fluctuation method,<sup>[10–12]</sup> magnetic field-induced orientation,<sup>[13]</sup> and micropipette aspiration method,<sup>[14,15]</sup> AFM can provide information on the following:

1. Adsorbed liposomes of small sizes between 20 and 100 nm;
2. Mechanical property variation at nanoscale;
3. Local deformation and rupture events induced by the tip; and
4. Surface and adhesive forces.

AFM measurements focus on the properties of vesicle population with the smallest sizes because large vesicles rupture into bilayers on adsorption. Small liposomes with sizes between 50 and 150 nm were found to passively target several different tumors because this size range is a compromise among loading efficiency (which increases with increasing size), stability (which

decreases with increasing size), and the ability to extravasate in tissues with enhanced vesicular permeability (which decreases with increasing size).<sup>[3]</sup> Size control may be a simple way for targeted drug delivery because vesicle distribution among different organs and tissues is related to its size.

## AFM IMAGING AND FORCE MEASUREMENT ON UNILAMELLAR VESICLES

In our work, sonicated unilamellar EggPC vesicles with diameters less than 50 nm, adsorbed on mica, were studied by AFM liquid tapping and liquid contact mode imaging as well as direct force measurement. The AFM tip was moved on top of individual vesicles so that the mechanical properties of the smallest vesicles could be measured at the nanoscale. The EggPC vesicle underwent reversible shape changes from convex to flattened and concave shape with increasing image force. In addition to the monotonic repulsion because of vesicle resistance to AFM tip advancement and compression, there existed several characteristic breaks in the force-vs.-distance curves. Hertz analysis of the slope of repulsion gave a measure of vesicle elastic properties. The breaks in the force curve were interpreted as the tip jumping across the bilayer. We attempt to gain a clear understanding of various factors that may affect the stability and morphology of small unilamellar vesicles on adsorption. We aim at perfecting the method to measure the mechanical properties of the vesicles based on AFM approach and retraction force curves. We report the Young's modulus and the bending modulus of adsorbed vesicles extracted from AFM force curves by Hertz analysis. The results are compared with those obtained on giant vesicles.

## EXPERIMENTAL METHODS

We followed a well-established recipe to prepare sonicated unilamellar vesicles (SUVs).<sup>[4]</sup> EggPC with 99% purity was purchased from Sigma. Deionized water with a resistivity of 18 M $\Omega$ cm was obtained from a Barnstead Nanopure water purification system. Grade 2 muscovite ruby mica from United Mineral and Chemical was used as support for vesicles because it is molecularly smooth and hydrophilic. MLV solution was obtained by dissolving appropriate amounts of EggPC lipids in chloroform/methanol (2:1 vol/vol) and by evaporating the solvent with nitrogen. After drying in a desiccator connected to a rotary vacuum pump for 30 min, the lipids were resuspended by stirring them in an aqueous buffer solution (20 mM NaCl) at a concentration of 0.5 mg/mL. SUVs were produced

from the MLV suspension by sonication to clarity (about 1 hr) in a Branson 2200 bath sonicator. The suspension was kept in an ice bath during the sonication process. Sonicated samples were centrifuged for 1 hr at 16,000 rpm to remove large lipid fragments by Sorvall OTD70B Ultraspeed Centrifuge. SPBs were prepared via the extrusion method. Multilamellar EggPC solution was extruded through a polycarbonate membrane with an average pore size of 200 nm using a LiposoFast extruder from Avestin. The extrusion method produced larger vesicles that ruptured into bilayers on adsorption.

AFM imaging and force measurement were conducted using a Nanoscope IIIA atomic force microscope from Digital Instruments equipped with an E scanner with a maximum scan area of  $16 \times 16 \mu\text{m}^2$ . The scanner was calibrated following the standard procedures provided by the manufacturer. The fluid cell (Digital Instruments) was washed with deionized water, ethanol, and deionized water before each experiment. Freshly cleaved mica was mounted onto a stainless steel disk using a sticky tab. After the substrate was brought to a close distance from the AFM tip, the freshly prepared EggPC vesicle solution was injected through a silicone rubber tubing into the fluid cell, sealed by a silicone rubber O-ring. The EggPC vesicle solution was allowed to incubate on mica at room temperature for 1 hr. Excess vesicles were removed by flushing the fluid cell with buffer solution followed by pure water, and the images were obtained in pure water. The microscope was allowed to thermally equilibrate for 30 min before imaging. Scanning rates between 1 and 5 Hz were used. Room temperature was maintained at  $22 \pm 1^\circ\text{C}$ . Images were recorded in liquid contact mode or liquid tapping mode using standard silicon nitride ( $\text{Si}_3\text{N}_4$ ) integral tips (NP type).

All force curves presented here were obtained with the same AFM tip so that the force values can be directly compared. The radius of the contact tip ( $33.2 \pm 6.6 \text{ nm}$ ) was calibrated by imaging the TGT01 gratings (Mikromasch).<sup>[29]</sup> The spring constant of the cantilever was calibrated using the deflection method against a reference cantilever (Park Scientific Instruments) of known spring constant ( $0.157 \text{ N/m}$ ).<sup>[30]</sup> The calibrated spring constant ( $0.17 \pm 0.05 \text{ N/m}$ ) was used in all force curve calculations. Force curves were obtained in liquid contact mode only. Multiple force curves were obtained on the vesicle layer and on the bilayer. It was impossible to locate the tip exactly on top of the center of a vesicle. Therefore multiple force curves were obtained around a vesicle, and the force curve with the largest repulsion onset was selected. The time to record an approach and retraction force curve cycle was about 1 sec. The force calibration plot is converted to a force-vs.-distance plot by defining the point of zero force and the

point of zero separation.<sup>[31]</sup> Zero force is determined by identifying the region at a large separation, where the deflection is constant. Zero separation is determined from the constant compliance region at high force where deflection is linear with the expansion of the piezoelectric crystal. Both the approaching and retracting force curves are reported, unless otherwise specified.

To determine the elastic properties of SUVs, the force-vs.-distance curve was fitted to the Hertz model  $\delta = AF^b$ , where  $\delta$  is the indentation on the vesicle and  $F$  is the load force. The Young's modulus  $E$  can be calculated from  $A$  using the following equation:<sup>[25]</sup>

$$|z - z_0| - (d - d_0) = 0.825 \times \left[ \frac{k^2(R_{\text{tip}} + R_{\text{ves}})(1 - \nu_{\text{ves}}^2)^2}{E_{\text{ves}}^2 R_{\text{tip}} R_{\text{ves}}} \right]^{1/3} (d - d_0)^{2/3} \quad (1)$$

The indentation  $\delta$  equals the difference between the cantilever distance  $z - z_0$  and the cantilever deflection  $d - d_0$ , where  $z$  is the z-scan position,  $z_0$  is the contact point,  $d$  is the deflection of the tip, and  $d_0$  is the non-contact deflection. The Poisson's ratio of the vesicle  $\nu_{\text{ves}}$  was assumed to be 0.5. The calibrated cantilever spring constant  $0.17 \text{ N/m}$  was used as the value of  $k$ .  $R_{\text{tip}}$  and  $R_{\text{ves}}$  are the radii of the AFM tip and vesicle, respectively. Only data with indentations less than 10 nm were used in our calculations to ensure elastic behavior. The bending modulus  $k_c$  is deduced from the Young's modulus.<sup>[32]</sup>

$$k_c = \frac{Eh^3}{12(1 - \nu_{\text{ves}}^2)} \quad (2)$$

where  $h$  is the bilayer thickness.

The size distribution of vesicles in the solution was studied by dynamic light scattering (Nicomp 370 Autodilute Submicron Particle Sizer; Pacific Scientific). Polystyrene (diameter =  $32 \pm 1.3 \text{ nm}$ , Nanosphere TM size standards; Duke Scientific) was used as the calibration standard. The light scattering cell was from VWR Scientific. A He-Ne laser (wavelength =  $632.8 \text{ nm}$ ) was used. Data were taken at  $23^\circ\text{C}$ .

## RESULTS

### Imaging in Liquid Tapping vs. Liquid Contact Mode

Images of EggPC vesicles were obtained in both liquid contact mode and liquid tapping mode. Fig. 1 shows the amplitude and deflection images for liquid tapping



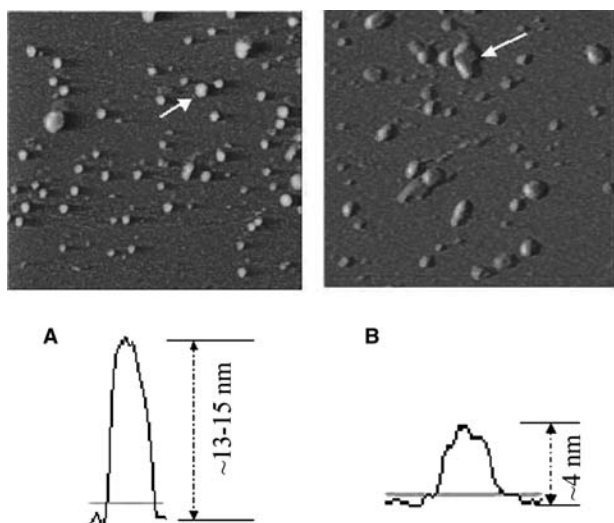


**Fig. 1** AFM images and cross-section profiles of EggPC vesicles on mica by tapping mode (A) and contact mode (B). The image size is  $1 \times 1 \mu\text{m}^2$ . The height profile belongs to the particle pointed by the arrow obtained in height image. (A) Amplitude image with  $z$ -scale = 20 nm. (B) Deflection image with  $z$ -scale = 5 nm.

and liquid contact, respectively, and the cross-sectional height profiles from the corresponding height images. The images consist of spherical objects on a flat background. The lateral width or diameter of the spheres was measured to be  $48.6 \pm 11.4$  and  $69.3 \pm 12.8$  nm on the sectional height profiles of tapping and contact, respectively. The diameter is taken from the width of the peak at the baseline in sectional height profiles. The lateral width values are higher than the vesicle diameter in solution ( $37.0 \pm 7.9$  nm), obtained by dynamic light scattering. The discrepancy is generally attributed to the flattening of vesicles on the surface

and the tip, casting its shadow over the object (the so-called tip convolution effect). The height of vesicles from sectional height profiles in tapping and contact mode was determined to be  $13.9 \pm 2.2$  and  $3.9 \pm 0.4$  nm, respectively. These values are consistent with previous studies<sup>[18,21,23]</sup>. The height value from tapping mode is about 40–50% of the vesicle diameter in solution. Causes for the unreasonably low height values from contact mode are postulated as follows:

1. Bound vesicles may move during contact mode imaging.
2. The vesicles are severely compressed by the tip.

The intermittent contact motion of the tapping tip is known to reduce frictional and adhesive forces on the sample surface. Our results show that by minimizing image force, it is possible to obtain stable images of unruptured vesicles in both liquid tapping and liquid contact mode. The vesicles were stable within 2 hr of observation, unless the area was repeatedly scanned. Tapping causes less deformation of the vesicle, and it can maintain a smaller image force than contact mode.

### Morphological Change of Vesicles

With increasing image force by decreasing the setpoint in tapping mode, EggPC vesicles exhibited three distinctive morphologies: convex-shaped vesicles, where the highest point is at the center, as shown in Fig. 2A; disk-shaped vesicles with uniform height across much of the vesicle, as shown in Fig. 2B; and concave-shaped vesicles, where the center is depressed, as shown in Fig. 2C. The lateral diameter of the vesicle increased from  $48.6 \pm 11.4$  nm for convex shape to  $73.7 \pm 11.5$  nm

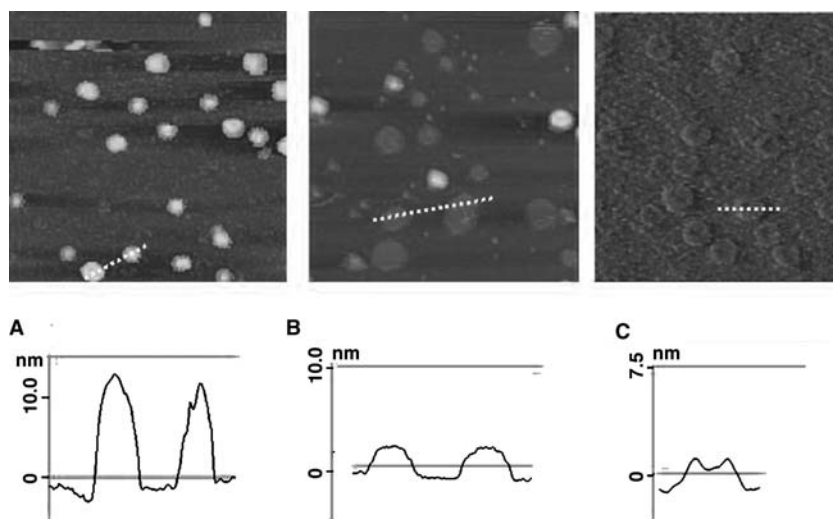


**Fig. 2** AFM height images obtained by tapping mode with different shapes. The image size is  $0.75 \times 0.75 \mu\text{m}^2$ .  $z$ -scale = 20 nm. The height profile across the dotted line is given. (A) Convex vesicles. (B) Planar vesicles. (C) Concave vesicles.

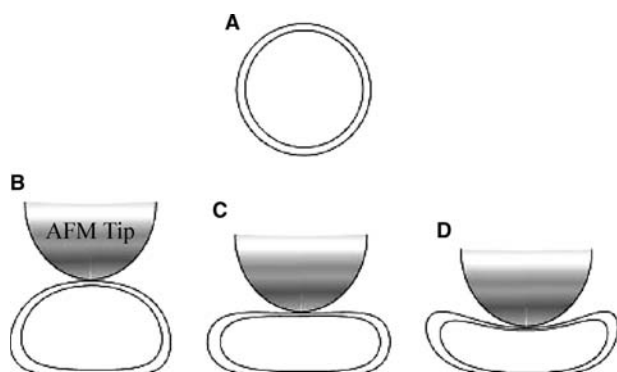


**Fig. 3** Tip compression scheme on vesicle morphology. (A) Vesicle in solution. (B) Convex vesicle imaged with minimum image force. (C) Planar vesicle imaged with intermediate indentation. (D) Concave vesicle imaged with the highest indentation.

for disk shape and to  $89.8 \pm 6.6$  nm for concave shape. The morphological change was reversible under varying image forces. The convex-shaped vesicles are similar to the conical relief and domelike structures in other studies.<sup>[19,23]</sup> The disk-shaped vesicles are similar to saucerlike vesicles.<sup>[23,24]</sup> There exists no prior report of concave-shaped SUVs by AFM, to the best of our knowledge. Although the saucerlike vesicles were cited as an intermediate state of vesicle fusion because of adhesion between the vesicle and the substrate, the morphological changes observed here could only be attributed to the compressive tip. The small size of the SUVs means that adhesion alone is not enough to collapse the vesicle edge to form saucerlike vesicles.<sup>[7]</sup> The morphological change because of tip compression is schematically illustrated in Fig. 3. A convex shape is obtained in the lowest indentation region of the force curve, a planar shape is obtained at an intermediate indentation, and a concave shape is obtained at the highest indentation. For the concave shape, when the tip moves across the vesicle with an

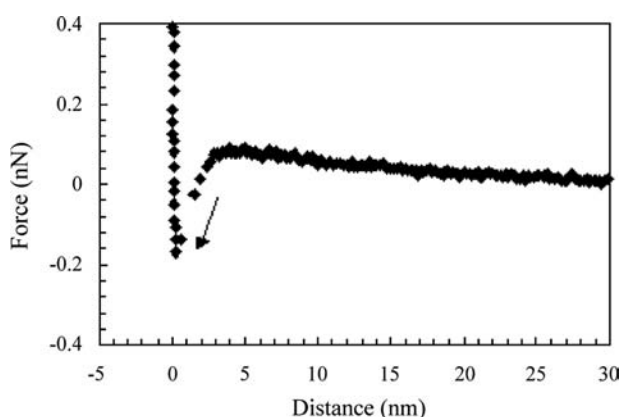


**Fig. 4** Force-vs.-distance curve in pure water between the tip and the mica during approach.

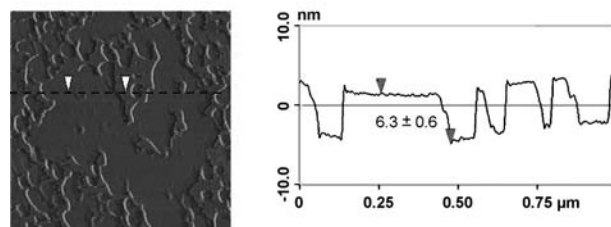
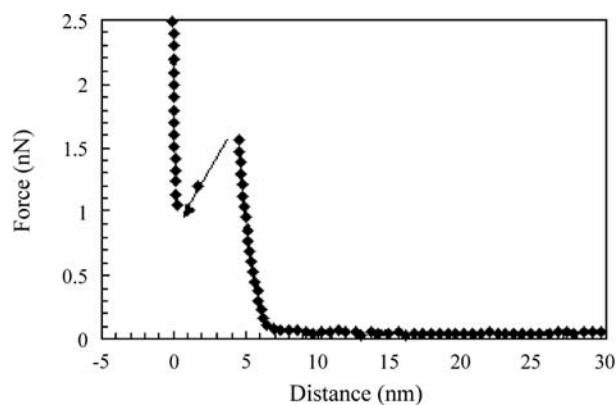


**Fig. 5** Force-vs.-distance curve and AFM amplitude image of EggPC bilayer patches. The arrow illustrates jump-in break. Section profile along the dotted line in the corresponding height image is shown. Scan size is  $1 \times 1 \mu\text{m}^2$ .  $z$ -scale = 20 nm.

applied force held more or less constant, the amount of indentation is largest at the center of the vesicle. Several factors may contribute to maximum depression at the center:

1. It is known that the mechanical response of thin films couples to the substrate, which results in an increase (50%) of the apparent modulus.<sup>[33]</sup> The coupling increases with decreasing film

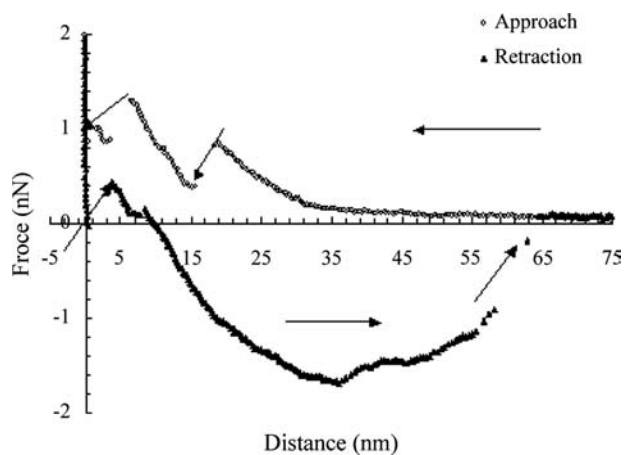


**Fig. 6** Force-vs.-distance curves on the EggPC vesicle. Two jump-in events during approach and two jump-out events during retraction are marked by arrows.

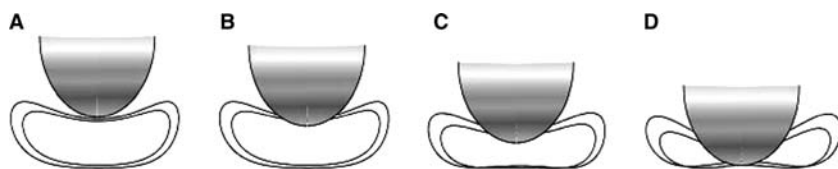


**Fig. 7** Scheme of the tip effect on vesicle during approach force measurement. (A) Elastic compression of vesicle top fraction. (B) Tip penetration of the upper bilayer. (C) Further compression with tip bridging the gap. (D) Tip penetration of the lower bilayer.

thickness. Therefore the tip indents more in the central region of a sessile droplet.

2. A high-volume percentage of material is bound by the surface near the edge of a droplet and spreads less on compression of the tip. Contrarily, at the center of the vesicle, less resistance exists against squeezing of the trapped liquid portion.

### Force Measurement on EggPC Vesicles

The force curve between the tip and the substrate was obtained in pure water as reference. Fig. 4 shows a weak and long-range repulsion with force maximum =  $0.11 \pm 0.02$  nN at separation =  $2.6 \pm 0.3$  nm, followed by a strong attraction with force minimum =  $-0.10 \pm 0.04$  nN just before contact. The discontinuity in the force curve, called the jump-in point, is because of an attractive force gradient exceeding the spring constant. The force profile, similar to reported ones, is attributed to electrostatic repulsion coupled to attractive van der Waals interaction.<sup>[34,35]</sup>

The force curves between the tip and the adsorbed vesicle layer were measured in pure water. To distinguish vesicles from bilayers, EggPC bilayer film was prepared by fusion of large extruded vesicles. Fig. 5A and B shows the force curve and image on the EggPC bilayer, respectively. Fig. 5A shows repulsion starting at  $6.6 \pm 0.4$  nm and a jump-in point at  $4.6 \pm 0.3$  nm with maximum force =  $1.8 \pm 0.3$  nN. This force curve agrees with previous force measurements on supported lipid bilayer films.<sup>[36,37]</sup> The sudden reduction in tip and substrate separation at jump-in corresponds to the removal of the bilayer segment from the gap, most probably by a lateral pushout mechanism. The maximum steric barrier was reported to be proportional to the surface excess of the film, and can be used to compare packing density within similar adsorption class.<sup>[38]</sup> The repulsion onset value coincides with thickness =  $6.3 \pm 0.6$  nm by AFM sectional analysis in Fig. 5B. The bilayer film thickness agrees with the hydrated bilayer thickness measured by x-ray diffraction.<sup>[39]</sup> The repulsion up to the jump-in point can be described as a combination of hydration, steric force, and mechanical deformation of bilayer films. The force curves measured on the lower, flat background in both extruded and sonicated

vesicle adsorption cases (not shown here) were similar to Fig. 4, without the distinct, short-ranged repulsion. It should be concluded that mica was not fully covered in either adsorption case.

Fig. 6 represents a typical force curve captured on vesicles. Although it is impossible to place the tip exactly at the center of the vesicle, the force curve with the largest onset repulsion distance was selected from a set of force curves obtained in the vicinity of a vesicle, and was used to represent the interaction between the apices of the AFM tip and the vesicle. The onset force distance = 32.2 nm in Fig. 6 falls in the range of measured vesicle sizes between 30 and 40 nm. The repulsion was not continuous, but displayed characteristic force breaks. During approach, one or two breaks were observed around 19 and 7 nm, respectively. Although the exact locations of the breaks varied somewhat, the gap distance between the beginning and the end point of the jump-in was constant at  $4.8 \pm 0.4$  nm. During retraction, a similar jump-out gap was also observed, although apparently not as well defined. This unique gap distance coincides with lipid bilayer thickness. We hypothesize that during approach, the bilayer portion at the top of the vesicle gives way to the pressing tip and slides aside, followed by continuous compression of the tip on the vesicle, until the tip approaches and breaks through the bottom portion of the bilayer enclosure. It is surprising that the vesicle maintains its enclosed shape, whereas the tip bridges

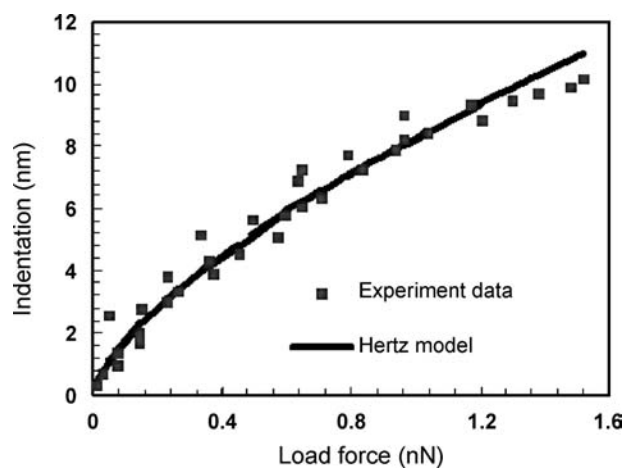


**Fig. 8** Indentation vs. load force for both experimental data and fit by the Hertz model.

**Table 1** Young's moduli of biological samples

Material	Young's modulus $E$ (MPa)	Method	Remarks	Reference
Synaptic vesicles	0.2–1.3	Force mapping	Size: 90–150 nm adsorbed on mica	[25]
DMPC/DOPC vesicles	15	Osmotic swelling	Size: 160–180 nm in solution	[40]
EggPC vesicles	$1.97 \pm 0.75$	Force plot	Size: < 60 nm adsorbed on mica	This work

DMPC = dimyristoylphosphatidylcholine; DOPC = dioleoylphosphatidylcholine.

across different parts of the bilayer shell. The stepwise deformation during approach is shown in Fig. 7:

1. Compression of vesicle
2. Breakthrough of top portion
3. Further compression of vesicle with tip bridging the top portion
4. Breakthrough of bottom portion with tip spanning the whole vesicle.

The process was reversed during retraction except that the vesicle was stretched to 150% of its intrinsic diameter before the final detachment of the tip from the vesicle. This adhesive interaction may also contribute to the shape stability of the vesicle bridged by the AFM tip. The force curves were repeated at the same spot, indicating that no permanent deformation occurred by tip breakthroughs. Vesicles are known to self-heal after perforation because of high line tension.

The initial slope in the approach force curve correlates to the local bending modulus of the vesicle, and therefore was used to calculate the Young's modulus of the adsorbed SUVs based on Hertz model, as in Eq. (1). The fit is shown in Fig. 8. The calibrated tip

radius value 33 nm was used for  $R_{\text{tip}}$ , and experimentally determined force onset distance  $z_0$  was used to calculate  $R_{\text{ves}} (= z_0/2)$ . The calculated Young's modulus is  $1.97 \pm 0.75$  MPa. Bending modulus is calculated (according to Eq. (2)) to be  $(0.21 \pm 0.08) \times 10^{-19}$  J, assuming that bilayer thickness  $h = 4.57 \times 10^{-9}$  m and Poisson's ratio  $\nu_{\text{ves}} = 0.5$ .

The calculated values are compared with literature values in Tables 1 and 2. The calculated Young's modulus for adsorbed SUVs is close to those measured on adsorbed synaptic vesicles between 0.2 and 1.3 MPa on mica.<sup>[25]</sup> The calculated value is one order of magnitude smaller than the value measured in solution by the osmotic pressure method (about 15 MPa).<sup>[40]</sup> The calculated value is affected by the choice of tip radius, spring constant, contact point, and liquid environment. The calculated bending modulus is in the same range as that reported in the literature, with different methods between  $10^{-20}$  and  $10^{-19}$  J (Table 2).<sup>[10–14,41–44]</sup> The variation in bending modulus values is attributed to the following:

1. Different experimental methods
2. Sample purity and

**Table 2** Comparison among bending moduli of EggPC obtained by different methods

Method	Shape (size)	Bending modulus $k_c$ ( $\times 10^{-19}$ J)	$T$ ( $^{\circ}\text{C}$ )	Reference
Phase contrast microscopy	Long unilamellar tubular vesicle ( $11\mu\text{m} < L < 34\mu\text{m}$ , $17 < L/r < 83$ )	$2.3 \pm 0.3$	22.0	[10]
	Cylindrical vesicle ( $>10\mu\text{m}$ )	1–2	25	[11]
	Quasi-spherical vesicle ( $>10\mu\text{m}$ )	1–2		[12]
	Spherical ( $>10\mu\text{m}$ )	0.4–0.5		[41,42]
Magnetic field-induced orientation	Cylindrical rods ( $5\text{--}30\mu\text{m}$ in diameter, $<200\mu\text{m}$ long)	0.4	25	[13]
A.C. electric field	Spherical vesicle (diameter $>20\mu\text{m}$ )	0.247		[43]
	Spherical vesicle ( $\sim 15\text{--}70\mu\text{m}$ in diameter)	$0.66 \pm 0.06$ , $0.45 \pm 0.05$		[44]
AFM force curve	Spherical vesicle (diameter $<60\text{nm}$ ) on mica substrate	$0.21 \pm 0.08$	$22 \pm 1$	This work

3. vesicle size
4. Surface-bound vs. free vesicles.

## CONCLUSION

This entry describes AFM imaging and force measurement on sonicated unilamellar EggPC vesicles whose diameter is less than 50 nm. AFM measurements on adsorbed vesicle layers on mica were conducted using liquid tapping and liquid contact mode. The small vesicles were remarkably stable and did not rupture under the scan conditions. The shape of the vesicle changed from a concave shape in the lowest indentation region of the force curve to a planar shape, and to a concave shape at higher indentations. The mechanical deformation of the vesicle was also apparent during force-vs.-distance measurements when a vesicle was gradually pressed against the AFM tip. The indentation curve converted from the force-vs.-distance curve was fitted to the Hertz spherical contact model to extract the Young's modulus of the vesicle. The calculated Young's modulus and the bending modulus of the small adsorbed vesicles are  $(1.97 \pm 0.75) \times 10^6$  Pa and  $(0.21 \pm 0.08) \times 10^{-19}$  J, respectively. The elastic constants are compared with literature values from various micromechanical tests of liposomes. The force curves showed various gaps with a fixed gap distance equal to the lipid bilayer thickness. These gaps are interpreted as an abrupt jump of the AFM tip across the top or bottom portion of the bilayer enclosure during approach and retraction. It can be inferred that the vesicle maintains its enclosed morphology during tip breaking by bridging the bilayer gaps. Adhesion between the tip and the cross-sectional contact of the bilayer is necessary for the apparent shape stability of penetrated vesicles. The retraction force curve and gaps need further mechanical analysis. The AFM method offers new insights into adsorption, spreading, fusion, self-healing, and mechanical properties of liposomes at the nanoscale. The AFM method may pave the way for incorporating genes, proteins, and medicines into specific cells and locations with molecular precision in drug delivery and gene therapy.

## ACKNOWLEDGMENTS

The authors acknowledge the National Science Foundation grant CTS-0221586 and the Petroleum Research Fund grants 36149-AC5 and 33036-ACS, administered by the American Chemical Society. The authors thank Jerome S. Jourdan at BASF (Wyandotte, MI) for help with the dynamic light scattering measurements.

## REFERENCES

1. Blumenthal, R.; Clague, M.J.; Durell, S.R.; Epanand, R.M. Membrane fusion. *Chem. Rev.* **2003**, *103*, 53–69.
2. Barenholz, Y. Liposome application: Problems and prospects. *Curr. Opin. Colloid Interface Sci.* **2001**, *6*, 66–77.
3. Lasic, D.D. Novel applications of liposomes. *Tibtech* **1998**, *16*, 307–321.
4. Huang, C.-H. Studies on phosphatidylcholine vesicles formation and physical characteristics. *Biochemistry* **1969**, *8*, 344–352.
5. Hope, M.J.; Bally, M.B.; Webb, G.; Cullis, P.R. Production of large unilamellar vesicles by a rapid extrusion procedure. Characterization of size distribution, trapped volume and ability to maintain a membrane potential. *Biochim. Biophys. Acta* **1985**, *821*, 55–65.
6. Lipowsky, R.; Seifert, U. Adhesion of membranes: A theoretical perspective. *Langmuir* **1991**, *7*, 1867–1873.
7. Seifert, U.; Lipowsky, R. Shapes of fluid vesicles. In *Handbook of Nonmedical Applications of Liposomes—Theory and Basic Sciences*; Lasic, D.D., Barenholz, Y., Eds.; CRC Press: Boca Raton, 1996; Vol. 1, 43–85. Chap. 2.
8. Svetina, S.; Žekš, B. Elastic properties of closed bilayer membranes and the shapes of giant phospholipid vesicles. In *Handbook of Nonmedical Applications of Liposomes—Theory and Basic Sciences*; Lasic, D.D., Barenholz, Y., Eds.; CRC Press: Boca Raton, 1996; Vol. 1, 1–42. Chap. 1.
9. Sackmann, E. Membrane bending energy concept of vesicle- and cell-shapes and shape-transitions. *FEBS Lett.* **1994**, *346*, 3–16.
10. Servuss, R.M.; Harbich, W.; Helfrich, W. Measurement of the curvature-elastic modulus of egg lecithin bilayers. *Biochim. Biophys. Acta* **1976**, *436*, 900–903.
11. Schneider, M.B.; Jenkins, J.T.; Webb, W.W. Thermal fluctuations of large cylindrical phospholipid vesicles. *Biophys. J.* **1984**, *45*, 891–899.
12. Schneider, M.B.; Jenkins, J.T.; Webb, W.W. Thermal fluctuations of large quasi-spherical bimolecular phospholipid vesicles. *J. Phys. (France)* **1984**, *45*, 1457–1472.
13. Sakurai, I.; Kawamura, Y. Magnetic-field-induced orientation and bending of the myelin figures of phosphatidylcholine. *Biochim. Biophys. Acta* **1983**, *735*, 189–192.
14. Evans, E.; Rawicz, W. Entropy-driven tension and bending elasticity in condensed-fluid membranes. *Phys. Rev. Lett.* **1990**, *64*, 2094–2097.
15. Waugh, R.E.; Song, J.; Svetina, S.; Žekš, B. Local and nonlocal curvature elasticity in bilayer membranes by tether formation from lecithin vesicles. *Biophys. J.* **1992**, *61*, 974–982.
16. Quate, C.F. The AFM as a tool for surface imaging. *Surf. Sci.* **1994**, *299/300*, 980–995.
17. Radmacher, M.; Tillmann, R.W.; Fritz, M.; Gaub, H.E. From molecules to cells: Imaging soft samples with the atomic force microscope. *Science* **1992**, *257*, 1900–1905.
18. Shibata-Seki, T.; Masai, J.; Tagawa, T.; Sorin, T.; Kondo, S. In-situ atomic force microscopy study of lipid

- vesicles adsorbed on a substrate. *Thin Solid Films* **1996**, *273*, 297–303.
19. Egawa, H.; Furusawa, K. Liposome adhesion on mica surface studied by atomic force microscopy. *Langmuir* **1999**, *15*, 1660–1666.
  20. Thomson, N.H.; Collin, I.; Davies, M.C.; Palin, K.; Parkins, D.; Roberts, C.J.; Tendler, S.J.B.; Williams, P.M. Atomic force microscopy of cationic liposomes. *Langmuir* **2000**, *16*, 4813–4818.
  21. Reviakine, I.; Brisson, A. Formation of supported phospholipid bilayers from unilamellar vesicles investigated by atomic force microscopy. *Langmuir* **2000**, *16*, 1806–1815.
  22. Pignataro, B.; Steinem, C.; Galla, H.-J.; Fuchs, H.; Janshoff, A. Specific adhesions of vesicles monitored by scanning force microscopy and quartz crystal microbalance. *Biophys. J.* **2000**, *78*, 487–498.
  23. Kumar, S.; Hoh, J.H. Direct visualization of vesicle-bilayer complexes by atomic force microscopy. *Langmuir* **2000**, *16*, 9936–9940.
  24. Jass, J.; Tjærnhage, T.; Puu, G. From liposomes to supported, planar bilayer structures on hydrophilic and hydrophobic surfaces: An atomic force microscopy study. *Biophys. J.* **2000**, *79*, 3153–3163.
  25. Laney, D.E.; Garcia, R.A.; Parsons, S.M.; Hansma, H.G. Changes in the elastic properties of cholinergic synaptic vesicles as measured by atomic force microscopy. *Biophys. J.* **1997**, *72*, 806–813.
  26. Weisenhorn, A.L.; Khorsandi, M.; Kasas, S.; Gotzos, V.; Butt, H.-J. Deformation and height anomaly of soft surfaces studied with an AFM. *Nanotechnology* **1993**, *4*, 106–113.
  27. Vinckier, A.; Semenza, G. Measuring elasticity of biological materials by atomic force microscopy. *FEBS Lett.* **1998**, *430*, 12–16.
  28. Heinz, W.F.; A-Hassan, E.; Hoh, J.H. *Applications of Force Volume Imaging with the NanoScope Atomic Force Microscope Application Note No. 20*; Digital Instruments, 1998. See also references therein.
  29. Villarrubia, J.S. Algorithms for scanned probe microscope image simulation, surface reconstruction, and tip estimation. *J. Res. Natl. Inst. Stand. Technol.* **1997**, *102*, 425–454.
  30. Tortonese, M.; Kirk, M. Characterization of application specific probes for SPMs. *SPIE* **1997**, *3009*, 53–60.
  31. Prater, C.B.; Maivald, P.G.; Kjoller, K.J.; Heaton, M.G. *Probing Nano-scale Forces with the Atomic Force Microscope, Application Note No. 8*; Digital Instruments, 1995. See also references therein.
  32. Evans, E.A. Bending resistance and chemically induced moments in membrane bilayers. *Biophys. J.* **1974**, *14*, 923–931.
  33. Domke, J.; Radmacher, M. Measuring the elastic properties of thin polymer films with the atomic force microscope. *Langmuir* **1998**, *14*, 3320–3325.
  34. Teschke, O.; de Souza, E.F.; Ceotto, G. Double layer relaxation measurements using atomic force microscopy. *Langmuir* **1999**, *15*, 4935–4939.
  35. Dong, J.; Mao, G. Direct study of C12E5 aggregation on mica by atomic force microscopy imaging and force measurements. *Langmuir* **2000**, *16*, 6641–6647.
  36. Franz, V.; Loi, S.; Müller, H.; Bamberg, E.; Butt, H.-J. *Colloids Surf., B* **2002**, *23*, 191–200.
  37. Defrêne, Y.F.; Boland, T.; Schneider, J.W.; Barger, W.R.; Lee, G.U. Characterization of the physical properties of model membranes at the nanometer scale with the atomic force microscope. *Faraday Discuss.* **1998**, *111*, 79–94.
  38. Eskilsson, K.; Ninham, B.W.; Tiberg, F.; Yaminsky, V.V. Effects of adsorption of low-molecular-weight triblock copolymers on interactions between hydrophobic surfaces in water. *Langmuir* **1999**, *15*, 3242–3249.
  39. McIntosh, T.J.; Magid, A.D.; Simon, S.A. Steric repulsion between phosphatidylcholine bilayers. *Biochemistry* **1987**, *26*, 7325–7332.
  40. Hantz, E.; Cao, A.; Escaig, J.; Taillandier, E. The osmotic response of large unilamellar vesicles studied by quasielastic light scattering. *Biochim. Biophys. Acta* **1986**, *862*, 379–386.
  41. Faucon, J.F.; Mitov, M.D.; Méléard, P.; Bivas, I.; Bothorel, P. Bending elasticity and thermal fluctuations of lipid membranes. Theoretical and experimental requirements. *J. Phys. (France)* **1989**, *50*, 2389–2414.
  42. Engelhardt, H.; Duwe, H.P.; Sackmann, E. Bilayer bending elasticity measured by Fourier analysis of thermally excited surface undulations of flaccid vesicles. *J. Phys. Lett. (France)* **1985**, *46*, L395–L400.
  43. Kummrow, M.; Helfrich, W. Deformation of giant lipid vesicles by electric fields. *Phys. Rev., A* **1991**, *44*, 8356–8360.
  44. Angelova, M.I.; Soléau, S.; Meleard, Ph.; Faucon, J.F.; Bothorel, P. Preparation of giant vesicles by external AC electric fields, kinetic and applications. *Prog. Colloid Polym. Sci.* **1992**, 127–131.



# Liquid Crystals and Nanostructured Surfaces: Detecting Protein Binding

Yan-Yeung Luk

Department of Chemical Engineering, University of Wisconsin–Madison,  
Madison, Wisconsin, U.S.A.

## INTRODUCTION

Studies of nanometer-scale phenomena represent one of the most flourished areas in science at the beginning of 21st century.<sup>[1]</sup> While the early activities have focused on fabricating well-defined nanomaterials and their novel properties, few have demonstrated a workable functional principle that can be developed into tangible applications. On the other hand, the protein binding events that orchestrate the biological activities in living cells (so-called cell signaling pathways (occur at nanometer scale. [Scheme 1](#) shows a schematic representation of the complexity of one of such signaling pathway. The protein binding events can be first induced at membrane proteins by either a physical or chemical signal or an internal stimulus such as hormone.<sup>[2]</sup> The dimerization or phosphorylation of membrane proteins leads to a series of protein binding events in the cytosol. The final binding event in the cytosol may lead to the transport of a protein into the nucleus that induces gene expression to produce a new protein. The new protein expressed signals a biological response in the form of new activities, such as cell death, proliferation, disease, or expression of white blood cells.

Deciphering the protein binding events in such complicated and interconnected signaling pathway will lead to molecular-level understanding of the physiology of living system as well as drug design. However, the scope of the problem demands a rapid and global approach. Because the quantity of protein involved on chip-based assay is little and the detection scheme can be highly parallel, surface-based proteomics tools have the potential to increase the rate of discovery and the scope of investigations aimed at understanding protein function, modification, and regulation in cell signaling processes as well as the study of protein–drug interactions.<sup>[3,4]</sup>

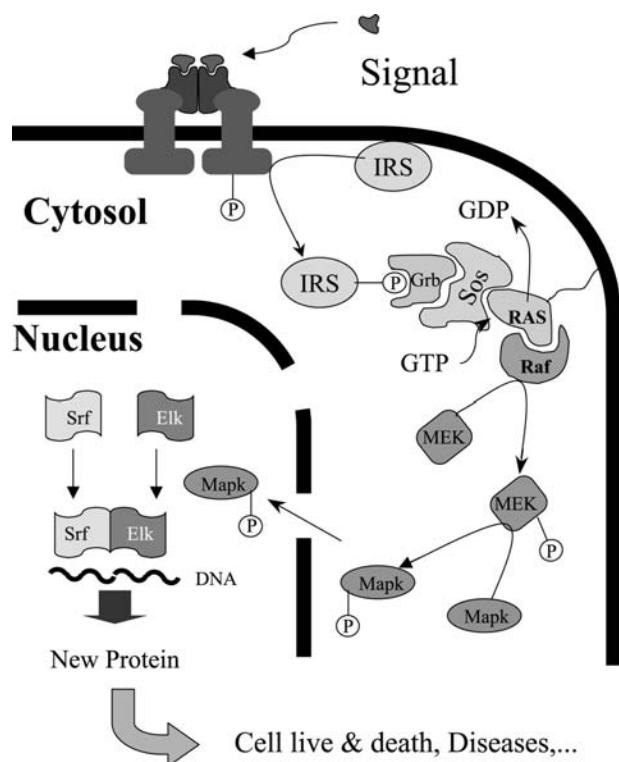
This entry describes a new detection method for protein binding events by using a well-controlled nanotopography on surface and the unique optical properties (birefringence) of liquid crystals. The development of this method integrated knowledge from multiple disciplines including self-assembled monolayers (SAMs),

liquid crystals, protein immobilization, and molecular biology. In the following, the effect surface topography and chemistry on the alignment of liquid crystal is first investigated. Then, the influence of surface-bound proteins on the alignment of liquid crystal is reported. Establishing the response of liquid crystal to surface-bound protein, a general scheme is designed to support biospecific protein binding on surface. Last, the binding activities of the immobilized protein on nanostructured surface toward specific and non-specific antibodies are detected by the molecular organization (orientations) of liquid crystals in contact with the surfaces where binding occurs.

## BACKGROUND

Self-assembled monolayers (SAMs) of alkanethiols on gold provide a class of versatile substrates for biological studies.<sup>[5]</sup> This class of surfaces is particularly useful because of several unique properties. First, monolayer formed from alkanethiols on gold substrate presents a structurally well-defined surface. Second, because of the powerfulness of organic synthesis developed over the past decades, almost any desired organic compound (including alkanethiols) could be synthesized so long as the compound is stable under condition of application. Hence a vast variety of functional groups can be presented on surfaces to tailor the surface chemistry at desire. [Scheme 2](#) shows the functionalized alkanethiols used in this review and a schematic representation of the SAMs. Recently, SAMs that resist protein adsorption and cell attachment are also developed providing a class of model surfaces for studying specific interactions of proteins and cells.

Liquid crystal is a delicate phase of materials that existed in between crystal and liquid.<sup>[6]</sup> This phase has the fluidic property of a liquid crystal and, at the same time, has the optical property of a crystal. The coexistence of these properties in liquid crystals rises from the orientational order of molecules. This orientational order gives each molecule a preferred orientation relative to each other that is absent in an isotropic liquid, while each molecule in liquid crystal



**Scheme 1** A schematic presentation of cell signaling pathway from cell membrane to nucleus.

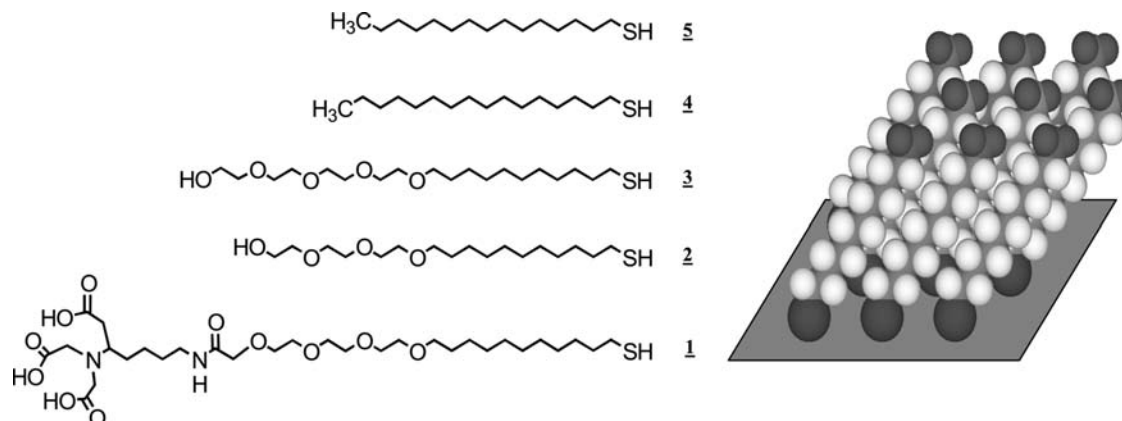
still bears the translocation freedom. Thus all the terms used for characterizing crystals such as packing, defect, and symmetry elements are also applicable to liquid crystal. Hence the texture of a liquid crystal, which reflects the organization of the mesogens and the degree of order in the bulk of the liquid crystal, can be readily viewed under a polarizing microscope. Based on the detailed molecular organization in the phase, liquid crystals are further classified into smectic (layer-like), nematic (thread-like), and discotic (disk-like).

**Scheme 3** demonstrates a schematic representation of the organization of a crystal, a smectic, a nematic liquid crystal, and an isotropic liquid. One character that is common to both crystal and liquid crystal is the almost ubiquitous existence of defects. These defects disrupt the local organization of molecules (or atoms in the case of crystals) preventing the crystal or liquid crystal from forming a perfect crystal. However, one of the most exquisite phenomena in liquid crystals is that the orientational order can transmit up to  $100\ \mu\text{m}$  or  $10^6$  before being disrupted by defects.

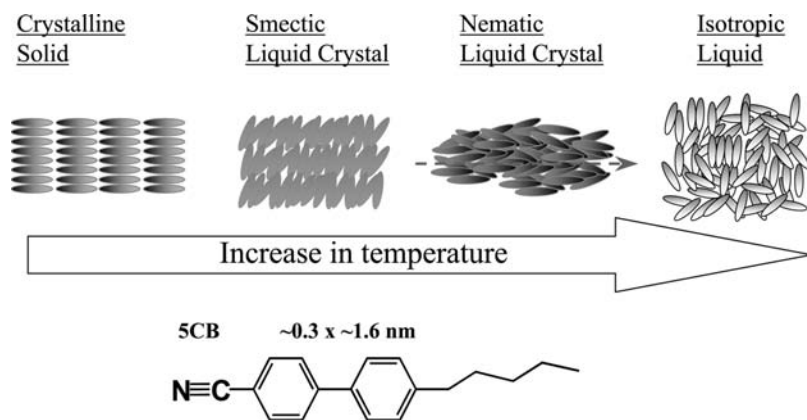
An implicit, but aptly useful aspect of the transmission of this orientational order of liquid crystals is that it bridges and amplifies the interactions at molecular level to micrometer-scale phenomena. Because most of the biological interactions occur at nanometer scale, and liquid crystalline phases exist ubiquitously in the membranes of cells, liquid crystals and biological systems share common characters such as they both break the symmetry of isotropy and bear structural order to different extent. In this entry, this unique property of orientational order in liquid crystal is explored to form the basis for a new detection scheme for protein binding events on nanostructured surfaces.

## NANOSTRUCTURED SURFACES

Vapor deposition of gold atoms on surfaces in high vacuum ( $\sim 10^{-7}$  to  $10^{-8}$  Torr) leads to polycrystalline gold films.<sup>[7]</sup> This polycrystalline gold film is particularly useful because it supports the self-assembly of alkanethiols that form well-organized monolayers with well-defined structure.<sup>[8]</sup> The exact detailed structure of these monolayers is still much in research, but it is generally known that the alkanethiols complex with surface at the (1,1,1) facet of the polycrystalline gold forming a two-dimensional crystalline with each



**Scheme 2** Chemical structure of alkanethiols used for protein immobilization and controls experiments, and a schematic presentation of the two-dimensional crystallinity of the SAMs.



**Scheme 3** Molecular order in different state of matter.

alkanethiol tilted  $30^\circ$  from the normal of the surface.<sup>[9]</sup> This well-organized and close-packed structure of alkanethiols on gold is absent from other monolayers. For example, on silica surface, the monolayer structure formed by alkyl silane is not close-packed and is poorly organized because of the large spacing between each alkyl silane.

Abbott et al.<sup>[7,10]</sup> further discovered that different experimental setups of the deposition of gold atoms also lead to subtle but significant topographical structures in the gold films. Fig. 1 demonstrates three different experimental setups of the deposition of gold

atoms that lead to different topography at nanometer scale on surfaces. These three different depositions are named as uniform deposition (Scheme 4A and B), oblique deposition (Scheme 4C and D),<sup>[7]</sup> and gradient deposition (Scheme 4E and F).<sup>[10]</sup> By uniform deposition, the substrates are positioned normal to the incidence of gold atoms, and the substrates are rotating during the time period of deposition. In this mode of deposition, the topography on the surface of the gold film is uniform or isotropic. By oblique deposition, the substrates are positioned at an oblique angle relative to the incidence of the gold atoms (Scheme 4C and D). In this mode of deposition, the gold atoms “hit” the substrate at a fixed oblique angle. Thus the surface features (topography) on the gold film parallel and perpendicular to the direction of gold deposition are no longer degenerate.

To characterize the gold films at a resolution of nanometer scale, Skaife and Abbott<sup>[11]</sup> applied atomic force microscopy (AFM) to sample the topography of the gold surfaces. Fig. 1A is an AFM micrograph showing the surface features of a gold film deposited at an angle of incidence of  $45^\circ$  measured from normal of the substrate. A coarse inspection of Fig. 1A indicates that the surface is rough and consisted of grains of gold crystalline with diameters of roughly 25 nm. However, by mere visual inspection of AFM micrograph, no anisotropy (or difference) can be observed in the texture/roughness between the direction parallel and perpendicular to the gold deposition.

To characterize the roughness quantitatively, Skaife and Abbott measured the contour lengths across a family of directions relative to the direction of gold deposition with different sample lengths. Fig. 1B shows an example of the cross-section profile of the roughness scanning across the direction parallel to the direction of gold deposition. The total length of this cross-section profile represents the contour length of the topography on the surface and thus a direct measure of the surface roughness. A long contour length implies high roughness and vice versa. The measured

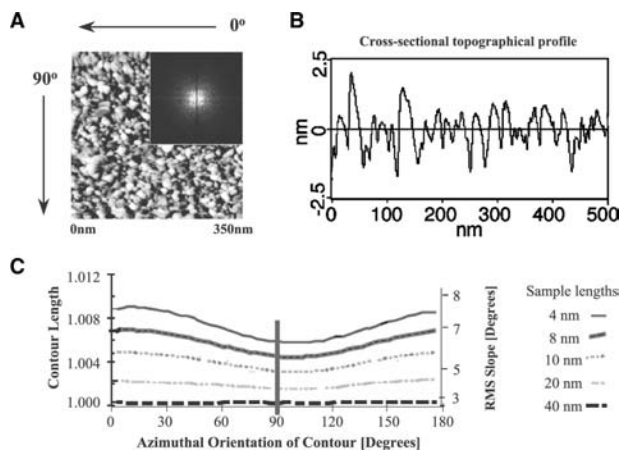
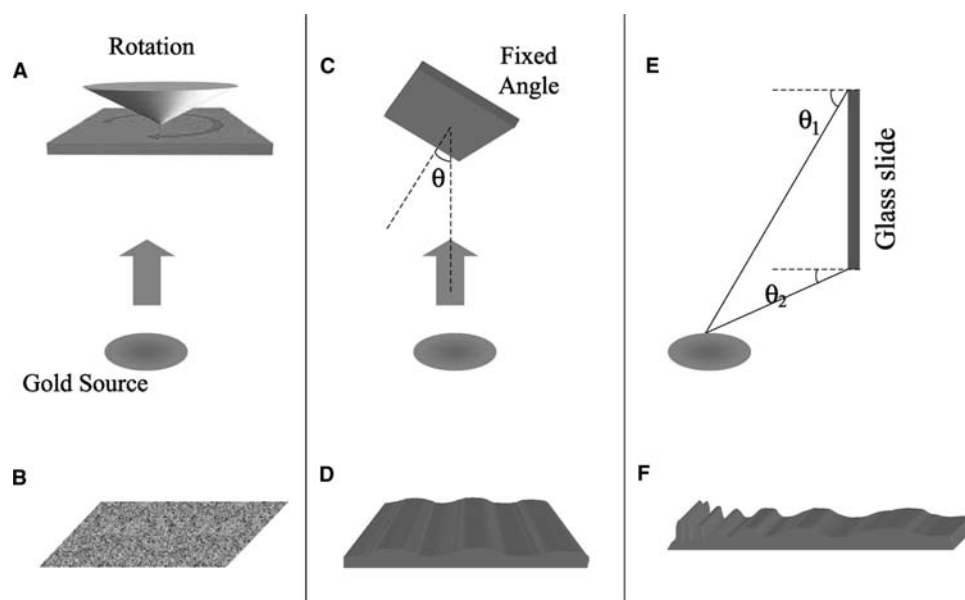


**Fig. 1** (A) Image ( $350 \times 350 \text{ nm}$ ) of an obliquely deposited film of gold obtained by AFM with the direction of deposition parallel to the scanning direction. The insets are fast Fourier transforms of the real-space images. The gray scale of contrast in the real-space images corresponds to a variation in height ( $z$ -axis) of 8 nm. Note that  $0^\circ$  denotes a direction parallel to the direction of gold deposition, and  $90^\circ$  denotes a direction perpendicular to the direction of gold deposition. (B) Cross-sectional topographical profile of the obliquely deposited gold film in (A). (C) Contour lengths calculated from AFM images of obliquely deposited films of gold shown in (A). Sampling lengths are 4, 8, 12, 20, and 40 nm. Source: From Ref.<sup>[11]</sup>.



**Scheme 4** Setups for vapor deposition of ultra-thin gold films by electron beam evaporator.

contour length (roughness) of the surface, however, depends on the dimension of the sample length that is used to measure the surface roughness. Similar to a ruler, if the sample length is much larger than the surface features, each measurement will cover multiple surface features (grains) and thus no longer measure the roughness on the surface. Fig. 1C plots a family of the contour lengths across different directions on the topography of an obliquely deposited gold film with different sample lengths ranging from 4 to 40 nm. The measured contour lengths increase with decrease in the sample lengths. This is consistent with the fact that a small sample length measures more the roughness at nanometer scale. However, more importantly, with small sample lengths (4 to 12 nm), the contour lengths are longer in the direction parallel to the gold deposition than perpendicular to the gold deposition. This anisotropy in the topography of obliquely deposited gold films starts to vanish when the sample lengths reach around 30 to 40 nm. This result indicates that the topography of surface on an obliquely deposited gold film bears a maximum roughness in the direction parallel to the direction of gold deposition and a minimum roughness in the direction perpendicular to the direction of gold deposition. Because the amplitude of the roughness is approximately 1 to 2 nm (Fig. 1B) and the anisotropic roughness appears on a minimum length scale of roughly 30 to 40 nm, the anisotropic topography can be idealized as a corrugation with the amplitude of 1–2 nm and the wavelength of 30–40 nm.

By gradient deposition, a substrate of 7 cm in length is positioned at an oblique angle close to the source of the gold atoms (Scheme 4E and F). Because at close proximity to the gold source, the oblique angle of gold

deposition onto the surface varies along the substrate following a simple equation:

$$\theta = \arctan[(x + b)/a]$$

where  $\theta$  is the oblique angle of incidence of gold atoms measured from normal,  $x$  is the position on the substrate measured from the bottom of the substrate,  $b$  is the vertical distance measured from the bottom substrate to the level of the gold source, and  $a$  is the horizontal distance measured from the horizontal position of the substrate to the gold source. In this mode of deposition, because the angle of deposition changes gradually and continuously along the substrate, a gradual and continuous change (gradient) in the anisotropic topography is created in the gold film.<sup>[10]</sup>

#### EFFECT OF ANISOTROPIC TOPOGRAPHY ON LIQUID CRYSTAL ALIGNMENT

While the anisotropy in the topography of the gold film prepared by oblique deposition (or gradient deposition) is subtle, it affords drastic effect on the alignment of liquid crystals. Studies using nematic liquid crystals show that when brought in contact with surfaces that do not have an anisotropic topography, nematic phase such as 4-cyano-4'-pentylbiphenyl (5CB) adopts random orientations on surfaces.<sup>[7]</sup> However, when brought in contact with anisotropic topography of gold films by oblique deposition, 5CB assumes a uniform orientation with the principal (long) axis of the mesogens lying in an azimuthal direction parallel to the direction of minimum roughness of

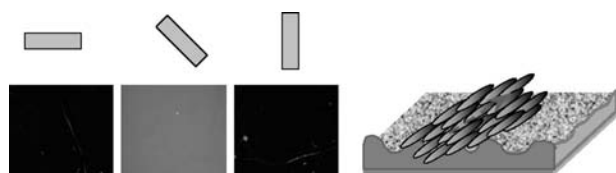


**Fig. 2** Optical appearance (crossed polars) of 5CB sandwiched between two obliquely deposited gold films with Saran wrap ( $12\ \mu\text{m}$ ). Both gold films were the direction of gold deposition parallel to each other. The orientation of the sample relative to one of the cross polars is indicated below the liquid crystal image. A schematic representation of the azimuthal orientation of the liquid crystal with respect to the topography is shown to the right. *Source:* From Ref.<sup>[15]</sup>.

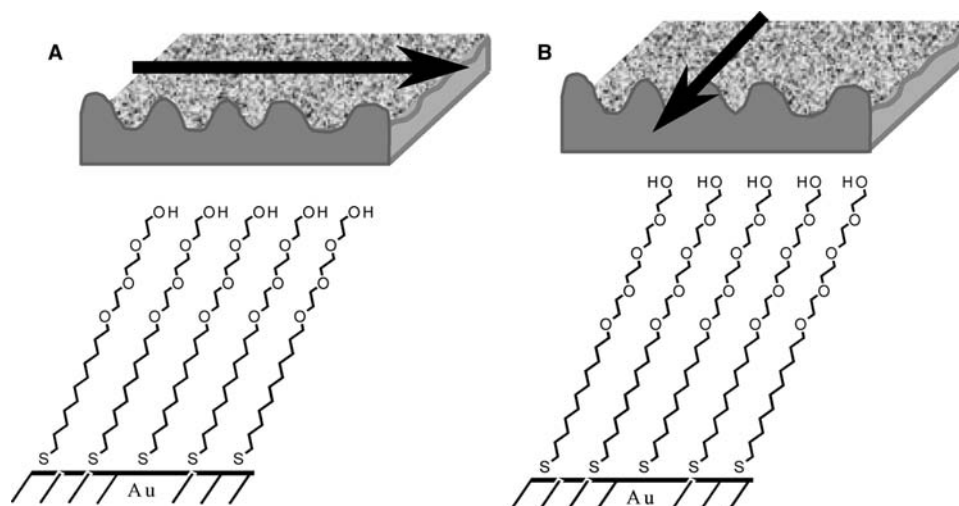
the anisotropic topography (Fig. 2).<sup>[7]</sup> This uniform orientation represents a single crystal without any defects giving a uniform texture under the polarizing microscope. Furthermore, much like a single solid crystal, liquid crystal with uniform orientation modulates the intensity of the polarized light with maximum extinction when the director of the liquid crystal is perpendicular to either one of the crossed polarizers, and minimum extinction with the director is  $45^\circ$  relative to either one of the crossed polarizers.

## EFFECT OF SURFACE CHEMISTRY ON LIQUID CRYSTAL ALIGNMENT

The mechanistic origin of the uniform orientation and azimuthal direction of the principle axis of liquid crystal as a result of such small, subtle anisotropy in the nanometer-scale topography is not entirely understood and is still the subject of on-going research. However,

the orientation of mesogens is known to minimize the elastic distortion within the liquid crystal when brought in contact with a surface. In general, it is most stable for the azimuthal direction of the principal axis in the uniform orientation of liquid crystal to lie in the direction of minimum roughness of the topography. It is important to note that the next energetic minimum (a metastable one) for liquid crystal alignment is actually the uniform orientation with the azimuthal alignment in the direction of *maximum* roughness. The energetic difference between the two azimuthal alignments is small, ca.  $0.015\ \text{mJ m}^{-2}$ .<sup>[11]</sup> Hence the azimuthal alignment of the uniform orientation turns out to be highly sensitive to the molecular details (and chemical functionality) of the monolayers of alkanethiols assembled on obliquely deposited gold film. For example, on obliquely deposited gold films, 5CB aligns in the azimuthal direction of minimum roughness on SAMs formed from pentadecanethiol, but aligns in the azimuthal direction of maximum roughness on SAMs formed from hexadecanethiols.<sup>[12]</sup> The subtle difference between the two SAMs is only the orientation of the terminal methyl groups at the surface of each monolayer.

A more important class of SAMs is oligo(ethylene glycol)-terminated alkanethiols on gold substrate (Scheme 5). Monolayers formed from these alkanethiols are particularly useful for biological researches and applications because they resist the non-specific adsorption of proteins and adhesion of cells.<sup>[13]</sup> The structure and dynamics of this class of SAMs are believed to be intimately related to their ability to resist protein adsorption and cell adhesion and thus are under intense research.<sup>[14]</sup> While methyl-terminated SAMs are well organized, the



**Scheme 5** Azimuthal orientation (indicated by arrow) of the uniform planar alignment of 5CB on oligo(ethylene glycol)-terminated SAMs.

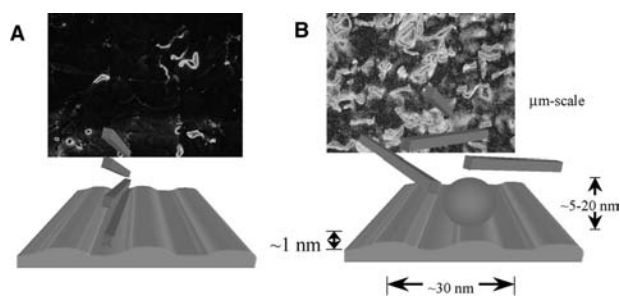


conformational homogeneity and flexibility of the terminal ethylene glycol groups are not definitely known.

Interestingly (and luckily), 5CB aligns uniformly on oligo(ethylene glycol)-terminated SAMs supported by gold films possessing an anisotropic topography (obliquely deposited at  $40^\circ$  measured from normal of the glass substrate). Furthermore, when supported on obliquely deposited gold films (Scheme 5B), 5CB aligns in the azimuthal direction of maximum roughness on tri(ethylene glycol)-terminated SAM (Scheme 5A), but aligns in the azimuthal direction of minimum roughness on tetra(ethylene glycol)-terminated SAMs.<sup>[15]</sup> This result is both significant and useful. First, it indicates that the oligo(ethylene glycol)'s are largely well organized at surface in contact with an organic phase (5CB) and thus shed light for the large effort of probing the structure of oligo(ethylene glycol) at surface. Because bare gold films uniformly align the nematic phase of 5CB in the azimuthal direction of minimum roughness, the azimuthal orientation observed on the surfaces covered with tri(ethylene glycol)-terminated SAMs suggests that molecular-level interactions between the SAMs and 5CB are important in determining the alignment of 5CB. Second, the uniform alignment of liquid crystals on these oligo(ethylene glycol)-terminated monolayers provides a great potential for combining use of liquid crystals with surfaces that supports exclusively bio-specific interactions.

## DETECTION OF PROTEINS BY MASKING THE TOPOGRAPHY

Because the sizes and dimensions of many proteins (5–20 nm in their longest dimension) are comparable to the spatial scale of the nanometer-scale topography of the obliquely deposited gold films, proteins bound to surfaces can mask or erase the topography of the surface. The uniform alignment of liquid crystal, on SAMs not supporting bound protein, can be disrupted by the presence of bound protein (Scheme 6).<sup>[16]</sup> The



**Scheme 6** Illustration of detection scheme for protein on nanostructured surfaces by the use of liquid crystals.

non-uniform alignment of the liquid crystal is readily distinguished from the uniform alignment by using polarized light microscopy. It should be noted that this scheme of detecting proteins on surface is direct and does not require any secondary interactant or labeling.

The magnitude of the anisotropy within the topography of the gold films depends on the oblique angle of deposition of the gold atoms.<sup>[17]</sup> At higher oblique angle (measured from normal of the substrate) of deposition, the magnitude of the anisotropy between the direction parallel and perpendicular to the direction of gold deposition is higher. By bringing the silica substrates closer to the source of gold for deposition, the end of the substrate that are farther from the gold source will have a larger oblique angle than the end of the substrate that are closer to the gold source (Scheme 4E). Thus a gradient in the anisotropy of the topography is created across the substrate. With this gradient in the topography, protein adsorbed on surface will mask the topography with low anisotropy to greater extent than the topography with high anisotropy.<sup>[10]</sup> An idealized representation of protein adsorbed on surface with gradient in the topography is shown in Fig. 3A.

Fig. 3B shows optical images of liquid crystal cell comprised of 5CB in contact with protein BSA adsorbed on gold film (7 cm in length) with gradient in topography. Two distinct regions are observed in Fig. 3B. First, in regions of the gold film deposited at  $56^\circ$  (gold thickness of  $\sim 13$  nm), BSA masks the topography of the surface resulting in nonuniform alignment of the liquid crystal. When the alignment of the liquid crystal is nonuniform, there is little modulation in the optical appearance of the liquid crystal when it is rotated between crossed polarizers. Second, in regions of the gold film deposited at  $63^\circ$  (gold thickness of  $\sim 7$  nm), the liquid crystals are uniformly oriented in contact with BSA on the surface. While the liquid crystal image is distinct in either region of the surface, the presence of the adsorbed BSA is confirmed by ellipsometry.<sup>[10]</sup> This result suggests that protein (BSA) adsorption on surface sufficiently masks the region of low anisotropy causing a nonuniform alignment of 5CB. But the topography of the gold film with high anisotropy is sufficiently pronounced that adsorption of BSA can no longer mask the topography that orients the liquid crystal. Furthermore, it indicates that the topography of the gold film can be adjusted by choosing particular angles of deposition for optimal reporting of the presence of protein on nanostructured surfaces.

This gradual change in the liquid crystal orientation represents continuous transformations in the orderliness, uniformity, and symmetry across the solvent structure at the interface. The essence of this transformation is demonstrated by the artwork by M.C.



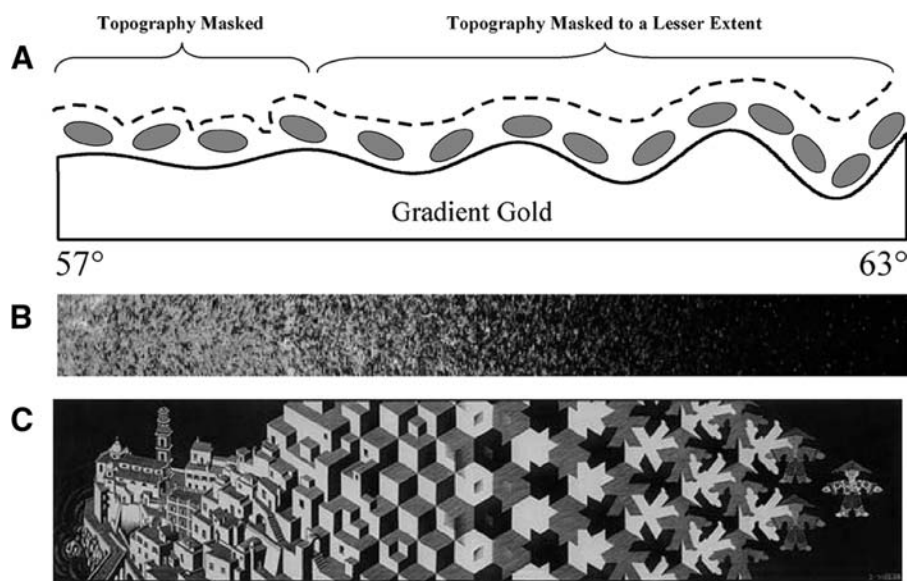


**Fig. 3** (A) Schematic representation of protein bound on surface with gradient topography. The extent of masking of the topography is indicated above the image. (B) Optical appearance (crossed polars) of liquid crystal sandwiched between two gold films supporting BSA. Both gold films were deposited at an angle of incidence that changes from 56.5° to 63.5° across the length of the slide. The image shows the entire length of a microscope slide. (C) The artwork “transformation” by M.C. Escher. Source: From Ref.<sup>[10]</sup>.

Escher (Fig. 3C). It is worth noting that while the artwork itself does not bear any specific scientific implication, the idea behind transcends across multiple areas in science from liquid crystal orientation on nanostructured surfaces (demonstrated here) to proposed Kibble mechanism in cosmology.<sup>[18]</sup>

### PROTEIN BINDING VIA NTA–Ni(II) HIS-TAG COMPLEXATION

Immobilization of oriented proteins and rapid detection of specific binding events on surfaces are two key challenges for surface-based proteomics tools. Conventional surface-based protein assays such as enzyme-linked immunoassays (ELISA) have typically relied upon rudimentary surface chemistries, such as the use of hydrophobic surfaces to promote antibody adsorption.<sup>[19]</sup> Adsorption of BSA is also often used to minimize non-specific adsorption. The nanometer-scale structure of surfaces used in conventional surface-based proteins assays is not typically controlled. Recently, however, advances have been reported on both fronts. First, surfaces with well-defined chemical functionalities have been reported for biological studies. These surfaces use self-assembled monolayers (SAMs) of  $\omega$ -functionalized alkanethiols on gold to oligo(ethylene glycol)<sup>[13]</sup> or polyol groups<sup>[20]</sup> that have been demonstrated to resist nonspecific protein adsorption and cell attachment. Second, preparation of surfaces with anisotropic nanometer-scale topography and the opportunities of using this topography in combination with liquid crystals on biological assays have also been reported.<sup>[12,21,22]</sup>

The regulation of proteins in cell signaling pathways often involves activation or deactivation. Activation,

such as phosphorylation, enables specific binding events between proteins that ultimately regulate cellular processes. Mitogen-activated and extracellular signal-related protein kinase (MEK) is one of such proteins in cell signaling pathways [mitogen-activated protein kinase (MAPK) cascade].<sup>[23,24]</sup> Detection and characterization of MEK are of substantial interest in cell biology. Here a general immobilization scheme is used to tether MEK on nanostructured surfaces, and liquid crystals are used to detect its presence on surface and further binding activities with antibodies.

Many immobilization schemes have been developed to afford oriented protein on surfaces.<sup>[25–27]</sup> The immobilization of protein on SAMs is guided by past work of Sigal et al.<sup>[28]</sup> This general scheme is based on the use of mixed SAMs presenting nitrilotriacetic (NTA) (**1**) and tri(ethylene glycol) (**2**) (Fig. 4). Nitrilotriacetic was used because, when complexed with Ni(II) ions via a tetravalent chelate, the NTA–Ni(II) complex can specifically bind proteins that present a sequence of six histidines (His-tag) at the amino end of the protein. His-tags are commonly incorporated into the amino end of the primary sequence of recombinant proteins to facilitate purification by metal-affinity chromatography.<sup>[29]</sup> The tri(ethylene glycol)-terminated alkanethiol, **2**, functions as a diluent of the NTA-terminated alkanethiol to prevent non-specific protein adsorption. With a background surface of ethylene glycols, all proteins bound to the surface were immobilized either by complexation to NTA–Ni(II) or by specific binding to the immobilized His-tag protein.

His-tag MEK were first immobilized on gold films that possessed nanometer-scale topography and presented mixed SAMs formed from **1** and **2** [following chelation of the Ni(II) with the surface]. Because the chelation of Ni(II) ions by **1** within the mixed

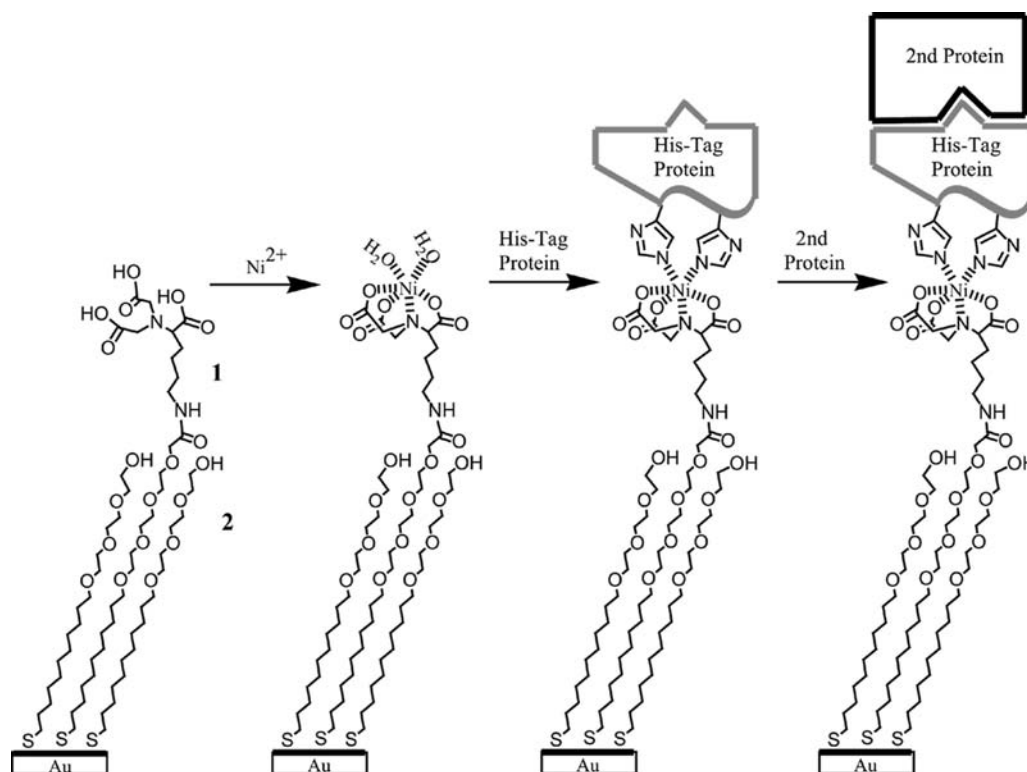


**Fig. 4** General scheme for immobilization of proteins on mixed SAMs formed from NTA-terminated alkanethiols, **1**, and tri(ethylene glycol)-terminated alkanethiols, **2**. Each nitrilotriacetic acid group on the SAM chelates a Ni(II) ion, which is subsequently recognized and bound by the histidine tags of the protein to be immobilized. The histidine-tagged protein functions as a receptor that binds a second protein. The tri(ethylene glycol)-terminated SAM resists nonspecific protein adsorption. *Source:* From Ref.<sup>[15]</sup>.

monolayer is a requirement for specific binding of the His-tag MEK, a control experiment was conducted by binding of His-tag MEK to mixed SAMs without Ni(II) ions. Because the sensitivity of liquid crystal to bound protein can be enhanced by decreasing the anisotropic topography within a gold film (achieved by decreasing the oblique angle of deposition of gold film),<sup>[17]</sup> gold films prepared by oblique deposition at a low angle (30° from normal) were used. Mixed SAMs formed with low percentages of the NTA-terminated alkanethiols (5% **1** and 95% of **2** in ethanol) were used to afford a low surface coverage of NTA so that two

experiments are aimed to detect difference as a result of small amount of protein specifically immobilized on surface.

The optical appearances of nematic phases of 5CB contacted with SAMs-treated NiSO<sub>4</sub> and then the His-tag MEK are shown in Fig. 5A. The optical appearance of the 5CB was nonuniform and the extent of modulation of light as the sample was rotated between the cross polarizers was low confirming that no preferred azimuthal orientation is present within the sample. In contrast, when the SAM was treated with deionized water instead of NiSO<sub>4</sub> solution and

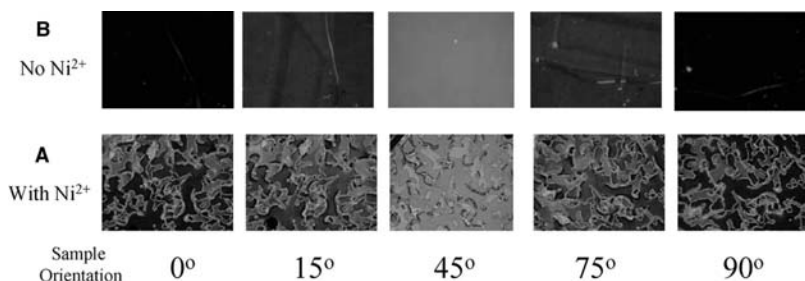


**Fig. 5** Optical images (crossed polarizers) of nematic 5CB supported on MEK-treated mixed SAMs (**1/2**: 20/80 in ethanol) on gold films obliquely deposited at 30°. The mixed SAMs were incubated in either (A) 50 mM NiSO<sub>4</sub> or (B) deionized water for 2 hr prior to incubation in 0.5 μM of His-tag MEK for 5 hr. The mixed SAMs supported on the anisotropic gold films were aligned with the direction of minimum roughness on each surface parallel to each other. *Source:* From Ref.<sup>[15]</sup>.

then His-tag MEK, 5CB assumed a uniform alignment on the surface. A strong modulation of the intensity of light was measured as the sample was rotated between cross-polarizers (Fig. 5B). By comparing the optical appearance of the liquid crystal in Fig. 5A and B, the orientation of 5CB is disrupted only when the surface is treated with both Ni(II) ions and His-tag MEK. This result indicates that His-tag MEK binds specifically to the Ni(II) NTA complex within the SAMs. This conclusion is further supported by the increase of ellipsometric thickness only after the surface is treated with both Ni(II) ions and His-tag MEK. Because the size of MEK is comparable to the scale of the topography on the obliquely deposited gold films, bound His-tag MEK masks the topography of the surface from the liquid crystal, thus resulting in nonuniform alignment of the liquid crystal.

### SPECIFIC BINDING OF ANTIBODIES TO IMMOBILIZED PROTEINS

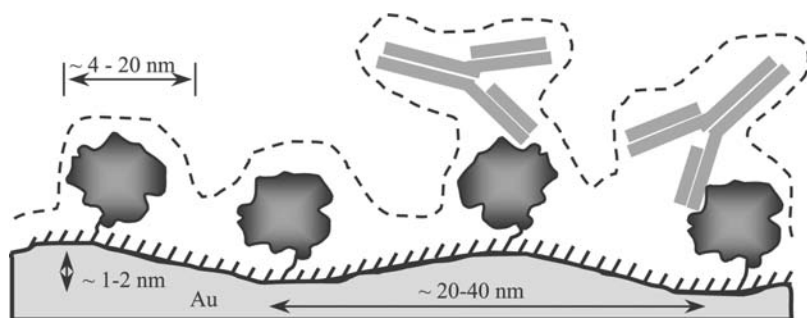
To investigate the binding activity of the immobilized MEK on surface, specific anti-MEK immunoglobulin G (IgG) and non-specific streptavidin immunoglobulin G (IgG) were used as model binding partners of MEK to demonstrate the possibility of using liquid crystals to detect binding events on surfaces that involve MEK. The presence of a second protein bind to the immobilized receptor will mask the nanometer-scale topography to greater extent. Fig. 6 demonstrates a schematic representation of changes in the topography upon binding of an antibody to the immobilized protein. Because the liquid crystal is sensitive to the magnitude of the anisotropy in the topography, the alignment of liquid crystal on surfaces supporting bound proteins can be made uniform by increasing the anisotropy of the topography on the surface. Whereas gold films deposited at an angle of  $30^\circ$  provide an anisotropic topography that is facile for reporting bound MEK using liquid crystal, gold films deposited at  $40^\circ$  instead of  $30^\circ$  are used to obtain uniform alignment of liquid crystal on the surface with

MEK present. On these gold films, mixed SAMs with higher surface density of NTA (1/2: 20/80 in ethanol) were used to investigate the orientational response of liquid crystal to IgG bound to His-tag MEK immobilized on the surface.

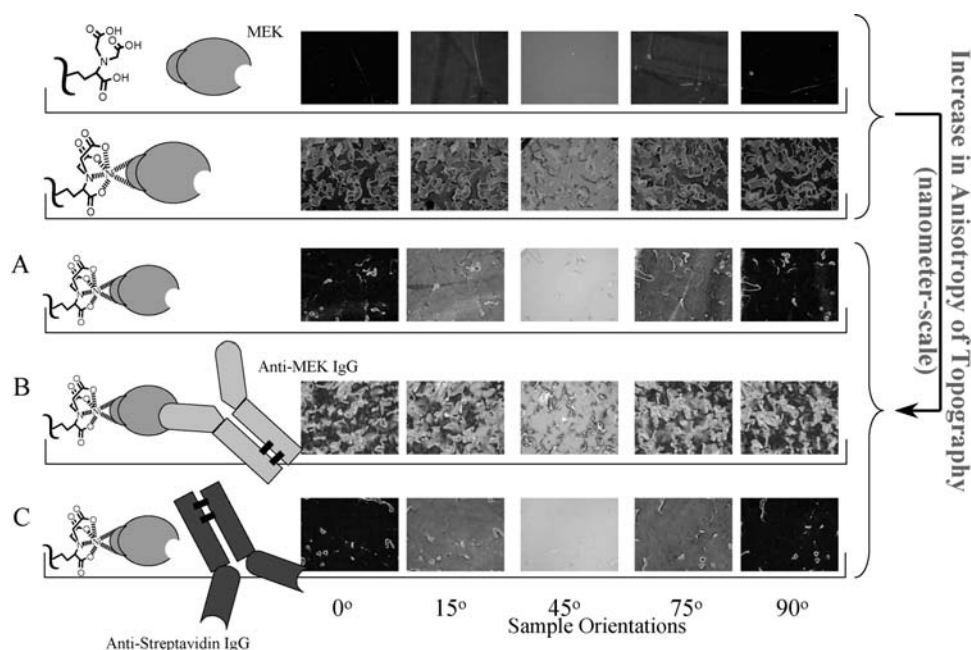
After incubating the SAMs in His-tag MEK ( $0.1 \mu\text{M}$  in PBS, pH 7.2) for 2 hr, ellipsometric measurement indicated a thickness of  $\sim 1.9 \text{ nm}$  of MEK. In contrast, a layer of MEK having a thickness of only  $\sim 0.9 \text{ nm}$  was bound to SAMs presenting low density of NTA (1/2: 5/95 in ethanol). Next, substrates immobilized with MEK were incubated with solutions containing either anti-MEK IgG ( $0.5 \mu\text{M}$ ) or antistreptavidin IgG ( $0.5 \mu\text{M}$ ) for 5 hr.

Fig. 7A shows the optical textures of nematic 5CB in contact with immobilized His-tag MEK on gold obliquely deposited at  $40^\circ$ . A strong modulation in the intensity of light was observed as the sample was rotated between crossed polarizers, indicating a largely uniform planar alignment of the liquid crystal. With the ellipsometric thickness of  $1.9 \pm 0.5 \text{ nm}$  of MEK bound on surface, this result shows that this amount of immobilized MEK is not sufficient to mask the influence of the topography of the gold film (obliquely deposited at  $40^\circ$ ) on the orientation of the liquid crystal.

Whereas 5CB on surfaces presenting immobilized His-tag MEK that was treated anti-MEK IgG ( $\sim 150 \text{ kD}$ ) assumed non-uniform orientations with little modulation of the intensity of polarized light (Fig. 7B), a control experiment in which antistreptavidin IgG was used instead of anti-MEK IgG yielded a liquid crystal with a uniform alignment (Fig. 7C). Ellipsometric measurement confirmed the increase of thickness only when specific anti-MEK IgG is used. Whereas surfaces with immobilized MEK treated with anti-MEK IgG showed an increase of  $\sim 3.3 \pm 1 \text{ nm}$  in thickness, no increase in thickness was detected after treatment with antistreptavidin IgG. Both of the experiments showed that the results are consistent with the specific binding between the immobilized MEK and the anti-MEK IgG in solution. Furthermore, specific binding of the second protein (anti-MEK IgG)



**Fig. 6** Schematic illustration of changes in the surface topography due to binding of an antibody to immobilized His-tag MEK on a SAM supported on a surface possessing nanometer-scale topography. The approximate topography of the surface supporting the bound protein is indicated by the dashed line. *Source:* From Ref.<sup>[15]</sup>.



**Fig. 7** Optical images (crossed polarizers) of nematic 5CB supported on MEK-treated mixed SAMs (1/2: 20/80 in ethanol) on gold films obliquely deposited at  $40^\circ$  that were exposed to PBS solution containing the following proteins prior to contact with nematic 5CB: (A) His-tag MEK, (B) His-tag MEK and anti-MEK IgG, and (C) His-tag MEK and anti-streptavidin IgG. The schematic representation of the protein binding events is shown to the left of the liquid crystal images. *Source:* From Ref.<sup>[15]</sup>.

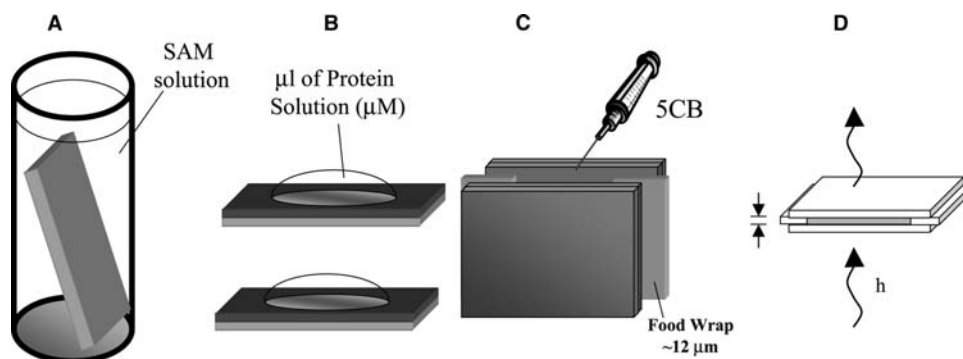
sufficiently masks the topography of gold films obliquely deposited at a higher angle ( $40^\circ$ ) and thus is readily reported by the nonuniform orientation of liquid crystal.

## EXPERIMENTAL

The experimental procedures such as organic synthesis, gold deposition, ellipsometry, and AFM measurements are well documented in the referenced literatures. However, the unique experimental procedures pertaining to protein binding assays using liquid crystals in this work bear a beauty of brevity and are described

here. Scheme 7 demonstrates a four-step procedure that completes an assay of protein binding starting from surface preparation. An example is shown below.

Mixed SAMs of **1** and **2** (prepared from 5% of **1** and 95% of **2** in ethanol) was immersed in 50 mM of  $\text{NiSO}_4$  for 2 hr (Scheme 7A) and then incubated the rinsed surfaces in PBS containing  $0.5 \mu\text{M}$  of His-tag MEK for 5 hr (Scheme 7B). Upon removal of the samples from contact with the His-tag MEK, the surfaces were rinsed with PBS buffer (pH 8.2). Two substrates with immobilized protein (or treated with second protein) were spaced with a Saran wrap ( $12 \mu\text{m}$ ) to create a liquid crystal optical cell. Nematic 5CB was injected



**Scheme 7** Experimental procedures for label-free protein assays on nanostructured surfaces for the use of liquid crystals.

into the cell at a temperature above the nematic-isotropic transition by capillary motion (Scheme 7C). Last, the cell was placed under a polarizing microscope, and the texture of the 5CB was examined and analyzed.

## CONCLUSION

In summary, using liquid crystal in combination with SAMs supported on nanostructured gold films, protein binding events can be readily detected without using secondary protein reporter or any labeling. Several unique characters make the use of liquid crystals with nanostructured gold films power for biological studies. First, the liquid crystal is sensitive to both the nanometer-scale topography and the molecular details of the organic monolayer on surface. Second, the liquid crystal can be masked from the nanometer-scale topography by the presence of surface-bound protein. Third, the anisotropy of the nanometer-scale topography can be adjusted by varying the angle of oblique deposition. Fourth, the combination of liquid crystal and nanostructured surfaces is completely compatible with sophisticated surface chemistry (mixed ethylene glycol monolayer) that prevents nonspecific protein adsorption and supports biospecific interactions. Fifth, by increasing the anisotropy of the topography of the nanostructured surfaces, multiple biospecific protein binding events can be detected. Together, these results suggest that nanostructured surfaces supporting biospecific interactions combined with liquid crystals form the basis of a general and facile method for detecting protein binding events on surfaces directly.

## ACKNOWLEDGMENTS

This research was supported by funding from the Office of Naval Research (Presidential Early Career Award for Science and Engineering to Professor Abbott, N00014-99-1-0250), Materials Research Science and Engineering Center on Nanostructured Materials and Interfaces (NSF-DMR-0079983) at University of Wisconsin, and the Biophotonics Partnership Initiative of NSF (ECS-0086902). The author would like to thank Professor Abbott for his support and encouragement throughout the course of some of the above research.

## REFERENCES

- Cava, R.J.; DiSalvo, F.J.; Brus, L.E.; Dunbar, K.R.; Gorman, C.B.; Haile, S.M.; Interrante, L.V.; Musfeldt, J.L.; Navrotsky, A.; Nuzzo, R.G.; Pickett, W.E.; Wilkinson, A.P.; Ahn, C.; Allen, J.W.; Burns, P.C.; Ceder, G.; Chidsey, C.E.D.; Clegg, W.; Coronado, E.; Dai, H.J.; Deem, M.W.; Dunn, B.S.; Galli, G.; Jacobson, A.J.; Kanatzidis, M.; Lin, W.B.; Manthiram, A.; Mrksich, M.; Norris, D.J.; Nozik, A.J.; Peng, X.G.; Rawn, C.; Rolison, D.; Singh, D.J.; Toby, B.H.; Tolbert, S.; Wiesner, U.B.; Woodward, P.M.; Yang, P.D. Future directions in solid state chemistry: report of the NSF-sponsored workshop. *Prog. Solid State Chem.* **2002**, *30* (1–2), 1–101.
- Helmreich, E.J.M. *The Biochemistry of Cell Signalling*; Oxford University Press: New York, 2001.
- Zhu, H.; Bilgin, M.; Bangham, R.; Hall, D.; Casamayor, A.; Bertone, P.; Lan, N.; Jansen, R.; Bidlingmaier, S.; Houfek, T.; Mitchell, T.; Miller, P.; Dean, R.A.; Gerstein, M.; Snyder, M. Global analysis of protein activities using proteome chips. *Science* **2001**, *293*, 2101.
- MacBeath, G.; Schreiber, S.L. Printing proteins as microarrays for high-throughput function determination. *Science* **2000**, *289*, 1760.
- Mrksich, M. A surface chemistry approach to studying cell adhesion. *Chem. Soc. Rev.* **2002**, *29* (4), 267–273.
- Collings, P.J.; Patel, J.S. *Handbook of Liquid Crystal Research*; Oxford University Press: New York, 1997.
- Gupta, V.K.; Abbott, N.L. Uniform anchoring of nematic liquid crystals on self-assembled monolayers formed from alkanethiols on obliquely deposited films of gold. *Langmuir* **1996**, *12* (10), 2587–2593.
- Poirier, G.E. Characterization of organosulfur molecular monolayers on Au(111) using scanning tunneling microscopy. *Chem. Rev.* **1997**, *97* (4), 1117–1127.
- Ulmon, A. *An Introduction to Ultra Thin Organic Films—From Langmuir–Blodgett to Self-Assembly*; Academic Press: New York, 1991.
- Tingey, M.L.; Luk, Y.-Y.; Abbott, N.L. Orientations of liquid crystals on chemically functionalized surfaces that possess gradients in nanometer-scale topography. *Adv. Mater.* **2002**, *14* (17), 1224–1227.
- Skaife, J.J.; Abbott, N.L. Quantitative characterization of obliquely deposited substrates of gold by atomic force microscopy: influence of substrate topography on anchoring of liquid crystals. *Chem. Mater.* **1999**, *11*, 612.
- Gupta, V.K.; Abbott, N.L. Design of surfaces for patterned alignment of liquid crystals on planar and curved substrates. *Science* **1997**, *276* (5318), 1533–1536.
- Mrksich, M.; Whitesides, G.M. Using self-assembled monolayers that present oligo(ethylene glycol) groups to control the interactions of proteins with surfaces. *A.C.S. Symp. Ser.* **1997**, *680*, 361–373.
- Feldman, K.; Hahner, G.; Spencer, N.D.; Harder, P.; Grunze, M. Probing resistance to protein adsorption of oligo(ethylene glycol)-terminated self-assembled monolayers by scanning force microscopy. *J. Am. Chem. Soc.* **1999**, *121* (43), 10,134–10,141.
- Luk, Y.-Y.; Tingey, M.L.; Hall, D.J.; Israel, B.A.; Murphy, C.J.; Bertics, P.J.; Abbott, N.L. Using liquid crystals to amplify protein–receptor interactions: design of surfaces with nanometer-scale topography that present histidine-tagged protein receptors. *Langmuir* **2002**, *19* (5), 1671–1680.



16. Gupta, V.K.; Skaife, J.J.; Dubrovsky, T.B.; Abbott, N.L. Design of surfaces for patterned alignment of liquid crystals on planar and curved substrates. *Science* **1998**, *279* (5318), 2077–2080.
17. Skaife, J.J.; Brake, J.M.; Abbott, N.L. Influence of nanometer-scale topography of surfaces on the orientational response of liquid crystals to proteins specifically bound to surface-immobilized receptors. *Langmuir* **2001**, *17* (18), 5448–5457.
18. Bowick, M.J.; Chandar, L.; Schiff, E.A.; Srivastava, A.M. The cosmological Kibble mechanism in the laboratory—string formation in liquid-crystals. *Science* **1994**, *263* (5149), 943–945.
19. Van Oss, C.J.; van Regenmortel, M.H.V. *Immunochemistry*; Dekker: New York, 1994.
20. Luk, Y.-Y.; Kato, M.; Mrksich, M. Self-assembled monolayers of alkanethiolates presenting mannitol groups are inert to protein adsorption and cell attachment. *Langmuir* **2000**, *16* (24), 9604–9608.
21. Skaife, J.J.; Abbott, N.L. Quantitative interpretation of the optical textures of liquid crystals caused by specific binding of immunoglobulins to surface-bound antigens. *Langmuir* **2000**, *16* (7), 3529–3536.
22. Skaife, J.J.; Abbott, N.L. Influence of molecular-level interactions on the orientations of liquid crystals supported on nanostructured surfaces presenting specifically bound proteins. *Langmuir* **2001**, *17* (18), 5595–5604.
23. Huang, C.-Y.F.; Ferrell, J.E. Ultrasensitivity in the mitogen-activated protein kinase cascade. *Proc. Natl. Acad. Sci. U. S. A.* **1996**, *93* (19), 10,078–10,083.
24. Asai, T.; Tena, G.; Plotnikova, J.; Willmann, M.R.; Chiu, W.L.; Gomez-Gomez, L.; Boller, T.; Ausubel, F.M.; Sheen, J. MAP kinase signalling cascade in Arabidopsis innate immunity. *Nature* **2002**, *415* (6875), 977–983.
25. Hodneland, C.D.; Lee, Y.S.; Min, D.H.; Mrksich, M. Selective immobilization of proteins to self-assembled monolayers presenting active site-directed capture ligands. *Proc. Natl. Acad. Sci. U. S. A.* **2002**, *99* (8), 5048–5052.
26. Yeung, C.; Leckband, D. Molecular level characterization of microenvironmental influences on the properties of immobilized proteins. *Langmuir* **1997**, *13* (25), 6746–6754.
27. Edmiston, P.L.; Saavedra, S.S. Molecular orientation distributions in protein films. 4. A multilayer composed of yeast cytochrome *c* bound through an intermediate streptavidin layer to a planar supported phospholipid bilayer. *J. Am. Chem. Soc.* **1998**, *120* (8), 1665–1671.
28. Sigal, G.B.; Bamdad, C.; Barberis, A.; Strominger, J.; Whitesides, G.M. A self-assembled monolayer for the binding and study of histidine tagged proteins by surface plasmon resonance. *Anal. Chem.* **1996**, *68* (7), 490–497.
29. Hochuli, E.; Dobeli, H.; Schacher, A.J. New metal chelate adsorbent selective for proteins and peptides containing neighboring histidine-residues. *J. Chromatogr.* **1987**, *411*, 177–184.



# Litho-to-Nano Link

**Gianfranco Cerofolini**

Post-Silicon Technology, STMicroelectronics, Agrate Brianza, Italy, and Department of Materials Science, University of Milano-Bicocca, Milan, Italy

**Dario Narducci**

**Elisabetta Romano**

CNISM and Department of Materials Science, University of Milano-Bicocca, Milan, Italy

## Abstract

External accessibility to the molecular world requires a hierarchy of devices and addressing protocols. The paradigmatic example is that of a molecular memory, arranged in about  $N^2$  cross-points (each containing  $10^3$  reprogrammable molecules), defined by  $2N$  nanoscopic wires, addressed by  $\log_2(2N)$  lithographically defined gates. For  $N = 10^5$ , this gives  $10^{13}$  molecules (the molecular scale),  $10^{10}$  cross-points and  $2 \times 10^5$  lines (the mesoscopic scale), and  $1 + 5 \log_2(10)$  addressing gates (the macroscopic scale). This complex hierarchy requires the development of new techniques able to merge the ones involved in the top-down route, characteristic of the macroscopic scale, with the ones involved in the bottom-up route, characteristic of the nanoscopic scale.

## INTRODUCTION

From the fundamental point of view, the properties of matter can be distinguished on the grounds of their scaling behavior:

- (Ma) On the *macroscopic scale* (the one described by classical physics), the properties of matter remain substantially unchanged when the size of the considered system is progressively reduced; replicas of the system have negligible statistical dispersion.
- (Me) On the *mesoscopic scale*, the properties of matter change substantially when the size of the system is progressively reduced; replicas of the systems have usually large statistical dispersion.
- (Mi) On the *microscopic scale* (the one described by quantum physics) matter cannot be shrunk; all replicas of the system are rigorously identical; the upper limit of this scale is the molecular one, (Mo).

## LITHOGRAPHY AND ITS LIMITS

Of course, this description is matched to the thermodynamic properties of simple systems. When the functional properties of the systems are prevailing over the thermodynamic ones, the system is usually referred to as a *device*—something “which is formed by design”.<sup>[1]</sup> It may happen that devices working on a certain length scale work, even better, on a lower length scale. The combination of better properties with lower cost of materials has led to the development of *miniaturization techniques*. The most spectacular achievement in this field has been the development of the integrated-circuit (IC) technology.

The evolution of ICs has been dominated by the idea of scaling down its basic constituent—the metal-oxide-semiconductor (MOS) field-effect transistor (FET). In turn, this has required the development of suitable lithographic techniques for its definition on smaller and smaller length scales. There are several generations of lithographic techniques, usually classified according to the medium required for the definition of the wanted features on photo- or electro-sensitive materials (resists): standard photolithography (436 nm, Hg *g*-line; refractive optics), deep ultraviolet (DUV) photolithography (193 nm, ArF excimer laser; refractive optics), immersion DUV photolithography (refractive optics), extreme ultraviolet (EUV) photolithography (13.5 nm, plasma-light source; reflective optics); electron beam (EB) lithography (electron wavelength controlled by the energy, typically in the interval  $10^{-3}$ – $10^{-2}$  nm).

This generation of techniques has grown to match what seems to be the fundamental issue of IC production: increase the integration scale by decreasing the MOS-FET size. The industrial system has succeeded in that, but the cost of ownership has in the meanwhile dramatically increased, because of either the required investment per machine,

DUV  $\ll$  immersion DUV  $\ll$  EUV,

or the throughput,

EB  $\ll$  DUV.

The dramatic cost explosion necessary for the reduction of the feature size (see Fig. 1) has thrown doubts on the possibility of continuing the current

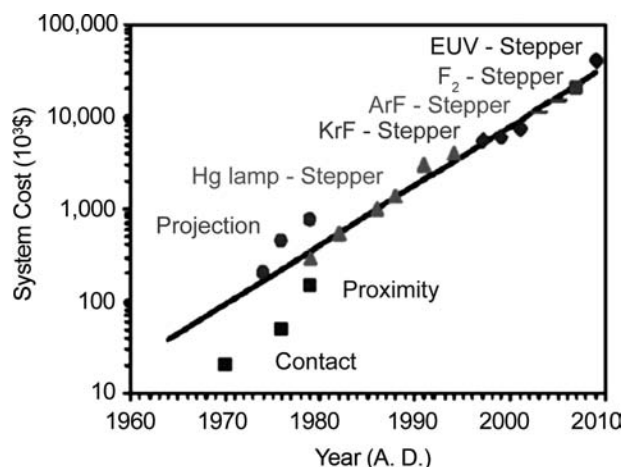


**Fig. 1** Exponential increase with time of the cost of lithographic systems.

increase of density (by a factor of 2 each 18 months for memories or each 24 months for microprocessors) beyond the next 10 years.

The impossibility of preparing horizontal features on the nanometer length scale via conventional lithography, the poor technical maturity of the advanced lithographic (extreme-ultraviolet, synchrotron-radiation in the X-ray region, or electron-beam) tools necessary for their preparation, and the huge investment cost expected for IC mass production, have generated a strong interest for the development of alternative lithographic methods or of non-lithographic techniques for the definition of geometries on the nanometer length scale.

To overcome these limits, other routes have been proposed as alternatives to the *top-down route* that has characterized the evolution of microelectronics; the *bottom-up route*, in which the circuit is generated via the self-assembly of nanoscopic (typically molecular) devices, and the *hybrid route*, in which such molecular devices are arranged in a hosting microelectronic frame to form a circuit.<sup>[2,3]</sup>

Since the architecture of the hybrid IC remains substantially controlled by its microelectronic part, the hybrid route does not require a complete rethinking of the circuit. The hybrid route may thus be seen as a *conservative extension of microelectronics into nanoelectronics*, where the nanoelectronic (molecular) devices are otherwise produced (with synthetic methods of chemistry) and assembled on a microelectronic frame. *The hybrid route may thus be seen as a kind of host-guest technology, in which the host is demanded to microelectronics while the guest is demanded to chemistry.*

The structure that seems to pose less problems for the integration of molecular devices in microelectronic circuits is the crossbar one, in which a lower array of  $N$

wires crosses an upper array of  $N$  wires and the  $N^2$  overlapping regions (*cross-points*) are prepared to host nanoscopic devices.

## PROCESSING CROSSBARS

The property that has attracted the maximum of interest for possible application of molecules in electronics is the bistability manifested by some of them: under the application of a suitable difference of electric potential, a molecule may undergo electronic and structural changes, in turn responsible for large conductance difference.<sup>[4]</sup> The ideal arrangement for the exploitation of bistable molecules is based on their insertion in a crossbar structure, in turn defined by two arrays of conducting wires arranged in parallel planes and oriented perpendicularly to one another.<sup>[5-8]</sup>

The first demonstrators of molecular crossbar memories exploited the spontaneous formation of monolayers of functional molecules with thiol termination(s) on metal films to produce their self-assembly inside the cross-points of the crossbar.<sup>[9]</sup> The process, according to which the first molecular memory was prepared, employed thiol-terminated rotaxanes as reprogrammable cells. The molecules were embedded between the metal layers forming the crossbar via a process that can be sketched as follows:

- (XB1), deposition and definition of the first-level (“bottom”) wire array;
- (XB2), deposition of the active reconfigurable molecules, working also as vertical spacer separating lower and upper arrays; and
- (XB3), deposition and definition of the second-level (“top”) wire array.

The above XB approach, with double metal strips, has however been found to have serious limits:

- The organic active element is incompatible with high-temperature processing, so that the top layer must be deposited at room or slightly higher temperature. This need implies a preparation based on physical vapor deposition, where the metallic electrode results from the condensation of metal atoms on the outer surface of the deposited organic films. This process, however, poses severe problems of compatibility, because isolated metal atoms, quite irrespective of their chemical nature, are mobile and decorate the molecule, rather than being held at its outer extremity.<sup>[10-12]</sup>
- A safe determination of the conductance state of bistable molecules requires the application of a voltage  $V$  appreciably larger than  $k_B T/e$  (with  $k_B$  being the Boltzmann constant,  $T$  the absolute

temperature, and  $-e$  the electron charge), say  $V = 0.1\text{--}0.2\text{ V}$ . Applied to molecules with typical length around 3 nm, this potential generates an electric field, of the order of  $5 \times 10^5\text{ V cm}^{-1}$ , sufficiently high to produce metal electromigration along the molecules.<sup>[13]</sup>

- The energy barrier for metal-to-molecule electron transfer is controlled by the polarity of the contact, in turn increasing with the electronegativity difference along the bond linking metal and molecule.<sup>[14]</sup> The use of thiol terminations for the molecule, as implicit in the XB approach, is expected to be responsible for high-energy barriers because of the relatively high electronegativity of sulfur.

A solution to the electromigration problem, eliminating metal contacts, can be achieved preparing the bottom electrodes in the form of silicon wires (as done in Ref.<sup>[15]</sup>) and the top electrodes in the form of conducting  $\pi$  conjugated polymers (as suggested in Ref.<sup>[16]</sup>).

- (XB<sup>+1</sup>), deposition and definition of the bottom array of poly-silicon wires;
- (XB<sup>+2</sup>), deposition of the active (reconfigurable) element, working also as vertical spacer separating lower and upper arrays; and
- (XB<sup>+3</sup>), deposition and definition of the top array of conducting  $\pi$ -conjugated polymer.

This process requires the development of grafting techniques to both poly-silicon and the  $\pi$ -conjugated polymer. The development of the process would certainly be simplified using the same material for upper and lower wires.

The use of poly-silicon as material also for the top array seems impossible because poly-silicon is almost uniquely prepared via chemical vapor deposition at temperatures (600–700°C) that are incompatible with organic molecules (certainly destroyed at a temperature of 400°C). The only way to overcome this difficulty consists thus in a process, XB\*, where the two poly-silicon arrays defining the crossbar matrix are prepared *before* the insertion of the organic element:

- (XB\*1), preparation of a bottom array of poly-silicon wires;
- (XB\*2), deposition of a sacrificial layer as vertical spacer separating lower and upper arrays;
- (XB\*3), preparation of a top array of poly-silicon wires crossing the first-floor array;
- (XB\*4), selective chemical etching of the spacer; and
- (XB\*5), insertion of the reconfigurable molecules in a way to link upper and lower wires in each cross-point.

Of the three considered processes (XB, XB<sup>+</sup>, and XB\*), the most conservative one is certainly based on

double-silicon strips and is thus expected to be of easiest integration in IC processing.

Limiting the attention to this structure, the hybrid circuit is formed by two zones: the *nano-zone*, containing the crossbar and hence hosting the molecular devices, and the *litho-zone*, hosting the conventional CMOS circuitry. Nano- and litho-zones are interconnected by the strips (addressing lines), which take the function of rows and columns of the crossbar memory.

The process for the production of the nano-IC should comprise a *zeroth mask*, protecting (with Si<sub>3</sub>N<sub>4</sub> or SiO<sub>2</sub>) the nano-zone from the *front-end initial stage*, where transistors, capacitors, and short-range poly-silicon interconnections are defined. At a certain point of this stage, the protection of the nano-zone is removed and the poly-silicon seed is allowed to cross the nano-litho frontier, thus initiating the construction of the crossbar. After its conclusion, the nano-zone is protected (once again with Si<sub>3</sub>N<sub>4</sub> or SiO<sub>2</sub>) and the *front-end final stage* is carried out. The process goes to completion as in standard IC process. After that, the dielectric layer protecting the nano-zone is selectively removed and the *grafting* of the active elements to the poly-silicon strips is achieved by the simple exposure to the organic molecules: the molecules are addressed to the wanted regions simply by the appropriate distribution of chemical potentials. In turn, that requires the ability to control the chemical terminations of the surfaces of the most important IC films. The passivation with organic resins of the overall nano IC completes the process.

In addition to the said reorganization of the IC process, the implementation of the hybrid silicon-organic architecture XB\* requires, however, the solution of a number of problems. The major ones seem the following:

1. the setup of an economically sustainable technology for the preparation of crossbar with cross-point density (say,  $10^{11}\text{ cm}^{-2}$ ) higher than the maximum bit density projected by the International Technology Roadmap for Semiconductors;<sup>[17]</sup>
2. the linkage of the addressing lines to the silicon circuitry for writing and sensing;
3. the design and synthesis of the reconfigurable molecules; and
4. the grafting of the functional molecules to those cross-points via batch processing.

This entry is devoted to analyze whether XB\* can be adapted to solve problems 1 and 2. Problems 3 and 4 are considered in articles<sup>[19,20]</sup> respectively.

## CROSSBAR PRODUCTION WITH GEOMETRIES ON THE NANOMETER LENGTH SCALE WITHOUT USING ADVANCED LITHOGRAPHY

Needless to say, the crossbar structure may be prepared with any lithographic method. The use of standard lithography (up to DUV) results in systems on the macroscopic scale. The use of advanced lithography (or even of the non-lithographic methods described in the following) produces instead systems on the mesoscopic scale. In view of the intrinsically large statistical variability of the properties of mesoscopic systems, the circuit architecture should be self-aligned.

The crossbar structure satisfies this need because the fabrication of cross-points does not require any alignment, being the self-aligned result of two subsequent definition. Moreover, the geometries of each mask are so simple (parallel lines) to allow their production on the mesoscopic scale with techniques not involving advanced lithography.

These non-conventional techniques are based on the following technological skills:

- the control of film thickness (say, along the “vertical” direction), which is possible down to

the sub-nanometer length scale provided that the film is sufficiently homogeneous; and

- the transformation of horizontal features (i.e., surface layers with thickness  $t$ ) into vertical features (i.e. columns, called spacers, of width  $t$ ).

### Collective Preparation

The first method (originally proposed by Natelson et al.<sup>[18]</sup> and later implemented practically by another collaboration<sup>[19]</sup>) is essentially based on the sequential alternate deposition of two films A and B, characterized by the existence of a preferential etch for one (say, A) of them. After cutting at 90°, polishing, and controlled etching of A, one eventually gets a mold that can be used as an imprinting mask, as sketched in Fig. 2. This technique is referred to as imprint lithography (IL); actually it is a *contact* (rather than proximity) lithography.

The first practical application of this idea was provided by Melosh et al., who prepared a contact mask for IL with pitch of 16 nm by growing on a substrate a quantum well via molecular beam epitaxy, cutting the sample perpendicularly to the surface, polishing the newly exposed surface, and etching selectively the different strata of the well.<sup>[21]</sup>

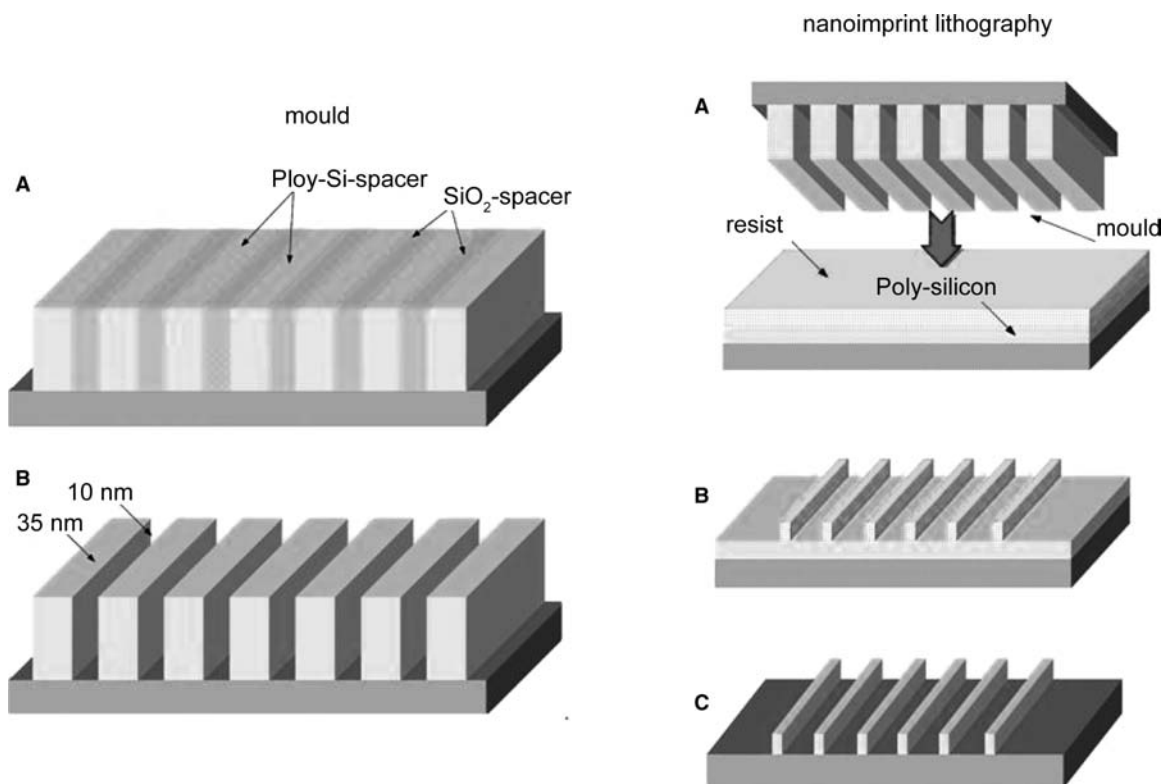


**Fig. 2** Preparation of a mold via selective etching in multilayered structure (*left*) and its use as a contact mask for imprint lithography (*right*).

## Sequential Preparation

Another route is the multi-spacer patterning technique (S<sup>3</sup>PT), in turn an extension of the spacer patterning technique (SPT).

The SPT is based on the definition of a suitable seed, the conformal deposition of a poly-silicon film of assigned thickness, and its anisotropic etching completed with the formation of a sidewall. The upper part of Fig. 3 sketches the process, whereas the lower part

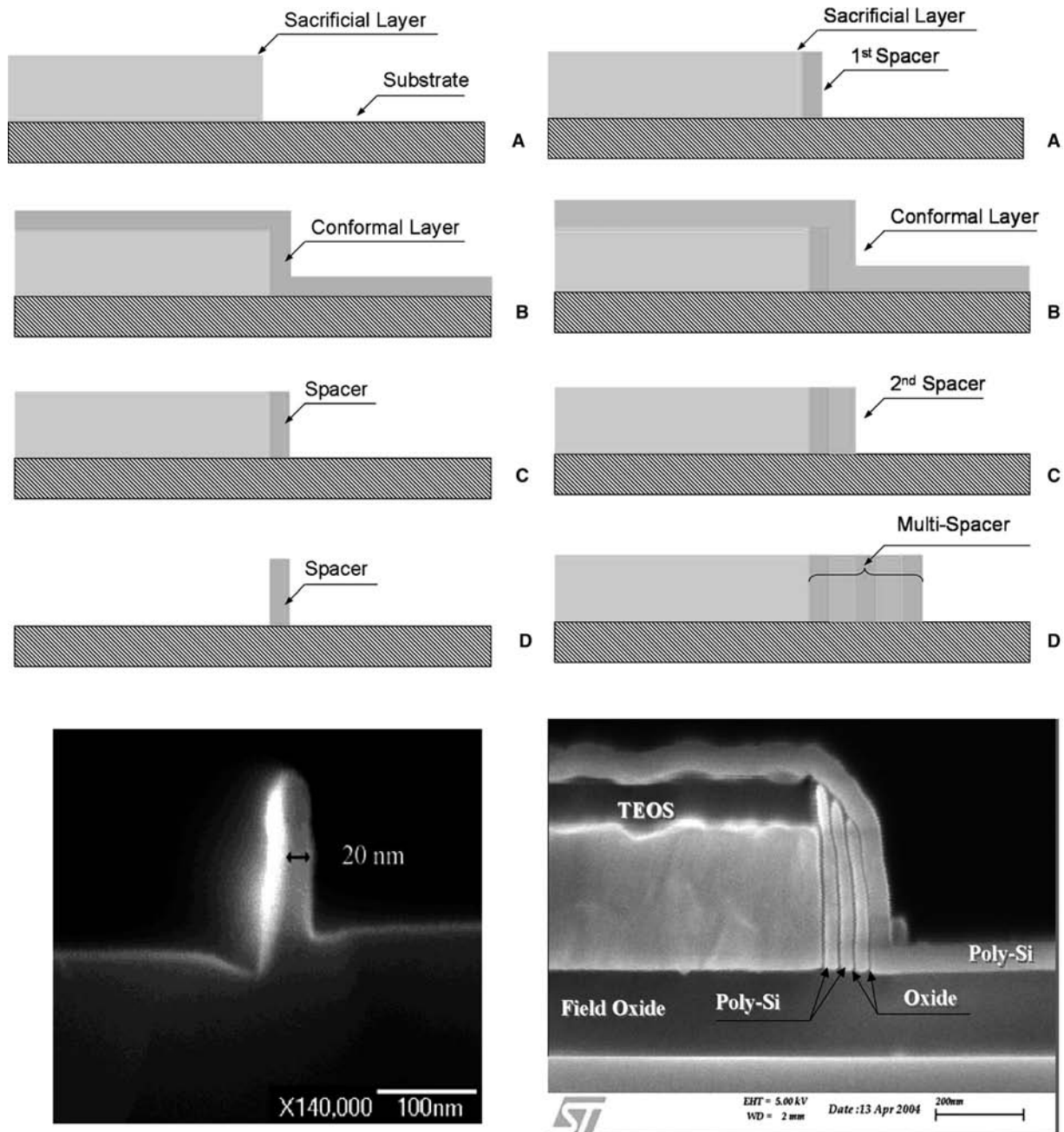


**Fig. 3** *Upper left:* A sequence for obtaining sublithographic features via the spacer patterning technique: (A) deposition of a layer and lithographic definition of a vertical step by means of an anisotropic etching; (B) deposition of a conformal layer; (C) anisotropic etching; (D) selective chemical etching of the sacrificial layer. *Lower left:* An example of structure produced via SPT [taken from Ref.<sup>[26]</sup>]. *Upper right:* The multi-spacer patterning technique: (A) fabrication of a first spacer by means of the SPT; (B) deposition of a novel conformal layer; (C) anisotropic etching and fabrication of a second array of another material; (D) iteration of the sequence (B)–(C). *Lower right:* An example of an S<sup>3</sup>PT multi-spacer (with pitch of 35 nm and formed by a double layer poly-Si|SiO<sub>2</sub>) resulting after three repetitions of the SPT. *Source:* Taken from Ref.<sup>[25]</sup>.

shows the cross-section of a wire produced via this technique.

The S<sup>n</sup>PT is just an extension of the SPT. It is based on the idea that a wire array of  $2n$  bars is produced via a sequence of  $n$  conformal depositions and anisotropic etchings. This idea, proposed and developed by Cerofolini et al.,<sup>[22–24]</sup> is shown on the right of Fig. 3: the upper right part sketches the process; the lower part shows instead how poly-silicon arrays separated by SiO<sub>2</sub> dielectrics with sub-lithographic pitch (35 nm) can indeed be produced. The minimum pitch reported as producible via this technique is 20 nm.<sup>[25,26]</sup>

### Comparing IL with S<sup>n</sup>PT

Although both IL and S<sup>n</sup>PT allow the preparation of deeply sub-lithographic features with comparable pitches; however, these techniques manifest large differences:

- Whereas in IL all wires are defined collectively, in S<sup>n</sup>PT they are constructed sequentially.
- In IL, all wires have the same height,<sup>[19]</sup> while in S<sup>n</sup>PT the wire height decreases progressively with the order of preparation.
- Similarly, the separation between bottom and top wires in IL is independent of the wire, whereas in S<sup>n</sup>PT it can be varied from one top wire to the subsequent one tuning the thickness of oxide before poly-silicon deposition.
- Moreover, the geometry obtained via IL is necessarily formed by parallel wires, while the geometry obtained via S<sup>n</sup>PT may be more complex in relation to the mask used to define the sacrificial layer.

### NANOWIRE DEMULTIPLEXING

If the availability of nanofabrication techniques is fundamental in establishing a nanotechnology, not less vital is the integration of the nanostructures with higher-level structures: Once the crossbar structure is formed, it is necessary to link it to the conventional silicon circuitry. As clearly stated in a scholium to Ref.<sup>[27]</sup>, “the difficulties in communication between the nanoworld and the macroworld represent a central issue in the development of nanotechnology.”

Although the importance of addressing nanoscale elements in arrays goes beyond the area of memories (and will be critical to the realization of other integrated nanosystems such as chemical or biological sensors, electrically driven nanophotonics, or even quantum computers), in the following the attention will however be limited to the problem of addressing cross-points in nanoscopic crossbar by means of

externally accessible lithographic contacts. This is a difficult task because the current devices at the forefront of the technology are characterized by a feature size of 45 nm (half pitch).

Several strategies have been adopted to attack this problem:

- The complicate circuitry required by binary-code demultiplexing is avoided using nanoscopic addressing circuits, embodying in themselves the ability to address single cells. In the first demonstrator, they were prepared by “vertical” growth of variously doped silicon wires, first chemical-vapor deposited and then randomly arranged horizontally to link the nanoscopic lines to the lithographic lines.<sup>[28,29]</sup> As far as the exact way such links cover the nanoscopic lines is not exactly known—this technique does not allow to know a priori which cell is addressed. “This was a rudimentary demonstration vehicle, and neither vehicle nor probably the programming technique could be extended to the much larger arrays required for practical interest”.<sup>[30]</sup> A conceptually similar technique was developed by the collaboration of Ref.<sup>[30]</sup>; however, using a consistent solution with the CMOS technology. In this solution, where one-to-one correspondence between nano- and litho-wires is achieved via rotation of a very small angle, the lithographic lines need to be defined with the same pitch as the nanoscopic lines.
- The idea of using small misalignment to access the nanoscopic circuitry was perhaps first proposed by Likharev with the name of cmol circuit (see Refs.<sup>[31–33]</sup> for recent reviews). In Likharev approach, the contact is achieved with the growth of pyramids whose base is matched to the lithographic feature and whose summit is matched to intersect one and only one nanoscopic line. The misalignment guarantees this occurrence but makes it impossible to know the correspondence between cross-point and wire pair.
- A misalignment-tolerant random-interconnect architecture was hypothesized by the proponent of the crossbar structure.<sup>[5,34]</sup> In this way, a large amount of cells are left out of control (being either not addressed or such that different cells are identified with a unique code) and a special logic must be employed to manage this situation, eliminating unaddressed cells and possibly exploiting redundancy (TERAMAC approach).<sup>[35]</sup> Needless to say, this deal is convenient only if the non-functioning cells are a minority and the circuitry required to manage the randomness remains relatively simple. That these conditions may really be satisfied in practice is not clear, especially if the expected cross-point density ( $10^{11} \text{ cm}^{-2}$ ) is compared with



the soon achievable density ( $10^{10} \text{ cm}^{-2}$ ) for NAND memories, whose control is deterministic.

In the following, the attention will only be focused on arrangements allowing a deterministic access to all cross-points and using two length scales—the sub-lithographic one (possibly down to a few nanometers) and the lithographic one. In particular, three methods will be discussed: one suitable for all kinds of nanoscopic crossbars (irrespective of their preparation procedure) and the others specific of crossbars prepared by the S<sup>n</sup>PT.

### The Horizontal Beveling Technique

The first technique is reminiscent of the beveling technique once used, together with micro-sectioning and staining, for the measurement of junction depth (and more recently of carrier concentration profiles using spreading resistance techniques); because of this, it will henceforth be referred to as horizontal beveling technique (HBT).

Consider as above an array of  $n$  conductive parallel wires aligned in the  $x$  direction with width  $l_y$  and pitch  $L_y$ , so densely arranged that they cannot be singularly accessed photolithographically and thus cannot be linked to the hosting microelectronic circuit.

A kind of hardware demultiplexing is possible via the following process: after the deposition of a protective insulating cap, a bar with width  $b$ , oriented in a direction tilted by a small angle  $\alpha$  with respect to the  $x$  direction and so long as to cross all wires, are defined and this pattern is used to etch the underlying insulating cap (see Fig. 4). This process will result in the exposition of  $N$  rhomboids with pitch  $\Delta_x$  and major side  $\delta_x$

in the  $x$ -direction given by

$$\Delta_x = L_y / \tan \alpha, \quad (1)$$

$$\delta_x = b / \sin \alpha, \quad (2)$$

the area of each open contact being thus  $bl_y / \sin \alpha$ . The orientation is chosen in such a way that both  $\delta_x$  and  $\Delta_x$  are in the reach of (not necessarily electron-beam) lithography. Because of Eqs. (1) and (2), which is certainly possible for sufficiently small  $\alpha$ . Since the method produces from an array with pitch  $L_y$  another array with pitch  $\Delta_x$  [controlled uniquely by the orientation angle  $\alpha$  of the cutting bar, see Eq. (1)], it may be viewed as a kind of *pitch converter*. This method is immediately extended from one to two arrays by defining two bars (one per row and one per column).

Even this method, proposed by Cerofolini and Mascolo,<sup>[36,37]</sup> is based on controlled misalignment. Compared with the one proposed by Likharev, it has the advantages of greater consistency with the current IC technology and of specifying exactly the location of the addressed cross-point. Since each cross-point can be addressed independent of the remaining ones, this architecture is suitable for random-access memories (RAMs).

### Fusing Adjacent Lines in S<sup>n</sup>PT

After the demonstration that the S<sup>n</sup>PT can be used for the preparation of nanowire arrays, Cerofolini and Mascolo proposed another addressing strategy exploiting specific features of this technology.<sup>[36,37]</sup> The process starts with deposition of a film (e.g., of  $\text{Si}_3\text{N}_4$ ) and its photolithographic definition to form a seed with the pattern shown in Fig. 5A. The pattern is

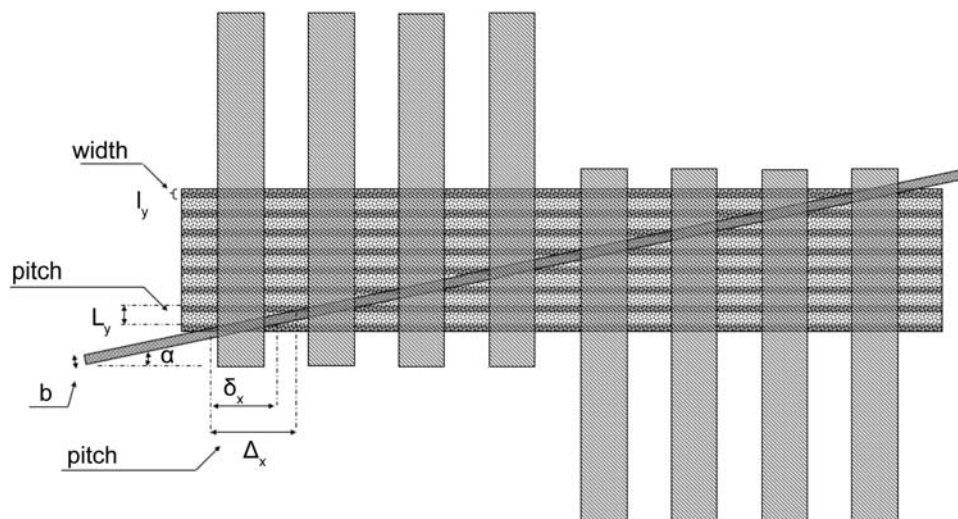
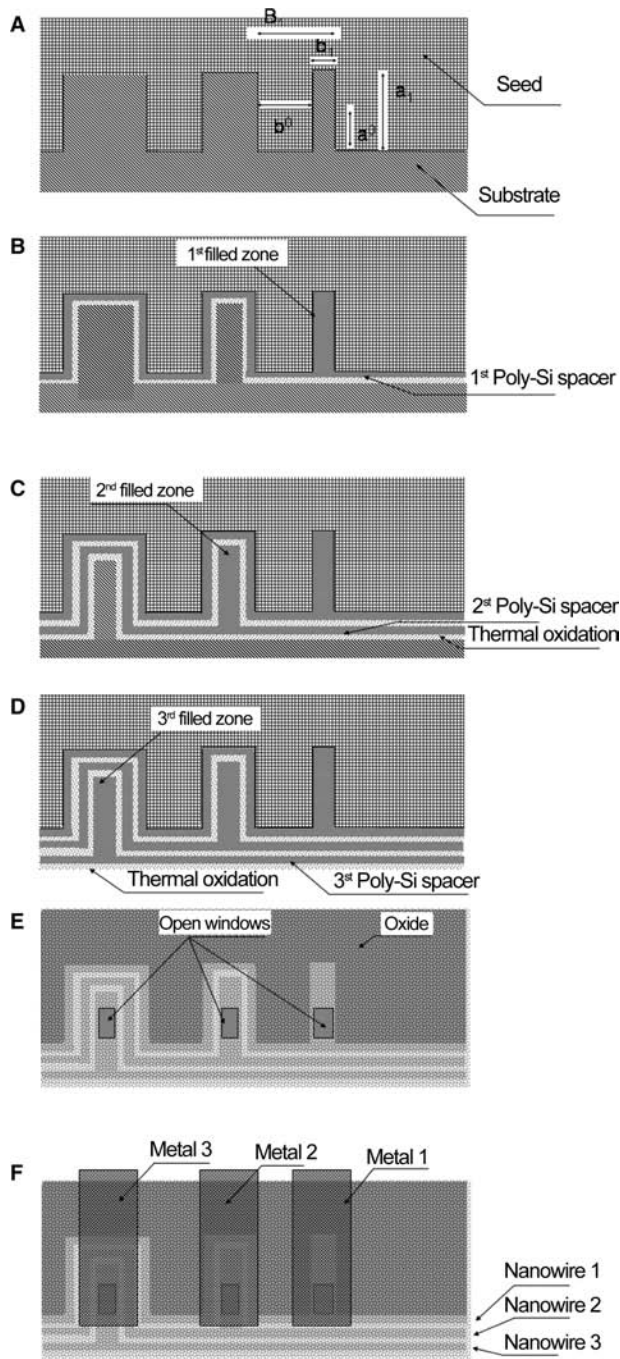


Fig. 4 The trick adopted for contacting each wire in the horizontal beveling technique.



**Fig. 5** Plan view of the mask able to contact single wires using the spacer patterning technique.

derived from the rectilinear edge required for the multi-spacer preparation with the addition of  $n$  rectangular indentations, of sides  $b_k$  (“width,” parallel to the border) and  $a_k$  (“depth,” perpendicular to the border);  $k$  runs from 1 to  $n$  and enumerates the wire in the array. The pitch  $B_k$  describing the indentation sequence is assumed to be given by

$$B_k = b^0 + b_k, \quad (3)$$

where  $b^0$ , the separation between vicinal indentations, does not vary with  $k$ ; instead  $a_k$  is assumed, at least temporarily, to be independent of  $k$  and given by

$$a_k = a^0 + (n - 1)t_{sp}, \quad (4)$$

where  $t_{sp}$  is the width of the double spacer formed by a poly-silicon spacer (with width  $t_{Si}$ ) and an oxide spacer (with width  $t_{ox}$ ),  $t_{sp} = t_{Si} + t_{ox}$ , and the meaning of  $a^0$  will be discussed later.

In  $S^nPT$ , alternate spacers of poly-silicon and oxide are grown after conformal deposition and anisotropic etching. This process results in the reproduction indentations only if  $b_n > 2nt_{sp}$ . If this condition is not satisfied, at a certain stage of the  $S^nPT$  the indentation is completely filled. Suppose now that the indentation width  $b_k$  satisfies the following condition:

$$b_k = 2t_{Si} + 2(k - 1)t_{sp}. \quad (5)$$

When condition (5) is satisfied, the first  $S^nPT$  step fills the first indentation (Fig. 5B); the inspection of Fig. 5 shows that this phenomenon extends progressively to the  $k^{\text{th}}$  indentation with the order  $k$  of bar deposition. After step  $k$ , the central region of each indentation up to the  $k^{\text{th}}$  is filled with a poly-silicon bar of width  $2t_{Si}$ ; the remaining part of the cave is filled with  $(k - 1)$  double layers each of width  $t_{sp}$ . At the end of the  $S^nPT$  (Fig. 5D) all indentations have their central zone connected with only one nanowire running out of the original indentation.

After the  $S^nPT$  completion, the process continues with the deposition of a dielectric film ( $\text{SiO}_2$ ) on the whole structure and with the definition of  $n$  rectangular windows (of nominal sides  $a^0$  and width  $2t_{Si}$ ) aligned on the central zone of each cave (Fig. 5E). The process is concluded with the deposition of a metal film and the definition of  $n$  metal strips contacting the single nanowires.

The functions  $a^0$  and  $b^0$  are now clear:  $a^0$  controls the area metal–poly-silicon contacts, whereas  $b^0$  is determined by the minimum allowed distance between metal strips (Fig. 5F).

The process described above has the great advantage of allowing the definition of the nano-litho contacts simultaneously to the formation of the wire array. It is, however, stressed that the considered architecture is quite demanding about the mask. To evaluate the tolerance, we observe that the maximum width  $b_k^{\text{max}}$  of the  $k^{\text{th}}$  indentation must be not so large as to allow the formation therein of filaments of the  $(k + 1)^{\text{th}}$  wire:

$$b_k^{\text{max}} = 2kt_{sp}; \quad (6)$$

the minimum width  $b_k^{\text{min}}$  of the  $k^{\text{th}}$  indentation must instead be so large as to guarantee that the  $k^{\text{th}}$  wire

therein is certainly connected to the wire forming the crossbar:

$$b_k^{\min} = 2(k - 1)t_{\text{sp}} + t_{\text{Si}}, \quad (7)$$

where the wire continuity has been assumed to be certain when the wire has a thickness  $t_{\text{Si}}$ . Combining Eqs. (6) and (7), one has

$$\begin{aligned} b_k^{\max} - b_k^{\min} &= 2t_{\text{sp}} - t_{\text{Si}} \\ &= t_{\text{sp}} + t_{\text{ox}}; \end{aligned} \quad (8)$$

In the case of Fig. 3 (with  $t_{\text{sp}} = 35$  nm and  $t_{\text{ox}} = 5$  nm), Eq. (8) gives a tolerance, of  $\pm 20$  nm, compatible with the current technology. It is however noted that the mask opening the contacts in the worst case (7) should have a maximum size (along the wire) of just  $t_{\text{sp}} + t_{\text{ox}}$ ; in the example of Fig. 3  $t_{\text{sp}} + t_{\text{ox}} = 40$  nm, inconsistent with the current technology. This value would run in the range achievable with standard photolithography only taking a larger value of  $t_{\text{ox}}$ .

The process is not optimized. Area occupancy can be reduced taking, instead of the constant value  $a_k$  of Eq. (4), a value varying with  $k$ . For instance, choosing

$$a_k = a^0 + (k - 1)t_{\text{sp}} \quad (9)$$

still allows the nano-to-micro link saving more space.

The crossing of these  $n$  nanowires with the analogue ones, perpendicularly oriented and lying on a parallel plane (obtained by the deposition or growth of an oxide of thickness adapted to the molecular size) results in the crossbar. Since the access to each single cross-point is independent of the other, the described addressing strategy is suitable for application to RAMs.

### Energetic Filtering

Whereas in IL all wires are defined collectively, in  $S^n$ PT they are constructed sequentially. The batch fabrication would make preferable IL over  $S^n$ PT unless one were able to use the sequential array deposition for the external recognition of single wires.

An inspection of the right side of Fig. 3 shows that multispacer patterning results in wires whose height is progressively reduced with the order of preparation (the reader will easily convince herself or himself that the amount of this decrease can be magnified in a controlled way via slight changes in the  $S^n$ PT). Cerofolini proposed to exploit this spatial difference for the recognition and separation of single nanoscopic wires by electrical probes.<sup>[38]</sup>

In this case, the crossbar is built before the addressing system, exactly as in “The Horizontal Beveling

Technique.” Let  $r_i$  and  $c_j$  denote the  $i^{\text{th}}$  row and  $j^{\text{th}}$  column, respectively, and  $(r_i, c_j)$  be the cross-point they define. All the rows  $r_i$  (columns  $c_j$ ) run below a photolithographically defined electrode  $\text{GE}_r$  ( $\text{GE}_c$ ) and finally terminate at a unique photolithographically defined contact  $C_r$  ( $C_c$ ), as it is well represented in the cross-sections in Fig. 6. The process is arranged in a way that electrodes  $\text{GE}_r$  and  $\text{GE}_c$  are separated from the underlying wires by an insulator of fixed thickness. Exploiting the electrodes as self-aligned masks, the nanowires are highly doped everywhere but below the electrodes via ion implantation and subsequent thermal activation of a suitable dopant.

This configuration reminds us of a transistor in depletion mode, where  $\text{GE}_r$  and  $\text{GE}_c$  operate as control

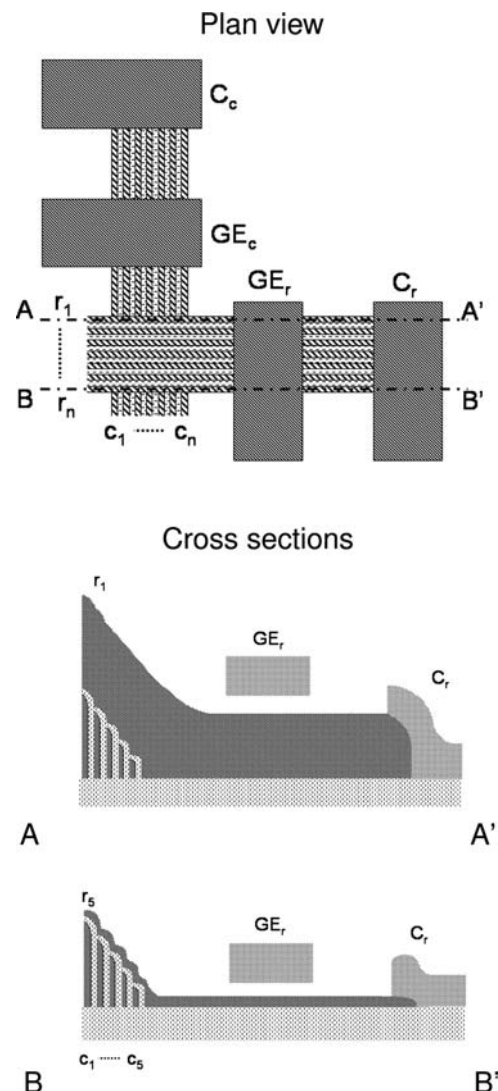


**Fig. 6** Plan view of the crossbar and of the lithographically defined contacts (*up*) and views projected on planes AA' and BB' perpendicular to the surface and crossing the tallest and smallest row lines, respectively (*down*).

gates, the underlying slightly doped sector of nanowire as the semiconductor channel, and the adjacent highly doped sectors as drain and source. If no voltage is applied on gates with respect to the body, the carriers are free to move in the whole nanowire; if a repulsive voltage is applied, the channel is depleted and no current flow between  $C_r$  and  $C_c$ . In principle, the voltage necessary to disable a nanowire decreases with its height.

For assigned poly-silicon nanowire doping and insulator thickness, it exists at least one couple of voltage values of  $GE_r$  and  $GE_c$ , which makes only the highest wires,  $r_1$  and  $c_1$ , not totally depleted. In this case, the current  $I_{(1,1)}$  flowing from the contact  $C_r$  to the contact  $C_c$  is controlled by the conduction state of cross-point ( $r_1$ ,  $c_1$ ) alone. If the voltage of  $GE_c$  is modified in such a way that even the wire immediately shorter,  $c_2$ , is enabled, the current flowing from  $C_r$  to  $C_c$  becomes the sum of the current  $I_{(1,1)\cup(1,2)}$  flowing through ( $r_1$ ,  $c_1$ ) and ( $r_1$ ,  $c_2$ ). If  $I_{(1,1)}$  was memorized, the current  $I_{(1,2)}$  flowing through ( $r_1$ ,  $c_2$ ) (giving its state) is obtained as difference  $I_{(1,1)\cup(1,2)} - I_{(1,1)}$ .

Reiterating the argument to all cross-points, the states of each of them can be determined provided that the information contents of all cross-points are memorized in a buffer memory. This implies that only a small part of the crossbars can be read in parallel, because each one needs the availability of a circuitry for analog-to-digital conversion and for the manipulation of the information.

By the time, the addressing system depends only on the different heights of the nanowires induced by the S<sup>PT</sup> technology. Some modification can be introduced to optimize the process. If the poly-silicon wires are doped singularly (for instance, via gas-phase doping during each poly-silicon deposition), the difference in the threshold voltage from one wire to the subsequent may be enlarged. Also the oxide thickness between wires and electrodes  $GE_r$  and  $GE_c$  can be varied, achieving the same result about threshold voltage tuning, even if this procedure is quite more demanding for technology.

## REFERENCES

- Simon & Schuster; *Webster's New Twentieth Century Dictionary*, 2nd Ed.; New York, 1979, item 1.
- Tour, J.M. Molecular wires and devices. In *Stimulating Concepts in Chemistry*; Vögtle, F., Stoddart, J.F., Shibasaki, M., Eds.; Wiley-VCH: Weinheim, 2000; 237.
- Cerofolini, G.F.; Ferla, G. Toward a hybrid micro-nanoelectronics. *J. Nanoparticle Res.* **2002**, *4*, 185–191.
- Chen, J.; Reed, M.A.; Rawlett, A.M.; Tour, J.M. Large on-off ratios and negative differential resistance in a molecular electronic device. *Science* **1999**, *286*, 1550–1552.
- Heath, J.R.; Kuekes, P.J.; Snider, G.S.; Williams, R.S. A defect-tolerant computer architecture: opportunities for nanotechnology. *Science* **1998**, *280*, 1716–1721.
- Ziegler, M.M.; Stan, M.R. CMOS/nano co-design for crossbar-based molecular electronic systems. *IEEE Trans. Nanotechnol.* **2003**, *2*, 217–230.
- DeHon, A. Array-based architecture for FET-based, nanoscale electronics. *IEEE Trans. Nanotechnol.* **2003**, *2*, 23–32.
- Mendes, P.M.; Flood, A.H.; Stoddart, J.F. Nanoelectronic devices from self-organized molecular switches. *Appl. Phys. A* **2005**, *80*, 1197–1209.
- Luo, Y.; Collier, C.P.; Jeppesen, J.O.; Nielsen, K.A.; Delonno, E.; Ho, G.; Perkins, J.; Tseng, H.R.; Yamamoto, T.; Stoddart, J.F.; Heath, J.R. Two-dimensional molecular electronics circuits. *Chem. Phys. Chem.* **2002**, *3*, 519–525.
- Service, R.F. Next-generation technology hits an early midlife crisis. *Science* **2003**, *302*, 556–559.
- Stewart, D.R.; Ohlberg, D.A.A.; Beck, P.; Chen, Y.; Williams, R.S.; Jepsen, J.O.; Nielsen, K.A.; Stoddart, J.F. Molecule-independent electrical switching in Pt/organic monolayer/Ti devices. *Nano Lett.* **2004**, *4*, 133–136.
- Lau, C.N.; Stewart, D.R.; Williams, R.S.; Bockrath, D. Direct observation of nanoscale switching centers in metal/molecule/metal structures. *Nano Lett.* **2004**, *4*, 569–572.
- Zhitenev, N.B.; Jiang, W.; Erbe, A.; Bao, Z.; Garfunkel, E.; Tennant, D.M.; Cirelli, R.A. Control of topography, stress and diffusion at molecule-metal interfaces. *Nanotechnology* **2006**, *17*, 1272–1277.
- Stewart, M.P.; Maya, F.; Kosynkin, D.V.; Dirk, S.M.; Stapleton, J.J.; McGuinness, C.L.; Allara, D.L.; Tour, J.M. Direct covalent grafting of conjugated molecules onto Si, GaAs and Pd surfaces from aryldiazonium salts. *J. Am. Chem. Soc.* **2004**, *126*, 370–378.
- Green, J.E.; Choi, J.W.; Boukai, A.; Bunimovich, Y.; Johnston-Halperin, E.; Delonno, E.; Luo, Y.; Sheriff, B.A.; Xu, K.; Shin, Y.S.; Tseng, H.R.; Stoddart, J.F.; Heath, J.R. A 160-kilobit molecular electronic memory patterned at  $10^{11}$  bits per square centimetre. *Nature* **2007**, *445*, 414–417.
- Akkerman, H.B.; Blom, P.W.M.; de Leeuw, D.M.; de Boer, B. Towards molecular electronics with large-area molecular junctions. *Nature* **2006**, *41*, 69–71.
- Semiconductor Industry Association (SIA); *International Technology Roadmap for Semiconductors*. 2005 Edition; available at: <http://public.itrs.net>
- Natelson, D.; Willett, R.L.; West, K.W.; Pfeiffer, L.N. Fabrication of extremely narrow metal wires. *Appl. Phys. Lett.* **2000**, *77*, 1991–1993.
- James, D.K.; Tour, J.M. Molecular electronics: Logic and memory. In *Dekker Encyclopedia of Nanoscience and Nanotechnology*, 2E; Schwarz, J.A., Contescu, C.I., Putyera, K., Eds.; Taylor & Francis: New York, NY, 2009; Vol. 4, 2303–2316.
- Cerofolini, G.F.; Narducci, D.; Romano, E. Silicon functionalization for molecular electronics. In *Dekker Encyclopedia of Nanoscience and Nanotechnology*, 2E;



- Gusev, E., Korkin, A., Labanowski, J., Luryi, S., Eds.; Taylor & Francis: New York, NY, 2009; Vol. 6, 4009–4020.
21. Melosh, N.A.; Boukai, A.; Diana, F.; Gerardot, B.; Badolato, A.; Heath, J.R. Ultrahigh-density nanowire lattices and circuits. *Science* **2003**, *300*, 112–115.
  22. Cerofolini, G.F.; Arena, G.; Camalleri, M.; Galati, C.; Reina, S.; Renna, L.; Mascolo, D.; Nosik, V. Strategies for nanoelectronics. *Microelectr. Eng.* **2005**, *81*, 405–419.
  23. Cerofolini, G.F.; Arena, G.; Camalleri, M.; Galati, C.; Reina, S.; Renna, L.; Mascolo, D. A hybrid approach to nanoelectronics. *Nanotechnology* **2005**, *16*, 1040–1047.
  24. Cerofolini, G.F. An extension of microelectronic technology to nanoelectronics. *Nanotechnol. E-Newslett.* **2005**, *7*, 5–6.
  25. Choi, Y.K.; King, T.J.; Hu, C. A spacer patterning technology for nanoscale CMOS. *IEEE Trans. Electron Devices* **2002**, *49*, 436–441.
  26. Choi, Y.K.; Zhu, J.; Grunes, J.; Bokor, J.; Somorjai, G.A. Fabrication of sub-10-nm silicon nanowire arrays by size reduction lithography. *J. Phys. Chem. B* **2003**, *107*, 3340–3343.
  27. Roukes, M. Plenty of room indeed. *Sci. Am. Rep.* **2007**, *17* (3), 4–11.
  28. Huang, Y.; Duan, X.; Cui, Y.; Lauhon, L.J.; Kim, K.H.; Lieber, C.M. Logic gates and computation from assembled nanowire building blocks. *Science* **2001**, *294*, 1313–1317.
  29. Zhong, Z.; Wang, D.; Cui, Y.; Bockrath, M.W.; Lieber, C.M. Nanowire crossbar arrays as address decoders for integrated nanosystems. *Science* **2003**, *302*, 1377–1379.
  30. Alley, R.; Cumbie, M.; Enck, R.; Huang, D.; Kornilovitch, P.; Ramamoorthi, S.; Wu, J.; Yang, X. Misalignment-tolerant H-hot demultiplexer for nanowire arrays. *MST News No. 4/06* **2006**, 8–10.
  31. Likharev, K.K. Electronics below 10 nm. In *Nano and Giga Challenges in Microelectronics*; Greer, J., Korkin, A., Labanowski, J., Eds.; Elsevier: Amsterdam, 2003; 27–68.
  32. Likharev, K.K.; Strukov, D.B. CMOL: Devices, circuits, and architectures. In *Introducing Molecular Electronics*; Cuniberti, G., Fagas, G., Richter, K., Eds.; Springer: Berlin, 2005; 447–477.
  33. Strukov, D.B.; Likharev, K.K. Prospects for terabit-scale nanoelectronic memories. *Nanotechnology* **2005**, *16*, 137–148.
  34. Beckman, R.; Johnston-Halperin, E.; Luo, Y.; Green, J.E.; Heath, J.R. Bridging dimensions: demultiplexing ultrahigh-density nanowire circuits. *Science* **2005**, *310*, 465–468.
  35. Wu, W.; Jung, G.Y.; Olynick, D.L.; Strasnick, J.; Li, Z.; Li, X.; Ohlberg, D.A.A.; Chen, Y.; Wang, S.Y.; Liddle, J.A.; Tong, W.M.; Williams, R.S. One-kilobit cross-bar molecular memory circuits at 30-nm half-pitch fabricated by nanoimprint lithography. *Appl. Phys. A* **2005**, *80*, 1173–1178.
  36. Cerofolini, G.F.; Mascolo, D. A hybrid micro-nano-molecular route for nonvolatile memories. *Semicond. Sci. Technol.* **2006**, *21*, 1315–1325.
  37. Cerofolini, G.F.; Mascolo, D. A hybrid route from CMOS to nano and molecular electronics. In *Nanotechnology for Electronic Materials and Devices*; Gusev, E., Korkin, A., Labanowski, J., Luryi, S., Eds.; Springer: New York, 2006; 1–65.
  38. Cerofolini, G.F. Realistic limits to computation. II. The technological side. *Appl. Phys. A* **2007**, *86*, 31–42.

# Low-Dielectric Constant Materials

**Robert D. Miller**

*Advanced Organic Materials, IBM Almaden Research Center,  
San Jose, California, U.S.A.*

## INTRODUCTION

While the prefix nano- became the scientific buzzword for the last decade of the 20th century, nanotechnology has become the technology driver for the 21st. Although nanotechnology really means the ability to fabricate and control functioning structures integrated over size scales ranging from nanometers to centimeters, “smaller” has captured the imagination of the public and funding agencies.

The semiconductor industry is an example built on the foundations of nanotechnology. Integrated semiconductor devices have become progressively smaller to improve performance and accommodate an increase in functional density. This obsession has driven the industry for the last 30–40 yr. As device densities increase and component dimensions shrink, the relative effect of the on-chip wiring on performance progressively increases. Many performance issues can be ameliorated by the introduction of low-*k* insulators as replacements for silicon dioxide, thus stimulating a flurry of interest in these materials.

In this entry, we have focused on the need for new low-*k* insulators, the timing for introduction of new materials and processes, the chemical nature of the dielectrics and methods of application, the role of porosity in future dielectric insulators and we end with opportunities beyond porous materials. We have tried to focus on the new materials and chemistry; the review does not deal extensively with the characterization and integration of low-*k* films, except in the context of current integration processes and concerns. The topic of the review is particularly timely given the key role that new materials will play in evolutionary complementary metal oxide semiconductor (CMOS) device performance and the fact that the first truly low-*k* materials are just now appearing in volume chip manufacturing.

## BACKGROUND

For many years, semiconductor manufactures have produced new generations of products according to Moore’s Law, which states that device densities on

chips should approximately double every 18–24 mo.<sup>[1,2]</sup> Fig. 1 shows a relative size comparison for a number of common objects. Scaling in semiconductors has required a continuous reduction in device dimensions. The transistors and other active electronic devices are integrated into the substrate (usually silicon) and are connected with each other and to the outside world by a myriad of on-chip wiring. This interconnect wiring, on-chip insulation, and local packaging is often referred to as the back-end-of-the-line (BEOL), while the active devices on the substrate constitute the front-end-of-the-line (FEOL) portion of the chip. Advanced chips many contain hundreds of millions of active devices with the interconnect wiring distributed over 8–10 vertical wiring levels and approaching 10,000 m in cumulative length. All of this is integrated on chips with 1–3 cm<sup>2</sup> total surface area. A typical BEOL configuration is illustrated schematically in Fig. 2, while Fig. 3 shows a number of chip cross-sections from some commercial processor chips. Both Figs. 2 and 3 also show an actual IBM seventh generation CMOS microprocessor from which the insulating oxide has been removed to reveal the copper BEOL wiring.

As device dimensions decrease and device densities increase, chip performance degrades owing to signal delays and cross talk between the conductor lines. Signal propagation delays are characterized by the product of metal resistance times the capacitance of the lines (RC), which has the dimensions of time.<sup>[3]</sup> Various equations describing the signal delays and power consumption are shown in Fig. 4. The RC delay depends on the resistivity of the wiring metallurgy, the dielectric constant(s) of the insulating media, and the dimensions and configuration of the metal lines. The relatively recent change in metallurgy from aluminum to copper has reduced the resistivity of the metal by about 30%, providing a significant improvement in performance.<sup>[4]</sup> Copper metallurgy is now standard for advanced logic devices and will remain so for the foreseeable future. The difficulty in gas phase etching of copper has necessitated the development of polishing processes [chemical mechanical polishing (CMP)] to planarize metallized structures. Such an integration technique is known as a damascene process and can



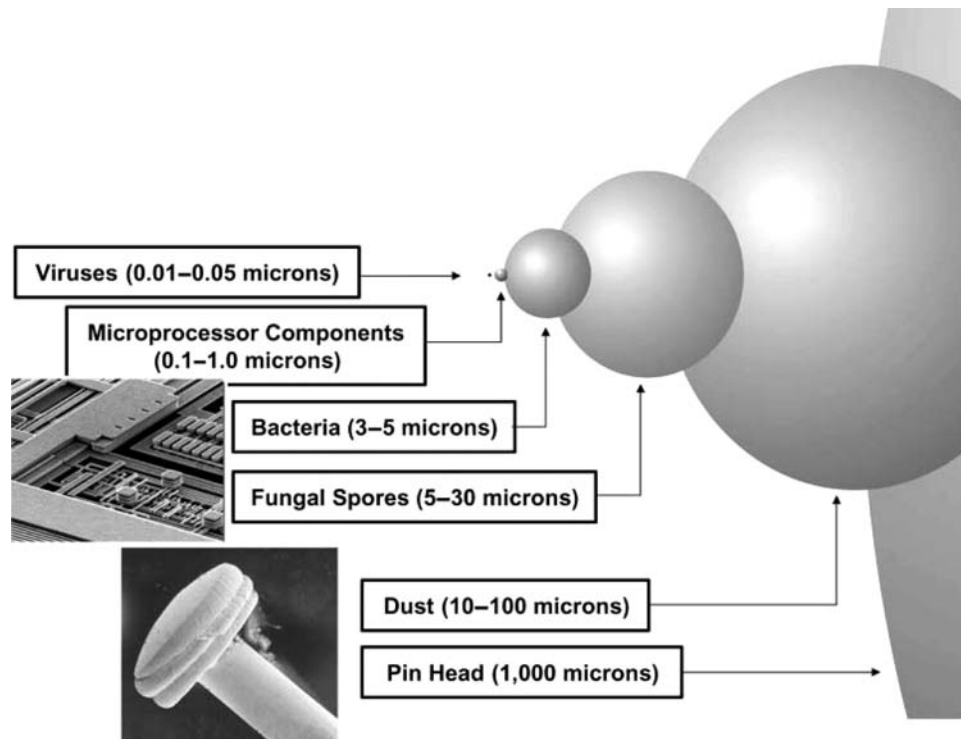


Fig. 1 Relative size comparison of common objects.

be further characterized as either single or dual damascene (Fig. 5) depending on whether the lines and layer-connecting vias are processed separately or together.<sup>[5]</sup> Further examination of Fig. 4 shows that the dielectric constant of the on-chip insulating media has a strong influence on both signal delays and power consumption. Until the end of the last decade, this insulator was invariably SiO<sub>2</sub> with a dielectric constant

ranging from 3.9 to 4.2 depending on the deposition and/or processing technique. Signal delays and power consumption are currently driving the search for low-*k* alternatives to SiO<sub>2</sub>. The replacement of silicon dioxide has proved much more difficult than anticipated. For example, the International Technology Roadmap for Semiconductors (ITRS) predicted in 1999 that the 90 nm device generation would employ insulators with

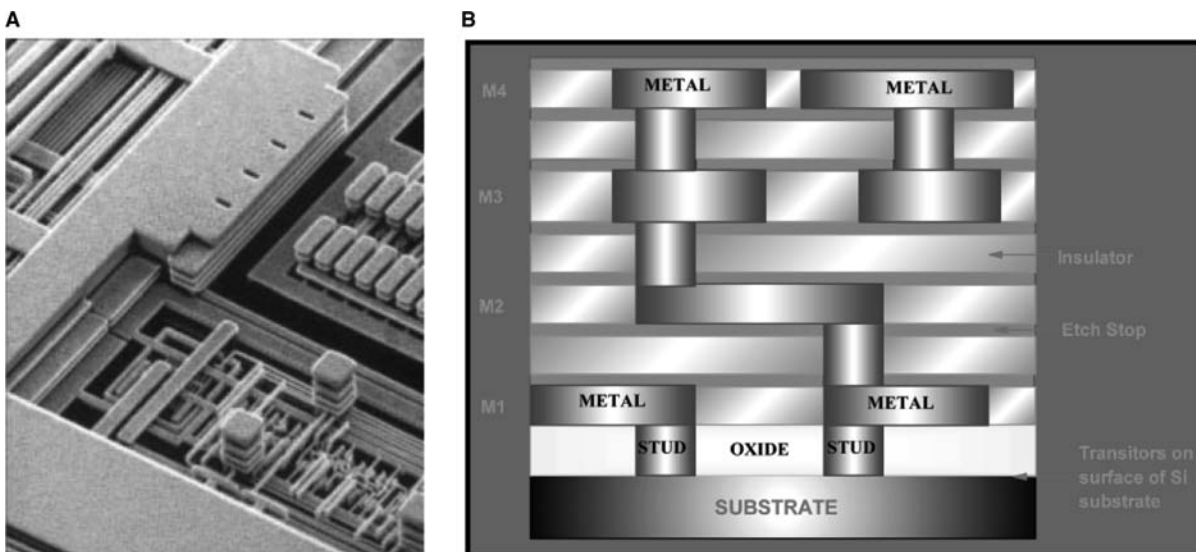


Fig. 2 (A) IBM CMOS seventh generation microprocessor with silicon dioxide insulator removed. (B) Schematic of on-chip BEOL wiring showing insulator and wiring levels.

Low-Dielectric Constant Materials for On-Chip Applications

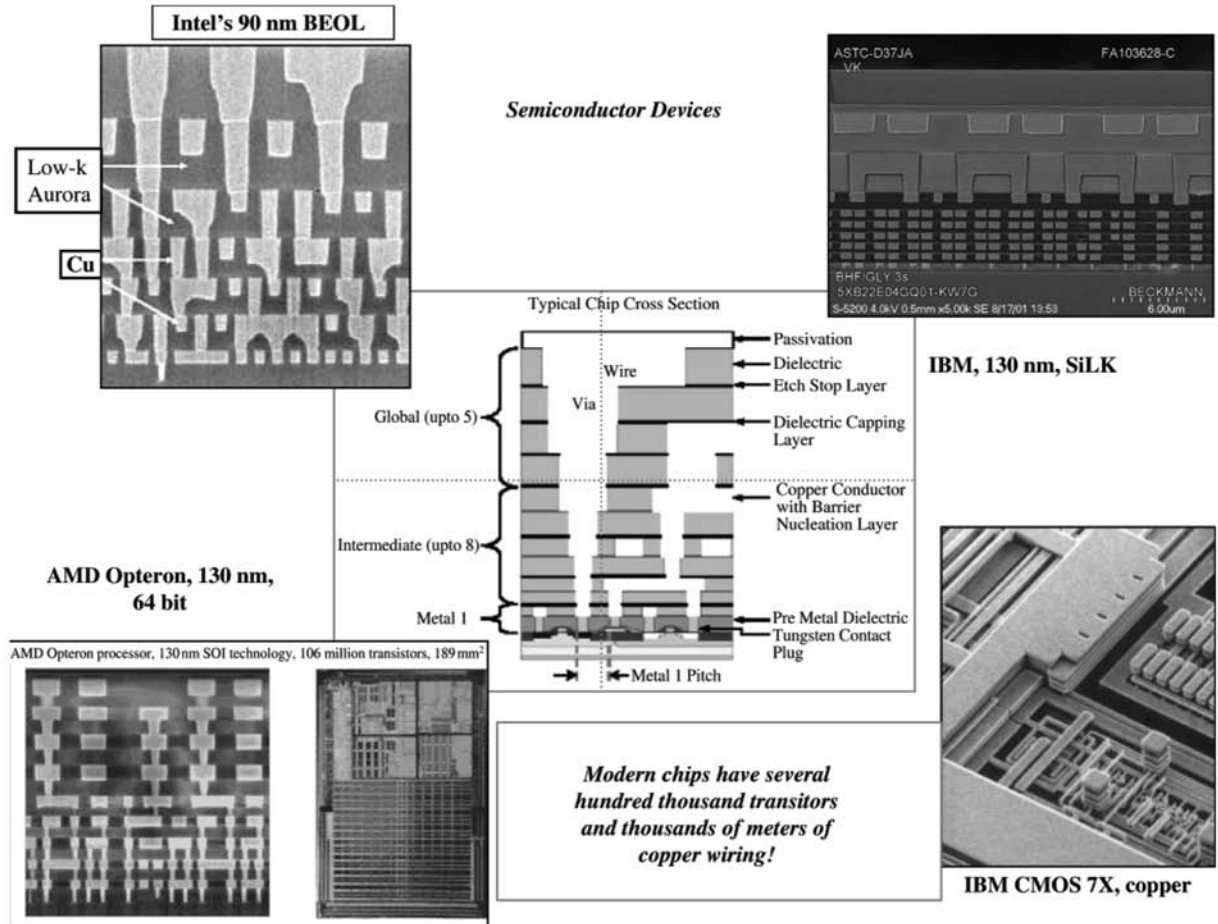


Fig. 3 Cross-section micrographs of commercial microprocessor chips; (center) schematic for BEOL wiring levels.

dielectric constants between 1.3 and 1.4 in 2005 (Table 1). Reality is that current 90 nm production node uses insulators with dielectric constants around 3.0<sup>[6,7]</sup> and the revised 2004 ITRS roadmap predicted

porous materials with  $k < 2.4$  at 65 nm in 2007.<sup>[8]</sup> In fact, the situation has changed again with most of the industry targeting a bulk dielectric  $k$  value of 2.7 (non-porous) for the 65 nm node and the first introduction of porous materials at the 45 nm node ( $k = 2.2-2.4$ ) projected for production in 2009-2010.

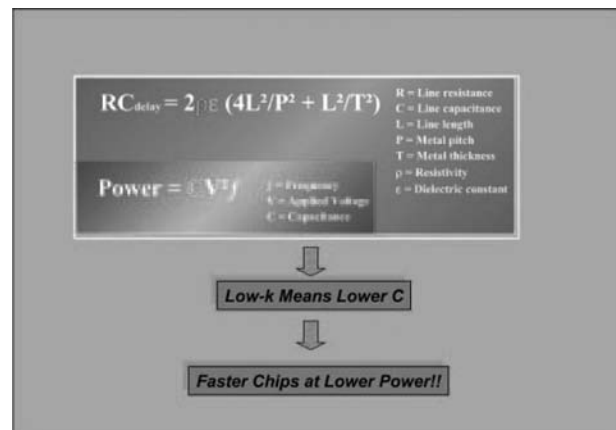
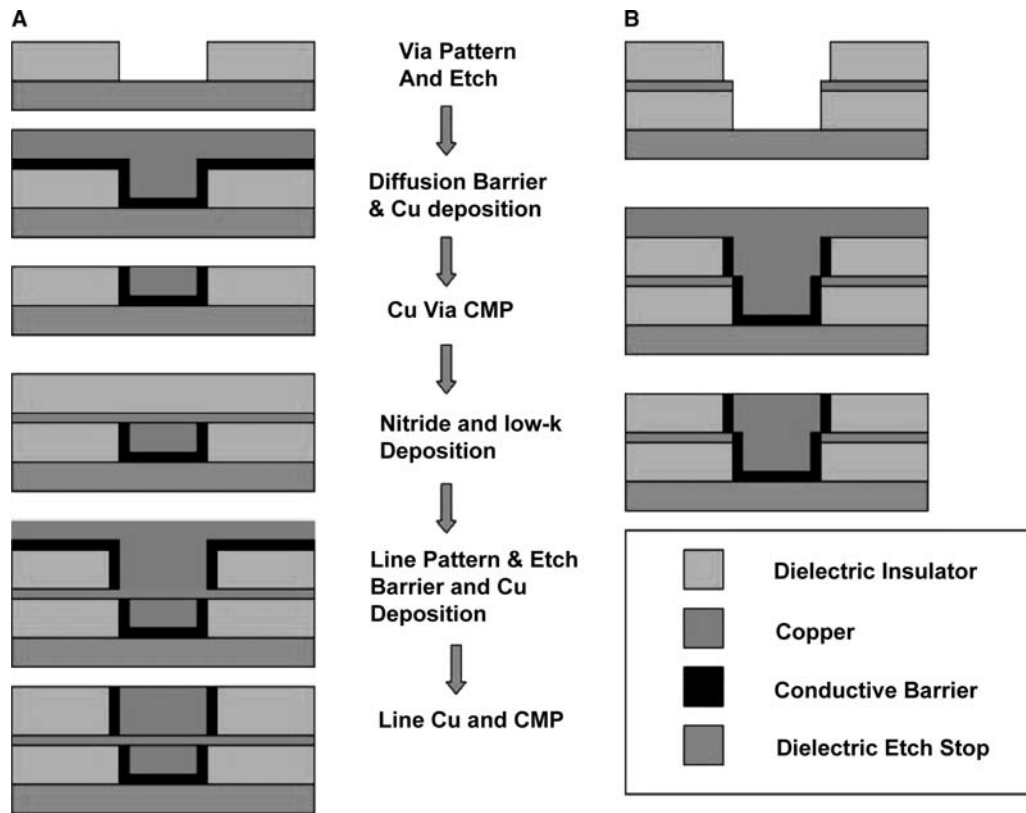


Fig. 4 RC delay and power consumption as a function of BEOL wiring capacitance.

LOW-K DIELECTRIC INSULATORS

Table 2 shows the types of materials that have been auditioned as replacements for silicon dioxide at various times. On the right hand side of the table are a set of challenging integration properties that have evolved primarily from the extensive use of SiO<sub>2</sub>. The materials in the table may be roughly divided into two classes: 1) those materials that are more inorganic in nature represented primarily by cross-linked organosilicates and 2) organic materials represented by various high-temperature organic polymers (polyarylenes, polyarylene ethers, and polyazoles). The former have good electrical and thermal properties, but are



**Fig. 5** Damascene processing for Cu interconnects; CMP is used for planarization of deposited metal (A), single damascene processing (B), and dual damascene (line and via) procedure.

fragile and prone to cracking, while the later are tough but soft with higher thermal coefficients of expansion and lower thermal stabilities. While initially both classes of materials were considered as candidates, the current situation is that the inorganic materials

have currently moved to the forefront and will be very difficult to displace. The difficulty in finding an acceptable replacement for silicon dioxide has placed a premium on dielectric extendibility i.e., maintaining a very similar elemental composition albeit with

**Table 1** ITRS BEOL Roadmap evolution from 1999 to 2003

<b>(2003)</b>							
Year of production	2003	2004	2005	2006	2007	2008	2009
Technology node		hp90			hp65		
MPU printed gate length (nm)	65	53	45	40	35	32	28
Physical gate length (nm)	45	37	32	28	25	22	20
Metal levels	9	10	11	11	11	12	12
Interconnect length (m/cm <sup>2</sup> )	579	688	907	1002	1117	1401	1559
Effective dielectric constant	3.3–3.6	3.1–3.6	3.1–3.6	3.1–3.6	2.7–3.0	2.7–3.0	2.7–3.0
Bulk dielectric constant	<3.0	<2.7	<2.7	<2.7	<2.4	<2.4	<2.4

<b>(1999)</b>					
Year of production	2002	2005	2008	2011	2014
Technology node	(130 nm)	(100 nm)	(70 nm)	(50 nm)	(35 nm)
ILDκ <sub>bulk</sub>	<2.6	<1.3–1.4	?	?	?
ILDκ <sub>eff</sub>	2.7–3.5	1.6–2.2	1.5	<1.5	<1.5

**Table 2** Material candidates for replacement of silicon dioxide BEOL insulator and integration requirements required based on the use of silicon dioxide on-chip insulators

Dielectric material	<i>k</i>	Integration requirements
Silicon dioxide	3.9–4.5	Thermal stability to 450°C
Fluorosilicate glass (FSG)	3.3–4.0	Dielectric constant <3.0 (dense)
Polyimides	3.1–3.4	<2.2 (porous)
HSSQ	2.9–3.2	High T <sub>g</sub>
Diamond-like carbon (DLC)	2.7–3.4	Low moisture absorption
Carbon-doped oxide/SiCOH	2.8–3.2	Good adhesion (caps hardmasks liners, substrates, etc.)
Parylene N	2.7	
Benzocyclobutenes	2.6–2.7	Good mechanical properties
Fluorinated polyimides	2.5–2.9	Chemical compatibility (no reaction with metallurgy, liners, etc.)
MSSQ	2.6–2.8	
Polyarylene ethers	2.7–2.9	vs. Solvent resistance
Polyarylenes	2.6–2.7	Compatibility with CMP
Fluorinated DLC (F-DLC)	2.4–2.8	High etch selectivity
Parylene-F4	2.4–2.5	Reasonable shelf life
Fluoropolymers	1.9–2.1	Environmental compliance Low cost
Porous organics	2.1–2.2	
Xerogels (silica)	2.0–2.3	Pores sizes <1/10 of minimum features
Mesoporous silica	2.0–2.2	
Porous HSSQ/MSSQ	1.4–2.2	

No single candidate meets all requirements.

progressively decreasing dielectric constants for subsequent device generations. There is no true dielectric extendibility without embracing the concept of porosity, which brings with it a new set of materials problems (e.g., pore size and distribution, poor mechanical properties, reduced thermal conductivity, and contamination issues). The only common dense organic polymers with dielectric constants in the 2.0–2.2 range are heavily fluorinated (e.g., Teflon and Teflon-AF). The presence of substantial amounts of fluorine bound to carbon causes thermal issues (temperatures >400°C) particularly in the presence of common interconnect metallurgy (Cu, Ta, TaN, W, etc.). For this reason, the use of porous materials eventually seems inevitable, although the industry will delay implementation as long as possible, certainly until the 45 nm technology node. In addition to the standard integration issues shown in Table 1, there are a number of porosity-specific integration criteria: e.g., pores must be small relative to minimum device dimensions, the pore distribution should be uniform, the porous surfaces must be uniformly covered by added integration layers (caps, hardmasks, etch barriers, liners, etc.), contaminant uptake must be minimized and localized, the materials must show high strength and toughness

under low density conditions, and others. Given the requirements, it is little wonder that the introduction of any new low-*k* materials and porous materials in particular into products has been progressively delayed.

### CVD vs. Spin-on

Dielectric materials can also be classified according to their method of application. In this regard, materials can either be deposited from the gas phase by CVD or plasma enhanced chemical vapor deposition (PECVD) or by spin-on techniques. Gas phase techniques were the mode of application of silicon dioxide and capital accumulation in semiconductor manufacturing heavily favors this technique for future low-*k* materials. On the other hand, spin-on techniques are well established and are currently used primarily for the application of liquid photoresists. Generally speaking, the equipment costs for CVD processes are higher, but the materials costs are lower than for spin-on applications. The CVD processes have already been adopted at the 90 nm node ( $k \sim 3.0$ )<sup>[6,7]</sup> and provide the strongest candidates for the 65 nm node ( $k \sim 2.7$ ). These materials

**Table 3** Common chemical vapor deposition (CVD) precursors to carbon-doped oxide films: 3-TMS monomer requires an oxidizing coreagent (e.g., N<sub>2</sub>O) to produce Si–O–Si bonds in film

Molecule	Si-CH <sub>3</sub> /Si	Si-O/Si	Si-H/Si	Structure
MTES	1/1	3/1	N/A	
DEMS	1:1	2:1	1:1	
DMOMS	1:1	2:1	1:1	
DMDMOS	2:1	2:1	N/A	
DMDOSH	2:1	2:1	N/A	
OMCATS	2:1	1:1	N/A	
3MS	3:1	N/A	1:1	

will not be significantly porous. The first appearance of porous materials will be at the 45 nm node and even there only at the levels where low-*k* materials provide the maximum performance benefits. Table 3 shows some typical CVD dielectric precursors. Most viable candidates contain the elements of C, H, O, and Si.

When oxygen is not present in the precursors, it is usually introduced in the form of a plasma oxidant e.g., oxygen, N<sub>2</sub>O, H<sub>2</sub>O<sub>2</sub>, CO<sub>2</sub>, etc. The film products have complicated cross-linked structures comprised of rings and chains and are known collectively as carbon-doped oxides (CDO) or SiCOH materials. The dielectric constants and 3-D structures can be tuned to some degree by varying the plasma and deposition conditions. Depending on the tool supplier and monomer(s) employed, the dielectric products are designated by various vendor names, e.g., Aurora (ASM), Black Diamond (Applied Materials), and Coral (Novellus). Some common CVD precursors are shown in Table 3, each with its own champion. In spite of the availability of spin-on candidates for *k* = 2.6–3.0, including polyarylene ethers (VELOX, Schumacher/Air Products,<sup>[9]</sup> and Flare, Honeywell<sup>[10]</sup>) and polyarylenes (SiLK, Dow Chemical),<sup>[11]</sup> CVD-deposited CDO materials will dominate both the 90 and 65 nm device generation nodes.<sup>[8]</sup> While the electrical and thermal properties of CVD-deposited CDO materials can be excellent, the

mechanical properties are less so—a situation that will be exacerbated by the transition from dense to porous materials. Fortunately, critical mechanical properties such as modulus, fracture toughness, and fracture energy can often be improved by postdeposition e-beam or UV treatment.<sup>[12,13]</sup> Such postdeposition treatment becomes essential for porous materials regardless of the mode of application (vide infra).

## Mechanical Properties

Fracture energies, fracture toughness, and cohesive energies are important parameters related to the mechanical properties of the film.<sup>[14]</sup> For fragile materials such as organosilicates, they are related to the formation and propagation of devastating cracks. However, measurement of fracture energies, fracture toughness, and cohesive energies is not trivial, often requires specialized equipment, and is time consuming and tedious. For this reason, the film modulus is often used as a predictor of mechanical properties. Modulus together with film stress are important contributors to the mechanical properties of thin films. Fracture toughness, fracture energy, and modulus are interrelated as shown below in Fig. 6. Modulus is the easiest of these properties to measure in thin, constrained films.

The most widespread measurement technique is nanoindentation, which produces values for both the modulus and the hardness.<sup>[15,16]</sup> This technique can, however, result in inaccurate values for very thin films, is prone to substrate effects, and is less applicable for fragile and crushable materials. More recently, surface acoustical wave spectroscopy (SAWS) has been used to study film properties in constrained systems, particularly for very thin films.<sup>[17–19]</sup> The numbers from SAWS measurements are almost always lower than those generated by nanoindentation, sometimes significantly so. The actual difference in the modulus values measured by the two techniques also depends on the structure and composition of the films. Techniques for the complete characterization of thin film insulators (thermal, mechanical, and electrical), both dense and porous, have been recently reviewed by Maex et al.<sup>[20]</sup> and will not be discussed in detail here.

## POROUS MATERIALS

The transition from dense to porous materials is inevitable for dielectric constants less than 2.4. Porous spin-on materials have a longer history starting with silica aerogels (formed by solvent extraction with supercritical CO<sub>2</sub>)<sup>[21,22]</sup> and evolving to xerogels where the solvent occupying the pores is removed by successive solvent exchange and careful thermal processing.<sup>[23–25]</sup> Higher boiling solvents have also been trapped in films that are cross-linked with gas phase catalysts (e.g., NH<sub>3</sub>) and serve ultimately as pore generators.<sup>[26]</sup> For silica xerogels, porosities of 70–80% are common and dielectric constants of <2.0 have been demonstrated, although the mechanical properties are quite poor. One problem with silica matrices, aside from the high dielectric constant of the dense matrix, is that they tend to be hydrophilic, leading to the uptake of water and other polar contaminants

during processing. A potential solution to this problem is post-porosity silylation<sup>[27,28]</sup> (hexamethyldisilazane is often utilized) to passivate the reactive sites. For this job, many reagents have been auditioned in the gas phase, in solution, or dissolved in supercritical CO<sub>2</sub>. The lack of surface tension effects in supercritical fluids (SCFs) allows the reagents to be introduced into small features without difficulty.<sup>[29,30]</sup> Silylation, particularly with multifunctional reagents, can also lead to improved mechanical properties of porous films. An alternative approach to the formation of porous hydrophobic materials is to substitute more hydrophobic monomers such as methyl triethoxysilane for tetraethyl orthosilicate either completely or in mixture in the sol–gel process. The result is the formation of an intrinsically more hydrophobic matrix (vide infra).

## Porosity without Added Pore Generators

In general, there are many ways of introducing porosity into thin films. A number of them can be used to generate nanoporous organic and inorganic films. These techniques may be roughly divided into those that do not require sacrificial pore generators (porogens) and those that do. Without porogens, the amount of porosity that can be introduced is limited although *k* values down to 2.2 seem to be attainable in some cases. There are a number of techniques that can be used to generate porosity without adding a sacrificial porogen. A non-comprehensive list would include: 1) introduction of free volume into the films via the use of large and poorly packing substituents;<sup>[31]</sup> 2) the use of SCFs, which dissolve in and plasticize the films such that nucleation sites can be produced to introduce nanoscopic porosity;<sup>[32]</sup> 3) the generation of particles with a predetermined shape and reactive functionality on the particle surface, which can subsequently be sintered to produce a matrix containing interstitial volume;<sup>[33,34]</sup> 4) the incorporation of particles containing meso and/or microporosity already into a reactive matrix followed by sintering to incorporate the particle into the matrix;<sup>[35]</sup> and 5) assembly of porous yet shape-persistent particles into a contiguous array to introduce porosity. Some of these techniques have been applied for the generation of both organic and inorganic porous films. For example, recently route (1) has been auditioned for the generation of thermally stable organic polymer films and dielectric constants as low as 2.4 have been demonstrated. Amorphous nanoporous polymer films have been produced using polyimides and supercritical CO<sub>2</sub> at high temperatures, although the procedure has yet to be demonstrated for thin films of <10 μm using route (2). There are a number of porous organosilicate materials where the porosity is introduced by

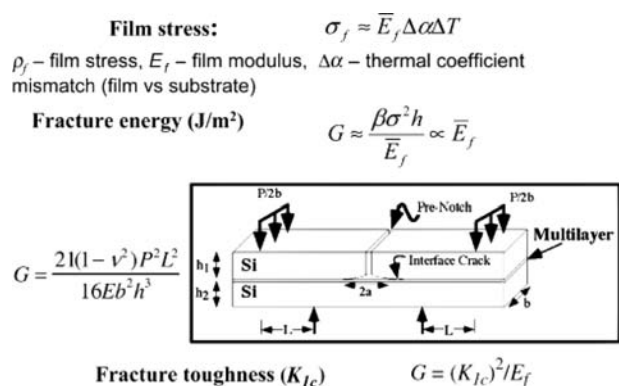


**Fig. 6** Mechanical properties of constrained thin films; (insert) four-point bending technique for measurement of fracture energies (*G*).



the interstitial packing of preformed functionalized particles. These particles can be composed of primarily surface functionalized silica or more hydrophobic versions containing substituted organosilicate particles. Using this technique, dielectric constants as low as 2.2 have been reported without the need for sacrificial porogens. This technique is capable of producing films with reasonable mechanical properties that can be further improved by post-porosity treatment.

### Porosity through Addition of Sacrificial Pore Generators

A large amount of effort has been devoted to the generation of porosity by the removal of a sacrificial pore generator (porogen). Using such an approach, sub-2.0 dielectric constants may be realized. This approach is applicable both for CVD and spin-on materials. The porogens may be small molecules, aggregates, oligomers or organic polymers; they can be chemically attached to the matrix<sup>[36,37]</sup> or not, but they must be easily removed without destroying the matrix material. This removal may be thermal, initiated by ionizing radiation, photochemically induced, or employ some combination of techniques. Removal of the porogens must be delayed until the mechanical properties of the matrix are developed (thermosetting resins) and can resist the potentially pore-collapsing capillary forces associated with the formation of the voids.

Early entries into the nanoporous polymer dielectric arena included porous organic polymers such as polyimides,<sup>[38,39]</sup> polyarylene ethers [Velox-ELK, Schumacher,<sup>[40]</sup> and GXP-3 (Honeywell)], polyarylenes (SiLK, Dow Chemical),<sup>[41]</sup> and others. With the exception of the polyimides, all viable candidates utilize thermosetting resins. The most advanced material is SiLK Y from Dow Chemical, which uses a polyarylene matrix and a thermally labile polymeric porogen.<sup>[41]</sup> While organic polymers can be thermally stable and are often quite tough, they are intrinsically soft and have higher expansion coefficients than inorganic-like materials. For these reasons, the industry has moved to organosilicates and the organic polymers have been utilized mainly in building hybrid structures<sup>[42]</sup> containing both inorganic and organic polymeric dielectrics—a compromise structure designed to mitigate the deficiencies of both material classes.

Porous organosilicates derived from porogens have received considerable attention and have recently been realized in CVD processes by the incorporation of small molecule porogens, often terpene derivatives or other unsaturated hydrocarbons.<sup>[43–45]</sup> Although the number of porous CVD candidates and amount of accumulated data lag far behind the spin-on materials

currently, a number of strong CVD candidates have arisen for the 45 nm technology node, which likely will utilize a material with dielectric constant in the 2.4–2.5 range. The history and options for porous organosilicates from spin-on materials are much more numerous. Porogens for spin-on organosilicates include small molecules,<sup>[46]</sup> polymers with various molecular architectures, amphiphilic block copolymers (vide infra), cross-linked nanoparticles,<sup>[47]</sup> and amphiphilic core shell materials that behave like nanoparticles without the need for extensive cross-linking.<sup>[48,49]</sup>

There is extensive literature on the formation of mesoporous films (defined by IUPAC convention as pores ranging from 2–50 nm in size) using self-organized amphiphiles to template the hydrolytic condensation of reactive monomers such as tetraethylorthosilicate.<sup>[50–55]</sup> For these examples, the templating surfactants have included cationic materials, non-ionic amphiphiles, amphiphilic block copolymers, and others. Regular structures can be produced in this manner and the process is adaptable to both spin and dip coating. In these cases, the structure is produced by evaporation-induced self-assembly and the hydrolytic process is templated by the organized structures. Calcination ultimately produces pores and the pore size can be tuned to some extent by the amphiphile. Such a process has recently been demonstrated with hydrophobic alkoxy silane monomers, obviating the need for post-porosity treatment characteristic of porous silica.<sup>[56–59]</sup> An interesting variant of this templated condensation uses preorganized block copolymer films, which are subsequently phase-selectively mineralized with hydrolyzing organosilicate monomers and water in  $\text{SCCO}_2$ .<sup>[60,61]</sup> The catalyst is selectively incorporated into the hydrophilic phase and the structure of the organized block copolymer is maintained upon mineralization. Also, recently it has been demonstrated that low-*k* porous films could be generated from colloidal zeolite nanocrystals produced using templating surfactants under hydrothermal conditions.<sup>[62–64]</sup> Upon calcination of thin films of solution-spun nanocrystals, low-*k* materials with surprising mechanical properties are formed.

Amorphous, randomly oriented porous organosilicates can also be produced using porogen molecules. For any sacrificial porogen process, the decomposition of the porogen must occur after the matrix has developed enough strength to resist the capillary forces associated with pore generation. These thermally labile porogens are often oligomers or polymers. A variety of thermosetting organosilicates have been employed. Many organosilicates are hydrolysis-condensates produced from alkyl- and aryl-substituted silane monomers. The most common candidates have been silsesquioxanes (SSQs,  $\text{RSiO}_{1.5}$ )<sub>n</sub> produced by acidic hydrolysis of appropriately substituted monomers.<sup>[65]</sup>

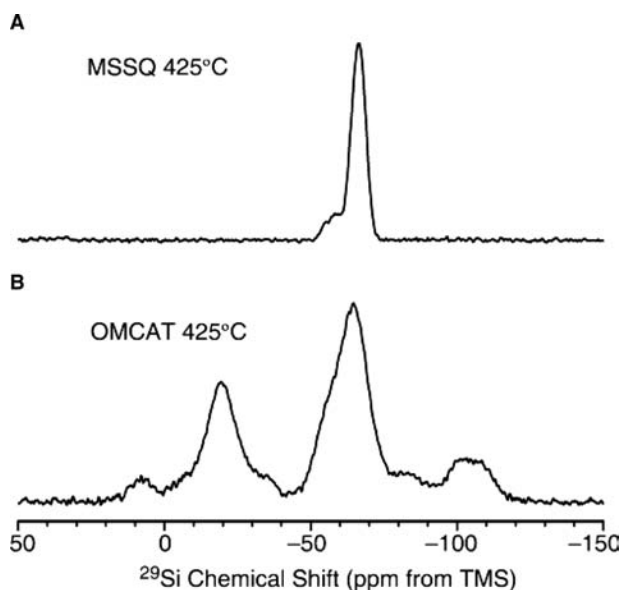


**Fig. 7** Solid state  $^{29}\text{Si}$  NMR spectra for organosilicate insulators: (A) spin-on methyl silsesquioxane spectra, sample cured to  $425^\circ\text{C}$ ; (B) PE-CVD-deposited CDO derived from OMCATS.

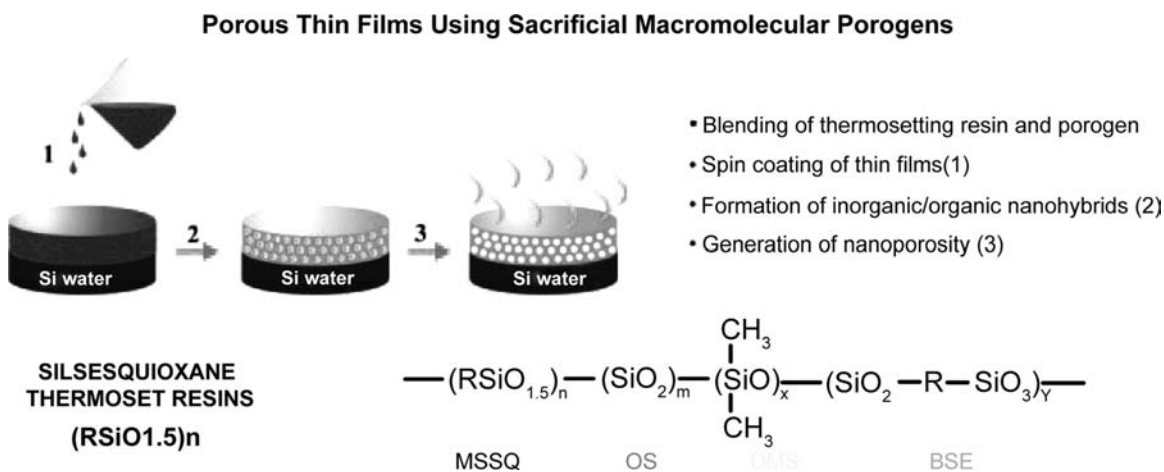
These structurally complex materials are available in a variety of structures and molecular weights, depending on the hydrolysis conditions. In general, these materials may be thermally cured to produce organosilicate films with acceptable thermal and electrical properties. Depending on the substitution, the dielectric constants of the densified organosilicates can range from 2.8 to 3.3, values substantially lower than those for silicon dioxide. Invariably, however, these materials form fragile films, which are prone to cracking, particularly in films thicker than  $1\ \mu\text{m}$ . The CVD-deposited CDOs often have similar elemental compositions, but are much more structurally complex. This is obvious in

Fig. 7, which shows solid state  $^{29}\text{Si}$  nuclear magnetic resonance (NMR) spectra of a cured, solution-spun MeSSQ material together with that of a CVD-deposited CDO derived from octamethylcyclotetrasiloxane (OMCATS). Although the functionality is similar in both cases, the CVD material is structurally much more complex. Because of the wide range of deposition parameters available for CVD and PE-CVD processes (temperature, pressure, reagent flow rates, plasma power, etc.), films with widely varying electrical and mechanical properties can be produced from the same precursor. This is not usually the case for spin-on materials where composition is fixed and the processing parameters are limited. NMR<sup>[66]</sup> and infrared<sup>[67,68]</sup> are the spectroscopic techniques that are most often used for structural analysis of cross-linked organosilicate films.

In general, both solution-spun and CVD-deposited organosilicates are fragile and must be enhanced by postcure treatment, usually using e-beams or energetic UV photons. Mechanical properties become an integration issue because of damascene processing, chip dicing, wire bonding, and other processes that require mechanically robust materials. Other troubling integration issues for organosilicates include dielectric damage upon plasma etching and plasma stripping of the developed photoresist. These issues are exacerbated in the transition from dense to porous materials. In spite of these problems, organosilicates are currently the materials of choice for the 90 nm technology and beyond.

### Nucleation and Growth vs. Templating

The simplest route to the generation of porous, spin-on organosilicates is a blending approach that involves



**Fig. 8** Blending scheme for the spin-on generation of organosilicate nanohybrids and nanoporous thin films; organosilicate resin and miscible/compatible porogen are mixed in a suitable spinning solvent.

mixing the thermosetting organosilicate that will become the matrix material with the organic porogen. Such a process is shown in Fig. 8. Although small molecules such as cyclodextrins<sup>[46]</sup> have been utilized, the most common porogen molecules are low-molecular-weight organic polymers. As most polymer mixtures are immiscible,<sup>[69]</sup> the porogen molecule must be tailored to be compatible with the organosilicate before vitrification. This usually requires strong interactions of the polymer functionality and/or the chain ends with the end groups of the SSQ prepolymers to prevent macroscopic phase separation.<sup>[70–72]</sup> As a result, low porogen molecular weights and high end-group functionality are beneficial. For this reason, stars, dendritic, and hyperbranched homo- and copolymers have been studied in some detail.<sup>[73–77]</sup> A requirement for the formation of nanoscopic hybrid domains and porosity is that the porogen must be either miscible or compatible with the organosilicate prior to curing. Phase separation must be limited until significant vitrification of the matrix has occurred, which limits domain growth (kinetically restricted). Such a process, where the components are initially miscible and phase separate after the matrix cures is called nucleation and growth (N&G), which leads to random pores, that can be quite small. A large number of blends that ultimately form porous organosilicates may be described as N&G processes. Characteristics of this type of process are random pore distributions

often with irregular shapes and dependence of the pore size and size distribution on parameters such as loading level, porogen and resin structure, porogen molecular weight, film processing conditions, etc. While N&G can be operationally simple with the right materials, control of the process is often not.

As mentioned, nucleation and growth formation of phase-separated nanodomains requires that the porogen be initially miscible in the resin precursor and phase separate after vitrification. Nanoporous organosilicates can also be made by a templating process using organic nanoparticles. For this, the nanoparticles must be compatible with the resin precursor, but not miscible. This usually requires a particle with a corona shell, which interacts strongly with the matrix precursors. Compatibilized, highly cross-linked nanoparticles have been prepared by microemulsion polymerization. These highly cross-linked examples have been used as porogens with SSQ precursors and nanoporous films with dielectric constants as low as  $k = 2.0$  have been demonstrated. Shipley has been sampling such materials for some time under the name of Zirkon.<sup>[47]</sup> The porosity in these samples seems to be randomly dispersed throughout the film and is sub-4 nm—a significant achievement using microemulsion polymerization techniques.

Recently it has been demonstrated that extensive cross-linking of organic nanoparticles is not always necessary for templating the condensation of

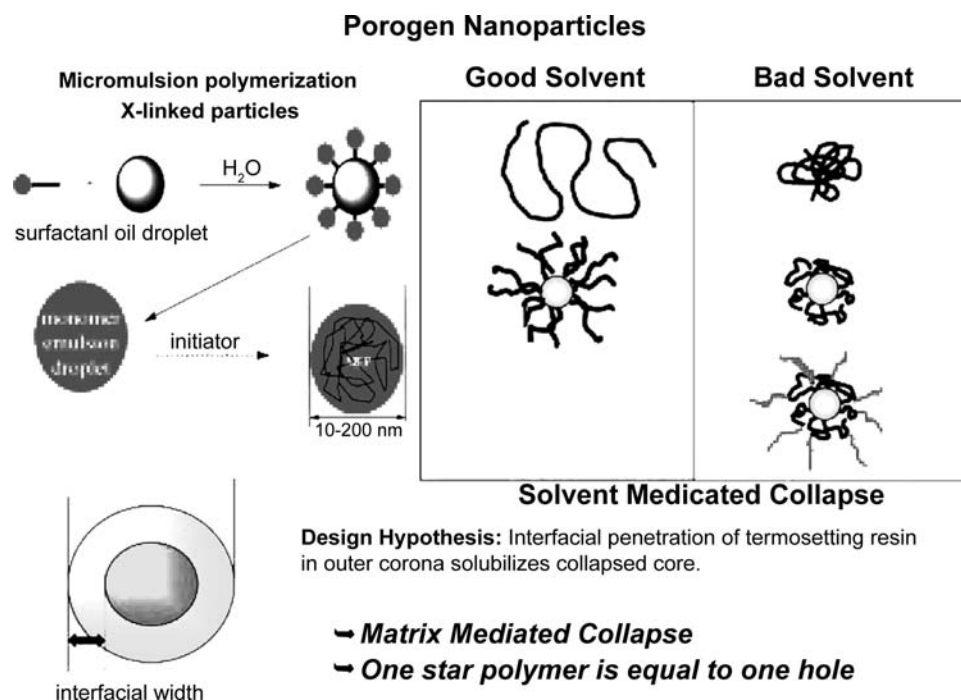


**Fig. 9** Templating particle-like behavior from core-shell amphiphiles with minimal cross-linking; hydrophobic core collapses in polar media but the particles are compatibilized by corona substitution to prevent aggregation; (top left) a schematic of a classic top-down approach to cross-linked nanoparticles by microemulsion polymerization.

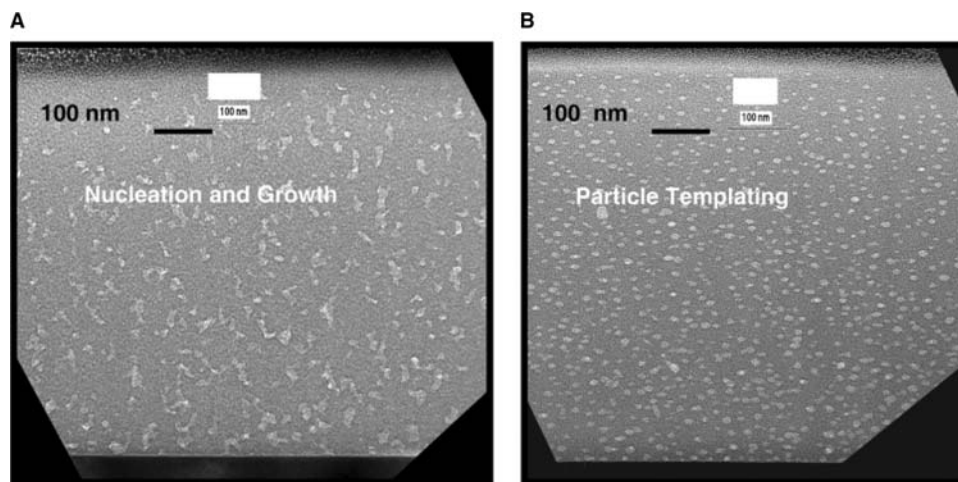


**Fig. 10** TEM cross-sections of porous MeSSQ films: (A) porosity generated by N&G porogen [poly(propylene glycol)]; (B) porosity generated by templating using core-shell amphiphilic stars (polystyrene core-PEG methacrylate corona).

organosilicates. In this regard, core-shell polymeric unimolecular amphiphiles with little or no cross-linking have been exercised as porogens in organosilicate thermosetting resins.<sup>[48,49]</sup> These materials are basically core-shell block copolymer amphiphiles where the hydrophobic core collapses in the presence of the polymer SSQ prepolymer, but aggregation is prevented by the polar, compatibilizing corona. This concept is illustrated schematically in Fig. 9. The core for the templating nanoparticle was polystyrene (anionic polymerization) while the corona was a polyethylene glycol (PEG) methacrylate shell (formed by atom transfer polymerization from the end-functionalized multiarm (20–40 arms) stars. A significant result for the templated polymerization is that one particle produces one pore (loading levels <30 wt.%) and that the size and shape of the pore is determined by the porogen molecule itself. A further distinguishing feature is that over a porogen range from 5% to 35%, the pore sizes are essential constant and only the number density changes. This is a significant difference relative to N&G processes. Fig. 10 shows a comparison of TEM micrographs for both N&G and templating porogens. In general, templating processes are easier to control and depend on fewer material and processing variables than N&G procedures. The main difficulty seems to be in the synthetic routes to small particles required for integration, which are compatible with the matrix polymers. This is a particular problem when the core-shell block copolymers are prepared by tandem polymerization processes. A more successful approach is surface small molecule or oligomer attachment, which limits the size of the polar corona. Most bottom-up procedures are easily applicable for particles in the 10–40 nm range while particles <5 nm or more than 50 nm present more of a synthetic challenge.

## CONCLUSIONS

In summary, continual evolutionary progress in CMOS devices with scaling requires progress in imaging techniques and lithographic materials, new high-*k* materials for the FEOL transistors, advances in processing, metallurgy, hardmasks, etch stops, liners, and especially low-*k* insulators for the BEOL. For the latter, the search has been driven mainly by the desire to minimize RC delays and cross talk, although power issues are becoming more important. However, the replacement of silicon dioxide as the BEOL insulator has proven much more difficult than anticipated, explaining the dramatic slip in the schedules as defined by the various ITRS roadmaps. At least 10 years after the realization that low-*k* replacements for silicon dioxide could be a major performance enhancer for devices beyond the 180 nm device node, people are still arguing whether spin-on or CVD provides the most versatility for the future. In the short term, at least for the 90 and 65 nm nodes, it appears that CVD processes have gained the upper hand. Even here, there is room for some imaginative chemistry in the development of precursors to address current materials and integration limitations. For porous materials required for the 45 nm node and beyond, there are still questions that remain, e.g., CVD vs. spin-on how much porosity, porogen vs. non-porogen approaches, bound vs. unbound porogens, etc. The key here will be dielectric extendibility over multiple technology nodes. This becomes critical because the integration of new materials is very difficult. It seems likely that CMOS technology will extend now at least through the 25 nm node generation. Although the use of porous materials seems inevitable, an important question is how much porosity is necessary for the future and if

and when we should gradually change over to the use of air gaps where air constitutes the volume bulk of the dielectric. In this regard, a number of imaginative schemes directed toward air gap dielectrics, some of which utilize sacrificial materials have already appeared.<sup>[78–82]</sup>

## ACKNOWLEDGMENTS

The author gratefully acknowledges the continuing contributions of colleagues in the Advanced Organic Materials Department at the IBM Almaden Research Center and also M. Sherwood for NMR studies on dielectric thin films. R.D. Miller acknowledges partial financial support from the NSF Materials Research Science and Engineering Center: Grant DMR-9400354 for the Center for Polymeric Interfaces and Macromolecular Assemblies (CPIMA).

## REFERENCES

- Moore, G.E. Cramming more components onto integrated circuits. *Electronics* **1965**, 38 (8).
- Moore, G.E. IDEM Tech. Digest **1975**, 11.
- Wilson, S.R. *Handbook of Multilevel Metallization for Integrated Circuits*; Chapt. 1; Wilson, S.R., Tracy, C.J., Freeman, J.L., Eds.; Noyes: Park Ridge, NJ, 1993.
- Edelstein, D.; Heidenreich, J.; Goldblatt, R.; Cote, W.; Uzoh, C.; Lustig, N.; Roper, P.; McDevitt, T.; Motsiff, W.; Simon, A.; Durkovic, J.; Wachnik, R.; Rathore, H.; Schultz, R.; Su, L.; Luce, S.; Slattery, J. Full copper wiring in a sub-0.25 micron CMOS ULSI technology. *Tech. Digest IEEE Int. Electron Devices Mtg.* **1997**, 773.
- Nguyen, V.H.; van Kranenburg, H.; Woerlee, P.H. Copper for advanced interconnect, Proceedings of the Third International Workshop on Materials Science (IWOMS'99), Nov 2–4; Hanoi Vietnam, 1999.
- Jan, C.-J.; Bielefeld, J.; Buehler, M.; Chikamanr, V.; Fischer, K.; Hepburn, T.; Jain, A.; Jeong, J.; Kielty, T.; Kook, S.; Marieb, T.; Miner, B.; Nguyen, P.; Schmitz, A.; Nasher, N.; Scherban, T.; Schroeder, B.; Wang, P.-H.; Wu, R.; Xu, J.; Zawadzki, K. 90 nm generation, 300 mm wafer low k ILD/Cu Interconnect Technology, IEEE International Interconnect Technology Conference (IITC) Proceedings, San Francisco CA, 2003.
- Rantala, J.T.; McLaughlin, W.; Reid, J.S.; Beery, D.; Hacker, N.P. Looking forward to 65nm: nonporous low-k dielectrics. *Solid State Technology*. **2003**, 46 (12), 34.
- <http://public.itrs.net/>.
- Vrtis, R.N.; Heak, K.A.; Burgoyne, W.F., Jr.; Robeson, L.M. Poly(arylene ethers) as low dielectric constant materials for ULSI interconnect applications. *Mat. Res. Soc. Proc.* **1997**, 443, 171.
- Sum, J.C.; Ray, G.W.; Ma, S.; Karai, R.; MacInnes, L.M.; Treadwell, C.A.; Dunne, J.; Hacker, N.P.; Figge, L.K.; Hendricks, N. Process integration of a direct-on-metal, non-etchback k = 2.5 spin-on polymer for the 0.18 micron CMOS technology node, *IEEE Int. Interconnect Technol. Conf. Proc.*, **1999**, May 24–26, 184.
- Martin, S.J.; Godschalx, J.P.; Mills, M.E.; Shaffer, E.O., III; Townsend, P.H. Development of a low-dielectric constant polymer for the fabrication of integrated circuit interconnect. *Adv. Mater.* **2000**, 12 (23), 1769.
- Forester, L.; Choi, D.K.; Kennedy, J.; Ross, M.; Livesay, W.R. Siloxane spin-on glass with low dielectric constant by e-beam treatment. *Mat. Res. Soc. Proc.* **1996**, ULSI XI, 89.
- Dharmadhikari, V.; Sims, J.S.; Vandarajan, B.; Chang, S.; Niu, D.; Shrinivasan, K. UV-assisted processing for advanced dielectric films. *Sol. State Technol.* **2005**, 48 (3), 43.
- Callister, W.D. *Materials Science and Engineering*, 5th Ed.; John Wiley and Sons: New York, 2000.
- Oliver, W.C.; Pharr, G.M. An improved technique for determining hardness and elastic modulus using load and displacement sensing indentation experiments. *J. Mater. Res.* **1992**, 7 (6), 1564.
- Volinsky, A.A.; Vella, J.B.; Gerberich, W.W. Fracture toughness, adhesion and mechanical properties of low-k dielectric thin films measured by nanoindentation. *Thin Sol. Films* **2003**, 429, 201.
- Flannery, C.M.; Baklanov, M.R. Nondestructive stiffness and density characterization of porous low-k films by surface acoustic wave spectroscopy. *Proc. IEEE Int. Interconnect Technical Conf. (IITC)* **2002**, 233.
- Schneider, D.; Witke, T.; Schwarz, T.; Schoneich, B.; Schultrich, B. Testing ultra-thin films by laser-acoustics. *Surf. Coat. Technol.* **2000**, 126, 136.
- Hess, P. Surface acoustic waves in materials science. *Phys. Today* **2002**, March, 42.
- Maex, K.; Baklanov, M.R.; Shamiryan, D.; Iacopi, F.; Brongersma, S.H.; Yanovitskaya, Z.S. Low dielectric constant materials for microelectronics. *J. Appl. Phys.* **2003**, 93 (11), 8793.
- Husing, A.N.; Schubert, U. Aerogels—airy materials: chemistry, structure and properties. *Angew. Chem. Int. Ed.* **1998**, 37, 22.
- Hrubesh, L.W.; Keene, L.E.; Latore, V.R. Dielectric properties of aerogels. *J. Mater. Res.* **1993**, 8 (7), 1736.
- Ramos, T.; Roderick, K.; Maskara, A.; Smith, D.M. Nanoporous silica for low-k dielectrics. *Mat. Res. Soc. Proc.* **1997**, 443, 91.
- Smith, D.M.; Anderson, J.; Cho, C.C.; Johnson, G.P.; Jeng, S.P. Preparation of low-density xerogels at ambient pressure for low-k dielectrics. *Mat. Res. Soc. Proc.* **1995**, 381, 261.
- Jain, A.; Rogojevic, S.; Nitta, S.V.; Pisupatti, V.; Gill, W.G.; Wayer, P.C., Jr.; Plawsky, J.L.; Standaert, T.E.F.M. Processing and characterization of silica xerogel films for low-dielectric applications. *Mat. Res. Soc. Proc.* **1999**, 565, 29.
- Moyer, E.S.; Deis, T.; Chung, K.; Spaulding, M.; Saha, C.; Boisvert, R.; Chen, W.; Bremmer, J. Ultra Low k Silsesquioxane-Based Resins, Proceedings of Conference on Concepts and Needs for Low Dielectric



- Constant (<150 nm) Interconnect Materials: now and the Next Millennium, Nov 14–17, 1999; Monterey, CA.
27. Oku, Y.; Nishiyama, N.; Tanaka, S.; Korekazu, H.; Hata, N.; Kikkawa, T. Novel periodic nanoporous silicate glass with high structural stability as low-k film. *Mat. Res. Soc. Proc.* **2002**, *716*, 587.
  28. Jung, S.-B.; Park, H.-A. Control of surface residual-OH polar sites in SiO<sub>2</sub> aerogel films by silylation. *Thin Sol. Films* **2002**, *420–421*, 503.
  29. Moreau, W.M.; McCullough, K.J.; Medeiros, D.R.; Simons, J.P.; Taft, C.J. Supercritical Fluid (SCF) Silylation Process. U.S. Patent Appl Publ 2003036023 A12003
  30. Gorman, B.P.; Orozco-Teran, R.A.; Zhang, Z. Rapid repair of plasma ash damage in low-k dielectrics using supercritical CO<sub>2</sub>. *J. Vac. Sci. Technol. B* **2004**, *22* (3), 1210.
  31. Long, T.M.; Swager, T.M. Molecular design of free volume as a route to low-k dielectric materials. *J. Am. Chem. Soc.* **2003**, *125*, 14,113.
  32. Krause, B.; Koops, G.-H.; van der Vegt, N.F.A.; Wessling, M.; Wubbenhorst, M.; van Turnhout, J. Ultralow-k dielectrics made by supercritical foaming of thin polymer films. *Adv. Mater.* **2002**, *14* (15), 1041.
  33. Nakashima, A.; Komatsu, M. Coating liquid for forming silica-containing film with a low dielectric constant. U.S. Patent # 6639015, 2003.
  34. Hayashi, E.; Hasegawa, K. Composition for film formation and silica-based film. US Patent # 6413647, 2002.
  35. Nishida, H.; Nakai, M.; Komatsu, M.; Yoshitome, H. Sol having fine particles dispersed and a method for preparing. US Patent # 6680040, 2004.
  36. Zhong, B.; Spaulding, M.; Albaugh, J.; Moyer, E. Porous ultralow-k dielectrics with ultra small pores. *Polym. Prepr.* **2002**, *87*, 440.
  37. Yamada, N.; Takahashi, T. Methylsiloxane spin-on glass films for low dielectric constant interlayer dielectrics. *J. Electrochem. Soc.* **2000**, *147* (4), 1477.
  38. Cha, H.-J.; Hedrick, J.L.; DiPietro, R.; Blum, T.; Beyers, R.; Yoon, D.Y. Structures and dielectric properties of thin polyimide films with nanofoam morphologies. *Appl. Phys. Lett.* **1996**, *68*, 1930.
  39. Hedrick, J.L.; Carter, K.; Richter, R.; Miller, R.D.; Russell, T.P.; Flores, V.; Mecerreyes, D.; Dubois, P.; Jerome, R. Polyimide nanofoams from aliphatic polyester-based copolymers. *Chem. Mater.* **1998**, *10*, 39.
  40. O'Neill, M.L.; Robeson, L.M.; Burgoyne, W.F., Jr.; Langsam, M. Low dielectric nanoporous polymer films and products thereof using a combination of high and low boiling solvents. EP **2000**, *1002830*, A2.
  41. Strittmatter, R.J.; Niu, Q.J.; Waeterloos, J.; Mohler, G.E.; Landes, B.G.; Lyons, J.-H.; Curphy, J.J.; Hahnfield, J.L.; Silvas, C.H. Porous SiLK semiconductor dielectric resin-impact of dramatically reduced pore size on integration of organic ultra-low k ILD materials. *Adv. Met. Conf. Proc.* **2003**, *159*.
  42. Matsunaga, N.; Nakamura, N.; Higashi, K.; Yamaguchi, H.; Watanabe, T.; Akiyama, K.; Nakao, S.; Fujita, K.; Miyajima, H.; Omoto, S.; Sakata, A.; Katata, T.; Kagawa, Y.; Kawashima, H.; Enototo, Y.; Hasegawa, T.; Shibata, H. BEOL Process Integration Technology for 45 nm Node Porous low-k/Copper Interconnect, IEEE International Interconnect Technical Conference (IITC) Proceedings, San Francisco, CA, 2005.
  43. Grill, P.V.; Rodbell, K.P.; Huang, E.; Baklanov, M.R.; Mogilnikov, K.P.; Toney, M.; Kim, H.-C. Porosity in plasma enhanced chemical vapor deposited SiCOH dielectrics: a comparative study. *J. Appl. Phys.* **2003**, *94* (5), 3427.
  44. Grill, A.; Patel, V. Ultralow-k dielectrics prepared by plasma-enhanced chemical vapor deposition. *Appl. Phys. Lett.* **2001**, *79* (6), 803.
  45. Vtris, R.N.; O'Neill, M.L.; Vincent, J.L.; Lukas, A.S.; Peterson, B.K.; Bitner, M.D.; Karwacke, E.J. Plasma-enhanced chemical vapor deposition of porous organosilicate glass ILD films with  $k < 2.4$ . *Mat. Res. Soc. Proc.* **2003**, *766*, 259.
  46. Yim, J.-H.; Lyu, Y.-Y.; Jeong, H.-D.; Song, S.A.; Hwang, H.; Lee, J.; Mah, S.K.; Park, J.-G.; Hu, Y.F.; Sun, J.N.; Gidley, D.W. The preparation and characterization of small mesopores in siloxane-based materials that use cyclodextrins as templates. *Adv. Funct. Mater.* **2003**, *13* (5), 382.
  47. Malhouitre, S.; Jehoul, C.; van Aelst, J.; Struyl, H.; Brongersma, S.; Carbonell, L.; Vos, I.; Beyer, G.; van Hove, M.; Gronbeck, D.; Gallagher, M.; Calvert, J.; Maex, K. Single damascene integration of Zirkon version 1 low-k dielectric film. *Microelectron Eng.* **2003**, *70*, 302.
  48. Connor, E.F.; Sundberg, L.; Kim, H.-C.; Cornelissen, J.J.; Magbitang, T.; Rice, P.R.; Lee, V.Y.; Hawker, C.J.; Volksen, W.; Hedrick, J.L.; Miller, R.D. Templation of silsesquioxane crosslinking using unimolecular self-organizing polymers. *Angew. Chem. Int. Ed.* **2003**, *42* (15), 3755.
  49. Miller, R.D.; Volksen, W.; Lee, V.Y.; Connor, E.F.; Magbitang, T.; Zafran, R.; Sundberg, L.; Hawker, C.J.; Hedrick, J.L.; Huang, E.; Toney, M.; Huang, Q.R.; Frank, C.W.; Kim, H.-C. Nanoporous low-dielectric constant organosilicates derived from inorganic blends. In *Polymers for Microelectronics and Nanoelectronics*; Lin, Q., Pearson, R.A., Hedrick, J.C., Eds.; ACS Symposium series 874; American Chemical Society: Washington, DC, 2004; 144 pp.
  50. Zhao, D.; Feng, J.; Huo, Q.; Melosh, N.; Fredrickson, G.H.; Chmelka, B.F.; Stuckey, G.D. Triblock copolymer synthesis of mesoporous silica with periodic 50–300 Angstrom pores. *Science* **1998**, *279*, 548.
  51. Bruinsma, P.J.; Hess, N.J.; Bontha, J.R.; Baskaran, S. Low-k mesoporous silica films through template-based processing. *Mat. Res. Soc. Proc.* **1996**, *443*, 105.
  52. Lu, Y.; Ganguli, R.; Drewien, C.A.; Anderson, M.T.; Brinker, C.J.; Gong, W.; Guo, Y.; Soyey, H.; Dunn, B.; Huang, M.H.; Zink, J.I. Continuous formation of supported cubic and hexagonal mesoporous films by sol-gel dip coating. *Nature* **1997**, *389*, 364.
  53. Mou, C.-Y.; Lin, H.-P. Control of morphology in synthesizing mesoporous silica. *Pure Appl. Chem.* **2000**, *72*, 137.
  54. Zhao, D.; Huo, Q.; Feng, J.; Chmelka, B.F.; Stuckey, G.D. Nonionic triblock and star diblock copolymer and oligomeric surfactant synthesis of highly ordered,



- hydrothermally stable mesoporous silica structures. *J. Am. Chem. Soc.* **1998**, *120*, 6024.
55. Doshi, D.A.; Gibaud, A.; Goletto, V.; Lu, M.; Gerung, H.; Ocko, B.; Han, S.M.; Brinker, C.J. Peering into the self assembly of surfactant templated thin-film silica mesophases. *J. Am. Chem. Soc.* **2003**, *125*, 11,646.
  56. Yu, S.; Wong, T.K.S.; Hu, X.; Pita, K. Sol-gel derived mesoporous silica films used as low dielectric constant materials. *Thin Sol. Films* **2004**, *462–463*, 311.
  57. Balkenende, A.R.; de Theije, F.K.; Kriege, J.C.K. Controlling dielectric and optical properties of ordered mesoporous organosilicate films. *Adv. Mater.* **2003**, *15* (2), 139.
  58. Cho, E.-B.; Kwon, K.-W.; Char, K. Mesoporous organosilicas prepared with PEO-containing triblock copolymers with different hydrophobic moieties. *Chem. Mater.* **2001**, *13*, 3837.
  59. Yu, K.; Wu, X.; Brinker, C.J.; Ripmeester, J. Mesostructured MTES-derived silica thin film with spherical voids investigated by TEM: 1. Mesostructure determination. *Langmuir* **2003**, *19*, 7282.
  60. Pai, R.A.; Humayun, R.; Schulberg, M.T.; Sengupta, A.; Sun, J.-N.; Watkins, J.J. Mesoporous silicates prepared using preorganized templates in supercritical fluids. *Science* **2004**, *303*, 507.
  61. Schulberg, M.T.; Humayun, R.; Sengupta, A.; Sun, J.-N. Deposition and integration of a novel ultra-low k (2.2) material. *Mat. Res. Soc. Proc.* **2004**, *812*, F6.1.1.
  62. Wang, Z.; Mitra, A.; Wang, H.; Huang, L.; Yan, Y. Pure silica Zeolite films as low-k dielectrics by spin-on of nanoparticle suspensions. *Adv. Mater.* **2001**, *13* (19), 1463.
  63. Wang, Z.; Wang, H.; Mitra, A.; Huang, L.; Yan, Y. Pure-silica zeolite low-k dielectric films. *Adv. Mater.* **2001**, *13* (10), 746.
  64. Li, S.; Sun, J.; Peng, H.; Gidley, D.; Ryan, E.T.; Yan, Y. Evaluation of pore structure in pure silica Zeolite MFI low-k thin films using positronium annihilation lifetime spectroscopy. *J. Phys. Chem.* **2004**, *108*, 11,689.
  65. Baney, D.H.; Itoh, M.; Sakakibara, A.; Suzuki, T. Silsesquioxanes. *Chem. Rev.* **1995**, *95*, 1409.
  66. Mabboux, P.-Y.; Gleason, K.K. Chemical bonding structure of low dielectric constant Si:O:C:H films characterized by solid state NMR. *J. Electrochem. Soc.* **2005**, *152* (1), F7.
  67. Wang, C.Y.; Shen, Z.X.; Zheng, J.Z. Thermal cure study of a low-k methyl silsesquioxane for intermetal dielectric application by FT-IR spectroscopy. *Appl. Spectroscopy*, **2000**, *54*, 209.
  68. Burkey, D.D.; Gleason, K.K. Temperature resolved Fourier transform infrared study of condensation reactions and porogen decomposition in hybrid organosilicon-porogen films. *J. Vac. Sci. Technol. A* **2004**, *22* (1), 61.
  69. Munk, P. *Introduction to Macromolecular Science*; John Wiley & Sons: New York, 1989, Chapter 4.
  70. Huang, Q.R.; Kim, H.-C.; Huang, E.; Mecerreyes, D.; Hedrick, J.L.; Volksen, W.; Frank, C.W.; Miller, R.D. Miscibility in organic/inorganic hybrid nanocomposites suitable for microelectronic applications: comparison of modulated differential scanning calorimetry and fluorescence spectroscopy. *Macromolecules* **2003**, *36* (20), 7661.
  71. Huang, Q.R.; Volksen, W.; Huang, E.; Toney, M.; Frank, C.W.; Miller, R.D. Structure and interaction of organic/inorganic hybrid nanocomposites for microelectronic applications: 1. MSSQ/P(MMA-co-DMAEMA) nanocomposites. *Chem. Mater.* **2002**, *14* (9), 3676.
  72. Miller, R.D.; Beyers, R.; Carter, K.R.; Cook, R.F.; Harbison, M.; Hawker, C.J.; Hedrick, J.L.; Lee, V.Y.; Liniger, E.; Nguyen, C.; Remenar, J.; Sherwood, M.; Trollsas, M.; Volksen, W.; Yoon, D.Y. Porous organosilicates for on-chip applications. *Mat. Res. Soc. Proc.* **1999**, *565*, 4.
  73. Hedrick, J.L.; Miller, R.D.; Hawker, C.J.; Carter, K.R.; Volksen, W.; Yoon, D.Y.; Trollsas, M. Templating nanoporosity in thin film dielectric insulators. *Adv. Mater.* **1998**, *10* (13), 1049.
  74. Hedrick, J.L.; Magbitang, T.; Connor, E.F.; Glauser, T.; Volksen, W.; Hawker, C.J.; Lee, V.Y.; Miller, R.D. Application of complex macromolecular architectures for advanced electronic materials. *Chem. Eur. J.* **2002**, *8* (15), 3309.
  75. Hawker, C.J.; Hedrick, J.L.; Miller, R.D.; Volksen, W. Supramolecular approaches to nanoscale dielectric foams for advanced microelectronic devices. *MRS Bull.* **2000**, April, 54.
  76. Nguyen, C.; Hawker, C.J.; Miller, R.D.; Huang, E.; Hedrick, J.L.; Gauderon, R.; Hilborn, J.G. Hyperbranched polyesters as nanoporosity templating agents for organosilicates. *Macromolecules* **2000**, *33* (11), 4281.
  77. Miller, R.D.; Volksen, W.; Hedrick, J.L.; Hawker, C.J.; Remenar, J.; Furuta, P.; Nguyen, C.; Yoon, D.Y.; Toney, M.; Rice, P.; Hay, J. Sacrificial macromolecular porogens: a route to porous organosilicates for on-chip applications. *Adv. Met. Conf. Mat. Res. Soc. Proc.* **2000**, 327.
  78. Kohl, P.A.; Bhusari, D.M.; Wedlake, M.; Case, C.; Klemens, F.P.; Miner, J.; Lee, B.-C.; Gutman, R.J.; Shick, R. Air-gaps in 0.3 micron electrical connections. *IEEE Device Lett.* **2000**, *21* (12), 557.
  79. Bhusari, D.J.; Wedlake, M.D.; Kohl, P.A.; Case, C.; Klemens, F.P.; Miner, J.; Lee, B.-C.; Gutmann, R.J.; Lee, J.J.; Shick, R.; Rhodes, L. Fabrication of air gaps between Cu interconnects for low intralevel k. *Mat. Res. Soc. Proc.* **2001**, *612*, D4.8/1–D4.8/6.
  80. Arnal, V.; Torres, J.; Reyanard, J.-P.; Gayet, P.; Verove, C.; Guillermet, M.; Spinelli, P. Optimization of CVD dielectric process to achieve reliable ultra-low-k air gaps. *Microelectronic Eng.* **2002**, *60*, 143.
  81. Uno, S.; Noguchi, J.; Ashihara, H.; Oshima, T.; Sato, K.; Konishi, N.; Saito, T.; Hara, K. Dual damascene process for air-gap Cu interconnects using conventional CVD films as sacrificial layers, IEEE International Interconnect Technology Conference (IITC) Proceedings, San Francisco, CA, 2005.
  82. Daamen, R.; Verheijden, G.J.A.M.; Bancken, P.H.L.; Vandeweyer, T.; Michelon, J.; Hoang, V.N.; Hoofman, R.J.O.M.; Gallagher, M.K. Air gap integration for the 45 nm node, IEEE International Interconnect Technology Conference (IITC) Proceedings, San Francisco, CA, 2005.

# Luminescence of Nanoparticle-Labeled Antibodies and Antigens

**Shaopeng Wang**

*Nomadics Inc., Stillwater, Oklahoma, U.S.A.*

**Nicholas A. Kotov**

*Department of Chemical Engineering, University of Michigan, Ann Arbor, Michigan, U.S.A.*

## INTRODUCTION

Bioconjugation of nanoparticles (NPs)<sup>[1–14]</sup> is the attachment of specific biological molecules or components to nanoparticles. The resulting structures represent the convolution of biotechnology and nanotechnology, and yield hybrid materials, processes, and devices that can utilize both the unique optical and magnetic properties of NPs and highly selective binding of biological interactions. The combination of these features can potentially make a prominent impact in current biomedical technologies, and possibly in nanoelectronics, microphotonics and related fields. Antigen and antibody interaction is a naturally occurring immunology interaction of the biological defense system, and has been widely used as molecular recognition method for medical diagnostics and detection of biological threat agents.<sup>[15]</sup> The bioconjugation of NPs with antigens and antibodies are interesting and important as a method for their organization in more complex structures, and as a pathway to new sensing and imaging technologies. In the viewpoint of biologically programmed assembly of nanostructures,<sup>[12,16,17]</sup> the similarity of sizes of NP and proteins limits the overall number of affinity ligands around one semiconductor core to a few proteins leading to, for instance, 1-, 2-, 3-, and 4-valent quantum dots. The practical aspect of NP-antigen/antibody conjugation is related to the further development of immunoluminescence as a technique that affords highly sensitive and specific detection of various biological and non-biological analytes of military and civilian importance.

Colloid gold nanoparticles have been used in labeling antigens and antibodies as contrasting agents of various immunoassays,<sup>[18–20]</sup> however, their sensitivity is limited by the nature of colorimetric detection. Luminescence spectroscopy is more sensitive than absorption spectroscopy because of its substantially better signal-to-noise ratio. We observed the excited-state

dipole–dipole coupling between NPs of different sizes in the constructed immunocomplex, which results in the excitation energy transfer from NPs of smaller diameters to those with bigger diameters, i.e., Förster resonance energy transfer (FRET). The detection limits of analytical processes based on FRET can be as low as 10 ppt, with a linear dynamic range of 0.1–1000 ppb,<sup>[21,22]</sup> while the utilization of antibodies enables the selective detection of substrates, which may differ only by a few atoms. Highly luminescent semiconductor NP, or quantum dots, are a new class of luminescence materials providing a number of advantages over organic dyes. They can be made in a single-step synthesis, with precisely controlled size distribution and tunable emission spectrum. Compared to organic dyes such as Rhodamine, this new class of luminescent material are 20 times brighter and 100 times more stable against photobleaching, and one-third as wide in spectra linewidth.<sup>[3]</sup> Therefore luminescence nanoparticles will have tremendous potential in biomedical imaging and diagnostic applications.

Typically, NPs are synthesized by arrested precipitation in the presence of organic molecules strongly coordinating to metal ions, such as thiols or phosphines.<sup>[23,24]</sup> The simplified description of the product is a semiconductor core coated with a monolayer of organic molecules attached to surface metal sites. The core of the NPs is highly crystalline, which is a prerequisite for strong luminescence. Many different thiol derivatives may be used for the stabilization of II–VI nanoparticles. The terminal end of the thiol can be conveniently used for further functionalization of nanoparticles and for conjugation to biological molecules by either nonspecific electrostatic absorption or specific conjugation reactions. Most antigens and antibodies are proteins, have a number of amino acids that provide functional groups which can be chemically conjugated, such as  $-\text{NH}_2$  (lysine, and N-terminal),  $-\text{COOH}$  (aspartic acid, glutamic acid, and C-terminal), and  $-\text{SH}$  (cysteine).

The direct NP–protein conjugation method frequently used is the 1-ethyl-3-(3-dimethylaminopropyl) carbodiimide hydrochloride (EDC)/*N*-hydroxysulfosuccinimide (sulfo-NHS) reaction (Scheme 1).<sup>[20,25–27]</sup> NHS-conjugated proteins have the highest bioactivity among other conjugates, as established by several comparative studies.<sup>[28–30]</sup> The carboxylic acid group of thiolglycolic acid-stabilized NPs will form amide bond with the primary amine groups of the protein, or, the amine groups of a cysteine-stabilized NPs can link to the carboxylic acid group of protein.

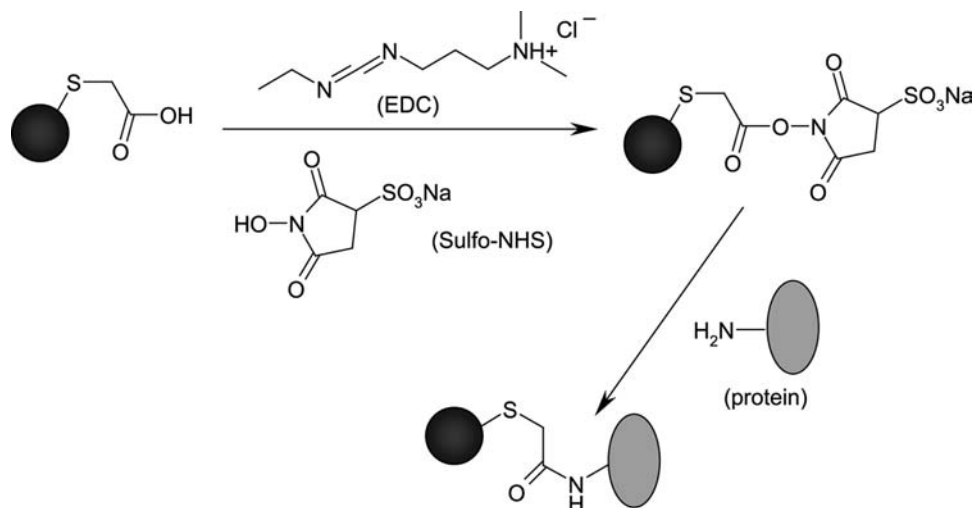
To explore and demonstrate the potential of NP Bioconjugates, we used EDC/sulfo-NHS reaction to conjugate different-sized CdTe NPs to two antigen/antibody systems: 1) bovine serum albumin (BSA) and anti-BSA IgG (immunoglobulin G)<sup>[8]</sup> and 2) *Brucella suis* and its antibody Bru-38 (Anti-GBa-O side chain). Antigens were conjugated to red-emitting CdTe NPs, while green-emitting NPs were attached to the corresponding antibodies. FRET was observed upon the formation of immunocomplex between the complementary antigens/antibodies. the competitive inhibition of FRET by unlabeled antigens was investigated.

## METHODOLOGY

The optimized EDC/sulfo-NHS conjugation protocol is as follows: a reaction mixture containing 0.05 mM CdTe NP, 1.5–2.5 mg/mL antigen or antibody, 0.05 M NHS, and 0.05 M EDC in pH 7.0 PBS buffer was prepared and kept in room temperature for 2–4 hr, then stored overnight at 4°C. This allows the unreacted EDC to hydrolyze and lose its activity. After

that, a small amount of precipitate is formed, likely consisting of unconjugated NPs, which are known to agglomerate and become non-emissive at fairly low pH. The precipitate (if any) is removed by centrifugation. The stock, ready-to-use solution of the product was stored at 4°C. Optionally, the conjugates can be dialyzed with Spectra/Por<sup>®</sup> 4 membrane with molecular weight cut-off 12,000–14,000 (Spectrum Laboratories, Inc.) in pH 7.4 phosphate-buffered saline (PBS) to remove the small molecules.

The NP bioconjugates were characterized by gel electrophoresis, gel permeation high-performance liquid chromatography (HPLC), circular dichroism (CD), fluorescence spectroscopy, and enzyme-linked immunosorbent assay (ELISA) test. Optical absorption spectra were obtained on a Hewlett-Packard 8453 diode array spectrophotometer using 1-cm quartz cuvettes. Fluorolog 3 and Fluoromax 2 from JY SPEX were used to register the luminescence spectra. The right-angle registration mode with no intermediate filters was utilized in all measurements. All FRET experiments were carried out after centrifugation of the solutions to remove all particles aggregated as a result of oxidation and coagulation. The quantum yield of NP luminescence was determined by using Rhodamine B in ethylene glycol ( $\lambda_{\text{max}} = 580 \text{ nm}$ , quantum yield 1) as a standard as described elsewhere.<sup>[7,8]</sup> The luminescence intensity does not decrease even after the samples were stored for over a month at 4°C. Gel permeation HPLC experiment was carried out on an HP-1090-II instrument equipped with Jordi GPC column 500A with physical dimensions of  $300 \times 7.8 \text{ mm}$ . Deionized 18 M $\Omega$  water was used as an eluent. The optical adsorption signal was monitored at 254 nm by a diode array detector.



**Scheme 1** Schematics of the sulfo-NHS/EDC conjugation reaction.

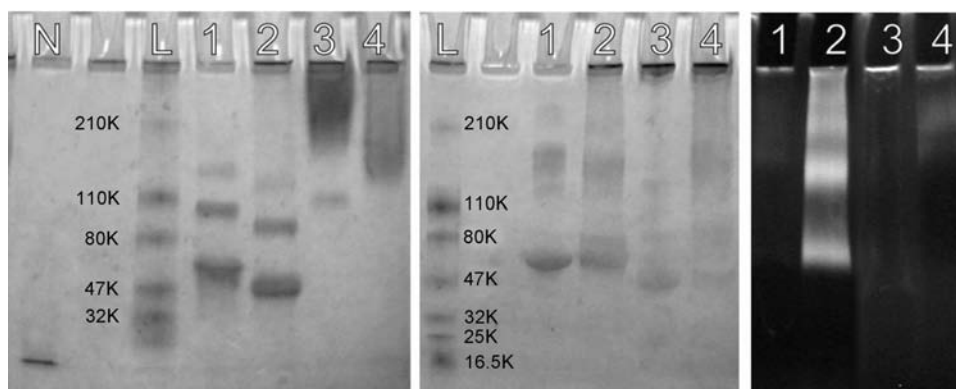


**Fig. 1** Native and SDS-PAGE electrophoresis of CdTe bioconjugates on 4–20% gradient Tris–HCl precast gels (Bio-Rad). Left panel—native, stained by Coomassie Blue. Center panel—SDS-PAGE, stained by Coomassie Blue. Right panel—SDS-PAGE, luminescence image (excitation 360 nm). Wells: 1) BSA; 2) green-emitting NP-BSA; 3) anti-BSA IgG; 4) red-emitting NP-IgG; N) Free CdTe NPs; L) standard protein ladder, molecular weight are marked on the side in kiloDaltons (kDa). Note that in native electrophoresis, the position of the band is not linearly proportional to the molecular weight, because of the different charge status of each sample. *Source:* From Ref.<sup>[8]</sup>. © 2002, American Chemical Society.

## RESULTS AND DISCUSSION

### Investigate the Formation of NP-BSA and NP-Anti-BSA Bioconjugates by Electrophoresis

The native electrophoresis results (Fig. 1, left panel) show that both NP-conjugated BSA (well 2) and anti-BSA IgG (well 4) bands become more mobile in the electric field than the unlabeled biospecific ligands (wells 1 and 3). The BSA monomer band shifts from the relative marker of 65 to 47 kDa, which demonstrates that the high negative charge of the NP and their compactness overcomes the increase of their mass as a result of labeling. Note that the commercial BSA shows two other bands at 100 and 150 kDa, corresponding to BSA–BSA dimer and globulins, respectively. This observation agrees with the specifications of Sigma; these compounds have minor influence on the biospecific reactions discussed below. Both of these bands shift synchronously with BSA monomer to smaller masses after the NP conjugation. By mixing NP with BSA and IgG without adding coupling reagents (EDC and sulfo-NHS), no evidence of nonspecific binding was observed in native gel electrophoresis.

The mobility of the proteins in sodium dodecyl sulphate-polyacrylamide gel electrophoresis (SDS-PAGE) (Fig. 1, center panel) is determined by the mass/charge ratio of denatured protein chains carrying SDS, which imparts negative charge to them. Interestingly, the band positions of NP-labeled and unlabeled proteins virtually coincide at the 65-kDa marker (Fig. 1, center panel). Similar to the native gel results, the increase of mass resulting from the addition of NPs to the protein is compensated by the

increase of the overall charge density of the conjugate. Unlike NP-BSA, the SDS-PAGE band of NP-IgG conjugate remains at 150 kDa, while the free IgG is mostly broken apart into small molecular weight fragments as a result of SDS and heating treatment (Fig. 1, center panel, wells 3–4). Considering the SDS-PAGE data, we emphasize three factors. 1) Estimates of molecular masses based on gel electrophoresis results can give erroneous outcomes for bioconjugates from highly charged NPs. Different experimental techniques must be used for this purpose. 2) A brief heat treatment (150 sec) at 96°C was used for the preparation of SDS-PAGE samples. Because high-temperature denaturation destroys the tertiary structure of the protein, little non-specific binding of NP and BSA is to be expected after that. Therefore the observation of NP luminescence in the SDS-PAGE bands demonstrates covalent linkage between protein and the semiconductor units. 3) Bioconjugation to NP may increase the stability of antibodies. The relative intensity of the SDS-PAGE bands indicates that the conjugated antibodies are more resilient to this temperature than the unlabeled ones. The unlabeled antibodies (well 3) are mostly broken apart by SDS and heating into small fragments, showing up as band at 40–50 kDa; whereas for NP-IgG conjugates, this band has significantly lower intensity—the antibody remains mostly intact. The latter effect was reproduced in several control experiments.

The direct evidence of the successful conjugation of CdTe to BSA and IgG can be found from the luminescence analysis of the gel plates. The NP conjugate bands show strong luminescence, while the free proteins do not show any detectable signal in the luminescence image (Fig. 1, right panel). As before,<sup>[7]</sup> the gel pieces cut out of the gel plates in the area of the

conjugate bands reveal the luminescence spectra with identical peaks to the original NPs.

### Confirm the Formation of NP-BSA and NP-Anti-BSA Bioconjugates by HPLC

The formation of NP bioconjugates was also confirmed by HPLC size exclusion chromatography (Fig. 2), which is complementary to electrophoresis. The original BSA revealed three HPLC peaks congruent to the three bands seen in gel electrophoresis (Fig. 1). Because the species with higher molecular weight are eluted at shorter retention times, the observed HPLC peaks at retention times 7.8, 6.8, and 5.4 min should be attributed to BSA monomer, BSA dimer, and globulins, respectively. After conjugation to CdTe, the same three peaks can be seen at 6.5, 5.3, and 4.2 min, all being shifted to higher molecular weight, as expected for the attachment of NPs to proteins. Considering that the approximate molecular weight of 5.0-nm red-emitting CdTe attached to BSA is 240 kDa (specific density of CdTe is 6.2 g/cm<sup>3</sup>), the HPLC peak shift for monomeric BSA shows that not more than one NP is attached to this protein. Similar behavior can be observed for the bioconjugates of IgG. An HPLC peak attributed to free IgG was observed at 6.7 min, while shifting to 6.1 min after conjugation to green-emitting NP of ca. 2.5 nm in diameter. Their molecular mass is estimated to be 30 kDa; therefore, the HPLC molecular weight shift corresponds to the attachment of about one quantum dot per IgG as well. We want to emphasize that the estimates of NP-protein composition of the conjugates should be taken with caution and should be treated as preliminary data. The retention of NPs and polymers/proteins in gel permeation media may

follow different scaling schemes, and therefore introduce an unforeseen error in them. No free BSA or large oligomeric NP-BSA agglomerates with gradually increasing molecular masses can be detected in elution curves (Fig. 2). Besides such oligomers, the luminescent bands seen at the starting line in gel electrophoresis can possibly originate from aggregates produced by accumulation on dust particles, rather than multiple chemical cross-linking because of BSA's tendency to adsorb on many surfaces.<sup>[31]</sup>

### Study Structure of NP-BSA and NP-Anti-BSA Bioconjugates by CD Spectroscopy

The integration of antigen and antibody structure after NP conjugation was confirmed by CD spectroscopy, which shows little change between both BSA and NP-BSA conjugate, as well as the anti-BSA and NP-anti-BSA pair. These data show that the tertiary structure of both proteins remains mostly intact after conjugation.<sup>[8]</sup>

### Examine Biological Activity of NP-BSA and NP-Anti-BSA Bioconjugates by ELISA

The antigen-antibody binding affinity was retained for both conjugates as evaluated by standard ELISA experiments.<sup>[8]</sup> NP-IgG retained 25–50% of binding affinity to free BSA, as compared to free IgG, while NP-BSA retained almost 100% of binding capability to unmodified antibody. The decrease in NP-IgG binding affinity is believed to be a result of partial blocking of binding sites 1) by NP positioned close to the N terminal of the IgG and 2) by other bioconjugates in forming dynamic aggregates. The luminescence properties of NPs remained unchanged in the conjugates as measured by fluorescence spectroscopy.

### FRET Study of NP-BSA and NP-Anti-BSA Bioconjugates

When NP-IgG (anti-BSA) with green luminescence are combined with NP-labeled BSA with red luminescence, the NP-IgG/BSA-NP immunocomplex should form. As expected, a significant enhancement of the NP-BSA's red emission at 611 nm and the corresponding quenching of the green emission of NP-IgG at 555 nm are observed after the self-assembly of the labeled biospecific ligands in the immunocomplex (Fig. 3). The mutual affinity of the antigen and antibody brought the NPs close enough together to allow the resonance dipole-dipole coupling required for

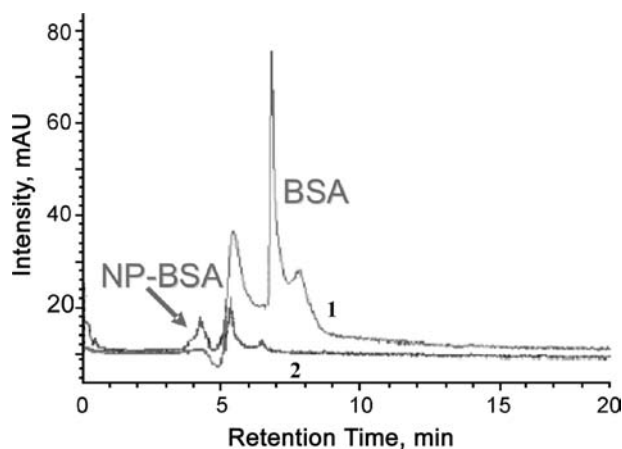


**Fig. 2** HPLC gel permeation elution curves for: 1) BSA and 2) NP-BSA. Source: From Ref.<sup>[8]</sup>. © 2002, American Chemical Society.

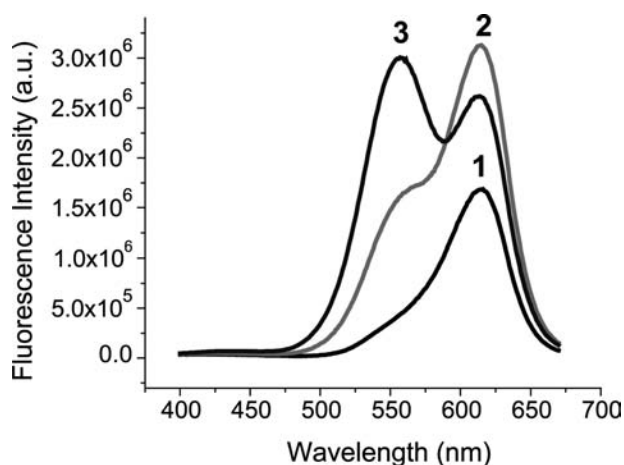


**Fig. 3** FRET-based detection of BSA in solution. 1) NP-BSA; 2) NP-BSA + NP-IgG; 3) BSA + NP-BSA + NP-IgG. Concentrations: NP-BSA  $5 \times 10^{-7}$  M, NP-IgG  $5 \times 10^{-7}$  M, BSA  $2 \times 10^{-6}$  M. Source: From Ref.<sup>[8]</sup>. © 2002, American Chemical Society.

FRET to occur. Thus the energy of the excitonic state in the green-emitting NP was transferred to the similar state of the red-emitting NP with lower exciton energy. FRET efficiency is particularly high for green/red NP pairs because of the strong overlap of their emission and absorption spectra. Importantly, when unlabeled BSA was added to the immunocomplex, it competitively bound to NP-IgG, and replaced NP-BSA in the immunocomplex, thereby inhibiting the FRET process. Consequently, the green emission peak of NP-IgG at 555 nm can be observed again, while the red emission peak at 610 nm shows decreased intensity.

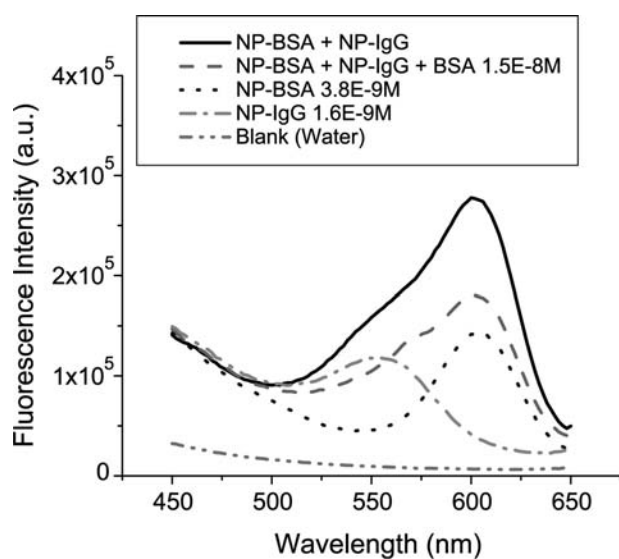


**Fig. 4** Result of FRET-based detection limit—concentrations:  $1.5 \times 10^{-8}$  M BSA, NP-BSA  $3.8 \times 10^{-9}$  M NP-BSA and  $1.6 \times 10^{-9}$  M NP-IgG.

Following this approach, we were able to clearly detect as low as  $1.5 \times 10^{-8}$  M BSA (Fig. 4). Unlike ELISA, the described detection process does not require the multiple binding and washing steps. High-concentration egg albumin, which does not bind to anti-BSA IgG, shows no influence on FRET between NP-IgG and NP-BSA. It demonstrates the high biospecificity of the prepared conjugates and virtually absent interference from the non-complimentary proteins.

### Study of NP-Conjugated *B. suis* and Its Antibody

After successfully demonstrating FRET-based detection in the BSA/anti-BSA model system, we examined it with a more practical antigen–antibody system. We obtained whole-cell killed *B. suis* and the corresponding antibody Bru 38 (anti-GBa-O side chain) and prepared the green NP-conjugated *B. suis* and red NP-conjugated Bru 38 according to the NP-anti-BSA protocol. We used CdTe/CdS NPs with green emission (561 nm) and red emission (601 nm) for the conjugation experiment. The concentration of Bru38 used in the synthesis was 3 mg/mL and the final concentration in the conjugation was 1.2 mg/mL. The concentration of *B. suis* (estimated from optical density, OD 600 nm absorption value) used in the synthesis was  $2.7 \times 10^{-12}$  M ( $1.6 \times 10^9$  cells/mL) and the final concentration in the conjugation was  $7 \times 10^{-13}$  M ( $4 \times 10^8$  cells/mL). The conjugated *B. suis* was purified by centrifuge and washed with 0.1 M PBS buffer three times. Native and SDS-PAGE gel electrophoresis

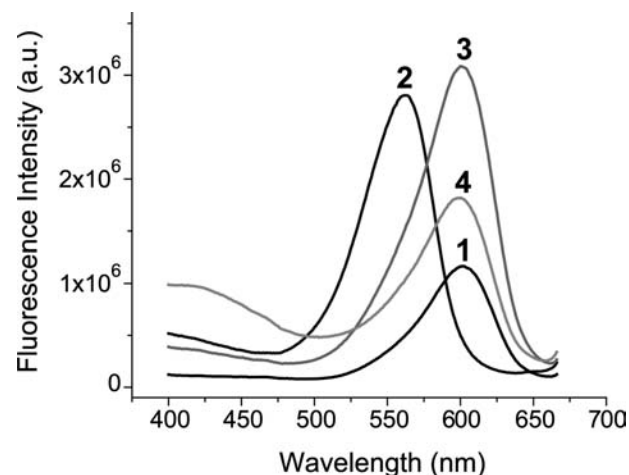


**Fig. 5** FRET-based detection of *Brucella suis* in solution. 1) NP-anti-*B. suis*; 2) NP-*B. suis*; 3) NP-*B. suis* + NP-anti-*B. suis*; 4) *B. suis* + NP-*B. suis* + NP = anti-*B. suis*. Concentration: NP-anti-*B. suis* (Bru38)  $2 \times 10^{-7}$  M, NP-*B. suis*  $3.3 \times 10^{-15}$  M ( $2 \times 10^6$  cells/mL), *B. suis*  $1.3 \times 10^{-14}$  M ( $8 \times 10^6$  cells/mL).



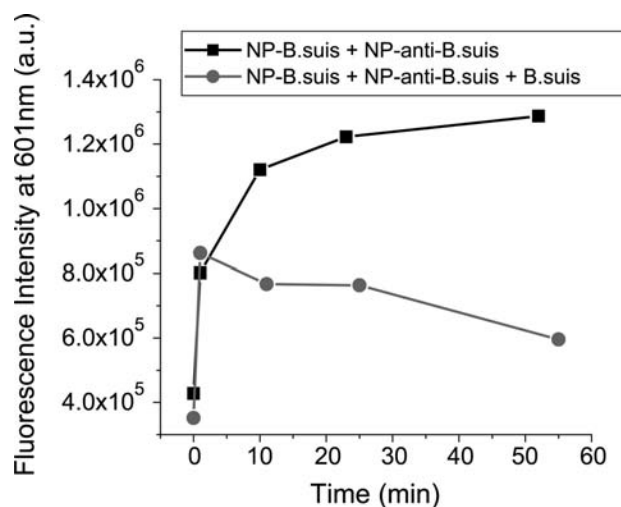


**Fig. 6** FRET transfer kinetics between NP-*B. suis* and NP-anti-*B. suis* showing the influence of the presence of *B. suis*. The FRET is qualified by the intensity of the red-emission peak (601 nm). Concentrations: NP-anti-*B. suis* (Bru38)  $8 \times 10^{-8}$  M; NP-*B. suis*  $1.6 \times 10^{-15}$  M ( $10^6$  cells/mL); *B. suis*  $6.5 \times 10^{-15}$  M ( $4 \times 10^6$  cells/mL).

results of the conjugated Bru 38 are very similar to the NP-anti-BSA conjugate. Although the surface of the bacteria is complex, it should contain numerous primary amine sites for the NP binding, and many of these binding sites should be close enough to the antibody-binding site to allow FRET to occur. Considering the much larger size of bacteria, multiple attachments of NPs on a single bacterium is expected; however, we did not verify it at this stage.

Similar to BSA results, we observed (Fig. 5) FRET as expected when we mixed NP-anti-*B. suis* with the NP-*B. suis* solution. It results as a fluorescence enhancement of the red-emission NP-anti-*B. suis* at 601 nm. The present unlabeled *B. suis* bound to NP-Bru 38 and competitively inhibited the FRET process, and dramatically reduced the fluorescence enhancement at 601 nm.

Binding kinetics, as well as specificity of the FRET, has been studied, and the results are shown in Fig. 6. The presence of unlabeled *B. suis* inhibited the FRET process. The full reaction takes about an hour to finish, because of the antigen/antibody binding nature. However, FRET and competitive inhibition effect can be clearly observed a few minutes after mixing the components together.

## CONCLUSION

Luminescence NPs represent a new class of biological labeling reagents with advantages over traditional dyes. To demonstrate the potential of this class of

materials, two complementary antigens and antibodies systems were labeled with thiol-stabilized green- and red-emitting CdTe NPs. They retain substantial bioactivity and can form the corresponding immunocomplex, which pairs NPs with different emission properties in a supramolecular assembly. Quenching of the green-emitting NPs and the enhancement of the luminescence of their red-emitting counterparts signify the presence of FRET in the immunocomplex. The introduction of unlabeled antigen into the complex solution induced the competitive inhibition of FRET. The exceptional specificity of immunocomplex reactions affords unique possibilities for assembling organized assemblies of NPs and other nanocolloids. After synthetic optimization such as enhancement of the luminescence quantum yield of the bioconjugates, FRET effects can be exploited in biosensing as well as in hybrid photoelectronic devices.

## ACKNOWLEDGMENTS

We thank NSF SBIR (grant #DMI-0109778), AFOSR STTR (grant #F49620-00-C-0058) and the Memorial Institute for Prevention of Terrorism (MIPT) for financial support of this research. We thank Natasha Mamedova, OSU Department of Chemistry, for performing some experiments, and Dr. John Wycoff, OSU College of Veterinary Medicine, for providing the *B. suis* bacteria sample.

## REFERENCES

- Bruchez, M., Jr.; Moronne, M.; Gin, P.; Weiss, S.; Alivisatos, A.P. Semiconductor nanocrystals as fluorescent biological labels. *Science* **1998**, *281*, 2013–2016.
- Mirkin, C.A.; Letsinger, R.L.; Mucic, R.C.; Storhoff, J.J. A DNA-based method for rationally assembling nanoparticles into macroscopic materials. *Nature (Lond.)* **1996**, *382*, 607–609.
- Chan, W.C.W.; Nie, S. Quantum dot bioconjugates for ultrasensitive nonisotopic detection. *Science* **1998**, *281*, 2016–2018.
- Mahtab, R.; Harden, H.H.; Murphy, C.J. Temperature- and salt-dependent binding of long DNA to protein-sized quantum dots: Thermodynamics of “inorganic protein”–DNA interactions. *J. Am. Chem. Soc.* **2000**, *122*, 14–17.
- Davis, S.A.; Burkett, S.L.; Mendelson, N.H.; Mann, S. Bacterial templating of ordered macrostructures in silica and silica-surfactant mesophases. *Nature (Lond.)* **1997**, *385*, 420–423.
- Willard, D.M.; Carillo, L.L.; Jung, J.; Van Orden, A. CdSe–ZnS quantum dots as resonance energy transfer donors in a model protein–protein binding assay. *Nano Lett.* **2001**, *1*, 469–474.

7. Mamedova, N.N.; Kotov, N.A.; Rogach, A.L.; Studer, J. Protein–CdTe nanoparticle conjugates: Preparation, structure and interunit energy transfer. *Nano Lett.* **2001**, *1*, 281–286.
8. Wang, S.; Mamedova, N.; Kotov, N.A.; Chen, W.; Studer, J. Antigen/antibody immunocomplex from CdTe nanoparticle bioconjugates. *Nano Lett.* **2002**, *2* (8), 817–822.
9. Santra, S.; Zhang, P.; Wang, K.; Tapeç, R.; Tan, W. Conjugation of biomolecules with luminophore-doped silica nanoparticles for photostable biomarkers. *Anal. Chem.* **2001**, *73*, 4998–4993.
10. Slocik, J.M.; Moore, J.T.; Wright, D.W. Monoclonal antibody recognition of histidine-rich peptide encapsulated nanoclusters. *Nano Lett.* **2002**, *2* (3), 169–173.
11. Winter, J.O.; Liu, T.Y.; Korgel, B.A.; Schmidt, C.E. Recognition molecule directed interfacing between semiconductor quantum dots and nerve cells. *Adv. Mater.* **2001**, *13* (22), 1673–1677.
12. Mann, S.; Shenton, W.; Li, M.; Connolly, S.; Fitzmaurice, D. Biologically programmed nanoparticle assembly. *Adv. Mater.* **2000**, *12*, 147–150.
13. Mattoussi, H.; Mauro, J.M.; Goldman, E.R.; Green, T.M.; Anderson, G.P.; Sundar, V.C.; Bawendi, M.G. Bioconjugation of highly luminescent colloidal CdSe–ZnS quantum dots with an engineered two-domain recombinant protein. *Phys. Status Solidi, B* **2001**, *224* (1), 277–283.
14. Wang, D.; Rogach, A.L.; Caruso, F. Semiconductor quantum dot-labeled microsphere bioconjugates prepared by stepwise self-assembly. *Nano Lett.* **2002**, *2* (8), 857–861.
15. Iqbal, S.S.; Mayo, M.W.; Bruno, J.G.; Bronk, B.V.; Batt, C.A.; Chambers, J.P. A review of molecular recognition technologies for detection of biological threat agents. *Biosens. Bioelectron.* **2000**, *15*, 549–578.
16. Alivisatos, A.P. Semiconductor clusters, nanocrystals, and quantum dots. *Science* **1996**, *271*, 933–937.
17. Alivisatos, A.P. Perspectives on the physical chemistry of semiconductor nanocrystals. *J. Phys. Chem.* **1996**, *100*, 13226–13239.
18. Miemeyer, C.M. Nanoparticles, proteins, and nucleic acids: Biotechnology meets materials science. *Angew. Chem., Int. Ed.* **2001**, *40*, 4128–4158.
19. Shipway, A.N.; Katz, E.; Willner, I. Nanoparticle arrays on surface for electronic optical and sensor applications. *ChemPhysChem* **2000**, *1*, 18–52.
20. Hermanson, G.T. *Bioconjugate Techniques*; Academic Press: San Diego, CA, 1996; 593–602.
21. Charles, P.T.; Kusterbeck, A.W. Trace level detection of hexahydro-1,3,5-trinitro-1,3,5-triazine (RDX) by microimmunosensor. *Biosens. Bioelectron.* **1999**, *14*, 387–396.
22. Bart, J.C.; Judd, L.L.; Kusterbeck, A.W. Environmental immunoassay for the explosive RDX using a fluorescent dye-labeled antigen and the continuous-flow immunosensor. *Sens. Actuators, B* **1997**, *B39*, 411–418.
23. Rogach, A.; Nagesha, D.; Koktysh, D.; Kotov, N.A. Synthesis of “raisin-bun”-type composite nanoparticle spheres. *Chem. Mater.* **2000**, *12*, 2676–2685.
24. Rogach, A.L.; Katsikas, L.; Kornowski, A.; Su, D.; Eychemueller, A.; Weller, H. Synthesis and characterization of thiol-stabilized CdTe nanocrystals. *Ber. Bunsen-Ges.* **1996**, *100*, 1772–1778.
25. Bragg, P.D.; Hou, C. Subunit composition, function, and spatial arrangement in the Ca<sup>2+</sup>- and Mg<sup>2+</sup>-activated adenosine triphosphatases of *Escherichia coli* and *Salmonella typhimurium*. *Arch. Biochem. Biophys.* **1975**, *167*, 311–321.
26. Lomant, A.J.; Fairbanks, G. Chemical probes of extended biological structures: Synthesis and properties of the cleavable protein cross-linking reagent [<sup>35</sup>S]dithiobis(succinimidyl propionate). *J. Mol. Biol.* **1976**, *104*, 243–261.
27. Staros, J.V. *N*-Hydroxysulfosuccinimide active esters: Bis(*N*-hydroxysulfosuccinimide) esters of two dicarboxylic acids are hydrophilic, membrane-impermeant, protein cross-linkers. *Biochemistry* **1982**, *21*, 3950.
28. Halliday, M.I.; Wisdom, G.B. A comparison of 3 methods for the preparation of enzyme antibody conjugates. *Biochem. Soc. Trans.* **1986**, *14*, 473–474.
29. Imagawa, M.; Yoshitake, S.; Hamaguchi, Y.; Ishikawa, E.; Niitsu, Y.; Urushizaki, I.; Knazawa, R.; Tachibana, S.; Nakazawa, N.; Ogawa, H. *J. Appl. Biochem* **1982**, *4*, 41.
30. Kishida, Y.; Olsen, B.R.; Berg, R.A.; Prockop, D.J. Two improved methods for preparing ferritin–protein conjugates for electron microscopy. *J. Cell Biol.* **1975**, *64*, 331–339.
31. Peters, T., Jr. *All About Albumin. Biochemistry, Genetics, and Medical Applications*; Academic Press: San Diego, 1995.

# Magnetic Ferrofluids

**Carlos Rinaldi**

*Department of Chemical Engineering, University of Puerto Rico,  
Mayagüez, Puerto Rico*

**Thomas Franklin**

**Markus Zahn**

*Department of Electrical Engineering and Computer Science, Massachusetts Institute of  
Technology, Cambridge, Massachusetts, U.S.A.*

**Tahir Cader**

*Isothermal Systems Research, Clarkston, Washington, U.S.A.*

## INTRODUCTION

Ferrofluids are synthesized colloidal mixtures of non-magnetic carrier liquids, typically water or oil, containing single-domain, permanently magnetized particles, typically magnetite, with diameters on the order of 5–15 nm and volume concentration up to about 10%.<sup>[1–6]</sup> A 10% by volume magnetite ferrofluid would have a saturation magnetization of about 0.0560 T = 560 G (1 T = 10,000 G). Brownian motion keeps the nanoscopic particles from settling under gravity and a surfactant layer, such as oleic acid, surrounds each particle to provide short-range steric hindrance and electrostatic repulsion between particles to prevent particle agglomeration. A polymeric layer surrounding each nanoparticle may also serve this purpose. These nanoparticle coatings allow ferrofluids to maintain fluidity even in intense, high-gradient magnetic fields. The study and application of ferrofluids, invented in the mid-1960s,<sup>[7]</sup> involves interdisciplinary science and technology integrating chemistry, fluid mechanics, and magnetism. Because of the small particle size, ferrofluids involved nanoscience and nanotechnology from their inception.

Conventional ferrofluid applications use d.c. magnetic fields from permanent magnets for use as liquid O-rings in rotary and exclusion seals,<sup>[8–10]</sup> bearings, as dampers in stepper motors and shock absorbers, in magnetorheological fluid composites,<sup>[11,12]</sup> for heat transfer in loudspeakers,<sup>[1–5]</sup> in inclinometers and accelerometers, for grinding and polishing, and in magnetocaloric pumps and heat pipes.<sup>[1,13]</sup> Ferrofluid is used in over 50 million loudspeakers each year. Almost every computer disk drive uses a magnetic fluid rotary seal for contaminant exclusion<sup>[14]</sup> and the semiconductor industry uses silicon crystal-growing furnaces that employ ferrofluid rotary shaft seals. A representative seal can withstand a pressure difference of up to

1.5 MPa (~15 atm) at a speed of 7000 rpm.<sup>[15]</sup> Ferrofluids are also used for the separation of magnetic from non-magnetic materials and for the separation of materials by their density using a non-uniform magnetic field to create a magnetic pressure distribution in the ferrofluid that causes the fluid to act as if it has a variable density that changes with height.<sup>[1,16]</sup> Magnetic materials are attracted to the regions of strongest magnetic field, whereas non-magnetic materials are displaced to the regions of low magnetic field with matching effective density. Magnetomotive separations use this selective buoyancy for sink–float separation of materials such as ore minerals,<sup>[16]</sup> one novel application being the separation of diamonds from beach sand.<sup>[17,18]</sup>

Ferrofluids are a multifunctional medium<sup>[2]</sup> that allow applications in each of its constituent disciplines of chemistry, fluid mechanics, and magnetism. With modern advances in understanding nanoscale systems, current research focuses on synthesis,<sup>[19–23]</sup> characterization,<sup>[20,22–27]</sup> and functionalization<sup>[21,22,28–34]</sup> of nanoparticles with magnetic and surface properties tailored for application as microelectromechanical/nanoelectromechanical sensors, actuators, in microfluidic/nanofluidic devices, as nanobiosensors, as targeted drug delivery vectors, in magnetocytolysis of cancerous tumors, in hyperthermia, in separations and cell sorting, for magnetic resonance imaging (MRI), and in immunoassays.

## FERROFLUID SYNTHESIS

### Ferrofluid Composition

The current “nanotechnology” focus on nanoscale devices is new, but the synthesis and formulation of magnetic nanoparticles in ferrofluids has been fairly well established in science and engineering over the last

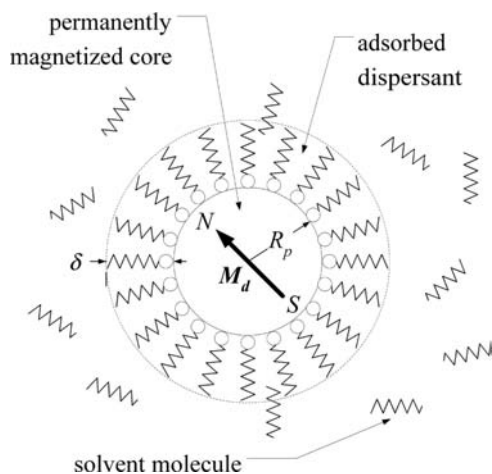


**Fig. 1** Ferrofluid as a colloidal dispersion of permanently magnetized nanoparticles of radius  $R_p$ , on the order of 5 nm, possessing a permanent dipole moment with domain magnetization  $M_d$ . A stabilizing dispersant layer of thickness  $\delta$ , on the order of 1–2 nm, is adsorbed on the magnetic particle's surface.

four decades.<sup>[1–6,17,32–38]</sup> As illustrated in Fig. 1, ferrofluids generally consist of suspensions of permanently magnetized nanoparticles up to about 10% by volume, with diameters on the order of 5–15 nm and with adsorbed surfactant/polymer dispersant layers of approximately 2 nm thickness,<sup>[39]</sup> undergoing rotational and translational Brownian motion in a suspending fluid. A transmission electron microscopy (TEM) electron micrograph at 500,000 $\times$  magnification of approximately 6-nm-diameter iron oxide particles to be utilized in commercial grade ferrofluid is shown in Fig. 2.

### Ferrofluid Colloidal Stability

Colloidal stability involves competition between thermal energy  $= kT$  and magnetic energy  $= \mu_0 M_d H V$ , where  $k = 1.38 \times 10^{-23}$  J/K is Boltzmann's constant,  $T$  is the absolute temperature [in K],  $\mu_0 = 4\pi \times 10^{-7}$  H/m is the magnetic permeability of free space,  $M_d$  is the particle magnetization [in A/m],  $H$  is the magnetic field [in A/m], and  $V = \pi D^3/6$  m<sup>3</sup> is the magnetic volume of a spherical ferrofluid nanoparticle of diameter  $D = 2R_p$  [in m<sup>3</sup>].<sup>[1]</sup>

Stability against settling in a magnetic field requires that the thermal energy be large compared to the magnetic energy:

$$\frac{kT}{\mu_0 M_d H (\pi D^3/6)} > 1 \Rightarrow D < (6kT/(\pi\mu_0 M_d H))^{1/3} \quad (1)$$

For the typical magnetite ferrofluid nanoparticle with  $M_d = 4.46 \times 10^5$  A/m (or, equivalently,

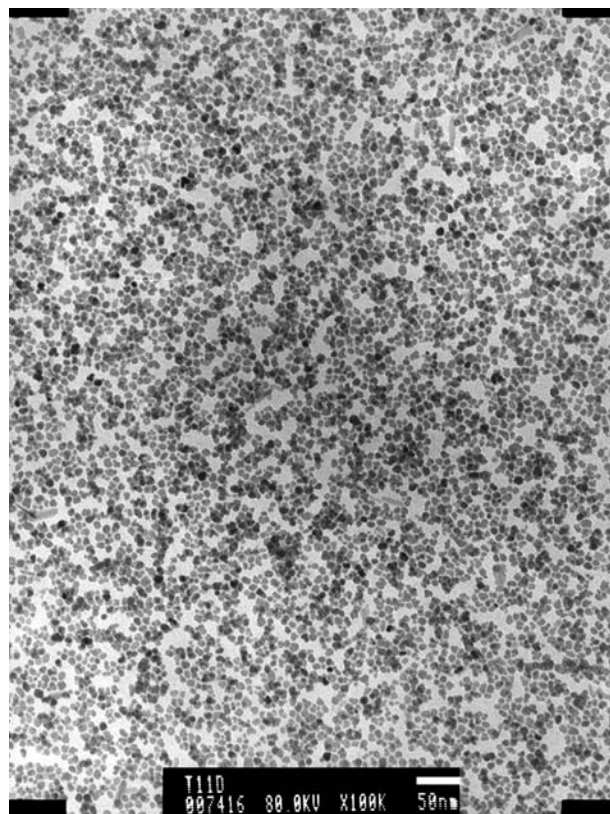


**Fig. 2** A TEM electron micrograph at 500,000 $\times$  magnification of a mixture of  $\text{Fe}_3\text{O}_4$  and  $\text{Fe}_3\text{O}_2$  iron oxide particles. The average diameter is  $5.9 \pm 0.4$  nm, with a standard deviation of 2.3 nm. Particles are coated with a surfactant and are utilized in the preparation of a commercial-grade ferrofluid. Source: Ferrotec Corporation.

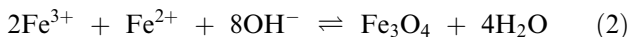
$\mu_0 M_d = 0.56$  T) in a magnetic field of  $H = 10^4$  A/m ( $\mu_0 H \approx 0.013$  T) at room temperature ( $T = 298$  K), Eq. (1) yields  $D < 11.2$  nm.

Commercially available ferrofluids with a volume concentration  $\phi$  of magnetic particles with magnetization  $M_d$  have a saturation magnetization  $M_s = \phi M_d$  up to about 0.1 T, but calculations show that an upper limit of saturation magnetization can be 0.21 T for 16-nm-diameter magnetite particles, 0.48 T for 8.7-nm cobalt particles, and 0.55 T for 7.8-nm iron particles.<sup>[40]</sup>

### Ferrofluid Preparation

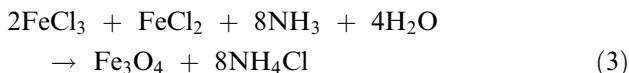
The two primary methods of preparing particles in the nanosize range are grinding<sup>[7]</sup> and precipitation.<sup>[41]</sup> The first commercial ferrofluid was prepared in the mid-1960s by wet grinding of magnetite in kerosene starting from micron-sized particles in a ball mill. It takes about 500–1000 hr to reach  $\sim 10$  nm diameter. Chemical precipitation methods are much faster, and thus are most often employed to produce small magnetic nanoparticles.<sup>[1–6]</sup> The overall chemical reaction for

precipitation of ferrofluid nanoparticles is:<sup>[41]</sup>



where  $\text{Fe}_3\text{O}_4$  is magnetite with a divalent/trivalent iron ion ratio of  $\text{Fe}^{\text{III}}/\text{Fe}^{\text{II}} = 2$ . Following precipitation, the small particles are resuspended in a mixture of a surfactant and an organic solvent.

An easy and economical method for preparing an aqueous ferrofluid in less than 2 hr reacts iron(II) and iron(III) ions in an aqueous ammonia solution to form magnetite ( $\text{Fe}_3\text{O}_4$ ):



The magnetite is then mixed with an aqueous tetramethylammonium hydroxide  $[(\text{CH}_3)_4\text{NOH}]$  solution to form a stabilizing surfactant coating.<sup>[17]</sup>

A ferrofluid using a liquid metal carrier is desirable for high thermal and electrical conductivity applications. A liquid mercury ferrofluid with 2% by weight iron was made with a saturation magnetization of about 700 G. However, stabilizing surfactants have not yet been found for liquid metals, and so, to date, no stable conducting ferrofluid has been made.<sup>[1,42,43]</sup>

Whereas conventional ferrofluids are opaque, Xerox has developed a new series of water-based ferrofluids based on hydrogel technology with high optical transparency for colored magnetic toner and ink applications.<sup>[44]</sup> Using maghemite ( $\gamma\text{-Fe}_2\text{O}_3$  particles) in the size range of 2–10 nm, Xerox produced transparent colloids ranging in color from light amber to dark red with saturation magnetization greater than 400 G.

## FERROFLUID MAGNETIZATION

### Magnetization Relaxation Time Constants

When a d.c. magnetic field  $\vec{H}$  is applied to a ferrofluid, just like a compass needle, each magnetic nanoparticle with magnetic moment  $\vec{m}$  experiences a torque  $\mu_0\vec{m} \times \vec{H}$ , which tends to align  $\vec{m}$  and  $\vec{H}$ . There are two important time constants that determine how long it takes  $\vec{m}$  to align with  $\vec{H}$ :<sup>[1,45]</sup>

$$\tau_B = 3\eta V_h/kT; \quad \tau_N = \tau_0 e^{(KV_p/kT)} \quad (4)$$

The Brownian rotational relaxation time  $\tau_B$  describes the hydrodynamic process when the magnetic moment is fixed to the nanoparticle and surfactant layer of total hydrodynamic volume  $V_h$ , and the whole rotates in a fluid of viscosity  $\eta$  to align  $\vec{m}$  and  $\vec{H}$ . For the spherical

nanoparticle in Fig. 1,  $V_h = 4\pi/3(R_p + \delta)^3$ . The Néel time constant  $\tau_N$  is the characteristic time for the magnetic moment to align along the particle's easy axis with  $\vec{H}$ , without particle rotation. The parameter  $K$  is the particle magnetic anisotropy and  $V_p = 4\pi/3R_p^3$  is the volume of magnetic material alone. The literature gives different values for the anisotropy constant of magnetite, over the range of 23,000–100,000 J/m<sup>3</sup>, whereas  $\tau_0$  approximately equals  $10^{-9}$  sec. Recent work<sup>[46]</sup> has used Mössbauer spectroscopy to show that the value of  $K$  is size-dependent, increasing as particle size decreases and gives a value of  $K = 78,000 \text{ J/m}^3$  for 12.6-nm-diameter magnetite nanoparticles. The total magnetic time constant  $\tau$  including both Brownian and Néel relaxation is given by:<sup>[1,45]</sup>

$$\frac{1}{\tau} = \frac{1}{\tau_B} + \frac{1}{\tau_N} \Rightarrow \tau = \frac{\tau_B \tau_N}{\tau_B + \tau_N} \quad (5)$$

The time constant  $\tau$  is dominated by the smaller of  $\tau_B$  or  $\tau_N$ . For  $K = 23,000 \text{ J/m}^3$  with 12.6-nm-diameter magnetite nanoparticles at  $T = 300 \text{ K}$ ,  $\tau_N$  approximately equals 336 nsec, whereas for the same size particles and temperature with  $K = 78,000 \text{ J/m}^3$ ,  $\tau_N$  approximately equals 368 msec. For a ferrofluid with a representative fluid viscosity of  $\eta = 0.001 \text{ Pa sec}$  and with a surfactant thickness  $\delta = 2 \text{ nm}$ ,  $\tau_B = 1.7 \mu\text{sec}$ . Thus we see that with  $K = 23,000 \text{ J/m}^3$ , the effective time constant is dominated by  $\tau_N$ , whereas for  $K = 78,000 \text{ J/m}^3$ , the effective time constant is dominated by  $\tau_B$ . Experiments with ferrofluid particles of the order of 10 nm diameter have found effective magnetic relaxation times by fitting theory to experimental measurements. The computed Brownian relaxation time<sup>[47]</sup> thus indicated that  $K$  has value on the order of  $78,000 \text{ J/m}^3$ , as recently reported<sup>[46]</sup> rather than previously used values on the order of  $23,000 \text{ J/m}^3$ . Brownian and Néel relaxation are lossy processes leading to energy dissipation and causing complex susceptibility to have an imaginary part measurable using spectroscopic magnetometry.<sup>[48]</sup> These losses lead to heat generation using time-varying magnetic fields, which can be used for localized treatment of cancerous tumors.

In rotating magnetic fields, the time constant  $\tau$  of Eq. (5) results in the magnetization direction lagging  $\vec{H}$ ; therefore a time average torque acts on each nanoparticle, causing the particles and surrounding fluid to spin.<sup>[1,49–62]</sup> This leads to new physics as the fluid behaves as if it is filled with nanosized gyroscopes that stir and mix the fluid. In a flow field, if the nanoparticles spin to cause secondary flow in the direction opposite to the local vorticity of the flow, the driving pressure must increase to maintain the initial flow, in the same way as if the fluid viscosity increased. Similarly, if the nanoparticles spin to cause secondary

flow in the same direction as the local vorticity of the flow, the driving pressure can decrease for the same initial flow, in the same way as if the fluid viscosity decreased. Thus the nanoscale flow field resulting from the spinning nanoparticles can result in an increase or decrease of effective magnetoviscosity. A decrease in viscosity that is controllable by magnetic field amplitude and frequency has been termed “negative viscosity.”<sup>[63–67]</sup> The torques described above can drive ferrofluid flow for microfluidic and nanofluidic pump applications, or generate heat by viscous dissipation of spinning nanoparticles.

### Langevin Magnetization Characteristic

Ferrofluid equilibrium magnetization is accurately described by the Langevin equation for paramagnetism:<sup>[1–6,45]</sup>

$$M = M_s \left[ \coth \alpha - \frac{1}{\alpha} \right]; \quad \alpha = \mu_0 m H / kT \quad (6)$$

where  $M$  and  $H$  are collinear,  $M_s = Nm = M_d \phi$  is the saturation magnetization when all magnetic dipoles with moment  $m = M_d V_p$  and magnetic nanoparticle volume  $V_p$  with magnetization  $M_d$  are aligned with  $H$ ,  $N$  is the number of magnetic dipoles per unit volume, and  $\phi$  is the volume fraction of magnetic nanoparticles in the ferrofluid. For the typically used magnetite nanoparticle ( $M_d = 4.46 \times 10^5$  A/m or  $\mu_0 M_d = 0.56$  T), a representative volume fraction of  $\phi = 4\%$  with nanoparticle radius  $R_p = 5$  nm ( $V_p = 5.24 \times 10^{-25}$  m<sup>3</sup>) gives a ferrofluid saturation magnetization of  $\mu_0 M_s = \mu_0 M_d \phi = 0.0244$  T and  $N = \phi / V_p \approx 7.6 \times 10^{22}$  magnetic nanoparticles/m<sup>3</sup>.

Fig. 3 shows Eq. (6) plotted together with magnetization measurements of four different ferrofluids at various temperatures.<sup>[68]</sup> At low magnetic fields, the magnetization is approximately linear with  $\bar{H}$ ,  $\bar{m} = \chi_m \bar{H}$ , where:

$$\chi_m = \mu_0 m^2 N / (3kT) \quad (7)$$

is the magnetic susceptibility, related to magnetic permeability as  $\mu = \mu_0(1 + \chi_m)$ . For our representative numbers at room temperature and 10-nm-diameter magnetite particles, we obtain  $\chi_m \approx 4.24$  and  $\mu / \mu_0 \approx 5.24$ . The universality of the Langevin curve of Eq. (6) for different ferrofluids, different nanoparticle sizes, and different temperatures is demonstrated in Fig. 3.

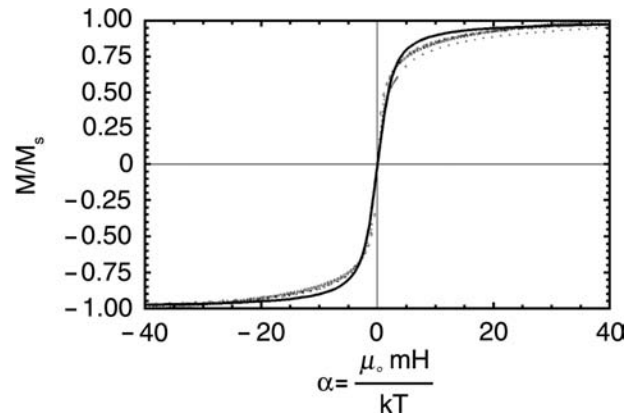


**Fig. 3** Measured magnetization (dots) for four ferrofluids containing magnetite particles ( $M_d = 4.46 \times 10^5$  A/m, or, equivalently,  $\mu_0 M_d = 0.56$  T) plotted with the theoretical Langevin curve (solid line). The data consist of Ferrotec Corporation ferrofluids: NF 1634 Isopar M at 25.4°C, 50.2°C, and 100.4°C, all with fitted particle size of 11 nm; MSG W11 water-based at 26.3°C and 50.2°C, with fitted particle size of 8 nm; NBF 1677 fluorocarbon-based at 50.2°C, with fitted particle size of 13 nm; and EFH1 (positive  $\alpha$  only) at 27°C, with fitted particle size of 11 nm. All data fall on or near the universal Langevin curve indicating superparamagnetic behavior. *Source:* From Ref.<sup>[68]</sup>.

### Magnetocaloric Effect

The temperature dependence of magnetization causes ferrofluids to exhibit the magnetocaloric effect whereby magnetic materials can heat up in a magnetic field and cool down when the magnetic field is removed.<sup>[1,69]</sup> This allows a direct and efficient conversion of magnetic work to heat with no mechanical moving parts, or, if the cycle is reversed, refrigeration or heat pumping is obtained. If the magnetic field  $H$  of a magnetic material with magnetization  $M(H, T)$  is increased by an amount  $\Delta H$ , adiabatic demagnetization results in a decrease of temperature:

$$\Delta T_{\text{decrease}} = \frac{T \Delta H}{C_H} \frac{\partial M(H, T)}{\partial T} \quad (8)$$

where  $C_H$  is the heat capacity at constant  $H$ .<sup>[38]</sup> For example, using iron in a 20-T magnetic field, the adiabatic temperature drop is 53°C.<sup>[1]</sup>

For a heated magnetic fluid with a change in magnetization of  $\Delta M$  in a magnetic field  $H$ , the pressure increase is:

$$\Delta p \approx (\mu_0 \Delta M) H \quad (9)$$

For  $\Delta M \approx 5 \times 10^4$  A/m in a  $\mu_0 H = 1$  T magnetic field, the pressure drop is  $\Delta p \approx 5 \times 10^4$  Pa ( $\approx 1/2$  atm).<sup>[1]</sup>



## Magneto-Optical Effects

Anisotropy from non-spherical nanoparticles orienting in an applied magnetic field causes birefringence (also known as the Cotton–Mouton effect, where the refractive index changes along axes parallel and perpendicular to the magnetic field), dichroism (change in light color dependent on direction of light polarization), and Faraday rotation (the plane of linearly polarized light is rotated when a magnetic field is applied parallel to the direction of light propagation).<sup>[70,71]</sup> Birefringence causes incident linearly polarized light to become elliptically polarized at some angle to the applied magnetic field. If the birefringent ferrofluid is placed in an optical polariscope, the transmitted light intensity varies with applied magnetic field magnitude and direction. Such a configuration can be used as a light shutter or as a magnetometer. After removing a magnetic field, the transient birefringence can be measured to determine the Brownian relaxation time of Eq. (4) from which the hydrodynamic nanoparticle size can be determined. Such magneto-optical relaxation measurements have also been used to determine the binding reactions of antibodies to their antigens through increases of nanoparticle size.<sup>[72]</sup>

## FERROHYDRODYNAMICS

### Ferrohydrodynamic Bernoulli's Law

The magnetic force density acting on an incompressible ferrofluid is:<sup>[1,73]</sup>

$$\bar{F} = \mu_0(\bar{M} \cdot \nabla)\bar{H} \text{ N/m}^3 \quad (10)$$

so that ferrofluids move in the direction of increasing magnetic field strength.

When  $\bar{M}$  and  $\bar{H}$  are collinear, this force density modifies Bernoulli's equation for inviscid and irrotational flow to:

$$-\rho \frac{\partial \psi}{\partial t} + p + \frac{1}{2} \rho v^2 - \rho \bar{g} \cdot \bar{r} - \mu_0 \int_0^H M dH = \text{constant} \quad (11)$$

where  $\rho$  is the ferrofluid mass density [in kg/m<sup>3</sup>],  $\psi$  is the velocity potential defined as  $\bar{v} = -\nabla\psi$ ,  $p$  is the pressure [in Pa],  $v|\bar{v}|$  is the magnitude of the fluid velocity  $\bar{v}$ ,  $\bar{g}$  is the gravitational acceleration vector, and  $\bar{r} = x\bar{i}_x + y\bar{i}_y + z\bar{i}_z$  is the position vector. The magnetic term in Eq. (11) is the magnetic contribution to fluid pressure and describes such magnetic effects as the shape of a ferrofluid meniscus; flow and instabilities

of a ferrofluid jet such as for magnetic fluid inkjet printing; operation of magnetic fluid seals, bearings, and load supports; magnetic fluid nozzles; and magnet self-levitation in a ferrofluid.<sup>[1,73]</sup> Ferrofluids in a non-uniform magnetic field can be used to separate material mixtures according to their densities, known as sink–float separation. With gravity directed in the  $-z$  direction, the apparent density of ferrofluid with density  $\rho$  when  $H = 0$  is:<sup>[35]</sup>

$$\rho_a = \rho - \frac{\mu_0 M}{g} \frac{dH}{dz} \quad (12)$$

## Fluid Instabilities

Ferrofluids exhibit a wide range of very interesting lines, patterns, and structures that can develop from ferrohydrodynamic instabilities.<sup>[61]</sup> Figs. 4 and 5 illustrate the ferrofluid hexagonal peaking behavior resulting from a magnetic field perpendicular to the free surface of a ferrofluid layer.<sup>[1,74,75]</sup> The peaks initiate when the magnetic surface force exceeds the stabilizing effects of fluid weight and surface tension. In Fig. 6, the gearlike structure results from the radial perpendicular field instability when a small magnet is placed behind a ferrofluid drop confined between closely spaced glass plates. In a rotating magnetic field, this “star wheel” will rotate and can function as a gear, flow stirrer, or pump. Possible further microdevice and nanodevice applications could result from solid

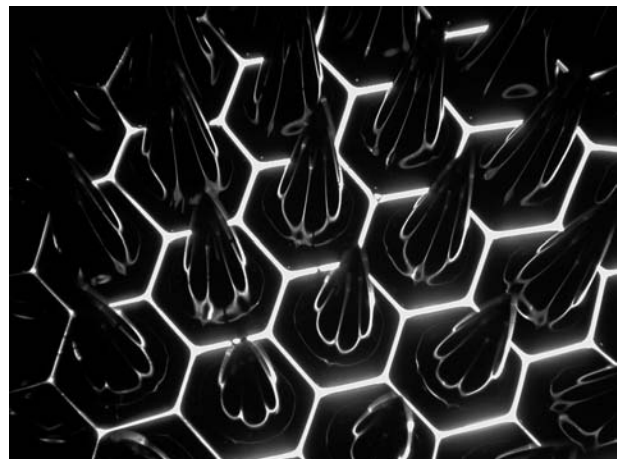


**Fig. 4** Hexagonal peaking patterns of about 1 cm spacing result when a perpendicular magnetic field is applied to a layer of Isopar M magnetic fluid with saturation magnetization of 400 G. The peaks initiate when the magnetic surface force exceeds the stabilizing effects of the fluid weight and surface tension. The image with a magnetic field of about 330 G shows the sharp peaks with a hexagonal base pattern. *Source:* From Ref.<sup>[61]</sup>.

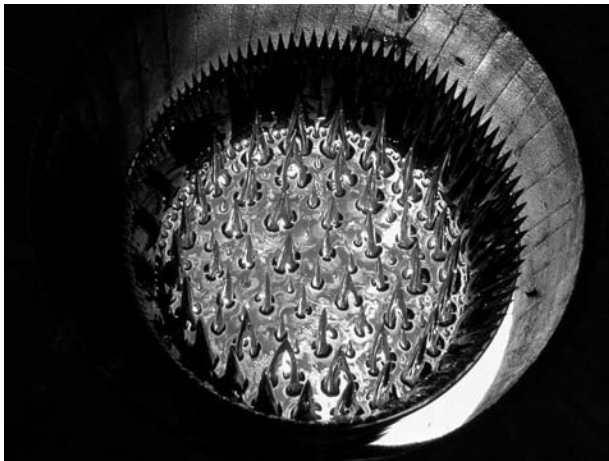


**Fig. 5** Another view of the perpendicular field instability including a crown of peaks on the glass container wall edge when a 400-G magnetic field is applied to Isopar M ferrofluid. The containing vessel has a 15-cm diameter. *Source:* From Ref.<sup>[61]</sup>.

structures made from a ferrofluid that is solid at room temperature but becomes liquid at slightly elevated temperature, such as by using a paraffin-based ferrofluid. If the ferrofluid is heated and then cooled in the presence of a magnetic field, solid magnetic nanostructures can be fabricated such as the gearlike structure in Fig. 6. Solid spiked structures with shapes like those in Figs. 4 and 5 may be useful for forming high electric fields at the tips that can be used in charge injection devices. Figure 7 shows the labyrinth instability that results when a magnetic field is applied tangent to the thin dimension of the ferrofluid layer confined between closely spaced glass plates.<sup>[76–78]</sup>

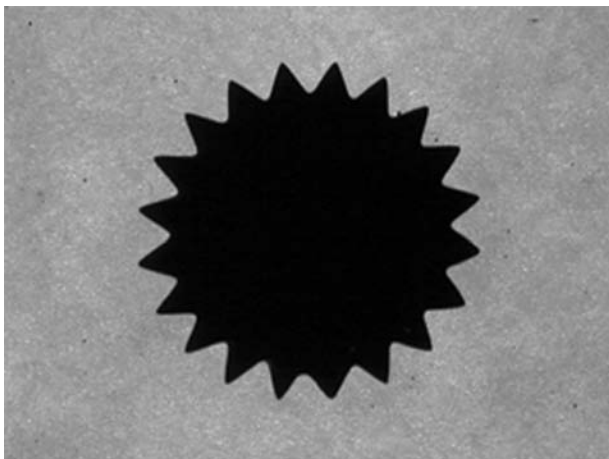


**Fig. 6** Gearlike structure that results when a small 5-mm-diameter permanent magnet, with strength of about 1200 G, is placed behind a small Isopar M ferrofluid droplet confined between glass plates with 1 mm gap. *Source:* From Ref.<sup>[61]</sup>.

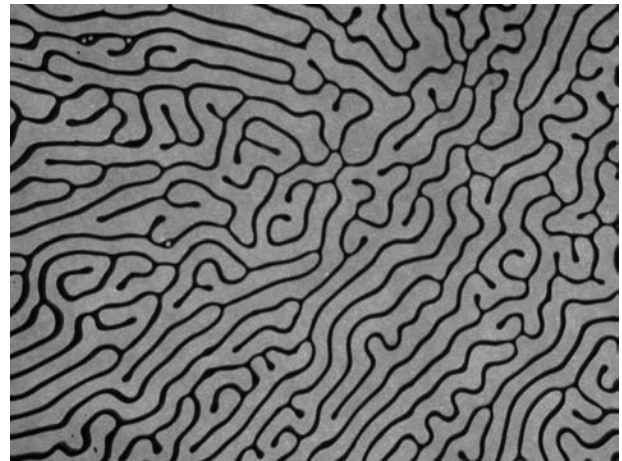


**Fig. 7** Labyrinth instability that results when a 1-mm-thick layer of Isopar M ferrofluid between glass plates is stressed by a magnetic field of about 150 G tangent to the thin dimension of the ferrofluid layer. The line thickness is about 200  $\mu\text{m}$ . *Source:* From Ref.<sup>[61]</sup>.

The labyrinth forms because the induced magnetic poles on the top and bottom surfaces of the ferrofluid create a magnetic field that opposes the applied field, the so-called demagnetization field, so that the magnetic field in the ferrofluid is less than the magnetic field in the non-magnetic region outside the ferrofluid. Because the ferrofluid is attracted to regions of strong magnetic field, a comblike interfacial instability develops and the interface forms thin lines that move away from the ferrofluid layer. Such fine lines may be useful for lithography and printing applications.

### Rotating Magnetic Field Torque-Driven Phenomena

Attention has shifted to rotating magnetic field phenomena, where the magnetization relaxation time constant of Eq. (5) creates a phase difference between magnetization and magnetic field, so that  $\bar{M}$  and  $\bar{H}$  are not in the same direction. This causes a magnetic torque density:<sup>[55–62,79]</sup>

$$\bar{T} = \mu_0 \bar{M} \times \bar{H} \quad \text{N/m}^2 \quad (13)$$

which causes the magnetic nanoparticles and surrounding fluid to spin. The concerted action on the order of  $10^{22}$ – $10^{23}$  nanoparticles/ $\text{m}^3$  leads to interesting microdrop behavior. A ferrofluid spherical microdrop, about 20  $\mu\text{m}$  in diameter, in a rotating magnetic field of intensity from 50 to 1000 A/m over a frequency range of 4 Hz–4 kHz forms a set of complicated shapes of loops, worms, and stars at intermediate strength fields and a “spinning starfish” shape with

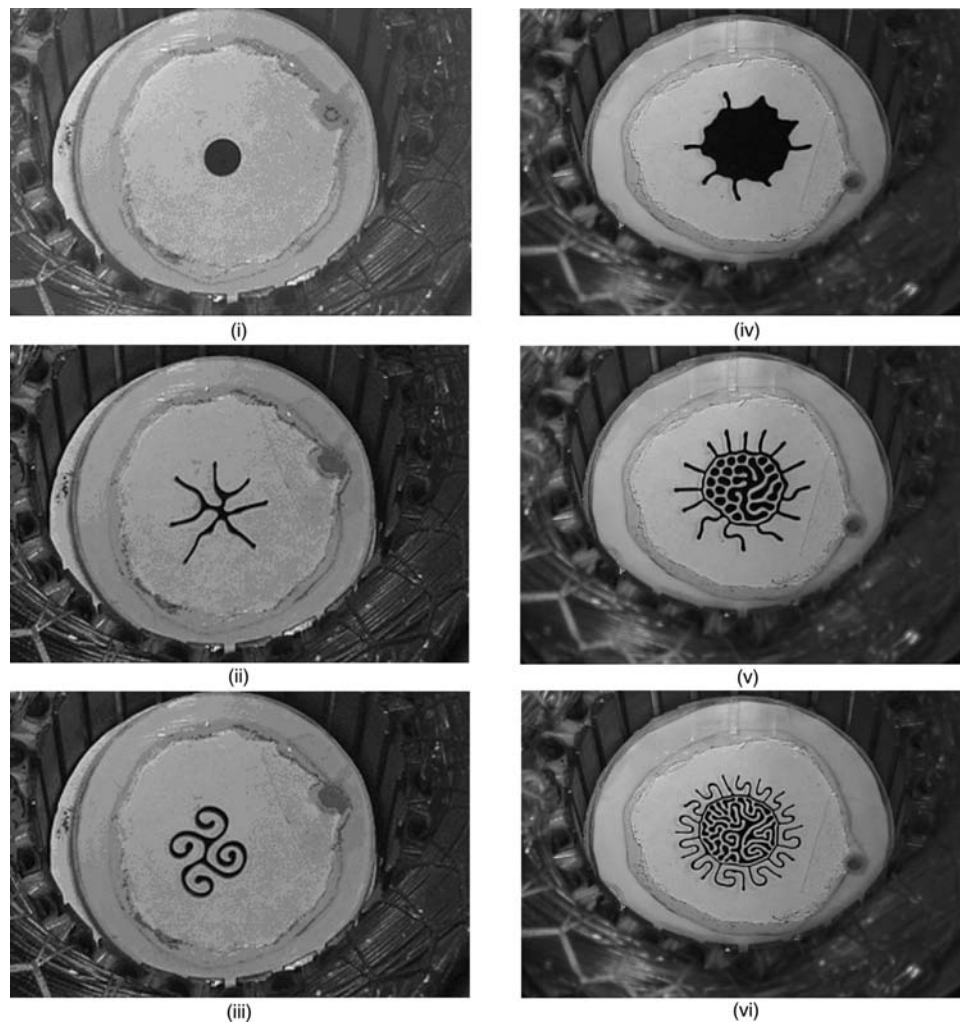


**Fig. 8** Spiral and intricate structure shapes with simultaneously applied d.c. and 20-G, 25-Hz rotating magnetic fields to fluorocarbon-based ferrofluid drops with  $\sim 400$  G saturation and low field magnetic susceptibility  $\sim 3$  confined between two glass plates with a 1.1 mm gap. The ferrofluid is surrounded by a 50/50 mixture of isopropyl alcohol and deionized water, which prevents ferrofluid wetting of the glass plates. (i)–(iii) have  $50 \mu\text{L}$  of ferrofluid. (i) shows the ferrofluid drop before the magnetic field is applied. (ii) The d.c. axial field is first increased to 100 G to cause the radially spiking labyrinth pattern. (iii) The clockwise rotating field is turned on and the spikes begin to curl in on themselves, forming a smooth spiral pattern. (iv)–(vi) have  $200 \mu\text{L}$  of ferrofluid. The test cell is first placed in the clockwise rotating field, which causes a counterclockwise flow that holds the fluid drop together without spikes. In (iv), a 100-G d.c. axial field is then gradually applied, causing the ferrofluid drop to appear to expand before the phaselike transition to (v) at a critical d.c. magnetic field strength around 100 G. (vi) The magnetic field is increased from 100 to 250 G. *Source:* From Ref.<sup>[81]</sup>.

many arms at high magnetic field, all corotating with the magnetic field.<sup>[53]</sup>

Other new ferrohydrodynamic phenomena with simultaneously applied d.c. and rotating magnetic fields are shown in Fig. 8 for a ferrofluid contained between glass plates with a 1.1 mm gap.<sup>[80,81]</sup> Two experiments are shown in Fig. 8. The first experiment, images (i)–(iii), uses  $50 \mu\text{L}$  of ferrofluid, brings the d.c. axial field up to 100 G, and then turns on the clockwise rotating field. Image (i) shows the circular ferrofluid drop before the magnetic field is applied, whereas image (ii) shows the spiking labyrinth pattern formed

by the ferrofluid after only the d.c. axial field has been applied. Then the clockwise rotating field is applied and the spikes begin to curl in on themselves, eventually forming the smooth spiral pattern shown in image (iii) after some of the spikes are absorbed into the larger structure. The smooth spirals form as the clockwise rotating magnetic field causes counterclockwise viscous shear flow on the outside ferrofluid surfaces, which returns on the inside surfaces.

The second experiment, with  $200 \mu\text{L}$  of ferrofluid, is seen in images (iv)–(vi) and is the result of first placing the cell in the clockwise rotating field and then

gradually applying a 100-G d.c. axial field. This results in the originally round ferrofluid drop appearing to expand in image (iv) before the phase transition to image (v) at a critical d.c. magnetic field strength around 100 G, evolving to image (vi) as the d.c. magnetic field is further increased to 250 G.

These intricate patterns can possibly have applications as self-assembling structures in fluidic devices, printing, separations, etc.

### Application to Power Transformer Cooling

With the development of a ferrofluid transformer oil that meets electrical property and breakdown requirements of high-power transformers,<sup>[82]</sup> there has been recent applied research<sup>[83–92]</sup> to use ferrofluid physical, mechanical, and thermal properties together with the magnetic body force density of Eq. (10) for enhanced cooling of power transformers. Heat generated by the windings and magnetic core produces temperature gradients in the ferrofluid, where there is also a non-uniform magnetic field. It is also thought that the high a.c. magnetic field in the vicinity of the windings and oil ducts can cause magnetic particle stirring that reduces ferrofluid thermal gradients. Measurements for 10- and 50-kVA transformers showed up to about 12°C lower operating temperature for ferrofluid transformer oil than for non-magnetic transformer oil.<sup>[88,89]</sup> Because the 10-nm-diameter ferrofluid particles are so small, they appear to have no deleterious effect on the oil electrical breakdown strength.<sup>[90]</sup> The enhanced cooling method uses the temperature dependence of ferrofluid magnetization described by the Langevin relation, so that the magnetic susceptibility  $\chi_m$  in Eq. (7) decreases as temperature increases. Thus, hot ferrofluid in the vicinity of the transformer windings has a lower magnetic permeability than cold ferrofluid. Then, cool (high magnetic permeability) ferrofluid is attracted to high magnetic field regions near the transformer windings as hot (low magnetic permeability) ferrofluid is displaced. Thus, the temperature gradients in a transformer can be used to induce magnetic permeability gradients that cause cooling ferrofluid motion and the resulting convective flow enhances transformer cooling. As an additive, a ferrofluid concentrate can be used to extend the lives of millions of aging transformers. As a new technology, ferrofluid transformers may be smaller, more efficient, and possess improved dielectric capabilities. A related analysis models a laminar and turbulent pipe flow that is applicable to transformer duct flows and validates a set of ferrohydrodynamic equations including the effects of nanoparticles interacting with magnetic fields and thermal/flow gradients.<sup>[93]</sup>

## APPLICATIONS TO NANOELECTROMECHANICAL AND MICROELECTROMECHANICAL SYSTEMS

### Advantages of Magnetic Field Devices

To demonstrate the advantages of magnetic field-based microelectromechanical systems (MEMS) and nanoelectromechanical systems (NEMS) devices over the usual electric-field based devices, we can compare representative electric and magnetic energy densities.<sup>[61]</sup> An electric field device is generally limited by the maximum allowed electric field without electrical breakdown, typically  $E \approx 10^8$  V/m for small-scale devices that take advantage of the Paschen curve at small gaps to raise the electrical breakdown strength of air (e.g., a variable capacitance micromotor may use 150 V across a 1.5- $\mu\text{m}$  gap).<sup>[94]</sup> Magnetic field devices have no limitations analogous to electrical breakdown and the maximum magnetic flux density is on the order of the saturation magnetization of single-domain magnetic nanoparticles, which is about  $B \approx 2.1$  T for single-domain iron particles. The resulting electric and magnetic energy densities are then:

$$\begin{aligned} W_e &= 0.5\epsilon_0 E^2 \approx 4.43 \times 10^4 \text{ J/m}^3; \\ W_m &= 0.5B^2/\mu_0 \approx 1.75 \times 10^6 \text{ J/m}^3 \end{aligned} \quad (14)$$

This possible increase in energy density and corresponding forces for magnetic devices has the added advantage of increased reliability as there are no catastrophic failure mechanisms analogous to electrical breakdown. Potential new NEMS applications using ferrofluid nanoparticles, with and without carrier fluid, include nanoduct flows, nanomotors, nanogenerators, nanopumps, nanoactuators, and other similar nanoscale devices.<sup>[61,95]</sup>

### Magnetic Nanoparticle Sensors and Actuators

The capability to actuate ferrofluids through magnetic fields and magneto-mechanical coupling makes them attractive for MEMS/NEMS applications,<sup>[61,96–99]</sup> as well as for energy conversion schemes.<sup>[95]</sup>

The essential principles of magnetic nanoparticle sensors and actuators are illustrated in Fig. 9. Single magnetic nanoparticles can be trapped in nanofabricated wells surrounded by a nanocoil. The nanocoil can then serve to sense a voltage when open-circuited, or a current when short-circuited, or, with imposed current, can drive nanoparticle rotation, much like in the operation of macroscopic generators or motors. Imposed flow over the nanowell would serve to drag the magnetic nanoparticle into rotation. Such rotation



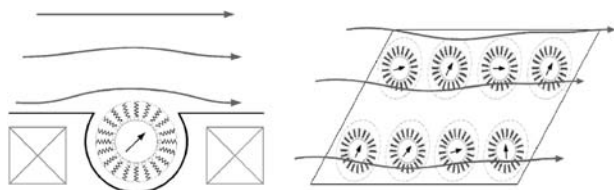


**Fig. 9** Proposed surface-immobilized magnetic nanoparticle-based flow sensors and actuators.

would result in a time-varying magnetic flux in the nanocoil, causing induced open-circuit voltage or short-circuit current. The induced voltage or current can be measured and used to determine the flow rate of the fluid, or can be used as a micropower source converting flow kinetic energy to electrical energy. The reverse operation with proper multiphase time-varying currents, through a set of such coils to cause a rotating magnetic field, would result in magnetic nanoparticle rotation and flow actuation. Both single wells and arrays are possible, allowing for sensing and actuation of flow over whole surfaces of a micro-electromechanical or nanoelectromechanical device consisting of nanoscale electromagnets, coupled with wells to hold the magnetic nanoparticles.

The fabrication procedure for micron-sized electromagnets and micron-sized gold wires has been demonstrated<sup>[100,101]</sup> and was successfully used to trap and manipulate collections of magnetic nanoparticles and atoms. At liquid nitrogen or helium temperatures in vacuum, the wires could carry currents of several amperes with a current density of  $\sim 10^8$  A/cm<sup>2</sup> and a power dissipation of  $\sim 10$  kW/cm<sup>2</sup>, producing magnetic fields to 0.3 T.

Representative present technology can fabricate gold coil windings that are about  $3\ \mu\text{m}$  thick and  $10\ \mu\text{m}$  wide, with center-to-center spacing of  $20\ \mu\text{m}$ , and can support a current density as high as  $10^{11}$  A/m<sup>2</sup>.<sup>[100]</sup> A representative maximum current of 3 A produces a magnetic field of about 0.1 T. Fig. 10 extends the concepts in Fig. 9 and shows a proposed micropower supply method for possible space applications. Waste heat is converted to ferrofluid flow using a vapor bubble pump that controllably causes magnetic particle rotation, which generates a time rate of change of magnetic flux through a nearby coil.<sup>[61]</sup> A 10-nm-diameter magnetite nanoparticle with a magnetization of 0.56 T would have a total magnetic flux of about  $4 \times 10^{-17}$  Wb. If this nanoparticle rotated next to our representative coil at an angular speed of 1000 rps with all the magnetic flux of the nanoparticle linking the coil, the induced peak voltage would be about  $3 \times 10^{-13}$  V. The conductivity of gold is  $4 \times 10^7$  S/m so that the resistance of a gold wire of length  $100\ \mu\text{m}$  with a cross section of  $10 \times 3\ \mu\text{m}^2$

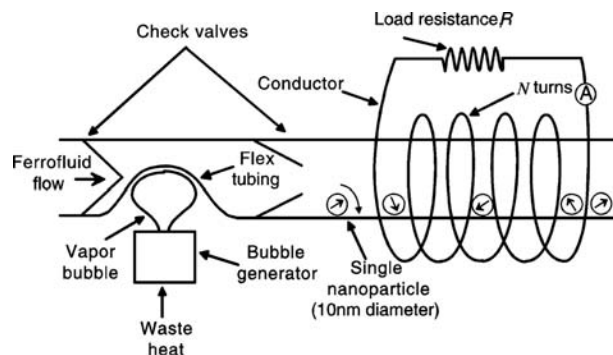


**Fig. 10** Schematic diagram of a proposed micropower supply method that takes waste heat to cause a time-varying flow that controllably rotates ferrofluid nanoparticles so that there is a time-varying magnetic flux through a coil that induces a current through a load. *Source:* From Ref.<sup>[61]</sup>.

would be about  $0.08\ \Omega$ . The short circuit peak current would be the ratio of the voltage divided by the coil resistance, or approximately 4 pA. The maximum power that could be delivered by this single nanoparticle generator would be about  $10^{-24}$  W. If confined to a single plane, there could be as many as  $10^{16}$  such single nanoparticle generators per square meter. If connected in series, the open circuit peak voltage could be as high as  $3000\ \text{V/m}^2$  of generator surface, whereas if connected in parallel, the short circuit peak load current could be as high as  $40,000\ \text{A/m}^2$  of generator surface, or in more practical units for nanoscale devices, about  $0.04\ \mu\text{A}/\mu\text{m}^2$  of generator surface area. The delivered time average power would then be on the order of  $10^{-8}\ \text{W/m}^2$ .

Of course, practical packing constraints, small wafer sizes, smaller nanoparticle rotation rates, magnetic flux leakage (so that the nanocoils do not link all the magnetic flux), nanoparticle sticking, nanoparticle confinement, and other non-idealities and problems of controlling motions of nanoparticles would lower these idealized large values, but these “back-of-the-envelope” preliminary calculations indicate the practical possibility of generating useful levels of micropower for selected applications, such as in space where plentiful waste heat can be used to cause ferrofluid flow to generate electricity, along the lines shown in Fig. 10.

Similar devices with submicron dimensions allow for single-particle manipulation and sensing. Trapping of nanoparticles would occur because of magnetophoretic forces,<sup>[102,103]</sup> analogous to dielectrophoretic trapping of particles,<sup>[104,105]</sup> where magnetic nanoparticles are attracted to the position of maximum magnetic field strength. A micromachined particle separator  $2 \times 3\ \text{mm}$  in size was fabricated on a silicon wafer. Electromagnetic coils using 500 mA of d.c. current generated a  $\sim 0.03$ -T magnetic field to separate  $\sim 1\text{-}\mu\text{m}$

magnetite particles from a water suspension at a velocity of  $\sim 1$  mm/sec in a channel that was  $90 \mu\text{m}$  deep and  $100 \mu\text{m}$  wide.<sup>[103]</sup>

### Microfluidics/nanofluidics

Ferrofluid devices can be a major component of a micro total analysis system ( $\mu\text{TAS}$ ), also known as “lab-on-a-chip.” The magnetic pressure generated in a ferrofluid is:<sup>[96–98]</sup>

$$p_m = \mu_0 \int_0^H M(H) dH \quad (15)$$

Ferrofluid plugs act as valves when placed near a stationary magnet and do not require any power. Hermetic sealing of a channel  $250 \mu\text{m}$  wide,  $150 \mu\text{m}$  deep, and  $9.5$  mm long has been achieved using a  $400$ -G hydrocarbon-based ferrofluid with  $42$  cP viscosity and a  $1200$ -G magnet, generating a magnetic field-induced change in pressure of  $p_m \approx 13.5$  Pa.<sup>[97]</sup> Ferrofluid microplugs have been able to sustain a pressure difference up to  $1700$  Pa.<sup>[99]</sup>

A number of micropumps use moving magnets to push ferrofluid microplugs that then displace non-magnetic fluids.<sup>[96–99]</sup> A circular channel of  $\sim 1$  cm diameter with  $250 \mu\text{m}$  depth and  $2$  mm channel width containing a  $125$ -G hydrocarbon-based ferrofluid pushing water had a flow rate of  $45.8 \mu\text{L}/\text{min}$  with an  $8$ -rpm motor rotating a  $3500$ -G permanent magnet at speed  $3.75$  mm/sec, generating a pressure of  $1200$  Pa.<sup>[99]</sup>

An electromagnetic ferrofluid pipette was designed to accurately dispense liquid volumes smaller than  $0.2 \mu\text{L}$ .<sup>[106]</sup> The pipette consisted of four electromagnets with a total of  $160$  turns around a  $1.8$ -mm air gap holding the pipette tube. A small hydrocarbon-based ferrofluid plug of  $600$  G saturation magnetization and  $1.43$  Pa sec viscosity in the pipette would move with  $0.6$  A total current applied to the electromagnets, causing a ferrofluid pressure rise up to  $770$  Pa. The ferrofluid would move at a speed of  $0.9$  cm/sec in about  $1.5$  sec and would dispense  $90$  nL of water. The position of the ferrofluid plug was controlled to within  $0.2$  mm.

### BIOMEDICAL APPLICATIONS

There are a number of methods in which magnetic nanoparticles can be used for biomedical applications:<sup>[107–110]</sup>

1. Magnetic nanoparticles can bind to drugs, proteins, enzymes, antibodies, or organisms.
2. Magnetic nanoparticles can be directed to organs, tissues, or tumors using an external magnet for therapeutic effect.

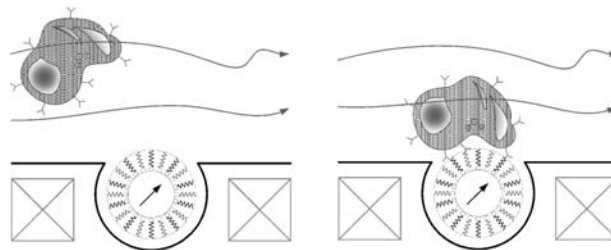


**Fig. 11** Proposed surface-immobilized magnetic nanoparticle-based nanobiosensor.

3. Dissipation in alternating and rotating magnetic fields can cause heating of magnetic nanoparticles for use in hyperthermia.

Such chemotherapeutic applications require particles to be able to pass through organ and tissue capillary systems without threat of vessel embolism and be able to transport pharmacologically active materials with an effective release mechanism of the drug at the target site. All components for the drug carrier system must be non-toxic, biodegradable, and/or removable.<sup>[111]</sup>

As an example application, Fig. 11 shows a surface-immobilized nanoelectromechanical flow sensor or actuator that may operate for detection of biological molecules and organisms. Magnetic nanoparticles functionalized with a surfactant coating for specific binding to a biological molecule or organism would be placed in the nanowells. A biological liquid medium would then flow over the nanosensor array. If the biological molecule or organism of interest is present in the medium, then specific binding with the magnetic nanoparticles would result, thus hindering their rotation. This, in turn, would result in a measurable change in the induced current through the nanocoils. In this way, a surface-immobilized flow-through nanobiosensor may be developed.

Magnetorelaxometry is a technique used to measure the binding or immobilization of a magnetic nanoparticle through measurement of changes in magnetic relaxation time following the removal of an applied magnetic field. Small free nanoparticles have magnetization decay because of Brownian relaxation, with time constant  $\tau_B$  of Eq. (4) increasing when additional molecules are bound to the nanoparticle because of the increased hydrodynamic volume  $V_h$ . The Néel relaxation time only depends on the magnetic material volume  $V_p$  and so is independent of non-magnetic material binding to a magnetic nanoparticle. If the nanoparticle is bound to a solid phase and has restricted motion, the magnetization predominantly decays by Néel relaxation. By determining if magnetization relaxation is occurring through Brownian or Néel



mechanisms, the binding conditions of nanoparticles to molecules or fixed material are determined.<sup>[112]</sup>

Suitability for biotechnological and biomedical applications of magnetic nanoparticles and ferrofluids is being determined through fundamental studies of magnetic nanoparticle cell toxicity, biocompatibility, and transport for such applications as separations, magnetic resonance imaging, drug delivery, cytolysis (cell destruction), hyperthermia, colloid extractants, cell sorting, and immunoassays. A brief summary of current research follows.

### Magnetocytolysis

Classical hyperthermia induces damage to cells and tissues, enhances radiation injury to tumor cells, and improves chemotherapeutic efficacy. A local thermal effect is desired within cancerous tissues while leaving normal tissues unaffected.<sup>[113,114]</sup> Heating between 41°C and 46°C generally reduces the viability of cancer cells and increases their sensitivity to radiation and chemotherapy. Temperatures up to 56°C (thermoablation) lead to cell death.<sup>[113–116]</sup> Magnetic materials for hyperthermia of biological tissues have been used since at least the late 1950s. Over a diameter range of 5–10 nm, the effective relaxation time of Eq. (5) in magnetite varies over two orders of magnitude. Ferrofluid subdomain particles (~10 nm diameter) absorb more power at reasonable a.c. magnetic fields than by hysteresis heating of multidomain particles (~1 μm).<sup>[114–118]</sup>

Small amounts of magnetic fine particles in radio-frequency (rf) magnetic fields can easily rise in temperature to cause cell death. For example, for a magnetic field intensity of 6.5 kA/m at 300 kHz, Néel relaxation has peak dissipated power density of about 10<sup>10</sup> W/m<sup>3</sup> for magnetite nanoparticles of about 9 nm radius, decreasing to about 10<sup>8</sup> W/m<sup>3</sup> at 7 nm radius and to 10<sup>6</sup> W/m<sup>3</sup> at 12 nm radius. Hysteresis losses are about 10<sup>6</sup> W/m<sup>3</sup> at 9 nm nanoparticle radius, rising to about 10<sup>10</sup> W/m<sup>3</sup> for nanoparticles larger than about 10 nm particle radius. Calculations and confirming measurements show that a temperature rise of about 16°C in about 30 min results from a 3-mm radius sphere of crushed magnetite embedded in a gel in a magnetic field of 17.6 kA/m at 300 kHz.<sup>[119]</sup>

To study the biological effects of a.c. magnetic field excited ferrofluids, both in vivo and in vitro studies have been done in cancer cell lines and spontaneously induced tumors in animal models.<sup>[118]</sup> The term magnetic fluid hyperthermia (MFH), which uses a.c. magnetic fields to heat target areas containing magnetic fluids, is suggested for this new cancer treatment method. It has been shown<sup>[120]</sup> that MFH is able to inactivate tumor cells in vitro to at least the same

extent as water bath hyperthermia and that there is no cytotoxic effect of intracellularly administered dextran-ferrite magnetic particles.<sup>[121,122]</sup> An in vivo study<sup>[123]</sup> using transplants of a mammary carcinoma showed that high doses of MFH were able to induce tumor control in 44% of the cases up to 30 days after therapy.

Trials carried out on human and mouse macrophages (leukocytes, white blood cells) without a magnetic field and in a constant magnetic field did not observe any cytolysis or toxic effects.<sup>[124]</sup> Under an alternating magnetic field of 100 G at a frequency of 1 MHz, the temperature of a concentrated ferrofluid increases from 37°C to 80°C in about 2 min. Magnetocytolysis experiments were carried out using very low concentrations of magnetic nanoparticles, such that no increase in the temperature of the bulk solution was evidenced. After being subjected to alternating fields for 5 min, it was observed that 40–50% of the mouse and human macrophages are killed, but only 3–6 hr after application of the oscillating field. It was found that binding of the magnetic nanoparticles to the cell membrane is essential for cytolysis.

For iron oxide nanoparticles of 10 nm diameter deposited into tumors in mice and exposed to a 6500-A/m, 400-kHz magnetic field for 4 min, the local heating, called “magnetic thermoablation,” raised the tumor temperature by ~62°C, causing therapeutic irreversible damage to the tumor.<sup>[125]</sup> Similar measurements in mice using water-based dextran-ferrite magnetic fluid in a 9300-A/m magnetic field at 0.88 MHz raised the tumor temperature by ~45°C, with 33% tumor regression and mouse life span increases of 150%.<sup>[126]</sup>

### Drug Delivery

The use of biocompatible ferrofluids as a delivery system for therapeutic drugs is commonly called “magnetic drug targeting.”<sup>[127–129]</sup> Mitoxantrone, a chemotherapeutic agent that inhibits DNA and RNA synthesis, was ionically bound to magnetic nanoparticles and was directed to cancerous tumor sites in rabbits using a 1.7-T magnet focused on the tumor. Complete tumor remissions with no adverse side effects were obtained using only 20% of the normal mitoxantrone dosage.<sup>[130]</sup> Similar success was achieved using ferrofluids labeled with iodine in a 0.6-T magnetic field.<sup>[131]</sup>

Magnetic targeting of anticancer drugs reversibly bound to magnetic fluids to locally advanced tumors can be achieved using magnetic fields directed to the tumor surfaces from outside the patient.<sup>[118,132]</sup> Phase I clinical trials using this approach in patients with advanced and unsuccessfully pretreated cancers or

sarcomas showed successful magnetic drug targeting with epirubin<sup>[118]</sup> and epirubicin.<sup>[132]</sup> Based on magnetic resonance tomographic techniques, pharmacokinetics, and the histological detection of magnetite, it was shown that ferrofluids could be successfully directed by externally imposed magnetic fields to the tumors in about one half of the patients.

Superparamagnetic nanoparticles were surface-modified with poly(ethylene glycol) (PEG) and folic acid, respectively, to improve their intracellular uptake and ability to target specific cells.<sup>[133]</sup> It was found that PEG modification of nanoparticles resulted in decreased uptake by macrophages, whereas folic acid modification did not result in any change in uptake by macrophages. However, both PEG and folic acid modification resulted in increased internalization of magnetic nanoparticles in breast cancer cells.

## Separations

Separation techniques are important for purification of biological materials and for identification of organisms, cells, and genomic materials. Application of a magnetic field to a suspension of magnetic nanoparticles confined between planar sheets causes the nanoparticles to self-organize into a regular array of columns. The column spacing can be controlled from submicron to 100  $\mu\text{m}$  by varying gap width, nanoparticle size, and concentration. Such a self-assembled array of magnetic particles was used to separate large DNA in a micro-channel in about 30 min, in contrast to the usual pulsed field agarose gel electrophoresis method, which takes about 12–24 hr.<sup>[134]</sup> Because pore size control from about 1–100  $\mu\text{m}$  can be obtained without the need for sophisticated microlithography, there are many separation applications envisioned for DNA, cells, proteins, organelles, and microparticles or nanoparticles.

Magnetic fluids have also been used as magnetically responsive extractants usable in treating aqueous media contaminated with organic compounds. In one study,<sup>[135]</sup> magnetite ( $\text{Fe}_3\text{O}_4$ ) nanoparticles of  $\sim 7.5$  nm nominal diameter coated with a  $\sim 9$ -nm bifunctional polymer layer composed of a hydrophilic poly(ethylene oxide) (PEO) outer region and a hydrophobic poly(propylene oxide) (PPO) inner region were prepared. With the advantages of very high surface area and decreased diffusion lengths, these magnetic fluids were shown to have high capacity for organic solutes, similar to that of analogous PEO–PPO–PEO block copolymer micelles. Efficient magnetic nanoparticle recovery using high-gradient magnetic field separation (HGMS) has been shown and incorporated into a proposed water purification process.<sup>[135]</sup>

Magnetic cell sorting schemes based on quadrupole fields<sup>[136]</sup> and in microfabricated magnetic arrays<sup>[137]</sup>

have been developed. The objective was to develop economical, high-throughput, high-purity, and high-recovery alternatives for separation of heterogeneous cell populations based on expression of particular surface markers.

An efficient magnetic vector/effector synthesis procedure was developed to target membrane receptors in target cells for subsequent separation.<sup>[118]</sup> This system was used to target, separate, and count damaged red blood cells. Applications of this technology include: 1) quality testing of human blood during storage in vitro;<sup>[138]</sup> 2) studies of the evolution of erythrocyte populations during parasitic pathologies such as *malaria*<sup>[139]</sup> and *Alzheimer's* disease;<sup>[140]</sup> and 3) detection of membrane modifications involved in complex biological processes such as apoptosis (programmed cell death).

## Immunoassays

Immunoassays are widely used in biology and medicine for the determination of the composition of complex samples such as blood by labeling one of the reaction components with radioisotopes, enzymes, or fluorescent dyes. Magnetic nanoparticle labels offer advantages as they are inexpensive to produce, are stable, and can be safely and easily stored, handled, and disposed of without problems of radioactivity or environmental contamination.<sup>[141]</sup>

Antibodies were coupled with magnetic nanoparticles and reacted with their solid-phase adsorbed antigen. The samples were first placed in a magnetic field of 1500 A/m and then the remanent magnetization in the absence of magnetic field was measured in a superconducting quantum interference device (SQUID) magnetometer. This measurement technique investigated the binding of monoclonal antibodies (MABs) to collagen type III using Dextran-coated iron oxide nanoparticles with 13 nm mean diameter. Then polystyrene tubes used as sample containers were incubated with the antigen collagen type III so that the antigen was adsorbed onto the tube wall. The measured magnetic moment after switching off the magnetic field is entirely caused by the remanent magnetization of nanoparticles with hindered mobility because of their binding to the antigen fixed at the tube wall. Unbound nanoparticles relax by Brownian relaxation and have no net remanent magnetization. For this method to work, the Néel relaxation time must be longer than the measurement period, typically about 100 sec, which requires larger size magnetic particles on the order of  $>20$  nm diameter for magnetite particles.<sup>[141,142]</sup>

## Magnetic Resonance Imaging

Magnetic materials are highly opaque to x-rays and, with 8–10% volume concentration in ferrofluid, offer

comparable image quality to conventional barium sulfate.<sup>[2,143]</sup> Magnetic nanoparticles, conjugated to various MABs, peptides, or proteins, show potential applications for in vivo monitoring of brain intercellular communication and target-oriented magnetic resonance imaging in animal and human brains.<sup>[144]</sup> Dextran-coated superparamagnetic iron oxide is commercially available for MRI and has been used for localization and diagnosis of brain and cardiac blood obstructions and for liver lesions or tumors, where the nanoparticles tend to accumulate because of the difference in tissue fluidity and endocytotic processes (incorporation of substances into cells).

Approximately 7-nm-sized magnetite nanoparticles coated with polymeric starch were injected into a rat brain. The magnetic nanoparticles were well distributed within the dorsal hippocampus, demonstrating the feasibility of using magnetite nanoparticles for in vivo MRI of the rat brain.

### Bacterial Threads of Nanomagnets

Magnetotactic bacterial threads can be used to direct the self-assembly of ordered magnetic microstructures.<sup>[145]</sup> *Bacillus subtilis* strain FJ7 is a mutant strain that can be cultured with intertwining filaments to form weblike structures. A thread was dipped into an aqueous colloidal suspension containing 10-nm-diameter magnetite nanoparticles between the cell strings to form threads of magnetic materials with an estimated nanoparticle density of  $10^{18}$  particles/cm<sup>3</sup> and a volume fraction of about 7%.

### CONCLUSION

This entry has described the integrated chemistry, fluid mechanics, and magnetic nanoscience and nanotechnology of magnetic fluids with summary reviews of ferrofluid synthesis: composition, colloidal stability, and preparation; ferrofluid magnetization: relaxation time constants, magnetization characteristic, magnetocaloric effect, and magneto-optical effects; ferrohydrodynamics: Bernoulli's law of pressure and flow, instabilities, and rotating magnetic field torque-driven phenomena; applications to microelectromechanical/nano-electromechanical systems: magnetic nanoparticle sensors, actuators, and microfluidic devices; and biomedical applications: drug delivery, hyperthermia, immunoassays, magnetic resonance imaging, separations, and cell sorting. These topics span the range from the nanosize magnetic nanoparticles to the concerted action from  $10^{22}$  to  $10^{23}$  magnetic nanoparticles/m<sup>3</sup> to cause macroscopic pressure and flow. Continuing research will integrate ferrofluid

nanotechnology to MEMS/NEMS fabrication capability by modification and tailoring of magnetic nanoparticle suspension properties for specific new high-technology applications as sensors, actuators, and biomedical tools.

### REFERENCES

1. Rosensweig, R.E. *Ferrohydrodynamics*; Dover Publications: New York, 1997.
2. Bashtovoy, V.G.; Berkovsky, B.M.; Vislovich, A.N. *Introduction to Thermomechanics of Magnetic Fluids*; Hemisphere Publishing Corporation: Washington, NY, 1988.
3. Berkovsky, B.M.; Bashtovoy, V.G. *Magnetic Fluids and Applications Handbook*; Begell House: New York, 1996.
4. Berkovsky, B.M.; Medvedev, V.F.; Krakov, M.S. *Magnetic Fluids, Engineering Applications*; Oxford University Press: Oxford, UK, 1993.
5. Blums, E.; Cebers, A.; Maiorov, M.M. *Magnetic Fluids*; Walter de Gruyter: Berlin, 1996.
6. Rosensweig, R.E. Magnetic fluids. *Sci. Am.* **1982**, *247* (4), 136–145.
7. Papell, S.S. Low Viscosity Magnetic Fluid Obtained by the Colloidal Suspension of Magnetic Particles. US Patent 3,215,572, 1965
8. Raj, K.; Chorney, A.F. Ferrofluid technology—an overview. *Indian J. Eng. Mater. Sci.* **1998**, *5* (6), 372–389.
9. Raj, K.; Moskowitz, B. Commercial applications of ferrofluids. *J. Magn. Magn. Mater.* **1990**, *85*, 233–245.
10. Raj, K.; Moskowitz, B.; Casciari, R. Advances in ferrofluid technology. *J. Magn. Magn. Mater.* **1995**, *149* (1–2), 174–180.
11. Popplewell, J.; Rosensweig, R.E. Magnetorheological fluid composites. *J. Phys., D, Appl. Phys.* **1996**, *29*, 2297–2303.
12. Rosensweig, R.E.; Popplewell, J.; Siller, J.K. Magnetorheology of ferrofluid composites. *J. Magn. Magn. Mater.* **1995**, *14*, 953–956.
13. Nakatsuda, N. Trends of magnetic fluid applications in Japan. *J. Magn. Magn. Mater.* **1993**, *122*, 387–394.
14. Chen, S.X.; Zhang, Q.D.; Chang, H.C.; Komatsu, T.; Kang, C.H. Some design and prototyping issues on a 20,000 rpm HDD spindle-motor with a ferro-fluid bearing system. *IEEE Trans. Magn.* **2001**, *37* (2), 805–809.
15. Jinbin, Z.; Yongping, L. Numerical calculations for ferrofluid seals. *IEEE Trans. Magn.* **1992**, *28* (6), 3367–3371.
16. Andres, U. *Magnetohydrodynamic & Magnetohydrostatic Methods of Mineral Separation*; John Wiley and Sons/Israel Universities Press: New York/Jerusalem, 1976.
17. Berger, P.; Adelman, N.B.; Beckman, K.J.; Campbell, D.J.; Ellis, A.B.; Lisensky, G.C. Preparation and properties of an aqueous ferrofluid. *J. Chem. Educ.* **1999**, *76* (7), 943–948.

18. Ogden, F. *The Last Book You'll Ever Read*; MacFarlane, Walter, and Ross: Toronto, 1993; 206.
19. Biddlecombe, G.B.; Gun'ko, Y.K.; Kelly, J.M.; Pillai, S.C.; Coey, J.M.D.; Venkatesan, M.; Douvalis, A.P. Preparation of magnetic nanoparticles and their assemblies using a new Fe(II) alkoxide precursor. *J. Mater. Chem.* **2001**, *11* (12), 2937–2939.
20. Burke, N.A.D.; Stover, H.D.H.; Dawson, F.P.; Lavers, J.D.; Jain, P.K.; Oka, H. Preparation and characterization of polymer-coated magnetic nanoparticles. *IEEE Trans. Magn.* **2001**, *37* (4), 2660–2662.
21. Chatterjee, J.; Haik, Y.; Chen, C.J. Polyethylene magnetic nanoparticle: a new magnetic material for biomedical applications. *J. Magn. Magn. Mater.* **2002**, *246* (3), 382–391.
22. Kim, D.K.; Zhang, Y.; Voit, W.; Rao, K.V.; Muhammed, M. Synthesis and characterization of surfactant-coated superparamagnetic monodispersed iron oxide nanoparticles. *J. Magn. Magn. Mater.* **2001**, *225* (1–2), 30–36.
23. Aquino, J.M.; Sandoval, M.P.G.; Yoshida, M.M.; Valenzuela, O.A. Synthesis and study of a magnetic fluid. In *Magnetism, Magnetic Materials and Their Applications; Vol. 302-3, Materials Science Forum*, Proceedings of the Fourth Latin American Workshop on Magnetism, Magnetic Materials and Their Applications, São Paulo, Brazil, June, 1998; Trans Tech Publication Inc.: Switzerland, 1999, 455–459.
24. Jonsson, T.; Nordblad, P.; Svedlindh, P. Dynamic study of dipole–dipole interaction effects in a magnetic nanoparticle system. *Phys. Rev., B* **1998**, *57* (1), 497–504.
25. Haller, A.; Hartwig, S.; Matz, H.; Lange, J.; Rheinlander, T.; Kötz, R.; Weitschies, W.; Trahms, L. Magnetic nanoparticle relaxation measured by a low- $T_c$  SQUID system. *Supercond. Sci. Technol.* **1999**, *12* (11), 956–958.
26. Lacava, Z.G.M.; Azevedo, R.B.; Martins, E.V.; Lacava, L.M.; Freitas, M.L.L.; Garcia, V.A.P.; Rebola, C.A.; Lemos, A.P.C.; Sousa, M.H.; Tourinho, F.A.; Da Silva, M.F.; Morais, P.C. Biological effects of magnetic fluids: toxicity studies. *J. Magn. Magn. Mater.* **1999**, *201*, 431–434.
27. Spinu, L.; Srikanth, H.; Wiemann, J.A.; Li, S.; Tang, J.; O'Connor, C.J. Superparamagnetism and transverse susceptibility in magnetic nanoparticle systems. *IEEE Trans. Magn.* **2000**, *36* (5), 3032–3034.
28. Carpenter, E.E. Iron nanoparticles as potential magnetic carriers. *J. Magn. Magn. Mater.* **2001**, *225* (1–2), 17–20.
29. Da Silva, M.F.; Tourinho, F.A.; Liebert, L.; Neto, A.M.F. Anisotropic magnetic fluid—a magnetic liquid-crystal. *J. Magn. Magn. Mater.* **1993**, *122* (1–3), 57–61.
30. Domingo, J.C.; Mercadal, M.; Petriz, J.; Garcia, J.; de Madariaga, M.A. Preparation of PEG-grafted immunomagneto liposomes and their application in cell sorting. *Cell. Mol. Biol. Lett.* **1999**, *4* (4), 583–597.
31. Halbreich, A.; Roger, J.; Pons, J.N.; Geldwerth, D.; Da Silva, M.F.; Roudier, M.; Bacri, J.C. Biomedical applications of maghemite ferrofluid. *Biochimie* **1998**, *80* (5–6), 379–390.
32. Maxwell, D.J.; Taylor, J.R.; Nie, S.M. Self-assembled nanoparticle probes for recognition and detection of biomolecules. *J. Am. Chem. Soc.* **2002**, *124* (32), 9606–9612.
33. Shen, L.F.; Stachowiak, A.; Hatton, T.A.; Laibinis, P.E. Polymerization of olefin-terminated surfactant bilayers on magnetic fluid nanoparticles. *Langmuir* **2000**, *16* (25), 9907–9911.
34. Pileni, M.P. Magnetic fluids: fabrication, magnetic properties, and organization of nanocrystals. *Adv. Funct. Mater.* **2001**, *11* (5), 323–336.
35. Rosensweig, R.E. Magnetic fluids. *Annu. Rev. Fluid Mech.* **1987**, *19*, 437–463.
36. Shen, L.F.; Laibinis, P.E.; Hatton, T.A. Aqueous magnetic fluids stabilized by surfactant bilayers. *J. Magn. Magn. Mater.* **1999**, *194* (1–3), 37–44.
37. Shen, L.F.; Laibinis, P.E.; Hatton, T.A. Bilayer surfactant stabilized magnetic fluids: synthesis and interactions at interfaces. *Langmuir* **1999**, *15* (2), 447–453.
38. Novotny, M.A.; Rikvold, P.A. *Magnetic Particles*, arXiv: Cond-mat/9806082VI; January 5, 1998.
39. Shen, L.F.; Stachowiak, A.; Fateen, S.E.K.; Laibinis, P.E.; Hatton, T.A. Structure of alkanolic acid stabilized magnetic fluids. A small-angle neutron and light scattering analysis. *Langmuir* **2001**, *17* (2), 288–299.
40. Scholten, P.C. How magnetic can a magnetic fluid be? *J. Magn. Magn. Mater.* **1983**, *39*, 99–106.
41. Rosensweig, R.E. Ferrofluids Introduction. In *Encyclopedia of Materials: Science and Technology*; Buschow, K.H.J., Cahn, R.W., Flemings, M.C., Ilshner, B., Kramer, E.J., Mahajan, S., Eds.; Pergamon/Elsevier Science Ltd.: Amsterdam, 2001.
42. Windle, P.L.; Popplewell, J.; Charles, S.W. The long term stability of mercury based ferromagnetic liquids. *IEEE Trans. Magn.* **1975**, *Mag-11* (5), 1367–1369.
43. Charles, S.W.; Popplewell, J. Ferromagnetic Liquids. In *Ferromagnetic Materials*; Wohlfarth, E.P., Ed.; North-Holland Publ. Co.: Amsterdam, 1980; 2, 509–559.
44. Ziolo, R.F.; Giannelis, E.P.; Weinstein, B.A.; O'Horo, M.P.; Ganguly, B.N.; Mehrotra, V.; Russell, M.W.; Heiffman, D.R. Matrix-mediated synthesis of nanocrystalline  $\gamma$ -Fe<sub>2</sub>O<sub>3</sub>: a new optically transparent magnetic material. *Science: New Ser.* **1992**, *257* (5067), 219–222.
45. Shliomis, M.I. Magnetic fluids. *Sov. Phys., Usp.* **1974**, *17* (2), 153–169. (English translation).
46. Lehlooh, A.F.; Mahmood, S.H.; Williams, J.M. On the particle size dependence of the magnetic anisotropy energy constant. *Physica, B* **2002**, *321*, 159–162.
47. Rosenthal, A.D.; Rinaldi, C.; Franklin, T.; Zahn, M. Torque measurements in spin-up flow of ferrofluids. *ASME J. Fluids Eng.* **March 2004**.
48. Fannin, P.C.; Scaife, B.K.P.; Charles, S.W. Relaxation and resonance in ferrofluids. *J. Magn. Magn. Mater.* **1993**, *122*, 159–163.
49. Laithwaite, E.R. The mysterious rolling cylinder. *Electr. Rev.* **1968**, *182*, 130–131.

50. Moskowitz, R.; Rosensweig, R.E. Nonmechanical torque-driven flow of a ferromagnetic fluid by an electromagnetic field. *Appl. Phys. Lett.* **1967**, *11* (10), 301–303.
51. Brown, R.; Horsnell, R.S. The wrong way round. *Electr. Rev.* **1969**, *184*, 235–236.
52. Mailfert, R.; Martinet, A. Flow regimes for a magnetic suspension under a rotating magnetic field. *J. Physique* **1973**, *34*, 197–198.
53. Bacri, J.C.; Cebers, A.; Perzynski, R. Behavior of a magnetic fluid microdrop in a rotating magnetic field. *Phys. Rev. Lett.* **1994**, *72* (17), 2705–2708.
54. Călugăru, G.; Cotaș, C.; Bădescu, R.; Bădescu, V.; Luca, E. A new aspect of the movement of ferrofluids in a rotating magnetic field. *Rev. Roum. Phys.* **1976**, *21* (4), 439–440.
55. Zahn, M.; Wainman, P.N. Effects of fluid convection and particle spin on ferrohydrodynamic pumping in traveling wave magnetic fields. *J. Magn. Magn. Mater.* **1993**, *122*, 323–328.
56. Zahn, M.; Greer, D.R. Ferrohydrodynamic pumping in spatially uniform sinusoidally time-varying magnetic fields. *J. Magn. Magn. Mater.* **1995**, *149*, 165–173.
57. Zahn, M.; Pioch, L.L. Ferrofluid flows in AC and traveling wave magnetic fields with effective positive, zero or negative dynamic viscosity. *J. Magn. Magn. Mater.* **1999**, *201*, 144–148.
58. Zahn, M.; Pioch, L.L. Magnetizable fluid behaviour with effective positive, zero, or negative dynamic viscosity. *Indian J. Eng. Mater. Sci.* **1998**, *5*, 400–410.
59. Rinaldi, C.; Zahn, M. Effects of spin viscosity on ferrofluid flow principles in alternating and rotating magnetic fields. *Phys. Fluids* **2002**, *14* (8), 2847–2870.
60. Rinaldi, C.; Zahn, M. Effects of spin viscosity on ferrofluid duct flow profiles in alternating and rotating magnetic fields. *J. Magn. Magn. Mater.* **2002**, *252*, 172–175.
61. Zahn, M. Magnetic fluid and nanoparticle applications to nanotechnology. *J. Nanopart. Res.* **2001**, *3* (1), 73–78.
62. Rinaldi, C.; Lee, J.H.; Rosenthal, A.D.; Franklin, T.; Zahn, M. *Ferrohydrodynamics in Time-Varying Magnetic Fields*, Proceedings of International Mechanical Engineering Conference and Exposition, New Orleans, LA, November 17–22, 2002.
63. Bacri, J.-C.; Perzynski, R.; Shliomis, M.I.; Burde, G.I. “Negative viscosity” effect in a magnetic fluid. *Phys. Rev. Lett.* **1995**, *75* (11), 2128–2131.
64. Rosensweig, R.E. “Negative viscosity” in a magnetic fluid. *Science* **1996**, *271*, 614–615.
65. Shliomis, M.I.; Morozov, K.I. Negative viscosity of ferrofluid under alternating magnetic field. *Phys. Fluids* **1994**, *6* (8), 2855–2861.
66. Zeuner, A.; Richter, R.; Rehberg, I. Negative Viscosity in a Dispersion of Magnetite, Abstracts of the 8th International Conference on Magnetic Fluids, Timisoara, Romania, 1998, 72–73.
67. Zeuner, A.; Richter, R.; Rehberg, I. On the consistency of the standard model for magnetoviscosity in an alternating magnetic field. *J. Magn. Magn. Mater.* **1999**, *201*, 191–194.
68. Franklin, T.A. *Ferrofluid Flow Phenomena*; Master’s Thesis in the Department of Electrical Engineering and Computer Science; Massachusetts Institute of Technology: Cambridge, MA, 2003.
69. Rosensweig, R.E. Thermodynamics of electromagnetism. In *Thermodynamics. An Advanced Text Book for Chemical Engineers*; Astarita, G., Ed.; Plenum Press: New York, 1989.
70. Charles, S.W. Some applications of magnetic fluid—use as an ink and in microwave systems. *J. Magn. Magn. Mater.* **1987**, *65*, 350–358.
71. Scholten, P.C. The origin of magnetic birefringence and dichroism in magnetic fluids. *IEEE Trans. Magn.* **1980**, *Mag-16* (2), 221–225.
72. Romanus, E.; Gro, B.C.; Glöckl, G.; Weber, P.; Weitschies, W. Determination of biological binding reactions by field-induced birefringence measurements. *J. Magn. Magn. Mater.* **2002**, *252*, 384–386.
73. Melcher, J.R. *Continuum Electromechanics*; MIT Press: Massachusetts, 1981.
74. Cowley, M.D.; Rosensweig, R.E. The interfacial stability of a ferromagnetic liquid. *J. Fluid Mech.* **1967**, *80* (4), 671–688.
75. Abou, B.; Wesfreid, J.-E.; Roux, S. The normal field instability in ferrofluids: hexagon–square transition mechanism and wavenumber selection. *J. Fluid Mech.* **2000**, *416*, 217–237.
76. Rosensweig, R.E.; Zahn, M.; Shumovich, R. Labyrinthine instability in magnetic and dielectric fluids. *J. Magn. Magn. Mater.* **1983**, *39*, 127–132.
77. Zahn, M.; Rosensweig, R.E. Magnetic and dielectric fluids in porous media. In *Advances in Porous Media*; Corapcioglu, M.Y., Ed.; Elsevier: Amsterdam, 1991; Vol. 1, 125–178.
78. Zahn, M.; Rosensweig, R.E. Magnetic field gradient effects on magnetic fluid stabilization. *J. Magn. Magn. Mater.* **1987**, *65*, 293–300.
79. Rinaldi, C. *Continuum Modeling of Polarizable Systems*; PhD Thesis in the Department of Chemical Engineering; Massachusetts Institute of Technology: Cambridge, MA, 2002.
80. Lorenz, C.; Zahn, M. *Hele-Shaw Ferrohydrodynamics for Rotating and Axial Magnetic Fields*, 55th Annual Meeting of the Division of Fluid Dynamics, Dallas, TX, November 24–26, 2002; American Institute of Physics: Maryland, 2002.
81. Lorenz, C.; Zahn, M. Hele-Shaw ferrohydrodynamics for rotating and dc axial magnetic fields. *APS Bull.* **2003**, *47* (11), DD11, 47; *Phys. Fluids* **2003**, Gallery of Fluid Motion, *15* (9), S4.
82. Raj, K.; Moskowitz, R. Ferro-Cooled Electromagnetic Device and Improved Cooling Method. US Patent 5,462,685, 1995.
83. Cader, T.; Bernstein, S.; Crowe, C. Magnetic Fluid Cooled Transformer. US Patent 5,898,353, April 1999.
84. Tangthieng, C.; Finlayson, B.A.; Maulbetsch, J.; Cader, T. Heat transfer enhancement in ferrofluids subjected to steady magnetic fields. *J. Magn. Magn. Mater.* **1999**, *201*, 252–255.
85. Cader, T.; Knoke, G.S. *Novel Concept for Heat Transfer Enhancement. Application of Ferrofluids in Oscillating Magnetic Fields: Amendment 3. Report on Ferrofluid-Filled Distribution Transformer*, Energy

- International Report No. B9453009, Electric Power Research Institute, 1999.
86. Cader, T. *Novel Concept for Heat Transfer Enhancement. Application of Ferrofluids in Oscillating Magnetic Fields: Amendment 2*, Energy International Report No. B9453004, Electric Power Research Institute, 1998.
  87. Segal, V. Colloidal Insulating and Cooling Fluid. US Patent 5,863,455, 1999.
  88. Segal, V.; Raj, K. *An Investigation of Power Transformer Cooling with Magnetic Fluid*, Abstract of Papers, Symposium on Recent Trends in Science and Technology of Magnetic Fluids, Zadeshwar, Bharuch (Gujarat), India, October 16–18, 1997; Narmada College of Science and Commerce, 2427.
  89. Segal, V.; Raj, K. *Indian J. Eng. Mater. Sci.* **1998**, *5* (6), 416–422.
  90. Segal, V.; Hjortsberg, A.; Rabinovich, A.; Natrass, D.; Raj, K. *AC (60 Hz) and Impulse Breakdown Strength of a Colloidal Fluid Based on Transformer Oil and Magnetite Nanoparticles*, Proceedings of the 1998 IEEE International Symposium on Electrical Insulation, Arlington, VA, 1998, 619–622.
  91. Segal, V.; Natrass, D.; Raj, K.; Leonard, D. *Accelerated Thermal Aging of Petroleum Based Ferrofluids*, Abstracts of the 8th International Conference on Magnetic Fluids, Timisoara, Romania, July, 1998, 43–44.
  92. Segal, V.; Natrass, D.; Raj, K.; Leonard, D. *J. Magn. Magn. Mater.* **1999**, *201*, 70–72.
  93. Schumacher, K.R.; Sellien, I.; Knoke, G.S.; Cader, T.; Finlayson, B.A. Experiment and simulation of laminar and turbulent ferrofluid pipe flow in an oscillating magnetic field. *Phys. Rev., E* **2003**, *67* (2).
  94. Mehregany, M.; Senturia, S.D.; Lang, J.H.; Nagarkar, P. Micromotor fabrication. *IEEE Trans. Electron Devices* **1992**, *39* (9), 2060–2069.
  95. Gazeau, F.; Baravian, C.; Bacri, J.-C.; Perzynski, R.; Shliomis, M.I. Energy conversion in ferrofluids: magnetic nanoparticles as motors and generators. *Phys. Rev., E* **1997**, *56* (1), 614–618.
  96. Pérez-Castillejos, R.; Plaza, J.A.; Esteve, J.; Losantos, P.; Acero, M.C.; Cane, C.; Serra-Mestres, F. The use of ferrofluids in micromechanics. *Sens. Actuators, A, Phys.* **2000**, *84* (1–2), 176–180.
  97. Menz, A.; Benecke, W.; Pérez-Castillejos, R.; Plaza, J.A.; Esteve, J.; Garcia, N.; Higuero, J.; Diez-Caballero, T. *Fluidic Components Based on Ferrofluids*, 1st Annual International IEEE-EMBS Special Topic Conference on Microtechnologies in Medicine and Biology, Lyon, France, 2000.
  98. Pérez-Castillejos, R.; Esteve, J.; Acero, M.C.; Menz, A.; Kriz, K. *Smart Passive Microfluidic Systems Based on Ferrofluids for  $\mu$ TAS Applications*, The 11th International Conference on Solid-State Sensors and Actuators, Munich, Germany, June 10–14, 2001.
  99. Hatch, A.; Kamholz, A.E.; Holman, G.; Yager, P.; Bohringer, K.F. A ferrofluidic magnetic micropump. *J. Microelectromech. Syst.* **2001**, *10* (2), 215–221.
  100. Lee, C.H.; Lee, H.; Westervelt, R.M. Microelectromagnets for the control of magnetic nanoparticles. *Appl. Phys. Lett.* **2001**, *79*, 3308–3311.
  101. Drndić, M.; Johnson, K.S.; Thywissen, J.H.; Prentiss, M.; Westervelt, R.M. Micro-electromagnets for atom manipulation. *Appl. Phys. Lett.* **1998**, *72* (22), 2906–2908.
  102. Drndić, M.; Lee, C.S.; Westervelt, R.M. Three-dimensional microelectromagnet traps for neutral and charged particles. *Phys. Rev., B* **2001**, *63*, 085321-1–085321-4.
  103. Ahn, C.H.; Allen, M.G.; Trimmer, W.; Jun, Y.-N.; Erramilli, S. A fully integrated micromachined magnetic particle separator. *J. Microelectromech. Syst.* **1996**, *5* (3), 151–156.
  104. Voldman, J.; Braff, R.A.; Toner, M.; Gray, M.L.; Schmidt, M.A. Holding forces of single-particle dielectrophoretic traps. *Biophys. J.* **2001**, *80* (1), 531–541.
  105. Gascoyne, P.R.C.; Vykoukal, J. Particle separation by dielectrophoresis. *Electrophoresis* **2002**, *23* (13), 1973–1983.
  106. Greivell, N.E.; Hannaford, B. The design of a ferrofluid pipette. *IEEE Trans. Biomed. Eng.* **1997**, *44* (3), 129–135.
  107. Connolly, J.; St. Pierre, T.G. Proposed biosensors based on time-dependent properties of magnetic fluids. *J. Magn. Magn. Mater.* **2001**, *225* (1–2), 156–160.
  108. Wilhelm, C.; Gazeau, F.; Roger, J.; Pons, J.N.; Salis, M.F.; Perzynski, R.; Bacri, J.C. Binding of biological effectors on magnetic nanoparticles measured by a magnetically induced transient birefringence experiment. *Phys. Rev., E* **2002**, *65* (3), 031404.
  109. Dias, A.F.; Dernick, G.; Valero, V.; Yong, M.G.; James, C.D.; Craighead, H.G.; Lindau, M. An electrochemical detector array to study cell biology on the nanoscale. *Nanotechnology* **2002**, *13* (3), 285–289.
  110. Perez, J.M.; O’Loughin, T.; Simeone, F.J.; Weissleder, R.; Josephson, L. DNA-based magnetic nanoparticle assembly acts as a magnetic relaxation nanoswitch allowing screening of DNA-cleaving agents. *J. Am. Chem. Soc.* **2002**, *124* (12), 2856–2857.
  111. Ruuge, E.K.; Rusetski, A.N. Magnetic fluids as drug carriers: targeted transport of drugs by a magnetic field. *J. Magn. Magn. Mater.* **1993**, *122*, 335–339.
  112. Lange, J.; Kötz, R.; Haller, A.; Trahms, L.; Semmler, W.; Weitschies, W. Magnetorelaxometry—a new binding specific detection method based on magnetic nanoparticles. *J. Magn. Magn. Mater.* **2002**, *252*, 381–383.
  113. Chan, D.C.F.; Kirpotin, D.B.; Bunn, P.A., Jr. Synthesis and evaluation of colloidal magnetic iron oxides for the site-specific radiofrequency-induced hyperthermia of cancer. *J. Magn. Magn. Mater.* **1993**, *122*, 374–378.
  114. Jordan, A.; Scholz, R.; Wust, P.; Fähling, H.; Felix, R. Magnetic fluid hyperthermia (MFH): cancer treatment with AC magnetic field induced excitation of biocompatible superparamagnetic nanoparticles. *J. Magn. Magn. Mater.* **1999**, *201*, 413–419.
  115. Hiergeist, R.; Andra, W.; Buske, N.; Hergt, R.; Hilger, I.; Richter, U.; Kaiser, W. Application of magnetite ferrofluids for hyperthermia. *J. Magn. Magn. Mater.* **1999**, *201*, 420–422.
  116. Fannin, P.C.; Scaife, B.K.P.; Giannitsis, A.T.; Charles, S.W. Determination of the radius of nano-particles in a magnetic fluid by means of a constant frequency



- measurement technique. *J. Phys., D, Appl. Phys.* **2002**, *35* (12), 1305–1310.
117. Kötitz, R.; Weitschies, W.; Trahms, L.; Semmler, W. Investigation of Brownian and Néel relaxation in magnetic fluids. *J. Magn. Magn. Mater.* **1999**, *201*, 102–104.
  118. Ramchand, C.N.; Pande, P.; Kopcansky, P.; Mehta, R.V. Application of magnetic fluids in medicine and biotechnology. *Indian J. Pure Appl. Phys.* **2001**, *39* (10), 683–686.
  119. Hergt, R.; Andrä, W.; d'Ambly, C.G.; Hilger, I.; Kaiser, W.A.; Richter, U.; Schmidt, H.-G. Physical limits of hyperthermia using magnetite fine particles. *IEEE Trans. Magn.* **1998**, *34* (5), 3745–3754.
  120. Jordan, A.; Wust, P.; Scholz, R.; Tesche, B.; Fahling, H.; Mitrovics, T.; Vogl, T.; Cervos-Navarro, J.; Felix, R. Cellular uptake of magnetic fluid particles and their effects on human adenocarcinoma cells exposed to AC magnetic fields in vitro. *Int. J. Hypertherm.* **1996**, *12* (6), 705–722.
  121. Autenshlyus, A.I.; Brusentsov, N.A.; Lockshin, A. Magnetic-sensitive dextran-ferrite immunosorbents (for diagnostic and therapy). *J. Magn. Magn. Mater.* **1993**, *122*, 360–363.
  122. Roath, S. Biological and biomedical aspects of magnetic fluid technology. *J. Magn. Magn. Mater.* **1993**, *122*, 329–334.
  123. Jordan, A.; Scholz, R.; Wust, P.; Fahling, H.; Krause, J.; Wlodarczyk, W.; Sander, B.; Vogl, T.; Felix, R. Effects of magnetic fluid hyperthermia (MFH) on C3H mammary carcinoma in vivo. *Int. J. Hypertherm.* **1997**, *13* (6), 587–605.
  124. Roger, J.; Pons, J.N.; Massart, R.; Halbreich, A.; Bacri, J.C. Some biomedical applications of ferrofluids. *Eur. Phys. J., Appl. Phys.* **1999**, *5* (3), 321–325.
  125. Hilger, I.; Andrä, W.; Hergt, R.; Hiergeist, R.; Kaiser, W.A. Treatment of breast cancers by magnetic thermoablation: in vivo experiments in mice. *Magneto-hydrodynamics* **2001**, *37* (3), 323–327.
  126. Brusentsov, N.A.; Nikitin, L.V.; Brusentsova, T.N.; Kuznetsov, A.A.; Bayburtskiy, F.S.; Shumakov, L.I.; Jurchenko, N.Y. Magnetic fluid hyperthermia of the mouse experimental tumor. *J. Magn. Magn. Mater.* **2002**, *252*, 378–380.
  127. Lubbe, A.S.; Alexiou, C.; Bergemann, C. Clinical applications of magnetic drug targeting. *J. Surg. Res.* **2001**, *95* (2), 200–206.
  128. Voltairas, P.A.; Fotiadis, D.I.; Michalis, L.K. Hydrodynamics of magnetic drug targeting. *J. Biomech.* **2002**, *35* (6), 813–821.
  129. Browning, V.M. Potential Department of Defense (DOD) applications of magnetic carriers. *Eur. Cells Mater.* **2002**, *3* (2), 5–6.
  130. Alexiou, C.P.; Arnold, W.; Hulin, P.; Klein, R.; Schmidt, A.; Bergemann, C.; Parak, F.G. Therapeutic efficacy of ferrofluid bound anticancer agent. *Magneto-hydrodynamics* **2001**, *37* (3), 318–322.
  131. Alexiou, C.; Schmidt, A.; Klein, R.; Hulin, P.; Bergemann, C.; Arnold, W. Magnetic drug targeting: biodistribution and dependency on magnetic field strength. *J. Magn. Magn. Mater.* **2002**, *252*, 363–366.
  132. Lubbe, A.S.; Bergemann, C.; Riess, H.; Schriever, F.; Reichardt, P.; Possinger, K.; Matthias, M.; Dorken, B.; Herrmann, F.; Gurtler, R.; Hohenberger, P.; Haas, N.; Sohr, R.; Sander, B.; Lemke, A.J.; Ohlendorf, D.; Huhnt, W.; Huhn, D. Clinical experiences with magnetic drug targeting: a phase I study with 4'-epidoxorubicin in 14 patients with advanced solid tumors. *Cancer Res.* **1996**, *56* (20), 4686–4693.
  133. Zhang, Y.; Kohler, N.; Zhang, M. Surface modification of superparamagnetic magnetite nanoparticles and their intracellular uptake. *Biomaterials* **2002**, *23*, 1553–1561.
  134. Doyle, P.S.; Bibette, J.; Bancaud, A.; Viovy, J.-L. Self-assembled magnetic matrices for DNA separation chips. *Science* **2002**, *295*, 2237.
  135. Moeser, G.D.; Roach, K.A.; Green, W.H.; Laibinis, P.E.; Hatton, T.A. Water-based magnetic fluids as extractants for synthetic organic compounds. *Ind. Eng. Chem. Res.* **2002**, *41*, 4739–4749.
  136. Sun, L.P.; Zborowski, M.; Moore, L.R.; Chalmers, J.J. Continuous, flow-through immunomagnetic cell sorting in a quadrupole field. *Cytometry* **1998**, *33* (4), 469–475.
  137. Berger, M.; Castelino, J.; Huang, R.; Shah, M.; Austin, R.H. Design of a microfabricated magnetic cell separator. *Electrophoresis* **2001**, *22*, 3883–3892.
  138. Sestier, C.; Sabolovic, D.; Geldwerth, D.; Moumaris, M.; Roger, J.; Pons, J.N.; Halbreich, A. Use of annexin V-ferrofluid to enumerate erythrocytes damaged in various pathologies or during storage in vitro. *C. R. Acad. Sci., Ser. 3 Sci. Vie* **1995**, *318* (11), 1141–1146.
  139. Halbreich, A.; Sabolovic, D.; Sestier, C.; Amri, A.; Pons, J.N.; Roger, J.; Geldwerth, D. Annexin V binding to mouse erythrocytes following infection with *Plasmodium* parasites. *Parasitol. Today* **1996**, *12* (7), 292–293.
  140. Sabolovic, D.; Roudier, M.; Boynard, M.; Pautou, C.; Sestier, C.; Fertil, B.; Geldwerth, D.; Roger, J.; Pons, J.N.; Amri, A.; Halbreich, A. Membrane modifications of red blood cells in Alzheimer's disease. *J. Gerontol., Ser. A, Biol. Sci. Med. Sci.* **1997**, *52* (4), B217–B220.
  141. Kötitz, R.; Matz, H.; Trahms, L.; Koch, H.; Weitschies, W.; Rheinländer, T.; Semmler, W.; Bunte, T. SQUID based remanence measurements for immunoassays. *IEEE Trans. Appl. Supercond.* **1997**, *7* (2), 3678–3681.
  142. Koneracká, M.; Kopčanský, P.; Antalík, M.; Timko, M.; Ramchand, C.N.; Lobo, D.; Mehta, R.V.; Upadhyay, R.V. Immobilization of proteins and enzymes to fine magnetic particles. *J. Magn. Magn. Mater.* **1999**, *201*, 427–430.
  143. Depeyrot, J.; Sousa, E.C.; Aquino, R.; Tourinho, F.A.; Dubois, E.; Bacri, J.-C.; Perzynski, R. Rare earth doped maghemite EDL-MF: a perspective for nanoradiotherapy?. *J. Magn. Magn. Mater.* **2002**, *252*, 375–377.
  144. Kim, D.K.; Viot, W.; Zapka, W.; Bjelke, B.; Muhammed, M.; Rao, K.V. Biomedical applications of ferrofluids containing magnetite nanoparticles. *Mater. Res. Soc. Symp. Proc.* **2001**, *676*, Y8.32.1–Y8.32.6.
  145. Smith, C.J.; Field, M.; Coakley, C.J.; Awschalom, D.D.; Mendelson, N.H.; Mayes, E.L.; Davis, S.A.; Mann, S. Organizing nanometer-scale magnets with bacterial threads. *IEEE Trans. Magn.* **1998**, *34* (4), 988–990.

# Magnetic Nanocarbon

T. L. Makarova

*Department of Experimental Physics, Institute of Physics, Umeå University, Umeå, Sweden*

## INTRODUCTION

Carbon is unique among the elements in the vast number of allotropies and compounds that it can form. The diversity of carbon's electronic structure is reflected in its electrical properties: carbon with a tetrahedral spatial structure (diamond) is an insulator; carbon with a planar structure (graphite) is classified either as a semi-metal or a zero-gap semiconductor; the linear structural form of carbon (carbyne) as well as spherical carbon molecules (fullerenes) are semiconductors; whereas, cylindrical forms of carbon (nanotubes) can be either semiconductors or metals, depending on their geometric structure. Theoretical studies have shown that specific features of the electronic structure of carbon could give rise to ferromagnetic or superconducting correlations retained at high temperatures.

There is no physical law that prohibits magnetic ordering in the structures containing only light elements such as carbon; however, there are strong reasons why high-temperature ferromagnetism in carbon is hard to expect. A major requisite for magnetism in an all-carbon structure is the presence and stability of carbon radicals. The occurrence of radicals that can introduce an unpaired spin is cut down by the strong ability of pairing all valence electrons in covalent bonds. These reasons may explain the difficulties experienced in the preparation of magnetic carbon compounds. Certain defects exist that drastically change magnetic properties of carbon. Bulk crystalline graphite is a strong diamagnet with magnetic susceptibility second only to superconductors. Theoretical works show that graphite containing certain types of defects can exhibit spontaneous magnetization. This review collects the experimental studies of the carbon-based magnets and describes the current status of the theoretical work.

## BASIC THEORIES ON CARBON MAGNETISM

Almost without exception, carbon modifications—graphite, diamond, fullerenes, and carbon nanotubes—are diamagnetic.

Diamagnetism of diamond<sup>[1]</sup> is described in a simple model based on magnetic contributions of localized

electrons: two Langevin diamagnetic terms,  $\chi_c$  and  $\chi_v$ , arising from the core and valence electrons, respectively, and a Van Vleck paramagnetic susceptibility  $\chi_{vv}$ . The Van Vleck term results from virtual magnetic dipole transitions between the valence band and the conduction band. The absence of Landau diamagnetism,  $\chi_L$ , and Pauli paramagnetism,  $\chi_P$ , is due to the absence of the states at the Fermi level. The magnetic moment of diamond is temperature independent.

Graphite has an anisotropic diamagnetic susceptibility.<sup>[2]</sup> If the magnetic field is perpendicular to the basal plane, the graphite susceptibility is larger than for any other substance, excluding superconductors. The in-plane susceptibility is very small as it is close to the diamagnetic susceptibility of a carbon atom. For graphite, only one contribution to  $\chi$ , namely the large and anisotropic orbital contribution of valence electrons  $\chi_v$ , is usually considered in theoretical approaches. Pauli paramagnetism in ideal graphite should be absent.

The electronic properties of graphite planes of finite size (graphenes) differ radically from those of bulk graphite. Calculating magnetic susceptibility of graphenes, one must take into account not only the sum of  $\chi_c$ ,  $\chi_v$  and  $\chi_{vv}$ , but also the Pauli paramagnetism  $\chi_P$ , Landau diamagnetism  $\chi_L$  of conduction electrons and the Curie paramagnetism  $\chi_C$ . The diamagnetic susceptibility of graphene planes of a finite size is primarily controlled by the concentration of charge carriers, and this concentration in turn depends on structural defects. Three types of defects in graphite can be recognized provisionally: edges of the planes, porosity, and so-called topological defects (Gaussian curvature).

Nanographene is defined as a nano-sized two-dimensional flat hexagon-network of  $\pi$ -electron system. According to theoretical suggestions, the presence of edges in nanographene produces an edge-inherited non-bonding  $\pi$ -electronic state (edge state) in addition to the  $\pi$ - and  $\pi^*$ -bands, resulting in an entirely different electronic structure from bulk graphite, where the localized spins of the edge state play an important role in the unconventional nanomagnetism.<sup>[3]</sup>

If graphite has a steplike surface, localized states, caused by the cut of a graphite sheet, appear at the Fermi level, localized near the step.<sup>[4]</sup> Two recognized

types of edges of a graphene plane are armchair and zigzag. Peculiar electronic properties of zigzag edges were first investigated by M. Fujita.<sup>[5]</sup> It is typically assumed that, in real conditions, a zigzag-type edge is stabilized by a single hydrogen atom. If each carbon atom of an edge is bonded to two hydrogen atoms, this type of edge is referred to as a *bearded edge*.<sup>[6]</sup>

Long and narrow graphenes are called *ribbons*, and can be characterized by the type of long edge and by the number of cells  $N$  between the edges. Zigzag-type ribbons are always metallic; whereas, the armchair ribbons are metallic only if  $N = 3m - 1$ , where  $m$  is an integer. Narrow and long graphene ribbons with zigzag edges feature a sharp peak in the density of states at the Fermi energy; whereas such a peak is not observed in the case of bulk graphite. A specific feature of the zigzag ribbons is the appearance of a pair of almost flat bands on the Fermi energy.<sup>[7]</sup> The charge density in the flat band state is strongly localized on the zigzag-edge sites. These edge states are of primary importance in the case of nanosized graphite.<sup>[8]</sup> The extremely high density of states at the Fermi level in graphite ribbons leads to paramagnetism. The presence of flat energy bands near the Fermi level has a considerable influence on the graphite electronic structure with zigzag edges. A consideration of the effects of electron–electron interactions in the frame of the Hubbard model shows that there can be a spontaneous magnetic ordering in nanographite. In the case of the zigzag-type strips, a ferrimagnetic structure is possible, the appearance of magnetic ordering controlled by the magnitude of the surface deformation caused by the electron–phonon interaction.<sup>[9]</sup>

A graphite *honeycomb* plane with hexagonal holes (porous graphite) has an electronic structure different from the ideal plane. Flat bands appear systematically in the electronic structure, implying the occurrence of spin ferromagnetism when the electron correlation is turned on. It is predicted that organic ferromagnetism can appear in a *superhoneycomb* bipartite structure.<sup>[10]</sup> It is shown theoretically that the energy-band structure of porous graphite allows for the separation of spin and charge.<sup>[11]</sup>

Variations in the graphene curvature due to the appearance of heptagons and pentagons instead of hexagons also change the magnetic properties of bulk graphite. This curvature occurs owing to the Stone–Wales rearrangement:<sup>[12]</sup> the rotation of two neighboring carbon bonds by an angle  $\pi/2$  transforms four hexagons into two pentagons and two heptagons. The periodic system of these defects completely changes the energy-band structure of graphite. A non-dispersive band is formed along one of the directions and the peak in the density of states caused by defects is located near the Fermi level.<sup>[13]</sup>

Bulk graphite is the most typical diamagnetic material, but nanographite is characterized by the dependence of electronic structure on edge structures. The electronic structure around the Fermi level may be highly degenerated, and this degeneracy can cause magnetic instability. It is suggested that the basic magnetic mechanism is spin polarization in these highly degenerate orbitals or in a flat band.<sup>[14]</sup>

## EXPERIMENTAL EVIDENCE

Magnetic ordering at high temperatures in carbon-based compounds has been persistently observed since 1986 with the main results summarized in Table 1. It is important to note that the structural unit giving rise to carbon ferromagnetism is unknown. Bulk carbon ferromagnets as recently as 2005 did not exist. The materials described in Table 1 contain only a small part of ferromagnetic substance and, therefore, the structural determination of the ferromagnetic phase is impossible. Therefore, Table 1 does not identify the structure of the material, but does indicate the substance chosen as the starting material for the production of magnetic carbon.

Table 1 also shows the room temperature values of magnetization, values of the Curie temperature, and the amount of transition metal impurities in the samples. Methods of impurity analysis are abbreviated as follows: inductively coupled plasma atomic emission spectroscopy (ICP); atomic absorption spectroscopy (AAS); electron probe microanalysis (EPMA); x-ray fluorescence analysis (XRF); Rutherford backscattering (RBS); mass spectroscopy (MS); energy dispersive spectroscopy (EDS), and particle-induced x-ray emission (PIXE). The abbreviation *ppm* indicates part per million in weight, i.e., mg/kg or  $\mu\text{g/g}$ . We assume that the abbreviation *ppb* in some papers also means *ppm*.

## CRITICAL ANALYSIS OF EXPERIMENTAL RESULTS

Analysing reports in the literature on the synthesis of carbon-based organic materials that exhibit magnetic ordering at room temperature and higher, it may be observed that the ferromagnetic carbonaceous compounds have several features in common.

Bulk magnetization is rather low. Low magnetization values apparently contradict to the high temperatures of the magnetic ordering transition.

In some instances, these values were increased by one to two orders of magnitude using the magnetic separation. In nearly all cases, the authors note that they could not find structural or chemical differences between the magnetic and non-magnetic parts. It is

**Table 1** Saturation ( $M_s$ ), remanence ( $M_r$ ), coercive force ( $H_c$ ) and the curie temperature values for magnetic carbons prepared from different organic materials

Starting material	Magnetization values	$T_c$	Impurity content	Reference
Poly-BIPO ( $C_{14}O_4N_2H_{14}$ )	$M_s = 0.022$ emu/g	420–460 K	Atomic absorption spectroscopy (AAS): 15 ppm	[15][16]
	$M_s = 0.2$ emu/g		Inductively coupled plasma atomic emission spectroscopy (ICP): 10 ppm	[17]
$C_3H_3N$ (pyro-PAN)	$M_s = 0.2$ emu/g decays in air by $\exp(-t/\tau)$ law, $\tau \approx 5 \times 10^5$ s	>RT	AAS: 100–400 ppm	[18][19]
Poly-triaminobenzen $C_6H_9N_3$		Decomposes at 400		[20]
Triarylmethane resin ( $C_{27}H_{31}N_2O_7S$ ) <sub>n</sub>	$M_s = 0.12$ emu/g; $H_c = 65$ Oe	>RT	AAS, 20 ppm of Fe, absence of Ni and Co	[21][22]
Indigo ( $C_{16}H_{10}N_2O_2$ )	$M_s = 0.7$ emu/g; $M_r = 0.08$ emu/g; $H_c = 120$ Oe	>200 C	ICP: 26–28 ppm	[23][24]
Adamantane $C_{10}H_{16}$	$M_s = 0.5$ emu/g; $M_r = 0.35$ emu/g; $H_c = 600$ Oe	>400 K	ICP: <25 ppm	[25]
	$M_s = 0.06$ emu/g	200 K	ICP: <25 ppm	[26][27]
Phenylendiamine $C_6H_8N_2$ and triazine $C_3H_3N_3$	$M_s = 0.624$ emu/g, $M_r = 0.0665$ emu/g, $H_c = 125$ Oe			[28][29]
Guanine $C_5H_5N_5O$	$M_s = 2.25$ emu/g	>RT	AAS: not found	[30]
Triazine $C_3H_3N_3$ and melamine $C_3H_6N_6$	$M_s$ about 20 emu/g	>RT	<0.5 ppm AAS	[31]
Tetraazadodecane	$M_s = 2.56$ emu/g	>RT		[32]
Cyclodecane	$M_s = 1.07$ emu/g; $M_r = 0.21$ emu/g; $H_c = 163$ Oe decomposed in one month	>RT	ICP and fluorescent x-ray:<50 ppm	[33]
	$M_s = 10.5$ emu/g	>500 K		[33]
1,2-Diaminopropane $C_3H_{10}N_2$	$M_s = 10.5$ emu/g	>500 K		[33]
Triethylboranes $C_6H_{15}B$ , tripropylboranes $C_9H_{21}B$ tributylboranes $C_{12}H_{27}B$	$M_s = 36.2$ emu/g at 4.5K, RT values are slightly lower $M_r/M_s < 0.1$	>RT		[34]
Hexane	$M_s = 1.08$ emu/g	>RT	Free from transition metals	[35–39]
Dicyclohexane	$M_s = 1.28$ emu/g			
Tetraazacyclotetradodecane	$M_s = 1.63$ emu/g			
Tetraazadodecane	$M_s = 1.92$ emu/g			
Triethylamine	$M_s = 2.63$ emu/g			

(Continued)

**Table 1** Saturation ( $M_s$ ), remanence ( $M_r$ ), coercive force ( $H_c$ ) and the curie temperature values for magnetic carbons prepared from different organic materials (*Continued*)

Starting material	Magnetization values	$T_c$	Impurity content	Reference
Diethylamine	$M_s = 6.69$ emu/g			
Dipropylamine	$M_s = 7.85$ emu/g			
Propanediamine	$M_s = 9.37$ emu/g			
Polyvinylchloride (PVC)	$M_s = 0.27$ emu/g			
Carbonized polyvinylchloride	$M_s = 3$ emu/g, $M_r = 0.6$ emu/g, $H_c = 400$ Oe			[40]
Phenylenediamines: poly ( <i>meta</i> -PDA), poly( <i>ortho</i> -PDA) poly ( <i>para</i> -PDA)	$M_s = 0.38$ emu /g; $M_s = 0.29$ emu/g; $M_s = 0.07$ emu/g	>RT	ICP<0.1% Fe	[41]
Ferromagnetic polyaniline	$M_s = 10$ emu/g	>RT	AAS: absence of transition metals	[42]
Polyaniline and tetracyanoquinodimethane	$M_s = 0.1$ J T <sup>-1</sup> kg <sup>-1</sup>	350 K	ICP: 7 ppm of Ni, trace of Fe	[43]
CIO <sub>4</sub> <sup>-</sup> doped poly (3-methylthiophene)	Decays in air	RT	AAS: 1 ppb of Fe, 2 ppb of Ni	[44]
Polyimide film Kapton	$M_s = 0.059$ emu/g, and $M_r = 9 \times 10^4$ emu/g, respectively, at 300 K	>300 K	Not found within the detection limit	[45][46]
C <sub>60</sub> in dimethylformamide and polyvinylidene fluoride	0.210 emu/g	370 K	Fe<10 ppm; Mn<5 ppm; Cr<100 ppm Co<2 ppm Ni<5 ppm	[47][48]
C <sub>60</sub> H <sub>36</sub>	$M_s = 0.04$ emu/g			[49]
C <sub>60</sub> H <sub>36</sub>	$M_s = 1.2$ emu/g, degrades to zero during 1 year		Fe:<100 ppm Ni<2 ppm Pd<100 ppm Al<50 ppm Cu:<1000 ppm	[50]
C <sub>60</sub> photolysed	$M_s = 1.4 \times 10^{-2}$ emu/g			[51]
	$M_s = 0.04$ emu/g		ICP:<100 parts per 10 <sup>9</sup>	[52]
C <sub>60</sub> pressure-polymerized	$M_s = 0.12$ emu/g	500 K	PIXE: 174 ppm Fe in the surface layer	[53][54]
	$M_s = 0.42$ emu/g	820 K		[55]
	$M_s = 0.045$ emu/g	>400 K		[56]
Glassy carbon	$M_s = 0.8 \times 10^{-2}$ emu/g		70 ppm transition metal impurities	[57][58]
Carbon particles in He plasma	$M_s = 0.67$ emu/g		Fe, Co, and Ni at the noise level in EPMA	[59]
Carbon nanofoam	$M_s = 0.4$ emu/g (freshly produced), decays during one day		RBS and MS (Fe+Ni)<110 ppm	[60]
Oxygen eroded graphite	$M_s = 0.58$ emu/g	320 K	AAS, x-ray fluorescence analysis (XRF), energy dispersive spectroscopy (EDS) 60–90 ppm Fe, 3–8 ppm Cu	[61][62]
Proton irradiated graphite	$M_s \cong 0,005$ emu/g $M_r = 0,00045$ emu/g		PIXE 2.1 ppm Fe 0.4 ppm Ni	[63][64]

likely that the only example where this difference is unquestionable is photopolymerized fullerene, as dissolving in toluene removes nonreacted monomeric fullerenes and the residue shows an increased magnetization.<sup>[52]</sup>

Remnant magnetization  $M_r$  is small compared to the saturated  $M_s$  value,  $M_r \leq 0.1 M_s$ . This feature may be attributed to a superparamagnetic behavior, although the coercive force is not zero and the temperature dependence of the value is small. We note, however, that carbon magnets are not expected to exhibit a large hysteresis because of the small spin-orbit coupling. Spin-orbit coupling is small or negligible for light atoms because it scales with the fourth power of the atomic number.

Saturation magnetizations in pyrolytic magnetic carbons are nearly temperature-independent up to temperatures well above 295 K. Curie temperature in several cases is close to the decomposition temperature.

Results are poorly reproduced. Organic magnetic materials are produced by the chemical processes that involve a large number of reactions, and the results are hard to duplicate. Recent results where the chemical methods are supplemented by the physical ones: proton bombardment, laser ablation, oxygen erosion, pressure-temperature treatment, and photolysis, appear to be more repeatable.<sup>[59–64]</sup>

Magnetic properties of the synthesized substances are very sensitive to the synthesis conditions, especially preparation temperature. Deviations from an optimal temperature, that is specific for a certain process, lead to a quick decay of bulk magnetization. Fig. 1A illustrates this effect.

In earlier attempts to produce ferromagnetic carbonaceous compounds, the most successful ones are the processes involving the pyrolysis of organic compounds. The common features of these processes are heating organic substances in a complex (steplike) way, sometimes in the presence of a magnetic field, and stopping the processes halfway to graphitization. This process yields a highly oriented graphite-like material with a high concentration of unpaired spins. Clear features of room temperature magnetic ordering were observed in some cases. Again, there is a series of similarities between the substances reported by different authors.

The choice of the starting material to be pyrolyzed is important. Several authors mention isomeric effect where magnetic carbons are produced from the branched isomers. In other words, the geometric arrangement of radicals is important for attaining an ordered spin structure.

The *ratio* between the concentrations of hydrogen and carbon [H] and [C] in the starting material is particularly critical. As soon as this ratio exceeds 1.5, a sharp increase in the saturation magnetization of the

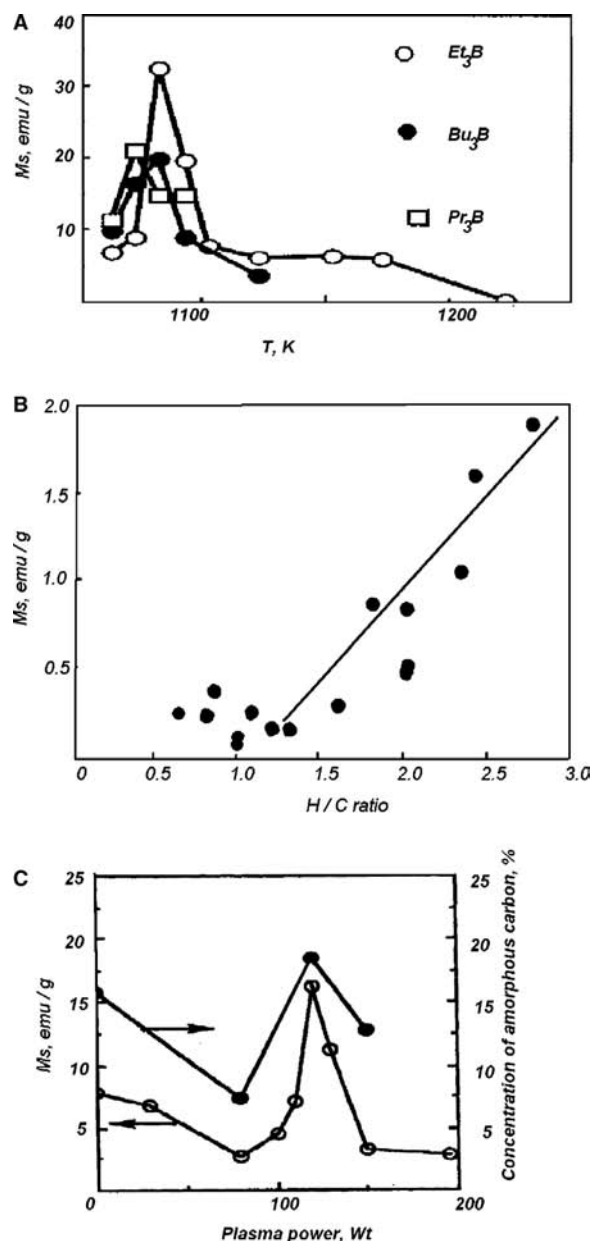


**Fig. 1** (A): Dependence of the observed saturation magnetization at 298 K on the pyrolysis temperature for triethylboranes ( $Et_3B$ ), tributylboranes ( $Bu_3B$ ) and tripropylboranes ( $Pr_3B$ ); (B): Dependence of saturation magnetization of carbon-based magnetic materials on the hydrogen-carbon ratio in the starting material; (C): Plasma power dependence of the saturation magnetization value at room temperature (solid circles) and amorphous carbon content of the carbon material (open circles).

reaction product is observed. A parallel between the hydrogen-related magnetic properties of pyrocarbons and the proton-induced magnetic ordering in graphite can be drawn (Fig. 1B).

Patents describing methods for preparing carbonaceous ferromagnets frequently include stopping the synthesis process at the mid-course to graphitization.



Properties of magnetic carbon materials made by pyrolysis of diverse organic compound monomers at around 1000°C are strongly related to the radicals and hydrogen atoms generated during the pyrolysis process and to the degree of amorphousness of the material.

Studies of a large number of ferromagnetic materials obtained from various nitrogen-containing substances showed that the structure of these materials is most often amorphous and disordered. In order to reveal the structural–magnetic correlations, samples of ferromagnetic carbon were subjected to various doses of plasma treatment, after which the percentage of amorphous carbon and the value of magnetization were measured. A one-to-one correspondence between the above two parameters was observed. The higher the content of amorphous carbon, the higher the spontaneous magnetization (Fig. 1C).

Some of the carbon magnets are unstable and lose the room-temperature ferromagnetic properties during one day, like carbon nanofoam, or in one year, like proton-bombarded graphite of hydrogenated fullerenes. The theoretical models should take into account metastable carbon structures.

## INFLUENCE OF IMPURITIES

It is seen from Table 1 that, in some cases, the experimental data does not give convincing proof for the intrinsic origin of the effect. In cases where the amount of impurities is given, the magnetization values are one or two orders of magnitude (but not several orders) larger than the value that could be expected if all impurities formed sufficiently large clusters. This value can be easily estimated from Table 2.

It cannot be excluded that part of the results listed in Table 1 can be caused by extrinsic reasons, especially taking into account the fact that the results are poorly

reproduced. Trivial sources of iron include air pollution, magnetic separations, grinding, and catalysts.<sup>[65]</sup> A nontrivial origin of magnetic behavior in contaminated carbon-based materials may result from the special arrangement of the spins of metallic ions being arranged in such a way that they are strongly coupled to an organic polymeric backbone.<sup>[65]</sup>

However, in order to contribute to the total magnetization of the samples, the impurities must interact magnetically. A good example of unconventional ferromagnetism is the one in diluted magnetic semiconductors where 1%–10% of transition metal ions are added to semiconductors or oxides. Ferromagnetism is induced in very rare occasions and only on the samples with special structure. Simple addition of transition metals does not lead to ferromagnetic properties, as no interaction pathway is provided. The incorporation of several atomic percents of transition metals, combined with the optimized synthesis conditions, leads to ferromagnetism. The mechanism, either carrier-induced, double-exchange or bound magnetic polaron formation, is still under debate. Various other theories (band ferromagnetism, carrier induced ferromagnetism, flat band theory, excitonic models, etc.)<sup>[66]</sup> have been reported as explanations for the ferromagnetism in these materials. A recent model of exchange in dilute ferromagnetic semiconductors suggests that the exchange is mediated by donor electrons in a spin-polarized impurity band.<sup>[67]</sup>

## NONTRIVIAL IMPURITY EFFECTS

Even if the extrinsic sample magnetization, calculated with the help of Table 2, is close to the experimental magnetization value, one cannot exclude non-trivial mechanisms. One of the mechanisms, contact-induced magnetism, was suggested by Cooley et al.<sup>[68]</sup> The effect of triggering carbon magnetism by the presence of

**Table 2** Maximum values of magnetization caused by 1 ppm of the impurities provided the impurities are in the ferromagnetic form

Type of impurity	Maximum magnetization, emu/g	Curie temperature, K	Comment
Iron, $\alpha$ -Fe	0.00022	1045	
Magnetite, $\text{Fe}_3\text{O}_4$	0.000092	860	Ferrimagnetic, Verwey transition at 118 K
Magnetite, $\text{Fe}_2\text{O}_3$	0.00008	880	Ferrimagnetic
Hematite, $\text{Fe}_2\text{O}_3$	0.0000004	950	Canted antiferromagnetic; Morin transition at 260 K
Iron carbide, $\text{Fe}_3\text{C}$	0.00013	483	
Trevorite $\text{NiFe}_2\text{O}_4$	0.00005	860	
Nickel, Ni	0.000055	630	
Cobalt, Co	0.000161	1400	

transition metals was found in extraterrestrial graphite,<sup>[68]</sup> carbon nanotubes,<sup>[69]</sup> and x-ray dichroism experiments on C/Fe layers.<sup>[70]</sup>

In some experimental works on organic compounds,<sup>[71–75]</sup> the authors indicate that the presence of ferromagnetic ions induces carbon ferromagnetism during the synthesis process. The procedure was as follows: charcoal was impregnated with the aqueous solution of cobalt acetate and, after adsorption of cobalt ions, the piece was hydrogenated and heated to 1000 K. Dilute hydrochloric acid treatment at 360 K during 48 h was used to dissolve cobalt from the specimen. After this, the x-ray fluorescence analyser did not detect any cobalt concentration in the carbon specimen. Magnetization measurements, before and after cobalt removal, indicated that the contribution of cobalt ions or cobalt metal in the signal is very small.

## NONMETALLIC IMPURITIES

There are many theoretical and experimental confirmations that, under certain conditions, magnetism arises without transition-metal elements. The best known example of a magnetic *p*-compound is molecular oxygen, which orders in antiferromagnetic fashion at 24 K. Non-metallic impurities, as well as intrinsic defects in metal-free compounds, may offer a path to realizing unique ferromagnetic materials. It is shown, theoretically, that ferromagnetism can be induced in CaO with calcium vacancies,<sup>[76]</sup> boron, carbon, or nitrogen-doped CaO,<sup>[77]</sup> calcium pnictides (i.e., CaP, CaAs, and CaSb with the zinc blend structure). The pnictides are the compounds of phosphorus, arsenic, antimony, and bismuth.<sup>[78]</sup> There are persistent indications of small ferromagnetic moments in CaB<sub>6</sub>,<sup>[79]</sup> that depend on sample stoichiometry and heat treatment<sup>[80]</sup> and are observed in impurity-free disordered thin films.<sup>[81]</sup> Lattice defects were suggested as a source of magnetism in another system with closed-shell configuration, HfO<sub>2-x</sub> films.<sup>[82]</sup>

In the case of carbon, two types of non-metallic impurities are considered. One type is trivalent elements like nitrogen and boron. The other type is hydrogen.

The role of hydrogen is particularly important. The entrapment of hydrogen by dangling bonds at the nanographite perimeter can induce a finite magnetization.<sup>[83]</sup> The same mechanism occurs in the case of hypergraphites, i.e., structures with edges where completely degenerate states appear.<sup>[84]</sup> Combination of the magnetic and non-magnetic edge structures (by means of hydrogenation, fluorination, or oxidation) is proposed as a guiding principle to design magnetic nanographite: a magnetic material made only from

light elements.<sup>[85]</sup> Another model includes absorption of hydrogen atoms on vacancies in graphite<sup>[86]</sup> and nanotubes.<sup>[87]</sup> A simple spin model was used to illustrate the mechanism through which chemically bonded hydrogen leads to a ferromagnetic ground state in polymerized fullerenes.<sup>[88]</sup>

Irradiation with hydrogen ions (protons) was shown to produce ferromagnetic spots on samples of highly oriented pyrolytic graphite. Magnetic force microscope studies showed that a magnetic signal appeared in an irradiated region and that this signal varied in an applied external field. Similar experiments on irradiation with helium ions do not yield a magnetic contrast. The explanations of the effects are based on the formation of di-hydrogenated and mono-hydrogenated edges or on the absorption of hydrogen atoms on irradiation-induced vacancies.

Non-metallic impurities like hydrogen, boron, and phosphorus are suggested to trigger ferromagnetism in diamond.<sup>[89]</sup> It has been shown experimentally that doping nanodiamond with nitrogen (<sup>15</sup>N) and carbon (<sup>12</sup>C) leads to ferromagnetic hysteresis behavior at room temperature. Doping was performed by means of ion implantation. Magnetic moment of nitrogen-implanted samples was higher than that of carbon-implanted samples.<sup>[90]</sup>

## MAGNETIC NATURE OF INTRINSIC CARBON DEFECTS

The magnetic properties of common bulk materials are determined mainly by choice of constituting elements from the periodic table. In nanometer-scale materials, the shapes or boundaries in nanostructures play important roles in determining the characteristics of electron states and generate various types of magnetic interactions, opening a possibility for the creation of nanoscale magnets consisting solely of nonmagnetic elements.<sup>[91]</sup>

The analysis of experimental and theoretical data shows that certain similarities between the magnetism of organic molecules and carbon-based structures can be found.

Long-range magnetic ordering requires the following conditions: the existence of spin carriers, the interaction among these spins, and the propagation of these interactions.

The first obvious problem is the occurrence and, more importantly, stability of carbon radicals. There are two ways to obtain unpaired spins in organic molecules.<sup>[92]</sup>

One way is based on the charge transfer process between the electron donor and the electron acceptor. The resulting open shell anions and cations bear unpaired spins.

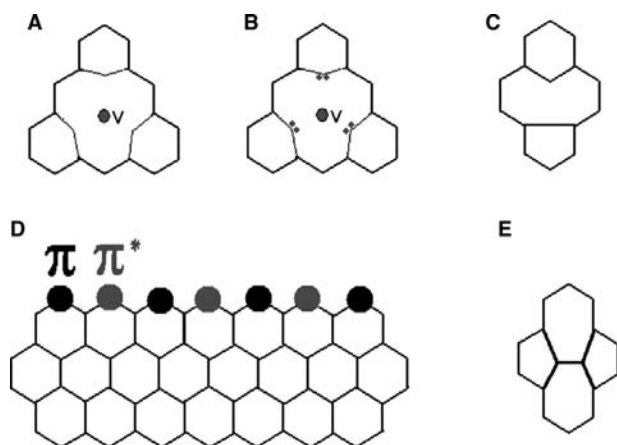


**Fig. 2** Magnetic nature of intrinsic carbon defects. (A): vacancy in graphite; (B): hydrogenated vacancy on graphite; (C): pentagon-one dangling bond; (D): zigzag edge carbon atoms; (E): Stone–Wales defect.

Another method of obtaining open shell molecules is the generation of free radicals. The main problem in this case is the stability of the radicals.<sup>[93]</sup> The stability can be increased by the steric protection of the unpaired electrons, the use of Coulombic electrostatic repulsions to keep the radicals apart, or the introduction of electronegative heteroatoms.

Similar ways have been proposed for the carbon-based materials. Proposed mechanisms leading to the generation of the unpaired electrons are the following:

- Vacancies in graphite, both ordinary (Fig. 2A) and hydrogenated (Fig. 2B), create new states below the Fermi level. The extra  $\pi$ -electrons are induced to the system when vacancies are introduced. For non-interacting vacancies, these extra electrons give rise to an unpaired spin associated with the vacancy.<sup>[94]</sup>
- Formation of pentagon-one dangling bond, also called 5-1db (Fig. 2C).<sup>[95]</sup>
- Edge states appearing on zigzag edge carbon atoms (Fig. 2D).<sup>[96–101]</sup> The localized spins are considered to originate from the nonbonding edge states of the  $\pi$ -electrons.
- Stone–Wales defects<sup>[102]</sup> (Fig. 2E) and related structures with negative Gaussian curvature.<sup>[103]</sup>

Is it realistic to expect ferromagnetism or ferrimagnetism as an intrinsic feature of a pure  $\pi$ -electron system like graphite?

Interaction between the magnetic centers without entering a chemical reaction seems to be the main problem for the organic magnets. Propagation of magnetic interactions largely depends on the arrangement of the radicals in the crystal.

Several strategies have been proposed in order to achieve this spontaneous magnetization:<sup>[92]</sup>

- Orthogonal orbitals.<sup>[104]</sup> When the overlap between the magnetic orbitals is zero, i.e., the orbitals are orthogonal, the magnetic interaction is ferromagnetic whereas, in the case of antiferromagnetic interaction, the kinetic term is dominant.
- Spin polarization (McConnell I mechanism)<sup>[105]</sup> for ferromagnetic coupling (not ordering). This involves a special spatial arrangement of neighboring radicals. Ferromagnetic coupling is expected when a region of negative spin density in one molecule overlaps with a region of positive spin density in another molecule.
- Chains of alternating electron-donor and electron-acceptor species. (McConnell II mechanism).<sup>[106]</sup> This mechanism for ferromagnetic coupling, not ordering, was proposed for charge-transfer salts where the single occupied molecular orbitals of the donor in the neutral state are degenerate. The triplet state of the neutral donor induces a triplet state in the charge-transfer state through a configuration admixing of an excited state with a ground state. Such a triplet state is propagated along the donor-acceptor chain.
- The ferrimagnetic approach is based on the construction of chains containing alternating magnetic centers with unequal spin values. This approach has led to the design of a novel class of organic magnets, coordination polymers.<sup>[107]</sup>
- Weak ferromagnetism<sup>[108,109]</sup> in an antiferromagnetic structure where there exists a canting angle between the magnetic moments of different sublattices with opposite signs of the magnetic moments.

The importance of topologically dependent  $\pi$ -electronic structure is emphasized by Sugawara and Matsushita.<sup>[110]</sup> An arrangement of  $sp^2$  carbons that creates a branched  $\pi$ -system exhibits magnetism due to the appearance of unpaired electrons. The researchers working on creating carbon-based magnets point out the necessity of branched precursors.

A theoretical prediction of a ferromagnetic carbon with magnetization higher than that of  $\alpha$ -Fe was published more than a decade ago.<sup>[111]</sup> The proposed intermediate graphite-diamond structure with alternating  $sp^2$ – $sp^3$  hybridized carbon atoms has never been realized technologically. A possible method for attaining this structure is the creation of defect-containing graphite or diamond structures.

The possibility of ferromagnetism in disordered graphite samples has been predicted on more than one occasion. The underlying mechanism is the existence of unpaired spins at defects, induced by a change in the coordination of the carbon atoms.<sup>[112]</sup> Several works discuss theoretical models that address the effects of electron-electron interactions and disorder in graphene planes.<sup>[113,114]</sup>

It has been shown experimentally that the peculiar, edge-related electronic states in nanographite lead to such novel phenomena as spin glass states, magnetic switching, and edge-state spin gas probing.<sup>[115]</sup> Direct observations of irradiation-induced magnetic ordering in graphite and nanodiamond raise hopes that this effect can lead to a development of a controllable method for producing magnetic carbon materials.

## CONCLUSIONS

Recently, it has become evident that pure carbon can show strong paramagnetism and even ferromagnetism. These properties appear to arise from specific features of the carbon structure and bonding, namely the edge states, dangling-bond states, sterically protected spins, carbon adatoms, and carbon vacancies. Production of bulk quantities of these materials is still at an early stage.

Magnetic systems based on nanostructured carbon are expected to display novel properties not found in metallic systems. There are two fundamental differences. First, the electrons in p-orbitals are delocalized, in contrast to the electrons in d- and f-orbitals. Second, spin-orbit coupling for the light elements is small or negligible. Inconvenient electronic properties of nanocarbon and experimentally observed novel magnetic phenomena are expected to find applications in molecular spintronic, as a large variety of magnetic functions can be produced by modifying its structure on nanoscale. We expect that the desired modifications will be produced by electron beam lithography, chemical modification, ion bombardment, or laser irradiation.

## ACKNOWLEDGMENTS

This work is supported by the Swedish Research Council and European FP6 program *Ferrocarbon*.

## REFERENCES

- Hudgens, S.; Kastner, M.; Fritzsche, H. Diamagnetic susceptibility of tetrahedral semiconductors. *Phys. Rev. Lett.* **1974**, *33*, 1552–1555.
- Ganguli, N.; Krishnan, K.S. The magnetic and other properties of the free electrons in graphite. *Proc. Roy. Soc. (London)* **1941**, *A177*, 168–171.
- Enoki, T.; Takai, K. Unconventional magnetic properties of nanographite. In *Carbon Based Magnetism*; Makarova, T.L., Palacio, F., Eds.; Elsevier: Amsterdam, 2006; 397–416.
- Kobayashi, K. Electronic structure of a stepped graphite surface. *Phys. Rev. B* **1993**, *48*, 1757–1760.
- Fujita, M.; Wakabayashi, K.; Nakada, K.; Kusakabe, K. Peculiar localized state at graphite edge. *J. Phys. Soc. Jpn* **1960**, *65*, 1920–1923.
- Klein, D.J.; Bytautas, L. Graphitic edges and unpaired pi-electron spins. *J. Phys. Chem. A* **1999**, *103*, 5196–5201.
- Nakada, K.; Fujita, M.; Dresselhaus, G.; Dresselhaus, M.S. Edge state in graphene ribbons: nanometer size effect and edge shape dependence. *Phys. Rev. B* **1996**, *54*, 17,954–17,961.
- Yoshizawa, K.; Okahara, K.; Sato, T. Molecular-orbital study of pyrolytic carbons based on small cluster-models. *Carbon* **1994**, *32*, 1517–1522.
- Wakabayashi, K.; Fujita, M.; Kusakabe, K.; Nakada, K. Localized electronic states on graphite edge. *Czech. J. Phys.* **1996**, *46*, 2429–2430.
- Shima, N.; Aoki, H. Electronic structure of superhoneycomb systems: a peculiar realization of semimetal/semiconductor classes and ferromagnetism. *Phys. Rev. Lett.* **1993**, *71*, 4389–4392.
- Takeda, H.; Kajii, H.; Yoshino, K. Pore symmetry dependence of band gap of nanoscale periodic porous graphites with different pore shapes. *Jpn J. Appl. Phys. Part 1* **2002**, *41*, 3782–3787.
- Stone, A.J.; Wales, D.J. Theoretical studies of icosahedral C<sub>60</sub> and some related species. *Chem. Phys. Lett.* **1986**, *128*, 501–503.
- Igami, M.; Nakada, K.; Fujita, M.; Kusakabe, K. Effect of topological defects in graphite. *Czech. J. Phys.* **1996**, *46*, 2715–2716.
- Kusakabe, K. Flat-band ferromagnetism in organic crystals. In *Carbon Based Magnetism*; Makarova, T.L., Palacio, F., Eds.; Elsevier: Amsterdam, 2006; 305–328.
- Korshak, Y.V.; Ovchinnikov, A.A.; Shapiro, A.M.; Medvedeva, T.V.; Spektor, V.N. Organic polymer ferromagnet. *JETP Lett.* **1986**, *43*, 309–312.
- Korshak, Y.V.; Medvedeva, T.V.; Ovchinnikov, A.A.; Spektor, V.N. Organic polymer ferromagnet. *Nature* **1987**, *326*, 370–373.
- Cao, Y.; Wang, P.; Hu, Z.; Li, S.; Zhang, L. Magnetic characterization of organic ferromagnet—poly-BIPO and its analog. *Synth. Met.* **1988**, *27*, B625–B628.
- Shulga, Y.M.; Boldyrev, A.I.; Ovchinnikov, A.A. Auger-electron spectroscopy and electron energy-loss spectroscopy study of ferromagnetic carbon. *Chem. Phys. Lett.* **1992**, *189*, 577–583.
- Lee, W.P.; Park, E.B.; Yoon, C.O.; Ovchinnikov, A.A.; Park, Y.W. The electromagnetic properties of conducting polymers and intercalated C<sub>60</sub>. In *Chemical Physics of Intercalation*; Bernier, P. et al., Eds.; Plenum Press: New York, 1993.
- Torrance, J.B.; Oostra, S.; Nazzari, A. A new, simple model for organic ferromagnetism and the first organic ferromagnet. *Synth. Met.* **1987**, *19*, 709–714.
- Ota, M.; Otani, M.; Igarashi, M. Evolution of ferromagnetic properties by dehydrogenation of triaryl-methane resin. *Chem. Lett.* **1989**, *7*, 1186–1183.

22. Ota, M.; Otani, M.; Kobayashi, K.; Igarashi, M. Magnetic properties of triarylmethane resins. *Mol. Cryst. Liq. Cryst.* **1989**, *176*, 99–108.
23. Tanaka, H.; Tokuyama, K.; Sato, T.; Ota, T. Preparation and properties of organic polymer ferromagnet with indigo unit. *Chem. Lett.* **1990**, *10*, 1813–1817.
24. Kawabata, K.; Mizutani, M.; Fukuda, M.; Mizogami, S. Ferromagnetism of pyrolytic carbon under low-temperature growth by the CVD method. *Synth. Met.* **1989**, *33*, 399–402.
25. Tanaka, H.; Sato, T.; Ota, C. Preparation of Organic Polymer Ferromagnet with Indigo Unit. Japanese Patent JP 04,008,731, 1996.
26. Mizogami, S.; Mizutani, M.; Fukuda, M.; Kawabata, K. Abnormal ferromagnetic behaviour for pyrolytic carbon under low temperature growth by CVD method. *Synth. Met.* **1991**, *43*, 3271–3273.
27. Tanaka, K.; Kobashi, M.; Sanekata, H. et al. Peculiar magnetic property of pyrolytic carbon prepared from adamantane. *J. Appl. Phys.* **1992**, *71*, 836–841.
28. Araki, H.; Matsuoka, R.; Yoshino, K. Ferromagnetic behaviour of pyrolyzed *ortho*-, *meta*-, *para*-phenylenediamine and triazine derivatives. *Solid State Commun.* **1991**, *79*, 443–446.
29. Araki, H.; Yoshino, K. Spontaneous magnetization phenomena in pyrolyzed organic compounds containing nitrogen atoms. *Jpn J. Appl. Phys.* **1992**, *31* (Part 2), L130–L133.
30. Araki, H.; Roh, Y.B.; Kuwamura, N.; Yoshino, K. Preparation of ferromagnetic organic compounds by pyrolysis of (2,4,6-triphenoxy-1,3,5-triazine melamine) in Ar atmosphere including a trace of dry air. *Jpn J. Appl. Phys.* **1992**, *31* (Part 2), L337–L340.
31. Murata, K.; Ushijima, H.; Ueda, H.; Kawaguchi, K. Magnetic properties of amorphous-like carbons prepared from tetraaza compounds by the chemical vapor-deposition (CVD) method. *J. Chem. Soc. Chem. Commun.* **1991**, *18*, 1265–1266.
32. Murata, K.; Ueda, H.; Kawaguchi, K. Preparation of carbon powders by pyrolysis of cyclododecane under vacuum and their magnetic properties. *Synth. Met.* **1991**, *44*, 357–362.
33. Murata, K.; Ushijima, H.; Ueda, H. A stable carbon-based organic magnet. *J. Chem. Soc. Chem. Commun.* **1992**, *7*, 567–569.
34. Murata, K.; Ushijima, H. Effect of pyrolysis temperature on the magnetic properties of the carbon materials prepared from trialkylboranes. *J. Appl. Phys.* **1996**, *79*, 978–981.
35. Ushijima, Y. Organic Magnetic Substance—Composed of Amorphous Carbide Containing Phosphorus and/or Boron. Japanese Patent J 06,251,924/1994.
36. Murata, K. Organic Ferromagnetic Substance. United States Patent US 5,135,673, 1990.
37. Murata, K. Production of Organic Magnetic Body with High Saturation Magnetization by Heating Organic Substance in Vacuum to Obtain Amorphous Carbide, and Treating with Plasma. Japanese Patent JP 0,519,842, 1993.
38. Murata, K.; Masuda, T.; Ueda, H. Magnetic carbon compounds prepared from polyvinyl chloride, phenol resin, pyrene-benzaldehyde copolymer. *Chem. Expr.* **1990**, *5*, 605.
39. Murata, K. Organic Ferromagnetic Substance and Process for Producing Same. United States Patent US 5,330,668, 1994.
40. Ueda, H. Strong Magnetic Carbon Free from Transition Metal-Heated from Below Decomposition Temperature Under Nitrogen Gas Flow then Burned in Vacuum Under Specific Temperature. Japanese Patent JP 156,433, 1994.
41. Trivedi, D.C. Observation of ferromagnetism in polyaniline. *Synth. Met.* **2001**, *121*, 1780–1783.
42. Zaidi, N.A.; Giblin, S.R.; Terry, I.; Monkman, A.P. Room temperature magnetic order in an organic magnet derived from polyaniline. *Polymer* **2004**, *45*, 568–571.
43. Correa, A.A.; Walmsley, L.; Bulhoes, L.O.S.; Ortiz, W.A.; de Oliveira, A.J.A.; Pereira, E.C. Weak ferromagnetism in poly(3-methylthiophene)(PMTh). *Synth. Met.* **2001**, *121*, 183–186.
44. Nascimento, R.; de Oliveira, A.J.A.; Correa, A.A. et al. Magnetic behavior of poly(3-methylthiophene): metamagnetism and room-temperature weak ferromagnetism. *Phys. Rev. B* **2003**, *67*, 144422.
45. Kaburagi, Y.; Hishiyama, Y. Ferromagnetism discovered on heat-treating the aromatic polyimide film Kapton. *J. Mater. Res.* **2002**, *17*, 2000–2006.
46. Spemann, D.; Schindler, K.; Esquinazi, P.; Diaconu, M.; Schmidt, H.; Hohne, R.; Setzer, A.; Butz, T. Magnetic force microscopy studies on the magnetic ordering in organic materials induced by high-energy proton irradiation. *Nucl. Instr. Meth. B* **2006**, *250*, 303–308.
47. Ata, M.; Machida, M.; Watanabe, H.; Seto, J. Polymer—C<sub>60</sub> composite with ferromagnetism. *Jpn J. Appl. Phys.* **1994**, *33*, 1865–1871.
48. Ata, M. Magnetic Body Having Good Magnetic Properties—Comprises Spherical Carbon Doped with Halogen Obtained from Alkali Halide or Solid Iodine. Japanese Patent J 0,512,912, 1993.
49. Lobach, A.S.; Shul'ga, Y.M.; Roshchupkina, O.S. et al. C<sub>60</sub>H<sub>18</sub>, C<sub>60</sub>H<sub>36</sub> and C<sub>70</sub>H<sub>36</sub> fullerene hydrides: Study by methods of IR, NMR, XPS, EELS and magnetochemistry. *Fullerene Sci. Technol.* **1998**, *6*, 375–391.
50. Antonov, V.E.; Bashkin, I.O.; Khasanov, S.S. et al. Magnetic ordering in hydrofullerite C<sub>60</sub>H<sub>24</sub>. *J. Alloys Comp.* **2002**, *330*, 365–368.
51. Murakami, Y.; Suematsu, H. Magnetism of C<sub>60</sub> induced by photo-assisted oxidation. *Pure Appl. Chem.* **1996**, *68*, 1463–1467.
52. Owens, F.J.; Iqbal, Z.; Belova, L.; Rao, K.V. Evidence for high-temperature ferromagnetism in photolyzed C<sub>60</sub>. *Phys. Rev. B* **2004**, *69*, 033403.
53. Makarova, T.L.; Sundqvist, B.; Esquinazi, P. et al. Magnetic carbon. *Nature* **2001**, *413*, 718–720.
54. Han, K.H.; Spemann, D.; Höhne, R. et al. Observation of intrinsic magnetic domains in C<sub>60</sub> polymer. *Carbon* **2003**, *41*, 785–792.

55. Narozhnyi, V.N.; Müller, K.H.; Eckert, D. et al. Ferromagnetic carbon with enhanced Curie temperature. *Physica. B* **2003**, *329*, 121–124.
56. Wood, R.A.; Lewis, M.H.; Lees, M.R.; Bennington, S.M.; Cain, M.G.; Kitamura, N. Ferromagnetic fullerene. *J. Phys. Condens. Matter* **2002**, *14* (22), L385–L391.
57. Wang, X.; Liu, Z.X.; Zhang, Y.L.; Li, F.Y.; Jin, C.Q. Evolution of magnetic behaviour in the graphitization process of glassy carbon. *J. Phys. Condens. Matter* **2002**, *14*, 10265–10268.
58. Jin, C.Q.; Wang, X.; Liu, Z.X.; Zhang, Y.L.; Li, F.Y.; Yu, R.C. The unusual morphology, structure, and magnetic property evolution of glassy carbon upon high pressure treatment. *Braz. J. Phys.* **2003**, *33*, 723–726.
59. Akutsu, S.; Utsushikawa, Y. Magnetic properties and electron spin resonance of carbon fine particles prepared in He plasma. *Mater. Sci. Res. Int.* **1999**, *5*, 110–115.
60. Rode, A.V.; Gamaly, E.G.; Christy, A.G. et al. Unconventional magnetism in all-carbon nanofoam. *Phys. Rev. B* **2004**, *70*, 054407.
61. Mombrú, A.W.; Pardo, H.; Faccio, R. et al. Multilevel ferromagnetic behavior of room-temperature bulk magnetic graphite. *Phys. Rev. B* **2005**, *71*, 100404(R).
62. Pardo, H.; Faccio, R.; Araújo-Moreira, F.M.; de Lima, O.F.; Mombrú, A.W. Synthesis and characterization of stable room temperature bulk ferromagnetic graphite. *Carbon* **2005**, *44*, 565–569.
63. Spemann, D.; Esquinazi, P.; Hohne, R. et al. Magnetic carbon: A new application for ion microbeams. *Nucl. Instrum. Method B* **2005**, *231*, 433–439.
64. Esquinazi, P.; Spemann, D.; Höhne, R.; Setzer, A.; Han, K.H.; Butz, T. Induced magnetic ordering by proton irradiation in graphite. *Phys. Rev. Lett.* **2003**, *91*, 227201.
65. Miller, J.S. The quest for magnetic polymers—Caveat emptor. *Adv. Mater.* **1992**, *4* (298–300), 435–438.
66. Pearton, S.J.; Heo, W.H.; Ivill, M.; Norton, D.P.; Steiner, T. Dilute magnetic semiconducting oxides. *Semicond. Sci. Technol.* **2004**, *19*, R59–R74.
67. Coey, J.M.D.; Venkatesan, M.; Fitzgerald, C.B. Donor impurity band exchange in dilute ferromagnetic oxides. *Nat. Mater.* **2005**, *4*, 173–179.
68. Coey, J.M.D.; Venkatesan, M.; Fitzgerald, C.; Douvalis, A.; Sanders, I. Ferromagnetism of a graphite nodule from the Canyon Diablo meteorite. *Nature* **2002**, *420*, 156–159.
69. Cespedes, O.M.; Ferreira, S.; Sanvito, S.; Kociak, M.; Coey, J.M.D. Contact induced magnetism in carbon nanotubes. *J. Phys. Condens. Matter* **2004**, *16*, L155–L158.
70. Mertings, H.C.; Valencia, S.; Gudat, W.; Oppeneer, P.M.; Zaharko, O.; Grimmer, H. Direct observation of local ferromagnetism on carbon in C/Fe multilayers. *Europhys. Lett.* **2004**, *66*, 743–748.
71. Ueda, H. The magnetization of poly (vinyl-chloride) heattreated in CCl<sub>4</sub> atmosphere. *Denki Kagaki* **1992**, *60*, 24–27.
72. Ueda, H. Magnetization of carbonized product of polyvinyl-chloride heat-treated in CCl<sub>4</sub> atmosphere. *Denki Kagaki* **1992**, *60*, 71–74.
73. Ueda, H. Magnetization of carbonized products of chrysene, triphenylene and violanthrone. *Denki Kagaki* **1994**, *62*, 69–73.
74. Ueda, H. Preparation of ferromagnetic carbon electrode from charcoal blocks. *J. Mater. Sci.* **2001**, *36*, 5955–5959.
75. Ueda, H. Carbonaceous Ferro Magnets and Method for the Preparation Thereof. US Patent US 5,556,570, 1996.
76. Elfimov, I.; Yunoki, S.; Sawatzky, G.A. Possible path to a new class of ferromagnetic and half-metallic ferromagnetic materials. *Phys. Rev. Lett.* **2002**, *89*, 2164.
77. Kenmochi, K.; Seike, M.; Sato, K.; Yanase, A.; Katayama-Yoshida, H. New class of diluted ferromagnetic semiconductors based on CaO without transition metal elements. *Jpn J. Appl. Phys.* **2004**, *43*, L934–L936.
78. Kusakabe, K.; Geshi, M.; Tsukamoto, H.; Suzuki, N. Design of new ferromagnetic materials with high spin moments by first-principles calculation. *J. Phys. Condens. Matter* **2004**, *16*, S5639–S5644.
79. Young, D.P.; Hall, D.; Torelli, M.E. et al. High-temperature weak ferromagnetism in a low-density free-electron gas. *Nature* **1999**, *397*, 412–414.
80. Lofland, S.E.; Seaman, B.; Ramanujachary, K.V.; Hur, N.; Cheong, S.W. Defect driven magnetism in calcium hexaboride. *Phys. Rev. B* **2003**, *67*, 020410(R).
81. Dorneles, L.S.; Venkatesan, M.; Moliner, M.; Lunney, G.; Coey, J.M.D. Magnetism in thin films of CaB<sub>6</sub> and SrB<sub>6</sub>. *Appl. Phys. Lett.* **2004**, 856377–856381.
82. Venkatesan, M.; Fitzgerald, C.B.; Coey, J.M.D. Unexpected magnetism in a dielectric oxide. *Nature* **2004**, *430*, 630.
83. Kusakabe, K.; Maruyama, M. Magnetic nanographite. *Phys. Rev. B* **2003**, *67*, 09240.
84. Kusakabe, K.; Takagi, Y. On possible surface magnetism in nanographite. *Mol. Cryst. Liq. Cryst.* **2002**, *387*, 231–235.
85. Maruyama, M.; Kusakabe, K. Theoretical prediction of synthesis methods to create magnetic nanographite. *J. Phys. Soc. Jpn.* **2004**, *73*, 656–663.
86. Lehtinen, P.O.; Foster, A.S.; Ma, Y.C.; Krasheninnikov, A.V.; Nieminen, R.M. Irradiation-induced magnetism in graphite: a density functional study. *Phys. Rev. Lett.* **2004**, *93*, 187202.
87. Ma, Y.C.; Lehtinen, P.O.; Foster, A.S.; Nieminen, R.M. Hydrogen-induced magnetism in carbon nanotubes. *Phys. Rev. B* **2005**, *72*, 085451.
88. Chan, J.A.; Montanari, B.; Gale, J.D.; Bennington, S.M.; Taylor, J.W.; Harrison, N.M. Magnetic properties of polymerized C<sub>60</sub>: the influence of defects and hydrogen. *Phys. Rev.* **2004**, *B70*, 041403.
89. Kenmochi, K.; Sato, K.; Yanase, A.; Katayama-Yoshida, H. Materials design of ferromagnetic diamond. *Jpn J. Appl Phys.* **2005**, *44*, L51–L53.
90. Talapatra, S.; Ganesan, P.G.; Kim, T. et al. Irradiation-induced magnetism in carbon nanostructures. *Phys. Rev. Lett.* **2005**, *95*, 097201.



91. Oshiyama, A.; Okada, S. Magnetism in nanometer-scale materials that contain no magnetic elements. In *Carbon Based Magnetism*; Makarova, T.L., Palacio, F., Eds.; Elsevier: Amsterdam, 2006; 329–353.
92. Campo, J.; Luzón, J.; Palacio, F.; Rawson, J. Spin density distribution and interaction mechanisms in thiazyl-based magnets. In *Carbon Based Magnetism*; Makarova, T.L., Palacio, F., Eds.; Elsevier: Amsterdam, 2006; 159–181.
93. Veciana, J. Molecular magnetism: from molecular assemblies to the devices. In *NATO ASI series. No. 425*; Coronado, E., Delhaes, P., Gatteschi, D., Miller, J.S., Eds.; Kluwer Academic Publishing: New York, 1996.
94. Hjort, M.; Stafstrom, S. Modeling vacancies in graphite via the Huckel method. *Phys. Rev. B* **2000**, *61*, 14089.
95. El-Barbary, A.A.; Telling, R.H.; Ewels, C.P.; Heggie, M.I.; Briddon, P.R. Structure and energetics of the vacancy in graphite. *Phys. Rev. B* **2003**, *68*, 144107.
96. Wakabayashi, K.; Fujita, M.; Ajiki, H.; Sigrist, M. Electronic and magnetic properties of nanographite ribbons. *Phys. Rev. B* **1999**, *59*, 8271.
97. Andersson, O.; Prasad, B.L.V.; Sato, H. et al. Structure and electronic properties of graphite nanoparticles. *Phys. Rev. B* **1998**, *58*, 16387.
98. Prasad, B.L.V.; Sato, H.; Enoki, T. et al. Heat-treatment effect on the nanosized graphite  $\pi$ -electron system during diamond to graphite conversion. *Phys. Rev. B* **2000**, *62*, 11209.
99. Affoune, A.M.; Prasad, B.L.V.; Sato, H.; Enoki, T.; Kaburagi, Y.; Hishiyama, Y. Experimental evidence of a single nano-graphene. *Chem. Phys. Lett.* **2001**, *348*, 17–20.
100. Shibayama, Y.; Sato, H.; Enoki, T.; Bi, X.X.; Dresselhaus, M.S.; Endo, M. Novel electronic properties of a nano-graphite disordered network and their iodine doping effects. *J. Phys. Soc. Jpn* **2000**, *69*, 754–767.
101. Shibayama, Y.; Sato, H.; Enoki, T.; Endo, M. Disordered magnetism at the metal-insulator threshold in nano-graphite-based carbon materials. *Phys. Rev. Lett.* **2000**, *84*, 1744–1747.
102. Kim, Y.; Choi, J.K.; Chang, J.; Tomanek, D. Defective fullerenes and nanotubes as molecular magnets: an ab initio study. *Phys. Rev. B* **2003**, *68*, 125420.
103. Park, N.; Yoon, M.; Berber, S.; Ihm, J.; Osawa, E.; Tomanek, D. Magnetism in all-carbon nanostructures with negative Gaussian curvature. *Phys. Rev. Lett.* **2003**, *91*, 23720.
104. Gadet, V.; Mallah, T.; Castro, I.; Veillet, P.; Verdagner, M. High- $T_c$  molecular-based magnets—a ferromagnetic bimetallic chromium (III) nickel (II) cyanide with  $T_c = 90$  K. *J. Am. Chem. Soc.* **1992**, *114*, 9213–9214.
105. McConnell, H.M. Ferromagnetism in solid free radicals. *J. Chem. Phys.* **1963**, *39*, 1910.
106. McConnell, H.M. Proceedings of the Robert A. Welch foundation conference. *Chem. Res.* **1967**, *144*, 11.
107. Miller, J.S. Organic magnets—a history. *Adv. Mat.* **2002**, *14*, 1105–1110.
108. Dzyaloshinsky, I. A thermodynamic theory of ‘weak’ ferromagnetism of antiferromagnetics. *J. Phys. Chem. Solids* **1958**, *4*, 241.
109. Moriya, T. Anisotropic superexchange interaction and weak ferromagnetism. *Phys. Rev.* **1960**, *120*, 91–98.
110. Sugawara, T.; Matsushita, M.M. Exchange-coupled localized spins with itinerant electrons in organic p-electronic system. In *Carbon Based Magnetism*; Makarova, T.L., Palacio, F., Eds.; Elsevier: Amsterdam, 2006; 1–22.
111. Ovchinnikov, A.A.; Shamovsky, I.L. The structure of the ferromagnetic phase of carbon. *J. Mol. Struct. (Theochem.)* **1991**, *251*, 133–140.
112. Guinea, F.; Pilar Lopez-Sancho, M.; Vozmediano, M.A.H. Interactions and disorder in 2D graphite sheets. In *Carbon Based Magnetism*; Makarova, T.L., Palacio, F., Eds.; Elsevier: Amsterdam, 2006; 353–371.
113. González, J.; Guinea, F.; Vozmediano, M.A.H. Electron–electron interactions in graphene sheets. *Phys. Rev. B* **2001**, *63*, 134421.
114. Stauber, T.; Guinea, F.; Vozmediano, M.A.H. Disorder and interaction effects in two dimensional graphene sheets. *Phys. Rev. B* **2005**, *71*, 041406(R).
115. Enoki, T.; Kobayashi, Y. Magnetic nanographite: an approach to molecular magnetism. *J. Mater. Chem.* **2005**, *15*, 3999–4002.

# Magnetic Nanomaterials: Conventional Synthesis and Properties

Dajie Zhang

Center for Nondestructive Evaluation, Johns Hopkins University,  
Baltimore, Maryland, U.S.A.

## INTRODUCTION

Nanophased magnetic materials have wide applications in magnetic recording device,<sup>[1]</sup> ferrofluids,<sup>[2–4]</sup> and biomedical science.<sup>[5–7]</sup> Nanoscale particles are considered to have a size range from 1 to 100 nm. Particles within this size range usually have hybrid properties different from those of the bulk solid or the molecular/atomic species. The unique properties of nanoscale particles can be attributed to two basic phenomena. The first is that the number of atoms at the surface and/or interface in these materials is comparable to that of atoms located in the crystal lattice. Therefore the chemical and physical properties, which are normally determined by the structure of the bulk lattice, become increasingly dependent upon the atoms at the surface and interface. The high number of atoms on the surfaces of nanoparticles form a layer of “damaged” lattice with a higher energy state; therefore these particles are highly unstable and more reactive. The second phenomenon is the “quantum-size effect” or “quantum confinement effect.” When particles approach the nanometer-size range, their electronic and photonic properties can be significantly modified as a result of the absence of a few atoms in the lattice and the regional relaxation of the lattice structure.<sup>[8,9]</sup>

The small size and rich surface/interface structure of magnetic nanomaterials can lead to properties quite different from those of the bulk. Studies on magnetic nanomaterials will not only provide information about the structure–property relations of magnetic nanomaterials but also help generating new ideas and technologies for the fabrication and application of these materials. The first part of this review will describe common fabrication techniques for magnetic nanomaterials. The second part will give a brief introduction to the theoretical aspects of fine particle magnetism; experimental results on some of these topics will also be discussed.

## FABRICATION OF MAGNETIC NANOMATERIALS

Magnetic nanomaterials can be categorized into three types based on their structural and compositional characteristics. The first types are magnetic nanoparticles or clusters. They are free-flowing magnetic powders of nanometer sizes. The second types of magnetic nanomaterials are nanostructured or nanophased magnetic materials. They are either bulk magnetic materials with nano-sized grains, or magnetic nanoparticles/clusters embedded in random within a non-magnetic bulk matrix. The later are often called magnetic nanocomposites. The third types of magnetic nanomaterials are nano-sized magnetic particles or magnetic “dots” organized in either two- or three-dimensional arrays in a long-range order. The various types of magnetic nanomaterials require different fabrication techniques; and in many cases, several techniques are combined to obtain a certain type of material.

Magnetic nanoparticles of metals, such as iron, cobalt, and nickel, can be prepared in many ways. The biggest challenge is to protect these particles from oxidation. The traditional methods for the preparation of ultrafine iron, cobalt, or nickel particles include the inert-gas evaporation method and the chemical reduction method. Small iron particles can be generated by evaporating iron metal in an inert gas atmosphere<sup>[10]</sup> or by chemical reduction of iron ions in solution or iron compounds in solid state. The obtained magnetic metal particles were stabilized by slowly exposing them to oxygen over a long period of time to form a layer of oxides on the surfaces of the particles. The common disadvantage of these methods is the reduction of average magnetization intensities of the particles. Iron particles obtained usually have magnetization intensities of about 700 to 900 emu/cm<sup>3</sup> and consist of as much as 50% to 70% of oxides by volume. Coating the surface of small magnetic metal particles

with a non-magnetic matrix to protect them from oxidation is a useful method to obtain air-stable nano-scale magnetic metal particles.<sup>[11]</sup> These coating materials can be metals, oxides, polymers, and surfactants. When metallic coating materials are used, these metals should be immiscible with iron, cobalt, or nickel, or intermetallic alloys would be formed which contain no single-phase nano-sized clusters of pure iron, cobalt, or nickel.

There are two important methods to fabricate small Fe, Co, or Ni clusters homogeneously within a matrix of coating material. The first is the coevaporation method. Fe, Co, or Ni can be coevaporated with a second component, which can be a metal, an oxide, or other types of materials. The evaporation is carried out either in vacuum or in an inert atmosphere. Electric heating is usually the first choice, while other heating methods such as sputtering can be applied to evaporate materials that are not easily evaporated by electric heating. Particle size can be selected from 1 to 1000 nm by controlling the pressure of the inert gas, the type of gas, and the evaporation rates of the starting materials. The diameter of the particles produced is roughly proportional to the pressure of the inert gas and the atomic weight of the gas. If evaporation rate is raised, the distribution of particle size becomes wider and the average particle size increases. Examples for the evaporation-produced particles include iron grains of sizes from 5 to 8 nm dispersed in an amorphous  $\text{Al}_2\text{O}_3$  matrix by cosputtering Fe and  $\text{Al}_2\text{O}_3$ ,<sup>[12]</sup> Fe– $\text{SiO}_2$  and Fe–BN granular solids obtained from Fe,  $\text{SiO}_2$ , and BN targets by using RF magnetron sputtering,<sup>[13]</sup> Fe(Co)/Ag particles with Fe of about 17 nm and Co of about 110 nm, and Fe/Mg particles with Fe of about 2.6 to 40 nm.<sup>[14]</sup>

Mechanical alloying, also known as high-energy ball milling, is another effective way to obtain a homogeneous mixture of two materials immiscible under normal conditions. The starting materials are fine powders in the sizes of a few to a few hundreds of microns produced by conventional methods. Often, the starting materials are either a mixture of a magnetic material and a non-magnetic matrix material, or a mixture that would undergo chemical reactions under milling to produce a magnetic phase. If no chemical reactions occur during the milling process, depending on the time of milling and energy applied, the as-milled samples can be either atomic mixtures of the starting materials or mixtures of small clusters of the starting materials, in which one or both of the components still maintain a short-range order. Heat treatment can be applied to the as-milled samples to introduce phase separation and increase the grain sizes. Examples of samples produced by mechanical alloying include Fe– $\text{SiO}_2$  nanocomposite materials,<sup>[15]</sup>  $\text{Al}_{100-x}\text{Fe}_x$  amorphous powder,<sup>[16]</sup>  $\text{Fe}_{100-y}\text{M}_y$  powder blends

with  $\text{M} = \text{Al}$ ,  $\text{Si}$ , and  $\text{Cu}$  and  $y < 50$ ,<sup>[17]</sup> nanocrystalline  $\text{Ni}_3\text{Al}$ ,<sup>[18]</sup> and  $\text{Sm}_2\text{CO}_{17}$  alloy nanoparticles and  $\text{BaFe}_{12}\text{O}_{19}$  synthesized by a mechanochemical process.<sup>[19,20]</sup>

The melt-spun method, which is a liquid-quenching technique, is often used to produce nanostructured magnetic materials such as amorphous or granular Fe-, Co-, or Ni-based metastable alloys. Fe-based nanostructured alloys were usually prepared with this method.<sup>[21,22]</sup> The amorphous alloys were prepared by arc melting of Fe together with a non-magnetic metal, followed by melt spinning in an inert atmosphere. Melt-spun techniques can produce metastable alloys of metals that are normally immiscible in liquid state. Heat treatment can later be applied to induce phase separation and grain growth of the metals.

Chemical reactions, such as liquid-phase reduction of metal ions,<sup>[23,24]</sup> hydrogen reduction of metal salts,<sup>[25]</sup> decomposition of organometallic compounds,<sup>[26,27]</sup> and hydrothermal or radiation-assisted reactions,<sup>[28,29]</sup> are very useful methods to produce amorphous metal powders or nanometer-sized metal crystallites. Simple chemical coprecipitation reactions are an economical way to produce various types of nanometer-sized oxides or mixed oxides magnetic particles such as iron oxides or ferrites.<sup>[30–33]</sup> Zeolites and graphitic materials are good matrices for the encapsulation of angstrom-sized metal clusters. Cobalt clusters of 7 Å were incorporated into zeolites by first subliming cobalt carbonyl compound  $\text{Co}_2(\text{CO})_8$  onto dehydrated Na-X zeolite at room temperature, and later decomposing the cobalt carbonyl compound by using an argon microwave plasma.<sup>[34]</sup> Superparamagnetic Fe particles with a size of about 4 Å dispersed in graphite matrices were also prepared by incorporating iron carbonyl compound  $\text{Fe}(\text{CO})_5$  and  $\text{Fe}_2(\text{CO})_9$  into matrix materials followed by thermal decomposition of the iron carbonyls.<sup>[35]</sup> Clusters of up to 28 Fe atoms were introduced into the supercages of NaY zeolite by ion exchange of  $\text{Fe}^{2+}$  for  $\text{Na}^+$  followed by reduction to  $\text{Fe}^0$  with solvated electrons and  $\text{Na}^-$  ions.<sup>[36]</sup> Small clusters of Fe were also fabricated within the pores of ZSM-5 zeolite.<sup>[37]</sup>

Metal clusters can also be coated with another metal by chemical reduction methods. Chatterjee et al.<sup>[38]</sup> produced iron particles with diameters of around 8 nm loosely packed within nanometer-sized copper particles by hydrogen reduction at 450°C of gel powders obtained from the aqueous solutions of ferric nitrate and copper nitrate. The chemical reduction of gels containing nickel and palladium salts also produced Pd-coated Ni nanoparticles.<sup>[39]</sup>

A sol–gel route followed by reduction treatment is an effective technique to produce metal–glass and metal–ceramic nanocomposites. For the preparation of Fe– $\text{SiO}_2$  or Ni– $\text{SiO}_2$  nanocomposites, hydrated Fe

or Ni chlorides or nitrates and an appropriate amount of silicon tetraethoxide were mixed into an alcohol-water solution and a clear gel was formed after a few hours or a few days. The gel was then dried and ground into small particles. Chemical reductions in a hydrogen atmosphere at high temperatures (500–800°C) were carried out to produce metal clusters within the silica gels. Metal particles with diameters ranging from a few to a few tens of nanometers could be obtained. Varying the metal ion concentrations and reduction temperature<sup>[40]</sup> can control the sizes of the metal particles.

The formation of alumina, aluminosilicate/iron, cobalt, and nickel magnetic nanocomposites followed a slightly different route.<sup>[41]</sup> Porous gels of alumina or aluminosilicate were prepared first. Then the metallic phase was introduced by immersing the gels in aqueous solutions of metal nitrates (iron, cobalt, or nickel nitrates) to allow the diffusion of metal ions into water trapped within the pores of the gels. After heat treatment in hydrogen at 600°C, nanocomposites with iron, cobalt, or nickel clusters of 5 to 70 nm were obtained.

Microemulsion is one of the latest techniques explored to prepare encapsulated magnetic clusters. Surfactant, S, dissolved in organic solvents, can form spherical aggregates.<sup>[42]</sup> These aggregates can be formed with and without the presence of water. When the medium is completely free of water, the aggregates are very small and polydisperse. Large and monodisperse surfactant aggregates can be formed in the presence of water. The amount of water present in the medium usually determines the sizes of the aggregates. As water molecules are attracted to the polar ends of the surfactants, a “water pool” is formed in the polar core of the surfactant aggregates, with its size being determined by the water-surfactant molar ratio  $w$  ( $w = [\text{H}_2\text{O}]/[\text{S}]$ ). According to Pileni,<sup>[43]</sup> aggregates containing only a small amount of water ( $w < 15$ ) are usually called reverse micelles, and they are called microemulsions when a large amount of water molecules ( $w > 15$ ) is contained in the droplets. However, the terms reverse micelle and microemulsion are often used as an equivalent description without the consideration of the values of the water-surfactant molar ratios.

The water-in-oil structure of reverse micelles makes them microreactors that can host chemical reactions to produce nanometer-sized inorganic clusters.<sup>[44]</sup> Coprecipitation reactions inside reverse micelles can produce nanometer-sized particles of compounds such as quantum-confined semiconductor clusters, and chemical reduction of metal ions performed in micelle solutions can produce surfactant-coated metal clusters. Rivas et al.<sup>[45]</sup> prepared iron particles with a diameter of less than 100 nm by using microemulsions consisting

of an aqueous solution, *n*-heptane, and surfactant AOT (Bis-2-ethyl hexyl sodium sulphosuccinate). At first two microemulsions were prepared, one with FeCl<sub>2</sub> and the other with the reducing reagent NaBH<sub>4</sub>. Then the two microemulsions were mixed and the chemical reduction took place through the exchange of matter by diffusion between the different droplets. A high-temperature reduction in hydrogen was later carried out at 500°C to prevent unwanted oxidation. Chen et al.<sup>[46]</sup> synthesized cobalt particles in the size range of 18 to 44 Å in diameter with the microemulsion technique. First, CoCl<sub>2</sub>·6H<sub>2</sub>O was dissolved in an 11 wt.% didodecyldimethylammonium bromide (DDAB) solution in toluene at concentrations of 0.005 to 0.02 M, where DDAB is a cationic surfactant. A blue solution was formed with Co<sup>2+</sup> ions trapped in H<sub>2</sub>O/DDAB micelles. Then an aqueous solution of NaBH<sub>4</sub> was added to reduce the Co<sup>2+</sup> ions into metallic cobalt particles. The small cobalt particles were coated with a layer of DDAB surfactant molecules when the toluene was removed. Other examples of magnetic nanoparticles synthesized in water-in-oil microemulsions include stable colloidal Fe<sub>3</sub>O<sub>4</sub> particles<sup>[47]</sup> and ultrafine barium ferrite powders.<sup>[48]</sup>

The latest effort in the production of nanophased magnetic materials involves the fabrication of highly ordered two- or three-dimensional nanophased magnetic material arrays or nanowires.<sup>[49–51]</sup> Such efforts will aid the development of magnetic devices based on magnetic nanomaterials, such as high-density magnetic storage media. When magnetic nanoparticles/nanowires uniform in size/shape are arranged into an ordered structure with identical spacing, each of these nanoparticles/nanowires could act as a single bit. This could greatly enhance the memory capacity of the magnetic device.

There are three general approaches that could lead to the formation of ordered magnetic nanostructures. The first approach is based on the tendency of some magnetic colloidal nanoparticles to settle into a long-range ordered structure through self-organization. Magnetic particles with uniform morphology and a narrow size distribution can be dispersed in a solvent, either with or without the aid of a surfactant. When such a dispersion of magnetic nanoparticles is placed on a solid substrate and let dry under controlled conditions (temperature, atmosphere), particle arrays of two- or three-dimensional long-range order can be formed through particle self-assembly when the solvent is removed. Cobalt nanoparticle arrays have been fabricated via such a process.<sup>[52,53]</sup> The second approach is the formation of ordered magnetic nanostructures with the aid of a template. Well-organized arrays of silica spheres of uniform size can be formed through the hydrolysis of Si(C<sub>2</sub>H<sub>5</sub>O)<sub>4</sub>. Under appropriate reaction conditions, perfect spherical microparticles with very

small size distribution can be formed.<sup>[54]</sup> These micro-particles of silica will form an array with periodic surface geometry when allowed to settle onto a glass substrate by natural sedimentation. Cobalt film was first grown onto the surface of the silica array by ultrahigh-vacuum electron-beam evaporation, then the formed cobalt film was allowed to undergo a controlled oxidation process. The oxidation will fully convert the thinner Co films on the side regions of the spheres into cobalt oxide but leave the thicker Co films on the top of the spheres only partially oxidized to allow the formation of an ordered array of isolated metallic cobalt “magnetic dots.”<sup>[54]</sup> Three-dimensional cobalt nanocrystal arrays were also deposited from a suspension of cobalt nanocrystals onto a highly oriented graphite substrate with the aid of an applied magnetic field parallel to the substrate.<sup>[55]</sup> When a magnetic field was not present during the deposition, the deposited films showed no long-distance order for the cobalt nanocrystals. With the presence of an applied magnetic field, the deposited cobalt nanocrystals formed regular stripe patterns.<sup>[55]</sup> Alumina membranes with ordered pore arrays could serve as templates for the formation of magnetic nanowire arrays. Such porous alumina films can be formed by the anodization of aluminum. Well-organized pores with diameters of nanometer in size and micron in length can be obtained within these films. Magnetic nanowire arrays of Fe, Co, and Co–Cu alloy were fabricated within the alumina pores by electrochemical deposition.<sup>[56–59]</sup> Nuclear track-etched polycarbonate membranes also have pore structures similar to those of anodized aluminum films; therefore they can also serve as templates for the formation of magnetic nanowire arrays.<sup>[60,61]</sup> However, unlike alumina templates, polycarbonates cannot allow annealing after the nanowires are formed.

The most practical and versatile method for the fabrication of nanomagnetic arrays may be the nanolithography process. Magnetic dots can either be evaporated onto a template produced by electron or ion-beam etching, or by etching of predeposited metal films on a substrate through a resist.<sup>[62,63]</sup> Scanning tunneling microscopy (STM) and atomic force microscopy (AFM) can also be employed to aid the formation of ordered nanoscale magnetic structures. In such processes, particles are deposited one by one with the aid of the STM or AFM tip.<sup>[64,65]</sup>

## PROPERTIES

### Magnetic Domain and Superparamagnetism

All magnetic effects are derived from the movements of particles that have both mass and electric charge.

These particles include electrons, holes, protons, as well as positive and negative ions. A spinning electric charged particle is called a magneton, or a magnetic dipole. The magnetic moment of an atom is the vector sum of all its electronic moments. Diamagnetism arises when the magnetic moments of all the electrons of an atom are so oriented that they cancel one another out, so the atom as a whole does not possess a net magnetic moment. When cancellation of electron moments is only partially achieved, the atom will have a net magnetic moment. The varieties of magnetism arise from the different magneton alignments. Based on its magnetic behavior toward an applied field, a magnetic matter can be described as paramagnetic, antiferromagnetic, ferromagnetic, or ferrimagnetic.<sup>[66]</sup>

In ferromagnetic materials, magnetons are associated in groups. A magnetic domain (also called a Weiss domain) refers to a volume of ferromagnetic material in which all magnetons are aligned in the same direction by the exchange forces. The concept of domains distinguishes ferromagnetism from paramagnetism. Also, the domain structure of a ferromagnetic material determines the size dependence of its magnetic behavior. When the size of a ferromagnetic material is reduced below a critical value, it would become a single domain. Fine particle magnetism has traditionally dealt with size effects, which are based on the magnetic domain structure of ferromagnetic materials. It assumes that the state of lowest free energy of ferromagnetic particles has uniform magnetization for particles smaller than a certain critical size and non-uniform magnetization for large particles. The former ones are generally referred to as single-domain particles, while the latter are called multidomain particles. In earlier studies, Kittel<sup>[67,68]</sup> estimated the critical single-domain size for spherical particles of some ferromagnetic materials to be roughly 150 Å. Kittel and his colleagues were also the first to clearly show the existence of single-domain particles through experiment.<sup>[69,70]</sup> According to the magnetic domain theory, the critical size of the single domain is affected by several factors including the value of the magnetic saturation, the strength of the crystal anisotropy and exchange forces, surface or domain-wall energy, and the shape of the particles.<sup>[67,71]</sup>

In magnetic studies on fine particles, the coercivity is the single property of most interest. It must be at least above several hundred oersterds (Oe) to be of any value for permanent magnetic application. The coercivity of fine particles is a good example for size-dependent characteristics. It has been found that as the particle size is reduced, the coercivity increases to a maximum, and then decreases toward zero (Fig. 1).<sup>[70,72]</sup> Although the magnetic behavior of small particles has not been fully understood, certain relationship between particle size and coercivity has

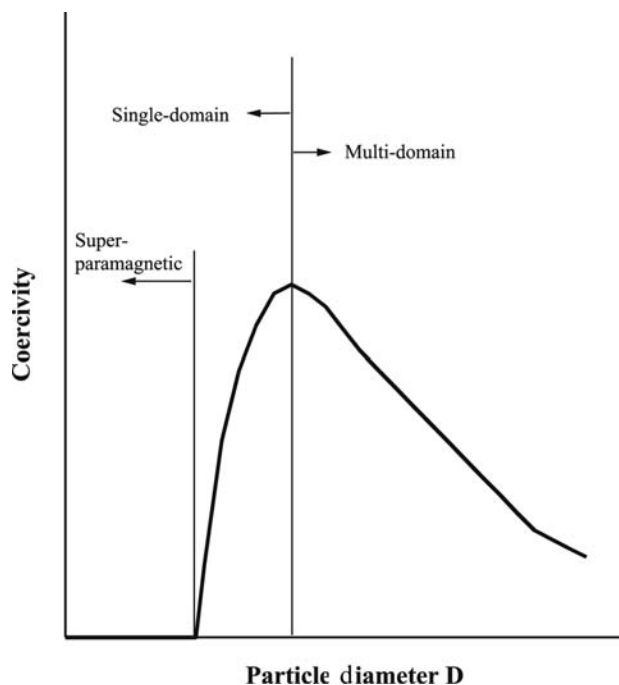


**Fig. 1** Schematic illustration of the coercivity–size relations of small particle systems. *Source:* From Refs.<sup>[70], [72]</sup>.

been established based on a uniaxial and monodispersed non-interacting particle system. As the particle size decreases below single-domain, the coercivity  $H_C$  of such particles is<sup>[70,71]</sup>

$$H_C = H_C(0)[1 - (D_S/D)^{3/2}] \quad (1)$$

and  $H_C(0)$  is given as  $2K/M_S$ , where  $D_S$  is the critical size for single-domain behavior,  $D$  is the particle size,  $H_C(0)$  is the coercivity when temperature  $T$  approaches zero,  $K$  is the anisotropy constant, and  $M_S$  is the saturation magnetization. Another version of the coercivity of single-domain particles, showing its temperature dependence, is written as<sup>[70]</sup>

$$H_C = H_C(0)[1 - (T/T_B)^{1/2}] \quad (2)$$

where  $T_B$  is the blocking temperature for ferromagnetism–superparamagnetism transition.

Single-domain size could be experimentally estimated when the coercivity reaches a maximum. Gong et al.<sup>[73]</sup> studied the magnetic properties of Fe, Co, and Ni ultrafine particles prepared by evaporation in an inert atmosphere. They found that the maximum  $H_C$  was 450, 1000, and 1500 Oe, respectively, for Ni (310 Å), Fe (210 Å), and Co (200 Å) at room temperature. They also calculated the sizes of these particles based on formula given by the domain theory, and the results were 424 Å (Ni), 196 Å (Fe), and 192 Å (Co), respectively. Zhang, Klabunde, and Sorensen<sup>[74]</sup>

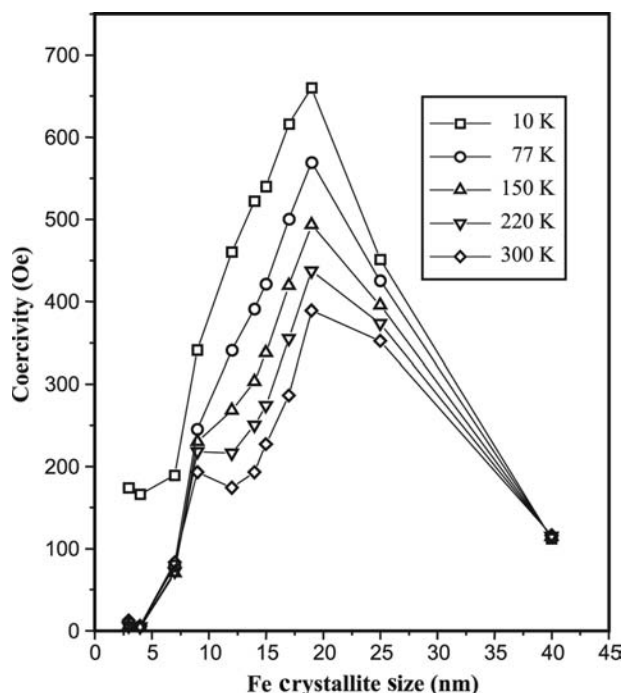


**Fig. 2** Size and temperature dependence of coercivities of iron crystallites in the [Mg]Fe systems. *Source:* From Ref.<sup>[74]</sup>.

examined the coercivities of [Mg]Fe particles at various temperatures. Coercivities reached maximum for Fe with size of about 20 nm (Fig. 2) for all the temperatures. Such behavior of coercivities was also observed in granular solids consisting of a magnetic element and a non-magnetic matrix, such as Fe–SiO<sub>2</sub><sup>[75]</sup> and Fe<sub>x</sub>Cu<sub>1-x</sub>.<sup>[76]</sup> In these magnetic granular solids, coercivity first reaches a maximum with the increase in the concentration of the magnetic element, then gradually decreases with the further increase in the magnetic element concentration. The behaviors of coercivities of granular solids could also be considered as a size effect. With the increase of concentration of the magnetic phase, the average size of the magnetic grains within these materials could increase from below single-domain size, through single-domain size, to multidomain size.

When the size of single-domain particles further decreases below a critical diameter, the coercivity becomes zero, and such particles become superparamagnetic. Thermal effects cause superparamagnetism. In superparamagnetic particles, thermal fluctuations are strong enough to spontaneously demagnetize a previously saturated assembly of particles. A superparamagnetic specimen has zero retentivity and coercivity. Therefore it has no hysteresis. Also, magnetization curves measured at different temperatures superimpose when  $M$  is plotted as a function of  $(H/T)$ .<sup>[70]</sup> These two aspects were well illustrated by the magnetic behavior of fine iron particles dispersed in solid mercury.<sup>[77]</sup>



Superparamagnetic behavior arises from the time-dependent thermal relaxation process of ferromagnetic materials. If a magnetic particle is very small (typically  $\leq 100$  Å), it will exhibit serious thermal relaxation effects which tend to reduce the coercivity force and lead to a time-dependent magnetization. For isolated uniaxial single-domain particles with negligible interactions, the Néel–Arrhenius law gives the relaxation time of the magnetic moment in zero-field:<sup>[71]</sup>

$$\tau = \tau_0 \exp(KV/k_B T) \quad (3)$$

In Eq. (3)  $\tau_0$  is a frequency factor related to gyromagnetic precession and is often taken as  $\tau_0 \cong 10^{-9}$ – $10^{-13}$  sec,  $K$  is the effective anisotropy constant,  $V$  is the particle volume, and  $k_B$  is Boltzmann's constant. For a bulk ferromagnetic material, the thermal relaxation time is much higher than the measurement time. When the relaxation time reaches the measurement time due to the decrease of particle size, the transition from ferromagnetic behavior to superparamagnetic behavior occurs.

The intrinsic time-dependent behavior of ferromagnetic materials at finite temperatures can be used to predict the critical size and the blocking temperature for superparamagnetism. However, this basic theory based on the Néel model of single-particle system is often insufficient to describe magnetic relaxation process because of the complex nature of most magnetic systems. In real systems, factors affecting the time-dependent relaxation of single-domain particles include particle size distribution,<sup>[78]</sup> anisotropy energy distribution,<sup>[79–81]</sup> dipole–dipole coupling between particles,<sup>[82–84]</sup> and the presence of an applied field.<sup>[85,86]</sup> For an individual real system, experimental results and theoretical studies are often combined to determine the dominating factors in the relaxation process in order to achieve the best description. The existence of a distribution of energy barriers leads to a logarithmic decay of magnetization in time and can be described as<sup>[83,87]</sup>

$$M(t) = M_0 - S \ln(t) \quad (4)$$

where  $S$  is called magnetic viscosity. For a system of particles with a distribution of anisotropy energies, there will be a distribution of blocking temperatures. For a measurement time  $\tau$ , the Néel law gives the median blocking temperature,  $T_B$ , as<sup>[86]</sup>

$$T_B = \frac{KV}{k_B [\ln(\tau/\tau_0)]} \quad (5)$$

When two measuring times  $\tau_1$  and  $\tau_2$  are selected, two median blocking temperatures  $T_{B1}$  and  $T_{B2}$  will be

obtained as

$$\frac{T_{B1}}{T_{B2}} = \frac{\ln(\tau_2/\tau_0)}{\ln(\tau_1/\tau_0)} \quad (6)$$

both  $\tau_0$  and the anisotropy energy  $KV$  can be determined.<sup>[86]</sup> For a system of previously saturated uniaxial particles with an applied field  $H$  along the easy axis, the relaxation time is given by<sup>[85]</sup>

$$\tau = \tau_0 \exp \left[ \frac{KV}{k_B T} \left( 1 - \frac{H}{H_K} \right)^2 \right] \quad (7)$$

where  $H_K$  is anisotropy field. For interacting particles, magnetic relaxation is a Curie-Weiss behavior and is described by a Vogel–Fulcher law<sup>[83]</sup>

$$\tau = \tau_0 \exp \left[ \frac{KV}{k_B T(T - T_0)} \right] \quad (8)$$

where  $T_0$  is the spin freezing temperature.

### Magnetization Temperature/Size Dependence and the Bloch Law

According to Bloch, the magnetization due to spin wave fluctuation is described as<sup>[88]</sup>

$$M(T) = M(0)(1 - BT^b) \quad (9)$$

In Eq. (9),  $M(T)$  is the temperature-dependent magnetization,  $B$  is the Bloch constant and  $b$  is the Bloch exponent. The exponent is given by  $b = 3/2$  for a three-dimensional bulk system and has been well defined.

By using calculation on spin waves, Mills and Maradudin<sup>[89–91]</sup> found Bloch exponent remained  $b = 3/2$  for “non-bulk” surface materials, and the Bloch constant for the surface was expected to be twice that of the bulk. By using spin wave simulations, Wildpaner et al.<sup>[92,93]</sup> studied particles of various sizes and found stronger temperature dependencies with decreasing size, and the magnetization temperature relation did not fit Eq. (9). More importantly, spin excitations were found to be inhomogeneous through the particle. Hendriksen, Linderoth, and Lindgård<sup>[94]</sup> considered the spin wave spectrum of nanometer-sized particles by solving the Heisenberg Hamiltonian. Again the excitations were a function of radial position in the particles, and the overall result was a prediction that the exponent  $b$  should increase above the bulk value of  $3/2$  inversely proportional to the particle size.

Experimental investigations of  $M(T)$  for nanoparticles gave a mixed story. Pierce et al.<sup>[95]</sup> studied the magnetization of macroscopic surfaces and found

results consistent with Mills and Maradudin. Linderoth et al.<sup>[96]</sup> followed up their calculations<sup>[94]</sup> with a measurement on Fe–C particles with a diameter of 3.1 nm and found  $b = 1.9$  in qualitative agreement with their theory. Xiao and Chien<sup>[97]</sup> studied iron imbedded in SiO<sub>2</sub> at ~50% volume fraction. The iron particle size was 2–3 nm. They found  $b = 3/2$  with  $B_{\text{surf}} \cong 10 B_{\text{bulk}}$ . Chen et al.<sup>[98]</sup> studied MnFe<sub>2</sub>O<sub>4</sub> particles and found  $b$  in the range 1.5–1.9 for sizes in the range 5–15 nm.

The effect of particle size on magnetization of magnetic nanoparticles has to be taken into consideration when magnetization–temperature dependencies of particles of various sizes are studied under various temperatures. In experimental investigations, the average magnetic moments of the magnetic atoms in these particles are either found enhanced or depressed compared to those of the atoms in bulk materials. Billas, Châtelain, and de Heer<sup>[99]</sup> used a molecular beam deflection method to study the magnetic moment of small Fe, Co, and Ni clusters containing several tens to several hundreds of atoms at temperatures between 80 and 1000 K. They found that clusters with fewer than 400 atoms generally had larger magnetic moments than the bulk. Douglas et al.<sup>[100]</sup> studied the magnetic properties of free cobalt clusters with a similar method, and they found an internal magnetic moment per atom of  $2.24 \pm 0.14 \mu\text{B}/\text{atom}$  for cobalt

clusters containing 65 to 215 atoms, which is substantially higher than the bulk value of cobalt.

Coevaporation of a magnetic metal with a non-magnetic matrix material can produce very small magnetic metal clusters embedded within the non-magnetic matrix.<sup>[101]</sup> This not only provides oxygen-free nanometer-sized magnetic clusters that can be studied in air but can also produce magnetic nanoparticles with various sizes by annealing these matrix-isolated metal clusters at different temperatures. Zhang et al.<sup>[102–104]</sup> prepared BCC-Fe nanoparticles by coevaporating Fe with Mg or MgF<sub>2</sub> in a pentane vapor, followed by annealing at various temperatures ranging from 100 to 600°C. Low-temperature annealing (below 430°C) produced a series of Fe nanoparticles ranging from 3 to 18 nm, as confirmed by XRD and TEM. The SQUID magnetometer was used for magnetic measurements. The saturation magnetization  $M_S$  was determined by  $H^{-1} \rightarrow 0$  extrapolation using fields of  $H \leq 55 \text{ K Oe}$  (Figs. 3 and 4). Both the [Mg]Fe and [MgF<sub>2</sub>]Fe systems show increasing temperature dependencies of  $M_S$  with decreasing particle size. The concave upward dependence of  $M_S$  vs.  $T$  in Fig. 4 for the 3-nm-diameter [MgF<sub>2</sub>]Fe sample even indicates a Bloch exponent  $b < 1$ . The [MgF<sub>2</sub>]Fe samples also show a significant magnetization quench, especially for smaller particles. It is believed that this quench is

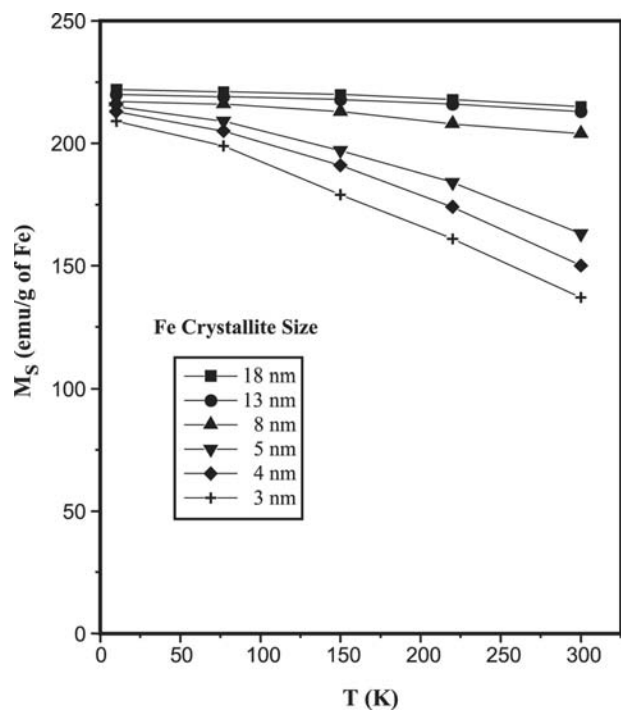


**Fig. 3** Saturation magnetization vs. temperature for different size iron crystallites in the [Mg]Fe systems. *Source:* From Ref.<sup>[102]</sup>.

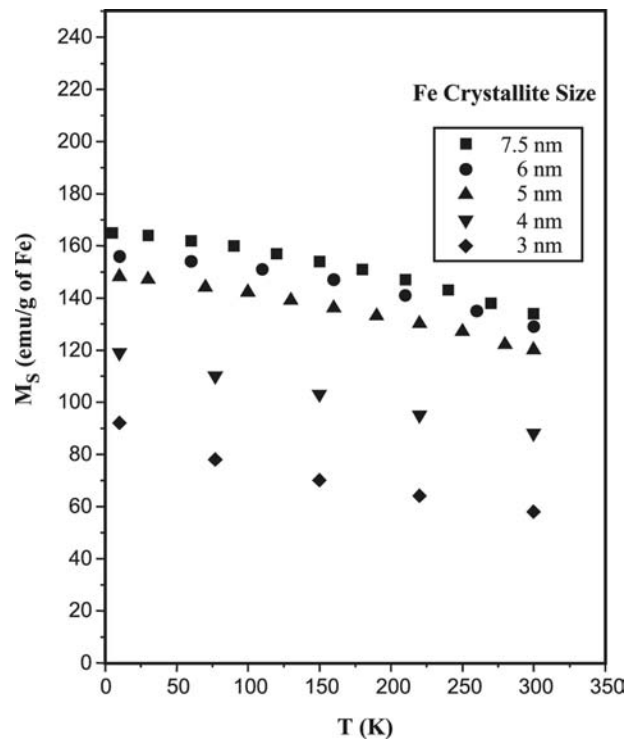


**Fig. 4** Saturation magnetization vs. temperature for different size iron crystallites in the [MgF<sub>2</sub>]Fe systems. *Source:* From Ref.<sup>[102]</sup>.

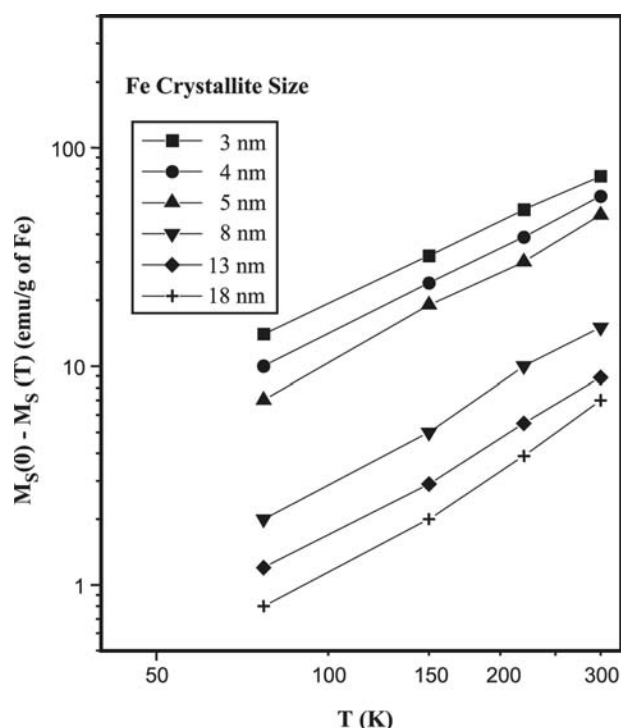


**Fig. 5** Saturation magnetization depression relative to its values at  $T = 0$  K vs. temperature for different size iron crystallites in the  $[\text{Mg}]\text{Fe}$  system. *Source:* From Ref.<sup>[102]</sup>.

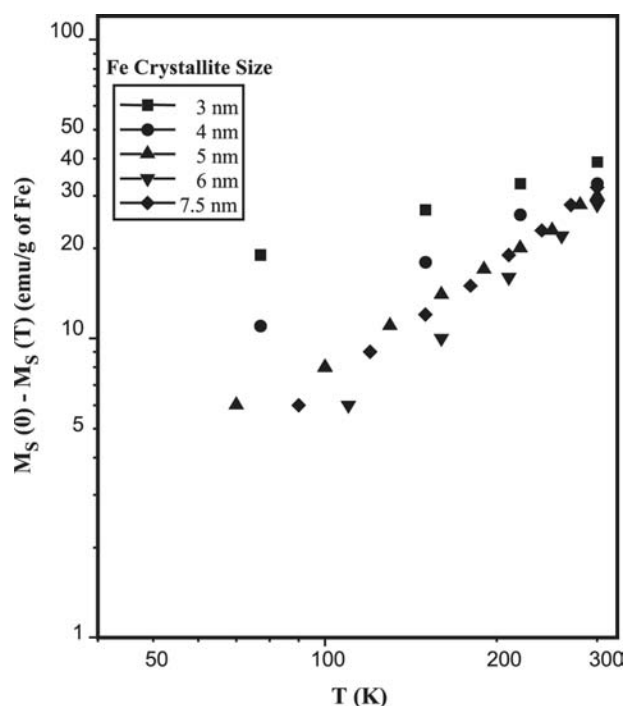


**Fig. 6** Saturation magnetization depression relative to its values at  $T = 0$  K vs. temperature for different size iron crystallites in the  $[\text{MgF}_2]\text{Fe}$  system. *Source:* From Ref.<sup>[102]</sup>.

due to an electron donation from  $\text{MgF}_2$  coating material to the unfilled minority d band of the iron.

Double logarithmic graphs of the magnetization depression vs.  $T$  were plotted for both the  $[\text{Mg}]\text{F}$  and  $[\text{MgF}_2]\text{Fe}$  systems (Figs. 5 and 6). The form of Bloch law [Eq. (9)] implies that the magnetization depression  $M_S(0) - M_S(T)$  is a power law with temperature ( $T$ ). Thus if Bloch law holds, a double logarithmic graph of these quantities will yield straight lines, the slopes of which will be the Bloch exponent  $b$  and with intercepts related to  $BM_S(0)$ . The data presented all fall in line to imply that Bloch's law holds for these particles.<sup>[102]</sup>

Linear fit of Eq. (9) to the data also yielded the Bloch parameters  $b$  and  $B$  plotted in Figs. 7 and 8. The results of both the  $[\text{Mg}]\text{Fe}$  and  $[\text{MgF}_2]\text{Fe}$  systems indicated that nanoparticles still obey the Bloch law, but with decreasing size, the Bloch exponent  $b$  falls from the bulk value of  $b = 3/2$  to smaller values, while the Bloch constant rises from the bulk values by orders of magnitude.<sup>[102]</sup> Also, the chemistry of the interface can affect the size-dependent properties of  $M(T)$ . Recent studies on the magnetic properties of oxide-coated iron nanoparticles by Banerjee et al.<sup>[105]</sup> provided some quantitative agreement to the results on the  $[\text{Mg}]\text{Fe}$  and  $[\text{MgF}_2]\text{Fe}$  systems. Four oxide-coated Fe samples, with sizes of 4.9, 5.5, 9.5, and 11.1 nm, were synthesized by an electrodeposition

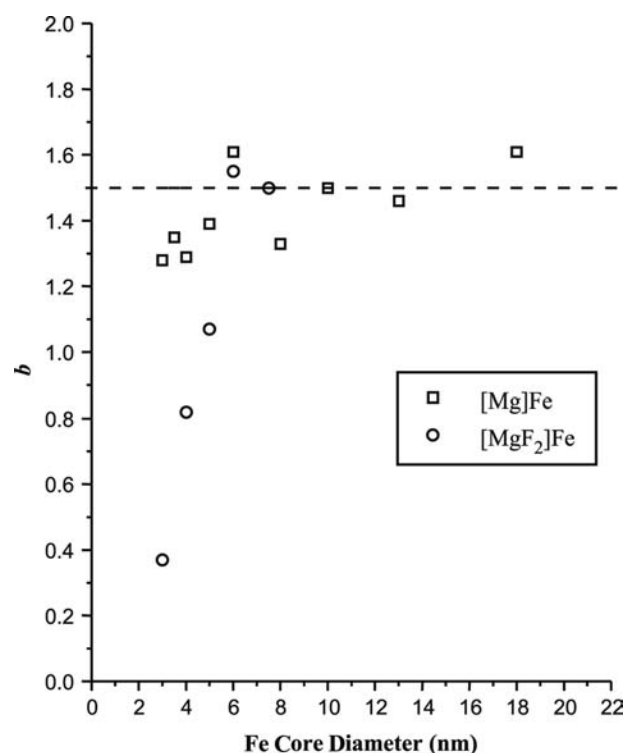


**Fig. 7** Bloch exponent  $b$  as a function of iron crystallite size. Dashed line is the bulk value. *Source:* From Ref.<sup>[102]</sup>.

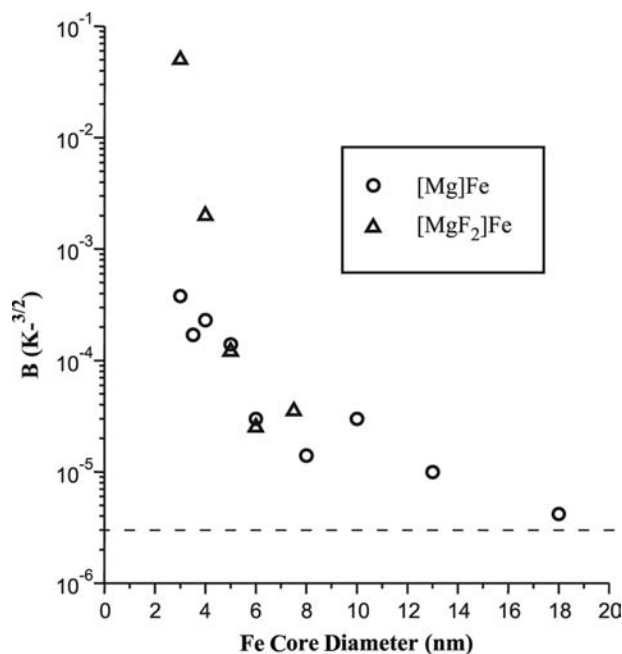


**Fig. 8** Bloch constant  $b$  as a function of iron crystallite size. Dashed line is the bulk value. Source: From Ref.<sup>[102]</sup>.

method. For the samples with the sizes of 4.9 and 11.1, the values of the Bloch exponent  $b$  were 0.79 and 1.1, both smaller than the bulk value of 3/2. The saturation magnetization values of these samples were also found depressed as compared with the theoretical value.

For a three-dimensional bulk system at a low temperature, Bloch law can also be written as<sup>[106]</sup>

$$M(T) \cong M(0)(1 - BT^{3/2} - CT^{5/2}) \quad (10)$$

Curve fitting by using the original Bloch law equation could give  $b \cong 2$ . And this may explain why  $b$  was near 2 in some nanoparticle systems such as Fe-C<sup>[96]</sup> and Ni.<sup>[107]</sup> Bloch's  $T^{3/2}$  law is based on an infinite ideal three-dimensional system and it is not always suitable for all real systems. The foundation of the Bloch law based on classical theories of solid-state physics should still hold for magnetic nanomaterials. However, the unique characteristics of the nanostructured materials should also be addressed when these theories are employed to describe the behaviors of nanomaterials. For a thin film, one of its dimensions is limited, for a nanowire, two dimensions could be reduced, and for very small particles, all three dimensions may be reduced. Nanoparticle systems have a high surface volume fraction. In order to emphasize the two-dimensional nature of the surface, Bloch law could be written as

$$M(T) = M_{\text{core}}(0)(1 - BT^{3/2}) + M_{\text{surface}}(0) \times (1 - CT) \quad (11)$$

If magnetic coupling exists between the surface and the soft core, and the surface becomes dominant in determining the overall magnetization process of the particle, then Bloch law could also be written as

$$M(T) \cong M(0)(1 - BT) \quad (12)$$

And for extremely long magnetic nanowires, they could be considered as one-dimensional systems and  $M(T)$  could be linear to  $T^{1/2}$ .

### The Effect of Particle Shape on Magnetic Properties

Single-domain magnetic nanoparticles can become the building blocks of high-density magnetic memory devices.<sup>[108–110]</sup> However, merely decreasing the size of the memory bits would not be adequate to form high-density magnetic recording systems. The signal/noise ratio is another important factor determining the quality of magnetic memory. For ordered single-domain magnetic particle arrays to become desirable magnetic memory elements, they should have both high remanence and high coercivity. Remanence and coercivity are determined by anisotropy forces, which are affected by many factors. One of the important anisotropies is shape anisotropy, which is directly associated with the shape of the nanomagnet.

Most magnetic nanoparticles in the size ranges of several nanometers do not have well-defined shapes and often appear spherical. Spherical particles do not have shape anisotropy; therefore their shapes do not affect important magnetic properties such as coercivity, remanence, hysteresis, and susceptibility. Studies of larger particles with stable and defined non-spherical geometric shapes could reveal the influence of shape on magnetic properties due to shape anisotropy. Arrays of magnetic particles in the size range from 35 to 500 nm with nearly uniform shapes and identical sizes were fabricated by using high-resolution electron beam lithography with a standard lift-off pattern transfer process.<sup>[111]</sup> The shapes of nanomagnets in these arrays include elliptical, triangular, square, pentagonal, and circular geometries, and adequate spacing between particles was allowed for some arrays to eliminate interparticle interaction. The influence of size, shape, and thickness on the magnetic properties of these nanomagnets was carefully examined with both theoretical modeling and experimental measurement by Cowburn.<sup>[111]</sup> It was found that there were two distinct phenomena that could be attributed to the shape and size effects on magnetic properties. The first is the small deviations from uniformity in the magnetization field within the nanostructures. Such deviations could give rise to higher-order anisotropy terms due to

configurational anisotropy, and these anisotropies could dominate the overall magnetic properties. The second phenomenon is the existence of competition between quantum mechanical exchange energy and classical magnetostatic energy. This competition will not only determine whether a nanoparticle exhibits single-domain behavior, but also control configurational anisotropy by defining non-uniformity in magnetization.

For smaller circular nanomagnets of 100 nm in diameter and 10 nm in thickness, hysteresis loops showed a high remanence and a low switching field, which is typical single-domain behavior. For larger circular nanomagnets of 300 nm in diameter and 10 nm in thickness, hysteresis loops showed a sudden loss of magnetization at near zero-field. This phenomenon indicates a “flux-closing” configuration that may be characterized by a “vortex” phase in which the magnetization vectors were parallel to the nearest edges at all positions along the particle surfaces. The hysteresis loops of magnetic arrays containing thin triangular, square, and pentagonal nanomagnets were very different from each other; and they were also different from the loops of conventional unstructured material. The multifold anisotropy fields of these materials were attributed to a phenomenon called configurational anisotropy, which was associated with the geometric shapes of the nanomagnets. The elliptically shaped nanomagnets clearly showed easy-axis behavior characterized by high remanence and high coercivity; therefore they are the best choice for patterned nanomagnet arrays.<sup>[111]</sup> He et al. compared the magnetization behaviors of single-domain and multidomain, square and elliptical cobalt nanomagnet arrays, and they also concluded that elliptical cobalt nanomagnets were preferred to form a single-domain demagnetization state.<sup>[112]</sup>

### Surface Effects and Interparticle Interactions

Fine particle magnetism has always been dealing with two very common aspects of small particle behavior, namely, the surface/interface effect and interparticle interactions. The reduced geometry at particle surface/interface often leads to the relaxation of crystal lattice. This will generate an inhomogeneous spin structure throughout the whole particle, with spins at the surface behaving very differently compared with those in the core. For a ferromagnetic particle, this type of non-linear spin structure can be described as a ferromagnetic core with aligned spins, and a structurally disordered surface spin structure. The surface spin structure resembles a spin-glass-like state, with the surface spins not oriented at random but inclined to the direction of the net magnetization through exchange

interaction with the core.<sup>[113]</sup> Surface spin canting has been demonstrated in 6-nm  $\gamma$ -Fe<sub>2</sub>O<sub>3</sub> prepared by chemical precipitation,<sup>[114]</sup> NiFe<sub>2</sub>O<sub>4</sub> nanoparticle prepared by grinding with oleic acid in kerosene,<sup>[115]</sup> NiFe<sub>2</sub>O<sub>4</sub> prepared by chemical precipitation,<sup>[116]</sup> and ball-milled CuFe<sub>2</sub>O<sub>4</sub>.<sup>[117]</sup> Surface/interface effects can also come from either magnetic or non-magnetic coatings formed due to the oxidation of metal particle surface or the presence of a surface coating or matrix. Many abnormalities of fine particle magnetism can be attributed to the surface effects. For example, for oxide-coated or matrix-hosted nanoscale Fe, Co, and Ni particles, interactions between particles and the coating materials may modify the coercivity of the system. Therefore magnetic coercivity in these systems is somewhat considered as a surface/interface property. Hadjipanayis et al. explained the coercivity behavior of the oxide-coated Fe clusters as the result of the interaction between the soft Fe<sub>2</sub>O<sub>3</sub> shell and the hard Fe core.<sup>[118]</sup> This gave the high coercivity at low temperature and its strong temperature dependence. The whole particle may become magnetically soft when the core is very small and fluctuation of the magnetic moment of the shell dominates the overall magnetic properties.

Non-interacting single-domain magnetic nanoparticles are superparamagnetic below certain temperatures. However, when particles are brought closer together, dipole/exchange interactions can occur. Such interactions will increase the effective energy barriers for spontaneous magnetization. For a densely packed but disordered assembly of superparamagnetic particles, the interparticle interactions can be inhomogeneous, thus giving rise to a distribution of effective energy barriers for spontaneous magnetization. Fiorani et al.<sup>[119]</sup> studied relaxation properties of 4.7-nm  $\gamma$ -Fe<sub>2</sub>O<sub>3</sub> with increasing strength of interparticle interaction and discovered that the very weakly interacting particles can be well described by the Néel–Brown model for superparamagnetism. For particles with weak to medium interaction, Néel–Brown model still applies if interparticle interaction is accounted for. For strongly interacting particles, the result of such distribution of energy barriers is the transformation from pure superparamagnetism to a glass collective state resembling spin glasses, but with its own distinct features. Zysler et al.<sup>[120]</sup> compared the blocking behaviors and hysteresis cycles of amorphous (Fe<sub>0.26</sub>Ni<sub>0.74</sub>)<sub>50</sub>B<sub>50</sub> nanoparticles (mean diameter 2 nm) and the same nanoparticles dispersed in a polymer with a 0.3 wt.% ratio for the nanoparticles. Results from the polymer-dispersed sample, with a mean interparticle center-to-center distance of 18 nm, showed good agreement with the model of non-interacting particles. For non-dispersed particles, strong interparticle interaction was observed. The  $M_{ZFC}$  had a maximum at a

temperature  $T_{\max} \approx 100$  K, which was higher than that of the dispersed sample (55 K). Above  $T_{\max}$ , the non-dispersed sample could still be described as superparamagnetic if interparticle interaction is considered. Below 50 K, the non-dispersed sample underwent a regime change as indicated by its magnetization and hysteresis behaviors. It is believed that the low-temperature state is a collective glassy-like state, which is characterized by a randomly frozen assembly of correlated particle moments.

The coupling particle moments of interaction of magnetic nanoparticles at low temperatures could give rise to a new magnetic order if the particle moments are parallel. Such magnetic ordering is called superferromagnetism.<sup>[121]</sup> Superferromagnetism should behave similarly to normal ferromagnetic materials, but with much higher magnetic moment.

### Giant Magnetoresistance Effect

Magnetoresistance is defined as the fractional change in resistance or resistivity of a material induced by an applied magnetic field relative to the resistivity either at zero field,  $\rho(0)$ , or at the saturation field  $H_s$ ,  $\rho(H_s)$ :<sup>[122,123]</sup>

$$\left(\frac{\Delta\rho}{\rho}\right)_0 = \frac{\rho(H) - \rho(0)}{\rho(0)} \quad (13)$$

or

$$\left(\frac{\Delta\rho}{\rho}\right)_{H_s} = \frac{\rho(H) - \rho(H_s)}{\rho(H_s)} \quad (14)$$

Giant magnetoresistance (GMR) was first discovered in Fe/Cr magnetic superlattices.<sup>[124]</sup> Baibich et al.<sup>[124]</sup> first suggested GMR in Fe/Cr magnetic superlattices as the result of spin-dependent electron transmission between Fe layers through the thin Cr interfaces. This spin-dependent electron transport between ferromagnetic Fe layers was facilitated by the interplay of orientation of the Fe layers induced by the magnetic field. The spin-dependent electron transmission through an interface, also referred to as spin-dependent scattering, is called the “two-current model.” Other effects, such as exchange coupling, spin-value effect, and periodic density of states, were also considered to be the reasons for GMR in thin films.<sup>[123]</sup>

Giant magnetoresistance effects in granular films were first discovered in heterogeneous granular Cu–Co alloys<sup>[125]</sup> and in Co–Cu and Fe–Cu granular alloys,<sup>[126]</sup> and were later observed in many other granular systems.<sup>[123,127–129]</sup> A granular magnetic metal system is generally referred to as a material consisting of nanoscale magnetic metal granules (clusters)

embedded in a non-magnetic matrix. Although magnetic granular films lack defined structures, the mechanism of spin-dependent scattering could still be applied to explain the GMR phenomenon in these materials. Rather than going through a layer-to-layer electron transport process, the neighboring magnetic granules, under an aligning magnetic field, could undergo electron transfer through the non-magnetic interfaces. Giant magnetoresistance in granular metals was found to be dependent upon the size, shape, as well as the concentration of the magnetic granules.<sup>[130]</sup> Initially, it was believed that GMR could only exist in granular metal/metal systems because of the absence of metallic conductivity in metal/insulator systems such as Fe–Al<sub>2</sub>O<sub>3</sub>.<sup>[123]</sup> Recent studies have shown that GMR can also be found in metal/insulator granular films. The magnetoresistance in these films is called tunneling magnetoresistance (TMR). Tunneling magnetoresistance in metal/insulator films occurs when electrons are transferred between magnetic clusters by a spin-dependent tunneling effect through tunneling junctions or grain boundaries. The probability of spin-dependent tunneling depends on many factors including particle size, shape, distribution, the nature of the particle/matrix interfaces, and film thickness.<sup>[131–133]</sup>

### Quantum Tunneling of Magnetization

Quantum tunneling of magnetization, or macroscopic quantum tunneling (MQT), is a phenomenon that describes quantum mechanically the non-conservation of magnetization along a certain axis between different energy configurations.<sup>[77,134–137]</sup> Consider the classical case of superparamagnetism to ferromagnetism transition in a single-domain particle. For a small single-domain ferromagnetic particle with its entire spins (magnetic moments) aligned along an easy axis in an applied field, the overall magnetic relaxation process of the particle can be described as a single macroscopic degree of freedom, with all the individual spins acting as a total moment (spin) of the particle. This is a thermodynamic process whereas magnetic relaxation of the system has a linear relation to temperature as described by the Arrhenius law  $\tau = \tau_0 \exp(\Delta E/k_B T)$ . When temperature drops below a certain point, all the individual spins in the small ferromagnetic particle will be frozen out because of crystal anisotropy, and the spontaneous magnetization  $M$  will be close to saturation magnetization value  $M_0$ . When a magnetic field  $H$  is applied along the opposite direction of the original spontaneous magnetization  $M$ , a metastable state arises with  $M$  being antiparallel to  $H$ . To overcome such a metastable state and achieve a stable magnetization state with  $M$  being parallel to  $H$ , spontaneous magnetization must overcome certain energy barriers.<sup>[134]</sup>



These potential energy barriers generally originate from two sources: anisotropy energy barriers due to intrinsic crystal anisotropies, and possible barriers caused by the pinning of domain walls by defects.<sup>[138]</sup> As these energy barriers have no direct relations with temperature, magnetic relaxation will no longer be temperature dependent. Chudnovsky and Gunther considered a simple spherical ferromagnetic system with an energy barrier  $E_a$  as<sup>[134]</sup>

$$E_a = (K_{\parallel} + K_{\perp} \sin^2 \phi) \sin^2 \theta - MH(1 - \cos \theta) \quad (15)$$

with  $H$  in the  $-z$  direction, and  $K_{\parallel}$  and  $K_{\perp}$  being parallel anisotropy and transverse anisotropy, respectively. By combining the classical equation for  $M$  and their own theory of quantum nucleation, they gave a crossover temperature  $T^*$  for quantum tunneling as<sup>[134]</sup>

$$T^* = (3/8)h\gamma(K_{\parallel}K_{\perp}\varepsilon)^{1/2}/k_B M_S \quad (16)$$

where  $\varepsilon$  is  $(1 - H/H_C)$  and  $H_C$  is coercivity. From the above we can see that a high crossover temperature is expected for a sample with high anisotropy energies and low saturation magnetization. Furthermore, the magnetic tunneling of a system at a certain temperature could also be achieved by controlling the external magnetic field. Tejada et al. estimated the range of  $T^*$  to be 0.1–5 K for small magnetic particles with high magnetic anisotropy.<sup>[139]</sup>

In real systems, there can be a broad distribution of energy barriers. Under such conditions, there is no longer a single crossover temperature below which quantum tunneling occurs, and the magnetic relaxation process theoretically could be both temperature and field dependent. The time-dependent magnetization for such systems would be<sup>[138,139]</sup>

$$M(\tau) = M_0[1 - S(T, H) \ln(\tau/\tau_0)] \quad (17)$$

where  $M_0$  is the magnetization at  $\tau_0$  and  $S(T, H)$  is magnetic viscosity. At high temperatures, magnetic viscosity is temperature dependent and is called thermal viscosity  $S_T$  and  $S_T \sim T$ . At very low temperatures, magnetic viscosity is independent of temperature and is called quantum viscosity  $S_Q$ .<sup>[139]</sup>

There are several types of magnetic tunneling mechanisms.<sup>[140]</sup> Although ample experimental evidence has been obtained to suggest the existence of these processes, it is not easy to achieve quantitative agreements between theory and experiment results in many systems. This may be because many systems studied have been assemblies of particles with heterogeneous parameters that lead to unknown barrier

energy distributions. These various energy barriers could be different crystal anisotropy energies originating from non-uniform particle sizes or shapes, or due to the simultaneous precipitation of different domain walls in the blocking process. In addition, other small particle behaviors, such as particle interactions, could be confused with macroscopic quantum tunneling without detailed analysis.<sup>[141,142]</sup> Tejada et al.<sup>[139]</sup> studied the magnetic relaxation of small ferrofluid particles  $\text{Fe}_3\text{O}_4$  (36 Å),  $\text{FeC}$  (60 Å), and  $\text{CoFe}_2\text{O}_4$  (50 Å) by examining the hysteresis loops, time-dependent magnetization, magnetization relaxation times, and magnetic viscosity at temperatures above and below the blocking temperature  $T_B$ . At  $T \geq T_B$ , these particles exhibited typical superparamagnetic thermal relaxation behaviors. At  $T \ll T_B$ ,  $S(T, H)$  became linear to  $T$ , suggesting weak interactions between the particles. At extremely low temperatures, relaxation time, coercivity, and magnetic viscosity  $S(T, H)$  all appeared independent of  $T$ , suggesting quantum tunneling of magnetization. The crossover temperatures,  $T_c$ , were estimated as about 0.5, 1, and 2.5 K for  $\text{Fe}_3\text{O}_4$ ,  $\text{FeC}$ , and  $\text{CoFe}_2\text{O}_4$ , respectively. Tejada and Zhang<sup>[138,140]</sup> studied several different types of materials including single-domain particles (SDPs) and granular solids with SDPs embedded within. These materials included  $\text{CrO}_2$  recording tapes, antiferromagnetic horse-spleen ferritin, and magnetic thin film of  $\text{TbFe}_3$ . They observed quantum magnetic tunneling effects in these systems with experimental values of  $T_c$  ranging from 2 to 5.5 K. Rather sharp crossover from thermal to quantum state for these samples was observed, suggesting that dissipation had very little effect on magnetic tunneling. Peng et al.<sup>[143]</sup> studied monodispersed ferromagnetic Co clusters coated with an antiferromagnetic  $\text{CoO}$  shell and observed enhanced coercivities (2–8.5 K Oe) and quantum magnetization behavior with a crossover temperature of 8 K. The high coercivities and high crossover temperature were attributed to the enhanced uniaxial anisotropy caused by the ferromagnetic–antiferromagnetic coupling between the Co core and the  $\text{CoO}$  shell.

Unlike assemblies of small magnetic particles with inhomogeneous sizes and properties, high-spin molecular clusters have uniform chemical characteristics and can be defined with certain parameters. Therefore they could be better candidates for the studies of quantum magnetic relaxation process. Friedman et al.<sup>[144]</sup> examined the low-temperature relaxation of a superparamagnetic and highly anisotropic molecular cluster compound  $\text{Mn}_{12}\text{O}_{12}(\text{CH}_3\text{COO})_{16}(\text{H}_2\text{O})_4$ , and they observed stepwise magnetization with periodic increase of external field, as well as much faster magnetization relaxation near these steps. They described this as a process called resonant tunneling of magnetization. They suggested that  $\text{Mn}_{12}$  molecule had two

symmetrical ground states  $m = S$  and  $m = -S$ , due to uniaxial anisotropy, with  $S$  being the total spin of the molecule ( $S = 10$ ). When an external field was applied, the symmetry between two ground states was destroyed and this led to the formation of a metastable state and a new ground state. The metastable state first resonated with an excited state associated with the new ground state, then degenerated into the new ground state. The energy levels of the states depend not only on temperature but also on the applied field; therefore such quantum tunneling is a “thermally assisted” and “field-tuned” process.

## CONCLUSION

The studies on the fabrication and properties of magnetic nanomaterials have made great progress. Many well-established techniques have found success in the preparation of magnetic nanomaterials of various sizes and structures. In the studies of magnetic properties, both theoretical and experimental efforts have demonstrated that fine particle magnetism is not only a result of the reduction of size, but also due to surface/interface effects and the interaction of particles. The fundamental theories of solid-state physics that describe the magnetic properties of bulk materials can still be applied to magnetic nanomaterials, if the unique structural aspects and collective behaviors of nanoparticles are taken into consideration. Theoretically, future effort should be focused on the improvement of the modeling of magnetic properties of nanometer-sized particles. Although theoretical modeling for clusters consisting of a few to a few tens of atoms has been well established, there is still a need for dependable approaches to the calculations of nanometer-sized particles. Experimentally, further improvement in the fabrication techniques should lead to more effective ways to generate particles with controllable size and uniform morphology, and better methods to handle and study individual particles. The availability of “identical” particles, and the techniques to put a single or a few of such particles under study, not only would enable closer examination of size-dependent magnetic properties, but could also, through nano-manipulation, enable them to become building blocks for magnetic devices.

## REFERENCES

1. McHenry, M.E.; Laughlin, D.E. Nano-scale materials development for future magnetic applications. *Acta Mater.* **2000**, *48*, 223–238.
2. Raj, K.; Moskowitz, R. Commercial applications of ferrofluids. *J. Magn. Magn. Mater.* **1990**, *85*, 233–245.

3. Raj, K.; Moskowitz, B.; Casciari, R. Advances in ferrofluid technology. *J. Magn. Magn. Mater.* **1995**, *149*, 174–180.
4. Shlioms, M.I.; Pshenichnikov, A.F.; Morozov, K.I.; Shurubor, I.Yu. Magnetic properties of ferrofluids. *J. Magn. Magn. Mater.* **1990**, *85*, 40–46.
5. Bergemann, C.; Müller-Schulte, D.; Oster, J.; Brassard, L.à.; Lübbe, A.S. Magnetic ion-exchange nano- and microparticles for medical, biomedical and molecular biological applications. *J. Magn. Magn. Mater.* **1999**, *194*, 45–52.
6. Grüttner, C.; Teller, J. New types of silica-fortified magnetic nanoparticles as tools for molecular biology applications. *J. Magn. Magn. Mater.* **1999**, *194*, 8–15.
7. Jordan, A.; Scholz, R.; Wust, P.; Fähling, H.; Felix, R. Magnetic fluid hyperthermia (MFH): cancer treatment with AC magnetic field induced excitation of biocompatible superparamagnetic nanoparticles. *J. Magn. Magn. Mater.* **1999**, *201*, 413–419.
8. Gleiter, H. Nanostructured materials: basic concepts and microstructure. *Acta Mater.* **2000**, *48*, 1–29.
9. Klabunde, K.J.; Stark, J.; Koper, O.; Mohs, C.; Park, D.G.; Decker, S.; Jiang, Y.; Lagadic, I.; Zhang, D. Nanocrystals as stoichiometric reagents with unique surface chemistry. *J. Phys. Chem.* **1996**, *100*, 12,142–12,153.
10. Jen, S.U.; Lee, C.Y.; Yao, Y.D.; Lee, K.C. Magnetic properties of ultra-fine particles. *J. Magn. Magn. Mater.* **1991**, *96*, 82–88.
11. Glavee, G.N.; Kerizan, C.F.; Klabunde, K.J.; Sorensen, C.M.; Hadjipanayis, G.C. Clusters of immiscible metals. Iron-lithium nanoscale bimetallic particles synthesis and behavior under thermal and oxidative treatments. *Chem. Mater.* **1991**, *3*, 967–976.
12. Dormann, J.L.; Sella, C.; Renaudin, P.; Gibart, P. Interface properties in granular compound films studied by Mössbauer spectroscopy. *Thin Solid Films* **1979**, *58*, 265–272.
13. Papaefthymiou, V.; Tsoukatos, A.; Hadjipanayis, G.C.; Simopoulos, A.; Kostikas, A.J. Mössbauer studies in Fe/(SiO<sub>2</sub>, BN) granular solids. *Magn. Magn. Mater.* **1995**, *140–144*, 397–398.
14. Gangopadhyay, S.; Hadjipanayis, G.C.; Sorensen, C.M.; Klabunde, K.J. Magnetism in ultrafine Fe and Co particles. *IEEE Trans. Magn.* **1993**, *29* (6), 2602–2607.
15. Giri, A.K.; de Julián, C.; González, J.M.J. Coercivity of Fe–SiO<sub>2</sub> nanocomposite materials prepared by ball milling. *Appl. Phys.* **1994**, *76* (10), 6573–6575.
16. Wang, G.; Zhang, D.; Wang, W.; Dong, Y.J. Investigation of Al<sub>1-x</sub>Fe<sub>x</sub> amorphous powders prepared by ball milling. *Magn. Magn. Mater.* **1991**, *97*, 73–78.
17. Kuhrt, C.; Schultz, L. Magnetic properties of nanocrystalline mechanically alloyed Fe–M (M = Al, Si, Cu). *IEEE Trans. Magn.* **1993**, *29* (6), 2667–2669.
18. Jang, J.S.C.; Koch, C.C. Amorphous and disordering of the Ni<sub>3</sub>Al ordered intermetallic by mechanical milling. *J. Mater. Res.* **1990**, *5* (3), 498–510.
19. Liu, W.; McCormick, P.G. Synthesis of Sm<sub>2</sub>Co<sub>17</sub> nanoparticles by mechanochemical processing. *J. Magn. Magn. Mater.* **1999**, *195*, L279–L283.

20. Ding, J.; Tsuzuki, T.; McCormick, P.G. Ultrafine BaFe<sub>12</sub>O<sub>19</sub> powder synthesized by mechanochemical processing. *J. Magn. Magn. Mater.* **1998**, *177–181*, 931–932.
21. Buschow, K.H.J.; van der Kraan, A.M. Magnetic properties of amorphous Th<sub>1-x</sub>Fe<sub>x</sub> alloys. *Phys. Status Solidi, A* **1979**, *53*, 665–669.
22. Buschow, K.H.J.; van der Kraan, A.M. Magnetic properties of amorphous rare-earth alloys. *J. Magn. Magn. Mater.* **1981**, *22*, 220–226.
23. Reike, R.D. Preparation of highly reactive metal powders and their use in organic and organometallic synthesis. *Acc. Chem. Res.* **1977**, *10*, 301–306.
24. Corrias, A.; Ennas, G.; Licheir, G.; Marongiu, G.; Paschina, G. Amorphous metallic powders prepared by chemical reduction of metal ions with potassium borohydride in aqueous solution. *Chem. Mater.* **1990**, *2*, 363–366.
25. Mauger, A.; Escorne, M.; Paul-Boncour, V.; Percheron-Guegan, A.; Achard, J.C.; Barrault, J. Magnetic anisotropy and granulometry of Ni/CeO<sub>2</sub> catalyst. *J. Appl. Phys.* **1988**, *63* (8), 3236–3238.
26. Suslick, K.S.; Choe, S.-B.; Cichowlas, A.A.; Grinstaff, M.W. Sonochemical synthesis of amorphous iron. *Nature* **1991**, *353*, 414–416.
27. Lin, J.-G.; Su, Y.; Shan, J.; Yang, J.-H.; Fu, K.-J. Ultrafine powders produced by UV laser photolysis of iron penta-carbonyls. *Chin. J. Phys.* **1988**, *8* (3), 659–663.
28. Chen, D.; Xu, R. Hydrothermal synthesis and characterization of nanocrystalline  $\gamma$ -Fe<sub>2</sub>O<sub>3</sub> particles. *J. Solid State Chem.* **1998**, *137*, 185–190.
29. Wang, S.; Xin, H.; Qian, Y. Preparation of nanocrystalline Fe<sub>3</sub>O<sub>4</sub> by  $\gamma$ -ray radiation. *Mater. Lett.* **1997**, *33*, 113–116.
30. Kang, Y.; Risbud, S.; Rabolt, J.; Stroeve, P. Synthesis and characterization of nanometer-sized Fe<sub>3</sub>O<sub>4</sub> and  $\gamma$ -Fe<sub>2</sub>O<sub>3</sub> particles. *Chem. Mater.* **1996**, *8*, 2209–2211.
31. Chen, J.P.; Sorensen, C.M.; Klabunde, K.J.; Hadjipanayis, G.C.; Devlin, E.; Kostikas, A. Size-dependent magnetic properties of MnFe<sub>2</sub>O<sub>4</sub> fine particles synthesized by coprecipitation. *Phys. Rev.* **1996**, *54*, 9288–9296.
32. Chen, Q.; Rondinone, A.J.; Chakoumakos, B.C.; Zhang, Z.J. Synthesis of superparamagnetic MnFe<sub>2</sub>O<sub>4</sub> nanoparticles by coprecipitation. *J. Magn. Magn. Mater.* **1999**, *194*, 1–7.
33. Yokoyama, M.; Ohta, E.; Sato, T.; Sato, T. Magnetic properties of ultrafine particles and bulk materials of cadmium ferrite. *J. Magn. Magn. Mater.* **1998**, *183*, 173–180.
34. Sam, S.S.; Iton, L.; Suib, S.L.; Zhang, Z. Particle size determination of cobalt clusters in zeolite. *Chem. Mater.* **1989**, *1*, 529–534.
35. Dyakonov, A.J.; McCormick, B.J.; Kahol, P.K.; Hamdeh, H.H. Magnetic materials based on iron dispersed in graphitic matrices: part I. Superparamagnetic iron in an amorphous matrix. *J. Magn. Magn. Mater.* **1994**, *137*, 11–17.
36. Cowen, J.A.; Tsai, K.L.; Dye, J.L. Magnetic properties of Fe clusters in NaY zeolite. *J. Appl. Phys.* **1994**, *76* (10), 6567–6569.
37. García, J.L.; Lázaro, F.J.; Martínez, C.; Corma, A. Zeolite supported magnetic clusters. *J. Magn. Magn. Mater.* **1995**, *140–144*, 363–364.
38. Chatterjee, A.; Datta, A.; Giri, A.K.; Das, D.; Chakravorty, D. Iron nanoparticles in copper matrix prepared by sol-gel routes. *J. Appl. Phys.* **1992**, *72* (80), 3822–3834.
39. Otani, Y.; Miyajima, H.; Yamaguchi, M.; Nozaki, Y.; Manago, T.; Fagan, A.J.; Coey, J.M.D. Hydrogenation characteristics and magnetic properties of fine Ni particles coated with Pd. *J. Magn. Magn. Mater.* **1995**, *140–143*, 403–404.
40. Roy, S.; Das, D.; Chakravorty, D.; Agrawal, D.C. Magnetic properties of glass-metal nanocomposites prepared by the sol-gel route and hot pressing. *J. Appl. Phys.* **1993**, *74* (4), 4746–4749.
41. Vendange, V.; Colomban, Ph. Elaboration and thermal stability of (alumina, aluminosilicate/iron, cobalt, nickel) magnetic nanocomposites prepared through a sol-gel route. *Mater. Sci. Eng.* **1993**, *A168*, 199–203.
42. Pileni, M.P.; Ed. *Structure and Reactivity in Reverse Micelles*; Elsevier: Amsterdam, 1989.
43. Pileni, M.P. Reverse micelles as microreactors. *J. Phys. Chem.* **1993**, *97*, 6961–6973.
44. Langevin, D. Microemulsions. *Acc. Chem. Res.* **1988**, *21* (7), 255–260.
45. Rivas, J.; López-Quintela, M.A.; López-Pérez, J.A.; Liz, L.; Duro, R.J. First steps towards tailoring fine and ultrafine iron particles using microemulsions. *IEEE Trans. Magn.* **1993**, *29* (6), 2655–2657.
46. Chen, J.P.; Sorensen, C.M.; Klabunde, K.J.; Hadjipanayis, G.C. Enhanced magnetization of nanoscale colloidal cobalt particles. *Phys. Rev., B* **1995**, *51* (17), 11,527–11,532.
47. Lee, K.M.; Sorensen, C.M.; Klabunde, K.J.; Hadjipanayis, G.C. Synthesis and characterization of stable colloidal Fe<sub>3</sub>O<sub>4</sub> particles in water-in-oil microemulsions. *IEEE Trans. Magn.* **1992**, *28* (5), 3180–3182.
48. Liu, X.; Wang, J.; Gan, L.-M.; Ng, S.-C.; Ding, J. An ultrafine barium ferrite powder of high coercivity from water-in-oil microemulsion. *J. Magn. Magn. Mater.* **1998**, *184*, 344–354.
49. Wirth, S.; von Molnár, S.; Field, M.; Awschalom, D.D. Magnetism of nanometer-scale iron particle arrays (invited). *J. Appl. Phys.* **1999**, *85* (8), 5249–5254.
50. Wirth, S.; von Molnár, S. Thermally and field driven magnetization processes in nanometer-scale particle systems. *IEEE Trans. Magn.* **2001**, *37* (4), 2182–2184.
51. Fert, A.; Piraux, L. Magnetic nanowires. *J. Magn. Magn. Mater.* **1999**, *200*, 338–358.
52. Sun, S.; Murray, C.B. Synthesis of monodisperse cobalt nanocrystals and their assembly into magnetic superlattices (invited). *J. Appl. Phys.* **1999**, *85* (8), 4325–4330.
53. Puentes, V.F.; Krishnan, K.M. Synthesis, structural order and magnetic behavior of self-assembled  $\epsilon$ -Co

- nanocrystal arrays. *IEEE Trans. Magn.* **2001**, *37* (4), 2210–2213.
54. Li, S.P.; Lew, W.S.; Xu, Y.B.; Hirohata, A.; Samad, A.; Baker, F.; Bland, J.A.C. Magnetic nanoscale dots on colloid crystal surfaces. *Appl. Phys. Lett.* **2000**, *76* (6), 748–750.
  55. Petit, C.; Legrand, J.; Russier, V.; Pileni, M.P. Three dimensional arrays of cobalt nanocrystals: fabrication and magnetic properties. *J. Appl. Phys.* **2002**, *91* (3), 1502–1508.
  56. Yang, S.; Zhu, H.; Yu, D.; Jin, Z.; Tang, S.; Du, Y. Preparation and magnetic property of Fe nanowire array. *J. Magn. Magn. Mater.* **2000**, *222*, 97–100.
  57. Peng, Y.; Zhang, H.-L.; Pan, S.-L.; Li, H.-L. Magnetic properties and magnetization reversal of  $\alpha$ -Fe nanowires deposited in alumina film. *J. Appl. Phys.* **2000**, *87* (10), 7405–7408.
  58. Metzger, R.M.; Konovalov, V.V.; Sun, M.; Xu, T.; Zangari, G.; Xu, B.; Benakli, M.; Doyle, W.D. Magnetic nanowires in hexagonally ordered pores of alumina. *IEEE Trans. Magn.* **2000**, *36* (1), 30–35.
  59. Schwarzacher, W.; Kasyutich, O.I.; Evans, P.R.; Darbyshire, M.G.; Yi, Ge.; Fedosyuk, V.M.; Rousseaux, F.; Cambril, E.; Decanini, D. Metal nanostructures prepared by template electrodeposition. *J. Magn. Magn. Mater.* **1999**, *198-199*, 185–190.
  60. Scarani, V.; Doudin, B.; Ansermet, J.-P. The microstructure of electrodeposited cobalt-based nanowires and its effect on their magnetic and transport properties. *J. Magn. Magn. Mater.* **1999**, *205*, 241–248.
  61. Blythe, H.J.; Fedosyuk, V.M.; Kasyutich, O.I.; Schwarzacher, W. SQUID studies of Co–Cu heterogeneous alloy nanowires. *J. Magn. Magn. Mater.* **2000**, *208*, 251–254.
  62. Savas, T.A.; Farhoud, M.; Smith, H.I.; Hwang, M.; Ross, C.A. Properties of large-area nanomagnet arrays with 100 nm period made by interferometric lithography. *J. Appl. Phys.* **1999**, *85* (8), 6160–6162.
  63. Xu, Y.B.; Hirohata, A.; Lopez-Diaz, L.; Leung, H.T.; Tselepi, M.; Gradiner, S.M.; Lee, W.Y.; Bland, J.A.C. Micromagnetism in mesoscopic epitaxial Fe dot arrays. *J. Appl. Phys.* **2000**, *87* (9), 7019–7021.
  64. Wirth, S.; von Molnár, S. Magnetic interactions in nanometer-scale particle arrays grown onto permalloy films. *J. Appl. Phys.* **2000**, *87* (9), 7010–7012.
  65. Liu, X.; Fu, L.; Hong, S.; Dravid, P.V.; Mirkin, C.A. Arrays of magnetic nanoparticles patterned via “dip-pen” nanolithography. *Adv. Mater.* **2002**, *14* (3), 231–234.
  66. Burke, H.E. *Handbook of Magnetic Phenomena*; van Nostrand Reinhold Company: New York, 1986; 45–48.
  67. Kittel, G. Theory of the structure of ferromagnetic domains in films and small particles. *Phys. Rev.* **1946**, *70* (11–12), 965–971.
  68. Kittel, G. Physical theory of ferromagnetic domains. *Rev. Mod. Phys.* **1949**, *21* (4), 541–583.
  69. Kittle, C.; Galt, J.K.; Campbell, W.E. Crucial experiment demonstrating single domain properties of ferromagnetic powders. *Phys. Rev.* **1950**, *77*, 725.
  70. Cullity, B.D. *Introduction to Magnetic Materials*; Addison Wesley Publishing Company, Inc., 1972; 384–389, 410–414.
  71. Neel, L. Influence des fluctuations thermiques sur l’aimantation de grains ferromagnétique très fins. *Comput. Rend Acad. Sci.* **1949**, *228*, 664–666.
  72. Luborsky, F.E.; Paine, T.O. Coercive force and remanence of 25-A to 2000-A diameter cobalt, iron, and iron–cobalt alloy. *J. Appl. Phys.* **1960**, *31* (5), 68S–70S.
  73. Gong, W.; Li, H.; Zhao, Z.; Chen, J. Ultrafine particles of Fe, Co, and Ni ferromagnetic metals. *J. Appl. Phys.* **1991**, *69* (8), 5119–5121.
  74. Zhang, D.; Klabunde, K.J.; Sorensen, C.M. unpublished results.
  75. Chien, C.L.; Xiao, G.; Liou, S.H.; Taylor, J.N.; Levy, A. Magnetic granular Fe–(SiO<sub>2</sub>) solids. *J. Appl. Phys.* **1987**, *61* (8), 3311–3313.
  76. Childress, J.R.; Chien, C.L. Granular cobalt in a metallic matrix. *J. Appl. Phys.* **1991**, *70* (1), 5885–5887.
  77. Bean, C.P.; Livingston, J.D. Superparamagnetism. *J. Appl. Phys., Suppl.* **1959**, *30* (4), 120S–133S.
  78. Harrell, J.W.; Khapikov, A.F. Temperature dependence of magnetic viscosity and irreversible susceptibility for aligned Stoner–Wohlfarth particles. *J. Appl. Phys.* **2000**, *87* (9), 5708–5710.
  79. El-Hilo, M.; Uren, S.H.; O’Grady, K.; Popplewell, J. Effects of anisotropy field distribution on magnetic viscosity in particulate recording media. *IEEE Trans. Magn.* **1990**, *26* (1), 244–246.
  80. Kronmüller, H.; Fischer, R.; Bachmann, M.; Leineweber, T. Magnetization process in small particles and nanocrystalline materials. *J. Magn. Magn. Mater.* **1999**, *203*, 12–17.
  81. Chantrell, R.W.; Fearon, M.; Wohlfarth, E.P. The time-dependent magnetic behavior of fine particle system. *Phys. Status Solidi, A* **1986**, *97*, 213–221.
  82. Holmes, M.; O’Grady, K.; Popplewell, J. A study of Curie–Weiss behaviour in ferrofluids. *J. Magn. Magn. Mater.* **1990**, *85*, 47–50.
  83. Humfeld, K.D.; Giri, A.K.; Majetich, S.A.; Venturini, E.L. Time dependent properties of iron nanoparticles. *IEEE Trans. Magn.* **2001**, *37* (4), 2194–2196.
  84. Aharoni, A. Effect of a magnetic field on the superparamagnetic relaxation time. *Phys. Rev.* **1969**, *177*, 793–796.
  85. O’Grady, K.; Chantrell, R.W.; Popplewell, J.; Charles, S.W. Time dependent magnetization of a system of fine cobalt particles. *IEEE Trans. Mater.* **1981**, *17* (6), 2943–2945.
  86. Chien, C.L. Granular magnetic solids (invited). *J. Appl. Phys.* **1991**, *69* (8), 5267–5272.
  87. Street, R.; Woolley, J.C. Study of magnetic viscosity. *Proc. Phys. Soc. A* **1949**, *62*, 562.
  88. Morrish, A.H. *The Physical Principles of Magnetism*; John Wiley & Sons, Inc.: New York, 1965; 527 pp.
  89. Mills, D.L.; Maradudin, A.A. Some thermodynamic properties of a semi-infinite Heisenberg ferromagnet. *J. Phys. Chem. Solids* **1967**, *28*, 1855–1874.
  90. Mills, D.L. The effect of a surface on the low-temperature properties of the Heisenberg ferromagnet. *I. Solid State Phys.* **1971**, *4*, 28–33.

91. Mills, D.L. The effect of a surface on the low-temperature properties of the Heisenberg ferromagnet. II. *Solid State Phys.* **1972**, *4*, 95–100.
92. Binder, K.; Rauch, H.; Wildpaner, V. Monte Carlo calculation of the magnetization of superparamagnetic particles. *J. Phys. Chem. Solids* **1970**, *31*, 391–397.
93. Wildpaner, V. Monte-Carlo study of small magnetic particles. *Z. Phys. A* **1974**, *270*, 215–223.
94. Hendriksen, P.V.; Linderroth, S.; Lindgård, P.-A. Finite-size modification of the magnetic properties of clusters. *Phys. Rev., B* **1993**, *48* (10), 7259–7273.
95. Pierce, D.T.; Celotta, R.J.; Unguris, J.; Siegmann, H.C. Spin-dependent elastic scattering of electrons from a ferromagnetic glass, Ni<sub>40</sub>Fe<sub>40</sub>B<sub>20</sub>. *Phys. Rev., B* **1982**, *26*, 2566–2574.
96. Linderroth, S.; Balcells, L.; Labarta, A.; Tejada, J.; Hendriksen, P.V.; Sethi, S.A. Magnetization and Mössbauer studies of ultrafine Fe–C particles. *J. Magn. Magn. Mater.* **1993**, *124*, 269–276.
97. Xiao, G.; Chien, C.L. Temperature dependence of spontaneous magnetization of ultrafine Fe particles in Fe–SiO<sub>2</sub> granular solids. *J. Appl. Phys.* **1987**, *61*, 3308–3310.
98. Chen, J.P.; Sorensen, C.M.; Klabunde, K.J.; Hadjipanayis, G.C.; Devlin, E.; Kostikas, A. Size-dependent magnetic properties of MnFe<sub>2</sub>O<sub>4</sub> fine particles synthesized by coprecipitation. *Phys. Rev., B* **1996**, *54*, 9288.
99. Billas, I.M.L.; Châtelain, A.; de Heer, W.A. Magnetism from the atom to the bulk in iron, cobalt, and nickel clusters. *Science* **1994**, *265*, 1682–1684.
100. Douglas, D.C.; Cox, A.J.; Bucher, J.P.; Bloomfield, L.A. Magnetic properties of free cobalt and gadolinium clusters. *Phys. Rev., B* **1993**, *47* (19), 12,874–12,889.
101. Klabunde, K.J.; Stark, J.V.; Koper, O.; Mohs, C.; Khaleel, A.; Glavee, G.; Zhang, D.; Sorensen, C.M.; Hadjipanayis, G.C. Chemical Synthesis of Nanophase Materials. In *Nanophase Materials*; Hadjipanayis, G.C., Siegel, R.W., Eds.; Kluwer Academic Publishers: Dordrecht; Boston, 1994; 1–9.
102. Zhang, D.; Klabunde, K.J.; Sorensen, C.M.; Hadjipanayis, G.C. Magnetization temperature dependence in iron nanoparticles. *Phys. Rev., B* **1998**, *58* (21), 14,167–14,170.
103. Klabunde, K.J.; Zhang, D.; Glavee, G.N.; Sorensen, C.M.; Hadjipanayis, G.C. Encapsulated nanoparticles of iron metal. *Chem. Mater.* **1994**, *6*, 784–787.
104. Zhang, D.; Klabunde, K.J.; Sorensen, C.M.; Hadjipanayis, G.C. Synthesis of nanoscale magnetic metal particles encapsulated in magnesium fluoride and the properties of these materials. *High Temp. Mater. Sci.* **1997**, *36*, 135–154.
105. Banerjee, S.; Roy, S.; Chen, J.W.; Chakravorty, D. Magnetic properties of oxide-coated iron nanoparticles synthesized by electrodeposition. *J. Magn. Magn. Mater.* **2000**, *219*, 45–52.
106. Herpin, A. *Theorie du magnetisme*; Presses Universitaires de France: Paris, 1968; 3327–3329.
107. Schaefer, H.-E.; Kisker, H.; Kronmüller, H.; Würschum, R. Magnetic properties of nanocrystalline nickel. *Nanostruct. Mater.* **1992**, *1*, 523–529.
108. Chou, S.Y.; Wei, M.S.; Krauss, P.R.; Fischer, P.B. Single-domain magnetic pillar arrays of 35 nm diameter and 65 Gbits/in.<sup>2</sup> density for ultrahigh density quantum magnetic devices. *J. Appl. Phys.* **1994**, *76* (10), 6673–6675.
109. Wei, M.S.; Chou, S.Y. Size effects on switching field of isolated and interactive arrays of nanoscale single-domain Ni bars fabricated using electron-beam nanolithography. *J. Appl. Phys.* **1994**, *76* (10), 6679–6681.
110. New, R.M.H.; Pease, R.F.W.; White, R.L. Lithography patterned single-domain cobalt islands for high-density magnetic recording. *J. Magn. Magn. Mater.* **1996**, *155*, 140–145.
111. Cowburn, R.P. Properties variation with shape in magnetic nanoelements. *J. Phys., D, Appl. Phys.* **2000**, *33*, R1–R16.
112. He, L.; Wang, F.Z.; Mapps, D.J.; Clegg, W.W.; Wilton, D.T.; Robinson, P. Size and shape effects of patterned polycrystalline islands. *IEEE Trans. Magn.* **1999**, *35* (5), 3508–3510.
113. Coey, J.M.D. Noncollinear spin arrangement in ultrafine ferromagnetic crystallites. *Phys. Rev. Lett.* **1971**, *27* (17), 1140–1142.
114. Gazeau, F.; Bacri, J.C.; Gendron, F.; Perzynski, R.; Raikher, Yu.L.; Stepanov, V.I.; Dubois, E. Magnetic resonance of ferrite nanoparticles: evidence of surface effects. *J. Magn. Magn. Mater.* **1998**, *186*, 175–187.
115. Kodama, R.H.; Berkowitz, A.E.; McNiff, E.J.; Finer, S. Surface spin disorder in ferrite nanoparticles. *J. Appl. Phys.* **1997**, *81* (8), 5552–5557.
116. Morrish, A.H.; Haneda, K. Magnetic structure of small NiFe<sub>2</sub>O<sub>4</sub> particles. *J. Appl. Phys.* **1981**, *52* (3), 2496–2498.
117. Goya, G.F.; Rechenberg, H.R.; Jiang, J.Z. Magnetic irreversibility and relaxation in CuFe<sub>2</sub>O<sub>4</sub> nanoparticles. *J. Magn. Magn. Mater.* **2000**, *218*, 221–228.
118. Gangopadhyay, S.; Hadjipanayis, G.C.; Sorensen, C.M.; Klabunde, K.J. Effect of oxide layer on the hysteresis behavior of fine Fe particles. *J. Appl. Phys.* **1991**, *70* (10), 5888–5890.
119. Fiorani, D.; Dormann, J.L.; Cherkaoui, R.; Tronc, E.; Lucari, F.; D’Orazio, F.; Spinu, L.; Nogues, M.; Garcia, A.; Testa, A.M. Collective magnetic state in nanoparticles systems. *J. Magn. Magn. Mater.* **1999**, *196–197*, 143–147.
120. Zysler, R.D.; Ramos, C.A.; Biasi, E.D.; Romero, H.; Ortega, A.; Fiornia, D. Effect of interparticle interactions in (Fe<sub>0.26</sub>Ni<sub>0.74</sub>)<sub>50</sub>B<sub>50</sub> magnetic nanoparticles. *J. Magn. Magn. Mater.* **2000**, *221*, 37–44.
121. Mørup, S.; Christiansen, G. Influence of magnetic anisotropy on the superferromagnetic ordering in nanocomposites. *J. Appl. Phys.* **1993**, *73* (10), 6955–6957.
122. Xiao, J.Q.; Jiang, J.S.; Chien, C.L. Giant magnetoresistive properties in granular transition metals. *IEEE Trans. Magn.* **1993**, *29* (6), 2688–2693.
123. Chien, C.L. Giant Magneto-transport Properties in Granular Magnetic Systems. In *Nanophase Materials*; Hadjipanayis, G.C., Siegel, R.W., Eds.; Kluwer Academic Publishers: Netherlands, 1994; 555–568.
124. Baibich, M.N.; Broto, J.M.; Fert, A.; Nguyen Van Dau, F.; Petroff, F. Giant magnetoresistance of (001)

- Fe/(001) Cr magnetic superlattices. *Phys. Rev. Lett.* **1988**, *61* (21), 2472–2475.
125. Berkowitz, A.E.; Mitchell, J.R.; Carey, M.J.; Young, A.P.; Zhang, S.; Spada, F.E.; Parker, F.T.; Hutten, A.; Thomas, G. Giant magnetoresistance in heterogeneous Cu–Co alloys. *Phys. Rev. Lett.* **1992**, *68* (25), 3745–3748.
  126. Xiao, J.Q.; Jiang, J.S.; Chien, C.L. Giant magnetoresistance in nonmultilayer magnetic systems. *Phys. Rev. Lett.* **1992**, *68* (25), 3749–3752.
  127. Xiong, P.; Xiao, G.; Wang, J.Q.; Xiao, J.Q.; Jiang, J.S.; Chien, C.L. Extraordinary Hall effect and giant magnetoresistance in the granular Co–Ag systems. *Phys. Rev. Lett.* **1992**, *69* (22), 3220–3223.
  128. Xiao, G.; Wang, J.Q.; Xiong, P. Giant magnetoresistance and anomalous Hall effect in Co–Ag and Fe–Cu, Ag, Au, Pt granular alloys. *IEEE Trans. Magn.* **1993**, *29* (6), 2694–2699.
  129. Song, W.; Yang, R. Giant magnetoresistance in magnetic granular systems. *Physica, B* **2000**, *279*, 181–184.
  130. Kuzminski, M.; Slawska-Waniewska, A.; Lachowicz, H.K.; Knobel, M. The effect of particle size and surface-to-volume ratio distribution on giant magnetoresistance (GMR) in melt-spun Cu–Co alloys. *J. Magn. Magn. Mater.* **1999**, *205*, 7–13.
  131. Xi, L.; Zhang, Z.-Z.; Wang, J.-B.; Li, C.-X.; Li, F.-S.; Ge, S.-H.; Xu, T.; Yang, S.-R. The influence of microstructure on tunneling magnetoresistance in Fe–SiO<sub>2</sub> granular films. *J. Phys., D, Appl. Phys.* **2000**, *33*, 621–626.
  132. Ge, S.H.; Zhang, S.B.; Chi, J.H.; Zhang, Z.G.; Li, C.X.; Gan, R.J. The giant magnetoresistance effect of Fe–Al–O nano-structured granular films. *J. Phys. D: Appl. Phys.* **2000**, *33*, 917–920.
  133. Itoh, H.; Nishimura, N.; Inoue, J. A theory of tunnel magnetoresistance through a magnetic grain boundary. *J. Magn. Magn. Mater.* **2002**, *240*, 121–123.
  134. Chudnovsky, E.M.; Gunther, L. Quantum theory of nucleation in ferromagnets. *Phys. Rev., B* **1988**, *37* (16), 9455–9459.
  135. Chudnovsky, E.M.; Gunther, L. Quantum tunneling of magnetization in small ferromagnetic particles. *Phys. Rev. Lett.* **1988**, *60* (8), 661–664.
  136. Garg, A.; Kim, G.-H. Dissipation in microscopic magnetization tunneling. *Phys. Rev. Lett.* **1989**, *63* (22), 2512–2515.
  137. Chudnovsky, E.M. Magnetic tunneling. *J. Magn. Magn. Mater.* **1995**, *140–141*, 1821–1824.
  138. Tejada, J.; Zhang, X.X. Experiments in quantum magnetic relaxation. *J. Magn. Magn. Mater.* **1995**, *140–141*, 1815–1818.
  139. Tejada, J.; Balcells, Ll.; Linderoth, S.; Perzynski, R.; Rigau, B.; Barbara, B.; Bacri, J.C. Quantum tunneling of magnetization in single domain particles. *J. Appl. Phys.* **1993**, *73* (10), 6952–6954.
  140. Tajada, J.; Zhang, X.X. Macroscopic Quantum Tunneling in Ferro and Antiferromagnetic Nanoscale Particles. In *Nanophase Materials*; Hadjipanayis, G.C., Siegel, R.W., Eds.; Kluwer Academic Publishers: Netherlands, 1994; 683–690 and references therein.
  141. Kodama, R.H. Magnetic nanoparticles. *J. Magn. Magn. Mater.* **1999**, *200*, 359–372.
  142. Batlle, X.; García del Muro, M.; Labarta, A. Interaction effects and energy barrier distribution on the magnetic relaxation of nanocrystalline hexagonal ferrites. *Phys. Rev., B* **1997**, *55* (10), 6440–6445.
  143. Peng, D.L.; Sumiyama, K.; Hihara, T.; Yamamuro, S. Enhancement of magnetic coercivity and macroscopic quantum tunneling in monodispersed Co/CoO cluster assemblies. *Appl. Phys. Lett.* **1999**, *75* (24), 3856–3858.
  144. Friedman, J.R.; Sarachik, M.P.; Tejada, J.; Ziolo, R. Macroscopic measurement of resonant magnetization tunneling in high-spin molecules. *Phys. Rev. Lett.* **1996**, *76* (20), 3830–3833.



# Magnetic Nanomaterials: Nonconventional Synthesis and Chemical Design

Luminita Patron

Ioana Mindru

*I.G. Murgulescu Institute of the Romanian Academy, Bucharest, Romania*

Gabriela Marinescu

*Institute of Physical Chemistry, I.G. Murgulescu Institute of the Romanian Academy, Bucharest, Romania*

## INTRODUCTION

The synthesis of nanomaterials presents a great interest not only for elucidation of basic research problems, but also for practical applications. Because of the presence of very small size nanoparticles, these materials acquire new properties that differ from those of bulk materials of the same composition.<sup>[1]</sup> As a result of the special magnetic properties of small particles, nanomaterials find promising use in various applications: ferrofluids, information storage media, magnetic refrigeration, magnetic resonance imaging, etc.<sup>[2]</sup>

Ferrites—magnetic materials—are composed of  $\alpha$ -Fe<sub>2</sub>O<sub>3</sub> and another metallic oxide MO<sub>n</sub>. The general formula of ferrites is  $x\text{MO}_n \cdot y\text{Fe}_2\text{O}_3$ . If M is a divalent metal ion with ionic radius,  $r < 1 \text{ \AA}$ , a spinel ferrite is formed:  $\text{MO} \cdot \text{Fe}_2\text{O}_3$  ( $n = 1$ ). The “spinel structure” proceeds from the natural combination MgAl<sub>2</sub>O<sub>4</sub> called “spinel.” Spinel ferrite structure consists of a cubic close-packed oxygen arrangement, in which the cations reside on tetrahedral and octahedral interstices. The unit cell is obtained by the union of two face-centered cubic oxygen sublattices along each of three directions. This results in 64 tetrahedral sites (A) and 32 octahedral sites (B). Only 8 sites A and 16 sites B are occupied by cations in a stoichiometric spinel. The spinel compounds mainly belong to the space group Fd3m and the lattice parameter is  $\approx 8.5 \text{ \AA}$ . Occupation of all the tetrahedral sites with divalent metal ions yields a normal spinel structure, while occupation of the octahedral sites with the divalent metal ions yields an inverse spinel structure. Ferrites can adopt both a normal spinel structure ( $\text{M}^{2+} = \text{Zn}^{2+}, \text{Cd}^{2+}, \text{Mn}^{2+}$ ) and an inverse spinel one ( $\text{M}^{2+} = \text{Fe}^{2+}, \text{Co}^{2+}, \text{Ni}^{2+}, \text{Cu}^{2+}$ ). Ferrites constitute a broad and important class of magnetic ceramic materials, with important technological applications which cover electronic and electrotechnical devices, heterogeneous catalysts, cement products, paints, and plastics.<sup>[3,4]</sup> The magnetic properties of ferrites (magnetic saturation, magnetization, and coercivity) change

drastically when the size of particles becomes very small.<sup>[5]</sup> For this reason, the idea that synthesizing ferrites with nanometer-sized particles (nanoferrites) would help obtaining materials with superior magnetic properties is of great interest.<sup>[6,7]</sup>

## THE COMPLEXATION METHOD FOR SYNTHESIS OF FERRITES

The method of preparation plays a very important role in determining the chemical, structural, and magnetic properties of spinel ferrites. Ferrites are commonly produced by the ceramic technique that involves high-temperature solid-state reactions between the constituent oxides, carbonates, or oxalates. The particles obtained by the ceramic method are large and of non-uniform size. The products obtained by sintering are, in most cases, nonreproducible in terms of their magnetic properties.<sup>[8–11]</sup> Because the average particle sizes and the particle size distribution of nanoferrites affect very much their magnetic properties, the control of these parameters is crucial. To overcome the difficulties arising from the ceramic route, wet chemical methods, such as coprecipitation,<sup>[6,7,12–14]</sup> hydrothermal processing,<sup>[4,15,16]</sup> and sol-gel technique,<sup>[17]</sup> were designed and employed. The control of colloid chemistry properties that determine the stability of microemulsions and self-assembling of nanoparticles is particularly recommended for the synthesis of nanoferrites.<sup>[2,18–21]</sup> The essential requirements of obtaining well-controlled uniformity and high-purity materials make these chemical methods the preferred choice.

The nature of precursors plays a very important role in the synthesis of nanoferrites. In many cases, the use of a particular precursor may affect the structure of materials at the molecular level, thus improving the homogeneity and increasing the dispersion of resulted products. Considerable efforts have been made to develop chemical synthesis routes that yield precursors having two or more metal ions included in the same

molecular entity. Synthesis routes, in which polynuclear coordination compounds with two or more metal ions are formed as precursors, are preferred because these compounds are capable of giving mixed oxides by thermal decomposition.<sup>[22–24]</sup>

Synthesis of nanoferrites by thermal decomposition of polynuclear complex compounds is a non-conventional chemical method that belongs to “chimie douce” (soft chemistry). This method is sometimes referred to as the complexation method for synthesis of ferrites.

Compared to classical methods, the complexation method offers a series of advantages:

- The distribution of chemical species is homogeneous at the molecular level.
- The decomposition of coordination compounds is simultaneous with, or is immediately followed by, formation of a ferrite.
- The temperature of ferrite formation is much lower than the temperature range of ceramic processes.
- Because of the relatively low temperature of formation, the ferrites obtained through the complexation method are characterized by ultrafine particle granulation and high specific surface areas.

Over the past 20 years, the chemistry of polynuclear coordination compounds has developed spectacularly and now it could be regarded as a well-established branch of coordination chemistry. In spite of all this progress, information regarding the use of polynuclear coordination compounds as precursors of ferrites is limited.

The successful application of the complexation method for synthesis of nanoferrites requires two important steps:

- A detailed study on the formation of the polynuclear complex compounds to establish the parameters that influence the synthesis, such as the combination ratio of elements, the nature of the ligand, the pH of the reaction medium, the temperature, etc.
- A study on the mechanism of their thermal decomposition, accompanied by the characterization of the obtained ferrites.

The polynuclear coordination compounds, which may successfully be used as precursors for ferrite formation, should generate by decomposition only volatile products. The ligands that largely satisfy this requirement are the anions of polycarboxylic and polyhydroxy carboxylic acids: citrate, acetate, oxalate, etc. Thus there are various variants of the complexation method for ferrite synthesis encountered in the literature, which are named according to the acid employed as the complexing agent (e.g., citrate, acetate, oxalate, and malate methods). In [Scheme 1](#), these alternative methods are presented together with the self-propagating

combustion. We consider this last method, in which the combustion occurs in situ, together with the group of methods based on thermal decomposition of polynuclear coordination compounds.

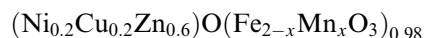
## FERRITES OBTAINED BY THERMAL DECOMPOSITION OF POLYNUCLEAR COORDINATION COMPOUNDS

### Citrate Method

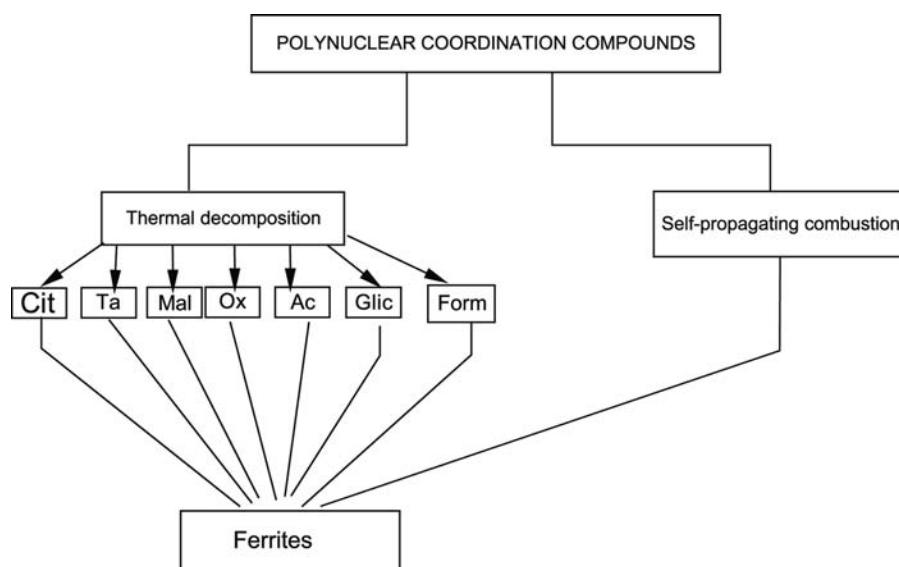
Synthesis of ultrafine ferrites by the citrate precursor technique is the only synthesis route that has enjoyed so far technological applications.<sup>[25–27]</sup> It requires the use of precursor solutions containing the metal ions and citric acid in the desired ratio. Dehydration is carried out in revolving evaporators under a pressure of a few millimeters of Hg at 70°C; it is stopped before the viscosity becomes high. Dehydration is completed by drying for an additional 3 to 24 hr in a vacuum oven at temperatures below 100°C. This procedure yields transparent glasses, uniformly colored, completely amorphous to X-ray diffraction. The materials present no evidence of non-homogeneity. Moderate temperatures are sufficient for the pyrolysis of the precursors (500–600°C). When the expected mixed oxides do not form at this temperature, pyrolysis is conducted at, or above, the lowest temperature necessary for product formation. Thus the  $\text{Fe}_2\text{Mn}_{0.5}\text{Zn}_{0.5}\text{O}_4$  nanoferrite was obtained after 2 hr of thermal treatment at 500°C. The X-ray pattern indicated formation of a pure, perfectly homogeneous phase, with particle sizes in the range between 30 and 100 Å.<sup>[25]</sup>

Verma et al.<sup>[28]</sup> have prepared by this method high-resistivity nickel–zinc ferrites:  $\text{Ni}_{1-x}\text{Zn}_x\text{Fe}_2\text{O}_4$  with  $x = 0.2, 0.35, 0.5,$  and  $0.6$ . They observed that these Ni–Zn ferrites have resistivity  $\geq 10^8 \Omega \text{ cm}$  which is higher by 2 orders of magnitude than that reported ( $\leq 10^6 \Omega \text{ cm}$ ) for ferrites prepared by the conventional ceramic method. This is attributed to better purity and homogeneity of these ferrite powders.

An alternative of this method was proposed for Ni–Cu–Zn ferrite powders with compositions:<sup>[29]</sup>



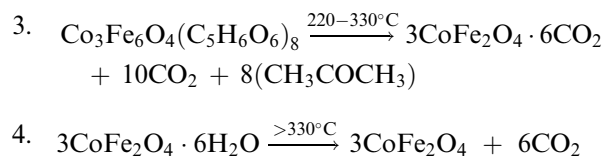
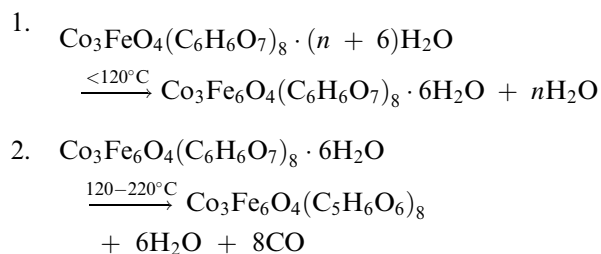
( $x = 0, 0.02, 0.04, 0.06$ ). A mixed solution containing metal nitrates and citric acid in a 1:1 ratio (pH value of the solution was adjusted to  $\sim 7$  using ammonia) was poured into a dish and heated at  $\sim 135^\circ\text{C}$  until it transformed into a dried gel. The dried gel burned in a self-propagating combustion to form a loose ash. The synthesized nanoferrites powders could be sintered by heating for 5 hr at  $900^\circ\text{C}$  in air. These nanoferrites are characterized by high magnetic permeability.



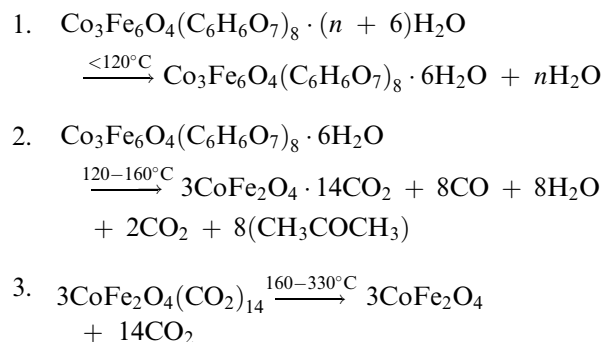
Cit = citrate method  
 Ta = tartarate method  
 Mal = malonate method  
 Ox = oxalate method  
 Ac = acetate method  
 Gli = glycolate method  
 Form = formate method

**Scheme 1** Polynuclear coordinator compounds-precursors for ferrites.

Attempts to separate complex citrates from the reaction medium were very difficult because of their high solubility. Prasad, Vijayalakshmi, and Gajbhiye [30] have succeeded the isolation of a citrate precursor with the general formula  $\text{Co}_3\text{Fe}_6\text{O}_4(\text{C}_6\text{H}_6\text{O}_7)_8 \cdot 6\text{H}_2\text{O}$ . Ultrafine particles of  $\text{CoFe}_2\text{O}_4$  were obtained by decomposition of this precursor. The citrate polynuclear compound was characterized through elemental chemical analysis and IR spectrum. It was difficult to predict the bonding positions of metal ion sites with the citric acid. Therefore based on thermal analyses, chemical analyses, and gas analyses and X-ray diffraction (XRD), infrared (IR), and nuclear magnetic resonance (NMR) data, the authors have proposed the following mechanism. The decomposition of the citrate complex compound occurs in one or two major steps, depending on the heating rate in static or in flowing air atmosphere. For heating rate of  $5^\circ\text{C}/\text{min}$ :



For heating rate of  $10^\circ\text{C}/\text{min}$



When the heating rate is  $5^\circ\text{C}/\text{min}$ , the hexahydrate cobalt iron citrate precursor was isolated by removing the lattice water around  $120^\circ\text{C}$ . The first step represents the major reaction in the thermal decomposition of the citrate precursor. During this process, the metastable acetonedicarboxylate complex,

$\text{Co}_3\text{Fe}_6\text{O}_4\text{-(C}_5\text{H}_6\text{O}_6)_8$ , is formed. In the second step, the complete internal conversion of carboxylate groups, methylene, and hydroxyl groups takes place to form acetone and  $\text{CO}_2$  gas. In the IR spectrum of this intermediate compound, the characteristic bands of  $\nu_{\text{sym}}\text{CH}$  ( $\sim 2900\text{ cm}^{-1}$ ),  $\nu_{\text{asym}}\text{COO}$  ( $1570\text{ cm}^{-1}$ ), and  $\nu_{\text{sym}}\text{COO}$  ( $1400\text{ cm}^{-1}$ ) are absent. Some amount of  $\text{CO}_2$  gas is adsorbed on the  $\text{CoFe}_2\text{O}_4$  lattice because of the large surface area.

When the heating rate is  $10^\circ\text{C}/\text{min}$ , the first and the second steps occur simultaneously at a lower temperature ( $120\text{--}160^\circ\text{C}$ ). At the same time, a large amount of gases ( $\text{CO}$ ,  $\text{CO}_2$ , water vapors, and acetone) is released. The compound  $3(\text{CoFe}_2\text{O}_4) \cdot 14\text{CO}_2$  obtained was X-ray-amorphous. The adsorbed  $\text{CO}_2$  gas disappears only by heating at  $250^\circ\text{C}$  for more than 1 day.

The complete crystallization of the  $\text{CoFe}_2\text{O}_4$  amorphous phase occurs above  $280^\circ\text{C}$ , as confirmed by its XRD pattern. This crystalline phase  $\text{CoFe}_2\text{O}_4$  shows the crystallite size in the range of  $7.5\text{--}34\text{ nm}$ .

Sainamthip and Amarakoon<sup>[31]</sup> synthesized ultra-fine ferrite powders (Mn–Zn ferrite) by alcoholic dehydration of citrate/formate solution. This method consists of spraying or atomizing an aqueous citrate/formate solution containing the metal ions in the desired ratio into a bath of a hygroscopic liquid (acetone or alcohol), which rapidly removes water. A bright yellow citrate complex is obtained. Thermal decomposition of this precursor yields a fine, high-purity, homogeneous ferrite. The success of powder preparation depends on the water content in the starting solution, the pH of the solution, the amount of alcohol used, and the drying step. Low-temperature calcination ( $350^\circ\text{C}$  in air) for decomposition, followed by calcinations at  $900^\circ\text{C}$  for 4 hr in an enclosed vessel, leads to submicrometer-sized ferrite powders with an important degree of agglomeration.

The citrate method is simple and inexpensive. It is a promising method for the synthesis of high-performance nanoferrites.

### Tartarate Method

The capacity of tartaric acid to form coordination compounds is well known. This capacity originates in the following structural characteristics:

- The presence of four potentially ionizable H atoms.
- The presence in the molecule of several coordination positions.
- The tendency of molecular association because of the polydentate nature of the tartarate anion.

Although the factors that influence the structure of the complex species are known, their individual

contribution in assuming one structure or another is hard to establish. Tapscott, Belford, and Paul<sup>[32]</sup> published an exhaustive study on the anionic homodinuclear species in which two metallic ions are bonded in bridged position through two tartarate tetradentate ligands. In the literature, there are relatively few studies concerning the coordination compounds in solid state with tartaric acid as ligand.<sup>[33]</sup> The multiple function of the ligand is responsible for its capacity to form heteropolynuclear coordination compounds.<sup>[34]</sup>

To establish to what extent such heteropolynuclear coordination compounds may represent the raw materials for spinel ferrites formation, the following systems have been studied:<sup>[35]</sup>

$2\text{Fe(III)} : \text{M(II)} : \text{tartaric acid}$

$\text{M(II)} = \text{M(II)}, \text{Co(II)}, \text{Zn(II)}$

and

$2\text{Fe(III)} : [0.5\text{M(II)} : 0.5\text{M'(II)}] : \text{tartaric acid}$

$\text{M(II)} = \text{Co(II)}; \text{M'(II)} = \text{Zn(II)}$

$\text{M(II)} = \text{Co(II)}; \text{M'(II)} = \text{Mn(II)}$

The study of the chemistry solution of the tartaric acid has evidenced the dependence of the nature of the polymeric species on the pH of the reaction medium. For this reason, the behavior of the above systems depended on the selected reaction medium pH (pH = 1–2 and pH = 6–7, respectively) at constant  $\text{M}^{n+}/\text{tartaric acid}$  ratio [ $2\text{Fe(III)}:1\text{M(II)}:4\text{-tartaric acid}$ ].

The following types of compounds were obtained:

pH = 1 – 2

$[\text{Fe(III)}_2\text{M(II)}(\text{C}_4\text{O}_6\text{H}_3)_2(\text{C}_4\text{O}_6\text{H}_4)] \cdot x\text{H}_2\text{O}$

$\text{M(II)} = \text{Co(II)}, \text{Zn(II)}, \text{Mn(II)}$

$[0.5\text{M(II)} + 0.5\text{M'(II)}] : \text{Co(II)} + \text{Zn(II)};$

$\text{Co(II)} + \text{Mn(II)}$

$x = 2 - 4$

pH = 6 – 7

$(\text{NH}_4)_2[\text{Fe(III)}_2\text{M(II)}(\text{C}_4\text{O}_6\text{H}_3)_2(\text{C}_4\text{O}_6\text{H}_2)] \cdot x\text{H}_2\text{O}$

$\text{M(II)} = \text{Mn(II)}, \text{Co(II)}, \text{Zn(II)}$

$[0.5\text{M(II)} + 0.5\text{M'(II)}] = \text{Co(II)} + \text{Zn(II)};$

$\text{Co(II)} + \text{Mn(II)}$

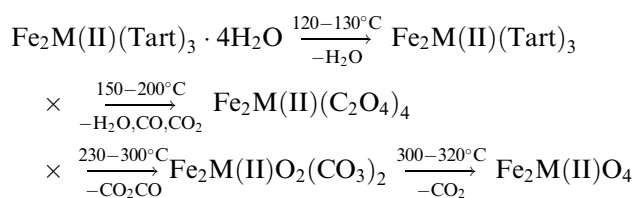
$x = 2 - 4$

The formula of these compounds was established by correlating elemental chemical analysis with physicochemical measurements (IR, UV-Vis spectra, and magnetic and thermogravimetric runs).

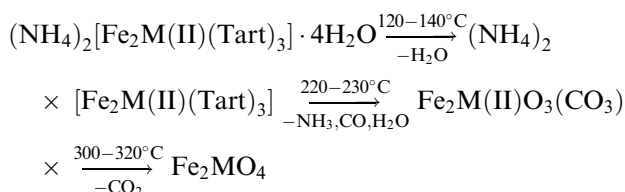
The IR spectra recorded for the two types of compounds suggest the coordination of both carboxylic groups existing in the molecule of tartaric acid at metal ions. The band at  $1750\text{ cm}^{-1}$  of tartaric acid, assigned to  $\nu_{\text{C=O}}$  is replaced in the spectra of the compounds by the two bands  $\nu_{\text{as(OCO)}}$  and  $\nu_{\text{s(OCO)}}$ . The analysis of these spectra within  $1000\text{--}1100\text{ cm}^{-1}$  range shows a considerable difference between the spectrum of free tartaric acid and those of the two compounds. In the tartaric acid spectrum, the peak at  $\sim 1097\text{ cm}^{-1}$  is assigned to the C-O stretching vibration of OH secondary group. In the spectra of complexes, this band splits and shifts toward lower frequencies ( $1085\text{--}1059\text{ cm}^{-1}$ ). The splitting could be assigned to a different bonding of the two secondary OH groups present in the molecule of the acid. Thus one can advance the hypothesis that the two secondary OH groups coordinate at two different metal ions.

The analysis of electronic spectra and their second derivatives recorded within  $9000\text{--}50000\text{ cm}^{-1}$  for both types of compounds supplied data about the stereochemistry of metal ions. For example, the spectrum of  $(\text{NH}_4)_2[\text{Fe}_2^{\text{III}}\text{Co}^{\text{II}}(\text{C}_4\text{O}_6\text{H}_3)_2(\text{C}_4\text{O}_6\text{H}_2)] \cdot x\text{H}_2\text{O}$  shows one low intensity absorption band at about  $11000\text{ cm}^{-1}$  which may be assigned to the spin-forbidden transition  ${}^6\text{A}_{1g} \rightarrow {}^4\text{T}_{1g}$  for Fe(III)( $d^5$ ) ion, in an octahedral high spin configuration. Another band at  $\sim 18560\text{ cm}^{-1}$  could be assigned to  ${}^4\text{T}_{1g} \rightarrow {}^4\text{T}_{1g}(\text{P})(\nu_3)$  transition, characteristic to Co(II) ion in a high spin octahedral configuration. All compounds are paramagnetic. The experimental values of magnetic moments are lower than the theoretical ones. This difference could be assigned to the antiferromagnetic interaction between metal ions.

The thermal decomposition of the intermediate complex compounds was further studied. For the first type of compounds, the following scheme was advanced:

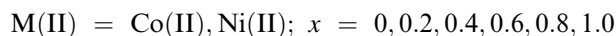


For the compounds from the second group, the following scheme was suggested:

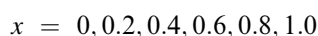
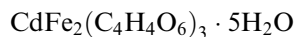


The spinel ferrites were formed at a temperature above  $320\text{--}350^\circ\text{C}$ , but the crystallinity was quite low. An additional thermal treatment was required to obtain a good crystallinity product (e.g., 7 hr at  $700^\circ\text{C}$  for  $\text{Fe}_2\text{ZnO}_4$ ; 5 hr at  $800^\circ\text{C}$  for  $\text{Fe}_2\text{CoO}_4$ ) (Fig. 1).

Also used for obtaining of mixed cadmium-cobalt and cadmium-nickel ferrispinel:<sup>[36,37]</sup>



the following tartarates complex precursors:



were obtained by adding a sodium tartarate solution to the mixture of metal-sulfate solutions. The pH of the reaction medium was adjusted to a low-enough value ( $\text{pH} < 6$ ). Acetone was added to ensure high yield of compounds. In addition, acetone influences

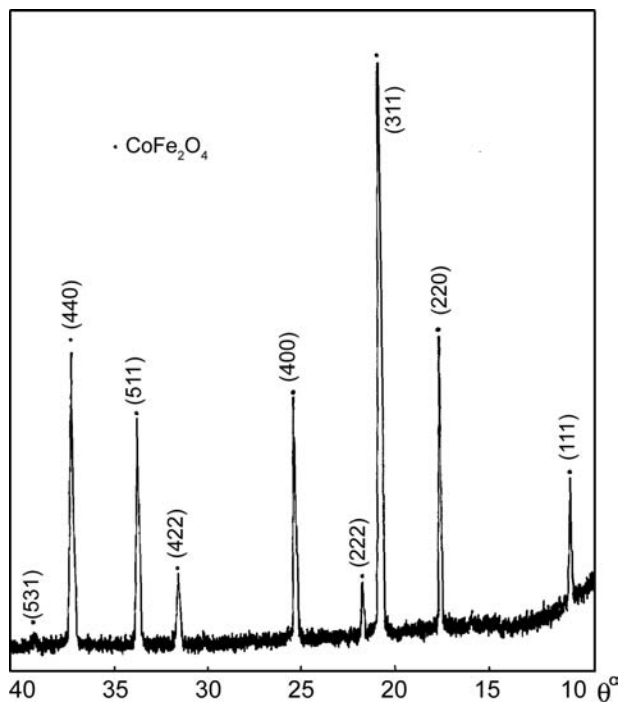


Fig. 1 Powder XRD patterns of the final thermolysis products of  $(\text{NH}_4)_2[\text{Fe}_2\text{Co}(\text{C}_4\text{O}_6\text{H}_4)_3(\text{OH})_4] \cdot 4\text{H}_2\text{O}$ .

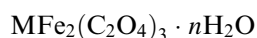
the homogeneity and the stoichiometry of the fine-grained powders. These tartarates precursors were decomposed and calcined for 2 hr at 700°C and slowly cooled afterward (3°C/min) to room temperature. The polycrystalline powders were reground and recalcined for 2 hr at 700°C. The X-ray diffraction patterns of all the compositions indicated the formation of a single-spinel phase with cubic structure. Mean crystallite size varied in the range of 24–35 nm ± 10%. The formation of these ferrispinel was also studied by electrical conductivity, thermoelectric power, magnetic susceptibility, magnetic hysteresis, and Mössbauer spectroscopy.

### Oxalate Method

Oxalic acid enjoyed a special attention, among the carboxylic acids that can operate as a ligand, because of its multiple coordination capacity, either as a monodentate ligand (bonded to the oxygen atoms of the same carboxylic group), as a bidentate ligand (bonded at one oxygen atom from each carboxylic group), or as a tetradentate ligand (double bridge between two or four metal ions).

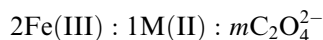
Although several investigations focused on coprecipitation processes as well as on decomposition of complex oxalates, the information regarding the precipitation and the decomposition conditions that decisively influence the purity of the final oxide phase are scarce.

Thermal analysis of complex oxalates of the type:



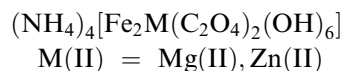
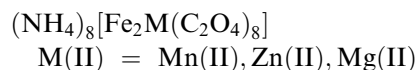
where M(II) = Ni(II), Co(II), (Ni, Zn), and (Mn, Co) leads to the conclusion that the decomposition is apparently a low-temperature phenomenon and the structure of spinelic phase depends to a great extent on the thermal treatment applied.<sup>[38]</sup>

In the systems:

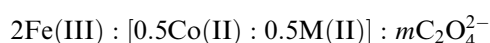
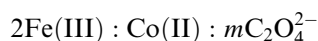


where M(II) = Mg(II), Zn(II), and Mn(II).

Brezeanu et al.<sup>[39–41]</sup> have synthesized and characterized the following series of polynuclear coordination compounds that serve as precursors of spinelic ferrites:



Extension of these studies to the systems:<sup>[42]</sup>



where M(II) = Zn(II), Mn(II) resulted in isolation and characterization of a wide range of complex compounds depending on the pH of the reaction medium, the  $M^{n+}/mC_2O_4^{2-}$  ratio, and the nature of precipitating agent (B = NH<sub>4</sub>OH 12.5%; KOH 40%) (Table 1). These compounds were characterized by IR and electronic spectra and by magnetic measurements. The optimal conditions of decomposition of these polynuclear coordination compounds for obtaining ferrites were established by means of thermal analysis data. The following decomposition route is advanced as an example:

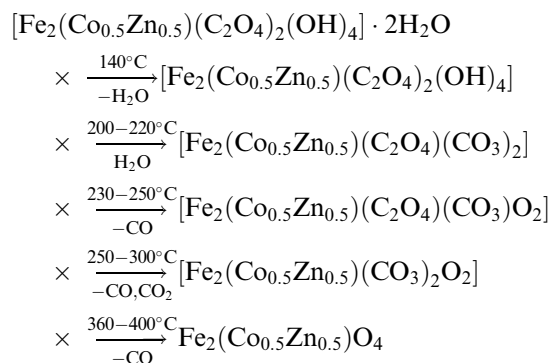


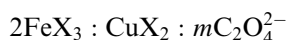
**Table 1** Coordination compounds obtained in 2Fe(III):(Co<sub>x</sub>M<sub>1-x</sub>):mC<sub>2</sub>O<sub>4</sub><sup>2-</sup> System (x = 0, 0.5; M(II) = Zn, Mn)

M <sup>n+</sup> :mC <sub>2</sub> O <sub>4</sub> <sup>2-</sup>	Condition of reaction			Compound
	pp. agent	pH	t (°C)	
2Fe(III):Co(II):10C <sub>2</sub> O <sub>4</sub> <sup>2-</sup>	NH <sub>4</sub> OH 25%	5–7	25	(NH <sub>4</sub> ) <sub>8</sub> [Fe <sub>2</sub> Co <sub>1-x</sub> M <sub>x</sub> (C <sub>2</sub> O <sub>4</sub> ) <sub>8</sub> ] · 3H <sub>2</sub> O
2Fe(III):(Co, M):10C <sub>2</sub> O <sub>4</sub> <sup>2-</sup>				
2Fe(III):Co(II):4C <sub>2</sub> O <sub>4</sub> <sup>2-</sup>	NH <sub>4</sub> OH 25%	5–7	25	[Fe <sub>2</sub> Co <sub>1-x</sub> M <sub>x</sub> (C <sub>2</sub> O <sub>4</sub> ) <sub>2</sub> (OH) <sub>4</sub> ] · 2H <sub>2</sub> O
2Fe(III):(Co, M):4C <sub>2</sub> O <sub>4</sub> <sup>2-</sup>		10	25/(100°C/10 hr)	[Fe <sub>2</sub> Co <sub>1-x</sub> M <sub>x</sub> (OH) <sub>8</sub> ] · 1H <sub>2</sub> O
2Fe(III):(Co, M):mC <sub>2</sub> O <sub>4</sub> <sup>2-</sup>	KOH	5–7	25	[Fe <sub>2</sub> Co <sub>1-x</sub> M <sub>x</sub> (C <sub>2</sub> O <sub>4</sub> ) <sub>2</sub> (OH) <sub>4</sub> ]
m = 2, 4	40%	12	25	[Fe <sub>2</sub> Co <sub>1-x</sub> M <sub>x</sub> (OH) <sub>8</sub> ] · H <sub>2</sub> O
		12	80–100°C/10 hr	[Fe <sub>2</sub> Co <sub>1-x</sub> M <sub>x</sub> O <sub>4</sub> ] · 0.5H <sub>2</sub> O



The IR spectrum of the intermediate product at 350°C shows the characteristic bands of carbonate anion [ $\nu_{\text{as}}(\text{CO}_3^{2-})$  at 1430  $\text{cm}^{-1}$ ,  $\delta(\text{CO}_3^{2-})$  at 880  $\text{cm}^{-1}$  (out of plane), and  $\delta(\text{CO}_3^{2-})$  at 700  $\text{cm}^{-1}$  (in plane)]. The IR spectrum of the final product shows strong absorption bands at  $\sim 580 \text{ cm}^{-1}$  ( $\nu_1$ ) and  $\sim 400 \text{ cm}^{-1}$  ( $\nu_2$ ) characteristic to  $\text{Fe}_2\text{Co}_{0.5}\text{Zn}_{0.5}\text{O}_4$  spinel ferrites. The X-ray diffraction pattern confirms the formation of Co–Zn ferrite (Fig. 2). Mean crystallite sizes of 90–100 Å were obtained.

Because the  $\text{CuFe}_2\text{O}_4$  is an important deep oxidation catalyst for volatile organic compounds removal and air purification, we tried to obtain this spinel oxide by the pyrolysis of polynuclear oxalate complexes.<sup>[43]</sup> To establish the optimal conditions of polynuclear compound isolation, the following systems were studied:



where  $x = \text{Cl}^-$ ,  $\text{NO}_3^-$  and  $m = 2, 10$ .

For a complete precipitation, the pH of the medium was adjusted with a solution of  $\text{NH}_4\text{OH}$  12.5% (pH  $\sim 5$ –6). The slurries were filtered, washed with water and ethanol, and dried in vacuum on  $\text{P}_4\text{O}_{10}$ . The polynuclear compounds have the following molecular formulae:

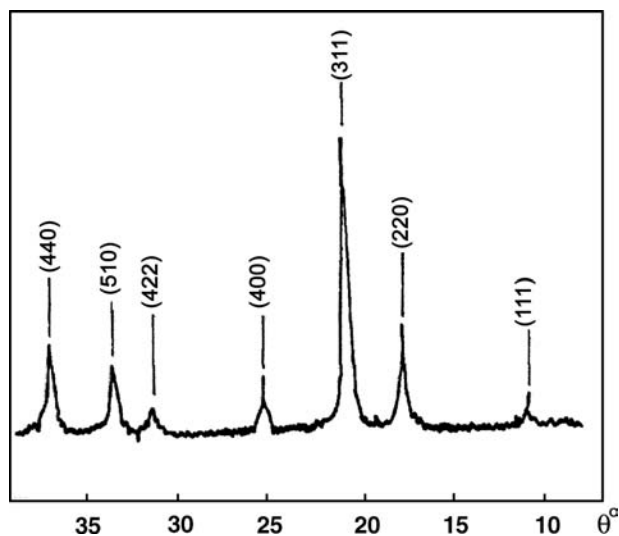
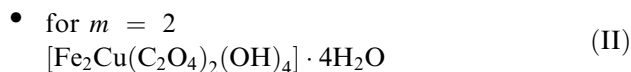
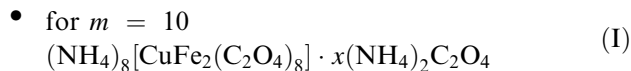


Fig. 2 Powder XRD patterns of the final thermolysis products of  $[\text{Fe}_2(\text{Co}_{0.5}\text{Zn}_{0.5})(\text{C}_2\text{O}_4)_2(\text{OH})_4] \cdot 2\text{H}_2\text{O}$ .

The IR spectra of the oxalate compounds are usually dominated by two strong bands in the 1650–1550 and 1400–1300  $\text{cm}^{-1}$  ranges, arising from C–O stretching vibrations. In the case of  $\text{C}_2\text{O}_4^{2-}$  anion, the band assignment is complicated by its multiple coordination ability. The spectra of these compounds are a proof. Thus the splitting of  $\nu_{\text{asym}}(\text{OCO})$  and  $\nu_{\text{sym}}(\text{OCO})$  vibrations in the spectrum of compound I suggests two different coordination modes for  $\text{C}_2\text{O}_4^{2-}$  anions: as a tetradentate bridge and as a chelate ligand. For compound II, only the chelate bonding is evidenced. The reflectance spectra reveal an octahedral high spin environment of the  $\text{Fe}^{3+}(\text{d}^5)$  ions and a pseudotetrahedral one of  $\text{Cu}^{2+}(\text{d}^9)$ . The stereochemistry of the  $\text{Fe}^{3+}$  and  $\text{Cu}^{2+}$  ions is supported also by Mössbauer and electron paramagnetic resonance (EPR) results.

The polynuclear oxalate compounds decompose in the temperature range 80–400°C. The X-ray diffraction patterns of the thermolysis products show:

- The formation of  $\text{CuFe}_2\text{O}_4$  (as the main product) together with  $\alpha\text{-Fe}_2\text{O}_3$  (hematite) and  $\text{CuO}$  (tenorite) by the pyrolysis of compound I.
- The formation of a single  $\text{CuFe}_2\text{O}_4$  tetragonal phase by the decomposition of compound II. The mean crystallite size was  $\sim 100 \text{ Å}$  (Fig. 3).

The results are supported by Mössbauer measurements on these powders (Fig. 4). In the case of the first thermolysis compound, the Mössbauer spectrum exhibits, besides the two characteristic sextets of  $\text{CuFe}_2\text{O}_4$ , a sextet belonging to a residual  $\alpha\text{-Fe}_2\text{O}_3$ . The Mössbauer spectrum of the second oxide exhibits only the two magnetic sextets characteristic of the  $\text{CuFe}_2\text{O}_4$  tetragonal phase. The value for the saturation magnetization (26.89  $\text{emu g}^{-1}$ ; 1  $\text{emu g}^{-1} = 1 \text{ A m}^2 \text{ kg}^{-1}$ ) for the pure  $\text{CuFe}_2\text{O}_4$  tetragonal phase is in accord with the literature data.<sup>[44]</sup>

These results reveal the importance of the precursor nature on the formation conditions and properties of the final product. The specific molecular architecture of compound II, which consists of a succession of Fe–Fe–Cu units with iron linked via OH bridges shorter than the length of oxalate ones, favors the solid-state ferritization during thermal decomposition.

### Malonate Method

The selection of malonic acid as a ligand is justified by its excellent coordination ability. Moreover, the multiple function of this ligand is responsible for its capacity to form species containing an unusual type of carboxylate bridge (this coordination mode is sometimes called “malonate coordination mode.”<sup>[45]</sup>)

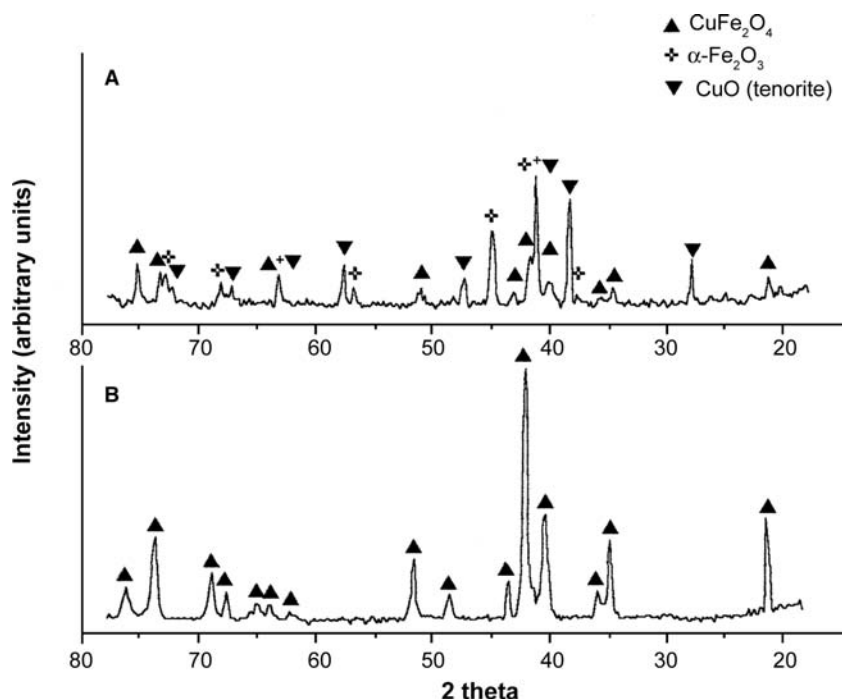
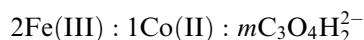
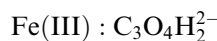
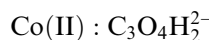


**Fig. 3** Powder XRD patterns of the final thermolysis products of (A)  $(\text{NH}_4)_8[\text{Fe}_2\text{Cu}(\text{C}_2\text{O}_4)_8]$  and (B)  $[\text{Fe}_2\text{Cu}(\text{C}_2\text{O}_4)_2(\text{OH})_4] \cdot 4\text{H}_2\text{O}$ .

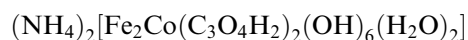
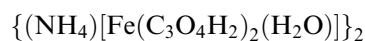
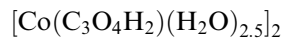
Lanthanide malonate and copper (II) malonate complexes have been extensively studied<sup>[46–48]</sup> but no detailed studies of the malonate complexes as precursors for spinel mixed oxides are available.

Our study<sup>[49]</sup> was focused on the use of malonate coordination compounds as precursors for the spinel ferrites. Furthermore, this idea was supported by the results obtained in a recent study about the thermal stability of malate cobalt complexes<sup>[50]</sup> where malonate–cobalt complexes as intermediates were formed.

To obtain the single and mixed compounds, the following systems were studied:



Elemental chemical analysis and physicochemical measurements (IR, UV–Vis spectra, and thermal analysis) have indicated that the coordination compounds correspond to the following general formulae:



Based on experimental data, and by similarity with the literature ones, the probable structure for these malonate complex compounds is proposed as shown in Fig. 5.

To identify the formation temperature of the cobalt ferrite, the thermal decomposition of the polynuclear malonate complex was investigated. The decomposition

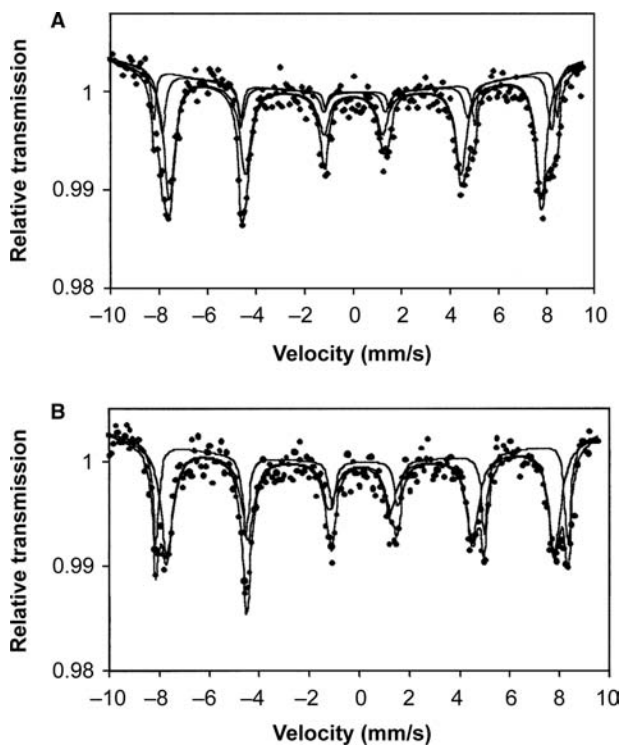


**Fig. 4** Mössbauer spectra of the final thermolysis products of (A)  $(\text{NH}_4)_8[\text{Fe}_2\text{Cu}(\text{C}_2\text{O}_4)_8]$  and (B)  $[\text{Fe}_2\text{Cu}(\text{C}_2\text{O}_4)_2(\text{OH})_4] \cdot 4\text{H}_2\text{O}$  at  $25 \pm 1^\circ\text{C}$ .

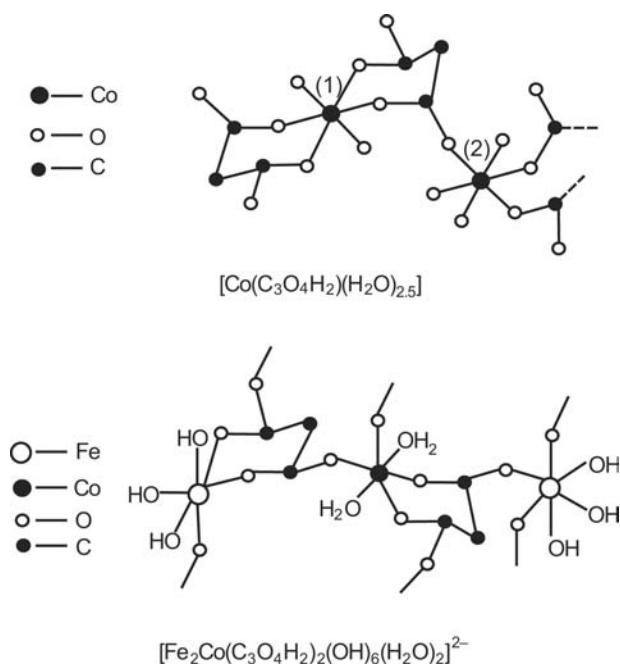
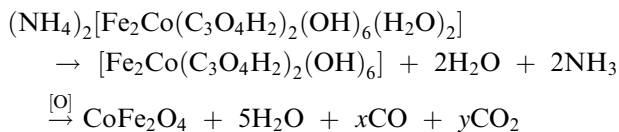


**Fig. 5** Probable structure of  $[\text{Co}(\text{C}_3\text{O}_4\text{H}_2)(\text{H}_2\text{O})_{2.5}]$  and  $(\text{NH}_4)_2[\text{Fe}_2\text{Co}(\text{C}_3\text{O}_4\text{H}_2)_2(\text{OH})_6(\text{H}_2\text{O})_2]$ .

starts at about  $55^\circ\text{C}$  with two partially overlapped endothermic stages. They are followed by the complex decomposition ( $138\text{--}300^\circ\text{C}$ ) for which the DTA curve evidenced three processes: an endothermic one first, followed by two exothermic ones. The following decomposition scheme may be written:



$$x + y = 6$$

The final product obtained after the pyrolysis of the complex compound was calcined for 5 hr at  $300^\circ\text{C}$ . The X-ray diffraction pattern confirmed the formation of ultrafine  $\text{CoFe}_2\text{O}_4$  (Fig. 6) with particles sizes ranging between 50 and 80 Å.

### Acetate Method

The homotrinnuclear acetates with mixed valence and the heterotrinnuclear ones are, at present, the largest group of isostructural compounds which offer a wide field of studies on possible interactions between metal ions.<sup>[51]</sup> These compounds represent also one of the most important sources of raw materials for spinelic ferrites. X-ray diffraction analysis of these compounds has revealed that the symmetric

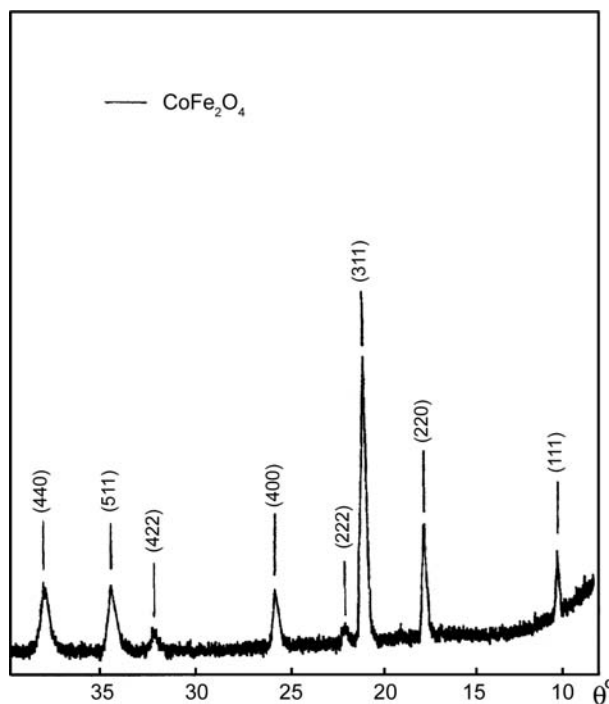


**Fig. 6** Powder XRD patterns of the final thermolysis products of  $(\text{NH}_4)_2[\text{Fe}_2\text{Co}(\text{C}_3\text{O}_4\text{H}_2)_2(\text{OH})_6(\text{H}_2\text{O})_2]$ .

$[\text{Fe}_2^{\text{III}}\text{M}^{\text{II}}\text{O}(\text{RCOO})_6\text{L}_3]$  cluster structures are unique (Fig. 7). The three iron atoms lie at the corners of an equilateral triangle with an oxygen atom in the middle. The carboxylate ions bridge the iron atoms so that each pair of iron atoms is connected by two bridges.

The selection as precursors for obtaining of ferrites of  $[\text{Fe}_2^{\text{III}}\text{M}^{\text{II}}\text{O}(\text{CH}_3\text{COO})_6(\text{H}_2\text{O})_3]$  compounds, where  $\text{M}(\text{II}) = \text{Fe}(\text{II}), \text{Co}(\text{II}), \text{Ni}(\text{II}), \text{Mn}(\text{II}),$  and  $\text{Zn}(\text{II})$ , is justified by a series of arguments, such as:

- The compounds contain the two metals in the exact 2:1 ratio  $[2\text{Fe}(\text{III}):1\text{M}(\text{II})]$  which is necessary to form the ferrite.

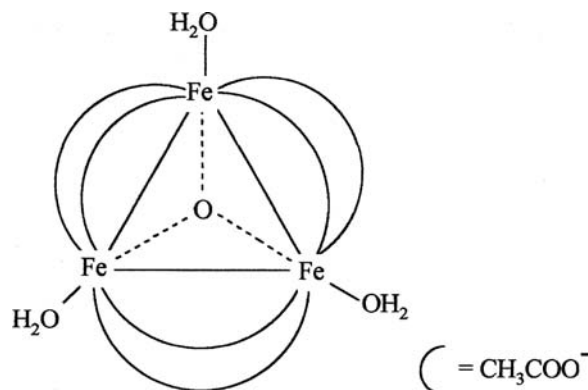


**Fig. 7** Structure of  $[\text{Fe}_3\text{O}(\text{CH}_3\text{COO})_6(\text{H}_2\text{O})_3]$ .

- The ligands decompose at low temperature and according to a simple mechanism.
- The reaction yield remains adequate even for variations within wide limits of the parameters that control the process.

The other two methods for ferrite synthesis (glycolate and formate methods) are based on the thermal decomposition of the oxotrinuclear compounds.

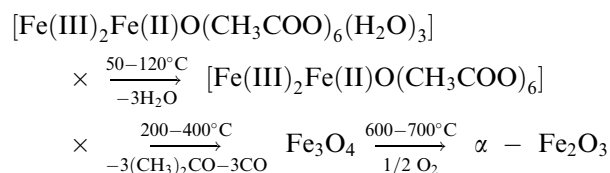
The homonuclear complex species:



where R = CH<sub>3</sub> and H were separated as intermediates in the process of obtaining magnetite.<sup>[52]</sup>

The thermolysis of the oxotrinuclear acetate occurs in three steps. The first step, between 50°C and 150°C, entails a weight loss of about 8%, which corresponds to the elimination of three coordinated water molecules. In the second step, between 200°C and 400°C, a weight loss of 52% is recorded, corresponding to the decomposition of [Fe<sub>3</sub>O(CH<sub>3</sub>COO)<sub>6</sub>] complex. This loss is accompanied on the differential thermal Analysis (DTA) curve by a strong exothermic effect. The residue (39.96%) corresponds to Fe<sub>3</sub>O<sub>4</sub> that is oxidized, turning into α-Fe<sub>2</sub>O<sub>3</sub>. X-ray analysis of the final product showed the characteristic lines of α-Fe<sub>2</sub>O<sub>3</sub>. The thermal analysis of this compound was coupled with identification of gaseous products resulted through mass spectrometry. The decomposition of the acetate complex shows loss of water in a first stage (maximum of 75%), followed by the loss of acetone in two steps (at about 280°C and 320°C), and finally by elimination of CO (~400°C) (Fig. 8).

The decomposition of the oxotrinuclear acetate supports the following scheme:



The study of the thermal decomposition of the polynuclear coordination compound [Fe(III)<sub>2</sub>Ni(II)O(CH<sub>3</sub>COO)<sub>6</sub>(H<sub>2</sub>O)<sub>3</sub>] showed in the temperature range of 350–400°C that the process ends up with the formation of the spinel phase. Thus the temperature required to form NiFe<sub>2</sub>O<sub>4</sub> is 400°C. The crystallinity of the samples was improved by 5-hr thermal treatment at 400°C.<sup>[53]</sup> At temperatures higher than 400°C, hematite was present, as an impurity, besides NiFe<sub>2</sub>O<sub>4</sub>. The mechanism of Ni-ferrite formation may be presented as in Scheme 2. The oxide phases were identified by Mössbauer spectroscopy. Formation of NiFe<sub>2</sub>O<sub>4</sub> from magnetite/maghemite, which was

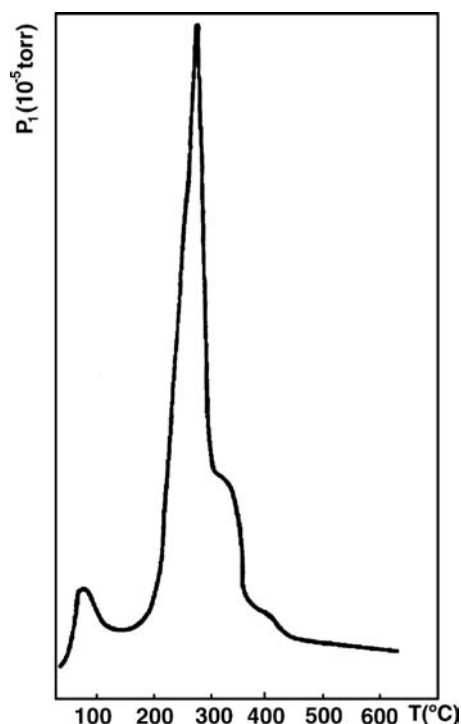


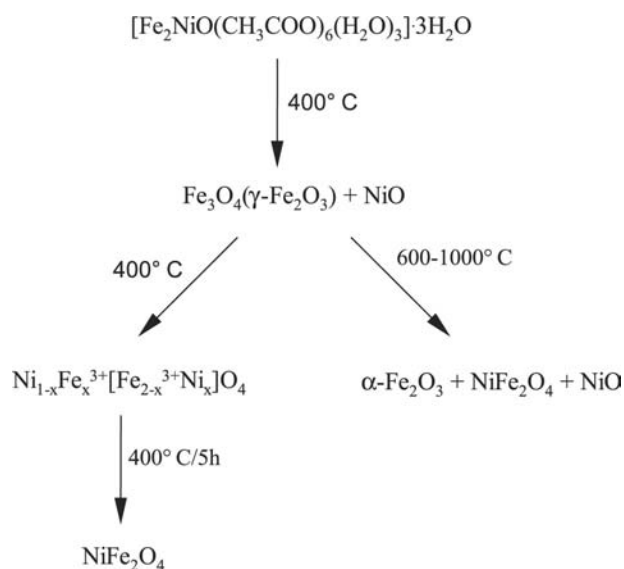
Fig. 8 Thermal decomposition in vacuum of [Fe<sub>3</sub>O(CH<sub>3</sub>COO)<sub>6</sub>(H<sub>2</sub>O)<sub>3</sub>], β = 16°/min.

visualized first, suggests its germ role in spinel lattice. The intermediate oxide phases react fast to form structurally ordered solid solutions of Fe<sub>3</sub>O<sub>4</sub>–NiFe<sub>2</sub>O<sub>4</sub> type that gradually convert into NiFe<sub>2</sub>O<sub>4</sub>. The inversion degree and the size of crystallites increase with the duration of the thermal treatment applied.

Walker, Breen, and Applett<sup>[54]</sup> have discovered a new class of metal carboxylates that appeared to be similar to the other basic carboxylates of iron: Fe<sub>3</sub>O(MEEA)<sub>7</sub> · 5.5H<sub>2</sub>O where MEEA = 2-[2-(2-methoxy)etoxy]etoxyacetate (MeOCH<sub>2</sub>CH<sub>2</sub>OCH<sub>2</sub>CH<sub>2</sub>OCH<sub>2</sub>COO<sup>-</sup>).

The similar composition of the iron MEEA salt to the basic carboxylate suggested that it might also have a similar trinuclear cluster. The mass spectroscopy of Fe<sub>3</sub>O(MEEA)<sub>7</sub> · 5.5H<sub>2</sub>O supports this hypothesis because the largest fragment observed corresponds to Fe<sub>3</sub>O(MEEA)<sub>7</sub> · H<sub>2</sub>O. However, the IR spectrum of Fe<sub>3</sub>O(MEEA)<sub>7</sub> · 5.5H<sub>2</sub>O indicates that the bonding is different from that of the acetate. The stability toward hydrolysis of Fe<sub>3</sub>O(MEEA)<sub>7</sub> · 5.5H<sub>2</sub>O is another factor that differentiates it from other “Fe<sub>3</sub>O” polynuclear carboxylates. [Fe<sub>3</sub>O-(RCOO)<sub>6</sub>L<sub>3</sub>] hydrolyzes to give dimers such as Fe<sub>6</sub>O<sub>2</sub>(RCOO)<sub>12</sub> or larger clusters such as Fe<sub>11</sub>O<sub>6</sub>(OH)<sub>6</sub>(RCOO)<sub>15</sub>, while Fe<sub>3</sub>O(MEEA)<sub>7</sub> · 5.5H<sub>2</sub>O may be dissolved in water without change in composition.

The precursor for the nickel ferrite was obtained by solving 0.5 M equivalent of Ni(NO<sub>3</sub>)<sub>2</sub> in Fe<sub>3</sub>O



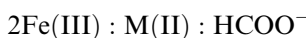
**Scheme 2** Mechanism of Ni-ferrite formation.

(MEEA)<sub>7</sub> · 5.5H<sub>2</sub>O solution. The formula of this liquid nickel ferrite precursor may be written as [Fe<sub>3</sub>O(MEEA)<sub>7</sub>][Ni(NO<sub>3</sub>)<sub>2</sub>] · 2H<sub>2</sub>O. Thermogravimetric analysis indicated dehydration at 125°C followed by burning out of the organic and nitrate ions over the range 150–330°C. The XRD pattern of the material showed that it is amorphous. However, a sample heated to 400°C demonstrated that a well-crystallized phase of pure nickel ferrites was formed. These results confirm our previous works on obtaining of NiFe<sub>2</sub>O<sub>4</sub> from oxotrinuclear acetate compounds.

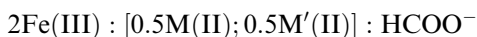
### Formate Method

The nature of formate compounds utilized as precursors of ferrites is influenced by the pH of the reaction medium.

For this reason, the following systems were studied:<sup>[55]</sup>

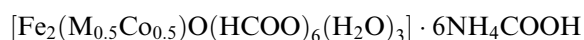
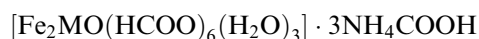


where M(II) = Mn(II), Co(II), Ni(II), and Fe(II)



where M(II) = Mn(II) and M'(II) = Co(II) in two different pH ranges (3–3.5 and 7–7.5, respectively).

- At pH = 3–3.5, oxotrinuclear formate compounds similar with the basic acetate complexes were obtained:



- At pH = 7–7.5, only the species (NH<sub>4</sub>)<sub>2</sub>[Fe<sub>2</sub>Co(HCOO)<sub>2</sub>(OH)<sub>8</sub>] was obtained.

The IR spectra of the oxotrinuclear formates evidenced strong bands at 580–590 and 585 cm<sup>-1</sup>, respectively, which could be assigned to ν<sub>as</sub>(M<sub>3</sub>O) units.

The thermal decomposition of the polynuclear compounds was investigated. The final products obtained at about 600–650°C were analyzed by X-ray diffraction. The diffractograms indicated the formation of spinelic ferrites (Fig. 9) with mean crystallite sizes of 70–90 Å.

The decomposition of the oxotrinuclear formate.<sup>[52]</sup>



supports the following scheme:

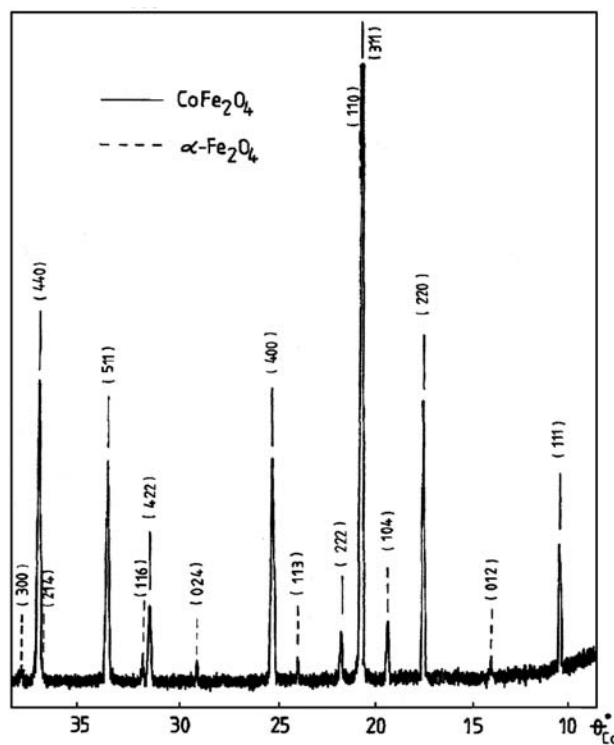
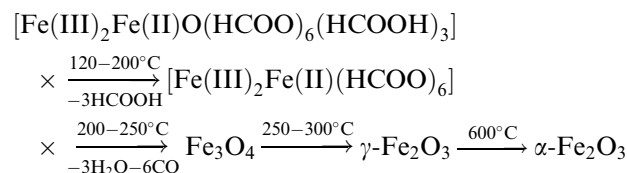


**Fig. 9** Powder XRD patterns of the final thermolysis products of (NH<sub>4</sub>)<sub>2</sub>[Fe<sub>2</sub>Co(HCOO)<sub>2</sub>(OH)<sub>8</sub>].

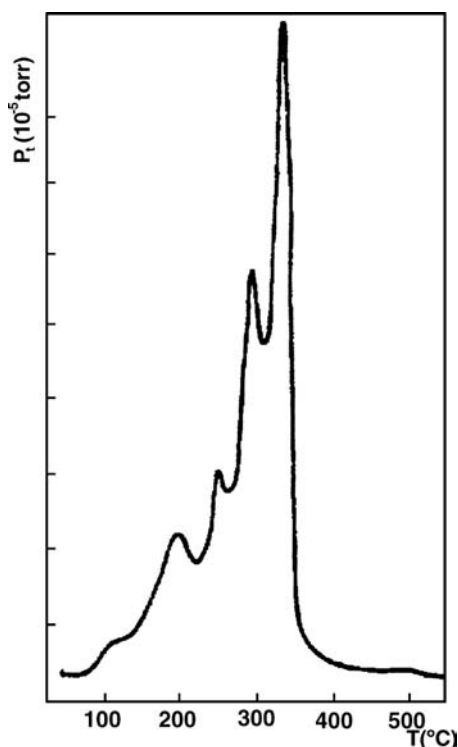


**Fig. 10** Thermal decomposition in vacuum of  $[\text{Fe}_3\text{O}(\text{CH}_2\text{COO})_6(\text{HCOOH})_3]$ ,  $\beta = 16^\circ/\text{min}$ .

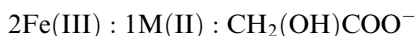
The decomposition of this compound (Fig. 10) shows the loss of  $\text{HCOOH}$  in a first stage (of two steps between  $100^\circ\text{C}$  and  $200^\circ\text{C}$ ) followed by a gradual loss (above  $200^\circ\text{C}$ ) of  $\text{HCOO}$  radical simultaneously with fragments originating from the decomposition of this radical.

Magnetite ( $\text{Fe}_3\text{O}_4$ ) is obtained at temperatures lower than  $250^\circ\text{C}$  (the lines characteristic of  $\text{Fe}_3\text{O}_4$  are present on the X-ray diagrams of the product obtained on calcination at  $220^\circ\text{C}$ ). The X-ray analysis of the oxide obtained at  $300^\circ\text{C}$  shows the lines characteristic of maghemite ( $\gamma\text{-Fe}_2\text{O}_3$ ). Calcination at  $600\text{--}700^\circ\text{C}$  results in the conversion of  $\gamma\text{-Fe}_2\text{O}_3$  into  $\alpha\text{-Fe}_2\text{O}_3$  modification.

### Glycolate Method

The glycolic acid (hydroxyacetic acid) is the simplest representative of the polyhydroxycarboxylic acids with many coordination possibilities because of the presence in the molecule of both carboxylic and hydroxy groups.

The isolation and the characterization of the polynuclear coordination compounds, potentially precursors for ferrites, were carried out from the systems<sup>[56]</sup>



where  $\text{M(II)} = \text{Co(II)}$  and  $\text{Ni(II)}$ .

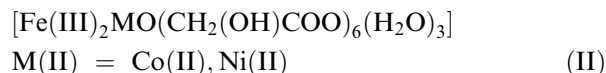
To determine the nature of the species formed and, especially, to establish the stability range of these species, three pH intervals have been selected for the synthesis: 2–2.5, 3–5, and 6.5–8.0.

The results of the elemental analysis indicated that the polynuclear compounds have the following composition as a function of the pH reaction medium:

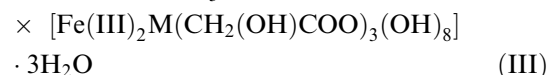
$$\text{pH} = 2 - 2.5$$



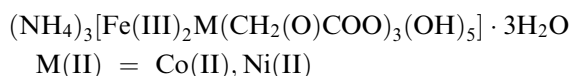
$$\text{pH} = 3 - 5.0$$



$$\text{pH} = 6.5 - 8.0(\text{NH}_4)_3$$



or



To obtain data concerning the ligand bonding, IR spectra were recorded over  $400\text{--}4000\text{ cm}^{-1}$  for all these compounds. These spectra were compared with those of the free ligand and of the sodium salt. The examination of these IR spectra has shown the coordination through the monodentate  $\text{COO}^-$  group and the OH group in compounds I and III and the coordination of the bidentate bridging  $\text{COO}^-$  group ( $\Delta\nu_{\text{as}} - \nu_{\text{s}} = 170\text{ cm}^{-1}$ ) in compound (II); this participation correlated to the existence of  $\nu(\text{M}_3\text{O})_{(\text{as})} \sim 590\text{ cm}^{-1}$  pleads for an oxotrinuclear configuration.

The electronic spectra were recorded in the  $400\text{--}1000\text{ nm}$  range. Analysis of all spectra suggests the assignment of an octahedral configuration to  $\text{Fe(III)}$  ions as well as to  $\text{M(II)} = \text{Co(II)}$  and  $\text{Ni(II)}$  for all the polynuclear compounds. The magnetic moments values of paramagnetic compounds ( $\mu = 7.27$  Bohr magnetons for  $[\text{Fe(III)}_2\text{CoO}(\text{CH}_2(\text{OH})\text{COO})_6(\text{H}_2\text{O})_3]$  and  $\mu = 6.38$  Bohr magnetons for  $(\text{NH}_4)_3[\text{Fe(III)}_2\text{Ni}(\text{CH}_2(\text{OH})\text{COO})_3(\text{OH})_8]$ ) are smaller than those obtained by summing up the magnetic moments of the metal ions. This indicates that antiferromagnetic interactions were present, as generally expected in such polynuclear compounds.

The thermal decomposition of these compounds was investigated to establish the decomposition steps and the optimal conditions for the conversion into spinelic phase. The first step corresponds to the loss of the three water molecules. The second step, a very complex one, corresponds to the decomposition



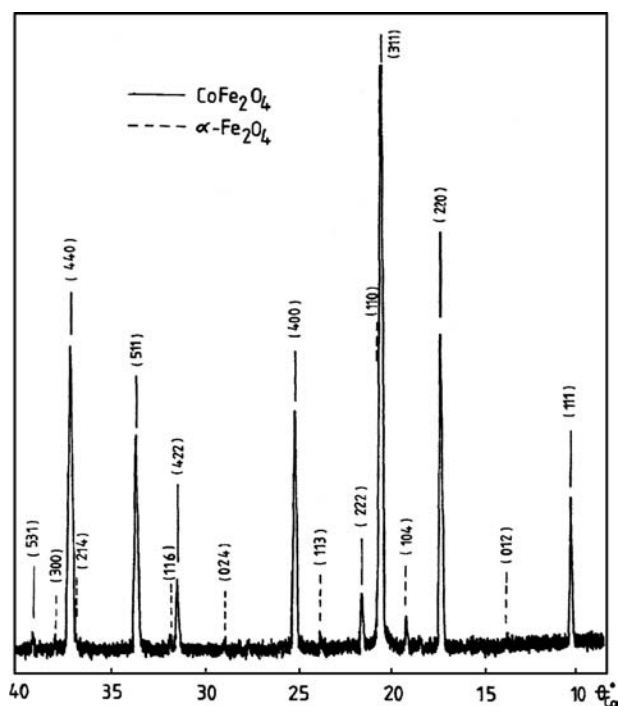


Fig. 11. Powder XRD patterns of the final thermolysis products of  $[\text{Fe}_2^{\text{III}}\text{CoO}(\text{CH}_2(\text{OH})\text{COO})_6(\text{H}_2\text{O})_3]$ .

of the glycolate ligands and the formation of the spinel phase. This final product was analyzed by X-ray diffraction. The diffractograms suggested the formation of spinel ferrite (Fig. 11).

## FERRITES OBTAINED BY COMBUSTION METHOD

Fine particles spinel ferrites are useful for the preparation of ferromagnetic liquids.<sup>[57]</sup> The synthesis of these nanoferrites continues to be a challenge to chemists and material scientists.

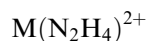
One of the most recent synthesis strategy used to eliminate the difficulties of classical methods is the “combustion synthesis,” also known as “self-propagating high-temperature synthesis” (SHS). The combustion method has been used in the preparation of a large number of technologically important oxides (refractory oxides, magnetic, semiconducting oxides, insulators, catalysts, sensors, etc.). In recent years, there is a growing interest in the combustion synthesis of materials because this method is simple, fast, economic, and yields high-purity products.

The SHS method was developed by Patil et al.<sup>[58–61]</sup> and during the last decade, a number of review works on the combustion method have already been published. The combustion method uses the energy produced by the exothermic redox decomposition of a

mixture of metal nitrates with an organic compound. In the combustion, the mixtures of nitrates and organic compounds behave similarly to conventional oxidants and fuels. The reaction is carried out by dissolving metal nitrates and fuel in a minimum amount of water and heating the mixture to evaporate water in excess. The resulting viscous liquid ignites and undergoes self-combustion, producing ashes that contain the oxide products. During the combustion, exothermic reactions take place. Gases such as  $\text{N}_2$ ,  $\text{H}_2\text{O}$ , and  $\text{CO}_2$  evolve, favoring the formation of fine particle ashes.<sup>[57]</sup>

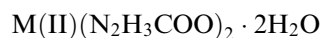
The exothermicity of the combustion is controlled by the nature of the fuel and the ratio oxidizer/fuel. Fuels are organic compounds: hydrazine (H) and its derivatives (monomethyl, unsymmetric disubstituted methyl hydrazines and hydrazides), hydrazine carboxylic acid ( $\text{N}_2\text{H}_3\text{COOH}$ ), oxalyldihydrazide (ODH) ( $\text{CON}_2\text{H}_3$ )<sub>2</sub>, maleic hydrazide ( $\text{C}_4\text{H}_4\text{N}_2\text{O}_2$ , MH), malonic dihydrazide ( $\text{C}_3\text{H}_8\text{N}_4\text{O}_2$ , MDH), tetraformyl tris-azine ( $\text{C}_4\text{H}_{16}\text{N}_6\text{O}_2$ , TFTA), urea ( $\text{CH}_4\text{N}_2\text{O}$ , U), etc. The stoichiometric composition of the metal nitrate–fuel mixture is given by the equivalence ratio  $\Phi_e$  which reflects the relative ratio fuel/oxidizer. In propellant chemistry, the species  $\text{M}^{2+}$ ,  $\text{M}^{3+}$ ,  $\text{M}^{4+}$ , C, and H are considered to be reducing with the corresponding valences +2, +3, +4, +4, and +1. Elemental oxygen is an oxidizing species with valence 2. All of these organic fuels are at the same time very good ligands. The strategy for using hydrazine and its derivatives, urea and tetraformyl tris-azine, as fuels involves complexation with appropriate metal ions. For this reason, we regard the combustion method as a thermal decomposition of polynuclear coordination compounds in situ.

The metal hydrazine compounds:<sup>[58,61]</sup>

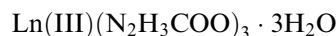


have low ignition temperature ( $<300^\circ\text{C}$ ) and, once ignited, decompose autocatalytically to yield fine particle oxides.

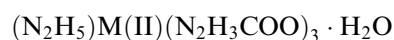
Hydrazine has a great affinity for  $\text{CO}_2$  and forms the hydrazine carboxylic acid ( $\text{N}_2\text{H}_3\text{COOH}$ ). The hydrazine carboxylate anion,  $\text{N}_2\text{H}_3\text{COO}^-$ , is a bidentate ligand, which can form coordination compounds such as:



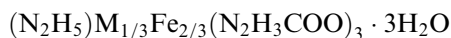
where  $\text{M}(\text{II}) = \text{Mg}(\text{II}), \text{Mn}(\text{II}),$  and  $\text{Zn}(\text{II})$



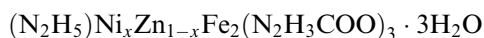
Together with hydrazine, it can form coordination compounds with mixed ligands:



where M(II) = Mg(II), Co(II), Mn(II), Fe(II), Ni(II), Cu(II), and Zn(II)



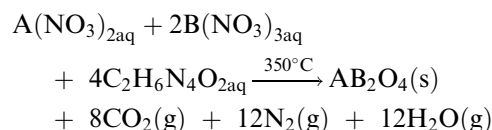
where M(II) = Mg(II), Mn(II), Co(II), Zn(II), and Cd(II)



$$x = 0.2, 0.4, 0.5, 0.6, 0.8$$

These complexes and their solid solution have low ignition temperatures (120–300°C) and decompose or combust in air with evolution of NH<sub>3</sub>, H<sub>2</sub>O, and CO<sub>2</sub> to yield fine particle oxides. These powders have a narrow size distribution with average agglomerate particles of 5–50 nm. The fine particulate nature is attributed to evolution of a large amount of gases (NH<sub>3</sub>, H<sub>2</sub>O, and CO<sub>2</sub>) that help to dissipate the heat, thereby preventing the oxides from sintering.

If the fuel is oxalyldihydrazide (CON<sub>2</sub>H<sub>3</sub>)<sub>2</sub>, the theoretical equations proposed by Suresh and Patil<sup>[59,62]</sup> for the complete combustion of the redox mixtures to obtain spinel oxides are:

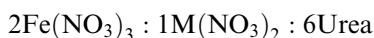


The formation of a spinel phase was confirmed by its characteristic powder XRD pattern. The spinel ferrites show considerable X-ray line broadening owing to the fine particle nature. The crystallite size of MFe<sub>2</sub>O<sub>4</sub> where M(II) = Mg(II), Mn(II), Co(II), Ni(II), Cu(II), and Zn(II) are in the range 15–30 nm.

Another important, very simple fuel is urea (CON<sub>2</sub>H<sub>4</sub>). The property of urea to form ureates with inorganic salts has been known for over 50 years. The usual way of their synthesis is the isothermal evaporation of aqueous solutions containing an inorganic salt and urea. The final product is a compound in which the water molecules may be partially or completely substituted by urea.

Using compounds containing urea and two or more metal ions as precursors of spinel ferrites opens very interesting reaction routes.<sup>[63,64]</sup>

For this reason, the following systems were investigated:

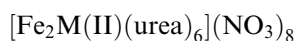


where M(II) = Ni(II), Co(II), and Zn(II).

The compounds containing Fe(III), M(II), and urea as ligand (in the best ratio 2:1:6) were separated by two synthesis methods:

- A solid-state method.
- A coprecipitation method.

Both synthesis methods lead to the formation of the same polynuclear compound:



where M(II) = Ni(II), Co(II), and Zn(II).

The IR spectra of these compounds compared with that of urea indicate the coordination of urea to metal ions through oxygen atoms. This coordination mode leads to a decrease of the CO stretching bands.<sup>[65]</sup> Bands assigned to the vibration mode of NO<sub>3</sub><sup>-</sup> anion were also identified.

The thermal analyses performed for these compounds showed that the decomposition occurs above 110°C in four stages of weight loss. The first one, associated with an endothermic effect, is a result of the release of four molecules of urea. The second one, a strong exothermic effect, is a complex process; the decomposition of the two remaining urea molecules takes place together with the nitrate anions. The last two steps correspond to the oxidation of the decomposition urea product.

The nanosized ferrite powders were obtained with crystallite sizes in the range of 40–60 nm. The Mössbauer spectra indicated superparamagnetic behavior. The combustion synthesis applied for the obtaining of nanoferrites is a very promising procedure. The combustion process is simple, rapid, and has the advantages of the wet chemical methods. As Prof. Patil himself described very eloquently this method,<sup>[61]</sup> “The materials arise from the combustion residues (ash) like a “Phoenix,” the mythological bird that burnt itself on pyre and arose from the ashes with renewed youth to live again.”

## CONCLUSION

The complexation method—comprising the thermal decomposition of the polynuclear complex compounds and the self-autocombustion method—is one of the most promising methods for obtaining of nanoferrites.

In the synthesis of nanoferrites, the precursors play a very important role. The use of a particular precursor may affect the materials' structure on a molecular level. Using appropriate precursors ensures the homogeneity and the highly dispersed state of the resulted materials.

The polynuclear coordination compounds with two or more metallic ions included in the same molecular entity satisfy all of these requirements:

- The atomic distribution is homogeneous at molecular level.

- The decomposition of compounds is simultaneous with, or is immediately followed by, formation of ferrite.
- The temperature of ferrite formation is much lower than that used in the classical methods.
- Because of this relatively low temperature of the formation, the ferrites are characterized by ultrafine granulation and high specific surface area.

In this entry, we emphasized the important role of the coordination chemistry in the nanoparticle science. As Busch<sup>[66]</sup> stated in his review, "Coordination chemistry is a field that spawns fields...; It is foundational to other burgeoning fields, for example solid-state chemistry, extended and mesoscopic materials, photonic materials, models for solid surface and molecular electronics, machines and devices. The enormous extension of the field reflect its fundamental nature: the principles are so basic that they have immediately application as undreamed of new substances..."

## REFERENCES

1. Zhou, Z.H.; Wang, J.; Liu, X.; Chan, H.S.O. Synthesis of Fe<sub>3</sub>O<sub>4</sub> nanoparticles from emulsions. *J. Mater. Chem.* **2001**, *11*, 1704–1709.
2. Liu, Ch.; Zou, B.; Rondinone, A.J.; Zhang, Z.J. Reverse micelle synthesis and characterization of superparamagnetic MnFe<sub>2</sub>O<sub>4</sub> spinel ferrite nanocrystallites. *J. Phys. Chem., B* **2000**, *104*, 1141–1145.
3. Sugimoto, M. The past, present and future of ferrites. *J. Am. Ceram. Soc.* **1999**, *82*, 269–279.
4. Rath, C.; Sahu, K.K.; Anand, S.; Date, S.K.; Mishra, N.C.; Das, R.P. Preparation and characterization of nanosize Mn–Zn ferrite. *J. Magn. Magn. Mater.* **1999**, *202*, 77–84.
5. Sen, D.; Deb, P.; Mazumder, S.; Basumallick, A. Microstructural investigations of ferrites nanoparticles prepared by nonaqueous precipitation route. *Mater. Res. Bull.* **2000**, *35*, 1243–1250.
6. Qiu, X.P. Synthesis and characterization of magnetic nanoparticles. *Chin. J. Chem.* **2000**, 834–837.
7. Dey, S.; Roy, A.; Ghose, J.; Bhowmik, R.N.; Ranganathan, R. Size dependent magnetic phase of nanocrystalline Co<sub>0.2</sub>-Zn<sub>0.8</sub>Fe<sub>2</sub>O<sub>4</sub>. *J. Appl. Phys.* **2001**, *90*, 4138–4142.
8. Choi, Y.; Shim, H.S.; Lee, J.S. Study on magnetic properties and structural analysis of Ni–Zn ferrite prepared through self-propagating high temperature synthesis reaction by neutron diffractometry. *J. Alloys Compd.* **2001**, *326*, 56–60.
9. Chinnasamy, C.N.; Narayanasamy, A.; Ponpandian, N. Grain size effect on the Neel temperature and magnetic properties of nanocrystalline NiFe<sub>2</sub>O<sub>4</sub> spinel. *J. Magn. Mater.* **2002**, *238*, 281–287.
10. El-Sawy, S.M.; Salah, S.H. The protective properties of nickel ferrite and its paint films against corrosion. *Corros. Prev. Control* **1997**, *147*, 135–139.
11. Jadhav, S.A. Magnetic properties of Zn-substituted Li–Cu ferrites. *J. Magn. Magn. Mater.* **2001**, *224*, 167–172.
12. Pathak, A.; Pramanik, P. A novel technique for the preparation of fine ceramic oxides. *Bull. Mater. Sci.* **1992**, *15*, 449–452.
13. Shin, H.C.; Choi, S.C.; Jung, K.D.; Han, S.H. Mechanism of M ferrites (M = Cu, Ni) in the CO<sub>2</sub> decomposition reaction. *Chem. Mater.* **2001**, *13*, 1238–1242.
14. Ramankutty, C.G.; Sugunan, S. Surface properties and catalytic activity of ferrosinels of nickel, cobalt and copper, prepared by soft chemical methods. *Appl. Catal., A Gen.* **2001**, *218*, 39–51.
15. Upadhyay, C.; Verma, H.C.; Rath, C.K.; Sahu, K.; Anand, S.; Das, R.P.; Mishra, N.C. Mössbauer studies of nanosize Mn<sub>1-x</sub>Cu<sub>x</sub>Fe<sub>2</sub>O<sub>4</sub>. *J. Alloys Compd.* **2001**, *218*, 94–97.
16. Sorescu, M.; Tarabasanu, D.; Diamandescu, L. Site and distributed hyperfine magnetite fields in synthetic magnetite. *Int. J. Inorg. Mater.* **2000**, *2*, 371–374.
17. Kim, W.Ch.; Kim, S.J.; Lee, S.W.; Kim, Ch.S. Growth of ultrafine NiZnCu ferrite and magnetic properties by a sol-gel method. *J. Magn. Magn. Mater.* **2001**, *226–230*, 1418–1420.
18. Rondinone, A.J.; Sania, A.C.; Zhang, Z.J. A chemometric approach for predicting the size of magnetic spinel ferrite nanoparticles from the synthesis conditions. *J. Phys. Chem., B* **2000**, *104*, 7919–7922.
19. Pileni, M.P. Magnetic fluids: Fabrication, magnetic properties and organization of nanocrystals. *Adv. Funct. Mater.* **2001**, *11*, 323–336.
20. Petit; Taleb, A.; Pileni, M.P. Cobalt nanosized particles organized in a 2D superlattice: synthesis, characterization and magnetic properties. *J. Phys. Chem., B* **1999**, *103*, 1805–1810.
21. O'Connor, Ch.I.; Seip, C.T.; Carpenter, E.E.; Li, S.; John, V.T. Synthesis and reactivity of nanophase ferrites in reverse micellar solutions. *Nanostruct. Mater.* **1999**, *12*, 65–70.
22. Spacu, P.; Brezeanu, M.; Patron, L.; Contescu, A.; Crisan, D. Coordination compounds as raw materials for mixed oxides. *Thermochim. Acta* **1991**, *178*, 231–239.
23. Carp, O.; Segal, E.; Brezeanu, M.; Patron, L.; Barjega, R.; Stanica, N. The synthesis of manganese zinc ferrite through the transformation of polynuclear coordination compounds. *J. Therm. Anal.* **1996**, *47*, 857–859.
24. Mindru, I.; Albu, T.; Patron, L.; Segal, E.; Brezeanu, M. Thermal stability and non-isothermal decomposition kinetics of a polynuclear metal-alkoxide precursor of cobalt ferrite. *Rev. Roum. Chim.* **1997**, *43* (7), 505–510.
25. Marcilly, C.; Courty, P.; Delmon, B. Preparation of highly dispersed mixed oxides and oxide solid solutions by pyrolysis of amorphous organic precursors. *J. Am. Ceram. Soc.* **1970**, *53*, 56–57.

26. Marcilly, C.; Delmon, B.; Sugier, A. *New Process for Obtaining Finely Divided Homogeneous Oxides of Many Elements*, P.V. 110, 438; June 14, 1967.
27. Courty, P.; Delmon, B.; Marcilly, C.; Sangier, A. *New Process for Obtaining Finely Divided Homogeneous Oxides of Many Elements and Products Obtained*, P.V. 157, 487; June 2, 1968.
28. Verma, A.; Goel, T.C.; Mendiratta, R.G.; Gupta, R.G. High-resistivity nickel–zinc ferrites by citrate precursor method. *J. Magn. Magn. Mater.* **1999**, *192*, 271–276.
29. Yue, Z.; Zhou, J.; Li, L.; Gui, Z. Effects on MnO<sub>2</sub> on the electromagnetic properties of NiCuZn ferrites prepared by sol-gel auto-combustion. *J. Magn. Magn. Mater.* **2001**, *233*, 224–229.
30. Prasad, S.; Vijayalakshmi, A.; Gajbhiye, N.S. Synthesis of ultrafine cobalt ferrite by thermal decomposition of citrate precursor. *J. Therm. Anal.* **1998**, *52*, 595–607.
31. Sainamthip, P.; Amarakoon, V.R.W. Preparation of Mn–Zn ferrite powders by alcoholic dehydration of citrate/formate solution. *J. Am. Ceram. Soc.* **1988**, *71*, C-92–C-95.
32. Tapscott, R.E.; Belford, R.L.; Paul, J.C. Stereochemistry of tartrato(4)-bridged binuclear complexes. *Coord. Chem. Rev.* **1969**, *4*, 323–359.
33. Onutu, C.; Albu, T.V.; Segal, E.; Patron, L. Coordination compounds with tartaric acid as ligand. I. Homobinuclear coordination compounds of Co(II). *Rev. Roum. Chim.* **1997**, *42*, 271–276.
34. Patron, L.; Pocol, V.; Carp, O.; Modrojan, E.; Brezeanu, M. New synthetic route in obtaining copper chromite. I. Hydrolysis of some soluble salts. *Mater. Res. Bull.* **2001**, *36*, 1269–1276.
35. Patron, L.; Mindru, I.; Tuna, F.; Ionescu, L.; Brezeanu, M. Polynuclear coordination compounds of Fe(III), Co(II), Zn(II) and Mn(II) with tartaric acid. *Rev. Roum. Chim.* **1994**, *39*, 1407–1413.
36. Nikumbh, A.K.; Nagawade, A.V.; Tadke, V.B.; Bakare, P.P. Electrical, magnetic and Mössbauer properties of Cd–Co ferrites prepared by the tartarate precursor method. *J. Mater. Sci.* **2001**, *36*, 653–662.
37. Nikumbh, A.K.; Nagawade, A.V.; Gugale, G.S.; Chaskar, M.G.; Bakare, P.P. The formation, structural, electrical, magnetic and Mössbauer properties of ferrispinel, Cd<sub>1-x</sub>Ni<sub>x</sub>Fe<sub>2</sub>O<sub>4</sub>. *J. Mater. Sci.* **2002**, *37*, 637–647.
38. Schröder, H. Zur kinetik der tieftemperaturspinellbildung von Nickelferrit durch mischoxalatzersetzung. *Z. Phys. Chem.* **1967**, *236*, 200–202.
39. Dinu, G.; Brezeanu, M.; Segal, E.; Mincu, V.; Patron, L. Process for the Obtaining of Mn Ferrite. RSR Patent 77973 August 31, 1981.
40. Brezeanu, M.; Safarica, E.; Segal, E.; Patron, L.; Mincu, V. Process for the Obtaining of Mn–Ni Ferrite. RSR Patent 88,045, May 24, 1985.
41. Carp, O.; Segal, E.; Brezeanu, M.; Patron, L.; Barjega, R.; Stanica, N. Physico-chemical characterization and non-isothermal decomposition kinetics of a precursor (polynuclear coordination compound) of manganese ferrite. *Thermochim. Acta* **1994**, *243*, 43–50.
42. Mindru, I.; Patron, L.; Crisan, D.; Brezeanu, M. Synthesis of Co(II)–Mn(II) ferrites from polynuclear oxalates. *Rev. Roum. Chim.* **1997**, *42*, 31–35.
43. Marinescu, G.; Patron, L.; Carp, O.; Diamandescu, L.; Stanica, N.; Meghea, A.; Brezeanu, M.; Grenier, J.C.; Etourneau, J. Polynuclear coordination compounds as precursors for CuFe<sub>2</sub>O<sub>4</sub>. *J. Mater. Chem.* **2002**, *12*, 1–6.
44. Buron, M.; Gougeon, M.; Rousset, A. Elaboration de particules submicroniques de ferrite de cuivre, variation de la coercivite avec le volume des particules. *C. R. Acad. Sci., Paris* **1996**, *322* (Iib), 775–782.
45. Marrot, F.; Trombe, J.C. Synthèse et étude structurale d'un malonate de lanthane [La<sub>2</sub>(H<sub>2</sub>O)<sub>3</sub>](C<sub>3</sub>H<sub>2</sub>O<sub>4</sub>)<sub>3</sub> · 2H<sub>2</sub>O. *C. R. Acad. Sci., Paris* **1993**, *317* (II), 319–321.
46. Yakomori, Y.; Hodgson, D.J. Calcium binding to  $\gamma$ -carboxyglutamate and  $\beta$ -carboxyaspargate residues: structure of a calcium complex of benzylmalonic acid. *Inorg. Chem.* **1988**, *27*, 2008–2011.
47. Marrot, F.; Trombe, J.C. Synthesis, characterization and structure of a diaqua lanthanum bimalonate malonate monohydrate. *Polyhedron* **1994**, *13*, 1931–1935.
48. Muro, G.; Mautner, F.A.; Ivsansti, M.; Lezama, L.; Ariortua, M.I.; Rojo, T. Study of the-dimensional [MM'(–CH<sub>3</sub>H<sub>2</sub>O<sub>4</sub>)<sub>2</sub>(H<sub>2</sub>O)<sub>4</sub>] (M = Ba, Sr and M' = Cu, Mn) systems: synthesis, structure, magnetic properties and thermal decomposition. *Inorg. Chem.* **1998**, *37*, 3243–3251.
49. Mindru, I.; Patron, L.; Carp, O.; Marinescu, G.; Brezeanu, M.; Segal, E. Spectral and thermal studies of some malonate complexes. A new synthetic route leading to spinel type oxides. *Rev. Roum. Chim.* **2000**, *45*, 601–608.
50. Albu, T.V.; Mindru, I.; Patron, L.; Segal, E.; Brezeanu, M. Thermal behavior of some solid coordination compounds with malic acid as ligand. *Thermochim. Acta* **1999**, *340–341*, 235–240.
51. Brezeanu, M.; Patron, L.; Andruh, M. *Polynuclear Coordination Compounds and Their Applications*; Ed. Acad.: Bucharest, 1986; 141 pp.
52. Patron, L.; Contescu, A.; Munteanu, G.; Brezeanu, M.; Segal, E. Coordination compounds as raw materials for mixed oxides. III. Trinuclear, oxo-centered carboxylate compounds containing Fe(II, III, III). *Rev. Roum. Chim.* **1986**, *31*, 811–818.
53. Ilie, I.; Patron, L.; Brezeanu, M.; Segal, E. Synthesis of Ni(II) ferrite from polynuclear complex compounds. *J. Mater. Sci. Lett.* **1987**, *6*, 932–935.
54. Walker, E.H., Jr.; Breen, M.L.; Apblett, A.W. Preparation of nickel ferrite using ligand metal carboxylate. *Chem. Mater.* **1998**, *10*, 1265–1269.
55. Mindru, I.; Patron, L.; Brezeanu, M. Ferrites obtained by thermal decomposition of polynuclear coordination compounds. *Roum. Chem. Quart. Rev.* **1996**, *4*, 167–181.
56. Mindru, I.; Patron, L.; Brezeanu, M. Polynuclear coordination compounds of transition metals with glycolic acid as precursors for ferrites. *Rev. Roum. Chim.* **1995**, *40*, 853–858.

57. Castro, S.; Gayoso, M.; Rodriguez, C. A study of the combustion method to prepare fine ferrite particles. *J. Solid State Chem.* **1997**, *134*, 227–231.
58. Patil, K.C. Advanced ceramics: Combustion synthesis and properties. *Bull. Mater. Sci.* **1993**, *16*, 541–553.
59. Suresh, K.; Patil, K.C. Perspectives in Solid State Chemistry. In *A Recipe for An Instant Synthesis of Fine Particle Oxide Materials*; Rao, K.J., Ed.; Narosa Publ. House: New Delhi, 1995; 376–388.
60. Aruna, S.T.; Patil, K.C. Combustion synthesis and magnetic properties of nanosize barium hexaferrite. *Trans. Indian Ceram. Soc.* **1996**, *55*, 147–150.
61. Patil, K.C.; Aruna, S.T.; Ekambaram, S. Combustion synthesis. *Curr. Opin. Solid State Mater. Sci.* **1997**, *2*, 158–165.
62. Suresh, K.; Patil, K.C. Combustion synthesis and properties of fine particle Mg–Zn ferrites. *J. Mater. Sci. Lett.* **1994**, *13*, 1712–1714.
63. Patron, L.; Carp, O.; Mindru, I.; Petre, L.; Brezeanu, M. Compounds containing urea-precursors of mixed oxides. I. Synthesis of nickel ferrite. *Rev. Roum. Chim.* **1998**, *43*, 993–996.
64. Carp, O.; Patron, L.; Diamandescu, L.; Reller, A. Thermal decomposition study of coordination compound  $[\text{Fe}(\text{urea})_6](\text{NO}_3)_3$ . *Thermochim. Acta* **2002**, *390*, 169–177.
65. Nakamoto, K. *Infrared Spectra of Inorganic and Coordination Compounds*, 4th Ed.; Wiley: New York, 1978; 268 pp.
66. Busch, D.H. The complete coordination chemistry—one practitioner’s perspective. *Chem. Rev.* **1993**, *93*, 847–880.

# Magnetic Nanoparticles

Valérie Cabuil

Université Pierre et Marie Curie, Paris, France

## INTRODUCTION

Magnetic particles are well known for their use in recording devices. For such an application that involves information storage, the nature, size, and shape of the particles are important parameters. These particles are usually made of magnetite ( $\text{Fe}_3\text{O}_4$ ), maghemite ( $\gamma\text{-Fe}_2\text{O}_3$ ), cobalt ferrite ( $\text{Fe}_2\text{CoO}_4$ ), or chromium dioxide ( $\text{CrO}_2$ ). They are spherical or acicular, and are usually micron-sized.<sup>[1]</sup> These particles are deposited on a substrate, and only magnetic properties of the systems are considered.

In this entry, we shall not focus on magnetic particles as magnetic pigments, but as special colloids. Indeed, we shall describe the synthesis and properties of particles whose diameters are smaller than 15 nm, and thus are subject to Brownian motion.

## OVERVIEW

Nanometric magnetic particles can be prepared by grinding a magnetic material, typically a ferrite, for several weeks using chemical synthesis.<sup>[2]</sup> Many synthesis procedures are used, according to the nature of the magnetic particles: iron oxide particles are usually obtained using a precipitation method; synthesis of metallic particles needs more subtle processes. The main difficulty is in getting monodispersed samples in a nanometric range. Nevertheless, it is an important point because the magnetic properties of particles vary based on their size. The materials constituting the particles are ferromagnetic or ferrimagnetic materials.<sup>[3]</sup> Because of their small diameters, the particles under consideration are magnetic monodomains, which means that each particle has a permanent magnetic moment whose intensity is proportional to the particle's volume and to the specific magnetization of the material. Depending on this volume, this moment is either blocked in the easy axes of magnetization, or is free to rotate inside the grain. In this last case, the grain is said to be "superparamagnetic."<sup>[4]</sup> For even smaller particles, the magnetic order will disappear.

Because of their small size, magnetic nanoparticles can be dispersed in a liquid carrier.<sup>[5]</sup> A superparamagnetic

colloidal dispersion (usually called ferrofluid) is then obtained.<sup>[6]</sup> Such a dispersion is stable for years, contrary to the so-called "bitter fluid" or to the magnetorheological fluids that are dispersions of micron-sized particles. It does not settle with time—neither when a magnetic force is applied and is not magnetic in zero field but becomes magnetized when a magnetic field is applied.<sup>[7]</sup> It is able to move under the action of a magnetic force and indeed finds numerous applications in the field of mechanics. Because the entry on "Magnetic Nanoparticles in Fluid Suspension: Ferrofluid Applications" covers this aspect in depth, this entry will only touch on this area of research. A key condition for the development of ferrofluid-based applications is that the colloidal dispersion has to be stable. To prevent particle aggregation because of van der Waals forces or magnetic dipolar interactions, interparticle repulsions have to be "chemically" created. Oxide particles can be directly dispersed in water, provided the pH value is such that the surface hydroxyl groups are ionized.<sup>[8]</sup> In this case, electrostatic repulsions prevent particles from aggregation.<sup>[9]</sup> Particles can also be coated by surfactants or polymers, especially when they have to be dispersed in oily media, and steric repulsions are, in this case, responsible for the stability of the system.<sup>[10]</sup> Obtaining stable dispersions of magnetic particles is an important point for applications, but on the theoretical point of view, such dispersions are also original examples of colloids, with additional interparticle interactions, that are tunable using an external parameter (i.e., the magnetic field). These dispersions have, in addition, many original properties because of their global response to a magnetic field. This response can be a "magnetic" one (the medium becomes magnetized), but also an optical one (the medium becomes birefringent) or a rheological one (the medium becomes structured).<sup>[6,7,9]</sup>

These properties can be transmitted to more complex media: glasses,<sup>[11]</sup> polymeric gels,<sup>[12]</sup> lyotropic systems (nematics<sup>[13]</sup> and smectics<sup>[14]</sup>), and microscopic colloids (emulsions,<sup>[15]</sup> latex,<sup>[16]</sup> and liposomes<sup>[17]</sup>), which then obtain a response to a magnetic field of small intensity. For example, orientational transition of self-organized phases of surfactants<sup>[18]</sup> and deformation of liposomes<sup>[19]</sup> have been observed in low-intensity magnetic fields. Magnetic nanoparticles have also been introduced in inorganic or polymeric gels



as viscosity probes, analyzing their magneto-optical response.<sup>[20]</sup>

These magnetic nanoparticles should find numerous applications. Nevertheless, until now, except for the “ferrofluid applications” in the field of commercial mechanics,<sup>[21]</sup> few applications have been developed. The challenge seems to be in the field of biomedical applications in the next few years.<sup>[22,23]</sup>

## PREPARATION PROCEDURES

According to the chemical nature of the particles (metallic or oxide particles), synthesis procedures will be very different.

## Chemical Nature of Particles

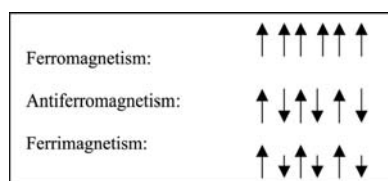
Magnetic nanoparticles are, of course, constituted of a magnetic material: a ferromagnetic material or a ferrimagnetic one.<sup>[3]</sup> In a ferromagnetic or ferrimagnetic material, specific interactions exist between the spins of atoms and lead to an ordering of the spins in parallel or antiparallel directions (Fig. 1). This spontaneous ordering of individual magnetic moments results in a magnetic moment per unit volume that is called its *specific magnetization*  $M_s$ , but it disappears above a given temperature, which is called *Curie temperature*. Please note that although ferromagnetism and ferrimagnetism are formally different, they lead to the same macroscopic magnetic properties, and the word “ferromagnetism” is often used in place of “ferrimagnetism,” even in this entry.

Table 1 lists several ferromagnetic or ferrimagnetic materials, in order of increasing magnetization.

Unfortunately, the more magnetic materials (metals) are, the more easily they are oxidized; this tendency to oxidation is enhanced when materials become powder. Consequently, the most commonly used magnetic materials as colloidal particles are iron oxides because they are cheap and easy to obtain.

## Magnetite and Maghemite Particles

The most widely known magnetic iron oxide is magnetite ( $\text{Fe}_3\text{O}_4$ ). Indeed, the first magnetic nanoparticles were



**Fig. 1** The three types of cooperative magnetism. Antiferromagnetism does not lead to macroscopic magnetism.

**Table 1** Some commonly used ferromagnetic or ferrimagnetic materials ( $T_c$  is the curie temperature, and  $M_s$  is the saturation magnetization of the material)

Material	Type of magnetism	$T_c$ (°C)	$M_s$ (kA/m)
Chromium dioxide ( $\text{CrO}_2$ )	Ferrimagnetic	117	410
Maghemite ( $\gamma\text{-Fe}_2\text{O}_3$ )	Ferrimagnetic	590	414
Cobalt ferrite ( $\text{CoFe}_2\text{O}_4$ )	Ferrimagnetic	520	422
Magnetite ( $\text{Fe}_3\text{O}_4$ )	Ferrimagnetic	585	470
Nickel $\text{Ni}(\alpha)$	Ferromagnetic	358	485
Cobalt $\text{Co}(\alpha)$	Ferromagnetic	1131	1400
Iron $\text{Fe}(\alpha)$	Ferromagnetic	770	1707

obtained by grinding magnetite grains in ball mills, in the presence of a surfactant and a liquid carrier. The surfactant, at the same time, helps in grinding and prevents particle aggregation. This process costs time (about 1000 hr) and leads only to surfactant-coated particles.<sup>[2,24]</sup>

Chemical synthesis of colloidal magnetite is now widely used. It has been known for a long time: aqueous mixtures of ferric and ferrous salts are mixed with an alkali to induce the precipitation of a black hydrophilic magnetic product, which is constituted of magnetite particles—negatively charged and associated with the counterions of the alkali.<sup>[25]</sup> According to the experimental conditions of the synthesis, the particle size can be roughly controlled.<sup>[26,27]</sup> The particles are rocklike (Fig. 2A) and the system is always polydispersed in size, but the average diameter can be monitored between 5 and 14 nm through the nature of the alkali, its concentration, the concentration of the ferric and ferrous salt, the  $\text{Fe(II)/Fe(III)}$  ratio, the ionic strength, the temperature, the way of admixing the reactants, and the efficiency of stirring.<sup>[26]</sup> Once all these parameters are fixed, the result of the synthesis is reproducible. Concerning magnetite, the situation can be summarized this way. Magnetite nanoparticles are obtained at room temperature and, for a given concentration of ferric and ferrous species, an increase of pH induces a decrease of particle size, sodium hydroxide leads to particles smaller than ammonia (for the same pH), an increase in ionic strength induces a decrease in particle size, and an increase in the  $\text{Fe(II)/Fe(III)}$  ratio increases the particle size. Another way to reduce particle size is to add to the synthesis mixture a molecule-chelating iron species. For example, it is known that carboxylate species interfere with the formation and growth of ferric oxides. Performing the synthesis of colloidal magnetite in citrate

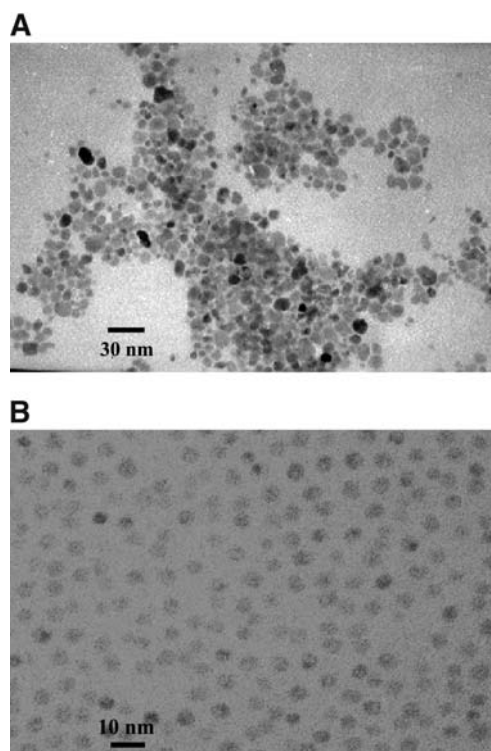


**Fig. 2** TEM pictures of ferrite nanoparticles (A) and iron particles (B).

or tartrate species allows the reduction of the average particle diameter to 3 nm.<sup>[28]</sup> However, particle size distribution remains rather wide. Synthesis using micelles has been proposed to control the size distribution.<sup>[29]</sup> Processes using iron(III) acetylacetonate in organic media have been recently proposed to produce monodisperse magnetite particles.<sup>[30]</sup> Please note that nature is also able to synthesize colloidal magnetite (e.g., magnetotacticum bacteria produce nanometric magnetite particles).<sup>[31]</sup>

Colloidal magnetite gets oxidized easily. If it is kept under usual atmosphere, it quickly oxidizes, and the product often called maghemite is, in fact, bertholide [i.e., a ferric oxide whose composition is between that of magnetite ( $\text{Fe}_3\text{O}_4$ ) and maghemite ( $\gamma\text{-Fe}_2\text{O}_3$ )]. That is the reason why magnetite is sometimes deliberately oxidized to maghemite, by dispersing the magnetic particles in acidic medium and stirring them with ferric nitrate.<sup>[10]</sup> The maghemite particles obtained are then chemically stable in alkaline or acidic medium. The saturation magnetization of maghemite is slightly lower than the one of magnetite, but the difference of magnetization is largely counterbalanced by the gain of chemical stability.

### Other Ferric Oxides

Many ferric oxide materials with a spinel-like structure ( $\text{MFe}_2\text{O}_4$ ,  $\text{M} = \text{Co}, \text{Mn}, \text{etc.}$ ) can be obtained as

nanoparticles. The synthesis of cobalt ferrite particles and manganese ferrite particles has been widely described.<sup>[32–35]</sup> The process is again a precipitation of the oxide using an alkali, but the synthesis conditions to obtain magnetic nanoparticles depend on the nature of the oxide synthesized. For example, cobalt ferrite particles are more rapidly obtained at 90°C, using sodium hydroxide or methylamine.<sup>[33]</sup> Such particles are highly unstable in acidic medium: they are completely dissolved, leading back to the initial mixture. The same problem exists with manganese ferrite particles. Coating particles with a thin amorphous ferric oxide shell prevent this dissolution and stabilize the samples in acidic media.<sup>[32]</sup>

M can stay for a mixture of two metallic species (e.g., Zn and Mn, Ni or Co). Compounds with such a composition  $\text{M}_{1-x}\text{Zn}_x\text{Fe}_2\text{O}_4$  have magnetic properties that are continuously dependent on the value of  $x$  (when  $x = 1$ , the compound  $\text{ZnFe}_2\text{O}_4$  is no more ferrimagnetic at room temperature). The problem is to control the particle size at the same time, which is dependent on  $x$  and the magnetic properties.<sup>[34]</sup>

Again synthesis using micelles has been described to produce calibrated cobalt ferrite,<sup>[33,36]</sup> or zinc–cobalt ferrite nanoparticles.<sup>[37]</sup> Surfactant of the type metal dodecyl sulfate [ $\text{Fe}(\text{DS})_2$ ,  $\text{Co}(\text{DS})_2$ , or  $\text{Zn}(\text{DS})_2$ ] are synthesized and mixed in micelles; addition of an alkali again induces the formation of particles.

### Metallic Particles

Metallic particles seem to be more interesting than oxides because their specific magnetization is higher (Table 1). Nevertheless, metallic particles are highly oxidizable and often lose their high magnetization because of oxidation. Different processes have been developed.

Decomposition of metal carbonyl compounds is a convenient method that allows one to obtain large amounts of monodisperse metal particles. Cobalt particles are prepared from dicobalt octacarbonyl ( $\text{Co}_2(\text{CO})_8$ ).<sup>[38–40]</sup> Iron particles are obtained from iron pentacarbonyl ( $\text{Fe}(\text{CO})_5$ ).<sup>[41,42]</sup> In the case of iron particles, the solvent is usually toluene or decalin, and the stabilizing agent is either oleic acid, or a polymer as polyisobutene. Usually, the metallic particles obtained this way have narrower size distributions than the ferrite particles (Fig. 2B). Nevertheless, their magnetization is always lower than the one of the bulk material because of surface oxidation and carbon incorporation. The surfactant or the polymer dispersed in the solvent is supposed to catalyze the reaction, to prevent particles from aggregating and to protect them against oxidation. Unfortunately, for this last point, the efficiency of the surfactants or polymers tested is not as promising.

Decomposition of iron octacarbonyl in the presence of ammonia has been described as leading to iron-nitride particles ( $\text{Fe}_3\text{N}$ ), which has a high saturation magnetization and a good chemical stability.<sup>[43]</sup> The particle diameter is monitored between 5 and 10 nm, through the  $\text{Fe}(\text{CO})_5$  content.

Reduction of metal salts by strong reducing agents such as borohydrides is another method to obtain metallic particles, but it is difficult to obtain colloidal objects with reasonable polydispersity without using reverse micelles. For example, nanosized particles, with diameters on the order of 6 nm, are obtained from the reduction of cobalt bis(2-ethylhexyl)-sulfosuccinate ( $\text{Co}(\text{AOT})_2$ ) involved in  $\text{Na}(\text{AOT})$  micelles.<sup>[44]</sup> Nearly monodispersed cobalt nanocrystals were obtained by reduction of cobalt chloride at high temperature in the presence of stabilizing agents.<sup>[45]</sup> A special case is the one of iron particles dispersed in mercury that have been obtained by electrolytic reduction of metal salt solutions, or of colloidal solutions of iron oxide in a supporting electrolyte.<sup>[46]</sup> Nanometric particles are obtained, but the prevention of particle agglomeration is the key problem and is still under study.

A third method uses the evaporation of metal in a vacuum in the presence of a solvent containing a surfactant.<sup>[47]</sup> This technique produces metal particles, the size of which depends on the time during which samples are heated and the amount of surfactant.

### Polydispersity of Samples

Polydispersity is the main problem encountered when working with nanoparticles. It can be solved, in some cases, by the choice of the synthesis process, or by size-sorting processes once the particles are synthesized.

In the case of ferric oxide particles, the average diameter is easily controlled through the experimental conditions of synthesis, but the system is always polydispersed. The particle size distribution is well described using a log-normal distribution of diameters (Fig. 3):

$$P(d) = \frac{1}{\sqrt{2\pi}\sigma} \exp\left(-\frac{\ln^2(d/d_0)}{2\sigma^2}\right)$$

In usual products synthesized by a coprecipitation method, the polydispersity  $\sigma$  ranges between 0.3 and 0.4. This corresponds to a rather wide distribution. Synthesis using micelles reduced polydispersities but never obtained monodisperse samples.<sup>[48]</sup> Centrifugation and magnetic separation can be alternative procedures.<sup>[49]</sup> A size-sorting process has been proposed to reduce significantly the polydispersity down to 0.15. It is based on the thermodynamic properties of colloidal dispersions ("Phase Behavior of Dispersions of

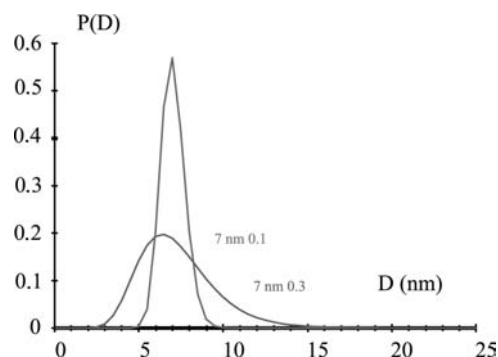


Fig. 3 Two examples of log-normal distribution of diameters.

Magnetic Nanoparticles") and has already been used to obtain monodispersed emulsions.<sup>[15]</sup> It is described in the case of positive or negative ferrite particles dispersed in water in Refs.<sup>[49,50]</sup> Such dispersions are stabilized by the electrostatic repulsions between particles. These repulsions depend on the ionic strength in the aqueous solution and can be reduced by addition of an electrolyte in the medium. The screening of the repulsions induces a reversible phase separation between a liquid phase dense in colloids and a liquid phase poor in colloids. If both phases are separated and analyzed, it is found that the dense phase contains the bigger particles, and the light phase contains the smallest ones. Performing this process two or three times, it is possible to fractionate the size distribution and obtain almost monodispersed samples with a reasonable yield.

Metallic particles are usually obtained with a very low polydispersity (Fig. 2) and size sorting is indeed unnecessary.

### MAGNETIC PROPERTIES

Because of their colloidal size, the magnetic particles under consideration here and whose synthesis is described above have magnetic properties that are strongly modified with respect to the properties of bulk materials.

#### Bulk Ferromagnetic Materials

In ferromagnetic or ferrimagnetic materials, the order results in high magnetostatic energy.<sup>[3,51]</sup> To reduce this energy, the bulk material divides into domains, called magnetic monodomains, separated by the so-called "Bloch walls." Each monodomain has a permanent magnetization vector, which is oriented, in zero field, to minimize this magnetostatic energy (Fig. 4). In zero field, this magnetization vector has a given crystallographic direction, which is one of the

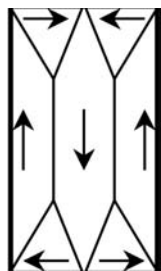


Fig. 4 Magnetic domains in zero field.

so-called “easy axes of magnetization.” In some materials, there are three easy axes of magnetization; in others, only there is only one axis. In the first case, it is told that the material has a cubic anisotropy; in the second instance, it has an axial anisotropy. Moving the magnetic vector away from an easy axis of magnetization costs energy, which is called the energy of anisotropy ( $E_a$ ). This energy depends on constants called the magnetocrystalline anisotropy constants (denoted  $K$ ), which are a function of the material under consideration.

On the macroscopic point of view, the magnetization of a ferromagnetic (or a ferrimagnetic) material in zero field is equal to zero, and its magnetization curve (magnetization as a function of the applied magnetic field) is a shape characteristic of a ferromagnetic material with a hysteresis loop (Fig. 5A).

### Magnetic Properties of Fine Particles

The diameter of the colloidal particles under consideration here are always smaller than the dimension of a

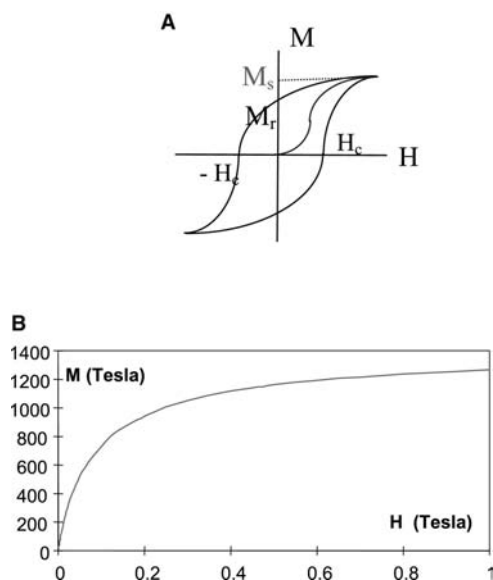


Fig. 5 (A) Scheme of the magnetization curve of a ferromagnetic (or ferrimagnetic) material. (B) Real magnetization curve of a superparamagnetic material.

magnetic domain. It means that each particle is a magnetic monodomain and has a permanent magnetic moment, whose intensity  $\mu$  is proportional to the specific magnetization of the material constituting the grain ( $M_s$ ), and to the volume of this grain ( $V$ ):

$$\mu = M_s V$$

$M_s$  is usually lower than the magnetization of the bulk material for several reasons. The first is relevant for oxidized materials; for example, metallic particles' specific magnetization, if submitted to oxidation, will fall down—and this change will be more dramatic as the particle surface increases. But even for particles stable with respect to oxidation, the local disorganization of the surface leads to a lowering of the specific magnetization.<sup>[7]</sup>

For 7-nm-diameter maghemite particles, a typical value of  $\mu$  is  $5.4 \times 10^{-20} \text{ A m}^2$ , which corresponds to about  $6000 \mu_B$ .<sup>[52]</sup>

The direction of this moment is fixed in the direction of an easy axis of magnetization. Nevertheless, the nature of the anisotropy (cubic one or uniaxial one) depends on the particles' shape and size. The value of the energy of anisotropy is also modified compared with the value of the bulk material. For an uniaxial anisotropy, it is given by:

$$E_a = K_{a \text{ eff}} V$$

where  $V$  is the volume of the monodomain, and  $K_{a \text{ eff}}$  is the anisotropy constant of the material in the grain. This anisotropy constant depends now on the particle shape, particle size, and the interactions between grains. It is difficult to propose a calculation of such an energy, but experimental magnetization or Mössbauer measurements have allowed estimations for ferrite particles.<sup>[37]</sup>

For a given material and a given temperature, the energy of anisotropy decreases when the particle size decreases. Under a given diameter, it becomes the same order of magnitude as the entropic term  $kT$ : this means that the magnetization vector fluctuates around the easy axis of magnetization, with a characteristic relaxation time (Néel relaxation time) such as  $\tau = \tau_0 \exp(E_a/kT)$  ( $\tau_0$  is on the order of  $10^{-10}$  sec). This phenomenon is called superparamagnetism (by comparison with the paramagnetic behavior of isolated magnetic moments, and by opposition to the ferromagnetic behavior of the bulk material) and the particle is called a “soft dipole.” For a given temperature, according to the nature of the material, the diameter below which superparamagnetism is observed differs. For example, at room temperature, 5-nm-diameter maghemite particles have a superparamagnetic behavior, although cobalt ferrite particles have a



ferromagnetic behavior. But please note that the colloids under consideration here are always polydispersed in size and, at a given temperature, an assembly of such colloids presents a rather large distribution of relaxation times. Some studies have tried to relate the anisotropy of cobalt ferrite grains to the particle size.<sup>[53,54]</sup> A complete description of the magnetic properties of nanoparticles needs to take into account surface effects: the surface disordered spins fluctuate and hinder the dynamics of the magnetic moment associated with a particle. Surface anisotropy can be more important than the volume.<sup>[55]</sup>

On a macroscopic point of view, the shape of the magnetization curve of a diluted assembly of superparamagnetic grains is well described by the Langevin formalism (Fig. 5B):

$$M(H) = M_s \left( \coth \frac{\mu H}{kT} - \frac{kT}{\mu H} \right)$$

The polydispersity has to be taken into account and can modify the shape of the curve because of its high influence on  $\mu$ .<sup>[52]</sup>

## COLLOIDAL DISPERSION OF MAGNETIC NANOPARTICLES

As mentioned earlier, because of their colloidal dimensions, magnetic nanoparticles can be dispersed in a liquid carrier, and a stable colloidal dispersion, usually called “magnetic fluid” or “ferrofluid,” can be obtained.<sup>[6]</sup> Such dispersions conjugate the properties of usual colloidal dispersions and the magnetic properties of the nanoparticles dispersed. Indeed, oily magnetic fluids have found many commercialized applications (special seals and bearings, moving coils speaker, inertia dampers, etc.)<sup>[56]</sup> and many other conceptual ones (captors, magnetic ink, magnetic levitation, magneto-optical devices, etc.).<sup>[57]</sup>

### Processes for the Dispersion of Magnetic Colloidal Particles in Liquid Carriers

#### Oily carriers

Organic solvents are often needed for commercialized applications. That is the reason why most of the particle synthesis processes involve a step during which a surfactant is added to the mixture, to adsorb on particles and to provide them an affinity for the oily media.<sup>[58,59]</sup> The surfactant avoids aggregation of particles in the oily liquid carrier, and the resulting product is a stable colloidal dispersion of magnetic particles. Surfactants are, for applications, commercial

products. Oleic acid is often used because it is one of the best surfactants for dispersing metal oxide particles in hydrocarbon media. But it cannot be used for dispersion of particles in aromatic oils or chlorinated solvents. In fact, the choice of a surfactant is not a trial-and-error work.<sup>[10,60,61]</sup> It is always a single-chain surfactant and the chemical nature of the chain is a function of the nature of the liquid carrier. For example, dispersion in aromatic oils is possible with surfactants having an aromatic cycle in their tail. The choice of the polar head is determined by the nature of the particle surface. Oleic acid is a good surfactant for ferric oxide particles because the carboxylic acid group is a good chelating agent of Fe species.<sup>[62]</sup> But even when the affinity of the surfactant for the surface is strong, it has to be kept in mind that desorption can occur (e.g., when diluting the colloidal dispersion with the liquid carrier). This is a serious limitation for applications as for theoretical studies.

Polymeric species, again introduced during the synthesis of particles, are sometimes described as stabilizers, in the case of metallic particles.<sup>[39,40]</sup> In some other cases, they are grafted as macrosurfactants on the particles after synthesis.<sup>[63]</sup>

Anyway, the result is that, at the present time, it is possible to obtain dispersions of magnetic nanoparticles in a wide variety of media: alkane, aromatic solvents, chlorated solvents, ketones, phthalates, and commercial oils derived from silicon oils, resins, etc. Some dispersions are commercialized; others are laboratory products.

#### Aqueous solvents

Aqueous solvents are also used for the dispersion of ferrite particles, usually for fundamental studies or biomedical applications.<sup>[64]</sup> In this case, the dispersions are stabilized, thanks to particle surface charges. Indeed, a metal oxide surface in water has a specific acid–base behavior, which leads to anionic or cationic surface charges according to the value of the pH, which are called “structural charges”.<sup>[8]</sup> When particles have a sufficient number of structural charges, electrostatic repulsions can stabilize their dispersion in water or in a brine solution. Unfortunately, for the magnetic ferric oxides constituting the magnetic particles under consideration (cobalt ferrite, maghemite, etc.), particles have a sufficient amount of surface charges only for strongly alkaline media (pH > 11) or strongly acidic ones (pH < 3).<sup>[9]</sup> As an example, it has been found that 7-nm-diameter maghemite particles have 80 structural charges at pH 2, 25 at pH 3, and only 8 at pH 4.<sup>[65]</sup>

Such a pH range is not suitable for applications, but can be modified by adsorption of small organic molecules (e.g., citrate species). The latter provide to the surface their own acid–base behavior and ensure negative surface charges for particles for any pH higher

than 3.<sup>[9,65]</sup> Moreover, it has been found that dispersions of citrate-coated particles were astonishingly stable in brine solution for electrostatically stabilized systems, indicating that adsorption of citrate leads to additional short-range repulsions of steric origin.<sup>[66]</sup> To modify the pH stability range of their dispersions, the particles can also be coated by silica or by molecules such as dimercaptosuccinic acid. This last molecule is of particular interest as it allows a further grafting of biological species through thiol bridges.<sup>[67]</sup>

The number of structural charges is not, in fact, the relevant parameter to explain the stability of electrostatically stabilized aqueous colloidal dispersions. As a matter of fact, the nature of the counterions of particles (charge and size) is of great importance because these counterions will condense on the charged surface, leading to an “effective surface” charge, inferior to the structural one and is the relevant parameter to quantify the electrostatic repulsions.<sup>[68]</sup> Highly charged and small counterions have to be avoided to obtain stable dispersions. That is the reason why tetramethylammonium has often been used in the case of dispersions of negatively charged ferrite particles, and nitrate anions in the case of positively charged particles.<sup>[25]</sup>

### Phase Behavior of Dispersions of Magnetic Nanoparticles

Dispersions of magnetic nanoparticles are special examples of colloidal dispersions because to the usual interparticle interactions (van der Waals attractions, electrostatic repulsions, or steric repulsions) are added the anisotropic dipolar magnetic interactions between the monodomains.<sup>[69]</sup> As a consequence, the total interparticle potential, which controls the structure and the phase behavior of the dispersion, becomes, theoretically, anisotropic. This is a rather original behavior and many theoretical papers dealing with dipolar fluids take dispersions of magnetic nanoparticles as an experimentally available example of dipolar fluid.<sup>[70–79]</sup> Theories predict for dipolar fluids in the high-dipole concentration regime the existence of a ferroelectric liquid phase,<sup>[73,75,76,80–84]</sup> or a ferroelectric crystal,<sup>[84]</sup> but, until now, such phases have never been observed. When the system is diluted, theories predict that the key parameter is the ratio of the dipolar attractions to the isotropic ones.<sup>[72,75–77,84]</sup> if this ratio is high, chains of dipoles, described as living polymers, are formed; if it is low, a “gas–liquid”-like phase transition can be observed. Application of a magnetic field to such systems has been considered for a long time. Authors who predict chains in zero field predict in magnetic field a phase transition between a “gas of chains” and a “liquid of chains,” or a phase separation leading to elongated drops of dense phase that

do not contain chains, according to the form given to the total interparticle potential.<sup>[75,76]</sup> Please note that refinements are now available to take into account the polydispersity.<sup>[78]</sup>

Interparticle interactions in magnetic fluids are van der Waals attractions, and dipolar magnetic interactions and repulsions, which depend on the nature of the dispersion:

1. The potential relative to the *van der Waals interactions* is isotropic and, for two spherical colloids of radius  $R$  separated by  $r$ , is given by:

$$U_{\text{vdw}} = -\frac{A}{6} \times \left[ \frac{2R^2}{r^2 - 4R^2} - \frac{2R^2}{r^2} + \ln \left( 1 - \frac{4R^2}{r^2} \right) \right]$$

where  $A$ , the Hamaker constant, can be estimated on the order of  $A = 10^{-19}$  J for metals and metallic oxides.<sup>[85]</sup>

2. The potential relative to *magnetic dipolar interactions* between two dipoles is anisotropic and is given by the formula:

$$\frac{U_{\text{dip}}(r)}{kT} = \frac{\gamma}{4\pi} (2 \cos \theta_1 \cos \theta_2 - \sin \theta_1 \sin \theta_2 \cos \varphi)$$

where  $\theta_i$  is the angle between the dipolar moment of a particle  $i$  and the vector joining the centers of two particles, and  $\varphi$  is the azimuthal angle between both dipoles. The reduced parameter  $\gamma = \mu_0 m_s^2 V^2 / kTr^3$  ( $V$  is the volume of a particle,  $m_s$  is the specific magnetization of the material, and  $r$  is the distance between particles) characterizes the strength of the magnetic coupling between particles. The average dipolar term is attractive and is usually calculated in two limit cases:<sup>[65,86]</sup> the case of low coupling in zero field ( $\gamma/4\pi \ll 1$ ), corresponding to the case of small moments or (and) large separations, and the case of high coupling ( $\gamma/4\pi \gg 1$ ), corresponding to the case of high moments separated by small distances.

For maghemite particles, with a diameter of 7 nm, the reduced parameter  $\gamma$  leads to a dipolar term in zero field, which is small compared with van der Waals attractions whatever the interparticle distance is.<sup>[65,87,88]</sup> Indeed, in zero field, usual ferrite magnetic fluids behave as isotropic systems. Thus as in any other colloidal dispersion, the range of attractions compared with the range of repulsions controls the phase



diagram of the system: if attractions are short-range, “fluid–solid”-like phase transitions are expected; if there are long-range attractions in the system, a critical point can exist, and “gas–liquid”-like, “liquid–solid”-like, and “gas–solid”-like transitions can be observed.<sup>[86,89–91]</sup> The theoretical treatment to describe such a behavior is not specific of magnetic fluids, and literature on this subject exceeds the present entry. We just emphasize here that aqueous dispersions of citrate-coated maghemite nanoparticles have allowed to experimentally investigate all the possible interactions regimes. At low ionic strength, electrostatic repulsions dominate interparticle interactions, and the phase diagram is one of an isotope-repulsive system. At high ionic strength, repulsions are screened and the interparticle potential is an isotope-attractive Lennard–Jones-like one in zero field.

The equation of state  $\Pi = f(\phi)$  of an aqueous dispersion of 7-nm-maghemite particles covered by citrate species has been constructed [using small-angle neutron scattering (SANS) and osmotic compression experiments] in several cases.<sup>[86–91]</sup> Such an equation is analogous to the equation of state of gases. Particles are compared with the molecules of a real gas, and the liquid carrier is compared with a continuum.  $\Pi$ , the osmotic pressure, is the pressure of the gas of particles.  $\Pi/\phi$  is a function of  $\phi$  that allows to check if the interactions between the particles are attractive or repulsive ones. It has been shown that it is possible with this unique system in zero field, varying the ionic strength and the temperature, to observe all the phase behaviors predicted by theories. At low ionic strength, the phase diagram is similar to the repulsive spheres and “gas–solid”-like transitions are observed for high-volume fractions of colloids. Nevertheless, the residual polydispersity, even if small, avoids to obtain a colloidal crystal and glasses are obtained.<sup>[90]</sup> At high ionic strength, the phase diagram is similar to the one of an atomic system and “gas–liquid”-like transitions are observed.<sup>[87]</sup> a phase dense in colloids nucleates inside a phase poor in colloids. A critical point has been localized. This noticeable richness of behaviors is because of the presence at the same time of monitorable electrostatic repulsions, strong steric repulsions because of the citrate coating, and long-range van der Waals attractions associated with the dipolar ones.<sup>[86]</sup>

In zero field, for these particles, chains have never been found. But using iron particles (that have a higher magnetic moment), chains have been observed even in zero field.<sup>[92,93]</sup>

The effect of a magnetic field depends on the range of the repulsions. In strongly repulsive systems, the application of a magnetic field will not macroscopically modify the aspect of the dispersions. Nevertheless, nanometric investigation, using SANS, shows that the structure of the suspensions is sensitive to the field,

a model of magnetic interactions explaining the under-field anisotropy of the SANS nuclear contribution.<sup>[94]</sup> However, in the regime of low repulsions, the dispersions are very sensitive to the application of a magnetic field, even macroscopically: “gas–liquid”-like phase transitions can be induced by the application of the field.<sup>[9]</sup>

### Some Properties of Dispersions of Magnetic Nanoparticles

The colloidal dispersion of magnetic nanoparticles has several original properties. Because the entry on “Magnetic Nanoparticles in Fluid Suspension: Ferrofluid Applications” covers this aspect in depth, here we shall only say few words on the magnetic and magneto-optical properties of these dispersions.

#### Magnetic properties

A colloidal dispersion of magnetic nanoparticles, whatever its nature, has a superparamagnetic behavior provided it is not too concentrated in particles in the absence of interparticle magnetic interactions (volume fraction lower than 1%).<sup>[7]</sup> Thus its magnetization curve is described by the Langevin formalism (Fig. 5B). This property has two origins. First, it may be because of the fact that the magnetic particles themselves are superparamagnetic (“Magnetic Properties of Fine Particles”). But even if all the particles were ferromagnetic, the behavior of their dispersion would be superparamagnetism because of the Brownian motion of particles in the carrier. Thus two characteristic times control the magnetic response of the colloidal dispersion—the Néel time (“Magnetic Properties of Fine Particles”) and the Brownian rotational relaxation time— $\tau_B = 3\eta V/kT$ , where  $\eta$  is the viscosity of the medium into which the particles are dispersed and  $V$  is their volume.<sup>[95]</sup> The relaxation process that is more rapid will control the relaxation. This provides magnetic fluids interesting frequency-dependent properties.<sup>[96,97]</sup>

#### Magneto-optical properties

These properties have been described for ferrite particles<sup>[98–106]</sup> and cobalt ferrite. In a zero magnetic field, a colloidal dispersion of such nanoparticles is an optically isotropic solution, but when a magnetic field is applied, it becomes anisotropic. When a beam of polarized light passes through a dispersion of nanometric ferrite particles (sufficiently diluted to limit absorption), according to the relative direction of the wave vector with respect to the magnetic field, linear anisotropy (field perpendicular to the wave vector) or circular anisotropy (field parallel to the wave vector)

will be observed. Linear anisotropy is characterized by linear birefringence and linear dichroism measurements. Circular anisotropy is characterized by Faraday rotation and ellipticity measurements. Both anisotropies increase as the magnetic field increases, and disappear without remanence when the magnetic field is cut off if the carrier is liquid. Nevertheless, they do not have exactly the same microscopic origin. Circular anisotropies behave as magnetization with respect to the magnetic field, although birefringence is related to the Brownian alignment of the particles (and not the Néel alignment of the moment) and follows the second Langevin law.<sup>[100]</sup> Trapped in a silica matrix, the dispersed magnetic nanoparticles can indeed be used to produce components for ellipsometry.<sup>[107]</sup>

### MAGNETIC COLLOIDAL PARTICLES ASSOCIATED WITH OTHER COLLOIDAL SYSTEMS

Magnetic nanoparticles have been introduced these last years in several complex media, either as probes to characterize the viscosity (and subsequently the structure) of the medium,<sup>[11,12,20,89,108]</sup> or to obtain field-dependent materials.<sup>[13–19]</sup> Such a mixture of a colloidal system with another has chemical and physico-chemical limitations.

### Hybrid Magnetic Materials: A Problem of Chemistry and of Physico-Chemistry

In any case, an eventual chemical incompatibility between the nanometric magnetic particles and the host colloid has to be examined first. A modification of the pH, an increase of the ionic strength, and adsorption or desorption of the charge-determining species or of the surfactants can occur during the mixing process or a few weeks after. The latter case is especially harmful because it can be unnoticed and leads to important interpretation errors. In the case of mixtures of self-assemblies of surfactants with particles, if the surfactant can adsorb on the ferrite particles, the properties of both the lyotropic system and the dispersion of nanoparticles will be modified. But even mixtures of purely inorganic systems can raise problems. For example, some clays are chemically stable only between pH 9 and pH 10: magnetic nanoparticles stable for these precise values have to be used to mix them with such a clay.<sup>[89,108]</sup> Chemistry of magnetic colloids is now sufficiently well developed to succeed in solving such problems.

As soon as the chemical stability of both colloidal systems is controlled, it has to be verified that one of the colloids will not “stress” the other one. As a matter

of fact, each colloidal system is characterized by its own osmotic pressure, and it can be roughly said that the system that has the higher osmotic pressure will impose its own pressure to the other one, which can then destabilize.<sup>[67]</sup>

### Magnetic Colloidal Particles as Viscosity Probes for the Characterization of Gels

As soon as particles can be dispersed in a medium, the medium will carry a magnetic field of induced birefringence (cf. “Some Properties of Dispersions of Magnetic Nanoparticles”). This birefringence disappears when the field is cut off, and its decrease is related to the Brownian motion of particles and their random orientations. The characteristic relaxation time is related to the diffusion coefficient of Brownian rotation of the particles in the carrier ( $\tau_B = 3\eta V/kT$ ) and becomes a measure of the local viscosity of the medium surrounding the particles, as soon as the latter are dispersed as individual grains in this medium ( $V$ , the hydrodynamic volume of the particles, must not vary during the experiment). This result makes the magnetic nanoparticles suitable probes to test the viscosity of several media at a nanometric scale<sup>[109]</sup> and allows, as a consequence, one to have an idea of the nanometric structure of a material. For example, if particles are able to rotate in a glass obtained by sol-gel process, it means that condensation is not complete or that heterogeneities exist into which nanometric objects are able to move. If the particles are really trapped in the silica matrix, a permanent birefringence can be remained.<sup>[11]</sup>

Another example is provided through the characterization of laponite gels.<sup>[89,108]</sup> Laponite is a synthetic clay, constituted by small discotic particles. These can be dispersed in water, but over a given volume fraction, a gel is obtained. Mixing nanometric maghemite particles in very low concentration with laponite particles (solving the problems of chemistry mentioned in “Hybrid Magnetic Materials: A Problem of Chemistry and of Physico-Chemistry”), it has been possible to investigate the local viscosity of laponite gels by measuring the relaxation decay of the birefringence signal of the probes. It has been found that in some macroscopically solid gels, the nanometric particles are able to rotate and feel the same viscosity as the one of water. This indicates the existence of mesoscopic liquid domains in the apparently homogeneous gels.

Magnetic polymeric hydrogels have also been synthesized, trapping nanometric maghemite or cobalt ferrite particles in polyacrylamide networks. Relaxation of a birefringence experiment has shown that according to the nature and amount of cross-linker

and to the particles' diameter, these particles are able or not able to rotate in the mesh of the network.<sup>[20,110,111]</sup>

### Magnetic Colloidal Particles to Induce a Magnetic Response to Lyotropic Systems

Magnetic fields or electric fields are often used to modify lyotropic systems: orientational transitions are induced in nematics or smectics,<sup>[112]</sup> liposomes are deformed by the application of an electric field.<sup>[113]</sup> Incorporation of a very small amount of magnetic colloidal particles in such systems can induce very impressive responses to low-intensity magnetic fields.

#### Magnetic liquid crystals

Several so-called "ferrosmeectics" have been synthesized. Surfactant-coated particles have been introduced in the cyclohexane part of the pseudo-ternary system water/sodium dodecyl sulfate/pentanol/cyclohexane.<sup>[14,114,115]</sup> Bidimensional packing of magnetic layers alternating with non-magnetic ones was obtained and it has been shown that this lamellar system, stabilized by Helfrich repulsions, can admit a great amount of particles and orientates in magnetic fields of low intensity. The origin of the coupling between the particles and the lyotropic systems is still not well established, with the coefficient of translational diffusion of the particles in the plane of the lamellae not modified by their confinement.<sup>[116]</sup> Later, negatively charged magnetic nanoparticles have been introduced in the aqueous part of the same system, and the role of the nature of the membrane interaction has been evidenced, modifying the system from a purely electrostatic one to a sterically stabilized one.<sup>[117]</sup> Indeed, pure electrostatic systems such as the binary one (didodecylammonium bromide/water) do not admit many particles, excluding them from the lamellar structure under the form of a dense magnetic aqueous phase.<sup>[63]</sup>

Ferromematics have also been obtained by mixing anisotropic micelles with maghemite nanoparticles.<sup>[13,118]</sup> The lyotropic system was, in this case, the ternary mixture potassium laurate/decanol/water and, surprisingly, stable ferromagnetic samples have been obtained by mixing this system with positively charged maghemite particles.<sup>[13]</sup> The phase diagram of the hybrid system has been constructed in the vicinity of the nematic area showing that the existence domain of the hybrid is very narrow.<sup>[119]</sup> Nevertheless, it exists and allows one to observe the so-called "Frederickz transitions" in low field (lower than 100 Oe).<sup>[118]</sup> Even if not explained on the microscopic point of view, the analysis of the dependence of the threshold magnetic field on the thickness of the sample and the volume fraction of magnetic oxide is explained by assuming a superparamagnetic behavior of the grains,

but a strong coupling between the latter and the nematic matrix.

### Liposomes, Emulsions, Capsules, and Latex

Incorporation of magnetic nanoparticles in lyotropic systems (as phospholipidic vesicles) or in polymeric ones (as latex) is usually performed in biotechnological applications. For example, magnetic latex is a commercial product used for cell labeling and cell sorting (i.e., for in vitro applications).<sup>[120,121]</sup> Magnetic liposomes have many conceptual applications especially for in vivo applications.<sup>[122–126]</sup>

Until now, the so-called "ferroliposomes," obtained by encapsulation of maghemite nanoparticles in dioleoylphosphatidylcholine (DOPC) vesicles, have been essentially considered for their unique physical properties.<sup>[19,127]</sup> They are able to move in a magnetic field gradient and giant liposomes elongate when a magnetic field is applied. From the analysis of the modification of the liposome shape, it is possible to obtain some information on the properties of the DOPC membrane bending modulus.<sup>[19]</sup> For applications, small unilamellar liposomes have now been considered. Several procedures are possible to encapsulate the particles in the liposomes, but, first of all, these particles have to be negatively charged to avoid a quick adsorption on the phospholipid on their surface, and to be citrate-coated to disperse in water at pH 7.<sup>[9,62]</sup> Then they can be introduced in the liposomes by a multiple emulsion process, either through a spontaneous swelling in water of phospholipidic bilayers stuffed with magnetic particles, or by swelling of the liposomes in a magnetic fluid, followed by the separation of the non-encapsulated particles.<sup>[17,127]</sup>

Magnetic multilamellar vesicles (oignons) can also be obtained by dilution of a lamellar phase containing magnetic particles.<sup>[128]</sup>

Synthesis of magnetic emulsions<sup>[15]</sup> and magnetic capsules<sup>[129]</sup> has also been described. These systems are interesting transpositions at the microscopic scale of nanoscopic particles. For example, chaining these magnetic objects with the application of a magnetic field is observed with a microscope or by light scattering and may have many interesting properties.<sup>[16]</sup> The main limitation of the technology at the present time is the polydispersity of the object synthesized.

## TECHNIQUES FOR THE CHARACTERIZATION OF MAGNETIC COLLOIDAL PARTICLES

### Particle Size

The particles under consideration here have diameters on the order of 10 nm. This implies the use of techniques

allowing size determination in the nanometric range. It has to be kept in mind that the systems are always polydispersed. Few techniques give the particle size distribution; most methods give average diameters, and it is repeated here that the log-normal size distribution given in “Metallic Particles” leads to average diameters such as:  $\langle d^n \rangle = d_0^n \exp(n^2 \sigma^2 / 2)$ .<sup>[130]</sup>

*Transmission electron microscopy (TEM)* allows one to calculate particle size and shape. It is well suited for magnetic particles as they are constituted of heavy metals such as iron or cobalt. Its data may provide a histogram of diameters, and log-normal size distribution can be adjusted to obtain  $d_0$  and  $\sigma$ .

*X-ray diffraction on powders* allows one to check the crystallographic nature of particles and provides an average diameter such as  $d_{RX} = d_0 \exp(2.5\sigma^2)$ .

*Magnetization measurements* allow one to obtain the particle size distribution also, through the analysis of the shape of the magnetization curve.<sup>[7,51]</sup> For sufficiently magnetic systems, this is constructed by using a vibrating magnetometer (called “Foner”). Particles have to be well dispersed in a solid or liquid carrier. The size obtained has to take into account the specific magnetization of the material constituting the particles.

*Small-angle neutron scattering and small-angle X-ray scattering (SAXS)* also allow one to find the particle size and shape, as soon as particles are dispersed in a carrier. The analysis of the form factor of diluted suspensions of magnetic nanoparticles allows one to verify that particles are well described as spheres [ $I(q)$  proportional to  $q^{-4}$  in the high  $q$  range], and the gyration radius found is usually in good agreement (taking into account the polydispersity effects) with the TEM results.<sup>[64,131]</sup>

The hydrodynamic radius of particles when dispersed in a solution can be obtained from *dynamic light scattering* but also from the experiment of *relaxation of birefringence* (cf. “[Magnetic Colloidal Particles as Viscosity Probes for the Characterization of Gels](#)”). Indeed, the relaxation time, when the viscosity is known, becomes a measure of the particle’s hydrodynamic volume.<sup>[98,132]</sup> The diameters obtained by these techniques are always much higher than the other ones because they are hydrodynamic diameters and because they are averages providing an important weight to the polydispersity. Relaxation of birefringence can, in that way, be used to characterize the binding of biological molecules on particles.<sup>[133]</sup>

### Nature of the Surface Coverage

Adsorption isotherms have to be constructed to determine the amount of species (surfactants, polymers, or ions) adsorbed on particles. It is not specific to magnetic particles and will not be developed here, but is

discussed in the entry on “Nanoparticles: Generation, Surface Functionalization, and Ion Sensing.” Please just note that the main difficulty in the case of nanometric particles is to separate the particles from the supernatant without modifying the adsorption phenomena.

### Interactions between Particles

Again the interactions between particles are not specific to magnetic particles and are discussed in “Nanoparticles in Solutions: General Interactions.” Nevertheless, these particles have been revealed to be good examples of colloidal systems. SAXS and SANS have allowed to determine the structure factor of several aqueous and non-aqueous dispersions of magnetic nanoparticles.<sup>[64,90,94]</sup> Direct measurements of osmotic pressure have also been performed.<sup>[65,86,90]</sup> Using these techniques, it has been possible to propose a reasonable form for the interparticle interaction potential.

### APPLICATIONS INVOLVING MAGNETIC NANOPARTICLES

As stated at the beginning of this entry, magnetic recording is not the only application of magnetic nanoparticles. As a matter of fact, superparamagnetic particles are not able to keep magnetic information. Applications involving magnetic nanoparticles can be classified in two categories: technological applications involving magnetic fluids (ferrofluids applications)<sup>[21]</sup> and applications taking advantage of some particular properties of the nanoparticles, especially the biomedical applications.<sup>[22,23]</sup>

Ferrofluids applications will not be detailed here because they are not really concerned with the colloidal aspect of the system. Nevertheless, they are the only applications of magnetic nanoparticles truly commercialized at this point.

The other application fields concerning magnetic nanoparticles are conceptual ones:<sup>[57]</sup> optics (realization of birefringent components) and microwave technology (dispersions of particles can be wave guides or microwave absorbants) are some examples.

Applications in the field of biotechnology and medical imaging are in full expansion<sup>[22,23,135]</sup> (e.g., Ref.<sup>[134]</sup>). Dispersion of magnetic nanoparticles is already commercialized as contrast agents for magnetic resonance imaging.<sup>[135–141]</sup> They can be used as drug carriers at the same time.<sup>[142]</sup> But the problem of the biodistribution of magnetic probes is not fully solved. Particle size and surface coating both are parameters that have to be controlled. Another promising application is the treatment of tumors using magnetothermolysis: an a.c.

magnetic field applied to magnetic nanoparticles that induces an increase of temperature and cell hyperthermia.<sup>[143]</sup> Concerning in vitro applications of magnetic nanoparticles, the latter are now commercialized.<sup>[22,23]</sup> Nevertheless, they have to challenge the magnetic latex and emulsions that are widely commercialized for rapid bioseparation processes. This area still leads to sparkling new results.<sup>[144]</sup>

## CONCLUSION

Magnetic nanoparticles are original colloids because of their magnetic properties. Improved manipulation of these properties is a permanent challenge for scientists involved in the chemistry of materials. On the theoretical point of view, it is interesting to note that colloidal dispersions of such particles have proven to be excellent experimental systems, allowing one to illustrate the phase behavior of colloids. More and more, these particles are used as probes to test other colloidal systems, and new colloids, hybrid ones, are born from these works. The development of their applications in the field of biotechnology is the new challenge now.

## REFERENCES

- Bate, G. Recording Materials. In *Ferromagnetic Materials*; Wohlfart, E.P., Ed.; 1980; Vol. 2, 381 pp.
- Charles, S.; Massart, R. Particles Suitable for Magnetic Colloids. In *Magnetic Fluids and Applications Handbook*; Berkovski, B., Ed.; 1996; 4 pp.
- Kittel, C. *Introduction to Solid State Physics*; John Wiley and Sons, Ed.; 1976.
- Charles, S. Magnetic Properties of Fine Particles. In *Magnetic Fluids and Applications Handbook*; Berkovski, B., Ed.; 1996; 64.
- Scholten, P.C. Some material problems in magnetic fluids. *Chem. Eng. Commun.* **1988**, *67*, 331.
- Rosensweig, R.E. *Ferrohydrodynamics*; Cambridge University Press, 1985.
- Bacri, J.C.; Perzynski, R.; Salin, D.; Cabuil, V.; Massart, R. Magnetic colloidal properties of ionic ferrofluids. *J. Magn. Magn. Mater.* **1986**, *62*, 31, and references therein.
- Stumm, W. *Chemistry of the Solid-Water Interfaces*; John Wiley and Sons, Ed.; 1992.
- Bacri, J.-C.; Perzynski, R.; Salin, D.; Cabuil, V.; Massart, R. Ionic magnetic fluids: A crossing of chemistry and physics. *J. Magn. Magn. Mater.* **1990**, *85*, 27.
- Lefébure, S.; Dubois, E.; Cabuil, V.; Neveu, S.; Massart, R. Monodisperse magnetic nanoparticles: Preparation and dispersion in water and oils. *J. Mater. Res.* **1998**, *13* (10), 2975.
- Chaput, F.; Boilot, J.-P.; Canva, M.; Brun, A.; Perzynski, R.; Zins, D. Permanent birefringence of ferrofluid particles trapped in a silica matrix. *J. Non-Cryst. Solids* **1993**, *160*, 177.
- Zrinyi, M.; Büki, A.; Barsi, A. *Electric and Magnetic Field-Sensitive Smart Polymer Gels in Polymer Gels and Networks*; Osada, Y., Khokhlov, A.R., Eds.; Marcel Dekker: New York, 2002; 309 pp.
- Berejnov, V.; Raikher, Yu.; Cabuil, V.; Bacri, J.-C.; Perzynski, R. Synthesis of stable lyotropic ferronematics with high magnetic content. *J. Colloid Interface Sci.* **1998**, *199*, 215.
- Fabre, P.; Casagrande, C.; Veyssié, M.; Cabuil; Massart, R. Ferrosmeectics: A new magnetic and mesomorphic phase. *Phys. Rev. Lett.* **1990**, *64* (5), 539.
- Bibette, J. Monodisperse ferrofluid emulsions. *J. Magn. Magn. Mater.* **1993**, *122*, 37.
- Fermigier, M.; Gast, A.P. Structure evolution in a paramagnetic latex suspension. *J. Magn. Magn. Mater.* **1993**, *122* (1/3), 46.
- Ménager, C.; Cabuil, V. Synthesis of magnetic liposomes. *J. Colloid Interface Sci.* **1995**, *169*, 251.
- Lyotropic ferronematics: Magnetic orientational transition in the discotic phase. *Europhys. Lett.* **1998**, *41* (5), 507.
- Bacri, J.-C.; Cabuil, V.; Cebers, A.; Ménager, C.; Perzynski, R. Elongation of ferro-vesicles along a magnetic field. *Europhys. Lett.* **1996**, *33* (3), 235.
- Galicía, J.A.; Sandre, O.; Cousin, F.; Guemghar, D.; Ménager, C.; Cabuil, V. Designing magnetic composite materials using aqueous magnetic fluids. *J. Phys., Condens. Matter* **2003**, *15*, S1379.
- Rajj, K. Magnetic Fluids and Devices: A Commercial Survey. In *Magnetic Fluids and Applications Handbook*; Berkovski, B., Ed.; 1996; 657 pp.
- Halbreich, A.; Roger, J.; Pons, J.-N.; Geldwerth, D.; Da Silva, M.F.; Roudier, M.; Bacri, J.-C. Biomedical applications of maghemite ferrofluid. *Biochimie* **1998**, *80*, 379.
- Halbreich, A.; Roger, J.; Pons, J.-N.; Da Silva, M.F.; Bacri, J.-C. *Functional Ferrofluids for Biomedical Applications. Radioactive and Magnetic Microparticles*; Arshady, R., Ed.; MML Series: Citus Book: London, 2001; Vol. 3, 459.
- Papell, S.S. Low Viscosity Magnetic Fluid Obtained by Colloidal Suspension of Magnetic Particles. U.S. Patent 3,215,572, 1965.
- Massart, R. Preparation of aqueous magnetic liquids in alkaline and acidic media. *IEEE Trans. Magn.* **1981**, *MAG-17* (2), 1247.
- Massart, R.; Cabuil, V. Synthèse en milieu alcalin de magnetite colloïdale: Contrôle du rendement et de la taille des particules. *J. Chim. Phys.* **1987**, *84*, 967.
- Veyssières, L.; Chaneac, C.; Jolivet, J.P. Size tailoring of magnetite particles formed by aqueous precipitation: An example of thermodynamic stability of nanometric oxide particles. *J. Colloid Interface Sci.* **1998**, *205* (2), 205.
- Bee, A.; Massart, R.; Neveu, S. Synthesis of very fine maghemite particles. *J. Magn. Magn. Mater.* **1995**, *149*, 6.
- Feltin, N.; Pileni, M.P. New technique for synthesizing iron ferrite magnetic nanosized particles. *Langmuir* **1997**, *13*, 3927.

30. Sun, S.; Zeng, H. Size-controlled synthesis of magnetic nanoparticles. *J. Am. Chem. Soc.* **2002**, *124*, 8204.
31. Mann, S. Biom mineralization and Biomimetic Materials Chemistry. In *Biomimetic Materials Chemistry*; Mann, S., Ed.; VCH Publishers, Inc., 1996; 1 pp.
32. Tourinho, F.; Franck, R.; Massart, R.; Perzynski, R. Synthesis and magnetic properties of manganese and cobalt ferrite ferrofluids. *Prog. Colloid Polym. Sci.* **1989**, *79*, 128.
33. Tourinho, F.; Franck, R.; Massart, R. Aqueous ferrofluids based on manganese and cobalt ferrites. *J. Mater. Sci.* **1990**, *25*, 3249.
34. Ngo, A.T.; Bonville, P.; Pileni, M.P. Nanoparticles of  $\text{Co}_x\text{Fe}_{1-x}\text{O}_4$ : Synthesis and superparamagnetic properties. *Eur. Phys. J., B* **1999**, *9*, 583, and references therein.
35. Zins, D.; Cabuil, V.; Massart, R. New aqueous magnetic fluids. *J. Mol. Liq.* **1999**, *83*, 217.
36. Moumen, N.; Pileni, M.P. New synthesis of cobalt ferrite particles in the range 2–5 nm: Comparison of the magnetic properties of the nanosized particles in dispersed fluid or in powder form. *Chem. Mater.* **1996**, *8*, 1128.
37. Hochepped, J.F.; Pileni, M.P. Magnetic properties of mixed cobalt–zinc ferrite nanoparticles. *J. Appl. Phys.* **2000**, *87* (5), 2472.
38. Hess, P.H.; Parker, P.H. Polymers for stabilization of colloidal cobalt particles. *J. Appl. Polym. Sci.* **1966**, *10*, 1915.
39. Papirer, E. Preparation de suspensions de particules de cobalt finement divisées. *C. R. Acad. Sci.* **1977**, *285*, 73.
40. Wagener, M.; Günther, B.; Blums, E. Preparation of oxidation resistant cobalt oil colloids. *J. Magn. Magn. Mater.* **1999**, *201*, 18.
41. Griffiths, C.H.; O'Horo, M.P.; Smith, T.W. The structure, magnetic characterization, and oxidation of colloidal iron dispersions. *J. Appl. Phys.* **1979**, *50*, 7108.
42. Butter, K.; Philipse, A.P.; Vroege, G.J. Synthesis and properties of iron ferrofluids. *J. Magn. Magn. Mater.* **2002**, *252*, 1.
43. Nakatani, I.; Hijikata, M.; Ozawa, K. Iron–nitride magnetic fluids prepared by vapor–liquid reaction and their magnetic properties. *J. Magn. Magn. Mater.* **1993**, *122*, 10.
44. Petit, C.; Taleb, A.; Pileni, M.P. Cobalt nanosized particles organized in a 2D superlattice: Synthesis, characterization and magnetic properties. *J. Phys. Chem., B* **1999**, *103*, 1805.
45. Sun, S.; Murray, C.B. Synthesis of monodisperse cobalt nanocrystals and their assembly into magnetic superlattices. *J. Appl. Phys.* **1999**, *85* (8), 4325.
46. Dubois, E.; Chevalet, J.; Massart, R. Magnetic conductive liquids: Preparation and properties of iron particles in mercury. *J. Mol. Liq.* **1999**, *83*, 243, and references therein.
47. Yamamoto, H.; Kanno, T.; Nakatani, I. Effects of heat treatment on properties of Co magnetic fluids. *J. Magn. Magn. Mater.* **1993**, *122*, 13.
48. Blums, E.; Chukhrov, A.Yu. Separation processes in polydisperse magnetic fluids. *J. Magn. Magn. Mater.* **1993**, *122*, 110.
49. Dubois, E.; Cabuil, V.; Massart, R.; Hasmonay, E.; Perzynski, R. Preparation of monodisperse magnetic fluids. *J. Magn. Magn. Mater.* **1995**, *149*, 1.
50. Lefébure, S.; Dubois, E.; Cabuil, V.; Neveu, S.; Massart, R. Monodisperse magnetic nanoparticles: Preparation and dispersion in several media. *Mater. Res.* **1998**, *13* (10), 2975.
51. Jiles, D. *Introduction to Magnetism and Magnetic Materials*; Jiles, D., Ed.; Chapman and Hall Publ., 1991.
52. Bacri, J.C.; Perzynski, R. Salin, magnetic and thermal behavior of  $\gamma\text{-Fe}_2\text{O}_3$  fine grains. *J. Magn. Magn. Mater.* **1988**, *71*, 246.
53. Popplewell, J.; Sakhini, L. The dependence of the physical and magnetic properties of magnetic fluids on particle size. *J. Magn. Magn. Mater.* **1995**, *149*, 72.
54. Pileni, M.P.; Moumen, N.; Hochepped, J.H.; Bonville, P.; Veillet, P. Control of the size of cobalt ferrite nanoparticles: Synthesis and properties. *J. Phys., IV (France)* **1997**, *7*, C1-505.
55. Gazeau, F.; Bacri, J.C.; Gendron, F.; Perzynski, R.; Raikher, Yu.; Stepanov, V.; Dubois, E. Magnetic resonance of nanoscopic ferrite particles in ferrofluids: Evidence of surface effects. *J. Magn. Magn. Mater.* **1998**, *186*, 175.
56. Raj, K. Magnetic Fluids and Devices: A Commercial Survey. In *Magnetic Fluids and Applications Handbook*; Berkovski, B., Ed.; 1996; 657.
57. Rosensweig, R.E. Conceptual Applications of Magnetic Fluids. In *Magnetic Fluids and Applications Handbook*; Berkovski, B., Ed.; 1996; 591 pp.
58. Reimers, G.W.; Khalafalla, S.E. Preparing magnetic fluids by a peptization method. U.S. Bur. Mines, Tech. Prog. Rep. **1972**, *59*, .
59. Wyman, J.E. Ferrofluid Composition and Method of Making and Using Them. U.S. 4,430,239, February 07, 1984.
60. Scholten, P.C. Some material problems in magnetic fluids. *Chem. Eng. Commun.* **1988**, *67*, 331.
61. van Ewijk, G.A.; Vroege, G.J.; Philipse, A.P. Convenient preparation methods for magnetic colloids. *J. Magn. Magn. Mater.* **1999**, *201*, 31.
62. Rocchicciolo-Deltcheff, C.; Franck, R.; Cabuil, V.; Massart, R. Surfacted ferrofluids: Interactions at the surfactant–magnetic iron oxide interface. *J. Chem. Res.* **1987**, (S)126, (M):1209.
63. Cabuil, V.; Hochart, N.; Perzynski, R.; Lutz, P.J. Synthesis of cyclohexane magnetic fluids through adsorption of end-functionalized polymers on magnetic particles. *Prog. Colloid Polym. Sci.* **1994**, *97*, 71.
64. Bacri, J.C.; Perzynski, R.; Salin, D.; Cabuil, V.; Massart, R.; Pons, J.N.; Roger, J. Ionic Ferrofluids: Physico-Chemical Aspects. In *Biophysical Effects of Steady Magnetic Fields*; Springer-Verlag, 1986; 59 pp.
65. Ménager, C.; Belloni, L.; Cabuil, V.; Dubois, M.; Gulik-Krzywicki, T.; Zemb, Th. Osmotic equilibrium between an ionic magnetic fluid and an electrostatic lamellar phase. *Langmuir* **1996**, *12* (14), 3516.
66. Dubois, E.; Cabuil, V.; Boué, F.; Perzynski, R. Structural analogy between aqueous and oily magnetic fluids. *J. Chem. Phys.* **1999**, *111* (15), 147.



67. Roger, J.; Pons, J.-N.; Massart, R.; Halbreicht, A.; Bacri, J.-C. Some biomedical applications of ferrofluids. *Eur. Phys. J., Appl. Phys.* **1999**, *5*, 321.
68. Belloni, L. Interacting Monodisperse and Polydisperse Spheres. In *Neutron, X-ray and Light Scattering*; Lindner, P., Zemb, Th., Eds.; Elsevier Science Publ., 1991; 135 pp.
69. Cabuil, V. Phase behavior of magnetic nanoparticles dispersions in bulk and confined geometries. *Curr. Opin. Colloid Interface Sci.* **2000**, *5*, 44.
70. De Gennes, P.G.; Pincus, P.A. Pair correlations in a ferromagnetic colloid. *Phys. Kondens. Mater.* **1970**, *11*, 189.
71. Kalikmanov, V. Statistical thermodynamic of ferrofluids. *Physica, A* **1992**, *183A*, 25.
72. Leeuwen, M.E.; Smit, B. What makes a polar liquid a liquid? *Phys. Rev. Lett.* **1993**, *71* (24), 3991.
73. Groh, B.; Dietrich, S. Long-ranged orientational order in dipolar fluids. *Phys. Rev. Lett.* **1994**, *72* (15), 2422.
74. Zhang, H.; Widom, M. Global phase diagrams for dipolar fluids. *Phys. Rev., E* **1994**, *49* (5), 3591.
75. Stevens, M.S.; Grest, G.H. Structure of soft spheres dipolar fluids. *Phys. Rev., E* **1995**, *51* (6), 5962.
76. Stevens, M.S.; Grest, G.H. Phase coexistence of a Stockmayer fluid in an applied field. *Phys. Rev., E* **1995**, *51* (6), 5976.
77. Osipov, M.A.; Teixeira, P.I.C.; Telo da Gama, M.M. Structure of strongly dipolar fluids at low densities. *Phys. Rev., E* **1996**, *54* (3), 2597.
78. Costa Cobral, B.J. Structure of polydisperse dipolar hard-sphere fluids. *J. Chem. Phys.* **2000**, *112* (9), 4351.
79. Weis, J.J. Simulation of quasi-two-dimensional dipolar systems. *J. Phys., Condens. Matter* **2003**, *15* (15), S1471.
80. Tejero, C.F.; Daanoun, A.; Lekkerkerker, H.N.W.; Baus, M. Phase diagrams of simple fluids with extreme pair potentials. *Phys. Rev. Lett.* **1994**, *73*, 752.
81. Wei, D.; Patey, G.N. Orientational order in simple dipolar liquids: Computer simulation of a ferroelectric nematic phase. *Phys. Rev. Lett.* **1992**, *68* (13), 2043.
82. Wei, D.; Patey, G.N. Ferroelectric liquid-crystal and solid phases formed by strongly interacting dipolar soft spheres. *Phys. Rev., A* **1992**, *46* (12), 7783.
83. Lesvesque, D.; Weis, J.J. Orientational and structural order in strongly interacting dipolar hard spheres. *Phys. Rev., E* **1994**, *49* (6), 5131.
84. Klapp, S.; Forstmann, F. Phase transitions in dipolar fluids: An integral equation study. *J. Chem. Phys.* **1997**, *106* (23), 742.
85. Scholten, P.C. *Colloid Chemistry of Magnetic Fluids in Thermodynamics of Magnetic Fluids*; Berkovsky, X., Ed.; Hemisphere Publishing Corporation: Bristol, PA, 1978; 1 pp.
86. Cousin, F.; Dubois, E.; Cabuil, V. Tuning the interactions of a magnetic colloidal suspension. *Phys. Rev., E* **2003**, *68*, 021405.
87. Dubois, E.; Perzynski, R.; Boué, F.; Cabuil, V. Liquid-gas transitions in charged colloidal dispersions: Small-angle neutron scattering coupled with phase diagrams of magnetic fluids. *Langmuir* **2000**, *16*, 5617.
88. Cousin, F.; Cabuil, V. Osmotic pressure of electrostatically stabilized magnetic liquids. *L. Mol. Liq.* **1999**, *83*, 203.
89. Cousin, F. *Comportement de Phase de Colloïdes Sphériques et Plaquettaires*; Thesis of the University Paris; September 31, 2000; Vol. VI.
90. Cousin, F.; Cabuil, V. Fluid-solid transitions in aqueous ferrofluids. *Prog. Colloid Polym. Sci.* **2000**, *115*, 77.
91. Cousin, F.; Dubois, E.; Cabuil, V. *J. Chem. Phys.* **2001**, *115*, 6051.
92. Butter, K.; Bomans, P.H.; Frederik, P.M.; Vroege, G.J.; Philise, A.P. *Nat. Mater.* **2003**, *2*, 88.
93. Butter, K.; Bomans, P.H.; Frederik, P.M.; Vroege, G.J.; Philise, A.P. Direct observation of dipolar chains in ferrofluids in zero magnetic field using cryogenic electron microscopy. *J. Phys., Condens. Matter* **2003**, *15* (15), S1451.
94. Gazeau, F.; Boué, F.; Dubois, E.; Perzynski, R. Static and quasi-elastic small angle scattering on biocompatible ionic ferrofluids: Magnetic and hydrodynamic interactions. *J. Phys., Condens. Matter* **2003**, *15* (15), S1305.
95. Kötz, R.; Weitschies, W.; Trahms, L.; Semmler, W. Investigation of Brownian and Néel relaxation in magnetic fluids. *J. Magn. Magn. Mater.* **2000**, *201*, 102, and references therein
96. Fannin, P.C.; Kinsella, L.; Charles, S.W. Wide-band complex magnetic susceptibility measurements of magnetic fluids as a function of temperature. *J. Magn. Magn. Mater.* **2000**, *201*, 91.
97. Fannin, P.C.; Vincent, D.; Massart, R.; Perov, P.; Neveu, S. A study of the frequency dependent susceptibility of colloidal suspension of manganese ferrite (MnFe<sub>2</sub>O<sub>4</sub>) nanoparticles. *Eur. Phys. J., Appl. Phys.* **1999**, *8*, 247.
98. Bacri, J.-C.; Cabuil, V.; Massart, R.; Perzynski, R.; Salin, D. Ionic ferrofluids: Optical properties. *J. Magn. Magn. Mater.* **1987**, *65*, 285.
99. Hasmonay, E.; Dubois, E.; Bacri, J.C.; Perzynski, R.; Raikher, Yu.L.; Stepanov, V.I. Static magneto-optical birefringence of size-sorted  $\gamma$ -Fe<sub>2</sub>O<sub>3</sub> nanoparticles. *Eur. Phys. J., B* **1998**, *5*, 859.
100. Monin, J.; Brevet, P.; Neveu, S.; Delaunay, L.; Gagnaire, H. A light polarization modulator using magnetic liquid intended for high precision optical instrumentation. *J. Magn. Magn. Mater.* **1993**, *122*, 403.
101. Donatini, F.; Jamon, D.; Monin, J.; Neveu, S. Experimental investigation of longitudinal magneto-optic in four ferrite ferrofluids in visible-near infrared spectrum. *IEEE Trans. Magn.* **1999**, *35* (5), 4311.
102. Neveu, S.; Tourinho, F.A.; Bacri, J.C.; Perzynski, R. Magnetic birefringence of cobalt ferrite ferrofluids. *Colloids Surf., A* **1993**, *80*, 1.
103. Donatini, F.; Neveu, S.; Monin, J. Measurements of longitudinal magneto-optic effect in ferrofluids: A dynamic method. *J. Magn. Magn. Mater.* **1996**, *162*, 69.
104. Jamon, D. *Thesis of the University Jean Monnet, Saint-Etienne, France*; July 2000.
105. Hasmonay, E.; Dubois, E.; Neveu, S.; Bacri, J.C.; Perzynski, R. Alternating magneto-birefringence of

- ionic ferrofluids in crossed magnetic fields. *Eur. Phys. J., B* **2001**, *21*, 19.
106. Raikher, Yu.; Stepanov, V.I.; Bacri, J.C.; Perzynski, R. Orientational dynamics of ferrofluids with finite magnetic anisotropy of the particle. Relaxation of magneto-birefringence in crossed fields. *Phys. Rev., E* **2002**, *66*, 021203.
  107. Jamon, D.; Robert, S.; Conatini, F.; Rousseau, J.J.; Bovier, C.; Roux, H.; Serrughetti, J.; Cabuil, V.; Zins, D. Optical investigation of  $\gamma$ -Fe<sub>2</sub>O<sub>3</sub> nanoparticle-doped silica gel matrix for birefringent components. *IEEE Trans. Magn.* **2001**, *37* (5), 3803.
  108. Cousin, F.; Cabuil, V.; Levitz, P. *Langmuir* **2002**, *18*, 1466.
  109. Bacri, J.C.; Dumas, J.; Gorse, D.; Perzynski, R.; Salin, D. Ferrofluid viscosimeter. *J. Phys. Lett.* **1985**, *46*, L1199.
  110. Mayer, C.; Cabuil, V.; Lalot, T.; Thouvenot, R. Incorporation of magnetic nanoparticles in new hybrid networks based on heteropolyanions and polyacrylamide. *Angew. Chem., Int. Ed. Engl.* **1999**, *38* (24), 3672.
  111. Mayer, C.; Cabuil, V.; Lalot, T.; Thouvenot, R. Magnetic nanoparticles trapped in pH 7 hydrogels as a tool to characterize the properties of the polymeric network. *Adv. Mater.* **2000**, *12* (6), 417.
  112. de Gennes, P.G.; Prost, J. *The Physics of Liquid Crystals*, 2nd Ed.; de Gennes, P.G., Prost, J., Eds.; Oxford University Press, 1993.
  113. Kummrow, M.; Helfrich, W. Deformation of giant lipid vesicles by electric fields. *Phys. Rev., A* **1991**, *44*, 409.
  114. Dabadie, J.C.; Fabre, P.; Veyssié, M.; Cabuil, V.; Massart, R. Magnetic lyotropic phases. *J. Phys., Condens. Matter* **1990**, *2*, 291.
  115. Fabre, P.; Ober, R.; Veyssié, M.; Cabuil, V. Smectic ferrofluid. *J. Magn. Mater.* **1990**, *85*, 77.
  116. Fabre, P.; Quillet, C.; Veyssié, M.; Nallet, F.; Roux, D.; Cabuil, V.; Massart, R. Anisotropy of the diffusion coefficients of submicronic particles embedded in lamellar phases. *Europhys. Lett.* **1992**, *20* (3), 229.
  117. Dubois, E.; Fabre, P.; Ramos, L. Compatibility between solid particles and lamellar phase: A crucial role of the membranes interactions. *J. Chem. Phys.* **1996**, *100* (11), 4533.
  118. Figueiredo Neto, A.M.; Saba, M.M.F. Determination of the minimum concentration of ferrofluid required to orient nematic liquid crystals. *Phys. Rev., A* **1986**, *34* (4), 3483, and references therein.
  119. Berejnov, V.; Cabuil, V.; Perzynski, R.; Raikher, Yu. Lyotropic system potassium laurate/1-decanol/water as a carrier medium for a ferronematic liquid crystal: Phase diagram study. *J. Phys. Chem., B* **1998**, *102*, 7132.
  120. Yanase, N.; Noguchi, H.; Asakura, H.; Suzuta, T. Preparation of magnetic latex particles by emulsion polymerization of styrene in the presence of a ferrofluid. *J. Appl. Polym. Sci.* **1993**, *50*, 765.
  121. Landfester, K.; Ramirez, R.B. Encapsulated magnetite particles for biomedical applications, 2003. *J. Phys., Condens. Matter* **2003**, *15*, S1345.
  122. de Cuyper, M. Magnetoproteoliposomes. *J. Magn. Mater.* **1993**, *122*, 340.
  123. De Cuyper, M.; Müller, P.; Lueken, H.; Hødenius, M. *J. Phys., Condens. Matter* **2003**, *15*, S1425.
  124. Babincova, M.; Altanerova, V.; Babinec, P. Site specific in vivo targeting of magnetoliposomes using externally applied magnetic field. *Z. Nat.forsch., C* **2000**, *55* (3/4), 278.
  125. Bacri, J.C.; Cabuil, V.; Cebers, A.; Ménager, C.; Perzynski, R. *Magn. Vesicles Mater. Sci. Eng., C* **1995**, *2*, 197.
  126. Lesieur, S.; Grabielle-Madlmont, C.; Ménager, C.; Cabuil, V.; Dadhi, D.; Pierrot, P.; Edwards, K. Evidence of surfactant-induced formation of transient pores in lipid bilayers by using magnetic fluid loaded liposomes. *J. Am. Chem. Soc.* **2003**, *125*, 5266.
  127. Sandre, O.; Ménager, C.; Prost, J.; Cabuil, V.; Bacri, J.C.; Cebers, A. Shape transitions of giant liposomes induced by an anisotropic spontaneous curvature. *Phys. Rev., E* **2000**, *62* (3), 3865.
  128. Letellier, D.; Cabuil, V. Dilution of 6-lauryl poly(oxethylene ether) lamellar phases doped with magnetic nanoparticles. *Prog. Colloid Polym. Sci.* **2000**, *115*, 5.
  129. Neveu-Prin, S.; Cabuil, V.; Massart, R.; Escaffre, P.; Dussaud, J. Encapsulation of magnetic fluids. *J. Magn. Mater.* **1993**, *122*, 42.
  130. Cabuil, V.; Perzynski, R. Particle Size Determination in Magnetic Fluids. In *Magnetic Fluids and Applications Handbook*; Berkovski, Ed.; Begell House Inc. Publ.: New York, 1996; 12 pp.
  131. Boué, F.; Cabuil, V.; Bacri, J.C.; Perzynski, R. Small-angle neutron scattering of ionic ferrofluids. *J. Magn. Mater.* **1993**, *122*, 78.
  132. Bacri, J.C.; Perzynski, R.; Salin, D.; Servais, J. Magnetic transient birefringence of ferrofluids: Particle size determination. **1987**, *48*, 1385.
  133. Wilhem, C.; Gazeau, F.; Roger, J.; Pons, J.N.; Salis, M.F.; Perzinsky, Bacri, J.-C. Binding of biologically effectors on magnetic nanoparticles measured by a magnetically induced transient birefringence experiment. *Phys. Rev., E* **2002**, *65*, 031404.
  134. Häfeli, U.; Schütt, W.; Teller, J.; Zborowski, M., Eds.; *Scientific and Clinical Applications of Magnetic Carriers*; Plenum Press: New York, 1997.
  135. Roger, J.; Pons, J.N.; Massart, R.; Halbreich, A.; Bacri, J.C. Some biomedical applications of ferrofluids. *Eur. Phys. J.* **1999**, *5*, 321.
  136. Weissleder, R.; Bogdanov, A.; Neuwelt, E.A.; Papisov, M. Long circulating iron oxides for MR imaging. *Adv. Drug Deliv.* **1995**, *167*, 321.
  137. Cambon, C.; Clement, O.; Le Blanche, A. Superparamagnetic iron oxide as positive contrast agents: In vitro and in vivo evidence. *J. Magn. Reson. Imaging* **1993**, *11* (4), 509.
  138. Enochs, W.S.; Harsh, G.; Hochberg, F.; Weissleder, R. Improved delineation of human brain tumors on MR images using a long-circulating, superparamagnetic iron oxide agent. *J. Magn. Reson. Imaging* **1999**, *9* (2), 228.
  139. Dodd, C.H.; Hsu, H.C.; Chu, W.J.; Yang, P.; Zhang, H.G.; Mountz, J.D., Jr.; Zinn, K.; Forder, J.;

- Josephson, L.; Weissleder, R.; Mountz, J.M.; Mountz, J.D.J. Normal T-cell response and in vivo magnetic resonance imaging of T cells loaded with HIV transactivator-peptide-derived superparamagnetic nanoparticles. *Immunol. Methods* **2001**, *256* (1–2), 89.
140. Portet, D.; Denizot, B.; Rump, E.; Lejeune, J.J.; Jallet, P. Non polymeric coating of iron oxide colloids for biological use as magnetic resonance imaging contrast agent. *J. Colloid Interface Sci.* **2001**, *238*, 37.
141. Billotey, C.; Wilhem, C.; Devaud, M.; Bacri, J.C.; Bittoun, J.; Gazeau, F. Cell internalization of anionic maghemite nanoparticles: Quantitative effect on magnetic resonance imaging. *Magn. Reson. Med.* **2003**, *49*, 646.
142. Pauser, S.; Reszka, R.; Wagner, S.; Wolf, K.J.; Biuhr, H.J.; Berger, G. Liposome-encapsulated superparamagnetic iron oxide particles as markers in an MRI-guided search for tumor-specific drug carriers. *Anti-cancer Drug Des.* **1997**, *12*, 125.
143. Jordan, A.; Scholz, R.; Maier-Hauff, K.; Johannsen, M.; Wust, P.; Nadobny, J.; Schirra, H.; Schmidt, H.; Deger, S.; Loening, S.; Lanksch, W.; Felix, R. Presentation of a new magnetic field therapy system for the treatment of human solid tumors with magnetic fluid hyperthermia. *J. Magn. Magn. Mater.* **2001**, *225*, 118.
144. Doyle, P.S.; Bibette, J.; Bancaud, A.; Viovy, J.L. Self-assembled magnetic matrices for DNA separation chips. *Science* **2002**, 2237.

# Magnetic Nanoparticles for Granular Recording Media

**David E. Nikles**

*Department of Chemistry, University of Alabama,  
Tuscaloosa, Alabama, U.S.A.*

**J. W. Harrell**

*Department of Physics and Astronomy, University of Alabama,  
Tuscaloosa, Alabama, U.S.A.*

## INTRODUCTION

Moore's Law has been the most famous symbol of the power of high technology in the last half of the 20th century. In 1965, Moore<sup>[1]</sup> predicted that the number of transistors on a computer chip would double every 18 months. Indeed, the number of transistors has grown at a compound annual rate of 39% per year (Fig. 1) for more than 30 years.<sup>[2]</sup> Meanwhile, the data storage density of magnetic hard drives has matched the pace of growth in data storage density (36% per year) until 1990, when it accelerated to 79% per year. Both technologies have grown at an amazing pace, providing higher-performance computing and higher-capacity data storage at lower costs, thereby fueling growth of the Internet. However, both technologies face scientific challenges that threaten to limit continued growth.

Modern magnetic data storage devices record data as magnetized bit cells in thin films, either polycrystalline metal films or particulate films (acicular iron particles in a polymer matrix).<sup>[3]</sup> Each bit cell contains many grains or particles, and the signal-to-noise ratio depends on the number of particles in the bit volume.<sup>[4]</sup> The data storage density of state-of-the-art hard disk drive systems is 100 gigabits per square inch,<sup>[5]</sup> and the information storage industry is now pursuing basic research aimed at densities beyond 1 terabit per square inch.<sup>[6]</sup> Increases in data storage density are achieved by scaling down the bit size, i.e., the bit length (increasing the bits per inch), the track width (increasing the track per inch), and the film thickness. In 2002, the bit cell dimension in state-of-the-art hard disk media was approximately  $50 \times 400$  nm. If densities were to increase at a rate of 41% per year over the next decade (less than the last decade), then the bit cell would be  $4 \times 4$  nm in 2012 (Fig. 2). This is less than the size of a single grain in current media and would necessitate a new paradigm in magnetic recording. The reduction in bit size using conventional recording methods means

that magnetic grains and particle sizes must be decreased. However, the superparamagnetic limit threatens to limit the bit sizes that can be achieved using conventional recording methods. Superparamagnetism arises when the thermal stability factor ( $KV/kT$ ) becomes small, where  $K$  is the anisotropy constant,  $V$  is the particle or grain volume,  $k$  is the Boltzmann constant, and  $T$  is the temperature.  $KV$  gives the magnetic anisotropy energy for a magnetic grain or particle, and as the volume decreases, the anisotropy energy decreases. As the ratio of anisotropy energy to thermal energy ( $KV/kT$ ) decreases, the thermal stability of the magnetization decreases (i.e., subject to thermally activated magnetization reversal). When  $KV/kT$  is less than about 60, long-term data storage (>10 years) is no longer reliable. Of course, the grain size can be decreased if  $K$  is increased. This has led to increased interest in materials with high values of magnetocrystalline anisotropy, and the  $L1_0$  phase of FePt has found particular scrutiny because of its very high value of  $K_u$  ( $6$  to  $10 \times 10^7$  erg/cm<sup>2</sup>).<sup>[7]</sup>

Here we report our progress on solving basic materials science problems, whose solution would enable self-assembled FePt nanoparticles to be used in high-density magnetic recording. We describe the synthesis of FePtAg, FePtAu, FePtCu, or FePtCo ternary alloy nanoparticles. The effect of added Ag, Au, or Cu on temperature required to transform the particles from the fcc phase to the  $L1_0$  phase is reported along with the effect of added Co on the magnetic properties.

## FePt NANOPARTICLES

A team from IBM first reported the synthesis of nearly monodisperse 3- to 4-nm diameter FePt nanoparticles and self-assembly of the particles into close-packed films and magnetic recording in the films.<sup>[8]</sup> We found that we could reliably reproduce their synthetic procedure.<sup>[9]</sup> The particles were prepared by heating

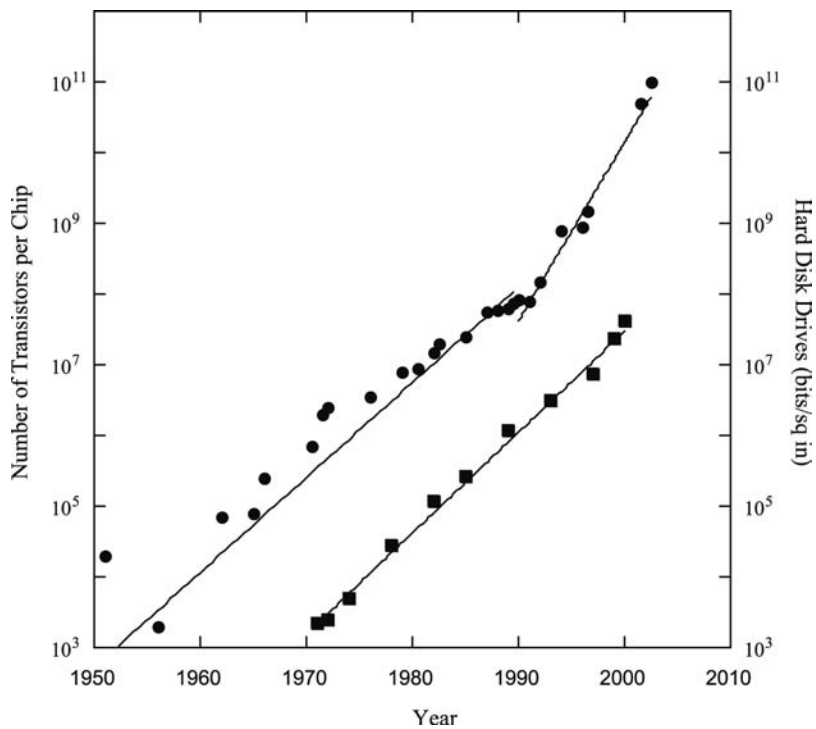


**Fig. 1** Comparison of the growth of data storage density for magnetic disks (solid circles) and the number of transistors on a computer chip (solid squares).

a solution of platinum acetylacetonate and 1,2-hexadecanediol in dioctyl ether to 100°C. Iron pentacarbonyl, oleyl amine, and oleic acid were added, and the reaction mixture was heated to boiling (~280°C) for 30 min, giving a black dispersion of FePt nanoparticles. Adding ethanol precipitated the particles, which were isolated by centrifugation. The particles were redispersed in hexane and reprecipitated by adding ethanol. Repeated cycles of dispersion and precipitation removed impurities and somewhat narrowed the size distribution.

As prepared, the FePt particles were single crystals with a disordered face-centered cubic structure and were superparamagnetic. The particles had an average diameter of 3.5 nm and a distribution of particle diameters of about 5% of the average. They had a coating of organic surfactants and could be dispersed in hydrocarbon solvents. When dispersions in a 50/50 mixture of hexane and octane were cast onto a solid substrate (either a silicon wafer or a carbon-coated copper TEM grid) and the solvent evaporated slowly, the particles self-assembled into films containing close-packed arrays (Fig. 3). If the solvent evaporated too rapidly, the particles had positional disorder. Using octane lowers the solvent evaporation, allowing the particles to find their lattice positions as the films form.

The X-ray diffraction curves for films containing Fe<sub>48</sub>Pt<sub>52</sub> particles showed two diffraction peaks, the 111 peak and the 200 peak, indicative of a disordered fcc phase. The films were heat-treated for 30 min either in a tube furnace with flowing 2% hydrogen in argon

( $T = 350^{\circ}\text{C}$  to  $500^{\circ}\text{C}$ ) or in a vacuum annealer ( $T = 550^{\circ}\text{C}$  to  $700^{\circ}\text{C}$ ). After heat treatment at temperatures above  $500^{\circ}\text{C}$  in an inert atmosphere, the L<sub>1</sub>0 001 and 110 peaks appeared. The fcc 200 peak split into two peaks, the L<sub>1</sub>0 200 and 002 diffraction peaks. The 111 peak moved to higher values of  $2\theta$  and the  $d$ -spacing decreased to the bulk value for FePt ( $d_{111} = 219.7$  pm). The position of the  $d_{111}$  peak could be used as a measure of the degree of transformation, which depended on the heating temperature (Fig. 4). While being heated at these temperatures, the organic surfactant decomposed, leaving a carbonaceous char.

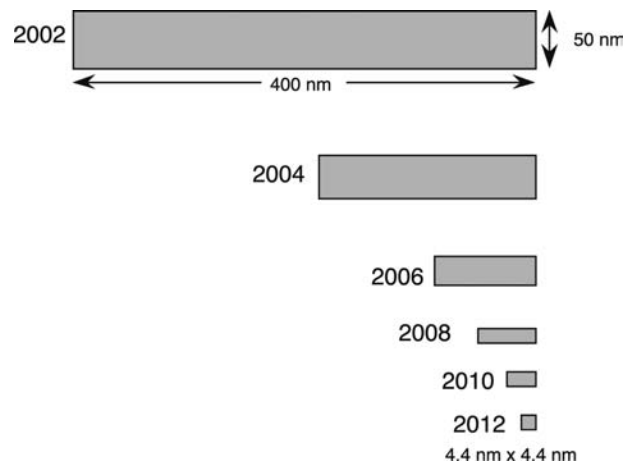


**Fig. 2** The incredible shrinking bit—road map for future bit cell dimensions in magnetic hard drive systems.

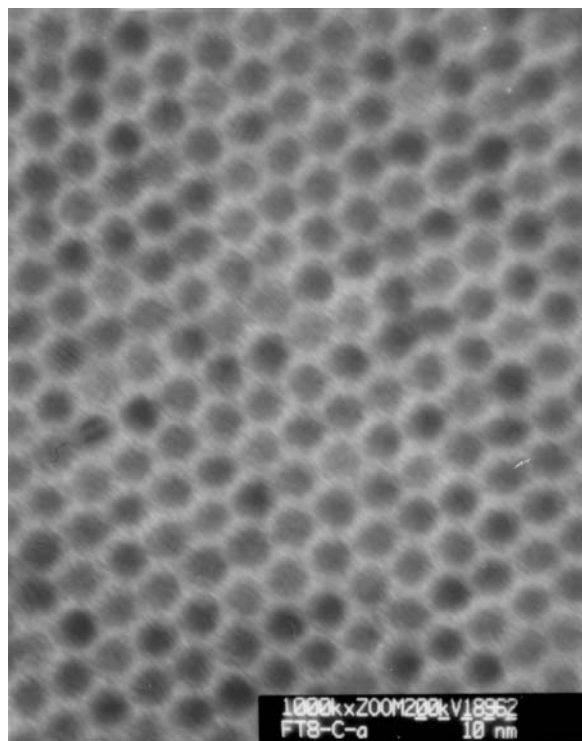


Fig. 3 TEM image of self-assembled FePt nanoparticles.

There was considerable loss in particle positional order and particle agglomeration.<sup>[10]</sup> This is a problem because it defeats the object of preparing small particles with a narrow distribution of sizes and self-assembling them into highly ordered structures.

As the particles transformed to the  $L1_0$  phase, the coercivity increased, reflecting the high anisotropy of the phase. For films containing weakly interacting

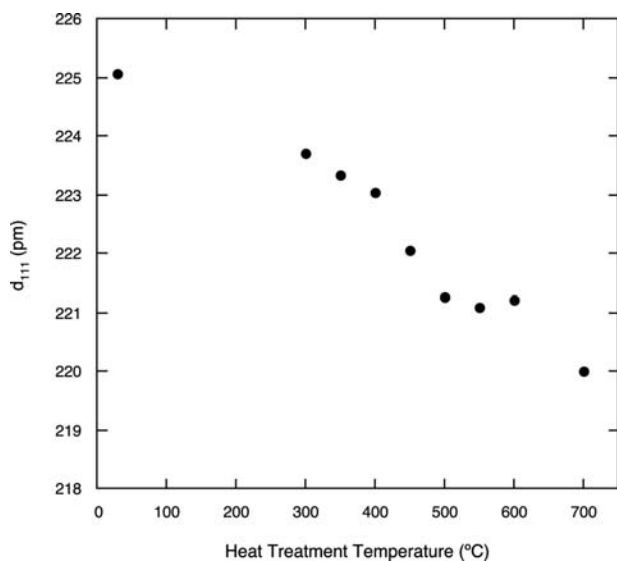


Fig. 4 Effect of heat treatment temperature on the value of the  $d$ -spacing for the 111 diffraction peak.

single-domain particles,  $H_c$  will depend on the magnetic anisotropy energy,  $K$ , and the volume,  $V$ , of the particle. As prepared, the spherical particles had very small anisotropy with  $KV < 25k_B T$ , the particles were superparamagnetic, and  $H_c = 0$ . The bulk anisotropy of fully ordered  $L1_0$  FePt is  $K \sim 6\text{--}10 \times 10^7$  erg/mL,<sup>[6]</sup> which, for fully ordered 4-nm diameter FePt particles, would give  $KV/k_B T \sim 48\text{--}81$  and the films would exhibit a high room-temperature coercivity. For films containing weakly interacting single-domain particles with randomly oriented easy axes, the coercivity would be expected to follow the Sharrock equation, given by<sup>[11]</sup>

$$H_c = H_0 \left\{ 1 - \left[ \frac{k_B T}{KV} \ln(f_0 t) \right]^{2/3} \right\} \quad (1)$$

where  $f_0$  is an attempt frequency of the order of  $10^9\text{--}10^{11}$  Hz and  $t$  is the effective measuring time.  $H_0$  is the low-temperature or short-time coercivity given by  $H_0 \sim K/M_s$ , where  $M_s$  is the saturation magnetization. For highly ordered FePt nanoparticles, Eq. (1) predicts high coercivities; however,  $H_c$  will depend on temperature and particle size. Fig. 5 shows a plot of the room-temperature coercivity as a function of heat treatment temperature for films containing self-assembled  $\text{Fe}_{48}\text{Pt}_{52}$  nanoparticles. After heat treatment at 350°C or 400°C, the films were still superparamagnetic, with no coercivity. Only after heat treatment at 450°C did the films become ferromagnetic and show some coercivity. Heat treatment at higher temperatures gave higher values of coercivity as the transformation to the  $L1_0$  phase was more complete. Scherrer analysis of the linewidth of the 111 diffraction peaks for the films heated to temperature over 500°C showed increased crystallite size, suggesting particle sintering.<sup>[12]</sup> Particle coalescence has also been shown in high-resolution TEM studies of FePt films that have been heat-treated at temperatures above 500°C.<sup>[10]</sup> Accordingly, in interpreting this increase in coercivity, it is difficult to separate the effect of increasing the magnetocrystalline anisotropy of the particles as a result of transforming to the  $L1_0$  phase from the effect of increasing particle volume as a result of sintering.

The problem of transforming the particles from the fcc phase to the  $L1_0$  phase is somewhat vexing. Heat treatment at temperature in excess of 500°C caused degradation of the organic surfactants, leading to loss in particle positional order. Furthermore, as the heat treatment temperature exceeds 550°C, there is extensive particle coalescence. Particle coalescence increases the switching volumes, which defeats the purpose of making small particles. The solution to this problem could be to heat-treat at lower temperatures, thereby decreasing the amount of particle coalescence.



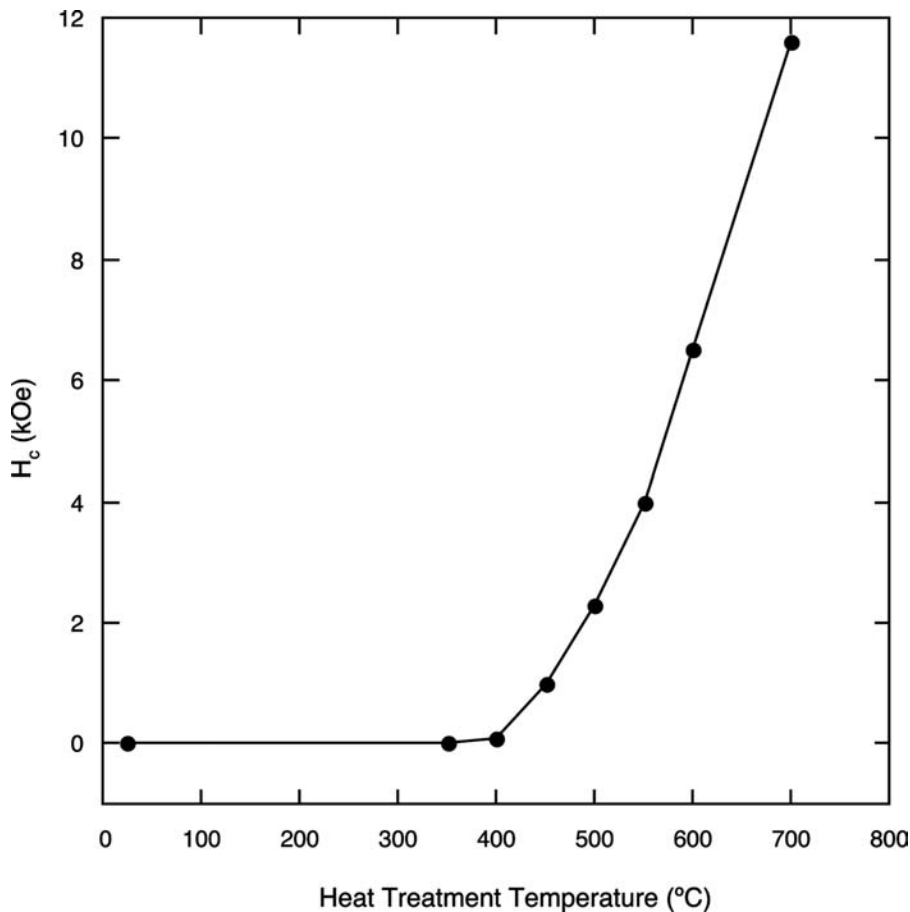


**Fig. 5** Effect of heat treatment temperature on the coercivity of films containing Fe<sub>48</sub>Pt<sub>52</sub> nanoparticles.

However, heat treatment at lower temperatures results in incomplete phase transformation, giving films with a distribution of order parameters and, in turn, a distribution of magnetic anisotropies, which is detrimental to high-density magnetic recording. It would be highly desirable if the fcc to tetragonal phase transformation could be carried out at lower temperature, at least below temperatures where the particles coalesce, preferably below temperatures where the surfactants decompose.

### FeCuPt NANOPARTICLES

Our interest in finding means of lowering the temperature required for transforming the FePt particles from the fcc to the L1<sub>0</sub> phase led us to add copper to the FePt nanoparticles. We were motivated by literature reports that adding copper to sputter-deposited FePt films greatly reduced the L1<sub>0</sub> ordering temperature. Maeda et al.<sup>[13]</sup> reported that for films containing [FePt]<sub>85</sub>Cu<sub>15</sub>, the coercivity was 5000 Oe after annealing at 300°C, while H<sub>c</sub> for FePt films was only a few hundred oersted after annealing at 300°C. Takahashi, Ohnuma, and Hono<sup>[14]</sup> found that adding 4 at.% Cu

into FePt sputtered films decreased the temperature required for fcc to L1<sub>0</sub> ordering from 500°C to 400°C. They suggested that the addition of Cu lowered the melting point for the alloy, increasing the atomic mobility, thereby enhancing the kinetics of ordering.

These reports suggest the possibility of lowering the temperature needed to bring about the fcc to L1<sub>0</sub> phase transformation for FePt nanoparticles by adding copper. This led us to devise a method to prepare FePtCu ternary alloy nanoparticles that was quite similar to the synthesis of FePt nanoparticles,<sup>[15]</sup> except for adding a source of Cu and using diphenyl ether as the solvent. A solution of platinum acetylacetonate, copper bis(2,2,6,6-tetramethyl-3,5-heptadionate), and 1,2-hexadecanediol in diphenyl ether was heated to 80°C. Iron pentacarbonyl, oleyl amine, and oleic acid were added and the mixture was heated to reflux (~260°C) for 30 min to give a black dispersion. After cooling to room temperature, the particles were precipitated by adding ethanol and isolated by centrifuging. As with the FePt nanoparticles, the FePtCu nanoparticles were repeatedly redispersed and reprecipitated to remove impurities and narrow the particle size distribution. Varying the relative ratio of Fe, Pt, and Cu charged to the reaction mixture varied the

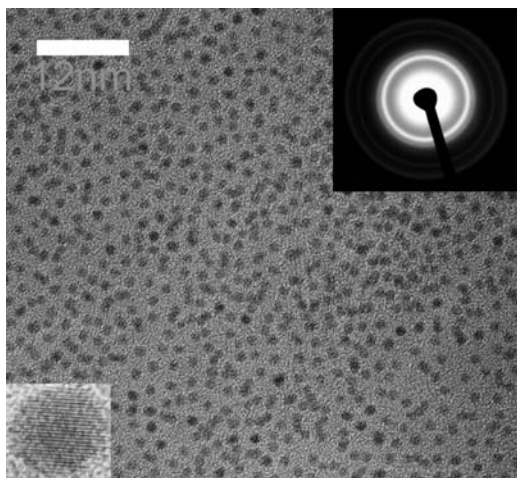


**Fig. 6** TEM image of self-assembled  $\text{Fe}_{45}\text{Pt}_{44}\text{Cu}_{11}$  nanoparticles.

particle composition. However, the amount of Fe in the particles was much less than the amount of Fe charged into the reaction as iron pentacarbonyl. Particles with the compositions  $\text{Fe}_{55}\text{Pt}_{35}\text{Cu}_{10}$ ,  $\text{Fe}_{45}\text{Pt}_{44}\text{Cu}_{11}$ ,  $\text{Fe}_{48}\text{Pt}_{40}\text{Cu}_{12}$ , and  $\text{Fe}_{35}\text{Pt}_{50}\text{Cu}_{15}$  were prepared.

Self-assembled films consisting of close-packed FePtCu nanoparticles were prepared in exactly the same manner as for the FePt nanoparticles (Fig. 6). The average particle size was 3.5 nm, and the particles were single crystalline with a disordered fcc structure. There was no evidence either in the TEM images or the X-ray diffraction curves (Fig. 7) for particles other

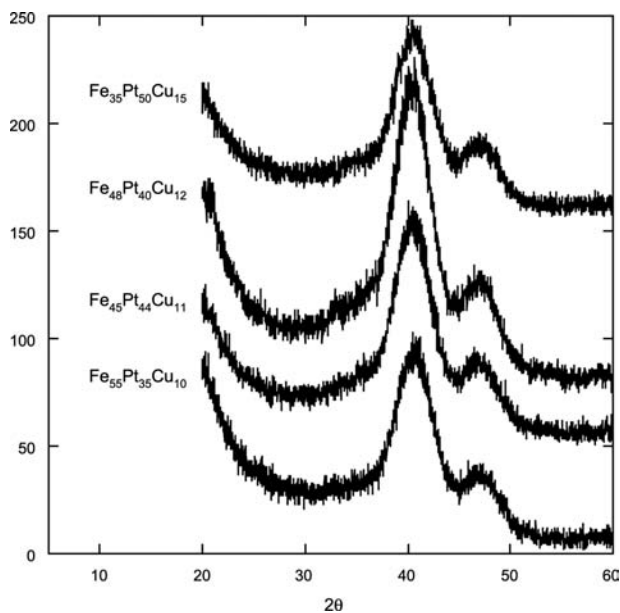


**Fig. 7** X-ray diffraction curves for films containing FePtCu nanoparticles as-prepared.

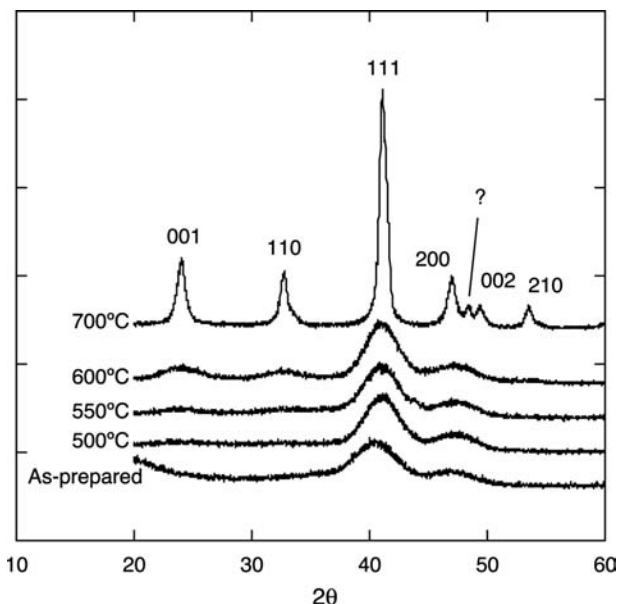


**Fig. 8** Effect of heat treatment temperature on the X-ray diffraction curves for films containing  $\text{Fe}_{45}\text{Pt}_{44}\text{Cu}_{11}$ .

than a ternary FePtCu alloy. There were no apparent diffraction peaks due to fcc copper. The films were heated in a tube furnace in an atmosphere containing 4%  $\text{H}_2$  in Ar, and X-ray diffraction was used to determine the amount of phase transformation. Results for the composition  $\text{Fe}_{45}\text{Pt}_{44}\text{Cu}_{11}$  (Fig. 8) were typical of the other compositions. Only after heat treatment above 550°C did the particles begin to transform to the  $L1_0$  phase. The copper remained in the particles; otherwise, the 111 peak for fcc Cu would have appeared near  $2\theta = 43^\circ$ . Only after heating at 700°C did the  $L1_0$  phase completely form, as seen by the sharp 001 and 110 diffraction peaks and the splitting of the fcc 200 peak into the  $L1_0$  200 and 002 peaks. The ternary Fe–Pt–Cu phase diagram shows a range of compositions for FePtCu where a single  $L1_0$  phase is formed and other compositions where the  $L1_0$  phase and the fcc phase coexist.<sup>[17]</sup> In both phases, Cu is substituting for iron. Careful examination of the X-ray diffraction curves for the films heat-treated at 700°C (Fig. 8) revealed an extra peak near  $2\theta = 48.5^\circ$ , between the  $L1_0$  200 and the 002 peaks. This peak may be a result of the presence of a small amount of the fcc phase. The extra peak was not seen for  $\text{Fe}_{48}\text{Pt}_{40}\text{Cu}_{12}$ .

The hysteresis curve in Fig. 9 was measured for the  $\text{Fe}_{45}\text{Pt}_{44}\text{Cu}_{11}$  particles heat-treated at 700°C and is typical of the curves for the other compositions also heat-treated at 700°C. The shape of the curve suggests a mixture of hard and soft magnetic phases, and it could be decomposed into hard and soft loops. The hard component coercivities of  $\text{Fe}_{45}\text{Pt}_{44}\text{Cu}_{11}$ ,  $\text{Fe}_{48}\text{Pt}_{40}\text{Cu}_{12}$ , and  $\text{Fe}_{35}\text{Pt}_{50}\text{Cu}_{15}$  were greater than 5000 Oe and were comparable to that of  $\text{Fe}_{48}\text{Pt}_{52}$ .

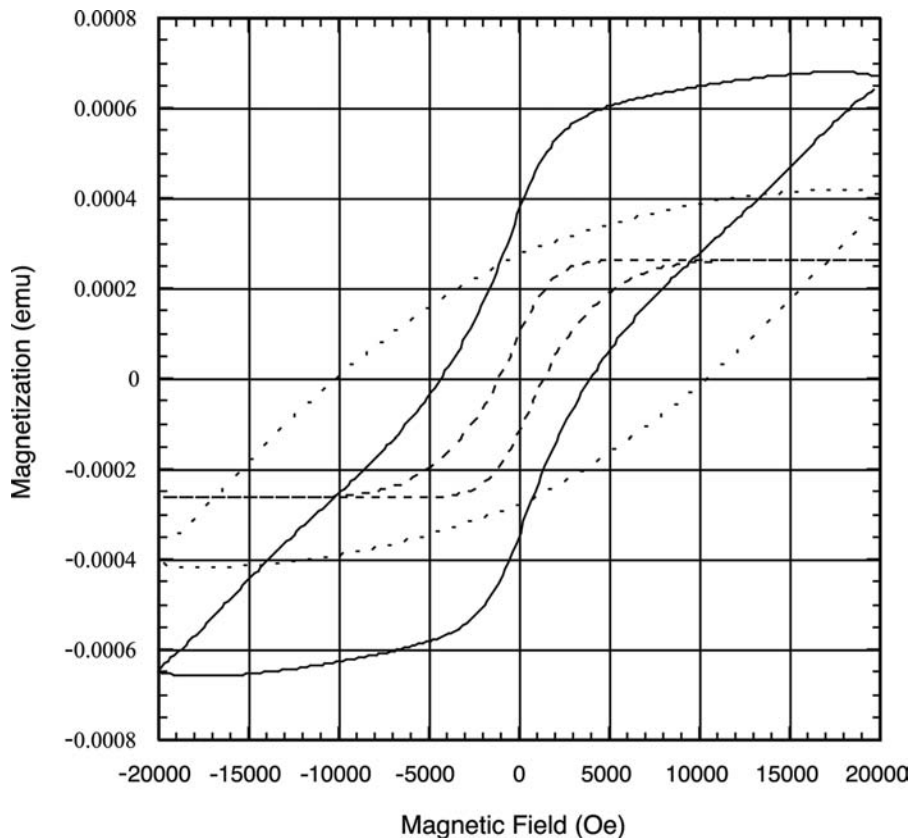


**Fig. 9** Magnetic hysteresis curve for  $\text{Fe}_{45}\text{Pt}_{44}\text{Cu}_{11}$  heat-treated at  $700^\circ\text{C}$  (solid curve). The curve was decomposed into a hard magnetic component (dotted curve) and a soft magnetic component (dashed curve).

The soft component coercivities were less than 1500 Oe. In all cases, the shape of the loops suggests that the maximum field of the magnetometer was not sufficient to saturate the loops and that the actual coercivities are higher. These results are in agreement with the X-ray diffraction results that suggest phase separation of the FePtCu particles into  $L1_0$  and disordered fcc phases. The hysteresis loop for the  $\text{Fe}_{48}\text{Pt}_{40}\text{Cu}_{12}$  particles had the smallest soft magnetic fraction (<20%), which was consistent with the fact that the X-ray diffraction (XRD) showed no evidence of a cubic phase. The soft magnetic phases may also consist of iron oxides, which if disordered, would not exhibit well-defined XRD peaks. The effect of heat treatment temperature on coercivity is plotted in Fig. 10, where the hard component coercivity was used at the highest annealing temperature for the films containing FePtCu particles. The coercivity for the  $\text{Fe}_{48}\text{Pt}_{52}$  nanoparticles began to increase after heat treatment above  $450^\circ\text{C}$ , while the coercivity for the FePtCu nanoparticles only increased after heating to  $550^\circ\text{C}$ . Only after heat treatment at  $650^\circ$ , where the X-ray diffraction curves indicated that the particles had largely transformed to the  $L1_0$  phase, did the coercivity for the hard component for the FePtCu nanoparticles match that for the FePt nanoparticles.

The addition of Cu to FePt nanoparticles did not lower the temperature required for the fcc to  $L1_0$  phase

transformation. This was unexpected because the transformation occurs at temperatures in the range of  $300^\circ\text{C}$  to  $400^\circ\text{C}$  in FePtCu sputtered films. Instead, the FePtCu nanoparticles had to be heated to temperatures as high or even higher than the temperature required to transform the FePt nanoparticles. The reason for the different effect of additive Cu in chemically synthesized nanoparticles and sputtered films is not well understood. One factor may be grain size. It has been shown that additive Cu promotes grain growth in sputtered FePt films and chemical ordering has been shown to increase with grain size.<sup>[16]</sup> There has been also a recent report that, for FePt sputtered films, relief of film stresses occurs in the course of the phase transformation process,<sup>[17]</sup> whereas there is no film stress for the self-assembled FePtCu nanoparticles.

Our FePtCu results led us to try to incorporate other metals into FePt particles. A recent report compared the effect of additive Cu, Ag, and Au on the chemical ordering of sputtered FePt films.<sup>[18]</sup> In agreement with previous reports,<sup>[10,11]</sup> Cu was found to promote the  $L1_0$  ordering for FePt. During annealing, copper did not appear to phase-segregate and large grain growth occurred. On the other hand, Ag and Au additives tended to phase-segregate from the FePt, thus limiting the FePt grain size. Adding silver to CoPt/ $\text{SiO}_2$  granular films was found to promote the CoPt  $L1_0$  ordering process, thereby reducing the

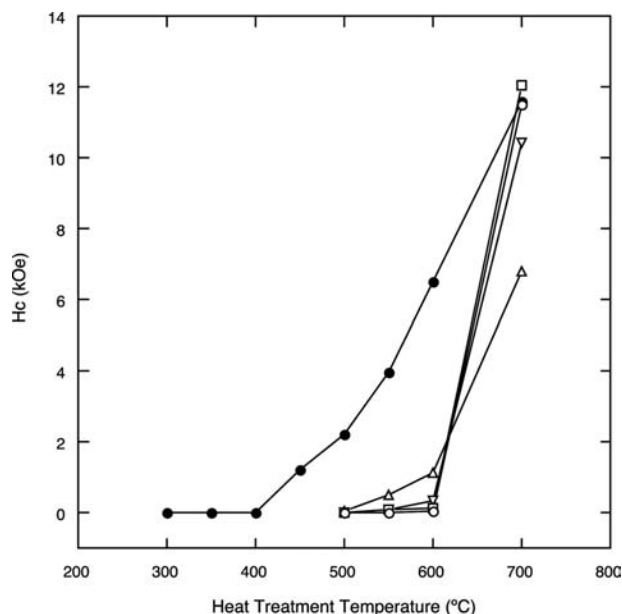


**Fig. 10** Effect of heat treatment temperature on the coercivity for films containing  $\text{Fe}_{48}\text{Pt}_{52}$  (filled circles),  $\text{Fe}_{55}\text{Pt}_{35}\text{Cu}_{10}$  (triangles),  $\text{Fe}_{45}\text{Pt}_{44}\text{Cu}_{11}$  (upside-down triangles),  $\text{Fe}_{48}\text{Pt}_{40}\text{Cu}_{12}$  (squares), or  $\text{Fe}_{35}\text{Pt}_{50}\text{Cu}_{15}$  (open circles) nanoparticles.

ordering temperature by  $100^\circ\text{C}$ , compared with  $\text{CoPt}$ .<sup>[19]</sup> This result encouraged us to prepare FePt nanoparticles containing Ag.

### FePtAg AND FePtAu TERNARY ALLOY NANOPARTICLES

FePtAg or FePtAu ternary alloy nanoparticles were made using the same procedure as for the preparation of FePtCu nanoparticles, except that silver acetate was used to prepare FePtAg nanoparticles<sup>[20]</sup> and gold acetate was used to prepare FePtAu nanoparticles.<sup>[21]</sup> The relative amount of Ag or Au in the particles could be systematically varied by varying the amount of silver acetate or gold acetate in the reaction mixture. For the case of Ag, we obtained compositions  $[\text{FePt}]_{100-x}\text{Ag}_x$ , where  $x = 0, 4, 15, 18,$  or  $30$ , while for  $[\text{FePt}]_{100-x}\text{Au}_x$ ,  $x = 8, 12,$  or  $24$ . In all cases, the particles had a disordered fcc lattice, were superparamagnetic, and self-assembled into films containing close-packed arrays of particles.

The FePtAg films were heat-treated under flowing 2% hydrogen in argon for 30 min at temperatures ranging from  $300^\circ\text{C}$  to  $500^\circ\text{C}$ . The X-ray diffraction pattern for the film containing  $[\text{FePt}]_{88}\text{Ag}_{15}$  heat-treated at  $350^\circ\text{C}$  (Fig. 11) showed a hint of the 001 and 110  $L1_0$  peaks. After heat treatment at  $400^\circ\text{C}$ , the peaks due to the  $L1_0$  phase were clearly present, and there was also a shoulder on the low  $2\theta$  side of the 111 peak. After heat treatment at higher temperatures, this

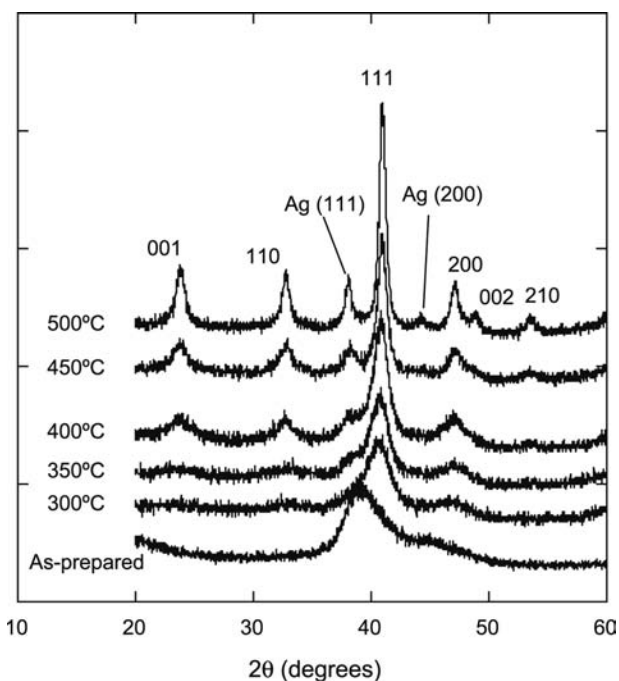


**Fig. 11** Effect of heat treatment temperature on the X-ray diffraction curves for films containing  $[\text{FePt}]_{88}\text{Ag}_{12}$  nanoparticles.

shoulder became a separate peak consistent with the Ag 111 diffraction peak, indicating that the Ag atoms had left the FePt particles. For the sample heat-treated at  $500^\circ\text{C}$ , the Ag 200 diffraction peak could also be seen. Similarly, the X-ray diffraction curves for

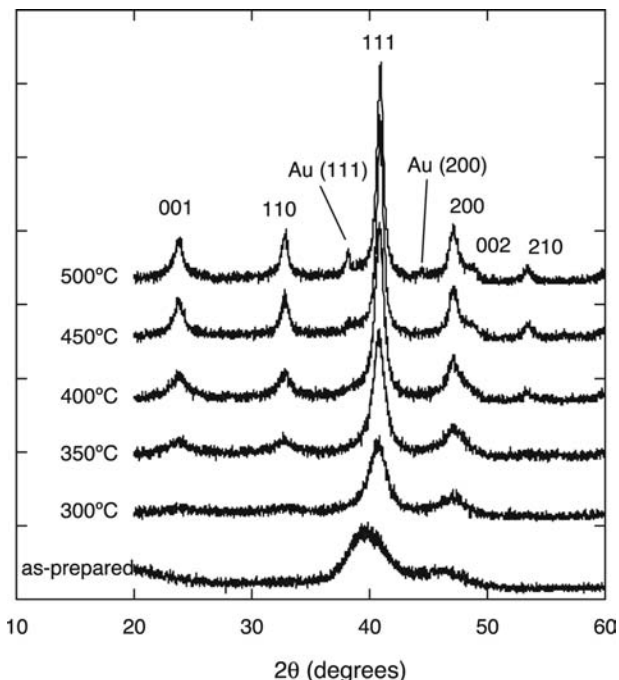


**Fig. 12** Effect of heat treatment temperature on the X-ray diffraction curves for films containing  $[\text{FePt}]_{85}\text{Au}_{15}$  nanoparticles.

[FePt]<sub>85</sub>Au<sub>15</sub> in Fig. 12 show the effect of heat treatment temperature on the fcc to L1<sub>0</sub> phase transformation. The L1<sub>0</sub> 001 and 110 diffraction peaks were apparent after heat treatment at 350°C and increased in intensity when heated to higher temperatures. After heating at 500°C, the Au 111 diffraction peak appeared at  $2\theta = 38.2^\circ$ , which indicated that gold had also phase-separated from the FePt particles. Adding Ag or Au to FePt nanoparticles lowers the temperature required to transform the particles to the L1<sub>0</sub> phase. In both cases, the Ag or Au atoms leave the particles, providing vacancies that allow the Fe and Pt atoms to move to their L1<sub>0</sub> lattice positions at lower temperatures than for pure FePt.

Magnetic measurements on annealed FePtAg and FePtAu films support the findings from the X-ray diffraction measurements that the addition of Ag and Au significantly reduces the required annealing temperature for obtaining L1<sub>0</sub> order. Fig. 13 compares the hysteresis loops for films containing [FePt]<sub>88</sub>Ag<sub>12</sub> and Fe<sub>48</sub>Pt<sub>52</sub> nanoparticles after heat treatment at 400°C for 30 min. The Fe<sub>48</sub>Pt<sub>52</sub> film was still superparamagnetic ( $H_c = 0$ ), while  $H_c$  for the [FePt]<sub>88</sub>Ag<sub>12</sub> film was 3400 Oe. A plot of film coercivity as a function of heat treatment temperature (Fig. 14) showed a clear benefit of adding Ag into the FePt nanoparticles. The [FePt]<sub>88</sub>Ag<sub>12</sub> films showed an increase in coercivity at heat treatment temperatures some 100°C to 150°C lower than that for the Fe<sub>48</sub>Pt<sub>52</sub> films. The effect of additive Ag on the coercivity enhancement depended on the concentration and was largest in the range 12–15%.

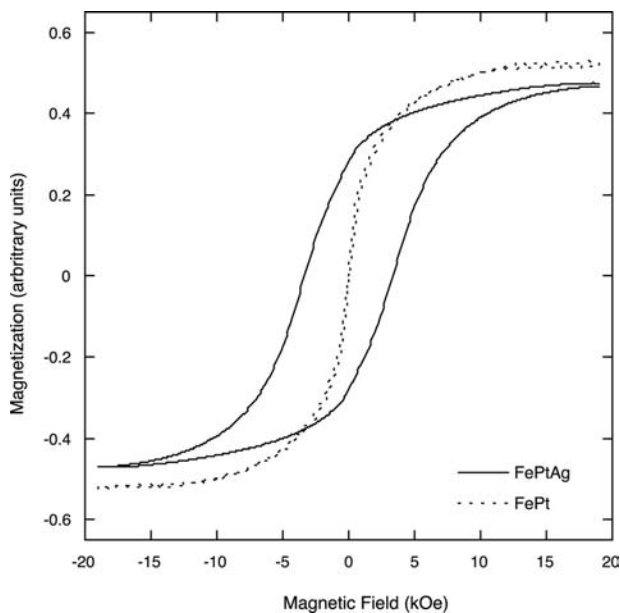


Fig. 13 Comparison of the magnetic hysteresis curves for films containing Fe<sub>48</sub>Pt<sub>52</sub> or [FePt]<sub>88</sub>Ag<sub>12</sub> nanoparticles.

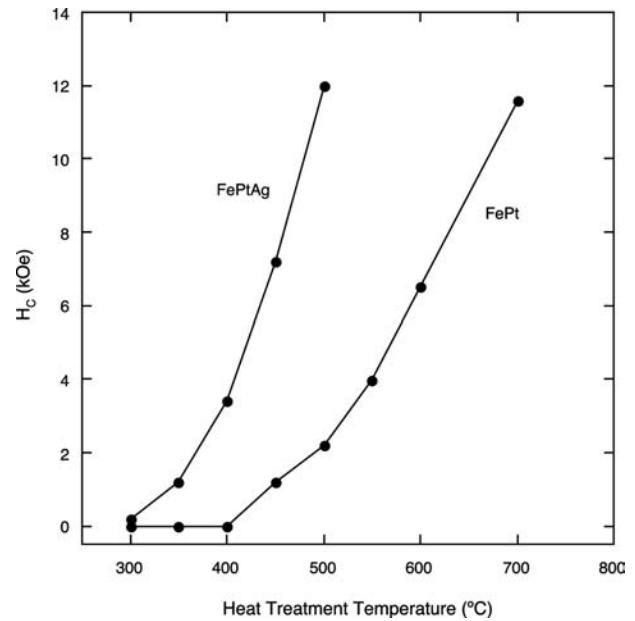


Fig. 14 Effect of heat treatment temperature on the coercivity of films containing either Fe<sub>48</sub>Pt<sub>52</sub> or [FePt]<sub>88</sub>Ag<sub>12</sub> nanoparticles.

Fig. 15 shows the coercivity as a function of annealing temperature for different Au concentrations. The coercivity increases as a function of Au concentration up to 24% Au. It can be seen that the effect of 15% and 24% Au is even greater than Ag up to an annealing temperature of 450°C. The coercivity enhancement for 24% Au occurs at temperatures about 150°C below that for FePt with no additive.

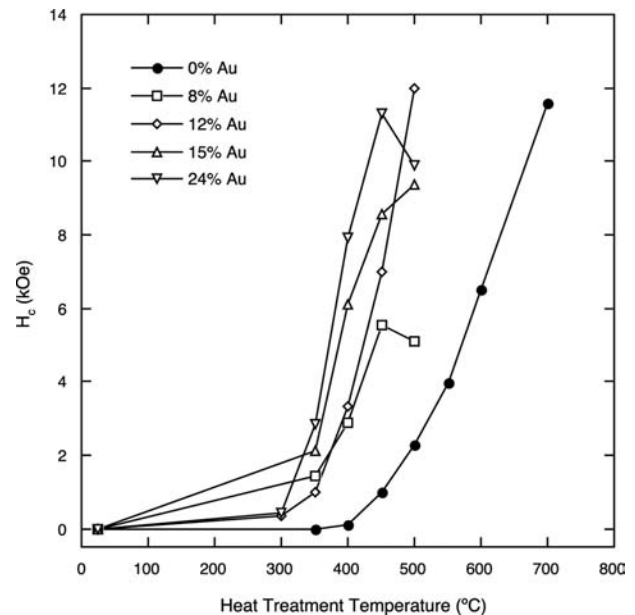
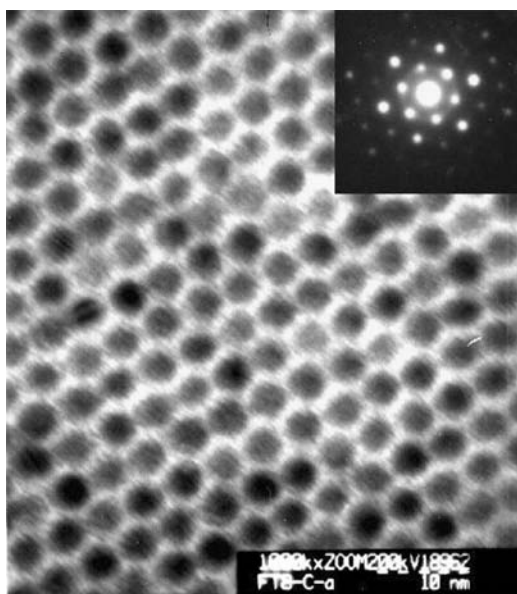


Fig. 15 Effect of heat treatment temperature on the coercivity of films containing FePt Au nanoparticles.



**Fig. 16** TEM image of self-assembled  $\text{Fe}_{49}\text{Co}_7\text{Pt}_{44}$  nanoparticles. The inset is the low-angle electron diffraction pattern.

### FeCoPt NANOPARTICLES

The FePt nanoparticle synthesis can also be modified to prepare FeCoPt nanoparticles by a simultaneous polyol reduction of platinum acetylacetonate and cobalt acetylacetonate and the thermal composition of iron pentacarbonyl.<sup>[22]</sup> The solvent was dioctyl ether, the reducing agent was 1,2-hexadecane diol, and a mixture of oleyl amine and oleic acid was the

surfactant. The FeCoPt particles were isolated and purified in the same manner as for FePt nanoparticles. This gave particles with an average diameter of 3.5 nm that self-assembled into close-packed arrays of particles (Fig. 16). The relative amounts of platinum acetylacetonate, cobalt acetylacetonate, and iron pentacarbonyl were varied to produce nanoparticles with different compositions (Table 1). As prepared, the particles had a disordered face-centered cubic structure and were superparamagnetic.

The films of the self-assembled FeCoPt nanoparticles were heat-treated in a tube furnace with flowing 2% hydrogen in argon to transform the particles to the  $L1_0$  phase. In this case, we used the quotient  $c/a$  as a measure of the degree of transformation to the  $L1_0$  phase, where  $a$  is the  $a$ -axis unit cell length and  $c$  is the  $c$ -axis unit cell length. For the films heat-treated at 600°C for 30 min, small increases in the amount of Co had little effect on the ability of the particles to transform to the tetragonal phase. Values of  $c/a$  in Table 1 were in the range 0.971 to 0.976 for  $\text{Fe}_{48}\text{Pt}_{52}$ ,  $\text{Fe}_{49}\text{Co}_7\text{Pt}_{44}$ , and  $\text{Fe}_{40}\text{Co}_{17}\text{Pt}_{43}$ . Heat treating at 700°C for 30 min decreased the values of  $c/a$  to 0.964–0.966. However, further increasing the Co content inhibited the transformation.  $\text{Fe}_{34}\text{Co}_{19}\text{Pt}_{47}$  or  $\text{Fe}_{23}\text{Co}_{27}\text{Pt}_{50}$  was only completely transformed after heat treatment at 700°C for 3 hr. Heat treatment also increased the average crystallite size, as measured by Scherrer analysis of the 111 peak in the X-ray diffraction. There was a slight increase in average crystallite size upon annealing at 550°C. The crystallite size increased greatly when annealing at temperatures beyond 600°C. These results are in agreement with a

**Table 1** Effect of heat treatment conditions on the structural and magnetic properties of FeCoPt nanoparticles

Temperature (°C)		550	600	700	700	700
Time (min)		30	30	30	60	180
$\text{Fe}_{48}\text{Pt}_{52}$	$c/a$	0.984	0.971	0.966	0.965	
	$d$ (nm)	4.7	7.9	16.4	21.2	
	$H_c$ (Oe)	3,790	6,500	>12,300		
$\text{Fe}_{49}\text{Co}_7\text{Pt}_{44}$	$c/a$	0.988	0.976	0.966	0.966	
	$d$ (nm)	4.5	6.4	16.2	21.6	
	$H_c$ (Oe)	2,430	4,500	8,700	9,170	
$\text{Fe}_{40}\text{Co}_{17}\text{Pt}_{43}$	$c/a$		0.971	0.964		
	$d$ (nm)		6.1	15.7		
	$H_c$ (Oe)		3,800	6,500		
$\text{Fe}_{34}\text{Co}_{19}\text{Pt}_{47}$	$c/a$		0.987		0.970	0.967
	$d$ (nm)		4.9		16.4	20.2
	$H_c$ (Oe)		2,180		6,630	6,990
$\text{Fe}_{23}\text{Co}_{27}\text{Pt}_{50}$	$c/a$		1.000		0.998	0.971
	$d$ (nm)		3.6		6.0	18.9
	$H_c$ (Oe)		242		4,590	9,090



recent paper by Dai, Sun, and Wang,<sup>[10]</sup> which reported that FePt nanocrystals coalesce to form larger grains when annealed at temperatures above 600°C. For films having small amounts of Co and annealed at 600°C, the average crystallite size decreased with increasing Co content. However, the films annealed at other temperatures showed little effect of composition on crystallite size. The films containing higher amounts of Co (Fe<sub>34</sub>Co<sub>19</sub>Pt<sub>47</sub> and Fe<sub>23</sub>Co<sub>27</sub>Pt<sub>50</sub>) were not as susceptible to coalescing. Annealing at 600°C for 30 min resulted in smaller increases in average crystallite size. Even after 1-hr annealing at 700°C, the average crystallite size was still smaller than that for the films containing lower amounts of Co.

After annealing, the films were ferromagnetic with an in-plane coercivity that depended on the annealing temperature and the composition (Table 1). The coercivity for the film containing Fe<sub>48</sub>Pt<sub>52</sub> and annealed at 700°C was so high that the electromagnet on the alternating gradient magnetometer (maximum field 18 kOe) could not saturate the sample and only a minor loop was obtained. For films heated at 600°C or 700°C, having similar values of *c/a* and similar average crystallite sizes, the coercivity decreased as the cobalt content increased. This can be qualitatively explained by the lower value of magnetocrystalline anisotropy for CoPt ( $K_u = 4.9 \times 10^7$  erg/cm<sup>3</sup>) relative to FePt (6.6 to  $10 \times 10^7$  erg/cm<sup>3</sup>). However, when completely transformed by annealing at 700°C for 3 hr, the film with the highest Co content, Fe<sub>23</sub>Co<sub>27</sub>Pt<sub>50</sub>, had a high coercivity ( $H_c = 9090$  Oe). This could not be explained by grain size because the average crystallite size was comparable (18.9 nm) to that for the samples annealed at 700°C for 1 hr. The magnetic properties of the films containing self-assembled Fe<sub>*x*</sub>Co<sub>*y*</sub>Pt<sub>100 - *x* - *y*</sub> particles were consistent with the properties of thin alloy films prepared by rf sputtering<sup>[23]</sup> or by electron beam evaporation.<sup>[24]</sup> Films prepared by rf sputtering at low temperatures (<400°C) had a disordered fcc structure and a low coercivity. After annealing at 650°C to 700°C in vacuum, the films transformed to the tetragonal phase and had high coercivities that decreased with increasing cobalt content. For the case of the particles described in our work, the relationship between the coercivity of the films and the cobalt content was complex, particularly for the films having high cobalt content.

Films containing self-assembled FePt alloy nanoparticles are promising candidates for granular thin film media in future high-density magnetic hard disk systems. A number of problems must be solved before they can find application. Perhaps the most challenging problem is how to maintain the highly ordered structure without particle coalescence/sintering after annealing to transform the particles to the tetragonal phase. We have also found that films containing

partially transformed FePt particles have a broad distribution of magnetic anisotropies.<sup>[9]</sup> One explanation is that there was extensive particle coalescing leading to a distribution of particle sizes. This underscores the need to find annealing conditions where the particles transform without coalescence. Another explanation is that the broad distribution of magnetic anisotropies arises from a broad distribution of degrees of transformation from the fcc to the L1<sub>0</sub> phase. This suggests that one must completely transform the particles to the tetragonal phase to achieve a narrow distribution of magnetic anisotropies. However, in the case of FePt, the magnetocrystalline anisotropy is so high that the completely transformed particles had coercivities in excess of 10,000 Oe, much too high to be useful in magnetic recording. The Fe<sub>*x*</sub>Co<sub>*y*</sub>Pt<sub>100 - *x* - *y*</sub> alloy particles described here provide an opportunity to prepare self-assembled films that are completely transformed but have lower coercivity.

## CONCLUSION: OUTLOOK FOR FePt NANOPARTICLES AS GRANULAR MAGNETIC RECORDING MEDIA

The large magnetocrystalline anisotropy, coupled with the ability to make very small particles that self-assemble into highly ordered arrays of particles, make FePt nanoparticles a serious candidate for future high-density magnetic recording systems. To realize this application, a number of materials science problems must be solved. Methods must be found to lower the temperature required for transformation to the L1<sub>0</sub> phase to avoid degradation of the particle positional ordering and sintering. We have made progress along those lines by incorporating Ag or Au into the particles. Better yet, it would be desirable to prepare the L1<sub>0</sub> phase directly, and other groups are pursuing this approach.<sup>[25]</sup> The very high magnetocrystalline anisotropy for FePt gives films with very high coercivity, perhaps too high for recording using current head technology. The industry is examining thermally assisted recording, where a laser locally heats the recording layer, thereby lowering the coercivity allowing writing lower fields. This raises issues including the temperature dependence magnetic properties of the FePt nanoparticles and the thermal stability (both chemical and physical) of both the particles and the matrix. A new matrix must be found that renders the films tribologically robust. The carbonaceous char arising from decomposition of the oleyl amine and oleic acid surfactants left after heat treatment would not be suitable.

Perpendicular recording, where the magnetization of the data bit is directed perpendicular to the plane of the film, is being given serious consideration as the

means to achieve very high bit densities.<sup>[26]</sup> To support a perpendicular recording scheme, the magnetic easy axis (i.e., the crystallographic *c*-axis) must be directed perpendicular to the film. No one has yet reported achieving either in-plane or perpendicular anisotropy for films containing FePt nanoparticles. An obvious approach would be to heat-treat the particles in a magnetic field, and we have attempted this without success. We suspect that heat treatment to transform the particles to the L<sub>1</sub><sub>0</sub> phase occurs at temperatures above the Curie temperature; therefore there is no force directing the magnetic anisotropy.

## ACKNOWLEDGMENT

The work was supported by the NSF Materials Research Science and Engineering Center awards DMR-98009423 and DMR-0213985.

## REFERENCES

- Moore, G.E. Cramming more components into integrated circuits. *Electronics* **1965**, 38 (8), April 19, 1965.
- Gelsinger, P.P.; Gargini, P.A.; Parker, G.H.; Yu, A.Y.C. Microprocessors circa 2000. *IEEE Spectrum* **1989**, 26 (10), 43–47.
- Bertram, H.N. *The Physics of Magnetic Recording*; Cambridge University Press: Cambridge, UK, 1994.
- Mallinson, J.C. Maximum signal-to-noise ratio of a tape recorder. *IEEE Trans. Magn.* **1969**, Mag-5 (3), 182–186.
- Zhang, Z.; Feng, Y.C.; Clinton, T.; Badran, G.; Yeh, N.-H.; Tarnopolsky, G.; Girt, E.; Munteanu, M.; Harkness, S.; Richter, H.; Nolan, T.; Tanjan, R.; Hwang, S.; Rauch, G.; Ghaly, M.; Larsan, D.; Singleton, E.; Vas'ko, V.; Ho, J.; Stageberg, F.; Kong, V.; Duxstad, K.; Slade, S. Magnetic recording demonstration over 100 Gb/in<sup>2</sup>. *IEEE Trans. Magn.* **2002**, 38, 1861–1866.
- Wood, R. The feasibility of magnetic recording at 1 terabit per square inch. *IEEE Trans. Magn.* **2000**, 36, 36–42.
- Weller, D.; Moser, A.; Folks, L.; Best, M.E.; Lee, W.; Toney, M.F.; Schwickert, M.; Thiele, J.-U.; Doerner, M.F. High K<sub>u</sub> materials approach to 100 Gbits/in<sup>2</sup>. *IEEE Trans. Magn.* **2000**, 36, 10–15.
- Sun, S.; Murray, C.B.; Weller, D.; Folks, L.; Moser, A. Monodisperse FePt nanoparticles and ferromagnetic FePt nanocrystal superlattices. *Science* **2000**, 287, 1989–1992.
- Harrell, J.W.; Wang, S.; Nikles, D.E.; Chen, M. Thermal effects in self-assembled FePt nanoparticles with partial chemical ordering. *Appl. Phys. Lett.* **2001**, 79, 4393–4395.
- Dai, Z.R.; Sun, S.; Wang, Z.L. Phase transformation, coalescence and twinning of monodisperse FePt nanocrystals. *Nano Lett.* **2001**, 1 (8), 443–447.
- Sharrock, M.P.; McKinney, J.T. Kinetic effects in coercivity measurements. *IEEE Trans. Magn.* **1981**, 17, 3020–3022.
- Chen, M.; Nikles, D.E. Effects of substrates on the self-assembly of FePt nanocrystals. *Mater. Res. Soc. Symp. Proc.* **2001**, 674, U4.8.
- Maeda, T.; Kai, T.; Kikitsu, A.; Nagase, T.; Akiyama, J. Reduction of ordering temperature of an FePt-ordered alloy by addition of Cu. *Appl. Phys. Lett.* **2002**, 80 (12), 2147–2149.
- Takahashi, Y.K.; Ohnuma, M.; Hono, K. Effect of Cu on the structure and magnetic properties of FePt sputtered film. *J. Magn. Magn. Mater.* **2002**, 246, 259–265.
- Sun, X.; Kang, S.; Harrell, J.W.; Nikles, D.E. Synthesis, chemical ordering and magnetic properties of FePtCu nanoparticle films. *J. Appl. Phys.* **2003**, 93 (10), 7237–7239.
- Takahashi, Y.; Ohnuma, M.; Hono, K. *Grain Size Effect on Ordering of FePt Sputtered Films*, Paper CH-04 at the 47th Annual Conference on Magnetism and Magnetic Materials, Tampa, FL, November, 2002.
- Wierman, K.W.; Platt, C.L.; Howard, K.J.; Spada, F. Evolution of Thin Film Stresses with L<sub>1</sub><sub>0</sub> Ordering in (FePt)<sub>100-x</sub>Cu<sub>x</sub> Films, Paper CH-02 at the 47th Annual Conference on Magnetism and Magnetic Materials, Tampa, FL, November, 2002.
- Platt, C.L.; Wierman, K.W.; Svedberg, E.B.; van de Veerdonk, R.; Roy, A.G.; Laughlin, D.E. L<sub>1</sub><sub>0</sub> ordering and microstructure of FePt thin films with Cu, Ag and Au additive. *J. Appl. Phys.* **2002**, 92, 6104–6109.
- Chen, C.; Kitakami, O.; Okamoto, S.; Shimada, Y. Ordering and orientation of CoPt/SiO<sub>2</sub> granular films with additive Ag. *Appl. Phys. Lett.* **2000**, 76, 3218–3220.
- Kang, S.; Nikles, D.E.; Harrell, J.W. Reduction of ordering temperature of self-assembled FePt nanoparticles by the addition of Ag. *Nano Lett.* **2002**, 2 (10), 1033–1036.
- Kang, S.; Jia, Z.; Nikles, D.E.; Harrell, J.W. Synthesis, self-assembly and magnetic properties of [FePt]<sub>1-x</sub>Au<sub>x</sub> nanoparticles. *IEEE Trans. Magn.* in press.
- Chen, M.; Nikles, D.E. Synthesis, self-assembly and magnetic properties of Fe<sub>x</sub>Co<sub>y</sub>Pt<sub>100-x-y</sub> nanoparticles. *Nano Lett.* **2002**, 2 (3), 211–214.
- Wang, P.W.; Kim, D.W.; Park, C.H.; Na, J.G.; Lee, S.R. Magnetic and structural properties of (Co<sub>1-x</sub>Fe<sub>x</sub>)Pt films. *J. Appl. Phys.* **1998**, 83 (11), 6614–6616.
- Kanazawa, H.; Lauhoff, G.; Suzuki, T. Magnetic and structural properties of (Co<sub>x</sub>Fe<sub>100-x</sub>)<sub>50</sub>Pt<sub>50</sub> alloy thin films. *J. Appl. Phys.* **2000**, 87 (9), 6143–6145.
- Balachandran, J.; Nallasamy, C.; Shinoda, K.; Tohji, K. Towards Direct Synthesis of fct-FePt Nanoparticles by Chemical Route, Paper ED-02 at the 47th Annual Conference on Magnetism and Magnetic Materials, Tampa, FL, November, 2002.
- Ouchi, K. Recent advancements in perpendicular magnetic recording. *IEEE Trans. Magn.* **2001**, 37 (4), 1217–1222.

# Membrane-Coated Nanoparticles: Photochemistry

**Ulrich Siggel**

*Max Volmer Institut für Physikalische Chemie, Technischen Universität Berlin, Berlin, Germany*

**Guangtao Li**

**Jürgen-Hinrich Fuhrhop**

*Institut für Organische Chemie, Freie Universität Berlin, Berlin, Germany*

## INTRODUCTION

The objective of this entry is to describe the different types of photochemical and photophysical reactions on nanoparticles and their application with special emphasis on recent work.

## OVERVIEW

Nanoparticles can be used as single particles in solution (colloids) or arrays of particles with a specially designed architecture again in solution or on a suitable support. Membrane coating is often necessary for stabilization of aqueous or organic solutions of isolated particles. In particle arrays, special linker molecules may be used in order to realize an optimal interparticle distance.

Membrane-coated nanoparticles are functionalized for optical functions by covalent attachment of chromophores to the membrane or to the particle surface. Mixed monolayers of lipids and amphiphilic dyes are also common. The enclosed or adsorbed dyes are used for the construction of photochemical reaction centers as well as in the analysis of special membrane properties such as rigidity and regioselective interaction with solutes.

Photochemical reaction centers are realized either by covalent dyads or by noncovalent long-distance dimers. Triads have also been realized. Nanoparticles provide a large surface to light-absorbing chromophores as well as the possibility to transfer electrons to electrodes. Functionalized membrane coatings allow the construction of long-distance dimers of redox active molecules for light-induced charge separation.

Three different types of colloidal particles are currently used: metals, semiconductors, and insulators. Colloids of noble metals (gold, silver, copper) are characterized by their chemical stability and by surface plasmon absorptions in the visible range, which interfere with the photophysics of dyes. Semiconductor

particles with a narrow bandgap absorb in the visible region and are prone to corrosion. Semiconductors with a wide bandgap, on the other hand, are more stable but absorb only in the UV region. Dyes absorbing visible light are then applied as sensitizers in order to use sunlight. Insulating particles are not appropriate for the construction of photochemical cells but are promising carriers for studies of charge separating molecular assemblies.

## GOLD AND OTHER METAL PARTICLES

Gold particles have been used most frequently. They can be easily prepared by different methods. The citrate reduction method<sup>[1]</sup> yields nearly monodisperse spheres with typical diameters of about 20 nm. Particles of this size remain dispersed for many days and their curvature is low enough to allow the construction of closed membrane systems in water. Weakly bound citrate leads to a negative surface charge. Particles of silver, palladium, and platinum may be prepared by the same method.<sup>[2–5]</sup> Borohydride reduction, on the other hand, yields much smaller particles (1–5 nm). Their high curvature does not allow the formation of a closed membrane. Monolayer-protected gold clusters (MPCs) are obtained by reaction with alkane thiols, which form a covalent bond to the gold surface. The surface of the nanoparticles can be varied from hydrophilic to hydrophobic by selecting appropriate head groups on the other end of the attached thiol.<sup>[6,7]</sup>

Other routes of particle production include the electrochemical synthesis of size-selective nanostructured palladium clusters in tetrahydrofuran<sup>[8]</sup> and a photochemical method of making size-controlled spherical metal particles in a nonaqueous, but highly polar and viscous medium. Complexes of gold, silver, palladium, and platinum have been reduced by the photochemically formed carbamoyl radicals.<sup>[9]</sup> Small particles were sterically stabilized by polyvinylpyrrolidone (PVP), the size being determined by the ratio PVP/metal complex.

A ratio of 5/1 yielded, for example, particles of 12 nm (Au), 15 nm (Ag), 10 nm (Pt), and 16 nm (Pd). The gold particles were pure enough to show single-electron tunneling (SET) in the current–voltage dependence (the 1.8-nm stabilizer shell serves as a tunnel junction). This makes the particles interesting for nanoscale electronic circuits.

The functionalization of the monolayer opens the way to a variety of photophysical and photochemical reactions, which are strongly influenced by the collective excitation of metal electrons, leading to the size-dependent plasmon absorption. This leads, however, to heating of the probe upon strong excitation, problems in the measurements of transient absorptions of adsorbed dyes, energy transfer to the metal, and reduced quantum yields for all the reactions of the chromophore from the excited singlet state. Analytically, the plasmon absorption has been used to probe the dielectric properties of surface-bound molecules,<sup>[10]</sup> and the distance between coupled particles if aggregation of the particles occurs.<sup>[11]</sup>

Photoreactions have been useful in exploring the properties of monolayers on planar gold surfaces. Photoextrusion of nitrogen from aryl azide<sup>[12,13]</sup> and diazoketones,<sup>[14,15]</sup> E-Z photoisomerization of stilbenes<sup>[16]</sup> and azocompounds<sup>[17]</sup> as well as photodimerization reactions<sup>[18–21]</sup> have been well characterized. On gold nanoclusters electron transfer reactions are very often examined; they occur from donors either to relay molecules or directly to the metal. *cis–trans* Isomerization of molecules with double bonds and cycloadditions have, however, also been studied. The latter are very much enhanced if the reporter molecules are close to each other and in proper orientation. If dimerization, followed by charge transfer, occurs in the excited state, excimer fluorescence may be studied as a measure of distance. As a further photophysical reaction, energy transfer can also be used to probe the membrane order.

## Energy Transfer

Singlet energy transfer is measured by fluorescence quenching of suitable chromophores. The plasmon absorption band of metallic particles is usually broad and energy transfer occurs with a wide range of fluorescent dyes. The transfer from donors to acceptors depends on the distance: the efficiency of a transfer between a point dipole and a nearby flat metal surface decreases with the third power; for extended molecules close to curved particle surfaces with an intermediate exponent between 3 and 6 is expected. Monolayers on small particles are usually fluid and the chain density decreases with increasing chain length because of the high curvature. Motional freedom, thermal

flexing, and chain folding lead to altered energy transfer efficiencies.

Imahori et al.<sup>[22]</sup> have shown that the energy transfer between tetraphenylporphyrin, coupled to a gold surface by a C12-alkanethiol spacer, and gold is much more effective in the case of a SAM on planar gold (111-surface) as compared to particles of 5-nm diameter (MPC). The lifetime of the porphyrin fluorescence is shortened from 9.5 nsec to 0.04 and 0.15 nsec, respectively. Additionally a 9.1-nsec phase (15% of total amplitude) appears on the particles, suggesting a second type of monolayer structure. The portion of unquenched porphyrin molecules is only 3% for mixed monolayers. Lifetime measurements thus result in additional information on the homogeneity of the monolayers. Energy transfer is more efficient in SAMs than in MPCs. The origin of this effect is not known.

Aguila and Murray<sup>[23]</sup> have investigated the energy transfer of dansyl chromophores bound to gold clusters of 5–8 nm (C2 to C15 linkers) in mixed monolayers. In this environment the fluorescence is reduced to 1% of that of the free dye by energy transfer. The emission intensity increased with the effective distance, provided that the linker had about the same length as the surrounding alkanethiolates (C4–C12). For longer linkers the emission decreased and became dependent on the load with the dansyl label, i.e., the stiffness of the outermost part of the disordered layer (Fig. 1).

The distance-dependent energy transfer from a methylene blue-type fluorophore (*Alexa 488*) to a metal surface<sup>[24]</sup> has been exploited to measure changes of chemisorption with respect to the electrode potential on a polycrystalline gold electrode. In the potential range of  $-0.7$  to  $+0.2$  V only reversible reorientation of the charged chromophore occurred. For potentials lower than  $-0.8$  V and higher than  $+0.2$  V, an exponential increase of fluorescence was observed. This was related to the reduction and oxidation of the Au–S bond and release of the fluorophore into the solution. An additional spacer of 12 C-atoms between the chromophore and the thiolate moiety decreased the sensitivity toward the potential, because the van der Waals forces between the alkane chains became dominating.

## Excimer Fluorescence

The excimer fluorescence of pyrene is a good tool to investigate order and dynamics of alkane monolayers on surfaces. Excimers are not formed in homogeneous solution of low concentration. The fluorescence behavior after the addition of a gold colloid depends on the nature of the pyrene side chain. If this does not contain a thiol group for binding to the gold the monomer fluorescence is somewhat decreased because of ineffective energy transfer to the gold. On binding

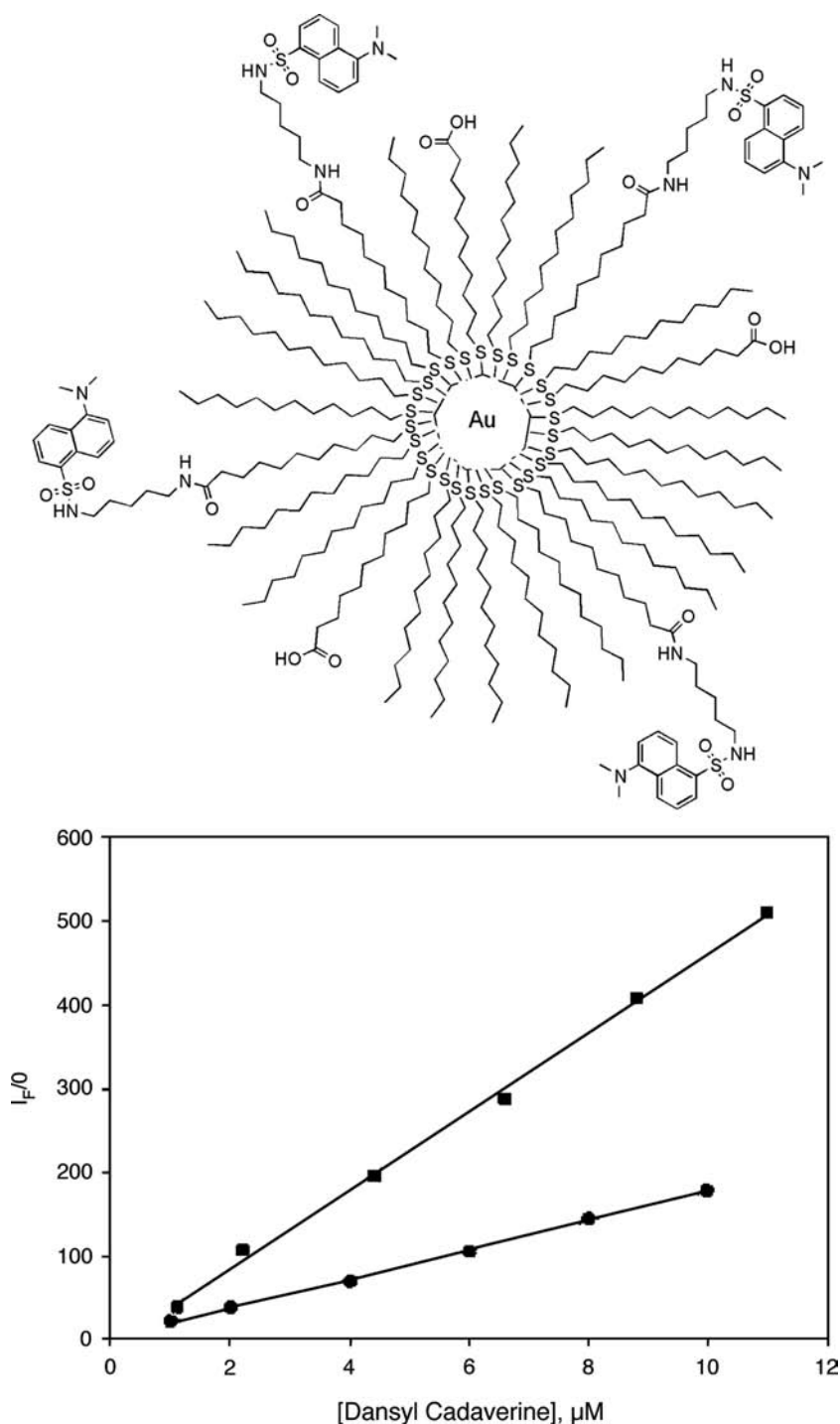


**Fig. 1** Monolayer protected cluster (“MPC”) of an HSC<sub>10</sub>-coated Brust gold particle after partial exchange with HSC<sub>10</sub>COO<sup>-</sup> and coupling with dansyl cadaverine and fluorescence intensities with 17 (upper curve) and 6 dansyls (lower curve) per MPC. Fluorescence increases linearly with concentration in both cases. The dye molecules do not interact. *Source:* From Ref.<sup>[23]</sup>.

through a thiol group hydrophobic aggregates are formed and a strong excimer fluorescence appears. This has been shown by Chen and Katz<sup>[25]</sup> for protected thiols. A pyrene-thioester and a pyrene-thiocarbonate bind noncovalently to the surface of 12.5-nm citrate-gold particles with binding constants of  $7.2 \times 10^7$  and  $1.7 \times 10^8 \text{ M}^{-1}$ , respectively. The change from excimer to monomer fluorescence has also been taken as a measure for the gold-catalyzed hydrolysis

of the ester and carbonate bonds, which leads to the appearance of the pyrene moieties in the bulk solution.

Pyrene excimer fluorescence has also been used to detect changes in interparticle interactions for capped gold particles.<sup>[26]</sup> Freshly prepared Brust-type gold particles (3.2–3.7 nm) capped with pyrenyl-decanethiol or -heptadecanethiol showed practically no excimer fluorescence. The monomer fluorescence was quenched by 99% by energy transfer to the gold particles.

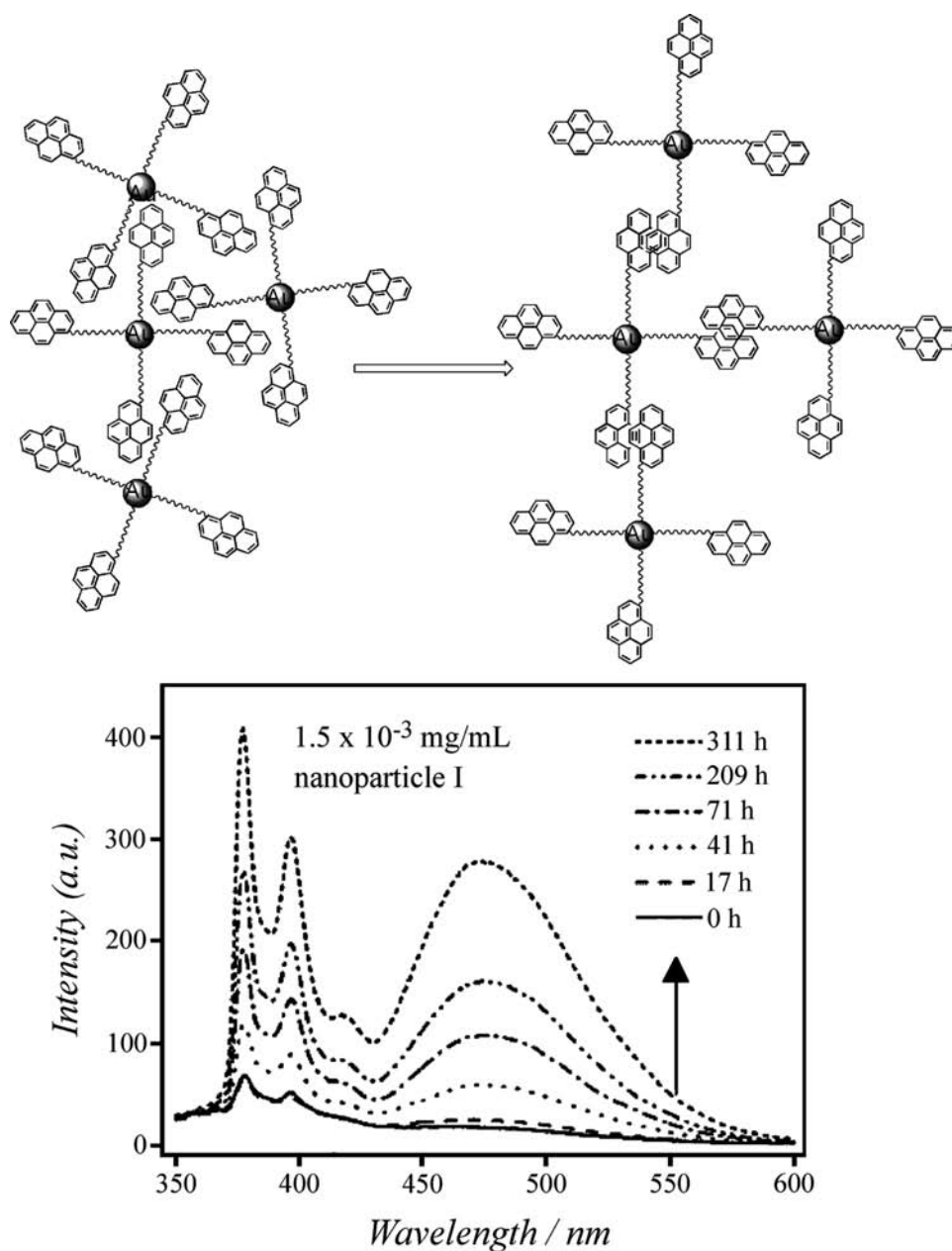


**Fig. 2** Fluorescence of pyrene-coated particles increases with ageing because interdigitation leads to excimers. *Source:* From Ref.<sup>[26]</sup>.

Although 43% (C-10) and 31% (C-17) of the surface gold atoms were covered with the thiol, most of the pyrene units were not oriented in a face-to-face manner. Upon ageing for up to 300 hr the fluorescence increased, especially the excimer emission. This was traced back to aggregation of the gold particles, leading to interdigitation of the alkyl chains resulting in a stacking of the pyrene units. The higher intensity of the excimer fluorescence for the short-chain pyrene provides further evidence for the chain density gradient for alkanethiolates on gold nanoparticles. The decay of the fluorescence was biexponential with lifetimes of 4.3 and 22 nsec for the monomer

fluorescence of fresh solutions. For aged samples only the lifetime of the longer-lived excited species was increased to 35 and 30 nsec for the two preparations. This indicates that there may be different binding sites on the gold surface leading to different excited states (Fig. 2).

#### **trans-cis Isomerization, Cyclodimerization, and Benzylic Cleavage**

The realization of dimerization necessitates two molecules in near neighborhood; isomerization, on the



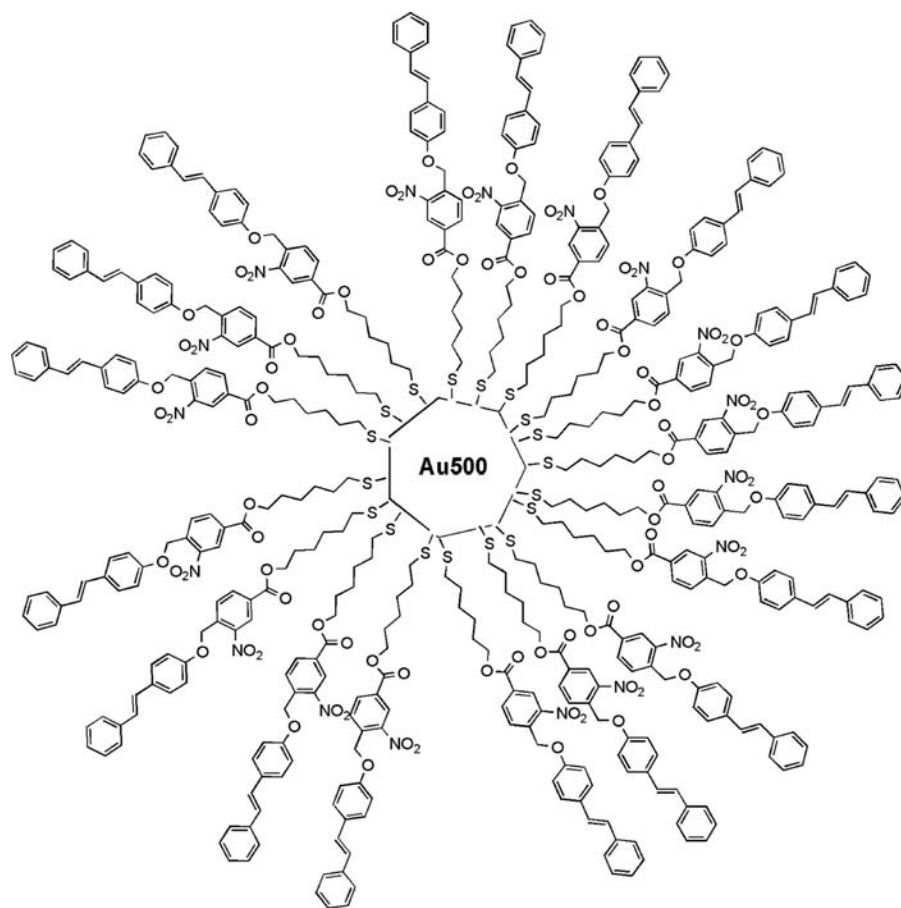


**Fig. 3** Photodimerization of stilbene chromophore was only observed in ordered and flexible domains on particles with high curvature. *Source:* From Ref.<sup>[28]</sup>.

other hand, needs some space around the molecule. Both reactions are optimized under opposite conditions. Fluid monolayer coatings favor cleavage reactions which are linked to release molecules.

The comparison of three photochemical reactions, *trans-cis* isomerization, cyclodimerization, and benzylic cleavage of thioalkyl-azobenzenes and -stilbenes in homogeneous solution and in monolayers on 2.5-nm gold particles and on planar gold,<sup>[27,28]</sup> yielded valuable information about the effects of monolayer packing. Photoisomerization was found to be independent of the alkyl chain length in homogeneous solution with quantum yields of  $10^{-1}$  and  $3 \times 10^{-4}$  for the azobenzene and stilbene species, respectively. In a tightly packed monolayer on planar gold it was sterically blocked. In the more loosely packed monolayers on the small gold particles, isomerization occurred with reduced quantum yield. An additional decrease of the yield was found after shortening the alkyl chain from 12 to 4  $\text{CH}_2$  groups. Quenching of the excited state by the metallic core became dominant. The dependence on the distance was exponential with an attenuation constant of  $\beta = 0.5$ , which is smaller than expected for through-bond coupling. If a nitrobenzyloxy group was

introduced into the alkyl chain, photocleavage occurred. Parallel observation of isomerization and cleavage pointed to strong metal-based non-radiative quenching of the excited state. The significance of packing and steric hindrance became evident in stilbene photodimerization experiments. It was not observed in solution or in monolayers on planar gold but occurred on gold particles with a very low quantum yield of  $2\text{--}4 \times 10^{-6}$ , depending on the distance (Fig. 3).

Similar conclusions with respect to the rigidity of the monolayers have been drawn by Evans et al.<sup>[29]</sup> Photoswitching between the *cis* and *trans* states of alkane-derivatized azobenzene was not possible in single-component monolayers on planar gold. It has only been realized in mixed monolayers with free volume introduced by a spacer molecule with three ethyleneoxy units and especially in mixed monolayers of C6-thiol-azobenzene and mercaptophenol on 3.2-nm particles.

The Norrish-Young type II photochemical reaction has been used to probe the properties of a variety of ordered media including cyclodextrins, zeolites, liquid crystals, and micelles. At first the reaction was investigated in an MPC capped with a mixed monolayer of

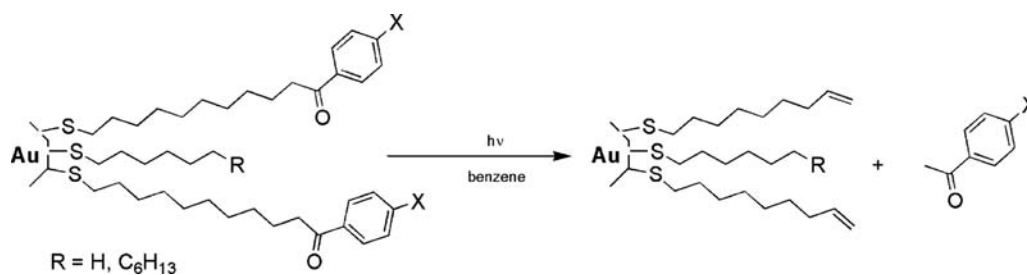


**Fig. 4** Benzophenone is only released, if the benzophenone head groups are separated by unreactive molecules and on curved surfaces. *Source:* From Ref.<sup>[30]</sup>.

short alkanethiol and mercaptoundecanophenone by Kell, Stringle, and Workentin.<sup>[30]</sup> Irradiation released free benzophenone, irrespective of the length of the spacer alkanethiol (C-6 or C-12), but not in its absence. Whether fragmentation or cyclization is the main pathway to products depends greatly on the conformational flexibility of the triplet 1,4-biradical, which is formed from the  $n,p^*$  triplet excited state of the carbonyl group. If the volume, which is necessary for cyclization motions, is not available, only fragmentation occurs. The resulting terminal vinyl group on the MPC can then be used for further modification (Fig. 4).

### Miscellaneous Reactions

An interesting example for the interaction of a chromophore with the metal particle is the binding of methylaminopyrene on spherical gold particles of 5–8-nm diameter.<sup>[31]</sup> Because of internal charge transfer, pyrene is only weakly fluorescent in THF solution. On binding to the gold surface the electron-donating ability of nitrogen was decreased. As a result the fluorescence yield was increased from 0.09 to 0.48 (chelation enhancement). A second indication of the binding was the appreciable red shift of the absorption and fluorescence bands.

A phthalocyanine thiol bound to Brust-type gold particles with diameters ranging from 2 to 4 nm and associated with the TOAB phase transfer reagent generated singlet oxygen upon irradiation with visible light more effectively than without gold. The quantum yield increased from 0.45 to 0.65. TOAB promotes solubility in polar solvents, which is essential for a possible application in photodynamic therapy.<sup>[32]</sup>

Upon illumination of thiocyanine (TC)-J aggregates in solution, an ultrashort excited state was formed. Its relaxation was intensity dependent and dominated by exciton-exciton annihilation. On bulk silver surfaces ultrafast quenching of the exciton and its fluorescence occurred. The same was true on gold nanoparticles. The binding of the dye aggregate via two sulfonate groups was reported originally by

Kometani et al.<sup>[33]</sup> who applied gold, silver, and composite Au/Ag particles with diameters of about 10 nm. The absorption spectra were measured and simulated using the Maxwell-Garnett treatment. On silver particles after fsec-excitation at 417 nm (140-fsec time resolution) a charge separated state with a lifetime of 300 psec was observed<sup>[34]</sup> by absorption changes at 475 nm close to the sharp absorption band of the J aggregate on silver at 481 nm. The exciton of the J aggregate is then of course strongly coupled to the silver particle plasmon. Photoexcitation of this resonance leads to very fast electron transfer of the TC aggregate to the metal. In the case of gold particles the plasmon energy is too low for such coupling (2.38 vs. 3.1 eV for Ag).

Rhodamine 6G has been used as a reporter molecule for changes in aggregation and morphological changes of the gold clusters. The 2-nm particles, prepared by rhodanide reduction,<sup>[35]</sup> did not exhibit surface plasmon absorption, for which the diameter must be at least 5 nm,<sup>[36]</sup> and bound rhodamins 6G as a monomer. On increasing the Au/dye ratio, aggregation was shown by a blue shift of the dye absorption (H aggregate) and the appearance of a plasmon band at 537 nm. Twenty-five minutes of laser irradiation at 532 nm lead to melting and growth of the particles, due to plasmon excitation.<sup>[37]</sup> This was indicated by the broadening of the plasmon band and by an increase of the monomer fluorescence of rhodamine at 545 nm, originating from molecules released into the bulk solution (Fig. 5).

### Well-Defined Assemblies of Nanoparticles

Arrays of nanoparticles have been prepared by salt-induced aggregation,<sup>[38–42]</sup> Langmuir techniques,<sup>[43]</sup> surface assembly,<sup>[44–46]</sup> or crystallization.<sup>[47]</sup> The motive for such preparations is the special nonlinear optical properties of collective metal nanoclusters. They show large surface-enhanced Raman signals<sup>[44–46]</sup> and large first hyperpolarizabilities.<sup>[38–42]</sup> A necessary condition is a well-defined symmetry and interparticle spacing, which is not always met in the preparations mentioned above.

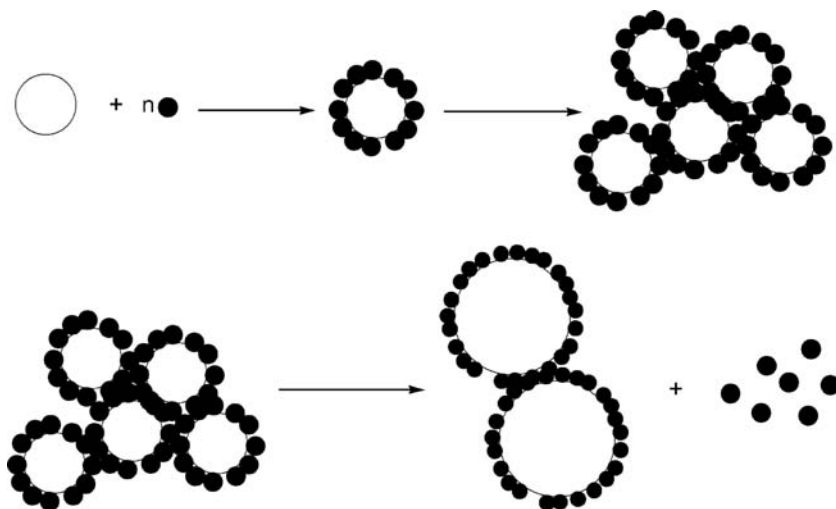


**Fig. 5** Model of possible morphological changes of gold-dye cluster arrays upon laser irradiation. *Source:* From Ref.<sup>[37]</sup>.

It may be realized more easily by covalent bridges between the particles.<sup>[48,49]</sup> Gold particles were connected, for example, by thiol-functionalized oligo-phenylacetylenes.<sup>[50]</sup> The intensity of hyper-Rayleigh scattering (HRS), i.e., incoherently scattered second harmonic light, was especially high for noncentrosymmetric trimers, which was traced back to enhanced values of first hyperpolarizability. These properties are also of interest for nanoscale electronics.

Defined aggregates can also be obtained by non-covalent interactions. Two-dimensional (2-D) assemblies with hexagonal packing of 5-nm gold particles (Bust-type) were formed by adsorption of tetrapyrrolylporphyrin to the surfaces. Optically, this was shown by the red shift (512 to 610 nm) and broadening of the plasmon absorption as well as of the porphyrin Soret band from 25 nm half width in solution to 45 nm. The porphyrin dye acts as a reporter molecule and as a trigger of a defined aggregation.<sup>[51]</sup> Surface-enhanced resonance Raman scattering (SERRS) was also observed (Fig. 6).

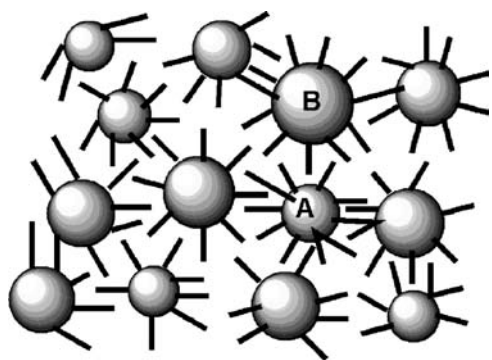


**Fig. 6**  $H_2TpyP$  stands perpendicular on the gold surface and causes aggregation. (From Ref.<sup>[51]</sup>.)

### Photoelectrochemical Cells

A photoelectrochemical cell consists of a charge separating system attached to a macroscopic electrode and a redox electrolyte carrying charges to a counter electrode. If self-assembled monolayers (SAMs) of electron transfer dyades or triades are directly bound to the working electrode, the light absorption in these 2-D arrays is normally low. The use of photosensitive nanoparticles in contact with the electrode yields 3-D array electrodes with high surface and high absorbance.

The conventional method to get a 3-D array of a charge separating system makes use of bifunctional bridge compounds and of electrostatic interactions to form a multilayered system. Lahav et al.<sup>[52,53]</sup> used indium-doped tin oxide (ITO) electrodes coated by aminosiloxane. Negatively charged gold nanoparticles (diameter: 13 nm) were self-assembled on the ITO electrode, followed by a positively charged charge-separating (CS) system. Repetition produced a multilayer system. The CS system consisted of either a Zn protoporphyrin–viologen dyade or a catenane, consisting of a cyclo-bis-viologen-phenylen and a Ru(bipy) derivative. Following excitation of the porphyrin the excited electron is conducted to the ITO electrode via the gold particles. The quantum yields of the corresponding photochemical cells [with ethylenediaminetetraacetic acid (EDTA) as electron donor and a graphite counter electrode] were  $\phi = 10^{-3}$  ( $\lambda = 544$  nm) for the porphyrin system and  $\phi = 10^{-4}$  ( $\lambda = 434$  nm) for the Ruthenium system. These numbers, referring to the short-circuit current, are relatively low. This is because of the poor contact between the CS system and the gold particles (Fig. 7).

Better results are obtained if the photosensitizer is directly bound to the gold particles. Sudeep et al.<sup>[54]</sup> electrodeposited functionalized gold particles on a nanostructured  $SnO_2$  electrode, made by annealing a  $SnO_2$

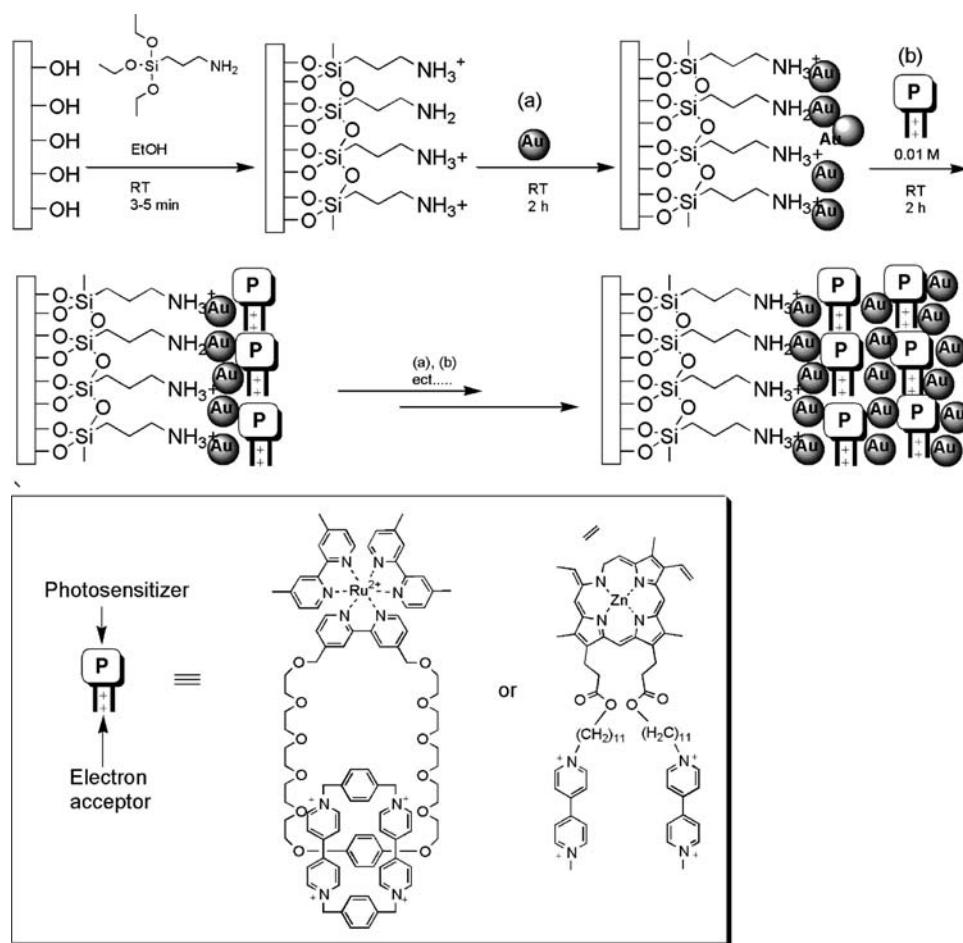


Fig. 7 Model of the gold-nanoparticle arrays on an ITO electrode for photocurrent production. Source: From Ref.<sup>[53]</sup>.

film on an optically transparent electrode (OTE). The charge separating system consisted of a light-absorbing fullerene electron donor bound to 3-nm gold particles via a modified alkanethiol chain. The light-induced electron transfer to the gold particles was optimized by the redox electrolyte  $J^-/J_3^-$  in high concentration. An incident photon to photocurrent efficiency (IPCE) of  $8 \times 10^{-3}$  (at 450 nm) was achieved (Fig. 8).

Another efficient approach is to precipitate the gold particles directly on a flat gold electrode and to bind an electron transfer dyade afterwards.<sup>[55]</sup> The dyade consisted, for example, of a rutheniumbipyridyl complex as light-absorbing electron donor, connected via a C7 bridge to viologen, as electron acceptor, and a second bridge (C6) to the final thiol group bound to the citrate gold particles. In such a photochemical cell with triethanolamine as electron donor and a Pt-counter electrode the photocurrent was 15 times higher than in a cell in which the RuVS dyade was directly bound to the flat gold electrode. This factor corresponds to the enhanced concentration of RuVS as achieved by binding to the nanoparticles. The photocurrent efficiency was  $8 \times 10^{-3}$  (at 460 nm).

High IPCE was, however, also achieved on flat gold electrodes without nanoparticles by increasing the absorption cross section of the sensitizing electron donor. Imahori et al.<sup>[56]</sup> prepared mixed SAMs of a ferrocene-porphyrin-fullerene electron transfer triad and of a boron-dipyrrin sensitizer, which transfers energy to the porphyrin. An IPCE as high as  $1.6 \times 10^{-2}$  (at 430 nm) was thus achieved.

### Construction of Form-Stable Gaps in Monolayers

Li and Fuhrhop<sup>[57]</sup> used a totally different approach for capping and functionalizing gold particles. Multiply charged derivatives of tetraphenylporphyrins were directly bound to the gold surface in a flat-lying position. Long-chain thiols with two secondary amide groups were then self-assembled around them. As a result of hydrogen bonding the monolayers were rigid and impermeable to compounds, which dissolve in fluid membranes. The diameter of above 20 nm of the particles allowed the formation of totally closed membranes. The curvature was not too high. Form-stable

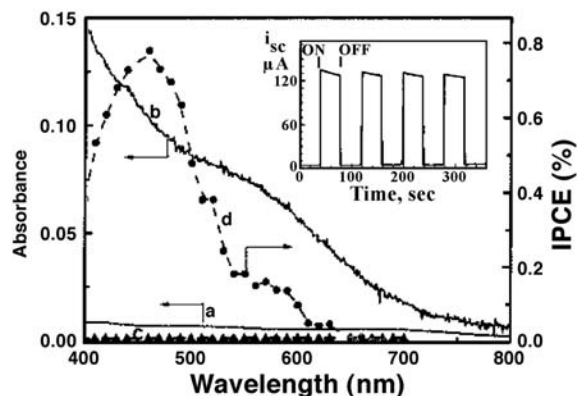
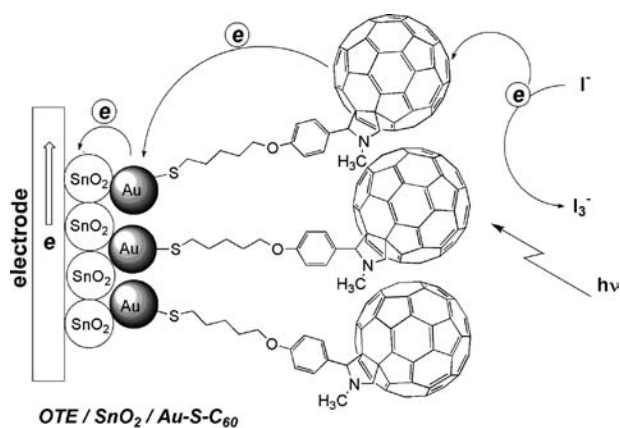


**Fig. 8** Model of fullerene-thiol-coated gold nanoparticles, their absorption spectrum (—) and photocurrent action spectrum (---). The inset shows the on-off response upon illumination at 400 nm. *Source:* From Ref.<sup>[54]</sup>.

gaps of  $2 \times 2 \times 2$ -nm size with rigid walls were thus formed. The rigidity has been proven by fluorescence quenching experiments. The porphyrins on the surface showed only a very weak rest fluorescence as a result of energy transfer quenching. It was totally quenched by paramagnetic metalloporphyrins of the same size as the porphyrin at the bottom of the gap by forming a heterodimer. Porphyrins with larger side groups were not able to enter the rigid gaps and quench the fluorescence. Such size discrimination did not take place when the surface layer around the porphyrins consisted of octadecanethiol without rigidifying amide groups. On flat gold electrodes, long-distance (1–2 nm) heterodimers were also established with a fitting porphyrin being attached to amine substituents at the rigid walls of the gap<sup>[58,59]</sup> (Fig. 9).

## SEMICONDUCTOR NANOPARTICLES

Semiconductors can be optically excited. But the internal charge separation is not stable. The electrons in the conduction band and the holes in the valence

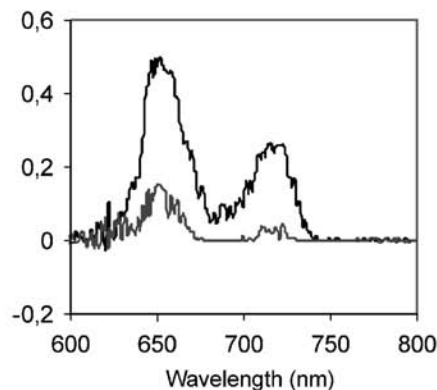
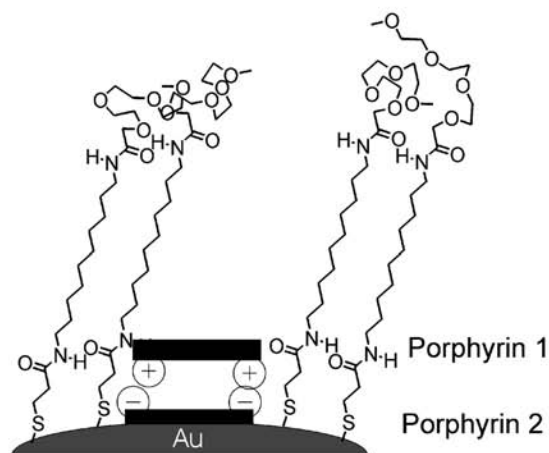
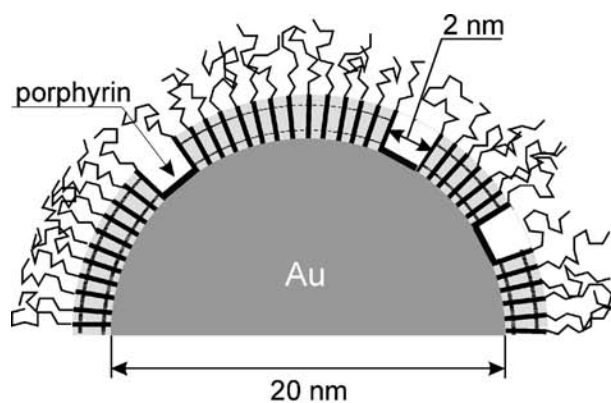


**Fig. 9** Model of a gold nanoparticle coated with a rigid diamide monolayer containing 2-nm gaps with a porphyrin at the bottom. The head group of the diamido amphiphile is an oligoethylene ether. *Source:* From Ref.<sup>[57]</sup>.

band have to be brought to reaction with added electron acceptors and donors, respectively. In this way charge separation can be stabilized. Much of the work with semiconductor particles is thus focused on the conversion of sunlight into chemical energy (e.g., hydrogen production) or electrical energy (photoelectrochemical cells). For the absorption of light the size of the bandgap is essential. The coupling to electron

acceptors and donors depends on the position of the conduction and the valence band. It must be noticed that these properties are size dependent in the quantum (Q) particles.<sup>[60]</sup> Narrow bandgap semiconductors such as cadmium sulfide (CdS),<sup>[61]</sup> cadmium selenide (CdSe),<sup>[62]</sup> lead sulfide (PbS),<sup>[63]</sup> and silver sulfide (Ag<sub>2</sub>S)<sup>[64]</sup> are excitable with visible light. Wide bandgap semiconductors such as titanium dioxide (TiO<sub>2</sub>),<sup>[65]</sup> zinc oxide (ZnO),<sup>[66]</sup> and tin dioxide (SnO<sub>2</sub>)<sup>[67]</sup> are only sensitive in the UV. Spectral sensitization is therefore an important approach to making wide band semiconductors attractive for solar energy conversion.<sup>[68,69]</sup> A chromophore absorbing in the visible range is attached to the particle surface. The excited electron of the chromophore is injected into the conduction band of the semiconductor. Thus in most cases the semiconductor surface is solely modified by dyes; additional monolayer coatings may improve solubility and longevity in the chosen solvent.

A different approach to enlarging the wavelength range of absorption is the coupling of two semiconductor particles with wide and narrow bandgap in mixed particle assemblies.<sup>[70]</sup> Either nanostructured films containing nanoparticles of different semiconductors (e.g., ZnO and CdS) are prepared by coprecipitation.<sup>[71]</sup> Heterostructures of the core-shell type are formed by controlled precipitation of semiconductor molecules of one type (shell) on the presynthesized nanoparticles of another type (core), e.g., CdSe/ZnS.<sup>[72]</sup> Photocatalytic water splitting with such systems was introduced by Henglein<sup>[73]</sup> and Duonghong, Ramsden, and Graetzel<sup>[74]</sup> both in 1982. It should be noted that in most cases the semiconductor particles used in photocatalytic studies (synthesis of organic compounds) are rather large (100 nm) with no quantum size effects.

## Spectral Sensitization

Charge ejection from excited dyes or charge injection into the conduction band of semiconductor particles is the key reaction for the construction of photoelectrochemical cells of technical interest. At first, electron injection was not determined directly. Photocurrents were measured in electrode systems with polycrystalline layers of TiO<sub>2</sub> loaded with different dyes.<sup>[75–80]</sup> From the current efficiency IPCE and the absorption of the dye quantum yields of injection from 87% to 100% were calculated. Direct measurement of the luminescence yield of the ruthenium complex on TiO<sub>2</sub> particles gave a value of only 60%.<sup>[75]</sup> Later,<sup>[81]</sup> fluorescence and transient absorption changes were measured on colloidal TiO<sub>2</sub> electrodes, consisting of SnO<sub>2</sub> conductive glass and a film of 25 nm TiO<sub>2</sub> particles. Chlorin e6 and Cu-chlorophyllin were used as sensitizers. Comparison of the fluorescence lifetime of

chlorin e6 on TiO<sub>2</sub> and ZrO<sub>2</sub>, where charge injection is not possible, yielded a rate constant for the electron injection of  $2.2 \times 10^9 \text{ sec}^{-1}$ . The constant was nearly 10 times smaller ( $3 \times 10^8 \text{ sec}^{-1}$ ) for the copper compound, where electron transfer starts from the triplet state and was determined from the phosphorescence lifetimes. Transient absorption changes after 10 nsec of excitation of the dye indicated the formation of its cation radical and of the electron injected into the TiO<sub>2</sub> conduction band. In the absence of a redox electrolyte (J<sup>-</sup>) the recovery of the ground-state absorption of the dye and the decay of the products of charge separation were identical. The addition of J<sup>-</sup> caused a fast reduction of the cation radical, whereas the absorption of the electron stayed for more than 100 msec.

Fsec-time resolution is necessary to the study of the dynamics of electron injection. This was done for fluorescein 27 adsorbed to 2.4-nm TiO<sub>2</sub> particles.<sup>[82]</sup> The absorption of the injected electrons had a rise time of 300 fsec, which is identical to the decay time of the stimulated emission of the dye. The recombination was much slower, which was explained by the validity of the Marcus formula in the inverted region. The kinetics was multiexponential with a very wide distribution of rates, ranging from 25 psec to nanoseconds and microseconds. Normally, in such a case, a distribution of energetically different trap sites for electrons is suggested. Here a red shift of the transient absorption within 25 psec was found, explained by vibrational cooling and perhaps solvation and structural relaxation of the initial product state, leading to a time-dependent  $\Delta G^0$ .

Ashbury et al.<sup>[83]</sup> studied the effect of the bridge length of the binding ligand of re-polypyridyl complexes. They also obtained evidence for the injection of hot excited state electrons.<sup>[84]</sup> Bonhote et al.<sup>[85]</sup> studied the structural effect of different Ru-dye molecules. The best yield of charge separation was obtained for the system in which the excited electron was localized on the ligand bound to the semiconductor surface.

Electron injection is expected to be especially effective from a highly polar excited state of the dye. This has been verified by comparison of two coumarin dyes bound to TiO<sub>2</sub> particles through a carboxyl group.<sup>[86]</sup> Coumarin C 343 is a four-ring-system and the electron injection occurs from a normal intramolecular charge transfer (ITC) state with a quantum yield of 0.6. In the second dye, 7-diethylaminocoumarin-3-carboxylic acid (D-1421), the ICT state was able to relax to the more polar twisted intramolecular charge transfer (TICT) state. The overall quantum yield of electron injection from both excited states was 0.9, i.e., 50% higher than for C343, for which rotation of the nitrogen moiety is not possible. The products of the reaction, the dye radical cation, and the electron



in the  $\text{TiO}_2$  conduction band were shown by picosecond laser flash photolysis.

### Photocurrents in Photoelectrochemical Cells

For a long time the construction of efficient photoelectrochemical cells was hampered by the fact that monolayers of dyes on planar electrodes absorb usually less than 1% of the incident light. Graetzel<sup>[75–80]</sup> used polycrystalline  $\text{TiO}_2$  (anatase) electrodes with a roughness of 200. Thus in the beginning the second problem, that of charge injection, was attacked.  $\text{Fe}(\text{CN})_6^{4-}$  which forms a charge transfer complex with  $\text{TiO}_2$  yielded an IPCE of 0.37 only;<sup>[76]</sup> the metalloporphyrin  $\text{ZnTPPC}$ <sup>[77]</sup> was only slightly better (0.42). A number of ruthenium complexes were examined.<sup>[87]</sup> The normal *tris*-bipyridin complex did not bind sufficiently. Carboxylic groups turned out to be necessary. Ruthenium complexes with two and three carboxy-bipyridin ligands were used and gave values of 0.62 and 0.73 for the IPCE.<sup>[75,78,79]</sup> For the latter ligand the importance of type and concentration of the redox electrolyte were determined.<sup>[79]</sup>  $\text{J}^-$  turned out to be better (0.73) than  $\text{Br}^-$  (0.56); and for hydroquinone the initially used concentration of 1 mM was too low (0.44) and had to be increased to 0.1 M (0.74). A very good value (0.83) was obtained with coumarin.<sup>[80]</sup> Other groups also tried merocyanines.<sup>[88]</sup> The importance of carboxyl groups for binding of a dye to the  $\text{TiO}_2$  surface was again shown by comparing the photocurrent action spectra of chlorophyll, chlorins, and mesoporphyrins.<sup>[89]</sup> Copper-chlorophyllin was not better than copper-chlorin, indicating that conjugation of the carboxyl group to the  $\pi$ -electron system of the dye was not advantageous.

O'Regan and Graetzel published in 1991 the design of the first photoelectrochemical cell which could compete with photovoltaic cells.<sup>[90]</sup> The progress was based on the use of a 3-D network of  $\text{TiO}_2$  nanoparticles (15 nm size), coated with a charge-transfer dye and fixed as a film of 10- $\mu\text{m}$  thickness on a conducting glass support. The large surface allowed binding of a higher amount of the dye than before. The dye was a trimeric ruthenium complex  $\text{RuL}_2 (\mu\text{-(CN)Ru(CN)L}_2')_2$ , with bipyridine and bipyridine-dicarboxylic acid as ligands. With lithium-iodide as a redox electrolyte an IPCE of 0.84 was achieved. The overall energy conversion yield was 7.1–7.9% in simulated solar light and 12% in diffuse daylight. The next step was to improve the redox electrolyte by changing to solid systems. P-type semiconductors<sup>[91]</sup> and organic materials<sup>[92]</sup> were tested with disappointing results. An amorphous organic hole transporting material, namely, tetrakis (*N,N'*-dimethoxyphenyl-amine)-spirobifluorene (OMeTAD), was then successful.<sup>[93]</sup> The energy efficiency was 33%

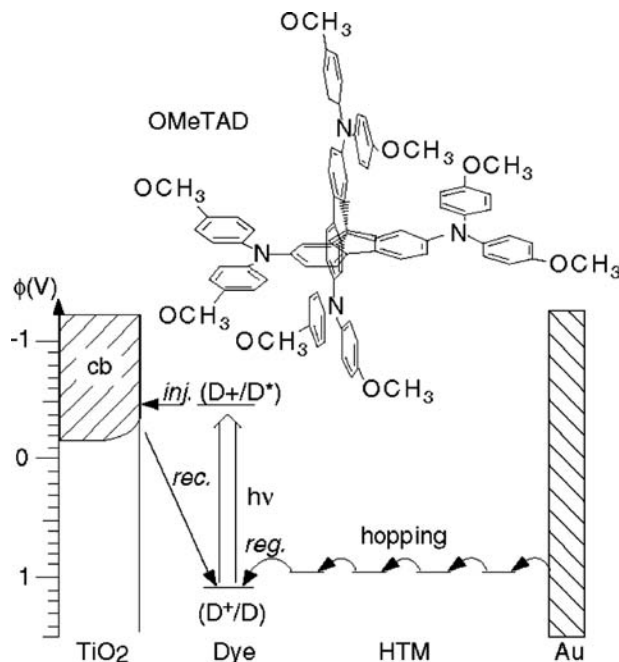


**Fig. 10** Model of the electron injection (inj.), regeneration (reg.), recapture (rec.), and hopping in the mesoporous  $\text{TiO}_2$  solar cell heterojunction. *Source:* From Ref.<sup>[93]</sup>.

with Ru-bis(dicarboxy-bipyridyl)-bis-rhodanid complex as a sensitizer (Fig. 10).

CdS nanoparticles were covered with thiolated oligonucleotides and then cross-linked with DNA. The assembly was connected with a gold electrode by double-stranded DNA.<sup>[94]</sup> Photocurrents were observed in the presence of TEOA upon irradiation at 405 nm where the CdS particles absorb. Conduction band electrons from particles near the electrode were directly ejected into the electrode. Electrostatic binding of  $\text{Ru}(\text{NH}_3)_6^{3+}$  to the DNA increased the current. Obviously, the ruthenium complex was active as electron relay (Fig. 11).

Nanocomposite Ni/ $\text{TiO}_2$  films were derivatized with hexacyanoferrate to form nickel salt (NHF).<sup>[95]</sup> Under chopped illumination photocurrent signals indicated photoelectron-hole recombination, mediated by the hexacyanoferrate redox electrolyte, if the potential was below the NHF redox regime. At higher potentials the oxidized NHF centers accepted electrons from the excited  $\text{TiO}_2$  with enhanced quantum yield. If a nickel electrode was derivatized with hexacyanoferrate and  $\text{TiO}_2$ , the electrode exhibited bipolar photoactivity: the photocurrent switched from cathodic to anodic. Below the NHF potential the photogenerated holes from  $\text{TiO}_2$  were transferred to reduced NHF sites; above the NHF potential, the electrons were transferred to oxidized NHF sites as in the composite film. This result underlines the importance of the microenvironment (Fig. 12).

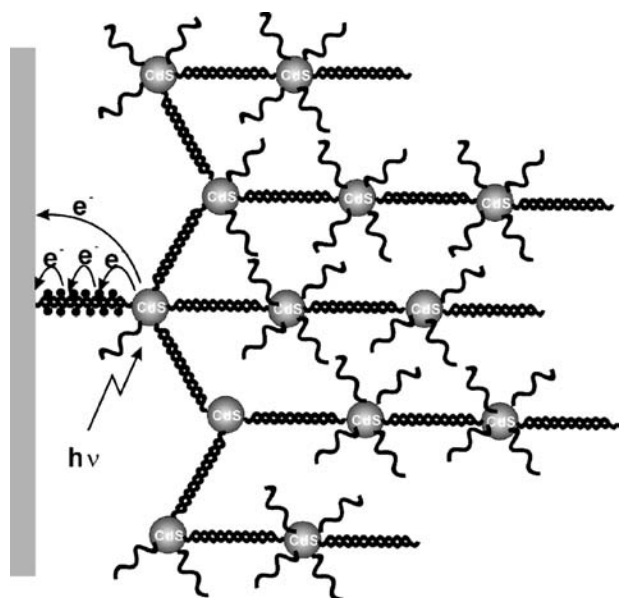


**Fig. 11** Model of oligonucleotide-DNA linked arrays of CdS nanoparticles. *Source:* From Ref.<sup>[94]</sup>.

### Hydrogen Production

After a burst of articles in the early 1980s, little work has been done on hydrogen production recently. TiO<sub>2</sub> and Nb<sub>2</sub>O<sub>5</sub> nanoparticles have been used in integrated systems for light-induced vectorial electron transfer and hydrogen production.<sup>[96]</sup> The electron

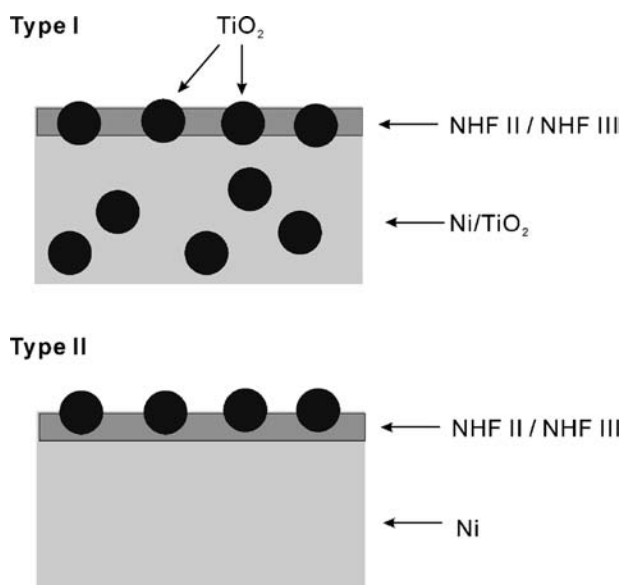


**Fig. 12** Model of nickel hexacyanoferrate (NHF) films on TiO<sub>2</sub> or nickel electrodes. Type I was photoactive above an applied potential of 0.4 V. Type II switches from cathodic to anodic photobehavior upon change of potential or Ni(II)/Ni(III) ratio.

transfer system consisted of an electron donor, Ruthenium-bipyridyl-dicarboxylate as a sensitizer, the semiconductor as initial electron acceptor, and a viologen as electron relay to the platinum catalyst. This system was spatially organized by a linear channel zeolite (zeolite L or mordenite), which was internally platinized. The semiconducting quantum particles were grown by hydrolysis within the channels and on the external surface of the zeolites. The channel openings (0.71- and 0.65-nm diameter) did not allow the entrance of the ruthenium complex, which was adsorbed exclusively on the surface of the external particles. The viologens were able to enter the channels. In this way the electron donors were separated from the hydrogen catalyst. Despite very efficient initial charge separation no hydrogen (TiO<sub>2</sub> system) or hydrogen with only 0.01% quantum yield (Nb<sub>2</sub>O<sub>5</sub>) was evolved in the presence of a reversible electron donor (e.g., J<sup>-</sup>). The quantum yield was, however, 1% at 450 nm for the system zeolite/TiO<sub>2</sub>/MV<sup>2+</sup>/RuL<sub>3</sub><sup>2+</sup> in the presence of sacrificial electron donors such as TEOA or EDTA. It should be noted that the initial charge injection from the Ru complex into the semiconductor particle is essential for the success. Without the particles with self-assembly of the MV<sup>2+</sup> and Ru(Bipy)<sub>3</sub><sup>2+</sup> onto/into the zeolites very little hydrogen was produced. On the other hand, the H<sub>2</sub>-evolution rate was highest in the case of direct bandgap excitation (Fig. 13).

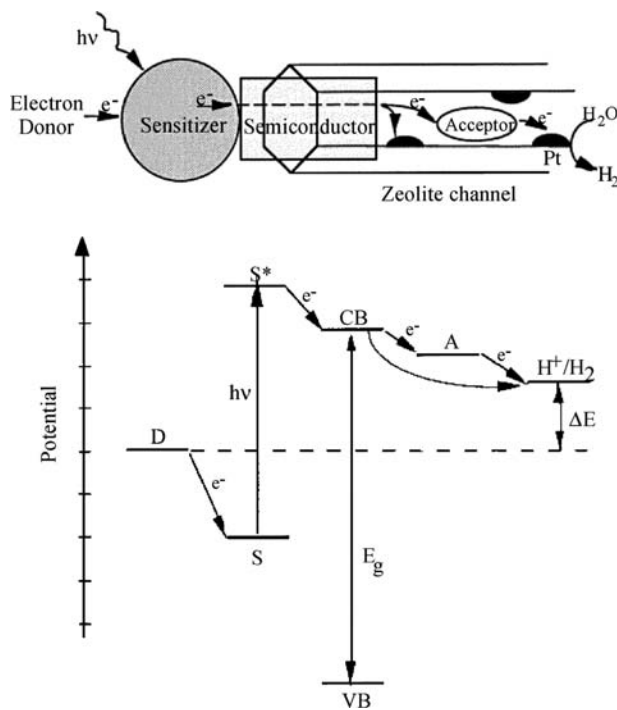


**Fig. 13** Model of a sensitized semiconductor-zeolite system for light-induced hydrogen production. *Source:* From Ref.<sup>[96]</sup>.

Magnetic - Mesoporous

## SILICA PARTICLES

Silica particles are usually prepared by the method of Stöber, Fink, and Bohn<sup>[97]</sup> which is the polycondensation of tetraethoxysilane (TES). It leads to a dense SiO<sub>2</sub> network, if the conversion of SiOEt groups and the cross-linking are perfect. Otherwise, the hydrophilic and charge stabilized particles contain nanosized pores. The negative surface charge has been used to stabilize the products of photo-induced charge separation.<sup>[98]</sup> More recently, interest has grown in concentrated dispersions of the silica particles. For this purpose sterically stabilized core-shell particles have been synthesized by surface esterification with octadecanol.<sup>[99]</sup> These organosilica particles are dispersed in organic solvents and several different colloid phases have been produced: colloidal fluids with only short-range positional order, colloidal glasses with a frozen-in fluid structure, colloidal crystals with long-range positional correlations, and thermotropic gels. These systems are of special interest, when single particles become visual by covalently bound fluorescent dyes. There are three possible positions for the dye: on the particle surface (type a), in a thin shell in the particle interior (type b), and distributed in the volume of an inner core (type c). All three types have been realized by introducing the dye at different stages of the particle synthesis. Isocyanate derivatives of fluorescein, coumarin, azobenzene, and pyrene have been used to be covalently bound to the silane coupling agent 3-aminopropyl-triethoxysilane (APS).<sup>[100]</sup> Type c particles<sup>[101,102]</sup> were applied in studies by fluorescence confocal scanning laser microscopy (FCSLM), type b particles<sup>[103]</sup> in fluorescence recovery after photobleaching (FRAP) experiments. Apart from these investigations centered around the question of interparticle structure and particle diffusion, photochemical studies have not been undertaken. A new method of preparing dye-labeled particles has recently been published.<sup>[104,105]</sup> Trimethoxymethylsilanes (TMOMS) were used for the synthesis together with chlorobenzyl-trimethoxysilane, leading to lower cross-link density and higher porosity as compared to the particles from TES. Thus carboxylate derivatives of the dyes were able to diffuse through the micropores and were bound by esterification with the chlorobenzyl group. For particles to be stable in aqueous medium, the coating has to be carried out with bifunctional compounds, one group being a terminal amino group.

Fuhrhop<sup>[106]</sup> started the Stöber synthesis with silicon tetrapropoxide and aminated the surface with a silylchloride derivative. Judging from TEM pictures the particles of at least 60-nm diameter had a smooth surface. In a further derivatization step gaps in monolayers, as already realized on gold particles, were constructed. Tetracarboxyphenylporphyrin was covalently

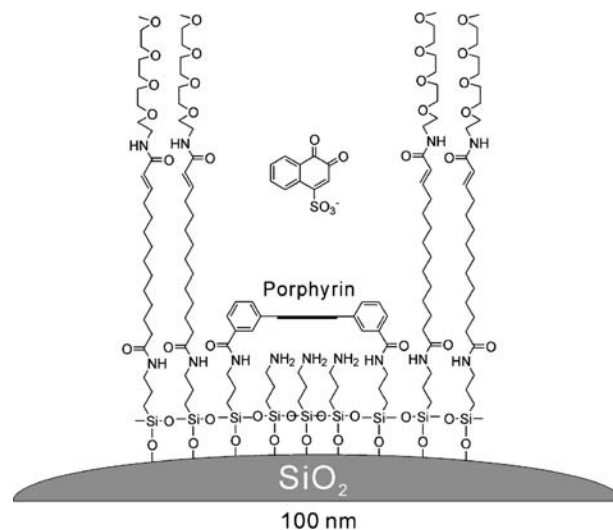


**Fig. 14** Model of a porphyrin-based membrane gap. (Fuhrhop, unpublished.)

bound to the surface through four amide bonds. Polyoxyethylene as terminal group rendered the particles especially hydrophilic. In contrast to the case of porphyrin bound to gold particles the photophysical properties of the porphyrin were similar to that of corresponding porphyrins in solution (e.g., the fluorescence yield). The triplet state was detected by absorption changes around 780 nm with a relaxation time larger than in solution. Negatively charged *o*-naphthoquinone-sulfonate was able to penetrate to the porphyrine and to accelerate the triplet relaxation by electron transfer (the singlet state was also affected) (Fig. 14).

Silica particles are commercially available in different qualities. Cab-O-Sil, which has been sintered at 500°C, is the least porous material and best suited for the attachment of monolayers. Mallouk<sup>[107]</sup> has formed multilayers by alternating assembly of  $\alpha,\omega$ -bis-phosphonic acid-bolaamphiphiles and Zr(IV)-salts on Cab-O-Sil particles terminated by phosphonic acid.

## CONCLUSION

Membrane coating of nanoparticles enables to vary the properties and interactions of individual particles, thereby also determining their stability in a given solvent. The ordering of these membranes is less than that of SAMs on planar surfaces and therefore a subject of intense research. Photochemical and photophysical reactions of dyes incorporated into the membranes help to elucidate the order and other properties of the membranous coatings, especially on gold particles. On silver and gold particles, surface-enhanced reactions such as Raman and resonance Raman scattering

are analytical tools. Fluorescent dyes on silica particles are used to investigate the structure of concentrated colloidal solutions. On semiconductor particles, dye coatings have a more practical purpose: sensitization for the absorption of visible light makes the particles interesting in the context of solar energy conversion. The construction of photoelectrochemical cells, the production of hydrogen, and the photochemical detoxification of waste materials, especially in water, are projects that will still become more important in the future. The general trend is to leave the single-particle systems and come to the design of assemblies of nanoparticles with a well-defined architecture. The particles are cross-linked by membranes or polymers, provided with dyes or other molecules, to realize defined distances and surfaces with special properties and finally to arrive at new complex composite materials. Until now for photochemical reactions the large surface of the particles has been the decisive advantage over planar surfaces. The size dependence of optical, electrochemical, and thermodynamic properties of quantum particles has scarcely been exploited and is surely more essential for the design of special optical materials for nonlinear optics and of nanoelectronic circuits.

## ACKNOWLEDGMENT

Financial support by the Deutsche Forschungsgemeinschaft (SFB 348 "Mesoscopic Systems"), the European TMR research network "Carbohydrate Recognition," the Fonds der Deutschen Chemischen Industrie and by the FNK of the Free University is gratefully acknowledged.

## REFERENCES

1. Turkevich, J.; Stevenson, P.C.; Hiller, J. A study of the nucleation and growth processes in the synthesis of colloidal gold. *Discuss. Faraday Soc.* **1951**, *11*, 55–75.
2. Cassagneau, T.; Fendler, J.H. Preparation and layer-by-layer self-assembly of silver nanoparticles capped by graphite oxide nanosheets. *J. Phys. Chem., B* **1999**, *103*, 1789–1793.
3. Hostetler, M.J.; Wingate, J.E.; Zhong, C.-J.; Harris, J.E.; Vachet, R.W.; Clark, M.R.; Londono, J.D.; Green, S.J.; Stokes, J.J.; Wignall, G.D.; Glish, G.L.; Porter, M.D.; Evans, N.D.; Murray, R.W. Alkanethiolate gold cluster molecules with core diameters from 1.5 to 5.2 nm: core and monolayer properties as a function of core size. *Langmuir* **1998**, *14*, 17–30.
4. Turkevich, J.; Kim, G. Palladium: preparation and catalytic properties of particles of uniform size. *Science* **1970**, *169*, 873–879.

5. Rampino, L.D.; Nord, F.F. Preparation of palladium and platinum synthetic high polymer catalysts and the relationship between particle size and rate of hydrogenation. *J. Am. Chem. Soc.* **1941**, *63*, 2745–2749.
6. Brust, M.; Walker, M.; Bethell, D.; Schiffrin, D.J.; Whyman, R. Synthesis of thiol-derivatized gold nanoparticles in a two-phase liquid-liquid system. *J. Chem. Soc., Chem. Commun.* **1994**, 801–802.
7. Hostetler, M.J.; Green, S.J.; Stokes, J.J.; Murray, R.W.J. Monolayers in three dimensions: Synthesis and electrochemistry of  $\omega$ -functionalized alkanethiolate-stabilized gold cluster compounds. *J. Am. Chem. Soc.* **1996**, *118*, 4212–4213.
8. Reetz, M.T.; Helbig, W. Size-selective synthesis of nanostructured transition metal clusters. *J. Am. Chem. Soc.* **1994**, *116*, 7401–7402.
9. Han, M.Y.; Queck, C.H. Photochemical synthesis in formamide and room-temperature coulomb staircase behavior of size-controlled gold nanoparticles. *Langmuir* **2000**, *16*, 362–367.
10. Link, S.; El-Sayed, M.A. Size and temperature dependence of the plasmon absorption of colloidal gold nanoparticles. *J. Phys. Chem., B* **1999**, *103*, 4212–4217.
11. Quinten, M.; Kreibig, U. Optical properties of aggregates of small metal particles. *Surf. Sci.* **1986**, *172*, 557–577.
12. Rozsnyai, L.F.; Wrighton, M.S. Selective electrochemical deposition of polyaniline via photopatterning of a monolayer modified substrate. *J. Am. Chem. Soc.* **1994**, *116*, 5993–5994.
13. Wollman, E.W.; Kang, D.; Frisbie, C.D.; Lorkovic, I.M.; Wrighton, M.S. photosensitive self-assembled monolayers on gold: Photochemistry of surface-C azide and cyclopentadienylmanganese tricarbonyl. *J. Am. Chem. Soc.* **1994**, *116*, 4395–4404.
14. Jocy, G.J.; Workentin, M.S.  $\alpha$ -Diazo ketone self-assembled monolayer modified electrode: a proposed photoreactive template for electrode derivatization. *Chem. Commun.* **1999**, 839–840.
15. Pitters, J.L.; Kovar, M.; Griffiths, K.; Norton, P.R.; Workentin, M.S. Reactive intermediates on metal surfaces: a ketene monolayer on single crystal platinum generated by photolysis of pyridyl  $\alpha$ -diazoketones. *Angew. Chem., Int. Ed.* **2000**, *39*, 2144–2147.
16. Wolf, M.; Fox, M.A. Photochemistry and surface properties of self-assembled monolayers of *cis*- and cyano-4'-(10-thiodeoxy)stilbene on polycrystalline gold. *J. Am. Chem. Soc.* **1995**, *117*, 1845–1846.
17. Willner, I.; Doron, A.; Katz, E. Gated molecular and biomolecular optoelectronic systems via photoisomerizable monolayer electrodes. *J. Phys. Org. Chem.* **1998**, *11*, 546–560.
18. Wolf, M.O.; Fox, M.A. Photoisomerization and photodimerization in self-assembled monolayers of *cis*- and *trans*-4-cyano-4'-(10-mercaptodeoxy)stilbene on gold. *Langmuir* **1996**, *12*, 955–962.
19. Kim, T.; Chan, K.C.; Crooks, R.M. Polymeric self-assembled monolayers: 4. Chemical, electrochemical, and thermal stability of  $\omega$ -functionalized, self-assembled diacetylenic and polydiacetylenic monolayers. *J. Am. Chem. Soc.* **1997**, *119*, 189–193.

20. Fox, M.A.; Wooten, M.D. Characterization, adsorption, and photochemistry of self-assembled monolayers of 10-thiodecyl 2-anthryl ether on gold. *Langmuir* **1997**, *13*, 7099–7105.
21. Li, W.; Lynch, V.; Thompson, H.; Fox, M.A. Self-assembled monolayers of 7-(10-thiodecoxy)coumarin on gold: Synthesis, characterization, and photodimerization. *J. Am. Chem. Soc.* **1997**, *119*, 7211–7217.
22. Imahori, H.; Arimura, M.; Hanada, T.; Nishimura, Y.; Yamazaki, I.; Sakata, Y.; Fukuzumi, S.J. Photoactive three-dimensional monolayers: Porphyrin-alkanethiolate-stabilized gold clusters. *Am. Chem. Soc.* **2001**, *123*, 335–336.
23. Aguila, A.; Murray, R.W. Monolayer-protected clusters with fluorescent dansyl ligands. *Langmuir* **2000**, *16*, 5949–5954.
24. Ruzgas, L.L.; Gaigalas, A.K. Fluorescence from Alexa 488 fluorophore immobilized on a modified gold electrode. *Langmuir* **1999**, *15*, 6358–6363.
25. Chen, M.M.Y.; Katz, A. Steady-state fluorescence-based investigation of the interaction between protected thiols and gold nanoparticles. *Langmuir* **2002**, *18*, 2413–2420.
26. Wang, T.; Zhang, D.; Xu, W.; Yang, J.; Han, R.; Zhu, D. Preparation, characterization, and photophysical properties of alkanethiols with pyrene units-capped gold nanoparticles: unusual fluorescence enhancement for the aged solutions of these gold nanoparticles. *Langmuir* **2002**, *18*, 1840–1848.
27. Zhang, J.; Whitesell, J.K.; Fox, M.A. Photoreactivity of self-assembled monolayers of azobenzene or stilbene derivatives capped on colloidal gold clusters. *Chem. Mater.* **2001**, *13*, 2323–2331.
28. Hu, J.; Zhang, J.; Liu, F.; Kittredge, K.; Whitesell, J.K.; Fox, M.A. Competitive photochemical reactivity in a self-assembled monolayer on a colloidal gold cluster. *J. Am. Chem. Soc.* **2001**, *123*, 1464–1470.
29. Evans, S.D.; Johnson, S.R.; Ringsdorf, H.; Williams, L.M.; Wolf, H. Photoswitching of azobenzene derivatives formed on planar and colloidal gold surfaces. *Langmuir* **1998**, *14*, 6436–6440.
30. Kell, A.J.; Stringle, D.L.B.; Workentin, M.S. Norrish type II photochemical reaction of an aryl ketone on a monolayer-protected gold nanocluster. Development of a probe of conformational mobility. *Org. Lett.* **2000**, *2* (21), 3381–3384.
31. Thomas, K.G.; Kamat, P.V. Making gold nanoparticles glow: enhanced emission from a surface-bound fluoroprobe. *J. Am. Chem. Soc.* **2000**, *122*, 2655–2656.
32. Hone, D.C.; Walker, P.I.; Evans-Gowing, R.; FitzGerald, S.; Beeby, A.; Chambrier, I.; Cook, M.J.; Russell, D.A. Generation of cytotoxic singlet oxygen via phthalocyanine-stabilized gold nanoparticles: A potential delivery vehicle for photodynamic therapy. *Langmuir* **2002**, *18*, 2985–2987.
33. Kometani, N.; Tsubonishi, M.; Fujita, T.; Asami, K.; Yonezawa, Y. Preparation and optical absorption spectra of dye-coated Au, Ag, and Au/Ag colloidal nanoparticles in aqueous solutions and in alternate assemblies. *Langmuir* **2001**, *17*, 578–580.
34. Hranisavljevic, J.; Dimitrijevic, N.M.; Wurtz, G.A.; Wiederrecht, G.P. Photoinduced charge separation reactions of J-aggregates coated on silver nanoparticles. *J. Am. Chem. Soc.* **2002**, *124*, 4536–4537.
35. Baschong, W.; Lucocq, J.M.; Roth, J. Thiocyanate gold: small (2–3 nm) colloidal gold for affinity cytochemical labelling in electron microscopy. *Histochemistry* **1985**, *83*, 409–411.
36. Henglein, A. Radiolytic preparation of ultrafine colloidal gold particles in aqueous solution: optical spectrum, controlled growth, and some chemical reactions. *Langmuir* **1999**, *14*, 6738–6744.
37. Chandrasekharan, N.; Kamat, P.V.; Hu, J.; Jones, G. Dye-capped gold nanoclusters: Photoinduced morphological changes in gold/rhodamine 6G nanoassemblies. *J. Phys. Chem., B* **2000**, *104*, 11,103–11,109.
38. Johnson, C.K.; Soper, J.A. Nonlinear surface-enhanced spectroscopy of silver colloids and pyridine: hyper-Raman and second-harmonic scattering. *J. Phys. Chem.* **1989**, *93*, 7281–7285.
39. Clays, K.; Hendricks, E.; Triest, M.; Persoons, A. Second-order nonlinear optics in isotropic liquids: hyper-Rayleigh scattering in solution. *J. Mol. Liq.* **1995**, *67*, 133–155.
40. Baranov, A.V.; Inoue, K.; Toba, K.; Yamanaka, A.; Petrov, V.I.; Fedorov, A.V. Resonant hyper-Raman and second harmonic scattering in a CdS quantum dot system. *Phys. Rev., B Condens. Matter* **1996**, *53*, R1721–R1724.
41. Vance, F.W.; Lemon, V.I.; Hupp, J.T. Enormous hyper-Rayleigh scattering from nanocrystalline gold particle suspensions. *J. Phys. Chem., B* **1998**, *102*, 10,091–10,093.
42. Johnson, R.C.; Hupp, J.T. *Metal Nanoparticles. Synthesis Characterization and Applications*; Feldheim, D., Foss, C., Eds.; Marcel-Dekker: New York, 2000.
43. Shiang, J.J.; Heath, J.R.; Collier, C.P.; Saykally, R.J. Cooperative phenomena in artificial solids made from silver quantum dots: The importance of classical coupling. *J. Phys. Chem., B* **1998**, *102*, 3425–3430.
44. Chumanov, G.; Sokalov, K.; Gregory, B.; Cotton, T.M. Colloidal metal films as a substrate for surface-enhanced spectroscopy. *J. Phys. Chem.* **1995**, *99*, 9466–9471.
45. Feilchenfeld, H.; Chumanov, G.; Cotton, T.M. Photo-reduction of methylviologen adsorbed on silver. *J. Phys. Chem.* **1996**, *100*, 4937–4943.
46. Moskovits, M. Surface-enhanced spectroscopy. *Rev. Mod. Phys.* **1985**, *57*, 783–826.
47. Harfenist, S.A.; Wang, Z.L.; Alvarez, M.M.; Vezmar, I.; Whetten, R.L. Highly oriented molecular Ag nanocrystal arrays. *J. Phys. Chem.* **1996**, *100*, 13,904–13,910.
48. Brousseau, L.C., III; Novak, J.P.; Marinakos, S.M.; Feldheim, D.L. Assembly of phenylacetylene-bridged gold nanocluster dimers and trimers. *Adv. Mater.* **1999**, *11*, 447–449.
49. Novak, J.P.; Feldheim, D.L. Assembly of phenylacetylene-bridged silver and gold nanoparticle arrays. *J. Am. Chem. Soc.* **2000**, *122*, 3979–3980.
50. Novak, J.P.; Brousseau, L.C., III; Vance, F.W.; Johnson, R.C.; Lemon, B.I.; Hupp, J.T.; Feldheim, D.L.

- Nonlinear optical properties of molecularly bridged gold nanoparticle arrays. *J. Am. Chem. Soc.* **2000**, *122*, 12,029–12,030.
51. Šluofová-Srnová, I.; Vlčková, B. Two-dimensional assembling of Au nanoparticles mediated by tetrapyrroldiporphine molecules. *Nano Lett.* **2002**, *2* (2), 121–125.
  52. Lahav, M.; Gabriel, T.; Shipway, A.N.; Willner, I. Assembly of a Zn(II)-porphyrin-bipyridinium dyad and Au-nanoparticle superstructures on conductive surfaces. *J. Am. Chem. Soc.* **1999**, *121*, 258–259.
  53. Lahav, M.; Heleg-Shabtai, V.; Wasserman, J.; Katz, E.; Willner, I.; Duerr, H.; Hu, Y.-Z.; Bossmann, S.H. Photoelectrochemistry with integrated photosensitizer-electron acceptor and Au-nanoparticle arrays. *J. Am. Chem. Soc.* **2000**, *122*, 11,480–11,487.
  54. Sudeep, P.K.; Ipe, B.I.; Thomas, K.G.; George, M.V.; Barazzouk, K.S.; Hotchandani, S.; Kamat, P.V. Fullerene-functionalized gold nanoparticles. A self-assembled photoactive antenna-metal nanocore assembly. *Nano Lett.* **2002**, *2* (1), 29–35.
  55. Kuwahara, Y.; Akiyama, T.; Yamada, S. Facile fabrication of photoelectrochemical assemblies consisting of gold nanoparticles and a *tris*(2,2'-bipyridine)ruthenium(II)-viologen linked thiol. *Langmuir* **2001**, *17*, 5714–5716.
  56. Imahori, H.; Norieda, H.; Yamada, H.; Nishimura, Y.; Yamazaki, I.; Sakata, Y.; Fukuzumi, S. Light-harvesting and photocurrent generation by gold electrodes modified with mixed self-assembled monolayers of boron-dipyrroin and ferrocene-porphyrin-fullerene triad. *J. Am. Chem. Soc.* **2001**, *123*, 100–110.
  57. Li, G.; Fuhrhop, J.H. Anticorrosive lipid monolayers with rigid walls around porphyrin-based 2 nm gaps on 20 nm gold particles. *Langmuir* **2002**, *18*, 7740–7747.
  58. Fudickar, W.; Zimmermann, J.; Ruhlmann, L.; Roeder, B.; Siggel, U.; Fuhrhop, J.-H. Fluorescence quenching and size selective heterodimerization of a porphyrin adsorbed to gold and embedded in rigid membrane gaps. *J. Am. Chem. Soc.* **1999**, *121*, 9539–9545.
  59. Skupin, M.; Li, G.; Fudickar, W.; Zimmermann, J.; Roeder, B.; Fuhrhop, J.-H. Methylammonium groups at the solid walls of nanometer-sized, water-filled monolayer gaps as binding sites for a tetraanionic porphyrin. *J. Am. Chem. Soc.* **2001**, *123*, 3454–3461.
  60. Alivisatos, A.P. Semiconductor clusters, nanocrystals, and quantum dots. *Science* **1996**, *271*, 933–937.
  61. Hickey, S.G.; Rilley, D.J. Photoelectrochemical studies of CdS nanoparticle-modified electrodes. *J. Phys. Chem., B* **1999**, *103*, 4599–4602.
  62. Klein, D.L.; Roth, R.; Kim, A.K.L.; Alivisatos, A.P.; McEuen, P.L. A single-electron transistor made from a cadmiumselenide nanocrystal. *Nature* **1997**, *389*, 699–701.
  63. Meldrum, F.C.; Flath, J.; Knoll, W. Chemical deposition of PbS on self-assembled monolayers of 16-mercaptohexadecanoic acid. *Langmuir* **1997**, *13*, 2033–2049.
  64. Spanhel, L.; Weller, H.; Fojtik, A.; Henglein, A. Photochemistry of semiconductor colloids: 17. Strong luminescing CdS and CdS-Ag<sub>2</sub>S particles. *Ber. Bunsenges. Phys. Chem.* **1987**, *91*, 88–94.
  65. Rizza, R.; Fitzmaurice, D.; Hearne, S.; Hughes, G.; Spoto, G.; Ciliberto, E.; Kerp, H.; Schropp, R. Self-assembly of monolayers of semiconductor nanocrystals. *Chem. Mater.* **1997**, *9*, 2969–2982.
  66. Hotchandani, S.; Kamat, P.V. Charge-transfer processes in coupled semiconductor systems. Photochemistry and photoelectrochemistry of the colloidal CdS–ZnO system. *J. Phys. Chem.* **1992**, *96*, 6834–6839.
  67. Bedja, I.; Hotchandani, S.; Kamat, P.V. Preparation and photoelectrochemical characterization of thin SnO<sub>2</sub> nanocrystalline semiconductor films and their sensitization with bis(2,2'-bipyridine) (2,2'-bipyridine-4,4'-dicarboxylic acid)ruthenium(II) complex. *J. Phys. Chem.* **1994**, *98*, 4133–4140.
  68. Gerischer, H.; Willig, F. Reaction of excited dye molecules at electrodes. *Top. Curr. Chem.* **1976**, *61*, 31–84.
  69. Nozik, Y.; Memming, R. Physical chemistry of semiconductor–liquid interfaces. *J. Phys. Chem.* **1996**, *100*, 13,061–13,078.
  70. Lawless, D.; Kapoor, S.; Meisel, D. Bifunctional capping of CdS nanoparticles and bridging to TiO<sub>2</sub>. *J. Phys. Chem., B* **1995**, *99*, 10329–10335.
  71. Vogel, R.; Pohl, K.; Weller, H. Sensitization of highly porous, polycrystalline TiO<sub>2</sub> electrodes by quantum sized CdS. *Chem. Phys. Lett.* **1990**, *174*, 241–246.
  72. Kortan, A.R.; Hull, R.; Opila, R.L.; Stams, D.A.; Thomas, T.D.; McLaren, D.C.; Ji, D.; Morton, T.H. Nucleation and growth of CdSe on ZnS quantum crystallite seeds, and vice versa, in inverse micelle media. *J. Am. Chem. Soc.* **1990**, *112*, 1327–1332.
  73. Henglein, A. Photochemistry of colloidal cadmium sulfide: 2. Effects of adsorbed methyl viologen and of colloidal platinum. *J. Phys. Chem.* **1982**, *86*, 2291–2293.
  74. Duonghong, D.; Ramsden, J.; Graetzel, M. Dynamics of interfacial electron-transfer processes in colloidal semiconductor systems. *J. Am. Chem. Soc.* **1982**, *104*, 2977–2985.
  75. Desilvestro, J.; Graetzel, M.; Kavan, L.; Moser, J. Highly efficient sensitization of titanium dioxide. *J. Am. Chem. Soc.* **1985**, *107*, 2988–2990.
  76. Vrachnou, E.; Vlachopoulos, N.; Graetzel, M. Efficient visible light sensitization of TiO<sub>2</sub> by surface complexation with Fe(CN)<sub>6</sub><sup>4-</sup>. *J. Chem. Soc., Chem. Commun.* **1987**, 868–870.
  77. Kalyanasundaram, K.; Vlachopoulos, N.; Krishnan, V.; Monnier, A.; Graetzel, M. Sensitization of TiO<sub>2</sub> in the visible light region using zinc porphyrins. *J. Phys. Chem.* **1987**, *91*, 2342–2347.
  78. Liska, P.; Vlachopoulos, N.; Nazeeruddin, M.K.; Comte, P.; Graetzel, M. *cis*-Diaquabis(2,2'-bipyridyl-4,4'-dicarboxylate)-ruthenium(II) sensitizes wide band gap oxide semiconductors very efficiently over a broad spectral range in the visible. *J. Am. Chem. Soc.* **1988**, *110*, 3686–3687.
  79. Vlachopoulos, N.; Liska, P.; Augustynski, J.; Graetzel, M. Very efficient visible light energy harvesting and conversion by spectral sensitization of high surface area polycrystalline titanium dioxide films. *J. Am. Chem. Soc.* **1988**, *110*, 1216–1220.
  80. Enea, O.; Moser, J.; Graetzel, M. Achievement of incident photon to electric current conversion yields



- exceeding 80% in the spectral sensitization of titanium dioxide by coumarin. *J. Electroanal. Chem.* **1989**, *259*, 59–65.
81. Kay, A.; Humphry-Baker, R.; Graetzel, M. Artificial photosynthesis: 2. Investigations on the mechanism of photosensitization of nanocrystalline TiO<sub>2</sub> solar cells by chlorophyll derivatives. *J. Phys. Chem.* **1994**, *98*, 952–959.
  82. Hilgendorff, M.; Sundstroem, V. Dynamics of electron injection and recombination of dye-sensitized TiO<sub>2</sub> particles. *J. Phys. Chem., B* **1998**, *102*, 10,505–10,514.
  83. Asbury, J.B.; Hao, E.; Wang, Y.; Lian, T. Bridge length-dependent ultrafast electron transfer from re polypyridyl complexes to nanocrystalline TiO<sub>2</sub> thin films studied by femtosecond infrared spectroscopy. *J. Phys. Chem.* **2000**, *104*, 11,957–11,964.
  84. Asbury, J.B.; Wang, Y.Q.; Hao, E.; Gosh, H.N.; Lian, T. Evidence of hot excited state electron injection from sensitizer molecules to TiO<sub>2</sub> nanocrystalline thin films. *Res. Chem. Intermed.* **2001**, *27*, 393.
  85. Bonhote, P.; Moser, J.E.; Humphry-Baker, R.; Vlachopoulos, N.; Zakeeruddin, S.M.; Walder, L.; Grätzel, M. Long-lived photoinduced charge separation and redox-type photochromism on mesoporous oxide films sensitized by molecular dyads. *J. Am. Chem. Soc.* **1999**, *121*, 1324–1336.
  86. Ramakrishna, G.; Ghosh, H.N. Efficient electron injection from twisted intramolecular charge transfer (TICT) state of 7-diethyl amino coumarin 3-carboxylic acid (D-1421) dye to TiO<sub>2</sub> nanoparticle. *J. Phys. Chem., A* **2002**, *106*, 2545–2553.
  87. Grätzel, M. Nanocrystalline electronic junctions. In *Semiconductor Nanoclusters—Physical Chemical and Catalytic Aspects*; Kamat, P.V., Meisel, D., Eds.; Elsevier: Amsterdam, 1997; 335pp.
  88. Khazraji, A.C.; Hotchandani, S.; Das, S.; Kamat, P.V. Controlling dye (merocyanine-540) aggregation on nanostructured TiO<sub>2</sub> films. An organized assembly approach for enhancing the efficiency of photosensitization. *J. Phys. Chem., B* **1999**, *103*, 4693–4700.
  89. Kay, A.; Graetzel, M. Artificial photosynthesis: 1. Photosensitization of TiO<sub>2</sub> solar cells with chlorophyll derivatives and related natural porphyrins. *J. Phys. Chem.* **1993**, *97*, 6272–6277.
  90. O'Regan, B.; Graetzel, M. A low-cost, high-efficiency solar cell based on dye-sensitized colloidal TiO<sub>2</sub> films. *Nature* **1991**, *353*, 737–739.
  91. O'Regan, B.; Schwarz, D.T. Large enhancement in photocurrent efficiency caused by UV illumination of the dye-sensitized heterojunction TiO<sub>2</sub>/RuLL'NCS/CuSCN: Initiation and potential mechanisms. *Chem. Mater.* **1998**, *10*, 1501–1509.
  92. Hagen, G.; Haarer, D.; Schaffrath, W.; Otschik, P.; Fink, R.; Bacher, A.; Schmidt, H.-W. Novel hybrid solar cells consisting of inorganic nanoparticles and an organic hole transport material. *Synth. Met.* **1997**, *89*, 215–220.
  93. Bach, U.; Lupo, D.; Comte, P.; Moser, J.E.; Weissoertel, F.; Salbeck, J.; Spreitzer, H.; Graetzel, M. Solid-state dye-sensitized mesoporous TiO<sub>2</sub> solar cells with high photon-to-electron conversion efficiencies. *Nature* **1998**, *395* (8), 583–585.
  94. Willner, I.; Patolsky, F.; Wasserman, J. Photoelectrochemistry with controlled DNA-cross-linked CdS nanoparticle arrays. *Angew. Chem.* **2001**, *113* (10), 1913–1916.
  95. de Tacconi, N.R.; Carmona, J.; Rejeshwar, K. Chemically modified Ni/TiO<sub>2</sub> nanocomposite films: charge transfer from photoexcited TiO<sub>2</sub> particles to hexacyanoferrate redox centers within the film and unusual photoelectrochemical behavior. *J. Phys. Chem., B* **1997**, *101* (49), 10,151–10,154.
  96. Kim, Y.I.; Keller, S.W.; Krueger, J.S.; Yonemoto, E.H.; Saupe, G.B.; Mallouk, T.E. Photochemical charge transfer and hydrogen evolution mediated by oxide semiconductor particles in zeolite-based molecular assemblies. *J. Phys. Chem., B* **1997**, *101*, 2491–2500.
  97. Stöber, W.; Fink, A.; Bohn, E. Controlled growth of monodisperse silica spheres in the micron size range. *J. Colloid Interface Sci.* **1968**, *26*, 62–69.
  98. Willner, I.; Yango, J.-M.; Laane, C.; Otvos, J.W.; Calvin, M. The function of SiO<sub>2</sub> colloids in photoinduced redox reactions. Interfacial effects on the quenching, charge separation, and quantum yields. *J. Phys. Chem.* **1981**, *85*, 3277–3282.
  99. van Helden, A.K.; Jansen, J.W.; Vrij, A. Preparation and characterization of spherical monodisperse silica dispersions in nonaqueous solvents. *J. Colloid Interface Sci.* **1981**, *81* (2), 354–368.
  100. van Blaaderen, A.; Vrij, A. Synthesis and characterization of colloidal dispersions of fluorescent, monodisperse silica spheres. *Langmuir* **1992**, *8*, 2921–2931.
  101. van Blaaderen, A.; Imhof, A.; Hage, W.; Vrij, A. Three-dimensional imaging of submicrometer colloidal particles in concentrated suspensions using confocal scanning laser microscopy. *Langmuir* **1992**, *8*, 1514–1517.
  102. Verhaegh, N.A.M.; van Blaaderen, A. Dispersions of rhodamine-labeled silica spheres: Synthesis, characterization, and fluorescence confocal scanning laser microscopy. *Langmuir* **1994**, *10*, 1427–1438.
  103. van Blaaderen, A.; Peetermans, J.; Maret, G.; Dhont, J.K.G. Long-time self-diffusion of spherical colloidal particles measured by fluorescence recovery after photobleaching. *J. Chem. Phys.* **1992**, *96*, 4591–4603.
  104. Graf, C.; Schaertl, W.; Maskos, M.; Schmidt, M. Tracer diffusion of polyorganosiloxane nanoparticles in solution: effects of tracer topology and particle concentration. *J. Chem. Phys.* **2000**, *112*, 3031–3039.
  105. Graf, C.; Schaertl, W.; Fischer, K.; Hugenberg, N.; Schmidt, M. Dye-labeled poly(organosiloxane) microgels with core-shell architecture. *Langmuir* **1999**, *15*, 6170–6180.
  106. Li, G.; Bhosale, S.V.; Wang, T.; Hackbarth, S.; Roeder, B.; Siggel, U.; Fuhrhop, J.-H. Nanowells on silica particles in water containing long-distance porphyrin heterodimers. *J. Am. Chem. Soc.* **2003**, *125*, 10,693–10,702.
  107. Yang, H.C.; Aoki, K.; Hong, H.-G.; Sackett, D.D.; Arendt, M.F.; Yau, S.-L.; Bell, C.M.; Mallouk, T.E. Growth and characterization of metal(II) alkane-bis-phosphate multilayer thin films on gold surfaces. *J. Am. Chem. Soc.* **1993**, *115*, 11855–11862.

# Mesoporous Materials

**James C. Vartuli**

**Wielsaw J. Roth**

*ExxonMobil Research and Engineering Company, Annandale, New Jersey, U.S.A.*

**Thomas F. Degnan, Jr.**

*Research Laboratory, ExxonMobil Research and Engineering Company, Annandale, New Jersey, U.S.A.*

## INTRODUCTION

The quest for new molecular sieves in the late 1980s led Mobil researchers to the discovery of a family of nanostructured mesoporous materials known as M41S.<sup>[1–3]</sup> MCM-41 is undoubtedly the best known and most widely studied of this family of materials, each synthesized via a self-assembled liquid crystal mechanism involving sol–gel precursors which form a hexagonally packed rod-shaped micelle structure.<sup>[4]</sup> The other members of the M41S family are the cubic (MCM-48) and lamellar (MCM-50) forms. This entry describes the progression of M41S materials from discovery through characterization and development. ExxonMobil has very recently commercialized MCM-41 for an undisclosed application. Its decade-long journey from initial identification to commercial application is similar in duration to that of many novel materials. Yet there were many unique challenges posed by the synthesis and development of such a novel material. This is its story.

## THE DISCOVERY OF THE M41S MATERIALS FAMILY

Like most discoveries of novel materials, the discovery of Mobil's M41S mesoporous molecular sieves was an unanticipated outcome of the application of observational skills, knowledge, and techniques developed over many years of effort in synthesizing large pore catalytically active frameworks. Like many major petroleum companies, Mobil had a material synthesis effort attempting to identify new zeolites that could selectively convert high molecular weight petroleum-based molecules. In the mid-1980s, Mobil Technology Company had a significant effort in developing pillared layered materials. This class of materials, theoretically, offered the ability to tune pore size, active site density,

and composition; variables that the traditional aluminosilicate zeolites did not possess. By varying the pillar size and pillar density, the Mobil researchers learned that pore systems could be tuned for the desired application. The pillar composition also appeared to be adjustable so various chemistries could be effected. Unfortunately, although significant progress was made in designing these pillared layered materials,<sup>[5]</sup> realistically these materials did not have sufficient thermal and hydrothermal stability or catalytic activity to be used in most petroleum processes. Furthermore, the pillar composition could not be as varied as initially conceived. Toward the end of the decade, a small group of researchers at Mobil's Paulsboro Laboratory approached this effort of discovering large pore frameworks by attempting to combine both the concepts of the pillared layered materials and the formation of zeolites. The approach was to consider that some zeolites were formed via layered intermediates. Thus if this intermediate could be isolated and used as a layered composition to form pillared porous materials; the resultant product would be composed of crystalline walls that would be thermally stable and catalytically active. This concept had credibility because of a new layered framework that was discovered during that time.<sup>[6]</sup> It was designated by Mobil as MCM-22 (MWW).

We noted that upon thermal treatment of the as-synthesized MCM-22, the X-ray diffraction pattern of the material shifted to higher  $2\theta$  values, similar to that of swollen layered materials when the intercalate is removed. In layered materials the low-angle lines associated with the interlayer distance shifted to lower  $d$ -spacings consistent with the removal of the organic template intercalate and the collapse of the layers. However, in the as-synthesized MCM-22 sample, this shift of the  $d$ -spacings, upon thermal treatment, was subtle,  $\sim 2\text{--}3 \text{ \AA}$ , and the base crystalline framework remained relatively unaffected. This suggested that

the MCM-22 zeolite was composed of crystalline layers that were linked together by weak chemical bonds during the synthesis. Upon thermal treatment, these chemical linkages became much stronger, as the layers condensed onto each other.

Using the as-synthesized zeolite material, with the template intact and prior to any thermal exposure, we attempted to delaminate or separate these crystalline layers of the MCM-22 “precursor.” A pillared layered material resulting from this delamination and subsequent pillaring was obtained and identified as MCM-36.<sup>[7,8]</sup> The process involved the initial intercalation of the layers using an alkyltrimethylammonium compound followed by the insertion of stable inorganic pillars using a reactive silica source such as tetraethylorthosilicate.

The layered zeolite precursors, exemplified by the MCM-22 case, differed from their layered predecessors such as clays and layered silicates in possessing layers with high zeolite activity and porosity. Obviously, these were very attractive from the catalyst standpoint. Another feature distinguishing the layered zeolite precursors from the other layered materials was their resistance to swelling by ion exchange with neutral or mildly basic media, such as quaternary ammonium salts or amines. It was only with the introduction of a quaternary ammonium surfactant in a hydroxide form, specifically cetyltrimethylammonium hydroxide solution obtained by anion exchange of the halide solution with hydroxide, that successful swelling of the layered zeolite precursor was demonstrated. The use of an apparently equivalent medium, a mixture of surfactant halide and another hydroxide, instead of the anion exchanged surfactant hydroxide, was ineffective.<sup>[9]</sup>

This general approach of interrupting zeolite syntheses, isolating the layered zeolite precursors, and using these potential crystalline layered materials as reagents to form large pore active catalysts was investigated for other zeolite families such as ZSM-35, or synthetic ferrierite. In this system, the ferrierite sheet, pre-Fer, may be the principal building unit of the resultant zeolite material. To optimize the formation of these layered precursors, several reaction conditions were identified and imposed on the traditional zeolite synthesis. The zeolite synthesis was interrupted prior to any X-ray diffraction evidence of crystallinity. The interruption could be initiated at any point within ~25% to 75% of the total expected synthesis time. High concentrations of the intercalate, an alkyltrimethylammonium salt, at high pH were added to this interrupted zeolite precursor media. In other syntheses, a reactive silica source, tetramethylammonium silicate, was also added as a potential pillaring agent. These new synthesis mixtures were then subjected to additional hydrothermal treatment in an attempt to form the zeolite-layered

hybrid. In many instances, the resulting product exhibited some very unusual properties.

The X-ray diffraction pattern was essentially featureless except for one broad low-angle peak at about  $2^\circ 2\theta$ . This X-ray diffraction pattern was intriguing because the original zeolite templating agent still existed in the synthesis composition. Apparently, the reaction conditions and time and temperature sequence were changed during the addition of the quaternary salt. This inhibited the formation of the originally intended zeolite. Normally, even this low-angle line might not have been observed, except that we were using a chromium X-ray source instead of the typical copper tube. The chromium source, which is very useful for low-angle peak detection, was a remnant from our pillared layered material research effort. The other unusual properties on this unknown material were the extremely high BET surface areas and hydrocarbon sorption capacities. These BET surface area values, typically  $>600 \text{ m}^2/\text{g}$ , were many times those normally observed for zeolite samples. The hydrocarbon (*n*-hexane and cyclohexane) sorption capacities were in excess of 50 wt.%, also abnormally high compared to our typical microporous samples. In fact, our analytical laboratories initially incorrectly believed that their test equipment was broken or out of standard because of the results obtained from these initial mesoporous materials.

In a separate and concurrent synthesis study, the cetyltrimethylammonium hydroxide was used directly as a structure-directing agent in zeolite-like hydrothermal syntheses. The product properties were similar to those generated in the layered zeolite precursor systems, i.e., characterized by a low-angle line in an X-ray diffraction pattern corresponding to large *d*-spacing and unusually high BET surface area and adsorption capacities. Thus both interrupted zeolite precursor systems and direct introduction of cetyltrimethylammonium hydroxide as a template resulted in the mesoporous molecular sieve products. As described below, subsequent detailed characterization studies allowed elucidation of the nature of these remarkable materials.

Obviously, these abovementioned unusual physical properties are characteristics of the mesoporous molecular sieves. However, with only one broad low-angle X-ray diffraction peak and the uniquely high values for both surface area and hydrocarbon sorption as data, this was insufficient to fully identify the nature of these materials. We initially concluded from this one broad X-ray diffraction peak material that we had completely disrupted the interlayer connectivity of layered zeolite hybrids, and the resulting X-ray diffraction was simply a repeat of the thickness of the layered precursor of about 4.0 nm. A key in the identification of this new class of porous materials was the observation, by TEM analyses, of a trace amount of MCM-41 in one

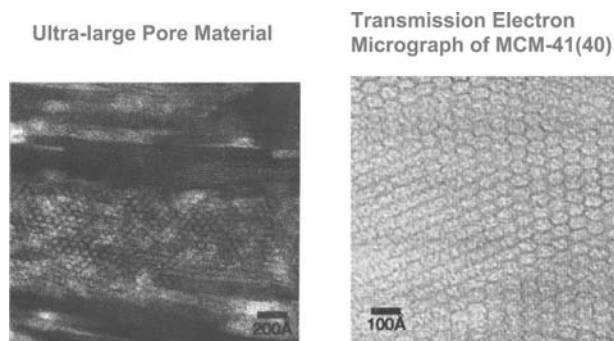


**Fig. 1** The initial discovery by TEM analysis of MCM-41. Source: From Ref.<sup>[1]</sup>.

of our samples. At this time, our small research group had the luxury of having as one of the members, a microscopist, Mike Leonowicz, who typically would conduct analyses on some of our more unusual samples. The observation of trace quantities of MCM-41, the uniform hexagonal pore structure, in one of the interrupted synthesis preparations provided us with hard evidence of this new class of materials (Fig. 1).

In a relatively short time, we were able to produce sufficient excellent quality samples of MCM-41 to characterize these materials by X-ray diffraction, pore size distribution, sorption capacities, and NMR and to evaluate them for catalytic applications. Many researchers at both the Paulsboro and Princeton Laboratories were involved in this effort. In all cases, we were analyzing a new class of materials that presented unique data. For example, the pore size distribution was remarkable; the narrow pore size appeared to be like that of microporous materials but within the mesopore range. As mentioned previously, the hydrocarbon sorption capacity was unique. Benzene sorption isotherms clearly indicated pore condensation inflections at benzene partial

pressures indicative of mesopore size channels. These inflections were typically not observed with microporous materials because of the low partial pressures needed. We were also able to synthesize various pore size materials using both different alkyl chain lengths of the cationic surfactant as well as taking advantage of micellar swelling.<sup>[10]</sup> These techniques improved our knowledge of micelles and liquid crystal chemistry improved. Both this knowledge base and the resultant samples helped to establish the basis for the mechanism of formation of these materials.

In retrospect, the synthesis conditions that we were using to try and obtain our layered zeolite hybrids, high pH, high surfactant concentration, and a reactive silica source, were synthesis conditions conducive to the formation of the mesoporous molecular sieves. The discovery and identification of other members of this new class of porous materials, MCM-48 and MCM-50, came several months later as a result of a detailed study relating the effect of surfactant concentration on the silica reagent (Fig. 2). The discovery of these additional two members of the mesoporous molecular sieve family was another key factor in developing the proposed mechanism of formation.

The discovery of this new class of materials, mesoporous molecular sieves, posed several challenges for our understanding of the formation of porous materials. Our first conclusion, based on both the hexagonal ordering of the pores, as seen in TEM analyses, and the XRD pattern, was that we had discovered one of the crystalline phases predicted by Smith and Dydrich,<sup>[11]</sup> known as the 81(n) family of frameworks. The theoretical XRD pattern of this family almost matched that of some of our best samples of MCM-41. It was not until we obtained the silica NMR data that we determined that our material was not typical of crystalline frameworks that we had expected. The realization that XRD patterns could be generated by the order of the

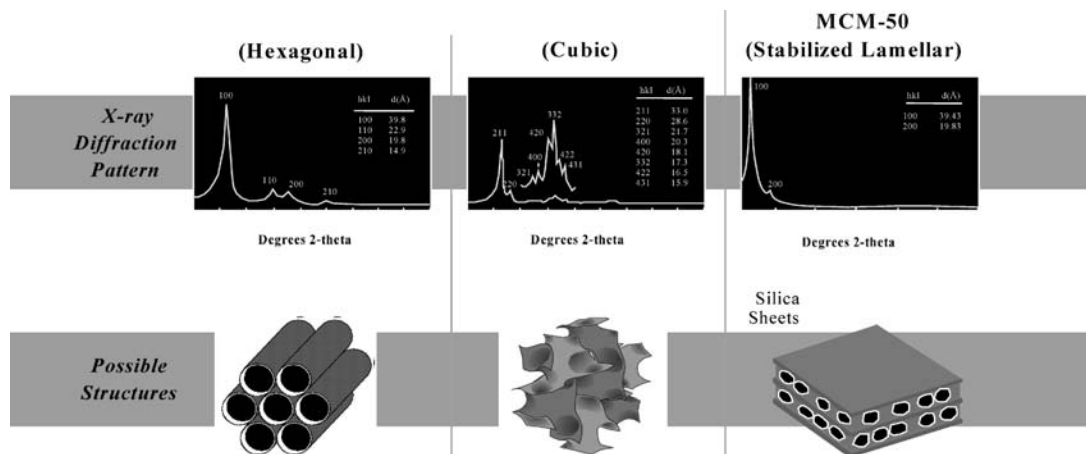


**Fig. 2** The M41S family of materials including MCM-41, MCM-48, and MCM-50.

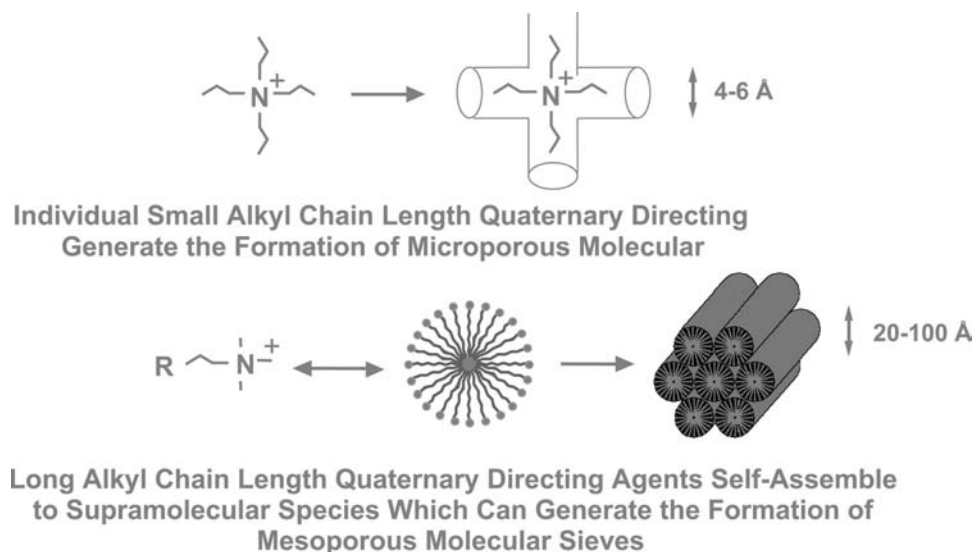


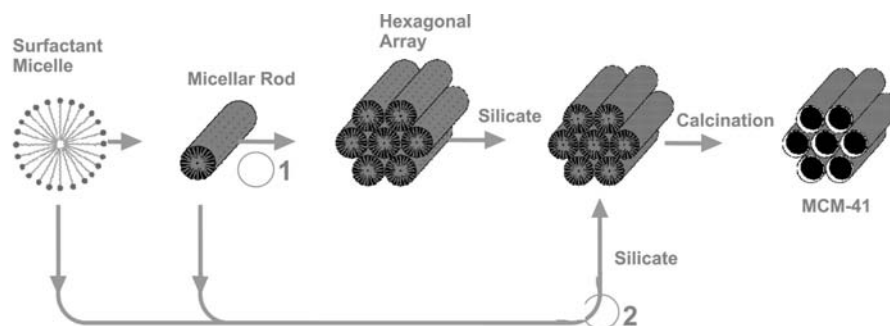
**Fig. 3** The role of quaternary directing agents. *Source:* From Refs.<sup>[1]</sup> and <sup>[4]</sup>.

pores and not the crystalline structure was another key feature of this new class of porous materials.

The mechanism of formation was also a challenge, which led to many long debates within our research group. We initially approached the concept of formation of these materials like traditional zeolite chemists. Our first premise was that the materials were formed by some sort of templating structure or pore filling agent. This meant, in the case of the mesoporous molecular sieves, that the templating agent was an aggregation of molecules and not the discrete molecules that normally template microporous structures (Fig. 3). Based on our limited knowledge of liquid crystal structures and micelles, we initially concluded that the liquid crystal structure existed prior to the formation of the molecular sieve. In the case of the MCM-41, this would be the hexagonal liquid crystal phase.

However, this simple mechanistic pathway was not universally accepted within our group of researchers.

Alternatively, it was proposed that the silicate reagent also affected the formation of these materials. And it was this proposed route that gathered more popularity as more data were obtained. A significant set of data appeared to help establish the preferred mechanistic route. This was a group of experiments that studied the effect of various levels of surfactant (SUR) as a function of silica. By changing the SUR/Si molar ratio we were able to synthesize MCM-41, -48, and -50 while keeping all of the other synthesis conditions the same.<sup>[12,13]</sup> These conditions would then exclude the possibility of any preformed liquid crystalline phase prior to the formation of the silicon phase, as we used the same surfactant solution and concentration for all experiments, only changing the amount of silica added. These data supported the concept that the anion, in this case, the silicate species, significantly affected the formation of the resultant template of the mesoporous molecular sieves (Fig. 4). These data were some of the



**Possible mechanistic pathways for the formation of MCM-41**  
1- liquid crystal phase initiated and 2 - silicate anion initiated.

**Fig. 4** The proposed mechanism of formation pathways. *Source:* From Ref.<sup>[1]</sup>.

evidence that led us to propose the possible mechanisms of formation that we published in our initial entries.<sup>[1,4]</sup>

In retrospect, both proposed pathways proved to be valid. The predominate pathway appears to be the anionic species initiated one (using cationic surfactants). This concept was explained and expanded upon by many researchers, specifically by the group at the University of Santa Barbara headed by Galen Stucky.<sup>[14,15]</sup> A Michigan State University group, headed by Tom Pinnavaia, expanded this mechanistic pathway further to include neutrally charged directing agents such as polymers.<sup>[16,17]</sup> Later, researchers at the University of South Hampton demonstrated the other proposed pathway, originally labeled the liquid crystal phase initiated pathway.<sup>[18,19]</sup> Attard and his co-researchers used a preformed liquid crystal phase to synthesize both a silica and a metal (platinum alloy) mesoporous molecular sieve.

### M41S SYNTHESIS DEVELOPMENT

When contrasted with the development of many high silica zeolites, MCM-41 posed several synthetic challenges that were immediately evident after its discovery. The first of these was the need to remove an inordinately large amount of surfactant that remained occluded in the pores of this mesoporous molecular sieve. Compared to a typical 5 to 8 wt.% organic component in most high silica zeolites, MCM-41 contained as much as 50 wt.% organic. Organic structure directing agents (SDA) are typically removed from zeolites by careful calcination or ion exchange. Calcination is normally preferred because of the ease with which the gaseous effluent can be handled. Ion exchange is normally more difficult either because of the ionic selectivity of the zeolite for the SDA or because the SDA may literally be locked inside of the zeolite by virtue of being situated at pore intersections or in the super cages. While the bulky hexadecyltrimethylammonium cation in MCM-41 was more amenable to ion exchange than the SDA in most unidimensional pore zeolites, the pH of the exchange step had to be carefully monitored. In the absence of CTMA the material was extremely sensitive to alkaline conditions. The ion exchange route was also attractive because it allowed us to recover the majority of the expensive surfactant. The surfactant recovered from the ion exchange step could be easily combined with that recovered from the residual mother liquor. In the initial synthesis preparations, a significant amount of the surfactant remained in the mother liquor. It was clear that organic recovery and subsequent recycle use would substantially reduce the manufacturing cost. Several routes for recovering the

surfactant from the as-synthesized MCM-41 were evaluated.

A second challenge was the need to develop an agreed upon protocol for determining MCM-41 product quality both during the synthesis and immediately following drying and post-processing. While MCM-41 is a highly ordered structure, its walls are amorphous. We found that the surface area, hydroxyl content, wall thickness, and even the pore diameter were highly dependent on synthesis conditions. Whereas X-ray powder diffraction can be used to very quickly quantify the crystallinity of zeolites, this was not the case in MCM-41 or any of the M41S materials. The pH of the synthesis liquor for zeolites can also be followed as a rough indicator of the crystallinity of these structured materials. However, this protocol was not useful for determining the precise degree to which a fully formed MCM-41 material is obtained. It remained for the final product to be treated to remove the surfactant before a good assessment of MCM-41 product quality could be made through adsorption capacity and low-angle X-ray peak location.

A third challenge was to change the silica reagents from expensive tetramethylammonium silicate (TMA-Si) and tetraethylorthosilicate (TEOS) to more reasonably priced sources. While cost was an important consideration, the availability, handling, and disposal issues associated with TEOS were most compelling. Identification of alternate reagents brought about a whole new series of problems associated with material and phase purity and the impacts on subsequent catalytic performance.

Fundamental studies of the mechanism of MCM-41S formation provided insight into a convenient laboratory synthesis route.<sup>[20]</sup> Our studies showed that high quality MCM-41 with consistently uniform 4.0-nm pores could be produced in the laboratory under very reasonable conditions. X-ray analyses showed that the preferred synthesis conditions produced materials exhibiting four peaks with positions corresponding to hexagonal symmetry. Subsequent analysis confirmed that the MCM-41 had high BET surface area, a large pore capacity, and very narrow pore size distribution as discerned by its nitrogen adsorption/desorption isotherm.

While much of the development was based upon our previous experience with the commercialization of high silica zeolites, one major difference was the apparent ease with which MCM-41 could be formed. Our initial studies showed that the M41S family of materials could be formed at much milder conditions than zeolites. In fact, it was quickly found that pure material could be formed even at ambient conditions and in relatively short duration (i.e., 6 to 12 hr) syntheses. However, the ease of making this material was deceptive, because the stability of MCM-41 varied



significantly with synthesis conditions. Usually, the stability increased with synthesis time and temperature.

Surprisingly, our analysis of fully dried “retained” samples that were placed in storage for several weeks with the occluded surfactant still present showed that the material became amorphous with time. This reversal produced a series of concerns regarding the stability of the material to storage even under mild conditions. Later studies showed that the synthesis conditions and the prompt removal of the surfactant were critical to improving the stability of mesoporous M41S. The studies also suggested that calcination was preferred to ion exchange for applications where hydrothermal stability was important.

Synthesis efforts within Mobil in the early and mid-1990s focused in two objectives: 1) identify and develop to a modest scale commercially attractive routes for producing MCM-41 materials with a range of pore diameters and acidity; and 2) broaden the compositional range and synthesis approaches to produce additional exploratory materials. The progress was closely linked to parallel catalytic evaluation studies looking at a range of applications (vide infra). Exploratory materials syntheses first focused on the production of both aluminosilicate and metalloaluminophosphate M41S materials including silicoaluminophosphate. Almost simultaneously, studies were initiated around the incorporation of metals either during the synthesis or post-synthesis. Later, in recognizing that these mesoporous materials were slightly less acidic than zeolites, we carried out studies aimed at incorporating acidity by post-treatment techniques such as impregnating MCM-41 with heteropoly acids.

We recognized very early on that these materials had uncharacteristically large surface silanol concentrations. NMR studies showed that nearly 40% of the silicon atoms located on the surface of the walls could be associated with hydroxyls. The silanols can be functionalized to modify M41S pore size and the hydrophobicity as well as serve as anchoring sites for attachment of selective groups for separation applications. The availability of large quantities of silanol groups led to a series of functionalization studies. The work provided the foundation for the synthesis of phase transfer catalysts built around M41S as well as the underlying concepts needed for anchoring the aforementioned heteropoly acid catalysts.

## FUNCTIONAL PRODUCT DEVELOPMENT CHALLENGES

The functional form of molecular-sieve-based catalysts and adsorbents is a tablet, pellet, or extrudate where the active material is incorporated as a component with materials such as binders, weighting agents, or

other active materials. Among the challenges addressed during development was the potential for collapse of the mesoporous structure under the pressures implicit in the forming steps. As crystalline structures, zeolites have the rigidity needed to withstand inordinately high point pressures. However, M41S materials with amorphous walls surrounding large amounts of occluded surfactant had to be viewed differently.

Binding of M41S materials where the surfactant had been removed prior to forming proved to be even more challenging. Not only was the collapse of the pores a more significant concern, but intrusion and pore blockage from some of the gel-type binder systems became an important consideration. Solubilization of the binder system and loss of physical integrity during ion exchange of uncalcined particles also had to be addressed. While calcination remained an attractive process option for removing the hexadecyltrimethylammonium structure directing agent post-forming, the burden on the gaseous effluent abatement systems proved a considerable obstacle.

Most commercial applications of molecular sieves are developed around volumetric constraints, where the challenge is to load as much of the active material as possible into a given volume. This drives product development programs toward formed products with higher levels of the active component and lower levels of binder or weighting components with the limits being set by physical (e.g., crush) strength. The framework density of M41S is approximately 70% of typical zeolites. This translates directly into a lower particle density. Thus, balancing the fraction of M41S in the formed particle with the fraction and type of binder and weighting agent in the finished particle became a key consideration in maximizing the amount of M41S in the process vessel.

## APPLICATIONS OF MCM-41

Because evaluations of larger pore exfoliated pillared layered materials were already under way at the time of its discovery, MCM-41 was able to be quickly screened for a number of applications of interest to Mobil. Not surprisingly, most of these focused on petroleum refining, polymer, and petrochemical manufacture applications. Later, applications outside of the core petroleum and petrochemical businesses were identified. Much of this story can be traced through the ExxonMobil patent literature.

Because the initial commercial application of MCM-41 remains undisclosed by ExxonMobil, and very few results from the applications directed research have been published, we will focus on information provided in issued US patents as well as on similar studies published in the open literature. That the first

commercial application of such a scientifically exciting new material required nearly a decade is an interesting story in itself. The protracted development resulted not nearly as much from the technical hurdles implicit in the identification of a commercially attractive route for synthesis, forming, and activation of MCM-41, as it did from the difficulty in identifying a commercial application with the technical incentives, inherent risk profile, and economics required to justify the introduction of such a unique new material.

In the following, MCM-41 is discussed in terms of its attributes as: 1) a refining catalyst or catalyst component; 2) a petrochemical catalyst or catalyst component; and 3) an adsorbent or material otherwise used for separation. Additional applications such as sensors, optical guides, and fuel cell electrodes are also highlighted. Unless otherwise indicated, the MCM-41 materials used in these studies had diameters of approximately 4.0 nm. However, this does not connote that the same material was used throughout. Composition (e.g., aluminum content) varied considerably depending upon targeted application and synthesis conditions. This review of applications examined by ExxonMobil is not intended to be exhaustive. Comprehensive surveys of potential applications of mesoporous materials, including MCM-41, have been published by On, Desplantes-Giscard, and Danumah<sup>[21]</sup> and Zhao, Lu, and Miller.<sup>[22]</sup>

## CATALYTIC APPLICATIONS OF MCM-41

### Refining and Polymerization Catalysis

Kresge et al.<sup>[23–25]</sup> describe a broad range of hydrocarbon conversion processes over MCM-41 including aromatic dealkylation, cracking, and hydrocracking. Their work established the catalytic activity of MCM-41 and its ability to perform both as a solid acid catalyst and as a catalyst support for hydrocarbon conversions in general. No performance comparisons were made with other solid acid catalysts.

### Catalytic Cracking

Catalytic cracking is the most widely deployed catalytic petroleum refining process. Nearly 35 wt.% of all gasoline is produced by cracking of gas oils and atmospheric resid over large pore ultrastable Y (USY) zeolite catalysts. The products include both fuel and petrochemical feedstocks. For many years, researchers have looked for larger pore alternatives to USY or to large pore materials to supplement the effectiveness of USY in fluidized catalytic cracking (FCC) particularly for processing heavy hydrocarbons. Aufdembrink et al.<sup>[26]</sup>

examined MCM-41 alone and in combination with USY for catalytic cracking vacuum gas oils and atmospheric resids. The catalysts were mildly steamed to simulate equilibrated FCC regeneration conditions. Their performance comparisons showed that equilibrated MCM-41 was superior to amorphous silica–alumina both in its cracking activity and in its propensity for producing larger amounts of gasoline at equivalent coke yield. Comparisons at equivalent conversions to gasoline, distillate, and light gases, showed that MCM-41 was more selective for heavy oil conversion, again producing more gasoline than the amorphous silica–alumina. This is shown in Table 1.

However, in a similar gas oil cracking comparison, MCM-41 was not nearly as active or as gasoline selective as USY, although it was more selective in converting the heavier fractions in fully formulated catalysts. This comparison is shown in Table 2.

Similar investigations by Corma et al.<sup>[27]</sup> suggested that fresh MCM-41 had unique cracking selectivities, producing significantly higher amounts of gasoline and less coke than USY, but that the selectivity disappeared once the material was steamed under simulated FCC regeneration conditions. Corma et al.<sup>[28]</sup> concluded that MCM-41 partially collapsed when steamed to produce a material resembling silica–alumina. The corollary was that MCM-41 lacked the hydrothermal stability needed for it to be useful as an FCC catalyst component.

Nickel and vanadium are present in small concentrations especially in heavier hydrocarbon feedstocks where they tend to degrade typical FCC catalyst performance as they accumulate on the catalyst. In a recent study, Balko, Chester, and Quinones<sup>[29]</sup> found that MCM-41 could be used as an FCC catalyst component to very effectively trap and concentrate the metals so that they are much less deleterious to FCC catalyst performance. MCM-41, when used at low levels (5 to 30 wt.%) in conjunction with the USY zeolite, acted as a metals “getter” and protected the cracking function by effectively passivating the metals. MCM-41 could be added as a component in the cracking catalyst particle or could be added as a separate particle.

### Oligomerization Catalysts

Pelrine et al.<sup>[30,31]</sup> evaluated a chromium-impregnated MCM-41 as an oligomerization catalyst for the production of high viscosity synthetic lubricants. Evaluations were carried out in a fixed bed reactor using 1-decene and reaction temperatures ranging from 120°C to 182°C at LHSV = 1.9 to 2.0 hr<sup>-1</sup>. The analysis showed that MCM-41 could produce a significantly higher viscosity product than, for example, a commercial Cr/SiO<sub>2</sub> polymerization catalyst under the same

**Table 1** Comparison of MCM-41 and silica–alumina catalysts in catalytic cracking of Joliet sour heavy gas oil (516°C, fixed-fluidized bed reactor; 1 min on stream, catalyst/oil = 2 to 6)

	Yields, wt.%		
	Silica–alumina <sup>a</sup>	MCM-41 <sup>a</sup>	Difference
<i>Comparison at equivalent coke yields (=4 wt.%)</i>			
Coke, wt.%	4.0	4.0	–
Conversion, wt.%	48.5	56.8	8.3
C4's, vol.%	9.7	13.3	3.6
C5's, vol.%	3.7	4.7	1.0
C <sub>5</sub> <sup>+</sup> gasoline, wt.%	32.6	37.2	4.6
Gasoline, RON	92	92	–
Light fuel oil, wt.%	36.7	32.2	(4.5)
Heavy fuel oil, wt.%	14.7	11.0	(3.7)
<i>Comparison at equivalent conversion (=55 wt.%)</i>			
Conversion, wt.%	55.0	55.0	–
Coke, wt.%	4.7	3.3	(1.4)
C5's, vol.%	3.8	4.6	0.8
C <sub>5</sub> <sup>+</sup> gasoline, wt.%	34.9	36.0	1.1
Gasoline, RON	92	92	–
Light fuel oil, wt.%	35.0	33.6	(1.4)
Heavy fuel oil, wt.%	13.1	11.3	(1.8)

<sup>a</sup>Both catalysts steamed for 4 hr, 45% steam, 650°C.

Source: From Ref.<sup>[26]</sup>.

reaction conditions. The same reaction catalyzed by chromium acetate-impregnated and calcined MCM-41 was used to demonstrate the concept and utility of functionalized MCM-41.<sup>[32]</sup> Bhore et al.<sup>[33]</sup> extended the oligomerization concept to Ni/MCM-41 catalysts for dimerization of lower molecular

weight olefins. The principal application was for C<sub>3</sub> to C<sub>10</sub> olefin dimerization primarily to produce gasoline. In their study the performance of Ni/MCM-41 catalysts compared favorably to Ni-based Dimersol® catalysts.

**Table 2** Comparison of 35% MCM-41 and 35% USY catalysts<sup>a</sup> in catalytic cracking of Joliet sour heavy gas oil (516°C, fixed-fluidized bed reactor; 1 min on stream, catalyst/oil = 2 to 6)

	Yields, wt.%		
	USY <sup>b</sup>	MCM-41 <sup>c</sup>	Difference
<i>Equivalent conversion</i>			
Conversion, vol.%	65.0	65.0	–
Coke, wt.%	2.4	6.0	3.6
C4's, vol.%	14.2	16.1	1.9
C5's, vol.%	10.2	9.7	(0.5)
C <sub>5</sub> <sup>+</sup> gasoline, wt.%	43.2	37.4	(5.8)
Gasoline, RON	92.1	91.6	(0.5)
Light fuel oil, wt.%	28.1	28.9	0.8
Heavy fuel oil, wt.%	9.8	8.3	(1.5)

<sup>a</sup>35 wt.% active component (MCM-41 or USY)/65 wt.% binder; spray dried catalysts.

<sup>b</sup>Steamed for 10 hr, 45% steam, 788°C.

<sup>c</sup>Steamed for 4 hr, 45% steam, 650°C.

Source: From Ref.<sup>[26]</sup>.

Le, Thompson, and Yokomizo<sup>[34]</sup> used MCM-41 to selectively react the C<sub>3</sub>–C<sub>5</sub> olefins in a mixed stream of lower molecular weight (MW) olefins and paraffins with the intent of producing a heavier oligomer stream that could be readily separated from the lower MW paraffin-enriched stream. Reaction conditions used in the study were 120°C, 10.3 MPa, and LHSV = 1.8 hr<sup>-1</sup>. The resulting oligomers were highly branched and could be converted to tertiary olefins suitable for a number of applications via subsequent selective disproportionation or cracking over, for example, a zeolitic catalyst. Specific applications are for the production of tertiary C<sub>4</sub> and C<sub>5</sub> olefins for subsequent paraffin-olefin alkylation or oxygenate production.<sup>[35]</sup>

Bhore et al.<sup>[36]</sup> investigated metals-free MCM-41 for the oligomerization of olefins for the production of higher molecular weight products as, for example, fuels, lubricants, fuel additives, and detergents. For acid-catalyzed propylene oligomerization, they found MCM-41 particularly selective for trimer and tetramer synthesis, materials that are well suited for clean gasoline. Reaction temperatures ranged from 40°C to 250°C and pressures ranged from 0.1 to 13 MPa.

## Hydrocracking

MCM-41 alone, or in combination with zeolites such as USY, has been examined as the active component in vacuum gas oil and lube hydrocracking catalysts. Degnan et al.<sup>[37–39]</sup> examined the performance of NiW-impregnated USY/MCM-41/Al<sub>2</sub>O<sub>3</sub> catalysts and found them to be superior in activity and comparable in selectivity to several commercial distillate selective hydrocracking catalysts. The work was further extended to hydrocracking heavier feedstocks to produce lubricants.<sup>[40–42]</sup> Fig. 5 compares the hydrocracking activity of NiW/MCM-41 and a conventional NiW/fluorided alumina lube hydrocracking catalyst

for conversion of heavy slack wax at 13.7 MPa, 1 LHSV. The comparison, at equivalent conditions of 13.8 MPa, LHSV = 1 hr<sup>-1</sup>, shows that MCM-41 is more active for conversion of this heavy hydrocarbon feed.

Work by Apelian et al.<sup>[40]</sup> and Marler and Mazzone<sup>[41–42]</sup> also showed that MCM-41 could be combined with a strong hydrogenation function to subsequently hydroisomerize the heavy hydrocrackate to produce high-quality, low pour point lubricants. In a similar study, Corma et al.<sup>[43]</sup> compared the mild hydrocracking performance of NiMo (12 wt.% MoO<sub>3</sub>, 3 wt.% NiO) supported on MCM-41 with that of amorphous silica-alumina and USY zeolite catalysts with the same Ni and Mo loadings. The feedstock was vacuum gas oil. The MCM-41 catalyst was superior to the other catalysts in hydrodesulfurization, hydrodenitrogenation, and hydrocracking activities in single-stage hydrocracking. When a hydrotreating stage was used in front of the hydrocracking stage, the USY catalyst became more active than the MCM-41 catalyst, but MCM-41 was still significantly more active than the amorphous silica-alumina catalyst. Most importantly, the MCM-41 catalyst distillate selectivity was better than that of USY and was very similar to the silica-alumina catalyst. A number of other studies have also pointed to MCM-41 as a superior distillate selective hydrocracking catalyst.<sup>[44–45]</sup>

## Hydrodemetallation

Vanadium, nickel, iron, and other trace metals pose problems in processing heavy oils because they foul catalysts and cause undesirable side reactions. Kresge et al.<sup>[46]</sup> showed that MCM-41 (*d*-spacing > 1.8 nm) was very active for removing trace metals from petroleum residua and shale oils. Nickel- or molybdenum-impregnated MCM-41 extrudates (MCM-

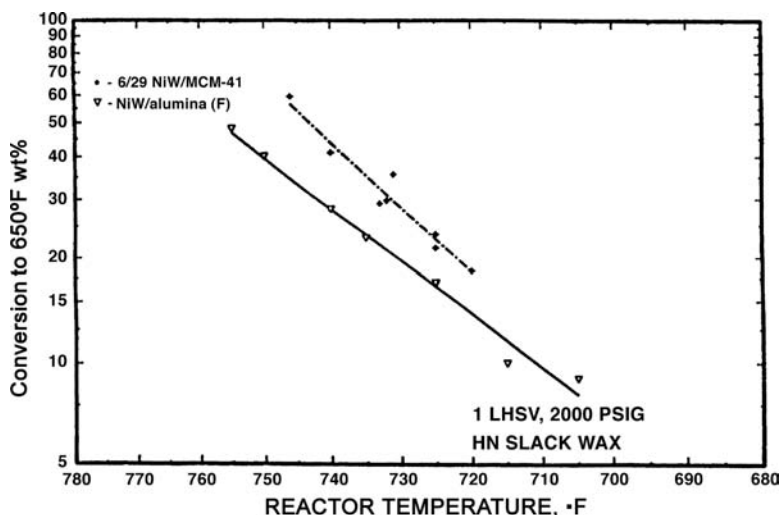


**Fig. 5** Comparison of the hydrocracking activities of NiW/MCM-41 and NiW/fluorided alumina demonstrating the superior cracking activity of the MCM-41 catalyst. Source: From Ref.<sup>[40]</sup>.

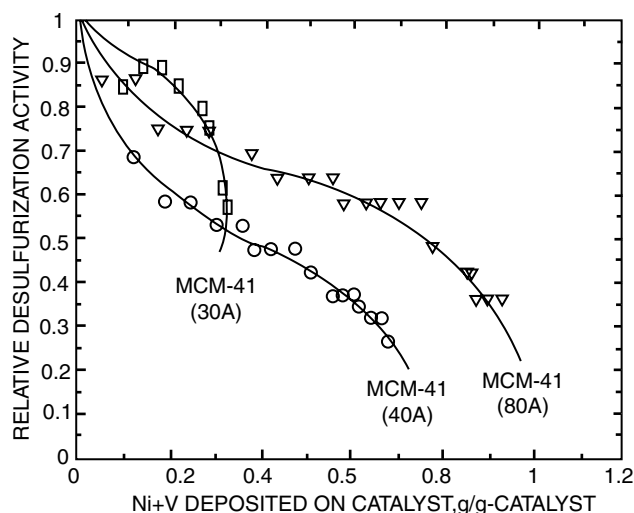


Fig. 6 Hydrodemetallation activity comparison—effect of MCM-41 pore diameter. (From Ref.<sup>[47]</sup>.)

41/Al<sub>2</sub>O<sub>3</sub>) were found to be particularly selective for the removal of iron, vanadium, nickel, and even arsenic. Shih also found that staging MCM-41 materials of different pore sizes, with the largest pore size material positioned first to see the oil, was a particularly effective strategy for hydrodemetallation.<sup>[47]</sup> Fig. 6, taken from Shih's patent, shows the effect of MCM-41 pore diameter on metals uptake effectiveness using hydrodesulfurization (HDS) activity as a basis for comparison. As metals accumulate on the catalyst they tend to poison HDS activity. The comparison shows that MCM-41 with 8.0-nm pores has a greater metals capacity than smaller pore MCM-41.

## Hydrogenation

Given its large surface area (>600 m<sup>2</sup>/g) and its large concentration of silanol groups that are easily functionalized or ion exchanged, MCM-41 is an obvious choice as a support material for metals in both precious and base metal hydrogenation catalysts. Evaluations by Baker et al.<sup>[48]</sup> and Degnan et al.<sup>[49]</sup> showed that MCM-41 was more active than other conventional supports for long-chain olefin and heavy aromatic hydrogenation. The specific applications cited are for polyalphaolefin (PAO) saturation for synthetic lube hydrofinishing and for alkylaromatics hydrogenation for color and viscosity index (VI) improvement. Similarly, Borghard et al.<sup>[50]</sup> demonstrated that metal impregnated MCM-41 is a very active catalyst for the saturation of highly aromatic feedstocks under relatively mild hydrogenation conditions. Hydrotreating highly aromatic cracked distillate stocks with NiMo- or CoMo/MCM-41 or other strong hydrogenation metals supported on MCM-41 to produce low

aromatic distillates, e.g., for high-quality diesel fuels, is described by Apelian, Degnan, and Shi<sup>[51]</sup>

Similarly, Corma, Martinez, and Martinez-Soria<sup>[52]</sup> found that MCM-41 provided an excellent medium for dispersion of Pt particles, and that the Pt/MCM-41 catalysts were superior in overall hydrogenation activity for naphthalene saturation when compared to Pt supported on amorphous silica-alumina, zeolite USY,  $\gamma$ -alumina, and silica. These investigators demonstrated that sulfur tolerance was a strong function of molecular sieve aluminum content. Pt supported on USY and Al-rich MCM-41 was superior in sulfur tolerance to Pt located on the other supports. They were able to confirm the sulfur tolerance in the hydrogenation of a mildly hydrotreated light cycle oil (LCO) containing approximately 70 wt.% aromatics and 400 ppm sulfur.

## Hydroisomerization

When combined with a strong hydrogenation function (e.g., Pt or Pd) MCM-41 is an effective long-chain paraffin isomerization catalyst once trace nitrogen and sulfur compounds are removed. This is shown in the aforementioned hydroprocessing patents<sup>[42,48]</sup> where Marler and Mazone demonstrated that MCM-41 could be used to improve the viscometric properties of hydroprocessed or synthetic lubricating oils. Del-Rossi, Hatzikos, and Huss<sup>[53]</sup> extended the hydroisomerization studies to lower molecular weight hydrocarbon feeds and found that noble metal MCM-41 catalysts are both active and selective for isomerization of C<sub>4</sub> to C<sub>8</sub> paraffins. Similar results were obtained by Chaudhari et al.<sup>[54]</sup> in their analysis of noble-metal-impregnated MCM-41 for *n*-hexane isomerization.

**Table 3** Comparison of isoparaffin–olefin alkylation selectivities and activities of high surface area heteropoly acid catalysts effect of supports

Conditions: Isobutane/2-butene ratio = 50:1; 3.4 MPa; 121°C; batch autoclave			
Support	MCM-41	SiO <sub>2</sub> (Cab-O-Sil)	Alumina
Support surface area, m <sup>2</sup> /g	738	159	207
H <sub>3</sub> PW <sub>12</sub> O <sub>40</sub> , wt.%	75	75	75
Olefin conversion, wt.%	87	60	66
Yield, gram C <sub>5</sub> + /gram 2-C <sub>4</sub> =	1.1	1.0	1.2
Total product distribution, wt.%			
C <sub>5</sub> –C <sub>7</sub>	9.1	2.8	5.5
C <sub>8</sub>	57.2	69.7	58.8
C <sub>9</sub>	34.0	27.5	35.7
C <sub>8</sub> product distribution, wt.%			
TMP (trimethylpentane)	23.9	13.8	13.2
DMH (dimethylhexane)	35.8	25.3	28.0
Unknown	40.3	60.9	58.9
TMP/DMH	0.7	0.5	0.5
TMP/ (C <sub>8</sub> -TMP)	0.3	0.2	0.2

Source: From Ref.<sup>[60]</sup>.

### Olefin Disproportionation

Higher molecular weight olefins can be converted to lower, more highly branched and often more valuable lower molecular weight olefins through disproportionation. The process is not used widely but has the potential for providing incremental lower molecular olefins as a feedstock for paraffin–olefin alkylation for fuels or for petrochemical applications. Le and Thompson<sup>[55,56]</sup> determined that MCM-41 was an attractive cracking catalyst for the conversion of light olefinic gasoline to propylene and isobutylene.

### Light Olefin-Paraffin Alkylation

MCM-41 is an attractive support for either Lewis or Bronsted acids used in the alkylation of C<sub>4</sub> to C<sub>12</sub> isoparaffins with <C<sub>10</sub> olefins.<sup>[57,58]</sup> The principal application of low molecular weight isoparaffin–olefin alkylation is for the production of high-octane C<sub>5</sub> to C<sub>12</sub> isoparaffins for gasoline. These studies highlighted the ability of MCM-41 to concentrate the acid and increase its effectiveness by nearly an order of magnitude over the free acid as measured by the amount of alkylate produced at the same volumetric acid to oil ratio. Typical reaction conditions for both Bronsted (H<sub>2</sub>SO<sub>4</sub>) and Lewis (BF<sub>3</sub>) acid/MCM-41 catalyzed paraffin–olefin alkylation were –20°C to 200°C, 0.7 to 1.4 MPa, and an isobutane/2-butene molar ratio of 10:1. The reactions were carried out in batch reactors for a preset duration.

Kresge et al.<sup>[59]</sup> and DelRossi et al.<sup>[60]</sup> found that the performance of MCM-41 for this application could be improved if the activity of MCM-41 could be increased through the addition of heteropoly acids via, for example, impregnation with phosphotungstic acid, H<sub>3</sub>PW<sub>12</sub>O<sub>40</sub>. In batch experiments with 50:1 isobutane/2-butene molar ratio, 121°C, 3.4 MPa, incorporation of 50 to 75 wt.% of the heteropoly anion, via impregnation, significantly improved both the catalyst activity and the yield of desirable trimethylpentane (TMP) and dimethylhexane (DMH) isomers. Comparison catalysts prepared by impregnation of equivalent loadings of H<sub>3</sub>PW<sub>12</sub>O<sub>40</sub> onto high surface silica and high surface alumina did not produce nearly equivalent activities or TMP and DMH yields. This comparison is shown in Table 3.

## PETROCHEMICAL CATALYSIS

### Aromatics Alkylation

MCM-41 is an effective catalyst for olefin alkylation of single-ring aromatics under milder conditions than are used in, for example, ZSM-5. Le<sup>[61]</sup> evaluated MCM-41 combined with an alumina binder for the production of ethylbenzene via benzene alkylation and found that the same ethylene conversion could be achieved at a reaction temperature that was 40°C lower than with ZSM-5. Polyalkylated benzene yields were higher, but MCM-41 produced no undesirable xylenes. Conditions



were 2.1–3.4 MPa and a benzene/ethylene (molar ratio = 10:1).

Le<sup>[62]</sup> also identified MCM-41 as an attractive catalyst for single- and multiring aromatic alkylation with higher molecular weight olefins. Higher molecular weight olefins are used to alkylate aromatics to produce linear alkyl benzenes (LABs). Linear alkyl benzenes are the basis for linear alkyl benzene sulfonate (LAS). Linear alkyl benzene sulfonate is used widely as a large component in liquid detergents. Le's work is focused on the alkylation of mono- and polycyclic aromatics for lube additive and detergent applications.

### PHASE TRANSFER CATALYSTS

Hellring and Beck<sup>[63]</sup> found that MCM-41 containing a stabilized onium ion, such as cetyltrimethylammonium (CTMA) cation, could effectively catalyze dual-phase reactions within the MCM-41 pores. To demonstrate the concept, Hellring and Beck reacted water insoluble bromopentane with potassium iodide in an agitated aqueous medium to produce iodopentane. Addition of CTMA-MCM-41 to the stirred dual-phase mixture greatly increased the reaction rate. The results implied that CTMA, which is amphiphilic, is able to concentrate bromopentane and increase its interaction with iodide, which is closely associated with the CTMA cation.

### CATALYTIC DECOMPOSITION OF NITROGEN OXIDES

Vanadium- and titanium-impregnated high surface area alumina or silica is a commercially attractive selective catalytic reduction (SCR) catalyst for NO<sub>x</sub> reduction. Beck et al.<sup>[64]</sup> compared several TiV/MCM-41 samples with conventional metal-oxide-based SCR catalysts and found the MCM-41 materials were comparable in both NO<sub>x</sub> removal selectivity and activity. The ability of the high surface area of MCM-41 to support large amounts of highly dispersed titanium and vanadium was believed to account for the high activity of the MCM-41 catalyst.

### APPLICATION OF MCM-41 TO SEPARATIONS

MCM-41 can be used to separate at least one component from a mixture of gaseous or liquid components as described in the patent of Beck et al.<sup>[65]</sup> The examples provided in this reference relate mainly to separation of higher and lower viscosity components of a mixture. The concept of using MCM-41 alone or as a composite in a membrane or as an active component in chromatographic separation media is described by

Herbst et al.<sup>[66]</sup> Among the contemplated uses are size exclusion applications such as the bioseparation of endotoxins or pyrogens. In another study, Kuehl<sup>[67]</sup> examined MCM-41 as a selective sorbate for the removal of large molecules such as polynuclear aromatics (PNAs) from fluids and gases. The applications range from wastewater and catalyst regeneration gas cleanup to the reduction of PNAs in hydrocarbon fuels.

### OTHER APPLICATIONS

A wide array of other MCM-41 applications have been investigated, each based on the unique composition, uniform pore size, and extraordinarily high surface area of the M41S family of materials. While the reviews by On et al.<sup>[21]</sup> and Zhao et al.<sup>[22]</sup> have described many of these, we want to highlight three applications to illustrate the breadth of potential applications outside the realm of catalysts and adsorbents. The first relates to the use of MCM-41 and M41S materials as key components in microoptical and microelectronic applications. Beck et al.<sup>[68]</sup> determined that M41S materials, when processed to include quantum clusters of semiconducting inorganic or organic compounds, have unique nonlinear optical properties useful as frequency mixers, frequency doublers, and parametric amplifiers. Extended uses are for beam steering, optical switching, and image processing.

In the second application, MCM-41 is used as a central component in a sensor device.<sup>[69]</sup> Electrical, optical, or gravimetric systems designed around MCM-41 detect, for example, the presence of specific gases, changes in pH, or the presence of metal ions. The examples describe a range of biological, chemical, and physical sensor applications including the selective detection of benzene, ammonia, nickel, formaldehyde, and carbon monoxide.

Finally, Ozin et al.<sup>[70]</sup> describe the use of M41S (nickel/platinum)-yttria-zirconia M41S materials as thermally stable electrode materials in solid oxide fuel cells. The mesoporous materials, which are synthesized in aqueous media using glycometallates and metal complexes, have the highest known surface area of any form of (metal)-yttria-stabilized zirconia and thus improve the efficiency of solid oxide fuel cells.

### CONCLUSION

For many new materials, traversing the path from discovery to commercial application can take as long as a decade. This was certainly true for MCM-41, the most widely studied representative of a new class of materials known as the M41S family. Commercialization of

MCM-41 required approximately 10 years as issues surrounding scale-up of the synthesis, raw materials selection, and post-processing had to be addressed. However, the major challenge was associated with identification of an application where the performance advantages justified the risks and costs associated with the targeted commercialization. Initial commercializations of truly new materials are, by their very nature, expensive and associated with a large degree of uncertainty. The initial application bears all of the developmental costs which normally represents a significant hurdle in the development of any truly "step out" material.

Now that MCM-41 is commercial, we anticipate that several new applications will be pursued. Work on mesoporous materials such as M41S continues in many laboratories around the world as witnessed by the consistent increase in both M41S-related patents and publications since the discovery of MCM-41, the first member of this family, in 1989.

## ACKNOWLEDGMENT

The authors would like to thank ExxonMobil Corporation for permission to publish this review.

## REFERENCES

- Kresge, C.T.; Leonowicz, M.E.; Roth, W.J.; Vartuli, J.C.; Beck, J.S. Ordered mesoporous molecular sieves synthesized by a liquid-crystal template mechanism. *Nature* **1992**, *359*, 710–712.
- Kresge, C.T.; Leonowicz, M.E.; Roth, W.J.; Vartuli, J.C. Synthetic Mesoporous Crystalline Material. US Patent 5,098,684, March 24, 1992, Mobil Oil Corporation.
- Kresge, C.T.; Leonowicz, M.E.; Roth, W.J.; Vartuli, J.C. Of Synthetic Porous Crystalline Material, Its Synthesis. US Patent 5,102,643, April 7, 1992, Mobil Oil Corporation.
- Beck, J.S.; Vartuli, J.C.; Roth, W.J.; Leonowicz, M.E.; Kresge, C.T.; Schmitt, K.D.; Chu, C.T.-W.; Olson, D.H.; Sheppard, E.W.; McCullen, S.B.; Higgins, J.B.; Schlenker, J.L. A new family of mesoporous molecular sieves prepared with liquid crystal templates. *J. Am. Chem. Soc.* **1992**, *114*, 10,834–10,843.
- Landis, M.E.; Aufdembrink, B.A.; Chu, P.; Johnson, I.D.; Kirker, G.W.; Rubin, M.K. Preparation of molecular sieves from dense layered metal oxides. *J. Am. Chem. Soc.* **1991**, *113*, 3189–3192.
- Leonowicz, M.E.; Lawton, J.A.; Lawton, S.L.; Rubin, M.K. MCM-22: A molecular sieve with two independent multidimensional channel systems. *Science* **1994**, *264*, 1910–1915.
- Kresge, C.T.; Roth, W.J.; Simmons, K.G.; Vartuli, J.C. Crystalline Oxide Material. US Patent 5,229,341, July 20, 1993, Mobil Oil Corporation.
- Roth, W.J.; Kresge, C.T.; Vartuli, J.C.; Leonowicz, M.E.; Fung, A.S.; McCullen, S.B. MCM-36: The first pillared molecular sieve with zeolite properties. In *Catalysis by Microporous Materials*; Studies in Surface Science and Catalysis; Beyer, H.K., Karge, H.G., Kiricsi, I., Nagy, J.B., Eds.; Elsevier Science, 1995; vol. 94, 301pp.
- Roth, W.J.; Vartuli, J.C. Preparation of exfoliated zeolites from layered precursors: The role of pH and the nature of intercalating media. *Stud. Surf. Sci. Catal.* **2002**, *141*, 273.
- Beck, J.S. Method for Synthesizing Mesoporous Crystalline Material. US Patent 5,057,296, October 15, 1991, Mobil Oil Corporation.
- Smith, J.V.; Dydrich, W.J. Nets with channels of unlimited diameter. *Nature* **1984**, *309*, 607–608.
- Vartuli, J.C.; Schmitt, K.D.; Kresge, C.T.; Roth, W.J.; Leonowicz, M.E.; McCullen, S.B.; Hellring, S.D.; Beck, J.S.; Schlenker, J.L.; Olsen, D.H.; Sheppard, E.W. Effects of surfactant/silica molar ratios on the formation of mesoporous molecular sieves: Inorganic mimicry of surfactant liquid-crystal phases and mechanistic implications. *Chem. Mater.* **1994**, *6*, 2317–2326.
- Beck, J.S.; Vartuli, J.C.; Kennedy, G.J.; Kresge, C.T.; Roth, W.J.; Schramm, S.E. Molecular or supramolecular templating: Defining the role of surfactant chemistry in the formation of microporous and mesoporous molecular sieves. *Chem. Mater.* **1994**, *6* (10), 1816–1821.
- Stucky, G.D.; Monnier, A.; Schueth, F.; Huo, Q.; Firouzi, D.I.; Janicke, M.; Chmelka, B.F. Molecular and atomic arrays in nano- and mesoporous materials synthesis. *Mol. Crystals Liq. Crystals* **1994**, *240*, 187–196.
- Firouzi, A.; Kumar, D.; Bull, L.M.; Besier, T.; Siegar, P.; Huo, Q.; Walker, S.A.; Zasadzinski, J.; Glinka, A.G.; Nicol, J.; Marogloese, D.; Stucky, G.D.; Chmelka, B.F. Cooperative organization of inorganic surfactant and biomimetic assemblies. *Science* **1995**, *267*, 1138–1143.
- Tanev, P.T.; Chibwe, M.; Pinnavaia, T.J. Titanium-containing mesoporous molecular sieves for catalytic oxidation of aromatic compounds. *Nature* **1994**, *368*, 321–324.
- Pinnavaia, T.J.; Zhang, W. Catalytic properties of mesoporous molecular sieves prepared by neutral surfactant assembly. *Stud. Surf. Sci. Catal.* **1998**, *117*, 23–36.
- Attard, G.S.; Glyde, J.C.; Goltner, C.G. Liquid-crystalline phases as templates for the synthesis of mesoporous silica. *Nature* **1995**, *378*, 366.
- Attard, G.S.; Leclerc, S.A.A.; Maniquet, S.; Russell, A.E.; Nandakumer, I.; Gollas, B.R.; Bartlett, P.N. Ordered mesoporous silicas prepared from both micellar solutions and liquid crystal phases. *Micro. Meso. Mater.* **2001**, *44–45*, 159–163.
- Roth, W.J.; Vartuli, J.C. The effect of stoichiometry and synthesis conditions on the properties of the mesoporous M41S family of silicates. *Stud. Surf. Sci. Catal.* **2001**, *135*, 134–139.
- On, D.T.; Desplantier-Giscard, D.; Danumah, C.; Kaliaguine, S. Perspectives in catalytic applications of mesostructured materials. *Appl. Catal., A Gen.* **2001**, *222*, 299–357.

22. Zhao, X.S.; Lu, G.Q.; Millar, G.J. Advances in mesoporous molecular sieve MCM-41. *Ind. Eng. Chem. Res.* **1996**, *35*, 2075–2090.
23. Kresge, C.T.; Leonowicz, M.E.; Roth, W.J.; Vartuli, J.C. Catalytic Conversion. US Patent 5,174,888, December 29, 1992, Mobil Oil Corporation.
24. Kresge, C.T.; Leonowicz, M.E.; Roth, W.J.; Vartuli, J.C. Catalytic Conversion. US Patent 5,196,633, March 23, 1993, Mobil Oil Corporation.
25. Beck, J.S.; Kresge, C.T.; McCullen, S.B.; Roth, W.J.; Vartuli, J.C. Hydrocarbon Conversion Process Employing a Porous Material. US Patent 5,370,785, Mobil Oil Corporation.
26. Aufdembrink, B.A.; Chester, A.W.; Herbst, J.A.; Kresge, C.T. Ultra Large Pore Cracking Catalyst and Process for Catalytic Cracking. US Patent 5,258,114, November 2, 1993, Mobil Oil Corporation.
27. Corma, A.; Grande, M.S.; Gonzalez-Alfaro, V.; Orchilles, A.V. Cracking activity and hydrothermal stability of MCM-41 and its comparison with amorphous silica-alumina and a USY zeolite. *J. Catal.* **1996**, *159* (2), 375–382.
28. Corma, A.; Fornes, M.T.; Navarro, M.T.; Perezpariente, J. Acidity and stability of MCM-41 crystalline aluminosilicates. *J. Catal.* **1994**, *148* (2), 569–574.
29. Balko, J.W.; Chester, A.W.; Quinones, A.R. FCC Metal Traps Based on Ultra Large Pore Crystalline Material. US Patent 5,965,474, October 12, 1999, Mobil Oil Corporation.
30. Pelrine, B.P.; Schmitt, K.D.; Vartuli, J.C. Production of Olefin Oligomer Lubricants. US Patent 5,105,051, April 14, 1992, Mobil Oil Corporation.
31. Pelrine, B.P.; Schmitt, K.D.; Vartuli, J.C. Olefin Oligomerization Catalyst. US Patent 5,270,273, December 14, 1993, Mobil Oil Corporation.
32. Beck, J.S.; Calabro, D.C.; McCullen, S.B.; Pelrine, B.P.; Schmitt, K.D.; Vartuli, J.C. Catalytic Conversion over Modified Synthetic Mesoporous Material. US Patent 5,200,058, April 6, 1993, Mobil Oil Corporation.
33. Bhore, N.A.; Johnson, I.D.; Keville, K.M.; Le, Q.N.; Yokomizo, G. Catalytic Oligomerization Process Using Modified Crystalline Material. US Patent 5,260,501, November 9, 1993.
34. Le, Q.N.; Thompson, R.T.; Yokomizo, G.H. Catalytic Olefin Upgrading Process Using Synthetic Mesoporous Crystalline Material. US Patent 5,134,242, July 28, 1992, Mobil Oil Corporation.
35. Le, Q.N.; Thompson, R.T.; Yokomizo, G.H. Multistage Olefin Upgrading Process Using Synthetic Mesoporous Crystalline Material. US Patent 5,134,241, July 28, 1992, Mobil Oil Corporation.
36. Bhore, N.A.; Le, Q.N.; Yokomizo, G.H. Catalytic Oligomerization Process Using Synthetic Mesoporous Crystalline Material. US Patent 5,134,243, July 28, 1993, Mobil Oil Corporation.
37. Degnan, T.F.; Keville, K.M.; Landis, M.E.; Marler, D.O.; Mazzone, D.N. Hydrocracking Process Using Ultra-Large Pore Size Catalysts. US Patent 5,183,557, February 2, 1993, Mobil Oil Corporation.
38. Degnan, T.F.; Keville, K.M.; Marler, D.O.; Mazzone, D.N. Hydrocracking with Ultra Large Pore Size Catalysts, US Patent 5,281,328 January 25, 1994, Mobil Oil Corporation.
39. Degnan, T.F.; Keville, K.M.; Landis, M.E.; Marler, D.O.; Mazzone, D.N. Hydrocracking Process Using Ultra-Large Pore Size Catalysts. US Patent 5,290,744, March 1, 1994, Mobil Oil Corporation.
40. Apelian, M.R.; Degnan, T.F.; Marler, D.O.; Mazzone, D.N. Production of Lubricants by Hydrocracking and Hydroisomerization. US Patent 5,264,116, November 23, 1993.
41. Marler, D.O.; Mazzone, D.N. Production of Hydrocracked Lubricants. US Patent 5,277,792, January 11, 1994, Mobil Oil Corporation.
42. Marler, D.O.; Mazzone, D.N. Production of High Viscosity Lubricants. US Patent 5,288,395, February 22, 1994, Mobil Oil Corporation.
43. Corma, A.; Martinez, A.; Martinezsoria, V.; Monton, J.B. Hydrocracking of vacuum gas oil on the novel mesoporous MCM-41 aluminosilicate catalyst. *J. Catal.* **1995**, *153* (1), 25–31.
44. Klemm, A.; Taouli, A.; Koch, H.; Reschetilowski, W. The preparation of hydrocracking catalysts using mesoporous aluminosilicates MCM-41—influence of the preparation conditions on the catalytic behavior. *Stud. Surf. Sci. Catal.* **1999**, *127*, 405–408.
45. Klemm, A.; Reschetilowski, W. New hydrocracking catalysts based on mesoporous Al-MCM-41 materials. *Chem. Eng. Technol.* **2002**, *25* (2), 137–139.
46. Kresge, C.T.; Leonowicz, M.E.; Roth, W.J.; Vartuli, J.C.; Keville, K.M.; Shih, S.S.; Degnan, T.F.; Dwyer, F.G.; Landis, M.E. Demetallation of Hydrocarbon Feedstocks With a Synthetic Mesoporous Crystalline Material. US Patent 5,183,561, February 2, 1993, Mobil Oil Corporation.
47. Shih, S.S. Upgrading of a Hydrocarbon Feedstock Utilizing a Graded Mesoporous Catalyst System. US Patent 5,344,553, September 6, 1994, Mobil Oil Corporation.
48. Baker, C.L.; Chu, C.T.-W.; Mazzone, D.N.; Page, N.M. Lubricant Hydrocracking Process. US Patent 5,468,368, November 21, 1995, Mobil Oil Corporation.
49. Degnan, T.F.; Dougherty, R.C.; Hatzikos, G.H.; Shih, S.S.; Yan, T.Y. Hydrogenation Process. US Patent 5,573,657, November 12, 1996, Mobil Oil Corporation.
50. Borghard, W.S.; Chu, C.T.-W.; Degnan, T.F.; Shih, S.S. Aromatics Saturation with Catalysts Comprising Crystalline Ultra-Large Pore Oxide Materials. US Patent 5,264,641, November 23, 1993, Mobil Oil Corporation.
51. Apelian, M.R.; Degnan, T.F.; Shih, S.S. Catalyst and Process for Producing Low-Aromatics Distillates. US Patent 5,451,312, September 19, 1995, Mobil Oil Corporation.
52. Corma, A.; Martinez, A.; Martinez-Soria, V. Hydrogenation of aromatics in diesel fuels on Pt/MCM-41 catalysts. *J. Catal.* **1997**, *169* (2), 480–489.
53. DelRossi, K.J.; Hatzikos, G.H.; Huss, A. Paraffin Isomerization Process Utilizing a Catalyst Comprising a Mesoporous Crystalline Material. US Patent 5,256,277, October 26, 1993, Mobil Oil Corporation.
54. Chaudhari, K.; Das, T.K.; Chandwadkar, A.J.; Sivasanker, S. Mesoporous aluminosilicate of the

- MCM-41 type: its activity in *n*-hexane isomerization. *J. Catal.* **1999**, *186* (1), 81–90.
55. Le, Q.N.; Thompson, R.L. Olefin Upgrading by Selective Conversion with Synthetic Mesoporous Crystalline Material. US Patent 5,191,144, March 2, 1993, Mobil Oil Corporation.
  56. Le, Q.N.; Thompson, R.T. Catalytic Process for Hydrocarbon Cracking Using Synthetic Mesoporous Crystalline Material. US Patent 5,232,580, August 3, 1993.
  57. Degnan, T.F.; Del Rossi, K.J.; Huss, A. Isoparaffin/Olefin Alkylation. US Patent 5,191,148, March 2, 1994, Mobil Oil Corporation.
  58. DelRossi, K.J. Isoparaffin/Olefin Alkylation. US Patent 5,191,147, March 2, 1994, Mobil Oil Corporation.
  59. Kresge, C.T.; Marler, D.O.; Rav, G.S.; Rose, B.H. Supported Heteropoly Acid Catalysts for Isoparaffin–Olefin Alkylation Reactions. US Patent 5,324,881, June 28, 1994, Mobil Oil Corporation.
  60. DelRossi, K.J.; Jablonski, G.A.; Kresge, C.T.; Kuehl, G.H.; Marler, D.O.; Rav, G.S.; Rose, B.H. Supported Heteropoly Acid Catalysts. US Patent 5,475,178, December 12, 1995, Mobil Oil Corporation.
  61. Le, Q.N. Production of Ethylbenzene. US Patent 5,118,894, June 2, 1992, Mobil Oil Corporation.
  62. Le, Q.N. Aromatics Alkylation Process. US Patent 5,191,134, March 2, 1993, Mobil Oil Corporation.
  63. Hellring, S.D.; Beck, J.S. Phase-Transfer Catalysis with Onium-Containing Synthetic Mesoporous Crystalline Material. US Patent 5,347,060, September 13, 1994, Mobil Oil Corporation.
  64. Beck, J.S.; Socha, R.F.; Shihabi, D.S.; Vartuli, J.C. Selective Catalytic Reduction of Nitrogen Oxides. US Patent 5,143,707, September 1, 1992, Mobil Oil Corporation.
  65. Beck, J.S.; Calabro, D.C.; McCullen, S.B.; Pelrine, B.P.; Schmitt, K.D.; Vartuli, J.C. Sorption Separation over Modified Synthetic Mesoporous Material. US 5,220,101, June 15, 1993, Mobil Oil Corporation.
  66. Herbst, J.A.; Kresge, C.T.; Olson, D.H.; Schmitt, K.D.; Vartuli, J.C.; Wang, D.I.C. Method of Separation of Substances. US Patent 5,378,440, January 3, 1995, Mobil Oil Corporation.
  67. Kuehl, G.H. Removal of Large Molecules from a Fluid. US Patent 5,583,277, December 10, 1996, Mobil Oil Corporation.
  68. Beck, J.S.; Kuehl, G.H.; Olson, D.H.; Schlenker, J.L.; Stucky, G.D.; Vartuli, J.C. M41S Materials Having Nonlinear Optical Properties. US Patent 5,348,687, September 20, 1994, Mobil Oil Corporation.
  69. Olson, D.H.; Stucky, G.D.; Vartuli, J.C. Sensor Device Containing Mesoporous Crystalline Material. US Patent 5,364,797, November 15, 1994, Mobil Oil Corporation.
  70. Ozin, G.A.; Mamak, M.; Coombs, N.A. Mesoporous Oxide Compositions and Solid Oxide Fuel Cells. US Patent 6,420,063, July 16, 2002, Mobil Oil Corporation.

# Metal Clusters on Oxides

Ivan Stensgaard

Department of Physics and Astronomy, University of Aarhus, Aarhus, Denmark

## INTRODUCTION

Metal clusters on oxides play a profound role in modern-day society because such systems are the basic ingredients in catalysts used for environmental protection, refining of fossil fuels, and production of chemicals. In the automotive three-way catalytic converter, for example, chemical reactions take place on nanometer-scale metal particles of Rh, Pt, and/or Pd distributed on an oxide of a high surface area, typically alumina.

Catalysis has thus been the main motivation for research on metal clusters on oxides. The improved ability to control the size and distribution of metal clusters coupled with the development of techniques for better characterization of the structural, electronic and chemical properties of metal clusters on oxides (primarily scanning probe techniques) has spurred an increased research activity in the field. Consequently, a series of interesting new results have been obtained, which have demonstrated how, e.g., the properties of the metal clusters may change in the nanometer-scale regime due to quantum size effects.

Atomic-scale investigations of industrial catalysts are hampered by the complexity of the systems. In this entry emphasis will therefore be on metal clusters on oxides prepared and investigated in laboratory research environments, i.e., under ultrahigh vacuum (UHV) conditions. The advantage of such model systems is that they lend themselves much more readily to investigations based on a large variety of surface science tools. The entry is intended to give the reader an overview of the techniques for synthesis and characterization of model systems, as well as to address important issues that are relevant for metal clusters on oxides in general. For further reading, reference is given to a number of reviews on metals on oxides.<sup>[1–5]</sup>

## SUBSTRATE PREPARATION, GROWTH, AND CLUSTER MORPHOLOGY

Fig. 1 shows an image of a ruthenium catalyst for ammonia synthesis recorded with high-resolution

transmission electron microscopy (HRTEM).<sup>[6]</sup> The Ru metal clusters appear as dark, almost circular regions on a lighter background of  $\text{MgAl}_2\text{O}_4$ . The experimental challenge of investigating (at the atomic level) systems of a structural complexity such as that in Fig. 1 is still so formidable that strong efforts are made to derive information from structurally simpler systems. In the following, focus will be on techniques for creating model systems of metal clusters on oxides.

## Substrate Preparation

Typically, the metal clusters are supported on low-index surfaces of crystalline metal or semiconductor oxides, such as MgO,  $\text{Al}_2\text{O}_3$ ,  $\text{TiO}_2$ ,  $\text{Fe}_2\text{O}_3$ , ZnO, and  $\text{SiO}_2$ . The surface science of metal oxides has been treated in an excellent monograph.<sup>[7]</sup> Unfortunately, the preparation of clean and well-ordered oxide surfaces on a bulk specimen still remains an experimental challenge.<sup>[1]</sup> The standard procedures for creating clean, well-ordered *metal* surfaces include polishing and etching, followed by ion sputtering to remove impurities and annealing to reestablish the crystal order. Such procedures, when applied to oxides, will, in many cases, lead to poor order or loss of stoichiometry due to preferential sputtering and/or thermally induced segregation.

As an alternative, in situ cleavage of bulk oxide specimens under UHV may be considered. However, materials such as  $\text{SiO}_2$ ,  $\text{Al}_2\text{O}_3$ , and  $\text{TiO}_2$  are difficult to cleave successfully in the sense that the cleavage plane will not coincide with an extended low-index plane, and that the surface may locally be very rough. Successfully cleaved surfaces can be used for one-shot experiments. To remove deposited metal, sputtering/annealing cycles are necessary.

Being large band gap materials the oxides are strongly insulating, adding to the difficulty and a severe drawback because when working with oxide surfaces most experimental techniques involve electron transfer, leading to charging effects. The charging problem has spurred the development of alternative schemes, where the oxide is made conductive by the introduction of point defects, or the oxide is grown

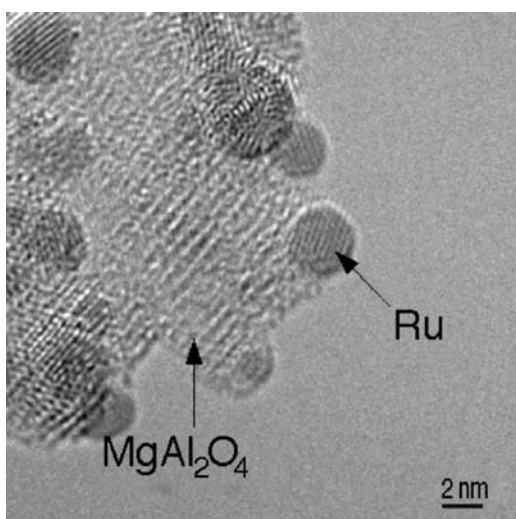


**Fig. 1** High-resolution TEM micrograph of a ruthenium catalyst for ammonia synthesis. The almost circular dark regions are Ru metal clusters. The oxide is  $\text{MgAl}_2\text{O}_4$ . Source: From Fig. 3 of Ref.<sup>[6]</sup>, with permission of Kluwer Academic Publishers.

in the form of an ultrathin film on a metallic substrate<sup>[1-4,8,9]</sup> that allows for electric transport through the film, e.g., in the form of a tunneling current.

Examples of the two types of alternative schemes are shown in Fig. 2 in the form of scanning tunneling microscopy (STM) images of a  $\text{TiO}_2$  bulk crystal surface and an  $\text{Al}_2\text{O}_3$  thin film surface. Titanium dioxide is used extensively, not only for heterogeneous catalysts, but in several other technologically important areas such as photocatalysis and sensor technology. Bulk  $\text{TiO}_2$  in its rutile form has a band gap of 3 eV, but thermal reduction under vacuum leads to oxygen

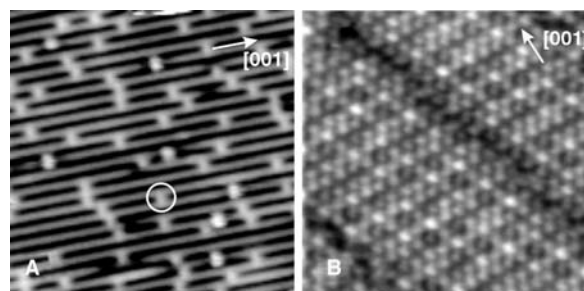


**Fig. 2** STM images of oxides. (A) A clean  $\text{TiO}_2$  (110) surface ( $13 \times 13 \text{ nm}^2$ ). The bright lines are rows of Ti atoms. The bright dots imaged between the Ti rows (see circle) are vacancies in rows of oxygen atoms which are in bridge positions relative to underlying Ti atoms. Source: Courtesy: Renald Schaub, CAMP, University of Aarhus. (B) A thin  $\text{Al}_2\text{O}_3$  film grown on  $\text{NiAl}(110)$  by oxidation. The two dark lines are antiphase domain boundaries relieving strain due to a mismatch between the film and the substrate ( $20 \times 20 \text{ nm}^2$ ).

deficiencies which create a shallow donor level in the gap, giving rise to a sufficiently increased conductivity for performing experiments such as STM on the surface.<sup>[7,8]</sup> The (110) surface of  $\text{TiO}_2$  in its rutile form shown in Fig. 2A is the most intensively studied  $\text{TiO}_2$  surface and it has become a prototype of a metal oxide.<sup>[10]</sup> Aluminum oxide (alumina),  $\text{Al}_2\text{O}_3$ , is extremely important in both ceramics and catalysis. A band gap of 8–9 eV makes  $\text{Al}_2\text{O}_3$  an excellent insulator, and  $\text{Al}_2\text{O}_3$  surfaces are not easily accessible for surface science experiments. Fortunately, thin alumina films can easily be prepared.<sup>[8,9]</sup> Oxidation at elevated temperatures, for example, of a (110) NiAl alloy single crystal surface results in the formation of an alumina film.<sup>[3,11]</sup> The ensuing film depicted in Fig. 2B has a thickness of only  $\approx 0.5 \text{ nm}$ , less than the thickness of a unit cell of  $\gamma\text{-Al}_2\text{O}_3$  or  $\alpha\text{-Al}_2\text{O}_3$ , but nevertheless sufficiently thick to have most of the properties of  $\gamma\text{-Al}_2\text{O}_3$ .<sup>[3]</sup> And importantly, electron transport through the film is easily achieved, facilitating, e.g., STM investigations.

## Metal Deposition

The standard technique for metal deposition on extended oxide surfaces is vapor deposition, where a metal in close proximity to the oxide is heated to a temperature at which the metal has a suitable vapor pressure. Metal atoms will then impinge on the oxide surface at thermal energy. At room temperature (RT), the reevaporation probability for metal atoms is generally very low, i.e., the sticking probability is close to unity.

After landing, the metal adatoms may diffuse on the surface with a diffusion constant  $D$  determined by

$$D = (\nu a^2/4) \exp(-E_d/kT) \quad (1)$$

for 2-D diffusion. Here  $\nu$  is a frequency factor of the order of  $10^{13} \text{ Hz}$ ,  $a$  is the distance between neighboring adsorption sites,  $E_d$  is the energy barrier for diffusion,  $k$  is the Boltzmann constant, and  $T$  the absolute temperature. Diffusion can therefore be enhanced by an increase in temperature.

In a time interval  $\tau$  the diffusing adatoms will travel a root-mean-square (rms) distance  $l$  given by

$$l = (4D\tau)^{1/2} \quad (2)$$

For sufficient metal coverage the diffusion process leads to nucleation. If the diffusing metal atom attaches itself to a surface defect (such as a step edge), the nucleation is heterogeneous. If, on the other hand, diffusing adatoms meet and form stable nuclei, the nucleation is termed homogeneous. In general, only a



few atoms need to agglomerate to form stable nuclei. The minimum number of other adatoms that a diffusing metal adatom must meet to form a stable nucleus is called the critical cluster (or island) size. Thus if a metal dimer is stable, the critical cluster size is one.

Continued metal evaporation does not lead to an ever-increasing density of clusters. The saturation density  $N$  is determined by parameters such as the rate  $R$  at which atoms impinge on the surface, the temperature  $T$ , the frequency factor  $\nu$  from the diffusion constant  $D$  (Eq. (1)), the diffusion barrier  $E_d$ , and the critical cluster size  $i$ .<sup>[12]</sup> It is important to realize that for a given metal–oxide system, the saturation density of clusters can be controlled by changing the substrate temperature during nucleation and/or the evaporation rate  $R$ .

When the saturation density of clusters has been reached, the clusters will grow by attachment of further adatoms. Although exceptions exist, the growth modes can conveniently be divided into three classes: *Frank van der Merwe* growth in which the metal grows layer-by-layer across the entire surface, *Volmer–Weber* growth in which metal grows as 3-D islands separated by bare oxide, and *Stranski–Krastanow* growth which starts as layer-by-layer growth, but with 3-D islands appearing after a few monolayers. Based on a model in which the cluster is treated as a liquid droplet on the support surface it is possible to have some preconception of the growth mode of a particular metal–oxide system. If  $\gamma_{\text{met}}$  and  $\gamma_{\text{ox}}$  denote the surface energies of the metal and the oxide, respectively, and  $\gamma_{\text{int}}$  the interface energy, the following rule can be established.<sup>[13]</sup>

$$\gamma_{\text{ox}} \geq \gamma_{\text{met}} + \gamma_{\text{int}} : \text{layer-by-layer growth} \quad (3a)$$

$$\gamma_{\text{ox}} < \gamma_{\text{met}} + \gamma_{\text{int}} : \text{3-D cluster growth} \quad (3b)$$

Expressions (3a) and (3b) apply to the thermodynamical equilibrium. It is important to note that film growth is a kinetic process which does not take place at thermodynamic equilibrium (growth is incompatible with equilibrium!). The expressions are therefore applicable only to growth conditions which are close to equilibrium. As the free energies of the mid-to-late transition metals and the noble metals are frequently larger than the free energies of the supporting oxides, 3-D growth rather than layer-by-layer growth is to be expected for such systems. This is, indeed, confirmed by experiments.<sup>[1]</sup> In the following, 3-D cluster growth is assumed.

### Cluster Morphology

The thermodynamic equilibrium shape of a *free* metal cluster can be found from the Wulff theorem<sup>[14]</sup> if the

surface free energies of the low-index surfaces are known. The basis of the theorem is that for a given volume, the equilibrium shape must be determined by minimizing the total surface free energy. The ensuing theorem states that the ratio between the real-space distance  $d_i$  from the cluster center to the facet plane  $i$  and the surface energy  $\gamma_i$  of this facet is a constant:

$$d_i/\gamma_i = c \text{ (constant)} \quad (4)$$

Fig. 3A shows a free cluster with a shape determined by the relative values of the surface energies  $\gamma_{100}$ ,  $\gamma_{110}$ , and  $\gamma_{111}$ . A cross section of the cluster along the (110) plane is shown in Fig. 3B. The relative area of the different facets clearly depends on the relative values of  $\gamma_{100}$ ,  $\gamma_{110}$ , and  $\gamma_{111}$ .

If the metal cluster is formed on an oxide, a metal–oxide interface is created. The free energy of the interface is given by the Dupré equation:

$$\gamma_{\text{int}} = \gamma_{\text{met}} + \gamma_{\text{ox}} - W_{\text{adh}} \quad (5)$$

where  $\gamma_{\text{int}}$  is the interface energy,  $\gamma_{\text{met}}$  and  $\gamma_{\text{ox}}$  the surface free energy of the contact facet of the cluster and the substrate, respectively, and  $W_{\text{adh}}$  the adhesion energy, i.e., the work per unit area needed to separate the cluster and the substrate.

The equilibrium shape of a *supported* cluster can now be found using a modified Wulff construction scheme,<sup>[15]</sup> by replacing the free energy of the surface in contact with the substrate with an effective surface energy  $\gamma^*$ , which is the difference between the interface energy and the surface energy of the oxide:

$$\gamma^* = \gamma_{\text{int}} - \gamma_{\text{ox}} \quad (6)$$

The height  $H$  of the supported cluster, relative to that of a free cluster, thus depends on  $\gamma^*$ . For a cluster residing on a {111} facet (Fig. 4), the cluster will adopt its free-space form on the oxide if  $\gamma^* = \gamma_{111}$ . For smaller

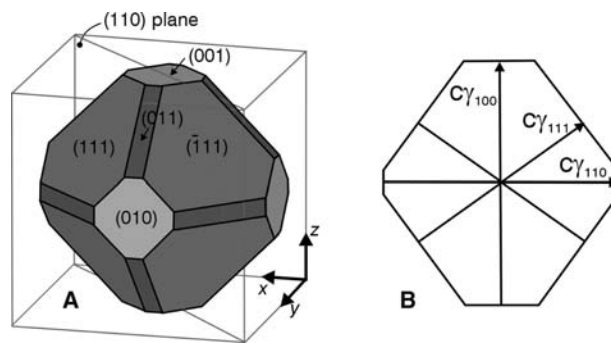


**Fig. 3** The Wulff construction. (A) Cluster displaying three types of facets. (B) Cross section of the cluster along the (110) plane.

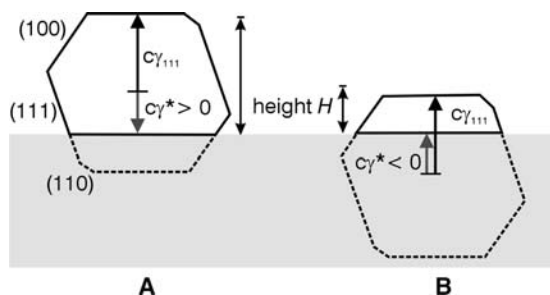


**Fig. 4** Cross section of a cluster supported on a {111} facet for a positive (A) and a negative (B) value of the effective surface energy  $\gamma^*$ .  $H$  denotes the height of the cluster.

values of  $\gamma^*$  the cluster gets truncated [Fig. 4A], and for negative values of  $\gamma^*$ , the height of the supported cluster becomes less than half the height of the free cluster, as illustrated in Fig. 4B. An experimental value of the  $\gamma^*$  can be derived from the observed, detailed morphology of the clusters in terms of the cluster surface energies.<sup>[16]</sup> From Eqs. (5) and (6)

$$W_{\text{adh}} = \gamma_{\text{met}} - \gamma^* \quad (7)$$

Again,  $\gamma_{\text{met}}$  denotes the surface free energy of the metal cluster facet in contact with the oxide. The work of adhesion can therefore be derived from experiments, if the surface energies are known.

The Wulff construction is basically a continuum description which does not consider the discrete nature (finite number of atoms) of the clusters, and neglects the formation energy of corner and edge atoms, which play an important role in small clusters. Nevertheless, the theorem has been extremely successful in predicting or rationalizing shapes of metal clusters on oxides.

## TWO CASE STUDIES

A large amount of metal/oxide combinations have been studied and an impressive amount of knowledge has been gained. In the following, focus will be on two different metal/oxide systems which have attracted special attention. The two systems will serve to illustrate fundamental properties, results, considerations, and problems related to research on metal clusters on oxides in general.

### Palladium on $\text{Al}_2\text{O}_3$

Palladium on alumina is an important catalyst for partial or complete oxidation in many catalytic processes. The system has therefore been studied extensively, both in the form of industrial catalysts and as a model system. Most laboratory studies of Pd on alumina have

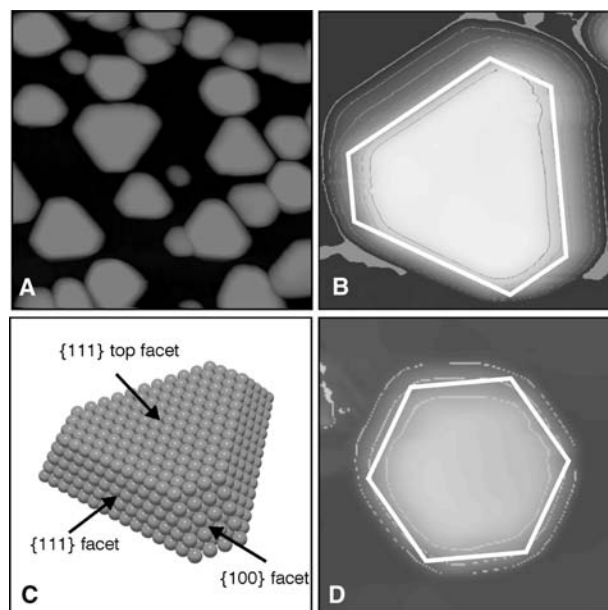


**Fig. 5** (A) STM image of nanoclusters on  $\text{Al}_2\text{O}_3/\text{NiAl}(110)$ . Note the characteristic hexagonal shape of many clusters. ( $50 \times 50 \text{ nm}^2$ ). (B) Height contours (thin lines) of a single Pd cluster. The thick line indicates the idealized, regular form. ( $15 \times 15 \text{ nm}^2$ ). (C) Ball model of a cluster displaying {100} and {111} facets. (D) Height contours (thin lines) of a Cu cluster, closely resembling a regular hexagon (thick line), ( $9 \times 9 \text{ nm}^2$ ). Source: (B) and (D) are reprinted from Ref.<sup>[17]</sup>, © 2001, with permission from Elsevier.

been carried out on  $\text{Al}_2\text{O}_3$  thin films because of the insulating nature of bulk  $\text{Al}_2\text{O}_3$ . Fig. 5A is an STM image showing the result of Pd evaporation onto a thin  $\text{Al}_2\text{O}_3$  layer formed by oxidation of  $\text{NiAl}(110)$  (cf. Fig. 2B). As expected from surface free energy considerations, Pd grows in the form of 3-D clusters (Volmer–Weber growth). For room temperature, low-coverage deposition of Pd on well-ordered films, the spatial distribution of the clusters is heavily influenced by the intrinsic defect structure of the film with a tendency for the clusters to nucleate at step edges and domain boundaries.

From Fig. 5A it is evident that a large fraction of the clusters are hexagonal in shape. On films with large domains up to 50% of the clusters are hexagonal in shape,<sup>[16]</sup> reflecting the fact that these clusters are crystalline. The remaining clusters have not necessarily adopted their thermodynamical equilibrium form because of incorporated defects, insufficient temperature, etc. Because of the finite size of the STM tip the clusters are imaged as a convolution of the cluster and the tip shapes. This leads to a certain rounding of edges and corners as illustrated in Fig. 5B which displays height contours of a single Pd cluster.<sup>[17]</sup> Based on atomic resolution STM,<sup>[16]</sup> the facets of the cluster can be identified: The top facet is of {111} orientation

while the sides are  $\{111\}$  and  $\{100\}$  facets. For comparison, Fig. 5C shows a ball model of a cluster. As discussed earlier, the general shape of the cluster is governed by the surface and interface energies (modified Wulff construction). The clusters do not display any  $\{110\}$  facet, either because  $\gamma_{110}$  is too large compared to  $\gamma_{100}$  and  $\gamma_{111}$  (cf. Fig. 3B), or because the cluster is too small to develop a genuine  $\{110\}$  facet. Fig. 5D shows the height contours of a Cu cluster formed under similar conditions.<sup>[17]</sup> In this case the shape of the top facet approaches a regular hexagon, illustrating how the surface energies influence the cluster morphology.

The principal objective for dispersing the active metal in a catalyst in the form of nanosized clusters is to increase the surface area. There are, however, several reasons why the dispersion, i.e., the formation of clusters, may influence the reactivity and make it deviate from that of corresponding, extended surfaces. First of all, the number of edge and corner sites will obviously increase dramatically. If such sites are active (see “Gold on  $\text{TiO}_2$ ” section), the dispersion will promote an increase in activity which is easily explained. Secondly, exposure to gases may have different effects on extended surfaces and clusters dispersed on oxides. As an example, exposure of an extended Pd(111) surface to  $\text{O}_2$  is known to result in the formation of a  $(2 \times 2)$  structure, i.e., a structure with a unit cell four times bigger than the substrate unit cell. Exposure of a clean Pd nanocrystal [Fig. 6A] to  $\text{O}_2$  has the same effect in the central portion of the top  $\{111\}$  facet, but an entirely new structure develops along the facet edge, as shown in Fig. 6B.<sup>[18]</sup> It is beyond the scope of this entry to discuss this phenomenon in detail; suffice it to state that the adsorption of gases on nanoclusters may cause reconstructions along facet edges, thereby creating new, possibly catalytically active sites. For very small clusters, the presence of gas may therefore influence the structure of the entire cluster.

The previous example is related to adsorption under static conditions, i.e., at a fixed temperature and in an

unchanging atmosphere of (low pressure) oxygen. What happens to the cluster morphology when the cluster is exposed to gases at a higher pressure and temperature, i.e., under industrial catalytic conditions? An answer was recently found based on an in situ investigation.<sup>[19]</sup> Model catalysts of Cu nanoparticles on ZnO (equivalent to the industrial methanol synthesis catalyst) were imaged with TEM in a high-pressure cell. The Cu nanocrystals were found to undergo dynamic, reversible shape changes in response to changes in the gaseous environment. The changes were found to be caused by adsorbate-induced changes in the surface energies and by changes in the interface energy. To describe and understand the catalytic properties of nanoscale clusters, *dynamic* effects on the nanocrystal morphology must therefore be included.

Dispersion may lead to effects of an even more subtle origin. Consider, for example, the sensitivity to changes in the lattice parameter. Because of the increased importance of the surface stress for smaller clusters, the lattice parameter is expected to decrease for decreasing cluster size.<sup>[20]</sup> Fig. 7 shows an experimental verification obtained for Pd on  $\text{Al}_2\text{O}_3$  on the basis of TEM measurements.<sup>[21]</sup> The smallest clusters (size  $\approx 1.5$  nm) show a 4–5% reduction in lattice parameter. A smaller lattice parameter results in a broadening of the d-band. Compared to the effect of bringing atoms together to form a solid: The atomic levels broaden and become energy bands. The closer the atoms the stronger the broadening. For transition metals with d-bands that are more than half-filled, such as Pd, the broadening results in a downward shift of the d-band center to maintain the degree of filling. According to the d-band model, a shift in the d-band center relative to the Fermi energy will be correlated with a change in binding energy.<sup>[22]</sup> Hence a change in the lattice parameter will influence the reactive properties of the cluster. An indisputable experimental

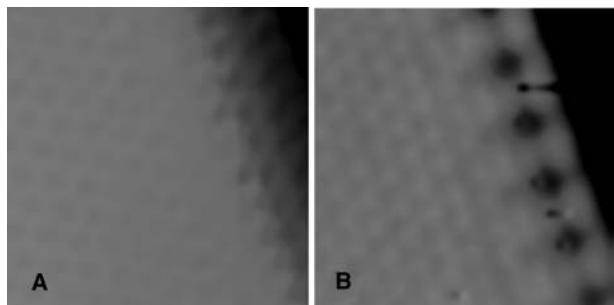


**Fig. 6** Two atomically resolved STM images ( $2.5 \times 2.5 \text{ nm}^2$ ) of a Pd cluster before (A) and after (B) exposure to  $\text{O}_2$ . The  $(2 \times 2)$  oxygen adlayer in (B) is not imaged by STM, but a severe reordering of the facet edge has taken place.

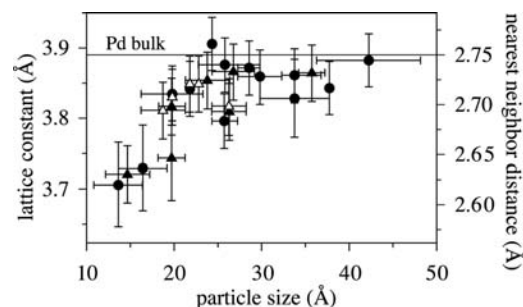


**Fig. 7** Atomic spacing in Pd clusters on  $\gamma\text{-Al}_2\text{O}_3/\text{NiAl}(110)$  as a function of cluster size. Horizontal bars illustrate the difference in length and width of the clusters whereas the vertical bars are estimated errors. *Source:* From Ref.<sup>[21]</sup>. © 1999, American Chemical Society.

verification of this effect on clusters is still lacking, but changes in the reactivity of a metallic surface induced by a change in lattice parameter has been reported for a (0001)-oriented Ru sample in an area where an edge dislocation intersects the surface.<sup>[23]</sup> On one side of the dislocation the lattice is compressed, and on the other side it is stretched. When analyzing the results of NO dissociation on the surface with STM, a much larger concentration of N atoms appeared at the stretched than at the compressed and the defect-free surface, signaling an enhanced reactivity of the stretched surface in accordance with the d-band model.<sup>[22]</sup>

For tiny (few-atom) clusters, the electronic structure cannot be properly described in a band structure model. Instead the energy levels may be described in a picture based on molecular orbitals. The energy levels, and hence the reactivity, will therefore be very sensitive to the detailed size and shape of the cluster.

In this section a number of concepts which are central in the description of catalytically active metal clusters have been described, whereas the role of the substrate has been neglected, apart from its part in providing a passive, high surface-area matrix (structural promoter) for the dispersed metal clusters. Increasing evidence has been found that the oxide in many cases plays a much more active and decisive role than hitherto expected. References to some aspects of metal-oxide interaction will be made in the next section.

### Gold on TiO<sub>2</sub>

Gold is generally accepted to be the noblest of all the metals because of its electronic structure with a filled 5d band.<sup>[24]</sup> Only little attention has therefore been paid to gold as a potential catalyst. Nevertheless, when gold is highly dispersed on select oxide surfaces in the

form of nanosized clusters, its chemistry changes dramatically and surprisingly a high activity and/or selectivity is exhibited in catalytic processes such as the low-temperature oxidation of CO.<sup>[25]</sup> The observation that the chemical properties of gold depend on the support and in particular on the size of the Au clusters has spurred an intense search for the underlying physical origin.

When Au is evaporated onto a TiO<sub>2</sub> surface (cleaned by Ar ion sputtering and vacuum annealed to  $\approx 1000$  K), the Au atoms form clusters that nucleate at defects. Apart from major defects such as steps, the main nucleation sites are the bridging-oxygen vacancies shown in Fig. 2A.<sup>[26]</sup> A single oxygen vacancy will bind up to three Au atoms and for larger Au clusters, the Au/TiO<sub>2</sub> interface will contain a high density of oxygen vacancies.

Fig. 8A shows an STM image of a 50  $\times$  50-nm area of a TiO<sub>2</sub> (110) surface with a large number of Au clusters (bright protrusions).<sup>[27]</sup> As already mentioned the average cluster size can be varied by adjusting the evaporation flux, temperature, and total dose. By measuring the turnover frequency (TOF), i.e., the number of reactions taking place per Au atom per second, for CO oxidation as a function of the Au cluster size, a clear correlation between the TOF and the cluster diameter was revealed, showing a distinct maximum for a Au cluster diameter of  $\approx 3$  nm.<sup>[27]</sup>

In the search for the origin of this effect, the electronic properties of the Au clusters were investigated with scanning tunneling spectroscopy (STS).<sup>[27]</sup> In this technique, the STM tip is positioned on top of a particular cluster, and the tunnel current  $I$  is recorded as a function of the tunnel voltage  $V$ . The resulting  $I$ - $V$  curves reflect the electronic properties of the clusters and can be correlated with cluster size and geometry, as shown in Fig. 8B. A perfectly metallic cluster on a conducting substrate should display a simple ohmic behavior, i.e., a straight line as  $I$ - $V$  curve. From

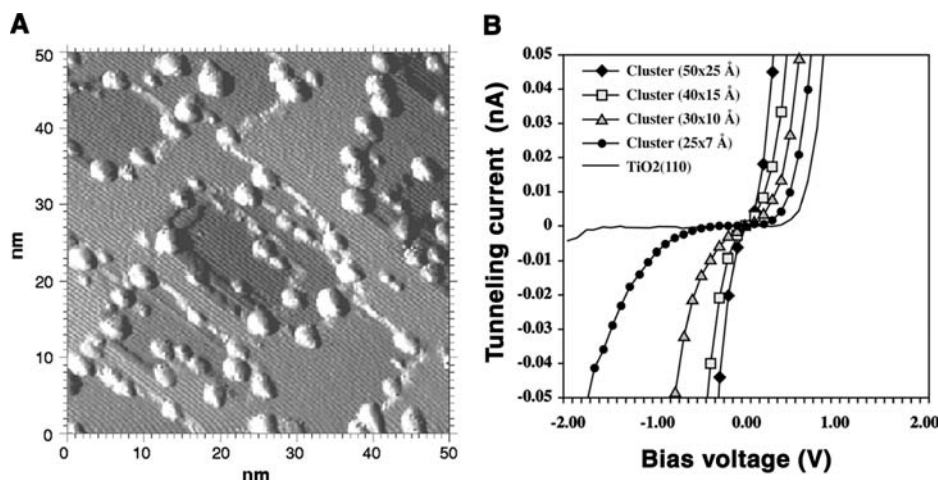


**Fig. 8** (A) Constant-current STM image of Au/TiO<sub>2</sub>(110). The total amount of Au corresponds to 0.25 monolayer. (B) Scanning tunneling spectroscopy data acquired for Au clusters of varying sizes on the TiO<sub>2</sub>(110) surface. For reference the STS data of the TiO<sub>2</sub> substrate are also shown. *Source:* From Ref.<sup>[27]</sup>. © 1998, American Association for the Advancement of Science.



Fig. 8B it is evident that the smaller the cluster the stronger the deviation from simple ohmic behavior is observed. When the dimension of the cluster is decreased, a plateau of zero tunnel current develops around zero bias voltage corresponding to the appearance of a band gap between the valence and the conduction band. For comparison, an STS curve for the TiO<sub>2</sub> substrate, having a wider band gap than the Au clusters, is also included in Fig. 8B. These measurements provide a fine illustration of how quantum size effects become important when the dimensions of metal clusters are reduced, but do not by themselves explain the peak in activity for a given cluster size.

To elucidate the mechanism behind the observed activity, the possible role of the substrate must also be considered. It is well known that the support may take part in reactions, for example via spillover effects where reactants may be formed at the metal clusters or the oxide and migrate from one to the other. The active role of an oxide support during CO oxidation over supported Au catalysts has been investigated theoretically and experimentally with conflicting results (see Ref.<sup>[28]</sup> and references therein). To illustrate the complexity of the problem, reference is made to a case study: a theory study based on density functional theory (DFT) calculations.<sup>[29]</sup> MgO rather than TiO<sub>2</sub> was chosen as a substrate because of its structural simplicity and appearance in the experimental literature (Au clusters on MgO have also been shown to be reactive to CO oxidation at RT and even below.)<sup>[30]</sup> The higher reactivity of supported nanometer-sized Au clusters was found to originate from two effects: 1) the oxide acts as a structural promoter, leading to the formation of small Au clusters with low-coordinated Au edge sites that readily bind CO; 2) the proximity of the oxide stabilizes a peroxo-like reaction intermediate CO·O<sub>2</sub>.

It remains to be seen how general such mechanisms are, but the example serves to illustrate how the catalytic process may rely on an intricate interplay between the metal cluster and the oxide, and how challenging it is to sort out the relative importance of different effects.

## CONCLUSION

In this entry, emphasis has been on the synthesis and characterization of metal clusters on relatively flat, extended oxides which mimic real, metal-based catalysts sufficiently well to be exploited as model systems. Based on two case stories, Pd/Al<sub>2</sub>O<sub>3</sub> and Au/TiO<sub>2</sub>, a number of issues relevant for such systems have been introduced and discussed. Many other fascinating applications of metal clusters on oxides may be developed in the near future. Examples can already be found in the literature, such as the fabrication of

single-electron transistors based on contacting Au nanoclusters on SiO<sub>2</sub> with carbon nanotubes.<sup>[31]</sup> While each example is of interest in its own area, the principal importance of metal clusters on oxides is unquestionably still in the field of catalysis.

## ACKNOWLEDGMENTS

Fruitful collaboration with K. Højrup Hansen is gratefully acknowledged. This work was supported by the Danish National Research Foundation through the Center for Atomic-Scale Materials Physics.

## REFERENCES

1. Campbell, C.T. Ultrathin metal films and articles on oxide surfaces: Structural, electronic and chemisorptive properties. *Surf. Sci. Rep.* **1997**, *27*, 1–111.
2. Henry, C.R. Surface studies of supported model catalysts. *Surf. Sci. Rep.* **1998**, *31*, 231–325.
3. Bäumer, M.; Freund, H.-J. Metal deposits on well-ordered oxide films. *Prog. Surf. Sci.* **1999**, *61*, 127–198.
4. Santra, A.K.; Goodman, D.W. Oxide-supported metal clusters: Models for heterogeneous catalysts. *J. Phys., Condens. Matter* **2002**, *14*, R31–R62.
5. Freund, H.-J. Clusters and islands on oxides: From catalysis via electronics and magnetism to optics. *Surf. Sci.* **2002**, *500*, 271–299.
6. Hansen, T.W.; Hansen, P.L.; Dahl, S.; Jacobsen, C.J.H. Support effect and active sites on promoted ruthenium catalysts for ammonia synthesis. *Catal. Letters* **2002**, *84*, 7–12.
7. Henrich, V.E.; Cox, P.A. *The Surface Science of Metal Oxides*; Cambridge University Press: Cambridge, Great Britain, 1994.
8. Chambers, S.A. Epitaxial growth and properties of thin films. *Surf. Sci. Rep.* **2000**, *39*, 105–180.
9. Franchy, R. Growth of thin, crystalline oxide, nitride and oxynitride films on metal and metal alloy surfaces. *Surf. Sci. Rep.* **2000**, *38*, 195–294.
10. Diebold, U. The surface science of titanium dioxide. *Surf. Sci. Rep.* **2003**, *48*, 53–229.
11. Libuda, J.; Winkelmann, F.; Bäumer, M.; Freund, H.-J.; Bertrams, T.; Neddermeyer, H.; Müller, K. Structure and defects of an ordered alumina film on NiAl(110). *Surf. Sci.* **1994**, *318*, 61–73.
12. Venables, J.A. Atomic processes in crystal growth. *Surf. Sci.* **1994**, *299/300*, 798–817.
13. Bauer, E. Phänomenologische Theorie der Kristallabscheidung an Oberflächen. *Z. Kristallogr.* **1958**, *110*, 372.
14. Wulff, G. Zur Frage der Geschwindigkeit des Wachstums und der Auflösung der Kristallflächen. *Z. Kristallogr.* **1901**, *34*, 449–530.
15. Winterbottom, W.L. Equilibrium shape of a small particle in contact with a foreign substrate. *Acta Metall.* **1967**, *15*, 303–310.

16. Højrup Hansen, K.; Worren, T.; Stempel, S.; Lægsgaard, E.; Bäumer, M.; Freund, H.-J.; Besenbacher, F.; Stensgaard, I. Palladium nanocrystals on  $\text{Al}_2\text{O}_3$ : Structure and adhesion energy. *Phys. Rev. Lett.* **1999**, *83*, 4120–4123.
17. Worren, T.; Højrup Hansen, K.; Lægsgaard, E.; Besenbacher, F.; Stensgaard, I. Copper clusters on  $\text{Al}_2\text{O}_3/\text{NiAl}(110)$  studied with STM. *Surf. Sci.* **2001**, *477*, 8–16.
18. Højrup Hansen, K.; Šljivančanin, Ž.; Lægsgaard, E.; Besenbacher, F.; Stensgaard, I. Adsorption of  $\text{O}_2$  and  $\text{NO}$  on Pd nanocrystals supported on  $\text{Al}_2\text{O}_3/\text{NiAl}(110)$ : Overlayer and edge structures. *Surf. Sci.* **2002**, *505*, 25–38.
19. Hansen, P.L.; Wagner, J.B.; Helveg, S.; Rostrup-Nielsen, J.R.; Clausen, B.S.; Topsøe, H. Atom-resolved imaging of dynamic shape changes in supported copper nanocrystals. *Science* **2002**, *295*, 2053–2055.
20. Henry, C. Growth, structure and morphology of supported metal clusters studied by surface science techniques. *Cryst. Res. Technol.* **1998**, *33*, 1119–1140.
21. Nepijko, S.A.; Klimenkov, M.; Adelt, M.; Kühlenbeck, H.; Schlögl, R.; Freund, H.-J. Structural investigation of palladium clusters on  $\gamma\text{-Al}_2\text{O}_3(111)/\text{NiAl}(110)$  with transmission electron microscopy. *Langmuir* **1999**, *15*, 5309–5313.
22. Hammer, B.; Nørskov, J.K. Theoretical surface science and catalysis—Calculations and concepts. *Adv. Catal.* **2000**, *45*, 71.
23. Winterlin, J.; Zambelli, T.; Trost, J.; Greely, J.; Mavrikakis, M. Atomic-scale evidence for an enhanced catalytic reactivity of stretched surfaces. *Angew. Chem., Int. Ed.* **2003**, *42*, 2850–2853.
24. Hammer, B.; Nørskov, J.K. Why gold is the noblest of all the metals. *Nature* **1995**, *376*, 238–240.
25. Haruta, M. Size- and support-dependency in the catalysis of gold. *Catal. Today* **1997**, *36*, 153–166.
26. Wahlström, E.; Lopez, N.; Schaub, R.; Thostrup, P.; Rønnau, A.; Africh, C.; Lægsgaard, E.; Nørskov, J.K.; Besenbacher, F. Bonding of gold nanoclusters to oxygen vacancies on rutile  $\text{TiO}_2(110)$ . *Phys. Rev. Lett.* **2003**, *90*, 026101-1-4.
27. Valden, M.; Lai, X.; Goodman, D.W. Onset of catalytic activity of gold clusters on titania with the appearance of non-metallic properties. *Science* **1998**, *281*, 1647–1650.
28. Schubert, M.M.; Hackenberg, S.; van Veen, A.C.; Muhler, M.; Plzak, V.; Behm, R.J. CO oxidation over supported gold catalysts—“Inert” and “Active” support materials and their role for the oxygen supply during reaction. *J. Catal.* **2001**, *197*, 113–122.
29. Molina, L.M.; Hammer, B. Active role of oxide support during CO oxidation at Au/MgO. *Phys. Rev. Lett.* **2003**, *90*, 206102-1-4.
30. Grisel, R.J.H.; Nieuwenhuys, B.E. Selective oxidation of CO, over supported Au catalysts. *J. Catal.* **2001**, *199*, 48–59.
31. Thelander, C.; Magnusson, M.H.; Deppert, K.; Samuelson, L.; Poulsen, P.R.; Nygård, J.; Borggren, J. Gold nanoparticles single-electron transistor with carbon nanotube leads. *Appl. Phys. Lett.* **2001**, *79*, 2108–2110.



# Metal Nanoparticle Catalysts

Naoki Toshima

Department of Materials Science and Engineering,  
Tokyo University of Science, Yamaguchi, Japan

## INTRODUCTION

“Metal nanoparticles” receive much attention because of their uniform size and sharp size distribution in nanometers, and because they are easily prepared as a result of recent developments in nanoscience and nanotechnology. In addition, catalysts based on such metal nanoparticles are highly active and selective. They also exhibit a long lifetime for several kinds of chemical reactions. In this entry, a background on the use of metal nanoparticles as catalyst is first briefly discussed. Then, preparation, characterization, structures, and catalyses of metal nanoparticles, especially of bimetallic nanoparticles, are described. The prospects on the use of metal nanoparticles as catalysts<sup>[1–8]</sup> are summarized in the last section.

## METAL NANOPARTICLES AS CATALYSTS

There is a long history since metal has been known to work as a catalyst for various kinds of reactions. The catalytic sites of metals are located on its surface. This means that metal nanoparticles of 1–10-nm size (thus, having a large surface-to-volume ratio) are expected to work as effective catalysts. The surface-to-volume ratio increases with decreasing particle size. In other words, the ratio of surface atoms with respect to all atoms in a particle increases with decreasing particle size. Fig. 1 shows the dependence of the ratio of surface atoms of Au nanoparticles on the radius of nanoparticles, assuming that Au nanoparticles have the same fcc (face-centered cubic) crystalline structure as that of the bulk gold. Fig. 1 shows that the smaller the size, the larger is the ratio. Another characteristic property of the nanoparticles is the quantum size effect. Although bulk metal has a band structure, the electronic energy levels of metal nanoparticles with size of a few nanometers are rather separated as shown in Fig. 2.<sup>[9]</sup> This may have an advantage as a catalyst.

When metal nanoparticles are used as catalysts, it is necessary for the metal nanoparticles to be stabilized under the catalytic reaction conditions. Otherwise, metal nanoparticles can very easily coagulate in solution to form aggregates, which are less effective

as catalysts than the original ones. There are two ways to stabilize metal nanoparticles: One is to immobilize the metal nanoparticles on inorganic supports, resulting in heterogeneous catalysts. The other method is to surround metal nanoparticles with stabilizers, resulting in homogeneous catalysts, or more precisely, homogenized heterogeneous catalysts.

In practical industries, heterogeneous catalysts are often used because they are easy to handle. They can be used in tubular reaction vessels for gaseous reactions in continuous reaction processes, and thus are effective for mass production of conventional chemicals. However, metal nanoparticles often cannot keep their shapes and properties when immobilized on inorganic supports. For example, interactions between metal particles and inorganic supports are often very strong in the supported catalysts. This strong interaction can sometimes increase the stability and activity of catalysts, but in some cases can make the catalytic properties worse.

In contrast, metal nanoparticles in solution, especially those stabilized by polymers, are less affected by the stabilizers than those immobilized on inorganic supports because the interaction between metal nanoparticles and capping polymers is usually very weak in comparison with that between metal nanoparticles and inorganic supports. The structure models of a conventional heterogeneous metal catalyst and a typical metal nanoparticle catalyst are shown in Fig. 3.

In metal nanoparticles stabilized by strong coordination with organic ligand molecules, the story is quite different from those stabilized by polymers. Because the strongly coordinating organic molecules can occupy the surface of metal nanoparticles, the reaction substrates cannot attack the surface of metal nanoparticles. Thus metal nanoparticles strongly coordinated by organic ligands cannot work as effective catalysts.

The advantages of using metal nanoparticles as catalysts are the following:<sup>[1,4]</sup>

1. The size and shape of metal nanoparticles are easily controlled by the preparation conditions.
2. Metal nanoparticles dispersed in solution can be used as catalysts in solution like homogeneous catalysts. Thus the temperature applied to the catalyst is below the boiling point of the solvent.

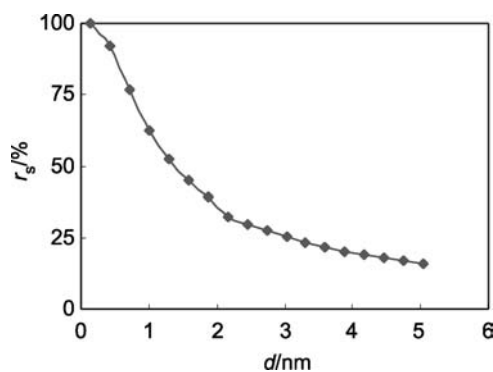


**Fig. 1** Dependence of the ratio of surface atoms ( $r_s$ ) on the radius ( $r$ ) of gold nanoparticles.

3. Metal nanoparticles dispersing in solution are transparent to light. Thus they can be used as photocatalysts.
4. Metal nanoparticles capped by organic polymers can be functionalized by modifying the organic polymers.
5. It is possible to prepare bimetallic and trimetallic nanoparticles with various compositions and structures. The catalytic activity and selectivity of these metal nanoparticles can be controlled by varying the composition and structure.
6. Metal nanoparticles immobilized on solid supports can be used as catalysts even for the reactions in a gaseous phase.
7. Metal nanoparticles dispersed in solution or immobilized on solid supports are usually more active and selective as catalysts under mild reaction conditions than the conventional industrial catalysts.

The metal nanoparticles dispersed in solution and used as catalysts can be characterized not only by their own structure but also by the structure of the organic layers surrounding them. Both structures provide various functions to the metal nanoparticles used as catalysts.

The structure of a metal nanoparticle capped by an organic layer is shown in Fig. 4. The diameter  $d$  of core

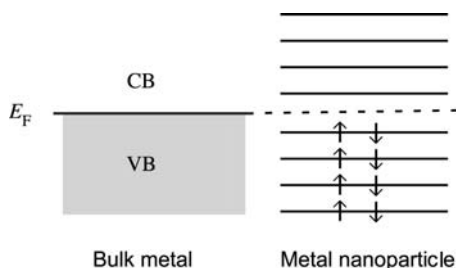


**Fig. 2** Formation of separated energy-levels of metal nanoparticles by a quantum size effect.

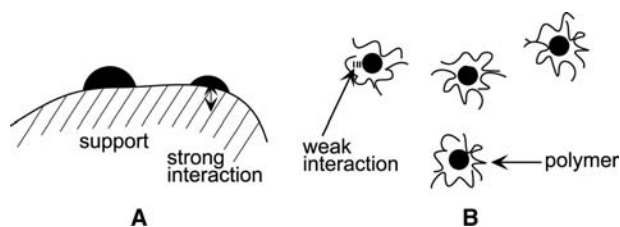


**Fig. 3** Schematic illustration of the structures of (A) conventional metal catalyst and (B) metal nanoparticles capped by polymers.

metal nanoparticles can be easily measured by transmission electron microscopy (TEM). The thickness  $\delta$  of the organic layer or the total diameter  $D$  including the organic layer can be measured by various methods depending on the kind of organic layer. In solution, hydrodynamic radius provides  $D/2$ . When the hydrodynamic radius is large enough, it can be measured by a light scattering method. However, when the hydrodynamic radius is small, it can still be measured by a Taylor dispersion method if the size is homogeneous or uniform enough.<sup>[10]</sup> When the organic layer is composed of soluble polymers, the direct measurement of  $D$  is not so easy. The thickness  $\delta$  was proposed to be measured by the amount of polymers adsorbed on the surface of metal nanoparticles.<sup>[11]</sup> Because it is not easy to measure  $D$  in solution, measurement using scanning tunnel microscopy (STM) was performed in the dry state.<sup>[12]</sup>

In solution, the metal nanoparticles interact with each other by weak interaction forces; they form “superstructures,” the size of which can be measured by small-angle X-ray scattering (SAXS).<sup>[13]</sup>

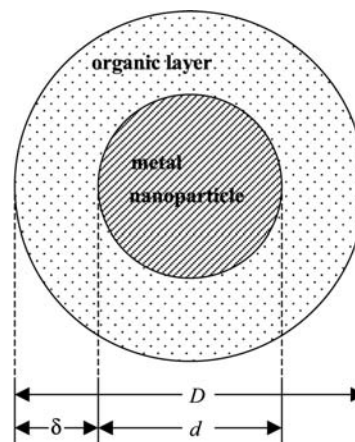


**Fig. 4** Illustration of the metal nanoparticle capped by an organic layer.

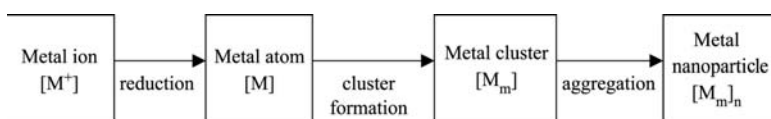


**Fig. 5** Formation of metal nanoparticles by a chemical method.

## PREPARATION AND CHARACTERIZATION OF METAL NANOPARTICLES

Metal nanoparticles are defined as metal particles of nanometer size, which have a rather uniform size in the range of 1–10 nm. Metal nanoparticles with rather strict structures are called metal nanoclusters. Metal nanoparticles immobilized on solid supports or dispersed in solution can be used as catalysts.

### Preparation of Metal Nanoparticles Used as Catalysts

Metal nanoparticles with a rather uniform size can be prepared by both physical and chemical methods. In the physical method, sometimes called the top-down-type method, metal nanoparticles are prepared by decomposition of bulk metal with mechanical force, vaporization, laser abrasion, and so on, which can provide higher energy to bulk metal than the bond energy of metal. In the chemical method, sometimes called a bottom-up-type method, the preparation process starts from reduction of metal ions to metal atoms, which is followed by aggregation resulting in metal nanoparticles Fig. 5. Both physical and chemical methods have their own advantages. However, chemical methods are now considered to be better than physical methods from the viewpoints of reproducibility, homogeneity (e.g., uniformity in size), and mass production.

The production of metal nanoparticles by chemical methods requires some techniques by which coagulation is prevented. For example, electrostatic and steric repulsions among metal nanoparticles are used for this purpose. To prevent coagulation and to keep the dispersity of metal nanoparticles by electrostatic repulsion, electrical charges are provided. Adsorption of ions on the surface of metal nanoparticles is a simple way to acquire such charges Fig. 6A. The typical conventional colloidal dispersions of metal nanoparticles are usually stabilized by this method.

The most satisfying method for stabilization of metal nanoparticles by steric repulsion is the dispersion of metal nanoparticles in solid such as glass. However, in this case, the metal nanoparticles cannot work as catalysts because the substrate molecules cannot attack the surface of metal nanoparticles. Thus adsorption of metal nanoparticles on the surface of inorganic supports or immobilization in porous solids is often used for stabilization of metal nanoparticles by steric repulsion on solids Fig. 6B and C.

For the stabilization of metal nanoparticles in solution by steric repulsion, attachment of organic molecules or organic macromolecules on the surface of metal nanoparticles is easily considered to be a favorite method. An organic molecule with S and/or N atom(s), for example, is used as a ligand, which strongly bonds to metal nanoparticles Fig. 6D. In the case of organic macromolecules, the molecule is strongly attached to the metal nanoparticle because the macromolecule interacts with the surface of a metal nanoparticle at many sites although each interaction may be weak Fig. 6E. Organic molecules with low molecular weight can occasionally act as if they were a macromolecule when the interactions among the organic molecules are strong enough. In micelles and reverse micelles, surfactant molecules aggregate and protect the metal nanoparticles from coagulation Fig. 6F.

One of the simplest and most reproducible methods for preparation of metal nanoparticles is alcohol reduction of precious metal ions in alcohol–water in the presence of water-soluble polymers such as

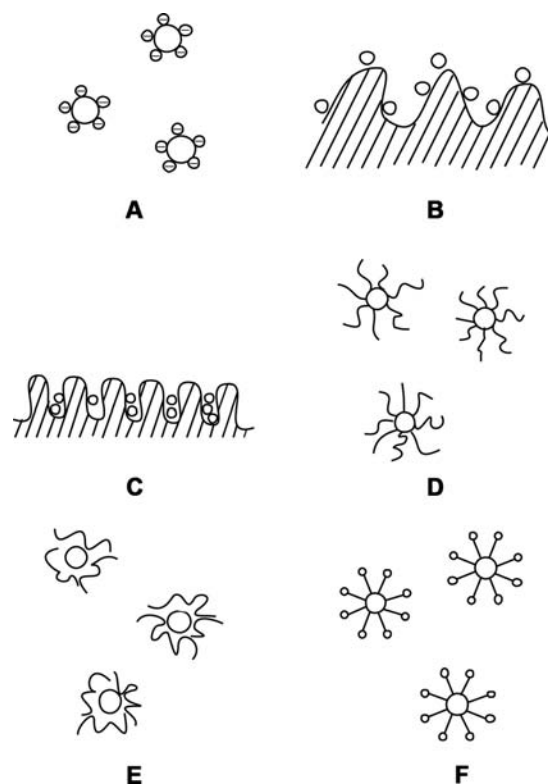


**Fig. 6** Various metal nanoparticles stabilized by (A) electric charge, (B) inorganic supports, (C) porous solids, (D) organic molecules, (E) soluble macromolecules, and (F) surfactants.

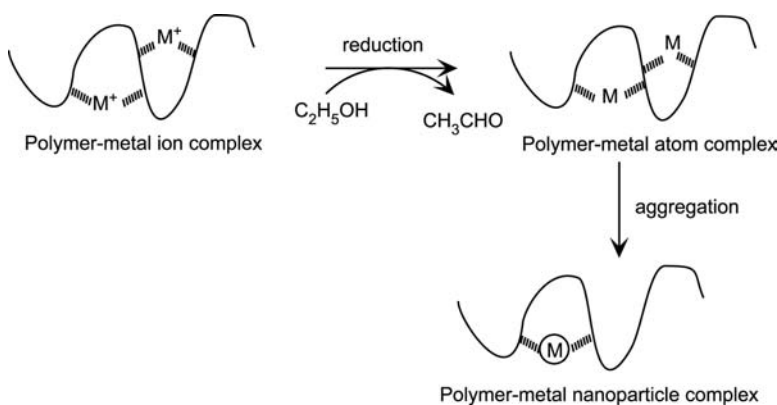


**Fig. 7** Preparation of polymer-capped metal nanoparticle by alcohol reduction.

poly(*N*-vinyl-2-pyrrolidone) (PVP).<sup>[14]</sup> This process is schematically shown in Fig. 7. Thus the precious metal ions form complexes with polymers at first. The metal ions can be reduced by alcohol to produce polymer-metal atom complexes accompanying aldehyde formation from alcohol.

Other chemical reductants, such as hydrazine, molecular hydrogen, glycol, sodium borohydride, etc., can be used instead of alcohol. Energy, such as photoenergy, X-ray,  $\gamma$ -ray, electron beam, microwave, ultrasonic wave, electrolysis, etc., can also be used in solution in the presence of stabilizers to break the bond or reduce the metal ions to 0-valent metal atoms resulting in metal nanoparticles.

Other stabilizers such as organic ligands can be used instead of protective polymers. In general, the presence of strong ligands requires a strong reductant if the reduction is carried out in the presence of stabilizers. Otherwise, stabilizers must be immediately added after the reduction and coagulation of metal atoms to form metal nanoparticles and before the aggregation of metal nanoparticles to form the precipitates.

Metal nanoparticles stabilized by weakly coordinating polymers are considered as the best metal nanoparticle catalyst because substrate molecules can easily

attack the surface of metal nanoparticles and the reaction smoothly occurs as shown in Fig. 8. Because the polymer molecule weakly coordinates with the metal nanoparticle, the substrate molecules can replace the polymer on the surface of metal nanoparticle. When the reaction occurs on the surface and the substrate changes to a product, then the product can easily be removed from the surface because it cannot strongly interact with the metal surface. Upon removal of the product, the parts of the polymer that were left on the metal surface can now interact with the metal surface again and cover the metal nanoparticle. This kind of reversible capping of the polymer on the metal surface cannot occur in organic ligands with low molecular weight, although organic ligands or ionic species play an important role to control the shape of metal nanoparticles.

The metal nanoparticles immobilized on solid supports can be prepared by immobilization of the separately prepared metal nanoparticles on solid supports. Immobilization can be carried out by chemisorption or chemical bond formation between metal nanoparticles and solid supports. The immobilized metal nanoparticles thus prepared work as industrial catalysts for reactions in solution as well as in gaseous phase.

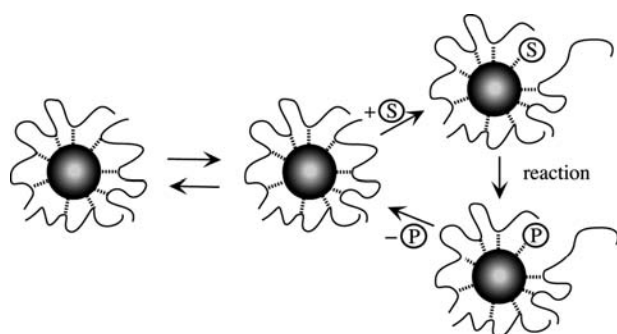


**Fig. 8** Illustration of the catalytic reaction process of a metal nanoparticle catalyst stabilized by weakly coordinating polymers. (S): reaction substrate; (P): reaction product. Source: From Ref.<sup>[7]</sup>.

## Characterization of Metal Nanoparticles

Metal nanoparticles can be characterized by a combination of the following methods:<sup>[2,3]</sup>

1. Transmission electron microscopy (TEM). This is the simplest and most reliable method to measure the size and shape of metal nanoparticles. The average size is usually calculated by counting the sizes of about 200 particles. High-resolution TEM (HR-TEM) can provide information not only on the particle size and shape but also on the crystalline structure of metal nanoparticles. When energy dispersive X-ray microanalysis (EDX) is used in

conjunction with TEM, elemental information of metal nanoparticles can be obtained. The localized elemental information is also obtained by electron energy-loss spectroscopy (EELS) in conjunction with energy-filtering TEM (EF-TEM).

2. Ultraviolet and visible absorption spectroscopy (UV/VIS). The color change is a very useful and convenient method to identify the chemical change from the solution of metal ions to the dispersion of metal nanoparticles. The colloidal dispersions of Au, Ag, and Cu (Group 11 elements) have a red to yellow color because of their plasmon absorption, the peak position of which varies depending on the particle size and the extent of coagulation. The plasmon absorption of other metal nanoparticles is located in a UV region and is often difficult to clearly detect.
3. Infrared spectroscopy (IR). The IR spectra can provide information on organic layers surrounding metal nanoparticles. For example, the coordination of poly(*N*-vinyl-2-pyrrolidone) (PVP) onto the surface of metal nanoparticles was revealed by a shift of C=O stretching vibration absorption in the IR spectra. The structure of organic layers and the interaction of organic layers with metal nanoparticles are effective in the catalysis of metal nanoparticles. Thus information given by the IR spectra is very important in some cases. The IR spectra can also be used to understand the surface structure of the metal nanoparticles. The IR spectra of carbon monoxide adsorbed on the surface metal are so often used to identify the element of the surface metal of bimetallic nanoparticles.
4. X-ray diffraction (XRD). The solid structure of metal nanoparticles can be investigated by XRD. For monometallic nanoparticles, XRD can give information on the phase changes depending on the particle size. X-ray diffraction can determine if the bimetallic system is composed of the mixtures of two kinds of monometallic nanoparticles or of single bimetallic nanoparticles in which two elements are included in one particle.
5. X-ray photoelectron spectroscopy (XPS). Photoelectron spectroscopy is used to obtain information on the state of metal, e.g., the oxidation state of metal on the surface. Metal on the surface is often oxidized by air. So the 0-valency of surface metal must be confirmed by using XPS or other methods. When polymers cover the metal nanoparticles, clear XPS spectra of the metal cannot be observed. In this case, the removal of covering polymers from the surface of metal nanoparticles is required. Etching of covering polymers could be useful for this purpose. The polymers can also be removed from the metal nanoparticles by washing the nanoparticles adsorbed on thiol-modified silica supports with a good solvent. The quantitative analysis of XPS spectra of bimetallic nanoparticles can suggest the elements present in the surface region of nanoparticles.
6. Surface enhanced Raman spectroscopy (SERS). The SERS spectra can be obtained in the case of nanoparticles containing Au, Ag, and/or Cu. Quantitative analysis of enhanced Raman spectra can provide information about the adsorbing structures of organic molecules on the metal nanoparticles. Not only monometallic nanoparticles but also bimetallic nanoparticles containing Au, Ag, or Cu can enhance Raman spectra.
7. Scanning probe microscopy (SPM). Scanning probe microscopy techniques such as scanning tunneling microscopy (STM) and atomic force microscopy (AFM) can give information on the total size of metal nanoparticles capped by organic layers and the coagulating structure (superstructure) of capped metal nanoparticles. The superstructure sometimes has an effect on catalysis of capped metal nanoparticles. Although SPM is usually used for observation of dry samples, the superstructure at dry state is often thought to be similar to that in solution.
8. Extended X-ray absorption fine structure (EXAFS). This is one of the most powerful characterization methods to determine the detailed structure of metal nanoparticles, especially bimetallic nanoparticles. Because big synchrotron radiation facilities are now available, the EXAFS technique becomes useful for structure analysis of nanoparticles of precious metals. EXAFS can provide the number of atoms surrounding the X-ray absorbing atom and their interatomic distances involved in the various coordination shells, as well as the electron density. However, to obtain exact information, the sample of metal nanoparticles should be homogeneous, i.e., uniform in size and narrow in size distribution. Because the number of atoms surrounding the X-ray absorbing atom and even their interatomic distances can vary with the size of metal nanoparticles, we succeeded to give a core/shell structure model for Pd/Pt (4:1, mol/mol) bimetallic nanoparticles capped by poly(*N*-vinyl-2-pyrrolidone) (PVP), because they are very homogeneous (monodispersed) and stable.
9. Small-angle X-ray scattering (SAXS). Analysis of SAXS data can give information on

rather long regularity, for example, size of superstructures.

10. Thermogravimetry (TG) and differential thermal analysis (DTA). Thermal analysis (TG and DTA) can give information not only on composition and structure of organic layers but also on the phase transition of metal.
11. Dynamic light scattering (DLS). This method gives the hydrodynamic radius; that is, the size of metal nanoparticles including organic layers.

## STRUCTURE CONTROL OF BIMETALLIC NANOPARTICLES

Bimetallic nanoparticles, in which each particle contains two metal elements, are very important and interesting from the viewpoint of catalysis of metal nanoparticles because catalytic performance is very often affected by the addition of another element to the metal. In addition, the structure of bimetallic nanoparticles is strongly related with the catalytic performance.

Typical structures of bimetallic nanoparticles are illustrated in Fig. 9. These bimetallic nanoparticles have two kinds of metal-metal bonds, i.e., a homobond and a heterobond. If the metal particles are composed of atoms A and B, the homobond is either an A-A bond or a B-B bond, while an A-B bond is a heterobond. If the binding energies of the homobonds are same with that of the heterobond, the random alloy or solid solution should be the thermodynamically most stable structure. If the homobonds are much stronger than the heterobond, no bimetallic particles may be produced but only the mixture of two kinds of monometallic particles will be favorably obtained. However, in practice, there are no such big differences between the two kinds of bonds in precious metals. When heterobonds are preferred over homobonds, a

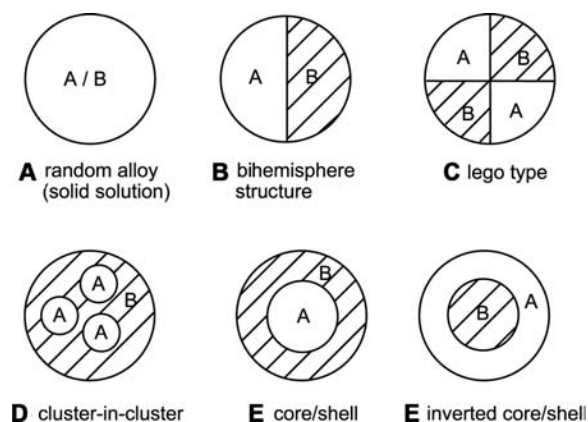


**Fig. 9** Various structures of bimetallic nanoparticles.

heterobondphilic structure may be obtained.<sup>[15]</sup> The opposite case gives a homobondphilic structure. Hence a core/shell structure, a kind of homobondphilic structure, is obtained as a thermodynamically stable structure. In contrast, an inverted core/shell structure is thermodynamically metastable. Such metastable structures can be constructed by the concept of kinetic control. Thus the structure of bimetallic nanoparticles depends on the kind of a couple of elements used.

## Bimetallic Nanoparticles Composed of a Couple of Platinum-Group Elements

Bimetallic nanoparticles of two kinds of platinum-group elements such as Pt, Pd, Au, etc. can be produced by coreduction of the corresponding metal ions in refluxing alcohol-water in the presence of water-soluble polymer. The coreduction usually gives colloidal dispersions of bimetallic nanoparticles with a core/shell structure, a kind of homobondphilic structure. For example, the solution of  $\text{PdCl}_2$  and  $\text{H}_2\text{PtCl}_6$  in refluxing ethanol-water in the presence of PVP gives colloidal dispersion of Pd/Pt bimetallic nanoparticles with a Pt-core/Pd-shell structures.<sup>[16]</sup> From  $\text{HAuCl}_4$  and  $\text{PdCl}_2$ , Au-core/Pd-shell structured bimetallic nanoparticles were obtained.<sup>[17]</sup>

The easiness of core formation increases in the order of  $\text{Rh} < \text{Pd} < \text{Pt} < \text{Au}$ . Thus Rh is the most easily shell-forming element. The core/shell structure is constructed via the complexes shown in Fig. 9. Two factors control the core/shell structure: 1) redox potential of metal ions; and 2) coordination ability of metal atom to the polymer.<sup>[18]</sup>

The PVP-protected Pd/Pt bimetallic nanoparticles work as a catalyst for partial hydrogenation of 1,3-cyclooctadiene to cyclooctene under mild conditions. The catalytic activity depends on the composition of Pd and Pt. The highest activity can be achieved by the Pd/Pt ratio (4:1, mol/mol) of bimetallic nanoparticles, in which 13 atoms of Pt form a core and 42 atoms of Pd surround the Pt core to form a shell.<sup>[16]</sup>

The mechanism of formation of Pd/Pt bimetallic nanoparticles with a thermodynamically stable Pt-core/Pd-shell structure has been proposed as shown in Fig. 10. In this process, easily reduced Pt(IV) ions are first reduced to produce Pt atoms that form a Pt core. Less easily reduced Pd(II) ions later produce Pd atoms, which deposit on the Pt core to form a Pd shell.

An inverted core/shell structure can be prepared by the so-called sacrificial hydrogen reduction method.<sup>[19]</sup> For example, Pd-core/Pt-shell bimetallic nanoparticles can successfully be prepared by this method. Successive reduction of Pd(II) and Pt(IV) ions cannot produce the inverted core/shell structured bimetallic nanoparticles, because addition of Pt(IV) ions to Pd(0) core



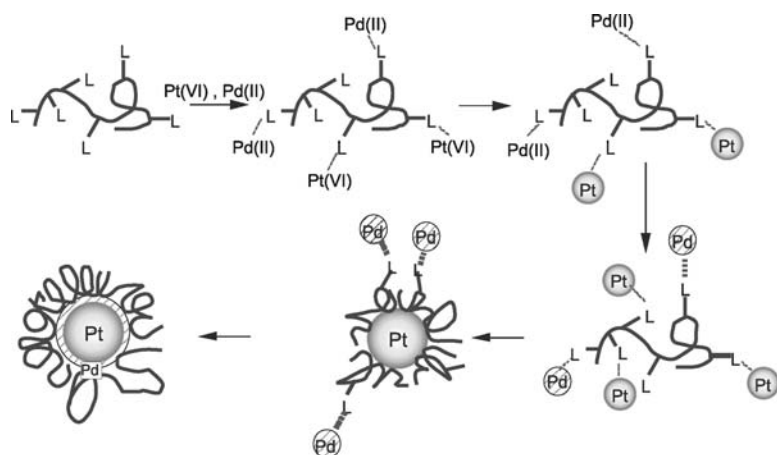


**Fig. 10** Proposed formation mechanism of Pt-core/Pd-shell-structured bimetallic nanoparticles. *Source:* From Ref.<sup>[18]</sup>.

nanoparticles results in redox reaction between them to form Pt(0) nanoparticles and Pd ions. Hence before the addition of Pt(IV) ions, the dispersion of Pd-core nanoparticles is treated with molecular hydrogen, forming hydride-covered Pd nanoparticles. Addition of Pt(IV) ions into the hydride-covered Pd nanoparticles produces Pt atoms, which immediately deposit on Pd cores to form Pd-core/Pt-shell, i.e., inverted core/shell structured bimetallic nanoparticles. This sacrificial hydrogen reduction method is useful for constructing other kinds of core/shell structured bimetallic nanoparticles.

### Bimetallic Nanoparticles Composed of an Iron-Group Element and a Platinum-Group Element

Reduction of ions of an iron-group element (transition metal in the third period) is more difficult than those of a platinum-group element. Nevertheless, ions of an iron-group element can easily be reduced to the corresponding atoms in the coexistence of nanoparticles of a platinum-group element. For example, copper(I) and palladium(II) can be reduced by ethylene glycol at ca. 200°C to produce the dispersions of Cu/Pd bimetallic nanoparticles,<sup>[20]</sup> which are surprisingly stable even

under air. The structure of Cu/Pd bimetallic nanoparticles is analyzed to be a random alloy (solid solution) on the basis of preliminary EXAFS measurements. The precise EXAFS analysis has recently concluded that the Cu/Pd bimetallic nanoparticles thus prepared have a heterobondphilic structure Fig. 11 rather than a random alloy structure.<sup>[15]</sup> The Cu/Pd bimetallic nanoparticles work as catalysts both for hydration of nitriles and hydrogenation of olefins, suggesting that both Cu and Pd atoms are located on the surface of the nanoparticles, because the Cu and Pd are generally known as active catalysts for the former and the latter reaction, respectively. Bimetallic nanoparticles with other combinations such as Cu/Pt, Ni/Pd, Ni/Pt, Fe/Pd, and Fe/Pt can be prepared by the same method.<sup>[21,22]</sup>

### Formation of Bimetallic Nanoparticles by Mixing Two Kinds of Monometallic Nanoparticles; Self-Organization of Metal Nanoparticles

Self-organization is one of the most important concepts in supramolecular science. In the formation of bimetallic nanoparticles from two kinds of metal atoms, the bimetallic structures, such as a core/shell, random alloy, and heterobondphilic structure, are controlled by self-organization in practice.

Another type of self-organization has recently been observed to produce pseudo-core/shell structured bimetallic nanoparticles by mixing two kinds of monometallic nanoparticles in solution.<sup>[23]</sup> Mixing of colloidal dispersions of PVP-protected Ag nanoparticles with those of PVP-protected Rh nanoparticles in solution at room temperature was found to result in a kind of “fusion” to produce colloidal dispersions of Ag/Rh bimetallic nanoparticles with a pseudo-core/shell structure in a few hours Fig. 12. Poly(*N*-vinyl-2-pyrrolidone) is suggested to play an important role for this self-organization. However, the driving force

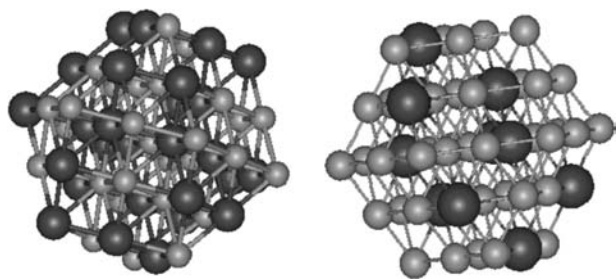


**Fig. 11** Model structures for Cu/Pd 1:1 (left panel) and Cu/Pd 4:1 (right panel) bimetallic nanoparticles. Big dark balls correspond to Pd. *Source:* From Ref.<sup>[15]</sup>.

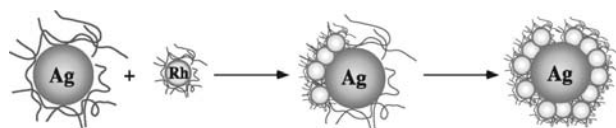


**Fig. 12** Formation of pseudo-Ag-core/Rh-shell-structured bimetallic nanoparticles. *Source:* From Ref.<sup>[23]</sup>.

as well as the conditions for this self-organization is not well understood yet.

Nevertheless, Pd/Ag/Rh and Pt/Pd/Rh trimetallic nanoparticles with a triple core/shell structure have recently been successfully prepared by this method.

## CATALYSES OF METAL NANOPARTICLES

Metal nanoparticles are used as catalysts for various kinds of reactions in dispersions or on supports, which are summarized here. Metal nanoparticles stabilized by weakly coordinating polymers are considered to be an effective catalyst, which works as shown in Fig. 8. As for polymer-protected metal nanoparticle catalysts, the catalytic performance, i.e., activity and selectivity, is affected not only by the structures of metal nanoparticles but also by those of the surrounding polymers.

## Reduction

Hydrogenation of C–C multiple bonds is catalyzed by many kinds of precious metal nanoparticles. The

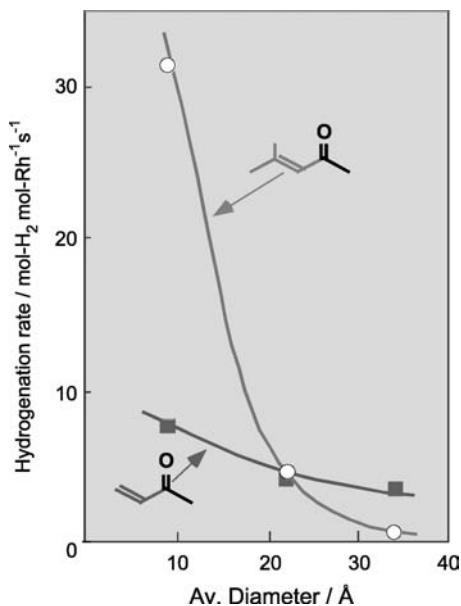
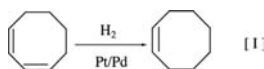


**Fig. 13** Size effect of catalytic activity of PVP-protected Rh nanoparticle catalysts for hydrogenation of internal and vinyl olefins. *Source:* From *Shokubai* **1985**, 27, 488.

activity depends not only on the kind of metal element but also on the size and shape of metal nanoparticles. One of the most significant examples of the size effect is shown for hydrogenation of internal olefins catalyzed by PVP-protected Rh nanoparticle catalysts prepared by an alcohol reduction method Fig. 13.<sup>[1]</sup>

In bimetallic nanometal catalysts, the activity depends on the composition and structure of bimetallic nanoparticles.<sup>[3]</sup> For example, PVP-protected Pd/Pt bimetallic nanoparticles with a core/shell structure show the highest catalytic activity for partial hydrogenation of 1,3-cyclooctadiene to cyclooctene Formula I at a 4:1 atomic ratio of Pd to Pt Fig. 14, in which the Pt core is covered by an atomic layer of Pd.<sup>[16]</sup> This means that the catalytic active site of the metal nanoparticles is located on the surface Pd atoms and that the Pt core adjacent to the Pd has an electronic effect on the surface Pd atoms. In other words, the additional Pt atoms do not have an ensemble effect, but a ligand effect, on the active Pd sites.



The catalytic selectivity of metal nanoparticles can sometimes be controlled by their sizes and shapes. The selectivity of partial hydrogenation of cyclopentadiene catalyzed by PPV-protected Pd nanoparticles rapidly increases when the diameter of Pd nanoparticles is below 2 nm.<sup>[1]</sup>

The selectivity is more often controlled by the organic layer surrounding metal nanoparticles. 10-Undecenoic

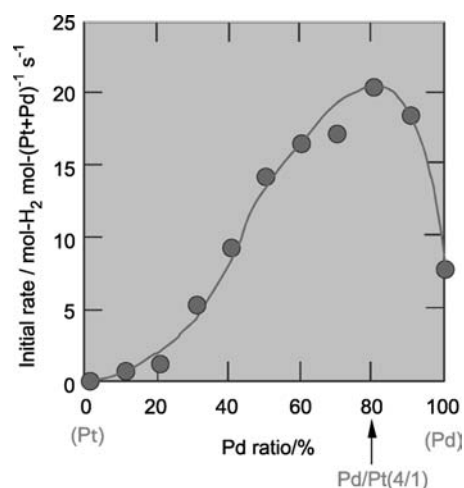


**Fig. 14** Dependence of the catalytic activity of PVP-protected Pd/Pt bimetallic nanoparticles for partial hydrogenation of cyclooctadiene to cyclooctene upon the composition of the nanoparticles. *Source:* From *J. Chem. Soc. Faraday Trans.* **1993**, 89, 2537.

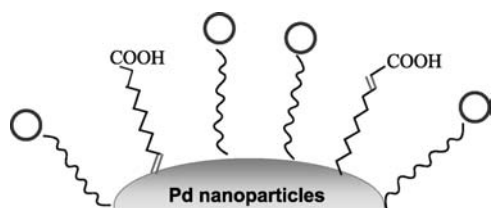
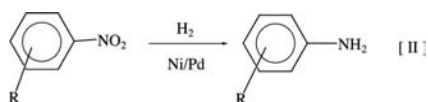


**Fig. 15** Schematic illustration of selectivity control of surfactant-protected Pd nanoparticle catalysts for hydrogenation of 2- and 10-undecenoic acid. *Source:* From Ref.<sup>[24]</sup>.

acid is much more easily hydrogenated than 2-undecenoic acid when catalyzed by Pd nanoparticles stabilized by nonionic surfactant molecules.<sup>[24]</sup> This selectivity control is shown in Fig. 15. Polycyclodextrin-covered metal nanoparticles are also effective catalysts for the reaction with high substrate selectivity because the cyclodextrin cavity can recognize the substrate molecule.

Enantioselective hydrogenation can be achieved by using metal nanoparticles capped by chiral stabilizers such as cinchonidine and dihydrocinchoxidine in dispersions and on inorganic supports.<sup>[25]</sup>

The reduction of C=O bond was reported to be catalyzed by Rh nanoparticles. The reduction of nitrobenzene to aniline by hydrogen at room temperature Formula II was catalyzed by PVP-protected Ni/Pd bimetallic nanoparticles, prepared by glycol reduction at 190°C. In nitrobenzene, the atomic ratio Ni/Pd = 1:4 gave the most active catalyst, while in the other substituted nitrobenzene, the ratio was 2:3.



### Visible-Light-Induced Hydrogen Generation

Because metal nanoparticles in dispersions are transparent to visible light, their application to catalyses for photochemical reactions is preferred over conventional solid catalysts. Colloidal dispersions of Pt nanoparticles in water was used for visible-light-induced hydrogen generation in the system of metal nanoparticles/methyl viologen (electron mediator)/trisbipyridineruthenium(II) dichloride (photosensitizer)/ethylenediaminetetraacetic acid disodium salt (electron donor) Formula III.

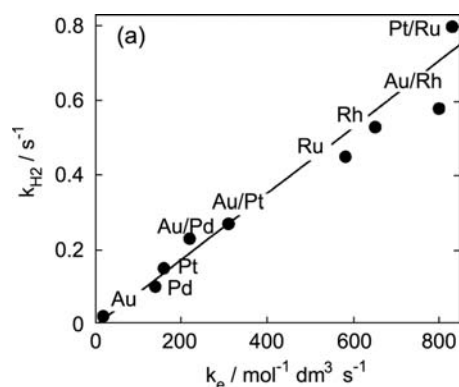
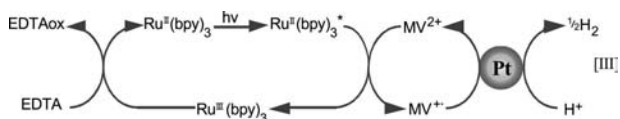


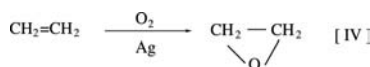
**Fig. 16** Relationship between hydrogen generation rate and electron transfer rate over various kinds of metal nanoparticle catalysts. *Source:* From Ref.<sup>[26]</sup>.

Various kinds of bimetallic nanoparticles were recently examined as catalysts of the above reaction. It was found that the hydrogen generation rate is proportional to the rate of electron transfer from methyl viologen cation radical to the metal nanoparticles as shown in Fig. 16, and that the bimetallic nanoparticles are more active as a catalyst than the corresponding monometallic nanoparticles.<sup>[26]</sup>

### Oxidation

Oxidation is one of the most general chemical reactions and is often applied to industrial processes. Nevertheless, there are few reports on the application of metal nanoparticle catalysts for oxidation reactions. This is because organic stabilizers are easily oxidized, resulting in their decomposition. Hence development of the stabilizers strong against oxidation is very important.

Oxidation of ethylene to ethylene oxide by molecular oxygen Formula IV is catalyzed by Ag nanoparticles stabilized by poly(sodium acrylate). The reaction proceeds under the pressure of ethylene and oxygen at 170°C.<sup>[27]</sup>



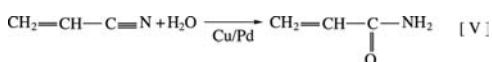
Catalytic oxidation is enhanced by the presence of Cs(I) and Re(VII) ions, which are immobilized on the stabilizer poly(acrylate). The catalytic activity of Ag nanoparticles depends on the protecting polymer. Polyacrylate-protected Ag nanoparticles have much higher activity than PVP-protected ones especially at high temperature. This is probably because of the stronger coordinations of polyacrylate to Ag nanoparticles.

Other examples include oxidation of cyclooctane to cyclooctanone and cyclooctanone by *t*-butyl hydroperoxide (*t*-BHP) catalyzed by Ru nanoparticles in a

biphasic system, and oxidation of D-glucose to D-gluconate by molecular oxygen catalyzed by tetraalkylammonium-stabilized Pd/Pt bimetallic nanoparticles on charcoal.<sup>[28]</sup>

## Hydration

Selective hydration of acrylonitrile, which is catalyzed by copper catalysts, is used for industrial production of acrylamide. The same reaction can proceed by using Cu nanoparticles as catalysts. The colloidal dispersions of PVP-protected Cu nanoparticles were prepared by NaBH<sub>4</sub> reduction of Cu(II) ions and applied to the catalyst for this reaction.<sup>[1]</sup> However, Cu nanoparticles are easily oxidized by the contaminant air and are not stable enough to be repeatedly used. To stabilize Cu nanoparticles, Cu/Pd bimetallic nanoparticles were prepared by coreduction of Cu and Pd ions by glycol at 190°C in the presence of PVP.<sup>[20]</sup> The bimetallic nanoparticles are more stable, and much more active as the catalyst for hydration of acrylonitrile to acrylamide Formula V than the simple Cu monometallic nanoparticles.



## C–C Bond Formation

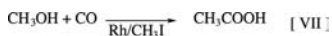
The C–C bond formation is a useful reaction in organic syntheses and is often catalyzed by homogeneous catalysts of organometallic complexes. Metal nanoparticles have recently been used instead of organometallic complexes as catalysts for C–C bond formation. Because these reactions are catalyzed by ionic species of precious metals in homogeneous catalysts, real active species of these metal nanoparticle catalysts are often considered to be the ionic species produced by oxidation of metal nanoparticles. Further research is required to understand the real reaction mechanism.

Heck reaction, the coupling between aromatic and vinyl carbons Formula VI, was found to be catalyzed by Pd nanoparticles in the presence of base at a rather high temperature.<sup>[29,30]</sup>



Because the reaction requires a rather high temperature, enough stable polymers are preferred as the stabilizer for the metal nanoparticles used as catalysts.

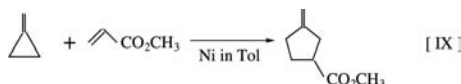
Carbonylation of methanol to directly produce acetic acid Formula VII is catalyzed by a homogeneous Rh catalyst. Poly(*N*-vinyl-2-pyrrolidone)-protected Rh nanoparticles were used as the catalyst of this reaction at 140°C under CO pressure.



Suzuki reaction, which is useful for direct coupling of two different benzene rings Formula VIII, were catalyzed by Pd and Pd/Ni nanoparticles.<sup>[31]</sup> The stability of the PVP-protected Pd nanoparticles was investigated as well.<sup>[32]</sup>



[3 + 2] Cycloaddition reaction between methylene-cyclopropane and methyl acrylate in reflux toluene Formula IX was catalyzed by Ni nanoparticles immobilized on alumina.<sup>[33]</sup>



In these C–C coupling reactions, the catalytic activity of metal nanoparticles is less than the corresponding homogeneous organometallic catalysts. However, metal nanoparticle catalysts have an advantage for repeated usage. For the practical use of metal nanoparticles as catalysts, further investigations of stable protective polymers and of immobilization on inorganic supports as well as of the reaction mechanism will be required.

## CONCLUSION

Catalysts based on metal nanoparticles have recently received much attention because investigations in the field of metal nanoparticles has rapidly developed. Now many techniques have been reported to control the structures of metal nanoparticles, not only the structures of metal parts but also the structure of organic layers surrounding them. By using these techniques, metal nanoparticles can be constructed according to the design.

Metal nanoparticles can be used as catalysts not only in dispersions but also on solid supports. In dispersions, metal nanoparticles can be used as catalysts only for reactions in a solution, while on solid supports they can be used both in solution and in gaseous phase. Thus metal nanoparticles are now applied to catalysts for various kinds of reactions. The number of the reactions for which metal nanoparticles are used as catalysts is going to rapidly increase. In the field of environmental

catalysts, which are the largest in the market of catalysts, conventional catalysts may be replaced by metal nanoparticles designed for this purpose.

## REFERENCES

- Hirai, H.; Toshima, N. Polymer-attached catalysis. In *Tailored Metal Catalysts*; Iwasawa, Y., Ed.; D. Reidel Pub. Co.: Dordrecht, 1975; 87–140.
- Schimid, G.; Ed. *Clusters and Colloids. From Theory to Application*; VCH: Weinheim, 1994.
- Toshima, N.; Yonezawa, T. Bimetallic nanoparticles—novel materials for chemical and physical application. *New J. Chem.* **1998**, *22*, 1179–1201.
- Toshima, N.; Shiraishi, Y. Catalysis by metallic colloids. In *Encyclopedia of Surface and Colloid Science*; Hubbard, A.T., Ed.; Marcel Dekker: New York, 2002; 879–886.
- Roucoux, A.; Schulz, J.; Patin, H. Reduced transition metal colloids: a novel family of reusable catalysts? *Chem. Rev.* **2002**, *102*, 3757–3778.
- Teranishi, T.; Toshima, N. Preparation, characterization, and properties of bimetallic nanoparticles. In *Catalysis and Electrocatalysis at Nanoparticles Surfaces*; Wieckowski, A., Sarinova, E.R., Vayenas, C.G., Eds.; Marcel Dekker: New York, 2003; 379–407.
- Toshima, N. Metal Nanoparticles for catalysis. In *Nanoscale Materials*; Liz-Marzán, L.M., Kamat, P.V., Eds.; Kluwer Academic Pub.: Boston, 2003; 79–96.
- Moreno-Nañas, M.; Pleixats, R. Formation of carbon-carbon bonds under catalysis by transition-metal nanoparticles. *Acc. Chem. Res.* **2003**, *36* (8), 638–643.
- Kobayashi, S.-I.; Goto, H.; Katsumoto, S. Kubo effects in small particles of metals. In *Mesoscopic Materials and Clusters*; Arai, T., Ed.; Springer: Berlin, 1999; 113–122.
- Yonezawa, T.; Tominaga, T.; Toshima, N. Novel characterization of the structure of surfactants on nanoscopic metal clusters by a physico-chemical method. *Langmuir* **1995**, *11*, 4601–4606.
- Hirai, H.; Yakura, N. Protecting polymers in suspension of metal nanoparticles. *Polym. Adv. Technol.* **2001**, *12*, 724–733.
- Reetz, M.T.; Helbig; Quaiser, S.A.; Stimming, U.; Breuer, N.; Vogel, R. Visualization of surfactants on nanostructured palladium clusters by a combination of STM and high-resolution TEM. *Science* **1995**, *267*, 367–369.
- Hashimoto, T.; Saijo, K.; Harada, M.; Toshima, N. Small-angle X-ray scattering analysis of polymer-protected platinum, rhodium, and platinum/rhodium colloidal dispersions. *J. Chem. Phys.* **1998**, *109* (13), 5627–5638.
- Hirai, H.; Nakao, Y.; Toshima, N.; Adachi, K. Colloidal rhodium in polyvinyl alcohol as hydrogenation catalyst of olefins. *Chem. Lett.* **1976**, 905.
- Bian, C.-R.; Suzuki, S.; Asakura, K.; Ping, L.; Toshima, N. EXAFS studies on the structure of the PVP-stabilized Cu/Pd nanoclusters colloiddally dispersed in solution. *J. Phys. Chem., B* **2002**, *106* (34), 8587–8598.
- Toshima, N.; Harada, M.; Yonezawa, T.; Kushihashi, K.; Asakura, K. Structural analysis of polymer-protected Pd–Pt bimetallic clusters as dispersed catalysts by using extended X-ray absorption fine structure spectroscopy. *J. Phys. Chem.* **1991**, *95*, 7448–7453.
- Toshima, N.; Harada, M.; Yamazaki, Y.; Asakura, K. Catalytic activity and structural analysis of polymer-protected Au–Pd bimetallic clusters prepared by the simultaneous reduction of HAuCl<sub>4</sub> and PdCl<sub>2</sub>. *J. Phys. Chem.* **1992**, *96*, 9927–9933.
- Yonezawa, T.; Toshima, N. Mechanistic consideration of formation of polymer-protected nanoscopic bimetallic clusters. *J. Chem. Soc., Faraday Trans.* **1995**, *91*, 4111–4119.
- Wang, Y.; Toshima, N. Preparation of Pd–Pt bimetallic colloids with controllable core/shell structures. *J. Phys. Chem., B* **1997**, *101*, 5301–5306.
- Toshima, N.; Wang, Y. Preparation and catalysis of novel colloidal dispersions of copper/noble metal bimetallic clusters. *Langmuir* **1994**, *10*, 4574–4580.
- Lu, P.; Teranishi, T.; Asakura, K.; Miyake, M.; Toshima, N. Polymer-protected Ni/Pd bimetallic nano-clusters; preparation, characterization and catalysis for hydrogenation of nitrobenzene. *J. Phys. Chem., B* **1999**, *103* (44), 9673–9682.
- Sun, S.; Murray, C.B.; Weller, D.; Folks, L.; Mosen, A. Monodisperse FePt nanoparticles and ferromagnetic FePt nanocrystal superlattices. *Science* **2000**, *287*, 1989–1992.
- Hirakawa, K.; Toshima, N. Ag/Rh bimetallic nanoparticles formed by self-assembly form Ag and Rh monometallic nanoparticles in solution. *Chem. Lett.* **2003**, *32* (1), 78–79.
- Toshima, N.; Takahashi, T. Colloidal dispersion of platinum and palladium cluster embedded in micelles. Preparation and application to catalysis for hydrogenation of olefins. *Bull. Chem. Soc. Jpn.* **1992**, *65*, 400–409.
- Bönnemann, H.; Braun, G.A. Enantioselective hydrogenations on platinum colloids. *Angew. Chem., Int. Ed. Engl.* **1996**, *35*, 1992–1995.
- Toshima, N.; Hirakawa, K. Polymer-protected bimetallic nanocluster catalysts having core/shell structure for accelerated electron transfer in visible-light-induced hydrogen generation. *Polym. J.* **1999**, *31* (11-2), 1127–1192.
- Shiraishi, Y.; Toshima, N. Oxidation of ethylene catalysed by colloidal dispersions of poly(sodium acrylate)-protected silver nanoclusters. *Colloids Surf., A* **2000**, *169* (1–3), 59–66.

28. Bönnehan, H.; Brojoux, W.; Tilling, A.S.; Siepen, K. Application of heterogeneous colloid catalysts for the preparation of fine chemicals. *Top. Catal.* **1998**, *4* (3,4), 217–227.
29. Beller, M.; Fischer, H.; Kuehlein, K.; Reisinger, C.P.; Herrmann, W.A. First palladium-catalyzed Heck reactions with efficient colloidal catalysts systems. *J. Organomet. Chem.* **1996**, *520* (1–2), 257–259.
30. Reetz, M.T.; Lohmer, G. Propylene carbonate stabilized nanostructured palladium clusters as catalysts in Heck reactions. *Chem. Commun.* **1996**, (16), 1921–1922.
31. Reetz, M.T.; Breinbaner, R.; Wanninger, K. Suzuki and Heck reactions catalyzed by preformed palladium clusters and palladium/nickel bimetallic clusters. *Tetrahedron Lett.* **1996**, *37* (27), 4499–4502.
32. Narayaman, R.; El-Sayed, M.A. Effect of catalysis on the stability of metallic nanoparticles; Suzuki reaction catalyzed by PVP–palladium nanoparticles. *J. Am. Chem. Soc.* **2003**, *125* (27), 8340–8347.
33. Reetz, M.T.; Breinbauer, R.; Wedemann, P.; Binger, P. Nanostructured nickel-clusters as catalysts in [3 + 2] cycloaddition reactions. *Tetrahedron* **1998**, *34* (7), 1233–1240.



# Metal Nanoparticle Ensembles: Collective Optical Properties

Alexander Wei

Department of Chemistry, Purdue University,  
West Lafayette, Indiana, U.S.A.

## INTRODUCTION

Ensembles of gold and silver nanoparticles in the 10- to 100-nm size range exhibit collective electromagnetic properties, which can be tuned according to particle size and interparticle spacing. Self-assembly is a critical enabling mechanism for organizing nanoparticles into ensembles with well-defined lattice structures or geometries, if particle dispersion forces can be adequately controlled. Presented here are several recent theoretical and experimental studies on metal nanoparticle assemblies with novel and technologically appealing optical properties. For example, gold nanoparticles with intense plasmon resonances can be organized into planar arrays or spherical ensembles around dielectric cores, and serve as substrates for surface-enhanced Raman scattering (SERS). Recent theoretical developments indicate that the electromagnetic field factors responsible for such enhancements can be further tuned by adjusting the diameter-spacing ratio, enabling the optimization of metal nanoparticle ensembles for various applications in sensing and nanophotonics.

## SURFACE PLASMONS

Gold and silver nanostructures are well known to exhibit electrodynamic phenomena commonly referred to as surface plasmons (see entry on “Surface Plasmon Spectra of Gold and Silver Nanoparticles”). These are generated by the collective excitation of free electrons in the metal particle, in response to a characteristic electromagnetic frequency. The surface plasmon modes of metal nanostructures have essentially the same function as radio antennas, except that they resonate in the optical and near-infrared (NIR) regions of the electromagnetic spectrum. Surface plasmons can be categorized into two types: localized plasmon resonances, in which incident light is absorbed or scattered by the oscillating electric dipoles within a metal nanoparticle, and surface plasmon polaritons, which propagate along metal surfaces in a waveguide-like fashion until released at some distance from their point of origin (Fig. 1). Localized plasmon resonances generate

electromagnetic field factors, which enhance linear and nonlinear optical effects near the metal surface. The localized plasmonic responses of individual metal nanoparticles are now quite well understood and have been summarized in several recent works.<sup>[1–3]</sup> On the other hand, metal nanoparticle ensembles can support both localized and propagating surface plasmon modes, whose physical relationships are less well defined. Regardless of the complexity of these phenomena, the plasmonic coupling of metal nanostructures with light enhances a broad range of useful optical phenomena, such as resonant light scattering (RLS), surface plasmon resonance (SPR), and SERS, all of which have tremendous potential for ultrasensitive chemical and biomolecular detection and analysis.

The plasmonic responses of coupled metal nanostructures are capable of intensifying local electromagnetic fields by many orders of magnitude. For example, many of the early SERS observations in the late 1970s and early 1980s were performed using kinetically formed aggregates of Ag and Au nanoparticles.<sup>[4]</sup> Interest in SERS has been further stoked by reports of single-molecule SERS spectroscopy,<sup>[5–7]</sup> however, the reproducibility of such activities has been poor. Despite strong evidence that aggregated nanoparticles can generate “hot spots” that produce enormous enhancements in Raman intensities, these vary widely from sample to sample and often disappear after a few days’ aging. The conditions that enable reproducibly high SERS enhancements have yet to be established, and constitute an important challenge in nanomaterials synthesis.

## FABRICATION OF NANOPARTICLE ASSEMBLIES

In the last few years, significant progress has been made in the fabrication and optical characterization of metal nanoparticle assemblies in one, two, and three dimensions. Much of this work has been directed toward the self-assembly and materials properties of nanoparticle assemblies in which the unit particle size is below 10 nm (radius  $R < 5$  nm); these have been



**Fig. 1** Incident light on nanostructured metal surfaces can result in localized (standing) plasmon resonances (A), propagation of surface plasmon waves (B), or a combination of the two (C). Excitation of conduction electrons produces local electromagnetic fields (pink) near the metal surfaces.

reviewed elsewhere.<sup>[8–10]</sup> More recently, several investigations have focused on metal nanoparticle assemblies with unit structures in the 10- to 100-nm range, the central theme of this entry. Both theoretical considerations and experimental investigations of discrete clusters and extended arrays of these midnanometer-sized nanoparticles will be discussed. It will become evident that in addition to particle size, structural parameters such as interparticle distance, lattice geometry, and periodic order also have important roles in the collective optical responses of these ensembles.

### Discrete Clusters of Metal Nanoparticles

Plasmon-resonant nanoparticles can experience significant dipolar coupling when their interparticle separation  $\delta$  is on the order of diameter  $2R$  or less where  $R$  is nanoparticle radius, giving rise to additional plasmon modes. Effective-medium theories such as the Maxwell–Garnett formula, which can accurately describe the plasmon resonance of isolated metal particles below 30 nm, can provide only a limited approximation of the optical responses by coupled nanoparticles.<sup>[11]</sup> These approximations lose their accuracy if  $\delta$  is much less than one particle diameter ( $\delta < 1.5R$ ), at which point evanescent (near-field) coupling becomes significant.

Simulations of discrete  $N$ -particle systems based on generalized Mie theory<sup>[1,12]</sup> or numerical approaches such as discrete dipole approximation<sup>[13,14]</sup> appear to provide more consistent models of coupled metal nanoparticles. These have been used to predict the extinction and absorption cross sections of specific aggregate structures, such as chained particles in linear or bent conformations (Fig. 2). Linear chains of Ag nanoparticles produce longitudinal plasmon resonances at strongly redshifted wavelengths, whereas close-packed aggregates exhibit less pronounced shifts in their collective plasmon resonance frequencies. The optical responses of these  $N$ -particle clusters in fact correlate closely with anisotropic metal particles of similar overall shape, such as nanorods<sup>[15,16]</sup> and nanoprisms.<sup>[13,14,17]</sup>

More recent theoretical treatments have given emphasis to the local electromagnetic fields generated near the metal nanoparticle surfaces, with the objective

of defining regions with the highest field factors (often quantified as a function of  $|E/E_0|$  where  $E$  and  $E_0$  are the plasmon-enhanced and incident electric field intensities) for a given frequency  $\omega$ . This is especially important for surface-enhanced spectroscopies such as SERS, in which signals are amplified as a function of  $G_{\text{EM}} = |E(\omega)/E_0(\omega)|^2 \cdot |E(\omega')/E_0(\omega')|^2$ , where  $G_{\text{EM}}$  is the local Raman enhancement factor and  $\omega$  and  $\omega'$  are the incident and Stokes-shifted frequencies, respectively.<sup>[18]</sup> In the simplest case of a two-sphere system, it is widely agreed that local field factors are greatest when the two particles are almost touching. Xu and coworkers have performed electrodynamic calculations on pairs of Au and Ag particles (10–90 nm) separated by as little as 1 nm, and suggested  $G_{\text{EM}}$  values more than  $10^{11}$  for the best cases.<sup>[19]</sup> These localized enhancements are exquisitely sensitive to interparticle spacing; changes in  $\delta$  by just a few nanometers can cause the local enhancements to drop by several orders of magnitude (Fig. 3). These calculations, in conjunction with experimental studies by the same group,<sup>[7,20]</sup> imply that nanoparticle dimers have potential as substrates for routine single-molecule SERS, given a reliable method for localizing analytes in regions of high field.

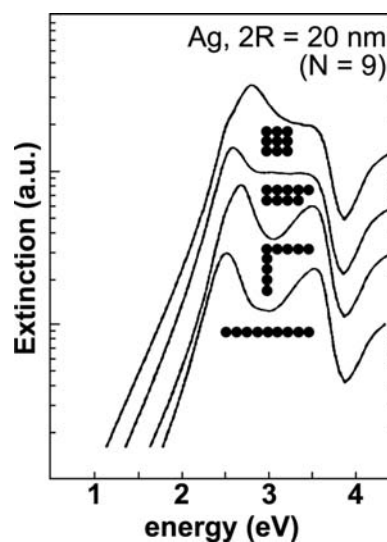


**Fig. 2.** Extinction spectra of 20-nm Ag particle aggregates in different geometries, as calculated by generalized Mie theory. *Source:* Adapted from Ref.<sup>[1]</sup>

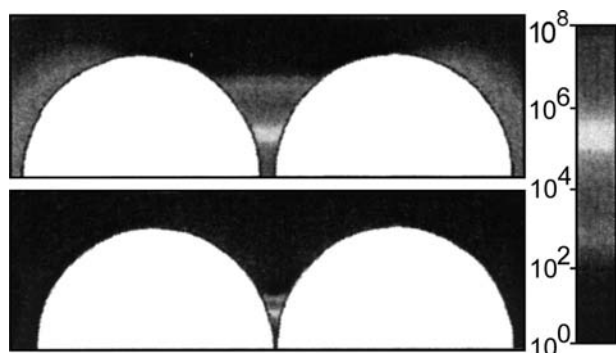


**Fig. 3** Electrodynamic simulation of local field enhancements ( $G_{EM}$ ) between two 90-nm Ag particles at interparticle separations of  $\delta = 5.5$  and 1.0 nm. *Source:* From Ref.<sup>[19]</sup>.

### Linear Arrays of Metal Nanoparticles

Linear (1-D) arrays of metal nanoparticles have attracted much interest for their potential to transport energy in an antenna-like fashion and serve as near-field optical waveguides at subwavelength dimensions, with the possibility of integrating nanophotonics with far-field optical devices.<sup>[21]</sup> Theoretical calculations of vectorial energy transport through chains of closely spaced 50-nm Au nanospheres suggest remarkably high levels of transmission at optical resonance, with optimized losses ranging between 10 and 25 dB per micron (Fig. 4).<sup>[22,23]</sup> Several methods for producing nanoparticle 1-D arrays have been reported, including self-assembly on prepatterned surfaces<sup>[24]</sup> and inside of nanoporous templates<sup>[25,26]</sup> as well as by directed assembly using scanning probe microscopy tips.<sup>[21]</sup>

Recent experimental studies on plasmonic 1-D nanoarrays have so far been promising. Proof of concept was established by Krenn and coworkers, who used photon scanning tunneling microscopy to image near-field excitations within Au nanoparticle chains.<sup>[27]</sup> Near-field optical transport in linear arrays of Au nanoparticles and Ag nanorods was also recently demonstrated by Maier et al.<sup>[23,28]</sup> The latter case was shown to support plasmon propagation with losses as

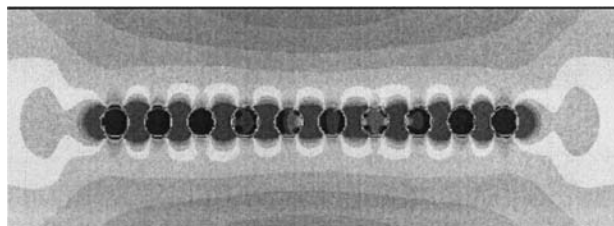


**Fig. 4** Finite-difference time-domain simulation of electric fields (red) localized within a linear array of 50-nm Au particles (blue), with interparticle separations of  $\delta = 75$  nm. *Source:* From Ref.<sup>[23]</sup>.

low as 6 dB per 200 nm, which suggests their feasible integration into all-photonic device architectures.

### Two-Dimensional Arrays of Metal Nanoparticles

Several methods have been employed for arranging metal nanoparticles into periodic and aperiodic two-dimensional (2-D) lattices. Periodically ordered 2-D arrays with relatively large interparticle spacings ( $D/2R = 1.5$  to 5, where center-to-center distance  $D = 2R + \delta$ ) have been fabricated by electron-beam lithography<sup>[29,30]</sup> or by self-assembly on lithographically defined surfaces<sup>[24]</sup> (for some recent examples see Refs. <sup>[31,32]</sup>). Aperiodic 2-D arrays of the same genre have also been produced by self-assembly techniques, mostly by random sequential adsorption onto charged surfaces.<sup>[33–37]</sup> For these cases, the collective optical properties of nanoparticles are dominated by dipolar coupling mechanisms; however, their responses are more complex than predicted by classical dipole–dipole interactions, whose strength varies with  $1/D^3$ . Particles larger than 30 nm can exhibit sizable retardation effects in their dipolar interactions, and this can impact both the wavelength and decay time of their coupled plasmon resonances.<sup>[29,38]</sup> For example, Chumanov et al. observed a remarkable blueshifting and narrowing of extinction maxima in submonolayer films of 100-nm Ag particles as a function of packing density.<sup>[33]</sup> This was later reproduced in lithographically defined Ag nanoparticle 2-D arrays, and reexamined as a function of particle diameter–spacing ratio.<sup>[37]</sup> Recent theoretical analyses by Zhao and coworkers suggest that the blueshifting and narrowing are largely due to radiative dipolar coupling, an electrodynamic term that scales largely with  $1/D$ .<sup>[39]</sup>

Aperiodic 2-D arrays may also provide a practical and straightforward method for preparing SERS substrates.<sup>[34–36]</sup> Submonolayer ensembles of colloidal metal particles can be prepared with packing densities of up to 30% (Fig. 5, left), which is well below the close-packing limit ( $\sim 90\%$ ) but sufficient to produce significant electromagnetic coupling and SERS.<sup>[34–36,40]</sup> Electrostatic self-assembly of Au nanoparticles on spherical submicron particles has also been reported recently;<sup>[41]</sup> in this case, packing densities on the order of 50% can be achieved by increasing the nanoparticles' surface potentials, with a concomitant enhancement in electromagnetic coupling (Fig. 5, right).

2-D nanoparticle arrays with much smaller interparticle spacings ( $D/2R < 1.1$ ) are likely to support strong near-field coupling as well as dipolar coupling, and should be excellent substrates for generating SERS and other surface-enhanced spectroscopies. In principle, such nanoparticle ensembles should also be

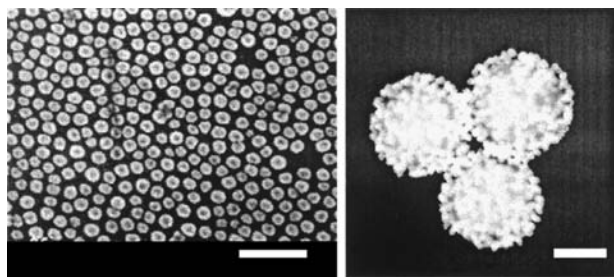


**Fig. 5.** Left: planar ensemble of 40-nm Au particles adsorbed onto thiol-functionalized SiO<sub>2</sub>. *Source:* From Ref.<sup>[40]</sup>. © 1995, American Chemical Society. Right: spherical core-shell ensembles of 30-nm particles adsorbed onto amine-functionalized 390-nm SiO<sub>2</sub> particles. *Source:* From Ref.<sup>[41]</sup>. Scale bar = 200 nm in both images.

accessible by thermodynamic self-assembly; however, metal particles in the midnanometer size range experience strong interaction potentials that can promote kinetic aggregation, resulting in poorly defined structures. This can be viewed as a problem in dispersion control: If repulsive interactions can offset particle self-attraction at close range, conditions for thermodynamically controlled self-organization can be achieved. Earlier demonstrations by Schmid et al.<sup>[42]</sup> and by Giersig and Mulvaney<sup>[43,44]</sup> have indicated that colloidal Au particles can be organized into close-packed domains with local 2-D order.

A general method for organizing metal nanoparticles into hexagonal close-packed 2-D arrays has recently been developed by Wei and coworkers, using multivalent macrocyclic surfactants known as resorcinarenes.<sup>[45,46]</sup> These compounds are capable of extracting colloidal Au particles from aqueous suspensions and dispersing them into organic solvents or at air-water interfaces.<sup>[47]</sup> In the latter case, resorcinarene-stabilized nanoparticles as large as 170 nm have been organized into 2-D arrays with excellent local order (Fig. 6). Here the  $D/2R$  ratios are well below 1.1; careful inspection of the TEM images reveals an inverse correlation between array periodicity and interparticle spacing  $\delta$ , most likely due to greater van der Waals attraction with unit particle size.

The periodic 2-D nanoparticle arrays exhibit size-dependent optical properties at visible and NIR

wavelengths. The gold nanoparticle films vary in hue from blue ( $2R = 16$  nm) to a faint gray ( $2R > 70$  nm), the latter being strongly absorptive in the NIR region (Fig. 7). The specular reflectance is also dependent on periodic structure, with maximum reflectance of white light observed for  $2R$  between 40 and 70 nm.<sup>[48]</sup> These variable reflectivities can be attributed to several effects: 1) an angular dependency in attenuated reflection as a function of surface roughness, a well-studied phenomenon in metallic thin films;<sup>[49]</sup> 2) size-dependent optical absorption, with significant absorptivities in the visible region for nanoparticle arrays with periodicities below 40 nm; and 3) size-dependent increases in Mie scattering, a phenomenon that has been characterized for nanoparticles and nanostructured metal surfaces with roughnesses on the order of 40 nm or more.<sup>[1,2,49]</sup>

The 2-D nanoparticle arrays also exhibit size-dependent SERS activities, with excellent levels of signal enhancement in many cases.<sup>[50]</sup> Surface-averaged Raman signals generated from the adsorbed resorcinarenes could be optimized as a function of periodicity and excitation wavelength, with enhancements as high as  $10^7$ . The observed trends are in accord with previous theoretical calculations describing electromagnetic SERS,<sup>[51–54]</sup> and also with SERS studies on disordered metal colloid aggregates.<sup>[55–57]</sup> However, the resorcinarene-stabilized nanoparticle arrays have considerable advantages in reproducibility and stability, and retain essentially all SERS activity more than a year after self-assembly. Additional signal enhancement could be obtained by increasing the solid angle of incidence and collection; the angle-dependent Raman intensities suggest that propagating surface plasmons in the Au nanoparticle films contribute significantly to the SERS effect.

The colloidal Au nanoparticle arrays are capable of detecting exogenous analytes by SERS and thus have potential as spectroscopic chemical sensors.<sup>[50]</sup> Volatile organic compounds adsorbed onto the array surface produce a detectable signal within seconds; removal of the surfactant layer by plasma treatment further increases the arrays' sensitivities and enables the reproducible detection of analytes in aqueous solutions at micromolar concentrations.<sup>[58]</sup> However, recent

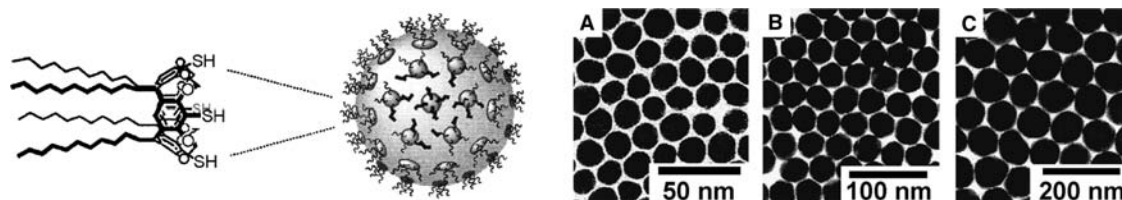


**Fig. 6** Self-organized 2-D arrays of resorcinarene-encapsulated Au nanoparticles. Unit particle sizes: (A) 16 nm; (B) 34 nm; (C) 87 nm. *Source:* From Ref.<sup>[45]</sup>. © 2001, American Chemical Society.



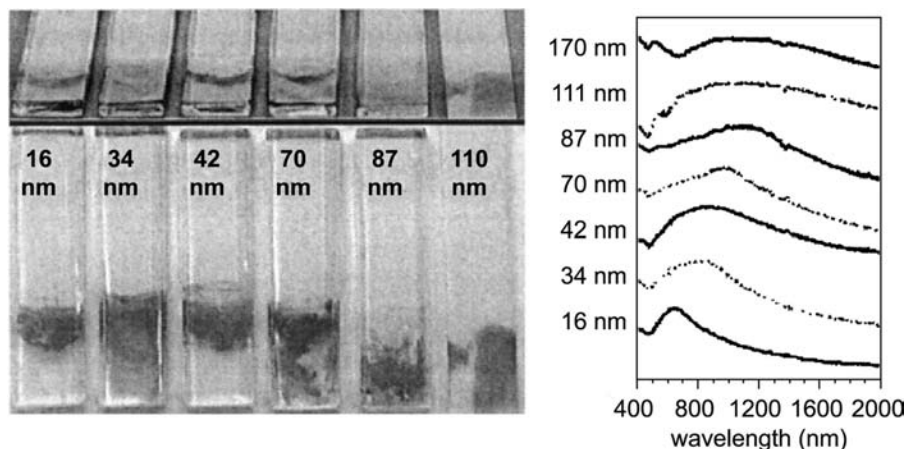


**Fig. 7** Size-dependent optical properties of Au nanoparticle arrays. *Source:* From Refs.<sup>[45,48]</sup>. Left: 2-D nanoparticle arrays transferred onto annealed quartz substrates, as viewed directly (bottom) and with specular reflectance (top,  $\theta_i = 60^\circ$ ). Substrates are approximately 1 cm wide. *Source:* Reproduced by permission of the Materials Research Society. Right: extinction spectra of 2-D nanoparticle arrays. *Source:* © 2001, American Chemical Society.

theoretical calculations indicate that detection limits can be further lowered by adjusting the interparticle spacing. An incremental change in  $\delta$  delocalizes field intensities but at the same time increases the available sampling space for analyte detection. Recent calculations by Genov et al. indicate that the surface-averaged enhancement factor  $G_R$  (as opposed to the local factor  $G_{EM}$ ) from periodic nanoparticle arrays can be maximized as a function of excitation wavelength at a given value of  $2R/\delta$ , and can surpass that produced by disordered metal–dielectric films by several orders of magnitude (Fig. 8).<sup>[59]</sup>

### 3-D Superlattices of Metal and Metalodielectric Nanoparticles

In addition to enhancing spontaneous emission events such as SERS, metal nanoparticle superlattices may also be capable of blocking electromagnetic radiation at select frequencies, i.e., a photonic band gap. Highly monodisperse particles on the order of an optical wavelength are well known to crystallize into 3-D superlattices, and often produce opalescent Bragg reflections. Colloidal crystals may also exhibit photonic band gaps in the visible to NIR range, and have been highly sought after as a way to manipulate the

flow of light.<sup>[60]</sup> In principle, a photonic band gap can be engineered from nearly any type of material by periodically modulating its dielectric properties. However, lattices with relatively low dielectric contrast are not optimal materials for designing photonic band gaps at optical wavelengths. Periodic metal–dielectric nanostructures are capable of much stronger optical modulation; “inverse-opal” metal-coated colloidal crystals have recently been fabricated and have some promise as photonic band-gap materials.<sup>[61]</sup>

Theoretical studies by Moroz indicate that plasmonic colloidal crystals can support a complete photonic band gap in the visible and even the near-UV range.<sup>[62]</sup> Close-packed, face-centered cubic (FCC) crystals of colloidal Ag particles were calculated to possess tunable band gaps, at frequencies defined by the particle radius and plasma wavelength ( $R/\lambda_p$ ) and with relative gap widths between 5% and 10% as defined by  $(\Delta\omega/\omega_c)$ , the gap width to mid-gap frequency ratio. The photonic band gaps were predicted to be greatest for colloidal crystals with  $R/\lambda_p > 0.9$ ; for Ag, 3-D arrays of large, submicron-sized particles would be needed to produce band gaps for visible wavelengths.

A related study by Zhang et al. suggests that tunable photonic band gaps can also be made using metal-coated, core–shell nanoparticles as 3-D array elements.<sup>[63]</sup> The band gaps of these materials are

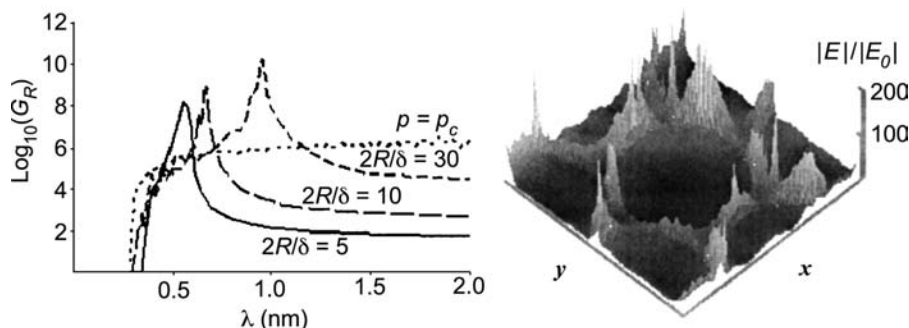


**Fig. 8** Left: numerical calculations of surface-averaged field enhancements ( $G_R$ ) from 2-D hexagonal superlattices, with diameter–spacing ratios of 5, 10 and 30, vs. a random metal–dielectric film at the percolation threshold ( $p = p_c$ ). *Source:* From Ref.<sup>[59]</sup>. © 2003, American Chemical Society. Right: local field distribution within a hexagonal lattice produced by  $p$ -polarized light ( $\lambda = 600$  nm,  $2R/\delta = 10$ ).

predicted to be less dependent on long-range order, a critical and challenging issue in the self-assembly of colloidal crystals. Photonic band gaps have been calculated for FCC lattices of SiO<sub>2</sub>/Ag core-shell nanoparticles of different sizes and packing densities: 500/50-nm core-shell particles at 45% packing density are expected to have a robust band gap centered at  $\lambda = 1.5 \mu\text{m}$ , whereas 160/50-nm core-shell particles at 42% packing density are expected to have a band gap across the visible spectrum. Graf and van Blaaderen have recently reported a closely related core-shell colloidal crystal, in which a second dielectric shell has been grown around the metal-coated nanoparticle.<sup>[64]</sup> The outermost SiO<sub>2</sub> shell reduces the van der Waals interactions considerably, and permits their self-organization into colloidal crystals with fractional densities close to that proposed by Zhang et al.<sup>[63]</sup>

## CONCLUSION

In closing, the controlled assembly of metal nanoparticles into well-defined structures can yield novel collective electromagnetic behavior, with excellent potential for function and application. Chemical and bioanalytical nanosensors have already reached a remarkably advanced stage of development, with detection and analysis bordering on the single-molecule limit, and the emerging area of nanophotonics may have long-term impact on telecommunications and device integration.

## ACKNOWLEDGMENTS

The author wishes to thank Beomseok Kim, Steven Tripp, and Bryce Sadtler for their valuable efforts toward the preparation and analysis of the planar and spherical Au nanoparticle arrays, and Dentcho Genov, Andrey Sarychev, and Vladimir Shalaev for related theoretical investigations. Financial support from the National Science Foundation, the National Institutes of Health, and Department of Defense are gratefully acknowledged.

## REFERENCES

- Kreibig, U.; Vollmer, M. *Optical Properties of Metal Clusters*; Springer: New York, 1995.
- Yguerabide, J.; Yguerabide, E.E. Light-scattering sub-microscopic particles as highly fluorescent analogs and their use as tracer labels in clinical and biological applications. I. Theory. *Anal. Biochem.* **1998**, *262*, 137–156.
- Wei, A. Plasmonic Nanomaterials: Enhanced Optical Properties from Metal Nanoparticles and their Ensembles. In *Nanoparticles: Building Blocks for Nanotechnology*; Rotello, V.M., Ed.; Kluwer Academic: New York, 2003; 173–200.
- Moskovits, M. Surface enhanced spectroscopy. *Rev. Mod. Phys.* **1985**, *57*, 783–826.
- Kneipp, K.; Wang, Y.; Kneipp, H.; Perelman, L.T.; Itzkan, I.; Dasari, R.R.; Feld, M.S. Single molecule detection using surface-enhanced Raman scattering. *Phys. Rev. Lett.* **1997**, *78*, 1667–1670.
- Nie, S.; Emory, S.R. Probing single molecules and single nanoparticles by surface-enhanced Raman scattering. *Science* **1997**, *275*, 1102–1106.
- Xu, H.X.; Bjerneld, E.J.; Käll, M.; Borjesson, L. Spectroscopy of single hemoglobin molecules by surface enhanced Raman scattering. *Phys. Rev. Lett.* **1999**, *83*, 4357–4360.
- Collier, C.P.; Vossmeier, T.; Heath, J.R. Nanocrystal superlattices. *Annu. Rev. Phys. Chem.* **1998**, *49*, 371–404.
- Shipway, A.N.; Katz, E.; Willner, I. Nanoparticle arrays on surfaces for electronic, optical, and sensor applications. *ChemPhysChem.* **2000**, *1*, 18–52.
- Pileni, M.P. Nanocrystal self-assemblies: Fabrication and collective properties. *J. Phys. Chem., B* **2001**, *105*, 3358–3371.
- Ung, T.; Liz-Marzan, L.M.; Mulvaney, P. Optical properties of thin films of Au@SiO<sub>2</sub> particles. *J. Phys. Chem., B* **2001**, *105*, 3441–3452.
- Quinten, M. Optical effects associated with aggregates of clusters. *J. Clust. Sci.* **1999**, *10*, 319–358.
- Jensen, T.; Kelly, L.; Lazarides, A.; Schatz, G.C. Electrodynamics of noble metal nanoparticles and nanoparticle clusters. *J. Clust. Sci.* **1999**, *10*, 295–317.
- Kelly, K.L.; Coronado, E.; Zhao, L.L.; Schatz, G.C. The optical properties of metal nanoparticles: The influence of size, shape, and dielectric environment. *J. Phys. Chem., B* **2003**, *107*, 668–677.
- van der Zande, B.; Böhmer, M.R.; Fokkink, L.G.J.; Schönenberger, C. Colloidal dispersions of gold rods: Synthesis and optical properties. *Langmuir* **2000**, *16*, 451–458.
- Link, S.; El-Sayed, M.A. Optical properties and ultrafast dynamics of metallic nanocrystals. *Annu. Rev. Phys. Chem.* **2003**, *54*, 331–366.
- Jensen, T.R.; Malinsky, M.D.; Haynes, C.L.; Van Duyne, R.P. Nanosphere lithography: Tunable localized surface plasmon resonance spectra of silver nanoparticles. *J. Phys. Chem., B* **2000**, *104*, 10549–10556.
- Weitz, D.A.; Garoff, S.; Gramila, T.J. Excitation spectra of surface-enhanced Raman scattering on silver-island films. *Opt. Lett.* **1982**, *7*, 168–170.
- Xu, H.; Aizpurua, J.; Käll, M.; Apell, P. Electromagnetic contributions to single-molecule sensitivity in surface-enhanced Raman scattering. *Phys. Rev., E* **2000**, *62*, 4318–4324.
- Xu, H.; Käll, M. Polarization-dependent surface-enhanced Raman scattering of isolated silver nanoaggregates. *ChemPhysChem.* **2003**, *4*, 1001–1005.



21. Maier, S.A.; Brongersma, M.L.; Kik, P.G.; Meltzer, S.; Requicha, A.A.G.; Atwater, H.A. Plasmonics—A route to nanoscale optical devices. *Adv. Mater.* **2001**, *13*, 1501–1505.
22. Quinten, M.; Leitner, A.; Krenn, J.R.; Aussenegg, F.R. Electromagnetic energy transport via linear chains of silver nanoparticles. *Opt. Lett.* **1998**, *23*, 1331–1333.
23. Maier, S.A.; Kik, P.G.; Atwater, H.A. Observation of coupled plasmon–polariton modes in Au nanoparticle chain waveguides of different lengths: Estimation of waveguide loss. *Appl. Phys. Lett.* **2002**, *81*, 1714–1716.
24. Li, H.-W.; Muir, B.V.O.; Fichet, G.; Huck, W.T.S. Nanocontact printing: A route to sub-50-nm-scale chemical and biological patterning. *Langmuir* **2003**, *19*, 1963–1965.
25. Hornyak, G.; Kröll, M.; Pugin, R.; Sawitowski, T.; Schmid, G.; Bovin, J.-O.; Karsson, G.; Hofmeister, H.; Hopfe, S. Gold clusters and colloids in alumina nanotubes. *Chem. Eur. J.* **1997**, *3*, 1951–1956.
26. Nagle, L.; Fitzmaurice, D. Templated nanowire assembly on the surface of a patterned nanosphere. *Adv. Mater.* **2003**, *15*, 933–935.
27. Krenn, J.R.; Dereux, A.; Weeber, J.C.; Bourillot, E.; Lacroute, Y.; Goudonnet, J.P.; Schider, G.; Gotschy, W.; Leitner, A.; Aussenegg, F.R.; Girard, C. Squeezing the optical near-field zone by plasmon coupling of metallic nanoparticles. *Phys. Rev. Lett.* **1999**, *82*, 2590–2593.
28. Maier, S.A.; Kik, P.G.; Atwater, H.A.; Meltzer, S.; Harel, E.; Koel, B.E.; Requicha, A.A.G. Local detection of electromagnetic energy transport below the diffraction limit in metal nanoparticle plasmon waveguides. *Nat. Mater.* **2003**, *2*, 229–232.
29. Lamprecht, B.; Schider, G.; Lechner, R.T.; Ditlbacher, H.; Krenn, J.R.; Leitner, A.; Aussenegg, F.R. Metal nanoparticle gratings: Influence of dipolar particle interaction on the plasmon resonance. *Phys. Rev. Lett.* **2000**, *84*, 4721–4724.
30. Haynes, C.L.; McFarland, A.D.; Zhao, L.; Van Duyne, R.P.; Schatz, G.C.; Gunnarsson, L.; Prikulis, J.; Kasemo, B.; Käll, M. Nanoparticle optics: The importance of radiative dipole coupling in two-dimensional nanoparticle arrays. *J. Phys. Chem., B* **2003**, *107*, 7337–7342.
31. Ivanisevic, A.; Im, J.-H.; Lee, K.-B.; Park, S.-J.; Demers, L.M.; Watson, K.J.; Mirkin, C.A. Redox-controlled orthogonal assembly of charged nanostructures. *J. Am. Chem. Soc.* **2001**, *123*, 12424–12425.
32. Lu, Y.; Yin, Y.; Li, Z.-Y.; Xia, Y. Synthesis and self-assembly of Au@SiO<sub>2</sub> core-shell colloids. *Nano Lett.* **2002**, *2*, 785–788.
33. Chumanov, G.; Sokolov, K.; Cotton, T.M. Unusual extinction spectra of nanometer-sized silver particles arranged in two-dimensional arrays. *J. Phys. Chem.* **1996**, *100*, 5166–5168.
34. Freeman, R.G.; Grabar, K.C.; Allison, K.J.; Bright, R.M.; Davis, J.A.; Guthrie, A.P.; Hommer, M.B.; Jackson, M.A.; Smith, P.C.; Walter, D.G.; Natan, M.J. Self-assembled metal colloid monolayers: An approach to SERS substrates. *Science* **1995**, *267*, 1629–1632.
35. Grabar, K.C.; Freeman, R.G.; Hommer, M.B.; Natan, M.J. Preparation and characterization of Au colloid monolayers. *Anal. Chem.* **1995**, *67*, 735–743.
36. Grabar, K.C.; Smith, P.C.; Musick, M.D.; Davis, J.A.; Walter, D.G.; Jackson, M.A.; Guthrie, A.P.; Natan, M.J. Kinetic control of interparticle spacing in Au colloid-based surfaces: Rational nanometer-scale architecture. *J. Am. Chem. Soc.* **1996**, *118*, 1148–1153.
37. Hanarp, P.; Käll, M.; Sutherland, D.S. Optical properties of short ranged ordered arrays of nanometer gold disks prepared by colloidal lithography. *J. Phys. Chem., B* **2003**, *107*, 5768–5772.
38. Meier, M.; Wokaun, A.; Liao, P.F. Enhanced fields on rough surfaces: Dipolar interactions among particles of sizes exceeding the Rayleigh limit. *J. Opt. Soc. Am., B* **1985**, *2*, 931–949.
39. Zhao, L.; Kelly, K.L.; Schatz, G.C. The extinction spectra of silver nanoparticle arrays: Influence of array structure on plasma wavelength and width. *J. Phys. Chem., B* **2003**, *107*, 7343–7350.
40. Chumanov, G.; Sokolov, K.; Gregory, B.W.; Cotton, T.M. Colloidal metal films as a substrate for surface-enhanced spectroscopy. *J. Phys. Chem.* **1995**, *99*, 9466–9471.
41. Sadtler, B.; Wei, A. Spherical ensembles of gold nanoparticles on silica: Electrostatic and size effects. *Chem. Commun.* **2002**, 1604–1605.
42. Schmid, G.; Lehnert, A.; Kreibitz, U.; Adamczyk, Z.; Belouschek, P. Synthese und elektronenmikroskopische untersuchung kontrolliert gewaschener, ligandstabilisierter Goldkolloide sowie theoretische Überlegungen zur Oberflächenbelegung durch Kolloide. *Z. Naturforsch.* **1990**, *45b*, 989–994.
43. Giersig, M.; Mulvaney, P. Formation of ordered two-dimensional gold colloid lattices by electrophoretic deposition. *J. Phys. Chem.* **1993**, *97*, 6334–6336.
44. Giersig, M.; Mulvaney, P. Preparation of ordered colloid monolayers by electrophoretic deposition. *Langmuir* **1993**, *9*, 3408–3413.
45. Kim, B.; Tripp, S.L.; Wei, A. Self-organization of large gold nanoparticle arrays. *J. Am. Chem. Soc.* **2001**, *123*, 7955–7956.
46. Wei, A.; Kim, B.; Pusztay, S.V.; Tripp, S.L.; Balasubramanian, R. Resorcinarene-encapsulated nanoparticles: Building blocks for self-assembled nanostructures. *J. Incl. Phenom. Macrocycl. Chem.* **2001**, *41*, 83–86.
47. Balasubramanian, R.; Kim, B.; Tripp, S.L.; Wang, X.; Lieberman, M.; Wei, A. Dispersion and stability studies of resorcinarene-encapsulated gold nanoparticles. *Langmuir* **2002**, *18*, 3676–3681.
48. Kim, B.; Tripp, S.L.; Wei, A. Tuning the optical properties of large gold nanoparticle arrays. *MRS Symp. Proc.* **2001**, *676*, 1–7. Y.6.1.
49. Raether, H. *Surface Plasmons on Smooth and Rough Surfaces and on Gratings*; Springer: Berlin, 1988.
50. Wei, A.; Kim, B.; Sadtler, B.; Tripp, S.L. Tunable surface-enhanced Raman scattering from large gold nanoparticle arrays. *ChemPhysChem* **2001**, *2*, 743–745.

51. Aravind, P.K.; Nitzan, A.; Metiu, H. The interaction between electromagnetic resonances and its role in spectroscopic studies of molecules adsorbed on colloidal particles or metal spheres. *Surf. Sci.* **1981**, *110*, 189–204.
52. Wang, D.-S.; Kerker, M. Enhanced Raman scattering by molecules adsorbed at the surface of colloidal spheroids. *Phys. Rev., B* **1981**, *24*, 1777–1790.
53. Liver, N.; Nitzan, A.; Gersten, J.I. Local fields in cavity sites of rough dielectric surfaces. *Chem. Phys. Lett.* **1984**, *111*, 449–454.
54. Zeman, E.J.; Schatz, G.C. An accurate electromagnetic theory study of surface enhancement factors for Ag, Au, Cu, Li, Na, Al, Ga, In, Zn, and Cd. *J. Phys. Chem.* **1987**, *91*, 634–643.
55. Blatchford, C.G.; Campbell, J.R.; Creighton, J.A. Plasma resonance-enhanced Raman scattering by adsorbates on gold colloids: The effects of aggregation. *Surf. Sci.* **1982**, *120*, 435–455.
56. Kneipp, K.; Dasari, R.R.; Wang, Y. Near-infrared surface-enhanced Raman scattering (NIR SERS) on colloidal silver and gold. *Appl. Spectrosc.* **1994**, *48*, 951–955.
57. Maxwell, D.J.; Emory, S.R.; Nie, S. Nanostructured thin-film materials with surface-enhanced optical properties. *Chem. Mater.* **2001**, *13*, 1082–1088.
58. Kim, B.; Wei, A. Unpublished results.
59. Genov, D.A.; Sarychev, A.K.; Shalaev, V.M.; Wei, A. Resonant field enhancements from metal nanoparticle arrays. *Nano Lett.* **2003**, *in press*.
60. Joannopoulos, J.D.; Meade, R.D.; Winn, J.N. *Photonic Crystals: Molding the Flow of Light*; Princeton University Press: Princeton, 1995.
61. Braun, P.B.; Wiltzius, P. Macroporous materials—Electrochemically grown photonic crystals. *Curr. Opin. Colloid Interface Sci.* **2002**, *7*, 116–123.
62. Moroz, A. Three-dimensional complete photonic band-gap structures in the visible. *Phys. Rev. Lett.* **1999**, *83*, 5274–5277.
63. Zhang, W.Y.; Lei, X.Y.; Wang, Z.L.; Zheng, D.G.; Tam, W.Y.; Chan, C.T.; Sheng, P. Robust photonic band gap from tunable scatterers. *Phys. Rev. Lett.* **2000**, *84*, 2853–2856.
64. Graf, C.; van Blaaderen, A. Metallodielectric colloidal core-shell particles for photonic applications. *Langmuir* **2002**, *18*, 524–534.

# Metal Nanoparticles Prepared in Supercritical Carbon Dioxide

Harry W. Rollins

Chemistry Department, Idaho National Engineering and Environmental Laboratory,  
Idaho Falls, Idaho, U.S.A.

## INTRODUCTION

The novel optical, electronic, and/or magnetic properties of metal and semiconductor nanoparticles have resulted in extensive research on new methods for their preparation. An ideal preparation method would allow the particle size, size distribution, crystallinity, and particle shape to be easily controlled, and would be applicable to a wide variety of material systems. Numerous preparation methods have been reported, each with its inherent advantages and disadvantages; however, an ideal method has yet to emerge. The most widely applied methods for nanoparticle preparation include the sonochemical reduction of organometallic reagents,<sup>[1,2]</sup> the solvothermal method of Alivisatos,<sup>[3]</sup> reactions in microemulsions,<sup>[4-6]</sup> the polyol method (reduction by alcohols),<sup>[7-9]</sup> and the use of polymer and sol-gel materials as hosts.<sup>[10-13]</sup>

In addition to these methods, there are a variety of methods that take advantage of the unique properties of a supercritical fluid.<sup>[14,15]</sup> Through simple variations of temperature and pressure, the properties of a supercritical fluid can be continuously tuned from gas-like to liquid-like without undergoing a phase change. Nanoparticle preparation methods that utilize supercritical fluids are briefly reviewed below using the following categories: Rapid Expansion of Supercritical Solutions (RESS), Reactive Supercritical Fluid Processing, and Supercritical Fluid Microemulsions. Because of its easily accessible critical temperature and pressure and environmentally benign nature, carbon dioxide is the most widely used supercritical solvent. Supercritical CO<sub>2</sub> is unfortunately a poor solvent for many polar or ionic species, which has impeded its use in the preparation of metal and semiconductor nanoparticles. We have developed a reactive supercritical fluid processing method using supercritical carbon dioxide for the preparation of metal and metal sulfide particles and used it to prepare narrowly distributed nanoparticles of silver (Ag) and silver sulfide (Ag<sub>2</sub>S). The preparation and characterization of these materials and the effects of processing conditions on particle properties is reported.

## NANOPARTICLE PREPARATION METHODS USING SUPERCRITICAL FLUIDS

### Rapid Expansion of Supercritical Solutions

The Rapid Expansion of Supercritical Solutions (RESS) process takes advantage of the pressure dependence of solute solubility in supercritical fluids. In this method, a supercritical solution of the solute is prepared by dissolving the solute in an appropriate solvent and then pressurizing and heating the solution to above its critical point. (Alternatively, the solute can be directly dissolved by the solvent at supercritical conditions.) The supercritical solution is rapidly expanded through a small nozzle or orifice into a region at lower pressure, where the solute is insoluble. The very rapid reduction in pressure results in the precipitation of the solute. The timescale for the precipitation has been estimated to be on the order of 10<sup>-7</sup> sec,<sup>[16]</sup> which results in the homogeneous nucleation and precipitation of the solute. A wide variety of organic, polymeric, and inorganic nanoparticles have been prepared by RESS.<sup>[17-23]</sup> Organic particles prepared using this method typically have a wide particle-size distribution and are in the ~1- $\mu$ m size range. Particle size is highly dependent on solute concentration, with smaller particles being produced at lower concentrations. Ginosar et al.<sup>[24]</sup> reported that the on-line particle-size analysis for the RESS preparation of phenanthrene nanoparticles from carbon dioxide solutions consists of a bimodal distribution of primary nanoparticles and much larger micron-sized aggregates. Processing by RESS using carbon dioxide solutions has primarily been used in the preparation of organic nanoparticles because of the limited solubility of inorganic salts and polymers in CO<sub>2</sub>. Smith, Matson, Petersen, and coworkers<sup>[18,20,25]</sup> have used supercritical water solutions for the RESS preparation of SiO<sub>2</sub> and GeO<sub>2</sub> nanoparticles. Processing of SiO<sub>2</sub> by RESS using a preexpansion temperature of 470°C at 590 bar and an expansion nozzle with an inner diameter of 60  $\mu$ m resulted in the formation of particles with diameters from less than 0.1 to 0.5  $\mu$ m. Variation of the

SiO<sub>2</sub> concentration from 10 to 500 ppm resulted in SiO<sub>2</sub> particles with diameters from less than 0.01 to 0.5 μm, with larger particles being produced at higher SiO<sub>2</sub> concentrations. Variation of the processing conditions has been used to generate thin films of the inorganic material. Supercritical carbon dioxide has been used for the RESS preparation of triiron dodecacarbonyl, dimanganese decacarbonyl, and chromium hexacarbonyl.<sup>[26]</sup> The triiron dodecacarbonyl particles ranged in diameter from 1 to 10 μm.

### Reactive Supercritical Fluid Processing

The RESS process is a precipitation process based on the pressure dependence of solute solubility in supercritical fluids. Unfortunately, metals and metal sulfides are insoluble in most solvents, thus precluding their direct preparation by RESS. Using aqueous solutions of metal salts, the RESS process has been used to prepare metal oxide nanoparticles. Processing of Fe(NO<sub>3</sub>)<sub>3</sub> solutions by RESS using water at 500°C and 100 MPa and orifices with diameters of 50–200 μm resulted in the formation of Fe<sub>2</sub>O<sub>3</sub> nanoparticles with diameters of 20–40 nm.<sup>[27]</sup> Oxidation of metal salts in pressurized water at high temperatures is typically referred to as hydrothermal processing and is a common method in the synthesis of metal oxides. Hydrothermal treatment using batch-type reactions affords little control over the solution temperature and duration of exposure and typically results in the formation of micron-scale particles. Careful control of the reaction conditions has been demonstrated using a flowing system in which the aqueous solution of the metal salt is rapidly mixed with a preheated water stream. Variation of the temperature and flow rate of each stream and the residence time at high temperature can be precisely controlled and limited to short exposure times. Using flowing systems, Poliakoff et al.<sup>[28,29]</sup> were able to prepare nanoparticles of Ce<sub>1-x</sub>Zr<sub>x</sub>O<sub>2</sub> and MFe<sub>2</sub>O<sub>4</sub> (M = Co, Ni, Zn) with particle sizes of ~10 nm. Solutions of metal salts in alcohols have also been processed using high temperatures and pressures to prepare nanoparticles of a variety of metals.<sup>[30,31]</sup>

Sun et al.<sup>[15,32–36]</sup> have developed a reactive supercritical fluid method for the preparation of metal and metal sulfide particles based on the RESS process. In this method, a metal salt is dissolved in a polar solvent, which is then pressurized and heated to supercritical conditions. The supercritical solution is then rapidly expanded through a small nozzle or orifice into a liquid solution containing a second reactant (e.g., reducing agent or sodium sulfide). The method is versatile and can be used with a variety of metal salts, supercritical fluids, and reagents. They have used

this method to prepare nanoparticles of the metals, Ag, Cu, Fe, Ni, and Co, as well as the metal sulfides, CdS, Ag<sub>2</sub>S, and PbS. The particles produced have average diameters of ≤10 nm with particle-size distributions of ~1 nm. Solvents used include methanol, ethanol, acetone, tetrahydrofuran, and ammonia. Particle aggregation is minimized by collecting the sample in liquid solution and can be further prevented through the use of polymer surfactants such as poly(*N*-vinyl-2-pyrrolodone) (PVP).

### Supercritical Fluid Microemulsions

To overcome the limited solubility of polar compounds, particularly metal salts, in carbon dioxide, several researchers have used reverse micelles. Wai et al.<sup>[37,38]</sup> reported the preparation of silver and copper nanoparticles using water-in-CO<sub>2</sub> reverse micelles. Silver and copper salts were dissolved in the aqueous core of reverse micelles formed with sodium bis(2-ethylhexyl) sulfosuccinate (AOT) and the cosurfactant perfluoropolyether phosphate in supercritical carbon dioxide. The cosurfactant perfluoropolyether phosphate is necessary to dissolve the AOT, which is not soluble in carbon dioxide. Addition of a reducing agent to the reverse micelle solutions resulted in the formation of metallic Ag or Cu nanoparticles with 5–15 nm diameters.<sup>[37,38]</sup> AgI, AgBr, and AgCl nanoparticles (3–15 nm) have been prepared by mixing two carbon dioxide microemulsions, one containing AgNO<sub>3</sub> and the other containing NaI, NaBr, or NaCl.<sup>[39]</sup> A fluorinated analog of AOT has been synthesized and used for the preparation of CdS and ZnS nanoparticles by mixing two CO<sub>2</sub> reverse micelle solutions, one containing the metal salt and the other Na<sub>2</sub>S.<sup>[40]</sup> The average diameter was calculated from the band gap and varied from 2.7 to 4.2 nm depending on the water to surfactant ratio. Formation of water-in-CO<sub>2</sub> microemulsions by perfluoropolyether surfactants has been demonstrated<sup>[41–44]</sup> and used to prepare CdS nanoparticles.<sup>[45]</sup> Sun, Atorngitjawat, and Mezziani<sup>[46]</sup> have used perfluoropolyether ammonium carboxylate water-in-CO<sub>2</sub> microemulsions to dissolve AgNO<sub>3</sub>, which was then rapidly expanded into a room temperature solution of sodium borohydride resulting in Ag nanoparticles.

## RESULTS AND DISCUSSION

We have developed a reactive supercritical fluid nanoparticle preparation method based on the RESS process that uses supercritical carbon dioxide as the solvent. In this method, neutral metal salts are dissolved in carbon dioxide using tributyl phosphate

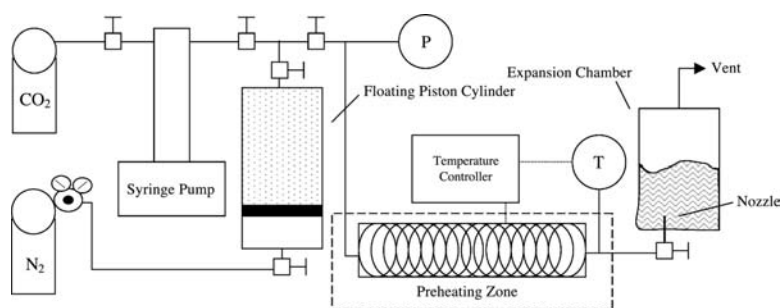


**Fig. 1** Experimental apparatus for the reactive RESS preparation of nanoparticles.

(TBP). The method can be used with a variety of metal salts and can be used for the preparation of both metal and metal sulfide nanoparticles. The particles thus prepared have average diameters of approximately 10 nm, with narrow size distributions. The preparation and characterization of silver and silver sulfide nanoparticles is presented.

### Silver Nanoparticles

The experimental apparatus for the reactive RESS preparation of nanoparticles is shown in Fig. 1. The system consists of an ISCO model 260D syringe pump, a floating piston cylinder (TEMCO model CFT-50-50, 300-cm<sup>3</sup> volume), a high-pressure nitrogen cylinder and regulator, a preheating zone with ~40 ft of 1/16-in. o.d. tubing in an aluminum clamshell, an Omega CN4800 temperature controller with k-type thermocouple in contact with the fluid, a 127- $\mu$ m i.d. by 10-cm-long nozzle, and an expansion chamber. For the preparation of silver nanoparticles, CF<sub>3</sub>SO<sub>3</sub>Ag solution in tributyl phosphate (TBP) was added to the floating piston cylinder, which was filled with liquid CO<sub>2</sub> and pressurized to 2000 psi at room temperature. The amount of CO<sub>2</sub> was gravimetrically determined. The floating piston cylinder was placed on a horizontal platform rocker and allowed to equilibrate for at least 2 hr. The preheating zone was brought to temperature and allowed to equilibrate. A solution of NaBH<sub>4</sub> in ethanol or methanol (150 ml) was immediately prepared before use and was placed in the expansion chamber. The polymer PVP (molecular weight 360,000, ~3.5 mg/mL) was also dissolved in the NaBH<sub>4</sub> alcohol solution to prevent particle aggregation. An excess of sodium borohydride was used for the preparation of all samples ( $[\text{NaBH}_4]/[\text{Ag}^+] = 3\text{--}5$ ). The CF<sub>3</sub>SO<sub>3</sub>Ag solution in CO<sub>2</sub>/TBP was pressurized to 3500 psi using nitrogen on the back side of the piston. The system temperature was equilibrated by flowing CO<sub>2</sub> at 3500 psi for ~5 min. The CO<sub>2</sub> flow was stopped and the CF<sub>3</sub>SO<sub>3</sub>Ag solution flow was initiated and expanded into the NaBH<sub>4</sub> solution.

The NaBH<sub>4</sub> solution immediately turned yellow upon addition of CF<sub>3</sub>SO<sub>3</sub>Ag solution, typical of silver

nanoparticle suspensions. The resulting suspension was then characterized using X-ray diffraction (XRD), transmission electron microscopy (TEM), and UV-Vis absorption spectroscopy. For TEM analysis, a drop of the suspension was placed on a carbon-coated Cu grid, allowed to dry, rinsed with hexane, and then dried in a vacuum oven at 100–120°C overnight to remove residual TBP. For UV-Vis analysis, the samples were diluted to an optical density <1 using 0.2-cm path length cuvettes. For XRD analysis, the sample was dried on a rotary evaporator at up to 80°C. Upon removal of the alcohol, the silver particles and PVP polymer precipitated and the remaining TBP liquid was decanted. The sample was rinsed with hexane and then dried in a vacuum oven. X-ray diffraction patterns for the samples matched the powder diffraction file reference patterns for face-centered cubic silver (04-0783).

Several silver nanoparticle samples were prepared using different expansion temperatures and concentrations of TBP. Transmission electron microscopy analysis and particle-size distributions are shown in Figs. 2–4 for several silver nanoparticle samples.

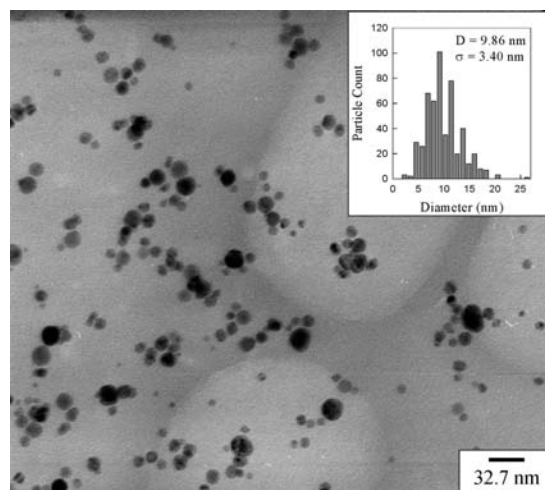


**Fig. 2** Transmission electron micrograph of silver nanoparticles prepared from supercritical CO<sub>2</sub> solution at 70°C, 3500 psi, with 0.22 wt.% TBP. The particle-size distribution is shown in the inset.

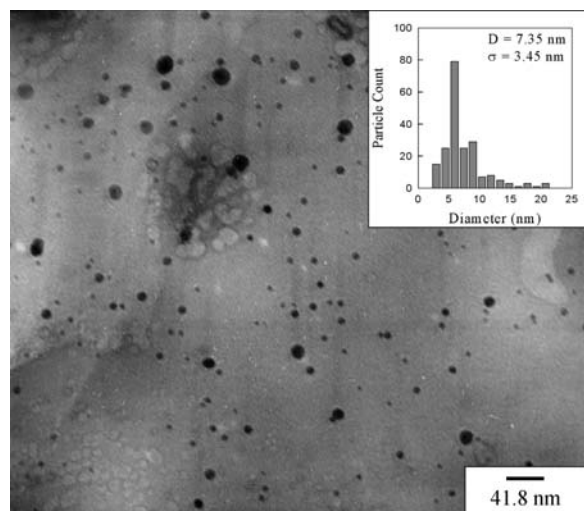


**Fig. 3** Transmission electron micrograph of silver nanoparticles prepared from supercritical CO<sub>2</sub> solution at 110°C, 3500 psi, with 0.24 wt.% TBP. The particle-size distribution is shown in the inset.

Particle diameters and size distributions were determined from the TEM micrographs and are based on a minimum of 200 particles. The samples shown in Figs. 2 and 3 were both prepared using 0.2 wt.% TBP. The sample prepared using a temperature of 70°C has an average particle diameter of 9.9 nm, while the sample prepared at 110°C has an average diameter of 7.4 nm. The particle diameter standard deviation is ~3.5 nm for both samples. Analysis by TEM of a sample prepared using a temperature of 104°C and [TBP]

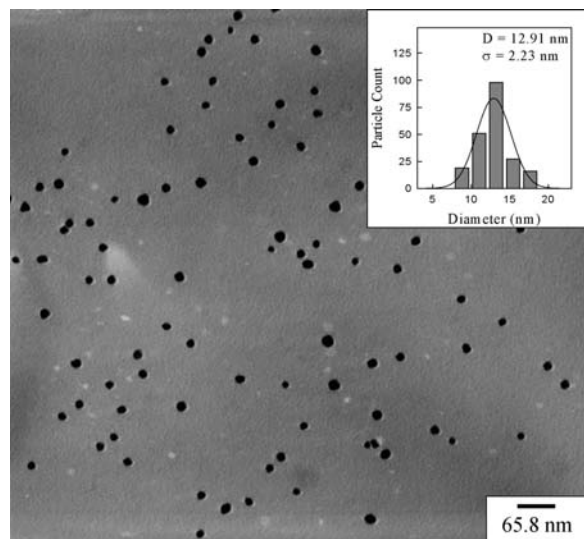


**Fig. 4** Transmission electron micrograph of silver nanoparticles prepared from supercritical CO<sub>2</sub> solution at 104°C, 3500 psi, with 1.41 wt.% TBP. The particle-size histogram and Gaussian-distribution analysis are shown in the inset.

**Table 1** Properties of silver and silver sulfide nanoparticles prepared by reactive RESS processing using CO<sub>2</sub> solutions

	Temperature (°C)	[TBP] (wt.%)	Diameter (nm)	$\sigma$ (nm)
Silver	70	0.22	9.9	3.4
Silver	110	0.24	7.4	3.5
Silver	104	1.41	12.9	2.2
Silver sulfide	50	0.23	3.1	1.2
Silver sulfide	70	0.23	3.0	1.0
Silver sulfide	110	1.38	7.2	1.8

of 1.41 wt.% has an average diameter of 12.9 nm and a standard deviation of 2.2 nm. Sample preparation conditions and results from TEM analysis are summarized in Table 1. Particle diameter shows a slight dependence on expansion temperature, with smaller particles produced at lower temperature. The particle size and distributions were highly dependent on TBP concentration, with larger, more uniform particles prepared at higher TBP concentrations. The absorption spectra of the 9.9- and 12.9-nm diameter silver nanoparticles are shown in Fig. 5, and both samples exhibit the characteristic surface plasmon absorption band. The 12.9-nm diameter sample is red shifted and broader than the 9.9-nm diameter sample. The absorption maximums are at 406.5 nm (68 nm FWHM) and 399.5 nm (62 nm FWHM) for the 12.9- and 9.9-nm samples, respectively.

### Silver Sulfide Nanoparticles

Silver sulfide nanoparticles were prepared using the reactive RESS processing method. The preparation conditions were the same as those used for the preparation of silver metal nanoparticles except that the expansion chamber contained a methanol solution of

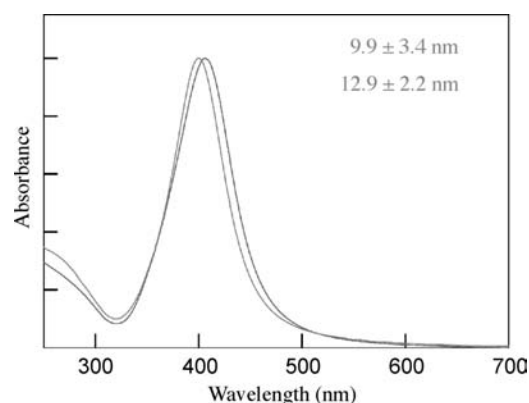


**Fig. 5** Normalized absorption spectra of silver nanoparticles prepared from supercritical CO<sub>2</sub> solutions.



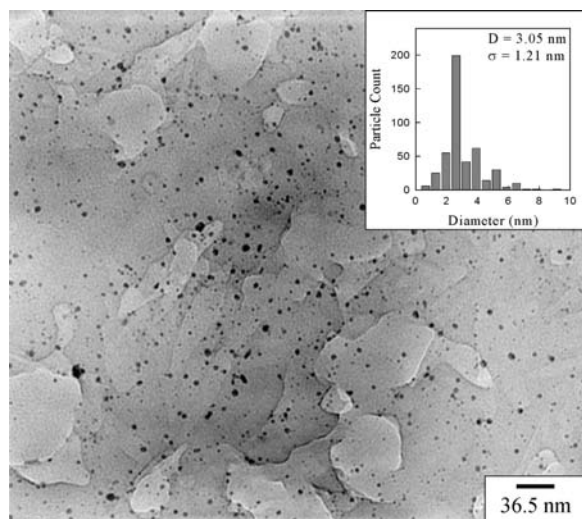


**Fig. 6** Transmission electron micrograph of silver sulfide nanoparticles prepared from supercritical CO<sub>2</sub> solution at 50°C, 3500 psi, with 0.23 wt.% TBP. The particle-size distribution is shown in the inset.

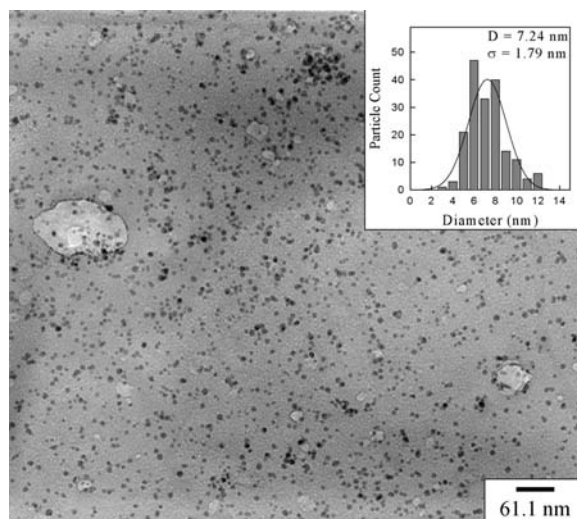


**Fig. 8** Transmission electron micrograph of silver sulfide nanoparticles prepared from supercritical CO<sub>2</sub> solution at 110°C, 3500 psi, with 1.38 wt.% TBP. The particle-size histogram and Gaussian-distribution analysis are shown in the inset.

Na<sub>2</sub>S with PVP. Excess Na<sub>2</sub>S was used in the preparation of all the samples ( $[S^{2-}]/[Ag^+] \approx 7.5$ ). X-ray diffraction analysis of the samples matched the reference pattern for monoclinic Ag<sub>2</sub>S (75-1061). Transmission electron micrographs and particle-size distributions for silver sulfide nanoparticles are shown in Figs. 6–8. Preparation conditions and TEM results are summarized in Table 1. The samples prepared using temperatures of 50°C (Fig. 6) and 70°C (Fig. 7) were both prepared using 0.2 wt.% TBP. The sample prepared using an expansion temperature of 50°C

had an average diameter of  $3.1 \pm 1.2$  nm and the sample prepared using 70°C had an average diameter of  $3.0 \pm 1.0$  nm. The expansion temperature had little, if any, effect on particle size; however, the sample prepared using 50°C had a slightly larger size distribution. Silver sulfide nanoparticles were considerably smaller than silver metal particles prepared using similar conditions. For samples prepared using an expansion temperature of 70°C and 0.2 wt.% TBP, silver nanoparticles were  $9.9 \pm 3.4$  nm, while silver sulfide nanoparticles were  $3.0 \pm 1.0$  nm. Silver sulfide nanoparticles prepared using an expansion temperature of 110°C and 1.38 wt.% TBP had an average diameter of  $7.2 \pm 1.8$  nm (Fig. 8). Particle size and size distribution are larger for the silver sulfide sample prepared using higher TBP concentration. The UV–Vis–NIR

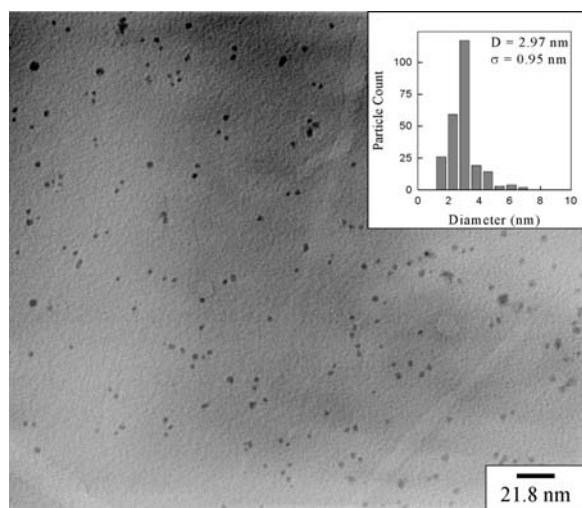


**Fig. 7** Transmission electron micrograph of silver sulfide nanoparticles prepared from supercritical CO<sub>2</sub> solution at 70°C, 3500 psi, with 0.23 wt.% TBP. The particle-size distribution is shown in the inset.

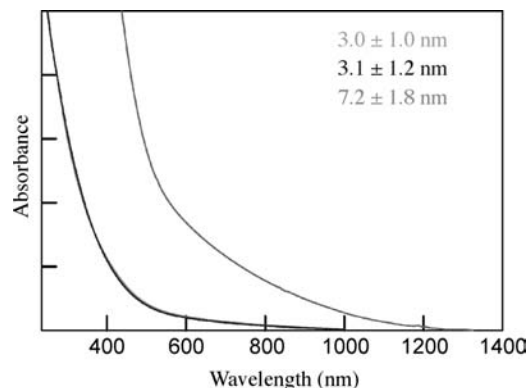


**Fig. 9** Absorption spectra of silver sulfide nanoparticles prepared from supercritical CO<sub>2</sub> solutions.

absorption spectra of the silver sulfide nanoparticle suspensions are shown in Fig. 9. The samples with average diameters of  $\sim 3$  nm have an absorption onset at  $\sim 950$  nm, while the sample with an average diameter of 7.2 nm has an absorption onset at  $\sim 1250$  nm. This is consistent with a shift in band gap (and absorption onset) to higher energies with decreasing particle size for semiconductor nanoparticles.

## CONCLUSION

Silver and silver sulfide nanoparticles with average diameters  $\sim 10$  nm with narrow size distributions have been prepared using a reactive supercritical fluid processing method. In this method, a neutral metal salt is dissolved in  $\text{CO}_2$  using tributyl phosphate. The supercritical solution of the metal salt is rapidly expanded into a liquid solution containing a second reactant, resulting in the formation of metal or metal sulfide nanoparticles. The nanoparticles have been characterized by powder X-ray diffraction, transmission electron microscopy, and absorption spectroscopy. The particle size and size distribution depend on preparation conditions, most notably on TBP concentration.

## ACKNOWLEDGMENTS

This work was supported by the U.S. Department of Energy through the INEEL Laboratory Directed Research and Development (LDRD) Program under DOE Idaho Operations Office Contract DE-AC07-99ID13727.

## REFERENCES

1. Suslick, K.S.; Fang, M.M.; Hyeon, T. Sonochemical synthesis of iron colloids. *J. Am. Chem. Soc.* **1996**, *118* (47), 11960–11961.
2. Suslick, K.S.; Choe, S.B.; Cichowlas, A.A.; Grinstaff, M.W. Sonochemical synthesis of amorphous iron. *Nature* **1991**, *353* (6343), 414–416.
3. Alivisatos, A.P. Semiconductor clusters, nanocrystals, and quantum dots. *Science* **1996**, *271* (5251), 933–937.
4. Motte, L.; Billoudet, F.; Pileni, M.P. Synthesis in situ of nanosize silver sulphide semiconductor particles in reverse micelles. *J. Mater. Sci.* **1996**, *31* (1), 38–42.
5. Petit, C.; Lixon, P.; Pileni, M.P. In-situ synthesis of silver nanocluster in AOT reverse micelles. *J. Phys. Chem.* **1993**, *97* (49), 12,974–12,983.
6. Lisiecki, I.; Pileni, M.P. Synthesis of copper metallic clusters using reverse micelles as microreactors. *J. Am. Chem. Soc.* **1993**, *115* (10), 3887–3896.
7. Chakroune, N.; Viau, G.; Ricolleau, C.; Fievet-Vincent, F.; Fievet, F. Cobalt-based anisotropic particles prepared by the polyol process. *J. Mater. Chem.* **2003**, *13* (2), 312–318.
8. Feldmann, C.; Metzmacher, C. Polyol mediated synthesis of nanoscale MS particles ( $M = \text{Zn}, \text{Cd}, \text{Hg}$ ). *J. Mater. Chem.* **2001**, *11* (10), 2603–2606.
9. Feldmann, C. Polyol-mediated synthesis of nanoscale functional materials. *Adv. Funct. Mater.* **2003**, *13* (2), 101–107.
10. Blackburn, J.M.; Long, D.P.; Cabanas, A.; Watkins, J.J. Deposition of conformal copper and nickel films from supercritical carbon dioxide. *Science* **2001**, *294* (5540), 141–145.
11. Cao, Y.; Hu, J.C.; Hong, Z.S.; Deng, J.F.; Fan, K.N. Characterization of high-surface-area zirconia aerogel synthesized from combined alcohothermal and supercritical fluid drying techniques. *Catal. Letters* **2002**, *81* (1–2), 107–112.
12. Casula, M.F.; Corrias, A.; Paschina, G. FeCo–SiO<sub>2</sub> nanocomposite aerogels by high temperature supercritical drying. *J. Mater. Chem.* **2002**, *12* (5), 1505–1510.
13. Watkins, J.J.; McCarthy, T.J. Polymer/metal nanocomposite synthesis in supercritical CO<sub>2</sub>. *Chem. Mater.* **1995**, *7* (11), 1991–1994.
14. Rollins, H.W. Ph.D. Dissertation; Clemson University, 1999.
15. Sun, Y.-P.; Rollins, H.W.; Jayasundera, B.; Meziani, M.J.; Bunker, C.E. *Supercritical Fluid Technology in Materials Science and Engineering: Synthesis, Properties, and Applications*; Sun, Y.P., Ed.; Marcel Dekker: New York, 2002; 491–576.
16. Lele, A.K.; Shine, A.D. Effect of RESS dynamics on polymer morphology. *Ind. Eng. Chem. Res.* **1994**, *33* (6), 1476–1485.
17. Eckert, C.A.; Knutson, B.L.; Debenedetti, P.G. Supercritical fluids as solvents for chemical and materials processing. *Nature* **1996**, *383* (6598), 313–318.
18. Matson, D.W.; Fulton, J.L.; Petersen, R.C.; Smith, R.D. Rapid expansion of supercritical fluid solutions—solute formation of powders, thin-films, and fibers. *Ind. Eng. Chem. Res.* **1987**, *26* (11), 2298–2306.
19. Blasig, A.; Shi, C.M.; Enick, R.M.; Thies, M.C. Effect of concentration and degree of saturation on RESS of a CO<sub>2</sub>-soluble fluoropolymer. *Ind. Eng. Chem. Res.* **2002**, *41* (20), 4976–4983.
20. Petersen, R.C.; Matson, D.W.; Smith, R.D. Rapid precipitation of low vapor-pressure solids from supercritical fluid solutions—the formation of thin-films and powders. *J. Am. Chem. Soc.* **1986**, *108* (8), 2100–2102.
21. Chernyak, Y.; Henon, F.; Harris, R.B.; Gould, R.D.; Franklin, R.K.; Edwards, J.R.; Desimone, J.M.; Carbonell, R.G. Formation of perfluoropolyether coatings by the rapid expansion of supercritical solutions (RESS) process. Part 1: Experimental results. *Ind. Eng. Chem. Res.* **2001**, *40* (26), 6118–6126.
22. Mawson, S.; Johnston, K.P.; Combes, J.R.; Desimone, J.M. Formation of poly(1,1,2,2-tetrahydroperfluorodecyl acrylate) submicron fibers and particles from supercritical carbon-dioxide solutions. *Macromolecules* **1995**, *28* (9), 3182–3191.

23. Debenedetti, P.G.; Tom, J.W.; Kwauk, X.; Yeo, S.D. Rapid expansion of supercritical solutions (RESS)—fundamentals and applications. *Fluid Phase Equilib.* **1993**, *82*, 311–321.
24. Ginosar, D.M.; Swank, W.D.; McMurtrey, R.D.; Carmack, W.J. Flow-Field Studies of the RESS Process, Proceedings of the 5th International Symposium on Supercritical Fluids, Atlanta, Georgia, Apr 8–12, 2000.
25. Matson, D.W.; Smith, R.D. Supercritical fluid technologies for ceramic-processing applications. *J. Am. Ceram. Soc.* **1989**, *72* (6), 871–881.
26. Williams, J.R.; Clifford, A.A.; Bartle, K.D.; Kee, T.P. The production of fine particles of metal complexes using supercritical fluids. *Powder Technol.* **1998**, *96* (2), 158–162.
27. Burukhin, A.A.; Churagulov, B.R.; Oleynikov, N.N.; Kolen'ko, Y.V. *Nanostructured Powders and Their Industrial Applications*; Mater. Res. Soc. Symp. Proc.; Materials Research Society: Warrendale, PA, 1998; Vol. 520, 171 pp.
28. Cabanas, A.; Poliakoff, M. The continuous hydrothermal synthesis of nano-particulate ferrites in near critical and supercritical water. *J. Mater. Chem.* **2001**, *11* (5), 1408–1416.
29. Cabanas, A.; Darr, J.A.; Lester, E.; Poliakoff, M. Continuous hydrothermal synthesis of inorganic materials in a near-critical water flow reactor; the one-step synthesis of nano-particulate  $Ce_{1-x}Zr_xO_2$  ( $x = 0-1$ ) solid solutions. *J. Mater. Chem.* **2001**, *11* (2), 561–568.
30. Pessey, V.; Garriga, R.; Weill, F.; Chevalier, B.; Etourneau, J.; Cansell, F. Core-shell materials elaboration in supercritical mixture  $CO_2$ /ethanol. *Ind. Eng. Chem. Res.* **2000**, *39* (12), 4714–4719.
31. Sheldrick, W.S.; Wachhold, M. Solventothermal synthesis of solid-state chalcogenidometalates. *Angew. Chem., Int. Ed. Engl.* **1997**, *36* (3), 207–224.
32. Sun, Y.P.; Rollins, H.W. Preparation of polymer-protected semiconductor nanoparticles through the rapid expansion of supercritical fluid solution. *Chem. Phys. Lett.* **1998**, *288* (2–4), 585–588.
33. Sun, Y.P.; Rollins, H.W.; Guduru, R. Preparations of nickel, cobalt, and iron nanoparticles through the rapid expansion of supercritical fluid solutions (RESS) and chemical reduction. *Chem. Mater.* **1999**, *11* (1), 7–9.
34. Meziani, M.J.; Rollins, H.W.; Allard, L.F.; Sun, Y.P. Protein-protected nanoparticles from rapid expansion of supercritical solution into aqueous solution. *J. Phys. Chem., B* **2002**, *106* (43), 11,178–11,182.
35. Sun, Y.P.; Guduru, R.; Lin, F.; Whiteside, T. Preparation of nanoscale semiconductors through the rapid expansion of supercritical solution (RESS) into liquid solution. *Ind. Eng. Chem. Res.* **2000**, *39* (12), 4663–4669.
36. Sun, Y.P.; Riggs, J.E.; Rollins, H.W.; Guduru, R. Strong optical limiting of silver-containing nanocrystalline particles in stable suspensions. *J. Phys. Chem., B* **1999**, *103* (1), 77–82.
37. Ohde, H.; Hunt, F.; Wai, C.M. Synthesis of silver and copper nanoparticles in a water-in-supercritical-carbon dioxide microemulsion. *Chem. Mater.* **2001**, *13* (11), 4130–4135.
38. Ji, M.; Chen, X.Y.; Wai, C.M.; Fulton, J.L. Synthesizing and dispersing silver nanoparticles in a water-in-supercritical carbon dioxide microemulsion. *J. Am. Chem. Soc.* **1999**, *121* (11), 2631–2632.
39. Ohde, H.; Rodriguez, J.M.; Ye, X.R.; Wai, C.M. Synthesizing silver halide nanoparticles in supercritical carbon dioxide utilizing a water-in- $CO_2$  microemulsion. *Chem. Commun.* **2000**, (23), 2353–2354.
40. Ohde, H.; Ohde, M.; Bailey, F.; Kim, H.; Wai, C.M. Water-in- $CO_2$  microemulsions as nanoreactors for synthesizing Cds and Zns nanoparticles in supercritical  $CO_2$ . *Nano Lett.* **2002**, *2* (7), 721–724.
41. Lee, C.T.; Ryoo, W.; Smith, P.G.; Arellano, J.; Mitchell, D.R.; Lagow, R.J.; Webber, S.E.; Johnston, K.P. Carbon dioxide-in-water microemulsions. *J. Am. Chem. Soc.* **2003**, *125* (10), 3181–3189.
42. Nagashima, K.; Lee, C.T.; Xu, B.; Johnston, K.P.; Desimone, J.M.; Johnson, C.S. NMR studies of water transport and proton exchange in water-in-carbon dioxide microemulsions. *J. Phys. Chem., B* **2003**, *107* (9), 1962–1968.
43. Da Rocha, S.R.P.; Johnston, K.P.; Rossky, P.J. Surfactant-modified  $CO_2$ -water interface: a molecular view. *J. Phys. Chem., B* **2002**, *106* (51), 13,250–13,261.
44. Meziani, M.J.; Sun, Y.P. Spectrophotometry study of aqueous salt solution in carbon dioxide microemulsions. *Langmuir* **2002**, *18* (10), 3787–3791.
45. Holmes, J.D.; Bhargava, P.A.; Korgel, B.A.; Johnston, K.P. Synthesis of cadmium sulfide Q particles in water-in- $CO_2$  microemulsions. *Langmuir* **1999**, *15* (20), 6613–6615.
46. Sun, Y.P.; Atorngitjawat, P.; Meziani, M.J. Preparation of silver nanoparticles via rapid expansion of water in carbon dioxide microemulsion into reductant solution. *Langmuir* **2001**, *17* (19), 5707–5710.

# Metal Nanoparticles: Self-Assembly into Electronic Nanostructures

**Venugopal Santhanam**

*Institut für Anorganische Chemie, Universität Duisburg-Essen, Essen, Germany*

**Ronald P. Andres**

*Purdue University, West Lafayette, Indiana, U.S.A.*

## INTRODUCTION

Nanotechnology is a catchword that evokes excitement in researchers and captures the imagination of laymen. The excitement in the research community stems from the fact that theoretically predicted variations in the physical properties of solid objects as their dimensions approach a few nanometers ( $1\text{ nm} = 10^{-9}\text{ m}$ )—viz. lowering of melting point, Coulomb charging, novel magnetic, optical phenomena, etc.—have been verified experimentally.<sup>[1–4]</sup> This experimental verification has been possible because of rapid strides made over the last two decades, both in techniques for synthesis and in tools for characterization of individual nanoscale objects. These advances have also opened up a vast array of potential technological applications and have occurred just as the limits of photolithography-based solid-state technology are being reached. Coupled with the revolutionary impact of solid-state electronic devices on our lives, advances in synthesis, manipulation, and characterization of nanomaterials have made nanotechnology—and in particular nanoelectronics—a cynosure of public interest.

There are two alternative approaches for fabricating nanoelectronic devices: the “top–down” and the “bottom–up” approaches. The top–down approach is similar to current photolithographic techniques used to produce microelectronic devices. It consists of “chiseling” nanometer-scale features in bulk materials. Using such techniques as e-beam lithography and x-ray phase shift lithography, this approach can now produce nanoscale features ( $<50\text{ nm}$ ) and has the decided advantage of being compatible with current microelectronic processing methods and design concepts. However, this approach suffers from two important drawbacks: 1) processing costs rise exponentially as feature size decreases; and 2) the surfaces and interfaces produced by this approach exhibit atomic-scale imperfections, which critically degrade device performance as feature size approaches nanometer dimensions. The bottom–up approach consists of “building” the device or circuit by assembling it from

preformed nanoscale “bricks.” Bottom–up processing, involving the serial manipulation of nanoscale objects, is technologically impractical. However, it is often possible to induce nanoscale objects to assemble themselves into desired structures. It is such biologically inspired self-assembly which holds the greatest promise.

There are a number of interesting nanoelectronic building blocks, viz. metal nanocrystals and nanowires (both magnetic and non-magnetic), semiconductor nanocrystals and nanowires, and carbon nanotubes. In this entry, we focus solely on non-magnetic metal nanocrystals. Two characteristics of metal nanoparticles are critical for assessing their usefulness in nanoelectronic applications: 1) the ease with which bare metal particles cold weld on contact to form hard aggregates; and 2) the tendency of metal particles to oxidize in an atmospheric environment especially in the presence of water molecules. The first characteristic means that the surface of a metal nanoparticle must be passivated by attachment of a monolayer of capping ligands or surfactant molecules before any attempt is made to assemble these particles into a uniform nanostructure. We will refer to such encapsulated particles as molecularly protected nanoparticles (MPNs). The second characteristic means that only noble metals such as Au and Ag will form nanoparticles that are not rapidly oxidized when exposed to an atmospheric environment. Linear alkanethiol molecules readily react in solution with both Au and Ag nanoparticles to form stable MPNs. These MPNs can be manipulated as stable physical species in a variety of organic solvents. The ability to manipulate Au and Ag MPNs in organic liquids, to synthesize macroscopic quantities of these particles with diameters in the 2–20 nm range, and to control the interparticle spacing in arrays of these particles by changing the length of the alkanethiol molecules coating the metal core make Au and Ag MPNs ideal building blocks for the self-assembly of nanoelectronic devices. To date, most studies of metal MPNs are of Au nanoparticles encapsulated by an alkanethiol monolayer.

## ELECTRONIC APPLICATIONS OF METAL NANOPARTICLES

The simplest metal nanoparticle-based electronic material is fabricated by suspending Au MPNs in an organic solvent such as toluene, casting or spraying this suspension on a solid substrate, and allowing the solvent to evaporate. The nanoparticles agglomerate as the solvent evaporates to form a loosely aggregated solid. If the original suspension is dilute and care is taken to allow the solvent to evaporate slowly, small 3-D superlattice domains or “ordered MPN crystals” form as the suspension becomes supersaturated; however, in general, the solid phase that forms is amorphous. The closest interparticle spacing in the solid is determined by the length of the alkanethiol molecules encapsulating the Au particles. Because this spacing is on the order of a nanometer, these amorphous solids are weak electrical conductors in which electrons tunnel through the organic layers separating the Au particles and hop from particle to particle. Snow and Wohltjen<sup>[5]</sup> have measured the electrical conductivity of amorphous films of Au MPNs as a function of the ratio of the diameter of the gold core to the length of the alkanethiol encapsulant. They measured electrical conductivities ranging from  $10^{-6}$  to  $10^{-12}$  ( $\Omega \text{ cm}$ )<sup>-1</sup> and found that the conductivity at a given temperature increases as this ratio is increased. They have also shown that, when such an MPN solid is exposed to volatile organic vapors, its electrical conductivity is a function of the partial pressure of the organic molecule.<sup>[6]</sup> This effect is most probably because of the absorption of the organic molecule into the alkanethiol layer surrounding the gold nanoparticles. Quantum tunneling varies exponentially with distance, and a small swelling of this layer results in a large variation in tunnel resistance. Thus even as simple a structure as an amorphous solid of Au MPNs constitutes an interesting electronic material, and a film of this nanostructured material can act as a chemiresistive sensor. Unfortunately, films of alkanethiol-coated Au nanoparticles are not strongly species-selective.<sup>[6]</sup> However, adding different chemical functionalities to

the ligand shell around the Au particles may be a way to increase the chemselectivity of the film.

Amorphous films of Au MPNs can also be used to fabricate low-resistance electrical conductors on flexible substrates. Low-resistance conductors are important components of high- $Q$  inductors, capacitors, tuned circuits, and interconnects. An inexpensive method for fabricating such conductors on flexible substrates is critical for the development of ultralow-cost microelectronic systems such as radiofrequency identification tags. Using a dense suspension of Au MPNs in a volatile organic liquid, it is possible to print micron-thick lines via either ink jet or silk screen techniques on a substrate. If the Au particle diameter and the alkanethiol encapsulant are optimized, these low-conductivity Au MPN lines can be converted into high-conductivity Au lines. This transformation is made possible by the low melting temperature and low shear resistance of Au nanoparticles.<sup>[2,7,8]</sup> It is accomplished either by thermally annealing the lines at a relatively low temperature ( $<150^\circ\text{C}$ ),<sup>[9]</sup> or by exposing them to laser radiation.<sup>[10]</sup>

Although the electrical conduction behavior of an amorphous film of Au MPNs has technological potential, placing a single Au MPN between two electrodes provides a much richer range of electronic behavior. In this configuration (Fig. 1), the nanoparticle is able to suppress all electrical conduction at low-bias voltages. This phenomenon is called “Coulomb blockade.” Coulomb blockade occurs when the electrostatic energy increase caused by adding a single electron on a capacitively coupled metal island is much larger than the thermal energy of the electrons:

$$e^2/2C \gg k_B T \quad (1)$$

where  $e$  is the charge on an electron,  $C$  is the effective capacitance of the metal island,  $k_B$  is the Boltzmann constant, and  $T$  is the absolute temperature of the metal island. In the case of metal MPNs, the capacitance  $C$  is directly proportional to the radius of the metal nanoparticle. For room temperature operation,

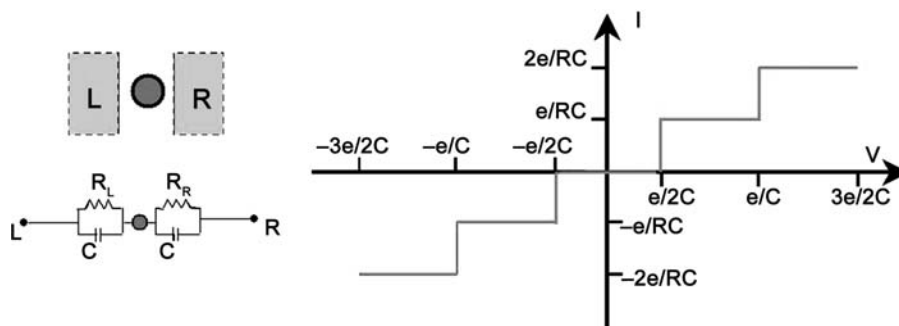


**Fig. 1** (A) Schematic representation and equivalent circuit of nanostructure consisting of a single metal MPN placed between two electrodes. (B) Ideal  $I$ - $V$  curve for this nanostructure illustrating Coulomb blockade at low bias and Coulomb staircase as bias is increased.



Eq. 1 is satisfied when the particle diameter is less than approximately 2–3 nm. Larger particles are able to suppress all electron transport only if their temperature is lowered. For Coulomb blockade to be observed, the tunneling resistance ( $R$ ) to and from the metal island must also be much greater than the resistance quantum ( $R_Q$ ):

$$R \gg R_Q \quad (2)$$

where  $R_Q = h/2e^2$  ( $\sim 12.9 \times 10^3 \Omega$ ), with  $h$  being the Planck's constant.

When both Eqs. 1 and 2 are satisfied, the  $I$ - $V$  curve for an asymmetric junction  $\{R_R \gg R_L \text{ or } R_L \gg R_R\}$  shows characteristic steps in the current, called "Coulomb staircase" (Fig. 1). The asymmetry in the resistance means that the flow of electrons is controlled either at the right or left tunnel junction, and so electrons tend to accumulate on the metal island. Because of the electrostatic energy associated with the charging of the island, an additional electron is not added at steady state until this excess energy is compensated for by increasing the external bias. Both Coulomb blockade and Coulomb staircase phenomena have been experimentally verified at room temperature using an Au MPN.<sup>[3,11]</sup> In this experiment, a scanning tunneling microscope (STM) was used to measure the  $I$ - $V$  characteristics of a vertical nanostructure, fabricated by depositing a single 2-nm-diameter gold particle on a gold substrate that had been coated with a self-assembled monolayer (SAM) of a double-ended thiol molecule.

The structure shown in Fig. 1 is the simplest example of a large class of nanoelectronic logic and data storage devices that are based on the controllable transfer of single electrons between small conducting islands separated by tunnel barriers.<sup>[12]</sup> For example, Tucker<sup>[13]</sup> proposed a nanoscale field effect transistor (FET) based on modulating the voltage range of the Coulomb blockade by applying an asymmetric bias on a conducting island transverse to the direction of

current propagation. Fabrication of such a single electron tunneling-field effect transistor (SET-FET), using metal nanoparticles, requires the ability to place 1-D chains of metal MPNs on an insulating substrate with variable interparticle spacing and the ability to address a nanoparticle having a diameter of  $\sim 2$  nm from three directions. At present, there does not appear to be any way to self-assemble such a device. Although, in principle, any SET architecture can be constructed using metal MPNs, the technical difficulties involved in self-assembling complex SET circuits that can operate at room temperature seem overwhelming.

Roychowdhury, Janes, Bandyopadhyay<sup>[14]</sup> have suggested a logic architecture (Fig. 2) involving metal MPNs that does not require room temperature Coulomb blockade for its operation. This architecture consists of a uniform 2-D array of Au MPNs with input and output addressing along the edges of the array. The nanoparticles are coupled through electron tunneling barriers both to each other and to a semiconductor substrate that is a resonant tunneling diode (RTD) structure. The computation is performed by allowing the array to relax to its ground state, which depends on the Coulomb interactions of adjacent islands for a particular set of input voltages. This 2-D array architecture is compatible with the self-assembly and microcontact printing techniques described later in the present entry, and recent reports on the formation of 8-nm-wide metallic lines<sup>[15]</sup> and addressable cantilever arrays<sup>[16]</sup> suggest that edge addressing issues and even readout of the charge state of individual nanoparticles may be tractable.

The weak interaction forces that exist between metal MPNs, although ideal for promoting self-assembly from solution, are not strong enough to produce 1-D, 2-D, or 3-D arrays that are structurally robust. Thus it is often necessary to strengthen the self-assembled structures formed by Au MPNs. This can be accomplished by displacing the monofunctional alkanethiol molecules coating the particles with difunctional molecules that bind the particles to each other or to the substrate. Both dithiol molecules and diisonitrile

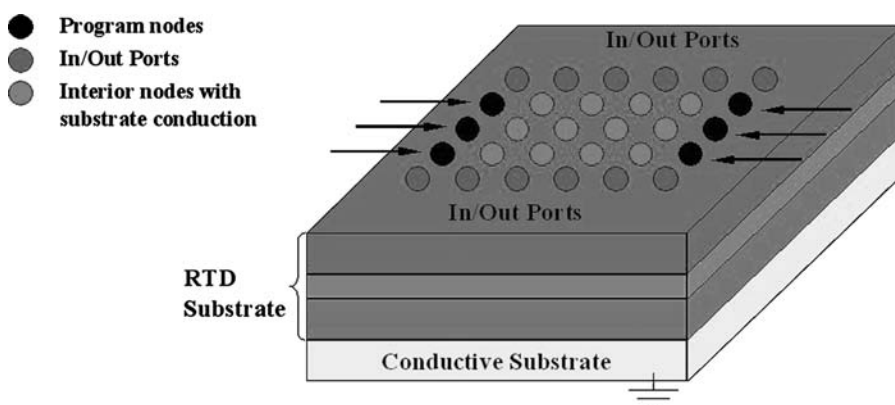


**Fig. 2** Schematic of nanoelectronic architecture proposed by Roychowdhury et al. for Boolean logic. Nanostructure consists of an ordered 2-D array of Au MPNs linked to a RTD substrate. *Source:* From Ref.<sup>[14]</sup>. ©IEEE, 1997.



molecules are able to displace monothiol molecules from Au.<sup>[17,18]</sup> Attaching conjugated molecules having distributed electronic states in the gap between adjacent metal nanoparticles in an array, or between a metal nanoparticle and a substrate, is also an attractive way to self-assemble another kind of electronic nanostructure. The metal–molecule–metal bridge that is established in this manner is the focus of the emerging field of molecular electronics.<sup>[19,20]</sup> The diode structure shown in Fig. 1 can now be thought of as being replaced by one in which the conjugated linking molecule takes the place of the Au MPN. To date, experimental measurements of electron transport through such metal–molecule–metal structures have been attempted either by introducing a “nano” gap between two metal electrodes and adsorbing the desired organic molecules on the electrodes, or by STM manipulation of metal atoms and a single organic molecule on a substrate. An elegant example of this latter type of experiment is reported in the recent paper by Nazin, Qiu, and Ho<sup>[21]</sup> Although interesting electronic behavior has been demonstrated,<sup>[22]</sup> the problem of how to self-assemble logic or memory circuits is still unsolved. A fruitful approach to this problem may be to self-assemble molecular electronic devices using “linked arrays” of metal MPNs.

Au MPNs have been used to fabricate lateral structures that are linked by conjugated molecules. Andres et al.<sup>[17]</sup> fabricated a linked monolayer of Au nanoparticles in the gap between lithographically defined electrodes by first self-assembling a uniform superlattice array of Au MPNs and then by replacing the alkanethiol molecules coating the Au particles with

difunctional conjugated molecules. They measured electron transport in this monolayer film. Datta et al.<sup>[23]</sup> have proposed the use of quasi-1-D conductive ribbons of linked metal nanoparticles, which they term “molecular ribbons,” as interconnects for semiconductor devices. It is difficult to fabricate linked monolayer films that are free of defects when the length of the linking molecule does not closely match the spacing in the original MPN array. One way to solve this problem is to fabricate a linked bilayer film, such as that shown in Fig. 3.<sup>[24]</sup> This bilayer consists of two monolayers of Au MPNs with a molecular interconnect covalently linking the two layers. This nanostructure has been proposed as the basis of a novel chemiresistive sensor.<sup>[24]</sup> It is hypothesized that target molecules that ligate with the linking molecules will shift the electronic energy levels of the linking molecules, thereby changing the tunnel resistance between the two layers and the electrical conductivity of the film. If this hypothesis is confirmed, this scheme would provide a generic method for fabricating chemiselective sensing elements.

Au MPNs have also been used to construct linked vertical structures. They have been utilized as nanoscale contacts on a semiconductor substrate<sup>[25]</sup> and as nanoscale switches on top of redox molecules.<sup>[26]</sup> Such linked vertical structures represent an attractive paradigm for molecular electronics-based devices.

Metal MPNs are also being studied for hybrid microelectronic applications such as floating gate memory cells and multiple tunnel junction devices.<sup>[27,28]</sup> Metal nanoparticles provide an attractive choice for these applications because of the abundance

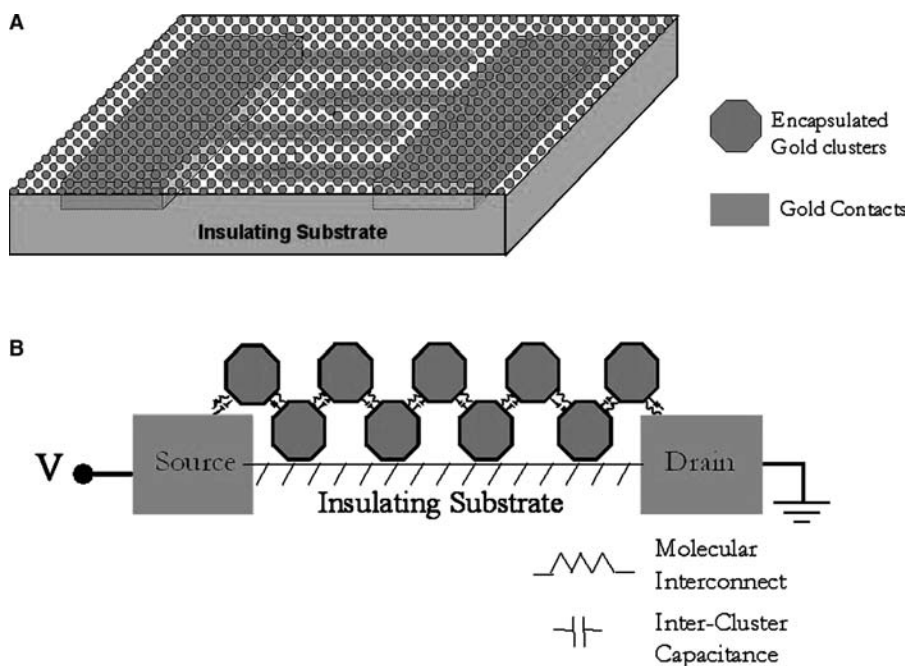


**Fig. 3** Schematic representation of a chemiresistive sensor element proposed by Santhanam. (A) Plane view and (B) cross-sectional view. Nanostructure consists of a uniform bilayer of Au MPNs in which the two layers are interconnected by adsorbate-specific organic molecules. This bilayer forms the channel of an electrical diode. *Source:* From Ref.<sup>[24]</sup>.

of electrons near the Fermi level and the ability to tune their work function by changing the metal.

## MPN SYNTHESIS

Metal MPNs can be synthesized either in the gas phase or in liquid solution. In either case, the essential requirement for synthesizing particles with a narrow size distribution is to initiate a temporally discrete homogeneous nucleation event followed by a slow growth regime, and to prevent particle aggregation. An apparatus for gas-phase synthesis of metal nanoparticles is shown schematically in Fig. 4.<sup>[29,30]</sup> Metal atoms, evaporated from a single crucible or a series of crucibles located in a resistively heated oven, are entrained in helium and induced to condense by mixing the hot flow from the oven with a room temperature stream of helium. Controlling conditions in the oven and helium flows controls the mean particle size. The particles are thermally annealed in the gas phase by passing the aerosol mixture through a tube furnace. They are scrubbed from the gas phase by contact with a mist of organic solvent containing surfactant molecules and collected as a stable colloidal suspension. The reactor shown in Fig. 4 also has provision for expanding a portion of the aerosol stream into a vacuum chamber to form a particle beam. Potential advantages of gas-phase synthesis are: 1) the ability to synthesize extremely small particles and to vary

the mean particle size over a wide range; 2) the ability to produce pure metal particles, which may then be encapsulated with a wide variety of surfactants; 3) the ability to produce mixed metal particles even when the constituent metals are immiscible at room temperature; and 4) the ability to thermally anneal metal particles before encapsulating them with an organic surfactant.

Solution-based techniques for the synthesis of metal nanoparticles are based on the reduction of positively charged metal ions or ion complexes in solution usually in the presence of a capping ligand to arrest particle growth at a desired size. The major advantage of solution synthesis is the simplicity of the required equipment. The major disadvantage is the need for removal of excess reactants and for isolation of the particles as pure MPNs. In the case of Au particles, encapsulation by alkanethiols simplifies the isolation and purification steps greatly. A general technique for solution synthesis of nanoparticles with a controlled size and a narrow size distribution is to isolate small volumes of aqueous solution in which particle growth takes place by means of nonionic inverse micelles.<sup>[31,32]</sup> However, two homogeneous solution methods are more commonly used for the production of Au MPNs. The first method is reported by Brust et al.<sup>[33]</sup> This is a two-phase (water–toluene) reduction of  $\text{AuCl}_4^-$  by sodium borohydride in the presence of an alkanethiol. The Au ions are transferred to the toluene phase using tetraoctylammonium bromide,

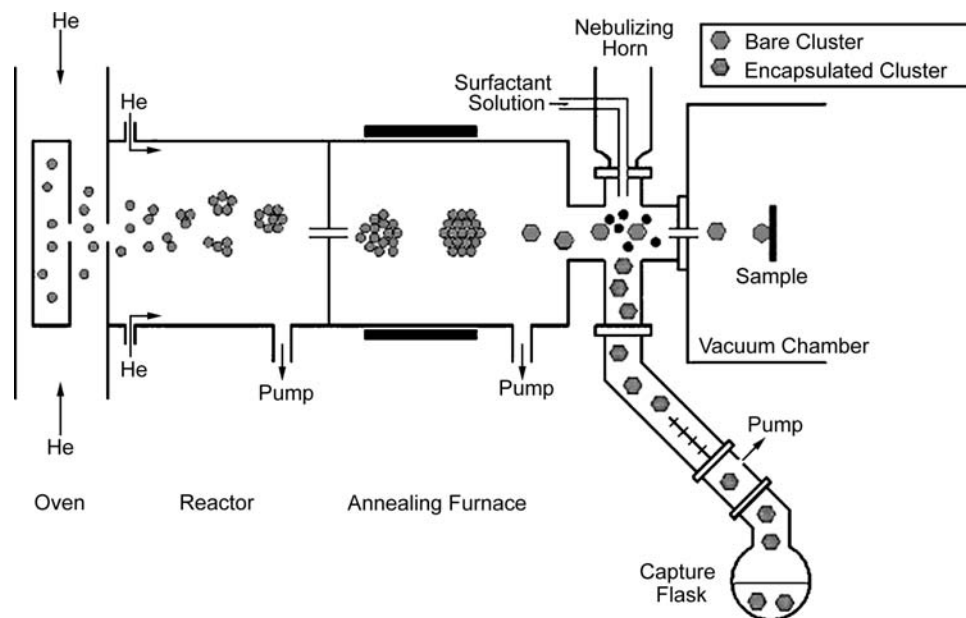


**Fig. 4** Schematic representation of an aerosol reactor used to produce metal MPNs with a narrow size distribution. Metal atoms are condensed in a helium flow to form bare metal clusters (nanoparticles). The aerosol containing the nanoparticles then passes through an annealing furnace, after which the particles are encapsulated with an appropriate surfactant molecule and captured as a colloidal suspension.

where they are simultaneously reduced by borohydride and capped by the alkanethiol. Once encapsulated Au particles have formed, they are precipitated from the toluene solution by the addition of a polar solvent, and then washed, dried, and resuspended in a non-polar solvent such as toluene, hexane, or chloroform. The second method is reported by Giersig and Mulvaney.<sup>[34]</sup> This method makes use of the classical method of Turkevich, Stevenson, and Hillier<sup>[35]</sup> which produces charge-stabilized Au particles by reduction of  $\text{AuCl}_4^-$  in water using trisodium citrate as the reducing agent. An alkanethiol dissolved in tetrahydrofuran (THF) is then added to this aqueous solution, causing encapsulation of the Au particles and their gradual flocculation. The capped Au particles can be extracted into cyclohexane. They are precipitated from cyclohexane by the addition of a polar solvent, and then washed, dried, and resuspended in a nonpolar solvent. Au MPNs produced by the Giersig method retain a residual charge before they are extracted into cyclohexane and can be deposited on a conducting substrate by electrophoresis.<sup>[34]</sup> After they have been washed, dried, and resuspended in a nonpolar solvent, there does not seem to be any difference between Au MPNs produced by the two methods; however, the Brust method appears to be more suitable for the synthesis of smaller particles (<5 nm) and the Giersig method appears to be more suitable for the synthesis of larger particles (>5 nm).

The standard deviation of the diameter distribution of particles synthesized by either the Brust method or the Giersig method is about 10%. The size distribution can be narrowed by fractional crystallization.<sup>[36]</sup> This involves selective precipitation of the particles in a solvent mixture containing a good solvent and a poor solvent such as toluene/acetone. Whetten et al.<sup>[37]</sup> have used selective precipitation in the presence of excess alkanethiol surfactants to refine the size distribution of Au MPNs synthesized by the Brust method. Starting with Au MPNs having a mean diameter in the 1- to 2-nm range, they were able to prepare monodispersed samples having a fixed number of gold atoms. Stoeva et al.<sup>[38]</sup> have found that it is possible to refine both the size distribution and faceting of Au MPNs simply by heating a concentrated suspension of the particles in a process they have termed “digestive ripening.”

Au MPNs produced by solution synthesis are compact, nearly spherical particles with a narrow size distribution that can be improved by size-selective precipitation; however, the gold cores are not necessarily faceted single crystals. Whetten et al.<sup>[37]</sup> report that in the 1.5- to 3.5-nm range, Au MPNs synthesized by the Brust method have faceted gold cores that are primarily single crystals with a face-centered cubic (FCC) lattice and a lattice constant close to the bulk gold value of 0.409 nm. High-resolution transmission

electron microscopy (HRTEM) analysis of Au MPNs that were synthesized by the Giersig method with diameters in the 5- to 20-nm range reveals that these particles are primarily polycrystalline.<sup>[39]</sup> This is also true for Au MPNs with diameters greater than a few nanometers that are synthesized by gas-phase condensation, unless they are thermally annealed by heating them above their melting temperature and then allowing them to recrystallize in the gas phase. Then they become predominately single crystals or singly twinned crystals with an FCC lattice and a lattice constant of 0.409 nm.<sup>[24,39]</sup>

The ultimate Au MPN as far as controlled size and crystal structure are concerned is the triphosphine ligand-protected 55-gold-atom particle synthesized by Schmid et al.<sup>[40]</sup> almost two decades ago. These particles have an icosahedral geometry and exhibit Coulomb blockade behavior at room temperature. They played an important role in establishing the quantum size behavior of metal MPNs and in suggesting possible electronic applications of encapsulated metal nanoparticles.<sup>[41,42]</sup> However, the complex synthesis of these particles, which requires anaerobic conditions and diborane as a reducing agent, and the difficulty of replacing the triphosphine ligands with other ligands have led to these particles being studied much less than alkanethiol-encapsulated Au particles. A more convenient synthesis technique and schemes for utilizing exchange reactions to modify the characteristics of these particles have been reported.<sup>[43]</sup>

Because of their simplicity and flexibility, the solution-based synthesis routes of Brust et al.<sup>[33]</sup> and Giersig and Mulvaney<sup>[34]</sup> are currently the methods of choice for preparing Au MPNs for electronic applications. Similar solution-based methods are available for preparing semiconductor and magnetic metal MPNs.<sup>[36,44]</sup> Methods utilizing safer solvents and biosynthetic routes are being explored to address environmental concerns.<sup>[45,46]</sup>

## FABRICATION OF ORDERED MPN ARRAYS

The ability to assemble nanometer-scale metal islands or particles into ordered arrays is a prerequisite for the successful fabrication of nanoscale electronic devices based on these building blocks. In what follows, we focus on self-assembly methods involving metal MPNs. “Top-down” approaches using resist-based lithographic patterning will not be discussed at all. However, two methods that do not make use of metal MPNs are worth mentioning. The first technique is to self-assemble an ordered monolayer of polystyrene or silica spheres on a substrate and thermally evaporate metal atoms onto this colloidal mask. This results in nanometer-scale metal deposits forming on

the areas of the substrate not masked by the colloidal spheres.<sup>[47]</sup> The second technique involves synthesis of metal nanoparticles inside structures formed using diblock polymers.<sup>[48,49]</sup> The major drawbacks of both of these schemes are that the metal islands or particles have largely uncontrolled shapes and typically have interparticle spacings much larger than molecular dimensions. Because of the ease by which Au nanoparticles can be thermally annealed, the first of these drawbacks may not be severe in the case of Au. Nevertheless, the large interparticle spacings make it difficult to see how electronic circuits can be fabricated using these methods. Self-assembly of MPNs that have been preselected as to size, shape, and surface chemistry into ordered arrays seems to be the most promising approach for fabricating nanoscale electronic devices.

### 3-D Arrays

Starting with metal MPNs that have a narrow size distribution, it is relatively easy to produce ordered 3-D arrays or superlattices, in which the MPNs take the place of atoms in conventional crystals. Ordered 3-D arrays are formed by supporting a drop of the colloidal nanoparticle suspension on a flat surface and slowly evaporating the solvent. Encapsulated metal nanoparticles typically self-assemble into an FCC or HCP superlattice.<sup>[38,50]</sup> Faceted, single-crystal Au MPNs often adopt preferred orientations in both 2-D and 3-D arrays in which the (111) atomic planes of each Au particle align parallel to the (111) atomic planes of all the other Au particles and to the surface of the supporting substrate.<sup>[38,39]</sup>

### 2-D Arrays

Uniform, close-packed monolayers of MPNs are an essential component of many proposed nanoelectronic

devices. There are several techniques for fabricating nanoparticle monolayers by self-assembly. These fall into three categories: 1) field-enhanced or molecular interaction-induced deposition from a colloidal solution of MPNs onto a solid substrate; 2) drop casting or spin coating of a suspension of MPNs onto a solid substrate and allowing of the solvent to evaporate; and 3) spreading of a suspension of hydrophobic MPNs in an organic solvent on a water surface, allowing of the solvent to evaporate, and transferring of the floating MPN film to a solid substrate.

Giersig and Mulvaney<sup>[34]</sup> employed electrophoretic deposition at field strengths of 1 V/cm to deposit a monolayer of Au MPNs on a carbon film-coated TEM grid. The monolayer was polycrystalline with small hexagonal close-packed domains. When the nanoparticles were deposited without an electric field, no ordering was observed. The adsorption of MPNs from solution onto functionalized surfaces has also been used to form nanoparticle monolayers. In this case, the substrate is coated with a “tether” molecule having a strong affinity for the particles. The substrate is immersed in a colloidal solution of MPNs, removed after a period of time, and rinsed to remove unbound particles. The MPN monolayer formed in this manner is amorphous and is seldom dense (Fig. 5A).<sup>[51,52]</sup> This approach can also be used to form multilayers if, after the deposition of each monolayer, the monofunctional molecule encapsulating the particles is replaced by a difunctional molecule such as a dithiol. The major drawback of these methods for electronic applications is the lack of long-range order in the particle film.

The simplest method of forming a monolayer of MPNs is to spread a thin film of a colloidal suspension containing the particles either by drop casting or spin coating on a substrate that is wet by the solvent, and to allow the solvent to evaporate.<sup>[17]</sup> As the solvent evaporates, small monolayer islands form on the substrate. These islands result from the breakup of the

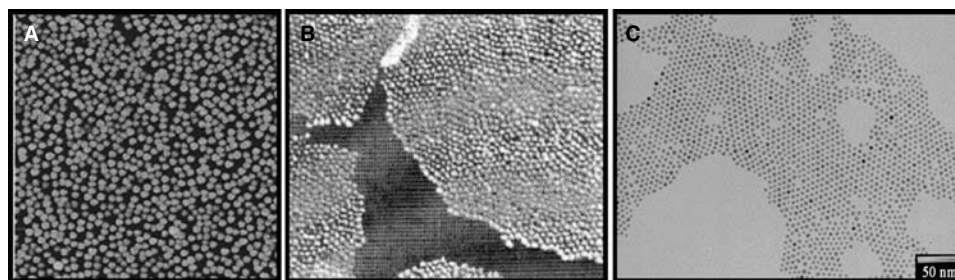


**Fig. 5** Examples of nanoparticle monolayers self-assembled by three different methods. (A) Scanning electron microscopy (SEM) micrograph of a monolayer formed by adsorption of the particles onto a substrate coated with a bifunctional tether molecule. (B) SEM micrograph of a monolayer produced by compression of nanoparticle rafts on a Langmuir trough. (C) TEM micrograph of a monolayer formed by drop casting a colloidal suspension of nanoparticles on a carbon film-coated TEM grid. *Source:* From Ref.<sup>[51]</sup>. ©ACS, 2000. From Ref.<sup>[56]</sup>. ©AIP, 2001.

liquid film because of dewetting as the film thickness approaches molecular dimensions. The monolayer islands are dense and consist of small hexagonal close-packed domains (Fig. 5C). An important parameter for optimizing the size and degree of order in these monolayer domains is the rate of evaporation of the solvent. However, the key to forming large ordered regions are the uniformity and smoothness of the substrate.<sup>[53]</sup> Surface nonuniformities arrest the lateral mobility of the nanoparticles and result in microscopic voids and grain boundaries in the particle film.

A liquid/liquid interface, because of its inherent uniformity in the lateral direction and non-uniformity in the vertical direction, provides an ideal surface for self-assembling 2-D arrays of nanoparticles. Usually the self-assembly process is carried out by casting an organic suspension containing nanoparticles, which are encapsulated by a hydrophobic molecule, on a water surface and by allowing the solvent to evaporate. The number of nanoparticles spread on the water surface is taken to be smaller than the number needed to form a dense monolayer. When the organic solvent evaporates, discrete monolayer rafts of nanoparticles form on the water surface. These monolayer domains are often well-ordered but cover only a fraction of the surface area. A dense monolayer is obtained by decreasing the area available to the particle rafts using a Langmuir trough.<sup>[54–56]</sup> As the area of the trough is decreased, the monolayer rafts collide with each other and coalesce. Without an organic solvent present, the monolayer domains typically exhibit solidlike behavior and resist deformation. Collier et al.<sup>[57]</sup> were able to make use of the rigid behavior of a nanoparticle film supported on a water surface to carefully compress a film of Ag MPNs and to measure a reversible insulator-to-metal transition as the film was compressed and the tunneling distance between adjacent particles was decreased. Unfortunately, this rigid behavior often results in microscopic voids (Fig. 5B) and multilayer domains in monolayers assembled using a Langmuir trough.<sup>[56]</sup>

Schmid and Beyer<sup>[58]</sup> have proposed an intriguing variation on the classical technique. They introduce an amphiphilic molecule that has a strong affinity for the nanoparticles to assist in the formation of an ordered particle monolayer. They first self-assemble a

layer of these molecules at an organic / water interface. When nanoparticles are introduced to the system, they adsorb on the amphiphilic layer and assemble into monolayer sheets or ribbons, depending on the experimental conditions.

Santhanam et al.<sup>[59]</sup> have also proposed a modification of the classical technique. They are able to self-assemble uniform, ordered 2-D arrays of Au MPNs on a water surface by controlling the nucleation and growth of the particle monolayer. This is accomplished by designing a cell that establishes a “concave” lens of colloidal solution on the water surface (Fig. 6). As the solvent evaporates, the organic layer thins fastest at the center of the cell and, at some point, a monolayer array of MPNs nucleates at this spot. The periphery of this 2-D array is defined by a circular contact line. As more solvent evaporates, additional MPNs deposit at the edge of the particle monolayer, and the contact line moves steadily outward. The advantage of this technique is that new particles are added to the growing monolayer in the presence of solvent molecules. This ensures enough particle mobility to largely eliminate microscopic holes and grain boundaries, and promotes the formation of a close-packed crystalline monolayer. Figure 7 shows a photograph of a film of 5-nm-diameter Au MPNs that was self-assembled on a water surface using this technique. The different hue seen near the edge of the cell arises from the increased curvature of the water interface at the cell wall, which leads to contact line instabilities. This results in alternating bands of multilayer regions surrounding the uniform monolayer region in the center of the cell. Figure 7 also shows TEM micrographs of samples of this Au MPN film taken near the center and the edge of the cell. These images clearly illustrate the long-range translational ordering of the monolayer that forms in the center of the cell and the nature of the multilayer bands that form at the edge of the cell. A bilayer film can be produced on the water surface simply by increasing the concentration of the particles in the initial colloidal solution.

Once a high-quality monolayer of MPNs is self-assembled on the water surface, if it is to be used for constructing an electronic device, it must be transferred to a solid substrate. This transfer has been accomplished by either dipping the substrate through the

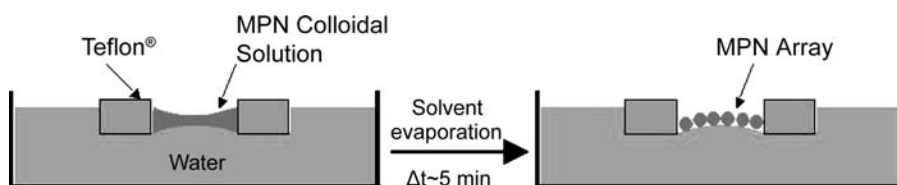


**Fig. 6** Schematic illustration of the process proposed by Santhanam et al. for self-assembly of a uniform close-packed monolayer of metal MPNs by controlling the nucleation and growth of the monolayer film on a water surface. *Source:* From Ref.<sup>[59]</sup>. ©ACS, 2003.

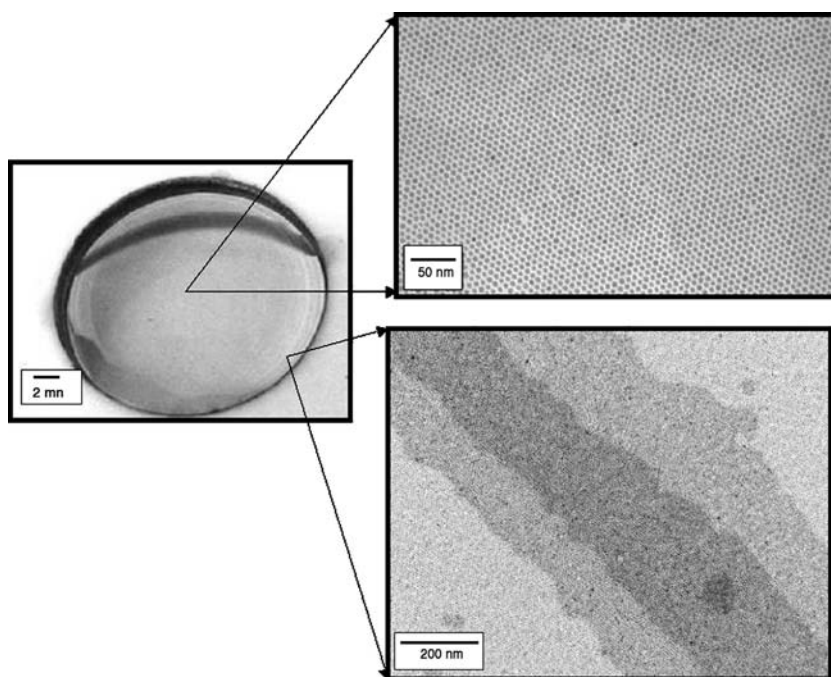


**Fig. 7** Photograph of a film of 5-nm-diameter Au MPNs that were self-assembled on a water surface using the method of Santhanam et al. The two inserts are TEM micrographs of samples of this nanoparticle film that were transferred to carbon film-coated TEM grids. The upper insert is taken from the central portion of the film, which is a uniform close-packed monolayer with a diameter of approximately 1 cm. The lower insert is taken from the outer edge of the film and shows one of the multilayer bands that form near the wall of the cell. *Source:* From Ref.<sup>[59]</sup>. ©ACS, 2003.

water surface and slowly withdrawing it [Langmuir–Blodgett (LB) method], or by holding the substrate parallel to the water surface and touching it to the nanoparticle film [Langmuir–Schaefer (LS) method]. Although Santhanam et al.<sup>[59]</sup> found the LS method preferable, it proved unsatisfactory when the substrate was large and/or hydrophilic. As a result, they developed a two-step transfer process. First, using the LS method, the nanoparticle film is transferred from the water surface to a polydimethylsiloxane (PDMS) pad. After carefully wicking off any water drops that adhere to the transferred nanoparticle film, the PDMS pad is then pressed conformally onto the desired substrate. This technique is analogous to conventional microcontact printing,<sup>[60]</sup> with the nanoparticle monolayer taking the place of the molecular ink. This two-step printing technique facilitates the formation of MPN films with a controlled number of layers. This

can be achieved either by repeating the process for a desired number of cycles and printing the monolayers one on top of the other, or by picking up the monolayers successively onto the same elastomeric pad and then using a single printing step. The use of a PDMS stamp also allows the formation of patterned monolayer and multilayer arrays of MPNs by using an appropriately structured elastomeric pad.<sup>[24,61]</sup> Fig. 8 shows TEM images at three different magnifications of a bilayer film of 5-nm-diameter Au MPNs that has been patterned into a series of micron-scale lines and printed on a  $\text{Si}_3\text{N}_4$  substrate.<sup>[24,61]</sup>

### 1-D Arrays

The ability to form 1-D arrays or thin ribbons of metal MPNs is important in the context of using linked metal

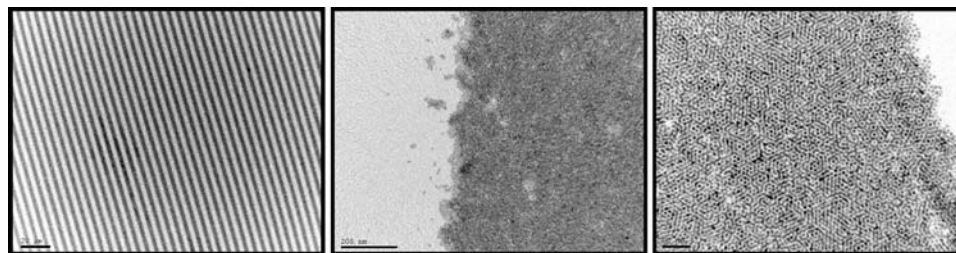


**Fig. 8** TEM micrographs of a bilayer film of 5-nm-diameter Au MPNs that were deposited as a pattern of parallel lines on a silicon nitride substrate using the two-step process proposed by Santhanam et al. The low-magnification micrograph on the left shows the lines printed on the substrate. The higher-magnification micrograph in the center shows the relatively sharp edge of one of the lines. The highest-magnification micrograph on the right shows the dense close-packed nanostructure of the film at the edge of one of the lines. (From Ref.<sup>[61]</sup>. ©ACS, 2003.)



MPNs as interconnects. However, because metal MPNs are nearly spherical in shape, this is a difficult pattern to produce by self-assembly and can be accomplished only with the help of appropriate templates to direct the self-assembly process. For example, carbon nanotubes, long-chain polymers, and DNA strands can be decorated with MPNs to produce quasi-1-D chains, and MPNs can be assembled inside a nanotube or adsorbed on a thin line fabricated on a substrate. Hornyak et al.<sup>[62]</sup> have synthesized nanoporous alumina membranes with controlled pore size and narrow pore size distribution, and used the pores as a template to form quasi-1-D chains of Au MPNs. A colloidal solution of the particles was drawn by means of a vacuum into the pores. On evaporation of the solvent, some of the pores were found to be filled with MPN chains. Gleich, Chi, and Fuchs<sup>[63]</sup> made use of the wetting instability of a monolayer transferred onto a solid substrate to produce channels on the order of 200 nm in width and were able to form quasi-1-D chains of MPNs by drop casting a colloidal solution onto this template. Quasi-1-D arrays or ribbons of MPNs have also been prepared by patterning a 2-D monolayer of MPNs using e-beam lithography.<sup>[64]</sup> In principle, the PDMS stamping technique described in “2-D Arrays” could be extended to produce nanometer-scale ribbons of metal MPNs using an appropriate master to mold the PDMS stamp. The technique of Melosh et al.,<sup>[15]</sup> which makes use of selective etching of a GaAs/AlGaAs superlattice to generate thin parallel trenches, could possibly be used as the master, or a master could be generated using e-beam lithography and PMMA resist.

## CONCLUSION

Au MPNs are attractive building blocks for fabricating nanoelectronic devices by self-assembly. The synthesis of Au MPNs with a mean diameter in the 2- to 20-nm range, with a narrow size distribution, and with a monolayer coating of alkanethiol molecules is, by now, a standard procedure. The assembly of these particles to form chemiresistive films and low-resistivity printable conductors is well established. Recent results describing the self-assembly of high-quality monolayer films of Au MPNs on a water surface and the discovery that these films can be transferred as patterned close-packed arrays onto any reasonably flat substrate have opened up a wide range of potential nanoelectronic applications. What remains is the need to establish methods to reproducibly link these ordered arrays of alkanethiol-encapsulated gold particles with conjugated organic molecules to form nanometer-scale interconnects and molecular electronic circuits.

## REFERENCES

- Andres, R.P.; Averback, R.S.; Brown, W.L.; Brus, L.E.; Goddard, W.A.; Kaldor, A.; Louie, S.G.; Moscovits, M.; Percy, P.S.; Riley, S.J.; Siegel, R.W.; Spaepen, F.; Wang, Y.J. Research opportunities on clusters and cluster-assembled materials. *J. Mater. Res.* **1989**, *4* (3), 704.
- Castro, T.; Reifengerger, R.; Choi, E.; Andres, R.P. Size-dependent melting temperature of individual nanometer-sized metallic clusters. *Phys. Rev., B* **1990**, *42* (13), 8548.
- Andres, R.P.; Bein, T.; Dorogi, M.; Feng, S.; Henderson, J.I.; Kubiak, C.P.; Mahoney, W.; Osifchin, R.G.; Reifengerger, R. Coulomb staircase at room temperature in a self-assembled molecular nanostructure. *Science* **1996**, *272*, 1323.
- Simon, U. Charge transport in nanoparticle arrangements. *Adv. Mater.* **1998**, *10* (17), 1487.
- Snow, A.W.; Wohltjen, H. Size-induced metal to semiconductor transition in a stabilized gold cluster ensemble. *Chem. Mater.* **1998**, *10* (4), 947.
- Wohltjen, H.; Snow, A.W. Colloidal metal-insulator-metal ensemble chemiresistor sensor. *Anal. Chem.* **1998**, *70* (14), 2856.
- Buffat, Ph.; Borel, J.-P. Size-effect on the melting temperature of gold particles. *Phys. Rev., A* **1976**, *13* (6), 2287.
- Schaefer, D.M.; Patil, A.; Andres, R.P.; Reifengerger, R. Nanoindentation of a supported Au cluster. *Appl. Phys. Lett.* **1993**, *63* (12), 1492.
- Huang, D.; Liao, F.; Moles, S.; Redinger, D.; Subramanian, V. Plastic-compatible low resistance printable gold nanoparticle conductors for flexible electronics. *J. Electrochem Soc.* **2003**, *150* (7), G412.
- Bieri, N.R.; Chung, J.; Haferi, S.E.; Poulikakos, D.; Grigoropoulos, C.P. Microstructuring by printing and laser curing of nanoparticle solutions. *Appl. Phys. Lett.* **2003**, *82* (20), 3529.
- Andres, R.P.; Datta, S.; Dorogi, M.; Gomez, J.; Henderson, J.I.; Janes, D.B.; Kolagunta, V.R.; Kubiak, C.P.; Mahoney, W.; Osifchin, R.F.; Reifengerger, R.; Samanta, M.P.; Tian, W. Room temperature Coulomb blockade and Coulomb staircase from self-assembled nanostructures. *J. Vac. Sci. Technol., A* **1996**, *14* (3), 1180.
- Likharev, K.K. Single-electron devices and their applications. *Proc. IEEE* **1999**, *87* (4), 606.
- Tucker, J.R. Complementary digital logic based on the Coulomb blockade. *J. Appl. Phys.* **1992**, *72* (9), 4399.
- Roychowdhury, V.P.; Janes, D.B.; Bandyopadhyay, S. Nanoelectronic architecture for Boolean logic. *Proc. IEEE* **1997**, *85* (4), 574.
- Melosh, N.A.; Boukai, A.; Diana, F.; Gerardot, B.; Badolato, A.; Petroff, P.M.; Heath, J.R. Ultrahigh-density nanowire lattices and circuits. *Science* **2003**, *300*, 112.
- Vettiger, P.; Cross, G.; Despont, M.; Dreschler, U.; Dürig, U.; Gotsmann, B.; Härberle, W.; Lantz, M.A.; Rothuizen, H.E.; Stutz, R.; Binnig, G. The Millipede—Nanotechnology entering data storage. *IEEE. Trans. Nanotechnol.* **2002**, *1* (1), 39.

17. Andres, R.P.; Bielefeld, J.D.; Henderson, J.I.; Janes, D.B.; Kolagunta, V.R.; Kubiak, C.P.; Mahoney, W.J.; Osifchin, R.G. Self-assembly of a two-dimensional superlattice of molecularly linked metal clusters. *Science* **1996**, *273*, 1690.
18. Henderson, J.I.; Ferrence, G.M.; Feng, S.; Bein, T.; Kubiak, C.P. Self-assembled monolayers of dithiols, diisocyanides, and isocyanothiols on gold: "Chemically sticky" surfaces for covalent attachment of metal clusters and studies of interfacial electron transfer. *Inorg. Chim. Acta* **1996**, *242*, 115.
19. Aviram, A.; Ratner, M.A. Molecular rectifiers. *Chem. Phys. Lett.* **1974**, *29* (2), 277.
20. Avouris, P. Molecular electronics with carbon nanotubes. *Acc. Chem. Res.* **2002**, *35* (12), 1026.
21. Nazin, G.V.; Qiu, X.H.; Ho, W. Visualization and spectroscopy of a metal-molecule-metal bridge. *Science* **2003**, *302*, 77.
22. Chen, J.; Reed, M.A.; Rawlett, A.M.; Tour, J.M. Large on-off ratios and negative differential resistance in a molecular electronic device. *Science* **1997**, *278*, 252.
23. Datta, S.; Janes, D.B.; Andres, R.P.; Kubiak, C.P.; Reifenberger, R.G. Molecular ribbons. *Semicond. Sci. Technol.* **1998**, *13* (12), 1347.
24. Santhanam, V. Fabrication of Nanoelectronic Devices Using Self-Assembled 2D Arrays of Monolayer Protected Clusters. In *Ph.D. Thesis*; Purdue University, 2002.
25. Lee, T.; Liu, J.; Janes, D.B.; Kolagunta, V.R.; Dicke, J.; Andres, R.P.; Lauterbach, J.; Melloch, M.R.; McInturff, D.; Woodall, J.M.; Reifenberger, R. An ohmic nanocontact to GaAs. *Appl. Phys. Lett.* **2000**, *74* (19), 2869.
26. Gittins, D.I.; Bethell, D.; Schiffrin, D.J.; Nichols, R.J. A nanometre-scale electronic switch consisting of a metal cluster and redox-addressable groups. *Nature* **2000**, *408*, 67.
27. Liu, Z.; Kim, M.; Narayanan, V.; Kann, E.C. Process and device characteristics of self-assembled metal nano-crystal EEPROM. *Superlattices Microstruct.* **2000**, *28* (5-6), 393.
28. Mizuta, H.; Müller, H.-O.; Tsukagoshi, K.; Williams, D.; Durrani, Z.; Irvine, A.; Evans, G.; Amakawa, S.; Nakazato, K.; Ahmed, H. Nanoscale Coulomb blockade memory and logic devices. *Nanotechnology* **2001**, *12* (2), 155.
29. Park, S.B. Optimal Design of a Reactor for Gas-Phase Generation of Metal Microclusters. In *Ph.D. Thesis*; Purdue University, 1988.
30. Patil, A.N. Synthesis and Characterization of Structured One and Two Component Clusters. In *Ph.D. Thesis*; Purdue University, 1994.
31. Pileni, M.P. Nanosized particles made in colloidal assemblies. *Langmuir* **1997**, *13* (13), 3266.
32. Martin, J.E.; Wilcoxon, J.P.; Odinek, J.; Provencio, P.J. Control of the interparticle spacing in gold nanoparticle superlattices. *Phys. Chem., B* **2000**, *104* (40), 9475.
33. Brust, M.; Walker, M.; Bethell, D.; Schiffrin, D.J.; Whyman, R. Synthesis of thiol-derivatized gold nanoparticles in a two-phase liquid-liquid system. *J. Chem. Soc., Chem. Commun.* **1994**, *7*, 801.
34. Giersig, M.; Mulvaney, P. Preparation of ordered monolayers by electrophoretic deposition. *Langmuir* **1993**, *9* (12), 3408.
35. Turkevich, J.; Stevenson, P.C.; Hillier, J. A study of the nucleation and growth processes in the synthesis of colloidal gold. *Discuss. Faraday Soc.* **1951**, *11*, 55.
36. Murray, C.B.; Norris, D.J.; Bawendi, M.G. Synthesis and characterization of nearly monodisperse CdE (E = S, Se, Te) semiconductor nanocrystallites. *J. Am. Chem. Soc.* **1993**, *115* (5), 8706.
37. Whetten, R.L.; Houry, J.T.; Alvarez, M.M.; Murthy, S.; Vezmar, I.; Wang, Z.L.; Stephens, P.W.; Cleveland, C.L.; Luedtke, W.D.; Landman, U. Nanocrystal gold molecules. *Adv. Mater.* **1996**, *8* (5), 428.
38. Stoeva, S.; Klabunde, K.J.; Sorensen, C.; Dragieva, I. Gram-scale synthesis of monodisperse gold colloids by the solvated metal atom dispersions method and digestive ripening and their organization into two- and three-dimensional structures. *J. Am. Chem. Soc.* **2002**, *124* (10), 2305.
39. Du, Y. TEM Characterization of Au Nanoclusters and Two-Dimensional Au Cluster Arrays. In *M.S. Thesis*; Purdue University, 2000.
40. Schmid, G.; Pfeil, R.; Boese, R.; Bandermann, F.; Meyer, S.; Calis, G.H.M.; van der Velden, J. Au<sub>55</sub>[P(C<sub>6</sub>H<sub>5</sub>)<sub>3</sub>]<sub>12</sub>C<sub>16</sub>—ein goldcluster ungewöhnlicher gröÙe. *Chem. Ber.* **1981**, *114*, 3634.
41. Schön, G.; Simon, U. A fascinating new field in colloid science: small ligand-stabilized metal clusters and possible application to microelectronics: part I. State of the art. *Colloid Polym. Sci.* **1995**, *273* (2), 101.
42. Schön, G.; Simon, U. A fascinating new field in colloid science: small ligand-stabilized metal clusters and possible applications to microelectronics: part II. Future directions. *Colloid Polym. Sci.* **1995**, *273* (3), 202.
43. Weare, W.W.; Reed, S.M.; Warner, M.G.; Hutchinson, J.E. Improved synthesis of small ( $d_{\text{core}} = 1.5$  nm) phosphine-stabilized gold nanoparticles. *J. Am. Chem. Soc.* **2000**, *122* (51), 12,890.
44. Murray, C.B.; Sun, S.; Gaschler, W.; Doyle, H.; Betley, T.A.; Kagan, C.R. Colloidal synthesis of nanocrystals and nanocrystal superlattices. *IBM J. Res. Develop.* **2001**, *45* (1), 47.
45. Ghosh, A.; Patra, C.R.; Mukherjee, P.; Sastry, M.; Kumar, R. Preparation and stabilization of gold nanoparticles formed by in situ reduction of aqueous chloroaurate ions within surface-modified mesoporous silica. *Microporous Mesoporous Mater.* **2003**, *58* (3), 201.
46. Pum, D.; Sleytr, U.B. The application of bacterial S-layers in molecular nanotechnology. *Trends Biotechnol.* **1999**, *7* (1), 8.
47. Hulteen, J.C.; Van Duyne, R.P. Nanosphere lithography: a materials general fabrication process for periodic particle array surfaces. *J. Vac. Sci. Technol., A* **1995**, *13* (3), 1553.
48. Spatz, J.P.; Roescher, A.; Moller, M. Gold nanoparticles in micellar poly(styrene)- $\beta$ -poly(ethylene oxide) films—size and interparticle control in monoparticulate films. *Adv. Mater.* **1996**, *8*, 337.

49. Spatz, J.P.; Mossner, St.; Moller, M. Mineralization of gold nanoparticles in a block copolymer microemulsion. *Chem. Eur. J.* **1996**, *2*, 1552.
50. Harfenist, S.A.; Wang, Z.L.; Whetten, R.L.; Vezmar, I.; Alvarez, M.M. Three-dimensional hexagonal close-packed superlattice of passivated Ag nanocrystals. *Adv. Mater.* **1997**, *9* (10), 817.
51. Zheng, J.W.; Zhu, Z.H.; Chen, H.F.; Liu, Z.F. Nanopatterned assembling of colloidal gold nanoparticles on silicon. *Langmuir* **2000**, *16* (10), 4409.
52. Sato, T.; Brown, D.; Johnson, B.F.G. Nucleation and growth of nano-gold colloidal lattices. *Chem. Commun.* **1997**, *11*, 1007.
53. Lin, X.M.; Jaeger, H.M.; Sorensen, C.M.; Klabunde, K.J. Formation of long-range-ordered nanocrystal superlattices on silicon nitride substrates. *J. Phys. Chem., B* **2001**, *105* (17), 3353.
54. Heath, J.R.; Knobler, C.M.; Leff, D.V. Pressure/temperature phase diagrams and superlattices of organically functionalized metal nanocrystal monolayers: the influence of particle size, size distribution, and surface passivant. *J. Phys. Chem., B* **1997**, *101* (2), 189.
55. Bourgoïn, J.-P.; Kergueris, C.; Lefevre, E.; Palacin, S. Langmuir–Blodgett films of thiol-capped gold nanoclusters: fabrication and electrical properties. *Thin Solid Films* **1998**, *327–329*, 515.
56. Huang, S.; Tsutsui, G.; Sakaue, H.; Shingubara, S.; Takahagi, T. Formation of a large-scale Langmuir–Blodgett monolayer of alkanethiol-encapsulated gold particles. *J. Vac. Sci. Technol.* **2001**, *19* (1), 115.
57. Collier, C.P.; Henrichs, S.; Shiang, J.J.; Saykally, R.J.; Heath, J.R. Reversible tuning of silver quantum dot monolayer through the metal–insulator transition. *Science* **1997**, *277*, 1978.
58. Schmid, G.; Beyer, N. A new approach to well-ordered quantum dots. *Eur. J. Inorg. Chem.* **2000**, *2000* (5), 835.
59. Santhanam, V.; Liu, J.; Agarwal, R.; Andres, R.P. Self-assembly of uniform monolayer arrays of nanoparticles. *Langmuir* **2003**, *19* (19), 7881.
60. Xia, Y.; Rogers, J.A.; Paul, K.E.; Whitesides, G.M. Unconventional methods for fabricating and patterning nanostructures. *Chem. Rev.* **1999**, *99*, 1823.
61. Santhanam, V.; Andres, R.P. Microcontact printing of uniform nanoparticle arrays. *Nano Lett.* **2004**, *in press*.
62. Hornyak, G.L.; Kröll, M.; Pugin, R.; Sawitowski, Th.; Schmid, G.; Bovin, J.-O.; Karsson, G.; Hofmeister, H.; Hopfe, S. Gold clusters and colloids in alumina nanotubes. *Chem. Eur. J.* **1997**, *3* (12), 1951.
63. Gleich, M.; Chi, L.F.; Fuchs, H. Nanoscopic channel lattices with controlled anisotropic wetting. *Nature* **2000**, *403* (2), 173.
64. Werts, M.H.V.; Lambert, M.; Bourgoïn, J.P.; Brust, M. Nanometer scale patterning of Langmuir–Blodgett films of gold nanoparticles by electron beam lithography. *Nano Lett.* **2002**, *2* (1), 43.

# Metal Nanostructures: Synthesis Controlled by Photoexcitation

Kei Murakoshi  
Yoshihiro Nakato

*Department of Chemistry, Osaka University, Osaka, Japan*

## INTRODUCTION

The current interest in the structural control of metal and semiconductor materials in the nanoscale region has been rapidly promoted in terms of construction of ultrasensitive and low-energy-consumption devices.<sup>[1]</sup> Recently developed nanodevice technologies using scanning probe microscopy have allowed us to construct ultrasmall structures on an atomic scale.<sup>[2]</sup> However, this method is not adaptable to mass production because it is too slow, especially for sizes of more than a few nanometers. This situation, together with the limitation of the size control to about a hundred nanometers for conventional photolithographic techniques, clearly indicates that the creation of nanodevices sized between a few nanometers and tens of nanometers remains an undeveloped aspect of the present nanotechnology (Fig. 1). Thus we should develop methods of effective and high-speed construction of desirable nanostructure in this size region.

To solve the problem, we have proposed the idea of applying localized photoexcitation at metal nanostructures for the structural controls. Generally, metal nanoparticles such as Au, Ag, and Cu show characteristic surface plasmon absorption in the visible–near-infrared wavelength region (Fig. 2).<sup>[3,4]</sup> The electric field induced by excited surface plasmons is highly localized, and the direction of its polarization can be controlled by changing the wavelength and polarization of illumination light. Thus if the localized field can be utilized to induce electrochemical reactions, such as metal dissolution and deposition, the effect can be applied to change and control the metal nanostructures (Fig. 3).

## OVERVIEW

There have been numerous reports on structural changes of metal nanoparticles under photoillumination,<sup>[5,6]</sup> unfortunately, most of them describe fragmentation and structural deformation of the particles. There are

few reports concerning structural control in a nanometer region by photoillumination. Generally, it is known that the quantum efficiency of photoelectrochemical reactions at metals is extremely low because of the very short lifetime of photoexcited electrons or holes in the system. But it should be noted that there are several interesting examples to prove the possibility of the plasmon-mediated photoinduced electron transfer phenomenon in photoemission experiments using roughened metal electrodes.<sup>[7–11]</sup> For example, Fedurco et al.<sup>[7]</sup> reported that increments in photocurrent reduced carbon dioxide in solution at roughened Ag electrode. The quantum yield of the photocurrent exhibited a sharp maximum at the peak wavelength of surface plasmon of Ag electrode. The results suggest that plasmon-mediated photoinduced electron transfer at metal electrode may be possible if an appropriate electron acceptor/donor exists at the interface. Metal deposition and dissolution could be involved in the reactions for the structural control.

In this review, we summarize our recent developments to control metal nanostructures via photoillumination. After brief summaries of the research, the possibilities of future applications will be discussed.

## PHOTOINDUCED ANISOTROPIC AGGLOMERATION OF GOLD NANOPARTICLES IN SOLUTION AND ON Au(111) SINGLE CRYSTAL SURFACE

One of the promising ways to construct well-organized periodic nanostructures is the use of self-assembling processes of colloidal crystal agglomeration.<sup>[12–16]</sup> When the surface charge of inorganic nanoparticles with a narrow size distribution are carefully controlled in the course of the preparations, the nanoparticles form agglomerates with a highly ordered superstructure. Examples of well-ordered colloidal particles composed of nanosized metal and semiconductor crystals have been reported. If one can control the interaction

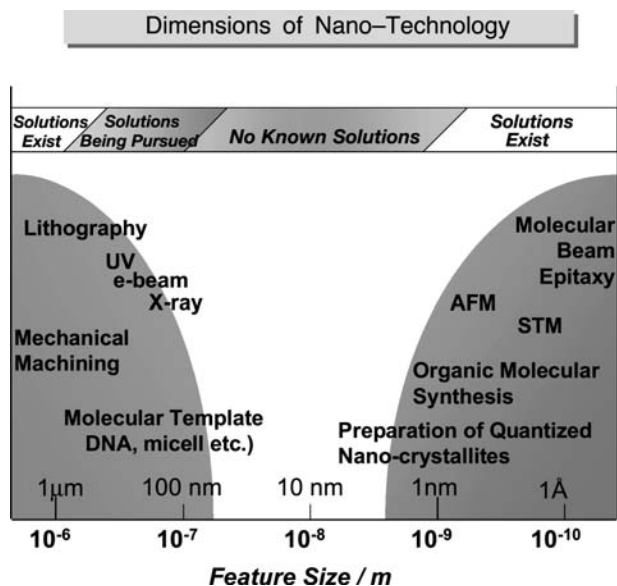


Fig. 1 Dimensions of nanotechnology.

between particles, desirable periodic superstructures and anisotropies can be introduced into the nanosized colloidal crystals. To demonstrate the possibility of combining photoexcitation for this aim, we investigated anisotropic agglomeration of gold nanoparticles (diameters ca. 6 nm) modified with organic thiols by

### Color of Spherical Metal Nano-particles in Solution ( $d = 10\text{--}20\text{ nm}$ )

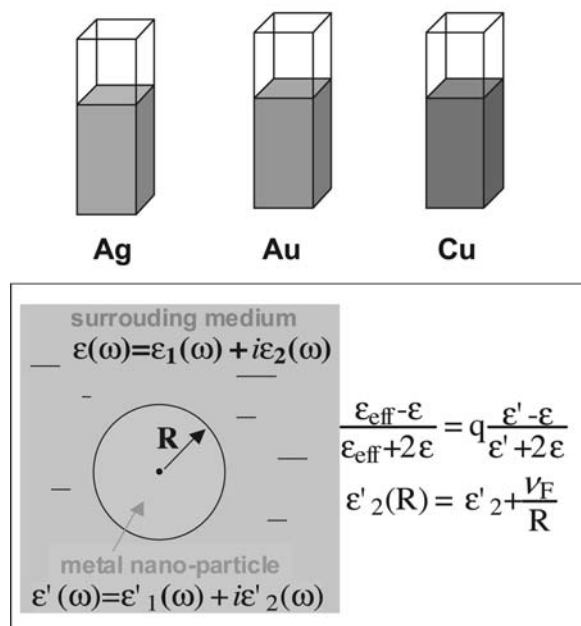


Fig. 2 Color of the plasmon absorption of metal nanoparticles.

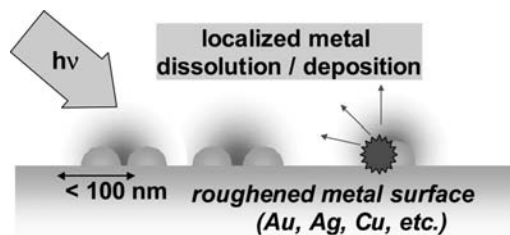
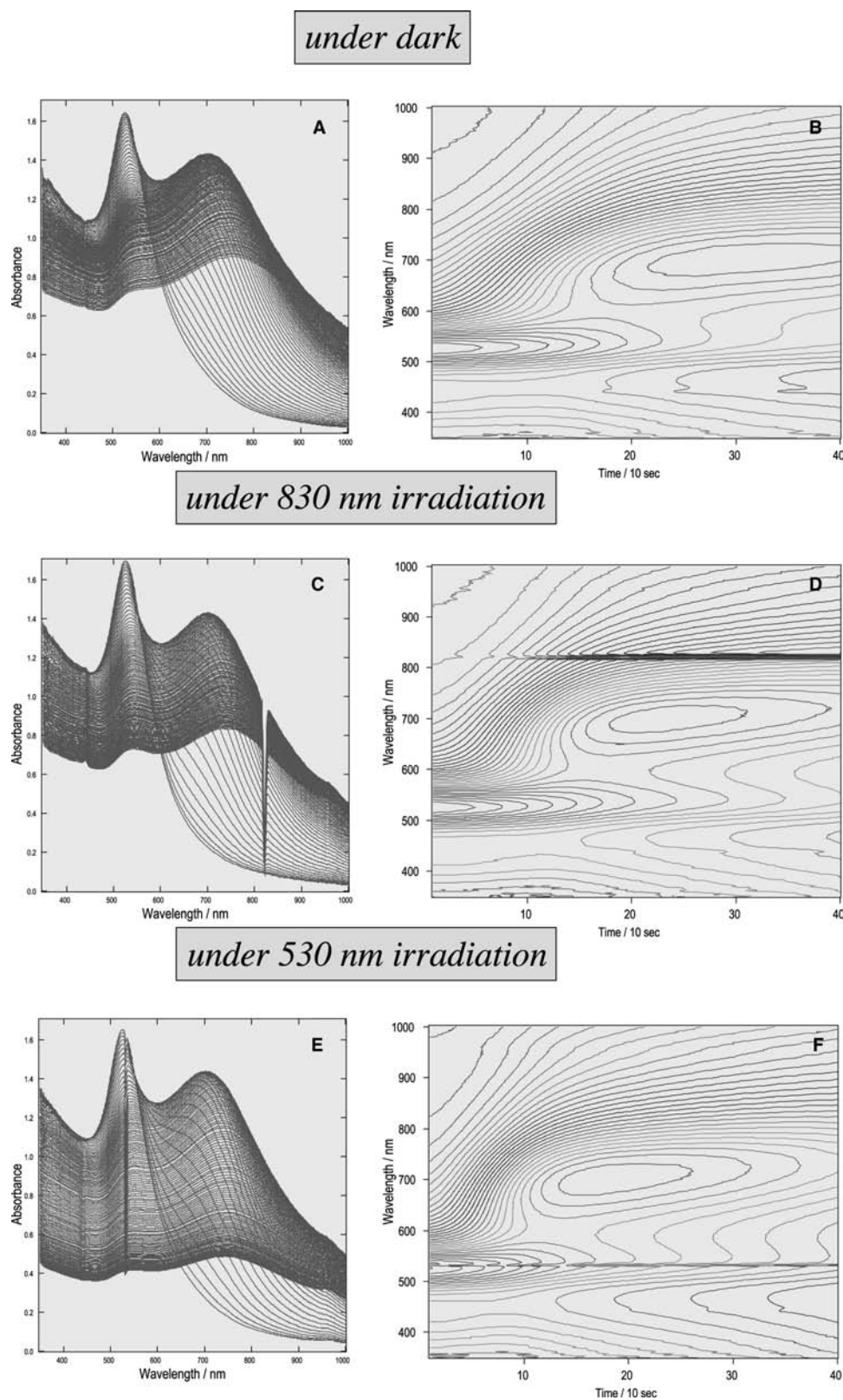


Fig. 3 Schematic presentation of electric field at roughened metal surface under illumination.

photoillumination with monochromatic light in aqueous media.<sup>[17]</sup>

Fig. 4 shows time-dependent spectral changes of gold nanoparticles after adding a surface-modifying reagent, thionicotinamide (TNA), in the dark and under illumination. In Fig. 4A and B, the initial spectrum with a single absorption peak at 520 nm in the dark is accompanied by evolution of an absorption band at wavelengths longer than 700 nm. After ca. 300 sec, the spectrum demonstrated double peaks at 520 and 720 nm. These changes can be attributed to agglomeration of gold nanoparticles by surface modification with the added reagent. The two absorption maxima of 520 and 720 nm can be attributed to the excitation of the transverse and longitudinal modes of surface plasmons in anisotropic agglomerates, respectively.<sup>[3,4]</sup> The modifying reagent should be bound on the gold surface via strongly interacting groups of thiol and/or amide.<sup>[18]</sup> The formation of such binding is expected to reduce or diminish anionic surface charges on the gold nanoparticles, leading to an increase in van der Waals attractive forces among the surface-modified gold nanoparticles, and hence resulting in agglomeration. Fig. 4(C)–(F) shows the effect of photoillumination on agglomeration of the gold nanoparticles. Under illumination at 830 nm, agglomeration was slightly accelerated. The evolution of the new absorption band above 700 nm became faster than that in the dark, showing the saturation in about 200 sec after the addition of TNA. In the case of 530-nm illumination, such acceleration of agglomeration was also observed, and further became faster than the illumination at 830 nm. The evolution of the new band above 700 nm reached saturation in about 180 sec. For the illumination at 830 and 530 nm, the absorption intensities also decreased after the saturation. The decreases reflect further aggregation and precipitation of the nanoparticles in solution. This result indicates that photoillumination accelerates the agglomeration of gold nanoparticles depending on the wavelength of the illumination light.

The above-presented photoinduced agglomeration reflects the change in the interaction between the gold nanoparticles by surface plasmon excitation.



**Fig. 4** Time-dependent absorption spectra of an aqueous solution containing gold nanoparticles modified with thionicotinamide. Measurements were performed 120 times at intervals of 10 sec, (A) in the dark, (C) under illumination at 830 nm, and (E) under illumination at 530 nm. Contour plots of time-dependent absorption spectra of the same systems, (B) in the dark, (D) under illumination at 830 nm, and (F) under illumination at 530 nm.



The interaction between colloidal particles was described by the total interaction potential consisting of an attractive van der Waals potential and a repulsive electrostatic potential in the DLOV theory.<sup>[19]</sup> The former potential contains a constant term determined by material- and geometry-dependent dispersion of coupled surface plasma oscillation frequencies. It was suggested that photoexcitation of the oscillations induces additional attractive forces via electromagnetic multipolar interactions. The results of the photoinduced agglomeration shown here should also be attributed to the photoinduced increase in the attractive force between the gold nanoparticles via surface plasmon excitation by illumination at 830 and 530 nm (Fig. 5). The wavelength dependence, i.e., slightly higher acceleration of agglomeration as well as earlier start of precipitation by 530-nm illumination than those by 830-nm illumination, may suggest another contribution of photoexcitation than the expected one. Illumination at 530 nm is known to cause not only plasmon excitation but also interband excitation of the gold nanoparticles, leading to photochemical reactions.<sup>[6]</sup> The relatively higher-energy excitation often results in destruction of the particles via electron ejection from them, fragmentation, and fusion. On the other hand, illumination at 830 nm under the present condition does not seem to cause structural deformation of individual particles. Furthermore, the excitation of the longitudinal mode at 830 nm is expected to induce anisotropic polarization along the long axis of the anisotropic agglomeration. Although the present results on the wavelength dependence of photoinduced agglomeration suggest that the 530-nm illumination is more effective in speed, it seems that the illumination at 830 nm is a more suitable perturbation to cause anisotropic agglomeration via plasmon excitation without any degradation of the gold nanoparticles.

The behavior of adsorption of the gold nanoparticles on Au(111) surfaces under photoillumination

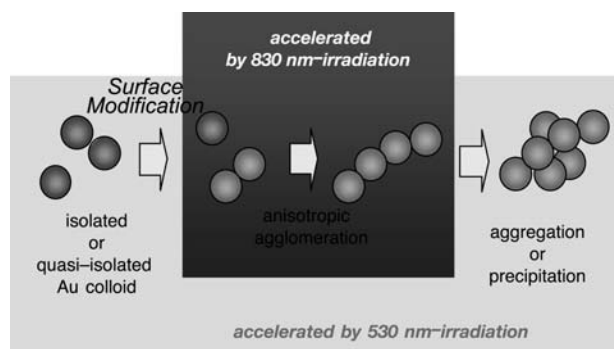


**Fig. 5** Agglomeration process of the gold nano-particles in solution.

was also investigated. Surface modified gold nanoparticles are adsorbed on Au(111) surface. We reported that their agglomerates on the Au(111) surface, prepared by immersion of the surface in the solution of gold nanoparticles, formed dot-interconnected lines of gold particles with a single particle width.<sup>[20]</sup> When the immersion conditions, such as the concentration of the gold nanoparticles and the immersion time, were changed, the coverage of the nanoparticles on the surface could be altered. Fig. 6 shows scanning tunneling microscopic (STM) images of the gold nanoparticles on the Au(111) surfaces prepared under 830-nm light illumination with different magnifications for different places. The images clearly show that each line of arrays is composed of the gold nanoparticles with the diameter of ca. 6 nm. Fig. 6(B) shows that the linear arrayed structure of the gold nanoparticles is formed on a typical structure of steps and terraces of the Au(111) surface with a monoatomic height at step edges crossing at 60° with each other, suggesting that the coverage of the nanoparticles should be a monolayer. It is also seen that the aligned arrays are parallel to the direction of one of the steps [Fig. 6(C)]. Although some vacancies or pits of the nanoparticles are observed, the alignment of the gold nanoparticles is not affected by such imperfections. It should be noted that this linearly arrayed structure was not observed at the surface prepared under dark or under illumination at 530 nm.<sup>[17]</sup>

As shown before, the photoillumination should cause an additional attractive interaction between the gold nanoparticles. The excitation at a long wavelength of 830 nm corresponds to the excitation of the longitudinal mode of surface plasmons in the anisotropic gold agglomerates, which propagates in the long-axis direction. The selective excitation of this mode is expected to cause an anisotropic electric field, leading to agglomeration in one specific direction. Isotropic excitation at 530 nm will not be able to induce such an anisotropic field, leading to random adsorption of nanoparticles. In addition, relatively strong excitation at 530 nm caused the destruction of the nanoparticles as observed in the solution experiments.

In this section, we have shown the promoting effect of photoillumination on agglomeration of surface-modified gold nanoparticles. The additional interactions between the particles were induced by photoillumination, and were controlled by changing the wavelength of illuminating light. In the case of adsorption onto the Au(111) surface, the illumination also affected the adsorption structure. The illumination at 830 nm led to the formation of a closed-packed and linearly arrayed superstructure on the surface. The results imply that photoillumination can be applied to control the superstructure of colloidal metal nanoparticles.

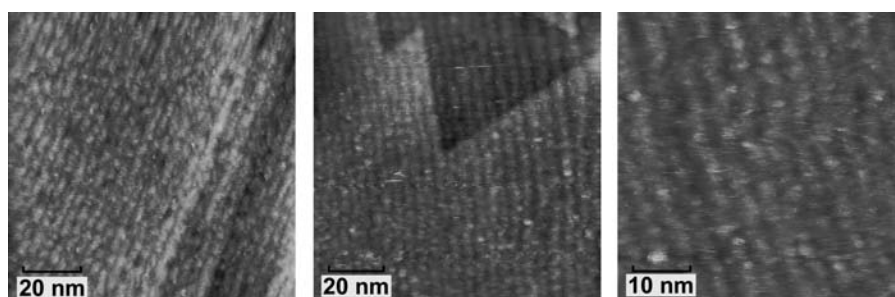


**Fig. 6** Scanning tunneling microscopic images of linear arrayed structures of gold nanoparticles adsorbed on a Au(111) surface prepared under illumination at 830 nm.

### NANOSCALE STRUCTURAL CHARACTERISTICS OF PHOTODISSOLVED Au(111) SINGLE CRYSTALLINE SURFACE

We investigated the effect of photoillumination on electrochemical dissolution of a gold electrode in KCl electrolyte. Structural changes in the surface morphology of metal electrodes by photoillumination have been recognized, especially in the field of surface-enhanced Raman scattering (SERS) spectroscopy.<sup>[21–23]</sup> Enhancement factors of the scattering signal are very sensitive to the surface microscopic morphology.<sup>[24–26]</sup> There are several reports on the change in SERS enhancement factors by photoillumination during electrochemical roughening in halide solutions.<sup>[21–23]</sup> The difference in the scattering intensity may reflect the structural characteristics of the surface prepared under the illumination. Thus the dissolution of metal electrode under photoillumination is expected to give some characteristic features, which differ from the

surfaces prepared under the dark. In this section, the structure of the photoilluminated electrode surface was characterized by STM. Comparison between the electrodes prepared under darkness and photoillumination conditions shows the effect of photoexcitation of metal on the electrochemical reaction.<sup>[27]</sup>

Several surface structures of Au(111) surface prepared by electrochemical dissolution were shown in Fig. 7. Under the dark conditions, it was found that the change of the surface structure was observed when the potential became more positive than 0.6 V vs. an Ag/AgCl reference electrode. Fig. 7A shows STM images of the surface after the positive polarization at 1.0 V under the dark. Formation of a random-valley structure at the terrace was shown in the image. Potential cycling between oxidation and reduction potentials (−0.1 and 1.0 V) resulted in a further roughened surface, consisting of spherical particles with the diameter of 20–30 nm as shown in Fig. 7B. The surfaces prepared in the dark had neither flat parts

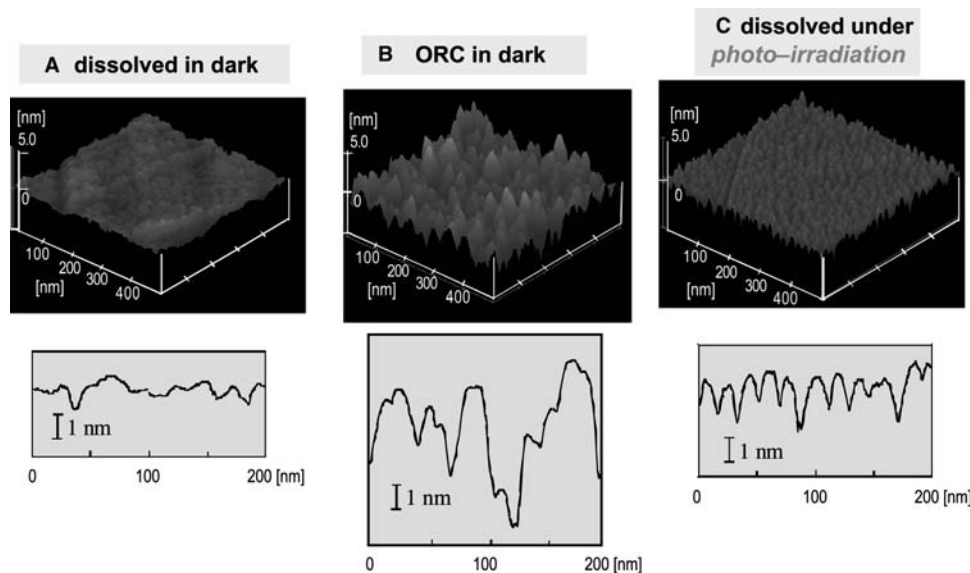


**Fig. 7** Scanning tunneling microscopic images and vertical sectional views of Au(111) surface kept at (A) 1.0 V for 5 sec under darkness, (B) −0.1 V for 5 sec after positive polarization at 1.0 V for 5 sec under darkness, and (C) 0 V for 5 sec under photoillumination; observed area was 500 × 500 nm.

nor residual step lines. Fig. 7(C) exhibits a photodissolved surface formed at a relatively negative potential of 0 V. The image shows that structural changes can be caused at much more negative potentials under the photoillumination than that in the dark. As the structural characteristics, homogeneous islands approximately 15 nm in size were found on the surface. The height of the islands was quite uniform, and the trace of the step edge was seen as a well-aligned dot-line structure of the islands. Comparison of the vertical sectional view of the surface to the surfaces prepared under the dark condition (Fig. 7A,B) shows that the size of the islands and the depth of the valleys are uniform.

Photoillumination of metal surfaces excites electrons and holes, and thus could induce electron transfer reactions if electron donors/acceptors exist at the interface. In the present system, a gold electrode dissolves via oxidation of gold forming  $\text{AuCl}_4^-$  when a sufficiently positive potential ( $>0.8$  V) is applied. Photoexcitation at 830 nm can generate excited holes with energy of 1.49 eV relative to the Fermi level, leading to the oxidative dissolution of the surface at a more negative potential. In addition to this effect of the potential, there were interesting structural characteristics observed at the dissolution under the dark. As shown in Fig. 7C, the island structure had a relatively narrow size distribution. Theoretical calculation of the electric field, taking into consideration strong electromagnetic coupling on the metal surface, predicted the creation of a very localized plasmon mode at the valley of the periodic superstructure.<sup>[28,29]</sup> Calculation results show that the strongest electric field is highly localized at the bottom of the valley between the particles. Thus, in the present case, after the formation of these randomly distributed valleys, some of them, whose separation distance is the same as the period of the photoexcited field induced by 830-nm light illumination, are selectively excited and form a localized field at the bottom of the valleys. Such a localized field could induce localized photodissolution of the metal via resonant electronic excitation. Formation of the periodic structure by photoillumination may be explained by the selective dissolution caused by a periodic electromagnetic field on the surface.

Scanning tunneling microscopic images proved that dissolution of the gold electrode was accelerated by photoillumination. At the surface prepared under the illumination, the size distribution of the islands was relatively small, and the heights of the islands were uniform. The selective dissolution caused by a periodic electromagnetic field on the surface may contribute to the formation of such uniform structure. The present results imply that the photoillumination can be applied to control the structure of metals in the size around 10 nm via photodissolution.

## PHOTOINDUCED SINGLE METAL-DOT DEPOSITION ONTO METAL SURFACE

Photoinduced electron transfer reactions via plasmon excitation have been reported in several roughened metal electrode systems.<sup>[7-11]</sup> For further developments as a novel method of nanostructural control in the size between a few nanometers and tens of nanometers, coupling the phenomenon with an electrochemical scanning tunneling microscope (EC-STM) system could prove interesting.<sup>[30,31]</sup> Several attempts have been reported on using photoirradiation for the tunneling gap of STM systems for nanostructure fabrication.<sup>[32-38]</sup> Although some of these studies succeeded in the preparation of nanostructures on solid surfaces, several problems still remain. When light is irradiated in the STM gap, thermal expansion of the tip and the sample substrates is observed as the most prominent effect.<sup>[32-34,36,39-49]</sup> This contribution is difficult to control, and often changes the distance of the gap leading to the deformation of the prepared structures. Thus it is important to identify the conditions that minimize the thermal expansion. Appropriate potential control of the electrodes in EC-STM systems is expected to improve the reaction efficiency of the photoinduced metal deposition.<sup>[50]</sup>

In this section, the effect of the photoirradiation on the gap between the Au(111) surface and the tip of the electrochemical STM was shown. Relatively weak light ( $100 \text{ mW/cm}^2$ ) was irradiated in the gap in the present experiment. During the irradiation for 10 msec, the position of the tip was fixed at the central part of the observed area under the constant tunneling current mode. After the irradiation, the tip was again scanned to obtain the surface image. This relatively weak light irradiation in the gap between the tip and the surface of the Au(111) electrode, whose potential was maintained at 0.4 V vs. Ag/AgCl in aqueous solution containing 0.1 M  $\text{CuSO}_4$ , resulted in the formation of a small island structure on the Au(111) surface in the vicinity of the tip (Fig. 8). The island structure was formed on the surface just below the tip only when the light was irradiated at the point of the gap. The island was dissolved when the potential of the electrode was maintained at 0.6 V, indicating that the island is a photodeposited Cu dot. This fact indicates that a Cu metal nanodot can be prepared by the photoirradiation of an atomically smooth surface of a metal electrode in the vicinity of the metal tip. The position of the dot can be controlled by changing the position of the metal tip of the electrochemical STM.

In this system, the contribution of the plasmon mode was successfully applied to construct a single metal-dot structure on the smooth Au(111) surface in the vicinity of the thin metal tip. Ukraintsev and Yates<sup>[40]</sup> proposed the possibility that the tip can work

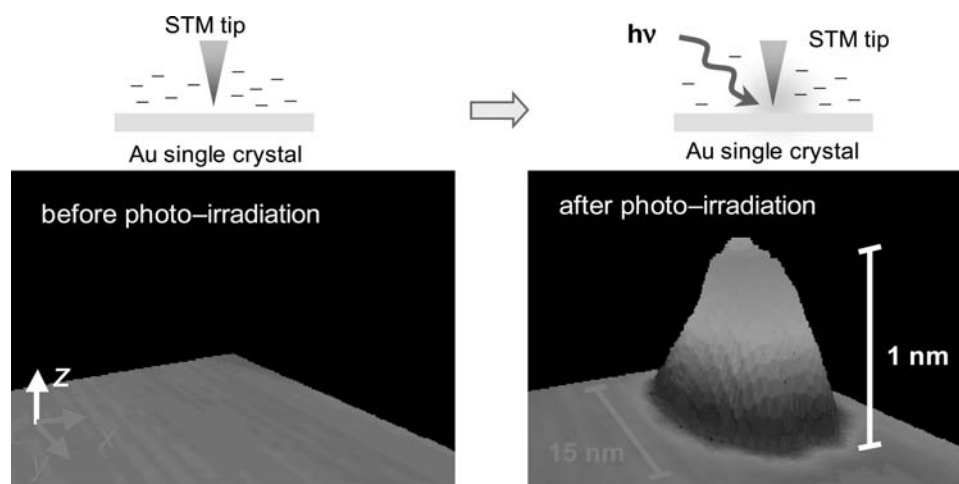


**Fig. 8** Electrochemical scanning tunneling microscope image of Cu nanodot on Au(111) single crystalline electrodes prepared by photoirradiation with power of  $100 \text{ mW/cm}^2$  for 10 msec.

as a conical antenna or a waveguide for the light under irradiation. Thus it is expected that the enhanced field was induced by photoirradiation in the gap between the smooth metal surface.<sup>[35,51–53]</sup> The field can induce the highly localized excitation of electrons at that point, leading to position-selective metal deposition onto the electrode surface, in the vicinity of the tip. As a result, a dot 15 nm in size and 1 nm in height was prepared on the Au(111) surface (Fig. 8). The fact that the preparation of the dot was achieved under relatively weak light irradiation proves the effective antenna effect of the tip in localizing the excitation. The method of position-selective photodeposition may be applied as a novel method to construct three-dimensional metal nanostructures on the solid surface.

### PHOTOINDUCED STRUCTURAL CHANGES OF SILVER NANOPARTICLES ON GLASS SUBSTRATE IN SOLUTION UNDER AN ELECTRIC FIELD

In the field of structural control of metal nanoparticles, several important topics remain unresolved. One of these areas involves the application of an external electric field for structural control. It is desirable to achieve control of metal nanostructures on surfaces of insulating materials, as metal nanostructures constructed for use as conducting materials. In this case, structural control of metals must be conducted via electrochemical dissolution and deposition without donation of charge from the substrate electrode. Numerous reports exist, describing sophisticated techniques pertaining to construction of metal nanostructures on electrodes of conducting materials,<sup>[54–56]</sup> as well as photoinduced

structural changes of dispersed metal nanoclusters in solution. However, little documentation occurs with respect to induction of the electrochemical reaction of metal dissolution/deposition to control the metal nanostructure adsorbed on insulating materials, in the absence of an external electric circuit.<sup>[57,58]</sup> Investigation of the combined effects of an external electric field and photoillumination is expected to give useful information on the structural control of metal nanostructures on insulating materials. The investigation shown here clarified the effect of photoirradiation of Ag nanoparticles adsorbed on a glass substrate under an electric field in solution.<sup>[59,60]</sup>

Application of an electric field to the Ag nanoparticles on glass immersed in solution was conducted employing a two-electrode cell (Fig. 9). Ag nanoparticles on a glass plate were prepared by the method of sputter deposition. The size of the hemispherical islands was approximately 20 nm in diameter (Fig. 10). The absorption spectrum of the film showed a plasmon absorption peak at 480 nm in air (Fig. 10). The absorption spectra of the Ag nanoparticles changed as a result of photoirradiation under an external electric field in water. Fig. 11 shows the time-dependent changes in the absorption spectra of the Ag nanoparticles on the glass plate during photoirradiation at various intensities (0.06, 0.26, and  $0.90 \text{ mW/cm}^2$ ) under applying an electric field of  $20 \text{ V/cm}$ . Absorption around the spectral peak wavelength (approximately 500 nm) decreased as a result of photoirradiation. Slight changes in the absorption were observed in the wavelength region below 420 nm.

The rate of the changes linearly increased as the intensity of the irradiated light increased. Fig. 12 displays the dependence of photoirradiation intensity on the change in the absorption of the nanoparticles.

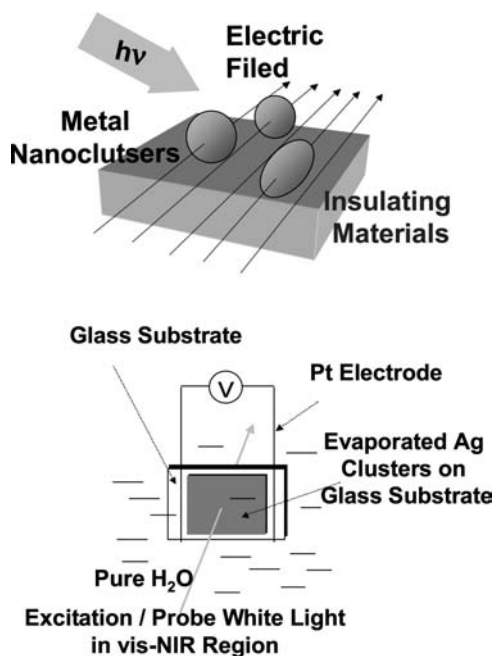


**Fig. 9** Schematic presentation of experimental setup and two-electrode cell.

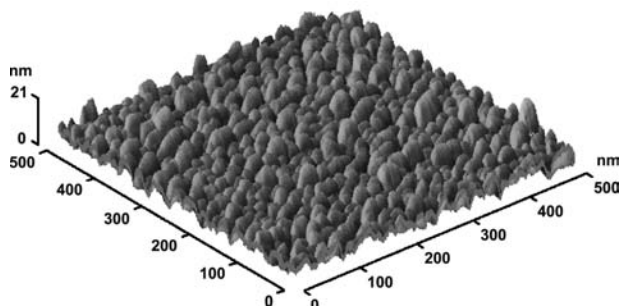
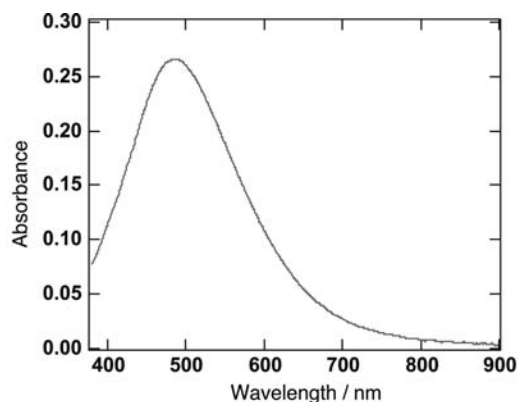


**Fig. 10** Absorption spectrum (top) and an atomic force microscopic image (bottom) of evaporated Ag nanoparticles on a glass substrate.

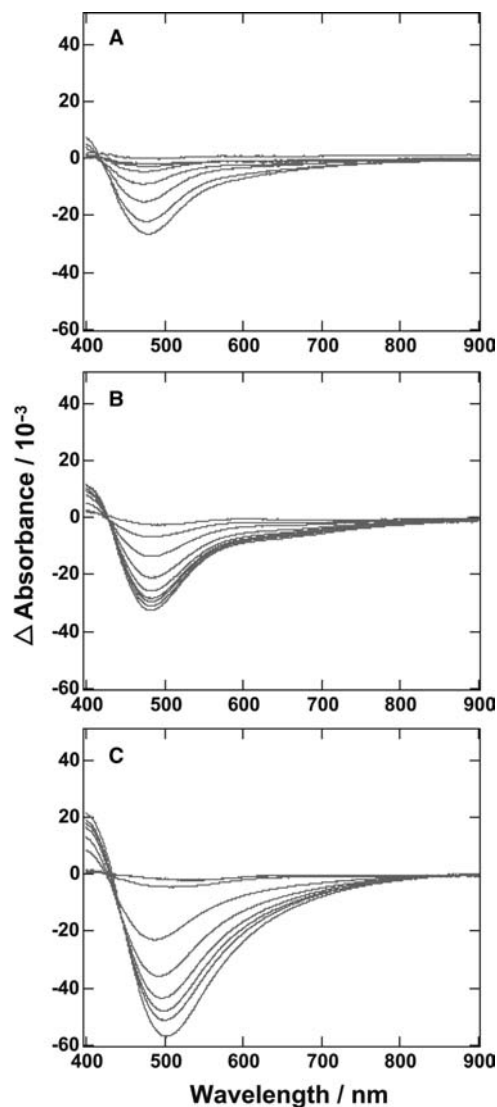


**Fig. 11** Time-dependent absorption spectral change of the evaporated gold nanoparticles on a glass substrate in pure water during irradiation at  $0.06 \text{ mW/cm}^2$  (A),  $0.26 \text{ mW/cm}^2$  (B), and  $0.90 \text{ mW/cm}^2$  (C). Applied electric field was  $20 \text{ V/cm}$ . Measurements were performed nine times at intervals of 15 sec.

The increase in the level of the changes was nearly linear with increasing intensity of irradiation. The effect of the applied electric field is also presented as the difference in the slope of the intensity dependence. The slope of an applied electric field of  $20 \text{ V/cm}$  was greater than twice that observed in the absence of an applied field. These results prove that photoirradiation induces dissolution of Ag particles even under relatively weak light irradiation in the range of  $\text{mW/cm}^2$ ; moreover, the findings indicate that photodissolution accelerates upon application of an external electric field in solution. It should be noted that dissolution



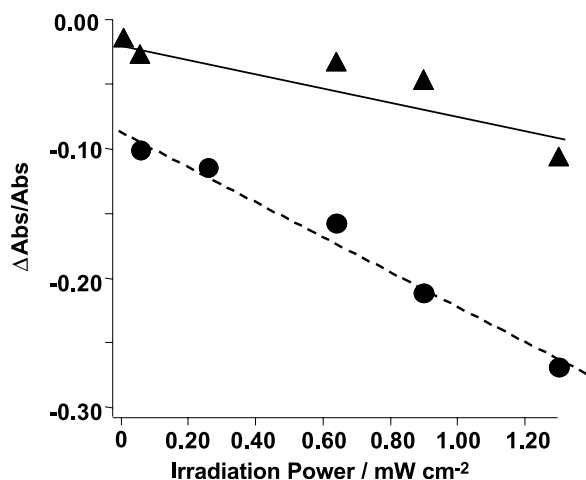


**Fig. 12** Dependence of irradiation power on the absorption change at 500 nm of the gold film observed in the absence of an electric field (solid line) and upon application of an external electric field (20 V/cm) (broken line) for 120 sec.

caused by application of an electric field alone without photoirradiation was minor, compared with the case involving the combination of an electric field and irradiation. Only slight incremental intrinsic dissolution of nanoparticles was evident upon application of an electric field in solution under darkness.

The synergetic effect of the weak light and the electric field was also detected in the structural changes. Fig. 13 displays AFM images of as-prepared Ag nanoparticles and those following treatment with light only, and with light and the electric field. The treatments with light only resulted in slight decreases in

the number of Ag nanoparticles without apparent size changes in the particles. On the other hand, the combined perturbations led to significant changes in particle size. The original size of approximately 20 nm in the prepared samples increased to 50–100 nm following polarization under irradiation. The particles were interconnected, forming anisotropic shapes. These changes in the size of the nanoparticles were more apparent when the irradiated light intensity became stronger (Fig. 13). This observed structural change suggests that photoirradiation under an external electric field induces deposition of Ag to specific particles as well as dissolution. This dissolution of the particles leads to an increase of the interparticle distance. The spectral blue shift shown in Fig. 3 seems to reflect this decrease in the interaction between the particles rather than the change in the size of the nanoparticles.

The effect of photoirradiation with respect to acceleration of dissolution under an electric field may be considered as follows. In comparison to the relatively large-sized metal particles, the present electric polarization of Ag nanoparticles approximately 20 nm in size should be much smaller, and would be on the order of  $10^{-5}$  V. Although this polarization appears to be insufficient to induce an electrochemical reaction, photoirradiation may assist the increase in polarization of the nanoparticles via photoexcitation. When resonant electronic excitation of nanoparticles is induced via plasmon excitation, the resultant polarization corresponding to several electron volts can generate electrochemical reactions such as metal dissolution and deposition (Fig. 14).

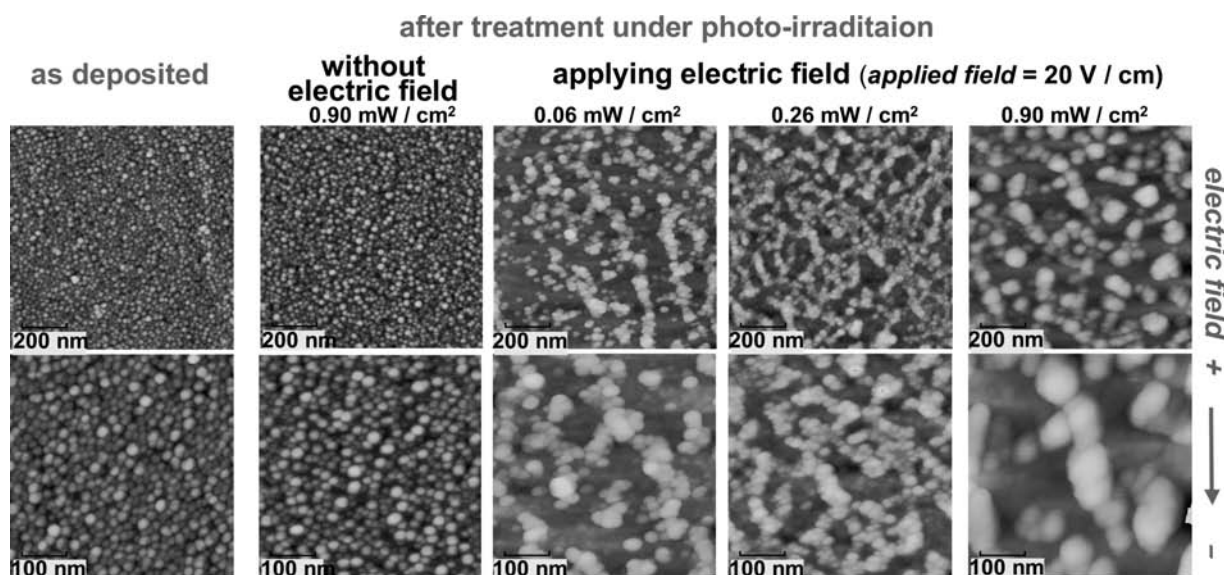


**Fig. 13** Atomic microscopic images of the evaporated Ag nanoparticles on a glass substrate, as-deposited, following only irradiation, and following irradiation and an electric field. Dimensions are indicated on the images.



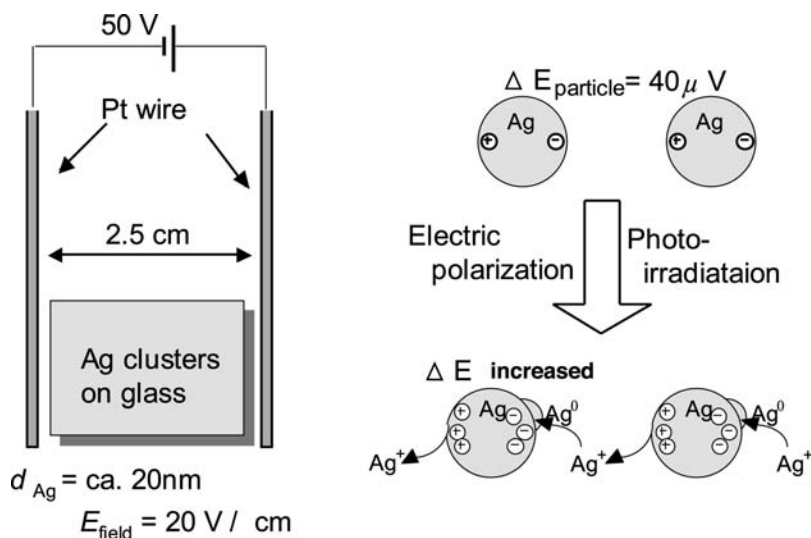
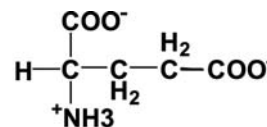


Fig. 14 Proposed mechanism of the photoinduced structural change under an external electric field in solution.

In the present system, possible electrochemical reactions in a single particle during the initial stage may include the oxidation reaction of Ag metal dissolution, the reductive reaction of hydrogen evolution, dissolved oxygen, and/or native oxide partially covering the surface of the Ag nanoparticle.<sup>[61]</sup> As the reaction proceeds, a Ag<sup>+</sup> ion is likely to be generated by dissolution, and diffuse to the neighboring particles. When a Ag<sup>+</sup> ion arrives at a neighboring particle, Ag deposition could occur as a dominant reductive reaction at the particles, leading to changes in the size of the Ag nanoparticles. The applied electric field can assist the migration of the Ag<sup>+</sup> ions; consequently, the electric field accelerates the present reactions.

The results shown here proved that photoirradiation of metal nanoparticles under polarization by an external electric field accelerates structural changes in Ag nanoparticles. The reaction can be attributed to the highly localized electrochemical reactions of metal dissolution/deposition on the surface of the Ag nanoparticles. This phenomenon can be utilized for structural control of Ag nanoparticles adsorbed on the surface of an insulating material, circumventing the need for an external electric circuit.



glutamic acid

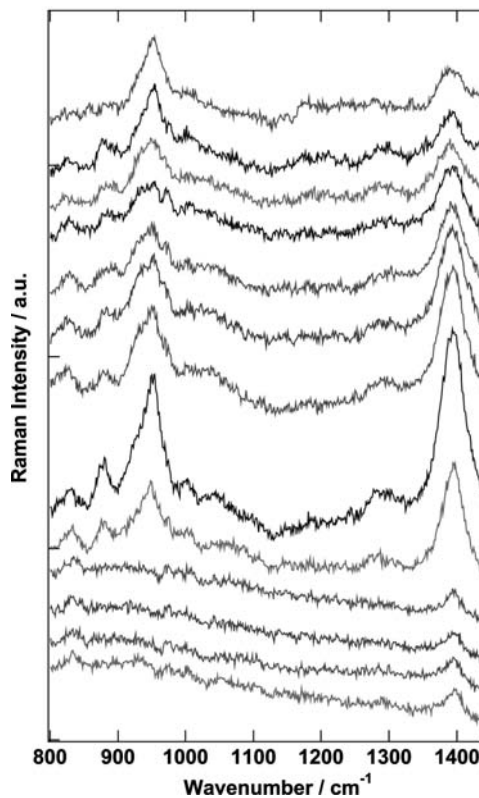
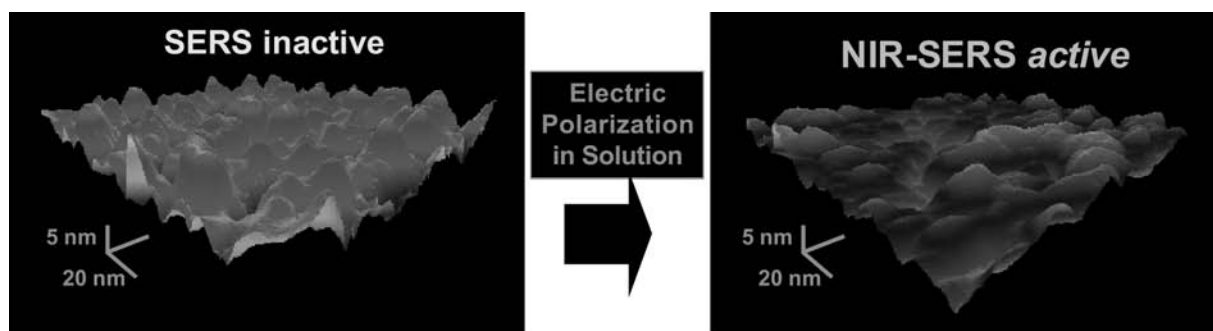


Fig. 15 Time-dependent SERS signals from the Ag on Au film during application of an external electric field. Measurements were performed at 20-sec intervals (from bottom to top). Two spectra at the top were at 420 and 480 sec after applying field.

#### CHANGES IN NEAR-INFRARED OPTICAL RESPONSE OF METAL THIN FILM ON GLASS SUBSTRATE BY ELECTRIC POLARIZATION IN SOLUTION

The technique of applying an external electric field to metal nanostructures could be used to control the optical properties of metal thin films on glass. One of the promising applications of metal nanostructures is their use as substrates for single molecular detection employing surface-enhanced Raman scattering



**Fig. 16** Surface structures of the Ag on Au film before and after the application of an external electric field.

(SERS).<sup>[62–65]</sup> The phenomenon utilizes localized electromagnetic fields at the metal nanostructure under photoirradiation. Although the SERS enhancement has often included visible excitation because of its very sensitive resonance condition, the importance of near-infrared (NIR) excitation has also been recognized because of the advantages associated with non-fluorescence properties and lower damage in photosensitive target molecules.<sup>[66,67]</sup> Recently, theoretical calculations proved that the effective electromagnetic enhancement via near-infrared excitation would be possible if some appropriate metal nanostructures were constructed.<sup>[29]</sup> Recent efforts have focused on preparation of the NIR-SERS active substrates using well-controlled structural units.<sup>[25,68]</sup> Although several sophisticated methods were successful with respect to generation of fully reproducible NIR-SERS activity, the preparations were often complicated because of the need for specialized synthetic or preparative techniques. Furthermore, additional tuning for optimized NIR-SERS activity is rather difficult following the preparation. Thus novel facile and controllable techniques to prepare NIR-SERS active substrates should be developed.<sup>[69]</sup>

Near-infrared SERS activity of the Ag on Au film on glass substrate under electric polarization was evaluated in aqueous solution containing 1 mM glutamic acid. Spectra were obtained in situ from the near-infrared laser Raman microscope system with excitation wavelength of 780 nm.<sup>[70]</sup> Intensity of the SERS significantly increased upon application of an external electric field to the film (Fig. 15). The empirical signal enhancement factor, which was determined from the peak integration ratio of the SERS vibration at  $1400\text{ cm}^{-1}$  to the unenhanced signal from the solution of a defined sample concentration, was found to be greater than  $10^7$ . The value is comparable to the recently reported value of the near-infrared SERS from carefully prepared gold nanoparticle superstructures possessing a precisely controlled periodic structure.<sup>[71,72]</sup> Strong enhancement of greater than  $10^7$  in the present systems could be attributable to the small

particle structure characterized by diameters of approximately 10–20 nm on the Ag on Au film.

In this investigation, the NIR-SERS activity of an Ag on Au thin film was controlled via application of an external field to the metal thin films on an insulating substrate in solution. We found a novel application of an external electric field to the control of metal nanostructures on an insulating material in solution. As the result of the structural change of the Ag on Au thin film, significant enhancement of the near-infrared Raman scattering of amino acid molecules in solution was achieved (Fig. 16). The method is an extremely facile and effective technique in terms of control of NIR optical properties of such thin metal films on an insulating material in solution. Moreover, this procedure should be applied in the preparation of substrates displaying optimized NIR-SERS activity for various highly sensitive molecular sensors.

## CONCLUSIONS AND FUTURE PERSPECTIVE

We have demonstrated that selective excitation of a specific surface plasmon mode of metal nanostructures can be employed as a perturbation for effective structural control. Useful effects on the particle interaction and highly localized electrochemical reaction were found in several nanostructured metal systems. The phenomena can be applied as a novel method to control metal nanostructures in the size region between a few nanometers and a hundred nanometers. As for the use of the method in future technologies, further optimization is required, utilizing the specificities of the wavelength and the polarization of the light for finer-size tuning at the metal nanostructures. Control in the contribution of the heat caused by photoillumination is also important for more precise structural control in the nanometer-size region. Despite these still unsolved issues, the structural control via localized photoexcitation should be one of the promising approaches to construct nanostructures in a size

region, which remains underdeveloped in the present nanotechnology.

## ACKNOWLEDGMENTS

We would like to thank our collaborators, Messrs. T. Kitamura, H. Tanaka, Y. Sawai, and M. Suzuki, and Dr. J. Li in Osaka University, who, together with the authors, performed most of the work presented here. Grateful acknowledgment is also made to Dr. K. Ajito, NTT Basic Research Laboratories, for stimulating discussion and his contribution for in situ confocal near-infrared Raman measurements. This work was partially supported by a Grant-in-Aid for Scientific Research from the Ministry of Education, Culture, Sports, Science and Technology, Japan.

## REFERENCES

1. Timp, G. *Nanotechnology*; Springer-Verlag: New York, 1999.
2. Nyffenegger, R.M.; Penner, R.M. Nanometer-scale surface modification using the scanning probe microscope: progress since 1991. *Chem. Rev.* **1997**, *97*, 1195–1230.
3. Quinten, M.; Kreibig, U. Optical properties of aggregates of small metal particles. *Surf. Sci.* **1986**, *172*, 557–577.
4. Kreibig, U. *Handbook of Optical Properties*; Hummel, R.E., Wismann, P., Eds.; CRC Press: New York, 1997; Vol. 2. Chap. 7.
5. Henglein, A. Small-particle research: physicochemical properties of extremely small colloidal metal and semiconductor particles. *Chem. Rev.* **1989**, *89*, 1861–1873.
6. Kamat, P.V. Photophysical, photochemical and photocatalytic aspects of metal nanoparticles. *J. Phys. Chem., B* **2002**, *106*, 7729–7744.
7. Fedurco, M.; Shklover, V.; Augustynski, J. Effect of halide ion adsorption upon plasmon-mediated photoelectron emission at the silver/solution interface. *J. Phys. Chem., B* **1997**, *101*, 5158–5165.
8. Kostecki, R.; Augustynski, J. Unusually strong cathodic photoeffect at silver in contact with aqueous solutions containing carbon dioxide. *Chem. Phys. Lett.* **1992**, *194*, 386–390.
9. Kostecki, R.; Augustynski, J. Photon-driven reduction reactions on silver. *J. Appl. Electrochem.* **1993**, *23*, 567–572.
10. Kostecki, R.; Augustynski, J. Effect of the surface roughness on the spectral distribution of photoemission current at the silver/solution contact. *J. Appl. Phys.* **1995**, *77*, 4701–4705.
11. Sass, J.K.; Laucht, H.; Kliewer, K.L. Photoemission studies of silver with low-energy (3 to 5 eV), obliquely incident light. *Phys. Rev. Lett.* **1975**, *35*, 1461–1464.
12. Fendler, J.H. Self-assembled nanostructured materials. *Chem. Mater.* **1996**, *8*, 1616–1624.
13. Motte, L.; Billoudet, F.; Lacaze, E.; Pileni, M.P. Self-organization of size-selected nanoparticles into three-dimensional superlattice. *Adv. Mater.* **1996**, *8*, 1018–1020.
14. Pileni, M.M. Nanosized particles made in colloidal assemblies. *Langmuir* **1998**, *13*, 3266–3276.
15. Murray, C.B.; Kagan, C.R.; Bawendi, M.G. Self-organization of CdSe nanocrystallites into three-dimensional quantum dot superlattices. *Science* **1995**, *270*, 1335–1338.
16. Kiely, C.J.; Fink, J.; Brust, M.; Bethell, D.; Schiffrin, D.J. Spontaneous ordering of bimodal ensembles of nanoscopic cluster. *Nature* **1998**, *396*, 444–446.
17. Murakoshi, K.; Nakato, Y. Formation of linearly arrayed structure of gold nanoparticles on gold single crystal surfaces. *Adv. Mater.* **2000**, *12*, 791–795.
18. Fujiwara, H.; Yanagida, S.; Kamat, P.V. Visible light induced fusion and fragmentation of TNA-modified gold nanoparticles. *J. Phys. Chem., B* **1999**, *103*, 2589–2591.
19. Eckstein, H.; Kreibig, U. Light induced aggregation of Au particles. *Z. Phys. D* **1993**, *26*, 239–241.
20. Murakoshi, K.; Nakato, Y. Anisotropic agglomeration of surface-modified gold nanoparticles in solution and on solid surfaces. *Jpn. J. Appl. Phys.* **2000**, *39*, 4633–4634.
21. Barz, F.J.G.G., II; Philpott, M.R.; Weaver, M.J. Effect of laser illumination during oxidation–reduction cycles upon surface-enhanced Raman scattering from silver electrodes. *Chem. Phys. Lett.* **1982**, *91*, 291–295.
22. Chen, T.T.; Raben, K.U.V.; Owen, J.F.; Chang, R.K.; Laube, B.L. Laser illumination effects on the surface morphology, cyclic voltammetry, and surface-enhanced Raman scattering of Ag electrodes. *Chem. Phys. Lett.* **1982**, *91*, 494–500.
23. Macomber, S.H.; Furtak, T.E.; Devine, T.M. Enhanced Raman characterization of adsorbed water at the electrochemical double layer on silver. *Chem. Phys. Lett.* **1982**, *90*, 439–444.
24. Brike, R.L.; Lombardi, J.R. Surface-enhanced Raman scattering. In *Spectroelectrochemistry*; Gale, R.J., Ed.; Plenum Press: New York, 1988; 263–348.
25. Lyon, L.A.; Keating, C.D.; Fox, A.P.; Baker, B.E.; He, L.; Nicewarner, S.R.; Mulvaney, S.P.; Natan, M.J. Raman spectroscopy. *Anal. Chem.* **1998**, *70*, 341R–361R.
26. Tian, Z.-Q.; Ren, B.; Wu, D.-Y. Surface-enhanced Raman scattering: from noble to transition metals and from rough surfaces to ordered nanostructures. *J. Phys. Chem., B* **2002**, *106*, 9463–9483.
27. Murakoshi, K.; Kitamura, T.; Nakato, Z.Z. Nanoscale structural characteristics of photodissolved gold (111) single crystalline surface. *Jpn. J. Appl. Phys.* **2001**, *40*, 1918–1922.
28. Garcia-Vidal, F.J.; Pendry, J.B. Collective theory for surface enhanced Raman scattering. *Phys. Rev. Lett.* **1996**, *77*, 1163–1166.
29. Xu, H.; Aizpurua, J.; Kall, M. Electromagnetic contributions to single-molecule sensitivity in surface-enhanced Raman scattering. *Phys. Rev., E* **2000**, *62*, 4318–4324.

30. Schindler, W.; Hugelmann, P.; Hugelmann, M.; Kartner, F.X. Localized electrochemical nucleation and growth of low-dimensional metal structures. *J. Electroanal. Chem.* **2002**, *522*, 49–57.
31. Itaya, K. In situ scanning tunneling microscopy in electrolyte solutions. *Prog. Surf. Sci.* **1998**, *58*, 121–248.
32. Dohnalek, Z.; Lyubinetsky, I.; Yates, J.T., Jr. Laser pulse desorption under scanning tunneling microscope tip—Cl removal from single site on Si(100). *J. Vac. Sci. Technol.* **1997**, *A15*, 1488–1492.
33. Liu, C.-Y.; Bard, A.J. Irradiation-induced nanometer-scale surface etching of a CdSe film with a scanning tunneling microscope. *Chem. Phys. Lett.* **1990**, *174*, 162–166.
34. Jersch, J.; Dickmann, K. Nanostructure fabrication using laser field enhancement in the near field of a scanning tunneling microscope tip. *Appl. Phys. Lett.* **1996**, *68*, 868–870.
35. Demming, F.; Jersch, J.; Dickmann, K.; Geshev, P.I. Calculation of the field enhancement on laser-illuminated scanning probe tips by the boundary element method. *Appl. Phys., B* **1998**, *66*, 593–598.
36. Jersch, J.; Demming, F.; Dickmann, K. Field enhancement of optical radiation in the nearfield of scanning probe microscope tips. *Appl. Phys., A* **1998**, *64*, 29–32.
37. Yau, S.-T.; Saltz, D.; Nayfeh, M.H. Laser-assisted deposition of nanometer structures using a scanning tunneling microscope. *Appl. Phys. Lett.* **1990**, *57*, 2913–2915.
38. Yau, S.-T.; Saltz, D.; Nayfeh, M.H. Scanning tunneling microscope-laser fabrication of nanostructures. *J. Vac. Sci. Technol., B* **1990**, *9*, 1371–1375.
39. Hamers, R.J.; Markert, K. Atomically resolved carrier recombination at Si(111)-(7\*7) surfaces. *Phys. Rev. Lett.* **1990**, *64*, 1051–1054.
40. Ukraintsev, V.A.; Yates, J.T., Jr. Nanosecond laser induced single atom deposition with nanometer spatial resolution using a STM. *J. Appl. Phys.* **1996**, *80*, 2561–2571.
41. Lyubinetsky, I.; Dohnalek, Z.; Ukraintsev, V.A.; Yates, J.T., Jr. Transient tunneling current in laser-assisted scanning tunneling microscopy. *J. Appl. Phys.* **1997**, *82*, 4115–4117.
42. Jersch, J.; Demming, F.; Fedotov, I.; Dickmann, K. Time-resolved current response of a nanosecond laser pulse illuminated STM tip. *Appl. Phys., A* **1999**, *68*, 637–641.
43. Jersch, J.; Demming, F.; Hildenhagen, L.J.; Dickmann, K. Field enhancement of optical radiation in the near-field of scanning probe microscope tips. *Appl. Phys., A* **1998**, *66*, 29–34.
44. Boneberg, J.; Tresp, M.; Ochmann, M.; Münzer, H.-J.; Leiderer, P. Time-resolved measurements of the response of a STM tip upon illumination with a nanosecond laser pulse. *Appl. Phys., A* **1998**, *66*, 615–619.
45. Boneberg, J.; Münzer, H.-J.; Tresp, M.; Ochmann, M.; Leiderer, P. The mechanism of nanostructuring upon nanosecond laser irradiation of a STM tip. *Appl. Phys., A* **1998**, *67*, 381–384.
46. Boneberg, J.; Lohrmann, M.; Böhmisch, M.; Burmeister, F.; Lux-Steiner, M.; Leiderer, P.Z. Electrical field induced growth of triangular nanometer structures on WSe<sub>2</sub>. *Phys. B* **1996**, *99*, 567–570.
47. Hiesgen, R.; Meissner, D. Nanoscale characterization of semiconductor surfaces by spatially resolved photocurrent measurements. *Fresenius' J. Anal. Chem.* **1997**, *358*, 54–58.
48. Hiesgen, R.; Meissner, D. Nanoscale photocurrent variations at metal-modified semiconductor surfaces. *J. Phys. Chem.* **1998**, *102*, 6549–6557.
49. Murakoshi, K.; Kitamura, T.; Nakato, Y. Localized photoresponses of nanostructured metal surfaces observed by a scanning tunneling microscope. *Phys. Chem., Chem. Phys.* **2001**, *3*, 4572–4577.
50. Sawai, Y.; Suzuki, M.; Murakoshi, K.; Nakato, Y. Photo-induced single metal-dot deposition onto an Au electrode.
51. Geshev, P.I.; Demming, F.; Jersch, J.; Dickmann, K. Calculation of the temperature distribution on laser-illuminated scanning probe tips. *Appl. Phys., B* **2000**, *70*, 91–97.
52. Kroo, N.; Thost, J.-P.; Völcker, M.; Krieger, W.; Walther, H. Decay length of surface plasmons determined with a tunnelling microscope. *Europhys. Lett.* **1991**, *15*, 289–293.
53. Moller, R.; Abrecht, U.; Boneberg, J.; Koslowski, B.; Leiderer, P.; Dransfeld. Detection of surface plasmons by scanning tunneling microscopy. *J. Vac. Sci. Technol.* **1991**, *B9*, 506–509.
54. Engelmann, G.E.; Ziegler, J.C.; Kolb, D.M. Electrochemical fabrication of large arrays of metal nanoclusters. *Surf. Sci.* **1998**, *401*, L420–L424.
55. Kolb, D.M.; Ullmann, R.; Will, T. Nanofabrication of small copper clusters on gold(111) electrodes by a scanning tunneling microscope. *Science* **1997**, *275*, 1097.
56. Schuster, R.; Kirchner, V.; Allongue, P.; Ertl, G. Electrochemical micromachining. *Science* **2000**, *289*, 98–101.
57. Bradley, J.-C.; Chen, H.-M.; Crawford, J.; Eckert, J.; Ernazarova, K.; Kurzeja, T.; Lin, M.; McGee, M.; Nadler, W.; Stephens, S.G. Creating electric contacts between Cu particles. *Nature* **1997**, *389*, 268–271.
58. Bradley, J.-C.; Crawford, J.; McGee, M.; Stephens, S.G. A contactless method for the directed formation of submicrometer copper wires. *J. Electrochem. Soc.* **1998**, *145*, L45–L47.
59. Murakoshi, K.; Tanaka, H.; Sawai, Y.; Nakato, Y. Photo-induced structural changes of silver nanoparticles on glass substrate in solution under an electric field. *J. Phys. Chem., B* **2002**, *106*, 3041–3045.
60. Murakoshi, K.; Tanaka, H.; Sawai, Y.; Nakato, Y. Effect of photo-irradiation and external electric field on structural change of metal nano-dots in solution. *Surf. Sci.*, 532–535, 1109–1115.
61. Peyser, L.A.; Vinson, A.E.; Bartko, A.P.; Dickson, R.M. Photoactivated fluorescence from individual silver nanoclusters. *Science* **2001**, *291*, 103–106.
62. Michaels, A.M.; Nirmal, M.; Brus, L.E. Surface enhanced Raman spectroscopy of individual rhodamine 6G molecules on large Ag nanocrystals. *J. Am. Chem. Soc.* **1999**, *121*, 9932–9939.

63. Maruyama, Y.; Ishikawa, M.; Futamata, M. Surface-enhanced Raman scattering of single adenine molecules on silver colloidal particles. *Chem. Lett.* **2001**, 834–835.
64. Kneipp, K.; Kneipp, H.; Kartha, V.B.; Manoharan, R.; Deinum, G.; Itzkan, I.; Dasari, R.R.; Feld, M.S. Detection and identification of a single DNA base molecule using surface-enhanced Raman scattering (SERS). *Phys. Rev., E* **1998**, *56*, R6281–R6284.
65. Nie, S.; Emory, S.R. Probing single molecules and single nanoparticles by surface-enhanced Raman scattering. *Science* **1997**, *275*, 1102–1106.
66. Ajito, K.; Torimitsu, K. Near-infrared Raman spectroscopy of single particles. *Trends Anal. Chem.* **2001**, *20*, 255–262.
67. Manfait, M.; Nabiev, I. *Raman Microscopy: Developments and Applications*; Turrell, G., Corset, J., Eds.; Academic Press: London, 1996; 379–420.
68. Vo-Dinh, T. Surface-enhanced Raman spectroscopy using metallic nanostructures. *Trends Anal. Chem.* **1998**, *17*, 557–582.
69. Murakoshi, K.; Ajito, K.; Jingze, L.; Sawai, Y.; Torimitsu, K.; Tanaka, H.; Nakato, Y. Control of near infrared surface-enhanced Raman scattering activity of Ag on Au thin film prepared on glass substrate by external electric polarization in solution. submitted.
70. Ajito, K.; Morita, M.; Torimitsu, K. Investigation of the molecular extraction process in single subpicoliter droplets using a near-infrared laser Raman trapping system. *Anal. Chem.* **2000**, *72*, 4721–4725.
71. Kim, B.; Tripp, S.L.; Wei, A. Self-organization of large gold nanoparticle arrays. *J. Am. Chem. Soc.* **2001**, *123*, 7955–7956.
72. Wei, A.; Kim, B.; Sadtler, B.; Tripp, S.L. Tunable surface-enhanced Raman scattering from large gold nanoparticle arrays. *Chem. Phys. Chem.* **2001**, *12*, 743–745.

# Metal Nanostructures: Synthesis by Soft Chemical Methods

**Yugang Sun**

*Department of Materials Science and Engineering, University of Illinois at Urbana-Champaign, Urbana, Illinois, U.S.A.*

**Younan Xia**

*Department of Chemistry, University of Washington, Seattle, Washington, U.S.A.*

## INTRODUCTION

This entry summarizes several approaches to the large-scale synthesis of metal nanostructures with various well-defined shapes by controlling the chemistry in solutions. The strategies include preferential adsorption of capping reagents on different crystallographic planes, use of self-assembled surfactant molecules as templates, control over the plasmonic excitation, and template-engaged replacement reaction. The as-synthesized nanostructures have well-controlled shapes and exhibit unique properties compared to their bulk material. They are promising candidates for applications in a range of fields that include optoelectronics, photonics, sensing, clinical diagnostics, catalysis, and energy storage/conversion.

## MOTIVATION FOR CONTROLLING THE SHAPE

Studies on metal nanoparticles have a long history since Faraday first observed the remarkable change of color associated with the size variation of gold colloids.<sup>[1]</sup> In addition to color tuning, properties of metal nanostructures have been extensively studied during the last two decades because of their promising uses in photography,<sup>[2]</sup> catalysis,<sup>[3]</sup> photonics,<sup>[4]</sup> electronics,<sup>[5]</sup> optoelectronics,<sup>[6]</sup> information storage,<sup>[7]</sup> chemical and biological sensing,<sup>[8,9]</sup> surface-enhanced Raman scattering (SERS),<sup>[10–12]</sup> clinic diagnosis,<sup>[13]</sup> and cancer therapy.<sup>[14]</sup> The performances of metal nanostructures in the aforementioned applications can be tailored by their chemical composition, size, shape, crystallinity, and structure (solid vs. hollow) because the intrinsic properties of a metal nanostructure are sensitive to any one of these parameters. The number of references in this multidisciplinary field

has increased dramatically and comprehensive reviews covering various aspects of the field have been published in recent years.<sup>[15–22]</sup> The first edition of this Encyclopedia includes overviews on “Nanocrystals Synthesized in Colloidal Self-Assemblies” and “Metal Nanostructures Synthesized by Photoexcitation.” However, this entry focuses on as much as possible a wider array of chemically synthetic approaches and how these techniques apply to the preparation of metal nanostructures with well-defined shapes and hollow interiors.

Controlling the shape of a metal nanostructure has been proven a powerful handle to fine-tune its properties. For example, the optical responses (e.g., surface plasmon resonance or SPR, and fluorescence) of gold or silver nanorods have been demonstrated to be highly sensitive to their aspect ratios.<sup>[15]</sup> Theoretic studies have suggested that the number of absorption peaks and effective spectral ranges for SERS are strongly dependent upon the exact morphology displayed by metal nanostructures.<sup>[23]</sup> With regard to catalysis, cubic platinum nanoparticles with their surfaces bound by  $\{1\ 0\ 0\}$  facets prefer to adsorb hydrogen molecules while carbon monoxide tends to strongly bond on the  $\{2\ 1\ 0\}$  facets of buckyball-shaped platinum nanoparticles.<sup>[24]</sup> Most recently, El-Sayed and Narayanan have comparatively studied the catalytic activity of platinum nanoparticles with different shapes (e.g., tetrahedron, cube, and quasi-sphere) toward the reaction between hexacyanoferrate (III) ions and thiosulfate ions in colloidal solution, and concluded that the activation energy decreased with the increase of percentage of surface atoms located on the corners and edges.<sup>[25]</sup> In case of magnetic property, the arrayed Ni nanowires with diameter of  $\sim 30$  nm that were prepared using the porous alumina membranes showed much enhanced coercivities, as high as 680 Oersteds, in comparison with bulk Ni (only



tens of Oersteds) and remnant magnetization up to 90%.<sup>[26]</sup> When metal nanostructures are developed into hollow ones, they can offer some advantages over their solid counterparts in making composites in terms of lighter weight, saving of material, and reduction of cost.<sup>[27]</sup> In particular, hollow nanostructures made of metals are intriguing to synthesize and study because they exhibit super tuning ability compared to their solid counterparts in surface plasmon resonance and catalytic activities. For example, Pd nanoshells have recently been demonstrated as an effective, recoverable catalyst for the Suzuki coupling reactions,<sup>[28]</sup> while solid Pd nanoparticles usually lose their catalytic activities after once cycle of operation.<sup>[29]</sup>

## OVERVIEW OF SYNTHETIC APPROACHES FOR CONTROLLING THE SHAPE

The fundamental and technological importance of metal nanoparticles with well-defined shapes has triggered the development of practical approaches that could produce nanostructures with desirable morphologies in large quantities. In principle, a metal can be generated by reducing its corresponding salt(s) with chemicals having relatively low redox potentials (e.g.,  $\text{NaBH}_4$ ,  $\text{H}_2$ , citric acid, and alcohols) and/or radicals generated from radiolysis of solvents or gases.<sup>[30,31]</sup> Pyrolysis of organometallic precursor is also an effective way to produce versatile metals in organic media.<sup>[32]</sup> This entry provides a brief overview of several solution-phase (which is referred to as “soft” medium) approaches that have been demonstrated for synthesizing metal nanostructures with well-defined shapes rather than spheres. It is further divided into four sections according to the properties of confinements that are used to direct the growth of metal nanocrystals. The first section explicitly discusses that the preferential adsorption of capping species (e.g., polymeric molecules and ions) onto different crystallographic planes can kinetically control the growth rates along different axes, resulting in various morphologies. The second section compares various metal structures synthesized by mediation of the self-assembled surfactant molecules (e.g., cetyltrimethylammonium bromide or CTAB, and sodium bis(2-ethylhexyl) sulfosuccinate or AOT). The third section represents that the plasmonic excitation induces the anisotropic transformation of metal nanoparticles into planar nanoprisms or nanodisks. The fourth section assesses the potential of template-engaged replacement reaction in synthesizing metal nanostructures with hollow interiors and complex multi-layered configurations. Finally, the entry is concluded with personal perspectives to the way in which this field is developing.

## PREFERENTIAL ADSORPTION OF CAPPING AGENTS

It is well known that the capping agents can protect metal nanoparticles from aggregating and are used to obtain well-dispersed sols of metal colloids. The capability of capping reagents in growing metal nanoparticles with selective shapes has been recognized in the last few years. To this end, the common sense is that the molecules could preferentially adsorb onto different crystallographic faces and mediate the relative growth rate along different crystal axes, resulting in the formation of nanoparticles with various shapes.<sup>[33,34]</sup>

With sharing this view, Sun and Xia developed a modified polyol process<sup>[35]</sup> involving poly(vinyl pyrrolidone) (PVP) that has been demonstrated a practical approach to synthesize nanowires (or nanorods) and nanocubes of silver.<sup>[36–38]</sup> In the synthesis, silver atoms are generated by reducing silver nitrate with ethylene glycol (which serves as both solvent and reducing agent) at elevated temperatures. The resultant atoms spontaneously assemble into small nanocrystals with different shapes and crystallinities depending on the reaction conditions (Fig. 1). We refer to this evolution process as the nucleation stage. These nanocrystals could serve as seeds for further addition of silver atoms (referred to as the growth stage). Although the exact function of PVP in the nucleation stage is still to be elucidated, it is believed that the preferential adsorption of PVP molecules to  $\{1\ 0\ 0\}$  facet of silver plays a critical role in growing one seed into larger structure. The shape of resultant nanoparticles is a

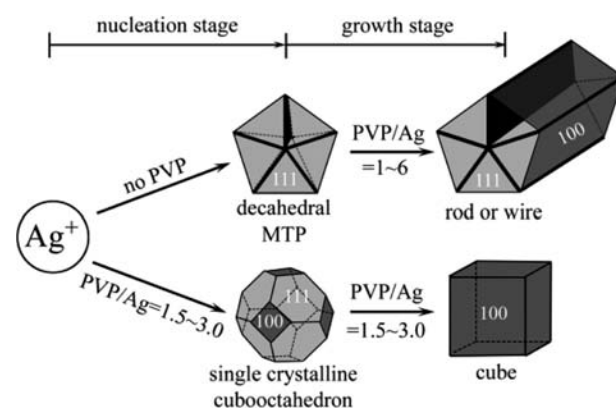


**Fig. 1** Schematic illustration on the formation of silver nanowires (or nanorods) and nanocubes via the PVP-modulated polyol process. The planes marked in gray with light and deep tones represent the facets bounded by  $\{1\ 1\ 1\}$  and  $\{1\ 0\ 0\}$  crystallographic planes, respectively. The twinned  $\{1\ 1\ 1\}$  planes and boundaries are filled in black color. “PVP/Ag” denotes the ratio between the amount of PVP (in terms of repeating unit) and silver nitrate.

manifestation of the crystallinity and morphology of the seed (see Fig. 1). For instance, multiple-twinned particles (MTPs) with the decahedral shape are produced when no PVP is introduced at the nucleation stage. Such a seed is comprised of five slightly deformed tetrahedrons by twinning their adjacent  $\{1\ 1\ 1\}$  faces. The seeds with fivefold symmetry would evolve into uniform nanowires characterized by pentagonal cross-section when their growth is assisted with PVP. In this case, the deposition of silver atoms on the twin boundaries leads to the uniaxial elongation of an MTP into a rod-shaped nanostructure under the confinement of twin planes (marked in black in Fig. 1). Meanwhile, the growth of rods in lateral directions is highly passivated by PVP through the strong co-ordination bonding between PVP and the side surfaces (exposing  $\{1\ 0\ 0\}$  facets). In comparison, the 10 end surfaces terminated with  $\{1\ 1\ 1\}$  facets retain high activity in attracting silver atoms because they are loosely covered by PVP. When a proper amount of PVP is added during nucleation, for example, when the molar ratio of the repeating unit of PVP to silver ions is between 1.5 and 2.0, single crystalline cubooctahedrons are formed. The passivation of  $\{1\ 0\ 0\}$  facets by PVP causes a much higher growth rate of  $\{1\ 1\ 1\}$  facets than that of  $\{1\ 0\ 0\}$  facets, and leads to the formation of nanocubes exposing only  $\{1\ 0\ 0\}$  facets.

The characterization results of silver nanowires and nanocubes were consistent with the evolution mechanism sketched in Fig. 1. Fig. 2A shows a typical SEM image of the as-obtained silver nanowires with diameter of 50–60 nm and lengths up to 50  $\mu\text{m}$ , indicating the abundant quantity that could be routinely achieved using this synthetic approach. Their cross-sections were directly observed from microtomed slices, which were prepared by cutting the nanowires embedded in cured epoxy. As shown in the inset of Fig. 2B, the nanowires exhibited a pentagonal profile with the fivefold contrast originated from the twinned boundaries. The stark contrast across each twin plane confirmed that each silver nanowire contained five single crystalline subunits (labeled as T1, T2, T3, T4, and T5). These subunits were equivalent and each had an untwinned side surface that tended to lie against the surface of TEM grid during sample preparation. As a result, the TEM image always displayed a straight twin boundary in the middle of a nanowire (as indicated by the arrow in Fig. 2B). Fig. 2C displays the selected-area electron diffraction (SAED) pattern recorded from the silver nanowire shown in Fig. 2B by aligning the electron beam perpendicular to the side surface of subunit T1. This pattern confirmed the formation of multitwinned crystalline structures.<sup>[39]</sup> Analysis of this pattern indicated that the side surfaces of each nanowire were terminated by  $\{1\ 0\ 0\}$  facets. The reactivity of the side surfaces and ends of as-prepared silver

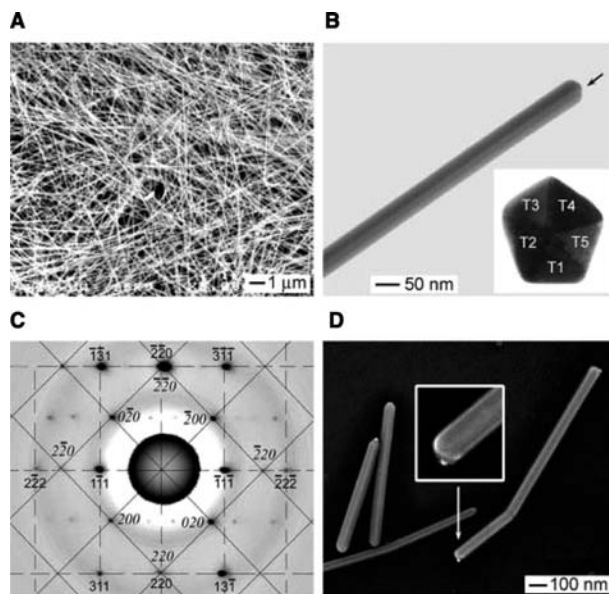


**Fig. 2** (A) An SEM image taken from the silver nanowires randomly assembled on a silicon substrate. (B) A TEM image recorded from the end of an individual nanowire showing the existence of a twin plane along the longitudinal axis (as indicated by the arrow). The inset in (B) is a TEM image of the cross-section of a Ag nanowire indicating that each wire had a fivefold twinned structure characterized by five single crystalline subunits (marked as T1, T2, T3, T4, and T5). (C) A selected-area electron diffraction pattern taken from an individual nanowire by directing the electron beam perpendicular to one of its five side surfaces. It corresponds to a superposition of square  $[0\ 0\ 1]$  (marked with italic characters, corresponding to T1) and rectangular  $[1\ \bar{1}\ \bar{2}]$  (marked with regular characters, corresponding to T3 and T4) zone patterns of face-centered cubic silver, together with the double diffraction reflections. The  $(2\ 2\ 0)$  and  $(2\ \bar{2}\ 0)$  reflections for these two zone patterns resulted in the same diffraction spots. (D) SEM image of several short silver nanowires after they had exchanged their PVP capping molecules with 1,12-dodecanedithiol (50 nM), and reacted with gold nanoparticles for 10 hr. The bright dots at the ends of the nanowires represent gold nanoparticles that had been attached through the dithiol linkage. Silver nanorods with relatively low aspect ratios were selected for this study in order to show both ends of each nanorod in the same image. The final concentration of  $\text{AgNO}_3$  and PVP ( $M_w \approx 55,000$ , calculated in terms of the repeating unit) were 0.027 and 0.05 M, respectively. The reaction temperature was  $160^\circ\text{C}$  and the reaction time was 60 min.<sup>[37]</sup>

nanowires was studied using the ligand-exchange experiment.<sup>[38]</sup> In a typical operation, gold nanoparticles were added to the dispersion of silver nanowires after they had been incubated in a very dilute solution of 1,12-dodecanedithiol. Fig. 2D shows the result, indicating that only the ends of each wire could adsorb gold nanoparticles. This observation implied that the interaction between PVP and the side surfaces of silver

nanowires was too strong to be replaced with the dithiol molecules when the concentration of dithiol was sufficiently low. In contrast, because the interaction between PVP and the ends of each nanowire was much weaker, the ends remained highly reactive for continuous addition of silver atoms during the growth stage.

Fig. 3A shows a typical SEM image of as-synthesized silver nanocubes with a mean edge length of 175 nm. The inset is the SEM image taken by tilting the sample stage of 20°, which clearly reveals that all the faces of each cube were smooth. The inset in Fig. 3B shows the electron diffraction pattern obtained by directing the electron beam perpendicular to one of the square faces of a cube. The square symmetry of the spots indicates that each silver nanocube was a single crystal bounded by {1 0 0} facets. Silver nanocubes with different sizes could be easily obtained by controlling the growth time. Fig. 3B shows a TEM image of the product obtained by shortening the growth time from 45 (the corresponding product as shown in Fig. 3A) to 14 min; the edge length decreased to 95 nm. The observation implied that the growth rate of all faces was almost the same once the cubic shape was formed. Thus, the further growth only increased its size without significant morphological change due to the equivalence of the six faces of each cube.

In contrast to the polyol process, silver nanoplates with triangular shapes can be obtained when ethylene glycol is replaced with *N,N*-dimethyl formamide (DMF). Liz-Marzán and Pastoriza-Santos have successfully synthesized silver nanoprisms by refluxing a DMF solution of silver nitrate (0.22 mol/L) in the presence of PVP (0.4 mmol/L).<sup>[40]</sup> The dependence of

morphology of silver nanostructures on solvent implies that the solvent molecules might compete with PVP molecules for preferential adsorption because both ethylene glycol and DMF have atoms (O for ethylene glycol and N for DMF) with lone electron pairs that could fill the empty orbitals of silver atoms to form co-ordination bonds. The synergetic adsorption of PVP and solvent molecules is similar to the synthesis of Co nanocrystals via pyrolysis of  $\text{Co}_2(\text{CO})_8$  in *o*-dichlorobenzene, a solvent having negligible interaction with Co.<sup>[41]</sup> In this system, the surfactant mixture of trioctylphosphine oxide (TOPO) and oleic acid was used to modulate the relative growth rates of different crystal facets. In addition to organic molecules, inorganic anions (e.g., halogenide and hydroxide) have also been found to dramatically change the shapes of metal nanostructures.<sup>[42,43]</sup> Pileni and coworkers systematically studied the effects of different anions on the shape of Cu nanoparticles synthesized from the  $\text{Cu}(\text{AOT})_2$ -isooctane-water system.<sup>[42]</sup> The addition of  $\text{Cl}^-$  led to the formation of Cu nanorods with high aspect ratios. Nanocubes became the dominated products by replacing  $\text{Cl}^-$  with  $\text{Br}^-$  and the size of nanocubes decreased significantly with addition of  $\text{F}^-$ . The preferential adsorption of capping reagents could enable us to synthesize metal nanoparticles with well-controlled shapes (for example, nanorods, nanowires, nanocubes, and nanoprisms) and in large quantities. However, the success systems are limited to only a few metals (e.g., Ag, Pt, Cu, Co, Fe<sup>[44]</sup>), and how the capping reagents work is still elusive.

## SELF-ASSEMBLED SURFACTANT MOLECULES

Surfactant molecules with polar hydrophilic heads and hydrophobic hydrocarbon chains tend to self-assemble into mesophase structures with various constructions when they are added to water. As shown in Fig. 4, cetyltrimethylammonium bromide (CTAB) could self-associate to different aggregates, depending on the pH value of medium. Weakly basic environment leads to the formation of rod-like micelles with double layers (process A), while planar lamellar phase is generated in strongly basic solution (process D). These assemblies provide a class of “soft” templates for synthesizing metal nanostructures with controlled shapes. Murphy and coworkers<sup>[45,46]</sup> have reported a seed-mediated route to the synthesis of metal nanorods with controllable aspect ratios in the presence of rod-like micelles. In this synthesis, small gold or silver nanoparticles stabilized with citrate ions were used as seeds. When a metal salt (e.g.,  $\text{HAuCl}_4$  or  $\text{AgNO}_3$ ), a weak reducing agent (e.g., ascorbic acid), and a base solution (e.g., NaOH) with relatively low concentration were mixed

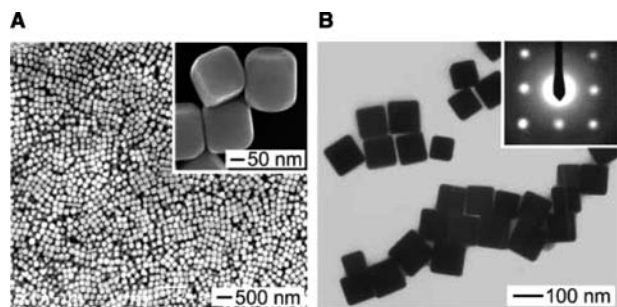


**Fig. 3** (A) SEM image of silver nanocubes obtained by growing silver nanocrystals via the polyol process for 45 min. The inset gives the high-magnification SEM image of the same sample taken at a tilting angle of 20°. (B) TEM image of the silver nanocubes obtained by shortening the growth time to 14 min. The inset shows diffraction pattern recorded by aligning the electron beam perpendicular to one of the square faces of an individual cube. The final concentration of  $\text{AgNO}_3$  and PVP were 0.068 and 0.10 M, respectively. The reaction temperature was 160°C.<sup>[36]</sup>

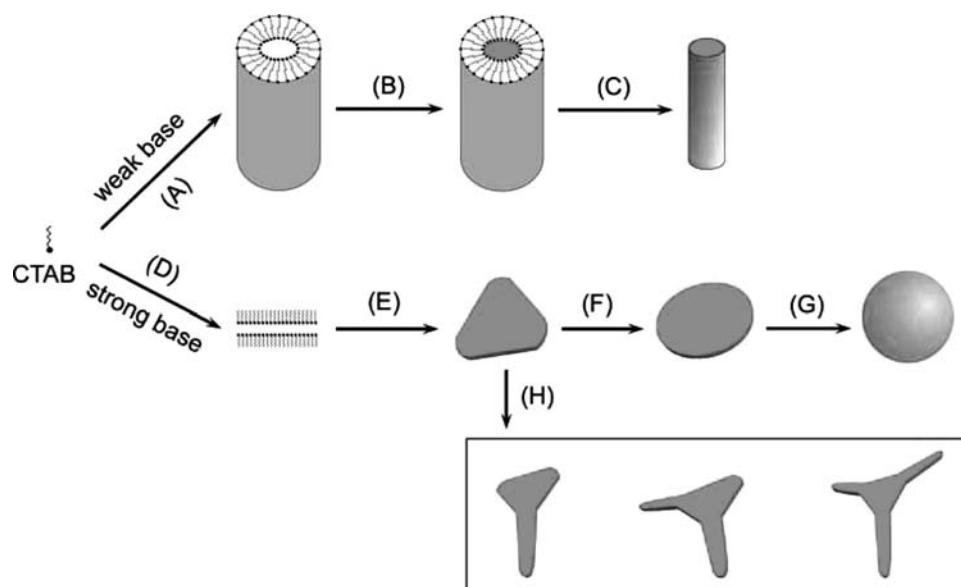


**Fig. 4** Depiction of metal nanostructures with various shapes formed by templating against self-assembled CTAB molecules in aqueous medium. (A) Formation of rod-like micellar phase; (B) reduction of metal ions which are encapsulated within the micellar cylinder; (C) removal of surfactant with appropriate solvents to collect pure nanorods or nanowires; (D) formation of planar lamellar mesophase; (E) generation of truncated triangular plates by templating against the lamellar phase; (F) aging of truncated triangular plates with formation of circular disks; (G) continuous aging of circular disks leading to the formation of spheres; (H) formation of armed structures (e.g., monopod, bipod, and tripod gold nanocrystals) by using the truncated triangular nanoplates of silver as seeds.

with the seeds, the seeds served as nucleation sites for the growth of nanorods within the confined micellar phase (see, process B). The lateral dimensions and aspect ratios of these one-dimensional (1D) nanostructures could be controlled by varying the concentration of seeds. Gold nanorods with more repeatable and higher quality could be obtained if the (CTAB)-capped seeds were used instead of citrate-capped ones.<sup>[47]</sup> Pure nanorods could be collected by removing the surfactant molecules after the reaction has completed (process C). The formation of rod-like structures was found to be independent of the reducing means. For example, Yang and coworkers and Esumi and coworkers<sup>[48,49]</sup> have prepared gold nanorods via the photochemical reactions induced by UV irradiation in the presence of rod-like CTAB micelles. Fourier-transform infrared spectroscopy (FTIR) and thermal gravimetric analysis (TGA) have been employed to study the structure of surfactant layers on the resultant gold nanorods.<sup>[50,51]</sup> The results indicated that CTAB adsorbed to the side surface of gold nanorods in a bilayer fashion, with the trimethylammonium headgroup of the inside monolayer of CTAB facing the gold surface. Chen and Carroll have demonstrated that the same approach could extend to synthesize truncated triangular silver nanoplates by increasing the pH value of reaction solution.<sup>[52]</sup> The TEM images of the closely stacked nanoplates revealed that the facial surfaces of

each nanoplate were covered with a monolayer of CTAB, consistent with the formation of a planar lamellar phase (processes D and E). The monolayer-protected silver nanoplates were not stable. The aging of triangular plates (with  $D_{3h}$  symmetry) at 40°C could transform them into various shapes with higher symmetries, such as circular disks (with  $C_{\infty,h}$  symmetry) and spheres (with  $C_s$  symmetry) (see processes F and G).<sup>[53]</sup> Most recently, these authors have successfully prepared gold nanocrystals with shapes of monopod, bipod, and tripod by using the as-synthesized silver nanoplates as seeds (process H).<sup>[54]</sup>

Another surfactant system used to successfully synthesize metal nanoparticles with various shapes was based on the reverse micelles formed in mixtures of sulfosuccinate (AOT), isooctane, and water.<sup>[55–57]</sup> In this case, the shape of surfactant assemblies was mainly determined by the ratio ( $w$ ) between water and surfactant. For examples, Pileni and coworkers have synthesized Cu nanorods by templating against the interconnected cylinders of AOT assembled at  $w = 10$ . When the value of  $w$  was increased to 20, supra-aggregates of AOT were formed, leading to the generation of Cu nanocrystals with various shapes, including MTPs and triangular plates. Metal nanoparticles could be synthesized in large quantities by using this kind of “soft” templates, albeit it is difficult and tedious to prepare micellar phase with controlled

morphologies as well as to remove the surfactant layers attached on the surface of metal nanostructures.

### CONTROLLED PLASMONIC EXCITATION

Plasmonic excitation has been suggested to provide the driving force that guides anisotropic growth of nanoparticles made of noble metals that exhibit strong surface plasmons.<sup>[58–62]</sup> Mirkin and coworkers<sup>[58,59]</sup> pioneered this approach to synthesize silver triangular nanoprisms with well-controlled size and monodispersity. In their synthesis, spherical silver nanoparticles with small size of 4.8–8.0 nm were firstly prepared by reducing silver nitrate with NaBH<sub>4</sub> in the presence of trisodium citrate and bis(*p*-sulfonatophenyl) phenylphosphine dehydrate dipotassium (BSPP). The resultant colloidal solution was transferred to transparent vessels and placed under the irradiation of light. The light fragmented silver nanospheres into much smaller clusters along with the formation of small silver nanoprisms. When subject to continuous illumination, the nanoprisms acted as seeds and grew until all the nanospheres had been consumed. If a lamp with monochromatic output (e.g., 550 nm) was used, the ultimate product contained bimodal silver nanoprisms with edge lengths around 70 and 150 nm, respectively. Each large prism was proposed to originate from four small ones through an edge-selective particle fusion mechanism.<sup>[58]</sup> In this case, the light wavelength (i.e., 550 nm) correlated to the dipole plasmon band (i.e., 640 nm) of silver nanoprisms with edge length of 70 nm. When a secondary beam with wavelength at either 340 or 450 nm was selected to excite the quadrupole plasmon (out-of-plane or in-plane mode) of the nanoprisms, the particle fusion process was inhibited, leading to the formation of nanoprisms with uniform size. Once the secondary beam was fixed to excite the quadrupole plasmon, the average edge length of the monodisperse nanoprisms correlated well with the wavelength of the primary excitation. Larger particles with in-plane dipole plasmon band located at longer wavelengths could be produced by increasing the wavelength of primary excitation. No matter which kind of silver source (small silver nanospheres vs. silver ions) was used, the plasmonic excitation could generate silver nanoprisms with shape and size related to the properties of exciting light.<sup>[60]</sup> Although this approach works only on the preparation of silver nanoprisms at the moment, it might be able to generate various morphologies of silver as well as other plasmonic metals when the role of light is thoroughly explored. The interested reader can find more details on the use of photoexcitation for structural control of metal nanoparticle assemblies in another review entry of the first edition of this Encyclopedia.

### TEMPLATE-ENGAGED REPLACEMENT REACTION

Galvanic replacement reaction has been demonstrated as a versatile and effective means for preparing metal nanostructures (e.g., thin films) by consuming the more reactive component.<sup>[63,64]</sup> Xia and coworkers have recently exploited the replacement reactions between silver nanostructures and desired metal salts that enable one to prepare metal nanostructures with hollow interiors.<sup>[65–71]</sup> For example, nanoboxes made of Au/Ag alloy could be synthesized by reacting silver nanocubes with aqueous chloroauric acid (HAuCl<sub>4</sub>) solution:

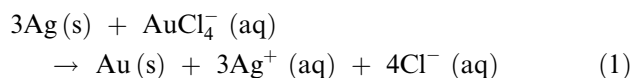
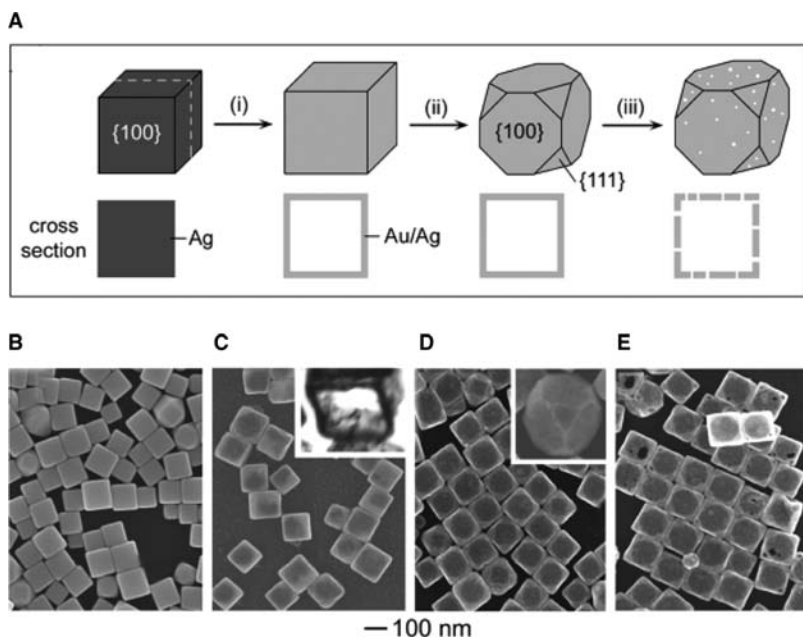


Fig. 5A summarizes the major steps involved in the galvanic replacement process that is performed at 100°C.<sup>[65]</sup> When the HAuCl<sub>4</sub> solution was mixed with the dispersion of silver nanocubes bounded by {1 0 0} facets (see a typical SEM image shown in Fig. 5B), the replacement reaction started from the sites with relatively high surface energies. The elemental gold generated from the replacement reaction tended to deposit on the surface of each template because their crystalline structures (both gold and silver are face-centered cubic) and lattice constants (4.0786 and 4.0862 Å for gold and silver, respectively) matched well. If the concentration of HAuCl<sub>4</sub> was high enough, the dissolution of silver could be continued until the whole silver template was completely consumed, leading to the formation of a box-like structure with uniform and homogeneous walls (Fig. 5C). The surface smoothness of each nanobox could be attributed to the Ostwald ripening process occurring at elevated temperature. The TEM image taken from a microtomed nanobox (inset of Fig. 5C) confirmed the formation of a void interior. Along with the replacement reaction, alloying also occurred between the deposited gold layer and the underlying silver surface because the interdiffusion rates of silver and gold atoms are relatively high at 100°C.

Silver atoms in the cubic boxes made of Au/Ag alloy (Fig. 5C) could be selectively removed when more HAuCl<sub>4</sub> was added to the reaction system. In this so-called *dealloying process*, numerous lattice vacancies would be formed because only one gold atom can be generated at the expense of three silver atoms, according to the stoichiometric relationship shown in Eq. (1). These lattice vacancies could be released via Ostwald ripening along with reconstruction of the morphology of the nanoboxes. As a result, each corner of the box became truncated to form new faces bounded by





**Fig. 5** (A) Summarization on the typical morphologies involved in the galvanic replacement reaction between a silver nanocube and an aqueous  $\text{HAuCl}_4$  solution. The major steps include following: (i) formation of a cubic nanobox with a uniform, smooth, homogeneous wall composed of Au/Ag alloy; (ii) dealloying of Au/Ag alloyed wall along with morphological reconstruction, resulting in the formation of a truncated nanobox of Au/Ag alloy; and (iii) continuation of dealloying, together with the formation of pores in the wall. The cross-sectional views correspond to the plane along dashed lines. (B–E) SEM images were taken from silver nanocubes (B) before and (C–E) after they had reacted with different volumes of 1 mM  $\text{HAuCl}_4$  solution: (C) 0.5, (D) 1.0, and (E) 2.0 ml.<sup>[65]</sup>

{1 1 1} crystallographic plane (step ii of Fig. 5A). Fig. 5D shows a typical SEM image of such truncated nanoboxes, and each of them was bounded by eight triangular faces and six octagonal ones. The inset shows the SEM image of a truncated nanobox sitting on the silicon substrate against its triangular faces, indicating that the newly formed triangular faces were also flat. Further dealloying could generate more lattice vacancies, and the Ostwald ripening process could not reconstruct the box and form a seamless box with ultrathin walls because such structures were not stable at  $100^\circ\text{C}$ . To this end, the lattice vacancies coalesced into pinholes in the wall (step iii of Fig. 5A). Fig. 5E shows a typical SEM image of such porous nanoboxes with cubic morphology. It is conclusive that the

template-engaged replacement reaction between silver nanocubes and  $\text{HAuCl}_4$  has the capability to generate hollow nanoboxes of Au/Ag alloys with various walls: cubic and seamless walls, truncated cubic and seamless walls, and truncated cubic and porous walls.

The template-engaged replacement reaction can be extended to silver templates with other shapes and crystallinities, such as polycrystalline spheres and multiple-twined wires. Fig. 6B shows a TEM image of Au/Ag alloyed nanoshells obtained by reacting the silver nanospheres of  $\sim 75$  nm in diameter with  $\text{HAuCl}_4$  in aqueous medium (step i of Fig. 6A). The surface of resultant Au/Ag alloyed nanoshell could be coated with a conformal, thin layer of pure Ag via an electroless plating process (step ii of Fig. 6A).

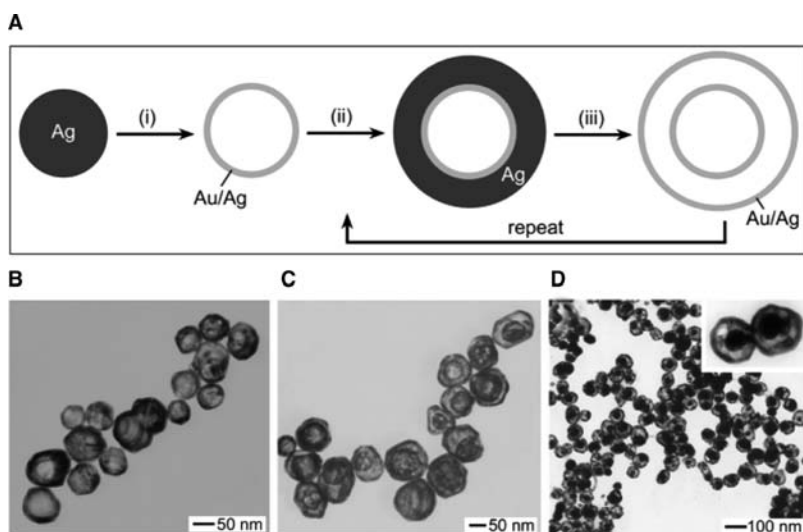


**Fig. 6** (A) Depiction of the procedure for synthesizing multiple-walled nanoshells composed of Au/Ag alloys: (i, iii) galvanic replacement reaction between Ag and  $\text{HAuCl}_4$  and alloying between Ag and Au; (ii) electroless deposition of pure silver on the surface of Au/Ag alloy shell. (B, C) Typical TEM images of Au/Ag alloy nanoshells that contained single (B), and double (C) walls, respectively. (D) TEM image of rattle-like nanostructures that were composed of solid Au/Ag alloyed nanoparticles encapsulated within Au/Ag alloyed nanoshells.<sup>[68]</sup>



When the replacement reaction was repeated one more time, a concentric Au/Ag alloyed layer with slightly larger dimension would be formed, and a double-walled Au/Ag nanoshell was finally obtained (step iii of Fig. 6A). Nanoshells with more than two walls could be readily prepared by repeating steps ii and iii.<sup>[68]</sup> Fig. 6C shows a TEM image taken from the bilayered nanoshells of Au/Ag alloys. It was believed that the inner shells were movable in the liquid medium because they could be located at the bottom of the outer shells as well as the top ceilings and/or other positions during the drying of sample. The spacing between outer and inner shells was determined by the thickness of silver layers deposited in the electroless plating process. If the Au/Ag alloyed nanoshells were replaced with solid Au/Ag alloyed nanoparticles to undergo the electroless plating of Ag and replacement reaction, nanorattles consisting of movable solid cores and hollow shells (both are made of Au/Ag alloys) could be prepared. Fig. 6D shows a typical TEM image of nanorattles that were prepared by using Au/Ag alloyed nanoparticles with diameter of  $\sim 30$  nm as templates. The average diameter of the outer shells was  $\sim 70$  nm, which was consistent with the thickness of silver layers deposited via electroless process. Statistical analysis over several hundred particles indicated that the yield of such nanorattles could be as high as 95% in each run of synthesis.

The approach which combines replacement reaction and electroless deposition could also enable us to prepare coaxial Au/Ag nanotubes with multiple layers by templating against silver nanowires.<sup>[71]</sup> Fig. 7A shows an SEM image of double-walled nanotubes consisting of Au/Ag alloys after they had been subjected to strong sonication. The inset of Fig. 7A clearly displays that each tube was composed of two coaxial sheaths characterized by a pentagonal cross-section similar to that of the silver template. If precursors rather than  $\text{HAuCl}_4$  were applied in the second round of replacement reaction, double-walled nanotubes made

of hybrid components could be generated. Fig. 7B gives an SEM image of the product obtained by reacting the Ag-coated Au/Ag nanotubes with aqueous  $\text{Pd}(\text{NO}_3)_2$  solution. In this sample, the inner and outer walls of each tube were constructed from Au/Ag and Pd/Ag alloys, respectively. The broken nanotube clearly shows that the side surfaces of Pd/Ag alloy tube (i.e., the outer wall) were rougher than those of Au/Ag alloy tube (i.e., the inner wall). The surface roughness could be attributed to the polycrystallinity of Pd/Ag sheath caused by the lattice mismatch between Pd and Ag ( $\sim 4.8\%$ ).

It is believed that the template-engaged replacement reaction could be easily extended to produce hollow nanostructures with numerous compositions because nanostructures made of many metals other than silver have been synthesized through various approaches. For example, hollow nanoshells composed of Pt nanoparticles with size of  $\sim 2$  nm had been prepared by reacting the Co nanoparticles with  $\text{H}_2\text{PtCl}_6$  in the nitrogen-saturated aqueous medium.<sup>[72]</sup> Different from the solid Pt nanoparticles with roughly the same size as that of nanoshells, nanoshells had relatively larger surface area, resulting in the increase of catalytic activity towards the electrochemical oxidation of methanol in acid solution.

## CONCLUSIONS

We have briefly discussed four classes of confinements that have been used to direct the anisotropic growth of metal nanostructures: 1) preferential adsorption of capping reagents onto different crystallographic planes; 2) self-assembled surfactant molecules; 3) controlled plasmonic excitation; and 4) template-engaged replacement reaction. Each method has been successful in preparing nanostructures consisting of specific components and having specific shapes. A comprehensive understanding of the complex chemical and physical processes involved in the synthetic strategies is still necessary to extend the present approaches to synthesize metal nanostructures with a broader number of shapes and compositions. The properties of a metal nanostructure have been suggested to be highly dependent on its shape and/or construction, but the novel properties associated with well-defined morphologies are still to be explored in order to improve its performance in the existing applications as well as to find new applications. In addition to systematic studies on the properties of the as-synthesized metal nanostructures, effective methods are sought for assembling individual nanostructures into ordered architectures (or superlattices) that might provide functional platforms in various applications such as chemical and

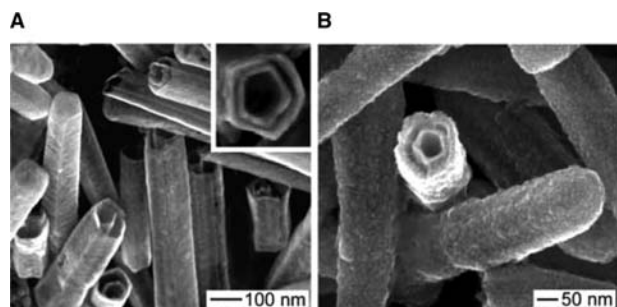


**Fig. 7** Metal nanotubes with double-layered walls: (A) both the inner and outer walls were composed of Au/Ag alloys; (B) the inner wall of each nanotube was made of Au/Ag alloy and the outer one was made of Pd/Ag alloy.<sup>[71]</sup>

biological sensing. For instance, Mirkin and coworkers have demonstrated that the oligonucleotide-modified gold nanoparticles could be selectively bonded to an arrayed substrate modified by the complementary oligonucleotide strand. This strategy has the ability to detect DNA with high sensitivity similar to that obtained from fluorophore-probe technique.<sup>[73]</sup> The recent results demonstrated by Yang and coworkers suggested that Langmuir–Blodgett (LB) process was a powerful technique to assemble 1D metal nanostructures (e.g., silver nanowires) into monolayered film with aligned orientation.<sup>[74]</sup> Such LB films of silver nanowires served as a kind of excellent substrate for SERS of 2,4-dinitrotoluene, the most common nitroaromatic component sought in detection of buried landmines and other explosives. There are still infinite opportunities to develop processes for synthesizing metal nanostructures and assembling them into ordered functional architectures. However, one who is working on metal nanostructures should take great caution because the particles with sizes on the nanometer scale have been proven pulmonary toxic.<sup>[75]</sup>

## ACKNOWLEDGMENT

The research on the synthesis of silver nanostructures with various shapes and template-engaged replacement reaction between silver templates and HAuCl<sub>4</sub> aqueous solutions had been supported in part by a Career Award from the NSF (DMR-9983893), an AFOSR-DURINT subcontract from SUNY-Buffalo, a DARPA-DURINT subcontract from Harvard University, and a David and Lucile Packard Foundation which were assigned to the Xia's group at the University of Washington.

## REFERENCES

- Faraday, M. The Bakerian lecture: experimental relations of gold (and other metals) to light. *Philos. Trans. R. Soc. Lond.* **1857**, *147*, 145–181.
- Lam, D.M.-K.; Rossiter, B.W. Chromoskedastic painting. *Sci. Am.* **1991**, *265* (5), 48–55.
- Lewis, L.N. Chemical catalysis by colloids and clusters. *Chem. Rev.* **1993**, *93*, 2693–2730.
- Maier, S.A.; Brongersma, M.L.; Kik, P.G.; Meltzer, S.; Requicha, A.A.G. Plasmonics—a route to nanoscale optical devices. *Adv. Mater.* **2001**, *13*, 1501–1505.
- Feldheim, D.; Keating, C.D. Self-assembly of single electron transistors and related devices. *Chem. Soc. Rev.* **1998**, *27*, 1–12.
- Kamat, P.V. Photophysical, photochemical and photocatalytic aspects of metal nanoparticles. *J. Phys. Chem. B* **2002**, *106*, 7729–7744.
- Murray, C.B.; Sun, S.; Doyle, H.; Betley, T. Monodisperse 3d transition-metal (Co, Ni, Fe) nanoparticles and their assembly into nanoparticle superlattices. *Mater. Res. Soc. Bull.* **2001**, *26*, 985–991.
- Kim, Y.; Johnson, R.C.; Hupp, J.T. Gold nanoparticle-based sensing of “spectroscopically silent” heavy metal ions. *Nano Lett.* **2001**, *1*, 165–167.
- Nicewarner-Peña, S.R.; Freeman, R.G.; Reiss, B.D.; He, L.; Peña, D.J.; Walton, I.D.; Cromer, R.; Keating, C.D.; Natan, M.J. Submicrometer metallic barcodes. *Science* **2001**, *294*, 137–141.
- Nie, S.; Emory, S.R. Probing single molecules and single nanoparticles by surface-enhanced Raman scattering. *Science* **1997**, *275*, 1102–1106.
- Cao, Y.C.; Jin, R.; Mirkin, C.A. Nanoparticles with Raman spectroscopic fingerprints for DNA and RNA detection. *Science* **2002**, *297*, 1536–1540.
- Dick, L.A.; McFarland, A.D.; Haynes, C.L.; Van Duyne, R.P. Metal film over nanosphere (MFON) electrodes for surface-enhanced Raman spectroscopy (SERS): improvements in surface nanostructure stability and suppression of irreversible loss. *J. Phys. Chem. B* **2002**, *106*, 853–860.
- Hirsch, L.R.; Jackson, J.B.; Lee, A.; Halas, N.J.; West, J.L. A whole blood immunoassay using gold nanoshells. *Anal. Chem.* **2003**, *75*, 2377–2381.
- Hirsch, L.R.; Stafford, R.J.; Bankson, J.A.; Sershen, S.R.; Rivera, B.; Price, R.E.; Hazle, J.D.; Halas, N.J.; West, J.L. Nanoshell-mediated near-infrared thermal therapy of tumors under magnetic resonance guidance. *Proc. Natl. Acad. Sci. U.S.A.* **2003**, *100*, 13549–13554.
- El-Sayed, M.A. Some interesting properties of metals confined in time and nanometer space of different shapes. *Acc. Chem. Res.* **2001**, *34*, 257–264.
- Badia, A.; Lennox, R.B.; Reven, L. A dynamic view of self-assembled monolayers. *Acc. Chem. Res.* **2000**, *33*, 475–481.
- Shipway, A.N.; Katz, E.; Willner, I. Nanoparticles arrays on surfaces for electronic, optical, and sensor applications. *ChemPhysChem.* **2000**, *1*, 18–52.
- Templeton, A.C.; Wuelfing, W.P.; Murray, R.W. Monolayer-protected cluster molecules. *Acc. Chem. Res.* **2000**, *33*, 27–36.
- Schmid, G. Large clusters and colloids. Metals in the embryonic state. *Chem. Rev.* **1992**, *92*, 1709–1727.
- Rao, C.N.R.; Kulkarni, G.U.; Thomas, P.J.; Edwards, P.P. Metal nanoparticles and their assemblies. *Chem. Soc. Rev.* **2000**, *29*, 27–35.
- Liz-Marzán, L.M. Nanoparticles: formation and color. *Mater. Today* **2004**, *7* (2), 26–31.
- Xia, Y.; Yang, P.; Sun, Y.; Wu, Y.; Mayers, B.; Gates, B.; Yin, Y.; Kim, F.; Yan, H. One-dimensional nanostructures: synthesis, characterization, and applications. *Adv. Mater.* **2003**, *15*, 353–389.
- Kottmann, J.P.; Martin, O.J.F.; Smith, D.R.; Schultz, S. Plasmon resonances of silver nanowires with a nonregular cross section. *Phys. Rev. B* **2002**, *64*, 235402.
- Falicov, L.M.; Somorjai, G.A. Correlation between catalytic activity and bonding and coordination-number of atoms and molecules on transition-metal surfaces—theory and experimental evidence. *Proc. Natl. Acad. Sci. U.S.A.* **1985**, *82*, 2207–2211.

25. Narayanan, R.; El-Sayed, M.A. Shape-dependent catalytic activity of platinum nanoparticles in colloidal solution. *Nano Lett.* **2004**, *4*, 1343–1348.
26. Whitney, T.M.; Jiang, J.S.; Searson, P.C.; Chien, C.L. Fabrication and magnetic properties of arrays of metallic nanowires. *Science* **1993**, *261*, 1316–1319.
27. Ohmori, M.; Matijevic, E. Preparation and properties of uniform coated colloidal particles 7. Silica on hematite. *J. Coll. Interface Sci.* **1992**, *150*, 594–598.
28. Kim, S.-W.; Kim, M.; Lee, W.Y.; Hyeon, T. Fabrication of hollow palladium spheres and their successful application to the recyclable heterogeneous catalyst for Suzuki coupling reactions. *J. Am. Chem. Soc.* **2002**, *124*, 7642–7643.
29. Li, Y.; Hong, X.M.; Collard, D.M.; El-Sayed, M.A. Suzuki cross-coupling reactions catalyzed by palladium nanoparticles in aqueous solution. *Org. Lett.* **2000**, *2*, 2385–2388.
30. Brust, M.; Walker, M.; Bethell, D.; Schiffrin, D.J.; Whyman, R. Synthesis of thiol-derivatised gold nanoparticles in a two-phase liquid-liquid system. *J. Chem. Soc. Chem. Commun.* **1994**, (7), 801–802.
31. Henglein, A. Reduction of  $\text{Ag}(\text{CN})_2^-$  on silver and platinum colloidal nanoparticles. *Langmuir* **2001**, *17*, 2329–2333.
32. Puentes, V.F.; Zanchet, D.; Erdonmez, C.K.; Alivisatos, A.P. Synthesis of hcp-Co nanodisks. *J. Am. Chem. Soc.* **2002**, *124*, 12874–12880.
33. Ahmadi, T.S.; Wang, Z.L.; Green, T.C.; Henglein, A.; El-Sayed, M.A. Shape-controlled synthesis of colloidal platinum nanoparticles. *Science* **1996**, *272*, 1924–1926.
34. Murphy, C.J. Nanocubes and nanoboxes. *Science* **2002**, *298*, 2139–2141.
35. Fievet, F.; Lagier, J.P.; Figlarz, M. Preparing monodisperse metal powders in micrometer and submicrometer sizes by the polyol process. *Mater. Res. Soc. Bull.* **1989**, *14* (12), 29–40.
36. Sun, Y.; Xia, Y. Shape-controlled synthesis of gold and silver nanoparticles. *Science* **2002**, *298*, 2176–2179.
37. Sun, Y.; Xia, Y. Large-scale synthesis of uniform silver nanowires through a soft, self-seeding, polyol process. *Adv. Mater.* **2002**, *14*, 833–837.
38. Sun, Y.; Mayers, B.; Herricks, T.; Xia, Y. Polyol synthesis of uniform silver nanowires: a plausible growth mechanism and the supporting evidence. *Nano Lett.* **2003**, *3*, 955–960.
39. Johnson, C.J.; Dujardin, E.; Davis, S.A.; Murphy, C.J.; Mann, S. Growth and form of gold nanorods prepared by seed-mediated, surfactant-directed synthesis. *J. Mater. Chem.* **2002**, *12*, 1765–1770.
40. Pastoriza-Santos, I.; Liz-Marzán, L.M. Synthesis of silver nanoprisms in DMF. *Nano Lett.* **2002**, *2*, 903–905.
41. Puentes, V.F.; Krishnan, K.M.; Alivisatos, A.P. Colloidal nanocrystal shape and size control: the case of cobalt. *Science* **2001**, *291*, 2115–2117.
42. Filankembo, A.; Giorgio, S.; Lisiecki, I.; Pileni, M.P. Is the anion the major parameter in the shape control of nanocrystals? *J. Phys. Chem. B* **2003**, *107*, 7492–7500.
43. Caswell, K.K.; Bender, C.M.; Murphy, C.J. Seedless, surfactantless wet chemical synthesis of silver nanowires. *Nano Lett.* **2003**, *3*, 667–669.
44. Park, S.-J.; Kim, S.; Lee, S.; Khim, Z.G.; Char, K.; Hyeon, T. Synthesis and magnetic studies of uniform iron nanorods and nanospheres. *J. Am. Chem. Soc.* **2000**, *122*, 8581–8582.
45. Murphy, C.J.; Jana, N.R. Controlling the aspect ratio of inorganic nanorods and nanowires. *Adv. Mater.* **2002**, *14*, 80–82.
46. Busbee, B.D.; Obare, S.O.; Murphy, C.J. An improved synthesis of high-aspect-ratio gold nanorods. *Adv. Mater.* **2003**, *15*, 414–416.
47. Nikoobakht, B.; El-Sayed, M.A. Preparation and growth mechanism of gold nanorods (NRs) using seed-mediated growth method. *Chem. Mater.* **2003**, *15*, 1957–1962.
48. Kim, F.; Song, J.H.; Yang, P. Photochemical synthesis of gold nanorods. *J. Am. Chem. Soc.* **2002**, *124*, 14316–14317.
49. Kameo, A.; Suzuki, A.; Torigoe, K.; Esumi, K. Fiber-like gold particles prepared in cationic micelles by UV irradiation: effect of alkyl chain length of cationic surfactant on particle size. *J. Colloid Interface Sci.* **2001**, *241*, 289–292.
50. Nikoobakht, B.; El-Sayed, M.A. Evidence for bilayer assembly of cationic surfactants on the surface of gold nanorods. *Langmuir* **2001**, *17*, 6368–6374.
51. Gao, J.; Bender, C.M.; Murphy, C.J. Dependence of the gold nanorod aspect ratio on the nature of the directing surfactant in aqueous solution. *Langmuir* **2003**, *19*, 9065–9070.
52. Chen, S.; Carroll, D. Synthesis and characterization of truncated triangular silver nanoplates. *Nano Lett.* **2002**, *2*, 1003–1007.
53. Chen, S.; Fan, Z.; Carroll, D.L. Silver nanodisks: synthesis, characterization, and self-assembly. *J. Phys. Chem. B* **2002**, *106*, 10777–10781.
54. Chen, S.; Wang, Z.L.; Ballato, J.; Foulger, S.H.; Carroll, D.L. Monopod, bipod, tripod, and tetrapod gold nanocrystals. *J. Am. Chem. Soc.* **2003**, *125*, 16186–16187.
55. Pileni, A.-P. The role of soft colloidal templates in controlling the size and shape of inorganic nanocrystals. *Nat. Mater.* **2003**, *2*, 145–150.
56. Maillard, M.; Giorgio, S.; Pileni, M.-P. Silver nanodisks. *Adv. Mater.* **2002**, *14*, 1084–1086.
57. Lisiecki, I.; Pileni, M.P. Synthesis of well-defined and low size distribution cobalt nanocrystals: the limited influence of reverse micelles. *Langmuir* **2003**, *19*, 9486–9489.
58. Jin, R.; Cao, Y.C.; Hao, E.; Métraux, G.S.; Schatz, G.C.; Mirkin, C.A. Controlling anisotropic nanoparticle growth through plasmon excitation. *Nature* **2003**, *425*, 487–490.
59. Jin, R.; Cao, Y.; Mirkin, C.A.; Kelly, K.L.; Schatz, G.C.; Zheng, J.G. Photoinduced conversion of silver nanospheres to nanoprisms. *Science* **2001**, *294*, 1901–1903.
60. Maillard, M.; Huang, P.; Brus, L. Silver nanodisk growth by surface plasmon enhanced photoreduction of adsorbed  $[\text{Ag}^+]$ . *Nano Lett.* **2003**, *3*, 1611–1615.
61. Callegari, A.; Tonti, D.; Chergui, M. Photochemically grown silver nanoparticles with wavelength-controlled size and shape. *Nano Lett.* **2003**, *3*, 1565–1568.

62. Sun, Y.; Xia, Y. Triangular nanoplates of silver: synthesis, characterization, and use as sacrificial templates for generating triangular nanorings of gold. *Adv. Mater.* **2003**, *15*, 695–699.
63. Lin, W.; Warren, T.H.; Nuzzo, R.G.; Girolami, G.S. Surface-selective deposition of palladium and silver films from metal-organic precursors: a novel metal-organic chemical vapor deposition redox transmetalation process. *J. Am. Chem. Soc.* **1993**, *115*, 11644–11645.
64. Porter, L.A., Jr.; Choi, H.C.; Ribbe, A.E.; Buriak, J.M. Controlled electroless deposition of noble metal nanoparticle films on germanium surfaces. *Nano Lett.* **2002**, *2*, 1067–1071.
65. Sun, Y.; Xia, Y. Mechanistic study on the replacement reaction between silver nanostructures and chloroauric acid in aqueous medium. *J. Am. Chem. Soc.* **2004**, *126*, 3892–3901.
66. Sun, Y.; Xia, Y. Alloying and dealloying processes involved in the preparation of metal nanoshells through a galvanic replacement reaction. *Nano Lett.* **2003**, *3*, 1569–1572.
67. Sun, Y.; Mayers, B.; Xia, Y. Metal nanostructures with hollow interiors. *Adv. Mater.* **2003**, *15*, 641–646.
68. Sun, Y.; Wiley, B.; Li, Z.-Y.; Xia, Y. Synthesis and optical properties of nanorattles and multiple-walled nanoshells/nanotubes made of metal alloys. *J. Am. Chem. Soc.* **2004**, *126*, 9399–9406.
69. Sun, Y.; Xia, Y. Increased sensitivity of surface plasmon resonance of gold nanoshells compared to that of gold solid colloids in response to environmental changes. *Anal. Chem.* **2002**, *74*, 5297–5305.
70. Sun, Y.; Mayers, B.T.; Xia, Y. Template-engaged replacement reaction: a one-step approach to the large-scale synthesis of metal nanostructures with hollow interiors. *Nano Lett.* **2002**, *2*, 481–485.
71. Sun, Y.; Xia, Y. Multiple-walled nanotubes made of metals. *Adv. Mater.* **2004**, *16*, 264–268.
72. Liang, H.-P.; Zhang, H.-M.; Hu, J.-S.; Guo, Y.-G.; Wan, L.-J.; Bai, C.-L. Pt hollow nanospheres: facile synthesis and enhanced electrocatalysts. *Angew. Chem. Int. Ed.* **2004**, *43*, 1540–1543.
73. Taton, T.A.; Mirkin, C.A.; Letsinger, R.L. Scanometric DNA array detection with nanoparticle probes. *Science* **2000**, *289*, 1757–1760.
74. Tao, A.; Kim, F.; Hess, C.; Goldberger, J.; He, R.; Sun, Y.; Xia, Y.; Yang, P. Langmuir–Blodgett silver nanowire monolayers for molecular sensing using surface-enhanced Raman spectroscopy. *Nano Lett.* **2003**, *3*, 1229–1233.
75. Warheit, D.B. Nanoparticles: health impacts? *Mater. Today* **2004**, *7* (2), 32–35.

## BIBLIOGRAPHY

1. Murakoshi, K.; Nakato, Y. Metal nanostructures: synthesis controlled by photoexcitation. In *Dekker Encyclopedia of Nanoscience and Nanotechnology*, 2E; Schwarz, J.A., Contescu, C.I., Putyera, K., Eds.; Taylor & Francis: New York, NY, 2009; Vol. 3, 2091–2104.
2. Pileni, M.P. Nanocrystals synthesized in colloidal self-assemblies. In *Dekker Encyclopedia of Nanoscience and Nanotechnology*, 2E; Schwarz, J.A., Contescu, C.I., Putyera, K., Eds.; Taylor & Francis: New York, NY, 2009; Vol. 4, 2581–2591.

# Metal–Oxide Interfaces: Design via Control of Defect Density

A. Bogicevic

Ford Motor Company, Dearborn, Michigan, U.S.A.

## INTRODUCTION

Ever since metals and ceramics were first joined together, mankind has striven to control this bond to enable the development of new and superior composite products. Transistors, catalytic converters, light bulbs, jet engine turbines, cutting tools, and dental implants are but a few examples of every day products that depend on the integrity of metal–ceramic interfaces. Further technology development is, in an increasing number of applications, rapidly reaching a point where precise atomic-level control of the composite interface is required. This is already a reality in the ever-shrinking world of microelectronics components, where device performance relies on metal–oxide junctions, often only a few atomic layers thick, and in emerging fields such as nano-fabricated catalysts and nano-electromechanical systems.

The ability to control the formation and stability of composite interfaces can be generally viewed as requiring two critical components: an adequate understanding of what factors determine interface formation and integrity, and the actual means to manipulate the interface using that insight. Atomic defects and impurities are well known to strongly influence interface formation and can, these days, be relatively well controlled experimentally. However, the poor understanding of *how* such defects affect individual metal–oxide systems currently represents a major obstacle for using defect control to one's advantage in tailoring interfaces. The large variations in system behavior with respect to any given defect situation indicate the complexity of the problem. This intricacy is ultimately rooted in the quantum mechanical nature of nano-sized components, which, in itself, can lead to the emergence of new properties, e.g., the onset of catalytic ignition of normally inert metals.<sup>[1]</sup> Therefore, first-principles parameter-free atomistic calculations are a useful complement to well-controlled experiments for shedding some light on this problem. Substantial progress has been made lately on both theoretical and

experimental ends, and this article highlights some of these developments with regard to simple point defects. While the focus here falls on applications involving thin metal films and dispersed metal particles on metal oxides, certain generalizations can be made for other materials, as well as the inverse situation encompassing the growth of oxides on metals.

In the following, a brief overview of metal–oxide bonding is given from a theorist's perspective, as an introduction to the important concepts of adhesion, wetting, and nucleation and growth processes. A natural division is made into thermodynamic and kinetic aspects of interface control, and the discussion then shifts to the role of common point defects and the prospects of defect-mediated control of metal–oxide interfaces.

## METAL–OXIDE INTERFACE

The nature and strength of the bond between a metal and an oxide varies, often sensitively, with the constituent materials and their preparation, e.g., surface morphology, metal coverage, gas phase atmosphere, etc. A number of different adhesion mechanisms have been reported, including weak van der Waals dispersion forces between induced surface dipoles, electrostatic polarization binding, and strong ionic and covalent bonding (the latter being more directional).<sup>[2–5]</sup> Several reviews on the general science of metal–oxide interfaces have been recently published. Recommended background literature includes the excellent reviews on the surface science of metal oxides by Henrich and Cox,<sup>[6]</sup> and on metal–oxide interfaces by Finnis<sup>[2]</sup> and by Campbell.<sup>[7]</sup>

Single metal atoms tend to form relatively strong chemical bonds to most oxide surfaces.<sup>[2,4,5]</sup> This is mainly the result of a severe under-coordination of the metal atom (compared to its favored bulk state), which is therefore reactive with the surface. These ionic or covalent metal–oxide bonds are correspondingly

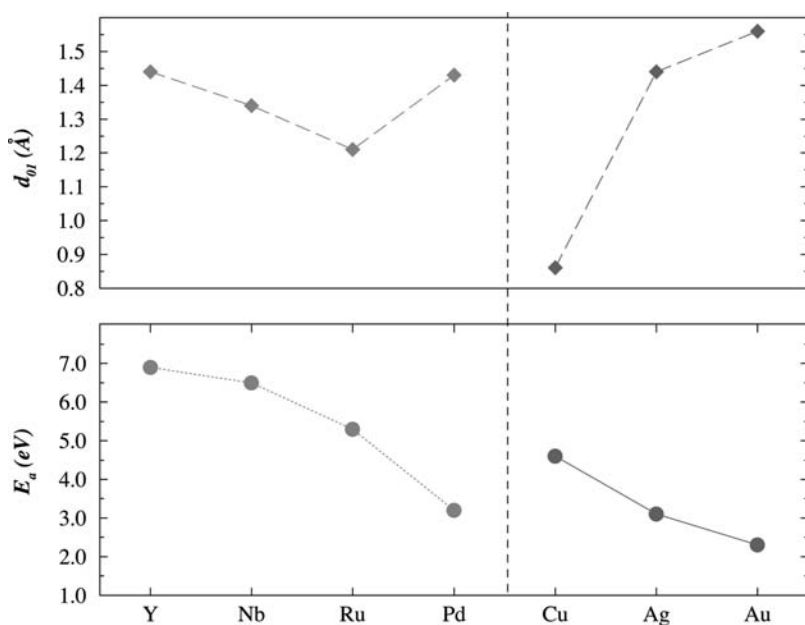


**Fig. 1** Low coverage metal–oxide bond lengths ( $d_{01}$ ) and metal adsorption energies ( $E_a$ ) for various metal atoms deposited on thin alumina films. The dashed line separates  $4d$  elements and the Group IB coinage metals. Note how the metal–oxide bond lengths ( $d_{01}$ ) increase down and to the left in the periodic table as the metal cation radii increase, with an attendant weakening of the adsorption energy. Note also the exception to this bond length–bond strength relation for the Ru–Nb–Y series, which is attributable to multiple ionization for Nb and Y (cf. Ru–Pd–Ag that are all singly ionized).

quite short, normally around 1–2 Å.<sup>[4,5,8,9]</sup> Typical bond strengths range from 1 to several eV, and are normally referred to as adsorption or desorption energies—defined as the energy required to remove a metal atom to the vacuum level. The metal–oxide bonds tend to further strengthen at various oxide surface defects, e.g., anion/cation vacancies, which can trap and immobilize diffusing metal atoms (as discussed in detail below). Figure 1 illustrates how the adsorbate–substrate bonds shorten and strengthen on ultrathin ( $\approx 5$  Å) alumina films as the adsorbate radius decreases (see Ref.<sup>[5]</sup>). For ionic adsorbate–substrate bonds, the metal atoms normally occupy the electrostatically favored position at low coverages,<sup>[3–5,9]</sup> although this rule of thumb weakens with oxide covalency. Strong chemical bonds tend to introduce new states in the band gap of the oxide, and one often finds a moderate to strong net spin polarization on the metal atom.<sup>[9]</sup>

As the metal coverage increases, metal–metal bonds are strengthened at the expense of weakened metal–oxide bonds. At some point, the very nature of the interfacial bond can change, and several theoretical studies have suggested simple polarization binding<sup>[10,11]</sup> as the origin of metal–oxide cohesion at coverages near and above 1 monolayer (ML).<sup>[5]</sup> This image interaction-based binding is considerably weaker than the ionic and covalent bonds typically found at low coverages. Fig. 2 illustrates the polarization binding found in a number of metal–oxide systems at the atomic level. The transition to increased metal coverage is marked by a lengthening of the metal–oxide bonds, typically by about 1 Å or more,<sup>[5,9]</sup> accompanied by a substantially weakened metal–oxide bond.

This is illustrated in Fig. 3 for single-layer ML thick metal films atop an ultrathin alumina substrate. The exact coverage at which metallic states appear depends on several factors, but has been estimated to be about 2/3 ML in certain systems.<sup>[5]</sup>

As the metal film or particle grows thicker, its cohesion to the oxide decreases only slightly in the case of polarization binding, and stabilizes already at about 2 ML.<sup>[5]</sup> This is a simple consequence of the image interaction bonding, which is to first order independent of the metal film thickness. The interface structure can change at any time during the film formation, as

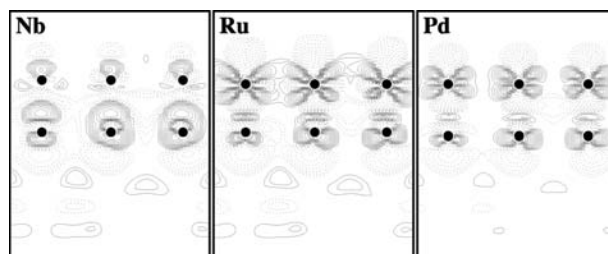


**Fig. 2** Charge density difference plot that illustrates how single-layer Nb, Ru, and Pd metal films adhere to a thin alumina support by means of polarization binding atop the oxide anions (see Ref.<sup>[5]</sup> for details). Solid lines indicate charge accumulation, dashed lines charge depletion, and the position of the topmost oxygen ions and the adsorbate atoms is indicated with (six) filled dots. As one moves to the right in the periodic table (PT),  $d$ -shell filling increases, there is more charge rehybridization, and less of the ionic core exposed, resulting in weakened metal–oxide bonds. Note the counterpolarization of the oxygen ions in the top layer of the oxide, which thus actively participate to some degree in the bond formation.



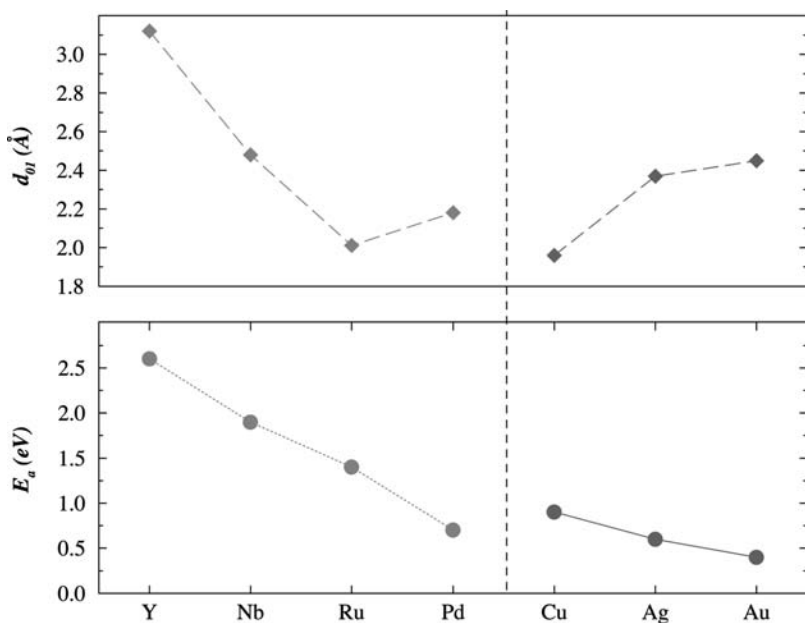


**Fig. 3** High coverage adhesion energies and film-oxide separations for various metal films deposited on ultrathin alumina films. The trends are similar to those at low coverage (cf. Fig. 1), which is largely attributable to atomic size arguments here as well, although the far-left elements again behave anomalously because of the rehybridization illustrated in Fig. 2.

existing bonds are broken and new ones are formed. During initial film formation, this tends to happen because of improving metal coordination. For example, Pt clusters on MgO(100) occupy initially both anion and cation sites to maximize their coordination, but spread out to anion sites only as the cluster becomes larger and starts forming a metal film.<sup>[9]</sup> In other circumstances, it is the variation in elastic strain energy within the growing metal film that leads to change of interface structure, as reported in a systematic study of metal film growth atop thin alumina films.<sup>[5]</sup> Here it was found that elastically soft single-layer films preferred a buckled adsorption atop cations, while at 2 ML and above, all metal films preferred unrumpled atop anion adsorption because of the accumulated strain energy penalty.<sup>[5]</sup> Overlayer strain is also often relieved through misfit dislocations, which can already appear at a few ML film thickness, leaving behind epitaxial interface domains.

### Adhesion and Wetting (Thermodynamics)

Thermodynamic analyses constitute a good starting point for assessing interface morphology and stability [kinetics are discussed in the section “Nucleation and Growth (Kinetics)”]. The work of adhesion  $W_{ad}$  describes the reversible free-energy change for cleaving an interface to produce surfaces in equilibrium with their environments. It is defined by the Dupré equation as

$$W_{ad} = \sigma_m + \sigma_o - \gamma_{mo} \quad (1)$$

where the three terms on the right-hand side of Eq. (1) denote the surface energies of the metal and the oxide,

and their mutual interface energy.<sup>a</sup> The work of adhesion is directly correlated to the degree to which a metal will wet an oxide, with the contact angle  $\theta$  given by

$$\cos \theta = \frac{\sigma_o - \gamma_{mo}}{\sigma_m} \quad (2)$$

The smaller the contact angle  $\theta$ , the greater the wettability of the oxide by the metal, as illustrated in Fig. 4.

In some applications, good wetting that results in a uniform metal film atop the oxide is desired (e.g., metal-oxide electronic junctions), while in other situations one instead strives to decrease the wetting to improve metal particle dispersion (e.g., catalysis applications). High oxide surface energies and low metal surface energies thus favor wetting of an oxide by the metal, as does increasing the interface energy.<sup>b</sup>

At this moment, it is useful to make a note about theoretical adhesion studies between metals and oxides. If one starts from unrealistic surfaces (e.g., non-stoichiometric oxides), which may not spontaneously reconstruct because of constraints, artificially strong interface energies will be computed because such surfaces are unstable and therefore very reactive. This is

<sup>a</sup>The work of adhesion is closely related to the work of separation  $W_{sep}$ , which is a fundamental interfacial quantity that establishes the minimum work needed to cleave a metal-oxide interface into two free surfaces. A detailed discussion on this topic is given in Ref.<sup>[2]</sup>.

<sup>b</sup>The sign conventions differ in the literature, so some caution must be taken when comparing the three relevant energies. While a higher surface free energy is typically associated with an energetic penalty, a higher interface energy is often taken to mean more energetically favored.

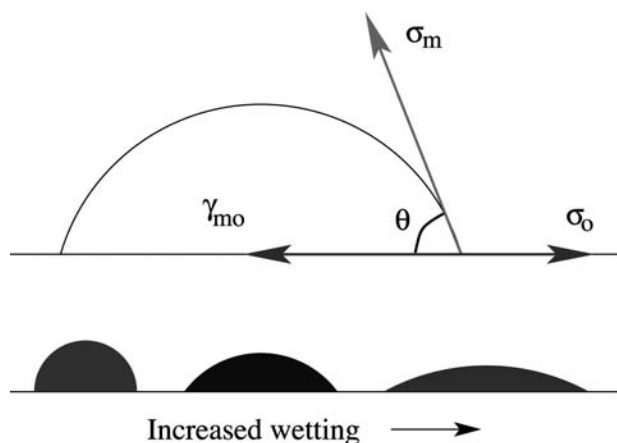


**Fig. 4** Schematic illustration of how the contact angle  $\theta$  is determined by surface/interface energies, and how wetting increases with a smaller contact angle. Non-wetting occurs for  $\theta > 90^\circ$ , wetting for  $<90^\circ$ , and perfect wetting or spreading for  $\theta = 0^\circ$ .

particularly important for oxide surfaces, and the simple recipe for avoiding such misconstructions is to ensure that the surface free energies are realistic, if not in agreement with experiment. The alternative is to include the energetic penalty of altering a realistic oxide into a reactive state by taking into account the displaced oxide material in the energetic balance.

### Nucleation and Growth (Kinetics)

Metal–oxide interfaces are, in a number of applications, manufactured through controlled growth of one component atop the other. The most common growth modes in epitaxial growth are layer-by-layer Frank–Van der Merwe (FV) growth, three-dimensional Volmer–Weber (VW) growth, and the Stranski–Krastanov (SK) growth mode that transitions from FV to VW growth after a few initial layers (Fig. 5). The two-dimensional FV growth mode corresponds to complete wetting, and is expected on thermodynamic grounds for systems in which  $\sigma_o - \gamma_{mo} > \sigma_m$ . Correspondingly, three-dimensional VW growth is expected for the opposite scenario where  $\sigma_o - \gamma_{mo} < \sigma_m$ , and the intermediate 2-D–3-D SK mode for situations in which  $\sigma_o - \gamma_{mo} \simeq \sigma_m$ .

These types of free-energy analyses outline the thermodynamic limits of achievable interface morphologies. In reality, it can be technically quite difficult to realize the desired interface properties within these limits. In addition, there is frequently a need to also join non-wetting materials. The fact that epitaxial growth is a highly non-equilibrium process is part of the problem with achieving thermodynamically stable interfaces, but also enables joining nominally non-wetting materials. This kind of interface manipulation

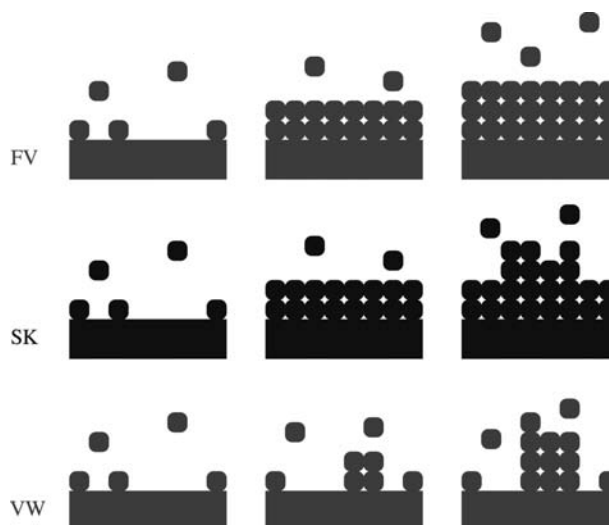


**Fig. 5** Schematic illustration of three common epitaxial growth modes. The SK growth mode starts out in a layer-by-layer FV fashion, and later transitions to a 3-D VW-type growth.

is enabled by kinetic control of the microscopic pathways that the system undergoes as one material is grown atop the other.

Mean-field nucleation theory provides a suitable mathematical framework for understanding the role that different atomic diffusion and reaction processes play in determining film morphology. As atoms arrive on the surface from the gas phase, they diffuse and meet to form the smallest stable island nuclei, e.g., dimers. As more atoms are deposited, the further growth of these nuclei competes with the formation of new nuclei. At the saturation density of stable nuclei, any further deposition leads exclusively to island growth. The mean-field assumption that the monomer density in between islands is homogeneous facilitates a simple analytical solution to the time evolution of island densities.

As an example illustrating the important concepts of a critical nucleus size and its relation to atomic processes that can be manipulated via defect density, the simple case of 2-D nucleation and growth with stable dimers is considered next. The rate equations for the density of single atoms  $n_1$  and stable metal islands  $n_x$  then read,<sup>[12]</sup>

$$\frac{dn_1}{dt} = F - 2\tau_1 D n_1^2 - \tau_x D n_1 n_x - \phi_x F (F t - n_1) - 2\phi_1 F n_1 \quad (3)$$

$$\frac{dn_x}{dt} = \tau_1 D n_1^2 + \phi F n_1 - 2n_x (F - dn_1/dt) \quad (4)$$

where the subscript  $x$  denotes the number of atoms in the island,  $\tau$  represents the capture rates,  $D$  is the

adatom diffusivity,  $F$  is the influx rate of atoms,  $t$  is the time, and  $\phi$  relates to direct impingement on existing islands. Incorporating the standard Arrhenius relation for thermally activated processes within transition state theory,  $\nu = \nu_0 \exp - E/k_B T$ , where  $\nu$  represents the process rate,  $\nu_0$  the vibrational prefactor,  $k_B$  the Boltzmann factor, and  $E$  the activation energy of the process, and using the approximate mean free path relation  $l \simeq (D/F)^{1/6}$ , one arrives at the general island density expression for 2-D islands in the complete condensation regime,

$$n_x = \eta(\theta, i) \left( \frac{D}{F} \right)^{-\chi} \exp \left( \frac{E_i}{(i+2)k_B T} \right) \quad (5)$$

with the scaling exponent  $\chi$  given by

$$\chi = \frac{i}{i+2} \quad (6)$$

and where  $\theta$  denotes the coverage and  $\eta$  represents a universal scaling function of the coverage  $\theta$ . The *critical* island size  $i$  represents the number of atoms in the smallest stable nucleus minus one, and  $E_i$  its binding energy ( $E_1 = 0$ ). From Eqs. (5) and (6), it is evident that these last two parameters, in particular, strongly affect the island density, which is the primary means to kinetic control of growth morphology. This is the primary subject of the remainder of this entry.

## ROLE OF DEFECTS

There are essentially two approaches to tailoring metal-oxide interfaces: manipulation of thermodynamic energies and manipulation of growth kinetics. In the first case, one strives to adjust the interface energy or the surface energies of the constituents, while the second approach encompasses adjusting the nucleation and growth kinetics. Point defects in particular were repeatedly shown to strongly influence or control both interface formation and interface stability<sup>[13-16]</sup> as well as the chemical reactivity of thus formed overlayers.<sup>[1,6,7,10,17-19]</sup> Even in well-controlled ultrahigh vacuum environments, relatively modest defect densities on the order of  $10^{12} \text{ cm}^{-2}$  (roughly 1 defect per 1000 surface atoms) have been known to dominate the nucleation and growth process of interface formation.<sup>[14,16]</sup> For example, it was recently shown that even low  $10^{-11}$  mbar pressure chambers allowed for low-level impurities to completely change the growth mode of Pt(111) from flat films (FW) to 3-D dispersed particles (VW).<sup>[20]</sup>

The presence of point defects is often noted indirectly, e.g., via sample coloration, or by the way the metal island density varies in growth experiments

(see below). Sometimes, it is discrepancies with other studies that eventually lead to the realization of defect-affected systems. In the Pt example above, new experiments prompted by variances with first-principles calculations revealed that 0.001 ML of adsorbed CO was responsible for the unexpected 3-D growth.<sup>[20]</sup> In other examples, hydroxyl groups from dissociated water were identified as nucleation centers in several metal-oxide systems,<sup>[21-24]</sup> as confirmed by first-principles theoretical calculations.<sup>[8,23]</sup> The mechanism by which hydroxyls tend to nucleate metal islands on oxides is discussed in some detail in Refs.<sup>[8,23,24]</sup> Other defects that have been commonly held responsible for affecting metal-oxide interface formation are hydrogen, carbon, sulphur, and other contaminants, as well as intrinsic oxide point defects such as oxide vacancies.

A common misconception in the literature is that the trapping ability of a defect is also a signature of its propensity to preferentially nucleate metal islands. If one ignores the interaction between the trapped atom and the sea of diffusing adatoms, there is actually *no* net effect whatsoever on the nucleation and growth process. All that would happen upon the trapping is that the population of diffusing adatoms and the availability of surface sites would decrease by the number of trapped atoms. In essence, this would be equivalent to considering a smaller portion of the growth area, resulting in no net perturbation.

Clearly then, at the very heart of nucleation and growth lies the interaction between metal adatoms, and its manipulation is grounded in the modification of these interactions. A defect will preferentially nucleate metal islands if, and only if, it stabilizes the metal-metal bond(s) of the cluster compared with the same cluster on the defect-free surface. Specifically, the defect must enhance the binding energy of the smallest stable cluster, henceforth referred to as the *core* cluster. The core cluster is what the critical cluster, introduced earlier, becomes upon the addition of a single atom. Thus, one distinguishes between unstable, critical, core, and stable clusters, which contain  $n < n_i$ ,  $n_i$ ,  $n_i + 1$ , and  $n > n_i + 1$  atoms, respectively, with  $i$  representing the critical cluster size.

It is evident from these arguments alone that the concept of critical and core clusters are central in any growth process, and that the trapping energy of clusters smaller than the core cluster are not (single atoms included). This is also reflected in the nucleation theory expressions for the island density, which carry an exponential dependence of the core cluster binding energy [cf. Eq. (5)]. Depending on the metal-oxide system and the overall growth conditions, the core cluster can consist of a dimer, trimer, tetramer, or even larger aggregates. In many instances, dimers (pairs of atoms) constitute the core cluster ( $i = 1$ ). In this case, the

appropriate quantity entering Eq. (5) is the dimer binding energy  $E_b$ , which is defined with respect to two infinitely separated adatoms. A good indication of whether a defect may preferentially nucleate metal islands for  $i = 1$ , is to thus consider whether it enhances  $E_b$ . For a discussion of how cluster mobility enters the picture, and the conditions under which larger clusters than dimers may become critical, the reader is referred to the excellent review of nucleation and aggregation by Brune.<sup>[12]</sup>

At this point, it is important to realize that, in some cases, even significant changes in core cluster binding energies brought about by defects can be absolutely irrelevant for the nucleation and growth process. The relevance of defect-mediated changes in the binding energy of the core nucleus depends on the degree of perturbation and on the relevant growth conditions. For example, a change in  $E_b$  of, say, 1 eV on top of an already strong dimer bond of several eVs will barely perturb the nucleation process under most growth conditions—once two atoms meet, they will stick together for a sufficiently long time to nucleate an island irrespective of the actual dimer binding energy. Conversely, the same change of 1 eV in a system with relatively weak dimer bonds of an eV or less will have a tremendous effect under the same growth conditions. Clearly, the relevant measure here is to consider the relative change the defect brings about in the core cluster binding energy compared with its absolute value on the pristine surface, and to view that perturbation in light of the growth conditions (e.g., temperature and flux), cf. Eq. (5).

## NUCLEATION AT OXIDE VACANCIES

The role of intrinsic oxide point defects in metal–oxide interface formation remains quite controversial. It has been suggested in several studies that surface anion vacancies serve as nucleation centers for metal islands by trapping metal adatoms, thereby strongly affecting the growth kinetics and consequent growth modes.<sup>[16,27–29]</sup> A number of theoretical first-principles studies have shown that both single metal atoms and metal films bind stronger, in the former case much stronger, to oxide surfaces containing intrinsic defects such as oxygen vacancies.<sup>[8,9,27,28,30–32]</sup> Oxygen vacancies in particular were suggested as the most likely candidate for nucleating metal islands.<sup>[16,30]</sup> However, there is, to this date, no direct experimental or theoretical evidence to support this supposition. Direct experimental verification remains elusive, not least because of the inherent difficulty in atomically resolving insulating oxide surfaces. Instead, indications of defect-controlled nucleation and growth often comes from noting that the metal island density  $n_x$  stays constant

over a wide range of deposition temperatures  $T$  and/or deposition fluxes  $F$ ,<sup>[15,16]</sup> cf. Eq. (5). Theoretical studies, while supporting the trapping model, have not adequately addressed the issue of nucleation, which involves the buildup of metal–metal bonds on the oxide surface. The first theoretical study to actually do so suggested that oxygen vacancies on MgO(100) do not preferentially nucleate Pt islands, contrary to prevailing speculations.<sup>[8]</sup> Subsequent studies of a number of other systems lend further support to these initial findings, and provide a physical explanation to why highly reactive vacancies do not necessarily nucleate metal islands.<sup>[9]</sup> In the following, these arguments are recounted and elaborated on to explain why the ability of oxygen vacancies (and other defects) to trap individual atoms is, in general, not a good indication of their propensity to preferentially nucleate metal islands.

Anion and cation vacancies can both exist in several charge states in most oxides. The  $F_s$  surface anion vacancy results from the removal of an oxygen atom, and contains two electrons that are weakly trapped by the electrostatic Madelung potential. These electrons give rise to electronic surface states, which at a sufficient (bulk) density of vacancies can often be seen by the naked eye through coloration of the oxide. The  $F_s$  center (the  $F$  stems from the German *Farbe* for color) can be viewed as a core-less oxygen ion, although a much more reactive one at that. In the case of divalent oxides, one can construe two additional types of anion vacancies, the singly charged paramagnetic  $F_s^+$  center and the doubly charged  $F_s^{2+}$  center, where one or both of the color center electrons are absent. The  $F_s$  center is typically the most stable of these anion vacancies,<sup>[25,26]</sup> and also the most well studied one. The generalization to oxides of other valency, and to the corresponding cation vacancies is analogous.

## Trapping of Individual Adatoms

The first thing to keep in mind when considering oxide vacancies is that they are undoubtedly more reactive than most, if not all, other sites on the otherwise pristine oxide surface. Their reactivity can be appreciated by considering the energetic penalty of creating the defects. The anion vacancy formation energy ( $F_s$  center) for MgO(100) is a huge 13.5 eV, which is a rather representative value for other oxides as well (the corresponding cation formation energy is reportedly 13.1 eV).<sup>[8]</sup> Therefore, it is not very surprising that both anion and cation vacancies are extremely reactive and will trap and immobilize nearly any metal (or non-metal) atom that comes near. The natural abundance of surface vacancies in thermodynamic

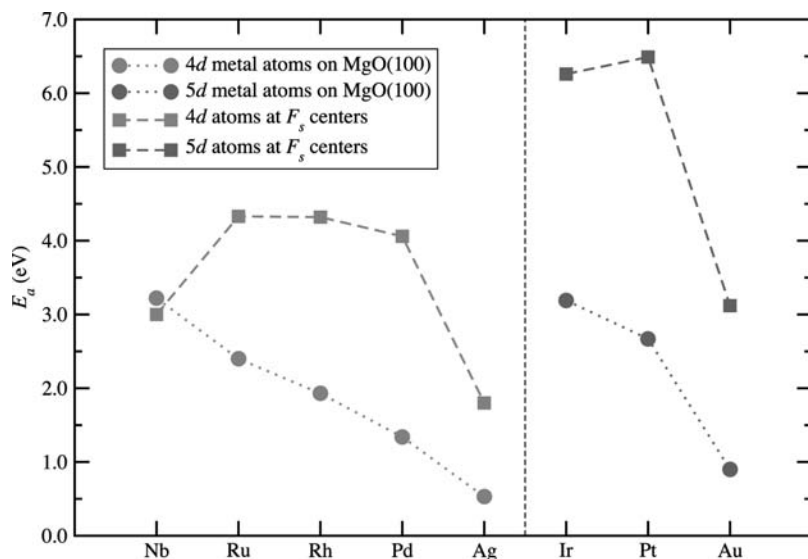


**Fig. 6** Adsorption energies  $E_a$  at regular sites (atop anions) on MgO(100) and at  $F_s$  centers at 1/36 ML coverage for a string of 4d and 5d metal elements across the periodic table, as computed within generalized gradient approximation of density functional theory (DFT-GGA). The main point of this figure is to illustrate the considerable strengthening of the metal–oxide bond at the oxygen vacancy, with the only exception Nb being due to its large size preventing sufficient penetration of the vacancy.<sup>c</sup> Source: From Ref.<sup>[9]</sup>.

equilibrium is obviously quite low because of their large formation energy. However, intentional creation of oxide vacancies can be accomplished using a variety of experimental techniques, including ultraviolet (UV) irradiation in reducing atmospheres, ion beam sputtering, and doping with aliovalent cations.<sup>[33,34]</sup>

The trapping ability of neutral oxygen vacancies is illustrated in Fig. 6, which shows the adsorption energy of individual metal atoms at regular sites (atop anions) and at  $F_s$  centers on MgO(100) (where they sit deeply inside the vacancy).<sup>[9]</sup> The adsorption energies increase substantially at the  $F_s$  defect compared with the surface in all cases except Nb, which is too large to fill the vacancy.<sup>c</sup> The color center electrons are largely transferred to the trapped metal atoms, which assume a negative charge. Similar results have been noted in several other systems,<sup>[8,9,27,28,30–32,35]</sup> several of which have also suggested that the trapped metal atoms develop a significantly enhanced activity toward other adsorbates.

### Impact on Cluster Stability

To assess whether there is a preference for metal islands to nucleate at oxide vacancies, it is thus appropriate to compare the dimer binding energies at the vacancy and on the defect-free surface. The dimer binding energy at the vacancy is defined with respect to one atom trapped in the vacancy and the other infinitely far apart on the defect-free surface. For details

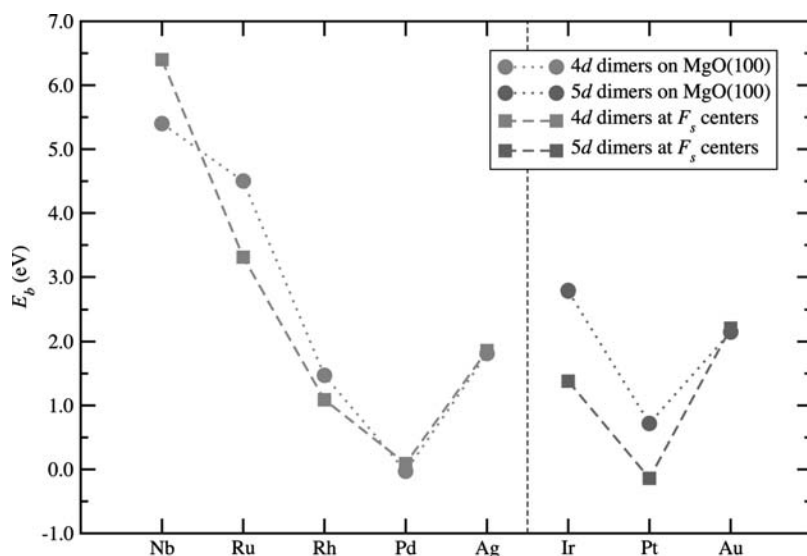
about adsorption geometries of dimers, the reader is referred to Ref.<sup>[9]</sup>.

Fig. 7 displays the dimer binding energy for a variety of metal dimers at regular sites and at  $F_s$  centers on MgO(100).<sup>[9]</sup> The dimer binding on the pristine surface is noted to increase to the left in the periodic table. This trend follows that of the bulk cohesive energy of these metals, and can be well understood by simple  $d$ -shell filling arguments: the strongest metal–metal bonds occur for half-filled  $d$ -shells, and so as the anti-bonding  $d$ -states become increasingly more occupied to the right of Nb, the bond strength decreases accordingly. Silver and gold both behave somewhat anomalously in this regard, a well-known fallacy of the  $d$ -shell model in alloy theory involving these elements.

Fig. 7 further shows that the dimer binding trend at the  $F_s$  vacancy is quite similar to that on the defect-free surface, and that, in several cases, the adatom–adatom bond is actually weakened at the defect. More importantly, it is evident from a comparison between Figs. 6 and 7 that there is no apparent relation between how well vacancies stabilize atoms (universally) vs. how they affect dimer bonds (quite varied). These results lend tangible support to the main conclusion of the previous section—that it is inappropriate to deduce a defect’s ability to nucleate islands based solely on how strongly it traps individual atoms.

A good part of these observations can be understood by simple bond-order and  $d$ -shell filling arguments. Bond-order and rebonding considerations state that the stronger one of the dimer atoms interacts with a third party, the weaker its bond becomes to its partner adatom, as noted in Fig. 7. The fact that the dimer binding trend at and away from vacancies is the same originates from the  $d$ -shell filling arguments outlined above. However, depending on the amount

<sup>c</sup>Atoms too large to sufficiently fill the vacancy may not bind as strongly because of the exponentially decaying Madelung field away from the surface.



**Fig. 7** Dimer binding energies  $E_b$  on the defect-free terrace of MgO(100) and at  $F_s$  centers at 1/18 ML coverage for various 4d and 5d metal elements, as computed within DFT-GGA. Source: From Ref.<sup>[9]</sup>.

of charge transfer to the dimer, one would expect a shift in the maximum, to the left in the periodic table for  $F_s$  vacancies. The reasoning here is as follows. As a second atom joins an already trapped atom at the  $F_s$  vacancy, electron density from the color center electrons is shared between the two atoms. This is evident from a lengthening of the adatom–adatom bond, by the dimer tilt angles being toward neighboring oxide cations, and from charge density analyses.<sup>[9]</sup> In Group VIII elements, this adds to antibonding levels because the  $d$ -shells are overfull, thereby weakening the adatom–adatom bonds. In contrast, the opposite happens to the far left in the periodic table (Nb and beyond), where added electron density to the underfilled  $d$ -shell strengthens the dimer bond. In the extreme case of complete transfer of the two color center electrons, one would therefore expect the maximum adatom–adatom binding to be shifted by one element to the left in the periodic table. The noble metals bind only weakly to the oxide, and their dimers are less prone to interact with the  $F_s$  defects. This results in a weak perturbation of the dimer bond due to lesser charge exchange, as attested by the dimer bond strengths being quite near gas phase values (e.g., 1.7 eV for Ag).<sup>[36]</sup>

As mentioned previously, changes in core cluster energies resulting from defects may or may not be relevant, depending on the magnitude of both relative and absolute energies, as well as the growth conditions, cf. Eq. (5). A closer examination of Fig. 7 suggests that  $F_s$  vacancies on MgO are unlikely to significantly affect the nucleation kinetics of, e.g., Nb, Ru, Ag, and Au, while Pd, Pt, and possibly also Ir, should be considerably more sensitive to such defects.

While  $d$ -shell filling arguments seem to provide a useful perspective on metal nucleation at defects, there are a number of other factors that likewise influence the core cluster binding energy. The size of the metal

atom has already been mentioned, as it affects its trapping and amount of charge transfer to the atom and subsequent clusters. The degree of covalency is another factor which varies depending on the type of metal bonding, e.g.,  $s$ - $p$  and  $s$ - $d_\sigma$  bonding, and which affects the ability to form multidirectional bonds<sup>[37]</sup> For large enough clusters, the ability to relieve mismatch strain becomes energetically competitive and is clearly affected by adsorption geometry. In addition, the  $d$ -shell filling arguments become less indicative as the cluster becomes bigger and the charge is shared over more atoms. Studies of how larger clusters are affected by  $F_s$  vacancies are reported elsewhere.<sup>[9]</sup>

## CONCLUSION

This entry emphasizes the need of a microscopic understanding of nucleation kinetics and adhesion energetics to facilitate defect-mediated engineering of metal–oxide interfaces. For example, it is shown via straightforward nucleation theory analyses that single-atom trapping is, by default, not a good indicator of a defect’s ability to preferentially nucleate metal islands as it omits the crucial aspect of metal–metal bond formation. The principal conclusions in this regard can be summarized as:

1. Defects affect metal–oxide interfaces by changing the nucleation kinetics, by modifying adhesion and thereby wetting energetics, or both.
2. To assess whether a defect serves as a preferential nucleation center, it is not sufficient to consider only single atom trapping. A better measure is how well the defect stabilizes the binding energy of the core cluster.



- The stabilization of the core cluster must be viewed in light of both the absolute core cluster binding energy and the growth conditions to assess its impact on nucleation dynamics.

The neutral oxygen vacancy defect, whose much-debated role as potential nucleation center remains a controversial topic, is considered in some detail within the nucleation theory framework. A series of first-principles calculations very clearly shows the disconnect between single-atom trapping and core cluster stabilization at  $F_s$  centers on magnesia. These calculations further demonstrate considerable variations in cluster formation energies depending on metal species, which is interpreted by using  $d$ -shell filling arguments. The computed energies suggest that, in several cases,  $F_s$  centers on magnesia do not, in fact, stabilize island formation. While nucleation theory and chemical arguments provide a reasonably well-grounded basis for interpreting the role of defects in metal–oxide interface formation, more studies are needed for quantitative predictions and generality assessments. In particular, it would be interesting to extend these studies to other metal–oxide systems, and to quantify the formation barriers for dimers at and away from defects where charge transfer to/from the adsorbates may play an important role. In addition, more studies are needed to assess whether defects that destabilize initial cluster formation may actually increase the monomer density between the defect sites, and thereby promote nucleation away from the defects. More studies are also needed to provide a better understanding of cluster geometries, to which the energetics underpinning all nucleation arguments are extremely sensitive.

## REFERENCES

- Valden, M.; Lai, X.; Goodman, D.W. Onset of catalytic activity of gold clusters on titania with the appearance of nonmetallic properties. *Science* **1998**, *281*, 1647–1650.
- Finnis, M.W. The theory of metal–ceramic interfaces. *J. Phys., Condens. Matter* **1996**, *8*, 5811–5836.
- Verdozzi, C.; Jennison, D.R.; Schultz, P.A.; Sears, M.P. Sapphire (0001) surface, clean and with  $d$ -metal overlayers. *Phys. Rev. Lett.* **1999**, *82*, 799–802.
- Yudanov, I.; Pacchioni, G.; Neyman, K.; Rösch, N. Systematic density-functional study of the adsorption of transition metal atoms on the MgO(001) surface. *J. Phys. Chem., B* **1997**, *101*, 2786–2792.
- Bogicevic, A.; Jennison, D.R. Variations in the nature of metal adsorption on ultrathin  $\text{Al}_2\text{O}_3$  films. *Phys. Rev. Lett.* **1999**, *82*, 4050–4053.
- Heinrich, V.E.; Cox, P.A. *The Surface Science of Metal Oxides*; Cambridge University Press: Cambridge, England, 1996.
- Campbell, C.T. Ultrathin metal films; particles on oxide surfaces: structural, electronic and chemisorptive properties. *Surf. Sci. Rep.* **1997**, *27*, 1–111.
- Bogicevic, A.; Jennison, D.R. Role of surface vacancies and water products for metal nucleation: Pt/MgO(100). *Surf. Sci. Lett.* **1999**, *437*, L741–L747.
- Bogicevic, A.; Jennison, D.R. Effect of oxide vacancies on metal island nucleation defect density. *Surf. Sci. Lett.* **2002**, *515*, L481–L486.
- Zhukovskii, Y.F.; Kotomin, E.A.; Jacobs, P.W.M.; Stoneham, A.M. Ab initio modeling of metal adhesion on oxide surfaces with defects. *Phys. Rev. Lett.* **2000**, *84*, 1256–1259.
- Finnis, M.W.; Stoneham, A.M.; Tasker, P.W. Approaches to Modelling Metal/Ceramic Interfaces. In *Metal–Ceramic Interfaces*; Rühle, M., Evans, A.G., Ashby, M.F., Hirth, J.P., Eds.; Pergamon: Oxford, 1990; 35–44.
- Brune, H. Microscopic view of epitaxial metal growth: nucleation and aggregation. *Surf. Sci. Rep.* **1998**, *31*, 121–230.
- Harsdorff, M. Heterogeneous nucleation and growth of thin films. *Thin Solid Films* **1982**, *90*, 1–14.
- Fahsold, G.; Pucci, A.; Rieder, K.H. Growth of Fe on MgO(001) studied by He-atom scattering. *Phys. Rev., B* **2000**, *61*, 8475–8483.
- Bäumer, M.; Frank, M.; Heemeier, M.; Rühnemuth, R.; Stemperl, S.; Freund, H.-J. Nucleation and growth of transition metals on a thin alumina film. *Surf. Sci.* **2000**, *454–456*, 957–962.
- Haas, G.; Menck, A.; Brune, H.; Barth, J.V.; Venables, J.A.; Kern, K. Nucleation and growth of supported clusters at defect sites: Pd/MgO(001). *Phys. Rev., B* **2000**, *61*, 11105–11108.
- Henry, C.R. Surface studies of supported model catalysts. *Surf. Sci. Rep.* **1998**, *31*, 235–325.
- Lodziana, Z.; Nørskov, J.K. Adsorption of Cu and Pd on  $\alpha\text{-Al}_2\text{O}_3(0001)$  surfaces with different stoichiometries. *J. Chem. Phys.* **2001**, *115*, 11261–11267.
- Hammer, B. Adsorbate–oxide interactions during the NO + CO reaction on MgO(100) supported Pd monolayer films. *Phys. Rev. Lett.* **2002**, *89*, 016102.1–016102.4.
- Kalff, M.; Comsa, G.; Michely, T. How sensitive is epitaxial growth to adsorbates? *Phys. Rev. Lett.* **1998**, *81*, 1255.
- Ertl, G.; Freund, H.-J. Catalysis and surface science. *Phys. Today* **1999**, *52*, 32–38.
- Libuda, J.; Frank, M.; Sandell, A.; Andersson, S.; Brühweiler, P.A.; Bäumer, M.; Mårtensson, N.; Freund, H.-J. Interaction of rhodium with hydroxylated alumina model substrates. *Surf. Sci.* **1997**, *384*, 106–119.
- Kelber, J.A.; Niu, C.; Shepherd, K.; Jennison, D.R.; Bogicevic, A. Copper wetting of  $\alpha\text{-Al}_2\text{O}_3(0001)$ : theory and experiment. *Surf. Sci.* **2000**, *446*, 76–88.
- Chambers, S.A.; Droubay, T.; Jennison, D.R.; Mattsson, T.R. Laminar growth of ultrathin metal films on metal oxides: Co on hydroxylated  $\alpha\text{-Al}_2\text{O}_3(0001)$ . *Science* **2002**, *297*, 827–831.
- Scorza, E.; Birkenheuer, U.; Pisani, C. The oxygen vacancy at the surface and in bulk MgO: an embedded-cluster study. *J. Chem. Phys.* **1997**, *107*, 9645–9658.

26. Pacchioni, G.; Pescarmona, P. Structure; stability of oxygen vacancies on sub-surface, terraces, and low-coordinated surface sites of MgO: An ab-initio study. *Surf. Sci.* **1998**, *412–413*, 657–671.
27. Ferrari, A.M.; Pacchioni, G. Metal deposition on oxide surfaces: a quantum-chemical study of the interaction of Rb, Pd, and Ag atoms with the surface vacancies of MgO. *J. Phys. Chem.* **1996**, *100*, 9032–9037.
28. Matveev, A.V.; Neyman, K.M.; Yudanov, I.V.; Rösch, N. Adsorption of transition metal atoms on oxygen vacancies and regular sites of the MgO(001) surface. *Surf. Sci.* **1999**, *426*, 123–139.
29. Kim, Y.D.; Stultz, J.; Wei, T.; Goodman, D.W. Interaction of Ag with MgO(100). *J. Phys. Chem., B* **2002**, *106*, 6827–6830.
30. Giordano, L.; Goniakowski, J.; Pacchioni, G. Characteristics of Pd adsorption on the MgO(100) surface: role of oxygen vacancies. *Phys. Rev., B* **2001**, *64*, 075417.1–075417.9.
31. Zhukovskii, Y.F.; Kotomin, E.A.; Jacobs, P.W.M.; Stoneham, A.M. Ab initio modeling of metal adhesion on oxide surfaces with defects. *Phys. Rev. Lett.* **2000**, *84*, 1256–1259.
32. Yang, Z.; Wu, R.; Zhang, Q.; Goodman, D.W. Adsorption of Au on an O-deficient MgO(001) surface. *Phys. Rev., B* **2002**, *65*, 155407.1–155407.8.
33. Tench, A.J. Temperature effects on the hyperfine coupling of a surface centre. *Surf. Sci.* **1971**, *25*, 625–632. See, e.g.
34. Bogicevic, A.; Wolverton, C. Nature and strength of defect interactions in cubic stabilized zirconia. *Phys. Rev., B* **2003**, *67*, 024106.1–024106.13.
35. Becker, T.; Boas, C.; Burghaus, U.; Wöll, C. Adsorption probability of CO on a metal oxide: The case of oxygen-terminated ZnO and the influence of defects. *Phys. Rev., B* **2000**, *61*, 4538–4541.
36. Ferrari, A.M.; Xiao, C.Y.; Neyman, K.M.; Pacchioni, G.; Rösch, N. Pd and Ag dimers and tetramers adsorbed at the MgO(001) surface: A density-functional study. *Phys. Chem., Chem. Phys.* **1999**, *1*, 4655–4661.
37. Bogicevic, A. Metal-on-metal bonding and rebonding revisited. *Phys. Rev. Lett.* **1999**, *82*, 5301–5304.

# Metal Oxide Nanoparticles

Ryan M. Richards

Department of Chemistry, International University of Bremen, Bremen, Germany

## INTRODUCTION

Metal oxides include materials with a wide range of properties and applications. When the size of these materials is brought down to the nanometer regime, a number of size-dependent properties arise primarily as a result of surface chemistry. This field of nanoscience is facilitated by the fact that many of the systems of interest have been extensively studied in the bulk form and therefore provide ready comparisons with the nanoparticulate systems.

The insulating oxides are made up of the metals from the left and right sides of the periodic table. Typical examples of insulating oxides include MgO, CaO, Al<sub>2</sub>O<sub>3</sub>, and SiO<sub>2</sub>. The oxides of the metals in the middle of the periodic table (Sc to Zn) make up the semiconducting or metallic oxides. Typical examples include ZnO, TiO<sub>2</sub>, NiO, Fe<sub>2</sub>O<sub>3</sub>, and Cr<sub>2</sub>O<sub>3</sub>. Additionally, the transition metal oxides, which include the oxides of Ru, Mo, W, Pt, V, and so forth, are of particular interest for applications in catalysis, sensor materials, and other potential applications.

## OVERVIEW

The surface chemistry effects result from the large number of atoms at the surface of nanoscale materials. In spherical nanoparticles, for example, at a size of 3 nm, 50% of the atoms or ions are on the surface, allowing the possibility of manipulation of bulk properties by surface effects and allowing near stoichiometric chemical reaction.<sup>[1]</sup> When strong chemical bonding is present, delocalization can vary with size; this, in turn, can lead to different chemical and physical properties.<sup>[2]</sup>

Because of the refractory nature of most of the metal oxides, the formation of the ultrasmall particles is facilitated.<sup>[2]</sup> The highly ionic nature of some materials, especially MgO, Al<sub>2</sub>O<sub>3</sub>, ZrO<sub>2</sub>, and TiO<sub>2</sub>, allows the formation of many stable defect sites, including edges, corners, and anion/cation vacancies. In choosing materials for study, MgO and CaO were found to be attractive because they are highly ionic and have high melting points, and it would be expected that samples of very small particle size might be stable and isolable.

Furthermore, reactive surface sites on these oxides have been extensively studied, especially for MgO crystals and powders.

It should also be noted that materials prepared via aerogel methods have very low densities, can be translucent or transparent, have low thermal conductivities, and have unusual acoustic properties. They have found various applications, including as detectors for radiation, superinsulators, solar concentrators, coatings, glass precursors, catalysts, insecticides, and destructive adsorbents. It has been shown that nanoparticles of ceramic materials (which includes some metal oxides) can be compressed at relatively low temperatures into solids that possess better flexibility and malleability than traditional ceramics.<sup>[2]</sup> It should also be noted that nanoparticles of crystalline substances have about 10<sup>19</sup> interfaces/cm<sup>3</sup> and range in surface area up to 800 m<sup>2</sup>/g. Upon compaction, but without growing the nanocrystals, solids with multitudinous grain boundaries are formed. In the case of TiO<sub>2</sub>,<sup>[3]</sup> solid samples are obtained that undergo plastic deformation at room temperature, presumably by diffusional creep. It has been proposed that further work in the area of consolidated nanophase materials may lead to ceramics with increased flexibility, less brittleness, and perhaps greater strength.<sup>[2]</sup> It may also be possible to form materials with a large fraction of atoms at grain boundaries, perhaps in arrangements that are unique. Additionally, it may be possible to produce binary materials of normally immiscible compounds or elements.

The very high surface areas of nanoscale particles gives rise to a number of defect sites. There have been numerous studies of their surfaces in an attempt to clarify the type of defect sites that can exist.<sup>[4–7]</sup> The most common defects are coordinatively unsaturated ions due to planes, edges, corners, anion/cation vacancies, and electron excess centers. Such sites are often attributed as the active sites for many useful and interesting reactions, including methane activation,<sup>[8]</sup> D<sub>2</sub>-CH exchange,<sup>[9]</sup> CO oligomerization,<sup>[10–12]</sup> oxygen exchange in CO<sub>2</sub>,<sup>[13]</sup> and H<sub>2</sub>O.<sup>[14]</sup>

## STRUCTURE AND BONDING

Determining the exact nature of structure and bonding in nanomaterials is particularly difficult because,

generally, these materials are made of very small crystallites or are amorphous. Recent advances in crystallography for powders and crystals employing X-ray, electron, and neutron diffraction have provided insight into the structures of metal oxides. Metal oxides crystallize in a variety of structures, and bonding in these materials can range from ionic ( $\text{MgO}$ ,  $\text{Fe}_{1-x}\text{O}$ ) to metallic ( $\text{TiO}$ ,  $\text{ReO}_3$ ).<sup>[15]</sup>

An understanding of not only the crystal structure and bonding, but also the local microstructures, which result from defects, is necessary to understand the structure of complex transition metal oxides. Of course, on the nanoparticulate scale, the number of defects due to edges, corners, centers, and other surface imperfections is greatly enhanced by the large surface area (Fig. 1). The pursuit of an understanding of the structure/property relationship is integral to the understanding of the unique properties observed on the nanoscale.

In bulk structures, five types of crystals can be defined based on bonding considerations: covalent, ionic, metallic, molecular (van der Waals), and hydrogen bonded. These structures are also present on the nanoscale; however, one must also consider the number of atoms at the surface when examining the structure of nanoscale materials. Ionic crystals are formed when highly electronegative and highly electropositive elements are combined in a lattice. It has been found that the ionic model is a poor approximation for crystals containing large anions and small cations (e.g., oxides and sulfides), where the covalent contribution to bonding becomes significant.<sup>[15]</sup> van der Waals interactions play a crucial role in many transition metal

oxides, especially those with layered structures. In many oxide hydrates or hydroxy oxides, hydrogen bonding also contributes to the cohesive energy. In most transition metal oxides, the bonding is only partly ionic; however, there are several examples that are primarily ionic such as  $\text{MgO}$  and  $\text{CaO}$ . In other words, there is a considerable overlap between the orbitals of the cations and anions. Many transition metal oxides also exhibit metallic properties.

Inorganic compounds of the formula  $\text{AB}$  can have the rock salt (B1), CsCl (B2), Zn blend (B3), Wurzite (B4), or NiAs (B8) structure.<sup>[16]</sup> Alkaline earth metal oxides, such as  $\text{MgO}$  and monoxides of 3d transition metals, as well as Lanthanides and Actinides, such as  $\text{TiO}$ ,  $\text{NiO}$ ,  $\text{EuO}$ , and  $\text{NpO}$ , exhibit the rock salt structure with the 6:6 octahedral coordination.

## Defects

Because of the number of atoms at the surface and the limited number of atoms within the lattice, the chemistry and bonding of oxide nanoparticles is greatly affected by the defect sites present. Point defects in crystals, such as vacancies and interstitials described by Schottky and Frenkel, account for the transport properties of ionic solids.<sup>[16]</sup> However, it appears that the point defect model is valid only when the defect concentration (or the deviation from stoichiometry) is extremely small. The defects that occur in the ionic solids are grouped into the following classes: point, linear, planar, and volumetric defects. Point defects are a result of the absence of one of the constituent atoms (or ions) on the lattice sites, or their presence in interstitial positions. Foreign atoms or ions present in the lattice represent another type of point defect. Point defects cause displacements on neighboring atoms or ions because of polarization in the surrounding region. A cationic vacancy in an ionic solid will have an electronegative charge, causing displacements of neighboring anions.<sup>[15]</sup> The energy of formation of a point defect mainly depends on the atomic arrangement in the immediate neighborhood of the corresponding to rows of atoms that do not possess the right coordination. Boundaries between small crystallites (grain boundaries), stacking faults, crystallographic shear planes, twin boundaries, and antiphase boundaries are planar defects. Three-dimensional volumetric defects are a result of segregating point defects.

The common point defects in ionic solids are Schottky pairs (pairs of cation and anion vacancies) and Frenkel defects (cation or anion interstitial plus a vacancy).<sup>[16]</sup> When there is a large concentration of Schottky pairs, the measured pycnometric density of the solid is considerably lower than the density calculated from the X-ray unit cell dimensions (e.g.,

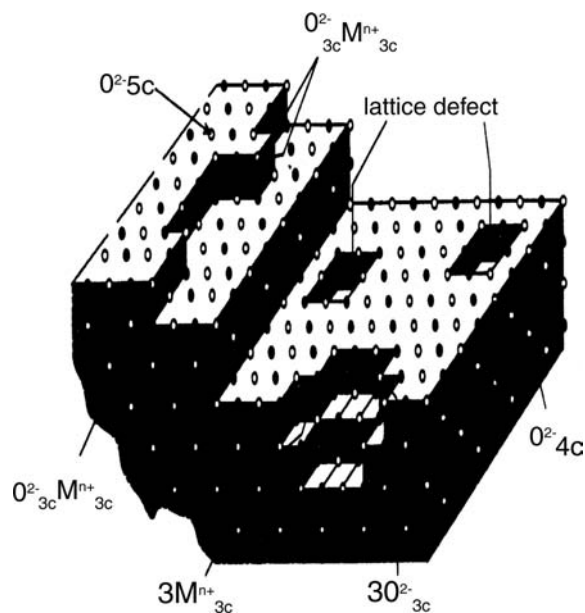


**Fig. 1** A representation of the various defects present on metal oxides. *Source:* From Ref.<sup>[162]</sup>.

$\text{VO}_x$ ).<sup>[15]</sup> Creation of defects is generally an endothermic process. Thus the formation energies of vacancies in ionic solids are generally 2 eV or more. Therefore, the intrinsic defect concentration in these solids is extremely low even at high temperatures.<sup>[15]</sup>

The surface of a crystal constitutes a planar, 2-D defect. The environment of atoms or ions on the surface of a crystal is considerably different from that in the bulk. In polycrystalline materials, there are grain boundaries between the particles. The interface between two solid phases is an important factor in determining the course of reactions, crystal growth, and so on. An interface may be coherent, incoherent, or semicoherent. It is coherent when the interface matches perfectly between the contact planes of two solid planes. Epitaxial growth occurs when there is considerable mismatch (semicoherent interface).

In close packed solids, one also often encounters stacking faults. For example, in a solid with cubic close packing, ABC ABC ABC, there can be a fault such as ABC AB ABC. Other types of planar defects include tilt boundary (array of periodically space of edge dislocations), twist boundary (array of screw dislocations), twin boundary (a layer with mirror plane symmetry with respect to the rotation of one part of the crystal, on a specific plane, with respect to another, and anti-phase boundary across which the sublattice occupation becomes interchanged).

The radius of the oxide anion (1.44 Å) given by Shannon and Prewitt is larger than most cations.<sup>[15]</sup> However, in crystals, the ionic radii correspond to free ions and not ions. The anions in crystals are subjected to a positive Madelung potential, which gives rise to a contraction of the charge cloud, while cations are subjected to negative potential causing an opposite effect.<sup>[15]</sup>

Generally, phase purity is hard to achieve, especially for phases containing more than one cation.<sup>[17]</sup> Often, phase segregation occurs, and so the particles are a mixture of other possible phases derivable from the precursors.

## SYNTHESIS

One of the areas of fundamental importance to the understanding and development of nanoscale materials, is the development of synthetic methods that allows the scientist control over such parameters as particle size, shape, and size distributions. While considerable progress has taken place in recent years, one of the major challenges to scientists is the development of a “synthetic toolbox,” which would afford access to size and shape control of structures on the nanoscale and conversely allow scientists to study the effects these parameters impart to the chemical and physical properties of the nanoparticles.

The syntheses of nanoscale particles are generally grouped into two broad categories: “bottom up” and “top down.” Those materials prepared from atomic precursors that come together to form clusters, and subsequently nanoparticles are referred to as “bottom up” preparations. Conversely, when the nanoscale is reached by physically tearing down larger building blocks, the process is referred to as “top down.”

“Bottom up” preparation methods are of primary interest to chemists and materials scientists because the fundamental building blocks are atoms. Gaining control over the way these fundamental building blocks come together and form particles are among the most sought-after goals of synthetic chemists. Therefore these methods will be the focus of this section. Interest in “bottom up” approaches to nanoscale oxides and other materials is clearly indicated by the number of reports and reviews on this subject.<sup>[18–34]</sup> Indeed, there are numerous “bottom up” approaches to the preparation of nanoscale materials and metal oxides are no exception. Generally, the preparations can be divided into two basic categories: physical and chemical. Several physical aerosol methods were reported for the synthesis of nano-size particles of oxide materials. These include gas condensation techniques,<sup>[35–41]</sup> spray pyrolysis,<sup>[39,42–48]</sup> thermochemical decomposition of metal–organic precursors in flame reactors,<sup>[41,49–51]</sup> and other aerosol processes named after the energy sources applied to provide the high temperatures during gas–particle conversion. The most common and widely used “bottom up” wet chemical method for the preparation of nanoscale oxides has been the sol–gel process. Other wet chemistry methods including novel microemulsion techniques, oxidation of metal colloids, and precipitation from solutions have also been used.

The methods of sample preparation are naturally the determining factors in producing different morphologies.<sup>[1]</sup> For example, burning Mg in  $\text{O}_2$  (MgO smoke) yields 40–80 nm cubes and hexagonal plates, while thermal decomposition of  $\text{Mg}(\text{OH})_2$ ,  $\text{MgCO}_3$ , and especially  $\text{Mg}(\text{NO}_3)_2$  yields irregular shapes often exhibiting hexagonal platelets. Surface areas can range from  $10 \text{ m}^2/\text{g}$  (MgO smoke) to  $250 \text{ m}^2/\text{g}$  for  $\text{Mg}(\text{OH})_2$  thermal decomposition, but surface areas of about  $150 \text{ m}^2/\text{g}$  are typical. In the case of calcium oxide, surface areas can range from 1 to  $100 \text{ m}^2/\text{g}$  when prepared by analogous methods, but typically about  $50 \text{ m}^2/\text{g}$  is typical.

## Physical/Aerosol Methods

### Vapor condensation methods

Gas condensation techniques to produce nanoparticles directly from a supersaturated vapor of metals are

among the earliest methods for producing nanoparticles. They generally involve two steps: first, a metallic nanophase powder is condensed under inert convection gas after a supersaturated vapor of the metal is obtained inside a chamber. A high pressure of inert gas is usually needed to achieve supersaturation, then the powder is oxidized by allowing oxygen into the chamber. This postoxidation is a critical step and very often it becomes necessary for this process is to be performed slowly. Because of the large exothermic reaction, particles heat up for short times (usually less than 1 sec) to temperatures as high as 1000°C, resulting in their agglomeration into large particles by rapid diffusion processes. A subsequent annealing process at higher temperature is often required to complete the oxidation. For further information on these processes, please see Refs.<sup>[52–57]</sup>

Supersaturated vapor has been achieved by many different vaporization methods. The most common techniques include thermal evaporation,<sup>[57–65]</sup> sputtering,<sup>[35,39,66,67]</sup> and laser methods.<sup>[36,41]</sup>

Gas condensation methods to prepare nanoparticles directly from supersaturated vapor have many advantages over other techniques including: versatility, ease in performance and analysis, and high-purity products. They can also be employed to produce films and coatings. In spite of the success of these methods, the drawback lies in the high production cost because of low yields and the difficulty in scaling-up. Heating techniques have other disadvantages that include the possibility of reactions between the metal vapors and the heating source materials. Furthermore, the operating temperature is limited by the choice of the source material, and because of that, they cannot be used to make a wide variety of materials. For further discussion on supersaturation, particle nucleation and growth, and the transport and collection of the particles, see Ref.<sup>[54]</sup>.

### Spray pyrolysis

Spray pyrolysis is another useful method for the synthesis of high-purity homogeneous oxide powders.<sup>[39,42–48]</sup> This technique has been known by several other names including solution aerosol thermolysis,<sup>[45]</sup> evaporative decomposition of solutions,<sup>[46]</sup> plasma vaporization of solutions,<sup>[47]</sup> and aerosol decomposition.<sup>[48]</sup> The starting materials in this process are chemical precursors, usually appropriate salts, in solution, sol, or suspension form. The process involves the generation of aerosol droplets by nebulizing or “atomization” of the starting solution, sol, or suspension. The generated droplets undergo evaporation and solute condensation within the droplet, drying, thermolysis of the precipitate particle at higher temperature to form a microporous particle, and finally, sintering to form a dense particle.

Aqueous solutions are usually used because of their low cost, safety, and the availability of a wide range of water-soluble salts. Metal chloride and nitrate salts are commonly used as precursors because of their high solubility. Precursors that have low solubility or those which may induce impurities, such as acetates that lead to carbon in the products, are not preferred.<sup>[43,46]</sup> For further details on atomization techniques, refer to Refs.<sup>[39,43–46]</sup>

During the transformation of the aerosol droplets into particles, different processes are involved including solvent evaporation, precipitation of dissolved precursor, and thermolysis of precipitated particles. One advantage to this process is that all of these processes take place in one step. Other advantages include the production of high-purity nano-size particles, the homogeneity of the particles as a result of the homogeneity of the original solution, the fact that each droplet/particle undergoes the same reaction conditions, and no subsequent milling is necessary. Disadvantages of spray pyrolysis include the large amounts of necessary solvents and the difficulty in scaling up the production. The use of large amounts of nonaqueous solvents increases production expenses because of the high cost of pure solvents and the need for proper disposal.

### Combustion methods

The combustion synthesis technique consists of bringing a saturated aqueous solution of the desired metals salts and suitable organic fuel to boil, until the mixture ignites a self-sustaining and rather fast combustion reaction takes off, resulting in a dry, usually crystalline, fine oxide powder. By simple calcination, the metal nitrates can, of course, be decomposed into melt oxides upon heating to or above the phase transformation temperature.

Flame processes have been widely used to synthesize nanosize powders of oxide materials. In this process, chemical precursors are vaporized and then oxidized in a combustion process using a fuel/oxidant mixture such as propane/oxygen or methane/air.<sup>[49]</sup> It combines the rapid thermal decomposition of a precursor/carrier gas stream in a reduced pressure environment with themophoretically driven deposition of the rapidly condensed product particles on a cold substrate.<sup>[51]</sup> The flame usually provides a high temperature (1200–3000 K), which promotes rapid gas-phase chemical reactions.<sup>[41]</sup> Several types of flame reactors have been used in research settings and have produced numerous types of nanoscale metal oxides.<sup>[41,49–51,68–73]</sup>

### Mechanochemical synthesis

Mechanochemical synthesis involves the mechanical activation of solid state displacement reactions. This process has been successfully used recently to make



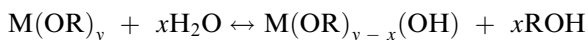
nanoparticles of a number of materials including ceramics, such as  $\text{Al}_2\text{O}_3$  and  $\text{ZrO}_2$ .<sup>[74–79]</sup> It involves the milling of precursor powders (usually a salt and a metal oxide) to form a nanoscale composite structure of the starting materials, which react during milling and subsequent heating, if necessary, to form a mixture of dispersed nanocrystals of the desired oxide within a soluble salt matrix.

## Chemical Methods

### Sol–Gel technique

Sol–gel techniques have long been known for the preparations of metal oxides and have been described in several books and reviews.<sup>[18–25,27–34]</sup> The process is typically used to prepare metal oxides via the hydrolysis of metal reactive precursors, usually alkoxides in an alcoholic solution, resulting in the corresponding hydroxide. Condensation of the hydroxide molecules by giving off water leads to the formation of a network of metal hydroxide. When all hydroxide species are linked in one network-like structure, gelation is achieved and a dense porous gel is obtained. The gel is a polymer of a three-dimensional skeleton surrounding interconnected pores. Removal of the solvents and appropriate drying of the gel results in an ultrafine powder of the metal hydroxide. Further heat treatment of the hydroxide leads to the corresponding ultrafine powder of the metal oxide. Because the process starts with a nanosized unit, and undergoes reactions on the nanometer scale, it results in nanometer materials.

The chemical and physical properties of the final product are primarily determined by the hydrolysis and drying steps. Hydrolysis of metal alkoxides ( $\text{M}(\text{OR})_z$ ) involve nucleophilic reactions with water as follows:



The mechanism of this reaction involves the addition of a negatively charged  $\text{HO}^{\delta-}$  group to the positively charged metal center ( $\text{M}^{\delta+}$ ). The positively charged proton is then transferred to an alkoxy group followed by the removal of  $\text{ROH}$ . Condensation occurs when the hydroxide molecules bind together as they release water molecules and a gel/network of the hydroxide is obtained, as demonstrated below.



The rates at which hydrolysis and condensation take place are important parameters affecting the properties of the final product. Slower and more controlled hydrolysis typically leads to smaller particle sizes and

more unique properties. Hydrolysis and condensation rates depend on the electronegativity of the metal atom, the alkoxy group, solvent system, and the molecular structure of the metal alkoxide. Those metals with higher electronegativities undergo hydrolysis more slowly than those with lower electronegativities. For example, the hydrolysis rate of  $\text{Ti}(\text{OEt})_4$  is about 5 orders of magnitude greater than that of  $\text{Si}(\text{OEt})_4$ . Hence the gelation times of silicon alkoxides are much longer (on the order of days) than those of titanium alkoxides (seconds or minutes).<sup>[43]</sup> The sensitivity of metal alkoxides toward hydrolysis decreases as the OR group size increases. Smaller OR groups lead to higher reactivity of the corresponding alkoxide toward water and, in some cases, results in uncontrolled precipitation of the hydroxide.

Because alcohol interchange reactions are possible, the choice of solvents in sol–gel processes is very important. As an example, when silica gel was prepared from  $\text{Si}(\text{OMe})_4$  and heated to  $600^\circ\text{C}$ , and when ethanol was used as a solvent, the surface area was  $300\text{ m}^2/\text{g}$  with mean pore diameter of  $29\text{ \AA}$ . However, when methanol was used, the surface area dropped to  $170\text{ m}^2/\text{g}$  and the mean pore diameter increased to  $36\text{ \AA}$ .<sup>[20]</sup>

The rate of hydrolysis also becomes slower as the coordination number around the metal center in the alkoxide increases. Therefore alkoxides that tend to form oligomers usually show slower rates of hydrolysis, and hence, are easier to control and handle. *n*-Butoxide ( $\text{O}-n\text{-Bu}$ ) is often preferred as a precursor to different oxides including  $\text{TiO}_2$  and  $\text{Al}_2\text{O}_3$  because it is the largest alkoxy group that does not prevent oligomerization.<sup>[21]</sup>

Careful handling in dry atmospheres is required to avoid rapid hydrolysis and uncontrolled precipitation because most metal alkoxides are highly reactive toward water. For alkoxides with low rates of hydrolysis, acid or base catalysts can be used to enhance the process. The relatively negative alkoxides are protonated by acids creating a better leaving group and eliminating the need for proton transfer in the transition state. Alternatively, bases provide better nucleophiles ( $\text{OH}^-$ ) for hydrolysis; however, deprotonation of metal hydroxide groups enhances their condensation rates.

Developments in the areas of solvent removal and drying facilitated the production of nanoscale metal oxides with novel properties. When drying is achieved by evaporation under normal conditions, the gel network shrinks as a result of capillary pressure that occurs and the hydroxide product obtained is referred to as xerogel. However, if supercritical drying is applied by using a high-pressure autoclave reactor at temperatures higher than the critical temperatures of solvents, less shrinkage of the gel network occurs as there is no capillary pressure and no liquid–vapor interface, which allows the pore structure to remain largely intact. The hydroxide product obtained in this manner is referred

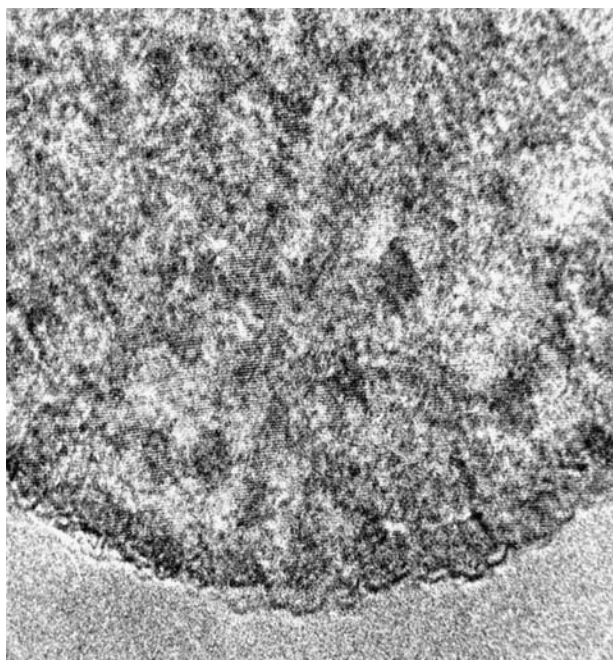


**Fig. 2** TEM micrograph of the nanostructure of CP MgO. Note that, here, there is no porosity and all of the nanocrystals have agglomerated together. *Source:* From Ref.<sup>[113]</sup>.

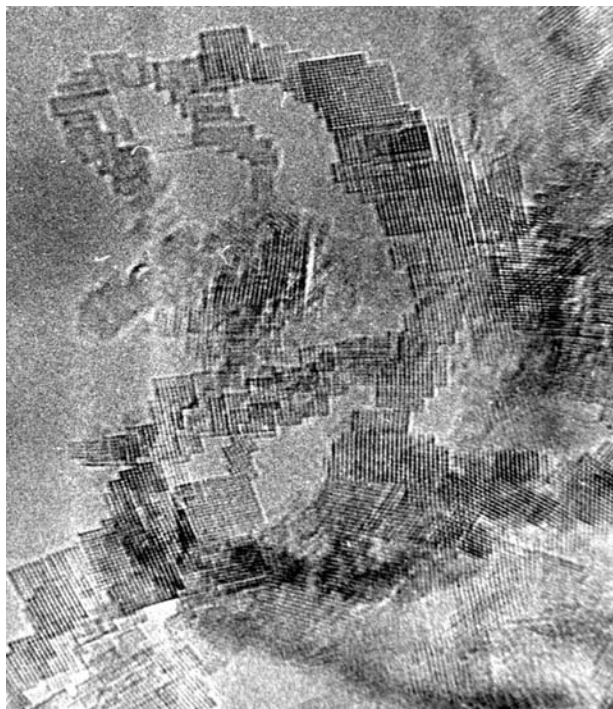


**Fig. 3** TEM micrograph of the nanostructure of AP MgO (supercritical solvent removal). Here the porosity is formed by the interconnected cubic nanocrystals of MgO. *Source:* From Ref.<sup>[113]</sup>.

to as an aerogel. Aerogel powders usually demonstrate higher porosities and larger surface areas compared to analogous xerogel powders. Aerogel processing has been very useful in producing highly divided powders of different metal oxides<sup>[18,26,80]</sup> (Figs. 2 and 3).

Sol-gel processes have several advantages over other techniques for the synthesis of nanoscale metal oxides. Because the process begins with a relatively homogeneous mixture, the resulting product is a uniform ultrafine porous powder. Furthermore, sol-gel processing has the advantage in that it can also be scaled up to accommodate industrial-scale production (personal Contact with Nantek Inc., Manhattan, KS, June 1999).

Numerous metal oxide nanoparticles were produced by making some modifications to the traditional aerogel method. One modification involved the addition of large amounts of aromatic hydrocarbons to the alcohol-methoxide solutions before hydrolysis and alcogel formation. This was carried out to further reduce the surface tension of the solvent mix and to facilitate solvent removal during the alcogel-aerogel transformation.<sup>[1,18,81]</sup> The resulting nanoparticles exhibited higher surface areas, smaller crystallite sizes, and more porosity for samples of MgO, CaO, TiO<sub>2</sub>, and ZrO<sub>2</sub> [these samples are often referred to as aerogel preparation (AP) samples for aerogel or autoclave preparation].<sup>[17,82]</sup>

#### Reverse microemulsions/micelles method

The reverse micelle approach is one of the recent promising routes to nanocrystalline materials. Several recent studies have shown that this approach is a potential candidate to synthesize nanocrystalline metal oxide powders with well-defined and controlled properties.<sup>[83-90]</sup> By carefully controlling reaction parameters, this technique affords a great deal of control over the particle size and shape.

Surfactants dissolved in organic solvents form spheroidal aggregates called reverse micelles. In the presence of water, the polar head groups of the surfactant molecules organize themselves around small water droplets, small water pools (~100 Å), leading to dispersion of the aqueous phase in the continuous oil phase as shown in Fig. 4.<sup>[91-93]</sup>

Reverse micelles are used to prepare nanoparticles by using a water solution of reactive precursors that can be converted to insoluble nanoparticles. Nanoparticle synthesis inside the micelles can be achieved by different methods including hydrolysis of reactive precursors, such as alkoxides, and precipitation reactions of metal salts.<sup>[84,85]</sup> Solvent removal and subsequent calcination leads to the final product. A variety of surfactants can be used in these processes such as, pentadecaoxyethylene nonylphenylether (TNP-35),<sup>[85]</sup>

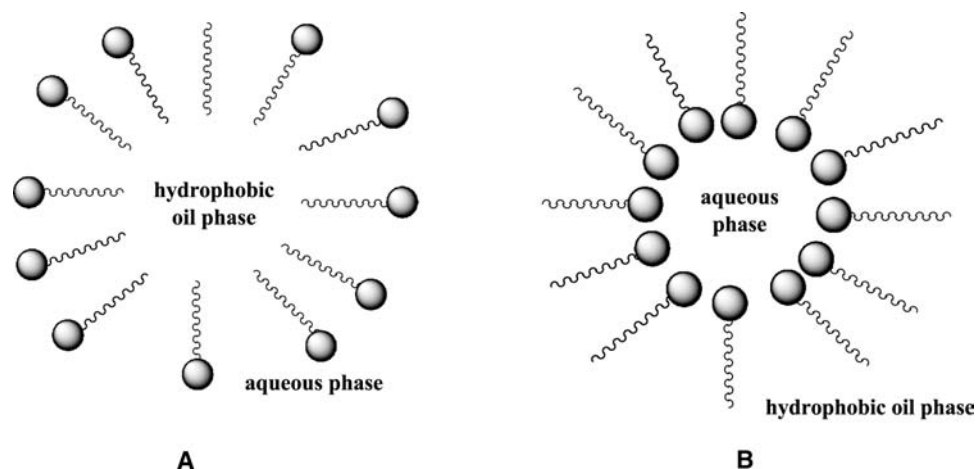


Fig. 4 Schematic representation of (A) micelle and (B) inverse micelle.

decaoxyethylene nonylphenyl ether (TNT-10),<sup>[85]</sup> poly(oxyethylene)<sub>5</sub> nonyl phenol ether (NP5),<sup>[90]</sup> and many others that are commercially available. Several parameters, such as the concentration of the reactive precursor in the micelle and the weight percentage of the aqueous phase in the microemulsion, affect the properties, including particle size, particle size distribution, agglomerate size, and phases of the final oxide powders. There are several advantages to using this method—the preparation of very small particles and the ability to control the particle size. Disadvantages include low production yields and the need to use large amount of liquids.

#### Low-temperature wet-chemical synthesis; precipitation from solutions

One of the conventional methods to prepare nanoparticles of metal oxide ceramics is the precipitation method.<sup>[94–96]</sup> This process involves dissolving a salt precursor, usually chloride, oxychloride, or nitrate, such as  $\text{AlCl}_3$  to make  $\text{Al}_2\text{O}_3$ ,  $\text{Y}(\text{NO}_3)_3$  to make  $\text{Y}_2\text{O}_3$ , and  $\text{ZrCl}_2$  to make  $\text{ZrO}_2$ . The corresponding metal hydroxides usually form and precipitate in water by adding a base solution such as sodium hydroxide or ammonium hydroxide solution. The resulting chloride

salts, i.e.,  $\text{NaCl}$  or  $\text{NH}_4\text{Cl}$ , are then washed away and the hydroxide is calcined after filtration and washing to obtain the final oxide powder. This method is useful in preparing composites of different oxides by coprecipitation of the corresponding hydroxides in the same solution. One of the disadvantages of this method is the difficulty to control the particle size and size distribution. Very often, fast (uncontrolled) precipitation takes place resulting in large particles.

#### Colloidal methods

Some nanostructured metal oxides can also be prepared through the oxidation of metal colloids. Nanosized (i.e., 3–5 nm) colloidal  $\text{Fe}(0)$ ,  $\text{Co}(0)$ , and  $\text{Ni}(0)$  particles are very oxophilic both in solution and in powder form, and cannot be redispersed after exposition to air. However, the precisely controlled, stoichiometric addition of argon-diluted air to an organic solution of a 3-nm  $\text{Fe}(0)$ -sol stabilized by  $\text{N}(\text{octyl})_4\text{Br}^-$  leads to a rusty-brown solution of colloidal  $\text{Fe}^{3+}$  oxide, which can be isolated and redissolved, e.g., in THF.<sup>[97]</sup> Colloidal  $\text{CoO}$  nanoparticles have also been prepared by air oxidation of  $\text{N}(\text{octyl})_4\text{Br}^-$  stabilized  $\text{Co}(0)$  particles<sup>[98]</sup> (Fig. 5).

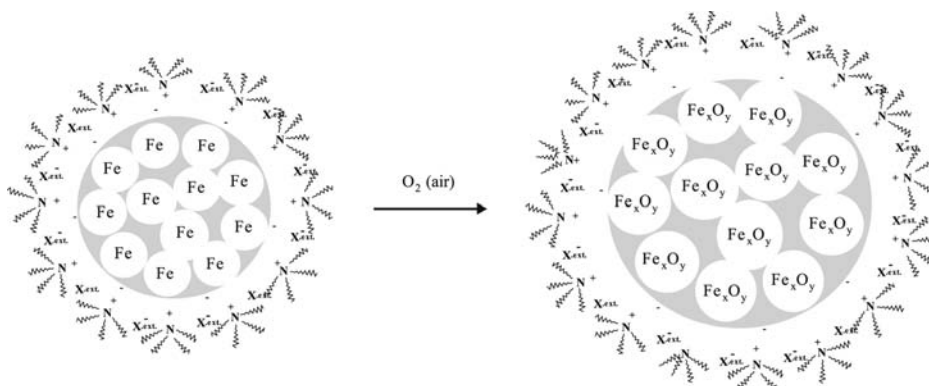


Fig. 5 Schematic representation of the oxidation of tetraalkylammonium stabilized colloids. Source: From Ref.<sup>[97]</sup>.

Particles prepared via the colloidal approach are also easily supported to form heterogeneous catalysts. It was shown that air oxidation at room temperature leads to surface passivation. Consequently, the resulting particles show a composite structure with a metallic core surrounded by an oxide surface layer.<sup>[99]</sup> Recently, a new process for the manufacture of a water-soluble PtO<sub>2</sub> colloid has been developed, which is significant because of its use as a water-soluble “Adams catalyst.”<sup>[100,101]</sup> Colloidal PtO<sub>2</sub> stabilized by carbo- or sulfobetaines, respectively, were prepared by simple hydrolysis/condensation of metal salts under basic aqueous conditions in the presence of the surfactants. This method was further exploited to give bi- and trimetallic colloidal metal oxides used as precursors for fuel cell catalysts, e.g., colloidal Pt/RuO<sub>x</sub> and Pt/Ru/WO<sub>x</sub>.<sup>[102]</sup>

## SPECIFIC PROPERTIES AND APPLICATIONS

As previously mentioned, the properties of nanoparticles are usually size-dependent. When prepared in nanometer size particles, materials exhibit unique chemical and physical properties that are remarkably different than those of the corresponding bulk materials. The study of physical and chemical properties of nanoparticles is of great interest as a way to explore the gradual transition from atomic or molecular to condensed matter systems.

As the size of a particle decreases, the percentage of atoms residing on the surface increases. As an example, a study on different samples of MgO nanoparticles has revealed that for particles ~4 nm in diameter, ~30% of the atoms are surface atoms.<sup>[18]</sup> Naturally, surface atoms/ions are expected to be more reactive than their bulk counterparts as a result of coordinative unsaturation. Because of this and the fact that the surface-to-volume ratio is large, it is not unusual to see unique behavior and characteristics for nanoparticles. This particle size effect is a characteristic of different nanomaterials including metal oxides.

In this section, we will briefly discuss some selected properties of nanophase metal oxides showing significant size dependence.

### Chemical Properties: Acid/Base Behavior of Metal Oxide Surfaces

Metal oxides are often hard acids or bases (e.g., MgO, Al<sub>2</sub>O<sub>3</sub>), so they possess sites capable of catalyzing acid/base chemistry. Several insulating oxides and oxide composites were found to be potential catalysts for a variety of important reactions as a result of their surface basicity or acidity.<sup>[103–107]</sup> Some selected

reactions typical to metal oxides include dehydration of alcohols, cracking of hydrocarbons, isomerization of olefins and paraffins, dehydrohalogenations, alkylations, and esterifications.

Acidity and basicity vary from one metal oxide to another. Several metal oxides exhibit surface basic behavior, such as MgO, CaO, and SrO, while others are considered to be acidic solids that possess more and stronger acidic sites on their surfaces, such as Al<sub>2</sub>O<sub>3</sub>. Acid/base behavior and the presence of several types of deficiencies in the lattice and on the surface are two major driving forces for surface reactivity of metal oxides. When metal oxides are prepared in nanostructures, the percentage of coordinatively unsaturated ions, especially on edges and corners, increases significantly. Consequently, surface chemistry effects, which are barely noticeable in large particle systems, become overwhelming in nanoparticle systems. These effects are demonstrated by enhanced surface reactivities and catalytic potentials possessed by many nanoparticle systems of metal oxides.<sup>[108–112]</sup>

Two of the most intensively studied nanoparticulate systems of the metal oxides are MgO and CaO. Two types of nanocrystalline oxides have been prepared and thoroughly studied; a “conventional preparation” (CP), and an “aerogel preparation” (AP).<sup>[1,17,18,81]</sup> Nanocrystalline MgO prepared by a modified aerogel procedure (AP), yields a fine, white powder of 400–500 m<sup>2</sup>/g and 4 nm average crystallite size. High-resolution transmission electron microscope (TEM) imaging of a single crystallite indicated a polyhedral structure suggesting the presence of high surface concentrations of edge/corner sites, and various exposed crystal planes (such as 002, 001, 111).<sup>[113]</sup> Conversely, the conventional preparation (CP) yields particles with surface areas of 150–200 m<sup>2</sup>/g and 8 nm average crystallites.

If intrinsic surface chemistry differences due to size are to be uncovered, consider that in bulk MgO the effective ionic charges are close to +2, whereas the MgO molecule is much more covalent with effective charges close to +1.<sup>[1]</sup> Lower coordination surface ions such as Mg<sub>3c</sub><sup>2+</sup>, Mg<sub>4c</sub><sup>2+</sup>, O<sub>3c</sub><sup>2-</sup>, and O<sub>4c</sub><sup>2-</sup> are expected to have effective charges between +1 and +2. Surface sites on crystalline and powdered MgO have been probed by theoretical as well as experimental efforts. Ab Initio calculations with H<sub>2</sub> have been used to probe perfect crystal surfaces and various defect sites. On the perfect (100) MgO surface, H<sub>2</sub> has a small adsorption energy and does not dissociate. However, temperature programmed desorption methods have shown that polycrystalline samples do dissociate H<sub>2</sub>, probably on O<sub>3c</sub>–Mg<sub>3c</sub> sites. These sites are apparently very active for heterolytic H<sub>2</sub> dissociation. The microfaceted (111) surface of MgO is

particularly reactive, and steps, kinks, and point defects (ion vacancies and substitutions) are also important. Indeed, the unique catalytic properties of defective MgO surfaces also depend on a plethora of unusual coordination sites.

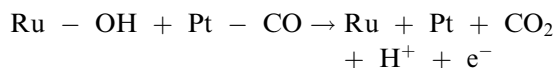
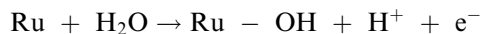
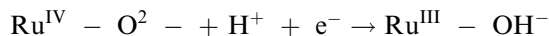
There have also been studies of the Lewis acid and base sites of metal oxide nanoparticles using a variety of techniques. For example, through the use of probe molecules, electron spin resonance (ESR) was used to quantify the Lewis acid and base site on AP-MgO.<sup>[114]</sup> Surprisingly, AP MgO was found to possess both types of Lewis sites, which is very interesting because MgO is not typically associated with acid catalysis, and it is believed that this is the first observation of this type of Lewis acid activity on MgO.<sup>[115]</sup>

### Catalytic properties of transition metal oxides

The development of nanoscale transition metal oxides has been of importance to several applications, especially in catalysis. Transition metal oxides that are electrically conductive are of fundamental importance to catalysis and, in particular, to fuel cells. Ion and electron transfer reactions required for these applications require high surface area materials with defective or charged surfaces.<sup>[116]</sup> Water-soluble PtO<sub>2</sub> (i.e., a colloidal “Adams catalyst”) has been applied in the immobilized form for the reductive amination of benzaldehyde by *n*-propylamine.<sup>[100,101]</sup> The selectivity in favor of the desired monobenzylated product was found to be >99% and the immobilized PtO<sub>2</sub> was found to be 4–5 times more active than the commercial Adams catalysts. The PtO<sub>2</sub> colloid was also effective in the hydrogenation of carbonyl compounds, or of olefins in solution or in immobilized form.

The most active and CO-tolerant fuel cell catalysts [direct methanol fuel cell (DMFC) and proton exchange membrane fuel cell (PEMFC)] have been shown to contain oxides and hydrous oxides of Pt and Ru. Recent studies have revealed that practical Pt–Ru blacks are not single phase materials, but are instead bulk mixtures of Pt metal, Pt hydrous oxides, and hydrous and dehydrated RuO. A proposed mechanism for the increased CO tolerance is that Pt-adsorbed CO is removed via an oxygen transfer step from electrogenerated Ru–OH because Ru(0) transfers oxygen more effectively than Pt(0). Additionally, recent studies have suggested that the presence of metal oxides (in particular, Ru, Sn, and Mo) in electrocatalysts working with a carbon containing feed show improved CO tolerance.<sup>[117,118]</sup> It is generally accepted that this is a result of the oxide interacting with the CO-poisoned metal (usually Pt) and oxidizing the CO to CO<sub>2</sub>. Because these metal oxides are

composed of metals with high oxidation potentials, the hydrous oxides are readily regenerated by water in the feed.



Furthermore, by combining Pt/Ru alloy catalysts with transition metal oxides (WO<sub>x</sub>, MoO<sub>x</sub>, VO<sub>x</sub>) improved DMFC catalysts have been produced. Electrochemical results demonstrated that the introduction of the oxides leads to an improvement of the catalytic activity toward methanol oxidation.<sup>[119]</sup> The addition of a transition metal oxide to the PtRu catalyst led to a decrease in the methanol oxidation and surface oxide formation with the most effective being VO<sub>x</sub>.

Ruthenium oxide, in particular, has been the subject of numerous investigations because of the numerous chemical and electrical applications it can be used for. Ruthenium oxide also catalyzes the Fischer Tropsch methanation of CO<sub>2</sub>, and selectively hydrogenates benzene and its derivatives to cyclohexane and relevant cycloalkenes.<sup>[120]</sup> Solid state nuclear magnetic resonance (NMR) investigations of hydrous ruthenium oxide prepared using LiOH have demonstrated that the mobility of water molecules and their interaction with ruthenium oxides play an important role in proton charge density.<sup>[121]</sup>

RuO<sub>2</sub>–TiO<sub>2</sub> aerogels have been prepared and the redistribution of electrical properties on the nanoscale have been studied. It was found that the electrical (electronic and protonic) transport properties of the bulk RuO<sub>2</sub>–TiO<sub>2</sub> are redistributed when synthesized as an aerogel. Electron transport dominates the characteristics of the dense form, while protonic transport of the hydrous oxide surfaces governs the electrical properties of the aerogel.<sup>[122]</sup> Anhydrous RuO<sub>2</sub> is also used as a thick film resistor but the hydrous oxide is preferred in electrocatalysis.<sup>[123]</sup> RuO<sub>2</sub> electrodes are generally prepared by the thermal decomposition of RuCl<sub>3</sub> · yH<sub>2</sub>O,<sup>[124]</sup> which produces hydrous materials that are more correctly described as RuO<sub>x</sub> · yH<sub>2</sub>O or RuO<sub>x</sub>H<sub>y</sub>.

### Adsorptive Properties

Compared to their conventionally prepared and commercial counterparts, nanoparticles of several metal oxides exhibit a significantly enhanced ability to chemically adsorb and dissociate a variety of organic

molecules on their surfaces. One of the great promises that nanoparticles of metal oxides hold in chemical applications is their remarkable ability to chemically adsorb a wide variety of molecules, especially organic molecules that are of concern as environmental hazards.

Several oxides have shown promise in this field including MgO, CaO, Al<sub>2</sub>O<sub>3</sub>, SiO<sub>2</sub>, and ZnO. A wide range of molecules including chlorinated hydrocarbons, phosphorous compounds, alcohols, aldehydes, ketones, and amines were found to strongly adsorb and chemically decompose on the surfaces of these oxides.<sup>[125–133]</sup> Details and examples on this subject are discussed in the literature.<sup>[1,134]</sup>

It has been proposed that as particles become smaller in size, they may take on different morphologies, which may alter their surface chemistry and adsorption properties in addition to increasing the surface area and porosities.<sup>[135]</sup> One of the most intriguing observations was that nanocrystals prepared by the altered aerogel approach have exhibited higher surface chemical reactivities than more conventionally prepared samples (precipitation of hydroxides followed by vacuum dehydration, herein referred to as CP samples).<sup>[135]</sup> For example, in the reaction of  $2\text{CaO} + \text{CCl}_4 \rightarrow 2\text{CaCl}_2 + \text{CO}_2$ , AP (aerogel prepared) samples demonstrated reaction efficiencies twice those of CP samples and 30 times higher than commercial samples.<sup>[1,136]</sup> For the adsorption of SO<sub>2</sub>, AP MgO adsorbed three times as much as CP MgO/nm<sup>2</sup>.<sup>[137,138]</sup> For the destructive adsorption of CH<sub>3</sub>(CH<sub>3</sub>O)<sub>2</sub>PO, the reaction efficiency was four times higher for AP MgO than CP MgO, and 50 times higher than for CM MgO.<sup>[139]</sup> This high reactivity observed at both room temperature and high temperatures observed for numerous reactions demonstrates that this is not an effect of higher surface area alone. Nanoparticles (especially the AP samples) have been shown to possess a much greater number of defect sites per unit surface area, which are believed to be responsible for the observed chemistry.

### Physical/Mechanical Properties

Many physical properties of nanoscale metal oxides are also size-dependent. Most of the physical properties are dominated by those of the surface, which differ from the bulk because of the different bonding geometries present in nanoscale materials. Several systems of nano-phase oxides have exhibited quite interesting and potentially useful mechanical properties, which creates the necessity for much more work on exploring their physical properties.

#### Improved sintering and hardness properties

Unique consolidation and compaction properties have been observed in ceramics produced from nanophase

powders. Ceramic is processed from nanophase powders by first compacting a powder composed of individual ceramic particles (usually less than 50 nm in size) into a raw shape (often called a green body), then it is heated at elevated temperatures. Densification occurs as a result of diffusion of vacancies out of pores (to grain boundaries) leading to sample shrinkage, which is referred to as pressureless sintering. Fortunately, nanophase powders were found to compact as easily as their analogous submicron particles. Samples have to be sintered at the lowest temperature possible for a time sufficient to remove the residual porosity and establish coherent grain boundaries to avoid particle size growth. Successful sintering enhances the hardness of materials. However, if, hardness decreases with sintering, only grain growth is occurring.<sup>[54]</sup>

Experimental evidence has demonstrated that nanophase powders densify at faster rates than commercial (submicron) particles. The slow densification of commercial samples is a result of their larger grain and pore sizes. It has also been found that faster densification rates allow achieving a given density at smaller grain sizes, before serious growth takes place. As a result of their small particle and pore sizes, nanocrystalline powders sinter to much greater densities than their conventional analogs at the same temperature. This also demonstrates that nanocrystalline powders, as compared to conventional powders, reach the same density at much lower temperatures, which eliminates the need for very high temperatures.<sup>[54,133,140–142]</sup>

Nonuniform heating where the outside layers of the particles densifies into a hard impervious shell, which constrains the inside of the sample from normal shrinking leading to some cracking as a result of strain incompatibility, is one disadvantage that can occur with fast densification. This problem can be avoided by several ways. The most efficient way is to heat the samples slowly to reduce the shrinkage in the outer shell while heat is transported to the inner regions.<sup>[143]</sup> Additionally, high-density nanostructured oxide systems including Y<sub>2</sub>O<sub>3</sub>, TiO<sub>2</sub> and ZrO<sub>2</sub> have been achieved via pressure-assisted sintering, and it has been shown that applying some pressure during sintering can increase the densification rate and suppress the particle growth.<sup>[144,145]</sup>

#### Reduced brittleness and enhanced ductility and superplasticity

The ability of some polycrystalline materials to undergo extensive tensile deformation without necking or fracture is referred to as superplasticity and ductility. Theoretical and experimental results provide evidence for the possibility that, traditionally, brittle materials can be ductilized by reducing their particle and grain sizes. Brittle ceramics can be superplastically



deformed at modest temperatures and then heat-treated at higher temperatures for high-temperature strengthening when made from nanocrystalline precursors. The great interest in this property stems from the fact that brittle fracture is a technical barrier in the use of ceramics in load-bearing applications. This interest in the superplasticity of oxide materials has been growing after it was experimentally demonstrated in 1986 that yttria-stabilized tetragonal zirconia polycrystals could be elongated by over 100% in tension.<sup>[145,146]</sup> Similar behavior was later demonstrated by other nanophase ceramic systems involving  $\text{Al}_2\text{O}_3$ ,  $\text{TiO}_2$ , and  $\text{ZnO}$ .<sup>[147–155]</sup>

One important use of superplasticity in ceramics is diffusion bonding, where two ceramic parts are pressed together at moderate temperatures and pressures to form a seamless bond through diffusion and grain growth across the interface. Diffusion bonds form more easily in nanocrystalline ceramics than in larger-grained ceramics as a result of both the enhanced plastic flow of nanocrystalline ceramics and the larger number of grain boundaries they provide for diffusional flux across the interface.<sup>[156,157]</sup>

Other properties of ceramics that are size-dependent include electrical and optical properties. An increase in the electrical resistance and dielectric constant was observed for nanophase ceramic materials as a result of their small particle sizes.<sup>[158,159]</sup> An effect on optical properties of ceramic materials was also found because of their nanometer particle sizes. As an example, nanoparticles of  $\text{TiO}_2$  were found to become a more efficient ultraviolet (UV) absorber.<sup>[160]</sup> In conclusion, nanophase ceramic powders and metal oxides hold great promise for better materials with unique desired properties and potential applications as compared to their large-grained counterparts.

#### Additional selected size dependent properties

Lead zirconate–titanate (PZT), a solution of ferroelectric  $\text{PbTiO}_3$  ( $T_c = 490^\circ\text{C}$ ) and antiferroelectric  $\text{PbZrO}_3$  ( $T_c = 230^\circ\text{C}$ ), belongs to the ferroelectric family of perovskite structure with a general formula of  $\text{ABO}_3$  (where A = mono or divalent, and B = tri to hexavalent ions).<sup>[158]</sup> Nanoscale PZT particles (25 nm) were synthesized by using an in situ method. Powder X-ray diffraction (XRD) studies of these particles found the sample X-ray amorphous and produced single phase PZT after heating at  $500^\circ\text{C}$ .

Nanophase powders of  $\text{Y}_x\text{Zr}_{1-x}\text{O}_{2-x/2}$  have been prepared from a mixture of commercially available  $\text{ZrO}_2$  and  $\text{Y}_2\text{O}_3$  powders.<sup>[161]</sup> It was found that, depending on the starting powder mixture composition, the yttrium content in the nanophases can be controlled and the tetragonal or cubic phases can be obtained. Tetragonal or a mixture of tetragonal and

cubic were observed for low yttria content (3.5% mol yttria), and cubic for higher yttria contents (19, 54, and 76% mol yttria). These powders were found to have a most probable grain radius of about 10–12 nm and the grains appear as isolated unstrained single crystals with polyhedral shapes. The grain shapes appeared to be polyhedral and not very anisotropic. Lattice fringes were parallel to the surfaces demonstrating that (100) and (111) faces dominate.

## CONCLUSION

Nanoscale metal oxides are of considerable importance to both the fundamental understanding of size-dependent properties and numerous applications. While, in many cases, a basic understanding of the bonding and structure present in these systems has been determined, there is still a great deal of work to be carried out. Additionally, the methods for the preparation of oxide systems is a continually evolving area of science. Ultimately, developments in the areas of synthesis, instrumentation, and modeling will aid scientists as we try to gain an understanding of the relationships between physical, electronic, and chemical properties.

Developing a “tool box” of synthetic methods, which would afford scientists the possibility to put atoms together into nanomaterials with predetermined shapes and sizes, is an ongoing effort among preparative chemists. Another ongoing effort is the search for relationships between these shapes and sizes, and the chemical and electronic properties observed. As rapid advances take place in these areas, we will begin to see the potential of nanoscience begin to realize its potential. Metal oxides should be at the forefront of these advances in nanoscience because of their stability and the amount of information that has been gathered about their bulk counterparts through the years.

## REFERENCES

1. Klabunde, K.J.; Stark, J.V.; Koper, O.; Mohs, C.; Park, D.G.; Decker, S.; Jiang, Y.; Lagadic, I.; Zhang, D. *J. Phys. Chem.* **1996**, *100*, 12,142–12,153.
2. Klabunde, K.J.; Mohs, C. Nanoparticles and nanostructural materials. In *Chemistry of Advanced Materials: An Overview*; Interrante, L.V., Hampden-Smith, M.J., Eds.; Wiley-VCH: New York, 1998; 317 pp, Chapter 7.
3. Siegel, R.W.; Ramasamy, S.; Hahn, H.; Zonquuan, L.; Timg, L.; Gronsky, R. *J. Mater. Res.* **1988**, *3*, 1367.
4. Liu, H.; Feng, L.; Zhang, X.; Xue, O. *J. Phys. Chem.* **1995**, *99*, 332.
5. Tanabe, K. *Solid Acids and Bases*; Academic Press: San Diego, CA, 1970.

6. Utiyama, M.; Hattori, H.; Tanabe, K. *J. Catal.* **1978**, *53*, 237.
7. Morris, R.M.; Klabunde, K.J. *Inorg. Chem.* **1983**, *22*, 682.
8. Driscoll, D.J.; Martin, W.; Wang, J.X.; Lunsford, J.H. *J. Am. Chem. Soc.* **1985**, 107.
9. Hoq, M.F.; Klabunde, K.J. *J. Am. Chem. Soc.* **1986**, *108*, 2114.
10. Morris, R.M.; Klabunde, K.J. *J. Am. Chem. Soc.* **1983**, *105*, 2633.
11. Nygren, M.A.; Pettersson, L.G.M.; Barandiaran, Z.; Siejo, L. *J. Phys. Chem.* **1994**, *100*, 2010.
12. Tashiro, T.; Ito, J.; Sim, R.B.; Miyazawa, K.; Hamada, E.; Toi, K.; Kobayashi, H.; Ito, T. *J. Phys. Chem.* **1995**, *99*, 6115.
13. Tsuji, H.; Shishido, T.; Okamura, A.; Gao, Y.; Hattori, H.; Kita, H. *J. Chem. Soc., Faraday Trans.* **1994**, 803.
14. Li, Y.X.; Klabunde, K.J. *Chem. Mater.* **1992**, *4*, 611.
15. Rao, C.N.R.; Raveau, B. *Transition Metal Oxides, Structure, Properties, and Synthesis of Ceramic Oxides*, 2nd Ed.; Wiley-VCH: New York, 1998; 4 pp.
16. Shriver, D.F.; Atkins, P.W.; Langford, C.H. *Inorganic Chemistry*; W.H. Freeman and Co.: New York, 1990.
17. Klabunde, K.J.; Stark, J.V.; Koper, O.; Mohs, C.; Khaleel, A.; Glavec, G.; Zhang, D.; Sorensen, C.M.; Hadjipanayis, G.C. *Nanophase Materials*; Hadjipanayis, G.C., Siegel, R.W., Eds.; Kluwer Academic Publishers: Dordrecht, The Netherlands, 1994.
18. Itoh, H.; Utamapanya, S.; Stark, J.V.; Klabunde, K.J.; Schlup, J.R. *Chem. Mater.* **1993**, *5*, 71.
19. Palkar, V.R. *Nanostruct. Mater.* **1999**, *11* (3), 369.
20. Interrante, L.V.; Hampden-Smith, M.J., Eds.; *Chemistry of Advanced Materials: An Overview*; Wiley-VCH: New York, 1998.
21. Barringer, E.A.; Bowen, H.K. *J. Am. Ceram. Soc.* **1982**, *65*, C-199.
22. Gesser, H.D.; Gosswami, P.C. *Chem. Rev.* **1989**, *89*, 765.
23. Bourell, D.L. *J. Am. Ceram. Soc.* **1993**, *76*, 705.
24. Chatry, M.; Henry, M.; Livage, J. *Mater. Res. Bull.* **1994**, *29*, 517.
25. Kumazawa, H.; Inoue, T.; Sasa, E. *Chem. Eng. J.* **1994**, *55*, 93.
26. Hatakeyama, F.; Kanzaki, S. *J. Am. Ceram. Soc.* **1990**, *73* (7), 2107.
27. Hench, L.L.; West, J.K. *Chem. Rev.* **1990**, *90*, 33.
28. Yi, G.; Sayer, M. *Ceram. Bull.* **1991**, *70*, 1173.
29. Avnir, D. *Acc. Chem. Res.* **1995**, *28*, 328.
30. Chandler, C.D.; Roger, C.; Hampden-Smith, M.J. *Chem. Rev.* **1993**, *93*, 1205.
31. Brinker, C.J.; Scherer, C.W. *Sol-Gel Science*; Academic Press: San Diego, CA, 1990.
32. Segal, D. *Chemical Synthesis of Advanced Ceramic Materials*; Cambridge University Press: Cambridge, UK, 1989.
33. Klein, L., Ed.; *Sol-Gel Optics: Processing and Applications*; Kluwer: Boston, MA, 1993.
34. Narula, C.K. *Ceramic Precursor Technology and Its Applications*; Marcel Dekker: New York, 1995.
35. Siegel, R.W.; Ramasamy, S.; Hahn, H.; Zongquan, L.; Ting, L.; Gronsky, R. *J. Mater. Res.* **1988**, *3*, 1367.
36. El-Shall, M.S.; Slack, W.; Vann, W.; Kane, D.; Hanely, D. *J. Phys. Chem.* **1994**, *98* (12), 3067.
37. Huibin, X.; Shusong, T.; Ngal, L.T. *Trans. NF Soc.* **1992**, *2*, 58.
38. Baraton, M.I.; El-Shall, M.S. *Nanostruct. Mater.* **1995**, *6*, 301.
39. Hadjipanayis, G.C.; Siegel, R.W.; Eds. *Nanophase Materials*; Kluwer Academic Publishers: Dordrecht, The Netherlands, 1994. 73, 85–88, 109–116.
40. Huh, M.Y.; Kim, S.H.; Ahn, J.P.; Park, J.K.; Kim, B.K. *Nanostruct. Mater.* **1999**, *11* (2), 211.
41. Cow, G.M.; Gonsalves, K.E.; Eds. *Nanotechnology, Molecularly Designed Materials*; American Chemical Society: Washington, DC, 1996. 64–78, 79–99.
42. Kodas, T.T. *Adv. Mater.* **1989**, *6*, 180.
43. Janackovic, D.; Jokanovic, V.; Kostic-Gvozdenovic, L.; Uskokovic, D. *Nanostruct. Mater.* **1998**, *10* (3), 341.
44. Messing, G.L.; Zhang, S.C.; Jayanthi, G.V. *J. Am. Ceram. Soc.* **1993**, *76* (11), 2707.
45. Jayanthi, G.V.; Zhang, S.C.; Messing, G.L. *J. Aerosol Sci. Technol.* **1993**, *19* (4), 478.
46. Messing, G.L.; Gardner, T. *J. Am. Ceram. Soc. Bull.* **1984**, *64*, 1498.
47. Pollinger, J.P.; Messing, G.L. *J. Aerosol Sci. Technol.* **1993**, *19* (4), 217.
48. Kodas, T.T.; Datye, A.; Lee, V.; Engler, E. *J. Appl. Phys.* **1989**, *65*, 2149.
49. Ulrich, G.D.; Riehl, J.W. *J. Colloid Interface Sci. Technol.* **1982**, *87*, 257.
50. Lindackers, D.; Janzen, C.; Rellinghaus, B.; Wassermann, E.F.; Roth, P. *Nanostruct. Mater.* **1998**, *10* (8), 1247.
51. Skanadan, G.; Chen, Y.-J.; Glumac, N.; Kear, B.H. *Nanostruct. Mater.* **1999**, *11* (2), 149.
52. Granqvist, C.G.; Buhrman, R.A. *J. Appl. Phys.* **1976**, *47*, 2200.
53. Ichinose, N.; Ozaki, Y.; Kashu, S. *Superfine Particle Technology*; Springer-Verlag: New York, 1992.
54. Edelstein, A.S.; Cammarato, R.C.; Eds. *Nanoparticles: Synthesis, Properties and Applications*; Institute of Physics Publishing: Philadelphia, PA, 1996; 13–54, 170.
55. Gleiter, H. *Prog. Mater. Sci.* **1989**, *33*, 223.
56. Birringer, R.; Herr, U.; Gleiter, H. *Trans. Jpn. Inst. Met. Suppl.* **1986**, *27*, 43.
57. Arai, T.; Mihama, K.; Yamamoto, K.; Sugano, S.; Eds. *Mesoscopic Materials and Clusters. Their Physical and Chemical Properties*; Arai, T., Mihama, K., Yamamoto, K., Sugano, S., Eds.; Springer-Verlag: New York, 1999; 275–283.
58. Pfund, A.H. *Phys. Rev.* **1930**, *35*, 1434.
59. Burger, H.; van Cittert, P.H. *Z. Phys.* **1930**, *66*, 210.
60. Harris, L.; Feffries, D.; Siegel, B.M. *J. Appl. Phys.* **1948**, *19*, 791.
61. Uyeda, R. *J. Cryst. Growth* **1974**, *24*, 69.
62. Chaudhari, P.; Matthews, J.W. *Appl. Phys. Lett.* **1970**, *17*, 115.
63. Kaito, C.; Fujita, K.; Shibahara, H.; Shiojiri, M. *Jpn. J. Appl. Phys.* **1977**, *16*, 697.
64. Kaito, C.M. *Jpn. J. Appl. Phys.* **1978**, *17*, 601.

65. Rouanet, A.; Solmon, H.; Pichelin, G.; Rouicau, C.; Sibieude, F.; Monty, C. *Nanostruct. Mater.* **1995**, *6* (1–4), 283.
66. Hahn, H.; Averback, R.S. *Appl. Phys. Lett.* **1990**, *67*, 1113.
67. Mayo, M.J.; Siegel, R.W.; Narayanasamy, A.; Nix, W.D. *J. Mater. Res.* **1990**, *5*, 1073.
68. Singhal, A.; Skandan, G.; Wang, A.; Glumac, N.; Kear, B.H.; Hunt, R.D. *Nanostruct. Mater.* **1999**, *11* (4), 545.
69. Wu, M.K.; Windeler, R.S.; Steiner, C.K.R.; Friedlander, S.K. *Aerosol Sci. Technol.* **1993**, *19*, 527.
70. Lindackers, D.; Strecker, M.G.D.; Roth, P.; Janzen, C.; Pratsinis, S.E. *Combust. Sci. Technol.* **1997**, *123*, 287.
71. Glumac, N.G.; Chen, Y.J.; Skandan, G.; Kear, B. *Mater. Lett.* **1998**, *34*, 148.
72. Zacharia, M.R.; Chin, D.; Semerjian, H.G.; Katz, J.L. *Combust. Flame* **1989**, *78*, 287.
73. Hung, C.H.; Katz, J.L. *J. Mater. Res.* **1992**, *7*, 1861.
74. Zeng, D.; Hampden-Smith, M.J. *Chem. Mater.* **1992**, *4*, 968.
75. Ding, J.; Tsuzuki, T.; McCormick, P.G. *Nanostruct. Mater.* **1997**, *8* (1), 75.
76. Ding, J.; Miao, W.F.; McCormick, P.G.; Street, R. *Appl. Phys. Lett.* **1995**, *67*, 3804.
77. Ding, J.; Tsuzuki, T.; McCormick, P.G.; Street, R. *J. Phys., D, Appl. Phys.* **1996**, *29*, 2365.
78. Ding, J.; Tsuzuki, T.; McCormick, P.G. *Nanostruct. Mater.* **1997**, *8* (6), 739.
79. Matteazzi, P.; Basset, D.; Miani, F. *Nanostruct. Mater.* **1993**, *2*, 70.
80. White, D.A.; Oleff, S.M.; Fox, J.R. *Adv. Ceram. Mater.* **1987**, *2* (1), 53.
81. Utampanya, S.; Klabunde, K.J.; Schlup, J.R. *Chem. Mater.* **1991**, *3*, 175.
82. Bedilo, A.; Klabunde, K.J. *Chem. Mater.* **1993**, *5*, 500.
83. Herrig, H.; Hempelmann, R. *Mater. Lett.* **1996**, *27*, 287.
84. Bruch, C.; Kruger, J.K.; Unruh, H.G. *Ber. Bunsenges. Phys. Chem.* **1997**, *101* (11), 1761.
85. Hartl, W.; Beck, C.; Roth, M.; Meyer, F.; Hempelmann, R. *Ber. Bunsenges. Phys. Chem.* **1997**, *101* (11), 1714.
86. Gan, L.M.; Chan, H.S.O.; Zhang, L.H.; Chew, C.H.; Loo, B.H. *Mater. Chem. Phys.* **1994**, *37*, 263.
87. Gan, L.M.; Zhang, L.S.; Chan, H.S.O.; Chew, C.H.; Loo, B.H. *J. Mater. Sci.* **1996**, *31*, 1071.
88. Wang, J.; Lee, S.E.; Ng, S.C.; Gan, L.M. *Mater. Lett.* **1997**, *30*, 119.
89. Lim, J.K.; Wang, J.; Ng, S.C.; Gan, L.M. *Mater. Lett.* **1996**, *28*, 431.
90. Fang, J.; Wang, J.; Ng, S.C.; Chew, C.H.; Gan, L.M. *Nanostruct. Mater.* **1997**, *8* (4), 499.
91. Rosano, H.L.; Claussen, M. *Microemulsion Systems*; Marcel Dekker Inc.: New York, 1987.
92. Martellucci, S.; Chester, A.N., Eds.; *Progress in Microemulsions*; Plenum Press: New York, 1989.
93. Pileni, M.P. *J. Phys. Chem.* **1993**, *97*, 6961.
94. Gao, L.; Wang, H.Z.; Hong, J.S.; Miyamoto, H.; Miyamoto, K.; Nishikawa, Y.; Torre, S.D.D.L. *Nanostruct. Mater.* **1999**, *11* (1), 43.
95. Qian, Z.; Shi, J.L. *Nanostruct. Mater.* **1998**, *10* (2), 235.
96. Rao, R.M.; Rao, K.; Prasada, A.V.; Komameni, S. *Mater. Lett.* **1996**, *1* (28), 463.
97. Boennemann, H.; Braun, G.; Brijoux, W.; Brinkmann, R.; Schulze Tilling, A.; Seevogel, K.; Siepen, K. *J. Organomet. Chem.* **1996**, *520*, 143–162.
98. Reetz, M.T.; Quaiser, S.; Winter, M.; Becker, J.A.; Schaefer, R.; Stimming, U.; Marmann, A.; Vogel, R.; Konno, T. *Angew. Chem. Int. Ed.* **1996**, *35*, 2092–2094.
99. Verelst, M.; Ould Ely, T.; Amiens, C.; Snoeck, E.; Lecante, P.; Mosset, A.; Respaud, M.; Broto, J.-M.; Chaudret, B. *Chem. Mater.* **1999**, *11*, 2702–2708.
100. PCT/EP 99/08594 (November 9, 1999), M.T. Reetz and M. Koch (to Studiengesellschaft Kohle m.b.H.).
101. Reetz, M.T.; Koch, M. *J. Am. Chem. Soc.* **1999**, *121*, 7933–7934.
102. Koch, M. *Ph.D. Thesis*; Verlag: Mainz, 1999; ISBN 3-89653-514-5.
103. Philipp, R.; Omata, K.; Aoki, A.; Fujimoto, K. *J. Catal.* **1992**, *134*, 422.
104. Ito, T.; Wang, J.-X.; Liu, C.-H.; Lunsford, J.H. *J. Am. Chem. Soc.* **1985**, *107*, 5062.
105. Driscoll, D.J.; Martir, W.; Wang, J.-X.; Lunsford, J.H. *J. Am. Chem. Soc.* **1985**, *107*, 58.
106. Peng, X.D.; Richards, D.A.; Stair, P.C. *J. Catal.* **1990**, *121*, 99.
107. Stakheev, A.Yu.; Shapiro, E.S.; Apijok, J. *J. Phys. Chem.* **1993**, *97*, 5668.
108. Mayo, M.J.; Seidensticker, J.R.; Hague, D.C.; Carim, A.H. *Nanostruct. Mater.* **1999**, *11* (2), 271.
109. Vishwanathan, B.; Tanka, B.; Toyoshima, L. *Langmuir* **1986**, *2*, 113.
110. Sun, N.; Klabunde, K.J. *J. Am. Chem. Soc.* **1999**, *121*, 5587.
111. Sun, N.; Klabunde, K.J. *J. Catal.* **1999**, *185*, 506.
112. Jiang, Y.; Decker, S.; Mohs, C.; Klabunde, K.J. *J. Catal.* **1998**, *180*, 24.
113. Richards, R.; Li, W.; Decker, S.; Davidson, C.; Koper, O.; Zaikovski, V.; Volodin, A.; Rieker, T.; Klabunde, K.J. *J. Am. Chem. Soc.* **2000**, *22* (20), 4921.
114. Richards, R.; Volodin, A.; Klabunde, K.J. in preparation.
115. Richards, R.M.; Volodin, A.M.; Bedilo, A.F.; Klabunde, K.J. *Phys. Chem. Chem. Phys.* **2002**, submitted.
116. Swider, K.E.; Merzbacher, C.I.; Hagans, P.L.; Rolison, D.R. *Chem. Mater.* **1997**, *9*, 1248–1255.
117. Rolison, D.; Hagans, P.; Swider, K.; Long, J. *Langmuir* **1999**, *15*, 774–779.
118. Long, J.; Stroud, R.; Swider-Lyons, K.; Rolison, D. *J. Phys. Chem., B* **2000**, *104*, 9772–9776.
119. Lasch, K.; Joerissen, L.; Garcke, J. *J. Power Sources* **1999**, *84*, 225–230.
120. Paseka, I. *Appl. Catal., A Gen.* **2001**, *207*, 257–265.
121. Ma, Z.; Zheng, J.; Fu, R. *Chem. Phys. Lett.* **2000**, *331*, 64–70.
122. Swider, K.E.; Merzbacher, C.I.; Hagans, P.L.; Rolison, D.R. *Chem. Mater.* **1997**, *9*, 1248–1255.
123. Trasatti, S. *Electrochim. Acta* **1991**, *36*, 225.
124. Battaglin, G.; Caarnera, A.; Della Mia, G. *J. Chem. Soc., Faraday Trans.* **1985**, *81*, 2995.

125. Klabunde, K.J.; Khaleel, A.; Park, D. *High Temp. Mater. Sci.* **1995**, *33*, 99.
126. Khaleel, A.; Klabunde, K.J. *Nanophase Materials*; Hadjipanayis, G.C., Siegel, R.W., Eds.; Kluwer Academic Publishers: Dordrecht, The Netherlands, 1994; 785pp.
127. Klabunde, K.J.; Li, Y.; Khaleel, A. *Nanophase Materials*; Hadjipanayis, G.C., Siegel, R.W., Eds.; Kluwer Academic Publishers: Dordrecht, The Netherlands, 1994; 757pp.
128. Khaleel, A.; Li, W.; Klabunde, K.J. *Nanostruct. Mater.* **1999**, *12*, 463.
129. Khaleel, A.; Kapoor, P.N. *Nanostruct. Mater.* **1999**, *11* (4), 459.
130. Koper, O.B.; Wovchko, E.A.; Glass, J.A.; Yates, J.T., Jr.; Klabunde, K.J. *Langmuir* **1995**, *11*, 2054.
131. Wagner, G.W.; Bartram, P.W.; Koper, O.; Klabunde, K.J. *J. Phys. Chem., B* **1999**, *103*, 3225.
132. Masel, R.I. *Principles of Adsorption and Reaction on Solid Surfaces*; John Wiley and Sons, Inc.: New York, 1996.
133. Henrich, V.; Cox, P.A. *Metal Oxides*; Cambridge University Press: New York, 1994.
134. Klabunde, K.J.; Mulukutla, R.S. *Chemical and Catalytic Aspects of Nanocrystals. Nanoscale Materials in Chemistry*; Wiley-Interscience: New York, 2001; 223–263.
135. Koper, O.; Lagadic, I.; Volodin, A.; Klabunde, K.J. *Chem. Mater.* **1997**, *9*, 2468.
136. Li, Y.X.; Koper, O.; Atteya, M.; Klabunde, K.J. *Chem. Mater.* **1992**, *4*, 323.
137. Stark, J.V.; Park, D.G.; Lagadic, I.; Klabunde, K.J. *Chem. Mater.* **1996**, 1904.
138. Stark, J.V.; Klabunde, K.J. *Chem. Mater.* **1996**, *8*, 1913.
139. Li, Y.X.; Klabunde, K.J. *Langmuir* **1991**, *7*, 1388.
140. Karch, J.; Birringer, R. *Ceram. Int.* **1990**, *16*, 291.
141. Apte, P.; Suits, B.H.; Siegel, R.W. *Nanostruct. Mater.* **1997**, *9* (1–8), 501.
142. Mayo, M.J. *J. Mater. Res.* **1990**, *5* (5), 1073.
143. Chen, D.-J.; Mayo, M.J. *Nanostruct. Mater.* **1993**, *2*, 469.
144. Hadjipanayis, G.C.; Siegel, R.W. *Nanophase Materials, Synthesis—Properties—Applications*; Kluwer Academic Publishing: London, 1994; 263–273.
145. Hahn, H.; Averbach, R.S. *Mater. Res. Soc. Symp.* **1991**, *206*, 561.
146. Nieh, T.G.; Wadsworth, J. *Acta Metall. Mater.* **1990**, *38*, 1121.
147. Wakai, F.; Kato, H. *Adv. Ceram. Mater.* **1988**, *3*, 71.
148. Nieh, T.G.; McNally, C.M.; Wadsworth, J. *Scr. Metall.* **1989**, *23*, 457.
149. Karch, J.; Birringer, R.; Gleiter, H. *Nature* **1987**, *330*, 556.
150. Hahn, H.; Averbach, R.S. *J. Am. Ceram. Soc.* **1991**, *74*, 2918.
151. Mayo, M.J.; Siegel, R.W.; Liao, Y.X.; Nix, W.D. *J. Mater. Res.* **1992**, *7*, 973.
152. Koch, C.C.; Morris, D.G.; Lu, K.L.; Inoue, A. *Mater. Res. Bull.* **1999**, *24* (2), 54.
153. Nieh, T.G.; McNally, C.M.; Wadsworth, J. *J. Met.* **1989**, 31.
154. Machara, Y.; Langdon, T.G. *J. Mater. Sci.* **1990**, *25*, 2275.
155. Nieh, T.J.; Wadsworth, J.; Wakai, F. *Int. Mat. Rev.* **1991**, *36*, 146.
156. Cross, T.H.; Mayo, M.J. *Nanostruct. Mater.* **1994**, *3*, 163.
157. Weertman, J.R.; Farkas, D.; Hemker, K.; Kung, H.; Mayo, M.; Mitra, R.; Swygenhoven, H.V. *Mater. Res. Bull.* **1999**, *24* (2), 44.
158. Das, R.N.; Pramanik, P. *Nanostruct. Mater.* **1998**, *10* (8), 1371–1377.
159. Saito, S. *Fine Ceramics*; Elsevier: New York, 1985; Ohmsha Ltd., Tokyo.
160. Gleiter, H. *Nanostruct. Mater.* **1995**, *6*, 3.
161. Rouanet, A.; Pichelin, G.; Roucau, C.; Snoeck, E.; Monty, C. *Nanophase Materials*; Hadjipanayis, G.C., Siegel, R.W., Eds.; Kluwer Academic Publishers: Dordrecht, The Netherlands, 1994; 85–88.
162. Dyrek, K.; Che, M. *Chem. Rev.* **1997**, *97*, 305–331.

# Metal Oxide Nanoribbons and Carbon Nanotubes: Modeling

Amitesh Maiti

Materials Science, Accelrys Inc., San Diego, California, U.S.A.

## INTRODUCTION

Nanotechnology<sup>[1–5]</sup> continues to be a rapidly emerging field in which new ideas are being born and discoveries are being made at a breathtaking pace. New materials systems with novel properties are being designed or invented at an incredible rate in laboratories throughout the world. Of nanosystems, two of the most intensely studied are carbon nanotubes (CNTs)<sup>[6,7]</sup> and metal–oxide nanoribbons.<sup>[8]</sup> CNTs have been a popular area of research for more than a decade because of the promise of a host of commercial applications, while metal–oxide nanoribbons, particularly those synthesized from inexpensive SnO<sub>2</sub> and ZnO, have been a materials system of great current interest because of their potential applications as chemical sensors for pollutant gas species and biomolecules. The well-characterized atomic structures of both these systems, as well as their high degree of structural purity, allow accurate computer modeling and *in silico* property prediction. In the following, we illustrate some of the modern techniques of molecular modeling to study technologically important applications such as displays, electromechanical sensing, and chemical sensing.

## ROLE OF MOLECULAR MODELING

As with any new technology, Nanotechnology has many challenges to overcome, typically associated with our control and precision at the nanoscale. Some of the challenges include: device integration (interconnect failure, addressability issues), growth and synthesis (difficulty in size-dispersion control, requirement of novel assembly techniques, presence of structural defects), contact resistance (necessity of atomic-level structural precision at junctions), functionalization (challenges with chemical inertness), and doping (non-uniformity of dopant levels). Molecular modeling is a great approach in surmounting some of the above obstacles because it often provides deeper insight into the system properties as a function of size/shape, structural defects, added functional groups, and system

surroundings. Often, the whole nanosystem/device can be modeled in full atomistic detail on the computer, and its properties studied with a level of precision not possible experimentally. The growing success of density functional theory (DFT),<sup>[9]</sup> availability of accurate interatomic potentials (force fields),<sup>[10]</sup> development of Green's function-based electronic transport codes,<sup>[11]</sup> and deployment of sophisticated graphics user interface (GUI) have all led to the emergence of molecular modeling as a powerful tool in Nanotechnology research. Molecular modeling applications to nanomaterials are too numerous to mention here, and we can only point to the literature for further reference.<sup>[12–17]</sup>

## CARBON NANOTUBES (CNTs)

### Atomic and Electronic Structure

A CNT can be geometrically thought of as a graphite sheet rolled into a seamless cylinder. A necessary condition for the cylinder to be seamless is that, upon rolling, a graphite lattice point ( $n_1, n_2$ ) coincides with the origin (0,0). Thus if  $a_1$  and  $a_2$  are the two lattice vectors of graphite, the CNT circumference is equal to the length of the vector ( $n_1 a_1 + n_2 a_2$ ), while the CNT chiral angle  $\theta$  is defined as the angle between vectors ( $n_1 a_1 + n_2 a_2$ ) and  $a_1$ . With the choice of lattice vectors as in Fig. 1A, the chiral angle and diameter of a CNT are given respectively by the formulas:

$$\theta = (\tan^{-1}[\sqrt{3}n_2/(2n_1 + n_2)]), \text{ and} \quad (1)$$

$$d = a\sqrt{(n_1^2 + n_1n_2 + n_2^2)}/\pi \quad (2)$$

where  $a = |a_1| = |a_2| \sim 2.45 \text{ \AA}$  is the lattice constant of graphite. The CNT diameter and chirality, and therefore its atomic geometry, are completely specified by the two integers ( $n_1, n_2$ ), which are referred to as the chiral indices of the CNT. Because of the symmetry of the graphite lattice, a nanotube of any arbitrary chirality can be defined in the range  $n_1 \geq n_2 \geq 0$  and  $n_1 > 0$ , which implies that the chiral angle  $\theta$  for all

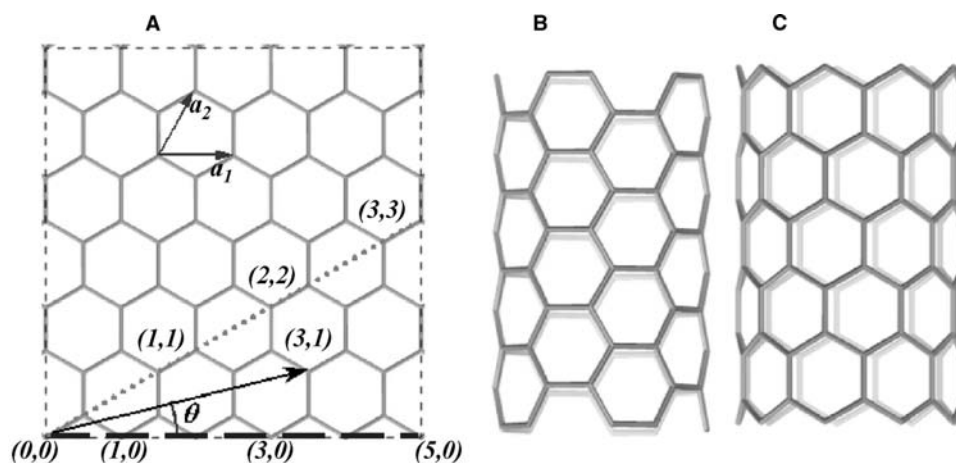


**Fig. 1** Carbon nanotube (CNT) basics. (A) A graphite sheet with lattice vectors  $a_1$ ,  $a_2$ . A few lattice points are indicated, as is the chiral angle  $\theta$  for a (3,1) CNT. Dotted and dashed lines are drawn along circumferences of armchair and zigzag tubes, respectively; (B) a (5,5) armchair tube; (C) a (9,0) zigzag tube.

CNTs lies between  $0^\circ$  and  $30^\circ$ . CNTs with the extreme chiral angles of  $0^\circ$  and  $30^\circ$  have special names: a CNT with  $\theta = 0$  (i.e.,  $n_2 = 0$ ) is called *zigzag*, while a CNT with  $\theta = 30^\circ$  ( $n_1 = n_2$ ) is called *armchair*. The names armchair and zigzag simply reflect the shape of the open edges of these CNTs (Fig. 1B,C). CNTs with any other chiral angles (i.e.,  $0 < \theta < 30^\circ$ ) are called *chiral*.

Armchair and zigzag CNTs possess short periodic repeat lengths along the nanotube axis, the repeat length being only  $a$  ( $\sim 2.45 \text{ \AA}$ ) for armchair tubes and  $\sqrt{3} a$  ( $\sim 4.24 \text{ \AA}$ ) for zigzag tubes. On the other hand, chiral CNTs can possess very long periodic repeat lengths depending on the ratio of its chiral indices. Thus electronic structure calculations, especially those employing first-principles Quantum Mechanics (QM) with periodic boundary conditions, are rarely performed on chiral tubes. However, this does not turn out to be a serious limitation. Because a CNT is just a rolled-up graphite sheet, one can obtain a good approximation to the CNT electronic structure simply by applying an appropriate boundary condition to the electronic structure of a graphite sheet, with a small perturbation resulting from the finite cylindrical *curvature* of the CNT surface. The boundary condition for a CNT with chiral indices  $(n_1, n_2)$  corresponds to the coincidence of the  $(n_1, n_2)$  lattice point of graphite with the origin  $(0,0)$ . It has been known for some time that a single sheet of graphite (also known as graphene) is neither a semiconductor nor a metal, but a semi-metal<sup>[18]</sup> (i.e., a zero-bandgap semiconductor). This peculiarity implies that the electronic states of graphene are very sensitive to additional boundary conditions that a CNT mandates. Taking into account small effects due to curvature, such boundary conditions lead to the important result<sup>[19–24]</sup> that: all *armchair* tubes are metallic; CNTs with  $n_1 - n_2 = 3n$  ( $n = \text{any positive}$

integer), which includes the  $(3n,0)$  *zigzag* tubes as a special class, are quasimetallic (small bandgap  $\sim 10 \text{ meV}$  or less, arising from curvature effects); and CNTs with  $n_1 - n_2 \neq 3n$  are semiconducting, with a bandgap decreasing as  $1/d$  as a function of tube diameter  $d$  (thereby converging to the zero bandgap of graphite in the limit  $d \rightarrow \infty$ ). Experimental measurements are often unable to make the distinction between metallic and quasimetallic tubes because of the presence of contact resistance and thermal effects. Thus, for simplicity, experimentalists often classify CNTs as either metallic or semiconducting, and we follow the same convention in the discussion below.

### Synthesis Methods, Properties, Potential Applications

CNTs were originally discovered by Sumio Iijima in 1991<sup>[25]</sup> in the soot produced by an arc discharge between graphite electrodes in a helium atmosphere. The original tubes<sup>[25–27]</sup> were multiwalled, i.e., they consisted of several concentric cylinders with successive layers separated by a distance approximately equal to the interlayer spacing of graphite. Subsequently, single-walled CNTs were synthesized in the same arc-discharge apparatus with the addition of transition-metal catalysts.<sup>[28,29]</sup> Presently, high-quality multiwalled and single-walled CNTs can be grown in well-defined directions via chemical vapor deposition (CVD),<sup>[30]</sup> while high-yield of single-walled CNTs can be obtained by several techniques, including: arc discharge of Ni–Y catalyzed graphite electrodes,<sup>[31]</sup> laser ablation of Ni–Co catalyzed graphite targets,<sup>[32]</sup> and vapor-phase pyrolysis of CO and  $\text{Fe}(\text{CO})_5$ <sup>[33]</sup> (the so-called HiPCO process).



Over the last decade, CNTs have become one of the hottest research areas in all of science and engineering because of a number of fascinating properties:

- Depending on their chiral indices, they can behave like metals or semiconductors, as discussed in the section “Atomic and Electronic Structure.”
- Single- or multiwalled CNTs are exceptionally strong, could possess a Young’s modulus as high as 1.2 TPa, six times the modulus of steel.
- CNTs are elastic to the highest degree, and do not display plasticity behavior even under large deformation including stretching, bending, or twisting.
- Metallic CNT are one-dimensional quantum conductors where electrons travel ballistically: there is no heat dissipation along the length of the CNT. All dissipation occurs at the contacts.
- CNTs can have huge aspect ratio (i.e., length-to-diameter ratio), as large as  $10^5$ . Therefore, field emission of electrons can be induced from the tip of long metallic CNTs in the presence of moderate electric fields.
- Depending on its chiral indices, metallic CNTs can undergo metal-to-semiconductor transition under small tensile or torsional strain. This effect is discussed in more detail in this section.
- With a magnetic field parallel to its axis, a CNT can exhibit the Aharonov–Bohm effect.
- Atoms/molecules can be enclosed inside a CNT.
- A CNT can be doped both p-type and (to a lesser degree) n-type.

All of the above properties come with the promise of a host of commercial applications,<sup>[34,35]</sup> including: field emission-based flat panel displays,<sup>[36–42]</sup> novel semiconducting devices and robust metallic interconnects in microelectronics,<sup>[43,44]</sup> hydrogen storage devices,<sup>[45]</sup> structural reinforcement agents,<sup>[46]</sup> chemical sensors,<sup>[47–49]</sup> electromechanical sensors,<sup>[47,50]</sup> nano-probes,<sup>[51]</sup> and nanotweezers.<sup>[52]</sup>

### Molecular Modeling of CNTs

Ever since they were discovered, CNTs have provided a fertile ground for theoretical simulations and analysis. In fact, the prediction of the dependence of CNT’s electronic structure on its chirality<sup>[19–21]</sup> came within just a few months of the experimental discovery.<sup>[25]</sup> Since then, there have been a huge number of theoretical investigations<sup>[14–16,53–55]</sup> of growth mechanisms, structure and energetics of topological defects, mechanical and electrical response to various kinds physical perturbation, field emission from tips of metallic CNTs, electronic effects of doping and gas adsorption, chemical reactivity, interaction with polymers,

capillary effects, CNT–metal contacts, H and Li storage, thermal conductivity, and encapsulation of organic as well as inorganic material. Computational approaches used in the above work include solving diffusion equations, QM simulations (DFT, tight binding, and semiempirical methods), classical molecular dynamics, kinetic Monte Carlo, genetic algorithms, and Green’s function-based electronic transport theory. The following two sections illustrate the use of some of the above techniques to explore two application areas of CNTs: 1) field-emission displays; and 2) nano-electromechanical sensors.

### CNT-Based displays: effect of adsorbates

Synthesis of CNTs with length-to-width ratio as large as  $10^5$ , as well as advanced fabrication methods for generating self-aligned or patterned nanotube films on glass<sup>[56]</sup> or silicon<sup>[40]</sup> substrates have pushed CNT-based flat-panel displays to the brink of commercial reality.<sup>[57–59]</sup> One major challenge to overcome is to reduce the threshold field, defined as the electric field necessary to induce a current of  $1 \text{ mA/cm}^2$ . One way to achieve this is to introduce adsorbates that might effectively lower the ionization potential (IP) and facilitate the extraction of electrons. An important experimental work in this regard was performed at Motorola,<sup>[60]</sup> which studied changes in field emission behavior in the presence of various gases, i.e., CO, CO<sub>2</sub>, H<sub>2</sub>, and water vapor. Adsorbed water was found to significantly enhance the emission current, while the other residual gases did not have any noticeable impact. Water also appeared to be present at the CNT tip up to very high temperatures ( $\sim 900 \text{ K}$ ), and field-emission current was more enhanced at higher partial pressures of water.

To understand the difference between H<sub>2</sub> and water on the field-emission properties of CNTs, first-principles electronic structure calculations were carried out on a (5,5) armchair tube, with a hemispherical tip represented by the half of a C<sub>60</sub> molecule. A uniform external field  $E_{\text{FE}}$ , directed toward the tube from above, was chosen to represent the electric field close to the tube tip under field emission conditions. Because the actual field close to the tip is radial rather than uniform,<sup>[61]</sup> the uniform field representation is appropriate only if the tube stem in the simulation is confined to the same size as the tube diameter. For this reason, a short stem of three atomic layers (30 atoms) was used. A more realistic field around the tip could perhaps be simulated via a large number of point charges situated at some distance from the tip. Such an effort was not undertaken for two reasons: 1) in all flat panel display designs, the field emission occurs not from isolated tubes, but from a film of closely spaced nearly

aligned tubes, with the resulting E-field more closely resembling a uniform field above the tip assembly; 2) the essential chemistry that drives the effect of adsorbates on field emission behavior can be extracted from calculations by using a uniform field, as illustrated below. For all calculations, a magnitude of  $E_{FE} = 1 \text{ V/\AA}$  was used as a ballpark figure, around which field emission is known to occur for these systems. Difference in electronegativities between H and C introduces an artificial dipole moment in the CNT if the dangling C atoms at the stem end are H-saturated. The C atoms at the stem end were therefore left unsaturated. In addition, these C atoms were fixed during the simulation to mimic the presence of a long stem in actual experiments. Structures of the CNT with or without adsorbates were optimized by using the DFT code DMol<sup>3</sup>,<sup>[62]</sup> in which the electronic wave functions are expanded as a linear combination of atom-centered basis functions defined on a numerical grid. The present calculations explicitly considered all electrons in the system (i.e., core electrons were included), with wave functions expanded in the double numeric polarized (DNP) basis set,<sup>[63]</sup> and the exchange-correlation part of the electron–electron interactions represented by the gradient-corrected Perdew–Burke–Ernzerhof (PBE) functional.<sup>[64]</sup> The main results from this study<sup>[65]</sup> can be summarized as follows:

1. A single H<sub>2</sub> molecule can either lie “flat” or “upright” on the CNT (Fig. 2A,B). A single water molecule adsorbs in such a way that its plane symmetrically cuts the CNT into two equal halves. The two H atoms are symmetrically equidistant from the tip, and could be

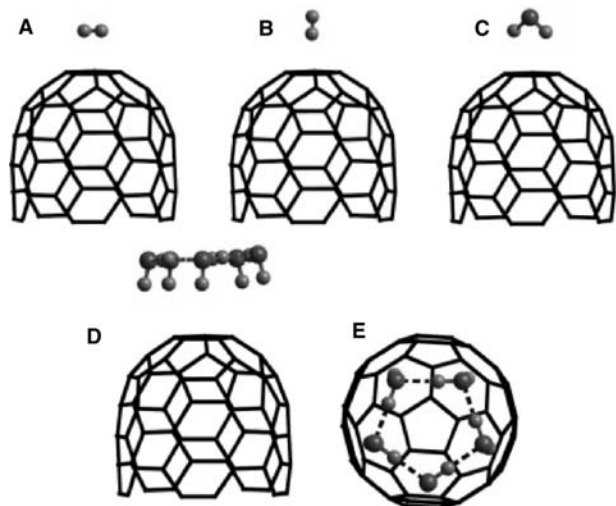


**Fig. 2** Optimized structures for adsorbates on a CNT tip in zero electric field: (A) H<sub>2</sub> (flat); (B) H<sub>2</sub> upright; (C) a single “down” water; (D) a cluster of five water molecules; (E) view of (D) from top.

either closer or further from the surface as compared to the O atom. We call these configurations “down” (Fig. 2C) and “up” water, respectively.

2. In zero electric field, none of the adsorbates show any significant binding to the CNT tip. The H<sub>2</sub> has less than 0.1 kcal/mol binding in either configuration, while a single water has  $\sim 0.7$  kcal/mol binding.
3. At a tip field of  $1 \text{ V/\AA}$ , the binding energies change significantly. Thus H<sub>2</sub> has a binding energy of 1.1 and 3.5 eV, in the flat and the upright configurations, respectively, while the “down” water has a binding energy of  $\sim 20$  kcal/mol, which is of the order of a chemical bond. The “up” water becomes unstable in the presence of a finite electric field at the CNT and spontaneously flips into a “down” water. Therefore “up” water is not considered further in the discussion below.
4. Because water molecules can form clusters through H bonding, it was also important to consider the structure and adsorption energy of a cluster of water molecules on the CNT tip. Because of the fivefold symmetry of the (5,5) CNT (with a C<sub>60</sub> half cap) about its axis, it was easy to determine the global minimum for a cluster of five water molecules. In the minimum energy structure, the five water molecules form a “crown” on the top of the CNT (Fig. 2D,E). Each water molecule in this crown is tilted with respect to the ideal “down” water configuration for a single water molecule. However, the resulting loss in interaction energy with the CNT tip is almost exactly recovered from the gain in H bonding to the nearest neighbor waters.
5. The adsorbate atoms in all cases are at a distance of 3 Å or more from the CNT surface. This strongly suggests that they are being physisorbed. This is supported by an analysis of charge density in the region between the adsorbate and the CNT tip, which is less than  $0.004 \text{ e/\AA}^3$ . Even at a field as large  $1 \text{ V/\AA}$ , the changes to the adsorbate and CNT structures are small. In particular, the distance between the adsorbate and the CNT changes by less than 0.07 Å, and the bond lengths change by less than 0.01 Å. The most significant geometrical change is in the H–O–H angle in water, which decreases from 103.7° in zero field to 98° on the tube tip at  $E_{FE} = 1 \text{ V/\AA}$ . Such a change in angle leads to only a 0.02 a.u. increase in the dipole moment of water.
6. An analysis of the various interaction energies and the dipole moments of the CNT as well as

the adsorbates yield the following picture: in the absence of an electric field, the CNT has a very small dipole moment. This small dipole has only negligible interaction with any of the adsorbates. However, under field-emission conditions, large E-field at the CNT tip induces a significant dipole moment. This dipole interacts with the dipole of the adsorbates. Water molecules having a large intrinsic dipole moment interacts strongly, while H<sub>2</sub> molecules have only a small field-induced dipole, and therefore a much weaker interaction.

- Finally, the highest occupied molecular orbital (HOMO) for the isolated CNT, one water molecule on CNT, and five water molecules on the CNT were analyzed (Fig. 3). The HOMO essentially remains confined to the CNT tip, and its shape does not significantly change because of the presence of the adsorbates. However, when the ionization potential (IP) is computed, it is found to be 0.1 and 0.6 eV lower for the one water and five water cases, respectively, compared to the adsorbate-free CNT. This also perfectly correlates to the instability of the HOMO orbital. Thus electrostatic interactions from the adsorbates make the HOMO level in the CNT more unstable, with a corresponding decrease in the IP, thereby lowering the operating voltage for field emission.

Table 1 displays computed IP of a (5,5) CNT tip (same as in Fig. 2) for a number of potential adsorbates,<sup>[66]</sup> including water. It is clear that as the lowering of IP becomes more pronounced, the larger the dipole moment of the adsorbate becomes. This work calls for further experiments on polar adsorbates to optimize the performance of CNT-based field-emission displays. It would also be interesting to compute *I-V* characteristics due to field emission from CNT tips<sup>[67]</sup> in the presence of adsorbates.

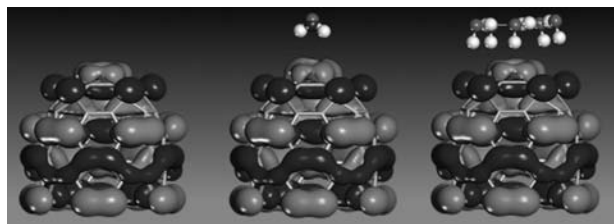


**Fig. 3** Highest occupied molecular orbital (HOMO) for: isolated CNT; CNT + 1 adsorbed water; and CNT + 5 adsorbed water. Although the position and shape of the HOMO is not significantly affected by the adsorbates, the energy level and ionization potential change markedly.

**Table 1** IP of a (5,5) CNT for various molecules physisorbed on its tip

Adsorbate	Dipole moment (Debye)	Ionization potential (eV)
H <sub>2</sub>	0.0	6.40
HCl	1.0	6.36
H <sub>2</sub> O	2.0	6.30
HCN	3.0	6.20
LiH	5.9	6.12

### CNT-based nano-electromechanical sensors

Interest in the application of carbon nanotubes as electromechanical sensors received a significant boost from the pioneering experiment of Tomblor et al.,<sup>[50]</sup> in which the middle part of the segment of a metallic CNT suspended over a trench was pushed with an Atomic Force Microscope (AFM) tip. Beyond a deformation angle of  $\sim 13^\circ$ , the electrical conductance of the tube dropped by more than 2 orders of magnitude. The effect was found to be completely reversible, i.e., through repeated cycles of AFM deformation and tip removal, the electrical conductance displayed a cyclical variation with constant amplitude. An interesting explanation was put forward by O(N) tight-binding calculations,<sup>[68]</sup> which show that beyond a critical deformation several C atoms close to the AFM tip become sp<sup>3</sup>-coordinated. This leads to the tying up of  $\pi$  electrons into localized  $\sigma$  states, which would explain the large drop in electrical conductance.

Considering the significance of the above result, it was important to carry out an independent investigation using first-principles QM. Unfortunately, the smallest models required to simulate the AFM deformation of a CNT typically involve a few thousand atoms, which makes first-principles QM simulations unfeasible. This necessitated a combination of first-principles DFT and classical molecular mechanics. Bond reconstruction, if any, is likely to occur only in the highly deformed, non-straight part of the tube close to the AFM tip. For such atoms ( $\sim 100$ – $150$  atoms including AFM-tip atoms), a DFT-based QM description was used, while the long and essentially straight part away from the middle was described accurately by using the Universal Forcefield (UFF),<sup>[69]</sup> which was previously used in CNT simulations.<sup>[70]</sup>

Because of known differences in the electronic response of zigzag and armchair tubes to mechanical deformation, the simulations were performed on a (12,0) zigzag and a (6,6) armchair tube, each consisting of 2400 atoms. The AFM tip was modeled by a 6-layer deep, 15-atom Li needle normal to the (100) direction, terminating in an atomically sharp tip. To simulate AFM tip deformation, the Li needle was initially

aimed at the center of a hexagon on the bottom side of the middle part of the tube. The Li needle tip was then displaced by an amount  $\delta$  toward the tube along the needle axis, resulting in a deformation angle  $\theta = \tan^{-1}(2\delta/l)$ ,  $l$  being the unstretched length of the tube. At each end of the tube, a contact region defined by a unit cell plus one atomic ring (a total of 36 and 60 atoms for the armchair and the zigzag tube, respectively) was then fixed, and the whole tube relaxed with the UFF, while constraining the needle atoms as well. The contact region atoms were fixed to simulate an ideal undeformed semiinfinite carbon nanotube lead, and to ensure that all possible contact modes are coupled to the deformed part of the tube. Following the UFF relaxation, a cluster of 132 C atoms for the (6,6) tube, and a cluster of 144 C atoms for the (12,0) tube were cut out from the middle of the tubes. These clusters, referred to below as the *QM clusters* (plus the 15 Li-tip atoms in tip deformation simulations) were further relaxed with Accelrys' DFT code DMol<sup>3</sup>,<sup>[62,63,71–73]</sup> with the end atoms of the cluster plus the Li-tip atoms fixed at their respective classical positions. To cut down on CPU requirements, the DFT calculations were performed by using the Harris functional<sup>[74,75]</sup> and the local exchange-correlation potential due to Vosko, Wilk, and Nusair.<sup>[76]</sup>

Fig. 4 displays the tip-deformed QM cluster for (6,6) and (12,0) tubes at the highest deformation angle of 25° considered in these simulations. Even under such large deformations, there is no indication of sp<sup>3</sup> bonding, and the structure was very similar to what was observed for a (5,5) tube in a previous work.<sup>[77]</sup> The absence of sp<sup>3</sup> coordination is inferred based on an analysis of nearest-neighbor distances of the atoms

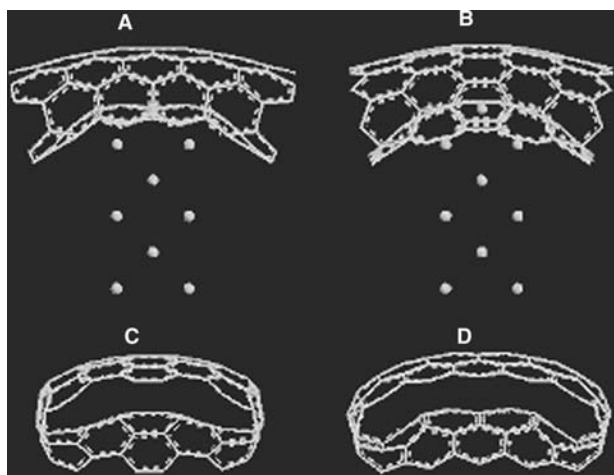


**Fig. 4** DMol<sup>3</sup>-relaxed Li-tip-deformed QM clusters for: (A) the (6,6) armchair (132 C atoms); and (B) the (12,0) zigzag (144 C atoms), in side views. The deformation angle is 25° for both tubes. Panels (C) and (D) are the respective views along the tube length, with the Li tip hidden for clarity.

with the highest displacements, i.e., the ones closest to the Li tip. *Although, for each of these atoms, the three nearest neighbor C–C bonds are stretched to between 1.45 and 1.75 Å, the distance of the fourth neighbor, required to induce sp<sup>3</sup> coordination is greater than 2.2 Å for all tubes in our simulations.*

Following the structural relaxation of the CNTs, the transmission and conductance were computed using the recursive Green's function formalism.<sup>[11,78]</sup> A nearest-neighbor sp<sup>3</sup> tight-binding Hamiltonian in a non-orthogonal basis was chosen, and ideal semiinfinite contacts assumed at both ends. The parameterization scheme explicitly accounts for the effects of strain in the system through a bond length dependence of the Hamiltonian and the overlap matrices  $\mathbf{H}_{ij}$  and  $\mathbf{S}_{ij}$ .<sup>[79]</sup> First, the retarded Green's function  $G^R$  of the whole CNT was determined by solving the following equation:

$$(E \cdot \mathbf{S}_{ij} - \mathbf{H}_{ij} - \Sigma_{L,ij} - \Sigma_{R,ij})G^{R,jk} = \delta_i^k \quad (3)$$

where  $\Sigma_{L,R}$  are the retarded self-energies of the left and the right semiinfinite contacts. The transmission at each energy was then obtained<sup>[80]</sup> from the equation:

$$T(E) = G^{R,ij}\Gamma_{L,jk}G^{A,kl}\Gamma_{R,li} \quad (4)$$

where  $\Gamma_{L,R} = i(\Sigma_{L,R}^R - \Sigma_{L,R}^A)$  are the couplings to the left and right leads. Finally, the total conductance of the tube was computed by using Landauer–Büttiker formula:

$$G = \frac{2e^2}{h} \int_{-\infty}^{\infty} T(E) \left( -\frac{\partial f_0}{\partial E} \right) dE \quad (5)$$

where  $f_0(E)$  is the Fermi–Dirac function. In Eqs. (3) and (4), summation over the repeating roman indices is implied. The lower and upper indices denote the covariant and contravariant components of a tensor.

The simulations (Fig. 5) indicate that the conductance remains essentially constant for the (6,6) armchair tube up to deformation as large as 25°. However, for the (12,0) zigzag tube, the conductance

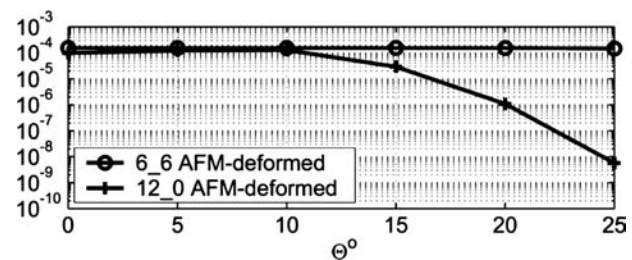


**Fig. 5** Computed conductance (in Siemens) of AFM-deformed (6,6) and (12,0) CNTs as a function of deformation angle  $\theta$  (in degrees).

drops significantly, by 2 orders of magnitude at  $20^\circ$  and 4 orders of magnitude at  $\theta = 25^\circ$ . Because  $sp^3$  coordination could be ruled out, what could be the cause for such a large conductance drop in the experiment of Ref.<sup>[50]</sup> as well as for the metallic zigzag tube in Fig. 5? Also, why did the armchair tube display no significant drop in conductance even up to large angles of deformation?

A simple explanation emerges if one zooms out from the middle of the tube and looks at the profile of the whole tube under AFM deformation. One immediately discovers an overall stretching of the tube under AFM deformation, as indicated schematically in Fig. 6. Fig. 7 compares drop in conductance in the (12,0) tube subjected to: 1) AFM deformation; and 2) uniform stretching. Such comparison makes it clear that tensile strain is the main reason behind the conductance drop in an AFM-deformed metallic zigzag tube. It was also verified that the (6,6) armchair tube does not undergo any significant conductance drop upon stretching.<sup>[81]</sup>

To explain the differences in conductance drops of the armchair (6,6) and the zigzag (12,0) tubes as a function of strain, it helps to revisit the literature where a considerable amount of theoretical work already exists.<sup>[82–86]</sup> An important result<sup>[86]</sup> is that the *rate of change* of bandgap as a function of strain depends on the CNT chiral angle  $\theta$ , more precisely as proportional to  $\cos(3\theta)$ . Thus stretched armchair tubes ( $\theta = 30^\circ$ ) do not open any bandgap, and always remain metallic. On the other hand, a metallic (3n,0) zigzag tube ( $\theta = 0$ ) can open a bandgap of  $\sim 100$  meV when stretched by only 1%. This bandgap increases linearly with strain, thus transforming the CNT into a semiconductor at a strain of only a few percent. In general, all metallic tubes with  $n_1 - n_2 = 3n$  will undergo the above metal-to-semiconductor transition, the effect being the most pronounced in metallic zigzag tubes. An experiment such as that in Ref.<sup>[50]</sup> is thus expected to show a decrease in conductance upon AFM deformation for all CNTs except the armchair

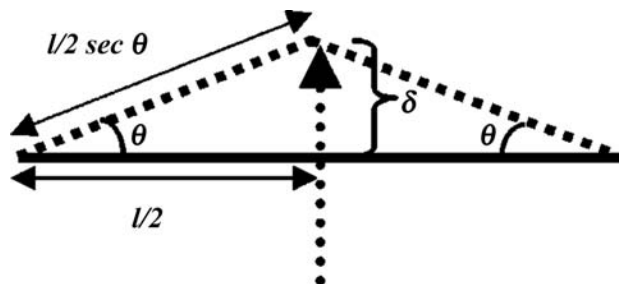


**Fig. 6** Schematic diagram representing deformation with an AFM tip. The tip-deformed tube undergoes a tensile strain. The deformation angle  $\theta$  is related to the tip displacement ( $\delta$ ) and non-deformed tube length ( $l$ ) by  $\theta = \tan^{-1}(2\delta/l)$ .

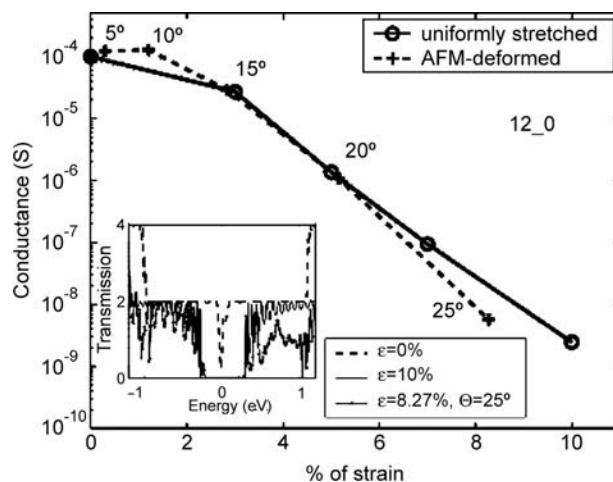


**Fig. 7** Conductance of an AFM tip-deformed (12,0) tube compared to the same tube under a uniform stretch. Actual angles of tip deformation are indicated. The % strain for the AFM-deformed tube is computed from the average C–C bond stretch in the middle of the straight portion of the tube. The inset shows transmission in the vicinity of the Fermi surface (energy = 0) for a uniform strain of 10% and a tip-deformation angle of  $25^\circ$ , compared to the non-deformed tube.

tubes. Researchers are also beginning to explore the electromechanical response of a squashed CNT,<sup>[87,88]</sup> where  $sp^3$  coordination is a possibility.

In addition to the above results for metallic CNTs, theory also predicts that for semiconducting tubes ( $n_1 - n_2 \neq 3n$ ), the bandgap can either increase (for  $n_1 - n_2 = 3n - 2$ ) or decrease (for  $n_1 - n_2 = 3n - 1$ ) with strain. These results have recently prompted more detailed experiments on a set of metallic and semiconducting CNTs deformed with an AFM tip,<sup>[89]</sup> as well as on CNTs under experimental tensile stretch.<sup>[90]</sup> Commercial applications from such work could lead to novel pressure sensors, transducers, amplifiers, and logic devices.<sup>[91]</sup>

## NANOWIRES AND NANORIBBONS

In spite of tremendous advances in carbon nanotube research, there remain a number of practical difficulties hindering many applications. Cheap mass production remains one of the biggest hurdles. Other technological challenges involve controlling CNT chirality, isolating/separating CNTs from bundles, alignment in nanocomposites, and so on. Chemical inertness of the CNT poses big problems in functionalization, sensor applications, and adhesion to structural materials. The above deficiencies have prompted researchers to explore other types of one-dimensional nanostructures. These efforts have recently led to the synthesis



of *nanowires* and *nanoribbons*. Nanowires are typically solid (i.e., not hollow) cylindrical objects with a nearly uniform diameter of a few tens of nanometers or less. So far, most nanowires<sup>[1]</sup> have been synthesized from standard semiconductors: Si, Ge, GaAs, GaP, GaN, InAs, InP, ZnS, ZnSe, CdS, CdSe, and mixed compounds. Semiconducting nanowires have great potential in electronic and optoelectronic applications at the nanoscale. In addition, conducting nanowires made of transition and noble metals, silicides ( $\text{ErSi}_2$ ), and polymeric materials have also been investigated in connection with interconnect applications.

Nanoribbons are a close cousin of the nanowires. As the name suggests, they possess a uniform rectangular cross-section with well-defined crystal structure, exposed planes, and growth direction (Figs. 8 and 9). So far, nanoribbons have primarily been synthesized from the oxides of metals and semiconductors. In particular,  $\text{SnO}_2$  and  $\text{ZnO}$ <sup>[92–94]</sup> nanoribbons have been materials systems of great current interest because of their potential applications as catalysts, in optoelectronic devices, and as chemical sensors for pollutant gas species and biomolecules.<sup>[95–97]</sup> Although they grow to tens of microns long, the nanoribbons are remarkably single-crystalline and essentially free of dislocations. Thus they provide an ideal model for the systematic study of electrical, thermal, optical, and transport processes in one-dimensional semiconducting nanostructures, and their response to various external process conditions.

### $\text{SnO}_2$ Nanoribbons: A Brief Introduction

$\text{SnO}_2$  nanoribbons are usually synthesized by evaporating  $\text{SnO}$  or  $\text{SnO}_2$  powder at high temperature, followed by deposition on an alumina substrate in the

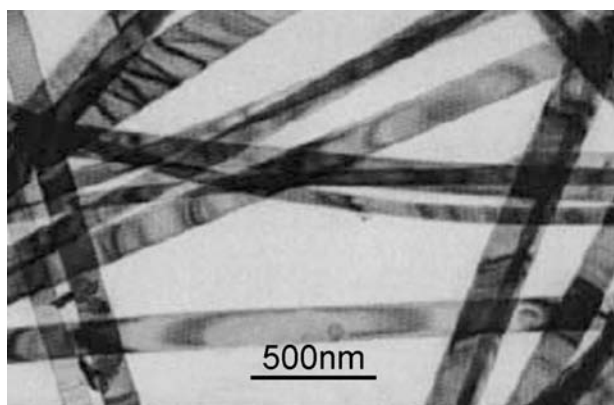


**Fig. 8** TEM bright-field image of  $\text{SnO}_2$  nanoribbons displaying strain contrast induced by bending of the ribbons. Each nanoribbon is single-crystalline without any dislocations. *Source:* From Ref.<sup>[93]</sup>.

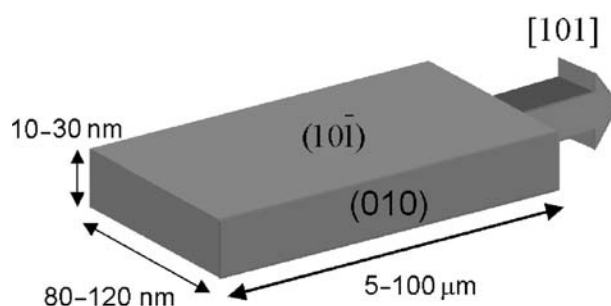


**Fig. 9** Schematic diagram of a  $\text{SnO}_2$  nanoribbon, showing typical dimensions, exposed planes, and growth direction.

downstream of an Ar gas flow.<sup>[92]</sup> Field-emission scanning electron microscopy (FE-SEM) and transmission electron microscopy (TEM) revealed that the ribbons: 1) possess a highly crystalline rutile structure; 2) grow tens of microns long in the  $\langle 10\bar{1} \rangle$  direction; 3) display a uniform quasirectangular cross-section perpendicular to the growth direction; and 4) present the  $(10\bar{1})$  and  $(010)$  rutile planes as surface facets along the growth axis, with dimensions ranging from 80 to 120 nm by 10 to 30 nm (Fig. 9). Rutile  $\text{SnO}_2$  is a wide bandgap (3.6 eV) n-doped semiconductor, with the intrinsic carrier density determined by the deviation from stoichiometry, primarily in the form of oxygen vacancies.<sup>[98]</sup>

### $\text{SnO}_2$ Nanoribbons as Chemical Sensors

Recent experiments with  $\text{SnO}_2$  nanoribbons<sup>[99]</sup> indicate that these are highly effective in detecting even very small amounts of harmful gases such as  $\text{NO}_2$ . Upon adsorption of these gases, the electrical conductance of the sample decreases by more than 1 order of magnitude. More interestingly, it is possible to remove the adsorbates by shining UV light, and the electrical conductance is completely restored to its original value. Such single-crystalline sensing elements have several advantages over conventional thin-film oxide sensors: low operating temperatures, no ill-defined coarse grain boundaries, and high active surface-to-volume ratio.

Electron-withdrawing groups such as  $\text{NO}_2$  and  $\text{O}_2$  are expected to deplete the conduction electron population in the nanoribbon, thereby leading to a decrease in electrical conductance. To investigate this, first-principles DFT calculations of the adsorption process of  $\text{NO}_2$ ,  $\text{O}_2$ , and  $\text{CO}$  on the exposed  $(10\bar{1})$  and  $(010)$  surfaces, as well as the edge atoms of a  $\text{SnO}_2$  nanoribbon, were carried out. The DFT code used was DMol<sup>3</sup><sup>[62,63,71–73]</sup> with the same basis set, parameter settings, and exchange-correlation functional as in the section “Atomic and Electronic Structure.” Nanoribbon surfaces were represented in periodic supercells (Figs. 10 and 11), and accurate Brillouin zone



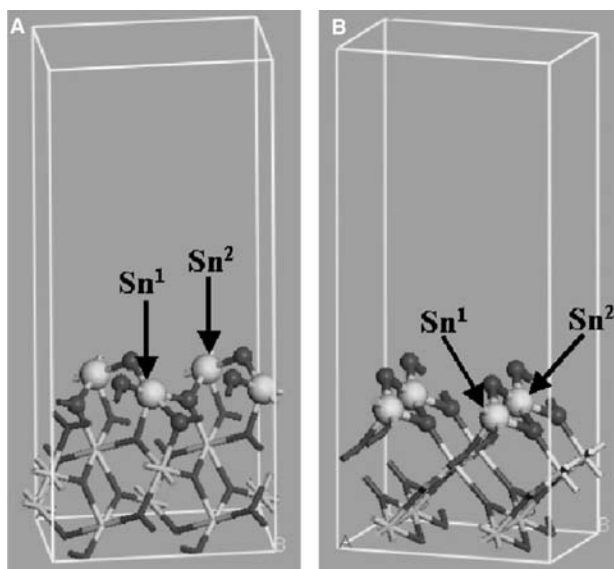


**Fig. 10** Simulation supercells representing exposed surfaces of a  $\text{SnO}_2$  nanoribbon: (A)  $(10\bar{1})$  surface; (B)  $(010)$  surface. Surface atoms are shown in ball representation. White (larger) balls and black (smaller) balls represent Sn and O atoms, respectively.  $\text{Sn}^1$  and  $\text{Sn}^2$  are neighboring Sn atoms connected with a bridging O.

integration was performed by careful sampling of  $k$ -points chosen according to the Monkhorst–Pack scheme,<sup>[100]</sup> with a  $k$ -point spacing of  $0.1 \text{ \AA}^{-1}$ . To estimate charge transfer to adatoms, the partial charge on each atom was computed by using the Mulliken population analysis.<sup>[101]</sup>

In bulk rutile  $\text{SnO}_2$ , the Sn atoms are octahedrally coordinated with six O neighbors, while each O atom is a threefold bridge between neighboring Sn centers. At both  $(10\bar{1})$  and  $(010)$  surfaces, the Sn atoms lose an O neighbor, thereby becoming fivefold coordinated (Fig. 10A,B). The surface O atoms become

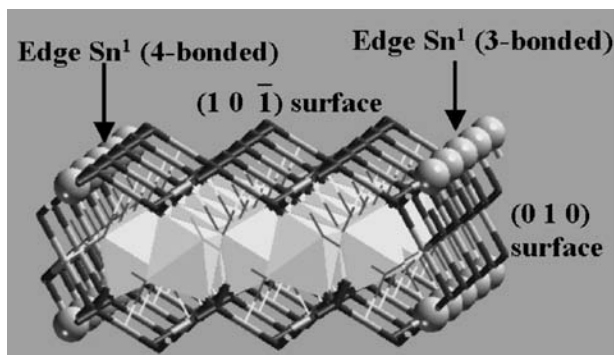


**Fig. 11** Simulation supercells representing  $\text{SnO}_2$  nanoribbon edges. For clarity, the periodic cell is not shown, and the interior atoms are represented by polyhedra. The edge (Sn) atoms are shown in ball representation.

twofold-coordinated bridges connecting neighboring surface Sn atoms (Fig. 10A,B). Both surfaces were represented by three layers of Sn, each layer being sandwiched between two O layers. The bottom  $\text{SnO}_2$  layer was fixed to simulate the presence of several bulk-like layers in the actual sample. To reduce interaction with periodic images, the surface unit cell was doubled in the direction of the smaller surface lattice constant, and a vacuum of  $15 \text{ \AA}$  was placed normal to the surface. To simulate nanoribbon edges [i.e., lines of intersection of  $(10\bar{1})$  and  $(010)$  planes], a structure similar to that in Fig. 11 was embedded in a periodic supercell with the smallest repeat period ( $5.71 \text{ \AA}$ ) along the length of the ribbon, and a vacuum of  $15 \text{ \AA}$  normal to both the  $(10\bar{1})$  surface ( $y$ -axis) and the  $(010)$  surface ( $x$ -axis). At the nanoribbon edges, the Sn atoms can be either threefold- or fourfold-coordinated (Fig. 11).

Details of the results on binding energy and charge transfer are discussed elsewhere.<sup>[102]</sup> Important results are summarized below:

1. All adsorbate structures involve one or more bonds to surface Sn atoms. The binding energy on different surfaces and edges increases in the sequence  $(010) < (10\bar{1}) < 3\text{-fold edge} < 4\text{-fold edge}$ .
2.  $\text{NO}_2$  adsorption displays a very rich chemistry because it can either form a single bond to a surface Sn, or can adsorb in the bidentate form through two single bonds to neighboring Sn atoms. The doubly bonded  $\text{NO}_2$  is 2–3 kcal/mol more stable than the single-bonded  $\text{NO}_2$ , and the binding energies are in general 4–5 kcal/mol higher on the  $(10\bar{1})$  surface than on the  $(010)$ . Activation barrier between the doubly bonded and single-bonded structures is expected to be low, which should make the  $\text{NO}_2$  species mobile on the exposed faces by performing a series of random walk steps along well-defined rows of Sn atoms on the surface.
3. When two  $\text{NO}_2$  molecules meet on the surface, either through random walk as described above, or through the incidence of a second  $\text{NO}_2$  from the gas phase in the vicinity of an already chemisorbed  $\text{NO}_2$ , there is a transfer of an O atom from one  $\text{NO}_2$  to the other, thus converting it to a surface  $\text{NO}_3$  species. The net disproportionation reaction  $\text{NO}_2 + \text{NO}_2 \rightarrow \text{NO}_3 + \text{NO}$  is well known in chemistry. The bidentate  $\text{NO}_3$  group has a substantially higher binding energy, especially on the  $(10\bar{1})$  surface, and should not, therefore, be mobile. The resulting NO species is only weakly bound to the surface and should desorb easily. Synchrotron measurements using X-ray absorption near-edge spectroscopy (XANES) have recently confirmed the

abundance of  $\text{NO}_3$  species on the nanoribbon surface following  $\text{NO}_2$  adsorption (Fig. 12).<sup>[102]</sup>

4. A CO likes to adsorb in the following manner: the C forms two single bonds to the surface—one with a surface Sn and another with a bridging O, while the O of the CO forms a double bond to the C and sticks out of the surface. This way, the C atoms attains its preferred 4-valency and the O has its bivalency satisfied.
5. On a defect-free surface (i.e., surface with no O vacancies), the  $\text{O}_2$  molecules can only weakly physisorb. In this configuration, there is no charge transfer to the  $\text{O}_2$ , and therefore a nanoribbon surface without surface O vacancies should be insensitive to atmospheric oxygen. However, at surface O-vacancy sites, the  $\text{O}_2$  molecule has a strongly bound chemisorbed structure in the form of a peroxide bridge.
6. Both  $\text{NO}_3$  groups and chemisorbed  $\text{O}_2$  (at O-vacancy sites) accept significant amount of

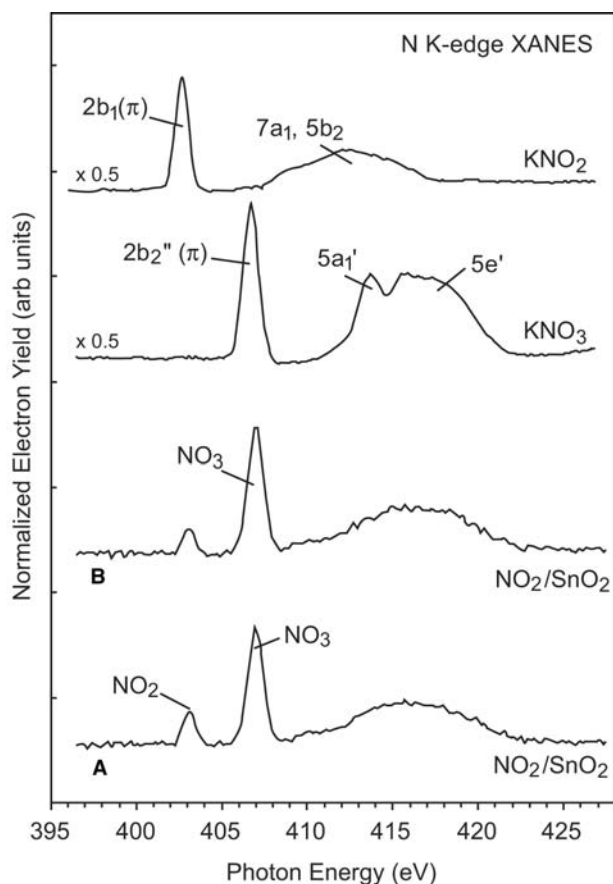


**Fig. 12** N K-edge XANES spectra acquired after exposing nanoribbons of  $\text{SnO}_2$  to  $\text{NO}_2$  at 300 K. Traces “A” and “B” correspond to two different nanoribbon samples, respectively. Included in the figure are the corresponding spectra for  $\text{KNO}_2$  and  $\text{KNO}_3$ . Source: The assignment of the features in these spectra is discussed in Refs.<sup>[103,104]</sup>

electronic charge from the surface. Therefore such adsorbates should lead to the lowering of electrical conductance of the sample. On the other hand, CO donates a moderate amount of electrons to the surface, and is therefore expected to increase the electrical conductance. All these results are consistent with direct experimental measurements of sample conductance.<sup>[96,99,105]</sup> Charge transfer between molecular species (donor or acceptor alike) and the nanoribbon surface could thus serve as a general mechanism for ultrasensitive chemical and biological sensing by using single-crystalline semiconductor nanowires.

## ACKNOWLEDGMENTS

The author thanks Accelrys Inc. for the support of this research, and would like to acknowledge collaborations with M.P. Anantram and Alexei Svizhenko (NASA, Ames), Paul von Allmen (Motorola), José Rodriguez (Brookhaven National Lab), Peidong Yang (UC, Berkeley), and Paul Kung and Jan Andzelm (Accelrys) for parts of the work reported here.

## REFERENCES

1. Ratner, M.; Ratner, D. *Nanotechnology—A Gentle Introduction to the Next Big Idea*; Prentice-Hall: Englewood Cliffs, NJ, 2002.
2. Gross, M. *Travels to the Nanoworld: Miniature Machinery in Nature and Technology*; Perseus Publishing: Cambridge, MA, 2001.
3. Wilson, M., Kannangara, K., Smith, G., Simmons, M., Crane, C., Eds.; *Nanotechnology: Basic Science and Emerging Technologies*; CRC Press: Boca Raton, FL, 2002.
4. Timp, G., Ed.; *Nanotechnology*; Springer-Verlag: New York, London, Heidelberg, 1999.
5. Drexler, K.E. *Nanosystems: Molecular Machinery, Manufacturing, and Computation*; John Wiley & Sons: New York, NY, 1992.
6. Harris, P.J.F. *Carbon Nanotubes and Related Structures*; Cambridge University Press: Cambridge, UK, 2002.
7. Dresselhaus, M.S., Dresselhaus, G., Avouris, P., Eds.; *Carbon Nanotubes: Synthesis, Structure, Properties, and Applications*; Springer-Verlag: New York, London, Heidelberg, 2001.
8. Wang, Z.L., Ed.; *Nanowires and Nanobelts: Materials, Properties, and Devices*; Kluwer Academic Publishers: Netherlands, 2003.
9. Parr, R.G.; Yang, W. *Density Functional Theory of Atoms and Molecules*; Oxford University Press: New York, NY, 1989.

10. Hill, J.-R.; Freeman, C.M.; Subramanian, L. Use of force fields in materials modeling. *Rev. Comp. Chem.* **2000**, *16*, 141.
11. Datta, S. *Electronic Transport in Mesoscopic Systems*; Cambridge University Press: Cambridge, UK, 1997.
12. Blochl, P.E.; Joachim, C.; Fisher, A.J., Eds.; *Computations for the Nano-Scale*; Kluwer Academic Publishers: Netherlands, 1993.
13. Reith, M. *Nano-Engineering in Science and Technology: An Introduction to the World of Nano-Design*; Imperial College Press: London, UK, 2003.
14. *Technical Proceedings of the 2003 Nanotechnology Conference and Trade Show*; NSTI Publications: Cambridge, MA, 2003; Vol. 3.
15. *Technical Proceedings of the 2002 International Conference on Computational Nanoscience and Nanotechnology*; NSTI Publications: Cambridge, MA, 2002; Vol. 2.
16. *Technical Proceedings of the 2001 International Conference on Computational Nanoscience and Nanotechnology*; NSTI Publications: Cambridge, MA, 2001; Vol. 2.
17. Merhari, L.; Wille, L.T.; Gonsalves, K.; Gyure, M.F.; Matsui, S.; Whitman, L.J.; Eds. *Materials Issues and Modeling for Device Nanofabrication*; MRS Proceedings, MRS Press: Warrendale, PA, 1999; Vol. 584.
18. Wallace, P.R. The band theory of graphite. *Phys. Rev.* **1947**, *71*, 622.
19. Mintmire, J.W.; Dunlap, B.I.; White, C.T. Are fullerene tubules metallic? *Phys. Rev. Lett.* **1992**, *68*, 631.
20. Hamada, N.; Sawada, S.; Oshiyama, A. New one-dimensional conductors: Graphitic microtubules. *Phys. Rev. Lett.* **1992**, *68*, 1579.
21. Saito, R.; Fujita, M.; Dresselhaus, G.; Dresselhaus, M.S. *Appl. Phys. Lett.* **1992**, *60*, 2204.
22. White, C.T.; Robertson, D.H.; Mintmire, J.W. Helical and rotational symmetries of nanoscale graphitic tubules. *Phys. Rev., B* **1993**, *47*, 5485.
23. Jishi, R.A.; Inomata, D.; Nakao, K.; Dresselhaus, M.S.; Dresselhaus, G. Electronic and lattice properties of carbon nanotubes. *J. Phys. Soc. Jpn.* **1994**, *63*, 2252.
24. White, C.T.; Mintmire, J.W.; Mowrey, R.C.; Brenner, D.W.; Robertson, D.H.; Harrison, J.A.; Dunlap, B.I. Predicting properties of fullerenes and their derivatives. In *Buckminsterfullerenes*; Billups, W.E., Ciufolini, M.A., Eds.; VCH Publishers: New York, 1993.
25. Iijima, S. Helical microtubules of graphitic carbon. *Nature* **1991**, *354*, 56.
26. Iijima, S.; Ichihashi, T.; Ando, T. Pentagons, heptagons and negative curvature in graphite microtubule growth. *Nature* **1992**, *356*, 776.
27. Ebbesen, T.W.; Ajayan, T.W. Large scale synthesis of carbon nanotubes. *Nature* **1992**, *358*, 220.
28. Bethune, D.S.; Klang, C.H.; de Vries, M.S.; Gorman, G.; Savoy, R.; Vazquez, J.; Beyers, R. Cobalt-catalysed growth of carbon nanotubes with single-atomic-layer walls. *Nature* **1993**, *363*, 605.
29. Iijima, S.; Ichihashi, T. Single-shell carbon nanotubes of 1-nm diameter. *Nature* **1993**, *363*, 603.
30. Dai, H. Growth and Characterization of Carbon Nanotubes. In *Carbon Nanotubes*; Dresselhaus, M., Dresselhaus, G., Avouris, P., Eds.; Springer-Verlag: New York, London, Heidelberg, 2000.
31. Journet, C.; Maser, W.K.; Bernier, P.; Loiseau, A.; de la Chapelle, M.L.; Lefrant, S.; Deniard, P.; Lee, R.; Fisher, J.E. Large-scale production of single-walled carbon nanotubes by the electric-arc technique. *Nature* **1997**, *388*, 756.
32. Thess, A.; Lee, R.; Nikolaev, P.; Dai, H.; Petit, P.; Robert, J.; Xu, C.; Lee, Y.H.; Kim, S.G.; Rinzler, A.G.; Colbert, D.T.; Scuseria, G.; Tománek, D.; Fischer, J.E.; Smalley, R.E. Crystalline ropes of metallic carbon nanotubes. *Science* **1996**, *273*, 483.
33. Nikolaev, P.; Bronikowski, M.J.; Bradley, R.K.; Rohmund, F.; Colbert, D.T.; Smith, K.A.; Smalley, R.E. Gas-phase catalytic growth of single-walled carbon nanotubes from carbon monoxide. *Chem. Phys. Lett.* **1999**, *313*, 91.
34. Articles on nanotubes. *Phys. World* **2000**, *13* (6), 29–53.
35. Terrones, M. Science and technology of the twenty-first century: Synthesis, properties, and applications of carbon nanotubes. *Annu. Rev. Mater. Res.* **2003**, *33*, 419–501.
36. de Heer, W.A.; Chatelain, A.; Ugarte, D. A carbon nanotube field-emission electron source. *Science* **1995**, *270*, 1179.
37. Rinzler, A.G.; Hafner, J.H.; Nikolaev, P.; Lou, L.; Kim, S.G.; Tománek, D.; Nordlander, P.; Colbert, D.T.; Smalley, R.E. Unraveling nanotubes: Field emission from an atomic wire. *Science* **1995**, *269*, 1550.
38. Collins, P.G.; Zettl, A. A simple and robust electron beam source from carbon nanotubes. *Appl. Phys. Lett.* **1996**, *69*, 1969.
39. Gulyaev, Y.V. Work function estimate for electrons emitted from nanotube carbon cluster films. *J. Vac. Sci. Technol., B* **1997**, *15*, 422.
40. Fan, S.; Chapline, M.G.; Franklin, N.R.; Tomblor, T.W.; Cassell, A.M.; Dai, H. Self-oriented regular arrays of carbon nanotubes and their field emission properties. *Science* **1999**, *283*, 512.
41. Küttel, O.M.; Groenig, O.; Emmenegger, C.; Schlapbach, L. Electron field emission from phase pure nanotube films grown in a methane/hydrogen plasma. *Appl. Phys. Lett.* **1998**, *73*, 2113.
42. Fransen, M.J.; van Rooy, Th.L.; Kruit, P. Field emission energy distributions from individual multiwalled carbon nanotubes. *Appl. Surf. Sci.* **1999**, *146*, 312.
43. Tans, S.J.; Verchueren, A.R.M.; Dekker, C. Room-temperature transistor based on a single carbon nanotube. *Nature* **1998**, *393*, 49.
44. de Heer, W.A.; Martel, R. Industry sizes up nanotubes. *Phys. World* **2000**, *13* (6), 49.
45. Liu, C.; Fan, Y.Y.; Liu, M.; Cong, H.T.; Cheng, H.M.; Dresselhaus, M.S. Hydrogen storage in single-walled carbon nanotubes at room temperature. *Science* **1999**, *286*, 1127.
46. Wong, E.W.; Sheehan, P.E.; Lieber, C.M. Nanobeam mechanics: Elasticity, strength, and toughness of nanorods and nanotubes. *Science* **1997**, *277*, 1971.

47. Dai, H. Controlling nanotube growth. *Phys. World* **2000**, *13* (6), 43.
48. Kong, J.; Franklin, N.R.; Dai, H. Nanotube molecular wires as chemical sensors. *Science* **2000**, *287*, 622.
49. Collins, P.G.; Bradley, K.; Zettl, A. Extreme oxygen sensitivity of electronic properties of carbon nanotubes. *Science* **2000**, *287*, 1801.
50. Tomblor, T.W.; Zhou, C.; Alexseyev, L.; Kong, J.; Dai, H.; Liu, L.; Jayanthi, C.S.; Tang, M.; Wu, S.Y. Reversible electromechanical characteristics of carbon nanotubes under local-probe manipulation. *Nature* **2000**, *405*, 769.
51. Guthold, M.; Falvo, M.R.; Matthews, W.G.; Paulson, S.; Washburn, S.; Erie, D.; Superfine, R.; Brooks, F.P.; Taylor, R.M. Controlled manipulation of molecular samples with the nanomanipulator. *IEEE ASME Trans. Mechatron.* **2000**, *5* (2), 189.
52. Kim, P.; Lieber, C.M. Nanotube nanotweezers. *Science* **1999**, *286*, 2148.
53. Bernholc, J.; Brenner, D.; Nardelli, M.B.; Meunier, V.; Roland, C. Mechanical and electrical properties of carbon nanotubes. *Annu. Rev. Mater. Res.* **2002**, *32*, 347–375.
54. Tománek, D., Enbody, R., Eds.; *Science and Applications of Nanotubes*; Kluwer Academic Publishers: Netherlands, 2000.
55. Papers in, *Physica B, Condens. Matter* **2002**, *323*. No. 1–4.
56. Ren, Z.F.; Huang, Z.P.; Xu, J.W.; Wang, J.H.; Bush, P.; Siegal, M.P.; Provencio, P.N. Synthesis of large arrays of well-aligned carbon nanotubes on glass. *Science* **1998**, *282*, 1105.
57. Wang, Q.H.; Setlur, A.A.; Lauerhaas, J.M.; Dai, J.Y.; Seelig, E.W.; Chang, R.P.H. A nanotube-based field-emission flat panel display. *Appl. Phys. Lett.* **1998**, *72*, 2912.
58. Saito, Y. Carbon nanotube field emitters. *Surf. Sci. Soc. Jpn.* **2002**, *23*, 38.
59. Choi, W.B.; Chung, D.S.; Kang, J.H.; Kim, H.Y.; Jin, Y.W.; Han, I.T.; Lee, Y.H.; Jung, J.E.; Lee, N.S.; Park, G.S.; Kim, J.M. Fully sealed, high-brightness carbon-nanotube field-emission display. *Appl. Phys. Lett.* **1999**, *75*, 3129.
60. Dean, K.; von Allmen, P.; Chalamala, B.R. Three behavioral states observed in field emission from single-walled carbon nanotubes. *J. Vac. Sci. Technol., B* **1999**, *17*, 1959.
61. Maiti, A.; Brabec, C.J.; Roland, C.; Bernholc, J. Growth energetics of carbon nanotubes. *Phys. Rev. Lett.* **1994**, *73*, 2468.
62. See <http://www.accelrys.com/mstudio/dmol3.html> for information on the latest version of DMol<sup>3</sup>.
63. Delley, B. An all-electron numerical method for solving the local density functional for polyatomic molecules. *J. Chem. Phys.* **1990**, *92*, 508.
64. Perdew, J.P.; Burke, K.; Ernzerhof, M. Generalized gradient approximation made simple. *Phys. Rev. Lett.* **1996**, *77*, 3865.
65. Maiti, A.; Andzelm, J.; Tanpipat, N.; von Allmen, P. Effect of adsorbates on field emission from carbon nanotubes. *Phys. Rev. Lett.* **2001**, *87*, 155502.
66. Grujicic, M. et al. Enhancement of field emission in carbon nanotubes through adsorption of polar molecules. *Appl. Surf. Sci.* **2003**, *206*, 167.
67. Buldum, A.; Lu, J.P. Electron field emission properties of single-walled carbon nanotubes: modeling and simulations. In *Technical Proceedings of the 2003 Nanotechnology Conference and Trade Show*; NSTI Publications: Cambridge, MA, 2003; Vol. 3, 297 pp.
68. Liu, L. et al. Controllable reversibility of an sp<sup>2</sup> to sp<sup>3</sup> transition of a single wall nanotube under the manipulation of an AFM tip: A nanoscale electromechanical switch? *Phys. Rev. Lett.* **2000**, *84*, 4950.
69. Rappe, K.; Casewit, C.J.; Colwell, K.S.; Goddard, W.A.; Skiff, W.M. UFF, a full periodic table force field for molecular mechanics and molecular dynamics simulations. *J. Am. Chem. Soc.* **1992**, *114*, 10024.
70. Yao, N.; Lordi, V. Young's modulus of single-walled carbon nanotubes. *J. Appl. Phys.* **1998**, *84*, 1939.
71. Delley, B. Fast calculation of electrostatics in crystals and large molecules. *J. Phys. Chem.* **1996**, *100*, 6107.
72. Delley, B. A scattering theoretic approach to scalar relativistic corrections on bonding. *Int. J. Quant. Chem.* **1998**, *69*, 423–433.
73. Delley, B. From molecules to solids with the DMol<sup>3</sup> approach. *J. Chem. Phys.* **2000**, *113*, 7756.
74. Lin, Z.; Harris, J. A localized-basis scheme for molecular dynamics. *J. Phys., Condens. Matter* **1993**, *5*, 1055.
75. Li, X.P.; Andzelm, J.W.; Harris, J.; Chaka, A. A fast density-functional method for chemistry. In *Chemical Applications of Density Functional Theory*; Laird, B.B., Ross, R.B., Zeigler, T., Eds.; ACS Symp. Ser., Oxford University Press: New York, NY, 1996; Vol. 629, 388–401.
76. Vosko, S.H.; Wilk, L.; Nusair, M. Accurate spin-dependent electron liquid correlation energies for local spin density calculations: A critical analysis. *Can. J. Phys.* **1980**, *58*, 1200.
77. Maiti, A. Application of carbon nanotubes as electromechanical sensors—Results from first-principles simulations. *Phys. Status Solidi, B* **2001**, *226*, 87.
78. Svizhenko, A.; Anantram, M.P.; Govindan, T.R.; Biegel, B.; Venugopal, B. Two-dimensional quantum mechanical modeling of nanotransistors. *J. Appl. Phys.* **2002**, *91*, 2343.
79. Papaconstantopoulos, D.A.; Mehl, M.J.; Erwin, S.C.; Pederson, M.R. *Tight-Binding Approach to Computational Materials Science, in MRS Proceedings* **491**; Turchi, P.E.A., Gonis, A., Colombo, L., Eds.; Materials Research Society: Warrendale, PA, 1998.
80. Lohez, D.; Lanoo, M. Generalization of the Green's-functions formalism to nonorthogonal orbitals: Application to amorphous SiO<sub>2</sub>. *Phys. Rev., B* **1983**, *27*, 5007.
81. Maiti, A.; Svizhenko, A.; Anantram, M.P. Electronic transport through carbon nanotubes: Effects of structural deformation and tube chirality. *Phys. Rev. Lett.* **2002**, *88*, 126805.
82. Kane, C.L.; Mele, E.J. Size, shape, and low energy electronic structure of carbon nanotubes. *Phys. Rev. Lett.* **1997**, *78*, 1932.

83. Heyd, R.; Charlier, A.; McRae, E. Uniaxial-stress effects on the electronic properties of carbon nanotubes. *Phys. Rev., B* **1997**, *55*, 6820–6824.
84. Yang, L.; Anantram, M.P.; Han, J.; Lu, J.P. Band-gap change of carbon nanotubes: Effect of small uniaxial and torsional strain. *Phys. Rev., B* **1999**, *60*, 13874–13878.
85. Yang, L.; Han, J. Electronic structure of deformed carbon nanotubes. *Phys. Rev. Lett.* **2000**, *85*, 154–157.
86. Kleiner, A.; Eggert, S. Band gaps of primary metallic carbon nanotubes. *Phys. Rev., B* **2001**, *63*, 073408.
87. Lammert, P.E.; Zhang, P.; Crespi, V.H. Gapping by squashing: Metal–insulator and insulator–metal transitions in collapsed carbon nanotubes. *Phys. Rev. Lett.* **2000**, *84*, 2453.
88. Lu, J.-Q.; Wu, J.; Duan, W.; Liu, F.; Zhu, B.E.; Gu, B.L. Metal-to-semiconductor transition in squashed armchair carbon nanotubes. *Phys. Rev. Lett.* **2003**, *90*, 156601.
89. Minot, E.D.; Yaish, Y.; Sazonova, V.; Park, J.-Y.; Brink, M.; McEuen, P.L. Tuning carbon nanotube band gaps with strain. *Phys. Rev. Lett.* **2003**, *90*, 156401.
90. Cao, J.; Wang, Q.; Dai, H. Electromechanical properties of metallic, quasimetallic, and semiconducting carbon nanotubes under stretching. *Phys. Rev. Lett.* **2003**, *90*, 157601.
91. Maiti, A. Carbon nanotubes: Bandgap engineering with strain. *Nat. Mater. (London)* **2003**, *2*, 440.
92. Dai, Z.R.; Pan, Z.W.; Wang, Z.L. Ultra-long single crystalline nanoribbons of tin oxide. *Solid State Commun.* **2001**, *118*, 351.
93. Huang, M.; Wu, Y.; Feick, H.; Tran, N.; Weber, E.; Yang, P. Catalytic growth of zinc oxide nanowires by vapor transport. *Adv. Mater.* **2001**, *13*, 113.
94. Huang, M.; Mao, S.; Feick, H.; Yan, H.; Wu, Y.; Kind, H.; Weber, E.; Russo, R.; Yang, P. Room-temperature ultraviolet nanowire nanolasers. *Science* **2001**, *292*, 1897.
95. Cui, Y.; Wei, Q.; Park, H.; Lieber, C.M. Nanowire nanosensors for highly sensitive and selective detection of biological and chemical species. *Science* **2001**, *293*, 1289.
96. Comini, E.; Faglia, G.; Sberveglieri, G.; Pan, Z.; Wang, Z.L. Stable and highly sensitive gas sensors based on semiconducting oxide nanobelts. *Appl. Phys. Lett.* **2002**, *81*, 1869.
97. Favier, F.; Walter, E.C.; Zach, M.P.; Benter, T.; Penner, R.M. Hydrogen sensors and switches from electrodeposited palladium mesowire arrays. *Science* **2001**, *293*, 2227.
98. Founstadt, C.G.; Rediker, R.H. Electrical properties of high-quality stannic oxide crystals. *J. Appl. Phys.* **1971**, *42*, 2911.
99. Law, M.; Kind, H.; Kim, F.; Messer, B.; Yang, P. Photochemical sensing of NO<sub>2</sub> with SnO<sub>2</sub> nanoribbon nanosensors at room temperature. *Angew. Chem., Int. Ed.* **2002**, *41*, 2405.
100. Monkhorst, H.J.; Pack, J.D. Special points for Brillouin-zone integrations. *Phys. Rev., B* **1976**, *13*, 5188.
101. Szabo, A.; Ostlund, N.S. *Modern Quantum Chemistry*; Dover: New York, 1996; 151.
102. Maiti, A.; Rodriguez, J.; Law, M.; Kung, P.; McKinney, J.; Yang, P. SnO<sub>2</sub> nanoribbons as NO<sub>2</sub> sensors: Insights from first-principles calculations. *Nano Lett.* **2003**, *3* (8), 1025.
103. Rodriguez, J.A.; Jirsak, T.; Sambasiban, S.; Fischer, D.; Maiti, A. Chemistry of NO<sub>2</sub> on CeO<sub>2</sub> and MgO: Experimental and theoretical studies on the formation of NO<sub>3</sub>. *J. Chem. Phys.* **2000**, *112*, 9929.
104. Rodriguez, J.A.; Jirsak, T.; Liu, G.; Hrbek, J.; Dvorak, J.; Maiti, A. Chemistry of NO<sub>2</sub> on oxide surfaces: Formation of NO<sub>3</sub> on TiO<sub>2</sub>(110) and NO<sub>2</sub>:O vacancy interactions. *J. Am. Chem. Soc.* **2001**, *123*, 3597.
105. Kind, H.; Yan, M.; Law, M.; Messer, B.; Yang, P. Nanowire ultraviolet photodetectors and optical switches. *Adv. Mater.* **2002**, *14*, 158.

# Metallic Nanopowders

## Frederick Tepper

*Argonide Corporation, Sanford, Florida, U.S.A.*

## Marat I. Lerner

*Design Technology Center, Russian Academy of Sciences, Tomsk, Russia*

## David S. Ginley

*National Renewable Energy Laboratory (NREL), Golden, Colorado, U.S.A.*

## INTRODUCTION

It is now widely recognized that the fundamental properties of materials strongly depend on the size of crystallites, especially if they are in the nanometer regime. Most of the physical, optical, and electronic properties of a bulk solid vary when the crystallites are in the nanoscale regime. If the grain size can be maintained at nanoscale dimensions, this creates major opportunities to design advanced materials with enhanced properties.

The emerging nanometals industry encompasses nanoparticles, nanolayers, thin films, nanofibers, and bulk nano-structured metals and alloys. This entry focuses on metal nanoparticles, their properties and uses, with special emphasis on those manufactured by the electroexplosion of metal wire (EEW), a process that is the most commercialized and has produced the greatest diversity of metal nanopowders.

Nanometals are in the process of becoming one of the major feedstocks for a host of emerging technologies and industries. The body of knowledge on nanosize particles has grown throughout the latter part of the twentieth century as various processes for producing them were developed. With the exception of precious metals, most of the focus has been on ceramics and non-metallic materials. More recently, there has been an increasing interest in other metallic nanoparticles. Handling them is problematic because they are highly reactive and difficult to produce, handle, and ship.

Nanosize precious metals have already had a long history of development and use as catalysts and in photography because of their chemical stability in water and air. Precious metal catalysts in a ceramic matrix, as in automotive catalysts, or dispersed homogeneously in media have had a profound affect on industrial processes. The increasing availability of other nanosize metals should lead to a plethora of new applications from composites to chemicals.

## NANOMETAL PROCESSES

There are over a dozen companies that are currently developing processes for nano metal particles, but only a few companies routinely manufacture and supply them. Production quantities are currently limited to only grams or a few kilograms but some companies claim they are building facilities to produce tens to hundreds of kilograms per day. As a result of the small quantities, the prices range from several hundred to a few thousand dollars per kilogram. Most companies do not stock nano metal powders but will produce them on a custom basis.

The manufacturing processes for micron-scale powders, such as water atomization, are generally not adaptable to nanometer size metal powders, mostly because the powders would be oxidized in the environment in which they are produced. The methods currently being developed for nanosize particles include the following:

- **Ball milling**—This method is capable of milling brittle materials to nanometer size, but fails for ductile metals such as copper unless milling is performed at cryogenic temperatures. Milling produces non-spherical particles with a broad particle size range. Dry milling of the more reactive metals can result in their contamination by air but wet milling under an organic fluid can protect the powder. Dry milling in an inert atmosphere is more complex and expensive.
- **Precipitation from aqueous solution**—Such processes are limited to precious metals because most other nanosize powders will react with water, causing surface contamination and, in the case of reactive metals, rapid and sometimes violent reaction. Metals that are precipitated from aqueous solutions generally tend to be porous and highly agglomerated. For example, silver particles can be



produced<sup>[1]</sup> via the reduction of acidic silver salt solutions using aldehydes in the presence of silica sol, but the powder is highly agglomerated. The silica is subsequently hydrolyzed in caustic, and aided by a surfactant, it is separated from the agglomerated silver powder. Bonet et al.<sup>[2]</sup> describe a method for producing deagglomerated precious metal particles smaller than 10 nm by heating a mixture of precious metal salts with hot (~150°C) ethylene glycol using polyvinylpyrrolidone (PVP) to minimize agglomeration.

- Organometallic synthesis in solution—This method employs the use of kinetically controlled reactions of organometallic precursors usually in non-aqueous solvents to product metal nanoparticles. The process can also utilize redox chemistry to reduce an inorganic precursor. The advantage of this process is that monodisperse populations of small (<50 nm) particles is possible, and the disadvantage is that Schlenk-type techniques may be necessary.
- Evaporation/condensation under vacuum—Vacuum-driven thermal evaporation is limited to low-boiling-point metals such as aluminum and copper. Higher-boiling-point materials can be evaporated by e-beam or laser heating, but the capital and operating costs of such processes are high, favoring the development of processes that operate at or near ambient pressure.
- Evaporation/condensation of the metal in an inert gas environment—Because most of the nanometals will react with oxygen or nitrogen to form oxides and nitrides, such processes require an inert gas cover. Generally, argon is used because of its lower cost compared to helium. Higher energy or impulse heating, such as laser bombardment or electric discharge, can attain higher temperatures and volatilize higher boiling metals compared to slower heating, e.g., via resistance heating of a crucible containing the molten metal. Ablation is well suited to refractory materials especially when employing laser-based heating. This has been performed both with excimer and CO<sub>2</sub> lasers for a variety of high melting materials. Once evaporated, the metal nucleates in the cold inert gas and coalesces to larger particles during transport to the collector. Eifert and Gunther<sup>[3]</sup> describe a pilot-scale reactor using a cryogenically cooled condenser with a scraper to remove product from the condenser. Other collection approaches involve an electrostatic filter and cyclone separators.
- Thermal decomposition of a salt or organometallic precursor in a flame or plasma—Axelbaum, Rosen, and Dufaux<sup>[4]</sup> produced nanosize metal particles submerged in a sodium chloride shell by flame reaction of a metal salt such as titanium tetrachloride with sodium vapor in argon. The NaCl

encapsulate is removed from the particles by both washing and subsequent sublimation at 800°C. There is potential for ionic contamination of the product, as well as sintering that could occur during sublimation of the salt.

- The electroexploded wire (EEW) process—The EEW process is a physical process converting wire into nano particles in the absence of any chemical reaction that could contaminate the product. It is capable of producing a wide spectrum of nanopowders including high and low boiling metals as well as complex alloys. The EEW process has a very long history. In 1773, Edward Nairne applied an electrical pulse to a wire, causing it to explode in air to form aerosols of metal oxide. The EEW phenomenon also occurs at the moment of burnout of an incandescent filament, when a thinned filament is explosively converted to aerosolized powders in the burned out bulb, producing a momentary brilliant flash. The EEW principal is also used in exploding bridge wire (EBW) explosive detonators. There was a considerable amount of research carried out on EBWs in the 1940s and 1950s, showing that the pulse duration is only a few microseconds long and reach temperatures higher than 15,000 K are reached at the moment of explosion.

In the 1970s and 1980s, institutes of the Russian Academy of Sciences located in Tomsk, Siberia, invested considerable effort in developing the EEW process. Their innovation included adaptation of the process within an inert gas chamber and an effective mechanism for feeding wire from an internal spool to an electrode. Prior to 1995, most of their emphasis was for producing nano aluminum for energetics and nano copper for use in lubricating oil.

In 1994, Argonide Corporation was founded to commercialize EEW nanopowders. In 1997, a cooperative research and development agreement (CRADA) between the Department of Energy (DOE) and Argonide funded these Russian groups to further develop the process. Funds were also provided to the National Renewable Energy and Los Alamos National Laboratories for characterization of the nano powders. With the exception of a 2-year halt during 1998–1999, the program continues to the present. The focus of this joint effort is on process improvement and applications development.

EEW powders can be produced from any metal that is available as ductile wire. Kilogram quantities have been produced with aluminum, copper, nickel, tin, indium, zinc, titanium, tungsten, niobium, tantalum, and silver and gram quantities with gold, palladium, and platinum. The alloys that have been produced include stainless steel, Hastelloy, and nickel–titanium.

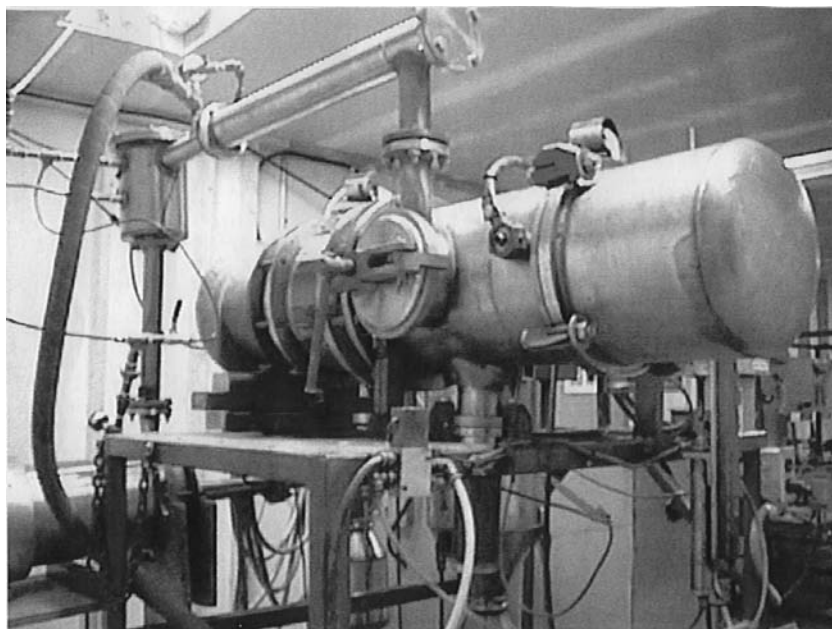


Fig. 1 Electroexplosion machine.

Fig. 1 shows an EEW machine, where the main reactor is seen in the upper center. The chamber and associated piping include either one or two cyclone separators (one is visible under the main chamber). A reel of wire is enclosed in the right side of the chamber and is then fed through an electrically insulated baffle. When the wire contacts a strike plate located in the center of the chamber, the circuit is closed causing a large pulse ( $10^2$ – $10^3$  J in 1  $\mu$ sec) to flow through the wire, creating a plasma. A very strong field is formed that contains the plasma during the microsecond pulse. When the vapor pressure of the metal exceeds the ability of the field to contain the plasma, there is an interruption in current flow, and containment by the field is lost, allowing clusters of metal atoms to be projected at supersonic speed through the argon. The metal clusters are less than about 10 nm, but coalescence occurs as flowing argon (at 2–3 atm) transports the clusters to a cyclone separator, where the now agglomerated particles are collected. At this point, further growth and coalescence is frozen, producing spherical particles with an average particle size of 40–150 nm, depending on the wire size, exploding regime, and freezing point of the metal. X-ray diffraction shows the powders to be relatively pure elemental metal.

Several hundred grams of powder per hour are produced in a single exploder with the rate proportional to the specific gravity of the metal. The energy density introduced in an exploding wire is one of the most important parameters in the process. Pulse energy is optimized by balancing the energy input with the diameter of the wire to produce electrical energy equivalent to the sublimation energy of the metal. With the current power supplies, the best trade-off between the particle size and production rate is achieved by using

0.3-mm diameter wire and results in nanopowders with an average size of 100 nm. Smaller particles (down to about 50 nm average particle size) are produced by substantial reduction in wire diameter, but at the cost of reduced throughput of metal powders. Below a critical energy density, no explosion will occur and the wire is evaporated leading to coarser particles.

Particle size can also be reduced by a higher rate of electrical explosions and by reducing the overpressure of inert gas. Low levels of active gases, such as nitrogen and oxygen, if added to the argon in the reactor, often result in reduced particle size without much contamination of the metal. The apparent mechanism is the formation of fine oxide coatings such as aluminum oxide on aluminum, inhibiting coalescence of the metal particles. Excessive oxygen will result in the production of nanosize metal oxides such as ( $\gamma$ ) aluminum and titanium oxides, with particle size about 30–50 nm in diameter.

Powder is collected in the separators until they contain about 1 kg. The collector is frequently emptied into a collection drum. The EEW process is scalable, and a newer reactor design increases the throughput of the reactor and minimizes downtime. In the newer device, the explosion frequency has been increased from about 0.5 to 3 Hz, as recirculation of the argon gas is increased. A feed-through system was developed so that a large spool of wire can be fed into the reactor without opening the chamber and interrupting the process. Also, the arrangement and length of the piping was altered to improve sedimentation, particularly of occasional large particles that are produced by the conventional process.

The EEW process is limited to particles with average sizes less than about 300 nm. Particles as small as 20 nm

have been made in experimental quantities. Virtually all the metals produced by this process are combustible, and several of them, such as aluminum, iron, titanium, and zirconium, are either pyrophoric or nearly so. The powders are collected and protected from oxidation by the argon in the reactor. The more reactive powders are transferred to liquid hydrocarbon. In the case of Alex<sup>®</sup> nanoaluminum, the particles are passivated by adding dry air before removing it from the chamber and are then packaged as a dry powder.

All EEW powders are handled and shipped as hazardous (combustible) metal powder. Alex<sup>®</sup> is the nanometal made in the greatest quantity, followed by nickel, copper, tungsten, stainless steel, silver, and zinc. While Ni, Cu, and W may oxidize when exposed to air, they are relatively well behaved compared to dry iron, stainless steel, or titanium powders. The preferred method of packaging dry metal powders is in glass ampoules, and they are offered in quantities of at least 100 g net weight of powder.

The principal advantages of the EEW process are:

1. As with gas condensation techniques, contamination by chemical reactants or by reaction with solvents is avoided.
2. Spherical particles are ordinarily produced.
3. As compared to other high-temperature processes, virtually all of the electrical energy in the EEW process is directly converted to heat. There is little opportunity for convection or

radiation heat loss during the very rapid ( $\sim 1 \mu\text{sec}$ ) pulse.

4. Alloys can be converted to nanopowder with no measurable segregation as compared to evaporative processes, where the composition of the particles will vary.
5. The process operates with pressurized inert gas, simplifying the weight and cost of the reactor and piping.

Alloys are produced on a custom basis, so long as the fine wire is either commercially available in a continuous filament or can be produced with sufficient ductility to be fed into the wire feed mechanism without breakage.

## PHYSICAL AND CHEMICAL PROPERTIES

Table 1 summarizes the surface area and crystallographic character of several EEW powders including aluminum oxide ( $\gamma$  phase) and aluminum nitride. As with other nano powders, the principal difference in the physical and chemical properties of nanometals results from their greater surface area as compared to fine (micron) size particles. The surface area is inversely proportional to the square of the diameter of the particle, so a 100-nm spherical particle has a surface 1000 times greater than a 10- $\mu\text{m}$  particle. This creates opportunity for creating materials with new and useful

**Table 1** Electroexploded nanopowders and their characteristics

Powder	Particle size distribution function	Average particle size [nm]	Metal content [%]	Surface area [ $\text{m}^2/\text{g}$ ]	Particle morphology	Crystalline defects
Al	Normal-logarithmic	80–150	Passivated $\geq 92$	8–18	Spherical	Numerous defects
Al	Normal Gaussian	30–50	Depends on particle size distribution	20–48	Crystallites	No information
Cu	Normal logarithmic	100–150	passivated $\geq 90$ non-passivated $\geq 96$	5–8	Spherical	Numerous defects
Cu	Normal Gaussian	30–50	passivated $\geq 90$ non-passivated $\geq 96$	$\sim 12$	Crystallite faces	Small amount of defects
Ni	Normal logarithmic	80–100	passivated $\geq 95$ non-passivated $\approx 99$	4.5–6	Spherical	Numerous defects
Ni	Normal Gaussian	30–50	passivated $\geq 95$ non-passivated $\approx 99$	$\sim 7.5$	Crystallite faces	Small amount of defects
Zn	Normal logarithmic	100–200	passivated $\geq 90$	4.1–6	Spherical	Numerous defects
$\gamma\text{-Al}_2\text{O}_3$	Normal Gaussian	30–50	Not applicable	20–45	Spherical	Small amount of defects
AlN	Normal Gaussian	50–60	Not applicable	$\sim 36$	Crystallite faces	Small amount of defects

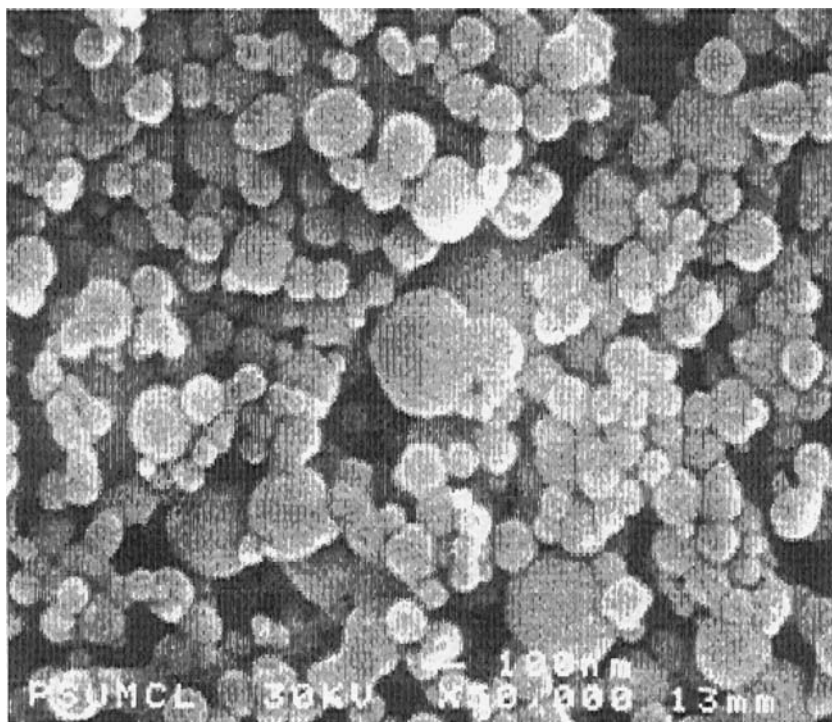


**Fig. 2** Field emission electron microscopic view of Alex<sup>®</sup> (50,000 $\times$ ).

properties, but also poses difficulty in handling, shipping, and storage.

A scanning electron microscopy photo of Alex<sup>®</sup> nanopowder is seen in Fig. 2. Surface area [Brunauer–Emmett–Teller (BET)] measurement is generally a good surrogate for determining average particle size because EEW powders are mostly spherical, fully dense, and smooth. The surface area of Alex<sup>®</sup> with 100 nm average particle size ranges from about 10 to 20 m<sup>2</sup>/g. Fig. 3 shows a sector of an Alex<sup>®</sup> particle with a passivation coating about 2.5–3 nm thick. X-ray powder diffraction shows these particles are primarily metallic aluminum, while the coating is principally aluminum oxide with minor amounts of nitride and an oxynitride. The amount of active aluminum for a 100-nm size average particle is approximately 88–90 wt.%. The oxide content rises with diminishing particle size, as the 3-nm oxide layer comprises an increasingly greater mass.

The thermal properties [differential thermal analysis (DTA)] of Alex<sup>®</sup> powder when heated in air, oxygen, and nitrogen was compared<sup>[5]</sup> to that of micron size aluminum. Alex<sup>®</sup> powder reacts rapidly with these gases, producing very sharp exotherms that occur well below the melting point (660°C) of aluminum, while 20- $\mu$ m-size aluminum does not react until about 1000°C.

An organic coating has been developed for many of the nanometals and is being used for coating aluminum and other reactive nanometals. The coating (called L-Alex<sup>®</sup>) is based on the reaction of a carboxylic acid (palmitic) acid with the aluminum powder rather than

coating it with oxide. The resistance of L-Alex<sup>®</sup> to moisture attack during accelerated aging was compared<sup>[6]</sup> to oxide-coated Alex<sup>®</sup> and to a 17- $\mu$ m-size aluminum powder (Cap45a). The test involved exposure of a thin layer of the aluminum particles in a dish within a temperature humidity chamber. Each day, a sample of each powder was removed and titrated for residual aluminum metal. The powder in the dish was mixed daily to expose fresh surface. Aging was performed at several temperatures and humidity levels from room temperature and dry conditions to a maximum of 60°C/75% relative humidity (RH). Fig. 4 shows a 20% and 70% aluminum metal loss, respectively, in the case of Cap45a and Alex<sup>®</sup> powders, but the L-Alex<sup>®</sup> showed little aluminum loss throughout the 40-day test exposure. The study also showed that bayerite (Al(OH)<sub>3</sub>) is the major product of hydrolysis rather than Al<sub>2</sub>O<sub>3</sub>. Degradation of the Cap45a powder ceased after day 12 when exposed to harsher conditions as a result of the buildup of a layer of bayerite.

Melting point is one of the properties that can be altered by reducing particle size down into the nanometer range. Fig. 5 shows the melting point of gold<sup>[7]</sup> as a function of particle size. Melting point reduction is not really significant until the particle size is less than about 10 nm.

EEW powders have crystal defects, faults, and twins caused by rapid quenching during the process. Fig. 6 shows a high-resolution transmission electron microscope (TEM) view of EEW nickel showing twins and polytwins. The clusters are propelled by electroexplosion

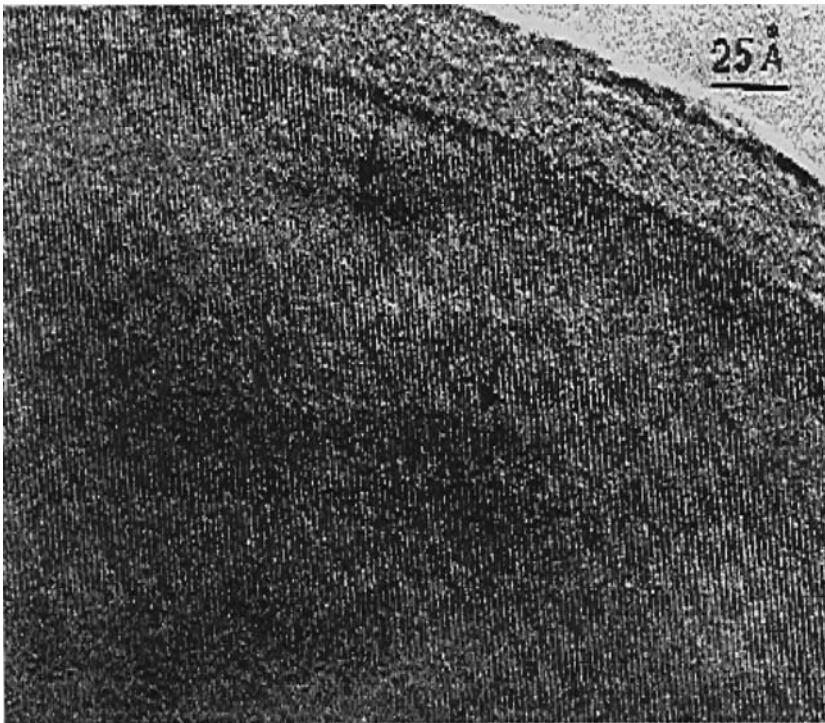


**Fig. 3** High-resolution (400,000 $\times$ ) transmission electron microscope of alumina layer on the surface of spherical Alex<sup>®</sup> particle.

at 2 km/sec through the cold argon, which results in a quenching rate of about  $10^8$  °C/sec. The disorder in the EEW aluminum crystal extends into the oxide outer layer, causing the powders to be physically metastable and more chemically reactive. Fig. 7 is a DTA of EEW silver showing an exotherm at about 220°C, far below the melting point (960°C) of silver. The internal energy is estimated to be about 40% of the heat of fusion. When alloy wire is electroexploded, the very high quench rates often produces non-equilibrium phases. For example, EEW 300-stainless steel can be heterogeneous, containing not only the expected austenite phase, but also alpha iron, nickel, and others components in the Fe–Ni–Cr phase diagram.

## APPLICATIONS

Nanomaterials and nanotechnology are currently receiving major attention and publicity as a future market. While certain ceramic nanopowders have reached commercial status, nano metals are still in the research stage and sales average about 1 kg per order. Prices are hundreds of dollars per kilogram, and while substantial reductions in cost are anticipated, nanopowders will always be more expensive than conventional size powders. In addition, they bear higher shipping and handling costs. Therefore the focus of nanopowder suppliers is on applications, in which there is high value added by the nanosize

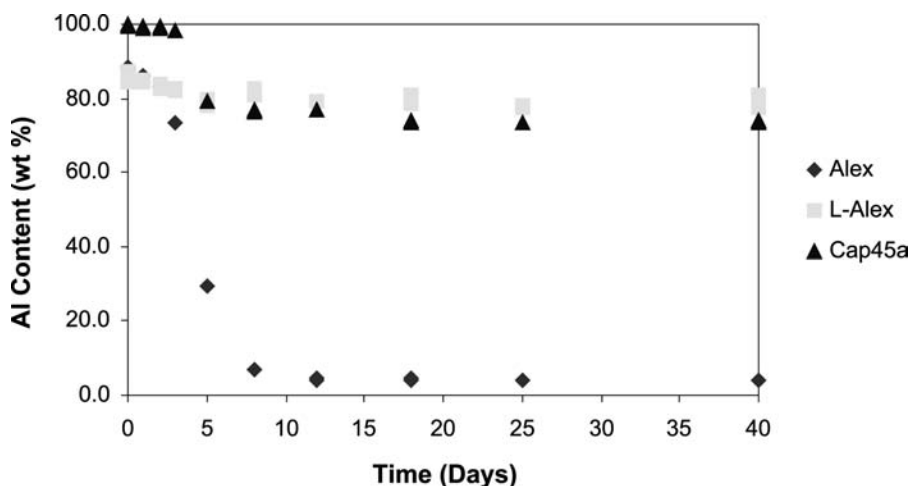


**Fig. 4** Aluminum powder accelerated aging in 60°C/75% RH air.



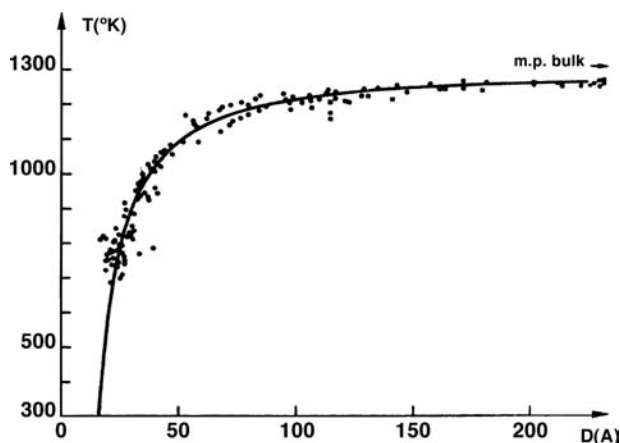


Fig. 5 Melting point of gold particles as a function of particle size.

particles. Target markets include energetics, microelectronics, metallurgical coatings, biotechnology, and niche powder metallurgy applications.

### Energetics

Aluminum is a highly energetic combustion fuel, particularly on a volumetric basis. For more than a century, it has been used as an additive in energetic compositions such as thermite, in explosives and pyrotechnics, and more recently, in rocket propellants. Because of its high surface area, nano aluminum provides a number of advantages over conventional aluminum powder, particularly with respect to burning rate. Fig. 8 shows that substituting Alex<sup>®</sup> for a conventional micron size

(~20  $\mu\text{m}$ ) aluminum in a mixture with ammonium perchlorate can increase the burning rate about 20 times.<sup>[8]</sup> Nano aluminum also ignites more rapidly. When combusted in an air shock tube, Alex<sup>®</sup> has an ignition delay of only 3  $\mu\text{sec}$  compared to 600  $\mu\text{sec}$  for 3- $\mu\text{m}$  diameter aluminum powder.

### Rocket Propellants

Rapid burning increases the thrust and speed of a rocket engine, and higher thrust is desired in many advanced missile systems. Several researchers<sup>[8-10]</sup> have noted a doubling of burning rate when Alex<sup>®</sup> is substituted for micron size aluminum in conventional solid rocket propellants such as Al/ammonium perchlorate/hydroxy-terminated isobutylene binder (Al/AP/HTPB). The rapid burning is attributed to the smaller particle size and (much) larger surface area. A model developed for aluminum particle combustion in a rocket engine predicts that nano aluminum would burn very rapidly. This model<sup>[11]</sup> describes the life of the burning particle as proportional to the square of the particle diameter. Experimental data shows that a 5- $\mu\text{m}$  aluminum particle survives for about 4 msec in a rocket engine. Extrapolation of the  $d^2$  model down to a 100-nm diameter predicts that the particle would be consumed in about 600 nsec, about 4 orders of magnitude shorter than the micron-size particle. High-speed photography of a burning propellant surface confirms that a nano aluminum particle is completely consumed at the surface of the burning grain rather than being propelled into the burning flow stream as in the case of the micron size aluminum.

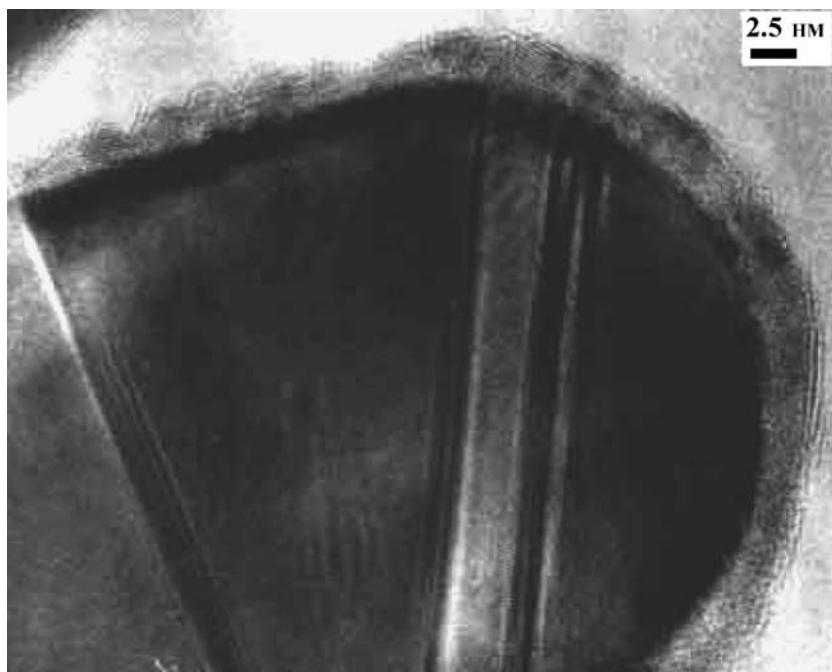


Fig. 6 Crystallographic defects in EEW nickel.



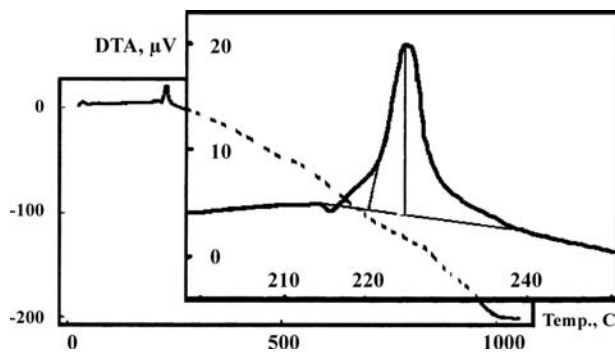


Fig. 7 DTA of EEW silver particles. Source: Los Alamos National Laboratory.

A faster burning grain is also more efficient because combustion is complete within the engine rather than in the exhaust stream of the rocket. The hybrid rocket engine would also benefit from nano aluminum as a fuel ingredient. The classic hybrid uses liquid oxygen with a rubber base binder (HTPB) grain that contains either no oxidizer, or just enough to react with the HTPB so as to be a gas generator. Pyrolysis of the rubber creates low-molecular-weight organic molecules that are forced into the engine and then react with liquid oxygen. If aluminum is added to a solid fuel such as HTPB, there is a theoretical increase in rocket performance, but unfortunately micron size aluminum does not burn effectively in such a hybrid. However, Chiavarinni et al.<sup>[12]</sup> found that adding 10 wt.% Alex<sup>®</sup> to an HTPB slab increased the regression rate by 70% and also resulted in smoother burning compared to the pure HTPB slab.

Aluminum, if gelled into kerosene, increases the volumetric energy density of the liquid rocket fuel. Unfortunately, micron size aluminum does not burn efficiently when immersed in kerosene; however, nano aluminum

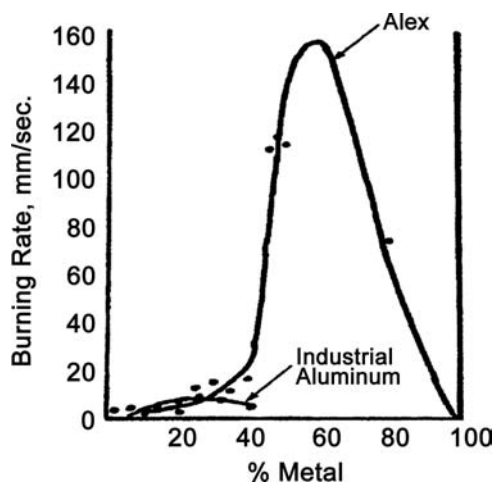


Fig. 8 Burning rate of aluminum/ammonium perchlorate powder mixes.

additive is completely combusted.<sup>[13]</sup> The higher temperatures created by combustion of nano aluminum also accelerates the combustion of the kerosene.

## Explosives

Reshetov, Shneider, and Yavorovski<sup>[14]</sup> were the first to notice that nano aluminum influences the detonation velocity of high explosives. When less than 30 wt.%, nano aluminum is added to hexamethyl-3-nitroamine (HMX) (Fig. 9), detonation velocity (VoD) decreased from 5400 to 4700 m/sec, about equivalent to that of explosives when micron size aluminum is added to HMX. However, beyond 30 wt.%, there is a rapid rise in VoD to 7000 m/sec. Even where the VoD is not affected, the force of the detonation is enhanced by the rapid reaction of the nano aluminum with the gases generated behind the detonation wave.

The affect of nano aluminum on enhanced detonation was demonstrated experimentally in the United States and Europe, and several organizations are studying Alex<sup>®</sup>'s use in explosives. When incorporated into ammonium dinitramide, Alex<sup>®</sup> was shown<sup>[15]</sup> to increase VoD from 4380 m/sec for a 97% dinitramide (balance Viton binder) to 5070 m/sec (73:24:3 ADN/Alex<sup>®</sup>/Viton). Identical loading of conventional aluminum had a detrimental effect on VoD. Similarly, detonation tube experiments comparing type 40XD flake aluminum and Alex<sup>®</sup> in N<sub>2</sub> gas dispersed lactose/Al/ammonium perchlorate compositions showed VoD enhancements for Alex<sup>®</sup> over the flake grade at four different Al concentrations.<sup>[16]</sup> Most recently, a collaborative program between Australian (DMSO-Adelaide) and Canadian (DREV) laboratories has

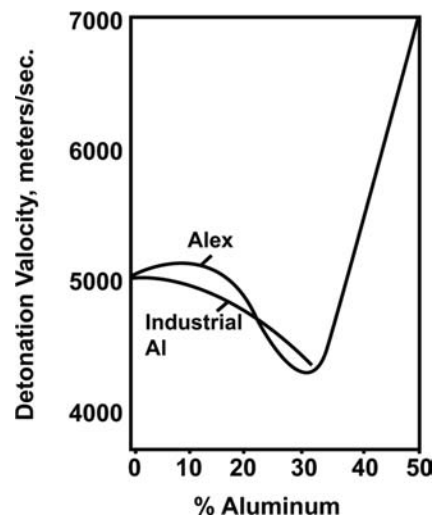


Fig. 9 Detonation velocity as a function of aluminum in HMX explosive.

demonstrated a beneficial enhancement for both VoD and brisance for a number of trinitrotoluene (TNT)-based tritonal and H-6 derivatives containing Alex<sup>®</sup>.<sup>[17]</sup> VoD enhancements of 200–300 m/sec and improvements in brisance of up to 27% were observed in a number of tritonal charges when conventional aluminum grades were substituted for Alex<sup>®</sup>.

### Gun Propellants

When Alex<sup>®</sup> is added to gun propellants, the burning rate was nearly doubled as compared to high caloric conventional double-base propellants.<sup>[18]</sup> Simultaneously, the pressure exponent of Vieille's burning law decreases from more than 0.8 for double base propellant to 0.66, resulting in more stable burning. Such aluminized gun propellants would be useful as a burning rate accelerator, as an igniter in high-pressure rocket propulsion, and as a booster.

### Miscellaneous Pyrotechnics

Metal/oxide pyrotechnic heat sources (thermite) are enhanced with faster burning nanosize aluminum. Mixtures of nano size aluminum and nano MoO<sub>3</sub> powder results in a very fast burning material. The reaction rate can be altered to develop energy release rates spanning the range between conventional explosives and conventional thermites. Such mixtures have application in advanced munitions, pyrotechnics, detonators, and primers.

### Self-Heating Synthesis (SHS)

Refractory compounds or alloys may be synthesized by direct reaction using the heat generated by metal/metal reaction or as in thermite, where a metal reduces an inorganic compound. Table 2<sup>[19]</sup> shows several reactions in which EEW powders were used to form intermetallic alloys. At 200°C, a pellet of EEW copper and micron zinc powder can react within a second producing light and forming brass. Pressed pellets of

Alex<sup>®</sup> and amorphous boron, when heated to 500°C and ignited by a hot wire, immediately forms aluminum diboride, while ordinary aluminum and boron would have to be heated above 1000°C for several hours to form the diboride. Nickel aluminide and alloys of aluminum with tungsten, iron, nickel, or molybdenum were produced at much lower temperatures and at shorter times than could be achieved by reacting micron size powders.

### Electrically Conductive Inks and Pastes

The goal of shrinking circuits and increasing functionality has resulted in a continuing search for new and improved processes in electronic packaging. Metal powders such as copper, gold, nickel, tin, and solder are formed into pastes and used for electronic interconnects. Copper pastes are used in the production of hybrid multi-chip module (MCM) circuits. The pastes are printed on ceramics such as aluminum oxide and more recently aluminum nitride to produce highly dense, thick film circuits. Nanosize powders provide a flatter surface topology and more precise edge definition and line spacing that would be attainable as compared to conventionally sized powders. Precise patterning ensures lower cross-talk between adjacent conductor lines. While such better edge definition is not attainable in silk screening patterns because of resolution limits of the process, newer patterning methods such as photo-patterned thick film processes could benefit from the smaller features of nanosize particles.

Metal-filled polymers also play an important role in microelectronics, including electrically conductive adhesives, polymers for shielding from radiofrequency radiation, and in magnetic polymeric layers. In most cases, high aspect ratio fibers and flakes are used because of the greater opportunity for conductor/conductor contact within the composite. Nano metal powders offer an advantage in increased electronic conductivity because of an increase in the number of point-to-point contacts. The authors developed silver-filled polyurethane and epoxy adhesives having

**Table 2** Alloying reactions in EEW pressed pellets

Metal 1	Metal 2	Reaction method	Product/comments
EEW Cu	Coarse Zn—30%	hot wire at 25°C	Brass verified by XRD
EEW Al	Amorphous B	hot wire at 500°C	AlB <sub>2</sub> produced
EEW Al	Coarse Ni	hot wire at 25°C	Al–Ni alloy principal phase
EEW Al	Coarse Fe	hot wire at 25°C	FeAl, FeAl <sub>3</sub> and Fe <sub>2</sub> Al <sub>5</sub>
EEW Al	EEW W (60 wt %)	self-ignited at 300°C	WAl <sub>4</sub> and WAl <sub>5</sub>
EEW Al	Coarse Mo	no reaction	
EEW Al	EEW Mo	self-ignited at 300°C	Al <sub>12</sub> Mo, Al <sub>5</sub> Mo and Al <sub>4</sub> Mo

an electronic conductivity of  $1 \times 10^{-5}$  and  $2 \times 10^{-6} \Omega\text{m}$ , respectively, which are improvements over silver flake-filled polymers. The conductivity of the composite is enhanced by agglomerated particles that are particularly prevalent in EEW silver.

## Nanostructures

Over the last few years, there have been extensive studies on nanostructures, with an expectation that they will form superplastic or ultrahigh strength, tough materials. Smaller grains result in greater strength, generally following the classic Hall–Petch relation, at least for grain sizes 50 nm and larger. Extrapolations forecast 2–7 times higher hardness and 2–3 times the tensile strength as compared to parts produced from conventional powders. Furthermore, the boundaries formed in a nanocrystalline structure tend to have higher ductility. Thus in contrast to most methods of strengthening metals, nanostructures have the potential dual benefit of increasing strength while also maintaining or increasing ductility.

There is a dilemma in that smaller grain size of a nano powder based compact recrystallize and grow at lower temperature, countering efforts to form nanostructures. Consolidation methods, such as equal channel angular extrusion (ECAE), that do not rely on much heating can densify the compact to greater than 99% while minimizing grain growth.

The breadth of potential applications for nanostructured metals and alloys is considerable. The higher tensile strength and fatigue strength, and even the enhanced ductility that have been reported in nanostructured metals can impact any application in which strength or strength-to-weight ratios are critical properties. Transportation, aerospace, sports products, implantable medical components, and chemical and food processing applications appear promising.

## Low-Temperature Sintering

The onset of sintering occurs substantially lower in temperature with nanosize particles. Eifert et al.<sup>[20]</sup> achieved a decrease in the onset of sintering of tantalum from about 1800 to 900°C when the particle size is reduced from 2  $\mu\text{m}$  to 50 nm. The onset of sintering of 40 nm iron powder is as low as 370 K, approximately 21% of the melting point as compared to  $\sim 900$  K, or 50% of melting for 2- $\mu\text{m}$ -size iron powder.<sup>[21,22]</sup> The challenge of the nanoparticulate approach is that the pores are readily formed in nano sinters at low temperatures, and they tend to slow full densification unless there is some strain induced in the porous compact to prevent the stabilization of larger pores.

## MISCELLANEOUS APPLICATIONS

Wear-resistant and microelectronic coatings can be formed from slurries of nanopowders. For example, the authors bonded a pattern of copper particles to glass by laser irradiation of a dried nanopowder paste deposited by silkscreen. The laser melted the individual particles to form circular disks approximately 1  $\mu\text{m}$  in diameter in a line pattern with resolution of approximately 5  $\mu\text{m}$ . The particles then provided a seed layer for the electroless deposition of additional copper to form a circuit pattern.

Selective laser sintering of metal powders is used for the computerized 3-D design and production of rapid tooling. Nanopowders are likely to be superior to conventional powders in that they sinter more readily and produce parts with tighter tolerance because of their smaller particle size.

Nanosize nickel–titanium alloys are being evaluated as source materials for producing memory alloy components.

Sintered metal disks are used in industrial filtration because of their capability to operate at elevated temperature and in corrosive environments. Disks produced from nanopowders would result in smaller pore size and would be more effective in filtering submicron particles.

A new class of heat transfer fluids is being developed where nanocrystalline particles are being suspended in liquids such as water or oil.<sup>[23]</sup> Copper oxide (5 vol.%) suspended in water results in an improvement in thermal conductivity of almost 60% as compared to water without nanoparticles. Direct evaporation of copper nanoparticles into pump oil results in similar improvements in thermal conductivity compared to oxide-in-water systems, but more importantly, requires far smaller concentrations of dispersed nanocrystalline powder.

Gold and other spheres are being considered for use as carriers of pharmaceutical and therapeutic agents through the blood stream to target organs. Colloidal gold particles have also been exploited in several bioanalytical methods, including a proposed DNA detection method.<sup>[24]</sup>

Iron powder, if injected into underground water plumes, will destroy trace halogenated solvents. “Iron walls,” which are permeable reactive barriers injected into the plumes, containing zerovalent iron, intercepts halogen-saturated solvents causing their dechlorination. For chlorinated ethenes [perchloroethylene (PCE) and trichloroethylene (TCE)], the products are mostly fully dechlorinated although some chlorinated alkanes yield partial dechlorination products that may still be a pollution problem. There have now been many feasibility studies, pilot tests, small- to medium-scale demonstration projects, and full-scale applications performed by numerous groups.

The authors have found that nano-iron is far more effective in converting perchlorethylene to dichlorethylene than micron size iron. Also, nano iron has potential for the conversion of trace As [+3] to As [+5] so that it could be filtered from drinking water.

Nanosize particles interact differently with the electromagnetic energy spectrum than do micron size particles. For instance, solid particles, with sizes substantially below  $<1/20$  of the wavelength of light are transparent so that the film can be strengthened by adding inorganic particles without affecting transparency.

Nanosize metallic silver is being considered as a biocide for water purification and in medical formulations.

Nanosize copper is used as an additive in lubricating oils and sold in Russia. Tarasov et al.<sup>[25]</sup> showed that adding 0.5% nano copper to lubricating oil reduces friction in rubbing surfaces, particularly when under high load as in heavy-duty engines, thereby extending their life. The lubricating mechanism is believed to be the deposition of nano copper particles onto the surfaces of a hot friction pair, producing a softer metal surface on the aggravated surface. Such mixtures may prove to be superior to existing lubricants such as those containing Teflon particles.

Nanosize metal particles also have potential as precursors for the synthesis of a wide variety of inorganic compounds such as oxides with complex stoichiometry and with unique sizes, shapes, and reactivities. Furthermore, they have potential as precursors in the direct synthesis of metal organic compounds.

## SAFETY, HANDLING, AND SHIPPING CONSIDERATIONS

Nano-metal powders are regarded as hazardous materials, particularly with respect to shipping regulations. Department of Transportation and International Air Transport Authority (IATA) require the user to test and categorize such powders relative to the combustion hazard prior to shipment. Should testing under the protocol show the powders to be pyrophoric in air, then shipment on passenger aircraft is disallowed. United Parcel Service and other carriers will not handle pyrophoric materials. The powders may be passivated by oxidizing their surface as in the case of nano aluminum, coating with an organic as in the case of L-Alex<sup>®</sup>, or immersion in a compatible liquid such as a hydrocarbon.

Working safety is also an issue with nano metal powders. Caution must be exercised to minimize the danger of untoward ignition and burning. Efforts should be directed to minimize the possibility of static ignition, *particularly when there is an oxidant mixed in with the powder*. Such oxidants include metal oxides and other oxidizing salts and halogenated organic

liquids and solids. For instance, magnesium or aluminum mixed with Teflon powder is a highly reactive pyrotechnic. Users should study Material Safety Data Sheets (MSDS) before using nano metals. High efficiency particulate air (HEPA)-type respiratory filters should be used in operations where there is an opportunity for encountering nanoparticulate dust.

An issue common to most forms of nano metal powders is packaging to assure purity. Glass ampoules are superior to packaging in plastic containers, although ampoules would still not be acceptable under Department of Transportation (DOT) or IATA rules if the powder is pyrophoric. In this case, the powders have to be submerged in liquid hydrocarbon and sealed to prevent the ingress of air to minimize contamination.

## CONCLUSION

The burgeoning field of nanotechnology is forecast to have an economic impact as great as biotechnology or microelectronics. Nano powders including nano metals are likely to be key source materials in this new industry. The EEW process is one of several methods being commercialized for manufacturing nano metal powders. EEW powders are readily produced from any metal or alloy that can be produced in the form of fine metal wire including elemental metals such as aluminum and copper, refractory metals such as titanium, tantalum, and tungsten, and alloys such as stainless steel and nickel-titanium.

Applications for nano metals include energetics such as rocket propellants, explosives and pyrotechnics, in self-heating synthesis of inorganic compounds and alloys, in high-strength nano structured metals, electrically conducting inks for microcircuits and in advanced capacitors, in environmental remediation, as carriers for bioactive and medical therapeutics, and in wear-resistant coatings. Most of the sales of nano powders are for small quantities to researchers investigating new properties with potential applications not discernable at this writing, but which are likely to add to the potential growth of this subindustry.

## ACKNOWLEDGMENTS

We are grateful for the support of the Department of Energy and its Incentives for Prevention of Proliferation (IPP) under the cooperative agreement. We are also grateful to the U.S. Industrial Coalition of Washington, DC, which has collaborated in the funding efforts.

We also appreciate the efforts of the team at the National Renewable Energy Laboratory including Ms. Tanya Rivkin, Mr. Alexander Miedaner, and Calvin Curtis as well as Dr. Joel Katz of Los Alamos

National Laboratory who contributed their time in characterizing the powders.

Lastly, we want to thank the many Russian scientists and engineers that contributed their knowledge and effort in developing the EEW technology and in manufacturing the powders.

## REFERENCES

- Tosun, G.; Glicksman, H.D. Process for Making Finely Divided Particles of Silver Metals. US Patent 5,188,660, Feb. 1993.
- Bonet, F.; Delmas, V.; Grugeon, S.; Herrera-Urbina, R.; Silver, P.Y.; Tekaiia-Elhissen, K. Synthesis of monodisperse Au, Pt, Pd, Ru and Ir nanoparticles in ethylene glycol in. *Nanostruct. Mater.* **1999**, *11* (8), 1277–1284.
- Eifert, H.; Gunther, B. Metallic nanopowders. *ASM Handb. Powder Metal Technol. Appl.* **1998**, *7*, 77–79.
- Axelbaum, R.L.; Rosen, L.J.; DuFaux, D.P. Method and Apparatus for Producing High Purity and Unagglomerated Submicron Particles. US Patent 5,498,446, March 1996.
- Mench, M.M.; Kuo, K.K.; Yeh, C.L.; Lu, Y.C. Comparison of thermal behavior of regular and ultra-fine aluminum powders (Alex<sup>®</sup>) made from plasma explosion process. *Combust. Sci. Technol.* **1998**, *135*, 269–292.
- Cliff, M.; Tepper, F.; Lisetsky, V. *Ageing Characteristics of Alex<sup>®</sup> Nanosize Aluminum*, 37th AIAA Joint Propulsion Meeting, Salt Lake City, July 8–11, 2001; AIAA-2001-3287.
- Buffat, Ph.; Borel, J.P. Size effect of the meeting temperature of gold particles. *Phys. Rev.* **1976**, *A 13*, 2287.
- Ivanov, G.V.; Tepper, F. *Activated Aluminum as a Stored Energy Source for Propellants. Challenges in Propellants and Combustion*, Symposium on Chemical Propulsion, Stockholm, May, 1996; Kuo, K.K., Ed.; Begell House: New York, 1997, 636–645.
- Mench, M.M.; Yeh, C.L.; Kuo, K.K. *Propellant Burning Rate Enhancement and Thermal Behaviour of Ultrafine Aluminium Powders (Alex<sup>®</sup>)*, The 29th International Annual Conference of ICT, Karlsruhe, Germany, June 30–July 3, 1998.
- Simonenko, V.N.; Zarko, V.E. *Comparative Studying the Combustion Behaviour of Composite Propellants Containing Ultrafine Aluminium*, The 30th International Annual Conference of ICT, Karlsruhe, Germany, 29 June–2 July, 1999.
- Law, C.K. A simplified theoretical model for the vapor-phase combustion of metal particles. *Combust. Sci. Technol.* **1973**, *7*, 197–212.
- Chiaverini, M.J.; Serin, N.; Johnson, D.K.; Lu, Y.C.; Kuo, K.K.; Risha, G.A. *Combustion Behavior of HTPB-Based Solid Fuels in a Hybrid Rocket Simulator*, 1996 JANNAF Propulsion Meeting, Albuquerque, Dec., 1996.
- Tepper, F.; Kaledin, L. *Nano Aluminum as a Combustion Accelerant for Kerosene in Air Breathing Systems*, 39th AIAA Aerospace Science Meeting, Reno, Jan. 10, 2001; AIAA-2001-0521.
- Reshetov, A.A.; Shneider, V.B.; Yavorovski, N.A. *Ultradispersed Aluminum's Influence on the Speed of Detonation of Hexagen*; Mendeleev All-Union Society: Chernogolovka, 1984; Vol. 1, Abstracts.
- Bedford, C.D.; Aumann, C.E.; Thompson, D.; Miller, P.J. *Effect of Metal Particle Size on the Detonation Properties of ADN/Aluminum*, TTCP WTP-4 Technical Workshop, Quebec, Canada, 1998.
- Tulis, A.J.; Sumida, W.K.; Dillon, J.; Comeyne, W.; Heberlein, D.C. Submicron aluminum particle size influence on detonation of dispersed fuel-oxidiser powders. *Arch. Combust.* **1998**, *18* (1–4), 157–164.
- Brousseau, P.; Cliff, M.D. *The Effect of Ultrafine Aluminum Powder on the Detonation Properties of Various Explosives*, The 32th International Annual Conference of ICT, Karlsruhe, Germany, July 3–6, 2001.
- Baschung, B.; Grune, D.; Licht, H.H.; Samirant, M. *Combustion Phenomena of a Solid Propellant Based on Aluminum Powder*, 5th International Symposium on Special Topics in Chemical Propulsion (5-ISICP), Stresa, Italy, June 19–22, 2000.
- Ivanov, G.V.; Lerner, M.I.; Tepper, F. *Intermetallic Alloy Formation from Nanophase Metal Powders Produced by Electro-Exploding Wires*; World Powder Metallurgy Congress: Washington, DC, June, 1996.
- Eifert, H.; Gunther, B.; Konig, T.; Meisel, R.L.; Winter, G. *CVR Production and Sinter Characteristics of Tantalum Nano-Powders*, Int. Conf. On Tungsten, Refractory Metals and Alloys, Orlando, FL, Nov. 16–19, 1997.
- Bourell, D.L.; Kaysser, W.A. Nanocrystalline iron sintering behavior and microstructured development. *Metall. Mater. Trans., A* **1994**, *25*, 677–685.
- Perez, R.J.; Huang, B.; Sharif, A.A.; Lavernia, E.J. Thermal stability of cryomilled Fe–10 wt.% Al. In *Synthesis and Processing of Nanocrystalline Powder*; Bourell, D.L., Ed.; The Minerals, Metals & Materials Society (TMS): Warrendale, PA, 1996; 273–280.
- Eastman, J.A.; Choi, U.S.; Li, S.; Thompson, L.J.; Lee, S. Enhanced thermal conductivity through the development of nanofluids. *Mater. Res. Soc. Symp. Proc.* **1997**, *457*, 3–11.
- Elghanian, R.; Storhoff, J.J.; Mucic, R.C.; Letsinger, R.L.; Mirkin, C.A. Selective colorimetric detection of polynucleotides based on the distance-dependent optical properties of gold nanoparticles. *Science* **1997**, *277*, 1078–1081.
- Tarasov, S.; Kolubaev, A.; Belyaev, S.; Lerner, M.; Tepper, F. Study of friction reduction by nanocopper additives to motor oil. *Wear* **2002**, *252*, 63–69.

# Metallic Nanopowders: Rocket Propulsion

Leonid Kaledin

Frederick Tepper

Argonide Corporation, Sanford, Florida, U.S.A.

## INTRODUCTION

Active metal powders are extensively used as fuels in most solid rocket propellants because of the high energy produced during their combustion. The specific impulse ( $I_{sp}$ ) of the rocket engine is proportional to  $(T_c/M)^{1/2}$ , where  $T_c$  is chamber temperature and  $M$  is molecular weight of combustion products. Thus the best propellants are those that produce the highest combustion temperature and the smallest possible molecular weight of the combustion products. Therefore the best oxidizers are fluorine and oxygen and the best fuels are lithium, beryllium, boron, aluminum, and magnesium. Lithium is extremely reactive and beryllium is extremely toxic so these are impractical in rocket applications. That leaves boron, aluminum, and magnesium powders as primary candidates.

Aluminum is a major ingredient in solid rocket fuels, often combined in a rubbery binder along with particles of oxidizer. When burning aluminum in solid propellants, the energy utilized can be diminished because the droplets agglomerate, producing larger droplets and slower combustion that can occur too late (after the nozzle) to be effective. The agglomerates, although partially oxidized, often slag up on the internal surfaces of the engine, reducing combustion efficiency and weighing down the vehicle.

As with solid propellants, adding aluminum to liquid fuels would also provide a theoretical advantage in higher volumetric energy density, but the metal must be uniformly dispersed and remain so in the hydrocarbon. As with solid propellants, aluminum combustion must be rapid enough so that it is consumed within the rocket engine. The most effective means of achieving complete combustion is to use powders with particle sizes at least an order of magnitude or two smaller than the metal powder ordinarily used in solid propellants. This entry focuses on Alex<sup>®</sup> nanosize aluminum particles manufactured by the electroexplosion of metal wire (“EEW”) and its use in liquid and solid rocket propellants.

## BACKGROUND

### Metal Powders for Solid Rocket Engines

Boron has been considered for many years as a candidate solid rocket fuel as it has a high energy content on both a gravimetric ( $I_{sp}$ ) and volumetric (density  $I_{sp}$ ) basis. In practice it has been difficult to realize these advantages as the combustion is severely hindered by a layer of oxide layer ( $B_2O_3$ ) on the particle surface and boron's vapor pressure is too low to escape the droplet, limiting the gas-phase oxidation to a much slower heterogeneous surface reaction.<sup>[1-3]</sup>

Aluminum has always been recognized as a highly energetic reactant for solid rocket fuels and one that can be more practically applied than boron. Because its specific gravity is high ( $2.7\text{ g/cm}^3$ ) relative to organic fuels, it is particularly advantageous for increasing density specific impulse, thereby reducing the size and therefore the weight of the rocket. It is generally used with ammonium perchlorate (AP) as a solid oxidizer and the two solid phases are held together with a rubber base binder such as hydroxy-terminated polybutadiene (HTPB) resin. Aluminum and its oxides are non-toxic and non-polluting. While AP has been the oxidizer of choice, it is a groundwater pollutant and it also produces large quantities of hydrogen chloride in rocket exhaust. Newer and more energetic oxidizers such as ammonium dinitramide (ADN) are being considered, primarily because they do not produce halogens in the exhaust. Also, there are efforts to replace HTPB with more energetic binders such as glycidyl azide polymer (GAP).

### Metal Powders for Liquid Rocket Engines

When burning aluminum in solid propellants, the delivered performance is affected because it agglomerates while molten. Duterque<sup>[4]</sup> collected the ash of aluminum from a solid propellant burn and found that it contained a significant amount of unburned aluminum. Despite this deficiency, aluminum is quite attractive



and it is used widely in solid propellants, particularly as the aluminum oxide particle reduces or suppresses combustion instability by damping of combustion waves.<sup>[5]</sup>

Dispersing metal particles as a gel in liquid propellants have been studied analytically and experimentally for more than 69 years<sup>[6]</sup> because of the higher specific impulse afforded by adding active metals such as aluminum. NASA<sup>[7-13]</sup> studied its use into gelled RP-1 (kerosene) for bi-propellant liquid propellant systems. It has also been considered as an additive to liquid hydrogen<sup>[14]</sup> because it would thicken the hydrogen, increasing safety in the event of leakage. Palaszewski and Rapp<sup>[11]</sup> suggest that given the suitable rheological tailoring, metallized propellants offer tremendous safety advantages. Design studies conducted for NASA missions show that aluminized gelled RP-1 with liquid oxygen can deliver rocket engine efficiencies that are comparable to that of traditional liquid propellants. Palaszewski and Rapp<sup>[11]</sup> discuss how using O<sub>2</sub>/RP-1/Al gel propellants as a replacement for the liquid rocket booster in the space shuttle boosters results in shorter boosters for the same payload size due to the increased propellant density. This in turn has the potential to deliver a higher payload mass over its solid counterpart. Fig. 1 shows the volumetric energy density calculated using the Propellant Evaluation Program (PEP) code<sup>[15]</sup> for aluminized RP-1 and ethanol fluids and compares these two fuels with nitrogen tetroxide/hydrazine, a highly energetic bi-propellant but one that is toxic and environmentally unfriendly. The computed energy available increases consistently with increasing aluminum content.

Unfortunately, conventional aluminum powder, when burning in liquid hydrocarbon fuel, also

agglomerates as in the case of solid propellants, reducing delivered specific impulse ( $I_{sp}$ ). Wong and Turns<sup>[16]</sup> noted significant Al agglomeration in burning JP-10 resulting in inefficient combustion. And as in the case of solid propellant engines using aluminum, this agglomeration would result in unburned combustion products deposited on engine walls.

### Metal Powders in Liquid Monopropellants

In the late 1950s and early 1960s, Atlantic Research studied the combustion of Arcogel, a gel of aluminum powder, ammonium perchlorate with dioctyl adipate as a liquid carrier. They found that such mixtures had adequate (6 months) shelf life and good stability under high acceleration loading and vibration. Arcogel was extensively characterized and found to be non-detonable and insensitive to ignition. They also conducted small motor tests. However, they found the viscosity to be unacceptably high at low temperatures ( $-55^{\circ}\text{C}$ ). In the early 1990s, this work was continued,<sup>[17]</sup> evaluating nitrated ester/AP/Al, hydrogen peroxide/Al, and HN/water/Al gels. All were found to have limited promise because of their sensitivity to premature ignition or detonation.

### Environmental Issues

Regulatory environmental requirements are forcing new choices for rocket propellant ingredients. For instance, ammonium perchlorate (AP), the oxidizer of choice for solid propellants, is falling out of favor because hydrogen chloride is a significant combustion

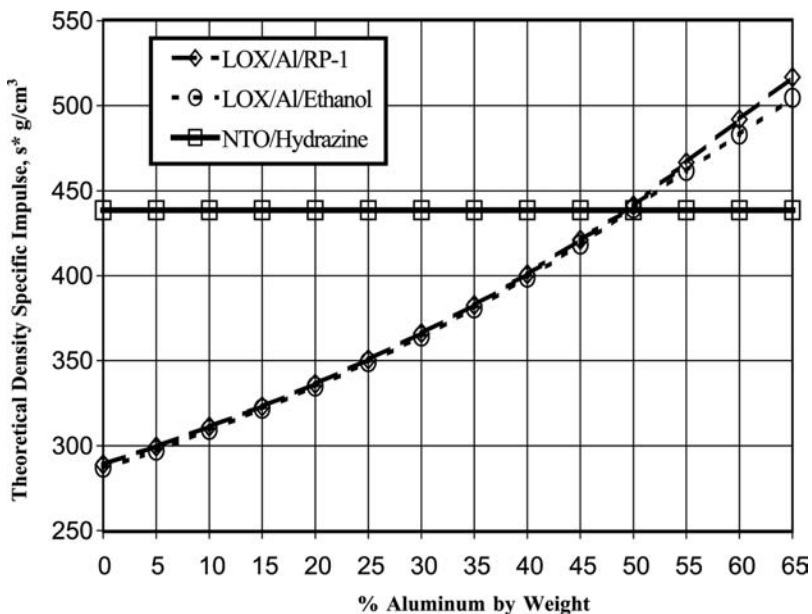


Fig. 1 Theoretical density specific impulse (vacuum, 100:1 expansion ratio) of aluminized bi-propellants.

product. Toxicological constraints are also affecting the choice of liquid propellants. For instance, hydrazine, which is extensively used, is very toxic, as is nitrogen tetroxide. Threshold limit value (TLV) concentrations for hydrazine are fractions of a part per million, often below the limits of detection (LOD) of continuous monitoring instruments. Those working with this fluid often have to wear completely encapsulated suits. In addition to AP, there are two other inorganic oxidizers that have potential for solid propellants—ammonium nitrate (AN) and ammonium dinitramide. Another oxidizer being developed in the Netherlands is hydrazinium nitroformate (HNF).

Fluids such as ethanol<sup>[18,19]</sup> and methanol<sup>[20]</sup> are being considered as non-toxic options in bi-propellant system. Boeing<sup>[21,22]</sup> reported on the hazardous and costly operations associated with monomethyl hydrazine (MMH) and nitrogen tetroxide propellants related to the Space Shuttle Orbiter OMS/RCS system which culminated in NASA's selection of ethanol/LOX as the bi-propellant. They designed such a propellant system and projected improvements in vehicle weight, complexity, and operational cost. They believe that the design solutions are applicable to other space-based cryogenic propulsion and power generation systems. Aluminizing these non-toxic fuels could substantially enhance propellant energy density without causing any environmental or toxic concerns.

Effect utilization of aluminum's combustion energy in propellants resolves a number of problems—improved performance, particularly on a volumetric basis, and achieving that with no penalty as a pollutant or a toxin.

## NANOMETAL POWDER FUELS

Many of the difficulties related to inefficient burning of aluminum powder in solid (as well as liquid) propellants could be ameliorated if the particle size of the powder were small enough. Nanosize aluminum was first prepared in the early 1970s by Russian scientists in Siberia,<sup>[23]</sup> who formed the powder by electroexploding metal wires (EEW). The EEW method is described in a separate entry of this Encyclopedia. Most of the Russian work was focused on producing nanosize aluminum for its potential use as a metal additive for rocket propellant fuel.

Electroexploding metal wire aluminum powder (Alex<sup>®</sup>) consists of spherical particles that are fully dense and about 100 nm in size. Because they are so active, during collection they form hard agglomerates. Because these particles are potentially pyrophoric, the final step in the manufacturing process involves controlled oxidation with dry air to form a passivating layer approximately 3 nm thick. Oxygen analysis shows

the coating to be about 92–95% aluminum (between about 85% and 89% as oxide). X-ray diffraction shows the crystallites to be essentially aluminum, while the coating has been found<sup>[24]</sup> to be principally aluminum oxide, with some aluminum nitride and some aluminum oxy-nitride. The passivation step is controllable and thinner passivation layers are readily obtained, but the U.S. Department of Transportation (DOT) and International Air Transport Association (IATA) prevent air shipment of pyrophoric materials, so sufficient coverage is necessary to assure no pyrophoricity.

When ignited in air Alex<sup>®</sup> appears to have two separate ignition steps. The first occurs at lower temperatures (400–500°C) and a second where the powder burns white hot. Mench et al.<sup>[25]</sup> studied the thermal behavior of Alex<sup>®</sup> powder and compared it to micron-size aluminum. Their data show that Alex<sup>®</sup> powder has very sharp exotherms when heated in air, oxygen, or nitrogen. These occur well below the melting point (660°C) of aluminum, while 20- $\mu$ m-size aluminum does not react with oxygen or air until about 1000°C.

A coated version of nano-aluminum (L-Alex<sup>®</sup>) is based on the replacement of the oxide coating by reaction with palmitic acid to form a monomolecular layer of palmitate. This version was tested by boiling the coated Alex<sup>®</sup> in water for an hour and the resulting coating appears to protect the metal, while ordinary Alex<sup>®</sup> would have reacted within minutes. Accelerated aging testing showed<sup>[26]</sup> L-Alex<sup>®</sup> to be superior in moisture and oxidation resistance to conventional Alex<sup>®</sup>.

## Alex<sup>®</sup> as an Additive to Solid Propellants

Ivanov and Tepper<sup>[23]</sup> reported a 10- to 20-fold increase in burning rate if air-passivated Alex<sup>®</sup> was substituted for ordinary propellant grade aluminum when mixed with ammonium perchlorate powder (no binder). Sigman and co-workers<sup>[27]</sup> also reported that the burning rate of Alex<sup>®</sup> with AP (again no binder) was 10 times greater than with other micron-size aluminum powders. Chiaverini et al.<sup>[28]</sup> reported that Alex<sup>®</sup> when added to HTPB binder produced a substantial increase in the burning rate in oxygen.

The agglomeration of aluminum droplets has been studied by Simonenko and Zarko<sup>[29]</sup> who noted that there was a growth in aluminum oxide particles collected from the combustion products of a solid propellant grain as compared to that of the original particle size of the aluminum. They also noted that there was a substantial amount of aluminum left within the residual products they collected. In a separate study Glotov, Zarko, Beckstead<sup>[30]</sup> noted that the replacement of commercial aluminum by Alex<sup>®</sup> in quantities as small as 8 wt.% increases burning rate and decreases agglomerate size as well as increases

the amount of oxidation. For example, total replacement of commercial aluminum by Alex<sup>®</sup> increases combustion efficiency to 99.2% as compared to 94.28% for coarse aluminum.

There have been considerable studies and modeling of the combustion of aluminum in a solid rocket engine. The Brooks and Beckstead model<sup>[31]</sup> estimates that the life of the particle is proportional to the particle size raised to the power of  $n$  with nominal values of approximately 1.5 to 1.8.<sup>[32]</sup> The life of a 35- $\mu\text{m}$  particle is about 6 msec. Extrapolating the Brooks and Beckstead equation for the burning time of a 100-nm-size particle (Alex<sup>®</sup>) results in a lifetime of only approximately 160 and 920 nsec, respectively, for  $n = 1.8$  and  $n = 1.5$ .

Experimental observations support the very short life computed for combustion of an Alex<sup>®</sup> particle that had originated from a solid propellant. Wang et al.<sup>[33]</sup> found that when Alex particles are flash-heated to the boiling point, 2740 K, in the presence of a nitrocellulose (NC) oxidizer, the energy release occurs in  $\sim 5$  nsec even much faster than predicted by the Brooks and Beckstead model. Ivanov and Tepper<sup>[23]</sup> noted from high-speed cinematographic photographs of a burning propellant that the combustion of Alex<sup>®</sup> is complete at the burning surface, while micron-size aluminum is known to burn throughout the throat and often past the nozzle.

### Alex<sup>®</sup> as an Additive to Hybrid Propellants

The classic hybrid technology uses LOX with an HTPB grain that contains either no oxidizer, or just enough to react with the HTPB so as to be a gas generator. This creates low molecular weight organics that are forced into the engine and then react with the liquid oxidizer. The hybrid fuel technology offers a number of advantages including the ability to throttle the engine in real time, stop and start and shift from combustion with on-board oxidizers to air. Should the mission require rapid launching, then the hybrid with storable oxidizers offers advantages over cryogenic fuels. Also, the grain case is smaller and much lighter without the heavy inorganic oxidizer that is in conventional solid propellants. Hybrid solid propellants are much easier, safer, and less costly to manufacture because the oxidizer is not combined into the grain. Also, there are fewer corrosion problems as the fuel is solid. These advantages would be very useful in a rocket-based combined-cycle (RBCC) engine.<sup>[34]</sup>

Hybrid problems include the fact that the distance of the flame to the burning surface is an order of magnitude larger than with solid propellant. This makes heat transfer an order of magnitude smaller and consequently the regression rate is an order of magnitude smaller. Because the main flow is rather

**Table 1** Specific impulse of aluminized HTPB resins with liquid oxygen (LOX)

Fuel			$I_{sp}$ (vacuum) <sup>a</sup> , sec	$I_{sp}^{\text{density}}$ , sec g/cm <sup>3</sup>
Metal	Carrier	Oxidizer		
0% Al	100% HTPB	LOX	371	392
25% Al	75% HTPB	LOX	376	423
50% Al	50% HTPB	LOX	370	458
	Hydrazine	N <sub>2</sub> O <sub>4</sub>	362	442

<sup>a</sup>At chamber pressure of 6.895 MPa (1000 psia) and expansion ratio of 100:1.

stratified, the mixing process and therefore the combustion can be incomplete. To achieve complete mixing and combustion of oxidizer and fuel, an aft combustion chamber is added to the hybrid motor.

However, many of these problems can be ameliorated by adding Alex<sup>®</sup>. Chiaverini et al.<sup>[28]</sup> added 10 wt.% Alex<sup>®</sup> to an HTPB slab and found an increase of 70% in the regression rate. They also noted much smoother burning in the case of Alex<sup>®</sup>-loaded HTPB. Table 1 shows how using Alex<sup>®</sup> increases the specific impulse and density-specific impulse of a hybrid and compares it to NTO/Hydrazine.

### Alex<sup>®</sup> as an Additive to Liquid Propellants

Palaszewski and Powell,<sup>[35]</sup> in some theoretical computations, demonstrated that 0-, 5-, and 55-wt.% aluminum loaded into RP-1 gel propellants provide benefits over neat RP-1. The 0-wt.% loading is attractive when safety over traditional RP-1 (ungelled) is desired and the 5-wt.% loading gave the maximum theoretical specific impulse. The 55-wt.% loading was chosen based on the fact that a liquid-based booster with O<sub>2</sub>/RP-1/Al could conform to the volume constraints of the current solid rocket booster even with potential two-phase flow losses taken into account. Palaszewski and Zakany<sup>[7,9]</sup> did some combustion experiments with these three mixes using micron-size aluminum for the 5% and 55% loadings. While relatively good performance was obtained, the engine efficiencies were not sufficient for NASA missions.

### Mechanisms of Combustion of Gelled Aluminized Propellants

The combustion of a heterogeneous two-phase gel of liquid fuel and aluminum particles is essentially a two-step process. The first step is the combustion of the liquid droplet, which involves boiling of the liquid. A vapor blanket of fuel exists around the two-phase droplet and the flame zone is at some distance beyond

the liquid–gas interface, protecting the aluminum from oxidation. At the temperatures and pressures that exist in the rocket engine, the aluminum will be molten. Aluminum combustion would be delayed until the hydrocarbon is burned away, and during that interval the micron-size aluminum droplets could coalesce. The smaller the hydrocarbon droplet the less time there is for the aluminum to agglomerate. The second step in the process involves the combustion of the now dry aluminum droplet. The mechanisms associated with this second step would be very similar to that occurring had the particles been generated from a solid propellant grain such as Al/organic binder/solid inorganic oxidizer. A nanosize aluminum particle would therefore be expected to have a life less than a microsecond, several orders of magnitude shorter than if micron-size aluminum had been dispersed into the kerosene.

### Development and Formulation of Aluminized Gels

The authors were sponsored by NASA to evaluate the benefits of using Alex<sup>®</sup> in lieu of micron-size aluminum powder as a dispersed phase in RP-1.<sup>[36]</sup> Wetting and gelling agents were used as additives to aid in homogenization and providing dynamic stability. Fumed silica (Cab-O-Sil<sup>®</sup> grade M5) was used as a gellant and the stability of the gel was determined by centrifugation for 1 hr at 1300 rpm. It was found that when Alex<sup>®</sup> loading was greater than about 25 wt.%, fumed silica was unnecessary as the powder acts as a pseudo-gellant. A 30 wt.% Alex<sup>®</sup> in RP-1 gel was found to be dynamically stable when stored for 2 years at room temperature. A non-anionic surfactant, specifically

Tween-85 (polyoxyethylene sorbitan trioleate), was used because it was more effective as a wetting and dispersing agent for the aluminum particles than anionic and cationic surfactants.

The viscosity of the gelled formulations was then measured so as to determine the practicality of pumping the mixture and spraying it into a combustion chamber. Spray characteristics of a given gas–liquid injector are a function of the liquid surface tension and the gas and liquid velocities, densities, and viscosities.<sup>[37]</sup> Liquid propellants typically have viscosities near 1 mPa sec and have Newtonian-type flow behavior.

Green, Rapp, Roncace<sup>[37]</sup> reported absolute viscosity value of 1.89 mPa sec for RP-1. This value remains constant in a wide range of applied shear rates from 1 to 100,000 sec<sup>-1</sup>. Gelled propellants typically have viscosity in the range of 20 to 50 mPa sec at the shear rates in the range of 10<sup>5</sup> to 10<sup>6</sup> sec<sup>-1</sup> that are typically encountered in engine injectors.<sup>[38]</sup> This is within the range of the pumping systems currently used in rocket engines. As the viscosity of a gelled fuel is a function of variables other than temperature (e.g., shear rate and temporal rheological effects such as thixotropy and gel relaxation time), the rheology is non-Newtonian, and viscometry is reported as “apparent” viscosity at a specific shear rate.

Fig. 2 shows the viscosity of Alexgel fluids and compares them with the viscosity measurements of Rapp<sup>[39]</sup> for micron-size aluminum/fumed silica/RP-1 gel permitting extrapolation to strains characteristic of the injector. Note the reduced viscosity when a surfactant is added to a 30% Alex<sup>®</sup>/RP-1. A power law rheological model ( $\tau = K \cdot \dot{\gamma}^n$ , where  $\tau$  is a shear stress,  $\dot{\gamma}$  is a shear rate,  $n$  is effective flow behavior index, and  $K$  is a constant of effective consistency) can be applied to

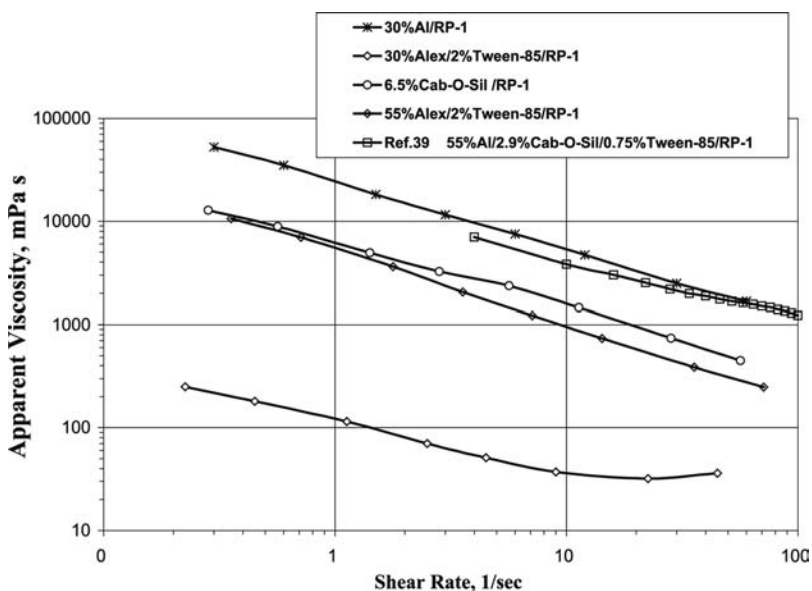


Fig. 2 Apparent viscosity of aluminized fuels.

model flow behavior. In general, power law is applicable to model flow behavior of pseudo-plastic fluids with zero yield point. Gelled fuels evaluated in Refs.<sup>[7,9,39]</sup>, and<sup>[40]</sup> have very small yield values ranging from 0.03 to 22 Pa. These yield points are greatly exceeded in injector fluid flow, so their contributions are negligible. By extrapolation of viscosity data to high shear rates using a power law rheological model to the large shear rates encountered in engine injectors, the gels have viscosity near kerosene and therefore within the capability of the pumping systems currently used in rocket engines.

### Ignition Delay Measurements

Fig. 3 is a stainless steel combustion bomb<sup>[41]</sup> used to measure ignition delay of kerosene and its aluminized versions. The injection port is water cooled to keep the gel (or neat RP-1) at ambient temperature. Fuel temperatures are monitored by a thermocouple at the nozzle close to the tip. The bomb, containing an oxidizing gas of known pressure, is preheated to a defined temperature. Using a piston powered by high-pressure argon, approximately  $0.3\text{ cm}^3$  of fuel is injected into the bomb and it auto-ignites at temperatures above about  $400^\circ\text{C}$ . An internal transducer measures pressure rise due to combustion. The time is measured from the first movement of the piston forcing the fluid into the chamber until there is a

rapid rise of pressure. Generally, the pressure rise due to combustion is 2–4 times the original pressure, depending upon whether the gas is air or oxygen. The inner length of the bomb is 10 cm, which is the maximum length of the spray pattern. The transit time of the spray to the farthest end of the internal space is approximately 25 msec. At lower temperatures where reaction was slow, the spray would deposit on the inner walls, and the ignition delay extended out to hundreds of milliseconds. This appears to be characteristic of the time for auto-ignition of the gel as a film on the wall of the chamber rather than during the spray interval.

### Combustion of Metallized RP-1

Fig. 4 shows chemical ignition delay times of neat RP-1, gelled RP-1, and aluminized gelled RP-1 in hot oxygen<sup>[40]</sup> at a fixed pressure at 0.8 MPa and at four different test temperatures ( $410^\circ\text{C}$ ,  $460^\circ\text{C}$ ,  $520^\circ\text{C}$ , and  $580^\circ\text{C}$ ). Gelled RP-1 was used as a control rather than neat RP-1, to attain equivalent viscosity and permit comparison of the combustion of control vs. the aluminized fluids under similar spray patterns as predicted by the power law model. The gelled RP-1 (6.5-wt.% silica) had a viscosity at high shear rates equivalent to 30% Alex<sup>®</sup>/RP-1. The data in Fig. 4 indicate that the 30-wt.% Alexgel ignites faster than gelled RP-1, but about equivalent to that of pure kerosene.

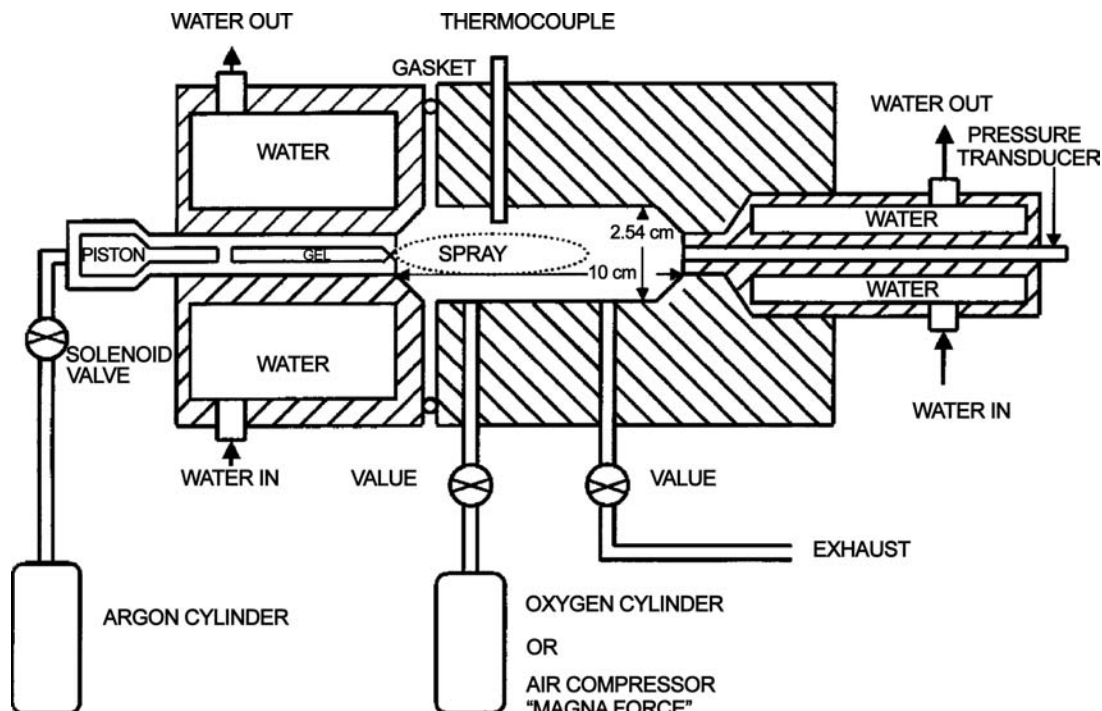


Fig. 3 Device for measuring ignition delay times of gels.

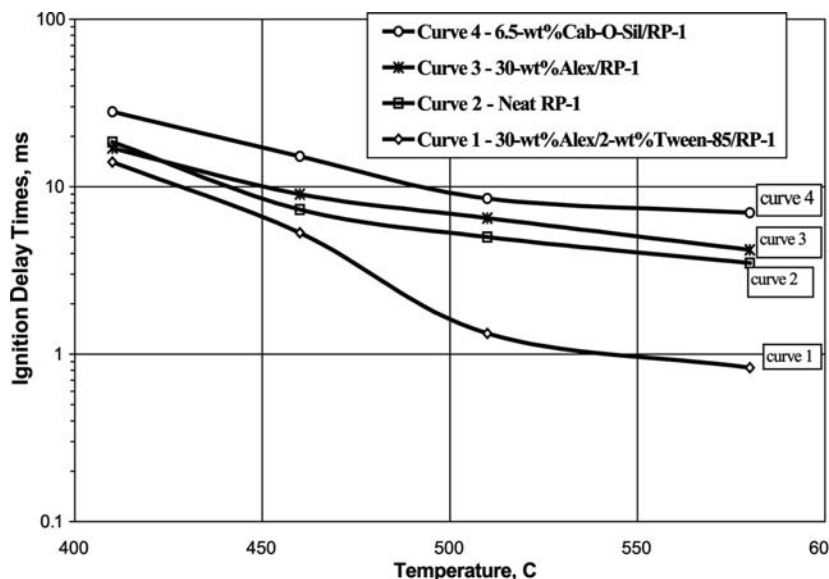


Fig. 4 Average ignition delay in hot oxygen vs. temperature.

However, a surfactant when added to the 30-wt.% Alexgel reduces ignition delay below that of pure RP-1 kerosene (compare curve 1 and curve 2), demonstrating that Alex<sup>®</sup> acts as combustion accelerant for kerosene. Estimations based on the power law model indicate that apparent viscosity of this gel is comparable to that of RP-1 at injector shear rates ( $6.3 \cdot 10^4 \text{ sec}^{-1}$ ). Gels produced from 5- $\mu\text{m}$  aluminum did not show any reduction in ignition delay.

Similar experiments were repeated except in air<sup>[40]</sup> rather than oxygen, and at an initial air pressure of 1.1 MPa. Four different fuels were examined: gelled RP-1, 25-wt.% Alexgel, neat RP-1, and 30-wt.% L-Alex<sup>®</sup>/2-wt.% Tween-85/RP-1 fuel. Tests were performed at four different temperatures (430°C, 550°C,

580°C, and 600°C). The data in Fig. 5 indicate that 25-wt.% Alexgel (curve 3) ignites faster by approximately 30% than gelled RP-1 (curve 4). Curve 1 shows that the L-Alex<sup>®</sup> version ignites faster by factor of 2–3 than neat RP-1 (curve 2). As it was noted earlier, these two fluids have similar fluidity at high shear rates, confirming that L-Alex<sup>®</sup> is even more superior as a combustion accelerant than Alex<sup>®</sup> in an air environment.

### “Combustion” in Nitrogen

Alex<sup>®</sup> is known to react rapidly with gaseous nitrogen and this is supported by the DTA data of Mench

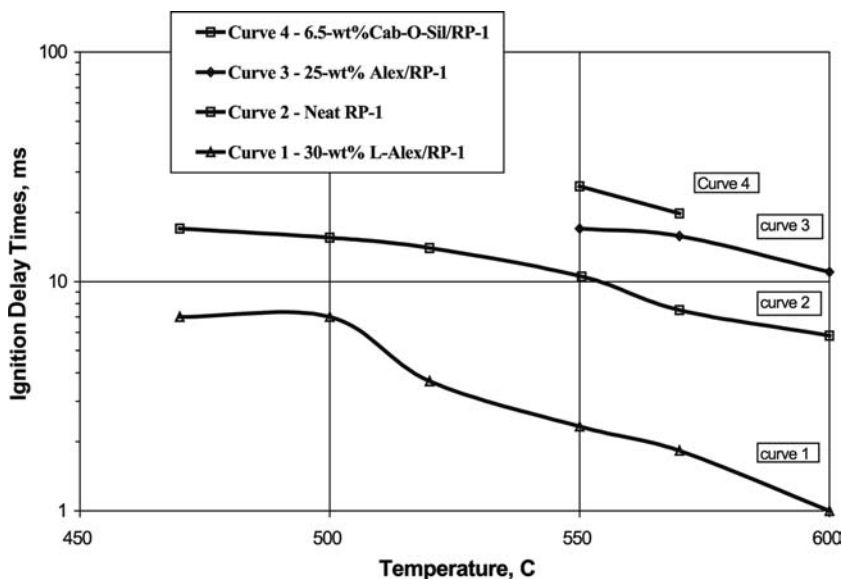


Fig. 5 Average ignition delay of different fuels in air vs. temperature.



et al.<sup>[25]</sup> This characteristic would be of benefit in air-breathing engines, permitting incipient combustion to occur and support these engines when they are starved for air. Alex<sup>®</sup>/RP-1 gels (55-wt.% Al) were sprayed into pure nitrogen at 750°C showing incipient combustion, but substantially slower than in air or oxygen. Nevertheless, the energy generated by this reaction can contribute to heat generation, while minimizing the opportunity for flame-out in air-breathing engines such as RBCC systems.

### Small Rocket Engine Tests

The combustion performance of Alexgels was measured in a small rocket engine by Mordosky et al.<sup>[42]</sup> The objective was to measure flame temperature, specific impulse, and  $c^*$  combustion efficiency (defined as  $P_c A_t / dm / dt$ ).<sup>[43]</sup>

In order to compare rocket test results obtained from different test engines, it is beneficial to have exactly the same fuel and oxidizer compositions as well as approximately the same operational conditions. The small rocket engine constructed by Mordosky et al.<sup>[42]</sup> was 30.5 cm long with an internal diameter of 12.0 cm. Combustion of Alexgels was done in gaseous oxygen. The aluminum loadings (Table 2) were the same, but there were some variations in the surfactant and gellant. Table 3 shows average values of adjusted  $c^*$  efficiency of the Penn State fuels as compared to the work of Palaszewski and Zakany.<sup>[7,9]</sup> They show that:

- i. The 5-wt.% Alex<sup>®</sup>/RP-1 gel burns more efficiently as compared to 5-wt.%Al/RP-1 gel using coarse aluminum.
- ii. The 55-wt.% Alex<sup>®</sup>/RP-1 gel burns more efficiently as compared to 55-wt.%Al/RP-1 gel.
- iii. The 5-wt.% Alex<sup>®</sup>/RP-1 gel burns with the same efficiency as neat RP-1, although the viscosity of the neat RP-1 is very much lower than that of gelled RP-1 or Alex<sup>®</sup>-loaded gels.

These data show that the combustion of the nano aluminum overcomes the deficiency of a larger droplet spray pattern associated with higher viscosity of the Alexgels. They also measured the aluminum oxide that is produced during combustion and found it to be submicron in size.

## APPLICATIONS OF ALEXGELS

### Hydrocarbon-Based Liquid Rocket Engines

Combustion bomb testing reinforced by small rocket engine tests shows that Alex<sup>®</sup> nano aluminum powder provides improvement in volumetric energy density over pure kerosene while micron-size aluminum burns inefficiently when dispersed in hydrocarbon. Another benefit is the reduction of metal slagging on the walls of the rocket engine.

### Hydrocarbon-Based RBCC Systems

Cryogenic hydrogen is being considered for RBCC engines. However, maintaining this cryogenic fuel over long duration flights, such as its use for re-entry, is problematic. Should hydrocarbon fuel be considered for RBCC engines, then adding Alex<sup>®</sup> would provide the same potential benefits as its use in hypersonics, i.e., flame stability and increased output in the air augmented mode, while providing increases in volumetric  $I_{sp}$  in the rocket mode as well.

### Pulse Detonation Engines

Another possible use for aluminizing kerosene is in pulse detonation engines (PDEs). The detonation of kerosene in air has yet to be demonstrated. The potential for reducing ignition delay into the submillisecond regime by adding Alex<sup>®</sup> is almost certain. Further reductions of particle size, enhanced by finer sprays as well as organic layered aluminum such as the

**Table 2** Compositions of the RP-1/Alex<sup>®</sup> gel propellants tested at Penn State

Metal loading weight percentage	Liquid fuel (RP-1)	Metal powder (Alex)	Gellant (SiO <sub>2</sub> )	Surfactant (Tween-85)
0 wt.%	95%	0%	5%	0%
5 wt.%	90%	5%	5%	0%
10 wt.%	86%	10%	4%	0%
30 wt.%	68.2%	30%	1.3%	0.5%
55 wt.%	43.3%	55%	0.4%	1.3%

**Table 3** Average values of normalized  $c_{avg}^*$  efficiency of NASA gels to the Penn State gels

Gel formulation	$c_{avg}^*$ (Alex <sup>®</sup> )	$c_{avg}^*$ (coarse Al, adjusted)	$c^*$ Ratio of nano/coarse aluminum [ $c_{avg}^*$ (Alex <sup>®</sup> )/ $c_{avg}^*$ (Al, adjusted)]
Neat RP-1	–	88.9 ± 1.8	–
5 wt.%	88.3 ± 1.7	78.1 ± 2.4	1.132 ± 0.036
55 wt.%	83.0 ± 2.2	77.8 ± 2.4	1.07 ± 0.04

L-Alex<sup>®</sup>, could result in overcoming the difficulty in detonating kerosene.

## Liquid Hydrogen Engines

Adding aluminum to cryogenic hydrogen to form gels has been suggested by Starkovich, Adams, and Palaszewski<sup>[14]</sup> as a means to increase volumetric energy density and at the same time increase the containment of a liquid hydrogen leak. Such benefits could also be useful for a liquid hydrogen RBCC engine, where Alex<sup>®</sup> could also serve to increase flame stability during the air cycle.

## CONCLUSION

Gels of Alex<sup>®</sup> in RP-1 are dynamically stable at least over the short term and matched the viscosity of coarse aluminum gelled into RP-1 (Fig. 2). Ignition delays of nano-aluminized gels were always shorter than gelled RP-1 (equivalent viscosity) as well as neat RP-1, which has lower viscosity. Alex<sup>®</sup> acts as a combustion accelerant for RP-1, and probably other kerosenes as well. An organic coated version of Alex<sup>®</sup> (L-Alex<sup>®</sup>) was developed and found to have ignition delays in air lower than RP-1 by a factor of 2–3. These findings are relevant to advanced rocket combined cycle engines, hypersonic (scramjet) engines, and perhaps pulse detonation engines. Coarse aluminum is not a combustion accelerant for RP-1 in oxygen.

Rocket engine testing at Penn State showed that the 5-wt.% and 55-wt.% Alexgels burn *substantially* more efficiently than coarse aluminum. The 5-wt.% Alex<sup>®</sup>/RP-1 gel burns with the same efficiency as neat RP-1, although the viscosity of the neat RP-1 is very much lower than that of gelled RP-1 or micron-size aluminized gels. Apparently, the kinetics of combustion of the nano aluminum overcomes the larger droplets of the spray caused by higher viscosity.

The overall conclusion is that loading Alex<sup>®</sup> into RP-1 improved its combustion kinetics and efficiency as compared to neat RP-1, and better than published values for micron-size aluminum gels. Moreover,

Alex<sup>®</sup> additions would result in improving the combustion of kerosene in air-breathing engines.

## ACKNOWLEDGMENTS

We appreciate the support of NASA Glenn Research Center under Contract No. NAS 3-99117, under the guidance of Brian Palaszewski, technical representative.

## REFERENCES

- Spalding, M.J.; Krier, H.; Burton, R.L. Chemical kinetics of boron combustion in high pressure Ar/F/O<sub>2</sub> mixtures, 34th AIAA/ASME/SAE/ASEE Joint Propulsion Conference & Exhibit, Cleveland, USA, July 13–15, 1998. AIAA-98-3823.
- Ulas, A.; Kuo, K.K.; Gotzmer, C. Effect of fluorine-containing species on ignition and combustion of boron particles: experiment and theory. In *Combustion of Energetic Materials*; Kuo, K.K., DeLuca, L.T., Eds.; Begell House: New York, 2002; 453–463.
- Vigot, C.; Cochet, A.; Guin, C. Combustion behavior of boron-based solid propellants in a ducted rocket. In *Combustion of Boron-Based Solid Propellants and Solid Fuels*; Kuo, K.K., Ed.; CRC: Boca Raton, 1993; 386–401.
- Duterque, J. Experimental studies of aluminum agglomeration in solid rocket motors. In *Challenges in Propellants and Combustion*; Kuo, K.K., Ed.; Begell House: New York, 1997; 693–705.
- Price, E.W. Solid rocket combustion instability. An American historical account. Nonsteady burning of combustion stability of solid propellants. *Prog. Astronaut.* **1992**, *143*, 1–16.
- Sanger, E. *Raketenflugtechnik*; R. Oldenburg: Berlin, Germany, 1933.
- Palaszewski, B.; Zakany, J.S. Metallized Gelled Propellants: Oxygen/RP-1/Aluminum Rocket Combustion Experiments, 31st AIAA/ASME/SAE/ASEE Joint Propulsion Conference and Exhibit, San Diego, CA, July 10–12, 1995. AIAA 95-2435.
- Rapp, D.C.; Zurawski, R.L. Characterization of Aluminum/RP-1 Gel Propellant Properties, 24th AIAA/ASME/SAE/ASEE Joint Propulsion Conference, Boston, MA, July 11–13, 1988. AIAA-88-2821.

9. Palaszewski, B.; Zakany, J.S. Metallized gelled propellants: Oxygen/RP-1/Aluminum rocket heat transfer and combustion measurements, 32nd AIAA/ASME/SAE/ASEE Joint Propulsion Conference, Lake Buena Vista, FL, July 1–3, 1996. AIAA-96-2622.
10. Galecki, D.L. Ignition and Combustion of Metallized Propellants, AIAA Propulsion Conf., Monterey, CL, July 10–12, 1989. AIAA-89-2883.
11. Palaszewski, B.; Rapp, D. Design issues for propulsion systems using metallized propellants, AIAA/NASA/OAI Conference on Advanced SEI Technologies, Cleveland, Sept 1991. AIAA-91-3484.
12. Palaszewski, B. Metallized gelled propellants experiences and lessons learned: Oxygen/RP-1/Aluminum Rocket Engine Testing, JANNAF/CPIA Gelled Propulsion Technology Symposium, Huntsville, AL, Sept 19–21, 1995.
13. Palaszewski, B.A. *Upper Stages Using Liquid Propulsion and Metallized Propellants*, NASA Tech. Paper 3191, 1992.
14. Starkovich, J.; Adams, S.; Palaszewski, B. Nanoparticulate gellants for metallized gelled liquid hydrogen with aluminum, NASA Tech. Memo 107280, 32nd AIAA/ASME/SAE/ASEE Joint Propulsion Conference, Lake Buena Vista, FL, July 1–3, 1996. AIAA-96-3234.
15. Cruise, D.R. *Theoretical Computations of Equilibrium Composition, Thermodynamic Properties, and Performance Characteristics of Propellant System*; Naval Weapon Center: Chana Lake, CA, 1991.
16. Wong, S.C.; Turns, S.R. Disruptive burning of aluminum/carbon slurry droplets. *Combust. Sci. Technol.* **1989**, *66*, 75–92.
17. Nieder, E.G.; Harrod, C.E.; Rapp, D.C.; Palaszewski, B.A. *Metallized Gelled Monopropellants*, NASA Tech. Memorandum 105418, April 1995.
18. Woodward, R.D.; Miller, K.L.; Bazarov, V.G.; Guerin, G.F.; Pal, S.; Santoro, R.J. Injector Research for Shuttle OMS Upgrade Using LOX/Ethanol Propellants, 34th AIAA Joint Propulsion Conference, Cleveland, OH, July 13–15, 1998. AIAA-98-3816.
19. Hurlbert, E.; Applewhite, J.; Nguyen, T.; Reed, B.; Baojiong, Z.; Yue, W. Nontoxic orbital maneuvering and reaction control systems for reusable spacecraft. *J. Propuls. Power* **1998**, *14* (5), 676–687.
20. Pellaccio, D.G.; Chew, G.; Lowther, S.E.; Zubrin, R.M. Low Cost, Methanol Fueled Rocket Propulsion Technology, AIAA/ASME/SAE/ASEE Joint Propulsion Conference, Cleveland, OH, July 12–15, 1998. AIAA-98-3209.
21. Lak, T.; Rodriguez, H.; Chandler, F.O.; Jenkins, D. Non-Toxic Cryogenic Storage for OMS/RCS Shuttle Upgrade, 34th AIAA/ASME/SAE/ASEE Joint Propulsion Conference, Cleveland, OH, July 12–15, 1998. AIAA-98-3818.
22. Rodriguez, H.; Cakiraga, T.; Olsen, A.; Rehagen, R. Non-Toxic System Architecture for Space Shuttle Applications, 34th AIAA/ASME/SAE/ASEE Joint Propulsion Conference, Cleveland, OH, July 12–15, 1998. AIAA-98-3821.
23. Ivanov, G.V.; Tepper, F. Activated aluminum as a stored energy source for propellants. In *Challenges in Propellants and Combustion*; Kuo, K.K., Ed.; Begell House: New York, 1997; 636–645.
24. Katz, J.; Tepper, F.; Ivanov, G.V.; Lerner, M.I.; Davidovich, V.I. 34th AIAA/ASME/SAE/ASEE Joint Propulsion Conference, Cleveland, OH, July 12–15, 1998.
25. Mench, M.M.; Kuo, K.K.; Yeh, C.L.; Lu, Y.C. Comparison of thermal behavior of regular and ultra-fine aluminum powders (Alex<sup>®</sup>) made from plasma explosion process. *Combust. Sci. Technol.* **1998**, *135*, 269–292.
26. Cliff, M.; Tepper, F.; Lisetsky, V. Ageing Characteristics of Alex<sup>®</sup> Nanosize Aluminum, 37th AIAA Joint Propulsion Meeting, Salt Lake City, July 8–11, 2001. AIAA-2001-3287.
27. Sigman, R.K.; Zachary, E.K.; Chakravarthy, S.R.; Freeman, J.M.; Price, E.W. Preliminary Characterization of the Combustion Behavior of Alex<sup>®</sup> in Solid Propellants, JANNAF Propulsion Meeting, West Palm Beach, FL, Dec 1997.
28. Chiaverini, M.J.; Serin, N.; Johnson, D.K.; Lu, Y.C.; Kuo, K.K. Instantaneous regression behavior of HTPB solid fuels burning with GOX in a simulated hybrid rocket motor. In *Challenges in Propellants and Combustion*; Kuo, K.K., Ed.; Begell House: New York, 1997; 719–733.
29. Simonenko, V.N.; Zarko, V.E. Comparative studying the combustion behavior of composite propellants containing ultra fine aluminum. In *Energetic Materials. Production, Processing and Characterization*, 30th International Annual Conference of ICT, Karlsruhe, Germany, June, 2000; 130 pp.
30. Glotov, O.G.; Zarko, V.E.; Beckstead, M.W. Agglomerate and oxide particles generated in combustion of Alex<sup>®</sup> containing solid propellants. In *Energetic Materials. Production, Processing and Characterization*, 31th International Annual Conference of ICT, Karlsruhe, Germany, June 1999; 21 pp.
31. Brooks, K.P.; Beckstead, M.K. The Dynamics of Aluminum Combustion, 30th JANNAF Combustion Subcommittee Meeting, Nov 1993; 337–356.
32. Beckstead, M.W.; Newbold, B.R.; Waroquet, C. A Summary of Aluminum Combustion, 50th JANNAF Propulsion Meeting, 2001, 201–220, Vol. 1.
33. Wang, S.; Yang, Ya.; Sun, Zh.; Dlott, D.D. Fast spectroscopy of energy release in nanometric explosives. *Chem. Phys. Lett.* **2003**, *368* (1), 183–188.
34. Hueter, U. Creating an airline to the stars. *Aerosp. Am.* April **1999**, 40–44.
35. Palaszewski, B.; Powell, R. Launch Vehicle Propulsion Using Metallized Propellants, AIAA 91-2050, 27th AIAA/ASME/SAE/ASEE Joint Propulsion Conference and Exhibit, Sacramento, CA, June 24–27, 1991.
36. Tepper, F.; Kaledin, L.A. Combustion Characteristics of Kerosene Containing Alex<sup>®</sup> Nano-Aluminum, Fifth International Symposium on Special Topics in Chemical Propulsion: Combustion of Energetic Materials, Stresa, Italy, June 18–22, 2000.

37. Green, J.M.; Rapp, D.C.; Roncace, J. Flow Visualization of a Rocket Injector Spray Using Gelled Propellant Stimulants, 27th AIAA/SAE/ASME/ASEE Joint Propulsion Conference, Sacramento, CA, June 24–27, 1991. AIAA-91-2198.
38. Thompson, D.M. Pressure Drop Model for Gel Propellants in Cylindrical Injectors Using Viscosity as a Parameter, JANNAF Propulsion Meeting, Cleveland, OH, July 15–17, 1998.
39. Rapp, D.C. Rheology of Aluminum/RP-1 Metallized Propellants Employing Gelling and Surface Active Agents. M.Sc. Thesis. Case Western Reserve University, 1989.
40. Tepper, F.; Kaledin, L.A. Combustion characteristics of kerosene containing Alex<sup>®</sup> nano-aluminum. In *Combustion of Energetic Materials*; Kuo, K.K., DeLuca, L.T., Eds.; Begell House: New York, 2002; 195–205.
41. Ryan, T.W., III; Stapper, B. *Diesel Fuel Ignition Quality as Determined in a Constant Volume Combustion Bomb*, SAE Paper 870586, February 1987.
42. Mordosky, J.W.; Zhang, B.Q.; Harting, G.C.; Kuo, K.K.; Tepper, F.; Kaledin, L.A. Combustion of gelled RP-1 propellant with Alex<sup>®</sup> particles in gaseous oxygen atomized sprays. In *Combustion of Energetic Materials*; Kuo, K.K., DeLuca, L.T., Eds.; Begell House: New York, 2002; 206–218.
43. Sutton, G.P. *Rocket Propulsion Elements: An Introduction to the Engineering of Rockets*, 6th Ed.; John Wiley and Sons, Inc.: New York, 1992.

# Metallic Quantum Dots

J. P. Wilcoxon

*Nanostructures and Advanced Materials Chemistry, Sandia National Laboratories, Albuquerque, New Mexico, U.S.A.*

## INTRODUCTION

Nanosize metal clusters occupy a position between the molecular and solid state and, because of the dominant role of their abundant surface area, provide a unique way to learn how metal-metal bonding, cluster shape, and packing are affected by ligands bound to the cluster surface. Such studies may give insights into complex issues in catalysis, such as selectivity of binding of substrates to vertex, edge, or face sites on a metal cluster, and how such binding affects the intermetal bond distances, essentially causing a surface reconstruction, mass redistribution, or shape change. Studies of the 3-D interface structure of nanosize metal clusters should yield information quite different from the extensive literature describing ligand interactions with extended, 2-D metal surfaces. Because clusters more closely resemble practical heterogeneous catalysts (e.g., hydrodesulfurization process, hydrogenation process), important new scientific and technical insights may be gained by their study.

The formation of metal colloids or clusters by the controlled reduction, nucleation, and growth from metal salts in aqueous solution has been investigated for over a century. In the case of gold colloids, the earliest scientific investigations were undertaken by Michael Faraday<sup>[1]</sup> and spanned over a decade. Human interest in the colors of such colloidal systems dates back to the Roman times, as pointed out by Kreibitz and Vollmer<sup>[2]</sup> in their excellent review of the optical properties of metal clusters. An example cited therein is a Roman goblet from the fourth century in the British Museum whose fame is attributed to the shining colors generated by a composition of Ag and Au clusters. The purple colors of colloidal Au and Cu dispersions are thought to be the origin of the association of purple with royal colors.

## OVERVIEW

The earliest methods of colloidal synthesis (e.g., Faraday method) rely on the chemical reduction of metal salts in aqueous solution. The remarkable

stability of these ancient wine-red sols was a result of charge stabilization via adsorbed citrate ions. In sealed vials, samples prepared by Faraday in the mid-1850s can be still be viewed in the Cavendish museum in Cambridge—a true testament to solution stability.

Only very recently have scientists developed non-aqueous methods of colloidal synthesis requiring steric, not charge, stabilization. An early example of this approach, which ultimately led to the development of magnetic particles for recording purposes, was that of Hoon et al.<sup>[3]</sup> They produced Co colloids (now called nanoclusters, nanocrystals, or nanoparticulates) in the 1–100 nm range by thermolysis of  $\text{Co}_2(\text{CO})_8$  in the presence of dispersant polymers. This seminal work provided the basis of nearly all subsequent methods for production of colloids from metallorganic precursors using high  $T$  decomposition. Other reports of base metal colloidal synthesis via thermal decomposition in the presence of surfactants or polymers soon followed.<sup>[4,5]</sup> With the advent of exotic organometallic precursors, even binary semiconductors could be produced by this approach.<sup>[6]</sup>

Although organometallic precursors are the basis of many current approaches to cluster synthesis in non-aqueous, low-dielectric constant solvents, there are several drawbacks to this approach. The toxicity, air sensitivity, cost, and unwanted by-products (e.g., metallic films) prevented the widespread adoption of such methods outside the chemical community.

Methods of systematic control of cluster size in organometallic decomposition routes are still lacking. Nevertheless, in certain cases, remarkable monodispersity can be achieved. One of the earliest and best-known examples of monodisperse metal cluster growth from atomic precursors in solution was the synthesis by Schmid<sup>[7]</sup> of  $\text{Au}(N = 55)$  clusters by diborane reduction of  $\text{Au}(\text{PPh}_3)\text{Cl}$  in benzene or methylene chloride. Fifty-five atoms of a metal corresponds to the closing of the second atomic shell of a  $\text{Au}(N = 13)$  cluster core with 42 Au atoms with a dozen  $\text{PPh}_3$  molecules weakly ligated to the faces of the inorganic core. Consequently, the role of the ligand used to sterically stabilize inorganic nanoclusters in a solvent was discovered to be critical in determining

the eventual structure and stable size of a given nanocluster. By a continuation of this growth process, Schmid has extended the range of sizes available to many thousands of atoms, utilizing a synthesis reminiscent of polymeric growth—one generation providing the “seeds” for the next.<sup>[8]</sup> His approach has also been extended to other metals such as Pd and Pt. However, the yields from each growth generation are low so, as in organic synthesis, the overall yield can be quite small for larger clusters. Also, the weak binding of the PPh<sub>3</sub> group means that the long-term stability (e.g., longer than a few days) of such clusters is severely compromised.

It would be very nice to have a general nanocluster chemical synthesis, which combines the advantages of low toxicity/cost precursors, and high yield of traditional aqueous-based colloidal chemistry with the size dispersion control and chemical versatility of organometallic methods. Possibly with this goal in mind, Boutonnet, Kizling, and Stenius<sup>[9]</sup> first used aqueous pools of water found in oil—continuous microemulsions to solubilize simple, ionic, metal salts of Au, Pd, Pt, and Rh, followed by chemical reduction using hydrazine or hydrogen gas to produce metal clusters dispersed in oils. Such new nanomaterials were later shown to have good catalytic activity for hydrogenation.<sup>[10]</sup>

A serious limitation of using water containing microemulsions as microscopic reactors for metal colloid formation was the limited types of reducing agents permitted (basically hydrazine or aqueous NaBH<sub>4</sub>), as well as the inherent polydispersity of microemulsions, which produced a fairly broad size dispersion in the final product. This limitation was overcome by the surprising discovery that ionic metal salts could be directly solubilized in a variety of newly discovered inverse micelle systems.<sup>[11–13]</sup> The most useful of these systems were reported in a series of papers and a patent, and form the basis of the most versatile method for the formation of nanoclusters, both semiconductor and metallic, in the 1–10 nm regime.<sup>[14–16]</sup> The complete absence of water and air in these systems allowed the use of very strong, even pyrophoric, reductants such as LiAlH<sub>4</sub> [in tetrahydrofuran (THF)] for the first time and permitted even exotic nanocrystalline species such as Si and Ge to be made by low-*T* chemical synthesis for the first time.<sup>[17–20]</sup> In addition, the well-defined interface and monodispersity inherent to inverse micelle systems resulted in narrow cluster size distributions.

Meanwhile, physicists were taking a different approach to cluster synthesis, based on their expertise in high-vacuum, molecular beam techniques coupled with the use of mass spectrometers for mass selection and analysis. An excellent example of the results that emerged from such endeavors is that of de Heer and coworkers, who utilized a supersonic expansion of an

atomic cluster source into a vacuum in the presence of an inert gas to create cluster beams.<sup>[21]</sup> Using a mass spectrometer they, and others,<sup>[22]</sup> discovered that certain masses of clusters were produced in relatively large abundance. These “magic” sizes corresponded to the closing of atomic shells, analogous to stable nuclear shells from nuclear chemistry,<sup>[23]</sup> or the electronic shells forming the basis of chemical bonding and the periodic table. Alkali metal clusters, in particular, were discovered to be well described by simple “jellium” models and their optical properties were investigated. Other interesting phenomena emerged from these studies, including the discovery of enhanced magnetic moments in small clusters of Co, Fe, and Ni compared to their bulk counterparts.<sup>[24]</sup>

The ability to compare the size-dependent physical properties (e.g., absorbance, PL, magnetic behavior, melting point, chemical reactivity) of clusters prepared by beam methods and those prepared by solution techniques is complicated by the very important role of the interface, also known as the embedding media effect.<sup>[2]</sup> “Naked” clusters in a vacuum have very different optoelectronic properties compared to those coordinated to a solvent or a ligand. Importantly, clusters in solution, in order to be perfectly dispersed, require tightly binding ligands to prevent association or “clumping” in solution, so one can never consider very small inorganic nanoclusters (1–3 nm) without also understanding their organic interface or “shell.” Even in a vacuum, a naked cluster has unsatisfied bonding at its surface, which probably requires some sort of structural “reconstruction” to minimize its energy, and this has not been taken into account in even the most refined theories of cluster structure. Thus, there is considerable controversy among theorists regarding the actual equilibrium shape of a cluster for a given number of atoms. In short, we have a long way to go before understanding the size- and interface-dependent properties of nanoclusters. Scientists may expect to be fruitfully employed in this enterprise for many years to come.

In this entry, we cannot possibly do justice to the enormous literature in the area of metallic nanoclusters or quantum dots. Accordingly, we primarily focus on metallic Q-dots of Au and Ag, which historically provided the earliest fascination with dispersed colloidal materials. In fact, the beautiful colors of colloidal sols, which differed so significantly from their bulk counterparts and organic dyes, influenced their medieval uses in stained glass, goblets, etc. Their synthetic preparation was a well-guarded alchemic secret. It is probably not surprising that the majority of scientific investigations of the optical properties of metal clusters have focused on the few metals with visible absorbance. This restricts studies to the alkalis and noble metals (Au, Ag, Cu). This is because strong collective



oscillations (plasmon resonances) require quasi-free electrons, as well as weak damping of these oscillations in the visible regime [i.e., the imaginary part of the dielectric constant  $\varepsilon(\omega)$  must be small]. A further preference for studies of Au and Ag colloids occurs because of their remarkable long-term stabilities in aqueous solutions under ambient conditions and their interesting size- and shape-dependent optical properties, which can often be described by the Mie theory<sup>[25]</sup> of electromagnetic scattering. In this review, we emphasize the important role of synthesis methods, advanced characterization tools for both feedback and understanding of size/optical properties, and formation of arrays of these dots. We discuss both alloys and core-shell nanoparticles of these materials. Only briefly discussed will be the magnetic and catalytic properties of nanoclusters.

## EXPERIMENTAL

### Nanocluster Synthetic methods

#### Inverse micelle method

The inverse micelle synthesis has been extensively described in a series of papers<sup>[11,13–20,26–28]</sup> and patent.<sup>[12]</sup> A key difference of this method from either liquid or gas atomic aggregation processes (e.g., high- $T$  thermal decomposition of organometallics) is that the cluster-cluster aggregation process, whose kinetically determined structures inevitably result in power-law or log normal cluster size distributions, is fundamentally altered by the microheterogeneous environment of the droplet-like inverse micelles. Because the ionic metal salt precursor is only soluble inside the micelle at typical precursor metal salt concentration of 0.01–0.1 M and surfactant concentrations of ~5–10 wt.% (~0.2 M), there are only about 1–4 precursor ions/micelle. Thus, growth to the final observed sizes of  $N = 10$ –10000 atoms must occur via micellar diffusion, micelle collision, temporary interface fusion, and atomic interchange. The micelle interior volume roughly determines the maximum size of the small atomic clusters, which may interchange during the growth or aggregation step of the synthesis. This cluster growth rate is set by the diffusion rate of the micelles, which is ~2 orders of magnitude slower than would occur in a continuous liquid phase (i.e., Schmid approach, gas-phase aggregation, etc.). So the opportunity for structural adjustments to atomic positions during atomic exchange and growth is enhanced, possibly favoring thermodynamic stabilities over metastable (e.g., disordered) cluster structures. For this reason, we have never observed disordered, and rarely<sup>[29]</sup> non-equilibrium nanoclusters as the final product

regardless of the melting point of the corresponding bulk material.

Our approach has changed only in minor ways since our first description of metal nanocluster synthesis in 1989.<sup>[11]</sup> The most significant change is the use of strongly binding surfactants, thiols, to passivate the surface during or after the chemical reduction, which allowed us to employ liquid chromatographic analysis of the nanocluster size and size dispersion.<sup>[30]</sup> When thiols are added prereduction, they can significantly alter the final nanocluster size, because they inhibit the cluster growth more strongly than the non-ionic and cationic surfactants we typically use to solubilize ionic gold, silver, or platinum salts in inverse micelles. However, the use of alkyl thiols as passivating agents presents other issues, which we have recently discussed—certain alkyl thiols act as etchants, reducing the size of the as-synthesized clusters.<sup>[31]</sup> They also fail to bind as effectively to larger (e.g.,  $D_c > 4$  nm) ( $D_c =$  inorganic core diameter) Au clusters compared to smaller ones (e.g.,  $D_c < 2$ –3 nm). The thiols, although present in much lesser amounts than the surfactants used to form the inverse micelles, compete very effectively for binding sites on the growing nanocluster surface. Because of their strong binding properties, thiol passivating agents also permit purification and removal of ionic byproducts and most of the surfactant micelles used to solubilize the metal salt precursors. The stabilization of the nanocluster surface by a strongly binding ligand is critical to the variety of purification approaches we have described.<sup>[30]</sup>

Numerous other papers describing Au nanocluster synthesis using so-called phase transfer catalysts (i.e., cationic surfactants)<sup>[32,33]</sup> have been published. There are some misconceptions about the role of the cationic surfactants used in this synthetic approach. The first is that the typical recipe requires water to first dissolve the salt (typically  $\text{HAuCl}_4$  or  $\text{NaAuCl}_4$ ) and then requires this aqueous salt solution to be brought into contact with an immiscible toluene solution containing a cationic surfactant [usually tetraoctylammonium bromide (TOAB)]. One needs to ask why only certain cationic surfactants will actually solubilize the gold salt into the organic phase? The reason is that very hydrophobic, long-alkyl chain surfactants are required to ensure both the formation of spherical micelles in the organic (toluene) phase and the total exclusion of water from that phase. Because such cationic surfactants spontaneously form inverse micelles in toluene, as was discovered several years ago by neutron scattering, they are capable of directly solubilizing a wide variety of metal salts without the use of water. We have described such an inverse micelle synthesis in Ref.<sup>[13]</sup> and in our original patent,<sup>[12]</sup> using didodecyldimethyl ammonium bromide (DDAB) in toluene. One can also use linear alkane solvents with these surfactants, but

geometric considerations in the tail group packing often require a cosurfactant such as hexanol be added to “fill in the gaps” in the micellar surfactant droplet interface with linear alkanes.

With this general understanding of the role of the cationic surfactant as a micelle forming agent, which can directly solubilize a variety of metal salts, water need not be introduced into the system, thus allowing the use of strong reducing agents such as  $\text{LiBH}_4$  in tetrahydrofuran (THF), or  $\text{LiAlH}_4$  in THF or toluene. These reducing agents are generally superior to  $\text{NaBH}_4$  in water, which must be used to reduce  $\text{HAuCl}_4$  in two-phase systems. Even if one chooses to use  $\text{NaBH}_4$  as a reductant, because  $\text{NaBH}_4$  in neutral aqueous solution is unstable with respect to hydrolysis, only highly alkaline solutions ( $\sim 4 \text{ NaOH}:\text{NaBH}_4$ ) should be used to effect reductions. Such caustic reducing solutions are quite stable and are actually sold by Aldrich as stock  $\sim 4.4 \text{ M NaBH}_4$  in  $\sim 14 \text{ M NaOH}$  solutions, and can be diluted into water, as desired.

In the case of gold or silver, the precursor metal salts are so easily reduced that the use of alkaline  $\text{NaBH}_4$  in water as we described in our early work is quite acceptable. However, this reducing agent is somewhat ineffective for the reduction of Pt or Pd salts, and is completely ineffective for formation of metallic Fe, Ni, Co, Si, or Ge. Instead, in the case of Fe, Ni, or Co, the corresponding metal boride will form.

### Metathesis method

In this cluster formation method, a chemical reduction of an organic soluble metal–organic precursor is used to produced metal clusters. This can be carried out in a coordinating or non-coordinating solvent, or some combination thereof. Alternatively, a surface-active (but not micelle forming) species such as dodecanthiol (C12SH) or tri-*n*-octylphosphine (TOP) may be added to prevent run-away growth during the chemical reduction. The best example of this approach is the one described by Schmid, and exemplified by the reaction that produces  $\text{Au}(N = 55)$  clusters. We refer the reader to his excellent review on this subject for further details.<sup>[8]</sup>

Another approach to the production of metal clusters in solution relies on the high-*T* reduction of organometallic precursors by glycols in coordinating solvents such as diphenyl ether. This “poly-ol” method was recently refined to produce base metal clusters of a variety of sizes of Co, Fe, and Ni. Generally, empirically chosen surfactants are used to stabilize the growing nanocluster. A review of this approach appeared recently.<sup>[34]</sup> Briefly, the nanocluster size is increased by increasing the amount of precursor and/or decreasing the amount of surfactant. There is usually some unwanted metallic film formation and/

or incomplete reduction so the yield is not 100%, and the method requires high boiling point solvents as the reduction typically takes place between 200 and 300°C. Some of these solvents may not allow solubilization of all the available components (metal–organic, poly-ol, stabilizer), so a fair amount of empirical variation is required before achieving an optimal synthesis.

### Thermal decomposition method

In this method, which is the oldest approach for non-aqueous synthesis of metallic Q-dots, a thermally labile, oil soluble, metal–organic precursor is thermally decomposed in the presence of a surfactant-like stabilizer, typically a block copolymer.<sup>[3]</sup> Under the proper conditions, fairly monodisperse colloids can result. However, the method is typically only used for base-metal nanocluster synthesis (Co, Fe, Ni) because an available thermally unstable metallorganic is required [e.g.,  $\text{Fe}(\text{CO})_5$ ,  $\text{Co}_2(\text{CO})_8$ ,  $\text{Ni}(\text{CO})_4$ ]. As these compounds are very air-sensitive and either mildly or severely toxic, all handling must be carried out in either a glove box, or by Schlenk-line methods. Additionally, because of the rapid growth rate compared to chemical reduction methods, the final clusters are highly defective, requiring significant annealing to produce high-quality samples. This means the final material properties (e.g., saturated magnetic response) are typically only a small fraction of that found in the corresponding bulk materials.<sup>[3–5]</sup>

### Nanocluster Characterization

#### Size exclusion chromatography (SEC)

We use a commercial Waters corporation autosampler, solvent pump, degasser, and detectors together with commercially available polystyrene microgel columns (Polymer Laboratories) with controlled pore sizes to separate and analyze organically passivated metal nanoclusters. The alkyl organic shell on the metal surface prevents specific chemical interaction with the hydrophobic column material. A single-channel output of an in-line photodiode array (PDA) detector at a particular wavelength near the classical plasmon resonance, ( $\sim 520 \text{ nm}$  for Au,  $\sim 400 \text{ nm}$  for Ag) was used as described in previous papers<sup>[30,35]</sup> to obtain the peak apex elution time and peak width, which together yield the average cluster size and size dispersion. A conductivity detector and refractive index (RI) detector were also used to demonstrate that the eluting metal clusters had no charge and were separated from the non-absorbing chemicals (surfactant micelles, salt byproducts, etc.) used in the synthesis. A chromatogram showing the separation  $D_c = 2 \text{ nm}$

Au nanoclusters from the solvents and surfactants used to produce them is illustrated in Fig. 1, taken from Ref.<sup>[30]</sup>.

The use of SEC to obtain cluster sizes and size distributions was explained in detail in a recent paper.<sup>[30]</sup> In that work, we demonstrated that the elution time  $t_e$  for a properly passivated Au nanocluster sample with a hydrodynamic diameter  $D_h$  obeyed the relation,  $\log D_h \sim t_e$ , allowing one to obtain a metal core diameter after subtraction of the thickness of the organic passivating layer. This thickness was determined by taking a sample with a single core size as determined by transmission electron microscopy (TEM) and adding a series of alkyl thiols, designated herein as CkSH, with chain lengths  $k$  of  $6 < k < 16$ , to the toluene mobile phase, and obtaining  $D_h$  from  $t_e$  and subtracting the known TEM core size. Fig. 2 shows an example of this size separation capability for a single core size,  $D_c = 2.0$  nm and  $k = 6, 10,$  and  $14$ . It illustrates that clusters with different total hydrodynamic sizes due to organic shell differences may be separated by using SEC.

The organic passivating shell thicknesses agree well with values calculated from known C–C bond lengths in linear alkanes and confirmed by SEC. A best fit to a series of linear alkanes and polystyrene polymer standards gave  $D_h$  (nm) =  $608 \exp(-0.62525t_e \text{ (min)})$  for the PL1000 column used in that reference. This relation was valid for  $1 \text{ nm} < D_h < 10 \text{ nm}$ . Columns are available with larger pore sizes, which extend this range to larger values. For further information, the reader should consult the excellent book by Yau Kitland, and Bly<sup>[37]</sup>

In the case of other nanoclusters such as Si, Ge, Co, Ni, and Fe, or semiconductors such as CdS, CdSe, FeS<sub>2</sub>, and MoS<sub>2</sub>, tetrahydrofuran (THF) or acetonitrile (ACN) appears to be the best mobile phase choice. It is highly recommended to use inhibited THF to

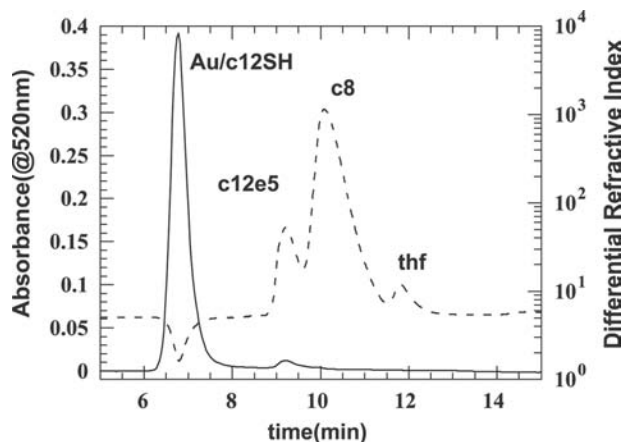


**Fig. 1** Chromatographic separation of capped Au nanoclusters stabilized using c12SH and containing the non-ionic surfactant c12e5. A PL500 column and a toluene mobile phase were used.

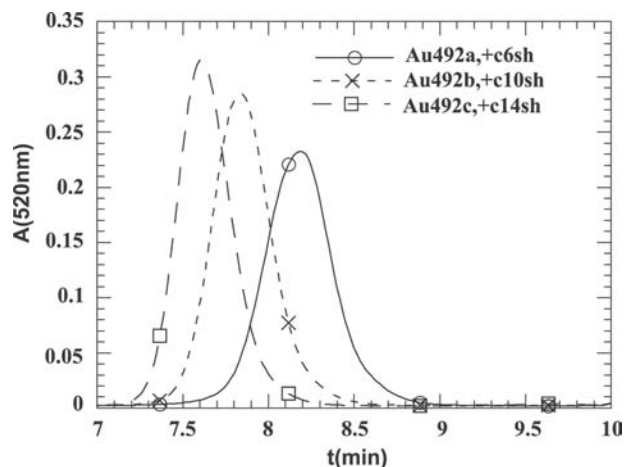


**Fig. 2** Effect of capping agents on the hydrodynamic diameter of Au nanoclusters. The HPLC chromatogram of Au nanoclusters with three alkyl thiols, CkSH,  $k = 6, 10, 14$ , added after reduction. The absorbance at 520 nm [ $A(520 \text{ nm})$ ] from the PDA vs. elution time is shown. The SEC column used was a Polymer Labs PL1000 and the mobile phase was toluene at 1 mL/min flow rate. Source: From Ref.<sup>[30]</sup>.

minimize oxidation as a result of peroxide formation. This is especially true if fraction collection of purified nanoclusters is desired. In our case, automatic vacuum removal of all gases occurs prior to the pump and injection system, so air-sensitive nanomaterials can be easily analyzed or fraction collected without degradation. In addition, an in-line filter and short “guard” column of the same column material is used to prevent retention time changes with age and/or injection of “bad” samples. With such an elaborate system (and many ruined columns during the learning process!), we can reproduce the retention time (i.e.,  $D_h$ ) of high-quality, stable nanocluster samples to within the instrument resolution of 0.01–0.02 min over periods exceeding 1 year. This corresponds to a size resolution (see Fig. 3) of  $\sim 1 \text{ \AA}$ ! Additionally, shape information is incorporated into the retention time, as we can achieve near baseline separation of C60 from C70 on a typical PL500 column, although these fullerenes differ in hydrodynamic size by only  $\sim 1 \text{ \AA}$ . Fig. 3 illustrates this point.

As we have discussed,<sup>[30,37]</sup> increasing the total pore volume for a pure SEC elution mechanism increases the resolving power of the separation. Preparative columns with diameters of 25.4 mm are available (i.e.,  $\sim 10\times$  the pore volume) that can separate clusters differing in size by only  $\sim 2\%$ . With such columns, large amounts (10–100 mg) of nanoclusters can be injected and fraction collected with great size selectivity ( $\sim 1$ – $2 \text{ \AA}$  separation). We have developed a custom-designed, anaerobic, automated fraction collection system which we will describe in future work.

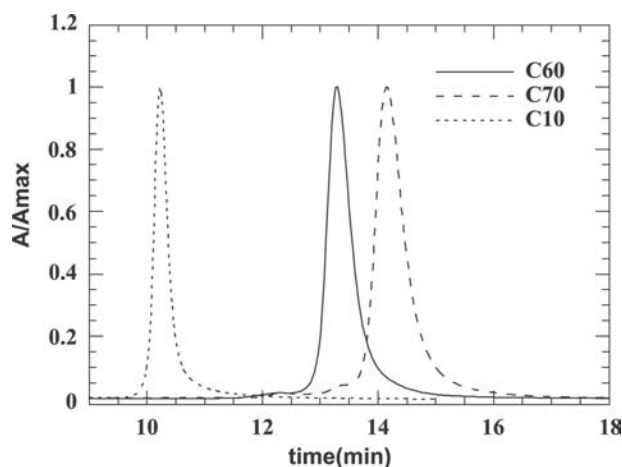


**Fig. 3** Chromatogram instrumental linewidth for samples of decane (C10), C60, and C70 run on a PL500 column in toluene. *Source:* From Ref.<sup>[30]</sup>.

There is an inherent elution peak width at half-height associated with the chromatography column itself even for monodisperse molecules such as octane (Fig. 3).<sup>[30]</sup> Unlike reverse-phase chromatography columns, for SEC columns the instrumental band-broadening does not depend on elution time, but simply on the average size of the microgel particles used to pack the column. For example, the high-resolution columns used in previous studies were packed with porous 5- $\mu\text{m}$  particles and had significantly narrower inherent band-broadening than less expensive columns packed with 10- $\mu\text{m}$  particles of the same material. This column band-broadening is experimentally determined by using a known monodisperse sample and the same column used for study of the unknown samples. Using decane C10, we found  $\Delta t_{1/2} = 0.25\text{--}0.27$  min while we found  $\Delta t_{1/2} = 0.40$  min for purified (99.9%, Strem Chemicals) buckyballs, C60 and C70.<sup>[30]</sup> From shape considerations, the latter standard seems more appropriate to compare to our spherical nanocluster samples. Any cluster elution peak whose width exceeds this value implies some polydispersity in the sample provided the sample does not have specific chemical interactions with the column. In fact, as shown in our previous work, reproduced in Fig. 4, our best metal cluster samples have  $\Delta t_{1/2} = 0.30\text{--}0.35$  min, slightly narrower than the best available C60, so there is some uncertainty ( $\sim 0.05$  min) as to which value best represents the inherent column broadening. Roughly speaking, the subpopulations of such a polydisperse sample with elution times lying outside  $t_e \pm 0.4/2$  will be separated from the clusters represented by the signal at the apex of the peak and contain additional spectral information. The optical spectra obtained from the size-selected population eluting at the peak apex represents

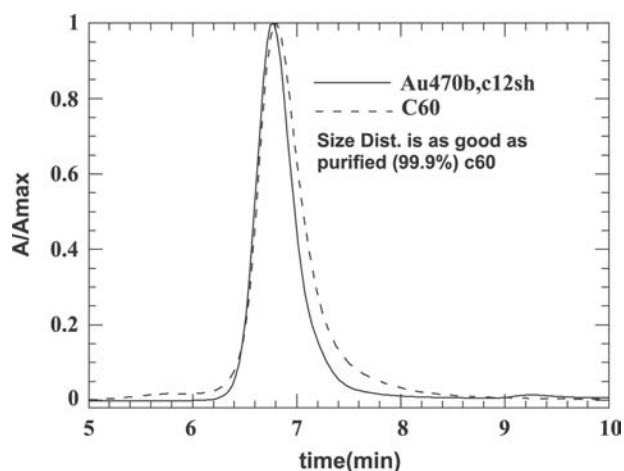


**Fig. 4** Size distribution of Au clusters is as narrow as buckyballs. Normalized absorbance chromatogram from PDA detector ( $A/A_{\text{max}}$ ) for C12SH-stabilized Au nanoclusters and 99.9% C60. HPLC conditions were a PL500 column using toluene as the mobile phase flowing at 1 mL/min. The C60 elution time has been shifted to coincide with that of the Au nanoclusters for ease of comparison. *Source:* From Ref.<sup>[30]</sup>.

a single size to within the  $\pm 2 \text{ \AA}$  resolution for our column. This resolution of  $\pm 2 \text{ \AA}$  may be increased by increasing the total pore volume of the column by adding an identical column in series.

Typically, a 10- $\mu\text{l}$  amount of  $\sim 0.01$  M nanocluster solution is injected from a crimp top vial using our Water's model 717 autoinjector and sampling loop. The total experimental time is 15 min, so complete size and optical analysis of 20 samples under automated control is quite feasible in a day. The retention time at the peak apex elution is measured by using the absorbance obtained from a chosen wavelength element of a 1024-channel, on-line, photodiode array (PDA), absorbance detector. The mobile-phase background absorbance, although not significant in the region of interest for most metal nanoclusters, is automatically removed. Organic chemicals (e.g., solvents, surfactants) that do not absorb at mobile-phase-transparent wavelengths, are detected by using an on-line differential refractometer (Water's model 410).

#### Transmission electron microscopy (TEM, HRTEM)

About 2  $\mu\text{l}$  of the purified  $\sim 0.01$  M solution of nanoclusters was deposited on a holey carbon grid, under which a porous filter paper was placed to quickly wick the solvent away to minimize cluster pile up on the grid. For core sizes larger than  $D_C \sim 2$  nm high-resolution TEM (HRTEM) was used to confirm the metal core size to an uncertainty of one lattice constant ( $\pm 2 \text{ \AA}$ ). However, in this size range, this

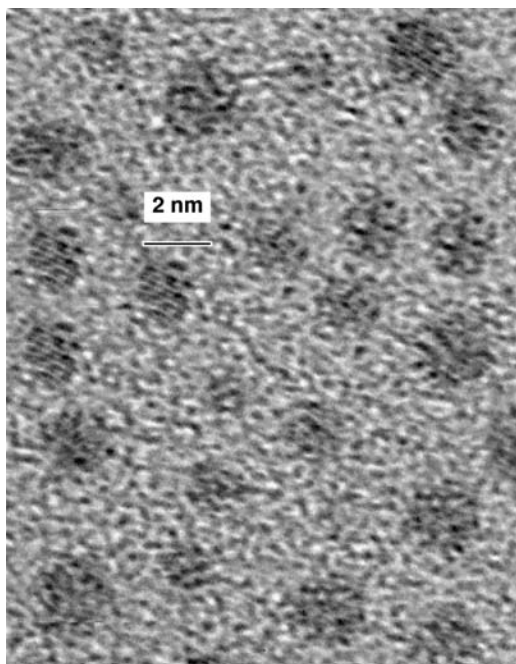


**Fig. 5** HRTEM of a region of a holey carbon grid on which a drop of sample Au,  $D = 1.8(2)$  nm was allowed to dry. Source: From Ref.<sup>[30]</sup>.

measurement uncertainty is as large as the SEC resolution, even assuming a perfectly monodisperse sample with all the clusters in an identical focal plane on the holey carbon grid and identical nanocrystal orientation.

Nanocrystal orientation is very important for small crystals. For example, if a randomly oriented distribution of monodisperse icosohedral Au crystals is examined with  $d\langle 111 \rangle = 2.1$  nm and  $d\langle 100 \rangle = 2.7$  nm, one obtains the number average  $D_c(\text{TEM}) \sim 2.4 \pm .3$  nm, but this is not a result of size dispersity. In addition, with the smallest clusters, especially Ag, there are e-beam cluster “melting” artifacts that make absolute size measurements difficult because the boundary with the grid becomes less sharp, in addition to causing some cluster fusion where their surfaces touch. For these reasons, size determination by high-resolution SEC, complemented by HRTEM, has major advantages. Fig. 5 shows an HRTEM of Au,  $D_c = 1.8$  nm particles, showing the atomic lattice fringes from this HPLC-purified sample, and illustrates the effects of crystallographic orientation and focal plane effects on the apparent cross-sectional diameter of this nearly monodisperse sample.

#### Absorbance spectra

The absorbance spectra of passivated metal nanoclusters was obtained by using an on-line photodiode array PDA with an adjustable bandwidth and wavelength

range. For the purpose of the studies reported in this review, the bandwidth was either 2.4 or 4.8 nm, and a wavelength range of 290–795 nm was used. Complete absorbance spectra were collected every 2 sec during the chromatography. A Cary 2300 ultraviolet (UV)–visible spectrometer was also used to verify selected results from the PDA. Both spectrometers were calibrated by using a holmium filter.

Because a typical cluster elution linewidth is about 0.3–0.4 min, between 10 and 15 complete spectra were available as a function of elution time (i.e., size). Thus, in addition to the information concerning how the absorbance spectra changes with cluster size at the peak of the elution, we also can determine the spectral homogeneity of an elution peak. A spectrally pure or homogeneous elution peak corresponds to one in which there is no variation in the absorbance spectral shape within the peak. Size or shape polydispersity would lead to size-dependent optical absorption spectra within the elution peak.

#### Synthesis Optimization with SEC Feedback

Perfecting the methods of inorganic nanocluster synthesis requires rapid, quantitative feedback concerning final cluster size, shape, optical properties, and their relationship to the myriad synthetic variables, which can affect the average cluster size and size distribution. A good analogy is with advances in organic synthesis which have been facilitated greatly by the advent of modern analysis methods, such as Fourier-transform infrared (FTIR), gas chromatography/mass spectrometry (GC/MS), liquid chromatography (LC)/PDA, nuclear magnetic resonance (NMR), etc. Without such feedback, the synthetic chemist is very much in the dark with respect to whether changes in synthetic protocol are making things better or worse. Another example comes from the application of liquid chromatography/mass spectrometry (LC/MS) and capillary gel electrophoresis approaches to DNA and protein analysis which, along with polymerase chain reaction (PCR) amplification, essentially enabled the rapid sequencing of the human genome. Unfortunately, carrying such analytic methods directly over into the field of inorganic nanocluster synthesis is not always straightforward. Perhaps, this is the reason for the limited number of nanomaterials that humans know how to synthesize in a predictable manner—the best examples being transition metal nanoclusters as pioneered by my group, and II–VI semiconductors (mainly CdSe) as pioneered by Murray, Bawendi, Alivisatos, and Brus.<sup>[6,38–40]</sup> These materials were explicitly chosen because they have clearly identifiable, size-dependent visible colors (absorbance) that allows rapid feedback regarding size and monodispersity.

For example, in the case of CdSe, size changes as small as 1–2 Å result in clear differences in the absorbance edge. In the case of nanosize Au or Ag, one can perceive, even with the naked eye, color changes corresponding to ~2–4 Å in size, and using an absorbance spectrometer, 1–2 Å size differences.

## RESULTS AND DISCUSSION

Our recognition of the dearth of rapid analysis techniques for inorganic nanomaterials led us to try to adapt some modern analytical methods to understand size/optical property relationships in both semiconductors and nanometals. These techniques include in situ elemental analysis of purified cluster solutions using X-ray fluorescence (XRF), which is very useful for composite nanoclusters, and size-exclusion liquid chromatography, which has recently become our most useful tool, supplanting even TEM in both size precision and utility. We now illustrate the power of these new analysis methods in improving nanocluster synthesis with several examples from our previous work.

### Nanocluster/Ligand Binding Studies

We have recognized for many years that at least four important factors control the final size of nanoclusters synthesized in inverse micelles:

1. The micelle size,
2. The binding strength of the surfactant micelle used,
3. The amount of precursor salt used in the synthesis,
4. The strength of the reducing agent used.

Variables 3) and 4) influence the final cluster size even in the absence of micelles as, e.g., in metathesis methods using metal–organic precursors in the presence of coordinating ligands. Perhaps, not surprisingly, increasing the concentration of metal salt precursor increases the final cluster size, while increasing the rate of reduction by using a stronger reducing agent decreases the cluster size. Also, increasing the strength of the binding of the micelle-forming surfactant decreases the final cluster size if all other variables remain fixed. However, it is very difficult to predict, a priori, which surfactants will bind most strongly to which metals, nor how much change in final size will be achieved by changing the precursor concentration or reducing strength.

By measuring the total amount of clusters eluting from a given column/mobile phase using measurement of the elution area at a given wavelength with and

without the column, one can study the competition for the organic ligand between the high surface area column and the high surface area nanoclusters. It is found that, for Au nanoclusters, thiol exchange does not occur on the time scale of the chromatography experiment (~15 min) even in the presence of an overwhelming amount of a different CkSH in the mobile phase [i.e., the clusters elute at the time expected for the chain length (thickness) of the alkyl thiol], while for Ag nanoclusters, complete exchange occurs under these conditions. Thus, Ag nanoclusters bind alkyl thiols significantly more weakly than Au. Pt, Pd, and Rh nanoclusters do not exchange thiols during the chromatography like Ag, but still have slightly more weak binding than in the case of Au clusters of the same size, as indicated by fewer (<100%) eluting clusters.<sup>[30]</sup>

One can learn about ligand metal cluster binding, so critical to catalysis, by examining the relative amount of clusters eluting from a column with a mobile phase of pure toluene. In this case, the column attempts to separate the ligand from the cluster. Failure to do so results in complete elution of the clusters, as judged from ratio of the area under the elution peak compared to the no-column case. In Fig. 6, one observes that the relative areas decrease with  $k$  for  $k = 6, 10,$  and  $14$ , indicating shorter chain thiols bind less strongly than longer ones.<sup>[30]</sup>

These types of subtle binding effects are nearly impossible to study by other methods. In fact, the organic ligand cannot be seen in TEM so its length

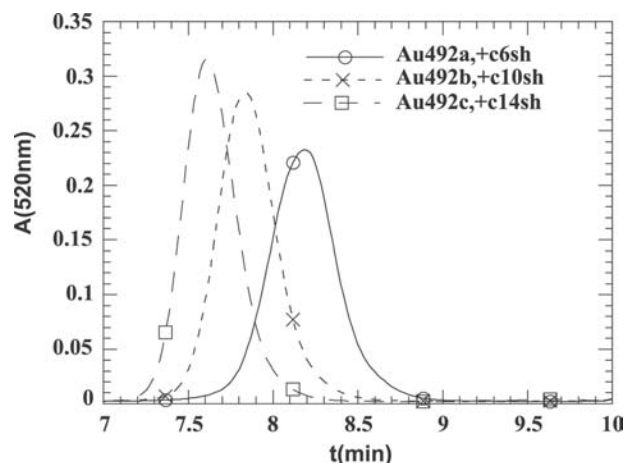


**Fig. 6** Effect of capping agent size on the hydrodynamic diameter of Au nanoclusters. HPLC chromatogram of Au nanoclusters with three alkyl thiols, CkSH,  $k = 6, 10, 14$ , added after reduction. The absorbance at 520 nm [ $A(520\text{nm})$ ] from the PDA vs. elution time is shown. The SEC column used was a Polymer Labs PL1000 and the mobile phase was toluene at 1 mL/min flow rate. Source: From Ref.<sup>[30]</sup>.



can only be indirectly inferred from the intercluster gap. An interesting prediction from our SEC ligand/cluster binding studies is that, under vacuum as in an electron microscope, only longer chain thiols will be able to retain their ligands, preventing cluster coalescence and allowing the formation of hexagonal or cubic quantum dot arrays (QDAs). This is indeed the case as we have shown in previous work on QDAs.<sup>[41,42]</sup> Another prediction based upon our SEC work is that Ag nanoclusters will more readily desorb even long chain alkyl thiol ligands under vacuum and so, the longevity of QDAs of Ag under TEM is significantly decreased relative to Au. Also, electron beam melting effects are more severe in QDAs of Ag than of Au although the melting temperatures of the two materials are very similar. As expected, QDAs of alkyl thiol ligated Pt, Pd, and Rh are more robust than Ag under vacuum.

A somewhat surprising observation common to all metal Qdots, which we have studied, is that monodentate ligands such as alkyl thiols, alkyl sulfides, and primary amines bind increasingly less effectively as the size of the nanocluster increases. In fact, for  $D_c > 10$  nm, one finds that displacement of a polydentate ligand such as a non-ionic alkylated polyethylene oxide by a more strongly binding alkyl thiol will result in complete irreversible aggregation of a Au or Ag nanocluster solution! Thus, one needs to develop more advanced polydentate ligands for larger nanoclusters.

Intuition often fails when choosing an appropriate multidentate ligand for a given metal Qdot. For example, we have found that alkyl chain disulfides aggregate these larger clusters, which surprised us greatly. This observation probably indicates that the hypothesis that alkyl thiolates form disulfides on nanocrystalline gold is wrong. Fortunately, non-ionic block copolymers, such as were employed in the first synthesis of Co via high- $T$  decomposition,<sup>[5]</sup> are obvious choices and, if selected appropriately, they stabilize a very broad range of transition and base metal Qdots extremely effectively. However, they do not allow efficient SEC analysis of the stabilized large nanoclusters as most columns are too effective at pulling them off the cluster surface, and such bulky stabilizers may prevent deposition of additional atoms to form core-shell particles, so they are not a panacea. Thus we are still searching for the most effective steric ligands for SEC analysis of large,  $D_c > 10$  nm nanoclusters.

### SEC Studies of Synthetic Variables

Traditionally, TEM or X-ray diffraction (XRD) was used to infer the nanocluster particle size. In the case of the former, between a few dozen particles to a few hundred are measured from a “chosen” area of the

grid and tediously counted. Many “representative” areas of the grid must be chosen by the microscopist, requiring significant expertise and time. To obtain a detailed analysis of even a single sample in a day’s time requires a dedicated graduate student or postdoctorate individual—highly motivated by the possibility of a permanent job! Considering that a skilled synthetic inorganic chemist can easily make a dozen samples in the same period of time, one can see where the roadblock to synthetic progress occurs.

Other traditional surface science methods of analysis often prove inadequate as well. For example, in XRD characterization of size, the first maximum in the low-angle diffraction pattern can be used to obtain the average interparticle spacing (assuming either hexagonal or cubic packing). Unfortunately, the interparticle gap depends on the organic ligand and its degree of interdigitization, so this method of core size determination is not ideal, although it is applicable to the smallest clusters with  $D_c < 2$  nm, and has been used with good precision for very monodisperse clusters.<sup>[43]</sup>

As we have extensive experience with small-angle neutron scattering (SANS), X-ray scattering (SAXS), and dynamic light scattering (DLS), I initially believed these methods would prove very useful for size and size dispersion analysis.<sup>[44]</sup> However, in the case of metal Qdots and DLS using visible light, the very strong absorbance and concomitant weak scattering requires very low nanocluster concentrations so that the signal-to-noise (S/N) ratio is exceptionally low for clusters with  $D_c < 4$  nm. This technical difficulty has precluded our routine use of this method. In the case of SANS, the scattering length density difference between solvent and typical metal Qdots is very low, again giving low S/N and long data collection times. SAXS is the best approach with respect to S/N from metallic Qdots, but typically requires an intense tunable (synchrotron) X-ray source, to avoid large (e.g., 24 hr) data collection times.<sup>[44]</sup> Thus until we had developed SEC for nanoclusters, our synthetic feedback was poor.

To illustrate the speed, precision, and high information content of SEC size/optical property analysis, we now review some selected cases of using SEC to determine the effect of variation of synthetic parameters on metal Qdot synthesis. We refer the reader to the results of a recently submitted manuscript for further examples.<sup>[31]</sup> First, we fix the solvent, metal precursor concentration, reductant, and inverse micelle surfactant, and examine the effect of alkyl thiol concentration on the final cluster size. Fig. 7 shows the SEC chromatograms from Au nanoclusters synthesized with various amounts of added C12SH from 0.0 to 0.03 M. As expected, having more of the tightly binding alkyl thiol restricts the growth more strongly.

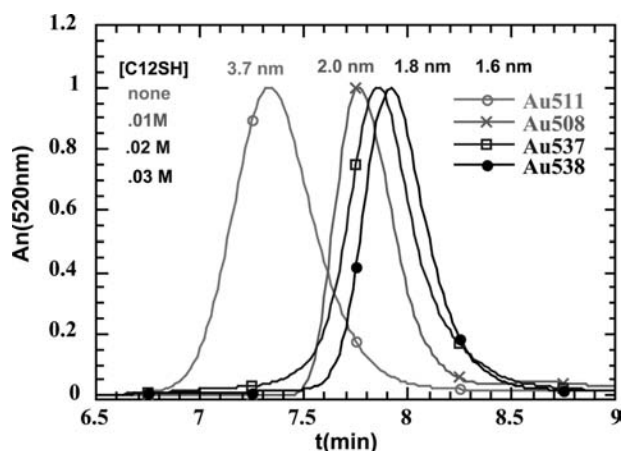


**Fig. 7** Effect of C12SH concentration on the final nanocluster size and size distribution of Au nanoclusters made by  $\text{NaBH}_4$  reduction of a two-component TOAB/toluene inverse micelle system with  $[\text{Au}] = 0.01 \text{ M}$ . The column is a PL1000 type and the mobile phase is toluene with C12SH added at 0.01 M. The SEC core sizes assume a core-size-independent 2.4-nm total organic shell, and are indicated above each curve. *Source:* From Ref.<sup>[31]</sup>.

The linewidths observed (size dispersions) only vary slightly once the thiol concentration exceeds 0.01 M. (The Au/C12SH ratio is 1:1 for this case.) In fact, once the Au/CkSH ratio exceeds 1.0, the samples are nearly monodisperse. It is noteworthy that although TEM easily gives the size of the largest cluster made with no alkyl thiol present, Au #511, as  $D_c \sim 3.8 \text{ nm}$ , the other three samples all appear to be around  $D_c \sim 1.8 \pm .2 \text{ nm}$  using HRTEM because identification of the cluster/substrate boundary combined with orientation effects obscure the true size differences, which SEC clearly demonstrates. ( $2 \text{ \AA}$  is one lattice fringe and thus is the inherent measurement uncertainty for a perfectly monodisperse sample.) Also noteworthy is that this information was obtained in 15 min/chromatogram by using only  $10 \mu\text{l}$  of a 0.01 M Au cluster sample! On this particular day, the effect of over 12 different synthetic variables were determined by SEC.

We obtain the complete absorbance spectra from our PDA array throughout the peak elution (every 2 sec, which corresponds to a size discrimination of only 1–2 Å). The spectra obtained at the peak apex represent the absorbance of the majority of the nanoclusters. The spectra normalized at a common value, 500 nm, are shown in Fig. 8 for each sample. One observes the characteristic blue shift of the plasmon, which we first identified in Ref.<sup>[13]</sup> and confirmed using SEC in a recent paper.<sup>[36]</sup> As the size decreases from  $\sim 2.0$  to 1.6 nm, additional non-classical features appear in the absorbance as a result of the discrete density of states of a gold cluster. For example,  $D_c = 1.6 \text{ nm}$  corresponds very closely to the magic,

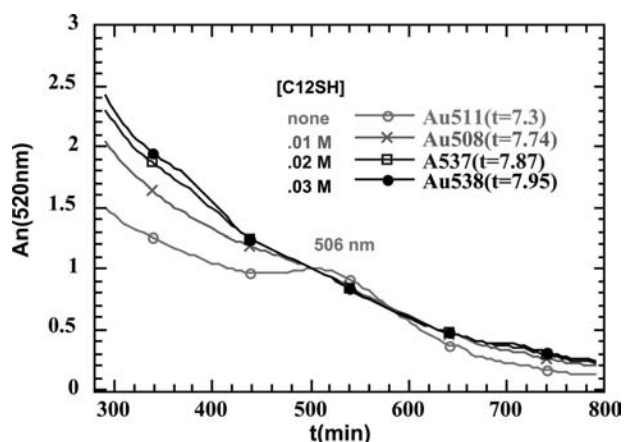


**Fig. 8** Absorbance at the elution peak of each of the chromatograms of Fig. 7, illustrating the blue shift and plasmon broadening with decreasing size. All the clusters are in toluene, which is also the mobile phase. *Source:* From Ref.<sup>[31]</sup>.

two fully closed shells icosahedra with  $N = 55$  having  $D_c = 1.5\text{--}1.6 \text{ nm}$  first synthesized and identified by Schmid.<sup>[7]</sup> Recently, Whetten has also identified this magic size using MALDI TOF mass spectroscopy.<sup>[45,46]</sup> The features of this smallest  $\sim 9 \text{ kDa}$  cluster fraction correspond closely to the spectra of Au #538 shown in Fig. 8. The enhancement of both the UV and near-infrared (NIR) absorbance is characteristic of the quantum confinement effects in ultrasmall metallic Qdots<sup>a</sup> and corresponds to the absorbance features which are observed in semiconductor Qdots.<sup>[6,47]</sup>

Both Au and Ag possess strongly size-dependent optical absorbance in the quantum confinement regime,  $D_c < 5 \text{ nm}$ , which allows us to assay the size homogeneity of the elution peaks of Fig. 7 by examining the “spectral homogeneity” of the peak. Measuring the uniformity of the spectral shapes of an eluting component is a commonly used approach to look for possible coelution of inhomogeneous species even with simple chemicals.<sup>[37]</sup> We have extended its use to Au, Ag, and Cu nanoclusters. In the case of metallic Qdots of Au or Ag, spectral inhomogeneity could arise from either size or shape effects. In fact, we find that only the largest component, Au  $D_c = 3.8 \text{ nm}$ , made without C12SH present during the synthesis, possesses any significant spectral inhomogeneity, as demonstrated by the spectra obtained at the peak apex time,  $t = 7.36 \text{ min}$ , and at the half-width at half maximum positions,  $t = 7.16$  and

<sup>a</sup>Quantum size effects are a result of the discrete nature of the electronic levels as a cluster is built up from atoms. The level splitting ( $\Delta E$  is roughly given by  $\Delta E \sim E_f/N$ , where  $E_f$  is the Fermi level of the metal and  $N$  is the number of atoms in the cluster. If  $E_f \sim 5 \text{ eV}$ , eV, then ( $\Delta E \sim 50 \text{ meV}$  for a 100-atom cluster. At room temperature, one might see these effects for Au at  $N \sim 400$  or  $d \sim 3 \text{ nm}$ .

$t = 7.56$  min (Fig. 9). The total variation of the plasmon position even for this sample is incredibly small, as the bandwidth of the detector was set to  $\pm 4.8$  nm for these experiments. However, it is certainly real and corresponds to size inhomogeneity of  $\sim \pm 0.5$  nm. Samples made with alkyl thiol present during the reduction have elution linewidths and spectral homogeneities consistent with complete monodispersity—a tribute to both the inverse micelle method and the role of alkyl thiols as etchants to narrow the size distribution.<sup>[31,45]</sup>

What is the role of inverse micelle type and solvent on the final cluster size? Both of these issues were the subject of a recent publication.<sup>[31]</sup> In that work, it was demonstrated that even in the presence of a strongly binding thiol, the size and/or strength of the micellar binding to the encapsulated precursor salt had a significant effect on the final size and size distribution. Fig. 10 shows the cluster size distribution obtained without deconvolution of the instrumental linewidth for nonionic, three types of cationic surfactant, and an anionic surfactant. In each case, the solvent was held constant, toluene, as was the reductant,  $\text{LiAlH}_4$ .

As was noted in the original reference, the structure and binding properties of the inverse micelle used is a competitive factor with the binding of the alkyl thiol surfactant. For example, the presence of the significantly weaker binding tetrahexylammonium chloride (THAC) results in much larger clusters than do bromide head group cationics didodecyldimethylammonium bromide (DDAB) or tetraoctylammonium bromide (TOAB). Didodecyldimethylammonium bromide has a smaller micelle interior volume and one could rationalize the smaller final cluster size compared to TOAB by this factor.

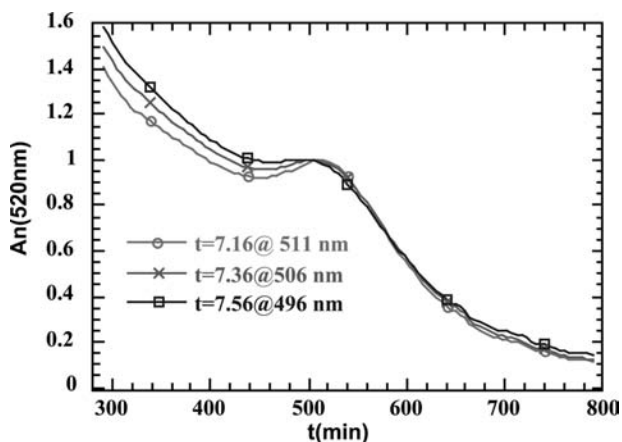


**Fig. 9** Elution peak spectral homogeneity of the sample Au,  $D_c = 3.8$  nm, with the broadest size distribution (linewidth) shows the population to be mildly inhomogeneous in size, but with only a spread of plasmon positions from 496 to 511 nm, a size dispersion of about  $\pm 0.5$  nm. *Source:* Previously unpublished work.

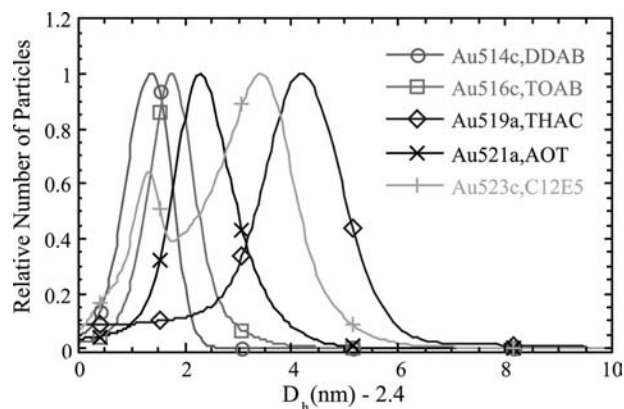


**Fig. 10** Plot of the Au core size  $D_c = D_h - 2.4$  obtained by assuming the previously measured total shell thickness of 2.4 nm, vs. normalized detector response at 520 nm (relative number of particles). The surfactants used in the synthesis are indicated. *Source:* From Ref.<sup>[31]</sup>.

A most surprising result was the formation of a bimodal population distribution from inverse micelles of the nonionic surfactant C12E5 in toluene, whereas only a narrow dispersion, monomodal distribution is produced when alkanes are used as the oil continuous phase, as has been reported previously.<sup>[35,36]</sup> This illustrates that the packing of the surfactant molecules into a droplet-like interface, and the lability of this interface is strongly affected by the interaction of the surfactant alkyl chains with the oil used.

Finally, one might wonder about the role of precursor salt concentration on the final size and size distribution in the inverse micelle synthesis. To study this we used a single cationic surfactant two component micelle system (TOPB/tol), where TOPB = tetraoctylphosphonium bromide and a fixed  $[\text{metal}]/[\text{surfactant}]$  ratio. As the  $[\text{HAuCl}_4]$  was varied from 0.01 to 0.1 M, no discernible change in size from  $D_c \sim 1.9$  nm was observed, nor did the size distribution alter as monitored by elution peak linewidth. This is in strong contrast to metastatic reduction reactions of organometallics in coordinating organic solvents, where an increase in  $[\text{precursor metal-organic}]$  leads to systematically greater final sizes with concomitant increases in size dispersion. For example, in the case of Fe(II) reduction in a coordinating solvent, an increase in size from  $D_c \sim 2.0$  to 14 nm occurs over the same concentration range. This illustrates the fundamentally different mechanism operating in the inverse micelle case.

### Optical Properties of Au, Ag, and Au/Ag Core-Shell Nanocrystals

In the proceeding section, we touched on the very interesting optical properties of Au, which exhibits a

non-classical (i.e., not explained by the Mie theory of electromagnetic scattering from metal colloids), blue shift and damping of the plasmon absorbance peak with decreasing size.

In Fig. 11, we show the absorbance chromatograms of several samples of Au nanocluster samples all stabilized with dodecanthiol to ensure a nearly constant shell thickness and interface environment. The peak heights have all been normalized to allow easy comparison of the elution shapes and widths. The elution peaks have *not* been deconvoluted with the instrumental band broadening. The size, as determined from the peak apex elution time, is given in Table 2. A constant shell thickness of  $2.4 \pm 0.1$  nm, as determined previously,<sup>[30]</sup> was used for all samples to obtain the metal core size.

The corresponding optical spectra for each sample at the peak of its elution are shown in Fig. 12. The spectra are normalized so that absorbance = 1.0 at 500 nm in each case. From this figure, we obtain the size-dependent blue shift and broadening of the optical plasmon as a function of size. This information is contained in Table 2.

The data from Fig. 12 and Table 2 demonstrate that, as the size decreases into the quantum size regime, a very rapid broadening and blue shift of the absorbance occurs between  $D_c = 3.0$  nm and  $D_c = 1.3$  nm. The classical Mie theory assumes no size dependence to the complex dielectric constant  $\epsilon(\omega)$  and so predicts that the optical plasmon for spherical Au clusters will blue shift with decreasing size until a size of  $D_c \sim 10$  nm is reached, at which point no further changes from the predicted peak position of 530 nm

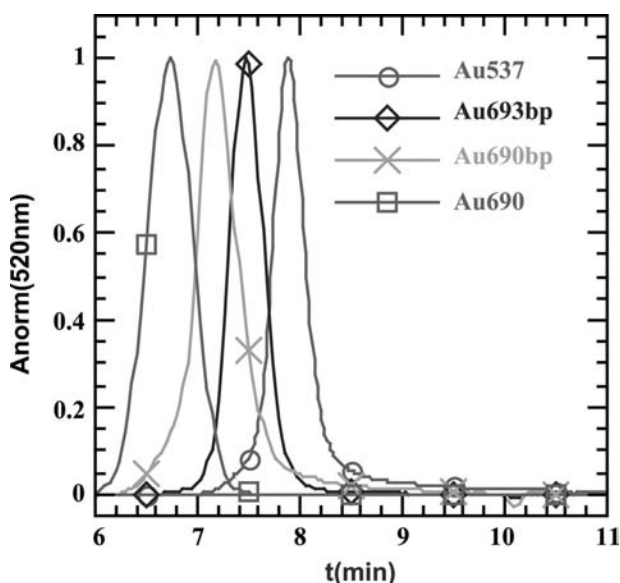


**Fig. 11** Normalized absorbance chromatograms of several differently sized Au nanocluster samples. *Source:* From Ref.<sup>[36]</sup>.

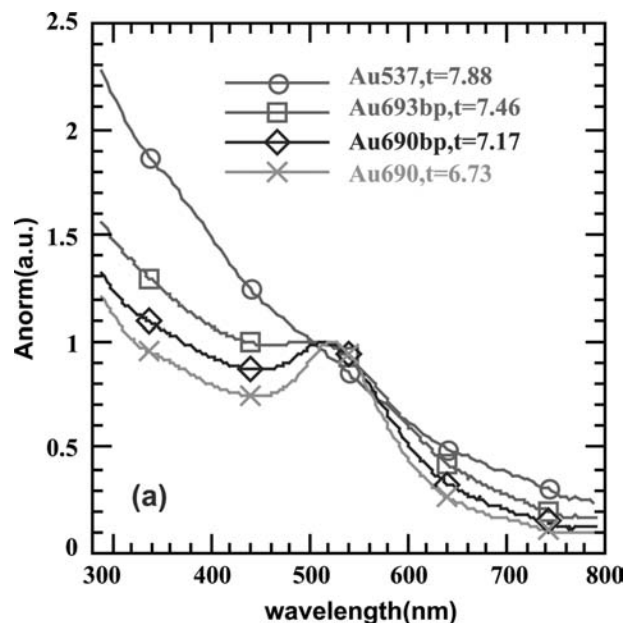


**Fig. 12** Normalized peak elution spectra from Fig. 11 demonstrate the effect of decreasing Au nanoclusters size (increasing elution time) on the optical absorbance in the visible. *Source:* From Ref.<sup>[36]</sup>.

(in toluene) or half-width should occur. Thus all the spectra shown in Fig. 12 are non-classical in character, exhibiting significant blue shifts and broadening compared to the Mie prediction. The effects of cluster size are usually accounted for by assuming that  $\epsilon(\omega)$  is size-dependent. This allows classical effects, such as increased electron scattering at the metal–dielectric interface, to be empirically incorporated into the theory, as well as quantum size effects (QSE) and the effect of chemical interface damping. Although all these effects are predicted to increase the linewidth, just as what has been observed in the present experiments, as well as the majority of experiments on embedded clusters, a prediction of the direction of the peak shift is much more problematic.<sup>[2]</sup>

The absorbance spectra in Fig. 12 have been normalized at a common wavelength, 500 nm, to allow easy comparison of the peak shapes. (See Table 1 for sample synthesis conditions and other details. Note that the sample number has nothing to do with the number of atoms in a cluster, which can only be approximately estimated even with TOF-MS.) Both the UV and, to a lesser extent, the NIR absorbance are enhanced as the cluster size decreases. We have also noted the development of new features in the absorbance profile of the smallest  $D_c = 1.7$  and  $D_c = 1.3$  nm clusters.<sup>[31,36]</sup> More recent work by others has confirmed this trend, which is attributed to the appearance of molecule-like density of states in small metal clusters.<sup>[45,46]</sup>

**Table 1** Ag and Au nanocluster synthesis

Sample name	Metal salt	Surfactant	Solvent	Reductant	Passivator
Au511p	HAuCl <sub>4</sub> (0.01 M)	TOAB (0.06 M)	Toluene	NaBH <sub>4</sub> (0.04 M)	C12SH
Au514cp	HAuCl <sub>4</sub> (0.01 M)	DDAB (0.1 M)	Toluene	LiAlH <sub>4</sub> (0.04 M)	C12SH
Au521a	HAuCl <sub>4</sub> (0.01 M)	AOT (0.2 M)	Toluene	LiAlH <sub>4</sub> (0.04 M)	C12SH
Au537	HAuCl <sub>4</sub> (0.01 M)	TOAB (0.06 M) C12SH (0.03 M)	Toluene	NaBH <sub>4</sub> (0.1 M)	N.A.
Au567p	HAuCl <sub>4</sub> (0.01 M)	TOAB (0.06 M) C16SH (0.03 M)	Toluene	LiAlH <sub>4</sub> (0.04 M)	N.A.
Au687bp	HAuCl <sub>4</sub> (0.01 M)	C12E5 (0.2 M)	Octane	LS-SelBH (0.04 M)	C12SH
Au690	HAuCl <sub>4</sub> (0.01 M)	C12E5 (0.2 M)	Hexadecane	SuperH (0.08 M)	N.A.
Au690bp	HAuCl <sub>4</sub> (0.01 M)	C12E5 (0.2 M)	Hexadecane	SuperH (0.08 M)	C12SH
Au693bp	HAuCl <sub>4</sub> (0.01 M)	C12E5 (0.2 M)	Hexadecane	LSelAlH (0.08 M)	C12SH
Ag114	AgNO <sub>3</sub> (0.01 M)	TOAB (0.12 M)	Toluene	NaBH <sub>4</sub> (0.02 M)	N.A.
Ag205	AgNO <sub>3</sub> (0.01 M)	TOAC (0.12 M)	Toluene	LiAlH <sub>4</sub> (0.02 M)	N.A.
Ag213	AgNO <sub>3</sub> (0.01 M)	TOPB (0.12 M)	Toluene	NaBH <sub>4</sub> (0.02 M)	N.A.

Surfactant abbreviations are: AOT = *bis*(2-ethylhexyl) sulfosuccinate sodium salt, C12E5 = penta-ethyleneglycol-mono-*n*-dodecyl ether, DDAB = didodecyldimethylammonium bromide, TOAB = tetraoctylammonium bromide, TOAC = tetraoctylammonium chloride; reductants prepared in anhydrous tetrahydrofuran (THF) as 1–2 M solutions, SuperH = LiB(C<sub>2</sub>H<sub>5</sub>)<sub>3</sub>H, LS-SelBH = LiB(CH(CH<sub>3</sub>)CH(CH<sub>3</sub>)<sub>2</sub>)<sub>3</sub>H; LSeAlH = LiAl[OC(CH<sub>3</sub>)<sub>3</sub>]<sub>3</sub>H, final concentrations are indicated in table.

One does not need separate, completely monodisperse samples to determine the optical absorbance behavior of metal nanoclusters as a function of size, because the SEC process will separate clusters with very small differences in size  $\sim \pm 2 \text{ \AA}$  and the PDA detector will provide the spectra corresponding to these sizes. The information obtained on samples exhibiting size polydispersity is very consistent with that

obtained from the peak apex spectra of the individual samples of Table 2, demonstrating the consistency of the SEC size analysis. For example, in Table 2, we show that Au693bp has a peak retention time of 7.5 min corresponding to an average size of 2.9 nm and a plasmon peak at 501 nm. This is within the experimental uncertainty of the data of Fig. 12 corresponding to a size of 2.8 nm and having a plasmon

**Table 2** Size-dependent optical properties of Au and Ag nanoclusters

Sample name	$t_e$ (min)	$D_{\text{core}}$ (nm, SEC)	$D_{\text{core}}$ (nm, TEM)	$\lambda_p$ (nm)	$\Delta\lambda_{1/2}$ (nm)
Au511p	7.24 ± .21	3.60	3.5	506 ± 2.4	110
Au514cp	8.02 ± .19	1.33	1.5	none	
Au521a	7.68 ± .21	2.21	2.4	none	
Au537	7.88 ± .19	1.67	1.8	none	
Au567p	7.80 ± .05	1.40	1.5	none	
Au687bp	7.50 ± .02	3.10	3.0	496 ± 2.4	120
Au690	6.73 ± .30	6.0	6.2	523 ± 2.4	69
Au690bp	7.17 ± .20	4.0	4.2	513 ± 2.4	86
Au693bp	7.47 ± .26	2.90	3.0	501 ± 2.4	120
Ag114	7.93 ± .17	1.55	1.8	486 ± 4.8	124
Ag205	7.24 ± .22	3.70	4.0	440 ± 4.8	60
Ag213	6.3 ± .25	7.6	7.5	423 ± 4.8	39
	7.73 ± .17	2.4	2.5	474 ± 4.8	91
Ag213	6.7	6.2	Not measured	423 ± 4.8	48
	7.0	4.7		428 ± 4.8	69
	7.2	3.9		443 ± 4.8	76
	7.4	3.1		457 ± 4.8	79
	7.6	2.5		467 ± 4.8	86

$\Delta\lambda_{1/2}$  (nm) = Half-width at half maximum determined on long wavelength side of asymmetrical plasmon peak.



peak at 496 nm because the spectra bandwidth was set at 2.4 nm. The size-selected cluster population of Au #511b, which elutes near the half-maximum at  $t = 7.14$  min, corresponds to a SEC size of 4.2 nm and has identical spectra to that at the peak apex of Au #690bp.

In a recently submitted paper, we demonstrate a synthesis based upon the seminal work of G. Schmid,<sup>[7]</sup> which illustrates the selection and optical characterization abilities of HRSEC for strongly polydisperse samples.<sup>[31]</sup> In that paper, we illustrated the effects of the emergence of a discrete, “molecule-like” density of states in Au “molecules” specifically, Au( $N = 13$ ), the smallest closed shell atomic configuration. Such molecular species had been previously shown by us<sup>[48]</sup> and subsequently by others<sup>[45,46]</sup> to have both visible and NIR photoluminescence (PL), which is a startling result! This relatively strong PL ( $\sim 10^{-4}$  Q.E.) can come from both s-to-d interband transitions (visible PL), or intra-d-band transitions (NIR and IR PL). Such unexpected optoelectronic properties illustrate the reason why very small nanoclusters are so interesting.

### Ag nanoclusters

We next examine the size dependence of the optical absorbance of Ag nanoclusters grown in inverse micelles and stabilized with the identical alkyl thiol (C12SH) used in our Au cluster studies. A strong motivation for this complementary study is the important difference in the optics of Au and Ag clusters arising from the different energies of the interband (filled d shell to conduction sp band) transition onsets in the two metals. The close proximity of the interband transition to the plasmon energy in Au (it lies to the red of the plasmon energy) is the reason why energy damping (peak broadening) is so much greater for Au clusters than for Ag, where the interband transition energy onset lies significantly to the blue of the conduction band plasmon. This makes a determination of the size dependence of the linewidth for small Au clusters difficult (i.e., the peak simply disappears). It also leads to a pronounced asymmetry to the peak shape.

There has been a matter of significant controversy regarding the direction of the plasmon absorbance energy shift with cluster size in the quantum size region. Depending on details and relative weights assigned to the various theoretical factors, one can “predict” either a blue or a red shift with decreasing size. We had demonstrated a blue shift in the case of monodisperse, spherical nanoclusters of gold, and this is the general consensus based on dozens of papers in this field. However, the case of Ag is not as well established, and both red and blue shifts have been reported. We were considerably surprised when SEC and on-line

optical characterization of our inverse micelle prepared Ag nanoclusters showed a clear red shift with decreasing size. The magnitude of this shift was truly astounding compared to gold. In the smallest clusters we studied, the damping of the very sharp and relatively symmetrical absorbance plasmon of Ag completely disappears—the first such observation in nanosize Ag. Fig. 13 shows the effect of size decreases on the position of the optical absorbance of Ag nanoclusters.

The main feature of the optical absorbance of nearly free-electron metals such as Cu, Au, or Ag is a condensation of the conduction electron oscillator strength into a narrow frequency band of plasmon polariton excitations, which are caused by the particle surface—the plasmon resonance. If the dielectric function for a metal cluster does not depend on its size, little or no variation in the position of energy maximum of the plasmon absorbance profile is predicted to occur below a size of 10 nm. So, for particles smaller than this size, as Kreibig and Genzel have pointed out,<sup>[49]</sup> the absorbance band shape only changes with size if intrinsic particle effects are important. It has been established by numerous experiments that, for sizes less than  $\sim 5$  nm,  $n(\omega, R) \sim 1/R$ .<sup>[2]</sup> This is, of course, just the surface-to-volume ratio.

Both classical effects [such as electron scattering at the metal/dielectric interface and quantum size effects (QSE)] become important at sizes below  $\sim 5$  nm. The latter effects, in particular, should become important when the level spacing near the Fermi level exceeds

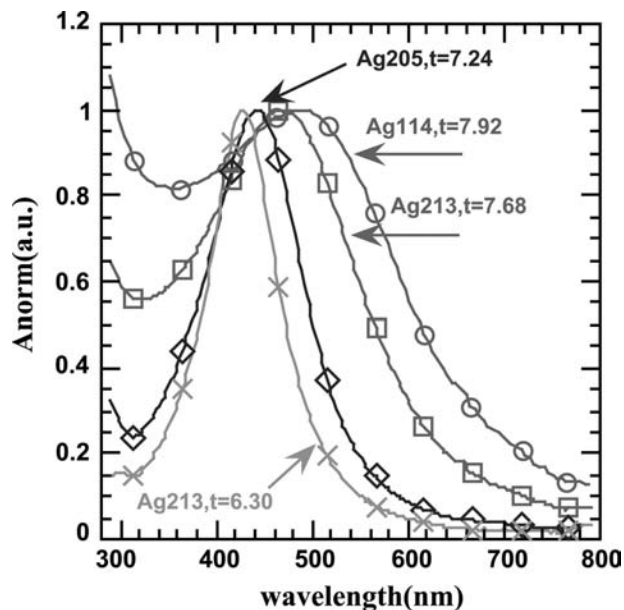


**Fig. 13** SEC separation and on-line characterization of Ag nanocluster solutions in toluene show the strong red-shift and extreme damping of the plasmon with decreasing size. See Table 1 for synthesis details and other information. Source: From Ref.<sup>[36]</sup>



the available thermal energy. This will occur at about 400 atoms of Au, or a size of about 2.5 nm, assuming the nanoclusters to have the density of the bulk material.<sup>a</sup> It turns out that both classical effects, such as the reduced free path of the electron and QSE effects, both predict a  $1/R$  dependence to the resonance linewidth, so an observation of a  $1/R$  behavior to the resonant linewidth does not, by itself, demonstrate a QSE. However, the emerging weak features in the spectra of our smallest clusters probably do indicate the onset of discrete bands, which is a true QSE.

A further complication in the interpretation of experimental observations in either classical (electron scattering) or quantum confinement (continuous bands becoming discrete) behavior occurs in the case of metals such as Au and Cu, in which the onset frequency of the interband transitions from d-type orbitals to the sp-type conduction band is close to the plasmon energy. In this case, there are major changes in the resonance energy just because of the importance of these transitions. For example, in the case of both Cu and Ag, the free-electron (Druid model) Mie theory predicts a resonance of  $\sim 9.2$  eV in a vacuum ( $\epsilon_m = 1$ ); however, the contribution of the 4d core electrons to the susceptibility shifts this to the experimental value of  $\sim 3.8$  eV for Ag but  $\sim 2$  eV for Cu! It may be that the different directions of the plasmon energy shift we have established for Au and Ag with the same passivating layer, embedded in an identical media, toluene, are a result of the relatively greater importance of the interband transitions in Au compared to Ag. For a more extensive discussion of our findings for nanosize Au and Ag, we refer the reader to Ref.<sup>[36]</sup> and the monograph by Vollmer and Kreibitz,<sup>[2]</sup> which is the definitive modern work on this subject.

The Ag samples whose spectra were shown in Fig. 13 are all coated with an identical ligand, C12SH, which gives keeps the clusters from aggregating even when deposited onto a holey carbon grid and inserted into the high vacuum of an electron microscope. Fig. 14 shows a TEM of Ag #205 illustrating the ready formation of arrays which we have termed quantum dot arrays—the next subject of this review.

We summarize our findings concerning the size-dependent optical properties of Au and Ag as follows. For both Au and Ag clusters in the size range  $D_c = 8$  to  $d = 1.5$  nm, the plasmon linewidth broadens following a  $1/R$  linewidth size dependence, whose slope

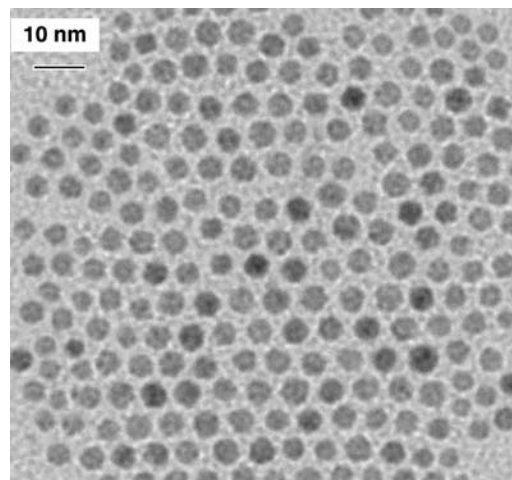


**Fig. 14** TEM of Ag #205,  $D_c = 4.0 \pm 0.5$  nm nanoclusters with a plasmon peak at 440 nm in toluene.

is greatest for Au. The peak asymmetry in the plasmon band shape is greatest for Au and increases with decreasing size for both Au and Ag clusters. The plasmon peak energy blue shifts with decreasing size for Au clusters, while in the case of Ag nanoclusters a red shift is observed.

### Core–Shell Particles and Alloys of Au and Ag

There are many scientific reasons to investigate core–shell or alloy nanoclusters. For example, even monolayer shell coverages can shift the Fermi level,  $E_f$ , via e-donation/acceptance by huge amounts (e.g.,  $\sim 20$ – $30\%$  donation/atom blue shifts  $E_f$  by  $\sim 1$  eV!). In the case of metals with dissimilar electron affinities, interface structures may form, which are similar to doping-induced depletion zones in bulk semiconductor materials. This effect may be a basis for metal rectification or spatial charge separation and thus of importance to nanocluster photocatalysis.<sup>[50,51]</sup> In view of the very interesting physics of such core–shell structures and the possibility of “reconstruction” occurring as the result of a heteroatomic deposition process, this area of nanometals should be very fecund and deserving of future investigation.

The coinage metals Au and Ag are a nearly an ideal system to study the effects of size and composition on the optical properties of nanoparticles because they have identical covalent radii, have simple fcc cubic lattice structures, and are miscible in all proportions. (However, this also means that diffraction-based methods such as TEM are not very useful for determining their structures.) One may pose a myriad of questions—some of which may even be theoretically treated—albeit, within the confines of classical electromagnetic Mie theory. For example, for fixed

<sup>a</sup>Quantum size effects are a result of the discrete nature of the electronic levels as a cluster is built up from atoms. The level splitting ( $\Delta E$  is roughly given by  $\Delta E \sim E_f/N$ , where  $E_f$  is the Fermi level of the metal and  $N$  is the number of atoms in the cluster. If  $E_f \sim 5$  eV, eV, then ( $\Delta E \sim 50$  meV for a 100-atom cluster. At room temperature, one might see these effects for Au at  $N \sim 400$  or  $d \sim 3$  nm.

composition and size, how does the order of deposition Au/Ag vs. Ag/Au (core-shell) affect the optical spectra? For equivalent atomic compositions and size, does a random nanocluster alloy of Au and Ag differ optically from the corresponding core-shell cluster? For a fixed total size, how does composition affect the optical absorbance?

First, a brief remark on the synthesis of core-shell vs. alloy nanometals. To make alloy-type materials, a chosen ratio of precursor salts (typically  $\text{NaAuCl}_4$  and  $\text{AgNO}_3$ ) are dissolved in a suitable inverse micelle solution. A reducing agent is then added to effect core-reduction. The agent chosen should approximately have the same reduction kinetics to avoid prenucleation of one material over the other, which would result in a core-shell type structure. By using an extremely aggressive reduction such as  $\text{LiAlH}_4$ , both metals undergo instantaneous reduction provided aggressive mixing is utilized.

To make core-shell structures, a simple variation on our newly developed solution epitaxial growth, which will be reported in a future work,<sup>[52]</sup> is employed. Specifically, a given seed nanocrystal, say  $D_c = 1.8$  nm Au, is purified via SEC or precipitation methods, and a metal organic precursor solution is slowly coinjected along with the reductant, typically  $\text{NaBH}_4$ , via a syringe pump. A slow injection rate, typically 1–2 mL/hr is used, to ensure hetero- vs. homogeneous nucleation of the growth solution. A key aspect is the choice of a suitable surface active agent as well as the organometallic atom source. In general, one wishes to avoid the use of micelle-forming surfactants because these may act as nucleation centers for homoatomic clusters from the feedstock. For Au/Ag and Ag/Ag core-shell nanocrystals, small amounts of long-chain alkyl thiols work quite well and allow facile SEC analysis to be performed.

### Effect of Alloying on Ligand Binding

Size exclusion chromatography can be used to determine the relative binding of ligands of a given size and metal type as mentioned earlier in this review. We demonstrated that no thiol exchange occurs for  $\text{C}_k\text{SH}$ ,  $k = 6, 10, 14$ , in the case of Au nanoclusters, when an overwhelming amount of  $\text{C}_{12}\text{SH}$  is in the mobile phase. In contrast, Ag nanoclusters with the identical thiols on their surface completely exchanged with the  $\text{C}_{12}\text{SH}$  in the mobile phase during the chromatography as evidenced by a common elution time in all cases, which corresponds to a shell of  $\text{C}_{12}\text{SH}$  (the core size is fixed in both cases). One must remove the completing thiol from the mobile phase and use a pure toluene eluant to observe the effect of various organic shell thicknesses on the elution time.

What is the effect of alloying or formation of a core-shell structure on the thiol binding behavior? We find that 1:1 (atomic ratio) alloys of a common core size,  $D_c \sim 2.0$  nm, elute at distinct times, which correspond to the organic shell thickness as shown in Fig. 15. So the effect of alloying Ag with Au is to prevent ligand exchange. At least two rationalizations of this observation are possible. The change in interatomic coordination and bonding distance in a spherical cluster alloy of Au/Ag affects the thiol metal binding strength, or, more likely, having Au sites at the surface of the metal alloy nanocluster allows the thiol to preferentially bind to these sites. In either case, our alloy AuAg binding results have obvious ramifications for issues in catalysis, where it is empirically known that even small amounts of metal atoms in a majority phase (e.g., Co in  $\text{MoS}_2$  hydrodesulfurization catalysts) has a profound effect on the catalytic activity by affecting the Mo substrate binding strength.

Despite the differences in total hydrodynamic size observed in Fig. 15 as a result of the alkyl chain length differences, the optical spectra of each 1:1 Au/Ag alloy nanocluster are indistinguishable, as demonstrated by the elution peak apex absorbance spectra shown in Fig. 16. For similar-sized nanoparticles of pure Ag, the plasmon would occur at 460 nm, while there would be no discernible plasmon peak as a result of damping effects in a pure Au sample of this size. So the effect of alloying on the optical properties of small noble metal nanoclusters is dramatic and constitutes the clearest evidence of a significant composition change from the corresponding pure metal Qdots of equivalent size.

Suppose we grow a 1:1 nanocrystal alloy of a smaller size. Which direction will the plasmon energy shift? If the cluster were pure Ag, a red-shift would be expected, while for pure Au, a blue shift is the norm.

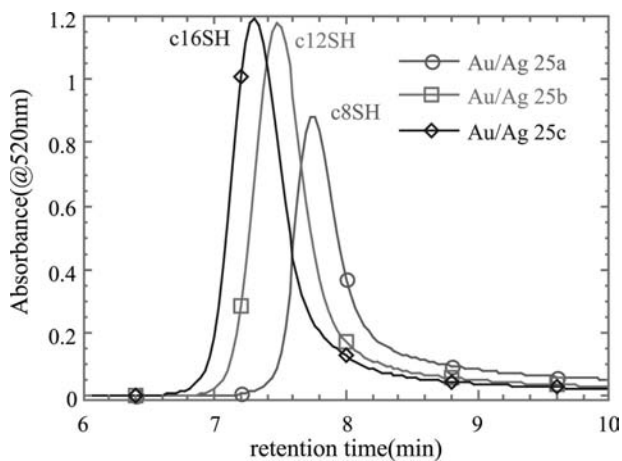


**Fig. 15** Effect of organic shell on the total hydrodynamic size of Au/Ag alloy nanoclusters formed by core-reduction of the precursor salts in inverse micelles. *Source:* Unpublished data.

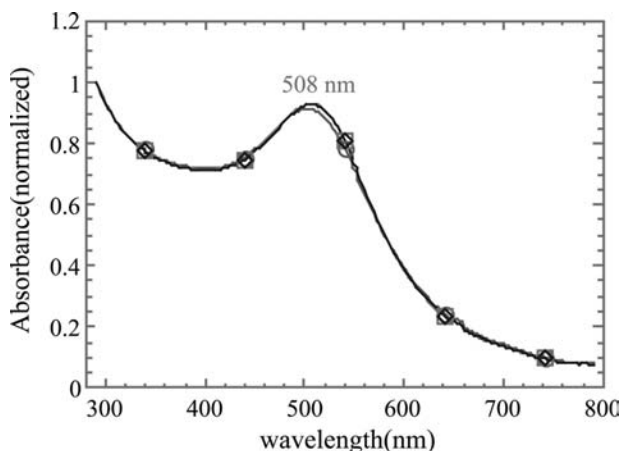


**Fig. 16** The peak apex absorbance spectra of a  $D_c = 2.4$  nm 1:1 Au/Ag alloy. *Source:* Unpublished data.

The results are shown in Fig. 17. The peak apex absorbance spectra of a 1:1 Au/Ag alloy blue shifts with decreasing size, so the Au component dominates its optical behavior. As expected, an increased damping of the plasmon occurs with decreasing size occurs; however, a distinct absorbance maximum is still observed even for  $D_c = 1.8$  nm clusters, apparently because of the silver component, a truly remarkable decrease in the dissipation of the electron plasmon oscillations! A complete theoretical explanation of the alloy behavior in the quantum size regime will prove most challenging, considering that even the extent of damping (peak broadening) and energy shift cannot be predicted currently for pure metal Qdots.

To impress upon the reader how distinct the optical absorbance behavior of the  $D_c = 1.8$  nm alloy Qdots are from the pure nanometals of the same size, coated with the identical organic thiol we show in Fig. 18 the spectra from such dots, obtained at the peak apex of the chromatograms.

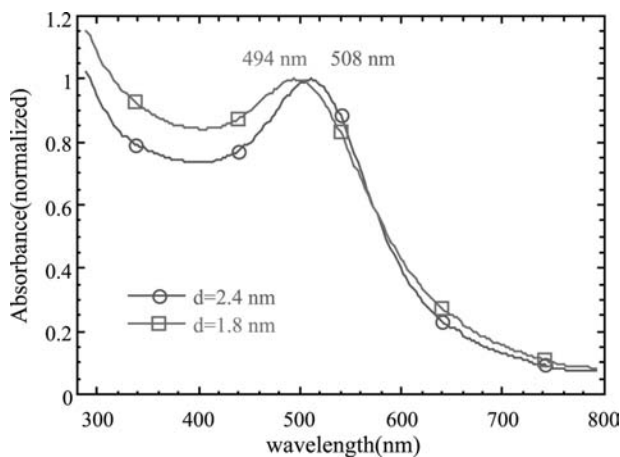


**Fig. 17** The peak apex absorbance spectra of a  $D_c = 2.4$  and 1.8 nm 1:1 Au/Ag alloy. *Source:* Unpublished data.

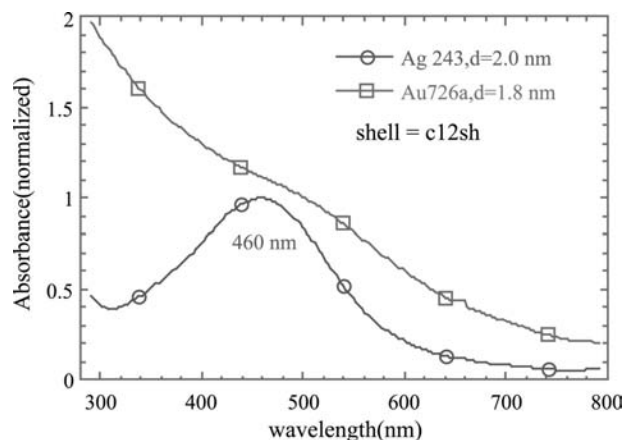


**Fig. 18** The peak apex absorbance spectra of  $D_c \sim 1.9$  nm pure metal nanoclusters. Compare with the spectra of Fig. 17. *Source:* Unpublished data.

As one might anticipate, Au/Ag and Ag/Au nanocrystals of the same size have very distinct optical absorbance signatures, which can be easily seen with the naked eye. Consider first the growth of Ag onto a purified seed solution of Au,  $D_c = 6.8$  nm, as shown in Fig. 19. The relatively large seed nanocrystals have a distinct absorbance peak at around 520 nm in benzene, which gives them a wine red color. As Ag is slowly deposited onto their surface the absorbance blue shifts, in the direction one would expect for Ag clusters, the peak becomes more symmetrical and narrows with increasing amounts of Ag deposition. In short, the Ag shell component begins to dominate the optical properties.

Fig. 20 shows the case of growth of a Au shell onto a  $D_c = 2.5$  nm Ag nanocluster seed. The relatively sharp and symmetrical resonance of the Ag homoatomic cluster broadens and red shifts as Au is

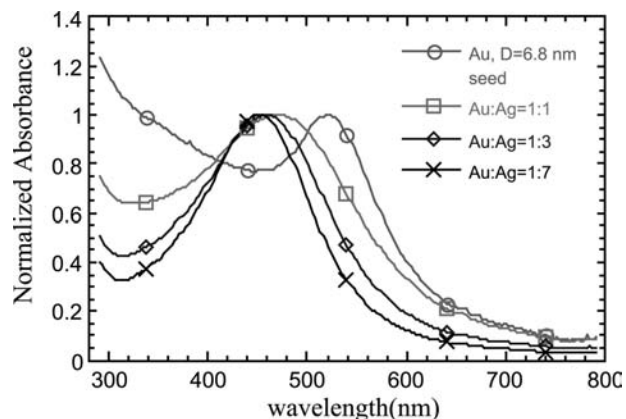


**Fig. 19** Optical absorbance for a series of Au/Ag nanoclusters starting from a  $D_c = 6.8$  nm Au nanocrystal. The atomic ratios of Au/Ag are indicated in the figure. *Source:* Unpublished data.

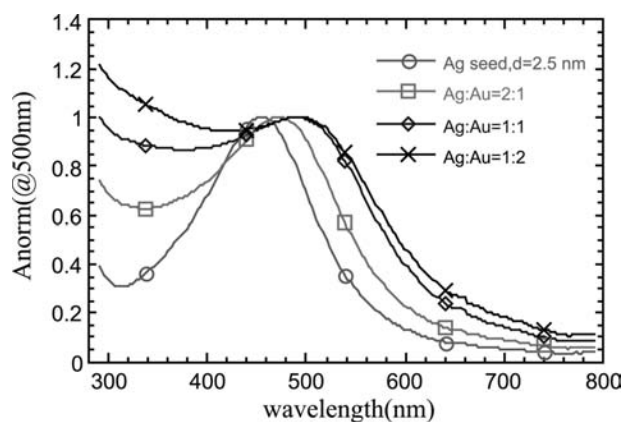


**Fig. 20** Optical absorbance for a series of Ag/Au nanoclusters starting from a  $D_c = 2.5$  nm Ag nanocrystal. The atomic ratios of Au/Ag are indicated in the figure.

deposited. The 1:1 ratio case is worth comparing to the 1:1 alloy of approximately the same size from Fig. 17. One notes that the alloy has both sharper and more red shifted ( $\lambda_{\max} \sim 508$  nm) compared to the core-shell spectra of Fig. 20. One observes also that the 1:2 Ag/Au nanocluster has not red shifted to the extent one would predict for a pure Au cluster of the same size, but exhibits considerably more dissipation (line broadening) and red-shift than expected for a corresponding homoatomic Ag nanocluster of equivalent size.

There is a considerable literature discussing thermal decomposition routes to the formation of base metal colloids, which has been recently reviewed.<sup>[34]</sup> These methods are based on the decomposition of metal carbonyls in the presence of a surfactant or polymer in a relatively high boiling point solvent such as xylene or triethyl benzene. In general, these methods are only effective in producing larger nanoclusters with  $D_c > 4-5$  nm with considerable nanocrystalline defects and polydispersity. Recent refinements in these methods have significantly improved on the polydispersity but, unfortunately, because of the rapid nature of the decomposition, significant defects are inevitable and are reflected in the poor magnetic response compared to the bulk counterparts (e.g.,  $\sim 0.2$  of  $M_{\text{sat}}$  for  $D_c \sim 6$  nm hcp Co).

What is very interesting is that different structural phases of these nanoclusters may be produced depending on the synthetic approach. We gave the first example of this in a paper describing the effect of surfactant on the formation of either  $\alpha$ -Fe (bcc phase) or  $\gamma$ -Fe (high  $T$ , fcc phase) using the inverse micelle process.<sup>[53]</sup> Later work by Sun and Murray<sup>[54]</sup> showed an even more surprising result for Co, which, when reduced by Superhydride at high  $T$ , produced the  $\varepsilon$ -Co phase, a complex 20-atom/unit cell structure related to  $\beta$ -Mn. These Co nanoparticles could be

converted to the hcp phase by annealing at  $>300^\circ\text{C}$ . However,  $\varepsilon$ -Co nanocrystalline Co showed significantly lower magnetic response than hcp Co of the same size.

### Base Metal Nanoclusters—Co, Fe, and Ni

A puzzle is the observation that, even in the case of directly synthesized nanocrystalline hcp Co, as the size reached the lower size limit of high- $T$  methods,  $D_c \sim 3$  nm, a saturation magnetism of only 8 emu/g was observed, about 5% of the bulk value.<sup>[34]</sup> Even for the largest  $D_c \sim 11$  nm Co clusters, a value of only about 60% of the bulk was observed. Likewise, the value of  $\sim 60\%$  is about what is the best achieved for nanocrystalline  $\alpha$ -Fe. Is the lowered magnetic response attributable to the surface, nanocrystalline defects, spin canting effects, or inadvertent formation of an oxide layer? Although lower density oxide is evident in TEMs of these nanomaterials, its thickness is probably not sufficient to explain the lowered magnetic response, so a likely explanation is poor spin exchange coupling as a result of nanocrystalline defects and/or spin canting near the surface.

By contrast, using the inverse micelle approach, which entails significantly lower nanocrystalline growth rates, we have recently observed saturation magnetism for  $D_c \sim 1.8$  nm Co nanoclusters slightly greater than bulk values. This implies full contribution of all the spins to the magnetism, including those at the cluster surface. This is a somewhat unexpected result and seems to depend very sensitively on the chemical nature of the surfactant used to grow the nanoclusters, as well as the time allowed for structural “reconstruction” of the as-synthesized cluster surface. Details will be presented elsewhere.<sup>[56]</sup> However, our results are consistent with previous observations of very small Co, Fe, and Ni nanoclusters made in cluster beams in vacuum and studied by magnetic deflection combined with mass selection.<sup>[24]</sup> The fact that magnetic clusters can be grown in solution with high magnetic response and no hysteresis (i.e., they a superparamagnetic at all  $T$ ) bodes well for potential applications requiring no energy dissipation [transformers and other high radio frequency (RF) inductors].

### Formation and Analysis of Quantum Dot Arrays

Hexagonal or cubic packed “rafts” or arrays of quasi-monodisperse spherical colloids [quantum dots arrays (QDAs)] can readily form on various types of substrates upon drying from the liquid phase. Many factors including the initial cluster concentration, the drying rate, the type and physical size of organic ligand “shell,” and the cluster core size itself affect the quality of the final cluster film. Just as in bulk crystallization,



defects and voids may be introduced if the drying rate is too rapid, trapping colloids in metastable positions. I highly recommend observing the drying of micron-size polystyrene spheres in water on a glass slide under a microscope to understand the role of various factors in the state of the final colloidal film. It is amazing to watch the spheres flow into the drying front and then find the best packing position (usually hexagonal) for themselves. Sometimes, a sphere will not remain mobile long enough to position itself in the ideal position. Subsequently, this point defect will propagate through the rest of the drying front creating a line defect. In other rare cases, a dumbbell-shaped dimer of two spheres will approach the drying front and, because of its strong intersphere interaction, cannot fit into the proper position in the lattice. Minority spheres of the wrong size and or shape will often be excluded from the lattice, a spontaneous form of size segregation. All of these factors are important on the nanoscale as well although we do not have the ability to observe the dynamics of lattice formation, only the final structures.

Au nanocluster superlattices were first reported in a 1993 entry by Giersig and Mulvaney,<sup>[56]</sup> who used a modified classical Faraday synthesis in water to produce ~14-nm diameter clusters. Because these samples were charged-stabilized with citrate ions, they were able to employ electrophoretic deposition to form monolayer arrays. Because of the small size of the citrate ion, the gap between particles was fixed and small at ~1 nm.

In 1994, Brust et al.<sup>[57]</sup> used an inverse micelle process in the presence of alkane thiols to make QDAs of 8-nm Au particles that were cross-linked with a bifunctional dithiol. Robert Whetten's group at Georgia Tech was the first to demonstrate the formation of QDAs with relatively small Au nanoparticles produced by using the inverse micelle technique with large amounts of thiol present during the reduction to severely limit the cluster growth. They also showed 3-D superlattices of significant (~1–10  $\mu\text{m}$ ) size.<sup>[58]</sup> Later work by Heath and coworkers utilizing inverse micelle techniques produced highly polydisperse dedecanthiol capped Au clusters which still formed ordered arrays in which they noted that size exclusion of smaller clusters occurred spontaneously during the drying process.<sup>[59]</sup>

In 2000, we reported the first quantitative studies of the effect of particle size and the organic capping thickness on the spacing and degree of ordering in Au QDAs.<sup>[41]</sup> These studies were enabled by the development of the first detailed digital image analysis methods for metallic nanocluster QDAs. Later, we reported similar studies on Pt QDAs, which had not been made previously.<sup>[42]</sup> We will summarize highlights of those entries now.

First, the formation and, in particular, the domain size of QDAs depend on many experimental factors. The successful formation of superlattices depends on the proper choice of oil, surface passivant, metal ligand binding strength, ligand chain length or structure, substrate type, and rate of drying.

Consider, for example, the effect of metal ligand binding strength on QDA stability. We have demonstrated via SEC that alkyl thiols bind considerably more strongly to Au and Pt nanoclusters of a fixed size than they do to Ag. This is reflected in the stability under TEM vacuum conditions of Au arrays compared to Ag ones. Although both initially form large, highly ordered hexagonal domains as observed in TEM, Ag QDAs rapidly (<1 day) deteriorate as a result of alkyl thiol desorption followed by cluster fusion or sintering.

We have also shown using SEC that the alkyl chain length affects the binding affinity of metallic Qdots for thiol surfactants. We find that longer chain length thiols bind more strongly, for example, to Au nanoclusters. TEM studies of QDAs, as a function of alkyl chain length  $k$ , confirm that short chain,  $k < 8$  thiols, fail to form large ordered domains. What is more surprising is that an optimal value,  $k = 10\text{--}14$ , is observed, with worse array formation despite stronger binding affinity for  $k = 16$ . Perhaps this is attributable to the observation that alkane ligands interdigitate and facilitate the QDA formation, and  $k = 16$  is approaching the length at which this process is still efficient.

The rate of drying and concentration of the initial cluster solution is also important in determining the structure of the final QDA. The effects here are a little more obvious, namely, faster drying and lower initial concentration favors the formation of monolayers of hexagonally or square packed Qdots, while higher concentrations and slower drying (less-volatile solvents) favors cluster pile-up and formation of bilayers and 3-D crystals on the substrate. In fact, 3-D crystals of Ag form so readily upon slow drying from solution that they can be observed on the glass surfaces of vials with inadequately sealed lids. Naturally, such molecular crystals dissolve readily into organic solvents.

Finally, we found that use of substrates such as Teflon was more effective than glass for the formation of large (~10–100  $\mu\text{m}$ ), supracrystals. See Fig. 21 is shown below. The triangular facets or crystal habit adopted by these QDA superlattices seems to depend on the nanocrystal core size, but this is a very complex issue (see Fig. 21). Graphite proved to be too porous for good QDA crystal superlattice formation, and holey carbon TEM grids, which are also relatively porous were more effective for the formation of either mono- or bilayer QDAs. However, these general observations are also particular to the metal type, with Ag

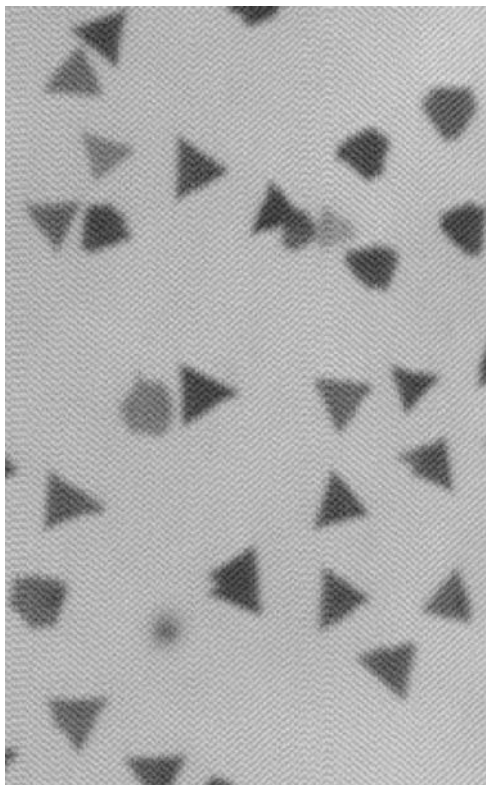


**Fig. 21** Optical micrograph of QDA 3-D superlattices made of Au nanocrystals with  $D_c \sim 4.6$  nm. *Source:* From Ref.<sup>[41]</sup>.

almost always showing both mono- and multilayer formation using holey carbon grids. One important technical point is that, for hydrophilic substrates such as glass, inert grease (Krytox) should be used to contain the non-wetting oil.

The nanocrystal size-dependent habit adopted by 3-D QDAs is amusingly illustrated in Fig. 22, for

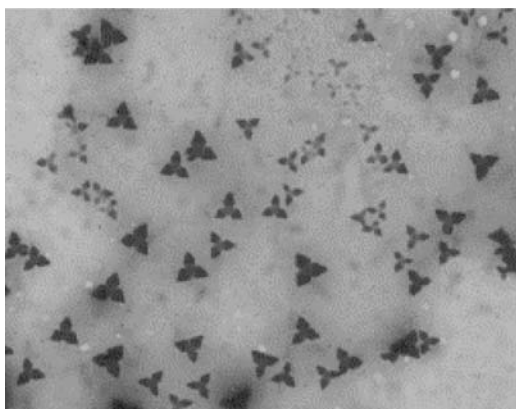


**Fig. 22** A tri-foil crystal motif is observed in an optical micrograph of  $D_c = 4.0$  Pt nanocrystals. It is reminiscent of a well-known Japanese corporate logo (although no funding was provided to influence this fortuitous observation). *Source:* From Ref.<sup>[42]</sup>.

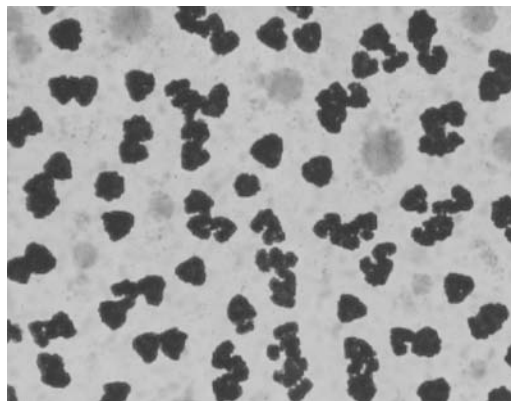


**Fig. 23** An optical micrograph of Pt QDAs formed by very small ( $D_c = 2.5$  nm) nanocrystals with slightly irregular shapes shows that crystal habit depends on the nanocrystal core size. *Source:* From Ref.<sup>[42]</sup>.

$D_c = 4.0$  nm Pt nanocrystals.<sup>[42]</sup> The “Mitsubishi” motif exhibited by these crystals is in marked contrast to that exhibited by smaller,  $D_c = 2.5$  nm crystals in Fig. 23. In both cases, dodecanthiol was used to passivate the surface, decane was used as the solvent, and an identical Pt concentration and substrate was used.

On larger-length scales still the QDAs of Fig. 21 form dendritic films, Fig. 24, of “cluster matter,” whose complex optical and electrical behavior was the subject of a fairly recent paper and is discussed in Kreibig and Vollmer’s monograph.<sup>[2]</sup> These dendritic films were shown to sinter into a metallic film with high optical reflectivity and electrical conductivity at low temperatures ( $\sim 200^\circ\text{C}$ ).<sup>[60]</sup>

Finally, it should be mentioned that, depending on growth conditions, many other crystal habits were observed, including large ( $\sim 1\text{--}10\ \mu\text{m}$ ) hexagonal motifs. The conditions that favor one habit over another are just as complex and difficult to understand as that of macrocrystalline growth from supersaturated solutions,

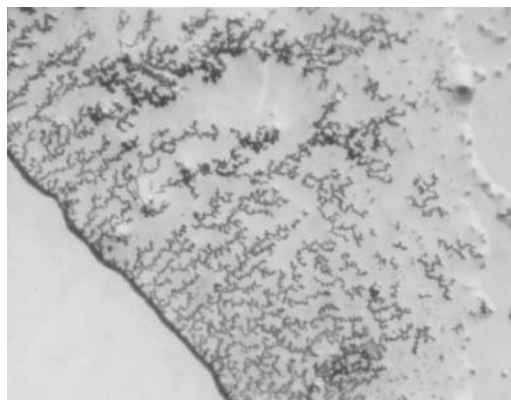


**Fig. 24** Optical micrograph at low magnification of the triangular Au QDAs shown in Fig. 21. *Source:* From Ref.<sup>[41]</sup>.



and growing QDAs of large size and high perfection is very much an art. An obvious goal would be to obtain crystals of sufficient size to perform single-crystal XRD and determine each atomic position in each identical nanocrystal to atomic resolution. This may well be possible in the future. It would answer some currently unknowable issues with respect to surface structure in nanocrystals with major impact on the design of nanometal catalysts, nanophosphors, etc.

### TEM image analysis

The qualitative observations of the preceding section can be augmented in the case of QDA monolayers by employing automated digital image analysis of large areas of TEM grids. Consider the TEM of Fig. 25. We first determine the center-of-mass position, and average size of all acceptable (i.e., non overlapping) nanocrystals in the image. These are then replaced with digital, color-coded balls of the same size, and the particle coordinates can be subsequently used to calculate both the 2-D and radial-averaged,  $g(r)$ , correlation functions. The latter is the Fourier transform of  $S(q)$ , the scattering structure factor which would be obtained from, for example, small-angle X-ray scattering (SAXS)<sup>[44]</sup> or neutron scattering (SANS). Balls that are sufficiently out of register with neighboring balls (e.g., in a hexagonal lattice) are then assigned colors that identify the coherent domains (analogous to the peak linewidth in SAXS). Fig. 26 shows the result of such assignments.

With the available domain and nanocrystal position information, one can then rotate each domain by the correct amount to obtain a coherent domain for the entire region (balls which fail to belong to any of

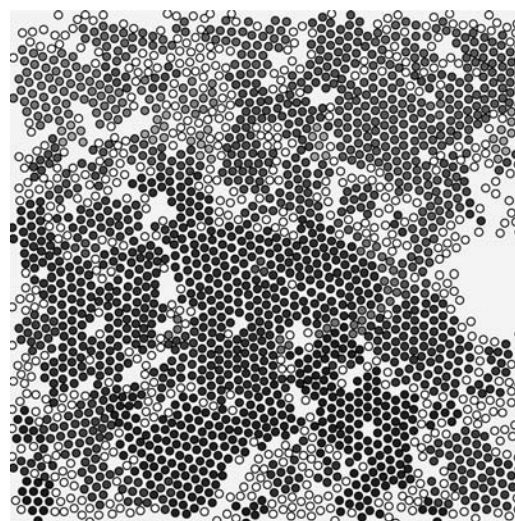


**Fig. 26** The digitized ball file containing the center-of-mass coordinates of the nanocrystals and whose ball color codes for the domain of a given ball is shown. *Source:* From Ref.<sup>[41]</sup>.

the domains are eliminated for simplicity). The resulting rotated 2-D correlation function is shown in Fig. 27. One easily observes the hexagonal symmetry of the QDA in this figure, and the very high degree of long-range order.

A radial average can then be performed to obtain  $g(r)$  and the average interparticle spacing. This is shown in Fig. 28. The hexagonal symmetry of the lattice is reflected in the splitting of the second peak, which is harder to observe when the domains are incoherent (i.e., not rotated). The average interparticle spacing and the gap can be very precisely determined from such analysis. This allowed us to perform a very precise

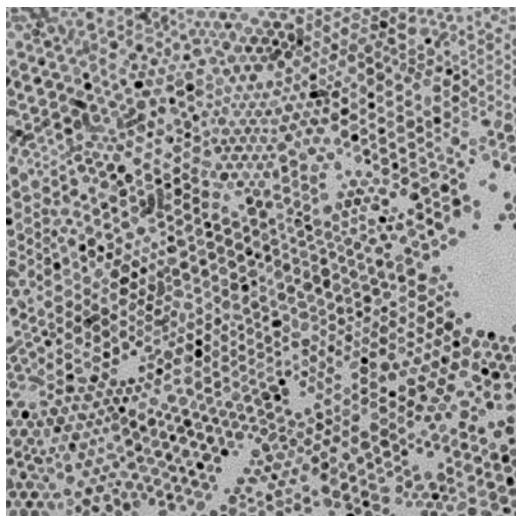


**Fig. 25** A monolayer of  $D_c = 4.6$  nm Au clusters that forms 3-D crystals as shown in Fig. 21. *Source:* From Ref.<sup>[41]</sup>.

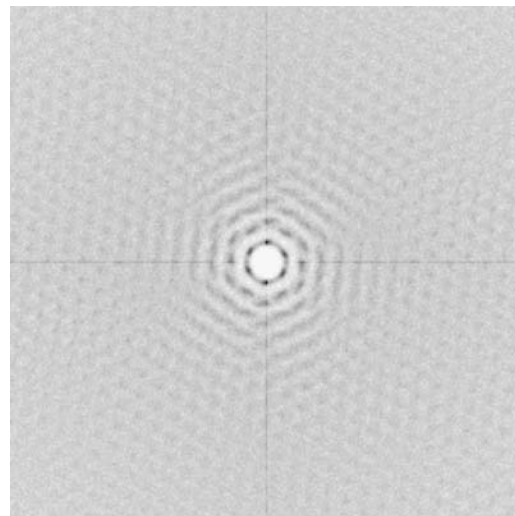


**Fig. 27** Rotated 2-D pair correlation function from Fig. 26. *Source:* From Ref.<sup>[41]</sup>.

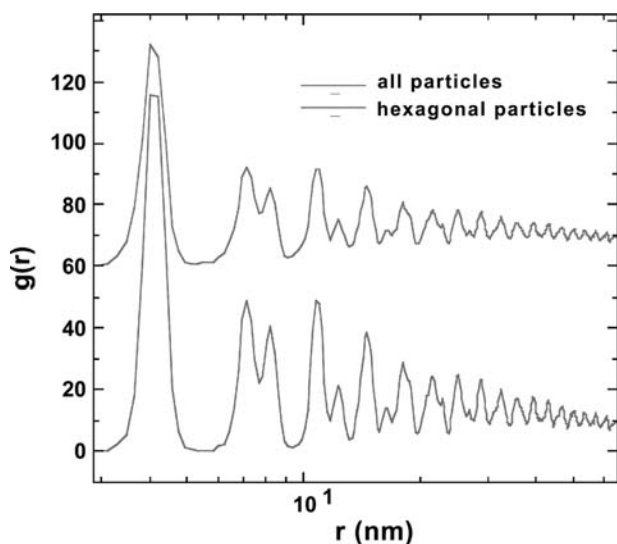


**Fig. 28** The radial pair correlation function,  $g(r)$  reflects both the degree of order (the number of periods or oscillations) and the symmetry of the QDA lattice. *Source: Source: From Ref.<sup>[41]</sup>.*

determination of the effect of alkyl chain length (organic shell thickness) on the interparticle spacing in Au and Pt QDAs for the first time. We reported a change of  $\sim 1.2 \text{ \AA}/\text{carbon}$  for alkyl chains C $_k$  with  $6 < k < 14$ , in the case of Au and  $1.4 \text{ \AA}/\text{carbon}$  in the case of Pt QDAs. For comparison, SEC determination of the organic shell thickness in Au alkylthiolate nanoconjugates found an increase of  $2.4 \text{ \AA}/2 \text{ carbon}$  atoms in the shell thickness in toluene—a very good agreement. It is important to note that substantial interdigitation of the alkyl groups is always observed

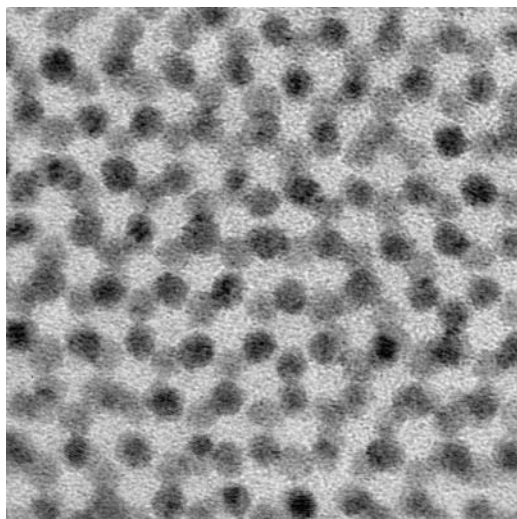


**Fig. 29** Pt QDA bilayer with the clusters deposited onto the low-energy trigonal sites above the first monolayer. *Source: Unpublished data.*

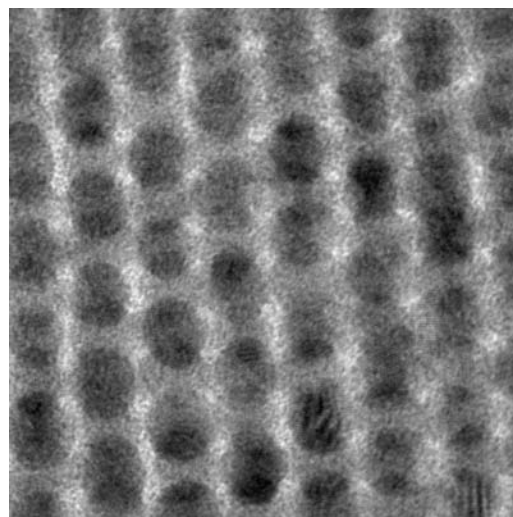


**Fig. 30** Pt Qdot bilayer has the second layer of clusters deposited onto twofold symmetry sites. *Source: Unpublished data.*

in the case of Au, Ag, Pt, and Pd QDAs, and plays an important role in the formation of the arrays. In the case of surfactants that do not easily pack or are too short, QDA formation is very rare. Also, for particles smaller than  $\sim 2.5 \text{ nm}$ , long-range order is rarely observed and the particles prefer to disperse randomly on the grid.

The symmetry of a monolayer lattice obtained from a given nanocluster solution is typically hexagonal; however, in the same preparation on the same grid, we have also observed and reported square lattice packings, so the symmetry cannot be solely dependent on organic layer thickness, nanocluster metal type, nor solvent because these are all identical. It does indicate that these two lattice types are of very similar energy.

Similarly, unexpected packing can occur in bilayers, as demonstrated by Figs. 29 and 30. In Fig. 29, a Pt PDA bilayer we observe the “expected” low-energy trigonal (threefold) locations of the second layer above the “holes” in the first hexagonal layer. But in other Pt QDA, Fig. 30, we observed that clusters in the second layer occupy the twofold sites.

### Nanocluster Matter and Nanotechnology

Cluster matter is obviously significantly more complex to study and understand than dilute solutions of individual Qdots acting independently. However, it does present some intriguing technological possibilities. Consider, for example, the effect of nanocrystal diameter and particle spacing on the effective dielectric constant of a fcc (or hexagonal) QDA. Fig. 31 shows that as the ratio of  $D_c/\text{gap}$  increases, the dielectric constant can become very large. This has implications for energy

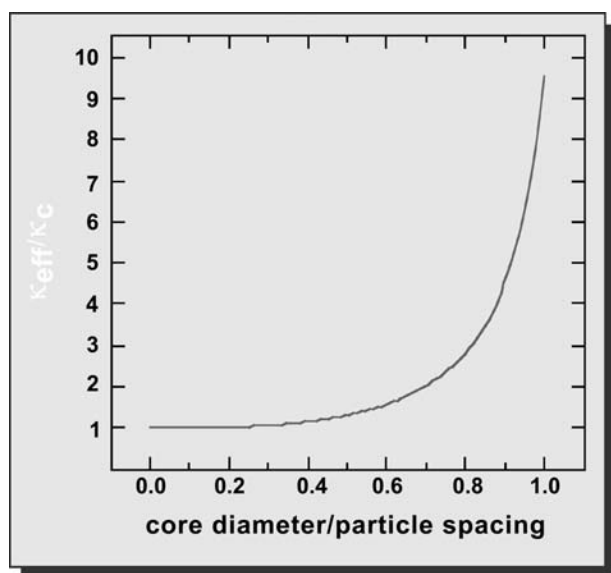


**Fig. 31** The calculated dielectric constant of an fcc QDA superlattice increases dramatically with core diameter/gap ratio. *Source:* From Ref.<sup>[41]</sup>.

storage in capacitors because cluster matter may not suffer the same problems with increased dielectric breakdown as those known for bulk powders. We discuss the reasons for these difference in Ref.<sup>[41]</sup>

Another area in which metallic nanoclusters are likely to have a significant impact in the future is in heterogeneous catalysis. As examples, we cite our work on nanosize Fe and FeS<sub>2</sub> as coal hydrogenation and hydrogenolysis catalysts, where the nanoclusters are directly deposited onto the coal powder, which acts both as a support and a substrate.<sup>[61,62]</sup> The coal is broken down under high-pressure H<sub>2</sub> into liquids, which may serve as either chemical feedstocks for advanced engineering materials or as fuels in energy production. A very significant amount of the chemical products are aromatic or naphthalenic in structure, a very desirable starting point for many engineering polymers and plastics.

We have also investigated nanosize MoS<sub>2</sub> as a photocatalyst demonstrating a size-dependent photooxidation of both phenol<sup>[50]</sup> and pentachlorophenol.<sup>[51]</sup> The latter is a major environmental contaminant as it has been widely employed as a fungicide and herbicide for wood preservation. As MoS<sub>2</sub> has a two-dimensional graphite-like structure with the catalytically active Mo sites at the “edge” of the cluster, making this material nanosize vastly increases its potential catalytic activity. Already, it is the most useful fuel hydrodesulfurization catalyst known. (This is the critical first step in crude refining, in which heteroatom compounds are removed to avoid poisoning subsequent expensive transition metal catalysts.) One would anticipate that nanosize MoS<sub>2</sub> would be even more effective (perhaps at lower temperature and H<sub>2</sub> pressures).

We have examined nanosize Pd, Pt, and Rh deposited on high surface area, commercially available supports such as alumina and carbon and found that not only can milder *T* and *P* conditions be utilized for hydrogenation, but that the product distribution (selectivity) can be tuned by nanocluster size and metal type. In fact, we have discovered that Pd nanoclusters on carbon can actually be more effective than more expensive Rh in the hydrogenation of pyrene. This is not true of commercially available Pd and Rh catalysts, and indicates the almost limitless possibilities in this largely unexplored area of nanotechnology.

## CONCLUSION

In this review, we discussed chemical preparation methods for the synthesis of metallic quantum dots, emphasizing the important role of surface active agents for the control of the average cluster size and size dispersion. Inverse micelle synthesis in non-polar oils using readily available, inexpensive ionic metal salts encapsulated in their interior is the most versatile method for metallic Qdot synthesis. We demonstrated the use of liquid chromatography for cluster size analysis and the role such rapid feedback plays in synthesis development. We demonstrated that special, thermodynamically stable cluster sizes are formed in the size regime  $D_c < 3$  nm, that the binding strengths of ligands to metal nanoclusters is stronger for Au than Ag, and that the length of the thiolate itself affects the binding affinity. We noted that short chain length alkyl thiolates may act as etchants to narrow the size distribution with time, and that, in general, an evolution of the cluster size distribution does occur, its rate being correlated with the bulk melting *T* of the material (i.e., slower evolution for Pt than for Au or Ag).

We next reviewed the size-dependent optical properties of Au and Ag nanoclusters, optical properties of core-shell particles, and the unexpected visible and NIR photoluminescence from molecular sized nanometals. A blue shift of the plasmon resonance was observed for nanosize Au, while the opposite behavior was found for Ag and attributed the greater role of inter-d-band transitions in Au than in the case of Ag. We reported the emergence of distinct molecule-like absorbance features in Au clusters approaching 1 nm in dimension. The optical properties of core-shell particles of equivalent size and atomic composition were shown to depend on whether Ag or Au was in the interior and were further shown to depend on whether an alloy or a true core-shell type structure was synthesized.

We next discussed the various synthetic approaches and resulting magnetic properties of the base itinerant metals, Co, Fe, and Ni. We discussed the possible

reasons for the heretofore low magnetic response of nanocrystals of these materials and also discussed soon-to-be published work on ultrasmall,  $D_c = 1.4$  and  $1.9$  nm Co nanocrystals exhibiting greater-than-bulk magnetic response. Possible reasons connected with surface magnetism and surface reconstruction in nanocrystals were given as explanations of our observations. We also discussed the synthesis of non-equilibrium crystal structures of nanoparticles of Fe and Co.

We next discussed the formation of QDAs of nanocrystals of Au, Pt, and Pd outlining the important parameters controlling the degree of order and whether mono-, bi-, or multilayer QDAs form. In particular, we reviewed novel digital-image analysis methods for obtaining the average domain size, interparticle spacing, and extent of long-range order in TEM images of QDAs. We noted that bilayers may exhibit either the predicted low-energy, threefold coordination or a twofold coordination in the second layer. We also commented that either hexagonal or square packing of nanocrystals can occur in the same sample on the same substrate.

We concluded our review with a discussion of the relationship between Qdots and nanotechnology. The ability to control the size, shape, and interface structure of Qdots is critical to their application in nanotechnology as new magnetic, dielectric, optical, and catalytic materials. As one example, we discussed the effect of core size to interparticle ratio on the dielectric constant and pointed out that one may expect nanosize clusters to eliminate some of the dielectric breakdown issues found in macroscopic materials, allowing significant increases in energy storage in capacitors. We particularly emphasized catalytic applications because we feel these may yield the most spectacular improvements on conventional technology. Two examples, the direct conversion of coal to chemicals and fuels using Fe and  $\text{FeS}_2$ , and solar-driven photocatalysis using  $\text{MoS}_2$  were given.

In any review, one must be quite selective in the topics covered. But we hope to have given the reader a good overview of the reasons for the large scientific interest in nanomaterials and nanotechnology, as well as the tools which are currently being developed to further these fields. Essentially, scientists are redoing all of materials research on a length scale in which interface is dominant. Thus these endeavors are likely to continue for many years and yield many unexpected observations.

## ACKNOWLEDGMENTS

This work was supported by the Division of Materials Sciences, Office of Basic Energy Sciences of the US Department of Energy under contract DE-AC04-

94AL8500. Sandia is a multiprogram laboratory operated by Sandia Corporation, a Lockheed-Martin Company, for the Department of Energy. The author would like to acknowledge the support of many collaborators over the years, especially my technical assistants, Edward Vernon, Sharon Craft, Judy Odinek, and James Mikkaelson. I would also like to recognize the fine TEM, XRD, and SAD work of Paula Provencio and my long-time friend and collaborator James Martin.

## REFERENCES

1. Faraday, M. Experimental relations of gold (and other metals) to light. *Philos. Trans. R. Soc. Lond.* **1857**, *147*, 145–185.
2. Kreibitz, U.; Vollmer, M. *Optical Properties of Metal Clusters*; Springer-Verlag: Berlin, 1995.
3. Hoon, S.R.; Kilner, M.; Russell, G.J.; Tanner, B.K. Preparation and properties of nickel ferrofluids. *J. Appl. Polym. Sci.* **1966**, *10*, 1915–1927.
4. Hess, P.; Parker, P.S., Jr. Polymers for stabilization of colloidal cobalt particles. *J. Appl. Polym. Sci.* **1966**, *10*, 1915–1927.
5. Griffiths, C.H.; O'Horo, M.P.; Smith, T.W. The structure, magnetic characterization, and oxidation of colloidal iron dispersions. *J. Appl. Phys.* **1979**, *50*, 7108–7115.
6. Murray, C.B.; Norris, D.J.; Bawendi, M.G. Synthesis and characterization of nearly monodisperse CdE ( $E = \text{S, Se, Te}$ ) semiconductor nanocrystallites. *J. Am. Chem. Soc.* **1993**, *115*, 8706–8715.
7. Schmid, G. Hexachlorodecakis(triphenyl-phosphine)pentapentacontagold,  $\text{Au}_{55}[\text{P}(\text{C}_6\text{H}_5)_3]_{12}\text{C}_{16}$ . *Angew. Chem.* **1978**, *90*, 417–420.
8. Schmid, G. *Developments in Transition Metal Cluster Chemistry—The Way to Large Clusters. Structure and Bonding*; Springer-Verlag: Berlin, 1985; Vol. 62, 52–82.
9. Boutonnet, M.; Kizling, J.; Stenius, P. The Preparation of monodisperse colloidal metal particles from microemulsions. *Colloids Surf.* **1982**, *5*, 209–225.
10. Boutonnet, M.; Kizling, J.; Mints-Eya, V.; Choplin, A.; Touroude, R.; Maire, G.; Stenius, P. Monodisperse colloidal metal particles from nonaqueous solutions: Catalytic behavior in hydrogenation of but-1-ene of platinum, palladium, and rhodium particles supported on pumice. *J. Catal.* **1987**, *103*, 95–104.
11. Wilcoxon, J.P.; Williamson, R.L. *Formation of Metal Colloids in Inverse Micelles and Microemulsions*; Proceedings of the MRS; 1989, Boston, MA.
12. Wilcoxon, J.P. Method for the Preparation of Metal Colloids in Inverse Micelles and Product Preferred by the Method. U.S. Patent #5,147,841, Sep. 15, 1992, issued.
13. Wilcoxon, J.P.; Williamson, R.L.; Baughman, R.J. Optical properties of gold colloids formed in inverse micelles. *J. Chem. Phys.* **1993**, *98* (12), 9933–9943.
14. Wilcoxon, J.; Sylwester, A.; Nigrey, P.; Martino, A.; Quintana, C.; Baughman, R. *Formation and Characterization*



- of Highly-Dispersed Iron Catalysts; Eighth Annual International Pittsburgh Coal Conference Proceedings; 1991; 703–708.
15. Wilcoxon, J.P.; Martino, R.I.; Baughmann, R.L.; Klavetter, E.; Sylwester, A.P. *Synthesis of Transition Metal Clusters and their Catalytic and Optical Properties*; Proceedings of the Fall MRS, Symposium J, Boston, MA; 1992.
  16. Wilcoxon, J.P.; Martino, T.; Klavetter, E.; Sylwester, A.P. Synthesis and Catalytic Properties of Metal and Semiconductor Nanoclusters. In *Nanophase Materials*; Hadjipanayis, Siegel, Eds.; 1993; 770–780.
  17. Martino, A.; Wilcoxon, J.P.; Kawola, J. Synthesis and characterization of Fe and FeS<sub>2</sub> (pyrite) coal liquefaction catalysts in inverse micelles. *Energy Fuels* **1994**, *8*, 1289–1294.
  18. Wilcoxon, J.P.; Samara, G.A.; Provencio, P.N. Optical and electronic properties of Si nanoclusters synthesized in inverse micelles. *Phys. Rev.*, **B** **1999**, *60*, 2704–2714.
  19. Wilcoxon, J.P.; Samara, G.A. Tailorable, visible light emission from silicon quantum dots. *Appl. Phys. Lett.* **1999**, *21*, 3164–3166.
  20. Wilcoxon, J.P.; Samara, G.A.; Provencio, P. Synthesis and optical properties of colloidal germanium nanocrystals. *Phys. Rev.*, **E** **2001**, *64*, 35417-1
  21. de Heer, W.A. Simple metal clusters. *Rev. Mod. Phys.* **1993**, *65*, 612–645.
  22. Brack, M. The physics of simple metal clusters: Self-consistent jellium model and semiclassical approaches. *Rev. Mod. Phys.* **1993**, *65*, 677–702.
  23. Friedlander, G.; Kennedy, J.W.; Miller, J.M. *Nuclear and Radiochemistry*, 2nd Ed. Ed. John Wiley & Sons: New York, 1966.
  24. Billas, I.M.L.; Chatelain, A.; De Heer, W.A. Magnetism of Fe, Co and Ni clusters in molecular beams. *J. Magn., Magn. Mater.* **1997**, *168* (1–2), 64–84.
  25. Mie, G. *Ann. Phys.* **1908**, *25*, 377.
  26. Wilcoxon, J.P.; Samara, G.A. Strong quantum-size effects in a layered semiconductor: MoS<sub>2</sub> nanoclusters. *Phys. Rev.*, **B Rapid Commun.** **1995**, *51*, 7299–7302.
  27. Wilcoxon, J.P.; Samara, G.A.; Newcomer, P. Strong quantum confinement effects in semiconductors: FeS<sub>2</sub> nanoclusters. *Solid State Commun.* **1996**, *98*, 581–585.
  28. Wilcoxon, J.P.; Newcomer, P.; Samara, G.A. Synthesis and optical properties of MoS<sub>2</sub> and isomorphous nanoclusters in the quantum confinement regime. *J. Appl. Phys.* **1997**, *81*, 7934–7940.
  29. Wilcoxon, J.P.; Provencio, P. Use of surfactant micelles to control the structural phase of nanosize iron clusters. *J. Phys. Chem.*, **B** **1999**, *103*, 9809–9813.
  30. Wilcoxon, J.P.; Martin, J.E.; Provencio, P. Size distributions of gold nanoclusters studied by liquid chromatography. *Langmuir* **2000**, *16* (25), 9912–9920.
  31. Wilcoxon, J.P.; Provencio, P. Etching and aging effects in nanosize Au clusters investigated using high resolution size-exclusion chromatography. *J. Am. Chem. Soc.* **2002**, submitted.
  32. Brust, M.; Fink, J.; Bethell, D.; Schrifin, D.J.; Kiely, C. Synthesis and reactions of functionalised gold nanoparticles. *J. Chem. Soc., Chem. Commun.* **1995**, 1655–1658.
  33. Whetten, R.L.; Khoury, J.T.; Alvarez, M.M.; Murthy, S.; Vezmar, I.; Wang, Z.L.; Stephens, P.W.; Cleveland, C.L.; Luedtke, W.D.; Landman, U. Nanocrystal gold molecules. *Adv. Mater.* **1996**, *8*, 428–437.
  34. Murray, C.B.; Sun, S.; Coyle, H.; Betley, T. Monodisperse 3d transition-metal (Co, Ni, Fe) nanoparticles. *MRS Bull.* **2001**, *26* (12), 985–990.
  35. Wilcoxon, J.P.; Craft, S.A. Liquid chromatographic analysis and characterization of inorganic nanoclusters. *NanoStructur. Mater.* **1997**, *9*, 85–88.
  36. Yau, W.W.; Kirkland, J.J.; Bly, D.D. *Modern Size-Exclusion Liquid Chromatography*; Wiley-Interscience: New York, 1979.
  37. Wilcoxon, J.P.; Martin, J.E.; Provencio, P. Optical properties of gold and silver nanoclusters investigated by liquid chromatography. *J. Chem. Phys.* **2001**, *115*, 998–1008.
  38. Norris, D.J.; Sacra, A.; Murray, C.B.; Bawendi, M.G. CdSe-TOP coated nanocrystals display band gap emission with room-T Q.Y. of a few percent. *Phys. Rev. Lett.* **1994**, *101*, 8455–8459.
  39. Dabbousi, B.O.; Rodriguez-Viejo, J.; Mikulec, F.V.; Heine, J.R.; Mattoussi, H.; Ober, R.; Jensen, K.F.; Bawendi, M.G. (CdSe)ZnS core-shell quantum dots: Synthesis and characterization of a size series of highly luminescent nanocrystallites. *J. Phys. Chem.*, **B** **1997**, *101*, 9463–9474.
  40. Peng, X.; Schlamp, M.C.; Kadavanich, A.V.; Alivisatos, A.P. Epitaxial growth of highly luminescent CdSe/CdSe core/shell nanocrystals with photostability and electronic accessibility. *J. Am. Chem. Soc.* **1997**, *119*, 7019–7029.
  41. Martin, J.E.; Wilcoxon, J.P.; Odinek, J.; Provencio, P. Control of the interparticle spacing in gold nanoparticle superlattices. *J. Phys. Chem.*, **B** **2000**, *40*, 9475–9486.
  42. Martin, J.E.; Wilcoxon, J.P.; Odinek, J.; Provencio, P. Superlattices of platinum and palladium nanoparticles. *J. Phys. Chem.*, **B** **2002**, *106*, 971–978.
  43. Schaaff, T.G.; Shafiqullin, M.N.; Khoury, J.T.; Vezmar, I.; Whetten, R.L.; Cullen, W.G.; First, P.N.; Gutierrez-Wing, C.; Ascnsio, J.; Jose-Yacamán, M.J. Isolation of smaller nanocrystal Au molecules: Robust quantum effects in optical spectra. *J. Phys. Chem.*, **B** **1997**, *101*, 7885–7892.
  44. Wilcoxon, J.P.; Thurston, T.R.; Craft, S. Performance of a high resolution Bonse-Hart SAXS instrument using a synchrotron source. *Rev. Sci. Instrum.* **1996**, *67* (9), 3021–3034.
  45. Schaaff, T.G.; Whetten, R.L. Controlled etching of Au:SR cluster compounds. *J. Phys. Chem.*, **B** **1999**, *103*, 9394–9396.
  46. Link, S.; Beeby, A.; FitzGerald, S.; El-Sayed, M.A.; Schaaff, T.G.; Whetten, R.L. Visible to infrared luminescence from a 28-atom gold cluster. *J. Phys. Chem.*, **B** **2002**, *106*, 3410–3413.
  47. Wilcoxon, J.P.; Provencio, P. Optical Properties of II–VI Semiconductor Nanoclusters for Use as Phosphors. Proceedings of the SPIE conference on “Optical Properties of Nanocrystals”, Seattle, WA, July, 7–11, 2002.
  48. Wilcoxon, J.P.; Martin, J.E.; Parsapour, F.; Wiedenman, B.; Kelley, D.F. Observation of photoluminescence from

- nanosize gold clusters. *J. Chem. Phys.* **1998**, *108*, 9137–9143.
49. Kreibig, U.; Genzel, L. Optical absorption of small metallic particles. *Surf. Sci.* **1985**, *156*, 678–682.
  50. Thurston, T.R.; Wilcoxon, J.P. Photo-oxidation of organic chemicals catalyzed by nanoscale MoS<sub>2</sub>. *J. Phys. Chem.* **1998**, *103*, 11–17.
  51. Wilcoxon, J.P. Catalytic photooxidation of pentachlorophenol using semiconductor nanoclusters. *J. Phys. Chem.* **2000**, *104*, 7334–7343.
  52. Wilcoxon, J.P.; Provencio, P. Heterogeneous nucleation and growth on metal nanoclusters. *Science*, in preparation.
  53. Wilcoxon, J.P.; Newcomer, P. Use of surfactant micelles to control the structural phase of nanosize iron clusters. *J. Phys. Chem., B* **1999**, *103*, 9809–9812.
  54. Sun, S.; Murray, C.B. Synthesis of monodisperse cobalt nanocrystals and their assembly into magnetic superlattices (invited). *J. Appl. Phys.* **1999**, *85*, 4325–4329.
  55. Wilcoxon, J.P.; Venturini, E.L.; Provencio, P. Enhanced magnetic response of dilute cobalt nanoparticles in an organic matrix—The effects of aging and interface structure. *Phys. Rev. Lett.*, in preparation.
  56. Goersig, M.; Mulvaney, P. Formation of ordered two-dimensional gold colloid lattices by electrophoretic deposition. *J. Phys. Chem.* **1993**, *97*, 6334–6336.
  57. Brust, A.; Bethell, D.; Schiffrin, D.J.; Kiely, C.J. Novel gold-dithiol nano-networks with non-metallic electronic properties. *Adv. Mater.* **1995**, *7*, 795–797.
  58. Fink, J.; Kiely, C.J.; Bethell, D.; Schiffrin, D.J. Self-organization of nanosized gold particles. *Chem. Mater.* **1998**, *10*, 922–925.
  59. Taleb, A.; Petit, C.; Pileni, M.P. Optical properties of self-assembled 2D and 3D superlattices of silver nanoparticles. *J. Phys. Chem., B* **1998**, *102*, 2214–2220.
  60. Martin, J.E.; Odinek, J.; Wilcoxon, J.P.; Anderson, R.A.; Provencio, P. Sintering of gold and platinum nanoclusters. *J. Phys. Chem. B* **2002**, *in press*.
  61. Wilcoxon, J.; Sylwester, A.; Nigrey, P.; Martino, A.; Quintana, C.; Baughman, R. *Formation and Characterization of Highly-Dispersed Iron Catalysts*; Eighth Annual International Pittsburgh Coal Conference Proceedings; 1991; 703–708.
  62. Martino, A.; Wilcoxon, J.; Sylwester, A.P.; Kawola, J.S. *Synthesis and Characterization of Fe and FeS<sub>2</sub> (pyrite) Catalysts Particles in Inverse Micelles*; Proceedings of the 205th National American Chemical Soc. Meeting; 1993.



# Metallomacrocyclic Selective Ion Receptors

Kay Severin

Institut de Chimie Moléculaire et Biologique, École Polytechnique Fédérale de Lausanne, Lausanne, Switzerland

## INTRODUCTION

Macrocyclic compounds, which are able to selectively bind ions, have received considerable attention because of applications in the fields of sensing, catalysis, and ion-transport, among others. Traditionally, covalent bonds are used for the construction of the macrocyclic framework. However, a drawback of this approach is that quite often, the synthesis is time-consuming and expensive. In the following, a unique class of receptors is described. These receptors are formed by self-assembly of three organometallic subunits and have a diameter of approximately 1 nm. They show an outstanding affinity and selectivity for lithium and sodium salts. This characteristic was used to construct specific chemosensors for lithium and fluoride ions, and to stabilize and characterize unusual molecules such as LiF.

## SELF-ASSEMBLY OF ORGANOMETALLIC HALF-SANDWICH COMPLEXES

Half-sandwich complexes of the general formula  $[(\pi\text{-ligand})\text{MCl}_2]_2 [(\pi\text{-ligand})\text{M}] = (\text{arene})\text{Ru}, \text{Cp}^*\text{Rh}, \text{Cp}^*\text{Ir}$  are common starting materials in organometallic synthesis and catalysis (Fig. 1). They are either commercially available or accessible via one-step synthetic procedures. In the solid state, they are not sensitive toward air and moisture, which facilitates the handling. The organic  $\pi$ -ligands are relatively inert toward substitution reactions. Consequently, they generally act as spectator ligands. On the other hand, the chloro ligands can be easily substituted with other neutral or anionic ligands.

The availability of three facial coordination sites can be utilized for self-assembly processes: upon addition of suited tridentate ligands, polynuclear complexes are obtained (Fig. 2). So far, macrocycles with two,<sup>[1–3]</sup> three (see below), four,<sup>[4–6]</sup> and six<sup>[7]</sup> metal fragments have been isolated and characterized. Generally, the compounds are formed in excellent yields. The number  $n$ , as well as the overall geometry, strongly depends on the nature of the bridging ligand.

In self-assembly reactions, there is a general bias toward the generation of aggregates with a small number of subunits due to reasons of entropy. On the other hand, the coordinate vectors of the ligand and the metal have to be matched, which may exclude the formation of very small assemblies such as dimers ( $n = 2$ ). For the combination of half-sandwich complexes with rigid tridentate ligands, the most common structural motif are trimers ( $n = 3$ ). First examples of such compounds were reported by Fish,<sup>[8]</sup> Annen et al.,<sup>[5]</sup> Korn and Sheldrick,<sup>[9]</sup> Beck et al.,<sup>[10,11]</sup> and Carmona et al.,<sup>[12]</sup> who used nucleobase derivatives and  $\alpha$ -amino acidates as bridging ligands. Structurally related compounds were subsequently reported by Yamanari et al.<sup>[13,14]</sup> In all cases, mono-anionic ligands were employed, which results in a charge of +3 for the trimeric assembly. As a consequence, an enhanced solubility in polar solvents such as methanol and water is observed but also a severely reduced affinity for cationic guest molecules. To obtain neutral macrocycles, our group has utilized *dianionic* tridentate ligands to bridge the half-sandwich complexes. After initial investigations using 3,4-dihydropyridine derivatives,<sup>[15]</sup> we have focused on the 2,3-dihydropyridine ligand. Upon addition of base, the chloro ligands of  $[(\pi\text{-ligand})\text{MCl}_2]_2$  undergo a substitution reaction to give the corresponding trimeric macrocycles in excellent yield (Fig. 3). The reaction can be performed with  $(\text{arene})\text{Ru}^{\text{II}}$  complexes (arene =  $\text{C}_6\text{H}_6$ ,  $p\text{-MeC}_6\text{H}_4\text{Pr}$ ,  $\text{C}_6\text{H}_3\text{Et}_3$ ,  $\text{C}_6\text{Me}_6$ ,  $\text{C}_6\text{H}_5\text{CO}_2\text{Et}$ ),<sup>[16–18]</sup> with  $\text{Cp}^*\text{Rh}^{\text{III}}$  complexes<sup>[17]</sup> and with  $\text{Cp}^*\text{Ir}^{\text{III}}$  complexes,<sup>[19]</sup> respectively. The solubility of the resulting compounds depends on the nature of the  $\pi$ -ligand: whereas the  $(\text{benzene})\text{Ru}$  complex displays a low solubility in organic solvents, such as dichloromethane, the  $(p\text{-MeC}_6\text{H}_4\text{Pr})\text{Ru}$ ,  $(\text{C}_6\text{H}_3\text{Et}_3)\text{Ru}$ ,  $\text{Cp}^*\text{Rh}$ , and  $\text{Cp}^*\text{Ir}$  complexes are well soluble in common organic solvents such as benzene and toluene.

The structures of the resulting macrocycles have been extensively studied by single crystal X-ray analysis.<sup>[16–19]</sup> In all cases, a pseudo- $C_3$ -symmetric geometry is observed. The tetrahedral metal fragments are connected via the pyridine N-atom and the two O-atoms of the pyridonate ligand. On average, the metal atoms

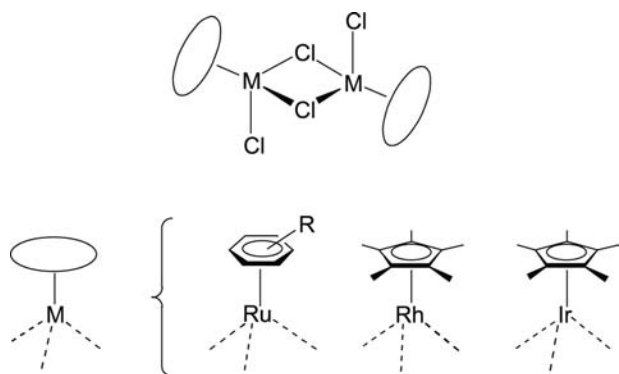


**Fig. 1** Chloro-bridged half-sandwich complexes of  $\text{Ru}^{\text{II}}$ ,  $\text{Rh}^{\text{III}}$ , and  $\text{Ir}^{\text{III}}$  as versatile starting materials for the construction of macrocyclic complexes.

are 0.54 nm apart from each other; the diameter of the complexes depends on the nature of the  $\pi$ -ligand and is approximately 1 nm. In Fig. 4, the structures of two representative macrocycles in the crystal are depicted.

The metal centers in these complexes are chiral and have the same absolute configuration. Because there is no chiral induction present during the synthesis, the macrocycles are obtained as a racemic mixture. Other isomers cannot be detected, indicating that the self-assembly process is completely diastereoselective. In solution, the complexes are configurationally stable on the nuclear magnetic resonance (NMR) time scale as evidenced by the observation of separate signals for the diastereotopic groups of the (*p*- $\text{MeC}_6\text{H}_4\text{Pr}$ )Ru complex ( $\text{CD}_3\text{OD}$  or  $\text{CDCl}_3$ ).

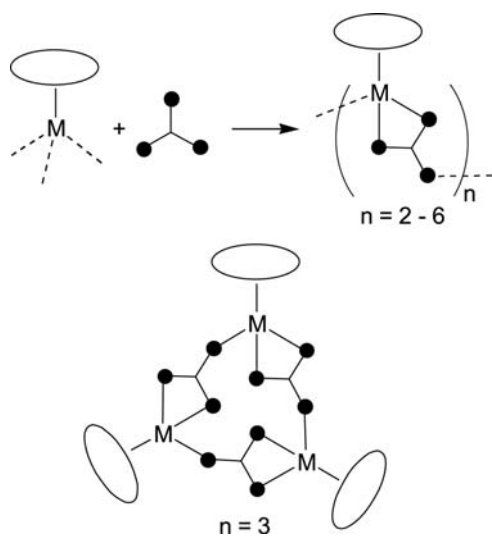


**Fig. 2** Self-assembly of half-sandwich complexes using tridentate ligands.

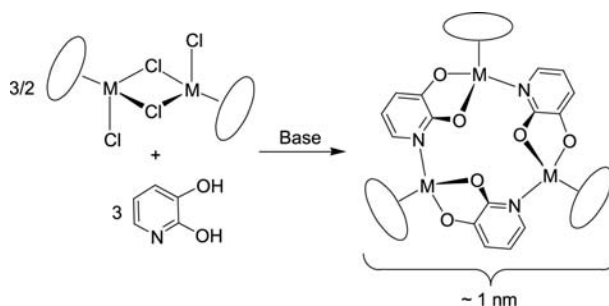


**Fig. 3** Synthesis of trinuclear metallamacrocycles by reaction of half-sandwich complexes with 2,3-dihydroxypyridine in the presence of base  $[(\pi\text{-ligand})\text{M}] = (\text{arene})\text{Ru}, \text{Cp}^*\text{Rh}, \text{Cp}^*\text{Ir}$ .

## METALLAMACROCYCLIC RECEPTORS FOR ION-PAIRS

### Selective Complexation of Lithium and Sodium Salts

Metallacrown complexes are analogues of crown ethers, in which metal atoms constitute an integral part of the macrocyclic framework. Compounds of this kind were first reported in 1989 by Pecoraro et al.<sup>[20,21]</sup> At present, metallacrown complexes with ring sizes between 9 and 30 atoms are known.<sup>[22]</sup> Similar to their organic counterparts, metallacrowns can selectively bind metal ions with high affinity. The trinuclear complexes depicted in Fig. 3 represent analogues of 12-crown-3. When investigated for their ability to bind alkali metal ions, it was found that the complexes display a very high affinity for lithium and sodium salts (Fig. 5).

The  $\text{Li}^+$  and  $\text{Na}^+$  adducts can be distinguished from the free receptors by  $^1\text{H}$  NMR: a significant downfield shift is observed for the signals for the bridging ligands as well as for the signals of the  $\pi$ -ligands. Because the exchange of the alkali guest is slow on the NMR time scale, quantitative information about adduct formation can be obtained by integration of the corresponding  $^1\text{H}$  NMR signals. Therefore, NMR spectroscopy can be used to investigate the affinity, the binding kinetics, and the selectivity of the 12-metallacrown-3 complexes.

To evaluate the affinity of the receptor  $[(p\text{-MeC}_6\text{H}_4\text{Pr})\text{Ru}(\text{C}_5\text{H}_3\text{NO}_2)]_3$  (**1**) for  $\text{LiCl}$  and  $\text{NaCl}$ , competition experiments with various organic ionophores were carried out.<sup>[16]</sup> These experiments showed that in chloroform, the binding affinity of **1** toward these salts is significantly higher than that of crown ethers (Fig. 6). A real competition situation, in which both the free receptor **1** and the adduct **1**·MCl can be detected, is only observed if extremely good ionophores, such as 2,1,1-cryptand, are employed as competing receptors.

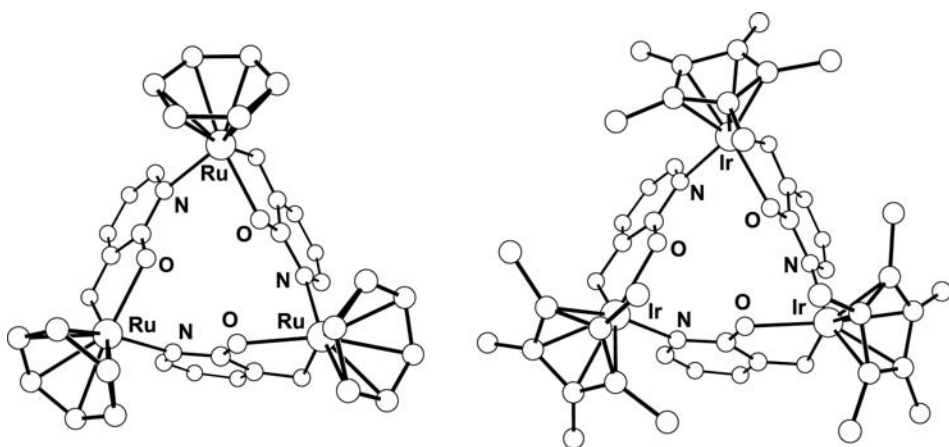


**Fig. 4** Ball and stick representation of the molecular structure of macrocyclic (benzene)Ru and Cp\*Ir complexes in the crystal. The hydrogen atoms are omitted for clarity.

To obtain more information about the binding kinetics, the time course of the reaction between the receptor **1** (11.4 mM) and a twofold excess of LiCl was investigated (Fig. 7).<sup>[23]</sup> Quantitative adduct formation is observed after approximately 2 days. This result confirms that the affinity of the receptor **1** for LiCl is very high, but also that the complexation reaction is unusually slow. Using a computational analysis, an apparent second-order rate constants of  $k_f = 1.6 \pm 0.3 \times 10^{-3} \text{ M}^{-1} \text{ sec}^{-1}$  was calculated. This value is very low compared to what has been measured for other ionophores. A formation rate constant of  $k_f = 4.8 \times 10^5 \text{ M}^{-1} \text{ sec}^{-1}$ , for example, has been determined for the Li<sup>+</sup>-specific [2,1,1]-cryptand.<sup>[24]</sup>

The selectivity of the metallacrown complexes strongly depends on the nature of the  $\pi$ -ligand. Whereas the (C<sub>6</sub>H<sub>6</sub>)Ru, (*p*-MeC<sub>6</sub>H<sub>4</sub>Pr)Ru and (C<sub>6</sub>H<sub>5</sub>CO<sub>2</sub>Et)Ru complexes bind both Li<sup>+</sup> and Na<sup>+</sup> salts, the (C<sub>6</sub>H<sub>3</sub>Et<sub>3</sub>)Ru, (C<sub>6</sub>Me<sub>6</sub>)Ru, Cp\*Rh, and Cp\*Ir complexes are specific for Li<sup>+</sup> salts. None of the receptors are able to bind K<sup>+</sup> salts. This pronounced selectivity for small cations is a result of the steric requirements of the  $\pi$ -ligands. A view along the pseudo-C<sub>3</sub> symmetry axis of the Li<sup>+</sup> and Na<sup>+</sup> adducts of receptor [(C<sub>6</sub>H<sub>6</sub>)Ru(C<sub>5</sub>H<sub>3</sub>NO<sub>2</sub>)<sub>3</sub>] (**2**) nicely illustrates the close encapsulation of the cations by the

benzene ligands of the receptor (Fig. 8). Given the rigidity of the host complex, it is evident that larger cations than Na<sup>+</sup> are not able to bind to the three adjacent O-atoms, which constitute the binding site.

Ionophores with high selectivity for Li<sup>+</sup> ions are of general interest because of potential applications as chemosensors. In this context, the ruthenium complex [(C<sub>6</sub>H<sub>5</sub>CO<sub>2</sub>Et)Ru(C<sub>5</sub>H<sub>3</sub>NO<sub>2</sub>)<sub>3</sub>] (**3**) displayed the most promising characteristics of all investigated receptors. Although this macrocycle is able to bind Na<sup>+</sup> ions, it shows an outstanding affinity and selectivity for Li<sup>+</sup> salts.<sup>[18]</sup> This is demonstrated by the following experiment: if an aqueous solution containing LiCl (0.05 M) and a large excess of NaCl, KCl, CsCl, CaCl<sub>2</sub>, and MgCl<sub>2</sub> (1.00 M each) is shaken with a chloroform solution of complex **3**, the exclusive and quantitative extraction of LiCl is observed (Fig. 9). This is remarkable because a) the extraction of LiCl from water is in principle a very difficult thing to accomplish due to the high enthalpy of hydration and b) the nearly perfect selectivity for Li<sup>+</sup>. Overall, the affinity and

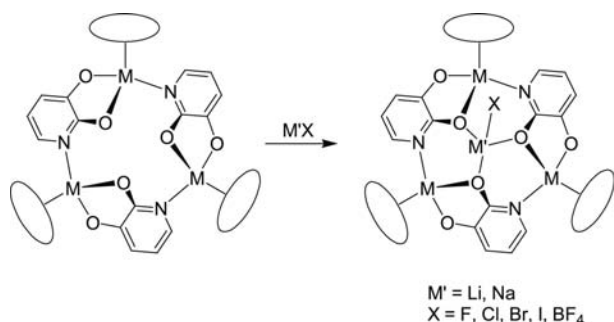


**Fig. 5** Selective complexation of lithium and sodium salts by 12-metallacrown-3 complexes.

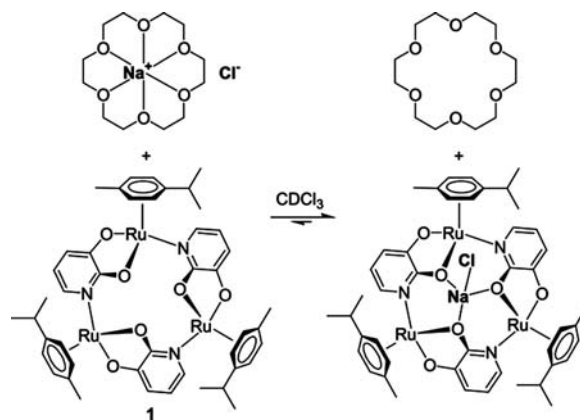


**Fig. 6** Competition experiment between receptor **1** and 18-crown-6: the 12-metallacrown-3 complex **1** has a significantly higher affinity for NaCl.

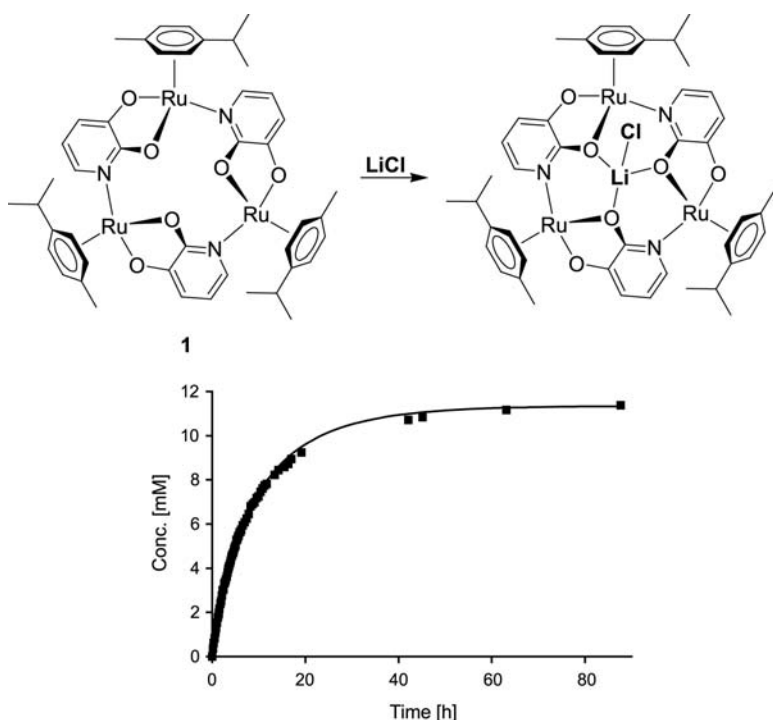


**Fig. 7** Time course of the reaction between the receptor **1** (11.4 mM) and LiCl (22.8 mM) in CD<sub>3</sub>OD to give the corresponding adduct **1** · LiCl (◆).

selectivity of complex **3** is comparable to the best receptors for Li<sup>+</sup> that have been reported so far.

Several MX (M<sup>+</sup> = Li<sup>+</sup>, Na<sup>+</sup>; X<sup>-</sup> = Cl<sup>-</sup>, Br<sup>-</sup>, I<sup>-</sup>) adducts have been characterized crystallographically. In all cases, the salt is bound as an ion pair with the alkali metal ion being coordinated to the three oxygen atoms of the metallacrown complexes (Fig. 10). The anion, which is tightly bound to the respective cation, is situated in close proximity to the  $\pi$ -ligands. The resulting tetrahedral coordination geometry is commonly found for LiX complexes but rarely found for NaX complexes. The unusually low coordination number results in Na–X bond length, which are among the shortest reported so far (e.g., Na–Cl = 253 pm for the NaCl complex of **1**).<sup>[17]</sup>

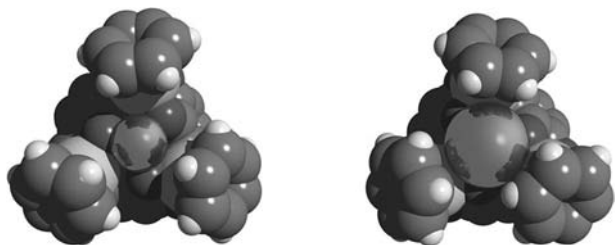


**Fig. 8** Space filling representation of the structures of **2** · LiCl (left) and **2** · NaCl (right) in the crystal (the Cl<sup>-</sup> anions are not depicted). Salts with larger cations such as KCl do not coordinate to **2** because they are efficiently blocked by the arene  $\pi$ -ligands, which encapsulate the binding site.

### Electronic Effects in 12-Metallacrown-3 Complexes

There are several effects that contribute to the exceptionally high affinity of 12-metallacrown-3 complexes for Li<sup>+</sup> and Na<sup>+</sup> salts in organic solvents: 1) The receptors are very rigid and the three O-donor atoms are ideally preorganized to bind small cations; 2) The salts are bound as an ion pair; 3) The energetic costs for the desolvation of the donor atoms are very small because

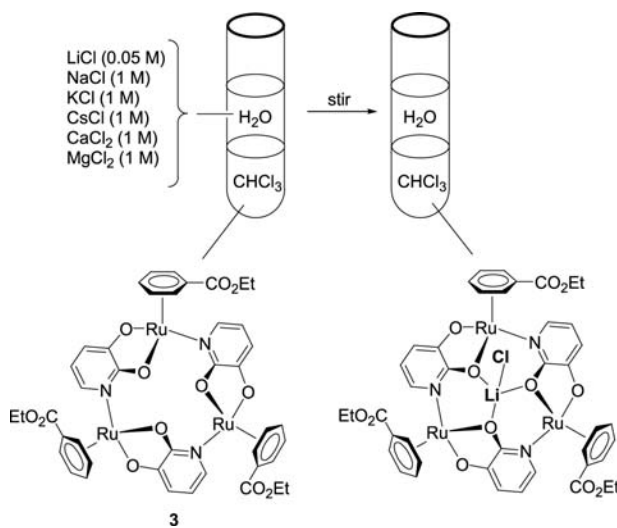


**Fig. 9** Selective extraction of LiCl from water containing a large excess of NaCl, KCl, CsCl, CaCl<sub>2</sub>, and MgCl<sub>2</sub>.

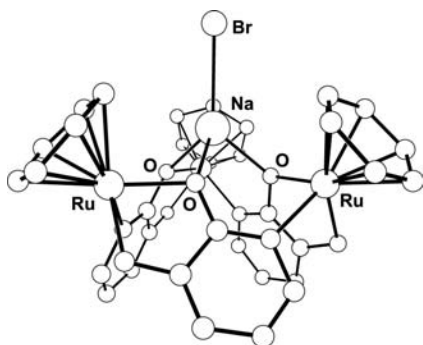


**Fig. 10** Ball and stick representation of the molecular structure of  $2 \cdot \text{NaBr}$  in the crystal. The hydrogen atoms are omitted for clarity.

the binding site is well shielded by the  $\pi$ -ligands. A fourth contribution is based on the peculiar electronic situation of metallacrown complexes. It is known that metal–oxygen bonds can be very polar, even in complexes of the late transition metals.<sup>[25]</sup> A computational study has revealed that the Ru–O bonds of receptor **2** are likewise highly polarized with a partial negative charge of  $-0.88$  for the oxygen atoms (Fig. 11).<sup>[23]</sup> For the organic counterpart 12-crown-3, on the other hand, significantly lower values were calculated ( $-0.59$ ). Because the O-donor atoms of the metallacrown complex are ideally preorganized, the increased negative charge is an important contribution to the high affinity for cationic guests. This result is of general importance because it points to an intrinsic advantage of metallacrown complexes: a highly polarized binding site.

To further address the question on how electronic effects influence the host–guest chemistry of 12-metallacrown-3 complexes, the derivative **4** having chloro-substituents at the bridging pyridonate ligands was synthesized (Fig. 12). The electron-withdrawing groups were expected to slightly reduce the partial negative charge on the O-donor atoms in *para* position. It was shown that this rather conservative

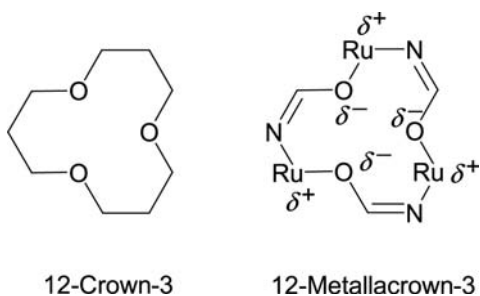


**Fig. 11** The highly polarized Ru–O bonds in 12-metallacrown-3 complexes favor the binding of cationic guest molecules for electrostatic reasons.

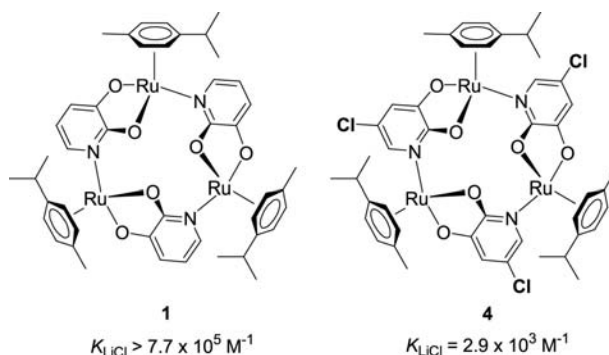


**Fig. 12** A 12-metallacrown-3 complex with chloro-substituents (**4**) displays a significantly lower binding constant for LiCl (values determined in  $\text{CD}_3\text{OD}/\text{D}_2\text{O}$ , 5:1).

change reduces the affinity of the receptor **4** for LiCl and NaCl by approximately 2 orders of magnitude, although only very small structural differences were observed.<sup>[23]</sup>

### Redox-Responsive Receptors

For applications in the field of sensing, it is necessary to transduce the binding of the analyte in some kind of signal output. Because of the sensitivity and accuracy of the measurement, electrochemical methods have found considerable attention in this context. Over the past years, many redox-responsive macrocycles have been synthesized to electrochemically recognize small ions.<sup>[26]</sup> Especially appealing are compounds with a responsive or signaling unit being an integral part of the receptor itself.

In the case of 12-metallacrown-3 complexes, electrochemical methods turned out to be ideally suited for the detection of lithium and sodium salts. The free receptor **1** is oxidized at a potential of  $+583$  mV when measured against a Ag/AgCl reference electrode. Upon addition of LiCl or NaCl, the metallamacrocycle is significantly more difficult to oxidize with a peak potential of  $940$  mV ( $1 \cdot \text{LiCl}$ ) and  $900$  mV ( $1 \cdot \text{NaCl}$ ), respectively.<sup>[17]</sup> A similar shift toward anodic potential is found for the other 12-metallacrown-3 complexes. The differences are large compared to what is observed for other redox-responsive ionophores such as ferrocene containing crown ethers,<sup>[26]</sup> and, in principle, sufficient to build an amperometric molecular sensor device.

The detection of guest molecules with 12-metallacrown-3 complexes can even be performed without employing electrochemical methods. That fact that the host–guest complexes are more difficult to oxidize was used to develop a colorimetric test: if the oxidation agent 2,3-dichloro-5,6-dicyano-1,4-benzoquinone (DDQ) is added to a solution of the



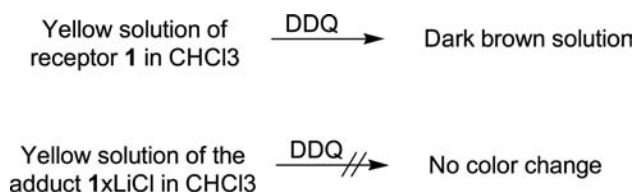


**Fig. 13** The different redox-potential of the free receptor **1** and the adduct **1**·LiCl can be used to detect lithium ions with a simple color test.

free receptor **1**, the originally yellow solution immediately turns dark brown because DDQ oxidizes the ruthenium complex. However, in the presence of LiCl, no reaction and thus no color change occurs (Fig. 13). A similar behavior is observed for the NaCl adduct. It is thus possible to detect lithium and sodium salts with a simple and fast color test.

### Stabilization of Unusual Molecules

Although hundreds of alkali metal halide complexes have been synthesized and structurally characterized,<sup>[27]</sup> complexes of molecular LiF are virtually unknown. There are some reports about compounds with Li···F contacts but here, the fluoride atom is either covalently bound to other atoms (e.g., in PF<sub>6</sub><sup>-</sup> salts) or coordinatively bound to very strong Lewis acids (e.g., to Ti<sup>4+</sup>).<sup>a</sup> The difficulty to stabilize complexes of molecular LiF is a result of the very high lattice energy of this salt. Consequently, the crystalline form represents a thermodynamic trap. A similar situation is found for the less common salt LiFHF containing the interesting FHF<sup>-</sup> anion.<sup>[29]</sup>

Our strategy to obtain complexes of these salts was to generate them in situ in the presence of the macrocyclic host. For this purpose, we first synthesized LiBF<sub>4</sub> adducts of the 12-metallacrown-3 complexes. The weakly bonded BF<sub>4</sub><sup>-</sup> anion was then exchanged with F<sup>-</sup> or FHF<sup>-</sup> in a salt metathesis reaction using potassium or tetraethylammonium salts (Fig. 14). After extraction with benzene to remove the KBF<sub>4</sub> or NEt<sub>4</sub>BF<sub>4</sub> biproducts, the LiF and LiFHF complexes were obtained in pure form.<sup>[30]</sup>

The physical properties of these encapsulated lithium salts were of special interest. In solution, the complexes were studied by heteronuclear NMR spectroscopy.<sup>[30]</sup> The first thing to point out is the strong scalar coupling between <sup>7</sup>Li and the adjacent <sup>19</sup>F atom observed for all complexes (90–103 Hz). The hydrogen bond of the FHF<sup>-</sup> anion was shown to be highly asymmetric: the value of <sup>1</sup>J<sub>HF</sub> of the distal fluorine

<sup>a</sup>For a cluster with the formula [(Cp\*TiF<sub>3</sub>)<sub>4</sub>(LiF)], see Ref.<sup>[28]</sup>.

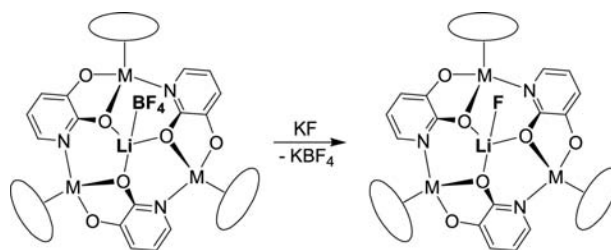


**Fig. 14** General strategy for the synthesis of LiF complexes by anion metathesis.

atom is large compared to that of the free FHF<sup>-</sup> anion, and coupling to the proximal fluorine atom was not observed. Therefore, an adequate description of the LiFHF complexes is a LiF complex hydrogen-bonded to a HF molecule (LiF···HF).

Several LiF and LiFHF complexes were examined by single crystal X-ray crystallography.<sup>[19,30]</sup> As what was found for other MX adducts, the lithium cation is bound to the three oxygen donor-atoms of the macrocyclic receptor with the fourth coordination site being occupied by the F<sup>-</sup> or FHF<sup>-</sup> anion (Fig. 15). The complexes show Li–F bond length between 176 and 181 pm. These values are among the shortest Li···F distances reported so far, highlighting the unique situation of molecular LiF and LiFHF inside the macrocyclic hosts.

The successful stabilization of LiF and LiFHF prompted us to investigate whether 12-metallacrown-3 complexes could capture unusual sodium salts. Similar to LiF, Na<sub>2</sub>SiF<sub>6</sub> displays a very low solubility in common solvents because of the high thermodynamic stability of the crystalline form. Thus it is not surprising that complexes of molecular Na<sub>2</sub>SiF<sub>6</sub> had not been described so far. The strategy to synthesize such a complex was related to that of the LiF complexes: a tetrafluoroborate adduct, **1**·NaBF<sub>4</sub>, was used as the starting material. Upon reaction with (NEt<sub>4</sub>)<sub>2</sub>SiF<sub>6</sub>, rapid anion exchange occurs and the dimeric complex

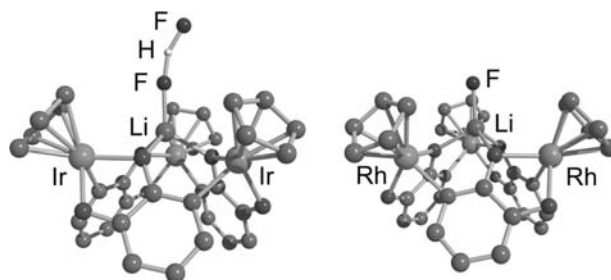


**Fig. 15** Ball and stick representation of the molecular structure of [Cp\*Ir(C<sub>5</sub>H<sub>3</sub>NO<sub>2</sub>)<sub>3</sub>]·LiFHF (left) and [Cp\*Rh(C<sub>5</sub>H<sub>3</sub>NO<sub>2</sub>)<sub>3</sub>]·LiF (right) in the crystal. The hydrogen atoms and the methyl groups of the Cp\* π-ligands are not shown for clarity.



$1 \cdot \text{Na}_2\text{SiF}_6 \cdot 1$  is obtained. The molecular structure in the crystal shows that two metallacrown complexes encapsulate the ion-paired  $\text{Na}(\mu\text{-F})_3\text{Si}(\mu\text{-F})_3\text{Na}$  guest molecule (Fig. 16).

In solution, two sets of signals are observed by  $^1\text{H}$ NMR spectroscopy, the relative ratio of which is 7:3. They correspond to the two diastereoisomers formed upon dimerization of the chiral hosts. The deviation from the statistical distribution shows that there is chiral recognition between the metallacrown complexes.

### Selective Complexation of Fluoride

Because the organometallic metallacrown complexes show a pronounced preference for the complexation of ion-pairs, they can also be used as specific receptors for anions. In particular, it is possible to use the  $\text{LiBF}_4$  adduct of the  $\text{Cp}^*\text{Ir}$  receptor  $[\text{Cp}^*\text{Ir}(\text{C}_5\text{H}_3\text{NO}_2)]_3$  (**4**) to construct a selective chemosensor for the fluoride anion.<sup>[19]</sup> As a result of the steric requirements of the large  $\text{Cp}^*$   $\pi$ -ligands, the lithium ion inside receptor **4** is well shielded. As a consequence, most anions (such as the  $\text{BF}_4^-$  counter ion) are efficiently blocked and  $\text{LiX}$  ion-pairs are not formed in solution. However, the small fluoride anion is able to enter the binding site and coordinate to the lithium ion (Fig. 17). The selective formation of  $\text{LiF}$  ion-pairs is further enhanced by the intrinsic affinity of  $\text{Li}^+$  to  $\text{F}^-$ .

The success of this approach was evidenced by the following NMR competition experiment: A mixture of  $\text{NBu}_4\text{X}$  ( $\text{X}^- = \text{Cl}^-, \text{Br}^-, \text{I}^-, \text{NO}_3^-$ ) and  $\text{NBu}_4\text{F}$  was added to a solution of complex **4**· $\text{LiBF}_4$  (receptor/ $\text{X}^-/\text{F}^- = 1:100:2$ ). In spite of the large excess of the competing anions  $\text{X}^-$ , the exclusive formation of **4**· $\text{LiF}$  was observed by NMR spectroscopy

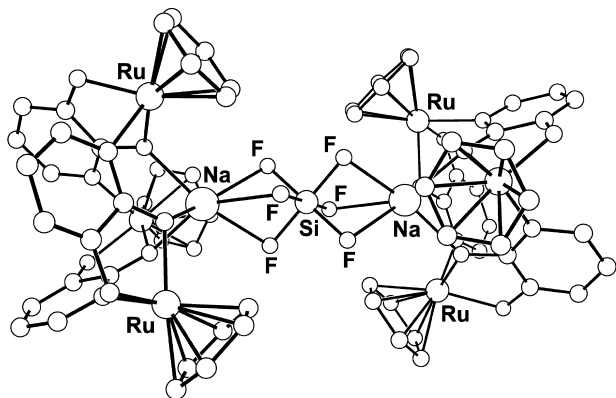


**Fig. 16** Stabilization of molecular  $\text{Na}_2\text{SiF}_6$  by encapsulation with two metallacrown complexes **1**. The ball-and-stick representation is based on the structure in the crystal. The hydrogen atoms and the side chains of the  $\pi$ -ligands are not shown for clarity.

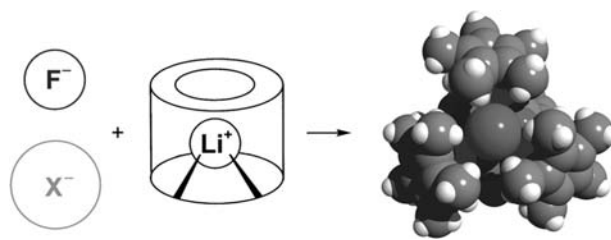


**Fig. 17** A lithium ion coordinated to a metallamacrocyclic host can act as a specific binding site for the fluoride anion. The space filling model of the  $\text{LiF}$  adduct of receptor **4** in the crystal (right) shows the close encapsulation of the fluoride anion by the  $\text{Cp}^*$   $\pi$ -ligands.

in all cases.<sup>[19]</sup> This indicates that the fluoride- $\text{X}^-$  selectivity is higher than 1000:1.

The presence of fluoride anions can also be detected by electrochemical methods. For **4**· $\text{LiBF}_4$ , the peak potential for the first oxidation is observed at  $890(\pm 3)$  mV when measured against a  $\text{Ag}/\text{AgCl}$  reference electrode.<sup>[19]</sup> Upon addition of five equivalents of  $\text{NBu}_4\text{F}$ , the complex is significantly easier to oxidize ( $\Delta E = -203$  mV). This can be explained by the reduced electron-withdrawing character of the ion-paired  $\text{LiF}$  guest as compared to the solvated lithium ion. In agreement with the NMR studies, only small changes are observed upon addition of other anions, such as  $\text{Cl}^-$ ,  $\text{Br}^-$ ,  $\text{NO}_3^-$ ,  $\text{HSO}_4^-$ , or  $\text{ClO}_4^-$  ( $\Delta E < 24$  mV). Similar results are obtained in solutions containing methanol in contrast to many other fluoride receptors, which have little or no affinity for  $\text{F}^-$  in protic solvents.

### CONCLUSION

Trinuclear metallamacrocycles of the general formula  $[(\pi\text{-ligand})\text{M}(\text{C}_5\text{H}_3\text{NO}_2)]_3$  [ $(\pi\text{-ligand})\text{M} = (\text{arene})\text{Ru}, \text{Cp}^*\text{Rh}, \text{Cp}^*\text{Ir}$ ] can easily be obtained via self-assembly by using commercially available starting materials. These nanometer-sized complexes are extremely good receptors for lithium and sodium salts with affinities and selectivities comparable to the best ionophores described so far. The possibility to vary the metal fragment was shown to be essential for the development of a chemosensor for lithium ions. Electronic effects are likewise important: subtle changes of the bridging ligand have a pronounced effect on the affinity for guest molecules. For the future design of metallacrown complexes, electronic effects should thus be considered as a powerful tool to modulate the binding affinities. A unique feature of the metallacrown complexes described in this article is the fact that the lithium and sodium salts are bound as an ion pair. As a result, it was not only possible to isolate unusual molecules

such as LiF and LiFHF but also to construct a highly specific chemosensor for the fluoride anion. It appears likely that the synthetic concept described here can be expanded to construct other 12-metallacrown-3 complexes with exciting new properties. Research along these lines is currently being pursued in our laboratory.

## ACKNOWLEDGMENTS

I am grateful to the following coworkers who have carried most of the experiments described in this overview: M.-L. Lehaire (syntheses), Z. Grote (syntheses), R. Scopelliti (X-ray analyzes), H. Piotrowski (X-ray analyses). The work was supported by the Swiss National Science Foundation.

## REFERENCES

1. Yamamoto, Y.; Settu, H.; Nishiyama, K.; Kuge, K.; Tatsumi, K. Unprecedented formation of dinuclear macrocyclic complexes by insertion of 2,3,5,6-tetrafluoro-7,7,8,8-tetracyanoquinodimethane (F4-tcnq) into a C–H bond and subsequent coordination to metal atoms. *Eur. J. Inorg. Chem.* **2002**, 2447.
2. Yamanari, K.; Fukuda, I.; Yamamoto, S.; Kushi, Y.; Fuyuhiko, A.; Kubota, N.; Fukuo, T.; Arakawa, R. Structural difference due to intramolecular stacking interactions in dinuclear rhodium(III) complexes  $[\{\text{Rh}(\eta^5\text{-C}_5\text{Me}_5)(\text{L})\}_2]^{n+}$  containing pyrimidine-2-thionate and related ligands. *J. Chem. Soc., Dalton Trans.* **2000**, 2131.
3. Haas, K.; Nöth, H.; Beck, W. Metallkomplexe mit biologisch wichtigen Liganden: CXX. Halbsandwich-Komplexe von Ruthenium(II) und Iridium(III) mit 3-(3-Pyridyl)-D-alanin. *Z. Naturforsch.* **1999**, 54b, 989.
4. Yamanari, K.; Ito, R.; Yamamoto, S.; Konno, T.; Fuyuhiko, A.; Fujioka, K.; Arakawa, R. Cyclic tetramers composed of rhodium(III), iridium(III), or ruthenium(II) half-sandwich and 6-purinethiones. *Inorg. Chim. Acta* **2002**, 41, 6824.
5. Annen, P.; Schildberg, S.; Sheldrick, W.S.  $(\eta^5\text{-Pentamethyl-cyclopentadienyl})\text{iridium(III)}$  complexes of purine nucleobases and nucleotides: a comparison with  $(\eta^6\text{-arene})\text{ruthenium}$  and  $(\eta^5\text{-pentamethylcyclopentadienyl})\text{rhodium(III)}$  species. *Inorg. Chim. Acta* **2000**, 307, 115.
6. Korn, S.; Sheldrick, W.S. Oligomeric  $(\eta^6\text{-arene})\text{ruthenium(II)}$  complexes of adenine and adenosine with N6,N7 coordination. *Inorg. Chim. Acta* **1997**, 254, 85.
7. Yamanari, K.; Yamamoto, S.; Ito, R.; Kushi, Y.; Fuyuhiko, A.; Kubota, N.; Fukuo, T.; Arakawa, R. Cyclic hexamer with a cubic cavity: crystal structure of  $[\{\text{Rh}(6\text{-purinethioneribosido})(\text{Cp}^*)\}_6](\text{CF}_3\text{SO}_3)_6$ . *Angew. Chem. Int. Ed.* **2001**, 40, 2268.
8. Fish, R.H. Bioorganometallic chemistry: synthesis, structure, and molecular recognition chemistry of  $(\eta^5\text{-pentamethylcyclopentadienyl})\text{-rhodium-DNA/RNA}$  complexes in water. *Coord. Chem. Rev.* **1999**, 185–186, 569, and refs. cited.
9. Korn, S.; Sheldrick, W.S. pH-Dependent competition between  $\kappa^2\text{N}^7, \text{O}(\text{P})$  macrochelation and  $\mu\text{-N}^1, \text{N}^7$  oligomer formation for  $(\eta^6\text{-arene})\text{Ru(II)}$  complexes of adenosine and guanosine 5'-mono-, -di- and -tri-phosphates. *J. Chem. Soc., Dalton Trans.* **1997**, 2191.
10. Sünkel, K.; Hoffmüller, W.; Beck, W. Metal complexes of biological important ligands: Part 107. Formation of tris(pentamethylcyclopentadienyl- $\mu\text{-L}$ -prolinato-iridium) tris(trifluoromethanesulfonate) with chiral self-recognition. *Z. Naturforsch.* **1998**, 53b, 1365.
11. Krämer, R.; Polborn, K.; Robl, C.; Beck, W. Metal complexes with biologically important ligands: Part LXIV. Pentamethylcyclopentadienyl-rhodium(III) complexes with  $\alpha$ -amino acid derivatives as bridging ligands and with several chiral metal centers: synthesis and structure of  $[\text{Cp}^*\text{Rh}(\mu\text{-L-phenylalaninato})_3](\text{BF}_4)_3$  and  $[\text{Cp}^*\text{Rh}(\mu\text{-NHCOCH}_2\text{NCO}_2\text{CH}_2\text{Ph})_2]$ . *Inorg. Chim. Acta* **1992**, 198–200, 415.
12. Carmona, D.; Lahoz, F.J.; Atencio, R.; Oro, L.A.; Lamata, M.P.; Viguri, F.; José, E.S.; Vega, C.; Reyes, J.; Joó, F.; Kathó, Á. Trimerisation of the cationic fragments  $[(\eta\text{-ring})\text{M}(\text{Aa})]^+$  ( $(\eta\text{-ring})\text{M} = (\eta^5\text{-C}_5\text{Me}_5)\text{Ir}$ ,  $(\eta^6\text{-p-MeC}_6\text{H}_4\text{Pr})\text{Ru}$ ; Aa =  $\alpha$ -amino acidate) with chiral self-recognition: synthesis, characterization, solution studies and catalytic reactions of the trimers  $[\{(\eta\text{-ring})\text{M}(\text{Aa})\}_3](\text{BF}_4)_3$ . *Chem. Eur. J.* **1999**, 5, 1544.
13. Yamanari, K.; Ito, R.; Yamamoto, S.; Konno, T.; Fuyuhiko, A.; Kobayashi, M.; Arakawa, R. Diastereomeric separations and crystal structure of rhodium(III) and iridium(III) complexes containing adenosine and related nucleosides. *Dalton Trans.* **2003**, 380.
14. Yamanari, K.; Ito, R.; Yamamoto, S.; Fuyuhiko, A. Diastereomeric separation of  $[\{\text{M}(\text{Cp}^*)(\text{ado})\}_3]^{3+}$  ( $\text{M} = \text{Rh}^{\text{III}}, \text{Ir}^{\text{III}}$ ; ado = adenosinato): Crystal structure of an inclusion compound  $[\{\text{Rh}(\text{Cp}^*)(\text{ado})\}_3](\text{CF}_3\text{SO}_3)_3 \cdot \text{MeOH}$ . *Chem. Commun.* **2001**, 1414.
15. Haberer, T.; Warchhold, M.; Nöth, H.; Severin, K. Chemically triggered assembly of chiral triangular metallomacrocycles. *Angew. Chem. Int. Ed.* **1999**, 38, 3225.
16. Piotrowski, H.; Polborn, K.; Hilt, G.; Severin, K. A self-assembled metallomacrocyclic ionophore with high affinity and selectivity for  $\text{Li}^+$  and  $\text{Na}^+$ . *J. Am. Chem. Soc.* **2001**, 123, 2699.
17. Piotrowski, H.; Hilt, G.; Schulz, A.; Mayer, P.; Polborn, K.; Severin, K. Self-assembled organometallic [12]metallacrown-3 complexes. *Chem. Eur. J.* **2001**, 7, 3196.
18. Piotrowski, H.; Severin, K. A self-assembled, redox-responsive receptor for the selective extraction of LiCl from water. *Proc. Natl. Acad. Sci. U. S. A.* **2002**, 99, 4997.
19. Lehaire, M.-L.; Scopelliti, R.; Piotrowski, H.; Severin, K. Selective recognition of fluoride anion using a  $\text{Li}^+$ -metallacrown complex. *Angew. Chem. Int. Ed.* **2002**, 41, 1419.
20. Lah, M.S.; Pecoraro, V.L. Isolation and characterization of  $\{\text{Mn}^{\text{II}}[\text{Mn}^{\text{III}}(\text{salicylhydroximate})]_4(\text{acetate})_2$

- (DMF)<sub>6</sub>·2DMF: An inorganic analogue of M<sup>2+</sup>(12-crown-4). *J. Am. Chem. Soc.* **1989**, *111*, 7258.
- Lah, M.S.; Kirk, M.L.; Hatfield, W.; Pecoraro, V.L. The tetranuclear cluster Fe<sup>III</sup>[Fe<sup>III</sup>(salicylhydroximato)(MeOH)(acetate)]<sub>3</sub> is an analogue of M<sup>3+</sup>(9-crown-3). *J. Chem. Soc., Chem. Commun.* **1989**, 1606.
  - Pecoraro, V.L.; Stemmler, A.J.; Gibney, B.R.; Bodwin, J.J.; Wang, H.; Kampf, J.W.; Barwinski, A. *Metallacrowns: A New Class of Molecular Recognition Agents*; Prog. Inorg. Chem.; Karlin, K., Ed.; Pergamon Press: New York, 1997; Vol. 45, 83.
  - Lehaire, M.-L.; Schulz, A.; Scopelliti, R.; Severin, K. Electronic effects in 12-metallacrown-3 complexes. A theoretical and experimental study. *Inorg. Chem.* **2003**, *42*, 3576.
  - Cox, B.G.; Garcia-Rosas, J.; Schneider, H. Solvent dependence of the kinetics of formation and dissociation of cryptate complexes. *J. Am. Chem. Soc.* **1981**, *103*, 1054.
  - Fulton, J.R.; Holland, A.W.; Fox, D.J.; Bergman, R.G. Formation, reactivity, and properties of nondative late transition metal–oxygen and –nitrogen bonds. *Acc. Chem. Res.* **2002**, *35*, 44.
  - Beer, P.D. Redox responsive macrocyclic receptor molecules containing transition metal redox centers. *Chem. Soc. Rev.* **1989**, *18*, 409.
  - Izatt, R.M.; Pawlak, K.; Bradshaw, J.S.; Bruening, R.L. Thermodynamic and kinetic data for macrocycle interaction with cations, anions, and neutral molecules. *Chem. Rev.* **1995**, *95*, 2529.
  - Demsar, A.; Pevec, A.; Golič, L.; Petriček, S.; Petrič, A.; Roesky, H.W. Lithium fluoride formed in situ is trapped by [TiF<sub>3</sub>(C<sub>5</sub>Me<sub>5</sub>)<sub>2</sub>]: an equilibrium with cleavage of a Ti–F–Ti bond and a model compound for molecular lithium fluoride. *Chem. Commun.* **1998**, 1029.
  - Kawahara, S.-I.; Uchimaru, T.; Taira, K. Electron correlation and basis set effects on strong hydrogen bond behavior: a case study of the hydrogen difluoride anion. *Chem. Phys.* **2001**, *273*, 207.
  - Lehaire, M.-L.; Scopelliti, R.; Severin, K. Stabilization of molecular LiF and LiFHF inside metallamacrocyclic hosts. *Inorg. Chem.* **2002**, *41*, 5466.

*Encyclopedia of*

# Nanoscience and Nanotechnology

*Second Edition*

## Volume IV

*Pages 2211 through 2922*

*Mica – Nanoparticles*

Mica – Mixed

Molecular Comp  
– Molecular Self

Molecular Simul  
– Motor

Nano –  
Nanocomposite

Nanocrystal –  
Nanocrystals

Nanodiamonds –  
Nanolithography

Nanomaterials –  
Nanomechanical

Nanoparticle –  
Nanoparticles

# Mica Surfaces: Charge Nucleation and Wear

**James M. Helt**

*Graduate Center, City University of New York, New York, New York, U.S.A.*

**James D. Batteas**

*Surface and Microanalysis Science Division, National Institute of Standards and Technology (NIST), Gaithersburg, Maryland, U.S.A.*

## INTRODUCTION

The area of nanotribology has advanced greatly in the past 17 years with the introduction of scanned probe microscopies<sup>[1]</sup> for the characterization of surface properties.<sup>[2–9]</sup> The ability to probe the details of structure, friction, and adhesion on a local atomic/molecular scale affords a definitive approach for understanding the mechanisms of wear at the most fundamental level. Muscovite mica, a layered aluminosilicate in the form of  $\text{KAl}_2(\text{Si}_3\text{AlO}_{10})(\text{OH})_2$ , has been a suitable standard for atomic force microscopy (AFM)<sup>[1]</sup> investigations of the atomic scale relationship between friction,<sup>[10–26]</sup> adhesion,<sup>[10,13,14,16,23,25,27–31]</sup> and wear<sup>[14–16,23,32,33]</sup> due to the ability to readily generate large areas of atomically smooth surface. The rich solution chemistry of mica, attributed to the Brønsted acid sites  $[\text{Si}-\text{O}(\text{H})-\text{Al}]$  within the basal (001) plane and its alternating sheet structure, combine with the vast atomically flat surface areas created when cleaved, to give a model substrate for examining a variety of phenomena. These include studies of double layer forces,<sup>[28,30,34–40]</sup> van der Waals forces,<sup>[38,41–43]</sup> ion binding and mobility,<sup>[35,44–46]</sup> monitoring the recoil tracks of alpha particles,<sup>[17,47]</sup> the characteristics of polymers at interfaces,<sup>[38,48,49]</sup> and ordering of discrete water layers.<sup>[38,43,50]</sup>

This review will be limited to a discussion on the wear of mica surfaces, with instructive comparisons drawn to other systems. The overall scope and outline of the chapter is detailed as follows.

As the area of nanotribology is too vast for us to cover in this review,<sup>[5,51,52]</sup> we shall endeavor to provide a perspective on studies as related to the mica surface, with a focus on direct observations of charge nucleation and defect formation, further limited to scanned probe microscopy studies. Relevant oxide and inorganic systems that have exhibited behavior paralleling that of mica will also be discussed. We will first begin with a description of the structure and chemistry of the mica surface followed by an overview of the scanned probe methodologies employed in the

investigation of nanotribological properties of mica surfaces. This includes the operating principles of the atomic force microscope (AFM), lateral force (or friction) measurements by AFM, as well as adhesion measurements. Moreover, as one wishes often to quantify such details we will also describe methodologies used to calibrate the signals retrieved from such experiments and then provide a brief description of a standardized approach for the measurement of wear at surfaces, whereby the details of the tip contact area will be explicitly taken into consideration when evaluating the number of scans needed to induce wear at an interface. After describing these approaches, we will then focus on the wear of the mica surface, including the impact of water, and functionalization of the mica surface with alkylsilanes.

## MICA SURFACES

The outermost mica surface typically exposes a hexagonally arrayed pattern of oxygen atoms, with a periodicity of 0.52 nm (Fig. 1A). Mica is comprised of a layered aluminosilicate structure with a periodicity of 1.0 nm normal to the (001) crystal basal plane (Fig. 1B), which is defined by a repeating boundary layer of  $\text{K}^+$ .<sup>[53,54]</sup> The  $\text{K}^+$  ions electrostatically bind the sheets together and act to neutralize the net negative charge associated with the partial substitution of Si with Al (on average one out of every four). It is at these boundaries that cleavage is preferred and is where shearing of the layers most readily occurs. Under aqueous conditions of low electrolyte concentrations, the outermost  $\text{K}^+$  layers are solvated into solution and exchanged with  $\text{H}^+$ .<sup>[19,30,34–36,44,46]</sup> This ready displacement has hindered direct imaging of the  $\text{K}^+$  terminated mica surface. The surface of mica may also be readily functionalized by a range of chemistries. Some of the most popular involve the organization of self-assembled monolayers of triethoxy- or trichloro-derivitized alkylsilanes, which can form densely packed structures on mica.<sup>[20,55–65]</sup> This provides

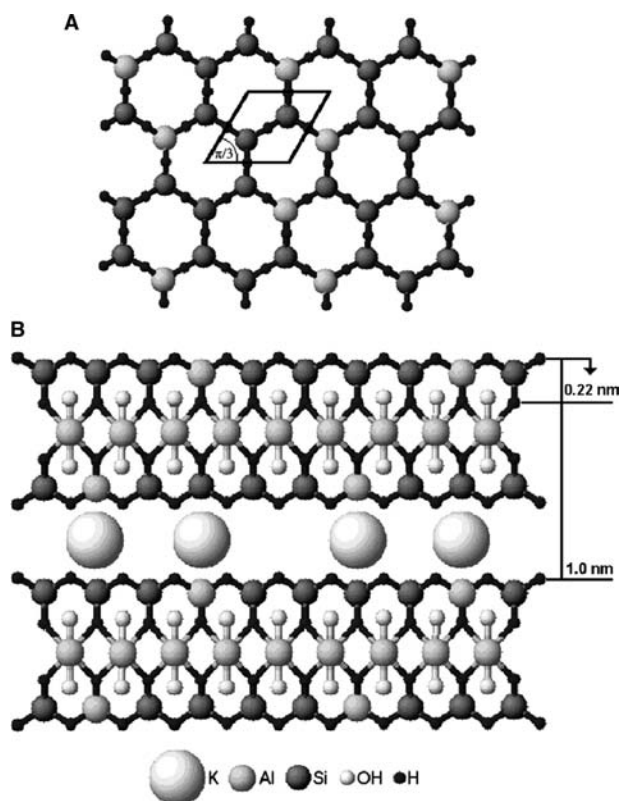


**Fig. 1** (A) Pictorial representation of the mica (001) cleavage plane showing the 0.52-nm lattice periodicity. (B) Repeating layered structure of mica along the *c* axis with interlayer distances referenced to the basal plane.

a means of investigating lubricant layers as protective barriers for the minimization of friction and wear.

To date, most surface wear studies have focused on the evaluation of surface structure before and after wear,<sup>[15,33,66–71]</sup> thus missing the key stage of the nucleation of defects that ultimately results in the gross structural changes observed. Although some studies have investigated the time evolution of wear using scanned probes,<sup>[14,16,72–77]</sup> the different approaches presented can make it difficult to compare experiments from different laboratories, and a more standardized approach is required. This is in part because of the typically large contact area between the AFM tip and the surface being worn, which frequently exceeds the area density of defects nucleated. Thus, an averaging over the contact renders the low population of defects “invisible” to the probe tip until gross wear has occurred.

Investigations of the wear of oxide surfaces such as mica and silica have unique difficulties when probing wear at the atomic level, which are associated with the chemical complexity of the surfaces, especially in the presence of water<sup>[71,78–87]</sup> where the surface charge density is highly pH dependent.<sup>[66,79–81,88,89]</sup> A recent demonstration by Maw et al. illustrates the incongruous

wear behavior that exists for ceramics in solution (pH = 7).<sup>[32]</sup> Specifically, they found that a Si<sub>3</sub>N<sub>4</sub> tip exhibited pronounced wear after being rastered against a quartz substrate for 25 scans at ~120 nN of force. However, under similar conditions the Si<sub>3</sub>N<sub>4</sub> tip exhibited little wear when the surface was mica. Here the disparity has been attributed to the relevant population of silanol (Si–OH) groups that can form bonds between the tip and substrate, which facilitates removal of tip materials. As the basal plane of mica possesses a Brønsted acid site, because of the 1 in 4 substitution of Si for Al, it is expected that the ionization potential of the surface is largely controlled by this site (at least at lower pH's), and therefore the chemically active Si–O<sup>−</sup> or M–OH should be in minute quantities.<sup>[40,46,65,90]</sup> Because the isoelectric point (IEP) of quartz is between pH 2 and 3, it is apparent that at pH 7 a significant number of Si–O<sup>−</sup> and Si–OH groups are available for condensation at the tip–quartz contact.<sup>[78]</sup> The influence of such tribochemically active species in initiating surface degradation is evident and illustrates the necessity to account for this when choosing material pairs for a given application, i.e., the chemistries should be complementary. This certainly applies to device applications such as microelectromechanical systems (MEMS) where interfacial chemical forces can readily dominate the moving contacts within the device.<sup>[70,91–96]</sup>

The organization of the water molecules<sup>[38,43,50]</sup> and counterions<sup>[19]</sup> immediately at the oxide surface may also impact the evolution of surface defects. Studies of the influence of water on the wear of oxide surfaces show a critical dependence on the amount of water present<sup>[14]</sup> and, in the case of solvation of the surface, the local pH of the surrounding water environment. Much of the wear processes present at oxides can be attributed to the catalytic activity of water (more appropriately the OH<sup>−</sup> ion) on the metal–oxygen and silicon–oxygen bonds present on such surfaces, the details of which have been investigated for many years.

## SCANNED PROBE METHODOLOGIES

### Atomic Force Microscopy: General Methodology

In atomic force microscopy, a sharp tip with a radius of curvature ranging between 10 and 50 nm is scanned over a surface using a piezoelectric translator to control the position of the tip relative to the sample. The forces acting between the tip and sample (these can be van der Waals, electrostatic, or magnetic in nature) act to attract or repel the tip to or from the surface, which in turn alters the bending of the lever to which the tip is attached. In most conventional AFMs, lever



deflections are detected by reflecting a laser beam off the back of the cantilever onto a quadrant photodiode. The photodiode signals are split to allow detection of the normal or torsional motions of the cantilever–tip assembly (Fig. 2). These motions can in turn (when appropriately calibrated, as discussed later) be translated into the normal and lateral forces acting between the tip and surface. The AFM can be operated in several imaging modes, including contact, non-contact/tapping, amplitude, and phase-modulated force or frictional force imaging. For nanotribological studies, contact and frictional force imaging modes are the most frequently used.

In contact mode the tip is brought in contact with the surface until the lever experiences a fixed amount of deflection. Assuming that this amount of deflection stays within a linear limit, then a Hooke's law response can be assumed. If the lever spring constant is known (see below) then the amount of deflection can be converted into the force applied between the tip and surface. During imaging, a feedback loop is then used to maintain a fixed amount of lever deflection (constant normal force) by repeatedly moving the piezoelectric translators up and/or down, hence following the topography of the surface. The lateral force signals are concomitantly acquired with the topographic images allowing for correlations to be drawn between the two. The lateral force signal is an excellent indicator of changes in local chemistry even when obvious topographic differences are not present. For example, the spatial organization of films consisting of both hydrophobic and hydrophilic end-groups, which have the same thickness and appear uniform in topography,

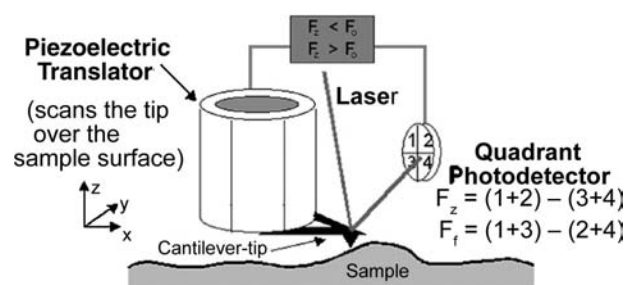


**Fig. 2** Schematic of an atomic force microscope. In this configuration, the tip is scanned over a fixed sample. The cantilever–tip assembly is mounted on a piezoelectric translator, which controls the tip position over the surface. In contact mode, the tip is pressed against the surface until a fixed set point force is reached ( $F_0$ ). The deflection of the lever is detected by a quadrant photodiode from which the normal force ( $F_z$ ) and torsional (frictional) force ( $F_f$ ) may be measured. As the tip is scanned over the surface a feedback loop raises and lowers the tip depending on whether the normal force is larger than or less than the set point force to maintain a constant force.

can be easily distinguished in the frictional images [Fig. 3A (2–3)].

### Lateral Force (Friction and Shear) Measurements

Eventhough qualitative lateral force, or frictional response, can be readily obtained by AFM, quantifying frictional forces can be a daunting task. This is due to the difficulties associated with calibration of the lateral spring constants for AFM cantilevers (see below). Here we briefly discuss the type of information, which may be obtained from lateral force or shear force measurements. In lateral force measurements, friction is assessed using a friction loop. The friction loop is generated from the forward and reverse scans plotting the lateral force data vs. distance (Fig. 3B). Initially, the tip sticks to the surface and the torsional force on the lever increases without the sliding motion of the tip. Once the static friction has been overcome, then the tip will begin to slide over the surface and the sliding friction may be determined (Fig. 3B). The shear modulus of the surface may also be measured using this same basic approach. To evaluate the shear modulus, the tip is oscillated in the scan direction and the slope of the friction force ( $F_f$ ) vs. distance signal is measured prior to sliding. This slope value contains the combined stiffness of the tip–sample contact [Eq. (1)] from which the shear modulus of the surface may be determined.

$$\frac{dF_f}{dx} = k_{\text{total}} = \left( \frac{1}{k_{\text{lever}}} + \frac{1}{k_{\text{contact}}} \right)^{-1} \quad (1)$$

A significant advantage of this measurement is that the details of the tip size ultimately fall out of the calculation, removing a potential source of error. The reader is directed to the literature for a more complete description of lateral stiffness measurements.<sup>[97]</sup>

## MAKING QUANTITATIVE MEASUREMENTS

### Calibration of AFM Cantilevers

AFM cantilevers can be bought from numerous sources and most frequently come as V-shaped or rectangular springboard-shaped levers. The levers are generally made from silicon and silicon nitride. Coatings are often applied to enhance the reflectivity of the laser beam. The reflective coating, however, can add strain to the levers when used in vacuum because of heating. The average lever spring constants provided by the manufacturer are often inaccurate and quantitative measurements should not be based on these

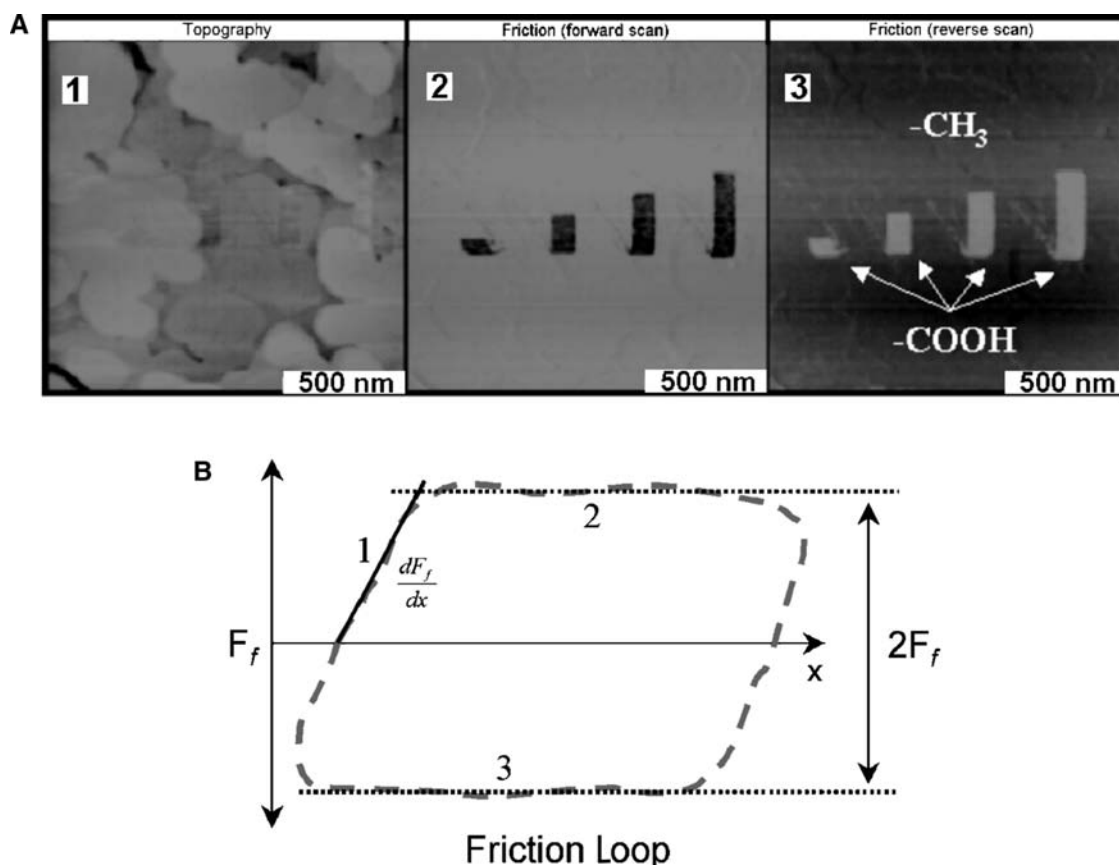


**Fig. 3** (A) Topographic (1) and forward and reverse friction images (2, 3) of mercaptoundecanoic acid grafted into a dodecanethiol self-assembled monolayer on Au. Whereas the topographic image shows almost no height contrast in the image because of the near equivalent heights of the two materials, the friction images clearly show the “chemical” contrast of the  $-\text{COOH}$  terminated regions vs. the  $-\text{CH}_3$  terminated regions. (B) Schematic of a friction loop. Initially the tip sticks to the surface (1) until the static friction between the tip and surface is overcome. The tip then enters a sliding friction regime (2). As the scan is reversed, the signal in the photodetector becomes negative (3) and a reverse trace is produced. The “frictional” force is the average of the forward and reverse friction traces. The stiffness of the contact may be deduced from the slope of the friction loop ( $dF_f/dx$ ) before sliding.

values. Therefore, each lever should be independently calibrated, preferably via an in situ methodology.

The determination of lever force constants is less demanding for a rectangular cantilever beam,<sup>[98]</sup> but it still requires non-trivial details of the lever’s dimensions and physical constants, e.g., modulus and Poisson ratio. These details become more difficult to define for metal-coated levers, as the coating significantly modifies the lever’s elastic properties. For a rectangular beam of length  $L$ , width  $w$ , thickness  $t$ , Young’s modulus  $E$ , the stiffness  $k$  is given by:

$$k_{\text{lever}} = \frac{Ewt^3}{4L^3} \quad (2)$$

Errors inherent to the determination of the spring constant come from difficulties in accurately measuring (by SEM) the thickness of the lever. In addition, for chemical vapor deposited silicon nitride levers,

variations in  $E$  can also occur. If a bulk value for  $E$  is used, the thickness can be determined by measuring the resonance frequency of the cantilever.<sup>[99]</sup> However, this method works only for uncoated monolithic cantilevers.<sup>[100]</sup> The formulae for the spring constants for V-shaped levers are much more complicated.<sup>[101]</sup> Uncoated, single-crystal silicon cantilevers are perhaps the best choice for which the force constant can be reliably determined by using Eq. (2) and the resonance frequency.<sup>[102]</sup>

A range of methods for the calibration of the normal<sup>[99–114]</sup> and torsional (lateral) force constants<sup>[101,105,110,115,116]</sup> of AFM cantilevers have been described. A recent method proposed by Sader, Chon, and Mulvaney appears to be reliable and simple to perform for rectangular levers.<sup>[107]</sup> It relies on measuring the resonance frequency and the quality factor of the cantilever in air. Use of the hydrodynamic function relates the damping of the lever resonance by air to the

quality factor, and the dependence of  $E$  and  $t$  are eliminated from the resulting formula for the force constant.

### Probe Tip Characterization

A problem of quite a different nature is an accurate measurement of the AFM tip shape and composition. With respect to tip geometry, continuum mechanics requires a priori knowledge of the probe shape, mechanical properties, and physical dimensions in order for the models to be properly applied.<sup>[117,118]</sup> Carpick et al. illustrated this point rather succinctly in an instructive set of experiments with non-parabolic Pt tips on a mica substrate in ultrahigh vacuum (UHV).<sup>[12]</sup>

There are several in situ methods to characterize the tip shape, where an AFM topographic image is used to deconvolute the tip and sample geometry.<sup>[119–121]</sup> Separation of the tip and sample contributions by contact imaging of known, or at least sharp, sample features allows determination of the tip.<sup>[104,105,120–131]</sup> Ex situ tip imaging by electron microscopy has also been performed.<sup>[103]</sup> Some of these measurements have revealed that a number of microfabricated cantilevers possess double tips and other unsuitable tip structures.<sup>[122,125,130,131]</sup> This demonstrates the importance of tip characterization in nanotribological measurements. Thin film coatings applied to the microfabricated levers can provide robust, smooth, and even conductive coatings.<sup>[132,133]</sup> Further work in this direction would be useful in providing a wider array of dependable tip structures and materials.

Detailed control of tip chemistry is still a difficulty of scan probe studies with commonly used tips (e.g., silicon nitride) possessing a variable stoichiometry.<sup>[89,112,134]</sup> Coating with inert metals (such as Au or Pt) or functionalization with alkylsilanes or alkanethiols is often useful; however, one must be aware of the “chemical” compatibility and how this can translate into “anomalous” wear behavior.<sup>[32]</sup> The chemical composition of the tip is equally important, but is also challenging to determine or control. Qian, Xiao, and Wen have shown that the AFM tip is readily chemically modified when scanned in contact with various materials,<sup>[25]</sup> even tips that have been coated with self-assembled monolayers to control their chemistry. They recommend “running in” the tip with a standard sample to give reproducible results. The stresses that take place in a nanocontact can be very large, and so modification of both the chemistry and structure of the tip is an important consideration.

### Adhesion Measurements

When quantifying adhesion and interfacial energies from AFM measurements, often the contact mechanics

model developed by Johnson, Kendall, and Roberts (JKR)<sup>[118,135]</sup> is used to analyze adhesion data from force–distance spectroscopy. Determination of the most appropriate continuum mechanics model to use, however, requires consideration of the range of forces and the materials operative at the contact. The JKR model is often applied to highly adhesive, compliant contacts, whereas the Derjauin–Müller–Toporov (DMT) model relates to stiff, weakly adhering contacts.<sup>[117,136]</sup> Attention has been given to identifying which model is most appropriate and therefore best describes the contact for a given material pair; the reader is directed to the references for the complete treatments.<sup>[135–138]</sup> The application of such models to AFM force of adhesion measurements ( $F_{adh}$ ) enables the number of interacting species (and consequently the average “unit” interaction force or energy) to be derived from the estimated contact area and the average molecular packing density. Using the JKR model, one can see that the  $F_{adh}$  (AFM pull-off force) is related to the work of adhesion,  $W_{adh}$ , and the reduced radius,  $R$ , of the tip–surface contact:

$$F_{adh} = -\frac{3}{2}\pi RW_{adh} \quad (3)$$

The work of adhesion, a formalism of Dupré from 1869, is a combination of the tip–surface ( $\gamma_{ts}$ ), tip–solvent ( $\gamma_{tl}$ ), and surface–solvent ( $\gamma_{sl}$ ) interfacial energies ( $W_{adh} = \gamma_{sl} + \gamma_{tl} - \gamma_{ts}$ ). For tip–surface combinations that have the same chemical composition, the surface energy may be estimated directly from the adhesion measurement ( $W_{adh} = 2\gamma_{sl}$ ) because  $\gamma_{sl} = \gamma_{tl}$ , with  $\gamma_{ts} = 0$ . Furthermore, the effective contact radius at separation,  $r_s$ , from the JKR model is given as:

$$r_s = \left( \frac{3\pi W_{adh} R^2}{2K} \right)^{1/3} \quad (4)$$

where  $K$  is the reduced elastic modulus of the tip and surface. Using the contact area at separation and the assumed packing density of the molecules at the surfaces in contact, an estimate of the adhesion force or interaction energy on a per molecule basis can be made.

The accuracy of the interfacial energies and per molecule values obtained with this approach must be carefully evaluated, as several sources of error exist in the various elements of the calculation. These include imprecise knowledge of the contact, including the tip radius, packing densities of molecular monolayers on the modified surfaces, as well as unknown elastic properties of the contact. Such properties are typically assumed to be dominated by those of the underlying substrate, and the bulk values of the surface and/or tip materials (Au, Si, mica,  $Si_3N_4$ ,

SiO<sub>2</sub>) are often used in these calculations.<sup>[59–61,139]</sup> Moreover, as mentioned earlier, if the molecular packing densities of the monolayers being evaluated are not known (as is frequently the case with a typical AFM tip), then estimations must be used.

### Watching Wear with the AFM (How Many Scans Does It Take?)

Atomic force microscopy tips, acting as single asperities, have proven indispensable in actively mediating the transition of a substrate surface from its native state to the defect nucleation regime (rupture of terminating surface bonds) and finally to the molecular-fragment abstraction (gross wear) regime.<sup>[14,73–77,140–142]</sup> Unifying empirical evidence pertaining to the intimate details of defect nucleation is essential to properly aid the current effort of wear map modeling on the micro- and macroscopic scales, situations with multiple asperity contacts, and a multitude of wear mechanisms operating in concert.<sup>[51,143]</sup> To ease comparison of data compiled from numerous research facilities within the field, guidelines outlining the optimal experimental protocol for an SPM study are desirable. Recent developments in modeling tip-activated dissolution of calcite and brushite by Dickinson et al. has given impressive results and holds promise for evaluating other “model” systems.<sup>[74–77]</sup> Salmeron and Kopta have recently used a model, similar to the one adopted by Dickinson et al., in their studies of tip induced mica surface degradation under low vacuum with variable humidity.<sup>[14]</sup> In this work, the objective was to evaluate the critical defect density necessary for the onset of gross surface degradation (abstraction of the surface terminating SiO<sub>3</sub> molecular fragments). The progressive layer removal illustrated the fidelity of inducing defects; however, linear regression analysis obtained a collected physical constant ( $B_0$ ) that was appreciably higher than anticipated. This could be attributed to scan overlap, which can lead to significant additional history of unintentional wear on the surface.

Here we outline a strategy for conducting wear trials with AFM, based on the Hertzian theory of *elastic* contacts,<sup>[144]</sup> to account for the degree of scan overlap in AFM wear trials, and arrive at an interesting *contact radius–line step* (CRLS) relationship.<sup>[145]</sup> This approach is intended to 1) account for additional scan history that line-scan overlap imparts to a surface and to experimentally quantify the impact of this overlap on the propagation of defects; 2) eliminate the systematic error in reported scan history (experimental number of scans,  $N_{\text{scans}}^{\text{Exp}}$ ) for wear trials performed with line-scan overlap; and 3) examine previous load ( $F_z$ ) and frequency ( $N_{\text{scans}}^{\text{Exp}}$ ) studies to reevaluate activation parameters for defect nucleation. Furthermore, the

extent of wear can be predicted with application of CRLS analysis for *paired* overlap and non-overlap wear trials, giving a unique perspective of the fundamental kinetics and thermodynamics of defect nucleation and growth.

### Contact Radius–Line Step Analysis

A brief description of CRLS analysis follows with a focus on its application rather than on the details of its derivation. A comprehensive discussion of CRLS model and experiments is described elsewhere.<sup>[145]</sup> First, consider the general case of obtaining an AFM micrograph or performing a wear trial. In either instance, one of many parameters set during image acquisition is the image resolution (res), the number of lines scanned per image. Typically, it is adjustable within the range of 8–1024 lines/image, depending on the design specifications of the microscope used. Although it is not generally thought of as an adjustable parameter for use in experimentation, it is readily illustrated that res can play an important role when assessing the number of scans required to induce wear. Its importance arises because res dictates the magnitude of the line step (LS), i.e., the distance the tip moves in the slow scan ( $L_{\text{sscan}}$ ) direction after each forward–reverse trace. Fig. 4 illustrates the inverse relationship between LS and res for the specified slow scan lengths ( $L_{\text{sscan}}$ ). Before we show how LS ties into defect production, we introduce the Hertzian definition of the contact radius ( $a$ ) as defined for an AFM tip compressed against flat elastic body without adhesion [Eqs. (5) and (6)].<sup>[118]</sup>

$$a = \left( \frac{3RF_z}{4\varepsilon} \right)^{1/3} \quad (5)$$

with

$$\varepsilon = \left( \frac{1 - \nu_1^2}{E_1} + \frac{1 - \nu_2^2}{E_2} \right)^{-1} \quad (6)$$

Here  $R$ ,  $F_z$ , and  $\varepsilon$  are the tip radius of curvature, the applied normal force, and the combined elastic modulus given in terms of the individual tip and substrate Poisson ratios ( $\nu_i$ ) and Young's moduli ( $E_i$ ). It is apparent that at a typical res of 256 lines/image, the LS is <4 nm for all  $L_{\text{sscan}}$  below  $\sim 1 \mu\text{m}$  in length. Thus, unless  $a \leq 2 \text{ nm}$ , overlap from successive scans will occur, and shows that avoidance of scan overlap and its effects are difficult to realize when probing regions with nanoscopic dimensions.

If we make the assertion that ideal scanning conditions for assessing wear as a function of the number of scans requires imaging conditions with no scan

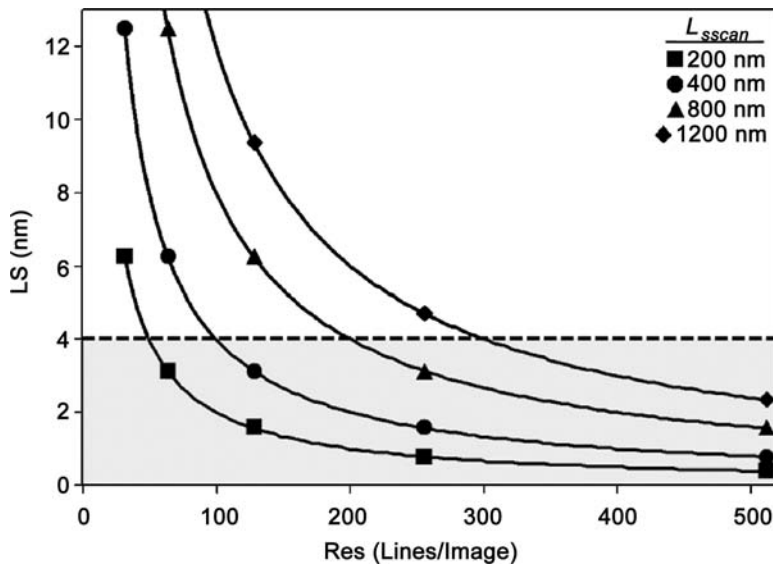


Fig. 4 Inverse relationship between image line step (LS) and image resolution (res) for several slow scan lengths  $L_{scan}$ . The dashed line and accompanying shaded region illustrate the occurrence of scan overlap during AFM imaging for contacts with a contact radius  $a \geq 2$  nm. For wear trials this implies that scan overlap will systematically contribute unaccounted attempts to defect production.

overlap, it is recognized that the line step (LS) must be greater than or equal to the contact diameter. Using the Hertz definition of  $a$  and the condition that ideal AFM wear trials have  $LS = 2a$ , the ideal ratio of contact radius to line step (CRLS) is 0.5. Furthermore, line-scan overlap is avoided (neglecting drift) when CRLS is  $\leq 1/2$ . This further implies that an ideal AFM wear trial, with  $LS = 2a$ , will have an ideal slow scan length,  $L_{scan}^{CRLS}$ , given by Eq. (7). Expression (7) reveals an important relationship between the AFM scanning parameters,  $L_{scan}^{CRLS}$  and res, and the applied normal load. A  $L_{scan}^{CRLS}$  vs.  $F_z$  plot is especially useful for conducting internally consistent load ( $F_z$ )-dependent studies.

$$L_{scan}^{CRLS} = 2a \times res = res \times \left(\frac{6RF_z}{\epsilon}\right)^{1/3} \quad (7)$$

We have used the term “ideal” quite ambiguously to describe  $L_{scan}^{CRLS}$ , the most appropriate scan size for defect generation. It is expected and empirically validated that the generated defects will be more uniformly (relative to overlapping trials) distributed over the wear area before the advent of other varieties of defects. This allows for the design of experiments to probe these low-density species (typically <1 defect within the tip-sample contact).<sup>[14]</sup>

To evaluate the effects of scan overlap we must account for the additional history overlap imparts to the surface; achieved by estimating a scan correction

( $scan_{cor}$ ) for overlapping studies. The  $scan_{cor}$  determines the additional number of scans contributed by overlap to the contact history and therefore can be used to estimate the number of scan cycles required to achieve an equivalent degree of wear, under identical loads, without scan overlap. The  $scan_{cor}$  is arrived at naturally by association to the force of overlap within overlapping contacts. The Hertz model defines the pressure distribution  $p(r)$  in terms of  $r$ , the distance from the center of contact via Eq. (8).<sup>[144]</sup>

$$\begin{aligned} F_z &= \int_0^{2\pi} \int_0^a p(r) r dr d\theta \\ &= \frac{1.5F_z}{\pi a^2} \int_0^{2\pi} \int_0^a \left(1 - \frac{r^2}{a^2}\right)^{1/2} r dr d\theta \\ &= \frac{2p_0\pi a^2}{3} \end{aligned} \quad (8)$$

Here  $p_0$  is the maximum Hertz pressure within the contact. Once the boundary of the overlapping area is defined (Fig. 5), the force of overlap can be calculated. The  $scan_{cor}$  is collectively calculated in terms of  $F_{ovlp}^{Total}$ , the total force within all successive overlapping contact areas.  $F_{ovlp}^{Total}$  is formulated from a geometric breakdown of overlapping circles of radii  $a$  (Fig. 5) and leads to the three integrals in Eq. (9), which have been converted to Cartesian coordinates. The  $(F_z \times res)$  term normalizes each experimental scan and the functions A, B, and C are given in Fig. 5.

$$\begin{aligned} scan_{cor} &= 1 \\ &+ \frac{2 \times \sum_{m_1}^{m_i} \{res - m_y\} \left(\frac{1.5F_z}{\pi a^2}\right) \left[ \int_0^{a \sin(\theta)} \int_0^{\sqrt{a^2-x^2}} p(x,y) dy dx - \int_A^{a \sin(\theta)} \int_0^B p(x,y) dy dx + \int_0^C \int_0^{-B} p(x,y) dy dx \right]}{res \times F_z} \end{aligned} \quad (9)$$

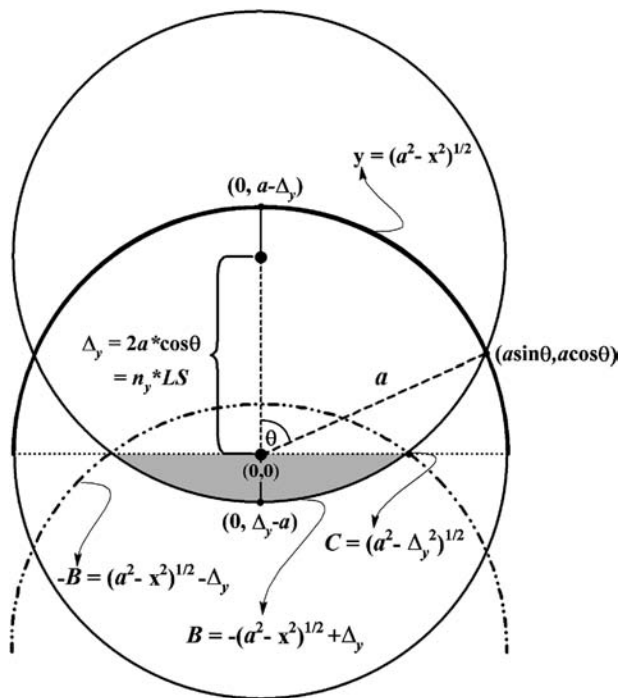


**Fig. 5** Geometry of overlapping scans according to Hertzian contact mechanics theory.

The center-to-center distance ( $\Delta_y$ ) along the slow scan axis for successive scans is referenced to the first scan line ( $n_0 = 0$ ) and is known a priori;  $n_y$  is a positive integer corresponding to the  $n$ th line step from  $n_0$

as shown in Fig. 6. The series is truncated at  $n_i$  ( $n_i = 2a/LS$ ) because overlap does not exist for the  $i$ th successive scan where  $\Delta_i \geq 2a$ . For simplicity, the summation is redefined in terms of  $m_y$  having an integer range of  $[m_1, m_i]$  with  $m_i = n_{i-1}$  because the 1 in Eq. (9) accounts for  $n_0$ . For the interested reader, more details on the theoretical workup can be found in Ref.<sup>[145]</sup>. We can now utilize the general, material independent result [ $scan_{cor}$  given in Eq. (10)] to explore how CRLS analysis is applied to previous wear trials with mica.

$$scan_{cor}(\theta, m_y) = 1 + \sum_{\theta(m_1)}^{\theta(m_i)} \left[ \frac{res - m_y}{res} \right] \times \left( 1.011 \exp \frac{-(\theta - 92.83)^2}{34.67^2} \right) \quad (10)$$

Completing the correction simply requires multiplying the experimental number of scans containing overlap ( $N_{scans}^{Exp}$ ) with  $scan_{cor}$  ( $scan_{cor} \times N_{scans}^{Exp} = N_{scans}^{Cor}$ ). Importantly, CRLS can be tested directly because it can predict wear for “paired” trials. In such circumstances, an experimental trial with overlap is taken as the primary trial from which the CRLS prediction and the secondary non-overlapping experiments are based. Experimentally, the secondary trials are conducted at a Hertz mean pressure ( $p_m$ ) equivalent to the primary run over a region with  $L_{sscans}^{CRLS}$  defined by Eq. (7). Therefore, the non-overlapping secondary wear trials

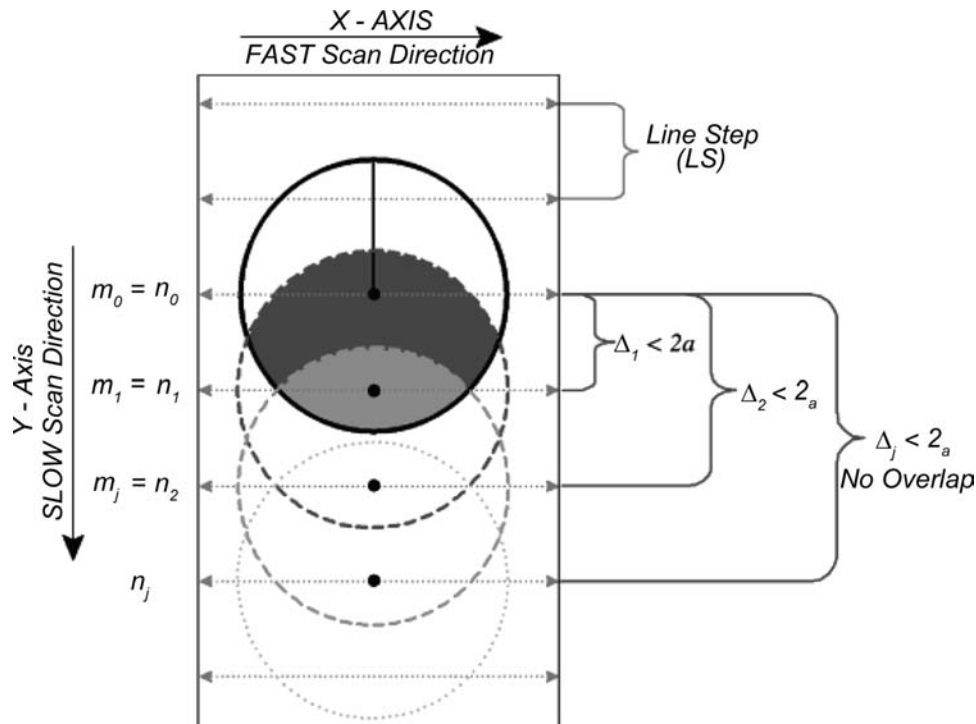


**Fig. 6** Definition of elements used for  $scan_{cor}$  analysis of sequential raster lines.



consist of  $N_{\text{scans}}^{\text{cor}}$  over a  $(L_{\text{sscans}}^{\text{CRLS}} \times L_{\text{fscan}})$  nm<sup>2</sup> region. The surface damage from both instances can be evaluated and compared with  $F_{\text{adh}}$  measurements, topography, and frictional force microscopy. In theory, the two wear experiments have “identical” scan history within this Hertzian approximation. Deviations from CRLS behavior are expected, however, because the tenets of elastic contact mechanics do not include inelastic energy dissipation pathways natural to a wearing contact. Numerical and experimental results clearly demonstrate that the systematic error attributed to scan overlap is considerable and affects fundamental wear processes acting at the tip–surface contact.<sup>[145]</sup> Work is currently under way to establish the relationship between scan overlap and defect nucleation and growth.

## WEAR OF MICA SURFACES

There have been many theoretical and experimental studies on wear of oxides and the generation and propagation of defects within condensed matter. Here we shall describe a few examples of crystalline systems within the context of tip induced defect nucleation and wear of mica surfaces in solution. The examples will focus on studies of defect nucleation that have revealed the prototypical behavior of what is to be expected (and what is detectable with AFM) of a surface reconstructing under the influence of an AFM tip. At the most fundamental level of defect nucleation, this includes *terminal* surface bond rupture for covalent systems as well as removal of ions from ionic surfaces.

### Native Mica Surfaces

Now we will briefly describe adhesion and wear of mica surfaces using silicon-nitride-based AFM tips. The complete experimental details are described elsewhere.<sup>[142]</sup> In these studies, oxidized and hydroxylated silicon nitride tips were used.<sup>[102,122]</sup> Under these conditions, the silicon nitride tip chemistry then varies with pH similar to that of silica,<sup>[146]</sup> where a neutral silanol-covered surface exists at the isoelectric point between pH 2 and 3, with a gradual surface charge increase via the formation of an anionic surface species with increasing pH ( $\sim 0.004\text{--}2$  charges/nm<sup>2</sup>) over the range of pH 3–10.<sup>[66,78]</sup> In aqueous solution, the adhesive force ( $F_{\text{adh}}$ ) vs. pH for native mica with an oxidized and hydroxylated silicon nitride tip is shown in Fig. 7. This pH dependence on adhesion is similar to that found for silica surfaces under the same conditions, with a shift in peak adhesion from pH  $\sim 4.5$ , for silica/silica, to pH  $\sim 6$  for the silica/mica interaction.<sup>[66]</sup> Based on this profile, alterations

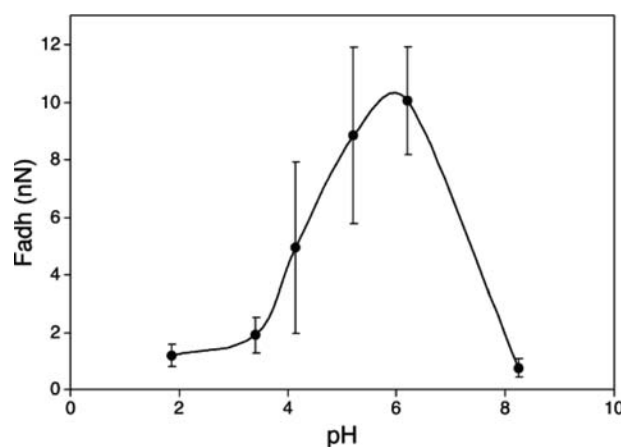


**Fig. 7** Mean  $F_{\text{adh}}$  vs. pH for muscovite mica with a  $\text{Si}_3\text{N}_4$  tip. Error bars correspond to the first standard deviation from the  $>180$  force distance curves collected for each point.

in adhesion, friction, and topography under various loads for three pH ranges (pH 2–3, 5–6, and  $>8$ ) can be assessed and related to the interfacial chemistry.

Typical of silicates, for the highest pH conditions (pH  $\geq 8$ ), the mica surface undergoes rapid wear.<sup>[78–81,85]</sup> Even under low loads (Hertz mean pressure,  $p_m \sim 1.2$  GPa) wear scars 0.22 nm in depth are formed. With additional scans ( $>10$ ) wear scars of 1.0 nm or more are rapidly formed (Fig. 8). Upon removal of a single repeat layer (1.0-nm-deep feature), the friction in the wear scar is equivalent to that of the contiguous unworn mica surface, indicating that we have progressed from the outermost oxygen-terminated layer to the next chemically equivalent repeat layer. This is a general observation for mica wear at any pH and has also been observed by Salmeron et al. under humid conditions.<sup>[14,16]</sup> Comparison of the threshold forces for removal of the  $\text{SiO}_3/\text{AlO}_3$  tetrahedral layer, i.e., generating 0.22-nm wear scars, illustrates the tribochemical influence hydroxide ions have on hydrolysis of surface bonds. Table 1 summarizes the threshold pressures and the ab initio calculated activation energies ( $E_a$ ) for water, acid, and base-catalyzed Si–O–M hydrolysis.<sup>[147,148]</sup> Once the  $\text{MO}_3$  (M=Si or Al) basal fragment is removed, the underlying aluminate (gibbsite) layer is exposed and should carry a net positive charge for pH  $\leq 10$ .<sup>[149,150]</sup> This is another “model” property of mica and the details on how this affects the tip–sample contact during friction imaging can be found in Ref.<sup>[142]</sup>

Conducting wear trials at pH 5 under lower loads ( $p_m \sim 0.74$  GPa; ca.  $\frac{1}{2} p_{\text{thresh}}$ ), the surface friction in the imaged region is observed to *decline* (Fig. 9A) relative to the unworn surface, before any noticeable wear (topographical) on the nanometer scale. This decrease in friction can be attributed to the accumulation

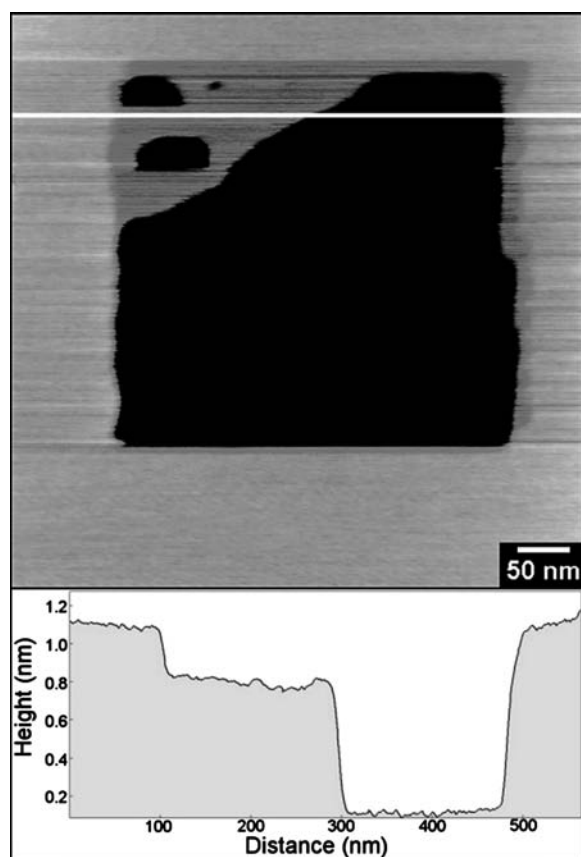


**Fig. 8** Topographic AFM images of a worn mica surface at pH 8 and the corresponding line trace across the surfaces showing both 1.0- and 0.22-nm wear regions.

of negative surface charge both on the tip and at the imaged surface through  $\text{OH}^-$  insertion into strained Al–O–Si and Si–O–Si bonds, yielding surface anions, such as siloxy ( $\text{Si-O}^-$ ) groups.<sup>[83,86]</sup> Analysis of the

**Table 1** Threshold pressures for mica wear under solution conditions, and ab initio calculated activation energies ( $E_a$ ) for acid-, base-, and  $\text{H}_2\text{O}$ -catalyzed hydrolysis

Conditions	$p_{\text{thresh}}^{[148]}$ (GPa)	Hydrolysis activation energy ( $E_a$ , kcal/mol)
Mica wear pH 3	2.1	–
Mica wear pH 5	1.5	–
Mica wear pH 8	1.2	–
Si–O–Si (OH catalyzed)	–	2–8 <sup>[148]</sup>
Si–O–Al ( $\text{H}^+$ catalyzed)	–	16 <sup>[147]</sup>
Si–O–Si ( $\text{H}^+$ catalyzed)	–	24 <sup>[147]</sup>
Si–O–Al ( $\text{H}_2\text{O}$ catalyzed)	–	26 <sup>[147]</sup>
Si–O–Si ( $\text{H}_2\text{O}$ catalyzed)	–	29 <sup>[147,160]</sup>

Threshold pressures ( $p_{\text{thresh}}$ ) were calculated with Hertz continuum mechanics theory.  $p_{\text{thresh}}$  corresponds to the gross deformation (abstraction) regime that is defined by removal of  $\text{SiO}_3$  and  $\text{AlO}_3$  basal tetrahedral units.

surface topography reveals a discernible increase by  $\sim 0.05$  nm (Fig. 9B), which is near the noise-level limit of  $\pm 0.03$  nm. This height increase would be consistent with capping of the surface dangling bonds by  $\text{OH}^-$  and  $\text{H}^+$  as the bonds are ruptured. Adhesion measurements, as summarized in Table 2, within the native and worn (“induced”) region show a marked shift to lower adhesive forces for the worn surface, which is expected for the proposed repulsive tip–sample interaction.

Although not a common observation, several groups have reported surface charging with little to no topography changes during wear experiments. Using the nanoscale Kelvin probe, capable of measuring variations in surface potential (work function mapping), DeVecchio and Bhushan have observed electron-deficient regions within the “zero-wear” regime for single-crystal aluminum under ambient conditions ( $\text{RH } 45 \pm 5\%$ ).<sup>[73]</sup> The topography and potential maps are given in Fig. 10 and illustrate the charging effect before catastrophic failure of the

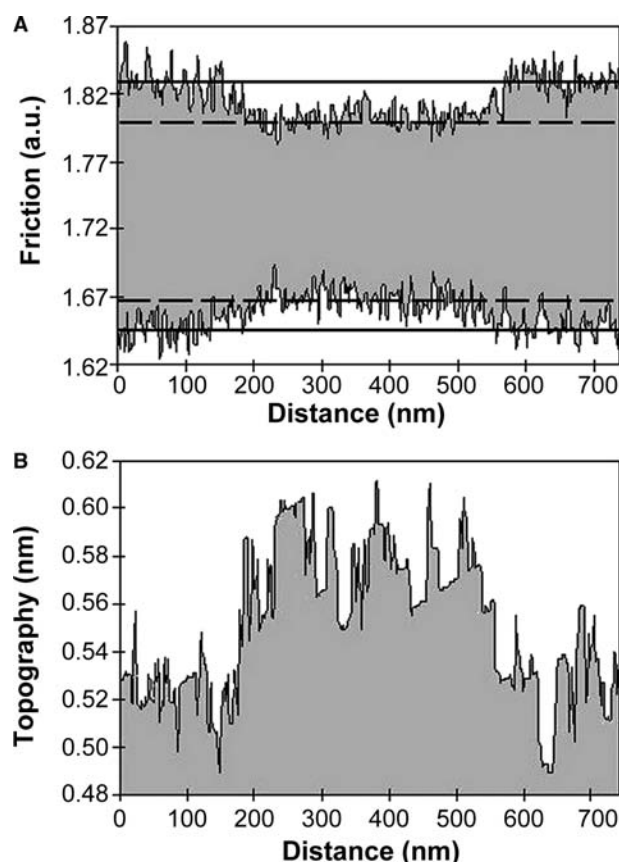


**Fig. 9** Friction (A) and topography (B) cursor profiles of the native and worn mica surface following defect nucleation (charging) of a  $(400 \times 400) \text{ nm}^2$  region under pH 5 conditions. The friction and topography profiles, respectively, indicate that the worn surface has become *negatively* charged and has *expanded* in height by  $\sim 0.05$  nm with respect to the unworn (neighboring) mica surface.

**Table 2** Tribological properties of mica and halide crystals

Specimen	Anion radius (nm)	Native periodic (nm)	Reconstructed periodicity (nm)	Nucleation height (nm)	$F_{adh}^{Induced}/F_{adh}^{Native}$	$F_f^{Induced}/F_f^{Native}$
Mica <sup>a</sup>	–	0.52 <sup>b</sup>	0.3	$\leq 0.05 \pm 0.03$	0.38–0.75 <sup>c</sup>	0.74–1 <sup>c</sup>
KF <sup>d</sup>	0.136	0.378	–	$0.2 \pm 0.03$	0.98	2.3
KCl <sup>d</sup>	0.181	0.445	–	$0.04 \pm 0.02$	0.93	1.79
KBr <sup>d</sup>	0.195	0.467	–	$< 0.02$	0.94	1.24

<sup>a</sup>From Refs.<sup>[142]</sup> and <sup>[145]</sup> with topography, friction, and adhesion data corresponding to the defect nucleation regime.

<sup>b</sup>For micas (001) crystal plane;  $F_{adh}^{Induced}/F_{adh}^{Native}$  is the ratio of force of adhesion measurements within the wear-induced region to the native surface;  $F_f^{Induced}/F_f^{Native}$  is the force of friction ratio of measurements within the wear-induced region to the native surface.

<sup>c</sup>Depends strongly on pH and the extent of surface charging.

<sup>d</sup>From Ref.<sup>[141]</sup>.

surface.<sup>[73]</sup> While studying the frictional properties of halide crystals (KF, KCl, and KBr) in UHV, Carpick et al. observed the evolution of “mysterious” high-friction regions for all crystal surfaces on AFM imaging. Table 2 provides a summary of the tribological properties of mica and the halide crystals. An interesting characteristic of the halide systems is that for KBr the increased friction was not accompanied with a change in topography; however, topographic contrast on the order of 0.2 nm was found to simultaneously occur for the KF crystal. It is believed that “defects” are triggered by the AFM contact; however, it is not clear why localization of the high-friction regions occurs and why the high- and low-friction regions have nearly identical adhesive forces. Further experiments are needed to address these questions and will be valuable contributions toward bridging simulation and experiment.<sup>[151–153]</sup>

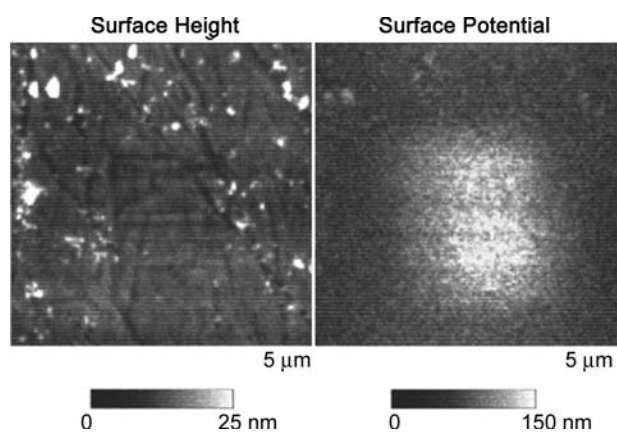


**Fig. 10** Topography (left) and surface potential (right) micrographs of single-crystal aluminum postwear trial under low loads. Although very little topographic contrast is present, the surface potential detects an electron deficient domain (bright central region) corresponding to the nucleation regime, i.e., pregress deformation of the surface. Source: From Ref.<sup>[73]</sup>.

For mica, under pH 5–6 imaging conditions, the tip induced surface charges have a temporal stability between 10 and 45 min, depending on the number of subsequent scans. Lattice-resolved images within a charged region, even with negligible topographic and friction contrast, portray a transforming mica lattice with two lattice constants. One periodicity corresponds to the native surface (0.52 nm) whereas the other corresponds to the defective, reconstructed surface (0.3 nm). This transition has been monitored in situ by scanning at a load  $\sim 75\%$  of the threshold force for SiO<sub>3</sub> abstraction. Exemplary friction micrographs of an in situ reconstruction, at pH 5 and under a load of 9 nN ( $p_m$  of 1.25 GPa), are given in Fig. 11. The progression from the 0.52- to the 0.3-nm periodicity (Fig. 11) provides explicit evidence as well as a characteristic structure of the metastable “nucleation” wear regime before the advent of gross deformation. An additional benefit of this in situ reconstruction is the ability to observe the transition regime, where a mixed population of the two discrete surface species are observed.<sup>[142]</sup> Such information may find applications in calculating the kinetic parameters of the reconstructing surface.

The lattice-resolved reconstruction clarifies that the change in the observed structure at the outermost surface is due to scission of the surface Si–O–Si and Al–O–Si bonds, along with the concomitant insertion of OH<sup>−</sup> and H<sup>+</sup> to terminate the surface. Appearance of the 0.3-nm lattice is intriguing, however, because AFM only gives a characteristic periodicity. The origin is difficult to assign unequivocally, although a simple geometric argument correlates well with AFM results.<sup>[142]</sup> There are interesting corollaries to work on high-silica zeolites,<sup>[83]</sup> silica,<sup>[154]</sup> cristobalite,<sup>[155]</sup> and kaolinite<sup>[156]</sup> that lend support to our current interpretation of the reconstruction; that is, hydrogen bonding is contributing significantly to the stability of the reconstructed surface.<sup>[156]</sup> For instance, Koller et al. have examined the siloxy–silanol (SiO<sup>−</sup> ··· HOSi) defect interaction in high-silica zeolites and found that

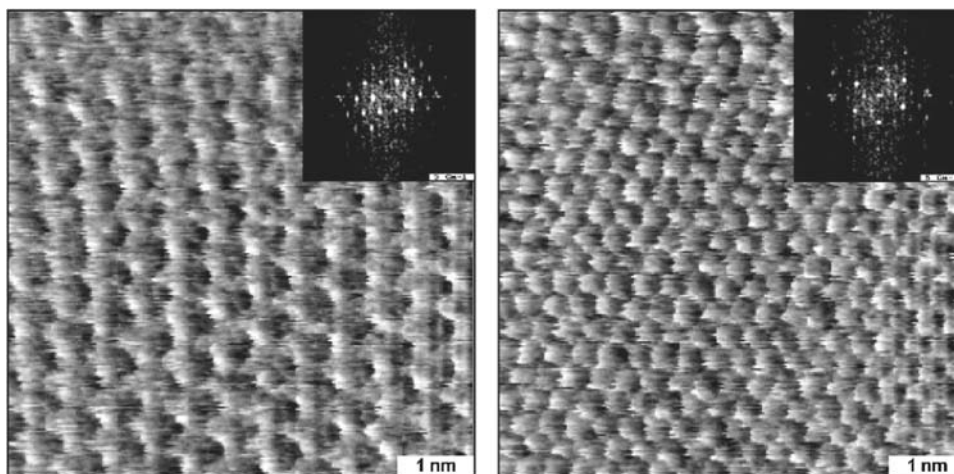


**Fig. 11** Frictional force images of in situ tribochemical surface reconstruction of the native mica lattice from a 0.52- (left) to a 0.3-nm (right) periodicity under the local stress of an AFM tip. The 2-D FFT inserts clearly illustrate the lattice reconstruction. This progression occurs over several scans and leaves no wear of the surface.

six-member rings are able to form stable conformations with multiple defects.<sup>[83]</sup>

For the lowest pH conditions ( $\text{pH} < 3$ ), wear of the surface is inhibited even though the surface is still immersed in water. In fact, the surface shows no wear under *identical loads* with over 8 times the number of scans required for wear at pH 5–6. Clearly, this is because of insufficient amounts of  $\text{OH}^-$  in the water to catalyze the Si–O–Si or Al–O–Si bond scission needed to initiate wear. Only after the load is increased to 23 nN ( $p_m \sim 2.1$  GPa) is any noticeable wear observed (in the limit of 10 scans). Interestingly the threshold force of  $\sim 70$ – $80$  nN ( $p_m \sim 2.25$  GPa), previously determined by Kopta and Salmeron with monolayer coverage of water on mica, is consistent with the range of our determinations in acidic solutions.<sup>[14]</sup>

Comparing the surface wear at pH 3, 5–6, and 8 (Table 1) shows that load (the local stress field) plays a more significant role under conditions where the  $\text{OH}^-$  concentrations are the lowest. Again, this is justified by the necessity to strain the bridging oxygen bonds more and induce cleavage in the absence of  $\text{OH}^-$  mediated bond scission. The critical load for this transition must then be linked with the minimum stress needed to facilitate bond scission in the presence of a particular  $\text{OH}^-$  concentration.

A brief comparison of mica wear<sup>[14,16,142,145]</sup> to the tip induced dissolution of calcite is instructive because there are distinct differences between these two systems. Dickinson, et al.<sup>[74–77]</sup> have elegantly explored calcite and brushite dissolution in supersaturated solutions with AFM. They have found strong correlations between theoretical and experimentally determined activated volumes and realistic activation energies using a relatively straightforward model. Application

of a similar model to mica has had some difficulties with agreement between empirically fitted material constants and their “known” values.<sup>[14]</sup> There is a fundamental difference between mica and calcite that may be limiting the model’s success. The basal mica plane is a covalent network of bridging oxygen bonds, which require scission in order for defect nucleation to occur. On the other hand, the nucleating stage for calcite (an ionic crystal) involves the displacement of individual surface ions into solution (separating ion pairs). As demonstrated by Dickinson, calcite wear does not exhibit a critical load where dissolution suddenly begins (Fig. 12). This is in stark contrast to mica, where in UHV and under  $3 \leq \text{pH} \leq 8$  conditions, a critical threshold pressure is observed, thus indicating that mechanical stress accounts for a significant portion of the energy required to cleave the surface bonds, and comparisons between the two systems should be conducted with caution, especially relating to adaptation of models.

### Mica Surfaces Functionalized with Alkylsilanes

There have been few frictional studies of modified mica surfaces by AFM. Alkylsilanes in the form of triethoxy- or trichlorosilanes can form mono- and multilayers on the mica surface. The formation of monolayers of alkylsilanes on mica and silicon surfaces has been heavily investigated especially for use as potential lubricant and protectant films in MEMS devices.<sup>[92,93,96,157,158]</sup> Unlike reactions of alkylsilanes on hydroxylated silicon surfaces, alkylsilane monolayers on mica do not form covalent bonds to the substrate, but rather become organized via an interconnected network of –Si–O–Si– linkages between



### Wear Track Growth Rate vs Contact Force During Repeated Linear Scanning

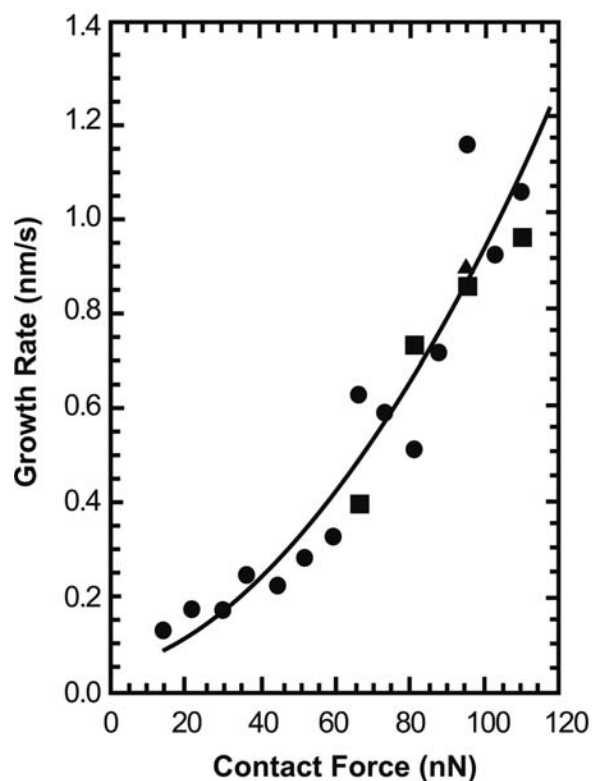


**Fig. 12** AFM scanning induced wear track growth of calcite as a function of applied load. Notice the absence of a critical load for dissolution, indicating the growth is reaction limited. This is unlike mica, which exhibits a threshold force in the abstraction regime for removal of  $\text{SiO}_3$  molecular fragments. *Source:* From Ref.<sup>[77]</sup>.

nearest neighbors. This produces monolayers with relatively lower packing densities as compared to other alkane-based SAMS such as alkanethiols on Au.<sup>[159]</sup> A key difficulty in the formation of alkylsilane monolayers is the precise control over the amount of water present during film formation. Sufficient water is required to carry out the condensation reactions on the surface for monolayer formation without inducing the production of micelles among unreacted alkylsilanes. Long-range ordered structures are in general not observed for alkylsilane films on mica surfaces.

Wear of the mica surface is inhibited by the presence of an alkylsilane film. The friction response of the surface, however, is highly dependent on the amount of water present in the environment during wear. The presence of water above 50% relative humidity rapidly increases the friction as a function of load, much as it does for the native mica surface as described above.<sup>[61]</sup> This impact of water on the frictional properties of the nominally hydrophobic coated surface clearly shows

that defects within the films can provide sufficient access of water to the underlying surface–film interface to catalyze film breakdown even under relatively low loads ( $\sim 10$  nN) as compared to the wear of the native surface ( $\sim 75$  nN).

## CONCLUSION

The area of nanotribology of oxides and the probing of defect nucleation at the atomic level by AFM is just beginning. Continuing developments in AFM technology via enhanced non-contact methodologies is advancing the ability of the AFM to probe even single atomic defects at crystal surfaces on non-conducting substrates. In this entry we have described how detailed control of the imaging environment and of the chemistry at the tip and sample surfaces can allow for atomic-level details of defect nucleation to be assessed and probed in situ before the onset of gross wear. This has permitted examination of tribochemically and mechanically enhanced wear processes of mica to be explored. We have also outlined a methodology for assessing the scan history dependence on wear of surfaces. Many avenues of oxide wear and charge nucleation at surfaces are unexplored and deserve attention, including the impact of temperature on wear at the nanoscale.

## ACKNOWLEDGMENTS

We acknowledge support for JH from The National Science Foundation (IGERT DGE-9972892) and the American Chemical Society Petroleum Research Fund (34792-G5). We also gratefully acknowledge Dr. Jayne Garino for comments on the work, as well as providing the images in Fig. 3.

## REFERENCES

1. Binnig, G.; Quate, C.F.; Gerber, C. Atomic force microscope. *Phys. Rev. Lett.* **1986**, *56*, 930–933.
2. Mate, C.M.; McClelland, G.M.; Erlandsson, R.; Chiang, S. Atomic-scale friction of a tungsten tip on a graphite surface. *Phys. Rev. Lett.* **1987**, *59*, 1942–1945.
3. Burnham, N.A.; Colton, R.J. Measuring the nanomechanical properties and surface forces of materials using an atomic force microscope. *J. Vac. Sci. Technol., A, Vac. Surf. Films* **1989**, *7*, 2906–2913.
4. Nyffenegger, R.M.; Penner, R.M. Nanometer-scale surface modification using the scanning probe microscope: progress since 1991. *Chem. Rev.* **1997**, *97*, 1195–1230.

5. Carpick, R.W.; Salmeron, M. Scratching the surface: fundamental investigations of tribology with atomic force microscopy. *Chem. Rev.* **1997**, *97*, 1163–1194.
6. Bhushan, B.; Israelachvili, J.N.; Landman, U. Nanotribology—friction, wear and lubrication at the atomic-scale. *Nature* **1995**, *374*, 607–616.
7. Landman, U.; Luedtke, W.D.; Burnham, N.A.; Colton, R.J. Atomistic mechanisms and dynamics of adhesion, nanoindentation, and fracture. *Science* **1990**, *248*, 454–461.
8. Dedkov, G.V. Experimental and theoretical aspects of the modern nanotribology. *Phys. Status Solidi, A Appl. Res.* **2000**, *179*, 3–75.
9. Singer, I.L. Friction and energy-dissipation at the atomic-scale—a review. *J. Vac. Sci. Technol., A, Vac. Surf. Films* **1994**, *12*, 2605–2616.
10. Tang, H.; Joachim, C.; Devillers, J. Interpretation of atomic-force microscopy images—The mica (001) surface with a diamond tip apex. *J. Vac. Sci. Technol., B* **1994**, *12*, 2179–2183.
11. Erlandsson, R.; Hadziioannou, G.; Mate, C.M.; McClelland, G.M.; Chiang, S. Atomic scale friction between the muscovite mica cleavage plane and a tungsten tip. *J. Chem. Phys.* **1988**, *89*, 5190–5193.
12. Carpick, R.W.; Agrait, N.; Ogletree, D.F.; Salmeron, M. Measurement of interfacial shear (friction) with an ultrahigh vacuum atomic force microscope. *J. Vac. Sci. Technol., B* **1996**, *14*, 1289–1295.
13. Carpick, R.W.; Agrait, N.; Ogletree, D.F.; Salmeron, M. Variation of the interfacial shear strength and adhesion of a nanometer-sized contact. *Langmuir* **1996**, *12*, 3334–3340.
14. Kopta, S.; Salmeron, M. The atomic scale origin of wear on mica and its contribution to friction. *J. Chem. Phys.* **2000**, *113*, 8249–8252.
15. Miyake, S. Atomic-scale wear properties of muscovite mica evaluated by scanning probe microscopy. *Appl. Phys. Lett.* **1994**, *65*, 980–982.
16. Hu, J.; Xiao, X.D.; Ogletree, D.F.; Salmeron, M. Atomic-scale friction and wear of mica. *Surf. Sci.* **1995**, *327*, 358–370.
17. Hagen, T.; Grafstrom, S.; Ackermann, J.; Neumann, R.; Trautmann, C.; Vetter, J.; Angert, N. Friction force microscopy of heavy-ion irradiated mica. *J. Vac. Sci. Technol., B* **1994**, *12*, 1555–1558.
18. Qian, L.M.; Luo, J.B.; Wen, S.W.; Xiao, X.D. The experimental rules of mica as a reference sample of AFM/FFM measurement. *Chin. Sci. Bull.* **2001**, *46*, 349–352.
19. Xu, L.; Salmeron, M. Effects of surface ions on the friction and adhesion properties of mica. *Langmuir* **1998**, *14*, 2187–2190.
20. Wei, Z.Q.; Wang, C.; Bai, C.L. Investigation of nano-scale frictional contact by friction force microscopy. *Langmuir* **2001**, *17*, 3945–3951.
21. Hoshi, Y.; Kawagishi, T.; Kawakatsu, H. Velocity dependence and limitations of friction force microscopy of mica and graphite. *Jpn. J. Appl. Phys.* **2000**, *39*, 3804–3807.
22. Piner, R.D.; Mirkin, C.A. Effect of water on lateral force microscopy in air. *Langmuir* **1997**, *13*, 6864–6868.
23. Schwarz, U.D.; Zworner, O.; Koster, P.; Wiesendanger, P. Quantitative analysis of the frictional properties of solid materials at low loads. 2. Mica and germanium sulfide. *Phys. Rev., B* **1997**, *56*, 6997–7000.
24. Tsujimichi, K.; Tamura, H.; Hirotsu, A.; Kubo, M.; Komiyama, M.; Miyamoto, A. Simulation of atomic force microscopy images of cleaved mica surfaces. *J. Phys. Chem., B* **1997**, *101*, 4260–4264.
25. Qian, L.M.; Xiao, X.D.; Wen, S.Z. Tip in situ chemical modification and its effects on tribological measurements. *Langmuir* **2000**, *16*, 662–670.
26. Gyalog, T.; Bammerlin, M.; Luthi, R.; Meyer, E.; Thomas, H. Mechanism of atomic friction. *Eur. Lett.* **1995**, *31*, 269–274.
27. Christenson, H.K. Adhesion and surface-energy of mica in air and water. *J. Phys. Chem.* **1993**, *97*, 12,034–12,041.
28. Teschke, O.; de Souza, E.F. Dielectric exchange: the key repulsive or attractive transient forces between atomic force microscope tips and charged surfaces. *Appl. Phys. Lett.* **1999**, *74*, 1755–1757.
29. Knarr, R.F.; Quon, R.A.; Vanderlick, T.K. Direct force measurements at the smooth gold/mica interface. *Langmuir* **1998**, *14*, 6414–6418.
30. Vakarelski, I.U.; Ishimura, K.; Higashitani, K. Adhesion between silica particle and mica surfaces in water and electrolyte solutions. *J. Colloid Interface Sci.* **2000**, *227*, 111–118.
31. Weisenhorn, A.L.; Maivald, P.; Butt, H.J.; Hansma, P.K. Measuring adhesion, attraction, and repulsion between surfaces in liquids with an atomic-force microscope. *Phys. Rev., B* **1992**, *45*, 11,226–11,232.
32. Maw, W.; Stevens, F.; Langford, S.C.; Dickinson, J.T. Single asperity tribochemical wear of silicon nitride studied by atomic force microscopy. *J. Appl. Phys.* **2002**, *92*, 5103–5109.
33. Liu, E.; Blanpain, B.; Celis, J.P.; Roos, J.R. Comparative study between macrotribology and nanotribology. *J. Appl. Phys.* **1998**, *84*, 4859–4865.
34. Pashley, R.M. DLVO and hydration forces between mica surfaces in Li<sup>+</sup>, Na<sup>+</sup>, K<sup>+</sup>, and Cs<sup>+</sup> electrolyte-solutions—a correlation of double-layer and hydration forces with surface cation-exchange properties. *J. Colloid Interface Sci.* **1981**, *83*, 531–546.
35. Raviv, U.; Laurat, P.; Klein, J. Time dependence of forces between mica surfaces in water and its relation to the release of surface ions. *J. Chem. Phys.* **2002**, *116*, 5167–5172.
36. Kjellander, R.; Marcelja, S.; Pashley, R.M.; Quirk, J.P. A theoretical and experimental-study of forces between charged mica surfaces in aqueous CaCl<sub>2</sub> solutions. *J. Chem. Phys.* **1990**, *92*, 4399–4407.
37. Teschke, O.; Ceotto, G.; de Souza, E.F. Dielectric exchange force: a convenient technique for measuring the interfacial water relative permittivity profile. *Phys. Chem. Chem. Phys.* **2001**, *3*, 3761–3768.
38. Israelachvili, J.N. *Intermolecular and Surfaces Forces*; Academic Press: New York, 1992.
39. Basu, S.; Sharma, M.M. Measurement of critical disjoining pressure for dewetting of solid surfaces. *J. Colloid Interface Sci.* **1996**, *181*, 443–455.



40. Toikka, G.; Hayes, R.A. Direct measurement of colloidal forces between mica and silica in aqueous electrolyte. *J. Colloid Interface Sci.* **1997**, *191*, 102–109.
41. Tabor, D.; Winterton, R.H.S. The direct force measurement of normal and retarded van der Waals forces. *Proc. R. Soc. Lond., A Math. Phys. Eng. Sci.* **1969**, *312*, 435–450.
42. Hutter, J.L.; Bechhoefer, J. Measurement and manipulation of van-der-Waals forces in atomic-force microscopy. *J. Vac. Sci. Technol., B* **1994**, *12*, 2251–2253.
43. Pashley, R.M.; Israelachvili, J.N. Molecular layering of water in thin-films between mica surfaces and its relation to hydration forces. *J. Colloid Interface Sci.* **1984**, *101*, 511–523.
44. Xu, L.; Salmeron, M. An XPS and scanning polarization force microscopy study of the exchange and mobility of surface ions on mica. *Langmuir* **1998**, *14*, 5841–5844.
45. Purton, J.A.; Allan, N.L.; Blundy, J.D. Impurity cations in the bulk and the {001} surface of muscovite: an atomistic simulation study. *J. Mater. Chem.* **1997**, *7*, 1947–1951.
46. Nishimura, S.; Biggs, S.; Scales, P.J.; Healy, T.W.; Tsunematsu, K.; Tateyama, T. Molecular-scale structure of the cation modified muscovite mica basal-plane. *Langmuir* **1994**, *10*, 4554–4559.
47. Snowdenifft, D.; Price, P.B.; Nagahara, L.A.; Fujishima, A. Atomic-force-microscopic observations of dissolution of mica at sites penetrated by keV/nucleon ions. *Phys. Rev. Lett.* **1993**, *70*, 2348–2351.
48. Terashima, H. Adsorption of polystyrene to mica/cyclohexane interfaces at the theta-temperature. *Phys. Chem. Chem. Phys.* **2000**, *2*, 5252–5258.
49. Heuberger, M.; Luengo, G.; Israelachvili, J.N. Tribology of shearing polymer surfaces. 1. Mica sliding on polymer (PnBMA). *J. Phys. Chem., B* **1999**, *103*, 10,127–10,135.
50. Cantrell, W.; Ewing, G.E. Thin film water on muscovite mica. *J. Phys. Chem., B* **2001**, *105*, 5434–5439.
51. Bhushan, B.; Ed. *Modern Tribology Handbook*; CRC Press: Boca Raton, 2001.
52. Hsu, S.M.; Ying, Z.C.; Eds. *Nanotribology: Critical Assessment and Research Needs*; Kluwer Academic: Boston, 2003.
53. Deer, W.A.; Howie, R.A.; Zussman, J. *Sheet Silicates*; Longmans, Green and Co.: London, 1962.
54. Wyckoff, R.W.G. *Crystal Structures*; Interscience: New York, 1971.
55. Woodward, J.T.; Ulman, A.; Schwartz, D.K. Self-assembled monolayer growth of octadecylphosphonic acid on mica. *Langmuir* **1996**, *12*, 3626–3629.
56. Eastman, T.; Zhu, D.M. Adhesion forces between surface-modified AFM tips and a mica surface. *Langmuir* **1996**, *12*, 2859–2862.
57. Demirel, A.L.; Granick, S. Transition from static to kinetic friction in a model lubricated system. *J. Chem. Phys.* **1998**, *109*, 6889–6897.
58. Barthel, E.; Roux, S. Velocity-dependent adherence: an analytical approach for the JKR and DMT models. *Langmuir* **2000**, *16*, 8134–8138.
59. Wurger, A. Comment on “relationship between friction and molecular structure: alkylsilane lubricant films under pressure”. *Phys. Rev. Lett.* **1999**, *83*, 1696.
60. Kopta, S.; Barrena, E.; Ogletter, D.F.; Charych, D.H.; Salmeron, M. Comment on “relationship between friction and molecular structure: alkylsilane lubricant films under pressure”—Kopta et al. reply. *Phys. Rev. Lett.* **1999**, *83*, 1697.
61. Barrena, E.; Kopta, S.; Ogletree, D.F.; Charych, D.H.; Salmeron, M. Relationship between friction and molecular structure: alkylsilane lubricant films under pressure. *Phys. Rev. Lett.* **1999**, *82*, 2880–2883.
62. Lio, A.; Charych, D.H.; Salmeron, M. Comparative atomic force microscopy study of the chain length dependence of frictional properties of alkanethiols on gold and alkylsilanes on mica. *J. Phys. Chem., B* **1997**, *101*, 3800–3805.
63. Tian, F.; Xiao, X.D.; Loy, M.M.T.; Wang, C.; Bai, C.L. Humidity and temperature effect on frictional properties of mica and alkylsilane monolayer self-assembled on mica. *Langmuir* **1999**, *15*, 244–249.
64. Chen, Y.L.; Helm, C.A.; Israelachvili, J.N. Measurements of the elastic properties of surfactant and lipid monolayers. *Langmuir* **1991**, *7*, 2694–2699.
65. Sterthaus, R.; Wegner, G. Ultrathin layers of polyelectrolytes on mica: preparation, characterization, and electrokinetic surface potential. *Langmuir* **2002**, *18*, 5414–5421.
66. Batteas, J.D.; Quan, X.H.; Weldon, M.K. Adhesion and wear of colloidal silica probed by force microscopy. *Tribol. Lett.* **1999**, *7*, 121–128.
67. Miyake, S. Improvement of mechanical properties of nanometer period multilayer films at interfaces of each layer. *J. Vac. Sci. Technol., B* **2003**, *21*, 785–789.
68. Prioli, R.; Reigada, D.C.; Freire, F.L. Nanoscale friction and wear mechanisms at the interface between a boron carbide film and an atomic force microscope tip. *J. Appl. Phys.* **2000**, *87*, 1118–1122.
69. Reigada, D.C.; Prioli, R.; Jacobsohn, L.G.; Freire, F.L. Boron carbide films deposited by a magnetron sputtering process: film composition and tribological properties. *Diamond and Related Materials* **2000**, *9*, 489–493.
70. Sundararajan, S.; Bhushan, B. Micro/nanotribological studies of polysilicon and SiC films for MEMS applications. *Wear* **1998**, *217*, 251–261.
71. Prioli, R.; Reigada, D.C.; Freire, F.L. The role of capillary condensation of water in the nanoscale friction and wear properties of boron carbide films. *J. Appl. Phys.* **2000**, *88*, 679–682.
72. Adams, J.B.; Hector, L.G.; Siegel, D.J.; Yu, H.L.; Zhong, J. Adhesion, lubrication and wear on the atomic scale. *Surf. Interface Anal.* **2001**, *31*, 619–626.
73. DeVecchio, D.; Bhushan, B. Use of a nanoscale Kelvin probe for detecting wear precursors. *Rev. Sci. Instrum.* **1998**, *69*, 3618–3624.
74. Scudiero, L.; Langford, S.C.; Dickinson, J.T. Scanning force microscope observations of corrosive wear on single-crystal brushite ( $\text{CaHPO}_4 \cdot 2\text{H}_2\text{O}$ ) in aqueous solution. *Tribol. Lett.* **1999**, *6*, 41–55.

75. Dickinson, J.T.; Hariadi, R.F.; Langford, S.C. Nanometer scale investigations of chemical mechanical polishing mechanisms using scanning force microscopy. *Ceram. Trans.* **1999**, *102*, 213–232.
76. Park, N.S.; Kim, M.W.; Langford, S.C.; Dickinson, J.T. Tribological enhancement of CaCO<sub>3</sub> dissolution during scanning force microscopy. *Langmuir* **1996**, *12*, 4599–4604.
77. Park, N.S.; Kim, M.W.; Langford, S.C.; Dickinson, J.T. Atomic layer wear of single-crystal calcite in aqueous solution using scanning force microscopy. *J. Appl. Phys.* **1996**, *80*, 2680–2686.
78. Iler, R.K. *The Chemistry of Silica*; Wiley-Interscience: New York, 1979.
79. Schmitz, I.; Schreiner, M.; Friedbacher, G.; Grasserbauer, M. Tapping-mode AFM in comparison to contact-mode AFM as a tool for in situ investigations of surface reactions with reference to glass corrosion. *Anal. Chem.* **1997**, *69*, 1012–1018.
80. Fischer, T.E.; Mullins, W.M. Chemical aspects of ceramic tribology. *J. Phys. Chem.* **1992**, *96*, 5690–5701.
81. Zirl, D.M.; Garofalini, S.H. Mechanism of alkali adsorption on silica surfaces. *Phys. Chem. Glasses* **1989**, *30*, 155–159.
82. Hunger, M.; Freude, D.; Pfeifer, H.; Schwieger, W. MAS NMR-studies of silanol groups in zeolites ZSM-5 synthesized with an ionic template. *Chem. Phys. Lett.* **1990**, *167*, 21–26.
83. Koller, H.; Lobo, R.F.; Burkett, S.L.; Davis, M.E. SiO<sup>-</sup> ··· HOSi hydrogen-bonds in as-synthesized high-silica zeolites. *J. Phys. Chem.* **1995**, *99*, 12,588–12,596.
84. Ruiz, J.M.; McAdon, M.H.; Garces, J.M. Aluminum complexes as models for Bronsted acid sites in zeolites: structure and energetics of [Al(OH)<sub>4</sub>]<sup>-</sup>, [Al(H<sub>2</sub>O)<sub>6</sub>]<sup>3+</sup>, and intermediate monomeric species [Al(OH)<sub>x</sub>(H<sub>2</sub>O)<sub>n-x</sub> ··· mH<sub>2</sub>O]<sub>3-x</sub> obtained by hydrolysis. *J. Phys. Chem., B* **1997**, *101*, 1733–1744.
85. Xu, H.; Van Deventer, J.S.J. Ab initio calculations on the five-membered alumino-silicate framework rings model: implications for dissolution in alkaline solutions. *Comput. Chem.* **2000**, *24*, 391–404.
86. Sokol, A.A.; Catlow, C.R.A.; Garces, J.M.; Kuperman, A. Local states in microporous silica and aluminum silicate materials. 1. Modeling structure, formation, and transformation of common hydrogen containing defects. *J. Phys. Chem., B* **2002**, *106*, 6163–6177.
87. Katsuki, F.; Kamei, K.; Saguchi, A.; Takahashi, W.; Watanabe, J. AFM studies on the difference in wear behavior between Si and SiO<sub>2</sub> in KOH solution. *J. Electrochem. Soc.* **2000**, *147*, 2328–2331.
88. Pal, S.; Banerjee, S. Friction-induced microstructure growth. *J. Phys., D Appl. Phys.* **2001**, *34*, 253–256.
89. Lin, X.Y.; Creuzet, F.; Arribart, H. Atomic-force microscopy for local characterization of surface acid–base properties. *J. Phys. Chem.* **1993**, *97*, 7272–7276.
90. Zembala, M.; Adamczyk, Z.; Warszycki, P. Influence of adsorbed particles on streaming potential of mica. *Colloids Surf., A Physicochem. Eng. Asp.* **2001**, *195*, 3–15.
91. Sniegowski, J.J.; de Boer, M.P. IC-compatible polysilicon surface micromachining. *Annu. Rev. Mater. Sci.* **2000**, *30*, 299–333.
92. Maboudian, R.; Ashurst, W.R.; Carraro, C. Tribological challenges in micromechanical systems. *Tribol. Lett.* **2002**, *12*, 95–100.
93. Maboudian, R.; Carraro, C. Surface engineering for reliable operation of MEMS devices. *J. Adhes. Sci. Technol.* **2003**, *17*, 583–591.
94. Malek, C.G.K.; Das, S.S. Adhesion promotion between poly(methylmethacrylate) and metallic surfaces for LiGA evaluated by shear stress measurements. *J. Vac. Sci. Technol., B* **1998**, *16*, 3543–3546.
95. Miller, S.L.; Rodgers, M.S.; La Vigne, G.; Sniegowski, J.J.; Clews, P.; Tanner, D.M.; Peterson, K.A. Failure modes in surface micromachined microelectromechanical actuation systems. *Microelectron. Reliab.* **1999**, *39*, 1229–1237.
96. Komvopoulos, K. Surface engineering and microtribology for microelectromechanical systems. *Wear* **1996**, *200*, 305–327.
97. Carpick, R.W.; Ogletree, D.F.; Salmeron, M. Lateral stiffness: a new nanomechanical measurement for the determination of shear strengths with friction force microscopy. *Appl. Phys. Lett.* **1997**, *70*, 1548–1550.
98. Timoshenko, S.P.; Goodier, J.N. *Theory of Elasticity*; McGraw-Hill: New York, 1987.
99. Cleveland, J.P.; Manne, S.; Bocek, D.; Hansma, P.K. A nondestructive method for determining the spring constant of cantilevers for scanning force microscopy. *Rev. Sci. Instrum.* **1993**, *64*, 403–405.
100. Sader, J.E.; Larson, I.; Mulvaney, P.; White, L.R. Method for the calibration of atomic-force microscope cantilevers. *Rev. Sci. Instrum.* **1995**, *66*, 3789–3798.
101. Neumeister, J.M.; Ducker, W.A. Lateral, normal, and longitudinal spring constants of atomic-force microscopy cantilevers. *Rev. Sci. Instrum.* **1994**, *65*, 2527–2531.
102. Tortonese, M.; Kirk, M. Characterization of application specific probes. *SPIE Proceedings—Micromatching and Imaging* **1997**, *3009*, 53–60.
103. Albrecht, T.R.; Akamine, S.; Carver, T.E.; Quate, C.F. Microfabrication of cantilever styli for the atomic force microscope. *J. Vac. Sci. Technol., A, Vac. Surf. Films* **1990**, *8*, 3386–3396.
104. Siedle, P.; Butt, H.J.; Bamberg, E.; Wang, D.N.; Kuhlbrandt, W.; Zach, J.; Haider, M. Determining the form of atomic-force microscope tips. *Inst. Phys. Conf. Ser.* **1993**, *130*, 361–364.
105. Ogletree, D.F.; Carpick, R.W.; Salmeron, M. Calibration of frictional forces in atomic force microscopy. *Rev. Sci. Instrum.* **1996**, *67*, 3298–3306.
106. Sader, J.E. Parallel beam approximation for V-shaped atomic-force microscope cantilevers. *Rev. Sci. Instrum.* **1995**, *66*, 4583–4587.
107. Sader, J.E.; Chon, J.W.M.; Mulvaney, P. Calibration of rectangular atomic force microscope cantilevers. *Rev. Sci. Instrum.* **1999**, *70*, 3967–3969.
108. Senden, T.J.; Ducker, W.A. Experimental-determination of spring constants in atomic-force microscopy. *Langmuir* **1994**, *10*, 1003–1004.

109. Torii, A.; Sasaki, M.; Hane, K.; Okuma, S. A method for determining the spring constant of cantilevers for atomic force microscopy. *Meas. Sci. Technol.* **1996**, *7*, 179–184.
110. Hazel, J.L.; Tsukruk, V.V. Friction force microscopy measurements: normal and torsional spring constants for V-shaped cantilevers. *J. Tribol.* **1998**, *120*, 814–819.
111. Hutter, J.L.; Bechhoefer, J. Calibration of atomic-force microscope tips. *Rev. Sci. Instrum.* **1993**, *64*, 1868–1873.
112. Walters, D.A.; Cleveland, J.P.; Thomson, N.H.; Hansma, P.K.; Wendman, M.A.; Gurley, G.; Elings, V. Short cantilevers for atomic force microscopy. *Rev. Sci. Instrum.* **1996**, *67*, 3583–3590.
113. Miyatani, T.; Fujihira, M. Bending of a rectangular cantilever of an atomic force microscope as a function of position along length. *Jpn. J. Appl. Phys.* **1997**, *36*, 5280–5281.
114. Levy, R.; Maaloum, M. Measuring the spring constant of atomic force microscope cantilevers: thermal fluctuations and other methods. *Nanotechnology* **2002**, *13*, 33–37.
115. Cain, R.G.; Biggs, S.; Page, N.W. Force calibration in lateral force microscopy. *J. Colloid Interface Sci.* **2000**, *227*, 55–65.
116. Green, C.P.; Sader, J.E. Torsional frequency response of cantilever beams immersed in viscous fluids with applications to the atomic force microscope. *J. Appl. Phys.* **2002**, *92*, 6262–6274.
117. Maugis, D. *Contact, Adhesion and Rupture of Elastic Solids*; Cardona, M., Fulde, P., von Klitzing, K., Merlin, R., Queisser, H.-J., Stromer, H., Eds.; Springer-Verlag: Berlin, 2000.
118. Johnson, K.L. *Contact Mechanics*; Cambridge University Press: Cambridge, 1987.
119. Villarrubia, J.S. Morphological estimation of tip geometry for scanned probe microscopy. *Surf. Sci.* **1994**, *321*, 287–300.
120. Westra, K.L.; Mitchell, A.W.; Thomson, D.J. Tip artifacts in atomic-force microscope imaging of thin-film surfaces. *J. Appl. Phys.* **1993**, *74*, 3608–3610.
121. Goss, C.A.; Brumfield, J.C.; Irene, E.A.; Murray, R.W. Imaging and modification of Au(111) monatomic steps with atomic-force microscopy. *Langmuir* **1993**, *9*, 2986–2994.
122. Sheiko, S.S.; Moller, M.; Reuvekamp, E.M.C.M.; Zandbergen, H.W. Calibration and evaluation of scanning-force-microscopy probes. *Phys. Rev., B* **1993**, *48*, 5675–5678.
123. Atamny, F.; Baiker, A. Direct imaging of the tip shape by AFM. *Surf. Sci.* **1995**, *323*, L314–L318.
124. Schneir, J.; Villarrubia, J.S.; McWaid, T.H.; Tsai, V.W.; Dixon, R. Increasing the value of atomic force microscopy process metrology using a high-accuracy scanner, tip characterization, and morphological image analysis. *J. Vac. Sci. Technol., B* **1996**, *14*, 1540–1546.
125. Dongmo, L.S.; Villarrubia, J.S.; Jones, S.N.; Renegar, T.B.; Postek, M.; Song, J.F. Experimental test of blind tip reconstruction for scanning probe microscopy. *Ultramicroscopy* **2000**, *85*, 141–153.
126. Jarausch, K.F.; Stark, T.J.; Russell, P.E. Silicon structures for in situ characterization of atomic force microscope probe geometry. *J. Vac. Sci. Technol., B* **1996**, *14*, 3425–3430.
127. Markiewicz, P.; Goh, M.C. Atomic-force microscope tip deconvolution using calibration arrays. *Rev. Sci. Instrum.* **1995**, *66*, 3186–3190.
128. Markiewicz, P.; Goh, M.C. Simulation of atomic-force microscope tip-sample reconstruction. *J. Vac. Sci. Technol., B* **1995**, *13*, 1115–1118.
129. Odin, C.; Aime, J.P.; Elkaakour, Z.; Bouhacina, T. Tip finite-size effects on atomic-force microscopy in the contact mode—simple geometrical considerations for rapid estimation of apex radius and tip angle based on the study of polystyrene latex balls. *Surf. Sci.* **1994**, *317*, 321–340.
130. Xu, L.; Yao, X.W.; Zhang, L.P.; Li, M.Q.; Yang, F.J. Effects of the long-range macroscopic forces on atomic-force-microscope images. *Phys. Rev., B* **1994**, *49*, 2875–2877.
131. Xu, S.; Amro, N.A.; Liu, G.Y. Characterization of AFM tips using nanografting. *Appl. Surf. Sci.* **2001**, *175*, 649–655.
132. Bietsch, A.; Schneider, M.A.; Welland, M.E.; Michel, B. Electrical testing of gold nanostructures by conducting atomic force microscopy. *J. Vac. Sci. Technol., B* **2000**, *18*, 1160–1170.
133. Trenkler, T.; Hantschel, T.; Stephenson, R.; De Wolf, P.; Vandervorst, W.; Hellemans, L.; Malave, A.; Buchel, D.; Oesterschulze, E.; Kulisch, W.; Niedermann, P.; Sulzbach, T.; Ohlsson, O. Evaluating probes for “electrical” atomic force microscopy. *J. Vac. Sci. Technol., B* **2000**, *18*, 418–427.
134. Sekimoto, M.; Yoshihara, H.; Ohkubo, T. Silicon-nitride single-layer X-ray mask. *J. Vac. Sci. Technol.* **1982**, *21*, 1017–1021.
135. Johnson, K.L.; Kendall, K.; Roberts, A.D. Surface energy and the contact of elastic solids. *Proc. R. Soc. Lond., A Math. Phys. Eng. Sci.* **1971**, *324*, 301–313.
136. Derjaguin, B.V.; Muller, V.M.; Toporov, Y.P. Effect of contact deformations on adhesion of particles. *J. Colloid Interface Sci.* **1975**, *53*, 314–326.
137. Maugis, D. Adhesion of spheres—the JKR–DMT transition using a Dugdale model. *J. Colloid Interface Sci.* **1992**, *150*, 243–269.
138. Greenwood, J.A. Adhesion of elastic spheres. *Proc. R. Soc. Lond., A Math. Phys. Eng. Sci.* **1997**, *453*, 1277–1297.
139. Weihs, T.P.; Nawaz, Z.; Jarvis, S.P.; Pethica, J.B. Limits of imaging resolution for atomic force microscopy of molecules. *Appl. Phys. Lett.* **1991**, *59*, 3536–3538.
140. Adamson, A.W. *Physical Chemistry of Surfaces*; Wiley & Sons: New York, 1990.
141. Carpick, R.W.; Dai, Q.; Ogletree, D.F.; Salmeron, M. Friction force microscopy investigations of potassium halide surfaces in ultrahigh vacuum: structure, friction and surface modification. *Tribol. Lett.* **1998**, *5*, 91–102.
142. Helt, J.M.; Batteas, J.D. Wear of mica under aqueous environments: direct observation of defect nucleation by AFM. *Langmuir*, to be submitted.

143. Hsu, S.M.; Zhang, J.; Yin, Z.F. The nature and origin of tribochemistry. *Tribol. Lett.* **2002**, *13*, 131–139.
144. Hertz, H. On the contact of elastic solids. *J. Reine Angew. Math.* **1881**, *92*, 156–171.
145. Helt, J.M.; Batteas, J.D. The contact radius–line step relationship: importance in atomic force microscopy wear experiments. *J. Chem. Phys.* to be submitted.
146. Bousse, L.; Mostarshed, S. The zeta-potential of silicon-nitride thin-films. *J. Electroanal. Chem.* **1991**, *302*, 269–274.
147. Xiao, Y.T.; Lasaga, A.C. Ab-initio quantum-mechanical studies of the kinetics and mechanisms of silicate dissolution— $H^+(H_3O^+)$  catalysis. *Geochim. Cosmochim. Acta* **1994**, *58*, 5379–5400.
148. Batteas, J.D.; Weldon, M.K.; Raghavachari, K. Bonding & inter-particle interactions of silica nanoparticles: probing adhesion at asperity-asperity contacts. In *Nanotribology: Critical Assessment and Research Needs*; Hsu, S.M., Ying, Z.C., Eds.; Kluwer Academic: Boston, 2003; 387–398.
149. Hiemstra, T.; Yong, H.; Van Riemsdijk, W.H. Interfacial charging phenomena of aluminum (hydr)oxides. *Langmuir* **1999**, *15*, 5942–5955.
150. Kavanagh, B.V.; Posner, A.M.; Quirk, J.P. Effect of polymer adsorption on properties of electrical double-layer. *Faraday Discuss.* **1975**, *59*, 242–249.
151. Shluger, A.L.; Rohl, A.L.; Wilson, R.M.; Williams, R.T. Atomistic modeling of imaging of ionic surfaces with a scanning force microscope. *J. Vac. Sci. Technol., B* **1995**, *13*, 1155–1162.
152. Loppacher, C.; Bennewitz, R.; Pfeiffer, O.; Guggisberg, M.; Bammerlin, M.; Schar, S.; Barwich, V.; Baratoff, A.; Meyer, E. Experimental aspects of dissipation force microscopy. *Phys. Rev., B* **2000**, *62*, 13,674–13,679.
153. Gnecco, E.; Bennewitz, R.; Gyalog, T.; Loppacher, C.; Bammerlin, M.; Meyer, E.; Guntherodt, H.J. Velocity dependence of atomic friction. *Phys. Rev. Lett.* **2000**, *84*, 1172–1175.
154. Pelmenchikov, A.; Leszczynski, J.; Pettersson, L.G.M. Mechanism of dissolution of neutral silica surfaces: including effect of self-healing. *J. Phys. Chem., A* **2001**, *105*, 9528–9532.
155. Pelmenchikov, A.; Strandh, H.; Pettersson, L.G.M.; Leszczynski, J. Lattice resistance to hydrolysis of Si–O–Si bonds of silicate minerals: ab initio calculations of a single water attack onto the (001) and (111) beta-cristobalite surfaces. *J. Phys. Chem., B* **2000**, *104*, 5779–5783.
156. Benco, L.; Tunega, D.; Hafner, J.; Lischka, H. Upper limit of the O–H···O hydrogen bond. AB initio study of the kaolinite structure. *J. Phys. Chem., B* **2001**, *105*, 10,812–10,817.
157. Maboudian, R. Surface processes in MEMS technology. *Surf. Sci. Rep.* **1998**, *30*, 209–270.
158. Maboudian, R.; Ashurst, W.R.; Carraro, C. Self-assembled monolayers as anti-stiction coatings for MEMS: characteristics and recent developments. *Sens. Actuators, A, Phys.* **2000**, *82*, 219–223.
159. Ulman, A. Formation and structure of self-assembled monolayers. *Chem. Rev.* **1996**, *96*, 1533–1554.
160. Kubicki, J.D.; Xiao, Y.; Lasaga, A.C. Theoretical reaction pathways for the formation of  $[Si(OH)_5]^{1-}$  and the deprotonation of orthosilicic acid in basic solution. *Geochim. Cosmochim. Acta* **1993**, *57*, 3847–3853.

# Micro- and Mesoporous Nanomaterials: Catalytic Properties

Johannes A. Lercher

Andreas Jentys

*Institut für Technische Chemie, Technische Universität München, Garching, Germany*

## INTRODUCTION

Micro- and mesoporous materials are unique materials having found widespread use as solid catalysts or catalyst components in areas ranging from petroleum refining to the synthesis of intermediates and fine chemicals. The reasons for the widespread use are related to the possibility to tailor the concentration and nature of catalytically active sites and their immediate environment, which allows controlling the nature of catalytically active sites and the access of molecules to these sites. Such strict control of access is only found in enzymes and similar biological catalysts, but has the inherent disadvantage that it restricts the size of molecules to be converted.

The materials are also special, because they may be nanostructured with respect to the pore diameters<sup>[1]</sup> and with respect to the overall size of the particles.<sup>[2,3]</sup> This may induce interesting properties, which are hardly explored at present. Nearly all solids with a high specific surface area contain micro- and mesopores, most of them being irregular arrays of void space defined by coalescing primary particles and voids generated upon the transformation of material precursors to the final material. The present entry will only discuss materials with regular pore structure, either being fully crystalline (zeotype materials) or showing at least significant long-range ordering (mesoporous materials).

## OVERVIEW

The pores of micro- and mesoporous materials range from a few tenths of a nanometer to pores with diameters of more than 10 nm.<sup>[4]</sup> The confinement of that surface represents the inverse of effects sometimes observed with solid materials of nanoscopic dimensions. As the largest fraction of the atoms in nanoparticles consists of surface atoms, the properties of nanomaterials are, among other effects, determined by the surface free energy and termination effects. In contrast, in crystalline microporous materials all atoms and, hence, also the pores are part of the crystalline structure.

This leads to the high thermal stability such porous materials have,<sup>[5]</sup> while solid nanoparticles tend to

reduce their free surface energy by coalescing and growing into larger entities. The stability originates from the thermodynamic stabilization by periodicity,<sup>[6]</sup> which indicates in consequence that the stabilization decreases with the size of the coherent domains.

Micro- and mesoporous materials act as catalysts by offering new reaction pathways via binding at least one of the reacting partners to an active site and/or increasing the concentration of reactants in a fraction of the total reaction volume. Thus, in addition to the nature of the solid material, three main processes have to be qualitatively and quantitatively described for understanding catalysis, i.e., the transport to and from the catalytically active sites (leading, for example, to shifts in the selectivity), the sorption and desorption at the active site (including preferential sorption and the relation between sorption in the pores and localized adsorption) and finally the transformation of the reacting molecules in the surface chemical reactions. All three processes may be distinctly different in micro- and mesoporous materials compared to processes at open surfaces, as the size of the molecules approaches the size of the material pores. The complexity of these problems receives only a sketchy treatment in this entry. The description will be primarily confined to microporous materials, because of their industrial importance. Whenever possible, reference will be made to more in-depth reviews on particular properties of the materials discussed.

## STRUCTURAL AND CHEMICAL PROPERTIES OF MICRO- AND MESOPOROUS MATERIALS

Crystalline microporous materials are characterized by structurally well-defined voids, whose diameters exceed typical atomic dimensions. The fact that a molecule has to be able to access these pores puts a lower limit to the pore diameter of approximately 0.25 nm. If these voids are below 2 nm in diameter the material is called microporous, above mesoporous (with an upper limit of approximately 50 nm). It should be noted that in mesoporous materials the pores are also periodically arranged; however, the confining material is typically amorphous.

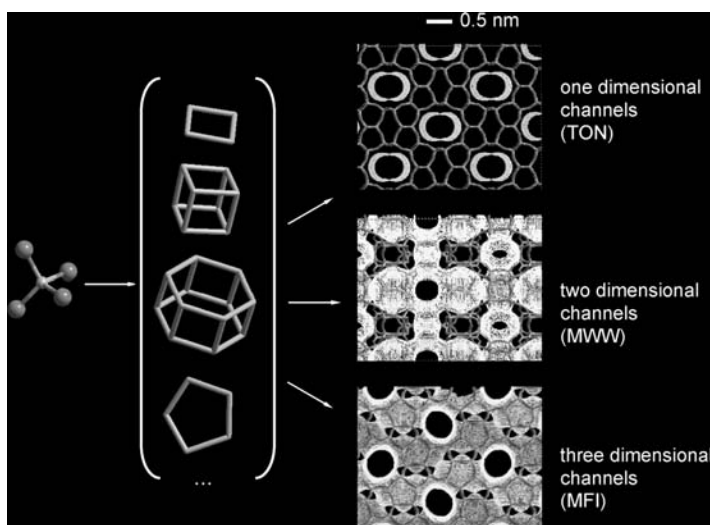


**Fig. 1** Examples for zeolite building blocks and one-, two-, and three-dimensional zeolite structures (T atoms are shown in orange, O atoms in red).

The crystalline materials may be of an inorganic or organic nature. Typical examples are zeolites and related tectosilicates for the inorganic materials<sup>[7]</sup> or cyclodextrine-type materials<sup>[8–10]</sup> and metal–organic frameworks.<sup>[11–13]</sup> Throughout this review, zeotypes (zeolites or aluminum phosphates) will be used as the examples to describe the interactions and catalytic actions. However, when the varying chemistry of the framework materials is kept in mind, the results can be extended to wide variations with respect to metal oxides/phosphates/sulfides or to (metal) organic entities.<sup>[14]</sup>

Common to zeolites and related materials is the principle of structures built by corner sharing  $\text{TO}_4$  tetrahedra or in some cases octahedra. T indicates the tetrahedrally coordinated cations such as  $\text{Si}^{4+}$  and  $\text{Al}^{3+}$  for zeolites or  $\text{Al}^{3+}$  and  $\text{P}^{5+}$  for aluminophosphates. These building blocks form a three-dimensional structure including a one-, two-, or three-dimensional pore network (see Fig. 1 for examples of zeolite building blocks and one-, two-, and three-dimensional zeolite structures). In some materials larger cages are formed at the intersections of the pores. Currently, about 140 framework types are known. To each framework type a three-letter code (Framework-Type Code) is assigned by the Structure Commission of the International Zeolite Association.<sup>[15]</sup> The framework type of a zeolite describes the connectivity of the framework tetrahedral atoms in the highest possible symmetry without reference to chemical composition and, therefore, defines the topology of the material with respect to size and shape of the pore openings, the dimensionality of the channels system, the volume and arrangement of the cages, and the type of cation sites available.<sup>[16]</sup>

Crystalline molecular sieves are often characterized by their smallest pore opening named after the number of T-atoms in the rings defining the size of the pore. A comparison between the diameters of the pore

openings and the size of typical reactant molecules is given in Fig. 2. Small pore zeolites, such as Zeolite A (LTA), Sodalite (SOD), and Zeolite P have pores build-up by 8-membered rings (8 MR pores). Medium pore zeolites, such as ZSM-5 (MFI), have minimum pore openings defined by 10-membered rings, while the pore openings of large pore zeolites, e.g., Zeolite Y (FAU), Mordenite (MOR), and Beta (BEA), are defined by 12-membered ring pores. Materials with pores of a larger minimum diameter are called ultra-large pores materials with 20 T-atom pores being the accepted upper limit. The materials with the largest pores are VPI-5 (18-MR pores)<sup>[17]</sup> and JDF-20 (20 MR pores).<sup>[18]</sup> Note that both materials are aluminophosphates. For siliceous materials UDT-1 (14-MR

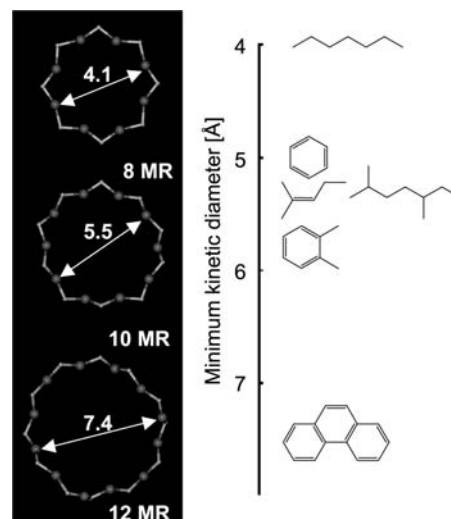


**Fig. 2** Comparison between the diameters of the pore openings and the size of typical reactant molecules.



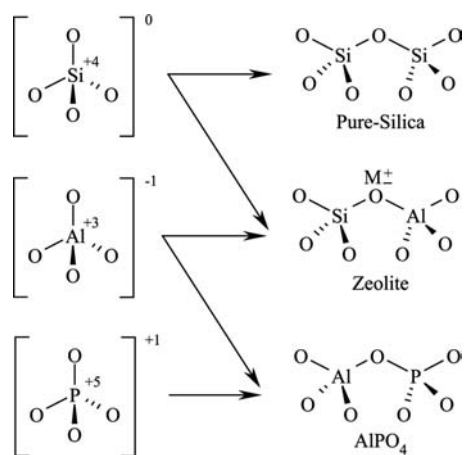


**Fig. 3** Possibilities of tailoring the zeolite by replacing framework  $\text{Si}^{4+}$  or  $\text{Al}^{3+}$  with different cations, i.e.,  $\text{P}^{5+}$ .

pore)<sup>[19]</sup> and CIT-5 (14 MR pores)<sup>[20]</sup> were among the materials with the largest pore sizes described.

The chemical composition determines the specific properties of microporous molecular sieves. Purely siliceous or aluminum phosphate molecular sieves are chemically inert. Chemical functionality and charge is introduced into such frameworks by substitution of cations with valences differing on the average from the value of four. Thus  $\text{Al}^{3+}$  as a T-atom in a silicate framework causes a negative framework charge, which has to be balanced by a proton (forming a hydroxy group, Brønsted acid site) or by a metal cation (forming a Lewis acid site).<sup>[21–23]</sup> The bare, negatively charged tetrahedron is the corresponding base anion. The differences in the charge of these tetrahedra determine the theoretically highest concentration of acid and base sites of the material. The possibilities of tailoring molecular sieves by replacing framework  $\text{Si}^{4+}$  or  $\text{Al}^{3+}$  with different cations, such as  $\text{P}^{5+}$ , are schematically shown in Fig. 3. Note that only cation exchange molecular sieves appear existing. For detailed information the reader is referred to excellent reviews.<sup>[16,24,25]</sup>

The chemical composition of the framework determines the polarity of the lattice and, in consequence, the acid–base properties of the material.<sup>[21,26–28]</sup> Because of the instability of Al–O–Al bonds (proximity of two positively charged atoms), only half of all silicon atoms can be replaced by aluminum in materials based on silica (lowest Si/Al ratio possible of 1). This has been expressed in the Loewenstein rule.<sup>[29]</sup> Consequently, each Al–O tetrahedron is surrounded by four Si–O tetrahedra. Adjacent Al–O tetrahedra are referred to as next nearest neighbors (NNN). Various models, reviewed by Barthomeuf,<sup>[27]</sup> relate the acid strength of Brønsted sites to the concentration of NNN Al atoms. The strongest acid sites are observed in the absence of NNN Al–O tetrahedra. The site strength decreases as the concentration of NNN

Al–O tetrahedra increases. Thus, in addition to long-range effects of the chemical composition, experiments and theoretical calculations<sup>[30]</sup> show that short-range effects influence the strength of acid sites. Additionally, more subtle factors such as the crystal structure leading to various angles between the tetrahedra (T–O–T bonding angle) and the nature of the metal cations at exchange sites can influence the strength of acid sites.<sup>[28,31,32]</sup>

Adjusting the combination of chemical composition, (partial) cation exchange, and the molecular sieve structure can lead to a wide variety of chemical properties. Depending upon the charge on the metal cation/proton and the oxygen, the acidic or basic properties of the molecular sieves will dominate and, consequently, the materials will act as a solid acid or base.<sup>[33]</sup>

Acid/base sites generated by substitution in crystalline materials are generally more stable than sites in mesoporous materials with amorphous walls, because the latter material does not face constraints in the relaxation of bonds.<sup>[34,35]</sup> In contrast to the crystalline materials, mesoporous materials have pores generated by the condensation of (X-ray amorphous) oxides<sup>[36]</sup> around medium and high molecular weight surfactants.<sup>[37]</sup> After forming a coherent structure, the surfactants are removed and the regular void structure with pore diameters between 20 and 100 nm remains. The large pores possess many hydroxyl groups,<sup>[38]</sup> which are well suitable for anchoring functional groups or metal–organic complexes.<sup>[39]</sup> The most prominent members of the family are the MCM41S-type materials (e.g., MCM-41, MCM-48) with hexagonally or cubic structures<sup>[40]</sup> and materials such as SBA15 synthesized using non-ionic triblock copolymers.<sup>[41,42]</sup> For postsynthetic modifications these materials are frequently used in their pure silica form.<sup>[43–45]</sup> Recently, mesoporous materials have been synthesized with fractions of crystalline materials as building blocks as part of the wall structure<sup>[46]</sup> or as delaminated and pillared zeolite entities.<sup>[47,48]</sup> These materials are able to combine the local structure of crystalline molecular sieve materials and, hence, the presence of stable and strong Brønsted acid sites with the accessibility for large molecules. The best examples for this are related to delaminated structures of MWW- or FER-type materials. When oxide pillars are used to stabilize the delaminated layers, widely differing chemical functions can be combined in one material, i.e., acidic and basic sites or acidic and redox sites.<sup>[49]</sup>

## FUNCTIONAL PROPERTIES

### Brønsted Acid Sites

As described above the strength of Brønsted acid sites varies markedly with the local and overall environment,

i.e., the chemical composition and the structure of the zeolite.<sup>[27,28]</sup> While the lengths of Al–O and Si–O bonds and the corresponding Al–O–Si and Si–O–Si angles<sup>[34]</sup> exert a subtle influence, the strongest sites are found in the absence of Al NNN atoms. For these materials Brønsted acid sites appear to be identical in strength and catalytic activity. This has been shown for protolytic cracking of *n*-hexane<sup>[50]</sup> and the isomerization of *m*-xylene<sup>[51]</sup> both being monomolecular reactions under the chosen reaction conditions. For *n*-hexane and *n*-hexene cracking this equivalency was shown also for materials with varying aluminum concentration.<sup>[50]</sup>

### Lewis Acid Sites

Lewis acid sites are electron pair acceptor sites formed by accessible metal cations stemming from lattice defects, oxide nanoparticles formed by lattice degradation, and cation exchange. The strength of Lewis acid sites is proportional to the ratio between the charge of the metal cation and its size,<sup>[52]</sup> but it can be reduced by limited accessibility (inability to assume minimum bond distance). Lewis acid sites formed by metal cation exchange are weak to moderately strong, because many of the exchangeable cations have a low electronegativity (e.g., alkali or alkali earth metals) or are relatively large (e.g., La<sup>3+</sup>). Together with the adjacent framework oxygen atoms they act as Lewis acid/base pair and may polarize bonds in reacting molecules.

Lewis acid sites originating from lattice defects or by degradations of the lattice are part of alumina or silica/alumina nanoparticles formed by the extraction of aluminum from the lattice (Fig. 4), which can be charged or neutral.<sup>[53,54]</sup> Al<sup>3+</sup> exists in octahedral and tetrahedral coordination and will have stronger Lewis acid sites than exchangeable metal cations.<sup>[26]</sup> The extra-framework alumina species (EFAL) are typically extracted from the zeolite lattice by steam treatment at higher temperatures and either block active sites by substituting for exchangeable cations, enhance the acidity by interacting with a Brønsted acid site, or block the access to micropores by forming voluminous oligomeric species.<sup>[55–58]</sup>

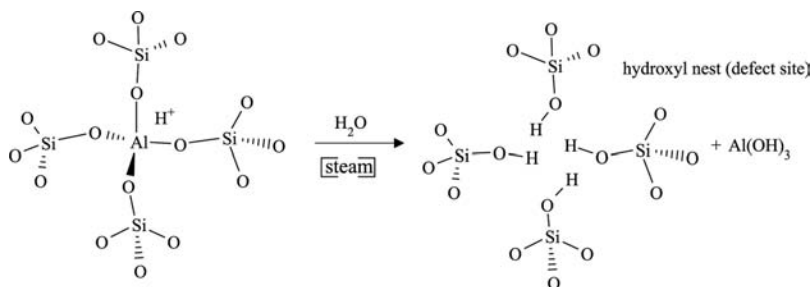


**Fig. 4** Hydrothermal extraction of aluminum from the zeolite lattice.

A third type of Lewis acid site has been recently described as Al<sup>3+</sup> reversibly and partially extracted from the lattice using a base molecule such as ammonia.<sup>[59,60]</sup> The Al<sup>3+</sup> cation assumes an octahedral coordination under such conditions. The reversibility is broken, however, once Al–O–Al bonds are formed, i.e., when the aluminum oxide species are completely detached from the lattice. Detailed information on such sites is not available, but it can be speculated that the drastic enhancement of catalytic activity for acid-catalyzed hydrocarbon conversion after mild steaming is associated with such reversible detached Lewis acid sites.<sup>[61]</sup>

It should be noted here that the interaction of the Lewis acid sites with electron pair donor molecules is very strong. The presence of the acid–base pairs allows polarizing molecules, which can potentially enhance their reactivity.<sup>[62,63]</sup> Lewis acid sites also act as hydride or anion receptors in a variety of reactions. Their presence seems also to stimulate dehydrogenation of alkanes to some degree.

### Basic Sites

Basic sites are proton accepting or electron pair donating oxygen atoms of the lattice. The strength is proportional to the negative charge on the oxygen. To a first approximation, this negative charge can be estimated with the help of the intermediate electronegativity using the Sanderson electronegativity principle<sup>[64]</sup> or the electronegativity equalization method (EEM).<sup>[30]</sup> It varies inversely to the intermediate electronegativity, i.e., materials with lower intermediate electronegativity and higher polarity show higher base strength.<sup>[65,66]</sup> The oxygen 1s binding energy can be used to confirm this trend experimentally.<sup>[67]</sup> Like the acid strength discussed above the base strength of the oxygen atoms in the lattice also depends subtly on T–O–T bond angles and on the local chemical environment (e.g., oxygen atoms in AlO<sub>4</sub> tetrahedra are more basic than in SiO<sub>4</sub> tetrahedra).<sup>[22,68]</sup> Additionally, the type of cation influences the polarity of the lattice.<sup>[69]</sup> Even when all cation exchange sites are exchanged with alkali cations, the overall chemical composition allows for the SiO<sub>2</sub>-based materials only

a weak base strength. Stronger base sites are therefore linked to clusters of alkaline or alkali-earth oxide hydroxides in the zeolite pores.<sup>[70,71]</sup> Very strong basic sites can be created by supporting metallic sodium in the zeolite pores,<sup>[25]</sup> which interact with framework oxygen atoms or react with trace humidity. Loading zeolites with alkali metal oxides utilizes the microporous material primarily as support.<sup>[72]</sup> Such materials show high activity in typical base-catalyzed reactions such as alcohol dehydrogenation or toluene side chain alkylation.<sup>[73]</sup> However, the low rates of base-catalyzed reactions make the materials always very susceptible to traces of catalytically more active protons, which then dramatically change the chemical reactivity.<sup>[73]</sup>

### Redox Sites

Redox sites can be introduced into micro- and mesoporous materials by isomorphous substitution of metal ions into framework positions, ion exchange with metal cations, and grafting metal complexes onto the surface of (mesoporous) molecular sieves. All three options lead to materials with unique properties that may be tailored for specific uses. While the first approach comes closest to mimicking enzyme catalysis, the ion exchanged materials are excellent redox catalysts for gas-phase reactions in environmental applications and the third group brings the wide variety of the metal-organic chemistry to mesoporous materials. For excellent reviews on the materials, see Refs.<sup>[43,74-77]</sup>

Examples for the first group of materials include Ti-silicalite (TS1-1),<sup>[78-80]</sup> vanadium silicates with MFI and MEL structure,<sup>[81]</sup> iron-containing MFI zeolites,<sup>[82]</sup> and Co and Cr incorporated into the framework of aluminum phosphate with AFI and AEL structure.<sup>[83]</sup> The uniqueness of these materials lies in the fact that isolated, identical, and stable sites are formed in a matrix that allows the proper adsorption of the reactants and provides sufficient space for the chemical transformations (with steric constraints of the molecular sieve directing the reaction). Most importantly, however, the materials can be tailored to have the proper hydrophobic/hydrophilic properties.<sup>[84]</sup>

Ti-silicalite (TS1-1) is an excellent catalyst for the oxidation of small molecules with H<sub>2</sub>O<sub>2</sub> and was the first commercially used zeolite-based partial oxidation catalyst. Experimental<sup>[78-80]</sup> and theoretical studies<sup>[85,86]</sup> suggest that the active sites in TS-1 are isolated and uniformly distributed Ti(IV) atoms in tetrahedral coordination, where each Ti(IV) is separated from other titanyl groups by at least two Si-O tetrahedra. The isolation of the Ti<sup>4+</sup> centers is required to obtain high selectivities (low rate of H<sub>2</sub>O<sub>2</sub> decomposition). Next to incorporation into the MFI or MEL structure, incorporation of Ti has also been reported,

e.g., for BEA (Ti-Beta), MTW (Ti-ZSM-12), and MWW (Ti-MCM-22).<sup>[87-89]</sup>

Transition metal cation exchanged materials have seen enormous interest as potential materials for reduction of NO<sub>x</sub> with hydrocarbons.<sup>[77,90-92]</sup> Most of the materials investigated are based on the MFI structure, and Cu, Co, and Fe are the most studied materials.<sup>[93]</sup> Such materials cannot be used in liquid-phase reactions as the metal cations at exchange places would be leached. Iron containing ZSM-5 materials are especially remarkable as their catalytic activity differs markedly from that of bulk Fe<sub>2</sub>O<sub>3</sub>.<sup>[82]</sup> Fe-ZSM-5 is unable to activate O<sub>2</sub>, but shows high activity for the decomposition of N<sub>2</sub>O<sup>[94]</sup> and utilizes the oxygen for selective gas-phase oxidation steps. Similar to the microporous Fe-ZSM-5, mesoporous iron-containing silicas with MCM-41-type structure<sup>[95,96]</sup> can be used to oxidize large hydrocarbons to oxygenates with N<sub>2</sub>O.

### UNDERSTANDING SIZE AND SHAPE OF MICRO- AND MESOPORES

In an ideal crystal the position of the atoms in the lattice and as a consequence also the void space between them are well defined. Thus in principle the pores can be assessed by experimental structure determining methods such as X-ray diffraction.<sup>[97,98]</sup> Practical problems are associated with the fact that the materials are not ideal frameworks and contain lattice defects and larger irregular void spaces (mesopores). Moreover, the accessible pore volume is defined by the van der Waals radii of the lattice oxygen atoms and of the sorbed molecules, both being flexible and temperature dependent.<sup>[99]</sup> Basically, understanding the pore volume and pore accessibility is based on five principal methods, including (high-resolution) transmission electron microscopy and tomographic methods,<sup>[100-102]</sup> adsorption of small inert molecules,<sup>[103]</sup> <sup>129</sup>Xe NMR spectroscopy,<sup>[104]</sup> adsorption of probe molecules of various sizes, and<sup>[105]</sup> lately on computer modeling the accessible pore space.<sup>[106]</sup> Typically, the combination of methods is mandatory to describe the properties of micro- and mesoporous nanomaterials.<sup>[107,108]</sup>

The complexity is seen in a comparison of the computer modeling of *n*-hexane, benzene, and 1,3-diethylbenzene adsorption in a zeolite with the MOR structure (Fig. 5) and the corresponding experimental

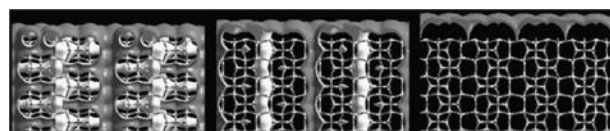


**Fig. 5** Accessible pore volume of mordenite for *n*-hexane and benzene and 1,3-diethylbenzene.

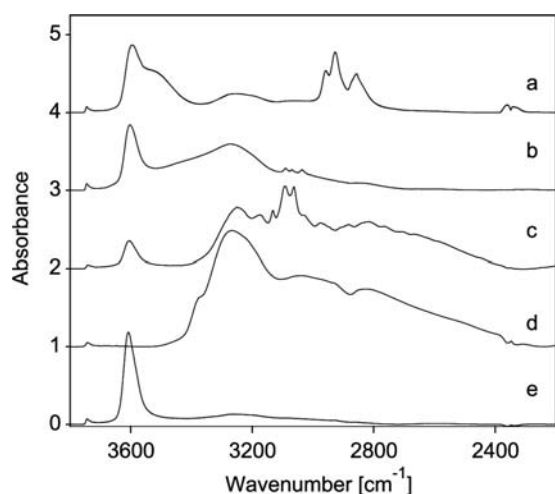


**Fig. 6** Adsorption of (A) *n*-octane, (B) benzene, (C) pyridine, and (D)  $\text{NH}_3$  on (E) H/MOR.

sorption experiment (Fig. 6). Unequivocally, the simulation presented in Fig. 5 shows that molecules with kinetic diameters larger than the pore diameter are excluded from accessing the pores (1,3-diethylbenzene). Computer modeling shows *n*-hexane may access also side pockets in this material, while benzene is unable to do so. Experiments show in contrast that neither molecule can approach sites in the side pockets. This indicates that very subtle changes in the interactions (linear amines access the side pockets) may lead to drastic changes in the sorption properties.

### TRANSPORT OF MOLECULES IN AND INTO MICRO- AND MESOPORES

Transport of molecules follows in the most cases configurational diffusion and in limited cases Knudsen diffusion for the largest pores. The mathematical principles and the methods to measure diffusion processes in microporous materials are excellently summarized in Ref.<sup>[109]</sup>. Configurational diffusion involves the transport of molecules between places of relatively long residence time (sorption sites) by hopping<sup>[110,111]</sup> between the pronounced sorption minima. The activation energies may be significant, as for each movement bonds have to be broken and energy maxima have to be overcome. The similarity of the minimum kinetic diameter of the diffusing molecule and the pore diameter makes it impossible or difficult for molecules to pass each other in the pore network. The resulting sequentially ordered transport of the molecules has been described as single-file diffusion<sup>[112,113]</sup> and is important to describe separation and catalysis in materials with one channel.<sup>[114,115]</sup>

Differences between the mobility of molecules at equilibrium or during forced movement through the pores can be substantial.<sup>[17,51,109]</sup> Significant slowdown of the transport process is induced by the crystal boundaries,<sup>[116,117]</sup> leading to faster transport through single crystal than polycrystalline H-ZSM-5.<sup>[118]</sup> This has been related recently to a weakly sorbed precursor state that allows adsorption of the aromatic molecules at the outer surface of the microporous particle and a subsequent entering into the pore system after arbitrary movement on the outer surface.<sup>[119]</sup>

### SORPTION IN MICRO- AND MESOPOROUS MATERIALS

Many of the unique properties of the microporous materials as sorbents and catalysts result from the proximity of the molecule to the surrounding wall. As a consequence, the molecules interact with the framework oxygen atoms by undirected short-range dispersion forces (physisorption), which can dominate over specific directed interactions for weakly polar and larger molecules. Such situations have been well demonstrated for alkanes in molecular sieves. Adsorption of more polar compounds may also include polar, field-dipole, and field gradient-quadrupole contributions to the interaction.

Adsorption of an alkane (as an example) in H-ZSM-5 has two energetic components of interaction, one related to the directed binding to hydroxy groups and another that results from the London dispersion forces.<sup>[120]</sup> The direct interaction results from a dipole-induced hydrogen-bridge of alkane hydrogens. To partition between these two groups of interactions, it is useful to compare microporous materials with and without Brønsted acid sites. The dependence of the heat of sorption of *n*-alkanes on their chain length is

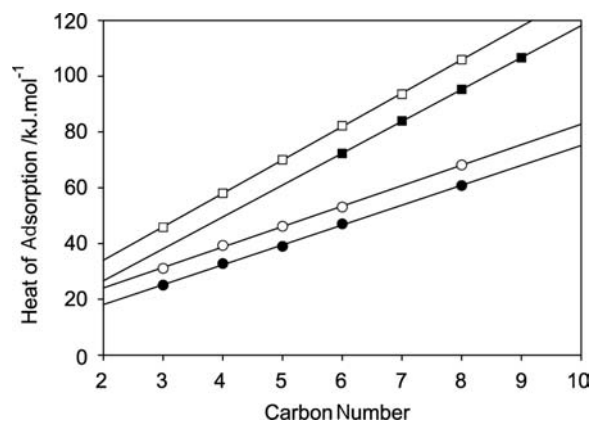


**Fig. 7** Heat of sorption of *n*-alkanes on (□) H-ZSM-5, (■) ZSM-5 (siliceous), (○) H-Y, and (●) Y (siliceous).

shown in Fig. 7 for two groups of molecular sieves, i.e., materials of MFI and FAU structure with and without strong Brønsted acid sites. The initial heat of sorption increases linearly with the chain length for ZSM-5 and zeolite Y.<sup>[105,121]</sup> However, the increment in the heat of sorption per carbon atom is larger for the medium pore ZSM-5 material compared to the large pore zeolite Y. Also, the modest contribution of polarization by strong Brønsted acid sites ( $7\text{--}10\text{ kJ mol}^{-1}$ ) is higher for ZSM-5 indicating higher acid strength. Overall, it can be concluded that the interaction between the alkane and the zeolite is governed by physisorption.

The sorption in the pores reduces the degrees of freedom (translatory and configurational) for the sorbed molecules (decrease of their entropy). Stronger bonding leads to a more pronounced reduction of the sorbate entropy. With increasing chain length of the alkane (increasing heat of sorption), indeed, also the entropy in the sorbed state decreases sympathetically. For a given heat of adsorption, the loss of entropy decreases with the pore size of the molecular sieve.<sup>[121]</sup> The slope of the resulting linear correlation between entropy and enthalpy can be used for unknown materials as characteristic value for the available pore diameter. Entropy plays also a significant role in ordering and sorbing molecules that can only partly access the pore system.<sup>[122]</sup>

Molecular sieves containing alumina are hydrophilic and are used as drying agents. However, in the pure silica form materials with the same structure and micropores interact very weakly with polar compounds (are hydrophobic). For practical measures a comparison of the sorption capacity for *n*-hexane and water has been introduced as hydrophobicity index.<sup>[123]</sup> The reason for this weak interaction lies in the low polarity of the pure silica lattice, which does not tend to form hydrogen bonds with polar molecules such as water or alcohols.<sup>[124]</sup> This is especially important for small molecules (water, ammonia, methanol, methylamine, etc.) that show a less pronounced interaction via dispersion forces than large molecules.

## CATALYSIS IN THE CONFINEMENT OF MICRO- AND MESOPORES

The dominating chemical functions, i.e., acid, base, or redox, determine the surface chemistry and the way reactions are catalyzed. The confinement of the pores does not lead to completely new chemistry, but the proximity of the lattice and the reacting molecules may stabilize some transition states similar to situations found in liquid phase or enzyme catalysis. It is impossible to review the wide variety of chemical reactions reported for microporous and mesoporous

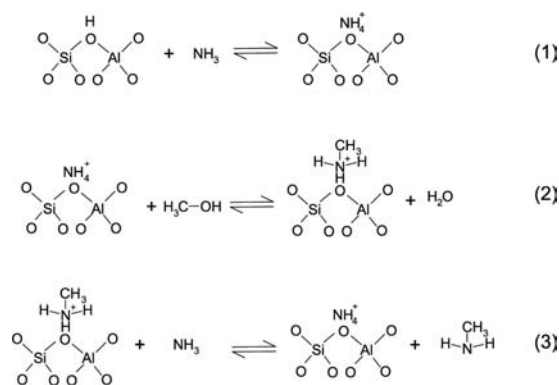
materials. Therefore, we will limit the review to those special situations, where the molecular sieves show special properties. For more general overviews the reader is referred to Refs.<sup>[7,125–131]</sup>

One of the most striking observations is the strong adsorption of even apolar molecules and the resulting high catalytic activity. This is most prominently seen in the conversion of light alkanes on various zeolites and mesoporous materials. At a particular temperature the rate of alkane cracking increases exponentially with the size of the alkane. This is not related to an easier breaking of the C–C bond (the true energies of activation are identical for all molecules) but is caused by the exponential increase of the adsorption equilibrium constant with the size of the molecule.<sup>[132,133]</sup> As the strength of adsorption is also related to the pore size, materials with larger pores adsorb fewer molecules at a given partial pressure. Indeed, the rate of *n*-alkane cracking is about an order of magnitude slower with materials of the FAU structure than with H-ZSM-5. The energy of activation, however, is identical for both reactants. The rates for cracking are even smaller for acidic mesoporous materials. As a consequence it is possible to selectively crack a heavy fraction of alkanes in the presence of light alkanes by choosing a large pore acidic material.

The variation of the chemical composition can be used to subtly influence the selectivity. It has been recognized for example that zeolites with higher concentration aluminum substituted into the lattice show appreciable hydride transfer activity, which not only maintains the cracking chain reactions, but also shifts the product distribution between olefins and aromatic molecules.<sup>[134]</sup> Now it could be shown with the reverse reaction, i.e., the alkylation of *iso*-butane with *n*-butene, that hydride transfer increases with the aluminum concentration over a much wider range of chemical indicating that a less strongly acidic material has the higher tendency to hydride transfer. This is surprising as it shows that the stability of the new bond between the carbon atom and the lattice oxygen is more important than the polarity of the C–O bond in the alkoxy group.<sup>[135,136]</sup>

While hydride transfer is important for hydrocarbon activation at low temperatures, deprotonation reactions by strong bases such as ammonia may help to release highly polar species such as alkylammonium compounds. Alkylammonium ions are generated by the reaction of ammonium ions with methanol, but are unable to leave the zeolite pores, because of their high base strength.<sup>[137]</sup> Scheme 1 shows that in the initial step an ammonium ion is formed, which donates a proton to the alcohol leading to an alkylammonium ion and water as a leaving group. Alkyl transfer reactions or adsorption-assisted desorption is necessary to allow the decomposition of the alkylammonium





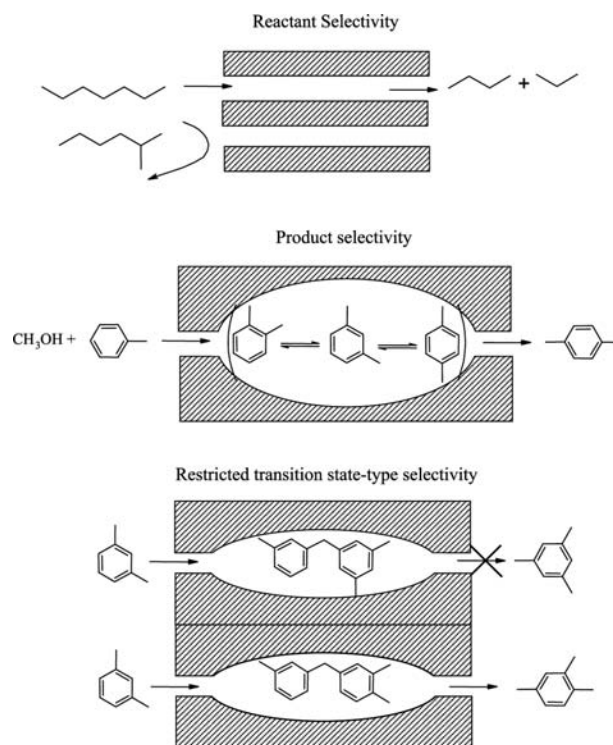
**Scheme 1** Acid-catalyzed methylamine synthesis.

ion and the desorption of alkylamines, while another ammonium ion is formed. The zeolite also binds the alkylammonium ions very strongly, but activates the alkyl groups on the other hand so that they can also react with strongly nucleophilic reactants.

The changes in the chemical composition can be used to modify the relative concentration of reactants in the pores by varying the polarity of the lattice and the strength of interaction with polar and apolar molecules. A nice academic example for that effect is reported by Namba et al.,<sup>[138]</sup> who studied the direct esterification of acetic acid with *n*-, *iso*-, and *tert*-butyl alcohol on different zeolites. The poisoning of the acid sites by water formed in the process was significantly weaker with the more hydrophobic high-Si/Al-ratio ZSM-5 catalysts. Materials with a low tendency to sorb polar compounds are therefore excellent catalysts for the synthesis and transformation of highly polar products.<sup>[139]</sup>

The weak interaction with water is also the main reason for the successful use of H<sub>2</sub>O<sub>2</sub> with Ti-silicalite materials. A significant concentration of water in the pores under reaction conditions would lead to the hydrolysis of, for example, epoxide groups formed from the reaction with olefinic molecules (Scheme 2). It should be noted that such subtle differences in the strength of interaction can be used to optimize polar and basic molecular sieves in order to adjust the ratio of methanol and toluene adsorbed in the pores of alkali exchanged zeolites during the side chain alkylation of toluene. In contrast to the well-tailored zeolites, the conversion over basic layered compounds such as hydrotalcites indicates that improper ratios between toluene and methanol lead to inactive catalysts.<sup>[140]</sup>

While there has been limited direct evidence, some results also suggest that it should be possible to use the polarization by the zeolite pores to activate molecules. Evidence includes the modification of the optical properties of sorbed naphthalene<sup>[141]</sup> and the variations in the cracking activity in aluminum phosphate molecular sieves because of local field gradients.<sup>[142]</sup>



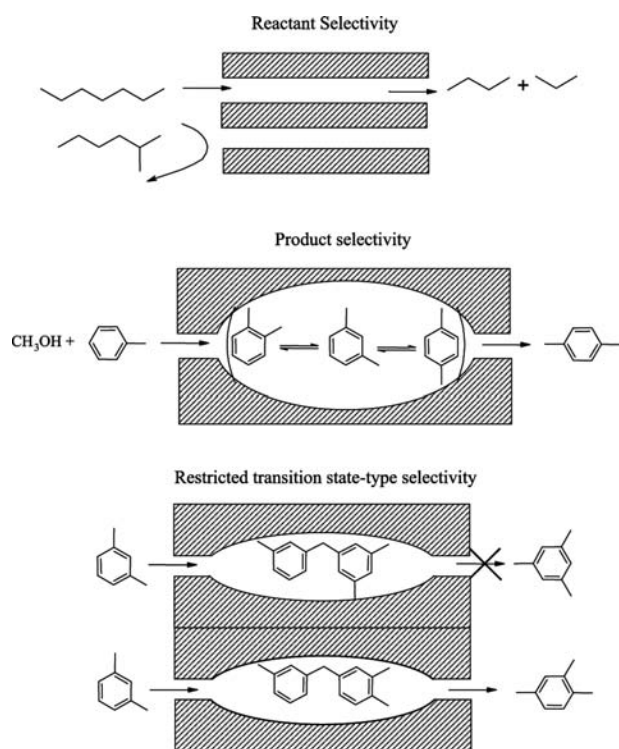
**Scheme 2** Epoxidation and hydrolysis.

The most pronounced and important effect in micro- and mesoporous materials, however, relates to its shape selectivity. It can be induced by limitations of the access of some of the reactants to the pore system (reactant selectivity), the limitation in the diffusion of some of the products out of the pores (product selectivity), and constraints in forming certain transition states (transition state selectivity) (see Scheme 3 for a comparison of the types of shape selectivity).<sup>[125,143–145]</sup>

Reactant selectivity occurs when the access of certain reactant molecules to the intercrystalline void space of the zeolite is suppressed on the basis of the diameter, while other (less bulky) molecules can enter and react. The first example of reactant shape selectivity was reported by Weisz and Frillette<sup>[146]</sup> for the dehydration of an *n*-butanol/*iso*-butanol mixture over LTA-type zeolites. Because of its larger minimum kinetic diameter *iso*-butanol is excluded from entering the zeolite pores, while *n*-butanol is easily dehydrated to butene. This demonstrates that the pores are able to realize a well-defined cutoff point with respect to the minimum kinetic diameter of the reacting molecules. This principle of size exclusion is frequently used in hydrocarbon processing to remove linear hydrocarbons from a mixture of hydrocarbons (e.g., selectofining).

Product selectivity is the result of the differences between the diffusivities of the reaction products in the pores of the zeolite. A typical example is the





**Scheme 3** Schematic representation of the three types of shape selectivity.

isomerization of alkylaromatics. Note that the diffusion constant of *p*-xylene in chemically modified ZSM-5 zeolites is about  $10^3$  times higher than that of *m*-xylene.<sup>[51,147]</sup> Therefore *p*-xylene will diffuse quickly out of the pores of the zeolite to the gas phase, while the more bulky product (*o*- and *m*-xylene) will undergo secondary isomerization reactions. As this type of shape selectivity results from the differences in the diffusivities it depends on the pore size but also on the crystal size of the zeolite particles.

Transition state shape selectivity occurs when the configuration of a potential transition state is spatially constrained compared to other transition states and therefore only certain reaction pathways are possible. *m*-Xylene isomerization is a well-documented example. It is interesting to note for this reactant that it diffuses slower through the pore channels of H-ZSM-5 than both reaction products, *o*-xylene and *p*-xylene. None of the products is adsorbed in a measurable degree during reaction. The *p*-xylene position is preferably formed as the transition state is smaller and, hence, entropically preferred. This is also confirmed kinetically by the temperature independence of the preference to *p*-xylene.<sup>[51]</sup>

Recently, it has also been shown that selectivity can be induced by the spacing between pore mouths of zeolites, although this has been strongly debated in relation to the hydroisomerization of alkanes.<sup>[148,149]</sup>

It has been shown that product patterns could be explained by invoking only the acid sites at the entrance of small pore materials such as erionite, ZSM-22, and Theta-1. The isomer distribution suggests that branching of *n*-alkanes occurs in approximately the distance between two pore openings.

## CONCLUSION

Crystalline nanostructured microporous and, to a lesser extent, mesoporous materials are broadly available providing a unique environment that allows to tailor the local reaction to an extent that is otherwise seen only in enzymes. This progress was and is based on the gradually developing understanding of chemical and physical processes and the material properties involved in the catalytic reactions. Rapidly advancing experimental capabilities and the progress in theoretical chemistry aided the speed of development greatly. The steric and chemical control of the environment of the active sites, the mobility of the reactants and products, and the interplay between these processes are understood at a level that makes it possible to design materials for specific purposes. The realization of controlled size and morphology of the microporous materials, the synthesis of stable larger pore materials, and the generation of well-defined outer surfaces and delaminated structures are three of the major challenges to be overcome. The introduction of chiral centers into the structure and the combination of organic and inorganic entities are other challenges that will see breakthroughs in the future.

## REFERENCES

1. Breck, D.W. *Zeolite Molecular Sieves, Structure, Chemistry and Use*; John Wiley & Sons, 1974.
2. van Grieken, R.; Sotelo, J.L.; Menendez, J.M.; Melero, J.A. Anomalous crystallization mechanism in the synthesis of nanocrystalline ZSM-5. *Microporous Mesoporous Mater.* **2000**, *39* (1–2), 135–147.
3. Reding, G.; Mäurer, T.; Kraushaar-Czarnetzki, B. Comparing synthesis routes to nano-crystalline zeolite ZSM-5. *Microporous Mesoporous Mater.* **2003**, *57*, 83–92.
4. Thomas, J.M.; Bell, R.G.; Catlow, C.R.A. Zeolites and Related Molecular Sieves. In *Handbook of Heterogeneous Catalysis*; Ertl, G., Knözinger, H., Weitkamp, J., Eds.; Wiley-VCH: Weinheim, 1997; Vol. 1, 286–310.
5. Beyerlein, R.A.; Choifeng, C.; Hall, J.B.; Huggins, B.J.; Ray, G.J. Effect of steaming on the defect structure and acid catalysis of protonated zeolites. *Catal. Lett.* **1997**, *4* (1–2), 27–42.
6. Moloy, E.C.; Davila, L.P.; Shackelford, J.F.; Navrotsky, A. High-silica zeolites: a relationship

- between energetics and internal surface areas. *Micro-porous Mesoporous Mater.* **2002**, *54* (1–2), 1–13.
7. Weitkamp, J. Zeolites and catalysis. *Solid State Ionics* **2000**, *131* (1–2), 175–188.
  8. Langley, P.J.; Hulliger, J. Nanoporous and mesoporous organic structures: new openings for materials research. *Chem. Soc. Rev.* **1999**, *28* (5), 279–291.
  9. Han, B.H.; Polarz, S.; Antonietti, M. Cyclodextrin-based porous silica materials as in situ chemical “nanoreactors” for the preparation of variable metal-silica hybrids. *Chem. Mater.* **2001**, *13* (11), 3915–3919.
  10. Polarz, S.; Smarsly, B.; Bronstein, L.; Antonietti, M. From cyclodextrin assemblies to porous materials by silica templating. *Angew. Chem., Int. Ed.* **2001**, *40* (23), 4417.
  11. Yaghi, O.M.; Li, G.M.; Li, H.L. Selective binding and removal of guests in a microporous metal–organic framework. *Nature* **1995**, *378* (6558), 703–706.
  12. Li, H.; Eddaoudi, M.; O’Keeffe, M.; Yaghi, O.M. Design and synthesis of an exceptionally stable and highly porous metal–organic framework. *Nature* **1999**, *402*, 276–279.
  13. Schuth, F. Non-siliceous mesostructured and mesoporous materials. *Chem. Mater.* **2001**, *13* (10), 3184–3195.
  14. Kaskel, S. Porous metal–organic frameworks. In *Handbook of Porous Solids*; Schüth, F., Sing, K.S., Weitkamp, J., Eds.; Wiley-VCH: Weinheim, 2002; Vol. 2, 1190–1249.
  15. <http://www.iza-structure.org/databases/>.
  16. McCusker, L.B.; Baerlocher, C. Zeolite Structures. In *Introduction to Zeolite Science and Practice*; van Bekkum, H., Flanigan, E.M., Jacobs, P.A., Jansen, J.C., Eds.; Elsevier: Amsterdam, 2001; Vol. 137, 37–67.
  17. Davis, M.E.; Saldarriaga, C.; Montes, C.; Garces, J.M.; Crowder, C.E. VPI-5-The 1st molecular-sieve with pores larger than 10 Angstroms. *Zeolites* **1988**, *8*, 362–366.
  18. Jones, R.H.; Thomas, J.M.; Chen, J.; Xu, R.; Huo, Q.; Li, S.; Ma, Z.; Chippindale, A.M. Structure of an unusual aluminium phosphate  $([Al_5P_6O_{24}H]^{2-} \cdot 2[N(C_2H_5)_3H]^+ \cdot 2H_2O)$  JDF-20 with large elliptical apertures. *J. Solid State Chem.* **1993**, *102* (1), 204–208.
  19. Freyhardt, C.C.; Tsapatsis, M.; Lobo, R.F.; Balkus, K.J.; Davis, M.E. A high-silica zeolite with a 14-tetrahedral-atom pore opening. *Nature* **1996**, *381* (6580), 295–298.
  20. Wagner, P.; Yoshikawa, M.; Lovallo, M.; Tsuji, K.; Taspatsis, M.; Davis, M.E. Cit-5-A high-silica zeolite with 14-ring pores. *J. Chem. Soc., Chem. Commun.* **1997**, *21* (22), 2179–2180.
  21. Ward, J.W. The nature of active sites on zeolites: I. The decationated Y zeolite. *J. Catal.* **1967**, *9*, 225–236.
  22. Barthomeuf, D. Basic zeolites—characterization and uses in adsorption and catalysis. *Catal. Rev., Sci. Eng.* **1996**, *38* (4), 521–612.
  23. Kühn, G.H. The coordination of aluminum and silicon in zeolites as studied by X-ray spectrometry. *J. Phys. Chem. Solids* **1977**, *38* (11), 1259–1263.
  24. Depmeier, W. Crystalline microporous Solids. In *Handbook of Porous Solids*; Schüth, F., Sing, K.S., Weitkamp, J., Eds.; Wiley-VCH: Weinheim, 2002; Vol. 2, 699–736.
  25. Martens, L.R.M.; Vermeiren, W.J.M.; Grobet, P.J.; Jacobs, P.A. *Preparation of Catalysts IV*; Delmon, B., Grange, P., Jacobs, P.A., Poncelet, G., Eds.; Stud. Surf. Sci. Catal.; Elsevier: Amsterdam, 1987; Vol. 31, 531 pp.
  26. Martens, J.A.; Souvrijns, W.; van Rhijn, W.; Jacobs, P.A. Acidity and basicity in zeolites. In *Handbook of Heterogeneous Catalysis*; Ertl, G., Knözinger, H., Weitkamp, J., Eds.; Wiley-VCH: Weinheim, 1997; Vol. 1, 324–365.
  27. Barthomeuf, D. Acidity and basicity in zeolites. In *Studies in Surface Science and Catalysis; Catalysis and Adsorption by Zeolites*; Ohlman, G., Pfeifer, H., Fricke, R., Eds.; Elsevier: Amsterdam, 1991; Vol. 65, 157–169.
  28. Haw, J.F. Zeolite acid strength and reaction mechanisms in catalysis. *Phys. Chem., Chem. Phys.* **2002**, *4* (22), 5431–5441.
  29. Loewenstein, W. The distribution of aluminum in the tetrahedra of silicates and aluminates. *Am. Mineral.* **1954**, *39*, 92.
  30. Mortier, W.J.; Ghosh, S.K.; Shankar, S. Electronegativity-equalization method for the calculation of atomic charges in molecules. *J. Am. Chem. Soc.* **1986**, *108*, 4315–4320.
  31. Uytterhoeven, L.; Mortier, W.J.; Geerlings, P. Charge-distribution and effective electronegativity of aluminophosphate frameworks—influence of the structure type. *J. Phys. Chem. Solids* **1989**, *50* (5), 479–486.
  32. Mortier, W.J. Zeolite electronegativity related to physicochemical properties. *J. Catal.* **1978**, *55* (2), 138–145.
  33. Tanabe, K.; Misono, M.; Ono, Y.; Hattori, H. *New Solid Acids and Bases, Studies in Surface Science and Catalysis*; Tanabe, K., Misono, M., Ono, Y., Hattori, H., Eds.; Elsevier: Amsterdam, New York, 1989; Vol. 51, 142 pp.
  34. van Santen, R.A. Quantum-chemistry of zeolite acidity. *Catal. Today* **1997**, *38* (3), 377–390.
  35. Brandle, M.; Sauer, J. Acidity differences between inorganic solids induced by their framework structure. A combined quantum mechanics molecular mechanics ab initio study on zeolites. *J. Am. Chem. Soc.* **1998**, *120* (7), 1556–1570.
  36. Kresge, C.T.; Leonowicz, M.E.; Roth, W.J.; Vartuli, J.C.; Beck, J.S. Ordered mesoporous molecular-sieves synthesized by a liquid-crystal template mechanism. *Nature* **1992**, *359*, 710–712.
  37. Beck, J.S.; Vartuli, J.C.; Roth, W.J.; Leonowicz, M.E.; Kresge, C.T.; Schmitt, K.D.; Chu, C.T.W.; Olson, D.H.; Sheppard, E.W.; McCullen, S.B.; Higgins, J.B.; Schlenker, J.L. A new family of mesoporous molecular sieves prepared with liquid crystal templates. *J. Am. Chem. Soc.* **1992**, *114*, 10,834–10,843.
  38. Jentys, A.; Kleestorfer, K.; Vinek, H. Concentration of surface hydroxyl groups on MCM-41. *Micro-porous Mesoporous Mater.* **1999**, *27* (2–3), 321–328.
  39. Corma, A.; Garcia, H. A unified approach to zeolites as acid catalysts and as supramolecular hosts exemplified. *J. Chem. Soc., Dalton Trans.* **2000**, *9*, 1381–1394.
  40. Schuth, F. Surface properties and catalytic performance of novel mesostructured oxides. *Ber. Bunsenges. Phys. Chem.* **1995**, *99* (11), 1306–1315.

41. Zhao, D.Y.; Huo, Q.S.; Feng, J.L.; Chmelka, B.F.; Stucky, G.D. Nonionic triblock and star diblock copolymer and oligomeric surfactant syntheses of highly ordered, hydrothermally stable, mesoporous silica structures. *J. Am. Chem. Soc.* **1998**, *120* (24), 6024–6036.
42. Antonietti, M. Surfactants for novel templating applications. *Curr. Opin. Colloid Interface Sci.* **2001**, *6* (3), 244–248.
43. Corma, A. Preparation and catalytic properties of new mesoporous materials. *Top. Catal.* **1997**, *4* (3–4), 249–260.
44. Landmesser, H.; Kosslick, H.; Storek, W.; Fricke, R. Interior surface hydroxyl groups in ordered mesoporous silicates. *Solid State Ionics* **1997**, *101* (Part 1), 271–277.
45. Moller, K.; Bein, T. Inclusion chemistry in periodic mesoporous hosts. *Chem. Mater.* **1998**, *10* (10), 2950–2963.
46. Liu, Y.; Zhang, W.Z.; Pinnavaia, T.J. Steam-stable MSU-S aluminosilicate mesostructures assembled from zeolite ZSM-5 and zeolite beta seeds. *Angew. Chem., Int. Ed.* **2001**, *40* (7), 1255.
47. Corma, A.; Fornes, V.; Martinez-Triguero, J.; Pergher, S.B. Delaminated zeolites: combining the benefits of zeolites and mesoporous materials for catalytic uses. *J. Catal.* **1999**, *186* (1), 57–63.
48. He, Y.J.; Nivarthi, G.S.; Eder, F.; Seshan, K.; Lercher, J.A. Synthesis, characterization and catalytic activity of the pillared molecular sieve MCM-36. *Microporous Mesoporous Mater.* **1998**, *25* (1–3), 207–224.
49. Barth, J.O.; Kornatowski, J.; Lercher, J.A. Synthesis of new MCM-36 derivatives pillared with alumina or magnesia–alumina. *J. Mater. Chem.* **2002**, *12* (2), 369–373.
50. Lago, R.M.; Haag, W.O.; Mikovsky, R.J.; Olson, D.H.; Hellring, S.D.; Schmitt, K.D.; Kerr, G.T. The nature of the catalytic sites in HZSM-5, activity enhancement. In *New Developments in Zeolite Science and Technology, Studies in Surface Science and Catalysis*; Murakami, Y., Iijima, A., Ward, J.W., Eds.; Elsevier: Amsterdam, New York, 1986; Vol. 28, 677–684.
51. Mirth, G.; Cejka, J.; Lercher, J.A. Transport and isomerization of xylenes over HZSM-5 zeolites. *J. Catal.* **1993**, *139*, 24.
52. Pearson, R.G. *Chemical Hardness*; Wiley-VCH: Weinheim, 1997.
53. Gomes, A.C.L.; Saguiar, E.F.; Cardosomenezes, S.C.; Cardoso, D. Influence of combined acid treatment on physico-chemical characteristics of ultrastable zeolite Y and on its catalytic properties in the disproportionation of ethylbenzene. *Appl. Catal., A Gen.* **1997**, *148* (2), 373–385.
54. Gola, A.; Rebours, B.; Milazzo, E.; Lynch, J.; Benazzi, E.; Lacombe, S.; Delevoye, L.; Fernandez, C. Effect of leaching agent in the dealumination of stabilized Y zeolites. *Microporous Mesoporous Mater.* **2000**, *40* (1–3), 73–83.
55. Narbeshuber, T.F.; Brait, A.; Seshan, K.; Lercher, J.A. The influence of extraframework aluminum on h-fau catalyzed cracking of light alkanes. *Appl. Catal., A Gen.* **1996**, *146* (1), 119–129.
56. Abbot, J.; Guertzoni, F.N. Roles of Brønsted and Lewis sites during cracking of *n*-octane on H-mordenite. *Appl. Catal., A Gen.* **1992**, *85* (2), 173–188.
57. Förster, H.; Evanics, F.; Kiricsi, I.; Tasi, G.; Foerster, H.; Fejes, P. Cracking of neopentane over acidic zeolites: influence of isobutane and isobutene admission. *J. Mol. Catal., A* **1995**, *95*, 267–269.
58. Lombardo, E.A.; Hall, W.K. Mechanism of isobutane cracking over amorphous and crystalline aluminosilicates. *J. Catal.* **1988**, *112*, 565–578.
59. Haouas, M.; Kogelbauer, A.; Prins, R. The effect of flexible lattice aluminium in zeolite beta during the nitration of toluene with nitric acid and acetic anhydride. *Catal. Lett.* **2000**, *70* (1–2), 61–65.
60. Oumi, Y.; Nemoto, S.; Nawata, S.; Fukushima, T.; Teranishi, T.; Sano, T. Effect of the framework structure on the dealumination–realumination behavior of zeolite. *Mater. Chem. Phys.* **2002**, *78* (2), 551–557.
61. Sano, T.; Uno, Y.; Wang, Z.B.; Ahn, C.H.; Soga, K. Realumination of dealuminated HZSM-5 zeolites by acid treatment and their catalytic properties. *Microporous Mesoporous Mater.* **2000**, *34* (3), 348.
62. Lonyi, F.; Lunsford, J.H. The development of strong acidity in hexafluorosilicate-modified Y-type zeolites. *J. Catal.* **1992**, *136* (2), 566–577.
63. Carvajal, R.; Chu, P.-J.; Lunsford, J.H. The role of polyvalent cations in developing strong acidity—a study of lanthanum-exchanged zeolites. *J. Catal.* **1990**, *125* (125), 123–131.
64. Sanderson, R.T. *Chemical Bonds and Bond Energy*; Academic Press: New York, 1976.
65. Barthomeuf, D. Conjugate acid–base pairs in zeolites. *J. Phys. Chem.* **1984**, *88* (1), 42–45.
66. Barthomeuf, D.; De Mallmann, A. Basicity and electronegativity of zeolites. In *Studies in Surface Science and Catalysis; Innovation in Zeolite Materials Science*; Grobet, P.J., Mortier, W.J., Vansant, E.F., Schulz-Ekloff, G., Eds.; Elsevier: Amsterdam, 1988; Vol. 37, 365–374.
67. Stoch, J.; Lercher, J.A.; Ceckiewicz, S. Correlations between XPS binding energies and the composition of aluminosilicates and phosphates. *Zeolites* **1992**, *12*, 81.
68. van Santen, R.A.; van Beest, B.W.H.; de Man, A.J.M. On lattice dynamics, stability and acidity of zeolites. In *Guidelines for Mastering the Properties of Molecular Sieves*; Barthomeuf, D., Ed.; Plenum Press: New York, 1990; 201 pp.
69. Rep, M.; Palomares, A.E.; Eder-Mirth, G.; van Ommen, J.G.; Rosch, N.; Lercher, J.A. Interaction of methanol with alkali metal exchanged molecular sieves: I. IR spectroscopy study. *J. Phys. Chem., B* **2000**, *104* (35), 8624–8630.
70. Wang, Y.; Zhu, J.H.; Cao, J.M.; Chun, Y.; Xu, Q.H. Basic catalytic behavior of MgO directly dispersed on zeolites by microwave irradiation. *Microporous Mesoporous Mater.* **1998**, *26* (1–3), 175–184.
71. Arishtirova, K.; Kovacheva, P.; Vassilev, S. BaO/NaX zeolite as a basic catalyst for oxidative methylation of toluene with methane. *Appl. Catal., A Gen.* **2001**, *213* (2), 197–202.

72. Hathaway, P.E.; Davis, M.E. Base catalysis by alkali-modified zeolites. *J. Catal.* **1989**, *116*, 263–278.
73. Ono, Y.; Baba, T. Selective reactions over solid base catalysts. *Catal. Today* **1997**, *38* (3), 321–337.
74. Sheldon, R.A.; Arends, I.; Lempers, H.E.B. Activities and stabilities of redox molecular sieve catalysts in liquid phase oxidations. A review. *Collect. Czechoslov. Chem. Commun.* **1998**, *63* (11), 1724–1742.
75. Rafelt, J.S.; Clark, J.H. Recent advances in the partial oxidation of organic molecules using heterogeneous catalysis. *Catal. Today* **2000**, *57* (1–2), 33–44.
76. Schuchardt, U.; Cardoso, D.; Sercheli, R.; Pereira, R.; de Cruz, R.S.; Guerreiro, M.C.; Mandelli, D.; Spinace, E.V.; Pires, E.L. Cyclohexane oxidation continues to be a challenge. *Appl. Catal., A Gen.* **2001**, *211* (1), 1–17.
77. Wichterlova, B.; Sobalik, Z.; Dedecek, J. Redox catalysis over metallo-zeolites—contribution to environmental catalysis. *Appl. Catal., B Environ.* **2003**, *41* (1–2), 97–114.
78. Notari, B. *Innovation in Zeolite Materials Science*; Stud. Surf. Sci. Catal.; Grobet, P.J., Mortier, W.J., Vansant, E.F., Schulz-Ekloff, G., Eds.; Elsevier: Amsterdam, 1988; Vol. 37, 413 pp.
79. Thomas, J.M.; Sankar, G. The role of synchrotron-based studies in the elucidation and design of active sites in titanium–silica epoxidation catalysts. *Acc. Chem. Res.* **2001**, *34* (7), 571–581.
80. Bolis, V.; Bordiga, S.; Lamberti, C.; Zecchina, A.; Carati, A.; Rivetti, F.; Spano, G.; Petrini, G. Heterogeneity of framework Ti(IV) in Ti-silicalite as revealed by the adsorption of NH<sub>3</sub>. Combined calorimetric and spectroscopic study. *Langmuir* **1999**, *15* (18), 5753–5764.
81. Rao, P.R.; Ramaswamy, A.V. Catalytic hydroxylation of phenol over a vanadium silicate molecular sieve with MEL structure. *Appl. Catal., A Gen.* **1993**, *93* (2), 113–123.
82. Panov, G.I.; Uriarte, A.K.; Rodkin, M.A.; Sobolev, V.I. Generation of active oxygen species on solid surfaces. Opportunity for novel oxidation technologies over zeolites. *Catal. Today* **1998**, *41* (4), 365–385.
83. Flanigen, E.M.; Lok, B.M.; Patton, R.L.; Wilson, S.T. New developments in zeolite science and technology. In *Studies in Surface Science and Catalysis*; Murakami, Y., Iijima, A., Ward, J., Eds.; Elsevier: Amsterdam, 1986; Vol. 28, 103 pp.
84. Thomas, J.M.; Raja, R.; Sankar, G.; Johnson, B.F.G.; Lewis, D.W. Single step, solvent-free processes: examples and prospects. *Chem. Eur. J.* **2001**, *7*, 2973.
85. deMan, A.J.M.; Sauer, J. Coordination, structure, and vibrational spectra of titanium in silicates and zeolites in comparison with related molecules. An ab initio study. *J. Phys. Chem. Solids* **1996**, *100* (12), 5025–5034.
86. Jentys, A.; Catlow, C.R.A. Structural properties of titanium sites in Ti-ZSM5. *Catal. Lett.* **1993**, *22*, 251.
87. Wu, P.; Tatsumi, T.; Komatsu, T.; Yashima, T. A novel titanosilicate with MWW structure: II. Catalytic properties in the selective oxidation of alkenes. *J. Catal.* **2001**, *202* (2), 245–255.
88. On, D.T.; Nguyen, S.V.; Hulea, V.; Dumitriu, E.; Kaliaguine, S. Mono- and bifunctional MFI, BEA and MCM-41 titanium-molecular sieves: part 1. Synthesis and characterization. *Microporous Mesoporous Mater.* **2003**, *57* (2), 169–180.
89. Brait, A.; Davis, M.E. Alkylation of 2-methoxynaphthalene with propylene oxide using titanium and zirconium containing molecular sieves. *Appl. Catal., A Gen.* **2000**, *204* (1), 117–127.
90. Traa, Y.; Burger, B.; Weitkamp, J. Zeolite-based materials for the selective catalytic reduction of NO<sub>x</sub> with hydrocarbons. *Microporous Mesoporous Mater.* **1999**, *30* (1), 3–41.
91. Armor, J.N. Catalytic removal of nitrogen oxides—where are the opportunities. *Catal. Today* **1995**, *26* (2), 99–105.
92. Iwamoto, M. Zeolites in environmental catalysis. Zeolites and related microporous materials. *State Art* **1994**, *84*, 1395–1410.
93. Sobalik, Z.; Dedecek, J.; Ikonnikov, I.; Wichterlova, B. State and coordination of metal ions in high silica zeolites. Incorporation, development and rearrangement during preparation and catalysis. *Microporous Mesoporous Mater.* **1998**, *21* (4–6), 525–532.
94. Ovanesyan, N.S.; Shteinman, A.A.; Dubkov, K.A.; Sobolev, V.I.; Panov, G.I. The state of iron in the Fe-ZSM-5-N<sub>2</sub>O system for selective oxidation of methane to methanol from data of Mossbauer spectroscopy. *Kinet. Catal.* **1998**, *39* (6), 792–797.
95. Grubert, G.; Hudson, M.J.; Joyner, R.W.; Stockenhuber, M. The room temperature, stoichiometric conversion of N<sub>2</sub>O to adsorbed NO by Fe-MCM-41 and Fe-ZSM-5. *J. Catal.* **2000**, *196* (1), 126–133.
96. Stockenhuber, M.; Hudson, M.J.; Joyner, R.W. Preparation, characterization, and unusual reactivity of Fe-MCM-41. *J. Phys. Chem., B* **2000**, *104* (14), 3370–3374.
97. Grosse-Kunstleve, R.W.; McCusker, L.B.; Baerlocher, C. Powder diffraction data and crystal chemical information combined in an automated structure determination procedure for zeolites. *J. Appl. Crystallogr.* **1997**, *30* (Part 6), 985–995.
98. Perego, G. Characterization of heterogeneous catalysts by X-ray diffraction techniques. *Catal. Today* **1998**, *41*, 251–259.
99. Cook, M.; Conner, W.M.C. How big are the pores of zeolites? *Mater. Res. Soc.* **1999**, *1*, 409–414.
100. Anderson, M.W. Surface microscopy of porous materials. *Curr. Opin. Solid State Mater. Sci.* **2001**, *5* (5), 407–415.
101. de Jong, K.P.; Koster, A.J. Three-dimensional electron microscopy of mesoporous materials—recent strides towards spatial imaging at the nanometer scale. *ChemPhysChem* **2002**, *3* (9), 776–780.
102. Janssen, A.H.; Van Der Voort, P.; Koster, A.J.; de Jong, K.P. A 3D-TEM study of the shape of mesopores in SBA-15 and modified SBA-15 materials. *J. Chem. Soc., Chem. Commun.* **2002**, *15*, 1632–1633.
103. Lippens, B.C.; Linsen, B.G.; de Boer, J.H. Studies on pore systems in catalysts: 1. The adsorption of nitrogen—apparatus and calculation. *J. Catal.* **1964**, *3* (1), 32–37.

104. Fraissard, J.; Ito, T. Xe-129 NMR-study of adsorbed xenon—a new method for studying zeolites and metal-zeolites. *Zeolites* **1988**, *8* (5), 350–361.
105. Eder, F.; Lercher, J.A. On the role of the pore size and tortuosity for sorption of alkanes in molecular sieves. *J. Phys. Chem., B* **1997**, *101* (8), 1273–1278.
106. Nagy, T.F.; Mahanti, S.D.; Dye, J.L. Computer modeling of pore space in zeolites. *Zeolites* **1997**, *19* (1), 57–64.
107. Jentys, A.; Lercher, J.A. Characterisation of Zeolites. In *Introduction to Zeolite Science and Practice*; van Bekkum, H., Flanigan, E.M., Jacobs, P.A., Jansen, J.C., Eds.; Elsevier: Amsterdam, 2001; Vol. 137.
108. Hunger, M.; Weitkamp, J. In situ IR, NMR, EPR, and UV/Vis spectroscopy: tools for new insight into the mechanisms of heterogeneous catalysis. *Angew. Chem., Int. Ed.* **2001**, *40* (16), 2954–2971.
109. Kärger, J.; Ruthven, D. *Diffusion in Zeolites and Other Microporous Solids*; John Wiley & Sons: New York, 1992.
110. Favre, D.E.; Schaefer, D.J.; Auerbach, S.M.; Chmelka, B.F. Direct measurement of intercage hopping in strongly adsorbing guest-zeolite systems. *Phys. Rev. Lett.* **1998**, *81* (26), 5852–5855.
111. Smit, B.; Loyens, L.D.J.C.; Verbist, G.L.M.M. Simulation of adsorption and diffusion of hydrocarbons in zeolites. *Faraday Discuss.* **1997**, *106*, 93–104.
112. Gupta, V.; Nivarthi, S.S.; McCormick, A.V.; Davis, H.T. Evidence for single file diffusion of ethane in the molecular sieve alpo4-5. *Chem. Phys. Lett.* **1995**, *247* (4–6), 596–600.
113. Sholl, D.S.; Lee, C.K. Influences of concerted cluster diffusion on single-file diffusion of CF<sub>4</sub> in AlPO<sub>4</sub>-5 and Xe in AlPO<sub>4</sub>-31. *J. Chem. Phys.* **2000**, *112* (2), 817–824.
114. Liu, H.; Lei, G.D.; Sachtler, W.M.H. Alkane isomerization over solid acid catalysts—effects of one-dimensional micropores. *Appl. Catal., A Gen.* **1996**, *137* (1), 167–177.
115. Okino, M.S.; Snurr, R.Q.; Kung, H.H.; Ochs, J.E.; Mavrouniotis, M.L. A consistent correlation approach to single file diffusion with reaction. *J. Chem. Phys.* **1999**, *111* (5), 2210–2221.
116. Kärger, J.; Heink, W.; Pfeifer, H.; Rauscher, M.; Hoffmann, J. NMR evidence of the existence of surface barriers on zeolite crystallites. *Zeolites* **1982**, *2*, 275.
117. Kocirik, M.; Struve, P.; Fiedler, K.; Bülow, M. A model for the mass-transfer resistance at the surface of zeolite crystals. *J. Chem. Soc., Faraday Trans. I* **1988**, *84*, 3001.
118. Müller, G.; Narbeshuber, T.F.; Mirth, G.; Lercher, J.A. IR microscopic study of sorption and diffusion of toluene in ZSM5. *J. Phys. Chem.* **1994**, *98*, 7436.
119. Tanaka, H.; Zheng, S.; Jentys, A.; Lercher, J.A. Kinetic processes during sorption and diffusion of aromatic molecules on medium pore zeolites studied by time resolved IR spectroscopy. In *Impact of Zeolites and Other Porous Materials on the New Technologies at the Beginning of the New Millennium*; Elsevier: Amsterdam, New York, 2002; Vol. 142, 1619–1626.
120. Eder, F.; Lercher, J.A. Alkane sorption in molecular sieves—the contribution of ordering, intermolecular interactions, and sorption on Bronsted acid sites. *Zeolites* **1997**, *18* (1), 75–81.
121. Eder, F.; Stockenhuber, M.; Lercher, J.A. Bronsted acid site and pore controlled siting of alkane sorption in acidic molecular sieves. *J. Phys. Chem., B* **1997**, *101* (27), 5414–5419.
122. Pieterse, J.A.Z.; Veefkind-Reyes, S.; Seshan, K.; Lercher, J.A. Sorption and ordering of dibranched alkanes on medium-pore zeolites ferrierite and TON. *J. Phys. Chem., B* **2000**, *104* (24), 5715–5723.
123. Stelzer, J.; Paulus, M.; Hunger, M.; Weitkamp, J. Hydrophobic properties of all-silica zeolite beta. *Microporous Mesoporous Mater.* **1998**, *22* (1–3), 1–8.
124. Mirth, G.; Lercher, J.A.; Anderson, M.W.; Klinowski, J. Adsorption complexes of methanol on zeolite ZSM-5. *J. Chem. Soc., Faraday Trans.* **1990**, *86* (17), 3039–3044.
125. Csicsery, S.M. Shape-selective catalysis in zeolites. *Zeolites* **1984**, *4*, 202–206.
126. Feast, S.; Lercher, J.A. Synthesis of intermediates and fine chemicals using molecular sieve catalysts. In *Recent Advances and New Horizons in Zeolite Science and Technology Studies in Surface Science and Catalysis*; Chon, H., Woo, S.I., Park, S.E., Eds.; Elsevier: Amsterdam, New York, 1996; Vol. 102, 363–412.
127. de Jong, K.P. Efficient catalytic processes for the manufacturing of high-quality transportation fuels. *Catal. Today* **1996**, *39*, 171–178.
128. Ribeiro, F.R.; Alvarez, F.; Henriques, C.; Lemos, F.; Lopes, J.M.; Ribeiro, M.F. Structure-activity relationship in zeolites. *J. Mol. Catal., A Chem.* **1995**, *96* (3), 245–270.
129. Corma, A. State of the art and future challenges of zeolites as catalysts. *J. Catal.* **2003**, *216* (1–2), 298–312.
130. Lercher, J.A.; Jentys, A. Application of microporous solids as catalysts. In *Handbook of Porous Solids*; Schüth, F., Sing, K.S., Weitkamp, J., Eds.; Wiley-VCH: Weinheim, 2002; Vol. 2, 699–736.
131. Holderich, W.F.; Roseler, J.; Heitmann, G.; Liebens, A.T. The use of zeolites in the synthesis of fine and intermediate chemicals. *Catal. Today* **1997**, *37* (4), 353–366.
132. Haag, W.O.; Dessau, R.M. *Proceedings 8th International Congress on Catalysis*, Berlin, 1984; Dechema: Frankfurt, 1984; Vol. 2, 305–316.
133. Narbeshuber, T.F.; Vinek, H.; Lercher, J.A. Monomolecular conversion of light alkanes over H-ZSM-5. *J. Catal.* **1995**, *157* (2), 388–395.
134. Gates, B.C.R.; Katzer, J.; Schuit, G.C.A. *Chemistry of Catalytic Processes*; McGraw-Hill: New York, 1979.
135. Nivarthi, G.S.; Feller, A.; Seshan, K.; Lercher, J.A. Alkylation of isobutane with light olefins catalyzed by zeolite beta. *Microporous Mesoporous Mater.* **2000**, *6*, 75–87.
136. Feller, A.; Lercher, J.A. Common mechanistic aspects of liquid and solid acid catalyzed alkylation of isobutane with *n*-butene. *J. Catal.* **2003**, *216* (1–2), 313–323.

137. Gründling, Ch.; Eder-Mirth, G.; Lercher, J.A. Surface species in the direct amination of methanol over Brønsted acidic mordenite catalysts. *Res. Chem. Intermed.* **1997**, *23*, 25.
138. Namba, S.; Wakushima, Y.; Shimizu, T.; Masumoto, H.; Yashima, T. *Catalysis by Acids and Bases*; Elsevier: Amsterdam, 1985.
139. Climent, M.J.; Corma, A.; Velly, A.; Susarte, M. Zeolites for the production of fine chemicals: Synthesis of the fructose fragrance. *J. Catal.* **2000**, *196* (2), 345–351.
140. Palomares, A.E.; Eder-Mirth, G.; Rep, M.; Lercher, J.A. Alkylation of toluene over basic catalysts—key requirements for side chain alkylation. *J. Catal.* **1998**, *180* (1), 56–65.
141. Marquez, F.; Zicovich-Wilson, C.M.; Corma, A.; Palomares, E.; Garcia, H. Naphthalene included within all-silica zeolites: Influence of the host on the naphthalene photophysics. *J. Phys. Chem., B* **2001**, *105* (41), 9973–9979.
142. Barthomeuf, D. Compared formation of light products in *n*-alkane cracking in Sap-37 and Si–Al faujasites. Energy gradient selectivity. *Appl. Catal., A Gen.* **1995**, *126* (1), 187–194.
143. Marcilly, C.R. Where and how shape selectivity of molecular sieves operates in refining and petrochemistry catalytic processes. *Top. Catal.* **2000**, *13* (4), 357–366.
144. Zones, S.I.; Harris, T.V. The constraint index test revisited: anomalies based upon new zeolite structure types. *Microporous Mesoporous Mater.* **2000**, *36*, 31–46.
145. Martens, J.A.; Jacobs, P.A. Introduction to acid catalysis with zeolites in hydrocarbon reactions. In *Studies in Surface Science and Catalysis, Introduction to Zeolite Science and Practice*; van Bekkum, H., Flanigan, E.M., Jacobs, P.A., Jansen, J.C., Eds.; Elsevier: Amsterdam, 2001; Vol. 137, 633–671.
146. Weisz, P.B.; Frilette, V.J. Intracrystalline and molecular shape selective catalysis by zeolite salts. *J. Phys. Chem.* **1960**, *64*, 382.
147. Kaeding, W.W.; Chu, C.; Young, L.B.; Weinstein, B.; Butter, S.A. A selective alkylation of toluene with methanol to produce para-xylene. *J. Catal.* **1981**, *67* (1), 159–174.
148. Souverijns, W.; Martens, J.A.; Froment, G.F.; Jacobs, P.A. Hydrocracking of isoheptadecanes on Pt/H-ZSM-22: an example of pore mouth catalysis. *J. Catal.* **1998**, *174* (2), 177–184.
149. Arroyo, J.A.M.; Martens, G.G.; Froment, G.F.; Marin, G.B.; Jacobs, P.A.; Martens, J.A. Hydrocracking and isomerization of *n*-paraffin mixtures and a hydrotreated gas oil on Pt/ZSM-22: confirmation of pore mouth and key-lock catalysis in liquid phase. *Appl. Catal., A Gen.* **2000**, *192* (1), 9–22.



# Microgel Dispersions: Colloidal Forces and Phase Behavior

**Jianzhong Wu**

*Department of Chemical and Environmental Engineering, University of California–Riverside, Riverside, California, U.S.A.*

**Zhibing Hu**

*Departments of Physics and Chemistry, University of North Texas, Denton, Texas, U.S.A.*

## INTRODUCTION

In many aspects, colloidal particles suspended in a liquid behave like large idealized atoms that exhibit liquid, glass, and crystal phases similar to those observed in atomic systems.<sup>[1–6]</sup> Phase transitions in colloidal systems have been intensively studied over the last decade not only because of the theoretical interest for addressing fundamental questions about the nature of liquids, crystals, and glasses, but also for many practical applications of colloids.<sup>[7–11]</sup> In recent years, colloidal dispersions have been used extensively for the fabrication of nanostructured materials such as photonic crystals, catalysts, membranes, and ceramics, and for device applications.<sup>[11–16]</sup> Current uses of colloidal particles as the building blocks of materials rely mostly on empirical approaches. Meanwhile, present knowledge on the structural and thermodynamic properties of colloidal dispersions is primarily based on an effective one-component model (OCM) where colloidal particles are represented by hard spheres and all remaining components in the dispersion, including solvent molecules, small ions, and polymers, are represented as a continuous medium.<sup>[17–23]</sup> Although the OCM approach is attractive because of its simplicity, application to practical systems is often limited by incomplete understanding of colloidal forces.<sup>[24–28]</sup>

Amid numerous conventional colloids, aqueous dispersions of poly-*N*-isopropylacrylamide (PNIPAM) microgel particles, first synthesized by Pelton and Chibante<sup>[29]</sup> in 1986, are of special interest for studying phase transitions and for the fabrication of colloid-based advanced materials.<sup>[30–36]</sup> Nearly monodispersed PNIPAM particles can now be routinely prepared in a wide range of colloidal sizes (50 nm up to 1  $\mu$ m) and with a variety of physiochemical characterizations.<sup>[35,37]</sup> Because the size of PNIPAM particles is

temperature-sensitive,<sup>[38]</sup> crystallization at different colloidal volume fractions can be conveniently measured by varying temperatures. By tuning the preparation conditions and the composition of the aqueous solution, the interaction potential between microgel particles can vary from star-polymer-like to hard-sphere-like potential for short-range repulsion, from electrostatically neutral to highly ionizable for long-range electrostatic interactions, and from essentially no attraction to strong attraction for van der Waals forces.<sup>[36,39]</sup> Furthermore, steric repulsion can be introduced by grafting polymers on the surface of PNIPAM particles.<sup>[40]</sup> The versatility in interaction potential makes PNIPAM microgel particles attractive for studying a broad variety of interesting phenomena in colloidal systems.<sup>[32,41–44]</sup> Although the practical values of PNIPAM particles have been long recognized, most previous studies on the physiochemical properties of PNIPAM dispersions have focused on particle preparations, swelling, rheology, and light (neutron) scattering measurements.<sup>[35,36,45–47]</sup> Little work has been reported on the relationship between the temperature-dependent interparticle potential and the phase behavior of PNIPAM dispersions. Unlike that in a conventional colloidal system, the interparticle potential in aqueous dispersions of PNIPAM microgel particles is sensitive to temperature changes. Consequently, the phase diagram of PNIPAM dispersions may be noticeably different from those for ordinary colloids where, in most cases, the interparticle potential is essentially invariant with temperature.

In this chapter, we report our recent investigations on the colloidal forces and phase behavior of neutral PNIPAM particles dispersed in pure water.<sup>[48–50]</sup> We will first discuss thermodynamic methods for the characterization of colloidal forces based on dynamic and static light scattering measurements. The analytical expression of colloidal forces allows us to construct a

theoretical phase diagram that can be compared with that obtained from spectroscopic measurements. In particular, we will illustrate how the volume transition of PNIPAM particles affects the interaction potential and determines a novel phase diagram that has not been observed in conventional colloids. Finally, we discuss briefly the kinetics of crystallization in an aqueous dispersion of PNIPAM particles.

### COLLOIDAL FORCES BETWEEN MICROGEL PARTICLES

Qualitatively, the pair potential between neutral microgel particles includes a short-range repulsion that is similar to the interaction between two polymer-coated surfaces, and a longer-ranged van der Waals-like attraction that arises from the difference in the Hamaker constants of the particle and the solvent.<sup>[51,52]</sup> To obtain a quantitative expression for the interparticle potential that covers a broad range of temperature, we assume that the interaction potential can be represented by a Sutherland-like function that includes a hard-sphere repulsion and a van der Waals attraction. A similar potential was used Senff and Richtering<sup>[43,53]</sup> for representing the phase behavior and rheological properties of PNIPAM microgel dispersions. Fig. 1 shows that the relative zero shear viscosity of PNIPAM dispersion can be approximately

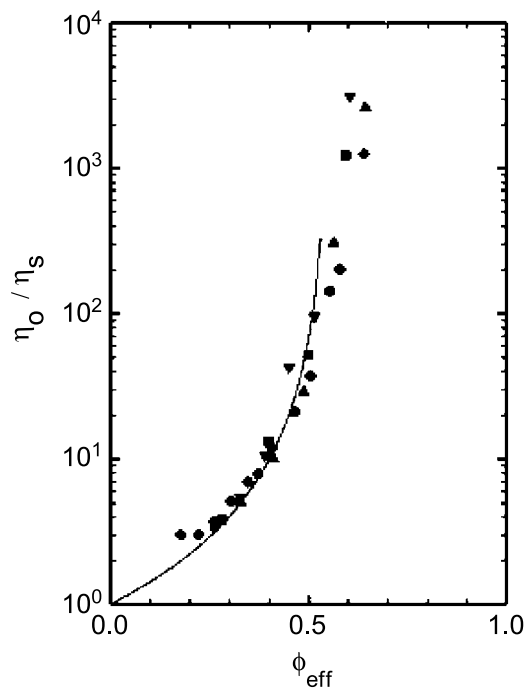


**Fig. 1** Relative zero shear viscosity at different temperatures vs. the effective volume fraction. The line represents the master curve of hard-sphere suspensions. *Source:* From Refs.<sup>[43,53]</sup>.

represented by that for hard spheres. Besides, as shown later, the kinetics of microgel crystallization also resembles that for hard spheres.

The variation of microgel diameter as a function of temperature is related to the swelling of microgel particles. The classical theory of gel swelling, proposed many years ago by Flory,<sup>[54]</sup> asserts uniform distributions of polymer segments and crosslinking points throughout the polymer network. However, recent experiments based on nuclear magnetic resonance (NMR) and light scattering investigations suggest the heterogeneous nature of PNIPAM particles.<sup>[51,55]</sup> To take into account the heterogeneity, we use an empirical modification of the Flory–Rehner theory proposed by Hino and Prausnitz.<sup>[56]</sup> This theory has been applied successfully to describing the volume transitions of bulk PNIPAM gels. Because the physics for the volume transition is irrelevant to the particle size as long as the surface effect is unimportant, and because the effect of the osmotic pressure of dispersion on the swelling of an individual particle is negligible,<sup>[42]</sup> we assume that the same thermodynamic model for bulk polymer gels is also applicable to microgel particles.

According to the modified Flory–Rehner theory,<sup>[56]</sup> the polymer volume fraction within the particle  $\phi$  is determined from:

$$\ln(1 - \phi) + \phi + \chi\phi^2 + \frac{\phi_0}{m} \times \left[ \left(\frac{\phi}{\phi_0}\right)^{1/3} - \left(\frac{\phi}{\phi_0}\right)^{5/3} + \left(\frac{\phi}{2\phi_0}\right) \right] = 0 \quad (1)$$

where  $m$  is the average number of segments between two neighboring crosslinking points in the microgel network, and  $\phi_0$  is the polymer volume fraction in the reference state where the conformation of network chains is closest to that of unperturbed Gaussian chains. Approximately,  $\phi_0$  is equal to the volume fraction of polymers within the microgel particles at the condition of preparation. The Flory polymer–solvent energy parameter  $\chi$  is given empirically as a function of temperature  $T$  and polymer volume fraction  $\phi$ :<sup>[56]</sup>

$$\chi = \frac{3}{1 - 0.65\phi} \times \left[ 2 \ln \left( \frac{5001}{1 + 5000 \exp(2458.867/T)} \right) - \frac{4566.468}{T} \right] \quad (2)$$

At a given temperature, Eq. (1) can be solved to find the polymer volume fraction  $\phi$  from which the diameter of PNIPAM particles ( $\sigma$ ) is calculated:

$$\frac{\sigma}{\sigma_0} = \left(\frac{\phi_0}{\phi}\right)^{1/3} \quad (3)$$

where  $\sigma_0$  is the particle diameter at the reference state. In this work, we fit the average chain length  $m$  and the volume fraction of polymer  $\phi_0$  at the reference state to the diameters of microgel particles obtained from static and dynamic light scattering measurements. Because the osmotic pressure of microgel dispersion is small in comparison to the gel swelling pressure, the microgel particle concentration has a negligible effect on the chemical potential of water. As a result, the size of microgel particles should be insensitive to the overall concentration of colloidal dispersions.

The van der Waals attraction beyond the hard-sphere diameter may be represented by a power law potential:

$$u_A(r) = -\frac{H}{r^n} \quad (4)$$

where  $H$  is the Hamaker constant. We assume that  $n = 8$  in considering that the range of attraction between colloidal particles (relative to the particle size) is shorter than that between atomic molecules. The calculated results are not sensitive to a small change in  $n$  if the Hamaker constant is obtained by fitting to osmotic second virial coefficients from static light scattering experiments. Because the interparticle attraction arises from the dispersion forces between polymeric segments from different particles, the Hamaker constant of microgel particles is approximately given by:<sup>[57]</sup>

$$H \propto \rho_m^2 \quad (5)$$

where  $\rho_m$  represents the number density of polymeric groups within each particle. The proportionality constant in Eq. (5) is independent of temperature and polymeric group density  $\rho_m$ . Following Eqs. (4) and (5), we obtain the attractive potential because of the van der Waals forces:

$$\frac{u_A(r)}{kT} = -k_A \left(\frac{T_0}{T}\right) \left(\frac{\sigma_0}{\sigma}\right)^{6+n} \left(\frac{\sigma}{r}\right)^n \quad (6)$$

where  $k_A$  is a dimensionless constant, and  $T_0$  is the reference temperature that is introduced for the purpose of dimensionality. In Eq. (6), the parameters  $T_0$ ,  $\sigma_0$ , and  $k_A$  are temperature-independent and they can be obtained by fitting to osmotic second virial coefficients from static light scattering measurements. An osmotic second virial coefficient in a colloidal dispersion is defined as:

$$B_2 = 2\pi \int_0^\infty [1 - e^{-u(r)/kT}] r^2 dr \quad (7)$$

where  $r$  stands for the center-to-center distance between colloidal particles,  $k$  is the Boltzmann constant, and  $u(r)$  is the interparticle potential.

The particle size and the osmotic second virial coefficients of microgel dispersions can be conveniently measured using static and dynamic light scattering. To correlate the radius of PNIPAM gel particles as a function of temperature, we combine the radius of gyration  $R_g$  with the hydrodynamic radius  $R_H$  from static and dynamic light scattering measurements, respectively. By assuming that the microgel particles are homogeneous spheres, we define the effective radius:

$$R = (\sqrt{5/3}R_g + R_H)/2 \quad (8)$$

This effective radius is introduced to represent the excluded volume of microgel particles as required in phase equilibrium calculations. Fig. 2 presents the radius of microgel particles near the volume transition temperature (approximately at 34.3°C). The error bars give the difference between the hydrodynamic radius and that calculated from the radius of gyration. The solid line is calculated by using the modified Flory–Rehner theory [Eqs. (1–3)]. In the calculation of the particle radius, the polymer fraction at the condition of preparation  $\phi_0 = 0.0884$ , the average number of segments between two neighboring crosslinking points  $m = 34$ , and the particle radius at the preparation condition  $R_0 = 125.8$  nm are obtained by fitting to the experimental data. These model parameters are in good agreement with experiments.

Fig. 3 presents the reduced osmotic second virial coefficients ( $B_2/B_2^{\text{HS}}$ ) for PNIPAM microgel particles dispersed in water. Here the open circles are data

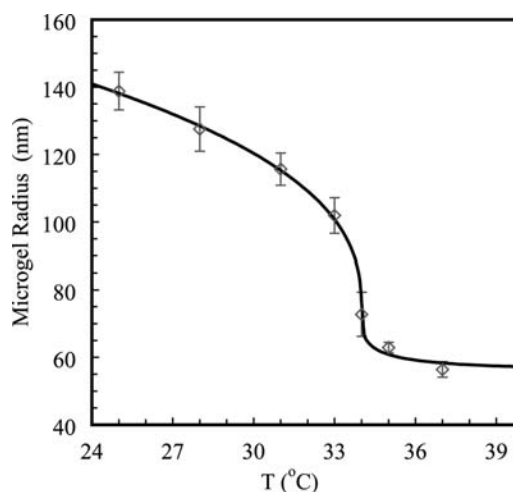


**Fig. 2** Radius of PNIPAM particles vs. temperature. The points are averages from dynamic and static light scattering measurements with the error bars showing the differences between the two. The line is calculated from [Eqs. (1–3)].

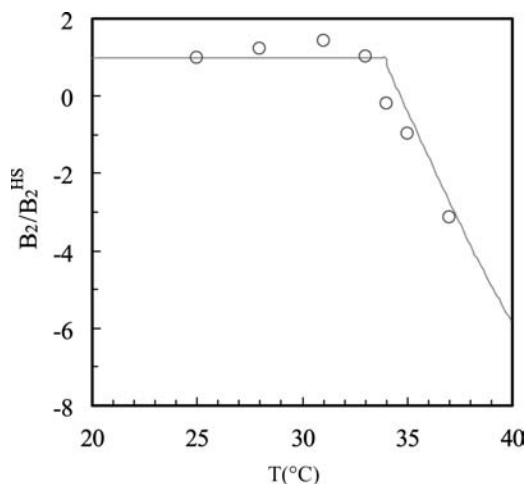


**Fig. 3** The reduced osmotic second virial coefficients ( $B_2/B_2^{HS}$ ) for PNIPAM particles dispersed in pure water. Points are from static light scattering and the line is calculated from Eq. (7) normalized by the second virial coefficient  $B_2^{HS} = (2\pi/3)\sigma^3$  for the corresponding hard spheres.

points from static light scattering measurements and the line is calculated using Eqs. (6) and (7), with the molecular weight  $M_W = 1.73 \times 10^7$  g/mol and the proportionality constant  $k_A = 6.43 \times 10^{-5}$  obtained by fitting to the experimental data. The hard-sphere second virial coefficient is related to the particle diameter  $\sigma$  by  $B_2^{HS} = (2\pi/3)\sigma^3$ . A positive osmotic second virial coefficient means that the overall interparticle potential is repulsive; otherwise, it is attractive. Fig. 3 indicates that below the volume transition temperature, the PNIPAM particles behave essentially like hard spheres. In this case, the microgel particles are in the swollen state and they contain up to 97% of water by volume. As a result, the van der Waals attraction between colloidal particles is negligible because of the close match in the Hamaker constants of the particle and the water. The reduced osmotic second virial coefficient exhibits a sharp change at the volume transition temperature, beyond which it turns to negative, indicating an increase in the van der Waals attraction as the particles collapse. Fig. 3 suggests that with temperature-dependent size and energy parameters, the Sutherland-type function captures the essential features of the interaction potential between microgel particles.

Because the number density of polymeric segments within each particle is closely related to the particle size, we expect that the attraction between microgel particles is highly temperature-sensitive. Fig. 4 shows the reduced energy parameter  $\varepsilon/(kT)$  near the volume transition temperature as obtained by correlation with the osmotic second virial coefficients from experiments. Experimental values for this parameter are

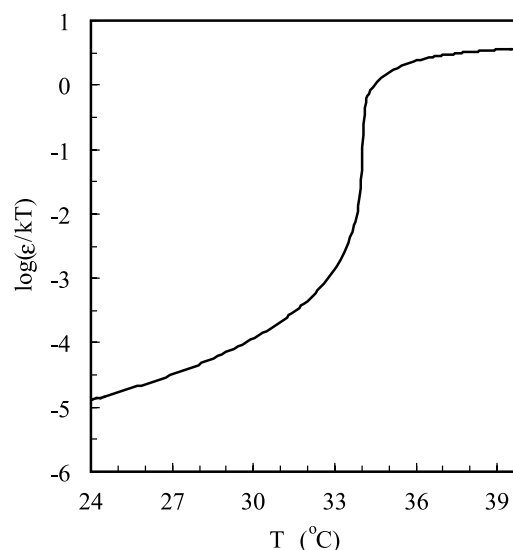


**Fig. 4** The reduced energy parameter ( $\varepsilon/kT$ ) for interparticle potential between PNIPAM particles near the volume transition temperature.

not included because it is difficult to make a direct (or indirect) measurement of the reduced energy parameter. But the credibility of calculated results is implied in the comparison of osmotic second virial coefficients, as shown in Fig. 3. Remarkably, the energy parameter increases by over six orders of magnitude as temperature changes from 24°C to 36°C, with the sharpest increase at the volume transition temperature of 34°C.

## THERMODYNAMIC MODELS FOR PHASE EQUILIBRIUM CALCULATIONS

To calculate the phase diagram, we need to have the thermodynamic models for both fluid and crystalline phases, as well as the structure of the crystal. It has been shown before by small-angle neutron scattering measurements that even at low crosslinker concentrations, aqueous dispersions of PNIPAM microgel particles crystallize like hard-sphere liquids.<sup>[42]</sup> Fig. 5 indicates that the structure factor of the colloidal crystal is well represented by that for a face centered cubic (fcc) structure. Therefore it is reasonable to assume that hard spheres provide a good reference system for representing the thermodynamic properties of microgel dispersions. Because the van der Waals attraction between microgel particles is short-ranged compared to the particle size, a first-order perturbation theory is appropriate for both phases. The higher-order terms are insignificant when the perturbation potential is short-ranged.<sup>[58]</sup>

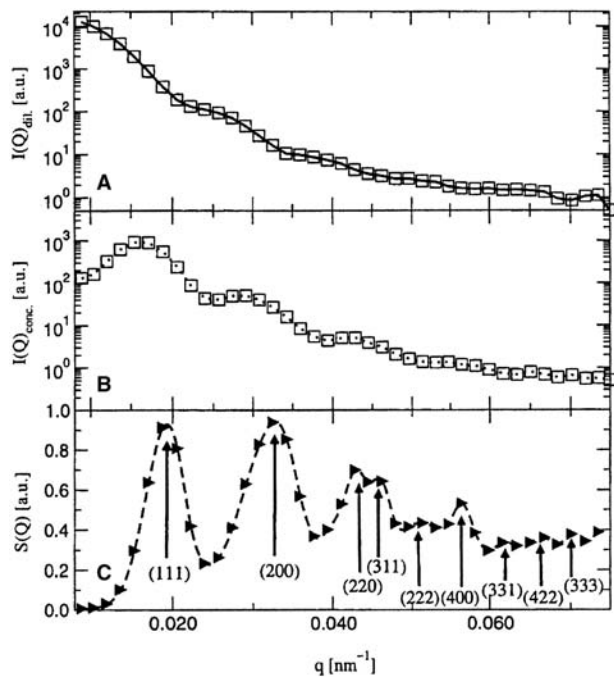


**Fig. 5** (A) Neutron scattering profile for a dilute microgel dispersion. (B) Scattering profile for a colloidal crystal of microgel particles. (C) Structure factor of the crystal. The Bragg peaks are interpreted according to the fcc lattice. Source: From Ref.<sup>[42]</sup>.

The Helmholtz energy of the fluid phase includes a hard-sphere contribution that is given by the Carnahan–Starling equation of state, and a perturbation that takes into account the van der Waals attraction. In dimensionless units, the Helmholtz energy is given by:

$$\frac{F}{NkT} = \ln(\eta) - 1 + \frac{4\eta - 3\eta^2}{(1 - \eta)^2} + 12\eta \int_1^{\infty} x^2 g_F^{\text{HS}}(x) \frac{u_A(x)}{kT} dx \quad (9)$$

where  $N$  represents the total number of particles,  $\eta = \pi\rho\sigma^3/6$  is the particle packing fraction,  $\rho$  is the particle number density, and  $g_F^{\text{HS}}(r)$  is the hard-sphere radial distribution function. For convenience, we correlate the integral in Eq. (9) as a function of particle packing fraction using the radial distribution function  $g_F^{\text{HS}}(r)$  obtained from the Percus–Yevick equation:<sup>[59]</sup>

$$I_F(\eta) \equiv \int_1^{\infty} x^{-6} g^{\text{HS}}(x) dx = 0.027224\eta^2 + 0.1642\eta + 0.2007 \quad (10)$$

The quadric form as given in Eq. (10) is applicable to the reduced density  $\rho\sigma^3 < 0.6$ . Replacement of the

integral in Eq. (9) with  $I_F(\eta)$  gives:

$$\frac{F}{NkT} = \ln(\eta) - 1 + \frac{4\eta - 3\eta^2}{(1 - \eta)^2} - 12\eta I_F(\eta) \varepsilon^* \quad (11)$$

where:

$$\varepsilon^* = \frac{\varepsilon}{kT} = k_A \left( \frac{T_0}{T} \right) \left( \frac{\sigma_0}{\sigma} \right)^{6+n} \quad (12)$$

Other thermodynamic properties can be derived from Eq. (11) following standard thermodynamic relations.

To describe the thermodynamic properties of the solid phase, we follow a perturbation approach similar to that for the fluid phase. The Helmholtz energy includes a contribution from the reference hard-sphere crystal and a perturbation taking into account the van der Waals attraction:

$$\frac{F}{NkT} = \frac{F^{\text{HS}}}{NkT} + 12\eta \int_1^{\infty} x^2 g_S^{\text{HS}}(x) \frac{u_A(x)}{kT} dx \quad (13)$$

where  $g_S^{\text{HS}}(r)$  is the radial distribution function of the hard-sphere solid. As in a hard-sphere system, an aqueous dispersion of PNIPAM microgel particles forms a face centered cubic lattice in the solid phase even when the particles are at low crosslinking density (“softer” particles).<sup>[42]</sup>

According to an improved cell theory,<sup>[60]</sup> the Helmholtz energy of the hard-sphere solid is given by:

$$\frac{F^{\text{HS}}}{NkT} = - \ln \left[ \frac{8}{\sqrt{2}} \left( (\rho/\rho_0)^{1/3} - 1 \right) \right] \quad (14)$$

Compared with the original cell model proposed many years ago by Lennard-Jones and Devonshire,<sup>[61]</sup> the improved cell model introduces a factor of 8, taking into account the fact that the neighboring particles share partially the free space. Unlike the original cell model, the modified cell model provides accurate freezing and melting densities for the fluid–solid transition of uniform hard spheres. The hard-sphere radial distribution function  $g_S^{\text{HS}}(r)$  can be calculated using a modified Gaussian model for density distributions.<sup>[49]</sup> Using the radial distribution function  $g_S^{\text{HS}}(r)$  for the hard-sphere solids, we numerically integrate the perturbation term in Eq. (13). The final expression for the Helmholtz energy of the solid phase is given by:

$$\frac{F}{NkT} = - \ln \left[ \frac{8}{\sqrt{2}} \left( (\rho/\rho_0)^{1/3} - 1 \right) \right] - 12\eta I_S(\rho) \varepsilon^* \quad (15)$$

where:

$$I_S(\rho) \equiv \int_1^\infty x^{-6} g_S^{HS}(x) dx = 0.451\rho^2 - 0.5253\rho + 0.5514 \quad (16)$$

Eq. (16) is applicable for the solid phase with the reduced density  $0.95 < \rho\sigma^3 < 1.27$ .

### EQUILIBRIUM PHASE DIAGRAM

Once we have an expression for the Helmholtz energy, the chemical potential  $\mu$  and the osmotic pressure  $P$  can be derived following standard thermodynamic relations:

$$\mu = \left( \frac{\partial F}{\partial N} \right)_{T,V} \quad (17)$$

$$P = - \left( \frac{\partial F}{\partial V} \right)_{T,N} \quad (18)$$

where “V” stands for the total volume. A fluid–fluid coexistence curve is obtained from the criteria of phase equilibrium:

$$\mu^\alpha = \mu^\beta \quad (19)$$

$$P^\alpha = P^\beta \quad (20)$$

where “ $\alpha$ ” and “ $\beta$ ” designate two distinguishable fluid phases. To calculate the pressure and the chemical potential in the fluid phase, the Helmholtz energy is given by Eq. (11). For each temperature, we solve for equilibrium densities  $\rho^\alpha$  and  $\rho^\beta$  using Eqs. (19) and (20). If no solution is found, the temperature is above the critical temperature for fluid–fluid equilibrium; in this case, there is only one fluid phase.

For fluid–solid equilibrium, we also use Eqs. (19) and (20). But now, for phase  $\alpha$ , we use Eq. (11) for the liquid-phase Helmholtz energy, whereas we use Eq. (15) for the solid-phase Helmholtz energy for phase  $\beta$ . Again, we search for densities  $\rho^\alpha$  and  $\rho^\beta$  that satisfy both equations of phase equilibrium [i.e., Eqs. (19) and (20)].

To calibrate the thermodynamic models proposed in this work, we first consider the phase behavior of a Yukawa system that is often used to represent colloidal dispersions with weak attractive interactions. Fig. 6 compares the fluid–solid as well as metastable fluid–fluid coexistence curves from simulation<sup>[62]</sup> and from the perturbation theory. The agreement is satisfactory except near the critical point of the fluid–fluid equilibrium where the long-range fluctuations become

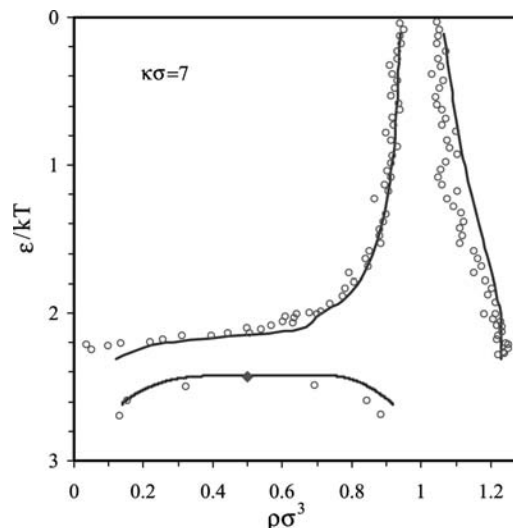


**Fig. 6** The phase diagram of a typical colloidal system with weak attractive forces. The points are from simulation data for Yukawa potential. Source: From Ref.<sup>[62]</sup>. The lines are from the theory.

significant. An improved prediction in this region can be achieved by applying the renormalization group theory.<sup>[63]</sup> Fig. 6 indicates that at high temperature, the system is dominated by short-range repulsion and it exhibits freezing transition similar to that for hard spheres, whereas at low temperature, freezing occurs at dilute conditions and is separated by a metastable liquid–liquid equilibrium.

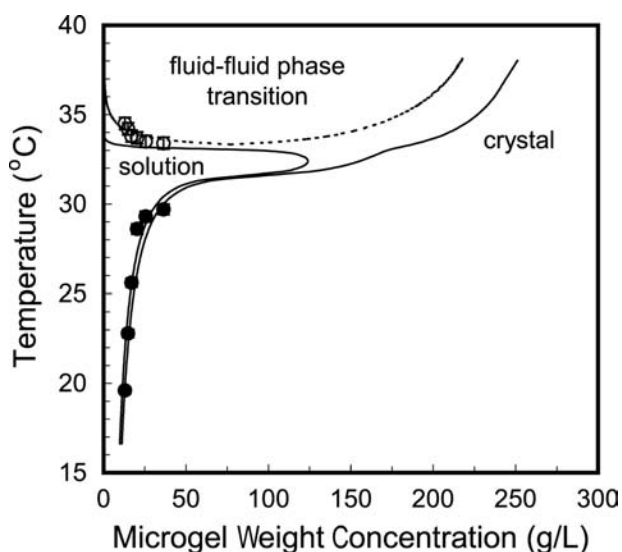


**Fig. 7** The phase diagram of aqueous dispersions of PNIPAM particles determined from turbidity measurements (symbols) and from the thermodynamic perturbation theory with an empirical correction of temperature (lines). The filled and open circles represent the melting and the second phase separation temperatures, respectively.



Fig. 7 shows the calculated phase diagram of PNIPAM microgel dispersion using the first-order perturbation theories for fluid and solid phases. Also shown in this figure are results determined from a UV-VIS spectrometer. In this calculation, the calculated temperature is rescaled empirically by  $T' = T(15/R_g)^{0.005}$  to match the experimental results quantitatively. The discrepancy is probably because of the slight size difference ( $\sim 2$  nm) between the microgel samples used in light scattering and in phase diagram measurements. Nevertheless, the theory and the experiment agree, at least semiquantitatively.

The phase diagram shown in Fig. 7 differs drastically from that of a conventional colloidal dispersion, or that of a colloid polymer mixture.<sup>[64]</sup> Below the volume transition temperature, the coexistence phases at the freezing and melting points have close particle densities, similar to that observed in a hard-sphere system. However, above the volume transition temperature, fluid–solid transition spans over a wide gap of particle concentrations. At high temperature, the fluid phase at the freezing point is highly dilute, whereas the solid phase at the melting point is highly concentrated. Interestingly, this phase diagram indicates that the microgel dispersion can freeze at temperatures both above and below the gel volume transition temperature. For instance, according to this phase diagram, a microgel dispersion with 7 g/L particle concentration is in the fluid state at 34.5°C; it becomes a solid of similar density when the temperature drops to about 34°C, and the dispersion will be separated into a dilute solution and a solid of much higher density (about 17 g/L) at about 35.3°C. The dashed line in Fig. 7 shows a metastable fluid–fluid coexistence curve with a low critical solution temperature. This coexistence curve is reminiscent of that for an aqueous solution of uncrosslinked PNIPAM polymer. Because of strong hydrogen bonding with water molecules from CO and NH groups, PNIPAM can be dissolved in water at low temperature. In this case, the isopropyl groups along the PNIPAM chain are caged by water molecules. When the temperature is increased, the cages of water molecules are partially melted, resulting in entropy increases. As a result, on increase of the temperature, the hydrophobic attraction caused by the isopropyl groups and the polymer backbone become more important and the solubility of PNIPAM in water drops.

## KINETICS OF CRYSTALLIZATION

As shown in Fig. 3, light scattering measurements indicate that when the particles are in the swollen state, the osmotic second virial coefficients of PNIPAM microgel dispersions are essentially the same as those for hard

spheres. The nucleation kinetics confirms further that the swollen PNIPAM particles behavior like hard spheres. We find that the kinetics of microgel crystallization can be represented quantitatively by the classical nucleation theory (CNT).

The classical theory of nucleation and crystal growth has been adapted by Russel<sup>[65]</sup> to hard-sphere colloids, and extended and evaluated numerically by Ackerson and Schatzel.<sup>[66]</sup> According to the CNT,<sup>[67]</sup> the crystal nucleation rate per unit volume  $I$  depends exponentially on the Gibbs energy barrier in the formation of a critical nucleus  $\Delta G_{\text{crit}}$ :

$$I = \zeta \exp(-\Delta G_{\text{crit}}/k_B T) \quad (21)$$

where the kinetic prefactor  $\zeta$  is usually expressed as  $A\phi^{5/3}(1 - \phi/\phi_g)^{2.6}$ , where  $A$  is a constant independent of the particle volume fraction  $\phi$ , and  $\phi_g$  is the glass transition concentration. The critical Gibbs energy of nucleation is related to the difference in the chemical potentials of the solution and the crystal  $\Delta\mu$ , the solution–solid interfacial tension  $\gamma$ , and the number density of the crystalline phase  $\rho_s$ :

$$\Delta G_{\text{crit}} = \frac{16\pi}{3} \frac{\gamma^3}{[\rho_s \Delta\mu]^2} \quad (22)$$

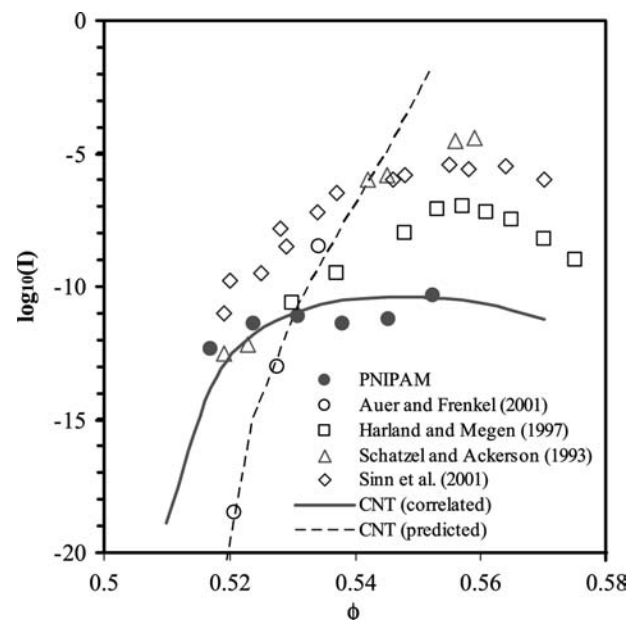


Fig. 8 The nucleation rates per unit volume as a function of the particle volume fraction in an aqueous dispersion of PNIPAM microgel particles and in various hard-sphere systems. The solid line is calculated from CNT with the prefactor  $A$  and the fluid–solid interfacial tension  $\gamma$  as adjustable parameters. The dashed line is the prediction of the CNT using  $A$  and  $\gamma$  from Monte Carlo simulation.

In most applications of the CNT to analyze crystal nucleation experiments, the parameter  $A$  in the kinetic prefactor and the interfacial tension are treated as adjustable variables.

In Fig. 8, we compare the rate of nucleation per unit volume in the microgel dispersion investigated in this work with previous studies for hard-sphere-like colloids.<sup>[7,68–70]</sup> Also shown in Fig. 8 are calculated results from CNT using  $A$  and  $\gamma$  as adjustable parameters, as well as the predictions of CNT with the kinetic prefactor and the fluid–solid interfacial tension obtained from Monte Carlo simulations.<sup>[71]</sup> In these calculations, the chemical potentials of the fluid and solid phases are calculated from Eqs. (11) and (15). Fig. 8 indicates that although the rate of nucleation for microgel dispersions is close to previous investigations on well-established hard-sphere-like colloids and it agrees well with CNT using  $\log_{10}(A) = -5.96$  and  $\gamma/k_B T = 0.45$ , it significantly deviates from simulation results for hard spheres. Similar observations have been reported by Schatzel and Ackerson for crystallization kinetics in a model hard-sphere system consisting of polymethyl methacrylate particles coated with a thin layer of hydroxystearic acid suspended in a mixture of decalin and tetralin.<sup>[68]</sup>

## CONCLUSION

The volume transition of PNIPAM particles significantly affects the interaction potential and determines a novel phase diagram that has not been observed in conventional colloids. Because both particle size and attractive potential depend on temperature, PNIPAM aqueous dispersion exhibits phase transitions at a fixed particle density by either increasing or decreasing temperature. At low temperature, freezing occurs at large particle volume fractions, similar to that in a hard-sphere system; whereas at high temperature, the freezing occurs at low particle concentration, driven by the strong van der Waals attraction caused by the collapsed microgel particles. Although the kinetics of nucleation in PNIPAM microgel dispersions is similar to that for hard-sphere-like colloids, it deviates significantly from the prediction of the CNT using the kinetic prefactor and the fluid–solid interfacial tension obtained from recent simulations for the crystal nucleation of hard spheres.

In many aspects, the phase behavior of colloidal dispersions reassembles that for simple fluids. However, a noticeable difference is that unlike the vapor–liquid equilibrium of a simple fluid, the equilibrium between a dilute and a concentrated colloidal dispersion is often metastable. Although that difference, arising from the short-ranged solvent-mediated attraction between colloidal particles, is now well-documented, not much

attention has been given to other features that are unique in colloidal systems. Temperature-dependent potential, as shown in this work, is special in colloidal systems. Because the interparticle potential is strongly temperature-dependent, the phase behavior of PNIPAM dispersions differs remarkably from that for simple fluids or for conventional colloids. In future work, it might be interesting to investigate other features that are special to colloidal dispersions, including the multibody effect on the phase behavior and dissimilarity of interparticle potentials in different phases.

## ACKNOWLEDGMENTS

J. W. gratefully acknowledges the financial support from the University of California Directed Research and Development. Z. H. gratefully acknowledges the financial support from the National Science Foundation (grant no. DMR-0102468), and the U.S. Army Research Office (grant no. DAAD19-01-1-0596). We thank G. Huang and B. Zhou for their help.

## REFERENCES

1. Weeks, E.R.; Crocker, J.C.; Levitt, A.C.; Schofield, A.; Weitz, D.A. Three-dimensional direct imaging of structural relaxation near the colloidal glass transition. *Science* **2000**, *287*, 627–631.
2. Russel, W.B.; Saville, D.A.; Schowalter, W.R. *Colloidal Dispersions*; Cambridge University Press: Cambridge, New York, 1989.
3. Pusey, P.N. *Liquid, Freezing, and the Glass Transition*; Les Houches, J.P., Levesque, H.D., Zinn-Justin, J., Eds.; Elsevier: Amsterdam, 1990.
4. Schatzel, K.; Ackerson, B.J. Observation of density fluctuations during crystallization. *Phys. Rev. Lett.* **1992**, *68*, 337–340.
5. Cheng, Z.D.; Chaikin, P.M.; Zhu, J.X.; Russel, W.B.; Meyer, W.V. Crystallization kinetics of hard spheres in microgravity in the coexistence regime: interactions between growing crystallites. *Phys. Rev. Lett.* **2002**, *8801*, art. no. 015501; pp. 5501, U5110–U5112.
6. Arora, A.K.; Tata, B.V.R. Interactions, structural ordering and phase transitions in colloidal dispersions. *Adv. Colloid Interface Sci.* **1998**, *78*, 49–97.
7. Pusey, P.N.; van Megen, W. Phase behavior of concentrated suspensions of nearly hard colloidal spheres. *Nature* **1986**, *320*, 340–341.
8. Denton, A.R.; Lowen, H. Stability of colloidal quasicrystals. *Phys. Rev. Lett.* **1998**, *81*, 469–472.
9. Cheng, Z.D.; Zhu, J.X.; Russel, W.B.; Chaikin, P.M. Phonons in an entropic crystal. *Phys. Rev. Lett.* **2000**, *85*, 1460–1463.
10. Pham, K.N.; Puertas, A.M.; Bergenholtz, J.; Egelhaaf, S.U.; Moussaid, A.; Pusey, P.N.; Schofield, A.B.; Cates, M.E.; Fuchs, M.; Poon, W.C.K. Multiple glassy

- states in a simple model system. *Science* **2002**, *296*, 104–106.
11. Xia, Y.N.; Gates, B.; Yin, Y.; Lu, Y. Monodispersed colloidal spheres: old materials with new applications. *Adv. Mater.* **2000**, *12*, 693–713.
  12. Blanco, A.; Chomski, E.; Grabtchak, S.; Ibisate, M.; John, S.; Leonard, S.W.; Lopez, C.; Meseguer, F.; Miguez, H.; Mondia, J.P.; Ozin, G.A.; Toader, O.; van Driel, H.M. Large-scale synthesis of a silicon photonic crystal with a complete three-dimensional bandgap near 1.5 micrometres. *Nature* **2000**, *405*, 437–440.
  13. Velev, O.D.; Tessier, P.M.; Lenhoff, A.M.; Kaler, E.W. Materials—a class of porous metallic nanostructures. *Nature* **1999**, *401*, 548.
  14. Dabbs, D.M.; Aksay, I.A. Self-assembled ceramics produced by complex-fluid templation. *Annu. Rev. Phys. Chem.* **2000**, *51*, 611–622, 601–U623.
  15. Giannelis, E.P.; Krishnamoorti, R.; Manias, E. Polymer–silicate nanocomposites: model systems for confined polymers and polymer brushes. *Adv. Polym. Sci.* **1999**, *138*, 107–147.
  16. Godovsky, D. Device applications of polymer-nanocomposites. *Adv. Polym. Sci.* **1999**, *153*, 163–205.
  17. Frenkel, D. Colloidal systems—playing tricks with designer “atoms”. *Science* **2002**, *296*, 65–66.
  18. Noro, M.G.; Frenkel, D. Extended corresponding-states behavior for particles with variable range attractions. *J. Chem. Phys.* **2000**, *113*, 2941–2944.
  19. Likos, C.N. Effective interactions in soft condensed matter physics. *Phys. Rep.* **2001**, *348*, 268–439.
  20. Dijkstra, M.; van Roij, R.; Evans, R. Effective interactions, structure, and isothermal compressibility of colloidal suspensions. *J. Chem. Phys.* **2000**, *113*, 4799–4807.
  21. Rosenbaum, D.; Zamora, P.C.; Zukoski, C.F. Phase behavior of small attractive colloidal particles. *Phys. Rev. Lett.* **1996**, *76*, 150–153.
  22. Asherie, N.; Lomakin, A.; Benedek, G.B. Phase diagram of colloidal solutions. *Phys. Rev. Lett.* **1996**, *77*, 4832–4835.
  23. Quesada-Perez, M.; Callejas-Fernandez, J.; Hidalgo-Alvarez, R. Interaction potentials, structural ordering and effective charges in dispersions of charged colloidal particles. *Adv. Colloid Interface Sci.* **2002**, *95*, 295–315.
  24. Hansen, J.P.; Lowen, H. Effective interactions between electric double layers. *Annu. Rev. Phys. Chem.* **2000**, *51*, 209–242.
  25. Attard, P. Recent advances in the electric double layer in colloid science. *Curr. Opin. Colloid Interface Sci.* **2001**, *6*, 366–371.
  26. Ninham, B.W. On progress in forces since the DLVO theory. *Adv. Colloid Interface Sci.* **1999**, *83*, 1–17.
  27. Walz, J.Y. The effect of surface heterogeneities on colloidal forces. *Adv. Colloid Interface Sci.* **1998**, *74*, 119–168.
  28. Ruckenstein, E. Attraction between identical colloidal particles caused by collective electrostatic repulsion. *Adv. Colloid Interface Sci.* **1998**, *75*, 169–180.
  29. Pelton, R.H.; Chibante, P. Preparation of Aqueous Lattices with *N*-isopropylacrylamide. *Colloids Surfaces* **1986**, *20*, 247–256.
  30. Weissman, J.M.; Sunkara, H.B.; Tse, A.S.; Asher, S.A. Thermally switchable periodicities and diffraction from mesoscopically ordered materials. *Science* **1996**, *274*, 959–960.
  31. Debord, J.D.; Eustis, S.; Debord, S.B.; Lofye, M.T.; Lyon, L.A. Color-tunable colloidal crystals from soft hydrogel nanoparticles. *Adv. Mater.* **2002**, *14*, 658–662.
  32. Debord, J.D.; Lyon, L.A. Thermoresponsive photonic crystals. *J. Phys. Chem., B* **2000**, *104*, 6327–6331.
  33. Okubo, T.; Hase, H.; Kimura, H.; Kokufut, E. Thermosensitive colloidal crystals of silica spheres in the presence of gel spheres of poly(*N*-isopropyl acrylamide). *Langmuir* **2002**, *18*, 6783–6788.
  34. Debord, S.B.; Lyon, L.A. Influence of particle volume fraction on packing in responsive hydrogel colloidal crystals. *J. Phys. Chem., B* **2003**, *107*, 2927–2932.
  35. Pelton, R. Temperature-sensitive aqueous microgels. *Adv. Colloid Interface Sci.* **2000**, *85*, 1–33.
  36. Saunders, B.R.; Vincent, B. Microgel particles as model colloids: theory, properties and applications. *Adv. Colloid Interface Sci.* **1999**, *80*, 1–25.
  37. Kawaguchi, H. Functional polymer microspheres. *Prog. Polym. Sci.* **2000**, *25*, 1171–1210.
  38. Hirotsu, S.; Hirokawa, Y.; Tanaka, T. Volume-phase transitions of ionized *N*-isopropylacrylamide gels. *J. Chem. Phys.* **1987**, *87*, 1392–1395.
  39. Fernandez-Nieves, A.; Fernandez-Barbero, A.; Vincent, B.; de las Nieves, F.J. Charge controlled swelling of microgel particles. *Macromolecules* **2000**, *33*, 2114–2118.
  40. Laukkanen, A.; Hietala, S.; Maunu, S.L.; Tenhu, H. Poly(*N*-vinylcaprolactam) microgel particles grafted with amphiphilic chains. *Macromolecules* **2000**, *33*, 8703–8708.
  41. Gao, J.; Hu, Z.B. Optical properties of *N*-isopropylacrylamide microgel spheres in water. *Langmuir* **2002**, *18*, 1360–1367.
  42. Hellweg, T.; Dewhurst, C.D.; Bruckner, E.; Kratz, K.; Eimer, W. Colloidal crystals made of poly(*N*-isopropylacrylamide) microgel particles. *Colloid Polym. Sci.* **2000**, *278*, 972–978.
  43. Senff, H.; Richtering, W. Temperature sensitive microgel suspensions: colloidal phase behavior and rheology of soft spheres. *J. Chem. Phys.* **1999**, *111*, 1705–1711.
  44. Hu, Z.B.; Wang, C.J.; Chen, Y.Y.; Zhang, X.M.; Li, Y. Spinodal decomposition in *N*-isopropylacrylamide gel. *J. Polym. Sci., B, Polym. Phys.* **2001**, *39*, 2168–2174.
  45. Gilanyi, T.; Varga, I.; Meszaros, R.; Filipcsei, G.; Zrinyi, M. Characterisation of monodisperse poly(*N*-isopropylacrylamide) microgel particles. *Phys. Chem., Chem. Phys.* **2000**, *2*, 1973–1977.
  46. Saunders, B.R.; Crowther, H.M.; Morris, G.E.; Mears, S.J.; Cosgrove, T.; Vincent, B. Factors affecting the swelling of poly(*N*-isopropylacrylamide) microgel particles: fundamental and commercial implications. *Colloids Surf., A Physicochem. Eng. Asp.* **1999**, *149*, 57–64.
  47. Wu, C.; Zhou, S.Q.; Auyeung, S.C.F.; Jiang, S.H. Volume phase transition of spherical microgel particles. *Angew. Makromol. Chem.* **1996**, *240*, 123–136.
  48. Hu, Z.B.; Tang, S.J.; Cheng, C.D.; Wu, J.Z. Crystallization kinetics of thermosensitive colloids probed by

- transmission spectroscopy. *Phys. Rev. Lett.* **2003**, submitted for publication.
49. Wu, J.Z.; Huang, G.; Hu, Z.B. Inter-particle potential and the phase behavior of temperature-sensitive microgel dispersions. *Macromolecules* **2003**, *36*, 440–448.
  50. Wu, J.Z.; Zhou, B.; Hu, Z.B. Phase behavior of thermally responsive microgel colloids. *Phys. Rev. Lett.* **2003**, *90*, art. no. 048304.
  51. Varga, I.; Gilanyi, T.; Meszaros, R.; Filipcsei, G.; Zrinyi, M. Effect of cross-link density on the internal structure of poly(*N*-isopropylacrylamide) microgels. *J. Phys. Chem., B* **2001**, *105*, 9071–9076.
  52. Berli, C.L.A.; Quemada, D. Prediction of the interaction potential of microgel particles from rheometric data. Comparison with different models. *Langmuir* **2000**, *16*, 10,509–10,514.
  53. Senff, H.; Richtering, W. Influence of cross-link density on rheological properties of temperature-sensitive microgel suspensions. *Colloid Polym. Sci.* **2000**, *278*, 830–840.
  54. Flory, P.J. *Principles of Polymer Chemistry*; Cornell University Press: Ithaca, 1953.
  55. Guillermo, A.; Addad, J.P.C.; Bazile, J.P.; Duracher, D.; Elaissari, A.; Pichot, C. NMR investigations into heterogeneous structures of thermosensitive microgel particles. *J. Polym. Sci., B, Polym. Phys.* **2000**, *38*, 889–898.
  56. Hino, T.; Prausnitz, J.M. Swelling equilibria for heterogeneous polyacrylamide gels. *J. Appl. Polym. Sci.* **1996**, *62*, 1635–1640.
  57. Israelachvili, J.N. *Intermolecular and Surface Forces*, 2nd Ed. Ed.; Academic Press: London, 1992.
  58. Gil Villegas, A.; Galindo, A.; Whitehead, P.J.; Mills, S.J.; Jackson, G.; Burgess, A.N. Statistical associating fluid theory for chain molecules with attractive potentials of variable range. *J. Chem. Phys.* **1997**, *106*, 4168–4186.
  59. Hansen, J.P.; McDonald, I.R. *Theory of Simple Liquids*, 2nd Ed.; Academic Press: London, 1986.
  60. Wu, J.Z.; Prausnitz, J. Phase equilibria in a system of “breathing” molecules. *Fluid Phase Equilib.* **2002**, *194*, 689–700.
  61. Hirschfelder, J.D.; Curtis, C.F.; Bird, R.B. *Molecular Theory of Gases and Liquids*; Wiley: New York, 1964.
  62. Hagen, M.H.J.; Frenkel, D. Determination of phase diagrams for the hard-core attractive Yukawa system. *J. Chem. Phys.* **1994**, *101*, 4093–4097.
  63. Lue, L.; Prausnitz, J.M. Renormalization-group corrections to an approximate free-energy model for simple fluids near to and far from the critical region. *J. Chem. Phys.* **1998**, *108*, 5529–5536.
  64. Poon, W.; Pusey, P.; Lekkerkerker, H. Colloids in suspension. *Phys. World* **1996**, *9*, 27–32.
  65. Russel, W.B. On the dynamics of the disorder order transition. *Phase Transit.* **1990**, *21*, 127–137.
  66. Ackerson, B.J.; Schatzel, K. Classical growth of hard-sphere colloidal crystals. *Phys. Rev., E* **1995**, *52*, 6448–6460.
  67. Harland, J.L.; van Meegen, W. Crystallization kinetics of suspensions of hard colloidal spheres. *Phys. Rev., E* **1997**, *55*, 3054–3067.
  68. Schatzel, K.; Ackerson, B.J. Crystallization of hard-sphere colloids. *Phys. Scr., T* **1993**, *49A*, 70–73.
  69. Sinn, C.; Heymann, A.; Stipp, A.; Palberg, T. Measurements in concentrated suspensions: solidification kinetics of hard-sphere colloidal suspensions. *Prog. Colloid Polym. Sci.* **2001**, *118*, 266–275.
  70. Vanmeegen, W.; Underwood, S.M. Glass-transition in colloidal hard-spheres—mode-coupling theory analysis. *Phys. Rev. Lett.* **1993**, *70*, 2766–2769.
  71. Auer, S.; Frenkel, D. Prediction of absolute crystal-nucleation rate in hard-sphere colloids. *Nature* **2001**, *409*, 1020–1023.

# Microweighing in Supercritical Carbon Dioxide

You-Ting Wu  
Christine S. Grant

*Chemical Engineering Department, North Carolina State University,  
Raleigh, North Carolina, U.S.A.*

## INTRODUCTION

Carbon dioxide (CO<sub>2</sub>), when heated and pressurized above its critical temperature (31°C) and pressure (7.377 MPa), is identified as being in a fourth, supercritical state with properties intermediate between liquid and gas (Table 1). At the critical point, the interface of CO<sub>2</sub> liquid and vapor starts to vanish (Fig. 1). Supercritical CO<sub>2</sub> (scCO<sub>2</sub>) has liquid-like densities providing good solvent capability, gas-like viscosities, and diffusivities to benefit mass transport, and a non-hazardous nature for the environment. Because of these properties and other advantages of CO<sub>2</sub> over organic solvents such as low surface tension and low cost,<sup>[1]</sup> scCO<sub>2</sub> has received increasing industrial<sup>[2]</sup> and research<sup>[1]</sup> attention in a variety of processes such as extraction,<sup>[3,4]</sup> cleaning,<sup>[5,6]</sup> polymer synthesis,<sup>[7,8]</sup> and more recently microelectronics processing.<sup>[9,10]</sup> CO<sub>2</sub> has been proposed to serve as an energy-efficient and environmentally benign solvent platform.<sup>[11]</sup> The real-time monitoring of the time-dependent mass change is crucial to understanding, characterizing, designing, and controlling the aforementioned processes. However, this monitoring presents a number of challenges because of the difficulty in applying various detection methods under high-pressure conditions.

In this entry, two microweighing techniques in scCO<sub>2</sub>, gravimetric and piezoelectric, are reviewed. A comparison is made between two representatives of these techniques: the magnetic suspension balance (gravimetric) and the quartz crystal microbalance (QCM, piezoelectric). The QCM theory in high-pressure fluids is briefly introduced, followed by a summary of recent research which includes 1) the experimental verification of QCM theory; 2) the scCO<sub>2</sub> adsorption on metal surfaces; and 3) the dissolution of polymer films for applications in scCO<sub>2</sub>-based lithography processes. Finally, the application of QCM in absorption, solubility, and other surface-specific processes in scCO<sub>2</sub> will be reviewed to highlight the versatility of the QCM technique.

## MICROWEIGHING TECHNIQUES: GRAVIMETRIC AND PIEZOELECTRIC

Many important physical and chemical processes can be monitored by observing the associated mass changes. Currently, two microweighing techniques, gravimetric and piezoelectric, have been widely used as an analytical tool for research and applied applications. Gravimetric microbalances are the most direct technique to measure mass variations at the microgram level. However, in a number of cases, most conventional gravimetric microbalances such as spring, beam, and torsional balances are not designed for the operation under extreme conditions. The extreme conditions are usually defined as conditions of high pressures (>1450 psi), viscous fluids, and/or high temperatures. In order to adapt the conventional gravimetric balances to work under extreme pressures, some researchers<sup>[12,13]</sup> have designed a high-pressure container to include both the microbalance and the sample. This not only greatly increases the system expenses, structural complexity, and operational difficulties, but also sacrifices the capability under high temperatures (>125°C) because of the microbalance working conditions. Jwayyed, Humayun, and Tomaska<sup>[13]</sup> modified a commercial high-pressure microbalance (Cahn C-1000 balance) by redesigning the container (nipple shape with 30 cm o.d. and 25 cm height) for use in scCO<sub>2</sub>. They were only able to extend the pressure limit from 1600 to 3000 psi.

In recent years, some researchers<sup>[14,15]</sup> have been able to design a unique balance, a magnetic suspension balance (MSB), for mass measurements under extreme conditions (>3000 psi). The MSB takes advantage of the principle of magnetic coupling to isolate the balance from the sample that is contained in a small pressure cell (Fig. 2), while maintaining most features of the traditional microbalances. Using this magnetic suspension coupling, the measured force is transmitted from the pressure cell to the microbalance that is located in the ambient environment. Such novel design eliminates the large container, enables the capability of mass determinations under extreme conditions, and



**Table 1** Physical properties of gas, liquid, and supercritical fluid (order of magnitude)

	Density (g/cm <sup>3</sup> )	Diffusivity (cm <sup>2</sup> /sec)	Viscosity (g/cm/sec)
Gas	1 × 10 <sup>-3</sup>	1 × 10 <sup>-1</sup>	1 × 10 <sup>-4</sup>
Liquid	1.0	5 × 10 <sup>-6</sup>	1 × 10 <sup>-2</sup>
Supercritical fluid	3 × 10 <sup>-1</sup>	1 × 10 <sup>-3</sup>	1 × 10 <sup>-4</sup>

Source: From Ref.<sup>[5]</sup>, with permission of William Andrew Publishing.

makes realistic applications of gravimetric techniques in CO<sub>2</sub>-based processes. The MSB has primarily been applied to determine the adsorption/absorption and diffusivity of scCO<sub>2</sub> in addition to other solutes on/in bulk solid materials under static conditions.<sup>[16–22]</sup> Applications of MSB for other chemical processes and applications under dynamic (flowing) conditions are rarely found in the literature.

Piezoelectric quartz crystal resonators take advantage of the electric polarization that occurs when the crystal is subjected to a mechanical stress.<sup>[23]</sup> Several different devices operate using the piezoelectric technique according to the modes of electromechanical coupling, such as modes of thickness shear, face shear, and surface acoustic wave.<sup>[24]</sup> The AT-cut thickness-shear mode resonator, commonly referred to QCM, is the most widely used piezoelectric mass sensor.<sup>[25]</sup> The QCM consists of a thin quartz disk with two metal electrodes plated on its two opposite surfaces (Fig. 3). The QCM is a powerful microweighing tool for detecting in situ the mass changes to the ng/cm<sup>2</sup> level of

sensitivity. In the last decade, there has been increased application of the QCM for studies of a wide range of chemical processes and chemistries on surfaces and in thin films.<sup>[23–29]</sup> There are few difficulties for QCM applications under extreme conditions, because of the rigidity and chemical inertness of the quartz crystals and the elimination of any connection except the supply of electricity. Rigid electrical leads are commonly used to hold the crystal in place and excite the sensor that is contained in the pressure cell (Fig. 4). The QCM has been applied to many scCO<sub>2</sub>-based processes and chemistries in bulk phases or at surface films; they will be summarized later in the following sections.

Table 2 summarizes a comparison of the performance of MSB with QCM for the microweighing in scCO<sub>2</sub>. As can be seen, the QCM is a more powerful and versatile microweighing tool in scCO<sub>2</sub> than the MSB, mainly owing to its low cost, conceptual simplicity, high mass sensitivity, wide range of applications, rapid time response, and miniature and simple construction. In particular, the nanogram-level sensitivity enables the QCM as a possible technique that can be utilized to study interfacial processes related to nanotechnologies and nanomaterials.

### QUARTZ CRYSTAL MICROBALANCE THEORY IN HIGH-PRESSURE FLUIDS

#### Fundamentals

As the QCM is piezoelectric, an external electrical potential applied across the electrodes produces internal mechanical stress. This stress induces an acoustic wave that propagates through the crystal and meets minimum impedance when the thickness of the crystal is a multiple of a half wavelength of the acoustic wave. A resonant oscillation is achieved by including the crystal into an oscillation circuit in which the electric and the mechanical oscillation are close to the fundamental frequency (*F*<sub>0</sub>) of the crystal.<sup>[25,26]</sup>

When a crystal is immersed in a fluid, any frequency shift from its fundamental value (*F*<sub>0</sub>) in vacuum can be observed because of contributions from 1) mass sorption or desorption from the crystal surface; 2) pressure; 3) density and viscosity of the fluid surrounding the crystal; and 4) surface roughness of the crystal. The following expression has been established to describe changes in the crystal frequency, Δ*F*, due to the aforementioned effects.<sup>[30]</sup>

$$\Delta F = F - F_0 = \Delta F_m + \Delta F_P + \Delta F_\eta + \Delta F_r \tag{1}$$

where *F* is the measured frequency of quartz, Δ*F*<sub>m</sub> relates to mass loading, Δ*F*<sub>P</sub> is dependent on pressure,

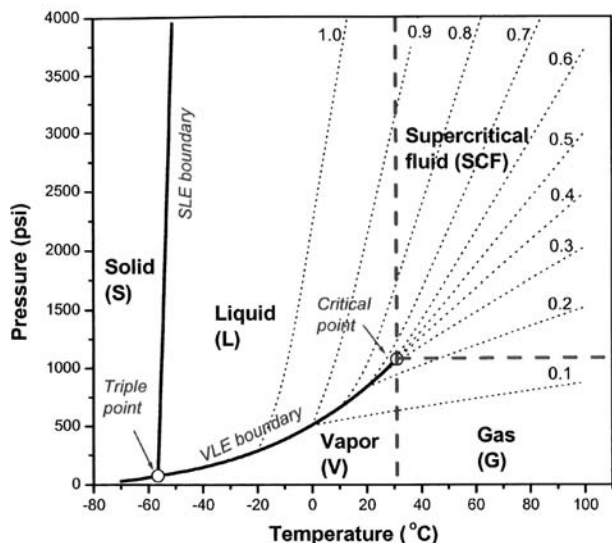


**Fig. 1** Phase diagram for CO<sub>2</sub> with constant density lines (dot lines, g/cm<sup>3</sup>). Above the critical point (31°C and 1070 psi), the vapor–liquid equilibrium (VLE) boundary vanishes, and the supercritical state is observed. The dash lines do not represent a boundary, but for the convenience to distinguish different states of CO<sub>2</sub>.



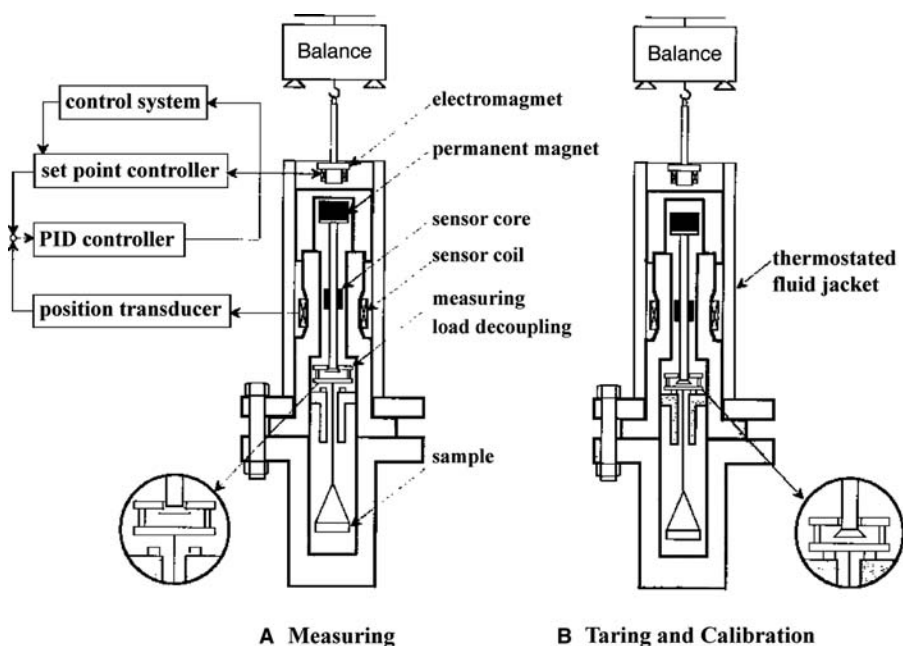


Fig. 2 A typical magnetic suspension balance (MSB). Source: From Ref.<sup>[21]</sup>.

$\Delta F_\eta$  changes with density and viscosity, and  $\Delta F_r$  is a function of surface roughness.

According to the well-known Sauerbrey equation,<sup>[31]</sup>  $\Delta F_m$  is directly proportional to the mass loading on the crystal:

$$\Delta F_m = -2nF_0^2 \Delta m / (\mu_q \rho_q)^{1/2} = -C_m \Delta m \quad (2)$$

where  $\mu_q$  is the shear modulus of quartz,  $\rho_q$  is the density of the crystal,  $\Delta m$  is the film mass per real surface

area,  $n$  is the number of faces of the crystal exposed, and  $C_m$  is the mass sensitivity of QCM, which is a function of the characteristic properties ( $F_0$ ,  $\mu_q$ , and  $\rho_q$ ) of the quartz crystal. Eq. (2) applies only if the adsorbed mass is much less than the mass of the crystal and it assumes this mass is firmly attached to the surface; hence the material moves together with the crystal. Such conditions are assumed to be fulfilled in cases of coated solid films and self-assembled monolayers.

The pressure dependence of frequency,  $\Delta F_p$ , increases with increasing pressure linearly, as shown by Stockbridge<sup>[32]</sup> for gases up to 15 psi. Susse<sup>[33]</sup> described a similar relationship for liquids up to  $1.5 \times 10^4$  psi. Thus  $\Delta F_p$  can be written as:

$$\Delta F_p = F_0 \alpha P = C_p P \quad (3)$$

where  $\alpha$  is the proportionality constant and  $C_p$  is the pressure sensitivity of QCM crystal, both of which are independent of the type of fluid in contact with the crystal.

The viscosity and density contribution,  $\Delta F_\eta$ , describes the interaction of the vibrating crystal with a Newtonian viscous fluid. The interaction leads to an additional loading of the crystal, causing a decrease in frequency.  $\Delta F_\eta$  is expressed to be proportional to the square root of the product of viscosity and density of the surrounding fluid:<sup>[32,34,35]</sup>

$$\Delta F_\eta = -0.5 C_m (\pi F_0)^{-1/2} (\rho_f \eta_f)^{1/2} \quad (4)$$

where  $\rho_f$  and  $\eta_f$  are the absolute density and viscosity of the fluid, respectively.

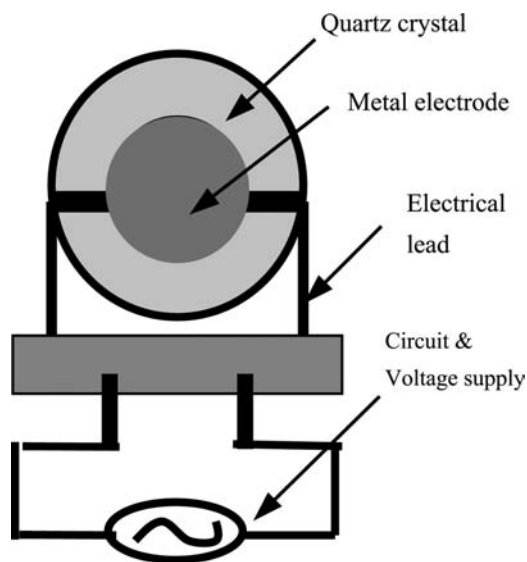
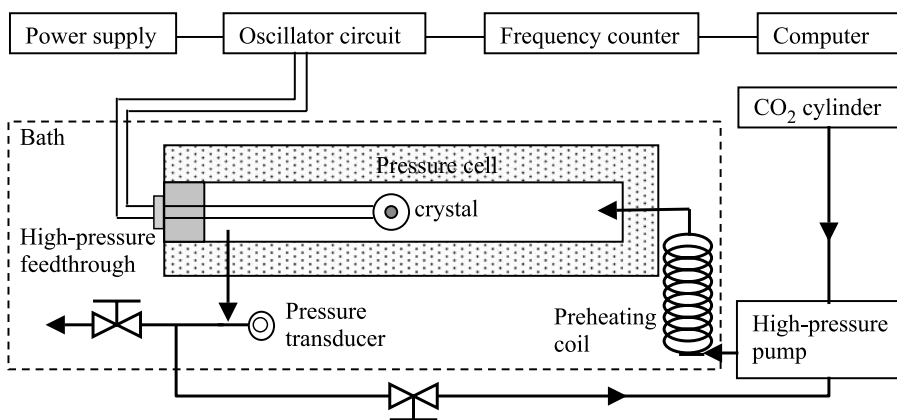


Fig. 3 Schematic view of a piezoelectric QCM crystal (only one side shown). A typical 5-MHz QCM from International Crystal Manufacturing consists of a thin quartz crystal (0.85 cm diameter) sputtered with a metal electrode (0.35 cm diameter) on each side. Both sides should be exposed to  $scCO_2$  because of high pressure.



**Fig. 4** Schematic view of an experimental setup of QCM measurement system in scCO<sub>2</sub>. Source: From Ref.<sup>[50]</sup>.

**Roughness Effect**

A common feature of the approaches to QCM theory as reviewed by Thompson et al.<sup>[27]</sup> is the neglect of microscopic properties of interfaces and surface roughness.<sup>[36]</sup> This leads to deviations of most experimental frequency shift data from the predictions by these approaches. Buttry and Ward<sup>[23]</sup> and Schumacher, Borges, and Kanazawa<sup>[37]</sup> observed that up to 80% of the observed frequency shifts for a crystal in contact with a liquid could be attributed to roughness effects.

As the microscopic properties of crystal–fluid interfaces change with the surface morphology, a predictive analytical expression for the roughness contribution to frequency,  $\Delta F_r$ , is not available. Urbakh and Dalkhin<sup>[36,38,39]</sup> formulated a model for surface roughness, assuming that a rough surface can be characterized by the average height ( $h$ ), lateral length ( $a$ ), and distance ( $l$ ) between the inhomogeneities of the surface (Fig. 5). They incorporated this model into a framework of perturbation theory<sup>[36,38]</sup> and derived a general

relationship for  $\Delta F_r$  as:

$$\Delta F_r = -0.5C_m(\pi F_0)^{-1/2}(\rho_f \eta_f)^{1/2} \Psi(a/\delta, a/l, h/a) \tag{5}$$

where  $\Psi$  is a scaling function, related to three dimensionless factors,  $a/\delta$ ,  $a/L$ , and  $h/a$ ;  $\delta$  is the decay length of fluid velocities,

$$\delta = [\eta_f/(\pi F_0 \rho_f)]^{1/2} \tag{6}$$

In particular, if one assumes a slowly varying roughness ( $h/a \ll 1$  and  $h/\delta \ll 1$ ) for the crystal surface with a limit of  $a/\delta \ll 1$  or  $a/\delta \gg 1$ , the scaling function  $\Psi$  is proportional to the ratio  $a/\delta$ .<sup>[36]</sup> Reformulating Eq. (5) yields:

$$\Delta F_r = -0.5C_m C_r \rho_f \tag{7}$$

where  $C_r = \Psi \delta$  is defined as the frequency–roughness correlation factor. This factor is only a function of sur-

**Table 2** Comparison of two microweighing methods

Characteristics	Gravimetric: MSB <sup>[21]</sup>	Piezoelectric: QCM <sup>[24]</sup>
Mass sensitivity	$10^{-5}$ – $10^{-6}$ g <sup>13</sup>	$<10^{-9}$ g
Time resolution of response	$5 \times 10^{-2}$ sec <sup>13</sup> (need fine damping control system)	$<10^{-3}$ sec
Measuring variables	Gravity	Frequency and/or impedance
Calculations	Simple	Simple
Construction	Complex, especially the designing of the magnetic coupling and fine damping control system	Very simple
Size	Medium size when comparing with the QCM	Miniature size (0.5–2.5 cm diameter)
Calibration	Required to correct buoyancy	Not necessary <sup>25</sup>
Cost	Expensive	Cheap ( $<\$30$ a QCM crystal) <sup>a</sup>
Operation conditions	Mainly static; <sup>13</sup> extreme conditions	Both static and dynamic; extreme conditions
Applications	Mainly for processes and chemistries in bulk phases	For processes and chemistries both in bulk phases and at thin films

<sup>a</sup>Price information was obtained from International Crystal Manufacturing.

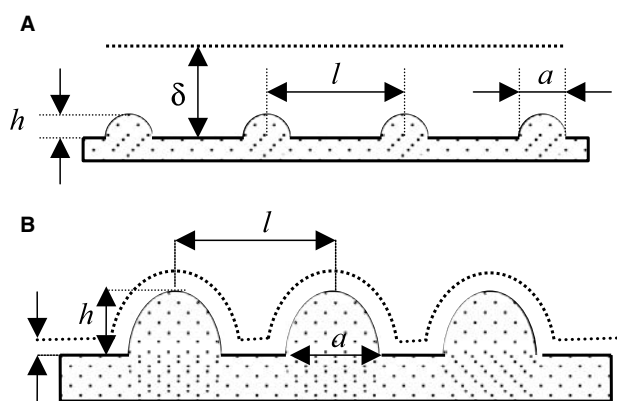


**Fig. 5** Two types of ideal surface roughness. (A) Slightly rough,  $h/\delta \ll 1$ ; (B) strongly rough,  $h/\delta \gg 1$ . Source: From Ref.<sup>[40]</sup>.

face roughness ( $h$  and  $a$ ), provided that the assumptions above are fully established. Otherwise,  $C_r$  should be additionally viewed as a weak function of  $\delta$ .

**EXPERIMENTAL EXAMINATION OF QUARTZ CRYSTAL MICROBALANCE THEORY AND ADSORPTION OF CO<sub>2</sub> ON METAL SURFACES**

As the frequency of a QCM crystal exposed to a high-pressure fluid is affected by different factors, it is critical to accurately separate out each influencing factor. Experimental verification of QCM theory enables the calculation of the actual mass change on the crystal surface. The investigation of CO<sub>2</sub> adsorption on metal electrodes of blank crystals is a required initial step for the successful use of the QCM technique to investigate the chemical and physical properties of surface films in scCO<sub>2</sub>.

**Separation of Contributions to Frequency**

As the microscopic properties of crystal–fluid interfaces complicate the QCM frequency behavior, a unique strategy<sup>[40]</sup> to verify the QCM theory in scCO<sub>2</sub> is to experimentally establish a relationship between the microscopic properties of crystal surfaces and frequency shifts. In a study reported here, the surface roughness of QCM crystals (three gold and three silver 5-MHz crystals; Table 3) was characterized using an AFM technique. Three groups of QCM experiments were performed on the six crystals to separate the following different contributions to QCM frequency:  $\Delta F_p$ ,  $\Delta F_m$ ,  $\Delta F_\eta$ , and  $\Delta F_r$ . The first set of experiments performed on Ag-polished and Ag-rough crystals utilized helium, the lightest inert gas considered nonabsorbing ( $\Delta F_m = 0$ ) on metals, to determine  $\Delta F_p$  and  $\Delta F_\eta$ . To evaluate the roughness contribution of frequency,  $\Delta F_r$ , the second set of experiments utilized N<sub>2</sub>, another nonabsorbing gas on the metal surfaces at room temperatures (i.e.,  $\Delta F_m$  negligibly small). The last group of experiments was conducted using low-density gaseous CO<sub>2</sub> ( $< 0.2 \text{ g cm}^{-3}$ ), an adsorbing gas at room temperatures, to test the adsorbed masses of CO<sub>2</sub> on the metal surfaces.

The first set of experiments in helium indicated that the frequency shifts of the smoothest silver crystal (Ag-polished) could be accurately predicted with the QCM theory for pressure and viscosity (Eqs. (3) and (4)) by neglecting the roughness effect. However, for the roughest silver crystal (Ag-rough), about 10% of the total frequency shifts could not be theoretically predicted with Eqs. (3) and (4). The variations in the prediction were attributed to the roughness effect. This is consistent with the experimental findings by Tsionsky et al.<sup>[30]</sup> who investigated frequency shifts of gold and nickel crystals in He, H<sub>2</sub>, Ar, and N<sub>2</sub>.

**Table 3** Some characteristic properties of six different QCM crystals

Crystals	RMS roughness <sup>a</sup> (10 <sup>-7</sup> cm)	$H$ (10 <sup>-7</sup> cm)	$a$ (10 <sup>-7</sup> cm)	$l$ (10 <sup>-7</sup> cm)	$C_r$ (10 <sup>-5</sup> cm) <sup>b</sup>	
					Eq. (8a)	Eq. (8b)
Ag-polished	3.7	12	180	190	1.32(1–2.65 $\rho_f$ )	0.398 + 4.96 × 10 <sup>4</sup> $\delta$
Ag-unpolished	26	85	1410	2180	1.79(1–3.48 $\rho_f$ )	0.322 + 7.44 × 10 <sup>4</sup> $\delta$
Ag-rough <sup>c</sup>	647	1030	–	–	7.28(1–1.27 $\rho_f$ )	5.16 + 1.05 × 10 <sup>5</sup> $\delta$
Au-polished	2.8	8	110	120	1.37(1–2.23 $\rho_f$ )	0.595 + 4.10 × 10 <sup>4</sup> $\delta$
Au-unpolished	115	210	1370	2120	3.22(1–2.37 $\rho_f$ )	1.41 + 9.17 × 10 <sup>4</sup> $\delta$
Au-rough <sup>3</sup>	681	1090	–	–	6.88(1–1.51 $\rho_f$ )	3.99 + 1.63 × 10 <sup>5</sup> $\delta$

<sup>a</sup>The rms roughness is defined as the root mean square (or standard deviation) of the  $Z$  values within a given AFM image area with respect to the average  $Z$  value.

<sup>b</sup>The units for  $\rho_f$  and  $\delta$  are g/cm<sup>3</sup> and cm, respectively.

<sup>c</sup>Lack of data for  $a$  and  $l$  because of no apparent periodic inhomogeneities in the AFM images of the strongly rough crystals.

Source: From Ref.<sup>[40]</sup>.

The second set of experiments in nitrogen showed that the roughness effect had a significant influence on the frequency even for the smoothest silver and gold crystals. The experimental roughness contribution,  $\Delta F_r$ , was calculated by subtracting theoretical  $\Delta F_p$  and  $\Delta F_\eta$  from the experimental  $\Delta F$  (Eq. (1)). The resulting  $\Delta F_r$  was plotted as a function of theoretical  $N_2$  density; the corresponding frequency shift corrected in this manner was found to be a nearly linear function of density, indicating the precision of the theoretical expression of  $\Delta F_r$  (Eq. (7)). Therefore the frequency-roughness correlation factor,  $C_r$ , can be obtained by correlating  $\Delta F_r$  with the  $N_2$  density ( $\rho_f$ ) or the decay length ( $\delta$ ), using Eqs. (8a) and (8b),

$$C_r = a_1(1 + b_1\rho_f) \tag{8a}$$

$$C_r = a_2 + b_2\delta \tag{8b}$$

where  $a$  and  $b$  are the constants assumed to be independent of the type of fluid. The values of  $a$  and  $b$  for each crystal are also shown in Table 3. Eqs. (8a) and (8b) represent accurate predictions of  $C_r$  with most correlation coefficients better than 0.999. Eq. (8a) is only applicable to gases because of the neglect of the influence of viscosity, while Eq. (8a) is suitable for dense gases ( $\rho_f > 0.2 \text{ g/cm}^3$ ) and liquids.<sup>[40]</sup>  $C_r$  was found to be dependent primarily on the rms roughness of crystals and, to a lesser degree, on  $a$  and  $l$ .<sup>[40]</sup>

In the last group of experiments, the frequency shifts ( $\Delta F$ ) of all six crystals in gaseous  $CO_2$  (pressure <1000 psi) were measured to evaluate the amount of  $CO_2$  adsorbed on the metal surfaces. The  $CO_2$  adsorption was calculated from  $\Delta F_m$  that was obtained by subtracting the theoretical  $\Delta F_p$ ,  $\Delta F_\eta$ , and  $\Delta F_r$  from  $\Delta F$ , using Eqs. (1) to (4), (7), and (8a). As can be seen (Fig. 6), all six crystals with different surface roughness values adsorbed similar amounts of gaseous  $CO_2$  per real surface area, which agrees well with the adsorption theory. This is additional evidence of the accuracy of the reformulated QCM theory by including the roughness contribution. It also implies that the  $a$  and  $b$  values obtained in  $N_2$  are independent of the type of fluid.

### Adsorption of Supercritical $CO_2$ on Metal Surfaces

Several researchers have determined the mechanisms of adsorption of  $scCO_2$  on metal surfaces. Otake et al.<sup>[41]</sup> determined the mass of  $CO_2$  adsorbed onto rough silver QCM electrodes at  $40^\circ C$  and at pressures up to 5800 psi. They concluded that  $scCO_2$  mass adsorption on metal surfaces could approach values as high as  $25 \mu\text{g/cm}^2$ . Guigard et al.<sup>[42]</sup> evaluated the

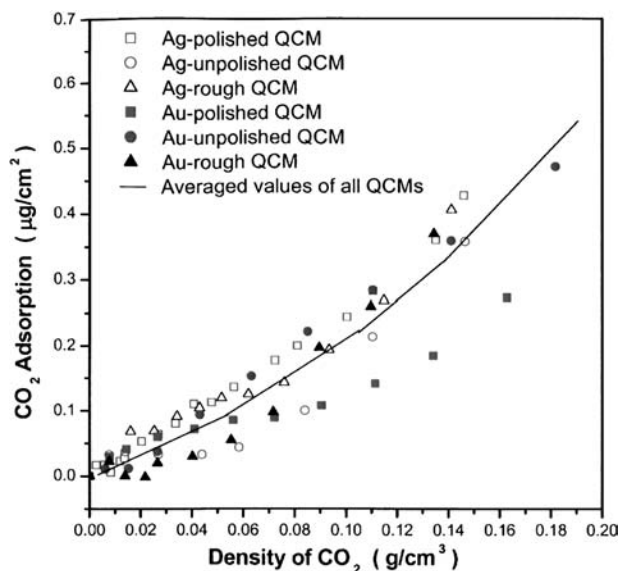


**Fig. 6** Adsorption of gaseous  $CO_2$  on silver and gold surfaces at  $40^\circ C$ , using the  $C_r$  values calculated with Eq. (8b). Source: From Ref.<sup>[40]</sup>.

adsorption of  $CO_2$  on rough gold electrodes at  $40^\circ C$  and  $45^\circ C$  and at pressures up to 1500 psi. They found the similar maximum amount of  $CO_2$  adsorption as by Otake et al. However, these researchers all neglected the roughness contribution to frequency in the calculation. In order to fully account for the roughness contribution, the Wu research group examined in greater detail the  $scCO_2$  adsorption on metal surfaces.<sup>[40]</sup>

The frequency shifts of Ag-polished and Ag-rough crystals (Fig. 7) in  $scCO_2$  were measured to evaluate

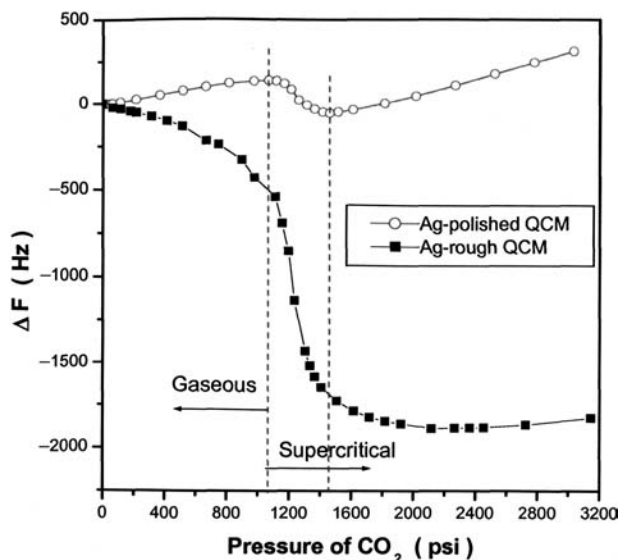


**Fig. 7** Frequency shift of Ag-polished and Ag-rough crystals in  $scCO_2$  at  $40^\circ C$  as a function of pressure. Source: From Ref.<sup>[40]</sup>.

the amount of CO<sub>2</sub> adsorbed on the surfaces (Fig. 8). The calculation procedure is the same as in the gaseous CO<sub>2</sub>. As the CO<sub>2</sub> density and the amount of adsorbed CO<sub>2</sub> increase with increasing pressure, the holes and valleys between the inhomogeneities on the crystal surface are gradually filled (Fig. 8, inset), which causes a gradual decrease of surface roughness.<sup>[36]</sup> Therefore  $C_r$  was corrected for the overestimation of the roughness contribution,<sup>[40]</sup>

$$C_r = (a_2 + b_2\delta)\xi/\xi_0 \quad (8c)$$

where  $\xi$  and  $\xi_0$  are the roughness in centimeters of the original substrate surface and the modified surface by the adsorbed molecules, respectively.  $\xi$  is a function of thickness (or mass) of adsorbed molecular layers. Analysis showed that it was appropriate to predict scCO<sub>2</sub> adsorption on the Ag-polished crystal by neglecting the roughness contribution ( $C_r = 0$  or  $\xi = 0$ ), when the density was larger than 0.4 g cm<sup>-3</sup> (Fig. 8). This was because the quantity (2.4 μg/cm<sup>2</sup>) of CO<sub>2</sub> mass absorbed at the density of 0.4 g cm<sup>-3</sup> could smooth the surface of Ag-polished crystal.<sup>[40]</sup> For the Ag-rough crystal, calculation showed that the two limits of  $\xi/\xi_0 = 1.0$  and 0.75 could fit the adsorption data of the Ag-polished crystal well in the regions of low and high densities (<0.4 and >0.7 g/cm<sup>3</sup>; Fig. 8). It was concluded that the use of rough QCM crystals (rms roughness >10 nm) required careful attention in scCO<sub>2</sub> adsorption studies, because of

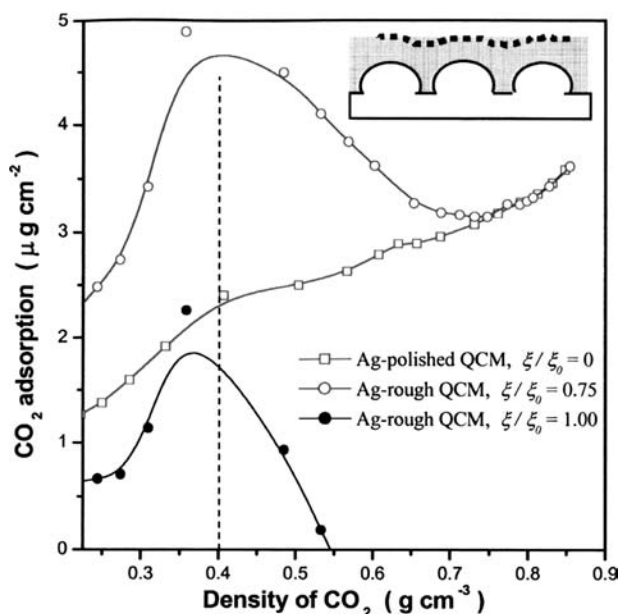


**Fig. 8** Adsorption of scCO<sub>2</sub> at 40°C on Ag-polished and Ag-rough QCM crystals. The inset on the upper right corner demonstrates how the adsorbed mass may alter the surface morphology. *Source:* From Ref.<sup>[40]</sup>.

the variation of  $C_r$ .<sup>[40]</sup> Only very smooth QCM crystals (several nanometers or less) are capable of accurately determining the adsorption of scCO<sub>2</sub> on the metal surfaces without considering the surface roughness contribution. The adsorption of scCO<sub>2</sub> on the silver and gold surfaces at 40°C ranges to 3.6 μg/cm<sup>2</sup>, but not up to 25 μg/cm<sup>2</sup> as determined by Otake et al.<sup>[41]</sup> and Guigard et al.<sup>[42]</sup> who used very rough crystals and neglected the roughness contribution.

## APPLICATIONS OF QUARTZ CRYSTAL MICROBALANCE FOR DISSOLUTION STUDY OF POLYMER FILMS IN SUPERCRITICAL CO<sub>2</sub>

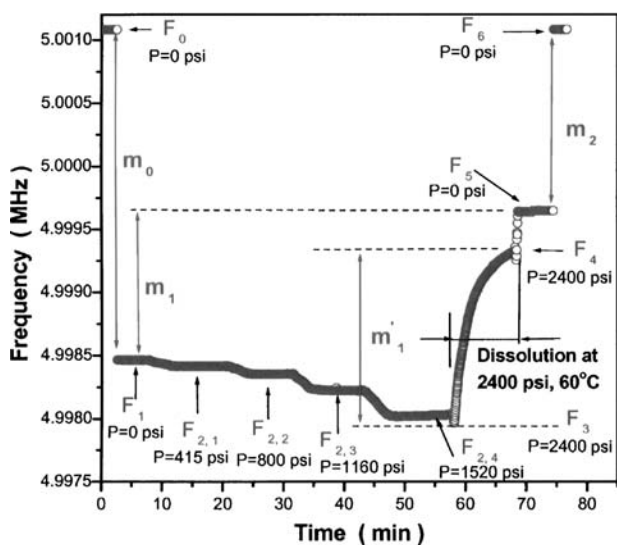
Polymer dissolution (or polymer desorption) in solvents is an important phenomena in polymer science and engineering. Applications of polymer dissolution or desorption are found in several areas such as microlithography, controlled drug delivery, and plastics recycling.<sup>[43]</sup> For example, the successful implementation of a microlithography process requires technical information on the dissolution of photoresist polymer films in specific solvents during 1) the development of the resist images and 2) the stripping of the remaining films after the lithography process.<sup>[44]</sup> Hinsberg, Willson, and Kanazawa<sup>[45,46]</sup> and Ito<sup>[47]</sup> applied the QCM techniques to determine the dissolution rate of novolac and poly(4-hydroxystyrene) films in aqueous developer solutions at atmospheric pressure. Mueller et al.<sup>[48]</sup> have used the QCM to investigate the diffusivity of casting organic solvents in photoresist films for the evaluation of the influence of the solvents on the polymer dissolution behavior. These researchers demonstrated that the QCM technique was a particular attractive tool for the evaluation of the dissolution of polymer films in organic and aqueous solutions.

The dissolution kinetics of polymer films in scCO<sub>2</sub> provides useful technical information for the development of scCO<sub>2</sub>-based interfacial processes that require excellent control of surface properties (e.g., thickness and morphology) at the micro- and nanometer scales. The recently proposed surface processing of microelectronics in scCO<sub>2</sub><sup>[9]</sup> is a typical field that requires information on polymer film dissolution. However, a search of the literature in this specific area revealed that there have been a very limited number of studies on the polymer dissolution kinetics in scCO<sub>2</sub> by the use of QCM technique. To date, the number of dissolution studies of polymer films in scCO<sub>2</sub> by other online techniques, e.g., interferometry,<sup>[49]</sup> is also limited. This is probably due to the lack of various detection techniques at extreme conditions and to the situation of such scCO<sub>2</sub>-based processes being in the stages of early development. Nevertheless, Wu and

Grant<sup>[50]</sup> have utilized the QCM for the evaluation of polymer film dissolution in  $scCO_2$ .

Based on the availability and applicability of the reformulated QCM theory in  $scCO_2$ , the dissolution study of polymer films in  $scCO_2$  was achieved utilizing the experimental high-pressure QCM apparatus (Fig. 4). Fig. 9 represents a typical experimental run using a Si-polished QCM crystal to evaluate the dissolution kinetics of poly(FOMA-r-THPMA) films (low MW polymer) at 60°C and 2400 psi. The fundamental frequency ( $F_0$ ; Fig. 9) of the blank crystal was determined in vacuum ( $P = 0$  psi). The crystal was removed from the vessel and the polymer film was cast onto the crystal by dip-coating in an 8 wt.% polymer-trifluorotoluene solution. After drying the film in vacuum for 30 min the stable frequency ( $F_1$ ; Fig. 9) of the coated crystal was measured. The total polymer mass ( $m_0$ ) coated on the crystal corresponded to the frequency difference of ( $F_1 - F_0$ ).  $CO_2$  was gradually pumped into the vessel via steep changes in pressure

(see abrupt steep changes in frequency curve in Fig. 9) and the frequency data ( $F_{2,i}, i = 1$  to 4) were continually recorded. As the polymer was insoluble at pressures lower than 1700 psi at 60°C, this set of frequency data at elevated pressures were used to evaluate the swelling (or  $CO_2$  absorption) of film and  $CO_2$  diffusivity in the polymer film. After the frequency of the crystal became stable at the last step change in pressure ( $P = 1520$  psi), the  $CO_2$  pressure was instantaneously raised to the required experimental pressure (2400 psi) by adding more  $CO_2$  into the vessel. The QCM frequency went through a minimum value ( $F_3$ ) and increased rapidly, indicating the removal of polymer film from the crystal surface. The minimum frequency is the point at which  $CO_2$  absorption (film swelling) and film dissolution are balanced. Therefore in the example presented here, the dissolution of polymer film in  $scCO_2$  consists of two steps: 1) absorption-dominating and 2) dissolution-dominating. After the polymer film dissolved in  $scCO_2$  at 2400 psi and 60°C for 10 min, the  $CO_2$  in the vessel was rapidly released and the QCM frequency ( $F_5$ ) was measured again in vacuum. The remaining polymer film was removed by dissolution in pure trifluorotoluene (TFT), and excess TFT was dried off in vacuum. The original fundamental frequency ( $F_6 = F_0$ ) of the crystal was recovered, indicating complete polymer removal. On the polymer dissolution graph, the line from  $F_3$  to  $F_4$  represents the dissolution curve that can be used to evaluate the kinetics. Wu and Grant<sup>[50]</sup> have evaluated the dissolution kinetics of poly(FOMA-r-THPMA) films under the conditions that will be required for static film-developing and stripping in the microelectronics processing. Studies are currently underway to evaluate the dissolution kinetics of polymer films in a flowing  $scCO_2$  environment.



Symbol	$\Delta F$	Note
$m_0$	$F_1 - F_0$	Polymer mass initially coated
$m_1$	$F_5 - F_1$	Polymer mass removed
$m_1'$	$F_4 - F_3$	Mass change during dissolution
$m_2$	$F_6 - F_5$	Polymer mass not removed during dissolution
—	$F_{2,i} - F_1$	$CO_2$ adsorption during step-pressurizing
—	$F_5 - F_4$	$CO_2$ desorption during the release of $CO_2$

**Fig. 9** A typical experimental QCM determination for the dissolution of poly(FOMA-r-THPMA) film in  $scCO_2$  at 2400 psi and 60°C under static conditions. Detailed explanation in the text. Source: From Ref.<sup>[50]</sup>.

### ADDITIONAL QUARTZ CRYSTAL MICROBALANCE APPLICATIONS IN SUPERCRITICAL $CO_2$

#### Absorption of Supercritical $CO_2$ and Other Analytes in Solid Films

The absorption and solubility of  $scCO_2$  or other analytes in solid films are important properties that can be used to understand many  $scCO_2$ -based processes and chemistries. The swelling of polymer films in  $scCO_2$  is a typical example of absorption processes. The QCM determination of absorption is realized by modification of the QCM surface with a coating that can interact with a desired analyte in a way that the mass and thickness of the coating are increased (Fig. 10A). To date, researchers<sup>[51-53]</sup> have successfully used the QCM technique to investigate the absorption



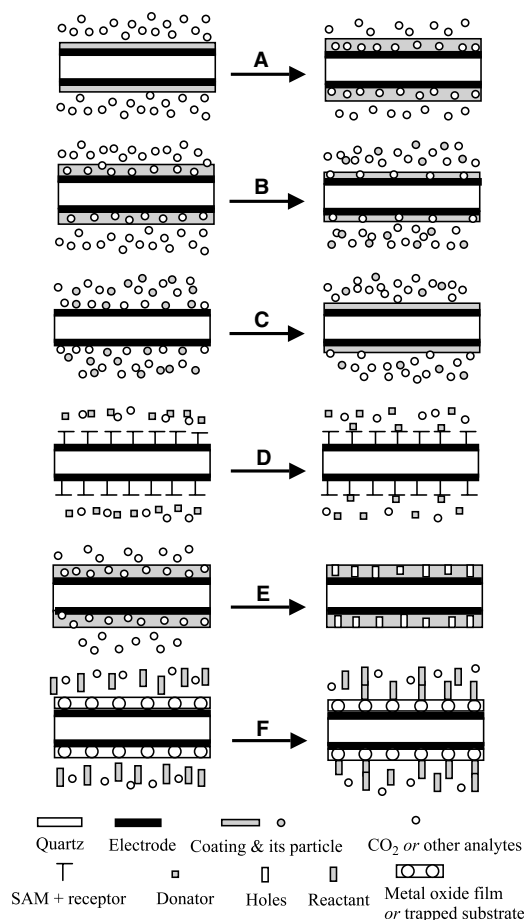


**Fig. 10** Schematic representations of some typical  $\text{scCO}_2$ -based processes or chemistries that can be investigated using the QCM. (A) Absorption or molecular recognition; (B) cleaning, developing, stripping, drying, dissolution, or solubility in  $\text{scCO}_2$ ; (C) deposition; (D) molecular recognition; (E) foaming; (F) surface reaction, or polymerization.

of  $\text{scCO}_2$  in polymers at elevated pressures with high performance. There are a limited number of QCM studies on the absorption of an analyte other than  $\text{CO}_2$  into a solid film, where both the analyte and the solid film are contained in a  $\text{scCO}_2$  environment.

Interestingly, based on the QCM, some dual techniques have been developed to measure other absorption-relevant physical properties. Hattori et al.<sup>[54,55]</sup> combined vapor-liquid partition chromatography with a piezoelectric QCM to measure vapor-liquid equilibrium (VLE) ratios of benzene and toluene at an infinite dilution state in a  $\text{scCO}_2$ -poly(vinyl acetate) system. The QCM indicated the solubility of organic solutes in the polymer phase while the chromatography analyzed the concentrations of solutes in the  $\text{scCO}_2$  phase. Good VLE data were obtained with this dual technique. Nakamura et al.<sup>[56]</sup> reported the determination of adsorption isotherms of  $\text{scCO}_2$  on several proteins and polysaccharides by a combination of two different

microbalances, gravimetric and piezoelectric. The QCM was used to measure the absorption of  $\text{CO}_2$  into the proteins and polysaccharides; the absolute adsorption could be accurately calculated from the gravimetric data by subtracting the absorption contribution.

### Precision Cleaning and Dissolution Using Supercritical $\text{CO}_2$

The QCM determination in cleaning and dissolution processes typically involves the partial or complete removal of a film or coating from the QCM surface by a liquid, gas, or a fluid in the supercritical state (Fig. 10B). Precision cleaning and precision decontamination can be defined as processes that result in a surface contaminant level of less than  $10 \mu\text{g}/\text{cm}^2$ .<sup>[57]</sup> However, most precision cleaning processes require a contaminant level of less than  $1 \mu\text{g}/\text{cm}^2$ .<sup>[58]</sup> A majority of recently developed  $\text{scCO}_2$ -based precision cleaning processes are found in the microelectronic industry. Some typical examples are 1) the decontamination of micromechanical devices;<sup>[59]</sup> 2) the initial removal of impurities such as organic soils and fingerprints from silicon wafers; 3) the stripping of resists from metallized silicon surfaces without damaging thin metallization patterns;<sup>[60]</sup> and 4) the direct development of resist films.<sup>[10,61]</sup> More recently, the  $\text{scCO}_2$ -drying of organic or aqueous rinse liquids from micro-electro-mechanical systems (MEMS) or other silicon structures were proposed to prevent the collapse of the fine features on the surfaces.<sup>[62,63]</sup> The QCM is capable of monitoring the mass changes in all these  $\text{CO}_2$ -based precision-cleaning processes at the nanogram scale.

### Solubility of Chemicals in Supercritical $\text{CO}_2$

A thermodynamic property that is essential to any application of supercritical fluids is chemical solubility. The application of the QCM in the determination of solubility (Fig. 10B) is, in principle, very close to the approach used for cleaning and dissolution studies. A critical difference is the amount of time required for the attainment of phase equilibrium. The QCM method is ideally suited for solutes that exhibit low solubility, or for measurements conducted at low  $\text{scCO}_2$  densities, a condition in which many solutes have low solubility. This is because the QCM theory (Eq. (2)) is considered accurate provided the mass of a coating does not exceed 2% of the crystal mass.<sup>[23]</sup> Guigard et al.<sup>[42]</sup> have applied the QCM technique to determine the solubilities of two metal chelates, bis(acetylacetonato) copper and bis(thenoyltrifluoroacetonato) copper, in  $\text{scCO}_2$  and described the methodology in detail. They found that the solubilities measured by the QCM were in excellent agreement with the four

sets of literature values obtained using other techniques, with a standard deviation of 25%.<sup>[42]</sup> This level of discrepancy is actually encouraging because of the extreme low solubility values on the order of  $10^{-5}$  mole fraction. Besides metal chelates, the QCM method can be extended to determine the solubilities of natural products (e.g., herbal medicines), photoresists, polymers, fats, biomaterials, and many other chemicals of interest for CO<sub>2</sub>-based processes. This is especially true in cases in which the traditional detection methodologies (e.g., spectroscopic techniques) are limited due to either their low sensitivity or the complexity of the associated apparatuses under extreme pressure conditions.

### Molecular Recognition in Supercritical CO<sub>2</sub>

Molecular recognition is of interest for biological processes because most biomolecules show selectivity and specificity when interacting with other species. This particular microweighing methodology involves either directly coating host molecules (insoluble in scCO<sub>2</sub>) on the surface of a QCM crystal (Fig. 10A) or modifying the surface with a self-assembled monolayer (SAM) (Fig. 10D). The SAM can be formed using thiols or other chain-like molecules that have two active groups at the two ends of the chain. The -SH group of the thiol or one end of the chain-like molecule is attached to the QCM surface, while the -OH group or the other end is grafted with the receptor molecule. When guest or donor molecules are supplied into the vessel together with CO<sub>2</sub>, they are bonded to the host or receptor molecules via molecular interactions, resulting in a mass increase of the coating. Naito et al.<sup>[64,65]</sup> successfully demonstrated two examples of molecular recognitions in scCO<sub>2</sub> using the QCM technique. In the first system, ethyl acetate and ethanol were selectively bound to anthracene-bis(resorcinol)tetraol that was coated on the crystal surfaces. In the second situation, nucleobases such as 9-ethyladenine and 2-pyrrolidone were recognized at different extents by thymine that was immobilized on the thiol-modified QCM surfaces. The equilibrium constants and the associated kinetics of molecular binding were easily obtained by the use of the QCM technique.

### Evaluation of Deposition in Supercritical CO<sub>2</sub>

Chemicals either previously dissolved in the scCO<sub>2</sub> phase or produced via reactions of other CO<sub>2</sub>-soluble chemicals may deposit onto surfaces, due to solubility variations with temperature and pressure or the insoluble characteristics. The dynamic mass of deposited surface films can be detected in situ using the QCM method (Fig. 10C). For example, the QCM technique can be directly used to evaluate the deposition of

metals (e.g., copper and nickel) on silicon wafers.<sup>[66]</sup> The metals were generated via the hydrogen reduction of organometallic compounds that are dissolved in a scCO<sub>2</sub> carrier. This deposition process was named as chemical fluid deposition (CFD), and the deposition of metals on pattern features less than 100 nm wide has been demonstrated using such CFD technique.<sup>[66]</sup>

### Polymer Foaming in Supercritical CO<sub>2</sub>

In recent years, scCO<sub>2</sub>-based polymer foaming has been of particular importance in the production of low dielectric films in electronics manufacturing and tissue engineering scaffolds for biological purposes.<sup>[67]</sup> Upon removal of the scCO<sub>2</sub> phase, the absorbed CO<sub>2</sub> is released from swollen polymer networks, resulting in free-standing porous foams. The foams have cell diameters of less than 1 μm and the process accomplishes density reductions of 97% relative to the parent polymers.<sup>[68]</sup> Quartz crystal microbalance can act as a useful tool for detecting the dynamic mass changes associated with such foaming processes (Fig. 10E). The dynamic mass changes can be correlated with the structure and morphology of the foams by evaluation using microscopic techniques, such as SEM and AFM. The combination of the QCM microweighing with the microscopic techniques can provide a comprehensive understanding of the foaming processes.

### Surface Reactions in Supercritical CO<sub>2</sub>

Reactions or polymerizations on metal oxide surfaces or other surfaces immobilized with active groups can be followed by detecting the mass increase on the surfaces with the QCM technique (Fig. 10F). When treated with acids, the metal oxide surfaces provide OH active groups to promote immobilization. The silylation of native oxide silicon surfaces in the preparation of coating for hydrophobic photoresists<sup>[69]</sup> is a typical example of surface reactions in scCO<sub>2</sub>. Supercritical CO<sub>2</sub> has been utilized as a carrier of silane reagents, thereby reducing the consumption of chemicals and improving the rate of surface coverage.

### CONCLUSION

Two techniques, MSB and QCM, have been developed primarily as microweighing tools for wide use under extreme conditions. In the literature, the MSB has been utilized mainly for the determination of adsorption/absorption and diffusivity of scCO<sub>2</sub> in bulk polymers under static conditions. When compared to the MSB technique, the QCM has found a wider range of applications for many scCO<sub>2</sub>-based static or

dynamic processes both in the bulk phase and at the surface film. This is primarily because of the intrinsic attributes of the QCM approach, such as the nanogram-level mass sensitivity, millisecond-level time resolution, miniature and simple construction, and low cost. The QCM can be successfully developed into a submicroweighing tool in  $\text{scCO}_2$  by the careful examination of the QCM theory in high-pressure fluids. Although the QCM has applications in various  $\text{CO}_2$ -based processes and chemistries, such as dissolution, solubility, adsorption/absorption, and molecular recognition, the reported efforts and application areas in the literature are limited to date. It is evident from the progress reviewed in this entry that the QCM demonstrates great potential for use in  $\text{scCO}_2$ .

Because  $\text{scCO}_2$  is a “green” solvent, it is expected that the use of this solvent in nanoscale processing will increase significantly in the next few decades. The complete scope of the QCM in actual nanoscale processing has not been realized either. Hence the QCM will serve as an excellent analytical tool for developmental studies on emerging nanotechnologies and nanomaterials.

## ACKNOWLEDGMENTS

This material is based upon work supported in part by the Science and Technology Center of the National Science Foundation under Agreement No. CHE-9876674. We acknowledge the DeSimone group at the University of North Carolina, Chapel Hill (UNC), the Carbonell group and Kenan Center at the NC State University for technical assistance and facility utilization. Finally, we acknowledge Professor Scott Wallen and Michael Hurrey at UNC for their contributions in AFM experiments.

## REFERENCES

- DeSimone, J.M. Practical approaches to green solvents. *Science* **2002**, *297* (5582), 799–803.
- McCoy, M. Industry intrigued by  $\text{CO}_2$  as solvent—“Green” processes based on supercritical carbon dioxide are moving out of the lab. *Chem. Eng. News* **1999**, *77* (24), 11–13.
- Mchugh, M.A.; Krukonis, V.J. *Supercritical Fluid Extraction: Principles and Practice*, 2nd Ed.; Butterworth-Heinemann: Stoneham, UK, 1993.
- Marsal, A.; Celma, P.J.; Cot, J.; Cequier, M. Supercritical  $\text{CO}_2$  extraction as a clean degreasing process in the leather industry. *J. Supercrit. Fluids* **2000**, *16* (3), 217–223.
- McHardy, J.; Sawan, S.P. *Supercritical Fluid Cleaning: Fundamentals, Technology, and Applications*; Noyes Publications: Westwood, NJ, 1998.
- Purtell, R.; Rothman, L.; Eldridge, B.; Chess, C. Precision parts cleaning using supercritical fluids. *J. Vac. Sci. Technol., A: Vac. Surf. Films* **1993**, *11* (4), 1696–1701.
- Desimone, J.M.; Guan, Z.; Elsbernd, C.S. Synthesis of fluoropolymers in supercritical carbon-dioxide. *Science* **1992**, *257* (5072), 945–947.
- Cooper, A.I. Polymer synthesis and processing using supercritical carbon dioxide. *J. Mater. Chem.* **2000**, *10* (2), 207–234.
- Weibel, G.L.; Ober, C.K. An overview of supercritical  $\text{CO}_2$  applications in microelectronics processing. *Microelectron. Eng.* **2003**, *65* (1–2), 145–152.
- Sundararajan, N.; Yang, S.; Ogino, K.; Valiyaveetil, S.; Wang, J.G.; Zhou, X.Y.; Ober, C.K.; Obendorf, S.K.; Allen, R.D. Supercritical  $\text{CO}_2$  processing for submicron imaging of fluouropolymers. *Chem. Mater.* **2000**, *12* (1), 41–48.
- Taylor, D.K.; Carbonell, R.; DeSimone, J.M. Opportunities for pollution prevention and energy efficiency enabled by the carbon dioxide technology platform. *Annu. Rev. Energy Environ.* **2000**, *25*, 115–146.
- Wong, B.; Zhang, Z.; Handa, Y.P. High-precision gravimetric technique for determining the solubility and diffusivity of gases in polymers. *J. Polym. Sci., Part B: Polym. Phys.* **1998**, *36* (12), 2025–2032.
- Jwayyed, A.M.; Humayun, R.; Tomasko, D.L. High pressure flow gravimetric apparatus for supercritical fluid extraction studies. *Rev. Sci. Instrum.* **1997**, *68* (12), 4542–4548.
- Lockemann, C.A.; Riede, T.; Magin, P. An experimental method to determine the sorption and swelling behavior of solids at high pressures. *Process Technol. Proc.* **1996**, *12*, 547–552.
- Wagner, W.; Brachthaeuser, K.; Kleinrahm, R.; Loesch, H.W. A new, accurate single-sinker densitometer for temperatures from 233 to 523 K at pressures up to 30 MPa. *Int. J. Thermophys.* **1995**, *16* (2), 399–411.
- Herbst, A.; Staudt, R.; Harting, P. The magnetic suspension balance in high pressure measurements of pure gases. *J. Therm. Anal. Calorim.* **2003**, *71* (1), 125–135.
- Areerat, S.; Hayata, Y.; Katsumoto, R.; Kegasawa, T.; Egami, H.; Ohshima, M. Solubility of carbon dioxide in polyethylene/titanium dioxide composite under high pressure and temperature. *J. Appl. Polym. Sci.* **2002**, *86* (2), 282–288.
- Von Schnitzler, J.; Eggers, R. Mass transfer in polymers in a supercritical  $\text{CO}_2$  atmosphere. *J. Supercrit. Fluids* **1999**, *16* (1), 81–92.
- Sato, Y.; Takikawa, T.; Yamane, M.; Takishima, S.; Masuoka, H. Solubility of carbon dioxide in PPO and PPO/PS blends. *Fluid Phase Equilib.* **2002**, *194–197*, 847–858.
- Sato, Y.; Takikawa, T.; Sorakubo, A.; Takishima, S.; Masuoka, H.; Imaizumi, M. Solubility and diffusion coefficient of carbon dioxide in biodegradable polymers. *Ind. Eng. Chem. Res.* **2000**, *39* (12), 4813–4819.
- Sato, Y.; Takikawa, T.; Takishima, S.; Masuoka, H. Solubilities and diffusion coefficients of carbon dioxide in poly(vinyl acetate) and polystyrene. *J. Supercrit. Fluids* **2001**, *19* (2), 187–198.

22. DeSimone, J.M.; Wojcinski, L.M., III; Kennedy, K.A.; Zannoni, L.; Saraf, M.; Charpentier, P.; Roberts, G.W. The polymerization of fluorinated monomers and the determination of phase equilibria in carbon dioxide. *Polym. Mater. Sci. Eng.* **2001**, *84*, 137.
23. Buttry, D.A.; Ward, M.D. Measurement of interfacial processes at electrode surfaces with the electrochemical quartz crystal microbalance. *Chem. Rev.* **1992**, *92* (6), 1355–1379.
24. Ward, M.D.; Buttry, D.A. In situ interfacial mass detection with piezoelectric transducers. *Science* **1990**, *249* (4972), 1000–1007.
25. Lu, C.; Czanderna, A.W. *Applications of Piezoelectric Quartz Crystal Microbalances; Methods and Phenomena, Their Applications in Science and Technology*; Elsevier: New York, 1984; Vol. 7.
26. O'Sullivan, C.K.; Guilbault, G.G. Commercial quartz crystal microbalances—Theory and applications. *Biosens. Bioelectron.* **1999**, *14* (8–9), 663–670.
27. Thompson, M.; Kipling, A.L.; Duncanhe Witt, W.C.; Rajakovic, L.V.; Cavicvlasak, B.A. Thickness-shear-mode acoustic-wave sensors in the liquid-phase—A review. *Analyst* **1991**, *116* (9), 881–890.
28. Wegener, J.; Janshoff, A.; Steinem, C. The quartz crystal microbalance as a novel means to study cell-substrate interactions in situ. *Cell Biochem. Biophys.* **2001**, *34* (1), 121–151.
29. O'Sullivan, C.K.; Vaughan, R.; Guilbault, G.G. Piezoelectric immunosensors—Theory and applications. *Anal. Lett.* **1999**, *32* (12), 2353–2377.
30. Tsionsky, V.; Daikhin, L.; Urbakh, M.; Gileadi, E. Behavior of quartz-crystal microbalance in nonadsorbed gases at high-pressures. *Langmuir* **1995**, *11* (2), 674–678.
31. Sauerbrey, G. Use of quartz vibration for weighing thin films on a microbalance. *Z. Phys.* **1959**, *155* (2), 206–222.
32. Stockbridge, C.D. Effects of Gas Pressure on Quartz Crystal Microbalances. In *Vacuum Microbalance Techniques*; Behrndt, K.H., Ed.; Plenum Press: New York, 1966; 147pp.
33. Susse, C. Variation des constantes elastiques du quartz en fonction de la pression jusqu'a 1000-atm. *J. Phys. Radium* **1955**, *16* (4), 348–349.
34. Kanazawa, K.K.; Gordon, J.G., II. The oscillation frequency of a quartz resonator in contact with a liquid. *Anal. Chim. Acta* **1985**, *175*, 99–105.
35. Kanazawa, K.K.; Gordon, J.G., II. Frequency of a quartz microbalance in contact with liquid. *Anal. Chem.* **1985**, *57* (8), 1770–1771.
36. Urbakh, M.; Daikhin, L. Influence of the surface-morphology on the quartz-crystal microbalance response in a fluid. *Langmuir* **1994**, *10* (8), 2836–2841.
37. Schumacher, R.; Borges, G.; Kanazawa, K.K. The quartz microbalance: A sensitive tool to probe surface reconstructions on gold electrodes in liquid. *Surf. Sci.* **1985**, *163* (1), L621–L626.
38. Urbakh, M.; Daikhin, L. Roughness effect on the frequency of a quartz-crystal resonator in contact with a liquid. *Phys. Rev., B* **1994**, *49* (7), 4866–4870.
39. Daikhin, L.; Urbakh, M. Effect of surface film structure on the quartz crystal microbalance response in liquids. *Langmuir* **1996**, *12* (26), 6354–6360.
40. Wu, Y.-T.; Akoto-Ampaw, P.-J.; Elbaccouch, M.; Grant, C.S.; Hurrey, M.; Wallen, S.L. Quartz crystal microbalance (QCM) in high pressure carbon dioxide—Experimental examination of QCM theory and adsorption of carbon dioxide on metal surfaces. *Langmuir* **2003**. Submitted.
41. Otake, K.; Kurosawa, S.; Sako, T.; Sugeta, T.; Hongo, M.; Sato, M. Frequency change of a quartz crystal microbalance at the supercritical condition of carbon dioxide. *J. Supercrit. Fluids* **1994**, *7* (4), 289–292.
42. Guigard, S.E.; Hayward, G.L.; Zytner, R.G.; Stiver, W.H. Measurement of solubilities in supercritical fluids using a piezoelectric quartz crystal. *Fluid Phase Equilib.* **2001**, *187*, 233–246.
43. Narasimhan, B.; Peppas, N.A. The physics of polymer dissolution: Modeling approaches and experimental behavior. *Polym. Anal., Polym. Phys.* **1997**, *128*, 157–207.
44. Dammel, R.; Reiser, A. Recent developments in the dissolution of novolak-based resists. *Polym. Mater. Sci. Eng.* **1993**, *68*, 49–51.
45. Hinsberg, W.D.; Willson, C.G.; Kanazawa, K.K. Use of a quartz crystal microbalance rate monitor to examine photoproduct effects on resist dissolution. *Proc. SPIE Int. Soc. Opt. Eng.* **1985**, *539*, 6–13.
46. Hinsberg, W.D.; Willson, C.G.; Kanazawa, K.K. Measurement of thin-film dissolution kinetics using a quartz crystal microbalance. *J. Electrochem. Soc.* **1986**, *133* (7), 1448–1451.
47. Ito, H. Dissolution behavior of chemically amplified resist polymers for 248-, 193-, and 157-nm lithography. *IBM J. Res. Develop.* **2001**, *45* (5), 683–695.
48. Mueller, K.E.; Koros, W.J.; Wang, Y.Y.; Willson, C.G. Diffusivity measurements in polymers: Part III. Quartz crystal microbalance techniques. *Proc. SPIE Int. Soc. Opt. Eng.* **1997**, *3049*, 871–878.
49. Pham, V.Q.; Weibel, G.L.; Rao, N.G.; Ober, C.K. Dissolution rate measurements for resist processing in supercritical carbon dioxide. *Proc. SPIE Int. Soc. Opt. Eng.* **2002**, *4690*, 425–431.
50. Wu, Y.-T.; Grant, C.S. Evaluation of the dissolution of photoresist polymer films in supercritical carbon dioxide using quartz crystal microbalance. *Langmuir* **2003**. Submitted.
51. Wang, N.H.; Takishima, S.; Masuoka, H. Solubility measurements of gas in polymer by the piezoelectric-quartz sorption method at high pressures and its correlation. Carbon dioxide + poly(vinyl acetate) and carbon dioxide + poly(butyl methacrylate) systems. *Kagaku Kogaku Ronbunshu* **1990**, *16* (5), 931–938.
52. Miura, K.; Otake, K.; Kurosawa, S.; Sako, T.; Sugeta, T.; Nakane, T.; Sato, M.; Tsuji, T.; Hiaki, T.; Hongo, M. Solubility and adsorption of high pressure carbon dioxide to poly(styrene). *Fluid Phase Equilib.* **1998**, *144* (1–2), 181–189.
53. Aubert, J.H. Solubility of carbon dioxide in polymers by the quartz crystal microbalance technique. *J. Supercrit. Fluids* **1998**, *11* (3), 163–172.
54. Hattori, K.; Wang, N.H.; Takishima, S.; Masuoka, H. Chromatographic measurement of vapor-liquid equilibrium ratios of organic solvents in supercritical carbon

- dioxide-poly(vinyl acetate) system. *Process Metall.* **1992**, *7B*, 1671–1676.
55. Wang, N.H.; Hattori, K.; Takishima, S.; Masuoka, H. Measurement and prediction of vapor–liquid equilibrium ratios for solutes at infinite dilution in carbon dioxide + poly(vinyl acetate) system at high pressures. *Kagaku Kogaku Ronbunshu* **1991**, *17* (6), 1138–1145.
  56. Nakamura, K.; Hoshino, T.; Suzuki, Y.; Yosizawa, H. Adsorption Isotherms for Supercritical Carbon Dioxide on Proteins and Polysaccharides. In *Proc. Int. Congr. Eng. Food*, 6th Ed.; Blackie: Glasgow, UK, 1994.
  57. Spall, W.D. Supercritical carbon dioxide precision cleaning for solvent and waste reduction. *Int. J. Environ. Conscious Des. Manuf.* **1993**, *2* (1), 81–86.
  58. McHardy, J.; Stanford, T.B.; Benjamin, L.R.; Whiting, T.E.; Chao, S.C. Progress in supercritical CO<sub>2</sub> cleaning. *SAMPE J.* **1993**, *29* (5), 20, 22–27.
  59. Douglas, M.A.; Wallace, R.M. Method of Cleaning and Treating a Micromechanical Device. US patent Number EP0746013, December 4, 1996.
  60. Rubin, J.B.; Davenhall, L.B.; Taylor, C.M.V.; Sivils, L.D.; Pierce, T. Carbon Dioxide-Based Supercritical Fluids as IC Manufacturing Solvents. In *IEEE International Symposium on Electronics and the Environment*; Danvers, MA, 1999.
  61. Lewis, H.G.P.; Weibel, G.L.; Ober, C.K.; Gleason, K.K. E-beam patterning of hot-filament CVD fluorocarbon films using supercritical CO<sub>2</sub> as a developer. *Chem. Vap. Depos.* **2001**, *7* (5), 195.
  62. Namatsu, H. Supercritical drying for water-rinsed resist systems. *J. Vac. Sci. Technol., B: Microelectron. Nanometer Struct.* **2000**, *18* (6), 3308–3312.
  63. Jafri, I.; Busta, H.; Walsh, S.T. Critical point drying and cleaning for MEMS technology. *Proc. SPIE Int. Soc. Opt. Eng.* **1999**, *3880*, 51–58.
  64. Naito, M.; Sasaki, Y.; Dewa, T.; Aoyama, Y.; Okahata, Y. Effect of solvation on induce-fit molecular recognition in supercritical fluid to organic crystals immobilized on a quartz crystal microbalance. *J. Am. Chem. Soc.* **2001**, *123* (44), 11037–11041.
  65. Mori, T.; Naito, M.; Irimoto, Y.; Okahata, Y. Nucleo-base molecular recognition in supercritical carbon dioxide by using a highly sensitive 27 MHz quartz-crystal microbalance. *Chem. Commun.* **2000**, (1), 45–46.
  66. Blackburn, J.M.; Long, D.P.; Cabanas, A.; Watkins, J.J. Deposition of conformal copper and nickel films from supercritical carbon dioxide. *Science* **2001**, *294* (5540), 141–145.
  67. Cooper, A.I. Recent developments in materials synthesis and processing using supercritical CO<sub>2</sub>. *Adv. Mater.* **2001**, *13* (14), 1111–1114.
  68. Shi, C.; Huang, Z.; Kilic, S.; Xu, J.; Enick, R.M.; Beckman, E.J.; Carr, A.J.; Melendez, R.E.; Hamilton, A.D. The gelation of CO<sub>2</sub>: A sustainable route to the creation of microcellular materials. *Science* **1999**, *286* (5444), 1540–1543.
  69. Cao, C.; Fadeev, A.Y.; McCarthy, T.J. Reactions of organosilanes with silica surfaces in carbon dioxide. *Langmuir* **2001**, *17* (3), 757–761.

# Mineral Nanoparticles: Electrokinetics

**Mehmet S. Celik**

*Mineral and Coal Processing Section, Istanbul Technical University, Istanbul, Turkey*

**Bahri Ersoy**

*Iscehisar Vocational School, Afyon Kocatepe University, Afyon, Turkey*

## INTRODUCTION

The term “electrokinetics” means the combined effects of motion and electrical phenomena. However, the term “electrokinetic properties” carry a wider connotation including zeta potential ( $\zeta$ ), the structure of electrical double layer (EDL), surface potential, and isoelectric point (iep) phenomena. The electrokinetic properties of a substance, inorganic or organic, are used to explain the mechanism of dispersion and agglomeration in a liquid phase and to identify the adsorption mechanisms of ions or molecules at a solid–liquid interface. Therefore they play an important role in a spectrum of applications including ceramics, food, mining, paper, medicine, water and wastewater treatment, emulsions, biochemistry, and detergents. In this entry, the type and significance of electrokinetic properties of mineral nanoparticles, the mechanism of particle–particle interactions in liquid systems, and the applications of electrokinetic phenomena are presented.

## DESCRIPTION OF ELECTROKINETIC PROPERTIES OF MINERAL PARTICLES

### Origin of Surface Charge

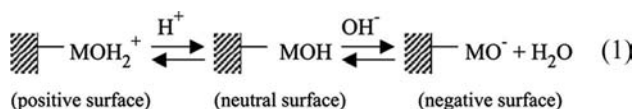
Each mineral particle in a liquid whether colloidal ( $<1\ \mu\text{m}$ ) or nanoparticle ( $<100\ \text{nm}$ ) carries electrokinetic charges depending on the properties of liquid phase such as pH and ionic strength.<sup>[1–3]</sup> The surface charge of minerals can originate as a result of a number of mechanisms discussed below.

### Dissociation of surface groups

In most solid minerals, dissociable functional surface groups such as carboxyl ( $-\text{COOH}$ ) and hydroxyl ( $-\text{OH}$ ) are present. These groups may be ionizable depending on the solution pH; a surface is

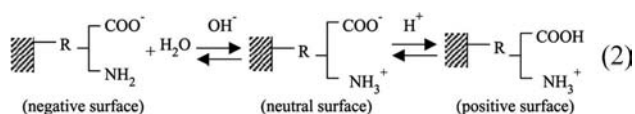
charged either negatively at high pHs or positively at low pHs.

For metal oxides and hydroxides: (see Eq. (1) below)



where M represents a metal cation at the surface.

For coal representing a typical hydrophobic mineral where R represents a hydrocarbon compound constituting the coal structure (see Eq. (2) below).



Consequently, for simple metal oxides and hydroxides, e.g.,  $\text{SiO}_2$ ,  $\text{Al}_2\text{O}_3$ ,  $\text{Fe}_2\text{O}_3$ , and  $\text{AlOOH}$ , complex metal oxides including clay minerals<sup>[4–6]</sup> and some hydrophobic minerals, e.g., coal,<sup>[7]</sup>  $\text{H}^+$ , and  $\text{OH}^-$  ions are considered as the potential determining ions (pdis) (see “[Potential Determining, Indifferent, and Specifically Adsorbed Ions](#)” section).

### Preferential dissolution of lattice ions

This type of charging mechanism is generally developed in aqueous solutions with some soluble ionic solids, viz.,  $\text{AgI}$ ,  $\text{CaCO}_3$ ,  $\text{BaSO}_4$ , and  $\text{CaF}_2$  as a result of the preferential release of certain constituent lattice ions from the solid into liquid phase as a result of hydration and lattice energies.<sup>[8]</sup> The concentrations of these ions at equilibrium state are dictated by the solubility product of the solid.<sup>[9]</sup> For  $\text{AgI}$  particles, for instance, the amount of  $\text{Ag}^+$  ions released into water from the particle surface at  $25^\circ\text{C}$  is more than that of  $\text{I}^-$  ions. Therefore the surface of  $\text{AgI}$  particle remains negatively charged. Thus the constituent lattice ions for these minerals are considered as the pdis.



### Preferential adsorption of ions from solution

This mechanism is most commonly observed and results from the differences in the affinity of two phases for some ions. Some specific ions (see “[Potential Determining, Indifferent, and Specifically Adsorbed Ions](#)” section) can strongly adsorb on a solid surface and charge the particle, or, vice versa, a charged particle can become noncharged through such adsorption, e.g., adsorption of  $H^+$  and  $OH^-$  on oxide minerals (Eqs. (3) and (4) in the case of  $SiO_2$ ),  $Ag^+$  and  $I^-$  adsorption on silver iodide particles, and  $Al^{3+}$  and  $HDTMA^+$  (hexadecyltrimethylammonium) adsorption on clinoptilolite.<sup>[10]</sup> It should be noted that especially for  $H^+$  and  $OH^-$  ions, it is difficult to distinguish whether the charging of a particle is generated from the adsorption or dissociation of these ions (see below).<sup>[2]</sup>



### Isomorphic substitutions

Almost all clay and zeolite minerals that are generally characterized as aluminum silicates exhibit negative charges in water, which results from the substitutions within the crystal lattice of  $Al^{3+}$  for  $Si^{4+}$  or  $Mg^{2+}$  for  $Al^{3+}$ .<sup>[11–14]</sup> Consequently, negative charges are developed in the lattice to compensate the so-called exchangeable cations, i.e.,  $Na^+$ ,  $K^+$ , and  $Ca^{2+}$  entering the crystal structure. When such minerals come in contact with water, some of these cations can easily dissociate, leading to negatively charged surfaces.

### Accumulation and transfer of electrons

Besides ion transfer, as explained above, electron transfer is also possible between solid and liquid phases depending on differences in the electron affinities of the two phases. Also, some molecules of dipole character may be oriented at the solid–liquid interface leading to charged surfaces,<sup>[2,3]</sup> this is mostly observed at the metal–solution interface.

### Electrical Double Layer and Double-Layer Models

When a mineral particle is immersed in a liquid, a surface charge will be developed through one of the mechanisms discussed above. Let us imagine a

negatively charged solid particle in an electrolyte solution; while the oppositely charged counterions will congregate in the vicinity of the particle, coions having the same sign with that of the particle will be repelled from the surface as a result of electrostatic interactions. Thus a charged surface layer (layer 1) and an ionic layer (layer 2) all the way to the bulk water constitute the electrical double layer with a thickness usually ranging from a few angstroms to a few hundred angstroms. To examine the structure of EDL, different models have been proposed.<sup>[3,15]</sup> These models are introduced below.

### Helmholtz compact layer model

The earliest model of the EDL, in which a rigid layer away from the surface in solution consists of oppositely charged ions, was proposed in 1879 by Helmholtz.<sup>[16]</sup> Also, the surface charge of particle is equal to that of rigid layer. Because this model ignores the disrupting effect of thermal agitation, it is unreasonable. This model is known as a molecular condenser model owing to its similarity to a parallel plate condenser.<sup>[1]</sup> Using the law of distribution of EDL, the potential  $\psi$  (V) across the double layer for this capacitor is

$$\psi = \sigma d / \epsilon \epsilon_0 \quad (5)$$

where  $\sigma$  is the charge density per unit area of a plate ( $C/m^2$ ),  $\epsilon$  (dimensionless) is the dielectric constant of the medium, and  $\epsilon_0$  is the permittivity of free space ( $8.854 \times 10^{-12} C^2/Jm$ ).

### Gouy–Chapman diffuse double-layer model

This is independently known as the Gouy–Chapman model. They expressed that, in addition to the electrostatic attraction of counterions to the charged surface, some of them tend to diffuse toward the bulk solution because of their thermal motion. Note that the EDL theory can be developed for different solid geometries such as flat plate, sphere, and cylinder. Because most studies for organic and inorganic solids in liquids assume the flat plate geometry,<sup>[17,18]</sup> here we also consider the flat plate to simplify the structure of EDL. The theory of Gouy–Chapman is based on the two fundamental equations: Poisson and Boltzmann.<sup>[16]</sup> The Poisson equation (Eq. (6)) for a flat surface given below is related to the potential distribution of an electric charge relative to the distance from the surface in a medium.

$$d^2\psi/dx^2 = \psi_{(x)} = -\rho_{(x)}/\epsilon\epsilon_0 \quad (6)$$

where  $\psi_{(x)}$  is the double-layer potential (V) at a point located a distance  $x$  from the surface,  $\rho_{(x)}$  is the

charge density per unit volume (C/m<sup>3</sup>) at the same point.

The Boltzmann equation is given by

$$n_i = n_i^0 \exp(-z_i e \psi / kT) \tag{7}$$

where  $n_i$  is the number of ions of type  $i$  per unit volume near the surface or in diffuse layer,  $n_i^0$  is the number of ions of type  $i$  per unit volume in the bulk solution,  $z_i$  is the valence number of  $i$  including its sign,  $e$  is the electronic charge ( $1.602 \times 10^{-19}$  C),  $k$  is the Boltzmann constant ( $1.381 \times 10^{-23}$  J/K), and  $T$  is the absolute temperature (K). The term  $z_i e \psi$  signifies the electrostatic (or coulombic) work required to bring the ion,  $i$ , from the bulk of the solution (where  $x \rightarrow \infty$  and  $\psi_0 = 0$ ) to a position where the potential is  $\psi$ .

The volume charge density near the surface is

$$\rho = \sum e z_i n_i = \sum e z_i n_i^0 \exp(-z_i e \psi / kT) \tag{8}$$

Substituting Eq. (8) into Eq. (6) yields the Poisson-Boltzmann equation (Eq. (9)).

$$d^2 \psi / dx^2 = (-1 / \epsilon \epsilon_0) \sum e z_i n_i^0 \exp(-z_i e \psi / kT) \tag{9}$$

Eq. (9) shows a non-linear differential equation without an explicit general solution but can be analytically solved by the Debye-Huckel approximation provided that  $z_i e \psi < kT$ , i.e., the potential ( $\psi$ )  $< 25.7 / z_i$  mV throughout the EDL. Thus Eq. (9) is converted to the following form<sup>[16]</sup>

$$d^2 \psi / dx^2 = \kappa^2 \psi \tag{10}$$

where  $\kappa$  is known as the Debye-Huckel parameter with a unit of reciprocal length (m<sup>-1</sup>) and given by

$$\kappa = \left[ \frac{e^2 \sum n_i^0 z_i^2}{\epsilon \epsilon_0 kT} \right]^{1/2} \tag{11}$$

For water at 25°C, Eq. (11) becomes

$$\kappa = 3.288 I^{1/2} \tag{12}$$

where  $I$  is the ionic strength ( $I = \frac{1}{2} \sum c_i z_i^2$ ) of the solution and  $c_i$  is the concentration of an ion,  $i$  in mol/L, and  $z_i$  is the valence number of  $i$ . Note that the inverse of  $\kappa$ ,  $1/\kappa$ , is a very important term in the stability of colloidal particles and is called as “the electrical double-layer thickness.” When the distance from surface reaches the value of  $1/\kappa$ , the double-layer (DL) potential ( $\psi$ ) equals  $\psi_0/e$  ( $e = 2.7182$ ). Eq. (12) clearly shows that the double-layer thickness is basically dependent on the ion concentration and the valency of the ion. An increase in both parameters results in

a decrease in double-layer thickness and potential as shown in Fig. 1.

For surface potentials ( $\psi_0$ )  $< 25$  mV, the solution of Eq. (10) yields<sup>[3]</sup>

$$\psi = \psi_0 \exp(-\kappa x) \tag{13}$$

where  $x$  is the distance from surface and  $\kappa$  is the Debye-Huckel parameter. For high surface potentials, i.e.,  $z_i e \psi > kT$ , the exact solution of Eq. (9) is required. The solution given by Gouy (1910) and Chapman (1913), for the case of a symmetrical electrolyte ( $z_{i+} = -z_{i-} = z$ , such as NaCl, CaSO<sub>4</sub>; and  $n_{i+}^0 = n_{i-}^0 = n^0$ ) and some mathematical manipulations, becomes<sup>[16]</sup>

$$\tanh(z e \psi / kT) = \tanh(z e \psi_0 / kT) \exp(-\kappa x) \tag{14}$$

or

$$\gamma = \gamma_0 \exp(-\kappa x)$$

where  $\gamma = \tanh(z e \psi / 4kT)$  and  $\gamma_0 = \tanh(z e \psi_0 / 4kT)$ .

Evidently, although Eq. (14) is relatively more complex than Eq. (13), it has wider applicability. The surface

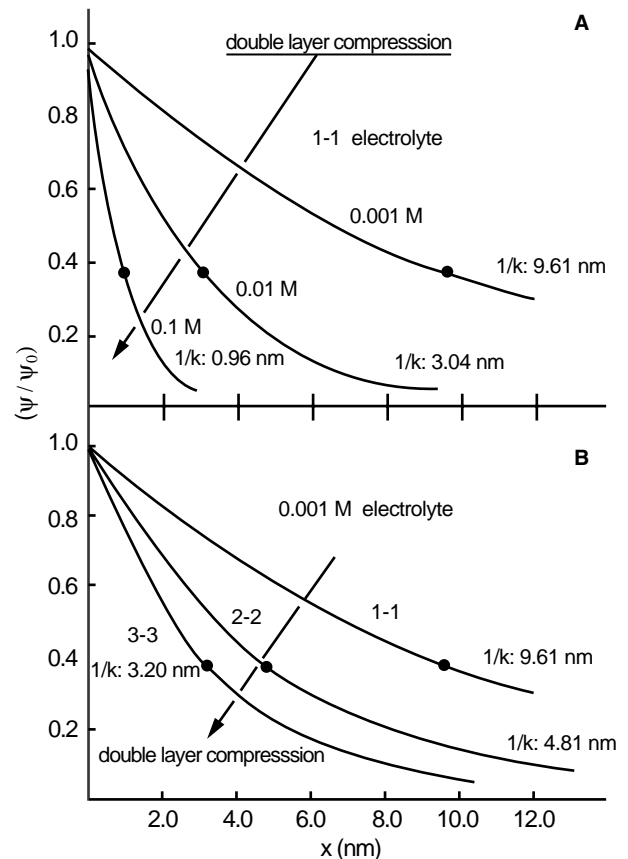


**Fig. 1** Variation of electrical double-layer thickness with electrolyte concentration. Source: From Ref.<sup>[16]</sup>.

charge density ( $\sigma_0$ ) of a particle in a liquid is given elsewhere.<sup>[3]</sup>

### Stern–Grahame model

The Gouy–Chapman model of EDL includes some unrealistic cases. For example, the ions are assumed as point charges and any specific effects related to the ion size are neglected. Therefore the adsorption densities on the solid surface calculated for moderate surface potentials and ionic strength values are so high that they are physically impossible. Also, the solvent is assumed to have continuous properties everywhere in solution; however, its properties such as the dielectric constant and the viscosity may be different in the EDL and the bulk solution.

Stern (1924)<sup>[19]</sup> modified the Gouy–Chapman model with an adsorbed layer of ions of thickness  $d$ , which is usually considered as 0.3–0.5 nm. This layer, assumed to be held fixed at the surface, is called the Stern layer. Thus the ion distribution in solution around the charged particle is divided into two parts: the Stern layer, which is the identical form in the Helmholtz model and consists of specifically adsorbed ions, and the diffuse (or Gouy) layer. The double layer in Fig. 2 essentially shows three layers, i.e., the layer of charged solid surface, the Stern layer, and the diffuse layer, but in the literature the commonly used term is “double layer.” Also, there is a shear plane in the diffuse layer at which the double layer potential ( $\psi$ ) is called the zeta ( $\xi$ ) potential.

Grahame<sup>[19]</sup> further divided the Stern layer into two parts: inner Helmholtz plane (IHP) and outer Helmholtz plane (OHP) (Fig. 2A,B). At the  $b$  plane, there are specifically adsorbed unhydrated ions known as the IHP, while that of the closest approach to the more weakly adsorbed hydrated ions at  $d$  is known as the OHP, the onset of the diffuse layer. This model, known as the Stern–Grahame model, is usually represented with low amounts of specifically adsorbed ions (Fig. 2A) while the modified version (Fig. 2B) incorporates the specifically adsorbed ions. In the former, the sign of particle surface cannot be reversed, but it is possible in the latter. The potential distribution in the diffuse layer for a symmetrical electrolyte (Eq. (14)) can be rewritten as;

$$\tanh(ze\psi/4kT) = \tanh(ze\psi_d/4kT) \times \exp[-\kappa(x - d)] \quad (15)$$

Note that, in the case of electrolyte concentrations less than 0.1 M, the zeta ( $\xi$ ) potential can be used instead of  $\psi_d$ . The composition of the double layer is usually inferred from a comparison between  $\sigma_0$  and  $\sigma_d$  or  $\psi_0$  and  $\psi_d$ , then computed by some model. The following

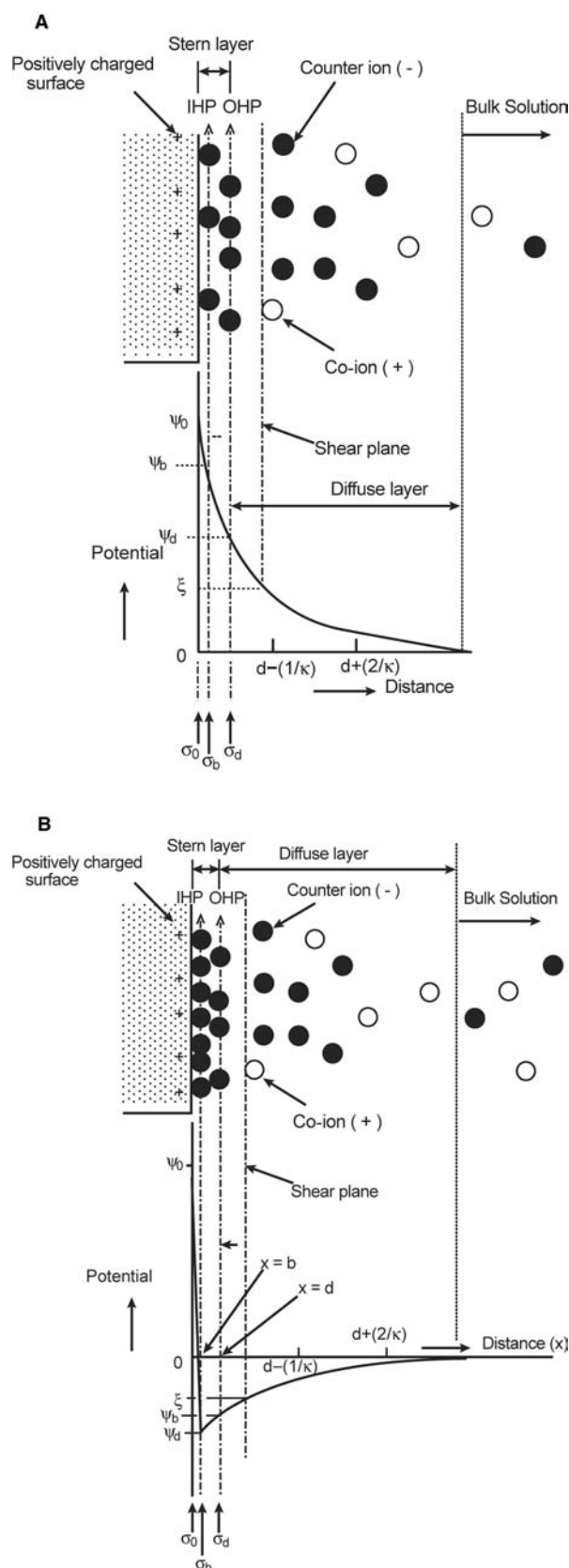


**Fig. 2** The Stern–Grahame model represented by (A) by low concentration of specifically adsorbed ions and (B) by higher concentration of the specifically adsorbed ions.

equation has a reasonably wide applicability if the amount of specifically adsorbed ions is low.

$$(\theta/1 - \theta) = (c_i/55.5) \times \exp[-(z_i e \psi_b + \Phi)/kT] \quad (16)$$

where  $\theta = \sigma_b/\sigma_0$  ( $0 \leq \theta \leq 1$ ),  $\sigma_b$  and  $\sigma_0$  are charge densities at the IHP and at the surface (in  $C/cm^2$ ), and  $\Phi$  stands for the specific adsorption free energy in units of  $kT$  and  $\psi_b$  is the potential at the IHP,  $c_i$  is the bulk concentration of ion  $i$  (mol/L). Eq. (16) is an extension of the familiar Langmuir equation.<sup>[2]</sup>

### Potential Determining, Indifferent, and Specifically Adsorbed Ions

Potential determining ions (pdi) are the major ions responsible for the establishment of the surface charge of particle.<sup>[3]</sup> Their activities in the liquid play a crucial role in the generation of potential difference across a solid-liquid interface. They are also able to reverse the sign of  $\zeta_p$  of the solid. As a simple recipe, for a cation to be the pdi, it must make the surface more positive upon increasing the cation concentration. Similarly, for an anion to be the pdi, it must impart the surface more negative charges with increasing anion concentration. While the pdi for ionic solids such as AgI, BaSO<sub>4</sub>, and CaCO<sub>3</sub>, etc. are the lattice constituent ions, i.e., Ag<sup>+</sup>, I<sup>-</sup>, Ba<sup>2+</sup>, SO<sub>4</sub><sup>2-</sup>, Ca<sup>2+</sup>, CO<sub>3</sub><sup>2-</sup>, H<sup>+</sup> and OH<sup>-</sup> ions are for metal oxides and hydroxides, silicate or clay minerals, some hydrophobic minerals (e.g., coal), and some synthetic polymers with sulfate groups.<sup>[1,3,5,6]</sup> Fig. 3 clearly shows the difference in

the behavior of a positively charged alumina surface toward (a) pdi: H<sup>+</sup> and OH<sup>-</sup>; (b) the indifferent ions Cl<sup>-</sup>, and NO<sub>3</sub><sup>-</sup>, Na<sup>+</sup>, and Ba<sup>2+</sup>; and (c) the specifically adsorbed ions SO<sub>4</sub><sup>2-</sup> and S<sub>2</sub>O<sub>3</sub><sup>2-</sup>. For metal oxides, for example, the surface potential is determined by the activities of pdis and expressed by Nernst-like equation

$$\psi_0 = (RT/F) \ln(a_{H^+}/a_{H^+}^0) \quad (17)$$

where  $F$  is the Faraday constant,  $a_{H^+}$  is the activity of H<sup>+</sup>, and  $a_{H^+}^0$  refers to the point of zero charge (pzc). The operational formula for aqueous solutions at 25°C is  $\psi_0 = 0.059 \text{ V (pH}^0 - \text{pH)}$ , where  $\text{pH}^0$  refers to the pzc.<sup>[19]</sup> For AgI, Eq. (17) can be written as

$$\psi_0 = (RT/F) \ln(a_{Ag^+}/a_{Ag^+}^0) \quad (18)$$

Indifferent ions are those that cannot specifically adsorb in the Stern layer of the EDL and unable to reverse the sign of surface charge of the particle but only compress the electrical double layer. For example, monovalent ions such as Na<sup>+</sup> and Cl<sup>-</sup> are indifferent ions for colemanite,<sup>[21]</sup> and Na<sup>+</sup>, Cl<sup>-</sup>, NH<sub>4</sub><sup>+</sup>, NO<sub>3</sub><sup>-</sup>, CaOH<sup>+</sup>, MgOH<sup>+</sup>, Al(OH)<sup>+</sup>, and Al(OH)<sup>2+</sup> are indifferent ions for clinoptilolite (natural zeolite).<sup>[10]</sup> Indifferent ions, which usually decrease the double-layer thickness ( $1/\kappa$ ), are used in electrokinetic studies to determine the point of zero charge (pzc) or isoelectric point (iep) of minerals (Fig. 3).

Specifically adsorbed ions possess special affinity for the solid surface through coulombic and non-coulombic forces. These noncoulombic forces may be chemical in nature, i.e., involving some degree of

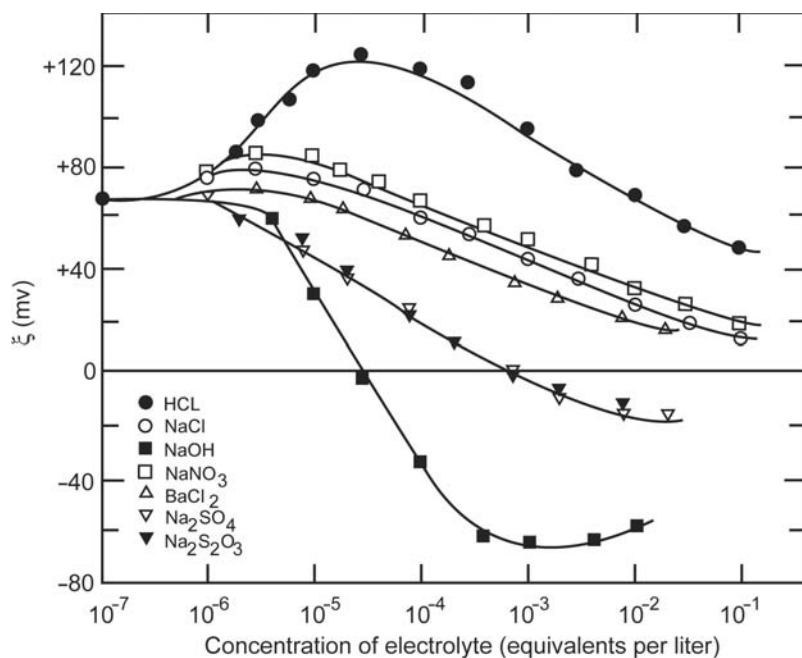


**Fig. 3** Zeta potential profile of a positively charged alumina surface in the presence of various ions. *Source:* From Ref.<sup>[3]</sup>.

covalent bonding with surface atoms or be more physical, e.g., van der Waals forces between the ion and the surface or between the hydrocarbon chains of surfactant ions adsorbed.<sup>[3]</sup>

### Isoelectric Point and/or Point of Zero Charge

Although the isoelectric point (iep) and the point of zero charge (pzc) are identical by definition, there are some differences between them. The iep or pzc of some typical minerals are given in Table 1. While the pzc denotes the state in which the net surface charge of the solid is zero, the iep describes the condition at which the potential at the shear plane, i.e., the zp obtained from electrokinetic measurements is zero; the iep and pzc are the same in the absence of the specific adsorption. But the pzc of a mineral need not coincide with the iep in most cases as seen in Table 1.

The iep of a mineral is directly obtained by electrokinetic measurements (see “Potential Determining, Indifferent, and Specifically Adsorbed Ions” section) against pH, usually in the presence of indifferent electrolytes (or ions) of various molarities seen in Fig. 4. This figure indicates that 1)  $\text{KNO}_3$  is an indifferent electrolyte for this system and 2) the iep in this case is the same as the pzc. The pzc is experimentally determined usually by potentiometric titration method of the adsorbed pdi.<sup>[40]</sup> For example, for oxides, hydroxides, and silicates, the surface charge density at pzc,  $\sigma_0$ , can be expressed as

$$\sigma_0 = F(\Gamma_{\text{H}^+} - \Gamma_{\text{OH}^-}) = 0 \quad (19)$$

where  $\Gamma_{\text{H}^+}$ , and  $\Gamma_{\text{OH}^-}$  are analytical surface excess for  $\text{H}^+$  and  $\text{OH}^-$  ions, respectively. Here it must be noted that iep and pzc of minerals depend on the heterogeneity of mineral surface and pretreatments of minerals such as leaching, washing, and ultrasonic scrubbing.<sup>[11,23,30,41]</sup> Interestingly, the iep of particularly semisoluble salt-type minerals has been found to vary with the solids concentration.<sup>[21]</sup>

### Zeta Potential (zp)

Zeta ( $\xi$ ) potential is an intrinsic property of a mineral particle in a liquid. It determines the strength of the EDL repulsive forces between particles and identifies the stability of a colloidal system. The zp is known as the measurable surface potential of a particle, viz., the potential at the shear plane. There is no direct experimental method for determining both the surface potential ( $\psi_0$ ) and Stern layer potential ( $\psi_d$ ).<sup>[3]</sup> So far, the exact position of the shear plane within the diffuse layer of the EDL could not be determined, but it is assumed that the position of the shear plane is very

close to the outer Helmholtz plane (OHP).<sup>[1]</sup> The  $\xi$  potential is fairly close to the Stern potential,  $\psi_d$ , in magnitude, and definitely less than the potential at surface,  $\psi_0$ .

## METHODS OF ZETA POTENTIAL MEASUREMENTS

Electrokinetic measurements using electrophoresis, electroosmosis, streaming potential, and sedimentation potential can be interpreted to yield a quantity known zeta or electrokinetic potential.<sup>[3,42]</sup> Of these four techniques, the electrophoresis is perhaps the best known and most commonly used technique to measure the zp of minerals. While the electrophoresis technique with modifications is extended for the measurement of very fine particles such as nanoparticles (<100 nm) and colloidal particles (<1  $\mu\text{m}$ ), other techniques are usually employed for larger particles. The size of mineral particles is independent of the charge and only identifies the measurement technique.

### Electrophoresis

When a charged mineral particle in a conducting liquid is applied an electrical field, it moves toward the oppositely charged electrode (relative to its charge). This is called electrophoresis. The method is based on the mobility ( $U$ ) of the particle under the applied electrical field ( $E$ ). The electrophoretic mobility of the particle represents the velocity ( $\nu$ ) per unit electric field ( $E$ ) and is given by

$$\begin{aligned} U \text{ (mobility)} &= \text{speed/electric field} = \nu/E \\ &= (\text{m/sec.})/(\text{V/m}) \end{aligned} \quad (20)$$

The mobility of particle is converted to the zp by the Henry equation

$$U = (\xi\epsilon/1.5\eta)f(\kappa a) \quad (21)$$

where  $\xi$  is the zeta potential,  $\epsilon$  is the dielectric constant of the medium relative to the vacuum,  $\eta$  is the viscosity of the medium,  $f(\kappa a)$  is the corrector factor depending on the product of  $\kappa$  (Debye–Huckel parameter), and  $a$  is the particle radius. For very small particles in dilute solution where the thickness of the DL ( $1/\kappa$ ) is large,  $\kappa a \ll 1$  and  $f(\kappa a) = 1$  (Huckel equation). For large particles in more concentrated solution,  $\kappa a \gg 1$  and  $1/\kappa$  is small, and  $f(\kappa a) = 1.5$  (Smoluchowski equation).<sup>[7]</sup>

If the particles are invisible, as in the case of some protein molecules, they are tracked by the Tiselius technique.<sup>[3,42]</sup> However, for particles of about 0.5  $\mu\text{m}$  in diameter or larger, direct observation is possible

**Table 1** iep and pzc of some typical natural and synthetic minerals

Mineral	Typical formula	iep or pzc	Reference
<i>Metal oxides and hydroxides</i>			
Corundum	Al <sub>2</sub> O <sub>3</sub>	pH 3 <sup>a</sup>	[5]
Quartz	SiO <sub>2</sub>	pH 2.2 <sup>a</sup>	[22]
Hematite	Fe <sub>2</sub> O <sub>3</sub>	pH 3 <sup>a</sup> , pH 7.1 <sup>b</sup>	[23]
Rutile	TiO <sub>2</sub>	pH 4.7 <sup>a</sup>	[5]
Zirconium	ZrO <sub>2</sub>	pH 10 <sup>a</sup>	[5]
Diaspore	γ-AlO(OH)	pH < 2 <sup>a</sup>	[5]
Goethite	α-FeOOH	pH 3.2 <sup>a</sup>	[5]
<i>Metal sulfides</i>			
Pyrite	FeS <sub>2</sub>	pH 6.5 <sup>a</sup>	[24]
Chalcopyrite	CuFeS <sub>2</sub>	PH 1.8 <sup>b</sup>	[25]
Sphalerite	ZnS	pH 2 <sup>b</sup>	[25]
Silver sulfide	Ag <sub>2</sub> S	pAg 10.2 <sup>b</sup>	[3]
<i>Soluble ionic minerals</i>			
Calcite	CaCO <sub>3</sub>	pH 8 <sup>a</sup>	[26]
Fluorite	CaF <sub>2</sub>	pCa 3 <sup>b</sup>	[3]
Silver iodide	AgI	pAg 5.6 <sup>b</sup>	[3]
<i>Complex minerals</i>			
Colemanite	Ca <sub>2</sub> B <sub>6</sub> O <sub>11</sub> .5H <sub>2</sub> O	pH 10.5 <sup>a</sup>	[21]
Kaolinite	Al <sub>2</sub> Si <sub>2</sub> O <sub>5</sub> (OH) <sub>4</sub>	pH 3.8 <sup>a</sup>	[11]
Dolomite	CaMg(CO <sub>3</sub> ) <sub>2</sub>	pH 8 <sup>a</sup>	[27]
Fluoroapatite	Ca <sub>5</sub> (PO <sub>4</sub> )(F,OH)	pH 6 <sup>b</sup>	[28]
Wolframite	(FeMn)WO <sub>4</sub>	pH 2.5 <sup>a</sup>	[29]
<i>Hydrophobic minerals</i>			
Coal	C	pH 1.5 <sup>a</sup> –4.8 <sup>a</sup>	[7,30]
Anthracite	C	pH 3.3 <sup>a</sup>	[31]
Talc	Mg <sub>3</sub> (Si <sub>4</sub> O <sub>10</sub> )(OH) <sub>2</sub>	pH 1.9 <sup>b</sup>	[1]
Sulfur	S	pH 2 <sup>b</sup>	[1]
Molybdenite	MoS <sub>2</sub>	pH 1 <sup>b</sup>	[1]
<i>Synthetic minerals and mineral mixtures (composites)</i>			
Silicon carbide	SiC	pH 3.3 <sup>a</sup>	[32]
Silicon	Si	pH 2.4 <sup>a</sup>	[32]
Hematite	α-FeOOH	pH 7.8 <sup>b</sup>	[33]
Boehmite	AlOOH	pH 9.2 <sup>a,c</sup>	[34]
Carbon (fiber)	C	pH 4.5 <sup>a</sup>	[35]
Rutile	TiO <sub>2</sub>	pH 5.9 <sup>a</sup>	[36]
Mixed metal oxide (40% Ni + 60% Co) <sup>c</sup>		pH 9.5 <sup>b</sup>	[37]
Mixed metal oxide (50% SiO <sub>2</sub> + 50% Al <sub>2</sub> O <sub>3</sub> ) <sup>d</sup>		pH 5.2 <sup>b</sup>	[38]

<sup>a</sup>The iep.<sup>b</sup>The pzc.<sup>c</sup>Samples of Ni and Co mixed oxide in the form of powders were synthesized by thermal decomposition of the nitrates at 400°C. Forty and sixty percent means the weight ratio of the composite material.<sup>d</sup>As starting materials, AlCl<sub>3</sub> and tetraethyl orthosilicate were used. They were mixed in an autoclave, and were calcined afterward at 500°C.

using an optic microscope illuminated with a strong light source. An ultramicroscope is useful for particles down to 0.1 μm. An electrical field is applied on the cell consisting of two electrodes and the movement of

mineral particles dispersed in a conducting liquid is observed. Thus the rate of movement of particles moving toward the opposite electrode is observed under an optical microscope using a light beam lamp.



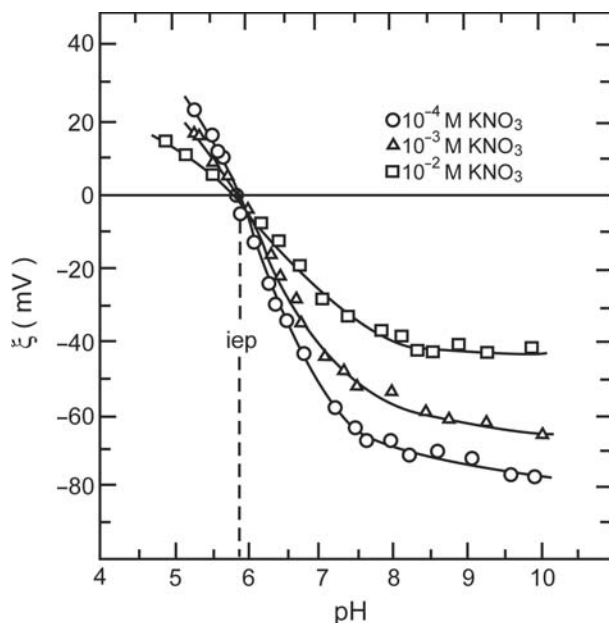


**Fig. 4** Determination of the iep by electrokinetic measurements against pH in the presence of indifferent electrolytes of various molarities. *Source:* From Ref.<sup>[39]</sup>.

Particle velocity is measured by timing individual particles on a microscope grid as they move from the start to the finish line. Ten to twenty particles are usually tracked with each traverse taking 3–15 sec. Thus the electrophoretic mobility of the particle is determined and then converted to the  $z_p$  using the Smoluchowski equation.

Electrokinetic measurements of nanoparticles can be performed by the Laser Doppler Electrophoresis method (LDE), the Phase Analysis Light Scattering Techniques (PALS), Tiselius technique, the Rotating Prism and Rotating Grating, and zone electrophoresis methods.<sup>[42,43]</sup> The LDE and PALS techniques can provide  $z_p$  or electrokinetic measurements of many millions of nanoparticles in a few seconds. The LDE is based on the mixing of scattered light from a sample of a suspension of colloidal particles moving in an electric field, with light directly from the source. The scattered light is frequency-shifted by the Doppler effect, and optical mixing of this with the “unshifted” reference beam light leads to a beating at a frequency dependent on the speed of the particles. The limitation of this method arises from the small displacement of the particles because of a low mobility. This problem can be somewhat overcome with the Phase Analysis Light Scattering Technique (PALS). In this technique, phase modulation is applied so that the Doppler frequency of zero mobility particle is equal to the modulation frequency  $\omega_0$ . It is possible then to measure the deviation of the actual frequency, present in the scattered light, by performing a phase comparison of the

detected signal with the imposed modulator frequency. If the mobility is truly zero, the relative phase of the two will be constant: If a small mobility is present, the relative phase will be shifted, and a small phase shift can be detected by a phase comparator.<sup>[43]</sup> At high ionic strengths where the conventional zeta meters fail to function, the PALS technique is becoming useful.

## Electroosmosis

This method is based on the measurement of liquid in a capillary (or in a system of capillaries such as a porous plug of compressed solid particles) under an applied electric field. When electric field or potential gradient,  $E$ , is applied via the working electrodes on the system, the electrolytes flow in response to the field and drag the liquid along with them. This movement of liquid can be conveniently observed by measuring the movement of a small bubble in the capillary, converting it to the flow rate from which the flow rate the  $z_p$  of the solid may be calculated using the following equation.<sup>[9]</sup>

$$\xi = 4\pi\eta\lambda V_e/\epsilon i \quad (22)$$

where  $V_e$  is the electroosmosis velocity of the liquid,  $i$  is the electric current passing through the capillary,  $\eta$  is the viscosity of the liquid,  $\epsilon$  is dielectric constant of the liquid, and  $\lambda$  is the specific conductance of the liquid.

## Streaming Potential

Streaming potential method may be considered as the converse of the electroosmosis. Here the electric field instead of the liquid velocity is measured. When a liquid is forced to flow through a capillary tube or porous plug by applying pressure, a potential difference is developed. This potential difference is called the streaming potential. The  $z_p$  of the solid (constituting the porous plug) from streaming potential data is given by the following Helmholtz–Smoluchowski equation (Eq. (23)).<sup>[19]</sup>

$$\xi = 4\pi\eta\lambda E_s/\epsilon P \quad (23)$$

where  $E_s$  is the streaming potential and  $P$  is the pressure applied for streaming the liquid. This equation is valid under the conditions where the flow is linear and the pore diameter is much greater than the value of  $1/\kappa$ .<sup>[3,9]</sup>

## Sedimentation Potential

This technique may be regarded as the converse of the electrophoresis method. When a particle in a liquid

settles through a suspending medium under the gravitational forces, it produces an electric field  $E$ . This electric field is measured by inserting reversible electrode probes at two different heights in the column of settling particles and then  $E = \Delta\phi/L$ , where  $\Delta\phi$  is the potential difference and  $L$  is the separation between the electrodes. The  $E$  value may be used to calculate the  $z_p$ , provided that the particle surface is nonconducting, the particles are of uniform size, and  $\kappa a \gg 1$ .<sup>[3,9]</sup>

$$E = (\xi\epsilon a^3/3\eta\lambda)(m_1 - m_2)ng \quad (24)$$

where  $a$  is the radius of the particle,  $m_1$  and  $m_2$  are the densities of particle and liquid respectively,  $n$  is the number of solid particles in a unit volume, and  $g$  is the gravitational constant.

## INTERACTION MECHANISMS BETWEEN MINERAL PARTICLES

### DLVO Theory and the Interaction Energy Curves

The DLVO (Derjaguin and Landau, 1941;<sup>[44]</sup> Verwey and Overbeek, 1948<sup>[45]</sup>) theory explains the stability of colloidal systems including nanosized particles considering the total potential energy of interaction between colloidal particles depending on the distance between them. The total or net interaction energy is equal to the summation of the EDL interaction energy ( $V_{ER}$ ) and the van der Walls interaction energy ( $V_{VA}$ ) and given as

$$V_T = V_{ER} + V_{VA} \quad (25)$$

The EDL interaction energy between two colloidal particles in an electrolyte solution results from the overlapping of their diffuse layers; that is, it results from an osmotic pressure of counterions in repulsive character when the two particles have the same sign of charge. But, when they are opposite in charge, the DL interaction energy becomes attractive in character. The van der Walls interaction energy ( $V_{VA}$ ) between the particles arises from the London–van der Walls forces. If the two particles are identical, the van der Walls interaction is always negative (attractive) but in the case of different particles, this may change depending on the Hamaker constant of the particles and the medium.<sup>[15,46]</sup>

For two spherical colloidal particles of equal size, which usually appear in most colloidal systems, the total interaction energy using the DLVO theory is

described provided that  $a \gg H$  as follows<sup>[15]</sup>

$$V_T = 32\pi\epsilon\epsilon_0 a(kT/ze)^2 \chi^2 \exp(-\kappa H) - (Aa/12H) \quad (26)$$

where  $a$  is the radius of colloidal particles,  $H$  is the shortest distance between them,  $A$  is the effective Hamaker constant depending on the Hamaker constants of the particles and the medium,  $\kappa$  is the Debye–Huckel parameter, and  $\chi$  is given by

$$\chi = \tanh(ze\xi/4kT) \quad (27)$$

Indeed, the right hand of Eq. (27) is identical with the term  $\tanh(ze\psi_d/4kT)$  in Eq. (15), only the zeta ( $\xi$ ) potential instead of  $\psi_d$  is used. In Eq. (26), the first term denotes the EDL repulsion energy ( $V_{ER}$ ) and the second term the van der Walls attraction energy ( $V_{VA}$ ). Note that here  $\xi$  is used as an effective surface potential of the particles. If  $V_T$ ,  $V_{ER}$ , and  $V_{VA}$  are plotted as a function of the distance ( $H$ ), the characteristic curves such as those in Fig. 5 are obtained. Here the  $V_T$  value at each distance is obtained by the summation of the  $V_{ER}$  and  $V_{VA}$  values; that is, the smaller energy is subtracted from the larger energy. If repulsive, the net value is plotted above; if attractive, the net value is plotted below. The  $V_T$  curve is then formed. As seen in Fig. 5, both repulsive and attractive interactions become weaker as the separation distance increases. At sufficiently large distances, the particles exert no influence on each other.

If the colloidal particles are very close, the van der Walls attractive forces take over with a resultant negative energy of interaction leading to the coagulation of particles. At contact state, the total interaction energy is known as the primary minimum. There is also another negative attraction energy usually beyond 3 nm known as the aggregation region or the secondary minimum.<sup>[46]</sup> But the coagulation in this region is not stable and reversible with respect to the case in the primary minimum.<sup>[9,47]</sup> Rheological properties such as thixotropy are closely related to coagulation at the secondary minimum.

If the particles are further away, van der Walls attraction forces sharply decrease because of the large exponent of inverse distance, and the EDL repulsion forces take over with an energy barrier occurring between the particles. If aggregation is required, the height of the energy barrier shown in Fig. 5 should be lowered or removed. Conversely, for a good dispersion, the height of the energy barrier must be enlarged. These two cases can be realized by changing the EDL repulsive forces, as it is perhaps impossible to change the van der Walls forces.

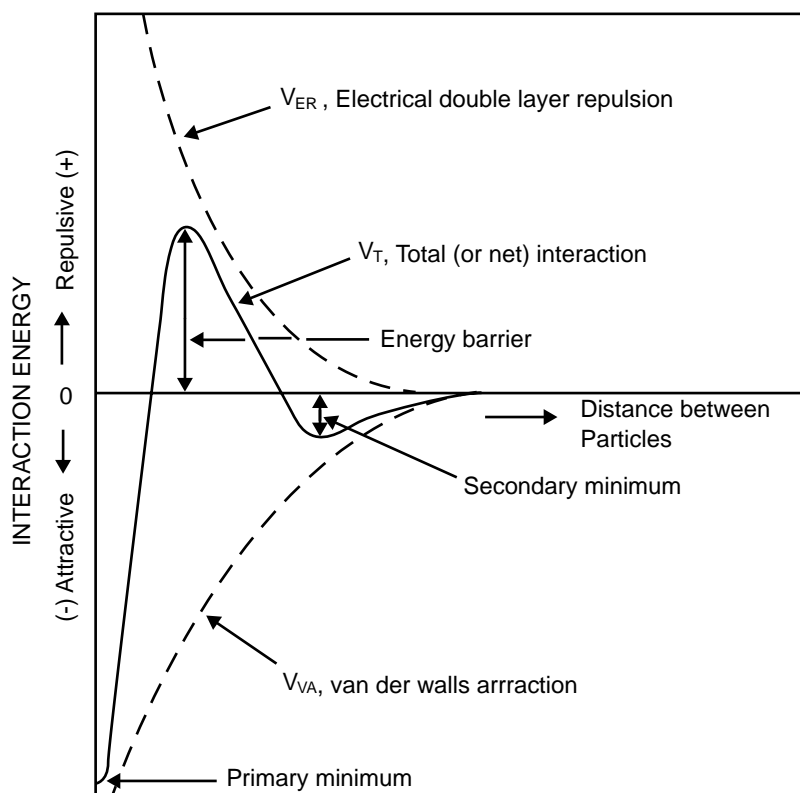


**Fig. 5** Repulsive and attractive forces as a function of distance of separation.

Now we can ask this question, how can we change the EDL repulsive forces? This is possible by changing the  $z_p$  of particles through changing parameters such as the type and concentration of electrolyte and solution pH. For example, for negatively charged colloidal silica particles in distilled water at 0,  $-14$ , and  $-30$  mV, the photomicrographs of the colloidal silica particles taken by Rosental<sup>[3]</sup> are given in Fig. 6A, B, and C, respectively. The total interaction energy ( $V_T$ ) curves are assumed to correspond to the cases in Fig. 6A, B, and C, respectively. As seen in Fig. 6A, silica particles with a  $z_p$  value of  $-30$  mV exhibit dispersion and the height of the energy barrier is considerably high. When KCl is added into water, the  $z_p$  of silica particles comes down to the  $-14$  mV (Fig. 6B) as a result of the double-layer compression with a resultant decrease in repulsive energy and in turn in the height of the energy barrier. Consequently, in this system, sometimes the van der Waals attractive forces may become dominant depending on the kinetic conditions and/or the existence of the non-DLVO forces such as hydration, hydrophobic forces, and steric forces. When a trivalent electrolyte,  $AlCl_3$ , is added into system, the  $z_p$  comes down to zero, which is called the isoelectric point (Fig. 6C), owing to the charge neutralization on the silica surface; the height of the energy barrier disappears and the van der Waals attractive forces become dominant in the system.<sup>[49]</sup> Accordingly, the colloidal particles come in contact and coagulate (Fig. 6C).

At the point where the energy barrier just disappears:

$$dV_T/dH = 0 \text{ and } V_T = 0 \quad (28)$$

Applying these conditions to Eq. (26) results in an expression for the critical coagulation (or flocculation) concentration,  $C_c$ , for a symmetrical ( $z_+ = -z_-$ ,  $z$  is the valence number of electrolyte, e.g., NaCl) electrolyte as follows:

$$C_c = K(P^4/A^2z^6) \quad (29)$$

where  $K$  is a constant that depends only on the properties of the dispersion medium and  $A$  is the effective Hamaker constant. When the  $z_p$  is very high, the term  $P$  approaches unity and the critical concentration becomes inversely proportional to the sixth power of the valency,  $z$ . This dependence of  $C_c$  on  $1/z^6$ , known as the Schultz–Hardy rule, is consistent with the DLVO theory. For instance, if coagulation occurs at 1 M with a 1:1 electrolyte, it will occur at  $1/2^6$  ( $\cong 0.016$ ) M with a 2:2 electrolyte, and at  $1/3^6$  ( $\cong 0.0014$ ) M with a 3:3 electrolyte.

## APPLICATIONS OF ZETA POTENTIAL AND ELECTROPHORETIC MOBILITY

As mentioned earlier, the  $z_p$  is a good indicator to explain the stability mechanisms of different colloidal

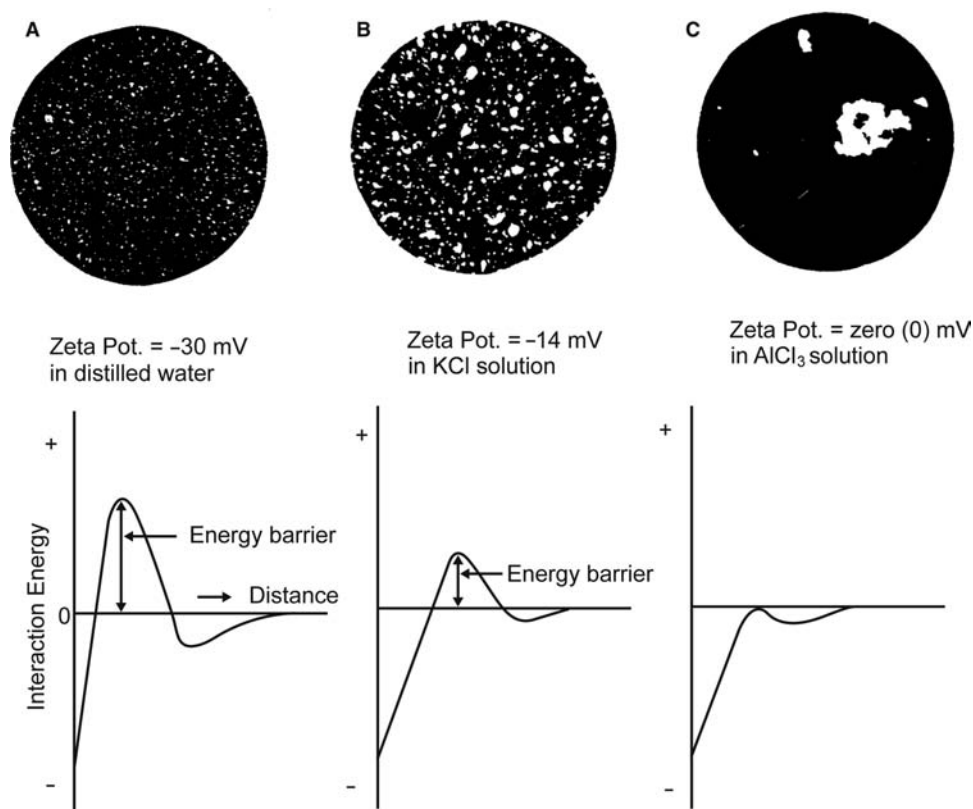


**Fig. 6** Total energy of interaction curves for silica particles and their corresponding coagulation behavior. *Source:* From Ref.<sup>[48]</sup>.

and emulsion systems, and the adsorption mechanism between any organic or inorganic species at any solid–liquid interface. The term stability, when applied to colloidal dispersions, is a relative term intended to express the resistance of the dispersion to change. In any colloidal system, colloidal particles may have different z<sub>p</sub> values depending on the conditions, i.e., solution pH, existence of electrolyte, type, and concentration. The z<sub>p</sub> is used mainly in the following areas as an indicator of the dispersion and coagulation of colloidal systems. Therefore it has a wide spectrum of applications, some of which will be briefly mentioned.

The preparation of a well-dispersed clay–water colloidal system in the slip casting molding method requires the z<sub>p</sub> of clay particles be sufficiently high to provide repulsion between the particles so that a dense packing with strong material is produced.<sup>[50]</sup> In the purification of municipal water and cleaning up of industrial wastes, it is usually necessary to remove solids from dilute suspension. The key to effective colloid removal is the reduction of z<sub>p</sub> of the colloidal particles to zero by adjusting solution pH, and type and concentration of electrolyte.<sup>[11,51]</sup>

The pigments in paint, consisting of fine particles or nanoparticles, colored or colorless solid particles, must be dispersed readily to maintain a stable dispersion.

The z<sub>p</sub> value of pigments in a solvent plays an important role in maintaining a good dispersion.<sup>[52]</sup> The pharmaceutical industry often prepares their product by suspending colloidal particles or nanoparticles of the drug uniformly throughout a liquid vehicle. A successful suspension remains stable and enjoys a long shelf life. This is often achieved by producing a stable dispersion that settles very slowly at maximum z<sub>p</sub>. Suspensions of paper stocks containing fine particles including filler or pigments are generally regarded as colloidal systems. If fine particles are agglomerated, they will attach to the fiber, leading to better drainage and improvement in total retention at a z<sub>p</sub> value of 0 mV.<sup>[53]</sup> The EDL repulsive forces and z<sub>p</sub> values between colloidal latex particles defining a sol of polymer particles such as polystyrene latex<sup>[50]</sup> have a decisive role in the preparation of monodisperse latex.<sup>[54,55]</sup>

The z<sub>p</sub> measurements are used to determine the optimum conditions for the stability of emulsions. In most emulsion systems such as cream in cosmetic industry (oil in water or water in oil emulsions), mayonnaise in food industry (solid in liquid emulsion), and toothpaste in pharmaceutical industry (solid in liquid emulsion), the stability is achieved through a good control of z<sub>p</sub>.<sup>[56]</sup> The z<sub>p</sub> values of fiber materials are used in the characterization of fiber materials such as carbon, polyethylene, cotton, and polyester in

liquids and identifying the adsorption capacity of different organic dye molecules.<sup>[42]</sup>

Flotation is a technique widely used in mining industry to separate valuable minerals from their ores or to separate the valuable minerals from each other. Finely ground minerals in water are coupled with an appropriate collector chemical and then floated with air bubbles. The  $z_p$  is used to select appropriate collector, elaborate the method of collector adsorption on minerals, and examine activation mechanism of minerals.<sup>[7,8,55]</sup>

Electrophoretic deposition is an important technique directly used to produce a thin or thick coating on a conducting base.<sup>[50,57]</sup> In this technique, charged particles migrate to an electrode of opposite charge under the influence of an electric field. Untirusting paint coatings on metal surfaces, composite coatings, production of superconductors,<sup>[48]</sup> and photocopying by electrodeposition<sup>[58]</sup> are further examples of this kind. Differences in electrophoretic mobilities of some proteins induce their separation in biological systems.<sup>[19,40,42,47,52–54,58–61]</sup> Similarly, analysis of the blood cells can reveal illness through electrophoretic mobility; a mobility of  $-1.1 \mu\text{m sec}^{-1}/\text{V cm}^{-1}$  is reported for fresh human red cells in blood at pH 7.4.<sup>[60]</sup> In addition, the intravascular coagulation diseases of human can be indirectly controlled by  $z_p$ .<sup>[48]</sup> Bacterial action is also governed by electrical potential.<sup>[62]</sup>

Detergency is the ability to remove dirt such as soil and oil adhering to fiber. The dirt removal from fabric by detergent is explained by the heterocoagulation theory including the EDL repulsion and van der Waals attraction energy between two different materials, fabric and dirt.<sup>[59,61]</sup> Soil used for agricultural purposes contains an appreciable fraction of colloidal material composed of both lyophobic and lyophilic colloids. When soil is treated with water, the soil must be kept in a flocculated state to impart porosity, a suitable medium for good plant growth; this condition is provided by adding some electrolyte into water. The permeability of oil-producing sandstones is governed by the clay particles present in sandstone material. The migration of clay particles is relevant to the properties of water used in the system and also the electrokinetic properties of clay particles.<sup>[63]</sup>

## CONCLUSION

It is clear from this review that electrokinetic properties of mineral particles are encountered in all walks of life. Understanding of electrokinetics of mineral nanoparticles in a liquid, in addition to the ionic composition of the solution, requires the knowledge of surface charge, zeta potential, surface potential, structure

of EDL at the mineral/liquid interface, and its double-layer thickness. This information is then used to identify the interaction mechanisms between two particles or between a particle surface and a substance (in ionic or non-ionic form), and in turn, the stability of solid-liquid system and the adsorption of an ion (or molecule) on a charged or non-charged mineral. Its practical implications are then explained in terms of the DLVO theory.

## REFERENCES

1. Leja, J. *Surface Chemistry of Froth Flotation*; Plenum Press: New York, 1983; 341–430, 2nd Ed.
2. Lyklema, J. Fundamentals of Electrical Double Layers in Colloidal Systems. In *Colloidal Dispersions*; Goodwin, J.W., Ed.; Dorset Press: Amsterdam, 1982; 48–69.
3. Hunter, J.R. *Zeta Potential in Colloid Science, Principles and Applications*; Academic Press: San Diego, 1988; 1–342, 3rd Ed.
4. Parks, G.A.; de Bruyn, P.L. The zero point of charge of oxides. *J. Phys. Chem.* **1962**, *66*, 967–972.
5. Parks, G.A. The isoelectric points of solid oxides, solid hydroxides, and aqueous hydroxo complex systems. *Chem. Rev.* **1965**, *65*, 177–198.
6. Somasundaran, P. Interfacial Chemistry of Particulate Flotation. In *Advances in Interfacial Phenomena*; AIChE Symp. Ser.; 1975; Vol. 71 (150), 1–15.
7. Laskowski, J.S. Coal Flotation and Fine Coal Utilization. In *Developments in Mineral Processing*; Fuerstenau, D.W., Ed.; Elsevier Science B.V.: Amsterdam, 2001; 35–44.
8. Dobias, B. Salt Type Minerals. In *Flotation Science and Engineering*; Matis, K.A., Ed.; Marcel Dekker Inc.: New York, 1995; 207–259.
9. Sennet, P.; Olivier, J.P. Colloidal Dispersions, Electrokinetic Effects and the Concept of Zeta Potential. In *Industrial and Eng. Chem., The Interface Symposium*, August, 12, 1965, Vol. 57, 32–50.
10. Ersoy, B.; Celik, M.S. Electrokinetic properties of clinoptilolite with mono and multivalent electrolytes. *Microporous Mesoporous Mater.* **2002**, *55*, 305–312.
11. Williams, D.J.A.; Williams, K.P. Electrophoresis and zeta potential of kaolinite. *J. Colloid Interface Sci.* **1978**, *65* (1), 80–87.
12. Fuerstenau, M.C. Oxide and Silicate Flotation. In *Flotation Science and Engineering*; Matis, K.A., Ed.; Marcel Dekker Inc.: New York, 1995; 89–126.
13. Grim, R.E. *Clay Mineralogy*; Mc-Graw-Hill Book Com. Inc.: New York, 1968; 184–233.
14. Kraepiel, A.M.L.; Keller, K.; Morel, F.M.M. On the acid-base chemistry of permanently charged minerals. *Environ. Sci. Technol.* **1998**, *32*, 2829–2838.
15. Gregory, J. Fundamentals of flocculation. *Crit. Rev. Environ. Control* **1989**, *13*, 185–230.
16. Hiemenz, P.C. *Principles of Colloid and Surface Chemistry*, 2nd Ed.; Marcel Dekker Inc.: New York, 1986; 677–789.

17. Harding, I.H.; Healy, T.W. Electrical double layer properties of latex colloids. *J. Colloid Interface Sci.* **1985**, *107* (2), 382–398.
18. Sridharan, A.; Satyamurty, P.V. Potential–distance relationships of clay–water colloidal systems considering the Stern theory. *Clays Clay Miner.* **1996**, *44* (4), 479–484.
19. Usui, S. Electrical Double Layer. In *Electrical Phenomena at Interfaces, Fundamentals, Measurements and Applications*; Watanable, A., Ed.; Marcel Dekker Inc.: New York, 1984; 15–46.
20. Modi, H.J.; Fuerstenau, D.W. Streaming potential studies on corundum in aqueous solutions of inorganic electrolytes. *J. Phys. Chem.* **1957**, *61*, 640–643.
21. Celik, M.S.; Yasar, E. Electrokinetic properties of some hydrated boron minerals. *J. Colloid Interface Sci.* **1995**, *173*, 181–185.
22. Fuerstenau, D.W.; Huang, P. The effect of the adsorption of lead and cadmium ions on the interfacial behavior of quartz and talc. *Colloids Surf., A Physicochem. Eng. Asp.* **2001**, *177*, 147–156.
23. Kulkarni, R.D.; Somasundaran, P. Mineralogical heterogeneity of ore particles and its effects on their interfacial characteristics. *Powder Technol.* **1976**, *14*, 279–285.
24. Pradeep, T.; Subramanian, S.; Rath, R.K. Surface chemical studies on pyrite in the presence of polysaccharide-based flotation depressants. *J. Colloid Interface Sci.* **2000**, *229*, 82–91.
25. Parks, G.A. Aqueous Surface Chemistry of Oxides and Complex Oxide Minerals, Isoelectric Point and Zero Point of Charge in Equilibrium Concepts in Natural Water Systems. In *Advances in Chemistry Series*; Gould, R.F., Ed.; American Chemical Society: Washington, DC; 1967, Vol. 67, 121–160.
26. Luevanos, A.M.; Salas, A.U.; Valdivieso, A.L. Mechanisms of adsorption of sodium dodecylsulfonate on celestite and calcite. *Miner. Eng.* **1999**, *12* (8), 919–936.
27. Pokrovsky, O.S.; Schott, J.; Thomas, F. Dolomite surface speciation and reactivity in aquatic systems. *Geochim. Cosmochim. Acta* **1999**, *63* (19/20), 3133–3143.
28. Somasundaran, P.; Ananthapadmanabhan, K.P. Physico-chemical aspects of flotation. *Trans. Indian Inst. Met.* **1979**, *32* (1), 177–194.
29. Xu, Z.; Wang, D.; Hu, Y. A study of interactions and flotation of wolframite with octyl hydroxamate. *Miner. Eng.* **1997**, *10* (6), 623–633.
30. Celik, M.S.; Somasundaran, P. Effect of pretreatments on flotation and electrokinetic properties of coal. *Colloids Surf.* **1980**, *1*, 121–124.
31. Unlu, M.; Doga, T.U. Electrokinetic properties of anthracite and morphology of its electrical double layer. *J. Eng. Environ.* **1987**, *11* (1), 62–77.
32. Rao, R.R.; Roopa, H.N.; Kannan, T.S. Dispersion, slip-casting and reaction nitridation of silicon–silicon carbide mixtures. *J. Eur. Ceram. Soc.* **1999**, *19*, 2145–2153.
33. Cromieres, L.; Moulin, V.; Fourest, B.; Giffaut, E. Physicochemical characterization of the colloidal hematite/water interface: Experimentation and modelling. *Colloids Surf., A Physicochem. Eng. Asp.* **2001**, *177*, 147–156.
34. Ersoy, B. Sol–Gel Coating of Al<sub>2</sub>O<sub>3</sub>–La<sub>2</sub>O<sub>3</sub> on Clay Based Substrate and Production of Ceramic Membrane. In M.Sc. Thesis; Dumlupinar University: Turkey, 1996; 66–107.
35. Springer, J.; Bismarck, A. Characterization of fluorinated PAN-based carbon fibers by zeta potential measurements. *Colloids Surf., A Physicochem. Eng. Asp.* **1999**, *159*, 331–339.
36. Webb, J.T.; Bhatnagar, P.D.; Williams, D.G. The interpretation of electrokinetic potentials and the inaccuracy of the DLVO theory for anatase sols. *J. Colloid Interface Sci.* **1974**, *49* (3), 346–361.
37. De Faria, L.D.; Prestat, M.; Koenig, J.F.; Chartier, P.; Trasatti, S. Surface properties of Ni + Co mixed oxides: A study by x-rays, xps, BET and pzc. *Electrochim. Acta* **1988**, *44*, 1481–1489.
38. Tscapek, M.; Tcheicvili, L.; Wasowski, C. The point of zero charge (pzc) of kaolinite and SiO<sub>2</sub>+Al<sub>2</sub>O<sub>3</sub> mixtures. *Clay Miner.* **1974**, *10*, 219–229.
39. Wiese, G.R.; Healy, T.W. *J. Colloid Interface Sci.* **1975**, *51*, 427.
40. Takahashi, K. Electrocapillary Measurements. In *Electrical Phenomena at Interfaces, Fundamentals, Measurements and Applications*; Watanable, A., Ed.; Marcel Dekker Inc.: New York, 1984; 147–182.
41. Kulkarni, R.D.; Somasundaran, P. Effect of pretreatment on the electrokinetic properties of quartz. *Int. J. Miner. Process.* **1977**, *4*, 89–98.
42. Kittaka, S. Electrokinetic Measurements. In *Electrical Phenomena at Interfaces, Fundamentals, Measurements and Applications*; Watanable, A., Ed.; Marcel Dekker Inc.: New York, 1984; 183–224.
43. Rowlands, W.N.; O'Brien, R.W.; Hunter, R.J.; Patrick, V.J. Surface properties of aluminum hydroxide at high salt concentration. *J. Colloid Interface Sci.* **1997**, *188*, 325–335.
44. Derjaguin, B.V.; Landau, L.D. Theory of the stability of strongly charged lyophobic sols and of the adhesion of strongly charged particles in solutions of electrolytes. *Acta Physicochim. URSS* **1941**, *14*, 622–633.
45. Verwey, E.J.W.; Overbeek, J.Th.G. *Theory of the Stability of Lyophobic Colloids*; Elsevier: Amsterdam, 1948; 168.
46. Israelachvili, J.N. *Intermolecular and Surface Forces*, 2nd Ed.; Academic Press: San Diego, 1995; 83–254.
47. Furusawa, K.; Matsumoto, M. Stability Measurement of Disperse Systems. In *Electrical Phenomena at Interfaces, Fundamentals, Measurements and Applications*; Watanable, A., Ed.; Marcel Dekker Inc.: New York, 1984; 225–268.
48. Riddick, T.M. *Control of Colloid Stability Through Zeta Potential*; Zeta-Meter Inc.: New York, 1968; 1–372.
49. Schwarz, J.A.; Driscoll, C.T.; Bhanot, A.K. The zero point of charge of silica–alumina oxide suspensions. *J. Colloid Interface Sci.* **1984**, *97* (1), 55–61.
50. Shanefield, D.S. *Organic Additives and Ceramic Processing*, 2nd Ed.; Kluwer Academic Publishers: Massachusetts, 1996; 131–251.
51. Grutsch, J.F. Wastewater treatment: The electrical connection. *Environ. Sci. Technol.* **1978**, *12* (9), 1023–1027.



52. Kumano, I. Pigments and Paints. In *Electrical Phenomena at Interfaces, Fundamentals, Measurements and Applications*; Watanable, A., Ed.; Marcel Dekker Inc.: New York, 1984; 355–368.
53. Yamada, H. Paper. In *Electrical Phenomena at Interfaces, Fundamentals, Measurements and Applications*; Watanable, A., Ed.; Marcel Dekker Inc.: New York, 1984; 323–338.
54. Usui, S.; Hachisu, S. Interaction of Electrical Double Layers and Colloid Stability. In *Electrical Phenomena at Interfaces, Fundamentals, Measurements and Applications*; Watanable, A., Ed.; Marcel Dekker Inc.: New York, 1984; 47–98.
55. Kydors, K.A.; Matis, K.A. Flotation of Iron Sulfide Minerals: Electrokinetic Aspects. In *Flotation Science and Engineering*; Matis, K.A., Ed.; Marcel Dekker Inc.: New York, 1995; 127–155.
56. Fukushima, S.C. Cosmetics. In *Electrical Phenomena at Interfaces, Fundamentals, Measurements and Applications*; Watanable, A., Ed.; Marcel Dekker Inc.: New York, 1984; 369–386.
57. Ferrari, B.; Moreno, R. Electrophoretic deposition of aqueous alumina slips. *J. Eur. Ceram. Soc.* **1997**, *17*, 549–556.
58. Karasawa, S. Reproduction in Copying and Electrophoretic Display. In *Electrical Phenomena at Interfaces, Fundamentals, Measurements and Applications*; Watanable, A., Ed.; Marcel Dekker Inc.: New York, 1984; 413–436.
59. Suzawa, T. Fibers. In *Electrical Phenomena at Interfaces, Fundamentals, Measurements and Applications*; Watanable, A., Ed.; Marcel Dekker Inc.: New York, 1984; 299–322.
60. Kondo, T. Electrokinetic Phenomena in Biological Systems. In *Electrical Phenomena at Interfaces, Fundamentals, Measurements and Applications*; Watanable, A., Ed.; Marcel Dekker Inc.: New York, 1984; 397–412.
61. Imamura, T.; Tokiwa, F. Detergency. In *Electrical Phenomena at Interfaces, Fundamentals, Measurements and Applications*; Watanable, A., Ed.; Marcel Dekker Inc.: New York, 1984; 269–284.
62. Poortinga, A.T.; Bos, R.; Norde, W.; Busscher, H.J. Electric double layer interactions in bacterial adhesion to surfaces. *Surf. Sci. Rep.* **2002**, *189*, 1–32.
63. Yen, T.F.; Kuo, J.F.; Sharma, M.M. Further investigation of the surface charge properties of oxide surfaces in oil-bearing sands and sandstones. *J. Colloid Interface Sci.* **1987**, *115* (1), 9–16.

# Mixed Metal Oxide Nanoparticles

**Pramesh N. Kapoor**

**Ajay Kumar Bhagi**

*Department of Chemistry, University of Delhi, Delhi, India*

**Ravichandra S. Mulukutla**

*Nanoscale Materials, Inc., Manhattan, Kansas, U.S.A.*

**Kenneth J. Klabunde**

*Department of Chemistry, Kansas State University,  
Manhattan, Kansas, U.S.A.*

## INTRODUCTION

Mixed metal oxide (MMO) nanoparticles (also called heterometal oxide nanoparticles) can play an appreciable role in many areas of chemistry and physics. The unique electronic and magnetic properties obtained when combining two metals in an oxide matrix have been well studied.<sup>[1,2]</sup> However, the most common use for MMOs has been in the area of catalysis, and here they have found use both as the catalyst and as catalyst supports.<sup>[3,4]</sup> Specifically, MMO containing aluminum has found many opportunities in catalysis.<sup>[5–7]</sup>

Mixed metal oxides are also used in many applications in the electronic industry as passive or active components in devices. These exhibit high dielectric, and ferro- or pyroelectric properties, e.g., BaTiO<sub>3</sub>, LiNbO<sub>3</sub>, KTaO<sub>3</sub>, Pb<sub>1-x</sub>La<sub>x</sub>Ti<sub>y</sub>Zr<sub>2</sub>O<sub>3</sub>, etc. The most remarkable MMO materials are surely the thermal-conducting superconductors based on YBa<sub>2</sub>Cu<sub>3</sub>O<sub>7-x</sub>. The technological interest in MMOs such as silica-titania and silica-zirconia arises from their chemical resistance and their thermomechanical or optical properties. SiO<sub>2</sub>-TiO<sub>2</sub> glasses and zircon, SrZrO<sub>4</sub>, are characterized by very low thermal expansion, which confer them a high thermal-shock resistance. SiO<sub>2</sub>-TiO<sub>2</sub> and SiO<sub>2</sub>-ZrO<sub>2</sub> glasses have high refractive indices and are wonderful catalysts or catalyst supports.<sup>[8]</sup> Owing to their refractoriness, these MMOs are difficult to produce by conventional melting techniques; thus, sol-gel technique is used for their preparation. The homogeneity of binary oxide has great influence on structural evolution of the gels during the heat treatment. Magnesium aluminate spinel (MgAl<sub>2</sub>O<sub>4</sub>) is expected to have applications as a structural material at high temperatures because it has a high melting point and superior thermal and chemical properties.

It is also of technological interest as a refractory materials at elevated temperatures. It is important to realize that improved properties are recorded for ceramic materials at nanoscale and these materials are expected to find the most important place in technology in the coming years.

In this entry, we have covered the most important and recent methods of preparation of nanocrystalline MMOs. Special emphasis has been given on sol-gel technique because of its popularity among researchers, resulting in homogeneous and pure MMO nanoparticles. Among physical methods, perhaps flame spray pyrolysis is gaining more importance in recent time. Structure, properties, and applications of MMO nanoparticles have also been discussed. This area of research is wide open and offers scope for development in synthetic and application fields.

## SYNTHESIS OF MIXED METAL OXIDE NANOPARTICLES

Developments in the field of MMO nanoparticles have produced many significant and interesting results in all areas investigated. This attracted attention toward the preparation of these potential new materials with variable composition having unique properties. Researches have explored and developed both physical and chemical methods by which such materials can be prepared.

### Physical Methods

Several physical aerosol methods have been reported for the synthesis of nanosized particles of ceramic materials. The most successful include gas condensation techniques,<sup>[9–12]</sup> spray pyrolysis,<sup>[13,14]</sup> thermochemical decomposition of metal-organic precursors

in flame reactors,<sup>[15,16]</sup> and some other aerosol processes named according to energy sources applied to reach the temperatures required for gas–particle conversion. The experimental details of these physical/aerosol methods have been outlined by Khaleel and Richards.<sup>[17]</sup>

### Vapor condensation method

It involves two steps. In the first step, a metallic nano-phase powder is condensed under an inert convection gas at high pressure, after the supersaturated vapor of metal is obtained inside a chamber. In the second step, the powder is oxidized by allowing oxygen into the chamber. It is a critical step in which the temperature is as high as 1000°C because of the exothermic nature of the reaction. High temperature results in agglomeration into large particles, and often annealing process at high temperature is required for completion of oxidation. Nanoparticles result when supersaturation is achieved above the vapor source. A collection surface cooled by liquid nitrogen is used to collect the particles.

### Spray pyrolysis

Some other techniques with slight modifications also work on same principle. They are aerosol thermolysis, evaporative decomposition of solutions, plasma vaporization of solutions, aerosol decomposition, flame pyrolysis, etc. A new broad name suggested for these techniques is flame spray pyrolysis (FSP) technology. The starting materials, or chemical precursors, are usually the appropriate salts, either in solution or in a sol or in suspension form. Aerosol droplets are generated by nebulizer or atomization technique of the starting chemical precursors. These droplets generated undergo evaporation with solute condensation within the droplet followed by drying and thermolysis of precipitate particles at high temperatures forming microporous particles. They are finally sintered to form dense particles. In this technique, various methods are used for atomization, including pressure, two-fluid, electrostatic, and ultrasonic atomizers. These methods give droplets of different sizes (2–15 μm) at various rates of atomization and various droplet velocities. Tal materials Inc. uses a patented flame spray pyrolysis process developed at the University of Michigan for the direct, large-scale production of inexpensive MMO nanopowders.<sup>[18,19]</sup>

The preparation of a variety of nanosized MMO powders from the thermolysis/flame pyrolysis of a new polymer-matrix-based precursor solution has been reported by Pramanic et al.<sup>[20]</sup> Spinel such as MgAl<sub>2</sub>O<sub>4</sub>, CuFe<sub>2</sub>O<sub>4</sub>, NiFe<sub>2</sub>O<sub>4</sub>, CoFe<sub>2</sub>O<sub>4</sub>, ZnFe<sub>2</sub>O<sub>4</sub>; orthoferrites such as LaFeO<sub>3</sub>; NdFeO<sub>3</sub>; GdFeO<sub>3</sub>;

SmFeO<sub>3</sub>; garnets such as Y<sub>3</sub>Al<sub>5</sub>O<sub>12</sub>, Gd<sub>3</sub>Al<sub>5</sub>O<sub>12</sub>, Gd<sub>3</sub>Fe<sub>5</sub>O<sub>12</sub>, Sm<sub>3</sub>Fe<sub>5</sub>O<sub>12</sub>; and composites such as Fe<sub>2</sub>O<sub>3</sub>·NiO, Fe<sub>2</sub>O<sub>3</sub>·CuO, and Fe<sub>2</sub>O<sub>3</sub>·TiO<sub>2</sub> have been reported.

### Thermochemical/flame decomposition of metal–organic precursors

This method is an example of another type of gas condensation technique. In this method, the starting material is a liquid chemical precursor. It is also known as chemical vapor condensation (CVC). It involves vaporization of chemical precursors, which are then oxidized with the help of a fuel–oxidant mixture (propane–O<sub>2</sub> or methane–O<sub>2</sub>). It combines the rapid thermal decomposition of a precursor carrier gas stream in a reduced pressure environment with thermophoretically driven deposition of the rapidly condensed product particles on a cold substrate.<sup>[16]</sup> The flame temperature varies between 1200 and 3000 K, which allows rapid gas phase chemical reactions. In rapid thermal decomposition of precursor in solution (RTDS), the precursor material dissolved in water undergoes rapid hydrothermal reactions in a near-critical and supercritical water environment. Due to the short residence time and extremely fast quenching rate, the particle growth in the reaction is limited. Both ultrafine metal oxides and MMOs using inexpensive water-soluble precursors are prepared using this method. Some examples of nanocrystalline powders produced using RTDS are (1) Fe<sub>3</sub>O<sub>4</sub> (magnetite) having grain size less than 12 nm from FeSO<sub>4</sub>/urea as precursors, (2) NiFe<sub>2</sub>O<sub>4</sub> (trevorite) having grain size less than 10 nm from Fe(NO<sub>3</sub>)<sub>3</sub>/Ni(NO<sub>3</sub>)<sub>2</sub>/urea as precursors, and (3) NiO/ZrO<sub>2</sub> having grain size nearly 10 nm from Ni(NO<sub>3</sub>)<sub>2</sub>/ZrO(NO<sub>3</sub>)<sub>2</sub>.

### Chemical Methods

The most potential and successful route for preparing homogeneous ceramic materials is liquid phase chemistry. The most widely used and perhaps most reliable method is the sol–gel method. There are many other wet chemistry methods known, such as microemulsion techniques and precipitation from solutions. Another novel technique is the mechanochemical synthesis method, which involves solid-state chemistry reactions.

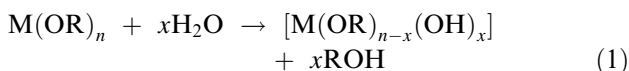
### Sol–gel technique

The synthesis of MMOs by sol–gel technique is one of several liquid phase methods that is the most widely employed and has been widely reviewed.<sup>[21–28]</sup> Reviews on the preparation of aerogels have also appeared in the literature.<sup>[29,30]</sup> Mainly, three routes are used to

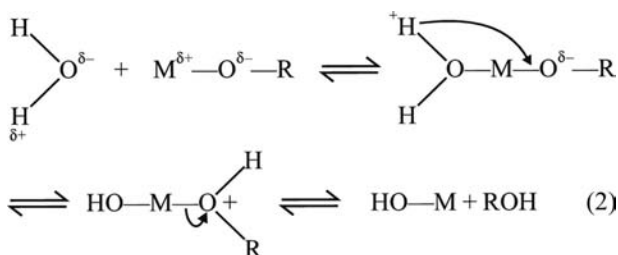
prepare sol-gel ceramic materials, which are distinguished by the nature of the starting material. They are (1) an aqueous solution of inorganic salt, (2) an aggregate of colloidal particles in a solvent, and (3) a network-forming species in organic or aqueous solution. The last route is the most acceptable because network formers can be tailor-made or modified to control the chemistry and processing of the gel, and ultimately its morphology. Usually, alkoxides, bimetallic- $\mu$ -oxoalkoxides, and heterometallic (double, *ter*-, *tert*-) alkoxides are used as precursors in alcoholic solutions. Other precursors include metal  $\beta$ -diketonates and metal carboxylates.

*Hydrolysis and condensation of metal alkoxides:*

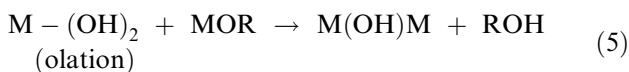
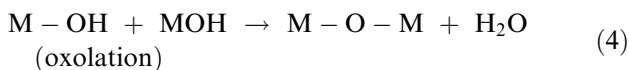
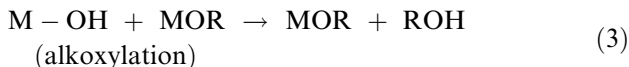
The sol-gel route is actually a two-step inorganic polymerization. In the first step, polymerization starts by hydrolysis at the metal-alkoxy linkage yielding alcohol and new reactants, hydroxylated metal centers (M-OH).



The mechanism of this reaction can be outlined as below:

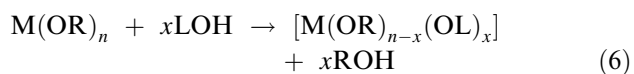


In the second step, condensation or three-dimensional propagation occurs when hydroxylated species condense to form oxypolymers. Polycondensation involves alkoxylation, oxolation, or ololation, a reaction that creates oxygen bridges and releases XOH species (where X=H or R).



The nature of the inorganic framework obviously then determines the relative rates of hydrolysis and

condensation at different centers. The rates of hydrolysis and condensation depend upon the nature of metal in terms of its electrophilicity and ability to expand its coordination number.<sup>[31]</sup> The hydrolysis rates of transition metal alkoxides are very high, as metal centers are highly electrophilic and exhibit several coordination numbers. This sometimes complicates the problem, especially in the case when heterobimetallic alkoxides are used as precursor, as precipitation occurs at different rates and often instantaneously. One of the suitable ways to overcome this problem is the modification of precursor by reacting alkoxide with other ligands when the exchange reaction takes place.<sup>[32]</sup> This results into a new precursor, which may undergo hydrolysis at a much slower rate.



Thus, at times when alkoxy ligands are quickly removed by hydrolysis, then chelating ligands such as acetyl acetone or other  $\beta$ -diketones act as terminating agents that limit the condensation reaction.<sup>[33]</sup> The major steps involved in sol-gel technique<sup>[21,22]</sup> for the preparation of MMOs as outlined in Fig. 1 are:

1. Preparation of a homogeneous solution of pure precursor in an organic solvent, which is miscible with water or the hydrolysis reagent.
2. Preparation of sol from solution by treating the homogeneous solution with H<sub>2</sub>O, or H<sub>2</sub>O with HCl/NaOH/NH<sub>4</sub>OH.
3. Allowing the sol to convert into gel by polymerization (aging).

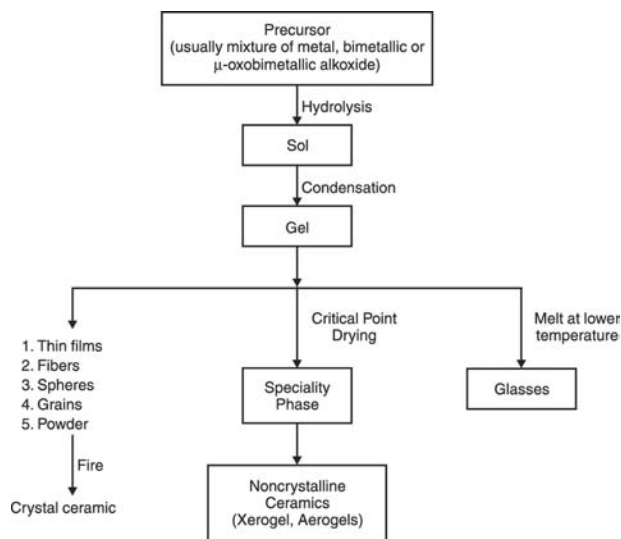
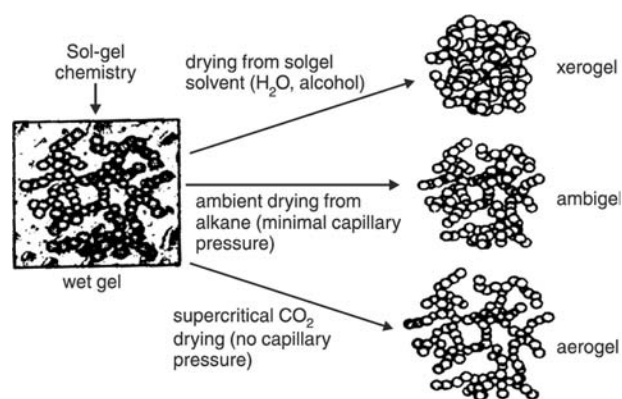


Fig. 1 Steps involved in sol-gel method.

- Shaping of gel into the desired form or shape followed by drying. In this step, solvent is removed. The manner in which the liquid phase is removed from wet gel determines whether the dried material is a highly porous aerogel or a denser xerogel. A xerogel is formed as the solvent evaporates from the wet gel, resulting in collapse of the wet-gel structure. If the network is compliant, the gel deforms because of capillary forces generated by the liquid phase as it recedes into the body of the gel. Supercritical drying (SCD) or ambient pressure upon wet gels results in aerogels. Aerogels are actually nano-scale mesoporous materials of low density and high surface area.

SCD preserves the porosity by bringing the solvent phase into its supercritical state (a state where no liquid–vapor interface exist), so that capillary pressures do not develop. There are two SCD methods. The sol–gel synthesis of  $(\text{Ru}_x\text{Ti}_{1-x})\text{O}_2$  ( $x = 0, 0.14, 0.20, 0.32$ ) involves modification of an alkoxide preparation of  $\text{TiO}_2$  with a ruthenium chloride,  $\text{RuCl}_3$ , refluxed in ethanol. Monolithic aerogels are formed using SCD method with  $\text{CO}_2$ . These were characterized after annealing treatment at  $400^\circ\text{C}$ , which removed the chloride and alkoxide. The resulting oxides consisted of  $\sim 10$  nm nanocrystallites of primarily phase-separated  $\text{TiO}_2$  and  $\text{RuO}_2$  (these rutile phases can form only a solid solution of a few mole percent  $\text{RuO}_2$  and  $\text{TiO}_2$ ). These MMO aerogels show surface areas of approximately  $85\text{ m}^2\text{ g}^{-1}$ .<sup>[34]</sup>

Ambient pressure method involves surface modifications as well as network strengthening.<sup>[35–38]</sup> Surface modification means, for example, that terminal silanols ( $\text{Si-OH}$ ) are replaced by nonreactive groups via silylation or esterification. These modifications inhibit condensation reactions, i.e., conversion of  $\text{Si-OH}$  centers to  $\text{Si-O-Si}$ , which locks in structural collapse by sealing compressed pores shut. This allows the porous network to almost retain its original volume. Network strengthening is done by either aging of wet gel in mother liquor (including thermal treatment in water) or soaking it in a precursor alkoxide [such as  $\text{Si}(\text{OR})_4$ ] during washing or aging steps. One can also use solvents with low surface tension so that pore liquid is exchanged with low-surface-tension solvents just before the ambient-pressure drying. The MMOs so obtained have been named as ambigels and are less porous than the corresponding SCD ceramics but have comparable surface area and pore volume (Fig. 2).<sup>[31]</sup> Finally, conversion of the shaped gel to the desired ceramic material by heating takes place at a much lower temperature than the conventional process of melting of oxides together.



**Fig. 2** The method used to extract the pore fluid from a wet gel creates a dry solid with variable porosity: strong capillary forces create a xerogel, weak capillary forces create an ambigel, and zero capillary force creates an aerogel that nominally retains the low-density framework for the wet gel. *Source:* Reprinted with permission from Ref.<sup>[31]</sup>.

Another widely used method for obtaining MMO aerogels is the prehydrolysis route.<sup>[39,40]</sup> In this method, two alkoxides with different rates of hydrolysis are used as precursors for obtaining MMO aerogels. However, before mixing these together, the one with the lower rate of hydrolysis is hydrolyzed or partially hydrolyzed separately and then mixed with the other alkoxide solution. This is to avoid phase segregation caused by different rates of hydrolysis. Similarly, hydrolysis of metal alkoxide with faster rate of hydrolysis can be slowed by suitable complexation. This is done to promote formation of  $\text{M-O-M}'$  mixed bond, which increases the homogeneity of MMO aerogel. A nonhydrolytic sol–gel route has also been used for preparation of MMO aerogels.<sup>[41]</sup> The  $\text{M-O-M}'$  bridges are obtained by condensation of  $\text{MX} + \text{M}'\text{-OR} \rightarrow \text{M-OM} + \text{RX}$ . In most cases, these reactions are thermally activated. Actually, the condensation completes with redistribution of the ligands, giving complicated halogenoalkoxides,<sup>[42]</sup> which ultimately leads to products after hydrolysis. The surface areas of oxides obtained after calcination was found to be quite high, but a low level of homogeneity on atomic scale was noticed. Syntheses of  $\text{MgAl}_2\text{O}_4$  spinel and  $\text{Mg}_2\text{SiO}_4$  spinel forsterite precursor from a heterogeneous alkoxide solution have been reported in the literature.<sup>[43,44]</sup> The preparation route is shown in Fig. 3. The obtained precursor was composed of a mixture of boehmite [ $\text{AlO}(\text{OH})$ ] and a mixed hydroxide [ $\text{Mg}_4\text{Al}_2(\text{OH})_{14}\cdot 3\text{H}_2\text{O}$ ]. The precursor was converted to a spinel phase through two steps: (1) decomposition of mixed hydroxide at  $\sim 400^\circ\text{C}$  and (2) solid-state reaction between  $\text{MgO}$  (which has decomposed from mixed hydroxide) and  $\gamma\text{-Al}_2\text{O}_3$  (which had been converted from boehmite at higher

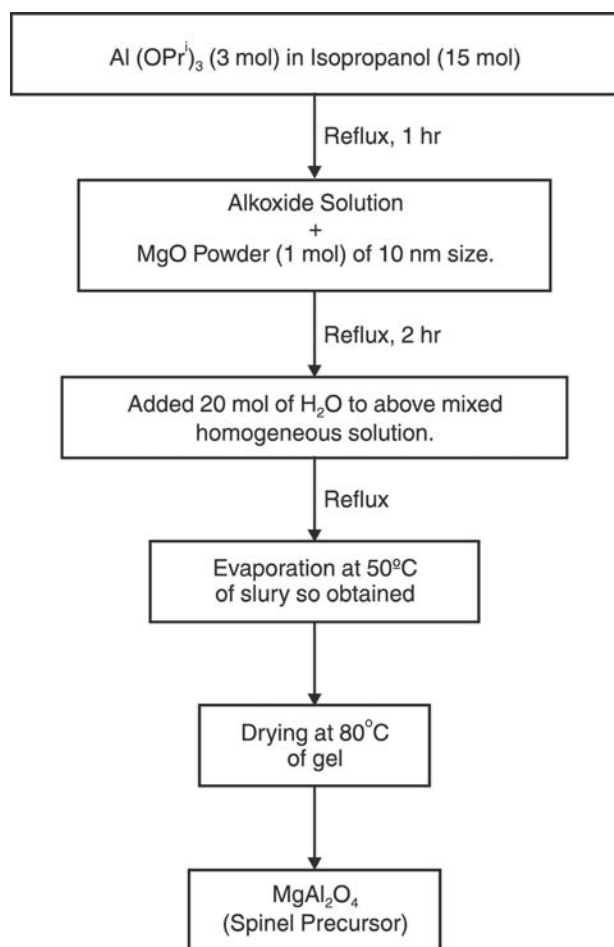


Fig. 3 Preparation route for spinel  $\text{MgAl}_2\text{O}_4$  precursor.

temperature). To prepare almost-monolithic spinel powder, calcination at a temperature of  $1300^\circ\text{C}$  was required. Powder that was calcined at  $1000^\circ\text{C}$  showed extraordinary sinterability, and fully dense polycrystalline spinel could be obtained at sintering temperature as low as  $1400^\circ\text{C}$ .

Synthesis of  $\text{La}_{0.7}\text{Sr}_{0.3}\text{MnO}_3$  (LSMO)/silica hybrid nanocomposites have been reported by Huang et al.<sup>[45]</sup> Homogeneous granular mixtures can be obtained through sol-gel chemical route in a single step. The precursors used are the following: (1) complexes of  $\text{La}^{3+}$ ,  $\text{Sr}^{2+}$ , and  $\text{Mn}^{2+}$  with EDTA and (2) tetraethoxysilane (TEOS). Silica is produced by an ammonia-catalyzed method, whereas LSMO is obtained by thermal decomposition of the complex precursors. When hydrolysis of silicon alkoxide to form silica oxyalkoxy oligomers takes place in the LSMO precursor solution, both are formed in the same system. Thus, effective combination of both phases achieves a satisfactory level. The microstructure of the composites can be controlled mainly through the calcination temperature. When calcined at  $800^\circ\text{C}$ , silica undergoes some interaction with LSMO, and

Si–O–metal bonds are formed. These bonds establish the connection between silica network and LSMO surface.

Synthesis of pure nanocrystalline  $\text{Al}_2\text{O}_3/\text{MgO}$  powder has been reported by Carnes, Kapoor, and Klabunde.<sup>[46]</sup> The two Mg and Al alkoxide solutions were mixed in desired molar ratios and then allowed to react with a mixture of water in ethanol to yield a hydroxide gel. Upon solvent removal, a fine powder was obtained, which was then heat-treated under dynamic vacuum. The powder has excellent surface area ( $790\text{--}830\text{ m}^2/\text{g}$ ) showing a completely amorphous XRD pattern.

*Bimetallic- $\mu$ -oxoalkoxides as precursors for sol-gel technique:* Homogeneously dispersed bimetallic oxides in nanocrystalline form, of the type  $\text{MAl}_2\text{O}_4$  (where  $\text{M}=\text{Mg}$ ,  $\text{Ca}$ ,  $\text{Mn}$ ,  $\text{Co}$ ,  $\text{Fe}$ ,  $\text{Ni}$ , and  $\text{Zn}$ ) were obtained by preparation of bimetallic- $\mu$ -oxo-bridged (Al–O–M–O–Al) alkoxides  $[(\text{RO})_2\text{Al–O–M–O–Al}(\text{OR})_2]$ , which upon thermal dehydration yield oxides  $[\text{Al–O–M–O–AlO}]$  such that M is homogeneously dispersed in M and  $\text{Al}_2$  ions of empirical formula  $\text{MAl}_2\text{O}_4$  in nanocrystalline form.<sup>[47]</sup> These materials were obtained in high-surface-area forms and were characterized by X-ray diffraction (XRD), electron microscopy (TEM), surface area analyses (BET), and solid-state  $^{27}\text{Al}$  NMR. Comparative studies of hydrolysis of  $\mu$ -alkoxo-bridged alkoxides yielded MMO phases of lower surface area. This method has proved advantageous over other traditional routes. One such method is coprecipitation of metal hydroxides followed by heat treatment at high temperature.

#### Reverse microemulsion/micelle method

It is a promising route for synthesis of MMO nanoparticles.<sup>[48–50]</sup> Surfactants dissolved in organic solvents form spheroidal aggregates called reverse micelles. The polar ends of surfactant molecules organize around small water pools ( $\sim 100\text{ \AA}$ ) in the presence of water. This leads to dispersion of aqueous phase in the continuous oil phase. These reverse micelles are used as water solutions of reactive precursors to prepare insoluble nanoparticles. Various reactive precursors such as alkoxides or metal salt mixtures can be used for synthesis of nanoparticles inside the micelles. Solvent removal followed by calcination lead to the final product.

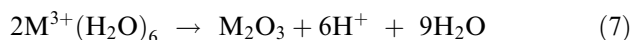
The above method was adopted to prepare the  $\text{ZnFe}_2\text{O}_4/\text{TiO}_2$  nanocomposite.<sup>[51]</sup> In this method,  $\text{ZnFe}_2\text{O}_4$  and  $\text{TiO}_2$  were prepared by coprecipitation and controlled hydrolysis methods, respectively.  $\text{ZnFe}_2\text{O}_4$  was coprecipitated from a mixed solution of  $\text{Zn}(\text{NO}_3)_2$  and  $\text{Fe}(\text{NO}_3)_2$  in a 1:2 molar ratio at pH 13 and temperature of  $100^\circ\text{C}$ .  $\text{TiO}_2$  was precipitated from mixed solution with a volume ratio of



Ti(OBu)<sub>4</sub>:C<sub>2</sub>H<sub>5</sub>OH:H<sub>2</sub>O ≡ 1:10:100 at pH 2. Both products were washed with deionized water. They were added separately to dodecyl benzene sulphonic acid (DBS), where ZnFe<sub>2</sub>O<sub>4</sub> or TiO<sub>2</sub> nanoparticles were capped with a layer of DBS. These then readily dispersed in organic solvents such as benzene or toluene. The capped ZnFe<sub>2</sub>O<sub>4</sub> and TiO<sub>2</sub> nanoparticles were mixed in various molar ratios, followed by extraction into toluene. Organic phase was removed by distillation, leaving mixed organic sol of ZnFe<sub>2</sub>O<sub>4</sub>/TiO<sub>2</sub>. This sol was distilled to remove toluene solvent and finally heated at 400°C for 2 hr to burn DBS, leaving behind nanocomposite ZnFe<sub>2</sub>O<sub>4</sub>/TiO<sub>2</sub> material. CoFe<sub>2</sub>O<sub>4</sub> nanoparticles were also synthesized by this technique. It uses Co- and Fe-containing surfactants as metal sources.<sup>[52,53]</sup>

#### Low-temperature wet chemical synthesis by precipitation from solutions

It involves dissolving salt precursors, usually chloride, oxychloride, nitrate, etc., in water followed by addition of base solution (NaOH or NH<sub>4</sub>OH) to coprecipitate hydroxides. The hydroxide mixtures are calcined to obtain MMO powder. Its disadvantage is poor control of particle size and size distribution, as fast (uncontrolled) precipitation often causes formation of larger particles and not nanoparticles. Mechanistically, in this solvation sheets of water around metal ion are dehydrated under alkaline conditions, e.g.,



The above scheme tells us the importance of alkaline conditions.<sup>[54]</sup> As an example, manganese ferrite (MnFe<sub>2</sub>O<sub>4</sub>) nanoscale particles ranging from 5 to 180 nm have been prepared from Fe<sup>3+</sup>, Fe<sup>2+</sup>, and Mn<sup>2+</sup> aqueous solution.

## STRUCTURE AND MORPHOLOGY

Control over structural and morphological properties are most crucial for performance of MMO nanoparticles in various applications. Mixed metal oxides are known to have different structural arrangement of constituent ions. The nature of these ions is important (size and charge) in the final adaptation of geometry; however, control over homogeneity, stoichiometry, phase, and crystallinity largely depend upon structure and reactivity of precursors in homogeneous solutions and their fate in subsequent processing steps. The stoichiometry and homogeneity depend upon the ability of mixed precursors, especially on addition of water to

form a single molecular species, so that the ions are distributed evenly.

Structural and morphological challenges initiated the search for suitable methods of preparation of various MMO ceramics. Several new and modified methods have been proposed for preparation of numerous ceramic nanoparticles. For example, in a modified aerogel method, addition of large amount of aromatic hydrocarbons to alcohol-methoxide solutions before hydrolysis to form gel yields ceramic materials with extraordinarily large surface area in comparison to materials obtained without adding it. This is probably because of reduced surface tension of the solvent mixture, which facilitates solvent-removed alcogel-aerogel transformation.<sup>[55,56]</sup>

Mixed metal oxide nanoparticles exhibit unusual surface morphologies and possess more reactive surface because of the presence of high concentrations of edge/corner sites and other defects. Morphological studies indicate that the nanocrystals are more polyhedral and thus possess more defects. Such defects could be of the Frankel or Schottky type (vacancies) or may be manifested as unusual configurations of edges, corners, or crystal planes. A ceramic material with high surface area displays 30–40% of the ceramic moieties on the surface, which allows surface gas reactions to approach the stoichiometric range.<sup>[17]</sup> As MMOs contain a variety of cations, the prediction of structure simply on the basis of radius ratios of cations and oxide ions becomes complicated. This means some simpler approach is required. For example, take a list of known structures and the radii of the ions present in them. The radii of two of the ions present in a given compound are plotted against each other. This is graphically related to arithmetic radius ratio approach. It is seen that compounds with similar structures are grouped together. In Fig. 4, compounds of the type A<sub>2</sub>BO<sub>4</sub> (where B is a higher-valent metal than A) are plotted as a function of radii A and B. In these materials, oxide ions form a closed packed array (framework) and sizes of A and B decide how they fit in (sometimes major distortion in closest-packed structure is noticed). On the basis of fields in Fig. 4, one can predict structures of newly discovered ceramic materials with known *r*<sub>A</sub> and *r*<sub>B</sub> values.<sup>[57]</sup>

### Spinel Structures

It consists of a face-centered cubic arrangement of oxygen ions. A unit cell contains 32 O<sup>2-</sup> ions, 64 tetrahedral, and 32 octahedral sites, which are occupied by A<sup>2+</sup> (A = Mg, Fe, Ca, Zn, etc.) and B<sup>3+</sup> (B = Al, Fe, etc.) cations. The general formula of spinel is written as A<sup>II</sup> B<sub>2</sub><sup>III</sup> O<sub>4</sub> [where A<sup>II</sup> is a Group 2 metal ion or transition metal in +2 oxidation state

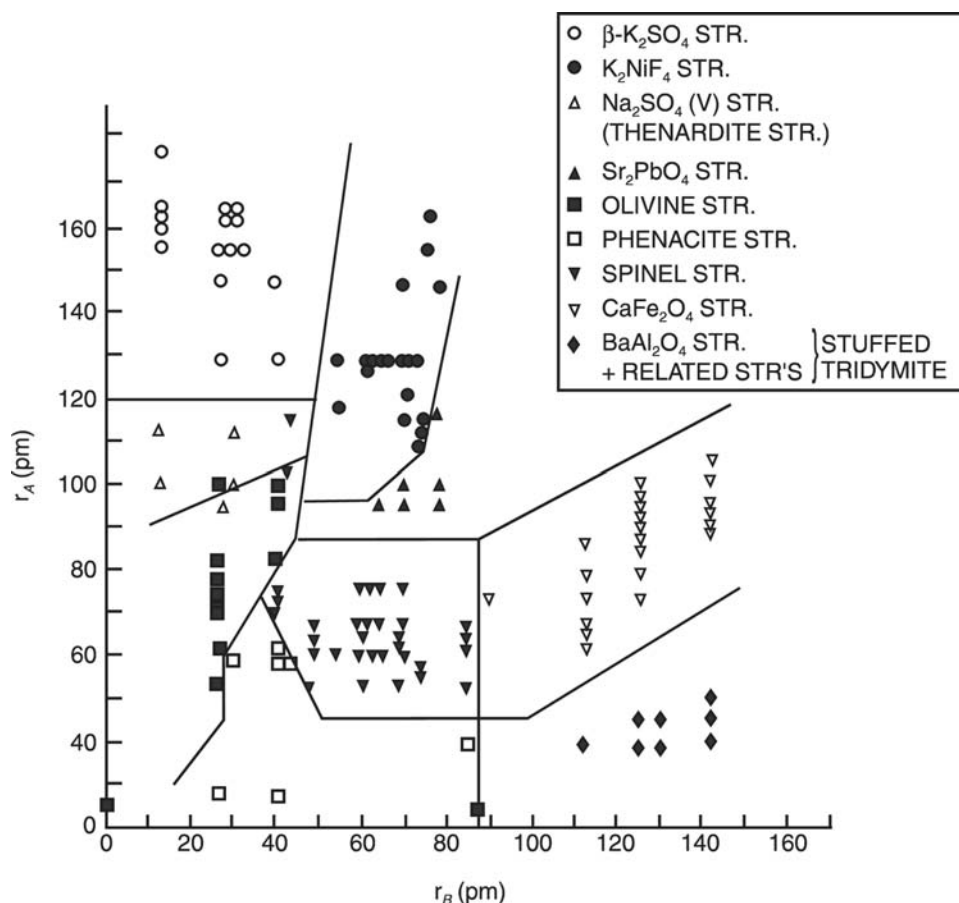


**Fig. 4** Classification of the structures of  $A_2BO_4$  ionic minerals as a function of cation radii. *Source:* Reproduced with permission from *Treatise on Solid State Chemistry*, Vol. 1, N.B. Hannay, ed., Plenum, New York, © 1973, Bell Telephone Laboratories, Inc.

and  $B^{III}$  is a Group 3B (B, Al, Ga, In) cation or transition metal ion in +3 oxidation state]. As a unit cell has 32  $O^{2-}$  ion and only 4 are present per molecule (from the formula), then spinel structure has 8 (64/8) tetrahedral and 4 (32/8) octahedral vacancies per molecule of  $AB_2O_4$ . When  $A^{2+}$  ions occupy one eighth of a tetrahedral (1 out of available 8) hole and  $B^{3+}$  ions occupy half (2 out of available 4) of an octahedral hole, the structure is called “normal” spinel, e.g.,  $MgAl_2O_4$ . This is a very stable arrangement even in terms of coordination, having tetrahedral arrangement about a divalent cation and octahedral arrangement about a trivalent cation. In some cases, one half of  $B^{3+}$  ions exchange their positions with  $A^{2+}$  ions. This is called “inverse” spinel, e.g.,  $NiFe_2O_4$ . In this arrangement, one eighth of tetrahedral sites are occupied by half of  $B^{3+}$ , whereas the rest of  $B^{3+}$  ions along with  $A^{2+}$  ions occupies half of the octahedral sites. If the general formula for “normal” spinel is written as  $(A)[B]_2O_4$  to suggest ( ) and [ ] representing tetrahedral and octahedral coordination, then the general formula for “inverse” spinel is written as  $(B)[AB]O_4$ . Many MMOs

also have intermediate cation distribution between these two extremes. The general formula for these structure is then written as  $(A_{1-x}B_x)[B_{2-x}A_x]O_4$ , where  $x$  is the “inversion parameter” ( $0 < x < 1$ ).<sup>[58,59]</sup>

Nanocomposites of  $ZnFe_2O_4$  and  $TiO_2$  were studied by Yuan and Zhang.<sup>[51]</sup>  $TiO_2$  (anatase phase) and  $ZnFe_2O_4$  (spinel phase) with broad diffractions were recorded (Fig. 5A). This means that in the composite,  $TiO_2$  and  $ZnFe_2O_4$  crystallite phases separate each other, having small size. Fig. 5B and C shows composite begins to form at 600°C. Anatase to rutile transformation takes place at 700°C. (Fig. 5D and E). The strongest peak ( $2\theta = 25.3^\circ$ ) disappears and, simultaneously, two new peaks of phases  $ZnTiO_3$  and  $Fe_2TiO_5$  appear. This shows the following solid-phase reaction might be taking place at annealing temperature.



Measurement of grain sizes in comparison with values of  $TiO_2$  and  $ZnFe_2O_4$  shows the following: (1) As

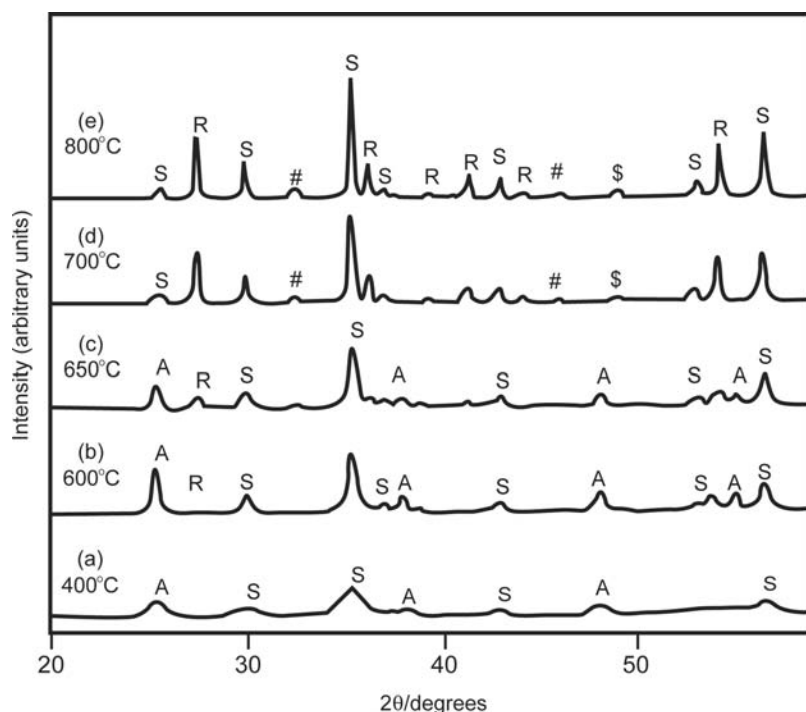


**Fig. 5** XRD patterns of the  $\text{ZnFe}_2\text{O}_4/\text{TiO}_2$  composite with a molar ratio of  $\text{Zn}:\text{Ti} = 0.1$  after annealing at various temperatures for 2 hr. A = anatase, R = rutile, S = spinel, \$ =  $\text{Fe}_2\text{TiO}_5$ , # =  $\text{ZnTiO}_3$ . Source: Reprinted with permission from Ref.<sup>[51]</sup>.

annealing temperature increases, the grain size of  $\text{TiO}_2$  increases. (2) In composite, an increase in temperature has the same effect of growth of  $\text{ZnFe}_2\text{O}_4$  as it does on pure  $\text{ZnFe}_2\text{O}_4$ . TEM analysis proved particles are distributed homogeneously and particles grow with uniform sizes.

### Perovskite Structures

Perovskite-phase MMO ceramics are important because of changes in their physical properties on application of an external electrical stimulus. These properties include ferroelectric, pyroelectric, piezoelectric, and dielectric behavior. These have led to numerous applications in electromechanical transducers, light modulation, charge storage, nonvolatile memory applications, etc.<sup>[23,24]</sup> The class of MMOs having the formula  $\text{ABO}_3$  (such as  $\text{CaTiO}_3$ ) is called perovskite. The structure of this mineral was first thought to be cubic but later confirmed as orthorhombic. The truly cubic form is referred to as “ideal perovskite” having a unit cell edge of  $\sim 4 \text{ \AA}$  containing one  $\text{ABO}_3$ . In perovskite structure, large cation A is surrounded by 12 oxide ions to form cuboctahedral coordination, while B cation is surrounded by 6 oxide ions in an octahedral coordination.

Nanophase powders of  $\text{Y}_x\text{Zr}_{1-x}\text{O}_{2-x/2}$  have been prepared from a mixture of  $\text{ZrO}_2$  and  $\text{Y}_2\text{O}_3$  powders.<sup>[60]</sup> It is shown that depending upon the starting powder mixture composition, the yttrium content in nanophases can be controlled to obtain tetragonal or

cubic phases. Tetragonal or a mixture of tetragonal and cubic were observed for low yttria content (3.5 mol% yttria), and cubic for higher yttria contents (19, 54, and 76 mol% yttria). These powders were found to have a most probable grain size of about 10–12 nm, and the grains appeared as isolated single crystals with polyhedral shape. The grain shape appeared to be polyhedral and not too anisotropic. Lattice figures were parallel to surfaces, showing that (100) and (111) face dominates.<sup>[17]</sup>

### PROPERTIES AND APPLICATIONS OF MIXED METAL OXIDE NANOPARTICLES

Properties of MMO nanoparticles are mainly size dependent, and their chemical and physical properties are unique in comparison to corresponding bulk materials. The study of physical and chemical properties is interesting as it allows gradual transition from atomic or molecular to condensed matter systems. As the particle size decreases, the percentage of atoms residing on the surface increases. This makes MMO nanoparticles more reactive, as atoms/ions are more reactive than their bulk counterparts because of coordinative unsaturation. Because of this and high surface-to-volume ratio, it is not unusual to see unique behavior and characteristics of MMO nanoparticles, including insulating oxides. When strong chemical bonding is present, delocalization varies with size; this in turn can lead to different chemical and physical properties.<sup>[17]</sup>

### Acid–Base Behavior (Catalysts)

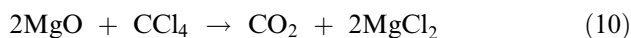
Several oxide composites have been found to be potential catalysts for a variety of important reactions because of different centers present in the same material and their basicity or acidity.<sup>[61,62]</sup> This behavior varies from one MMO to another. Some exhibit surface basic behavior and some surface acidic behavior, whereas mixtures show unusual properties. The mixing of two oxides can enhance the catalytic activity many fold because of synergistic effects, as seen in the mixed aerogel of titania/zirconia. The acid strength increases and active sites are more than pure titania and zirconia. This is probably because of oxide–oxide interaction at molecular level, suggesting that co-gelling two metal oxides is an effective way to bring two oxides in close contact.<sup>[17]</sup>

### Unusual Adsorptive Properties

Perhaps one of the greatest promises of MMO nanoparticles in chemistry is their ability to chemically adsorb a wide range of organic molecules or inorganic gases that are considered as hazardous environment pollutants. They not only adsorb but also dissociate these to nonhazardous substances on their surface. Carnes, Kapoor, and Klabunde<sup>[46]</sup> studied the adsorption of CCl<sub>4</sub>, SO<sub>2</sub>, and paraoxon on both Al<sub>2</sub>O<sub>3</sub> and Al<sub>2</sub>O<sub>3</sub>/MgO.

#### Reaction of Al<sub>2</sub>O<sub>3</sub> and (1/1) Al<sub>2</sub>O<sub>3</sub>/MgO with CCl<sub>4</sub>

The reaction of CCl<sub>4</sub> with Al<sub>2</sub>O<sub>3</sub> and Al<sub>2</sub>O<sub>3</sub>/MgO was carried out to understand the destructive adsorption abilities of the metal oxides toward a model chlorocarbon at elevated adsorption temperatures.



Thermodynamics predicts that the samples containing or being made of MgO will be more reactive than the Al<sub>2</sub>O<sub>3</sub> samples.<sup>[31]</sup> However, surface area, crystallite size, and morphology play important roles.

#### Sulfur dioxide adsorption on aluminum and aluminum/magnesium oxide

Adsorption of SO<sub>2</sub> was carried out to learn if the adsorption properties are different for nanocrystals (NC) when compared to commercial microcrystals (MC).<sup>[46]</sup> The experimental results showed that at atmospheric pressure and room temperature, SO<sub>2</sub> adsorbed onto NC-Al<sub>2</sub>O<sub>3</sub> up to 3.5 molecules

SO<sub>2</sub>/nm<sup>2</sup>; similarly, on CM-Al<sub>2</sub>O<sub>3</sub> there were 3.5 molecules SO<sub>2</sub>/nm<sup>2</sup> adsorbed, and on NC- (1/1) Al<sub>2</sub>O<sub>3</sub>/MgO there were 6.8 molecules SO<sub>2</sub>/nm<sup>2</sup>, whereas on CM-MgO there were only 0.68 molecules SO<sub>2</sub>/nm<sup>2</sup> adsorbed. These data indicate that NC-Al<sub>2</sub>O<sub>3</sub>/MgO efficiently adsorb SO<sub>2</sub> in slightly more than one layer. After adsorption, the samples were subjected to dynamic vacuum to remove the physisorbed species. The vacuum treatment removed most of the adsorbed SO<sub>2</sub> from the CM-MgO, whereas the NC-Al<sub>2</sub>O<sub>3</sub>/MgO sample retained 3.9 chemisorbed molecules of SO<sub>2</sub>/nm<sup>2</sup>.

### CONCLUSION

Mixed metal oxide nanoparticles can provide great diversity of substances and phenomena. Different metals in their various oxidation states can combine in different ratios to produce a variety of materials. These new materials with variation in physical, chemical, and morphological properties can be exploited in various fields of science and technology. The compression of nanoscale ceramic particles yields more flexible solid objects, apparently because of the multitude of grain boundaries that exist. After further development of compression techniques so that highly densified nonporous MMO nanomaterials can be prepared, these may find uses as replacements for metals in many applications including electrochemistry. These materials, beyond doubt, would be environment friendly, not only by themselves but also as future water purifiers and destructive adsorbents. These MMO nanoparticles are finding use in antichemical/biological warfare, in air purification, and as an alternative to incineration of toxic substances. Mixed metal oxide nanoparticles would also be replacing many heterogeneous catalysts known today because of high surface area, which increases their efficiency many fold. Research on the effect of particle size (percent dispersion as a measure of the fraction of metal atoms on the surface and thus available to incoming reactants) and shape (crystal faces, edges, corners, defects that lead to enhanced surface reactivity) has been and continues to be a potential field. In general, the ability to prepare MMO nanoparticles for use in high surface area catalysis has certain inherent advantages, and further progress is sure to come in the near future. It has been proposed that further work in the area of nanophase ceramics may lead to increased flexibility, less brittleness, and greater strength. It may also be possible to form materials with a large fraction of atoms at grain boundaries, maybe in unique arrangements. It may also be possible to produce binary materials of normally immiscible oxides. This entry has explored the synthetic, structural, and application

prospects that MMO nanoparticles provide. Although relatively few examples have been chosen, all relevant areas have been covered.

## REFERENCES

- Amigó, R.; Asenjo, J.; Krotenko, E.; Torres, F.; Tejada, J. Electrochemical synthesis of new magnetic mixed oxides of Sr and Fe: composition, magnetic properties, and microstructure. *Chem. Mater.* **2000**, *12* (2), 573–579.
- Rodriguez, J.A.; Hanson, J.C.; Chaturvedi, S.; Maiti, A.; Brito, J.L. Phase transformations and electronic properties in mixed metal oxides; experimental and theoretical studies on the behavior of NiMoO<sub>4</sub> and MgMoO<sub>4</sub>. *J. Chem. Phys.* **2000**, *112* (2), 935–945.
- Heinz, D.; Hoelderich, W.F.; Krill, S.; Boeck, W.; Huthmacher, K. V<sub>2</sub>O<sub>5</sub>/TiO<sub>2</sub> catalysts for the vapor-phase oxidation of  $\beta$ -picoline: Influence of the TiO<sub>2</sub> carrier. *J. Catal.* **2000**, *192*, 1–10.
- Watanabe, H.; Koyasu, Y. New synthesis route for Mo–V–Nb–Te mixed oxide catalyst for propane ammoxidation. *Appl. Catal. A* **2000**, *194–195*, 479–485.
- Corma, A. Inorganic solid acids and their use in acid catalyzed hydrocarbon reactions. *Chem. Rev.* **1995**, *95*, 559–614.
- Reddy, B.N.; Subrahmanyam, M. Ammoxidation of 3-picoline over highly dispersed vanadia on alumina–silica mixed support. *Langmuir* **1992**, *8*, 2072–2073.
- Kiessling, D.; Went, G.; Hagenau, K.; Schoellner, R. Dimerization of n-butenes on amorphous nickel oxide–alumina/silica catalysts. *Appl. Catal.* **1991**, *71*, 69–78.
- Andrianainarivelo, M.; Corrin, R.; Laclercq, D.; Mutin, P.H.; Vioux, A. Mixed oxides SiO<sub>2</sub>–ZrO<sub>2</sub> and SiO<sub>2</sub>–TiO<sub>2</sub> by a non-hydrolytic sol–gel route. *J. Mater. Chem.* **1996**, *6* (10), 1665–1671.
- Siegel, R.W.; Ramaswami, S.; Hahn, H.; Zongquan, L.; Ting, L.; Grousky, R. Synthesis, characterization, and properties of nanophase titanium dioxide. *J. Mater. Res.* **1988**, *3*, 1367–1372.
- El-Shall, M.S.; Slack, W.; Vann, W.; Kane, D.; Hanely, D. Synthesis of nanoscale metal oxide particles using laser vapourisation/condensation in diffusion cloud chamber. *J. Phys. Chem.* **1994**, *98* (12), 3067–3070.
- Edelstein, A.S.; Hadjipanayis, G.C.; Siegel, R.W.; Eds. *Nanophase Materials*; Kluwer Academic Publishers: Dordrecht, 1994, 73–80 and 85–88.
- Cow, G.M.; Gonsalves, K.E.; Eds. *Nanotechnology, Molecularly Designed Materials*; American Chemical Society: Washington, DC, 1996; 79–99.
- Kodas, T.T. *Adv. Mater.* **1989**, *6*, 180.
- Messing, G.L.; Zhang, S.C.; Jayanthi, G.V. Ceramic powder synthesis by spray pyrolysis. *J. Am. Ceram. Soc.* **1993**, *76* (11), 2707–2726.
- Cow, G.M.; Gonsalves, K.E.; Eds. *Nanotechnology, Molecularly Designed Materials*; American Chemical Society: Washington, DC, 1996; 64–78.
- Skanadan, G.; Chen, Y.I.; Glumac, N.; Kear, B.H. Ceramic powder synthesis by spray pyrolysis. *Nanostruct. Mater.* **1999**, *11* (2), 149–158.
- Khaleel, A.; Richards, R.M. *Ceramics*. In *Nanoscale Materials in Chemistry*; Klabunde, K.J., Ed.; Wiley-Interscience: New York, 2001; 85–120.
- Laine, R.M.; Waldner, K.; Bickmore, C.; Treadwell, D.R. Ultrafine powders by flame spray pyrolysis. U.S. Patent, 5, 958, 361, September 28, 1999.
- Laine, R.M.; Rand, S.C.; Hinklin, T.; Williams, G. Ultra-fine powders as lasing media. WO 0038282 HOIS 20000629.
- Pramanik, P.; Roy, J.C.; Sen, A.; Pati, R.K. Novel chemical methods for preparation of nanosized oxide ceramics. In *International Symposium on Metastable, Mechanically Alloyed and Nanocrystalline Materials*; Proceedings of ISMANAM-2000, Oxford, UK, Material Science Forum; 2001; Vols. 360–362, 623–630.
- Mehrotra, R.C.; Singh, A. Recent trends in metal alkoxide chemistry. In *Progress in Inorganic Chemistry*; Karlin, K.D., Ed.; John Wiley & Sons Inc., 1997; 239–454.
- Mehrotra, R.C.; Singh, A.; Tripathi, U.M. Recent advances in alkoxo and aryloxo chemistry of scandium, yttrium and lanthanoids. *Chem. Rev.* **1991**, *91*, 1287–1303.
- Chandler, E.D.; Roger, C.; Smith, M.J.H. Chemical aspects of solution routes to perovskite-phase mixed-metal oxides from metal–organic precursors. *Chem. Rev.* **1993**, *93*, 1205–1241.
- Liliane, G.H.P. Heterometallic alkoxides and oxoalkoxides as intermediates in chemical routes to mixed metal oxides. *Polyhedron* **1994**, *13*, 1185–1195.
- Interrante, L.V.; Hampden, M.J.; Eds. *Chemistry of Advanced Materials: An Overview*; Wiley-VCH: New York, 1998.
- Hench, L.L.; West, J.K. Aerogels—airy materials: chemistry, structure, and properties. *Chem. Rev.* **1990**, *90*, 33–72.
- Brinker, C.J.; Scherer, C.W. *Sol–Gel Science*; Academic Press: San Diego, CA, 1990.
- Narula, C.K. *Ceramic Precursor Technology and Its Applications*; Marcel Decker: New York, 1995.
- Husing, N.; Schubert, U. Aerogels—airy materials: chemistry, structure, and properties. *Angew. Chem. Int. Ed.* **1998**, *37*, 22–45.
- Schneider, M.; Baiker, A. Titania-based aerogels. *Catal. Today* **1997**, *35*, 339–365.
- Rolison, D.R.; Dunn, B. *Electrically Conductive Oxide Aerogels: New Materials in Electrochemistry*; J. Mater. Chem.; Royal Chemical Society, 2001; Vol. 11, 963–980.
- Sanchez, C.; Livage, J.; Henry, M.; Babonneau, F. J. Non-Cryst. Solids **1998**, *100*, 65.
- Ribot, F.; Toledano, P.; Sanchez, C. *Chem. Mater.* **1991**, *3*, 759.
- Swider, K.E.; Hagans, P.L.; Merzbacher, C.I.; Rolison, D.R. Synthesis of ruthenium dioxide–titanium dioxide aerogels: redistribution of electrical properties on the nanoscale. *Chem. Mater.* **1997**, *9*, 1248–1255.
- Prakash, S.S.; Brinker, C.J.; Hurd, A.J.; Rao, S.M. Silica aerogel films prepared at ambient pressure by using surface derivatisation to reduce reversible drying shrinkage. *Nature* **1995**, *374*, 439–443.
- Gerben, T. The subcritical preparation of aerogels based on sodium water glass. *J. Sol-Gel Sci. Technol.* **1998**, *13*, 323.

37. Haereid, S.; Anderson, J.; Einarsrud, M.A.; Hua, D.W.; Smith, D.M. *J. Non-Cryst. Solids* **1995**, *185*, 221.
38. Haereid, S.; Nilsen, E.; Einarsrud, M.A. Properties of silica gels aged in TEOS. *J. Non-Cryst. Solids* **1996**, *204*, 228–234.
39. Yoldas, B.E. Formation of titania–silica glasses by low temperature chemical polymerization. *J. Non-Cryst. Solids* **1980**, *38 & 39*, 81–86.
40. Miranda Salvado, I.M.; Fernandez Navarro, J.M. *J. Non-Cryst. Solids* **1992**, *147–148*, 256.
41. Andrianainarivelo, M.; Corriu, R.; Leclercq, D.; Mutin, P.H.; Vionx, A. Mixed oxides SiO<sub>2</sub>–ZrO<sub>2</sub> and SiO<sub>2</sub>–TiO<sub>2</sub> by non-hydrolytic sol–gel route. *J. Mater. Chem.* **1996**, *6* (10), 1665–1671.
42. Bradley, D.C.; Hancock, D.C.; Wardlaw, H. Titanium chloride alkoxides. *J. Chem. Soc.* **1952**, 2773–2778.
43. Shino, T.; Shiono, K.; Miyamoto, K.; Pezzotti, G. Synthesis and characterization of MgAl<sub>2</sub>O<sub>4</sub> spinel precursor from a heterogeneous alkoxide solution containing fine MgO powder. *J. Am. Ceram. Soc.* **2000**, *83* (1), 235–237.
44. Shiono, T.; Migamoto, K.; Sugishima, Y.; Okamoto, Y.; Hayashi, K.; Nishikawa, T. Preparation and sinterability of forsterite powders derived from heterogeneous alkoxide solution containing fine MgO powders. *J. Jpn. Soc. Powder Metall.* **1994**, *41* (5), 573–576.
45. Huang, Y.H.; Yan, C.H.; Wang, S.; Luo, F.; Wang, Z.M.; Liao, C.S.; Xu, G.X. Chemical synthesis of La<sub>0.7</sub>Sr<sub>0.3</sub>MnO<sub>3</sub>/silica homogeneous nanocomposites. *J. Mater. Chem.* **2001**, *11*, 3296–3299.
46. Carnes, C.L.; Kapoor, P.N.; Klabunde, K.J. Synthesis, characterisation and adsorption studies of nanocrystalline aluminium oxide and a bimetallic nanocrystalline aluminium oxide/magnesium oxide. *Chem. Mater.* **2002**, *14*, 2922–2929.
47. Kapoor, P.N.; Heroux, D.; Mulukutla, R.S.; Klabunde, K.J. High surface area homogeneous nanocrystalline bimetallic oxides obtained by hydrolysis of bimetallic- $\mu$ -oxoalkoxides. *J. Mater. Chem.* **2003**, *13*, 410–414.
48. Herrig, H.; Hempelmann, R. *Mater. Lett.* **1996**, *27*, 287.
49. Fang, J.; Wang, J.; Ng, S.C.; Chew, C.H. *Nanostruct. Mater.* **1997**, *8* (4), 499.
50. Gan, L.M.; Zhang, L.S.; Chan, H.S.O.; Chew, C.H.; Loo, B.H. A novel method for the synthesis of perovskite-type mixed metal oxides by the inverse microemulsion technique. *J. Mater. Sci.* **1996**, *31*, 1071–1079.
51. Yuan, Z.; Zhang, L. *Synthesis, Characterisation and Photocatalytic Activity of ZnFe<sub>2</sub>O<sub>4</sub>/TiO<sub>2</sub> Nanocomposite*; J. Mater. Chem.; Royal Chemical Society, 2001; 11, 1265–1268.
52. Davies, K.J.; Wells, S.; Upadhyay, R.V.; Charles, S.W.; O’Grady, K.; Hilo, M.E.; Meaz, T.; Morep, S. The observation of multi-axial anisotropy in ultrafine cobalt ferrite particles used in magnetic fluids. *J. Magn. Magn. Mater.* **1995**, *149*, 14–18.
53. Pillai, V.; Shah, D.O. Synthesis of high-coercivity cobalt ferrite particles using water-in-oil microemulsions. *J. Magn. Magn. Mater.* **1996**, *163*, 243–248.
54. Thimmaiah, S.; Rajamathi, M.; Singh, N.; Bera, P.; Meldrum, F.; Chandershekar, N.; Seshadsi, R. A solvothermal route to capped nanoparticles of  $\gamma$ -Fe<sub>2</sub>O<sub>3</sub> and CoFe<sub>2</sub>O<sub>4</sub>. *J. Mater. Chem.* **2001**, *11*, 3215–3221.
55. Klabunde, K.J.; Stark, J.V.; Koper, O.; Mohs, C.; Khaleel, A.; Glavee, G.; Zhang, D.; Soresen, C.M.; Hadipanayis, G.C. *Nanophase Materials*; Hadjipangyis, G.C., Siegel, R.W., Eds.; Kluwer Academic Publishers: Dordrecht, 1994; 1–21.
56. Bedilo, A.; Klabunde, K.J. Synthesis of catalytically active zirconia aerogels. *J. Catal.* **1998**, *176*, 448–458.
57. Huheey, J.E. Ionic bonding and the nature of solids. In *Inorganic Chemistry, Principles of Structure and Reactivity*, 2nd Ed.; Harper International Edition; Harper & Row Publishers: New York, 1978; 86–87.
58. Bragg, W.H. The structure of the spinel group of crystals. *Philos. Mag.* **1915**, *176* (30), 305–315.
59. Sickafus, K.E.; Wills, J.M. Structure of spinel. *J. Am. Ceram. Soc.* **1999**, *82* (12), 3279–3292.
60. Rouanet, A.; Pichelin, G.; Roucau, C.; Snoeck, E.; Monty, C. *Nanophase Materials*; Hadjipanayis, G.C., Siegel, R.W., Eds.; Kluwer Academic Publishers: Dordrecht, 1994; 85–88.
61. Philipp, R.; Omate, K.; Aoki, A.; Fujimoto, K. On the active site of magnesia/calcium oxide mixed oxide for oxidative coupling of methane. *J. Catal.* **1992**, *134*, 422–433.
62. Stakheev, A.; Yu Shapiro, E.S.; Apijok, J. XPS and XAES study of TiO<sub>2</sub>–SiO<sub>2</sub> mixed oxide system. *J. Phys. Chem.* **1993**, *97*, 5668–5672.



# Molecular Computing Machines

Yaakov Benenson

Ehud Shapiro

*Department of Computer Science and Applied Mathematics, Weizmann Institute of Science, Rehovot, Israel*

## INTRODUCTION

Biopolymers such as nucleic acids and proteins encode biological data and may be viewed as strings of chemical letters. While electronic computers manipulate strings of 0's and 1's encoded in electric signals, biologically encoded data might, in principle, be manipulated by biochemical means. During the last decade, several approaches to compute with biomolecules were developed, and the field has become known as biomolecular or DNA computing. The approaches varied widely with respect to the model of computation they employed, the problems they attempted to solve, and the degree of human intervention. One approach focused on the application of the Turing machine model and, more generally, string-processing automata to biomolecular information processing. Its goal is to construct computers made of biomolecules that are capable of autonomous conversion of an input data-encoding molecule to an output molecule according to a set of rules defined by a molecular program. Here we survey the field of biomolecular computing machines and discuss possible future directions.

## BACKGROUND

The seminal work of Adleman<sup>[1]</sup> demonstrated that commonly used biochemical manipulations of DNA can be utilized to solve real-world computational problems and initiated the field of biomolecular computing. In the biomolecular approach to computing, the computational paradigm is chosen to fit the capabilities of biomolecules, rather than adapting the biomolecular machinery to computational schemes borrowed from electronic computers.<sup>[2]</sup> The problems initially solved by DNA computing were so-called “combinatorial problems.” An example of such a problem is the traveling salesman problem, which is to find the most efficient route through several cities given a distances chart between them, passing through each city exactly once. Solving the problem can be performed by calculating all possible routes that pass

exactly once through each city, comparing them and choosing the shortest one. As the number of potential routes is exponential in the size of the problem, this computation may require an exponential number of steps. More efficient solution methods are not known for the traveling salesman problem and for similar such problems, termed NP-hard. It was hoped that the potential massive parallelism of DNA manipulation could speed up the solution of NP-hard problems. The DNA computing technique employed to solve the traveling salesman problem included 1) generation of all possible solution candidates (e.g., various routes) encoded in DNA strands and selection of the correct ones, 2) their amplification and detection by known molecular biology techniques, and 3) isolation and characterization of the shortest one. Computational problems solved in vitro with variations of this approach encompassed instances of Hamiltonian Path,<sup>[1]</sup> SAT,<sup>[3]</sup> maximal clique,<sup>[4]</sup> and “knight move”<sup>[5]</sup> problems. The computer, i.e., the physical system that produced a solution, comprised the biomolecules themselves, the laboratory equipment required to realize their biochemical manipulation, and the laboratory personnel who operated the laboratory equipment, performing the operations required to execute the computation. Therefore while these computing systems used biomolecules for computation, they realized laboratory-scale, rather than molecular-scale, computers.

A second direction in DNA computing, proposed by Winfree,<sup>[6,7]</sup> uses self-assembly of DNA tiles.<sup>[8,9]</sup> It relies on the mathematical theory of tiling. One result of this theory discovered by Wang<sup>[10]</sup> is that aperiodic assembly of appropriately designed tiles emulates the operation of a Turing machine, a universal computer. The tiles have colored edges, and they may be assembled once two adjacent tiles have edges of the same color. DNA tiles<sup>[8]</sup> are relatively rigid flat constructs with four sticky ends, with one sticky end emulating one edge of a tile and different sticky ends emulating different colors. DNA tiles make contact through complementary sticky ends, emulating recognition by the same color. Initial breakthrough in this area was achieved by constructing a periodic

two-dimensional crystal from DNA tiles, based on Wang assembly rules. The first actual computation performed by this technique was a cumulative XOR (exclusive OR) logical operation on a string of four binary bits.<sup>[9]</sup> In this experiment, an input string was built from alphabet tiles (either “0” or “1”) and then a second row of tiles self-assembled upon it. The first tile of the second row contained the result of the XOR operation between the first two bits, and each subsequent tile performed the operation between the intermediate cumulative result and the next unprocessed bit. Besides the potential to realize universal computation through Turing machine emulation, the technique of DNA tiles self-assembly may become a basis for fabrication of smart, aperiodic materials on a nanoscale, as suggested by several recent results.<sup>[11,12]</sup>

A third direction in DNA computing is an attempt to realize the vision,<sup>[13]</sup> recalled by Adleman in the conclusion to his seminal paper of a programmable, autonomous, molecular-scale computer: “In the future, research in molecular biology may provide improved techniques for manipulating macromolecules. Research in chemistry may allow for the development of synthetic designer enzymes. One can imagine the eventual emergence of a general purpose computer consisting of nothing more than a single macromolecule conjugated to a ribosomelike collection of enzymes that act on it.” This paradigm of biomolecular computers is the focus of our review. It views a DNA strand as a string or a tape that functions as the input as well as the memory storage for *automata* such as a finite automaton or a Turing machine.<sup>[13]</sup> This paradigm is inspired by the realization that some biomolecular machines in the living cell are essentially simple automata operating on digital information encoded in directional biopolymers.<sup>[14,15]</sup> An automaton operates by scanning a tape of symbols one symbol at a time, possibly modifies one symbol in each step, moving to an adjacent symbol and changing its state according to a predefined set of the transition rules. The tape of symbols may be naturally encoded in a polar biopolymer such as DNA or RNA. The transition rules of the machine may be encoded by transition molecules similar to tRNA. A transition, i.e., the physical modification of the input according to the transition rules, may be accomplished, in principle, by a combination of different processing enzymes. Taking this viewpoint, DNA and RNA polymerases, the ribosome, and recombinases can all be viewed as simple molecular automata. For example, RNA polymerase is, mathematically speaking, a so-called finite state transducer, which translates a string over the alphabet {A, T, C, G} into a string over the alphabet {A, U, C, G} according to a simple translation table. An artificial molecular automaton may be able to operate autonomously, realizing a truly molecular-scale

computer. Such a computer could have several important applications, discussed below.

The concept of a biomolecular computer was first introduced by Bennett<sup>[13]</sup> in 1982 as a hypothetical design for an energy-efficient computer. In this conceptual design, a set of artificial enzymes encoded the transition table of the machine and operated on RNA-based data tape. The design did not include any concrete implementation details. Several detailed designs were proposed since then. Rothmund<sup>[16]</sup> and Smith<sup>[17]</sup> proposed models for molecular implementations of Turing machines. Garzon et al.<sup>[18]</sup> designed a model of finite automata and Sakamoto et al.<sup>[19,20]</sup> implemented a semiautonomous state machine that could perform state transitions.

## MOLECULAR AUTOMATA

### Automata

Generally, an automaton consists of 1) a data tape divided into cells, each containing a symbol selected from the tape alphabet, and 2) a finite-state device driven by transition rules. The device is positioned over one of the cells and is in one of a finite number of internal states. Depending on the symbol read and the internal state, a transition rule instructs the device to write a new symbol, change state, and move one cell to the left or to the right. The Turing machine<sup>[21]</sup> is the most general automaton, capable of writing on the tape as well as moving in either direction. Fig. 1A demonstrates a Turing machine with two symbols and two states, with the upper part of the panel showing the application of one transition rule. Each rule is of the form *initial state, current symbol* → *new state, new symbol, direction of movement* (R = right, L = left). A more restricted, yet important, class of automata is called finite-state acceptors (finite automata for short).<sup>[22]</sup> A finite automaton is a unidirectional read-only Turing machine. Its input is a finite string of symbols. It is initially positioned on the leftmost input symbol in a default initial state and, in each transition, moves one symbol to the right, possibly changing its internal state (Fig. 1B is an example of a computation step of a finite automaton). Each of its transition rules specifies a next state based on the current state and current symbol. The computation terminates after the last input symbol is processed. Alternatively, it may suspend without completion when no transition rule applies. Some states are deemed accepting and the automaton accepts an input if there is a computation with this input that ends in an accepting final state. Otherwise, it is said to reject the input.

A finite automaton with two states and an alphabet of two symbols is shown in Fig. 1C. It determines

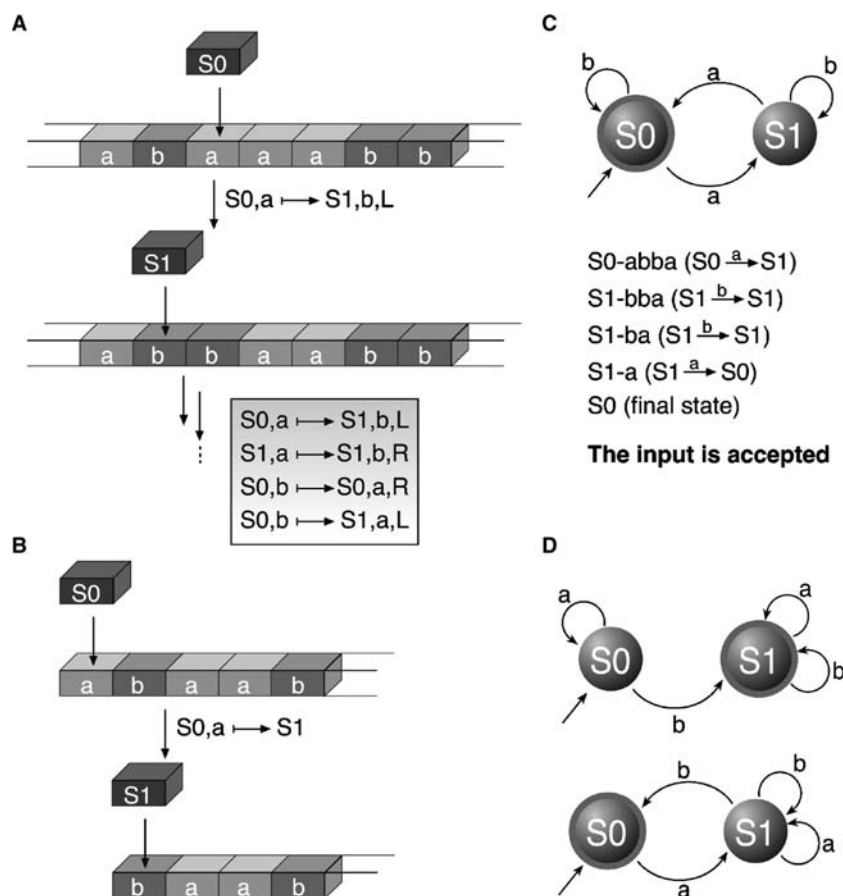


Fig. 1 Examples of automata.

whether a string of symbols over the alphabet  $\{a, b\}$  contains an even number of  $a$ 's. On a diagram, an incoming arrow represents an initial state, and a double circle represents an accepting state. Below the diagram, a sample computation over an input  $abba$  shows the intermediate configurations obtained during the sequential application of the transition rules.

A two-state, two-symbol automaton can have eight possible transition rules. The programming of such an automaton amounts to selecting the transition rules and determining the accepting states. Figure 1D shows some examples of additional final automata. The top-most automaton determines whether an input string contains at least one  $b$  symbol. A second one determines if an input string begins with  $a$  and ends with  $b$ . It is an example of a non-deterministic automaton with two transitions ( $S1, b \rightarrow S0$  and  $S1, b \rightarrow S1$ ) applicable to the same configuration. A computation ending in an accepting state uses  $S1, b \rightarrow S1$  for all  $b$  symbols except the last, and uses  $S1, b \rightarrow S0$  for the last  $b$ .

### Early Designs of Molecular Automata

Bennett<sup>[13]</sup> described a “truly chemical Turing machine” with a linear tape analogous to RNA, where

the internal state and head location are realized by a special chemical modifier attached to one of the nucleotides. Each transition rule is realized by a hypothetical “enzyme” that exclusively recognizes a unique combination of a nucleotide and its modifier, replaces a nucleotide by an output symbol, and attaches a next-state modifier to one of the adjacent nucleotides, according to the desired head movement (Fig. 2).

In Fig. 2, a transition molecule **7** that recognizes a combination of the symbol  $a$  and the state  $S0$  loads itself with the molecule for the symbol  $b$  and a molecule for the state  $S1$ . The loaded molecule **2** reversibly attaches itself to a data tape **1**. An intermediate complex **3** forms through new chemical bonds between the transition molecule and the symbol  $a$  and state  $S0$ , between the new symbol  $b$  and the data tape, and between the adjacent symbol  $b$  and the new state  $S1$  (dotted lines). In the next intermediate **4**, the old symbol  $a$  and state  $S0$  become attached to the transition molecule and are detached from the data tape; the new symbol  $b$  is inserted into the data tape; the new state  $S1$  attaches to the symbol  $b$  that lies to the right of the site of newly inserted symbol. The transition molecule **6** dissociates from the completely modified data tape **5** and is subsequently stripped of the attached old state and symbol.

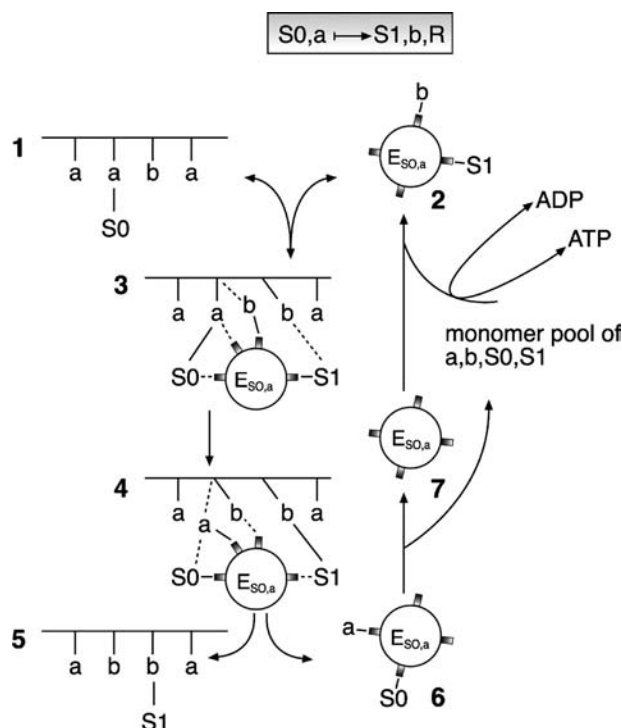


**Fig. 2** An example of a single transition performed by Bennett's hypothetical chemical Turing machine. The rule implemented is  $S0, a \rightarrow S1, b, R$ . Source: From Ref.<sup>[13]</sup> © Kluwer Academic/Plenum Publishers.

Bennett introduced several logical elements that remain relevant till this day. First, he proposed to encode a data tape in a single biopolymer, using a natural "alphabet." Second, he introduced the important concept of a "transition molecule," i.e., representation of each transition rule by a separate molecule or molecular assembly.

Following work on molecular automata dealt with realizing this concept. Different ways to encode tape symbols and machine states and to build transition molecules were proposed and various biochemical transition mechanisms were considered.

Rothemund<sup>[16]</sup> proposed a detailed design for a molecular Turing machine that utilized a common DNA structural motif known as a "cohesive terminus" or a "sticky end." A sticky end is a short (one to six nucleotides) stretch of single-stranded DNA emerging from the double-stranded DNA molecule of a potentially unlimited length. The advantage of a sticky end as compared with the dsDNA is that it is reactive and may interact once the DNA sequences of their sticky ends are complementary, irrespective to the sequence of their double-stranded part. This technique is extensively used in recombinant DNA technology. Rothemund's hypothetical computer comprised a data tape and transition molecules made of DNA

and hardware containing DNA ligase and restriction enzymes. Ligase is an enzyme that may glue together fragments of DNA that have complementary sticky ends. Restriction enzymes recognize specific locations in the double-stranded DNA and cut inside or near this location, forming two fragments with complementary sticky ends. Rothemund pioneered an encoding system of "frame shifts," where a long stretch of double-stranded DNA encoded a symbol while shorter sticky ends derived from this stretch encoded state-symbol combinations. This entailed a particular design of the transition molecules, using SII-type restriction enzymes that cut DNA outside their recognition sequence. The machine was not designed to be autonomous as it required a number of manual steps to perform a single transition (Fig. 3).

Figure 3 describes a single transition  $S0, a \rightarrow S1, b, R$  as implemented by Rothemund's hypothetical Turing machine. In this design, each data symbol is represented by a stretch of dsDNA flanked by invariant left (**L**) and right (**R**) short sequences. The starting circular double-stranded DNA structure **1** represents a data string  $bab$  and a Turing machine head, located at a symbol  $a$ . Inside a "head," there are two SII-type enzyme recognition sites. One is denoted **Inv** and another **St** for "state enzyme." **Inv** enzyme invariantly cuts in the **R** region of a symbol that lies to the left of the head. **St** enzyme cuts inside the current symbol  $a$ , and the exact restriction site is determined by the length of a spacer between the **St** recognition site and an **L** region of the current symbol. This spacer is denoted as **S0**.

After double restriction by **Inv** and **St**, the enzymes are removed and a modified data tape **2** with two sticky ends is formed. One is inside the **R** region of the leftmost  $b$  symbol. Another lies within the coding sequence of a current  $a$  symbol. Because the exact structure of this sticky ends depends on both the current symbol and the current state. This sticky end is recognized by the transition molecule **3**, which encodes a rule  $S0, a \rightarrow S1, b, R$ . It contains two sticky ends: one recognizes the current state-symbol sticky end of the data tape, and another one recognizes the sticky end within the **R** region of the left-hand symbol. Its dsDNA region contains, from left to right, an encoding for a new symbol  $b$ , a spacer and a recognition site of the **Inv** enzyme, a recognition site of the **St** enzyme, a new state spacer (**S1** in this case), **L** region, another spacer, two recognition sites of the auxiliary SII-type enzymes **X** and **Y**, and another **L** region.

The solution containing the transition molecules is added to the cleaved data tape **2**. Because real computation would require many different kinds of transition molecules, the existence of an invariant sticky end in a data tape would allow it to react non-selectively with

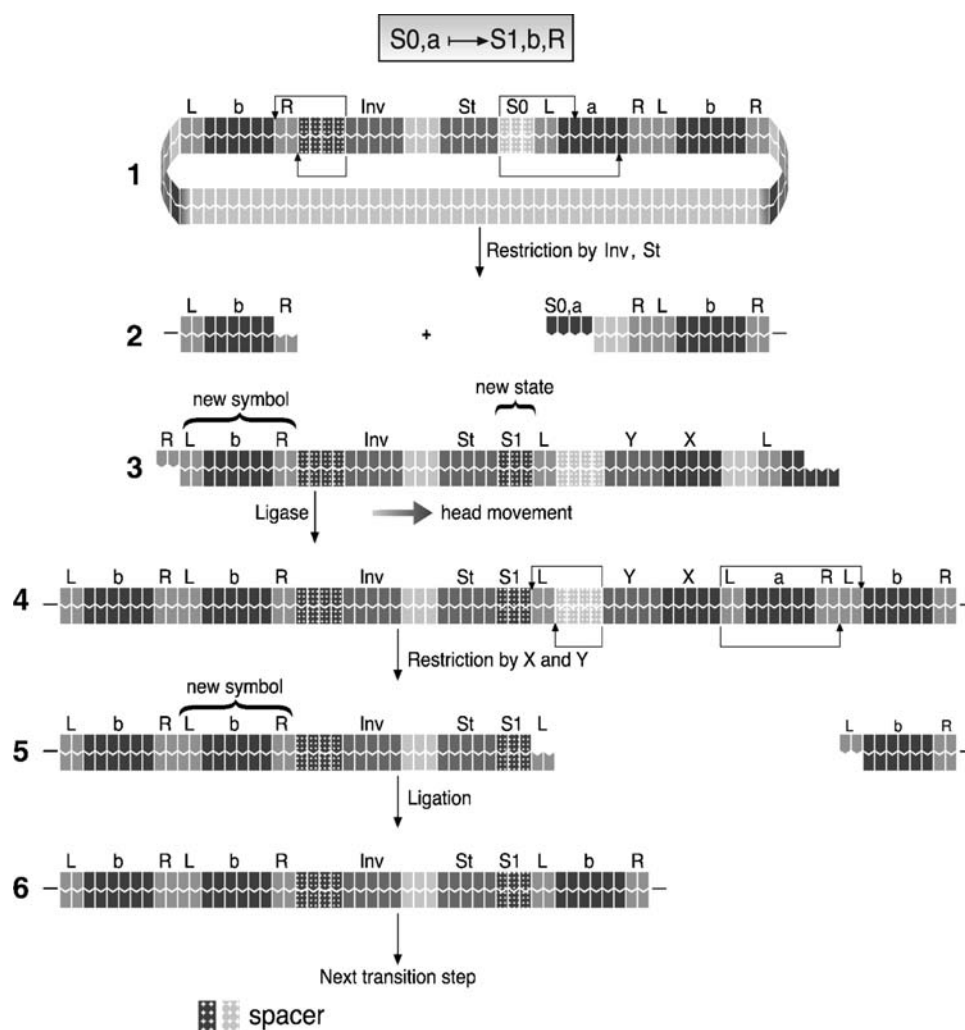


**Fig. 3** A single transition  $S_0, a \rightarrow S_1, b, R$  as implemented by the Rothemund's hypothetical Turing machine. *Source:* From Ref.<sup>[16]</sup> © American Mathematical Society.

different transition molecules. Therefore the original design contained only right-hand state-symbol specific sticky end. The left-hand sticky end was exposed by yet another restriction enzyme after correct ligation to the state-symbol sticky end and washout of the useless transitions (not shown on the figure). Following double ligation and insertion of the transition molecule, an intermediate structure **4** is formed. At this stage, the new symbol  $b$  is inserted into the tape. The head is also inserted, with the new state encoded by the new state spacer. However, the previous symbol  $a$  is regenerated. It needs to be excised by means of the enzymes  $X$  and  $Y$ . The enzymes form two complementary sticky ends in the intermediate **5**: one in the  $L$  region of the right-hand symbol  $b$ , and another one in the  $L$  region preinserted in the transition molecule. After their ligation, the next legal configuration **6** is formed. The  $St$  enzyme is now positioned at the correct distance from the next symbol  $b$ . Thus this multistep

transition process results in an insertion of a new symbol  $b$ , excision of a previous symbol  $a$ , and change of the machine state from  $S_0$  to  $S_1$ .

Sakamoto et al.<sup>[19,20]</sup> described a different approach to biomolecular state machines. While their system implemented only a fixed state-to-state transition scheme, which is not dependent on any input, it had the advantage of semiautonomous operation. The system was experimentally verified and shown to perform several transitions (Fig. 4).

Figure 4A shows a set of transition rules. Panel B depicts the molecular transition table. Each state is encoded by unique sequence of a ssDNA of 20–30 nt long. A transition between  $S_1$  and  $S_2$  is represented by a concatenation of two sequences, one complementary to  $S_1$  and another one—to  $S_2$ . The “stop” segment does not allow DNA polymerase to pass through. Figure 4C shows the initial configuration of the machine. A transition table is concatenated to the



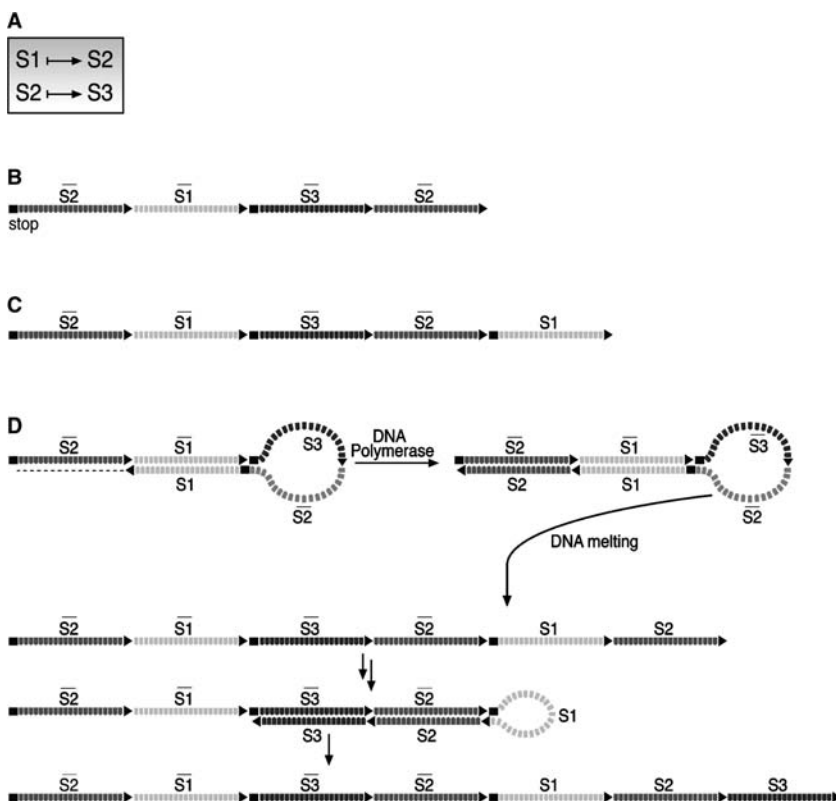


**Fig. 4** A molecular state machine of Sakamoto et al.

initial state S1. Figure 4D describes a sample computation. Initial state S1 is annealed to its complementary counterpart in the rule  $S1 \rightarrow S2$  of the transition table and then extended by DNA polymerase to form a DNA stretch for S2. After denaturation and another annealing, the S2 stretch is annealed to its counterpart in the rule  $S2 \rightarrow S3$  and extended to S3 stretch. The whole process is performed in the PCR-like manner, termed “Whiplash PCR” with cycles of denaturing, annealing, and polymerase extension.

Shapiro<sup>[14,15]</sup> proposed a detailed logical design for a molecular Turing machine, with an emphasis on a general-purpose programmable computer that may operate in vivo and interact with its biochemical environment. The design was realized in a working mechanical implementation.

The structural blocks of the design proposed by Shapiro are depicted in Fig. 5. The mechanical computer employs a chain of basic building blocks (Fig. 5A), referred to as *alphabet monomers*, to represent the Turing machine’s tape (Fig. 5B), and uses another set of building blocks (Fig. 5C), referred to as *transition molecules*, to encode the machine’s transition rules. The computer operates on two polymers simultaneously: the *tape polymer*, representing the Turing machine’s tape, and the *trace polymer*, which is a byproduct of the computation constructed incrementally from displaced transition molecules and displaced alphabet monomers and has no analog in

the theoretical Turing machine. A transition molecule loaded with an alphabet monomer specifies a computational step of the computer similarly to the way an aminoacyl-tRNA specifies a translation step of the ribosome.<sup>[23]</sup> The transition encoding is similar to a Wang tile construction<sup>[10]</sup> which is also at the basis of DNA computing via self-assembly.<sup>[6–9]</sup> The set of loaded transition molecules constitutes the computer *program* (Fig. 1A). A description of the design and mechanism of operation is shown in Figs. 5 and 6. Figure 5C shows the formation of a transition molecule and Fig. 5D shows an active transition molecule. An active transition molecule joins the two data polymers. It is embedded in the tape polymer and represents the location of the Turing machine’s read/write head as well as the machine’s internal state. At the same time, the active transition molecule is the terminal molecule of the trace polymer, representing the most recent transition of the computation. Figure 5E schematically depicts the computer (hardware). The computer is made of two subunits, referred to as *small* and *large*, each with a tunnel called the *small tunnel* and the *large tunnel*, respectively. The small tunnel provides incoming loaded transition molecules with access to the active transition molecule and to its adjacent alphabet monomer. Access is controlled by gating mechanisms that block transition molecules that are ill-formed or do not match the current state and current tape symbol. These mechanical analogs of



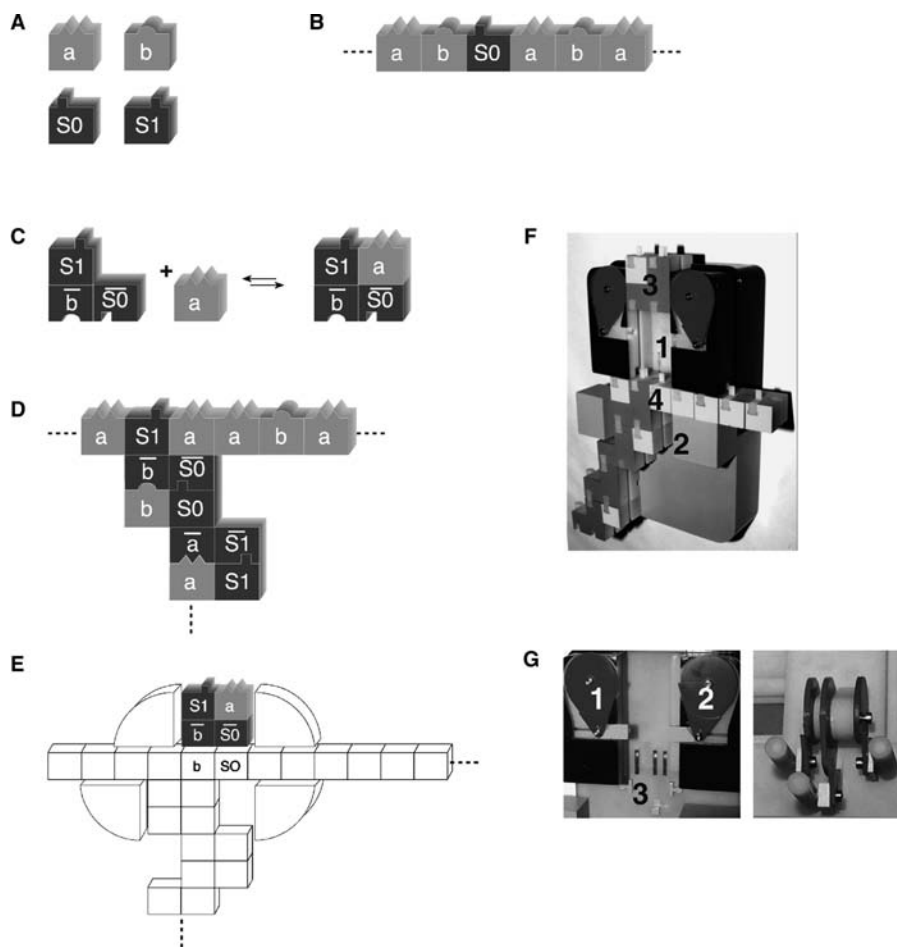


**Fig. 5** Structural blocks of the Shapiro's mechanical Turing machine.

allosteric conformational changes open the channel only when a valid incoming transition molecule approaches. The large tunnel holds the active transition molecule and the tail of the trace polymer being constructed.

The actual mechanical computer is  $18 \times 29 \times 9$  cm as shown in Fig. 5F. The small tunnel **1** is part of the small subunit and is 2 units wide. The large tunnel **2** is part of the large subunit and is 3 units wide, so that it can accommodate the displaced transition molecule and the new active transition molecules. The small and large subunits can move one unit sideways relative to each other. Such movement is necessary following a change of direction of the computation. An incoming transition molecule **3** is approaching the active transition molecule **4** and the alphabet molecule to its right. The tape polymer can move left or right 1 unit, aligning the active transition molecule to the left or to the right side of the large tunnel. Such movement is necessary to accommodate consecutive transitions in the same direction. The hardware as well as the data tapes and the incoming transition molecule are shown.

Figure 5G shows the mechanical implementation of the gating mechanisms, front (left) and back views.

Five mechanisms in the small tunnel prevent erroneous transitions from occurring. All mechanisms are based on a spring-loaded bell crank/cam which is connected to a linkage which, in its free state, blocks passage of the approaching transition molecule. Each bell crank/cam checks for a certain condition and, if the condition is met, is rotated. The connected linkage then moves out of the way of the approaching transition molecule, essentially effecting a conformational change in the tunnel. Two mechanisms **1** and **2** detect that the (left or right) transition molecule is loaded with an alphabet molecule. Mechanism **3** detects that the recognition site of the incoming transition molecule matches the state side group of the active transition molecule and the alphabet symbol to its right. Additional two mechanisms check for the blank transition.

The computer operates in cycles (Fig. 6), processing one transition molecule per cycle. In each cycle, an incoming loaded transition molecule **2** that matches the current state and its adjacent alphabet monomer of the data polymer **1** becomes the new active transition molecule and its accompanying alphabet monomer is incorporated into the tape polymer via the intermediate **3**. This is achieved by displacing the

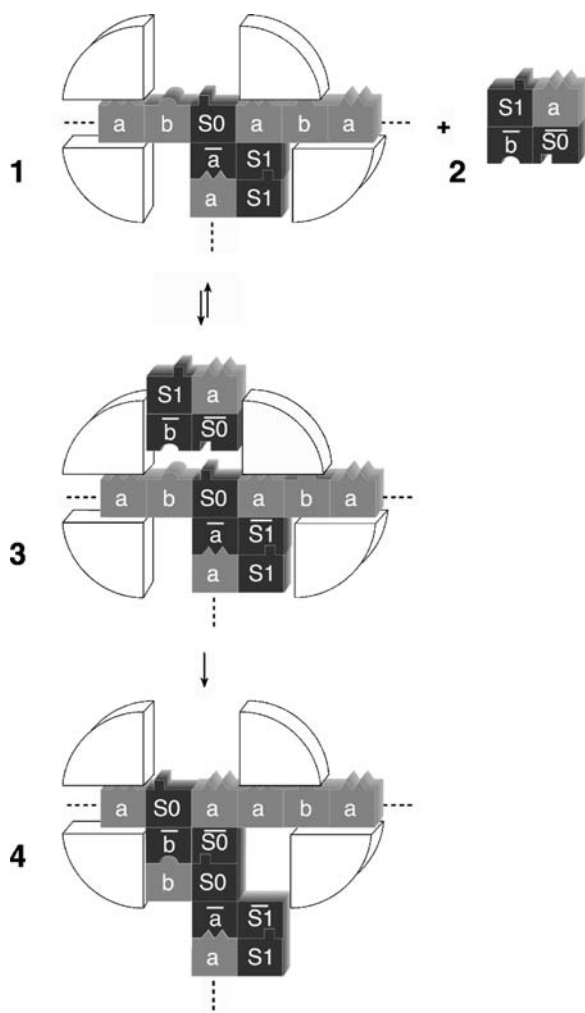


**Fig. 6** Operational cycle of the Shapiro's mechanical Turing machine.

currently active transition molecule and the matched alphabet monomer, effectively editing the tape polymer, and elongating the trace polymer by the displaced molecules to form the next configuration 4. Specifically, when processing a left transition molecule, the computer moves left to accommodate the molecule, if necessary, and displaces the currently active transition molecule and the alphabet monomer to its left by the new molecule. The computer processes a right transition molecule similarly by moving right and displacing the alphabet monomer to the right of the active transition molecule.

The trace polymer created during the computation represents past state changes and head movements, as well as the symbols that were “erased” from the tape during each transition, and as such has several important advantages. First, the trace polymer renders the computer reversible. Because the trace polymer embodies a complete record of the computation, a molecular implementation of the computer will be

subject to the speed/energy consumption tradeoff of reversible devices. Second, computation traces, in general, and the trace polymer, in particular, enable many “software” program analysis and debugging tools,<sup>[24]</sup> which are critically needed for large-scale applications. Third, the trace polymer enables “hardware” error detection and correction. One expects that any biomolecular implementation of the computer may exhibit non-negligible error rate. Such errors can be detected, and possibly also corrected, by cascading several computers along the same trace polymer, each detecting, and possibly also correcting, errors produced by its predecessor.

The most important property of the mechanical computer is that it is reactive:<sup>[25]</sup> it can have an ongoing, program-controlled, interaction with its environment. This capability is a result of the biologically inspired architecture of the computer rather than inherited from the theoretical Turing machine, which was conceived as a “batch” computing device that receives its input at the beginning of the computation and produces an output if and when the computation ends. The ribosome, for example, suspends the construction of a polypeptide chain when a required amino acid is unavailable. Similarly, this computer can be “programmed” to suspend until a specific molecule is available. The availability of such a control molecule can be tied to other relevant environmental conditions, thus triggering a computation only when these conditions prevail.

The Turing machine is a non-deterministic computing device in that it can make choices during a computation, and so is the mechanical computer. In a biomolecular implementation, this capability can be used to have the environment affect the course of a computation, based on the relative concentrations of molecules that enable one computational step compared with molecules enabling a different computational step. Using these two capabilities, the computer can be programmed so that both the timing and the course of a computation are affected and controlled by the biochemical environment.

The computer is endowed with an output device as follows. A simple extension to the Turing machine design is an instruction that erases the tape segment to the right of the read/write head. This instruction would mean in this context: “cleave the tape polymer to the right of the active transition molecule and release this tape polymer segment to the environment.” With this instruction, the computer can create and release any effectively computable polymer of alphabet monomers, in any number of copies, in the course of a computation. A cleaved tape polymer segment released by one computer can serve as the initial tape for the computation of another computer, or it can be ligated under certain conditions to the tape of

another computer, thus enabling parallel processing, communication, and synchronization among multiply operating computers.

The computer design allows it to respond to the availability and to the relative concentrations of specific molecules in its environment and to construct program-defined polymers and release them into the environment. Hence if implemented using biomolecules, the computer can be part of biochemical pathways. In particular, given a biomolecular implementation of the computer that uses ribonucleic acids as alphabet monomers, one can envision how cleaved tape polymer segments can function as messenger-RNA, effecting program-directed synthesis of proteins in response to specific biochemical conditions within the cell. Such an implementation can provide a family of computing devices with broad biological and pharmaceutical applications.

### Molecular Finite Automata

Two programmable, autonomous finite automata made of biomolecules were demonstrated by Benenson et al.<sup>[26,27]</sup> Both use a DNA molecule as input, DNA molecules as software, encoding the automaton transitions, and DNA-manipulating enzymes as hardware. The differences between the two are the source of energy for the computation and the reuse of software molecules. The first automaton relies on ATP as an energy source and consumes its software molecules during computation, while the second utilizes solely the energy stored in the chemical bonds of its DNA input molecule and its software molecules are reusable. While having similar logical structures, these versions differ in the implementation details. The design of the molecular finite automaton incorporates ideas from designs for molecular Turing machines.<sup>[15,16]</sup> The hardware of the first automaton consists of a mixture of the class IIS restriction nuclease *FokI*, T4 DNA ligase, and ATP, while the second automaton utilizes only *FokI*.

The structure of the latter automaton is shown in Fig. 7. Figure 7A shows the encoding of *a*, *b*, and terminator (sense strands) and the <state, symbol> interpretation of exposed 4-nucleotide sticky ends, the leftmost representing the current symbol and the state S1, similarly the rightmost for S0. Fig. 7B shows the hardware: the *FokI* restriction enzyme, which recognizes the sequence GGATG and cleaves 9 and 13 nucleotides apart on the 5' → 3' and 3' → 5' strands, respectively. The software comprises eight short double-stranded (ds) DNA molecules, the transition molecules encoding the eight possible transition rules (Fig. 7C). It consists of a <state, symbol> detector (light gray), a *FokI* recognition site (dark gray), and a spacer

(intermediate gray) of variable length that determines the *FokI* cleavage site inside the next symbol, which, in turn, defines the next state. Empty spacers effect S1 to S0 transition, single base-pair (bp) spacers maintain the current state, and 2-bp spacers transfer S0 to S1.

A dsDNA molecule encodes the initial state of the automaton and the input (Fig. 7D), with five to six base pairs (bp) coding for one input symbol (Fig. 7A), with the exposed sticky end at the 5'-terminus encoding the initial state and the first symbol. The ligase-based system may also contain "peripherals," two output-detection molecules of different lengths, each of which can ligate selectively with a different output molecule to form an output-reporting molecule that indicates a final state and can be readily detected by gel electrophoresis. In the ATP-free system, the output is detected by examining the length of the remainder of a processed input molecule. The computation starts when the hardware, software, and input are all mixed together and runs autonomously, if possible till termination. The automaton processes the input as shown in Fig. 7E. The computation proceeds via a cascade of transition cycles. In each cycle, the sticky end of an applicable transition molecule may ligate to the sticky end of the input molecule, detecting the current state and the current symbol. Alternatively, it may hybridize non-covalently. In both cases, the product is cleaved by *FokI* inside the next symbol encoding, exposing a new four-nucleotide sticky end. The design of the transition molecules ensures that the encodings of the input symbols *a* and *b* are cleaved by *FokI* at only two different "frames",<sup>[16]</sup> the leftmost frame encoding the state S1 and the rightmost frame encoding S0 (Fig. 7A). The exact next restriction site and thus the next internal state are determined by the current state and the size of the spacers (Fig. 7C, intermediate gray) in an applicable transition molecule. The computation proceeds until no transition molecule matches the exposed sticky end of the input or until the special terminator symbol is cleaved, forming an output molecule that has a sticky end encoding the final state. In a step extraneous to the computation and analogous to a "print" instruction of a conventional computer, this sticky end may ligate to one of two output detectors and the resultant output reporter may be identified by gel electrophoresis.

The ATP-free automaton has several advantages over the ligase-based version. First, the software molecule used in a transition is recycled because it undergoes no modification. Thus a finite number of software and hardware molecules may, in principle, process an input of any length. Second, much better performance characteristics may be achieved with the ATP-free automaton because the processing does not involve the usually slow ligation step. Using stoichiometric amounts of the software and the hardware

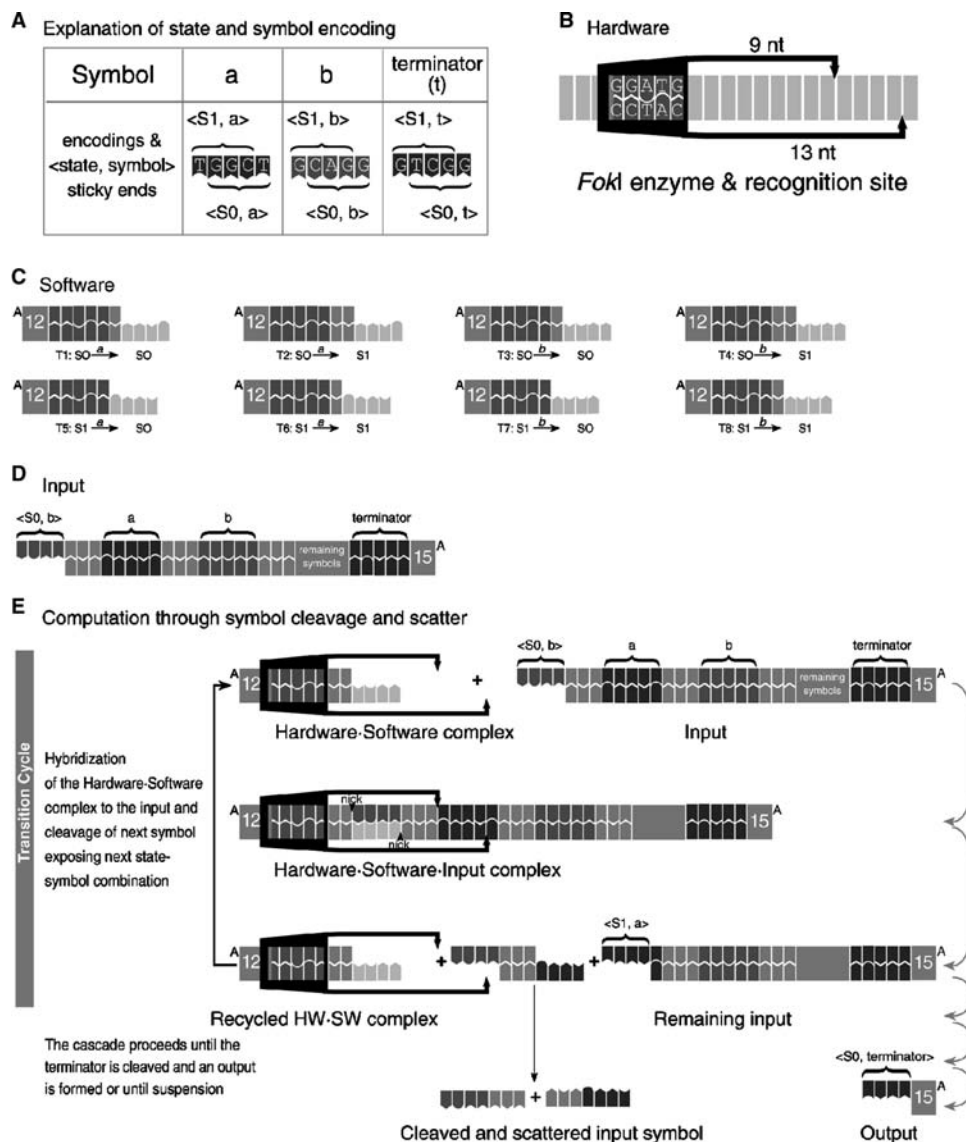


**Fig. 7** Design details and mechanism of operation of the molecular automata of Benenson et al. *Source:* From Ref.<sup>[27]</sup> © PNAS.

molecules, it is possible to process a single symbol in a few seconds. On the other hand, the ligase-based automaton is less structurally restricted. It may utilize different SII-type restriction enzymes as a hardware, including those that require a covalently bonded substrate. More importantly, it was found<sup>[27]</sup> that the ability of *FokI* to cleave DNA with its recognition and cleavage sites attached by sticky-end hybridization was limited to specific hybridization complexes. Long spacers and low GC content often resulted in cleaving only one of the input strands, producing a computationally illegal configuration. Correct performance was achieved with short spacers and high GC content of the sticky ends. The final design used the shortest possible spacers of 0, 1, and 2 bp (Fig. 7C), which dictated a particular symbol encoding (Fig. 7A) and the introduction of spacers between the symbols

(Fig. 7D). Using ligase may relax some of these constraints.

These molecular automata may be viewed from two perspectives. On one hand, the computations were performed with bulk amounts of the input molecules. Each molecule was processed independently and in parallel, thus the inputs could potentially be distinct. The parallel character of the computation could be employed in a hypothetical process of screening of DNA libraries. Large libraries of molecules could be filtered through the same software, for a search of certain sequence feature. Traditional approach to the same problem would require (non-parallel) sequencing of the whole library and then running non-parallel computer algorithms on the sequences. To analyze parallel performance of our system, the cumulative number of unit operations in a unit time per unit

volume was measured. This would represent an upper limit on the complexity of the libraries that could be analyzed. The parallel performance of the ligase-based version was in the order of  $8.3 \times 10^6$  operations/sec/ $\mu\text{L}$ , while in the ATP-free case, the performance was improved almost 8000-fold and reached  $6.6 \times 10^{10}$  operations/sec/ $\mu\text{L}$ .

Another approach is to try and scale down the system to run it in a very small compartment such as living cell. Then the question is what are the minimal requirements from the operational system. It is not unfeasible that a mixture of a single input molecule, four software molecules, and one or two *FokI* molecules could form a functioning computer while placed in a sufficiently small volume (to avoid dilution). While such possibility still requires experimental demonstration, it is possible to estimate its characteristics from the process performed in the bulk. Scaling down the concentrations, such a “minimal computer” would fit in a cube with a side length of 100 nm. The size of each component is in the range of several nanometers, with long inputs being tens of nanometers long. Such a computer would be a truly nanoscale computer. A computation on a single input molecule would proceed at a rate of 1000 sec per step in the ligase-based version and about 20 sec in the ATP-free version. While such rates seem slow compared with the electronic computers, they reflect the properties of biological systems. Once these computers would be able to operate in a cell, their performance would be competitive with respect to other cellular processes.

## CONCLUSION

The notion of a biomolecular computing machine has evolved gradually over the past decades. Theoretical designs proposed for such machines eventually led to simple molecular computing machines functioning in the test tube. The field may develop in several directions. First, more complex computing machines could be designed and built. This includes general finite automata, string transducers, stack automata, and, ultimately, the Turing machine. Currently, progress in this direction seems to be hampered by the lack of DNA- and RNA-manipulating enzymes; we hope that an eventual progress in enzyme engineering may supply the tools required to develop more complex machines. Another important issue relevant to many machine designs is symbol encoding. Current experimental realizations utilize artificial alphabet of pre-designed DNA sequences. However, the computer should “understand” natural alphabets of either single nucleotides or amino acid codons to be biologically relevant. Designing even the simplest finite automaton that would operate on an arbitrary DNA sequence

remains a major challenge. A third future direction is a search for application that would clearly demonstrate qualitative edge of a molecular computer over competing technologies.

We believe that the application potential of autonomous biomolecular computers is not to surpass electronic computers with performance; in fact, it is hard to believe they ever will. The advantage is that biomolecular computers process information encoded in molecules rather than in electric signals. Any *direct* computing over biomolecular inputs could only be performed by the computers of the same format, i.e., made of biomolecules. As we already mentioned, running sequence analysis algorithms on DNA libraries without actually sequencing all library members could be conveniently performed by a molecular state machine whose alphabet is composed of single nucleotides or codons. Another broad range of application may emerge once the molecular computer is successfully “plugged into” cellular molecular environment. By “plugging into” we mean that some of the computer components would be able to respond to certain changes in the environment, affecting the result of the computation. While the most obvious component to communicate with the environment seems to be the software, both the hardware and input could be affected as well. Once the communication between the intracellular compounds and the computer is established, the computer may, in principle, perform complex analysis of the environmental conditions. The complexity of such analysis would increase with the complexity of the computing machine and the sensitivity of the communication channels. However, even the simplest finite automata seem to provide enough computational power to make rather complex diagnostics.

## REFERENCES

1. Adleman, L.M. Molecular computation of solutions to combinatorial problems. *Science* **1994**, *266* (5187), 1021–1024.
2. Kari, L. DNA computing: arrival of biological mathematics. *Math. Intell.* **1997**, *19* (2), 9–22.
3. Lipton, R.J. DNA solution of hard computational problem. *Science* **1995**, *268* (5210), 542–545.
4. Ouyang, Q.; Kaplan, P.D.; Liu, S.; Libchaber, A. DNA solution of the maximal clique problem. *Science* **1997**, *278* (5337), 446–449.
5. Faulhammer, D.; Cukras, A.R.; Lipton, R.J.; Landweber, L.F. Molecular computation: RNA solutions to chess problems. *Proc. Natl. Acad. Sci. U. S. A.* **2000**, *97* (4), 1385–1389.
6. Winfree, E. On the computational power of DNA annealing and ligation. In *DNA Based Computers: Proceedings of the DIMACS Workshop, April 4, 1995, Princeton University*; Lipton, R.J., Baum, E.B., Eds.;

- American Mathematical Society: Providence, RI, 1996; 199–221.
7. Winfree, E. Algorithmic Self Assembly of DNA. In *Ph.D Thesis*; Caltech, 1998.
  8. Winfree, E.; Liu, F.; Wenzler, L.; Seeman, N.C. Design and self-assembly of two-dimensional DNA crystals. *Nature* **1998**, *394* (6693), 539–544.
  9. Mao, C.; LaBean, T.H.; Reif, J.H.; Seeman, N.C. Logical computation using algorithmic self-assembly of DNA triple-crossover molecules. *Nature* **2000**, *407* (6803), 493–496.
  10. Wang, H. Proving theorems by pattern recognition. Part II'. *Bell Syst. Tech. J.* **1961**, *40*, 1–41.
  11. Feng, L.; Park, S.; Reif, J.; Yan, H. A two-state DNA lattice switched by DNA nanoactuator. *Angew. Chem.* **2003**, *115* (36), 4478–4482.
  12. Yan, H.; Park, S.; Finkelstein, G.; Reif, J.; LaBean, T. DNA-templated self-assembly of protein arrays and highly conductive nanowires. *Science* **2003**, *301* (5641), 1882–1884.
  13. Bennett, C.H. The thermodynamics of computation—a review. *Int. J. Theor. Phys.* **1982**, *21* (12), 905–940.
  14. Shapiro, E. A mechanical turing machine: blueprint for a biomolecular computer. In *Proc. 5th Int. Meeting on DNA Based Computers*; DIMACS Series in Discrete Mathematics and Theoretical Computer Science; Winfree, E., Giffrod, D., Eds.; American Mathematical Society: Providence, RI, 1995; 229–230.
  15. Shapiro, E.; Karunaratne, K.S.G. Method and System of Computing Similar to a Turing Machine. US Patent 6,266,569, 2001.
  16. Rothmund, P.W.K. A DNA and restriction enzyme implementation of turing machine. In *DNA Based Computers: Proceedings of the DIMACS Workshop, April 4, 1995, Princeton University*; Lipton, R.J., Baum, E.B., Eds.; American Mathematical Society: Providence, RI, 1996; 75–119.
  17. Smith, W.D. DNA computers in vivo and in vitro. In *DNA Based Computers: Proceedings of the DIMACS Workshop, April 4, 1995, Princeton University*; Lipton, R.J., Baum, E.B., Eds.; American Mathematical Society: Providence, RI, 1996; 121–185.
  18. Garzon, M.; Gao, Y.; Rose, J.A.; Murphy, R.C.; Deaton, R.; Franceschetti, D.R.; Stevens, S.E. In vitro implementation of finite-state machines. In *Automata Implementation: Lecture Notes in Computer Science 1436*; Wood, D., Yu, S., Eds.; Springer: Berlin, 1998; 56–74.
  19. Sakamoto, K.; Kiga, D.; Komiya, K.; Gouzu, H.; Yokoyama, S.; Ikeda, S.; Sugiyama, H.; Hagiya, M. State transitions by molecules. *Biosystems* **1999**, *52* (1–3), 81–91.
  20. Sakamoto, K.; Gouzu, H.; Komiya, K.; Kiga, D.; Yokoyama, S.; Yokomori, T.; Hagiya, M. Molecular computation by DNA hairpin formation. *Science* **2000**, *288* (2469), 1223–1226.
  21. Turing, A.M. On computable numbers, with an application to the Entcheidung problem. *Proc. Lond. Math. Soc., II Ser.* **1936**, *42*, 230–265.
  22. Hopcroft, J.E.; Motwani, R.; Ullmann, J.D. *Introduction to Automata Theory, Languages, and Computation*, 2nd Ed.; Addison Wesley: Boston, 2000.
  23. Alberts, B.; Johnson, A.; Lewis, J.; Raff, M.; Roberts, K.; Walter, P. *Molecular Biology of the Cell*, 4th Ed.; Garland: New York, 2002.
  24. Shapiro, E. *Algorithmic Program Debugging*; MIT Press: Cambridge, MA, 1982.
  25. Harel, D.; Pnueli, A. On the Development of Reactive System. In *Logics and Models of Concurrent Systems*; Apt, K.R., Ed.; Springer-Verlag: New York, 1985; 477–498.
  26. Benenson, Y.; Paz-Elizur, T.; Adar, R.; Keinan, E.; Livneh, Z.; Shapiro, E. Programmable and autonomous computing machine made of biomolecules. *Nature* **2001**, *414* (6862), 430–434.
  27. Benenson, Y.; Adar, R.; Paz-Elizur, T.; Livneh, Z.; Shapiro, E. DNA molecule provides a computing machine with both data and fuel. *Proc Natl. Acad. Sci. U. S. A.* **2003**, *100* (5), 2191–2196.



# Molecular Electronics: Logic and Memory

Dustin K. James

James M. Tour

Chemistry Department, Rice University, Houston, Texas, U.S.A.

## INTRODUCTION

Electronic logic chips are used in many products today, from cell phones to robotic toys to automobiles and trucks, dishwashers and freezers, thermostats, and coffee makers. The most visible application of course is in our desktop and laptop computers. To enable further miniaturization of the circuitry used in these devices, recent research has focused on developing molecular-based logic and memory. In this entry, we will review the state of the art in the development and characterization of molecular electronic logic and memory, with discussions of the quantum cellular array approach (QCA) (and the related electrostatic repulsion architecture) and the crossbar approach to building molecular circuits followed by a more in-depth look at very recent results from our laboratory concerning the NanoCell approach to molecular logic and memory.

## MOLECULAR ELECTRONICS

The rapidly developing field of molecular electronics is one of the driving forces behind the interest in molecular-based circuits.<sup>[1–9]</sup> The limitations of the present “top-down” method of producing semiconductor-based devices have been the subject of debate and conjecture since Gordon Moore’s prediction that the number of components per integrated circuit would double every 18 months.<sup>[10]</sup> It is thought that the inherent limitations of the present technology will lead to a dead-end in the next few years. For instance, silicon’s band structure disappears when silicon layers are just a few atoms thick. Lithographic techniques that are used to produce the circuitry on the silicon wafers are limited, in part, by the wavelengths at which they work. However, leaders in the semiconductor manufacturing world are still making advances that appear to be pushing “Moore’s Law” beyond its prior perceived limits. In the commercial technology of 2001, the copper wires in Intel’s Pentium® 4 logic chip

are 0.13  $\mu\text{m}$  wide.<sup>[11]</sup> Intel is developing technology to create logic chips with wires 90 nm wide to be commercialized in 2003.<sup>[12]</sup>

For comparison’s sake, a typical molecular electronics candidate synthesized in our laboratory is calculated to be 0.3 nm wide and 2.5 nm in length (Fig. 1).<sup>[5]</sup> It would take 300 of these molecules, positioned side by side, to span the 90-nm metal line in the most advanced logic chip in development. The small size of these molecules is emphasized when one considers that 500 g (about 1 mol) would contain  $6 \times 10^{23}$  molecules, or more molecules than the number of transistors ever made in the history of the world. This amount of material could be produced by using relatively small 22-L laboratory reaction flasks. Changing the physical characteristics of this molecule is as easy as changing the raw materials used to make it. The small size, the potential of synthesizing huge numbers in small reactors, and the ease of modification of the physical characteristics of the molecules are good reasons for pursuing molecular electronics research. As an example of how far the technology has come, molecular electronics is discussed in the “Emerging Research Devices” section of the most recent International Technology Roadmap for Semiconductors<sup>[13,14]</sup> and molecules that may act as wires are a large part of the emerging technology. Molecular electronics was named the “breakthrough of the year” by *Science Magazine* for 2001.<sup>[15]</sup> Instead of replacing the present silicon-based technology, nanoelectronic architectures could prove to be a complement to traditional solid-state devices.<sup>[1,5,16,17]</sup>

To take advantage of the ultrasmall size of molecules, one needs an interconnect technology that 1) scales from the molecular dimensions; 2) can be structured to permit the formation of the molecular equivalent of large-scale diverse modular logic blocks as found in very large-scale interconnect (VLSI) architectures; and 3) can be selectively connected to mesoscopically (100 nm scale) defined input/output leads.

The first approach to molecular computing is based on quantum cellular automata (QCA) and related

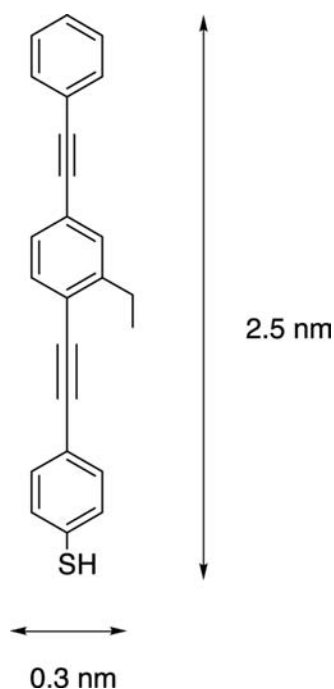


**Fig. 1** The dimensions of a typical molecule studied in molecular electronic applications are calculated to be 0.3 nm in width and 2.5 nm in length using molecular mechanics to determine the energy-minimized structure. *Source:* From Ref.<sup>[5]</sup>.

electrostatic information transfers.<sup>[18–20]</sup> This method relies on electrostatic field repulsions to transport information throughout the circuitry. One major benefit of the QCA or electrostatics approach is that heat dissipation is less of an issue because only a few or fractions of an electron are used for each bit of information.

The second approach is based on the massively parallel solid-state Teramac computer developed at Hewlett-Packard (HP),<sup>[9,21]</sup> and involves building a similarly massively parallel computing device using molecular electronics based on crossbar technologies that are proposed to be defect-tolerant. A Teramac-like crossbar-based approach called the “NanoFabric” architecture deals more effectively with the numbers of wires emanating from the array.<sup>[22]</sup> When applied to molecular systems, the crossbar approaches propose to use single-walled carbon nanotubes (SWNTs)<sup>[23–27]</sup> or synthetic nanowires (NWs)<sup>[28–31]</sup> for the crossbars. Logic functions are performed either by sets of crossed and specially doped nanowires, or by molecular switches placed at each crossbar junction.

The third approach involves using molecular scale switches as part of a NanoCell.<sup>[32]</sup> The NanoCell relies on disordered arrays of molecular switches to perform logic functions. It does not require that each switching molecule be individually addressed, and furthermore

utilizes the principles of chemical self-assembly in construction of the logic circuitry, thereby reducing complexity. While fabrication constraints are greatly eased, programming difficulties increase dramatically.

## QUANTUM CELLULAR AUTOMATA (QCA) AND ELECTROSTATIC ARCHITECTURES

Quantum dots have been called “artificial atoms” or “boxes for electrons”<sup>[33]</sup> because they have discrete charge states and energy level structures that are similar to atomic systems and can contain from a few thousand to one electron. They are typically small, electrically conducting regions, 1  $\mu\text{m}$  or less in size, with a variety of geometries and dimensions. Because of the small volume, the electron energies are quantized. No shell structure exists; instead, the generic energy spectrum has universal statistical properties associated with quantum chaos.<sup>[34]</sup> Several groups have studied the production of quantum dots.<sup>[35]</sup> Heath et al. discovered that hexane solutions of Ag nanoparticles, passivated with octanethiol, formed spontaneous patterns on the surface of water when the hexane was evaporated,<sup>[36]</sup> and has prepared superlattices of quantum dots.<sup>[37,38]</sup> Lieber has investigated the energy gaps in “metallic” single-walled carbon nanotubes<sup>[23]</sup> and has used an atomic force microscope to mechanically bend SWNT to create quantum dots less than 100 nm in length. He found that most metallic SWNT are not true metals, and that by bending the SWNT, a defect was produced that had a resistance of 10–100 k $\Omega$ . Placing two defects less than 100 nm apart produced the quantum dots.

In the QCA approach toward molecular electronic computing systems, four quantum dots in a square array are placed in a cell such that electrons are able to tunnel between the dots but are unable to leave the cell.<sup>[39]</sup> Coulomb repulsion will force the electrons to occupy dots on opposite corners. The two ground state polarizations are both energetically equivalent and can be labeled logic “0” or “1.” Flipping the logic state of one cell, for instance, by applying a negative potential to a lead near the quantum dot occupied by an electron, will result in the next-door cell flipping ground states in order to reduce Coulomb repulsion. In this way, a line of QCA cells can perform computations.<sup>[40]</sup> A QCA fan-out structure has been proposed; however, when the ground state of the input cell is flipped, the energy imposed into the system may not be enough to flip all the cells of both branches of the structure, producing long-lived metastable states and erroneous calculations. Switching the cells using a quasiadiabatic approach prevents the production of these metastable states.<sup>[41]</sup>

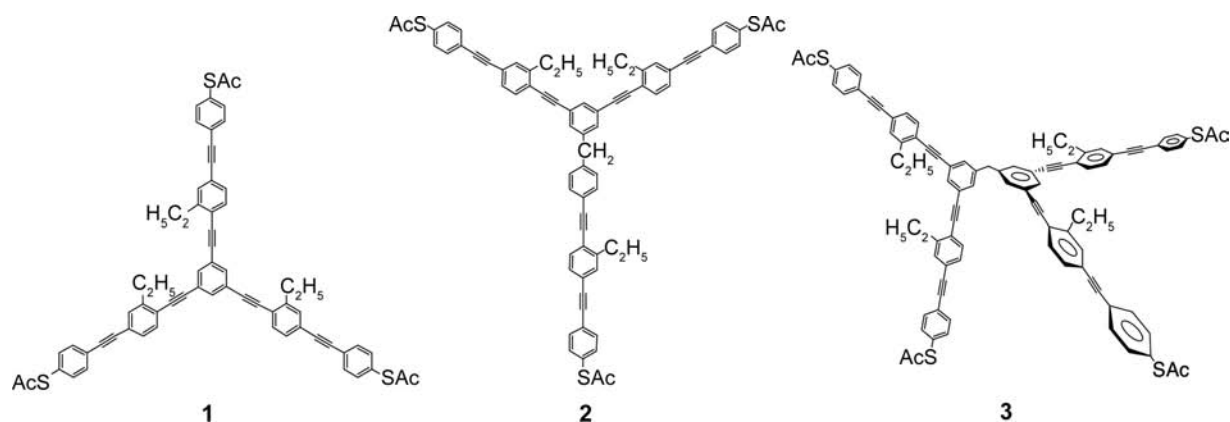


**Fig. 2** Three compounds that were synthesized for studies in computing using electrostatic potentials. **1** is a molecular three-terminal junction that could be used as a molecular interconnect. **2** is a molecular-sized switch for which there is a corresponding equivalent of a source, drain, and gate terminals of a bulk solid state FET. **3** can be an active OR or a passive NOR gate if positive logic is used, or an AND or NAND gate if negative logic is used.

While the use of quantum dots in the demonstration of QCA is a good first step in reduction to practice, the ultimate goal is to use individual molecules to hold the electrons and pass electrostatic potentials down QCA wires. We have synthesized molecules that were shown by ab initio computational methods to have the capability of transferring information from one molecule to another through electrostatic potentials (Fig. 2). The potentials use a millionth of an electron per bit of information. This is quite attractive because a major consideration in molecular devices is the energy consumption/dissipation needs. Considering the fact that there are  $10^8$  gates/cm<sup>2</sup> (in presently sized silicon-based systems) functioning at the rate of  $10^{-9}$  sec (present speeds), those gates afford  $10^{17}$  electrons/sec ( $\sim 0.02$  A/cm<sup>2</sup>) if only one electron per gate is used to transport, indicate, fetch, or represent a binary digit. At this point, heat considerations are already extreme: if the average resistance of the circuit is  $30\ \Omega$ , this represents  $20\ \text{W}/\text{cm}^2$ . If an increase of several orders of magnitude in performance is expected with molecular circuits, this would imply a proportional increase in power dissipation. Such levels of power dissipation rule out most conventional current or electron transfer methods for practical molecular devices wherein large numbers of devices are densely configured.

Electrostatic interactions are produced by small reshapes of the electron density as a result of the input signals. In turn, electrostatic potential interactions between molecules could transport the information throughout the central processing unit (CPU). When this approach is used, there is no need for electron currents or electron transfers as in present devices; a small change in the electrostatic potential of one molecule could be enough to send the information to another molecule. These perturbations of the electrostatic

potential imply a very small amount of charge transfer, substantially less than one electron.

Although we synthesized molecules that included three-terminal molecular junctions, switches, and molecular logic gates to demonstrate the electrostatics methodology, none of the molecules were incorporated into an actual assembly. Because the electrostatics method has major obstacles to overcome before even simple laboratory tests can be attempted, all results were based on computation only. While relatively large quantum dot arrays can be fabricated by using existing methods, a major problem is that placement of molecules in precisely aligned arrays at the nanoscopic level is very difficult to achieve with accuracy and precision. Another problem is that degradation of only one molecule in the array can cause failure of the entire circuit. There has also been some debate about the unidirectionality (or lack thereof) of QCA designs.<sup>[42–44]</sup> Examples of two-dot QCA arrays have yet to be demonstrated using molecules, because addressing the molecular-sized inputs and the recording of a signal based on fractions of an electron are enormous hurdles.

## CROSS-BAR ARRAYS

Heath et al.<sup>[9]</sup> reported on a massively parallel experimental computer that contained 220,000 hardware defects yet operated 100 times faster than a high-end single processor workstation for some configurations. The solid-state-based (not molecular electronics) Tera-mac computer, built at HP, relied on its fat-tree architecture for its logical configuration. The minimum communication bandwidth needed in the fat-tree architecture was determined by utilizing Rent's rule, which states that the number of wires coming out of a region of a circuit should scale as the power of the number of

devices ( $n$ ) in that region, ranging from  $n^{1/2}$  in two dimensions to  $n^{2/3}$  in three dimensions. The HP workers built in excess bandwidth, putting in many more wires than needed. The reason for the large number of wires can be understood by considering a simple city map. To get from point A to point B, one can take local streets, main thoroughfares, freeways, interstate highways, or any combination thereof. If there is a roadblock at any point C between A and B, then renavigation can be assessed by using the map to arrive to point B. In the Teramac computer, “street blockages” are stored in a defect database; when one device needs to communicate with another device, it uses the database and the map to determine how to get there. Therefore the Teramac design can tolerate defects.

In the Teramac computer (or a proposed molecular computer based on the Teramac design), the wires that comprise the address lines controlling the settings of the configuration switches and the data lines that link the logic devices are the most important and plentiful part of the computer. It is logical that a large amount of research has been performed to develop NWs that could be used in the massively parallel molecular computer. This approach is dependent on precise order in devices with exact arrays of nanostructures, including nanowires or nanotubes, sometimes bridged by molecules, and interfaced with microstructure in order to communicate with the outside world.<sup>[9,18,45]</sup> Advancements have been made in the art since our last review,<sup>[3]</sup> many of which have been reviewed by Luo et al.<sup>[46]</sup> and by us. (See the entry “Molecular Wires,” for our review of this related area.)

Lieber has reviewed the work carried out in his laboratory to synthesize and determine the properties of NWs and nanotubes.<sup>[23]</sup> He used Au or Fe catalyst nanoclusters to serve as the nuclei for NWs of Si and GeAs with diameters of 10 nm and lengths of hundreds of nanometers. By choosing specific conditions, Lieber was able to control both the length and the diameter of the single crystal semiconductor NW.<sup>[28]</sup> Silicon NWs doped with B or P were used as building blocks by Lieber to assemble semiconductor nanodevices. Active bipolar transistors were fabricated by crossing n-doped NWs with p-type wire base. The doped wires were also used to assemble complementary inverter-like structures.

Lieber used Langmuir–Blodgett (LB) techniques to transfer multiple layers of nanowires onto planar substrates, followed by spin coating a photoresist layer onto the lattice.<sup>[47]</sup> The photoresist was patterned and developed, and the exposed nanowires were removed by sonication in deionized water. The remaining photoresist covering the nanowire arrays was dissolved in acetone. Large arrays were built.

Yu, Chung, and Heath<sup>[48]</sup> reported the synthesis of silicon NWs by chemical vapor deposition using  $\text{SiH}_4$  as the Si source and An or Zn nanoparticles as the

catalytic seeds at 440°C. The wires produced varied in diameter from 14 to 35 nm, and were grown on the surface of silicon wafers. After growth, isolated NWs were mechanically transferred to wafers and Al contact electrodes were put down by standard e-beam lithography and e-beam evaporation such that each end of a wire was connected to a metallic contact. In some cases, a gate electrode was positioned at the middle of the wire. Tapping-mode atomic force microscopy (AFM) indicated the wire in this case was 15 nm in diameter.

Heath found that annealing the Zn–Si wires at 550°C produced increased conductance attributed to better electrode/nanowire contacts. Annealing Au–Si wires at 750°C for 30 min increased current about  $10^4$ , an effect attributed to doping of the Si with Au, and lower contact resistance between the wire and Ti/Au electrodes.

More recently, Melosh et al.<sup>[49]</sup> reported on a method of obtaining aligned metal and semiconductor nanowires, based on the process of first growing nanowires in a selectively etched GaAs/ $\text{Al}_{0.8}\text{Ga}_{0.2}\text{As}$  superlattice, and then releasing them onto a 10-nm epoxy adhesion layer on an oxidized silicon wafer. After heat curing of the epoxy layer, the GaAs template was removed by treatment with  $\text{KI}/\text{I}/\text{H}_2\text{O}$ . The wafer was then rinsed with ultrapure water and dried, and the exposed epoxy adhesion layer was removed by using an  $\text{O}_2$  plasma etch. This process produced nanowire arrays with center-to-center distances as small as 16 nm and high aspect ratios (up to  $10^6$ ). Multiple cycles produced crossed nanowires with a junction density  $>10^{11}$  per  $\text{cm}^2$ . No molecules were placed at the junctions of the nanowires.

Much research has been performed to determine the efficacy of SWNTs as NWs in molecular computers. One problem with SWNTs is their lack of solubility in common organic solvents. In their synthesized state, individual SWNTs form ropes,<sup>[50]</sup> from which it is difficult to isolate individual tubes. In our laboratory, a measure of the solubility of the tubes was seen in 1,2-dichlorobenzene.<sup>[51]</sup> An obvious route to higher solubility is to functionalize SWNTs by attachment of soluble groups through covalent bonding. Mickelson et al.<sup>[52]</sup> found that fluorinated SWNTs were soluble in alcohols, while Chen et al.<sup>[53]</sup> were able to dissolve SWNTs by ionic functionalization of the carboxylic acid groups present in purified tubes.

We have found that SWNTs can be functionalized by electrochemical reduction of aryl diazonium salts in their presence.<sup>[54]</sup> Using this method, about 1 in 20 carbon atoms of the nanotube framework are reacted. We have also found that the SWNTs can be functionalized by direct treatment with aryl diazonium tetrafluoroborate salts in solution, or by in situ generation of the diazonium moiety using an alkyl nitrite reagent.<sup>[55]</sup> These functional groups give us handles

with which we can direct further, more selective derivatization (Fig. 3) and we recently reviewed the area of covalent sidewall derivatization of SWNTs.<sup>[56]</sup>

From an electronics perspective, the good thing about SWNTs is that all the carbons on the sidewalls are essentially the same; therefore, there is no location for an electron to localize during electronic transport. However, most of organic synthetic chemistry is predicated upon the ability to distinguish different carbon atoms in a molecule based on their subtle electronic and/or steric differences. Thus, from a synthetic perspective, the bad thing about SWNTs is that all the carbons on the sidewalls are essentially the same; therefore, one cannot use the plethora of synthetic techniques that favor formation of one type of carbon-carbon bond over another. However, if one did have a crossbar array of nanotubes, where the voltage between the two tubes could be selectively addressed at discrete locations, then the bridging on the specified cross-junctions might be possible; this has not yet been demonstrated.

Unfortunately, fluorination and other sidewall functionalization methods can perturb the electronic nature of the SWNT. An approach by Smalley et al.<sup>[50,57]</sup> and Stoddart and Heath<sup>[27]</sup> to increasing the solubility without disturbing the electronic nature

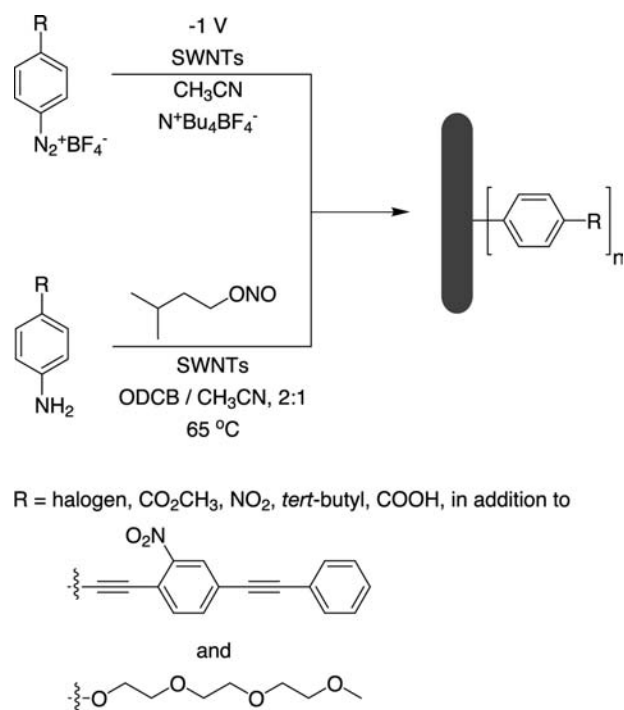


**Fig. 3** Reaction of SWNTs with aryl diazonium compounds. Shown are the electrochemical reactions with pre-formed diazonium salts, and the thermally activated reaction with in situ generated diazonium compounds. Also shown are a number of specific moieties that have been attached via these methods.

of the SWNTs was to wrap polymers around the SWNTs, but leave individual tubes' electronic properties unaffected. Stoddart and Heath found that the SWNT ropes were not separated into individually wrapped tubes; the entire rope was wrapped. Smalley found that individual tubes were wrapped with polymer; the wrapped tubes did not exhibit the roping behavior. Although Smalley was able to demonstrate removal of the polymer from the tubes, it is not clear, however, how easily the SWNTs can be manipulated and subsequently used in electronic circuits. In any case, the placement of SWNTs into controlled configurations has been, for the most part, a top-down methodology. Significant advances will be needed to take advantage of controlled placement at dimensions that exploit a molecule's small size.

Lieber proposed a SWNT-based non-volatile random access memory device comprising a series of crossed nanotubes, wherein one parallel layer of nanotubes is placed on a substrate and another layer of parallel nanotubes, perpendicular to the first set, is suspended above the lower nanotubes by placing them on a periodic array of supports.<sup>[24]</sup> The elasticity of the suspended nanotubes provides one energy minima, wherein the contact resistance between the two layers is zero, and the switches (the contacts between the two sets of perpendicular NWs) are OFF. When the tubes are transiently charged to produce attractive electrostatic forces, the suspended tubes flex to meet the tubes directly below them, and a contact is made, representing the ON state. The ON/OFF state could be read by measuring the resistance at each junction, and could be switched by applying voltage pulses at the correct electrodes. This theory was tested by mechanically placing two sets of nanotube bundles in a crossed mode and measuring the  $I(V)$  characteristics when the switch was OFF or ON. Although nanotube bundles with random distributions of metallic and semiconductor properties were used, the difference in resistance between the two modes was a factor of 10, enough to provide support for their theory. In another study, Lieber used scanning tunneling microscopy (STM) to determine the atomic structure and electronic properties of intramolecular junctions in SWNTs samples.<sup>[25]</sup> Metal-semiconductor junctions were found to exhibit an electronically sharp interface without localized junction states, while metal-metal junctions had a more diffuse interface and low-energy states.

A major problem with using SWNTs or NWs is how to guide them in formation of the device structures, i.e., how to put them where you want them. Lieber has studied the directed assembly of NWs by using fluid flow devices in conjunction with surface patterning techniques, and found that it was possible to deposit layers of NWs with different flow directions for

sequential steps.<sup>[28]</sup> For surface patterning, Lieber used  $\text{NH}_2$ -terminated surface strips to attract the NWs; in between the  $\text{NH}_2$ -terminated strips were either methyl-terminated regions or bare regions, to which the NW had less attraction. Flow control was achieved by placing a poly(dimethylsiloxane) (PDMS) mold, in which channel structures had been cut into the mating surface, on top of the flat substrate. Suspensions of the NWs (GaP, InP, or Si) were then passed through the channels. The linear flow rate was about 6.40 mm/sec. In some cases, the regularity extended over mm length scales, as determined by scanning electron microscopy (SEM).

In a similar fashion, the assembly of individual SWNTs onto substrates was realized by functionalizing substrate surfaces with polar and non-polar chemical groups in adjacent areas.<sup>[58]</sup> SWNTs deposited from a suspension tended to self-assemble into the polar regions of the substrate, with a lateral-directional force, probably as a result of electrostatic interactions, rotating the SWNTs so that they were confined with the polar area of the substrate. At low concentrations of 0.02 mg/mL, only single nanotubes were found at the center of each microscale polar molecular pattern. Although there was room for more than one SWNT on each patterned area, it was postulated that the hydrophobic surface of the first SWNT prevented additional SWNTs from being attracted to the underlying hydrophilic functionality. A problem with using carbon nanotubes is that they are always formed as mixtures of conducting tubes (0 eV bandgaps), semimetallic or “mod-3” tubes ( $\sim 1$  meV bandgaps), and semiconducting tubes (1 eV bandgaps). Most protocols form semiconducting tubes as  $\sim 60$ – $70\%$  of the mixture, therefore, one has to hope that the desired tube type would form or assemble in the desired device region. Of course, for a large array, the formation of the desired structure with the proper tube type is statistically prohibitive. Collins, Arnold, and Avouris at IBM have developed a method of engineering both multiwalled nanotubes (MWNTs) and SWNTs using electrical breakdown methods.<sup>[59]</sup> Shells in MWNT can vary between metallic or semiconductor character. Using electrical current in air to rapidly oxidize the outer shell of MWNTs, each shell can be removed in turn because the outer shell is in contact with the electrodes and the inner shells carry little or no current. Shells are removed until arrival at a shell with the desired properties. We recently published a process for selectively reacting the metallic and semimetallic tubes to the exclusion of the semiconducting tubes.<sup>[60]</sup> Therefore there is the hope, within a few years, that macroscopic quantities of homogeneous tube types will become available.

While Lieber has shown that it is possible to use the crossed NWs themselves as switches, Stoddart and

Heath have synthesized molecular devices that would bridge the gap between the crossed NWs and act as switches in memory and logic devices.<sup>[61]</sup> The UCLA/Caltech researchers have synthesized catenanes and rotaxanes that can be switched between states using redox chemistry. For instance, LB films were formed from the catenane, and the monolayers were deposited on polysilicon NWs etched onto a silicon wafer photolithographically. A second set of perpendicular Ti NWs were deposited through a shadow mask, and the  $I(V)$  curve was determined. The data, when compared to controls, indicated that the molecules were acting as solid-state molecular switches. As yet, however, there have been no demonstrations of combining the Stoddart switches with NWs.

The defect-tolerant approach to molecular computing using crossbar technology faces several hurdles before it can be implemented. Large numbers of nano-sized wires are used to obtain defect tolerance. How are each of these wires going to be accessed by the outside world? Multiplexing, the combination of two or more information channels into a common transmission medium, will have to be a major component of the solution to this dilemma. The directed assembly of the NWs and attachment to the multiplexers will be complicated, nonetheless, HP and CalTech researchers are making strides in this arena. Another hurdle is signal strength degradation as it travels along the NWs. Gain is typically introduced into circuits by the use of transistors. However, placing a transistor at each NW junction is an untenable solution because the silicon transistor would be much larger than the NW junction. Likewise, in the absence of a transistor at each cross point in the crossbar array, molecules with very large ON:OFF ratios will be needed. For instance, if a switch with a 10:1 ON:OFF ratio were used, then 10 switches in the OFF state would appear as an ON switch. Hence isolation of the signal via a transistor is essential. Researchers are hoping to insert diodes to sidestep this hurdle.

Additionally, if SWNTs are to be used as crossbars, connection of molecular switches via covalent bonds introduces  $\text{sp}^3$ -hybridized carbon atom linkages at each junction, disturbing the electronic nature of the SWNT and possibly rendering the SWNTs useless in the first place. Non-covalent bonding of the device molecule to the SWNT will probably not provide the conductance necessary for the circuit to operate. Therefore continued work is being carried out to devise and construct crossbar architectures that address these challenges.

## THE NANOCELL

This NanoCell architecture involves an approach where molecular switches are not specifically directed



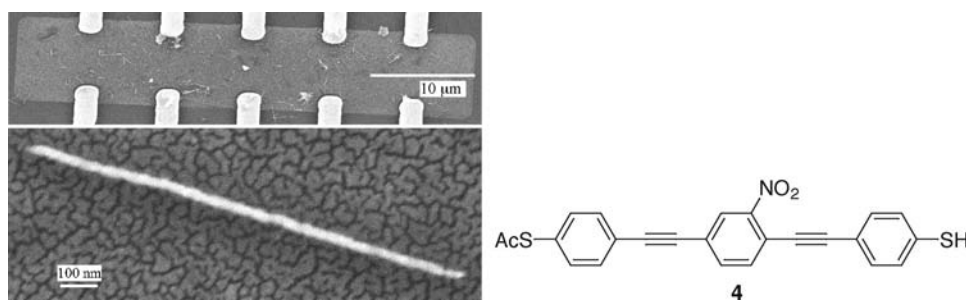


**Fig. 4** SEM image of the NanoCell after assembly of the Au nanowires and **4**. The top image shows the five juxtaposed pairs of fabricated leads across the NanoCell, and some Au nanowires are barely visible on the internal rectangle of the discontinuous Au film. The lower image is a higher magnification of the NanoCell's central portion showing the disordered discontinuous Au film with an attached Au nanowire that is affixed via the OPE-dithiol (not observable) derived from **4**.

to a precise location and the internal topology is generally disordered. A NanoCell is a two-dimensional (three-dimensional models could also be considered) network of self-assembled metallic particles or islands connected by molecules that show reprogrammable (can be turned ON or OFF) switching and/or memory properties. The NanoCell is surrounded by a small number of lithographically defined access leads at the edges of the NanoCell. Unlike typical chip fabrication, the NanoCell is not constructed as a specific logic gate and the internal topology is, for the most part, disordered. Logic is created in the NanoCell by training it postfabrication, similar in some respects to a field-programmable gate array (FPGA). Even if this process is only a few percent efficient in the use molecular devices, very high logic densities will be possible. Moreover, the NanoCell has the potential to be reprogrammed, thereby creating a real-time dynamic reconfigurable hard-wired logic. The CPU of the computer would be composed of arrays of NanoCells, wherein each NanoCell would have the functionality of many transistors working in concert. A regular array of NanoCells is assumed to manage complexity, and ultimately, a few NanoCells, once programmed, should be capable of programming their neighboring NanoCells through bootstrapping heuristics. Alternatively, arrays could be programmed one NanoCell at a time via an underlying complementary metal oxide semiconductor (CMOS) platform.

Within the fabricated NanoCell, the input and output leads could be repetitively interchanged based on the programming needs of the system, thereby demonstrating the pliability of the architecture. Naturally, issues of gain will eventually have to be addressed through either an underlying CMOS layer or clocked circuits programmed into the NanoCell.<sup>[62]</sup> Even if one CMOS transistor were used for gain at the output from each NanoCell, enormous space savings could be attained because a NanoCell could possess the functionality of numerous transistors working in concert

to produce a specified logic function. Furthermore, by capitalizing on the NDR properties of the molecular switches, internal gain elements based on NDR/nanoparticle/NDR stacks (Goto pairs) could be efficacious.<sup>[63,64]</sup>

The functionality of a NanoCell depends largely on the  $I(V)$  characteristics and placement of its molecular switches with respect to the nanoparticles. We have demonstrated NDR with a large ON:OFF ratio from several types of molecular switches based on nitro-containing OPEs (similar to **4** in Fig. 4). We will exploit this switching behavior (rise, then decline in the current with increased voltage) to build logic devices that exhibit negating functionality such as NAND or XOR responses from these two-terminal devices because two voltage inputs that are high could set the device into an OFF state (right side of the  $I(V)$  curve). Switches that do not exhibit the NDR characteristic cannot provide the negating functionality needed for the NanoCell approach.

The object in programming or training a NanoCell is to take a random, fixed NanoCell and turn its switches ON and OFF until it functions as a target logic device. The NanoCell is then trained postfabrication by changing the states, ON or OFF, of the molecular switches by imposing voltages at the surrounding input/output leads.

## NANOCELL MEMORIES

The NanoCell approach, as previously described and simulated,<sup>[1,32]</sup> is not dependent on placing molecules or nano-sized metallic components in precise orientations or locations. The internal portions are, for the most part, disordered and there is no need to precisely locate any of the switching elements. The nano-sized switches are added in abundance between the micron-sized input/output electrodes, and only a small percentage of them need to assemble in an orientation

suitable for switching. The result of the NanoCell architecture is that the patterning challenges of the input/output structures become far less exacting because standard micron-scale lithography can afford the needed address system. Also, fault tolerance is enormous.<sup>[32]</sup> However, programming is significantly more challenging than when using ordered ensembles. We describe here an example in which a NanoCell has been successfully assembled and tested. Remarkably, the NanoCell exhibits reproducible switching behavior with excellent peak-to-valley (PVR) ratios,<sup>[65]</sup> peak currents in the milliamperage range and reprogrammable memory states that are stable for more than a week with substantial 0:1 bit level ratios.

A NanoCell is a two-dimensional unit of juxtaposed electrodes fabricated atop a Si/SiO<sub>2</sub> substrate. In the embodiment described here, five Au electrode pairs were patterned on opposing sides of the NanoCell (Fig. 4, top). A discontinuous gold film was vapor deposited onto the SiO<sub>2</sub> in the central region (Fig. 4, bottom). The chips were always treated with UV ozone and ethanol-washed immediately prior to use to remove exogenous organics. Electrical measurements of up to 30 V DC confirmed there was  $\leq 1$  pA conduction across the discontinuous Au film between the five juxtaposed pairs of  $\sim 5$ - $\mu\text{m}$  spaced electrodes. In this study, each juxtaposed pair serves as an independent memory bit address system.

The assembly of molecules and nanowires in the central portion of the NanoCell was then carried out under N<sub>2</sub> to provide a current pathway across the NanoCell. Compounds similar to the mononitro oligo(phenylene ethynylene) (OPE) **4**<sup>[66]</sup> have been previously shown to exhibit switching and memory storage effects when fixed between proximal Au probes.<sup>[66,67]</sup> Au nanowires (diameter of 30 nm and length of 300–2000 nm, grown in a polycarbonate membrane by electrochemical reduction at 1.2 Coulombs)<sup>[68]</sup> were added to a vial containing **4** in CH<sub>2</sub>Cl<sub>2</sub>. The vial was agitated for 40 min to dissolve the polycarbonate membrane and to form **4**-encapsulated Au nanowires via chemisorption of the thiols to the nanowires.<sup>[69]</sup> Because the thiol groups are far more reactive toward Au than thioacetyl groups,<sup>[70]</sup> this procedure leaves the latter projecting away from the nanowire surfaces. NH<sub>4</sub>OH and ethanol were added, and the vial was agitated for 10 min to remove the acetyl group.<sup>[71]</sup> A chip containing 10 NanoCell structures was placed in the vial (active side up), and the vial was further agitated for 27 hr to permit the nanowires to interlink the discontinuous Au film via the OPEs (Fig. 4). The chip was removed, rinsed with acetone, and gently blown dry with N<sub>2</sub>.

The assembled NanoCells were electrically tested on a probe station with a semiconductor parameter analyzer at room temperature (297 K) under vacuum

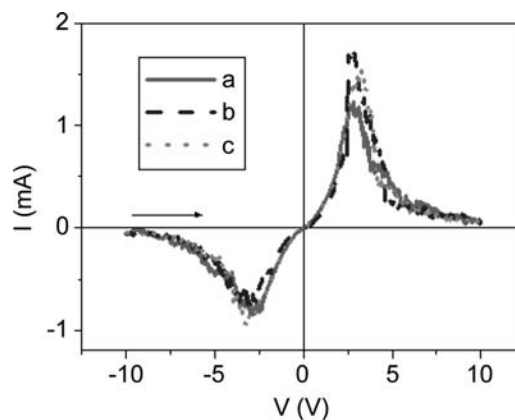


**Fig. 5**  $I(V)$  characteristics of the NanoCell at 297 K. The curves for a, b, and c are the first, second, and third sweeps, respectively ( $\sim 40$  s/scan). The PVRs in C are 23:1 and 32:1 for the negative and positive switching peaks, respectively. The arrow indicates the sweep direction of negative to positive.

( $10^{-5}$  mm Hg). Typical  $I(V)$  characteristics of the NanoCell devices are shown in Fig. 5. Two stable and reproducible switching peaks are observed in a bias range of  $-10$  and  $+10$  V. The shape of the  $I(V)$  curve is asymmetric because the molecule, as a result of the nitro-group orientation, is asymmetrically oriented, and/or the contacts are likely to be slightly different on each end. After about 300 scans, the switching responses further stabilized in peak voltage; the device showed no degradation to  $>2000$  scans over a 22-hr period of continuous sweeping. Also, after testing, an assembled NanoCell was stored in a capped vial (air) for 2 months with little, if any, signal variations relative to the readings recorded at the initial testing.

A juxtaposed pair of electrodes, as described above, showed little variation in its behavior over several thousand scans. However, there were notable differences when comparing different electrode pairs in that they showed variations in peak current position (occurring typically within a range of 3–15 V), peak current (typically 0.1–1.7 mA), and PVR (typically 5–30). The differences are undoubtedly related to the variations in the conduction pathways of these disordered arrays.

If a voltage sweep is conducted on a NanoCell in a bias range that is up to or not far beyond the peak of the  $I(V)$  curve (switching event), a pseudo-linear trace is observed, as shown by curve **a** (0-state) in Fig. 6. However, if three voltage pulses at  $-8$  V (100 msec width, 104 msec period) are then applied to the same pair of leads, a peak appears (1-state) in the first scan after the voltage pulses, as shown by curve **b** in Fig. 6. Apparently, the voltage pulses set the system into a new state that is then read by the bias sweep **b**. This is being termed the switch-type memory effect. However, the following scans **c** and **d** produced  $I(V)$

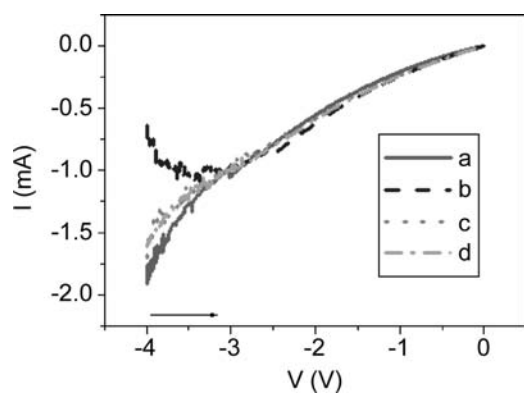


**Fig. 6**  $I(V)$  characteristics of the NanoCell before (a) and after (b–d) three voltage pulses at  $-8$  V at 297 K. Curves b, c, and d were the first, second, and third scans (after the  $-8$  V reset pulses), respectively. Scans a–d were run at  $\sim 40$  s/scan. The results here are from the same device used to generate the  $I(V)$  curve in Fig. 5.

responses similar to curve **a**, the scans before the voltage pulses, suggesting that the state set by the voltage pulse was erased after reading it by scan **b**. In other words, the switch-type memory effect has a destructive-read property [as seen with present-day dynamic random-access memory (DRAM)]. A positive voltage pulse, i.e.,  $+8$  V, can also set the system into the 1-state. Voltages higher than  $\pm 8$  V always worked, but voltages lower than  $\pm 8$  V did not reset this particular NanoCell into the 1-state. All of the active NanoCells showed this rewritable behavior, although the magnitudes and set voltages varied between different NanoCells as described above.

On the same device as shown in Figs. 5 and 6, another type of memory effect was found which has a non-destructive-read, the so-called conductivity-type memory, which operates by the storage of a high- or low-conductivity ( $\sigma$ ) state. The difference between the switch-type memory and the conductivity-type memory is based on the voltage-sweep range:  $-4$  to  $0$  V for the former and  $-2$  to  $0$  V for the latter. An initially high conductivity state (high  $\sigma$  or 0-state) was observed in a bias range of  $-2$  to  $0$  V as shown in Fig. 7, curves **a–c**. The high  $\sigma$  state is changed (written) into a low  $\sigma$  state (1-state) upon application of three voltage pulses at  $-8$  V (100 msec width, 104 msec period), as shown by curves **d–f**. The low  $\sigma$  state persists as a stored bit, which is essentially unaffected by successive read sweeps. There is a 400:1 0-state/1-state ratio in current levels between the high and low  $\sigma$  states recorded at  $-2$  V for this NanoCell device. The ratios may vary between different electrode pairs but the ratio here is representative. The highest observed 0:1 ratio was 12,500:1 ( $198 \mu\text{A}$ :  $16$  nA at  $-2.0$  V) for a  $5\text{-}\mu\text{m}$  gap electrode pair, and the lowest observed ratio was 10:1 at the same voltage.

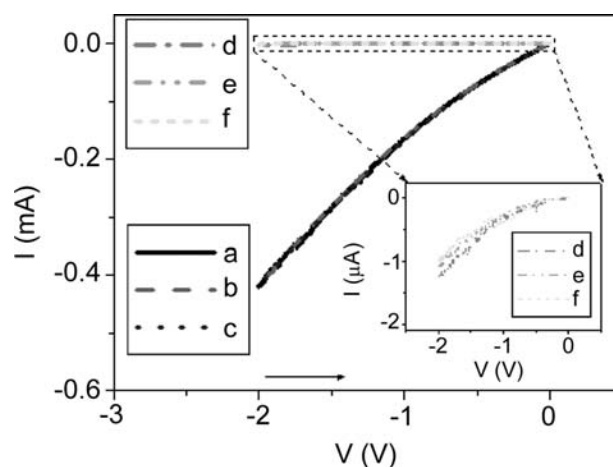


**Fig. 7**  $I(V)$  characteristics of the NanoCell before (scans a–c) and after (scans d–f) three voltage set-pulses of  $-8$  V at 297 K. The initial high  $\sigma$  state (0-state) is represented by curves a, b, and c, which are the first, second, and third scans before the set-pulse, respectively. The low  $\sigma$  state (1-state) is represented by curves d, e, and f, which are the first, second, and third scans after the  $-8$  V set-pulses, respectively. The inset shows scans d–f in the  $\mu\text{amp}$  range. Scans a–c were run at  $\sim 40$  s/scan. Scans d–f were run at  $\sim 50$  s/scan. This is the same device depicted in Figs. 5 and 6.

The conductivity-type memory effect is independent of bias sweep directions. Once set into the low  $\sigma$  state upon application of voltage-set (write) pulses, the system holds the low  $\sigma$  state regardless of negative bias sweep from  $0$  to  $-2$  V or positive bias sweep from  $0$  to  $2$  V. Several routes were investigated to erase the stored low  $\sigma$  state (written bit). Voltage pulses at  $-3$  to  $-4$  V ( $\sim 20$  pulses at 1 msec pulse width, 10-msec pulse period) reset the memory into the original high  $\sigma$  state (use a voltage pulse that comes near the peak of the switching event, but not far past the peak). Although the overall write, read, erase sequence used in the screening of these devices was rather slow because of the resetting time of the probing electronics, the inherent switching may be on the order of milliseconds, or faster, for each operation if customized electronics were used. The switch-type and conductivity-type memory effects are shown here in the negative bias regions; however, they apply in the positive bias region as well.

The bit retention time for the switch-type memory is at least 11 days and with  $\sim 10\%$  change in the voltage peak position of the curves when compared to the read-tests run seconds after setting the written state; however, there was no decline in the magnitude of the response. The conductivity-type memory persisted for at least 9 days. Over this period, the 0:1 signal magnitudes interestingly increased, although the reset voltages also drifted higher ( $\sim 10\%$ ) over this period. Therefore the two types of memory effects can have

much longer retention times, but these are merely the time periods over which they have been tested. Longer durations were not studied. During waiting periods over which these retention times were recorded, the NanoCells had been occasionally exposed to air at 1 atm for periods of up to 30 min, as more samples were moved through the testing chamber. Therefore the stored written states are robust even with short exposure to air. Yields of functioning NanoCells that have been prepared via the protocol described here seemed to be electrode gap-dependent. A NanoCell produced by using the described protocol chip showed 100%, 65%, and 30% yields for devices with 5-, 10-, and 20- $\mu\text{m}$  spacings between the juxtaposed electrodes, respectively.

The assembled chips were tested in the probe station both in the dark, by covering the observation window with aluminum foil, and in the presence of the room light with the station's fiber optic observation light projected through the observation window  $\sim 10$  cm above the chip. The same electrical responses were obtained regardless of the lighting, thereby excluding a photoconductive mechanism.

Several control experiments were conducted to investigate the mechanism of action for the NanoCell memories. When the same assembly process was conducted but **4** was not added, all the leads were "open" and no switching behavior was observed over the tested 15 juxtaposed electrodes (5 pairs at 5- $\mu\text{m}$  spacings, 5 pairs at 10- $\mu\text{m}$  spacings, and 5 pairs at 20- $\mu\text{m}$  spacings). Therefore the process is **4**-dependent. When the assembly procedure was conducted but the nanowires were not present (only **4**, polycarbonate devoid of nanowires,  $\text{CH}_2\text{Cl}_2$ ,  $\text{NH}_4\text{OH}$ , and ethanol were added), two out of three juxtaposed 5- $\mu\text{m}$  spacings showed switching between them; however, the switching effect signal degraded nearly completely after 3–10 scans. Therefore some molecules may have bridged the discontinuous Au film, but the connections were not as abundant or stable. A similar behavior was observed at 10- $\mu\text{m}$  spacings between the electrodes. When an alkyl system,  $\text{AcS}(\text{CH}_2)_{12}\text{SH}$  (**5**),<sup>[72]</sup> was substituted for **4** in the standard assembly process, and 30 juxtaposed electrode pairs were studied, 28 showed no device behavior. Interestingly, however, one 5- $\mu\text{m}$  electrode pair showed the characteristic switching that dissipated after three scans, while a second electrode pair showed reproducible switching behavior but the onset and peak currents occurred at 14 V. Therefore **1** is not unique among molecule types.

Concerning the mechanism underlying the programmable memories, a molecular electronic effect was first considered. Several mechanisms were proposed for molecular electronic switching<sup>[73–75]</sup> based upon charging of the molecules, which results in changes in the contiguous structure of the lowest unoccupied molecular

orbital (LUMO). This can be accompanied by conformational changes that would modulate the current based on changes in the extended  $\pi$ -overlap. Conversely, as some have pointed out, the so-called "molecular-based" switching might not be an inherently molecular phenomenon, but may result from surface bonding rearrangements that are molecule/metal contact in origin. For example, a sulfur atom changing its hybridization state, or subangstrom shifts between different Au surface atom bonding modes, or molecular tilting.<sup>[76,77]</sup> An estimate of the number of molecular junctions between a set of juxtaposed electrode pairs is difficult to gauge; however, based on the size of the nanowires and the Au islands, which can be 0.3–1  $\mu\text{m}$  long, the number of molecular junctions could be as few as four in a 5- $\mu\text{m}$  electrode gap. The number of molecules in parallel, per junction, could be as few as 30 or as many as several thousand, based on the nanowire diameters and lengths. Note that the quantum conductance of each molecule is  $\sim 0.08$  mA/V.

In addition to a molecular electronic process, electrode migration was considered as a cause for the high currents and reset operations that are analogous to filamentary metal memories.<sup>[78–81]</sup> To investigate this possibility, the exposed organic material was stripped from a working NanoCell by treating the assembled chip with UV ozone for 10–30 min. Remarkably, the device behavior of the NanoCell remained and often improved. In some cases, the 0:1 bit level ratios for the conductivity memory even increased up to  $10^6:1$  (2.53 mA:0.76 nA at  $-3.0$  V). This could suggest that the ozone was not able to reach the small amount of active organic molecules in the key nanodomains that are sandwiched between the nanowires and the Au islands, and that the more exposed leakage routes were destroyed by the ozone. Conversely, it could suggest that, indeed, filamentary metal had grown along the molecules and that these metal filaments were causing the observed switching behavior, with any molecular leakage routes being destroyed by the ozone. It was previously shown by modeling that the NanoCell should exhibit extraordinary defect tolerance because of the abundance of molecules available for switching; furthermore, if one molecule degrades, another could slip into place from the self-assembled monolayers that cover all the surrounding metal surfaces.<sup>[32]</sup> Consider also that, at the atomistic level, a molecular change in either conformation or hybridization at the metal–molecule interface, due to voltage changes or charging, could give electronic response characteristics that are analogous to filamentary metals (atoms moving in and out of alignment for current flow), and thereby resemble negative differential resistance-like behavior. In other words, metallic nanofilaments forming during a voltage sweep, then on increasing the voltage, they could exhibit a sudden break, causing a decline in the current.

Additionally, a mechanical motion involving the molecule-covered nanowires was considered. However, it was deemed less likely because of the highly cross-linked nature of the micron-sized matrix.

None of the former data was conclusive enough to exclude either the molecular electronic-based mechanism or the nanofilament mechanism. However, a later finding pointed toward the nanofilament-based mechanism being the dominant or exclusive pathway. As described above, we had never seen the switch-like behavior from the bare chips; they just showed open circuits. As customary to ensure open circuits before we begin the molecule/nanowire assembly, while probing an older chip (4 months storage at room temperature in a Fluoroware™ container) from the same lot of chips that was used to prepare the NanoCell described here, we notice switching with magnitudes similar to the levels outlined in Fig. 5. Neither nanowires nor molecules had been added; it was merely the aged discontinuous Au film vapor-deposited between electrodes. Possibly, while the film had aged, the islands migrated across the gaps sufficiently close together to form nanofilaments upon voltage scanning, and then metal filament breakage occurred at higher voltages, giving responses similar to that shown in Fig. 5. The metallic island migration was not obvious by microscopic analysis of the discontinuous Au films because the resolution needed within the topologically non-planar arrays cannot be achieved with either SEM or AFM. We carried out  $I(V,T)$  (current as a function of voltage and temperature,  $-2$  to  $2$  V,  $280$  to  $80$  K and back to  $280$  K) measurements to assess the possible conduction mechanism of the high  $\sigma$  conductivity-type memory state on the bare chip. The data suggested “dirty” or modified-metal conduction: metallic conduction with trace impurities. However, in the low conductivity state, only thermionic emission was observed. The same type of  $I(V,T)$  measurements on a molecule/nanowire assembled NanoCell showed both a temperature dependence and a non-temperature dependence based on the particular juxtaposed electrode set studied. Albeit confusing, there may be a duality of mechanisms coexisting on the same chip, namely, metallic filaments in the high  $\sigma$  state and molecular phenomena in the low  $\sigma$  state. Further studies are ongoing to better discern this process. Fabrication of NanoCells with more refractory metals such as Pt or Pd will be carried out to further test this point. Additionally, we are currently making chips with a  $193$ -nm stepper to yield juxtaposed electrode gap spacings of  $<1\ \mu\text{m}$  with smaller Au-film islands and appropriately sized nanowires, with the hope of attaining higher degrees of consistency between electrode pairs. With the presently sized embodiments, write/erase speeds, and the lack of isolation and fan-out, the NanoCell is not a harbinger for DRAM, flash,

or magnetic random access memory (MRAM) replacements. However, it demonstrates the first fabrication of a disordered nanoscale ensemble for high-yielding switching and memory, while mitigating the painstaking task of nanoscale lithography or patterning; thereby furthering the promise of disordered programmable arrays for complex device functionality.

## CONCLUSION

Of the three basic approaches to building a molecular computer—QCA, crossbar array, and NanoCell, two approaches appear to be at the forefront of the advancing science—the crossbar array approach and the NanoCell approach. The crossbar approach has seen many advances in the fabrication and assembly of nanowire arrays on surfaces. The NanoCell approach has also been swiftly advanced, and includes molecules in its assembly, but whether the device properties are due to the molecules themselves or to the formation of metal nanofilaments facilitated by the molecules remains unknown at this time. Work continues on many fronts to advance the idea of using molecules to meet the future computing needs of an ever more complex world. We are amazed and delighted to see this research unfold around us.

## ACKNOWLEDGMENTS

We thank the Defense Advanced Research Projects Agency (DARPA) administered by the Office of Naval Research (ONR); the ONR Polymer Program; the US Department of Commerce, National Institute of Standards and Technology; the Army Research Office; NASA; and the Air Force Office of Scientific Research (AFOSR F49620-01-1-0364) for financial support of this work.

## REFERENCES

1. Tour, J.M. *Molecular Electronics: Commercial Insights, Chemistry, Devices, Architecture, and Programming*; World Scientific Publishing: New Jersey, 2003.
2. Heath, J.R.; Ratner, M.A. Molecular electronics. *Phys. Today* **May 2003**, 2003, 43–49.
3. Tour, J.M.; James, D.K. Molecular electronic computing architecture. In *Handbook of Nanoscience, Engineering, and Technology*; Goddard, W.A., III, Brenner, D.W., Lyshevski, S.E., Iafate, G.J., Eds.; CRC Press: Boca Raton, FL, 2002; 4-1–4-28.
4. Ward, M.D. Chemistry and molecular electronics: new molecules as wires, switches, and logic gates. *J. Chem. Educ.* **2001**, 78 (3), 321–328.



5. Tour, J.M. Molecular electronics. Synthesis and testing of components. *Acc. Chem. Res.* **2000**, *33* (11), 791–804.
6. Heath, J.R. Wires, switches, and wiring. A route toward a chemically assembled electronic nanocomputer. *Pure Appl. Chem.* **2000**, *72* (1–2), 11–20.
7. Reed, M.A.; Tour, J.M. Computing with molecules. *Sci. Am.* **June 2000**, *2000*, 68–75.
8. Overton, R. Molecular electronics will change everything. *Wired* **2000**, *8* (7), 242–251.
9. Heath, J.R.; Kuekes, P.J.; Snider, G.S.; Williams, R.S. A defect-tolerant computer architecture: opportunities for nanotechnology. *Science* **12 June 1998**, *280*, 1716–1721.
10. Moore, G.E. Cramming more components onto integrated circuits. *Electronics* **1965**, *38* (8). Available on the web. <http://www.intel.com/research/silicon/moorepaper.pdf> (accessed September 2002).
11. Intel press release. <http://www.intel.com/pressroom/archive/releases/20011017man.htm> (accessed September 2002).
12. Intel press release. <http://www.intel.com/pressroom/archive/releases/20020813tech.htm> (accessed September 2002).
13. International Technology Roadmap for Semiconductors web pages. <http://public.itrs.net/Files/2001ITRS/PIDS.pdf> (accessed September 2002).
14. Wang, K.L. Issues of nanoelectronics: a possible roadmap. *J. Nanosci. Nanotechnol.* **2002**, *2* (3–4), 235–266.
15. Service, R.F. Molecules get wired. *Science* **21 December 2001**, *294*, 2442–2443.
16. Carroll, R.L.; Gorman, C.B. The genesis of molecular electronics. *Angew. Chem., Int. Ed.* **2002**, *41*, 4378–4400.
17. Goldhaber-Gordan, D.; Montemerlo, M.S.; Love, J.C.; Opitek, G.J.; Ellenbogen, J.C. Overview of nanoelectronic devices. *Proc. IEEE* **1997**, *85* (4), 521–540.
18. Lent, C.S.; Tougaw, P.D. A device architecture for computing with quantum dots. *Proc. IEEE* **1997**, *85* (4), 541.
19. Tougaw, P.D.; Lent, C.S.; Porod, W. Bistable saturation in coupled quantum-dot cells. *J. Appl. Phys.* **1993**, *74*, 3558.
20. Tour, J.M.; Kozak, M.; Seminario, J.M. Molecular scale electronics: a synthetic/computational approach to digital computing. *J. Am. Chem. Soc.* **1998**, *120*, 8486.
21. Heath, J.R. Wires, switches, and wiring: a route toward a chemically assembled electronic nanocomputer. *Pure Appl. Chem.* **2000**, *72*, 11.
22. Goldstein, S.C.; Budiu, M. Nanofabrics: spatial computing using molecular electronics. In *Proc. 28th Annual Int. Symp. On Comp. Arch.*; June 2001.
23. Hu, J.; Odom, T.W.; Lieber, C.M. Chemistry and physics in one dimension: Synthesis and properties of nanowires and nanotubes. *Acc. Chem. Res.* **1999**, *32*, 435.
24. Rueckes, T.; Kim, K.; Joselevich, E.; Tseng, G.Y.; Cheung, C.-L.; Lieber, C.M. Carbon nanotubes-based nonvolatile random access memory for molecular computing. *Science* **2000**, *289*, 94.
25. Ouyang, M.; Huang, J.-L.; Cheung, C.-L.; Lieber, C.M. Atomically resolved single-walled carbon nanotubes intramolecular junctions. *Science* **2001**, *291*, 97.
26. Bozovic, D.; Bockrath, M.; Hafner, J.H.; Lieber, C.M.; Park, H.; Tinkham, M. Electronic properties of mechanically induced kinks in single-walled carbon nanotubes. *Appl. Phys. Lett.* **2001**, *78*, 3693.
27. Star, A.; Stoddart, J.F.; Steuerman, D.; Diehl, M.; Boukai, A.; Wong, E.W.; Yang, X.; Chung, S.-W.; Choi, H.; Heath, C.M. Preparation and properties of polymer-wrapped single-walled carbon nanotubes. *Angew. Chem., Int. Ed. Engl.* **2001**, *40*, 1721.
28. Huang, Y.; Duan, X.; Wei, Q.; Lieber, C.M. Directed assembly of one-dimensional nanostructures into functional networks. *Science* **2001**, *291*, 630.
29. Gudixsen, M.S.; Wang, J.; Lieber, C.M. Synthetic control of the diameter and length of single crystal semiconductor nanowires. *J. Phys. Chem., B* **2001**, *105*, 4062.
30. Cui, Y.; Lieber, C.M. Functional nanoscale electronic devices assembled using silicon nanowire building blocks. *Science* **2001**, *291*, 851.
31. Chung, S.-W.; Yu, J.-Y.; Heath, J.R. Silicon nanowire devices. *Appl. Phys. Lett.* **2000**, *76*, 2068.
32. Tour, J.M.; Van Zandt, W.L.; Husband, C.P.; Husband, S.M.; Wilson, L.S.; Franzon, P.D.; Nackashi, D.P. Nanocell logic gates for molecular computing. *IEEE Trans. Nanotechnol.* **2002**, *1*, 100.
33. McEuen, P.L. Artificial atoms: new boxes for electrons. *Science* **1997**, *278*, 1729.
34. Stewart, D.R.; Sprinzak, D.; Marcus, C.M.; Duruoz, C.I.; Harris, J.S., Jr. Correlations between ground state and excited state spectra of a quantum dot. *Science* **1997**, *278*, 1784.
35. Rajeshwar, K.; de Tacconi, N.R.; Chenthamarakshan, C.R. Semiconductor-based composite materials: preparation, properties, and performance. *Chem. Mater.* **2001**, *13*, 2765.
36. Sear, R.P.; Chung, S.-W.; Markovich, G.; Gelbart, W.M.; Heath, J.R. Spontaneous patterning of quantum dots at the air–water interface. *Phys. Rev., E* **1999**, *59*, 6255.
37. Markovich, G.; Collier, C.P.; Henrichs, S.E.; Remacle, F.; Levine, R.D.; Heath, J.R. Architectonic quantum dot solids. *Acc. Chem. Res.* **1999**, *32*, 415.
38. Weitz, I.S.; Sample, J.L.; Ries, R.; Spain, E.M.; Heath, J.R. Josephson coupled quantum dot artificial solids. *J. Phys. Chem., B* **2000**, *104*, 4288.
39. Snider, G.L.; Orlov, A.O.; Amlani, I.; Zuo, X.; Bernstein, G.H.; Lent, C.S.; Merz, J.L.; Porod, W.J. Quantum dot cellular automata: review and recent experiments (invited). *Appl. Phys.* **1999**, *85*, 4283.
40. Snider, G.L.; Orlov, A.O.; Amlani, I.; Bernstein, G.H.; Lent, C.S.; Merz, J.L.; Porod, W. Quantum-dot cellular automata: line and majority logic gate. *Jpn. J. Appl. Phys., Part I: Reg. Pap. Short Notes* **1999**, *38*, 7227.
41. Toth, G.; Lent, C.S. Quasiadiabatic switching for metal-island quantum-dot cellular automata. *J. Appl. Phys.* **1999**, *85*, 2977.
42. Orlov, A.O.; Amlani, I.; Toth, G.; Lent, C.S.; Bernstein, G.H.; Snider, G.L. Experimental demonstration of a binary wire for quantum-dot cellular automata. *Appl. Phys. Lett.* **1999**, *74*, 2875.



43. Lent, C.S. Molecular electronics: bypassing the transistor paradigm. *Science* **2000**, *288*, 1597.
44. Bandyopadhyay, S. Debate response: What can replace the transistor paradigm? *Science* **29 June 2000**, 288.
45. Huang, Y.; Duan, X.; Cui, Y.; Lauhon, L.J.; Kim, K.-H.; Lieber, C.M. Logic gates and computations from assembled nanowire building blocks. *Science* **2001**, *294*, 1313.
46. Luo, Y.; Collier, C.P.; Jeppesen, J.O.; Nielsen, K.A.; Delonno, E.; Ho, G.; Perkins, J.; Tseng, H.-R.; Yamamoto, T.; Stoddart, J.F.; Heath, J.R. Two-dimensional molecular electronics circuits. *ChemPhysChem* **2002**, *3*, 519–525.
47. Whang, D.; Jin, S.; Wu, Y.; Lieber, C.M. Large-scale hierarchical organization of arrays for integrated nano-systems. *Nano Lett.* **2003**, *3*, 1255–1259.
48. Yu, J.-Y.; Chung, S.-W.; Heath, J.R. Silicon nanowires: preparation, devices fabrication, and transport properties. *J. Phys. Chem., B* **2000**, *104*, 11,864.
49. Melosh, N.A.; Boukai, A.; Diana, F.; Geradot, B.; Badolato, A.; Petrof, P.M.; Heath, J.R. Ultra-high density nanowire lattices and circuits. *Science* **2003**, *300*, 112–115.
50. Ausman, K.D.; O'Connell, J.J.; Boul, P.; Ericson, L.M.; Casavant, M.J.; Walters, D.W.; Huffman, C.; Saini, R.; Wang, Y.; Haroz, E.; Billups, E.W.; Smalley, R.E. In *Roping and Wrapping Carbon Nanotubes*, Proceedings of XVth International Winterschool on Electronic Properties of Novel Materials Euroconference, Kirchberg, Tirol, Austria, 2000.
51. Bahr, J.L.; Mickelson, E.T.; Bronikowski, J.J.; Smalley, R.E.; Tour, J.M. Dissolution of small diameter single-wall carbon nanotubes in organic solvents? *Chem. Commun.* **2001**, *2001*, 193.
52. Mickelson, E.T.; Chiang, I.W.; Zimmerman, J.L.; Boul, P.J.; Lozano, J.; Liu, J.; Smalley, R.E.; Hauge, R.H.; Margrave, J.L. Solvation of fluorinated single-wall carbon nanotubes in alcohol solvents. *J. Phys. Chem., B* **1999**, *103*, 4318.
53. Chen, J.; Rao, A.M.; Lyuksyutov, S.; Itkis, M.E.; Hamon, M.A.; Hu, H.; Cohn, R.W.; Eklund, P.C.; Colbert, D.T.; Smalley, R.E.; Haddon, R.C. Dissolution of full-length single-walled carbon nanotubes. *J. Phys. Chem., B* **2001**, *105*, 2525.
54. Bahr, J.L.; Yang, J.; Kosynkin, D.V.; Bronikowski, M.J.; Smalley, R.E.; Tour, J.M. Functionalization of carbon nanotubes by electrochemical reduction of aryl diazonium salts: a bucky paper electrode. *J. Am. Chem. Soc.* **2001**, *123*, 6536.
55. Bahr, J.L.; Tour, J.M. Highly functionalized carbon nanotubes using *in situ* generated diazonium compounds. *Chem. Mater.* **2001**, *13*, 3823.
56. Bahr, J.L.; Tour, J.M. Covalent chemistry of single-wall carbon nanotubes. *J. Mater. Chem.* **2002**, *12*, 1952–1958.
57. O'Connell, M.J.; Boul, P.; Ericson, L.M.; Huffman, C.; Wang, Y.; Haroz, E.; Kuper, C.; Tour, J.; Ausman, K.D.; Smalley, R.E. Reversible water-solubilization of single-walled carbon nanotubes by polymer wrapping. *Chem. Phys. Lett.* **2001**, *342*, 265.
58. Rao, S.G.; Huang, L.; Setyawan, W.; Hong, S. Large-scale assembly of carbon nanotubes. *Nature* **2003**, *425*, 36–37.
59. Collins, P.G.; Arnold, M.S.; Avouris, P. Engineering carbon nanotubes and nanotubes circuits using electrical breakdown. *Science* **2001**, *292*, 706.
60. Strano, M.S.; Dyke, C.A.; Usrey, M.L.; Barone, P.W.; Allen, M.J.; Shan, H.; Kittrell, C.; Hauge, R.H.; Tour, J.M.; Smalley, R.E. Electronic structure control of single walled carbon nanotube functionalization. *Science* **2003**, *301*, 1519–1522.
61. Pease, A.R.; Jeppesen, J.O.; Stoddart, J.F.; Luo, Y.; Collier, C.P.; Heath, J.R. Switching devices based on interlocked molecules. *Acc. Chem. Res.* **2001**, *34*, 433.
62. Nackashi, D.P.; Franzon, P.D. Moletronics: a circuit design perspective. *Proc. SPIE* **2000**, *4236*, 80.
63. Goto, E. The parametron: a digital computing element which utilizes parametric oscillation. *Proc. IRE* **1959**, *47*, 1304.
64. Ellenbogen, J.C.; Love, J.C. Architectures for molecular electronic computers: 1. logic structures and an adder designed from molecular electronic diodes. *Proc. IEEE* **2000**, *88*, 386.
65. Chen, J.; Reed, M.A.; Rawlett, A.M.; Tour, J.M. Large on-off ratios and negative differential resistance in a molecular electronic device. *Science* **1999**, *286*, 1550.
66. Yao, Y.; Flatt, A.K.; Maya, F.; Tour, J.M. submitted for review.
67. Chen, J.; Wang, W.; Reed, M.A.; Rawlett, A.M.; Price, D.W.; Tour, J.M. Room-temperature negative differential resistance in nanoscale molecular junctions. *Appl. Phys. Lett.* **2000**, *77*, 1224.
68. Mbindyo, J.K.N.; Mallouk, T.E.; Mattzela, J.B.; Kratochvilova, I.; Razavi, B.; Jackson, T.N.; Mayer, T.S. Template synthesis of metal nanowires containing monolayer molecular junctions. *J. Am. Chem. Soc.* **2002**, *124*, 4020.
69. Martin, B.R.; St. Angelo, S.K.; Mallouk, T.E. Interactions between suspended nanowires and patterned surfaces. *Adv. Funct. Mater.* **2002**, *12*, 759.
70. Tour, J.M.; Jones, L., II; Pearson, D.L.; Lamba, J.S.; Burgin, T.P.; Whitesides, G.W.; Allara, D.L.; Parikh, A.N.; Atre, S. Self-assembled monolayers and multilayers of conjugated thiols, *a,w*-dithiols, and thioacetyl-containing adsorbates. Understanding attachments between potential molecular wires and gold surfaces. *J. Am. Chem. Soc.* **1995**, *117*, 9529.
71. Cai, L.; Yao, Y.; Yang, J.; Price, D.W., Jr.; Tour, J.M. Chemical and potential assisted assembly of thioacetyl-terminated oligo(phenylene ethynylene)s on gold surfaces. *Chem. Mater.* **2002**, *14*, 2905.
72. Bain, C.D.; Troughton, E.B.; Tao, Y.-T.; Evall, J.; Whitesides, G.M.; Nuzzo, R.G. Formation of monolayer films by the spontaneous assembly of organic thiols from solution onto gold. *J. Am. Chem. Soc.* **1989**, *111*, 321.
73. Seminario, J.M.; Derosa, P.A.; Bastos, J.L. Theoretical interpretation of switching in experiments with single

- molecules. *J. Am. Chem. Soc.* **2002**, *124*, 10,266–10,267.
74. Cornil, J.; Karzazi, Y.; Bredas, J.L. Negative differential resistance in phenylene ethynylene oligomers. *J. Am. Chem. Soc.* **2002**, *124*, 3516–3517.
75. Fan, F.-R.R.; Yang, J.; Cai, L.; Price, D.W.; Dirk, S.M.; Kosynkin, D.; Yao, Y.; Rawlett, A.M.; Tour, J.M.; Bard, A.J. Charge transport through self-assembled monolayers of compounds of interest in molecular electronics. *J. Am. Chem. Soc.* **2002**, *124*, 5550.
76. Donhauser, Z.J.; Mantooh, B.A.; Kelly, K.F.; Bumm, L.A.; Monnell, J.D.; Stapleton, J.J.; Price, D.W., Jr.; Rawlett, A.M.; Allara, D.L.; Tour, J.M.; Weiss, P.S. Conductance switching in single molecules through conformational changes. *Science* **2001**, *292*, 2303.
77. Rawlett, A.M.; Hopson, T.J.; Nagahara, L.A.; Tsui, R.K.; Ramachandran, G.K.; Lindsay, S.M. Electrical measurement of a dithiolated electronic molecule via conducting atomic force microscopy. *Appl. Phys. Lett.* **2002**, *81*, 3043.
78. Buckley, W.D. Process of Making a Filament-Type Memory Semiconductor Device. US Patent 3,980,505, September 14, 1976
79. Chesnys, A.; Karpinskas, S.-A.; Urbelis, A. Current-voltage characteristic and parameters of the current filament region of an amorphous gallium telluride-crystalline silicon barrier register structure. *Tech. Phys. (Translation of Zhurnal Tekhnicheskoi Fiziki)* **2002**, *47*, 58.
80. Simmons, J.G.; Verderber, R.R. Conduction and reversible memory phenomena in thin insulating films. *Proc. R. Soc. Lond., A Math. Phys. Sci.* **1967**, *301*, 77.
81. Thurstans, R.E.; Oxley, D.P. The electroformed metal-insulator-metal structure: a comprehensive model. *J. Phys., D, Appl. Phys.* **2002**, *35*, 802.

# Molecular Electronics: Models of Switchable and Programmable Devices

Pedro A. Derosa  
Vandana R. Tarigopula  
Jorge M. Seminario

*Department of Electrical Engineering, University of South Carolina,  
Columbia, South Carolina, U.S.A.*

## INTRODUCTION

The process of scaling down modern semiconductor devices faces serious obstacles, mainly because of device-addressing problems. Practical limitations in fabrication and extraordinary increases in production costs will also be limiting issues. Small molecules, easy to tailor, are the natural candidates to complement semiconductor components in the generation of hybrid circuits, giving birth to a completely new area of electronics, molecular electronics or Moletronics. Experimental characterization is highly challenging, and only a few experiments in which only one molecule is addressed have been performed,<sup>[1–3]</sup> because technical possibilities of success become greatly diminished with the minuscule system size. Fortunately, modern quantum-chemistry-theoretical-based computational techniques are able to accurately solve molecular systems using precise natural laws, and this ability increases substantially as systems become smaller.

This entry investigates recent results on molecular systems that can potentially be used as electronic devices. It is particularly focused on molecules that can behave as controllable switches (a characteristic that allows programmability) and the theoretical techniques available for their analysis, design, and simulation. Switching has been studied before but not with the purpose of programmability. For instance, Collier et al.<sup>[4]</sup> studied switching based on the translation degrees of freedom of mechanical bonds, and more elaborate molecular circuits have been proposed, such as a flash-like, single-electron memory cell,<sup>[5]</sup> however, they are hardly useful for a paradigm of a chemically random assembly of molecules governed mostly by thermodynamic and some kinetic controls where programmability features at the level of devices are of paramount importance.<sup>[6]</sup> The studies cited focused on electrical features and their correlation to

conformational properties, the metallic contacts characterization, and the metal–molecule interface. Determining the correlation between transport characteristics and molecular electronic and geometrical configuration is particularly important, because this correlation provides a mechanism to control electron transport in molecular and atomistic systems.

## THEORY-BASED APPROACHES FOR THE CALCULATION OF MOLECULAR SYSTEMS

In this section, we describe several approaches used for the analysis of molecular electronic systems. We briefly summarize the common methods and tools that allow researchers to theoretically characterize, design, model, and simulate moletronics systems.

### Methods

The main methods used in moletronics are borrowed from quantum chemistry and solid state physics, and in particular, density functional theory (DFT) is used for discrete and extended systems as well as their interconnection using the Green function (GF) scattering technique.

#### Ab initio density functional theory for molecules

In the study of molecules presenting highly non-linear features, the Kohn–Sham molecular orbitals (MOs) can provide a qualitative picture of the molecular mechanisms of operation and how they are affected by its boundaries. The solution of the Schrödinger equation for the system under consideration should provide an exact solution if an exact Hamiltonian is used; however, such a solution is very tedious because

of the massive computational resources it demands. One way to bypass this difficulty is to use DFT where the solution of the wave function replaces the solution of the electron density. Electron density is obtained from auxiliary systems of non-interacting electrons whose total electron density is forced to be identical to the electron density of the interacting or real electrons. The advantage of this approach is that the system of non-interacting electrons can be easily separated into individual one-electron MOs, also called Kohn–Sham MOs. Each MO is associated to individual energies that can be roughly correlated with the excitation energies of the molecular system. The shape and energy of these MOs have been widely used in the qualitative explanation of electron transport (vide infra) in single molecules. However, the use of MOs is only for qualitative purposes. MOs from DFT, or any other theory, can never precisely describe the exact wave function of a real system because real electrons are not independent particles. For most practical purposes, DFT calculations using functionals based on ab initio approaches and beyond the local approximation have been very successful in describing the main features of molecular systems with acceptable precision. This fact has converted DFT into the main computational tool in modern quantum chemistry, and into the preferred tool for the study of molecular electronics.

Integration of several tools is often necessary. Single molecules are first treated by using ab initio density functional theory (DFT) as implemented in the Gaussian-98 program,<sup>[7]</sup> or its recent version, Gaussian-03.<sup>[8]</sup> The molecular geometry is optimized with no constraint (except for special cases) until all eigenvalues of the Hessian matrix are positive, ensuring that the molecule is in a minimum energy configuration. The Becke-3 Perdew–Wang 91 (B3PW91) procedure, which consists of the Becke3 hybrid exchange functional combined with the generalized gradient approximation (GGA) Perdew–Wang-91 correlation,<sup>[9–11]</sup> is used in combination with different basis set selected according to the system. In general, systems with metallic atoms are treated using LANL2DZ,<sup>[12–14]</sup> an effective core potential and basis set. The LANL2DZ basis set explicitly considers all the valence electrons, rather than just those in last electronic shell. Core electrons are treated in an approximate way by using pseudopotentials that include relativistic effects allowing an excellent description of heavy metal atoms.<sup>[15]</sup> The level of theory B3PW91/LANL2DZ has been used in several works, and further details can be found in Refs.<sup>[16–20]</sup> In some cases, where no metallic atoms are present, 6-31G\* basis or higher sets are also used.

Atomic charges are estimated by using Mulliken population analysis, which associates charge to each atom by integrating the basis functions assigned to each

individual atom and assigning equally to each atom of each pair their overlap contributions. Mulliken charges can only provide complementary information. Mulliken values do not support conclusions, but provide a qualitative picture of the quantitative results; atomic charges are not expectation values but mere indicators highly dependent on the method and basis set used to solve the Schrödinger equation. Nevertheless, if properly balanced basis sets are used, Mulliken analysis can provide an excellent tool for qualitative analysis and interpretations of charge transfer effects.

## Green functions

*I*–*V* characteristics are calculated by combining the DFT results with a Green function technique originally designed for mesoscopic systems.<sup>[21–27]</sup> This approach considered the molecule attached to infinite contacts that modify its electronic structure, the new modified electronic structure is, in turn, used to calculate the system (molecule plus contacts) *I*–*V* characteristic. The electron transport properties of a molecule under a bias voltage *V* are described by its Green function,  $G_M$ , obtained from the molecular Hamiltonian,  $H(V)$ , which is obtained by reoptimizing the molecular electronic structure under the presence of an external electrical field. The transport of electrons takes place through the MOs, which are affected by interaction with the contacts and with the applied voltage.<sup>[28,29]</sup> MOs may be affected by an applied external field or by the charge state on the molecule. For instance, delocalized MOs can become localized, or vice versa, when the molecule traps one electron. The molecule is in a conducting state (low impedance) if delocalized MOs are available in the energy range for which one contact has occupied levels and the other unoccupied ones. The molecule is in a non-conducting state (high impedance) if those MOs are localized, i.e., they do not connect both ends of the molecule to the contacts. When the molecule is open shell (electrons are unpaired), both  $\alpha$  and  $\beta$  spin states are considered to obtain the molecular *I*–*V* characteristics.

The Green function is obtained from Eq. (1),

$$G_M = [E\mathbf{1} - H_{MM} - H_{M1}g_1H_{1M} - H_{M2}g_2H_{2M}]^{-1} \quad (1)$$

where subscripts *i* and *j* in  $H_{ij}$  [submatrices of *H* in Eq. (2)] refer to the molecule (M), contact 1 (1), and contact 2 (2).

$$H = \begin{bmatrix} H_{11} & H_{1M} & H_{12} \\ H_{M1} & H_{MM} & H_{M2} \\ H_{21} & H_{2M} & H_{22} \end{bmatrix} \quad (2)$$

Information about the macroscopic nature of the contacts is introduced by a Green function for a semi-infinite medium ( $g_i$ ), whereby  $s$ ,  $p$ , and  $d$  contributions<sup>[30]</sup> to the density of states (DOS) of the Au metal are explicitly considered. Derosa and Seminario represented the metallic contacts by assuming a density of states with  $s$ ,  $p$ , and  $d$  contributions, but energy-independent. This approach, although not perfect, was an improvement compared to available applications (see, for example, Refs.<sup>[31,32]</sup>) that considered only an  $s$ -character, also energy-independent DOS. These descriptions of the contacts were finally improved by calculating at DFT level, the DOS of a metallic system extended using periodic boundary conditions (vide infra).<sup>[33]</sup>

From the molecular Green function, the transmission function (TF), which is the sum of the transmission probabilities of all channels (MOs) available at energy  $E$ , is obtained, as described by Eq. (3), and the current is obtained from Eq. (4),<sup>[25]</sup> where  $f_i$  is the Fermi–Dirac function for a voltage  $V_i$  at contact  $i$  ( $V = V_2 - V_1$ ).

$$T(E, V) = \text{trace}[\Gamma_1(V)G_M(E, V)\Gamma_2(V)G_M^+(E, V)] \quad (3)$$

$$I(V) = \frac{2e}{h} \int_{-\infty}^{\infty} dE T(E, V)[f_1(E, V_1) - f_2(E, V_2)] \quad (4)$$

As a first approximation, the experimental work function of the metal making the contact,  $-5.31$  eV for Au, was used for some calculations of neutral systems.<sup>[34]</sup> In previous works,<sup>[29,35]</sup> this value was also used to study the anions. An average of the highest occupied molecular orbital (HOMO)–lowest unoccupied molecular orbital (LUMO) midgap energy from several neutral organic molecules attached to Au atoms yielded an energy of  $-5.2$  eV, which is in excellent agreement with the experimental work function of Au. However, the midgap average energy for the single anions and dianions is  $-1.55$  and  $0.88$  eV, respectively. The HOMO and LUMO energies obtained from DFT is an approximation (with a minus sign) of the ionization potential and the electron affinity of the molecule, respectively. Thus it is not surprising that both energies are higher (in absolute value) for anions than for neutral; however, this situation will not reflect the position of the HOMO–LUMO gap (HLG) relative to the metal Fermi level. This shift in position of the HLG, which was not considered in our original model, was later accounted for to estimate the electrical characteristics of the anion and dianion.

The density of states (DOS) is also obtained from the Green function formalism,<sup>[25]</sup> as shown by Eq. (5).

$$\text{DOS}(E, V) = \text{trace}[(i[G_M(E, V) - G_M^+(E, V)])] \quad (5)$$

A full description of this procedure is published elsewhere,<sup>[29]</sup> where more detailed information and useful references can be found.

### Ab initio calculations for crystals and extended systems

CRYSTAL-98<sup>[36]</sup> is used to study the metallic contacts within the linear combination of atomic orbital approximations. Macroscopic properties (band structure, DOS, etc.) are obtained by reproducing the unit cell to infinite, following the rules of the corresponding crystal structure. CRYSTAL-98 is a suite of programs that can calculate the electronic structure, total energy, and wave functions, including its band structure, density of states, electron charge distribution, electron momentum distribution, Compton profile, Mulliken charges, electrostatic potentials, and X-ray structure factors<sup>[37]</sup> by using a DFT approach for periodic systems.<sup>[38]</sup> The basis set expands the Bloch functions built  $\Psi_k(r)$  by using  $s$ ,  $p$  and  $d$  Gaussian functions, as can be observed in Eq. (6).

$$\Psi_k(r + g) = \Psi_k(r) \exp(ik \cdot g) \quad (6)$$

The electron density of the  $N$ -electron system<sup>[38]</sup> is given by Eq. (7), where  $\theta$  is the Heaviside step function, and  $\varepsilon_i(k)$  is the eigenvalue of the  $i$ th crystalline orbital.  $\varepsilon_F$  is the Fermi energy.

$$\rho(r) = \int_{\text{Brillouin zone}} dk \sum_i^{\text{Occupied bands}} |\varphi_{ki}(r)|^2 \theta(\varepsilon_F - \varepsilon_i(k)) \quad (7)$$

The Bloch functions described above are used to expand the crystalline orbitals that are linear combinations of atom-centered Gaussian-type functions,  $\varphi_{ki}(r)$ . The coefficients for the linear expansion are adjusted such that  $\varphi_{ki}(r)$  are the solutions of the one-particle equations [Eq. (8)],

$$\hat{h}_i \varphi_{ki}(r) = \varepsilon_{ki} \varphi_{ki}(r) \quad (8)$$

where  $\hat{h}$  is the single particle Hamiltonian operator shown in Eq. (9), which includes the contributions from kinetic, external potential, Coulomb, and

exchange-correlation potential operators, respectively.

$$\hat{h}_{\text{KS}} = \hat{t} + \hat{v} + \hat{J}[\rho(r)] + \hat{v}_{\text{xc}}(r) \quad (9)$$

The exchange-correlation operator is expanded in a basis of Gaussian-type functions, as seen in Eq. (10), where  $g$  is the cell (vectors) containing the  $j$ th basis function centered at the atomic position  $s_j$ .

$$v_{\text{xc}}^{i,jg} = \int dr \chi_i(r - s_i) v_{\text{xc}}(r) \chi_j(r - s_j - g) \quad (10)$$

This integral is solved analytically because the exchange-correlation potential is expanded with Gaussian auxiliary basis functions,  $G_a(r)$ ; thus the integral is transformed into a linear combination of integrals of the form given by Eq. (11), which is solved only once then stored for subsequent use.

$$g_a^{i,jg} = \int dr \chi_i(r - s_i) G_a(r) \chi_j(r - s_j - g) \quad (11)$$

At each step, the coefficients are recalculated so the exchange-correlation potential fits the analytic form that depends on the charge density. In addition, the exchange potential is calculated by using the Hartree–Fock prescription, yielding a fully non-local functional, and when combined with the PW91 correlation functional, yields one of the so-called hybrid functionals. We use the hybrid functional approach with the gradient-corrected PW91 functionals<sup>[10]</sup> for the correlation potential together with the SBKJC VDZ ECP (8s 8p 6d)/[4s 4p 3d]<sup>[39,40]</sup> ECP and basis set. The Au bulk is treated as an infinite periodic system with face centered cubic (fcc) crystalline structure, thus realistic density of states for a metal is obtained to construct the Green function for the contacts.

## Tools for Molecular Calculations

This section describes tools employing the ab initio based techniques described in the last section.

### Nonlinear circuit solver

Recently, an algorithm able to calculate the current–voltage characteristics of combinations of single molecules has been developed.<sup>[6]</sup> In general, the algorithm is able to determine all possible solutions of an electrical circuit with devices having highly nonlinear characteristics, such as negative differential resistance or resonant tunneling. The solutions to these circuits are multivalued functions, which cannot be obtained with the traditional programs to solve electrical circuits.

The DFT, GF, and their combination, DFT–GF, provide quantitative information needed for the design and testing of programmable molecular circuits. Once the molecule is characterized, the  $I$ – $V$  curve is used as the device characteristic. The analysis is systematically applied branch by branch, such as sweeping a suitable range of currents and determining all compatible voltages from the  $I$ – $V$  of the device in the branch, then all possible voltage drops in the branch (each configuring one possible state) are determined by combining voltage drops on each device.

The method does not scale very well at this stage of development; the scaling depends on the number of solutions for each branch and the number of branches. However, this method can systematically solve any combination of molecular devices irrespective of the particular  $I$ – $V$  characteristic and provide all possible solutions; this feature is not available in any current software for circuit solution.

### Interpretation using molecular orbitals

A powerful technique for the analysis of molecular circuits, i.e., the use of the quantum chemistry techniques, including MOs and their energies, as indexes for the estimation of electron transport was recently introduced into the field of molecular electronics.<sup>[28,29,35]</sup> Delocalized MOs are expected to provide a more suitable path for electron transport, because they simultaneously connect the molecule to the metallic atoms at both ends. Thus analyzing MO qualitative predictions on how easy it is for a molecule to conduct electrons can be inferred. MOs can explain, without calculating the currents, the behavior of several oligomers and the effect of their substituents. Furthermore, using MOs can identify groups in the molecule responsible for a particular observed behavior, information that can be used in the design of new molecular devices; for instance, using them to explain the electrical behavior of  $\pi$ -conjugated organic molecules resembling a resonant tunneling diode.<sup>[28]</sup>

Figure 1 shows some of the conformations studied using DFT. The HOMO–LUMO gap (HLG) energy for planar and rotated  $\pi$ -conjugated organic molecules is reported in this figure at the bottom of the corresponding case. Calculations were extended to include gold clusters at both ends of these molecules. This work determined the mechanism of operation of the molecular resonant tunneling diode (MRTD),<sup>[28]</sup> where the electron transport occurs through the lowest unoccupied molecular orbital and so the shape of the LUMO determines the transport characteristics of the molecule presenting negative differential resistance (NDR). These analyses explained qualitatively<sup>[28]</sup> the peak found experimentally at 2.1 V at a temperature of 60 K,<sup>[41]</sup> and explained the observed reduction in



	A	B	C	D
Q = 0				
HLG $\tau$	3.70 0°	4.68 90°	3.48 0.4°/2.8°	4.01 89.6°/89.7°
Q = -1				
HLG $\tau$	1.09/1.13 0°	0.53/0.80 90°	1.25/1.17 0.2°/1.9°	0.78 <sup>a</sup>
Q = -2				
HLG $\tau$	1.30/1.59 0°	0.10 <sup>a</sup>	0.80/1.02 0.1°/1.7°	0.36 <sup>a</sup>

**Fig. 1** LUMO plots, HLG energies (in eV), and torsion angles ( $\tau$ ) for the optimized neutral and for the vertical and adiabatic structures of the anions. Only one LUMO is shown if the vertical and adiabatic shapes are similar. *Source:* See Ref.<sup>[28]</sup> for further details.) <sup>a</sup>Only vertical HLG is shown because the structure becomes planar during the optimization.

peak voltage as temperature increases. One of the key findings of this research is that Seminario and Derosa analyzed single molecules providing the effect of amplification.<sup>[42]</sup> Subsequently, electronic transport was fully investigated, and it was concluded that the molecular chemical potential determines the conduction barrier, and that the molecule becomes charged as the external potential increases.<sup>[33]</sup> In earlier studies, Seminario, Zacarias, and Tour<sup>[28]</sup> were able to explain the non-linear character of the current–voltage ( $I$ – $V$ ) characteristic of the molecule and its temperature dependence.

The effect of the bias voltage on the electron transmission of a molecular device, negative differential resistance

A bias voltage applied to a molecule attached to metallic contacts has two effects. On one hand, it changes the Fermi level in the contacts; electrons lower their energy on the positive electrode and increase their energy in the negative electrode and, as a result, electrons are available on the negatively polarized contact at energies for which empty states are available in the

positive electrode. If these electrons find a delocalized molecular level that connects both ends, electron transport occurs. On the other hand, the electric field created across the molecule affects MOs and can change not only their energy, but also the degree of localization; thus a MO that is localized at zero voltage may become delocalized by the electric field and vice versa.

One of the most interesting effects observed in some of the molecules studied is the negative differential resistance (NDR). NDR means negative slope in the  $I$ - $V$  curve. NDR can occur for two main reasons. One is charge or conformational-induced NDR; at a given voltage, the molecule can become charged, or change its structure such that current decreases after the voltage is increased. The other, intrinsic NDR, is produced by a change in the molecular electronic structure that reduces the electron transport capabilities of the MOs involved in conduction. Intrinsic NDR cannot be predicted if a bias voltage is not included in the calculations and cannot be predicted if the correct chemistry of the molecule is not considered. The current is calculated via Eq. (4) (in the section "Green functions"), where  $T$ , the transmission function, would only depend on  $E$  if a field is not applied to the molecule to account for the effect of the voltage. In such a case,  $V$  only enters in the Fermi factors that control the "window"; as a consequence, the current can only monotonically increase with  $V$ , and NDR would not be predicted.

Figure 2 shows the current-vs.-voltage curve for two test molecules; both molecules have three benzene rings separated by a C-C triple bond group. Molecule **1** ( $\text{NO}_2$  in Fig. 2) has two nitro groups as substituents in the central ring; molecule **2** ( $\text{NH}_2$ ) has one nitro and one amino group in the central ring. We used density functional theory (DFT) calculations to explain the electrical behavior of these  $\pi$ -conjugated organic

molecules with current-voltage characteristics resembling a resonant tunneling diode.<sup>[33]</sup>

Considering the behavior of the neutral of these molecules (blue curve solid and dotted, respectively, for **1** and **2**), intrinsic NDR is observed for **2** at around 1.3 V, while no NDR is observed for **1**. Figure 3 shows the transmission function at voltages relevant for the observed NDR effect. The NDR is observed between 1 and 1.5 V; the integration range to obtain the current at 1 V is from  $-5.81$  to  $-4.81$  eV [Fig. 3 and Eq. (3)], and from  $-6.06$  and  $-4.56$  eV for 1.5 V.

For **2**, a peak in the TF observed between  $-6.06$  and  $-5.81$  eV increases in height and approximately maintains its width when the voltage rises from 1 to 1.3 V (position of the NDR peak). Then the area below TF decreases considerably as the voltage increases further, thus explaining the decrease in the current (NDR). No similar effect is observed for **1**. This effect would have gone unnoticed if an electrical field had not been considered; the observed effect on the TF is entirely attributable to the changes in the molecular electronic structure (changes in MO localization and energy) due to the effect of an external field.

The need to implement the present methods is attributable to the impossibility of using simple model barriers able to represent the potential of small molecules acting on the conducting electrons. There are two ways that NDR and RT can be obtained from a single molecule. 1) The first is by charging the molecule or changing its geometry. Because the ion of a molecule has totally different characteristics than its neutral, charging a molecule is equivalent to substituting a molecule for another in the circuit. 2) Changing the shape of a molecule, for instance, by rotating a ring with respect to the other, which will very likely change the electron transport characteristics of molecule **2** via the intrinsic resonant tunneling (IRT) inherent to most

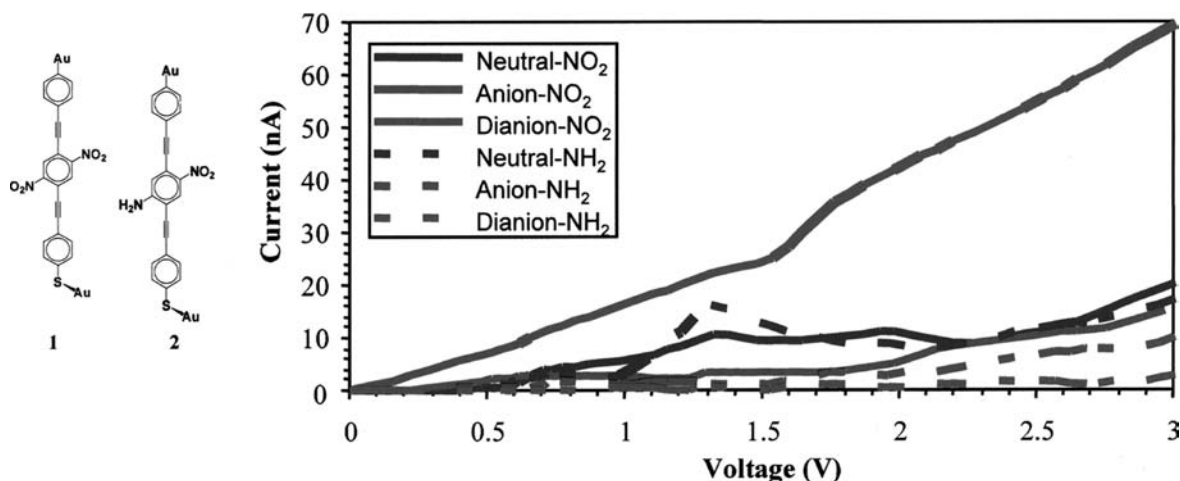
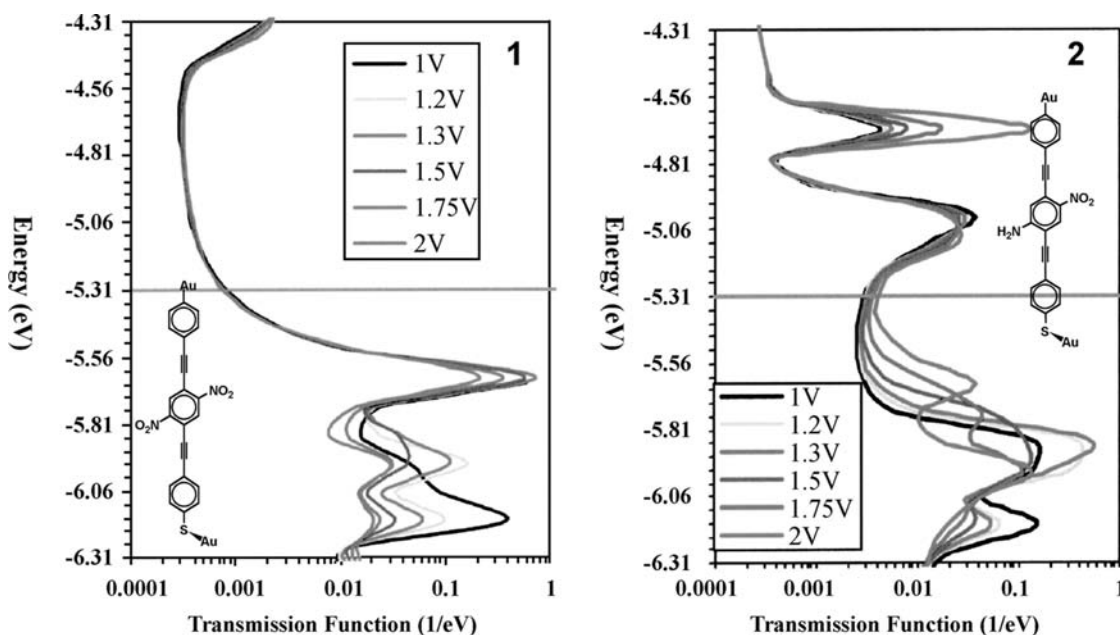


Fig. 2 Current-voltage of the neutrals (blue), anions (red), and dianions (green) for **1** (continuous lines) and **2** (dashed lines).



**Fig. 3** Transmission function vs. energy of incoming electrons at several bias voltages for the neutral of **1** and **2**. *Source:* Adapted from Ref.<sup>[33]</sup>.

molecular systems. The former yields sharp changes in the currents, and the latter yields smoother and symmetric curves, such as those in a typical resonance case.

### Molecular electrostatic potentials

Molecular electrostatic potential (MEP) is another important piece of information needed to understand the electronic properties of molecules. Areas of the molecule with specific properties (such as electron donation or electron-withdrawing capabilities) can be easily identified from an MEP map; this information is extremely useful in understanding molecular interactions and in molecular design. With MEPs, the

well-exploited electronic configuration analysis is able to accurately explain a switching experiment,<sup>[43]</sup> complementing the conclusions drawn by experimentalists, with a further explanation that include concepts and all the factors influencing the switching of the molecule, and raising research goals for subsequent experiments.

MEP does not show a smooth behavior across the molecule. For instance, when a bias voltage is applied, the voltage profile shows a complicated topology, which is very different from monotonous decrease that is expected from simple linear or bilinear devices. An example of an MEP profile across a molecule is shown in Fig. 4. Figure 4A shows the MEP profile across a single benzene ring at 2 Å above the benzene plane,

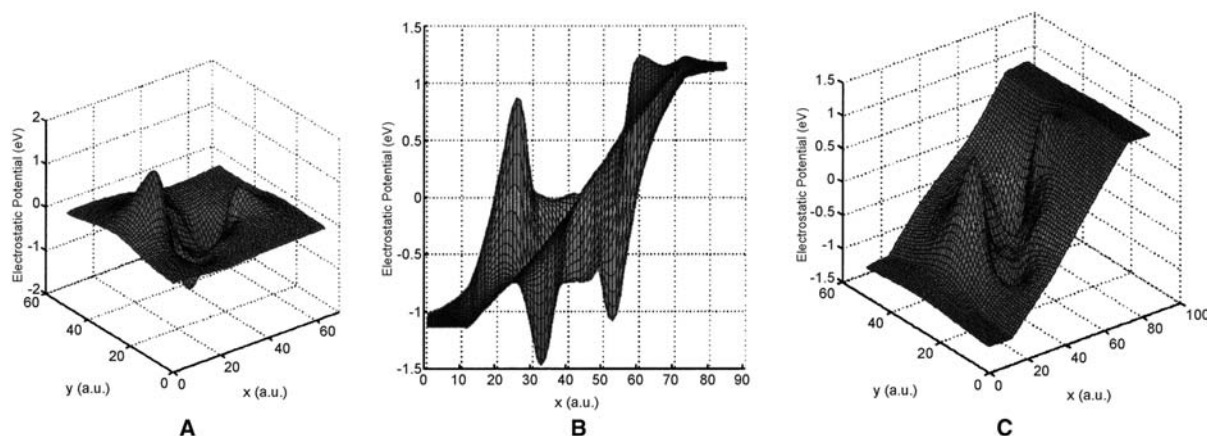


**Fig. 4** Molecular electrostatic potential profile at 2 Å above the molecular plane. (A) No voltage applied across the molecule; (B) side view of the MEP profile when 2 V are applied across the molecule; (C) like (B) but from a different view angle: view of the MEP profile showing the distribution on the plane.

while (B) and (C) are two different views of the MEP topology when a bias potential of 2 V is applied across the molecule. This picture dramatically changes the idea that molecules are simple barriers, and indicates that more precise studies should be performed to properly describe electron transport properties in molecules.

Tour, Kosaki, and Seminario<sup>[44,45]</sup> have also theoretically determined the first precise electrostatic potential profile obtained on a single molecule in the presence of an external potential source.

Seminario and Derosa have heavily investigated the behavior of benzene rings substituted with nitro and amine groups. It has been already determined that these groups render the negative ions of the ring stable with respect to the neutral state of the same molecule, thus they are able to exist as single, stable molecules. In addition, for some of these molecules, electron transport characteristics are different for the anion than for the neutral state. If this is the case, these molecules are able to behave by themselves as memory devices. Our calculations indicate that some of these molecules are able to store a second electron when bonded to metallic atoms.<sup>[28,33,35]</sup> The main advantage of this behavior for molecular electronics is that these molecules present storage characteristics at three levels (charge = 0, -1, and -2), therefore they could behave as devices without the need for a control gate because

we have one extra state available forming a two-terminal, three-state device that could be substituted for a three-terminal, two-state device.<sup>[35,46]</sup>

## APPLICATIONS

The following discussion reviews several applications of the tools and techniques described above.

### DFT-Based $I$ - $V$ Calculations

As a preliminary approach to calculating the  $I$ - $V$  characteristic of single molecules, a purely ab initio approach for the calculation of molecular current-voltage characteristics was developed.<sup>[17]</sup>

This method only uses molecular calculations to estimate the  $I$ - $V$  through a molecule, thus formulating a new prescription can obtain current-voltage characteristics via the use of precise quantum chemistry techniques. As shown by the results in Fig. 5, the agreement of calculations<sup>[17]</sup> with the experiments on single molecules<sup>[1]</sup> is very encouraging. Figure 5 shows results labeled as Au-S-(p-C<sub>6</sub>H<sub>4</sub>)-S-Au to be within the two experimental curves exp1 and exp2. This technique does not require any experimental feedback to predict

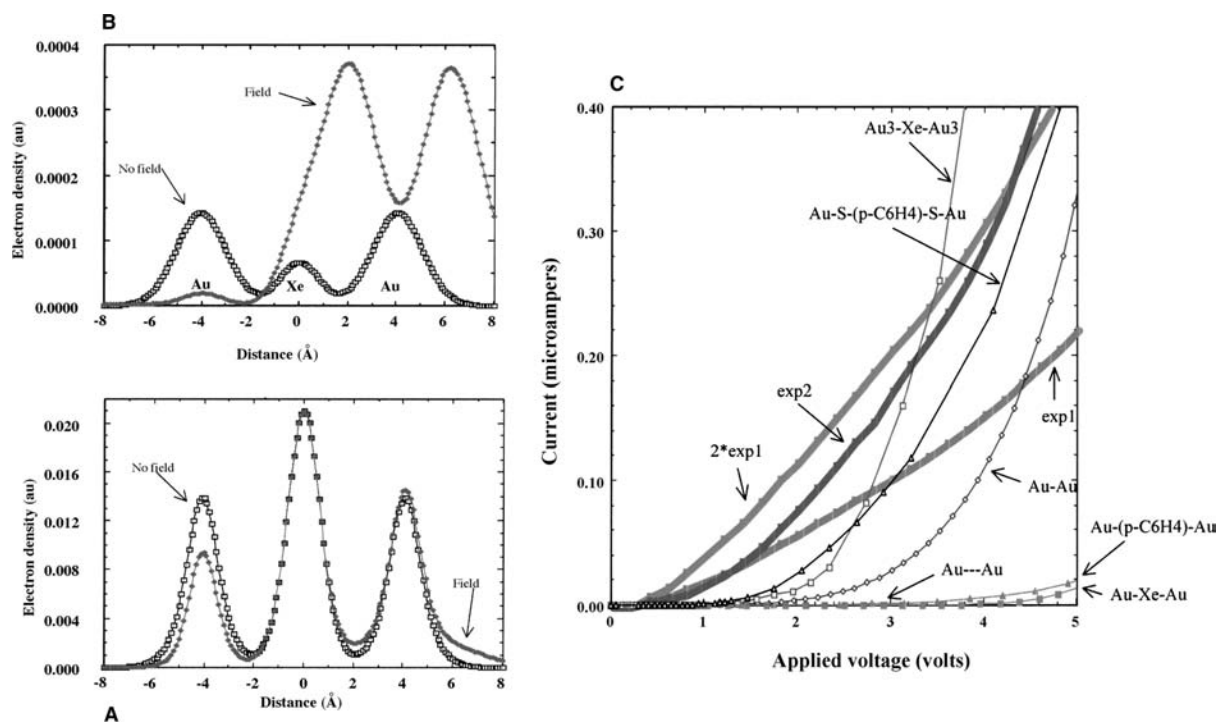


**Fig. 5** Panels (A) and (B) show electron densities along parallel axes to the molecule (Au-Xe-Au) axis at 1.5 and 3 Å, respectively. Cases when the external applied field is able to transfer one electron from the Au atom on the right side of the junction to the Au atom on the left side are shown. (C) Molecular  $I(V)$  characteristics. exp1 and exp2 correspond to the experimentally determined values of  $I(V)$ . Source: Adapted from Ref.<sup>[17]</sup>.

the  $I$ - $V$  characteristics. In addition, these studies have determined that the position of the molecule with respect to the metal tips has a strong effect on the charge transfer process.

### NDR and Memory

Some molecules have been found to present a particular response, such as NDR, to an applied voltage. This simply means that above a certain voltage, the current through the device decreases when the applied voltage increases. It is experimentally<sup>[41,47]</sup> and theoretically<sup>[28]</sup> known the nitroamine molecule **1** shows a strong negative differential resistance; its  $I$ - $V$  is characterized by a threshold at low voltage, followed by a steady and pronounced increase in the current until it reaches a maximum, then it sharply decreases. The steady increase in current is partly attributable to the increase in the TF of the neutral molecule, but is mainly a result of a simultaneous charge of the molecule to  $-1$ . The current for the negative ion is relatively small compared to the corresponding current that could be obtained with the neutral state; however, this is in qualitative agreement with the experiment where only 1 nA is obtained at the peak of the curve through  $\sim 1000$  molecules. The sharp drop observed in the experiment is attributable to a second electron charging the molecule, and yielding a current lower

than the currents for neutral and anion as shown in Fig. 2. These characteristics, together with the fact that the presence of Au atoms stabilizes the first two anions, make this molecule suitable for use as a memory device. Based on experimental observations,<sup>[41,47]</sup> the molecule probably charges with one electron at a voltage between 0.5 and 1.5 V, and most likely one electron is stored at a voltage closer to 0.5 V as a result of the position of the LUMO (Fig. 6), which is accessible for conduction at a bias voltage of 0.6 V, while the second electron is stored at a voltage closer to 1.5 V.

A bias voltage charges (writes) the neutral, and a pulse below 0.5 V allows reading the state of the molecule without altering its charge state—thus the “memory” can be read. If uncharged, the molecule will be in a low impedance state; but if charged, it will be in a high impedance state. The predicted position of the NDR peak is not exactly identical to the experimental observation, probably because of temperature effects<sup>[28]</sup> that we had not considered, and the fact that the experimental setting corresponds to a statistical average of ca. 1000 molecules in parallel.

Molecule **2** (dinitro) had not been experimentally tested (to the best of our knowledge); therefore, its characteristics were inferred from this study. Its anion and dianion were also predicted to be stable against electron ejection. If we assume that the molecule remains uncharged for low voltages, a threshold for conduction is observed. The LUMO of this molecule

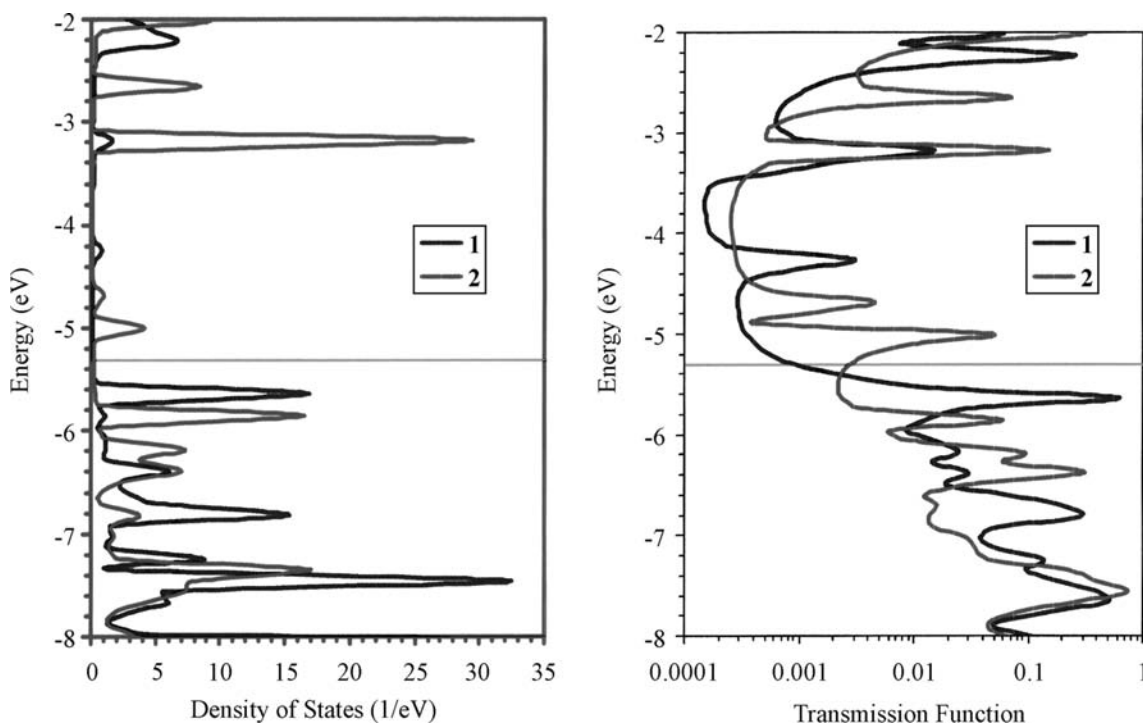


**Fig. 6** Density of states (A) and transmission function (B) for the neutral of **1** (blue) and **2** (red). The position of  $E_F$ , i.e., the interface between the occupied and unoccupied levels, is a 5.31 eV (light blue). *Source:* Adapted from Ref.<sup>[33]</sup>.

is accessible for conduction of electrons from the metal contacts at bias voltage of 2V, thus this molecule will not become charged for lower bias voltages. The storage of one electron in this molecule yields a sharp increase of current. If another electron is stored, a sharp decrease takes place.

NDR is expected in the dinitro molecule, although with a different mechanism than for the nitroamine. Unlike the latter, a range of voltages might be predicted in which the dinitro molecule is in a high conductance state, rather than just a peak. As a result, charged and uncharged states can be easily identified. The dinitro molecule can also perform as memory device. Its neutral shows high impedance, while its single ion shows low impedance. A read pulse should be lower than 2V, the conductance of the neutral and the single charged state are perceptibly different in that range, and the applied voltage is insufficient to charge the molecule if it is uncharged. However, if the write pulse is large enough to doubly charge the molecule, an ambiguity can result, because both neutral and double charge states of the molecule show high impedance.

The nitro groups are known to be electron-withdrawing groups; therefore, when the dinitro is connected to macroscopic tips, electrons are available in the contact flow and could charge the molecule even without an applied voltage, resulting in a current-voltage characteristic that is different from what is expected for the neutral. High conductance is expected at low voltages, with a sudden drop when a second electron is stored. This molecule is stable under the ejection of the second electron, thus keeping the charge until it is forced to discharge. A voltage pulse of more than 2 V writes a nonconducting state in the molecule, and a low voltage pulse will read the molecule statically, i.e., without changing its charge state.

### Molecular Gain

An interesting manifestation of molecular gain was discovered,<sup>[48]</sup> and later calculated by using high levels of theory<sup>[42]</sup> considering two different modes of operation of a single molecule with two phenyl rings. The relative position of these rings, perpendicular or parallel with respect to each other, determines the magnitude of the impedance.

The observed rotational barrier for this molecule is about 0.05 eV, which is the energy needed to shift from the parallel conformation to the perpendicular one. However, when such a shift occurs, the HLG increases to 0.85 eV—in other words, by investing 0.05 eV, the transmission barrier can be changed to 0.85 eV, which corresponds to an amplification factor of 17.

Another important finding of this calculation is the switching capabilities of this molecule, the coplanar

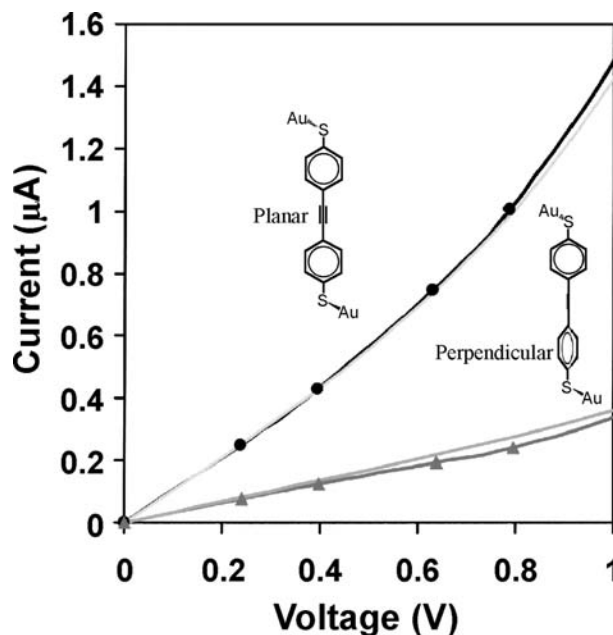


Fig. 7 Demonstration of molecular gain in a thiolane system.

conformation present an impedance of  $\sim 50 \text{ K}\Omega$  at 1 V, whereas for the perpendicular conformation, the impedance is almost  $3 \text{ M}\Omega$ , i.e.,  $\sim 60$  times greater (Fig. 7).

Figure 7 shows the  $I$ - $V$  for both conformations, the planar and rotated conformations. The solid line corresponds to the  $I$ - $V$  obtained after the application of an electric field to the molecule, the dotted line represents the zero-field approximation, i.e., the Hamiltonian at zero bias is used for the entire voltage range. No significant difference between the two approaches is observed for this molecule up to 1 V. Thus the zero-field approximation, unlike that for other molecules, works fairly well here.

### Conducting and Insulating Molecular Devices

Seminario, DeLa Cruz, and Derosa<sup>[49]</sup> demonstrated that molecules of nanometer sizes could still be characterized as low- and high-impedance devices by using quantum ab initio techniques. Low-impedance and high-impedance devices are needed as building blocks for circuits and systems in molecular electronics. Small alkanes and polyene chains with  $\sigma$  and  $\pi$  bonding, respectively, yield a high-low impedance relation of 2 orders of magnitude for changes of 1 nm in length, of 3 orders of magnitude for changes of 1.3 nm in length, and with exponential growth after 0.9 nm. A substantial difference between polyenes and alkanes is observed at small lengths; this difference is unpredictable from what is known about the larger chains.



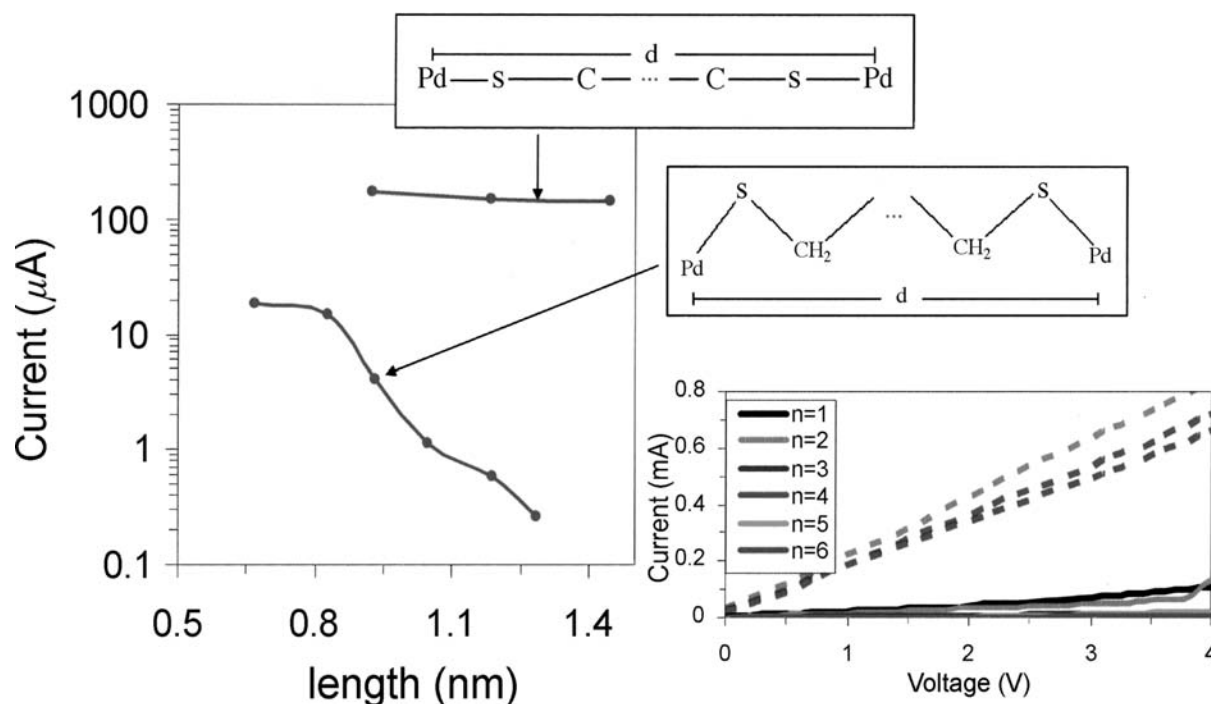


Fig. 8 Variation of the current in the alkanes and polyynes.

The current in the alkanes is relatively low compared with the current in the polyynes. The current in the polyynes increases linearly with the voltage, as shown in Fig. 8, but it does not change too much with the size of the polyyne.

On the other hand, the current through the alkanes is smaller and it decreases very rapidly with the number of C atoms in the chain. Figure 8 also shows, in logarithmic scale, the current at 1 V for all cases. While polyynes do not show a significant change with the size of the chain, the current through alkanes decreases rapidly and almost exponentially for the larger alkanes.

### A Programmable Diode

In searching for new possible molecular devices, Derosa, Guda, and Seminario<sup>[50]</sup> studied the molecule depicted in Fig. 9, the molecule 3-nitro-2-(3'-nitro-2'-ethynylpyridine)-5-pyridinethiol (DNNDP) has two pyridine rings with a nitro group each in a meta position with respect to the N atom in the pyridine. The two rings are separated by a phenylene group. The neutral state of this molecule has a stable configuration for which the rings are almost perpendicular to each other ( $\sim 87^\circ$ ).

To the best of the author's knowledge, this molecule is the only six-member-rings-based molecule separated by phenylene groups that presents a stable configuration for which the rings are not coplanar. Even more interesting, the anion and dianion for the DNNDP are

coplanar, thus the same molecule has a stable state with planar and nonplanar conformations. Figure 10 depicts a comparison with other similar molecules: A) is the DNNDP, B) shows the same molecule but without the nitro groups, i.e. two pyridine rings separated by a phenylene, C) shows a molecule similar to DNNDP but with two phenyl rings instead of pyridines, and D) shows the tolane. The only case where the rings are not parallel is A), the DNNDP.

Provided the anion (or the dianion) are low impedance states, a molecule with this characteristic is desirable as a controllable switch—in which switching can be achieved by controlling the charge or the conformation in the molecule. It can also be used as a

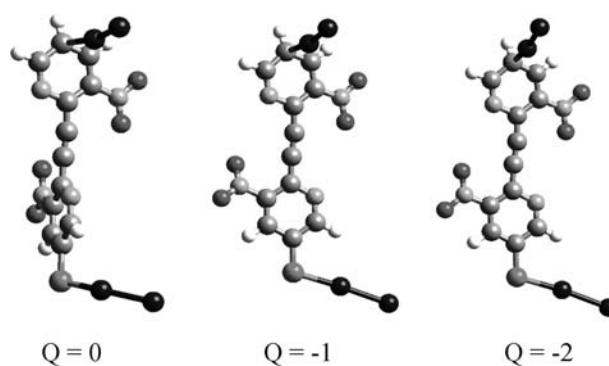
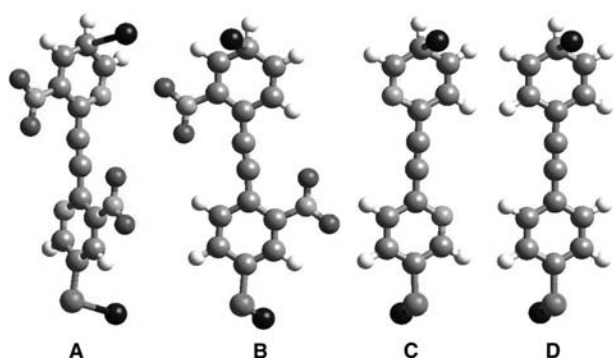


Fig. 9 The dinitro dipyridine molecule. Neutral (left), anion (center), and dianion (right) are shown. Au, C, H, N, and O atoms are green, gray, white, blue, and red respectively.



**Fig. 10** Comparison between related molecules, all of them consisting of two six-member rings separated by a phenylene group: (A) both rings are pyridines and each has a nitro group, (B) both rings are pyridines, (C) both rings are phenyls and each has a nitro group, (D) a toluene molecule. Au, C, H, N, and O atoms are green, gray, white, blue, and red respectively.

memory device when connected to two contacts—the molecule can be written by using an external field to control the relative rotation of the rings; this is possible because the presence of the nitro group gives the rings a dipole moment that will interact with the external field. To write a *zero*, we need to induce the non-coplanar conformation; to write a *one*, we need to force the rings to be coplanar and the molecule will grab a charge from the contacts because it is energetically favorable. To read the molecule, we need to sense its current by attaching the molecule ends to contacts: high impedance means zero (rings noncoplanar and the molecule is neutral), low impedance means one (rings coplanar, and the molecule is ionized). Alternatively, this molecule can be a nanoactuator, if we control the charge state; we can induce rotation by charging or discharging the molecule.

The  $I$ - $V$  for this molecule was calculated by attaching two Au atoms on one end to a S atom, and attaching another two Au atoms to the other end, directly bonded to the pyridine ring. The  $I$ - $V$  curves are shown in Fig. 11, as expected, the neutral is a poor conductor

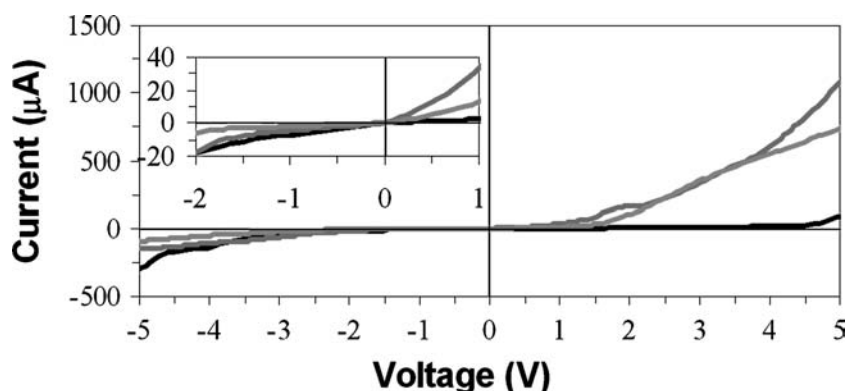


**Fig. 11** Current-vs.-voltage curves for the neutral (black), anion (orange), and dianion (blue). The inset shows details at the low voltage range.

while the anion and dianion conduct very well for positive bias (“+” on the vapor deposited end-top in the figure, and “-” on the self-assembly end) and poorly for negative bias. The different nature of the contacts provides this system with an even more attractive application—it can work as a programmable diode; it will behave as a diode if charged, but it can be turned off if we uncharge the molecule.

The idea of using an external field to induce switching was not born with this molecule, molecules with three phenyl rings were modified by attaching substituents to give this central ring a finite dipole moment to interact with the external field.<sup>[41,51]</sup> Switches based on this idea are schematically represented in Fig. 12.

### Metal Alligator Clip Interactions

Several works were devoted to understand the nature of the molecule–contact interface, and several other models have been proposed.<sup>[23,52–57]</sup> Through the characterization of different metallic contacts as they interact with the molecular device through different alligator clips, it was demonstrated that the best alligator clip corresponds to S, which is, however, not much better than the isonitryl (NC) alligator clip. It was predicted that the best metal for the metal–molecule interface corresponds to Pd, followed by Ni and Pt. Cu can be considered intermediate, and the worst cases correspond to Au and Ag (Fig. 13).

The impact of this study has been accepted at several research environments, including experimental ones, in which Pd and Pt have been considered as main substituents for Au, the metal that had been extensively used as contact for many nanotechnology approaches.<sup>[58]</sup>

A benzene ring bonded through a S or CN group to six different metallic atoms (Ni, Cu, Pd, Ag, Au, and Pt) at each end was fully studied. The  $I$ - $V$  curves were compared with each other, and conclusions were drawn about the best clip–metal combination. For this particular calculation, no electric field was applied to

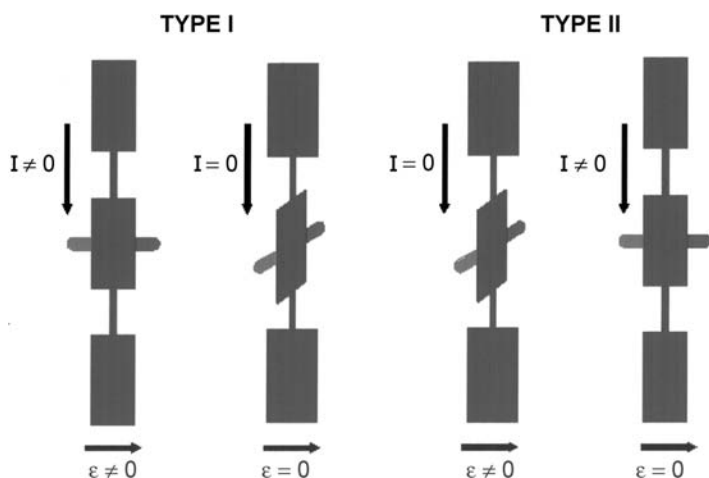


**Fig. 12** Complementary molecular field effect transistors (CMolFETs): The current through molecules is controlled by an external electric field able to rotate the central part of the molecule. To perform an electronic function, complementary types of molecules are required: Type I are ON when no field is applied and OFF when a field is applied, whereas the opposite takes place for type II molecules.

the molecule, and complementary calculations indicated that frontier MOs of a single benzene ring are hardly affected by the external field, thus unimportant differences would have been found if a field had been applied.

### The Metal–Molecule Interface

Derosa and Seminario also provided the theoretical proof that solved a controversial issue for both experimentalists and theoreticians, which involved the metal–molecule interface geometry.<sup>[29,33]</sup> They demonstrated through the geometrical optimization of different systems that the interaction between the clip and the gold surface is achieved through only one Au atom, rather than through two or three Au atoms, i.e., S tends to bond to one Au atom only. The system analyzed was a single benzene ring attached through a S clip to Au

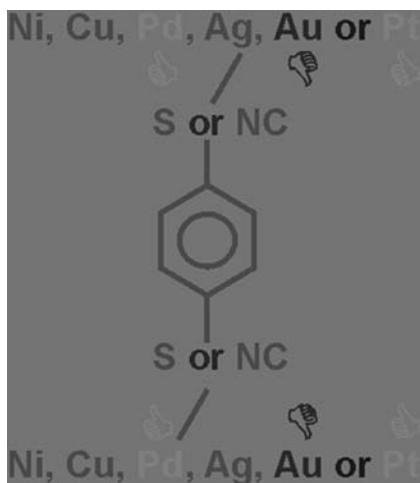


**Fig. 13** The study of the molecule–contact interfaces provided information about the best way to interconnect molecular systems.

atoms (we considered from one Au atom to five Au atoms). Benzene was chosen because it represents the end group of many molecules very commonly used for molecular electronics, a series of phenyl-based oligomers, and provided an insight into the nature of the metal–molecule interface on a self-assembled monolayer, and the metal–molecule interface on a vapor-deposited metal from *ab initio* DFT.<sup>[59]</sup> The analysis is based on the ability of the Kohn–Sham MOs to determine the electron transport characteristics of single molecules when they are attached to metallic contacts. The geometry optimization performed for all the studied systems used a high-accuracy convergence criterion, and one of the best tradeoffs between precision and cost. Furthermore, the theoretical results reasonably reproduce available experimental evidence.

The self-assembly process consists of the deposition of the molecules over a Au surface; thus, the metallic surface suffers minimal perturbations by the presence of the deposited structure. Accordingly, results show that the interaction between the clip and the gold surface is achieved through only one Au atom, rather than through two or three Au atoms. We predicted a S–Au bond of  $\sim 2.45$  Å and a C–S–Au of  $\sim 105^\circ$ . Considering S in a hollow site attached to three Au atoms in the exact center of the triangle, it is not compatible with the geometry we predicted; if S–Au is 2.45 Å, then the angle C–S–Au is  $137^\circ$  (Au–Au distance in a crystal is 2.88 Å). On the other hand, if the angle C–S–Au is considered  $105^\circ$ , in agreement with our predictions, then the S–Au distance should be  $\sim 1.7$  Å. Either way, we end up with a very high strain configuration, thus a very unstable bond, which is incompatible with the experimental finding that S is a good clip to attach organic molecules to metal surfaces. S, even when it can be above a triangle of Au atoms, cannot be in the center but mainly attached to one of the Au atoms. In short, even if S is above a triangle of three metal

atoms, it will not be in the bare center, but closer to one of the atoms in the triangle; such a Au atom is the one with the highest interaction with the S alligator *clip*. In some cases, the S clip is bonded to two Au atoms; however, the structure becomes energetically less favorable.

### Charge Effect on the Contacts

In a study of the dinitro and nitroamine molecule, Seminario, Zacarias, and Derosa<sup>[33]</sup> determined that all the charge transferred from the Au atoms to the molecule is taken from the Au directly connected to the phenyl ring, and almost no charge is taken from or added to the Au bonded to the S. Therefore, there will be substantial differences when S connects the molecule to the Au atoms at both ends. A calculation of nitroamine molecule, but with two Au atoms in the upper ring instead of one, yields a total charge of 0.38 in the two Au atoms. When three Au atoms are connected at each end of the molecule, the S–Au<sub>3</sub> group at the S end is neutral, while the Au<sub>3</sub> group at the other end bears a total charge of 0.48. This structure has two Au atoms directly connected to the S on one end, and one Au atom connected to the aryl ring on the other end. On the S side, the Au atom not directly connected to S has a charge of –0.2, while the S is positive by the same amount. The Au atoms directly attached to the S are neutral. On the other end, the Au directly attached to the C in the ring holds almost all the charge at that end (+0.46), while the other two Au are almost neutral. This indicates that, even when each nitro group can store up to half an electron, the molecule only takes less than half an electron from the contact with no S. When the nitroamine and the dinitro molecules are charged, part of the charge is stored in the Au atoms rather than in the molecule. For dianions, almost one electron for the dinitro and over one electron for the nitroamine are stored in the Au atoms, plus the sulfur. The fact that the Au atoms adsorb part of the charge does not imply that the molecule cannot become charged with two electrons; in fact, there is no definite limit in the real system where we can distinguish the molecule from the contacts. Certainly, the few first Au atoms making contact to the molecule have to be considered part of the molecule. Most of the charge transferred to the molecule comes from the Au atoms directly attached to the upper ring, irrespective of how many Au atoms are directly connected to the upper ring, or whether there are other Au atoms connected to them. Independently of how the molecule is connected to Au, the amount of charge in the molecule is half of an electron. The Au atoms attached to the upper ring are positive, and compensate the charge in the rest of the molecule.

Even if the molecule is not intrinsically charged at 0 V, it can be easily precharged before its use by applying a bias voltage, and therefore this molecule can operate in another mode with two charge states, –1 and –2.

### Geometry Effects of the Metallic Contacts

To make sure that a more detailed representation of the interface geometry does not strongly affect the electrical characteristics of the molecule, the original geometry in the dinitro and nitroamine molecules, described in the previous sections, was modified by adding one H atom bonded to the C on the vapor deposited end and two more Au atoms on the self-assemble monolayer (SAM) side, such that the S atom is on a hollow site of three Au atoms. The geometries for Au–(2'-nitro-4-ethynylphenyl-4'-ethynylphenyl-5'-nitro-1-benzenethiolate)–Au<sub>3</sub> (**1''**) and Au–(2'-amino-4-ethynylphenyl-4'-ethynylphenyl-5'-nitro-1-benzene thiolate)–Au<sub>3</sub> (**2''**) were partially optimized in the following manner: one Au atom is placed randomly close to a fully optimized benzene ring; then the calculation runs until a local minimum is obtained and it is confirmed by a second derivative calculation of the energy. This full benzene ring plus Au atom system is substituted into the molecules. This forms molecules that are most likely more realistic than those used before. For the S-ended side of the molecule, a triad of Au atoms is optimized and an S atom is placed on the hollow site and optimized with a constraint of C<sub>3v</sub> symmetry. Such a structure is unstable, thus the constraint is needed to represent a possible (111) surface hollow site of an Au crystal. Next, a benzene ring is attached to the S of the Au<sub>3</sub>S system, keeping the Au<sub>3</sub>S base fixed and letting the benzene ring to reach its most stable configuration with respect to the Au<sub>3</sub>S system.

The addition of a C–H bond to the system does not change the frontier MOs or those around them, as shown in Fig. 14. Therefore electrical characteristics, such as the *I*–*V* curve, are not affected. As long as the electronic structure around the Fermi level is the same, drastic changes in the geometry of the system only slightly affect the results. The metal geometry at the interface may add impedance, but the main features, such as NDR, are mostly governed by the molecular conformation in the central ring. This is supported by experiments, which show good reproducibility in the electrical characteristics when measuring several samples of the same molecule. It is expected that the geometry of the vapor deposited Au is different from sample to sample; however, results are reproducible as shown in Ref.<sup>[46]</sup>. On the other hand, it has been shown that the shape of the *I*–*V* curves changes radically when the substituents in the central ring,

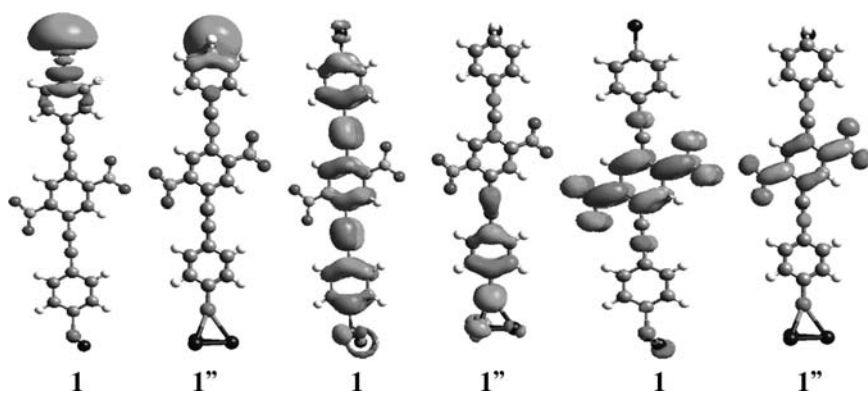


**Fig. 14** MOs of **1** and **1''** showing the effects of adding one H and two Au atoms to **1**. (A) LUMO + 3 of **1** and HOMO of **1''**, (B) HOMO of **1** and **1''**, (C) LUMO of **1** and **1''**. Source: Adapted from Ref.<sup>[33]</sup>.

which are those that strongly modify the frontier MOs, are changed. The substituents determine the nature of the molecular device. Thus the contacts do not affect the main characteristic of the device. Conduction is practically attributable to antibonding orbitals, rather than bonding ones, which are much more stable and much lower in energy than the Fermi energy of the metallic contacts. Neither the H bonded to a C nor the addition of more Au atoms contribute to the main channels of conduction through the molecule, because they only contribute with very stable bonding or very unstable antibonding MOs, all of them well localized. Nevertheless, the presence of the C–H or C–Au bonds provides marked and contrasting suggestions on how the contacts were created. A cleavage of the C–H bond could lead to strong damage of the nanopore, and this is certainly of paramount importance for a study of metal vapor deposition. On the other hand, the addition of more gold atoms simply increases the number of localized MOs, but they do not contribute to electron conduction.

Although the correct geometry in the experiment is unknown, the authors believe that the geometry with the S symmetrically centered on a hollow site, sometimes used in theoretical calculations, is chemically and physically impossible. This assertion is based on experimental<sup>[1]</sup> information and theoretical calculations,<sup>[29]</sup> which determine that S should be bonded to just one Au atom. Notice that constraining the geometry is the only way a S atom can be kept in the geometric center of Au triangle—thus confirming our affirmation that this geometry is not realistic. The extended nature of the surface may not be really relevant because the attachment of the molecule to the surface is strongly dominated by local effects. Even assuming that the SAM was performed on a perfect (111) surface, there is evidence that the angles are the correct ones. For instance, an angle of 107° is reported for the bond angle of Au–S–C when alkanes are used.<sup>[60]</sup> This is in agreement with calculations yielding 102° in a slightly different environment. There is experimental evidence indicating that the metal–S–C

angle is 104°,<sup>[61]</sup> which agrees with the theoretical predictions described in this section. Angles on the order of ~150° are certainly a possibility, but they yield substantially less stable structures as observed experimentally<sup>[60]</sup> and theoretically.<sup>[29]</sup>

In summary, interpreting that S is in a hollow site might lead to confusion. The fact is that S does not position itself symmetrically above the center of an Au<sub>3</sub> triangle. The geometry suggested in this section is compatible and in perfect agreement with the experimental findings that S is on a hollow site. However, the S atom does not remain at the center of the triad. We assume two possible and realistic bond angles for S, 90° and 100°, connecting an oligomer chain, thus making a tilt angle of 30° with the normal to the surface, as is already established experimentally for some alkanes.<sup>[60,62]</sup>

### Search for Minimum Molecular Programmable Units

Molecular electronics can be developed if we are able to program a RANDOM arrangement of molecules or a field programmable molecular random array. Preliminary simulations have shown that programming this molecular arrays is possible,<sup>[63–65]</sup> however, schemes for implementing these programming techniques still need to be realized and that starts by characterizing the smallest molecular system with programmable features. Present programs for the calculation of current–voltage characteristics of electronic circuits, needed for such demonstrations, are only able to predict single-valued characteristics. A procedure exists to incorporate molecular physics procedures with a practical analysis of molecular circuits having strong non-linearities.<sup>[6]</sup> The highly non-linear current–voltage (*I*–*V*) characteristics shown by some molecules open up a complete new set of possibilities for operational circuits. However, the engineering design becomes more complex and new approaches should be developed because traditional tools for circuit analysis are prepared to deal mostly with linear

components. Combinations of nonlinear systems yield circuits with multivalued characteristics. Thus determining all the possible states of the circuits is of fundamental importance to characterize operational modes defined as set of states allowed under normal operation. A special signal, usually large in magnitude, above a threshold, can be used to drive this system from one operational mode to another. This flexibility allows more than one  $I$ - $V$  curve for each device, facilitating the programming of molecular circuits.

The first step in the design flow of moletronics systems is to determine the electrical properties of single molecules. Theoretical methods allow scientists to study systems comprising a molecular system interconnected by small metal clusters. Triangular patterns made of gold clusters interconnecting molecules are expected to be the building blocks of moletronics functional units, for which all of their possible functional states need to be characterized. The analysis of possible configurations allowed by self-assembly procedures needs to be performed to find possible programmable units. When programmable molecular units of a given geometrical structure are found, the candidate molecule goes through the simulation loop until the simulated system yields programmable characteristics, otherwise the molecule is discarded and another, with different  $I$ - $V$  characteristics, is chosen. Molecules with

highly non-linear current–voltage ( $I$ - $V$ ) curves are preferred because of their ability to create switchable states. The simulation loop, looking for a programmable molecular unit, begins with the proposal of new single molecular devices and their characterization utilizing ab initio principles. The next step is the characterization of simple combinations of series and parallel circuits of a few units, then functional units can be studied. These minimum programmable units are then combined in larger circuits with more versatility, leading to field programmable molecular random arrays.<sup>[65]</sup>

### Testbed for Molecular Architectures

Having made a considerable effort to characterize the molecular device, a design paradigm for molecular electronics is simulated to demonstrate that clusters of devices showing negative differential molecular impedance can be used as minimum programmable units.<sup>[6,64,66]</sup> These molecular-scale resonant tunneling devices show features of multiple-valued logic and memory. The plausibility of programmability of minimum molecular units arranged in triangular structures, which are similar to the (111) surface of a face centered cubic crystal, are shown in Fig. 15. In general,

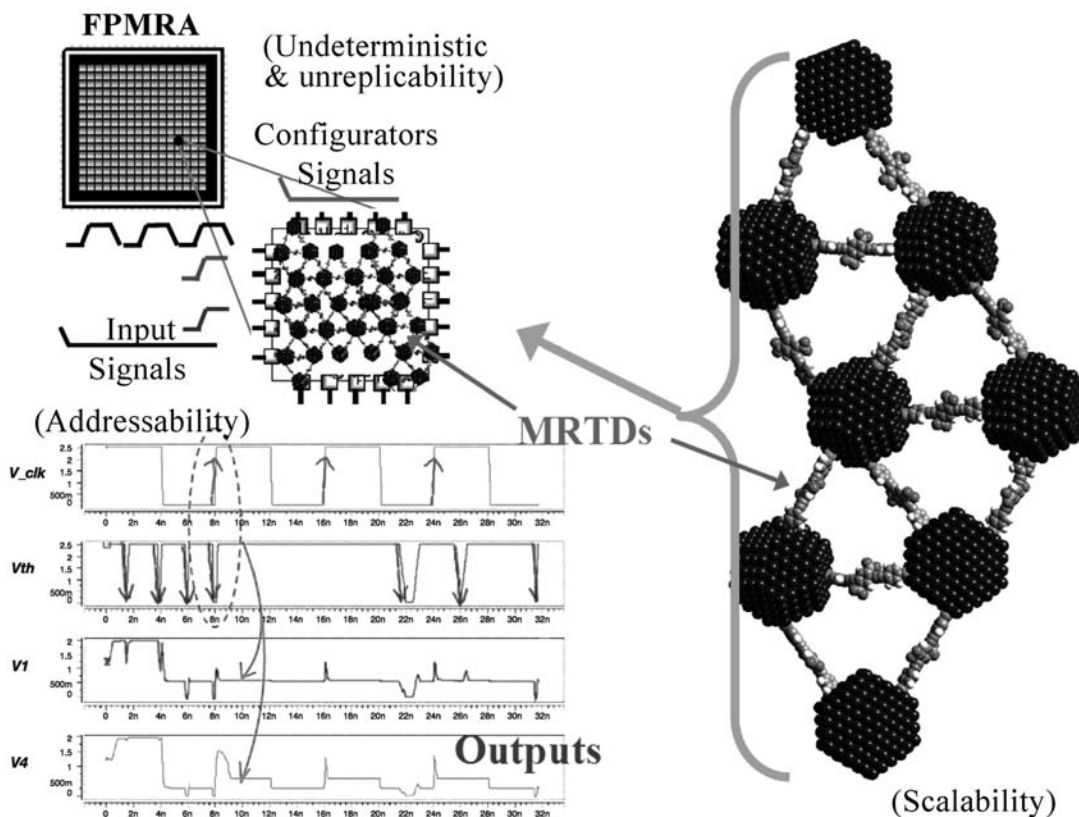


Fig. 15 Design of configurable random molecular logic units.



minimum units can be used as multivalued logic blocks.<sup>[64,66,67]</sup> Input, output, and control signals can be used to program the molefabric to a specific function, which can be accomplished by using artificial intelligence techniques such as neural networks and evolutionary techniques. Future work is needed to test other individual molecules until an optimum molecule, with adequate  $I$ - $V$  characteristics, is found for an efficient learning process of the molefabric.

## CONCLUSION

The field of moletronics is certainly exciting. Modern semiconductor devices are already facing complications with further size reduction, and are now forced to consider quantum mechanical effects as transistor sizes become increasingly smaller. It is believed that the semiconductor industry will soon hit a practical device size limit, and at that point, it will be necessary to pursue alternate computing strategies to further reduce size and power consumption, while providing increased computing power. Moletronics is one such alternative. Because molecules are on the nanometer scale, using them as electrical switches will provide an innate reduction in size, and the high molecular densities that can be achieved should lead to increased computing power. However, it is not expected that moletronics will replace conventional electronics; rather, it will complement it. The small molecular size also introduces many difficulties that must be overcome before moletronic devices can become a reality.

In this entry, we have discussed the methods used to calculate the electronic and electron transport properties of moletronic systems with programmability characteristics, as well as some applications of these methods. Theoretical results showed excellent consistency with experiments and explained experimental phenomena that were observed prior to these simulations, and recently theory was also able to predict experimental outcomes before the actual experiment were performed. This predictive capability enables molecular simulations to actually design molecular components and recommend to experimentalists the most appropriate systems to be tested. Finally, the search for minimum molecular programmable units and how these units may be used for computing purposes were discussed to explain the analysis and design flow of molecular devices.

## ACKNOWLEDGMENTS

We acknowledge Angelica Zacarias, Luis Cordova, Cecilia de la Cruz, Suneel Guda, Hernan Figueroa, and Jimena Bastos, who participated in an earlier work

being reviewed in this article. We also thank David McClard, Nagendra Vadlamani, and Sridhar Bingi for their assistance with the details of the manuscript. We thank James Tour from Rice University for his invaluable contribution to some of the work referred to in this manuscript. We highly appreciate the support of ARO under grants DAAD19-00-1-(0154, 0592, 0634) and DAAD19-99-1-0085, DARPA/ONR under grant N00014-01-1-0657, and the USC NanoCenter.

## REFERENCES

1. Reed, M.A.; Zhou, C.; Muller, C.J.; Burgin, T.P.; Tour, J.M. Conductance of a molecular junction. *Science* **1997**, *278*, 252–254.
2. Llang, W.; Shores, M.P.; Bockrath, M.; Long, J.R.; Park, H. Kondo resonance in a single-molecule transistor. *Nature* **2002**, *417*, 725–729.
3. Park, J.; Pasupathy, A.N.; Goldsmith, J.I.; Chang, C.; Yaish, Y.; Petta, J.R.; Rinkoski, M.; Sethna, J.P.; Abruñas, H.D.; McEuen, P.L.; Ralph, D.C. Coulomb blockade and the Kondo effect in single-atom transistors. *Nature* **2002**, *417*, 722–725.
4. Collier, C.P.; Mattersteig, G.; Wong, E.W.; Luo, Y.; Beverly, K.; Sampaio, J.; Raymo, F.M.; Stoddart, J.F.; Heath, J.R. A [2]catenane-based solid state electronically reconfigurable switch. *Science* **2000**, *289*, 1172–1175.
5. Türel, Ö.; Likharev, K. CrossNet: Possible neuro-morphic networks based on nanoscale components. *Int. J. Circuit Theory Appl.* **2003**, *31*, 37–53.
6. Seminario, J.M.; Cordova, L.E.; Derosa, P.A. An ab initio approach to the calculation of current–voltage characteristics of programmable molecular devices. *Proc. IEEE* **2003**, *91*, 1958–1975.
7. Frisch, M.J.; Trucks, G.W.; Schlegel, H.B.; Scuseria, G.E.; Robb, M.A.; Cheeseman, J.R.; Zakrzewski, V.G.; Montgomery, J.A., Jr.; Stratmann, R.E.; Burant, J.C.; Dapprich, S.; Millam, J.M.; Daniels, A.D.; Kudin, K.N.; Strain, M.C.; Farkas, O.; Tomasi, J.; Barone, V.; Cossi, M.; Cammi, R.; Mennucci, B.; Pomelli, C.; Adamo, C.; Clifford, S.; Ochterski, J.; Petersson, G.A.; Ayala, P.Y.; Cui, Q.; Morokuma, K.; Malick, D.K.; Rabuck, A.D.; Raghavachari, K.; Foresman, J.B.; Cioslowski, J.; Ortiz, J.V.; Stefanov, B.B.; Liu, G.; Liashenko, A.; Piskorz, P.; Komaromi, I.; Gomperts, R.; Martin, R.L.; Fox, D.J.; Keith, T.; Al-Laham, M.A.; Peng, C.Y.; Nanayakkara, A.; Gonzalez, C.; Challacombe, M.; Gill, P.M.W.; Johnson, B.; Chen, W.; Wong, M.W.; Andres, J.L.; Gonzalez, C.; Head-Gordon, M.; Replogle, E.S.; Pople, J.A. *GAUSSIAN-98*; Gaussian Inc.: Pittsburgh, PA, 1998.
8. Frisch, M.J.; Trucks, G.W.; Schlegel, H.B.; Scuseria, G.E.; Robb, M.A.; Cheeseman, J.R.; Montgomery, J.A., Jr.; Vreven, T.; Kudin, K.N.; Burant, J.C.; Millam, J.M.; Iyengar, S.S.; Tomasi, J.; Barone, V.; Mennucci, B.; Cossi, M.; Scalmani, G.; Rega, N.; Petersson, G.A.; Nakatsuji, H.; Hada, M.; Ehara, M.; Toyota,

- K.; Fukuda, R.; Hasegawa, J.; Ishida, M.; Nakajima, T.; Honda, Y.; Kitao, O.; Nakai, H.; Klene, M.; Li, X.; Knox, J.E.; Hratchian, H.P.; Cross, J.B.; Adamo, C.; Jaramillo, J.; Gomperts, R.; Stratmann, R.E.; Yazyev, O.; Austin, A.J.; Cammi, R.; Pomelli, C.; Ochterski, J.W.; Ayala, P.Y.; Morokuma, K.; Voth, G.A.; Salvador, P.; Dannenberg, J.J.; Zakrzewski, V.G.; Dapprich, S.; Daniels, A.D.; Strain, M.C.; Farkas, O.; Malick, D.K.; Rabuck, A.D.; Raghavachari, K.; Foresman, J.B.; Ortiz, J.V.; Cui, Q.; Baboul, A.G.; Clifford, S.; Cioslowski, J.; Stefanov, B.B.; Liu, G.; Liashenko, A.; Piskorz, P.; Komaromi, I.; Martin, R.L.; Fox, D.J.; Keith, T.; Al-Laham, M.A.; Peng, C.Y.; Nanayakkara, A.; Challacombe, M.; Gill, P.M.W.; Johnson, B.; Chen, W.; Wong, M.W.; Gonzalez, C.; Pople, J.A. *GAUSSIAN-2003*; Gaussian, Inc.: Pittsburgh, PA, 2003.
9. Becke, A.D. Density-functional thermochemistry. III. The role of exact exchange. *J. Chem. Phys.* **1993**, *98*, 5648–5652.
  10. Perdew, J.P.; Chevary, J.A.; Vosko, S.H.; Jackson, K.A.; Pederson, M.R.; Singh, D.J.; Fiolhais, C. Atoms, molecules, solids, and surfaces: applications of the generalized gradient approximation for exchange and correlation. *Phys. Rev., B* **1992**, *46*, 6671–6687.
  11. Perdew, J.P.; Wang, Y. Accurate and simple analytic representation of the electron-gas correlation energy. *Phys. Rev., B* **1992**, *45*, 13,244–13,249.
  12. Wadt, W.R.; Hay, P.J. Ab initio effective core potentials for molecular calculations. Potentials for main group elements Na to Bi. *J. Chem. Phys.* **1985**, *82*, 284–298.
  13. Hay, P.J.; Wadt, W.R. Ab initio effective core potentials for molecular calculations. Potentials for the transition metal atoms Sc to Hg. *J. Chem. Phys.* **1985**, *82*, 270–283.
  14. Hay, P.J.; Wadt, W.R. Ab initio effective core potentials for molecular calculations. Potentials for K to Au including the outermost core orbitals. *J. Chem. Phys.* **1985**, *82*, 299–310.
  15. Foresman, J.B.; Frisch, A. *Exploring Chemistry with Electronic Structure Methods*; Gaussian: Pittsburgh, 1996.
  16. Seminario, J.M.; Zacarias, A.G.; Tour, J.M. Molecular alligator clips for single molecule electronics. Studies of group 16 and isonitriles interfaced with Au contacts. *J. Am. Chem. Soc.* **1999**, *121*, 411–416.
  17. Seminario, J.M.; Zacarias, A.G.; Tour, J.M. Molecular current–voltage characteristics. *J. Phys. Chem., A* **1999**, *103*, 7883–7887.
  18. Zacarias, A.G.; Castro, M.; Tour, J.M.; Seminario, J.M. Lowest energy states of small Pd clusters using density functional theory and standard ab initio methods. A route to understanding metallic nanoprobles. *J. Phys. Chem., A* **1999**, *103*, 7692–7700.
  19. Seminario, J.M.; Zacarias, A.G.; Castro, M. Systematic study of the lowest energy states of Pd, Pd<sub>2</sub>, and Pd<sub>3</sub>. *Int. J. Quantum Chem.* **1997**, *61*, 515–523.
  20. Balbuena, P.B.; Derosa, P.A.; Seminario, J.M. Density functional theory study of copper clusters. *J. Phys. Chem., B* **1999**, *103*, 2830–2840.
  21. Mujica, V.; Kemp, M.; Ratner, M.A. Electron conduction in molecular wires. I. A scattering formalism. *J. Chem. Phys.* **1994**, *101*, 6849–6855.
  22. Mujica, V.; Kemp, M.; Ratner, M.A. Electron conduction in molecular wires. II. Application to scanning tunneling microscopy. *J. Chem. Phys.* **1994**, *101*, 6856–6864.
  23. Yaliraki, S.N.; Kemp, M.; Ratner, M.A. Conductance of molecular wires: Influence of molecule–electrode binding. *J. Am. Chem. Soc.* **1999**, *121*, 3428–3434.
  24. Yaliraki, S.N.; Roitberg, A.E.; Gonzalez, C.; Mujica, V.; Ratner, M.A. The injecting energy at molecule/metal interfaces: Implications for conductance of molecular junctions from an ab initio molecular description. *J. Chem. Phys.* **1999**, *111*, 6997–7002.
  25. Datta, S. *Electronic Transport in Mesoscopic Systems*; Cambridge University Press: Cambridge, UK, 1995.
  26. Samanta, M.P.; Tian, W.; Datta, S.; Henderson, J.I.; Kubiak, C.P. Electronic conduction through organic molecules. *Phys. Rev., B* **1996**, *53*, R7626–R7629.
  27. Datta, S.; Tian, W.; Hong, S.; Reifenberger, R.; Henderson, J.; Kubiak, C.P. Current–voltage characteristics of self-assembled monolayers by scanning tunneling microscopy. *Phys. Rev. Lett.* **1997**, *79*, 2530–2533.
  28. Seminario, J.M.; Zacarias, A.G.; Tour, J.M. Theoretical study of a molecular resonant tunneling diode. *J. Am. Chem. Soc.* **2000**, *122*, 3015–3020.
  29. Derosa, P.A.; Seminario, J.M. Electron transport through single molecules: Scattering treatment using density functional and green function theories. *J. Phys. Chem., B* **2001**, *105*, 471–481.
  30. Papaconstantopoulos, D.A. *Handbook of the Band Structure of Elemental Solids*; Plenum Press: New York, 1986.
  31. Tian, W.; Datta, S.; Hong, S.; Reifenberger, R.; Henderson, J.I.; Kubiak, C.P. Conductance spectra of molecular wires. *J. Chem. Phys.* **1998**, *109*, 2874–2882.
  32. Ventra, M.D.; Kim, S.-G.; Pantelides, S.T.; Lang, N.D. Temperature effects on the transport properties of molecules. *Phys. Rev. Lett.* **2001**, *86*, 288–291.
  33. Seminario, J.M.; Zacarias, A.G.; Derosa, P.A. Analysis of a dinitro-based molecular device. *J. Chem. Phys.* **2002**, *116*, 1671–1683.
  34. Lide, D.R. *CRC Handbook of Chemistry and Physics*; CRC Press: Boca Raton, 1998. Vol. 79th Edition 1998–1999.
  35. Seminario, J.M.; Zacarias, A.G.; Derosa, P.A. Theoretical analysis of complementary molecular memory devices. *J. Phys. Chem., A* **2001**, *105*, 791–795.
  36. Roetti, C. The CRYSTAL Code. In *Lecture Notes in Chemistry*; Pisani, C., Ed.; Springer-Verlag: Berlin, 1996; Vol. 67, 125–137.
  37. Dovesi, R.; Roetti, C.; Causa, M.; Apra, E.; Orlando, R.; Saunders, V.R.; Harrison, N.M. *Crystal* 98, [http://www.ccwp.ac.uk/ccwp/cg\\_crystal.html](http://www.ccwp.ac.uk/ccwp/cg_crystal.html)
  38. Towler, M.D.; Zupan, A.; Causa, M. Density functional theory in periodic systems using local Gaussian basis sets. *Comput. Phys. Commun.* **1996**, *98*, 181–205.
  39. Cundari, T.R.; Stevens, W.J. Effective core potentials methods for the lanthanides. *J. Chem. Phys.* **1993**, *98*, 5555–5565.
  40. Stevens, W.J.; Krauss, M.; Basch, H.; Jasien, P.G. Relativistic compact effective potentials and efficient,

- shared-exponent basis-sets for the 3rd-row, 4th-row, and 5th-row atoms. *Can. J. Chem.* **1992**, *70*, 612–630.
41. Chen, J.; Reed, M.A.; Rawlett, A.M.; Tour, J.M. Large on–off ratio negative differential resistance in a molecular electronic device. *Science* **1999**, *286*, 1550–1552.
  42. Seminario, J.M.; Derosa, P.A. Molecular gain in a thiotolane system. *J. Am. Chem. Soc.* **2001**, *123*, 12,418–12,419.
  43. Donhauser, Z.J.; Mantooh, B.A.; Kelly, K.F.; Bumm, L.A.; Monnell, J.D.; Stapleton, J.J.; Price, D.W., Jr.; Rawlett, A.M.; Allara, D.L.; Tour, J.M.; Weiss, P.S. Conductance switching in single molecules through conformational changes. *Science* **2001**, *292*, 2303–2307.
  44. Tour, J.M.; Kosaki, M.; Seminario, J.M. Molecular scale electronics: a synthetic/computational approach to digital computing. *J. Am. Chem. Soc.* **1998**, *120*, 8486–8493.
  45. Tour, J.M.; Kozaki, M.; Seminario, J.M. Use of molecular electrostatic potential for molecular scale computation. . US Patent 6,259,277, 2001.
  46. Reed, M.A.; Chen, J.; Rawlett, A.M.; Price, D.W.; Tour, J.M. Molecular random access memories. *Appl. Phys. Lett.* **2001**, *78*, 3735–3737.
  47. Chen, J.; Wang, W.; Reed, M.A.; Rawlett, A.M.; Price, D.W.; Tour, J.M. Room-temperature negative differential resistance in nanoscale molecular junctions. *Appl. Phys. Lett.* **2000**, *77*, 1224–1226.
  48. Seminario, J.M.; Zacarias, A.G.; Tour, J.M. Theoretical interpretation of conductivity measurements of thiotolane sandwich. A molecular scale electronic controller. *J. Am. Chem. Soc.* **1998**, *120*, 3970–3974.
  49. Seminario, J.M.; De La Cruz, C.; Derosa, P.A. Nanometer-size conducting and insulating molecular devices. *Chem. Phys. Lett.* **2003**. Submitted.
  50. Derosa, P.A.; Guda, S.; Seminario, J.M. A programmable molecular diode driven by charge-induced conformational changes. *J. Am. Chem. Soc.* **2003**, *125*, 14,240–14,241.
  51. Chen, J.; Calvet, L.C.; Reed, M.A.; Carr, D.W.; Grubisha, D.S.; Bennett, D.W. Electronic transport through metal-1,4-phenylene diisocyanide–metal junctions. *Chem. Phys. Lett.* **1999**, *313*, 741–748.
  52. Vondrak, T.; Wang, H.; Winget, P.; Cramer, C.J.; Zhu, X.-Y. Interfacial electronic structure in thiolate self-assembled monolayers: implication for molecular electronic. *J. Am. Chem. Soc.* **2000**, *122*, 4700–4707.
  53. Yaliraki, S.N.; Ratner, M.A. Molecule-interface coupling effects on electronic transport in molecular wires. *J. Chem. Phys.* **1998**, *109*, 5036–5043.
  54. Emberly, E.G.; Kirczenow, G. Theoretical study of electrical conduction through a molecule connected to metallic nanocontacts. *Phys. Rev., B* **1998**, *58*, 10,911–10,920.
  55. Selzer, Y.; Salomon, A.; Cahen, D. The importance of chemical bonding to the contact for tunneling through alkyl chains. *J. Phys. Chem., B* **2002**, *106*, 10,432–10,439.
  56. Cahen, D.; Hodes, G. Molecules and electronic materials. *Adv. Mater.* **2002**, *14*, 789–798.
  57. Onipko, A.; Klymenko, Y.; Malysheva, L. Conductance of molecular wires: analytical modeling of connection to leads. *Phys. Rev., B* **2000**, *62*, 10480–10493.
  58. Shashidhar, R. *Report to DARPA Moletronics Program*; 2002.
  59. Derosa, P.A.; Zacarias, A.C.; Seminario, J.M. Application of density functional theory to the study and design of molecular electronic devices: the metal–molecule interface. In *Reviews in Modern Quantum Chemistry*; Sen, K.D., Ed.; World Scientific: Singapore, 2002; 1537–1567.
  60. Ulman, A. Formation and structure of self-assembled monolayers. *Chem. Rev.* **1996**, *96*, 1533–1554.
  61. Heister, K.; Rong, H.-T.; Buck, M.; Zharnikov, M.; Grunze, M. Odd–even effects at the S–metal interface and in the aromatic matrix of biphenyl-substituted alkanethiol self-assembled monolayers. *J. Phys. Chem., B* **2001**, *105*, 6888–6894.
  62. Haag, R.; Rampi, M.A.; Holmlin, R.E.; Whitesides, G.M. Electrical breakdown of aliphatic and aromatic self-assembled monolayers used as nanometer-thick organic dielectrics. *J. Am. Chem. Soc.* **1999**, *121*, 7895–7906.
  63. Tour, J.M.; VanZandt, W.L.; Husband, C.P.; Husband, S.M.; Wilson, L.S.; Franzon, P.D.; Nackashi, D.P. NanoCell logic gates for molecular computing. *IEEE Trans. Nanotechnol.* **2002**, *1*, 100–109.
  64. Seminario, J.M.; Cordova, L.E.; Derosa, P.A. Search for minimum molecular programmable units. *Proc. IEEE Nanotechnol. Conf.* **2002**, *2*, 421–424.
  65. Seminario, J.M.; Cordova, L.E. Toward multiple-valued configurable random molecular logic units. *Proc. IEEE Nanotechnology Conf.* **2001**, *1*, 146–150.
  66. Seminario, J.M.; Derosa, P.A.; Cordova, L.E.; Bozard, B.H. A molecular device operating at terahertz frequencies: theoretical simulations. *IEEE Trans. Nanotechnol.* **2003**, *in press*.
  67. Seminario, J.M. A theory guided approach to molecular electronics: analysis, design and simulation. *Proc. IEEE Nanotechnol. Conf.* **2003**.

# Molecular Manipulator: Dynamic Design Criteria

Andrés Jaramillo-Botero

School of Engineering, Pontificia Universidad Javeriana, Cali, Colombia

## INTRODUCTION

The ability to intentionally manipulate three-dimensional (3-D) irregular-shaped matter with atomic precision, abiding to physical laws, is considered as one of the ultimate goals of nanoscience and engineering. Nature has given us a vast assortment of biological molecular machines that demonstrate the viability of this goal, including, among others, the ribosome (which can translate mRNA instructions into proteins) and kinesin, an enzyme that acts as a molecular motor which pulls things toward the outer reaches of the cell. In nerve cells, it is kinesin that pulls vesicles or other cellular materials from the cell body to the nerve endings. These biological systems are primarily “application-specific molecular machines.” They are not universal assemblers that could, in principle, be used in a programmable fashion to perform alternate functions at the molecular level. Self-replicating programmable manufacturing systems able to arrange atoms for multiple “applications” would require a universal assembler with an appropriate end-effector and a corresponding controller. The scope of this entry explores design criteria for such a universal assembler (Fig. 1).

This entry reviews the literature on the creation of nanometer-scale spatial positioners, from a kinematic and dynamic standpoint, as one of the basic building blocks for an atomic-scale manipulator (to arrange differently functionalized molecular building blocks into a lattice or any other nanometer-scale object in a specified and complex pattern, it is necessary to introduce positional control). The development of theoretical criteria for the design of reduced constrained dynamic complexity of a nanoscale positioning device (nanomanipulator), based on the equations of motion (EOM) for spatial serially articulated rigid multibodies, is presented in this entry. By using a rigid-body semiclassical mechanics approach, it is shown how dynamic complexities, such as coupling and non-linearities introduced by high-speed operation, complicate the control task and deteriorate performance. The first section of the entry introduces the reader to appropriate state space forms of the EOM for a serially coupled set of rigid bodies using internal

coordinates. This allows a compact mathematical description of the problem at hand and exposes the intended solution by permitting concise physical insight. The second section develops the complete set of EOM for both the Newton–Euler and Lagrange–Euler formulations. From the state space equivalence of both methods, the EOM are then expressed as a function of the articulated body inertia operator for the multibody, leading to a highly dependent form of the EOM on this operator. The internal matrix structure of the articulated body inertia is then revealed. The third section presents the analysis that leads to a reduced set of EOM from the structural simplification of the articulated body inertia matrix and develops the general kinematics and mass distribution criteria for doing so. From the resulting analysis, a set of compliant manipulator configurations that could, in principle, be built from carbon nanotubes, linked by direct-driven rotational molecular joints, is shown. Finally, the last section concludes on the obtained results and describes current and future work.

## NEED FOR A UNIVERSAL MOLECULAR ASSEMBLER

Today, atomic force microscopy (AFM) provides capabilities that allow scientist to characterize matter at the nanometer-scale (e.g., electrically, mechanically, and chemically) while correlating it to structure.<sup>[1]</sup> But perhaps its most notable capability is that of allowing the manipulation of nanometer-scale objects efficiently on 2-D surfaces,<sup>[2,3]</sup> making it possible to explore substrate–sample interactions<sup>[4]</sup> or the creation of devices incorporating nanometer-scale objects.<sup>[5]</sup> Atomic force microscopy is indeed an important tool for the study of nanodevices, but as impressive as it may be, it is not likely to become the type of atomic manipulator expected to permit the aforementioned goal, leading to the shift in paradigm proposed by molecular manufacturing: bottom-up atomic-scale construction. For this, a new set of devices is required to allow for atomic level manipulation in 3-D space, autonomous/commanded self-replication,

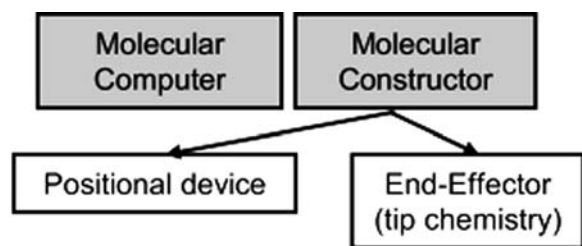
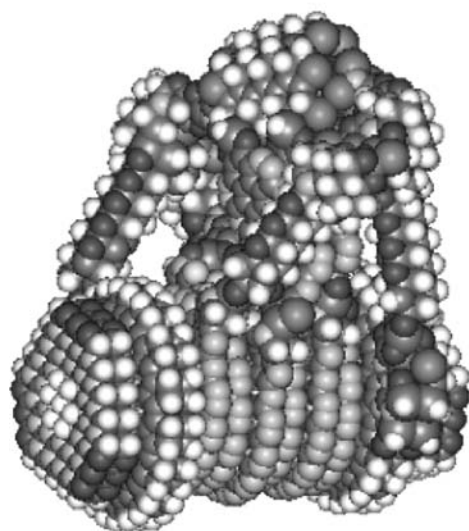


Fig. 1 Universal molecular assembler.

nanometer/submicrometer-scale size, increased spatial dexterity, and higher operational energy efficiency, among others.

Currently proposed nanoscale molecular devices inherit their design, for the most part, from macroscopic counterparts.<sup>[6,7]</sup> Little regard is taken to consider atomic-scale effects (in particular, non-bonded interactions or the discrete nature of the atoms spherical contact surfaces)<sup>[6]</sup> other than mere static structural stability of the molecular components or the undesired dynamic properties being ported from the macroscopic systems to the nanoscale that increase controller complexities and, in some cases, impose serious constraints on performance. Nanometer-scale manipulator designs tend to favor particular characteristics (e.g., force magnitude at the end-effector or stretching stiffness—refer to Fig. 2) while sacrificing other properties that are also fundamental at the nanoscale, such as dexterity (for molecular obstacle avoidance), reachable workspace, or operational speed, among others.



## New Approach

This entry is concerned with the theoretical criteria for the design of a nanoscale positioning device (nanomanipulator), based on the equations of motion (EOM) for spatial serially articulated rigid multibodies, in particular, by using a rigid-body semiclassical mechanics approach. The resulting equations for the corresponding microcanonical or canonical ensembles make it evident that the key operator affecting the complexity of the EOM is the articulated body inertia of the system.

This entry analyzes the necessary conditions under which the spatial articulated body inertia operator for the system can be made decoupled (diagonal) and configuration-invariant (independent of joint coordinates). Simplifying its structure via design, by considering the kinematics and mass distribution of the system, proves to be a major advantage for reducing the complexity of the forward dynamics solution (used in molecular simulations) and the inverse dynamics solution (used in the design of appropriate controllers). The proposed devices are presumed to be fully actuated; that is, joint motion depends on an individual actuator, located directly or remotely on the joint origin.

Although some research has been devoted in the past to highly speculative designs and concepts,<sup>[7,9,10]</sup> some with adequate functionality (evaluated via molecular simulations using first principles), it is worth pointing out that advances into the design of robust modular mechanosynthesis nanodevices are still very limited. This work provides a new direction in this



Fig. 2 Nanometer scale Stewart platform manipulator (left picture—©K.E. Drexler, Institute of Molecular Manufacturing—<http://www.imm.org>) and macroscopic commercial counterpart (right picture—by Physik Instrumente GmbH). Both designs trade off controllability (highly coupled designs that limit speed), dexterity (useful in obstacle avoidance), and reachable workspace for higher payload.

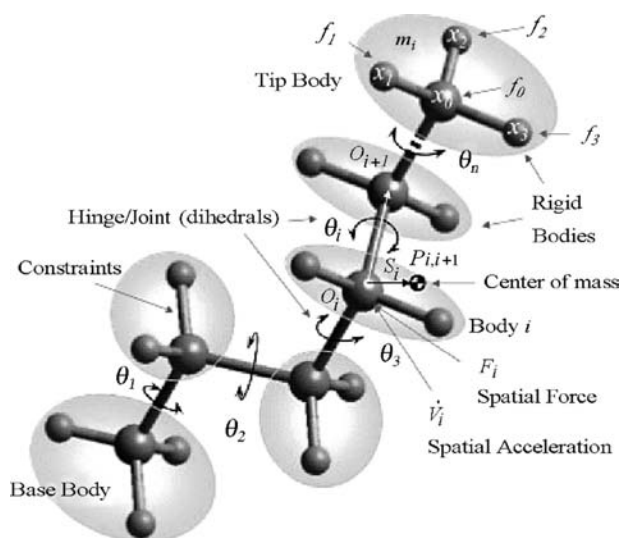


**Fig. 3** Rigid body (atomic clusters) molecular system representation.

quest by proposing novel designs for a positioning device for molecular mechanosynthesis with high dexterity, large workspace (ratio to manipulator size), and improved dynamic performance at high speed that could, in principle, be synthesized from modular self-assembled parts. Furthermore, the proposed designs can be actuated at the corresponding joints by existing polymeric muscles at the nanometer scale. It is assumed that arbitrary positioning of atoms in 3-D space requires at least 3 degrees of freedom, while that of complex macromolecules requires a minimum of 6 degrees of freedom to account for the added complexity of arbitrary orientation of manipulated bodies.

The approach presented here considers a semiclassical dynamics formulation of the constrained EOM for a serial set of articulated rigid molecular bodies, analogous in structure to a human manipulator arm. The notion of rigid body is employed at the molecular level in the context of clusters of atoms (refer to Fig. 3) that make up the primary components of the nanoscale positioning device (e.g., a single atom, a phenyl ring, an alpha helix, or even an entire protein domain). In turn, the notion of constrained dynamics comes from introducing constraints on molecular structural properties such as bond lengths and bond angles to shift focus onto the dihedrals that distinguish conformations, in this way reducing the number of atomic degrees of freedom (DOF).

Consequently, the description and analysis of the molecular system are simplified without losing nanoscale properties, and the real-time requirements for control or simulation of the device are significantly reduced (intracluster motions are neglected). Articulated motion comes from clusters interconnected via

hinges or joints. Joints do not have to be bonded atomically as shown in Fig. 3.

## STATE SPACE REPRESENTATION OF THE EQUATIONS OF MOTION

Assume that the state of the system is known and defined by the collection of generalized coordinates ( $Q$ ,  $\dot{Q}$ ,  $\ddot{Q}$ ) corresponding to effective joint positions, velocities, and accelerations, respectively. Furthermore, assume that the mass distribution of each rigid element of the multibody is completely characterized, given a localized center of mass and a known inertia tensor. It then follows that for a constrained molecular dynamics model, the EOM under Newton's formulation are represented in state space as

$$F(Q) = M(Q)\ddot{Q} + C(Q, \dot{Q}) + N(Q, \dot{Q}) \quad (1)$$

where  $F$  denotes the vector of generalized forces (e.g., torques) applied at the joint,  $N$  are any other conservative forces (e.g., potential) acting on each generalized coordinate,  $M$  denotes the articulated body inertia matrix, and  $C$  denotes the non-linear velocity-dependent terms of force (e.g., Coriolis, centrifugal, and gyroscopic forces). Solving Eq. (1) leads to a direct calculation of joint actuator forces required for the system to follow a specific spatial trajectory. On the other hand, the dynamics of motion are obtained by solving Eq. (1) for effective joint accelerations,

$$\ddot{Q} = M^{-1}(Q)[F(Q) - C(Q, \dot{Q}) - N(Q, \dot{Q})] \quad (2)$$

This entry explores the dependence of both Eqs. (1) and (2) on the articulated body inertia operator  $M$  and particular forms of this operator that lead to reduced complexities in both the inverse and forward dynamics solutions expressed above.

## Canonical Ensemble

Standard Newtonian dynamics leads to conservation of total energy along a motion trajectory; thus the collection of points for this type of molecular dynamics (MD) describes a microcanonical ensemble (NVE: number of particles, volume, and energy are conserved). To deal with normal experimental conditions, it is necessary to add contact with a heat bath at constant temperature. An appropriate ensemble to simulate these conditions (NVT and NPT) is the canonical ensemble. The corresponding extensions to support a canonical ensemble were carried out by Nosé<sup>[11]</sup> and Hoover<sup>[12]</sup> for Cartesian dynamics. Nosé introduced an additional time-scaling variable, and



its conjugate momentum, into the system to represent its interaction with the heat bath. The resulting EOM drive the velocity changes with time which, in turn, drive the changes in thermal energy (kinetic), leading to its proper canonical description. However, Nosé's EOM involve virtual time, which implies unequal time steps in real time. This is inconvenient for the analysis of dynamic properties of the system (e.g., Fast Fourier Transform (FFT)), so Hoover proposed transforming the Nosé EOM into real variables. A concise form of the Hoover dynamics EOM follows,

$$F(Q) = M(Q)\ddot{Q} + C(Q, \dot{Q}) + \Phi_X^{\text{nb}} + \xi M(Q)\dot{Q} \quad (3)$$

where  $\Phi_X^{\text{nb}}$  is the sum of gradients of the non-bond and external potentials  $\Phi$  with respect to Cartesian coordinates and  $\xi$  denotes the baths friction coefficient. For simulation purposes, the friction coefficient,  $\xi$ , is integrated for each time step using a modified leap frog verlet from the relation between the ratio of instantaneous temperature to bath temperature and the inescapable of relaxation of the bath variables.<sup>[13]</sup>

It should be noted that Eq. (3) has the same form as that for the microcanonical ensemble [Eq. (1)], except that it includes one additional term: a friction term as a result of the atomic interaction with a heat bath.

### The Articulated Body Inertia Using Spatial Operator Algebra

This section presents an overview of the development of the EOM for a serial chain multibody (Fig. 3) using spatial operator algebra. For additional detail on spatial algebra in multibody dynamics, see Refs.<sup>[14,15]</sup>. From the equivalence between the Newtonian and Lagrangian formulations, a particular form of the EOM is found to express the non-linear velocity-dependent terms in  $C$  [Eq. (1)] as a function of the articulated body inertia of the system,  $M$ . This form of the EOM conduces to a straightforward explanation of why altering the structure of  $M$ , by design, is critical for the dynamic complexity of the system.

### Spatial Transformations

To operate and manipulate 6-D physical quantities on a common coordinate reference frame, 6-D spatial transformation operators are required. For any generic 3-D distance vector from point 1 to point 2,  $t_{1,2}$ , the translation operator is defined as

$$\hat{T}_{1,2} = \begin{bmatrix} U & \tilde{t}_{1,2} \\ 0 & U \end{bmatrix} \quad (4)$$

where

$$\tilde{t}_{1,2} = \begin{bmatrix} 0 & -t_z & t_y \\ t_z & 0 & -t_x \\ -t_y & t_x & 0 \end{bmatrix} \quad (5)$$

is the skew symmetric equivalent to the vector cross product and  $U$  is the 3-D identity matrix.

To simplify notation, a coordinate free form representation of the EOM is adopted, hence the orientation transformation is not made explicit. For an actual implementation of the solution, such an operator is required.

### Newton–Euler Formulation

Assuming a base to tip propagation of kinematic parameters (refer to Fig. 3), the spatial (translational and rotational components stacked in a single 6-D operator) velocities ( $V$ ), from body  $i = 1 \dots n$ , are expressed as

$$V_i = \hat{P}_{i-1,i}^T V_{i-1} + H_i \dot{Q}_i \quad (6)$$

where  $H_i$  denotes the projection matrix onto the joint ( $i$ ) DOF. Differentiating with respect to time results in the spatial accelerations ( $\dot{V}$ ),

$$\dot{V}_i = \hat{P}_{i-1,i}^T \dot{V}_{i-1} + H_i \ddot{Q}_i + \dot{\hat{P}}_{i-1,i}^T V_{i-1} + \dot{H}_i \dot{Q}_i \quad (7)$$

A reverse (or downward) propagation from body  $i = n \dots 1$  of the spatial forces follows to complete the EOM,

$$F_i = \hat{P}_{i,i+1} F_{i+1} + I_i \dot{V}_i + [\dot{I}_i + I_i \dot{\hat{S}}_{O_i,cm}^T] V_i \quad (8)$$

where the spatial inertia matrix for body  $i$ ,  $I_i \in \mathfrak{R}^{6 \times 6}$ , is obtained from the scalar mass and the moments of inertia with respect to a point of interest on the body. Boundary conditions are set accordingly for the type of base (floating/fixed) and for the existence of external forces. Assuming for body  $i$  a mass  $m_i$  and a tensor of inertia  $J_{i,cm}$  about its center of mass, cm, the spatial inertia operator is defined as

$$I_{i,cm} = \begin{bmatrix} J_{i,cm} & 0 \\ 0 & m_i U \end{bmatrix} \in \mathfrak{R}^{6 \times 6} \quad (9)$$

It then follows from the parallel axis theorem that the spatial inertia of the body about the hinge origin,

O<sub>i</sub>, I<sub>i</sub> is given by

$$I_i = \begin{bmatrix} J_{O_i} & m_i \tilde{s}_{O_i,cm} \\ -m_i \tilde{s}_{O_i,cm} & m_i U \end{bmatrix} \quad (10)$$

Finally, spatial forces are projected onto the DOF of each joint to obtain the effective forces,

$$F_i = H_i^T F_i \quad (11)$$

By assuming, for notational simplicity, that EOM are found at the center of mass and by defining higher level physical operators as follows,

$$I = \text{diag}[I_n, I_{n-1}, \dots, I_1] \in \mathfrak{R}^{6n \times 6n}$$

$$H = \text{diag}[H_n, H_{n-1}, \dots, H_1]^T \in \mathfrak{R}^{6n \times m}$$

$$V = [V_n, V_{n-1}, \dots, V_1]^T \in \mathfrak{R}^{6n \times m}$$

$$\dot{Q} = [\dot{Q}_n, \dot{Q}_{n-1}, \dots, \dot{Q}_1]^T \in \mathfrak{R}^{n \times m}$$

$$\dot{V} = [\dot{V}_n, \dot{V}_{n-1}, \dots, \dot{V}_1]^T \in \mathfrak{R}^{6n \times m}$$

$$\ddot{Q} = [\ddot{Q}_n, \ddot{Q}_{n-1}, \dots, \ddot{Q}_1]^T \in \mathfrak{R}^{n \times m}$$

$$F = [F_n, F_{n-1}, \dots, F_1]^T \in \mathfrak{R}^{6n \times m}$$

$$S = \text{diag}[\hat{S}_n, \hat{S}_{n-1}, \dots, \hat{S}_1] \in \mathfrak{R}^{6n \times 6n}$$

$$P = \begin{bmatrix} U & 0 & 0 & \cdots & 0 \\ -\hat{P}_{n,n-1} & U & 0 & \cdots & 0 \\ 0 & -\hat{P}_{n-1,n-2} & U & \cdots & 0 \\ \vdots & \vdots & \ddots & \ddots & \vdots \\ 0 & 0 & \cdots & -\hat{P}_{2,1} & U \end{bmatrix} \quad (12)$$

where  $m$  is the number of DOF per joint and  $U$  is the 6-D identity matrix. Then, Eqs. (6–8) and 11 are rewritten in indexless spatial notation.

$$P^T V = H \dot{Q} \quad (13)$$

Solving for spatial velocities in Eq. (13)

$$V = P^{T^{-1}} H \dot{Q} \quad (14)$$

where

$$P^{-1} = \begin{bmatrix} U & 0 & 0 & \cdots & 0 \\ \hat{P}_{n-1,n} & U & 0 & \cdots & 0 \\ \hat{P}_{n-2,n} & \hat{P}_{n-2,n-1} & U & \cdots & 0 \\ \vdots & \vdots & \ddots & \ddots & \vdots \\ \hat{P}_{1,n} & \hat{P}_{1,n-1} & \cdots & \hat{P}_{1,2} & U \end{bmatrix} \in \mathfrak{R}^{6n \times 6n} \quad (15)$$

Because  $P^{T^{-1}}$  (upper triangular) is nilpotent,  $P_{0,n}^{T^{-1}} = 0$ , then  $P^{T^{-1}} = P^{-1}$ . For simplicity, let  $\rho \equiv P^{-1}$ , then,

$$V = \rho^T H \dot{Q} \quad (16)$$

From the above equation, it follows that the manipulator Jacobian ( $J$ ), relating the joint state with the end-effector position and orientation, is given by

$$J = \rho^T H \quad (17)$$

In turn, spatial accelerations are written as follows,

$$\dot{V} = \dot{\rho}^T H \dot{Q} + \rho^T \dot{H} \dot{Q} + \rho^T H \ddot{Q} \quad (18)$$

and the spatial forces expressed with respect to joint origin,

$$PF = \dot{I}V + I\dot{V} - \dot{S}IV \quad (19)$$

Solving for spatial forces,

$$F = \rho[\dot{I}V + I\dot{V} - \dot{S}IV] \quad (20)$$

and from projecting onto the axes of motion from Eq. (11), the effective forces are obtained,

$$F = H^T \rho[\dot{I}V + I\dot{V} - \dot{S}IV] \quad (21)$$

Replacing Eqs. (14) and (18) in Eq. (21),

$$F = H^T \rho[\dot{I} \rho^T H \dot{Q} + I[\dot{\rho}^T H \dot{Q} + \rho^T \dot{H} \dot{Q} + \rho^T H \ddot{Q}] - \dot{S} I \rho^T H \dot{Q}] \quad (22)$$

Grouping terms of  $\ddot{Q}$  and  $\dot{Q}$ ,

$$F = [H^T \rho I \rho^T H] \ddot{Q} + H^T \rho \times [\dot{I} \rho^T H + I \dot{\rho}^T H + I \rho^T \dot{H} - \dot{S} I \rho^T H] \dot{Q} \quad (23)$$

Recognizing that Eq. (23) is equivalent, in state space, to Eq. (1), then the articulated body inertia operator for the system is given by

$$M = H^T \rho I \rho^T H \quad (24)$$

Clearly,  $M$  is strictly dependent only on the kinematics and mass distribution of the multibody. Note that it can also be written in terms of the manipulator Jacobian, from Eq. (17)

$$M = JIJ^T \quad (25)$$

The non-linear-dependent (quadratic in velocity) terms (Coriolis, centrifugal, and gyroscopic) in Eq. (23) are extracted as

$$C = H^T \rho [I \dot{\rho}^T H + I \dot{\rho}^T H + I \rho^T \dot{H} - \dot{S} I \rho^T H] \dot{Q} \quad (26)$$

### Lagrange–Euler Formulation

Using the same operators already found, we will express the EOM in terms of the Lagrangian operator,  $L = T - U$ , where  $T$  is the kinetic energy and  $U$  is the potential energy.

#### The kinetic energy of the serial multibody

The kinetic energy for the entire system is the sum of the kinetic energy of each of the links, equivalent to

$$T_i = \frac{1}{2} \sum_{i=1}^n V_i^T I_i V_i \quad (27)$$

This can be expressed in simplified spatial form from the higher level operators in Eqs. (12) and (16), using the above equation,

$$T(Q, \dot{Q}) = \frac{1}{2} \dot{Q}^T H^T \rho(Q) I \rho^T(Q) H \dot{Q} \quad (28)$$

From Eq. (18), it then follows that the kinetic energy is given as a function of  $M$  by

$$T(Q, \dot{Q}) = \frac{1}{2} \dot{Q}^T M(Q) \dot{Q} \quad (29)$$

#### The potential energy of the serial multibody

The potential energy of each link is a function of the geometry of the manipulator. Let  $h_i(Q)$  be the height of the center of mass of the  $i$ th link (position of the center of mass opposing the direction of gravity). The total potential energy for the manipulator is given by the sum of contributions from each link:

$$U(Q) = \sum_{i=1}^n m_i g h_i(Q) \quad (30)$$

where  $m_i$  is the mass of the  $i$ th link and  $g$  is the gravitational constant. For simplicity, the systems potential energy is denoted in spatial notation as

$$U(Q) = \Phi(Q) \quad (31)$$

No gravity pull is assumed at the nanoscale.

The Lagrangian operator for the serial articulated multibody is then written as

$$L(Q, \dot{Q}) = T - U = \frac{1}{2} \dot{Q}^T M(Q) \dot{Q} - \Phi(Q) \quad (32)$$

Yang and Tzeng<sup>[16]</sup> proposed a simple method to “linearize” serial chain robot manipulators based on the Lagrange–Euler formulation. The method consists of eliminating by design the terms in  $T$  and  $U$  that depend on joint coordinate variables. By doing so, differentiation of both kinetic and potential energy leads to complete independence of the EOM on joint rates (velocity-dependent terms) for simple manipulators of up to 3 DOF and simplified dynamics for higher DOF. Nonetheless, the resulting configurations are still joint-coupled.

Applying variational principles to the Lagrangian operator results in the Lagrange–Euler dynamic EOM,

$$F_i = \frac{d}{dt} \frac{\partial L}{\partial \dot{Q}_i} - \frac{\partial L}{\partial Q_i} \quad (33)$$

where  $F_i$  represents the spatial forces acting on the  $i$ th joint.

It will be convenient to express the kinetic energy as a sum,

$$L(Q, \dot{Q}) = \frac{1}{2} \sum_{i,j=1}^n M_{ij}(Q) \dot{Q}_i \dot{Q}_j - \Phi(Q) \quad (34)$$

From Eqs. (29–31), the first term in Eq. (33) is given by

$$\begin{aligned} \frac{d}{dt} \frac{\partial L}{\partial \dot{Q}_i} &= \frac{d}{dt} \left( \sum_{j=1}^n M_{ij} \dot{Q}_j \right) \\ &= \sum_{j=1}^n (\dot{M}_{ij} \dot{Q}_j + M_{ij} \ddot{Q}_j) \end{aligned} \quad (35)$$

On the other hand, the first partial derivative of the Lagrangian operator with respect to joint variables is

$$\frac{\partial L}{\partial Q} = \frac{1}{2} \sum_{j,k=1}^n \frac{\partial M_{kj}(Q)}{\partial Q_i} \dot{Q}_k \dot{Q}_j - \frac{\partial \Phi(Q)}{\partial Q_i} \quad (36)$$

Subtracting Eq. (36) from Eq. (35) results in the EOM. Because the potential energy is dependent only on  $Q$ , these are not expanded (our interest lays on non-linear

velocity-dependent terms)

$$F_i = \sum_{j=1}^n (\dot{M}_{ij} \dot{Q}_j + M_{ij} \ddot{Q}_j) - \frac{1}{2} \times \sum_{j,k=1}^n \frac{\partial M_{kj}(Q)}{\partial Q_i} \dot{Q}_k \dot{Q}_j + \frac{\partial \Phi(Q)}{\partial Q_i} \quad (37)$$

This is expressed in higher-level spatial operators as

$$F = M\ddot{Q} + \dot{M}\dot{Q} - \frac{1}{2}\dot{Q}^T M_Q \dot{Q} + \frac{\partial \Phi}{\partial Q} \quad (38)$$

where  $M_Q$  corresponds to the partial derivative of  $M$  with respect to joint variables.  $\dot{M}_{ij}$  in Eq. (37) can be expanded in terms of partial derivatives to yield

$$\sum_{j=1}^n \dot{M}_{ij}(Q) = \sum_{j,k=1}^n \frac{\partial M_{ij}(Q)}{\partial Q_k} \dot{Q}_k \quad (39)$$

Rewriting Eq. (37) using the above result yields

$$F_i = \sum_{j=1}^n M_{ij}(Q) \ddot{Q}_j + \frac{\partial \Phi(Q)}{\partial Q_i} + \sum_{j,k=1}^n \left( \frac{\partial M_{ij}}{\partial Q_k} \dot{Q}_j \dot{Q}_k - \frac{1}{2} \frac{\partial M_{kj}(Q)}{\partial Q_i} \dot{Q}_k \dot{Q}_j \right) \quad (40)$$

From Eq. (37), the non-linear velocity-dependent terms are given by

$$C(Q, \dot{Q}) = \dot{M}\dot{Q} - \frac{1}{2}\dot{Q}^T M_Q \dot{Q} \quad (41)$$

By inspection, Eq. (37) is equivalent in state space to Eq. (1). It must then follow that Eq. (41)  $\equiv$  Eq. (26),

$$H^T \rho [\dot{I} \rho^T H + I \rho^T \dot{H} + I \rho^T \dot{H} - \dot{S} I \rho^T H] \dot{Q} \equiv \dot{M}\dot{Q} - \frac{1}{2}\dot{Q}^T M_Q \dot{Q} \quad (42)$$

The proof of this equality is reached in a straightforward manner from the time derivatives of the spatial operators.

The key issue here is noting the dependence of  $F$  on  $M$  in Eq. 40. By doing so, the following can be said about simplifying the complexity of  $F$  via careful structural design of the multibody.

1. Obtaining a decoupled form of the articulated body inertia operator (i.e., a diagonalized form of it) eliminates joint actuator interactions.
2. Obtaining a configuration-invariant form of the articulated body inertia operator eliminates the dependence of  $M$  on joint coordinates ( $Q$ ), hence non-linear velocity-dependent terms in

the EOM ( $C$ ) vanish, except non-bonded potential components and friction term.

## STRUCTURAL SIMPLIFICATIONS ON $M$ THAT LEAD TO SIMPLIFIED CONSTRAINED DYNAMICS

The existence of a diagonalized composite body inertia form for serially articulated rigid-body spatial manipulators can be proven given that the representing mass operator for the system defines a metric tensor.<sup>[17]</sup> If this tensor is made to be metric Euclidean (i.e., with constant coefficients) by design, based on kinematic and mass distribution characteristics, then its configuration manifold is flat and the associated curvature tensor vanishes<sup>[21]</sup> (i.e., global diagonalizing transformation exists).

$$R_{hijk} = \frac{1}{2} \times \left[ \frac{\partial^2 M_{hk}}{\partial Q_i \partial Q_j} + \frac{\partial^2 M_{ij}}{\partial Q_h \partial Q_k} - \frac{\partial^2 M_{hj}}{\partial Q_i \partial Q_k} - \frac{\partial^2 M_{ik}}{\partial Q_h \partial Q_j} \right] + \sum_l \left[ \left\{ \begin{matrix} l \\ ij \end{matrix} \right\} [hk, l] - \left\{ \begin{matrix} l \\ ik \end{matrix} \right\} [hj, l] \right] = 0 \quad (43)$$

where  $R$  is the curvature tensor of  $M$ ,  $R_{hijk}$  is the corresponding  $n(n+1)/2$  Riemannian symbols of the first kind,<sup>[18]</sup> and the quantities

$$[ij, k] \text{ and } \left\{ \begin{matrix} k \\ ij \end{matrix} \right\}$$

are the Christoffel symbols of the first and second kind,<sup>[18]</sup> respectively, which are computed from the corresponding first derivatives of the mass matrix operator with respect to the joint angles.

On the other hand, the existence of a configuration-invariant form of the articulated body inertia can be proven and the corresponding criteria can be derived when the first-order partial derivative of the corresponding metric tensor with respect to joint coordinates vanishes ( $M_Q = 0$ ),

$$M_{Q_i} = \frac{\partial H^T}{\partial Q_i} \rho I \rho^T H + H^T \frac{\partial \rho}{\partial Q_i} I \rho^T H + H^T \rho \frac{\partial I}{\partial Q_i} \rho^T H + H^T \rho I \frac{\partial \rho^T}{\partial Q_i} H + H^T \rho I \rho^T \frac{\partial H}{\partial Q_i} = H^T \rho [\tilde{H}_\delta^i \rho I - I \rho^T \tilde{H}_\delta^i] \rho^T H \quad (44)$$

where the matrix  $\tilde{H}_\delta^i$  is the  $6n \times 6n$  matrix whose elements are all zero, except for the  $6 \times 6$  block corresponding to the  $\tilde{H}_i$  at the  $i$ th location on the diagonal. The index  $i$  corresponds to the joint-angle  $Q_i$  with respect to which the sensitivity derivative of the mass matrix  $M_Q$  is being taken.

An alternate approach comes from the structure of  $M$ . By analytically determining the joint

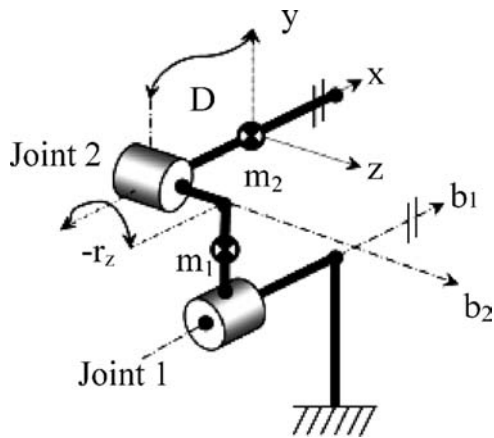


Fig. 4 Schematic of two rotational DOF arm and corresponding kinematic and mass parameters (cylinders indicate rotating joint).

coordinate-dependent terms in  $M$  and explicitly eliminating these, or inducing their constancy, through design criteria, configuration invariance can be achieved. Additionally, the off-diagonal terms in  $M$  can be explicitly removed by design. Expanding the spatial operator form of  $M$ , found in Eq. (24), into its diagonal and off-diagonal components leads to

$$M_{i,i} = H_i^T \left[ I_i + \sum_{k=i+1}^n \hat{P}_i^k I_k \hat{P}_i^{kT} \right] H_i \quad (45)$$

$$M_{i,j} = H_i^T \left[ \hat{P}_j^i I_j + \sum_{k=j+1}^n \hat{P}_i^k I_k \hat{P}_j^{kT} \right] H_j \quad i > j \quad (46)$$

For a serial chain,  $M$  is symmetric positive definite, then,  $M_{j,i} = M_{i,j}^T, j < i$ . Clearly, Eq. 45 cannot be null because of the principal moments of inertia.

**Structural Manipulator Building Blocks**

Simple two DOF cases can serve as building blocks for more complex articulated multibodies. For 2 DOF arms with open kinematic chain structure, the articulated body inertia cannot be decoupled unless the joint axes are orthogonal to each other (refer to Fig. 4). Possible mass distribution properties for decoupledness assuming joints with a rotational single degree of freedom,  $r$  as the distance vector between the two joints,  $b_i$  as the direction cosines of the joint axes ( $z_i$  as the joint axis), and a tensor of inertia given by

$$J = \begin{bmatrix} I_{xx} & I_{xy} & I_{xz} \\ I_{yx} & I_{yy} & I_{yz} \\ I_{zx} & I_{zy} & I_{zz} \end{bmatrix} \quad (47)$$

are shown in Fig. 5.

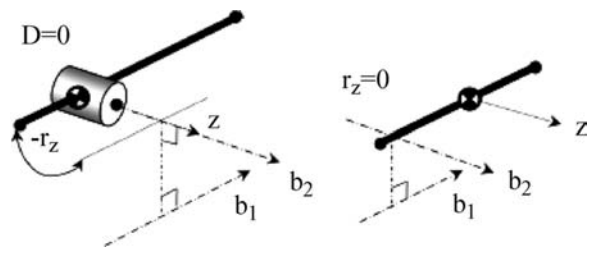


Fig. 5 Decoupled configurations resulting from Fig. 4.

For arms with open kinematic chain structure, the articulated body inertia can only be invariant iff one of the conditions expressed in Fig. 6 or Fig. 7 is met.

The necessary and sufficient conditions for a 2 DOF open kinematic chain structure and mass distribution to possess a decoupled and invariant articulated body inertia are given in Fig. 8. For higher DOF, the above 2 DOF cases can be used as building blocks. On the other hand, one way to relax the orthogonality condition for decoupling is to relocate the actuators to reduce the reaction torques exerted by an actuator. The above configurations assume actuators acting directly on each joint, hence reaction torques are present. From the conditions for decoupling, it can be deduced that decoupling the inertia tensor for more than 2 degrees of freedom requires modification of the structure of the arm mechanism. This was also demonstrated by Asada and Youcef-Toumi<sup>[20]</sup> and Youcef-Toumi<sup>[24]</sup> for macroscopic manipulators with fixed base. Fig. 8 shows a possible 4 DOF multibar spatial mechanism configuration that can be controlled

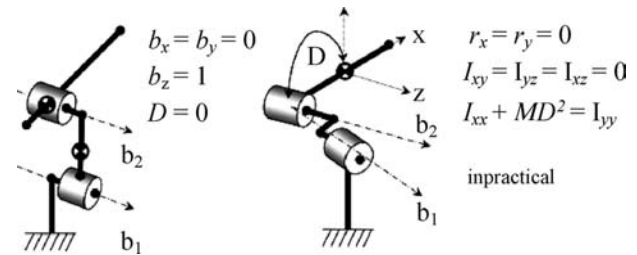


Fig. 6 Invariant configurations resulting from Fig. 4.

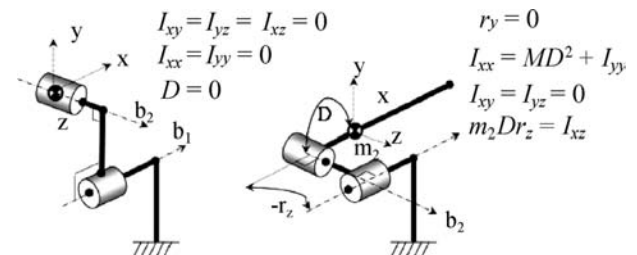
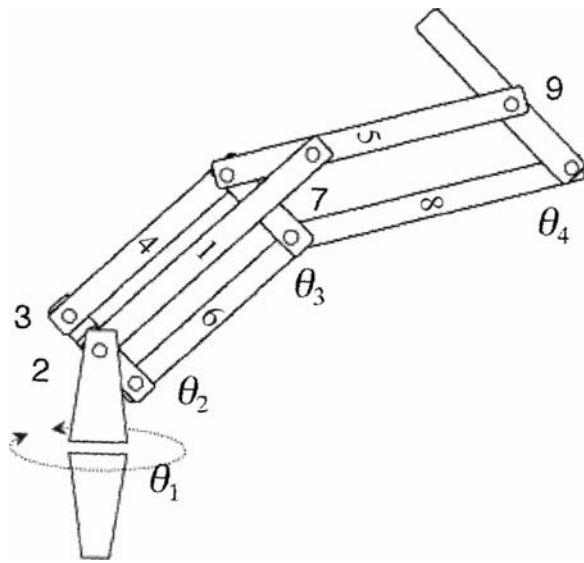


Fig. 7 Decoupled and/or invariant configurations resulting from Fig. 4.



**Fig. 8** Four DOF decoupled and invariant inertia manipulator for simultaneous motions involving  $\theta_{2-4}$ .

in a single plane (fixed waist rotation during motion of  $\theta_2$ ,  $\theta_3$ , and  $\theta_4$ ) with full decoupled and invariant inertia. The rotation of any link is a result of 1 and only 1 actuator [i.e.,  $\theta_1(1,4,6)$ ,  $\theta_2(2,5,8)$ ,  $\theta_3(3,7,9)$ ].

### Thermal Noise and Positional Variance (Uncertainty)

Thermal noise at the molecular level affects the positional accuracy. One of the key issues in achieving good positional accuracy at the nanoscale is controlling temperature or conversely controlling the structural stiffness of the elements that make up the manipulator. The latter is preferred, given the need to operate these nanodevices at room temperature. Because the presented designs have bending forces applied to their structural elements, we wish to evaluate their stiffness with respect to deflection of their ends as a consequence of thermal noise.

This has been shown by Ref.<sup>[19]</sup> from classical statistical mechanics. Let the probability density function for one position coordinate of a particle, say  $x$ , subject to the potential energy function  $V(x)$  be  $f_x(x)$ .

$$f_x(x) = \frac{\exp[-V(x)/k_B T]}{\int_{-\infty}^{\infty} \exp[-V(x)/k_B T] dx} \quad (48)$$

where  $k_B = 1.38 \times 10^{23}$  J/K is the Boltzmann constant and  $T$  is the temperature. From the potential energy for a simple case, say the harmonic potential,

$$V(x) = \frac{1}{2} k_s x^2 \quad (49)$$

it is shown that the probability density function is Gaussian:

$$\begin{aligned} f_x(x) &= \frac{\exp[-k_s x^2 / 2k_B T]}{\int_{-\infty}^{\infty} \exp[-k_s x^2 / 2k_B T] dx} \\ &= \frac{1}{\sqrt{2\pi\sigma_{\text{class}}^2}} \exp\left(\frac{-x^2}{2\sigma_{\text{class}}^2}\right) \end{aligned} \quad (50)$$

Yielding the classical value for the positional variance (=standard deviation squared = mean square displacement = RMS positional error squared),

$$\sigma^2 = \frac{k_B T}{f_R} \quad (51)$$

showing clearly that thermal noise can be controlled by decreasing the temperature  $T$  or by increasing the restoring force  $f_R$  (measured by the stiffness  $k_s$ ).

The positional uncertainty in quantum statistical mechanics for a harmonic oscillator shows that “quantum effects” do not pose a fundamental problem either,

$$\sigma^2 = \frac{\hbar\omega}{k_s} \left[ \frac{1}{2} + [\exp(\hbar\omega/kT) - 1]^{-1} \right] \quad (52)$$

Describing the frequency,  $\omega$ , in terms of the mechanical parameters ( $\omega = \sqrt{k_s/m}$ ) leads to

$$\sigma^2 = \frac{\hbar}{\sqrt{k_s m}} \left[ \frac{1}{2} + [\exp(\hbar\omega/kT) - 1]^{-1} \right] \quad (53)$$

Applying Eq. (51) to a cylindrical rod of radius  $r$ , length  $L$ , and traverse stiffness given by

$$k_s = \frac{3\pi r^4 E}{4L^3} \quad (54)$$

where  $E$  is the material’s Young modulus (e.g.,  $E = 10^{12}$  Pa for diamond), we can deduce that the positional error squared is given as

$$\sigma^2 = \frac{k_B T 4L^3}{3\pi r^4 E} \quad (55)$$

For a rod at room temperature (300 K) of  $E = 10^{12}$  N/m<sup>2</sup> (diamond),  $r = 8$  nm, and  $L = 50$  nm, the RMS positional error is  $\sigma = 0.007$  nm, much less than an atomic diameter. For the quantum mechanical version in Eq. (53), positional variance is again acceptable.

Single-wall carbon nanotubes (SWCN) are good candidates as structural elements. In general, diamond-oid structures are favored for nanomechanical systems because of their fundamental physical properties (strength and stiffness, among others).



Consequently, the structural elements that make up the manipulator must be chosen according to the systems kinematics and the calculated positional error of the end-effector. A simple kinematic analysis shows the calculation of the RMS positional error at the end-effector as a function of the propagation of deflections of the composing structural elements because of thermal noise. Using the cylindrical rods defined previously as structural elements for the kinematic configuration found in Fig. 8, and assuming an equal positional variance in all Cartesian coordinates, the worst-case RMS positional error of the manipulator's end-effector can be computed from Eq. (16) for a joint differential change on all 4 degrees of freedom. Using Denavit–Hartenberg's (DH) convention for coordinate frame assignment and parameterization,<sup>[22]</sup> the Jacobian for such a configuration can be computed algebraically from the kinematics equations,

$$A_1^0 A_2^1 A_3^2 A_4^3 = T_4^0 \quad (56)$$

where

$$A_i^{i-1} = \begin{bmatrix} \cos \theta_i & -\cos \alpha_i \sin \theta_i & \sin \alpha_i \sin \theta_i & a_i \cos \theta_i \\ \sin \theta_i & \cos \alpha_i \cos \theta_i & -\sin \alpha_i \cos \theta_i & a_i \sin \theta_i \\ 0 & \sin \alpha_i & \cos \alpha_i & d_i \\ 0 & 0 & 0 & 1 \end{bmatrix} \quad (57)$$

where  $a_i$  and  $d_i$  represent the Cartesian distance between joint axes  $i$  and  $i-1$ ,  $\alpha_i$  is the angle between adjacent joint axis,  $\theta_i$  is the  $i$ th joint angle, and  $T_4^0$  represents the orientation and position of the end-effector with respect to the inertial reference frame.

$$T_4^0 = \begin{bmatrix} n_x & o_x & a_x & p_x \\ n_y & o_y & a_y & p_y \\ n_z & o_z & a_z & p_z \\ 0 & 0 & 0 & 1 \end{bmatrix} \quad (58)$$

where  $n$ ,  $o$ , and  $a$  represent the 3-D vectors associated with the orientation of the manipulators' end-effector with respect to the inertial frame  $x$ ,  $y$ , and  $z$  and  $p$  represents the position of the end-effector with respect

**Table 1** Denavit–hartenberg parameters for the manipulator shown in Fig. 8

$a_i$ (rad)	$a_i$ (nm)	$\theta_i$ (rad)	$d_i$ (nm)
$\pi/2$	0	$\theta_1$	50
0	50	$\theta_2$	0
0	50	$\theta_3$	0
0	0	$\theta_4$	0

to the same reference frame. For this particular configuration, the DH parameters are given in Table 1.

The Jacobian can then be calculated from the column vectors that relate the differential Cartesian change of the end-effector with the differential change in each  $i$  joints,

$$\frac{dT_n}{d\theta_i} = \begin{bmatrix} -n_x p_y + n_y p_x \\ -o_x p_y + o_y p_x \\ -a_x p_y + a_y p_x \\ n_x \\ n_y \\ n_z \end{bmatrix} \quad (59)$$

Solving Eq. (16) for  $V$ , the maximum end-effector differential translational deviation in any given coordinate is 0.028 nm (still less than an atomic diameter). This does not account for the additional error introduced by joint backlash.

## CONCLUSION

Two and three DOF configurations with movable base are currently being designed at the molecular level, from modular parts (carbon nanotubes). Decoupled inertia is achievable for manipulators of up to 3 DOF, via structural redesign of the serial chain, while configuration-invariant inertia is manageable for higher DOF systems. These results become the basis for designing manipulators with reduced complexity dynamics, improved stability, and controllability, given that 1) for a hypothetical fully decoupled system, the dynamic control equations could then be computed under strict parallelism in  $O(1)$  with  $O(n)$  processors using a single input single output (SISO) controller (given precomputation of  $\Phi_X^{nb}$ ) and/or 2) for a configuration-invariant system, the computation of the inverse mass matrix does not need to be explicitly addressed at every control/integration time step. Having both conditions met results in the following simplified EOM,

$$F = M\ddot{Q} + \Phi_X^{nb} + \xi M\dot{Q} \quad (60)$$

$$\ddot{Q} = M^{-1}[F - \Phi_X^{nb} - \xi M\dot{Q}] \quad (61)$$

where  $M$  is diagonal and can be precalculated only once.

## ACKNOWLEDGMENTS

This work was performed under partial support of the Institute of Pure and Applied Mathematics (IPAM), an NSF Institute at the University of California at Los Angeles, California.

## REFERENCES

1. Falvo, M.R.; Clary, G.; Helser, A.; Paulson, S.; Taylor, R.M., II; Chi, V.; Brooks, F.P., Jr.; Washburn, S.; Superfine, R. Nanomanipulation experiments exploring frictional and mechanical properties of carbon nanotubes. *Microsc. Microanal.* **1998**, *4*, 504–515.
2. Falvo, M.R.; Finch, V.; Washburn, S.; Taylor, R.M., II; Brooks, F.P., Jr.; Superfine, R. *The Nanomanipulator: A Teleoperator for Manipulating Material at the Nanometer Scale*, Proc. 5th International Symp. Scie. Eng. Atomically Engineered Matter. World Scientific, Richmond, VA, November, 5, 1995.
3. Foster, J.S.; Frommer, J.E.; Arnett, P.C. Molecular manipulation using a tunnelling microscope. *Nature* **1988**, *331*, 324–327.
4. Sheehan, P.E.; Lieber, C.M. Nanotribology and nanofabrication of MoO<sub>3</sub> structures by atomic force microscopy. *Science* **May 24 1996**, *272*, 1158–1161.
5. Postma, H.W.C.; de Jonge, M.; Yao, Z.; Dekker, C. Electrical transport through carbon nanotube junctions created by mechanical manipulation. *Phys. Rev., B* **2000**, *62* (16), R10653–R10656.
6. Gao, P.; Swei, S. A six-degree-of-freedom micro-manipulator based on piezoelectric translators. *Nanotechnology* **1999**, *10*, 447–452.
7. Merkle, R. A new family of six degree of freedom positional devices, Ralph Merkle. *Nanotechnology* **June 1997**, *8* (2), 47–52.
8. Cagin, T.; Jaramillo-Botero, A.; Gao, G.; Goddard, W.A., III. Molecular mechanics and molecular dynamics analysis of Drexler–Merkle gears and neon pump. *Nanotechnology* **1998**, *9* (3), 143–152.
9. Montemagno, C.; Bachand, G. Constructing nanomechanical devices powered by biomolecular motors. *Nanotechnology* **1999**, *10*, 225–231.
10. Sohlberg, K.; Tuzun, R.E.; Sumpter, B.G.; Noid, D.W. Application of rigid-body dynamics and semiclassical mechanics to molecular bearings. *Nanotechnology* **1997**, *8* (1997), 103–111.
11. Nosé, S. *J. Chem. Phys.* **1984**, *81*, 511.
12. Hoover, W.G. *Phys. Rev.* **1985**, *A31*, 1695.
13. Vaidehi, N.; Jain, A.; Goddard, W.A., III. Constant temperature constrained molecular dynamics: the Newton–Euler inverse mass operator method. *J. Phys. Chem.* **1996**, *100*, 10508–10517.
14. Featherstone, R. The calculation of robot dynamics using articulated-body inertias. *Int. J. Rob. Res.* **1983**, *2* (1).
15. Jaramillo-Botero, A.; Crespo, A. *A Unified Formulation for Massively Parallel Rigid Multibody Dynamics of O(Log<sup>2</sup> N) Computational Complexity*; Journal of Parallel and Distributed Computing; Academic Press, June 1, 2002; Vol. 62 (6).
16. Yang, D.C.H.; Tzeng, S.W. Simplification and linearization of manipulator dynamics by the design of inertia distribution. *Int. J. Rob. Res.* **1986**, *5* (3).
17. Spong, M. *Remarks on Robot Dynamics: Canonical Transformations and Riemannian Geometry*, Proc. IEEE International Conference on Robotics and Automation, Nice, France, 1992, 554–559.
18. Eisenhart, L. *Riemannian Geometry*; Princeton University Press: Princeton, NJ, 1960.
19. Drexler, K.E. *Nanosystems: Molecular Machinery, Manufacturing, and Computation*; Wiley and Sons, 1992.
20. Asada, H.; Youcef-Toumi, K. *Decoupling of Manipulator Inertia Tensor by Mass Redistribution*, Proceedings ASME Mechanisms Conference, 1984.
21. Bedrossian, N. *Linearizing Coordinate Transformations and Euclidean Systems*, Workshop on Nonlinear Control of Articulated Flexible Structures, Santa Barbara, CA, Oct., 1991.
22. Denavit, J.; Hartenberg, R.S. A kinematic notation for lower-pair mechanisms based on matrices. *J. Appl. Mech.* **1955**, 215–221.
23. Lovelock, D.; Rund, H. *Tensors, Differential Forms, and Variational Principles*; Dover: New York, 1989.
24. Youcef-Toumi. Analysis and design of manipulators with decoupled and configuration-invariant inertia tensors using remote actuation. *Trans. ASME* **1992**, *114*.

# Molecular Motor-Powered Nanodevices: Control Mechanisms

Jacob J. Schmidt

Carlo D. Montemagno

*Department of Bioengineering, University of California–Los Angeles,  
Los Angeles, California, U.S.A.*

## INTRODUCTION

Although the biophysical and biochemical properties of motor proteins have been well studied, only recently have attempts been made to develop them as mechanical components in hybrid nanoengineered systems.<sup>[1–4]</sup> The motor protein  $F_1$ -ATPase is the smallest rotary motor known and can generate forces compatible with currently producible nanomechanical structures; we have previously fabricated and operated hybrid organic–inorganic nanodevices powered by  $F_1$ -ATPase (Fig. 1).<sup>[4]</sup> Control of device activity is a critical aspect in the engineering and deployment of integrated nanomachines. There are a variety of possible control mechanisms, including mechanical, optical, electrical, and chemical. We have previously implemented chemical controls into  $F_1$ -ATPase.<sup>[5]</sup> These controls followed from the design and construction of allosteric metal-binding sites that constituted a reversible and repeatable on/off switch of motor activity which was demonstrated in the bulk and at the single molecule level. For biomolecular motor-powered hybrid devices to fully realize their potential, progressing beyond scientific experiments and low-functioning curiosities, the devices and device components should be entirely reimagined from an engineering perspective. Development of a library of controls acting directly on motor proteins, their fuel, the components interfaced with them, or a combination of all of these will be highly useful toward increasing the utility, applicability, and range of operation of engineered biomotors.

In this entry, we will address these issues, describing the results of current research in which control of mechanical proteins incorporated into hybrid devices has been addressed for the first time. We will also discuss our recent work in which chemical controls were incorporated into the  $F_1$ -ATPase, able to reversibly start and stop the mechanical motion at the single molecule level. We will conclude with an outlook of the field as a whole and future directions.

## MECHANISMS AND STRATEGIES FOR CONTROL OF MOTOR PROTEINS

The  $F_1$ -ATPase is a biomolecular rotary motor deriving its mechanical energy from the hydrolysis of ATP. The loaded motor has been measured at the single molecule level to generate a constant torque of  $\sim 40$  pN nm while operating at high (50–100%) efficiency.<sup>[6,7]</sup> The no-load rotational velocity of  $F_1$ -ATPase has been measured to be over 7800 rpm.<sup>[8]</sup> In addition, genetic modification of  $F_1$ -ATPase has allowed the precise (sub-50 nm) positioning of single  $F_1$ -ATPase molecules on engineered nanofabricated substrates of nickel-capped posts.<sup>[4,9]</sup> Such advantageous natural and engineered characteristics of  $F_1$ -ATPase make it an ideal candidate for precision orientation and attachment to nanomechanical structures.<sup>[4,10,11]</sup>

Potential applications of devices using the  $F_1$ -ATPase and other motor proteins are currently limited because of the lack of control over the motor motion. The capability of the motor to reversibly turn on and off in response to an external signal represents an important first step in rational and useful device design for the next generation of biomolecular devices. Motor activity must be directed for device manipulation and efficient use of fuel. In natural biological systems such as the cell, thousands of proteins work interdependently, regulating themselves and others to ensure that the cell can adapt to changing external conditions, wasting no resources and ensuring that essential functions are carried out. These natural biological control mechanisms of proteins and protein complexes regulate their function in response to a variety of external stimuli: chemical, thermal, and mechanical, among others.

Commonly occurring natural controls include conformational changes in some proteins occurring in certain ranges of pH or ionic strength. These shape changes can alter the catalytic or hydrolytic activity of the protein, slow it down, or affect its interactions

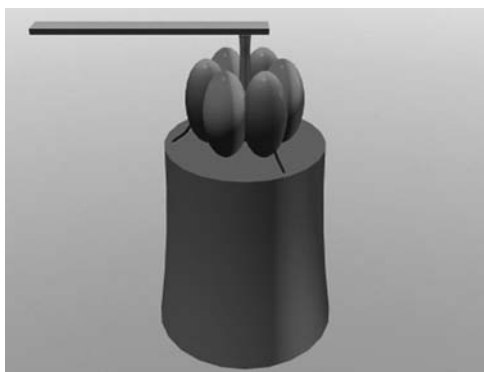


**Fig. 1** Depiction of the hybrid nanodevice constructed previously.<sup>[4]</sup> Electron beam lithography was used to construct 50-nm Ni-capped SiO<sub>2</sub> posts on which individual 10 × His-tagged F<sub>1</sub>-ATPase motors were mounted. Ni rods, 75 × 750 nm, were linked to the rotor of the motor through a peptide/biotin/streptavidin/biotin bond. Upon addition of ATP, the rods were observed to rotate using conventional optical microscopy.

with other proteins. These conformational changes can also be induced through the application of electric fields. The advantages of engineering these kinds of responses in motor protein-based hybrid devices draw upon the capability of micro- and nanoelectromechanical systems, MEMS and NEMS, fabrication to place arrays of electrodes at arbitrary positions on a substrate surface. Electric fields produced by such electrodes would give the power to individually address single motors. Electrical control has been shown to exist naturally in the family of porins. Porins are pore proteins that transport water and other solutes across cell membranes, controlling concentration-dependent properties such as osmolarity and acidity. Some porins have been shown to open and close physically in response to an applied voltage, a shape change that activates and deactivates the proteins' transporting ability.<sup>[12–14]</sup> These shape changes are a result of charged or polar groups in the protein responding to an external electric field and, on a small scale, occur in every ligand-receptor binding event. It may be possible to engineer similar responses on other proteins using polar or charged residues to enhance these responses. Proteins not containing the necessary functional groups to respond to the applied fields can be engineered to contain the groups or to further tune their response, much in the same way as the chemical binding sites discussed above were created. Electrical control mechanisms have the promise of addressability, control of activity, and easy interfacing with external instrumentation.

Motor activity can also be controlled without changing the protein conformation. Attachment of cargo presenting variable loads resulting from viscous, electric, or magnetic forces will result in a change of the

motor speed for molecular motors with constant torque output, such as F<sub>1</sub>-ATPase. Although this will not be possible in every case, it is a powerful and flexible method of motor control. Any moving part attached to the motor, if susceptible to an external field, may be used to increase controllably the drag force experienced by the motor. Work by Noji et al.<sup>[15]</sup> have used this principle to study the rotation characteristics of F<sub>1</sub>-ATPase. In these experiments, magnetic beads were attached to F<sub>1</sub>-ATPase motors lying on a substrate while observed by optical microscopy. As the rotary shaft of the motor turned, the bead turned with it. An external magnetic field with controllable direction and magnitude was applied to this system, creating a counterforce opposing the rotation of the motor. Fields large enough to slow and stall the motor were used, with the result that the rotary energy potential of the motor was determined.

There are several different strategies for the implementation of controls into hybrid biomotor devices. In contrast to natural systems, primitive engineered hybrid nanosystems to date have contained only a few proteins removed from their natural environments and therefore also removed from their natural control mechanisms. As a consequence, much regulation of the function of motor proteins is often possible only through regulation of the fuel supply. Fuel-based control techniques are able only to activate motors, with the motors functioning until the fuel is exhausted. In the regime of Michaelis–Menten kinetics (i.e., in a steady state when the substrate concentration is much greater than the enzyme concentration),  $V = V_{\max}[S]/(K_M + [S])$ , where  $V$  is the catalytic turnover rate,  $V_{\max}$  is the maximum rate,  $[S]$  is the substrate concentration, and  $K_M$  is the Michaelis constant. Therefore the enzyme velocity can be controlled by the substrate concentration, for substrate concentrations small compared with  $K_M$  ( $K_M$  for unloaded F<sub>1</sub>-ATPase is 15 μM). There are significant shortcomings with an approach based on the regulation of the fuel supply: other ATP-utilizing molecules will also be affected, there is no differential motor control, and fine control of operational parameters such as speed is not possible.

Recent work in chemical control mechanisms has utilized light-activated “caged” ATP, a chemical derivative of ATP in a non-hydrolyzable form, which is able to release a defined amount of ATP related to the intensity, duration, and location of optical illumination.<sup>[16]</sup> This technique has controlled the operation of kinesin motors for proscribed periods of time as they proceeded along microtubule tracks (Fig. 2).<sup>[1]</sup> Alternative mechanisms of fuel-based control include myosin mutants with engineered binding sites having sensitivities for analogs of ADP with bulky side

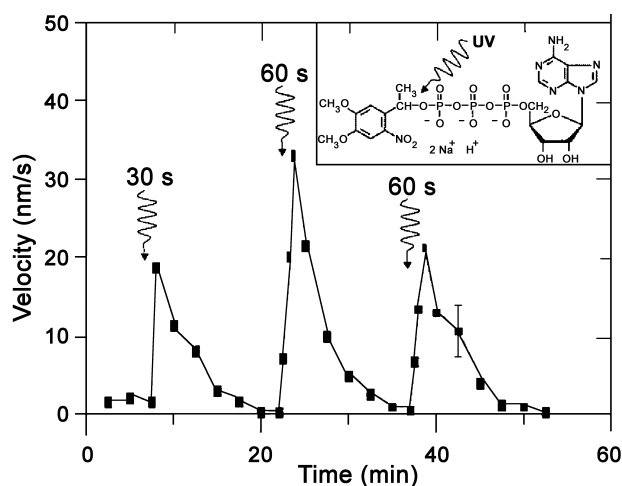


**Fig. 2** Average speed of microtubules after exposure of caged ATP to UV light for 30, 60, and 60 sec converting 20%, 30%, and 20% of the initial caged ATP into free ATP. The presence of the ATP-consuming enzyme, hexokinase, leads to a rapid decline of the microtubule velocity. The inset shows the structure of DMNPE-caged ATP. *Source:* From Ref.<sup>[1]</sup>.

chains such as *N*<sup>6</sup>-(2-methylbutyl) ADP, allowing differential control between specific motor types.<sup>[17]</sup>

Alternatively, chemical control of the motors apart from fuel regulation may be effected through chemical modification of the motor itself. By engineering peptides which bind directly to each other, the motor can be stopped in the presence of the appropriate chemical reagents, as in reversible disulfide cross-linking of kinesin.<sup>[18]</sup> Alternatively, enzyme activity may be altered by engineering metal ion-binding sites (e.g., the addition or substitution of histidine, aspartate, or lysine residues)<sup>[19]</sup> into appropriate regions of the protein. The presence of these metal-binding sites can fix adjacent regions of the protein to each other by introduction of metal ions into these binding sites. This induces strong bonding between the ions and adjacent residues. Because ions can bind several amino acids simultaneously, it is possible to attach two separate, independent regions to the ion—in effect, altering the local elasticity of these subunits by fixing them to each other. If movement of these regions is necessary for protein activity, this activity can be impaired or entirely halted. This is an illustration of an allosteric control mechanism, a mechanism in which enzyme function is controlled without affecting substrate availability or reactivity. With this aim, we genetically modified the F<sub>1</sub>-ATPase, engineering pockets in the enzyme with high affinity for binding zinc ions. When the protein binds the zinc, it is incapable of performing the conformational changes necessary for rotation of its central shaft, the  $\gamma$  subunit, therefore stopping the motor from further motion.

## IMPLEMENTATION OF ALLOSTERIC CHEMICAL CONTROLS INTO F<sub>1</sub>-ATPASE

Isolated F<sub>1</sub>-ATPase is composed of five different subunits with stoichiometry of  $\alpha_3\beta_3\gamma\delta\epsilon$ . The  $\alpha_3\beta_3\gamma$  sub-complex of F<sub>1</sub>-ATPase has been identified as a minimum ATPase-active complex with characteristics and stability similar to native F<sub>1</sub>-ATPase.<sup>[20–22]</sup> The X-ray crystallographic structures of the F<sub>1</sub> fragment of the bovine mitochondrial ATPase (BF<sub>1</sub>) have revealed the nature of the conformational changes involved in ATP hydrolysis in atomic detail.<sup>[23]</sup> The crystal structures of BF<sub>1</sub> show that three  $\alpha$  and three  $\beta$  are arranged alternately forming a hexameric aggregate having one nucleotide binding site each, with the long coiled-coil structure of the  $\gamma$  subunit inserted into the central cavity of the ring. There are three catalytic sites, located on  $\beta$  subunits at  $\alpha/\beta$  interfaces, and three non-catalytic sites, located on  $\alpha$  subunits at different  $\alpha/\beta$  interfaces. The  $\beta$  subunits assume two conformations in the crystal structures, an open and a closed state, that interconvert via a hinge-bending motion. In the closed state, the  $\beta$  subunit binds ATP ( $\beta_T$ ) or ADP ( $\beta_D$ ); in the open state, the active site is empty ( $\beta_E$ ). The corresponding conformations of the  $\alpha$  subunits are designated as  $\alpha_T$ ,  $\alpha_D$ , and  $\alpha_E$ . The conformations of  $\alpha_T$ ,  $\alpha_D$ , and  $\alpha_E$  are nearly identical. In contrast, the structures of  $\beta_T$  and  $\beta_D$ , which are quite similar to each other, are completely different from that of  $\beta_E$ . The  $\beta_T$  and  $\beta_D$  are in the “closed” conformation, the C-terminal domain of which is elevated, closed to the nucleotide binding domain, while the  $\beta_E$  is in the “open” conformation, with its substrate binding site open.<sup>[23–25]</sup> Although  $\beta_T$  and  $\beta_D$  adopt the same overall state, there are structural differences in several surface loops related to the critical role of these states in the rotary motion of this complex.

During ATP synthesis, the three non-catalytic sites are homogeneously liganded with MgAMP-PNP (an ATP analog), whereas the three catalytic sites are heterogeneously bound to ligands during normal enzyme operation. These structural features, in addition to the direct observation of  $\gamma$  rotation in F<sub>1</sub>-ATPase,<sup>[26]</sup> strongly support the binding change model established by Boyer.<sup>[27]</sup> The rotary mechanism postulated by this model assumes that the sequential participation of the three catalytic sites and alternate interchange of their roles during ATP hydrolysis drive the counterclockwise rotation of the  $\gamma$  subunit.<sup>[28,29]</sup> In other words, the intrinsic conformational changes induced by the heterogeneous nucleotide affinities to catalytic sites, coupled with the rotation of  $\gamma$ , are crucially necessary for the catalysis of ATP hydrolysis.

The binding change mechanism suggests that F<sub>1</sub>-ATPase activity can be controlled by blocking the conformational changes necessary for ATP hydrolysis.

Because the six  $\alpha/\beta$  interfaces (three interdimer and three intradimer) are all different, and the rotation of the  $\gamma$  subunit relies on sequential interchange between different conformational and substrate ligation states, we hypothesized that reversible inhibition of the catalytic and rotation cycle may be achieved through insertion of secondary metal binding site capable of interfering with the sequential cycle (Fig. 3). When the open/closed conformational interconversion of the  $\beta$  subunits is hindered, the nucleotides that have been bound (MgATP or MgADP) are trapped and free nucleotides are prevented from entering the binding sites. Because the conformational states of  $\alpha_T$ ,  $\alpha_D$ , and  $\alpha_E$  are identical, they provide an immobile substrate to which the  $\beta$  subunits can be fixed, physically preventing switching between cooperative nucleotide binding sites and the rotational movement of the  $\gamma$  subunit. The effect of this hypothetical conformational lock is to fully inhibit the operation of F<sub>1</sub>-ATPase. Such a site is therefore predicted to function as a classic allosteric inhibitor of enzyme activity<sup>[30]</sup> and should provide a chemical switch for the control of motor activity in a nanomechanical device.

Obviously, a strong permanent binding of the  $\alpha$  and  $\beta$  subunits directly to each other would permanently immobilize the protein, possibly irreversibly. However, binding them each to a multivalent ligand in effect

binds them to each other, accomplishing the same immobilization. Furthermore, removal of the ligands restores the protein to its initial state and reverses the immobilization. With this in mind, we modeled bovine mitochondrial F<sub>1</sub>-ATPase and designed binding sites in the protein intended to have high affinities for zinc ions. We chose to construct an allosteric control element based on a zinc-binding site, as these domains are relatively compact, consisting of three or four amino acids that chelate the metal.<sup>[31]</sup> Moreover, computational design methods have been developed that reliably predict and construct de novo metal centers into proteins of known structure.<sup>[32–34]</sup> Reversible inhibition of the enzymatic activity may be readily achieved by the addition of extrinsic metal chelators (e.g., 1,10-phenanthroline) that sequester zinc, but not the Mg<sup>2+</sup> required for ATP binding and hydrolysis. The bovine protein was modeled because the crystal structures of the F<sub>1</sub>-ATPase in empty, ATP-bound, and ADP-bound states are known. Such structures of the F<sub>1</sub>-ATPase from thermophilic *Bacillus* PS3 (TF<sub>1</sub>), used in our previous experiments, are not available. However, TF<sub>1</sub> also has a functional asymmetry among the three catalytic subunits, although it does not contain any endogenously bound nucleotide.<sup>[35]</sup> Therefore the binding change model-based design for the fixation of conformational change in bovine F<sub>1</sub>-ATPase

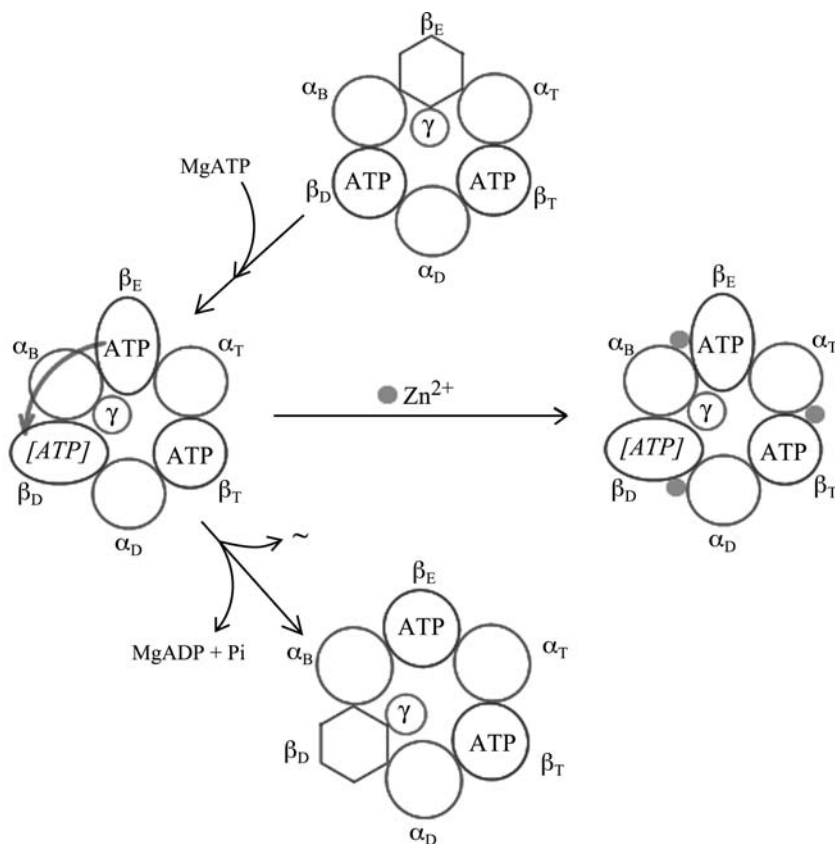


**Fig. 3** Model for zinc switch-controlled ATPase. Counterclockwise rotation of the  $\gamma$  subunit from  $\alpha_E$  to  $\beta_D$  initiates a conformational change. Blue circles represent  $\alpha$  subunits liganded with MgATP (omission of ATP for clarity). Green circles represent  $\beta$  subunits at different states: circles represent  $\beta$  liganded with MgATP, ellipses represent  $\beta$  in the transition from closed to open conformation, and hexagons represent  $\beta$  in open conformation. [ATP] represents the transition state of  $\beta_D$  converting from closed to open conformation.  $\sim$  represents the energy released during the hydrolysis. While the zinc binds to the engineered additional binding site, the conformation of  $\alpha_3\beta_3\gamma$  is locked in one state, so that neither ATP nor ADP can enter in or exchange out.



is suitable to be applied to TF<sub>1</sub>. The binding sites were produced through the replacement of selected glycine, glutamine, and aspartate residues with histidine.

To design locations for allosterically active zinc-binding sites in BF<sub>1</sub>, we first identified regions in the interfaces that undergo local conformational changes, but are not part of the active site. In collaboration with Hellinga et al.<sup>[36]</sup> at Duke University, protoallosteric sites were identified using C<sub>α</sub>-C<sub>α</sub> double-difference distance maps comparing β<sub>E</sub> and β<sub>T</sub> structures. These binding sites were placed at locations in each α/β interface having large relative motions during catalytic activity but separate from nucleotide binding sites. The DEZYMER algorithm protein design program<sup>[32]</sup> was used to carry out the calculations and refinement of site design for the construction of a tetrahedral zinc center at the interface between each pair of α and β subunits. The idealized tetrahedral zinc primary coordination sphere consists of three histidines and a water molecule. The zinc is allowed to coordinate with either the N<sub>δ</sub> or N<sub>ε</sub> nitrogens of the histidines and is constrained within the plane of the imidazole rings.<sup>[33,37,38]</sup>

The algorithm predicted a set of sites that were then rank-ordered and examined by inspection. The geometry of the interaction between the metal and the histidine side chains is derived from visual inspections of natural protein structures.<sup>[39]</sup> We chose a site located in the interdimer interface between β<sub>D</sub> and α<sub>E</sub>. This designed site replaces glutamine α405, glycine β392, and aspartate β400 in BF<sub>1</sub> with histidine residues. The initial design phase yielded a site with approximate tetrahedral geometry. This site was then optimized using a combination of molecular dynamics and conjugate gradient energy minimizations to satisfy the metal coordination geometry resulting in movement of the loop in this region. Mutations were chosen to satisfy both the desired metal binding geometry and the steric compatibility of the protein folding (Fig. 4).

Using site-directed mutagenesis, the peptide replacements were made to the gene encoding a mutant F<sub>1</sub>-ATPase (named DEMHZ) with 10 × His tags on the β subunits and a lone cysteine on the γ subunit, described previously.<sup>[4]</sup> The modified α, β, and γ coding sequence of TF<sub>1</sub>, DEMH, which contains five additional mutations as a working wild type, was cloned into the expression plasmid pETBlue<sup>TM</sup> (Novagen) with a T7 lac promoter. The vector-encoded *Nhe*I site (3434) was eliminated (gctagc to gcgagc). Three histidines for creating the zinc binding sites were introduced by standard PCR oligonucleotide-directed mutagenesis techniques using Pfu DNA polymerase (Stratagene). Specifically, they are Gln-397-His on α and Gly-398-His and Asp-406-His on β (calculated with the inclusion of the 10 × His tags). Expression of the recombinant protein, DEMHZ, was conducted in *Escherichia coli* Tuner<sup>TM</sup> (λDE3) pLacI (Novagen).

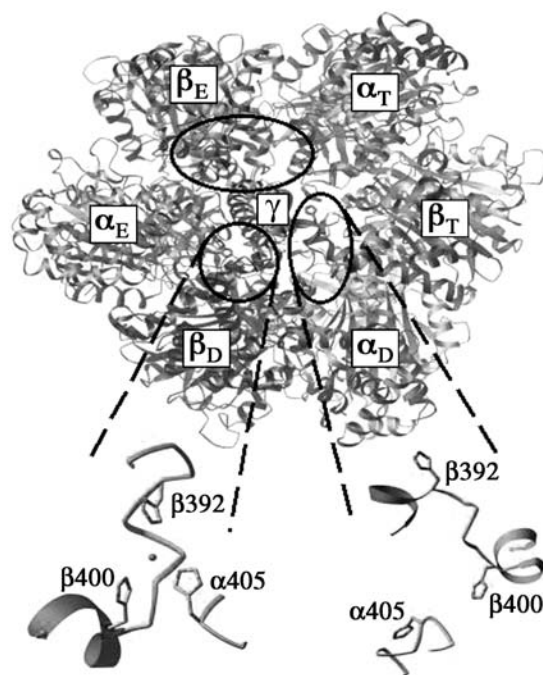


**Fig. 4** Molecular model of the computationally designed Zn<sup>2+</sup> binding site in BF<sub>1</sub> ATPase. The histidines in the three interdimer interface locations are shown in red. The circle indicates the site in the β<sub>D</sub> / α<sub>E</sub> interface predicted to form a tetrahedral Zn<sup>2+</sup>-binding site (left insert). The ovals indicate that the sites in the other two interdimer interfaces do not form a geometry predicted to favor metal binding (right insert).

The mutations on pETBlue-DEMZHZ were checked by restriction enzyme digestion and confirmed by DNA sequencing, which failed to reveal any additional mutations or frameshifts. DEMHZ protein was over-expressed in *E. coli* Tuner<sup>TM</sup> (λDE3) by IPTG induction and purified to homogeneity by Ni-NTA affinity chromatography. There was some concern about the endogenous ATPase genes in the host strain Tuner<sup>TM</sup> (λDE3) pLacI. However, because the recombinant protein was stable to 100°C, and the crude lysate was prepared by heating the extracts at 60°C for 45 min, the native protein subunits should have denatured completely under such conditions. Moreover, the use of Ni-NTA affinity chromatography also ensured the purification of His-tagged constructs only. So it was very unlikely that chimeric F<sub>1</sub>-ATPase was purified.

Following the generation of the mutant, the motor was grown in large quantities in a bacterial expression system, harvested, and purified. *E. coli* Tuner<sup>TM</sup> (λDE3) pLacI containing the F<sub>1</sub>-ATPase mutant expression plasmid, pETBlue-DEMZHZ, was cultured at 37°C in LB medium (with 1% glucose, 50 μg/ml carbencillin, and 34 μg/ml chloramphenicol). When the growth of this transformant reached the mid-logarithmic phase (OD<sub>600</sub> = 0.6), 1 mM of

isopropyl- $\beta$ -thiogalactopyranoside (IPTG) was added to induce endogenous T7 polymerase, and the cells were cultured successively for 4 hr. Purification of the mutant  $\alpha_3\beta_3\gamma$  subcomplex was carried out following the methods by Matsui and Yoshida<sup>[40]</sup> with some minor modifications. Cells were harvested by centrifugation at  $6000 \times g$  for 20 min at 4°C. The collected cells (7.5 g out of 2 L culture) were resuspended in buffer A (50 mM Tris-SO<sub>4</sub>, 1 mM EDTA), incubated with lysozyme on ice for 30 min. The suspension was disrupted by sonication, and then heated at 60°C for 15 min. The precipitate was removed by centrifugation at  $105,000 \times g$  (Beckman JA-30.50) for 15 min. The supernatant was saved and heated at 60°C for 30 min and then centrifuged at  $105,000 \times g$  for another 45 min. The supernatant fraction was applied to HiPrep<sup>®</sup> 16/10 DEAE column (Pharmacia) that was pre-equilibrated with buffer A. The column was washed with 200 mL of buffer A containing 150 mM NaCl and eluted with 80 mL of a 300–330 mM linear NaCl gradient. The eluted fractions were concentrated by adding ammonium sulfate to a final concentration of 75% saturation. The resuspended pellet was mixed with nickel-nitrilotriacetic acid (Ni-NTA) Superflow<sup>™</sup> resin (QIAGEN), following a batch purification procedure.<sup>[41]</sup> After washing the unbound proteins, the bound proteins (with  $10 \times$  His tags) were eluted out with 1 M imidazole. The purity of the DEMHZ was analyzed by sodium dodecyl sulfate-polyacrylamide gel electrophoresis (SDS-PAGE) using a 12% polyacrylamide gel. Protein concentrations of the  $\alpha_3\beta_3\gamma$  complex were determined by measuring the absorbance at 280 nm using coefficient factor 0.45 of absorbance for 1 mg/mL of F<sub>1</sub>-ATPase. Steady-state ATPase activity was determined spectrophotometrically at 25°C in the presence of an ATP-regenerating system.<sup>[42]</sup>

Bulk ATPase activity assays using an ATP-regenerating coupled enzyme system were performed to determine if Zn(II) could effectively inhibit the activity of the engineered ATPase, as well as the minimum Zn(II) concentration for full activity inhibition. To investigate the zinc effect on the DEMHZ, the indicated amount of ZnSO<sub>4</sub> was added to the assay mixture, which contained 50 mM Tris-HCl (pH 7.4), 100 mM KCl, 2.5 mM phosphoenolpyruvate, 50  $\mu$ g/mL double enzyme composed of pyruvate kinase and lactate dehydrogenase (Roche), 0.2 mM NADH (Sigma), 2 mM Na<sub>2</sub>ATP, and 4 mM MgCl<sub>2</sub>. One unit of activity was defined as the activity that hydrolyzed 1  $\mu$ mol ATP/sec/ $\mu$ mol ATPase. Assessment of zinc effect on ATP binding affinity to catalytic sites was carried out in the same assay system, except with a fixed concentration (800  $\mu$ M) of zinc that could effectively inhibit ATPase activity, and various concentrations of ATP. An experiment reversibly activating and deactivating the F<sub>1</sub>-ATPase was carried out by

adding 800  $\mu$ M of zinc and about 10% excess of the specific metal ion chelator 1,10-phenanthroline.

A summary of our previous work comparing ATPase activity of the mutant and wild-type<sup>[5]</sup> is shown in Fig. 5. In the absence of Zn<sup>2+</sup>, DEMH and DEMHZ exhibited similar specific activity, indicating that the histidine mutations did not affect catalysis. Addition of Zn<sup>2+</sup> to DEMHZ reduced the activity by 60% at saturating concentrations, but did not affect wild-type TF<sub>1</sub>. Zn<sup>2+</sup> bound hyperbolically with an apparent dissociation constant of  $8.6 \pm 1.2 \mu$ M. The Scatchard plot was linear (not shown) and consistent with noncooperative binding of Zn<sup>2+</sup>. An Eadie-Hofstee transformation of the steady-state kinetics with respect to ATP at various Zn<sup>2+</sup> concentrations revealed a pattern that is consistent with a linear mixed inhibition mode, in which both  $K_m(\text{ATP})$  and  $V_{\max}$  are affected by Zn<sup>2+</sup>. This finding is consistent with binding of Zn<sup>2+</sup> to both the free enzyme and the enzyme-substrate complex,<sup>[43]</sup> as expected. Repeated cycles of Zn<sup>2+</sup> addition followed by chelation with 1,10-phenanthroline demonstrated that the Zn<sup>2+</sup> inhibition of the enzyme's hydrolytic activity was reversible. This deactivation/reactivation cycle could be repeated many times. Taken together, these data suggest that we have successfully designed a Zn<sup>2+</sup>-dependent allosteric effector site that reversibly modulates TF<sub>1</sub> activity, as predicted.

Enzyme kinetics derived from these studies indicated that the mutant DEMHZ  $\alpha_3\beta_3\gamma$  has much higher propensity than wild type to bind Zn(II). However, quantification of the effect of the zinc on the mutant and wild-type protein was complicated by the discovery that the coupled enzyme assay itself was affected by the addition of zinc. We also conducted phosphorus colorimetric detection assays, an alternative method of measuring ATPase activity, and found possible effects on wild-type activity, but the sensitivity of that technique was poor and formed a precipitate at certain reagent concentrations. We did not use the P<sub>i</sub> release method for measuring ATPase activity because it is not able to monitor rate fluctuations.<sup>[44]</sup>

Several conclusions can be made from the data. 1) Zn(II) did not alter the affinities of catalytic sites of the wild-type  $\alpha_3\beta_3\gamma$  complex for ATP significantly, suggested by  $K_m = 210 \mu$ M in the presence of zinc vs.  $K_m = 159 \mu$ M in the absence of zinc. 2) Zn(II) has a strong effect on the ATPase activity of the mutant complex. In the presence of Zn(II), the activity was nearly fully inhibited; however, it was noticed that at low ATP concentrations, a precipitate formed upon addition of Zn(II), complicating the measurement of ATP hydrolysis rate. Therefore it remains unclear whether Zn(II) alters the ATP affinity to the mutant  $\alpha_3\beta_3\gamma$  complex, apart its direct effect on hydrolysis. 3) ATP hydrolysis of both the mutant and wild-type

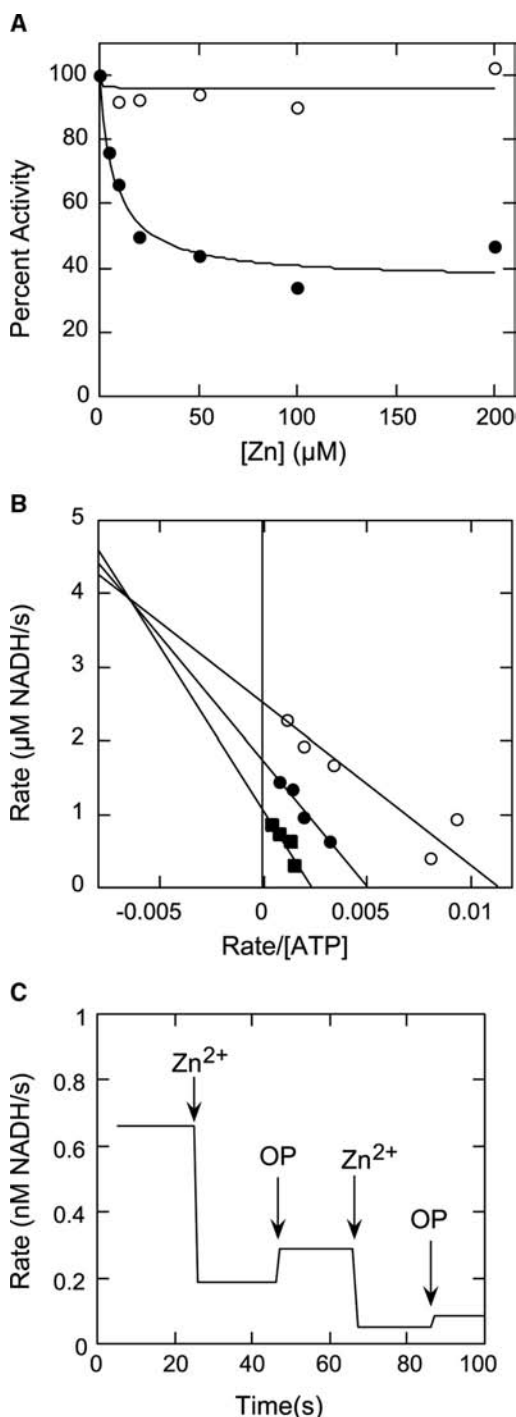


**Fig. 5** Steady-state kinetics of ATP hydrolysis in the wild-type and mutant TF<sub>1</sub> enzymes. (A) The effect of Zn<sup>2+</sup> addition on the activity of wild-type (DEM<sub>H</sub>; open circles) and mutant (DEM<sub>HZ</sub>; closed circles) enzymes. For DEM<sub>HZ</sub>, Zn<sup>2+</sup> binding is modeled with a hyperbolic binding isotherm 19, with <sup>app</sup>K<sub>d</sub> = 8.6 μM. (B) Eadie-Hofstee transformation of the steady-state kinetics of DEM<sub>HZ</sub> with respect to ATP concentration in the presence of different Zn<sup>2+</sup> concentrations (open circles, 0 μM; closed circles, 5 μM; squares, 200 μM). (C) Two cycles of successive additions of 100 μM Zn<sup>2+</sup> and 150 μM 1,10-phenanthroline (OP). Source: From Ref.<sup>[5]</sup>.

$\alpha_3\beta_3\gamma$  complex exhibited negative cooperativity as a function of ATP concentration, as indicated by the Eadie-Hofstee plots, consistent with reported literature.<sup>[24,40]</sup> 4) This zinc switch mutant had a  $K_m$  (1490 μM) over 9 times bigger than wild-type  $K_m$  (159 μM) in the absence of Zn(II), which might be a result of some intrinsic changes made by introducing the zinc-binding site in the mutant  $\alpha_3\beta_3\gamma$  complex. 5) It is possible that Zn(II) substitutes in a functional manner for Mg<sup>2+</sup>. If this was true, Zn(II) competitively bound to ATP as well as to the mutant  $\alpha_3\beta_3\gamma$  complex, which led to a full inhibition of ATPase activity of the mutant. The actual number of bound Zn(II) equivalents to the mutant  $\alpha_3\beta_3\gamma$  complex remains to be determined.

To overcome the shortcomings of the bulk activity assays and also demonstrate the ability of the engineered mutation to enable control of the motors on the single molecule level, we observed fluorescent actin filaments attached to individual molecules of TF<sub>1</sub>. A flow chamber was constructed consisting of one (22 × 40 mm #0) coverslip attached to a microscope slide using double-sided tape. In buffer A (50 mM KCl, 5 mM MgCl<sub>2</sub>, 10 mM MOPS-KOH, pH 7) (1:10), 0.1% Ni-NTA-coated polystyrene beads<sup>[45]</sup> (0.22 μm) was infused into the flow cell and incubated for 15 min, resulting in a bead density of several beads in a 5 × 5 μm<sup>2</sup> area. Nonadherent beads were removed through rinsing 3 times with 2 volumes of buffer B (buffer A + 10 mg/mL BSA). The His-tagged biotinylated ATPase (28 nM) in buffer B was then incubated for 5 min and rinsed 3 × with 2 volumes of buffer B. Streptavidin (180 nM) in buffer B was incubated for 12–15 min and rinsed 3 × with 2 volumes of buffer B. Actin filaments (fluorescently labeled with Phalloidin-TRITC, polymerized, and biotinylated<sup>[26]</sup>) were diluted to 50 nM in buffer B and incubated in the flow chamber for 12–15 min. The chamber was washed twice with 2 chamber volumes of buffer B and a third wash of 2 chamber volumes of buffer C [buffer B with an oxygen scavenger (0.5% 2-mercaptoethanol, 30 U/mL catalase, 6 mg/mL glucose, and 0.2 mg/mL glucose oxidase) and an ATP regenerating system (2 mM Na<sub>2</sub>ATP, 0.2 mg/mL creatine kinase, and 2.5 mM creatine phosphate)]. The actin filaments were observed using a Nikon E800 upright optical microscope in epifluorescent mode. ZnSO<sub>4</sub> (800 μM) in buffer C was added to measure any inhibition on the mutant and wild-type protein. 1,10-Phenanthroline (800 μM) in buffer C was added to determine the reversibility of the zinc switch.

Upon addition of ATP, some filaments were observed to rotate clockwise (as expected because the motors were attached to the top surface and viewed from the motor side “upside-down”), although the majority were stationary or fluctuated around a central

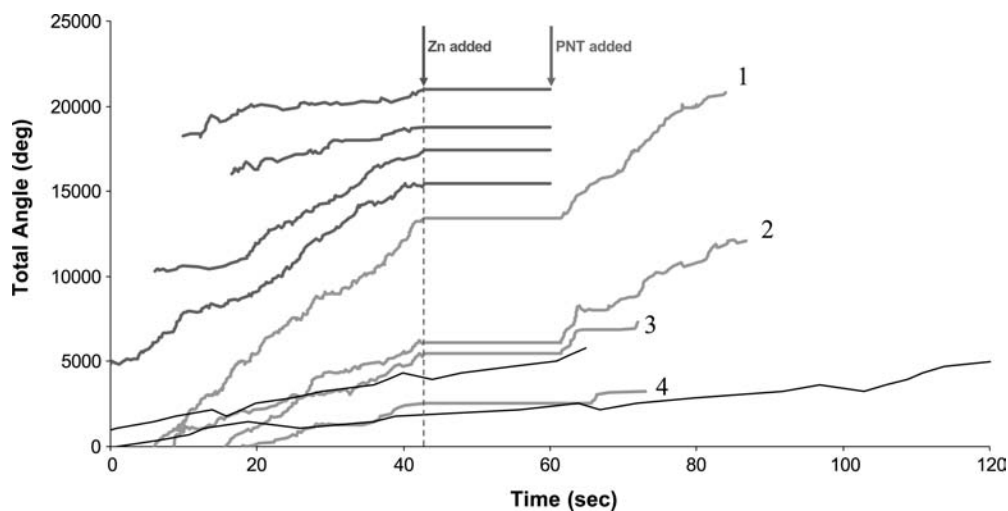


**Fig. 6** Measurements of single molecule rotation and control. The movements of rotating fluorescent actin filaments were recorded and digitized. The rotation angle vs. time is shown for eight filaments attached to the mutant ATPase and two filaments attached to motors without the zinc mutation (black lines). The filaments rotated continuously in the presence of ATP. After the addition of  $800\ \mu\text{M}$   $\text{ZnSO}_4$  (blue arrow), the filaments attached to the mutant motor stopped, whereas the filaments attached to the wild-type motor continued rotating at the same rate. 1,10-Phenanthroline ( $800\ \mu\text{M}$ ) was added to the stopped filaments (red arrow), restarting the motor motion. There was an interval of about 3 sec after the addition of both the  $\text{Zn}^{2+}$  and the phenanthroline in which the filaments were unfocused because of disturbance of the stage position, preventing a more precise determination of the times of cessation and reinitiation of motion. Some filaments dislodged from the surface during the replacement and so rotation data following the PNT addition is not available (green lines). The data for all filaments have been shifted in time to synchronize the  $\text{Zn}^{2+}$  addition times. There appear to be no lasting effects of the  $\text{Zn}^{2+}$  on the motors. The rotational rates before  $\text{Zn}^{2+}$  addition and after  $\text{Zn}^{2+}$  removal are similar, as linear fits of each of the pink traces show: (1) before  $\text{Zn}^{2+}$  0.96 rotations/sec, after  $\text{Zn}^{2+}$  0.97 rotations/sec; (2) 0.61, 0.61; (3) 0.36, 0.32; (4) 0.27, 0.19. The differences between the numbers are within the variations of rotational rate of each before Zn addition. The lengths of filaments 1–4 are 1.75, 2.0, 2.25, and 2.25  $\mu\text{m}$ , respectively.

position. There were no filaments observed rotating in the counterclockwise direction. The rotating filaments were then incubated with  $800\ \mu\text{M}$   $\text{ZnSO}_4$  and 2 mM ATP. Some filaments detached from the surface during this buffer exchange, but all rotating filaments (and some fluctuating filaments) remaining were observed to stop after introduction of the Zn. After several minutes, the filaments remained immobilized and  $800\ \mu\text{M}$  1,10-phenanthroline, a Zn chelator, and 2 mM ATP were introduced in the chamber. The filaments which were formerly rotating and were not dislodged during the fluid exchange restarted their motion (likewise with the formerly fluctuating filaments). Experiments with the wild-type motor showed no effects resulting from the presence of zinc; rotating filaments continued their motion at the same rate both before and after Zn addition. To verify that the rotation mechanism of the filaments was because of the motor proteins, introduction of 0.5 M imidazole resulted in the detachment of all moving actin filaments in both the wild type and mutant experiments. In addition, although the wild-type motors were not inhibited by zinc, addition of 10 mM sodium azide halted filament rotation. Plots of the rotation angle vs. time for several filaments are shown for both the mutant and wild type

in Fig. 6. The process of Zn addition and removal from the mutant protein does not appear to have any permanent effect on the mechanical properties of the mutant ATPase; that is, the rotation rates before zinc addition and after zinc removal are very close. Furthermore, the mutation to the ATPase has not appeared to alter its mechanical characteristics when compared with the wild type; that is, the motors rotate filaments of the same length at the same rate, indicating that the torque output and efficiency of the motor are unchanged.

## CONCLUSION

In summary, we have genetically engineered a zinc switch in the  $\alpha_3\beta_3\gamma$  complex of  $\text{TF}_1$ . Through introducing or removing the Zn(II), the conformations of the  $\alpha_3\beta_3\gamma$  complex were correspondingly fixed or freed, such that the  $\text{F}_1$ -ATPase activity could be turned on and off. This allowed us to switch the nanodevice coupled with this genetically modified  $\text{F}_1$ -ATPase on and off in a well-controlled way. Regarding the creation and implementation of control mechanisms in general, each type of control mechanism has unique advantages and disadvantages relative to the intended

application. Chemically controlled motors could result in devices that respond to their environment variables, such as pH, ionic concentration, and temperature, and are not tied to any specific location, although all engineered motors would be affected. Immobile substrate-bound devices may be best served by electrical contacts integrated into the surface; this allows for differential control, in which some devices are operational while others are not. These contacts have the advantages of easy and configurable connections to the outside world and rapid conveyance of signals from the controller to the device. Some proteins can be both electrically and chemically controlled. This flexibility in choices allows the design and application requirements to dictate the components and not vice versa. Exploration and development of artificial protein binding sites, determination of optimal electrode configurations, electric field magnitudes and frequencies, and buffer compositions utilize computational calculations and simulations. These techniques are necessary for screening large numbers of variables and exploring regions of parameter space prohibitive from a cost and time perspective. Establishment of a library of controls and control techniques is a crucial step toward a wider array of useful hybrid bionanodevices.

## ACKNOWLEDGMENTS

The tireless work of Haiqing Liu resulted in the successful generation of the mutant, biochemical assays, and single molecule measurements. We also thank Homme Hellinga, Loren Looger, and Shahir Rizk at Duke University for their assistance in binding site design and biochemical assays.

## REFERENCES

- Hess, H.; Clemmens, J.; Qin, D.; Howard, J.; Vogel, V. Light-controlled molecular shuttles made from motor proteins carrying cargo on engineered surfaces. *Nano Lett.* **2001**, *1* (5), 235–239.
- Bohm, K.J.; Stracke, R.; Muhlig, P.; Unger, E. Motor protein-driven unidirectional transport of micrometer-sized cargoes across isopolar microtubule arrays. *Nanotechnology* **2001**, *12*, 238–244.
- Hiratsuka, Y.; Tada, T.; Oiwa, K.; Kanayama, T.; Uyeda, T. Controlling the direction of kinesin-driven microtubule movements along microlithographic tracks. *Biophys. J.* **2001**, *81*, 1555–1561.
- Soong, R.K.; Bachand, G.D.; Neves, H.P.; Olkhovets, A.G.; Craighead, H.G.; Montemagno, C.D. Powering an inorganic nanodevice with a biomolecular motor. *Science* **2000**, *290* (5496), 1555–1558.
- Liu, H.; Schmidt, J.J.; Bachand, G.D.; Rizk, S.S.; Looger, L.L.; Hellinga, H.W.; Montemagno, C.D. Control of a biomolecular motor-powered nanodevice with an engineered chemical switch. *Nat. Mater.* **2002**, *1* (3), 173–177.
- Kinosita, K.; Yasuda, R.; Noji, H.; Ishiwata, S.; Yoshida, M. F<sub>1</sub>-ATPase: a rotary motor made of a single molecule. *Cell* **1998**, *93* (1), 21–24.
- Noji, H.; Yoshida, M. The rotary machine in the cell, ATP synthase. *J. Biol. Chem.* **2001**, *276*, 1665–1668.
- Yasuda, R.; Noji, H.; Yoshida, M.; Kinosita, K.; Itoh, H. Resolution of distinct rotational substeps by submillisecond kinetic analysis of F<sub>1</sub>-ATPase. *Nature* **2001**, *410*, 898–904.
- Soong, R.K.; Stelick, S.J.; Bachand, G.D.; Montemagno, C.D. Evaluating adhesion strength of biological molecules to nanofabricated substrates. In *Technical Proceedings of the Second International Conference on Modeling and Simulation of Microsystems*; Computational Publications: San Juan, Puerto Rico, 1999.
- Montemagno, C.D.; Bachand, G.D. Constructing nanomechanical devices powered by biomolecular motors. *Nanotechnology* **1999**, *10*, 225–331.
- Bachand, G.D.; Montemagno, C.D. Constructing organic/inorganic NEMS devices powered by biomolecular motors. *Biomed. Microdevices* **2000**, *2*, 179–184.
- Muller, D.; Engel, E. Voltage and pH-induced channel closure of porin OmpF visualized by atomic force microscopy. *J. Mol. Biol.* **1999**, *285*, 1347–1351.
- Durell, S.R.; Hao, Y.; Guy, H.R. Structural models of the transmembrane region of voltage-gated and other K<sup>+</sup> channels in open, closed, and inactivated conformations. *J. Struct. Biol.* **1998**, *121*, 263–284.
- Bainbridge, G.; Gokce, I.; Lakey, J.H. Voltage gating is a fundamental feature of porin and toxin  $\beta$ -barrel membrane channels. *FEBS Lett.* **1998**, *431*, 305–308.
- Noji, H.; Itoh, H.; Adachi, K.; Yoshida, M.; Kinosita, K. Rotary torque of stalled F<sub>1</sub>-motor. *Biophys. J.* **2001**, *80* (1 Part 2), 655.51.
- Dantzig, J.A.; Higuchi, H.; Goldman, Y.E. Studies of molecular motors using caged compounds. *Methods Enzymol., Caged Compd.* **1998**, *291*, 307–348.
- Gillespie, P.G.; Gillespie, S.K.H.; Mercer, J.A.; Shah, K.; Shokat, K.M. Engineering of the myosin-I $\beta$  nucleotide-binding pocket to create sensitivity to N<sup>6</sup>-modified ADP analogs. *J. Biol. Chem.* **1999**, *274* (44), 31,373–31,381.
- Tomishige, M.; Vale, R.D. Controlling kinesin by reversible disulfide cross-linking: identifying the motility-producing conformational change. *J. Cell Biol.* **2000**, *151* (5), 1081–1092.
- Kasianowicz, J.; Burden, D.; Han, L.; Cheley, S.; Bayley, H. Genetically engineered metal ion binding sites on the outside of a channel's transmembrane  $\beta$ -barrel. *Biophys. J.* **1999**, *76*, 837–845.
- Senior, A.E. The proton-translocating ATPase of *Escherichia coli*. *Annu. Rev. Biophys. Chem.* **1990**, *19*, 7–41.
- Oster, G.; Wang, H. ATP synthase: two motors, two fuels. *Structure* **1999**, *7* (4), R67–R72.
- Nakamoto, R.K.; Ketchum, C.J.; Kuo, P.H.; Peskova, Y.B.; Al-Shawi, M.K. Molecular mechanisms of

- rotational catalysis in the F<sub>0</sub>F<sub>1</sub> ATP synthase. *Biochim. Biophys. Acta* **2000**, *1458* (2–3), 289–299.
23. Abrahams, P.; Leslie, A.G.W.; Lutter, R.; Walker, J.E. Structure at 2.8 Å resolution of F<sub>1</sub>-ATPase from bovine heart mitochondria. *Nature* **1994**, *370*, 621–628.
  24. Tsunoda, S.P.; Muneyuki, E.; Amano, T.; Yoshida, M.; Noji, H. Cross-linking of two beta subunits in the closed conformation in F<sub>1</sub>-ATPase. *J. Biol. Chem.* **1999**, *274*, 5701–5706.
  25. Ren, H.; Dou, C.; Stelzer, M.S.; Allison, W.S. Oxidation of the alpha(3)(beta D311C/R333C)(3)gamma subcomplex of the thermophilic *Bacillus PS3F(1)*-ATPase indicates that only two beta subunits can exist in the closed conformation simultaneously. *J. Biol. Chem.* **1999**, *274* (44), 31,366–31,372.
  26. Noji, H.; Yasuda, R.; Yoshida, M.; Kinoshita, K. Direct observation of the rotation of F<sub>1</sub>-ATPase. *Nature* **1997**, *386* (6622), 299–302.
  27. Boyer, P.D. The binding change mechanism for ATP synthase—some probabilities and possibilities. *Biochim. Biophys. Acta* **1993**, *1140*, 215–250.
  28. Allison, W. F<sub>1</sub>-ATPase: A molecular motor that hydrolyzes ATP with sequential opening and closing of catalytic sites coupled to rotation of its subunit. *Acc. Chem. Res.* **1998**, *31*, 819–826.
  29. Kaibara, C.; Matsui, T.; Hisabori, T.; Yoshida, M. Structural asymmetry of F<sub>1</sub>-ATPase caused by the g subunit generates a high-affinity nucleotide binding site. *J. Biol. Chem.* **1996**, *271*, 2433–2438.
  30. Perutz, M.F. Mechanism of cooperativity and allosteric regulation in proteins. *Q. Rev. Biophys.* **1989**, *22*, 139–237.
  31. Glusker, J.P. Structural aspects of metal liganding to functional groups in proteins. *Adv. Protein Chem.* **1991**, *42*, 1–76.
  32. Hellinga, H.W.; Richards, F.M. Construction of new ligand-binding sites in proteins of known structure. 1. Computer-aided modeling of sites with predefined geometry. *J. Mol. Biol.* **1991**, *222* (3), 763–785.
  33. Marvin, J.S.; Hellinga, H.W. Conversion of a maltose receptor into a zinc biosensor by computational design. *Proc. Natl. Acad. Sci. U. S. A.* **2001**, *98*, 4955–4960.
  34. Benson, D.; Haddy, A.E.; Hellinga, H.W. Converting a maltose receptor into a nascent binuclear copper oxygenase by computational design. *Biochemistry* **2002**, *41*, 3262–3269.
  35. Shirakihara, Y.; Leslie, A.G.W.; Abrahams, J.P.; Walker, J.E.; Ueda, T.; Sekimoto, Y.; Kambara, M.; Saika, K.; Kagawa, Y.; Yoshida, M. The crystal structure of the nucleotide-free subcomplex of F<sub>1</sub>-ATPase from the thermophilic *Bacillus PS3* is a symmetric trimer. *Structure* **1997**, *5* (6), 825–836.
  36. Marvin, J.; Corcoran, E.; Hattangadi, N.; Zhang, J.; Gere, S.; Hellinga, H. The rational design of allosteric interactions in a monomeric protein and its applications to the construction of biosensors. *Proc. Natl. Acad. Sci. U.S.A.* **1997**, *98*, 4366–4371.
  37. Wisz, M.S.; Garrett, C.Z.; Hellinga, H.W. Construction of a family of Cys2His2 zinc binding sites in the hydrophobic core of thioredoxin by structure-based design. *Biochemistry* **1998**, *37*, 8269–8277.
  38. Christianson, D.W.; Cox, J.D. Catalysis by metal-activated hydroxide in zinc and manganese metalloenzymes. *Annu. Rev. Biochem.* **1999**, *68*, 33–57.
  39. Pavletich, N.P.; Pabo, C.O. Zinc finger-DNA recognition: crystal structure of a Zif268-DNA complex at 2.1 Å. *Science* **1991**, *252*, 809–817.
  40. Matsui, T.; Yoshida, M. Expression of the wild-type and the Cys-/Trp-less  $\alpha_3\beta_3\gamma$  complex of thermophilic F<sub>1</sub>-ATPase in *Escherichia coli*. *Biochim. Biophys. Acta* **1995**, *1231*, 139.
  41. Qiagen *The QIAexpressionist™. A Hand Book for High-Level Expression and Purification of 6 His-Tagged Protein*; QIAGEN, 2000.
  42. Pullman, M.E.; Penefsky, H.S.; Datta, A.; Racker, E. Partial resolution of the enzyme catalyzing oxidative-phosphorylation. I. Purification and properties of soluble, dinitrophenol-stimulated adenosine triphosphatase. *J. Biol. Chem.* **1960**, *235*, 3322–3329.
  43. Segel, I.H. *Enzyme Kinetics*; Wiley & Sons: New York, 1975.
  44. Matsui, T.; Muneyuki, E.; Honda, M.; Allison, W.S.; Dou, C.; Yoshida, M. Catalytic activity of the  $\alpha_3\beta_3\gamma$  complex of F<sub>1</sub>-ATPase without noncatalytic nucleotide binding site. *J. Biol. Chem.* **1997**, *272*, 8215–8221.
  45. Yasuda, R.; Noji, H.; Kinoshita, K.; Yoshida, M. F<sub>1</sub>-ATPase is a highly efficient molecular motor that rotates with discrete 120 degrees steps. *Cell* **1998**, *93* (7), 1117–1124.



# Molecular Orientation at Interfaces: Vibrational Spectroscopy

Zhan Chen

Department of Chemistry, University of Michigan,  
Ann Arbor, Michigan, U.S.A.

## INTRODUCTION

Sum frequency generation (SFG) vibrational spectroscopy has been developed into a powerful technique to detect molecular conformation and chemical group orientation at different interfaces. This entry will focus on recent SFG research of interfacial polymers and proteins. Understanding of molecular structures and conformations at interfaces involving polymer and/or protein molecules is widely desired because they determine the interfacial properties that play crucial roles in many important applications.<sup>[1–5]</sup> For example, the interfaces between polymer implants and proteins determine the biocompatibility of such devices. Consequently, improved control of these interfaces can increase human life expectancy.<sup>[3]</sup> The interfaces between antibiofouling polymer coatings and underwater glue proteins secreted by marine organisms such as mussels and barnacles dictate the performance of these coatings. Characterization of the molecular structures of such interfaces can aid in the design of environmentally benign polymer coatings with better antifouling properties, saving energy required to operate marine vessels.<sup>[4]</sup> The use of polymer-based adhesives is of major importance in a variety of modern microelectronic and photonic applications.<sup>[5]</sup> Understanding the molecular structures of these adhesives at interfaces is essential for the design of better adhesive materials.

The molecular-level understanding of structures of surfaces/interfaces involving polymers and/or proteins has been a challenge, as such structures are usually considered to be complicated and hard to examine in situ. Here we will present recent advances in characterizing molecular conformations and chemical group orientations of polymer surfaces and protein molecules at various interfaces using SFG. We will introduce the SFG technique, discuss SFG studies on buried polymer interfaces, and show SFG detection of interfacial protein conformations.

## EXPERIMENTAL: SUM FREQUENCY GENERATION TECHNIQUE

Sum frequency generation is a process in which two input beams at frequencies  $\omega_1$  and  $\omega_2$  mix in a medium and generate an output beam at the sum frequency  $\omega = \omega_1 + \omega_2$ . As a second-order non-linear optical process, it is forbidden under the electrical dipole approximation in media with inversion symmetry. At surfaces or interfaces where inversion symmetry is broken, SFG is naturally allowed, and can therefore be used as an effective surface probe. Typically, SFG vibrational spectroscopy uses a tunable infrared (IR) input  $\omega_2$  overlapping with a fixed visible input  $\omega_1$  on a surface/interface to generate a surface/interface vibrational spectrum by plotting SFG intensities vs. the IR input frequency.<sup>[6–22]</sup> Using different input/output polarization combinations with respect to beam and sample geometries, orientation information on surface/interfacial molecules can be obtained.<sup>[23–26]</sup>

A representative experimental arrangement for SFG is depicted schematically in Fig. 1. In our laboratory, the visible beam at 532 nm was generated by frequency-doubling fundamental output pulses of 20 psec pulse width from an EKSPLA Nd:YAG laser. The IR beam, tunable from 650 to 4300  $\text{cm}^{-1}$ , was generated from an EKSPLA optical parametrical generation/amplification and difference frequency system based on LBO and AgGaS<sub>2</sub> or GaSe crystals. Both beams were focused on the sample with diameters of about 0.5 mm. The sum frequency signal from the polymer surface was collected by a photomultiplier tube and processed with a gated integrator. Sum frequency generation spectra with different polarization combinations including ssp (s-polarized sum frequency output, s-polarized visible input, and p-polarized IR input), ppp, pss, and sps were collected. There are variations of SFG setups used in different research laboratories, depending on the types of lasers employed.<sup>[21]</sup>

### A second order, nonlinear optical Process

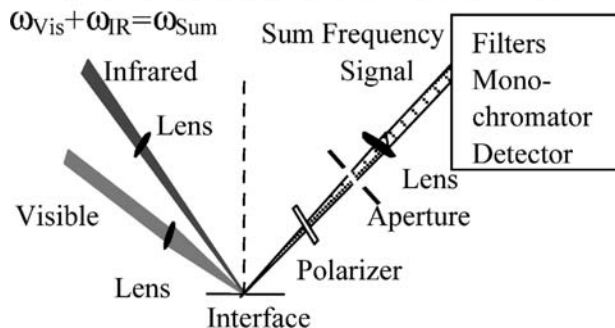


Fig. 1 Sum frequency generation experimental geometry.

Various experiments show that SFG is indeed a submonolayer surface-specific polymer surface probe. Such experiments include comparing reflected and transmitted SFG spectra, modifying a polymer surface by immersing it in liquids or by exposing it to plasma treatment for a short time, and evaluating SFG spectral intensity from polymer films with different thickness.<sup>[7]</sup> The surface specificity of SFG studies on interfacial proteins will be discussed later.

## RESULTS AND DISCUSSION

### Polymer/Water Interfaces

It is important to study polymer/water interfaces because many polymers such as biomedical or bio-fouling control polymers are used in aqueous environments. Unfortunately, most surface science techniques are operable only with the sample under ultrahigh vacuum.<sup>[27,28]</sup> Freeze-drying X-ray photoelectron spectroscopy (XPS) has been developed to study polymer surface restructuring in water, but it cannot provide molecular conformational information.<sup>[29]</sup> Contact angle measurements show that many polymer surfaces reconstruct in liquid, but they cannot show how the polymer surfaces change at the molecular level.<sup>[30]</sup> Here, we report our SFG studies on interfaces between polymethacrylates, which are widely used as biomaterials, and water.

Three polymethacrylates with different lengths of alkyl side chains—poly(methyl methacrylate) (PMMA), poly(*n*-butyl methacrylate) (PBMA), and poly(*n*-octyl methacrylate) (POMA)—were investigated. Their glass transition temperatures are 105°C, 17°C, and -70°C, respectively,<sup>[12]</sup> showing that the molecules have different bulk mobilities. Through this study, we hope to correlate the surface restructuring behavior of these three polymethacrylates in water to their bulk mobility or glass transition temperatures.

Both ssp and sps SFG spectra of PMMA in water are dominated by the signals from ester methyl groups, similar to those of the PMMA/air interface, although they are much weaker.<sup>[12]</sup> Analysis of the spectra shows that the weaker spectra are mainly because of the changes of the Fresnel coefficients for the two interfaces. There is little structural change for the ester methyl, alpha methyl, and methylene groups at the PMMA surface after contacting water.

Experimental and fitted SFG spectra indicated that PBMA surfaces in both air and water are dominated by the methyl groups of the ester side chains (Fig. 2). The average orientation and orientation distribution of these methyl groups at the PBMA/air and PBMA/water interfaces can be deduced by the SFG absolute intensity and intensity ratio measurements (Fig. 3).<sup>[14]</sup> Fig. 3 shows that methyl groups have different orientation distributions on PBMA surfaces in air and water, indicating that surface restructuring occurs when the PBMA sample contacts water. Methyl groups tend to stand up on the PBMA surface in air, and tend to lie down on the surface in water. The orientation distribution of side chain methyl groups

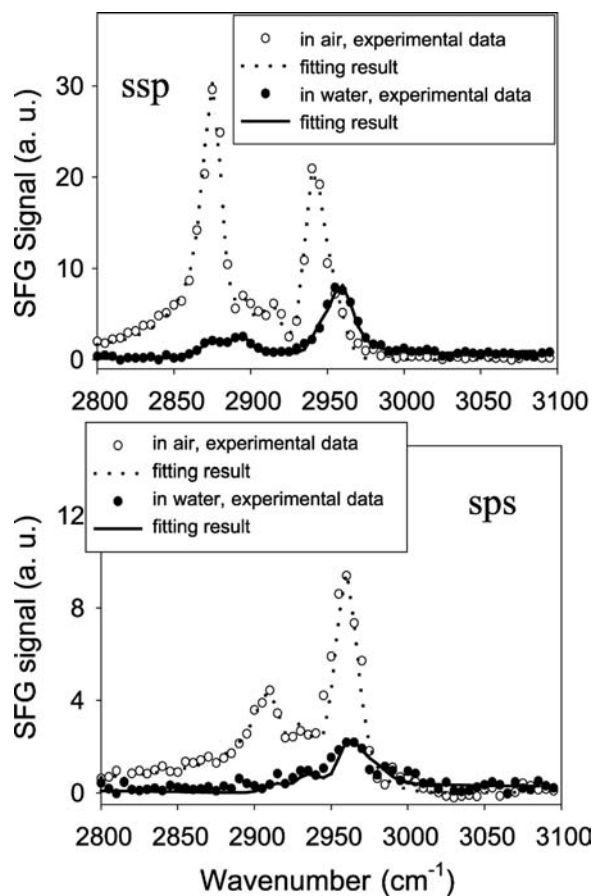
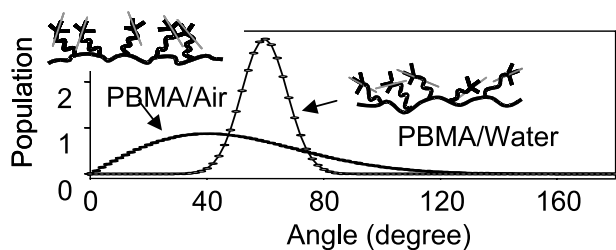


Fig. 2 Sum frequency generation spectra collected from the PBMA / air and PBMA / water interfaces. Source: From Ref.<sup>[14]</sup>; © American Chemical Society, 2002.



**Fig. 3** Orientation distribution of methyl groups on the PBMA surface in air and water. *Source:* From Ref.<sup>[14]</sup>; © American Chemical Society, 2002.

on the PBMA surface is narrower in water than that in air, indicating that the PBMA surface can be more ordered in water. To our knowledge, this is the first time that quantitative comparisons between molecular surface structures of polymers in air and water have been made. It has been found that the orientation angle distribution function deduced by the Gaussian distribution and the maximum entropy distribution are quite similar, showing that the Gaussian distribution is a good approximation of the angle distribution. When the PBMA surface was removed from water, the SFG spectra recovered, indicating that restructuring of the PBMA surface in water is reversible.

Sum frequency generation spectra of POMA show that the POMA/air interface is dominated by the methyl and methylene groups.<sup>[12]</sup> When POMA makes contact with water, its SFG spectra immediately disappear. With the sample out of water and dried, the spectra reappear, but are very different from those before contacting water. We believe that the polymer backbones of POMA change immediately after contacting water because POMA has a very low  $T_g$  ( $-70^\circ\text{C}$ ) and thus the backbones are very mobile. The molecules on the surface in water become randomly oriented so that no SFG signal can be detected.

We showed here that different polymers can have different surface restructuring behaviors in water. The PMMA surface has no detectable changes in water because of its rigid surface structures and hydrophilic surface-dominating ester methyl groups.<sup>[11]</sup> For PBMA, the surface had a reversible side group reorientation in water. Poly(*n*-octyl methacrylate) has a low glass transition temperature and thus molecules are very mobile. Its surface exhibited irreversible restructuring after contact with water.

In addition to these three polymethacrylates, surface restructuring of another polymethacrylate, cross-linked poly(2-hydroxyethyl methacrylate) (PHEMA), a widely used contact lens material hydrogel, has been studied using SFG.<sup>[31]</sup> Sum frequency generation measurements demonstrate that PHEMA can adopt two

discrete surface states depending on the environment. When PHEMA is exposed to air, polar side chains turn into the bulk, leaving the nonpolar methyl groups to project out of the surface to form a “hydrophobic conformation.” In water, polar ethylene glycol groups migrate to the surface and coexist with methyl groups at the surface, creating a “hydrophilic conformation” (Fig. 4).

Sum frequency generation studies on polymer surfaces in water demonstrate that it can provide molecular conformation and chemical group orientation information about polymer molecules at polymer/water interfaces in situ. Both qualitative and quantitative understanding of surface restructuring behaviors of polymer surfaces in water can be achieved.

### Solid/Liquid Polymer or Polymer Solution Interfaces

In addition to buried polymer/water interfaces, SFG has also been applied to study polymer/polymer interfaces. We will first report the SFG research on polymer structures at the solid/liquid interfaces. The polymers that will be examined here include poly(ethylene oxide) (PEO), poly(propylene oxide) (PPO), and PEO–PPO–PEO block copolymers.

Poly(ethylene oxide)–PPO–PEO block copolymers or pluronics are well-known non-ionic and water-soluble macromolecular surfactants. Their behavior in micelle formation, emulsification, drug stabilization, or drug delivery is determined by different interfacial conformations of PEO and PPO blocks at various solid/liquid interfaces. The adsorption behavior of pluronic surfactants at the solid/solution interface has been studied by several different techniques such as ellipsometry, total internal reflectance fluorescence (TIRF), XPS, and surface plasmon resonance (SPR).<sup>[32]</sup> However, it is still not clear how the polymer chains and chemical groups are arranged at different interfaces and how these molecules interact with the

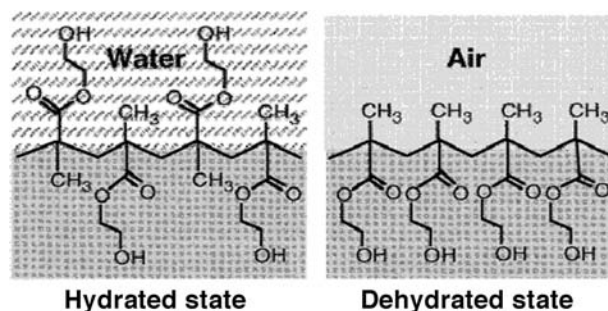


**Fig. 4** Schematics describing surface structures of PHEMA in air and water. *Source:* From Ref.<sup>[31]</sup>; © American Chemical Society, 1999.

contacting media. Here we want to elucidate the interfacial structures of pluronics at various interfaces. Before that, we first discuss the conformations of various components of pluronics, including PEO and PPO, at various interfaces.

#### Conformation of poly(ethylene oxide) and poly(propylene oxide) at different solid/liquid polymer interfaces

Sum frequency generation spectra were collected from interfaces between PEO or PPO liquid and several solid materials, including fused silica, deuterated polystyrene (d-PS), and deuterated PMMA (d-PMMA) (Fig. 5). We found that the intensity of the dominating peak (symmetrical C–H stretch for both PEO and PPO) decreases from the d-PS interface to the d-PMMA interface and drops to zero for the fused silica/liquid polymer interface. At the d-PS/polyether interfaces, strong SFG signals show that polyethers should have ordered conformations, with CH<sub>2</sub> (for PEO) or CH<sub>3</sub> groups (for PPO) oriented along the interface normal. This indicates that the hydrophobic polystyrene (PS) surface, which is dominated by phenyl groups, interacts favorably with CH<sub>2</sub> groups on PEO or methyl groups on PPO molecules, forming ordered conformations of PEO and PPO at the interface. At the fused silica/polyether interface, no SFG signal can be detected, showing that both polyethers have random conformations. This shows that the interactions between fused silica and CH<sub>2</sub> groups on PEO

molecules or methyl groups on PPO molecules are unfavorable. Because of the surface-dominating ester methyl groups,<sup>[11]</sup> the hydrophobicity of d-PMMA is between d-PS and fused silica, thus polyethers have intermediate conformations compared to those contacting d-PS and fused silica, evidenced by SFG spectra with intermediate intensities. Sum frequency generation studies of solid/polyether interfaces clearly demonstrate that polyethers can have different conformations while contacting different solid materials.

#### Interfacial activity and conformation of poly(ethylene oxide) and poly(propylene oxide) at solid/solution interfaces

Poly(ethylene oxide), PPO, and their copolymers are mostly used in aqueous solutions. Similar to the solid/pure liquid polymer interfaces mentioned above, SFG spectra (ssp) were collected from solid/polymer solution interfaces. No SFG signals corresponding to PEO molecules were detected for any solid/PEO solution interface. Further research indicated that PEO molecules do not segregate to the interfaces.<sup>[16]</sup> Because of strong hydrogen bonding between PEO and water, PEO tends to interact with the water phase, is surrounded by water molecules, and stays in the bulk.

Poly(propylene oxide) is more surface-active or interface-active than PEO. Sum frequency generation spectra collected from a solid/PPO solution interface is quite similar to the solid/PPO liquid polymer interface.

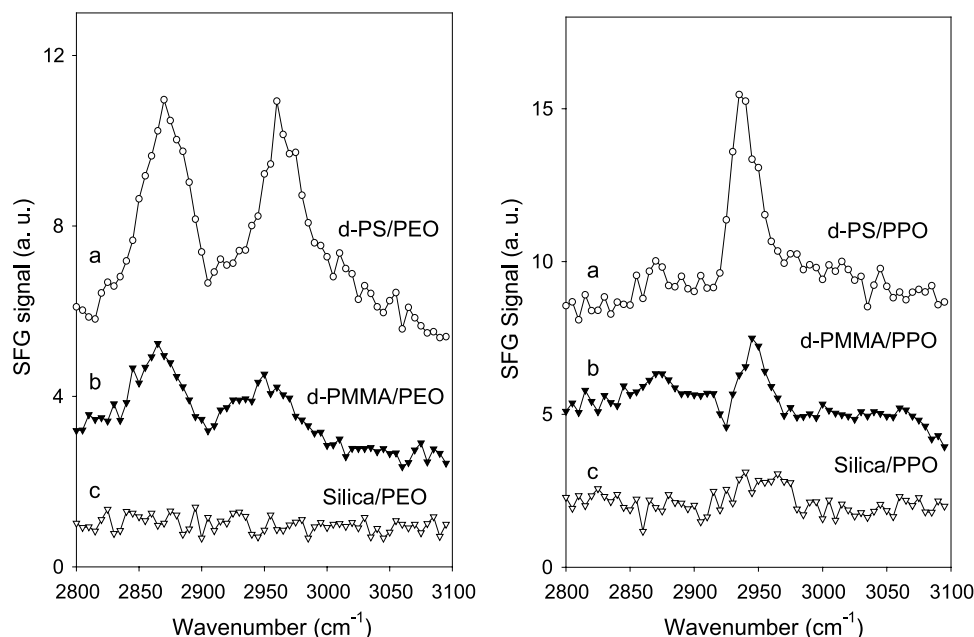


**Fig. 5** Sum frequency generation spectra collected from solid/PEO interfaces (left) and solid/PPO interfaces (right). *Source:* From Ref.<sup>[17]</sup>; © American Chemical Society, 2002.

For example, SFG signals of PPO collected from d-PS/PPO solution interfaces are very similar to those of d-PS/pure PPO liquid interfaces, showing that the d-PS/PPO solution interface is covered by a layer of PPO molecules, with ordered methyl groups standing up along the interface normal. Compared to those at the d-PS/PPO solution interface, the molecules at the d-PMMA/PPO solution interface are less ordered. At the fused silica/PPO solution interface, no SFG signal is detected. Further research indicated that this is because of the fact that PPO has a random conformation at this interface.<sup>[17]</sup>

#### Molecular structures of copolymers at the solid/solution interface

The interfacial SFG spectra of various pluronic copolymers with different block lengths of PEO and PPO (PEO ratio varying from 20% to 80%) have been collected from the d-PS/solution and d-PMMA/solution interfaces.<sup>[32]</sup> Plurionics with different PEO ratios show similar interfacial spectra. It was found that interfacial structures of plurionics at solid/solution interfaces are dominated by PPO blocks and the orientation of methyl groups varies with different solid contacting media. A stronger signal is detected when the liquid contacts d-PS, showing that the methyl groups are more ordered at the d-PS/solution interface. However, at the d-PMMA/solution interface, the methyl groups are not very ordered as shown by the weak signals from the SFG spectra. Different conformations of the copolymers at different interfaces are related to molecular interactions at these interfaces (Fig. 6). The favorable interactions between hydrophobic surfaces with phenyl groups and hydrophobic methyl groups on PPO blocks cause more ordered conformations with these groups preferentially orientated along the interface normal. The interactions between less hydrophobic media with ester methyl or C=O groups and hydrophobic methyl groups are not very favorable, causing a less ordered methyl group arrangement at the interface. Through this research, we have demonstrated that SFG is an appropriate technique to observe molecular-level structures such as chain conformation and group orientation of plurionics at solid/solution interfaces.

#### Solid Polymer/Solid Polymer Interfaces

Understanding interface structures between solid polymer materials is crucial to evaluate the miscibility and bulk properties of polymer blends, and adhesion at polymer/polymer interfaces. Such knowledge of polymer/polymer interfaces can be applied to many important industrial applications including coatings, lithography, microelectronic devices, and liquid crystal displays. In this section, we investigate the PBMA/PS interface as an example to demonstrate that SFG is a powerful technique to elucidate molecular-level structures of buried interfaces between solid polymers in situ.

The SFG spectra were collected with two input laser beams traveling through the substrate and the thin PS (or d-PS) film to the PS/PBMA interface (Fig. 7). We have ensured that the spectra we collected came from the polymer/polymer interface, not from the PS/substrate or PBMA/air interfaces.<sup>[16]</sup> As with the PBMA/air and PBMA/water interfaces,<sup>[14]</sup> orientation information of ester side chain methyl groups at the “buried” PBMA/PS (or d-PS) interface can be deduced after fitting these SFG spectra. Our detailed analysis clearly shows that the range of possible orientation of ester side chain methyl groups at the PBMA/PS (or d-PS) interface is between the two extremes of the PBMA/air and PBMA/water interfaces. On the PBMA surface in air, the ester side chain methyl groups have greater freedom and tend to extend into the air, leading to a small average orientation angle vs. the surface normal. Upon contacting water, the strong repulsion between the methyl groups and water molecules directs the methyl groups away from the surface normal, resulting in a larger average orientation angle. At the PBMA/PS (d-PS) interface, the ester side chain methyl groups interact with the phenyl groups, but the repulsion must be weaker compared to the situation in water. Therefore the orientation of ester side chain methyl groups is between the two extremes of the PBMA/air and PBMA/water interfaces. The repulsion force between the side chain methyl groups and the phenyl groups also directs the phenyl groups away from the interface normal compared to the PS/air interface, shown by different aromatic C–H signals at the PS/PBMA and PS/air interfaces.

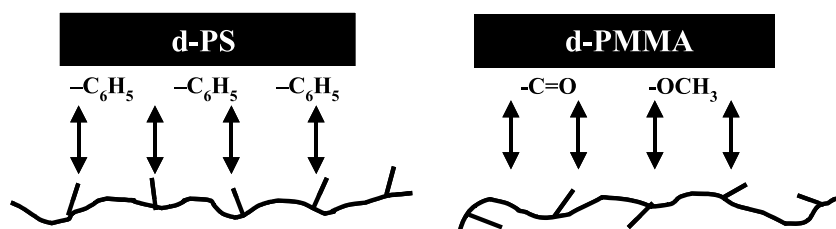


**Fig. 6** Schematics of group interactions at plurionics solution/solid interfaces. *Source:* From Ref.<sup>[32]</sup>; © American Chemical Society, 2003.

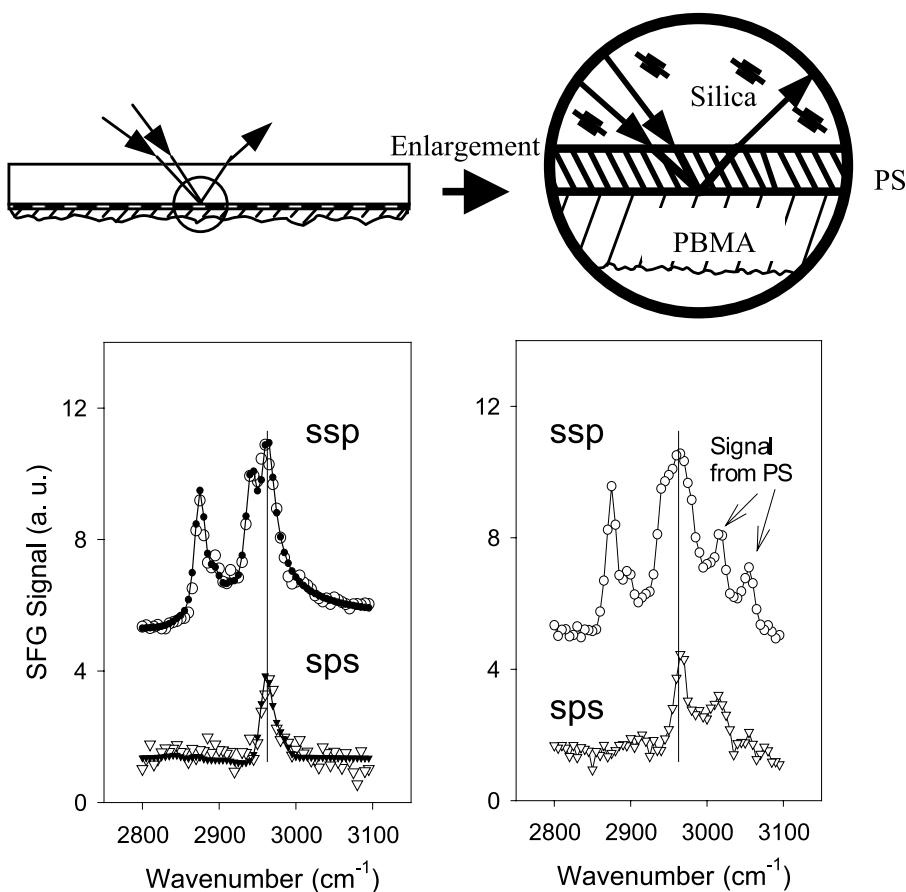


**Fig. 7** Sum frequency generation spectra collected from the PBMA/d-PS interface (lower left panel) and the PBMA/PS interface (lower right panel). Both ssp and sps spectra collected from the two interfaces are shown. The upper panel shows the experimental geometry.

Research has also been conducted on the structure of the PS/PMMA interface using SFG, showing ordered ester methyl groups at the interface.<sup>[18]</sup> Sum frequency generation studies on the

poly(vinyl-*N*-octadecylcarbamate-co-vinyl acetate) (Comb)/PS interface indicated that features of SFG spectra collected from this interface are broader than those from the Comb/air interface.<sup>[19]</sup> Phenyl,

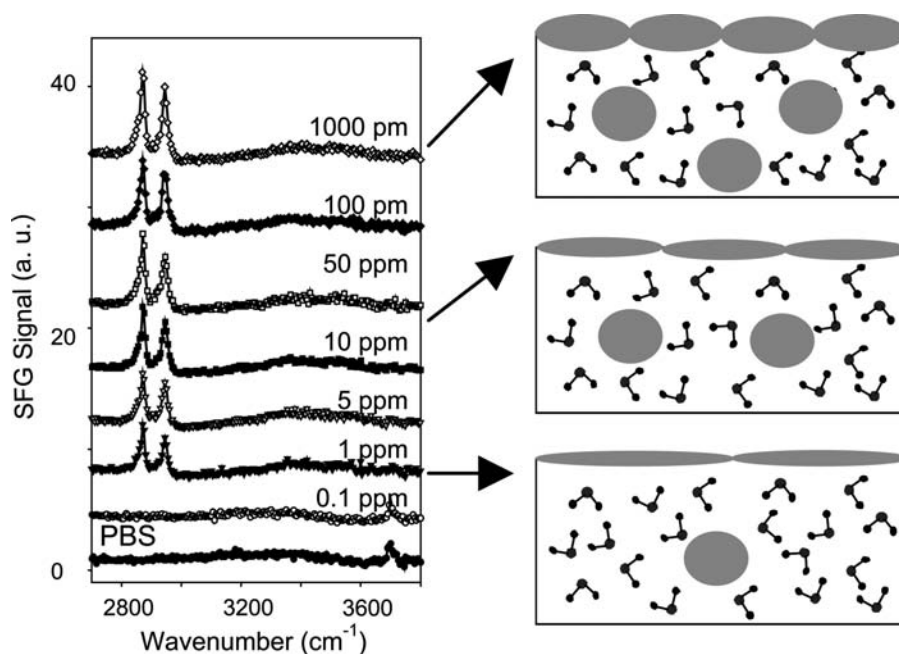


**Fig. 8** Left: Sum frequency generation spectra of BSA solution/air interfaces with different bulk concentrations. Right: Proposed schematics of different surface structures of BSA at the solution/air interfaces with different bulk concentrations.



methylene, and methyl groups were detected. Analyses of the SFG spectra indicate that Comb alkyl side chains are more disordered with a large population of gauche defects, and the crystallinity of the alkyl side chains is disrupted at these interfaces.

### Polymer/Inorganic Solid Interfaces

The PS/sapphire interface was studied using SFG in a total internal reflection geometry.<sup>[13]</sup> By carefully choosing the incident angles of the input beams, PS conformation at the PS/air surface and the buried PS/sapphire interface can be explored separately. Analyses of the spectra show that the phenyl rings are orientated approximately parallel to the surface normal at the PS/air interface, in comparison to nearly perpendicular to the surface normal at the PS/sapphire interface. Similarly, SFG was applied to investigate molecular structures of poly(*n*-alkyl acrylates)/sapphire interfaces as a function of temperature.<sup>[33]</sup> Upon heating, SFG spectral intensity decreased and one sharp transition close to bulk melting temperature was observed, showing that interfacial melting occurs at the same bulk melting temperature.

A different method was developed using SFG to detect the buried PS/spin-on-glass (SOG) interface by spin coating a thin layer of SOG on a gold film. A PS film was spin-coated on top of the SOG surface.<sup>[34]</sup> By varying the SOG thickness, the PS/air interface or the buried PS/SOG interface can be probed. The phenyl groups at the buried interface point away from the PS film toward the SOG/Au substrate, with an almost identical orientational distribution as that of the PS/air interface. In addition, the hydrophobic SOG surface was modified by UV ozone to create a hydrophilic SOG surface. Sum frequency generation studies on the PS/hydrophilic SOG interface show that the interface has a different structure from the PS/unmodified hydrophobic SOG interface.<sup>[20]</sup> Such structural differences can be correlated to the different adhesion properties of the two interfaces.

### Polymer/Protein Interfaces

Protein adsorption is the first process that happens when a biomaterial interacts with a biological system; the structure of adsorbed proteins determines finally whether an implanted material will be accepted or rejected by the body (biocompatible or not). Because of its critical importance, protein adsorption has been studied by a myriad of surface-sensitive methods for decades.<sup>[35–37]</sup> However, it is still difficult to determine chemical and structural information about adsorbed protein molecules, and details about how protein

molecules respond to different interfacial environments are still not clear. Recently, SFG has been shown to be a powerful technique to elucidate interfacial protein structures at the molecular level in situ.

We have studied structures and conformations of bovine serum albumin (BSA) at various interfaces including BSA solution/air, BSA solution/fused silica, BSA solution/d-PS, and BSA solution/d-PMMA interfaces.<sup>[15,38–40]</sup> Sum frequency generation is used mostly to study simple surfaces/interfaces and small molecule adsorptions, and models have been developed for the interpretation of such SFG spectra. Because BSA is a large protein (~65 kDa), a new interpretation model is needed. Instead of using a simple interface, we have successfully applied the more general thin film model to interpret protein

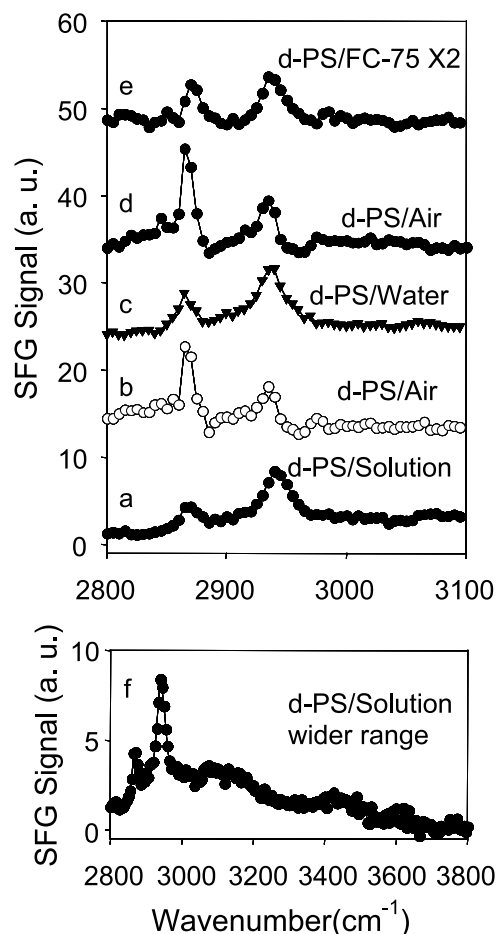


**Fig. 9** SFG spectra collected from A. d-PS/BSA solution interface; B. d-PS/air interface after the sample was removed from solution and washed by water; C. d-PS/water interface after the sample contacted water; D. d-PS/air interface again; E. d-PS/FC-75 interface after procedures a and b and contacting the sample with FC-75; F. d-PS/BSA solution interface in the wide spectral range. The spectral intensity in 2e has been multiplied by 2.

SFG spectra.<sup>[38,39]</sup> Using theoretical calculations as well as experimental results, we demonstrated that SFG spectra can be used to determine interfacial protein structure and conformation. The thin film model considers that SFG signals are contributed from functional groups in the whole adsorbed protein film, as long as inversion symmetry is broken.<sup>[38,39]</sup>

### BSA solution/air interfaces

Extensive research has been done regarding the dependence of BSA adsorption at the solution/air interface on bulk protein concentration. However, no investigations in this area have determined the bulk concentration's effect on molecular interfacial protein structure. Fig. 8 displays SFG spectra collected from BSA solution/air interfaces in situ. The peaks in the range from 2800 to 3100  $\text{cm}^{-1}$  are indicative of aliphatic and aromatic C–H stretches from hydrophobic side chains on BSA. The broad peaks at higher wavenumbers are O–H stretches of surface water molecules. We have confirmed that these SFG signals come from the adsorbed interfacial BSA, not from BSA in bulk solutions.<sup>[15,38]</sup> Using SFG intensity measurements, we have elucidated structural changes of BSA molecules at solution/air interfaces with different BSA bulk solution concentrations (Fig. 8).<sup>[40]</sup> Bovine serum albumin molecules are denatured more at the solution/air interface of lower concentration solutions.<sup>[40]</sup>

### BSA solution/fused silica interfaces

We have collected SFG spectra directly from BSA solution/solid interfaces. The solid media that we investigated include fused silica, d-PS, and d-PMMA. Our SFG results show clearly that the conformation of adsorbed BSA molecules at different interfaces can be varied.<sup>[15,38]</sup> No C–H stretching signals from albumin molecules are detected from the BSA solution/fused silica interface because of the lack of a net alignment of protein C–H groups at the fused silica/BSA solution interface. At this interface, the adsorbed BSA adopts a hydrophilic conformation; the hydrophobic groups tend to stay inside the BSA film with no net alignment. Thus no SFG signal is detected. We have contacted the BSA adsorbed on fused silica with different chemical environments, including air, water, and hydrophobic solvents. Sum frequency generation spectra collected from various interfaces indicate that BSA has different conformations when interfacial environments are changed.<sup>[15,38]</sup>

### BSA solution/polymer interfaces

An SFG spectrum was collected from the d-PS/BSA solution interface (Fig. 9A and F). In this spectrum, strong C–H signals are detected, demonstrating that the adsorbed BSA molecules do not adopt the hydrophilic conformation as found in the case of fused silica.

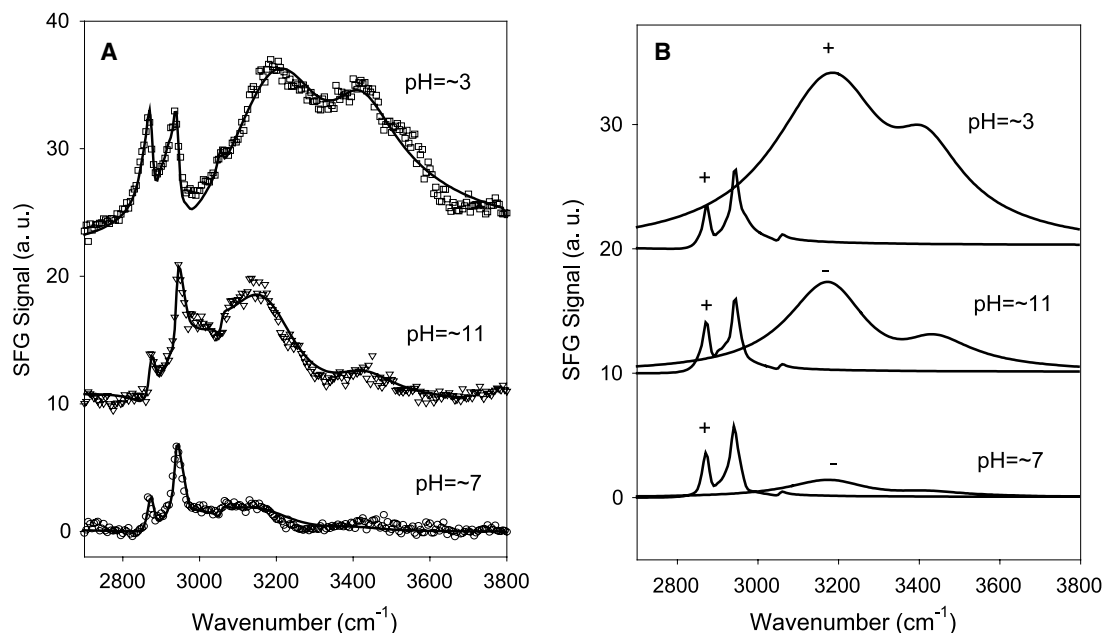


**Fig. 10** Sum frequency generation experimental spectra (A) and fitting spectra (B) of the PS/BSA solution interface with different solution pH values. *Source:* From Ref.<sup>[38]</sup>; © American Chemical Society, 2002.

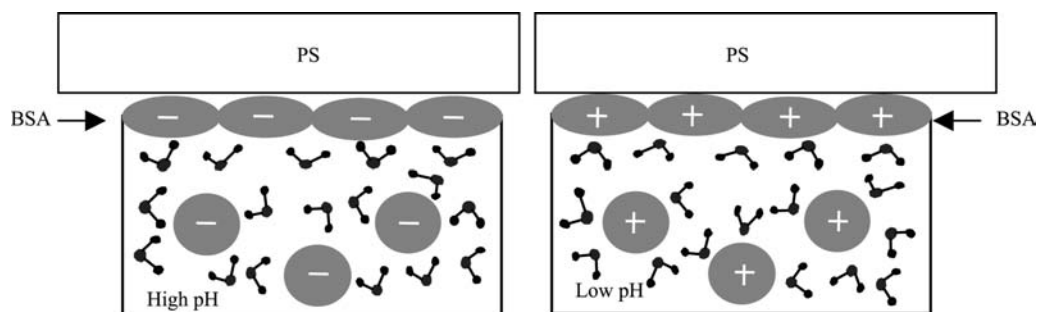


**Fig. 11** Schematic plot of the orientation of surface water molecules at different solution pH values. The water molecules at the interface have varying orientations because the surface BSA molecules have different charges at different pH levels above or below the BSA isoelectric point.

Bovine serum albumin adopts a conformation that allows for its hydrophobic components to maximize the favorable interaction with the surface. When the sample is removed from the BSA solution, washed by water, and exposed to air, SFG signals are still visible (Fig. 9B). When the sample is exposed to water again, strong C–H signals are detected (Fig. 9C), with different features as compared to the spectrum collected from the d-PS/air interface. C–H signals repeatedly change as we continue to alternately contact the sample with water and air (e.g., Fig. 9D). This phenomenon shows that the changes are reversible. When the sample is in contact with a hydrophobic fluorinated solvent FC-75 instead of water, C–H signals are still detected (Fig. 9E), but with weaker intensity. This research shows that BSA on PS can adopt different conformations in different chemical environments.

The SFG spectra of BSA solution/d-PS interfaces at different solution pH values are displayed in Fig. 10A, shown as dots. The detailed fitting results shown in Fig. 10B indicate that the C–H stretching signals collected from solutions of different pH values are quite similar, but spectral features in the O–H stretching region are different from spectrum to spectrum.<sup>[38]</sup> In addition, the relative phases between the C–H and O–H signals are quite different, resulting in distinct spectral differences in Fig. 10A. The phase differences between C–H and O–H signals at different solution pH values are because of opposite relative orientations between methyl or phenyl groups of BSA molecules and water molecules at the interface (Fig. 11).

#### Comparison of protein conformation at various interfaces

Our results show that BSA molecules have different conformations at various interfaces. The behavior of BSA on d-PS is totally different from the case of BSA on fused silica, showing the dependence of the protein conformations on material surface properties. We have also studied BSA structures at other polymer/BSA

solution interfaces. For example, the results at the d-PMMA/BSA solution interface are intermediate to those from interfaces involving fused silica and d-PS. This result is reasonable because the surface of d-PMMA is dominated by ester methyl groups and thus is more hydrophilic than d-PS but not as hydrophilic as fused silica. The adsorbed BSA film can form a “hydrophilic” conformation between two hydrophilic media (fused silica/BSA solution), and a “hydrophobic” conformation between two hydrophobic media (polymer/air or polymer/hydrophobic solvent) (Fig. 12). Nevertheless, such “hydrophobic” or “hydrophilic” characterization of interfacial protein structure is too crude. More molecular details of different “hydrophobic” or “hydrophilic” conformations need to be addressed in the future.

Sum frequency generation supplemented by fluorescence microscopy has also been applied to investigate different proteins including lysozymes, fibrinogen, and BSA adsorbed on fused silica and PS surfaces after removing the samples from solution and exposing

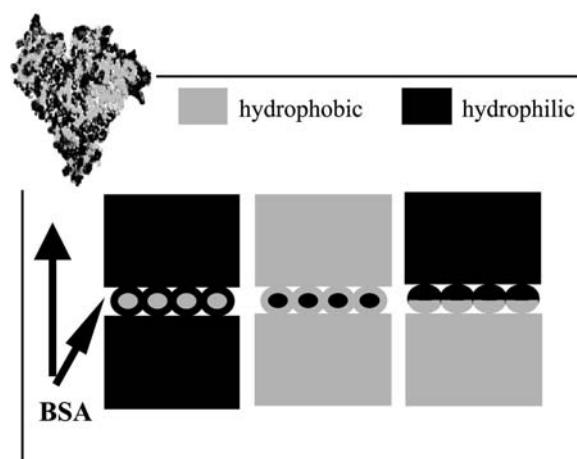


**Fig. 12** Schematics of different structures of BSA in contact with surfaces of different hydrophobicities. *Source:* From Ref.<sup>[15]</sup>; © American Chemical Society, 2002.

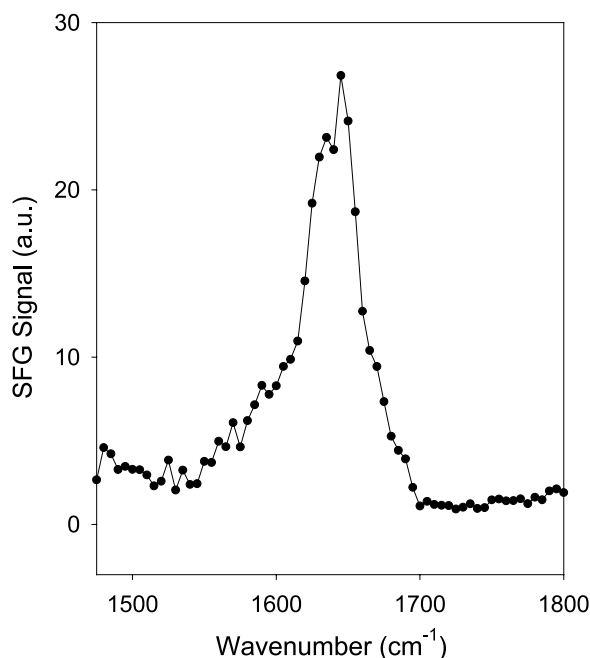


**Fig. 13** Sum frequency generation amide spectra collected from the PS / BSA solution interface in situ.

them to air.<sup>[41]</sup> Research shows that these proteins have different adsorption behaviors and conformations on various surfaces. On hydrophilic surfaces, the orientation of methyl groups in lysozymes is concentration-independent, but those of BSA and fibrinogen become less tilted with respect to the surface normal with increasing protein concentration. However, methyl groups in proteins adsorbed on hydrophobic PS surfaces appear more randomly

oriented and produce a weaker SFG signal. Sum frequency generation studies on lysozymes at fused silica/water interfaces with various water pH values indicate that when the pH value of water was varied, lysozymes changed conformations at the interface. At low pH, lysozymes have a hydrophilic conformation, whereas at high pH, they have a hydrophobic conformation.<sup>[42]</sup>

**Future direction: sum frequency generation studies on amide bands and isotope-labeled proteins**

The results shown above demonstrate that SFG is a powerful technique to deduce protein conformations at various interfaces. All the SFG signals shown above are signals from the C–H stretching region, which provide some structural information about interfacial protein molecules. However, for the determination of more detailed protein structures, the amide I band is more useful because it provides more specific information on the protein's secondary structure. We have demonstrated the feasibility to detect amide SFG signals of interfacial proteins at the solution/polymer interface in situ (Fig. 13). Research on correlating SFG amide signals to detailed conformation of proteins at various interfaces is underway.

Sum frequency generation C–H stretching signals and amide bands are generated from many functional groups in many amino acid residues of a protein molecule. To acquire conformation details of an interfacial protein, we need to know the orientation of every small segment of the protein. We have proven that SFG is sufficiently sensitive to detect even a few amino acid

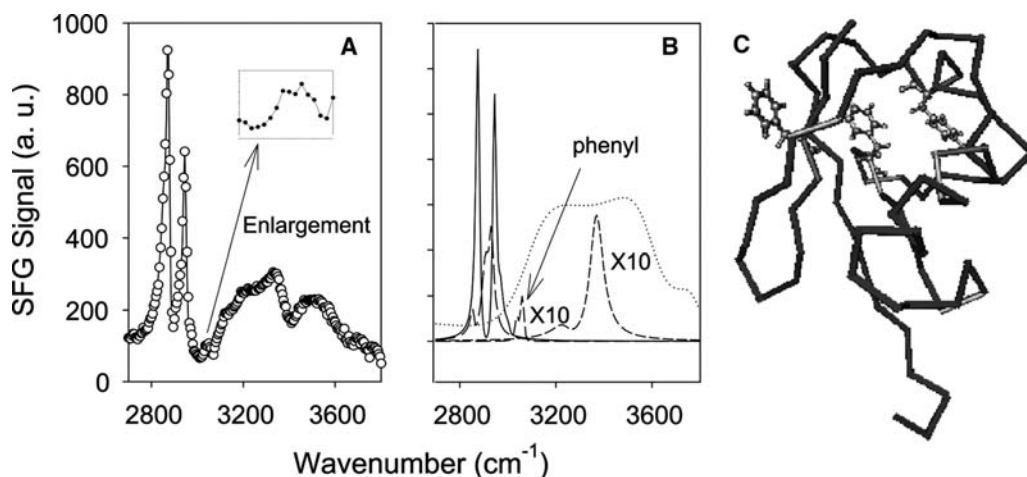


**Fig. 14** (A) Sum frequency generation spectrum collected from ubiquitin on fused silica in air. Dots: Experimental data. The enlarged phenyl signal is shown at the upper right corner. Lines: The overall fitted spectrum. (B). Fitted results of various functional groups for the entire spectrum shown in (A). These various functional groups include CH<sub>3</sub>, CH<sub>2</sub>, phenyl, N–H, and O–H groups. The fitted result for the phenyl group was multiplied by a factor of 10. (C). Ubiquitin structure: three phenyl groups are clearly indicated. This figure shows that it is feasible to detect SFG signals from three phenyl groups of ubiquitin molecules at the interface.

residues at the interface. Fig. 14A shows the SFG spectrum collected from ubiquitin adsorbed on the fused silica prism in air using a total reflection optical geometry. There are only three phenyl groups in a ubiquitin molecule (Fig. 14C). Both original and fitted spectra in Fig. 14 show clearly the SFG signal from three phenyl groups. Various isotope labeling techniques can be used to label different parts of a protein. Sum frequency generation can be developed into a powerful technique to provide detailed protein molecular interfacial structures by studying such isotope-labeled proteins.

## CONCLUSION

Sum frequency generation has been developed into a powerful technique to reveal conformations and orientations of polymer and protein molecules at various interfaces at the molecular level in situ. Sum frequency generation studies on polymer/water interfaces indicate that different polymers can have different surface changes in water. Quantitative surface restructuring behavior, such as surface functional group orientation distribution change, of polymers in water can be understood by SFG measurements. Polymer conformations at different solid/liquid polymer or solution interfaces observed by SFG provide more insights in understanding the interfacial performance of polymer surfactants. Sum frequency generation studies on solid polymer/solid interfaces show polymer conformation and chemical group orientation at various interfaces, elucidating interfacial interactions and polymer adhesion at the molecular level. Different conformations of interfacial proteins at various interfaces have been determined using SFG in situ. The effect of solution concentration, hydrophobicity of contacting surfaces, and pH value of protein solutions on interfacial protein conformation has been revealed. Sum frequency generation has been proven to be a unique and powerful submonolayer surface-sensitive molecular spectroscopy to examine conformations and orientations of large molecules such as polymers and proteins at various buried interfaces in situ.

## ACKNOWLEDGMENTS

I want to thank Dr. Jie Wang, Chunyan Chen, and Mark A. Even, who contributed substantially to this work. This research is supported by the Office of Naval Research, the National Science Foundation, the American Chemical Society Petroleum Research Fund, Dow Corning Corporation, and the University of Michigan.

## REFERENCES

1. Feast, W.J.; Munro, H.S.; Richards, R.W. *Polymer Surfaces and Interfaces II*; Wiley: New York, 1992.
2. Carbassi, F.; Morra, M.; Occhiello, E. *Polymer Surfaces: From Physics to Technology*; Wiley: Chichester, 1994.
3. Park, J.B.; Lakes, R.S. *Biomaterials: An Introduction*; Plenum Press: New York, 1992.
4. Wynne, K.J.; Guard, H. Introduction. *Nav. Res. Rev.* **1997**, *49* (4), 2–3.
5. Yacobi, B.G.; Martin, S.; Davis, K.; Hudson, A.; Hubert, M. Adhesive bonding in microelectronics and photonics. *J. Appl. Phys.* **2002**, *91* (10), 6227–6262.
6. Shen, Y.R. *The Principles of Nonlinear Optics*; Wiley: New York, 1984.
7. Chen, Z.; Shen, Y.R.; Somorjai, G.A. Studies of polymer surfaces by sum frequency generation vibrational spectroscopy. *Annu. Rev. Phys. Chem.* **2002**, *53*, 437–465.
8. Scatena, L.F.; Brown, M.G.; Richmond, G.L. Water at hydrophobic surfaces: weak hydrogen bonding and strong orientation effects. *Science* **2001**, *292* (5518), 908–912.
9. Kim, J.; Cremer, P.S. IR–visible SFG investigations of interfacial water structure upon polyelectrolyte adsorption at the solid/liquid interface. *J. Am. Chem. Soc.* **2000**, *122* (49), 12,371–12,372.
10. Bain, C.D. Sum-frequency vibrational spectroscopy of the solid–liquid interface. *J. Chem. Soc., Faraday Trans.* **1995**, *91* (9), 1281–1296.
11. Wang, J.; Chen, C.Y.; Buck, S.M.; Chen, Z. Molecular chemical structure on poly(methyl methacrylate) (PMMA) surface studied by sum frequency generation (SFG) vibrational spectroscopy. *J. Phys. Chem., B* **2001**, *105* (48), 12,118–12,125.
12. Wang, J.; Woodcock, S.E.; Buck, S.M.; Chen, C.Y.; Chen, Z. Different surface-restructuring behaviors of poly(methacrylate)s detected by SFG in water. *J. Am. Chem. Soc.* **2001**, *123* (38), 9470–9471.
13. Gautam, K.S.; Schwab, A.D.; Dhinojwala, A.; Zhang, D.; Dougai, S.M.; Yeganeh, M.S. Molecular structure of polystyrene at air/polymer and solid/polymer interfaces. *Phys. Rev. Lett.* **2000**, *85* (18), 3854–3857.
14. Wang, J.; Paszti, Z.; Even, M.A.; Chen, Z. Measuring polymer surface ordering differences in air and water by sum frequency generation vibrational spectroscopy. *J. Am. Chem. Soc.* **2002**, *123* (24), 7016–7023.
15. Wang, J.; Buck, S.M.; Even, M.A.; Chen, Z. Molecular responses of proteins at different interfacial environments detected by sum frequency generation vibrational spectroscopy. *J. Am. Chem. Soc.* **2002**, *124* (44), 13,302–13,305.
16. Chen, C.Y.; Wang, J.; Even, M.A.; Chen, Z. Sum frequency generation vibrational spectroscopy studies on “buried” polymer/polymer interfaces. *Macromolecules* **2002**, *35* (21), 8093–8097.
17. Chen, C.Y.; Even, M.A.; Wang, J.; Chen, Z. Sum frequency generation vibrational spectroscopy studies

- on molecular conformation of liquid polymers poly(ethylene glycol) and poly(propylene glycol) at different interfaces. *Macromolecules* **2002**, *35* (24), 9130–9135.
18. Liu, Y.; Messmer, M.C. Molecular orientation at the interface of polystyrene/poly(methyl methacrylate) blends: evidence from sum-frequency spectroscopy. *J. Am. Chem. Soc.* **2002**, *124* (33), 9714–9715.
  19. Harp, G.P.; Gautam, K.S.; Dhinojwala, A. Probing polymer/polymer interfaces. *J. Am. Chem. Soc.* **2002**, *124* (27), 7908–7909.
  20. Wilson, P.T.; Richter, L.J.; Wallace, W.E.; Briggman, K.A.; Stephenson, J.C. Correlation of molecular orientation with adhesion at polystyrene/solid interfaces. *Chem. Phys. Lett.* **2002**, *363* (1–2), 161–168.
  21. Briggman, K.A.; Stephenson, J.C.; Wallace, W.E.; Richter, L.J. Absolute molecular orientation distribution of the polystyrene surface. *J. Phys. Chem., B* **2001**, *105* (14), 2785–2791.
  22. Chen, C.; Wang, J.; Woodcock, S.E.; Chen, Z. Surface morphology and molecular chemical structure of poly(*n*-butyl methacrylate)/polystyrene blend studied by atomic force microscopy (AFM) and sum frequency generation (SFG) vibrational spectroscopy. *Langmuir* **2002**, *18* (4), 1302–1309.
  23. Guyot-Sionnest, P.; Hunt, J.H.; Shen, Y.R. Sum-frequency vibrational spectroscopy of a Langmuir film: study of molecular orientation of a two-dimensional system. *Phys. Rev. Lett.* **1987**, *59* (14), 1597–1600.
  24. Hirose, C.; Akamatsu, N.; Domen, K. Formulas for the analysis of surface sum-frequency generation spectrum by CH stretching modes of methyl and methylene groups. *J. Chem. Phys.* **1992**, *96* (2), 997–1004.
  25. Hirose, C.; Akamatsu, N.; Domen, K. Formulas for the analysis of the surface SFG spectrum and transformation coefficients of Cartesian SFG tensor components. *Appl. Spectrosc.* **1992**, *46* (6), 1051–1072.
  26. Zhuang, X.; Miranda, P.B.; Kim, D.; Shen, Y.R. Mapping molecular orientational and conformation at interfaces by surface nonlinear optics. *Phys. Rev., B* **1999**, *59* (19), 12,632–12,640.
  27. Woodruff, D.; Delchar, T. *Modern Techniques of Surface Science*; Cambridge University Press: Cambridge, 1986.
  28. Somorjai, G.A. *Introduction to Surface Chemistry and Catalysis*; Wiley: New York, 1994.
  29. Lewis, K.B.; Ratner, B.D. Observation of surface rearrangement of polymers using ESCA. *J. Colloid Interface Sci.* **1993**, *159* (1), 77–85.
  30. Ruckenstein, E.; Gourisankar, S.V. Surface restructuring of polymeric solids and its effect on the stability of the polymer–water interface. *J. Colloid Interface Sci.* **1986**, *109* (2), 557–566.
  31. Chen, Q.; Zhang, D.; Somorjai, G.A.; Bertozzi, C.R. Probing the surface structural rearrangement of hydrogels by sum frequency generation spectroscopy. *J. Am. Chem. Soc.* **1999**, *121* (2), 446–447.
  32. Chen, C.Y.; Even, M.A.; Chen, Z. Detecting molecular-level chemical structure and group orientation of amphiphilic PEO–PPO–PEO copolymers at solution/air and solid/solution interfaces by SFG vibrational spectroscopy. *Macromolecules* **2003**, *36* (12), 4478–4484.
  33. Gautam, K.S.; Dhinojwala, A. Melting alkyl side chain comb polymer interfaces. *Phys. Rev. Lett.* **2002**, *88* (14), 145501.
  34. Wilson, P.T.; Briggman, K.A.; Wallace, W.E.; Stephenson, J.C.; Richter, L.J. Selective study of polymer/dielectric interfaces with vibrationally resonant sum frequency generation via thin film interface. *Appl. Phys. Lett.* **2002**, *80* (17), 3084–3086.
  35. Horbett, T.A.; Brash, J.L. *Proteins at Interfaces: II. Fundamentals and Applications*; ACS Symposium Series; American Chemical Society: Washington, DC, 1995; Vol. 602.
  36. Baier, R.E. *Applied Chemistry at Protein Interfaces*; American Chemical Society: Washington, DC, 1975.
  37. Brash, J.L.; Horbett, T.A.; Eds. *Proteins at Interfaces, Physicochemical and Biochemical Studies*; American Chemical Society: Washington, DC, 1987.
  38. Wang, J.; Buck, S.M.; Chen, Z. Sum frequency generation vibrational spectroscopy studies on protein adsorption. *J. Phys. Chem., B* **2002**, *106* (44), 11,666–11,672.
  39. Wang, J.; Paszti, Z.; Even, M.A.; Chen, Z. Interpretation of sum frequency generation vibrational spectra of interfacial proteins by the thin film model. submitted for publication.
  40. Wang, J.; Buck, S.M. The effect of surface coverage on conformation changes of bovine serum albumin molecules at the air–solution interface detected by sum frequency generation vibrational spectroscopy. *Analyst* **2003**, *128* (6), 773–778.
  41. Kim, J.; Somorjai, G.A. Molecular packing of lysozyme, fibrinogen, and bovine serum albumin on hydrophilic and hydrophobic surfaces studied by infrared–visible sum frequency generation and fluorescence microscopy. *J. Am. Chem. Soc.* **2003**, *125* (10), 3150–3158.
  42. Kim, G.; Gurau, M.; Kim, J.; Cremer, P.S. Investigations of lysozyme adsorption at the air/water and quartz/water interfaces by vibrational sum frequency spectroscopy. *Langmuir* **2002**, *18* (7), 2807–2811.



# Molecular Probes of Cation–Arene Interactions

George W. Gokel

Departments of Molecular Biology and Pharmacology and Chemistry, Washington University  
School of Medicine, St. Louis, Missouri, U.S.A.

## INTRODUCTION

The three phases of matter are gas phase, liquid (or condensed), and solid state. In recent years, the stunning advances in computational studies have led some to refer to it in a jocular sense as the fourth: “the computational state.” Some of the studies discussed in this entry concern gas phase results determined by mass spectrometry and by calculation. Additionally, data have been derived from solution and solid-state studies. Important inferences can be drawn from computations, work undertaken in the gas phase, in solution, and in the solid state. Significant as all of these methods are, only X-ray crystallographic data permit unambiguous analysis and comparison of structural information. The emphasis of this entry is therefore on the evidence for cation– $\pi$  interactions that is available from solid-state structures.

## ISSUES AND INTERACTIONS

The three major species considered in chemistry are anions, cations, and neutral species. Anions are negatively charged and therefore Lewis-basic. Arenes are electron-rich and also considered to be Lewis bases. The interaction between two Lewis bases is usually repulsive rather than attractive. The term “neutral” means uncharged, but a neutral compound may be either Lewis-basic (e.g., dimethyl ether) or Lewis-acidic (e.g., aluminum chloride). Our major concern in this entry will be with interactions of the type illustrated in the lower panel of Fig. 1. Such interactions involve the arene’s  $\pi$ -cloud as a Lewis (base) donor and the cation as a Lewis acid. The cation is represented as  $M^+$ , and most of the discussion herein will concern metallic cations. Other cations are certainly possible and will be noted where appropriate (Fig. 1).

Although this article is limited to interactions of cations with arenes, there is much to be considered. Arenes may possess sigma-donors in addition to the  $\pi$ -system that is the primary focus of the present discussion. Sigma-donors may be substituents on the

arene or they may be an integral part of the arene. They may enhance the arene’s Lewis basicity or they may detract from it. The top row of Fig. 2 shows benzene, the archetype aromatic, at the left, followed by pyridine, nitrobenzene, and methoxybenzene (anisole). The nitro group is electron-withdrawing and the methoxy group is electron-donating. Thus nitrobenzene is a weaker  $\pi$ -base than is benzene and anisole is stronger. In both cases, however, the oxygen atoms can function as sigma-donors in their interactions with cations.<sup>[1]</sup> The pyridine nitrogen atom is also a good sigma-donor, and its presence in the heterocycle makes the aromatic ring about as weak a  $\pi$ -base as nitrobenzene.

The second line of Fig. 2 shows, from left to right, furan, thiophene, imidazole, and cyclopentadienide anion. The latter is formed by deprotonating cyclopentadiene. When two cyclopentadienide (Cp) anions react with ferrous ion [Fe(II)], ferrocene (third line of Fig. 2) is formed. Ferrocene is the prototype for cyclopentadienyl- $\pi$  complexes, whether they involve a sandwich structure or only one Cp ring. Organometallic structures of this general type number in the thousands (Fig. 2).

The remaining two structures shown on the third line of Fig. 2 are indole and phenol. Neither is a “simple” arene. Both are important in nature as the side-chain arenes of tryptophan (Trp, W) and tyrosine (Tyr, Y), respectively. The other two arenes that occur as side chains of the common amino acids are imidazole (second line) and benzene (first structure). These arenes are side-chain elements of histidine (His, H) and phenylalanine (Phe, F), respectively. Imidazole is electron-poor and has two potentially sigma-donating nitrogen atoms. As a result, it has not generally been of interest, as a  $\pi$ -donor has not been explored. Interest in the arenes benzene, phenol, and indole, however, has been high. The amino acids phenylalanine, tyrosine, and tryptophan comprise about 8.5% of the amino acids in all known protein structures. Thus along any given protein chain, one amino acid out of every dozen is capable of interacting with ubiquitous sodium, potassium, or other cations (Fig. 3).

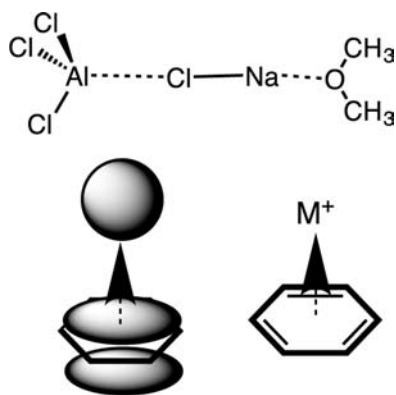


**Fig. 1** Lewis acid-base interactions. Top panel: The Lewis acid  $\text{AlCl}_3$  interacts with the Lewis base chloride of  $\text{NaCl}$  while  $\text{Na}^+$  interacts with dimethylether. Bottom: Two representations of a cation-pi interaction between a metal cation ( $\text{M}^+$ ) and benzene.

## GAS PHASE AND COMPUTATIONAL STUDIES

Pioneering studies of the cation–arene interaction were reported by Sunner, Nishi Zawa, and Kebarle,<sup>[2]</sup> in 1981. They used mass spectrometric methods to show that the interaction of  $\text{K}^+$  with benzene in the gas phase was similar energetically to the interaction of this cation with either a molecule of water or of methanol. Similar results were disclosed for  $\text{Na}^+$  by Castleman et al.<sup>[3,4]</sup> and by Cabarcos, Weinheimer, and Lisy,<sup>[5,6]</sup> some time later. Fig. 4 shows the presumed orientation of a benzene ring (shown in the CPK i.e., Corey-Pauling-Koltunorspace-filling metaphor) and  $\text{Na}^+$  (left) and  $\text{K}^+$  ions. Benzene is symmetrical and the ion's position with respect to the pi-cloud is predictable. This is not necessarily the

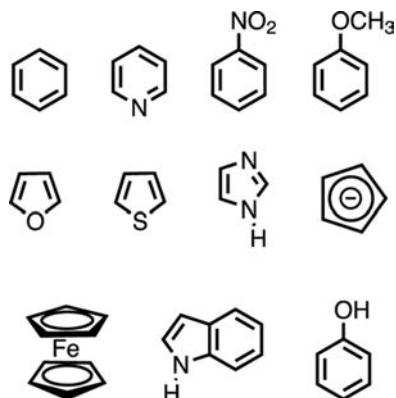


**Fig. 2** The top row shows from left to right benzene, the archetype aromatic, pyridine, nitrobenzene, and methoxybenzene (anisole). The second line shows, from left to right, furan, thiophene, imidazole, and cyclopentadienide anion. When two cyclopentadienide (Cp) anions react with ferrous ion  $[\text{Fe(II)}]$ , ferrocene (third line) forms. It is shown with indole and phenol.

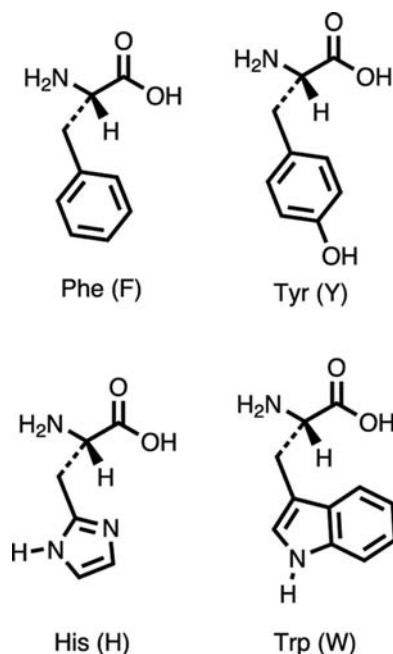


**Fig. 3** The four "essential" amino acids that have aromatic side chains. The amino acids are phenylalanine (F), tyrosine (Y), histidine (H), and tryptophan (W).

case with more complex arenes such as phenol or indole.

In recent years, a number of computational studies have been conducted,<sup>[7–11]</sup> in some cases, in concert with mass spectral analyses<sup>[12–14]</sup> (Table 1). In general, the conclusions are the expected and reasonable findings. Smaller cations of like charge, e.g.,  $\text{Na}^+$  compared with  $\text{K}^+$ , interact more strongly with an arene. Likewise, more electron-rich arenes, e.g., indole compared with benzene, are better donors for the same cation.

An example of how mass spectrometry may be used to study cation–pi interactions may be found in the study of pyxophanes.<sup>[15]</sup> The diacetylene, **1**, shown in Fig. 5 was prepared so that it would have a pi-rich interior of a size appropriate to bind  $\text{Na}^+$  but too small to bind  $\text{K}^+$ . These size notions were confirmed by a solid-state structure of **1**. The intriguing pyxophane has a molecular weight of 320 Da, but its  $^1\text{H-NMR}$  spectrum shows only two types of protons.

When the electrospray mass spectrum of the pyxophane was determined in the presence of equimolar

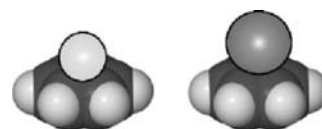


**Fig. 4** The presumed orientation of a benzene ring (shown in the CPK metaphor) and  $\text{Na}^+$  (left) and  $\text{K}^+$  ions.

**Table 1** Values reported for sodium and potassium cation interactions with benzene

Interaction	$-\Delta H$ (kcal/mol)	Method(s) used	Reference
$\text{Na}^+ + \text{C}_6\text{H}_6$	$28.0 \pm 0.1$	Mass spectrometry	[17]
$\text{Na}^+ + \text{C}_6\text{H}_6$	24.7–28.1	Computational methods	[9]
$\text{Na}^+ + \text{CH}_3\text{OH}$	26.6	Mass spectrometry	[17]
$\text{Na}^+ + \text{H}_2\text{O}$	24.0	Mass spectrometry	[17]
$\text{Na}^+ + \text{C}_6\text{H}_6$	21.5–21.8	Mass spectrometry and computational methods	[9][14]
$\text{K}^+ + \text{C}_6\text{H}_6$	18.3	Mass spectrometry and computational methods	[2]
$\text{K}^+ + \text{H}_2\text{O}$	17.9	Mass spectrometry and computational methods	[2]

$\text{Na}^+$  and  $\text{K}^+$ , a peak corresponding to  $[\mathbf{1}\cdot\text{Na}]^+$  was observed at  $m/e$  343. No peak corresponding to  $\mathbf{1} + \text{K}^+$  was observed at  $m/e$  359. This suggested selective pi-complexation of the smaller  $\text{Na}^+$  ion by  $\mathbf{1}$  and exclusion of larger  $\text{K}^+$ . These structural conclusions are reasonable based on known shapes, sizes, and interactions. Details cannot be known because they simply are not revealed in a mass spectral study. Notwithstanding, a structure was proffered shortly after the results appeared.<sup>[16]</sup> The conclusion was based on computational analysis, which is useful and, in this case, seemed reasonable. Thus one gains insight from both studies but actual structural data from neither.

### ARENE INTERACTIONS WITH NON-METALLIC CATIONS

Ammonium ( $\text{R}_4\text{N}^+$ ), phosphonium ( $\text{R}_4\text{P}^+$ ), sulfonium ( $\text{R}_3\text{S}^+$ ), and some others are common in nonmetallic cations. Their chemistry is both extensive and important. From the biological perspective, however, ammonium cations are the most important of these. The amine side chain of lysine (Lys, K) is protonated at physiologic pH as is the guanidinium residue of arginine (Arg, R). The potential of nonmetallic cations to interact with arenes was recognized in the early 1980s. Meot-Ner and Deakyne<sup>[17]</sup> used mass spectrometric studies to explore the interaction between -onium salts and arenes. At about the same time, Burley and Petsko<sup>[18]</sup> surveyed the Protein Data

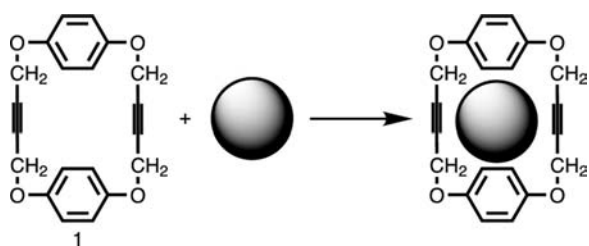


**Fig. 5** Diacetylene,  $\mathbf{1}$ , has a pi-rich interior of a size appropriate to bind  $\text{Na}^+$  but too small to bind  $\text{K}^+$ .

Bank (PDB) to see if -onium ion interactions with arenes could be identified. They were successful in identifying such interactions, but the structural database was limited.

### SOLUTION STUDIES OF ORGANIC CATION–PI INTERACTIONS

Solution studies involving synthetic receptor molecules have also been reported, which confirmed cation–pi interactions in aqueous solution.<sup>[19]</sup> These have involved several types of receptors, and their function has been studied in various solvents. The receptor shown at the right incorporates the essential elements for studies of this type. It is shown with an included adamantanyltrimethylammonium cation. Receptor  $\mathbf{2}$  is cyclic and contains an internal cavity. It is soluble in water by virtue of its 4 carboxylate anions that are present as cesium salts. The four sides of the receptor system are composed of pi-surfaces. The carboxylates are potential sigma-donors, but they are turned outward. The four oxygen atoms are also potential sigma-donors, but their attachment to an aromatic system enhances the pi-donicity of the arene at the expense of sigma-donation by the oxygen.

The use of water as a solvent has the potential advantage of driving together the organic receptor and substrate. The concern in such systems is that water will so strongly solvate one or both of the components that complexation between them will prove to be too weak to detect. Gas phase studies (mass spectrometry or computation) are unencumbered by solvation issues but may be criticized as unrealistic. This is especially true if inferences in the chemistry are to be applied to biological systems, which function in water.

Modern NMR techniques permit structural information to be obtained from these complexation studies. Nuclear Overhauser enhancements (NOEs) indicate proximity of certain atoms or groups. The aromatic receptors are especially amenable to study by NMR methods as the arenes have shielding and deshielding zones that affect adjacent nuclei. Numer-

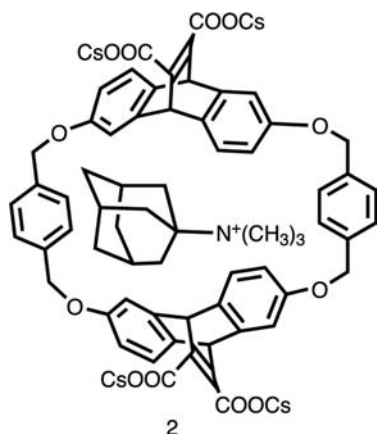


**Fig. 6** This figure shows a cyclic receptor (2), with an adamantyltrimethylammonium cation included in its internal cavity.

ous examples of and additional details concerning organic receptor molecules that have been studied in solution may be found in a review by Ma and Dougherty (Fig. 6).<sup>[20]</sup>

### SOLID-STATE STRUCTURAL STUDIES OF CATION–PI INTERACTIONS INVOLVING ANIONIC ARENES

The salt potassium tetraphenylborate [ $K^+B^-(C_6H_5)_4$ ] has been known for many years.<sup>[21]</sup> When it crystallizes, it forms a repeating unit that is packed to maximize the

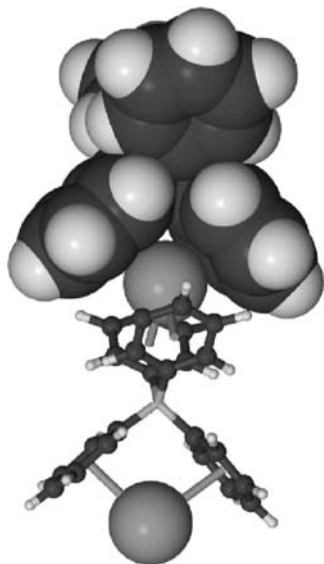


**Fig. 7** Rendering of two molecules of  $KB(C_6H_5)_4$  showing the cation–anion contacts. The boron atom's negative charge is shared among the four benzene rings in each salt, making each arene a stronger donor than it would be if neutral.

stabilizing forces and to minimize any unfavorable steric and electronic interactions. A two-molecule segment of its crystal structure, rendered in mixed ball and stick and CPK metaphor, is shown in Fig. 7. The  $K^+$  ion is nestled in an electron-rich pocket created by two benzene rings of one anion and two from an adjacent anion. The lines at the left of the figure from  $K^+$  to the arene indicate the line of contact between the cation and the arene's centroid. The distance from  $K^+$  to the centroid is 2.986 Å, and the centroid–K–centroid angle is  $\sim 100^\circ$ .

The boron atom's negative charge is shared among the four benzene rings in each salt, making each arene a stronger donor than it would be if neutral. The packing of the arenes is such that the space between them would probably be empty if the spherical cation failed to occupy it. This structure illustrates many of the issues of interest in cation–pi complexation. It is also clear that such precise distance and angle information cannot be gleaned from other analytical methods.

A number of other salts have been studied that reveal similar results. These include  $NaBPh_4$  and  $RbBPh_4$ . The latter was reported in 1962<sup>[22]</sup> and is recorded in the Cambridge Structural Database (CSD) using their six-letter code<sup>a</sup> as “RBPBOR.” The structure of  $NaBPh_4$ , which is similar to the  $K^+$  and  $Rb^+$  structures, is recorded in the CSD as ZZZUPI<sub>10</sub>.

Early efforts to demonstrate cation–pi interactions involved using an alkali metal cation as a reducing agent for an arene. Brooks et al. treated 1,4-dihydronaphthalene with *n*-butyllithium to afford dilithium naphthalenide as a dark purple solid. Its solid-state structure (CSD code: NAPLIM) is shown in Fig. 8A.<sup>[23]</sup> The arene is in contact with two lithium ions, which are present on opposite sides of the naphthalenide (Fig. 8). The lithium ions are  $\sim 2$  Å from the benzene ring centroids, and each cation is stabilized by tetramethylethylenediamine. It is interesting to note in this case that the van der Waals thickness of a benzene ring is  $\sim 3.5$  Å and the ionic radius for  $Li^+$  is  $\sim 0.7$  Å, suggesting that a Li–arene contact should be about  $(1.75 + 0.7 =) 2.45$  Å. In this structure, the distance is  $\sim 2$  Å, suggesting a very strong cation–pi interaction.

A similar approach involved treating fluorene with *n*-butylsodium and pentamethyldiethylenetriamine to give orange crystals of the sodium fluorene complex

<sup>a</sup>Each of the CSD's more than 250,000 crystal structures is assigned a unique code, usually consisting of six letters but sometimes followed by a number. Where possible, and especially for early structures, the code was suggestive of the structure as RBPBOR suggests rubidium and tetraphenylborate. As expected, most of the burgeoning number of structures do not have identifiable or suggestive names.

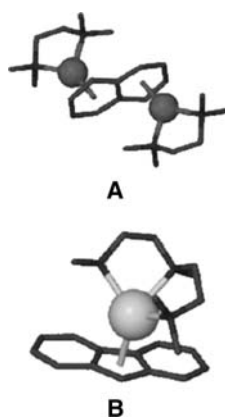


**Fig. 8** Dilithium naphthalenide's solid-state structure (CSD code: NAPLIM) is shown in Fig. 7A. The arene is in contact with two lithium ions, which are present on opposite sides of the naphthalenide. A similar approach gives orange crystals of the sodium fluorene complex shown in Fig. 7B.

shown in Fig. 7B.<sup>[24]</sup> The solid-state structure is recorded in the CSD as VOKPUG. It is interesting that the cation– $\pi$  interaction occurs with the central ring rather than either of the benzene rings. The Na-centroid distance is 2.562 Å. The ionic radius of Na<sup>+</sup> is about 1 Å, so the observed distance is once again shorter than the calculated value of (1.75 + 1 =) 2.75 Å.

### SOLID-STATE STRUCTURAL STUDIES OF CATION– $\pi$ INTERACTIONS INVOLVING NEUTRAL ARENES

The importance of an early and revealing structural study by Hrcir, Rogers, and Atwood<sup>[25]</sup> was not generally recognized at the time it appeared. The K–benzene distance is 3.369 Å. The ionic radius of K<sup>+</sup> is approximately 1.35 Å, giving an expected K<sup>+</sup>–arene contact distance of (1.75 + 1.35 =) 3.1 Å. In this



**Fig. 9** Crystal structure of potassium cation complexed by dibenzo-18-crown-6- and axially-solvated by neutral benzene. The K<sup>+</sup> ion is pulled out of the plane formed from the 6 oxygen atoms in the crown ether.

example, the K–arene contact is longer than the sum of the van der Waals distances, but the arene is not charged in this case. An interesting feature of this structure is that the K<sup>+</sup> ion is pulled out of the plane formed from the 6 oxygen atoms in the crown ether (Fig. 9).

Many solid-state structures show close contacts between arenes and cations.<sup>[26]</sup> One example is found in zeolites, which trap cations and arenes within their intricate molecular structure.<sup>[27]</sup> Another is found in numerous calixarene complexes<sup>[28]</sup> in which one or more cations are in proximity to the numerous arenes in the receptor molecule.<sup>[29,30]</sup>

### LARIAT ETHERS AS MOLECULAR PROBES OF CATION–ARENE INTERACTIONS

Examples of designed cation– $\pi$  receptor molecules are not yet common. A number of such compounds have been developed for gas phase and solution studies, but these do not provide definitive structural information. On the other hand, a solid-state structure is always suspected on the grounds that packing forces may exert an unexpected influence on the molecular arrangement. Even so, crystal structures are generally persuasive and provide details not available by other methods.

Lariat ethers are crown ethers that have flexible side chains attached to the macroring. Donors present on the side chains may further stabilize cations bound in the macrocycle's cavity. In principle, both sigma- and pi-donors may be incorporated to serve this purpose. Four bibracchial (two-armed) lariat ethers are shown as compounds **3–6** (Fig. 10). Each is a diaza-18-crown-6 macrocycle that has an arene-terminated ethylene sidearm. The arenes on **3**,<sup>[31]</sup> **5**,<sup>[32]</sup> and **6**<sup>[33]</sup> correspond to the side-chain residues of phenylalanine, tyrosine, and tryptophan, respectively. Compound **4**<sup>[34]</sup> is structurally very similar to **3**, but the arene is electron-deficient owing to the strong electron-withdrawing effect of fluorine (Fig. 10).

The solid-state structures of **3–6** as their KI complexes are shown in Fig. 11A–D, respectively. In all cases, K<sup>+</sup> is complexed in the crown's central cavity or hole. From the electrostatic perspective, the iodide ion should be the best anionic donor and it should be in essentially direct contact with the ring-bound cation. Instead, the sidearm arenes appear to be the axial donors in **3**-KI, **5**-KI, and **6**-KI. Such a result might be caused by crystal packing forces. Note that the iodide ion is in approximately the same position in a, c, and d, although H-bond interactions with hydroxyl (c) or amino (d) groups are possible only with **5** and **6**,



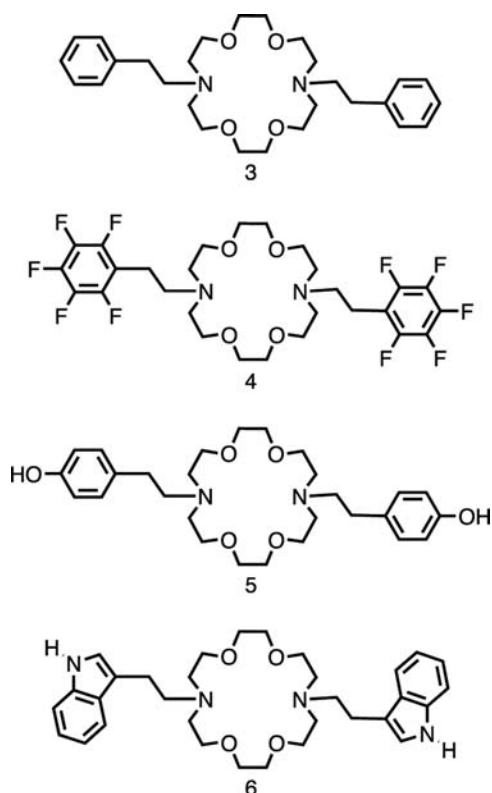


**Fig. 10** Bibracchial (two-armed) lariat ethers having arene-terminated side arms: 3, benzene; 4, penta fluoro benzene; 5, phenol; and 6, indole.

respectively. The concern about packing forces is dispelled by the result shown in Fig. 9B. In this case, the benzene ring of **3** has been replaced by pentafluorophenyl groups. These are only slightly larger than benzene, but they may be considered pi-acids rather than pi-bases. Thus they are expected *not* to interact with bound  $K^+$ . As shown in Fig. 11, panel b, the two arenes are turned away from the macrocycle and the cation interacts directly with the iodide anion. Two iodide ions are shown in Fig. 11B. They actually comprise part of an infinite chain of  $(-K-I)_n$  ion pairs within the crystal (Fig. 11).

To further clarify these interactions, the diaza-18-crown-6 compound (**7**) was prepared that has 2-methoxyethyl and 2-phenylethyl side chains.<sup>[35]</sup> The compound and the complex observed by X-ray crystallography are illustrated schematically in Fig. 12. The complex possesses no obvious H-bonding residue in the sidearms, but iodide anion in **7**·KI is excluded from the cation's solvation sphere. Because there is only one arene available to serve as an axial donor, the other site is occupied by the ether oxygen. When a single sidearm is present (*N*-2-phenylethylaza-18-crown-6), iodide occupies the axial position opposite the single arene.<sup>[36]</sup>

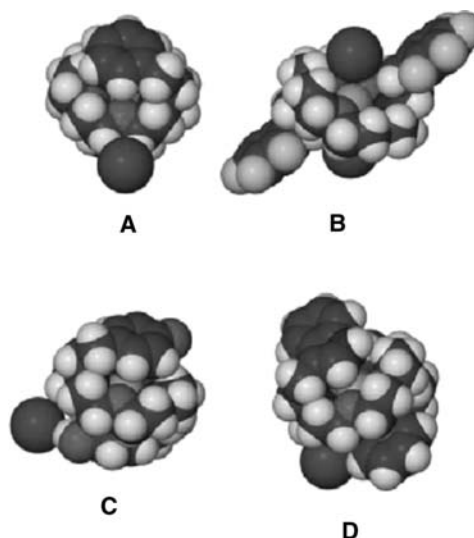


**Fig. 11** The solid state structures of **3–6** complexing KI are shown as A–D, respectively. In panel B, the two Lewis acidic arenes are turned away from the macrocycle and the cation interacts directly with iodide anion whereas iodide is excluded from the solvation sphere in A, C, and D.

An interesting feature of the solid-state structural studies is that the bound cation in **6** was closer to the 5-membered ring instead of the more electron-rich 6-membered ring. Computational studies showed a clear preference for the benzo, rather than the pyrrolo subunit, of indole to serve as the pi-donor. Similar experimental results were observed for both  $Na^+$  and  $K^+$  in concert with a variety of counteranions. When the position of attachment between the macrocycle and the arene was moved, benzene became the cation's axial donor.<sup>[37]</sup> This suggests that indole is indeed a versatile pi-donor.

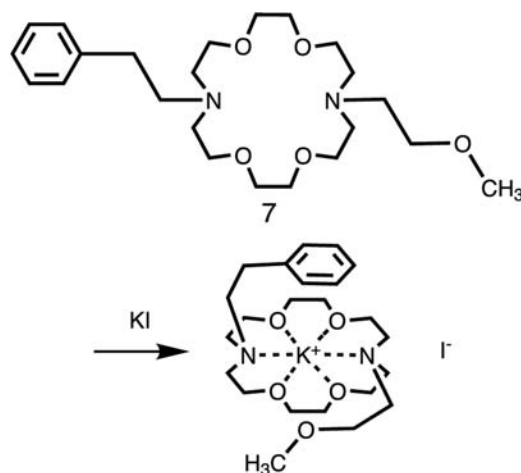


**Fig. 12** The diaza-18-crown-6 compound (**7**) was prepared to have 2-methoxyethyl and 2-phenylethyl side chains.



## CONCLUSION

Arenes are predicted by computational methods to bind cations. The first evidence for such interactions came from mass spectrometric studies conducted in the gas phase. Subsequent studies undertaken with designed receptor molecules gave evidence for cation–arene interactions in various solvents. Recently, numerous solid-state structural data have confirmed these interactions and have provided distance and angle information upon which to base more sophisticated receptor design efforts.

## ACKNOWLEDGMENTS

The author gratefully acknowledges that his work in this area has been supported by grants from the National Institutes of Health, the National Science Foundation, and the Petroleum Research Fund.

## REFERENCES

- Nicholas, J.B.; Hay, B.P. Anisole as an ambidentate ligand: ab initio molecular orbital study of alkali metal cations binding to anisole. *J. Phys. Chem., A* **1999**, *103*, 9815–9820.
- Sunner, J.; Nishizawa, K.; Kebarle, P. Ion–solvent interactions in the gas phase. The potassium ion and benzene. *J. Phys. Chem.* **1981**, *85*, 1814–1820.
- Guo, B.C.; Purnell, J.W.; Castleman, A.W., Jr. The clustering reactions of benzene with sodium and lead ions. *Chem. Phys. Lett.* **1990**, *168*, 155–160.
- Gilligan, J.J.; McCunn, L.R.; Leskiw, B.D.; Herman, Z.; Castleman, A.W., Jr. Associative ionization of excited sodium species with various ligands: assessing relative bonding strengths of ion–ligand interactions. *Int. J. Mass Spectrom.* **2001**, *204*, 247–253.
- Cabarcos, O.M.; Weinheimer, C.J.; Lisy, J.M. Competitive solvation of K<sup>+</sup> by benzene and water: cation–pi interactions and pi-hydrogen bonds. *J. Chem. Phys.* **1998**, *108*, 5151–5154.
- Cabarcos, O.M.; Weinheimer, C.J.; Lisy, J.M. Size selectivity by cation–p interactions: Solvation of K<sup>+</sup> and Na<sup>+</sup> by benzene and water. *J. Chem. Phys.* **1999**, *110*, 8429–8435.
- Dunbar, R.C. Binding of Na<sup>+</sup>, Mg<sup>+</sup>, and Al<sup>+</sup> to the pi faces of naphthalene and indole: ab initio mapping study. *J. Phys. Chem., A* **1998**, *102*, 8946–8952.
- Nicholas, J.B.; Hay, B.P.; Dixon, D.A. Ab initio molecular orbital study of cation–pi binding between the alkali-metal cations and benzene. *J. Phys. Chem., A* **1999**, *103*, 1394–1400.
- Hoyau, S.; Norman, K.; McMahan, T.B.; Ohanessian, G. A quantitative basis for a scale of Na<sup>+</sup> affinities of organic and small biological molecules in the gas phase. *J. Am. Chem. Soc.* **1999**, *121*, 8864–8875.
- Wouters, J. Use of theoretical descriptors to characterize cation–pi binding sites in (macro)molecules. *J. Comput. Chem.* **2000**, *21*, 847–855.
- Hay, B.P.; Nicholas, J.B.; Feller, D. Novel binding modes in tetramethoxycalix[4]arene: Implications for ligand design. *J. Am. Chem. Soc.* **2000**, *122*, 10083–10089.
- Ryzhov, V.; Dunbar, R.C. Interactions of phenol and indole with metal ions in the gas phase: models for Tyr and Trp side-chain binding. *J. Am. Chem. Soc.* **1999**, *121*, 2259–2268.
- Ryzhov, V.; Dunbar, R.C.; Cerda, B.; Wesdemiotis, C. Cation–pi effects in the complexation of Na<sup>+</sup> and K<sup>+</sup> with Phe, Tyr, and Trp in the gas phase. *J. Am. Soc. Mass Spectrom.* **2000**, *11*, 1037–1046.
- Armentrout, P.B.; Rodgers, M.T. An absolute sodium cation affinity scale: threshold collision-induced dissociation experiments and ab initio theory. *J. Phys. Chem., A* **2000**, *104*, 2238–2247.
- Behm, R.; Gloeckner, C.; Grayson, M.A.; Gross, M.L.; Gokel, G.W. Pyxophanes: Selective gas phase ion complexation by 1,6,13,18-tetraoxa[6.6]paracyclophane-3,15-diyne. *Chem. Commun.* **2000**, 2377–2378.
- Yoshida, M.; Tsuzuki, S.; Tamaoki, N. Induced-fit conformational changes in the cation–pi complexes of pyxophane: A DFT study. *Perkin 2* **2001**, 1021–1023.
- Meot-Ner, M.; Deakyne, C.A. Unconventional ionic hydrogen bonds. 2. NH<sup>+</sup>...pi. Complexes of onium ions with olefins and benzene derivatives. *J. Am. Chem. Soc.* **1985**, *107*, 474–479.
- Burley, S.K.; Petsko, G.A. Amino-aromatic interactions in proteins. *FEBS Lett.* **1986**, *203*, 139–143.
- Kearney, P.C.; Mizoue, L.S.; Kumpf, R.A.; Forman, J.E.; McKurdy, A.; Dougherty, D.A. Molecular recognition in aqueous media. New binding studies provide further insights into the cation–pi interaction and related phenomena. *J. Am. Chem. Soc.* **1993**, *115*, 9907–9919.
- Ma, J.C.; Dougherty, D.A. The cation–pi interaction. *Chem. Rev.* **1997**, *97*, 1303–1324.
- Hoffmann, K.; Weiss, E. Ueber metall-alkyl- und -arylverbindungen. XVI. Die kristallstrukturen von kaliumtetraphenylborat, K[B(C<sub>6</sub>H<sub>5</sub>)<sub>4</sub>] und tetramethylammonium-tetraphenylborat, [N(CH<sub>3</sub>)<sub>4</sub>][B(C<sub>6</sub>H<sub>5</sub>)<sub>4</sub>]. *J. Organomet. Chem.* **1974**, *67*, 221–228.
- Ozol, Y.; Vimba, S.; Levins, A. Crystal structure of RbBPh<sub>4</sub>. *Krystallografiya* **1962**, *7*, 362
- Brooks, J.J.; Rhine, W.; Stucky, G.D. Pi groups in ion pair bonding. Stabilization of the dianion of naphthalene by lithium tetramethylenediamine. *J. Am. Chem. Soc.* **1972**, *94*, 7346–7351.
- Corbelin, S.; Kopf, J.; Weiss, E. Monomeres, tetrameres und polymeres natriumfluorenid S [s = Me<sub>2</sub>N(CH<sub>2</sub>)<sub>2</sub>-N(Me)(CH<sub>2</sub>)<sub>2</sub>NMe<sub>2</sub>, Me<sub>2</sub>N(CH<sub>2</sub>)<sub>n</sub>NMe<sub>2</sub> (n = 2, 3)]. *Chem. Ber.* **1991**, 2417–2422.
- Hrcir, D.C.; Rogers, R.D.; Atwood, J.L. New bonding mode for a bridging dioxygen ligand: the crystal and molecular structure of [K.dibenzo-18-crown-6]-[Al<sub>2</sub>Me<sub>6</sub>O<sub>2</sub>].2C<sub>6</sub>H<sub>6</sub>. *J. Am. Chem. Soc.* **1981**, *103*, 4277.
- Gokel, G.W.; Wall, S.L.D.; Meadows, E.S. Experimental evidence for alkali metal cation–pi interactions. *Eur. J. Org. Chem.* **2000**, 2967–2978.

27. Hashimoto, S.; Ikuta, S.; Asahi, T.; Masuhara, H. Fluorescence spectroscopic studies of anthracene adsorbed into zeolites: from the detection of cation– $\pi$  interaction to the observation of dimers and crystals. *Langmuir* **1998**, *14*, 4284–4291.
28. Ikeda, A.; Shinkai, S. On the origin of high ionophoricity of 1,3-alternate calix[4]arenes:  $\pi$ -donor participation in complexation of cations and evidence for metal-tunneling through the calix[4]arene cavity. *J. Am. Chem. Soc.* **1994**, *116*, 3102–3110.
29. Arduini, A.; Casnati, A.; Pochini, A.; Ungaro, R. Recognition of cationic species with synthetic receptors. *Curr. Opin. Chem. Biol.* **1997**, *1*, 467–474.
30. Casnati, A.; Sansone, F.; Ungaro, R. Peptido- and glycolixarenes: playing with hydrogen bonds around hydrophobic cavities. *Acc. Chem. Res.* **2003**, *36*, 246–254.
31. Meadows, E.S.; De Wall, S.L.; Barbour, L.J.; Gokel, G.W. Alkali metal cation– $\pi$  interactions observed by using a lariat ether model system. *J. Am. Chem. Soc.* **2001**, *123*, 3092–3107.
32. De Wall, S.L.; Barbour, L.J.; Gokel, G.W. Cation– $\pi$  complexation of potassium cation with the phenolic sidechain of tyrosine. *J. Am. Chem. Soc.* **1999**, 8405–8406.
33. De Wall, S.L.; Meadows, E.S.; Barbour, L.J.; Gokel, G.W. Solution and solid state evidence for alkali metal, cation– $\pi$  interactions with indole, the sidechain of tryptophan. *J. Am. Chem. Soc.* **1999**, *121*, 5613–5614.
34. De Wall, S.L.; Meadows, E.S.; Barbour, L.J.; Gokel, G.W. Synthetic receptors as models for alkali metal cation– $\pi$  binding sites in proteins. *Proc. Natl. Acad. Sci. U. S. A.* **2000**, *97*, 6271–6276.
35. Hu, J.; Barbour, L.J.; Gokel, G.W. Sigma-donor,  $\pi$ -donor, and anion competition in  $\pi$ -complexation of alkali metal cations. *Chem. Commun.* **2002**, 1808–1809.
36. Hu, J.; Barbour, L.J.; Gokel, G.W. Probing alkali metal– $\pi$  interactions with the side chain residue of tryptophan. *Proc. Natl. Acad. Sci. U. S. A.* **2002**, *99*, 5121–5126.
37. Hu, J.; Barbour, L.J.; Gokel, G.W. The indole sidechain of tryptophan as a versatile  $\pi$ -donor. *J. Am. Chem. Soc.* **2002**, *124*, 10,940–10,41.

# Molecular Receptor-Modified Metal Nanoparticles

Jian Liu

Department of Chemistry, Michigan Technological University, Houghton, Michigan, U.S.A.

## INTRODUCTION

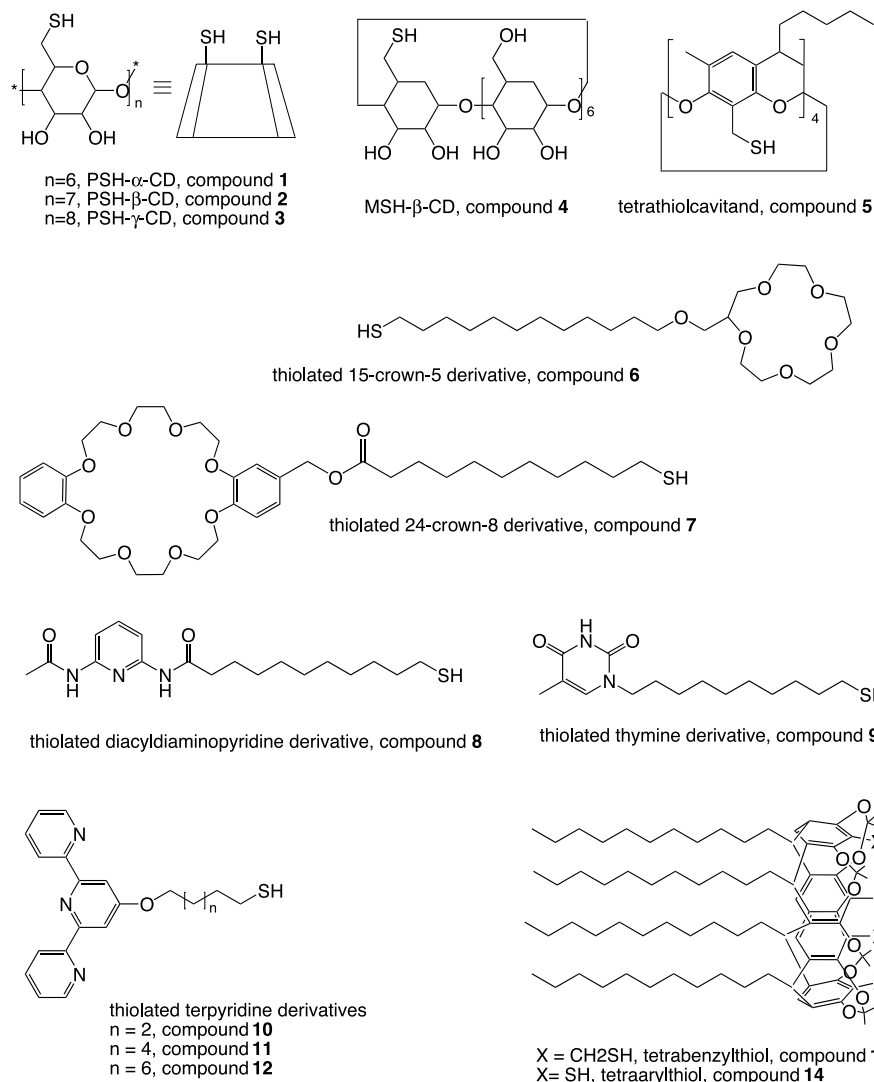
Presently, monolayer-protected metal nanoparticles (MPNPs) are the subjects of some exciting and very active interdisciplinary research because of the rapid development of preparation methods using organic thiols as stabilizers. The organic monolayer not only protects the particles from agglomeration, but also furnishes a scaffold for the construction of different functional entities on their surfaces leading to a broad range of interesting applications. Among these studies, the attachment of molecular receptors capable of engaging in well-defined host–guest interactions is receiving considerable attention.<sup>[1]</sup> This article summarizes recent advancements in the development and applications of artificial receptor-modified metal nanoparticles. The research work on metal nanoparticles modified with biological species, such as DNA, was reviewed recently,<sup>[2]</sup> thus this topic will not be included here.

## PREPARATION OF RECEPTOR-MODIFIED METAL NANOPARTICLES

There has been a great advance<sup>[3]</sup> in the development of synthetic methodology for the preparation of MPNPs after a seminar report from Brust et al.<sup>[4]</sup> In their approach, metal nanoparticles were prepared by chemical reduction of corresponding salts under a mild condition using NaBH<sub>4</sub> as the reducing agent. The presence of thiol ligands with various stoichiometries to metal salt in the reaction resulted in metal nanoparticles ranging in size between 2 and 8 nm. Molecular receptors on metal nanoparticles can be introduced by directly using the thiolated receptor as the capping agent during the particle formation. An alternative approach uses the ligand-exchange<sup>[3]</sup> method to further elaborate the preformed MPNPs with thiolated receptors. In the first case, a crucial consideration is the solubility of the receptor in the reaction media because metal salts are not soluble in nonpolar organic solvents. For example, Kaifer et al. developed a special method to prepare the water-soluble Au,<sup>[5]</sup> Pt,<sup>[6]</sup> and Pd<sup>[6,7]</sup> nanoparticles modified with perthiolated cyclodextrins (PSH-CDs, Chart 1). In this approach, the

special solvent, dimethyl sulfoxide (DMSO) or dimethylformamide (DMF), was used as the reaction media to bring all reacting components, the PSH-CD, the corresponding metal salt, and NaBH<sub>4</sub> in the same phase. This one-phase, one-step (1P-1S) approach eliminates the use of phase transfer reagents in a typical two-phase, one-step (2P-1S) method.<sup>[4]</sup> In the 1P-1S method, the final particle size is influenced not only by the concentration of thiols<sup>[5]</sup> but also by the nature of these molecules. For instance, a “macro-cyclic effect” was observed during the preparation of Ag nanoparticles in DMF.<sup>[8]</sup> Perthiolated  $\beta$ -CD (PSH- $\beta$ -CD) was found to be more efficient as a capping ligand than monothiolated  $\beta$ -CD (MSH- $\beta$ -CD, Chart 1). Similarly, a tetrathiol cavitand derivative (Chart 1) was also more efficient than a simple monothiol model compound. This sort of “macro-cyclic effect” probably results from an increased probability of surface attachment for the multidentate thiols, as they possess more functional groups capable of initiating their chemisorption process. In addition, once the surface attachment starts, their multidentate character may lead to a more robust, multipoint anchoring of the ligand. Therefore, this macrocyclic effect in metal nanoparticle capping reactions may have both a kinetic and a thermodynamic origin.

PSH-CD-modified metal nanoparticles prepared by 1P-1S approach have a diameter less than 10 nm. To obtain PSH- $\beta$ -CD-modified gold nanoparticles (PSH- $\beta$ -CD-Au) larger than 10 nm, a 2S method was applied. Preprepared, citrate-stabilized gold nanoparticles (13 nm in diameter)<sup>[9]</sup> were further modified with PSH- $\beta$ -CDs by ligand exchange with citrate on the particle surface in the aqueous solution.<sup>[10]</sup> A similar strategy was used by Lin et al.<sup>[11]</sup> to prepare Au nanoparticles (18 nm in diameter) modified with thiolated crown ether derivatives (Chart 1). Interestingly, surface-modified gold nanoparticles with even larger size (16–87 nm in diameter) were prepared by extracting citrate-stabilized particles in aqueous solutions into toluene or chloroform with thiolated resorcinarene derivatives (Chart 1),<sup>[12]</sup> the compounds relevant to some macrocyclic receptors. These tetrathiolated resorcinarenes improved the dispersion and robustness of midnanometer-sized gold nanoparticles in organic solvents. However, the authors clearly demonstrated that



the tetraaryltiol adsorbed on the surface is much weaker as compared to tetrabenzylthiol. This is another case that shows how the nature of the thiol compound affects the passivation on metal nanoparticles. Direct modification of Au particles (4 nm in diameter) with another type of crown derivative (Chart 1) was also achieved<sup>[13]</sup> by adapting Brust's 2P-1S approach.<sup>[4]</sup> Rotello et al.<sup>[14–16]</sup> introduced their organic receptors (Chart 1) by using ligand exchange approach to preformed, alkanethiol-modified Au particles in organic solvents. Multivalent receptors were also introduced by the same group on Au particles with similar methodology.<sup>[17]</sup> In the sense of practical application, the ligand exchange approach provides an easier way to control the number of receptors on each particle, which is one of the key factors for molecular recognition at particle surfaces.

Particle size characterization is usually carried out by transmission electron microscopy (TEM). The

solubility of MPNPs in various solvents affords a unique opportunity to characterize them by using standard solution-phase techniques such as nuclear magnetic resonance (NMR) and UV-vis spectroscopies. For example, a <sup>1</sup>H NMR spectrum of gold nanoparticles modified with perthiolated  $\gamma$ -CD (PSH- $\gamma$ -CD-Au) in D<sub>2</sub>O affords the broadened proton resonances from surface-immobilized  $\gamma$ -CDs (Fig. 1).<sup>[18]</sup> Such phenomenon is consistent with the observation obtained by Templeton and coworkers.<sup>[3]</sup> In these systems, the resonances of those protons closer to the metal surface are more seriously broadened, whereas the effect is less pronounced for the protons that are farther away. Fast relaxation and environmental heterogeneities are thought to be responsible for these line-broadening effects. The UV-vis spectroscopic study revealed that PSH- $\beta$ -CD-AuNPs with small size (3 nm in diameter) presented a relatively weak surface plasmon band (SP band) around 520 nm. In contrast, the bigger particles

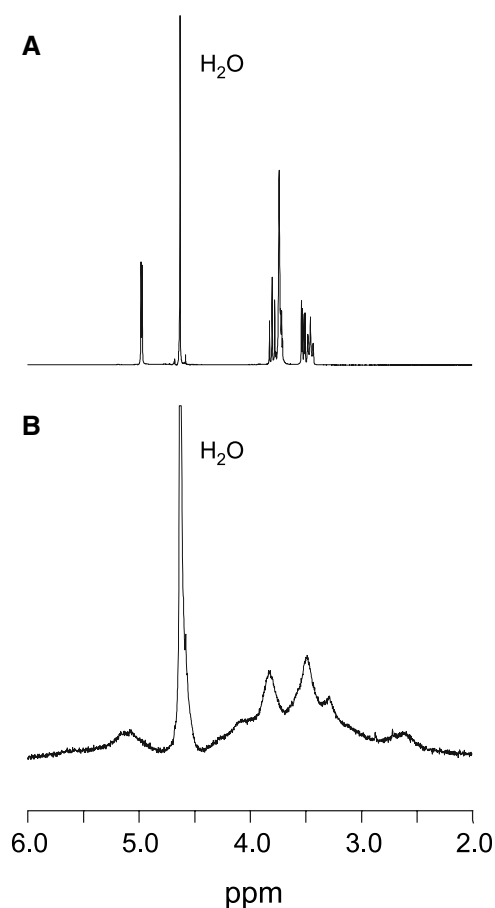


**Fig. 1**  $^1\text{H}$  NMR spectra (400 MHz,  $\text{D}_2\text{O}$ ) of (A) free  $\gamma$ -CD and (B) PSH- $\gamma$ -CD-Au. Source: From Ref.<sup>[29]</sup>. © 2001, American Chemical Society.

(13 nm in diameter) gave a strong SP band, which may serve as a signal for visibly probing chemical and biological species in the solution.

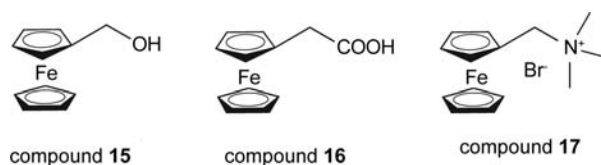
### MOLECULAR RECOGNITION AT THE SURFACES OF RECEPTOR-MODIFIED METAL NANOPARTICLES

The purpose of introducing molecular receptors on metal nanoparticle surfaces is to endow these nano-scale entities with the capability of engaging molecular recognition. Electrochemistry and UV-vis spectroscopy are the two common techniques used to study the molecular recognition events on particle surfaces in various solutions. Several aspects in this scenario are addressed as follows.

#### Recognition of Redox-Active Species

An important feature of cyclodextrin (CD)-modified metal nanoparticles is their excellent aqueous solubility.

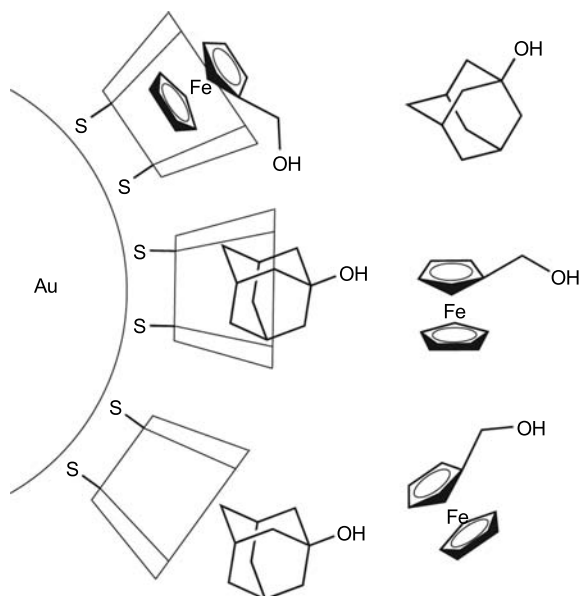
This property is probably contributed by the polarity of the secondary hydroxyl groups on CD receptors, which afford a polar character to the surface of nanoparticles. Surface attachment of the CD hosts through their primary faces necessarily leaves the wider, secondary faces exposed to the solution phase, a configuration that favors binding between the immobilized CDs and appropriate guests in the solution.



Liu et al. used some water-soluble, electroactive molecules (Chart 2) to study the complexation ability of surface-immobilized  $\beta$ -CDs on metal nanoparticles in aqueous solutions. For example, addition of PSH- $\beta$ -CD-Au led to two pronounced effects on the electrochemical response of ferrocenemethanol.<sup>[5]</sup> 1) it decreased the current of the voltammetric wave, and 2) it shifted the apparent half-wave potential to more positive values. Both effects clearly indicated that ferrocenemethanol was forming inclusion complexes with the CD receptors immobilized on the gold nanospheres. This was further verified by addition of 1-adamantanol to the same solution. Adamantanol, being also an excellent guest for inclusion complexation by  $\beta$ -CD,<sup>[19]</sup> competed effectively with ferrocenemethanol for the available CD binding sites on the surface of the gold particles (Scheme 1). As a result, most of the ferrocenemethanol molecules were displaced from their binding sites and released back to the bulk solution, giving rise to a voltammetric response very similar to that recorded in the absence of the  $\beta$ -CD-Au.

The host-binding ability of  $\beta$ -CD immobilized on gold nanoparticles was further verified using compound 17 as guest probe in a  $^1\text{H}$  NMR study.<sup>[18]</sup> The displacement and broadening of the ferrocene proton resonance in the presence of PSH- $\beta$ -CD-Au were attributed to the formation of the inclusion complexes on the nanoparticle surfaces, as they were similar to those observed upon the addition of free  $\beta$ -CD to solutions of ferrocene derivatives. The substantial line broadening must have resulted also from the association of the ferrocene guest to the massive nanoparticles, and was probably related to chemical exchange (free ferrocene going to bound ferrocene and back), as well as to relaxation effects in the bound state. Note that when the ferrocene guest was bound to a CD cavity, it became a part of a rather large supramolecular assembly.

A similar redox-controlled recognition event on receptor-modified metal nanoparticles was also demonstrated by Boal and Rotello in a different nanoparticle

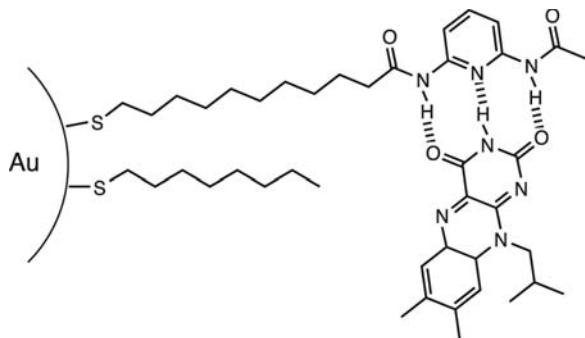


**Scheme 1** Competitive binding of ferrocenemethanol and 1-adamantanol to the  $\beta$ -CD hosts immobilized on a gold nanoparticle.

system. Reversible complexation between flavin ( $\text{Fl}_{\text{ox}}$ ) and diaminopyridine (DAP) tethered on gold nanoparticles was successfully controlled electrochemically in chloroform (Scheme 2).<sup>[14]</sup> Moreover, the same group investigated the multitopic recognition at gold nanoparticles by creating multivalent recognition sites through tethering both DAP and pyrene on the same particle surface. A stronger recognition of electron-deficient  $\text{Fl}_{\text{ox}}$  on particle surfaces was achieved through hydrogen bonding to DAP units and favorable  $\pi$  stacking with the electron-rich pyrene units.<sup>[17,20]</sup>

### Recognition of Cations

Lin et al.<sup>[11]</sup> reported an efficient recognition of  $\text{K}^+$  by 15-crown-5-modified gold nanoparticles (18 nm in



**Scheme 2** Recognition of flavin by surface-immobilized diacyldiaminopyridine.

diameter) in aqueous solution containing physiologically important cations, such as  $\text{Li}^+$ ,  $\text{Cs}^+$ ,  $\text{NH}_4^+$ ,  $\text{Mg}^{2+}$ ,  $\text{Ca}^{2+}$ , and an excess amount of  $\text{Na}^+$ . Upon exposure to  $\text{K}^+$ , the color of the nanoparticle solution changed from red to blue corresponding to the surface plasmon absorption of dispersed and aggregated nanoparticles. The authors postulated that one potassium ion efficiently bound to two crown moieties tethered to two different nanoparticles forming a sandwichlike 2:1 complex, which led to the aggregation of nanoparticles.

### Recognition of Anions

Gold nanoparticles modified with a mixed monolayer of alkanethiols and amidoferrocenylalkanethiol were used as effective exoreceptors for electrochemically sensing  $\text{H}_2\text{PO}_4^-$  and  $\text{HSO}_4^-$ .<sup>[21]</sup> The authors found that the redox potential of amidoferrocenyl group was perturbed by the synergy among the hydrogen bonding, electrostatic interaction, and topology of mixed monolayer to recognize  $\text{H}_2\text{PO}_4^-$  and  $\text{HSO}_4^-$  on particle surfaces. However, the potential change is much smaller for  $\text{HSO}_4^-$  than for  $\text{H}_2\text{PO}_4^-$ , showing certain selectivity of the recognition of these particles. The same group extended this work to gold nanoparticles modified with thiol dendrons containing three redox-active amidoferrocenyl or silylferrocenyl units.<sup>[22]</sup> These surface-functionalized particles could effectively recognize  $\text{H}_2\text{PO}_4^-$ . More insights about the stereoelectronic effect of amidoferrocenyl group on the recognition of oxoanions at gold nanoparticle surfaces were reported recently from the same group.<sup>[23]</sup> The recognition properties were weakened by permethylation of one Cp ring (electron releasing and sterically demanding) on amidoferrocenyl moiety but enhanced by acetylation of the same ring (electron withdrawing). Thus, the authors claimed, the stereoelectronic property of the amidoferrocenyl group acted as the key role for the recognition by the amidoferrocenium form through the hydrogen bonding between the  $-\text{NH}-$  amido group and the charged terminal oxygen atom of the oxoanions. The recognition properties of gold nanoparticles functionalized with metallodendrons were further discussed in a recent report.<sup>[24]</sup> Gold nanoparticles modified with up to 360 silylferrocenyl units on each particle were achieved. These dendronized gold nanoparticles combine the advantages of dendrimers and nanoparticles as sensors for the selective recognition of  $\text{H}_2\text{PO}_4^-$  and adenosine-5'-triphosphate ( $\text{ATP}^{2-}$ ) even in the presence of other anions. A dendritic effect on the recognition properties was clearly observed; in other words, the shift of the ferrocenyl redox potential upon introduction of the anion became larger as the generation number of dendrons increased.



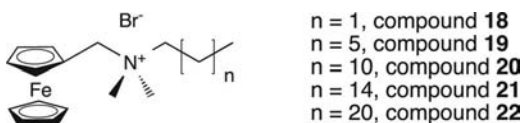
Watanabe et al. developed amide-functionalized gold nanoparticles as a prototype for optical recognition of various anions, such as  $\text{H}_2\text{PO}_4^-$ ,  $\text{HSO}_4^-$ ,  $\text{AcO}^-$ , and  $\text{NO}_3^-$ , in organic solvents.<sup>[25]</sup> Interestingly, the addition of anions initially caused a decrease in the surface plasmon absorption of gold nanoparticles. However, the intensity of this SP band increased when excess anion existed in the  $\text{CH}_2\text{Cl}_2$ . The authors reasoned that initial decrease of the SP band was because of the anion-induced aggregation of gold nanoparticles. Further addition of anion caused the disaggregation of the suprananoparticles composed of particles and anions.

### RECEPTOR-MODIFIED METAL NANOPARTICLES AS BUILDING BLOCKS IN THE SELF-ASSEMBLY OF ORGANIC-INORGANIC NANOCOMPOSITES

Metal nanoparticles modified with molecular receptors are excellent candidates as “building blocks” for the bottom-up construction of organic/inorganic hybrid nanocomposites in solution phase by using the non-covalent molecular interactions at particle surfaces. Such nanoscale systems may serve as the initial prototypes in the fabrication of nanoelectronic devices. Several aspects of this scenario will be summarized in this section. A detailed discussion about the research work on this topic from Shenhar and Rotello can be found in a recent review.<sup>[26]</sup>

#### Receptor-Modified Metal Nanoparticles as Templates for the Construction of Micellar Structures

In a recent report, Liu et al.<sup>[18]</sup> reasoned that the introduction of molecular species by molecular recognition at PSH-CD-Au might lead to reversible functionalization of particle surfaces. Therefore, a series of ferrocene derivatives with different lengths of aliphatic chains (Chart 3) were used to examine this idea.

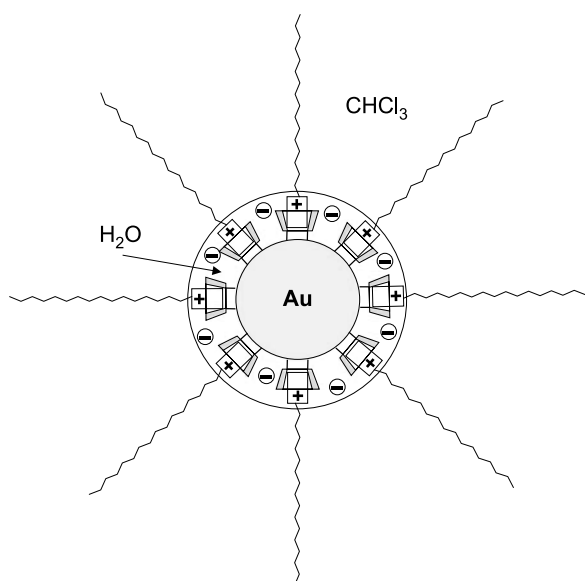


Mixing a chloroform phase containing **22** with an aqueous solution containing PSH- $\beta$ -CD-Au caused a color change of the organic phase from initial yellow to brown. The visible absorption spectrum of this solution clearly revealed two distinct bands residing at 430 and 510 nm, corresponding to the absorptions

by the ferrocene residues and the nanoparticles (SP band), respectively. The obvious conclusion from these results was that compound **22** acted as an efficient phase transfer agent for the water-soluble PSH- $\beta$ -CD-Au and enabled their solubilization in the chloroform phase. Further study showed that only compounds **20**, **21**, and **22** (with aliphatic chains of 12, 16, and 22 carbon atoms) effectively promoted the solubilization of the PSH- $\beta$ -CD-Au in the chloroform phase; compounds **18** and **19** (with shorter aliphatic chains of 3 and 7 carbon atoms) were ineffective. This finding strongly suggested that the long aliphatic chains of ferrocene derivatives could effectively cover the particle surfaces after the complexation with surface-immobilized  $\beta$ -CDs leading to more hydrophobic aggregates, which favored organic solvents. The effectiveness of phase transfer was enhanced when the initial concentration of either ferrocene derivatives or PSH- $\beta$ -CD-Au increased, which perfectly matched the transfer mechanism that involved the formation of interfacial complexes between the CD hosts on the nanoparticles and the ferrocene residues of the amphiphilic guests. Notably, PSH- $\beta$ -CD-Au were more effectively solubilized in the organic phase than PSH- $\alpha$ -CD-Au under identical experimental conditions. This finding was in excellent agreement with the well-established selectivity of ferrocene derivatives for  $\beta$ -CD hosts compared to  $\alpha$ -CD (or  $\gamma$ -CD) and provided additional support to the proposed involvement of nanoparticle/CD-ferrocene complexation in the phase transfer mechanism. Photon correlation spectroscopy (PCS) measurements verified that no aggregation happened after the phase transfer of PSH-CD-Au in chloroform. Gold nanoparticles still stayed individually in the solution with long-term stability.

Based on these findings, such phase transfer was believed to be accomplished by host-guest complexation between surface-immobilized CDs and ferrocene derivatives at gold nanoparticle surfaces. As the formation of inclusion complexes took place in the aqueous solution, water molecules were also transferred along with the nanoparticles into the chloroform solution leading to the stable complex in this organic solvent. The presence of the positively charged nitrogen atoms near the ferrocene subunits probably assisted in transferring water molecules and counterions to the organic phase. Further experiments supported this proposed mechanism. Thus, the proposed idealized structure of the nanoparticles after their transfer to the chloroform phase had some similarities with the structure of reverse micelles. Liu et al.<sup>[18]</sup> concluded that these nanoparticle-centered assemblies were conceptually similar to *gold-filled reverse micelles* (Scheme 3).

A similar micellar structure was also fabricated in Frankamp's group.<sup>[16]</sup> The hydrogen bonding between

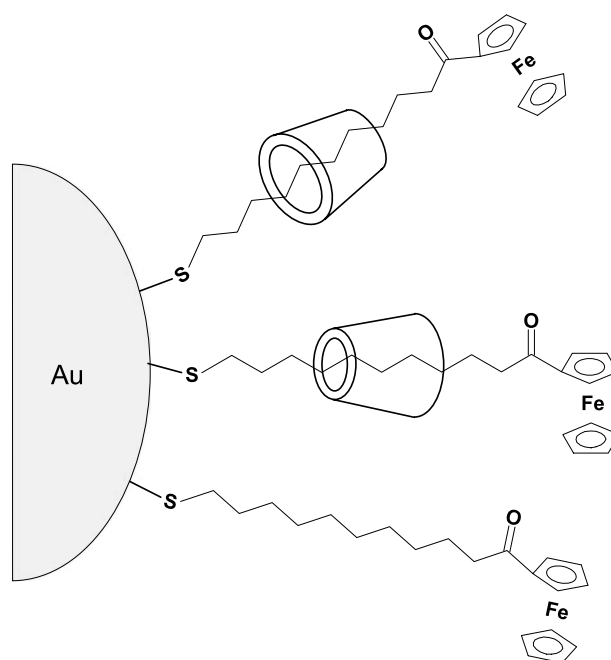


**Scheme 3** Proposed structure for the assemblies formed upon transfer of the PSH- $\beta$ -CD-Au into chloroform solution.

the thymine tethered on gold nanoparticles and the complementary diaminotriazine on a copolymer yielded a polymer/nanoparticle composite in which the polymer blocks bearing the diaminotriazine closely interacted with nanoparticles resulting in a spherical core, whereas the polystyrene units acted as the hydrophobic tails projecting out into the solution. Lala et al.<sup>[27]</sup> also reported a relevant result in which gold nanoparticles capped with inclusion complexes of  $\alpha$ -CD and alkanethiols were transferred into the chloroform phase by using a similar strategy discussed above.

### Fabrication of Rotaxanes on Metal Nanoparticles

One of the fast-growing research fields in nanochemistry is the construction of molecular architectures on nanoparticle surfaces. By employing the well-known host-guest chemistry between CDs and organic molecules, Liu, Xu, and Kaifer built, for the first time, a nanoparticle-supported rotaxane system,<sup>[28]</sup> which provides an interesting example of molecular structure for the further development of the functional nanoscopic systems at nanoparticle scaffolds. Ligand exchange of a thiolated ferrocene derivative solubilized by  $\alpha$ -CD with the citrate on citrate-stabilized gold nanoparticle (13 nm) in an aqueous solution led to the attachment of this compound on the particle surfaces. Further study of these materials revealed that some  $\alpha$ -CDs were trapped on particles. On the other hand, when long-chain aliphatic thiols were used under identical conditions for the preparation of thiol-modified gold nanoparticles, no  $\alpha$ -CD was detected



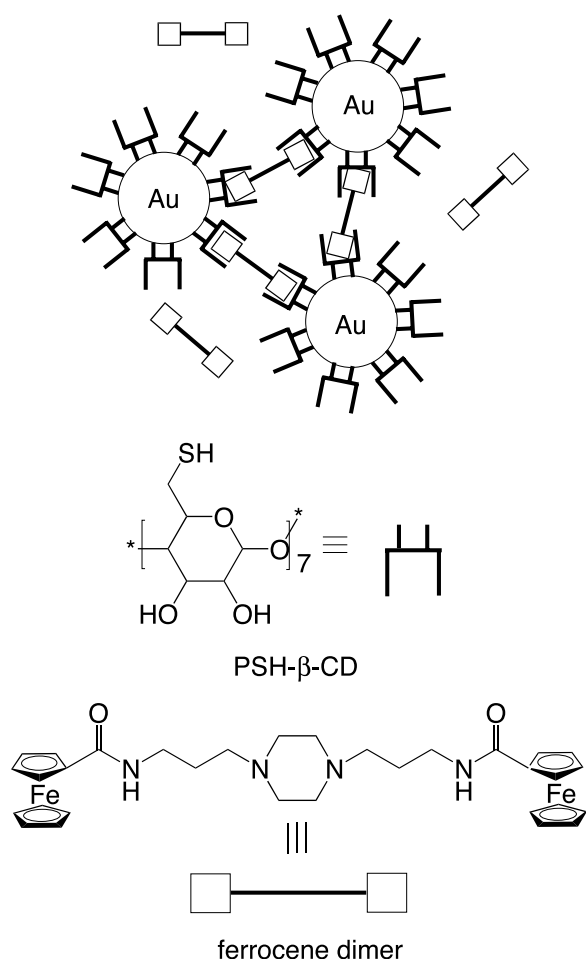
**Scheme 4** Nanoparticle-supported rotaxane.

after the necessary purification. These data suggested that the dynamic character of the complex between CD and alkanethiol allowed dissociation to take place after attachment to the gold surface, whereas the bulky ferrocene group at one end of the thiolated ferrocene derivative precluded  $\alpha$ -CD dissociation from the complex after its attachment on the particle. Thus, a novel molecular structure obtained in this study was a “gold-supported rotaxane” in which one of the rotaxanes’ stopper groups was the gold nanosphere itself (Scheme 4). Interestingly, Fitzmaurice and coworkers reported<sup>[13]</sup> a pseudorotaxane system on gold nanoparticles by binding dibenzylammonium cation in a crown derivative tethered on particle surfaces.

### Fabrication of Nanoparticle Networks in Solutions

Host-guest chemistry has been used as the general strategy to self-assemble receptor-modified metal nanoparticles in aqueous solutions. Liu et al. reported their first attempt in this research direction by using PSH- $\beta$ -CD-Au (12.5 nm) as building blocks and ferrocene dimers (Scheme 5) as “linkers” in aqueous solutions.<sup>[10]</sup>

It was found that the addition of a ferrocene dimer to an aqueous PSH- $\beta$ -CD-Au solution initially caused a red shift of the SP band. Almost immediately, slow precipitation of a red solid took place, accompanied by the attenuation of the intensity of the SP band. After several control experiments, the authors verified

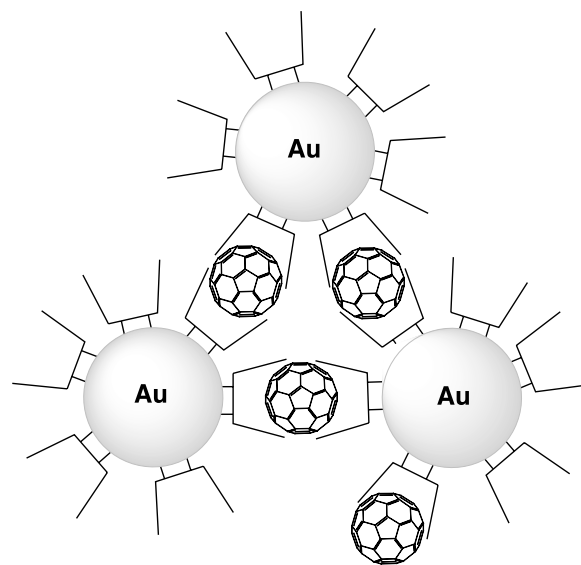


**Scheme 5** Gold nanoparticle aggregate driven by molecular recognition between surface-immobilized PSH- $\beta$ -CD and ferrocene dimer.

that such flocculation was driven by the host-guest interaction between  $\beta$ -CDs anchored on gold nanoparticle surfaces and the ferrocene dimers in the aqueous solution. In the process of complexation, two ferrocene sites in the same molecule bound with two  $\beta$ -CDs on different particles resulting in the network nanoparticle aggregates. Thus, the ferrocene dimer acted as the linker in self-assembly of nanoparticles in aqueous solutions. In addition, such aggregation process could be tuned by the addition of free host or guest molecules in the solution. For instance, introduction of  $\beta$ -CD in the same solution slowed and even shut down the aggregation process as free CD competed with surface-attached CD hosts for the available ferrocene groups. Thus, the flocculation was hindered because the dimers could not form a significant number of linkages between nanoparticles. Temperature also played an important role. Increasing the temperature diminished the extent of flocculation, resulting from the decrease in binding constant between the ferrocene residues and the  $\beta$ -CD hosts.

By using similar host-guest chemistry, another type of interesting organic/inorganic nanocomposites was constructed in the aqueous solution.<sup>[29]</sup> Direct mixing of PSH- $\gamma$ -CD-Au (3 nm) and solid  $C_{60}$  in water led to large nanoparticle aggregates with average size of around 290 nm as characterized by PCS analysis and TEM measurement. In an alternative approach, mixing a toluene phase of  $C_{60}$  with a PSH- $\gamma$ -CD-Au aqueous solution at 0°C also yielded similar nanoparticle aggregates in aqueous media. It is known that  $\gamma$ -CD can form stable 2:1 complex with  $C_{60}$  in aqueous solution.<sup>[30]</sup> Therefore, the authors reasoned that the solubilization of  $C_{60}$  in aqueous solution was attributed to its complexation by the nanoparticle-attached  $\gamma$ -CD hosts. Interestingly, the 2:1 stoichiometry of this complex suggests that the fullerene molecules may behave as *non-covalent linkers* between the nanoparticles, leading to their aggregation (Scheme 6).

Boal's group developed a "brick and mortar" approach in the fabrication of three-dimensional organic/inorganic nanostructures using receptor-modified gold nanoparticles as building blocks and polymers tethered with complementary recognition units as the glue. The three-point hydrogen bonding between the thymine-functionalized gold nanoparticles and diaminotriazine-functionalized polystyrene poly-Triaz yielded microspheric structures  $97 \pm 17$  nm in diameter.<sup>[31]</sup> The temperature had a profound effect on the assembly process. At -20°C, the largest micro-scale clusters were obtained, which were 10 times larger than the aggregates formed at 23°C. Each of these clusters was composed of 0.6–5.0 million individual gold nanoparticles representing the most complex synthetic structures known. Norsten's group also reported a



**Scheme 6** Fullerene-induced network of PSH- $\gamma$ -CD-Au in aqueous solution.

nanoparticle network system by using metal ions as the linkage. The chelation of various metal ions, Fe(II), Zn(II), Cu(II), and Ag(I), with two terpyridines that were tethered to separate nanoparticles resulted in the network aggregates.<sup>[15]</sup> The stability of these structures could be controlled by changing the solvent, adding excess terpyridine, or through the choice of bridging metal.

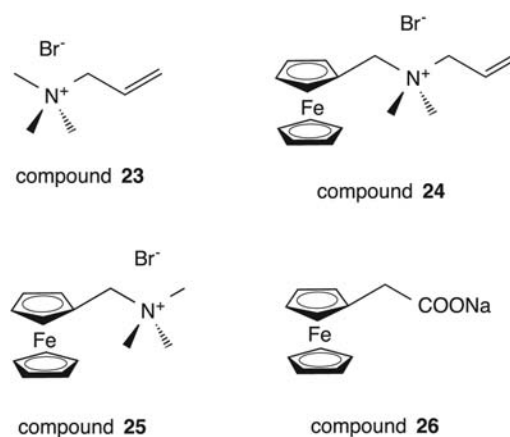
Ryan and coworkers reported that silver nanocrystals stabilized by chemisorption of a mixture of an alkane thiol and a thiolated dibenzo-24-crown-8 could form the nanoparticle aggregates by adding a small amount of bis-dibenzylammonium through the formation of crown-ammonium pseudorotaxane assembly.<sup>[32]</sup> It was also shown that the addition of excess dibenzylammonium cation or dibenzo-24-crown-8 inhibited further aggregation. This novel demonstration of controlled nanocrystal aggregation pointed the way toward the programmed assembly of complex nanocrystal architectures in solution. In a subsequent work, the same group reported the first example of binary nanostructures composing two different types of inorganic nanoparticles by using a similar recognition-directed templating strategy.<sup>[33]</sup> Dibenzo-24-crown-8-modified Ag nanoparticles (7 nm in diameter) recognized and bound to dibenzylammonium cation modified silica nanosphere (180 nm in diameter) via pseudorotaxane formation. Such templating process was proved to be reversibly controlled.

## RECEPTOR-MODIFIED METAL NANOPARTICLES AS NOVEL CATALYSTS

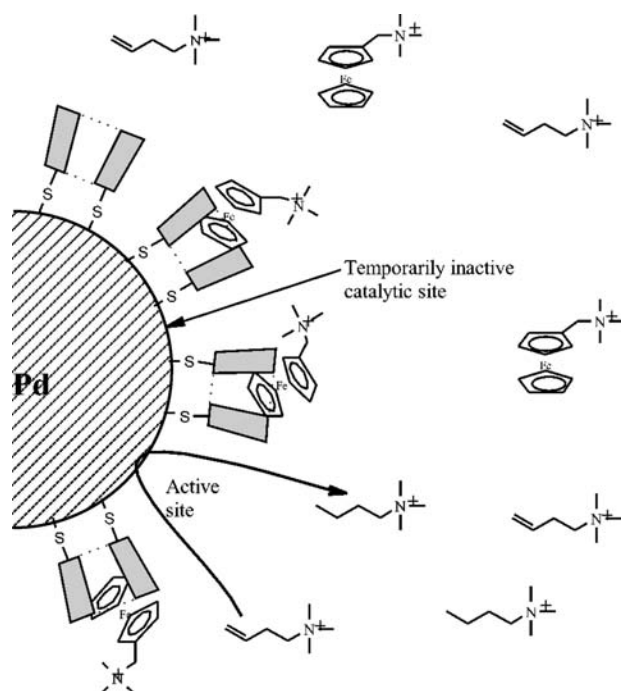
The increasing interest in using metal nanoparticles as catalysts is due to their high surface to volume ratio. In a recent and elegant work, Crooks and coworkers have prepared catalytically active metal nanoparticles encapsulated inside dendrimers.<sup>[34]</sup> The dendrimer effectively stabilizes the nanoparticles without passivating their surfaces, and its branched structure acts as a “molecular filter” imparting selectivity to the catalyst assembly. Recently, Kaifer et al.<sup>[6,7]</sup> reported several research works on the development of CD-modified Pt and Pd nanoparticles for catalytic reactions in aqueous solutions. Special effort has been made in tuning the catalytic activity of these CD-modified nanoparticles through introduction of host-guest interactions on their surfaces.

In an initial attempt,<sup>[6]</sup> water-soluble PSH- $\beta$ -CD-modified Pt and Pd nanoparticles (13 to 15 nm in diameter) were prepared in DMSO-H<sub>2</sub>O mixed solvents by reducing corresponding metal salts using borohydride as reducing agent. Both Pt and Pd nanoparticles prepared here could successfully catalyze the

hydrogenation of allylamine to propylamine in aqueous solutions. The ease of recovering the metal catalysts through precipitation with ethanol from the reaction medium provided an opportunity to recycle the catalyst for the hydrogenation reactions. The authors then focused their attention on the “selectivity” in the catalytic process. In this case, smaller Pd nanoparticles (3 nm) modified with  $\beta$ -CD were made in DMF. These  $\beta$ -CD-modified Pd nanoparticles (PSH- $\beta$ -CD-Pd) behaved as efficient catalysts for the selective hydrogenation of different substrates (Chart 4) in aqueous media. Interestingly, adding millimolar concentrations of **25** to the reaction mixture substantially decreased the rate of hydrogenation of **23**. However, the addition of similar concentrations of tetramethylammonium bromide or tetraethylammonium bromide had a much smaller effect on the rate of hydrogenation of **23**. Similarly, the negatively charged ferrocene derivative **26** and adamantanol (a neutral  $\beta$ -CD guest) were considerably less effective than **25** as catalyst inhibitors. All these data support the idea that **25** acts as an effective inhibitor of the catalytic activity of the PSH- $\beta$ -CD-Pd because of (1) its ability to act as a guest with the CD cavities and (2) its positive charge.



Further evidence of the strong correlation between inhibition by **25** and its binding ability with the CDs that decorated the Pd nanoparticles was obtained by investigating the concentration dependence of the reaction rate. The data obtained showed the saturation behavior that was clearly associated with the binding isotherm of the ferrocene derivatives in the binding sites (CD cavities) on the surface of the nanoparticles. The authors also found out that the actual effect of compound **25** to inhibit the hydrogenation of substrates **23** and **24** differed. Compound **25** was a more effective inhibitor with **23** than **24**. This was probably because of the ferrocene group present in **24**, which increased its affinity to the CD-modified nanoparticles.



**Scheme 7** Complexation control of the accessibility of reacting sites on PSH- $\beta$ -CD-Pd for hydrogenation reaction. Source: From Ref.<sup>[7]</sup>. © 2001, American Chemical Society.

Thus, **25** competed with the substrate itself (**24**) for the available binding sites, and its overall inhibition effect was strongly curtailed. The results presented in that work clearly showed that (1) PSH- $\beta$ -CD-Pds were active catalysts for the hydrogenation of water-soluble alkenes **23** and **24**, (2) catalytic activity could be substantially decreased by addition of the cationic ferrocene derivative **25**, and (3) the inhibiting character of **25** was due to its ability to create Coulombic barriers for the approach of the positively charged substrates (Scheme 7), resulting in the decrease in the surface density of catalytic active sites. These Pd nanoparticles served as heterogeneous catalysts while their small sizes and solubility properties approach those of homogeneous catalysts. These Pd nanoparticles were further used as the efficient catalysts for Suzuki reactions in aqueous media.<sup>[35]</sup>

## CONCLUSION

This article summarizes the recent advancement on the preparation and applications of molecular receptor-modified metal nanoparticles. Although, substantial progress has been achieved in these past years, this research field is still in its infancy. More work needs to be done in the future to reveal fundamental insights and explore more applications for these

nanoscale materials. For example, water solubility of these receptor-modified metal nanoparticles is the key factor for the development of chemical and biological sensors. To make three-dimensional nanocomposites self-organized by molecular recognition with long-range order and the controllable interparticle space is still a big challenge. High stereoselectivity provided by molecular receptors on metal particle surfaces is desired for the development of ecoefficient, environmentally benign heterogeneous catalysts. The author expects a great advancement in this research field in the next few years.

## REFERENCES

- Liu, J.; Alvarez, J.; Kaifer, A.E. Metal nanoparticles with a knack for molecular recognition. *Adv. Mater.* **2000**, *12*, 1381–1383.
- Storhoff, J.J.; Mirkin, C.A. Programmed materials synthesis with DNA. *Chem. Rev.* **1999**, *99*, 1849–1862.
- Templeton, A.C.; Wuelfing, W.P.; Murray, R.W. Monolayer-protected cluster molecules. *Acc. Chem. Res.* **2000**, *33*, 27–36.
- Brust, M.; Walker, M.; Bethell, D.; Schiffrin, D.J.; Whyman, R. Synthesis of thiol-derivatized gold nanoparticles in a two-phase liquid–liquid system. *Chem. Commun.* **1994**, 801–802.
- Liu, J.; Ong, W.; Roman, E.; Lynn, M.J.; Kaifer, A.E. Cyclodextrin-modified gold nanospheres. *Langmuir* **2000**, *16*, 3000–3002.
- Alvarez, J.; Liu, J.; Roman, E.; Kaifer, A.E. Water-soluble platinum and palladium nanoparticles modified with thiolated  $\beta$ -cyclodextrin. *Chem. Commun.* **2000**, 1151–1152.
- Liu, J.; Alvarez, J.; Ong, W.; Roman, E.; Kaifer, A.E. Tuning the catalytic activity of cyclodextrin-modified palladium nanoparticles through host–guest binding interactions. *Langmuir* **2001**, *17*, 6762–6764.
- Liu, J.; Ong, W.; Kaifer, A.E.; Peinador, C. A “macro-cyclic effect” on the formation of capped silver nanoparticles in DMF. *Langmuir* **2002**, *18*, 5981–5983.
- Grabar, K.C.; Freeman, R.G.; Hommer, M.B.; Natan, M.J. Preparation and characterization monolayers. *Anal. Chem.* **1995**, *67*, 735–743.
- Liu, J.; Mendoza, S.; Roman, E.; Lynn, M.J.; Xu, R.; Kaifer, A.E. Cyclodextrin-modified gold nanospheres. Host–guest interactions at work to control colloidal properties. *J. Am. Chem. Soc.* **1999**, *121*, 4304–4305.
- Lin, S.-Y.; Liu, S.-W.; Lin, C.-M.; Chen, C.-h. Recognition of potassium ion in water by 15-crown-5 functionalized gold nanoparticles. *Anal. Chem.* **2002**, *74*, 330–335.
- Balasubramanian, R.; Kim, B.; Tripp, S.L.; Wang, X.; Lieberman, M.; Wei, A. Dispersion and stability studies of resorcinarene-encapsulated gold nanoparticles. *Langmuir* **2002**, *18*, 3676–3681.
- Fitzmaurice, D.; Rao, S.N.; Preece, J.A.; Stoddart, J.F.; Wenger, S.; Zaccheroni, N. Heterosupramolecular

- chemistry: Programmed pseudorotaxane assembly at the surface of a nanocrystal. *Angew. Chem., Int. Ed.* **1999**, *38*, 1147–1150.
14. Boal, A.K.; Rotello, V.M. Redox-modulated recognition of flavin by functionalized gold nanoparticles. *J. Am. Chem. Soc.* **1999**, *121*, 4914–4915.
  15. Norsten, T.B.; Frankamp, B.L.; Rotello, V.M. Metal directed assembly of terpyridine-functionalized gold nanoparticles. *Nano Lett.* **2002**, *2*, 1345–1348.
  16. Frankamp, B.L.; Uzun, O.; Ilhan, F.; Boal, A.K.; Rotello, V.M. Recognition-mediated assembly of nanoparticles into micellar structures with diblock copolymers. *J. Am. Chem. Soc.* **2002**, *124*, 892–893.
  17. Boal, A.K.; Rotello, V.M. Fabrication and self-optimization of multivalent receptors on nanoparticle scaffolds. *J. Am. Chem. Soc.* **2000**, *122*, 734–735.
  18. Liu, J.; Alvarez, J.; Ong, W.; Roman, E.; Kaifer, A.E. Phase transfer of hydrophilic, cyclodextrin-modified gold nanoparticles to chloroform solutions. *J. Am. Chem. Soc.* **2001**, *123*, 11,148–11,154.
  19. Godínez, L.A.; Schwartz, L.; Criss, C.M.; Kaifer, A.E. Thermodynamic studies on the cyclodextrin complexation of aromatic and aliphatic guests in water and water–urea mixtures. Experimental evidence for the interaction of urea with arene surfaces. *J. Phys. Chem., B* **1997**, *101*, 3376–3380.
  20. Boal, A.K.; Rotello, V.M. Radial control of recognition and redox processes with multivalent nanoparticle hosts. *J. Am. Chem. Soc.* **2002**, *124*, 5019–5024.
  21. Labande, A.; Astruc, D. Colloids as redox sensors: Recognition of  $\text{H}_2\text{PO}_4^-$  and  $\text{HSO}_4^-$  by amidoferrocenylalkylthiol–gold nanoparticles. *Chem. Commun.* **2000**, *12*, 1007–1008.
  22. Daniel, M.-C.; Ruiz, J.; Nlate, S.; Palumbo, J.; Blais, J.-C.; Astruc, D. Gold nanoparticles containing redox-active supramolecular dendrons that recognize  $\text{H}_2\text{PO}_4^-$ . *Chem. Commun.* **2001**, *19*, 2000–2001.
  23. Labande, A.; Ruiz, J.; Astruc, D. Supramolecular gold nanoparticles for the redox recognition of oxoanions: syntheses, titrations, stereoelectronic effects, and selectivity. *J. Am. Chem. Soc.* **2002**, *124*, 1782–1789.
  24. Daniel, M.-C.; Ruiz, J.; Nlate, S.; Blais, J.-C.; Astruc, D. Nanoscopic assemblies between supramolecular redox active metallodendrons and gold nanoparticles: synthesis, characterization, and selective recognition of  $\text{H}_2\text{PO}_4^-$ ,  $\text{HSO}_4^-$ , and adenosine-5'-triphosphate ( $\text{ATP}^{2-}$ ) anions. *J. Am. Chem. Soc.* **2003**, *125*, 2617–2628.
  25. Watanabe, S.; Sonobe, M.; Arai, M.; Tazume, Y.; Matsuo, T.; Nakamura, T.; Yoshida, K. Enhanced optical sensing of anions with amide-functionalized gold nanoparticles. *Chem. Commun.* **2002**, *23*, 2866–2867.
  26. Shenhar, R.; Rotello, V.M. Nanoparticles: scaffolds and building blocks. *Acc. Chem. Res.* **2003**, *36*, 549–561.
  27. Lala, N.; Lalbegi, S.P.; Adyanthaya, S.D.; Sastry, M. Phase transfer of aqueous gold colloidal particles capped with inclusion complexes of cyclodextrin and alkanethiol molecules into chloroform. *Langmuir* **2001**, *17*, 3766–3768.
  28. Liu, J.; Xu, R.; Kaifer, A.E. In situ modification of the surface of gold colloidal particles. Preparation of cyclodextrin-based rotaxanes supported on gold nanoparticles. *Langmuir* **1998**, *14*, 7337–7339.
  29. Liu, J.; Alvarez, J.; Ong, W.; Kaifer, A.E. Network aggregates formed by  $\text{C}_{60}$  and gold nanoparticles capped with  $\gamma$ -cyclodextrin hosts. *Nano Lett.* **2001**, *1*, 57–60.
  30. Yoshida, Z.; Takekuma, H.; Takekuma, S.; Matsubara, Y. Molecular recognition of  $\text{C}_{60}$  with  $\gamma$ -cyclodextrin. *Angew. Chem., Int. Ed.* **1994**, *33*, 1597–1599.
  31. Boal, A.K.; Ilhan, F.; DeRouchey, J.E.; Thurn-Albrecht, T.; Russell, T.P.; Rotello, V.M. Self-assembly of nanoparticles into structured spherical and network aggregates. *Nature* **2000**, *404*, 746–748.
  32. Ryan, D.; Rao, S.N.; Rensmo, H.; Fitzmaurice, D.; Preece, J.A.; Wenger, S.; Stoddart, J.F.; Zaccheroni, N. Heterosupramolecular chemistry: Recognition initiated and inhibited silver nanocrystal aggregation by pseudorotaxane assembly. *J. Am. Chem. Soc.* **2000**, *122*, 6252–6257.
  33. Ryan, D.; Nagle, L.; Rensmo, H.; Fitzmaurice, D. Programmed assembly of binary nanostructures in solution. *J. Phys. Chem., B* **2002**, *106*, 5371–5377.
  34. Crooks, R.M.; Zhao, M.; Sun, L.; Chechik, V.; Yeung, L.K. Dendrimer-encapsulated metal nanoparticles: synthesis, characterization, and applications to catalysis. *Acc. Chem. Res.* **2001**, *34*, 181–190.
  35. Strimbu, L.; Liu, J.; Kaifer, A.E. Cyclodextrin-capped palladium nanoparticles as catalysts for the Suzuki reaction. *Langmuir* **2003**, *19*, 483–485.



# Molecular Self-Assembly: Environmental and Sensing Applications

Glen E. Fryxell

R. Shane Addleman

S. V. Mattigod

Yuehe Lin

T. S. Zemanian

H. Wu

Jerome C. Birnbaum

*Pacific Northwest National Laboratory, Richland, Washington, U.S.A.*

J. Liu

*Sandia National Laboratory, Albuquerque, New Mexico, U.S.A.*

X. Feng

*Ferro Corporation, Independence, Ohio, U.S.A.*

## INTRODUCTION

In the last decade, we have witnessed many exciting new discoveries in the ability to manipulate and measure matter at the nanometer scale—honeycombed pores structures, spheres, icosahedra, nanotubes and nanorods, and self-assembled structural hierarchies; the esthetics of the nanometer regime offers Nature's elegance in its purest form. Understanding the driving forces behind these shapes and the self-assembly processes provides key understanding for this chemistry to be exploited for positive impact on our daily lives. For this to take place, we must not only understand how the nanoscopic structures impact the structural and chemical properties of these novel new materials, but we must also understand the critical problems that we face today and how these nanoscopic properties can be tailored to address these specific needs and critical problems. The purpose of this entry is to show how this understanding can be applied to the synthesis of nanostructured hybrid materials that can address needs in the areas of drinking water purification, environmental remediation, and enhancing the sensitivity of analytical methods for detecting heavy metal contamination.

## DIMENSIONS OF THE PROBLEM

The most important factor in determining quality of life in human society is the availability of pure, clean

drinking water. Wars have been fought, and will continue to be fought, over access and control of clean water. Drinking water has two major classes of contamination: biological contamination and chemical contamination. Bacterial contamination can be dealt with by a number of well-established technologies [e.g., chlorination, ozone, ultraviolet (UV), etc.], but chemical contamination is a somewhat more challenging target. Organic contaminants, such as pesticides, agricultural chemicals, industrial solvents, and fuels, can be removed by treatment with UV/ozone, activated carbon, or plasma technologies. Toxic heavy metals such as mercury, lead, and cadmium can be partially addressed by using traditional sorbent materials such as alumina, but these materials bind metal ions non-specifically and can be saturated with harmless, ubiquitous species such as calcium, magnesium, and zinc (which are actually nutrients, and do not need to be removed). Another weakness of these traditional sorbent materials is that metal ion sorption to a ceramic oxide surface is an equilibrium process, meaning they can easily desorb back into the drinking water supply. Heavy metal contamination can also be removed via flocculation/precipitation, but these methods are far more effective at high contaminant concentrations, and commonly fail at lower metal concentrations, which is where most drinking water problems are found.

Heavy metal contamination comes from many sources, both natural and industrial. Geological contamination of drinking water with arsenic is a

major problem in Bangladesh<sup>[1-3]</sup> and in North America (e.g., the central valley of California<sup>[4,5]</sup> and New Hampshire.)<sup>[6]</sup> Industrial arsenic contamination has been found in New England<sup>[7]</sup> and the Pacific Northwest.<sup>[8]</sup> Stringent new Environmental Protection Agency (EPA) guidelines for arsenic in drinking water<sup>[9,10]</sup> make this a high-priority issue. Industrial activity has led to mercury contamination in many parts of the world.<sup>[11-13]</sup> Lead contamination from lead-based paints and burning leaded gasoline resulted in significant blood lead concentrations for children in the United States.<sup>[14]</sup> Aboveground nuclear weapons testing by the United States and the Soviet Union in the early 1960s and nuclear accidents (e.g., Chernobyl) have spread low levels of radioactive actinides and radiocesium throughout the world environment.<sup>[15]</sup>

## NANOSCIENCE AND ITS ROLE

Clearly, all these toxic metals form a significant threat to the water supplies of the world. How can nanoscience address this problem? A chemically specific sorbent material capable of permanently sequestering these toxic metal ions from groundwater supplies is needed to purify contaminated drinking water. Because we consume vast quantities of drinking water every day, the kinetics of heavy metal sorption need to be fast, allowing for high throughput in the process stream. A high binding capacity for the target heavy metal is clearly of value. In addition, as acceptable drinking water contamination limits becomes

increasingly lower, more sensitive analytical methods are needed in order to detect such contamination.

## Nanostructured Materials

There has been a great deal of recent developments in the synthesis of nanostructured materials, particularly in the area of surfactant templated synthesis of mesoporous ceramic materials.<sup>[16,17]</sup> Synthetic methods have been developed to prepare these materials in a variety of morphologies (lamellar, cubic, hexagonal, etc.) with structural features ranging from about 20 Å up to 300 Å.<sup>[18]</sup> The micelle shape and structure dictates pore size and structure (Fig. 1).<sup>[19,20]</sup> A huge amount of surface area is condensed into a very small volume in these nanoporous ceramics, making them well suited for catalytic, sorbent, and sensing applications. In addition, the rigid ceramic backbone precludes solvent swelling and allows facile diffusion throughout the entire porous matrix. The ceramic backbone is also structurally more robust than a polymer-based ion exchange resin, so particle attrition is less of an issue.

## Functionalization of Mesoporous Ceramics

Recently, a great deal of research has been performed exploring the synthetic elaboration of the pore surfaces of mesoporous materials.<sup>[21]</sup> Generally, these efforts fall into three approaches: cocondensation, surfactant displacement (or extraction), and postcalcination modification.<sup>[22]</sup> When a suitable metal precursor

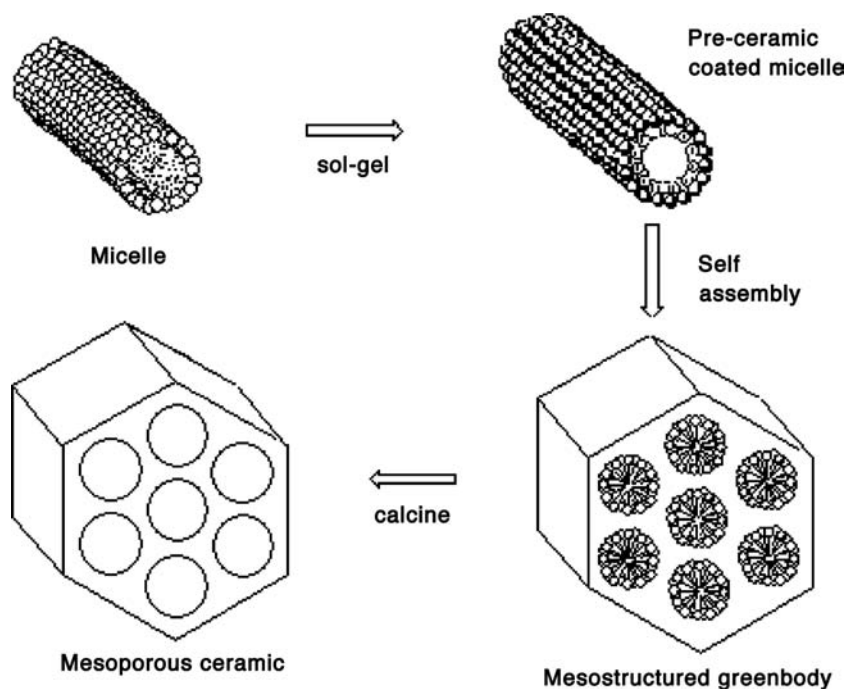


Fig. 1 Micelle templated synthesis of mesoporous ceramics.

(e.g., metal salt, alkoxide, etc.)<sup>[23]</sup> or alkyl siloxane is included in the original sol–gel mixture and subjected to hydrolysis, this is referred to as “cocondensation.”<sup>[24]</sup> In this case, the dopant is entrapped within the mesostructured greenbody, and because most of the ceramic material is at, or very close to, an interface, the dopant is also usually close to an interface. For metal dopants, the surfactant can be removed by calcining the greenbody, resulting in an anchored metal silicate. Alkyl siloxanes will not survive calcination conditions, and therefore the surfactant template must be removed by low-temperature methods such as acid extraction. Doping levels as high as 40% have been reported.<sup>[24]</sup> However, it is important to recognize that the dopant represents a defect in the wall structure of the nanoporous ceramic, and therefore, higher doping levels result in weaker and more defective materials. The advantages of the cocondensation strategy are its simplicity and the direct access it provides to functionalized mesoporous materials; the disadvantages include the relatively high defect density and somewhat limited doping levels of the functionalized products.

A second method for the preparation of functional mesoporous materials is by surfactant displacement. In this method, the surfactant laden greenbody has the quaternary ammonium surfactant molecules displaced by a suitable cationic species<sup>[25,26]</sup> or by acid extraction (which is simply displacement by a proton).<sup>[27]</sup> This route provides easy access to functionalized mesoporous materials, especially those involving cationic transition metal complexes. Displacement by a proton affords a native silica surface that is not dehydrated, or silanol-depleted, and is therefore highly receptive to silanation. Like cocondensation, the advantages of surfactant displacement/acid extraction are the simplicity of the procedure and the direct access to functionalized nanomaterials. The disadvantage of these approaches is that, by avoiding the calcination phase of the procedure, the silicic acid backbone is never fully condensed (crosslinked) to form a robust ceramic, and hence these materials are susceptible to structural degradation over time.

Most commonly, the mesostructured greenbody is calcined to burn off the surfactant template and the interface modified thereafter.<sup>[28–32]</sup> This strategy has the advantage of providing a well-defined, structurally robust, rigid pore structure. Unfortunately, calcination drives off most of the surface silanols and all of the surface water, leaving the interface poorly suited to functional elaboration. As a result, direct silanation of this desiccated interface leads to very limited surface coverage because there is only small fraction of the original surface silanols left to be capped. For catalytic applications requiring high turnover numbers and minimal steric congestion, this limited surface coverage can be highly beneficial.

## Self-Assembled Monolayers

The self-assembly of a monolayer is the spontaneous aggregation of molecules into an ordered, organized macromolecular array a single molecule thick. The self-assembly process is driven by the attractive forces between the molecules themselves (e.g., van der Waals interactions, hydrogen bonding, or dipole–dipole interactions), as well as the attractive forces between the molecule and interface (e.g., hydrogen bonding, acid/base interactions, etc.). It is important to recognize that the molecular spacing in a self-assembled monolayer is dictated by the aggregation efficiency and the molecular “footprint” of the monomer. In the silanol capping chemistry discussed above, the molecular spacing of the monomer on the surface is dictated by the number and distribution of hydroxyl groups on the ceramic surface. At first glance, self-assembly and surface capping are very similar processes, but in the final analysis, self-assembly is controlled by the chemistry and behavior of the monomer component, while surface capping chemistry is ultimately controlled by the hydroxyl population of the surface. Each reaction pathway can be favored by suitable choice of the reaction conditions. If the solvent chosen swamps out the attractive forces between the monomer molecules, then self-assembly is kinetically disfavored and surface capping chemistry tends to dominate, leaving vacancies between the individual silanes. In addition, there must be sufficient water on the interface to hydrolyze the silane, but if the water is present in solution and not at the interface, then this leads to bulk solution polymerization of the silane, which precludes organized assembly on the surface. Inadequate amounts of water at the interface prevent silane hydrolysis. Because tris(hydroxy)silane is the active species in this self-assembly, if it is not formed then self-assembly (and crosslinking) is retarded, and once again the surface chemistry is limited to silanol capping reactions. Only through the judicious choice of reaction conditions (i.e., solvent identity, water concentration, water location, and reaction temperature) can self-assembly take place, resulting in a dense, uniform coating of the surface (Fig. 2).

Supercritical fluids are a particularly powerful reaction medium in which to carry out silane self-assembly within mesoporous ceramics.<sup>[33]</sup> Supercritical carbon dioxide (SCCO<sub>2</sub>) effectively solvates the siloxane monomers, but it also does not inhibit the attractive (van der Waals) forces between the hydrocarbon chains because CO<sub>2</sub> is a small linear molecule, allowing self-assembly to proceed smoothly. In addition, any associative process can be accelerated by carrying it out under conditions of high pressure.<sup>[34]</sup> Self-assembled monolayer formation is an associative process and is significantly accelerated when carried

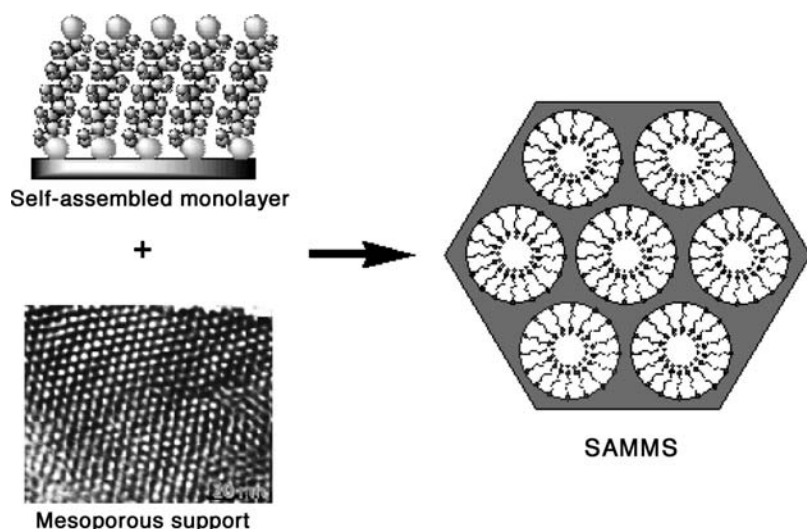


**Fig. 2** The marriage of self-assembled monolayers with mesoporous supports has created a powerful new class of heavy metal sorbent materials.

out in  $\text{SCCO}_2$ . In addition, the monolayers so formed have a lower defect density as a result of some novel annealing mechanisms that come into play under these conditions.<sup>[35]</sup> The low viscosity of  $\text{SCCO}_2$  also facilitates mass transport of silane throughout the nanoporous ceramic matrix. When the monolayer deposition is complete, the pores of the self-assembled monolayers on mesoporous supports (SAMMS) are clear and dry, and not filled with residual solvent that must be removed before the materials can be used.  $\text{SCCO}_2$  is such a powerful functionalization protocol that it has even been successfully applied to the subnanometer pores of zeolites!<sup>[35]</sup>

## SAMMS AS SORBENT MATERIALS

### Soft Heavy Metals

Our initial forays into developing SAMMS as a metallic sorbent focused on the sequestration of mercury because of its impact on the environment and human health. Because Hg is a “soft” Lewis acid,<sup>[36]</sup> we targeted the installation of “soft” Lewis bases, in particular alkyl thiols, to take advantage of the thiol’s legendary affinity for mercuric species. Preparation of thiol SAMMS is straightforward, and creates a powerful new class of mercury sorbent. The distribution coefficient ( $K_d$ ) is defined as a mass-weighted partition coefficient and provides a way of gauging the effectiveness of a sorbent material. Sorption distribution coefficients are determined by the following equation, where  $C_0$  is the initial concentration of the target analyte,  $C_f$  is the final equilibrium concentration,  $V$  is the volume of the testing solution (mL), and  $M$  is

the mass of SAMMS used (g).

$$K_d = [(C_0 - C_f)/C_f](V/M) \quad (1)$$

The  $K_d$  values obtained in our studies of thiol SAMMS binding mercury were typically in the  $10^7$  range.<sup>[37]</sup> This means that, for a solution/solids ratio of 10,000, at equilibrium there is 1000 times as much mercury in the small amount of SAMMS as there is in the supernatant solution. The  $K_d$  values were found to not vary significantly over a pH range from about 3 to 9. Below 3, the  $K_d$  values started to drop off significantly because of protonation of the ligand, and above pH of 10, the mesoporous silica begins to breakdown. The loading capacity is greater than 500 mg Hg, per gram of SAMMS (or 2.5 mmol/g). The sorption kinetics are quite fast, generally reaching equilibrium in about 3 min. Existing commercially available polymer systems require several hours to reach equilibrium. Extended X-ray absorption fine structure (EXAFS) characterization of the SAMMS–Hg adduct indicates that Hg is predominantly found bridging between two thiol groups.<sup>[38]</sup> Ubiquitous cations such as Na, K, Ca, Mg, Fe, and Zn were found to provide no competition for the thiol binding sites, as predicted by hard–soft acid/base theory. The binding affinity of thiol SAMMS for Hg is so high that even complexants such as ethylenediaminetetraacetic acid (EDTA) cannot compete!<sup>[39]</sup>

Other “soft” heavy metals of environmental concern, such as Cd, Cu, and Pb, are also bound by thiol SAMMS, although not as steadfastly as Hg ( $K_d$ ’s of several thousand to tens of thousands). Tl is also a suitable target for thiol SAMMS (Fig. 3).

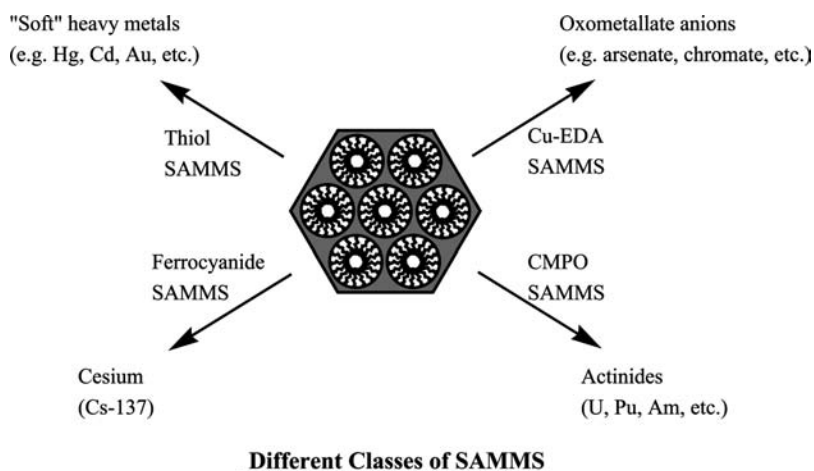


**Fig. 3** By tailoring the chemical nature of the monolayer interface, it is possible to selectively sequester a variety of metallic contaminants of environmental concern.

### Oxometallate Anions

The beauty of the SAMMS concept is that it arises from a convergent synthesis, one branch leading to the mesoporous backbone, one branch forms the monolayer support, and conceivably, a third branch to form the functional interface. As a result, modification to tailor the sorbent material for a different target species is very easily accomplished. By lining the pore surfaces of SAMMS with cationic metal complexes, a powerful new class of anion exchange material has been realized (Fig. 3).<sup>[40]</sup> By judicious choice of the metal center and ligand field, it is possible to create chemical selectivity not only at the stereochemical level, but also a level of selectivity based upon the solubility of the metal–anion adduct. For example, copper (II) is known to have a very high affinity for amine ligands; however, being a  $d^9$  species, it tends to undergo Jahn–Teller distortion to alleviate orbital degeneracy, distorting its geometry away from an ideal octahedral coordination sphere. Thus, a monolayer interface composed of a copper (II)–ethylenediamine (Cu–EDA) complexes has a firmly bound metal center, but the third EDA ligand (or water molecule) is readily displaced by an incoming anion to take the Cu (II) center to a trigonal bipyramidal geometry. If the copper–anion salt is soluble (e.g., copper (II) sulfate), then this ligand displacement is reversible, and the anion can be displaced. If not, however, then the anion is effectively sequestered. The latter condition holds true for anions such as chromate and arsenate, both of which are of significant environmental concern.  $K_d$  values for chromate are commonly  $10^5$  or higher, with a loading capacity of 130 mg (or 1.12 mmol) chromate per gram of Cu–EDA SAMMS. Similar loading capacity is observed for arsenate anion (140 mg/g or 1.0 mmol/g). Given the 3:1 stoichiometry of the initially Cu(II)EDA complex, this correlates quite well with the initial silane population density on the mesoporous silica, indicating that

all of the Cu (II) binding sites are effectively utilized. The kinetics of arsenate sorption are quite fast with equilibrium being reached in about 5 min. Clearly, diffusion into the mesoporous matrix is not a significant limitation.

### Radiocesium

Cesium-137 is a radioactive by-product of weapons-grade Pu production and fallout from aboveground nuclear weapons testing. Once released into the environment, Cs is quite mobile. Methods to sequester Cs include calixcrown-modified supports<sup>[41,42]</sup> and the crystalline silicotitanates (CST).<sup>[43]</sup> The crown ethers offer modest selectivity for Cs over other monovalent cations, but are sensitive to reaction conditions (pH, competing ions, etc.) and are sensitive to radiolytic breakdown of the polymer backbone. The CSTs provide excellent selectivity and high binding affinity, but sorption kinetics may be quite slow (because of diffusion through the microporous matrix), and once the Cs is bound it cannot be removed, making the CSTs a single-use-and-dispose technology. Transition metal ferrocyanides form insoluble Cs salts, and this was exploited by modifying support materials with ferrocyanides.<sup>[44–46]</sup> Treatment of the Cu–EDA SAMMS described above with ferrocyanide provides unprecedented Cs binding capability (Fig. 3).<sup>[47]</sup> Binding affinities, even in the presence of huge excesses of Na or K ion, are greater than  $10^5$ . The Cs loading capacity of the ferrocyanide SAMMS is 179 mg per gram of SAMMS (or 1.35 mmol/g), once again indicating that almost all of the ferrocyanide binding sites are effectively used to sequester the Cs target [X-ray photoelectron spectroscopy (XPS) analysis reveals that some of the ferrocyanide groups are bridging between two adjacent Cu–EDA complexes, which slightly limits the Cs capacity; however, the metathesis of Cs for Na

is quantitative]. Sorption kinetics are facile, with equilibrium being reached in approximately 20 min.

## Actinides

The Cold War led to 40 years of weapons-grade plutonium production. In the wake of this massive chemical production effort, the United States has been left with millions of gallons of highly radioactive waste. Currently, the ultimate plan is to combine this waste with a suitable silica source, melt the mixture to glassify it, and store the glass logs in a suitable subterranean repository, such as Yucca Mountain, Nevada. The majority of this waste is relatively innocuous (e.g., sodium nitrate, sodium aluminate, tributyl phosphate, etc.), and does not need to be glassified for long-term disposition. Clearly, it would save much time, effort, and money if the small amount of radioisotopes could be removed from the bulk of the waste and only the small amount of radionuclides is subjected to vitrification. Thus, the need to selectively sequester actinides from complex mixtures exists, and sorely needs to be addressed. Actinide separations have historically been accomplished by solvent extraction methods, and much has been learned in terms of ligand design from these efforts. One of the most effective ligands for actinide extraction is the carbamoylphosphine oxide (CMPO) class of ligands.<sup>[48–51]</sup> We have decorated the monolayer interface of SAMMS with CMPO analogs to make acetamidophosphonate SAMMS, and found an exceptional new actinide sorbent material (Fig. 3).<sup>[52]</sup> The acid form of this sorbent not only has excellent binding affinities for actinides such as Pu (IV) and U (VI) ( $K_d$  values are usually in excess of 20,000, and sometimes as high as 300,000), but there is no competition from transition metal cations, or common complexants (e.g., EDTA). The binding affinity is dependent on pH, but the phosphonic acid SAMMS are still effective sorbents down to below a pH of 0.5. Sorption kinetics are very rapid, with equilibrium being achieved in about 1 min. An added advantage of using SAMMS to extract actinide from Department of Energy (DOE) nuclear waste is that SAMMS is a silica-based sorbent system, and is therefore directly compatible with glassification.<sup>[53]</sup>

## PRECONCENTRATION FOR ANALYTICAL APPLICATIONS

What we know is typically bound by what we can confidently measure. Consequently, there are ongoing efforts to improve the sensitivity, selectivity, and speed of analytical methods. One approach to improving any analytical method is to separate the analyte(s) for the sample matrix and concentrate them into a smaller

volume prior to measurement. When this preconcentration is carried out with small quantities of sorbents, the method is typically referred to as a solid-phase microextraction (SPME). Another method is to preconcentrate the analyte directly upon the transducer of the detector. In either case, the amount of extracted analyte is limited by the magnitude of the partition coefficient of the analyte between the sample matrix and the sorbent material.

Self-assembled monolayers on mesoporous supports can be ideal materials for selective preconcentration and SPME. The mesostructure endows SAMMS with high surface areas and short diffusional path lengths. The monolayer provides a high density of complexation sites. This combination results in a sorbent material with rapid uptake kinetics and very large loading capacities. The wide range of monolayer chemistries allows significant flexibility in the target analyte(s). However, application of SAMMS for preconcentration and SPME must coordinate the monolayer chemistry with the target analyte and sample matrix.

The target analyte(s) must have a high partition coefficient from the sample matrix to enable significant preconcentration. Moreover, the analyte partition coefficient must be much higher than any competing material(s) commonly occurring in the sample matrix, or equilibrium processes will displace it. The morphology of the SAMMS material must be matched to the analytical application. The SAMMS material must be available to extraction or analysis and the mesoporous structure is not immune to fouling issues (i.e., suspended sediments, organics, etc.) that plague other preconcentration methods.

## X-Ray Fluorescence and Heavy Metal Assay

X-ray fluorescence (XRF) spectroscopy involves the measurement of characteristic elemental X-rays emitted from an atom after bombardment by higher energy photons. The technique is not capable of direct trace level assay but can quickly perform part per million (ppm)-level multielemental analyses of solids. SPME with SAMMS provides not only a mechanism to preconcentrate the target (significantly enhancing detection limits) but also mitigates two primary factors limiting XRF sensitivity: the heterogeneity of the sample matrix and the particle sizes. The typically small, and potentially uniform, SAMMS particles (<200  $\mu\text{m}$ ) allow the excitation radiation and subsequent characteristic X-rays to efficiently and uniformly pass through the silica SAMMS structure.

As mentioned in a previous section, the partition coefficient for mercury with thiol SAMMS is over  $10^7$  for typical aquatic pHs ranging from 5 to 8, and the material has no affinity for common ions



such as sodium, calcium, and iron. This selectivity enables effective SPME from complex environmental matrices. We have found that, for high  $K_d$  and high capacity systems, such as mercury uptake with thiol SAMMS, trace analyte uptake is linear over very large preconcentration ranges. Selective SPME preconcentration from actual river and aquifer water up to a factor of  $10^6$  has been demonstrated. Sorbent material morphology can be very important for uptake dynamics. Small particulates ( $<5\ \mu\text{m}$ ) can block flow in packed microfluidic SPME columns. The hydrophobic nature of some mesostructured monolayers can create difficulty in wetting the surfaces of the nanopores and reduce analyte uptake. Humic acids, suspended organics, and colloids in surface and ground waters can significantly reduce analyte uptake by plugging the SPME column. However, these problems can be resolved with intelligent application of techniques such as particle sorting, sequential solvent washing, and in-line filtration methods.

X-ray fluorescence coupled with SAMMS SPME enable the rapid detection of trace levels of toxic metals. Table 1 shows the concentration of trace metals in an SPME thiol SAMMS column (15 mg) after only 200 mL of river water (pH 8) spiked with of 1 ppb of selected metals was pumped through at 1 mL/min. The difference in the preconcentration of the metals in the SPME SAMMS column is a result of the competitive equilibrium processes between the sample solution and monolayer surface. However, the SAMMS SPME clearly preconcentrated all the metals from a level (1 ppb) well below their EPA drinking water limits (listed in the right column) to a range easily measurable by the XRF. Using Cu-EDA SAMMS, we have obtained similar results for the toxic chromate and arsenate anions. The actual limit of detection for metals in environmental samples with this approach will depend upon a number of variables including the target metal, the sample matrix, the type of SAMMS,

the relative volumes of sample and sorbent, and the sensitivity of the XRF system. However, it is clear the SPME with SAMMS-type materials can be a powerful tool for environmental assay.

### Electrochemical Heavy Metal Detection

Electrochemistry is a well-established method for the measurement of ionic species. Concentration of the target analytes upon the electrode followed by voltammetric stripping is one of the most sensitive electrochemical methods. Chemical modification of the electrode can produce improvements in both sensitivity and selectivity. The voltammetric response of a carbon paste electrode modified with thiol SAMMS has been found to provide an effective electrochemical sensor for the in-situ detection of  $\text{Pb}^{2+}$  and  $\text{Hg}^{2+}$  in aqueous solutions. Factors affecting the performance of the chemically modified electrodes include electrode activation and precondition, electrode composition, preconcentration time, electrolysis time, as well as electrolysis and stripping mediums. To date, the best electrode contained 20% thiol SAMMS in the carbon paste and the optimum operating conditions were a 120-sec preconcentration period followed by a 60-sec cathodic electrolysis of the preconcentrated species in 0.2 M  $\text{HNO}_3$ . This was followed by a square wave anodic stripping voltammetry in 0.2 M  $\text{HNO}_3$ . Under these conditions, the areas of the peak responses were linear to metal ion concentrations in the within a range of 1–1000 ppb  $\text{Pb}^{2+}$  and 500–5000 ppb  $\text{Hg}^{2+}$  (of the original solution). The detection limits for  $\text{Pb}^{2+}$  and  $\text{Hg}^{2+}$  were 0.5 ppb  $\text{Pb}^{2+}$  and 100 ppb  $\text{Hg}^{2+}$  after a 20-min preconcentration period.

### Enhancement of Nuclear Assay Methods

SPME with SAMMS provides the same advantages to nuclear assay techniques as it has been shown to provide for chemical measurement methods. Coupling high-performance chemical sorbents with nuclear detection systems enhances the selectivity and sensitivity for detection of radioactive materials. In addition to concentrating the target radionuclide(s), the sorbent can exclude interferents and provide a uniform, well-defined sample geometry, which can be a critical issue for isotopic assay. The detection scheme employed depends on the type of radiation (alpha, beta, gamma, neutron) emitted from the radionuclide and whether or not isotopic information is desired. To date, we have found SPME with SAMMS very effective for determination of gamma-, beta-, and alpha-emitting radionuclides in environmental samples.

**Table 1** Performance of thiol SAMMS and XRF

Metal	SAMMS concentration <sup>a</sup> (ppm)	XRF LOD <sup>b</sup> (ppm)	EPA DWS <sup>c</sup> (ppm)
Hg	7.2	2	0.002
Cu	57.5	2	1.3
Pb	7	2.4	0.015
Ag	16.3	7	0.1
Cd	18.7	7	0.005

<sup>a</sup>200 mL of river water spiked with 1 ppb of metals and flowed through a 15 mg SPME thiol SAMMS column.

<sup>b</sup>Limit of detection (LOD) for XRF system utilized.

<sup>c</sup>EPA drinking water standards (DWS) from [www.epa.gov/safewater/mcl.html](http://www.epa.gov/safewater/mcl.html).

Because gamma radiation can pass through a significant amount of mass without attenuation, the configurations of the SAMMS material is not particularly critical for assay. As previously discussed, the ferrocyanide SAMMS is a very effective sorbent for radiocesium. Measurement of the  $^{137}\text{Cs}$  and  $^{134}\text{Cs}$  isotopes is significant for environmental monitoring and treaty compliance issues associated with the Cold War nuclear legacy. In addition to improving the sensitivity of standard assay methods, using ferrocyanide SAMMS for SPME enables several novel options for detection of radiocesium isotopes. Detectors with no spectral resolution [such as the ubiquitous Gieger–Muller (GM) counters] or detectors with limited resolution [such as NaI(Tl) scintillators] can be used for rapid and sensitive assay of radiocesium—if ferrocyanide SAMMS is used first for selective SPME. Second, small, portable, room-temperature semiconductor detectors (such as CdZnTe) with limited sensitivity due to their size become capable of environmental level assay when combined with SAMMS SPME.

Alpha radiation is composed of heavy, energetic, highly charged particles that interact strongly with surrounding matter. Consequently, alpha radiation is quickly attenuated by surrounding material and has very short ranges. Therefore, accurate assay of alpha emitters typically involves extensive matrix separation and sample preparation to eliminate interfering material. SPME with SAMMS selective for actinides, such as those with AcPhos and PropPhos monolayers, have been found to be a fast, single-step preparation method for the radiochemical assay of alpha emitters in aquatic samples.

Fig. 4 shows the alpha energy spectrum of an electrostatically immobilized particulate layer of Ac-Phos SAMMS that was exposed to a solution

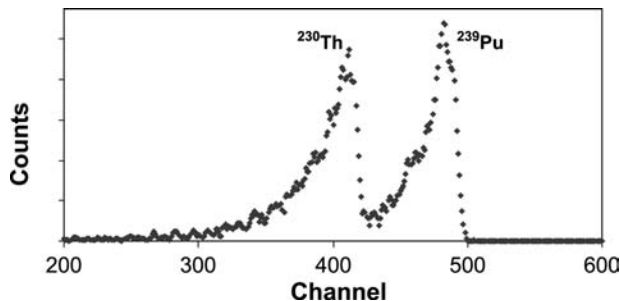


**Fig. 4** Alpha energy spectrum of electrostatically immobilized particulate layer of Ac-Phos SAMMS after exposure to a solution of  $^{230}\text{Th}$  and  $^{239}\text{Pu}$ . The films were dried and data directly collected with a standard laboratory alpha spectrometer (under vacuum).

with  $^{230}\text{Th}$  and  $^{239}\text{Pu}$ . The film was dried and spectra directly collected with a standard laboratory alpha spectrometer (under vacuum) with a diode detector. This data demonstrates SAMMS materials can be clearly used to rapidly preconcentrate actinides from liquid samples and then directly analyze for isotopic content by using standard laboratory equipment. The spectral resolution for this sample is approaching the quality of many electroplated sources and exceeds that of many standard sample preparation methods based on precipitation. Spectral resolution could no doubt be improved with a true mesoporous thin film of uniform thickness.

Actinide-loaded SAMMS can also be measured with other nuclear counting methods. For SAMMS materials with small particle sizes (less than a  $10\ \mu\text{m}$ ), liquid scintillation counting (LSC) was found to be easy, effective, and efficient. Consequently, selective preconcentration by SAMMS materials followed by direct LSC is a rapid, convenient, extremely sensitive, and somewhat selective method for nuclear assay.

Portable alpha monitors (PAMs) are ubiquitous survey devices in all radiation facilities with actinides. Despite the loss of spectral capability and reduced efficiency, there are advantages to using PAM devices for alpha screening of SAMMS materials including low cost, universal availability, and scalable surface area. Moreover, actinide selectivity is not necessarily lost because the SAMMS materials can provide significant chemical selectivity. We found that PAMs could very effectively measure the activity of actinide-loaded SAMMS materials. Accounting for differences in instrument efficiency, the count rate of actinide-loaded SAMMS thin films was the same when measured with PAMs or with the more sophisticated silicon diode-based spectrometers.

Unlike alpha and gamma radiation, beta radiation does not have any peak structure in the energy continuum. This increases the advantages of using a chemical selectivity SPME sorbent because spectral discrimination between isotopes is not possible. We have found that beta radiation from radionuclides selectively sorbed into SAMMS materials can be measured with many standard methods including silicon diodes, plastic scintillators, standard survey equipment (GM), and liquid scintillation counting (LSC). Of particular interest is using Cu–EDA SAMMS for the extraction of  $^{99}\text{Tc}$ , a beta-emitting fission product isotope. This long-lived isotope exists in groundwater, principally as the pertechnetate anionic species that is highly mobile in aquifers. Cu–EDA SAMMS has been found to be effective for SPME and assay of  $^{99}\text{Tc}$  with all of the aforementioned mentioned nuclear assay methods.

Nanostructured sorbent materials coupled with the selected detection methods can be used for either real-time analysis of the signature species or as a rapid screening method to flag which samples require more detailed analysis, or as archival samples. SAMMS coupled with rugged, compact instrumentation will provide portable, highly sensitive field analyzers/samplers that could be quickly reconfigured for new analytes simply by changing the sorbent material. Sorbents used may be reusable, renewable, or disposable, depending on the configuration and chemistries involved.

## CONCLUSION

Novel synthetic methodologies in the area of templated nanomaterials and molecular self-assembly have created a powerful new class of sorbent materials that can make a significant impact on environmental remediation and analytical sensing and detection. The rigid open pore structure of SAMMS allows for facile diffusion of the target analyte into the mesoporous matrix, providing for fast sequestration kinetics. Self-assembled monolayers terminated in highly specific ligands allow the sorbent to be tailored to the specific environmental target, providing excellent chemical selectivity. The close proximity of the ligands to one another allows for multiple analyte/ligand interactions, enhancing binding affinity and specificity. Novel SCCO<sub>2</sub> synthetic methodology allows us to make SAMMS substantially faster, and clearly enhances the stability of these hybrid nanomaterials toward alkaline conditions. By varying the interface of the self-assembled monolayer, it has been possible to tailor these sorbent materials to selectively sequester a variety of different environmental targets such as mercury, plutonium, arsenate, and cesium. This exact same chemistry can be used to enhance the selectivity and sensitivity of analytical methodology by using the SAMMS as a preconcentrating interface. This enhancement has been demonstrated via X-ray fluorescence, electrochemical sensing, and radioanalytical methods. Further work developing SAMMS for environmental remediation and analytical enhancement is currently underway.

## ACKNOWLEDGMENTS

This research was supported in part by the Department of Energy (DOE) Environmental Managed Science Program. This work was performed at Pacific Northwest National Laboratory, which is operated for the DOE by Battelle Memorial Institute under contract DE AC06-76RLO 1830.

## REFERENCES

1. Nordstrom, D.K. Worldwide occurrences of arsenic in ground water. *Science* **2002**, *296*, 2143–2145.
2. Smith, A.H.; Lingas, E.C.; Rahman, M. Contamination of drinking-water by arsenic in Bangladesh: A public health emergency. *Bull. W.H.O.* **2000**, *78*, 1093–1103.
3. Meharg, A.A.; Rahman, M. Arsenic contamination of Bangladesh paddy field soils: Implications for rice contribution to arsenic consumption. *Environ. Sci. Technol.* **2003**, *37* (2), 229–234.
4. Wilkie, J.A.; Hering, J.G. Rapid oxidation of geothermal arsenic (III) in streamwaters of the Eastern Sierra Nevada. *Environ. Sci. Technol.* **1998**, *32* (5), 657–662.
5. Kneebone, P.E.; Hering, J.G. Behavior of arsenic and other redox-sensitive elements in Crowley Lake, CA: A reservoir in the Los Angeles aqueduct system. *Environ. Sci. Technol.* **2000**, *34* (20), 4307–4312.
6. Peters, S.C.; Blum, J.D.; Klaue, B.; Karagas, M.R. Arsenic occurrence in New Hampshire groundwater. *Environ. Sci. Technol.* **1999**, *33* (9), 1328–1333.
7. Ahmann, D.; Krumholz, L.R.; Hemond, H.F.; Lovley, D.R.; Morel, F.M.M. Microbial mobilization of arsenic from sediments of the Aberjona watershed. *Environ. Sci. Technol.* **1997**, *31* (10), 2923–2930.
8. Davis, A.; De Curnou, P.; Eary, L.E. Discriminating between sources of arsenic in the sediments of a tidal waterway, Tacoma, Washington. *Environ. Sci. Technol.* **1997**, *31* (7), 1985–1991.
9. Guriuan, P.L.; Small, M.J. Addressing uncertainty and conflicting cost estimates in revising the arsenic MCL. *Environ. Sci. Technol.* **2001**, *35* (22), 4414–4420.
10. National Primary Drinking Water Regulations; Arsenic and Clarifications to Compliance and New Source Contaminants Monitoring U.S. EPA. *Fed. Regist.* **2001**, *66* (14), 6976–7066.
11. Wang, Q.; Shen, W.; Ma, Z. Estimation of mercury emission from coal combustion in China. *Environ. Sci. Technol.* **2000**, *34* (13), 2711–2713.
12. Ganguli, P.M.; Mason, R.P.; Abi-Saba, K.E.; Anderson, R.S.; Flegal, A.R. Mercury speciation in drainage from the New Idria Mercury Mine, California. *Environ. Sci. Technol.* **2000**, *34* (22), 4773–4779.
13. Balogh, S.J.; Engstrom, D.R.; Almendinger, J.E.; Meyer, M.L.; Johnson, D.K. History of mercury loading in the upper Mississippi river reconstructed from the sediments of Lake Pepin. *Environ. Sci. Technol.* **1999**, *33* (19), 3297–3302.
14. *Screening Young Children for Lead Poisoning*; Centers for Disease Control and Prevention, November, 1997.
15. Radiation in the Environment. In *Cleaning Our Environment: A Chemical Perspective*, 2nd Ed.; American Chemical Society: Washington, DC, 1978; 378–452.
16. Kresge, C.T.; Leonowicz, M.E.; Roth, W.J.; Vartuli, J.C.; Beck, J.S. Ordered mesoporous molecular sieves synthesized by a liquid-crystal template mechanism. *Nature* **1992**, *359*, 710–712.
17. Beck, J.S.; Vartuli, J.C.; Roth, W.J.; Leonowicz, M.E.; Kresge, C.T.; Scmitt, K.D.; Chu, C.T.W.; Olson, D.H.;

- Sheppard, E.W.; McCullen, S.B.; Higgins, J.B.; Schlenker, J.L. A new family of mesoporous molecular sieves prepared with liquid crystal templates. *J. Am. Chem. Soc.* **1992**, *114*, 10834–10843.
18. Zhao, D.; Huo, Q.; Feng, J.; Chmelka, B.F.; Stucky, G.D. Non-ionic triblock and star diblock copolymer and oligomeric surfactant syntheses of highly ordered, hydrothermally stable, mesoporous silica structures. *J. Am. Chem. Soc.* **1998**, *120* (24), 6024–6036.
  19. Alberius, P.C.A.; Frindell, K.L.; Hayward, R.C.; Kramer, E.J.; Stucky, G.D.; Chmelka, B.F. General predictive syntheses of cubic, hexagonal, and lamellar silica and titania mesostructured thin films. *Chem. Mater.* **2002**, *14* (8), 3284–3294.
  20. Landry, C.C.; Tolbert, S.H.; Gallis, K.W.; Monnier, A.; Stucky, G.D.; Norby, P.; Hanson, J.C. Phase transformations in mesostructured silica/surfactant composites. Mechanisms for change and applications to materials synthesis. *Chem. Mater.* **2001**, *13* (5), 1600–1608.
  21. Moller, K.; Bein, T. Inclusion chemistry in periodic mesoporous hosts. *Chem. Mater.* **1998**, *10* (10), 2950–2963.
  22. Fryxell, G.E.; Liu, J. Designing Surface Chemistry in Mesoporous Silica. In *Adsorption on Silica Surfaces*; Papirer, E., Ed.; Marcel Dekker: New York, 2000; 665–687.
  23. Antonelli, D.M.; Ying, J.Y. Mesoporous materials. *Curr. Opin. Colloid Interface Sci.* **1996**, *1* (4), 523–529.
  24. Burleigh, M.C.; Markowitz, M.A.; Spector, M.S.; Gaber, B.P. Direct synthesis of periodic mesoporous organosilicas: Functional incorporation by co-condensation with organosilanes. *J. Phys. Chem., B* **2001**, *105* (41), 9935–9942, and references cited therein.
  25. Yonemitsu, M.; Tanaka, Y.; Iwamoto, M. Metal ion-planted MCM-41. 1. Planting of manganese(II) ion into MCM-41 by a newly developed template-ion exchange method. *Chem. Mater.* **1997**, *9* (12), 2679.
  26. Badiei, A.R.; Bonneviot, L. Modification of mesoporous silica by direct template ion exchange using cobalt complexes. *Inorg. Chem.* **1998**, *37* (16), 4142–4145.
  27. Mercier, L.; Pinnavaia, T.J. Heavy metal ion adsorbents formed by the grafting of a thiol functionality to mesoporous silica molecular sieves: Factors affecting Hg(II) uptake. *Environ. Sci. Technol.* **1998**, *32* (18), 2749–2754.
  28. Antonchshuk, V.; Jaroniec, M. Functionalized mesoporous materials obtained via interfacial reactions in self-assembled silica-surfactant systems. *Chem. Mater.* **2000**, *12* (8), 2496–2501.
  29. Kruk, M.; Jaroniec, M.; Antochshuk, V.; Sayari, A. Mesoporous silicate-surfactant composites with hydrophobic surfaces and tailored pore sizes. *J. Phys. Chem., B* **2002**, *106* (39), 10096–10101.
  30. Bibby, A.; Mercier, L. Mercury(II) ion adsorption behavior in thiol-functionalized mesoporous silica microspheres. *Chem. Mater.* **2002**, *14* (4), 1591–1597.
  31. Mercier, L.; Pinnavaia, T.J. Direct synthesis of hybrid organic-inorganic nanoporous silica by a neutral amine assembly route: Structure-function control by stoichiometric incorporation of organosiloxane molecules. *Chem. Mater.* **2000**, *12* (1), 188–196.
  32. Mercier, L.; Pinnavaia, T.J. Access in mesoporous materials: Advantages of a uniform pore structure in the design of a heavy metal ion adsorbent for environmental remediation. *Adv. Mater.* **1997**, *9* (6), 500–507.
  33. Zemanian, T.S.; Fryxell, G.E.; Liu, J.; Mattigod, S.; Franz, J.A.; Nie, Z. Deposition of self-assembled monolayers in mesoporous silica from supercritical fluids. *Langmuir* **2001**, *17* (26), 8172–8177.
  34. Savage, P.E.; Gopalan, S.; Mizan, T.I.; Martino, C.J.; Brock, E.E. Reactions at supercritical conditions: Applications and fundamentals. *AIChE J.* **1995**, *41*, 1723–1778.
  35. Shin, Y.; Zemanian, T.S.; Fryxell, G.E.; Wang, L.Q.; Liu, J. Supercritical processing of functionalized size selective microporous materials. *Microporous Mesoporous Mater.* **2000**, *37* (1–2), 49–56.
  36. March, J. *Advanced Organic Chemistry*, 4th Ed.; Wiley-Interscience: New York, 1992; 261 and references cited therein.
  37. Chen, X.; Feng, X.; Liu, J.; Fryxell, G.E.; Gong, M. Mercury separation and immobilization using self-assembled monolayers on mesoporous supports (SAMMS). *Sep. Sci. Technol.* **1999**, *34* (6–7), 1121–1132.
  38. Kemner, K.M.; Feng, X.; Liu, J.; Fryxell, G.E.; Wang, L.-Q.; Kim, A.Y.; Gong, M.; Mattigod, S.V. Investigation of the local chemical interactions between Hg and self assembled monolayers on mesoporous supports. *J. Synchrotron Radiat.* **1999**, *6*, 633–635.
  39. Mattigod, S.V.; Feng, X.; Fryxell, G.E.; Liu, J.; Gong, M. Separation of complexed mercury from aqueous wastes using self-assembled mercaptan on mesoporous silica. *Sep. Sci. Technol.* **1999**, *34* (12), 2329–2345.
  40. Fryxell, G.E.; Liu, J.; Gong, M.; Hauser, T.A.; Nie, Z.; Hallen, R.T.; Qian, M.; Ferris, K.F. Design and synthesis of selective mesoporous anion traps. *Chem. Mater.* **1999**, *11* (8), 2148–2154.
  41. Arena, G.; Contino, A.; Magri, A.; Sciotto, D.; Spoto, G.; Torrisi, A. Strategies based on calixcrowns for the detection and removal of cesium ions from alkali-containing solutions. *Ind. Eng. Chem. Res.* **2000**, *39*, 3605–3610.
  42. Guillon, J.; Leger, J.-M.; Sonnet, P.; Jarry, C.; Robba, M. Synthesis of cone, partial-cone, and 1,3-alternate 25,27-bis[1-(2-ethyl)hexyl]- and 25,27-bis[1-(2-tert-butoxy)ethyl]calix[4]arene-crown-6 conformers as potential selective cesium extractants. *J. Org. Chem.* **2000**, *65*, 8283–8289.
  43. Nyman, M.; Bonhomme, F.; Teter, D.M.; Maxwell, R.S.; Gu, B.X.; Wang, L.M.; Ewing, R.C.; Nenoff, T.M. Integrated experimental and computational methods for structure determination and characterization of a new, highly stable cesium silicotitanate phase. Cs<sub>2</sub>TiSi<sub>6</sub>O<sub>15</sub> (SNL-A). *Chem. Mater.* **2000**, *12*, 3449–3458.
  44. Prout, W.E.; Russell, E.R.; Groh, H.J. Ion exchange absorption of cesium by potassium hexacyanocobalt (II) ferrate (II). *J. Inorg. Nucl. Chem.* **1965**, *27*, 473–479.
  45. Sebesta, F.; John, J.; Motl, A. *Phase II Report on Evaluation of PAN as a Binding Polymer for Absorbers used to Treat Liquid Radioactive Wastes*; SAND96-1088, Sandia National Laboratory, 1996.

46. Strelko, V.V.; Mardanenko, V.K.; Yatsenko, V.V.; Patrilyak, N.M. Sorption of cesium and strontium on native vermiculite and vermiculite modified with copper ferrocyanide. *Russ. J. App. Chem.* **1998**, *71* (10), 1746–1749.
47. Lin, Y.; Fryxell, G.E.; Wu, H.; Englehard, M. Selective sorption of cesium using self-assembled monolayers on mesoporous supports. *Environ. Sci. Technol.* **2001**, *35*, 3962–3966.
48. Peters, M.W.; Werner, E.J.; Scott, M.J. Enhanced selectivity for actinides over lanthanides with CMPO ligands secured to a  $C_3$ -symmetric triphenoxymethane platform. *Inorg. Chem.* **2002**, *41*, 1707–1716.
49. Nash, K.L.; Choppin, G.R. Separations chemistry for actinide elements: Recent developments and historical perspective. *Sep. Sci. Technol.* **1997**, *32*, 255–274.
50. Horwitz, E.P.; Kalina, D.G.; Diamond, H.; Vandergrift, G.F.; Schulz, W.W. The TRUEX process—A process for extraction of the transuranic elements from nitric acid wastes utilizing modified PUREX solvent. *Solvent Extr. Ion Exch.* **1985**, *3*, 15.
51. Schulz, W.W.; Horwitz, E.P. The TRUEX process and the management of liquid TRU wastes. *Sep. Sci. Technol.* **1988**, *23*, 1191.
52. Birnbaum, J.C.; Busche, B.; Lin, Y.; Shaw, W.J.; Fryxell, G.E. Synthesis of carbamoylphosphonate silanes for the selective sequestration of actinides. *Chem. Commun.* **2002**, 1374–1375.
53. Fryxell, G.E. Actinide Specific Interfacial Chemistry of Monolayer Coated Mesoporous Ceramics. In *Final Report for the Environmental Managed Science Program, Project #65370*; U.S. Dept. of Energy, 2001.

# Molecular Simulations of DNA Counterion Distributions

Alexander Lyubartsev

*Division of Physical Chemistry, Stockholm University,  
Stockholm, Sweden*

## INTRODUCTION

One of the remarkable physical properties of a DNA molecule is that it is a strongly charged polyelectrolyte. In solution, DNA dissociates, forming a negatively charged polyion surrounded by an atmosphere of mobile, positively charged counterions. Although positive counterions are attracted to DNA, they screen the negative charge of DNA, decreasing the attractive force for other positive counterions. Additionally, ions of different valency and size interact with DNA in a different manner, leading to effects of competition between ions of different species. There is always a delicate balance of forces forming the equilibrium ion distribution around DNA. The functionality of DNA in the cell is, in a decisive degree, determined by electrostatic forces, which in turn are dependent on the presence of different charged components in the surrounding solution. It is clear that understanding of DNA functionality is impossible without an understanding of electrostatic interactions of DNA with the environment.

The aim of the present review is to show how molecular computer simulations can contribute to our understanding of the basic features of the interaction of DNA with its ionic environment, what kind of information can be obtained by computer simulations, and how this information can be used to bridge experimental and theoretical studies of DNA. First, some common polyelectrolyte models of DNA will be briefly reviewed, and a survey of available computer simulation techniques will be given. Then, applications of computer simulations to describe the ionic environment of DNA on different levels of precision will be discussed: Monte Carlo (MC) and Brownian dynamics (BD) simulations within the continuum dielectric models, molecular dynamics (MD) simulations with explicit treatment of solvent, as well as a combination of these techniques, giving rise to the “multiscale modeling” approach.

Several reviews devoted to different aspects of DNA-ion interactions and computer simulations of DNA have recently appeared.<sup>[1–3]</sup> A more general and detailed review of the computer simulation of polyelectrolytes is presented in Ref.<sup>[4]</sup>

## DNA POLYELECTROLYTE MODELS AND THEORIES

A theoretical description of the ionic environment of DNA is not a simple task. In fact, in any condensed matter system, the more detailed and closer to reality the molecular model is, the more complicated (and often including even more approximations) is the theory that has to be applied to obtain meaningful results. There exist several levels of theoretical descriptions of polyelectrolyte systems. In the simplest approach (the so-called “primitive model”), a DNA is presented as a rigid cylinder, and mobile ions as point charges or small rigid charged spheres. Within the primitive model, the solvent is described as a uniform dielectric continuum, described by a dielectric permittivity of this solvent. The interaction between ions is described by the Coulombic potential scaled by the value of the dielectric permittivity.

The most commonly used approach to describe the properties of polyelectrolyte solutions at this level is the Poisson–Boltzmann (PB) (mean field) theory.<sup>[5]</sup> This approach implies a Boltzmann distribution of the mobile ion species in the average field of other ions. For a simple cylindrical geometry, the PB equation can be rather easily solved by numerical methods. If the electrostatic potential is small, the exponent term in the standard PB equation may be linearized, resulting in the linearized PB equation that allows an analytical solution. In this context, the counterion condensation (CC) model formulated by Manning<sup>[6]</sup> can also be mentioned. According to the CC model, for a highly charged cylindrical polyion, a certain amount of counterions remains in close proximity to the polyion. These counterions neutralize a given fraction of the total polyion charge, whereas the remaining counterions reside in the bulk phase. Because most of the charge of the polyion (76% in the case of DNA) is neutralized, the distribution of ions in the bulk phase may be described by the linearized PB equation. Because of its simplicity, the Manning CC model has had a profound impact on practical, as well as theoretical, studies of polyelectrolyte solutions.

The major problem with theories based on the PB approximation is that the Boltzmann expression for



the ion density cannot be strictly derived from the statistical-mechanical theory; therefore the accuracy of the PB theory should be checked by more rigorous theories, or by simulations. The PB theory neglects the small ion correlations within the model. The effect of correlations can be explained as follows. If a counterion is present at some point near the polyion surface, it will decrease the probability for other counterions to be around it. Therefore near this point, the counterion density will be lower than that given by the PB theory. The decrease in local counterion density causes an effective attractive force (in addition to the mean force) that draws the counterions closer to the polyion surface. Clearly, the effect becomes stronger with increase of the ion valency. Ion correlation effects can considerably change the behavior of the polyelectrolyte systems in quantitative as well as qualitative ways.

There exist a number of liquid state theories, based on integral equations, which go beyond the PB approximation: the hypernetted chain approximation (HNC),<sup>[7,8]</sup> the BBGY chain equations,<sup>[9,10]</sup> the mean spherical approximation,<sup>[5]</sup> the modified PB theory,<sup>[11]</sup> as well as some others. A discussion of these theories and a comparison of predictions of such models to both the PB model and that of computer simulations can be found in a recent review.<sup>[12]</sup>

More elaborate DNA models may include specific details of its structure. One example is the so-called "grooved" model of DNA,<sup>[13]</sup> in which the charged groups of DNA are located outside the cylindrical hard core, on the sites corresponding to the phosphate groups of DNA. In addition, full-atomic molecular models of DNA or other polyelectrolytes in continuum solvent have been considered. In such cases, the PB equation becomes three-dimensional, but its solution is still rather straightforward.<sup>[14,15]</sup> Sometimes effects of polarization and hydration are included by considering a distant-dependent and field-dependent dielectric constant. The relevant theory to treat this class of models is the modified PB equation.<sup>[16]</sup> Stricter statistical-mechanical theories become too complicated to be of any practical use in this case.

The above-discussed analytical theories have to resort to approximations already at the level of the primitive model. Comparison of theory with experiment is, in such cases, inconclusive; if discrepancies occur, it may be difficult to attribute them to the approximations within the model, or to approximations during the mathematical treatment of the model. Computer simulations can help to answer the questions because they may provide an accurate, asymptotically exact, statistical-mechanical solution for a given model. Moreover, computer simulations allow to treat even more accurate and detailed models, with a proper account of effects caused by hydration,

dielectric saturation, and the molecular structure of the solvent by considering explicit solvent molecules.

The main computer simulation methods are MC and MD. The MC method<sup>[17]</sup> is based on a stochastic procedure, which generates molecular configurations with probabilities equal to that in the canonical (or another statistical) ensemble. By calculating simple arithmetic averages over generated molecular configurations, it is possible to define average values of physical properties in the canonical ensemble and to obtain exact (in statistical sense) answers to a statistical-mechanical problem. An important kind of MC simulation technique is the grand canonical Monte Carlo (GCMC) method, which allows to perform simulations in the grand canonical ensemble at constant chemical potential.<sup>[18]</sup>

The MC method is very suitable for a description of electrolyte and polyelectrolyte systems within the frame of continuum solvent models (i.e., when solvent molecules are not explicitly included in the simulations). However, for models with explicit solvent molecules, the MC method is not so efficient. The main reason is that in the liquid state, the molecules are closely packed and the fraction of the accepted MC steps becomes too small. For molecular all-atom models of the solvent, the MD simulation scheme is then more efficient.

The MD simulation technique implies a numerical solution of the Newtonian equations of motion for all atoms in the simulated molecular system. At each step of the MD simulation, the coordinates and velocities of the particles are recalculated according to equations of classical mechanics where forces are computed from some predefined expressions, called the force field. The time step is usually chosen at about  $10^{-15}$  sec and a typical MD simulation covers a time interval of  $10^{-8}$ – $10^{-10}$  sec. In addition to structural and thermodynamic properties, the dynamics of the molecular system can be studied, including time correlation functions, diffusion, and other transport properties.

At present, MD simulation is the most commonly used simulation method for studying molecules and molecular interactions in the liquid state. However, because MD implies simulation of all atoms in the system including solvent molecules, it becomes too expensive for studies of polyelectrolytes. A simplified description of polyelectrolyte systems, in terms of continuum solvent models, is still a preferable option. For such models, either the MC method or the stochastic analogue of MD-BD is used. In BD, the solvent molecules are not explicitly accounted for, but enter the equations of motion for solute molecules by two terms: a friction force and a random force. The third term in forces describes interactions with other solute particles in the system (e.g., other ions or polyions). Because the

solvent molecules are not treated explicitly in BD, it allows simulation of substantially larger systems than full-atomic MD simulation. Moreover, compared with MC simulations, the dynamic properties of the ions can be determined. For example, the effect of polyions on ion diffusion can be studied.

## SIMULATION OF COUNTERIONS AROUND DNA WITHIN CONTINUUM SOLVENT MODELS

### Evaluation of Analytical Theories

The first attempts of computer simulations of DNA-like polyelectrolytes were made in the beginning of the 1980s using the MC method.<sup>[19,20]</sup> More systematic studies, with varying salt concentrations and/or ion type, have been carried out later.<sup>[21–27]</sup> The primary objective of these earlier computer simulation studies was to evaluate the applicability of analytical theories describing ionic distributions around DNA. In most of these works, the primitive model was used [i.e., the DNA was modeled as a hard body (cylinder) with a uniform distribution of surface charge, and the ions were represented as point charges or charged hard spheres]. In some of these works, a soft short-range ion–ion or ion–DNA interaction potential,<sup>[23]</sup> or a specific location of the charges on the polyion surface<sup>[22]</sup> has been used. The main outcome of the early simulations was that the PB approximation is generally valid if only monovalent ions are present in the solution. In subsequent works with more detailed and more accurate (in the sense of longer runs) simulations, it was shown that deviation of the PB theory from the simulations does not exceed 10% for the ion distribution or the electrostatic potential in the relevant range of ion concentrations.

For ions of higher valency and their mixtures, the PB approximation often fails. The typical behavior is that the PB approximation underestimates the ion density in the nearest layer next to the polyion surface, which is a result of neglecting ion–ion correlations. An example is given in Fig. 1, which shows the ion density distributions for a cylindrical model of DNA in the presence of a mixture of divalent counterions and monovalent coions. One can see an increased simulated concentration of counterions compared with the PB result within about 5 Å from the polyion surface. This feature may seem not large on the figure, but given the facts of the logarithmic scale of *Y*-axis and steep slope of the curve, it results in a noticeable higher affinity of divalent ions to DNA.

An additional attraction of counterions to DNA can be seen more clearly in the “integrated charge” curve, which represents ion distribution integrated from the surface of polyion to some distance *r*. The sense of this

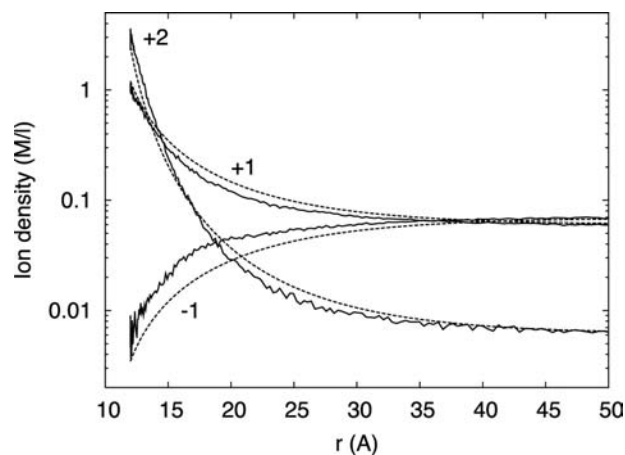


**Fig. 1** Ion distribution profile around a cylindrical DNA model for a mixture of divalent and monovalent counterions and monovalent coions, obtained in MC simulation (solid lines) and PB approximation (dashed lines). Radius of all ions in MC simulations, 2 Å. The simulation was set up as in Ref.<sup>[37]</sup>.

curve is the total counterion charge (per length of the polyion) within the cylinder of radius *r* around the polyion. An example of the integral charge curve is shown in Fig. 2 for the mixture of monovalent and divalent counterions with monovalent coions.<sup>[23]</sup> It is seen that for the given case (0.022 M MgCl<sub>2</sub> and 0.155 M NaCl mixture), the amount of divalent ions within 5 Å from the DNA surface in the PB approximation is underestimated by about 20%. In other cases (e.g., higher concentrations) deviations may reach 40% or even more.

Besides quantitative differences, computer simulations can, in some cases, predict a qualitatively different behavior as compared with the PB model. An example is the so-called “charge reversal” or “overneutralization,” which may happen if the total charge of the counterions in the close vicinity of a polyion exceeds the charge of the polyion itself, which then leads to an alternating sign of the electrostatic potential. Such behavior is typically observed for divalent or higher-valence counterions under certain thermodynamic conditions,<sup>[25]</sup> but it may happen even for monovalent ions if the salt concentration is high enough.<sup>[13]</sup> The charge reversal cannot be obtained in the PB theory. There is no clear experimental evidence of the charge reversal, except perhaps for a rather old work by Strauss et al.,<sup>[28]</sup> who observed a cationic polyion (poly-4-vinylpyridine) moving against the electric field at high salt concentration.

More accurate statistical–mechanical theories, such as the HNC or the modified PB theory, were found to reproduce properties of the ion distributions relatively well even for multivalent ions.<sup>[8,11,23]</sup> Fig. 2, reproduced from the work of Murthy, Bacquet, and Rossky,<sup>[23]</sup> shows the integral charge computed for a

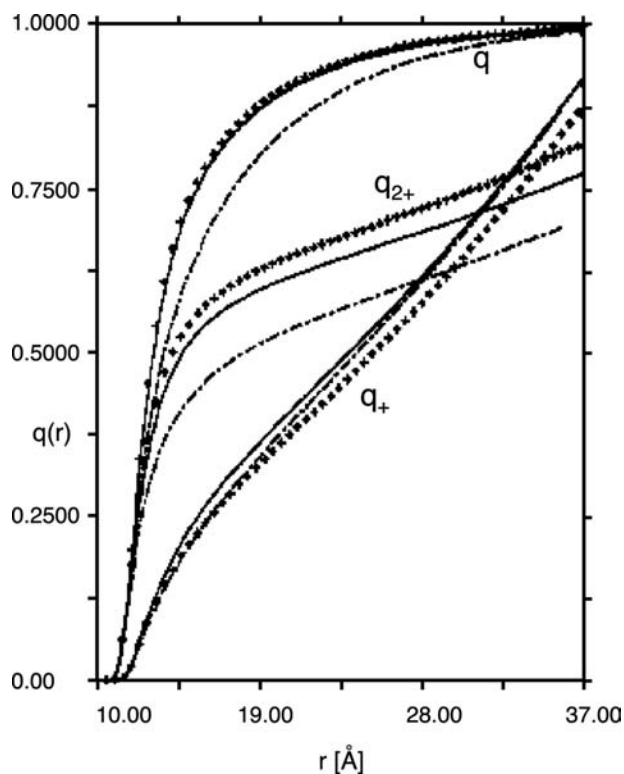


**Fig. 2** Radially integrated counterionic ( $q_{2+}$  and  $q_{+}$ ) and total ( $q$ ) charge for a 0.155 M NaCl and 0.022 M MgCl<sub>2</sub> salt mixture around a cylindrical model of DNA. Points are MC simulation result; dash-dot lines and solid lines are PB and HNC theories, respectively. *Source:* From Ref.<sup>[23]</sup>. © American Chemical Society, 1985.

mixture of divalent and monovalent ions by the PB and HNC theories as well as by MC simulations. Clearly, the HNC result is much closer to the simulation data than that obtained by the PB theory. The HNC theory, as well as some other more elaborated theories, are able to reproduce even such effects as charge reversal.<sup>[8]</sup> However, these theories are difficult to apply in the case of more complicated (non-cylindrical) geometries (e.g., for a model with specific location of the charges on the polyion).

Manning condensation theory is often considered as a further simplification of the PB theory. Still, it catches some basic features of ion distributions. Lamm, Wong, and Pack<sup>[27]</sup> compared the fraction of electrostatically bound ions using the MC, PB, and CC methods. If the bound fraction of counterions is determined as those residing within a region around the DNA where the electrostatic potential is less than  $kT$ , the MC results are found to quantitatively reproduce the bound fraction predicted by the Manning condensation theory. Another interesting feature of ion distribution, also related to the CC theory, is that the concentration of counterions just next to the DNA surface depends very weakly on the salt

concentration, and remains high (a few molars per liter) even at very low salt concentrations. According to the CC theory, a fraction of DNA counterions remains condensed to DNA even at infinite dilution. This feature was also confirmed by the computer simulations.

### Dielectric Effects

MC computer simulations within the primitive electrolyte model imply uniform continuum dielectrics with dielectric permittivity of liquid water ( $\epsilon \approx 80$ ). In fact, dielectric permittivity of DNA itself is substantially lower. It is also often argued that because the water molecules around the DNA are strongly oriented in the electrostatic field of DNA, their reorientation mobility is reduced, which must make the dielectric permittivity lower than in the bulk solution. Some estimations show that the effective dielectric constant may be as low as 6–30 in the first one to two molecular layers near a DNA surface<sup>[29,30]</sup> compared with the bulk value of about 80. Non-uniform dielectric permittivity is a source of polarization forces, and their effect on ionic distribution is a priori unclear.

MC simulations, incorporating the effect of dielectric discontinuity<sup>[31,32]</sup> at the polyion surface and using alternative dielectric saturation models,<sup>[33]</sup> have investigated the effects of the assumption of a constant dielectric permittivity, finding minor effects on the counterion distributions. Moreover, the effect may be different—it may drive ions out of the DNA grooves,<sup>[31]</sup> or, at the opposite, increase their concentration near the DNA surface,<sup>[32]</sup> depending on the details of the DNA model (shape) and the way how the dielectric effects are incorporated.

In fact, at distances on the order of a few angstroms, the concept of dielectric permittivity is not well defined. Within the primitive model, the interaction potential is the Coulombic potential scaled by the value of the dielectric constant. This potential is an approximation of the exact solvent-mediated potentials between the ions in the solution, which in fact represents the free energy of ion–solvent interactions. From this point of view,  $\epsilon$  in the interaction potential can be regarded as a parameter of the potential, which may differ from the local dielectric constant related, for example, to the water dipole fluctuation or the dielectric response. Evaluation of solvent-mediated potentials may be performed from the all-atom MD simulations, which showed that the effective dielectric constant—as a parameter of the effective potential—remains high even at high-enough salt concentrations and near the DNA surface.<sup>[33,34]</sup> The effects caused by an explicit account of the solvent in computer simulations on ion distribution around the DNA will be discussed in more detail below.

### Effect of Specific Distribution of Charges

The effects caused by a specific distribution of charges on the polyion surface were studied in a number of works<sup>[13,31,35–38]</sup> with applications to DNA. Quite evidently, a different structure of the charge distribution on the polyion may cause a rather different distribution of the ion density in the close vicinity of the polyion. Typically, one puts charges of  $-1$  on the sites corresponding to the phosphate groups of DNA. Additionally, helical grooves may be set, mimicking the minor and major grooves of DNA. In some cases, the DNA is presented with all-atom resolution.<sup>[39]</sup>

A detailed study of different ways to mimic helical grooves on DNA was presented by Montoro and Abascal.<sup>[13]</sup> These authors observed that specific interactions of ions with DNA (soft repulsion potential), the incorporation of the discrete charge distribution, and the grooved nature of the DNA surface may change the ion density profile around DNA considerably (Fig. 3). For example, in a “groove model” of DNA, in which explicit grooves on DNA were introduced, a double hump on the counterion density profile was observed,

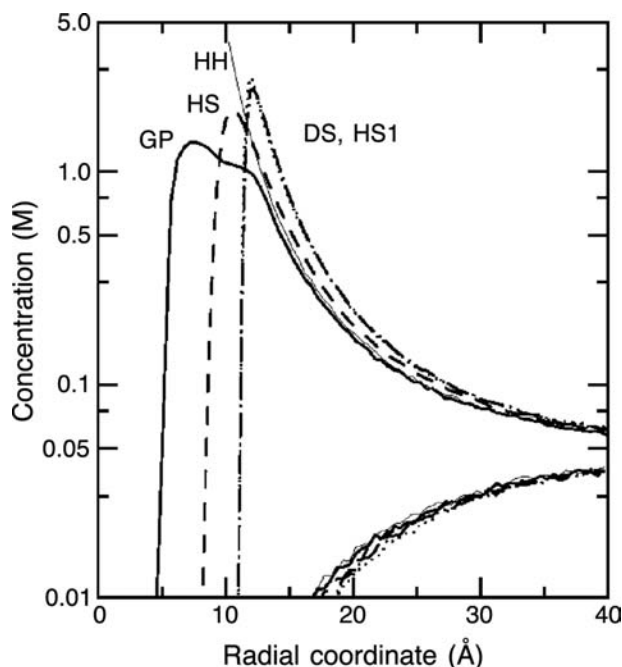


**Fig. 3** Ion distribution profiles at 0.05 M monovalent salt, calculated in MC simulations for different DNA models. HH is “homogeneous hard cylinder,” HS is “homogeneous soft cylinder” (ions interact with the polyion with repulsive  $1/r^9$  potential), HS1 is homogeneous soft cylinder with a displaced axis of short-range repulsion, DS is discretely charged, soft repulsion model with charges located on sites of phosphate groups, GP is grooved DNA model with explicit grooves. *Source:* From Ref.<sup>[13]</sup>. © American Institute of Physics, 1995.

which even transformed to a double maximum at higher concentrations. This is in agreement with BD simulations of a full-atomic description of DNA.<sup>[40,41]</sup> In addition, substantial penetration of counterions in the minor and major grooves was observed.<sup>[36]</sup> Enhanced concentration of counterions in the grooves (with stronger effect in the minor groove) has been observed also in several works.<sup>[37,38]</sup> However, distribution of counterions far from the DNA depends only weakly on the structure of the DNA surface.

An MC study of a DNA model with an all-atom resolution in a continuum solvent was carried out by Mills, Rashid, and James<sup>[39]</sup> for different forms of DNA. It was found that the grooved structure of both A-DNA and the B-DNA affects the details of the ion distribution in the center region of the polyion dramatically. However, the total number of bound ions at a particular added salt value differs only slightly among the conformations.

A general conclusion from the studies on the effect of the specific charge location on DNA is that although it may affect strongly the details in ion distribution near the polyion, the distribution of counterions far from the polyion (at distances more than 20 Å from the DNA axis) remains largely invariant. Furthermore, the integral properties of the ion distribution, such as the amount of ions within a certain distance around the polyion, depend very little on how the charges are located on the polyion surface. This is illustrated in Fig. 4, where the integrated charge is displayed for the same ion distributions as shown in Fig. 3. The integrated charge curves are determined

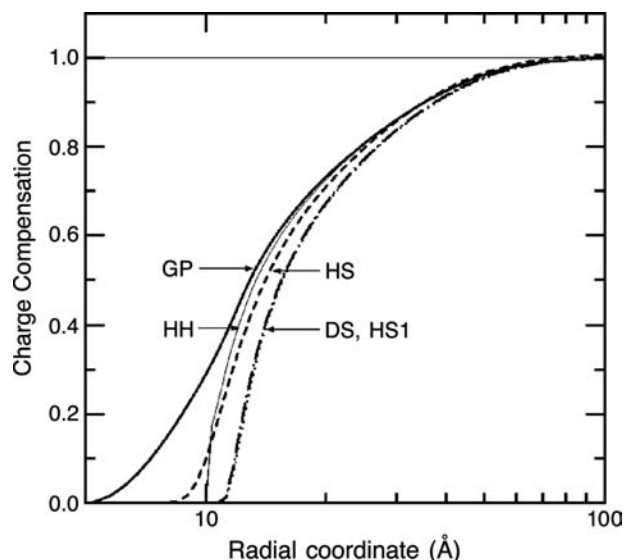


**Fig. 4** Integrated charge (charge compensation) function, calculated in MC simulations for different DNA models. Notations are the same as in Fig. 3. *Source:* From Ref.<sup>[13]</sup>. © American Institute of Physics, 1995.

mostly by the total charge density of the polyion and by the ion composition. The primary reason for the weak sensitivity of the global properties of the ion distribution to the details of charge location is the long-range character of electrostatic interactions, which effectively averages contributions from all the charges of the polyion and makes the total electrostatic field similar to that of a uniformly charged cylinder.

### Ion Competition

The interaction of mobile ions with polyions depends strongly on the ion type, charge, and size. Counterions of higher valency are more strongly attracted to polyions than monovalent ions—that is why they force low-valency ions out from the nearest vicinity of the polyelectrolyte. The size of the ions additionally plays a role and becomes especially important in the discussion of the competition of ions of the same valency. Smaller ions can come closer to the polyion surface and lower the electrostatic energy as compared with larger ions. However, within the primitive electrolyte model, the size of ions in simulations is not directly related to their real “crystallographic” sizes. Rather, it is a parameter that, in an average way, takes into account the effective hydration shell of water molecules around the ion. Reasonable values of the ion hydration radii can be obtained by fitting to available experimental data on ion osmotic and activity coefficients.<sup>[42]</sup> Other ways of choosing effective ion radii are discussed in a recent work by Banavali and Roux.<sup>[43]</sup>

The problem of ion competition has received much attention because of its importance in biological and technological applications. (For more information, see, for example, Ref.<sup>[44]</sup>.) Typically, one determines a “competition coefficient,” which has a sense of an equilibrium constant of the ion exchange process.<sup>[45]</sup> The competition coefficient may be determined experimentally from nuclear magnetic resonance (NMR) relaxation measurements,<sup>[45]</sup> or from direct ion exchange experiments.<sup>[46,47]</sup> The competition parameter may be also determined from computer simulations, or other theoretical approaches in a standard manner: For a given concentration of ions of different species, the ion density profiles are calculated and from these data, the amount of ions of each species within some distance from the polyion surface is obtained. Some uncertainty arises when one tries to define which ions are “bound” and which are “free.” Usually, one considers ions within some cutoff distance  $r_B$  from the surface of DNA (which is on the order of a few angstroms) as “bound.” Paulsen, Anderson, Record<sup>[45]</sup> analyzed the dependence of the competition coefficient on the cutoff radius and found that it is almost independent of  $r_B$  if  $r_B$  is chosen in reasonable limits.

In this way, the competition of ions of several divalent counterions with  $\text{Na}^+$  around the DNA was studied in the work<sup>[45]</sup> where a comparison of the PB model, MC simulations, and NMR experiments has been made. It was found that simulation results were closer to the experimental data than the PB results. Other studies of the ion competition effects are reported in a number of more recent MC simulations.<sup>[38,48,49]</sup> It was shown that the PB approximation underestimates binding of higher-valency ions and that this underestimation increases with ion valency.<sup>[38,45]</sup>

In the case of concentrated polyelectrolyte systems (e.g., oriented DNA fibers in equilibrium with a bulk electrolyte solution), the situation is different. The simulation cell, in this case, cannot include the “bulk” solution, so the concentration of the ions in the bulk is not directly known. The problem can be solved by performing GCMC simulations both in the polyelectrolyte gel phase and in the bulk solution (without polyions), at the same chemical potential.<sup>[50]</sup> The GCMC approach has been applied for studying the competition of monovalent, divalent, and trivalent ions in a series of works by Korolev et al.<sup>[46,47,51]</sup> In these works, competition coefficients of different ions, computed in GCMC simulations, were compared with the experimental ones measured by ion exchange experiments for DNA fibers, which were stabilized by the presence of ethanol. In computer simulations, the presence of ethanol was modeled as a lower (than in pure water) dielectric constant. The competition coefficients for the ions of different valencies and sizes have been computed and a good agreement with the ion exchange measurements has been observed.

### Interaction of DNA with Multivalent Ligands

Studies of DNA interacting with complex multivalent molecular ions is of considerable interest because of the role of such ions (e.g., polyamines) in living systems. Additionally, polyamines are often used as condensing agents in the preparation of condensed samples of DNA. Other interesting and important applications are related to binding of charged intercalative drugs to DNA and to protein–DNA binding.

Application of standard polyelectrolyte theories to complex multivalent ions faces additional difficulties related to the spatial distribution of the ion charges and the internal degrees of freedom. In analytical theories, these additional features are usually either ignored<sup>[52]</sup> or treated in some approximate manner.<sup>[53,54]</sup> In computer simulations, on the contrary, inclusion of the internal structure of the ionic ligand does not pose any principal complications. In Ref.<sup>[37]</sup>, the polyamine spermidine<sup>3+</sup> was modeled as a chain of three monovalent ions connected by harmonic bonds. It was

shown that because of the effects of the non-local charge distribution and internal degrees of freedom, the binding affinity of spermidine to DNA was reduced compared with that of a simple trivalent (metal) ion. The binding was reduced even below the predictions of the PB theory, which generally underestimates the binding affinities of higher valency ions for simple ions. Existing NMR diffusion studies qualitatively confirm this result.<sup>[55]</sup>

The binding of an octavalent rodlike ligand to DNA in the presence of monovalent salt has been studied by Olmstedt et al.<sup>[56]</sup> using GCMC simulations. Such highly charged ligand binds strongly to DNA, forming a stable complex. A strong reduction in the surface counterion (e.g., Na<sup>+</sup>) concentration over a region including—but extending well beyond—the location of the ligand binding site has been observed.

### Brownian Dynamics of Counterions Around DNA

BD simulations allow, alongside ion distribution, computation of dynamic and transport properties of ions. The presence of a polyion makes the diffusion of ions slower than in the bulk solution, because of both the steric obstacles imposed by the polyion and the electrostatic interactions. Thus the retardation of the diffusion provides information on the binding of ions to the polyelectrolyte. An advantage of diffusion studies is that the self-diffusion coefficient is a quantity that is directly available from experiments measuring macroscopic self-diffusion.

The diffusion properties of counterions in the presence of DNA were studied by BD simulations in a number of works.<sup>[40,57,58]</sup> The self-diffusion coefficient can also be obtained within the PB mean field approximation, using the PB–Smoluchowski diffusion model.<sup>[59]</sup> A comparison of lithium counterion diffusion coefficients determined in BD simulations, in the PB–Smoluchowski model, and in the experiment was performed in Ref.<sup>[57]</sup>. The comparison of the two polyelectrolyte theories with the experiment clearly demonstrated the effect of ion correlations included in the BD simulations, which substantially improve agreement with the experiment.

Apart from the general interest as to how the presence of DNA affects ion dynamics, such simulations provide valuable information for the interpretation of NMR relaxation experiments. For example, BD may provide data on the time correlation function of the electric field gradients<sup>[40,58]</sup> experienced by Na<sup>+</sup> counterions associated with DNA, for which the NMR quadrupolar relaxation of the <sup>23</sup>Na nuclei is determined by the time-dependent fluctuation of these field gradients.

## SIMULATIONS OF COUNTERIONS AROUND DNA WITH EXPLICIT ACCOUNT OF SOLVENT

### Molecular Dynamics of DNA

The studies of the ionic environment of DNA discussed above have been carried out within continuum solvent models. The effects of solvent and hydration can be taken into account rather straightforwardly in computer simulations by introducing explicit solvent (water) molecules. However, an all-atom description makes the simulations very time-consuming and reduces the size of the system that can be considered. At the present level of computer power, the maximum number of atoms that can be simulated long enough to obtain meaningful results is on the order 10<sup>4</sup>, which corresponds to a simulation box size of 50–60 Å. This size is not enough to study polyelectrolyte aspects of ion distribution. Still, all-atom simulations are extremely important for understanding ion–DNA interactions in close proximity to the DNA.

The preferable method in all-atom simulations is MD, although the first attempt to simulate such model was performed by the MC method.<sup>[60]</sup> Earlier MD simulations of DNA<sup>[61–63]</sup> were too short to produce information on ionic distribution. Given the diffusion of counterions around DNA on the order 10<sup>−6</sup> cm/sec<sup>2</sup>, at least nanosecond time scale is needed for the counterions to sample the space around DNA. Such simulations became possible from the second part of 1990s, when a large number of works on MD simulations of DNA, with full-atomic description of solvent and ions, appeared.<sup>[64–71]</sup> In the majority of these studies, the main interest was in the DNA molecule itself, investigating DNA backbone structure and dynamics, base stacking, phosphate orientation, overall nucleic acid structure, and so on. (For more information on these issues, the reader is referred to recent reviews.)<sup>[3,72]</sup> Below, we shall concentrate on works dealing with MD simulations of ion distributions around DNA. Note first that results on MD simulations are dependent on the force field used. The force fields used in macromolecular simulations are usually empirically parameterized to reproduce some set of experimental results. At present, the most often used force fields for DNA simulations are AMBER<sup>[73]</sup> and CHARMM.<sup>[74]</sup> It was found that these force fields may give somewhat different DNA structures.<sup>[70]</sup> However, the hydration structure and ion distribution are very similar in AMBER and CHARMM simulations.<sup>[71,75]</sup> This is because of the fact that these force fields differ mainly by parameters describing intramolecular DNA interactions, whereas parameters describing forces between water, ions, and DNA are almost the same.



## Specific Binding of Ions

A major issue in molecular dynamic studies of the ionic environment of DNA is the problem of specific ion binding to different sites on the DNA surface. Whether this binding is sequence-specific or purely electrostatic is still to be determined. X-ray experiments carried out in the 1980s have suggested that there exists a “spin of hydration” of DNA,<sup>[76]</sup> which is a sequence of water molecules in the minor and major grooves that is impenetrable to cations. Cations, according to this picture, form a diffuse cloud around, which is defined by electrostatic interactions. However, MD simulations, made in the 1990s, have shown that Na<sup>+</sup> counterions may intrude the spin of hydration of DNA and substitute for water molecules.<sup>[66–68,77]</sup> This was also confirmed by newer, high-resolution X-ray data.<sup>[78]</sup>

The question of sequence-specific counterion binding to DNA has a principal importance to our understanding of mechanisms of DNA recognition. When counterions bind to DNA in a sequence-specific manner, they form a mosaic of non-uniform charge distribution depending on the DNA sequence. Moreover, it was supposed that direct ion binding to DNA affects the DNA structure,<sup>[78]</sup> although this point of view is under debate.<sup>[79]</sup> Molecular computer simulation can provide valuable information to this discussion.

Most of the mentioned MD simulations of DNA have been carried out with Na<sup>+</sup> counterions. In some works, other counterions were also studied. In Ref.<sup>[68]</sup>, a comparative study of Li<sup>+</sup>, Na<sup>+</sup>, and Cs<sup>+</sup> around DNA was performed. It was found that these monovalent alkali ions interact with DNA in a very different manner. Li<sup>+</sup> ions bind almost exclusively to the phosphate groups of DNA. Na<sup>+</sup> ions bind prevailing bases in the minor groove through one water molecule, although a smaller fraction of ions binds directly to the bases at some specific sites (AT step in the minor groove and guanine bases in the major groove). Cs<sup>+</sup> ions bind directly to sugar oxygen in the minor groove. It was shown also that the specific character of ion bonding is, to a large extent, determined by the hydration structure of water around DNA. A stronger binding of Li<sup>+</sup> ions to DNA was also confirmed by NMR studies of the diffusion of Li<sup>+</sup> and Cs<sup>+</sup> ions in oriented DNA fibers.<sup>[80]</sup>

DNA oligomers d(TpA)<sub>12</sub> in the presence of K<sup>+</sup> counterions were simulated in Ref.<sup>[81]</sup>. Comparing with Na<sup>+</sup> counterions, a stronger preference of K<sup>+</sup> ions to the major groove has been observed.

MD of DNA with divalent ions Mg<sup>2+</sup> and Ca<sup>2+</sup> was performed in some recent works.<sup>[63,64,82]</sup> However, the slow diffusion of Mg<sup>2+</sup> ions makes it difficult to perform a reliable estimation of distribution of these ions around the DNA.

Recently, some works appeared on the distribution of multivalent polyamine ions around DNA.<sup>[83–85]</sup> It was found that flexible polyamine molecules (spermine or spermidine) have several binding modes, interacting with different sites on the DNA in an irregular manner. That is why polyamine molecules are not seen in X-ray diffractions of DNA. Spermine<sup>4+</sup> ions compete with Na<sup>+</sup> ions and water molecules in binding to bases in the minor groove, and they influence the structure of the DNA hydration shell in different ways.<sup>[85]</sup>

## Comparison with Continuum Solvent Models

An interesting question that MD simulation could answer is: How reliable are computations within the continuum solvent model, for example, in the prediction of overall ion density around DNA? The angularly averaged density profile of counterions (Na<sup>+</sup> mostly) has been calculated in some recent works.<sup>[66–68]</sup> At short distances (within 5 Å from the DNA surface), these density profiles are defined mainly by the details of DNA structure and hydration forces. Naturally, the distributions are very different from the density profiles calculated for the cylindrical model of DNA within the continuum solvent model (both in analytical approaches and MC simulations). Such comparison, from Ref.<sup>[68]</sup>, is shown in Fig. 5, where angularly averaged distributions of different monovalent counterions around the DNA are displayed, together with the PB theory result. Introducing details of the DNA structure within the continuum dielectric model may make the counterion distribution closer to

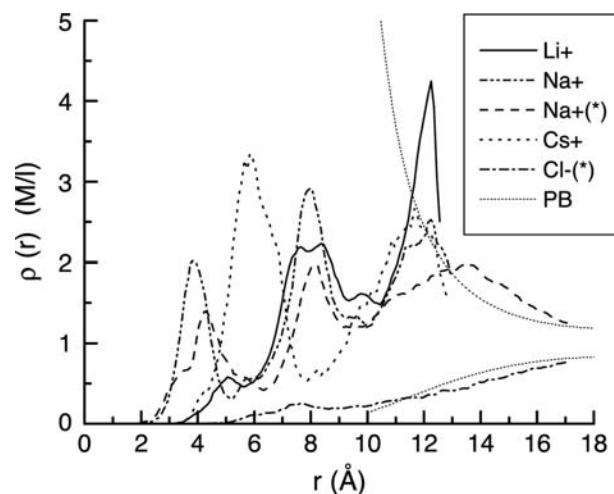


**Fig. 5** Density profile of different ions around DNA obtained in all-atom MD simulations. The results marked with (\*) are from a simulation with a larger simulation cell than the other data. The thin dotted line shows the PB results with a cell radius corresponding to the system marked (\*). Source: From Ref.<sup>[68]</sup>. Adenine Press.

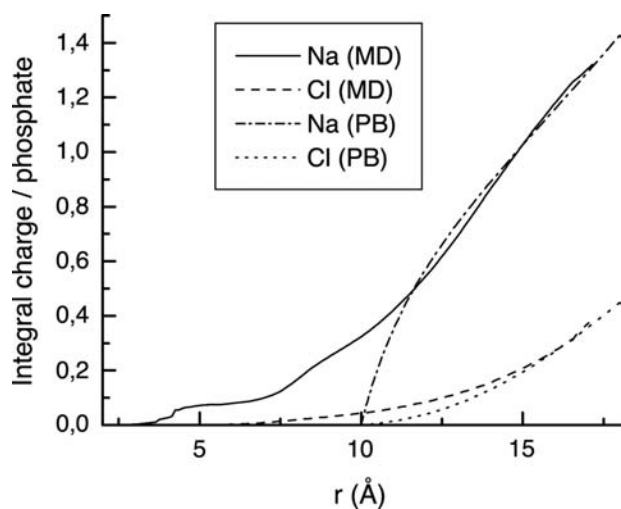


**Fig. 6** Integral charge for  $\text{Na}^+$  and  $\text{Cl}^-$  ions per phosphate obtained in all-atom MD simulations and PB approximation. Source: From Ref.<sup>[68]</sup>. Adenine Press.

that obtained in MD simulations. For example, a maximum in ion density is observed at about 8 Å from the DNA axis, corresponding to a high probability for counterions to be inside the DNA grooves.<sup>[38]</sup>

On larger distances from the DNA, the ion distribution, computed in MD simulations, became more similar to that calculated in the PB theory, or obtained in continuum solvent simulations. In addition, the integral charge for  $\text{Na}^+$  ions turned out to be very similar already on distances greater than 12 Å from the DNA surface (Fig. 6). This means that cylindrical PB equation, despite many inherent approximations, is still able to evaluate amounts of ions that are attracted (or “non-specifically” bound) to DNA.

### Multiscale Simulation Approach

However, direct simulation of ion density in MD simulation is a tedious task and can be performed only at relatively small distances from the DNA surface. These distances do not include the true “bulk” phase, where neither water nor ions are affected by the electrostatic field of DNA. On the other hand, the problem of finding the ion distribution in the whole range (from the DNA surface to the bulk solution) is the important one. The “bulk” ion concentration in the living cell is determined by the work of ion channels in the membrane; however, only ions that are in close proximity to DNA affect their properties. Although continuum solvent models allow to compute for the ion distribution in the whole range, they contain adjustable parameters, such as the effective ion radius, and are unable to describe the effects of specific ion binding (e.g., specific binding of  $\text{Li}^+$  ions to the phosphate groups).

In Refs.<sup>[33]</sup> and <sup>[34]</sup>, an approach was suggested to link together the two levels of simulations of electrolyte or polyelectrolyte systems (i.e., the all-atom MD simulations and the MC simulations without explicit solvent). The main idea is that detailed all-atom MD simulations provide information on how to parameterize parameters for the continuum solvent model. In practice, as a first step, an MD simulation of size as large as can be afforded is performed. From this simulation, the radial distribution function (RDF) between ions as well as between ions and some sites of DNA is determined. Then, an inverse MC procedure is performed,<sup>[34,86]</sup> which finds the effective interaction potentials that match the RDF obtained in the MD simulations. The great benefit of effective potentials is that they can be used for simulation of the very same system but of substantially larger scale because the solvent molecules are not included. The typical behavior of the effective potentials is that they have a few oscillations at short distances, reflecting the molecular structure of the solvent, and then—at distances of more than 10 Å—approach the Coulombic potential with the dielectric constant of water.<sup>[33,34]</sup> The short-range part of the effective potentials is rather ion-specific, thus the specific features of ion–DNA interactions are automatically included in the model.

In Ref.<sup>[34]</sup>, the effective potentials between different alkali ions and DNA have been determined and used for MC simulations of the ion environment of DNA. The computed ion distributions are shown in Fig. 7. One can notice clear similarities with the ion distribution obtained in all-atom MD simulations in Fig. 5. Another interesting observation is that for  $\text{Na}^+$  and  $\text{K}^+$  ions, the density profiles follow very closely the

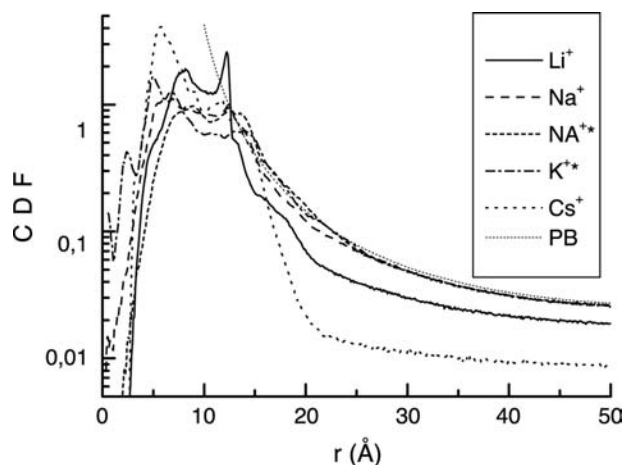


**Fig. 7** Density profile of different ions around DNA obtained by MC simulation with effective solvent-mediated potentials. The notations for the curves are the same as in Fig. 5. Source: From Ref.<sup>[34]</sup>. American Institute of Physics. Simulation details are given in this reference.

solution of the PB equation for distances larger than 15 Å from the DNA axis (of course, they were rather different at closer distances). For two other ions, Li<sup>+</sup> and Cs<sup>+</sup>, the deviations from the solution of the PB equation were more significant because of specific interactions of these ions with DNA. From the simulations, the relative binding affinity of these ions to DNA was determined as Cs<sup>+</sup> > Li<sup>+</sup> > Na<sup>+</sup> ≥ K<sup>+</sup>, in agreement with the experimental results.

The multiscale modeling approach may be used to take into account solvent and hydration effects in studies of ion binding and competition, as well as of the interaction of DNA with other ligands and proteins. Work in this direction is now in progress.

## CONCLUSION

The aim of the present review has been to show that computer simulation techniques are becoming increasingly important in the description of the ionic environment of DNA as well as other properties of biomacromolecular systems. Computer simulations allow us to follow the motion of every atom in the studied system, thus providing very detailed information and contributing to our general understanding of the physical mechanisms that govern the behavior of these biologically, as well as technologically, important systems. With the rapid development of computer technology, allowing larger systems to be studied on a longer time scale and enabling also a more accurate and detailed description of molecular interactions, the importance of molecular simulations in this area will grow further. Furthermore, new developments in experimental techniques including “single-molecule” experiments, as well as an interest in more and more complicated systems related to new areas of biotechnology, biomaterials, and nanotechnology additionally enhance the importance of computer simulation methods.

## ACKNOWLEDGMENTS

The author is thankful to Jose Abascal for providing electronic copies of the figures. Many thanks to Lars Nordenskiöld, Aatto Laaksonen, and Nikolai Korolev for stimulating discussions. This work was supported by the Swedish Research Council.

## REFERENCES

1. Anderson, C.F.; Record, M.T. Salt–nucleic acid interactions. *Annu. Rev. Phys. Chem.* **1995**, *46*, 657–700.
2. Jayram, B.; Beveridge, D.L. Modeling DNA in aqueous solutions: theoretical and computer simulation studies on the ion atmosphere of DNA. *Annu. Rev. Biophys. Biomol. Struct.* **1996**, *25*, 367–394.
3. Cheatham, T.E.; Kollman, P.A. Molecular dynamics simulations of nucleic acids. *Annu. Rev. Phys. Chem.* **2000**, *51*, 435–471.
4. Lyubartsev, A.P.; Nordenskiöld, L. *Computer Simulations of Polyelectrolytes*; Handbook of Polyelectrolytes and Their Applications; Tripathy, S.K., Kumar, J., Nalwa, H.S., Eds.; American Scientific Publishers, 2002; Vol. 3, 309–326.
5. Fixman, M. The Poisson–Boltzmann equation and its application to polyelectrolytes. *J. Chem. Phys.* **1979**, *70* (11), 4995–5005.
6. Manning, G.S. Limiting laws and counterion condensation in polyelectrolyte solutions. *J. Chem. Phys.* **1969**, *51*, 924–933.
7. Vlachy, V.; McQuarrie, D. A theory of cylindrical polyelectrolyte solution. *J. Chem. Phys.* **1985**, *83* (4), 1927–1932.
8. Tovar, E.G.; Losada-Gassou, H.; Henderson, D. Hypernetted chain approximation for cylindrical polyelectrolytes. *J. Chem. Phys.* **1985**, *83* (1), 361–372.
9. Croxton, T.; McQuarrie, D.A. The electrical double layer in the Born–Green–Yvon approximation. *Mol. Phys.* **1981**, *42*, 141–151.
10. Ramanathan, G.V. Statistical mechanics of electrolytes and polyelectrolytes: II. Counterion condensation on a line charge. *J. Chem. Phys.* **1982**, *77* (8), 4133–4140.
11. Outhwaite, C.W. A modified Poisson–Boltzmann equation for the ionic atmosphere around a cylindrical wall. *J. Chem. Soc., Faraday Trans. II* **1986**, *82*, 789–794.
12. Vlachy, V. Ionic effects beyond Poisson–Boltzmann theory. *Annu. Rev. Phys. Chem.* **1999**, *50*, 145–165.
13. Montoro, J.C.G.; Abascal, J.L.F. Ionic distribution around simple DNA models: I. Cylindrically averaged properties. *J. Chem. Phys.* **1995**, *103* (18), 8273–8284.
14. Klein, B.J.; Pack, G.R. Calculation of the spatial distribution of the charge density in DNA environment. *Biopolymers* **1983**, *22*, 2331–2352.
15. Cortis, C.M.; Friesner, R.A. Numerical solution of the Poisson–Boltzmann equation using tetrahedral finite-element meshes. *J. Comput. Chem.* **1997**, *18* (13), 1591–1608.
16. Gavryushov, S.; Zielenkiewicz, P. Electrostatics of a DNA-like polyelectrolyte: effects of solvent dielectric saturation and polarization of ion hydration shells. *J. Phys. Chem., B* **1999**, *103* (28), 5860–5868.
17. Metropolis, N.; Rosenbluth, A.W.; Rosenbluth, M.N.; Teller, A.H.; Teller, E. Equation of state calculations by fast computing machines. *J. Chem. Phys.* **1953**, *21*, 1087–1092.
18. Wood, W.W. *Physics of Simple Liquids*; North-Holland: Amsterdam, 1968.
19. Vlachy, V.; Dolar, D. Monte Carlo studies of polyelectrolyte solutions at low degrees of polymerization. *J. Chem. Phys.* **1982**, *76* (4), 2010–2014.
20. Bratko, D.; Vlachy, V. Distribution of counterions in the double layer around a cylindrical polyion. *Chem. Phys. Lett.* **1982**, *90* (6), 434–438.

21. Mills, P.; Anderson, C.; Record, M.T. Monte Carlo studies of counterions–DNA interactions. Comparison of the radial distribution of counterions with predictions of other polyelectrolyte theories. *J. Phys. Chem.* **1985**, *89*, 3984–3994.
22. LeBret, M.; Zimm, B. Monte Carlo determination of the distribution of ions around a cylindrical polyelectrolyte. *Biopolymers* **1984**, *23*, 271–286.
23. Murthy, C.S.; Bacquet, R.J.; Rossky, P.J. Ionic distribution near polyelectrolytes. A comparison of theoretical approaches. *J. Phys. Chem.* **1985**, *89*, 701–710.
24. Guldbbrand, L.; Nilsson, L.G.; Nordenskiöld, L. A Monte Carlo simulation study of electrostatic forces between hexagonally packed DNA double helices. *J. Chem. Phys.* **1986**, *85* (11), 6686–6698.
25. Vlachy, V.; Haymet, A.D.J. A grand canonical Monte Carlo simulation study of polyelectrolyte solutions. *J. Chem. Phys.* **1986**, *84* (10), 5874–5880.
26. Mills, P.; Anderson, C.; Record, M.T. Grand canonical Monte Carlo calculations of thermodynamic coefficients for a primitive model of DNA–salt solutions. *J. Phys. Chem.* **1986**, *90*, 6541–6548.
27. Lamm, G.; Wong, L.; Pack, G.R. Monte Carlo and Poisson–Boltzmann calculations of the fraction of counterions bound to DNA. *Biopolymers* **1994**, *34* (2), 227–237.
28. Strauss, U.P.; Gershfeld, N.L.; Spiera, H. Charge reversal of cationic poly-4-vinylpyridine derivatives in KBr solution. *J. Am. Chem. Soc.* **1954**, *76*, 5909–5911.
29. Hansen, W.N. The immersed double layer. *J. Electroanal. Chem.* **1983**, *150*, 133–140.
30. Young, M.A.; Jayaram, B.; Beverige, D.L. Local dielectric environment of B-DNA in solution: result from a 14 ns molecular dynamics trajectory. *J. Phys. Chem., B* **1998**, *102*, 7666–7669.
31. Conrad, J.; Troll, M.; Zimm, B. Ions around DNA: Monte Carlo estimates of distribution with improved electrostatic potentials. *Biopolymers* **1988**, *27*, 1711–1732.
32. Jayaram, B.; Swaminathan, S.; Beveridge, D.L.; Sharp, K.; Honig, B. Monte Carlo simulation studies on the structure of the counterion atmosphere of B-DNA. Variations on the primitive dielectric model. *Macromolecules* **1990**, *23*, 3156–3165.
33. Lyubartsev, A.P.; Laaksonen, A. Osmotic and activity coefficients from effective potentials for hydrated ions. *Phys. Rev., E* **1997**, *55* (5), 5689–5696.
34. Lyubartsev, A.P.; Laaksonen, A. Effective potentials for ion–DNA interactions. *J. Chem. Phys.* **1999**, *111* (24), 11207–11215.
35. Montoro, J.C.G.; Abascal, J.L.F. Discrete charge effects in the structure of ions around polyelectrolyte model. *Mol. Phys.* **1996**, *89* (4), 1071–1086.
36. Montoro, J.C.G.; Abascal, J.L.F. Ionic distribution around simple B-DNA models: II. Deviations from cylindrical symmetry. *J. Chem. Phys.* **1998**, *109* (14), 6200–6210.
37. Lyubartsev, A.P.; Nordenskiöld, L. Monte Carlo simulation study of DNA polyelectrolyte properties in the presence of multivalent polyamine ions. *J. Phys. Chem., B* **1997**, *101*, 4335–4342.
38. Abascal, J.L.F.; Montoro, J.C.G. Ionic distribution around simple B-DNA models: III. The effect of ionic charge. *J. Chem. Phys.* **2001**, *114* (9), 4277–4284.
39. Mills, P.A.; Rashid, A.; James, T.L. Monte Carlo calculations of ion distributions surrounding the oligonucleotide *d(atatataat)<sub>2</sub>* in the B, A and wrinkled D conformations. *Biopolymers* **1992**, *32*, 1491–1501.
40. Guldbbrand, L. The distribution and dynamics of small ions in simulations of ordered polyelectrolyte solutions. *Mol. Phys.* **1989**, *67* (1), 217–237.
41. Guldbbrand, L.E.; Forester, T.R.; Lynden-Bell, R.M. Distribution and dynamics of mobile ions in systems of ordered B-DNA. *Mol. Phys.* **1989**, *67* (1), 473.
42. Triolo, R.; Grigera, J.R.; Blum, L. Simple electrolytes in the mean spherical approximation. *J. Phys. Chem.* **1976**, *80* (17), 1858–1861.
43. Banavali, N.K.; Roux, B. Atomic radii for continuum electrostatics calculations on nucleic acids. *J. Phys. Chem., B* **2002**, *106*, 11,026–11,035.
44. Record, M.T.; Zhang, W.; Anderson, C.F. Analysis of effects of salts and uncharged solutes on protein and nucleic acids equilibria and processes: a practical guide to recognizing and interpreting polyelectrolyte effects, Hofmeister effects, and osmotic effects of salts. *Adv. Protein Chem.* **1998**, *51*, 281–353.
45. Paulsen, M.D.; Anderson, C.F.; Record, M.T. Counterion exchange reactions on DNA: Monte Carlo and Poisson–Boltzmann analysis. *Biopolymers* **1988**, *27*, 1249–1265.
46. Korolev, N.; Lyubartsev, A.P.; Rupprecht, A.; Nordenskiöld, L. Experimental and Monte Carlo simulation studies on the competitive binding of Li<sup>+</sup>, Na<sup>+</sup> and K<sup>+</sup> ions to DNA in oriented DNA fibers. *J. Phys. Chem., B* **1999**, *103*, 9008–9019.
47. Korolev, N.; Lyubartsev, A.P.; Rupprecht, A.; Nordenskiöld, L. Competitive binding of Mg<sup>2+</sup>, Ca<sup>2+</sup>, Na<sup>+</sup> and K<sup>+</sup> ions to DNA in oriented fibers: experimental and Monte Carlo simulation results. *Biophys. J.* **1999**, *77*, 2736–2749.
48. Das, T.; Bratko, D.; Bhuiyan, L.B.; Outhwaite, C.W. Polyelectrolyte solutions containing mixed valency ions in the cell model: a simulation and modified Poisson–Boltzmann theory. *J. Chem. Phys.* **1997**, *107* (21), 9197–9207.
49. Ni, H.; Anderson, C.F.; Record, M.T. Quantifying the thermodynamic consequences of cation (M<sup>2+</sup>, M<sup>+</sup>) accumulation and anion (X<sup>−</sup>) exclusion in mixed salt solutions of polyanionic DNA using Monte Carlo and Poisson–Boltzmann calculations of ion–polyion preferential interaction coefficient. *J. Phys. Chem., B* **1999**, *103*, 3489–3504.
50. Lyubartsev, A.P.; Nordenskiöld, L. Monte Carlo simulation study of ion distribution and osmotic pressure in hexagonally oriented DNA. *J. Phys. Chem.* **1995**, *99*, 10,373–10,382.
51. Korolev, N.; Lyubartsev, A.P.; Rupprecht, A.; Nordenskiöld, L. Competitive substitution of hexamine cobalt for Na<sup>+</sup> and K<sup>+</sup> ions in oriented DNA fibers. *Biopolymers* **2001**, *58*, 268–278.

52. Wilson, R.W.; Rau, D.C.; Bloomfield, V.A. Comparison of polyelectrolyte theories of the binding of cations to DNA. *Biophys. J.* **1980**, *30*, 317–325.
53. Rouzina, I.; Bloomfield, V.A. Influence of ligand spatial organisation on competitive electrostatic binding to DNA. *J. Phys. Chem.* **1996**, *100*, 4305–4313.
54. Stigter, D.; Dill, K.A. Binding of ionic ligands to polyelectrolytes. *Biophys. J.* **1996**, *71*, 2064–2074.
55. Andreasson, B.; Nordenskiöld, L.; Schultz, J. Interactions of spermidine and methylspermidine with DNA studied by nuclear magnetic resonance self-diffusion measurements. *Biophys. J.* **1996**, *70*, 2847–2856.
56. Olmstedt, M.C.; Bond, J.P.; Anderson, C.F.; Record, M.T. Grand canonical Monte Carlo molecular and thermodynamic predictions of ion effects on binding of an oligocation ( $L^{8+}$ ) to the center of DNA oligomers. *Biophys. J.* **1995**, *68*, 634–647.
57. Guldbrand, L.; Nordenskiöld, L. Brownian dynamics simulation of counterion dynamics in cylindrical polyelectrolyte solution. *J. Phys. Chem.* **1987**, *91*, 5714–5718.
58. Reddy, M.R.; Rossky, P.J.; Murthy, C.S. Counterion spin relaxation in DNA solutions: a stochastic dynamics simulation study. *J. Phys. Chem.* **1987**, *91*, 4923–4933.
59. Nilsson, L.G.; Nordenskiöld, L.; Stilbs, P.; Braunlin, W.H. Macroscopic counterion diffusion in solutions of cylindrical polyelectrolytes. *J. Phys. Chem.* **1985**, *89*, 3385–3391.
60. Clementi, E.; Corongiu, G. B-DNA structural determination of  $Na^+$  counterions at different humidities, ionic concentrations, and temperatures. *J. Quant. Chem.* **1982**, *22*, 595–630.
61. Seibel, G.L.; Singh, U.C.; Kollman, P.A. A molecular dynamics simulation of double-helical DNA including counterions and water. *J. Am. Chem. Soc.* **1985**, *82*, 6537–6540.
62. Swaminathan, S.; Ravishanker, G.; Beveridge, D.L. Molecular dynamics of B-DNA including water and counterions: a 140-ps trajectory for d(CGCGAATTCGCG) based on the GROMOS force field. *J. Am. Chem. Soc.* **1991**, *113*, 5027–5040.
63. York, D.M.; Darden, T.; Deerfield, D.; Pedersen, L.G. The interaction of Na(I), Ca(I), and Mg(II) metal ions with duplex DNA: a theoretical modeling study. *Int. J. Quant. Chem.* **1992**, *19*, 145–166.
64. MacKerell, A.D. Influence of magnesium ions on duplex DNA structural, dynamics and solvation properties. *J. Phys. Chem., B* **1997**, *101*, 646–650.
65. Cheatham, T.E., III; Kollman, P. Molecular dynamics simulations highlight the structural differences among DNA:DNA, RNA:RNA, and DNA:RNA hybrid duplexes. *J. Am. Chem. Soc.* **1997**, *119*, 4805–4825.
66. Young, M.A.; Ravishanker, D.; Beveridge, D.L. A 5-nanosecond molecular dynamics trajectory for B-DNA: analysis of structure, motions and solvation. *Biophys. J.* **1997**, *73*, 2313–2336.
67. Young, M.A.; Jayaram, B.; Beveridge, D.L. Intrusion of counterions into the spine of hydration in the minor groove of B-DNA: fractional occupancy of electronegative pockets. *J. Am. Chem. Soc.* **1997**, *119*, 59–69.
68. Lyubartsev, A.P.; Laaksonen, A. Molecular dynamics simulations of DNA in solution with different counterions. *J. Biomol. Struct. Dyn.* **1998**, *16* (3), 579–591.
69. Young, M.A.; Beveridge, D.L. Molecular dynamics simulations of an oligonucleotide duplex with adenine tracts phased by a full helix turn. *J. Mol. Biol.* **1998**, *281*, 675–687.
70. Feig, M.; Pettitt, B.M. A molecular simulation picture of DNA hydration around A- and B-DNA. *Biopolymers* **1998**, *48*, 199–209.
71. Feig, M.; Pettitt, B.M. Modelling high-resolution hydration patterns in correlation with DNA sequence and conformation. *J. Mol. Biol.* **1999**, *286*, 1075–1095.
72. Beveridge, D.L.; McConnel, K.J. Nucleic acids: theory and computer simulation, Y2k. *Curr. Opin. Struct. Biol.* **2000**, *10*, 182–196.
73. Cornel, W.D.; Cieplak, P.; Bayly, C.I.; Gould, I.R.; Merz, K.M.; Ferguson, D.M.; Spellmeyer, D.C.; Fox, T.; Caldwell, J.W.; Kollman, P.A. A second generation force field for the simulation of proteins, nucleic acids, and organic molecules. *J. Am. Chem. Soc.* **1995**, *117*, 5179–5197.
74. Mackerell, A.D.; Bashford, D.; Bellott, M.; Dunbrack, R.L.; Evanseck, J.D.; Field, M.J.; Fischer, S.; Gao, J.; Guo, H.; Ha, S.; Joseph-McCarthy, D.; Kuchnir, L.; Kuczera, K.; Lau, F.T.K.; Mattos, C.; Michnick, S.; Ngo, T.; Nguyen, D.T.; Prodhom, B.; Reiher, W.E.; Roux, B.; Schlenkrich, M.; Smith, J.C.; Stote, R.; Straub, J.; Watanabe, M.; Wiórkiewicz-Kuczera, J.; Yin, D.; Karplus, M. All-atom empirical potential for molecular modeling and dynamics studies of proteins. *J. Phys. Chem., B* **1998**, *102*, 3586–3616.
75. Feig, M.; Pettitt, B.M. Sodium and chlorine ions as part of the DNA solvation shell. *Biophys. J.* **1999**, *77*, 1769–1781.
76. Drew, H.R.; Dickerson, R.E. Structure of a B-DNA dodecamer: III. Geometry of hydration. *J. Mol. Biol.* **1981**, *151*, 535–556.
77. Steffl, R.; Koca, J. Unrestrained molecular dynamics simulations of  $[d(AT)_5]_2$  duplex in aqueous solution: hydration and binding of sodium ions in the minor groove. *J. Am. Chem. Soc.* **2000**, *122*, 5025–5033.
78. McFail-Isom, L.; Sines, C.C.; Williams, L.D. DNA structure: cations in charge? *Curr. Opin. Struct. Biol.* **1999**, *9*, 298–304.
79. McConnell, K.J.; Beveridge, D.L. DNA structure: What's in charge? *J. Mol. Biol.* **2000**, *304*, 803–820.
80. van Dam, L.; Lyubartsev, A.P.; Laaksonen, A.; Nordenskiöld, L. Self-diffusion and association of  $Li^+$ ,  $Cs^+$ , and  $H_2O$  in oriented DNA fibers. An NMR and MD simulation study. *J. Phys. Chem., B* **1998**, *102*, 10,636–10,642.
81. Auffinger, P.; Westhof, E. Water and ion binding around r(UpA)<sub>12</sub> and d(TpA)<sub>12</sub> oligomers—comparison with RNA and DNA (CpG)<sub>12</sub> duplexes. *J. Mol. Biol.* **2001**, *305*, 1057–1072.

82. Bevan, D.R.; Lee, L.; Pedersen, L.G.; Darden, T.A. Molecular dynamics simulations of the d(ccaacgttg)<sub>2</sub> decamer: influence of the crystal environment. *Biophys. J.* **2000**, *78*, 668–682.
83. Bryson, K.; Greenall, R.J. Binding sites of the polyamines putrescine, cadaverine, spermidine and spermine on A- and B-DNA located by simulated annealing. *J. Biomol. Struct. Dyn.* **2000**, *18*, 393–412.
84. Korolev, N.; Lyubartsev, A.P.; Nordenskiöld, L.; Laaksonen, A. Spermine: an “invisible” component in the crystals of B-DNA: A grand canonical Monte Carlo and molecular dynamics simulation study. *J. Mol. Biol.* **2001**, *308* (5), 907–917.
85. Korolev, N.; Lyubartsev, A.P.; Laaksonen, A.; Nordenskiöld, L. On the competition between water, sodium ions and spermine in binding to DNA: a molecular dynamics computer simulation study. *Biophys. J.* **2002**, *82*, 2860–2875.
86. Lyubartsev, A.P.; Laaksonen, A. Calculation of effective interaction potentials from radial distribution functions: a reverse Monte Carlo approach. *Phys. Rev., E* **1995**, *52* (4), 3730–3737.



# Molecular Switches

Jean-Pierre Launay  
Christophe Coudret  
Christian Joachim

*Centre d'Elaboration de Matériaux et d'Etudes Structurales (CEMES),  
Centre National de la Recherche Scientifique (CNRS), Toulouse, France*

## INTRODUCTION

A switch is an ensemble of pieces whose function is to stop and/or establish the electrical current in a circuit.<sup>[1]</sup> This 19th century definition of a switch continues to be valid in our days. But because of the requirement of better communication means during the 20th century, the pieces of our modern switches are no more mechanical or electromechanical in nature. In our information society era which uses plenty of communication and computation machines, the many switches constituting those machines are now made of solid-state semiconducting materials. After the relay and the vacuum tube, the microfabricated transistor is the modern reference of an integrated switch at the surface of a silicon wafer. Furthermore, not only electrical current, but also photons flux, magnetic flux, etc. have now their own switches, expanding the possibility of miniaturizing a switch to other types of material, such as dielectrics and ferromagnets.

A human operator was supposed to operate a switch in the 19th century. The increasing complexity of circuitry made this operator to disappear to the benefit of a third electrode per switch. In electronics, a switch is now a three-terminal device. The “on/off” triggering information is generally provided to a given switch by another one inside the circuit, without involving the operator. Taking the transistor as reference for switch performances, there is now a continuous demand for a further reduction of the weight, the size, the power consumption, and the switching time of the solid-state switches.

One solution is to reduce the amount of material required to fabricate a transistor by improving the lithographic technique, engraving a transistor on an always smaller and smaller portion of the surface of a semiconductor wafer. A radically new approach was proposed by Aviram and Ratner in 1974.<sup>[2]</sup> Instead of continuing the miniaturization of the transistor at the surface of a wafer by inventing new lithography techniques, why not go all the way down to the atomic scale. Here the next big step is to create switches whose

pieces are simple organic molecules and even a few atoms bound together to form a single molecule. Those switches are called molecular switches. In principle, they can control an electron flux or, for example, a photon flux in a photonic circuit.

What remains unchanged is the kernel of the definition of a switch: whatever the amount of material assembled or bonded to fabricate a switch (a condensed phase, a macromolecule, a few molecules, a single molecule), a switch must have two states (the “on” and “off” states) well separated to ensure the stability of both the “on” and the “off” states. Behind the scene, there is often an internal physical or chemical variable to describe the state of the material assembled to constitute the switch. This is independent of the physical or chemical effect triggering the switch and whatever the flux to be controlled. Along a reaction coordinate proper to each kind of switch, a double-well energy curve can often be plotted (Fig. 1) defining the “on,” the “off” states of the switch, and the transition region. But in simple monostable molecular switches, only one well is existing. The well is simply deformed or displaced by the triggering effect. The double-well case gives rise to bistable molecular switches: in a few examples, the same value of the triggering parameter can maintain both the “on” and the “off” state depending on the history of the switching event, i.e., there is a memory effect (note that conventional switches for domestic applications are usually bistable, but electronic switches such as transistors are only monostable). The memory corresponds to a hysteresis effect related to a cooperative phenomenon often obtained with molecular material molecular switches.<sup>[3]</sup>

In practice, mainly molecular electronic switches are explored. The reason is that the exchange of information between a given molecular switch and other molecular switches in the same circuit requires communication and interconnections means adapted to the size of ultimately a single molecule. Electrons have a much more practical wavelength than photons for this purpose. Furthermore, a tunnel junction is a very useful source of tunneling electrons where a

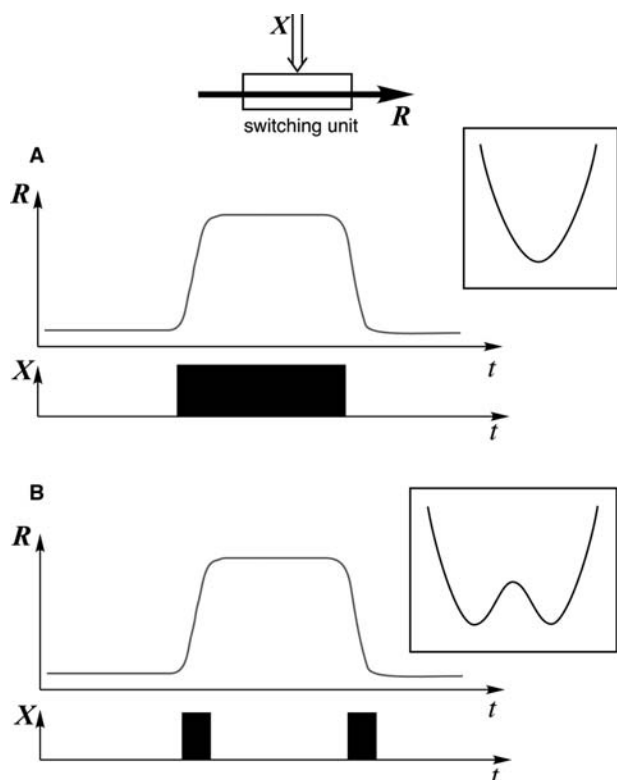


**Fig. 1** Topology of a switch.  $R$  is the response and  $X$  the switching action. (A) Monostable switch: the response comes back to its original value as soon as the switching action ceases; (B) bistable switch: the response remains modified after the end of the switching action (memory effect). Inserts: energy curves describing the state of a switch as a function of an internal coordinate. In the case of the bistable switch, an energy barrier separates the two states, permitting the memory effect.

molecule can be positioned on, like a jumper. Of course, such positioning is still very delicate to perform experimentally, taking into account the necessity to know exactly at the atomic scale the conformation and the exact position of the molecule in the junction. The invention of the scanning tunnel microscope (STM) in 1981<sup>[4]</sup> arrived exactly on time to show experimentally as early as in 1988<sup>[5]</sup> that such electrical interconnection between a single molecule and a macroscopic operator was possible.

Many experiments on molecular switches are still performed by averaging the answer of the molecules over many and even billions of the same type. This increases the signal-to-noise ratio and amplifies the signal to be measured. In those experiments, each molecule is supposed to be non-interacting with the others, so that the switching ability depends only on one class of molecules. Using many instead of one is not only a matter of convenience. This approach can speed up the exploration of new molecular switches, by separating two otherwise intricate problems: obtaining a switching effect and positioning one molecule on a surface.

In this entry, we shall consider first “chemical switches,” i.e., systems based on a chemical reaction, or on a cooperative process involving many molecules. Thus although the change in properties between the “on” and “off” states can be spectacular, it is not, in principle, possible to reach the truly monomolecular scale. Then we shall see the case of monomolecular switches, this latter goal being now strongly boosted by technological and fundamental purposes. There will be two variants: first “intrinsic” molecular switches, i.e., molecules which present a special sensitivity to an external perturbation, with a bistable character, and can be studied in solution, in particular for screening purposes; the second variant will be “surface bound” molecular switches, really interconnected to an electrical circuit, which implies a strong interaction with the surface, so that the switching effect comes actually from the molecule–surface ensemble.

## CHEMICAL SWITCHES

### Simple Chemical Conversions

A frequently encountered concept of molecular switch in chemistry is based on the abrupt variation of a property linked to a chemical concentration of some species, that could be detected by various optic or electrochemical measurement. In the most common approach, this is achieved by selecting a reversible chemical reaction for which the two processes back and forward are kinetically very fast compared to the time scale of the experiment. This is strongly reminiscent of colored indicators used in classic analytical chemistry. If we consider a set of species  $A$ ,  $B$ , and  $X$ , the concentrations of which are controlled by the following equilibrium  $A = B + X$ , then one can easily show that the concentrations of species  $A$  and  $B$  (and thus any macroscopic property linked to their concentrations, such as color, etc.) will vary quickly over a limited domain of  $-\log [X]$  values. Thus the latter parameter can be used as a control parameter. It is usually  $\text{pH}$  ( $X = \text{H}^+$ ), it can also be  $\text{pX}$  for another ion or the potential of an electrode. The switching effect is obtained by circulating around the “threshold” value  $-\log K$  (Fig. 2).

Sophisticated systems have been designed in order to exploit the output signal. One can indeed read out the switching by light (either in absorption, i.e., a color change, or in emission, i.e., a luminescence change) or by an electrochemical way, or by both. Many molecules have been proposed<sup>[6–8]</sup> for which an output signal, typically fluorescence, is triggered by chemical stimuli (Fig. 3). When several input conditions must be fulfilled, such systems even behave as logical gates.<sup>[8]</sup>

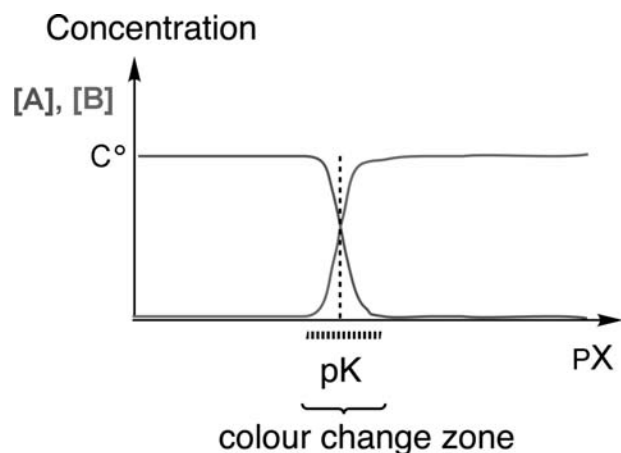


**Fig. 2** Abrupt variation of the concentration of a species (and thus of the related macroscopic property) around the threshold value.

However, as these switches are based on a quantitative conversion of a macroscopic population of molecules, in practice one has to add a sufficient amount of species X to the solution in order to read the signal related to compound A, then to add a chemical that has a better affinity toward X to set free the compound B. Thus a “switching cycle” involves an *ordered* sequence of *irreversible* mixing steps and reversible chemical reactions steps. This leads to the accumulation of the products resulting from the necessary second chemical reaction and of solvent. Thus the

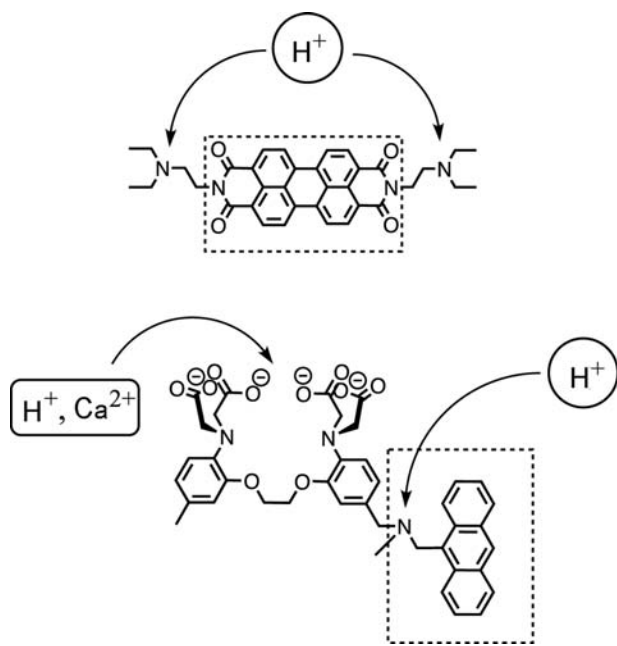


**Fig. 3** Switching of fluorescence by either  $H^+$ , (From Ref.<sup>[7]</sup>) or a combination of  $H^+$  and  $Ca^{2+}$  Source: From Ref.<sup>[8]</sup>.

intervention of an operator is absolutely necessary, to open or close taps to add chemicals, playing the same role as ancient telephone operators from the 19th century, before the introduction of the third terminal on each switch.

Ways to suppress the use of an external operator have been proposed. First, the states of different switches or molecules can be coupled by the exchange of another chemical species, for instance  $H^+$ .<sup>[9]</sup> In addition, it is possible to devise systems based on chemical reactors with reactions far from equilibrium, where several steady states can exist. For instance, in the case of “kinetic bistability,”<sup>[10]</sup> an abrupt variation can occur when the system passes through a bifurcation. Finally, the most spectacular developments would be the control of the state of the switch by an oscillating reaction. Such reactions have been used as a way to design logic gates, based on the propagation of chemical waves in a two-dimensional (2-D) non-stirred reactor containing an excitable media.<sup>[11]</sup> This would represent an archetype of a neuronal computer, because a living cell such as a neuron can be viewed as an out-of-equilibrium reactor.

### Molecules in Interaction: Cooperativity

A large class of works is related to switching effects involving molecules in interaction, constituting a molecular material. In some circumstances, one can achieve appealing characteristics for information storage, such as a sharp transition and even a hysteresis. The most typical example is given by spin-transition systems.<sup>[3]</sup> They involve paramagnetic coordination complexes with two possible states, a low-spin one and a high-spin one, the high-spin situation being favored by temperature. If the molecules are without interaction, the state of an individual molecule is governed by Boltzmann statistics, and only a gradual transition occurs when the temperature is raised. But an interesting situation arises when a positive cooperativity occurs, i.e., when the high-spin state of a molecule is favored by the presence of other high-spin molecules in its vicinity. Then, as shown by a simple model, the transition from low-spin to high-spin can be very sharp, and in some cases, a hysteresis appears, corresponding to a memory effect (Fig. 4). This has been the basis of a number of propositions to realize memory devices. In particular, the possibility to switch the system state by light, and not only temperature, has greatly expanded the potential for applications.<sup>[3]</sup>

However, in such systems, the switching effect relies inherently on the cooperativity parameter, i.e., the presence of many molecules. There is strictly no way to downsize the device to one molecule.

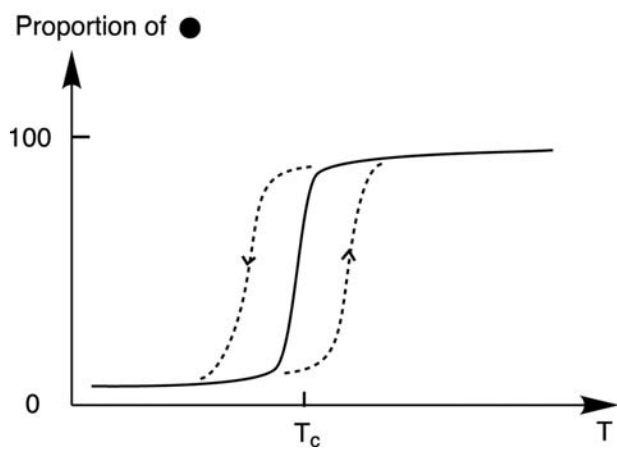
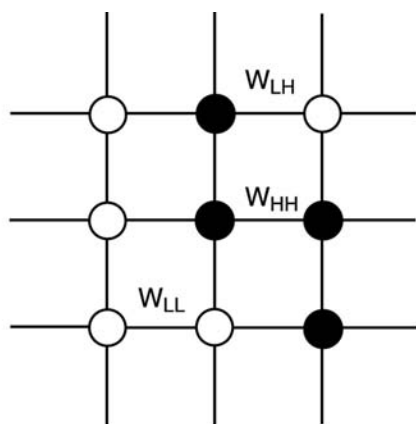


**Fig. 4** Cooperativity and abrupt transition. Up: array of interacting molecules, each presenting two states, for instance  $\circ$  = low-spin state (L), and  $\bullet$  = high-spin state (H).  $W_{LH}$ ,  $W_{HH}$ , and  $W_{LL}$  designate the interaction energies between molecules. Bottom: response (proportion of  $\bullet$ ) as a function of temperature. An abrupt transition occurs, as shown, when the cooperativity parameter is positive, i.e.,  $\frac{1}{2}(W_{HH} + W_{LL}) > W_{HL}$ . In some cases a hysteresis can appear (dotted lines).

### Chemical Bimolecular Reactions Involving a Change of an Intramolecular Process

En route for miniaturization, let us consider now the attempts to switch “on” and “off” an intramolecular transfer process of electrons. In this section we wish to present some examples of switches operated by a bimolecular reaction where the switching unit requires a modification of its composition or electronic configuration (Fig. 5), usually by a *chemical* reaction.

All of the chemical approaches of the problem imply the synthesis of rather complicated molecules made of a pair of groups A, B, the energetic or electronic configuration of which will prove the transfer, and a switching unit able to respond to a chemical stimulation such as an ion complexation, a redox reaction, or even a more “classic” organic chemistry

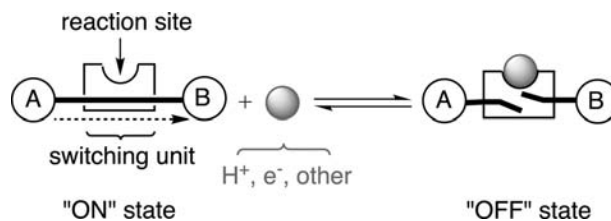


**Fig. 5** Switch made of two outer sites and a central switching unit sensitive to a chemical agent.

reaction. Following natural phenomena, two types of transfer have also been explored: energy transfer and electron transfer.

Energy is a rather difficult communication vector to control, because, after light absorption by a molecule, creating an electronically excited state, the energy tends to relax as heat to other parts of the molecule or to the surrounding. This dissipation is unavoidable. However, smart molecules have been devised, allowing cascading the energy through an array of chromophores. The switching effect is then obtained either by uncoupling the chromophores, or most commonly by creating a temporary energy sink. Some examples<sup>[12,13]</sup> are given in Fig. 6.

Switching an electron transfer along a molecular wire may sound easier as the electron should not vanish. Among the best systems explored are mixed valence systems, basically composed of at least two almost identical redox centers: they are differing only by one excedentary electron. Hence such a molecule undergoes a permanent intramolecular redox reaction, reflecting the electron quantum exchange between the two sites. This redox process is simply described in terms of a double wellled energy landscape as a function of a reaction coordinate. Switching is now based on changing the coupling between the two redox states. This can be achieved for example by changing the set of molecular orbital of the bridge by an acid–base reaction<sup>[14]</sup> or even a Diels–Alder reaction<sup>[15]</sup> (Fig. 7).

Finally, for such chemically sensitive switches, although the molecules do not interact with themselves, the input requires a chemical reaction and the output is a population-averaged property. Consequently, these switches will be hardly downsized to a single molecule.

### MONOMOLECULAR SWITCHES (I): INTRINSIC MOLECULAR SWITCHES

#### Model Molecules Studied in Solution

Here we consider molecules for which the barrier is large enough (Fig. 1), defining two states, “on” and “off,” that we assume of nearby energies. This

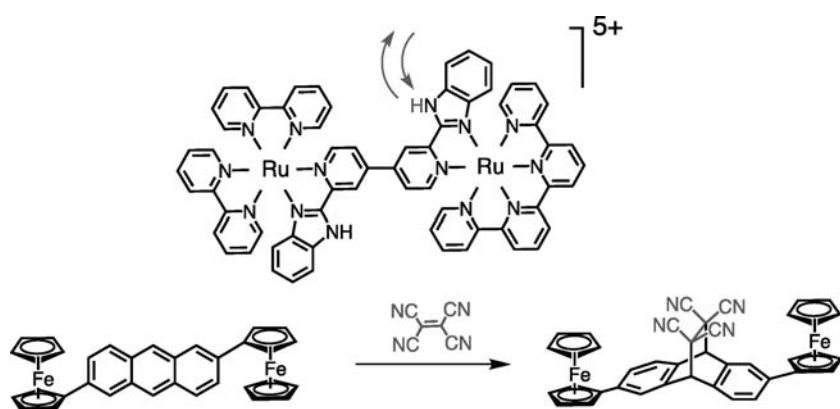
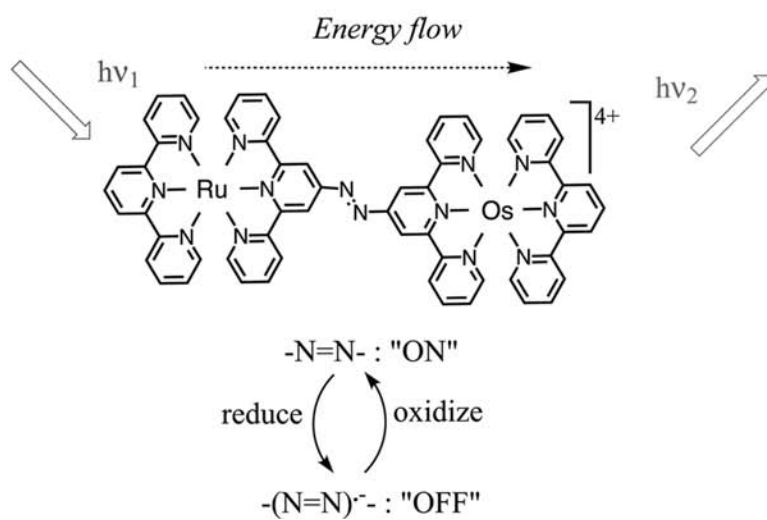
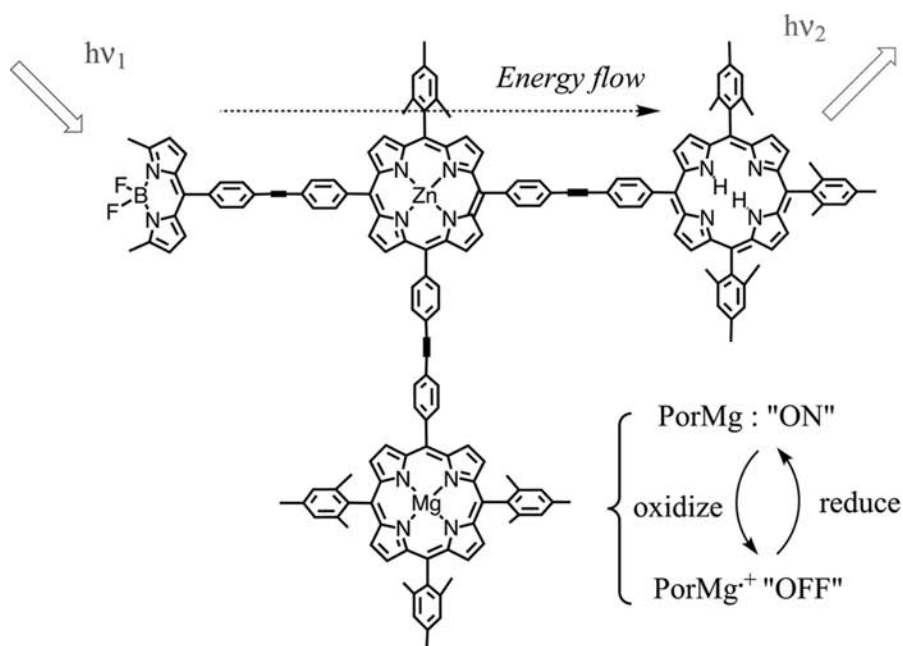


**Fig. 6** Switches based on the control of an intramolecular energy flow by a redox group. Up: association of porphyrins. From Ref.<sup>[13]</sup>. Bottom: use of an azo group. Source: From Ref.<sup>[13]</sup>.

**Fig. 7** Switches based on the control of an intramolecular electron transfer by a chemical agent. Up: protonation/deprotonation. From Ref.<sup>[14]</sup>. Bottom: adduct formation. Source: From Ref.<sup>[15]</sup>.



corresponds to an intrinsic bistability, which persists even when the molecules are isolated. The transformation is actually an isomerization reaction, i.e., a unimolecular process that does not require the reactant molecules, but can be activated by a physical process. The description is based on a simple double-well energetic landscape.

Certain compounds undergo a light-induced one. This usually leads to a deep change in the light absorption properties and is therefore called photochromism. In such a process, a molecule is brought in its Franck-Condon excited state upon absorbing a suitable photon  $h\nu_1$  and then starts to relax back to its ground state (Fig. 8). However, for this type of compound two isomeric ground states are available. A careful choice of the system can lead to a quantitative isomerization of the starting compound. An identical process but with another light of energy  $h\nu_2$ , or if the activation barrier is low, simply heating can be used as a way to reverse the populations.

Photochromism has been widely used to demonstrate the basic principle of switching, because the photochemical transformation is an elegant way to transform, at the macroscopic scale, one form into another, and these forms remain usually unchanged

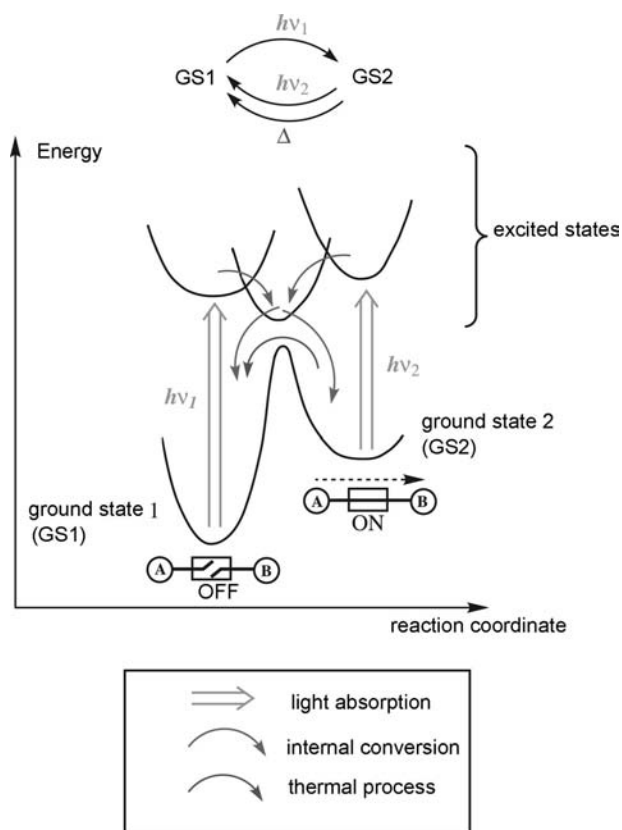


**Fig. 8** Potential energy curves involved in photochromic switches. The switching action drives the system from one potential well to the other, via high energy excited states.

after the irradiation. Following the approach mentioned in the previous section, several teams have presented molecules able to switch “on” and “off” an intramolecular “interaction” parameter.

Regarding the switching unit, any photochromic moiety could be used in principle, but the recent work has focused on diarylethene-based molecules, in which a photocyclization/ring reopening process occurs. They present indeed distinct advantages: they show excellent photochromic characteristics (stability, reversibility, quantum yield, etc.), but above all, the two states correspond to very different states of conjugation of an extended framework, thus heralding very different electronic properties, and finally, the geometry does not change very much during the photocyclization process, thus facilitating their incorporation in large supermolecules or assemblies.

The first members of the series were described independently by Irie,<sup>[16]</sup> and Gilat, Kawai, and Lehn<sup>[17]</sup> and this initiated a bunch of studies where photochromism has been associated to other properties. The change in absorption properties between the two photoisomers is already a signature of the large change in delocalization along the molecular skeleton. But, upon connection of redox sites of the pyridinium family, it is possible in addition to modifying the electrochemical properties.<sup>[17]</sup> Other variants have been described. For instance, the introduction of a fluorescent unit allows the change in the emission response.<sup>[18]</sup> The association with a hyperpolarizable group led to a modification of the non-linear optical properties.<sup>[19]</sup> Chiro-optical switching effects have also been described.<sup>[20]</sup> Grafting paramagnetic sites on each side of the central unit allowed the demonstration of switching an intramolecular exchange interaction parameter.<sup>[21]</sup> Finally, with redox sites of the Ruthenium(cyclometallated) family, it has been possible to switch “on” and “off” an intramolecular intervalence electron transfer,<sup>[22]</sup> i.e., a process which constitutes for mixed-valence molecules the equivalent of the conductance for a nanojunction (Fig. 9).

Thanks to the versatility of diarylethene chemistry, it is even possible to realize more complex functions than just switching. Playing with electrochemical and photophysical properties can lead to elaborate responses such as write/read/erase, which could be useful for the realization of molecular-based memories.<sup>[23]</sup>

As photochromic compounds are addressed by light, the response is typically the one of an ensemble of molecules, usually without interactions. But it is possible in principle to record signals corresponding to a unique isolated molecule. This has been achieved quite recently by Irie et al. who observed by confocal microscopy the signal of single molecules of a dithienylethene-bis(phenylethynylanthracene) dyad embedded in a polymer film.<sup>[24]</sup>



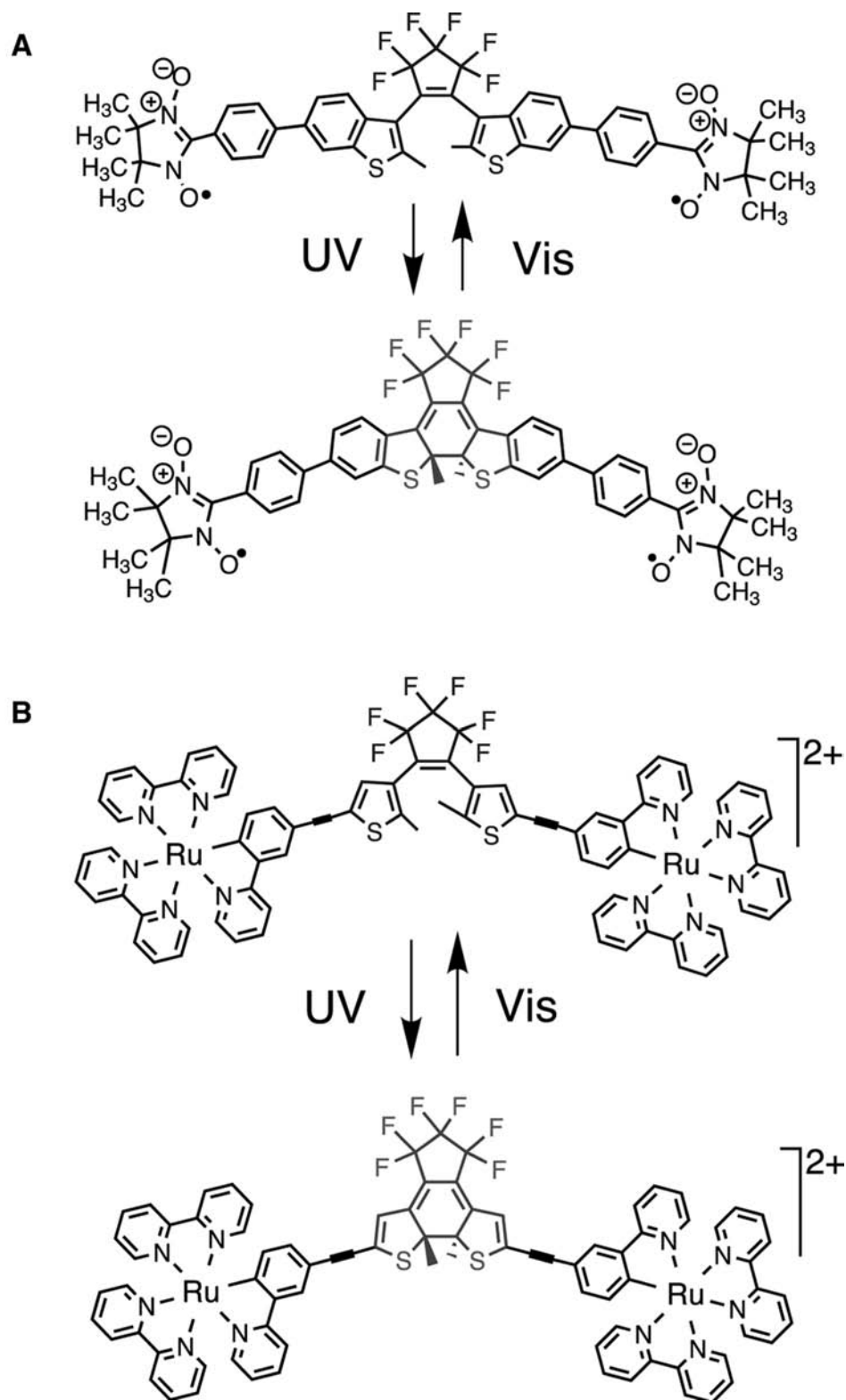


**Fig. 9** Photochromic switches based on diarylethenes. (A) Control of an exchange interaction between magnetic centers; From Ref.<sup>[21]</sup>. (B) control of an intramolecular electron transfer between redox sites. *Source:* From Ref.<sup>[22]</sup>.

## Electrical Studies on an Ensemble of Molecules

In this section, more recent molecules with an intrinsic “bistable” design are presented. They are destined to be supported by a surface, following the recent evolution of the technology to manipulate molecules at the surface of a solid. Therefore they can be triggered from the “on” to the “off” states by the application of an electric field when sandwiched between two metallic electrodes. As they are chemically designed to be adsorbed on a surface, the ultimate goal here is to electronically connect one molecule at a time. This field was opened by Aviram who synthesized in the 1980s a hemiquinone molecule well adapted to be attached to a surface. The switch was intrinsic and triggered by an electric field with double-well-potential-like characteristics. The first STM measurements were attempted in 1987 in IBM laboratories.<sup>[5]</sup> But at that time, the available equipment did not permit to reach a firm conclusion about the switching effect.<sup>[25]</sup>

This first experiment was nevertheless a prelude to studies aiming at the demonstration of electronic functions of molecules when disposed as thin monomolecular layers, in particular rectification. This latter goal was finally achieved by Metzger in 1997.<sup>[26]</sup> Since then and in relation to the switching problem, a large number of fascinating families of molecules equipped with different groups have been synthesized for this purpose. For example, the catenanes and rotaxanes molecular switches are based on the concept of “threading,” i.e., they contain two parts which cannot separate without breaking a bond.<sup>[27,28]</sup> The active parts used to control a motion are donor and acceptor moieties which can be associated through weak interactions, but because these moieties are kept in proximity by the special topology of the molecule and cannot fully separate, the association reaction is actually a monomolecular reaction analogous to an isomerization. Despite the flexibility inherent to large molecules presenting a large number of possible torsions, the number of pertinent conformations they can adopt is relatively limited, typically two, because of the unique topology of the system. They correspond to the location of a mobile part (the “shuttle”) in front of two possible “stations” (Fig. 10). Such molecules can be studied first in solution, where the acceptor/donor character of a moiety can be reversed by electrochemistry, and then can be transferred and used in solid-state devices.

Many examples have been described by Luo et al. The active molecules were deposited as Langmuir-Blodgett (LB) monolayers on an *n*-polycrystalline silicon substrate and covered by a Ti/Al top electrode, thus giving a two-terminal device of monomolecular thickness. The response was then probed by a method analogous to the remnant polarization method used

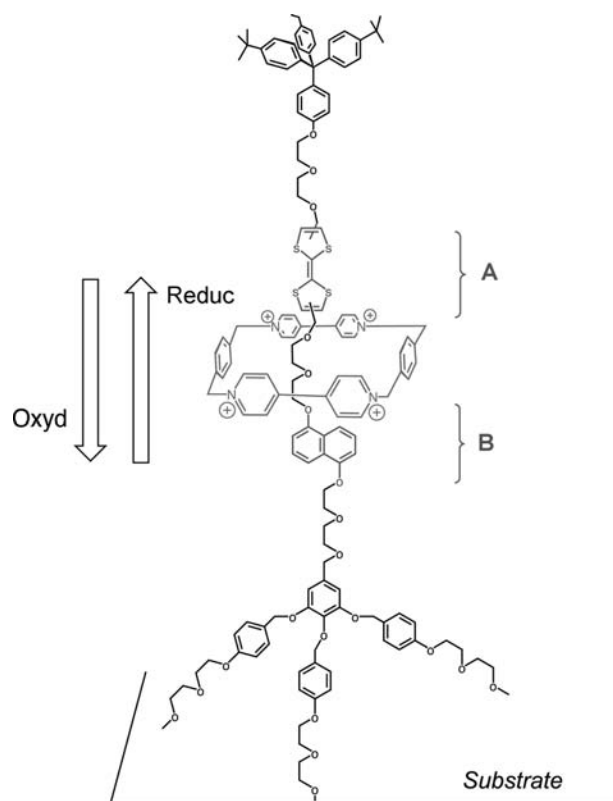
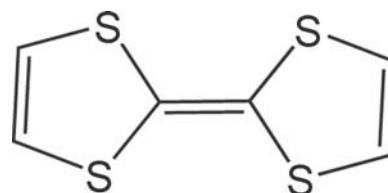


**Fig. 10** Molecular shuttle with two stations, A and B. The motion is controlled by the electrochemical oxidation of the TTF unit (station A). *Source:* From Ref.<sup>[29]</sup>.

for ferroelectric devices, i.e., scanning a voltage range while measuring the current at a low perturbing voltage, to avoid capacitance effects.<sup>[29]</sup> The basic signature of a switching effect is then the appearance of a hysteresis curve, associated with the existence of two possible conformations with different electron transport properties. Note that the perturbation here is an oxidation/reduction of a moiety, transforming, for instance, a donor tetrathiafulvalene (TTF) Scheme 1 into an acceptor (TTF<sup>+</sup>). This is basically an electrochemical process, requiring in solution the intervention of a counter ion. It is not clear how such a process occurs in the solid-state device based on a monolayer.

Although several control experiments show that a two-station structure is necessary to obtain a switching



**Scheme 1**

effect, the exact interpretation remains obscure, because the molecules contain several other flexible parts, and their exact orientation in the LB layer, as well as the geometry of the contacts with the interfaces, is not readily accessible to experiment.

Another series of molecules was designed and studied by Tour, Reed, et al.<sup>[30,31]</sup> They are made of several (phenylene ethynylene) groups with thiol end groups for attachments on electrodes (“alligator clips”). These molecules are then used either in a nanopore cell (Fig. 11), allowing the contacting of an ensemble of molecules (ca.  $10^3$ ) between a substrate and an evaporated upper electrode. The molecules form a self-assembled monolayer (SAM) and, because of the small size of the pore (30–50 nm), a defect-free ensemble can be expected. The interesting behavior resides in the appearance of a negative differential resistance effect (NDR), an effect tentatively assigned to the rotation of a phenylene group and/or charge injection under the influence of the applied voltage.

Looking further, although these devices are two-terminal ones, they can be of some use in electronics circuitry. The construction of a 2-D crossbar arrangement, with such layers of molecules at the nodes, would give an electronic circuit with a little amount of molecular material at the node in a defect-tolerant architecture similar to what was proposed in the 1960s.

## MONOMOLECULAR SWITCHES (II): SURFACE MOLECULAR SWITCHES

The end of the miniaturization roadmap for molecular switches is a single molecule connected between two, or if possible three, electrodes. This requires an underneath surface that will support the molecule and the nanoelectrodes. The surface can be active or passive in the definition of the molecular switch. The switching ability of the molecule can be intrinsic to the molecule, as mentioned in the previous section, or it can be created by the interaction of the molecule with the surface.

As an example of the first possibility, we can mention the recent experiment by Dulic et al.<sup>[32]</sup> who succeeded in contacting a photochromic switch of the diarylethene family with two electrodes, by the “break-junction” technique. The switching of the nanojunction conductance was observed, but in one direction only (from “on” toward “off”), due to the quenching effect of the metal surface.

We now consider the second possibility, i.e., systems strongly dependent on the interaction with a surface. The first real demonstration that an object of the size of a single atom can switch “on” and “off” a current was experimentally observed by Eigler et al. using a Xe atom switching back and forth under the tip of an STM at very low temperature.<sup>[33]</sup> This is a surface atomic switch whose double-well potential is created

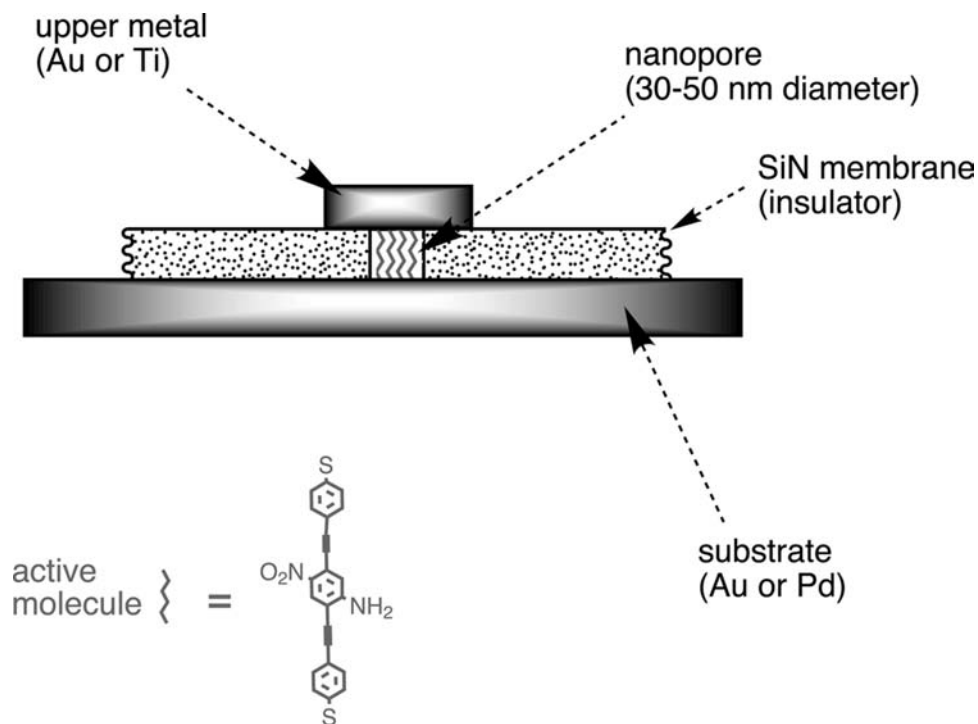


**Fig. 11** The “nanopore” setup. Each nanopore is filled by several thousands of active molecules. *Source:* From Ref.<sup>[30]</sup>.

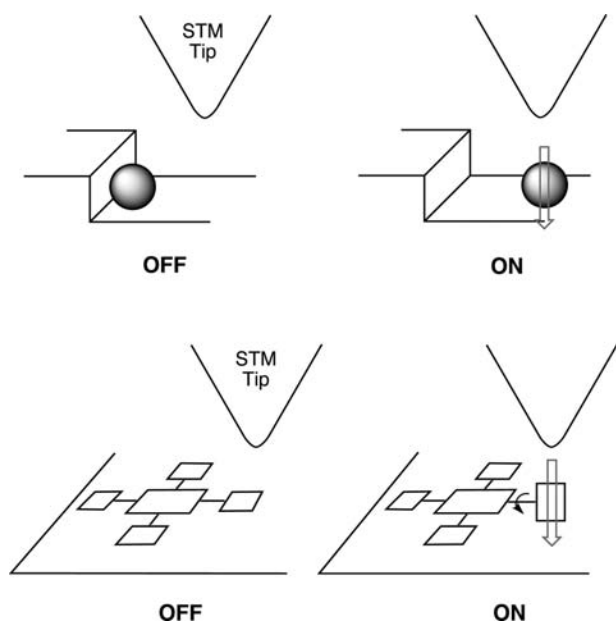


**Fig. 12** Atomic and molecular switch on a surface. Up: Eigler's atomic switch using the positioning of a Xe atom. From Ref.<sup>[33]</sup>. Bottom: molecular switch based on the rotation of a porphyrin "leg" out of the molecular plane. Source: From Ref.<sup>[34]</sup>.

on the surface by the van der Waals trap created by the tip apex for the "on" state and by a nearby monoatomic step edge for the "off" state. The tip-apex-to-surface applied electric field is used to pass the atom from one well to the other (Fig. 12).

The first double-well, truly single-molecular switch was experimentally observed in 2001.<sup>[34]</sup> It results from a peculiar property of the adsorption of a leg porphyrin molecule on metal surface. On a Cu(100) surface, the four legs of this molecule are almost perpendicular to the surface. On a Cu(111) surface, the four legs are flat on the surface, the central porphyrin being attracted by the 111 surface state of copper. The fabrication procedure was to adsorb the molecule on a Cu(211) surface which presents 111 facets separated by monoatomic steps. Some molecules adsorb on the edge of a step with three legs on the 111 facet and one at the step edge. The three legs are flat but the fourth one is found in a metastable state. Its most stable position is, of course, flat on the lower terrace. But this leg is now a bit too far to the down facet compared to the three others legs. Therefore it prefers to stay perpendicular to the surface (Fig. 12, bottom part). This creates a double-well potential for the

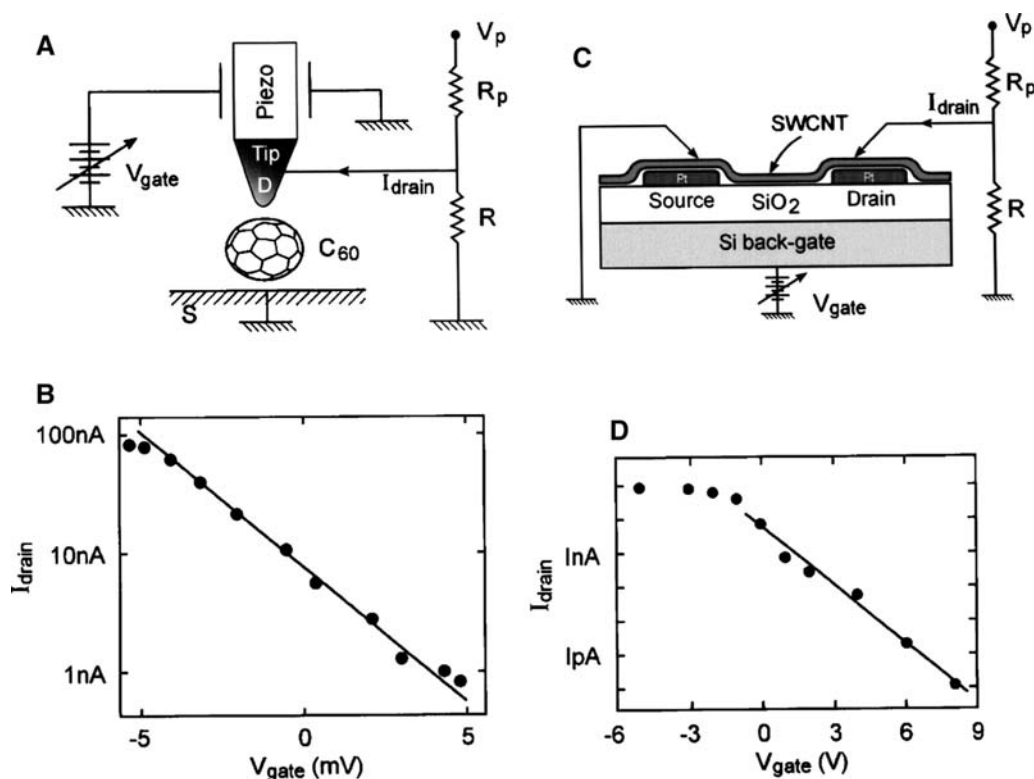


**Fig. 13** The variation of the drain-source current intensity as a function of the gate voltage for the original  $C_{60}$  single-molecule amplifier and the original single-carbon nanotube transistor. This variation corresponds to the slope of the passage from an "off" to an "on" state in a mono-stable switch (Fig. 1). Source: Reproduced with permission from Nature, 2000, 408, p. 541. © 2000, McMillan Magazines Limited.

configuration energy of this leg. The barrier can be overcome by pushing on the leg by the tip apex of the STM. The “on” and “off” states are defined for the same altitude of the tip apex on the switching leg. The “on” and “off” electrical resistance of this single intramolecular switch has been measured together with the energy required to switch on/off the leg. The on/off current difference in this molecular switch is due to a control of the electronic coupling between the tip and the surface through the molecular legs. It is large when the leg is perpendicular to the surface and low when parallel.

Another way to change the electronic coupling between the tip and the surface using a single molecule is to change the homo–lumo gap of the molecule. A simple experimental way is to deform the molecule by pressing on it with the tip apex. The  $C_{60}$  single-molecule amplifier is an example of such a device<sup>[35,36]</sup> as shown in Fig. 13. Used in its blocked-saturated mode, this is a monostable molecular switch. The  $C_{60}$  device beneficiaries from the high degeneracy of its homo and lumo orbitals, a degeneracy yielding to a low transparency toward electrons because of destructive interference effects through the molecule. By compressing the  $C_{60}$ , this degeneracy is raised, giving rise to a very fast increase of the tunnel current through the  $C_{60}$  molecule in this compressed state. A  $C_{60}$  molecular device can be used as a switch but also as a transistor. This had opened the way to simulate very complex hybrid molecular circuits made of more than 600  $C_{60}$  transistors interconnected together by a standard metallic circuit to test how high impedance and low gain transistors may still be used to design simple processors.<sup>[37]</sup>

A macromolecular version of the  $C_{60}$  single molecule switch was proposed in 2003 using a single-wall carbon nanotube positioned on a mesoscopic junction.<sup>[38]</sup> To create a monostable switch, the tip of an AFM is brought from the top of the device to deform the tube in the center of the device (Fig. 12). Depending on the chirality of the tube, its band gap can be closed or opened, modifying the resistance of the junction. With a good trans-conductance, carbon nanotube electronic transistors have also been fabricated using a third top metallic electrode like the grid of a field effect transistor.<sup>[39]</sup> Those mesoscopic devices are at the down limit of microelectronics where the source–drain distance of the transistor is of the dimension of a macromolecule.

## CONCLUSION

The different approaches of “molecular switches” are displayed in Fig. 14, according to the type of switching action and the type of measured response. In addition,

		Response (R)			
		electrical	mechanical	optical	magnetic
Switching action (X)	electrical	○ a ○ b		● k ● l	
	mechanical	☺ c ☺ e ☺ d			
optical	☺ f ● g	☺ j	● m ● n ☺ o	● q	
chemical	● h ● i		● p		

**Fig. 14** Chart of the different types of molecular switches, according to the type of switching action, and the type of response. ●: Experiments performed on a statistical ensemble, leading to a relatively large device; ○: on a few molecules (ca. 1000); on one molecule. *Source:* From the following teams: a: Pease, Luo;<sup>[27,29]</sup> b: Tour, Donhauser;<sup>[30,31]</sup> c: Joachim and Gimzewski;<sup>[35,36]</sup> d: Moresco;<sup>[34]</sup> e: Tans;<sup>[39]</sup> f: Dulic;<sup>[32]</sup> g: Fraysse;<sup>[22]</sup> h: Gonzalo;<sup>[15]</sup> i: Haga;<sup>[14]</sup> j: Hugel;<sup>[40]</sup> k: Akasaka;<sup>[13]</sup> l: Holten;<sup>[12]</sup> m: Irie;<sup>[16]</sup> n: Gilat;<sup>[17]</sup> o: Irie;<sup>[24]</sup> p: Daffy, de Silva;<sup>[7,8]</sup> q: Matsuda.<sup>[21]</sup>

a third characteristic is important, i.e., the scale at which the system works: a large statistical ensemble, a few molecules, or ultimately one. Only in this last case can we expect to take the full benefit of miniaturization and really reach the domain of molecular electronics, where the major question is about the fundamental limits.

Like any devices, a molecular switch is characterized by its performance such as its switching time and the energy required to change the status of the switch. For a single molecular switch interconnected between two electrodes, it has not yet been possible to measure the switching time. This is due to the large resistance of a metal–molecule–metal tunnel junction of the order of  $1\text{ G}\Omega$  for a single organic molecule, down to a few megaohms for macromolecule molecular switches such as a single-wall carbon nanotube (SWCNT). The RC constant of the switch is mainly controlled by the product of this resistance by the line capacitance, the latter of the order of a few picofarads. This leads to a minimum observable switching time of a few microsecond. Of course, the isomerization of a single molecule takes less than a few picoseconds. Here it is the way the device is built which sets up the limit, not the intrinsic limitation of the molecule itself.

Measuring the energy associated with a single-molecule geometrical change is a technological challenge but has been realized, for instance, with azobenzene molecules by monitoring their mechanical properties.<sup>[40]</sup> In the case of a surface electrical molecular switch, the energy required to switch “on” and “off” has been recently measured using a new

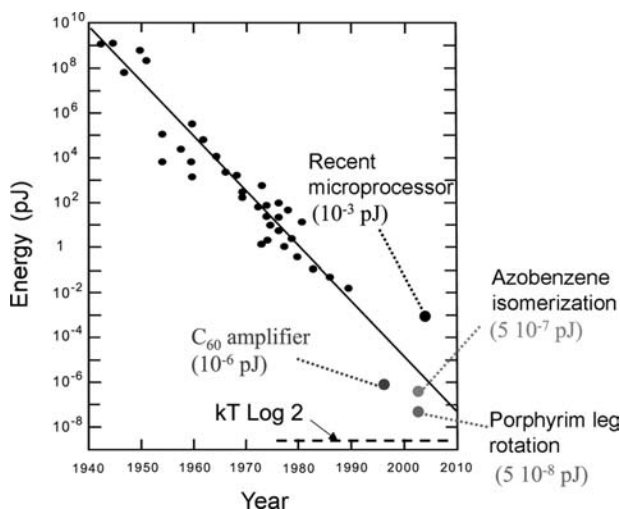


Fig. 15 Switching energy as a function of time. The approach of fundamental limits. Source: From Ref.<sup>[42]</sup>.

near-field microscope: the non-contact UHV AFM microscope.<sup>[41]</sup> The tip apex of the AFM oscillates on the surface and the tip apex altitude is decreased progressively toward the surface. This permits in a dynamic way to record the interaction force between the tip apex and the surface, giving access to the interaction energy. This instrument was used on the leg porphyrin switch to record the energy required to switch “off” the switch. The tip apex is located on the chosen switchable leg of the molecule and the force–distance curve recorded. The switching energy found is about  $5 \times 10^{-20}$  J (7 kcal/mol), which is four orders of magnitude lower than the state-of-the-art semiconductor technology transistor. It is interesting to report this value on the diagram proposed some years ago by Keyes,<sup>[42]</sup> in which the energy dissipated per logic operation is displayed (in logarithmic units) as a function of date (Fig. 15). One sees that the trend toward smaller and smaller energy consumption continues and raises the question of the absolute limit.

Thus aside from its technological applications, a molecular switch is becoming a very interesting nano-device to study the thermodynamic limits of switching. With a value as low as 7 kcal/mol, one is very close to the  $kT \log 2$  limit, considered as the minimum energy necessary to drive any switching device interacting with a thermal bath at a temperature  $T$ .<sup>[43]</sup>

## REFERENCES

1. The Academic Press Dictionary of Science and Technology, Academic Press: San Diego, 1991.
2. Aviram, A.; Ratner, M.A. Molecular rectifiers. *Chem. Phys. Lett.* **1974**, *29*, 277–283.
3. Kahn, O.; Martinez, C.J. Spin transition polymers: from molecular materials toward memory devices. *Science* **1998**, *279* (5347), 44–48.
4. Behm, R.J.; Garcia, N.; Rohrer, H. *Scanning Tunneling Microscopy and Related Methods*; Kluwer Academic Publishers: Dordrecht, 1990.
5. Aviram, A.; Joachim, C.; Pomerantz, M. Evidence of switching and rectification by a single molecule effected with a scanning tunneling microscope. *Chem. Phys. Lett.* **1988**, *146*, 490.
6. Rurack, K.; Resch-Genger, U. Rigidization, preorientation and electronic decoupling—the magic triangle for the design of highly efficient fluorescent sensors and switches. *Chem. Soc. Rev.* **2002**, *31* (2), 116–127.
7. Daffy, L.M.; de Silva, A.P.; Gunaratne, H.Q.N.; Huber, C.; Lynch, P.L.M.; Werner, T.; Wolfbeis, O.S. Arenedicarboximide building blocks for fluorescent photoinduced electron transfer pH sensors applicable with different media and communication wavelengths. *Chem. Eur. J.* **1998**, *4* (9), 1810–1815.
8. de Silva, A.P.; McClenaghan, N.D. Proof-of-principle of molecular-scale arithmetic. *J. Am. Chem. Soc.* **2000**, *122* (16), 3965–3966.
9. Raymo, F.M.; Giordani, S. Signal communication between molecular switches. *Org. Lett.* **2001**, *3* (22), 3475–3478.
10. Reckley, J.S.; Showalter, K. Kinetic bistability in the permanganate oxidation of oxalate. *J. Am. Chem. Soc.* **1981**, *103* (23), 7012–7013.
11. Steinbock, O.; Kettunen, P.; Showalter, K. Chemical wave logic gates. *J. Phys. Chem.* **1996**, *100* (49), 18,970–18,975.
12. Holten, D.; Bocian, D.F.; Lindsey, J.S. Probing electronic communication in covalently linked multiporphyrin arrays. A guide to the rational design of molecular photonic devices. *Acc. Chem. Res.* **2002**, *35* (1), 57–69.
13. Akasaka, T.; Otsuki, J.; Araki, K. Redox-responsive molecular switches based on azoterpyridine-bridged Ru/Os complexes. *Chem. Eur. J.* **2002**, *8* (1), 130–136.
14. Haga, M.-a.; Meser Ali, M.; Koseki, S.; Fujimoto, K.; Yoshimura, A.; Nozaki, K.; Ohno, T.; Nakajima, K.; Stufkens, D.J. Proton-induced tuning of electrochemical and photophysical properties in mononuclear and dinuclear ruthenium complexes containing 2,2'-bis(benzimidazol-2-yl)-4,4'-bipyridine: Synthesis, molecular structure and mixed-valence state and excited-state properties. *Inorg. Chem.* **1996**, *35* (11), 3335–3347.
15. Gonzalo, V.; Coudret, C.; Patoux, C.; Launay, J.P. Modulation of intramolecular electronic coupling in 2,6-diferrocenylanthracene via a Diels–Alder reaction with TCNE. *C. R. Acad. Sci., Ser. IIC* **1999**, *2* (5–6), 321–328.
16. Irie, M. Diarylethenes for memories and switches. *Chem. Rev.* **2000**, *100* (5), 1685–1716.
17. Gilat, S.L.; Kawai, S.H.; Lehn, J.M. Light-triggered molecular devices: Photochemical switching of optical and electrochemical properties in molecular wire type diarylethene species. *Chem. Eur. J.* **1995**, *1* (5), 275–284.
18. Fernandez-Acebes, A.; Lehn, J.M. Optical switching and fluorescence modulation properties of photochromic



- metal complexes derived from dithienylethene ligands. *Chem. Eur. J.* **1999**, *5* (11), 3285–3292.
19. Majumdar, D.; Lee, H.M.; Kim, J.; Kim, K.S.; Mhin, B.J. Photoswitch and non linear optical switch: theoretical studies on 1,2-bis-(3-thienyl)-ethene derivatives. *J. Chem. Phys.* **1999**, *111* (13), 5866–5872.
  20. Feringa, B.L.; van Delden, R.A.; Koumura, N.; Geertsema, E.M. Chiroptical molecular switches. *Chem. Rev.* **2000**, *100* (5), 1789–1816.
  21. Matsuda, K.; Matsuo, M.; Mizoguti, S.; Higashiguchi, K.; Irie, M. Reversed photoswitching of intramolecular magnetic interaction using a photochromic bis(2-thienyl)ethene spin coupler. *J. Phys. Chem., B* **2002**, *106* (43), 11,218–11,225.
  22. Fraysse, S.; Coudret, C.; Launay, J.P. Synthesis and properties of dinuclear complexes with a photochromic bridge: an intervalence electron transfer switching “on” and “off”. *Eur. J. Inorg. Chem.* **2000**, (7), 1581–1590.
  23. Kawai, S.H.; Gilat, S.L.; Ponsinet, R.; Lehn, J.M. A dual-mode molecular switching device: Bisphenolic diarylethenes with integrated photochromic and electrochromic properties. *Chem. Eur. J.* **1995**, *1* (5), 285–293.
  24. Irie, M.; Fukaminato, T.; Sasaki, T.; Tamai, N.; Kawai, T. A digital fluorescent molecular photoswitch. *Nature* **2002**, *420* (6917), 759–760.
  25. Aviram, A.; Joachim, C.; Pomerantz, M. Erratum to “evidence of switching and rectification by a single molecule effected with a scanning tunneling microscope”. *Chem. Phys. Lett.* **1989**, *162*, 416.
  26. Metzger, R.M. Unimolecular electrical rectifiers. *Chem. Rev.* **2003**, *103* (9), 3803–3834.
  27. Pease, A.R.; Jeppesen, J.O.; Stoddart, J.F.; Luo, Y.; Collier, C.P.; Heath, J.R. Switching devices based on interlocked molecules. *Acc. Chem. Res.* **2001**, *34* (6), 433–444.
  28. Raehm, L.; Sauvage, J.-P. Molecular machines and motors based on transition metal-containing rotaxanes and catenanes. *Struct. Bond.* **2001**, *99*, 55–78.
  29. Luo, Y.; Collier, C.P.; Jeppesen, J.O.; Nielsen, K.A.; Delonno, E.; Ho, G.; Perkins, J.; Tseng, H.R.; Yamamoto, T.; Stoddart, J.F.; Heath, J.R. Two-dimensional molecular electronics circuits. *ChemPhysChem* **2002**, *3* (6), 519–525.
  30. Tour, J.M.; Rawlett, A.M.; Kozaki, M.; Yao, Y.X.; Jagessar, R.C.; Dirk, S.M.; Price, D.W.; Reed, M.A.; Zhou, C.W.; Chen, J.; Wang, W.Y.; Campbell, I. Synthesis and preliminary testing of molecular wires and devices. *Chem. Eur. J.* **2001**, *7* (23), 5118–5134.
  31. Donhauser, Z.J.; Mantooh, B.A.; Kelly, K.F.; Bumm, L.A.; Monnell, J.D.; Stapleton, J.J.; Price, D.W.; Rawlett, A.M.; Allara, D.L.; Tour, J.M.; Weiss, P.S. Conductance switching in single molecules through conformational changes. *Science* **2001**, *292* (5525), 2303–2307.
  32. Dulic, D.; van der Molen, S.J.; Kudernac, T.; Jonkman, H.T.; de Jong, J.D.; Bowden, T.N.; van Esch, J.; Feringa, B.L.; van Wees, B.J. One-way optoelectronic switching of photochromic molecules on gold. **2003**, *91*, 207–402.
  33. Eigler, D.M.; Lutz, C.P.; Rudge, W.E. An atomic switch realized with a scanning tunneling microscope. *Nature* **1991**, *352*, 600–603.
  34. Moresco, F.; Meyer, G.; Rieder, K.H.; Tang, H.; Gourdon, A.; Joachim, C. Conformational changes of single molecules induced by scanning tunneling microscopy manipulation: A route to molecular switching. *Phys. Rev. Lett.* **2001**, *86* (4), 672–675.
  35. Joachim, C.; Gimzewski, J.K. An electromechanical amplifier using a single molecule. *Chem. Phys. Lett.* **1997**, *265* (3-5), 353–357.
  36. Joachim, C.; Gimzewski, J.K.; Tang, H. Physical principles of the single-C-60 transistor effect. *Phys. Rev., B* **1998**, *58* (24), 16,407–16,417.
  37. Ami, S.; Joachim, C. Logic gates and memory cells based on single C<sub>60</sub> electromechanical transistor. *Nanotechnology* **2001**, *12*, 44.
  38. Minot, E.D.; Yaish, Y.; Sazonova, V.; Park, J.Y.; Brink, M.; McEuen, P.L. Tuning carbon nanotube band gaps with strain. *Phys. Rev. Lett.* **2003**, *90*, 156401.
  39. Tans, S.J.; Devoret, M.H.; Dai, H.; Thess, A.; Smalley, R.E.; Geerligs, L.J.; Dekker, C. Individual single wall carbon nanotubes as quantum wires. *Nature* **1997**, *386*, 474.
  40. Hugel, T.; Holland, N.B.; Cattani, A.; Moroder, L.; Seitz, M.; Gaub, H.E. Single-molecule optomechanical cycle. *Science* **2002**, *296* (5570), 1103–1106.
  41. Loppacher, C.; Guggisberg, M.; Pfeiffer, O.; Meyer, E.; Bammerlin, M.; Luthi, R.; Schlittler, R.; Gimzewski, J.K.; Tang, H.; Joachim, C. Direct determination of the energy required to operate a single molecule switch. *Phys. Rev. Lett.* **2003**, *90* (6), art. no.-066107.
  42. Keyes, R.W. Miniaturization of electronics and its limits. *IBM J. Res. Develop.* **1988**, *32* (1), 24–28.
  43. Landauer, R. Dissipation and noise immunity in computation and communication. *Nature* **1988**, *335*, 779–784.

# Molecular Switches and Motors

Richard A. van Delden

Ben L. Feringa

Department of Organic and Molecular Inorganic Chemistry,  
University of Groningen, Groningen, The Netherlands

## INTRODUCTION

The fascinating principles exploited by nature to control organization, switching, and motion are a major source of inspiration for the design and synthesis of artificial molecular systems with such functions. The highly efficient retinal *cis-trans* photoisomerization in the process of vision is a superior example of a molecular switch,<sup>[1,2]</sup> and the intriguing biomolecular motors<sup>[3]</sup> set an extremely high standard for the development of synthetic counterparts. The bottom-up construction of switches and motors, with the realization of machines and robotics of nanosize dimensions as the ultimate goal, offers a formidable challenge to scientists. Synthetic approaches toward artificial machinery have already resulted in several molecular systems whereby switching and/or motion is controlled by means of chemical, electrochemical, photochemical, or thermal input.<sup>[4–6]</sup> For instance, molecular propellers,<sup>[7]</sup> brakes,<sup>[8]</sup> switches,<sup>[9]</sup> turnstiles,<sup>[10]</sup> ratchets,<sup>[11]</sup> and shuttles<sup>[12,13]</sup> have been constructed. Catenanes and rotaxanes have shown to be particularly promising systems in the development of molecular machines.<sup>[14–17]</sup> Jimenez, Dietrich-Buchecker, and Sauvage,<sup>[18]</sup> for example, reported the contraction and stretching of a linear rotaxane dimer resembling a natural muscle at work,<sup>[19]</sup> and Chia et al.<sup>[20]</sup> demonstrated the threading and dethreading of rotaxanes assembled on a surface. Recently, Hugel et al.<sup>[21]</sup> reported the first single molecule machine based on photoactive azo dyes.

In this entry, we do not attempt to give a complete and detailed overview of all molecular switches and motors developed thus far and the reader is referred to various reviews. Molecular switches, based on a large variety of principles, have been reviewed extensively.<sup>[9]</sup> Molecular motors found in nature as well as synthetic counterparts are reviewed elsewhere.<sup>[22]</sup> We will focus on systems based on sterically overcrowded alkenes, in which light is used to induce switching or motion, to illustrate several of the key principles involved.

## STERICALLY OVERCROWDED ALKENES AS CHIROPTICAL MOLECULAR SWITCHES

In a chiral approach toward molecular switches, the unique properties associated with stereoisomers of chiral photoresponsive molecules are exploited. The two stereoisomers of such photochromic compounds represent the distinct states of a light-switchable digital molecular system (Fig. 1).

Chiroptical techniques offer the attractive feature that the change in chirality of the photochromic system<sup>[23]</sup> can be detected. A major advantage of chiroptical switches is that nondestructive readout is feasible by monitoring the change in optical rotation at wavelengths remote from the wavelengths used for switching. Another important advantage of using chiral photochromic compounds is that they can be employed to control other (chiral) properties, e.g., the organization of a liquid crystalline phase.

### Chiral Switches Based on Enantiomers

A direct way of controlling chirality in a molecular switching system is by using the interconversion between two enantiomers by chiral light (Fig. 2). Schuster et al.<sup>[24,25]</sup> have published switchable systems which function under the influence of circularly polarized light. The switching process we envisioned involves the interconversion of the (*P*)- and (*M*)-enantiomers of helically shaped, inherently dissymmetric alkenes.

The possible photoisomerization steps are the following: 1) irradiation with circularly polarized light (CPL) will lead to a small excess of one of the two enantiomers starting from a racemate; 2) alternating irradiation with (*l*)- and (*r*)-CPL at a certain wavelength will result in a modulation between both enantiomers; and 3) irradiation with linear polarized or unpolarized light results again in a racemic (*P,M*)-mixture.

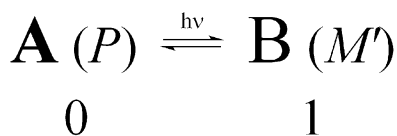


**Fig. 1** Chiroptical molecular switch based upon stereoisomers A and B with different chirality.

Decisive factors for a successful molecular switch based on enantiomers are as follows: 1) irradiation with CPL should not cause any photodestruction; 2) the enantiomers should have sufficiently high  $g$ -values ( $g$  = anisotropy factor); and 3) the quantum efficiency for photoracemization should be high, as the rate of photoresolution is exponentially related to this quantity. Out of a large number of sterically overcrowded chiral alkenes that were synthesized and resolved, helically shaped alkene **1** meets these requirements (Scheme 1).<sup>[26]</sup> The enantiomers of **1** are stable at ambient temperatures and are fatigue-resistant. This overcrowded alkene shows structural resemblance to helicenes, and large CD absorptions and optical rotations are found. A stereospecific photoisomerization takes place that reverses the helicity of the molecules.

Starting from racemic **1**, switching between photostationary states with small enantiomeric excesses (0.07%) of (*P*)- and (*M*)-**1** was accomplished by irradiation with (*l*)- and (*r*)-CPL, respectively. This demonstrates that chiral light can be used to switch a molecular system from one handedness to the other. Such a switching behavior on the molecular level might have potential in developments toward molecular integrated systems or optical data storage units, for example, by employing liquid crystalline matrices (vide infra). The selectivity of switching is, however, severely limited by the theoretical limitations of the concept.<sup>[27]</sup>

### Chiral Switches Based on Pseudoenantiomers

A way of circumventing the major limitations predicted and encountered in enantiomeric switches is by the use of pseudoenantiomeric photochromic molecules. Inspired by the efficient switching of retinal in the human eye,<sup>[28]</sup> the design of pseudoenantiomeric chiroptical switches is again based on sterically overcrowded alkenes (Scheme 2).<sup>[29,30]</sup> As for **1**, the intrinsic (helical) chirality originates from a distortion of the molecular framework leading to (*M*)- and (*P*)-helices.

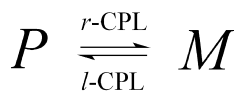
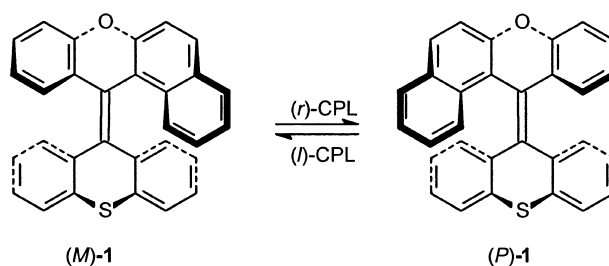


**Fig. 2** Schematic representation of a molecular switch based on enantiomers.

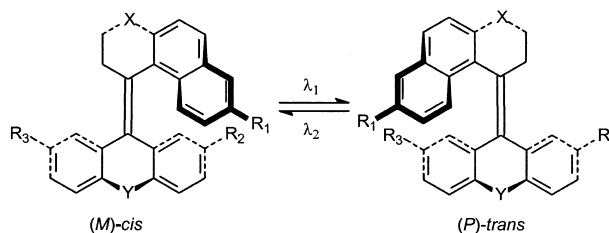


**Scheme 1** Circularly polarized light switch based on sterically overcrowded alkene **1**.

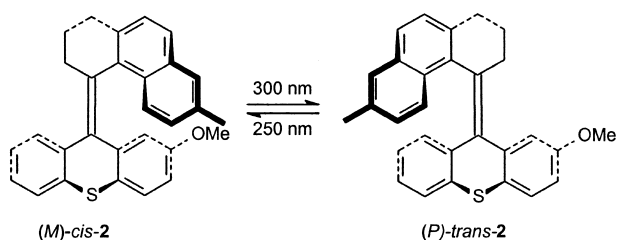
Both forms of the overcrowded alkene feature a *cis*- and a *trans*-stilbene chromophore in the same molecule. A photochemically induced *cis*–*trans* isomerization results in reversal of the helicity. Because of the near mirror-image relation of the two pseudoenantiomers, such a system offers a way to control molecular chirality merely by changing the wavelength of the light employed.

The first chiroptical switching process was realized with thioxanthene-based alkenes (*M*)-*cis*-**2** and (*P*)-*trans*-**2** (Scheme 3).<sup>[31]</sup> Irradiation of enantiomerically pure (*M*)-*cis*-**2** in *n*-hexane solution at 300 nm resulted in a photostationary state consisting of 64% (*M*)-*cis*-**2** and 36% (*P*)-*trans*-**2** because of different UV absorptions of the (*M*)-*cis* and (*P*)-*trans*-isomers (vide infra). Using 250-nm wavelength light, a photostationary state of 68% (*M*)-*cis*-**2** and 32% (*P*)-*trans*-**2** was reached. Alternated irradiation at 250 and 300 nm resulted in a photomodulation between these two photostationary states. It should be noted that after 20 switching cycles, 10% racemization was observed because of a relatively low racemization barrier. A second drawback is the relatively low switching efficiency of this prototype system. Both drawbacks can be overcome by synthetic modification.

It was found that the racemization barriers could be tuned over a range of approximately 50 to above 125 kJ mol<sup>-1</sup> by modification of the bridging atoms X and Y in the upper and lower half of the inherently dissymmetric alkenes (Scheme 2).<sup>[32]</sup> The effect of increasing the size of X and Y is that the naphthalene



**Scheme 2** General scheme of a chiroptical molecular switch based on pseudoenantiomers of a sterically overcrowded alkene.



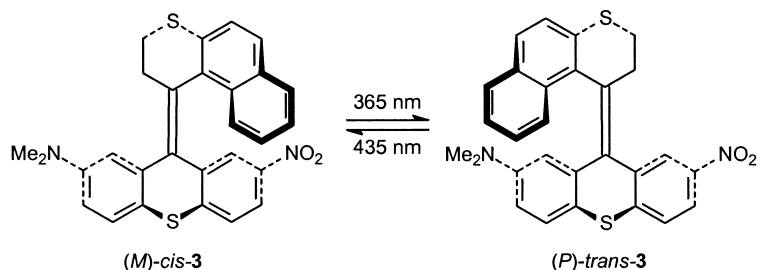
**Scheme 3** The first chiroptical molecular switch based on a sterically overcrowded alkene **2**.

unit of the upper half is pushed toward the lower half, and as a consequence, the steric hindrance at the so-called *fjord region* and the barrier for racemization are increased. For instance, going from  $Y = O$  to  $S$ , the Gibbs energy of activation for the racemization process increases from 91.2 to 120.9 kJ mol<sup>-1</sup>.

In a switching process, which is based on the difference in UV/Vis absorption of two states of a photochromic molecular system, the switching efficiency is linearly related to the ratio of the UV/Vis absorptions of the isomers [following Eq. (1)]. The ratio of the two extinction coefficients at a certain wavelength, together with the ratio of the quantum yields ( $\Phi$ ) for interconversion of the two forms, determines the photostationary state ratios. The ratio of the two extinction coefficients of a photochromic switch is wavelength-dependent, and this is a decisive factor for the selectivity of the switch.

$$\frac{[cis]}{[trans]} = \frac{\epsilon_{trans}}{\epsilon_{cis}} \frac{\Phi_{trans \rightarrow cis}}{\Phi_{cis \rightarrow trans}} \quad (1)$$

To increase the stereoselectivity of the photochromic process, a dimethylamino electron-donating substituent and a nitro electron-withdrawing substituent were introduced in the lower half (Scheme 4).<sup>[33,34]</sup> This asymmetric substitution results in relatively large differences in the UV/Vis absorption characteristics of the two pseudoenantiomers (Fig. 3A). Maxima in the ratio of extinction coefficients of the two pseudoenantiomers are found at 365 and 435 nm. With this system, in *n*-hexane, switching between a photostationary state of 90% (*M*)-*cis*-**3** and 10% (*P*)-*trans*-**3** (435 nm) and



**Scheme 4** Donor-acceptor substituted chiroptical molecular switch **3** showing high stereoselectivity.

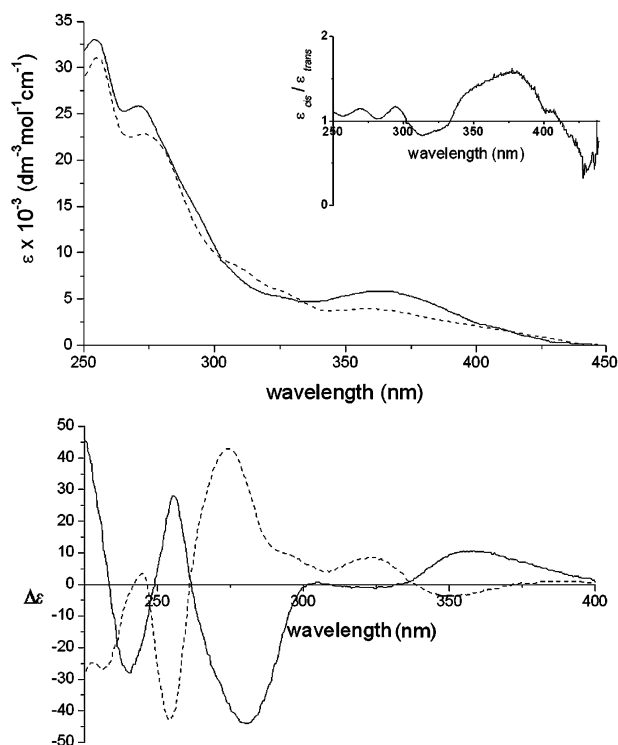


**Fig. 3** UV/Vis (top) and CD (bottom) absorption spectra of donor-acceptor switch **3** (inset: the ratio of the two extinction coefficients  $\epsilon_{cis}/\epsilon_{trans}$ ). The solid lines correspond to (*M*)-*cis*-**3** and the dashed graphs correspond to (*P*)-*trans*-**3**.

30% (*M*)-*cis*-**3** and 70% (*P*)-*trans*-**3** (365 nm) is achieved.<sup>[33]</sup> It was possible to perform 80 switching cycles without any deterioration or racemization.

Of utmost importance for further applications of chiroptical molecular switches is the pseudoenantiomeric relationship between the two isomers. This pseudoenantiomeric relation is evident from the circular dichroism (CD) spectra of the two forms (Fig. 3B). With this system, molecular chirality can effectively be controlled by changing only the wavelength of light used.

To obtain information on the necessity of both a donor and an acceptor moiety in the same molecule to induce efficient switching, the acceptor-only nitro-substituted and donor-only dimethylamine-substituted switches **4** and **5**, respectively, were synthesized

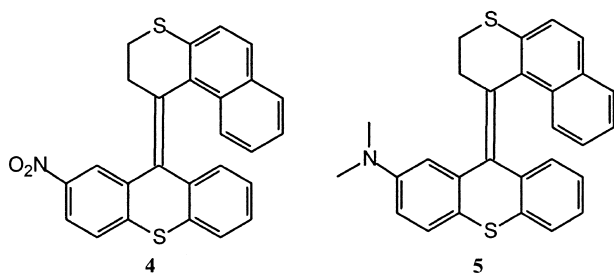


**Fig. 4** Simplified analogs of the donor–acceptor switches; acceptor-only compound **4** and donor-only compound **5**.

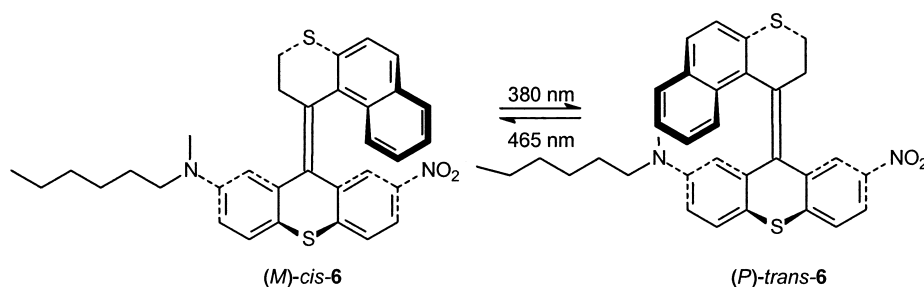
(Fig. 4). For both compounds, the wavelengths for the most selective switching process are considerably blue-shifted compared with the donor–acceptor switches because of the absence of a charge transfer absorption band, and switching selectivities for both **4** and **5** are lower than for the donor–acceptor substituted analog. Apparently, a combination of donor and acceptor substituents is a prerequisite for selective chiroptical switching in sterically overcrowded alkene systems. Therefore the concept of donor–acceptor substituted switches was further exploited.

The major drawback of **3**, which becomes of considerable importance especially when the molecule is incorporated in a liquid crystalline matrix, is low solubility and compatibility. Low compatibility leads to severe limitations with respect to the applicability of the system in an organized environment (vide infra). Donor–acceptor compound **6** was designed to increase the solubility without interfering with the switching efficiency (Scheme 5).<sup>[35]</sup> Although the UV/Vis spectra of **6** are comparable to those of its parent compound **3**, there are subtle differences resulting in slightly different photochemical behavior.

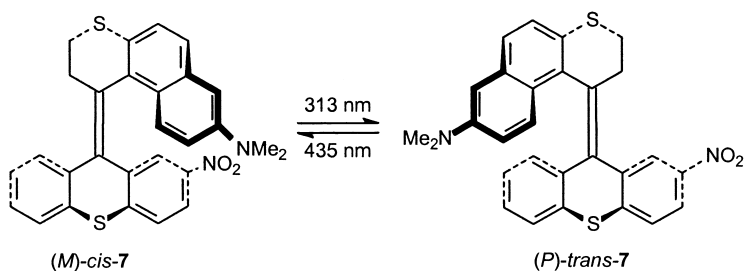
Irradiation of **6** in *n*-hexane solution at the most efficient wavelength of 380 nm resulted in the formation of a photostationary state consisting of 70% (*P*)-*trans*-**6** and 30% (*M*)-*cis*-**6**. Subsequent irradiation at 465 nm resulted in the formation of a photostationary state consisting of 98% (*M*)-*cis*-**6** and 2% (*P*)-*trans*-**6**. This system thus shows nearly quantitative switching to a *cis* photostationary state because of a slight bathochromic shift of the UV/Vis curve of the *trans*-isomer

relative to the *cis*-isomer. Although this is only a minor effect, it allows irradiation at the red edge of the spectrum to almost exclusively excite the *trans*-isomer resulting in a near quantitative switching to the *cis* photostationary state.

In another approach to change the photophysical properties of donor–acceptor switches, the relative position of the donor and acceptor substituents can be changed (Scheme 6).<sup>[36]</sup> By introducing a dimethylamino-substituent in the upper half of the switch as in **7**, the difference between the two isomers was expected to increase. In case of (*M*)-*cis*-**7**, where the donor and acceptor substituents are close together, a strong dipolar interaction between the donor and acceptor moieties is expected. The possibility for this direct interaction is absent in case of (*P*)-*trans*-**7**. Nevertheless, efficient photoisomerization was only observed in one direction strongly depending on solvent polarity. In toluene, for example, a remarkable *cis*/*trans* ratio of 99:1 was found upon irradiation at 435 nm. Switching to a state of excess, (*P*)-*trans*-**7**, however, was only possible in highly polar solvents such as, for example, dichloromethane, and even then, a maximum *trans*/*cis* ratio of only 55:45 was achieved. Although at certain wavelengths the extinction coefficient of the *cis*-isomer is higher than that of the *trans*-isomer, there is a preference for the *cis*-isomer throughout the entire spectrum and in almost any solvent. Because absorption characteristics are similar to those of **3**, in this case, apparently, the quantum yield ratio is the predominant factor for the switching selectivity. As a result of favorable donor–acceptor interaction in the excited state, a *cis*-like geometry will be preferred leading to a *cis*-ground state only slightly dependent on the wavelength used for excitation. This assumption is supported by the fact that in more polar solvents, where intramolecular dipole interactions become less important, the photostationary states are increasingly shifted to the *trans*-isomer. Compound **7** can, in principle, be used in a write-once type of molecular information storage system where, starting from the *trans*-state, information is written very efficiently with a diastereomeric ratio up to 99:1 (in toluene solution) in preference of the *cis*-state.



**Scheme 5** *n*-Hexyl modified donor–acceptor switch **6**.



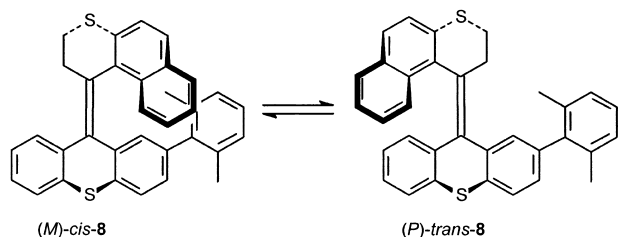
**Scheme 6** Alternative chiroptical molecular switch **7** with donor group in upper half and acceptor group in lower half of the molecule.

## Special Molecular Switches

The above examples show that sterically overcrowded alkenes allow control of molecular chirality and offer a binary switch system on a molecular level. The next examples aim to further exploit this chiroptical switching concept toward control over other functions or toward more sophisticated photochromic systems.

### Controlled Molecular Rotation

An approach toward a functional switch involves the control of the rotation around a single bond in a photoswitchable molecule modified with a biaryl-type rotor.<sup>[37]</sup> Photoisomerization between the (*M*)-*cis*-**8** and the (*P*)-*trans*-**8** form should cause a distinct difference in rotation rate for the biaryl rotation because steric hindrance on the rotor is completely different for the two pseudoenantiomers (Scheme 7). Dynamic nmr studies revealed barriers for the biaryl rotation of  $\Delta G^\ddagger = 4.54$  and  $4.71 \text{ kJ mol}^{-1}$  for the *cis*- and *trans*-isomer, respectively. In contrast with expectation, but in agreement with semiempirical calculations, the barrier for the *trans*-compound was higher than for the *cis*-compound. The observed isomerizations were attributed to distinct differences in the chiral conformations and steric effects associated with folding in the molecules. Particularly, the methyl groups of the xylyl rotor meet severe steric hindrance of the  $\text{CH}_2$  groups of the upper half in *trans*-**8**, whereas the nearly planar naphthalene moiety in *cis*-**8** simply bends away during the rotary process. This system can be considered a molecular gear but suffers from



**Scheme 7** Controlled intramolecular rotation of a biaryl propeller unit in a chiroptical molecular switch **8**.

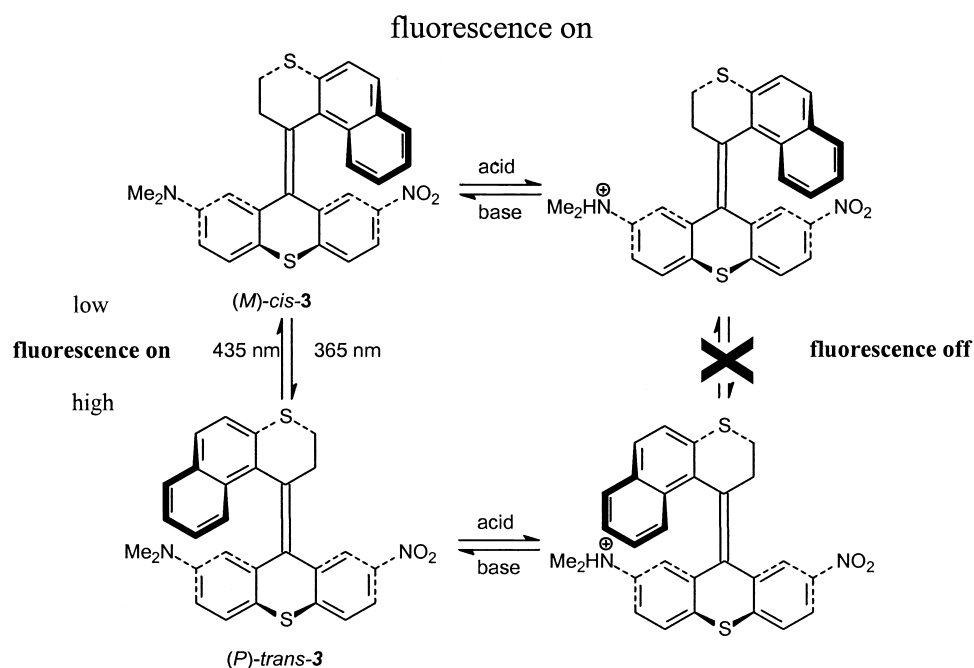
a small difference in energy barriers and inefficient photoswitching.

### Gated Response and Dual-Mode Photoswitching of Luminescence

Locking of written information is absolutely essential for optical data storage based on molecular switches. Donor–acceptor switch **3**, as a result of the presence of a basic dimethylamino-substituent, allows gated photoswitching (Scheme 8).<sup>[34]</sup> The photochemical isomerization process of both (*M*)-*cis*-**3** and (*P*)-*trans*-**3** was effectively blocked by protonation of the dimethylamine moiety which changes the lower half of the molecule from a *push–pull* donor–acceptor system to a *pull–pull* acceptor–acceptor system. The photoisomerization behavior can be restored upon subsequent deprotonation.

This protonation–deprotonation protocol does not only lead to gated response, but also has an effect on the fluorescence of the molecule, leading to a dual-mode photoswitching of luminescence. For (*M*)-*cis*-**3** in *n*-hexane, a weak fluorescence is found around 528 nm, whereas for (*P*)-*trans*-**3b**, a relatively strong fluorescent emission is observed around 531 nm. The fluorescence was found to be highly solvent-dependent. Protonation of these photochromic compounds resulted in complete quenching of the emission for both forms, whereas after deprotonation, fluorescence intensities were fully recovered. Combined with the photochemical switching, this allows for switching between three fluorescent states *on* (*trans*), *dimmed* (*cis*), and *off* (both protonated forms) by simultaneous use of light and acid/base stimuli. In circularly polarized luminescence studies, it was found that the chirality of the fluorescent excited states strongly depends on the polarity of the solvent.<sup>[38]</sup> In *n*-hexane, both (*M*)-*cis*-**3** and (*P*)-*trans*-**3** show circularly polarized luminescence of the same handedness, while in benzene, circular polarization of luminescence is opposite for (*M*)-*cis*-**3** and (*P*)-*trans*-**3**. This remarkable behavior was explained by the existence of a mutual *trans*-like luminescent excited state in *n*-hexane, where in benzene, clearly, *cis*-like as well as *trans*-like excited states can be observed. In benzene solution, this system





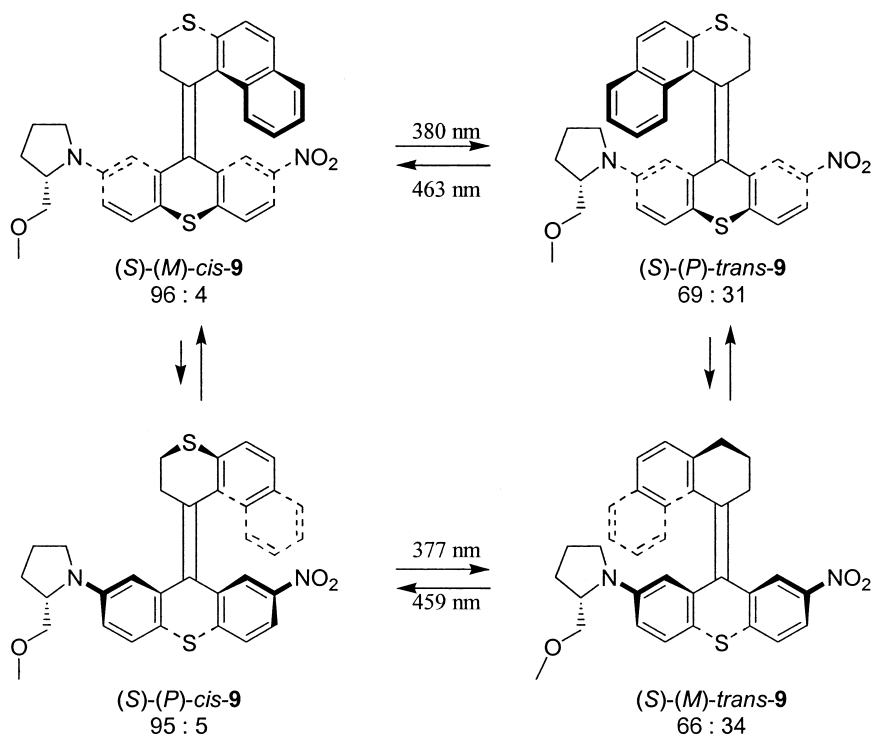
**Scheme 8** Gated photoswitching and fluorescence based on reversible protonation.

can function as a molecular modulator of circularly polarized luminescence.

### Pyrrolidine-Functionalized Molecular Switch

En route toward further functionalization of the switch skeleton in compound **9**, a chiral (*S*)-2-methoxymethyl-

pyrrolidine group was introduced as the electron donor moiety (Scheme 9). The additional stereogenic center in this molecular switch results in four distinct diastereomeric forms. As a result, the two photoequilibria are now different, and a difference in energy for the two separate *cis*- [(*S*)-(*M*)-*cis*-**9**]/[(*S*)-(*P*)-*cis*-**9**] and *trans*- [(*S*)-(*M*)-*trans*-**9**]/[(*S*)-(*P*)-*trans*-**9**] isomers of **9**



**Scheme 9** Four diastereoisomers of pyrrolidine-based chiroptical switch **9** and the isomerization pathways.

can be anticipated. For both pseudoenantiomeric couples, the ideal switching wavelengths and photostationary state ratios are summarized in Scheme 9. Switching selectivities are similar for the two diastereomeric bistable switching pairs, and functionalization of the donor part of the molecular switch has only a minor influence on the switching selectivity. This offers attractive possibilities for the use of these switch molecules in multicomponent photoactive materials.

Another interesting feature of **9** when compared with donor–acceptor switch **3** (Scheme 4) is that because of the diastereomeric relation between the respective *cis*- and *trans*-isomers, the thermal helix inversion steps are no longer true racemizations. The steady-state ratios are not 50 : 50, indicating that there is a small but significant energy difference between the two *cis*- and the two *trans*-forms of **9** (Scheme 9). This effect can be used to induce directionality in molecular rotation which might lead to molecular motors.

### Chiroptical Switching in Polymeric Matrices

In order for any molecular switch to be useful in future nanotechnological applications, the system should retain its properties when incorporated in a processable matrix. Incorporation into a polymer matrix would, for example, offer a photoswitchable film for reversible data storage. For this purpose, a polymer-bound sterically overcrowded alkene **10** was designed (Fig. 5).<sup>[39]</sup> Irradiation of thin films of this chiral photochromic polymer results in distinct changes in the CD spectrum, but **10** suffers from low switching selectivity and long irradiation times.

Photochemical switching of polymers doped with sterically overcrowded alkenes revealed that photo-switching was possible in a polymer matrix. The isomerization processes, however, critically depend on the mobility in the matrix. The restrictive polymer matrix slows down this process to a large extent, and more effective applications of the sterically overcrowded alkenes as chiroptical molecular switches were found with more flexible liquid crystalline host materials.

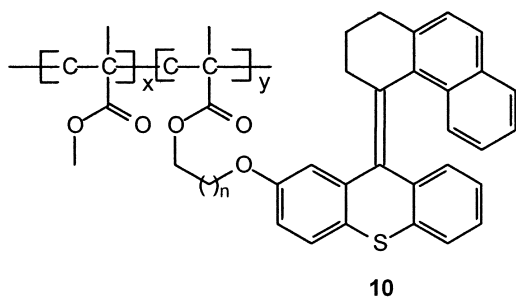


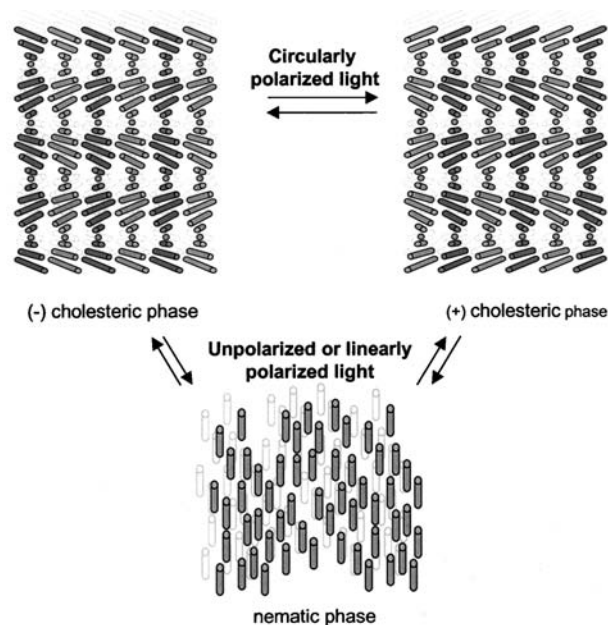
**Fig. 5** Polymer-bound chiroptical molecular switch **10** ( $n = 1-5$ ;  $x/y \geq 95.3:4.7$ ).

### TOWARD APPLICATIONS: SWITCHING OF LIQUID CRYSTALLINE PHASES

Liquid crystals (LCs), which are already widely applied in, for example, display technology, form excellent host materials for chiral molecular switches. When doped with a suitable molecular switch as a guest, liquid crystals offer a processable photoswitchable material, with essential features for application of these systems. Nematic liquid crystals are especially appealing for use in combination with these chiral guest compounds because they are extremely sensitive toward chiral perturbations forming chiral nematic or cholesteric phases. In their cholesteric packing, the mesogenic host molecules amplify the molecular chirality of the guest material resulting in a macroscopic chiral helical packing. Cholesteric phases can be assigned by a helical packing of the mesogens with a certain sign and a certain pitch.<sup>[40–42]</sup> This pitch is a measure of the chirality of the system. An important property of cholesteric liquid crystals for potential technological application is that they show unique optical properties when the pitch is of the same magnitude as the wavelengths of visible light. When illuminated with white light, cholesteric phases reflect light of a certain wavelength (color) dependent on the pitch of the LC phase. The interest in colored doped cholesteric phases in the research on chiroptical molecular switches is twofold. When chiroptical molecular switches can induce pitch lengths resembling the dimensions of the wavelength of visible light, a direct color readout of written information is possible. On the other hand, direct tuning of the color of the cholesteric phase opens the opportunity to develop color liquid crystal display materials addressable by light, i.e., color pixel formation.

### Enantiomeric Switches in a Liquid Crystal Matrix

A main goal of the research on enantiomeric switches has been the development of a potential liquid crystal phototrigger based on CPL. Because nematic materials are extremely sensitive to chiral perturbations, changes in LC films can even reflect enantiomeric excesses as small as 0.07% as found for **1**.<sup>[26]</sup> Irradiation with (*l*)-CPL (313 nm) of racemic **1** doped in a nematic LC host M15 resulted in the formation of a negative cholesteric phase. The molecular chirality controlled by circularly polarized light is amplified by the liquid crystalline environment. Accordingly, irradiation with (*r*)-CPL (again 313 nm) resulted in a cholesteric phase of opposite positive screw sense. The amount of dopant needed to obtain a measurable cholesteric phase is relatively large (20 wt.%) because of the small enantiomeric excesses reached in the photostationary state. Irradiation of the cholesteric film with linear polarized



**Scheme 10** Schematic representation of CPL switching between different liquid crystalline phases.

light at 313 nm resulted in an achiral compensated nematic phase. The two chiral influences (*l*- and *r*-)CPL at the most efficient wavelength stimulate the two extreme photostationary states. Actually, this macroscopic switchable material represents a multistate switch in which the cholesteric phases with intermediate pitches can be addressed by changing, for example, the irradiation time or wavelength (Scheme 10).

### Pseudoenantiomeric Switches in a Liquid Crystal Matrix

The photochemical modulation of the helical screw sense and the pitch of a cholesteric phase was also realized with the combination of a nematic liquid crystalline host and donor–acceptor switch **3**.<sup>[43]</sup> Different liquid crystals can be used as a host and show comparable results. For example, doping of liquid crystalline compound M15 with (*P*)-*trans*-**3** (2.4 wt.%) converts the nematic phase into a cholesteric phase. Irradiation at 365 or 435 nm of a thin film of this cholesteric phase led to photostationary states with an excess of (*M*)-*cis*-**3** or an excess of (*P*)-*trans*-**3**, comparable to the system in *n*-hexane solution. These two cholesteric phases show different pitches and opposite screw sense (+8.5 and –12.2 μm), as expected from the pseudoenantiomeric relationship of the two forms of the photoswitchable dopant. Switching efficiencies in a liquid crystalline environment and in solution are more or less equal, but irradiation times have increased. Doping concentrations are, however, limited for this particular system. For this reason, compound **6** with

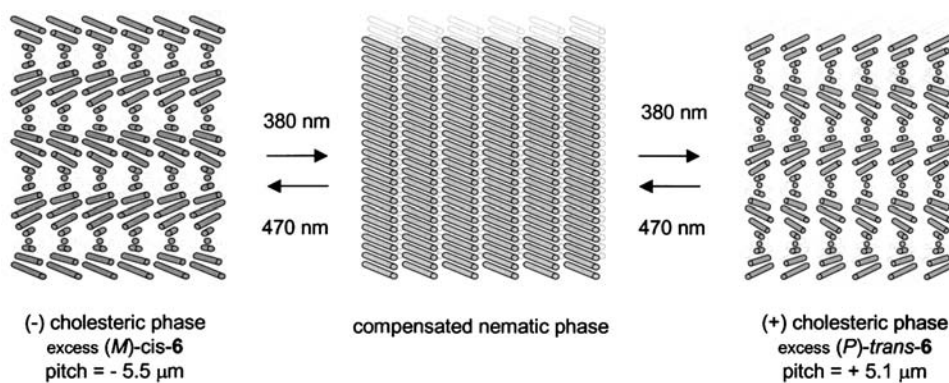
a solubilizing *n*-hexyl tail was synthesized (*vide supra*) and an increase in compatibility was observed in all tested nematic host materials.

For compound **6**, a cholesteric phase was readily induced by doping with either one of the enantiomerically pure forms of **6** in all tested nematic liquid crystalline hosts. The molecular chirality of the dopant was amplified to provide a macroscopic chirality of the liquid crystalline phase comparable to compound **3**. Using a 2.6-wt.% sample of **6** in M15, for example, switching between cholesteric phases with pitches of +10.1 and –12.0 μm was achieved using 380- and 435-nm light, respectively. A material of choice for further improvement of the system is E7, a commercially applied LC mixture which is liquid crystalline at room temperature. Ideal switching wavelengths in this LC host were determined to be 380 and 470 nm. Using again a 2.6-wt.% sample, switching between cholesteric phases with pitches of +5.1 and –5.5 μm was possible. These values represent the minimum pitches that can be reached for a 2.6-wt.% sample. By changing the irradiation time or the irradiation wavelength, cholesteric phases with intermediate pitches, including a compensated nematic phase, are addressable (Scheme 11).

### Controlling the Color of Cholesteric Phases

As indicated above, to obtain colored LC phases, pitches in the range of nanometers are required. Although the dopant concentration for **6** in E7 can be further increased, for LC color application, a different host system has to be used. For two important reasons, the system of choice was a chiral polymerizable cholesteric acrylate mixture (**11** and **12**) developed by Philips Research (Fig. 6).<sup>[44–47]</sup> First of all, because of the presence of a chiral diacrylate, the LC host already shows a colored cholesteric phase. Upon doping with a chiroptical switch, the color of the LC phase only has to be influenced rather than fully induced. A second important property of this system is that because of the presence of an achiral monoacrylate and a chiral diacrylate, this system can undergo photopolymerization when a suitable photoinitiator is present. This photopolymerization process locks the cholesteric phase to generate a stable polymeric matrix reflecting the optical properties of the initial liquid crystal matrix. This could allow stable storage of information. The principle was demonstrated using a mixture of 40% chiral (*S,S*)-diacrylate **11** with 60% achiral monoacrylate **12** (forthwith denoted as **11/12**). This mixture forms a green cholesteric phase with a maximum reflection wavelength of about 440 nm.

Switching properties of **6** were retained in this acrylate mixture.<sup>[35]</sup> Upon 435-nm irradiation, a photostationary



**Scheme 11** Schematic representation of the switching of the chirality of a doped cholesteric liquid crystal.

state was reached with a ratio *cis*-**6**/*trans*-**6** of 67:33. Irradiation at 380 nm resulted in a photostationary state of 31% *cis*-**6** and 69% *trans*-**6**. In all doped cases, the reflection wavelength was red-shifted compared with the undoped mixture.

Switching experiments were performed on an aligned sample with 12.5 wt.% of enantiomerically pure (*M*)-*trans*-**6** in the presence of 1 wt.% of photoinitiator (Irgacure 651) and 1 wt.% of inhibitor (*p*-methoxyphenol) at 435-nm irradiation. At this wavelength, no polymerization is initiated and a *trans* to *cis* isomerization of the chiral dopant is the only process observed. Upon photoisomerization, the reflection band of the LC film was gradually shifted to shorter wavelength. Starting at a reflection wavelength of 666 nm (red), a blue shift of the reflection wavelength to 541 nm (green) was observed at the photostationary state after about 150 sec of irradiation (Fig. 7). When increasing the irradiation wavelength using a 450-nm cutoff filter, the wavelength of reflection could further be decreased to a value of 526 nm. This blue shift of 140 nm can also be induced directly by >450 nm irradiation of the initial pure (*M*)-*trans*-**6** doped film.

Photopolymerization of the LC film was effected by 5-min irradiation at 365 nm in vacuo. At this wavelength, photoisomerization of the dopant is expected to some extent. After the irradiation, the liquid crystalline phase was polymerized and a rigid polymer matrix was obtained. For the 12.5-wt.% sample of pure (*M*)-*trans*-**6** in **11/12**, photopolymerization resulted in a blue shift of the reflection from 666 nm in the monomeric state to 632 nm for the polymerized state. The photostationary mixture obtained after 450-nm irradiation, which showed a reflection of 526 nm in the monomeric state, gave a polymerized matrix with a 518-nm reflection. The obtained polymeric phases in all cases reflect the photostationary state of the chiral dopant. Furthermore, the polymerized phases are completely inert to prolonged irradiation and the photochemically written color information is effectively locked.

This system constitutes a “write and lock” mechanism for color information (Fig. 7). Writing is performed by light, and cholesteric phases with pitches between 666 and 526 nm can be induced by varying the irradiation time. Color inspection (red to green)

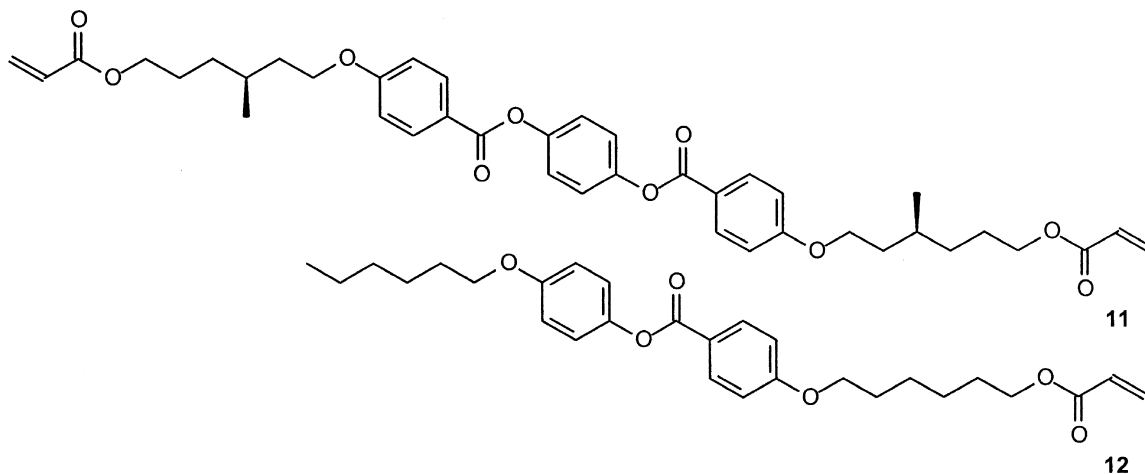


**Fig. 6** Photopolymerizable cholesteric mixture of monomeric acrylates **11** and **12**.

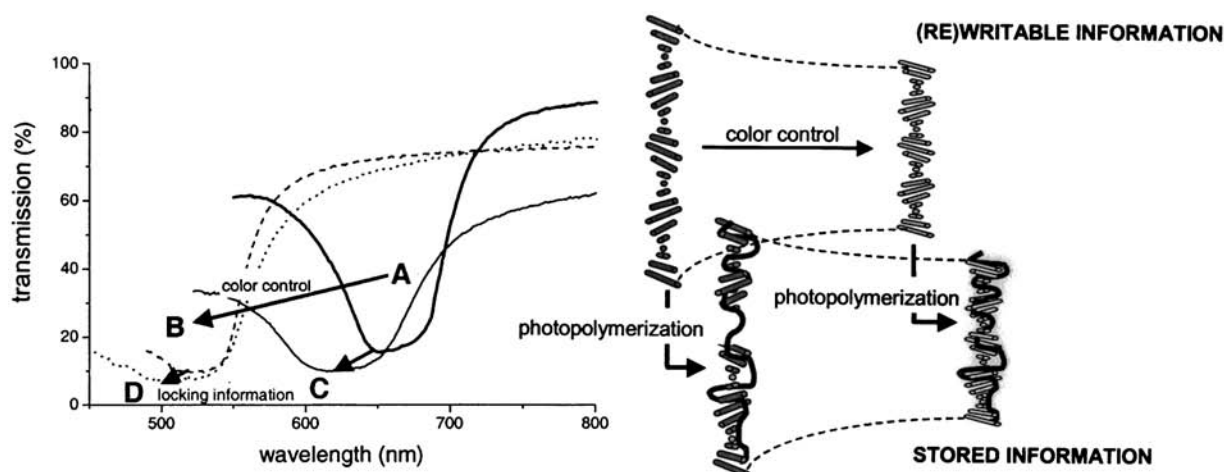


**Fig. 7** Color control of LC film: writing and locking information for a 12.5-wt.% sample of (*M*)-*trans*-6 in 11/12. Wavelength of reflection at different stages of the process: (A) initial sample; (B) photostationary state after 450-nm irradiation; (C) polymerized sample after 365-nm irradiation of the initial sample (A); (D) polymerized sample after 365-nm irradiation of the photostationary state (B) and a schematic representation of color control and storage of information by photopolymerization of a cholesteric liquid crystal.

offers an easy readout procedure. Further irradiation of this LC phase results in a change in the (*M*)-*trans*-6 to (*P*)-*cis*-6 ratio and, as a consequence, a change in the wavelength of reflection (the color) of the LC film, as long as the 450-nm photostationary state is not reached. This monomeric state can be considered a rewritable state. Upon photopolymerization, the LC matrix will harden and the written information is locked. Again, color inspection (orange to green) offers an easy readout procedure which is now absolutely non-destructive. The information is locked and there is no change in cholesteric pitch observed upon further irradiation.

### STERICALLY OVERCROWDED ALKENES AS UNIDIRECTIONAL ROTARY MOTORS

The design and synthesis of molecular motors are among the major endeavors in nanoscience. Inevitable motor functions will be needed to power nanomachines, although the design and functioning might be completely different from any known macroscopic or biological motor. We formulated three basic requirements for a molecular motor system: 1) repetitive 360° rotary motion; 2) consumption of energy; and 3) unidirectional rotation. The first chemically driven<sup>[48–50]</sup> and photochemically driven unidirectional rotary motors<sup>[51]</sup> were reported simultaneously.<sup>[52]</sup> Until these accomplishments, no synthetic system could be classified as a molecular motor according to the prerequisites formulated above.

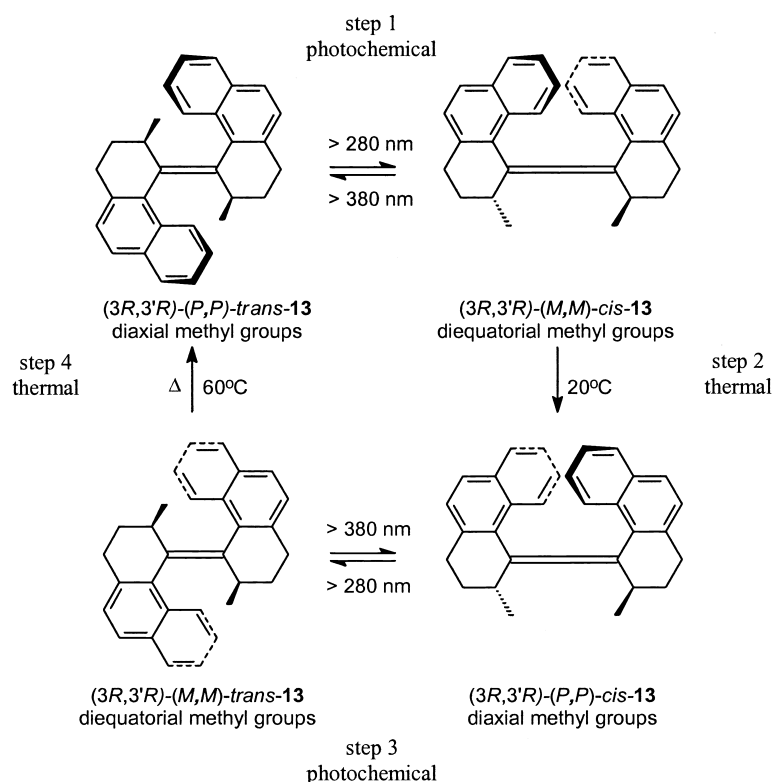
The chiroptical molecular switches already show a unidirectional rotation of about 105° where the

direction of the movement is solely governed by the helicity in the initial state, and this process is driven by light. In the design of molecular motors, using sterically overcrowded alkenes as the basic structure, an extension of the rotary movement is necessary and the light-induced motion during the switching event should continue in the same direction. Realizing that these sterically overcrowded alkenes consist of four stereoisomers, i.e., the pseudoenantiomeric forms that constitute the two switching stages and their enantiomers, the possibility of full 360° rotation arises as illustrated briefly for compound 9 (vide supra).

### The First Light-Driven Unidirectional Molecular Motor

Following extensive study on the thermal and photochemical isomerization processes of biphenanthrylidene,<sup>[53–56]</sup> it was demonstrated that the intrinsic chirality associated with sterically overcrowded alkenes can be used to accomplish unidirectional rotary motion.<sup>[57–59]</sup> In compound (*3R*, *3'R*)-13 (Scheme 12), the sterically overcrowded alkene skeleton bears two additional stereogenic centers besides the (*P,P*)-helical structure. In its most stable conformation (*P,P*)-*trans*-13, the two methyl substituents adopt an energetically favored axial orientation because of steric hindrance (Scheme 12). Irradiation with light ( $\lambda \geq 280$  nm) results in an isomerization process (step 1) to form (*M,M*)-*cis*-13. Inherent to the nature of such an isomerization, the methyl substituents are forced to adopt an energetically unfavorable equatorial orientation. At room temperature, a fast helix inversion





**Scheme 12** Light-driven unidirectional molecular motor **13**.

(step 2) takes place resulting in *(P,P)-cis-13* where the methyl substituents again adopt an axial orientation. A second photoisomerization step (step 3) results in the formation of *(M,M)-trans-13* with the methyl substituents again in their energetically unfavorable equatorial position. A second helix inversion (step 4) is induced by heating at  $60^\circ\text{C}$  and results in the formation of the initial *(P,P)-trans-13* isomer.

These four discrete steps add up to a full  $360^\circ$  unidirectional rotation of one (rotor) half of the molecule relative to the other (stator) half. Two photochemical energetically uphill isomerizations driving the rotary movement (steps 1 and 3) are each followed by two irreversible energetically downhill thermal helix inversions (steps 2 and 4). The release of internal energy of the system that takes place during helix inversion, to place the methyl substituents again in the more favorable axial orientation, ensures the unidirectionality of the process. The direction of rotation is solely governed by the configuration of the stereogenic centers because this determines the axial or equatorial orientation of the methyl groups. Essential features of the rotating system are the central olefinic bond, the helicity of the overcrowded alkene, the absolute configuration of the stereogenic centers, and the conformational flexibility of the cyclohexenyl rings. Because of the same wavelength used for both photoisomerization steps, a repetitive unidirectional rotation can be induced by continuous irradiation at elevated

temperature. This is the first example of a light-driven unidirectional molecular motor as illustrated in Fig. 8.

### Second-Generation Molecular Motor

One drawback of the first-generation motor is the thermal requirement of the system, and although photon energy is the driving force, heating to about  $60^\circ\text{C}$  is necessary to continue the rotary motion. A second drawback is that this system has little opportunities for structural variation. To overcome these drawbacks, a so-called second-generation motor concept was

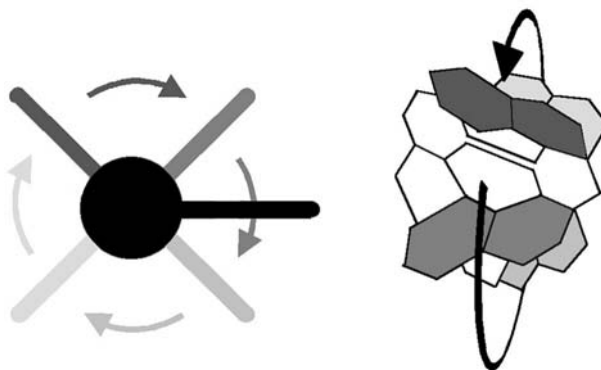


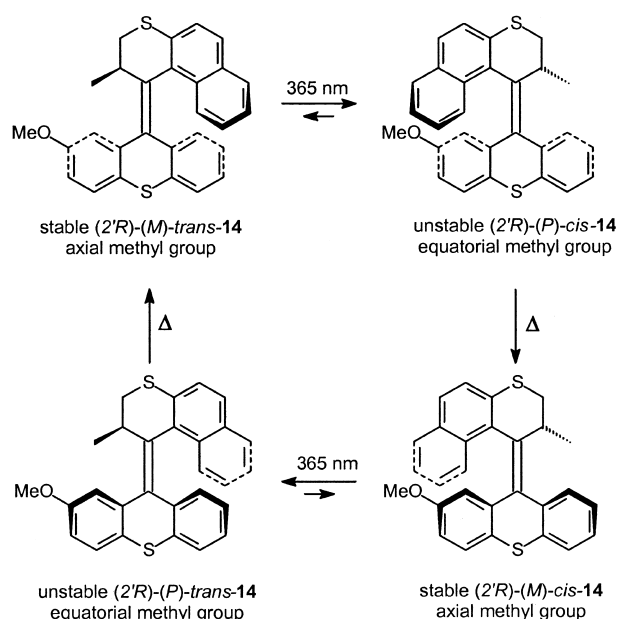
**Fig. 8** Continuous unidirectionally rotating molecular motor **13**.



developed combining the design versatility of our chiroptical molecular switches with the unique rotary behavior of the first-generation molecular motor (Fig. 9). In this concept, one-half of the molecule (a chiral 2-methyl-2,3-dihydrothiopyran upper part) would function as the rotor part, while the other could be used for adjusting the molecular properties by synthetic modifications. The main question was whether the presence of a single stereogenic center would suffice to induce unidirectional rotation.

The prototype system that was synthesized is compound (*2'R*)-**14**.<sup>[60]</sup> Analogous to the first-generation molecular motor, for **14**, a strong preference for an axial conformation of the methyl group at the stereogenic center was established. This stereochemical feature is essential to achieve unidirectional rotation. Starting from the energetically favored (*2'R*)-(*M*)-*trans*-**14** isomer, by irradiation with 365-nm light, a *trans* to *cis* isomerization was induced. This resulted in the corresponding less stable isomer (*P*)-*cis*-**14**, completely analogous to the first-generation molecular motor. Upon heating to 60°C, the unstable *cis*-isomer (*P*)-*cis*-**14** is converted to the stable (*2'R*)-(*M*)-*cis*-form. A second energetically uphill photoisomerization step yields the unstable (*2'R*)-(*P*)-*trans*-form which, upon heating, reverts again to stable (*2'R*)-(*M*)-*trans*-**14**, completing a full unidirectional 360° rotation of the rotor upper half relative to the stator lower half of the molecule (Scheme 13).

The direction of rotation in this second-generation motor is again dictated by the orientation of the methyl substituent at the stereogenic center. The process is solely driven by two light-induced energetically uphill photoisomerization processes, forcing the methyl substituent in the upper half of the molecule



**Scheme 13** First example of unidirectional rotation controlled by a single stereogenic center; the prototype of the second-generation motor **14**.

in an energetically unfavorable equatorial conformation. The release of internal energy is accomplished by a helix inversion step where the methyl substituent adopts the favorable axial conformation. These two energetically downhill processes ensure the unidirectionality of the entire rotary motion.

Following this proof of principle, an important objective was to decrease the barrier for the thermal helix inversion steps to allow rotation at room temperature. The approach focused on modification of the bridging groups X and Y (Fig. 9) to tune the steric

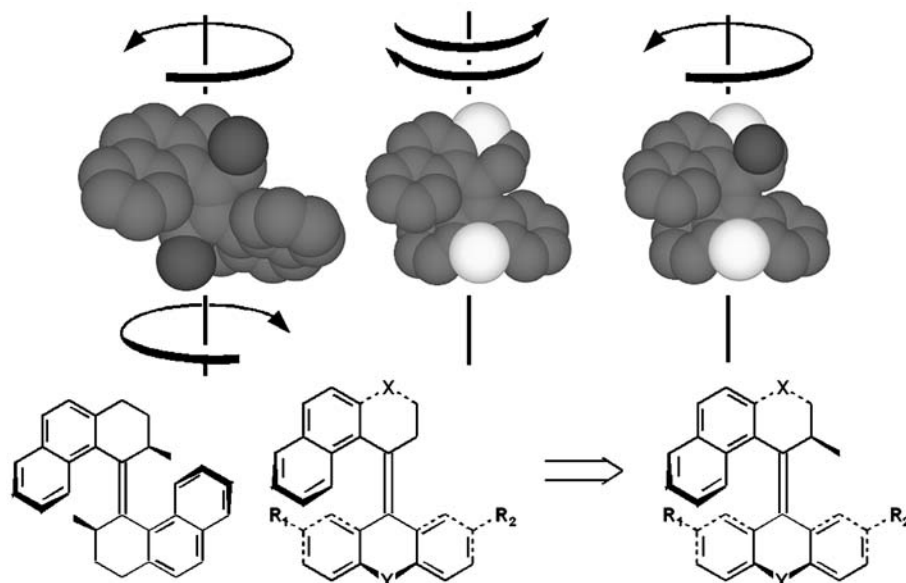


**Fig. 9** Design of second-generation motors.

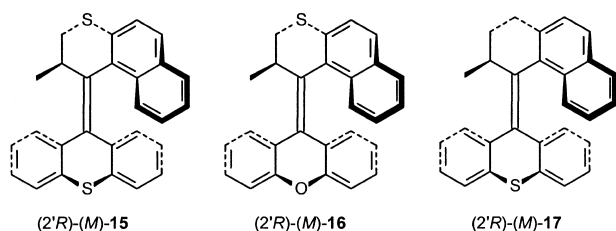


**Fig. 10** Second-generation motor: unidirectional rotation controlled by a single stereogenic center and structural modifications that allow control of rotary behavior.

hindrance at the fjord region of the molecules. Based on the experience with the molecular switches, compounds **15**, **16**, and **17** were synthesized in which, because of decreased dimensions of the (hetero-)atoms X and Y (O and CH<sub>2</sub> compared with S), helix inversion was expected to be facilitated (Fig. 10).<sup>[61]</sup> Changing the sulfur atom (in **15**) for an oxygen atom in the lower half (in **16**) resulted in a decrease in the half-life (in *n*-hexane) at room temperature by a factor of about 8. Replacing a sulfur by a carbon atom in the upper half decreased the half-life by a factor of about 320. This resulted in a motor **17** with a half-life for thermal helix inversion of about 2400 sec at room temperature allowing unidirectional rotation under ambient conditions.

In an attempt to further reduce these energy barriers, a new motor **18** with a tetrahydronaphthalene instead of a tetrahydrophenanthrene upper part used in the other second-generation motors including parent compound **19** was synthesized (Fig. 11).<sup>[62]</sup> Counterintuitively, for motor system **18**, the rotary motion is severely slowed down. This remarkable effect was attributed to a higher ground state energy of motor **19** compared with **18**. It is evident that there is a delicate balance between ground-state distortion and steric and electronic effects on the photochemical and thermal isomerization processes in these sterically overcrowded alkenes.

Another objective is the design of a system that can function under the influence of visible light. For this purpose, the absorption of the molecules has to be shifted from the UV region to the visible region.

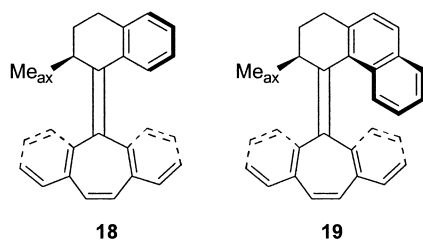


**Fig. 11** Tetrahydronaphthalene (**18**) and tetrahydrophenanthrene-based (**19**) motor.

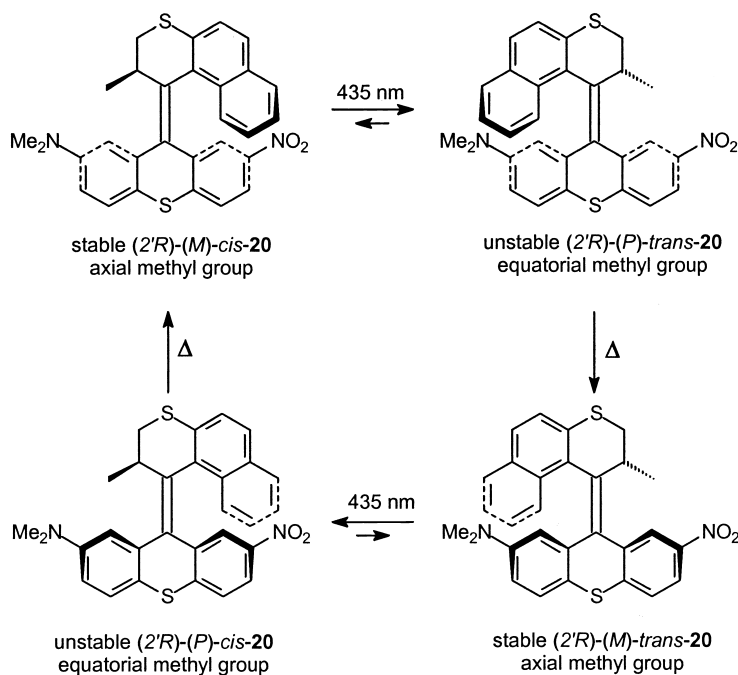
Asymmetric donor–acceptor substitution in **20** was expected to induce a red shift in UV/Vis absorption (Scheme 14).<sup>[63]</sup> Fig. 12 clearly shows that the UV/Vis absorption of both isomers of **20** extends to about 500 nm implying the possibility of excitation of these photoisomerizable compounds in the visible region of the spectrum.

Completely analogous to other second-generation motors, irradiation of enantiomerically pure (2'*R*)-(M)-*cis*-**20** with visible light of 435 nm resulted in the formation of less stable (2'*R*)-(P)-*trans*-**20** (Scheme 14). In this compound, the methyl substituent is forced to adopt an equatorial orientation. Subsequent heating at 50°C resulted in the formation of the stable (2'*R*)-(M)-*trans*-**20**. Irradiation of (M)-*trans*-**20** with visible (435 nm) light induced a second isomerization and the formation of energetically unfavorable (P)-*cis*-**24**. Heating the system to 50°C resulted in a helix inversion to form (M)-*cis*-**20** again. The combined four-step rotary cycle ensures that compound **20** functions as a molecular motor that can be driven by visible light.

## UNIDIRECTIONAL ROTARY MOTION IN A LIQUID CRYSTALLINE ENVIRONMENT

In the first-generation molecular motor, the energy of the irradiation light is used to exert mechanical motion. The next step toward any nanotechnological application of such a motor would be to actually drive other functions or perform work. In addition, for future application of these molecular motors, conservation of the molecular properties in an organized medium is essential. Combining the properties of our first molecular motor **13** with those of liquid crystalline materials is a first step in the direction of a nanotechnological application. The essence of the research is to examine whether the control of molecular rotation that can be exerted by light irradiation can be amplified to control the motion of a large ensemble of molecules and, as a consequence, the macroscopic (chiral) properties in a liquid crystalline phase, thereby allowing indirect macroscopic visualization of rotary motion.

Compound **13** (Scheme 12) efficiently induces cholesteric phases for different mesogenic host compounds. A helical twisting power of +69 μm<sup>-1</sup>, for example, was found for (P,P)-*trans*-**13** in E7.<sup>[64]</sup> The rotary process in the liquid crystalline matrix was tested using a drop-casted sample of E7 doped with 2.4 wt.% of (P,P)-*trans*-**13** and was shown to be analogous to solution experiments (Scheme 12). Unidirectional rotation was proven to be possible in a liquid crystalline matrix. It should be noted, however, that during the heating step, the LC material was in an isotropic stage, and as a consequence, the orientation is



**Scheme 14** Visible light-driven unidirectional rotation of donor-acceptor motor **20**.

temporarily lost. The whole light-driven process is less efficient in a liquid crystal than in solution for two important reasons: 1) the absorption of the LC material reduces the amount of photons that will actually reach the photoisomerizable material, which is evident from the strong dependence of isomerization efficiency on substrate thickness; and 2) because of the absorption of the LC material, the wavelength range that actually reaches the compound is  $>340$  nm which causes a shift in the two photoequilibria.

The high helical twisting powers for (*P,P*)-**trans-13** open up the possibility to generate cholesteric phases with pitch lengths in the range of the wavelength of visible light. Doping of E7 with only 6.16 wt.% of (*P,P*)-**trans-13** resulted in a violet cholesteric phase with a pitch of 234 nm and a reflection wavelength (at an angle of  $45^\circ$ ) of 357 nm. From the ratio and the pitches

of the 2.4-wt.% sample discussed above, the helical twisting powers of (*P,P*)-**cis-13** and (*M,M*)-**trans-13** could be calculated to be  $+12$  and  $-5 \mu\text{m}^{-1}$ , respectively. The dramatic decrease in the helical twisting power going from (*P,P*)-**trans-13** to the other isomers is essential for generating light-induced macroscopic changes by unidirectional rotation. Upon irradiation ( $\lambda \geq 280$  nm) of the violet film of 6.16 wt.% of (*P,P*)-**trans-13** in E7, a fast bathochromic shift of the reflection wavelength was induced. In only 80 sec, the color of the film changed from violet via blue, green, yellow, and orange to red as can be readily detected by visual inspection. The time-dependent quantitative change in reflection wavelength measured at a  $45^\circ$  angle is presented in Fig. 13.

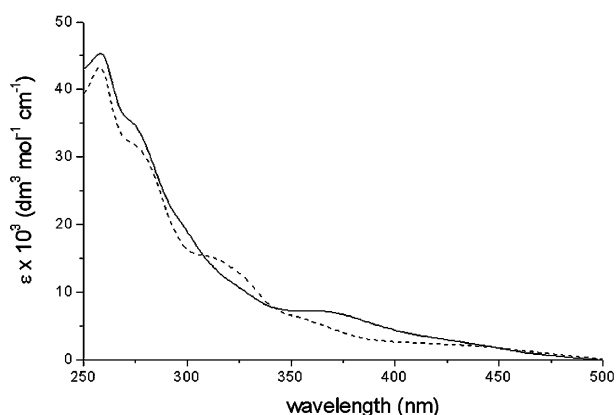


**Fig. 12** UV/Vis absorption of *cis*-**20** (solid) and *trans*-**20** (dashed) in chloroform.

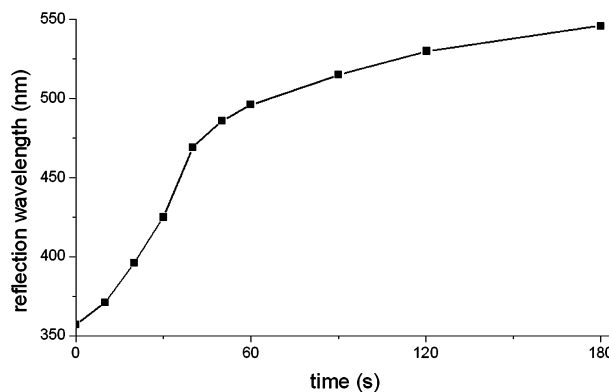


**Fig. 13** Wavelength of reflection at a  $45^\circ$  angle of a molecular motor doped LC phase (6.16 wt.% in E7) as a function of time starting from (*P,P*)-**trans-13** upon irradiation with  $>280$  nm.

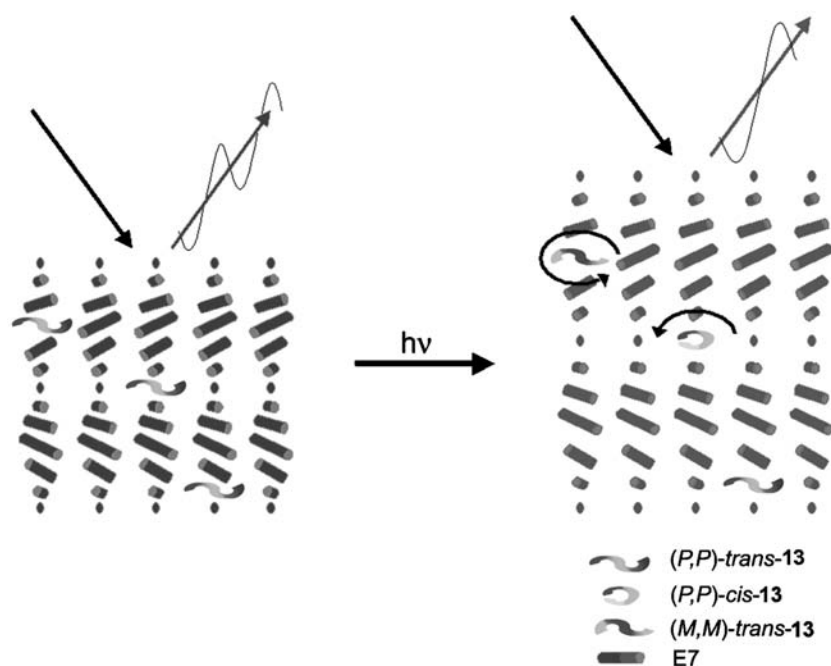


**Fig. 14** Schematic representation of unidirectional rotation of the guest molecular motor **13**, the induced elongation of the pitch of the LC host matrix, and the change in reflection wavelength of the light.

After heating the sample to 60°C at any time of irradiation, the *(M,M)*-*trans*-**13** isomer is converted to *(P,P)*-*trans*-**13** with a concomitant hypsochromic shift of the reflection wavelength. Again, during the heating process, the LC material was in an isotropic stage, and as a consequence, the orientation is temporarily lost.

These results show that unidirectional rotary motion could be performed in a LC matrix, as is schematically illustrated in Fig. 14. The light-driven motion in the dopant induces the motion of a large ensemble of rod-like molecules during the reorganization in the LC film. This indirectly allows visual observation of the rotary motion, but, more importantly, shows that rotation on a molecular level can be used to drive a reorganization of a macroscopic liquid crystalline film. Furthermore, it demonstrates that the molecular motor can perform actual work.

## CONCLUSION

It has been shown that chiral sterically overcrowded alkenes are extremely suitable for functioning as molecular switches and motors. Chiroptical switches based on sterically overcrowded alkenes were constructed that could function both in solution as well as in a liquid crystalline matrix. These switches might be used as molecular trigger elements or as reversible data storage units at the molecular level. The first light-driven molecular motors were also based on an overcrowded alkene. By combining two chiral elements (helical structure and stereogenic center) in the same photoactive molecule, the fundamental properties of

a molecular motor, energy consumption resulting in unidirectional rotary motion, were demonstrated. This prototype system led to the development of a second-generation of molecular motors for which tuning of the rotation speed and irradiation wavelength was proven to be possible. All the systems developed are still far from actual application, but they offer a solid basis for the development of future generations of switches and motors to meet the numerous challenges ahead on the road toward nanomechanical machinery.

## REFERENCES

1. Astumian, R.D. *Sci. Am.* **2001**, 285, 56.
2. Struct., Bond.; Sauvage, J.-P.; Ed. *Molecular Machines and Motors*; Struct. Bond.; Springer: New York, 2001; Vol. 99.
3. Goodsell, D.S. *Our Molecular Nature: The Body's Motors, Machines and Messages*; Springer: New York, 1996.
4. Molecular machines. *Acc. Chem. Res.* **2001**, 34, 409.. Special issue.
5. Balzani, V.; Gomez-Lopez, M.; Stoddart, J.F. *Acc. Chem. Res.* **1998**, 31, 405.
6. Sauvage, J.-P. *Acc. Chem. Res.* **1998**, 31, 611.
7. Mislow, K. *Chemtracts, Org. Chem.* **1989**, 2, 151.
8. Kelly, T.R.; Boyer, M.C.; Bhaskar, K.V.; Bebbington, D.; Garcia, A.; Lang, F.; Kim, M.H.; Jette, M.P.A. *J. Am. Chem. Soc.* **1994**, 116, 3657.
9. Feringa, B.L.; Ed. *Molecular Switches*; Wiley-VCH: Weinheim, 2001.
10. Bedard, T.C.; Moore, J.S. *J. Am. Chem. Soc.* **1995**, 117, 10,662.

11. Kelly, T.R.; Tellitu, I.; Sestero, J.P. *Angew. Chem., Int. Ed.* **1997**, *36*, 1866.
12. Sauvage, J.-P.; Dietrich-Buchecker, V. *Molecular Catenanes, Rotaxanes and Knots*; Wiley-VCH: Weinheim, 1999.
13. Balzani, V.; Credi, A.; Raymo, F.M.; Stoddart, J.F. Artificial molecular machines. *Angew. Chem., Int. Ed.* **2000**, *39*, 3348.
14. Pease, A.R.; Jeppesen, J.O.; Stoddart, J.F.; Luo, Y.; Collier, C.P.; Heath, J.R. Switching devices based on interlocked molecules. *Acc. Chem. Res.* **2001**, *34*, 433.
15. Bermudez, V.; Capron, N.; Gase, T.; Gatti, F.G.; Kajzar, F.; Leigh, D.A.; Zerbetto, F.; Zhang, S. Influencing intramolecular motion with an alternating electric field. *Nature* **2000**, *406*, 608.
16. Brouwer, A.M.; Frochot, C.; Gatti, F.G.; Leigh, D.A.; Mollier, L.; Paolucci, F.; Rofia, S.; Wurlpel, G.W.H. Photoinduction of fast, reversible translational motion in a hydrogen-bonded molecular shuttle. *Science* **2001**, *291*, 2124.
17. Raymo, F.M.; Stoddart, J.F. Switchable catenanes and molecular shuttles. In *Molecular Switches*; Feringa, B.L., Ed.; Wiley-VCH: Weinheim, 2001; 219.
18. Jimenez, M.C.; Dietrich-Buchecker, C.; Sauvage, J.-P. Towards synthetic molecular muscles: Contraction and stretching of a linear rotaxane dimer. *Angew. Chem., Int. Ed.* **2000**, *39*, 3284.
19. Feringa, B.L. Nanotechnology: In control of molecular motion. *Nature* **2002**, *408*, 151.
20. Chia, S.; Cao, J.; Stoddart, J.F.; Zink, J.I. Working supramolecular machines trapped in glass and mounted on a film surface. *Angew. Chem., Int. Ed.* **2001**, *40*, 2447.
21. Hugel, T.; Holland, N.B.; Cattani, A.; Moroder, L.; Seitz, M.; Gaub, H.E. Single-molecule optomechanical cycle. *Science* **2002**, *296*, 1103.
22. Schliwa, M.; Ed. *Molecular Motors*; Wiley-VCH: Weinheim, 2003.
23. Dürr, H.; Bouas-Laurent, H.; Ed. *Photochromism, Molecules and Systems*; Elsevier: Amsterdam, 1990.
24. Lemieux, R.P.; Schuster, G.B. *J. Org. Chem.* **1993**, *58*, 100.
25. Zhang, Y.; Schuster, G.B. *J. Org. Chem.* **1995**, *60*, 7192.
26. Huck, N.P.M.; Jager, W.F.; de Lange, B.; Feringa, B.L. Dynamic control and amplification of molecular chirality by circular polarized light. *Science* **1996**, *273*, 1686.
27. Stevenson, K.L. *J. Am. Chem. Soc.* **1972**, *94*, 6652.
28. Hampp, N. Bacteriorhodopsin as a photochromic retinal protein for optical memories. *Chem. Rev.* **2000**, *100*, 1755.
29. Feringa, B.L.; van Delden, R.A.; ter Wiel, M.K.J. *Molecular Switches*; Feringa, B.L., Ed.; Wiley-VCH: Weinheim, 2001; 123–163 Chapter 5.
30. Feringa, B.L.; van Delden, R.A.; Koumura, N.; Geertsema, E.M. Chiroptical molecular switches. *Chem. Rev.* **2000**, *100*, 1789.
31. Feringa, B.L.; Jager, W.F.; de Lange, B.; Meijer, E.W. *J. Am. Chem. Soc.* **1991**, *113*, 5468.
32. Feringa, B.L.; Jager, W.F.; de Lange, B. Resolution of sterically overcrowded ethylenes; a remarkable correlation between bond lengths and racemization barriers. *Tetrahedron Lett.* **1992**, *33*, 2887.
33. Jager, W.F.; de Jong, J.C.; de Lange, B.; Huck, N.P.M.; Meetsma, A.; Feringa, B.L. *Angew. Chem., Int. Ed. Engl.* **1995**, *34*, 348.
34. Huck, N.P.M.; Feringa, B.L. *J. Chem. Soc., Chem. Commun.* **1995**, 1095.
35. van Delden, R.A.; van Gelder, M.B.; Huck, N.P.M.; Feringa, B.L. Controlling the color of cholesteric liquid-crystalline films by photoirradiation of a chiroptical molecular switch used as dopant. *Adv. Funct. Mater.* **2003**, *13*, 319.
36. van Delden, R.A.; Schoevaars, A.M.; Feringa, B.L. *Mol. Cryst. Liq. Cryst.* **2000**, *344*, 1.
37. Schoevaars, A.M.; Kruizinga, W.; Zijlstra, R.W.J.; Veldman, N.; Spek, A.L.; Feringa, B.L. *J. Org. Chem.* **1997**, *62*, 4943.
38. van Delden, R.A.; Huck, N.P.M.; Warman, J.M.; Meskers, S.C.J.; Dekkers, H.P.J.M.; Feringa, B.L. *J. Am. Chem. Soc.* **2003**, *125*, 15,659.
39. Oosterling, M.L.C.M.; Schoevaars, A.M.; Haitema, H.J.; Feringa, B.L. *Isr. J. Chem.* **1996**, *36*, 341.
40. Dunmar, D.; Taniyama, K. *Handbook of Liquid Crystals Vol 1: Fundamentals*; Demus, D., Goodby, J., Gray, G.W., Spiess, H.-W., Vill, V., Eds.; Wiley-VCH: Weinheim, 1998; 215–239.
41. Meier, G. *Applications of Liquid Crystals*; Springer Verlag: Berlin, 1975; 1–21.
42. Chandrasekhar, S. *Liquid Crystals*; Cambridge University Press: Cambridge, 1977.
43. Feringa, B.L.; Huck, N.P.M.; van Doren, H.A. *J. Am. Chem. Soc.* **1995**, *117*, 9929.
44. Lub, J.; van der Veen, J.H.; van Echten, E. *Mol. Cryst. Liq. Cryst.* **1996**, *287*, 205.
45. Lub, J.; van der Veen, J.H.; ten Hoeve, W. *Recl. Trav. Chim. Pays-Bas* **1996**, *115*, 321.
46. Hikmet, R.A.M.; Lub, J.; Tol, A.J.W. *Macromolecules* **1995**, *28*, 3313.
47. Hikmet, R.A.M.; Zwerver, B.H.; Lub, J. *Macromolecules* **1994**, *27*, 6722.
48. Kelly, T.R.; de Silva, H.; Silva, R.A. Unidirectional rotary motion in a molecular system. *Nature* **1999**, *401*, 150.
49. Kelly, T.R.; Silva, R.A.; de Silva, H.; Jasmin, S.; Zhao, Y. A rationally designed prototype of a molecular motor. *J. Am. Chem. Soc.* **2000**, *122*, 6935.
50. Kelly, T.R. Progress toward a rationally designed molecular motor. *Acc. Chem. Res.* **2001**, *34*, 514.
51. Koumura, N.; Zijlstra, R.W.J.; van Delden, R.A.; Harada, N.; Feringa, B.L. Light-driven monodirectional molecular rotor. *Nature* **1999**, *401*, 152–155.
52. Davis, A.P. Nanotechnology: Synthetic molecular motors. *Nature* **1999**, *401*, 120.
53. Harada, N.; Saito, A.; Koumura, N.; Uda, H.; de Lange, B.; Jager, W.F.; Wynberg, H.; Feringa, B.L. *J. Am. Chem. Soc.* **1997**, *119*, 7241.
54. Harada, N.; Saito, A.; Koumura, N.; Roe, D.C.; Jager, W.F.; Zijlstra, R.W.J.; de Lange, B.; Feringa, B.L. *J. Am. Chem. Soc.* **1997**, *119*, 7249.
55. Harada, N.; Koumura, N.; Feringa, B.L. *J. Am. Chem. Soc.* **1997**, *119*, 7256.
56. Zijlstra, R.W.J.; Jager, W.F.; de Lange, B.; van Duijnen, P.T.; Feringa, B.L.; Goto, H.; Saito, A.; Koumura, N.; Harada, N. Chemistry of unique chiral olefins. 4. Theoretical studies of the racemization mechanism of

- trans*- and *cis*-1,1',2,2',3,3',4,4'-octahydro-4,4'-biphenanthrylidene. *J. Org. Chem.* **1999**, *64*, 1667.
57. van Delden, R.A.; ter Wiel, M.K.J.; Koumura, N.; Feringa, B.L. *Molecular Motors*; Schliwa, M., Ed.; Wiley-VCH: Weinheim, 2003; 559–577 Chapter 23.
  58. Feringa, B.L.; Koumura, N.; van Delden, R.A.; ter Wiel, M.K.J. *Appl. Phys., A* **2002**, *75*, 301.
  59. Feringa, B.L. In control of motion: from molecular switches to molecular motors. *Acc. Chem. Res.* **2001**, *34*, 504.
  60. Koumura, N.; Geertsema, E.M.; Meetsma, A.; Feringa, B.L. Light-driven molecular rotor: unidirectional rotation controlled by a single stereogenic center. *J. Am. Chem. Soc.* **2000**, *122*, 12005.
  61. Koumura, N.; Geertsema, E.M.; van Gelder, M.B.; Meetsma, A.; Feringa, B.L. Second generation light-driven molecular motors. Unidirectional rotation controlled by a single stereogenic center with near-perfect photoequilibria and acceleration of the speed of rotation by structural modification. *J. Am. Chem. Soc.* **2002**, *124*, 5037.
  62. Geertsema, E.M.; Koumura, N.; ter Wiel, M.K.J.; Meetsma, A.; Feringa, B.L. In control of the speed of rotation in molecular motors. Unexpected retardation of rotary motion. *Chem. Commun.* **2002**, 2962.
  63. van Delden, R.A.; Koumura, N.; Schoevaars, A.M.; Meetsma, A.; Feringa, B.L. A donor acceptor substituted molecular motor: unidirectional rotation driven by visible light. *Org. Biomol. Chem.* **2003**, *1*, 33.
  64. van Delden, R.A.; Koumura, N.; Harada, N.; Feringa, B.L. Supramolecular chemistry and self-assembly special feature: unidirectional rotary motion in a liquid crystalline environment: color tuning by a molecular motor. *Proc. Natl. Acad. Sci. U. S. A.* **2002**, *99*, 4945.



# Molecular Wires

Dustin K. James

James M. Tour

Chemistry Department, Rice University, Houston, Texas, U.S.A.

## INTRODUCTION

Electrical wiring is used all around us in today's world. Metallic wiring 1 cm in diameter facilitates the flow of electrons that power our household lighting, radios, televisions, and other appliances such as computers. Within those appliances and computers, wires 1 mm wide on printed circuit boards connect electronic devices such as resistors, rheostats, and logic chips. Inside those logic chips, wires tenths of a micrometer wide connect solid-state transistors, carved out of silicon, and allow them to act in concert with thousands of similar transistors to carry out computations. This last size reduction nearly reaches what is thought to be the limit of present semiconductor manufacturing technology. To enable further miniaturization, recent research has produced molecular-scale wires, ranging in length from 1 to 100 nm. In this entry, we will review the state of the art in the synthesis and characterization of molecular wires and examine theoretical work concerning how they are thought to conduct electricity.

## Molecular Electronics

The rapidly developing field of molecular electronics is one of the driving forces behind the interest in molecular wires.<sup>[1–8]</sup> The limitations of the present “top-down” method of producing semiconductor-based devices have been the subject of debate and conjecture since the prediction of Moore<sup>[9]</sup> that the number of components per integrated circuit would double every 18 months. It is thought that the inherent limitations of the present technology will lead to a dead end in the next few years. For instance, silicon's band structure disappears when silicon layers are just a few atoms thick. Lithographic techniques that are used to produce the circuitry on the silicon wafers are limited by the wavelengths at which they work. However, leaders in the semiconductor manufacturing world are still making advances that appear to be

pushing “Moore's law” beyond its prior perceived limits. In the commercial technology of 2001, the copper wires in Intel's Pentium® 4 logic chip are 0.13 μm wide.<sup>[10]</sup> Intel is developing technology to create logic chips with wires 90 nm wide to be commercialized in 2003.<sup>[11]</sup>

For comparison's sake, a typical molecular wire synthesized in our laboratory is calculated to be 0.3 nm wide and 2.5 nm long (Fig. 1).<sup>[4]</sup> It would take 300 of these molecules, side by side, to span the 90-nm metal line in the most advanced logic chip in development. The small size of these molecules is emphasized when one considers that 500 g (about 1 mol) of this wire would contain  $6 \times 10^{23}$  molecules, or more molecules than the number of transistors ever made in the history of the world. This amount of material could be produced using relatively small 22-L laboratory reaction flasks. Changing the physical characteristics of this wire is as easy as changing the raw materials used to make it. The small size, the potential of synthesizing huge numbers in small reactors, and the ease of modification of the physical characteristics of the molecules are good reasons for pursuing molecular wire research. As an example of how far the technology has come, molecular electronics is discussed in the “Emerging Research Devices” section of the most recent International Technology Roadmap for Semiconductors<sup>[12,13]</sup> and new molecular wires are a large part of the emerging technology. Molecular electronics was named the “breakthrough of the year” by Science<sup>[14]</sup> for 2001.

## Optoelectronics

Because of their chemical structure, some highly conjugated molecular wires have applications in optoelectronics.<sup>[15–17]</sup> Poly(phenylene vinylene)s are being used as components in organic light-emitting diodes (OLEDs) in displays such as those used in cellular phones and other electronic devices. Various other polymeric materials and small molecules are also being used or are in development.

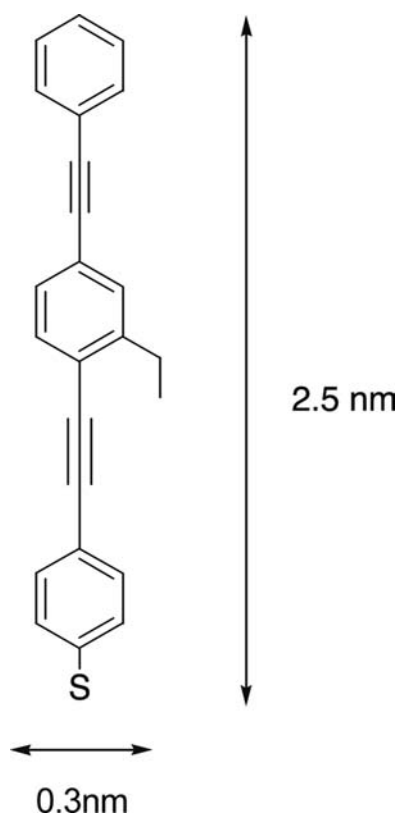


**Fig. 1** The dimensions of a typical molecular wire are calculated to be 0.3 nm in width and 2.5 nm in length using molecular mechanics (Spartan) to determine the energy-minimized structure. *Source:* From Ref.<sup>[4]</sup>.

These materials are applied in very thin layers about 100 nm thick, with the organic small molecules forming crystalline phases. This is quite different from the molecular electronics field, where it is envisioned that single molecules will eventually be used in circuits. However, much of the literature we will review addresses the optoelectronics applications of the molecular wires, and so we have included leading references for that area of research.

## MOLECULAR WIRES

In this work, when we say “molecular wires,” we mean discrete molecules, not crystals or films. We accept the statement of Cotton et al.<sup>[18]</sup> that linear chains of metal atoms that exist only in the solid state via the stacking of flat molecules, or through the formation of  $\mu$ -bridged chains of octahedral molecules (such as  $\text{NbCl}_4$ ) should not be called molecular wires. The extremely interesting inorganic crystalline nanowires being developed by Hu, Odom, and Lieber<sup>[19]</sup> Chung, Yu, and Heath<sup>[20]</sup> Cui and Lieber,<sup>[21]</sup> and Gudiksen, Wang, and Lieber<sup>[22]</sup> may eventually be used as wiring

in molecular electronics-based circuitry, but the fact that they comprise crystalline phases and not discrete molecules precludes their inclusion in this review.

In our survey of the literature, we find two general types of molecular wires. The largest portion of the literature, including most of our work, covers organic molecular wires. A smaller portion of the literature covers organometallic molecular wires. We include what some may call inorganic molecular wires in the organometallic class because of the ease of classification and the small number of inorganic molecular wires in the literature.

Molecular wires are meant to conduct electricity between two points of a circuit. However, a majority of the molecular wires intended for molecular electronics have never been tested in an actual circuit. One reason for this is that it is difficult to do so because of their small size. Another reason is that there is not one generally accepted test-bed that is readily available to all researchers. Rather, there are several different test-beds in the literature,<sup>[23–26]</sup> and the results from those molecular wires that have been tested are, in many cases, not comparable. These devices are difficult to make, yields are low, and obtaining reproducible results requires care and patience. Drawing conclusions about the activity of the classes of compounds, or building structure–activity relationships among several classes using the data generated can be a difficult exercise. However, because it has been shown that aromatic thiols are much higher conducting than alkane thiols<sup>[27]</sup> when bonded to Au surfaces, much attention has focused on conjugated aromatic molecular wires (*vide infra*).

## Organic Molecular Wires

### Oligo(2,5-thiophene ethynylene)s

Our group has focused on the synthesis of organic molecular wires. One class of compounds synthesized are the oligo(2,5-thiophene ethynylene)s (OTEs), several examples of which are compounds **1–5**, as shown in Fig. 2.<sup>[28–31]</sup> This class of rigid-rod oligomeric molecular wires was made through an iterative divergent–convergent synthesis method that allowed the quick assembly of the products, doubling their length at each step. The longest molecular wire synthesized was 12.8 nm in length. Note that these wires have thioester groups at one or both ends. When deprotected *in situ*, the thiol groups enable the molecular wires to adhere to Au (or other metal) surfaces,<sup>[27]</sup> thus serving as “alligator clips.” When large numbers of molecular wires bond to Au in a regular packed array, through this self-assembly process, the group of molecules is called a self-assembled monolayer (SAM). The bonding of

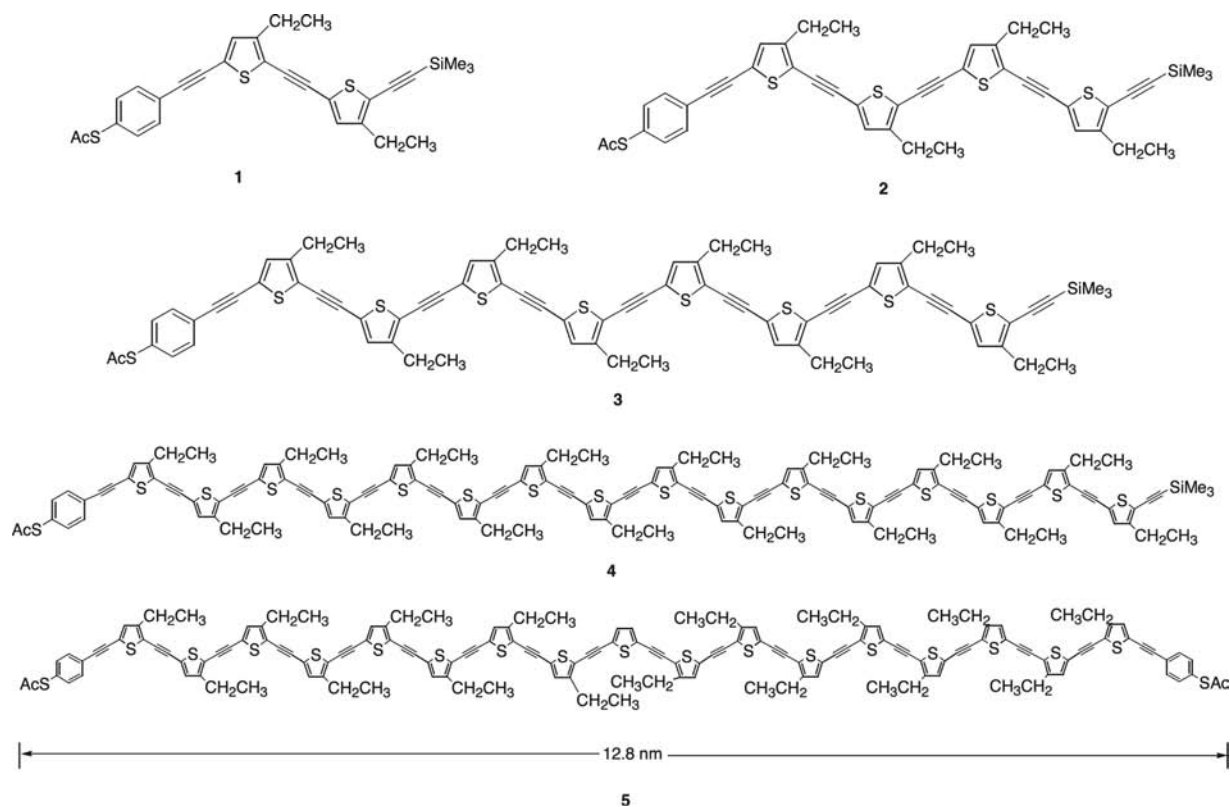


**Fig. 2** Oligo(2,5-thiophene ethynylene) molecular wires **1–5** synthesized by the authors. *Source:* From Ref.<sup>[28]</sup>. Note that **1–4** have thioester termini on one end only, whereas molecular wire **5** has thioester termini on both ends. The length of **5** is 12.8 nm for its energy-minimized conformation.

the S atom to Au enables the flow of electricity from the Au metal Fermi levels through the S molecular orbitals to the molecular orbitals formed by the conjugated portion of the molecule (see “[Theory and Measurement of Conduction](#)” and references cited therein for a discussion of this phenomena). The ethynyl units in between the aromatic molecules are used to maintain a maximum overlap of the orbitals and to keep the molecules in a rodlike shape. The various side chains appended to the thiophene cores were intended to increase the organic solvent solubility of the wires. Unfunctionalized rigid rod oligomers of this length suffer from severe solubility problems.

#### Oligo(1,4-phenylene ethynylene)s

A second class of molecules that has been studied extensively in our laboratory<sup>[32]</sup> and by others<sup>[33,34]</sup> are the oligo(1,4-phenylene ethynylene)s (OPEs). The molecule shown in [Fig. 1](#) is of this class, as are the molecules shown in [Fig. 3](#). As with the OTEs, the OPEs can be rapidly synthesized using transition metal-catalyzed coupling reactions. In this case, the compounds were synthesized in both solution phase and on a polymer-based solid resin. Compounds **6–9**

of [Fig. 3](#) are intermediates that were produced by cleaving the products from the resin using iodomethane and by coupling the resulting aryl iodides to the alligator clip acetyl(4-ethynylthiophenol) using typical transition metal-catalyzed coupling reactions.<sup>[32]</sup> The removal of the trimethylsilyl-protecting groups from the alkynes produced compounds **10–12** (from **6**, **7**, and **9**, respectively), and the coupling of the terminal alkyne in each case to acetyl(4-iodothiophenol) produced compounds **13** and **14** (from **10** and **12**, respectively). As in the OTEs, the C<sub>12</sub> side chains were used to impart organic solubility to the products. The use of longer side chains such as C<sub>16</sub> can result in side-chain interdigitation, leading to insolubility problems rather than increasing solubility.

In a series of syntheses of molecules in OPE subclasses, we have made products with more than two terminals and derivatives that are meant to test the necessity for a completely conjugated system.<sup>[35]</sup> [Fig. 4](#) shows a three-terminal molecular wire **15**. Note that all three terminals are functionalized with a protected thiol alligator clip, and that three of the aromatic nuclei have ethyl side chains to provide additional organic solvent solubility to the molecule. [Fig. 5](#) shows a three-terminal molecular wire **16** that contains an

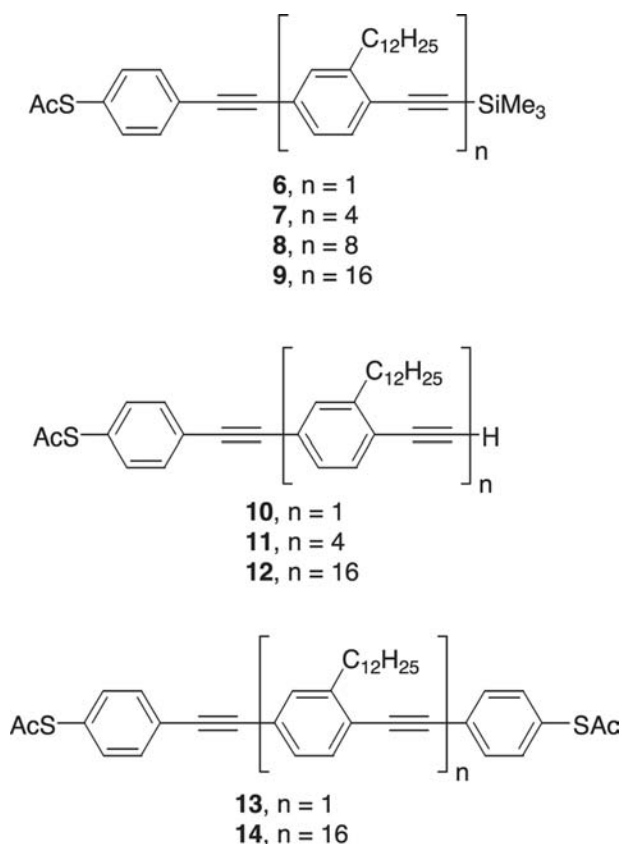


**Fig. 3** A series of oligo(phenylene ethynylene)s (OPEs) was synthesized using a polymer support to increase the yields and to facilitate purification. *Source:* From Ref.<sup>[32]</sup>.

interior methylene group as a possible barrier to current. **Fig. 6** shows two four-terminal molecular wires **17** and **18**, each with one methylene group interior current barrier. **Fig. 7** shows two four-terminal molecular wires **19** and **20**, each with two methylene group interior current barriers. The unfortunate circumstance is that, presently, no reliable system exists for testing these three-terminal and four-terminal molecular wires, so it is unknown whether or not the interior methylene group barriers are indeed resistant to current. However, the conductance of alkanethiolates (containing no aromatic conjugation whatsoever) on Au surfaces has been determined and has been shown to be less than that of conjugated systems (vida infra).

To further explore the organic functionality necessary for molecular wires to carry current, we have synthesized a group of two-terminal molecular wires **21–26**, shown in **Fig. 8**, which contains interior methylene or ethylene group barriers to electrical conduction, and which could be tested using presently known testbeds.<sup>[35]</sup> Each of these was synthesized using relatively straightforward chemistry, a fact that illustrates our earlier claim that it is easy to explore molecular wire

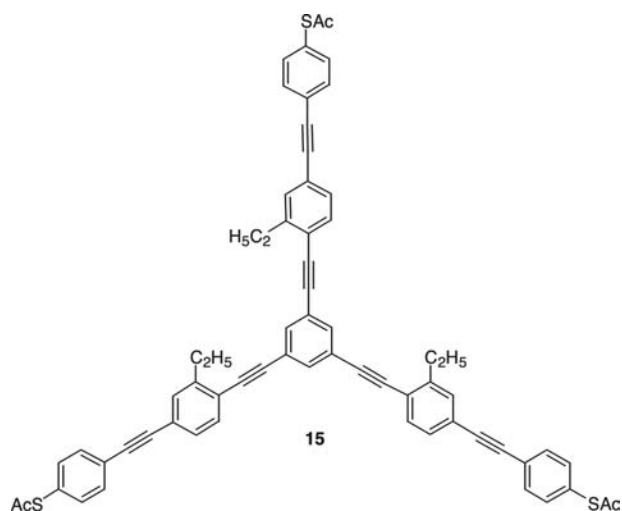


**Fig. 4** A three-terminal molecular wire that is functionalized with an alligator clip at each terminus and contains side-chain ethyl groups for solubility. *Source:* From Ref.<sup>[35]</sup>.

space by changing just one or two aspects of the synthesis. We also synthesized a series of OPEs with different alligator clips to see what effect that variation would have on the conductance of the molecular wire,<sup>[36]</sup> and we have developed combinatorial chemistry routes that will be capable of the synthesis of tens to hundreds of new molecular wires at one time.<sup>[37]</sup>

When members of the OPE family were functionalized with groups other than aliphatic ones (see **Fig. 9**),

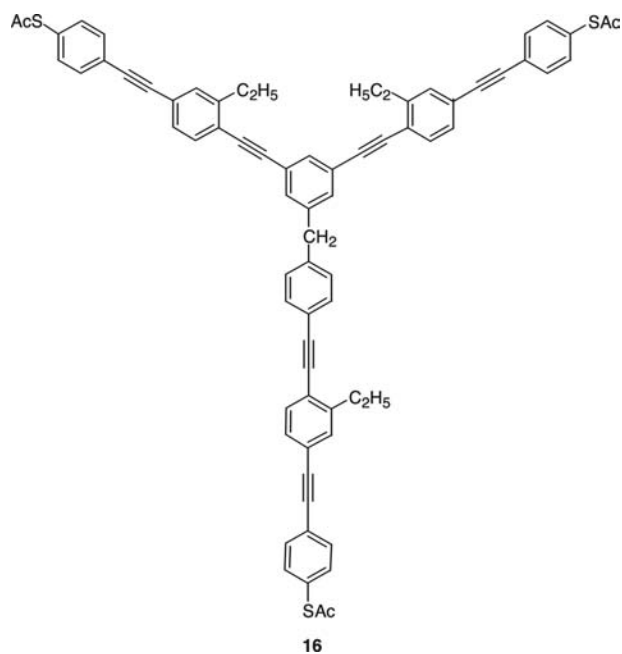


**Fig. 5** A three-terminal molecular wire containing an interior methylene group meant to serve as a possible small gate-like barrier to electrical current. *Source:* From Ref.<sup>[35]</sup>.

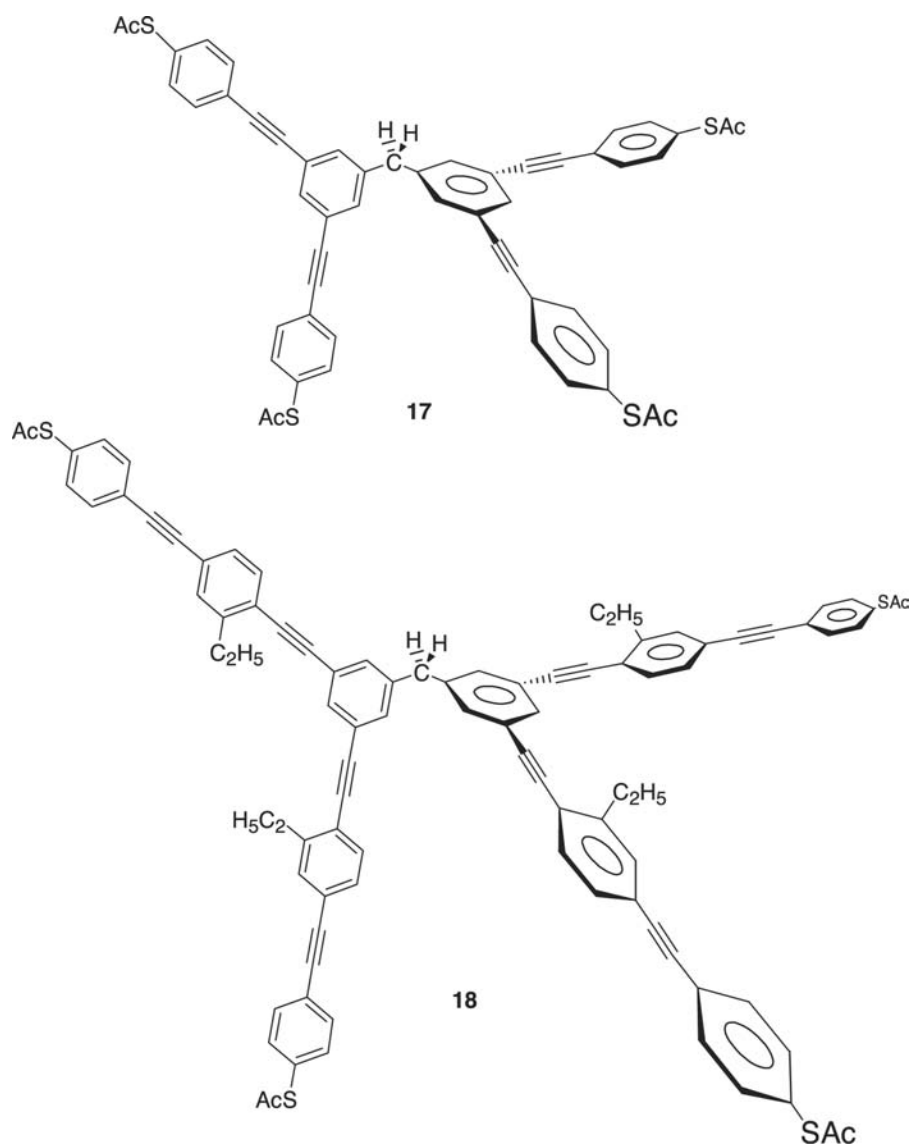


**Fig. 6** Two four-terminal molecular wires **17** and **18**, each containing an interior methylene group intended to be a gate-like barrier to current. *Source:* From Ref.<sup>[35]</sup>.

we began to see switching behavior,<sup>[24,38,39]</sup> although there is some question about whether the switching behavior results from molecular tilting modulations in the metal/molecule contact,<sup>[38]</sup> or from molecularly inherent features.<sup>[24]</sup> In the nanopore,<sup>[24]</sup> molecular wire **27** and amine-functionalized **29** had no activity,

whereas nitro-functionalized **28** and **30** were both active switches; conversely, analysis by scanning tunneling microscopy (STM)<sup>[38]</sup> indicated that all three of **27**, **28**, and **30** underwent conformational-based switching (**29** was not tested in the STM experiment) (see Refs.<sup>[1,2]</sup> for more information on switching). This

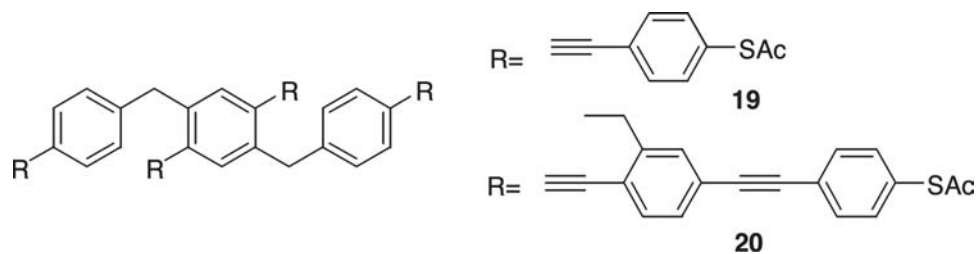


**Fig. 7** Two four-terminal molecular wires **19** and **20**, with each terminal having a protected alligator clip and each molecular wire having two interior methylene group current barriers. *Source:* From Ref.<sup>[35]</sup>.

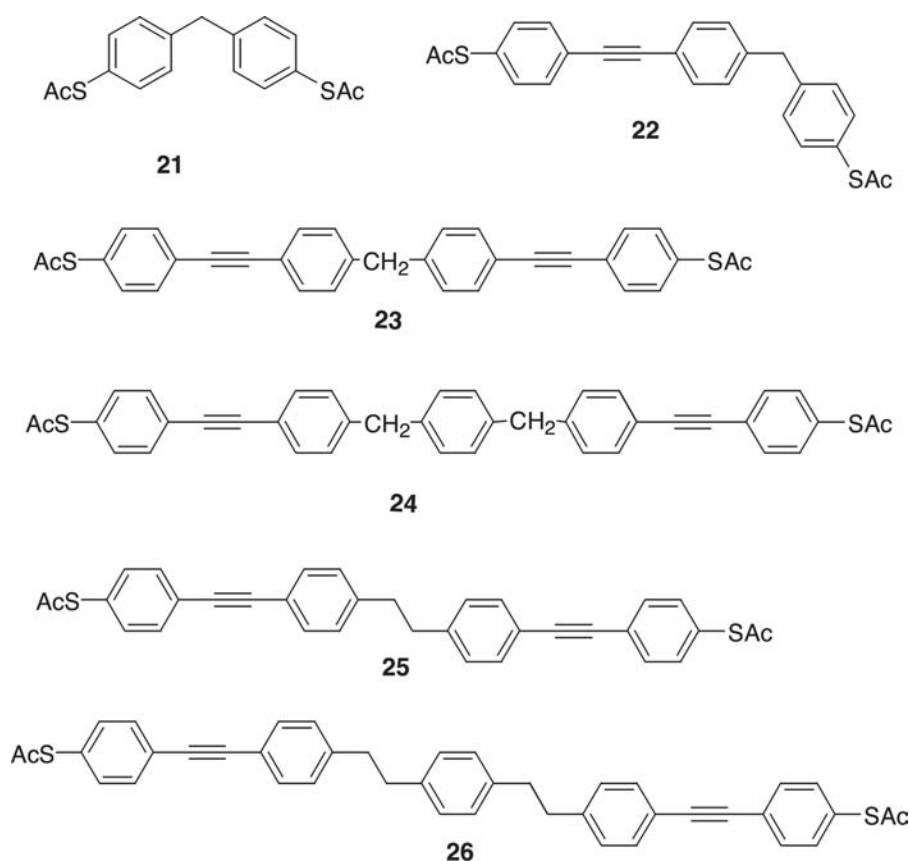


**Fig. 8** Molecular wires **21–26**, each containing an interior methylene or ethylene group barrier to conduction. *Source:* From Ref.<sup>[35]</sup>.

underscores that fact that varying test-beds can afford widely different results.

### Oligo(phenylene vinylene)s

A third class of compounds that has been studied in our laboratories as well as in others' are the oligo-

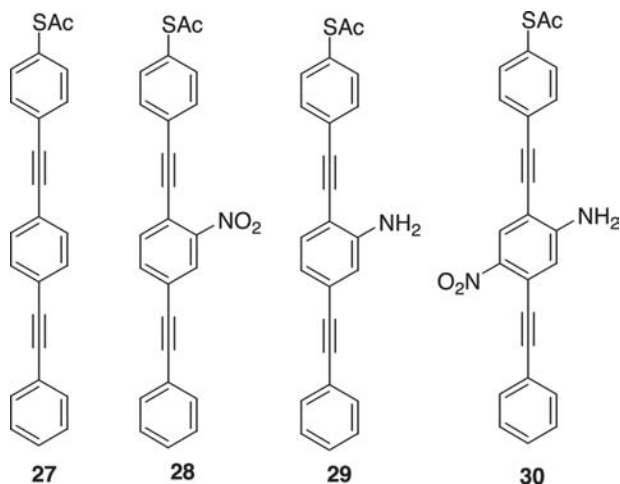


**Fig. 9** Unfunctionalized OPE **27** and functionalized OPEs **28–30**. *Source:* From Refs.<sup>[24]</sup> and <sup>[38]</sup>.

(phenylene vinylene)s (OPVs).<sup>[40–46]</sup> As mentioned earlier, the majority of others' works on OPVs have been geared toward applications in the optical and OLED field.<sup>[41–44,46]</sup> Our work produced molecular wires targeted for molecular electronics applications, and involved the synthesis of the three OPVs **31–33**, shown in Fig. 10. Note that **31** is unfunctionalized, containing only a protected thiol alligator clip for later SAM formation. After formation of the SAM, Au or other metals would be deposited, under vacuum, for the formation of the top contact to complete the circuit through the  $\pi$ -framework. We functionalized **32** with a nitro group on the interior aromatic core to determine if **32** would then act as a switch. Compound **32** is undergoing testing in a collaborator's laboratory. Finally, **33** was synthesized with both a nitro functional group and protected thiol groups at both ends so that it could span two Au contacts and form a circuit via a self-assembly process. This type of self-assembly process is important in our nanocell research program,<sup>[1]</sup> and is quite different from the approaches of others, who have not necessarily designed OPVs that are meant to connect two proximal probes, an interface to the present solid state-based technology.

Detert and Sugiono<sup>[46]</sup> synthesized a series of readily soluble OPVs shown in Fig. 11 to study their electronic spectra. They found that appending various



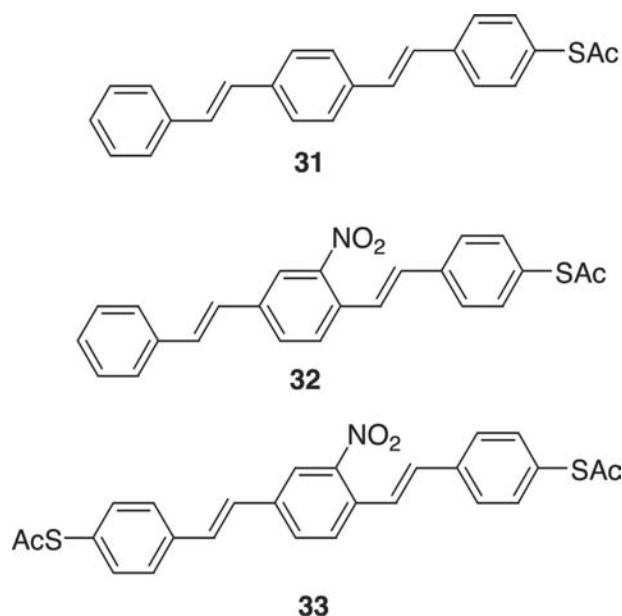


**Fig. 10** Three OPVs **31–33** synthesized by the authors. Source: From Ref.<sup>[40]</sup>.

electron-withdrawing groups to the terminal aromatic rings allowed the tuning of the electron affinity of the chromophore without significant changes in the spectra. When those same substituents were placed on the vinylene segments of the OPV molecules, strong bathochromic shifts were observed. Wong et al.<sup>[42]</sup> investigated similar substituent effects. Syamakumari, Schenning, and Meijer<sup>[41]</sup> and Gu et al.<sup>[43]</sup> synthesized large assemblies of OPVs attached to other molecules and measured their optical, electronic, and aggregation behaviors.

Sikes et al.<sup>[45]</sup> and Davis, Ratner, and Wasielewski<sup>[44]</sup> have used OPVs as core components of molecules (Fig. 12) synthesized to test electron tunneling and long distance electron transfer, respectively. Of the

compounds Sikes et al. synthesized, **35** spanned the most distance, 3.3 nm. The OPVs were assembled on a Au electrode and the tethered ferrocene redox species at the other end of the OPV bridge was exposed to an aqueous electrolyte. They used laser-induced temperature jump techniques to measure the rate constants of thermal interfacial electron transfer through the system and observed transfer through the OPV. They found that OPVs up to 2.8 nm in length were good conductors, with the transfer limited by structural reorganization.

In their study of a series of compounds including **36** (Fig. 12), the longest molecule tested, Davis, Ratner, and Wasielewski<sup>[44]</sup> found that electron transfer over long distances depends critically on the low-frequency torsional motions of the molecular wires (i.e., when the molecules twist and turn, their molecular orbitals do not line up in a fashion that favors fast electron transfer). But their tests were in solution rather than the more device-realistic molecule-surface attached patterns.

### Aromatic ladder oligomers

Our group has synthesized a vast array of aromatic ladder polymers<sup>[47,48]</sup> for use in conducting polymer and optoelectronic applications. However, we realized that for molecular electronic applications, the molecules we synthesized needed to have defined length and composition to be commercially useful as molecular wires.

As shown in Fig. 13, Gourdon<sup>[49]</sup> have synthesized two classes of conjugated ladder oligomers that maintain similar guidelines for molecular wires, including a defined length, rigidity, extended  $\pi$ -conjugation for good electron transfer, and good electronic coupling with metallic contacts. The oligo(quinoxaline) derivative **37** and oligo(benzoanthracene) molecular wire **38** were synthesized using standard condensation and coupling reactions. The oligo(quinoxaline) **37** has

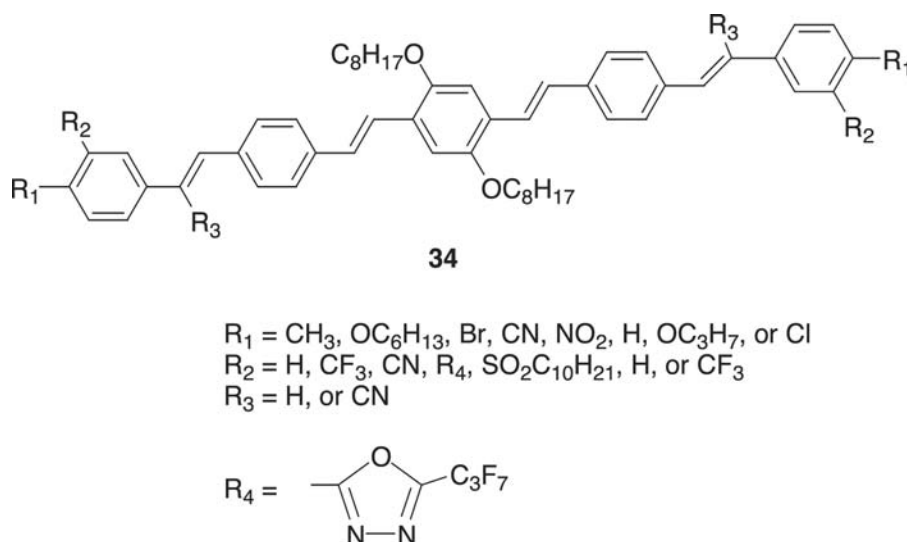


**Fig. 11** A series of OPVs **34** synthesized by Detert and Sugiono<sup>[46]</sup> to study the effect that variation of substituents  $R_1$ ,  $R_2$ ,  $R_3$ , and  $R_4$  had on the electronic spectra.

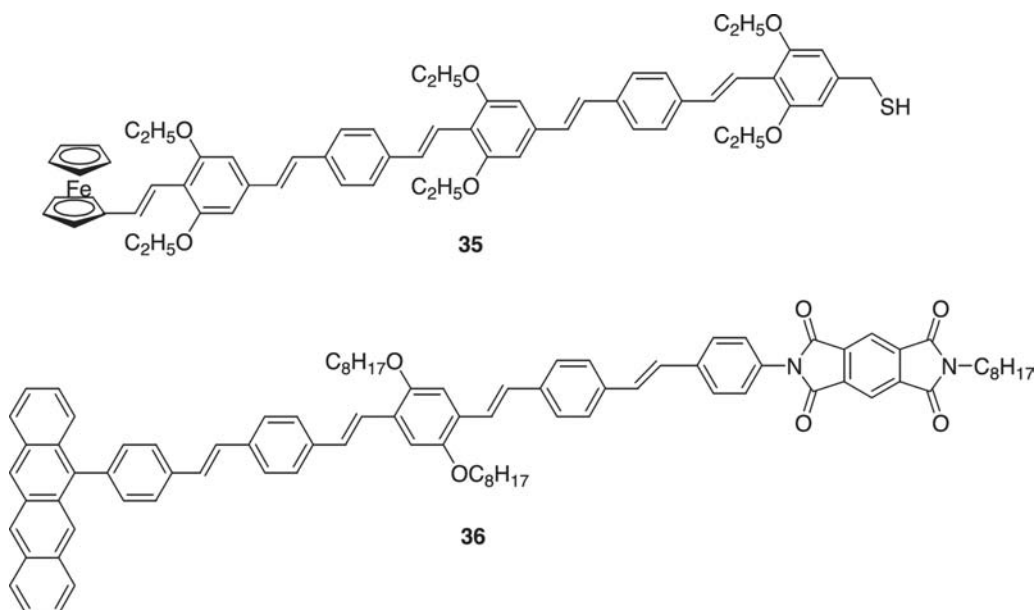


**Fig. 12** Sikes et al.<sup>[45]</sup> synthesized a series of OPVs including **35** to test electron tunneling whereas Davis et al.<sup>[44]</sup> synthesized a series of OPVs including **36** to measure long distance electron transfer.

built-in alligator clips in the terminal 1,10-phenanthroline moieties. We have also synthesized molecular wires containing terminal pyridine and other nitrogen-containing functional groups.<sup>[36]</sup> Calculations have supported their use as alligator clips.<sup>[50]</sup> An iterative crossed divergent–convergent process that leads to rapid growth of the oligomers was developed to synthesize the oligo(benzoanthracene) **38**.

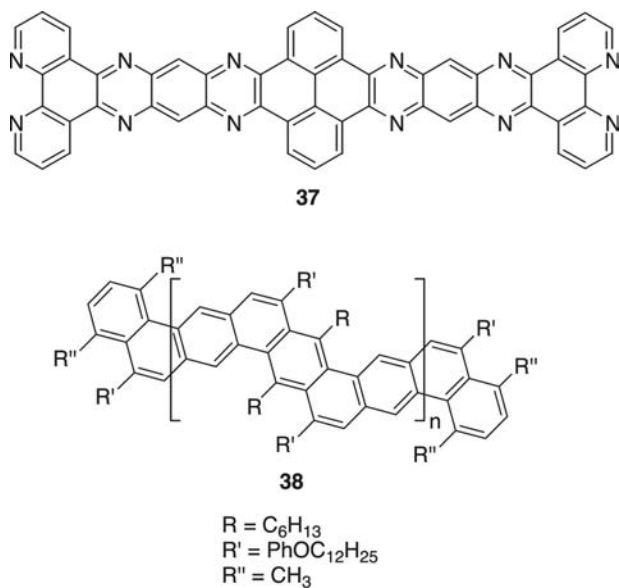


**Fig. 13** Gourdon<sup>[49]</sup> synthesized the aromatic ladder oligomers oligo(quinoxaline) **37** and the oligo(benzoanthracene) **38**.

### Oligophenylenes and polyphenylenes

The oligophenylene and polyphenylene classes of molecules, possessing a continuous overlap of molecular orbitals through extended conjugation without intervening groups such as alkynes or olefins, has been an active area of research for our group.<sup>[51–53]</sup> Grimsdale and Müllen<sup>[54]</sup> have synthesized a series of one-dimensional polyphenylenes including polyindeno-fluorene **39** and poly(9,9-diarylfuorene) **40**, shown in Fig. 14. The photoluminescence (PL) spectra of the series of polyindeno-fluorenes **39** all have maxima around 430 nm, making them possible candidates for OLED materials as well as molecular wires, although for applications in molecular electronics, one would normally want to be able to synthesize molecular wires with known lengths and constitutions because of concerns about homogeneity and materials handling. We have synthesized many oligophenylene derivatives<sup>[35,36]</sup> and generally find that the torsional twisting caused by the steric hindrance between the hydrogen atoms at the *ortho* positions of adjacent phenyl rings leads to decreased orbital overlap, and possibly lower conductance.

### Acetylene oligomers

Schenning et al.<sup>[55]</sup> and Livingston et al.<sup>[56]</sup> have synthesized the acetylene oligomer class of organic molecular wires. Their work included producing acetylene oligomers that are insulated via dendritic encapsulation (see Fig. 15). They found that the insulated

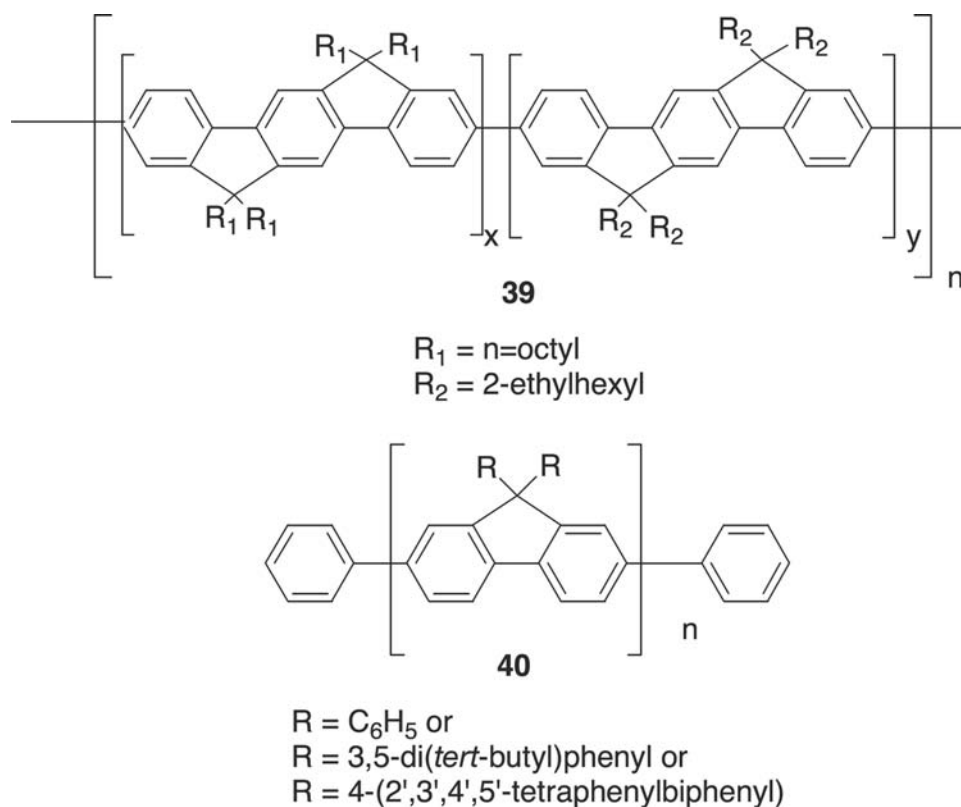


**Fig. 14** One-dimensional polyphenylene polymers **39** and **40** that have been synthesized by Grimsdale and Müllen.<sup>[54]</sup>

product **41** underwent ready isomerization around the double bond, producing a mixture of *E* and *Z* isomers that made purification of the materials difficult. Oligomeric acetylenic molecular wires that have been encapsulated within zeolites and other mesoporous materials show high electrochemical charge uptake.<sup>[57]</sup>

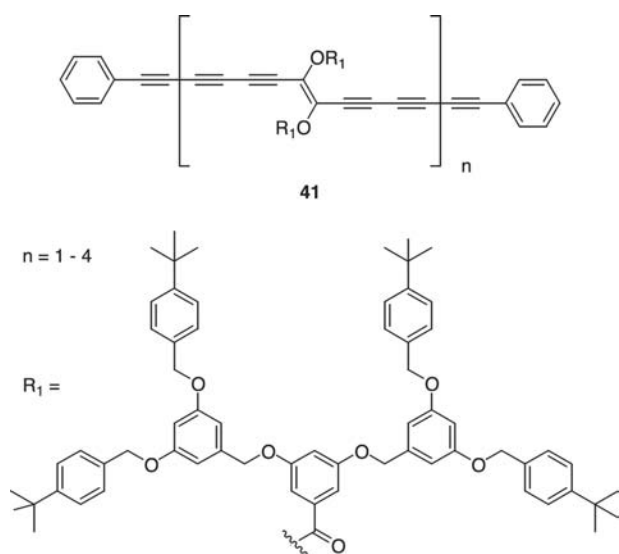


**Fig. 15** Encapsulated oligo(pentaacetylene) molecular wire **41** synthesized by Schenning et al.<sup>[55]</sup>

Taylor et al.<sup>[58]</sup> have published an approach to insulated molecular wires of the oligo(phenylene) class.

### Carbon nanotubes

Carbon nanotubes have been attractive candidates for use as molecular wires.<sup>[59,60]</sup> The so-called “cross-bar” approach to the development of a molecular electronics-based computer has, as one approach, the use of carbon nanotubes for the wiring between the molecular switches<sup>[5,8]</sup> of the circuitry. It is unfortunately difficult to work with carbon nanotubes because of their insolubility in most organic solvents,<sup>[61]</sup> and their tendency to form bundles of tubes that are difficult to separate. Several methods for the functionalization of the carbon nanotubes that may make it easier to handle the carbon nanotubes have been developed.<sup>[62,63]</sup> However, the same functionalization techniques can also destroy the electrical properties of the molecules.<sup>[2]</sup> Calculations by Seifert, Köhler, and Fravenheim<sup>[64]</sup> indicate that sidewall fluorination of carbon nanotubes could produce products with a wide range of characteristics from insulating to metallic-like behavior. It is possible that nanowires<sup>[19]</sup> will be used in the cross-bar computing devices instead of carbon nanotubes because of the easier synthesis and handling of the nanowires.

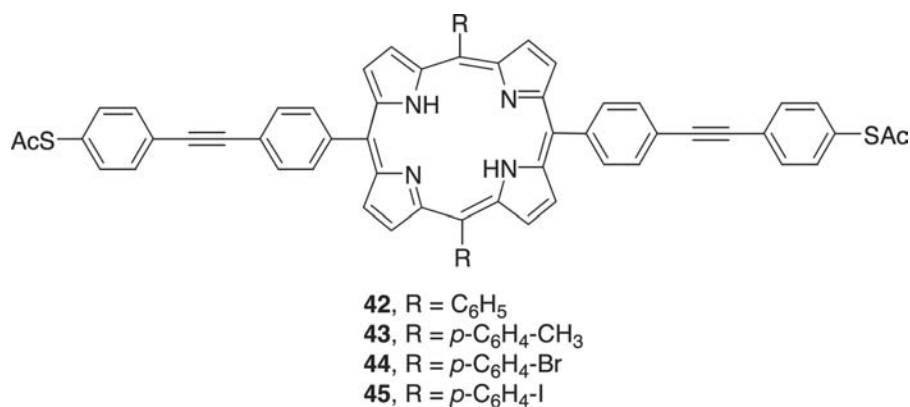


**Fig. 16** Porphyrins **42–45** synthesized by the authors. *Source:* From Ref.<sup>[35]</sup>. Zn, Cu, and Co metal atoms were inserted into **42**. Subsequent deprotection of the thiol acetates resulted in no metal ion loss.

### Organometallic Molecular Wires

We have synthesized molecules in the porphyrin class of molecular wires<sup>[35]</sup> and have recently returned to this work.<sup>[65]</sup> Fig. 16 shows four porphyrin derivatives made in our laboratories. Zn, Cu, and Co were all inserted into **42** using the corresponding hydrated metal acetates. Deprotection of the thiol acetates by NH<sub>4</sub>OH resulted in no loss of metal, as indicated

by subsequent nuclear magnetic resonance (NMR) analysis. Although being interesting compounds in and of themselves, **44** and **45** could also be intermediates in the synthesis of more complex molecular wires. A four-terminal porphyrin shown in Fig. 17 was also synthesized.

Ambroise et al.<sup>[66]</sup> have published a large body of work concerning the synthesis and testing of molecular “photonic” wires based on porphyrin molecules linked

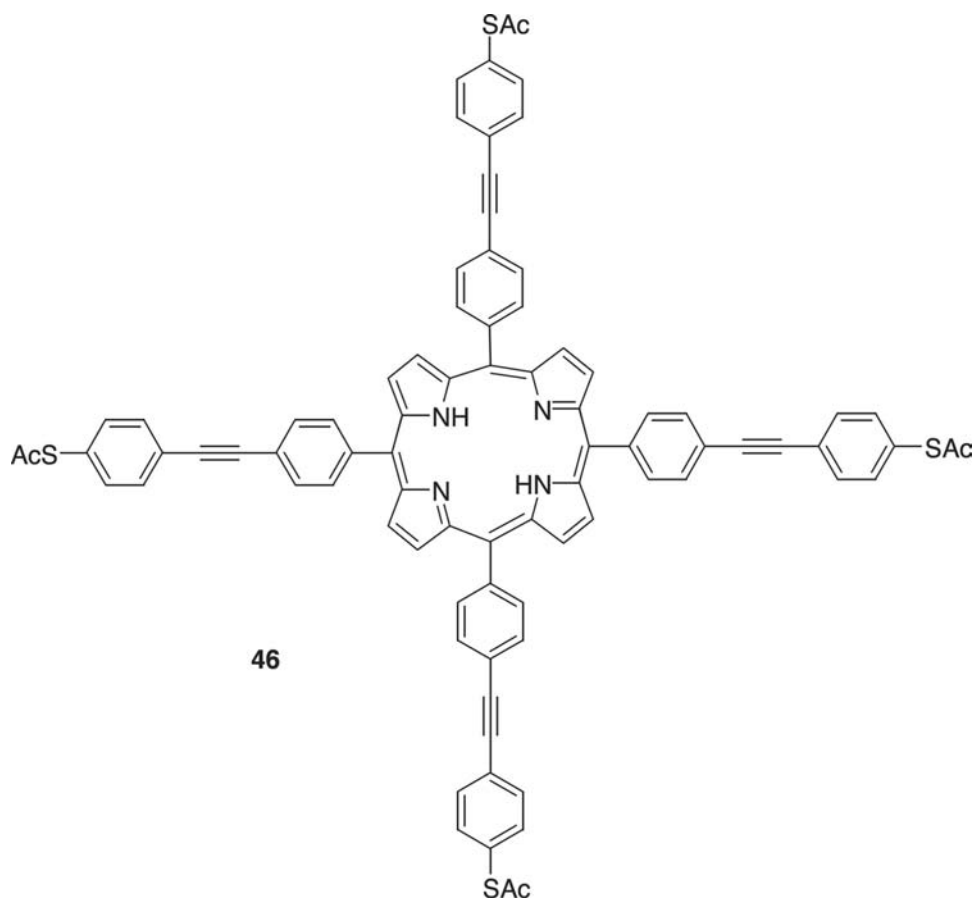


**Fig. 17** A four terminal porphyrin-based molecular wire **46** synthesized by the authors. *Source:* From Ref.<sup>[35]</sup>.

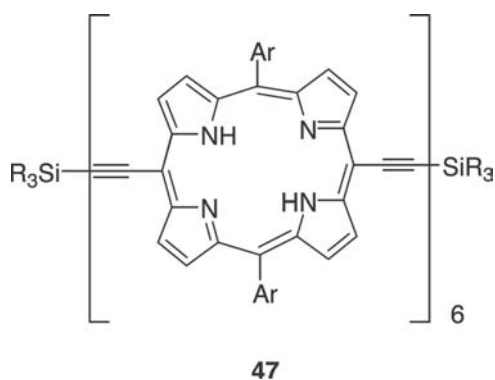


**Fig. 18** The porphyrin hexamer **47** synthesized by Anderson,<sup>[67]</sup> with six porphyrin units linked through dialkynes.

by diaryl ethyne units to light-absorbing dyes. The energy absorbed by the dyes is transmitted through the porphyrin-diaryl-ethyne wires to a free-base porphyrin transmission unit. The quantum efficiency was determined to be very high, from 81 to >99%.

Anderson<sup>[67]</sup> has reviewed the synthesis and optoelectronic properties of conjugated porphyrin molecular wires. As with the OPTs, OPEs, and oligomeric acetylenes, alkyne moieties have been used to link porphyrin units to make longer molecular wires, such as **47** in Fig. 18. The estimated length of **47** is 8.3 nm from Si atom to Si atom. Anderson's work has shown that the electronic behavior of these types of systems can be attributed to strong interporphyrin conjugation in the ground state. This strong interaction is amplified in the excited states, and also in the oxidized and reduced forms of the porphyrin core.

Iengo et al.<sup>[68]</sup> have used self-assembly techniques to synthesize large metallacycles of porphyrins. By synthesizing porphyrins having two peripheral pyridine appendages at either 90° or 180° to each other, and by adding the requisite ionic metallic component such as the RuCl<sub>2</sub> complex of dimethylsulfoxide (DMSO), supramolecular structures are produced. This self-assembly process proceeds with two porphyrin and two RuCl<sub>2</sub> complexes forming (as one example) the molecule **48** shown in Fig. 19. The substitution of CO for DMSO in the RuCl<sub>2</sub> raw material forms a similar metallacycle with CO instead of DMSO as Ru ligands. By inserting Zn into the resulting porphyrin core and by exposing the mixture to 4,4'-bipyridine (which acts as a ligand for the Zn atoms at the porphyrin cores), a stacked complex was formed. The authors envisioned that such complexes, with their extended conjugation and metal centers, could harvest light energy and act as molecular wires.

The self-assembly of inorganic molecular wires in solution has been described by Kimizuku.<sup>[69]</sup> However, it is unknown whether this process would produce products usable in constructing devices.

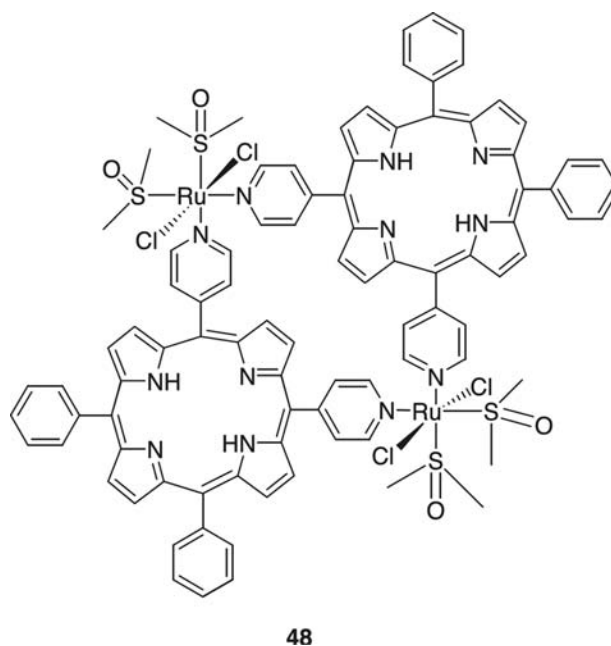


**Fig. 19** The porphyrin metallacycle **48** synthesized by Iengo et al.<sup>[68]</sup>

Pyridine ligands are common in organometallic molecular wires,<sup>[70–72]</sup> with a review recently appearing.<sup>[73]</sup> For instance, Constable et al.<sup>[70]</sup> synthesized the molecular wire **49** shown in Fig. 20. The [Ru(terpy)<sub>2</sub>]<sup>2+</sup> salts by themselves are nonluminescent, whereas adding the 2,5-thiophenediyl spacers produces a molecular wire that is luminescent. Shiotsuka et al.<sup>[71]</sup> made a Ru–Au–Ru triad by using a bis-σ-Au-acetylide to connect two Ru complexes. The resulting molecular wire showed an intense emission at 620 nm upon excitation at 360 nm, suggesting some energy transfer from the Au to the Ru site via the π-conjugation offered by the ethynyl units. Berry et al.<sup>[72]</sup> synthesized a trinickel complex of the ligand di-2,2'-pyridylamide that had a deep blue color and showed metal–metal bonding interaction in the crystal structure.

An interesting mixed-valence molecular wire pair **50** and **51** synthesized by Stang, Paul, and Lapinte<sup>[74]</sup> is shown in Fig. 21. As we have seen in many of the molecular wires, both the thiophenyl and the alkynyl units are present in this molecular wire.

## THEORY AND MEASUREMENT OF CONDUCTION

### Theory of Conduction in Molecular Wires

The difficulties in obtaining direct measurements of current in molecular wires have not deterred theoretical chemists from developing models of the conductive

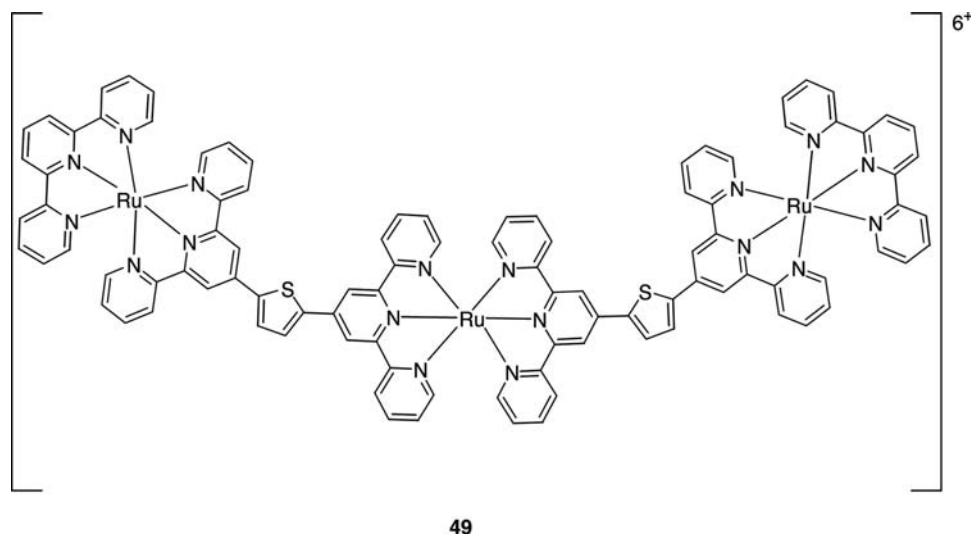


**Fig. 20** The molecular wire **49** synthesized by Constable et al.<sup>[70]</sup> that showed luminescence because of the presence of 2,5-thiophenediyl spacers.

process. This has been a very fruitful area of research. The editors of *Chemical Physics* recently devoted an entire issue to “Transport in Molecular Wires.”<sup>[75]</sup> We will briefly review the relevant literature here.

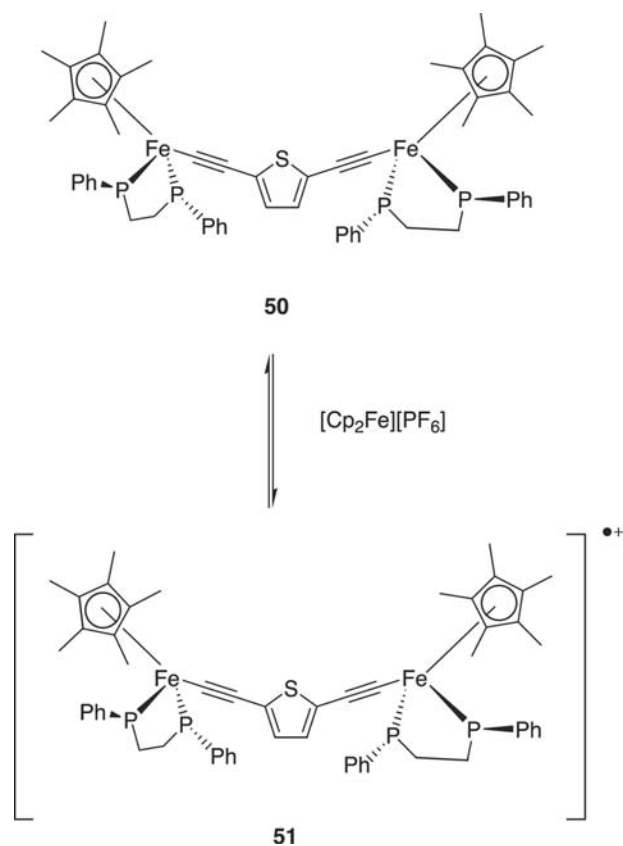


**Fig. 21** A mixed-valence complex pair of molecular wires **50** and **51** as synthesized by Stang et al.<sup>[74]</sup>

### The molecular wire–electrode interface

One of the most important aspects of the application of molecular wires is developing a method for contacting the molecular wire with the electrode that will be carrying the current to the molecular wire. Several researchers have examined the theoretical aspects of this connection.<sup>[76–79]</sup> Yaliraki, Kemp, and Ratner<sup>[76]</sup> examined the bonding of 1,4-bis(thiomethyl)benzene (**52** in Fig. 22) to metal surfaces using Green’s function and the extended Hückel Hamiltonian, and found that, except for the length of the surface bond, conductance through the molecule was not affected by the angle of the S-metal bond to the surface. They found that if Se substituted for S in the molecular wire, the conductance through the wire was larger (O substitution produced conductance of the same magnitude as S). They also found that Au made a better electrode than Ag. Note that a methylene node was between the terminal S atom and the aromatic benzene molecule, unlike other models where the S atom is directly bonded to the aromatic nucleus.

Using ab initio Hartree–Fock calculations, Johansson and Stafström<sup>[77]</sup> found that for a benzenethiol bonded to Au, the conducting states of the organic molecular wire interacted directly with the electronic system of the Au substrate, forming an ohmic contact. Onipko, Klymenko, and Malysheva<sup>[78]</sup> presented a detailed analytical approach to modeling the connection of the contacts to molecular wires that is applicable to a variety of functionalized systems. Seminario, De La Cruz, and Derosa<sup>[79]</sup> used the Green function coupled with the B3PW91/LANL2DZ level of theory to calculate the behavior of S and isonitrile (–NC) alligator clip bonds to Ni, Cu, Pd, Ag, Pt, and Au. They found that



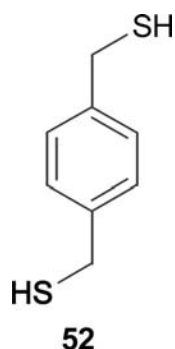


**Fig. 22** The structure of 1,4-bis(thiomethyl)benzene **52**, the molecule studied by Yaliraki et al.<sup>[76]</sup>

the best metal for the metal–molecule interface was Pd, followed by Ni and Pt. Cu was intermediate whereas Au and Ag were worst. The S-based alligator clip was slightly better than the isonitrile alligator clip. The bond angle of the metal–alligator clip bond did make a difference in the calculated conductance of the molecular wire, apparently because of various levels of overlap with the extended  $\pi$  system of the aromatic nucleus.

The theoretical use of molecular wires to transport spin-dependent information in an area of molecular electronics called “spintronics” has been studied by Emberly and Kirczenow.<sup>[80]</sup> Spintronics utilizes the electron’s spin degree of freedom as well the charge of the electron to store, transmit, and process data. Based on their calculations, spin valve behavior should be observable in SAMs formed from 1,4-benzenedithiol between two Ni wires (a “break-junction” test-bed).

Recall that in Figs.<sup>[5–8]</sup> were several examples of synthesized molecules that contained methylene or ethylene group spacers to break up the extended conjugation of the OPEs. Karzazi, Cornil, Brédas<sup>[81,82]</sup> have published quantum-chemical calculations that were used to describe qualitatively the mechanism leading to resonant tunneling diodes (RTDs) with negative differential resistance (NDR; a switching phenomena) in molecular wires with such spacers as part of their molecular structures. It was theorized that having an ethylene spacer versus a methylene spacer led to better NDR characteristics, with larger on–off ratios.

### Conductance theory of molecular wires

A large body of work has been published regarding the theoretical aspects of conductance of molecular wires.<sup>[83–96]</sup> We will highlight several aspects of the work here, and invite the reader to explore the cited literature for more information.

Seminario et al.<sup>[83,85,88]</sup> and Derosa and Seminario<sup>[87]</sup> have used density function theory and Green

function theory to model the molecular orbitals of simple 1,4-benzenedithiol and more complex conjugated OPE systems. Calculations show that the highest occupied molecular orbitals (HOMOs) and the lowest unoccupied molecular orbitals (LUMOs) of a system can be localized (i.e., confined to certain atoms of the molecule) or delocalized (i.e., distributed over the entire molecular system depending on the charge). The localization of molecular orbitals will tend to prevent conductance through the molecule, whereas delocalization will tend to favor conductance. The addition of substituents and/or addition or subtraction of electrons from the system can change not only the shape (localization or delocalization) of the LUMOs and HOMOs but their energy levels. Changes in energy levels will affect whether the LUMOs and/or HOMOs overlap with the Fermi levels of the metal contact, also affecting the conduction through the molecules. The values of conductance for these systems with various charges determined by calculation agreed with experimentally derived data. The change in the LUMOs and HOMOs brought about by the injection of electrons into the molecular system was the reason that they could act as switches, turning on or off to current.

Mujica, Ratner, and Nitzan<sup>[89]</sup> have examined the theoretical aspects of molecular rectification.<sup>[97]</sup> Rectification occurs when the shape of the forward  $I(V)$  curve is not the inverse of the reverse bias  $I(V)$  curve when determining the conductance of a molecular wire as related to the applied voltage. The work of Mujica et al. suggested that the rectification is difficult to achieve because the finite voltages in the system cause the deformation of the structure, leading to effectively symmetrical voltage profiles for the forward and reverse biases. Interestingly, many have observed rectification because the two contacts between the ends of the molecular wires are different.

Avouris and Lang<sup>[98]</sup> have done an interesting theoretical study on the effect of coadsorption of contaminants on the conductance of molecular wires. Avouris and Lang had observed experimentally that the conductance of semiconducting carbon nanotubes changed when metal/semiconducting nanotube/metal devices were exposed to oxygen. Density function theory was used to determine that adsorption of electropositive Li atoms or electronegative O atoms perturbed the molecular orbitals of biphenyl. This work has wide-ranging implications, as it has been thought that the development of molecular electronics-based computers might not require the ultra pure water (UPW) and expensive clean rooms that the semiconductor manufacturing industry needs to produce the high yields of working devices of the present commercial technology. However, purity of the chemicals and cleanliness of the tools and reaction chambers could be of paramount importance to the commercialization of

the molecular wire technology. This calculation also has implications for experimental work, as contamination could easily introduce artifacts and false positives or negatives into laboratory testing.

Granger et al.<sup>[99]</sup> have recently predicted that carbon nanotubes and other linear molecular conductors can support electronic states that are localized far from their surface. Hill and McLean<sup>[100]</sup> have published experimental evidence for such states around an In nanowire. This work could have implications in answering the question: "Just how close does a molecular wire have to be to a connection to conduct electricity?" Carbon nanotubes or inorganic nanowires placed in near proximity may have electronic effects on circuitry and devices.

### Measurement of Conductance in Molecular Wires

A large body of work has also been published concerning the measurement of conductance in molecular wires.<sup>[101–112]</sup> We will touch on the highlights in this review.

Reed et al.<sup>[23]</sup> and Chen and Reed<sup>[103]</sup> have studied the conductance of both single molecules and of SAMs of molecules formed in a nanopore device. Stable and reproducible switching and memory effects were seen in the nanopore devices, with demonstrated NDR and charge storage with bit retention times of greater than 15 min at room temperature.

Patrone et al.<sup>[105]</sup> compared the electronic coupling efficiency of S and Se alligator clips on Au surfaces and found Se to be the better coupling link. Rampi and Whitesides<sup>[107]</sup> have developed a test-bed for measuring conductance in molecular wires using two metal electrodes sandwiching two SAMs, with the top metal electrode being Hg for convenience of formation. There are three different forms of this test-bed; the first comprises two Hg drops, each covered with the same SAM; the second test-bed comprises a Hg drop covered with a SAM interacting with a SAM formed on Ag; the third test-bed is similar to the first, only with redox-active molecules trapped between the two SAMs to do electrochemical measurements on them.

Avouris<sup>[108]</sup> has carried out extensive conductance measurements on carbon nanotubes and has constructed electronic devices containing them, including carbon nanotube field effect transistors (CNTFETs). Nanotubes are known to have either metallic or semiconducting properties. One problem with single-walled nanotube (SWNT) bundles is separating the metallic tubes from the semiconducting tubes. Avouris has developed a process that removes the metallic nanotubes, leaving the semiconducting behind.

Kushmerick et al.<sup>[110]</sup> have developed a test-bed device in which a SAM of the molecule of interest is formed on one of two 10- $\mu\text{m}$  Au wires that are crossed, and brought into contact by the Lorentz force (i.e., DC current in one wire deflects it in a magnetic field). Using this device,  $I(V)$  characteristics were measured for three molecules **53–55** shown in Fig. 23. Normalizing the conductance of the  $\text{C}_{12}$  alkanethiol **53** to 1, the conductance of the OPE molecular wire **54** was measured at 15 and the conductance of the OPV molecular wire **55** was measured at 46. Note that **55** has benzylic thioester moieties with methylene barrier groups to disrupt the molecular orbital overlap of the rest of the conjugated system. The researchers attribute the increased conductivity of the OPV molecule to both the increased coplanarity of the molecule (the alkynes in the OPEs allow the phenyl rings to be more freely rotating when compared to the vinylene group-linked OPVs), thus the population of OPE molecules existing in fully conjugated form is lower than the population of OPV molecules existing in fully conjugated form at the same temperature), and to the more regular periodicity of the conjugated molecular backbone of the OPV molecular wire. Compare the short 0.1218-nm alkyne linkage in the OPE molecular wire to the 0.1352-nm vinylene linkage of the OPV molecular wire and the  $0.141 \pm 0.001$  nm periodicity of the  $\pi$ -conjugated molecular backbone.

Rawlett et al.<sup>[111]</sup> used conducting atomic force microscopy (cAFM) to measure the conductance of

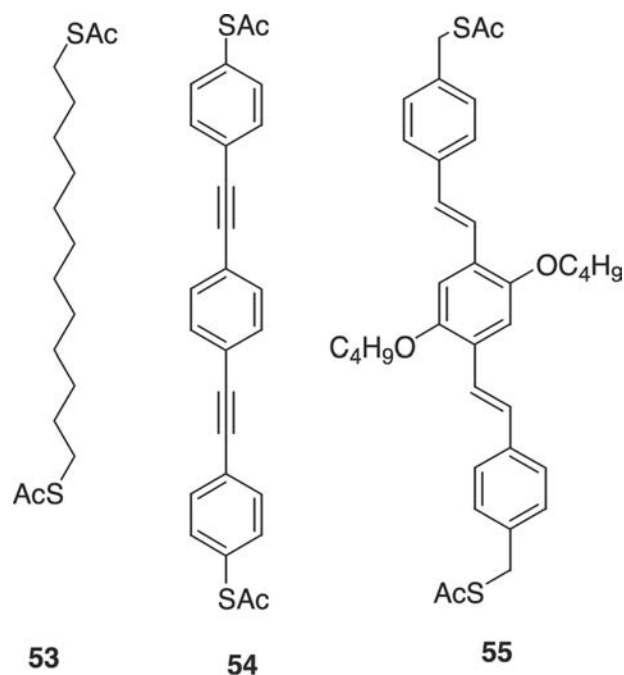


**Fig. 23** The molecular wires **53–55** tested by Kushmerick et al.<sup>[110]</sup> using a crossed-wire tunnel junction test-bed.

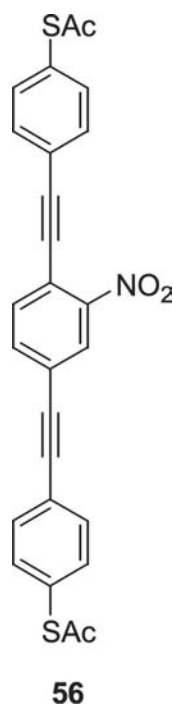


**Fig. 24** The molecular wire **56**, the conductance of which was tested by Rawlett et al.<sup>[11]</sup> using cAFM.

two different molecules that had been inserted into the naturally occurring defect sites of a dodecanethiol SAM on Au. The molecular wires **54** (Fig. 23) and **56** were (Fig. 24) constrained to be standing upright, parallel to the surface of the Au, because of the tight packing of the dodecanethiol SAM. Au nanoparticles were attached to the projecting deprotected thiol groups, and the nanoparticle was contacted by a Au-coated AFM tip to measure the conductance through what are thought to be individual molecules based on evidence not discussed here. Reproducible NDR effects were seen only for molecular wire **56**, not for **54**, indicating that the functionalization of the wire with the  $-\text{NO}_2$  group leads to the NDR effect.

Wang, Lee, and Reed<sup>[12]</sup> have completed a systematic temperature-dependent study of the conductance of alkanethiolates in SAMs and have shown conclusively that direct tunneling is the dominant transport mechanism.

## CONCLUSION

Based on the wealth of literature cited, fully conjugated completely organic aromatic molecular wires are the best candidates for introduction into new electronic devices as replacements for the Al or Cu wiring presently used in logic and memory devices. The OPE and OPV classes of molecular wires with S alligator clips have the highest conductances, both theoretical

and measured. Recent data indicate that OPV molecular wires are better than OPE molecular wires. Many more questions remain to be answered, the most important of which is how these molecular wires will be integrated into processes to build the molecular electronic and optoelectronic devices of the future. Problems raised by such integration efforts will likely require several iterations in molecular wire research. As we have pointed out, the beauty of organic chemistry is that simple changes to the raw materials used in synthesizing the molecular wires can yield products with vastly different physical properties. The molecular wire(s) that eventually appears in commercial devices may bear no resemblance to those we have discussed. Thus research in this area can still yield much fruit.

## ACKNOWLEDGMENT

We thank DARPA administered by the Office of Naval Research (ONR); the ONR Polymer Program; the U.S. Department of Commerce, National Institute of Standards and Technology; the Army Research Office; NASA; and the Air Force Office of Sponsored Research (AFOSR F49620-01-1-0364) for financial support of this work.

## REFERENCES

1. Tour, J.M. *Molecular Electronics: Commercial Insights, Chemistry, Devices, Architecture, and Programming*; World Scientific Publishing: New Jersey, 2003, *in press*.
2. Tour, J.M.; James, D.K. Molecular Electronic Computing Architecture. In *Handbook of Nanoscience, Engineering, and Technology*; Goddard, W.A., III, Brenner, D.W., Lyshevski, S.E., Iafate, G.J., Eds.; CRC Press: Boca Raton, FL, 2002; 4-1-4-28.
3. Ward, M.D. Chemistry and molecular electronics: New molecules as wires, switches, and logic gates. *J. Chem. Educ.* **2001**, *78* (3), 321-328.
4. Tour, J.M. Molecular electronics. Synthesis and testing of components. *Acc. Chem. Res.* **2000**, *33* (11), 791-804.
5. Heath, J.R. Wires, switches, and wiring. A route toward a chemically assembled electronic nanocomputer. *Pure Appl. Chem.* **2000**, *72* (1-2), 11-20.
6. Reed, M.A.; Tour, J.M. Computing with molecules. *Sci. Am.* June **2000**, *2000*, 68-75.
7. Overton, R. Molecular electronics will change everything. *Wired* **2000**, *8* (7), 242-251.
8. Heath, J.R.; Kuekes, P.J.; Snider, G.S.; Williams, R.S. A defect-tolerant computer architecture: Opportunities for nanotechnology. *Science* June 12 **1998**, *280*, 1716-1721.
9. Moore, G.E. Cramming more components onto integrated circuits. *Electronics* **1965**, *38* (8). Available

- on the web: <http://www.intel.com/research/silicon/moorespaper.pdf> (accessed September 2002).
10. Intel press release: <http://www.intel.com/pressroom/archive/releases/20011017man.htm> (accessed September 2002).
  11. Intel press release: <http://www.intel.com/pressroom/archive/releases/20020813tech.htm> (accessed September 2002).
  12. International Technology Roadmap for Semiconductors web pages: <http://public.itrs.net/Files/2001ITRS/PIDS.pdf> (accessed September 2002).
  13. Wang, K.L. Issues of nanoelectronics: A possible roadmap. *J. Nanosci. Nanotech.* **2002**, *2* (3/4), 235–266.
  14. Service, R.F. Molecules get wired. *Science* December 21, **2001**, *294*, 2442–2443.
  15. Patel, N.K.; Cinà, S.; Burroughes, J.H. High-efficiency organic light-emitting diodes. *IEEE J. Sel. Top. Quantum Electron.* **2002**, *8* (2), 346–361.
  16. Popovic, Z.D.; Aziz, H. Reliability and degradation of small molecule-based organic light-emitting devices (OLEDs). *IEEE J. Sel. Top. Quantum Electron.* **2002**, *8* (2), 362–371.
  17. Matthews, S.J. Organically grown. *Laser Focus World* **2001**, *37* (8), 169–170, 172, 175.
  18. Cotton, F.A.; Daniels, L.M.; Murillo, C.M.; Wang, X. Getting the right answer to a key question concerning molecular wires. *Chem. Commun.* **1999**, *1999*, 2461–2462.
  19. Hu, J.; Odom, T.W.; Lieber, C.M. Chemistry and physics in one dimension: Synthesis and properties of nanowires and nanotubes. *Acc. Chem. Res.* **1999**, *32* (5), 435–445.
  20. Chung, S.-W.; Yu, J.-Y.; Heath, J.R. Silicon nanowire devices. *Appl. Phys. Lett.* **2000**, *76* (15), 2068–2070.
  21. Cui, Y.; Lieber, C.M. Functional nanoscale electronic devices assembled using silicon nanowire building blocks. *Science*, February 2 **2001**, *291*, 851–853.
  22. Gudixsen, M.S.; Wang, J.; Lieber, C.M. Synthetic control of the diameter and length of single crystal semiconductor nanowires. *J. Phys. Chem., B* **2001**, *105* (19), 4062–4064.
  23. Reed, M.A.; Zhou, C.; Muller, C.J.; Burgin, T.P.; Tour, J.M. Conductance of a molecular junction. *Science*, October 10, **1997**, *278*, 252–254.
  24. Chen, J.; Reed, M.A.; Rawlett, A.M.; Tour, J.M. Large on–off ratios and negative differential resistance in a molecular electronic device. *Science*, November 19, **1999**, *286*, 1550–1552.
  25. Ranganathan, S.; Steidel, I.; Anariba, F.; McCreery, R.L. Covalently bonded organic monolayers on a carbon substrate: A new paradigm for molecular electronics. *Nano Lett.* **2001**, *1* (9), 491–494.
  26. Fan, F.-R.F.; Yang, J.; Cai, L.; Price, D.W., Jr.; Dirk, S.M.; Kosynkin, D.V.; Yao, Y.; Rawlett, A.M.; Tour, J.M.; Bard, A.J. Charge transport through self-assembled monolayers of compounds of interest in molecular electronics. *J. Am. Chem. Soc.* **2002**, *124* (19), 5550–5556.
  27. Bumm, L.A.; Arnold, J.J.; Cygan, M.T.; Dunbar, T.D.; Burgin, T.P.; Jones, L., II; Allara, D.L.; Tour, J.M.; Weiss, P.S. Are single molecular wires conducting? *Science* **1996**, *271*, 1705–1706.
  28. Pearson, D.L.; Tour, J.M. Rapid syntheses of oligo(2,5-thiophene ethynylene)s with thioester termini: Potential molecular scale wires with alligator clips. *J. Org. Chem.* **1997**, *62* (5), 1376–1387.
  29. Pearson, D.L.; Jones, L., II; Schumm, J.S.; Tour, J.M. Molecular scale electronics. Synthesis and testing. *Synth. Met.* **1997**, *84*, 303–306.
  30. Pearson, D.L.; Jones, L., II; Schumm, J.S.; Tour, J.M. In *Synthesis of Molecular Scale Wires and Alligator Clips*, Proceedings of the NATO Advanced Research Workshop on Atomic and Molecular Wires, Les Houches, France, May, 6–10, 1996; Joachim, C., Roth, S., Eds.; Kluwer Academic Publishers: Dordrecht, 1997; Vol. 341, 81–87. Applied Science Series E.
  31. Tour, J.M. Molecular wires for electronic applications. *Polym. News* **2000**, *25* (10), 329–336.
  32. Jones, L., II; Schumm, J.S.; Tour, J.M. Rapid solution and solid phase synthesis of oligo(1,4-phenylene ethynylene)s with thioester termini: Molecular scale wires with alligator clips. Derivation of iterative reaction efficiencies on a polymer support. *J. Org. Chem.* **1997**, *62* (5), 1388–1410.
  33. Collman, J.P.; Zhong, M.; Conzanzo, S.; Sunderland, C.J.; Aukauloo, A.; Berg, K.; Zeng, L. A practical route to functionalized (phenylethynyl)phenylthiol acetates for self-assembled monolayer studies. *Synthesis* **2001**, *2001* (3), 367–369.
  34. Gu, T.; Nierengarten, J.-F. Synthesis of fullerene-oligophenyleneethynylene hybrids. *Tetrahedron Lett.* **2001**, *42*, 3175–3178.
  35. Tour, J.M.; Rawlett, A.M.; Kozaki, M.; Yao, Y.; Jagessar, R.C.; Dirk, S.M.; Price, D.W.; Reed, M.A.; Zhou, C.-W.; Chen, J.; Wang, W.; Campbell, I. Synthesis and preliminary testing of molecular wires and devices. *Chem. Eur. J.* **2001**, *7* (23), 5118–5134.
  36. Dirk, S.M.; Price, D.W., Jr.; Chanteau, S.; Kosynkin, D.V.; Tour, J.M. Accoutrements of a molecular computer: Switches, memory components and alligator clips. *Tetrahedron* **2001**, *57*, 5109–5121.
  37. Hwang, J.-J.; Tour, J.M. Combinatorial synthesis of oligo(phenylene ethynylene)s. *Tetrahedron* **2002**, *58*, *in press*.
  38. Donhauser, Z.J.; Mantooth, B.A.; Kelly, K.F.; Bumm, L.A.; Monnell, J.D.; Stapleton, J.J.; Price, D.W., Jr.; Rawlett, A.M.; Allara, D.W.; Tour, J.M.; Weiss, P.S. Conductance switching in single molecules through conformational changes. *Science*, June 22, **2001**, *292*, 2303–2307.
  39. Chen, J.; Wang, W.; Klemic, J.; Reed, M.A.; Axelrod, B.W.; Kaschak, D.B.; Rawlett, A.M.; Price, D.W.; Dirk, S.M.; Tour, J.M.; Grubisha, D.S.; Bennett, D.W. Molecular wires, switches, and memories. *Ann. N.Y. Acad. Sci.* **2002**, *960*, 69–99.
  40. Flatt, A.F.; Dirk, S.M.; Henderson, J.C.; Shen, D.E.; Su, J.; Reed, M.A.; Tour, J.M. Synthesis and testing of new end-functionalized oligomers for molecular electronics., submitted for review.
  41. Syamakumari, A.; Schenning, A.P.H.J.; Meijer, E.W. Synthesis, optical properties, and aggregation behavior

- of a triad system based on perylene and oligo(*p*-phenylene vinylene) units. *Chem. Eur. J.* **2002**, *8* (15), 3353–3361.
42. Wong, M.S.; Li, Z.H.; Shek, M.F.; Samroc, M.; Samoc, A.; Luther-Davies, B. Synthesis and third-order nonlinear optical properties of end-functionalized oligo-phenylenevinylenes. *Chem. Mater.* **2002**, *14* (7), 2999–3004.
  43. Gu, T.; Ceroni, P.; Marconi, G.; Armaroli, N.; Nierengarten, J.-F. Synthesis and electronic properties of covalent assemblies of oligophenylenevinylene units arising from a calyx[4]arene core. *J. Org. Chem.* **2001**, *66* (19), 6432–6439.
  44. Davis, W.B.; Ratner, M.A.; Wasielewski, M.R. Conformational gating of long distance electron transfer through wire-like bridges in donor–bridge–acceptor molecules. *J. Am. Chem. Soc.* **2001**, *123* (32), 7877–7886.
  45. Sikes, H.D.; Smalley, J.F.; Dudek, S.P.; Cook, A.R.; Newton, M.D.; Chidsey, C.E.; Feldberg, S.W. Rapid electron tunneling through oligophenylenevinylene bridges. *Science*, February 23, **2001**, *291*, 1519–1523.
  46. Detert, H.; Sugiono, E. Soluble oligo(phenylenevinylene)s with electron withdrawing substituents for the use in light emitting diodes. *Synth. Met.* **2000**, *115* (1–3), 89–92.
  47. Zhang, C.Y.; Tour, J.M. Synthesis of highly functionalized pyrazines by ortho-lithiation reactions. Pyrazine ladder polymers. *J. Am. Chem. Soc.* **1999**, *121* (38), 8783–8790.
  48. Yao, Y.; Tour, J.M. Synthesis of imine-bridged phenylene-pyridine ladder polymers. Optical band gap widening through intramolecular charge transfer in planar polymers. *Macromolecules* **1999**, *32* (8), 2455–2461.
  49. Gourdon, A. In *Synthesis of Conjugated Ladder Oligomers*, Proceedings of the NATO Advanced Research Workshop on Atomic and Molecular Wires, Les Houches, France, May, 6–10, 1996; Joachim, C., Roth, S., Eds.; Kluwer Academic Publishers: Dordrecht, 1997; Vol. 341, 81–87. Applied Science Series E.
  50. Billić, A.; Reimers, J.R.; Hush, N.S. Adsorption of pyridine on the gold(111) surface: Implications for “alligator clips” for molecular wires. *J. Phys. Chem., B* **2002**, *106* (26), 6740–6747.
  51. Tour, J.M. Soluble oligo- and polyphenylenes. *Adv. Mater.* **1994**, *6* (3), 190–198.
  52. Tour, J.M.; John, J.A. Synthesis of polyphenylenes via Bergman cyclization and polymerization of enediyne monomers. *Polym. Prepr. (Am. Chem. Soc., Div. Polym. Chem.)* **1993**, *34* (2), 372–373.
  53. Tour, J.M.; Lamba, J.J.S. Synthesis of planar poly(*p*-phenylene) derivatives for maximization of extended  $\pi$ -conjugation. *J. Am. Chem. Soc.* **1993**, *115* (11), 4935–4936.
  54. Grimsdale, A.C.; Müllen, K. 1-, 2-, and 3-Dimensional polyphenylenes—From molecular wires to functionalized nanoparticles. *Chem. Rec.* **2001**, *1*, 243–257.
  55. Schenning, A.P.H.J.; Arndt, J.-D.; Ito, M.; Stoddart, A.; Schrieber, M.; Siemsen, P.; Martin, R.E.; Boudon, C.; Gisselbrecht, J.-P.; Gross, M.; Gramlich, V.; Diederich, F. Insulated molecular wires: Dendritic encapsulation of poly(triacetylene) oligomers, attempted dendritic stabilization of novel poly(pentaacetylene) oligomers, and an organometallic approach to dendritic rods. *Helv. Chim. Acta* **2001**, *84*, 296.
  56. Livingston, R.C.; Cox, L.R.; Gramlich, V.; Diederich, F. 1,3-diethynylallenes: New modules for three-dimensional acetylenic scaffolding. *Angew. Chem., Int. Ed. Engl.* **2001**, *40* (12), 2334–2337.
  57. Alvaro, M.; Ferrer, B.; García, M.; Lay, A.; Trinidad, F.; Valenciano, J. Remarkably high electrochemical charge uptake for modified electrodes of polyacetylene molecular wires encapsulated within zeolites and mesoporous MCM-41 aluminosilicate. *Chem. Phys. Lett.* April 26, **2002**, *356*, 577–584.
  58. Taylor, P.N.; O’Connell, M.J.; McNeill, L.A.; Hall, M.J.; Aplin, R.T.; Anderson, H.L. Insulated molecular wires: Synthesis of conjugated polyrotaxanes by Suzuki coupling in water. *Angew. Chem., Int. Ed. Engl.* **2000**, *39* (19), 3456–3460.
  59. Kong, J.; Franklin, N.R.; Zhou, C.; Chapline, M.C.; Peng, S.; Cho, K.; Dai, H. Nanotube molecular wires as chemical sensors. *Science*, January 28, **2000**, *287*, 622–625.
  60. Franklin, N.R.; Li, Y.; Chen, R.J.; Javey, A.; Dai, H. Patterned growth of single-walled carbon nanotubes on full 4-inch wafers. *Appl. Phys. Lett.* **2001**, *79* (21), 4571–4573.
  61. Bahr, J.L.; Mickelson, E.T.; Bronikowski, M.J.; Smalley, R.E.; Tour, J.M. Dissolution of small diameter single-wall carbon nanotubes in organic solvents? *Chem. Commun.* **2001**, *2001*, 193–194.
  62. Bahr, J.L.; Tour, J.M. Covalent chemistry of single-wall carbon nanotubes—A review. *J. Mater. Chem.* **2002**, *12*, 1952–1958.
  63. Bahr, J.L.; Tour, J.M. Highly functionalized carbon nanotubes using in situ generated diazonium compounds. *Chem. Mater.* **2001**, *13*, 3823–3824.
  64. Seifert, G.; Köhler, T.; Frauenheim, T. Molecular wires, solenoids, and capacitors by sidewall functionalization of carbon nanotubes. *Appl. Phys. Lett.* **2000**, *77* (9), 1313–1315.
  65. Cizek, J.; Tour, J.M. unpublished results.
  66. Ambroise, A.; Kirmaier, C.; Wagner, R.W.; Loewe, R.S.; Bocian, D.F.; Holten, D.; Lindsey, J.S. Weakly coupled molecular photonic wires: Synthesis and excited state energy-transfer dynamics. *J. Org. Chem.* **2002**, *76* (11), 3811–3826. and references cited therein.
  67. Anderson, H.L. Building molecular wires from the colours of life: Conjugated porphyrin oligomers. *Chem. Commun.* **1999**, *1999*, 2323–2330.
  68. Iengo, E.; Zangrando, E.; Minatel, R.; Alessio, E. Metallacycles of porphyrins as building blocks in the construction of higher order assemblies through axial coordination of bridging ligands: Solution- and solid-state characterization of molecular sandwiches and molecular wires. *J. Am. Chem. Soc.* **2002**, *124* (6), 1003–1013.
  69. Kimizuku, N. Toward self-assembling inorganic molecular wires. *Adv. Mater.* **2000**, *12* (19), 1461–1463.
  70. Constable, E.C.; Housecroft, C.E.; Schofield, E.R.; Encinas, S.; Armaroli, N.; Barigelletti, F.; Flamigni, L.;

- Figgemeier, E.; Vos, J.G. Luminescent molecular wires with 2,5-thiophenediyl spacers linking {Ru(terpy)<sub>2</sub>} units. *Chem. Commun.* **1999**, *1999*, 869–870.
71. Shiotsuka, M.; Yamamoto, Y.; Okuno, S.; Kitou, M.; Nozaki, K.; Onaka, S. Construction of molecular wires based on a gold (I) bis- $\sigma$ -acetylide building block incorporated into ruthenium(II) polypyridyl complexes. *Chem. Commun.* **2002**, *2002*, 590–591.
  72. Berry, J.F.; Cotton, F.A.; Daniels, L.M.; Murillo, C.A. A trinickel dipyridylamido complex with metal–metal bonding interaction: Prelude to polynickel molecular wires and devices? *J. Am. Chem. Soc.* **2002**, *124* (13), 3212–3213.
  73. Barigelletti, F.; Flamigini, L. Photoactive molecular wires based on metal complexes. *Chem. Soc. Rev.* **2000**, *29* (1), 1–12.
  74. Stang, S.L.; Paul, F.; Lapinte, C. Molecular wires: Synthesis and properties of the new mixed-valence complex [Cp\*(dppe)Fe–C $\equiv$ C–X–C $\equiv$ C–Fe(dppe)Cp\*][PF<sub>6</sub>] (X = 2,5-C<sub>4</sub>H<sub>2</sub>S) and comparison of its properties with those of the related all-carbon-bridged complex (X = –C<sub>4</sub>–). *Organometallics* **2000**, *19* (6), 1035–1043.
  75. Hänggi, P.; Ratner, M.; Yaliraki, S. Transport in molecular wires. In *Chem. Phys.*; Elsevier Science B.V.: The Netherlands, 2002; Vol. 281, 111.
  76. Yaliraki, S.N.; Kemp, M.; Ratner, M.A. Conductance of molecular wires: Influence of molecule–electrode binding. *J. Am. Chem. Soc.* **1999**, *121* (14), 3428–3434.
  77. Johansson, Å.; Stafström, S. Interactions between molecular wires and a gold surface. *Chem. Phys. Lett.* May 26, **2000**, *322*, 301–306.
  78. Onipko, A.; Klymenko, Y.; Malysheva, L. Conductance of molecular wires: Analytical modeling of connection to leads. *Phys. Rev., B* **2000**, *62* (15), 10480–10493.
  79. Seminario, J.M.; De La Cruz, C.E.; Derosa, P.A. A theoretical analysis of metal–molecule contacts. *J. Am. Chem. Soc.* **2001**, *123* (23), 5616–5617.
  80. Emberly, E.G.; Kirczenow, G. Molecular spintronics: Spin-dependent electron transport in molecular wires. *Chem. Phys.* **2002**, *281*, 311–324.
  81. Karzazi, Y.; Cornil, J.; Brédas, J.L. Negative differential resistance behavior in conjugated molecular wires incorporating spacers: A quantum-chemical description. *J. Am. Chem. Soc.* **2001**, *123* (41), 10076–10084.
  82. Karzazi, Y.; Cornil, J.; Brédas, J.L. Resonant tunneling diodes based on molecular wires incorporating saturated spacers: A quantum-chemical study. *Nanotechnology* **2002**, *13*, 336–340.
  83. Seminario, J.M.; Zacarias, A.G.; Tour, J.M. Molecular current–voltage characteristics. *J. Phys. Chem., A* **1999**, *103* (39), 7883–7887.
  84. Emberly, E.; Kirczenow, G. Electrical conductance of molecular wires. *Nanotechnology* **1999**, *10*, 285–289.
  85. Seminario, J.M.; Zacarias, A.G.; Tour, J.M. Theoretical study of a molecular resonant tunneling diode. *J. Am. Chem. Soc.* **2000**, *122* (13), 3015–3020.
  86. Emberly, E.G.; Kirczenow, G. Current-driven conformational changes, charging, and negative differential resistance in molecular wires. *Phys. Rev., B* **2001**, *64*, 125318-1–125318-5.
  87. Derosa, P.A.; Seminario, J.M. Electron transport through single molecules: Scattering treatment using density functional and green function theories. *J. Phys. Chem., B* **2001**, *105* (2), 471–481.
  88. Seminario, J.M.; Zacarias, A.G.; Derosa, P.A. Theoretical analysis of complimentary molecular memory devices. *J. Phys. Chem. A* **2001**, *105* (5), 791–795.
  89. Mujica, V.; Ratner, M.A.; Nitzan, A. Molecular rectification: Why is it so rare? *Chem. Phys.* **2002**, *281*, 147–150.
  90. Xue, Y.; Datta, S.; Ratner, M.A. First-principles based matrix Green's function approach to molecular electronic devices: General formalism. *Chem. Phys.* **2002**, *281*, 151–170.
  91. Lehmann, J.; Ingold, G.-L.; Hänggi, P. Incoherent charge transport through molecular wires: Interplay of Coulomb interaction and wire population. *Chem. Phys.* **2002**, *281*, 199–209.
  92. Petrov, E.G.; May, V.; Hänggi, P. Controlling electron transfer processes through short molecular wires. *Chem. Phys.* **2002**, *281*, 211–224.
  93. Ness, H.; Fisher, A.J. Coherent electron injection and transport in molecular wires: Inelastic tunneling and electron–phonon interactions. *Chem. Phys.* **2002**, *281*, 279–292.
  94. Nitzan, A.; Galperin, M.; Ingold, G.-L.; Grabert, H. On the electrostatic potential profile in biased molecular wires. *ArXiv Phys.*, July 31, **2002**, *1*, 1–6. 0207124.
  95. Sendt, K.; Johnston, L.A.; Hough, W.A.; Crossley, M.J.; Hush, N.S.; Reimers, J.R. Switchable electronic coupling in model oligoporphyrin molecular wires examined through the measurement and assignment of electronic absorption spectra. *J. Am. Chem. Soc.* **2002**, *124* (31), 9299–9309.
  96. Pourtois, G.; Beljonne, D.; Cornil, J.; Ratner, M.A.; Brédas, J.L. Photoinduced electron-transfer processes along molecular wires based on phenylenevinylene oligomers: A quantum-chemical insight. *J. Am. Chem. Soc.* **2002**, *124* (16), 4436–4447.
  97. Zhou, C.; Deshpande, M.R.; Reed, M.A.; Jones, L., II; Tour, J.M. Nanoscale metal/self-assembled monolayer/metal heterostructures. *Appl. Phys. Lett.* **1997**, *71* (5), 611–613.
  98. Avouris, P.; Lang, N.D. Effects of coadsorption on the conductance of molecular wires. *Nano Lett.* **2002**, *10*.1021/nl020202o.
  99. Granger, B.E.; Král, P.; Sadeghpour, H.R.; Shapiro, M. Highly extended image states around nanotubes. *Phys. Rev. Lett.* **2002**, *89* (13), 135506-1–135506-4.
  100. Hill, I.G.; McLean, A.B. Strongly anisotropic band dispersion of an image state located above metallic nanowires. *Phys. Rev. Lett.* **1999**, *82* (10), 2155–2158.
  101. Lehmann, J.; Kohler, S.; Hänggi, P.; Nitzan, A. Molecular wires acting as coherent quantum ratchets. *Phys. Rev. Lett.* **2002**, *88* (22), 228305-1–228305-4.
  102. Weber, H.B.; Reichert, J.; Weigend, F.; Ochs, R.; Beckmann, D.; Mayer, M.; Ahlrichs, R.; Löhneysen, H.V. Electronic transport through single conjugated molecules. *Chem. Phys.* **2002**, *281*, 113–125.



103. Chen, J.; Reed, M.A. Electronic transport of molecular systems. *Chem. Phys.* **2002**, *281*, 127–145.
104. Agraït, N.; Untiedt, C.; Rubio-Bollinger, G.; Vieira, S. Electron transport and phonons in atomic wires. *Chem. Phys.* **2002**, *281*, 231–234.
105. Patrone, L.; Palacin, S.; Bourgoïn, J.P.; Laboute, J.; Zambelli, T.; Gauthier, S. Direct comparison of the electronic coupling efficiency of sulfur and selenium anchoring groups for molecules adsorbed onto gold electrodes. *Chem. Phys.* **2002**, *281*, 325–332.
106. Davis, W.B.; Ratner, M.A.; Wasielewski, M.R. Dependence of electron transfer dynamics in wire-like bridge molecules on donor–bridge energetics and electronic interactions. *Chem. Phys.* **2002**, *281*, 333–346.
107. Rampi, M.A.; Whitesides, G.M. A versatile experimental approach for understanding electron transport through organic materials. *Chem. Phys.* **2002**, *281*, 373–391.
108. Avouris, P. Carbon nanotube electronics. *Chem. Phys.* **2002**, *281*, 429–445.
109. Cuniberti, G.; Fagas, G.; Richter, K. Fingerprints of mesoscopic leads in the conductance of a molecular wire. *Chem. Phys.* **2002**, *281*, 465–476.
110. Kushmerick, J.G.; Holt, D.B.; Pollack, S.K.; Ratner, M.A.; Yang, J.C.; Schull, T.L.; Naciri, J.; Moore, M.H.; Shashidhar, R. Effect of bond-length alternation in molecular wires. *J. Am. Chem. Soc.* **2002**, *124* (36), 10654–10655.
111. Rawlett, A.M.; Hopson, T.J.; Nagahara, L.A.; Tsui, R.K.; Ramachandran, G.K.; Lindsay, S.M. Electrical measurements of a dithiolated electronic molecule via conducting atomic force microscopy. *Appl. Phys. Lett.* **2002**, *81* (16), 3043–3045.
112. Wang, W.; Lee, T.; Reed, M.A. Characterization of electron tunneling in self-assembled alkanethiol monolayer devices. **2002**. Submitted for publication.

# Monolayer-Protected Metal Nanoparticles: Chemical Sensing and Gas Chromatography

Jay W. Grate  
David A. Nelson  
Rhonda Skaggs

*Pacific Northwest National Laboratory, Richland, Washington, U.S.A.*

Robert E. Synovec  
Gwen M. Gross

*Department of Chemistry, University of Washington,  
Seattle, Washington, U.S.A.*

## INTRODUCTION

Nanoparticles and nanoparticle-based materials are of considerable interest for their unique properties and their potential for use in a variety of applications. Metal nanoparticles, in which each particle's surface is coated with a protective organic monolayer, are of particular interest because the surface monolayer stabilizes them relative to aggregation and they can be taken up into solutions.<sup>[1-4]</sup> As a result, they can be processed into thin films for device applications. We will refer to these materials as monolayer-protected nanoparticles (MPNs). Typically, the metal is gold and the organic layer is a self-assembled thiol layer, and this composition will be assumed throughout the remainder of this chapter. A diversity of materials and properties is readily accessible by straightforward synthetic procedures, either by the structures of the monolayer-forming thiols used in the synthesis, or by postsynthetic modifications of the monolayers. A particularly promising application for these materials is as selective layers on chemical vapor sensors. In this role, the thin film of MPNs on the device surface serves to collect and concentrate gas molecules at the sensor's surface. Their sorptive properties also lend them to use as new nanostructured gas chromatographic stationary phases. This chapter will focus on the sorptive properties of MPNs as they relate to chemical sensors and gas chromatography (GC).

## BACKGROUND

The use of a sorptive layer to collect and concentrate vapor molecules at a sensor's surface is shown schematically in Fig. 1. The presence of these sorbed vapor molecules can then be detected in a variety of ways, depending on the transduction mechanism of the

sensor device. Acoustic wave devices, such as the thickness shear mode (TSM) device or the surface acoustic wave (SAW) device, transduce the presence of the vapor as an increase in mass detected by a change in the acoustic wave velocity.<sup>[5-8]</sup> Typically, the acoustic wave velocity change is measured as a change in oscillator frequency.

A schematic diagram of an MPN as an individual particle, its component parts, and a film is shown in Fig. 2. The film represents a cross section where gold cores are separated by the organic monolayers, with areas of lower density suggested between the MPNs. As a sorptive layer, molecules could sorb into the thiol material and/or the free volume associated with areas of lower density.

Chemiresistor devices measure a change in the resistance of the applied thin films as a function of the sorbed gas or vapor.<sup>[9-12]</sup> Because an MPN film on such a device carries the current, it participates directly in the transduction mechanism.<sup>[12]</sup> These films consist of metal particles separated from one another, insulating monolayers on their surfaces (Fig. 2). The current observed as electrons travel through a film from particle core to particle core can be modulated by the sorption of vapor molecules in the insulating regions. These insulating regions are of molecular dimensions, hence the sorption of molecules can represent a significant perturbation. Wohltjen and Snow<sup>[12]</sup> described MPN-sensing films as metal-insulator-metal ensembles (MIMEs) in recognition of the nanostructure of the films.

Regardless of the transduction mechanism chosen, the sorption of a vapor into the MPN film represents a significant aspect of the sensor response. The amount of vapor uptake and the rate of vapor uptake by these film materials provide useful information for understanding and interpreting sensor response behavior. Differences in the sorption of various vapors (i.e.,

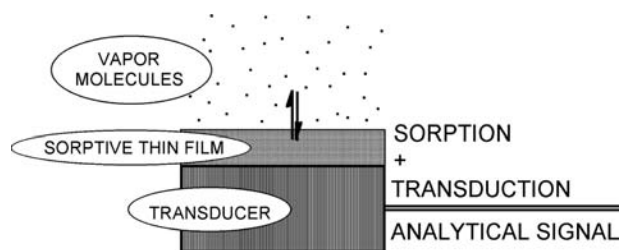


**Fig. 1** Schematic diagram of the mechanism for a chemical vapor sensor where the sorption of a vapor from the gas phase into a sorptive layer on the transducer surface results in an analytical signal.

selectivity) provide the basis for discriminating among vapors using arrays of such sensors, and for separating vapors using GC.

## SYNTHESIS AND PROPERTIES

The typical synthesis procedure for MPNs involves the reduction of gold salts in the presence of a monolayer-forming thiol. A two-phase water/toluene process with a phase transfer salt was first reported by Brust et al.<sup>[2]</sup> and has been used by many others as well.<sup>[12–15]</sup> For example, alkanethiol-protected gold nanoparticles are typically prepared starting with solutions of  $\text{HAuCl}_4 \cdot \text{H}_2\text{O}$  in water, alkanethiol in toluene, sodium borohydride as the reducing agent in water, and tetraoctylammonium bromide as the phase transfer salt in toluene. The aqueous  $\text{HAuCl}_4$  solution is added to the toluene solution containing tetraoctylammonium bromide. After thorough stirring to transfer  $\text{AuCl}_4^-$  anions into the toluene, the dodecanethiol/toluene solution is added followed by the aqueous  $\text{NaBH}_4$  solution. The product MPNs are recovered from the toluene phase.

MPNs can also be prepared in one-phase procedures that have been used, for example, for a variety

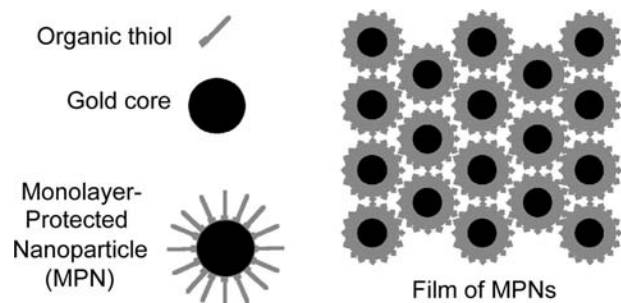


**Fig. 2** Schematic diagram of a gold nanoparticle protected with organic thiol monolayer, along with a hypothetical film where the gold cores are black, the monolayer material is gray, and there are areas of potentially lower density between the particles that may facilitate vapor diffusion and sorption.

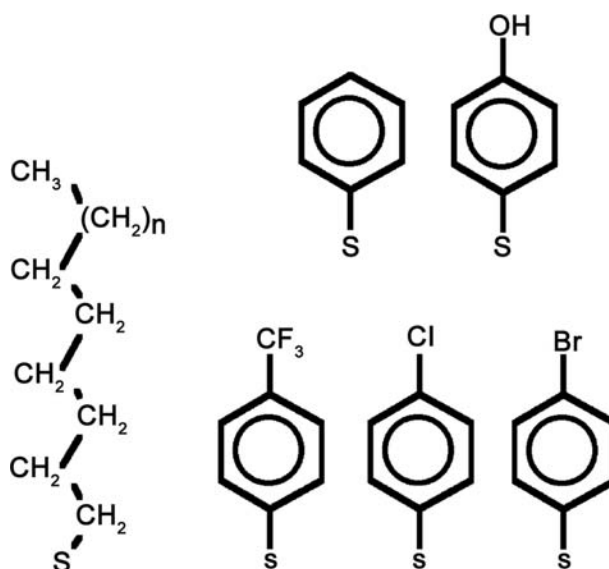


**Fig. 3** A selection of thiol structures that have been used as monolayers on gold nanoparticles. The alkanethiols indicated on the left typically range from octanethiol to dodecanethiol ( $n = 1-5$ ).

of arene thiol-protected gold nanoparticles. The single-phase methanol/water synthesis was developed by Brust et al.<sup>[1]</sup> and used by others.<sup>[15,16]</sup> A synthesis method from solvated metal atoms has also been described, where vaporized metal atoms and solvent vapors are codeposited as a frozen mixture, followed by reaction with the thiol.<sup>[17]</sup> This method is effective at generating gram quantities of MPNs that are unambiguously free of ionic impurities from reducing agents or phase transfer reagents.

A great variety of thiol ligands have been used in the synthesis of MPNs, some of which are shown in Fig. 3. Alkanethiols have been particularly popular, whereas the substituted arene thiols provide a facile method to incorporate varying functionality in the structure. In addition, the ligand shell can be synthetically modified by organic reactions with organic ligands. Additional examples of thiols used and postsynthetic modifications can be found in Ref.<sup>[3]</sup>.

Preparations are typically polydisperse in particle size. The metal cores can be observed and measured by high-resolution transmission electron microscopy (TEM). An example of a TEM of a monolayer of MPNs is shown in Fig. 4. Particle core sizes in most studies average between 1.5 and 5 nm in diameter. It is believed that the cores prefer to reach discrete sizes with closed-shell structures (i.e., completed outermost layers of gold on the particle or crystal), although non-equilibrium structures may be produced under kinetically controlled growth conditions.<sup>[3]</sup> A number of studies have described the ripening of nanoparticle

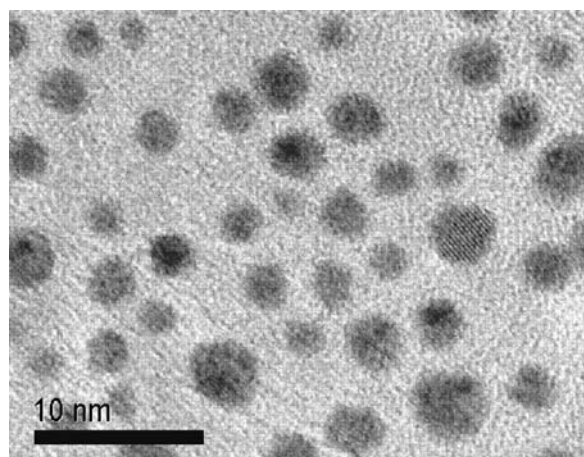


**Fig. 4** TEM image of a polydisperse sample of bromobenzenethiol-protected gold nanoparticles.

sizes after synthesis.<sup>[17–22]</sup> Particle sizes may increase with time and heating under appropriate conditions; however, reduction in gold core size has also been described by heating in neat thiol. Ripening of nanoparticles appears to lead to a more uniform size distribution than that obtained during synthesis.

A variety of additional characterization methods are also frequently applied. Thermogravimetric analysis (TGA) provides a measure of the mass percentages of gold and organic material in the prepared sample. Ideally, the organic material is all gold-bound thiol; however, impure samples may also contain excess free thiol, the corresponding disulfide, or phase transfer salt. Infrared spectra are sometimes used to look for the presence of phase transfer salt. Free thiol or disulfide can be observed by chromatographic methods including thin layer chromatography and liquid chromatography.

Additional techniques that have been applied to the study of MPNs include small-angle X-ray scattering (SAXS), conventional and synchrotron X-ray diffraction, mass spectrometry, scanning tunneling microscopy (STM), atomic force microscopy (AFM), differential scanning calorimetry, and nuclear magnetic resonance (NMR), to name a few. Detailed structural studies of carefully crystallized samples of alkanethiol-protected gold nanoparticles have been described.<sup>[4]</sup>

Of particular interest with regard to sorption are the relative proportions of the organic thiol material serving as a sorptive medium and the gold cores whose volume excludes sorbed molecules. The mass ratios of gold and thiol can be determined from TGA, where the organic material burns off, leaving gold. From our own data<sup>[15]</sup> as well as data in the literature,<sup>[13,14,23]</sup> it is found that MPN materials are typically 75–90% metal by mass and only 10–25% organic by mass. Nevertheless, these proportions are reversed when

volume fractions are considered. We have estimated that typical volume fractions are 70–90% organic material by volume and only 10–30% metal by volume, using the densities of bulk gold and condensed phase thiols to convert mass fractions to volume fractions.<sup>[15]</sup> Thus despite the low mass percentage of sorptive organic material, these materials are actually primarily sorptive organic material by volume.

Low-volume fractions of gold—and hence high-volume fractions of thiol—are also indicated by structural studies.<sup>[4]</sup> In studies of crystalline samples of MPNs with alkanethiol ligands, the gold cores have been assumed to have the density of bulk gold metal, and the volume not occupied by gold has been found to have a density very close to that of the bulk thiol.<sup>[24]</sup>

## SORPTIVE PROPERTIES AS MEASURED USING ACOUSTIC WAVE SENSORS

### Sorption, the Partition Coefficient, and Chemical Sensor Response

The analytical signal of a coated microsensors entails the sorption of the vapor and transduction of the presence of the vapor in the film.<sup>[25,26]</sup> The vapor sensor's response  $R$  is empirically expressed as a function of the gas-phase concentration of the test vapor  $C_v$  as in Eq. (1), and this is the basis of the calibration curve:

$$R = f(C_v) \quad (1)$$

Nevertheless, the sensor's response is more directly a function of the concentration of the vapor in the sorptive coating  $C_s$  as indicated in Eq. (2):

$$R = f(C_s) \quad (2)$$

The ratio of the concentrations  $C_v$  and  $C_s$  is given by the thermodynamic partition coefficient  $K$  [Eq. (3)]:

$$K = C_s/C_v \quad (3)$$

Consequently, the response function to the vapor concentration in the film [Eq. (2)] can be expressed as a function of the product of the gas-phase vapor concentration and the partition coefficient [Eq. (4)]:

$$R = f(KC_v) \quad (4)$$

Hence knowledge of the partitioning of vapors into sensor films (i.e., absorption) is fundamental to understanding sensor performance and mechanism.<sup>[25,26]</sup> We are particularly interested on how this knowledge can help to elucidate the relative roles of sorption and transduction in observed sensitivities and detection

limits. Partition coefficients are also fundamental to the separation of vapors by GC.

### Vapor Sorption by Nanoparticle Films

Four MPN materials were selected for detailed studies on sorptive behavior.<sup>[15]</sup> These four were satisfactorily characterized and all gave rapid and reversible sorption of the test vapors considered. They were MPNs with dodecanethiol, benzenethiol, chlorobenzenethiol, and trifluoromethylbenzenethiol ligands.

Vapor sorption measurements were made on TSM devices spray-coated with an amount of MPN material, yielding approximately 10 kHz frequency shifts (an indication of film thickness).<sup>[15]</sup> Impedance measurements were made to assure that the MPN layers on the TSM devices yield gravimetric sensors and valid vapor uptake measurements can be made. The test sensors were evaluated against four vapors: *n*-hexane, toluene, 2-butanone, and 1-butanol. These vapors represent a diverse set of properties to probe differences in behavior and chemical selectivity among the nanoparticle materials. Sensor responses to the test vapors were generally rapid and reversible, with exposures leading to steady-state or near-steady-state responses within the 6-min exposure period. Examples of such responses are shown in Fig. 5.

Calibration curves for vapor on four MPN a selected coatings are shown in Fig. 6. This figure includes calibration curves for two polymers selected for comparison. Polymers are widely used in chemical sensing

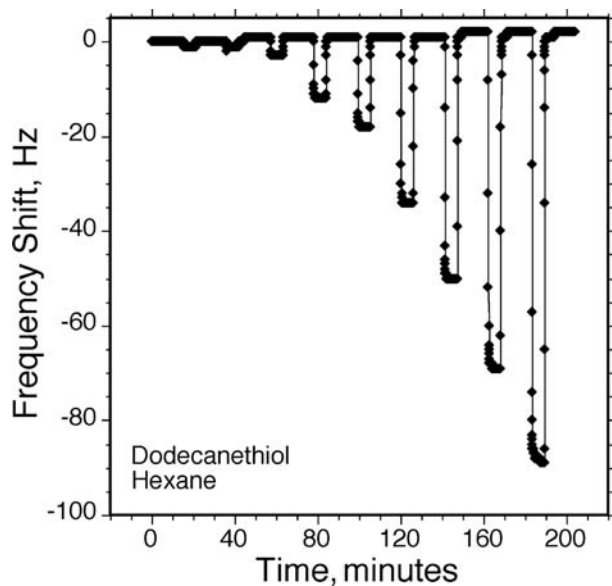


**Fig. 5** Response of a dodecanethiol-protected gold nanoparticle film on a TSM device to increasing concentrations of hexane. Data points are shown 2 sec apart.

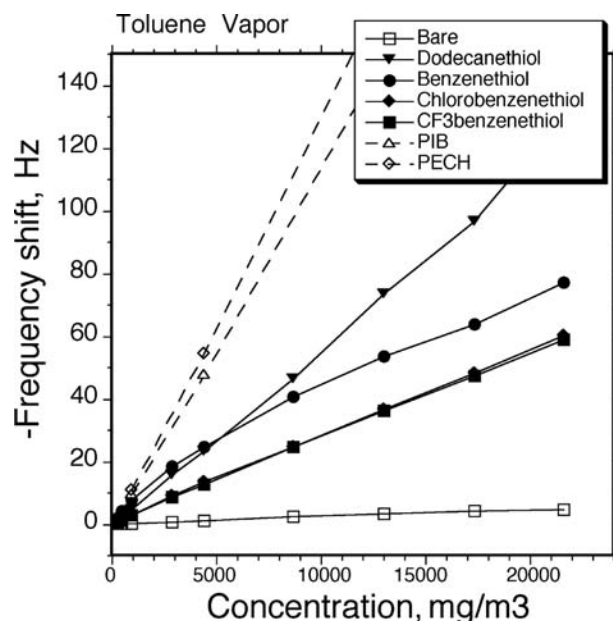


**Fig. 6** Calibration curves for toluene on a series of mono-layer-protected gold nanoparticles with data for two polymers, PIB and PECH, included for comparison.

and their sorptive properties have been examined in detail. The selected polymers—poly(isobutylene), PIB, and poly(epichlorohydrin), PECH—have been used in a variety of vapor-sensing studies, including sorption measurements on 10-MHz TSM devices.<sup>[27]</sup> They represent simple prototypical sorptive polymers whose structures and sorptive properties have been described in detail elsewhere.<sup>[26–29]</sup> The data for the polymers were normalized to 10-kHz films to match the film amounts applied to the MPN-coated sensors.

The calibration curves show two main points. First, the curves are linear or nearly linear in the vapor concentration range considered. We found that TSM sensors with dodecanethiol, chlorobenzenethiol, and trifluoromethylbenzenethiol yielded calibration curves with small intercepts (typically 1 Hz or less) and high correlation coefficients (typically 0.998 or higher for  $R^2$  as evidence for linearity).<sup>[15]</sup> For gravimetric sensors at a fixed temperature, linear calibration curves indicate linear sorption isotherms over the test concentration ranges.

Second, from the results in Fig. 6 and others we have published,<sup>[15]</sup> it is apparent that the sorption of the test vapors by the MPN films is typically less than the sorption of vapors by the selected polymers. The most sorptive nanoparticle films for any test were less sorptive on a per-mass basis than the best sorptive polymer considered within the concentration range studies, the polymer being better by a factor of 2–2.5. This analysis compares the sorptive properties on a mass of vapor sorbed per mass of sorbent material.

Nevertheless, vapor sorption is often quantified based on the partition coefficient defined in Eq. (3), where the concentration of vapor in the sorbent phase is in grams per liter; thus quantification of sorption is measured on a mass-per-volume basis. The partition coefficient is related to gravimetric sensor responses according to Eq. (5):<sup>[30]</sup>

$$\Delta f_v = \Delta f_s C_v K / \rho \quad (5)$$

The frequency shifts indicated by  $\Delta f_s$  and  $\Delta f_v$  refer to the shift obtained on coating the bare sensor with the sorptive coating, and the shift observed when the sorptive coating absorbs a vapor. This relationship assumes that the observed frequency shifts are caused by the bulk absorption of vapor in the film. The  $\rho$  parameter is the sorptive material density. Densities of the applied films are required to convert observed frequency shifts to partition coefficients for vapor sorption. Based on the mass fractions of gold and thiol in the film materials as determined by TGA, and the bulk densities of the condensed-phase gold and thiol materials, estimates of the required densities were determined for the calculation of partition coefficients according to Eq. (5).<sup>[15]</sup> On a per-volume basis, the sorption of organic vapors by these MPN materials is of the same order of magnitude as the polymers at this concentration. Thus it appears unlikely that the nanoparticle-based materials considered are more sorptive than the conventional polymers. If the actual densities of the film materials were lower than the estimated values used in the calculations (i.e., because of inefficient packing and/or large free volumes), then the actual partition coefficients would be proportionately lower, and it would still be true that these nanoparticle-based materials are not more sorptive than the polymers used for comparison.

The sorptive properties of these nanoparticle films prepared by monothiols can also be compared with networked nanoparticle films containing bridging dithiols. Quantitative data on vapor uptake of the latter films as measured on TSM devices by Han et al.<sup>[31]</sup> were compared with our quantitative data on vapor uptake by the monothiol-based MPNs.<sup>[15]</sup> After converting the reported data to similar units, it appears that the networked films sorb organic vapors with gravimetric sensitivity of the same order of magnitude as the monothiol-based materials, with the sorption by the particular alkanethiol-based film in our study being somewhat greater than the particular alkanedithiol-based film in their study.<sup>[32]</sup>

## NANOPARTICLE FILMS AS GAS CHROMATOGRAPHIC PHASES

Our interest in the sorptive behavior of these nanoparticle materials prompted us to investigate them as gas

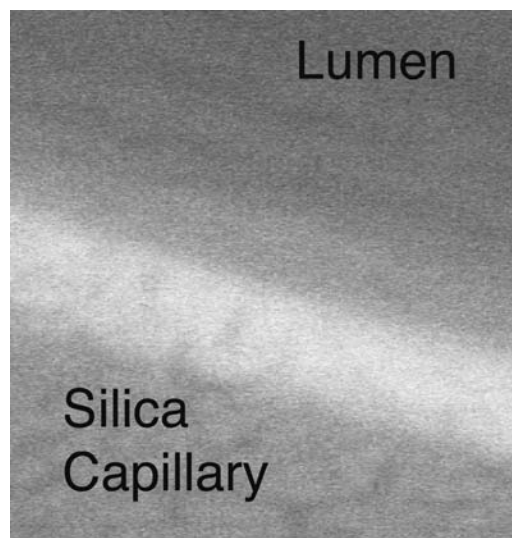


**Fig. 7** Scanning electron microscope image of a cross section of the open tubular GC column coated with the dodecanethiol-protected gold nanoparticles, shown as the light band between the silica column material and the column lumen. The band is 60 nm thick.

chromatographic phases. Dodecanethiol-protected gold nanoparticles were examined using an open tubular column configuration.<sup>[33]</sup> The nanoparticles were deposited on the inner walls of a deactivated silica capillary (0.530 mm i.d.) by deposition from a dichloromethane solution passed as a plug through the length of the column. This process was repeated until a layer yielding a uniform brown color was obtained. Scanning electron microscopy was used to characterize the thickness and consistency of the nanoparticle film. A film of 60 nm thickness in a 2-m column was used for subsequent chromatographic experiments. A cross-sectional image of the MPN film in the capillary is shown in Fig. 7.

Several test mixtures were separated on the open tubular GC column using both isothermal and temperature-ramped protocols. Rapid separations with good peak shapes and resolution were obtained.<sup>[33]</sup> Figs. 8 and 9 illustrate the separation of an eight-component mixture under isothermal and temperature-ramped conditions. Determination of reduced plate height as function of linear flow velocity indicated an efficient open tubular system. The performance of the MPN-coated column was compared with a commercial polymer stationary phase AT-1 in the same column length and inside diameter, and comparable phase thickness (100 vs. 60  $\mu\text{m}$  for the MPN phase). These two columns were found to have comparable separation efficiencies. These experiments demonstrate that MPN materials can be successfully coated as chromatographic phases for open tubular GC, yielding chromatographically efficient columns.<sup>[33]</sup>



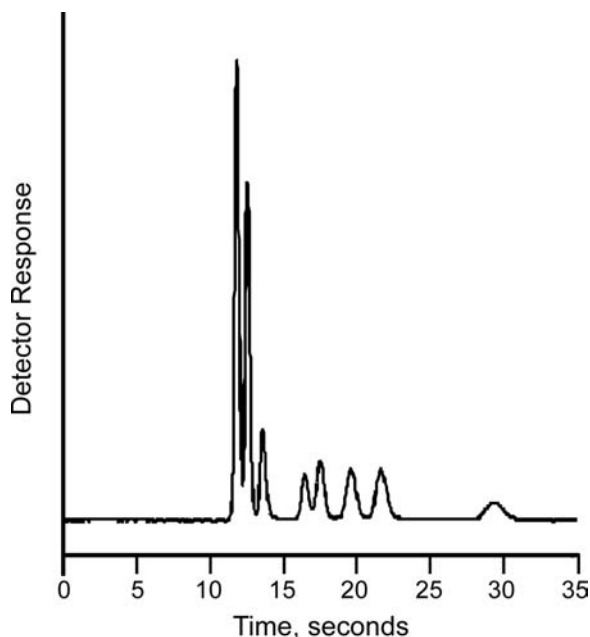


**Fig. 8** Separation of an eight-component mixture on the nanoparticle-coated GC column under isothermal conditions at 50°C. The eight vapors were ethanol, benzene, 1-butanol, 3-heptanone, chlorobenzene, 3-octanone, anisole, and decane.

We have further demonstrated that MPNs can be coated in  $100 \times 100 \mu\text{m}^2$  square-bore capillaries.<sup>[34]</sup> Polymeric stationary phases present problems in the columns with noncircular channels because the material tends to be thicker in the corners than on the other sides. Using the MPN materials, this effect was greatly

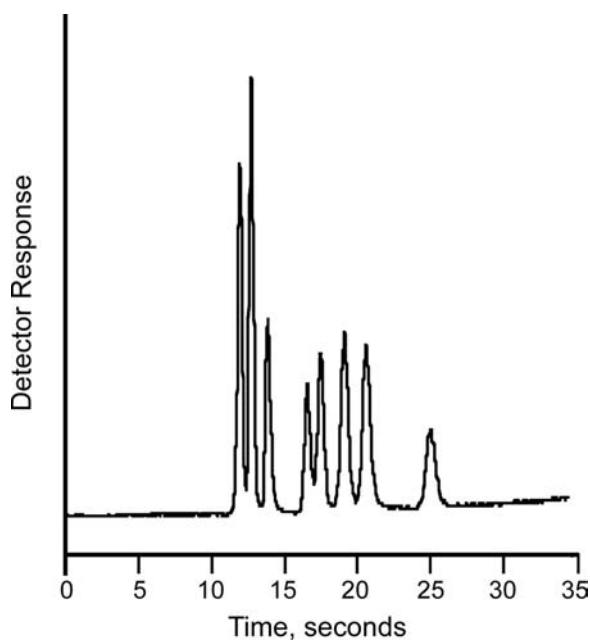


**Fig. 9** Separation of the same eight-component mixture as in Fig. 8 under temperature-ramped conditions from 40°C to 80°C at 70°C/min.

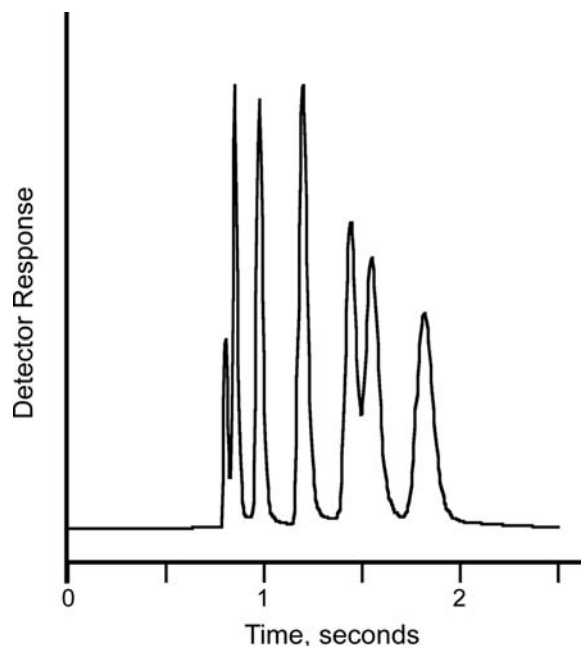


**Fig. 10** High-speed separation of seven components using the dodecanethiol MPN stationary phase within the  $100\text{-}\mu\text{m}^2$  square-bore capillary. The retention order is: methyl ethyl ketone, benzene, octane, chlorobenzene, anisole, 3-octanone, and decane. The separations were obtained by using a 1.3-m column at 75°C operated under constant pressure conditions at 25 psi ( $\sim 200$  cm/sec hydrogen gas).

reduced and an efficient chromatographic system was obtained. The phase thickness on the column sidewalls was 15 nm. A seven-component mixture representing four compound classes was separated in 2 sec on a 1.3-m column. These results are shown in Fig. 10.

Columns with noncircular channels are of interest because microfabricated GC columns (i.e., microGC or GC-on-a-chip) typically have angular channels as a result of the etching and capping process. Thus the square bore capillary GC columns just described serve as a model for microGC angular channels, while focusing on the performance of the stationary phase and not on the rest of a microGC system. Our result demonstrated that the MPN materials have advantageous coating properties for microGC systems.

#### NANOPARTICLE FILMS AS CONDUCTIVE SENSING LAYERS ON CHEMIREซิสТОР SENSORS

As noted in the background material, MPN films can be used as the selective layer on chemiresistor sensors, which measure changes in the electrical conductivity of the films as a function of changing vapor concentration. Initial investigations by a number of groups have demonstrated the potential of MPN-based films for chemical vapor sensing by this mechanism.

Wohltjen and Snow<sup>[12]</sup> reported the first use of MPN-coated chemiresistors as vapor sensors, demonstrating large decreases in the conductance of an octanethiol-based MPN film in response to toluene and trichloroethene.<sup>[35]</sup> Snow and Wohltjen have observed that MPN-coated chemiresistors can offer detection limits that are significantly better than those of polymer-coated SAW devices (A. W. Snow, Naval Research Laboratory, 2000, personal communication).<sup>a</sup> Subsequently, Evans et al.<sup>[16]</sup> demonstrated that chemiresistor devices with four different arenethiol-based MPN films yielded different patterns for each of the eight vapors, although it was observed that reproducibility was a concern for some vapors on some sensors. Additional work by this group attributed MPN-coated chemiresistor responses to film permittivity changes at low vapor concentrations and to film swelling that increases core–core distance at high vapor concentrations.<sup>[38]</sup>

Han et al.<sup>[31]</sup> investigated novel networked nanoparticle film materials containing bridging dithiols between gold cores as layers on both chemiresistor and TSM devices. Vapor uptake as measured on the TSM device was correlated with film resistance changes as measured by the chemiresistor. Zamborini et al.<sup>[39]</sup> also described both chemiresistor and TSM sensor measurements on networked nanoparticle materials; these authors concluded that film swelling as a result of vapor uptake leads to reduced electron-hopping rates. Gold nanoparticle/dendrimer composites have also been used as layers on chemiresistor vapor sensors.<sup>[40–43]</sup> Joseph et al.<sup>[44]</sup> have also examined gold nanoparticle alkanedithiol films prepared by a layer-by-layer assembly process directly on sensor surfaces. These films showed linear current–voltage characteristics and reversible responses to toluene and tetrachloroethene. Responses were consistent with a film swelling mechanism. In experiments with alkylene chains of varying lengths, it was found that the normalized vapor responses increased exponentially with increasing alkanedithiol length.

Cai and Zellers<sup>[45]</sup> described the vapor-sensing performance of MPN-coated chemiresistors with either octanethiol-protected gold nanoparticle or 2-phenylethanedithiol-protected gold nanoparticles. Rapid and reversible responses to most of the 11 test vapors were observed in direct exposures. Detection limits were reported to be 10- to 90-fold (with 20 as a typical value) better than those of selected polymer-coated SAW sensors. The sensors were also used as detectors for GC.

<sup>a</sup>Comparisons between chemiresistor vapor sensors coated with monolayer-protected nanoparticles and surface acoustic wave vapor sensors coated with polymers have been presented by Refs.<sup>[36,37]</sup>

## CONCLUSION

Vapor sorption by a sensing film on a chemical microsensor is a fundamental influence on sensor response and performance. Our studies have examined the sorption of vapors by gold nanoparticle materials protected with organic thiols, where the organic thiol represents the largest volume fraction of the material and its structure influences vapor sorption and selectivity. The nanoparticle-based films considered here were less sorptive than the selected polymers on a per-mass basis. Partition coefficients, which measure the mass of vapor sorbed per volume of the sorptive phase, were estimated for these MPN materials and were found to be comparable with, or less than, those of the polymer layers. Strictly from the standpoint of sorption, these materials do not appear to have advantages over polymers as sensing layers.

Nevertheless, others have reported that chemiresistor sensors coated with MPN films can offer better detection limits than polymer-coated vapor sensors,<sup>[36,37,45]</sup> such as those based on SAW devices or those based on chemiresistors coated with carbon black-containing polymers. If this is the case, and the MPN layers and polymer layers absorb similar amounts of vapor, then it follows that the lower detection limits for MPN-coated chemiresistors must be because of more signal-to-noise ratio per sorbed vapor molecule. Apparently, the electron transfer from one nanoparticle to another is very sensitive to the sorption of vapors into the spaces between the conducting gold nanoparticle cores. These spaces are of molecular dimensions. The implications are that nanostructure materials and can be used in the design of new chemical sensors with superior properties.

As sorptive materials, MPN films may also be used in other microanalytical applications. We have demonstrated that these materials can be advantageously used as sorptive stationary phases in GC. In addition, they appear to offer advantages over conventional polymers with respect to angular chromatographic channels; thus they may be useful in microfabricated channels and structures.

## ACKNOWLEDGMENTS

The authors thank Dr. Scott Elder for initial syntheses of some of the nanoparticle materials and Alice Dohnalkova for TEM images. J. W. G. thanks Dr. Arthur Snow for informative and motivating discussion of the work on nanoparticle-coated sensors at the Naval Research Laboratory in March 2000 as well as helpful discussions subsequently, and Dr. Laura Hughes for a review of the manuscript. This work was funded by the U.S. Department of Energy via the Laboratory Directed Research and Development funds administered

by the Pacific Northwest National Laboratory. A portion of the research was performed at the W. R. Wiley Environmental Molecular Sciences Laboratory, a national scientific user facility sponsored by the U.S. Department of Energy's Office of Biological and Environmental Research and located at the Pacific Northwest National Laboratory. The Pacific Northwest National Laboratory is operated for the U.S. DOE by the Battelle Memorial Institute.

## REFERENCES

1. Brust, M.; Fink, J.; Bethell, D.; Schiffrin, D.J.; Keily, C. Synthesis and reactions of functionalized gold nanoparticles. *J. Chem. Soc., Chem. Commun.* **1995**, 1655–1656.
2. Brust, M.; Walker, M.; Bethell, D.; Schiffrin, D.J.; Whyman, R. Synthesis of thiol-derivatized gold nanoparticles in a two-phase liquid–liquid system. *J. Chem. Soc., Chem. Commun.* **1994**, 801–802.
3. Templeton, A.C.; Wuelfing, W.P.; Murray, R.W. Monolayer-protected cluster molecules. *Acc. Chem. Res.* **2000**, *33*, 27–36.
4. Whetten, R.L.; Shafiqullin, M.N.; Khoury, J.T.; Shcaaff, T.G.; Vezmar, I.; Alvarez, M.M.; Wilkinson, A. Crystal structures of molecular gold nanocrystal arrays. *Acc. Chem. Res.* **1999**, *32*, 397–406.
5. Grate, J.W. Acoustic wave microsensor arrays for vapor sensing. *Chem. Rev.* **2000**, *100*, 2627–2647.
6. Grate, J.W.; Frye, G.C. Acoustic wave sensors. *Sens. Update* **1996**, *2*, 37–83.
7. Grate, J.W.; Martin, S.J.; White, R.M. Acoustic wave microsensors. *Anal. Chem.* **1993**, *65*, 940A.
8. Grate, J.W.; Martin, S.J.; White, R.M. Acoustic wave microsensors, Part II. *Anal. Chem.* **1993**, *65*, 987A–996A.
9. Barger, W.R.; Klusty, M.A.; Snow, A.W.; Grate, J.W.; Ballantine, D.S.; Wohltjen, H. Surface acoustic wave sensors, chemiresistor sensors and hybrids using both techniques simultaneously to detect vapors. *Proc. Electrochem. Soc.* **1987**, *87-15*, 198–217.
10. Grate, J.W.; Rose-Pehrsson, S.; Barger, W.R. Langmuir–Blodgett films of a nickel dithiolene complex on chemical microsensors for the detection of hydrazine. *Langmuir* **1988**, *4*, 1293–1301.
11. Grate, J.W.; Klusty, M.; Barger, W.R.; Snow, A.W. Role of selective sorption in chemiresistor sensors for organophosphorus detection. *Anal. Chem.* **1990**, *62*, 1927–1934.
12. Wohltjen, H.; Snow, A.W. Colloidal metal–insulator–metal ensemble chemiresistor sensor. *Anal. Chem.* **1998**, *70*, 2856–2859.
13. Hostetler, M.J.; Wingate, J.E.; Zhong, C.-J.; Harris, J.E.; Vachet, R.W.; Clark, M.R.; Londono, J.D.; Green, S.J.; Stokes, J.J.; Wignall, G.D.; Glish, G.L.; Porter, M.D.; Evans, N.D.; Murray, R.W. Alkanethiolate gold cluster molecules with core diameters from 1.4 to 5.2 nanometers: core and monolayer properties as a function of core size. *Langmuir* **1998**, *14*, 17–30.
14. Chen, S.; Murray, R.W. Arenethiolate monolayer-protected gold clusters. *Langmuir* **1999**, *15*, 682–689.
15. Grate, J.W.; Nelson, D.A.; Skaggs, R. Sorptive behavior of monolayer-protected gold nanoparticle films: implications for chemical vapor sensing. *Anal. Chem.* **2003**, *75*, 1868–1879.
16. Evans, S.D.; Johnson, S.R.; Cheng, Y.L.; Shen, T. Vapour sensing using hybrid organic–inorganic nanostructured materials. *J. Mater. Chem.* **2000**, *10*, 183–188.
17. Stoeva, S.; Klabunde, K.J.; Sorensen, C.M.; Dragieva, I. Gram-scale synthesis of monodisperse gold colloids by the solvated metal atom dispersion method and digestive ripening and their organization into two- and three-dimensional structures. *J. Am. Chem. Soc.* **2002**, *124*, 2305–2311.
18. Prasad, B.L.V.; Stoeva, S.I.; Sorensen, C.M.; Klabunde, K.J. Digestive-ripening agents for gold nanoparticles: alternatives to thiols. *Chem. Mater.* **2003**, *15*, 935–942.
19. Maye, M.M.; Zheng, W.X.; Leibowitz, F.L.; Ly, N.K.; Eichelberger, H.H.; Zhong, C.J. An investigation of temperature-manipulated size and shape evolution of preformed core–shell nanoparticles. *Mater. Res. Soc. Symp. Proc.* **2000**, *580*, 201–206.
20. Prasad, B.L.V.; Stoeva, S.I.; Sorensen, C.M.; Klabunde, K.J. Digestive ripening of thiolated gold nanoparticles: the effect of alkyl chain length. *Langmuir* **2002**, *18*, 7515–7520.
21. Lin, X.M.; Sorensen, C.M.; Klabunde, K.J. Digestive ripening, nanophase segregation and superlattice formation in gold nanocrystal colloids. *J. Nanopart. Res.* **2000**, *2*, 157–164.
22. Zhong, C.J.; Zhang, W.X.; Leibowitz, F.L.; Eichelberger, H.H. Size and shape evolution of core–shell nanocrystals. *Chem. Commun. (Cambridge)* **1999**, 1211–1212.
23. Snow, A.W.; Wohltjen, H. Size-induced metal-to-semiconductor transition in a stabilized gold cluster ensemble. *Chem. Mater.* **1998**, *10*, 947–949.
24. Shaaff, T.G.; Shafiqullin, M.N.; Khoury, J.T.; Vezmar, I.; Whetten, R.L. Properties of a ubiquitous 29 kDa Au:SR cluster compound. *J. Phys. Chem., B* **2001**, *105*, 8785–8796.
25. Grate, J.W.; Abraham, M.H. Solubility interactions and the design of chemically selective sorbent coatings for chemical sensors and arrays. *Sens. Actuators, B* **1991**, *3*, 85–111.
26. Grate, J.W.; Abraham, M.H.; McGill, R.A. Sorbent polymer materials for chemical sensors and arrays. *Handb. Biosens. Electron. Noses* **1997**, 593–612.
27. Grate, J.W.; Kaganove, S.N.; Bhethanabotla, V.R. Examination of mass and modulus contributions to thickness shear mode and surface acoustic wave vapor sensor responses using partition coefficients. *Faraday Discuss.* **1997**, *107*, 259–283.
28. Abraham, M.H.; Andonian-Haftvan, J.; Du, C.M.; Diart, V.; Whiting, G.S.; Grate, J.W.; McGill, R.A. Hydrogen bonding: part 29. Characterization of 14 sorbent coatings for chemical microsensors using a new solvation equation. *J. Chem. Soc., Perkin Trans. 2* **1995**, 369–378.
29. Grate, J.W.; Kaganove, S.N.; Bhethanabotla, V.R. Comparison of polymer/gas partition coefficients calculated from responses of thickness shear mode and surface acoustic wave vapor sensors. *Anal. Chem.* **1998**, *70*, 199–203.

30. Grate, J.W.; Snow, A.; Ballantine, D.S., Jr.; Wohltjen, H.; Abraham, M.H.; McGill, R.A.; Sasson, P. Determination of partition coefficients from surface acoustic wave vapor sensor responses and correlation with gas-liquid chromatographic partition coefficients. *Anal. Chem.* **1988**, *60*, 869–875.
31. Han, L.; Daniel, D.R.; Maye, M.M.; Zhong, C.-J. Core-shell nanostructured nanoparticle films as chemically sensitive interfaces. *Anal. Chem.* **2001**, *73*, 4441–4449.
32. Grate, J.W. Sorptive behavior of monolayer-protected gold nanoparticle films containing alkanethiols and alkenedithiols. *Anal. Chem.* **2003**, *75*, 6759.
33. Gross, G.M.; Nelson, D.A.; Grate, J.W.; Synovec, R.E. Monolayer-protected gold nanoparticles as a stationary phase for open tubular gas chromatography. *Anal. Chem.* **2003**, *75*, 4558–4564.
34. Gross, G.M.; Grate, J.W.; Synovec, R.E. Monolayer-protected gold nanoparticles as an efficient stationary phase for open tubular gas chromatography using a square capillary: a model for chip-based GC in square cornered microfabricated channels. **2003**. Submitted for publication.
35. Materials, Method and Apparatus for Detecting and Monitoring Chemical Species, provisional filing date of November 24, 1997.
36. Snow et al. Defense Applications of Nanomaterials, ACS Meeting, San Diego, April, 2001.
37. Snow et al. AVS Topical Conference on Understanding and Operating in Threat Environments, Monterey, CA, April 30–May 2, 2002.
38. Zhang, H.L.; Evans, S.D.; Henderson, J.R.; Miles, R.E.; Shen, T.H. Vapour sensing using surface functionalized gold nanoparticles. *Nanotechnology* **2002**, *13*, 439–444.
39. Zamborini, F.P.; Leopold, M.C.; Hicks, J.F.; Kulesza, P.J.; Malik, M.A.; Murray, R.W. Electron hopping conductivity and vapor sensing properties of flexible network polymer films of metal nanoparticles. *J. Am. Chem. Soc.* **2002**, *124*, 8958–8964.
40. Krasteva, N.; Guse, B.; Besnard, I.; Yasuda, A.; Vossmeier, T. Gold nanoparticle/PPI-dendrimer based chemiresistors. Vapor-sensing properties as a function of the dendrimer size. *Sens. Actuators, B, Chem.* **2003**, *92*, 137–143.
41. Krasteva, N.; Krustev, R.; Yasuda, A.; Vossmeier, T. Vapor sorption in self-assembled gold nanoparticle/dendrimer films studied by specular neutron reflectometry. *Langmuir* **2003**, *19*, 7754–7760.
42. Krasteva, N.; Besnard, I.; Guse, B.; Bauer, R.E.; Muellen, K.; Yasuda, A.; Vossmeier, T. Self-assembled gold nanoparticle/dendrimer composite films for vapor sensing applications. *Nano Lett.* **2002**, *2*, 551–555.
43. Vossmeier, T.; Guse, B.; Besnard, I.; Bauer, R.E.; Mullen, K.; Yasuda, A. Gold nanoparticle/polyphenylene dendrimer composite films. Preparation and vapor-sensing properties. *Adv. Mater.* **2002**, *14*, 238–242.
44. Joseph, Y.; Besnard, I.; Rosenberger, M.; Guse, B.; Nothofer, H.-G.; Wessels, J.M.; Wild, U.; Knop-Gericke, A.; Su, D.; Schloegl, R.; Yasuda, A.; Vossmeier, T. Self-assembled gold nanoparticle/alkanedithiol films: Preparation, electron microscopy, XPS-analysis, charge transport, and vapor-sensing properties. *J. Phys. Chem., B* **2003**, *107*, 7406–7413.
45. Cai, Q.-Y.; Zellers, E.T. Dual-chemiresistor GC detector employing monolayer-protected metal nanocluster interfaces. *Anal. Chem.* **2002**, *74*, 3533–3539.

# Monolayer-Protected Metal Nanoparticles: Synthesis

Young-Seok Shon

Department of Chemistry, Western Kentucky University, Bowling Green, Kentucky, U.S.A.

## INTRODUCTION

The basic synthetic methods of monolayer-protected metal nanoparticles including Au, Ag, Cu, Pt, and Pd particles are presented. (There is also an article on “Metal Nanoparticles Protected with Monolayers: Applications for Chemical Vapor Sensing and Gas Chromatography,” which explores the sorptive properties in depth.) This entry introduces the fundamentals about protective monolayers from various organic compounds containing reactive functional groups such as thiol, disulfide, sulfide, thiosulfate, xanthate, ammonium, amine, phosphine, phosphine oxide, carboxylate, selenide, isocyanide, etc.

## BACKGROUND

Nanoparticles (particles of 1–100 nm in diameter) have generated intense interest over the past decades because of their unique electronic, optical, photoreponsive, and catalytic properties. However, nanoparticles are subject to the irreversible particle aggregation and the oxidation reactions. Thus the stabilization of nanoparticles against these problems is a requirement for further advancement in nanoparticle science and technology. In 1981, Schmid et al.<sup>[1]</sup> synthesized the first example of the ligand-stabilized gold nanoparticles,  $\text{Au}_{55}(\text{PPh}_3)_{12}\text{Cl}_6$ . However, the dependable and practical formation of more stable and isolable monolayer-protected gold nanoparticles was achieved about a decade ago by Brust et al.<sup>[2]</sup> The organic monolayers, which bind to the surface of metal nanoparticles, not only prevent aggregation of the metal nanoparticles, but also stabilize them from harsh reaction conditions and enhance the solubility in various solvents.<sup>[3–5]</sup> Subsequent investigations were extended to different metal particles including Au,<sup>[1–53]</sup> Ag,<sup>[31,38,54–68]</sup> Cu,<sup>[38,59,69–71]</sup> Pt,<sup>[72–79]</sup> Pd,<sup>[76,80–86]</sup> Ni,<sup>[85,87]</sup> and alloy particles.<sup>[88,89]</sup> Other organic compounds with different reactive head groups, such as thiol,<sup>[8–29]</sup> disulfide,<sup>[30,31]</sup> sulfide,<sup>[32–35]</sup> thiosulfate,<sup>[36,37]</sup> xanthate,<sup>[38]</sup> phosphine,<sup>[1,39–41]</sup> phosphine oxide,<sup>[42]</sup> ammonium,<sup>[43,44]</sup> amine,<sup>[45–47]</sup> carboxylate,<sup>[48–50]</sup> selenide,<sup>[51,52]</sup> and isocyanide,<sup>[53]</sup> can protect metal nanoparticles by self-assembly. Monolayers with different

functional groups and moieties can also be incorporated onto the surface of metal nanoparticles.<sup>[3–5]</sup> The modification of nanoparticles by the incorporation of a functional group is of potential significance for the expansion of chemical and biological applications of these nanomaterials. This entry focuses on the synthesis of various metal nanoparticles protected with monolayers containing different reactive head groups and functional tail groups.

## GOLD NANOPARTICLES

Gold nanoparticles have drawn remarkable interest in the last few years because of their high stability to oxidation and their optical and well-defined size-related electronic (e.g., quantized charging) properties.<sup>[6,7]</sup> Biological applications of hybrid Au nanoparticles have also shown a great promise for the use of these nanomaterials in biotechnology.<sup>[4]</sup> The synthesis of monolayer-protected gold nanoparticles will be described based on the reactive head groups, which provide self-assembly of organic monolayers onto the nanoparticle surface.

### Gold Nanoparticles Protected with Thiols

The stabilization of gold nanoparticles with alkanethiols was a direct result of advancement in the passivation of two-dimensional gold surfaces using alkanethiols in the late 1980s and early 1990s, which results in the formation of self-assembled monolayers on gold substrates.<sup>[90]</sup> The first report regarding the capping of Au nanoparticles with alkanethiols was made by Giersig and Mulvaney<sup>[8]</sup> in 1993. Brust et al.<sup>[2]</sup> reported a convenient two-phase synthesis of isolable and soluble alkanethiolate-protected gold nanoparticles in 1994, which had a huge impact on the nanoparticle research. In this reaction (Fig. 1),  $\text{AuCl}_4^-$  was transferred to toluene using tetraoctylammonium bromide as the phase-transfer reagent. Addition of dodecanethiol to organic-phase  $\text{AuCl}_4^-$  followed by the reduction with  $\text{NaBH}_4$  generated dodecanethiolate-protected gold nanoparticles. The research was extended to the alkanethiols with different chain lengths (C3–C24).<sup>[3]</sup>





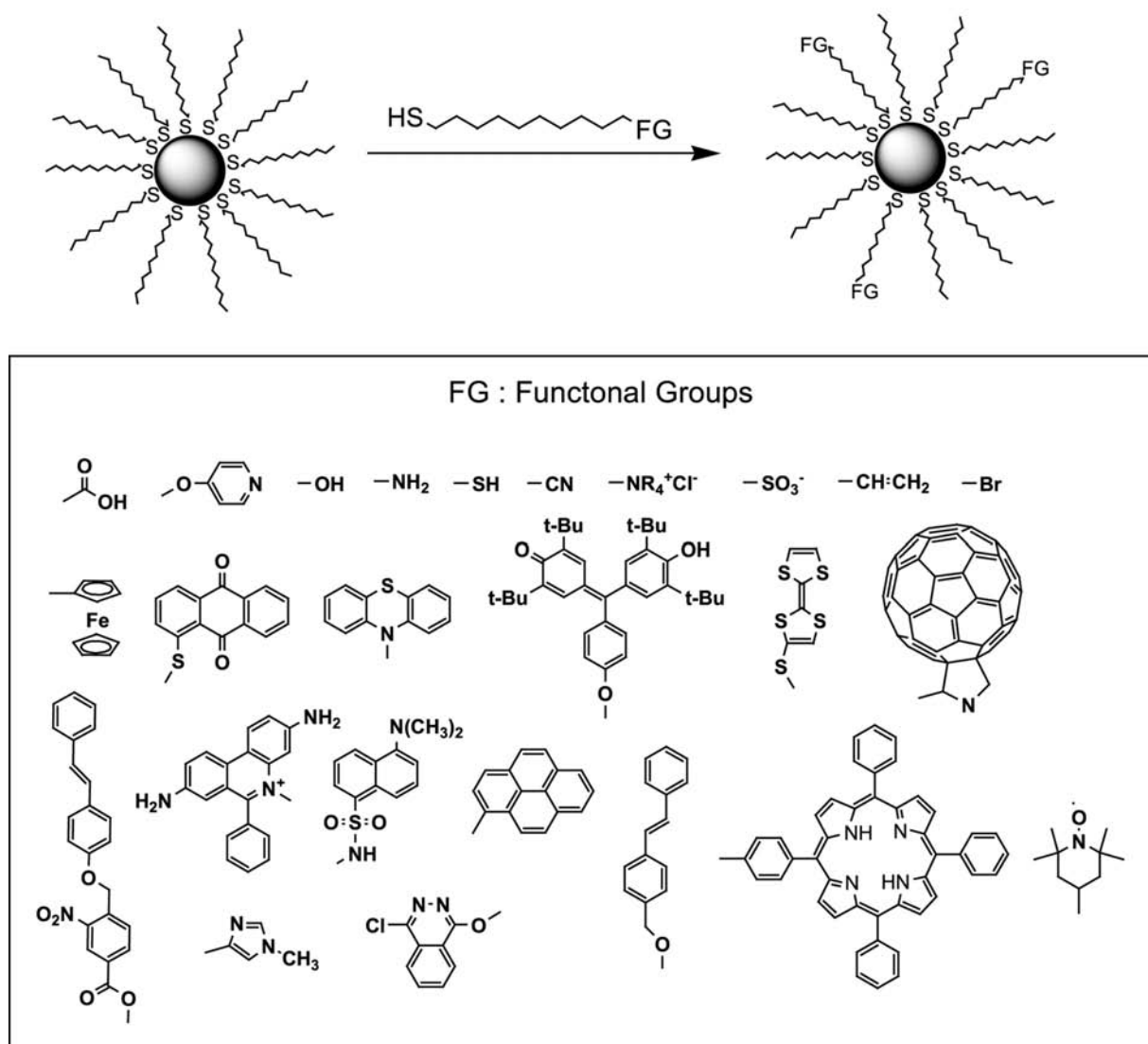


Fig. 3 General scheme and examples of functionalized thiols for the ligand-exchange reactions.

Templeton et al.<sup>[3]</sup> reported the “ligand-exchange” method to modify the composition of the monolayer-protected nanoparticles. This research enabled incorporation of many different functional groups and moieties onto the surface of gold nanoparticles (Fig. 3). In the exchange reaction, the incoming ligands replace the thiolate ligands on nanoparticles by an associative reaction, and the displaced thiolate becomes a thiol. The rate of ligand exchange depends on the chain length and/or steric bulk of the initial monolayers and electronic charge on nanoparticles. Various functional groups ranging from simple organic functional groups to functional complexes (electroactive or photochemical groups) were incorporated into the nanoparticles using ligand-exchange reactions.<sup>[3–5]</sup>

Reactions of functionalized gold nanoparticles were also frequently used for the incorporation of more specific organic groups and moieties having electroactive, photoresponsive, catalytic, mechanical, and biological properties (Fig. 4).<sup>[3–5]</sup>

### Gold Nanoparticles Protected with Other Sulfur-Containing Species

Other sulfur-containing species such as disulfides,<sup>[30,31]</sup> sulfides,<sup>[32–34]</sup> episulfides,<sup>[35]</sup> thiosulfates,<sup>[36,37]</sup> and xanthates<sup>[38]</sup> have been used for the synthesis of monolayer-protected gold nanoparticles (Fig. 5). The formation of alkanethiolate-protected gold nanoparticles generated by the adsorption of dialkyl disulfides

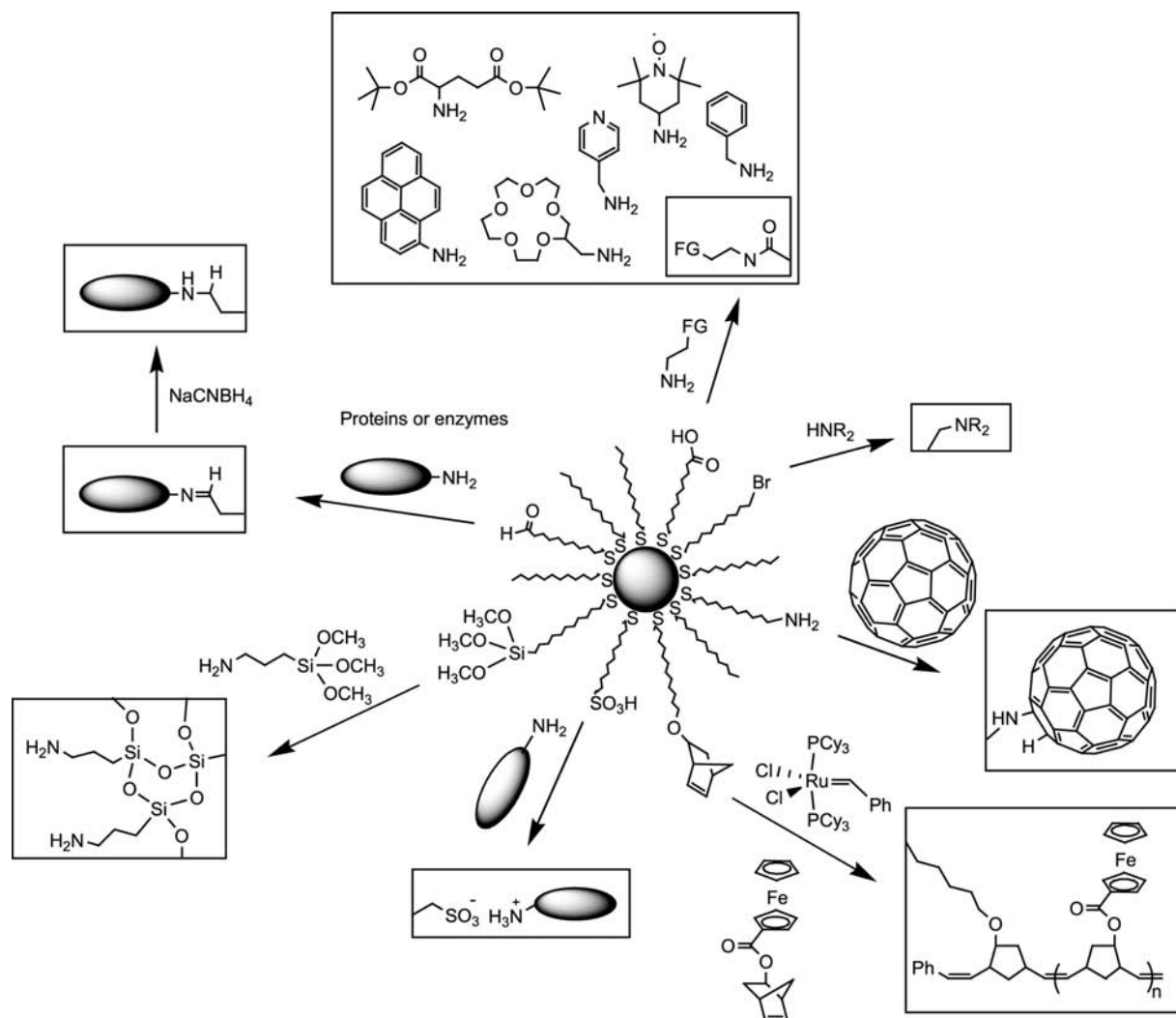


Fig. 4 General scheme and examples of organic reactions of functionalized metal nanoparticles.

showed that the characteristics (monolayer crystalline structure, core size, stability, and solubility) of these particles were identical to the nanoparticles generated by the adsorption of alkanethiols.<sup>[30,31]</sup>

Dialkyl sulfide-protected gold nanoparticles exhibited lower aggregation stability than alkanethiolate-protected gold nanoparticles because of the non-covalent bonding interactions between the gold surface and sulfur atoms. Because of low reactivity of sulfide groups, the average core size of dialkyl sulfide-protected gold nanoparticles was larger than that of alkanethiolate-protected nanoparticles prepared under the same conditions.<sup>[32]</sup> Alkyl sulfide-protected gold nanoparticles underwent ligand exchange by both thiols and disulfides.<sup>[33]</sup> In the case of thiol exchange of weakly adsorbed sulfides, it was found that intact thiols (RSH) rather than thiolates (RS<sup>-</sup>) were present on the surface of the nanoparticles. Tetradentate thioether was used for the spherical assembly of gold

nanoparticles that could be readily assembled and disassembled.<sup>[34]</sup>

The synthesis of alkanethiolate-protected gold nanoparticles using sodium *S*-dodecylthiosulfate resulted in the production of particles with larger average core dimensions (caused by low reactivity of thiosulfates) but indistinguishable Au-S bond compared with those prepared using dodecanethiol.<sup>[36]</sup> Xanthate-protected gold nanoparticles were found to be much less hydrophobic and temperature sensitive.<sup>[38]</sup>

#### Gold Nanoparticles Protected with Phosphorus-Containing Species (Phosphine and Phosphine Oxide)

The ligand-stabilized gold nanoparticles, Au<sub>55</sub>(PPh<sub>3</sub>)<sub>12</sub>Cl<sub>6</sub>, synthesized by Schmid et al.<sup>[1]</sup> were

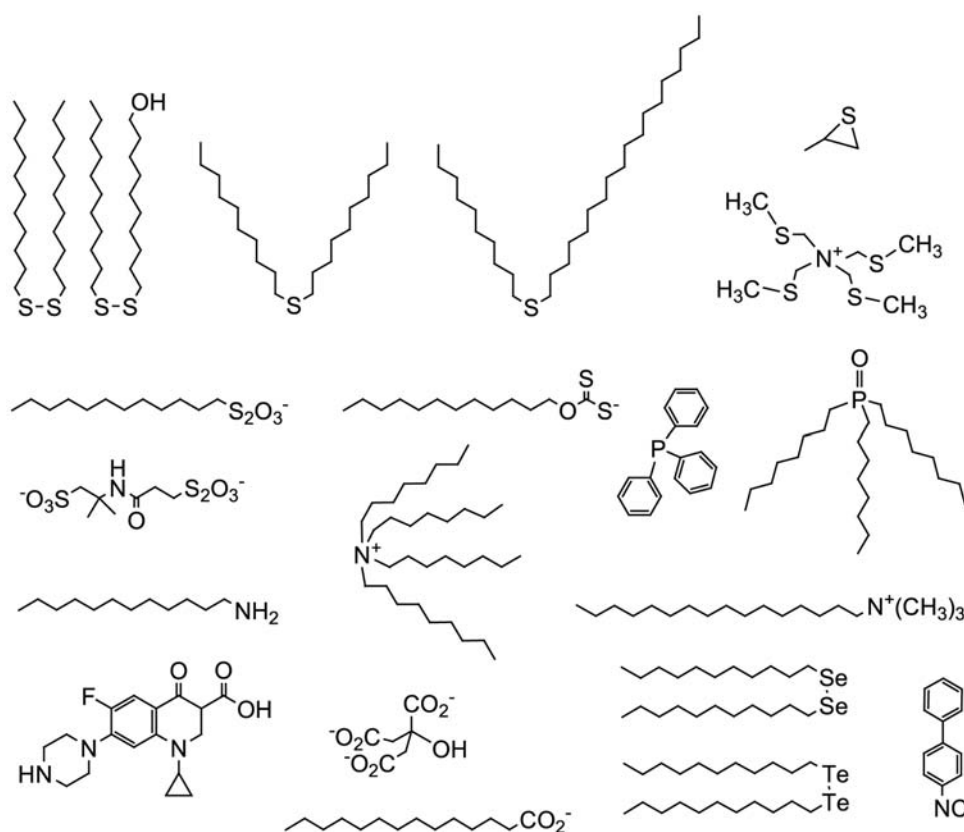


Fig. 5 Various organic compounds used for the protection of metal nanoparticles.

the first example of phosphine-stabilized quantum-dot particles. Weare et al.<sup>[39]</sup> improved the initial cumbersome procedure (anaerobic conditions and diborane gas as a reducing agent) with a more convenient and safer method using a two-phase system similar to the Schiffrin reaction to produce Au<sub>101</sub>(PPh<sub>3</sub>)<sub>21</sub>Cl<sub>5</sub> particles. This improved synthetic method allows size control and is tolerant of a variety of functionalized phosphine ligands. These phosphine-stabilized gold nanoparticles underwent ligand-exchange with  $\omega$ -functionalized alkanethiols producing alkanethiolate-protected gold nanoparticles.<sup>[40]</sup> Subnanometer phosphine-stabilized undecagold nanoparticles were synthesized by the NaBH<sub>4</sub> reduction of AuCl(PPh<sub>3</sub>). Ligand-exchange reactions of these Au<sub>11</sub> nanoparticles with alkanethiols and  $\omega$ -functionalized alkanethiols resulted in the formation of thiol-protected Au<sub>11</sub> nanoparticles.<sup>[41]</sup>

The reduction of gold (IV) chloride by sodium borohydride in hot tri-*n*-octylphosphine oxide (TOPO) at ca. 190°C resulted in gold nanoparticles with core sizes of 10–100 nm.<sup>[42]</sup> TOPO acts as both a reaction medium and passivating ligand. Particle synthesis in a mixture of TOPO and octadecylamine at ca. 190°C produced smaller and stable gold nanoparticles (ca. 8.5 nm).

### Gold Nanoparticles Protected with Nitrogen-Containing Species (Amines and Ammonium Salts)

Au nanoparticles capped with tetraoctylammonium bromide were prepared by the NaBH<sub>4</sub> reduction using the modified two-phase protocol (without the presence of thiols).<sup>[43]</sup> Binding of these gold nanoparticles with organic molecules containing functional groups such as -SCN or -NH<sub>2</sub> was found to dampen the surface plasmon bands of gold. Cetyltrimethylammonium bromide (CTAB)-capped gold nanoparticles were also synthesized using CTAB as both a phase-transfer reagent and stabilizer in a two-phase system.<sup>[44]</sup>

Alkylamine-stabilized gold nanoparticles were synthesized and used for the formation of ordered superlattices.<sup>[45]</sup> Thermal decomposition of organometallic gold (I) amine complexes produced gold nanoparticles protected with a monolayer of alkylamines.<sup>[46]</sup> The antibacterial drug ciprofloxacin (cfH) has been used to protect gold nanoparticles synthesized by citrate reduction in water.<sup>[47]</sup> The release of the drug (cfH) molecule from the nanoparticles showed the possible drug delivery application of gold nanoparticles.

## Gold Nanoparticles Protected with Other Organic Compounds

Citrate reduction of  $\text{HAuCl}_4$  in water led to less stable citrate-capped gold nanoparticles with core sizes ranging from 15 to 150 nm. The core size of gold nanoparticles was based on the ratio of trisodium citrate to gold.<sup>[48]</sup> This method is typically useful when a rather loose shell of ligands is required around the gold core.<sup>[49]</sup> Thermal decomposition of  $\text{Au(I)(C}_{13}\text{H}_{27}\text{COO)PPH}_3$  at 180°C resulted in the formation of myristate-capped gold nanoparticles.<sup>[50]</sup> The core size (10–45 nm) of these particles increased with reaction time and increasing reaction temperature.

Gold nanoparticles stabilized by alkyl selenides and alkyl tellurides could be prepared by using a two-phase Schiffrin reaction.<sup>[51,52]</sup> Passivation by alkyl selenide was characterized by greater chain density and stronger Au–Se bond strength. Particle size was, however, uniform in the cases when different ligand/substrate ratios were employed.<sup>[52]</sup>

The adsorption behavior of 4-biphenylisocyanide on gold nanoparticles has been studied using surface-enhanced Raman scattering (SERS).<sup>[53]</sup> The result showed that the isocyanides adsorbed on gold via the carbon lone pair electrons.

## SILVER NANOPARTICLES

Recently, research efforts have been intensified for the synthesis of Ag nanoparticles because of important roles played by Ag particles in antimicrobial applications, catalysis, and as a substrate for SERS. Thiols<sup>[54–58]</sup> have been the most popular choice of capping reagents for Ag nanoparticles because of a higher stability over other capping reagents, such as amines<sup>[59,60]</sup> and carboxylates,<sup>[61–63]</sup> which are weakly anchored to Ag particle cores. Other organic compounds, such as dialkyl disulfides,<sup>[31,64]</sup> dialkyl sulfides,<sup>[65]</sup> thiosulfates,<sup>[66]</sup> thiosalicylic acids,<sup>[67]</sup> and xanthates,<sup>[38]</sup> have been used to generate monolayer-protected Ag nanoparticles.

### Silver Nanoparticles Protected with Sulfur-Containing Species

Alkanethiolate-protected Ag nanoparticles were synthesized using the modified two-phase Schiffrin reaction.<sup>[54,55]</sup> Two-dimensional ordered superlattices of the Ag nanoparticles could be formed by evaporating a drop of the particle solutions on carbon films.<sup>[55]</sup> The fluorinated thiol-capped Ag nanoparticles could be prepared using the  $\text{NaBH}_4$  reduction of  $\text{AgNO}_3$  in the presence of perfluorodecanethiol in acetone/water. These particles could be redispersed in acetone and

liquid and supercritical  $\text{CO}_2$ .<sup>[56]</sup> Thiolated  $\beta$ -cyclodextrin-protected Ag nanoparticles were also synthesized from  $\text{AgNO}_3$ .<sup>[57]</sup> *N,N*-Dimethylformamide (DMF) was used as both the solvent and the reducing agent in this reaction. Synthesis of water-soluble tiopronin-protected Ag nanoparticles was also reported.<sup>[58]</sup>

Unlike Au nanoparticles functionalized by the adsorption of dialkyl disulfides, the monolayers of alkanethiolate-protected Ag nanoparticles derived from dialkyl disulfides were somewhat less crystalline than those prepared similarly from alkanethiols.<sup>[31]</sup> Positively charged Ag nanoparticles were synthesized by the  $\text{NaBH}_4$  reduction of  $\text{AgNO}_3$  in the presence of quaternary ammonium dialkyl disulfides.<sup>[64]</sup> Adsorption of benzyl phenyl sulfide on silver nanoparticles in water has been studied.<sup>[65]</sup> Alkanethiolate-protected Ag nanoparticles were synthesized from sodium *S*-dodecylthiosulfate in aqueous solution.<sup>[66]</sup> Silver nanoparticles, produced by the borohydride reduction of  $\text{AgNO}_3$  in  $\text{H}_2\text{O}$ , were stabilized by the adsorption of *S*-dodecylthiosulfate followed by the removal of the  $\text{SO}_3^-$  moiety.

Alkyl xanthates were also used for the capping of Ag nanoparticles.<sup>[38]</sup> Xanthate-capped Ag particles are less hydrophobic than alkanethiol-protected Ag nanoparticles and less stable than the oleate-capped particles (but still stable in aqueous solutions for over a month). Thiosalicylic acid (TSA)-functionalized silver nanoparticles were synthesized from  $\text{NaBH}_4$  reduction of TSA- $\text{AgNO}_3$  in aqueous ethanol solution.<sup>[67]</sup>

### Silver Nanoparticles Protected with Other Organic Species

A synthesis of alkylamine-capped silver nanoparticles was developed using thermal decomposition of  $[\text{Ag}(\mu\text{-mesityl})_4]$  (mesityl = 2,4,7- $\text{Me}_3\text{C}_6\text{H}_2$ ) derivatives in alkylamine solution.<sup>[59]</sup> Two-phase (*n*-heptane/water)  $\text{NaBH}_4$  reduction of *N*-hexadecylethylenediamine silver nitrate complex produced *N*-hexadecylethylenediamine-protected silver nanoparticles.<sup>[60]</sup> The colloidal solution of diamine-protected silver nanoparticles was free from flocculation and aggregation for several months.

Long-chain carboxylates (or fatty acids) have been one of the most commonly used ligands for silver particles.<sup>[61–63]</sup> The simple dissolution of silver 2-ethylhexanoate in DMSO (as both a solvent and reducing agent) produced silver nanoparticles.<sup>[61]</sup> Addition of stabilizing agent, sodium citrate, produced stable yet catalytic monolayer-protected silver nanoparticles. Thermal reduction of silver trifluoroacetate in isoamyl ether in the presence of oleic acid generated Ag nanoparticles with diameters in the range of 7–11 nm with narrow size distribution.<sup>[62]</sup>

Surface-enhanced Raman scattering studies of 4-biphenylisocyanide of silver nanoparticles proved the adsorption of isocyanide on silver surfaces.<sup>[53]</sup> Dye-protected silver nanoparticles were prepared through the reduction of metallic Ag ions by NaBH<sub>4</sub> in aqueous media.<sup>[68]</sup> The dye used was a cyanine derivative, 5,5'-dichloro-3,3-disulfopropylthiacyanine sodium salt.

## COPPER NANOPARTICLES

Because of the inexpensive nature of copper precursors and the expected optical, electronic, and catalytic properties of copper nanoparticles, there has been an increased interest in the synthesis of stable monolayer-protected copper nanoparticles. Monolayer-protected copper nanoparticles have been synthesized using alkanethiols,<sup>[69,70]</sup> alkylamines,<sup>[59]</sup> tetra-alkyl ammonium complexes,<sup>[71]</sup> and alkyl xanthates<sup>[38]</sup> as their stabilizing ligands. However, progress has been limited because of the instability (oxidation) of these copper nanoparticles.

### Copper Nanoparticles Protected with Sulfur-Containing Species

Alkanethiolate-protected copper nanoparticles with the size of 1–2 nm in diameter were prepared in a one-phase tetrahydrofuran (THF) system using lithium triethylborohydride (superhydride) as the reducing agent.<sup>[69]</sup> The aged particles typically failed to maintain their electronic and optical properties because of the oxidation of the copper core. Thermal annealing of copper nanoparticles in solid state produced large (>10 nm) nanoparticles with distinct shape evolutions. Thermolysis of copper complexes in the presence of alkanethiols in supercritical water produced small monodisperse Cu nanoparticles.<sup>[70]</sup> Alkyl xanthate stabilization also enabled the preparation of copper nanoparticles in aqueous solution.<sup>[38]</sup>

### Copper Nanoparticles Protected with Other Organic Species

Alkylamine-protected copper nanoparticles (8–9 nm) were synthesized by thermolysis of [Cu(*μ*-mesityl)<sub>5</sub>] (mesityl = 2,4,7-Me<sub>3</sub>C<sub>6</sub>H<sub>2</sub>) derivatives in octylamine followed by injection into a hot hexadecylamine solution.<sup>[59]</sup> A sonochemical approach was used for the preparation of elongated copper nanoparticles coated with cetyltrimethylammonium *p*-toluene sulfonate.<sup>[71]</sup>

## PLATINUM NANOPARTICLES

Platinum nanoparticles have drawn quite an interest because of their catalytic properties and promising fuel

cell application. Ligand-stabilized platinum nanoparticles with alkanethiols,<sup>[72–75]</sup> thiolated  $\beta$ -cyclodextrins,<sup>[76]</sup> alkyl xanthates,<sup>[77]</sup> alkylamines,<sup>[78]</sup> and alkyl isocyanides<sup>[79]</sup> have been reported.

### Platinum Nanoparticles Protected with Sulfur-Containing Species

Alkanethiols have been the choice of protecting ligands for Pt particles. The reduction of H<sub>2</sub>PtCl<sub>6</sub> by a small (10%) stoichiometric excess of sodium borohydride in the presence of a toluene solution containing 1-dodecanethiol produced dodecanethiolate-protected platinum nanoparticles, which were transferred to the toluene layer.<sup>[72]</sup> Transmission electron microscopy (TEM) results showed that these Pt nanoparticles have a mean diameter of 2.6 nm and a nearly monodispersed particle size distribution. Concentrated HCl was sometimes added to transfer Pt hydrosol, prepared by the NaBH<sub>4</sub> reduction in water, to the organic phase for thiolation.<sup>[73]</sup> The platinum nanoparticles synthesized in this manner have an average diameter of 4.4 nm. One-phase synthesis of alkanethiol-protected platinum nanoparticles using tetrahydrofuran as the solvent and superhydride as the reducing agent generated Pt nanoparticles with an average size of ~3 nm.<sup>[74]</sup> Water-dispersible mercaptosuccinic acid-protected platinum nanoparticles were prepared by one-phase reduction of chloroplatinic acid with sodium borohydride in either water or methanol.<sup>[75]</sup> The average particle diameter changes from 2.5 to 4.7 nm depending on the thiol/Pt ratio from 0.7 to 0.1, respectively.

Thiolated  $\beta$ -cyclodextrin-protected platinum nanoparticles were synthesized by NaBH<sub>4</sub> reduction of PtCl<sub>4</sub><sup>2-</sup> in DMSO–H<sub>2</sub>O in the presence of per-6-thio- $\beta$ -cyclodextrin.<sup>[76]</sup> These water-soluble platinum nanoparticles exhibit catalytic activity for the hydrogenation of allylamines. Alkyl xanthate-capped platinum nanoparticles were produced by the addition of alkyl xanthates in an aqueous solution containing uncapped platinum particles (4.0 nm).<sup>[77]</sup> Xanthate-capped platinum nanoparticles were found to be more stable than alkanethiol-protected platinum nanoparticles toward chemical corrosion and heating.

### Platinum Nanoparticles Protected with Other Organic Species

The use of hexylamine as an intermediate labile capping reagent for 4-mercaptoaniline-protected platinum nanoparticles has been reported.<sup>[78]</sup> *tert*-Butylammonium-stabilized platinum nanoparticles were prepared by a two-phase chemical reduction method. The addition of dodecyl isocyanide to this solution produced alkyl isocyanide-protected platinum nanoparticles.<sup>[79]</sup>

## PALLADIUM NANOPARTICLES

Research efforts to synthesize palladium nanoparticles have been increased because of the important roles played by palladium in catalysis. The catalytic activity of palladium nanoparticles is very sensitive to the particle size, shape, and ligand structure and density. Palladium nanoparticles were protected with alkanethiols,<sup>[80–82]</sup> thiolated  $\beta$ -cyclodextrins,<sup>[76,83]</sup> tetra-alkylammonium salts,<sup>[84,85]</sup> and alkyl phosphines.<sup>[86]</sup>

### Palladium Nanoparticles Protected with Sulfur-Containing Species

Alkanethiol-protected palladium nanoparticles can be synthesized using either the two-phase Schiffrin reaction<sup>[80]</sup> or one-phase superhydride reduction.<sup>[81,82]</sup> The size and morphology of palladium nanoparticles are sensitive to the thiol/Pd precursor ratio used in the reaction mixture.  $\omega$ -Functionalized monolayer-protected Pd nanoparticles can be synthesized by the ligand-place exchange reaction. Further organic reactions of functionalized Pd nanoparticles allow for the preparation of ferrocene-functionalized Pd nanoparticles.<sup>[80]</sup> Pd nanoparticles can be modified with thiolated  $\beta$ -cyclodextrin receptors by the reduction of  $\text{PdCl}_4^{2-}$  in DMF, yielding water-soluble Pd nanoparticles with good catalytic activity for the hydrogenation of various alkenes in aqueous media.<sup>[76,83]</sup>

### Palladium Nanoparticles Protected with Other Organic Species

Palladium nanoparticles stabilized by tetra-alkylammonium salts are prepared by the electrochemical reduction of Pd complex in the presence of tetra-alkylammonium surfactants.<sup>[84]</sup> Glycolate-stabilized Pd and Ni nanoparticles were synthesized by hydrogen reduction of  $\text{Pd}(\text{NO}_3)_2$  in the presence of tetraoctylammonium glycolates.<sup>[85]</sup> Monodisperse Pd nanoparticles with core dimensions of 3.5, 5, and 7 nm were synthesized by the thermal decomposition of Pd-trioctylphosphine (TOP) complex in an argon atmosphere.<sup>[86]</sup> The core size of Pd nanoparticles was controlled by varying the concentration of TOP.

## APPLICATIONS

Because the precise control over the chemical and structural composition of a monolayer surrounding a metal nanoparticle can dramatically affect its macroscopic properties and functions, monolayer-protected metal nanoparticles have found increased use in many recent applications including electronics, optics, catalysis, and

chemical recognition. Quantized double-layer charging has been one of the more interesting properties of alkanethiolate-protected metal nanoparticles. Optical properties of metal nanoparticles could be tuned by the incorporation of photoactive ligands. Optoelectronic properties of metal nanoparticles related to the surface plasmon absorption have also drawn increased interests. Catalytic properties of monolayer-protected metal nanoparticles are now being investigated in the broad field of catalysis including simple organic reactions, polymerization, and electrocatalysis. Functionalized monolayer-protected metal nanoparticles recognize molecules, bioconjugates, supramolecules, and metals based on various interactions (e.g., hydrogen-bonding, van der Waals, and electrostatic interactions). The combination of electronic and/or optical properties of metal nanoparticles with sensing capability results in the development of excellent sensory devices. The article on “Metal Nanoparticles Protected with Monolayers: Applications for Chemical Vapor Sensing and Gas Chromatography” touches on some of these particular applications.

## CONCLUSION

The synthesis of monolayer-protected metal nanoparticles has undoubtedly expanded the available diversity of the nanomaterials as functionalized chemical reagents. Various monolayer-protected metal nanoparticles including Au, Ag, Cu, Pt, and Pd particles have been prepared in different reaction conditions. However, there is still a great demand for new and convenient techniques that allow environmentally benign and cost-effective preparation of monolayer-protected metal nanoparticles and other hybrid nanoparticles. More extensive and systematic studies are essential for further advancement in the nanoparticle-related research field.

## ACKNOWLEDGMENTS

Y.-S. Shon thanks supports from Research Corporation (Cottrell College Science Award) and Kentucky Science and Engineering Foundation.

## REFERENCES

- Schmid, G.; Pfeil, R.; Boese, R.; Bandermann, F.; Meyer, S.; Calis, G.H.M.; van der Velden, J.A.W.  $[\text{Au}_{55}\{\text{P}(\text{C}_6\text{H}_5)_3\}_{12}\text{Cl}_6]$ —A gold cluster of unusual size. *Chem. Ber.* **1981**, *114*, 3634–3642.
- Brust, M.; Walker, M.; Bethell, D.; Schiffrin, D.J.; Whyman, R.J. Synthesis of thiol-derivatized gold



- nanoparticles in a two-phase liquid-liquid system. *J. Chem. Soc., Chem. Commun.* **1994**, 801–802.
- Templeton, A.C.; Wuelfing, W.P.; Murray, R.W. Monolayer-protected cluster molecules. *Acc. Chem. Res.* **2000**, *33*, 27–36.
  - Daniel, M.-C.; Astruc, D. Gold nanoparticles: Assembly, supramolecular chemistry, quantum-size-related properties, and applications toward biology, catalysis, and nanotechnology. *Chem. Rev.* **2004**, *104*, 293–346.
  - Shon, Y.-S.; Choo, H. Organic Reactions of Monolayer-Protected Metal Nanoparticles. In *Dendrimers and Nanosciences*; Astruc, D., Ed.; C. R. Chime: Paris, 2003; *6*, 1009–1018.
  - Quinn, B.M.; Liljeroth, P.; Ruiz, V.; Laaksonen, T.; Kontturi, K. Electrochemical resolution of 15 oxidation states for monolayer protected gold nanoparticles. *J. Am. Chem. Soc.* **2003**, *125*, 6644–6645.
  - Kelly, K.L.; Coronado, E.; Zhao, L.L.; Schatz, G.C. The optical properties of metal nanoparticles: the influence of size, shape, and dielectric environment. *J. Phys. Chem. B* **2003**, *107*, 668–677.
  - Giersig, M.; Mulvaney, P. Preparation of ordered colloid monolayers by electrophoretic deposition. *Langmuir* **1993**, *9*, 3408–3413.
  - Leff, D.V.; Ohara, P.C.; Heath, J.R.; Gelbart, W.M. Thermodynamic control of gold nanocrystal size: Experiment and theory. *J. Phys. Chem.* **1995**, *99*, 7036–7041.
  - Hostetler, M.J.; Wingate, J.E.; Zhong, C.-J.; Harris, J.E.; Vachet, R.W.; Clark, M.R.; Londono, J.D.; Green, S.J.; Stokes, J.J.; Wignall, G.D.; Glish, G.L.; Porter, M.D.; Evans, N.D.; Murray, R.W. Alkanethiolate gold cluster molecules with core diameters from 1.5 to 5.2 nm: core and monolayer properties as a function of core size. *Langmuir* **1998**, *14*, 17–30.
  - Jana, N.R.; Gearheart, L.; Murphy, C.J. Evidence for seed-mediated nucleation in the chemical reduction of gold salts to gold nanoparticles. *Chem. Mater.* **2001**, *13*, 2313–2322.
  - Clarke, N.Z.; Waters, C.; Johnson, K.A.; Satherley, J.; Schiffrin, D.J. Size-dependent solubility of thiol-derivatized gold nanoparticles in supercritical ethane. *Langmuir* **2001**, *17*, 6048–6050.
  - Hicks, J.F.; Miles, D.T.; Murray, R.W. Quantized double-layer charging of highly monodisperse metal nanoparticles. *J. Am. Chem. Soc.* **2002**, *124*, 13,322–13,328.
  - Zhong, C.J.; Zhang, W.X.; Leibowitz, F.L.; Eichelberger, H.H. Size and shape evolution of core-shell nanocrystals. *Chem. Commun.* **1999**, 1211–1212.
  - Wei, G.-T.; Liu, F.-K.; Wang, C.R.C. Shape separation of nanometer gold particles by size-exclusion chromatography. *Anal. Chem.* **1999**, *71*, 2085–2091.
  - Zanchet, D.; Micheel, C.M.; Parak, W.J.; Gerion, D.; Alivisatos, A.P. Electrophoretic isolation of discrete au nanocrystal/DNA conjugates. *Nano Lett.* **2001**, *1*, 32–35.
  - Brust, M.; Fink, J.; Bethell, D.; Schiffrin, D.J.; Kiely, C.J. Synthesis and reactions of functionalised gold nanoparticles. *J. Chem. Soc., Chem. Commun.* **1995**, 1655–1656.
  - Paulini, R.; Frankamp, B.L.; Rotello, V.M. Effects of branched ligands on the structure and stability of monolayers on gold nanoparticles. *Langmuir* **2002**, *18*, 2368–2373.
  - Foos, E.E.; Snow, A.W.; Twigg, M.E.; Ancona, M.G. Thiol-terminated di-, tri-, and tetraethylene oxide functionalized gold nanoparticles: A water-soluble, charge-neutral cluster. *Chem. Mater.* **2002**, *14*, 2401–2408.
  - Kim, K.-S.; Demberelnyamba, D.; Lee, H. Size-selective synthesis of gold and platinum nanoparticles using novel thiol-functionalized ionic liquids. *Langmuir* **2004**, *20*, 556–560.
  - Yonezawa, T.; Onoue, S.; Kimizuka, N. Formation of uniform fluorinated gold nanoparticles and their highly ordered hexagonally packed monolayer. *Langmuir* **2001**, *17*, 2291–2293.
  - Fitzmaurice, D.; Rao, S.N.; Preece, J.A.; Stoddart, J.F.; Wenger, S.; Zaccheroni, N. Heterosupramolecular chemistry: programmed pseudorotaxane assembly at the surface of a nanocrystal. *Angew. Chem., Int. Ed.* **1999**, *38*, 1147–1150.
  - Choo, H.; Cutler, E.; Shon, Y.-S. Synthesis of mixed monolayer-protected gold clusters from thiol mixtures: Variation in the tail group, chain length, and solvent. *Langmuir* **2003**, *19*, 8555–8559.
  - Link, S.; Beeby, A.; FitzGerald, S.; El-Sayed, M.A.; Schaaff, T.G.; Whetten, R.L. Visible to infrared luminescence from a 28-atom gold cluster. *J. Phys. Chem. B* **2002**, *106*, 3410–3415.
  - Tan, Y.; Li, Y.; Zhu, D. Fabrication of gold nanoparticles using a trithiol (thiocyanuric acid) as the capping agent. *Langmuir* **2002**, *18*, 3392–3395.
  - Resch, R.; Baur, C.; Bugacov, A.; Koel, B.E.; Echter-nach, P.M.; Madhukar, A.; Montoya, N.; Requicha, A.A.G.; Will, P. Linking and manipulation of gold multi-nanoparticle structures using dithiols and scanning force microscopy. *J. Phys. Chem. B* **1999**, *103*, 3647–3650.
  - Félidj, N.; Aubard, J.; Lévi, G.; Krenn, J.R.; Hohenau, A.; Schider, G.; Leitner, A.; Aussenegg, F.R. Optimized surface-enhanced Raman scattering on gold nanoparticle arrays. *Appl. Phys. Lett.* **2003**, *82*, 3095–3097.
  - Balasubramanian, R.; Kim, B.; Tripp, S.L.; Wang, X.; Lieberman, M.; Wei, A. Dispersion and stability studies of resorcinarene-encapsulated gold nanoparticles. *Langmuir* **2002**, *18*, 3676–3681.
  - Liu, J.; Alvarez, J.; Ong, W.; Román, E.; Kaifer, A.E. Phase transfer of hydrophilic, cyclodextrin-modified gold nanoparticles to chloroform solutions. *J. Am. Chem. Soc.* **2001**, *123*, 11,148–11,154.
  - Shon, Y.-S.; Mazzitelli, C.; Murray, R.W. Unsymmetrical disulfides and thiol mixtures produce different mixed monolayer-protected gold clusters. *Langmuir* **2001**, *17*, 7735–7741.
  - Porter, L.A., Jr.; Ji, D.; Westcott, S.L.; Graupe, M.; Czernuszewicz, R.S.; Halas, N.J.; Lee, T.R. Gold and silver nanoparticles functionalized by the adsorption of dialkyl disulfides. *Langmuir* **1998**, *14*, 7378–7386.
  - Shelley, E.J.; Ryan, D.; Johnson, S.R.; Couillard, M.; Fitzmaurice, D.; Nellist, P.D.; Chen, Y.; Palmer, R.E.; Preece, J.A. Dialkyl sulfides: novel passivating agents for gold nanoparticles. *Langmuir* **2002**, *18*, 1791–1795.

33. Hasan, M.; Bethell, D.; Brust, M. The fate of sulfur-bound hydrogen on formation of self-assembled thiol monolayers on gold:  $^1\text{H}$  NMR spectroscopic evidence from solutions of gold clusters. *J. Am. Chem. Soc.* **2002**, *124*, 1132–1133.
34. Maye, M.M.; Chun, S.C.; Han, L.; Rabinovich, D.; Zhong, C.-J. Novel spherical assembly of gold nanoparticles mediated by a tetradentate thioether. *J. Am. Chem. Soc.* **2002**, *124*, 4958–4959.
35. Suzuki, M.; Miyazaki, T.; Hisamitsu, H.; Kadoma, Y.; Morioka, Y. Study on chemical reaction of methylthiirane on gold colloid by surface-enhanced Raman scattering. *Langmuir* **1999**, *15*, 7409–7410.
36. Shon, Y.-S.; Gross, S.M.; Dawson, B.; Porter, M.; Murray, R.W. Alkanethiolate protected gold clusters generated from sodium s-dodecylthiosulfate (bunte salts). *Langmuir* **2000**, *16*, 6555–6561.
37. Shon, Y.-S.; Wuelfing, W.P.; Murray, R.W. Water soluble, sulfonic acid-functionalized, monolayer-protected nanoparticles and an ionically conductive molten salt containing them. *Langmuir* **2001**, *17*, 1255–1261.
38. Tzhayik, O.; Sawant, P.; Efrima, S.; Kovalev, E.; Klug, J.T. Xanthate capping of silver, copper, and gold colloids. *Langmuir* **2002**, *18*, 3364–3369.
39. Weare, W.W.; Reed, S.M.; Warner, M.G.; Hutchison, J.E. Improved synthesis of small (dCORE  $\approx$  1.5 nm) phosphine-stabilized gold nanoparticles. *J. Am. Chem. Soc.* **2000**, *122*, 12,890–12,891.
40. Warner, M.G.; Reed, S.M.; Hutchison, J.E. Small, water-soluble, ligand-stabilized gold nanoparticles synthesized by interfacial ligand exchange reactions. *Chem. Mater.* **2000**, *12*, 3316–3320.
41. Woehrl, G.H.; Warner, M.G.; Hutchison, J.E. Ligand exchange reactions yield subnanometer, thiol-stabilized gold particles with defined optical transitions. *J. Phys. Chem. B* **2002**, *106*, 9979–9981.
42. Green, M.; O'Brien, P. A simple one phase preparation of organically capped gold nanocrystals. *Chem. Commun.* **2000**, 183–184.
43. Thomas, K.G.; Zajicek, J.; Kamat, P.V. Surface binding properties of tetraoctylammonium bromide-capped gold nanoparticles. *Langmuir* **2002**, *18*, 3722–3727.
44. Cheng, W.; Dong, S.; Wang, E. Synthesis and self-assembly of cetyltrimethylammonium bromide-capped gold nanoparticles. *Langmuir* **2003**, *19*, 9434–9439.
45. Brown, L.O.; Hutchison, J.E. Controlled growth of gold nanoparticles during ligand exchange. *J. Am. Chem. Soc.* **1999**, *121*, 882–883.
46. Gomez, S.; Philippot, K.; Collière, V.; Chaudret, B.; Senoeq, F.; Lecante, P. Gold nanoparticles from self-assembled gold(I) amine precursors. *Chem. Commun.* **2000**, 1945–1946.
47. Tom, R.T.; Suryanarayanan, V.; Reddy, P.G.; Baskaran, S.; Pradeep, T. Ciprofloxacin-protected gold nanoparticles. *Langmuir* **2004**, *20*, 1909–1914.
48. Frens, G. Controlled nucleation for the regulation of the particle size in monodisperse gold suspensions. *Nat. Phys. Sci.* **1973**, *241*, 20–22.
49. Watson, K.J.; Zhu, J.; Nguyen, S.B.T.; Mirkin, C.A. Hybrid nanoparticles with block copolymer shell structures. *J. Am. Chem. Soc.* **1999**, *121*, 462–463.
50. Yamamoto, M.; Nakamoto, M. New type of monodispersed gold nanoparticles capped by myristate and  $\text{PPh}_3$  ligands prepared by controlled thermolysis of  $[\text{Au}(\text{C}_{13}\text{H}_{27}\text{COO})(\text{PPh}_3)]$ . *Chem. Lett.* **2003**, *32*, 452–453.
51. Brust, M.; Stuhr-Hansen, N.; Nørgaard, K.; Christensen, J.B.; Nielsen, L.K.; Bjørnholm, T. Langmuir-Blodgett films of alkane chalcogenide (S, Se, Te) stabilized gold nanoparticles. *Nano Lett.* **2001**, *1*, 189–191.
52. Yee, C.K.; Ulman, A.; Ruiz, J.D.; Parikh, A.; White, H.; Rafailovich, M. Alkyl selenide- and alkyl thiolate-functionalized gold nanoparticles: chain packing and bond nature. *Langmuir* **2003**, *19*, 9450–9458.
53. Bae, S.J.; Lee, C.; Choi, I.S.; Hwang, C.-S.; Gong, M.; Kim, K.; Joo, S.-W. Adsorption of 4-biphenylisocyanide on gold and silver nanoparticle surfaces: surface-enhanced Raman scattering study. *J. Phys. Chem. B* **2002**, *106*, 7076–7080.
54. Mitra, S.; Nair, B.; Pradeep, T.; Goyal, P.S.; Mukhopadhyay, R. Alkyl chain dynamics in monolayer-protected clusters (MPCs): a quasielastic neutron-scattering investigation. *J. Phys. Chem. B* **2002**, *106*, 3960–3967.
55. He, S.; Yao, J.; Jiang, P.; Shi, D.; Zhang, H.; Xie, S.; Pang, S.; Gao, H. Formation of silver nanoparticles and self-assembled two-dimensional ordered superlattice. *Langmuir* **2001**, *17*, 1571–1575.
56. Shah, P.S.; Holmes, J.D.; Doty, R.C.; Johnston, K.P.; Korgel, B.A. Steric stabilization of nanocrystals in supercritical  $\text{CO}_2$  using fluorinated ligands. *J. Am. Chem. Soc.* **2000**, *122*, 4245–4246.
57. Liu, J.; Ong, W.; Kaifer, A.E. A “macrocylic effect” on the formation of capped silver nanoparticles in DMF. *Langmuir* **2002**, *18*, 5981–5983.
58. Huang, T.; Murray, R.W. Luminescence of tiopronin monolayer-protected silver clusters changes to that of gold clusters upon galvanic core metal exchange. *Langmuir* **2003**, *107*, 7434–7440.
59. Bunge, S.D.; Boyle, T.J.; Headley, T.J. Synthesis of coinage-metal nanoparticles from mesityl precursors. *Nano Lett.* **2003**, *3*, 901–905.
60. Manna, A.; Imae, T.; Iida, M.; Hisamatsu, N. Formation of silver nanoparticles from a *N*-hexadecylethylene-diamine silver nitrate complexes. *Langmuir* **2001**, *17*, 6000–6004.
61. Rodriguez-Gattorno, G.; Diaz, D.; Rendón, L.; Hernández-Segura, G.O. Metallic nanoparticles from spontaneous reduction of silver(I) in DMSO. Interaction between nitric oxide and silver nanoparticles. *J. Phys. Chem. B* **2002**, *106*, 2482–2487.
62. Lin, X.Z.; Teng, X.; Yang, H. Direct synthesis of narrowly dispersed silver nanoparticles using a single-source precursor. *Langmuir* **2003**, *19*, 10,081–10,085.
63. Wang, W.; Chen, X.; Efrima, S. Silver nanoparticles capped by long-chain unsaturated carboxylates. *J. Phys. Chem. B* **1999**, *103*, 7238–7246.
64. Yonezawa, T.; Onoue, S.; Kimizuka, N. Preparation of highly positively charged silver nanoballs and their stability. *Langmuir* **2000**, *16*, 5218–5220.
65. Kim, S.J.; Kim, T.G.; Ah, C.S.; Kim, K.; Jang, D.-J. Photolysis dynamics of benzyl phenyl sulfide adsorbed on silver nanoparticles. *J. Phys. Chem. B* **2004**, *108*, 880–882.

66. Shon, Y.-S.; Cutler, E. Aqueous synthesis of alkanethiolate-protected metal nanoparticles using bunte salts. *Langmuir* **2004**, *20*, 6626–6630.
67. Tan, Y.; Wang, Y.; Jiang, L.; Zhu, D. Thiosalicylic acid-functionalized silver nanoparticles synthesized in one-phase system. *J. Colloid Interface Sci.* **2002**, *249*, 336–345.
68. Hranisavljevic, J.; Dimitrijevic, N.M.; Wurtz, G.A.; Wiederrecht, G.P. Photoinduced charge separation reactions of J-aggregates on silver nanoparticles. *J. Am. Chem. Soc.* **2002**, *124*, 4536–4537.
69. Chen, S.; Sommers, J.M. Alkanethiolate-protected copper nanoparticles: spectroscopy, electrochemistry, and solid-state morphological evolution. *J. Phys. Chem. B* **2001**, *105*, 8816–8820.
70. Ziegler, K.J.; Doty, R.C.; Johnston, K.P.; Korgel, B.A. Synthesis of organic monolayer-stabilized copper nanocrystals in supercritical water. *J. Am. Chem. Soc.* **2001**, *123*, 7797–7803.
71. Salkar, R.A.; Jeevanandam, P.; Kataby, G.; Aruna, S.T.; Koltypin, Y.; Palchik, O.; Gedanken, A. Elongated copper nanoparticles coated with a zwitterionic surfactant. *J. Phys. Chem. B* **2000**, *104*, 893–897.
72. Yang, J.; Lee, J.Y.; Dievaraj, T.C.; Too, H.-P. An improved procedure for preparing smaller and nearly monodispersed thiol-stabilized platinum nanoparticles. *Langmuir* **2003**, *19*, 10,361–10,365.
73. Zhao, S.-Y.; Chen, S.-H.; Wang, S.-Y.; Li, D.-G.; Ma, H.-Y. Preparation, phase transfer, and self-assembled monolayers of cubic Pt nanoparticles. *Langmuir* **2002**, *18*, 3315–3318.
74. Yee, C.; Scotti, M.; Ulman, A.; White, H.; Rafailovich, M.; Sokolov, J. One-phase synthesis of thiol-functionalized platinum nanoparticles. *Langmuir* **1999**, *15*, 4314–4316.
75. Chen, S.; Kimura, K. Synthesis of thiolate-stabilized platinum nanoparticles in protolytic solvents as isolable colloids. *J. Phys. Chem. B* **2001**, *105*, 5397–5403.
76. Alvarez, J.; Liu, J.; Román, E.; Kaifer, A.E. Water-soluble platinum and palladium nanoparticles modified with thiolated  $\beta$ -cyclodextrin. *Chem. Commun.* **2000**, 1151–1152.
77. Sawant, P.; Kovalev, E.; Klug, J.T.; Efrima, S. Alkyl xanthates: new capping agents for metal colloids. Capping of platinum nanoparticles. *Langmuir* **2001**, *17*, 2913–2917.
78. Perez, H.; Pradeau, J.-P.; Albouy, P.-A.; Perez-Omil, J. Synthesis and characterization of functionalized platinum nanoparticles. *Chem. Mater.* **1999**, *11*, 3460–3463.
79. Horswell, S.L.; Kiely, C.J.; O'Neil, I.A.; Schiffrin, D.J. Alkyl isocyanide-derivatized platinum nanoparticles. *J. Am. Chem. Soc.* **1999**, *121*, 5573–5574.
80. Zamborini, F.P.; Gross, S.M.; Murray, R.W. Synthesis, characterization, reactivity, and electrochemistry of palladium monolayer protected clusters. *Langmuir* **2001**, *17*, 481–488.
81. Quiros, I.; Yamada, M.; Kubo, K.; Mizutani, J.; Kurihara, M.; Nishihara, H. Preparation of alkanethiolate-protected palladium nanoparticles and their size dependence on synthetic conditions. *Langmuir* **2002**, *18*, 1413–1418.
82. Yee, C.K.; Jordan, R.; Ulman, A.; White, H.; King, A.; Rafailovich, M.; Sokolov, J. Novel one-phase synthesis of thiol-functionalized gold, palladium, and iridium nanoparticles using superhydride. *Langmuir* **1999**, *15*, 3486–3491.
83. Liu, J.; Alvarez, J.; Ong, W.; Roman, E.; Kaifer, A.E. Tuning the catalytic activity of cyclodextrin-modified palladium nanoparticles through host-guest binding interactions. *Langmuir* **2001**, *17*, 6762–6764.
84. Reetz, M.T.; Helbig, W.; Quaiser, S.A.; Stimming, U.; Breuer, N.; Vogel, R. Visualization of surfactants on nanostructured palladium clusters by a combination of STM and high-resolution TEM. *Science* **1995**, *267*, 367–369.
85. Bradley, J.S.; Tesche, B.; Busser, W.; Maase, M.; Reetz, M.T. Surface spectroscopic study of the stabilization mechanism for shape-selectively synthesized nanostructured transition metal colloids. *J. Am. Chem. Soc.* **2000**, *122*, 4631–4636.
86. Kim, S.-W.; Park, J.; Jang, Y.; Chung, Y.; Hwang, S.; Hyeon, T. Synthesis of monodisperse palladium nanoparticles. *Nano Lett.* **2003**, *3*, 1289–1291.
87. Chen, D.-H.; Wu, Z.-H. Synthesis of nickel nanoparticles in water-in-oil microemulsions. *Chem. Mater.* **2000**, *12*, 1354–1360.
88. Shon, Y.-S.; Dawson, G.B.; Porter, M.; Murray, R.W. Monolayer-protected bimetal cluster synthesis by core metal galvanic exchange reaction. *Langmuir* **2002**, *18*, 3880–3885.
89. Hutter, E.; Fendler, J.H. Size quantized formation and self-assembly of gold encased silver nanoparticles. *Chem. Commun.* **2002**, 378–379.
90. Ulman, A. Formation and structure of self-assembled monolayers. *Chem. Rev.* **1996**, *96*, 1533–1554.

# Moore's Law: Performance and Power Dissipation

Laszlo B. Kish

Department of Electrical Engineering, Texas A&M University,  
College Station, Texas, U.S.A.

## INTRODUCTION

Moore's law predicts that the number of transistors in a chip will grow exponentially in time. Exponents giving the best fit of various chip families suggest an 18-month transistor number doubling time. If Moore's law of miniaturization will be followed below the size of 40 nm, physics will impose fundamental and practical limits of performance because of shrinking noise margin, increasing and quickening noise, and increasing power dissipation. It is important to locate the fundamental aspects of the problem, to explore relevant practical problems and possible solutions, and to investigate this situation not only in microelectronics, such as complementary metal oxide semiconductor (CMOS), but also in single-electron transistor (SET)-based nanoelectronics and even in quantum informatics applications. Recent studies show that quantum computers are not satisfactory tools to solve these problems of *general-purpose* data handling, and that the fundamental limits governing classical (CMOS) computers allow a much better performance than possible quantum computers.

## FUTURE OUTLOOK

We all have been enjoying the fast growth of speed and memory size of computers during the last decades. Recently, the emerging fields of quantum computing and nanoelectronics have suggested that the future will be even more brilliant.

However, as soon as we confront physical laws and reality with expectations, the future becomes more realistic. In this entry, we briefly outline some of the key issues.

## GENERAL CONSIDERATIONS

Thermal noise is an omnipresent small-voltage fluctuation on resistors. It has been thought that thermal noise will never be an issue in digital electronics. This view has been reevaluated and changed recently by

Kish.<sup>[1]</sup> On a parallel resistor–capacitor (RC) unit, the effective thermal noise voltage  $U_n$  is given as:

$$U_n = \sqrt{kT/C} \quad (1)$$

and the bandwidth  $f_c$  of this noise is:

$$f_c = \frac{1}{2\pi RC} \quad (2)$$

Gaussian noise processes, such as thermal noise, can cross large amplitude levels, provided that sufficiently long time is available. In a logic circuitry, noise amplitudes reaching beyond the noise margin  $U_{th}$  cause false bit flips that can result in bit errors. For a single band-limited noise process, the mean frequency  $\nu(U_{th})$  of bit errors can be obtained from the Rice formula:<sup>[1]</sup>

$$\nu(U_{th}) = \frac{2}{\sqrt{3}} \exp\left(\frac{-U_{th}^2}{2U_n^2}\right) f_c \quad (3)$$

where  $U_n$  is the effective noise voltage and  $f_c$  is the bandwidth.

So, what happens during miniaturization? In CMOS technology, the resistors are two-dimensional conductors; thus the resistance stays (roughly) constant. Therefore the supply voltage has to be decreased to keep the electrical field and dissipation at acceptable levels. The capacitances decrease. Together, these effects yield the following trends:

1. Shrinking noise margin (because  $U_{th}$  is only a fraction of the supply voltage)
2. Growing noise [because of Eq. (1)]
3. Growing bandwidth [quickening of the noise; Eq. (2)].

All these phenomena (1, 2, and 3) act toward radically increasing the frequency of bit errors via Eq. (3). To have a feeling of the nature of this problem, on Fig. 1, the bit error frequency vs. the noise margin normalized to the noise voltage is shown for different bandwidths (clock frequency) and different numbers of transistor. The practical limit of usability is a certain

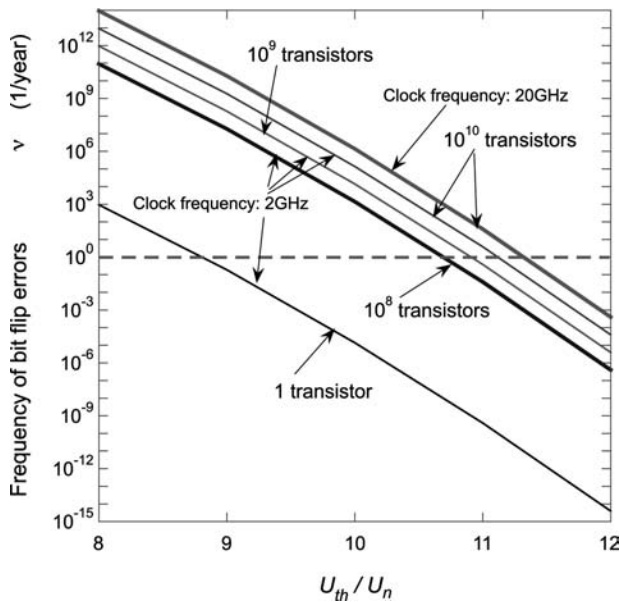


**Fig. 1** Bit errors vs. the ratio of noise margin and effective noise voltage. *Source:* From Ref.<sup>[1]</sup>.

$U_{th}/U_n$  ratio when the bit error rate is around 1 error/year. Even a 10% decrease of the  $U_{th}/U_n$  ratio compared with its critical value yields an error rate increase to  $10^5$  when we consider all transistors in a modern PC ( $3 \times 10^9$ – $10^{10}$  transistors).

Utilizing these results and a prediction of the evolution of capacitance and noise margin using present trends, recently, a prediction of the end of Moore's law was reported by Kish<sup>[1]</sup> (Fig. 2).

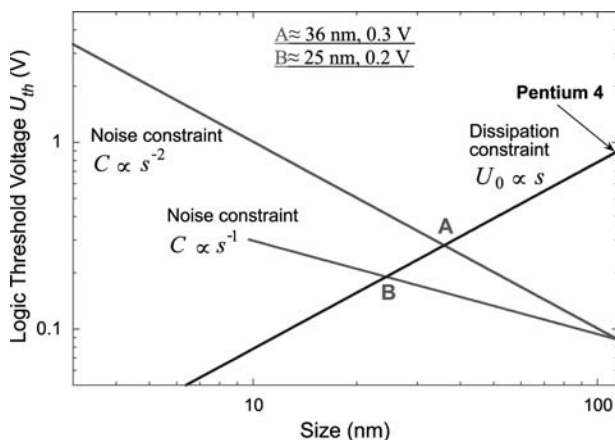


**Fig. 2** Prediction of the end of Moore's law. *Source:* From Ref.<sup>[1]</sup>. The technology faces a difficult problem when the upper limit of noise margin set by the dissipation/field constraint and the lower limit of noise margin required by the noise/error constraint cross each other (between points A or B, depending on the evolution of gate oxide thickness).

The shrinking noise margin (logic threshold voltage) and the increasing noise margin required by the increasing and quickening noise pose conflicting requirements, which would stop miniaturization in 6–8 years if the trends of the last year continue.

In the rest of this article, we outline the objectives that need further analysis and give some initiatives for extended research in the future.

### REFINEMENTS OF PREDICTIONS FOR CMOS TECHNOLOGY

It has been pointed out in Ref.<sup>[1]</sup> that the prediction was based on strong approximations to keep generality and because of lack of information about certain device parameters. Since Ref.<sup>[1]</sup> was published, new information from microprocessor makers about some previously unknown parameters has emerged and some new efforts have been made to reduce the supply voltage with a rate less than previously supposed. However, these efforts are controversial because many large-scale users (e.g., in aviation electronics)<sup>[2]</sup> would like to increase the rate of supply voltage reduction to improve device failure rate, which has been steadily growing because of high electric fields in chips.

Therefore theoretical efforts have been made on refining the prediction for the bit error problem because of thermal noise. The refined model takes into the account the following aspects:

- Further noise margin decrease because of the opening threshold voltages of the P-type and N-type MOSFET transistors
- Somewhat reduced noise because of parallel gate circuits
- Various supply voltage reduction strategies (predictions are controversial)
- The fact that the internal supply voltage and noise margin of microprocessors in 2002 were already less than supposed in Ref.<sup>[1]</sup>.

Interestingly, preliminary investigations indicate that the size range, where the problems begin, remains the same because the different corrections act in different directions and the effects compensate for each other. Thus the conclusions obtained in the context of Fig. 2 remain the same.

### THE CASE OF SINGLE-ELECTRON TRANSISTORS

The next question is the bit error situation of microprocessors based on SETs.<sup>[3]</sup> SETs work with tunneling, which is not dissipative, but the processes

coupled to it are dissipative. The electrons at the tunnel junction of a closed SET can be excited by thermal energy fluctuations to the energy level where tunneling can occur and a single electron can cause a single bit error in a SET. Similarly, an open SET can be temporarily shut down by thermal fluctuations. Thus the tentative expectation is that SETs will have a similar nature of bit error characteristics as CMOS. However, the picture is more complex.<sup>[3]</sup>

- Instead of a single capacitance, three different capacitances influence bit errors: the two tunnel junction capacitances and the quantum dot capacitance (gate capacitance).
- The noise margin cannot be increased arbitrarily by increasing supply voltage. It has a practical maximum that is equal to the voltage difference between the totally closed and totally open transistors. Higher voltages cause multiple-electron operation mode, and large noise and dissipation.
- There are two different working ranges vs. the quantum dot size: larger sizes (Coulomb blockade controls the current transport) and smaller sizes (<10 nm; quantum confinement effects dominate).

Preliminary studies<sup>[3]</sup> show that the requirement for small quantum dot size becomes much harder to satisfy when not only the d.c. characteristics but also the bit errors matter in a microprocessor with  $10^8$  or more SETs. To have SET-based microprocessors, the characteristic quantum dot size has to be less than 1 nm.

### ULTIMATE LIMITS OF ENERGY DISSIPATION VS. PERFORMANCE IN CLASSICAL AND QUANTUM COMPUTING

Heat problems with today's microprocessors have made it very clear that the ultimate and most fundamental questions of viability of the technology are related to power requirement information processing. This is the ultimate question for general-purpose classical or quantum computers. If CMOS and SET fail, it is a natural question if quantum computing and quantum information can help us out and—if yes—how. Because, so far, the existing quantum computing architectures have been neither practical nor general purpose, the only question we may be able to answer is the ultimate limits of performance. Performance includes error rate (accuracy), speed (bandwidth), and power dissipation. It is very important to take temperature into account, and to compare the ultimate performance limits of classical and quantum computers at the same temperature.<sup>[4]</sup> If it is room temperature, both the classical and quantum computers

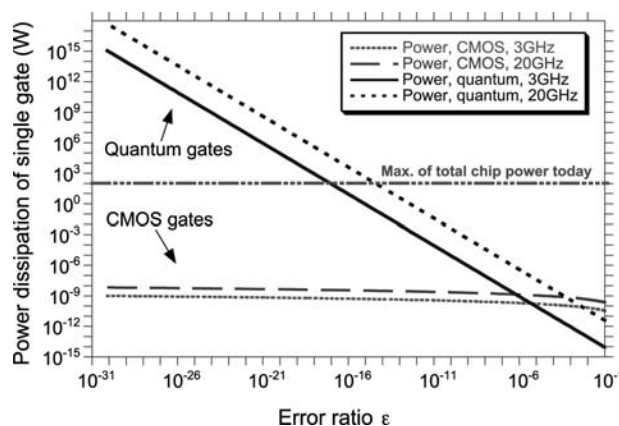


**Fig. 3** Minimal power dissipation of a single logical gate, classical (CMOS) and quantum, vs. the error ratio of the gate. *Source:* From Ref.<sup>[4]</sup>.

should be tested at room temperature; if it is the microkelvin temperature range, than the same conditions are required for both.

Recent studies<sup>[5]</sup> show that quantum computers have energy requirement problems at high accuracy because of arguments similar to Heisenberg's uncertainty principle. Classical computers perform much better when accuracy is concerned; however, quantum computers can balance this deficiency by a greater speed.<sup>[4]</sup> (For a comparison of the energy requirements of a classical and a quantum gate when they run at the same clock frequency, see Fig. 3.<sup>[4]</sup>)

Realistic estimations<sup>[6]</sup> based on existing quantum error correction methods indicate that a general-purpose quantum computer, which would use the best known quantum error correcting methods, would dissipate at least 100 times more energy than its classical counterpart.

Concerning future research aspects, we think that the ultimate focus of this study will not be the accuracy (error rate) of classical and quantum computers, but the energy requirements of processing Shannon information (bit). This aspect induces many new questions, including the problem of computer architectures that are not sensitive to noise. An important question is the energy and complexity requirement of error-correcting coding, and the ultimate measure should be energy requirement vs. Shannon information.

### REFERENCES

1. Kish, L.B. End of Moore's law: thermal (noise) death of integration in micro and nanoelectronics. *Phys. Lett.* **2002**, *305*, 144–149.
2. Huang, B.; Qin, J.; Walters, J.; Bernstein, J.B. Development of Derating Guidelines for Semiconductor Devices.



- In *Aerospace Vehicle Systems Institute Report*; 2003; unpublished.
3. Kim, J.; Kish, L.B. Can Single Electronic Microprocessors Ever Work at Room Temperature? In *Proceedings of SPIE, Vol. 5115*, Conference on Noise in Nanoelectronics, Sensors and Standards, Santa Fe, NM, June, 1–4, 2003; Kish, L.B., Green, F., Innaconne, G., Vig, J., Eds.; 2003, 174–182.
  4. Kish, L.B. Moore's Law is Killed by Classical Physics; can Quantum Information Save It? In *Proceedings of SPIE, Vol. 5115*, Conference on Noise in Nanoelectronics, Sensors and Standards, Santa Fe, NM, June, 1–4, 2003; Kish, L.B., Green, F., Innaconne, G., Vig, J., Eds.; 2003, 167–173.
  5. Gea-Banacloche, J. Minimum energy requirements for quantum computation. *Phys. Rev. Lett.* **2002**, *89*, 217901.
  6. Gea-Banacloche, J.; Kish, L.B. Comparison of energy requirements for classical and quantum information processing. *Fluct. Noise Lett.* **2003**, *3*, C3–C7.

# Motor Proteins in Synthetic Materials and Devices

**Henry Hess**

*Department of Bioengineering, University of Washington, Seattle, Washington, U.S.A.*

**George Bachand**

*Biomolecular Materials and Interfaces, Sandia National Laboratories, Albuquerque, New Mexico, U.S.A.*

**Viola Vogel**

*Institute for Biologically Oriented Materials, Department of Materials, Swiss Federal Institute of Technology, Zurich, Switzerland*

## INTRODUCTION

After billions of years of evolution, biological nanomotors and, in particular, motor proteins have achieved a level of performance unmatched by current synthetic nanomotors. Motor proteins in hundreds of specific designs perform a wide range of functions in biology, while achieving more than 50% efficiency in the conversion of chemical energy to mechanical work.<sup>[1,2]</sup>

The research discussed in this entry aims at utilizing motor proteins in hybrid “bio/nano” devices to explore the potential of nanomotors in technological applications. Challenges for this approach include the design of suitable synthetic environments, the interfacing of biological components with synthetic structures, the controlled modification of biological motors using recombinant techniques, and in general, the difficulty of engineering at a size scale where random fluctuations due to Brownian motion are an integral part of the system.

At this point, an international group of research teams has utilized a variety of rotational and linear motor proteins to demonstrate the first devices integrating motor proteins. These devices illustrate the important role that motor proteins can play in nanotechnology.

## MOTORS IN NANOTECHNOLOGY

Technological revolutions often involve access to new materials, and the mastery of a new material is so fundamental to mankind that historic ages are defined by the state-of-the-art material, hence the “stone age” or “bronze age.” However, some technological revolutions are characterized by the newfound ability of

man to convert energy into mechanical work, based, for example, on the invention of the steam engine, which powered the industrial revolution. Can nanotechnology become a revolution of energy conversion in addition to a materials revolution, driven by a nanomotor, which will power the “Nanofactory” and the “Nanoautomobile” of tomorrow?

Currently, no man-made nanomotor exists that can impact nanotechnology in the way that the steam engine defined the industrial revolution. However, while the first prototypes of synthetic nanomotors are studied,<sup>[3,4]</sup> nature provides us with a wide range of biological nanomotors, which have evolved to perform a wide range of functions with an amazing efficiency.<sup>[5]</sup> While the center stage is occupied by motor proteins such as myosin, which is, for example, responsible for muscle contraction, biological motor designs include motors based on ribonucleic acid (RNA) pulling on double-stranded deoxyribonucleic acid (DNA) to package it into the protein shell of a virus,<sup>[6]</sup> ribosomes moving along RNA while synthesizing a new protein, or even an electrostrictive membrane protein aiding the process of hearing.<sup>[7]</sup> The mechanism by which biological motors, in particular motor proteins, generate force is a very active field of research, and significant progress has been made.<sup>[8]</sup> Nowadays, motor proteins can be readily isolated and are even commercially available.

Biomolecular motors, in particular motor proteins, are a gift of nature to the nanotechnologist. They can be used in hybrid “bionano” devices to explore the potential of nanomotors. At this point, a small number of prototypical nanodevices based on motor proteins has been assembled, and in the following, we will introduce the biological motors used, and discuss the progress in the design of hybrid devices.

## BIOLOGICAL FUNCTIONS OF MOTOR PROTEINS

Motor proteins represent a unique class of enzymes and enzyme complexes that convert chemical energy into mechanical work with relatively high efficiency. In these proteins, energy associated with catalysis (or an electrochemical gradient) is linked to conformational changes in the structure. As with man-made motors, these molecular machines can be categorized as either rotary or linear motors, depending on their mode of translation.

Two true rotary molecular motors were identified, and extensively studied in terms of the biochemical and biophysical properties of these protein complexes. The bacterial flagellar motor is a classic example of a rotary motor used by certain bacteria to move in a fluid environment. The complex uses a proton gradient to propel a large flagellum at speeds of up to 300 rps, and produces a rotary torque in excess of 550 pN nm.<sup>[9]</sup> A second rotary motor, ATP synthase ( $F_0F_1$ -ATPase), is a ubiquitous enzyme complex responsible for proton-powered production of adenosine 5'-triphosphate (ATP) in living system.<sup>[10]</sup> Translocation of  $H^+$  across a membrane results in the rotation of a central shared subunit, and synthesis of three molecules of ATP per revolution. Moreover, the cytoplasmic  $F_1$ -ATPase domain may independently function as an ATP-fueled rotary motor;<sup>[11]</sup> construction of integrated devices with this motor protein will be discussed later (Fig. 1).

A number of linear motors were extensively studied in terms of their biomechanical characteristics,<sup>[8,13,14]</sup> as well as their potential use in hybrid nanodevices.<sup>[15]</sup> Linear motors can be chosen from three principal families: myosins—moving along actin filaments toward the barbed end; kinesins—moving along microtubules toward the plus end; and dyneins—moving along microtubules toward the minus end<sup>[16]</sup> (Fig. 2).

Actin filaments, which are double-stranded twisted ropes polymerized from 5.5-nm-long actin monomers, are highly flexible and can branch into a dense mesh. Microtubules are stiff, unbranched, proteinaceous tubes with an outer diameter of  $\sim 30$  nm, consisting of 8–18 parallel protofilaments assembled from 8-nm-long tubulin dimers. While motors of the myosin family are the molecular actuators responsible for the contraction of muscles, specialized motors of all families participate in the intracellular transport of membrane organelles and protein complexes. The morphology and biochemistry of the different types of motors is closely coupled to their function. For example, myosin II has evolved to act in a large array of motors in fast skeletal muscle. Consequently, the biochemical cycle of binding ATP, hydrolyzing ATP, and releasing the products adenosine 5'-diphosphate (ADP) and phosphate is tuned toward a short time

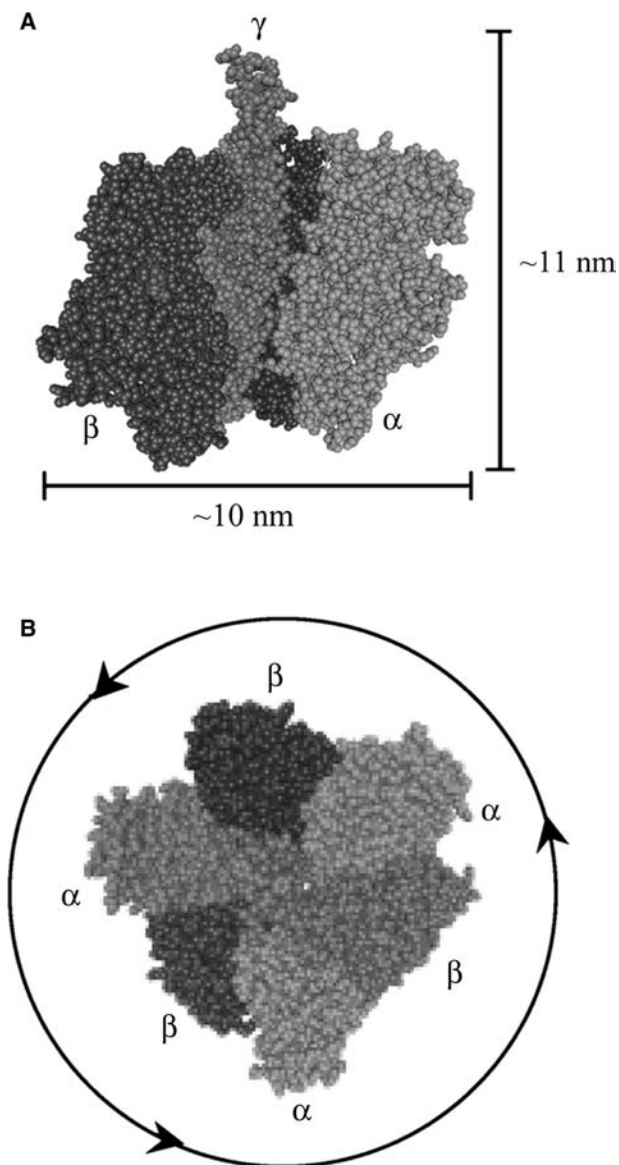


**Fig. 1** (A) Side view of the crystal structure of the bovine  $F_1$ -ATPase reported by Braig et al.<sup>[12]</sup> Adjacent  $\alpha$  and  $\beta$  subunits were removed to show the  $\gamma$  subunit and bound ADP (red). (B) Top of the  $F_1$ -ATPase motor showing the alternating  $\alpha/\beta$  hexamer (stator) and central  $\gamma$  subunit (rotor). The  $\gamma$  subunit rotates counterclockwise in a three-step process during ATP hydrolysis. The  $F_0$  portion of ATP synthase, which inserts into a membrane and converts a proton flow into a rotary motion, is not shown.

of attachment to the actin filament (non-processive motion). In contrast, the step size of a conventional kinesin motor (transporting as a single motor, e.g., synaptic vesicles) matches exactly the 8-nm spacing between adjacent tubulin binding sites on a protofilament of a microtubule, which, together with a coordinated hydrolysis cycle of the two heads of the motor, facilitates a large number of consecutive steps without detaching from the microtubule (processive motion).<sup>[5]</sup>

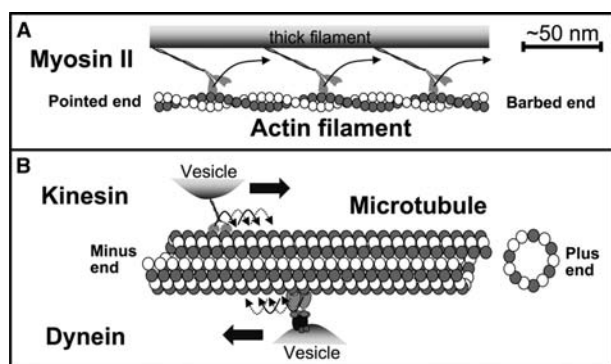


**Fig. 2** (A) Myosin II, the myosin type present, e.g., in skeletal muscle, assembles into a thick filament. The collective, unsynchronized motion of the myosin motors along the actin filament causes the contraction of muscle cells. Each myosin motor attaches only intermittently to the actin filament (non-processive motion), “running” along with a velocity of up to  $8 \mu\text{m}/\text{sec}$ . Actin filaments consist of two helical strands polymerized from actin monomers with a full period of  $72 \text{ nm}$ . (B) Conventional kinesin is a two-headed motor moving toward the “plus” end of a microtubule. The two heads move in coordinated fashion, covering a distance of  $8 \text{ nm}$  with each step, hydrolyzing one ATP molecule per step, and generating a maximum force of  $7 \text{ pN}$ . In vitro, kinesin takes up to 100 steps/sec. At least one of the kinesin heads is attached at any point in time (processive motion). Cytoplasmic dynein is a processive, two-headed motor moving toward the “minus” end of the microtubule. It is a particularly large protein complex, consisting of more than eight subunits with a combined mass of more than  $1000 \text{ kDa}$ . Microtubules are tubular structures with an outer diameter of  $30 \text{ nm}$ , which are polymerized from individual tubulin monomers with a length of  $8 \text{ nm}$ . Microtubules assembled in vitro can reach a length of up to  $100 \mu\text{m}$ . In vivo, microtubules constantly assemble and disassemble; however, the use of drugs like taxol can stabilize microtubules for weeks by slowing the depolymerization.

The large number of natural designs of linear motors for functions ranging from muscle contraction to vesicle transport can serve as a tool chest for hybrid devices. It is also an inspiration for artificial modifications to existing motors, for example, by integrating chemical switches or by changing their processivity.<sup>[17,18,61]</sup> Currently, conventional kinesins and microtubules are a motor/filament combination, which is often utilized for reasons related to the robustness of the proteins, the successful expression of kinesin in *Escherichia coli*,<sup>[19]</sup> and the easy modification of tubulin.<sup>[20]</sup>

## MOTOR PROTEINS IN A SYNTHETIC ENVIRONMENT

Controlling the interaction between the motor proteins and the synthetic materials is a major challenge in the

design of hybrid devices.<sup>[21]</sup> While regions of the surface intended as motor protein-coated tracks or islands have to have a high affinity for protein adsorption, denaturation and concomitant loss of function of the protein after adsorption to the surface has to be avoided as well. It is equally important for the defined positioning of motors in a device to prevent the adsorption of motors to regions surrounding the intended motor protein-rich regions, a challenging task because of the general tendency of proteins to stick to many synthetic surfaces.

A variety of approaches to reduce denaturation were developed, ranging from precoating surfaces with a generic protein (albumin, casein),<sup>[22]</sup> which restricts the surface–motor contact to small patches in-between the preadsorbed proteins, to coating the surface with polymer brushes with functionalized ends,<sup>[23]</sup> which prevents motor adsorption directly to the surface while providing a designated binding site on the polymer. The most sophisticated approach toward attaching a motor (discussed in more detail in the subsection “Rotational Systems”) relied on genetically engineering specific anchor sites into the protein, which connect to a patterned nickel film on the surface.<sup>[11,24]</sup> The adsorption of motors has been selectively prevented by either empirically identifying materials, which together with added detergents in the solution reduce protein adsorption,<sup>[25]</sup> or by using surface modification strategies originally developed for non-fouling surfaces.<sup>[26]</sup>

The lifetime of hybrid bionanodevices is a frequent concern. To maintain motor proteins in a functional state, the temperature, ionic strength, pH, and salt concentration of the surrounding solution have to be controlled.<sup>[27]</sup> Microtubules and actin filaments depolymerize over time,<sup>[28]</sup> a process which can be slowed but not entirely prevented. In addition, proteins are subject to degradation by proteases, and they sustain photodamage during observation under the fluorescence microscope. In combination, these factors currently limit the lifetime of actively operating devices to hours or a few days at room temperature. However, for a large number of applications, this lifetime, together with adequate storage at low temperatures before operation, is sufficient.

## REGULATING BIOMOLECULAR MOTOR ACTIVITY

A fundamental element in the engineering of biomolecular motor-powered devices and materials is the ability to modulate the activity of the motors. To date, two strategies have been used to regulate the functionality of biomolecular motors in synthetic systems. The first strategy involved the controlled release of caged ATP

into solution to modulate the linear translation of conventional kinesin.<sup>[29]</sup> Because the density of tethered kinesin was relatively low, an ATP-consuming enzyme, hexokinase, was used to rapidly reduce the liberated ATP in solution, and produce discrete spikes of available ATP. In this manner, the magnitude of velocity and distance could be regulated based on the intensity of light exposure.<sup>[29]</sup> This strategy has direct application for controlling any molecular motor that utilizes ATP as a fuel source. A primary advantage in this system is the ability to produce discrete spikes in ATP that, in turn, may be used to regulate the velocity/distance traveled by linear motors, or the speed/number of cycles for rotary motors.

The second strategy for controlling motor functionality involved genetically engineering an allosteric effector site into the catalytic domain of the F<sub>1</sub>-ATPase molecular motor.<sup>[30]</sup> This site was engineered to bind Zn<sup>2+</sup> such that the conformation changes necessary for ATP hydrolysis and  $\gamma$  subunit rotation would be reversibly inhibited when the site was occupied; chelation of the Zn<sup>2+</sup> would subsequently restore activity. In single molecule assays, rotation of all (i.e., 100%) mutated F<sub>1</sub>-ATPase was observed in the presence of 800  $\mu$ m ZnSO<sub>4</sub>, whereas bulk activity assays indicated a 60% inhibition in catalytic activity at saturating levels of Zn<sup>2+</sup>. This suggests that the complete inhibition of hydrolytic activity is not requisite for tight control of motor rotation in ATPase. Repeated cycles of Zn<sup>2+</sup> inhibition, followed by chelation with 1,10-phenanthroline, demonstrated the ability to reversibly control the functionality of the F<sub>1</sub>-ATPase motor.<sup>[30]</sup> A unique advantage in this strategy is the ability to tailor the allosteric binding site, which may serve as a recognition element in sensor-type applications.

## NANODEVICES

### Rotational Systems

The F<sub>0</sub>F<sub>1</sub>-ATPase enzyme complex consists of eight subunits ( $\alpha$ ,  $\beta$ ,  $\gamma$ ,  $\alpha$ ,  $\beta$ ,  $\gamma$ ,  $\epsilon$ , and  $\delta$ ) that are arranged in two distinct domains, the cytoplasmic F<sub>1</sub> and hydrophobic F<sub>0</sub> domains. The F<sub>1</sub>-ATPase domain can function independently as an ATP-powered rotary motor,<sup>[11,31]</sup> and offers a potential source of actuation in nanoscale device architectures.<sup>[24,32]</sup> During ATP hydrolysis, the central rotor (i.e.,  $\gamma$  subunit) of F<sub>1</sub>-ATPase rotates in response to the conversion of ATP to ADP + P<sub>i</sub> at each of the three catalytic sites. This three-step process that results in rotation of the  $\gamma$  subunit was confirmed by a number of methods.<sup>[32–34]</sup> The precise mechanism of mechanical coupling of ATP hydrolysis and rotation of the  $\gamma$  subunit has yet to be determined.

In general, a prerequisite technology for utilizing molecular motors as functional components of nanoscale devices is the ability to interface biological and non-biological components. To this end, the F<sub>1</sub>-ATPase from thermophilic bacterium *Bacillus* PS3 was genetically engineered to express a 10x histidine (His) tag on the N-terminus of the  $\beta$  subunits.<sup>[24,32]</sup> The His-tagged motors were subsequently used to precisely position individual F<sub>1</sub>-ATPase motors on arrays of nanoscale nickel dots.<sup>[35]</sup> Because the His-tags were located on the N-terminal of the  $\beta$  subunit, the motors were positioned such that the base of the stator was adjacent to the surface, and the rotor was positioned perpendicular to the surface and fully accessible for attachment of additional components. A single cysteine (Cys) was also engineered at position 107 in the  $\gamma$  subunit to provide a unique chemical “handle” for attaching synthetic cargo.<sup>[24,32]</sup> The ability to genetically engineer the motors for specified interactions with synthetic components represents a powerful tool for tailoring the interaction of various components.

As a basic proof-of-principle, a simple device was designed and constructed, in which the F<sub>1</sub>-ATPase motors provided a source of actuation to nanoscale metallic components.<sup>[36]</sup> This device has three primary components: 1) a lithographically defined surface of Ni posts, 2) F<sub>1</sub>-ATPase motors, and 3) functionalized nanoscale “propellers” (Fig. 3). The device was assembled by sequential addition of individual components; however, yield was relatively poor (i.e., 1%, defined as the number of rotating propellers divided by the number of propellers distributed on the surface). Rotation was initiated with the addition of ATP, and stopped with sodium azide, an inhibitor of ATPase activity. The mean frequency of rotation was 4.8 Hz and directly correlated with the length of the propeller,

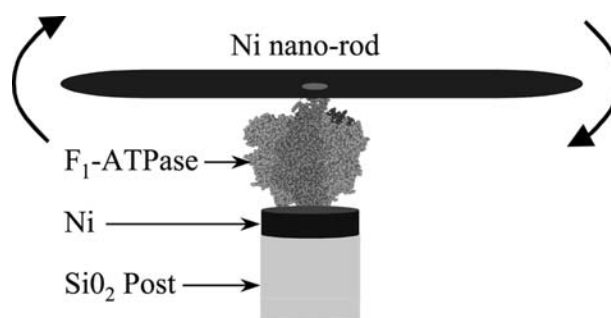


**Fig. 3** Schematic representation of the integrated nanoscale device that provided a proof-of-principle with regard to actuating nanomechanical devices with a biomolecular motor.<sup>[36]</sup> In the presence of ATP, the rotary motor F<sub>1</sub>-ATPase spins the nickel nanorod (10 × 150 × 1000 nm) with an angular velocity of 4 Hz while providing a torque of 20 pN nm. Elevating the motor on a post reduces the viscous drag on the moving nanorod, which increases near a surface.

suggesting that the torque was constant. The work performed by the  $F_1$ -ATPase motor to rotate a propeller through one complete revolution was calculated to be  $\sim 120$  pN nm, with an efficiency of 50%.<sup>[36]</sup> The device functioned for over 2 hr, at which point the propeller broke free from the motor. Overall, this experiment demonstrated the ability of this biomolecular motor to function as an actuator in a nanoscale mechanical device.

The force tolerances of these devices were characterized by using dynamic force spectroscopy to understand and potentially design integrated nanodevices with an increased assembly yield and lifetime.<sup>[37]</sup> In these experiments, the relative order of bond strengths (strongest to weakest) based on the magnitudes of their lifetimes were: biotin-streptavidin,  $(\text{His})_6$ -Ni-NTA,  $(\text{His})_6$ -Ni, and  $(\text{His})_6$ -gold. Based on these findings, the weakest bond in the  $F_1$ -ATPase-powered devices resides in the interaction between histidine and Ni, and likely represents a critical factor resulting in device failure. Improvements in device assembly and longevity may be engineered through further analysis and redesign of the interaction used to adhere the  $F_1$ -ATPase motors to the substrate, as well as to the propellers (or other components).

Overall, the  $F_1$ -ATPase biomolecular motor represents a highly efficient rotary actuator in integrated, nanomechanical devices. A number of enabling technologies were developed and used to construct a simple nanodevice powered by  $F_1$ -ATPase motors. Further characterization of this device by force measurements of binding strengths has determined the key linkages that likely result in poor assembly yields as well as device failure. As a whole, these data provide a foundation for the continued engineering and analysis of biomolecular motor-powered nanodevices.

## Transport Systems

One of the first ideas for a hybrid bionanodevice was a nanoscale transport system, a “molecular shuttle,” with the ability to move single molecules along tracks under user control.<sup>[15]</sup> The close analogy to the biological motor protein-based transport mechanisms<sup>[38]</sup> provided a clear vision of the feasibility and utility of such a system. Conceptually, a transport system requires solutions to the questions of how to direct the movement, how to load and unload cargo, and how to control the speed of the system.<sup>[29]</sup> The guiding issue was addressed with two different approaches (Fig. 4): either the actin filaments or microtubules are selectively immobilized on the surface and support the movement of motors attached to the cargo (bead assay),<sup>[39]</sup> or the motors are selectively adsorbed to the surface and move the corresponding filament, which in turn connects to the cargo (gliding assay).<sup>[40]</sup>

While the initial experiments by Turner et al.<sup>[41]</sup> yielded unpolarized patterns of aligned and immobilized microtubules capable of supporting kinesin motility, later experiments demonstrated polarized alignment of microtubules on surfaces using a variety of methods based on fluid flow.<sup>[42–44]</sup> Kinesin motors nonspecifically bound to the cargo surface then supported the directed transport of micrometer-sized objects across the array of microtubules.

The inverse arrangement, using microtubules as shuttle modules that move across a surface coated with motors and link specifically to the cargo, requires the structuring of the surface in order to create tracks. A variety of strategies including chemical modification,<sup>[45,46]</sup> guiding channels,<sup>[29,47]</sup> and combinations of surface chemistry and topography<sup>[25,48,49]</sup> has been employed to direct the shuttles along predetermined

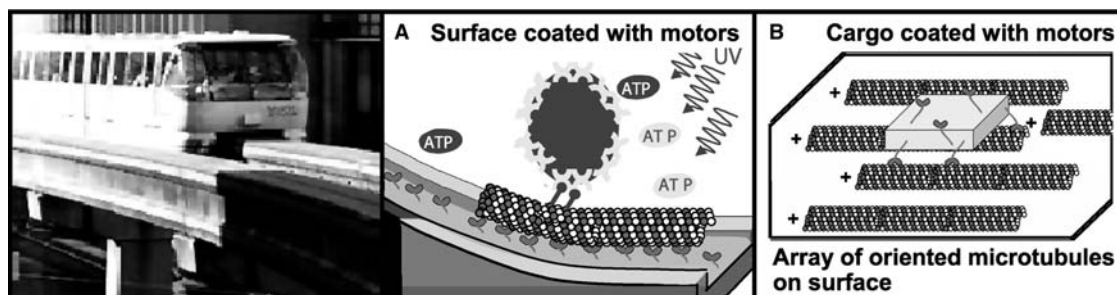


**Fig. 4** Nanoscale transport systems based on motor proteins face three principal challenges: guiding the movement, loading the cargo, and controlling the speed.<sup>[15]</sup> Two approaches toward guiding the movement have emerged: (A) motor proteins are selectively adsorbed to a structured surface and guide the movement of microtubules or actin filaments serving as shuttle modules, or (B) an oriented array of microtubules is assembled on a surface by adsorption or polymerization and support the directed movement of motor proteins connected to the cargo. Selective loading of cargo and control of movement has been demonstrated for approach (A) by using biotin/streptavidin links for cargo attachment and controlled release of ATP from an inactive, “caged” precursor using UV light. *Source:* From Ref.<sup>[29]</sup>. © 2001 Am. Chem. Soc.



paths. In addition, flow fields<sup>[50]</sup> and electric fields<sup>[51]</sup> can influence the path of the shuttle. The choice between these guiding strategies is, in large part, determined by the physical properties of the filaments used as shuttles. For example, the large stiffness of microtubules<sup>[52]</sup> precludes effective guiding by motors adsorbed in tracks on a chemically modified surface.<sup>[53]</sup> Unidirectional motion of the shuttles propelled by surface adsorbed motors can be achieved by suitable track geometries.<sup>[25,53]</sup> Conveniently, the orientation of the surface adsorbed motors does not have to be controlled, because the flexible tail region of the kinesin motor allows the motor heads to find a suitable position for microtubule binding independent of the original orientation.<sup>[54,55]</sup> Microtubules can be readily functionalized with fluorescent dyes or biotin linkers,<sup>[54]</sup> which facilitates the observation of their movement as well as the attachment of cargo if the microtubules are employed as shuttles.

In summary, the basic challenges of guiding, loading, and controlling can be addressed by using a variety of approaches to achieve directed transport, by linking cargo to microtubules or motors, and by controlling motor activity as described in the section on controlling motor functionality. By integrating these approaches, a nanoscale transport system can be assembled and, in the future, combined with other modular systems such as assembly and packaging stations.

### Surface Imaging

The self-propelled movement of microtubules with a diameter of 30 nm on a kinesin-coated surface provides us with a novel nanoscale probe, which can explore a surface in a radically different fashion compared to the tip of a scanning probe microscope. While scanning probe microscopes use a single tip, which scans the surface in a controlled, linear movement, the microtubule movement per se is random. Therefore it is necessary to synthesize an image of the surface based on the random paths of a large number of microtubules exploring the unknown surface at the same time. A basic implementation of this new approach to surface imaging (Fig. 5) was demonstrated for a surface with a structured topography,<sup>[56]</sup> but the research into guiding mechanisms for nanoscale transport systems indicates that the microtubule path is influenced by surface chemistry or fluid flow as well. Despite its limitations due to the sensitivity of the proteins and the optical detection of the microtubule position, the described technique is an example of how the availability of self-propelled nanoprobe enables the implementation of a new scanning method with similarities to mathematical Monte Carlo methods. Nanotechnology is

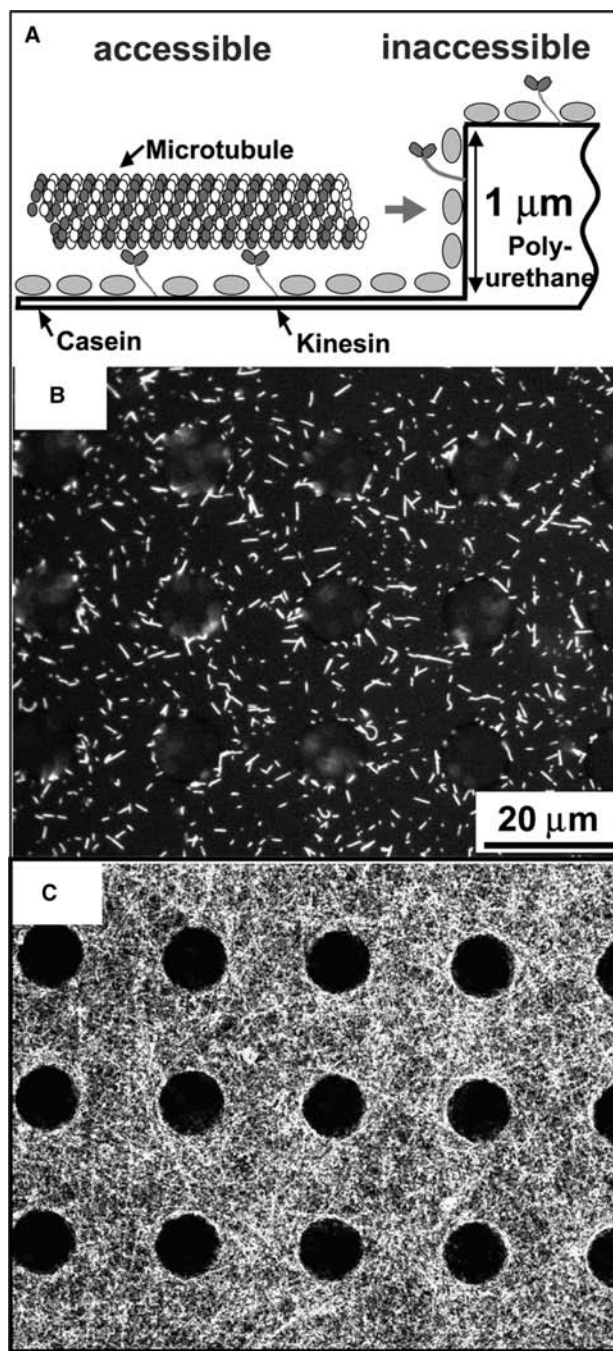


**Fig. 5** Fluorescently labeled microtubules transported by surface-adsorbed kinesins can serve as nanoscale probes exploring the surface. The sensitivity of the microtubule path to the topography allows us to image an unknown surface.<sup>[56]</sup> This is illustrated in (A), where a microfabricated pattern of 1- $\mu\text{m}$ -high posts divides the surface into an accessible and an inaccessible region, because microtubules move on the bottom surface and are unable to climb a steep incline. Repeated observation of microtubule positions under the fluorescence microscope as shown in (B) yields information about the path of several hundred microtubules. The superposition of 500 images taken every 5 sec reveals the surface topography (C). *Source:* From Ref.<sup>[56]</sup>. © 2002 Am. Chem. Soc.

not always “the same but smaller.” Instead, sometimes “small is different” (Uzi Landman) applies, which creates opportunities to utilize nanosystems for innovative technologies.

## Actuators

While nanoscale transport systems are the technological equivalent to the biological tasks of kinesin in intracellular transport, nanoactuators are inspired by the biological application of myosin motors in muscles. Evidently, molecular motors can be assembled into large arrays and exert many Newtons of force, and it is an interesting question if highly efficient engines built from macroscopic arrays of molecular motors may replace electric motors or heat engines in the future. However, for the purposes of nanotechnology, even single biomolecular motors generate forces, which are sufficient to overcome typical loads.<sup>[57,58]</sup>

Recently, a miniaturized forcemeter for the measurement of intermolecular bond strengths was demonstrated.<sup>[59]</sup> In this forcemeter, several kinesin motors provide the force to strain the bond between a receptor–ligand pair, while the magnitude of the strain is reflected in the bending of a microtubule attached to the ligand, which serves as a nanoscale cantilevered beam of known stiffness (Fig. 6). The forcemeter with lateral dimensions of less than 10  $\mu\text{m}$  can generate and detect forces on the order of several piconewtons, which is sufficient to rupture most single molecule receptor/ligand bonds within seconds. The strain generated by the action of motor proteins

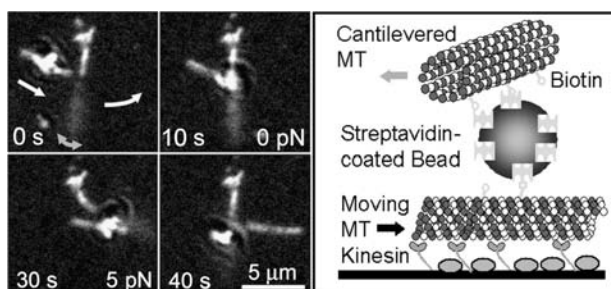


**Fig. 6** A microscopic forcemeter for the measurement of intermolecular forces on the order of a few piconewtons can be assembled from microtubules functionalized with ligands, beads coated with receptors, and kinesins (0 and 10 sec). It consists of a cantilevered microtubule that binds to a streptavidin-coated bead loaded onto a microtubule moved by kinesins.<sup>[59]</sup> The kinesins push the moving microtubule (30 sec), straining the bond between streptavidin and biotin until it ruptures (40 sec). Observation of the concurrent bending of the cantilevered microtubule allows the determination of the strain forces based on the known stiffness of microtubules. *Source:* From Ref.<sup>[59]</sup>. © 2001 Am. Chem. Soc.

inherently matches the low rate of force application characteristic for in vivo conditions, a situation that is difficult to duplicate with other approaches to molecular force measurements.<sup>[60]</sup> In addition, the small size of the instrument suggests the assembly of an array of forcemeters, capable of drastically reducing the time required for a statistically significant number of force measurements.

This forcemeter points the way to more sophisticated nanodevices, which aid in the measurement of properties of nanoscale objects, and can play an active role in the assembly and disassembly of nanoscale structures.

## CONCLUSION

Motor proteins are fast and versatile nanomotors with high energy efficiency and interface in a very specific manner with “road”-like filaments and various objects serving as “cargo.” At this point, this makes them superior to any man-made nanomotor, and allows us to explore the technological applications of nanomotors in hybrid nanodevices. Inspired by the biological applications of motor proteins in intracellular transport and as actuators, a number of devices have been designed. Challenges regarding the interface between biological and synthetic elements in the hybrid devices are addressed, and artificial elements, such as “anchors” or a “throttle,” are directly integrated into the motor protein. Nature has mastered not only the design of nanoscale functional units but also the integration of these units into the sophisticated multipurpose subcellular or cellular systems. This research attempts to learn nature’s lessons and translate them into valuable engineering.

## ACKNOWLEDGMENTS

Partial funding through NASA grant NAG5-8784 is gratefully acknowledged. This work was also partially supported through the Materials Science and Engineering Division, Office of Basic Energy Sciences, Department of Energy. Sandia is a multiprogram laboratory operated by Sandia Corporation, a Lockheed Martin Company, for the United States Department of Energy under contract DE-AC04-94AL85000.

## REFERENCES

1. Kinosita, K., Jr.; Yasuda, R.; Noji, H.; Adachi, K. A rotary molecular motor that can work at near 100% efficiency. *Philos. Trans. R. Soc. Lond., B Biol. Sci.* **2000**, *355* (1396), 473–489.

2. Kawaguchi, K.; Ishiwata, S. Temperature dependence of force, velocity, and processivity of single kinesin molecules. *Biochem. Biophys. Res. Commun.* **2000**, *272* (3), 895–899.
3. Stoddart, J.F. Molecular machines. *Acc. Chem. Res.* **2001**, *34* (6), 410–411.
4. Feringa, B.L. In control of motion: from molecular switches to molecular motors. *Acc. Chem. Res.* **2001**, *34* (6), 504–513.
5. Howard, J. *Mechanics of Motor Proteins and the Cytoskeleton*; Sindauer: Sunderland, MA, 2001.
6. Smith, D.E.; Tans, S.J.; Smith, S.B.; Grimes, S.; Anderson, D.L.; Bustamante, C. The bacteriophage straight phi29 portal motor can package DNA against a large internal force. *Nature* **2001**, *413* (6857), 748–752.
7. Zheng, J.; Shen, W.; He, D.Z.; Long, K.B.; Madison, L.D.; Dallos, P. Prestin is the motor protein of cochlear outer hair cells. *Nature* **2000**, *405* (6783), 149–155.
8. Vale, R.D.; Milligan, R.A. The way things move: looking under the hood of molecular motor proteins. *Science* **2000**, *288* (5463), 88–95.
9. DeRosier, D.J. The turn of the screw: the bacterial flagellar motor. *Cell* **1998**, *93* (1), 17–20.
10. Boyer, P.D. A research journey with ATP synthase. *J. Biol. Chem.* **2002**, *277* (42), 39045–39061.
11. Noji, H.; Yasuda, R.; Yoshida, M.; Kinoshita, K. Direct observation of the rotation of F1-ATPase. *Nature* **1997**, *386* (6622), 299–302.
12. Braig, K.; Menz, R.I.; Montgomery, M.G.; Leslie, A.G.; Walker, J.E. Structure of bovine mitochondrial F(1)-ATPase inhibited by Mg(2+) ADP and aluminium fluoride. *Struct. Fold. Des.* **2000**, *8* (6), 567–573.
13. Howard, J. Molecular motors: Structural adaptations to biological functions. *Nature* **1997**, *389*, 561–567.
14. Fisher, M.E.; Kolomeisky, A.B. Simple mechanochemistry describes the dynamics of kinesin molecules. *Proc. Natl. Acad. Sci. U. S. A.* **2001**, *98* (14), 7748–7753.
15. Hess, H.; Vogel, V. Molecular shuttles based on motor proteins: active transport in synthetic environments. *Rev. Mol. Biotechnol.* **2001**, *82*, 67–85.
16. Alberts, B.; Bray, D.; Lewis, J.; Raff, M.; Roberts, K.; Watson, J.D. *Molecular Biology of the Cell*; Garland: New York, 1994.
17. Thorn, K.S.; Ubersax, J.A.; Vale, R.D. Engineering the processive run length of the kinesin motor. *J. Cell Biol.* **2000**, *151* (5), 1093–1100.
18. Tomishige, M.; Vale, R.D. Controlling kinesin by reversible disulfide cross-linking. Identifying the motility-producing conformational change. *J. Cell Biol.* **2000**, *151* (5), 1081–1092.
19. Gilbert, S.P.; Johnson, K.A. Expression, purification, and characterization of the drosophila kinesin motor domain produced in *Escherichia coli*. *Biochemistry* **1993**, *32* (17), 4677–4684.
20. Hyman, A.A.; Drechsel, D.N.; Kellog, D.; Salsler, S.; Sawin, K.; Steffen, P.; Wordeman, L.; Mitchison, T.J. Preparation of modified tubulins. *Methods Enzymol.* **1991**, *196*, 478–485.
21. Malmsten, M.; Ed. *Biopolymers at Interfaces*; Marcel Dekker: New York, 1998.
22. Howard, J.; Hunt, A.J.; Baek, S. Assay of microtubule movement driven by single kinesin molecules. *Methods Cell Biol.* **1993**, *39*, 137–147.
23. deCastro, M.J.; Ho, C.H.; Stewart, R.J. Motility of dimeric ncd on a metal-chelating surfactant: Evidence that ncd is not processive. *Biochemistry* **1999**, *38* (16), 5076–5081.
24. Bachand, G.; Montemagno, C.D. Constructing organic/inorganic NEMS devices powered by biomolecular motors. *Biomed. Microdevices* **2000**, *2–3*, 179–184.
25. Hiratsuka, Y.; Tada, T.; Oiwa, K.; Kanayama, T.; Uyeda, T.Q. Controlling the direction of kinesin-driven microtubule movements along microlithographic tracks. *Biophys. J.* **2001**, *81* (3), 1555–1561.
26. Hoffman, A.S. Non-fouling surface technologies. *J. Biomater. Sci., Polym. Ed.* **1999**, *10* (10), 1011–1014.
27. Bohm, K.J.; Stracke, R.; Unger, E. Speeding up kinesin-driven microtubule gliding in vitro by variation of cofactor composition and physicochemical parameters. *Cell Biol. Int.* **2000**, *24* (6), 335–341.
28. Kristofferson, D.; Mitchison, T.; Kirschner, M. Direct observation of steady-state microtubule dynamics. *J. Cell Biol.* **1986**, *102* (3), 1007–1019.
29. Hess, H.; Clemmens, J.; Qin, D.; Howard, J.; Vogel, V. Light-controlled molecular shuttles made from motor proteins carrying cargo on engineered surfaces. *Nano Lett.* **2001**, *1* (5), 235–239.
30. Liu, H.; Schmidt, J.J.; Bachand, G.D.; Rizk, S.S.; Looger, L.L.; Hellinga, H.W.; Montemagno, C.D. Control of a biomolecular motor-powered nanodevice with an engineered chemical switch. *Nat. Mater.* **2002**, *1* (3), 173–177.
31. Yoshida, M.; Muneyuki, E.; Hisabori, T. ATP synthase—a marvelous rotary engine of the cell. *Nat. Rev., Mol. Cell Biol.* **2001**, *2* (9), 669–677.
32. Montemagno, C.; Bachand, G. Constructing nanomechanical devices powered by biomolecular motors. *Nanotechnology* **1999**, *10*, 225–331.
33. Yasuda, R.; Noji, H.; Kinoshita, K., Jr.; Yoshida, M. F1-ATPase is a highly efficient molecular motor that rotates with discrete 120 degree steps. *Cell* **1998**, *93* (7), 1117–1124.
34. Adachi, K.; Yasuda, R.; Noji, H.; Itoh, H.; Harada, Y.; Yoshida, M.; Kinoshita, K., Jr. Stepping rotation of F1-ATPase visualized through angle-resolved single-fluorophore imaging. *Proc. Natl. Acad. Sci. U. S. A.* **2000**, *97* (13), 7243–7247.
35. Bachand, G.-D.S., R.-K.; Neves, H.-P.; Olkhovets, A.; Craighead, H.-G.; Montemagno, C.-D. Precision attachment of individual F1-ATPase biomolecular motors on nanofabricated substrates. *Nano Lett.* **2001**, *1* (1), 42–44.
36. Soong, R.K.; Bachand, G.D.; Neves, H.P.; Olkhovets, A.G.; Craighead, H.G.; Montemagno, C.D. Powering an inorganic nanodevice with a biomolecular motor. *Science* **2000**, *290* (5496), 1555–1558.
37. Schmidt, J.J.; Jiang, X.; Montemagno, C.D. Force tolerances of hybrid nanodevices. *Nano Lett.* **2002**. web released 9/28/02.
38. Goldstein, L.S.; Philp, A.V. The road less traveled: emerging principles of kinesin motor utilization. *Nat. Rev., Mol. Cell Biol.* **1999**, *15*, 141–183.

39. Block, S.M.; Goldstein, L.S.; Schnapp, B.J. Bead movement by single kinesin molecules studied with optical tweezers. *Nature* **1990**, *348* (6299), 348–352.
40. Harada, Y.; Yanagida, T. Direct observation of molecular motility by light microscopy. *Cell Motil. Cytoskeleton* **1988**, *10* (1–2), 71–76.
41. Turner, D.C.; Chang, C.; Fang, K.; Brandow, S.L.; Murphy, D.B. Selective adhesion of functional microtubules to patterned silane surfaces. *Biophys. J.* **1995**, *69*, 2782–2789.
42. Bohm, K.J.; Stracke, R.; Muhlig, P.; Unger, E. Motor protein-driven unidirectional transport of micrometer-sized cargoes across isopolar microtubule arrays. *Nanotechnology* **2001**, *12* (3), 238–244.
43. Limberis, L.; Stewart, R.J. Polarized alignment and surface immobilization of microtubules for kinesin-powered nanodevices. *Nano Lett.* **2001**, *1* (5), 277–280.
44. Brown, T.B.; Hancock, W.O. A polarized microtubule array for kinesin-powered nanoscale assembly and force generation. *Nano Lett.* **2002**, *2* (10), 1131–1135.
45. Suzuki, H.; Yamada, A.; Oiwa, K.; Nakayama, H.; Mashiko, S. Control of actin moving trajectory by patterned poly(methylmethacrylate) tracks. *Biophys. J.* **1997**, *72*, 1997–2001.
46. Nicolau, D.V.; Suzuki, H.; Mashiko, S.; Taguchi, T.; Yoshikawa, S. Actin motion on microlithographically functionalized myosin surfaces and tracks. *Biophys. J.* **1999**, *77* (2), 1126–1134.
47. Clemmens, J.; Hess, H.; Howard, J.; Vogel, V. Analysis of microtubule guidance by microfabricated channels coated with kinesin. *Langmuir* **2003**, *19* (5), 1738–1744.
48. Suzuki, H.; Oiwa, K.; Yamada, A.; Sakakibara, H.; Nakayama, H.; Mashiko, S. Linear arrangement of motor protein on a mechanically deposited fluoropolymer thin film. *Jpn. J. Appl. Phys., Part 1* **1995**, *34* (7B), 3937–3941.
49. Dennis, J.R.; Howard, J.; Vogel, V. Molecular shuttles: directing the motion of microtubules on nanoscale kinesin tracks. *Nanotechnology* **1999**, *10*, 232–236.
50. Stracke, P.; Bohm, K.J.; Burgold, J.; Schacht, H.J.; Unger, E. Physical and technical parameters determining the functioning of a kinesin-based cell-free motor system. *Nanotechnology* **2000**, *11* (2), 52–56.
51. Stracke, R.; Bohm, K.J.; Wollweber, L.; Tuszyński, J.A.; Unger, E. Analysis of the migration behaviour of single microtubules in electric fields. *Biochem. Biophys. Res. Commun.* **2002**, *293* (1), 602–609.
52. Gittes, F.; Mickey, B.; Nettleton, J.; Howard, J. Flexural rigidity of microtubules and actin filaments measured from thermal fluctuations in shape. *J. Cell Biol.* **1993**, *120* (4), 923–934.
53. Hess, H.; Clemmens, J.; Matzke, C.M.; Bachand, G.D.; Bunker, B.C.; Vogel, V. Ratchet patterns sort molecular shuttles. *Appl. Phys., A* **2002**, *75*, 309–313.
54. Hunt, A.J.; Howard, J. Kinesin swivels to permit microtubule movement in any direction. *Proc. Natl. Acad. Sci. U. S. A.* **1993**, *90* (24), 11,653–11,657.
55. Hua, W.; Chung, J.; Gelles, J. Distinguishing inchworm and hand-over-hand processive kinesin movement by neck rotation measurements. *Science* **2002**, *295* (5556), 844–848.
56. Hess, H.; Clemmens, J.; Howard, J.; Vogel, V. Surface imaging by self-propelled nanoscale probes. *Nano Lett.* **2002**, *2* (2), 113–116.
57. Hunt, A.J.; Gittes, F.; Howard, J. The force exerted by a single kinesin molecule against a viscous load. *Biophys. J.* **1994**, *67*, 766–781.
58. Meyhofer, E.; Howard, J. The force generated by a single kinesin molecule against an elastic load. *Proc. Natl. Acad. Sci. U. S. A.* **1995**, *92* (2), 574–578.
59. Hess, H.; Howard, J.; Vogel, V. A piconewton force-meter assembled from microtubules and kinesins. *Nano Lett.* **2002**, *2* (10), 1113–1115.
60. Clausen-Schaumann, H.; Seitz, M.; Krautbauer, R.; Gaub, H.E. Force spectroscopy with single biomolecules. *Curr. Opin. Chem. Biol.* **2000**, *4* (5), 524–530.
61. Tomishige, M.; Vale, R.D. Controlling kinesin by reversible disulfide cross-linking: identifying the motility-producing conformational change. *J. Cell Biol.* **2000**, *151*, 1081–1092.

# Nano–Mesoscopic Interface: Hybrid Devices

Gianfranco Cerofolini

Post-Silicon Technology, STMicroelectronics, Agrate Brianza, Italy, and Department of Materials Science, University of Milano–Bicocca, Milan, Italy

## INTRODUCTION

The continuous size reduction associated with the development of microelectronics will, sooner or later, face the need of manipulating single molecules, addressing and contacting them to wanted regions of the device. Although the manipulation of individual molecules is already possible using the scanning tunneling microscope and their functional characterization is usually achieved for thiol-terminated molecules grafted to gold electrodes, both the process (individual management by scanning tunnel microscopy) and material (gold) are, however, incompatible with the integrated-circuit (IC) technology. Batch processing requires that the molecules are addressed to (photolithographically predefined) regions by a difference of chemical potentials. In turn, that requires a control of the chemical terminations of the surfaces of the most important IC films. Among them, the unique single crystalline surface is that of the silicon substrate, which makes it the most serious candidate for the growth of ordered functional films. Of the several producible orientations of silicon, the (100) surface is that with the largest applications. In usual technological cases, the (100) surface of silicon is hydrogen-terminated (immediately after aqueous HF etching) or covered by oxo terminations (after the formation of the native oxide). Although neither one nor the other has the necessary chemical and crystalline order required to be a seed for the deposition of molecular devices, they can, however, be used to prepare clean silicon surfaces with  $2 \times 1$  reconstruction or hydrogen-terminated silicon surfaces with  $2 \times 1$  or  $1 \times 1$  reconstruction. Alkenes or alkynes can be used to functionalize the silicon via cycloaddition to the clean  $2 \times 1$ -reconstructed surface or via hydrosilylation on the hydrogen-terminated surfaces.

## THE CONCEPTUAL POSSIBILITY OF MOLECULAR ELECTRONICS

With the synthesis of rotaxanes, catenanes, Möbius strips, etc., topological chemistry has changed from a visionary view<sup>[1,2]</sup> (one of the founding papers, Ref.<sup>[1]</sup>, circulating as a preprint at the Reaction Mechanisms Conference held in Princeton, NJ, at the

end of summer 1960, was summarily rejected as not being chemistry<sup>[3]</sup>) to a consolidated discipline for the synthesis of molecules able to mimic, on a molecular scale, the behavior of macroscopic machines.<sup>[4,5]</sup> In a way, those molecules may be considered as molecular machines.

Although the first molecular machines mimicked mechanical machines, a number of molecules able to perform even sophisticated electrical functions have been also synthesized.

Fig. 1 shows an example of molecule<sup>[6]</sup> with interesting electrical properties. The molecule is formed by a bipyridinium core, two alkane chains, and two thiol terminations. The bipyridinium core works as a Schmitt trigger, the alkane chains behave as wires, and the thiol terminations provide alligator clips to external electrodes. Once grafted to gold electrodes (through its thiol terminations), the molecule displays or not resonant electronic conduction, according to the charge state on one nitrogen atom in the bipyridinium core: if both nitrogen atoms are positively charged, the molecule does not display conduction; if one nitrogen is reduced (by injection, controlled by an external electrode, of one electron), the molecule displays conduction. In a way, the molecule performs as an electronic device (a Schmitt trigger), but has a size of the order of  $3 \text{ nm}^3$ .

The molecule in Fig. 1 is certainly not unique in possessing interesting electronic properties: the review of Ref.<sup>[7]</sup> reports wires, rectifiers, memories, etc. listing 106 references. The availability of such a molecular scaffold has kindled the interest toward an application of molecular devices for a new electronics—*molecular electronics*.

Molecular electronics has, however, a chance to become interesting for large-volume applications (and thus a potential competitor of microelectronics) only if it goes beyond the current and expected future limits of the IC technology.

## MICROELECTRONICS AND THE EVOLUTION OF THE INTEGRATED CIRCUIT

At present (end of 2002 A.D.), ICs have bit density of the order of  $10^8 \text{ bit cm}^{-2}$  (for microprocessors). This density has been achieved by an increase by a factor





certain ICs may operate as measuring devices is demonstrated by the detection of single photons through p–i–n diodes supplied at a voltage just above the breakdown<sup>[14]</sup> and of alpha particles through the soft errors of dynamic random access memories.<sup>[15]</sup> The first example is particularly interesting because it applies to a situation in which the event to be detected (the presence of a photon) has an energy (say, 1 eV) not exceedingly higher than the thermal unit (say, 25 meV). This occurrence thus suggests the possibility of using suitable microelectronic devices for the detection of the state (e.g., the oxidation number) of microscopic systems (e.g., molecules) hosted on the IC.

Actually, scanned probe techniques [such as the scanning tunneling microscope (STM)] have already been proven to have the necessary sensitivity to image single electrons in nanostructures<sup>[16]</sup> (although “they almost invariably alter the properties of the system they are measuring”<sup>[17]</sup>). Even assuming the ability to reduce the STM size in the micrometer length scale (to be compatible with the IC circuitry), its use for the detection and modification of the electronic state of an ordered array of molecules (considered as a molecular memory) will require dramatic changes in circuit architecture. In present ICs, all bits are matrix-ordered and are singularly accessible by specifying row and column; the use of STM as sensing-writing element suggests the need of organizing the memory as a shift register.

The STM is not the unique apparatus able to detect the electronic state of single molecules; in recent years, the single electron transistor has been proven to work. Such a transistor, based on the concept of Coulomb blockade<sup>[18,19]</sup> has the advantage over STM to be producible with the methods of the IC technology and not to require dramatic changes in circuit architecture.

This state of affairs suggests that molecular electronics will necessarily involve a combination of microtechnologies and nanotechnologies<sup>[20]</sup> and identifies in *self-assembly* (i.e., the deposition of functional molecules in wanted regions of the microelectronic device) and in *grafting* (i.e., the selective bonding of certain groups of the molecules to electrodes in the microelectronic regions) the key problems of molecular electronics. Actually, the few examples of logic devices prepared exploiting the electronic properties of molecules are hybrid devices with photolithographically defined electrodes.<sup>[21–23]</sup>

Determining the conductance of individual molecules is a difficult task. The case of DNA is emblematic of this difficulty—depending on the study, DNA is indeed said to be an insulator, semiconductor, conductor, or proximity-induced superconductor.<sup>[24]</sup> The usual approach to allow electrical testing of organic molecules is to terminate them with thiol (–SH) groups, which behave as alligator clips to gold. Gold electrodes with parallel-plate geometry are now

currently prepared down to separations of 4 nm. While useful for the determination of the electrical characteristics of the molecules (allowing the assessment of their conduction mechanism), this arrangement is, however, largely incompatible with silicon-based ICs, for which gold should be avoided.

Although it may seem difficult to insert functional molecules between two electrodes with a controlled separation in the nanometer length scale (say, 3 nm), a solution to this problem, fully compatible with the IC technology, has recently been proposed.<sup>[25]</sup> The MOS transistor provides indeed a parallel-plane geometry with silicon plates separated by just the gate-oxide thickness—3 nm in the current technology. To allow the insertion of functional molecules therein, it is sufficient to define the gate geometry with an etch sequence formed by a plasma etch of the unmasked polysilicon followed by a wet (aqueous HF) etch of the underlying SiO<sub>2</sub>. This process, initiated with a “vertical” attack, does not complete with the total dissolution of the unmasked SiO<sub>2</sub> but rather proceeds laterally overetching a portion of the SiO<sub>2</sub> covered by the polysilicon. The width of the overetched region (the “recessed region”) is controlled by the exposure of the structure to the etching solution. Of course, this is only one of the several possibilities offered by microelectronics, and it is expected that the region hosting the molecular electronics will be obtained exploiting features (such as overetches) hitherto ignored (or even demolished) in IC processing.

Accepting this view, the development of any nanotechnology for data processing does necessarily require the ability to control a number of IC surfaces to allow self-assembly, while still providing the functions of power supply, addressing, sensing, etc. To a large extent, the materials of microelectronics are limited to Si, SiO<sub>2</sub>, Si<sub>3</sub>N<sub>4</sub>, Al, and Ti; of them, only silicon is single crystalline and is thus the most natural candidate as the seed for ordered organic layers.

## THE (100) SURFACE OF SILICON AND ITS USUAL CHEMICAL STATES

Silicon surfaces are producible in various orientations: (111), (100), (110), (113), etc. Of them, the (100) surface is the most used in IC processing. In practical conditions, the (100) silicon surface is mainly oxygen-terminated or hydrogen-terminated.

### The Surface Resulting After Aqueous HF Etching of Sacrificially Grown SiO<sub>2</sub>

Silicon and fluorine combine to form one of the most stable bonds, the Si–F bond energy  $E_b[\text{Si–F}]$  being

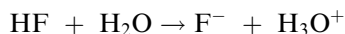
6.9 eV.<sup>[26]</sup> It does not surprise, therefore the astonishment when etching by HF-concentrated aqueous solutions of thermally grown SiO<sub>2</sub> was discovered to leave hydrogen-terminated silicon surfaces.<sup>[27]</sup>

The first explanation of this fact was given by Ubara, Imura, and Hiraki<sup>[27]</sup> in terms of polarization of Si-Si backbonds to Si-F bonds. Assuming that the strength of the Si-F bond derives from an electrostatic reinforcement because of electron transfer from silicon to fluorine, the ionicity of the Si-F bond polarizes the Si-Si backbonds, which allows an easy insertion of HF into the weakened Si-SiF bond. If this bond is cleaved with the addition of fluorine to the SiF site and of hydrogen to the other silicon atom, the ionicity is increased and so is the polarization of the residual backbonds. Reiterating this argument, one obtains that the formation of a SiF<sub>n</sub> moiety becomes easier the higher is *n*, and that the process is concluded with the formation of a volatile molecule, SiF<sub>4</sub>, and of hydrogen terminations at the silicon surface.<sup>[27]</sup>

This scheme was investigated quantum mechanically on model molecules (such as H<sub>3</sub>Si-SiH<sub>2</sub>F or H<sub>3</sub>SiF) by Trucks et al.<sup>[28]</sup> They showed that the activation energy, 1.0 eV, of the process leading to two fluorine atoms attached to the same silicon atom is lower than the activation energy, 1.4 eV, of the process transferring the fluorine to the adjacent silicon atom. Although the Si-H bond is spontaneously destroyed by reaction with HF (the reaction being exothermic by 1.3 eV), an activation energy of 1.2 eV was calculated for this process. Although small, the difference of 0.2 eV, between the activation energies for the destruction of the Si-H bond and that for the attachment of another fluorine atom to fluorinated silicon, is so high as to make the time constant of the former reaction 4 orders of magnitude higher than that of latter reaction. These calculations support therefore the opinion, first formulated by Ubara, Imura, and Hiraki<sup>[27]</sup> that the formation of hydrogen-terminated surfaces is kinetically, rather than thermodynamically, controlled.

The assumption that undissociated HF is the etching agent is, however, contradicted by the following facts:

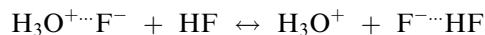
1. In diluted aqueous solution, HF is completely dissociated,



its behavior as a weak acid is a result of the reduction of the H<sub>3</sub>O<sup>+</sup> activity resulting from tight ion pairing H<sub>3</sub>O<sup>+</sup>⋯F<sup>-</sup> between the oxonium and fluoride ions (Ref.<sup>[29]</sup>, Chapter 3).

2. In concentrated aqueous solution, the H<sub>3</sub>O<sup>+</sup> activity is increased because of the formation of the hydrogen-bonded adduct F<sup>-</sup>⋯HF

via the equilibrium



the concentrated aqueous solution does therefore contain undissociated HF, but its binding energy to F<sup>-</sup> is so high (Eb[F<sup>-</sup>⋯HF] = 2.2 eV; Ref.<sup>[30]</sup>, p. 76) that the adduct F<sup>-</sup>⋯HF is considered a well-defined ion HF<sub>2</sub><sup>-</sup> (Ref.<sup>[29]</sup>, Chapter 3).

3. In gas phase (where the etching species is undissociated HF), the attack results mainly in fluorine-terminated silicon surfaces.<sup>[31]</sup>

Following the criticism of Ref.<sup>[32]</sup> and using the results of high-level quantum mechanical calculation of the stability of the Si-Si bond in relation to its terminations,<sup>[33]</sup> Cerofolini thus proposed an ionic route able to account for the observed hydrogen termination resulting after attack by HF-concentrated aqueous solution to thermally oxidized silicon. The route is constituted by three cycles each composed by four consecutive steps, the rate-determining one being F<sup>-</sup> transfer from the etching solution to the coma of SiF<sub>n</sub> termination.<sup>[34]</sup> Even the gas-phase attack, leading to fluorine-terminated silicon, seems to be controlled by the presence of adsorbed water.<sup>[31]</sup>

## The “Native Oxide” and Its Growth Kinetics

An ideally hydrogen-terminated surface is presumed to be indefinitely stable (in the laboratory timescale) in air.

Although the (100) surface resulting after aqueous HF etching of the overlying oxide is expected to be terminated with silicon dihydride, the hydrogen terminations actually form, however, a heterogeneous family of monohydride, dihydride, and trihydride species,<sup>[35,36]</sup> and the surface still contains an appreciable amount of silicon-oxygen centers, roughly corresponding to 0.2–0.5 monolayers, depending on the preparation.<sup>[37]</sup> Such oxygen-containing centers are responsible for the environmental instability of these surfaces via the oxidation of the backbonds to Si-O bonds; this process, initiated at oxygen defects and mediated by adsorbed water, proceeds with an island growth and is eventually responsible for surface roughening.<sup>[38]</sup>

Once the first layer has grown (at a characteristic time τ<sub>1</sub>), further oxidation occurs in a layer-by-layer fashion; the characteristic time τ<sub>n</sub> required for the formation of the *n*th layer increasing exponentially with *n* is given by:

$$\tau_n = \tau_1 a^{n-1}$$

where  $a$  is a suitable constant.<sup>[37]</sup> The native oxide so formed is the final result of a complex oxidation process, in which  $H_2O$  and  $O_2$  both play a crucial role.<sup>[37]</sup>

Understanding such a behavior is not a trivial task. A microscopic model for it was proposed by Cerofolini et al. in a series of papers in terms of tunneling either of a proton from adsorbed water<sup>[39,40]</sup> or of an electron to adsorbed oxygen.<sup>[41,42]</sup> The development of the kinetic description of layer-by-layer growth does not require the detailed knowledge of the tunneling species (for that it suffices to assume that the process is limited by a tunneling-assisted step); rather, the kinetic model provides a practical example for a self-similar process, in which the rates of growth from layer to layer are scaled by a subunitary positive Grossmann factor.<sup>[43]</sup>

Grafting of organic molecules to  $SiO_2$  is a relatively simple task.<sup>[44]</sup> For that it suffices first to cleave (by immersion in water or in water solutions of ammonia) the surface siloxanic bridges  $Si-O-Si$ , thus forming an array of silanols  $Si-OH$ , and then to expose the surface to alcohols; grafting occurs via condensation:



Because  $R$  can contain practically any functional group, this route seems to offer an interesting possibility for the functionalization of silicon.<sup>[45]</sup> However, two factors play against it:

1. No process is known for the preparation of a complete ordered layer of silanols, either at the  $SiO_2$  or silicon surface.
2. The oxo bridge between silicon and carbon undergoes readily hydrolysis, so that the condensation reaction above is somewhat reversible, that renders the grafted species environmentally weak.

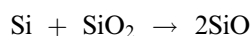
It is generally believed that the production of environmentally robust, ordered organic layers requires a preparation of the surface somewhat different from the current ones and a grafting through  $Si-C$  bonds.

### TRYING TO CONTROL THE CHEMICAL AND CRYSTALLINE ORDER OF THE (100) SURFACE OF SILICON

The “technological” surfaces discussed in the previous section do not preserve either the crystalline order of the underlying substrate or its chemical homogeneity; they are not useful as seed for ordered organic layers.

### The Clean, $2 \times 1$ -Reconstructed, (100) Silicon Surface

Clean (100) silicon surfaces with  $2 \times 1$  reconstruction [referred to as  $2 \times 1$  (100) Si, in which neighboring pairs of surface atoms form double-bonded dimers, and the dimers are organized in a two-dimensional lattice] can be prepared by suitable heat treatment in an ultrahigh vacuum (UHV) of technological surfaces. If the surface is covered by a native oxide, the oxo groups can be destroyed by heating at high temperature  $T$  (above  $1000^\circ C$ ); in the absence of oxygen, interfacial silicon reacts with  $SiO_2$  forming volatile  $SiO$ :



If the surface is mainly hydrogen-terminated (because it is prepared via aqueous HF etching of a sacrificial  $SiO_2$  film), the hydrogen terminations may be demolished at somewhat lower temperature (say,  $T < 800^\circ C$ ) with the formation of  $H_2$ .

Experimental evidence for the presence of the double-bonded dimers at the (100) silicon surface can be obtained from the presence of a satellite peak shifted by  $0.2\text{ eV}$  toward lower binding energies in the  $Si\ 2p$  spectrum obtained by X-ray photoemission spectroscopy (XPS).<sup>[46]</sup>

### The Hydrogen-Terminated, $2 \times 1$ - or $1 \times 1$ -Reconstructed, (100) Silicon Surfaces

Hydrogen-terminated,  $2 \times 1$ -reconstructed, (100)-oriented silicon surfaces [referred to as  $2 \times 1$  (100)H Si, in which the  $\pi$  bond of the surface dimer is broken and the two radicals are saturated by bonding to hydrogen] can be obtained by exposing, without breaking the vacuum, the clean  $2 \times 1$  (100) surface kept at ca.  $400^\circ C$  to a few langmuirs of atomic hydrogen, in turn obtained by the dissociation of  $H_2$  after contact with a hot tungsten filament.

The overall process (requiring a treatment in an UHV and an exposure to atomic hydrogen) is, however, complicated and may be simplified as follows. The surfaces prepared by aqueous HF etching can indeed be used for the preparation of highly ordered hydrogen-terminated surfaces via exposure to an  $H_2$  atmosphere at relatively high temperature. In fact, the oxygen terminations remaining after the HF attack are totally demolished after heating at  $T > 750^\circ C$ ; this treatment destroys the preexisting heterogeneous distribution of trihydride, dihydride, and monohydride terminations and eventually results in monohydride terminations and  $2 \times 1$  reconstruction<sup>[36]</sup> or in dihydride terminations and  $1 \times 1$  reconstruction<sup>[47]</sup> (for which even the residual  $\sigma$  bond of the surface dimer

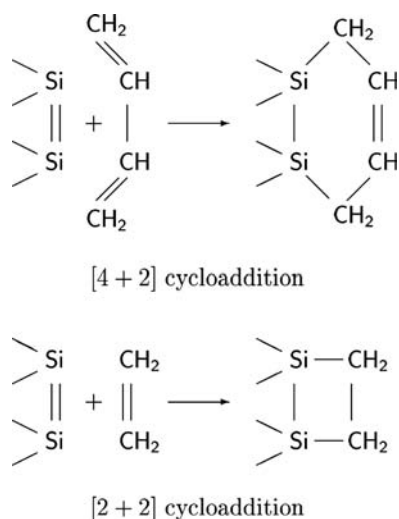


**Fig. 2** Addition of an alkene ([2 + 2] cycloaddition, bottom) or a conjugated diene ([4 + 2] cycloaddition or Diels–Alder reaction, top) to the clean,  $2 \times 1$ -reconstructed, (100) silicon surface.

is broken and the radicals are saturated with hydrogen atoms), according to the process. The surfaces so prepared are flat down to the atomic level.

## USING CONTROLLED SURFACES TO FUNCTIONALIZE SILICON

### Functionalization of Clean (100) Silicon via Cycloaddition

The clean,  $2 \times 1$ -reconstructed, (100) silicon surface can be used to functionalize the silicon via [2 + 2] or [4 + 2] cycloaddition.<sup>[48,49]</sup> Fig. 2 sketches both these reactions for the simplest alkene and diene.

Dienes are particularly interesting because, irrespective of whether they undergo [4 + 2] cycloaddition (as sketched in Fig. 2) or [2 + 2] cycloaddition (as performed in Ref.<sup>[50]</sup> using 1,4-cyclohexadiene), they may be used to insert a second functional group (the C=C double bond) on  $2 \times 1$  (100) Si. An ordered layer of intact functional groups allows the possibility of preparing hybrid organosilicon devices. Cycloaddition reactions must, however, be carried out in an UHV because the  $2 \times 1$  (100) Si surface is very reactive

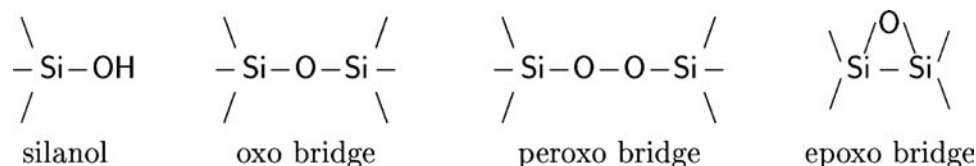


**Fig. 3** Silicon–oxygen moieties at the silicon surface.

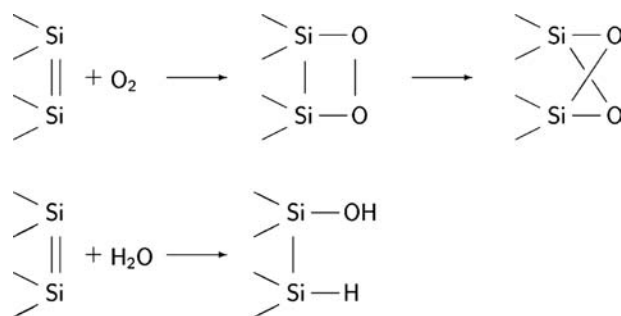


**Fig. 4** Expected reactions of water (bottom) and oxygen (top) at the  $2 \times 1$  (100) Si surface, showing how silanols, peroxy, and oxo centers may be formed after exposure to air of the clean,  $2 \times 1$ -reconstructed, (100) surface of silicon.

and, when exposed to air, forms quickly a disordered native oxide, characterized by the copresence of silanic and silanolic terminations in addition to oxo, peroxy, and perhaps epoxo bridges (Figs. 3 and 4).

### Functionalization of Hydrogen-Terminated (100) Silicon via Hydrosilation

In view of its relative inertness, it is not easy to graft organic molecules to hydrogen-terminated silicon. The preferred way for that is the *hydrosilation* reaction (Ref.<sup>[29]</sup>, p. 1255). This reaction occurs between 1-alkenes and hydrogen-terminated silicon.

Hydrosilation is a reaction involving hydrogen shift from silicon to a carbon atom involved in the  $\pi$  bond and bond formation between the silicon atom and the other carbon atom (Fig. 5). If the number  $n$  of carbon atoms in the alkane chain is small (say,  $n < 8$ ), the alkene hydrosilation occurs only in the presence of a catalyst ( $\text{H}_2\text{PtCl}_6$ )<sup>[44]</sup> or after activation (radical formation);<sup>[51]</sup> for long chains (say,  $n > 10$ ), the reaction occurs spontaneously at a temperature of about  $200^\circ\text{C}$ .<sup>[44,52]</sup>

Because hydrosilation involves only one silicon atom, it was mainly studied on the hydrogen-terminated,  $1 \times 1$ -reconstructed, (111) silicon surface [denoted as  $1 \times 1$  (111)H Si], and only few works have been devoted to study alkene hydrosilation on  $1 \times 1$  (100)H Si.<sup>[52,53]</sup> The hydrosilation of 1-alkenes at  $1 \times 1$  (100)H Si is expected to occur according to pathways (I') or (I'') in Fig. 6.

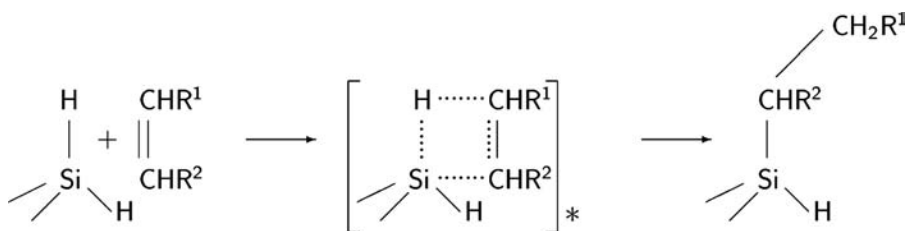


**Fig. 5** Hydrosilylation of 1-alkenes as a concerted reaction. One between  $R^1$  and  $R^2$  denotes hydrogen; the other may be either hydrogen or an alkane chain.

The C=C bond is not unique in undergoing hydrosilylation. This reaction is indeed known to occur for the C=N, C=O, and C≡C bonds also (Ref.<sup>[29]</sup>, p. 1256).

Although the reactivity of 1-alkynes is similar to that of 1-alkenes, there is, however, an important difference: after the first addition (II), the formed species,  $2'$  and  $2''$  in Fig. 6, contain a double bond in the vicinity of another hydrogen termination of silicon, so that the reaction can, in principle, proceed, via (III) or (IV), with the formation of the species 3 or 4. Understanding the nature of the interfacial species is not without interest: for instance, if the reaction stopped after (II), the silicon surface would be equipped with a

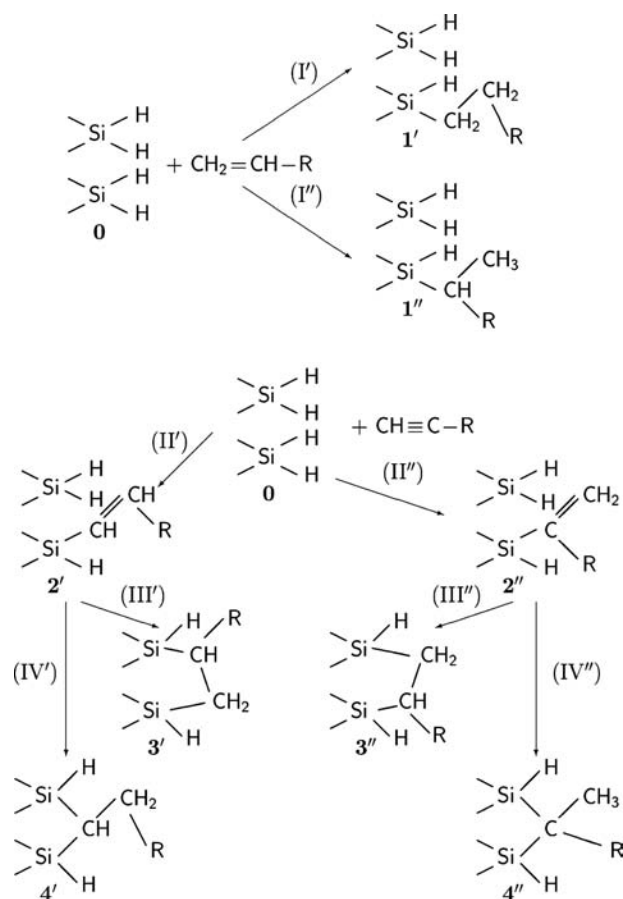


**Fig. 6** Hydrosilylation of 1-alkene [pathway (I)] and 1-alkyne [pathway (II)] at the hydrogen-terminated,  $1 \times 1$ -reconstructed, (100)-oriented, silicon surface; R denotes a suitably terminated alkane chain.

second reactive group (the C=C group) in addition to the one, if any, carried by R.

The only characterizations we know of the hydrogen-terminated,  $1 \times 1$ -reconstructed, (100) silicon surface derivatized with 1-alkyne are the ones due to Sieval et al.<sup>[54]</sup> and Cerofolini et al.<sup>[55]</sup> The first collaboration, basing their conclusions on infrared spectroscopy and quantum mechanical calculations, arrived to the conclusion that the grafting of 1-hexadecyne at 200°C on the technological hydrogen-terminated surface occurs mainly with the formation of the adducts 3 and 4. The second collaboration, basing their conclusions on XPS, arrived to the conclusion that the grafting of 1-octyne at 170°C on  $2 \times 1$  (100)H Si occurs with the formation of the adducts 2. At the present level of investigation, it is not clear if the different reported behaviors are a result of the nature of the surface, length of the alkyne, or reaction temperature or simply to an inadequate interpretation of the experimental data.

## CONCLUSION

The evolution of molecular electronics via the hybrid route requires the functionalization of the (100) surface of silicon. Two states of the (100) silicon surface seem to have the necessary characteristics of crystalline and chemical order required for the deposition of molecular devices with size in the nanometer length scale: the clean  $2 \times 1$ -reconstructed surface and the hydrogen-terminated  $1 \times 1$ - or  $2 \times 1$ -reconstructed surfaces. Alkenes or alkynes may be used for their functionalization: via cycloaddition to the clean surface or via hydrosilylation at the hydrogen-terminated surfaces.

## REFERENCES

1. van Gulick, N. Theoretical aspects of the linked ring problem. *New J. Chem.* **1993**, *17*, 619–625.
2. Frisch, H.L.; Wasserman, E. Chemical topology. *J. Am. Chem. Soc.* **1961**, *83*, 3789–3795.
3. Walba, D.M. Preface to van Gulick paper. *New J. Chem.* **1993**, *17*, 618.

4. Lehn, J.-M. Supramolecular chemistry—Scope and perspectives. *Molecules, supermolecules and molecular devices*. *Angew. Chem., Int. Ed. Engl.* **1988**, *27*, 89–112.
5. Balzani, V.; Credi, A.; Raymo, F.M.; Stoddart, J.F. Artificial molecular machines. *Angew. Chem., Int. Ed.* **2000**, *39*, 3348–3391.
6. Gittins, D.I.; Bethell, D.; Schiffrin, D.J.; Nichols, R.J. A nanometre-scale electronic switch consisting of a metal cluster and redox-addressable groups. *Nature* **2000**, *408*, 67–69.
7. Joachim, C.; Gimzewski, J.K.; Aviram, A. Electronics using hybrid-molecular and mono-molecular devices. *Nature* **2000**, *408*, 541–548.
8. Semiconductor Industry Association (SIA) *International Technology Roadmap for Semiconductors*; SIA: San Jose, CA, 2001.
9. Packan, P.A. Pushing the limits. *Science* **1999**, *285*, 2079–2081.
10. Ito, T.; Okazaki, S. Pushing the limits of lithography. *Nature* **2000**, *406*, 1027–1031.
11. Bohr, N. The quantum postulate and the recent development of atomic theory. *Nature* **1928**, *121*, 580–590. Reprinted in *Quantum Theory and Measurement*, edited by J.A. Wheeler and W.H. Zurek (Princeton Univ. Press, Princeton, NJ, 1983) p. 87–126.
12. Daneri, A.; Loinger, A.; Prosperi, G.M. Quantum theory of measurement and ergodicity conditions. *Nucl. Phys.* **1962**, *33*, 297–319.
13. Daneri, A.; Loinger, A.; Prosperi, G.M. Further remarks on the relations between statistical mechanics and quantum theory of measurement. *Nuovo Cim., B* **1966**, *44*, 119–128.
14. McIntyre, R.J. The distribution of gains in uniformly multiplying avalanche photodiodes: Theory. *IEEE Trans. Electron Devices* **1972**, *ED-19*, 703–713.
15. Cerofolini, G.F.; Ferla, G.; Foglio Para, A. A proposal: Dynamic RAMs as particle detectors. *Nucl. Instrum. Methods* **1980**, *169*, 125–128.
16. Lemay, S.G.; Janssen, J.W.; van den Hout, M.; Mooij, M.; Bronikowski, M.J.; Willis, P.A.; Smalley, R.E.; Kouwenhoven, L.P.; Dekker, C. Two-dimensional imaging of electronic wavefunctions in carbon nanotubes. *Nature* **2001**, *412*, 617–620.
17. Woodside, M.T.; McEuen, P.L. Scanned probe imaging of single-electron charge states in nanotube quantum dots. *Science* **2002**, *296*, 1098–1101.
18. Devoret, M.H.; Schoelkopf, R.J. Amplifying quantum signals with the single-electron transistor. *Nature* **2000**, *408*, 1039–1046.
19. Postma, H.W.Ch.; Teepen, T.; Yao, Z.; Grifoni, M.; Dekker, C. Carbon nanotube single-electron transistors at room temperature. *Science* **2001**, *293*, 76–79.
20. Cerofolini, G.F. Beyond Silicon? Perspectives for Molecular Electronics. In *Chemistry for Innovative Materials*; Cerofolini, G.F., Mininni, R.M., Schwarz, P., Eds.; EniChem: Milano, 1991; 84–97.
21. Collier, C.P.; Wong, E.W.; Belohradsky, M.; Raymo, F.M.; Stoddart, J.F.; Kuekes, P.J.; Williams, R.S.; Heath, J.R. Electronically configurable molecular-based logic gates. *Science* **1999**, *285*, 391–394.
22. Huang, Y.; Duan, X.; Cui, Y.; Lauhon, L.J.; Kim, K.-H.; Lieber, C.M. Logic gates and computation from assembled nanowire building blocks. *Science* **2001**, *294*, 1313–1317.
23. Bachtold, A.; Hadley, P.; Nakanishi, T.; Dekker, C. Logic circuits with carbon nanotube transistors. *Science* **2001**, *294*, 1317–1320.
24. Hippy, K.W. It's all about contacts. *Science* **2001**, *294*, 536–537.
25. Cerofolini, G.F.; Ferla, G. Toward a hybrid micro-nanoelectronics. *J. Nanopart. Res.* **2002**, *4*, 185–191.
26. Walsh, R. Bond dissociation energy values in silicon-containing compounds and some of their implications. *Acc. Chem. Res.* **1981**, *14*, 246–252.
27. Ubara, H.; Imura, T.; Hiraki, A. Formation of Si–H bonds on the surface of microcrystalline silicon covered with SiO<sub>x</sub> by HF treatment. *Solid State Commun.* **1984**, *50*, 673–675.
28. Trucks, G.W.; Raghavachari, K.; Higashi, G.S.; Chabal, Y.J. Mechanism of HF etching of silicon surfaces: A theoretical understanding of hydrogen passivation. *Phys. Rev. Lett.* **1990**, *65*, 504–507.
29. Cotton, F.A.; Wilkinson, G. *Advanced Inorganic Chemistry*, 5th Ed.; Wiley: New York, NY, 1988.
30. March, J. *Advanced Organic Chemistry*, 4th Ed.; Wiley: New York, NY, 1992.
31. Miki, N.; Kikuyama, H.; Kawanabe, I.; Miyashita, M.; Ohmi, T. Gas-phase selective etching of native oxide. *IEEE Trans. Electron Devices* **1990**, *37*, 107–115.
32. Cerofolini, G.F.; Meda, L. Chemistry at silicon crystalline surfaces. *Appl. Surf. Sci.* **1995**, *89*, 351–360.
33. Cerofolini, G.F.; Re, N. Chemical Perspectives on Growth and Properties of Ultrathin SiO<sub>2</sub> Layers. In *Fundamental Aspects of Ultrathin Dielectrics on Si-Based Devices*; Garfunkel, E., Gusev, E., Vul, A., Eds.; Kluwer: Dordrecht, 1998; 117–129.
34. Cerofolini, G.F. A study of the ionic route for hydrogen terminations resulting after SiO<sub>2</sub> etching by concentrated aqueous solutions of HF. *Appl. Surf. Sci.* **1998**, *133*, 108–114.
35. Niwano, M.; Kageyama, J.; Kinashi, K.; Takashi, I.; Miyamoto, N. Infrared spectroscopy study of initial stages of oxidation of hydrogen-terminated Si surfaces stored in air. *J. Appl. Phys.* **1994**, *76*, 2157–2163.
36. Aoyama, T.; Goto, K.; Yamazaki, T.; Ito, T. Silicon (001) surface after annealing in hydrogen ambient. *J. Vac. Sci. Technol., A* **1996**, *14*, 2909–2915.
37. Morita, M.; Ohmi, T.; Hasegawa, E.; Kawakami, M.; Ohwada, M. Growth of native oxide on a silicon surface. *J. Appl. Phys.* **1990**, *68*, 1272–1281.
38. Usuda, K.; Kanaya, H.; Yamada, K.; Sato, T.; Sueyoshi, T.; Iwatsuki, M. Scanning tunneling microscopy of hydrogen-terminated Si(111) surfaces at room temperature. *Appl. Phys. Lett.* **1994**, *64*, 3240–3242.
39. Cerofolini, G.F. Kinetics of tunnel-assisted multilayer chemisorption on homogeneous surfaces. *J. Colloid Interface Sci.* **1994**, *167*, 453–456.
40. Cerofolini, G.F.; Meda, L.; Falster, R. A Model for Room-Temperature Wet Oxidation of Silicon.



- In *Semiconductor Silicon 1994*; Huff, H.R., Bergholz, W., Sumino, K., Eds.; The Electrochemical Society: Pennington, NJ, 1994; 379–388.
41. Cerofolini, G.F.; La Bruna, G.; Meda, L. Gas-phase room-temperature oxidation of (100) silicon. *Appl. Surf. Sci.* **1996**, *93*, 255–266.
  42. Cerofolini, G.F. Room-Temperature Oxidation of Single-Crystalline Silicon. In *Silicon for the Chemical Industry III*; Oye, H.A., Rong, H.M., Ceccaroli, B., Nygaard, L., Tuset, J.K., Eds.; Tapir: Trondheim, 1996; 117–127.
  43. Vlad, M.O.; Cerofolini, G.F.; Ross, J. Temporal logarithmic oscillations in self-similar multilayer aggregation: Shlesinger–Hughes renormalization with application to the tunnel-assisted wet oxidation of silicon. *J. Phys. Chem., A* **1999**, *103*, 4798–4807.
  44. Tertykh, V.A.; Belyakova, L.A. Solid-Phase Hydrosilation Reactions with Participation of Modified Silica Surface. In *Adsorption on New and Modified Inorganic Sorbents*; Dabrowski, A., Tertykh, V.A., Eds.; Elsevier: Amsterdam, 1996; 147–189.
  45. Cleland, G.; Horrocks, B.R.; Houlton, A. Direct functionalization of silicon via the self-assembly of alcohols. *J. Chem. Soc., Faraday Trans.* **1995**, *91*, 4001–4003.
  46. Himpfel, F.J.; McFeely, F.R.; Taleb-Ibrahimi, A.; Yarnoff, J.A.; Hollinger, G. Microscopic structure of the SiO<sub>2</sub>/Si interface. *Phys. Rev., B* **1988**, *38*, 6084–6096.
  47. Cerofolini, G.F.; Galati, C.; Lorenti, S.; Renna, L.; Viscuso, O.; Bongiorno, C.; Raineri, V.; Spinella, C.; Condorelli, G.G.; Fragala, I.L.; Terrasi, A. The early oxynitridation stages of hydrogen-terminated (100) silicon after exposure to N<sub>2</sub>:N<sub>2</sub>O. III. The initial condition. *Appl. Phys., A* **2003**, *17*, 403–409.
  48. Bent, S.F. Organic functionalization of group IV semiconductor surfaces: Principles, examples, applications, and prospects. *Surf. Sci.* **2002**, *500*, 879–903.
  49. Buriak, J. Organometallic chemistry on silicon and germanium surfaces. *Chem. Rev.* **2002**, *102*, 1271–1308.
  50. Yamashita, Y.; Hamaguchi, K.; Machida, S.; Mukai, K.; Yoshinobu, J.; Tanaka, S.; Kamada, M. Adsorbed states of cyclopentene, cyclohexene, and 1,4-cyclohexadiene on Si(100)(2 × 1): Towards the fabrication of novel organic films/Si hybrid structures. *Appl. Surf. Sci.* **2001**, *169/170*, 172–175.
  51. Lopinski, G.P.; Wayner, D.D.M.; Wolkow, R.A. Self-directed growth of molecular nanostructures on silicon. *Nature* **2000**, *406*, 48–51.
  52. Sieval, A.B.; Demirel, A.L.; Nissink, J.W.M.; van der Maas, J.H.; de Jeu, W.H.; Zuilhof, H.; Sudholter, E.J.R. Highly stable Si–C linked functionalized monolayers on the silicon (100) surface. *Langmuir* **1998**, *14*, 1759–1768.
  53. Sieval, A.B.; Vleeming, V.; Zuilhof, H.; Sudholter, E.J.R. An improved method for the preparation of organic monolayers of 1-alkenes on hydrogen-terminated silicon surfaces. *Langmuir* **1999**, *15*, 8288–8291.
  54. Sieval, A.B.; Opitz, R.; Maas, H.P.A.; Schoeman, M.G.; Meijer, G.; Vergeldt, F.J.; Zuilhof, H.; Sudholter, E.J.R. Monolayers of 1-alkynes on the H-terminated Si(100) surface. *Langmuir* **2000**, *16*, 10359–10368.
  55. Cerofolini, G.F.; Galati, C.; Reina, S.; Renna, L. Functionalization of the (100) surface of hydrogen-terminated silicon via hydrosilation of 1-alkyne. *Mater. Sci. Eng., C* **2003**, *23*, 253–257.

# Nanoarrays: Electrochemically Self-Assembled

S. Bandyopadhyay

Department of Electrical Engineering, Virginia Commonwealth University,  
Richmond, Virginia, U.S.A.

## INTRODUCTION

Nanotechnology is currently a major scientific and engineering undertaking. It has been described with such plaudits as the “third industrial revolution,” the “final frontier,” and so on. Only a few research laboratories in the world will not have a focus on this field. On a global scale, investment in nanotechnology dwarfs those in many other important fields of scientific enterprise.

Nanotechnology is the science and engineering of few nanometer-sized objects endowed with unique properties not commonly encountered in larger “bulk” objects. To study these objects and exploit their special properties, one must first be able to produce them using techniques that are relatively inexpensive, reliable, and have a rapid throughput. This entry is concerned with electrochemically “self-assembled” nanostructures that are made cheaply, rapidly, and with high yield using a technique based on simple beaker electrochemistry.

## NANOFABRICATION

Traditionally, nanostructures have been made by fine-line lithography. Lithography is the workhorse of microfabrication. Computer chips, or other microelectronic circuits such as those found in supermarket laser scanners, are all made with standard lithography. In this approach, a circuit pattern with micron-sized features is transferred to a silicon chip by a series of processes that involves masking selected regions of the surface of a wafer and exposing the rest to light to make them either more amenable or less amenable to etching. In the case of nanometer-sized features, one would need X-ray light for this purpose. An alternate technique is to directly write the patterns on the surface of a wafer using an electron or ion beam. The problem with this approach is twofold. First, direct writing is a slow process. It is also *serial* in nature, whereby each wafer is patterned one at a time, resulting in an exceedingly slow throughput. Second, the patterning beams (electron beam or ion beam) can cause radiation damage to the nanostructures. In the

case of semiconductor structures, these damages cause the structures to become depleted of electrical carriers, so that they cannot function properly. Hence there is a great interest in non-lithographic techniques for nanosynthesis.

Among the non-lithographic techniques, one technique of interest is “nanostamping.” Here one makes a “stamp pad” using standard electron beam lithography. This stamp pad is then used to “stamp” the pattern on the surface of a wafer using pressure just like an ordinary rubber stamp. This technique does not cause radiation damage and has a fast throughput. As long as a single level of pattern definition is required (so that there is no requirement to align two patterns), it is an excellent technique for nanosynthesis. Its only drawback is that it cannot produce very small features because it is, after all, a stamping technique.

An even gentler technique, causing even less damage and capable of producing very small nanostructures is the process of “self-assembly.” Roughly speaking, self-assembly is the process in which the natural evolution of a physical or chemical system to its thermodynamic ground state results in the spontaneous formation of nanostructures on a surface. Normally, the nanostructures would nucleate with random size and at random locations on the surface. However, there are some processes where the size can be made uniform and even the locations can be controlled to the point where the structures that are spontaneously formed have some degree of spatial ordering. In our laboratory, we work with an electrochemical process that produces nanostructures with less than 1% standard deviation in surface area, and the structures form a nearly periodic two-dimensional array (hexagonal close packed structure). This entry is concerned with a description of this process and two specific applications of the structures. The applications we have chosen are 1) infrared (IR) photodetection and 2) neural networks for image processing.

## ELECTROCHEMICAL SELF-ASSEMBLY

We self-assemble regimented arrays of quasi one-dimensional nanostructures (so-called “quantum wires”)

and quasi zero-dimensional nanostructures (known as “quantum dots”) via a simple electrochemical technique. It consists of first self-assembling a thin (typically  $\sim 1 \mu\text{m}$  thick) nanoporous alumina film by anodization of aluminum. This film has a nearly periodic two-dimensional array of pores with hexagonal close packed arrangement. The next step is to electrodeposit the materials of interest within the pores to create a quasi-periodic, two-dimensional array of quantum dots or wires in an alumina matrix. It is now possible to synthesize *device-quality nanostructures* with this simple and inexpensive electrochemical technique. The advantages of this method are low cost, high throughput, and sometimes even improved quality.

This technique is now widely used for self-assembling semiconducting or metallic quantum dots and wires of uniform diameter (see, e.g., Refs.<sup>[1–3]</sup>). The structures that are formed are automatically (electrically) isolated from each other by the intervening alumina layer so that no etching or diffusion steps are needed to isolate neighboring structures. Furthermore, the boundaries of the structures are well-defined, sharp, and comparatively free of interface defects. Fig. 1 shows the top and side views of the alumina films (templates) used in this process. Note the excellent degree of ordering within domains that are about  $1 \mu\text{m}^2$  in size. Also note that the diameter of the pores is extremely uniform. Detailed microscopy and image analysis have shown that the standard deviation in the pore diameter is less than 1% of the average diameter.

For most optical applications, one does not need to make electrical contacts to the individual nanostructures, so that the structures in Fig. 1 are already adequate for many optical devices. For electronic devices, it is necessary to establish electrical contacts to the nanostructures. Electrical access to the dots or wires can be established by removing the alumina from the bottom of the dots/wires (the so-called “barrier layer” in Fig. 1) following a sequence of steps described later, and then contacting both top and bottom of the structures with metal (usually gold) contacts. It is obvious that this process of nanosynthesis is “parallel” in nature, whereby several wafers can be simultaneously processed resulting in fast throughput. It is also very inexpensive and easily accessible for academic laboratories with rather modest resources. The only disadvantage of this method, common to all self-assembly techniques, is the inability to create arbitrary patterns. For some device applications (including the ones discussed in this entry), this is not a serious drawback. Ultimately, the ideal nanosynthesis technique will be an optimum blend of lithography and self-assembly exploiting the merits of both approaches.

### Anodization

As mentioned before, the first step in electrochemical self-assembly of quantum dots or wires is the formation of the nanoporous alumina film. This is produced by controlled anodization of aluminum.

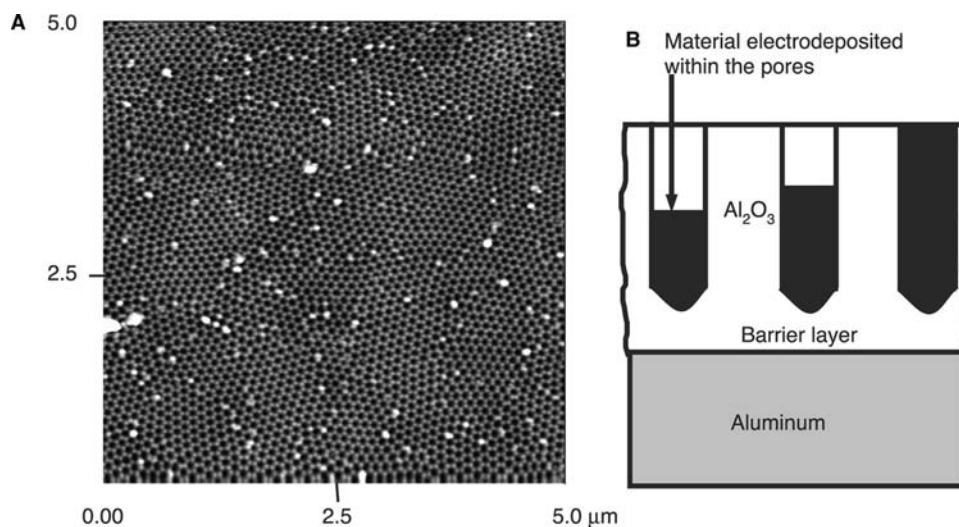


**Fig. 1** (A) Atomic force micrograph of a porous alumina film produced by anodizing aluminum in oxalic acid. The pore diameter for oxalic acid anodization is  $\sim 50 \text{ nm}$ , whereas for sulfuric acid anodization, it is  $\sim 10 \text{ nm}$ . A bright field TEM micrograph of the pores for sulfuric acid anodization can be viewed in Fig. 7 of Ref.<sup>[9]</sup>. The dark areas are the pores and the surrounding light areas are alumina. (B) The side view of the porous structure is sketched showing the barrier layer. Note that when the pores are filled with electrodeposition, they are filled to various heights.

A 99.999% pure 100- $\mu\text{m}$  aluminum foil is first degreased in trichloro-ethylene, washed in distilled water, and electropolished at 30 V for 60 sec in LECO-1 solution consisting of perchloric acid, ethanol, butyl cellulose, and water. The foil is then d.c.-anodized in either sulfuric, oxalic, or phosphoric acid at room temperature using a dc current density of  $\sim 25 \text{ mA}/\text{cm}^2$ . This results in the formation of a porous alumina film on the surface of the aluminum. The film is stripped off by soaking in phosphoric acid, and the anodization is repeated a few times. With the first few anodizations, the ordering of the pores in the film dramatically improves.<sup>[4,5]</sup> Finally, after the third or fourth iteration, the pores form a nearly perfect periodic (hexagonal close packed) array within domains that are 1–10  $\mu\text{m}$  in diameter. This self-ordering is usually best for oxalic acid anodization, and worst for sulfuric acid anodization. For anodization in sulfuric acid, the average pore diameter is about 8 nm<sup>[6]</sup> (with  $\sim 10\%$  standard deviation), resulting in an areal pore density of  $\sim 10^{11}/\text{cm}^2$ . For oxalic acid anodization, the pore diameter is  $50 \pm 1 \text{ nm}$  and the pore density is  $\sim 10^{10}/\text{cm}^2$ . For phosphoric acid anodization, the pore diameter is  $\sim 100 \pm 2 \text{ nm}$  and the pore density is less than  $10^9/\text{cm}^2$ . An atomic force micrograph (top view) of a porous film produced by anodization in oxalic acid is shown in Fig. 1A.

In Fig. 1B, we show the side view of a pore. If the pore is filled up with a material to a depth that is about equal to the diameter of the pore, we would have created a “quantum-dot.” On the other hand, if the pore is filled up to a depth that is much larger than the diameter, we would have created a short “quantum wire.” Thus, whether a dot or a wire is produced can be simply determined by the duration of the pore-filling action—electrodeposition. Care must be taken not to overfill the pores or allow the material to spill over the brim, which creates electrical shorts between neighboring wires. If this happens, the surface can be etched in phosphoric acid to reestablish electrical isolation between neighboring wires.

### Electrodepositing a Metal

The technique to electrodeposit a metal within the pores is well known and has been practiced for many years.<sup>[2,3,7–9]</sup> To electrodeposit a metal  $M$  in the pores, the porous anodic alumina film (along with the aluminum substrate) is immersed in a suitable non-cyanide aqueous electrolyte containing a dissolvable salt of  $M$ , such as  $\text{MSO}_4$  (we assume  $M$  is a divalent element). An alternating signal of 20–50 V rms amplitude and 100–1000 Hz frequency is imposed between the aluminum foil (substrate) and a platinum counterelectrode. Because the alumina structure preferentially conducts

in only one direction (the cathodic direction), it is called a “valve metal oxide”.<sup>[2,3]</sup> Metal ions ( $M^{2+}$ ) are reduced to zero-valent metal during the cathodic half-cycles of the imposed a.c. signal, and are selectively deposited within the pores because the pores offer the least impedance path (largest capacitance path) for the a.c. (displacement) current to flow. These ions are not reoxidized during the anodic half cycles to  $M^{2+}$  because alumina is a valve metal oxide. Once the metal is electrodeposited to the desired depth (controlled by the duration of the electrodeposition step), the pores are sealed by a 10-min immersion in boiling water, which covers the surface with a layer of  $\text{Al}(\text{OH})_3$ . This prevents or retards surface oxidation of the metal particles.

The presence of electrodeposited material in the pores were verified numerous times in the past by energy-dispersive analysis of X-ray,<sup>[10]</sup> cross-section TEM,<sup>[10]</sup> and variable-angle spectroscopic ellipsometry.<sup>[11]</sup> The last two techniques also yield information about the shapes of the metal nanostructures. They appear to resemble rotational ellipsoids (the shape of a football).

### Electrodepositing a Compound Semiconductor

There are different approaches to electrodepositing compound semiconductors within the pores.<sup>[10,12]</sup> Here we outline one of our approaches.

In our laboratory, we typically electrodeposit two different compound semiconductors within the pores: CdS and ZnSe. CdS is electrodeposited by immersing the alumina film (along with the aluminum substrate) in an electrolyte consisting of a non-aqueous solution of dimethylsulfoxide comprising 50 mM cadmium perchlorate, 10 mM lithium perchlorate, and 10 mM sulphur powder, whereas in the case of ZnSe deposition, cadmium perchlorate is replaced by zinc perchlorate and sulfur powder with selenium powder. Electrodeposition is carried out at 100°C with an a.c. signal of 20 V at 250 Hz. During the negative half of the a.c. cycle, the  $\text{Cd}^{2+}$  or  $\text{Zn}^{2+}$  ions in the solution are reduced to zero-valent Cd or Zn and are selectively deposited in pores offering the least impedance path for the electric current to flow. During the positive cycle, the zero-valent metals are not reoxidized into the ions. The high temperature of the solution then allows Cd or Zn in the pores to react with S or Se in the solution to produce CdS or ZnSe nanowires within the pores.

### Contacting Nanowires

The nanowires produced by the above method are not directly suitable for current–voltage measurements because they cannot be contacted easily. Particularly

bothersome is the presence of an alumina “barrier layer” in contact with the aluminum substrate (see Fig. 1), which presents a large potential barrier to current flow along the wire axis (perpendicular to the surface of the porous alumina film). Therefore, we carry out a series of steps to remove the barrier layer and make the wires electrically accessible. These steps are shown in Fig. 2. First, the top surface of the sample is etched for a few minutes in 0.2 M  $\text{H}_2\text{CrO}_4$ /0.4 M  $\text{H}_3\text{PO}_4$  solution. This dissolves the alumina and exposes the top of some of the semiconductor wires. Not all wires are exposed as the wires have varying length. A thin coating of Au (10–20 nm) is then applied on the surface, followed by a thick organic layer which provides mechanical strength to the film during later processing steps. The aluminum substrate is then dissolved in  $\text{HgCl}_2$  to expose the barrier layer of alumina, which is subsequently removed in 5%  $\text{H}_3\text{PO}_4$  (several minutes of soaking), thereby exposing some of the semiconductor nanowires from the bottom. The sample is flipped over and the bottom layer is coated with 10–20 nm of Au. The final structures are arrays of parallel nanowires with Au ohmic contacts at both ends.

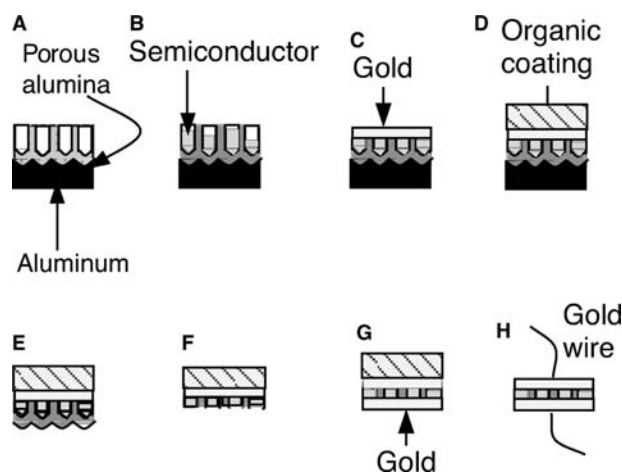


**Fig. 2** (A) Anodized aluminum foil with the porous alumina film on top, showing the “barrier layer” between the aluminum substrate and the bottom of the pore, (B) after filling the pores with semiconductor to create buried nanostructures, (C) etching away the top layer of alumina in phosphoric acid to expose the tips of a few nanostructures, followed by deposition of 50-nm gold electrode by e-beam evaporation, (D) coating with an organic binder to provide mechanical stability during later processing steps, (E) after dissolving the aluminum substrate in  $\text{HgCl}_2$  to expose the barrier layer, (F) after etching the alumina bottom barrier layer in phosphoric/chromic acid to expose the other end of the nanostructures, (G) after evaporating gold on the bottom for the second electrode, and (H) after dissolving away the organic binder in a solvent and attaching wires for current measurement. *Source:* From Ref.<sup>[13]</sup>. American Institute of Physics.

Gold wires and silver paint are used to connect the Au contacts with the measuring equipment.

## QUANTUM WIRE BASED ROOM TEMPERATURE INFRARED PHOTODETECTORS

There are many device applications of electrochemically self-assembled nanostructures. They span such diverse areas as optics, electronics, magnetism, and superconductivity. In this section, we will discuss an application in sensors—infrared photodetectors.

Infrared photodetectors have widespread applications in remote sensing, terrain mapping, night vision, missile defense, automobile collision avoidance systems, etc. There are a large number of devices that detect infrared radiation. However, solid-state detectors such as  $\text{HgCdTe}$  (the workhorse of infrared photodetectors),  $\text{InSb}$  photodiodes, quantum well photodetectors, and Stranski–Krastanow-grown quantum dot photodetectors all suffer from one common shortcoming. They do not work at room temperature, but require cooling down to about 77 K. In contrast, we have produced self-assembled quantum wire photodetectors that work well at room temperature with a very high signal-to-noise ratio of 45 dB. Moreover, their conductance is so low that the noise-equivalent power is also very low (it is less than  $10^{-18}$  W at room temperature). That translates to an extraordinarily high detectivity  $D^*$  approaching  $10^{14}$   $\text{cm} \sqrt{\text{Hz}}/\text{W}$ .

There is one peculiarity in our infrared photodetectors—they are “inverse” photodetectors. Normal photodetectors are those whose conductance *increases* when illuminated with infrared radiation. Ours exhibit the opposite effect; the conductance *decreases* when illuminated with infrared radiation. This has to do with the origin of infrared photoreponse in our structures, which is quite different from that of other photodetectors. However, they are just as effective in photodetection because they successfully transduce an infrared signal into an electrical signal. They are ideally suited for focal plane arrays.

We prepared 10- and 50-nm diameter nanowires of  $\text{CdS}$  and  $\text{ZnSe}$  by the electrodeposition of the compounds in porous alumina templates produced by anodization in sulfuric and oxalic acid, respectively. The d.c. current–voltage characteristics of both 10- and 50-nm diameter wires are measured using an HP 4140B electrometer in the dark and in the presence of infrared radiation. The infrared (IR) source is the glowbar of a BOMEM Fourier-transform IR (FTIR) spectrometer, which produces radiation in the wavelength range of 1.8–50  $\mu\text{m}$  covering the photon energy range of 0.025–0.686 eV. The radiation is always normally incident on the sample surface (direction of



wave propagation is along the length of the wires to maximize absorption). The intensity of the radiation is not enough to produce any significant sample heating. Results of these measurements are shown in Fig. 3A. The resistance of all samples increase significantly, by up to a factor of 160, when exposed to IR radiation. This is not a sample heating effect, which can only produce a few percent change in resistance. In any case, the radiation intensity is low enough to avoid measurable sample heating. In Fig. 3B, we show the characteristics for a “blank” alumina film (with no

semiconductor in it) to ascertain that the photoresponse is indeed attributable to the semiconductor and not to the alumina. Note that the alumina shows a weak increase in the conductance, i.e., the behavior is opposite to that of semiconductors; the conductance is slightly larger, rather than smaller, when the IR radiation is on. The ratio of dark to illuminated current ( $I_{\text{dark}}/I_{\text{IR}}$ ) for 10- and 50-nm diameter CdS and ZnSe nanowires is shown in Fig. 3C as a function of applied voltage. This ratio is essentially the signal-to-noise ratio which approaches 45 dB at the highest biases used in this experiment.

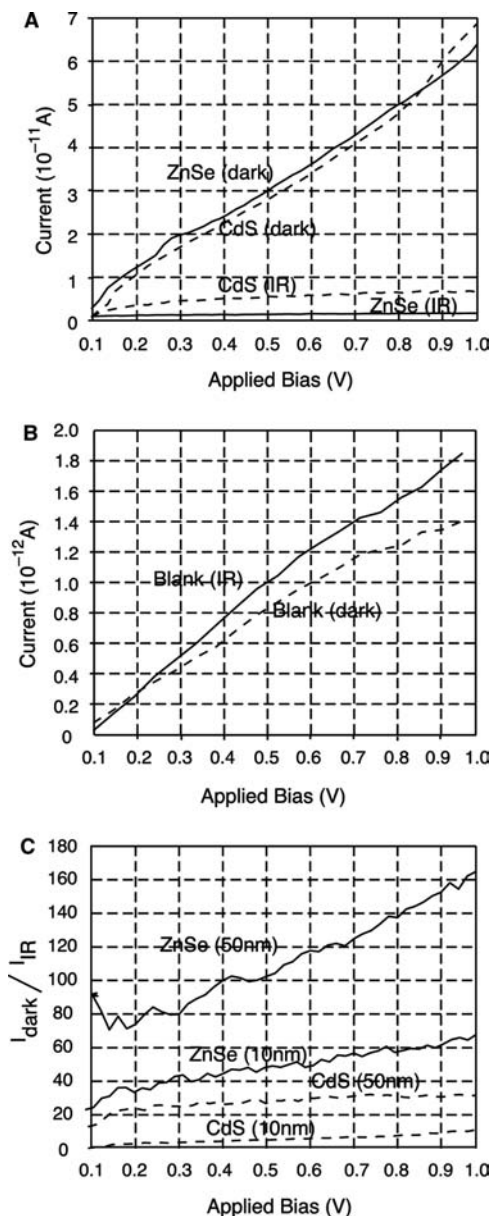


**Fig. 3** (A) The current–voltage characteristics of 10-nm diameter wires, (B) the current–voltage characteristics of blank alumina templates, and (C) the ratio of dark-to-illuminated current as a function of applied bias. Source: From Ref.<sup>[13]</sup>. American Institute of Physics.

## Origin of Photoresponse

The photoresistive behavior described here most likely accrues from photoassisted real-space transfer of electrons from the semiconductor nanowires into traps in the surrounding alumina. The majority carriers in the semiconductor nanowires are electrons as has been verified in the past by capacitance–voltage spectroscopy.<sup>[14]</sup> Many of these electrons absorb infrared photons and are excited to trap levels in the alumina where they become trapped and can no longer contribute to conduction. As a result, the resistance rises. This process is depicted in Fig. 4A. It is an indirect process in real-space, but the wavefunctions of electrons in the semiconductors penetrate a short distance into the alumina, thereby making the matrix element for this process significant at the interface between the semiconductor and alumina.

An interesting feature is that the larger-diameter (50 nm) wires show a stronger photoresistive effect (larger ratio of dark-to-illuminated conductance) than the smaller-diameter (10 nm) wires. This can be explained within a simple band picture (see Fig. 4B). When the wire is narrower, the subband level in the wire is higher up in energy so that fewer trap levels in the insulator are now *above* the subband level and accessible. Thus, fewer carriers can transfer out of the wire into the traps, and the photoresistive effect is weaker. This picture is substantiated by the IR absorption spectra for 10- and 50-nm diameter wires shown in Fig. 5A and B. The integrated absorption is always much larger for the wider-diameter wires showing that more trap levels are participating in their case.

Note that if there is a “dominant trap level” causing a dominant absorption peak, then it will be *red-shifted* in the narrower wire because the energy separation between the subband level and the trap states *decreases* as the wire becomes narrower. The red-shift is clearly observed in the CdS wires (Fig. 5A), where there is a dominant peak. On the other hand, the spectrum for ZnSe is much more complex (obviously because of a more complex distribution of traps in



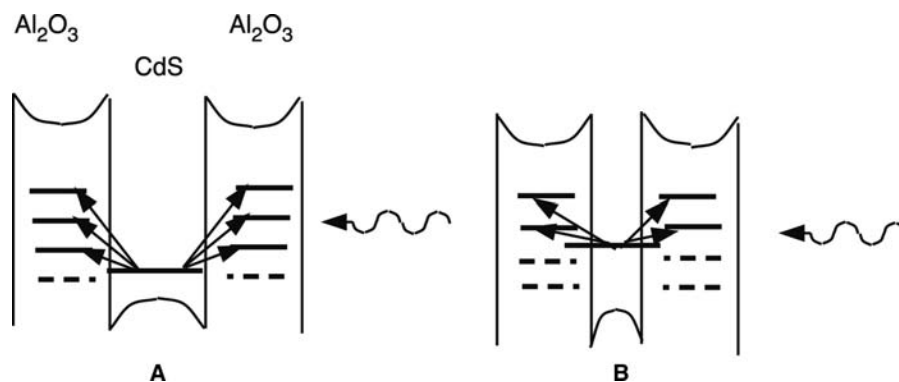


**Fig. 4** (A) Energy band diagram explaining photoabsorption of electrons from the semiconductor conduction band states into traps in the bandgap of alumina. (B) Fewer traps states are available as final states in narrower wires. Traps below the lowest subband level in the semiconductor wire (and therefore not accessible as final states) are shown with broken lines. *Source:* From Ref.<sup>[13]</sup>. American Institute of Physics.

energy space) and does not show a dominant peak, indicating that there is no single dominant trap level at the ZnSe/Al<sub>2</sub>O<sub>3</sub> interface. Little, if anything, is known about trap levels at the interface of electrodeposited semiconductors and anodic alumina. They are probably sensitive to electrodeposition and anodization conditions. There are trap states at the Au–semiconductor interface as well, but this interface is much smaller in area than the interface between

the semiconductor and alumina, so that these traps are unlikely to have a dominant effect.

In the past, a weak photoresistive effect, where the conductance dropped by a mere  $\sim 10\%$  (as opposed to the 160-fold drop reported here), was observed in *bulk* CdS and ZnSe samples,<sup>[15,16]</sup> but was attributed to an entirely different mechanism. There, electrons were photoexcited by the IR radiation from the valence band into intentionally created empty traps in the bandgap. The resulting holes in the valence band recombined with electrons in the conduction band to reduce the conductance by 10%. We do not have any intentionally created traps. Furthermore, capacitance voltage spectroscopy has shown<sup>[14]</sup> that the trap concentration is small enough in our samples that the Fermi level is completely unpinned. In any case, all traps in the bandgap must be filled because we have significant electron concentration in the conduction band, meaning that the Fermi level must be close to the conduction band edge. Thus, our effect cannot be explained by the same mechanism as that of Refs.<sup>[15,16]</sup> That mechanism is a two-step process: photoexcitation of electrons into traps (or, equivalently, photoemission of holes from traps), followed by recombination of those holes with electrons in the conduction band. Ours is a one-step process that only involves trapping and no recombination.

More recently, we have measured the current–voltage characteristics of a sample using an HP 4145B semiconductor parameter analyzer. A SiO filter was used to cut off any visible light from the infrared source. The results are shown in Fig. 6. In this particular sample, the signal-to-noise ratio is over 45 dB before breakdown occurs. There is some variability in the signal-to-noise ratio from sample to sample (in some samples, it is as low as 5 dB) and a concerted research effort will be required to standardize this nascent technology. The variability most likely accrues from the variability of the traps in the alumina, which are acquired during the processing steps. Traps are difficult to control, but a correct sequence of annealing

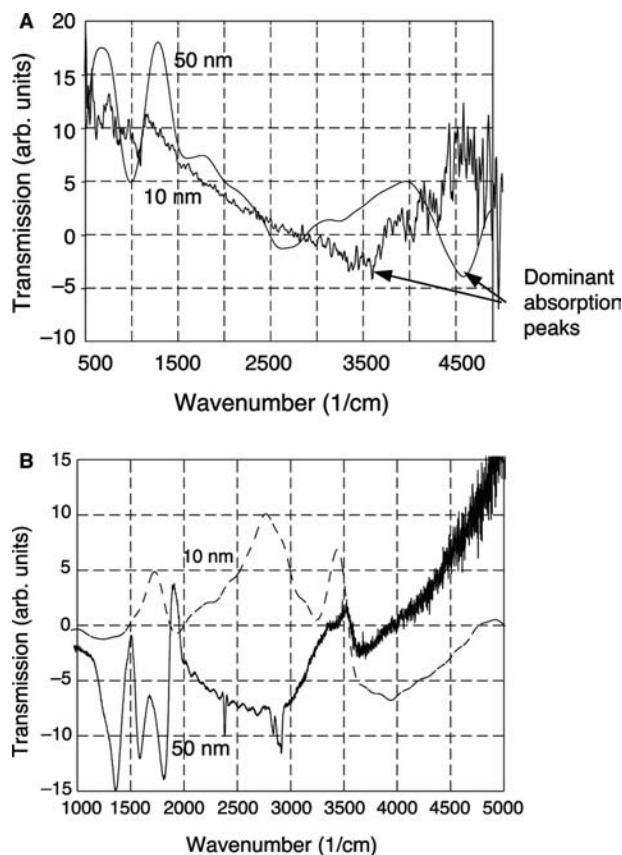


**Fig. 5** Infrared absorption spectra in (A) CdS nanowires and (B) ZnSe nanowires. In some cases, the spectrum was smoothed to eliminate spurious interference effects. *Source:* From Ref.<sup>[13]</sup>. American Institute of Physics.

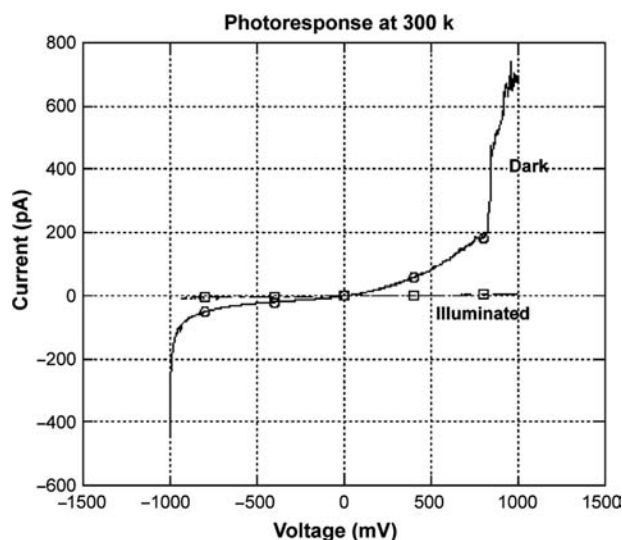


**Fig. 6** The current–voltage characteristic of a 50-nm diameter CdS wires in the dark and under infrared illumination. A filter was used to cut off all visible light.

steps may mitigate this problem somewhat. This is a topic of current research.

Another shortcoming of these photodetectors is the response time. Because the response time is associated with the response of traps, it is slow. Based on our measurements, we know that the photoresponse cannot be modulated any faster than 1 kHz (the lowest limit of our equipment); hence the response time is slower than 1 msec. Whether this becomes a serious limitation depends on the application. For most commercial applications, this is probably not a limitation at all.

## QUANTUM DOT IMAGE PROCESSORS

A holy grail of nanoelectronics is to find suitable paradigms where structures such as quantum dots and wires can perform signal processing tasks, particularly Boolean logic operations, such as transistors. However, this is a very tall order because transistors are a

unique find; they have properties that are not easy to duplicate. Two very important properties of transistors that are well appreciated in the electrical engineering community but seldom appreciated elsewhere are: 1) a transistor has a “gain” between its output and input terminals, i.e., the output can be a magnified (or amplified) version of the input. This property, which can be attained with three-terminal active devices such as transistors, is important for logic applications because it is necessary to restore logic signals that are corrupted by noise and other imperfections to their correct values. 2) Gain alone is not sufficient. Transformers have voltage gain, but nobody has successfully produced logic circuits with transformers alone. An additional property that is needed is “isolation” between the input and output terminals of the device, so that the input signal determines the output signal and not the other way around. Electrical engineers often call this property “unidirectionality,” that is, logic signal flows unidirectionally from the input terminal to the output terminal. Transistors have this property. Any undergraduate student of electrical engineering is familiar with the small signal equivalent model of a transistor, which is shown in Fig. 7. There is a dependent source at the output end, which depends on the input signal. However, the input does not depend on the output. This model follows from Ebers–Moll equations describing a transistor, and if one traces back the origin of this unidirectionality, one will ultimately find that this unidirectionality comes about because of the Fermi distribution of carriers (electrons and holes) in a transistor’s emitter (or source) that is driven not too far from equilibrium. Thus, the unidirectionality has its origin in thermodynamics (Fermi–Dirac statistics). Thermodynamics has a character trait to cause unidirectionality. It is somewhat responsible for the unidirectionality of time and it is also responsible for the unidirectionality of signal propagation in a transistor!

Many proposals have been forwarded (and published in major journals) to replace the transistor with quantum dots and other exotic devices, in hopes that

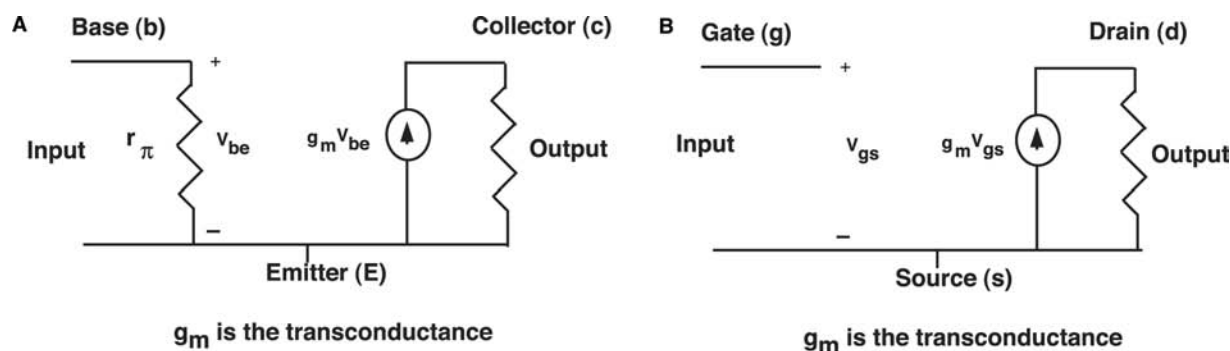


**Fig. 7** The simplest small signal equivalent models of a transistor: (A) bipolar junction transistor, (B) field effect transistor.

they will perform logic operations. There are widely publicized but flawed proposals for logic gates realized with quantum dots. Unfortunately, most of these proposals are wrong because these exotic devices do not have the properties of transistor, namely gain and unidirectionality.<sup>a</sup> As of now, nobody has made logic gates with quantum dots in spite of all the initial tall claims. Nonetheless, it is still attractive to look for ways to replace transistors with quantum dots because there can be tremendous savings in device density on a chip (quantum dots are much smaller than transistors), power dissipation (quantum dots typically dissipate much less power than a transistor), and cost (quantum dots are much easier to fabricate than a transistor).

### Quantum Dot–Based Neuromorphic Architectures

In 1995, Roychowdhury and coworkers proposed a revolutionary new idea for utilizing quantum dots for signal processing and computation.<sup>[17,18]</sup> Their scheme was not based on logic circuits, so that they did not need the properties necessary to build logic circuits. Instead, they proposed to build a neural network architecture. They also realized that making connections to quantum dots will be a nearly insurmountable challenge because quantum dots are so small that aligning multiple (or for that matter *any*) contact to them is very difficult. They overcame this problem by proposing a locally interconnected architecture, where every device is connected only to its nearest neighbors. Thus, in a rectangular lattice structure, every device will be connected to at most four nearest neighbors. The connections did not have to be metallic lines (wires) either. They could simply be the resistive and capacitive couplings between neighboring quantum dots that exist whenever the dots are embedded in a semiinsulating medium. For certain applications, the exact values of the resistances and capacitances of these couplings also did not matter so much as long as they were relatively uniform. Therefore, this architecture did not present much of a fabrication challenge at all to self-assembly (in fact, it was partly inspired by advances in self-assembly). We now describe this architecture.

Consider the system shown in Fig. 8. It consists of a two-dimensional periodic array of nanometer-sized metallic islands (or clusters), with nearest neighbor electrical interconnections, self-assembled (and self-aligned) on mesas whose current–voltage characteristics (for vertical transport) have a *non-monotonic* non-linearity.

<sup>a</sup>There are five basic requirements for a logic device. They are listed in the textbook: David A. Hodges and Horace G. Jackson, *Analysis and Design of Digital Integrated Circuits*, 2nd edition, McGraw-Hill, New York, 1988, Chapter 1, p. 2.

The above system displays a fundamental kind of computational effect based on non-linear cooperative charge interactions between the dots and the underlying non-ohmic substrate. A number of publications<sup>[17–20]</sup> have shown that this system realizes the content addressable models of associative memory, can exhibit image-processing capability, and can solve combinatorial optimization problems. It is a *neuromorphic network* inspired by the simple realization that, in any large-scale system, comprising tens of billions of nanoscale devices, there will be inherent randomness. It is easier to exploit that in realizing computational activity through collective computational models, than to strive against it to realize logic. Moreover, this network is massively parallel and fault-tolerant. Even a 100% variation in the size of an individual device is quite tolerable. The relative insensitivity to size variation stems from the fact that the size determines the capacitance of an individual device. A 100% variation in the size of an individual device will result in a similar variation in the capacitance and this does not affect the performance of the circuit very much as a whole because of the “collective” nature of the computation. Here the collective activities of all devices acting cooperatively matter, rather than the characteristic of a single device. Similar ideas were later proposed by Wu, Shibata, and Amemiya.<sup>[21]</sup>

We will not discuss the detailed theory of this architecture because that has already been described in Refs.<sup>[17–20]</sup>. Instead, we will focus on the realization of this system based on our technique of electrochemical self-assembly.

### Self-Assembling a Neural Network

Basically, the quantum dot network of Fig. 8A has two main components: 1) a 2-D periodic array of metallic islands, each interfaced with a mesa (resistor) displaying a negative differential resistance, and 2) a resistive/capacitive coupling between nearest neighbor islands. This network can be self-assembled electrochemically. We start with a  $n^+$  silicon substrate, evaporate a thin titanium layer, and evaporate or sputter a 1- $\mu\text{m}$ -thick layer of aluminum on it. The titanium layer allows the aluminum layer to adhere to the surface. Then, we anodize the aluminum in sulfuric or oxalic acid to convert it to a porous alumina film containing a *nearly periodic* regimented array of nanopores. When all of the aluminum is anodized into a porous alumina layer, the anodizing current begins to change rapidly, at which point the anodization is terminated. Then, we remove the alumina “barrier layer” by soaking in phosphoric acid. Next, we sequentially electrodeposit a semiconductor (e.g., CdS) and a metal (e.g., Cu) selectively within the pores. The metal dots are then

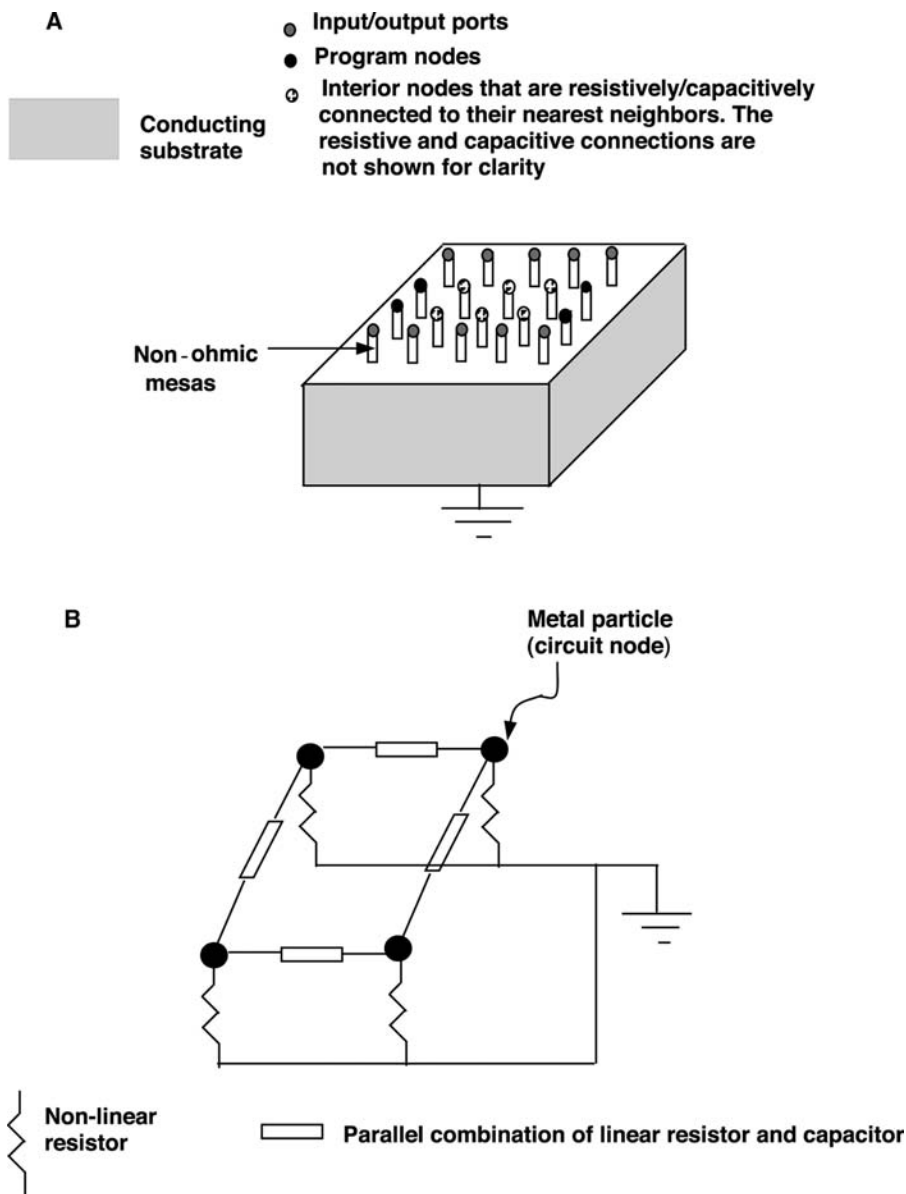


**Fig. 8** (A) A generic array of metallic islands deposited on a non-ohmic layer, which has been grown on a conducting substrate. It is assumed that all islands have direct resistive and capacitive links to nearest neighbors. A subset of the islands serves as program nodes, which are driven by external current sources. Another subset of islands serves as input/output ports, and the remaining islands introduce complexity to the system through non-linear conductive links to the substrate. The substrate non-linearity could arise, e.g., from resonant tunneling, which causes the substrate current-voltage characteristic to have a *non-monotonicity*. (B) A non-planar circuit representation of the network.

partially exposed by controlled etching of the alumina in phosphoric acid. Neighboring dots are electrically isolated by the intervening alumina layer, which is a semiinsulator. In the case of sulfuric acid anodization, the thickness of the semiinsulating layer is about 10 nm and in the case of oxalic acid anodization, the thickness is about 20 nm. Once complete, the structure is a self-assembled experimental realization of the system shown in Fig. 8A.

### Measurements of Circuit Parameters

#### Interdot resistance

To obtain an estimate for the interdot resistances, we need to measure the resistance of the alumina layer

separating neighboring pores. Two contact pads, spaced  $100\ \mu\text{m}$  apart, were delineated on the surface of a  $1\text{-}\mu\text{m}$ -thick porous alumina film produced by anodization of aluminum in sulfuric acid. The pores were filled with a semiconductor. The resistance measured between the pads, which were  $1\ \text{mm}$  wide, was about  $80\ \text{M}\Omega$ .<sup>[22]</sup> In this experiment, the effective width of the alumina between the pads was approximately one-half of the distance between the pads, namely  $50\ \mu\text{m}$ . Therefore, the resistivity of the alumina is  $80\ \text{M}\Omega \times 1\ \text{mm} \times 1\ \mu\text{m}/50\ \mu\text{m} = 160\ \text{K}\Omega\text{cm}$ . Conduction through the alumina was found to be ohmic<sup>[22]</sup> (probably conduction takes place through impurity bands in the alumina), so that the alumina resistivity can be assumed to be a constant. Therefore, when the alumina layer thickness between neighboring pores is 10 nm and the pore diameter is 10 nm (sulfuric acid

anodization), the interdot resistance will be of the order of  $1.6\text{ G}\Omega$ . If the anodization is carried out in oxalic acid instead of sulfuric acid, the alumina barrier between neighboring pores is  $20\text{ nm}$  wide and the pore diameter is  $50\text{ nm}$ . In that case, the interdot resistance is  $640\text{ M}\Omega$ . These parameters can change somewhat, depending on anodization conditions.

### Negative Differential Resistance

When metals or semiconductors are electrodeposited within pores, they tend to break up in small crystalline grains. Each grain is a few nanometers in diameter.<sup>[23]</sup> Neighboring grains are separated by amorphous regions, which are also a few nanometers thick. The amorphous regions are much more resistive than the crystalline regions, so that an amorphous–crystalline–amorphous combination acts like an effective double-barrier resonant tunneling diode. A series of these diodes will result in a “pass-bands” of energies separated by “stop-bands.” As a result, we expect the current–voltage characteristic to exhibit a weak negative differential resistance. In fact, we have observed negative differential resistance in vertical conduction through CdS nanowires electrodeposited within  $50\text{-nm}$  pores produced by anodization in oxalic acid. Two current–voltage characteristics showing negative differential resistance are given in Fig. 9. They were measured at room temperature. In the first sample, we probed about 100 mesas in parallel.<sup>[24]</sup> The peak-to-valley ratio is 1.5:1 and the peak current is  $1.5\text{ nA}$  for the 100-mesa ensemble. Therefore, the peak current per dot is  $15\text{ pA}$ . In the second sample shown in Fig. 9, we probed about 10 wires and observed *multiple* negative differential resistance peaks at room temperature.

### Dot Capacitance

In the past, we have observed room-temperature single electron charging (Coulomb blockade) effects in these systems.<sup>[24]</sup> From those measurements, we estimate that the dot-to-substrate capacitance (i.e., the capacitance of the CdS nanowire) is of the order of  $0.5\text{ aF}$  in sulfuric acid anodized templates. This value agrees nicely with what we would have calculated if we viewed the CdS wire as a parallel-plate capacitor. The wire has the shape of a cylinder with a diameter of  $10\text{ nm}$  and height of  $1\text{ }\mu\text{m}$ . The relative dielectric constant of bulk CdS is 5.4. Therefore, the “parallel-plate” capacitance of the mesa is  $0.1\text{ aF}$ , which is of the same order as what we measured. We have also observed Coulomb blockade in the oxalic acid anodized structures. There, the Coulomb blockade picture is somewhat more complicated because the semiconductor within the pores breaks up into small crystalline grains separated by

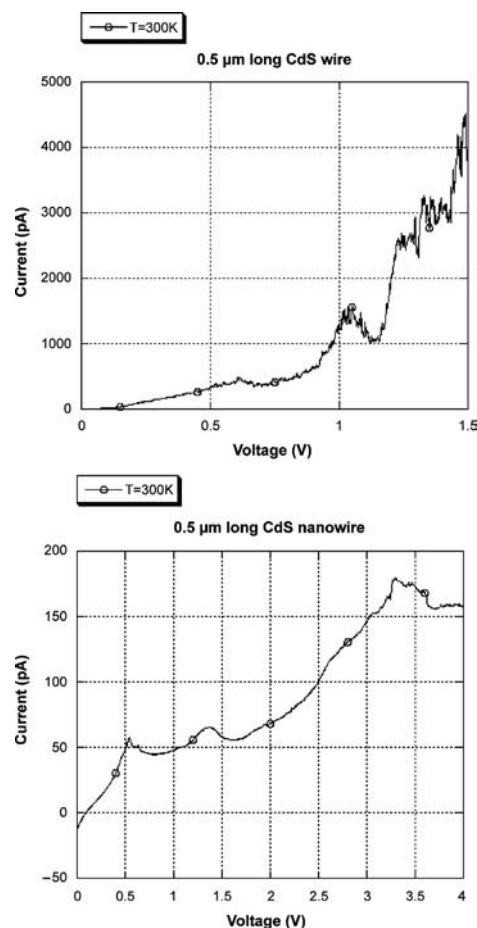


**Fig. 9** The current–voltage characteristics of two arrays of  $0.5\text{-}\mu\text{m}$ -long cylindrical CdS quantum wire samples of diameter  $50\text{ nm}$  showing negative differential resistance at room temperature. In the top figure, about 100 wires in parallel are probed, and in the bottom figure, roughly 10 wires in parallel are probed. The non-zero current at zero voltage in the bottom figure is an artifact of the measurement process. The non-zero current is purely a displacement current that flows through sample at zero voltage when the voltage source is scanned at a finite rate. The capacitance of the sample causes a displacement current  $C(dV/dt)$  to flow through the sample at zero voltage. In the top figure, this current is not visible because the current magnitude is more than 20 times larger. The positions and heights of the peaks change with repeated electrical cycling and finally after many cycles may tend towards stabilizing. The data shown here is after 3 cycling. Ref.<sup>[25]</sup> shows the data after many cycles when the I–V characteristics tend towards stabilizing. However, the peak-to-valley ratio surprisingly does not change perceptibly from one run to another.

amorphous regions. Consequently, they form a series of capacitors (or tunnel junctions). In fact, we have observed Coulomb staircase in oxalic acid anodized systems<sup>[24]</sup> because they comprise multiple capacitors in series. Based on the observed Coulomb staircase, we found that the effective dot-to-substrate capacitance in

oxalic acid anodized templates is actually 5 times smaller than what it is in sulfuric acid anodized templates, even though the pore area in oxalic anodized templates is 25 times larger. This apparently unexpected result can be explained by the fact that, in the case of oxalic acid templates, the dot-to-substrate capacitance is a series combination of many capacitors, which reduces the effective capacitance between the dot and the substrate.

### The Concept of “Superdot” for Image-Processing Applications

The pitch of the 2-D quantum dot array (dot diameter plus interdot separation) in oxalic acid anodized templates is about 70–80 nm. Considering that the edge of a pixel in an image should be perhaps 10 times the wavelength of light (we will assume light of wavelength 550 nm which is in the middle of the visible range), therefore the edge of a pixel is  $5500/70 = 80$  times larger than the pitch of the quantum dot array. Therefore, approximately  $80 \times 80 = 6400$  dots will represent a pixel. Thus, we will assume that a dot cluster of about 6400 dots can be approximated as an equivalent “superdot,” which will act as a single node interacting with the light wave in image-processing applications. Hence, its dynamical behavior can be modeled by treating it as a single dot if the circuit parameter values are modified accordingly. This means that the superdot-to-substrate capacitance is 6400 times the single dot capacitance, i.e.,  $6400 \times 0.5 = 3.2$  fF, the intersuperdot resistance is 80 times smaller than the interdot resistance (because the edge of the superdot contains 80 single dots), i.e.,  $640/80 = 8$  M $\Omega$ , and the peak current for a superdot is  $6400 \times 15$  pA = 0.1  $\mu$ A. The peak-to-valley ratio can be improved by annealing the structures at some optimum temperature to promote uniform grain growth. This requires a systematic study, which is reserved for future work. It stands to reason that the peak to valley ratio can be improved to at least 10:1. One parameter that we have not been able to measure is the interdot capacitance. Therefore, we will estimate it assuming a parallel-plate geometry for simplicity. The relative dielectric constant of alumina is roughly 4; therefore, the interdot capacitance is 5 aF if the anodization is carried out in oxalic acid. Here we have assumed that the quantum dot is 50 nm wide for oxalic acid anodization and 50 nm thick (to electrodeposit 50 nm of metals within the pores takes only a few seconds of electrodeposition). Based on this, the inter-superdot capacitance is 4 fF for oxalic acid anodization. The circuit parameters for the superdot are given in Table 1.

Circuit theorists have simulated the system architecture described here for image-processing applications

**Table 1**

Circuit parameter	Value
Superdot-to-substrate capacitance	3.2 fF
Intersuperdot capacitance	4 fF
Intersuperdot resistance	8 M $\Omega$
Peak current in a superdot	0.1 $\mu$ A
Valley current in a superdot	0.01 $\mu$ A

using the circuit parameter values of Table 1.<sup>[25]</sup> They found that the simple self-assembled architecture, in its most primitive form, can perform image-processing tasks. The natural dynamics of the system result in a response similar to edge detection. A preprocessing of input images may be necessary to handle more specific tasks. The response time of the circuits is few tens of nanoseconds. Together with the immense processing density, this makes the quantum dot array a fast and high-resolution image processor candidate for several applications.

### CONCLUSION

In this entry, we have provided a glimpse of how electrochemically self-assembled templates and nanostructures can be used for various device and circuit applications. This is a rapidly maturing field and can soon emerge as a competitive technology for high-throughput nanosynthesis.

### ACKNOWLEDGMENTS

Many sections of this review entry have been excerpted from work published by the author and coworkers. I am indebted to our Russian collaborators Drs. S. Tereshin, A. Varfolomeev, and D. Zaretsky, who measured the interdot resistances; Drs. Latika Menon and Nikolai Kouklin, who self-assembled many of the structures and made current–voltage, photoresponse, and capacitance–voltage measurements; Dr. Koray Karahaliloglu and Prof. Sina Balkir for circuit simulations; and Prof. Vwani Roychowdhury for stimulating discussions on the image-processing architecture. The atomic force micrograph in this entry was provided by Dr. Feng Yun and the current–voltage characteristics showing negative differential resistance, as well as some photoresponse data, were provided by Mr. Sandipan Pramanik.

Various facets of this work were supported by the Army Research Office, National Science Foundation, Office of Naval Research, and the State of Nebraska under the Nebraska Research Initiative.



## REFERENCES

1. Bandyopadhyay, S.; Miller, E. *Handbook of Advanced Electronic and Photonic Materials and Devices*; Nalwa, H.S., Ed.; Academic Press: San Diego, 2000; Vol. 6, 1–27. Chapter 1 and references therein.
2. Moskovitz, M. US Patent 5,202,290, April 1993.
3. AlMawlawi, D.; Coombs, N.; Moskovitz, M. *J. Appl. Phys.* **1991**, *70*, 4421.
4. Masuda, H.; Satoh, M. *Jpn. J. Appl. Phys.* **1996**, *35*, L126.
5. Masuda, H.; Fukuda, K. *Science* **1995**, *268*, 1466.
6. Menon, L.; Zheng, M.; Zeng, H.; Sellmyer, D.J.; Bandyopadhyay, S. *J. Electron. Mater.* **2000**, *29*, 510.
7. Kawai, S.; Ueda, R. *J. Electrochem. Soc.* **1975**, *122*, 32.
8. Zangari, G.; Lambeth, D.N. *IEEE Trans. Magn.* **1997**, *33*, 3010.
9. Wegrowe, J.E.; Kelly, D.; Fromck, A.; Gilbert, S.E.; Ansermet, J.-Ph. *Phys. Rev. Lett.* **1999**, *82*, 3681.
10. Bandyopadhyay, S.; Miller, A.E.; Chang, H.-C.; Banerjee, G.; Yuzhakov, V.; Yue, D.-F.; Ricker, R.E.; Jones, S.; Eastman, J.A.; Baugher, E.; Chandrasekhar, M. *Nanotechnology* **1996**, *7*, 360.
11. Balandin, A. *Ph.D. Thesis*; University of Notre Dame, 1996.
12. Routkevich, D.; Biglioni, T.; Moskovitz, M.; Xu, J.M. *J. Phys. Chem.* **1996**, *100*, 14037.
13. Kouklin, N.; Menon, L.; Wong, A.Z.; Thompson, D.W.; Woollam, J.A.; Williams, P.F.; Bandyopadhyay, S. *Appl. Phys. Lett.* **2001**, *79*, 4423.
14. Kouklin, N.; Bandyopadhyay, S. *2000 IEEE International Symposium on Compound Semiconductors*; IEEE Press: Piscataway, NJ, 2000; 303–308.
15. Schoenbach, K.H.; Lakdawala, V.K.; Germer, R.K.F.; Ko, S.T. *J. Appl. Phys.* **1988**, *63*, 2460.
16. Germer, R.K.F.; Schoenbach, K.H.; Pronko, S.G.E. *J. Appl. Phys.* **1988**, *64*, 913.
17. Bandyopadhyay, S.; Roychowdhury, V.P.; Wang, X. *Phys. Low-Dimens. Struct.* **1995**, *8–9*, 29.
18. Roychowdhury, V.P.; Janes, D.B.; Bandyopadhyay, S.; Wang, X. *IEEE Trans. Electron Devices* **1996**, *43*, 1688.
19. Roychowdhury, V.P.; Janes, D.B.; Bandyopadhyay, S. *Proc. IEEE* **1997**, *85*, 574.
20. Bandyopadhyay, S.; Roychowdhury, V.P.; Janes, D.B. *Quantum Based Electronic Devices and Systems*; Dutta, M., Stroschio, M.A., Eds.; World Scientific: Singapore, 1998; 1–36. Chapter 1.
21. Wu, N.J.; Shibata, N.; Amemiya, Y. *Appl. Phys. Lett.* **1998**, *72*, 3214.
22. Kouklin, N.; Bandyopadhyay, S.; Tereshin, S.; Varfolomeev, A.; Zaretsky, D. *Appl. Phys. Lett.* **2000**, *76*, 460.
23. Zeng, H.; Skomski, R.; Menon, L.; Liu, Y.; Bandyopadhyay, S.; Sellmyer, D.J. *Phys. Rev., B* **2002**, *65*, 134426.
24. Kouklin, N.; Menon, L.; Bandyopadhyay, S. *Appl. Phys. Lett.* **2002**, *80*, 1649.
25. Karahaliloglu, K.; Balkir, S.; Pramanik, S.; Bandyopadhyay, S. *IEEE Trans. Elec. Dev.* **2003**, *50*, 1610–1616.

# Nanobiological Sensors

Nathaniel Cady

Anand Gadre

Alain E. Kaloyeros

*College of Nanoscale Science and Engineering, State University of New York at Albany,  
Albany, New York, U.S.A.*

## Abstract

Nanobiological sensors are playing an increasingly important role in diagnosing disease, monitoring biological and chemical processes, and elucidating important biological and physical mechanisms. Nanotechnology has advanced our ability to create biosensors that interrogate, interact with, and examine biological targets at the molecular scale. This entry discusses the basic principles of biological sensing and illustrates how nanotechnology and nanoscale material and process technologies have helped shape a new class of “nanobiosensors.” Similar to larger-scale biosensors, nanobiosensors rely on two basic components, a recognition element and a signal transduction element. To illustrate the role of nanotechnology in these elements, specific biological targets and mechanisms of signal transduction are presented and discussed. A strong emphasis is placed on how nanomaterials can enhance both specificity and sensitivity in these systems.

## INTRODUCTION

Nanotechnology is defined as the ability to manage and control individual atoms and molecules at the nanoscale, leading to the design and fabrication of real-life functional physical, chemical, and biological systems at the macroscale. Nanotechnology offers a host of new materials and novel functionalities that can be exploited for biological and chemical sensors. In many cases, materials at the nanoscale have unusual optical, magnetic, catalytic, and mechanical properties, which differ greatly from their bulk material counterparts.<sup>[1]</sup> These unique properties are beginning to be harnessed for the development of novel sensors and transduction systems with improved spatial resolution, reduced detection volumes, higher sensitivity levels, and faster response times. Since a majority of biological processes occur at the nanoscale, these characteristics are highly desirable for biological sensing applications. In a typical cell, most of the major building blocks are nanoscale molecules that interact at nanometer length scales. Cell membranes and DNA are only a few nanometers wide, while the largest cellular proteins can be tens of nanometers in diameter. Such small dimensions require nanoscale sensors to accurately and sensitively probe highly complex biological systems.

Nanoscale biological sensors, or nanobiosensors, are biological sensing systems that have at least one feature size of 100 nm or smaller or perform measurements over nanometer length scales. Like most sensors, nanobiosensors are composed of both a recognition element and a transduction element, which define their mode of operation. The recognition element, which is often a biological molecule or biologically (chemically)

reactive compound, specifies the interaction between the sensor and the biological target. The transduction element converts the recognition event into a measurable signal through electrical, optical, or mechanical processes. To date, nanobiosensors have utilized each of these signal transduction mechanisms, although a majority has been based on optical and electrical mechanisms. In what follows, this description of nanobiosensors will first cover the range of biological targets that can be detected and will then outline specific transduction mechanisms that have been used. Examples of current nanobiosensor technologies will be covered for each transduction mechanism.

## BIOLOGICAL TARGETS

In its simplest form, a biosensor is a biological sensing element coupled to a transducer that generates a signal proportional to the concentration of its target.<sup>[2]</sup> Biosensors can be used to detect specific biological molecules, the products of biological reactions, or even whole cells. Nanobiosensors operate at a smaller length scale than conventional biosensors, giving them distinct advantages in precision, accuracy, sensitivity, and response time. Recently described nanobiosensors have been used to detect a wide range of biological targets including nucleic acids, proteins, lipids, and carbohydrates. To this end, each of these potential targets is described briefly.

Nucleic acids, which include DNA and RNA, are the information storage molecules of all biological organisms. Using four different nucleotide building blocks, adenine, guanine, cytosine, and thymine

(replaced by uracil in RNA), nucleic acids have the ability to encode a vast number of sequences that are responsible for the construction of individual proteins and entire organisms. A typical double-stranded DNA strand has a width of 2 nm (a nanometer is a billionth of a meter) and a length, which is dependent on the number of nucleotides in its sequence. In the past two decades, understanding of DNA structure and function has grown and the amount of sequence information has increased exponentially.

This understanding is useful for a variety of reasons, including identification of harmful mutations and detection of potentially dangerous microorganisms. For sensor applications, nucleic acids can be specifically captured through sequence-specific hybridization between a target strand and an immobilized capture strand. Nucleic acids are compatible with various amplification strategies, including the polymerase chain reaction (PCR), which can be used to generate multiple copies of the target. Such amplification can be particularly useful for nanobiosensors that have limited interaction volumes with limited numbers of target molecules for detection.

Proteins, which are composed of long chains of amino acids, can also be detected using nanobiosensing strategies. Proteins can serve a variety of functions within living organisms, including structural, catalytic, and regulatory roles. Other proteins mediate biological interactions and can bind or attach to specific molecular targets. Small proteins can be as small as a few nanometers in diameter while larger proteins can approach tens of nanometers in size. This size makes proteins amenable for both attachment to nanobiosensors, and detection by these systems. Antibodies, which are of particular interest for many biosensors, are proteins with unique specificity to a nearly infinite number of potential targets. They can be used as specific recognition elements for the detection of chemical compounds, biological molecules, or even inorganic materials. Enzymes, which are catalytic proteins, are also useful for biosensing since they can mediate biochemical reactions that produce detectable reaction products. Multiple biosensor technologies utilize immobilized enzymes as high specificity biological recognition elements and catalysts for the detection of biochemical reaction substrates. Structural and regulatory proteins are also good biosensing targets since they can be used as unique biological indicators. Cellular production of certain proteins can indicate the status and viability of a biological system, while the presence of particular proteins on the surface of a cell or virus can be used for identification.

Lipids and carbohydrates are essential components of many biological systems and can be used for identification and as biological indicators. Cell membranes and viral envelopes are constructed from lipid bilayers

that form an amphiphilic, water impermeable barrier. These lipid bilayers can be studded with membrane-soluble proteins that serve as receptors, pores, or regulatory elements and are excellent biosensing targets. Typical lipid bilayers in cells have a thickness of approximately 2 nm and can span large areas as continuous films. Carbohydrates, on the other hand, are typically small organic molecules (6 carbon rings such as glucose) but can be polymerized into linear and branching chains known as polysaccharides.

In addition to being energy storage molecules, carbohydrates can often be found in the form of polysaccharides, which are linked to both proteins and lipids for a variety of purposes. In Gram-negative bacteria, lipopolysaccharides (LPS) are commonly found on the external face of the outer membrane. These LPS molecules contain complex polysaccharide chains that are often strain-specific and can be used for identification purposes. Eukaryotic cells (including animals, plants, and some fungi) commonly attach carbohydrates to proteins in a process called glycosylation. These uniquely attached carbohydrates can also be used for identifying specific proteins and to differentiate different cell types or whole organisms. Carbohydrates can also be used as indicators of metabolic activity for living systems. For instance, glucose, which is used by many cells for energy production, can be detected and quantified with enzymatic biosensors.

Nanobiosensors have also been used to probe and analyze whole cells. Owing to their small size, these whole cell analytical sensors can be used without harming cells and without disrupting normal cellular functions. Whole cells can be attractive targets for high-sensitivity applications since they can contain large concentrations of target biomolecules and their larger size can affect more substantial transduction events than smaller biomolecular targets. Bacterial (prokaryotic) cells are typically within the 0.5–5  $\mu\text{m}$  size range, while plant, animal, and fungal (eukaryotic) cells can range from 1  $\mu\text{m}$  to 100  $\mu\text{m}$  in size. At this size scale, cellular analyses with nanobiosensors typically involve the manipulation of a single cell, or interrogation of individual components of the cell. This can yield important information about cellular structure and function, which would not be possible with macro-scale and microscale analysis (see Fig. 1).

## ELECTRICAL NANOBIOSENSORS

The use of nanoscale materials (nanomaterials) for electrochemical biosensing has seen an explosive growth in the past 5 years and there are several comprehensive reviews available that cover the use of nanomaterials for amperometric or voltammetric electrochemical detection.<sup>[3–7]</sup> Most developmental efforts

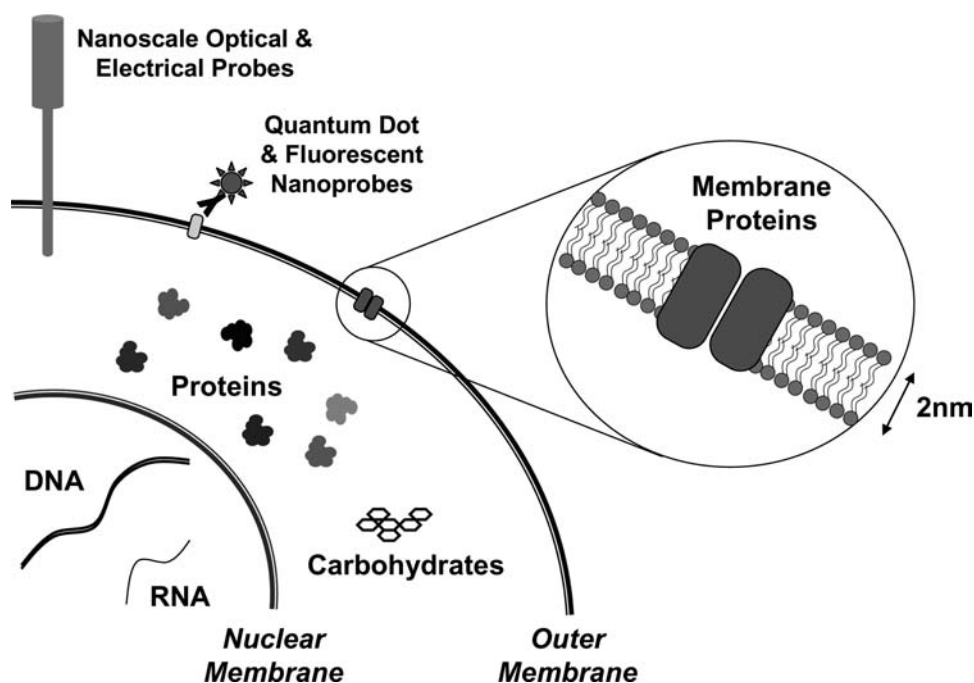


**Fig. 1** An example of a generic eukaryotic cell structure and key biological targets for nanobiosensors. Physical nanoprobe, such as optical and electrical fibers, can be used to make intracellular and extracellular measurements, while diffusible probes, such as fluorescent quantum dots, can be used for protein, carbohydrate, and nucleic acid labeling.

for electrochemical nanobiosensors have focused on the use of nanomaterials for electrode fabrication and for direct wiring of biological molecules to the sensor. This use of nanomaterials is aimed at promoting electrochemical reactions and amplifying the signal of biorecognition events. These systems can integrate protein machinery for sensitivity and specificity, peptide, or nucleic acid chemistry for aligning the various electron-transducing elements, and nanoelectrodes for enhancing sensitivity of electrical detection. The fundamental basis of electrochemical biosensing is to electrically monitor biochemical processes, including biochemical reactions, and the detection of electrically charged biomolecules. Many enzymatic biochemical reactions result in the oxidation or reduction of chemical compounds.

When coupled to an electrode surface, electrons can be transferred from the compound to the electrode (or vice versa), resulting in a measurable change in electrical current. Electrically charged biomolecules can also be detected using potentiometric methods. If the proper recognition elements (such as proteins or nucleic acids) are linked to an electrode, binding events with charged biomolecular targets could result in a measurable change in electrical potential. Incorporating nanoscale components into these types of electrochemical sensors enables active components of the sensor to approach the size and scale of biological molecules. This section focuses on electrochemical

nanobiosensors developed for detecting biologically relevant compounds.

Sensors based on carbon nanotubes are an excellent example of how nanotechnology can be used for electrochemical sensing applications. The advantages of using carbon nanotubes include high surface area, favorable electronic properties and electrocatalytic effects. These properties make nanotubes attractive for the construction of electrochemical enzyme-based biosensors. Carbon nanotube biosensors for glucose detection have utilized immobilized enzymes, such as glucose oxidase, to catalyze glucose oxidation in proximity to the nanotube.<sup>[8]</sup> When glucose is oxidized, electrons are transferred to the nanotube, generating a measurable electrical current.

Electrochemical nanobiosensors have also been based on conductive nanoparticles that are heavily functionalized with DNA molecules that could be used for the detection of specific target DNA sequences.<sup>[9]</sup> Hybridization events between target DNA and immobilized DNA can result in nanoparticle condensation. If condensation occurs between two electrodes, the conductivity of the condensate can be measured, yielding information about the original concentration of target DNA. Alternative nanomaterials, such as nanowire arrays can also be used for nanobiosensing applications. Nanowires can be formed by template synthesis methods involving electro- and electroless depositions that can be used to develop electrochemical

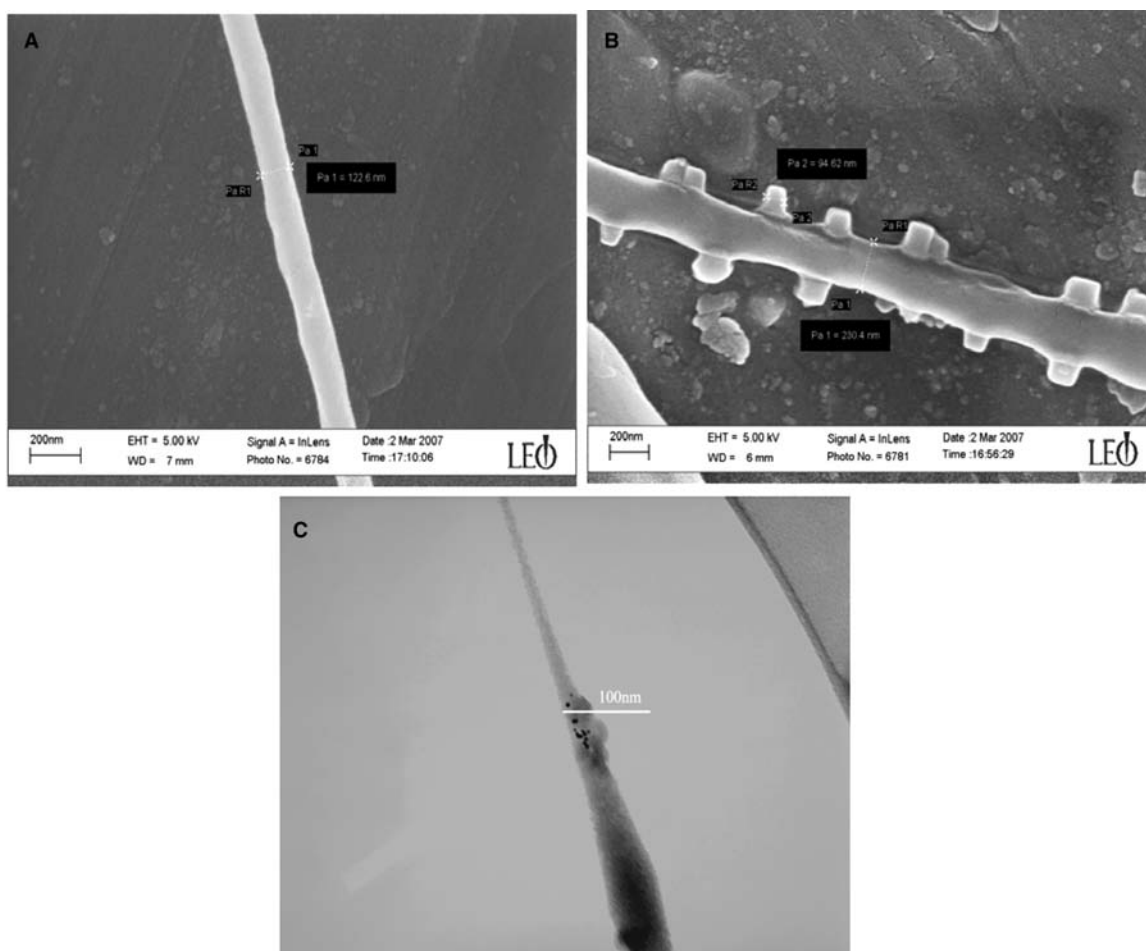


**Fig. 2** (A) Scanning electron micrograph (SEM) of Chitosan + PEO nanofibers without gold nanoparticles, (B) SEM of Chitosan + PEO nanofibers with gold nanoparticles, (C) transmission electron micrograph (TEM) of Chitosan + PEO nanofibers with gold nanoparticles.

nanobiosensors for the detection of hydrogen and *E. coli* bacteria.<sup>[10]</sup>

Another class of electrochemical nanobiosensors includes sensors based on electrospun polymeric nanofibers. Electrospun nanofibers are high surface area filaments that range from 35 nm to few hundreds of microns in diameter and can be formed from both conducting and non-conducting polymers. Electrospun nanofibers can be functionalized with capture molecules (including nucleic acid probes, antibodies, proteins) for electrical detection of various biomolecules. Such sensors can report real-time electrical signals indicative of electrically charged biological targets using conductive-insulating polymeric nanofibrous composites. Furthermore, the conductivity of such nanofibers can be enhanced by incorporating either gold or silver nanoparticles during the electrospinning process. Figure 2 shows the incorporation of gold nanoparticles (15–20 nm in diameter) into the Polyethylene Oxide (PEO) + Chitosan composite nanofibers.

Figure 2A shows a scanning electron microscope (SEM) image of PEO + chitosan nanofibers without any gold nanoparticles, while Fig. 2B shows the SEM image of nanofibers with gold nanoparticles, and Fig. 2C shows a transmission electron microscope (TEM) image of nanoparticles dispersed in the nanofiber matrix.

Investigations concerning the sensing performance as a function of surface modifying groups, polymer chemistry, nanofiber diameter, degree of alignment, pore size, and surface functionalization is currently being undertaken to achieve high levels of sensitivity, selectivity, and reliability. These fiber-based sensors have the potential to be intrinsically more rapid and sensitive sensors than thicker (> 100 nm) films of the same polymer matrix because of i) low steric hindrance of the attached biomolecules by the polymer matrix, ii) reduced need for target molecule diffusion through a microporous polymer matrix, and iii) the high surface to volume ratio that exponentially increases the

electrical and optical response of the polymer for the binding of the biomolecules.

## OPTICAL NANOBIOSENSORS

Optical nanobiosensing techniques include a wide range of nanoscale materials and devices. Similar to larger-scale optical detection systems, optical nanobiosensors rely on signal generation through fluorescence, absorbance, luminescence, or optical scattering. Many nanomaterials have unique optical properties that are the result of their size, and are not observed in the bulk material. For instance, compound semiconductor quantum dots have become popular tags for biological imaging and detection. These nanoscale particles exhibit enhanced fluorescence properties that are far superior to conventional organic dyes<sup>[11]</sup> and are dependent on the elemental composition and discrete particle size.

Other types of nanoparticles, including those made from gold and silver, can be used for simple colorimetric assays with extremely high sensitivity.<sup>[12]</sup> These particles can be linked to biological molecules, including nucleic acids and proteins, which can then bind specifically to biological targets. A simple color change can be observed when the biological molecules form molecular complexes, creating aggregates of the nanoparticles. This relatively simplistic detection method can be further enhanced by precipitation of other materials onto these aggregates, which can further modify optical and electrical properties for detection.<sup>[12]</sup>

Gold and silver nanoparticles are also useful for enhancing the sensitivity of spectroscopic techniques, including signal enhancement for Raman spectroscopy. Surface Enhanced Raman Spectroscopy (SERS) is a relatively new technique that utilizes nanoparticle-based spectral signal enhancement for high-sensitivity detection.<sup>[11]</sup> To perform SERS-based analyses, Raman-active compounds are placed in proximity to nanoscale metallic particles or nano-textured metallic surfaces where surface-generated plasmons can greatly enhance the Raman spectral signal.<sup>[13]</sup> For each of these techniques, detectable signal generation depends on the unique properties of nanoscale materials. While some nanomaterials simply enhance existing signals, such as the case for SERS, other nanomaterials such as quantum dots have optical properties that are dependent on their nanometer size scale and that are not present in the bulk material.

In addition to utilizing nanoscale materials for signal generation or signal enhancement, nanobiosensors can also use nanoscale tools for obtaining optical signals. For many colorimetric and spectroscopic detection assays, nanoscale lipid vesicles, known as liposomes,

have been used to contain high concentrations of dye molecules or optically active reagents.<sup>[14]</sup> In their simplest form, liposomes are small spheres that are composed of monolayers or bilayers of amphiphilic lipids and can range from a few nanometers to many microns in diameter. Similar to a cell membrane, liposomes can contain small volumes of materials, such as fluorescent dyes, and can have proteins or other biological molecules embedded in the lipid layer.

These embedded molecules can be used to link liposomes to specific targets or mediate biological recognition events. Because the liposomes can be filled with high concentrations of dyes and other reagents, they provide superior signal over targets labeled with individual molecules. Although many liposome-based detection assays utilize fluorophores or chromophores, liposomes can also be filled with enzymes or other catalytic species that can mediate fluorescence-generating or colorimetric reactions. Biological interactions between liposomes and their targets can cause release of catalysts into the solution or entry of substrates into the interior of the liposome. Through either mechanism, catalysts can be exposed to their substrates to generate an optical signal. This type of biosensing reaction can greatly amplify the signal due to the catalytic nature of the process.

Optical tools have also been developed for probing nanoscale features of biological systems. Nanometer-sized optical fibers are currently used for Near-field Scanning Optical Microscopy (NSOM) applications and for direct insertion into living cells.<sup>[15]</sup> To create these nanometer sized probes, optical fibers are stretched or etched to reduce their diameter to 50 nm or less. This dimension is typically smaller than the wavelength of light used for sample interrogation, which can greatly increase resolution. The sharpened optical probe can be used to collect light from an illuminated sample or can be used for localized, nanoscale illumination.

In either method, raster scanning of the probe across the sample can be used to create a high-resolution image that greatly exceeds the limits of traditional light microscopy. Spatial resolution on the order of 12 nm has been achieved with this type of optical probe system, making a true nanoscale technique.<sup>[15]</sup> Another use for these nanoscale optical probes is to insert them into living cells for observation of intracellular processes. Unlike larger probes, nanoscale probes can penetrate a living cell without causing cellular damage or cell death. This creates a unique opportunity to observe the cellular interior without the need for destructive preparation techniques. By coupling biomolecules or capture agents to the tip of these optical fibers, these nanoprobe can also be used as sensitive detectors. Biomolecular interactions with the tip can mediate a change in optical signal, which



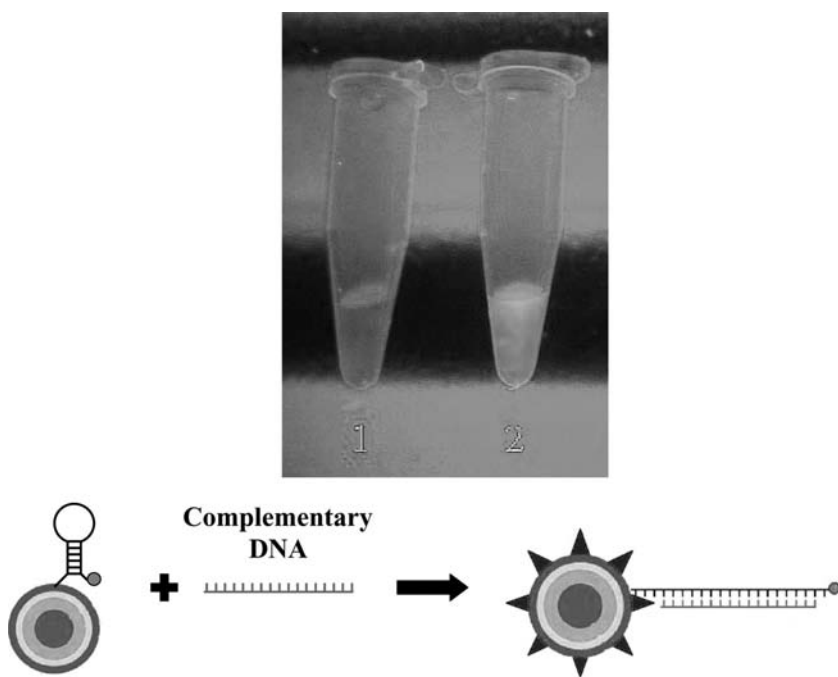


**Fig. 3** Quantum dot molecular beacons for sequence-specific DNA detection. In their native state, quantum dot molecular beacons form a stable hairpin complex that brings the quencher molecule in proximity with the fluorescent quantum dot. When exposed to target DNA, the DNA hairpin can open, hybridizing with the target and spatially distancing the quantum dot from the quencher. This significantly decreases FRET efficiency, resulting in reduced quenching and a significant increase in fluorescence. The upper image shows quenched (1) and un-quenched (2) quantum dots, demonstrating the large difference in fluorescence. The lower image schematically depicts a quantum dot molecular beacon target interacting with its complementary target DNA.

can be correlated to the presence or absence of a particular target or target concentration.

In most optical systems, the sensitivity of target detection is a function of the intensity of the signal and the background noise of the system. One method of increasing signal-to-noise ratios involves the use of fluorescence resonance energy transfer (FRET). Fluorescence resonance energy transfer is a distance-dependent phenomenon that occurs when a donor fluorophore and an acceptor chromophore (quencher) are in proximity.<sup>[16]</sup> When the fluorophore and quencher are within a certain distance from each other, excitation energy can be transferred from the fluorophore to the quencher, preventing fluorescence emission.

Multiple biological detection strategies have been devised to harness this effect, and often include the use of nucleic acid and proteins. Molecular beacons<sup>[17–20]</sup> are one of the most well-known nucleic acid-based biosensing elements that utilize FRET. Molecular beacons are composed of a fluorophore and a quencher moiety attached to opposite ends of a single-stranded DNA oligonucleotide. The sequence of the oligonucleotide is designed such that it preferentially base pairs with itself, forming a stem-loop structure. Included inside the loop region is a probe sequence that can bind to a complementary target DNA sequence. This hybridization event causes the stem-loop structure to open and spatially distance the fluorophore from the quencher. This decreases the FRET efficiency and results in increased emission from the fluorophore. To increase the fluorescence signal of molecular beacons, semiconductor quantum

dots have been used, replacing traditional organic fluorophores<sup>[11]</sup> (Fig. 3), creating novel, molecular-level nanobiosensors.

## MECHANICAL NANOBIOSENSORS

Mechanical observation and detection of biological targets has been used for many years at the macro- and micro-scale. Quartz crystal microbalances and other oscillatory platforms can be used to detect picogram and lower quantities of biological targets. These systems, however, do not measure nanoscale mechanical forces and do not have the resolution to measure nanometer length-scale events. Current cantilever-based technologies, such as atomic force microscopy (AFM), do perform measurements at the nanoscale and are capable of measuring both nanoscale topographical features and nanoscale forces. These nanomechanical biosensors are typically designed as a single-sensing element, biomechanical devices targeted for a specific measurement.

Recent efforts have focused on the development of cantilever-based sensors for the detection of biomolecular recognition events.<sup>[21]</sup> The high mechanical quality factors associated with resonant micro- and nanomechanical cantilever systems<sup>[22–25]</sup> have proven useful in a number of application areas ranging from signal processing,<sup>[26]</sup> to nanobiotechnology.<sup>[27]</sup> Such biosensors can be label-free systems and can also be applied to the detection of viruses,<sup>[28,29]</sup> single cells, and individual strands of DNA. In these “dynamic mode” systems, the amount of attached mass is

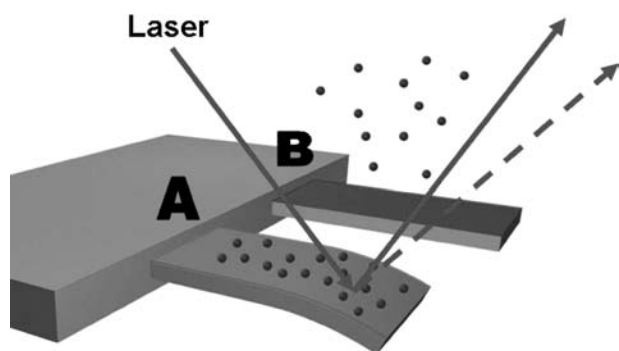


**Fig. 4** Detection of biomolecular interactions using microcantilevers. Cantilevers can be modified with biorecognition elements that are specific to certain biological targets. In this example, cantilever “A” is modified with a recognition element that can bind to the spherical molecular targets. This binding event causes a measurable deflection of the cantilever, which can be measured by the change in position of a laser beam focused on its surface. Cantilever “B” is coated with a recognition element that does not interact with the target and is not deflected.

typically determined by observing changes in the resonant frequency of the oscillator. Cantilever readout is often performed optically, in which case spatial multiplexing is relatively easy.

Piezoelectric technology, which is responsible for generating mechanical oscillation in most nanomechanical sensors, can also be employed for the development of a novel class of smart nanodevices that mimic biological design. In piezoelectric materials, an electro-mechanical transduction process takes place within a given material. It is worth noting that some biological molecules, including certain proteins, are naturally piezoelectric. Systems that incorporate these biomimetic, piezoresistive structures can perform localized, high-resolution molecular recognition measurements.<sup>[30]</sup> The microcantilevers translate the molecular recognition of biomolecules into nanomechanical motion ranging from a few to hundreds of nanometers (see Fig. 4).<sup>[21]</sup> This mechanical response by the cantilever is commonly coupled to an optical or piezoresistive read-out system.<sup>[31,32]</sup>

## CONCLUSIONS

Nanobiosensors are increasingly becoming a powerful new class of sensors that can probe biological systems at the molecular scale and enhance sensitivity through the use of novel nanomaterials. The measurement of biological processes with such devices can provide new insights into biomolecular structure, function, and interactions. The novel properties of integrated nanomaterials can also improve our ability to interface

physical sensors with biological systems. A large number of electrical and optical nanobiosensors have been described and active research continues for the integration of nanomaterials into these transduction mechanisms. Although there are fewer reports of nanobiosensors based on nanomechanical signal transduction, it is expected that future efforts will expand our abilities to mechanically probe biological systems at the nanoscale.

## REFERENCES

1. Yonzon, C.R.; Stuart, D.A.; Zhang, X.; McFarland, A.D.; Haynes, C.L.; Van Duyne, R.P. Towards advanced chemical and biological nanosensors—an overview. *Talanta* **2005**, *67*, 438–448.
2. Junhui, Z.; Hong, C.; Ruifu, Y. DNA based biosensors. *Biotechnol. Adv.* **1997**, *15*, 43–58.
3. Bakker, E.; Qin, Y. Electrochemical sensors. *Anal. Chem.* **2006**, *78*, 3965–3984.
4. Jain, K.K. Nanotechnology in clinical laboratory diagnostics. *Clin. Chim. Acta* **2005**, *358*, 37–54.
5. Wang, J. Nanomaterial-based electrochemical biosensors. *Analyst* **2005**, *130*, 421–426.
6. Patolsky, F.; Zheng, G.; Lieber, C.M. Nanowire-based biosensors. *Anal. Chem.* **2006**, *78*, 4260–4269.
7. Pumera, M.; Sanchez, S.; Ichinose, I.; Tang, J. Review of electrochemical nanobiosensors. *Sensors Actuators B* **2007**, *123*, 1195–1205.
8. Fei, J.; Wu, K.; Wang, F.; Hu, S. Glucose nanosensors based on redox polymer/glucose oxidase modified carbon fiber nanoelectrodes. *Talanta* **2005**, *65*, 918–924.
9. Zhu, N.; Chang, Z.; He, P.; Fang, Y. Electrochemical DNA biosensors based on platinum nanoparticles combined carbon nanotubes. *Anal. Chim. Acta* **2005**, *545*, 21–26.
10. Jiang, J. Electrochemical studies of nanostructured materials: the synthesis and size effect dependence of the adsorption of organic molecules and applications to biosensors. *Notre Dame*.
11. Cady, N.C.; Strickland, A.D.; Batt, C.A. Optimized linkage and quenching strategies for quantum dot molecular beacons. *Mol. Cell Probes* **2007**, *21*, 116–124.
12. Thaxton, C.S.; Georganopoulou, D.G.; Mirkin, C.A. Gold nanoparticle probes for the detection of nucleic acid targets. *Clin. Chim. Acta* **2006**, *363*, 120–126.
13. Orendorff, C.J.; Gearheart, L.; Jana, N.R.; Murphy, C.J. Aspect ratio dependence on surface enhanced Raman scattering using silver and gold nanorod substrates. *Phys. Chem. Chem. Phys.* **2006**, *8*, 165–170.
14. Vamvakaki, V.; Chaniotakis, N.A. Pesticide detection with a liposome-based nano-biosensor. *Biosens. Bioelectron.* **2007**, *22*, 2848–2853.
15. Cullum, B.M.; Vo-Dinh, T. The development of optical nanosensors for biological measurements. *Trends Biotechnol.* **2000**, *18*, 388–393.
16. Epstein, J.; Biran, I.; Walt, D.R. Fluorescence-based nucleic acid detection and microarrays. *Anal. Chim. Acta* **2002**, *469*, 3–36.

17. Tyagi, S.; Kramer, F.R. Molecular beacons: probes that fluoresce upon hybridization. *Nat. Biotechnol.* **1996**, *14*, 303–308.
18. Tan, L.; Li, Y.; Drake, T.J.; Moroz, L.; Wang, K.; Li, J.; Munteanu, A.; Chaoyong, J.Y.; Martinez, K.; Tan, W. Molecular beacons for bioanalytical applications. *Analyst* **2005**, *130*, 1002–1005.
19. Vet, J.A.; Marras, S.A. Design and optimization of molecular beacon real-time polymerase chain reaction assays. *Methods Mol. Biol.* **2005**, *288*, 273–290.
20. Tsourkas, A.; Behlke, M.A.; Rose, S.D.; Bao, G. Hybridization kinetics and thermodynamics of molecular beacons. *Nucleic Acids Res.* **2003**, *31*, 1319–1330.
21. Fritz, J.; Baller, M.K.; Lang, H.P.; Rothuizen, H.; Vettiger, P.; Meyer, E.; Guntherodt, H.; Gerber, C.; Gimzewski, J.K. Translating biomolecular recognition into nanomechanics. *Science* **2000**, *288*, 316–318.
22. Erickson, D.; Mandal, S.; Yang, A.H.J. Nanobiosensors: optofluidic, electrical and mechanical approaches to biomolecular detection at the nanoscale. *Microfluidics Nanofluidics* **2007**, *4*, 1613–4982.
23. Craighead, H.G. Nanoelectromechanical systems. *Science* **2000**, *290*, 1532–1536.
24. Majumdar, A. Bioassays based on molecular nanomechanics. *Dis. Markers* **2002**, *18*, 167–174.
25. Ekinci, K.L.; Huang, X.M.H.; Roukes, M.L. Ultrasensitive nanoelectromechanical mass detection. *Appl. Phys. Lett.* **2004**, *84* (22), 4469–4471.
26. Shim, S.B.; Imboden, M.; Mohanty, P. Synchronized oscillation in coupled nanomechanical oscillators. *Science* **2007**, *316*, 95–99.
27. Cleland, A.N.; Roukes, M.L. A nanometre-scale mechanical electrometer. *Nature* **1998**, *392*, 160–162.
28. Ilic, B.; Craighead, H.G.; Krylov, S.; Senaratne, W.; Ober, C.; Neuzil, P. Attogram detection using nanoelectromechanical oscillators. *J. Appl. Phys.* **2004**, *95*, 3694–3703.
29. Gupta, A.K.; Nair, P.R.; Akin, D.; Ladisch, M.R.; Broyles, S.; Alam, M.A.; Bashir, R. Anomalous resonance in a nanomechanical biosensor. *Proc. Natl. Acad. Sci. USA* **2006**, *103*, 13362–13367.
30. McKendry, R.; Zhang, J.; Arntz, Y.; Strunz, T.; Hegner, M.; Lang, H.P.; Baller, M.K.; Certa, U.; Meyer, E.; Guntherodt, H.J.; Gerber, C. Multiple label-free biodection and quantitative DNA-binding assays on a nanomechanical cantilever array. *Proc. Natl. Acad. Sci. USA* **2002**, *99*, 9783–9788.
31. Carrascosa, L.G.; Moreno, M.; Ivarez, M.A.; Lechuga, L.M. Nanomechanical biosensors: a new sensing tool. *Trends Anal. Chem.* **2006**, *25*, 196–206.
32. Minne, S.; Manalis, S.R.; Quate, C.F. Integrated piezoresistive and piezo-actuator based parallel scanning probe microscope. *Appl. Phys. Lett.* **1995**, *67*, 3918.

# Nanobridges: Thermal Properties

Jeong Won Kang

Computational Semiconductor Laboratory, Chung-Ang University, Seoul, South Korea

Ho Jung Hwang

Institute of Technology and Science, Chung-Ang University, Seoul, South Korea

## INTRODUCTION

As the scale of electronic devices continues to shrink, fundamental interest has focused on the nature of the mechanical, optical, and electrical behavior of one-dimensional nanometer-scale channels such as quantum wires<sup>[1]</sup> and carbon nanotubes.<sup>[2,3]</sup> The development of new experimental techniques such as mechanically controllable break junctions (MCBJs) and scanning tunneling microscopy (STM) has made it possible to form and to study atomic-sized junctions or contacts between macroscopical metals. The mechanical and electrical properties of nanocontacts between metallic bodies have been a subject of intensive research.<sup>[4–13]</sup> Quantum point contacts are structures in which a ‘neck’ of atoms, of just a few atomic diameters, bridges two electrical contacts. The results prepared by contacting a metal surface with an STM<sup>[7–14]</sup> and by other methods<sup>[15–19]</sup> have typically displayed a conductance quantized in steps of  $2e^2/h$ , where  $e$  is the electron charge and  $h$  is Planck’s constant. The mechanical properties of nanocontacts have shown that before the first yielding, nanowires preserve the elastic stage and, after that, the elongation deformation proceeds in alternating quasi-elastic and yielding stages.<sup>[12,13,20,21]</sup>

The thermal properties of infinite nanowires with periodical boundary conditions (PBCs) along the nanowire axis have been investigated using molecular dynamics (MD) simulations. For example, the MD methods were used to investigate the premelting of infinite Pb nanowires with the axis along a (110) direction<sup>[22]</sup> and the melting of infinite Au nanowires with a multishelled structure.<sup>[23]</sup> However, previous works<sup>[22,23]</sup> have not been enough to provide the thermal properties of nanocontacts and nanobridges, such as the melting and the breaking of nanobridges. Nanobridges can be sustained by supporting layers in contact with both ends of the nanobridges. This condition is considered as a similar situation to that in which a string, such as a guitar string, is connected between two clamps separated by a fixed distance. Therefore the nanobridge can also make an oscillation at a

resonant frequency to set up a standing wave pattern. Copper is an important engineering material, so in this investigation, we use MD simulations to investigate ultrathin Cu nanobridges. In this entry, we show the thermal properties of nanobridges in Sections ‘‘Oscillations of Nanobridges’’ and ‘‘Melting and Breaking of Nanobridges,’’ using a classical MD simulation.

## METHODS

In our MD simulations, we have used the same MD methods that we employed previously in studies on the cluster deposition and the structural motifs of Cu nanowires.<sup>[20,21,24–27]</sup> The MD time step is 0.5 fsec. The MD code uses the velocity Verlet algorithm, a Gunstern–Berendsen thermostat to keep temperature constant, a PBC along the wire axis, and neighbor lists to improve computing performance.<sup>[28]</sup> For Cu, we have used a many-body potential function of the second-moment approximation of the tight-binding (SMA-TB) scheme,<sup>[29]</sup> which has already been tested in nanoclusters and nanowires,<sup>[20,21,24–27,30]</sup> etc. The potential reproduces many basic properties of crystalline and non-crystalline bulk phases and surfaces,<sup>[31]</sup> and gives a good insight into the structures and thermodynamics of metal clusters.<sup>[32,33]</sup> The total potential energy of the system  $E_{\text{tot}}$  can be expressed as a sum of the potential energies of each atom  $i$ . The energy of each atom  $E_i$  is expressed as the sum of the attractive band energy determined by the occupied local density of states  $E_i^{\text{band}}$  and the repulsive term determined by the ion core–core interaction  $E_i^{\text{rep}}$ . The total energy of system  $E_{\text{tot}}$  can be written as:

$$E_{\text{tot}} = \sum_i E_i = \sum_i (E_i^{\text{rep}} + E_i^{\text{band}}) \quad (1)$$

$$E_i^{\text{rep}} = \sum_j A \exp[-p(r_{ij}/r_0 - 1)] \quad (2)$$

$$E_i^{\text{band}} = \left[ \sum_j \zeta_0^2 \exp[-2q(r_{ij}/r_0 - 1)] \right] \quad (3)$$

where  $r_0$  and  $r_{ij}$  are the nearest-neighbor bond length in a perfect crystal and the distance between  $i$  and  $j$  atoms, respectively.  $A$ ,  $\xi$ ,  $p$ , and  $q$  are adjustable parameters, which are determined by fitting the calculated values of cohesive energy, lattice constant, and elastic constants to the experimental values. The parameters are the same as those in Ref.<sup>[29]</sup>. The cutoff distance is set to the value between the fourth and fifth nearest neighbors of a perfect crystal.

## INITIAL STRUCTURES

The nanostructures we studied have two supporting layers that are connected with both ends of the nanobridges. The last layers at both supporting ends are rigid; all the atoms in these layers are kept fixed during the MD simulations. These fixed layers at both ends are assumed to be connected to the external agent. Atoms in the following two layers adjacent to the fixed atoms and those of the nanobridges are identified as dynamic atoms and are fully relaxed during the MD steps. We considered eight different structures, which are described in Table 1.  $D$  and  $L$  in Table 1 and Fig. 1 denote the diameter and the length of the nanobridges, respectively. The nanowires with a face-centered cubic (fcc) structure have been observed in a previous work<sup>[23]</sup> and the ultrathin nanowires also have a type of cylindrical multishell (CMS) structure.<sup>[24,30]</sup> Therefore we have selected nanobridges with fcc or CMS-type structures. The supporting layers have the same structures as those of the nanobridges. To describe CMS-type nanowires, we use the notation  $n - n' - n'' - n'''$  introduced by Ohnishi, Kondo, and Takayanagi<sup>[11]</sup> when the nanowire consists of coaxial tubes with  $n$ ,  $n'$ ,  $n''$ ,  $n'''$  helical atom rows ( $n > n' > n'' > n'''$ ). Because the structures of the CMS-type nanobridges are closely related to the  $\{111\}$  plane,<sup>[24]</sup> they are connected to the supporting layers with  $\{111\}$  planes. Nanobridges with different diameters were simulated under conditions of the same structure and the same length.

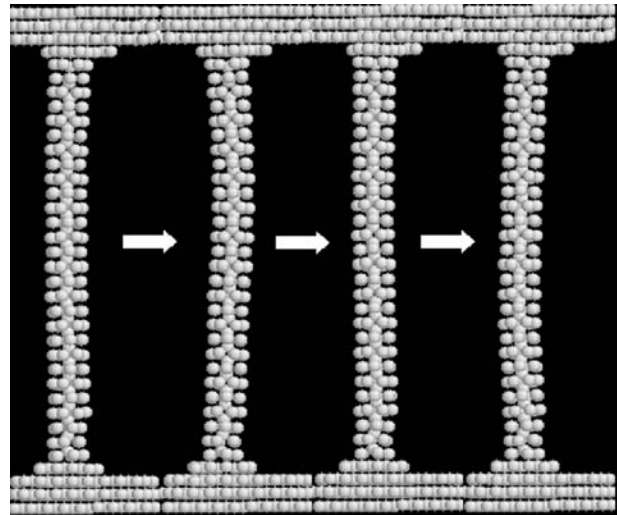


Fig. 1 Oscillation of the D1 nanobridge.

## OSCILLATIONS OF NANOBRIDGES

The MD simulations of all nanobridges in Table 1 have been performed during 1 nsec at room temperature. Fig. 1 shows four cuts representing the oscillations of the D1 nanobridge. The momentum of supercells for bulk systems is almost zero. However, the supercells for one-dimensional systems can have nonzero momentum in a specific condition and, in this situation, if tension is exerted on the one-dimensional system, the one-dimensional system will oscillate. Nanobridges can exist in this state. The mean kinetic temperature  $k_B T$  is calculated as follows:

$$k_B T = [2/(3N - 6)] \left\langle \sum_{i=1}^N (mv_i^2/2) \right\rangle \quad (4)$$

where the angular brackets denote averaging over time and  $k_B$  is the Boltzmann constant. It supplies the energy to atoms in the nanobridges, and the collective

Table 1 Structures of ultrathin Cu nanobridges

	Supporting layer	Nanobridge	$D$ (Å)	$L$ (Å)	Number of atoms in nanobridge
A1	{100}	{100}	10.2	61.449	425
A2	{100}	{100}	15.0	61.449	969
B1	{110}	{110}	10.2	42.452	323
B2	{110}	{110}	15.0	42.452	731
C1	{111}	{111}	10.2	70.956	492
C2	{111}	{111}	15.0	70.956	1102
D1	{111}	CMS 6-1	4.9	64.294	209
D2	{111}	CMS 11-6-1	10.2	64.294	534

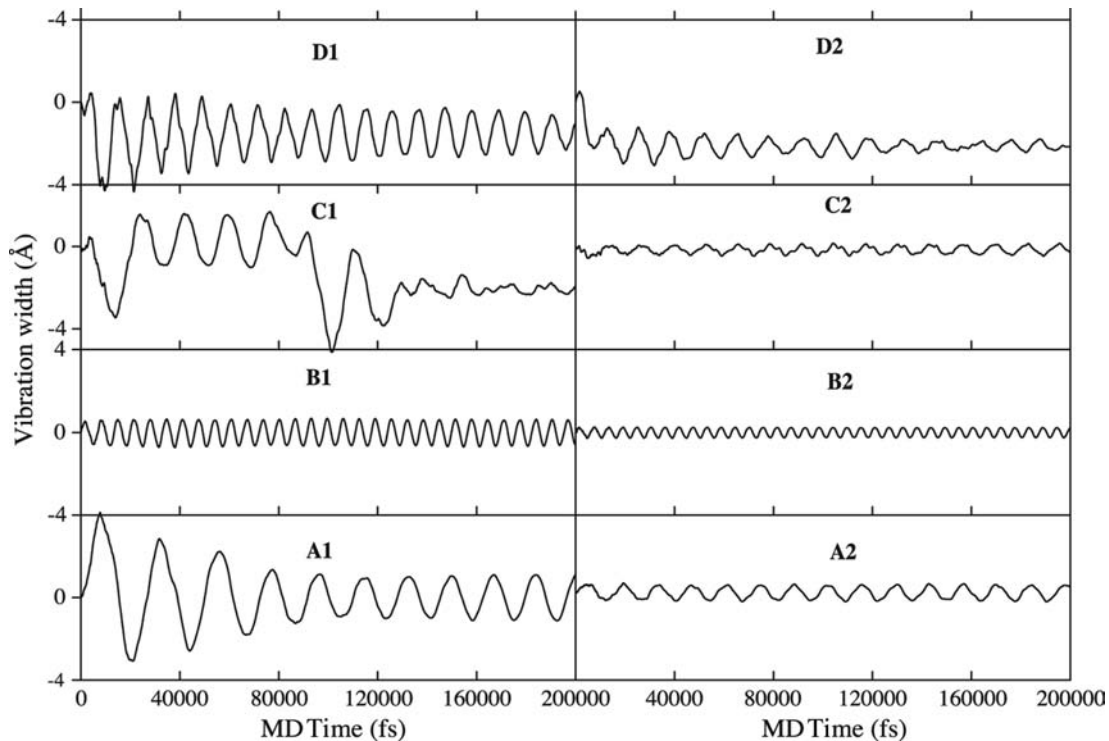


Fig. 2 Vibrations of the center of the nanobridge during the initial 200 psec for all cases in Table 1.

motion of the atoms in the nanobridges is discovered by the oscillation of the nanobridge.

Figure 2 shows the vibrations of the center of the nanobridges during the initial 200 psec for all cases. The thermal energy can make the nanobridges oscillate at a certain frequency. In the cases of A1, A2, B1, B2, and C2, the vibrations of the nanobridges show sinusoidal waves, such as resonance. In the A1 case, the resonance is stabilized after 100 psec. However, in the cases of C1, D1, and D2, the sinusoidal vibrations of the nanobridges disappear as the MD time increases. In classical oscillation systems, for certain frequencies, the interference produces a standing wave pattern or oscillation mode, and then the string resonates at a certain frequency, called resonant frequency. If the string oscillates at some frequencies other than a resonant frequency, a standing wave is not set up. In our simulations of nanobridges, if the nanobridges are in the mode of the certain resonant frequency at the beginning of the MD simulation, the standing waves of nanobridges are maintained. However, during the MD simulations, when the structures of the nanobridges are changed, the standing waves are not set up in our simulations, and atoms in the contact region between the supporting layer and the nanobridge are rearranged. The standing waves have been damped by structural rearrangements taking place. As the diameter of the nanobridge increases, because the tension in the nanobridge increases, the displacements

of its center decrease and, at the same time, the amplitude of the wave decreases.

Figure 3 shows the structures after the MD simulations of 1 nsec. In the A1 case, the neck of the nanobridge connected by the bottom supporting layer became narrow, as pointed out by the arrow. Therefore the rearrangements of the A1 nanobridge before 100 psec led to the damping of the sinusoidal wave, as shown in Fig. 2. However, because its final structure was the same as the original structure, the resonance was maintained in the nanobridge. In the C1 case, the nanobridge that originally had a {111} structure has been transformed into a complex nanobridge with

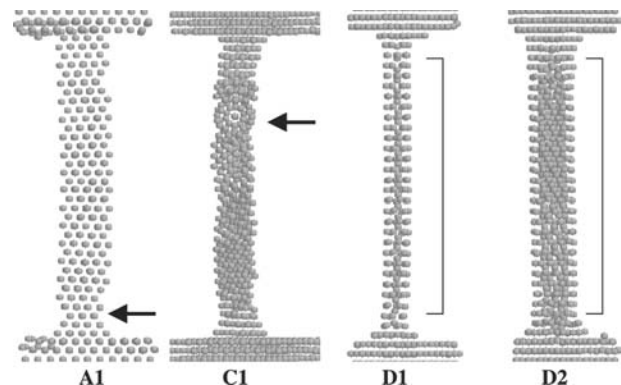


Fig. 3 Structures after MD simulations of 1 nsec.



diverse structures. Especially, the region pointed to by the arrow is a multishell-type 10-5-1 structure. Considering the 10-5-1 multishell nanoparticle, the pentagonal small particles, such as decahedron and icosahedron particles, have been extensively investigated and reviewed in Ref.<sup>[34]</sup>. The decahedron and icosahedron nanoclusters, called multiple twinned particles, are different from single crystalline particles and are composed of tetrahedrons, which consist of only triangular {111} faces.

In the D1 and D2 cases, at the early stage of the MD simulations, structural rearrangements were achieved in the contact regions between the supporting layer and the CMS-type nanobridge. As results of the structural rearrangements, the deviations of the center of the nanobridges are shown in the waves of Fig. 2. Most of all, the CMS-type nanobridges maintained their structures between the supporting layers with {111} planes. However, one or two layers of the nanobridge contacting the supporting layers were transformed into the {111} structure and the other regions of the nanobridges preserved the CMS-type structure.

We also performed MD simulations of 100 psec using the nanobridges, which have been obtained from simulations as explained in Fig. 2. The waves on the nanobridge can have two modes, such as longitudinal and transverse modes, because of their structural property. The waves shown in Fig. 2 are closely related to the transverse waves on the nanobridges. Because the transverse wave on the nanobridge makes a resonance, as shown in Fig. 2, the lowest resonant frequency of the nanobridge is calculated by the following method. Atoms in the center regions of the nanobridges were initially applied to the external force, 0.01 nN, during 1 psec at room temperature. Then we monitored the displacements of the center region of the nanobridge. Table 2 shows the lowest resonant frequency of the nanobridges at room temperature. In the C1 case, the

resonance did not appear. Therefore it is assumed that the nanobridges, which are not well-defined structures, cannot resonate at a certain frequency.

From the theory of the classical oscillation system, the relation between the wave length  $\lambda$  and  $L$  for a standing wave on a string can be summarized as:

$$\lambda = \frac{2L}{n}, \quad n = 1, 2, 3, \dots \quad (5)$$

The resonant frequencies that correspond to these wavelengths follow from Eq. (5):

$$f = \frac{v}{\lambda} = n \frac{v}{2L}, \quad n = 1, 2, 3, \dots \quad (6)$$

where  $v$  is the speed of the travelling waves on the string. The lowest resonant frequency is  $f = v/2L$ , which corresponds to  $n = 1$ .

The speed of the waves on the string is also expressed as follows:

$$v = \sqrt{\frac{\tau}{\mu}} \quad (7)$$

where  $\tau$  is the tension in the string and  $\mu$  is the linear density of the string. In the case of the first harmonic, the tension is calculated by Eqs. (6) and (7):

$$\tau = v^2 \mu \quad (8)$$

In Table 2, the larger the diameter of the nanobridge is, the larger is the lowest resonant frequency. When the wavelength is the same, the speed of the travelling wave on the nanobridge increases in linear proportion with the lowest resonant frequency. We can also calculate the linear density by using the mass of the nanobridge against the length of the nanobridge. From these

**Table 2** Lowest resonant frequency, speed of the traveling wave, linear density, and tension in the nanobridge of ultrathin Cu nanobridges

Nanobridge	Lowest resonant frequency (GHz)	Speed of the traveling wave (m/sec)	Linear density ( $\mu$ ) ( $10^{-16}$ kg/m)	Tension in the nanobridge ( $10^{-11}$ kg m/sec <sup>2</sup> )	
				Eq. (8)	MD simulation
A1	5.6	68.9	73.0	3.46546	6.95621
A2	7.2	89.2	166.5	13.24780	18.18869
B1	15.6	131.0	80.3	13.78028	10.03054
B2	18.5	155.4	118.8	28.68920	26.23471
C2	8.3	117.8	163.9	22.75958	17.25665
D1	4.7	60.2	34.3	1.24304	1.50018
D2	7.8	99.8	87.7	8.73495	10.44815

values, the tensions in the nanobridges were calculated by Eq. (8) and were compared with those obtained from the MD simulations. As the diameter of the nanobridge increases, the tension in the nanobridge increases. The tensions obtained directly from the MD simulations are the forces acting on the supporting layers and are in agreement, within the limits, with those calculated using the continuum theory [Eq. (8)]. For all cases, the tensions obtained from the MD simulations are slightly higher or lower than those obtained from the continuum theory. Because the tensions calculated by Eq. (8) reflect only upon the transverse waves, this difference could be derived from the interference of the longitudinal waves on the nanobridges. As the diameter of the nanobridge increases, the tension in the nanobridge increases. In spite of this difference, our simulations have shown an aspect of nanobridges in the state of the art. The oscillation of nanobridges can be understood by the classical oscillation theory.

### THE MELTING AND BREAKING OF NANOBRIDGES

We have also investigated the properties of nanobridges as the temperature is raised. The initial structures of the nanobridges were the structures obtained from Oscillations of Nanobridges and were equilibrated at 300 K. Each system was heated by uniformly scaling the atomic velocities. The MD runs of 20,000 time steps were performed with each temperature step from 300 K. Therefore the average temperature ascent rate is 0.1 K/psec. We monitored the internal energy as a function of temperature.

The caloric curves for some of the ultrathin Cu nanobridges in Table 1 are shown in Fig. 4. To compare nanobridges with semi-infinite nanowires, Fig. 4 includes the caloric curve of the CMS 16-11-6-1 applied to the PBC from Ref.<sup>[35]</sup>. The caloric curve of the CMS 16-11-6-1 nanowire close to the one-dimensional system is in the regime of the pseudo-first-order transitions and the jump in the caloric curve is apparent. The slope of the caloric curve of the CMS 16-11-6-1 corresponds to the Dulong–Petit specific heat.<sup>[35]</sup> The  $M_{\text{point}}$  and  $B_{\text{point}}$  indicate the temperatures of pronounced upward and downward points in the caloric curve, which are related to the melting and the breaking of the nanowire. The downward curvature in the caloric curve has not been observed until now. The caloric curve of the CMS 16-11-6-1 nanowires is divided into five regions. The first region ranges below the  $M_{\text{point}}$ , where the ultrathin nanowire is solid. The second region is the  $M_{\text{point}}$  at which the caloric curve exhibits an upward curvature, where the specific heat markedly increases at the beginning of

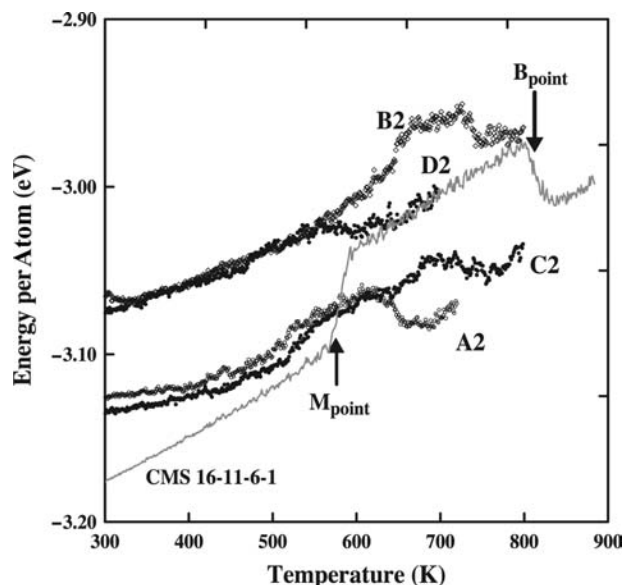


Fig. 4 Caloric curves of some of nanobridges and the CMS 16-11-6-1 nanowire.  $M_{\text{point}}$  and  $B_{\text{point}}$  indicate temperatures of upward and downward points in the caloric curve, respectively.

the surface melting. This upward curvature is associated with the loss of the solid rigidity of the nanowire. The third region is between the  $M_{\text{point}}$  and the  $B_{\text{point}}$ , where the ultrathin nanowire is in the melting state, and the slope is the same as that in the first region. The fourth region is the  $B_{\text{point}}$  at which the ultrathin nanowire is broken and then the spherical cluster is formed. In the last region, a spherical cluster has been maintained in the MD simulation applied to the PBC. The slope in the caloric curve of the CMS 16-11-6-1 nanowire is always the same as those in the first, third, and fifth regions. Thus properties of the caloric curve of nanowires are in excellent agreement with previous works on nanowires<sup>[22,23,35]</sup> and nanoclusters.<sup>[36]</sup> The melting temperatures of the ultrathin Cu nanowires and nanobridges are much lower than the bulk melting temperature.

The properties of the caloric curves of nanobridges are generally similar to those of nanowires or nanoclusters.<sup>[22,23,35,36]</sup> However, the caloric curves of nanobridges are different from those of nanowires for the slopes of the caloric curves. The caloric curves of nanobridges make it difficult to define both the  $M_{\text{point}}$  and the  $B_{\text{point}}$ . The difference of the slopes in the caloric curves is because of the supporting layers. As investigated in Oscillations of Nanobridges, the attractive force between the supporting layer and the nanobridge could maintain the nanobridges. Therefore the caloric curves of the nanobridges include effects of structure dependence related to the tension on the nanobridge as well as temperature dependence. In the

**Table 3** The  $M_{\text{point}}$  and  $B_{\text{point}}$  of Nanobridges

	$M_{\text{point}}$ (K)	$B_{\text{point}}$ (K)
A1	–	$350 \pm 7$
A2	$530 \pm 10$	$650 \pm 10$
B1	–	$420 \pm 7$
B2	$645 \pm 15$	$745 \pm 10$
C1	–	$410 \pm 8$
C2	$535 \pm 15$	$730 \pm 25$
D1	–	$330 \pm 5$
D2	$475 \pm 10$	$600 \pm 10$

The graph in the table shows the curve fitted with Eq. (8).

case of the CMS 16-11-6-1 semi-infinite nanowire, because its caloric curve is dependent only on temperature, the slopes of the solid and melting states in the caloric curve are fixed. However, in the cases of the nanobridges, because their caloric curves are dependent on both the structure and the temperature, their caloric curves before the breaking of the nanobridges are different from the caloric curves of semi-infinite nanowires. The slopes of caloric curves in the melting states of nanobridges are closer to the slopes of caloric curves in nanowires than to the slopes in the solid state of nanobridges. When the kinetic temperature of the nanobridge reaches its  $M_{\text{point}}$ , the nanobridge enters a quasi-melting state and then the tension in the nanobridge gradually decreases. The slopes of the caloric curves after the breaking of nanobridges come to have the same value as those of nanowires.

The  $M_{\text{point}}$  and the  $B_{\text{point}}$  of nanobridges are shown in Table 3. In the cases of A1, B1, C1, and D1, the  $M_{\text{point}}$  was not observed in our simulations but the  $B_{\text{point}}$  was observed. We can see that the  $M_{\text{point}}$  of nanobridges is closely related to the linear density and diameter of nanobridges in Fig. 5. In cluster science, the melting temperature depends on the cluster size and is expressed in the following form:<sup>[23]</sup>

$$T_{\text{mc}} = T_b - c/D_c \tag{9}$$

where  $T_{\text{mc}}$  is the melting temperature of the spherical nanoparticle of radius  $D_c$ ,  $T_b$  is the bulk melting temperature, and  $c$  is a constant. From our results, the melting temperature of nanobridges is expressed approximately as follows:

$$T_{\text{mn}} = T_b - n/D_n \tag{10}$$

where  $T_{\text{mn}}$  is the melting temperature of the nanobridge with linear density  $D_n$ , and  $n$  is a constant. The upper graph of Fig. 5A shows the  $T_{\text{mn}}$  with the line fitted by Eq. (10) originating at the  $T_b$  obtained from the SMA-TB potential (1490 K).<sup>[22]</sup>

Because the breaking temperature of nanobridge can be dependent on the diameter of nanobridges, linear density of nanobridges, crystallographical orientation, shapes in different directions, etc., our simulation results in this paper are not enough to provide some physical properties of the breaking of nanobridges because of thermal energies. However, in our simulation results, if we assume that the  $B_{\text{point}}$  of nanobridges depends on the diameters of nanobridges, the form of Eq. (9) could express those. Therefore the bottom graph of Fig. 5A shows the  $B_{\text{point}}$  with the solid

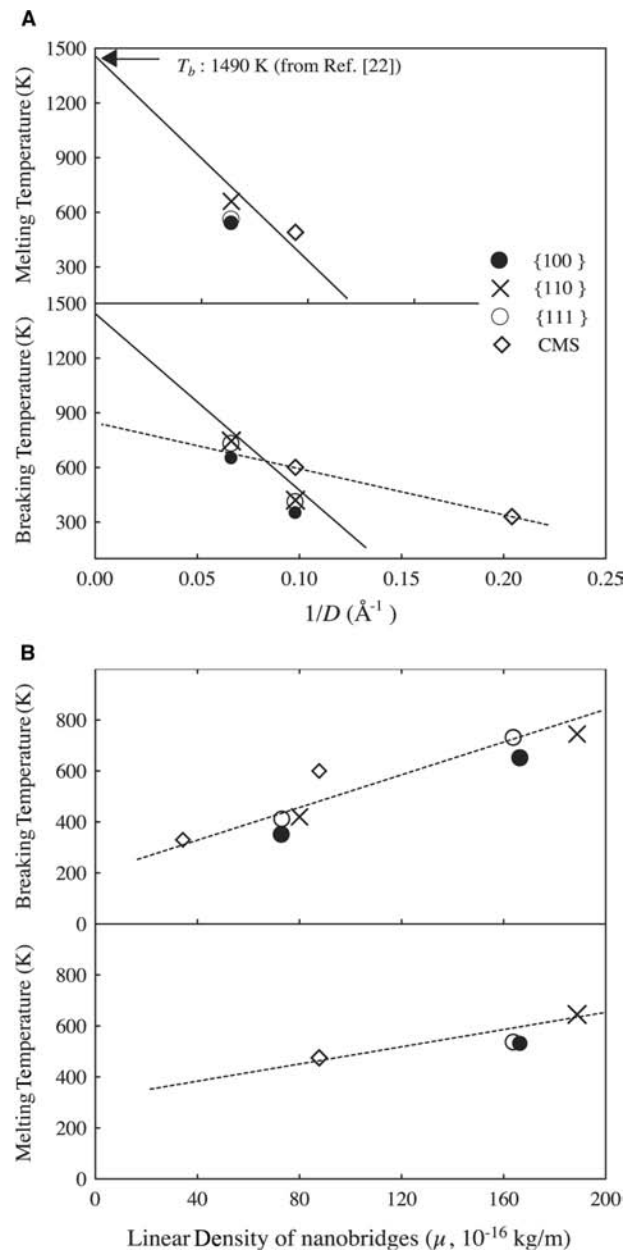


**Fig. 5** (A) The  $M_{\text{point}}$  and  $B_{\text{point}}$  of nanobridges with curves fitted by Eq. (10). (B) The  $M_{\text{point}}$  and  $B_{\text{point}}$  of nanobridges as a function of the linear density of nanobridges.

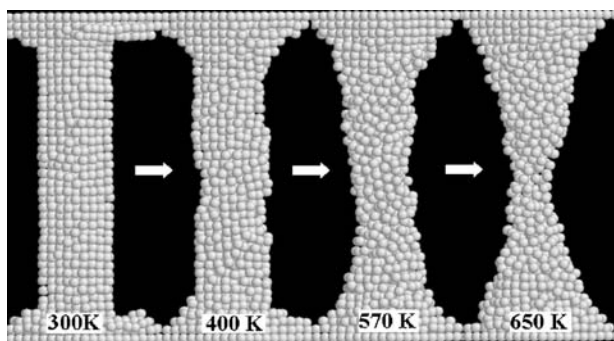


Fig. 6 Structures of A2 nanobridge for temperature.

line fitted by Eq. (10) originating at the  $T_b$  obtained from the SMA-TB potential. For ultrathin nanobridges, because it has been well known that the CMS-type structures are more stable than the other structures, the  $M_{\text{point}}$  and  $B_{\text{point}}$  of the CMS-type nanobridges are higher than those of the other nanobridges. However, for larger nanowires, because the nanobridges with fcc structure are more stable than the CMS-type nanobridges, the dashed line of Fig. 5A, the line fitted for the CMS-type nanobridges, originates near 900 K. Fig. 5B shows  $M_{\text{point}}$  and  $B_{\text{point}}$  as a function of the linear densities of nanobridges. The  $M_{\text{point}}$  and  $B_{\text{point}}$  of nanobridges are linearly proportional with the linear density of nanobridges.

Figure 6 shows the structures of the A2 nanobridge for various temperatures. As the temperature increases, the diameter of the neck of the nanobridge and the tension in the nanobridge decrease because atoms in the nanobridge migrate to the supporting layers. When the temperature reaches the  $B_{\text{point}}$ , the nanobridge is broken and, at the same time, atoms are swiftly accumulated on the supporting layers because of tension just before breaking. Therefore the breaking point  $B_{\text{point}}$  can also be defined by the variation of atomistic mobility as a function of temperature. The corresponding diffusion coefficient is evaluated for each temperature as:

$$(1/6t) \left\langle \left\langle \sum_{i=1}^N |r_i(t) - r_i(0)|^2 \right\rangle \right\rangle \quad (11)$$

where  $r_i(0)$  and  $r_i(t)$  are the vector positions of the  $i$ th atom at time=0 and  $t$ , respectively.

Figure 7 shows the atomistic diffusivity of nanobridges in Arrhenius form. The maximum points of the diffusivity of A1 and C1 are their  $B_{\text{point}}$ . Figure 7B compares the diffusivities of nanobridges and nanowires with that of bulk, which are the experimental values for liquid Cu, the melting point more or less.<sup>[37]</sup> At low temperature, the diffusivities of atoms in nanobridges and nanowires are higher than those of atoms in bulk. The reason is that in a one-dimensional

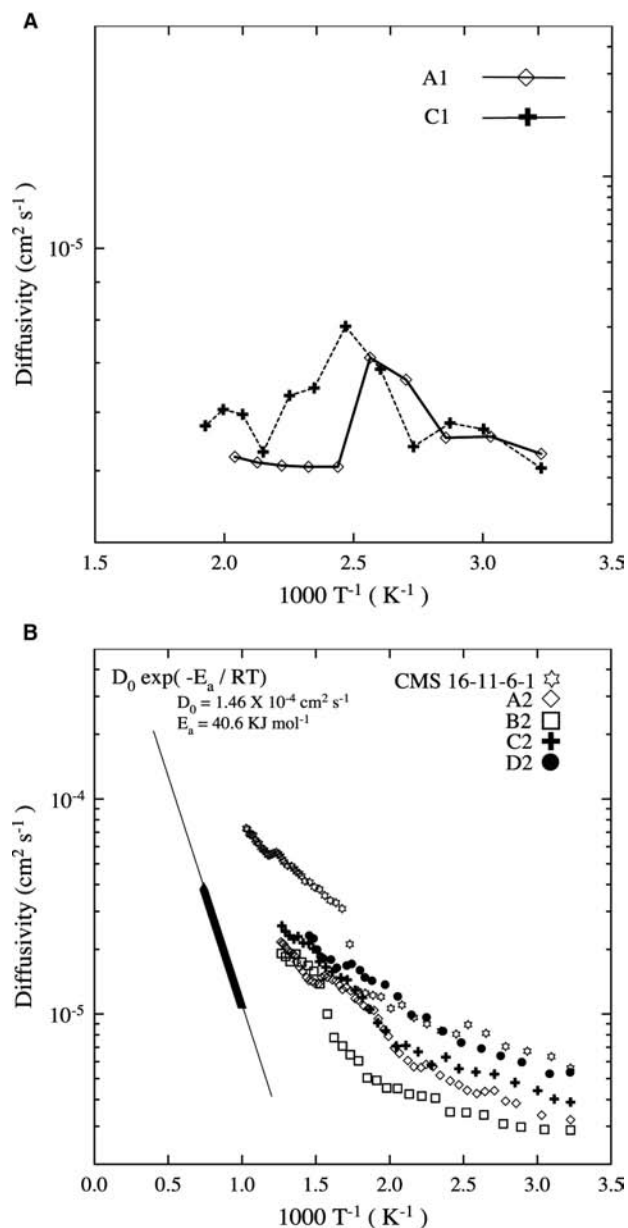


Fig. 7 Diffusivity of nanobridges. (A) A1 and C1. (B) A2, B2, C2, D2, and the CMS 16-11-6-1 nanowires. The diffusivities of nanobridges and nanowires are compared with that of the bulk for melting temperature more or less.

system, the surface area is the main region contrary to the bulk system. The variations of diffusivity before the breaking of nanobridges and nanowires are in good agreement with those of clusters<sup>[36]</sup> and nanowires.<sup>[23]</sup> Although the diffusivities of the CMS 16-11-6-1 nanowire slowly increase until the  $M_{\text{point}}$ , the diffusivities at the  $M_{\text{point}}$  show pronounced upward curvature. The diffusivities after the  $M_{\text{point}}$  show a more rapid increase than those before the  $M_{\text{point}}$  as the temperature is raised. This is because atoms in the CMS 16-11-6-1 nanowire, due to the surface melting at the  $M_{\text{point}}$ ,

rapidly migrate along the wire axis. However, the upward curvatures in the diffusivity curves of nanobridges at their  $M_{\text{point}}$  are less obvious than those of the CMS 16-11-6-1. As investigated in the caloric curves of nanobridges, atoms on the surfaces of nanobridges are gradually accumulated on the supporting layers, as shown in Fig. 5. Therefore, after their  $M_{\text{point}}$ , atoms in nanobridges begin to migrate to the supporting layers. This migration is a major factor in diffusivity ascension. Although the atoms of the CMS 16-11-6-1 nanowire applied to the PBC freely move in both directions along the wire axis, the atoms of the nanobridges lay thick on the supporting layers. The diffusivities of the nanobridges after their  $M_{\text{point}}$  are in good agreement with the experimental values of the diffusivity of liquid Cu, which is indicated by the thick line in Fig. 7B.

When the temperature reaches the  $B_{\text{point}}$  of the nanobridges, the nanobridge is broken and, at the same time, atoms are swiftly piled up on the supporting layers because of the tension just before breaking. Therefore the diffusivities of nanobridges just after their  $B_{\text{point}}$  decrease. However, as the temperatures of the nanobridge system increase above the  $B_{\text{point}}$ , diffusivities again increase. In the case of the CMS 16-11-6-1 nanowires, the nanocluster is formed from the nanowire just after the  $B_{\text{point}}$ , and then the diffusivities of the system also decrease. As the temperatures of the CMS 16-11-6-1 nanowire increase above the  $B_{\text{point}}$ , the diffusivities again increase. Previous studies on nanoclusters<sup>[36]</sup> and semi-infinite nanowires<sup>[22,23,35]</sup> have shown the physical phenomena related to only the melting point  $M_{\text{point}}$  of nanoclusters and nanowires. However, in this entry, we have shown various physical phenomena of ultrathin nanobridges, such as melting, breaking, variance of the diffusion constant, and the role of the supporting layers of ultrathin nanobridges.

## CONCLUSION

Nanobridges have attracted much interest for several reasons. One of the main reasons is that the nanobridge is the fundamental element used to fabricate nanometer-scale electronic devices. Another is the issue of their mechanical, optical, electrical, and thermal properties. This study has disclosed some interesting features of nanobridges using classical MD simulations. We have shown the resonance of nanobridges at room temperature and the physical phenomena of nanobridges because of the thermal energy. When nanobridges have a well-defined structure, the resonance frequency is defined and the resonance phenomenon is in common with classical oscillation systems. The caloric curves and diffusivities of nanobridges

have shown information on the melting and breaking points of nanobridges. The supporting layers of nanobridges have played important roles in the dynamics and thermal properties of nanobridges. Although our study has disclosed some interesting features of nanobridges, because this study was confined within eight systems of nanobridges, further study should be done and will give a more complete understanding of nanobridges.

## ACKNOWLEDGMENT

This work was supported by Korea Research Foundation grant KRF-2002-075-C00006.

## REFERENCES

1. Webb, R.A.; Washburn, S.; Umbach, C.P.; Laibowitz, R.B. Observation of  $h/e$  Aharonov–Bohm oscillations in normal-metal rings. *Phys. Rev. Lett.* **1985**, *54* (25), 2696–2699.
2. Iijima, S. Helical microtubules of graphitic carbon. *Nature* **1991**, *354*, 56–58.
3. Bockrath, M.; Cobden, D.H.; McEuen, P.L.; Chopra, N.; Zettl, A.; Thess, A.; Smalley, R.E. Single-electron transport in ropes of carbon nanotubes. *Science* **1997**, *275*, 1922–1925.
4. Agrait, N.; Rubio, G.; Vieira, S. Plastic deformation of nanometer-scale gold connective necks. *Phys. Rev. Lett.* **1995**, *74* (20), 3995–3998.
5. Krans, J.M.; Muller, J.C.; Yanso, I.K.; Govaert, Th.C.M.; Hesper, R.; van Ruitenbeek, J.M. One-atom point contacts. *Phys. Rev.*, **B 1993**, *48* (19), 14,721–14,724.
6. Krans, J.M.; van Ruitenbeek, J.M.; Fisun, V.V.; Yanson, I.K.; de Jongh, L.J. The signature of conductance quantization in metallic point contacts. *Nature* **1995**, *375*, 767–769.
7. Agrait, N.; Rodrigo, J.G.; Vieira, S. Conductance steps and quantization in atomic-size contacts. *Phys. Rev.*, **B 1993**, *47* (18), 12,345–12,348.
8. Olesen, L.; Lagsgaard, E.; Stensgaard, I.; Besenbacher, F.; Schiøtz, J.; Stoltze, P.; Jacobsen, K.W.; Nørskov, J.K. Quantized conductance in an atom-sized point contact. *Phys. Rev. Lett.* **1994**, *72* (14), 2251–2254.
9. Pascual, J.I.; Mendex, J.; Gomez-Herrero, J.; Baro, A.M.; Garcia, N.; Landman, U.; Luedtke, W.D.; Bogachek, E.N.; Cheng, H.P. Properties of metallic nanowires: from conductance quantization to localization. *Science* **1995**, *267*, 1793–1795.
10. Diaz, M.; Costa-Kramer, J.L.; Escobar, A.L.; Leon, N.; Correia, A. Breakage dynamics and quantized conductance of gold nanowires in the presence of lubricants. *Nanotechnology* **2002**, *13* (1), 43–46.
11. Ohnishi, H.; Kondo, Y.; Takayanagi, K. Quantized conductance through individual rows of suspended gold atoms. *Nature* **1998**, *395*, 780–783.
12. Rubio, G.; Agrait, N.; Vieira, S. Atomic-sized metallic contacts: mechanical properties and electronic transport. *Phys. Rev. Lett.* **1996**, *76* (13), 2302–2305.



13. Untiedt, C.; Rubio, G.; Vieira, S.; Agrait, N. Fabrication and characterization of metallic nanowires. *Phys. Rev., B* **1997**, *56* (4), 2154–2160.
14. Costa-Krammer, J.L. Conductance quantization in nanowires formed between micro and macroscopic metallic electrodes. *Phys. Rev., B* **1997**, *55* (8), 5416–5424.
15. Muller, C.J.; Krans, J.M.; Todorov, T.N.; Reed, M.A. Quantization effects in the conductance of metallic contacts at room temperature. *Phys. Rev., B* **1996**, *53* (3), 1022–1025.
16. Landman, U.; Luedtke, W.D.; Salisbury, B.E.; Whetten, R.L. Reversible manipulations of room temperature mechanical and quantum transport properties in nanowire junctions. *Phys. Rev. Lett.* **1996**, *77* (7), 1362–1365.
17. Costa-Krammer, J.L.; Garcia, N.; Garcia-Mochales, R.; Serena, P.A. Nanowire formation in macroscopic metallic contacts: quantum mechanical conductance tapping a table top. *Surf. Sci.* **1995**, *342* (1–3), L1144–L1149.
18. Hansen, K.; Lagsgaard, E.; Stensgaard, I.; Besebacher, F. Quantized conductance in relays. *Phys. Rev., B* **1997**, *56* (4), 2208–2220.
19. Yasuda, H.; Sakai, A. Conductance of atomic-scale gold contacts under high-bias voltages. *Phys. Rev., B* **1997**, *56* (3), 1069–1072.
20. Kang, J.W.; Hwang, H.J. Molecular dynamics simulation study of the mechanical properties of rectangular Cu nanowires. *J. Korean Phys. Soc.* **2001**, *38* (6), 695–700.
21. Kang, J.W.; Hwang, H.J. Mechanical deformation study of copper nanowire using atomistic simulation. *Nanotechnology* **2001**, *12* (3), 295–300.
22. Gulseren, O.; Ercolessi, F.; Tosatti, E. Premelting of thin wires. *Phys. Rev., B* **1995**, *51* (11), 7377–7380.
23. Bilalbegovic, G. Structures and melting in infinite gold nanowires. *Solid State Commun.* **2000**, *115* (2), 73–76.
24. Hwang, H.J.; Kang, J.W. Structures of cylindrical ultra-thin copper nanowires. *J. Korean Phys. Soc.* **2002**, *40* (2), 283–288.
25. Kang, J.W.; Hwang, H.J. Molecular-dynamics study of the interaction between energetic Al clusters and an Al surface. *Phys. Rev., B* **2001**, *64* (1), 014108.
26. Kang, J.W.; Choi, K.S.; Byun, K.R.; Hwang, H.J. Molecular dynamics study of Al atom and Al<sub>55</sub> cluster deposition on Al substrates. *J. Korean Phys. Soc.* **2000**, *36* (4), 248–250.
27. Kang, J.W.; Choi, K.S.; Kang, J.C.; Hwang, H.J. Molecular dynamics simulation of film growth by energetic aluminum cluster impact. *J. Korean Phys. Soc.* **2001**, *38* (2), 158–161.
28. Allen, M.P.; Tildesley, D.J. *Computer Simulation of Liquids*; Clarendon: Oxford, 1987.
29. Cleri, F.; Rosato, V. Tight-binding potentials for transition metals and alloys. *Phys. Rev., B* **1993**, *48* (1), 22–33.
30. Wang, B.; Yin, S.; Wang, G.; Zhao, J. Structures and electronic properties of ultrathin titanium nanowires. *J. Phys., Condens. Matter* **2001**, *13* (20), L403–L408.
31. Guillope, M.; Legrand, B. (110) Surface stability in noble metals. *Surf. Sci. Lett.* **1989**, *215* (3), 577–595.
32. Lee, Y.J.; Maeng, J.Y.; Lee, E.K.; Kim, B.; Kim, S.; Han, K.K. Melting behaviors of icosahedral metal clusters studied by Monte Carlo simulations. *J. Comput. Chem.* **2000**, *21* (5), 380–387.
33. Lee, Y.J.; Lee, E.K.; Kim, S.; Nieminen, R.M. Effect of potential energy distribution on the melting of clusters. *Phys. Rev. Lett.* **2001**, *86* (6), 999–1002.
34. Gryaznov, V.G.; Heydenreich, J.; Kaprelov, A.M.; Nepijko, S.Q.; Romanov, A.E.; Urban, J. Pentagonal symmetry and disclinations in small particles. *Cryst. Res. Technol.* **1999**, *34* (9), 1091–1119.
35. Kang, J.W.; Hwang, H.J. Molecular dynamics simulation study of the melting of ultra-thin copper nanowires. *J. Korean Phys. Soc.* **2002**, *40* (5), 946–948.
36. Cleveland, C.L.; Luedtke, W.D.; Landman, U. Melting of gold clusters. *Phys. Rev., B* **1999**, *60* (7), 5065–5077.
37. Mei, J.; Davenport, J.W. Molecular-dynamics study of self-diffusion in liquid transition metals. *Phys. Rev., B* **1990**, *42* (15), 9682–9684.



# Nanoceramics

Abbas Khaleel

Department of Chemistry, United Arab Emirates University, Al-Ain, United Arab Emirates

## INTRODUCTION

Ceramics is one of the fields where nanoscience and nanotechnology have shown remarkable progress, producing a variety of advanced materials with unique properties and performance. Nanoceramics is a term used to refer to ceramic materials fabricated from ultrafine particles, i.e., less than 100 nm in diameter. In this field, a great deal of research has been accomplished in the last 20 years and has resulted in significant outcomes that are of great impact academically as well as industrially.

## OVERVIEW

Advanced ceramics include inorganic and non-metallic solid materials composed of polycrystalline sintered bodies, fine powders, single crystals, non-crystalline materials, thin or thick films, and fibers with various morphologies. Systems of metal oxides, carbides, borides and nitrides compose most of the important ceramic materials. Traditional ceramics, or old ceramics, such as tile pottery, are made from minerals such as clay; however, industrial ceramics, or advanced ceramics, are made of highly pure well-chosen materials such as silicon carbide and alumina. Many people think that ceramic materials are used for artistic objects and tableware only. In fact ceramic products are now very important in a wide range of industrial and advanced technical applications in several fields including electronics, medicine, nuclear industry, magnetic applications, and several others.

It has been well proven that the bulk behavior of materials can be dramatically altered when constituted of nanoscale building blocks. Mechanical, magnetic, optical, and other properties of materials have been found to be favorably affected. Hardness and strength, as an example, can be greatly enhanced by consolidating ceramic materials from nanoscale particles. Ductility and superplastic-forming capabilities of nanophase ceramics have now become possible, leading to new processing routes that will be more cost-effective than traditional methods.

In this entry, our focus will be on advanced ceramics fabricated from nanometer-sized powders.

Preparation, properties, and applications will be the main directions of focus and a special attention will be given to the effect of the particle size in these materials.

## PREPARATION

Remarkable progress in synthetic chemistry has led to significant advances in material science, making possible the synthesis of various substances and materials. The manufacture of ceramics involves heat treatment of tightly squeezed powders. The size of the building block of these powders has been found to affect the properties of the final product. The method of preparation is very often a determining factor in shaping the material and its properties. For example, burning Mg in O<sub>2</sub> (MgO smoke) yields 40–80-nm cubes and hexagonal plates, whereas thermal decomposition of commercial Mg(OH)<sub>2</sub>, MgCO<sub>3</sub>, and especially Mg(NO<sub>3</sub>)<sub>2</sub> yields irregular shapes often exhibiting hexagonal platelets. Surface areas can range from 10 m<sup>2</sup>/g (MgO smoke) to 150 m<sup>2</sup>/g for Mg(OH)<sub>2</sub> thermal decomposition. On the other hand, aerogel-prepared Mg(OH)<sub>2</sub> can lead to MgO with surface areas as high as 500 m<sup>2</sup>/g.

Because the main focus of this article is ceramics fabricated from nanometer-sized building blocks, different methods for preparing ultrafine ceramic powders will be discussed. The steps in manufacturing ceramics from powders, which include molding, extrusion, and densification, will not be discussed here.

## Physical Methods

### Vapor condensation methods

Gas-condensation techniques to produce nanoparticles directly from a supersaturated vapor of metals are among the earliest methods for producing nanoparticles. They generally involve two steps: First, a metallic nanophase powder is condensed under inert convection gas after a supersaturated vapor of the metal is obtained inside a chamber. Second, the powder is oxidized by allowing oxygen into the chamber (to produce metal oxide powder). A subsequent annealing process at high temperatures is often required to complete the oxidation. The system consists of a vapor source inside a

vacuum chamber containing a mixture of an inert gas, usually argon or helium, mixed with another gas, which is selected based on the material to be prepared. Oxygen is mixed with the inert gas to produce metal oxides.  $\text{NH}_3$  is usually used to prepare metal nitrides and an appropriate alkane or alkene, as a source of carbon, is usually used to prepare metal carbides. Nanoparticles are formed when supersaturation is achieved above the vapor source. A collection surface, usually cooled by liquid nitrogen, is placed above the source. The particles are transported to the surface by a convection current or by a combination of a forced gas flow and a convection current, which is set up by the difference in the temperature between the source and the cold surface. Some improved systems involve a way to scrap the nanoparticles from the cold collection surface so that the particles would fall into a die and a unit where they can be consolidated into pellets. Supersaturated vapor can be achieved by many different vaporization methods. The most common techniques include thermal evaporation, sputtering, and laser methods. A variety of nanoscale metal oxides and metal carbides have been prepared using laser-vaporization techniques.

The advantages of vapor condensation methods include versatility, ease in performance and analysis, and high-purity products. On the other hand, they can be employed to produce films and coatings. Furthermore, laser-vaporization techniques allow for the production of high-density, directional, and high-speed vapor of any metal within an extremely short time. Despite the success of these methods, they have the disadvantage that the production cost is still high because of low yields. Heating techniques have other disadvantages that include the possibility of reactions between the metal vapors and the heating source materials.

### Spray pyrolysis

This technique is known by several other names including solution aerosol thermolysis, evaporative decomposition of solutions, plasma vaporization of solutions, and aerosol decomposition. The starting materials in this process are chemical precursors, usually appropriate salts, in solution, sol, or suspension. The process involves the generation of aerosol droplets by nebulizing or “atomization” of the starting solution, sol, or suspension. The generated droplets undergo evaporation and solute condensation within the droplet, drying, thermolysis of the precipitate particle at higher temperature to form a microporous particle, and, finally, sintering to form a dense particle.

Different techniques for atomization are employed including pressure, two-fluid, electrostatic, and ultrasonic atomizers. These atomizers differ in droplet size (2–15  $\mu\text{m}$ ), rate of atomization, and droplet velocity (1–20 m/sec). These factors affect the heating rate and

residence time of the droplet during spray pyrolysis which, in turn, affect some of the particle characteristics including particle size. For a specific atomizer, particle characteristics, including particle size distribution, homogeneity, and phase composition depend on the type of precursor, solution concentration, pH, viscosity, and the surface tension.

Aqueous solutions are usually used because of their low cost, safety, and the availability of a wide range of water-soluble salts. Metal chloride and nitrate salts are commonly used as precursors because of their high solubility. Precursors that have low solubility or those that may induce impurities, such as acetates that lead to carbon in the products, are not preferred.

The advantages of this method include the production of high-purity nanosized particles, homogeneity of the particles as a result of the homogeneity of the original solution, and the fact that each droplet/particle goes through the same reaction conditions. The disadvantages of spray pyrolysis include the need for large amounts of solvents and the difficulty to scale-up the production. The use of large amounts of non-aqueous solvents increases the production expenses because of the high cost of pure solvents and the need for proper disposal.

### Thermochemical/flame decomposition of metalorganic precursors

Flame processes have been widely used to synthesize nanometer-sized particles of ceramic materials. This is another type of gas-condensation technique with the starting material being a liquid chemical precursor. The process is referred to as chemical vapor condensation (CVC). In this process, chemical precursors are vaporized and then oxidized in a combustion process using a fuel-oxidant mixture such as propane-oxygen or methane-air. It combines the rapid thermal decomposition of a precursor-carrier gas stream in a reduced pressure environment with thermophoretically driven deposition of the rapidly condensed product particles on a cold substrate. The flame usually provides a high temperature (1200–3000 K), which promotes rapid gas-phase chemical reactions.

A variety of chemical precursors can be used including metal chlorides, such as  $\text{TiCl}_4$  to prepare  $\text{TiO}_2$  and  $\text{SiCl}_4$  to prepare  $\text{SiO}_2$ , metal-alkyl precursors, metal alkoxides, and gaseous metal hydrides, such as silane as a source of silicon to prepare silica. Chlorides have been the most widely used precursors in the industry and the process is sometimes referred to as the “chloride process.” The high vapor pressure of chlorides and the fact that they can be safely stored and handled make them excellent potential precursors. The disadvantages of using chloride precursors are the formation of acidic gases and contamination of the products with halide residues. Flame processes

are used industrially to produce commercial quantities of ceramic particulates, such as silica and titania. This is because of the low cost of production as compared to all other methods. The disadvantage of flame synthesis is that the control of particle size (both primary particle and aggregates size), morphology, and phase composition is difficult and limited.

## Chemical Methods

### Sol–gel technique

The sol–gel process is typically used to prepare nanometer-sized particles of metal oxides. This process is based on the hydrolysis of metal reactive precursors, usually alkoxides in an alcoholic solution, resulting in the corresponding hydroxide. Condensation of the hydroxide by giving off water leads to the formation of a network-like structure. When all hydroxide species are linked, gelation is achieved and a dense porous gel is obtained. The gel is a polymer of a three-dimensional skeleton surrounding interconnected pores. Removal of the solvents and appropriate drying of the gel result in an ultrafine powder of the metal hydroxide. Further heat treatment of the hydroxide leads to the corresponding powder of the metal oxide. As the process starts with a nanosized unit and undergoes reactions on the nanometer scale, it results in nanometer-sized powders. For alkoxides that have low rates of hydrolysis, acid or base catalysts can be used to enhance the process.

When drying is achieved by evaporation under normal conditions, the gel network shrinks as a result of capillary pressure that occurs and the hydroxide product obtained is referred to as xerogel. However, if supercritical drying is applied using a high-pressure autoclave reactor at temperatures higher than the critical temperatures of solvents, less shrinkage of the gel network occurs as there is no capillary pressure and no liquid–vapor interface, which better protects the porous structure. The hydroxide product obtained is referred to as an aerogel. Aerogel powders usually demonstrate higher porosities and larger specific surface areas than analogous xerogel powders.

Sol–gel processes have several advantages over other techniques to synthesize nanopowders of metal oxide ceramics. These include the production of ultrafine porous powders and the homogeneity of the product as a result of homogeneous mixing of the starting materials on the molecular level.

### Reverse microemulsions/micelles method

The reverse micelle approach is one of the recent promising routes to nanocrystalline materials including ceramics. Surfactants dissolved in organic solvents

form spheroidal aggregates called reverse (or inverse) micelles. In the presence of water, the polar head groups of the surfactant molecules organize themselves around small water pools ( $\sim 100 \text{ \AA}$ ), leading to dispersion of the aqueous phase in the continuous oil phase.

Reverse micelles are used to prepare nanoparticles by using a water solution of reactive precursors that can be converted to insoluble nanoparticles. Nanoparticle synthesis inside the micelles can be achieved by different methods including hydrolysis of reactive precursors, such as alkoxides, and precipitation reactions of metal salts. Solvent removal and subsequent calcination lead to the final product. Several parameters, such as the concentration of the reactive precursor in the micelle and the weight percentage of the aqueous phase in the microemulsion, affect the properties, including particle size, particle-size distribution, agglomerate size, and the phases of the final ceramic powders. There are several advantages to using this method including the ability to prepare very small particles and the ability to control the particle size. Disadvantages include low production yields and the need to use large amounts of liquids.

### Precipitation from solutions

Precipitation is one of the conventional methods to prepare nanoparticles of metal oxide ceramics. This process involves dissolving a salt precursor, usually chloride, oxychloride or nitrate, such as  $\text{AlCl}_3$  to make  $\text{Al}_2\text{O}_3$ ,  $\text{Y}(\text{NO}_3)_3$  to make  $\text{Y}_2\text{O}_3$ , and  $\text{ZrCl}_4$  to make  $\text{ZrO}_2$ , in water. The corresponding metal hydroxides are usually obtained as precipitates in water by adding a base solution such as sodium hydroxide or ammonium hydroxide solution. The remaining counter-ions are then washed away and the hydroxide is calcined after filtration and washing to obtain the final oxide powder. This method is useful in preparing ceramic composites of different oxides by coprecipitation of the corresponding hydroxides in the same solution. Solution chemistry is also used to prepare non-oxide ceramics or pre-ceramic precursors that can be converted to ceramics upon pyrolysis.

One of the disadvantages of this method is the difficulty in controlling the particle size and size distribution. Very often, fast and uncontrolled precipitation takes place resulting in large particles.

### Chemical synthesis of pre-ceramic polymers coupled with physical processing techniques

This method is based on the use of molecular precursors, which facilitates the synthesis of nanomaterials containing phases of desired compositions. It involves a chemical reaction to prepare an appropriate polymer, which is then converted into ceramic material upon

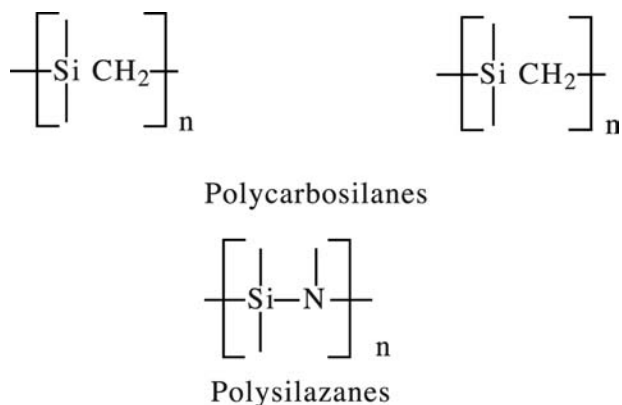
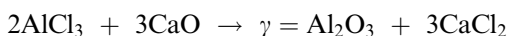


**Fig. 1** General structural formulas of polycarbosilanes and polysilazanes.

pyrolysis. Using chemical reactions to prepare the pre-ceramic polymer not only allows for control of phase compositions but also overcomes the limitation of low production yields of the physical methods. This method has been very useful in preparing non-oxide ceramics such as silicon carbide and silicon nitride. The conversion of an organometallic precursor into a ceramic depends on different parameters such as the molecular structure of the precursor and the pyrolysis conditions (temperature, duration, and atmosphere). Metal carbides and metal nitrides have been obtained by pyrolysis of polymers containing the appropriate elements such as Si or Al and C or N. These polymers are called pre-ceramic polymers and are prepared from simpler chemical precursors. A considerable amount of free carbon from the thermolysis process is very often a problem. Silicon carbide (SiC) and silicon nitride (Si<sub>3</sub>N<sub>4</sub>) are the most studied ceramic materials prepared via this route. They are usually synthesized by the pyrolysis of polycarbosilanes and polysilazanes, for which general structural formulas are shown in Fig. 1, at temperatures between 1000°C and 1200°C.

### Mechanochemical synthesis

Mechanochemical synthesis involves mechanical activation of solid-state displacement reactions. This process has been successfully used recently to make nanoceramic powders such as Al<sub>2</sub>O<sub>3</sub> and ZrO<sub>2</sub>. It involves the milling of precursor powders (usually a salt and a metal oxide) to form a nanoscale composite of the starting materials, which react during milling, and subsequent heating, if necessary, to form a mixture of dispersed nanoparticles of the desired oxide within a soluble salt matrix. Nanoparticles of Al<sub>2</sub>O<sub>3</sub> (10–20 nm), for example, can be prepared by milling AlCl<sub>3</sub> with CaO.



## BONDING CONSIDERATIONS

Understanding chemical bonding and structures in ceramic materials is necessary in order to understand their chemical and physical behavior. When materials are composed of nanometer-sized building blocks, they deviate considerably from structural perfection and stoichiometry. As a result, the number of defects due to edges, corners, f-centers, and other surface imperfections is greatly enhanced, which, in turn, affects several physical and chemical properties as will be discussed below.

A range of cohesive forces contribute to the nature of bonding in ceramic materials including ionic (MgO, Fe<sub>1-x</sub>O), covalent, metallic, van der Waals, and hydrogen bonding. Ionic compounds are formed when highly electronegative and highly electropositive elements are combined in a lattice. Pure ionic model is a reasonable approximation for some systems while it is a poor approximation for crystals containing large anions and small cations. In such systems, covalent contribution to bonding becomes significant. van der Waals interactions play a crucial role in many ceramic systems, especially those with layered structures. In many oxide hydrates or hydroxy oxides, hydrogen bonding also contributes to the cohesive energy. For further reading on structure and bonding, the reader is referred to structural inorganic chemistry books.

## SELECTED PROPERTIES

Ceramics possess their own chemical, physical, mechanical, and magnetic properties that are different from those of other materials such as metals and plastics. The properties of ceramics depend mainly on the type and the amounts of materials in their composition. However, the size of the building blocks of a ceramic material has been found to play an important role in its properties (see Ref.<sup>[1]</sup> and references therein).

When materials are prepared from nanometer-sized particles, a significant portion of the atoms become exposed on the surface. As a result, such materials exhibit unique properties that are remarkably different from those of the corresponding bulk. The physical and chemical properties of nanoparticles show the gradual transition from atomic or molecular to condensed matter systems.

### Chemical Properties

Ceramic materials are relatively inert, especially crystalline materials that tend to have perfect structures with minimum amount of defects. Most of the reactivity of these materials involves the surfaces where coordinatively unsaturated as well as defect sites exist.

The behavior of the surface toward other species and the nature of interaction depend on the composition and the morphology, which determine the nature and the degree of surface interactions with other substances. Most of the time, interactions are limited to adsorption on the surface, which does not affect the bulk making these materials good corrosion-resistant.

The possibility of preparing ceramic powders in high surface areas with high porosity makes them well desired in some advanced applications. One example is the use of ceramic materials as supports for heterogeneous catalysts. Another example is the use of such materials in biomedical applications, where the surface of nanophase ceramics exhibits a remarkably improved biomedical compatibility compared to conventional ceramics, as discussed below.

### Mechanical Properties

Ceramics are very strong materials showing considerable resistance against compression and bending. Some ceramic materials are similar to steel in strength. Most ceramics retain their strength at high temperatures. Silicon carbides and silicon nitrides, as an example, retain their strength at temperatures as high as 1400°C. As a result, such materials are used in high-temperature applications. Many of the physical and mechanical properties are particle-size dependent. As a result, several systems of nanophase ceramics have exhibited quite interesting and favorably enhanced mechanical properties.

#### Improved sintering and hardness properties

Nanoceramics are processed from nanophase powders by compacting first powders composed of individual ceramic particles (usually less than 50 nm in size) into a raw shape (often called a green body). This compacted powder is then heated at elevated temperatures. Densification occurs as a result of diffusion of vacancies out of pores (to grain boundaries), which lead to shrinkage of the sample. This process is referred to as pressure-less sintering. Fortunately, nanophase powders were found to compact as easily as their analogous submicron particles. To avoid particle size growth, samples have to be sintered at the lowest temperature possible for a time sufficient to remove the residual porosity and establish coherent grain boundaries. Successful sintering enhances the hardness of the final material.

Experimental evidence shows that nanophase powders densify at faster rates as compared to commercial (submicron) particles.<sup>[1]</sup> Faster densification rates allow achieving a given density at smaller grain sizes, before serious growth takes place. As a result of their

small particle and pore sizes, nanocrystalline powders sinter to much greater densities than their conventional analogs at the same temperature. This also establishes that nanocrystalline powders, as compared to conventional powders, reach the same density at much lower temperatures. This, of course, eliminates the need for very high temperatures.

One disadvantage that can accompany fast densification though is inhomogeneous heating where the outside layers of the particles densify into a hard impervious shell which constrains the inside of the sample from normal shrinking, leading to some cracking as a result of strain incompatibility. This problem can be avoided by several ways. The most efficient way is to heat the samples slowly to reduce the shrinkage in the outer shell while heat is transported to the inner regions. On the other hand, high-density nanostructured ceramic systems including  $Y_2O_3$ ,  $TiO_2$ , and  $ZrO_2$  have been achieved by means of pressure-assisted sintering. Applying some pressure during sintering can increase the densification rate and suppress the particle growth.

Nanoscale powders of non-oxide ceramics such as metal carbides and nitrides show similar behavior. Conventional SiC, as an example, is difficult to sinter. Addition of some additives such as boron or carbon is very often necessary to densify SiC. Ultrafine powder of SiC sinters at lower temperatures and densifies without additives. On the other hand, mechanical properties can be fairly improved by the introduction of metallic nanoparticles dispersed within the matrix grains. Such systems are referred to as nanocomposites. Tungsten, nickel, or molybdenum nanoparticles dispersed within  $Al_2O_3$  matrix grains, as an example, can enhance the mechanical properties of alumina, including the fracture strength and hardness.

#### Reduced brittleness and enhanced ductility and superplasticity

Superplasticity and ductility refer to the capability of some polycrystalline materials to undergo extensive tensile deformation without necking or fracture. Ceramic brittleness is the biggest technical barrier in practical applications, especially in load-bearing applications. Theoretical and experimental results provide evidence for the possibility that traditional brittle materials can be ductilized by reducing their grain sizes.<sup>[1]</sup> When made from nanoparticles, brittle ceramics can be superplastically deformed at modest temperatures and then heat treated at higher temperatures for high-temperature strengthening.

The capability to synthesize superplastic ceramic materials is now established. Nanocrystalline ceramics deform at faster rates, lower stresses, and lower temperatures. One important use of superplasticity in

ceramics is diffusion bonding, where two ceramic parts are pressed together at moderate temperatures and pressures to form a seamless bond through diffusion and grain growth across the interface. Diffusion bonds form more easily in nanocrystalline ceramics than in larger grained ceramics as a result of both the enhanced plastic flow of nanocrystalline ceramics and the larger number of grain boundaries they provide for diffusional flux across the interface.

### Electrical Properties

Ceramics include electrical conducting, insulating, and semiconducting materials. Chromium oxide is an electrical conductor, aluminum oxide is an insulator, while silicon carbide behaves as a semiconductor. As a result, ceramic materials have been used in a variety of electronic applications based on their electrical behavior.

Several electrical properties are particle-size and composition dependent. Electrical resistance and dielectric constant, as an example, for some systems increased as a result of small particle size. Conductivity of some mixed oxide ceramics, such as lithium aluminosilicate, is higher than that of their constituent oxides.

### Magnetic Properties

Some ceramic materials possess magnetic properties. These include iron oxide-based ceramics and oxides of chromium, nickel, manganese, and barium. Ceramic magnets are known to exhibit high resistance to demagnetization. As a result, several ceramic powders have been employed in a wide range of electronic and magnetic applications as discussed below.

The fabrication of such materials from ultrafine particles can significantly enhance their magnetic behavior. The fact that in nanometer-sized particles a large portion of the atoms are on the surface, where the coordination numbers are less than that for bulk atoms, affects several parameters including unique surface/interface behavior and different band structure, which both lead to magnetism enhancement. It is now well established that one of the requirements to achieve appropriate coercivity and high magnetization saturation is to fabricate such materials in highly divided particles, preferably in the nanometer-sized range, with homogeneity and narrow size distribution. For further reading on nanoscale magnetism, the reader is referred to Sorensen's chapter "Magnetism" in Ref.<sup>[1]</sup>.

Many other properties are also particle-size dependent. The optical properties, as an example, of some ceramic materials have been found to depend on particle sizes. Nanoparticles of  $\text{TiO}_2$ , as an example, are more efficient UV absorber than powders of large particles.

## APPLICATIONS

Ceramic materials are of great value in a variety of applications as a result of their unique properties compared to other materials. Because of their electrical and magnetic properties, ceramics are important in several electronic applications, where they are used as insulators, semiconductors, conductors, and magnets. Ceramic materials also have important uses in the aerospace, biomedical, construction, and nuclear industries. In many of these applications, ceramic materials have shown significantly better performance when fabricated from nanometer-sized particles.

### Mechanical Applications

Industrial ceramics are widely employed in applications that require strong, hard, and abrasion-resistant materials. Metal-cutting tools, tipped with alumina, and tools made from silicon nitrides for cutting, shaping, grinding, and sanding iron, nickel-based alloys, and other metals are very commonly used. Other ceramics such as silicon nitrides and carbides are used to make components for high-temperature use such as valves and turbocharger rotors. Ceramic materials and metal-based ceramics (cermets) are used to make components for space vehicles, including heat-shield tiles for the space shuttle and nosecones for rocket payloads.

### Electrical Applications

Ceramics are used as insulators, semiconductors, and conductors. Aluminum oxide ( $\text{Al}_2\text{O}_3$ ), for example, does not conduct electricity at all and is used to make insulators. Other ceramics, such as barium titanate ( $\text{BaTiO}_3$ ), are used as semiconductors in electronic devices. Some copper oxide-based ceramics are superconductive at temperatures higher than those at which metals become superconductive. Superconductivity refers to the ability of a cooled material to conduct an electric current with no resistance. This phenomenon can occur only at extremely low temperatures, which are difficult to maintain. Transition metal nitrides, carbides, and borides are of interest as cathodes in electrochemical applications. This interest stems from the favorable properties of these materials including electronic conductivity and good thermal conductivity, which when coupled with their mechanical strength and high melting points suggest that such materials can be stable in a range of environments.

Some ceramics such as strontium titanate ( $\text{SrTiO}_3$ ) are employed in the form of thin films as capacitors in several electronic devices because of their capability to store large amounts of electricity in extremely small



**Table 1** Examples of electronic ceramics

Functions	Examples of materials	Applications
Insulation	Al <sub>2</sub> O <sub>3</sub> , SiC + BeO	IC substrate
Dielectricity	BaTiO <sub>3</sub>	Capacitor
Semiconducting	SiC, LaCrO <sub>3</sub> , SnO <sub>2</sub> , ZnO + Bi <sub>2</sub> O <sub>3</sub>	Gas defector, thermistor, varistor
Piezoelectricity	ZnO, SiO <sub>2</sub>	Piezolighter, piezofilter, surfacewave transducer, piezovibrator, flexible piezodetector
Pyroelectricity	PZT	IR detectors
Ferroelectricity	PLZT	Optical shutter, optical memory
Ionic conduction	$\beta$ -Al <sub>2</sub> O <sub>3</sub> , ZrO <sub>2</sub>	Na-S battery, O <sub>2</sub> sensor
Luminescence	Y <sub>2</sub> O <sub>3</sub> :S:Eu, ThO <sub>2</sub> :Nd, Al <sub>2</sub> O <sub>3</sub> :Cr	Cathode luminescence, IR laser
Light guide	SiO <sub>2</sub>	Optical communication fiber
Polarization	PLZT	Optical shutter
Soft magnetism	$\gamma$ -Fe <sub>2</sub> O <sub>3</sub> , Zn <sub>1-x</sub> Mn <sub>x</sub> Fe <sub>2</sub> O <sub>4</sub>	Magnetic tape
Hard magnetism	SrO·6Fe <sub>2</sub> O <sub>3</sub>	Magnet seal

PZT: lead zirconate–titanate ceramics. PLZT: lanthanum-modified lead zirconate–titanate ceramics.

volumes. Lithium aluminosilicate ceramics have potential applications as solid electrolytes for utilization in solid high-energy density lithium battery systems. Piezoelectric ceramics are now key electronic components for television, FM radio, and the like. Very recently, piezoelectric ceramic displays have been developed in Japan, where microceramic actuators for activating the pixels are used. Piezoelectric effect refers to the appearance of an electric potential across certain faces of a crystal when it is subjected to mechanical pressure.

Other examples of functions and applications of advanced ceramics in the field of electronics are shown in Table 1.<sup>[2]</sup>

### Magnetic Applications

Iron oxide-based ceramics (ferrites) are widely employed as low-cost magnets in electric motors. Such magnets help in converting electric energy into mechanical energy. Unlike metal magnets, ferrites conduct high-frequency currents, and as a result, they do not lose as much power as metal conductors do. Manganese zinc ferrites are used in magnetic recording heads, and ferric oxides are the active component in several magnetic recording media, such as recording tapes and computer diskettes.

### Biomedical Applications and Bioceramics

Some advanced materials are used in the biomedical field to make implants for use within the body. The main requirement of biomaterials for this application

is the ability of their surfaces to support new bone growth. Ceramic materials are known to possess exceptional biocompatibility properties with bone cells and tissues. Specially made porous ceramic materials such as alumina, titania, zirconia, and others bind with bone and other natural tissues. Such ceramics are used to make hip joints, dental caps, and bridges. Other advanced ceramics such as hydroxyapatite, Ca<sub>10</sub>(PO<sub>4</sub>)<sub>6</sub>(OH)<sub>2</sub>, which is the principal component of bones and teeth, have excellent biocompatibility and bone in-growth capabilities and are used in reconstructing fractured bones and as replacement materials.

Recent research on long-term functions of osteoblasts on nanophase ceramics has shown evidence for unique and significant behavior.<sup>[3]</sup> Compared to conventional ceramics, nanophase ceramics has shown enhanced osteoblast adhesion and proliferation, alkaline phosphatase synthesis, and concentration of extracellular matrix calcium.

### Coatings

Because of its unique hardness and corrosion resistance, ceramic enamel is often used in coating metals. Thin hard wear-resistant coatings of ceramics include materials such as titanium nitride and titanium carbonitride. An emerging class of new hard protecting coatings beyond homogeneous layers of a ceramic nitride material is layered coating structures such as superlattices or multilayers of different nitrides. Such multilayer coating has been successfully applied in several applications such as bearings, pumps, and

compressors. Non-nitride coatings, such tungsten carbide/carbon, are also of interest because of their high elasticity and chemical inertness.

Several techniques are being employed for protective ceramic coating. These include thermal spraying, chemical vapor deposition (known as CVD), and plasma spraying.

### Nuclear Industry

Lithium-based ceramics are now considered as potential solid tritium breeders in nuclear fusion reactors. Potential breeder materials include  $\text{LiAlO}_2$ ,  $\text{Li}_2\text{O}$ ,  $\text{Li}_2\text{ZrO}_3$ , and  $\text{Li}_4\text{SiO}_4$ . Solid breeders are safer during operation than liquid lithium systems, which are highly reactive.

### CONCLUSION

Nanoceramics is one of the great outcomes of the evolutionary research in the field of nanoscience and nanotechnology, where fabrication of materials from nanometer-sized building blocks has resulted in a wide range of industrially useful materials. Recent research has proven that ceramic materials fabricated from ultrafine powders can be obtained through several physical as well as chemical methods that can be scaled up to produce commercial amounts. These unique materials have exhibited very remarkable behavior as compared with their bulk counterparts. Significant characteristics include chemical, mechanical, magnetic, electrical, and optical properties. As a result, improved performance of ceramic materials has been observed in a variety of applications including chemical, mechanical, magnetic, electrical, and biomedical. The new properties and improved performance of nanoceramics that are being discovered stimulate the development and improvement of ceramic processing, which, in turn, open the doors wide for the use of ceramics in a wide range of new technologies.

Directions of current interests include the preparation and processing of ultrafine (nanometer-sized) powders, the development of new synthetic routes to materials of homogeneous sintered bodies, and the preparation of ceramics made of several composites.

### REFERENCES

1. Khaleel, A.; Richards, R. Ceramics. In *Nanostructured Materials in Chemistry*; Klabunde, K.J., Ed.; John Wiley and Sons, Inc.: New York, 2001; 85–120.
2. Yanagida, H. Electronic Ceramics. In *Fine Ceramics*; Saito, S., Ed.; Elsevier: New York, 1988; 239–261.
3. Webster, T.J.; Ergun, C.; Doremus, R.H.; Siegel, R.W.; Bizios, R. Enhanced functions of osteoblasts on nanophase ceramics. *Biomaterials* **2000**, *21* (17), 1803–1810.

### BIBLIOGRAPHY

1. Brinker, C.J.; Scherer, W. *Sol-Gel Science*; Academic Press: San Diego, USA, 1990.
2. Cow, G.M.; Gonsalves, K.E. *Nanotechnology, Molecularly Designed Materials*; American Chemical Society: Washington, DC, 1996.
3. Edelstein, A.S.; Cammarato, R.C. *Nanoparticles: Synthesis, Properties and Applications*; Institute of Physics Publishing: Philadelphia, 1996.
4. Hadjipanayis, G.C.; Siegel, R.W. *Nanophase Materials*; Kluwer Academic Publishers: Dordrecht, 1994.
5. Ichinose, N.; Ozaki, Y.; Kashu, S. *Superfine Particle Technology*; Springer: London, 1992.
6. Interrante, L.V.; Hampden-Smith, M.J. *Chemistry of Advanced Materials: An Overview*; Wiley-VCH: New York, 1998.
7. Jolivet, J.-P. *Metal Oxide Chemistry and Synthesis. From Solution to Solid State*; John Wiley and Sons, Ltd.: New York, 2000.
8. Narula, C.K. *Ceramic Precursor Technology and Its Applications*; Marcel Dekker, Inc.: New York, 1995.
9. Segal, D. *Chemical Synthesis of Advanced Ceramic Materials*; Cambridge University Press: Cambridge, 1989.

# Nanoceramics: Thermal Conductivity

Paul G. Klemens

Department of Physics, University of Connecticut, Storrs, Connecticut, U.S.A.

## INTRODUCTION

The heat carriers in ceramic insulators are lattice waves. The thermal conductivity is governed by their attenuation length or mean free path. Scattering of these waves by grain boundaries can reduce the mean free path and thus decrease the thermal conductivity. The lattice waves, which carry heat range over a wide frequency spectrum, and only waves of the lower part of that spectrum are scattered by grain boundaries. This will be discussed with emphasis on thermal barrier coatings, where nanoscale grains and point defects, acting on different parts of the spectrum, each cause an independent thermal conductivity reduction. In coatings protecting against wear one can use nanoscale inclusions to enhance mechanical properties without reducing the thermal conductivity. Finally, there are applications where the thermal conductivity of ceramics is to be enhanced by appropriate high-conductivity inclusions, such as carbon nanotubes.

## LATTICE THERMAL CONDUCTIVITY

The thermal vibrations of solids can be described by a superposition of plane progressive displacement waves, which transport heat energy.<sup>[1,2]</sup> The frequency of these waves extends over a wide spectrum. Each wave of frequency  $f$  has energy  $E$  and energy flow  $Ev$ , where  $v$  is its group velocity. In the limit of low frequencies, and wavelengths large compared to interatomic distances, these waves are identical to elastic waves in the corresponding continuum. For higher frequencies or shorter waves, the dependence of  $f$  on direction and wavelength is modified.

In a solid of perfectly periodic structure and with perfectly harmonic interatomic forces, these waves would be normal modes of vibration; that is, the energy content of each wave would remain constant with time. In real solids there are structural lattice imperfections, which also include external and internal boundaries. In addition, all solids are somewhat anharmonic: the interatomic forces as function of relative displacements between atoms are not strictly a linear function of these displacements but contain

higher-order terms. The corresponding potential energy of displacement contains not only quadratic or harmonic terms, but higher-order or anharmonic terms. All these departures from perfection cause slow energy transfer among the waves. The multiplicity of these possible interactions in macroscopic solids tends to establish thermal equilibrium. In thermal equilibrium each wave in a group of frequency  $f$  has an average energy  $E(f)$ , a function of frequency but the same for all directions, and there is no net energy transport: for every wave  $f$  and  $v$  there is a wave  $f$  and  $-v$ . It is sufficient to know that interactions occur so that thermal equilibrium can be attained. For non-equilibrium properties such as the thermal conductivity one must also know at what rate equilibrium is restored, once equilibrium is disturbed. This requires knowledge of the interaction processes.

Whereas  $E(f)$  depends on both  $f$  and absolute temperature  $T$ , the equipartition value  $E = k_B T$  independent of frequency  $f$  is attained if  $T/f$  is sufficiently high. Here  $k_B$  is the Boltzmann constant. This limit applies for all waves that transport heat at ordinary and high temperatures, and will be used in the present discussion.

Each wave makes a contribution  $k_B$  to the specific heat. The number of waves in a given frequency interval varies as  $f^2 df$ . Therefore, the major contribution to the specific heat, of the waves with high group velocity and thus carry heat, come from the highest frequencies  $f_m$  of those waves, the acoustic branch.<sup>[3]</sup> This part of the specific heat, for a solid of unit volume and containing  $N$  molecular units, is

$$C = \int C(f) df = \int_0^{f_m} 9Nk_B \frac{f^2}{f_m^3} df = 3Nk_B \quad (1)$$

A temperature gradient slightly enhances the energy of waves propagating toward the colder side, and vice versa. The thermal conductivity is composed of contributions from each frequency interval. If  $l(f)$  is the attenuation length of waves of frequency  $f$ , the thermal conductivity  $\kappa$  has the form

$$\kappa = \frac{1}{3} \int C(f) v l(f) df = \frac{3Nk_B}{f_m^3} \int_0^{f_m} v f^2 l(f) df \quad (2)$$

The attenuation length plays here the same role as a mean free path in the corresponding expression in the kinetic theory of gases. It is important that in general  $l(f)$  increases with decreasing frequency, so that low frequencies play a larger role in the lattice thermal conductivity than they do in the specific heat or thermal energy of vibrations. This will enhance the effect of grain boundary scattering on the thermal conductivity.

## INTERACTION PROCESSES

In all real solids there is an interchange of energy among the waves because of the anharmonic terms (cubic or higher in the potential energy as function of strain), in addition to the harmonic terms, quadratic in strain and defining the elastic moduli. The corresponding intrinsic attenuation length is  $l_i(f, T)$ . Waves can also be attenuated by scattering from the various structural imperfections. These include extended obstacles, such as external and internal boundaries, and defects of atomic dimensions (point defects such as solute atoms, vacancies, interstitials, and small aggregates thereof). Platelets, tubes, and dislocations may also be significant. Each obstacle or defect, labeled  $\alpha$ , has its characteristic magnitude and frequency dependence, and some are listed in Table 1. All these processes contribute to the overall attenuation per unit path length for waves of a given frequency  $f$ :

$$\frac{1}{l(f)} = \frac{1}{l_i(f, T)} + \sum_{\alpha} \frac{1}{l_{\alpha}(f)} \quad (3)$$

The intrinsic thermal conductivity  $\kappa_i$  can be obtained from Eq. (2) by substituting  $l_i = (Bf^2T)^{-1}$  for  $l(f)$ . The integrand is independent of  $f$ , so that equal frequency intervals make equal contributions to the intrinsic conductivity. The coefficient  $B$  can be calculated from theory in terms of density, elastic moduli, and anharmonicity parameters.<sup>[1,2]</sup> Alternatively, it can be derived from measured conductivities, since

$$\kappa_i(T) = \frac{3Nk_B v}{Bf_m^2 T} \quad (4)$$

**Table 1** Inverse attenuation lengths

Processes	$1/l(f)$	$f$ dependence
Cubic anharmonic	$1/l_i(f, T)$	$Bf^2T$
Point defects	$1/l_p(f)$	$Af^4$
Line defects	$1/l_{\text{cyl}}(f)$	$Af^3$
Thin sheets, thickness $t$	$1/l_{\text{sh}}(f)$	$t^2 f^2$
Boundaries	$1/l_B$	$1/L$

Source: Ref.<sup>[1]</sup>.

## THERMAL CONDUCTIVITY REDUCTIONS

Of the imperfections that lower the thermal conductivity, two are important and are discussed here: point defects and large obstacles, including internal boundaries. The first reduces  $l(f)$  mainly at high frequencies, the second mainly at low frequencies. These reductions are practically independent of each other, so that

$$\kappa = \kappa_i(T) - \delta\kappa_p - \delta\kappa_B \quad (5)$$

Here  $\delta\kappa_p$  is the reduction in thermal conductivity due to point defects, and  $\delta\kappa_B$  is that due to internal boundaries and large obstacles. For grain boundary scattering it is provisionally assumed that it is frequency independent, although this assumption will have to be modified later. It is convenient to define a frequency  $f_o$  such that  $l_p(f_o) = l_i(T, f_o)$ , making  $f_o \propto T^{1/2}$ , and define a frequency  $f_B$  such that  $L = l_i(T, f_B)$ , hence  $f_B \propto (LT)^{-1/2}$ . Substituting each scattering mechanism in turn into  $l(f)$  of Eq. (3), and this into Eq. (2), one finds for the usual case when  $f_B \ll f_o$

$$\kappa - \delta\kappa_p = \kappa_i(f_o/f_m) \arctan(f_m/f_o) \quad (6a)$$

$$\begin{aligned} \delta\kappa_B &= \kappa_i(f_B/f_m) \arctan(f_m/f_B) \\ &\approx \frac{\pi}{2} \kappa_i(f_B/f_m) \end{aligned} \quad (6b)$$

The reductions due to these two scattering processes are additive. This differs from the frequently used approximation of adding their corresponding thermal resistances to give the total thermal resistance  $1/\kappa$ . Using Eq. (5) yields a larger reduction in conductivity than one obtains from adding resistances.

From this theory, two conclusions emerge: 1) The fractional reduction  $\delta\kappa_i/\delta\kappa_B$  is significant, even when the average intrinsic mean free path  $\langle l_i \rangle$  is very small compared to  $L$ . One would have expected, at first sight, a fractional reduction of the order  $\langle l_i \rangle/L$  or  $(f_B/f_m)^2$ , but the reduction from Eq. (6b) is of the order  $f_B/f_m$ . Because  $f_B < f_m$ , this reduction is much larger. 2) The fractional decrease due to small grain size  $\delta\kappa_B/\kappa$  is enhanced if  $\kappa$  is already significantly reduced by point defects. This was first seen in measurements on polycrystalline silicon of micron-sized grains.<sup>[4]</sup>

In the case of stabilized zirconia there is a large concentration of oxygen vacancies, which are responsible for the low thermal conductivity. It was suggested that a further reduction could be obtained if the grain size could be reduced below the micrometer into the nanometer regime. This assumes, of course, that the grain boundaries scatter the relevant phonons of frequencies  $f < f_B$  strongly, so that their mean free path is indeed limited by the grain size  $L$ . Using Eqs. (5) and 6(b), the thermal conductivities were calculated;<sup>[5]</sup> similar

calculations were made for other materials. The crucial assumption was of course that in calculating  $f_B$  in terms of  $L$ , the magnitude of  $L$  was given by the grain size, even for nanometer-sized grains. Unfortunately, this turned out not to be the case for nanometer-grained zirconia stabilized by 7 wt.% of yttria, a widely used composition for thermal barrier coatings<sup>[6]</sup> (Figs. 1 and 2). Therefore, it is necessary to look more closely at the scattering of lattice waves by grain boundaries.

## SCATTERING BY GRAIN BOUNDARIES

Because scattering by grain boundaries affects mainly the lattice waves at low frequencies, measurements of thermal conductivity at low temperatures provides much relevant information, because at low temperatures only the low frequencies contribute to the specific heat and the thermal conductivity. The important frequencies are then  $f < nk_B T/\hbar$ , where  $\hbar$  is the Planck constant and  $n$  ranges between 3 and 4. At very low temperatures, typically below 20 K, the thermal conductivity of single crystals is limited by the scattering of lattice waves at external boundaries. The corresponding mean free path  $L$  is comparable to the shortest linear dimension of the crystal.<sup>[7]</sup> Because the specific heat  $C$  is then proportional to  $T^3$ , the thermal conductivity  $\kappa = CvL/3$  also varies as  $T^3$ . If the crystal contains some imperfections, in some cases even a mixture of isotopes, this variation can be reduced somewhat; however, an average mean free path of

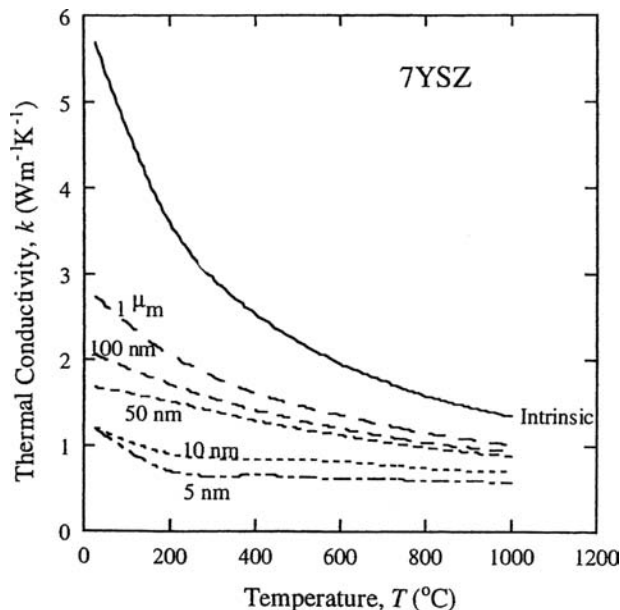


**Fig. 1** Theoretical reductions in the thermal conductivity of  $ZrO_2$  containing 7 wt.%  $Y_2O_3$  due to point defects and grain boundary scattering for various grain sizes. *Source:* From Klemens, P.G., Gell, M. *Mater. Sci. Eng., A* 245, 143 (1998).

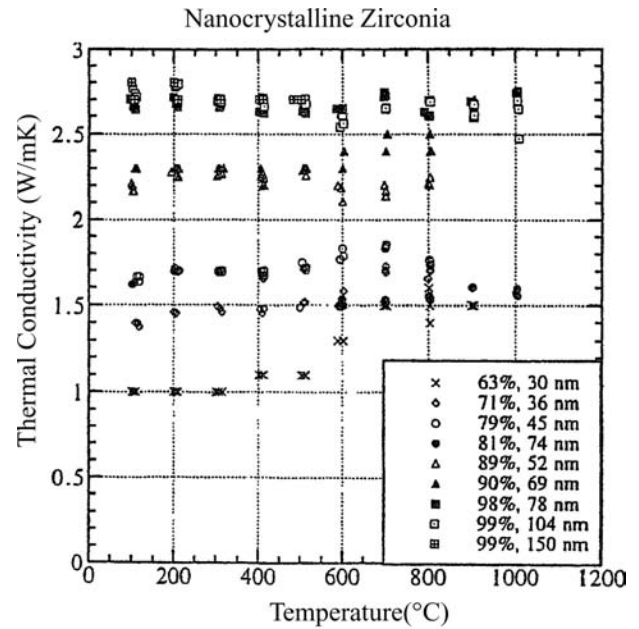


**Fig. 2** Thermal conductivity as a function of temperature in nanocrystalline tetragonal zirconia (5.8 wt.% yttria). Densities (% of theoretical) and grain diameters (in nanometers) are also indicated. *Source:* From Ref.<sup>[6]</sup>.

the order of the shortest linear dimension is frequently clearly observed.

This conductivity is substantially reduced when there are grain boundaries, as observed, e.g., by Berman,<sup>[8]</sup> who first compared a single crystal of  $Al_2O_3$  (sapphire) with polycrystalline alumina at low temperatures. The thermal conductivity varied more slowly than  $T^3$ , suggesting that the mean free path increased with decreasing phonon frequency. This, and similar results, need to be reconciled with calculations of phonon scattering by grain boundaries. The back reflection coefficient of a boundary between two materials is of the order  $(v_1 - v_2)^2/v^2$ , where  $v_1$  and  $v_2$  are the wave velocities on either side, and  $v$  is their average. For tilt boundaries this factor is generally no more than about 0.03, except for some very anisotropic materials. Thus the difference in orientation is not the major source of grain boundary scattering.<sup>[9,10]</sup>

This suggests that grain boundary scattering is due to a thin region between the grains of thickness  $t$  (believed to be around 2 nm), where the material is less compact than inside the grains, and where the local wave velocity is decreased by an amount  $\Delta v$ . This phonon-scattering problem, originally done for nitrogen platelets in diamond,<sup>[11]</sup> leads to a reflection probability for an infinite sheet of thickness  $t$  well below the wavelength  $\lambda$ ,

$$R \approx \frac{2}{3} (2\pi)^2 \left(\frac{t}{\lambda}\right)^2 \left(\frac{\Delta v}{v}\right)^2 \quad (7)$$

For short wavelengths  $\lambda < 2\pi t$  or frequencies greater than  $2\pi v/t$ ,  $R$  reaches a saturation value

$$R \approx \frac{2}{3}(\Delta v/v)^2 \quad (8)$$

These equations give an order-of-magnitude agreement with grain boundary scattering at both low and ordinary temperatures.<sup>[10]</sup> They are based on the assumption that a grain boundary acts as a set of thin plates, each plate having a diameter that is large compared to the wavelength of the lattice wave to be scattered, i.e., waves of frequencies around  $f_B$ . This holds approximately for grains that have a diameter  $D$  above 100 nm, but not smaller. For smaller grains, even if the intergrain regions remained 2 nm thick, they could no longer be regarded as thin plates of diameter large compared to the thickness. The theory of Ref.<sup>[11]</sup> also deals with plates of small  $D$ : the scattering is reduced in such cases. In the extreme case the plates become small obstacles or pores. This accounts for the observation in Ref.<sup>[6]</sup> that for very small grains the conductivity depends not on grain size but on overall porosity.

## WAVE SCATTERING BY OBSTACLES

Obstacles can be pores or inclusions of foreign material, but in contrast to thin plates, their linear dimensions are similar in all directions. For very long waves, scattering varies as the square of the volume, and does not depend on shape. The obstacles are thus approximated by spheres of diameter  $D'$ . If  $D'$  is small compared to the important wavelength  $\lambda$ , scattering is in the Rayleigh regime, and the scattering cross section area,  $\Sigma$ , is proportional to  $f^4$  or to

$$\Sigma \propto (\Delta v/v)^2 (D')^6 / \lambda^4 \quad (9)$$

Here  $\Delta v$  is the difference between the wave velocities in the matrix and in the material of the obstacle,  $v$  is that of the matrix. The extreme case of an obstacle of atomic size is the point defect, treated earlier. In the opposite case, when  $\lambda < D$ , it is the geometric cross section

$$\Sigma \approx \pi(D')^2/4 \quad (10)$$

Scattering in the intermediate region, Mie scattering, depends on the details of the obstacle, as it does in the corresponding case of light scattering. Because the lattice thermal conductivity involves an integration over a wide-frequency spectrum, it is not too bad an approximation to disregard this complication and to take scattering to vary as  $f^4$  at low frequencies, and be independent of frequency and given by the

geometric cross section at high frequencies, with a sharp transition at  $f_c$ , the frequency where both expressions are equal. Thus, one uses Eq. (10) for  $f > f_c$ , whereas for  $f < f_c$  one uses

$$\Sigma \approx \pi/4(D')^2(f/f_c)^4 \quad (11)$$

where

$$f_c \approx \frac{v}{D'} \left( \frac{\Delta v}{v} \right)^{-1/2} \quad (12)$$

for pores  $\Delta v = -v$ , so that  $f_c \approx v/D$ . For solid obstacles,  $\Delta v$  is smaller and  $f_c$  is larger.

It is the volume fraction  $\phi$  of the obstacles or pores that is usually known. Still assuming them to be spheres of diameter  $D'$ , the phonon mean free path for  $f > f_c$  becomes

$$L = \frac{2}{3} \frac{D'}{\phi} \quad (13)$$

This follows from expressing  $L$  and  $\phi$  in terms of the number of obstacles per unit volume, then eliminating that number. The obstacles reduce the thermal conductivity provided  $f_B > f_c$ . Since  $f_B \propto (LT)^{-1/2} \propto (D'T/\phi)^{-1/2}$  while  $f_c \propto (D'/\phi)^{-1/2}$ , obstacles will reduce the thermal conductivity the more, the lower the temperature and the higher their fractional volume.

## RADIATIVE COMPONENT

At very high temperatures, infrared radiation makes an additional contribution to thermal conduction. This component depends on layer thickness and can be reduced by pores, by internal absorption and by scattering. The effective thermal conductivity between two parallel slabs, acting as black bodies, separated by a distance  $L$  (in meter) and filled with a non-absorbing medium of refractive index  $n$ , is given by the Stefan–Boltzmann constant and the average temperature  $T$  (in Kelvin) as

$$\lambda_{\text{rad}} = 2.27 \times 10^{-7} n^2 L T^3 \text{ W m}^{-1} \text{ K}^{-1} \quad (14)$$

For dense yttria-stabilized zirconia,  $n = 2.7$ . At 1300 K and for a thickness  $L = 1$  mm, this yields a conductivity of about  $3 \text{ W m}^{-1} \text{ K}^{-1}$ . In flash-diffusivity measurements, this value is substantially reduced by a coating on the front that absorbs the heat of the radiative flash, and that has a reduced but unknown emissivity into the ceramic, so that the radiative component may be only about  $1 \text{ W m}^{-1} \text{ K}^{-1}$ .<sup>[12]</sup> Scattering of infrared radiation by submicron pores



is small, but all pores, irrespective of size, reduce the average value of  $n^2$  and thus the radiative component. The fractional reduction is comparable to the corresponding reduction in the lattice thermal conductivity.<sup>[13]</sup> In thermal barrier coatings, where  $L$  is substantially less than in the specimens used in flash-diffusivity measurements, the radiative component of the conductivity is correspondingly reduced.

## REDUCTIONS BY INCLUSIONS AND THIN LAYERS

Whereas nanometer-scale grains do not meet the original expectations of reducing the thermal conductivity of ceramics because grain boundaries do not scatter lattice waves when grains are small, this does not apply to small obstacles composed of a foreign material. Of course, these obstacles should not just reside at the boundaries between larger grains, although this would result in some reductions, but should be distributed uniformly throughout the ceramic. This implies that the ceramic must have been composed of very fine grains at some stage, when preexisting obstacles were incorporated, or that the obstacles were formed by some precipitation process, perhaps at some centers formed by irradiation. If the desired distribution of very small obstacles could be achieved, the reductions are given in terms of Eqs. (12) and (13), with the factor  $(\Delta v/v)$  appropriately reduced.

Greater reductions can be obtained if the foreign material is deposited as very thin sheets, preferably oriented across the direction of heat flow, interleaved with thin sheets of the ceramic. Sheets present a larger scattering cross section than spheres for the same volume. It was found that an array of alternating thin layers of tungsten and alumina, each 1 to 2 nm thick, have a thermal conductivity in the normal direction as low as  $0.4 \text{ W m}^{-1} \text{ K}^{-1}$  at room temperature, if the temperature at which the layers were deposited was low enough.<sup>[14]</sup>

For thermoelectric power conversion and refrigeration, one needs a low thermal conductivity combined with sufficient electrical conductivity and large thermoelectric power. Because these properties are interdependent, the coefficient of performance of these materials, intermediate between semiconductors and semimetals, requires not only careful control of the carrier concentration, but also a reduction of the parasitic lattice thermal conductivity, to be less than the electronic component of the thermal conductivity. It was pointed out earlier here that the lattice thermal conductivity is made up of contributions from a wide spectrum of lattice waves. It is necessary to reduce the mean free path of phonons over the entire spectrum. The reduction of the mean free path of waves

at high frequencies is achieved by solute atoms of the same valence (e.g., Ge in Si). The waves of low frequency interact with the carriers: their mean free path is also short. There remains a wide range of intermediate frequencies with a mean free path as large as in a perfect crystal. Their mean free path could be reduced when scattered by electrically inert obstacles of nanometer dimension.<sup>[15]</sup> Early attempts to realize this improvement were only marginally successful.<sup>[16]</sup> At that time the obstacles that were inserted into the material were not small enough and their diameter was not well controlled. The optimum diameter would be around 1–2 nm. Obstacles of larger size would reduce the electrical conductivity and the thermopower and be counterproductive.<sup>[17]</sup> Modern techniques may allow better control of obstacle size and may give better results.

## INCREASING THE THERMAL CONDUCTIVITY

It has been suggested to increase the thermal conductivity of an electrically insulating matrix by dielectric inclusions of high thermal conductivity. In packaging applications the matrix material is small, so that the inclusions should be even smaller, of submicron size. Unfortunately the thermal conductivity of these inclusions is then reduced well below the bulk value. Thus, the overall thermal conductivity is not enhanced, even if the inclusions occupy a significant volume fraction. This difficulty can be overcome by using small inclusions having a phonon gas of low dimensionality, such as graphite, graphene, or carbon nanotubes.

In three dimensions, the spectral specific heat varies as  $C(f) \propto f^2$  and the intrinsic mean free path  $l_i \propto f^{-2}$ , so that in Eq. (2) equal frequency intervals make equal contributions to the intrinsic thermal conductivity  $\kappa_i$ . However, for a two-dimensional phonon gas  $C(f) \propto f$ , but  $l_i$  still has the same dependence on  $f$  and on temperature  $T$ .<sup>[18]</sup> Thus

$$\kappa_i \propto \frac{1}{2} \int C(f) v \frac{B}{T f^2} df \propto \int_{f_{\min}}^{f_D} \frac{df}{T f} \quad (15)$$

Here  $f_{\min}$  is the lowest frequency for which the phonon gas is two-dimensional, either because there are lattice waves in a third direction or because the waves of lower frequency are scattered by another interaction, e.g., by boundaries. In graphite the phonon spectrum becomes three-dimensional below  $4 \times 10^{12}$  Hz, while  $f_D \approx 46 \times 10^{12}$  Hz. Thus,  $\ln(f_D/f_{\min}) = 2.44$  and the intrinsic thermal conductivity is

$$\kappa_i = \frac{5.71 \times 10^5}{T} \times 2.44 \text{ W m}^{-1} \text{ K}^{-1} \quad (16)$$

This agrees with measurements on pyrolytic graphite and single crystals.<sup>[18]</sup> Small graphite flakes of limited size in the  $a$  plane would have a lower  $f_{\min}$  and their conductivity would be reduced, as would graphite containing a large point defect concentration that reduces the effective value of  $f_D$ .

A graphene sheet, consisting of a single atomic layer of graphite or a small number of such layers, has a phonon gas that is two-dimensional down to zero frequencies. Here the logarithmic low-frequency divergence is removed by the condition that at very low frequencies the mean free path is limited by the shortest linear dimension  $L$  in the plane of the sheet, and  $f_{\min}$  is the frequency at which  $l_i = L$ . If  $L$  is given in meters, and for a free-standing graphene sheet

$$f_{\min} = \left[ \frac{8.5 \times 10^{21}}{LT} \right]^{1/2} \text{ Hz and}$$

$$\lambda(\text{graphene}) = \frac{1.17}{T} \ln((f_D^2 + f_{\min}^2)/f_{\min}^2)$$

For  $L = 1 \mu\text{m}$  and  $T = 300 \text{ K}$ ,  $f_{\min} = 5.3 \times 10^{12} \text{ Hz}$ , and  $\lambda(\text{graphene}) = 1.7 \times 10^3 \text{ W m}^{-1} \text{ K}^{-1}$ . However, for a graphene sheet or thin stack lying on a substrate, phonon energy can leak into the substrate, reducing the thermal conductivity.<sup>[19]</sup>

Similar considerations apply to carbon nanotubes, where a long graphene sheet but only  $N$  atomic units wide is rolled into a cylinder. The longitudinal modes are continuous, but the circumferential modes have discrete frequencies, multiples of  $f_D/N$ . Unless  $N$  is very small, this discreteness does not significantly change the value of  $l_i$ . Thus, the thermal conductivity of a free-standing nanotube is very similar to that of a free graphene sheet.<sup>[19]</sup> Again,  $f_{\min}$  is given by the length of the tube and is increased if the nanotubes are enclosed in a matrix, allowing wave energy to slowly leak into the matrix. Note that we have discussed the

conductivity of a single tube; the conductance is proportional to the cross-sectional area of the tube. A significant enhancement of the overall conductivity requires a large filling factor of the tubes in the matrix.

## REFERENCES

1. Klemens, P.G. *Thermal Conductivity*; Tye, R.P., Ed.; Academic Press: London, 1969; Vol. 1, 1.
2. Berman, R. *Thermal Conductivity of Solids*; Clarendon Press: Oxford, 1976.
3. Debye, P. *Ann. Phys. (Leipz.)* **1912**, *39*, 789.
4. Savvides, N.; Goldsmid, H. *J. Phys.* **1980**, *C13*, 4657, 4671.
5. Klemens, P.G. *Thermal Conductivity 23*; Wilks, K.E., Dinwiddie, R.B., Graves, R.S., Eds.; Technomics Publ. Co.: Lancaster, PA, 1996; 209 pp.
6. Raghavan, S.; Wang, H.; Dinwiddie, R.B.; Porter, W.D.; Mayo, M.J. *Scr. Mater.* **1998**, *39*, 1119.
7. Casimir, H.B.G. *Physica* **1938**, *5*, 459.
8. Berman, R. *Proc. Phys. Soc. Lond.* **1952**, *A65*, 1029.
9. Klemens, P.G. *Proc. Phys. Soc. Lond.* **1955**, *A68*, 1113.
10. Klemens, P.G. *Int. J. Thermophys.* **1994**, *15*, 1345.
11. Turk, L.A.; Klemens, P.G. *Phys. Rev., B* **1974**, *9*, 4422.
12. Klemens, P.G. *Int. J. Thermophys.* **2001**, *22*, 265.
13. Schlichting, K.W.; Padture, N.P.; Klemens, P.G. *J. Mater. Sci.* **2001**, *36*, 3003.
14. Costescu, R.M.; Cahill, D.G.; Fabreguette, F.H.; George, S.M. Thermal conductivity of nanolaminates. *Science*, *in press*.
15. White, D.P.; Klemens, P.G. *J. Appl. Phys.* **1992**, *71*, 4258.
16. Beaty, J.S.; Rolfe, J.L.; Vandersande, J.W. *Mater. Res. Soc. Symp. Proc.* **1991**, *234*, 105.
17. Klemens, P.G. 15th International Conference on Thermoelectrics, Piscataway, NJ; IEEE, 1966, 206, Catalogue No. 96 TH 8169.
18. Klemens, P.G.; Pedraza, D.F. *Carbon* **1994**, *32*, 735.
19. Klemens, P.G. Graphite, Graphene and Carbon Nanotubes. In *Thermal Conductivity 26*, *in press*.

# Nanocolloidal Gold Films: Self-Assembly

**E. Stefan Kooij**

*Faculty of Science and Technology, Department of Solid State Physics,  
University of Twente, Enschede, The Netherlands*

**E.A. Martijn Brouwer**

*Solid State Physics, University of Twente, Enschede, The Netherlands*

**Agnes A. Mewe**

*Faculty of Applied Physics, University of Twente, Enschede, The Netherlands*

**Herbert Wormeester**

*Faculty of Science and Technology, University of Twente, Enschede, The Netherlands*

**Bene Poelsema**

*Faculty of Applied Physics, University of Twente, Enschede, The Netherlands*

## INTRODUCTION

The unique and new optical, electrical, and magnetic properties of colloidal superstructures as opposed to the bulk characteristics of the constituent materials is attracting the attention of an increasing number of both fundamental scientists and technology-oriented industry. The colloid size used in the assembled structures varies over approximately 3 orders of magnitude and is closely related to the specific application. For photonic band gap materials, the particle size is of the same order of magnitude as the wavelength of light, while for magnetic applications, such as ultrahigh density storage devices, the particle radius is in the low-nanometer range. A combination of the aforementioned physical properties of colloidal matter introduces even more exciting fields of research. Electron transport through monolayers of magnetic nanocrystals or tunable photonic band gap materials, both controlled by applying a magnetic field, are only two examples of the many possibilities.

Nanotechnology is characterized by a continuous decrease of feature sizes, e.g., in electronic devices. Top-down fabrication methods, such as the well-established photolithography techniques, are being pushed toward their physical limits. Increasingly more research effort is presently being devoted to bottom-up fabrication methods. Instead of reducing the size of much larger, bulk materials, as is done with photolithography in combination with etching techniques, the focus is turning toward building up superstructures of much smaller building blocks. Self-assembly of single molecules or nanocolloidal particles into larger arrangements, employing intrinsic, extrinsic, or even externally induced

interactions, seems to be a most promising method, which is not hampered by problems related to scaling the processes to production scale. Much of the research activities in the field are focused on gold nanoparticles, as these systems are stable in a large number of environmental conditions and are relatively easy to prepare and control. In the first part of this contribution, we will summarize the different self-assembly methods with which nanocolloidal gold particles are composed into monolayers or multilayered superstructures.

In the second part of this contribution, we show how non-imaging, single wavelength reflectometry measurements can be applied to in situ study the formation of nanocolloidal gold monolayers at derivatized silicon surfaces. The kinetics of particles with dimensions in the low-nanometer range are investigated using a radial impinging jet setup, also referred to as a stagnation point flow geometry. We compare our results to similar adsorption experiments using micrometer-sized silica particles. For these large particles, the random sequential adsorption (RSA) model adequately describes the overall deposition kinetics. However, for considerably smaller particles in the 10–100 nm range, this relatively simple model fails. Here we show that a generalized adsorption model is in perfect agreement with deposition transients of particles in the low-nanometer range over the entire coverage range.

## SELF-ASSEMBLY METHODS TO GROW NANOCOLLOIDAL GOLD FILMS

Many different ways have been employed to assemble colloidal particles into disordered structures or highly

ordered superlattices. Most of these methods have also been applied to nanometer-sized gold particles, but because their size is orders of magnitude smaller than, for example, the particles used in photonic band gap applications, the results are often different.

One of the most frequently used methods, and without doubt the most often described<sup>[1–20]</sup> assembly technique, involves the chemical modification of the substrate onto which the nanocolloidal gold particles are adsorbed. Amino ( $\text{NH}_2$ )- and thiol ( $\text{SH}_2$ )-terminated surfaces lead to a high affinity for irreversible deposition of gold entities from solution. Additionally, the adsorption is self-limiting, as only submonolayer coverage can be achieved. Amino- or thiol-functionalized surface can be produced either by attaching aminosilane or thiolsilane molecules to oxidic surfaces, such as silicon and aluminum oxide, or by adsorbing bifunctional amino–thiol or dithiol molecules onto gold substrates. In the latter case, short-chain molecules are used because long-chain molecules with a sufficient degree of freedom will attach to the gold surface with both ends. In most cases, immersion of the substrate into a solution of the functionalizing substance is adequate, but also evaporation/sublimation of the amino or thiol compounds is employed.

The interaction between the functional groups on the surface and the gold nanocrystals in solution is generally considered to be electrostatic, which enables relatively simple tuning of the surface potential by varying the pH of the solution. Once the gold particles are adsorbed on the substrate, the strong bonding, which is of a covalent character, prevents desorption. Also, the lateral mobility is negligible and the deposition is governed by a random sequential adsorption (RSA) process. For this reason, ordering does not take place and the spatial arrangement of the nanocrystals is random. The maximum surface coverage corresponding to an RSA event is approximately 55%.

To increase the coverage, e.g., to grown conducting gold layers, several routes can be taken. One of these involves the specific enlargement of the adsorbed gold nanoparticles by electroless deposition of gold or any other desired method. This seeded growth has been described in several publications.<sup>[9,10]</sup> In Fig. 1, we show scanning electron microscopy images of a monolayer of gold nanoparticles before and after seeded growth for 5 min in a  $\text{AuCl}_4^-/\text{NH}_2\text{OH}$  aqueous solution. It is clear that the particles are enlarged to form a nearly percolating network. Additional growth leads to closed, conductive layers of gold.

Closely related to the aforementioned chemical functionalization of the substrates to enhance the specific affinity for gold nanoparticles is the use of DNA.<sup>[21,22]</sup> A major advantage of using DNA is that

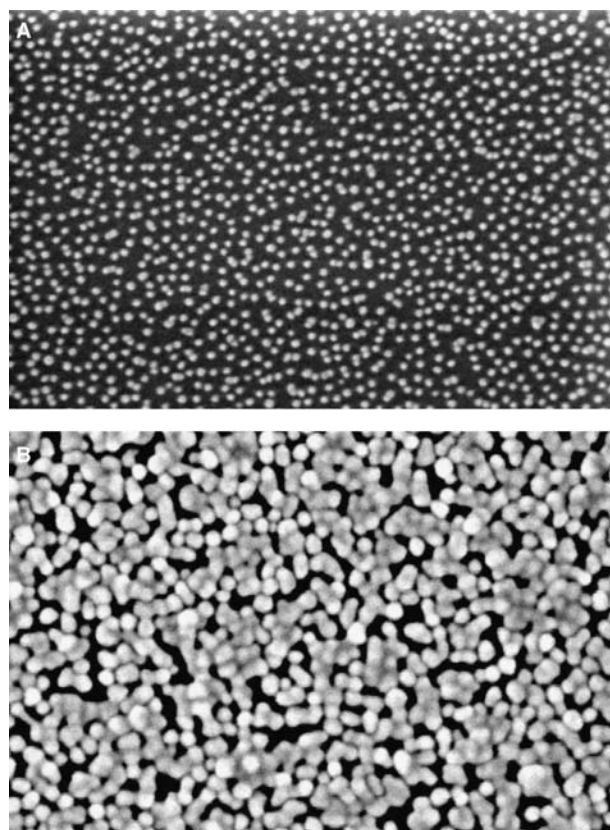


**Fig. 1** Scanning electron microscopy images of colloidal gold particles irreversibly adsorbed at silicon/silicon oxide substrates, derivatized with APTES. The image size amounts to  $1200 \text{ nm} \times 800 \text{ nm}$ . Prior to seeded growth (A), the average spacing between the isolated nanocrystals is tunable via the ionic strength. Seeded growth for 5 min in a  $\text{AuCl}_4^-/\text{NH}_2\text{OH}$  aqueous solution (B) gives rise to homogeneous particle enlargement.

a specific network can be generated using specific DNA molecules. Thiol-terminated DNA molecules can be built into the structure; the location and the density can be determined by the ratio of various DNA types in solution.

As mentioned above, specific functionalization of the surface onto which the gold entities are adsorbed limits the coverage to submonolayer values. To overcome this restriction, the layer-by-layer (LBL) technique can be employed.<sup>[3,5,6,9,11–13,17,18,23–25]</sup> For example, adsorbed gold nanoparticles can be covered with a layer of cross-linker molecules, such as amino–thiols or dithiols. One end of these molecules attaches to the gold nanocrystal surface, while the other end generates new functionalized adsorption sites for additional colloidal particles. Not only the aforementioned chemical interaction can be used in LBL deposition, but also electrostatic interactions are employed to form multilayers of gold nanoparticles.

In this case, the cross-linker entities are polyelectrolyte molecules, or oppositely charged nanoparticles. In principle, the number of deposition cycles, and therewith the thickness of the superstructure, is not restricted. However, the roughness of the structure substantially increases, which limits the application in many cases.

The aforementioned derivatization, either chemical or electrostatic, of the substrate enables patterning of the substrate and thus also of the superstructure of nanocolloidal gold particles.<sup>[12,19,26,27]</sup> Examples of ways to locally functionalize substrates include microcontact printing and scanning probe microscopy (SPM)-based methods. In the former case, a polydimethylsiloxane (PDMS) stamp is generally used to apply the amino-thiol molecules or polyelectrolytes to predefined areas on the substrate surface. After rinsing, the gold nanocolloidal particles adsorb only onto the derivatized patterned regions. With SPM, the approach is somewhat different. A surface is completely functionalized with, for example, amino endgroups. Subsequently, specific regions on the surface are defunctionalized by oxidizing or removing the molecules, therewith destroying the local affinity of the surface for gold adsorption. Although it allows complicated patterns to be made, the latter method is intrinsically slow as all structures have to be “written” onto the surface.

A completely different method used to form dense monolayers of gold nanoparticles is by electrophoretic deposition.<sup>[27–30]</sup> An external electric field is applied to drive the particles toward the surface. Although very impressive results have been obtained for micrometer-sized colloidal systems, the work on nanocolloidal gold particles is limited to a few reports of experimental results. In principle, highly ordered monolayers, and possible also multilayers, can be formed as the lateral mobility of the gold nanocrystals is not hindered.

Finally, hydrodynamic interactions can also be employed to form superstructures of gold nanoparticles.<sup>[4,16,31–33]</sup> The simplest approach is to simply dry the colloidal suspension on a substrate. This already generates a short-range order in the deposited layers. Control over the spatial extent of the ordering can be achieved by lowering the evaporation rate of the solvent, therewith giving the particles the opportunity to find a suitable spot in the superstructure while it is forming. The volume fraction also plays an important role. Modifications of this method, specifically for gold nanoparticles, have been described. The nanocrystals are first adsorbed onto amino- or thiol-derivatized surface, after which they are “liberated” by a ligand-exchange reaction. This is considered to increase the lateral mobility of the particles on the surface, which then allows them to “dry” in an ordered monolayer.

## KINETICS OF IRREVERSIBLE GOLD NANOCRYSTAL DEPOSITION

A prerequisite for studying any system in general, but nanocolloidal systems in particular, is the ability to unambiguously characterize them under relevant conditions. Among the large number of methods available for characterizing colloids and their superstructures, electron microscopy [scanning electron microscopy (SEM)/transmission electron microscopy (TEM)] is by far the most popular. Both for very small as well as relatively large particles, this encompasses the most employed *ex situ* technique. Among colloid scientists, the use of scanning probe microscopy [atomic force microscopy (AFM), scanning tunneling microscopy (STM), magnetic force microscopy (MFM)] is increasing, but also in this case experiments are typically performed *ex situ*. In fact, the only techniques that have been used *in situ* to study colloidal systems are optical methods. Imaging techniques such as conventional or confocal microscopy are used for large colloids. For particles with dimensions well below the diffraction limit of (visible) light, such as with gold nanoparticles, only non-imaging (lateral averaging) *in situ* experiments are available. These include primarily UV/*vis* absorption spectroscopy, but also optical waveguide lightmode spectroscopy, and reflection techniques as reflectometry and ellipsometry.

### Single Wavelength Reflectometry Results

We employed single wavelength reflectometry to characterize the adsorption of nanocolloidal gold particles onto substrates derivatized with aminopropyltriethoxysilane (APTES).<sup>[20]</sup> Gold colloids are prepared by standard citrate reduction of  $\text{HAuCl}_4$  in aqueous solution at  $100^\circ\text{C}$ , which yields colloidal particles with an average radius of  $a = 6.7\text{ nm}$ .<sup>[1,5]</sup> In all our reflectometry measurements, the as-prepared nanocolloidal gold suspension is diluted by a factor of 4, which leads to a particle concentration of approximately  $c_0 = 1.85 \times 10^{18}\text{ m}^{-3}$  and an ionic strength of  $3.6\text{ mM}$ .

The homebuilt reflectometer setup consists of a He-Ne laser, the stagnation point flow cell, a beamsplitter, and two photodiodes for detecting the intensities  $I_p$  and  $I_s$  of the parallel and perpendicular components of the reflected light. A more extensive description of our specific setup is given by Dijt et al.<sup>[34]</sup> The intensity ratio  $S = I_p/I_s = (I_{0p}/I_{0s})(R_p/R_s)$  is measured, where  $I_{0p}$  and  $I_{0s}$  are the initial intensities and  $R_p$  and  $R_s$  are the intensity reflection coefficients. The angle of the incident beam can be adjusted and is set to  $71^\circ$  with respect to the normal of the sample surface. The volume flow during the experiments was approximately  $1.0\text{ mL min}^{-1}$ .

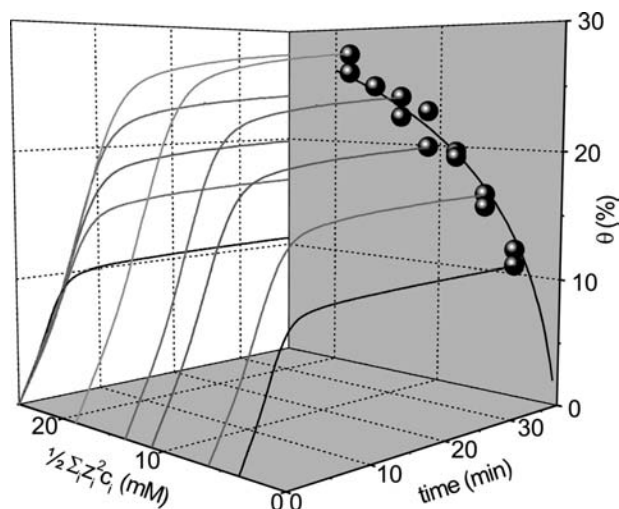


**Fig. 2** Three-dimensional representation of the ionic-strength-dependent adsorption kinetics of gold nanocolloidal particles in stagnation point flow geometry. The coverage is obtained by polarized reflectometry. The data on the back panel indicate the evolution of the saturation coverage with increasing ionic strength for a number of reflectometry experiments; the solid line is a guide to the eye.

For the reflectometry experiments, we used substrates cut from *p*-type silicon (100) wafers with a deposited oxide layer of 45 nm. When the oxide layer is too thin,  $R_p$  is very small and the initial sensitivity of the setup is low. With too thick oxide layers, the reflectometer signal flattens and even decreases above a certain surface concentration. The reflectometer signal has been calculated as a function of the gold nanocrystal coverage using the thin island film theory,<sup>[35,36]</sup> the relation between signal and coverage is used as a calibration to obtain an absolute surface coverage from the optical response.

In Fig. 2, we show typical reflectometry transients, obtained during colloidal gold deposition in the aforementioned stagnation point flow cell at various ionic strengths. For  $t < 0$ , only water flows through the cell, and a constant baseline is measured. At  $t = 0$ , the gold suspension is injected into the cell. When the flow is switched back to water at  $t = 38$  min, no significant decrease of the surface coverage is observed, indicating the absence of particle detachment. Two distinct regimes are observed in the measured curves in Fig. 2, which will be discussed in the next section.

### Two Limiting Regimes in the Deposition Transients

At longer deposition times, the deposition process leads to saturation at coverage values, which show a

clear dependence on the ionic strength.<sup>[15]</sup> This will be discussed at the end of this section. For short times, the deposition rate is similar for all ionic strengths, which implies that the deposition process is initially limited by the supply of colloidal particles to the surface. The hydrodynamics of colloid deposition in a stagnation point flow cell have been extensively described.<sup>[37,38]</sup> The initial particle flux toward the surface is in good approximation given by

$$j_0 = 0.776c_0 \left( \frac{D^2 \alpha V_m}{R^2} \right)^{\frac{1}{3}} = k_c c_0 \quad (1)$$

where  $c_0$  is the bulk particle concentration,  $D$  is the diffusion coefficient of the nanocolloidal particles,  $R = 0.64$  mm is the radius of the inlet tube and  $V_m = \nu Re/R$  is the average flow velocity, with  $Re$  the Reynolds number and  $\nu$  the kinematic viscosity of the fluid. The dimensionless flow parameter  $\alpha$  depends on the Reynolds number and the cell geometry parameter  $h/R$ . In our case, a value  $\alpha = 4.2$  is obtained from the work of Dabros and Van de Ven<sup>[37]</sup> using  $Re = 8.3$  and  $h/R = 1.7$ . The mass transfer coefficient  $k_c$  will be discussed in a later section.

Assuming pure random sequential adsorption (RSA), with a sticking probability of 1, the above considerations imply a constant deposition rate  $d\theta/dt$  from the moment the colloidal suspension is inserted. After a short transition time, this linear regime is indeed observed. The adsorption rate  $d\theta/dt = \pi a^2 j_0 = 0.0225 \text{ min}^{-1}$  in Fig. 2 is used to calculate the particle diffusion coefficient  $D$  from Eq. (1). For lower ionic strengths, the value of  $D$  is less accurate but within an experimental error of 5%, the aforementioned value  $d\theta/dt = 0.0225 \text{ min}^{-1}$  does not vary with ionic strength. Inserting the known values for particle density and cell geometry parameters, we find  $D = 6.9 \times 10^{-12} \text{ m}^2 \text{ sec}^{-1}$ . We now compare this result to the diffusion coefficient obtained using the Stokes–Einstein relation

$$D = \frac{kT}{6\pi\eta a} \quad (2)$$

where  $kT$  is the thermal energy and  $\eta$  is the dynamic viscosity of the fluid (for water,  $\eta = 1.00 \times 10^{-3} \text{ kg m}^{-1} \text{ sec}^{-1}$ ). With a particle radius  $a = 6.7$  nm, the Stokes–Einstein relation yields a diffusion coefficient  $D = 3.2 \times 10^{-11} \text{ m}^2 \text{ sec}^{-1}$ . Our experimentally determined value is about 4–5 times lower than this value. The apparent discrepancy is reasonable, considering the following arguments. One reason is that Eq. (2) represents an approximation<sup>[38]</sup> that is only valid in the infinitely small stagnation point in the center of the cell, whereas an elliptical area of



about  $1 \times 2 \text{ mm}^2$  is probed in the experiments. From SEM data, Böhmer, van der Zeeuw, Kopel<sup>[39]</sup> estimated that in the initial stage of nanocolloidal film growth, the adsorption rate is underestimated by a factor of 1.5. Numerical calculations based on the flow field in the cell<sup>[38]</sup> confirm that indeed the average flux on a probe area of  $1 \times 2 \text{ mm}^2$  is approximately  $0.7j_0$ . This implies an underestimation of the diffusion coefficient  $D$  in our experiments by approximately a factor of 2. Furthermore, the gold nanocolloids have a relatively large surface charge, which leads to an increased hydrodynamic radius, and thus a lower diffusion constant [Eq. (2)]. The particle concentration has been determined to have a small error, so we do not believe this interferes with our determination of the diffusion coefficient.

Let us now turn to the saturation regime of the deposition curves in Fig. 2. For higher ionic strengths, the maximum attainable coverage increases, in agreement with the Derjaguin-Landau-Verwey-Overbeek (DLVO) theory. This theory describes the accumulation of ions near charged interfaces, in this case the colloid-solvent interface, which results in a double layer around every particle. When the double layers of two particles overlap, the ions around the particles are confined to a smaller volume, which results in an entropic repulsion. This repulsion prevents coagulation of the particles, and also defines the distance of closest approach of two particles. When particles adsorb on a surface, this distance determines the maximum attainable coverage.<sup>[15]</sup>

More quantitatively, the double-layer interaction potential  $U_{pp}(r/a)$  in units  $kT$  is described by,<sup>[40,41]</sup>

$$\frac{U_{pp}\left(\frac{r}{a}\right)}{kT} = B_{pp} \frac{a}{r} e^{-\kappa(r-2a)} \quad (3)$$

where  $r$  is the particle-particle distance and  $\kappa$  is the Debye screening parameter, given by

$$\kappa^2 = \frac{e^2 \sum_i n_i z_i^2}{\epsilon \epsilon_0 kT} \quad (4)$$

with  $n_i$  and  $z_i$  being the number density and valence of ions  $i$ , respectively,  $e$  the elementary charge, and  $\epsilon \epsilon_0$  the dielectric permittivity of the electrolyte. The particle-particle interaction coefficient is defined as

$$B_{pp} = \left( \frac{4\pi\epsilon\epsilon_0 kT a}{e^2} \right) \left( \frac{y_p + 4\gamma\Omega\kappa a}{1 + \Omega\kappa a} \right)^2 \quad (5)$$

with  $\gamma = \tanh(y_p/4)$ ,  $\Omega = [(y_p - 4\gamma)/2\gamma^3]$ , and  $y_p = \psi_p(e/kT)$  the dimensionless surface potential. This yields an interaction potential that is valid over a large range of  $\kappa a$  provided  $r$  is larger than about

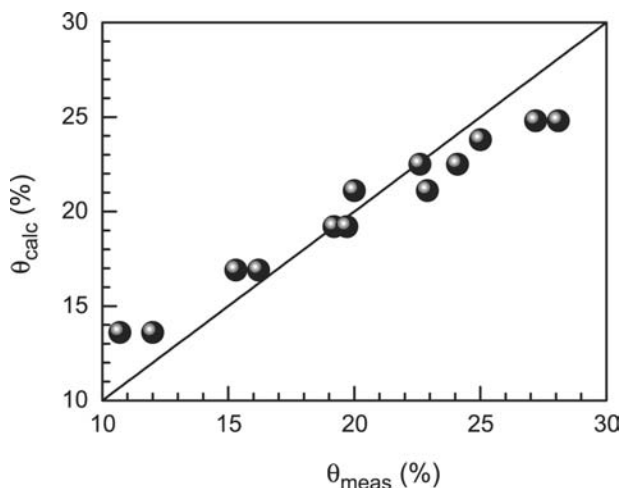


**Fig. 3** Saturation coverage  $\theta_{\text{calc}}$  calculated from the ionic strength using the DLVO theory as a function of the experimentally determined maximum coverage  $\theta_{\text{meas}}$  from the reflectometry measurements. The line has a slope of 1.

$a + (3/2)\kappa^{-1}$ . Assuming a constant surface potential, the distance  $r_{kT}$  between particles when their interaction energy drops below  $(3/2)kT$  can be numerically determined as a function of  $\kappa a$ , i.e., as a function of the ionic strength. The choice for the interaction energy is justified by the fact that particles have an average thermal energy of  $(3/2)kT$ , which competes with their electrostatic repulsion upon approaching each other.

In Fig. 3, the saturation coverage  $\theta_{\text{calc}}$ , calculated using Eqs. (3)–(5) with a particle surface potential  $y_p, kT/e = -85 \text{ mV}$ .<sup>[42,43]</sup> is plotted as a function of the surface concentration  $\theta_{\text{meas}}$  obtained from Fig. 2. The calculated coverage is obtained from the double-layer thickness defined as  $\Delta a = r/2 - a$ . Using the thus determined effective double-layer thickness  $\Delta a$ , the saturation coverage  $\theta_{\text{calc}}$  is obtained from

$$\theta_{\text{sat}} = \theta_{\text{jam}} \left( \frac{a}{a + \Delta a} \right)^2 \quad (6)$$

in which  $\theta_{\text{jam}} = 54.7\%$  represents the jamming limit for irreversible random deposition of hard spheres.<sup>[41,44,45]</sup>

The data in Fig. 3 exhibit a good one-to-one relation between experiment and the DLVO theory. However, at large values of the ionic strengths and thus high surface concentrations, the measured coverages are higher. One cause is that the linear approximation of the Poisson-Boltzmann equation underestimates the potential drop near the particles. When a far-field potential is used, as it is here, the potential at short distances is overestimated. This results in an overestimation of the distance where the particle-particle

interaction drops below  $(3/2)kT$ , and consequently leads to an underestimation of the surface concentration. The effect will become important when  $r < a + (3/2)\kappa^{-1}$ , which is approximately 10 nm for the highest ionic strengths. This value corresponds to a surface coverage of 25%, which is approximately the value at which the data in Fig. 3 start to deviate from the one-to-one relation (the solid line). Another possible explanation for the deviation at higher ionic strengths may be the formation of clusters on the sample surface. A cluster has a larger volume on a relatively small area, thereby accounting for a larger optically determined surface concentration.

### Modeling the Deposition Transients

The deposition kinetics of colloidal particles can be described in terms of the adsorption rate  $d\theta/dt$  by

$$\frac{d\theta}{dt} = \pi a^2 j_0 B(\theta) \quad (7)$$

where  $\pi a^2$  is the geometrical particle surface area and  $j_0$  represents the limiting deposition flux for uncovered surfaces. The quantity  $B(\theta) = j(\theta)/j_0$ , with  $j(\theta)$  being the actual deposition flux for a given coverage, is usually referred to as the overall kinetic blocking function. This designation is somewhat misleading as  $B(\theta) = 1$  for low coverages, while in the limit of saturating coverages  $B(\theta) \rightarrow 0$ ; so in fact  $B(\theta)$  represents an effective, coverage-dependent available surface. More correctly, it is also referred to as the “available surface function.”<sup>[46]</sup> The function  $B(\theta)$  not only depends on the coverage, but also on many additional factors such as particle–particle interactions, the mechanism of particle transport, and the reversibility of particle adsorption.

In principle, the overall kinetic blocking function can only be determined empirically from the particle deposition rate as a function of time, i.e., curves similar to those presented in Fig. 2. If we assume that all deposition transients for our system (nanocolloidal gold particles irreversibly deposited on APTES-derivatized silicon oxide surfaces) are characterized by a single, coverage-dependent overall kinetic blocking function  $B(\theta/\theta_{\text{sat}})$ , where  $\theta_{\text{sat}}$  is the saturation coverage defined in Eq. (6), the general adsorption Eq. (7) can be rewritten in terms of the dimensionless variables

$$\bar{\theta} = \theta/\theta_{\text{sat}} \quad (8a)$$

$$\bar{t} = \frac{\pi a^2 j_0}{\theta_{\text{sat}}} t \quad (8b)$$

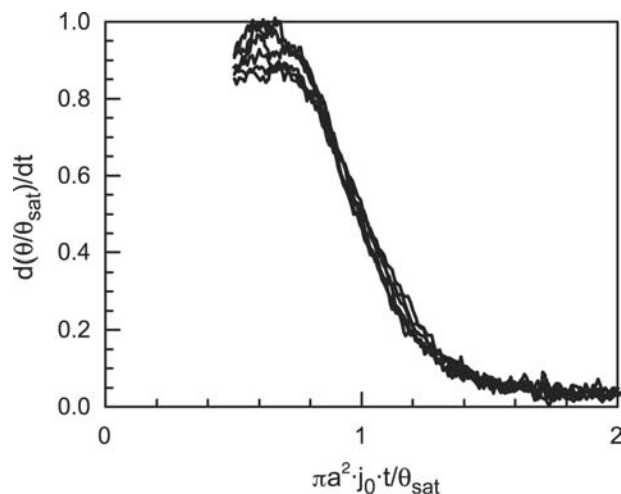


Fig. 4 Deposition transients of Fig. 2, scaled according to Eq. (9), using the dimensionless variables  $\bar{\theta}$  and  $\bar{t}$  as given by Eqs. (8a) and (8b).

to yield

$$\frac{d\bar{\theta}}{d\bar{t}} = B(\bar{\theta}) \quad (9)$$

The result of this scaling, applied to the deposition curves in Fig. 2, is shown in Fig. 4 where we have plotted the data according to Eq. (9). Apart from the initial first minutes (not shown in Fig. 4), it is clear that all curves collapse to a single curve, verifying that indeed a single overall kinetic blocking function governs the deposition process, irrespective of the ionic strength.

### A Generalized Adsorption Model

A theory, which is more specifically applicable to our system of colloidal particles, irreversibly deposited under forced convection conditions (stagnation point flow geometry), has been extensively described by Adamczyk.<sup>[47,48]</sup> A similar model was also described by Faraudo and Bafaluy.<sup>[49]</sup> In this generalized adsorption model, the deposition is considered to consist of two processes, i.e., 1) the actual adsorption, and 2) the convective supply of nanocrystals to the surface. The convective supply of colloidal particles to the outer edge of the adsorption layer, at a distance  $\delta_a$  from the surface, is described by the rate constant  $k_c = j_0/c_0$ , where  $j_0$  is equal to the particle flux. For the well-defined flow conditions in our stagnation point flow setup,  $k_c$  is given by Eq. (1).

The adsorption process is described by

$$\frac{d\theta}{dt} = \pi a^2 k_a c(\delta_a) B'(\theta) \quad (10)$$

and is governed by a rate constant  $k_a$  and a particle concentration  $c(\delta_a)$  at distance  $\delta_a$  from the surface.<sup>[50]</sup>

The available surface function  $B'(\theta)$ , also often referred to as the generalized blocking function, describes the transport resistance of the adsorbed layer to adsorbing particles; effectively, it is equal to the overall sticking probability. In fact, Eq. (10) is similar to Eq. (7), in which the actual adsorption process is taken into account by the overall kinetic blocking function  $B(\theta)$  considering a constant supply of colloidal particles. In Eq. (10), the adsorption process is considered and the supply of colloidal particles is described by the time dependence of  $c(\delta_a)$ . Within the adsorption layer of thickness  $\delta_a$ , convection effects can be neglected. The thickness  $\delta_a$  is comparable to the range of specific interactions, in principle electrostatic interactions, the extent of which is governed by the double-layer thickness. For our nanocolloidal particles, this implies that  $\delta_a$  is of the same order of magnitude as the particle radius.

For the irreversible adsorption of particles at uniformly accessible surfaces, Adamczyk<sup>[47]</sup> derived an expression for the kinetic overall blocking function, given by

$$B(\theta) = \frac{KB'(\theta)}{1 + (K - 1)B'(\theta)} \quad (11)$$

where  $K = k_a/k_c$  represents the coupling between adsorption and convection processes. In the case of strong particle–particle interactions,  $B'(\theta)$  can be approximated by the RSA available surface function  $B_0(\theta)$ . It is not possible to analytically evaluate  $B_0(\theta)$ , but a good approximation is given by<sup>[47,51]</sup>

$$B'(\theta) = \left[ 1 + 0.812 \frac{\theta}{\theta_{\text{sat}}} + 0.426 \left( \frac{\theta}{\theta_{\text{sat}}} \right)^2 + 0.0716 \left( \frac{\theta}{\theta_{\text{sat}}} \right)^3 \right] \left( 1 - \frac{\theta}{\theta_{\text{sat}}} \right)^3 \quad (12)$$

With this expression, the overall kinetic blocking function  $B(\theta)$  can be calculated, using Eq. (11), which now only depends on the maximum coverage  $\theta_{\text{sat}}$  obtained after saturation and the coupling constant  $K$ .

In practice,  $K \sim 1$  for micrometer-sized particles.<sup>[47]</sup> However, our colloidal particles are markedly smaller, which leads to a significant increase of the value of  $K$ . This can be understood by considering that from Eq. (2),  $D$  is inversely proportional to the particle radius  $a$ . Therewith the convective flux, expressed by the rate constant  $k_c$  in Eq. (1), varies as  $a^{-2/3}$ . An analytical expression for the adsorption constant  $k_a$  is given by Adamczyk and Szyk<sup>[52]</sup>

$$k_a = \frac{D}{2a} \frac{1}{1 + \frac{1}{2} \ln(1 + \frac{\Delta a}{a})} \quad (13)$$

where  $\Delta a$  represents the extent of the repulsive interactions, i.e., the effective thickness of the double layer. With Eq. (2), we obtain for the coupling constant  $K = k_a/k_c \sim a^{-4/3}$ ; that is, for smaller particles,  $K$  is expected to become considerably larger than 1.

In Fig. 5A, the coverage dependence of the overall kinetic blocking function is plotted for different values of  $K$ . A large value of  $K$  ( $\gg 1$ ) implies that the adsorption rate is considerably larger than the convective supply of particles. Thus up to relatively large coverages, the deposition is transport-limited, which is expressed by the considerable coverage range over which  $B(\theta/\theta_{\text{sat}}) \approx 1$ . Only near the saturation coverage,  $B(\theta/\theta_{\text{sat}})$  rapidly drops to 0. In the opposite case when  $K = 1$ , corresponding the pure RSA, the adsorption itself becomes

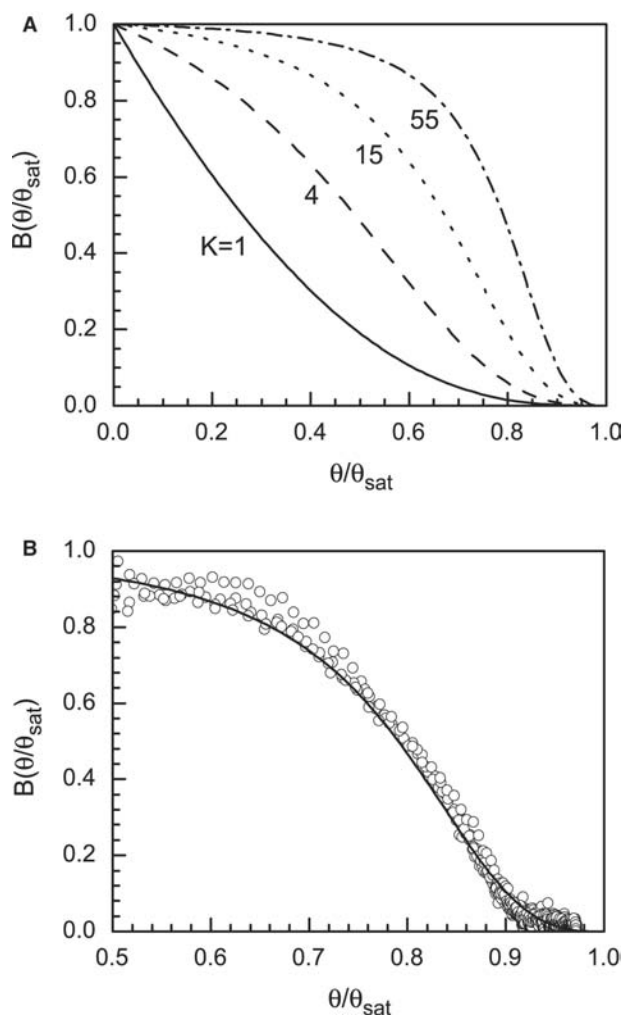


**Fig. 5** (A) The overall kinetic blocking function  $B(\theta/\theta_{\text{sat}})$  for different values of the coupling constant  $K$ , as a function of the normalized coverage  $\theta/\theta_{\text{sat}}$ . The solid line represents the RSA limit ( $K = 1$ ). The broken lines correspond to calculations using the generalized adsorption model with values for  $K$  as indicated. In (B), the data in Fig. 4 are replotted (symbols) and compared to the calculation for  $K = 55$ .

rate-limiting. Accordingly, for low  $K$  values,  $B(\theta/\theta_{\text{sat}})$  exhibits a sharp decrease already at low coverages.

From the deposition curves in Fig. 2, it is obvious that for a large coverage range, the deposition is dominated by mass transport of particles to the adsorption layer. The deposition rate  $d\theta/dt$  only decreases upon approaching the saturation coverage. This indicates that for our system of nanocolloidal gold particles, irreversibly deposited in a stagnation point flow geometry,  $K$  is considerably larger than 1. To obtain more quantitative information, we fitted the generalized adsorption model, expressed by Eqs. (7), (11), and (12), to the deposition transients in Fig. 2. As fitting parameters, a single value for both the coupling constant  $K$  and the initial, limiting deposition flux  $j_0$  is used for all ionic strengths. Only the saturation coverage  $\theta_{\text{sat}}$  is allowed to vary with ionic strength. Over the entire coverage range, there is a perfect correspondence between the measured and calculated deposition curves. This is also shown in Fig. 5B where the data obtained from the deposition transients are compared to the overall kinetic blocking function obtained from the fits. In agreement with results presented in the previous section, the initial deposition rate  $d\theta/dt = \pi a^2 j_0$  amounts to  $0.0225 \text{ min}^{-1}$ , while the saturation coverages  $\theta_{\text{sat}}$  are identical to the values given in Figs. 2 and 3. The fits yield a value  $K = 55 \pm 5$  for the coupling constant. Using the value  $k_c = 1.44 \times 10^{-6} \text{ m sec}^{-1}$  for our specific system, determined from Eq. (1), we obtain a value for the adsorption rate constant  $k_a = 7.91 \times 10^{-5} \text{ m sec}^{-1}$ . Using Eq. (13) with  $\Delta a = 2 \text{ nm}$ , we obtain a value of  $k_a = 2.9 \times 10^{-4} \text{ m sec}^{-1}$ , somewhat higher than our experimentally determined value but of the same order of magnitude.

### Comparison to Similar Nanoparticle Adsorption Experiment

Using the aforementioned generalized adsorption model, Adamczyk<sup>[48]</sup> collected adsorption rate constants for typical proteins [bovine serum albumin (BSA), fibrinogen, and IgG], which are of the same order of magnitude as our colloidal particles. Comparison with the  $k_a$  values for these proteins indicates that our aforementioned value for the irreversible deposition of nanocolloidal gold is in line with other systems of similar dimensions but of very different nature. As far as we are aware, the absolute value of the adsorption rate constant  $k_a$  has not been determined for colloidal systems with particle sizes in the low-nanometer range. In two papers,<sup>[39,53]</sup> Böhmer et al. describe similar measurements of silica particles with diameters between 32 and 200 nm. Their transients are very similar to our results for nanocolloidal gold, as presented in Fig. 2. In the analysis, the authors conclude that they are able to

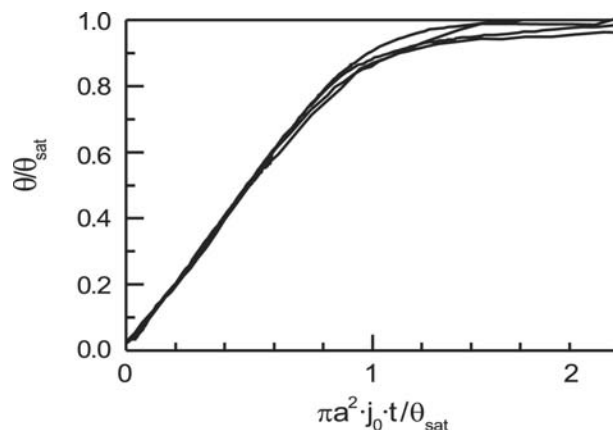


**Fig. 6** Deposition transients for 32-nm-diameter silica particles, scaled according to Eq. (9), using the dimensionless variables  $\bar{\theta}$  and  $\bar{t}$  as given by [Eqs. (8a) and (8b)] Source: From Ref.<sup>[39]</sup>.

quantitatively analyze the limiting regimes in their deposition transients. However, the overall transients could not be adequately described.

We have taken the data from the aforementioned work and analyzed them as we have described above for gold nanocrystal adsorption. The curves all scale onto a single, universal transient, similar to our results. This is shown in Fig. 6 for a deposition experiment using silica particles with a radius  $a = 16 \text{ nm}$ . Using Eqs. (1), (7), (11), (12), and (13), we obtain the size-dependent diffusion coefficient  $D$  and the adsorption rate constant  $k_a$ . The results are shown in Fig. 7, and compared to our results for nanocolloidal gold particles. Both the diffusion coefficient and the adsorption rate constant are lower than the trends observed for silica particles. Also, it is clear from Fig. 6 that the diffusion coefficients determined for the silica particles are in perfect agreement with the Stokes–Einstein relation [Eq. (2)], represented by the solid line. The origin of the discrepancy between the deposition parameters of gold nanocrystals and nanocolloidal silica particles is unclear and needs further investigation.

### CONCLUSION

The formation of nanocolloidal thin films consisting of assembled gold nanocrystals with diameters in the low-nanometer range has been reviewed. The different methods to produce monolayers as well as multi-layered superstructures are briefly summarized.

Also, a more detailed study of the kinetics of irreversible deposition of gold nanocrystals from colloidal suspensions onto silicon/silicon oxide substrates is presented. Using a stagnation point flow geometry, the

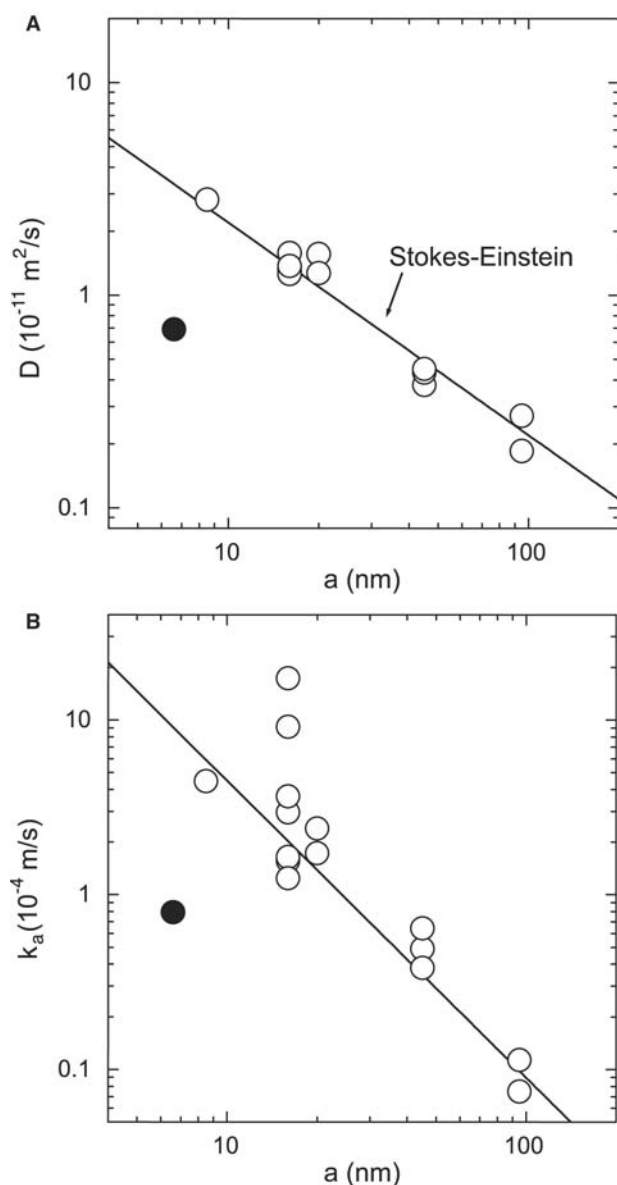


**Fig. 7** Size-dependent (A) diffusion coefficient  $D$  and (B) adsorption constant  $k_a$  for silica particles, obtained from analysis of results from Refs.<sup>[39,53]</sup>. For comparison, the values for nanocolloidal gold from our work (solid symbol) are compared to the silica results (open symbols). The solid line in (A) represents the Stokes–Einstein relation in Eq. (2); the line in (B) is a guide to the eye.

convective supply of colloidal particles is controlled. The deposition process is simultaneously monitored by in situ single wavelength reflectometry, as imaging optical methods cannot be used for such small particles. The absolute coverage is measured as a function of time for different ionic strengths. Two regimes are distinguished, related to two different processes in the adsorption process. Initially, the deposition is merely governed by mass transport limited supply of colloidal particles. The ionic strength of the suspension only

affects the deposition process in the saturation regime at higher coverages.

The coupling between the convection and adsorption processes, i.e., the transition from mass transport limitation to the regime where surface blocking effects dominate, is analyzed using a generalized adsorption theory. In this theory, the deposition rate is expressed in terms of an overall kinetic blocking function. For the irreversible deposition of particles, the adsorption is treated on the basis of the random sequential adsorption model. Using the generalized adsorption model, the measured deposition curves can be adequately described, and the rate constant for particle adsorption is determined. The experimental results are compared to those for proteins and also silica particles of similar dimensions as our nanocrystals. Although there is qualitative agreement, there is a discrepancy between the results for nanocolloidal gold and the other systems. The origin of the difference is unclear.

## ACKNOWLEDGMENTS

We thank Z. Adamczyk for valuable discussions regarding the quantitative analysis of the reflectometry experiments. This work is part of the research program of the Stichting voor Fundamenteel Onderzoek der Materie (FOM), financially supported by the Nederlandse Organisatie voor Wetenschappelijk Onderzoek (NWO) and Philips Research.

## REFERENCES

1. Grabar, K.C.; Freeman, R.G.; Hommer, M.B.; Natan, M.J. Preparation and characterization of Au colloid monolayers. *Anal. Chem.* **1995**, *67*, 735–743.
2. Grabar, K.C.; Smith, P.C.; Musick, M.D.; Davis, J.A.; Walter, D.G.; Jackson, M.A.; Guthrie, A.P.; Natan, M.J. Kinetic control of interparticle spacing in Au colloid-based surfaces: rational nanometer-scale architecture. *J. Am. Chem. Soc.* **1996**, *118*, 1148–1153.
3. Sato, T.; Ahmed, H.; Brown, D.; Johnson, B.F.G. Single electron transistor using a molecularly linked gold colloidal particle chain. *J. Appl. Phys.* **1997**, *82* (2), 696–701.
4. Sato, T.; Brown, D.; Johnson, B.F.G. Nucleation and growth of nano-gold colloidal lattices. *Chem. Commun.* **1997**, (11), 1007–1008.
5. Brust, M.; Bethell, D.; Kiely, C.J.; Schiffrin, D.J. Self-assembled gold nanoparticle thin films with nonmetallic optical and electronic properties. *Langmuir* **1998**, *14*, 5425–5429.
6. Schmitt, J.; Mächtle, P.; Eck, D.; Möhwald, H.; Helm, C.A. Preparation and optical properties of colloidal gold monolayers. *Langmuir* **1999**, *15* (9), 3256–3266.



7. Zhu, T.; Fu, X.; Mu, T.; Wang, J.; Liu, Z. pH-dependent adsorption of gold nanoparticles on *p*-aminothiophenol-modified gold substrates. *Langmuir* **1999**, *15* (16), 5197–5199.
8. Keating, C.D.; Musick, M.D.; Keefe, M.H.; Natan, M.J. Kinetics and thermodynamics of Au colloid monolayer self-assembly. *J. Chem. Educ.* **1999**, *76* (7), 949
9. Musick, M.D.; Peña, D.J.; Botsko, S.L.; McEvoy, T.M.; Richardson, J.N.; Natan, M.J. Electrochemical properties of colloidal Au-based surfaces: multilayer assemblies and seeded colloid films. *Langmuir* **1999**, *15*, 844–850.
10. Brown, K.R.; Lyon, L.A.; Fox, A.P.; Reiss, B.D.; Natan, M.J. Hydroxylamine seeded growth of colloidal Au nanoparticles. 3. Controlled formation of conductive Au films. *Chem. Mater.* **2000**, *12*, 314–323.
11. Shipway, A.N.; Lahav, M.; Willner, I. Nanostructured gold colloid electrodes. *Adv. Mater.* **2000**, *12* (13), 993–998.
12. Musick, M.D.; Keating, C.D.; Lyon, L.A.; Botsko, S.L.; Peña, D.J.; Holliway, W.D.; McEvoy, T.M.; Richardson, J.N.; Natan, M.J. Metal films prepared by stepwise assembly. 2. Construction and characterization of colloidal Au and Ag multilayers. *Chem. Mater.* **2000**, *12*, 2869–2881.
13. Kumar, A.; Mandale, A.B.; Sastry, M. Sequential electrostatic assembly of amine-derivatized gold and carboxylic acid-derivatized silver colloidal particles on glass substrates. *Langmuir* **2000**, *16*, 6921–6926.
14. Reincke, F.; Hickey, S.G.; Kelly, J.J.; Braam, T.W.; Jenneskens, L.W.; Vanmaekelbergh, D. Electrochemical and topological characterization of gold(111)|oligo(cyclohexylidene)|gold nanocrystal interfaces. *J. Electrochim. Acta* **2002**, *522*, 2–10.
15. Kooij, E.S.; Brouwer, E.A.M.; Wormeester, H.; Poelsema, B. Ionic strength mediated self-organization of gold nanocrystals: an AFM study. *Langmuir* **2002**, *18* (20), 7677–7682.
16. Liu, S.; Zhu, T.; Hu, R.; Liu, Z. Evaporation-induced self-assembly of gold nanoparticles into a highly organized two-dimensional array. *Phys. Chem. Chem. Phys.* **2002**, *4*, 6059–6062.
17. Hicks, J.F.; Seok-Shon, Y.; Murray, R.W. Layer-by-layer growth of polymer/nanoparticle films containing monolayer-protected gold clusters. *Langmuir* **2002**, *18* (6), 2288–2294.
18. Zhang, H.L.; Evans, S.D.; Henderson, J.R. Spectroscopic ellipsometry evaluation of gold nanoparticle thin films fabricated using layer-by-layer self assembly. *Adv. Mater.* **2003**, *15* (6), 531–534.
19. Li, Q.; Zheng, J.; Liu, Z. Site-selective assemblies of gold nanoparticles on an AFM tip-defined silicon template. *Langmuir* **2003**, *19*, 166–171.
20. Cant, N.E.; Critchley, K.; Zhang, H.L.; Evans, S.D. Surface functionalization for the self-assembly of nanoparticle/polymer multilayer films. *Thin Solid Films* **2003**, *426*, 31–39.
21. Maeda, Y.; Tabata, H.; Kawai, T. Two-dimensional assembly of gold nanoparticles with a DNA network template. *Appl. Phys. Lett.* **2001**, *79* (8), 1181–1183.
22. Kumar, A.; Pattarkine, M.; Bhadbhade, M.; Mandale, A.B.; Ganesh, K.N.; Datar, S.S.; Dharmadhikari, C.V.; Sastry, M. Linear superclusters of colloidal gold particles by electrostatic assembly on DNA templates. *Adv. Mater.* **2001**, *13* (5), 341–344.
23. Ung, T.; Liz-Marzán, L.M.; Mulvaney, P. Optical properties of thin films of Au–SiO<sub>2</sub> particles. *J. Phys. Chem., B* **2001**, *105*, 3441–3452.
24. Ung, T.; Liz-Marzán, L.M.; Mulvaney, P. Gold nanoparticle thin films. *Colloids Surf., A* **2002**, *202*, 119–126.
25. Kolny, J.; Kornowski, A.; Weller, H. Self-organization of cadmium sulfide and gold nanoparticles by electrostatic interaction. *Nano Lett.* **2002**, *2* (4), 361–364.
26. Parker, A.J.; Childs, P.A.; Palmer, R.E.; Brust, M. Deposition of passivated gold nanoclusters onto prepatterned substrates. *Appl. Phys. Lett.* **1999**, *74* (19), 2833–2835.
27. Bailey, R.C.; Stevenson, K.J.; Hupp, J.T. Assembly of micropatterned colloidal gold thin films via microtransfer molding and electrophoretic deposition. *Adv. Mater.* **2000**, *12* (24), 1930–1934.
28. Giersig, M.; Mulvaney, P. Preparation of ordered colloid monolayers by electrophoretic deposition. *Langmuir* **1993**, *9* (12), 3408–3413.
29. Trau, M.; Saville, D.A.; Aksay, I.A. Field-induced layering of colloidal crystals. *Science* **1996**, *272*, 706–709.
30. Smith, P.A.; Nordquist, C.D.; Jackson, T.N.; Mayer, T.S.; Martin, B.R.; Mbindyo, J.; Mallouk, T.E. Electric-field assisted assembly and alignment of metallic nanowires. *Appl. Phys. Lett.* **2000**, *77* (9), 1399–1401.
31. Kim, B.; Tripp, S.L.; Wei, A. Self-organization of large gold nanoparticle arrays. *J. Am. Chem. Soc.* **2001**, *123*, 7955–7956.
32. Lu, Y.; Yin, Y.; Li, Z.Y.; Xia, Y. Synthesis and self-assembly of Au–SiO<sub>2</sub> core-shell colloids. *Nano Lett.* **2002**, *2* (7), 785–788.
33. Jana, N.R.; Gearheart, L.A.; Obare, S.O.; Johnson, C.J.; Edler, K.J.; Mann, S.; Murphy, C.J. Liquid crystalline assemblies of ordered gold nanorods. *J. Mater. Chem.* **2002**, *12*, 2909–2912.
34. Dijt, J.; Cohen Stuart, M.; Hofman, J.; Fleer, G. Kinetics of polymer adsorption in stagnation point flow. *Colloids Surf., A* **1990**, *51*, 141.
35. Kooij, E.S.; Wormeester, H.; Brouwer, E.A.M.; van Vroonhoven, E.; van Silfhout, A.; Poelsema, B. Optical characterization of thin colloidal gold films by spectroscopic ellipsometry. *Langmuir* **2002**, *18* (11), 4401–4413.
36. Bedeaux, D.; Vlieger, J. *Optical Properties of Surfaces*; Imperial College Press: London, 2001.
37. Dabros, T.; Van de Ven, T.G.M. A direct method for studying particle deposition onto solid surfaces. *Colloid Polym. Sci.* **1983**, *261*, 694–707.
38. Adamczyk, Z.; Siwek, B.; Warzyński, P.; Musia, E. Kinetics of particle deposition in the radial impinging-jet cell. *J. Colloid Interface Sci.* **2001**, *242*, 14–24.
39. Böhmer, M.R.; van der Zeeuw, E.A.; Koper, G.J.M. Kinetics of particle adsorption in stagnation point flow studied by optical reflectometry. *J. Colloid Interface Sci.* **1998**, *197* (2), 242–250.
40. Sader, J.E. Accurate analytic formulae for the far field effective potential and surface charge density of a uniformly charged sphere. *J. Colloid Interface Sci.* **1997**, *188* (2), 508–510.



41. Yuan, Y.; Oberholzer, M.R.; Lenhoff, A.M. Size does matter: Electrostatically determined surface coverage trends in protein and colloid adsorption. *Colloids Surf., A* **2000**, *165* (1–3), 125–141.
42. Chow, M.K.; Zukoski, C.F. Gold sol formation mechanisms: role of colloidal stability. *J. Colloid Interface Sci.* **1994**, *165* (1), 97–109.
43. Van der Zande, B.M.I.; Dhont, J.G.K.; Böhmer, M.R.; Philipse, A.P. Colloidal dispersions of gold rods characterized by dynamic light scattering and electrophoresis. *Langmuir* **2000**, *16* (2), 459–464.
44. Adamczyk, Z.; Zembala, M.; Siwek, B.; Warszyński, P. Structure and ordering in localized adsorption of particles. *J. Colloid Interface Sci.* **1990**, *140* (1), 123–137.
45. Onoda, G.Y.; Liniger, E.G. Experimental determination of the random-parking limit in two dimensions. *Phys. Rev., A* **1986**, *33* (1), 715–716.
46. Schaaf, P.; Voegel, J.; Senger, B. From random sequential adsorption to ballistic deposition: a general view of irreversible deposition processes. *J. Phys. Chem., B* **2000**, *104* (10), 2204–2214.
47. Adamczyk, Z. Particle adsorption and deposition: role of electrostatic interactions. *Adv. Colloid Interface Sci.* **2003**, *100–102*, 267–347.
48. Adamczyk, Z. Kinetics of diffusion-controlled adsorption of colloid particles and proteins. *J. Colloid Interface Sci.* **2000**, *229* (2), 477–489.
49. Faraudo, J.; Bafaluy, J. Distribution function approach to irreversible adsorption of interacting colloidal particles. *J. Chem. Phys.* **2000**, *112*, 2003–2015.
50. Adamczyk, Z.; Senger, B.; Voegel, J.; Schaaf, P. Irreversible adsorption/deposition kinetics: a generalized approach. *J. Chem. Phys.* **1999**, *110*, 3118–3128.
51. Schaaf, P.; Talbot, J. Surface exclusion effects in adsorption processes. *J. Chem. Phys.* **1989**, *91*, 4401–4409.
52. Adamczyk, Z.; Szyk, L. Kinetics of irreversible adsorption of latex particles under diffusion-controlled transport. *Langmuir* **2000**, *16* (13), 5730–5737.
53. Hayes, R.A.; Böhmer, M.R.; Fokkink, L.G.J. A study of silica nanoparticle adsorption using optical reflectometry and streaming potential techniques. *Langmuir* **1999**, *15*, 2865–2870.

# Nanocomposite Magnetic Materials: Shock-Induced Synthesis

N. N. Thadhani

School of Materials Science and Engineering, Georgia Institute of Technology, Atlanta, Georgia, U.S.A.

Z. Q. Jin

Department of Physics, University of Texas at Arlington, Arlington, Texas, U.S.A.

## INTRODUCTION

Dynamic compaction utilizing high-pressure shock waves offers the possibility of fabricating bulk nanocrystalline materials via consolidation of amorphous or nanocrystalline alloy powders, while retaining the metastable structure and/or the nanoscale grain-size of the starting powders. Shock compression also has the potential of confining the movement of magnetic domain walls to the inside of grain boundaries in nanocrystalline magnetic materials, thereby providing an alternate method for design and fabrication of magnetic materials. With the anticipation of the next generation of high-performance permanent magnets produced at lower costs, in recent years, nanocomposite magnetic materials based on exchange-coupled nanoscale hard and soft magnetic phases have attracted the most attention owing to the combination of high magnetocrystalline anisotropy of magnetically hard phase, e.g.,  $R_2Fe_{14}B$  ( $R = \text{rare earth}$ ) and large saturation polarization of magnetically soft phase, e.g.,  $\alpha\text{-Fe}$ . Exchange-coupled magnets have usually been synthesized as thin films or as powders made by melt spinning and mechanically alloying off-stoichiometric alloys, which are then subjected to controlled crystallization to produce a mixture of the desired phases. Samples crystallized from amorphous precursors and those sintered to obtain bulk magnets usually result in non-uniform phase-separated structures with coarse grain size that limits exchange coupling, and, thus, significantly degrades magnetic properties. In fact, *fabrication of bulk nanocrystalline materials* has been the main obstacle that has limited the commercialization of such otherwise unique materials for a variety of applications.

In this entry, the shock consolidation approach employed for fabrication of high-performance magnetic nanocomposite  $R_2Fe_{14}B/\alpha\text{-Fe}$  ( $R = \text{Nd, Pr}$ )

hard-/soft-phase powders, using gas-gun impact and explosive shock-loading methods, will be described. The structure-property characteristics of highly dense compacts (up to 97–99% of full density) of  $R_2Fe_{14}B/\alpha\text{-Fe}$  ( $R = \text{Nd, Pr}$ ) nanocomposite magnets with a laminar particle morphology, solid-state interparticle bonding, and complete retention of nanoscale grain size and concomitant magnetic properties will be discussed. Effects of subsequent heat treatment on the improvement of coercive field and energy product will also be described. It will be illustrated that the control of starting powder characteristics, shock consolidation conditions, and postshock annealing treatments are necessary for fabrication of exchange-coupled nanocomposite bulk magnets with optimized magnetic properties.

## EXCHANGE-COUPLED NANOCOMPOSITE PERMANENT MAGNETS

One of the most important properties of permanent magnets is the maximum energy product,  $(BH)_{\text{max}}$ , which is a measure of the maximum stored energy. In the last 50 years,<sup>[1,2]</sup> remarkable evolutionary and revolutionary progress made in permanent magnet materials has resulted in the development of AlNiCo's with  $(BH)_{\text{max}} \sim 8 \text{ MGOe}$ , strong rare earth  $\text{SmCo}_5$  (1:5) and  $\text{Sm}(\text{Co, Fe, Cu, and Zr})_z$  (2:17) with  $(BH)_{\text{max}} \sim 30 \text{ MGOe}$ , and the new R-Fe-B supermagnets, which have large values of magnetization and magnetocrystalline anisotropy because of the highly *anisotropic* tetragonal  $R_2Fe_{14}B$  phase ( $a = 0.8792 \text{ nm}$  and  $c = 1.2177 \text{ nm}$  for  $\text{Nd}_2\text{Fe}_{14}\text{B}$ ). These single-phase Nd-Fe-B magnets have the highest energy product  $[(BH)_{\text{max}} \sim 54 \text{ MGOe}]$  of all existing magnets.<sup>[3]</sup>

The revolutionary progress has allowed dramatic miniaturization of devices in which the magnet was

previously a major part of the device volume and weight. High-energy permanent magnets are crucial for devices/components used in civilian and military systems and subsystems that require large and stable magnetic fields over a wide variety of environmental conditions. Examples of some of these applications include generators, actuators, electric drives (in tanks and automobiles), quieter and more efficient motors [unmanned undersea vehicles (UUV) propulsion], permanent magnet-based bearings for lubeless motors, holding and coupling devices, magnetic amplifiers, open magnetic resonance imaging (MRI), and faster spindle motors for hard drives (in which hard drive capacity increases by 60% a year).

Nanostructured magnetic materials show unique and interesting properties<sup>[4]</sup> that have been found to be scientifically and technologically very challenging to fully realize. Most of the endeavor in the development of magnetic materials in recent years has been placed in the exploration of nanocomposite magnets,<sup>[5]</sup> as this category of materials provides significant potential in obtaining a much higher remanence magnetization  $M_r$  and a large value of the theoretical maximum energy product  $(BH)_{\max}$  as compared to that in current commercial magnets. The unique properties of nanocomposite magnets originate from the exchange coupling between neighboring magnetic nanosize hard and soft phases, where the former provides high magnetocrystalline anisotropy and the latter contributes to the large saturation polarization. However, the grain size of soft and hard phases in these materials should be below a critical dimension of  $\sim 10$  nm to ensure effective exchange coupling and maximum fraction of the soft magnetic phases. It is anticipated that if the theoretical expectation of  $(BH)_{\max}$  for achieving  $1 \text{ MJ/m}^3$  is realized practically based on optimal exchange coupling,<sup>[6]</sup> then the overall volume and cost of magnets would be significantly reduced. Hence, the biggest challenge is to come up with an appropriate approach for fabricating bulk nanocomposites with sufficiently small and uniform grain size distribution to ensure the exchange interactions between neighboring grains.<sup>[7]</sup>

Magnetic nanocomposites such as  $\text{R}_2\text{Fe}_{14}\text{B}/(\alpha\text{-Fe, Fe}_3\text{B})$  ( $\text{R} = \text{rare earth}$ ) and  $\text{FePt}/\text{Fe}_3\text{Pt}$ <sup>[8]</sup> have to date been generally prepared in the form of powder particles, thin films, or rapidly quenched flakes via processes involving mechanical alloying/milling, sputtering, or melt spinning, chemical approaches, and subsequent heat treatment.<sup>[9–12]</sup> Bulk magnets are generally produced by resin bonding, sintering, extrusion, and hot isostatic pressing, etc. However, these approaches are not the preferred methods for fabricating bulk nanocomposite magnets, owing to the practical difficulty of attaining high density while also controlling the structure of the material at the nanoscale; hence the  $(BH)_{\max}$  values obtained are still far below the theoretical predictions.

## DYNAMIC SHOCK CONSOLIDATION OF POWDERS

Dynamic consolidation of powders using high-pressure shock waves is a potentially important method for the fabrication of bulk nanocrystalline or metastable materials.<sup>[13–17]</sup> The one-stage densification/bonding process occurring in the microsecond duration of the shock pulse involves the intense heterogeneous deposition of energy into particles, resulting in annihilation of the voids via plastic flow, and interparticle bonding. With this approach, it is possible to fabricate nanocomposite bulk magnets without introducing grain growth, as the localized heat generated at interparticle regions is dissipated into particle interiors in extremely short-time duration ( $\sim$  tens of microseconds). Shock waves can be generated through the impact of a projectile on to a powder-containing target, with the projectile being accelerated using a gas-gun or explosive devices, or by detonating explosive charges in contact with the powder container.<sup>[18]</sup> While the shock-densification conditions can be controlled by the initial packing density and by changing the impact velocity in the case of gas-gun compaction or explosive type in the case of explosive compaction, proper design of the shock-loading geometry (powder containment fixture) is essential to minimize variations in pressure distribution, and, therefore, ensure recovery of well-densified and crack-free powder compacts.

Recent work has illustrated that with typical shock pressures in the order of a few to tens of GPa, magnetic nanocrystalline powders can be successfully shock consolidated (with  $\sim 95\%$  of theoretical density) without significant grain growth.<sup>[19–23]</sup> However, these studies have employed shock compression under more excessive conditions, leading to the decomposition of the hard phase and even formation of undesired phases, causing significant deterioration of the hard-phase magnetic properties.

We have investigated shock consolidation of magnetic nanocomposite  $\text{R}_2\text{Fe}_{14}\text{B}/\alpha\text{-Fe}$  ( $\text{R} = \text{Pr, Nd}$ ) powders,<sup>[24–26]</sup> using a three-capsule plate-impact gas-gun compaction recovery fixture and a double-tube cylindrical-implosion explosive loading geometry, designed based on appropriate models for powder densification and optimizing shock-wave interactions across materials of dissimilar impedance. The gas-gun method involves planar-wave propagation through the powders, while in the explosive geometry, radial shock-wave implosion leads to powder densification. Fully dense, bulk nanostructured magnets have been successfully fabricated by optimization of compaction parameters (shock pressure and initial packing density), proper design of fixtures, and use of appropriate starting powder morphology. Amorphization and ultrafine-scale recrystallization along localized shear bands forming under

coupled high strain rate and high-pressure conditions have been observed to lead to grain-size refinement, which provides insight into the process of deformation of nanocrystalline materials and possibly its control for design of structures for optimized properties.

### Shock Consolidation of Hard-/Soft-Phase Nanocomposites

Nanocomposite ribbons with hard-phase  $\text{Pr}_2\text{Fe}_{14}\text{B}$  and 20 wt% soft-phase  $\alpha\text{-Fe}$  were prepared by melt spinning and subsequent heat treatment under conditions that ensured nanoscale phase retention. The ribbons were then pulverized to 10–200  $\mu\text{m}$  powder flakes, prior to packing (at predetermined green densities) in the powder containers for shock consolidation. Figure 1A and B are scanning electron microscopy (SEM) images

illustrating the morphology of the starting  $\text{Pr}_2\text{Fe}_{14}\text{B}/\alpha\text{-Fe}$  particles, and Fig. 1C and D are bright-field (BF) and dark-field (DF) transmission electron microscope (TEM) images showing the nanocrystalline (25–30 nm) grain size.

For gas-gun impact experiments, the nanocomposite powders were statically pressed in capsules at various packing densities. Impact experiments were conducted using an 80 mm diameter single-stage gas-gun facility where a stainless steel flyer-plate mounted on an aluminum sabot was accelerated at various velocities (500–1000 m/sec) to impact the target containing the three-capsule fixture. A schematic illustration of the three-capsule fixture and a photograph of the 80-mm diameter Georgia Tech gas-gun are shown in Fig. 2A and B, respectively. To minimize radial wave-focusing effects (and buildup of extreme pressure), originating because of differences in

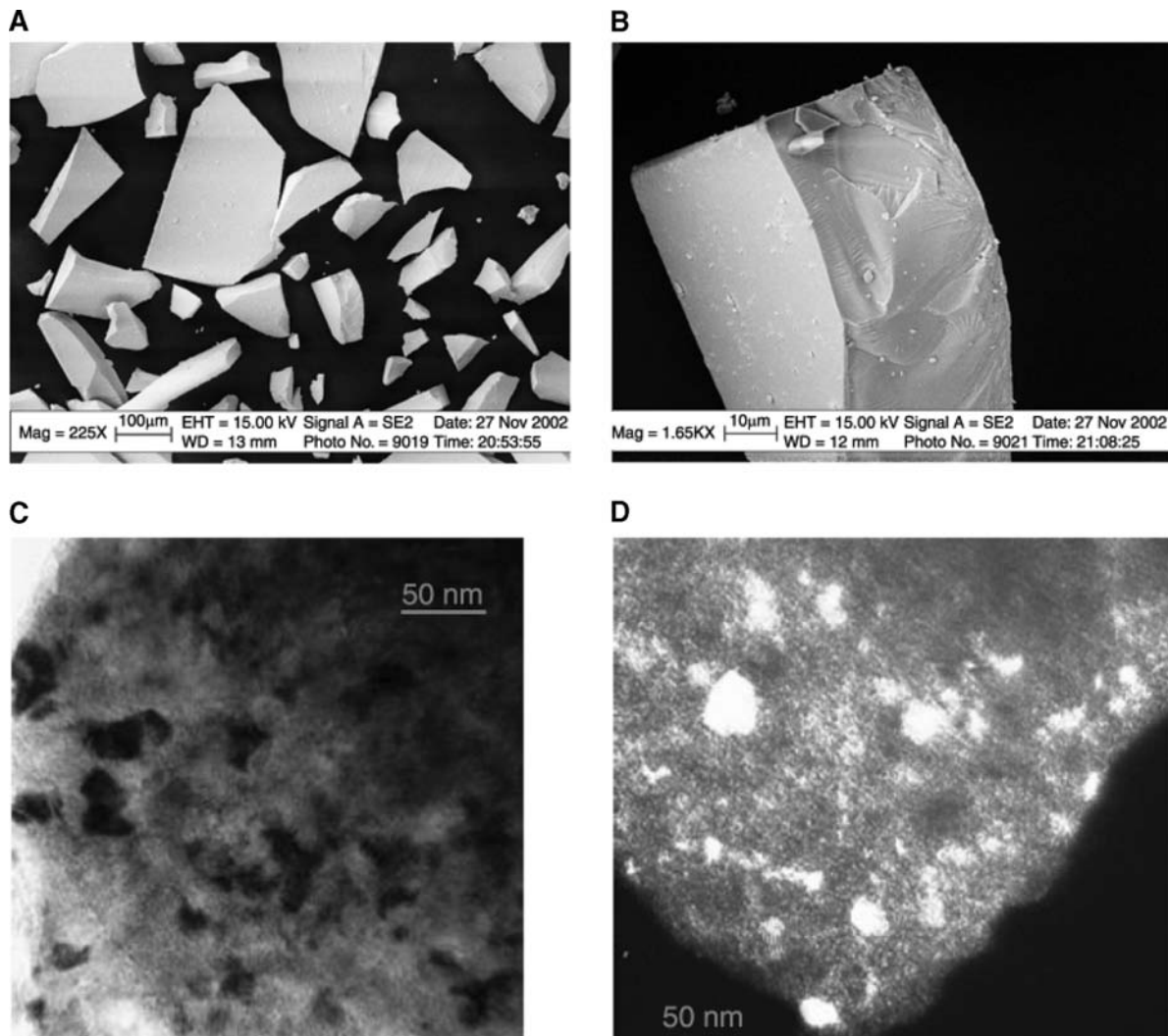


**Fig. 1** (A) and (B) SEM images illustrating the morphology of melt-spun and ground  $\text{Pr}_2\text{Fe}_{14}\text{B}/\alpha\text{-Fe}$  particles, and (C) and (D) BF and DF TEM images showing the nanocrystalline (25–30 nm) grain size of the starting powders.

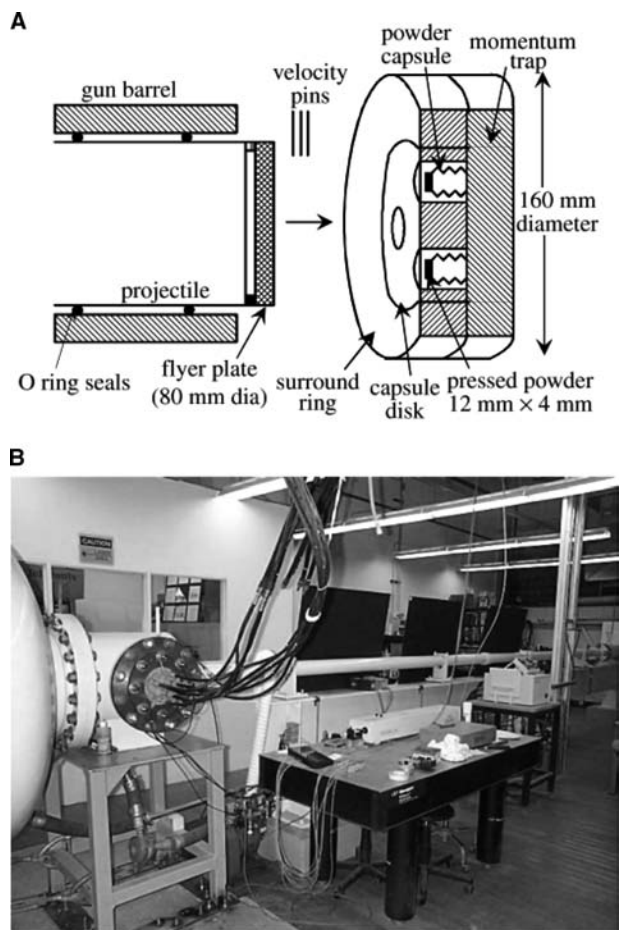


**Fig. 2** (A) Schematic illustration of three-capsule plate-impact fixture used for shock-consolidation of powders. (B) Photograph of 80-mm diameter Georgia Tech gas-gun.

the impedance between powder and steel container, the powder-containing capsules were designed with a surrounding void (air gap).

For explosive compaction, a cylindrical geometry consisting of two concentric tubes was used, as illustrated in Fig. 3. The internal steel tube contained the powder and the external steel tube acted as the flyer tube, which accelerated inwards upon detonation of the surrounding explosive ammonium nitrate and fuel oil mixed with low-density perlite diluent (ANFOIL). Upon ignition, the detonation wave sweeps along the flyer tube and accelerates it inwards resulting in a convergent shock wave propagating through the length of the cylinder.

With both geometries, corresponding maximum peak shock pressures generated upon impact were calculated, using AUTODYN-2D<sup>[27]</sup> and the  $P$ - $\alpha$  model of powder densification.<sup>[28]</sup>

Following shock compression, the compacts were recovered as 12-mm diameter by 3-mm thick discs (in the case of gas-gun experiments) and 25-mm diameter

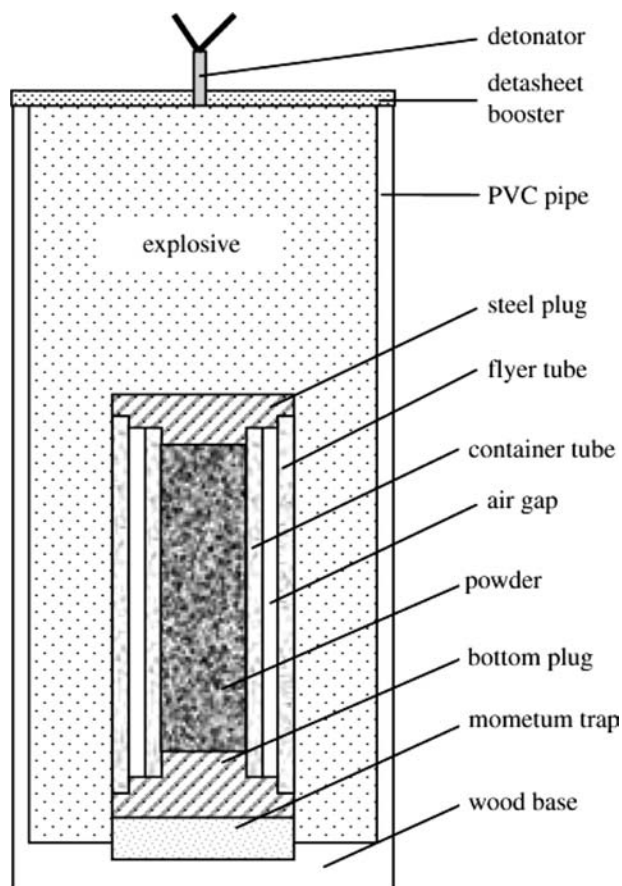


**Fig. 3** Schematic illustration showing the geometry of the explosive-loading fixture used for making rod-shaped bulk nanocomposite magnets.

by 120-mm long cylinders (in the case of explosive-loading configuration). The compact densities were determined using the Archimedeian method, and microhardness measurements were performed using the Leco DM-400F microhardness tester. The compacted magnets were analyzed by X-ray diffraction (XRD) using  $\text{Cu K}\alpha$  radiation, SEM, and TEM. The magnetic properties were measured using a superconducting quantum interference device (SQUID) magnetometer with a maximum applied field of 70 kOe. The measured magnetic properties were corrected by using effective demagnetization factor (estimated according to the sample morphology) of 0.33 and 0.14 for starting powders and shock-compacted samples, respectively.

### Physical and Structural Characteristics of Shock-Consolidated Bulk Magnets

Figure 4 shows a plot illustrating the shock compaction conditions and resulting characteristics of the  $\text{Pr}_2\text{Fe}_{14}\text{B}/\alpha\text{-Fe}$  nanocomposite compacts. The shock

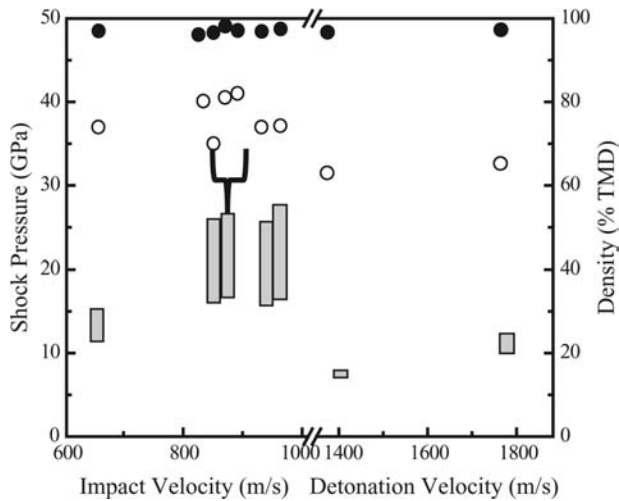


**Fig. 4** Plot of shock pressure and final density of compacts of  $\text{Pr}_2\text{Fe}_{14}\text{B}/\alpha\text{-Fe}$  nanocomposites shown as a function of compaction conditions (initial packing density and gas-gun impact velocity or explosive-detonation velocity). The rectangular bars correspond to the shock pressure range for the corresponding gas-gun impact and explosive-loading experiments. The initial packing densities of starting powders are marked as hollow circles. The solid circles denote the compact density of the final recovered shock-consolidated magnets. Note: The bracket indicates three samples of different initial packing densities compacted at same velocity of 880 m/sec.

pressure is a function of the compaction geometry (gas-gun impact or explosive loading), impact/detonation velocity, and initial powder packing “green” density. The degree of densification of  $\text{Pr}_2\text{Fe}_{14}\text{B}/\alpha\text{-Fe}$  powders depends on the shock pressure and the green density, with the final compact density approaching up to  $\sim 99\%$  of theoretical maximum density (T.M.D.), particularly in the case of the powders pressed at an initial green density of  $\sim 76\%$  T.M.D with the gas-gun geometry. The shock-consolidated compacts also had high hardness values (9–12 GPa), revealing the nature of strong interparticle bonding between the powders. While gas-gun experiments yielded disc-shaped compacts, the explosive compaction experiments provided compacts in the form of cylinders with uniform density of 97–98% T.M.D throughout the compact length. Compaction at very high shock pressures ( $\sim 12$  GPa) led to formation of an axial cavity owing to Mach stem effects.<sup>[29]</sup>

Figure 5 illustrates typical SEM images of the fracture surfaces of the  $\text{Pr}_2\text{Fe}_{14}\text{B}/\alpha\text{-Fe}$  compacts shock-consolidated using the gas-gun at the same impact velocity (880 m/sec), but starting with three different initial packing densities (64%, 76%, and 78% T.M.D). It can be seen from the images that the individual flaky powders are substantially compressed and deformed to fill the interstitial spaces. Because the starting ribbon

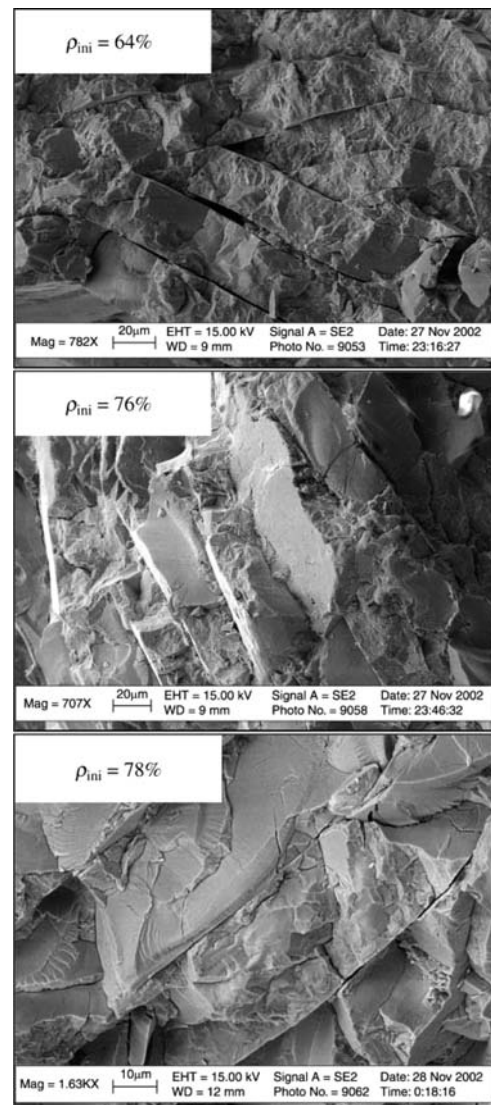


**Fig. 5** SEM images of fracture surfaces of  $\text{Pr}_2\text{Fe}_{14}\text{B}/\alpha\text{-Fe}$  compacts shock-consolidated using the gas-gun at the same impact velocity (880 m/sec), but starting with three different initial packing densities (64%, 76%, and 78% TMD). The 64% initial density compact shows incomplete bonding between particles, and the 78% initial density compact shows intraparticle cracking. The 76% initial density compact shows the highest degree of densification with solidstate intimate bonding.

powders have flat flake morphology, the initial uniaxial pressing causes the flakes to become aligned with the flat surfaces perpendicular to the pressing direction. The flat flakes retain their alignment even after shock compression. Archimedean-density measurements revealed that each of the 64%, 76%, and 78% initial density compacts had final densities of 94%, 99%, and 98%, respectively. As shown in Fig. 5, the 64% initial density compact indeed has incomplete bonding between particles, and the 78% initial density



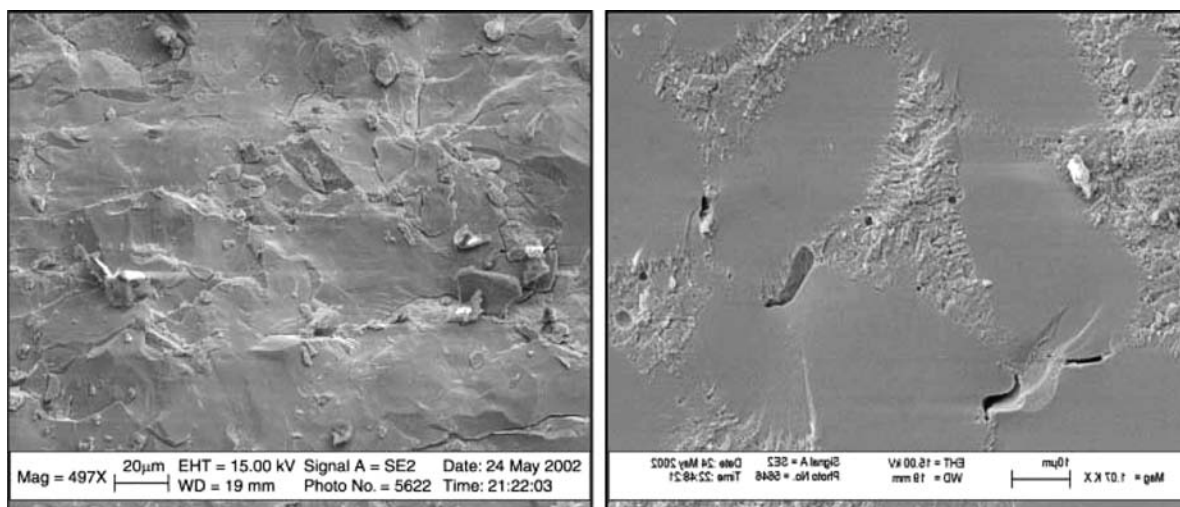


**Fig. 6** SEM images of planar surface of compacts made at two different impact velocities (660 and 950 m/sec for left and right images). The micrograph of the 950-m/sec impact velocity sample shows the presence of melted and resolidified interparticle regions, evidenced by the presence of microcrystalline and solidification shrinkage voids.

compact while being almost fully dense shows intraparticle cracking. The 76% initial density compact, in fact, shows the highest degree of densification with intimate solid-state bonding of particle interfaces.

In general, the SEM images of the fracture surfaces reveal partitioning of shock energy, with a significant amount of energy being localized at particle surfaces leading to interparticle bonding in the process of collapsing the voids. Excessive deposition of energy at interparticle regions, owing to low initial packing density or extreme shock-loading conditions (e.g., owing to high gas-gun impact velocity) can lead to interparticle bonding via surface melting and resolidification. Figure 6 shows SEM images of planar surfaces of compacts made at two different impact velocities (660 and 950 m/sec). The micrograph of the higher impact velocity sample clearly shows the presence of melted and resolidified interparticle regions, which is detrimental to the retention of nanoscale structure and optimum magnetic properties.

Figure 7 shows XRD patterns comparing the structure of the starting material and the recovered shock-compacted samples. The diffraction patterns of the starting specimen match the peaks corresponding to those of the 2:14:1 hard phase and the  $\alpha$ -Fe soft phase. Upon shock compression, the respective peak intensity ratios for both hard and soft phases do not change much, indicating no grain rotation and no preferred texture formation under the shock conditions employed. However, the recovered samples show broadening of peaks for both magnetic phases, more so for soft  $\alpha$ -Fe phase grains. The XRD peak broadening for as-compressed samples is associated with either lattice deformation/microstrain or a decrease in the grain size as a result of the uniaxial strain compression

during the rapid shock-energy dissipation. Calculations based on Williamson-Hall diffraction peak-width analysis showed microstrain of  $3\text{--}5 \times 10^{-3}$ , which is of same order of magnitude as heavily cold-worked materials. It is important to note that the crystallite size (15–20 nm) measured in the gas-gun compacts was found to be slightly lower than that of the starting powders ( $\sim 24$  nm in grain size). The retention of fine

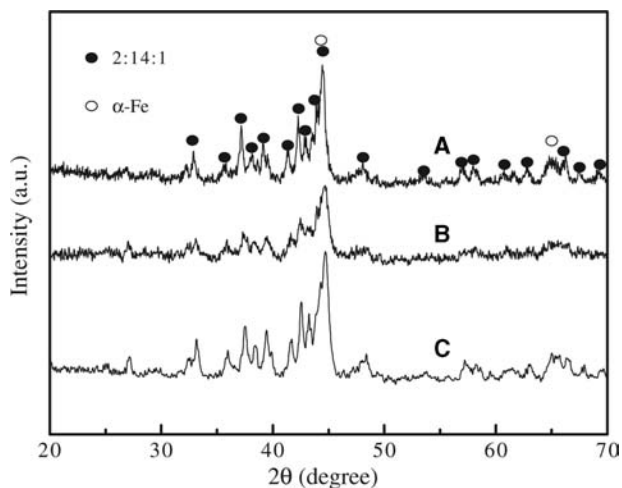


**Fig. 7** XRD patterns comparing the structure of (A) starting material and recovered shock-compacted samples prepared by (B) gas-gun compaction and (C) double-tube explosive compaction. The diffraction pattern of starting specimen matches the peaks corresponding to those of the 2:14:1 hard phase and the  $\alpha$ -Fe soft phase. Upon shock compression, respective peak intensity ratios for both hard and soft phases do not change much, indicating no grain rotation and no preferred texture formation under the shock compaction conditions employed.

grain size in the compacts is attributed to the rapid deposition of energy in time durations of fractions of a microsecond. When the powders are packed at a lower initial density; however, a higher temperature rise associated with the annihilation of a larger volume fraction of voids can result in grain growth.

BF and DF TEM observations shown in Figs. 8 and 9 confirm the retention of nanoscale structure in the recovered  $\text{Pr}_2\text{Fe}_{14}\text{B}/\alpha\text{-Fe}$  samples, obtained both in the gas-gun and in the explosive compaction experiments, respectively. It can be seen from Fig. 8 that the starting  $\text{Pr}_2\text{Fe}_{14}\text{B}/\alpha\text{-Fe}$  powder has a mean grain size of  $\sim 25$  nm; however, some coarse  $\alpha\text{-Fe}$  grains are also visible. Following shock compaction with the gas-gun at 880 m/sec, the grains have a size distribution of 20–25 nm, and even more fine grains of 10–15 nm are evident, consistent with XRD

line-broadening analysis. The explosively consolidated compacts also showed similar retention and refinement of grain size. As illustrated by the TEM images shown in Fig. 9, both the top and the bottom parts of the rod-shaped compact have the same uniform bimodal 20–25 and 15–20 nm grain size distribution. In fact the nanocrystalline grain size of the compacts is quite stable and even upon annealing at 750°C for 2 hr, the same grain size is retained as illustrated by the TEM images of the annealed explosively shock-consolidated compact.

The retention, and, most significantly, the refinement of nanometric grain size appear to be because of fragmentation of the larger grains by shear bands generated during dynamic compaction,<sup>[19]</sup> which is an important attribute of this technique. Figure 10 shows a TEM micrograph illustrating parallel nanoscale

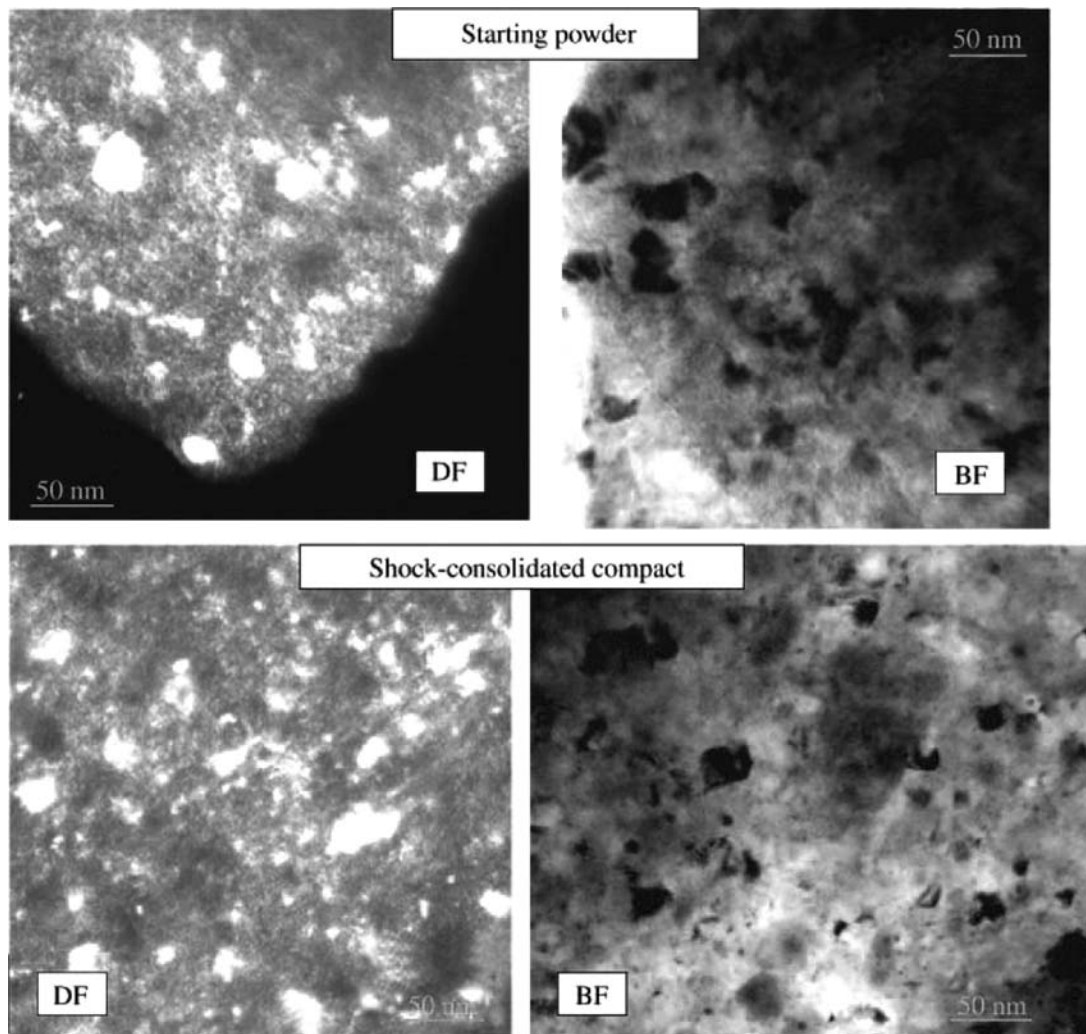


**Fig. 8** TEM DF and BF images illustrate that the starting  $\text{Pr}_2\text{Fe}_{14}\text{B}/\alpha\text{-Fe}$  powder has a mean grain size of  $\sim 25$  nm along with some coarse  $\alpha\text{-Fe}$  grains. Following shock compaction with the gas-gun at 880 m/sec, the grains have a bimodal size distribution of 20–25 nm (same as that of starting powder), in addition to finer grains of 10–15 nm size believed to have been formed during shock compaction.

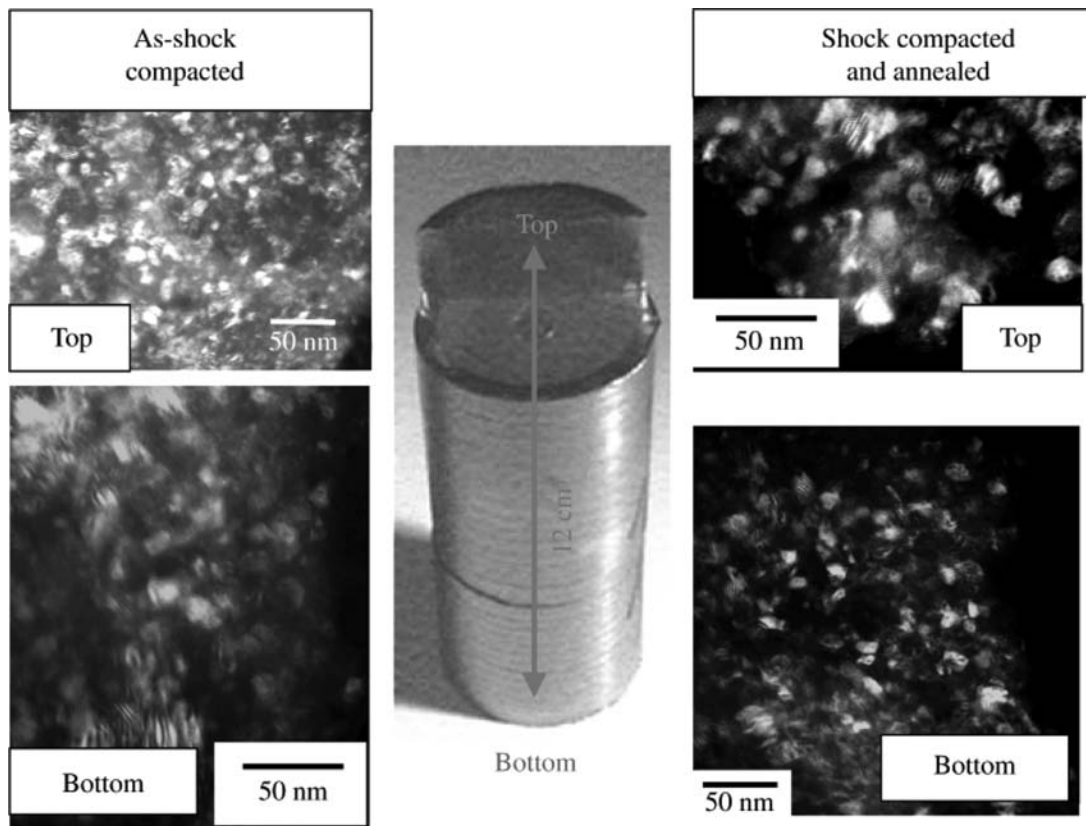


**Fig. 9** TEM images showing retention of similar 20–25 and 15–20 nm grain size distribution in the top and bottom parts of the 12 cm long by 2 cm diameter rod-shaped as shock-consolidated (explosively) compact. TEM images of the same annealed explosively shock-consolidated compact illustrate that the nanocrystalline grain size is quite stable (with no grain growth) even upon annealing at 750°C for 2 hr.

shear bands that span through multiple grain lengths but are confined within particle interiors. The very narrow “nanometer” scale of the shear bands is an indication that these are formed under an extremely high strain rate.<sup>[30]</sup> The shear bands have a shiny appearance quite different from the surrounding matrix because of its different structure where plastic deformation becomes highly concentrated often producing a precursor or a path to fracture. High-resolution transmission electron microscope (HRTEM) images shown in Fig. 10 reveal that the shear bands consist of a mixture of very fine  $\alpha$ -Fe nanocrystallites and amorphous  $\text{Pr}_2\text{Fe}_{14}\text{B}$  phase. The even higher magnification image also reveals the presence of amorphous phase inside the shear band. The strain rate estimated within the shear band is  $\sim 10^9$ /sec, which is close to the critical value of the strain rate determined by MD simulations for amorphization of metallic monocrystal nanowire.<sup>[31]</sup> Formation of other defects, including dislocations and twinning, is also commonly observed during shock compression of powders.<sup>[8,9,12]</sup> In the case of the shock-consolidated hard/soft phase nanocrystalline powder compacts, these structural defects were

indeed observed as revealed in the TEM images of the explosively compacted samples, shown in Fig. 11.

### Magnetic Properties of Shock-Consolidated Bulk Nanocomposite Magnets

Figure 12 shows typical hysteresis loops for the gas-gun compacted  $\text{Pr}_2\text{Fe}_{14}\text{B}/\alpha\text{-Fe}$  nanocomposite samples of different compact densities. Although all the samples consist of magnetically hard and soft phases, the smooth hysteresis loops reveal a single-phase-like behavior and a high remanence ratio of over 50% in these shock-consolidated compacts, indicating an effective exchange coupling between hard-magnetic  $\text{Pr}_2\text{Fe}_{14}\text{B}$  and soft-magnetic  $\alpha\text{-Fe}$  phases. The values of saturation magnetization for the various compacts are very close to that of starting materials, indicating that shock compaction does not affect the phase constitution of the material, as was also confirmed by XRD analysis, which showed the same phase structures before and after compaction. In addition, it can be seen that the difference in coercivity is minor

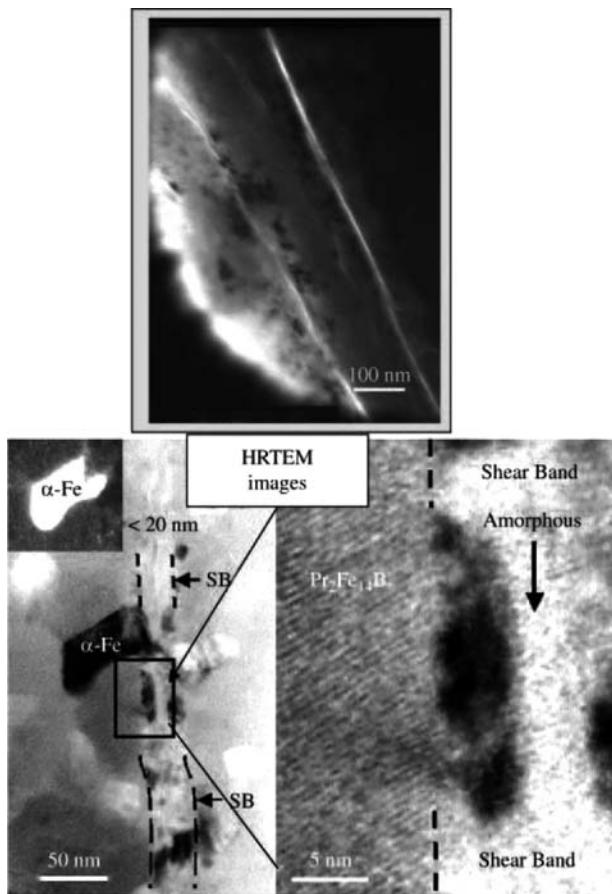


**Fig. 10** TEM micrograph illustrating parallel, nanoscale, shiny, shear bands spanning through multiple grain lengths, but confined within particle interiors. HRTEM images reveal that the shear bands consist of a mixture of very fine  $\alpha$ -Fe nanocrystallites and amorphous  $\text{Pr}_2\text{Fe}_{14}\text{B}$  phase. The even higher magnification image also reveals presence of amorphous phase inside the shear band.

and independent of the initial green density, although it is slightly lower than the value (550 kA/m) of the preshock samples. However, it appears that the remanent magnetization scales with the final compact density, with the 99% dense compact having the highest remanence value ( $M_r = 0.96 \text{ T}$ ) and the largest energy product  $(\text{BH})_{\text{max}} = 111 \text{ kJ/m}^3$ . After considering the effect of demagnetization factor, an energy product of  $\sim 128 \text{ kJ/m}^3$  was obtained, which is comparable to that of the starting materials.

An even higher energy product of  $142 \text{ kJ/m}^3$  was obtained in the explosive-compacted samples (made at a shock pressure of  $\sim 1 \text{ GPa}$ ). However, in the case of the explosively compacted rods, it was found that too high a shock pressure results in demagnetization of the hard magnetic phase and loss of coercivity, possibility owing to amorphization of crystallites caused by the intense shock compaction conditions.

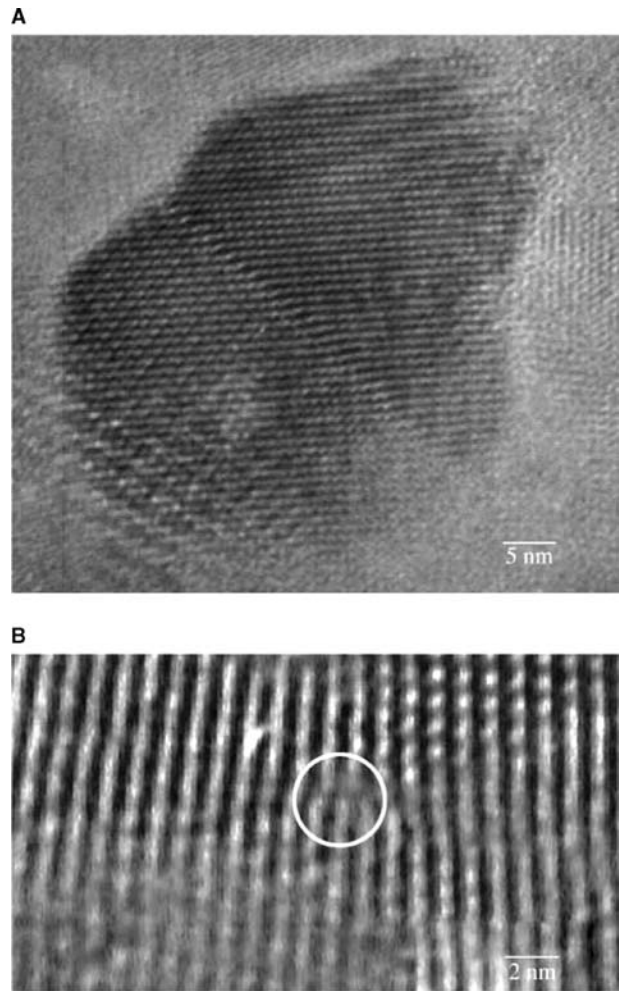


**Fig. 11** HRTEM image of shock-compacted nanocomposite  $\text{Pr}_2\text{Fe}_{14}\text{B}/\alpha\text{-Fe}$  compact showing the presence of (A) twinning and (B) edge dislocation in a hard-phase crystal.

Hence, the effect of subsequent heat treatment on the magnetic properties of the shock-compressed bulk magnets was investigated. As shown in Fig. 13, the coercivity and energy product are observed to increase with subsequent annealing at  $750^\circ\text{C}$ , which is slightly higher than the crystallization temperature. The increase of coercivity may be attributed to the crystallization of preexisting amorphous phase and formation and retention of nanostructure. Annealing at temperatures above  $750^\circ\text{C}$  lowers the coercivity, possibly because of grain growth and existence of free zones within the soft-phase grains where the exchange coupling is quite weak. The free zones act as reversal nucleation center, and magnetization reversal nucleates at relatively lower fields over the soft phase, resulting in the reduction of the coercivity. These observations suggest that the magnetic properties of shock-consolidated nanocomposite compacts can actually



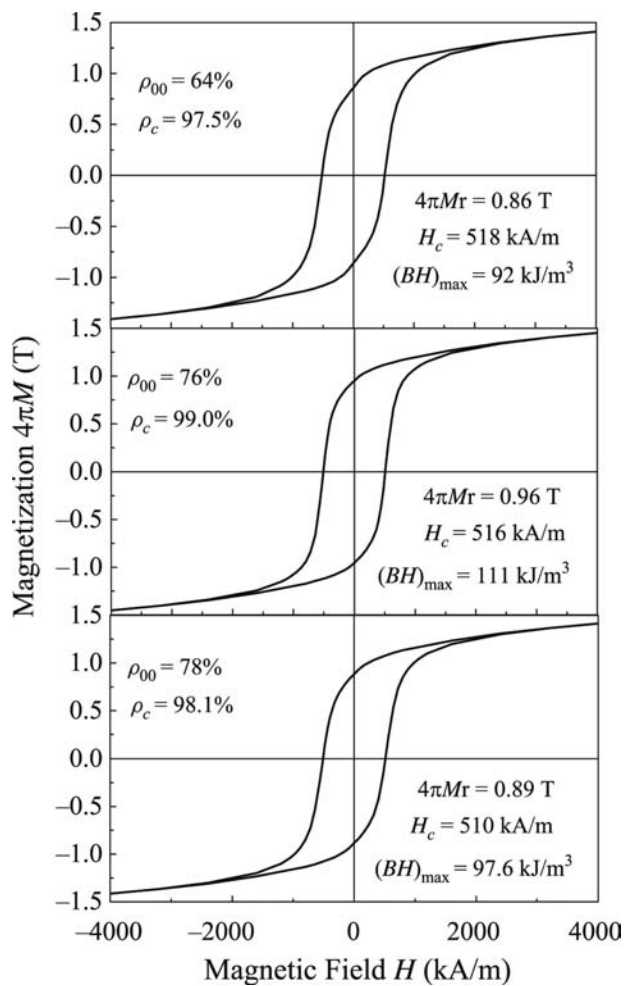


**Fig. 12** Hysteresis loops obtained for recovered  $\text{Pr}_2\text{Fe}_{14}\text{B}/\alpha\text{-Fe}$  samples shock consolidated at 880 m/sec starting with different initial densities  $\rho_c$  and attaining varying final compact densities  $\rho_c$ . The smooth hysteresis loops indicate exchange coupling between hard and soft phases. Varying density does not seem to significantly influence the coercivity, but the remnance and energy product are significantly influenced.

be optimized by proper control of subsequent annealing treatment conditions.

It is well established that in the case of nanocomposite magnets, polarization reverses by a mechanism of nucleation and further expansion of inverse domains. These inverse domains nucleate at sites exhibiting a non-uniform magnetization distribution, such as grain boundaries, internal pores, and high stress concentrations. Shock compression results in large amounts of highly strained and defected regions, which can be energetically preferred locations for nucleation and growth of inverse domain nuclei, and thus result in a lowered reversal field and the reduction of coercivity. However, the coercivity is easily recovered with

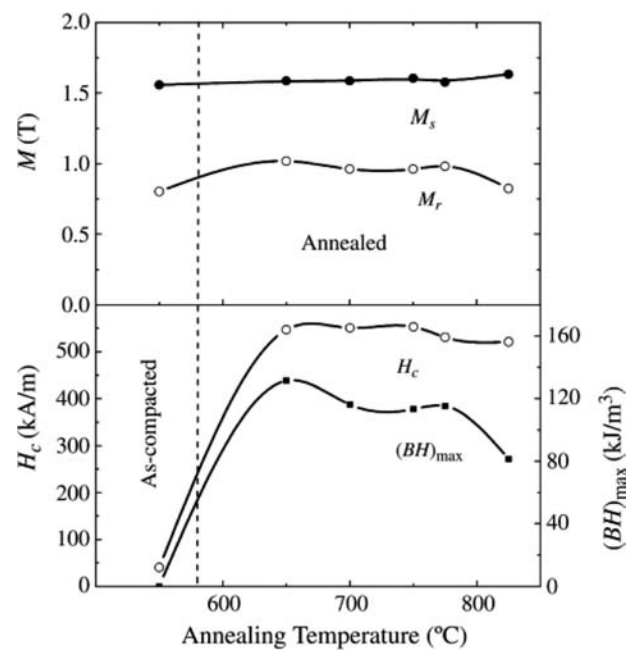


**Fig. 13** Annealing temperature dependence of the magnetic properties for the explosive-compacted  $\text{Pr}_2\text{Fe}_{14}\text{B}/\alpha\text{-Fe}$  samples.

subsequent annealing treatment. The refinement of grain size, owing to shock compression, plays an important role in the increase of coercivity and the enhancement of exchange coupling. Therefore, appropriate control of shock conditions and postcompaction annealing treatments can allow further improvements in magnetic properties. It should be noted that the magnetic properties of the shock-consolidated nanocomposite bulk compacts reported in this entry are higher than those of commercially available resin-bonded nanocomposite magnets ( $\rho < 80\%$  TMD,  $(\text{BH})_{\text{max}} < 100 \text{ kJ/m}^3$ ) because non-magnetic resins in these bonded magnets lower the bulk density, and, hence, reduce the energy product. The optimal magnetic properties are also closely associated with the retention of nanostructure and strong exchange coupling between hard- and soft-magnetic phases at nanoscale. Further refinement in grain size can be expected to provide more significant improvement in magnetic properties.

## CONCLUSIONS

Shock compression processing via gas-gun impact and explosive-loading geometries is shown to be an effective method for producing fully dense, bulk nanocomposite magnets while retaining nanocrystalline grain

size, and without grain growth. The investigation of the structural and magnetic properties as a function of shock-loading conditions (initial powder-packing density and impact velocity) shows that proper control can result in complete densification and retention (or even refinement) of nanostructure of both the soft and the hard phases. The grain refinement occurs because of the formation of shear bands during shock compression. The magnetic properties of compacts are also found to be sensitive to shock pressure, packing density, and shock compaction geometry. The understanding of amorphization and recrystallization in shear bands provides insight into the deformation response of nanocrystalline materials under coupled high strain rate and high-pressure conditions.

## ACKNOWLEDGMENTS

The results reported in this entry have been obtained from work supported by US DoD/DARPA through ARO under grant DAAD-19-01-1-0546. We are thankful to all collaborators with whom we have had the opportunity to interact with in this program. We are particularly grateful to Prof. J. P. Liu at the University of Texas at Arlington and Prof. Z. L. Wang at Georgia Institute of Technology for their collaborations and discussions during the course of this work.

## REFERENCES

- Parker, R.J. *Advances in Permanent Magnetism*; John Wiley: New York, 1990.
- Stadelmaier, H.H.; Reinsch, B. Magnetic applications. In *Intermetallic Compounds*; Westbrook, J.H., Fleischer, R.L., Eds.; John Wiley: New York, 1994; Vol. 2, 303pp.
- Buschow, K.H.J. Permanent magnet materials based on 3d-rich ternary compounds. In *Ferromagnetic Materials*; Wohlfarth, E.P., Buschow, K.H.J., Eds.; Elsevier Science Publishers: North Holland, Amsterdam, 1988; Vol. 4, 1–130.
- Hadjipanayis, G.C. Nanophase hard magnets. *J. Magn. Magn. Mater.* **1999**, *200*, 373–391.
- Kneller, E.F.; Hawig, R. The exchange-spring magnet—a new material principle for permanent-magnets. *IEEE T Magn.* **1991**, *27* (4), 3588–3600.
- Skomski, R.; Coey, J.M.D. Giant energy product in nanostructured 2-phase magnets. *Phys. Rev. B* **1993**, *48*, 15,812–15,816.
- Fischer, R.; Schrefl, T.; Kronmüller, H.; Fidler, J. Grain-size dependence of remanence and coercive field of isotropic nanocrystalline composite permanent magnets. *J. Magn. Magn. Mater.* **1996**, *153* (1–2), 35–49.
- Zeng, H.; Li, J.; Liu, J.P.; Wang, Z.L.; Sun, S. Exchange-coupled nanocomposite magnets by nanoparticle self-assembly. *Nature* **2002**, *420*, 395–398.
- McCormick, P.G.; Miao, W.F.; Smith, P.A.I.; Ding, J.; Street, R. Mechanically alloyed nanocomposite magnets. *J. Appl. Phys.* **1998**, *83*, 6256–6261.
- Liu, J.P.; Luo, C.P.; Liu, Y.; Sellmyer, D.J. High energy products in rapidly annealed nanoscale Fe/Pt multilayers. *Appl. Phys. Lett.* **1998**, *72*, 483–485.
- Jin, Z.Q.; Okumura, H.; Wang, H.L.; Hadjipanayis, G.C. Microstructure refinement and significant improvements of magnetic properties in Pr<sub>2</sub>Fe<sub>14</sub>B/alpha-Fe nanocomposites. *J. Magn. Magn. Mater.* **2002**, *248*, 216–222.
- Goll, D.; Seeger, M.; Kronmüller, H. Magnetic and microstructural properties of nanocrystalline exchange coupled PrFeB permanent magnets. *J. Magn. Magn. Mater.* **1998**, *185*, 49–60.
- Thadhani, N.N. Shock-induced and shock-assisted solid-state chemical-reactions in powder mixtures. *J. Appl. Phys.* **1994**, *76*, 2129–2138.
- Meyers, M.A. *Dynamic Behavior of Materials*; John Wiley & Sons, Inc.: New York, 1994; 382 pp.
- Chau, R.; Maple, M.B.; Nellis, W.J. Shock compaction of SmCo<sub>5</sub> particles. *J. Appl. Phys.* **1996**, *79*, 9236–9244.
- Thadhani, N.N.; Graham, R.A.; Royal, T.; Dunbar, E.; Anderson, M.U.; Holman, G.T. Shock-induced chemical reactions in titanium-silicon powder mixtures of different morphologies: time-resolved pressure measurements and materials analysis. *J. Appl. Phys.* **1997**, *82*, 1113–1128.
- Shkuratov, S.I.; Talantsev, E.F.; Dickens, J.C.; Kristiansen, M.; Baird, J. Longitudinal-shock-wave compression of Nd<sub>2</sub>Fe<sub>14</sub>B high-energy hard ferromagnet: the pressure-induced magnetic phase transition. *Appl. Phys. Lett.* **2003**, *82*, 1248–1250.
- Thadhani, N.N. Shock compression processing of powders. *Adv. Mater. Process.* **1988**, *3* (4), 493–550.
- Chandramouli, M.; Thomas, G.; Nellis, W.J. Shock compaction of Fe-Nd-B. *J. Appl. Phys.* **1993**, *73*, 6494–6496.
- Ando, S.; Mine, Y.; Takashima, K.; Itoh, S.; Tonda, H. Explosive compaction of Nd-Fe-B powder. *J. Mater. Process. Tech.* **1999**, *85*, 142–147.
- Mashimo, T.; Huang, X.; Hirokawa, S.; Makita, K.; Mitsudo, S.; Motokawa, M. Magnetic properties of fully dense Sm<sub>2</sub>Fe<sub>17</sub>Nx magnets prepared by shock compression. *J. Magn. Magn. Mater.* **2000**, *210*, 109–120.
- Saito, T. *IEEE Trans Magn.* Production of bulk materials of an Nd<sub>4</sub>Fe<sub>77.5</sub>B<sub>18.5</sub> alloy and their magnetic properties **2001**, *37*, 2561–2563.
- Leonowicz, M.; Kaszuwara, W.; Jezierska, E.; Januszewski, D.; Mendoza, G.; Davies, H.A.; Paszula, J. Application of the shock compaction technique for consolidation of hard magnetic powders. *J. Appl. Phys.* **1998**, *83* (11), Part 2, 6634–6636.
- Jin, Z.Q.; Chen, K.H.; Li, J.; Zeng, H.; Cheng, S.-F.; Liu, J.P.; Wang, Z.L.; Thadhani, N.N. Shock compression



- response of magnetic nanocomposite powders. *Acta Mater.* **2004**, *52*, 2147–2154.
25. Jin, Z.Q.; Thadhani, N.N.; McGill, M.; Li, J.; Ding, Y.; Wang, Z.L.; Zeng, H.; Chen, M.; Cheng, S.F.; Liu, P. Grain size dependence of magnetic properties in shock synthesized bulk  $\text{Pr}_2\text{Fe}_{14}\text{B}/\alpha\text{-Fe}$  nanocomposites. *J. Appl. Phys.* **2004**, *96* (6), 3452–3457.
  26. Li, J.; Jin, Z.Q.; Liu, J.P.; Wang, Z.L.; Thadhani, N.N. Amorphization and ultrafine-scale recrystallization in shear bands formed in shock-consolidated  $\text{Pr}_2\text{Fe}_{14}\text{B}/\alpha\text{-Fe}$  nanocomposite magnets. *Appl. Phys. Lett.* **2004**, *85*, 2223–2225.
  27. AUTODYN-2D. Century Dynamics Inc.: Concord, CA, 1995, <http://www.centdyn.com>.
  28. Hermann, W.J. Constitutive equation for the dynamic compaction of ductile porous materials. *J. Appl. Phys.* **1969**, *40*, 2490–2499.
  29. Jin, Z.Q.; Thadhani, N.N.; McGill, M.; Ding, Y.; Wang, Z.L.; Chen, M.; Zeng, H.; Chakka, V.M.; Liu, J.P. Explosive shock processing of  $\text{Pr}_2\text{Fe}_{14}\text{B}/\alpha\text{-Fe}$  exchange-coupled nanocomposite bulk magnets. *J. Mater. Res.* **2005**, *20* (3), 599–609.
  30. Meyers, M.A. *Dynamic Behavior of Materials*; Wiley-Interscience: New York, 1994; 448 pp.
  31. Ikeda, H.; Qi, Y.; Çagin, T.; Samver, K.; Johnson, W.L.; Goddard, W.A., III. Strain rate induced amorphization in metallic nanowires. *Phys. Rev. Lett.* **1999**, *82*, 2900–2903.

# Nanocrystal Arrays: Self-Assembly and Physical Properties

**Xiao-Min Lin**

*Material Science Division, Chemistry Division and Center for Nanoscale Materials,  
Argonne National Laboratory, Argonne, Illinois, U.S.A.*

**Raghuveer Parthasarathy**

*James Franck Institute, University of Chicago, Chicago, Illinois, U.S.A., and  
University of California–Berkeley, Berkeley, California, U.S.A.*

**Heinrich M. Jaeger**

*Department of Physics, University of Chicago,  
Chicago, Illinois, U.S.A.*

## INTRODUCTION

Over the last few years, research in the area of nanoscience has blossomed into an independent and highly interdisciplinary area.<sup>[1]</sup> Materials in the nanometer scale (size range 10 Å to 1 μm) are typically referred to as nanoparticles, nanocrystals, nanorods, or nanowires, depending on their crystallinity and shape. Here we refer to them simply all as nanocrystals, without distinguishing the differences. The unique material properties in this size range come from several sources: 1) quantum size effects,<sup>[2]</sup> where confinement of charge carriers in a small space leads to discrete energy levels; 2) classical charging effects,<sup>[3]</sup> which originate from the discrete nature of the electrical charge; and 3) surface/interface effects,<sup>[4]</sup> where the properties of surface or interface atoms become much more significant, as the surface-to-volume ratio increases with decreasing of particle size. Many novel properties of single, isolated nanocrystal have been investigated during the past two decades, such as size-dependent optical absorption and luminescence in semiconductors,<sup>[5,6]</sup> coulomb blockade phenomena in charge transfer,<sup>[7]</sup> or enhanced surface magnetic moments in magnetic nanocrystals.<sup>[8]</sup>

By comparison, assemblies of nanocrystals have only begun to be studied in a systematic fashion in recent years. The exciting aspect of nanocrystal arrays is that they form a truly new class of materials, where the basic building blocks are nanocrystals instead of atoms.<sup>[9]</sup> The properties of these materials not only depend on which chemical elements are used to form the building blocks, but also depend on how many atoms are in each building block and how strongly coupled these building blocks are. Traditional materials can be either crystalline or amorphous, depending on the arrangement of the constituent atoms. Similarly, nanocrystal arrays

can also be ordered or disordered. In the former case, they are referred to as nanocrystal superlattices (NCSs).

The purpose of this entry is to introduce several recent developments in the field, focusing on the experimental point of view. In “Formation of Nanocrystal Arrays,” experimental issues regarding the formation of nanocrystal arrays will be discussed and, in particular, the conditions for controlled formation by self-assembly. In “Electronic Transport” and “Optical Properties,” we consider electronic and optical transport properties of nanocrystal arrays, with the main theme being the collective phenomena in these systems, rather than behavior related to the individual nanocrystal. “Conclusion” contains a brief discussion of outstanding issues and concluding remarks. Because of the limited space, we will focus our entry on arrays formed by chemically synthesized nanocrystals only. Therefore lithographically patterned quantum dot arrays will not be discussed. For aspect not covered here and for additional, in depth information on nanocrystal arrays, we refer the reader to Refs.<sup>[9–12]</sup>

## FORMATION OF NANOCRYSTAL ARRAYS

The ultimate goal of nanocrystal self-assembly is the fabrication of highly ordered two-dimensional (2-D) or three-dimensional (3-D) superlattices or other well-defined structures.<sup>[12,13]</sup> One of the earliest research efforts in this direction can be found in the work of Bentzon et al.<sup>[14]</sup> who observed uniformly sized Fe<sub>2</sub>O<sub>3</sub> particles to spontaneously form hexagonal arrays. The discovery of high-temperature routes for high-quality semiconductor nanocrystals synthesis further stimulated the development of this field.<sup>[15]</sup> By now, nanocrystals made of metals,<sup>[16–20]</sup> semiconductors,<sup>[21,22]</sup> and

oxides<sup>[14,23,24]</sup> have been shown to form ordered NCS under proper experimental conditions, although the degree of ordering can still vary rather significantly.

In general, the spontaneous formation of nanocrystal superlattices via self-assembly requires the following: 1) a high degree of monodispersity in nanocrystal diameter (typically a relative size deviation in nanocrystal core diameters of less than 5%); 2) a complete coating of core surface with ligand molecules; and 3) suitable physical mechanisms to promote ordered packing. In the following, we discuss the relevant issues associated with the nanocrystal cores, the ligand shells surrounding the cores, and the self-assembly mechanisms.

### Nanocrystal Core

There are several different techniques to obtain monodisperse nanocrystals. High-temperature synthesis is the

most widely used since Murray, Norris, and Bawendi<sup>[15]</sup> in 1993 obtained high-quality semiconductor nanocrystals by this method. The basic principle behind this kinetically controlled process was actually proposed quite some time earlier.<sup>[25]</sup> The idea is to oversaturate the nucleating species in a very short period of time, so that there is a burst of nucleation sites at the beginning of the chemical reaction (Fig. 1A). If the concentration of the nucleating species is kept below the saturation level afterward, there will be no new nucleation sites. Subsequently, only the existing nucleation sites can grow. By monitoring the growth of particles, different sizes of nanocrystals can be synthesized with high monodispersity. Sugimoto<sup>[26]</sup> used this idea to synthesize uniform micron-sized spheres. Murray et al. extended this technique to semiconductor nanocrystals by using a high boiling point solvent (mixture of long chain alkylphosphines, alkylphosphine oxides, and alkylamines). High reaction temperature, necessary to decompose the organometallic precursor,

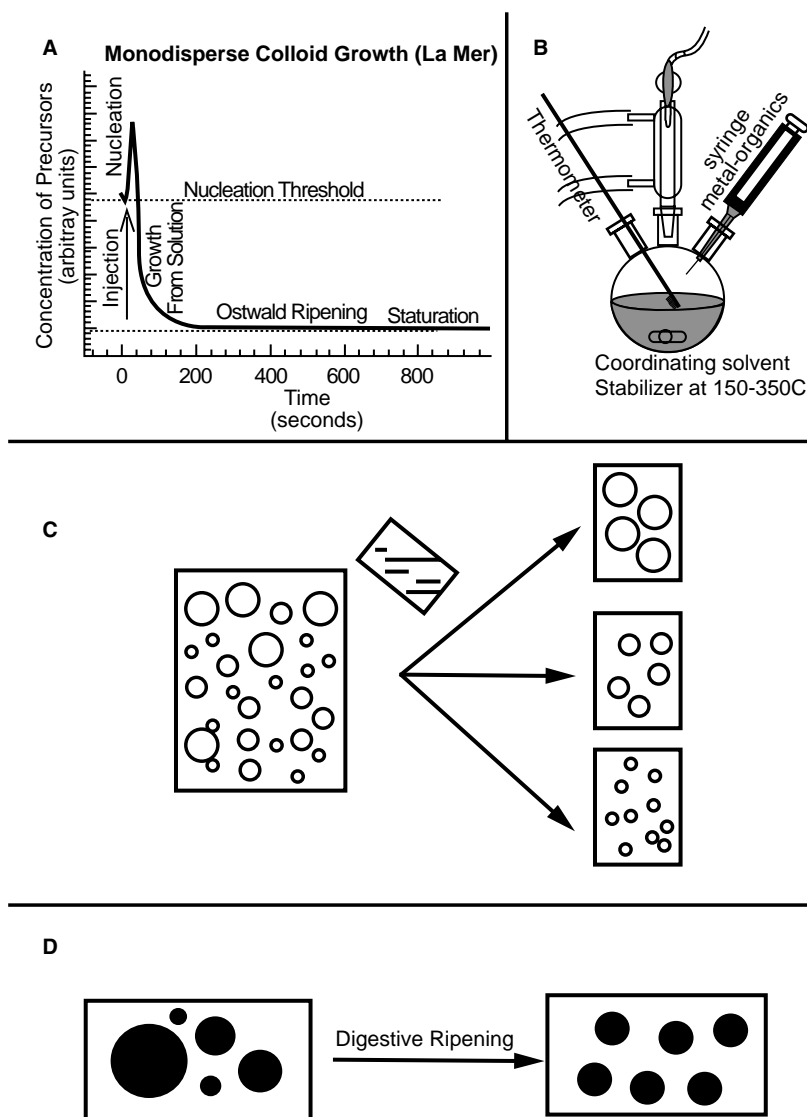


**Fig. 1** Schematic diagrams of various approaches to synthesize monodisperse colloidal nanocrystals. (A) Nucleation rate diagram of high-temperature synthesis.<sup>[9]</sup> (B) Experimental setup of high-temperature synthesis.<sup>[9]</sup> (C) Size-selective precipitation technique through solvent replacement.<sup>[20]</sup> (D) Digestive ripening process.<sup>[30]</sup> Source: Parts A and B are reprinted with permission from Ref.<sup>[9]</sup>. © 2000, Annual Review of Materials Science.

also results in high crystallinity of the final product (Fig. 1B). The relative size distribution of nanocrystals can, furthermore, be “focused” in situ by adjusting the concentration of reaction species during the growth.<sup>[27]</sup>

The second technique that is frequently used is the size-selective precipitation method (Fig. 1C).<sup>[28,29]</sup> This method exploits the fact that the solubility of nanocrystals in a solvent–non-solvent mixture is highly size-dependent. By slowly adding a nonsolvent into a polydisperse colloid, large particles typically become destabilized and are the first to precipitate out from the solution, which can be separated and redissolved into the original solvent. Increasing the concentration of non-solvent gradually causes smaller particles to precipitate. By repeating this process, different fractions become increasingly more monodisperse. Whetten et al.<sup>[20,29]</sup> have coupled this process with mass spectroscopy to obtain nanocrystals of highly precise mass.

Different from the above two methods is a recently developed process called digestive ripening which can transform a polydisperse colloid directly into a more monodisperse colloid through a thermodynamic pathway (Fig. 1D). Lin, Sorensen, and Klabunde<sup>[30]</sup> first demonstrated this process by heating a polydisperse gold colloid in an environment of excess dodecanethiol molecules. The large particles break up into smaller ones upon heating, and the initially polydisperse colloid evolves into a much more uniform system. This is in sharp contrast to the Ostwald ripening process, which favors large particles because of their lower surface energy. Stoeva, Klabunde, and Sorensen<sup>[31]</sup> recently showed that this process is not limited to the gold colloid synthesized by the inverse micelle technique, but works as well for gold colloid prepared by the solvate metal atom dispersion (SMAD) method. This ripening process explains why thiolated gold colloid typically gives particle sizes in the range of 4–6 nm. Although it has been reported that different thiol–gold ratios can be used to adjust the particle sizes,<sup>[32]</sup> they may be formed in kinetically trapped metastable sizes at room temperature. Reflux heating would eventually drive these particles into thermodynamically favored size ranges.<sup>[33]</sup> Although the detailed mechanism behind digestive ripening is still under investigation, it has been speculated that intermolecular interaction and molecular surface interaction might induce a specific ligand packing curvature on the nanocrystal surface, which, in turn, determines the particle size.<sup>[31]</sup>

## Ligand Shell

In aqueous solution, nanocrystals are typically stabilized by double layers of ions adsorbed on the surface.<sup>[34]</sup> Nanocrystals in the organic solvent generally require coating with an organic ligand shell.

There has been quite a variety of ligand molecules used in the literature, such as alkanethiol,<sup>[35,36]</sup> amine,<sup>[37]</sup> and carboxylic acid.<sup>[38]</sup> Ligand shells have several functions. First, and most importantly, they prevent nanocrystals from sintering upon colliding in the solution or on the substrate. The resulting steric repulsive force between ligand molecules is essential to the ordered packing of nanocrystals into arrays.<sup>[34]</sup> Molecular dynamics simulation by Luedtke and Landman<sup>[39]</sup> showed that ligand molecules interdigitate and even bundle together to form a robust structure that separates nanocrystals in the array. Subsequent high-resolution transmission electron microscopy experiments supported this claim.<sup>[40]</sup>

An important point is that the array packing order will depend not only on the particle size dispersion, but also on the integrity of the ligand shells. Adsorption of ligand molecules in the solution is a reversible process, and there is frequent exchange between molecules adsorbed on the nanocrystal surface and molecules in the solution. Therefore repeated precipitation and washing can remove some ligand molecules from nanocrystal surface, which causes incomplete coating of ligand molecules on the surface. Depending on the number of attached ligands and their interactions with those of neighboring nanocrystals, the interparticle spacings will vary when nanocrystals self-assemble on the surface. As a result, for incomplete ligand coating, the average interparticle spacing is typically smaller and has a wider distribution. As shown in Fig. 2, arrays formed by nanocrystals surrounded by an incomplete ligand shell exhibit a much reduced long-range ordering as compared with arrays formed by nanocrystals that have their surface saturated with ligands.<sup>[41]</sup>

Ligand molecules can also affect the nanocrystal solubility and induce specific interaction with complementary molecules adsorbed on other nanocrystals or surface. Alkanethiol with carboxylic acid group on one end can replace straight alkanethiol molecules, therefore allowing nanocrystals synthesized in the organic phase be transferred to aqueous solution.<sup>[38]</sup> DNA-labeled nanocrystals can form aggregates when complementary strands of DNA are added and result in a color change that is easy to detect.<sup>[42]</sup> Streptavidin-labeled nanocrystals can form a large array through biotin–streptavidin linkage.<sup>[43]</sup>

The physical properties of nanocrystals can also be changed by the ligand molecules. For example, electron-donating ligand such as pyridine or CO can change the unpaired electron density of a magnetic nanocrystal, quenching the magnetic moment of surface atoms attached.<sup>[44]</sup> On the other hand, enhanced surface moments were observed for nanocrystals formed in the gas phase without electron-donating ligands on the surface.<sup>[45]</sup>

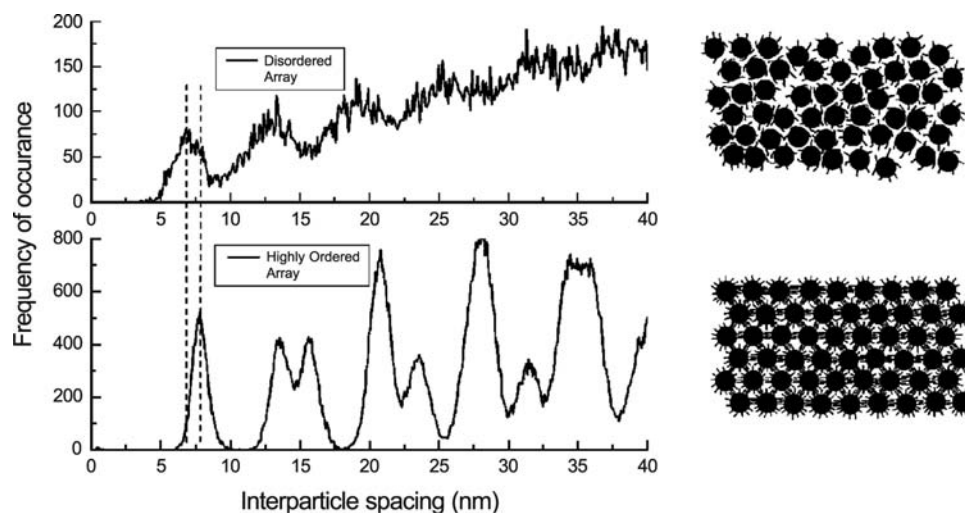


**Fig. 2** Interparticle spacings for a highly ordered array formed by monodisperse 5-nm Au nanocrystals with complete ligand shell and for a disordered array formed by the same nanocrystals but with incomplete ligand shells. *Source:* Image analysis based on transmission electron micrographs was done by N. Mueggenburg.

### Self-Assembly Mechanism

The driving forces for self-assembly of nanocrystals in solution and on surfaces have been extensively studied in a variety of systems.<sup>[46–51]</sup> The mechanisms are, however, quite complicated, depending on the specific materials, the size and shape of the particles, the charges on their surfaces, and on the physical environment during the self-assembly process. They can be roughly categorized into the following types.

1. Entropy-driven systems. Colloidal particles with strong repulsive interaction can crystallize when the concentration of particles exceeds a critical limit.<sup>[46–48]</sup> This is because the entropy gain associated with local motions around the regular lattice point compared with motion around random sites is sufficient to compensate the entropy loss arising from long-range ordering. In some cases, the structure of colloidal crystals grown from the surface can also be controlled by prefabricated patterns on the surface.<sup>[49]</sup>
2. Attraction-driven systems. For neutral, uncharged particles of sufficiently large size, van der Waals interaction can be strong enough to induce aggregation. At large distance, the attraction force varies as  $-AR^6/D^6$ , where  $A$  is the Hamaker constant,  $R$  is the particle radius, and  $D$  is the interparticle distance. At small distance, the functional form changes into  $-AR/D$ .<sup>[50–52]</sup> If the attraction force is the only force that acts upon the particles or it is significantly stronger than any other interaction that is present, it will cause irreversible, diffusion-limited aggregation. Ligand coating on nanocrystal

surfaces can act as a “bumper” or buffer layer to prevent such irreversibility. Diffusion of nanocrystals under the influence of the attractive force can lead to formation of large ordered arrays.<sup>[16]</sup> Care must be taken to minimize the disruptive effect of solvent dewetting to obtain high-quality arrays (Fig. 3).<sup>[16]</sup> Temperature also plays an important role to anneal out some defect sites during the self-assembly process. For a pair of 6-nm gold particles separated by a gap of 1.7 nm (dodecanethiol chain length), a simple calculation shows that the interparticle van der Waals force is roughly 46 meV, which is comparable to the thermal energy at room temperature. Fig. 4 shows the edge of a self-assembled gold nanocrystal array. Particle sizes are more polydisperse at the edge than in the interior of the domain, presumably because of the thermal annealing effect during the assembly process.

3. Other physically driven systems. Assembly of micron spheres and nanocrystals can also be accomplished by electrophoretic deposition.<sup>[53,54]</sup> The assembly of particles on the electrode surface is a result of electrohydrodynamic fluid flow arising from an ionic current flowing through the solution. By adjusting the electric field strength or frequency, the lateral attraction force between particles can be modulated. This facilitates the reversible formation of two-dimensional fluid and crystalline states on the surface.

### ELECTRONIC TRANSPORT

Charge transfer through nanocrystal arrays is of great importance not only because of the fundamental new

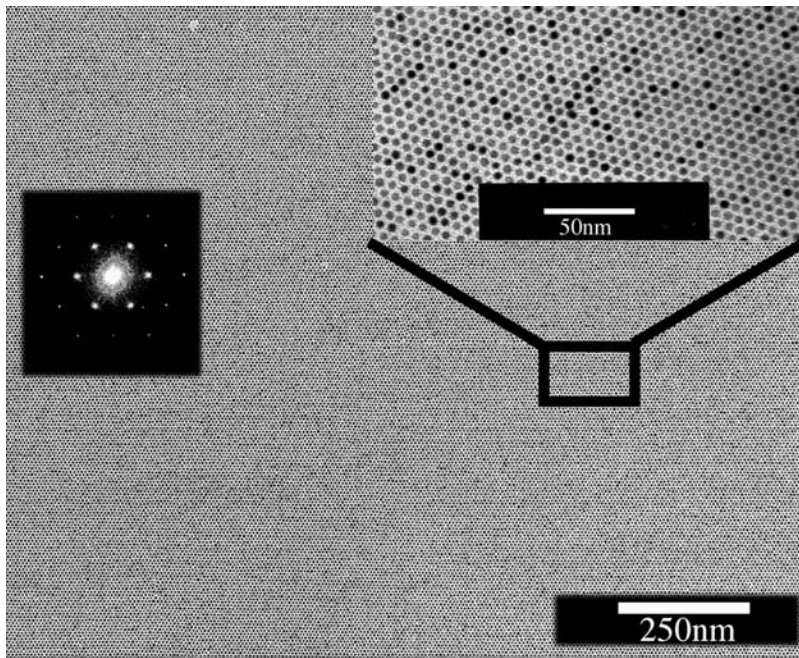


**Fig. 3** Long-range-ordered gold nanocrystal superlattices formed on silicon nitride substrate by controlling solvent dewetting. Each individual nanocrystal is about 5 nm in diameter.<sup>[16]</sup> Inset shows the Fourier transformation of a small portion of the image.

physics involved in such highly correlated system, but also because the modern electronic components are approaching the size limit of standard photolithography techniques.<sup>[55]</sup> Self-assembled structures based on chemically synthesized nanocrystals have the potential to circumvent such limitations and thus be used as alternative future electronic components.<sup>[56]</sup>

The transport through individual nanocrystals has been well-studied both theoretically and experimentally (by both scanning tunneling microscopy<sup>[57,58]</sup>

and two-terminal measurements).<sup>[59]</sup> For metal nanocrystal, its main feature is the Coulomb blockade effect, in which transfer of a single electron on or off a nanocrystal is strongly affected by electrostatic interaction with the nanocrystal's charge. Because of the large number of free electrons in metal nanocrystals, the discrete level spacing as a result of quantum confinement effects is small and becomes significant only at very low temperatures, typically  $\ll 1$  K. For semiconductor nanocrystals, the number of free carriers is much

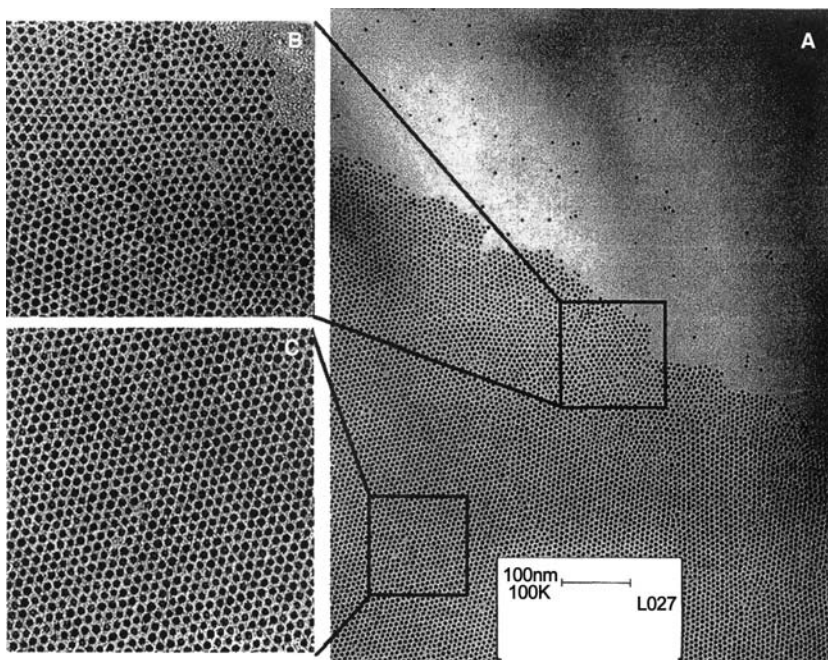


**Fig. 4** (A) The edge of self-assembled gold nanocrystal superlattices shows a sharp boundary, indicating that diffusion under the influence of interparticle van der Waals forces is responsible for the assembly process. (B–C) The edge of the domain exhibits a large-size polydispersity in size than the interior of the domain, indicating thermal annealing effect during the assembly process.



smaller and quantum confinement effects, together with the Coulomb blockade, determine transport properties.<sup>[59]</sup>

Many-particle systems, on the other hand, are not as well understood and are more complex because of the intricacies of coupling between constituent nanocrystals, effects of structural order and disorder, and charge transfer between nanocrystal cores and ligands. A variety of phenomena have been reported in different systems, including spin-dependent tunneling in magnetic particle assemblies,<sup>[18]</sup> hopping-type transport in dithiol linked arrays,<sup>[60]</sup> and metal-insulator-like transitions in silver nanocrystal monolayers.<sup>[61–63]</sup> Arrays of semiconductor particles exhibit interesting time- and illumination-dependent transport which, furthermore, shows striking slow relaxation behavior, reminiscent of glasses.<sup>[64]</sup>

Our own work has focused on weakly coupled metallic nanocrystal system—monolayers of 5 nm diameter 1-dodecanethiol-ligated gold nanocrystals, self-assembled on silicon nitride substrates—and we will begin our discussion with these arrays as our focus.<sup>[65,66]</sup> By “weakly coupled” we mean that the Coulomb blockade energy, associated with the transfer of individual electrons between individual nanocrystals, dominates transport—the Coulomb or single electron charging energies are large compared with  $k_B T$ , and the electron wavefunctions, consequently, are localized on the scale of single nanocrystals. A typical current–voltage ( $I$ – $V$ ) curve at 12 K, from an array of length  $N \approx 50$  particles separating the electrodes and width  $M \approx 270$  particles, is shown in Fig. 5. There is a significant voltage threshold ( $V_T = 4.2$  V) below

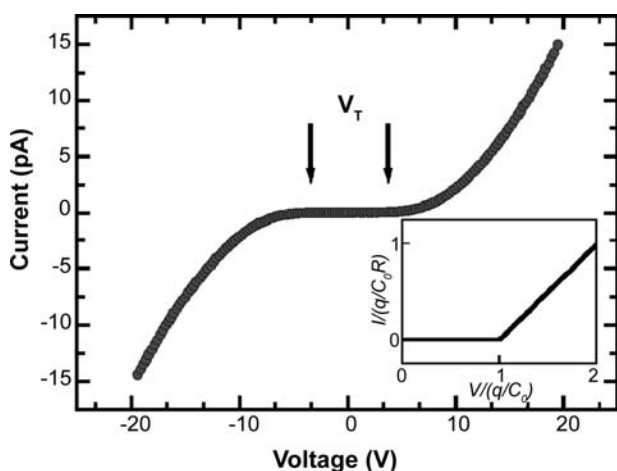


**Fig. 5** Current–voltage ( $I$ – $V$ ) characteristic for a weakly coupled gold nanocrystal superlattice array at low temperature (12 K). The distance between the in-plane electrodes was 330 nm and the array width was 2  $\mu$ m. The lower inset shows a schematic  $I$ – $V$  curve for a single nanocrystal. Source: From Ref.<sup>[65]</sup>.

which no current flows. The voltage threshold is the direct consequence of the Coulomb blockade. For each particle, an energetic cost  $V_0 \sim e/\epsilon r = e/C_0$ , where  $r$  is the particle radius,  $\epsilon$  is the dielectric constant of the medium surrounding the metal core, and  $C_0$  is the self-capacitance of the metal sphere, must be paid to transport a single electron onto the charged nanocrystal. For the particles in Fig. 5,  $V_0$  is around 100 mV, and  $V_T$  arises as the sum of this single electron charging energy over all nanocrystals traversed in crossing from one electrode to the other.  $V_T$  grows linearly with array length:  $V_T = \alpha N(e/C_0)$ , where the parameter  $\alpha$  ( $\alpha < 1$ ) accounts for interparticle capacitive coupling and the randomness of the offset charges in the underlying substrate that give rise to the Coulomb blockade repulsion.<sup>[65–68]</sup>

Current can flow when the voltage threshold is exceeded—but how, microscopically, do electrons move from nanocrystal to nanocrystal? This can be answered by detailed measurements of the non-linear current–voltage characteristics as a function of temperature. In the following, we start with a discussion of the low-temperature limit, in which thermal energies can effectively be neglected, and then consider the influence of finite temperatures.

### Low-Temperature Limit

There is a distinctive threshold voltage in this temperature range. Beyond the array’s threshold, current rises as a power law in voltage:

$$I \sim M \frac{V_0}{R} \left[ \frac{(V - V_T)}{V_T} \right]^\zeta$$

where  $R$  is the interparticle resistance,  $M$  is the array width,  $V_0$  is the charging voltage ( $e/C_0$ ), and  $V_T$  is the threshold voltage. This power-law form was predicted independently nearly a decade ago by Middleton and Wingreen (MW)<sup>[67]</sup> and by Roux and Herrmann (RH).<sup>[68]</sup> Middleton and Wingreen pointed out that local charge disorder (i.e., random offset charges) gives each nanocrystal a different single-electron charging energy, uniformly distributed in the interval  $(0, V_0)$ . The path between the electrodes with the lowest total Coulomb blockade cost determines the voltage threshold. Beyond threshold, the applied voltage allows an increasing number of paths to conduct current. As the current–voltage relation in each one-dimensional path is linear, the resulting array  $I$ – $V$  curve (beyond threshold) is superlinear. In fact, MW provided an analogy between the branched, meandering flow of current in this sort of arrays to Kardar–Parisi–Zhang (KPZ) models.<sup>[69]</sup> This deterministic growth model was originally used to describe

interface growth in disordered media, such as cluster formation, liquid front in fluid flow, and surface roughness of growing crystal. From this analogy, MW's theory gives a value of the scaling exponent:  $\zeta = 5/3$ .

Experiments on highly ordered superlattices show robust power-law scaling (Fig. 6A), in accord with the MW model. However, the measured scaling exponent,  $\zeta = 2.2$ , differs from the theoretical prediction,  $\zeta = 5/3$ . The cause for the discrepancy between theory and experiment remains an open question, although it may arise from dispersity in the interparticle resistances or from inadequacies in the analogy to KPZ-type models.

Structurally disordered arrays display different behavior beyond threshold. Fig. 6 compares ordered

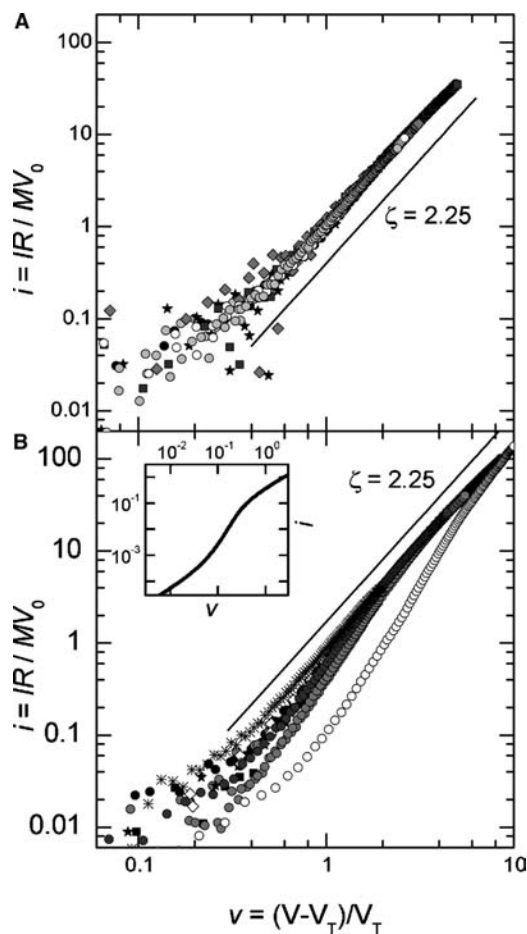


**Fig. 6** Log-log plots of  $I$ - $V$  curves above the voltage threshold for both highly ordered nanocrystals arrays (A) and disordered nanocrystals array caused by solvent dewetting (B). A single power law with an exponent of 2.25 fits all the highly ordered arrays, while structural disorder causes significant deviations from power-law behavior. Inset to (B) shows simulated  $I$ - $V$  curves for parallel one-dimensional chains of nanocrystals with randomly distributed thresholds. Source: From Ref.<sup>[65]</sup>.

arrays with disordered arrays in which voids were caused by solvent dewetting, thereby breaking up the monolayer. Rather than exhibiting robust scaling with a single exponent  $\zeta$  over several orders of magnitude, the current-voltage data for the disordered samples are not well fit by a single power law and display significant sample-to-sample variations. The lack of scaling behavior can be understood by considering disordered arrays as two-dimensional patches connected by one-dimensional “bottlenecks” which disturb the branching and growth of current-carrying paths. Accurate determination of array scaling exponents thus can only be performed in structurally ordered arrays.

### Finite Temperatures

Fig. 7 shows a set of  $I$ - $V$  curves measured at different temperatures. A careful examination of this data reveals that, at low temperatures ( $<100$  K), there is a very weak temperature dependence. In this temperature region, the  $I$ - $V$  characteristics above  $V_T$  appear simply shifted along the voltage axis with increasing temperature, while the current scale is untouched.<sup>[70,71]</sup> Based on the experimental results, we can write  $V_T(T) = V_T(0) \left(1 - b \frac{k_B T}{e^2/C_0}\right)$ , where  $V_T(T)$  is the threshold voltage at temperature  $T$  and  $b$  is a numerical factor. In other words, temperature contributes energy of order  $k_B T$  per nanocrystal, which assists the electrons in “paying” the coulomb blockade cost for transport. Quantitatively,  $b = 13.9$ , both from experiments and from a model of thermally assisted

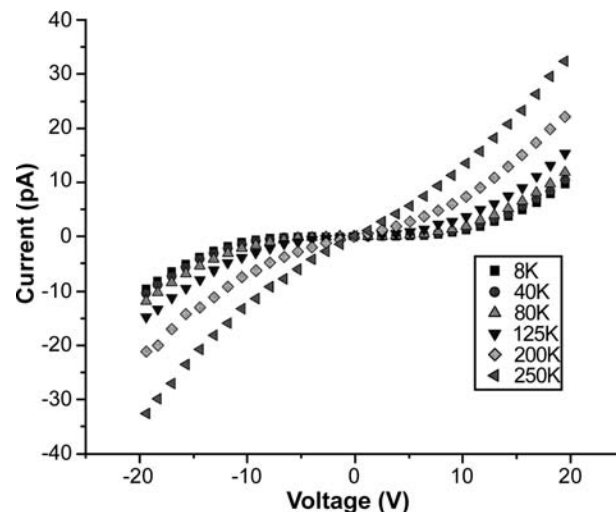


**Fig. 7**  $I$ - $V$  curves for a gold nanocrystal array as a function of temperature. In the low-temperature limit (below 100 K), a clear threshold exists, with a weak, linear temperature dependence. At high temperatures (above 100 K), there is a finite zero-biased conductance. Source: From Ref.<sup>[70]</sup>.

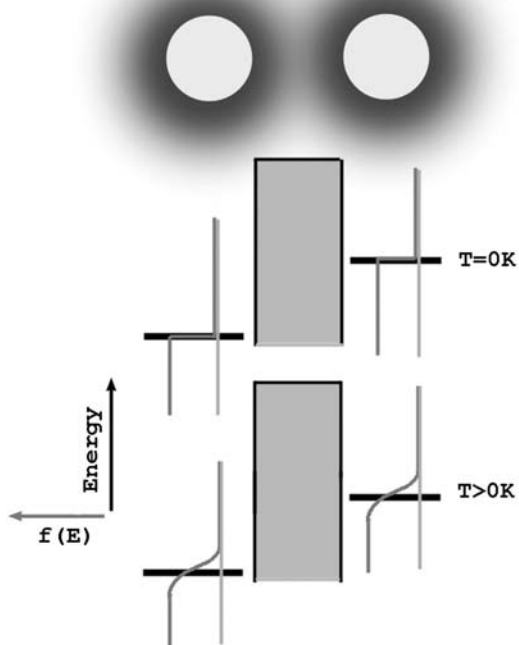


**Fig. 8** Schematic diagram of thermally-assisted tunneling at finite temperatures. The offset between energy levels involved in tunneling is caused by the single-electron charging energy. Source: From Ref.<sup>[70]</sup>.

tunneling.<sup>[69]</sup> Fig. 8 is a schematic picture of thermally assisted tunneling in metal nanocrystals. This correspondence, combined also with the absence of exponentially activated conduction in this region, implicates as the transport mechanism tunneling from metal core to metal core through large barriers (eV) provided by the ligands.<sup>[69]</sup>

At high temperatures, in our array around 100 K,  $V_T$  is lowered to zero, and the zero-bias conductance ( $g_0 = dI/dV$  at  $V = 0$ ) is found to obey an Arrhenius form:  $g_0 = \exp(-U/T)$ . In certain other nanocrystal systems, only this exponential form is seen at the temperatures examined.<sup>[60]</sup> One must be wary of equating Arrhenius-like conductance with, for example, activated hopping over a barrier, as it also follows from a direct tunneling scenario at temperatures which overwhelm the Coulomb blockade energy.

We have referred to the arrays above as “weakly coupled,” meaning several things: First, the tunneling amplitudes between particles are low, leading to only picoamperes of current flow at biases of several volts. Second, the interparticle capacitances (determined by both the interparticle spacings and the nanocrystal sizes) are less than or equal to the single-particle capacitance  $C_0$ . Third, transport is dominated by coulomb blockade effects, as shown by a finite

voltage threshold at low temperatures. Experiments on strongly coupled nanocrystal arrays have also been performed, as we will now discuss.

Interparticle coupling can be increased by the use of more complex conjugated or aromatic ligands<sup>[60]</sup> or by compressing arrays in Langmuir–Blodgett troughs. The latter technique has been used extensively by Heath et al.<sup>[61,62]</sup> Characteristic of transport data from these systems is the lack of a voltage threshold, i.e., a finite zero-bias conductance, down to the lowest temperatures examined.

The most dramatic feature of compressed nanocrystal monolayers, discovered by Heath’s group, is the appearance of shiny, metallic optical reflectivity beyond a certain critical compression.<sup>[61,62]</sup> This has been referred to as a metal-insulator transition; we will discuss it also in the next section in the context of plasmon coupling. At present, simultaneous optical and electronic transport data do not exist. However, a wide range of transport data from these films (transferred from Langmuir troughs onto solid substrates), from compressions at both sides of the optical transition, show resistivity which increases exponentially with decreasing temperature, indicating insulating behavior. Although not technically metallic, the arrays show a rich variety of transport characteristics, with conductivity ( $\sigma$ ) following activated hopping forms [ $\sigma \sim \exp(-U/T)$ ],<sup>[72]</sup> variable-range hopping of interacting electron forms [ $\sigma \sim \exp(-U/T^{1/2})$ ],<sup>[73]</sup> and other forms depending on variables such as compression and disorder.<sup>[73]</sup> We will return to some of the issues raised by these experiments in the final section of this entry.

## OPTICAL PROPERTIES

The optical properties of small particles have received considerable attention during the past decade because of potential applications in optical sensors<sup>[74]</sup> and lasing devices.<sup>[75]</sup> Research has mainly focused on semiconductor nanocrystals and their assemblies. Size-dependent optical absorption and photoluminescence as a result of the creation and recombination of excitons have been studied extensively.<sup>[5,6]</sup> In nanocrystal arrays, it has been found that interactions between nanocrystals can lead to long-range resonance transfer (LRRT).<sup>[22,76]</sup> This process is schematically sketched in Fig. 9. When two different sizes of CdSe nanocrystals, for example, are combined in a mixed nanocrystal array, excitation in the small particles (donors) can resonantly excite large particles (acceptors). If the transferred excitation can be trapped in a low energy state of the large particle, then the reverse process cannot occur and a unilateral energy transfer process has taken place. Photoluminescence (PL) quantum yield (QY) of both the donor and acceptor

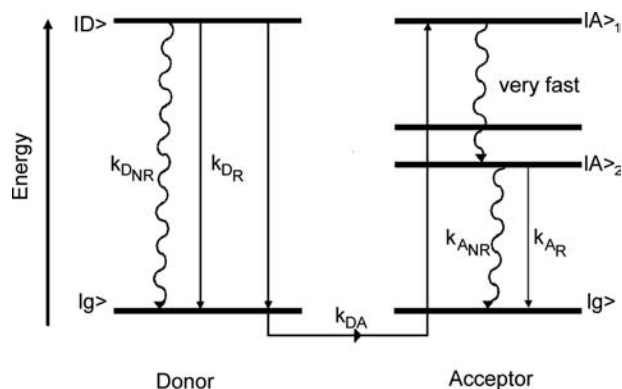


**Fig. 9** Schematic diagram of electronic energy transfer between two different size nanocrystals in a close-packed nanocrystal array. The smaller particles that have large bandgaps are donors of excitation, while large particles with smaller bandgaps are acceptors of excitation. Different pathways of both radiative (R) relaxation and non-radiative (NR) relaxation are also indicated. *Source:* From Ref.<sup>[9]</sup>. Copyright 2000, Annual Review of Materials Science.

in a mixed nanocrystal array showed a quenching of QY for the small particles and an enhancement for the large particles and thus confirm that the energy transfer process indeed takes place.<sup>[76]</sup> Even in a highly uniform nanocrystal array with size deviation less than 5%, the intrinsic inhomogeneity can lead to energy transfer among particles with different sizes. As a result, the PL spectrum of nanocrystals in solid form red-shifts compared with the same nanocrystals in colloidal form (Fig. 10).

Optical properties of metallic nanocrystals are dominated by surface plasmon phenomena, where spatially confined electrons oscillated in resonance with incident electromagnetic waves. For specific metals, such as silver and gold, the plasmon absorption occurs in the visible wavelength range, giving rise to the visible colors for these colloids. For example, 5-nm gold nanocrystals are deep maroon in color. The frequency-dependent polarizability of a single nanocrystal is given by the Clausius–Mossotti equation:<sup>[77]</sup>

$$\alpha_A(\omega) = R^3 \frac{\varepsilon(\omega) - \varepsilon_m}{\varepsilon(\omega) + 2\varepsilon_m}$$

where  $R$  is the radius of the particle,  $\varepsilon(\omega)$  is the dielectric function of the particle, and  $\varepsilon_m$  is the dielectric function of the medium. Using the dielectric function of metals, the polarizability of a single nanocrystal is

$$\alpha_A(\omega) = \frac{R^3}{1 - \omega(\omega + i/\tau)/\Omega^2}$$

where  $\Omega = \omega_p/\sqrt{3}$  and  $\omega_p$  is bulk plasmon frequency. The single particle therefore behaves like a harmonic

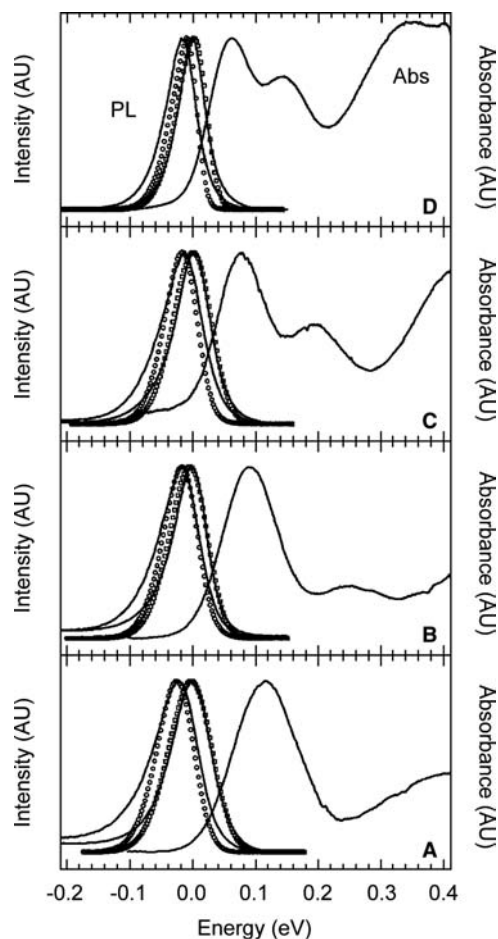


**Fig. 10** Absorption and photoluminescence spectra (PLs) for different sizes of CdSe nanocrystals (A) 30.3, (B) 39.4, (C) 48.0, and (D) 62.1 Å diameters. PL spectra for nanocrystals in a close-packed array are red-shifted compared to spectra obtained from particles in solution. Open squares and circles are theoretical fitting curves taking into account the inhomogeneous distribution of emitting energies. *Source:* From Ref.<sup>[9]</sup>. © 2000, Annual Review of Materials Science.

oscillator of frequency  $\Omega$  and damping constant  $\tau$ . The dipolar oscillation produces a strong electrical field near the surface, which is responsible for the surface-enhanced Raman scattering (SERS) of small molecules adsorbed on surfaces.<sup>[78]</sup> When nanocrystals are brought into close vicinity, interparticle coupling can lead to additional resonances.<sup>[79]</sup> Fig. 11 shows, in a schematic diagram, how light at normal incidence can induce a coupled mode where neighboring particles are oscillating in phase. This coupling causes addition absorption peaks in the long wavelength region. This coupling resonance depends not only on the particle size and interparticle spacing, but also on the polarization of the incident light and the structure of the nanocrystals lattices.<sup>[80]</sup> Persson and Liebsch<sup>[81]</sup> performed a theoretical calculation of a  $p$ -polarized

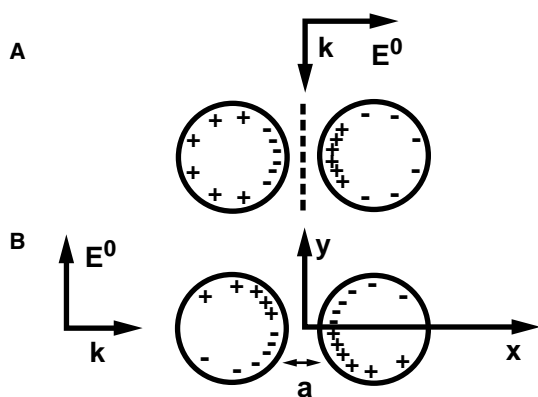


**Fig. 11** Schematic diagram of surface plasmons induced by a polarized plane wave incident upon two adjacent nanocrystals from different directions. (A) The external electric field is parallel to the line joining the nanocrystals. (B) The external field is perpendicular to the line joining the nanocrystals.

light incident on a two-dimensional square lattice (Fig. 12). Two resonant peaks in the imaginary part of the polarizability correspond to coupled plasmon oscillations, either parallel or perpendicular to the array. The frequencies of these resonances are given by:

$$\Omega_{//} = \Omega^2 \left( 1 - \frac{1}{2} R^3 U_0 \right)$$

$$\Omega_{\perp} = \Omega^2 (1 + R^3 U_0)$$

where  $U_0$  is a geometric factor that depends on the structure of the array. In the case of disordered particle arrangements, the same calculation based on a coherent potential approximation shows that both of these

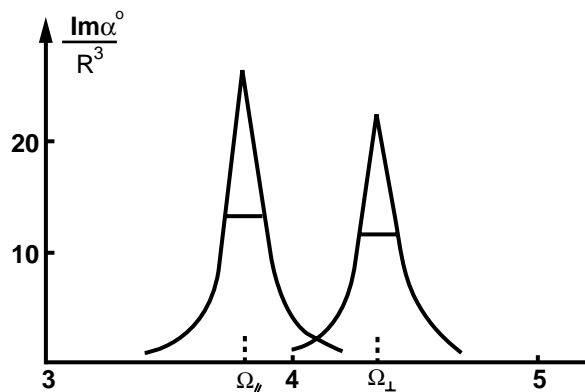


**Fig. 12** Calculated imaginary part of the polarizability of nanocrystals arranged on a square lattice. Resonance frequencies  $\Omega_{\perp}$  and  $\Omega_{//}$  correspond to surface plasmon oscillations perpendicular and parallel to the plane of nanocrystals. *Source:* From Ref.<sup>[81]</sup>. © 1983, American Physical Society.

absorption peaks are broadened. Experiments on disordered nanocrystal arrays confirmed that prediction.<sup>[82]</sup>

A promising scheme of utilizing surface plasmons of coupled nanocrystals for optical applications was proposed by Quinten et al.<sup>[83]</sup> In their model, a linear chain of metal nanocrystals was used to transmit electromagnetic waves through interparticle dipolar coupling. The field intensity of the transmitted electromagnetic wave depends strongly on the polarization of the incident light. Traditional dielectric optical waveguides have a fundamental wavelength limitation. In comparison, small particle arrays have the potential to become functional units for guiding, modulation, and amplification of light signals on a length scale that is much smaller than the wavelength of light.

In the case of strongly coupled nanocrystal arrays, such as Ag nanocrystal arrays compressed on the Langmuir trough, the optical properties also undergo dramatic changes when metal-insulator-like transitions occur.<sup>[61,62]</sup> The real part of the dielectric constant turns negative, indicating more metallic features. However, the derived value of the dielectric constant is about 10 times larger than typical values for an ordinary Ag film. This indicates that the “metallic” state caused by the strong coupling of neighboring nanocrystals is still quite different from the bulk metallic states that we are familiar with.

## CONCLUSION

The controlled assembly of nanocrystals into large arrays and superlattices opens the door to a new class of artificial materials whose properties can be tuned by choosing different core materials, by varying the core sizes and shapes, and by tuning the interparticle coupling strength. In particular, the ability to vary independently the properties of the individual nanocrystal building blocks and the type and strength of the interactions between them allows for new and unprecedented control. As a result, materials with electronic or optical properties not obtainable from bulk can be designed “bottom up” by nanocrystal assembly.

At present, the main challenge still lies in our ability to tune all of the key physical parameters of a nanocrystal array at will. As far as electronic transport is concerned, weakly coupled arrays are dominated by single electron Coulomb blockade effects. Strongly coupled arrays, on the other hand, are considerably different. Understanding the strongly coupled state and the transitions between strong and weak coupling are two pressing issues in this field. Experimentally, it is difficult to controllably adjust interparticle couplings. Compression in Langmuir troughs has yielded the

fascinating data described above, but it suffers from the disadvantage of simultaneously altering both the voltage and current scales of transport. As nanocrystals are brought closer together, their capacitive coupling increases, lowering the Coulomb blockade cost for electron transport.<sup>[67]</sup> Also, the tunneling barrier separating the metal cores narrows, increasing the interparticle tunneling amplitudes. Techniques to independently manipulate these two effects would do much to further our understanding. One possible route is a better grasp of the role of ligands in nanocrystal systems, perhaps designing metal core/ligand particles with specific tunneling rates. (Such feats have been accomplished in the context of electron tunneling through proteins.)<sup>[84]</sup> voltage scaling relations. For strongly coupled arrays, the paucity of studies is even more pronounced. It is not yet clear to what extent such well-known concepts such as variable-range hopping, metal-insulator transitions, localization, etc. developed for microscopic disorder in semiconductors or disordered thin metal films carry over directly to nanocrystal arrays. For example, it is not obvious that anything besides fixed-range, nearest-neighbor hopping should even occur in metal nanocrystal arrays because of the large, mesoscopic distances involved and because, in contrast to hopping between sharp impurity levels in semiconductors, in metals, at any finite temperatures, the spectrum of available states is broad. Furthermore, the interplay of several types of disorder (random offset charges and variations in the particle size modulating the local charging energy and variations in the particle spacings giving rise to coupling strength disorder) as well as the potentially complex roles played by any electronic states inside the ligands make application of these established, but more microscopic concepts nontrivial.

Controlling the optical response on a nanometer scale is another emerging direction of much promise. With strong coupling between nanocrystals, theoretical models have predicted that coherent transfer of electromagnetic energy along nanocrystal arrays should be possible, despite significant radiative loss. Experiments have not unambiguously demonstrated this phenomenon so far largely because of the difficulty of creating the desired array structures on a very small length scale and also because of current limitations with near-field optical detection schemes.

Several of the recently developed approaches discussed in this article provide new pieces to the expanding toolkit for nanocrystal array assembly: The digestive ripening method can produce size dispersions significantly below 5%; fully ligand-saturated Au nanocrystals can assemble into extended monolayer superlattices with unprecedented degree of long-range order; nanocrystal arrays can be patterned into arbitrary 2-D shapes by electron beam exposure or can

be interfaced with lithographically defined electrodes; and the use of membrane substrates allows for transport measurements and, with the same samples, for characterization of the local structural order by transmission electron microscopy.

## ACKNOWLEDGMENTS

We would like to thank fruitful discussion with Prof. David Grier about the manuscript. This work has been supported by the U.S. Department of Energy, BES-Materials Sciences, under Contract W-31-109-ENG-38, University of Chicago-Argonne National Laboratory Consortium for Nanoscience Research (CNR), and by the MRSEC program of National Science Foundation under Award Number DMR-0213745.

## REFERENCES

1. Timp, G., Ed. *Nanotechnology* 1st Ed.; Springer-Verlag: New York, 1999.
2. Halperin, W.P. Quantum size effects in metal particles. *Rev. Mod. Phys.* **1986**, *58* (3), 533–606.
3. Kastner, M.A. The single-electron transistor. *Rev. Mod. Phys.* **1992**, *64* (3), 849–858.
4. Pool, R. Clusters: strange morsels of matter. *Science* **1990**, *248*, 1186–1188.
5. Empedocles, S.; Bawendi, M. Spectroscopy of single CdSe nanocrystallites. *Acc. Chem. Res.* **1999**, *32*, 389–396.
6. Nirmal, M.; Brus, L. Luminescence photophysics in semiconductor nanocrystals. *Acc. Chem. Res.* **1999**, *32*, 407–414.
7. Chen, S.; Ingram, R.S.; Hostetler, M.J.; Pietron, J.J.; Murray, R.W.; Schaaff, T.G.; Khoury, J.T.; Alvarez, M.M.; Whetten, R.L. Gold nanoelectrodes of varied size: transition to molecule-like charging. *Science* **1998**, *280*, 2098–2101.
8. Bucher, J.; Douglass, D.C.; Bloomfield, L.A. Magnetic properties of free cobalt clusters. *Phys. Rev. Lett.* **1991**, *66* (23), 3052–3055.
9. Murray, C.B.; Kagan, C.R.; Bawendi, M.G. Synthesis and characterization of monodisperse nanocrystals and close-packed nanocrystal assemblies. *Annu. Rev. Mater. Sci.* **2000**, *30*, 545–610.
10. Collier, C.P.; Vossmeier, T.; Heath, J.R. Nanocrystal superlattices. *Annu. Rev. Phys. Chem.* **1998**, *49*, 371–404.
11. Pileni, M.P. Nanocrystal self-assembly: fabrication and collective properties. *J. Phys. Chem., B* **2001**, *105*, 3358–3371.
12. Weller, H. Self-organized superlattices of nanoparticles. *Angew. Chem., Int. Ed. Engl.* **1996**, *35* (10), 1079–1081.
13. Ohara, P.C.; Gelbart, W.M. Interplay between hole instability and nanoparticle array formation in ultrathin liquid films. *Langmuir* **1998**, *14* (12), 3418–3424.
14. Bentzon, M.D.; Wouterghem, J.V.; Morup, S.; Tholen, A.; Koch, C.J.W. Ordered aggregates of ultrafine iron



- oxide particle: 'Super crystals'. *Philos. Mag.*, **B 1989**, *60* (2), 169–178.
15. Murray, C.B.; Norris, D.J.; Bawendi, M.G. Synthesis and characterization of nearly monodisperse CdE (E = sulfur, selenium, tellurium) semiconductor nanocrystallites. *J. Am. Chem. Soc.* **1993**, *115* (11), 8706–8715.
  16. Lin, X.M.; Jaeger, C.M.; Sorensen, C.M.; Klabunde, K.J. Formation of long-range-ordered nanocrystal superlattices on silicon nitride substrates. *J. Phys. Chem.*, **B 2001**, *105* (17), 3353–3357.
  17. Wang, Z.L.; Harfenist, S.A.; Vezmar, I.; Whetten, R.L.; Bentley, J.; Evans, N.D.; Alexander, K.B. Superlattices of self-assembled tetrahedral Ag nanocrystals. *Adv. Mater.* **1998**, *10* (10), 808–812.
  18. Black, C.T.; Murray, C.B.; Sandstrom, R.L.; Sung, S. Spin-dependent tunneling in self-assembled cobalt-nanocrystal superlattices. *Science* **2000**, *290*, 113.
  19. Motte, L.; Billoudet, F.; Lacaze, E.; Douin, J.; Pileni, M.P. Self-organization into 2D and 3D superlattices of nanosized particles differing by their size. *J. Phys. Chem.* **1997**, *101*, 138–144.
  20. Whetten, R.L.; Khoury, J.T.; Alvarez, M.M.; Murthy, S.; Vezmar, I.; Wang, Z.L.; Stephens, P.W.; Cleveland, C.L.; Luedtke, W.D.; Landman, U. Nanocrystal gold molecules. *Adv. Mater.* **1996**, *8* (5), 428–433.
  21. Murray, C.B.; Kagan, C.R.; Bawendi, M.G. Self-organization of CdSe nanocrystallites into three dimensional quantum dot superlattices. *Science* **1995**, *270*, 1335–1338.
  22. Kagan, C.R.; Murray, C.B.; Bawendi, M.G. Electronic energy transfer in CdSe quantum dot solids. *Phys. Rev. Lett.* **1996**, *76*, 1517–1520.
  23. Cusack, L.; Rizza, R.; Gorelov, A.; Fitzmaurice, D. Self-assembly and subsequent self-organization of a semiconductor nanocrystallite superlattice. *Angew. Chem., Int. Ed. Engl.* **1997**, *36* (8), 848–851.
  24. Yin, J.S.; Wang, Z.L. Ordered self-assembling of tetrahedral oxide nanocrystals. *Phys. Rev. Lett.* **1997**, *79* (13), 2570–2573.
  25. Johnson, I.; LaMer, V.K. The determination of the particle size of monodispersed systems by the scattering of light. *J. Am. Chem. Soc.* **1947**, *69*, 1184.
  26. Sugimoto, T. Preparation of monodispersed colloidal particles. *Adv. Colloid Interface Sci.* **1987**, *28*, 65.
  27. Peng, X.G.; Wickham, J.; Alivisatos, A.P. Kinetics of II–V and III–V colloidal semiconductor nanocrystal growth: "Focusing" of size distribution. *J. Am. Chem. Soc.* **1998**, *120* (21), 5343–5344.
  28. Frens, G. Particle size and sol stability in metal colloids. *Kolloid-Z. Z. Polym.* **1972**, *250*, 736–741.
  29. Schaaff, T.G.; Knight, G.; Shafiqullin, M.N.; Bor, R.F.; Whetten, R.L. Isolation and selected properties of 10.4 kDa gold: glutathione cluster compound. *J. Phys. Chem.* **1998**, *102*, 10,643–10,646.
  30. Lin, X.M.; Sorensen, C.M.; Klabunde, K.J. Digestive ripening, nanophase segregation and superlattice formation in gold nanocrystal colloids. *J. Nanopart. Res.* **2000**, *2*, 157–164.
  31. Stoeva, S.; Klabunde, K.J.; Sorensen, C.M.; Dragieva, I. Gram-scale synthesis of monodisperse gold colloids by the solvated metal atom dispersion method and digestive ripening and their organization into two- and three-dimensional structure. *J. Am. Chem. Soc.* **2002**, *124* (10), 2305–2311.
  32. Leff, D.V.; Ohara, P.C.; Heath, J.R.; Gelbart, W.M. Thermodynamic control of gold nanocrystal size: experiment and theory. *J. Phys. Chem.* **1995**, *99* (18), 7036–7041.
  33. Lin, X.M. From Nanocrystals to Nanocrystal Superlattices: Synthesis and Properties *Ph.D Thesis*. Kansas State University, 1999.
  34. Schmid, G., Ed.; Clusters and Colloids, From Theory to Application; VCH: Weinheim, 1994.
  35. Hostetler, M.J.; Wingate, J.E.; Zhong, C.J.; Harris, J.E.; Vachet, R.W.; Clark, M.R.; Londono, J.D.; Green, S.J.; Stokes, J.J.; Wignall, G.D.; Glish, G.L.; Porter, M.D.; Evans, N.D.; Murray, R.W. Alkanethiolate gold cluster molecules with core diameters from 1.5 nm to 5.2 nm: core and monolayer properties as a function of core size. *Langmuir* **1998**, *14*, 17–30.
  36. Brust, M.; Walker, M.; Bethell, D.; Schiffrin, D.J.; Whyman, R. Synthesis of thiol-derivatised gold nanoparticles in a two-phase liquid–liquid system. *J. Chem. Soc. Chem. Commun.* **1994**, 801–802.
  37. Brown, L.O.; Hutchison, J.E. Formation and electron diffraction studies of ordered 2-D and 3D superlattices of amine-stabilized gold nanocrystals. *J. Phys. Chem.*, **B 2001**, *105*, 8911–8916.
  38. Schmitt, H.; Badia, A.; Dickinson, L.; Reven, L.; Lennox, R.B. The effect of terminal hydrogen bonding on the structure and dynamics of nanoparticle self-assembled monolayers (SAMs): an NMR dynamics study. *Adv. Mater.* **1998**, *10* (6), 475–480.
  39. Luedtke, W.D.; Landman, U. Structure, dynamics, and thermodynamics of passivated gold nanocrystallites and their assemblies. *J. Phys. Chem.* **1996**, *100* (32), 13,323–13,329.
  40. Wang, Z.L.; Harfenist, S.A.; Whetten, R.L.; Bentley, J.; Evans, N.D. Bundling and interdigitation of adsorbed thiolate groups in self-assembled nanocrystal superlattices. *J. Phys. Chem.* **1998**, *103*, 3068–3072.
  41. Lin, X.M.; Jaeger, H.M. (unpublished results).
  42. Mirkin, C.A.; Letsinger, R.L.; Mucic, R.C.; Storhoff, J.J. A DNA-based method for rationally assembling nanoparticles into macroscopic materials. *Nature* **1996**, *382*, 607–611.
  43. Grabar, K.C.; Freeman, R.G.; Hommer, M.B.; Natan, M.J. Preparation and characterization of Au colloid monolayers. *Anal. Chem.* **1995**, *67*, 735–743.
  44. Van Leeuwen, D.A.; Van Ruitenbeek, J.M.; De Jough, L.J. Quenching of magnetic moments by ligand–metal interactions in nanosized magnetic metal clusters. *Phys. Rev. Lett.* **1994**, *73*, 1432–1435.
  45. Apsel, S.E.; Emmert, J.W.; Deng, J.; Bloomfield, L.A. Surface-enhanced magnetism in nickel clusters. *Phys. Rev. Lett.* **1996**, *76*, 1441–1444.
  46. Alder, B.J.; Wainwright, T.E. Phase transition for a hard sphere system. *J. Chem. Phys.* **1957**, *27*, 1208–1209.
  47. Van Megen, W.; Underwood, S.M. Glass transition in colloidal hard spheres: model coupling theory analysis. *Phys. Rev. Lett.* **1993**, *70*, 2766–2769.

48. Hoover, W.G.; Ree, F.H. Melting transition and communal entropy for hard sphere. *J. Chem. Phys.* **1968**, *49*, 3609–3617.
49. Van Blaaderen, A.; Rue, R.; Wiltzius, P. Template-directed colloidal crystallization. *Nature* **1997**, *385* (6614), 321–324.
50. Bargeman, D.; Van Voorst Vader, F. Van der Waals forces between immersed particles. *J. Electroanal. Chem.* **1972**, *37*, 45–52.
51. Korgel, B.A.; Fitzmaurice, D.A. Condensation of ordered nanocrystal thin film. *Phys. Rev. Lett.* **1992**, *80* (16), 3531–3534.
52. Ohara, P.C.; Leff, D.V.; Heath, J.R.; Gelbart, W.M. Crystallization of opals from polydisperse nanoparticles. *Phys. Rev. Lett.* **1995**, *75* (19), 3466–3469.
53. Trau, M.; Saville, D.A.; Aksay, I.A. Field-induced layering of colloidal crystals. *Science* **1996**, *272*, 706–709.
54. Giersig, M.; Mulvaney, P. Formation of ordered two-dimensional gold colloid lattices by electrophoretic deposition. *J. Phys. Chem.* **1993**, *97*, 6334–6336.
55. Service, R.F. Optical lithography goes to extremes and beyond. *Science* **2001**, *293*, 785–786.
56. Simon, U. Charge transport in nanoparticle arrangements. *Adv. Mater.* **1998**, *10* (17), 1487–1992.
57. Dorogi, M.; Gomez, J.; Osifchin, R.; Andres, R.P.; Reifenberger, R. Room-temperature coulomb blockade from a self-assembled molecular nanostructure. *Phys. Rev., B* **1995**, *52* (12), 9071–9077.
58. Wang, B.; Wang, H.; Li, H.; Zeng, C.; Hou, J.G.; Xiao, X. Tunable single-electron tunneling behavior of ligand-stabilized gold particles on self-assembled monolayers. *Phys. Rev., B* **2000**, *63* (3), 35,403–35,407.
59. Klein, D.L.; Roth, R.; Lim, A.K.L.; Alivasatos, A.P.; McEuen, P.L. A single-electron transistor made from a cadmium selenide nanocrystals. *Nature* **1997**, *389*, 671–699.
60. Andress, R.P.; Bielefeld, J.D.; Henderson, J.I.; Janes, D.B.; Kolagunta, V.R.; Kubiak, C.P.; Mahoney, W.J.; Osifchin, R.G. Self-assembly of a two-dimensional superlattice of molecularly linked metal clusters. *Science* **1996**, *273*, 1690–1693.
61. Collier, C.P.; Saykally, R.J.; Shinag, J.J.; Henrichs, S.E.; Heath, J.R. Reversible tuning of silver quantum dot monolayers through the metal-insulator transition. *Science* **1997**, *277*, 1978–1981.
62. Markovich, G.; Collier, C.P.; Heath, J.R. Reversible metal-insulator transition in ordered metal nanocrystal monolayers observed by impedance spectroscopy. *Phys. Rev. Lett.* **1998**, *80* (17), 3807–3810.
63. Doty, R.C.; Yu, H.; Shih, C.K.; Korgel, B.A. Temperature-dependent electron transport through silver nanocrystal superlattices. *J. Phys. Chem., B* **2001**, *105* (35), 8291–8296.
64. Leatherdale, C.A.; Kagan, C.R.; Morgan, N.Y.; Empeocles, S.A.; Kastner, M.A.; Bawendi, M.G. Photoconductivity in CdSe quantum dot solids. *Phys. Rev., B* **2000**, *62* (4), 2669–2680.
65. Parthasarathy, R.; Lin, X.M.; Jaeger, H.M. Electronic transport on metal nanocrystal arrays: The effect of structural disorder on scaling behavior. *Phys. Rev. Lett.* **2001**, *87*, 186807–186810.
66. Parthasarathy, R. Electronic Transport in Arrays of Gold Nanocrystals. In *Ph.D. Thesis*; Univ. of Chicago, 2002.
67. Middleton, A.A.; Wingreen, N.S. Collective transport in arrays of small metallic dots. *Phys. Rev. Lett.* **1993**, *71*, 3198.
68. Roux, S.; Herrmann, H.J. Disorder-induced nonlinear conductivity. *Europhys. Lett.* **1987**, *4* (11), 1227–1231.
69. Kardar, M.; Parisi, G.; Zhang, Y.C. Dynamic scaling of interface growth. *Phys. Rev. Lett.* **1986**, *56*, 889–892.
70. Parthasarathy, R.; Lin, X.M.; Eltero, K.; Rosenbaum, T.F.; Jaeger, H.M. *Phys. Rev. Lett.* in press.
71. Bezradin, A.; Westervelt, R.M.; Tinkham, M. Self-assembled chains of graphitized carbon nanoparticles. *Appl. Phys. Lett.* **1999**, *74* (18), 2699–2701.
72. Sampaio, J.F.; Beverly, K.C.; Heath, J.R. DC transport in self-assembled 2D layers of Ag nanoparticles. *J. Phys. Chem., B* **2001**, *105* (37), 8797–8800.
73. Beverly, K.C.; Sampaio, J.F.; Heath, J.R. Effects of size dispersion disorder on the charge transport in self-assembled 2-D Ag nanoparticle arrays. *J. Phys. Chem., B* **2002**, *106* (9), 2131–2135.
74. Elghanian, R.; Storhoff, R.C.; Mucic, R.C.; Letsinger, R.L.; Mirkin, C.A. Selective colorimetric detection of polynucleotides based on the distance-dependent optical properties of gold nanoparticles. *Science* **1997**, *277*, 1078.
75. Klimov, V.I.; Mikhailovsky, A.A.; Xu, S.; Malko, A.; Hollingsworth, J.A.; Leatherdale, C.A.; Eisler, H.-J.; Bawendi, M.G. Optical gain and stimulated emission in nanocrystal quantum dots. *Science* **2000**, *290*, 314–317.
76. Kagen, C.R.; Murray, C.B.; Bawendi, M.G. Long-range resonance transfer of electronic excitations in close-packed CdSe quantum-dot solids. *Phys. Rev., B* **1996**, *54*, 8633–8643.
77. Jackson, J.D. *Classical Electrodynamics*, 2nd Ed. John Wiley & Sons: New York, 1975.
78. Chang, R.K.; Furtak, T.E., Eds. *Surface Enhanced Raman Scattering*; Plenum: New York, 1982.
79. Kreibig, U.; Vollmer, M. *Optical Properties of Metal Clusters*; Springer-Verlag: Berlin, 1995.
80. Kottmann, J.P.; Martin, O.J. Retardation-induced plasmon resonances in coupled nanoparticles. *Opt. Lett.* **2001**, *26* (14), 1096–1098.
81. Persson, B.N.J.; Liebsch, A. Optical properties of two-dimensional systems of randomly distributed particles. *Phys. Rev., B* **1983**, *28* (8), 4247–4254.
82. Yamaguchi, T.; Yoshida, S.; Kinbara. Optical effect of the substrate on the anomalous absorption of aggregated silver films. *Thin Solid Films* **1974**, *21*, 173.
83. Quinten, M.; Leitner, A.; Krenn, J.R.; Aussenegg, F.R. Electromagnetic energy transport via linear chains of silver nanoparticles. *Opt. Lett.* **1998**, *23* (17), 1331–1333.
84. Winkler, J.R.; Di Bilio, A.J.; Farrow, N.A.; Richards, J.H.; Gray, H.B. Electron tunneling in biological molecules. *Pure Appl. Chem.* **1999**, *71* (9), 1753–1764.

# Nanocrystals Synthesized in Colloidal Self-Assemblies

M. P. Pileni

*Laboratoire des Matériaux Mésoscopiques et Nanométriques,  
Université Pierre et Marie Curie, Paris, France*

## INTRODUCTION

During this last decade, because of the emergence of a new generation of high-technology materials, the number of groups studying nanomaterials has increased exponentially.<sup>[1,2]</sup> The electrical, optical, and magnetic properties of inorganic nanomaterials vary widely with their sizes and shapes. Nanomaterials are used in several domains such as chemistry, electronics, high-density magnetic recording media, sensors, and biotechnology. This is, in part, because of their novel material properties, which differ from both the isolated atoms and the bulk phase. An ultimate challenge in materials research is the creation of perfect nanometer-scale crystallites identically replicated in unlimited quantities in a state than can be readily handled and can behave as pure macromolecular substances. Thus the ability to systematically manipulate these is an important goal in modern materials chemistry. Optimizing this ability requires an understanding of nanocrystal growth, which turns out to be a complex process. The essential first step in the study of their physical properties and the use of nanomaterials in various technologies is their production. Several approaches to manipulate inorganic nanocrystals have been undertaken. The major contribution was to produce spherical nanocrystals with a very low size distribution. Deposition processes include use of microwave plasma,<sup>[3]</sup> low-energy cluster beam deposition,<sup>[4]</sup> inorganic chemistry,<sup>[5]</sup> ball milling,<sup>[6]</sup> sonochemical reactions,<sup>[7]</sup> sol-gel,<sup>[8]</sup> and flame by vapor phase reaction and condensation.<sup>[9]</sup> In 1986, we developed a method based on reverse micelles (water-in-oil droplets) to prepare nanocrystals.<sup>[1,2]</sup> Normal micelles make it possible to produce ferrite magnetic fluids.<sup>[10]</sup>

To control the shapes of nanocrystals, several procedures are now being studied. Hard templates are employed to direct 1-D nanostructure growth. The nanometer-sized pores in membranes and zeolites are utilized to confine the growth of wires.<sup>[11–14]</sup> Alternatively, lithography and deposition are combined to create quantum wires on single-crystal surfaces.<sup>[15–17]</sup> Electrochemical synthesis is used to produce well-defined nanorods.<sup>[18–20]</sup> In 1993 and again in 1995,

we were able to partially control the shape of nanocrystals by using colloidal solutions as templates.<sup>[21,22]</sup>

In the following, we will concentrate mainly on nanocrystal growth in colloidal self-assemblies and describe discrepancies in the control of size and shape.

## COLLOIDAL SELF-ASSEMBLIES OF SURFACTANTS

### Direct Micelles

Surfactants are molecules with a polar hydrophilic head (attracted to water) and a hydrophobic hydrocarbon chain (attracted to oil). If a surfactant is solubilized in water, the chains tend to self-associate to form various aggregates.<sup>[23,24]</sup> Of course, if the solvent is able to solubilize simultaneously the polar head and the alkyl chains, no aggregates are formed. The shape of the surfactant plays an important role in forming the assembly. If the surfactant molecules have a very large polar head and a small chain, the chains tend to self-associate and form a spherical aggregate that is called a direct micelle. When the direct (or normal) micelle is formed at low concentrations, it is spherical and the length of the hydrocarbon chain and the size of the polar head fix its diameter. On increasing the surfactant concentration, various aggregate shapes are formed. The most commonly used surfactants are sodium dodecyl sulfate [Na(DS)], cetyl trimethyl ammonium chloride (CTAC), or cetyl trimethyl ammonium bromide (CTAB).

### Reverse Micelles

If the surfactant has the shape of a champagne cork (small polar head and branched hydrocarbon chains), spherical water-in-oil droplets are formed. These are usually called reverse micelles.<sup>[25]</sup> They are a thermodynamically stable mixture of water, oil, and surfactant, where water and oil regions are separated by a surfactant monolayer. Because of the amphiphilic nature of

the surfactant, numerous disordered or partially ordered phases are formed, depending on temperature and concentration.<sup>[26]</sup> The surfactant most frequently used is sodium di(2-ethylhexyl) sulfosuccinate, usually called Na(AOT). The water/isooctane/Na(AOT) ternary-phase diagram shows a large zone where the reverse micellar phase is found. In this liquid-like phase, the ratio of water to surfactant concentration  $w = [\text{H}_2\text{O}]/[\text{Na}(\text{AOT})]$  determines the reverse micelle size. At  $w$  values lower than 15, water mobility is greatly reduced (bound water). Above  $w = 15$ , the linear increase of the water pool radius  $r_w$  with  $w$  (from 4 to 18 nm) is explained by a geometrical model,<sup>[27]</sup> which assumes a constant area per surfactant molecule and that all surfactant molecules participate in the reverse micelle interface. They are able to exchange their water content during collision between two droplets. The volume of water added to the solution is the only parameter controlling the droplet diameter. Hence, the droplet size remains unchanged in various bulk oil solvents. The intermicellar potential, modeled by an adhesive sphere potential, depends on the particle diameter ( $d$ ), the attractive range ( $\Delta$ ), and the sticky parameter ( $\tau^{-1}$ ) describing the attractive strength between two droplets.<sup>[28]</sup> The latter increases with the length of the bulk oil alkyl chain. It is related to the decrease in percolation threshold with oil chain length, and is explained in terms of an increase in intermicellar droplet interactions. This is caused by penetration of solvent molecules into the interface screening the AOT-alkyl chain interactions. In the case of long-chain oil solvents, steric hindrance does not allow solvent molecules to penetrate the interface, inducing an increase in attractive interactions.<sup>[29–32]</sup> The kinetic exchange process<sup>[33]</sup> is directly related to the sticky parameter and to the modulus binding of the film at the water-oil interface. Hence, the solvent used tunes the kinetic exchange process: for short-chain solvents, the surfactant alkyl chain is well solvated and the micellar interactions are weak, inducing a low kinetic exchange rate constant. Conversely, large molecules are poor solvents for alkyl chains inducing strong interactions between micelles (i.e., high kinetic rate constants). Hence, by replacing cyclohexane by isooctane as the bulk oil solvent, the kinetic rate constant, at fixed droplet size, increases by a factor of 10.<sup>[34]</sup> These two properties (size and exchange process) make it possible by mixing two micellar solutions containing the reactants to produce nanomaterials.

### Colloidal Self-Assemblies Made of Divalent Surfactant

Following our paper<sup>[35]</sup> in 1991, a great deal of work has been performed with divalent bis(2-ethylhexyl)

sulfosuccinate  $[\text{X}(\text{AOT})_2]$ . We demonstrated that, at low water content, spherical reverse micelles are formed. It was found that, with  $\text{Cu}(\text{AOT})_2$ ,  $\text{Co}(\text{AOT})_2$ , and  $\text{Cd}(\text{AOT})_2$ , on increasing the water content, spherical water-in-oil droplets turn into cylinders. This study has been extended by other groups; Eastoe et al.<sup>[36–39]</sup> confirm these data and show this for other surfactants such as  $\text{Zn}(\text{AOT})_2$ ,  $\text{Ni}(\text{AOT})_2$ , and  $(\text{C}_7\text{H}_{14})_4\text{N}(\text{AOT})_2$ . In the oil-rich region, the phase behavior of copper(II) bis(2-ethylhexyl)sulfosuccinate  $[\text{Cu}(\text{AOT})_2]$ -isooctane-water is known over a wide domain.<sup>[40–43]</sup> When the surfactant is not totally solvated, the various structures are governed by the hydration of the head polar group with a progressive increase in the surfactant parameter  $s = v_s/a_s l_s$ , where  $v_s$ ,  $a_s$ , and  $l_s$  are the volume of the surfactant, the surface area, and the length of the alkyl chain, respectively. All these divalent surfactants behave similarly: At low water content, reverse micelles are formed. On increasing the water content, the system evolves to interconnected cylinders, to an equilibrium between lamellae and interconnected cylinders, to an onion-phase region, and, finally, to reverse micelles.<sup>[40–43]</sup> Hence, these structures are made with the same surfactant and differ by their shapes. In the region where the head polar group is totally hydrated, spontaneously formed thermodynamically stable emulsions in equilibrium with other microstructure phases are observed. These spontaneous emulsions are comprised of supra-aggregates,<sup>[43]</sup> lamellar spherulites in which the interior and exterior are phases of interconnected cylindrical nanostructures. In another part of the phase diagram, clumps of interdigitated micelles are surrounded by an interconnected cylinder phase. The phase boundaries emerge qualitatively from elementary considerations that require only notions of local and global packing constraints.

### SYNTHESES OF NANOCRYSTALS IN SELF-ASSEMBLIES DIFFERING BY THEIR SIZES AND SHAPES

In the oil-rich region, the reactants are confined in the water pool. Because of this, the chemical reaction (i.e., production of nanocrystals) takes place in the supersaturation regime, thus allowing the formation of particles having a very high crystallinity. Such self-assemblies are either droplets (reverse micelles), or bicontinuous phases such as interconnected cylinders or lamellar phases. In aqueous solutions, a functionalized surfactant is used to make normal micelles that are the chemical media for nanocrystal growth. In this case, the reactants are localized at the water-oil interface of the micelles, creating a supersaturation regime.

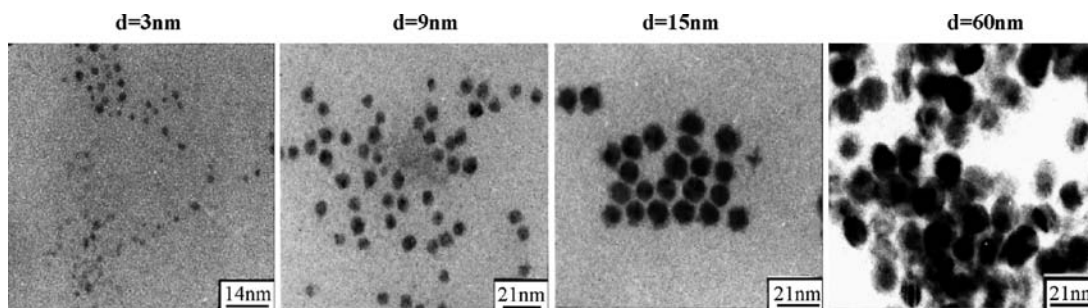


**Fig. 1** Change of the copper nanocrystal sizes with the reverse micelle diameter. Reverse micelles are made with 0.1 M Na(AOT) surfactant solubilized in isoctane. One solution contains  $10^{-2}$  M  $\text{Cu}(\text{AOT})_2$ , whereas the second one contains  $2 \times 10^{-2}$  M hydrazine. The water content is fixed by the amount of water added to the solution and controls the droplet size. By mixing the two reverse micelles, copper nanocrystals are formed. A drop of solution is deposited on grid and the transmission electron microscopy (TEM) patterns are presented for various water droplet sizes.

### Syntheses in Reverse Micelles with Formation of Spherical Nanocrystals

Fifteen years ago,<sup>[44]</sup> we discovered that reverse micelles are good candidates for templates. Coprecipitation reactions and chemical reduction occur in reverse micelles by using the two properties described above (change in the droplet size with the water content and micellar exchange process). Let us consider A and B solubilized in two micellar solutions. On mixing them and because of the exchange process, A and B are in contact and react. Thus it is possible to fabricate a very wide range of spherical nanomaterials<sup>[1]</sup> such as semiconductors, metals, oxides, and various metal and semiconductor alloys. The control of the template size, by changing the water content, enables control of the spherical nanocrystal size.<sup>[21,44]</sup> Fig. 1 shows the control of copper nanocrystal size with the water content. It is of interest to note that this nanoreactor makes it possible to produce metal nanocrystals without any detectable oxide. The nanocrystals are characterized by a very high crystallinity when one of the reactants used is a functionalized surfactant (the surfactant has one of the reactants as the counterion). Otherwise, when the two highly hydrated reactants are solubilized in the two droplets, amorphous nanomaterials are formed and metals are produced in their oxide form. The size of the produced material, under the same experimental conditions, is not that of the droplet used as a template.<sup>[1,2]</sup> In fact, for II–VI semiconductors<sup>[45]</sup> (CdS, CdTe, and CdMnS), the particle size varies from 2 to 4 nm, whereas for metals, it increases from 2 to 6 nm for silver<sup>[46]</sup> and from 2 to 10 nm for copper<sup>[21]</sup> and silver sulfide.<sup>[47]</sup> This control of the particle size is obtained for the smallest water-in-oil droplets (varying from 0.6 to 6 nm), whereas for larger template sizes (from 6 to 12 nm), no changes in the particle size are observed (Fig. 2). This is well demonstrated for large numbers of nanocrystals and is explained in terms of

water structure.<sup>[48]</sup> An exception is found for silver sulfide nanocrystals with a linear increase in the particle size with that of the template and similar sizes of the droplets and the material.<sup>[47]</sup> By changing the length of the solvent alkyl chain, we know that the droplet size remains the same, whereas the intermicellar interactions change. Syntheses at constant droplet size and in various bulk oil solvents induce a change in the produced nanocrystal size. This is observed for a large variety of nanocrystals and is well demonstrated with copper nanocrystals made in reverse micelles having isoctane and cyclohexane as the bulk phase (Fig. 2). This change in the particle size, keeping the same droplet radius, is explained in terms of efficiency in the exchange control process: Because cyclohexane is a

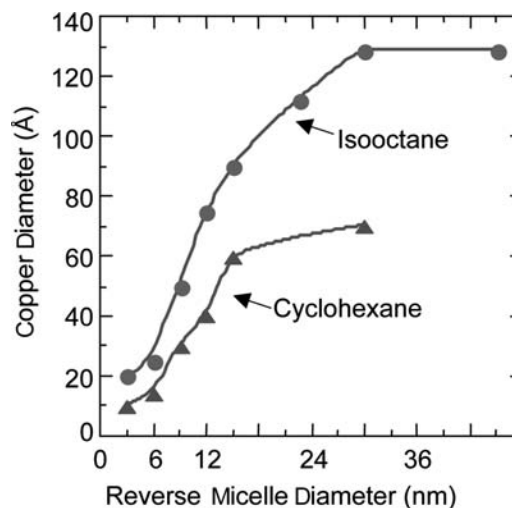


**Fig. 2** Variation of the copper nanocrystal size with the droplet diameters by using either isoctane or cyclohexane as the bulk oil solvent. The same procedure as described in Fig. 1 is used. Isooctane is replaced by cyclohexane. From the TEM pattern, the average diameter of nanocrystal sizes is measured.

good solvent for surfactant chains, intermicellar interactions between droplets and then the kinetic exchange rate constant are smaller with cyclohexane than isooctane.

### Discrepancies in the Use of Reverse Micelles as Templates

The method described above makes it possible to obtain a very large number of spherical nanomaterials, indicating that reverse micelles are efficient templates. However, note that some of them do not exist in the bulk phase and others can never be produced. Hence, in equilibrium states, the solid solubility between Fe and Cu is negligibly small. Their mixing enthalpy is positive and they form no intermetallic compounds even though their atomic radii are quite similar. On the nanoscale, reverse micelles produce Fe/Cu alloys.<sup>[49]</sup> With semimagnetic semiconductors<sup>[45]</sup> such as  $\text{Cd}_y\text{Mn}_{1-y}$ , it is possible to include, as in the bulk phase, 50% of  $\text{Mn}^{2+}$  ions in the CdS matrix, whereas with CdTe, there are no detectable manganese ions in the nanocrystals<sup>[50]</sup> and telluride nanorods are formed. No obvious explanations can be given. However, this indicates that physical chemistry in colloidal and homogeneous solutions differs.

The experimental mode used to prepare the nanocrystals is one of the key parameters. This is also described below for controlling nanocrystal shape. Let us consider spherical reverse micelles made of functionalized surfactants such as cadmium bis(2-ethylhexyl) sulfosuccinate [ $\text{Cd}(\text{AOT})_2$ ]. By adding a given amount of water, the water pool diameter reaches 10 nm. By replacing pure water with a solution containing sodium sulfide, spherical CdS nanocrystals are produced. Conversely, bubbling  $\text{H}_2\text{S}$  diluted with nitrogen gas results in formation of flat triangles of CdS nanocrystals<sup>[51]</sup> (Fig. 3). High-resolution electron microscopy shows formation of well-defined

monocrystals. The formation of flat triangles could be explained by the fact that the nucleation process is slower in using diluted  $\text{H}_2\text{S}$  gas. This enables selective adsorption of hydronium ( $\text{H}^+$ ) on specific faces. Such nanocrystal growth cannot be explained by surfactant impurity: The same reverse micelles produce spheres and triangles. This shape control by the presence of  $\text{H}^+$  in the solution can be related to the formation of cubic platinum nanocrystals<sup>[52]</sup> from aqueous solutions containing  $\text{PtCl}_4^{2-}$  and bubbled with hydrogen ( $\text{H}_2$ ). With time, hydrogen and chloride ions are formed in the solution and a precipitate of cubic platinum nanoparticles appears. It must be noted that the particles are well defined and faceted. Coalescence is prevented by selective adsorption of  $\text{H}^+$  or  $\text{Cl}^-$  on the facets. Other examples in the literature show formation of non-spherical nanoparticles: hence, spherical reverse micelles made of CTAB/butanol/octane produce cubic  $\text{KMnF}_3$  nanocrystals.<sup>[53]</sup> Details of the synthesis are not given and it is rather difficult to explain which parameter plays the determinant role. However, we have to keep in mind that bromide derivatives of CTAB are present during the synthesis. This will be discussed below. Similarly, elongated and rod-shaped  $\text{BaCrO}_4$  and  $\text{CaCO}_3$  nanocrystals are produced by using reverse micelles.<sup>[54-57]</sup> This could be caused by selective adsorption on various faces during the nanocrystal growth of either reactive products or impurities coming from the preparation of functionalized surfactants used to form reverse micelles. From this, it is reasonable to conclude that reverse micelles can be used as nanoreactors to produce nanoparticles. In most cases, a spherical template produces nanospheres. Hydration of the water pool, procedure mode, and size of the template control the nanocrystal growth. However, production of various species during the chemical reaction and the presence of some impurities prevent the control of spherical particles and induce the formation of nanoparticles having various shapes.

### Colloidal Solutions Used as Template to Produce Nanocrystals

Instead of using reverse micelles, let us consider a phase diagram made of a functionalized surfactant such as  $\text{Cu}(\text{AOT})_2$ -water-isooctane. The confinement of the reactant is still one of the major parameters. As (already) described above, the phase diagram markedly differs with the water content: At low water content, reverse micelles are formed. On increasing the water content, the system evolves to interconnected cylinders, then to an equilibrium between lamellae and interconnected cylinders, to an onion-phase region, and, finally, to reverse micelles.<sup>[41,42]</sup> Hence, the polar volume fraction controls the shape of

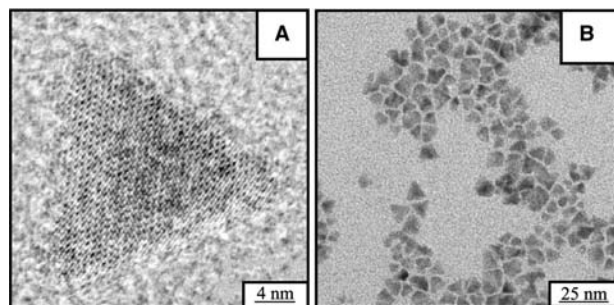


**Fig. 3** Triangles of CdS nanocrystals at various enhancements. Reverse spherical micelles of 0.1 M  $\text{Cd}(\text{AOT})_2$  solubilized in isooctane at water content equal to 31 are submitted to a slow bubbling of  $\text{H}_2\text{S}$ . CdS nanocrystals are formed.



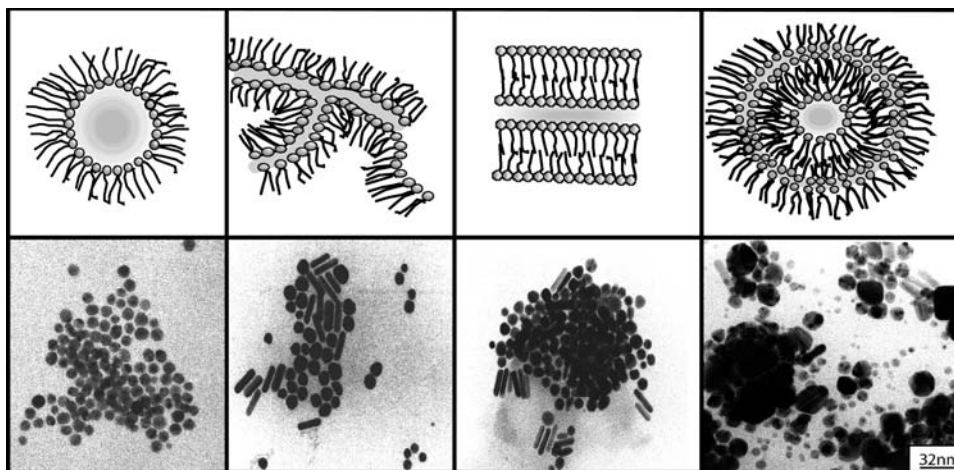


**Fig. 4** Change in the shape of copper nanocrystals in various colloidal solutions differing by their structures. The colloidal solution is made of 0.1 M  $\text{Cu}(\text{AOT})_2$  in isoctane and hydrazine is injected in the colloidal solution. At low water content (below 3), spherical reverse micelles are formed, inducing formation of spheres. On increasing the water content to  $w = 5$ , interconnected cylinders are produced with the formation of a mixture of spherical and cylindrical copper nanocrystals. In lamellar phase obtained at  $w = 11$ , a mixture of spheres and cylinders is produced, whereas at  $w = 30$ , supra-aggregates are formed and a large variety of copper nanocrystals differing by their shapes are produced.

colloids. To make nanocrystals and to determine if the shape of the template controls that of the nanocrystals, water is replaced by hydrazine in the aqueous solution, keeping the same polar volume fraction colloidal shapes described above. Fig. 4 shows that the shape of the template partially controls that of copper nanocrystals.<sup>[57]</sup> The crystallinity of these nanomaterials is very high. In the interconnected cylinder region, spheres and cylinders are formed: The cylinder structure is characterized by a fivefold symmetry.<sup>[58]</sup> In the

region of the phase diagram consisting of an onion phase containing internal and external interconnected cylinders, a large variety of shapes are observed.<sup>[59]</sup> This control of the nanocrystal shape by that of the template has been recently confirmed by Simmons et al.<sup>[60]</sup> Syntheses of CdS nanoparticles in such colloidal assemblies characterized by various structures make it possible to vary the morphology of the nanocrystals from spheres to nanorods with a switch in the crystal structure from cubic to hexagonal. However,

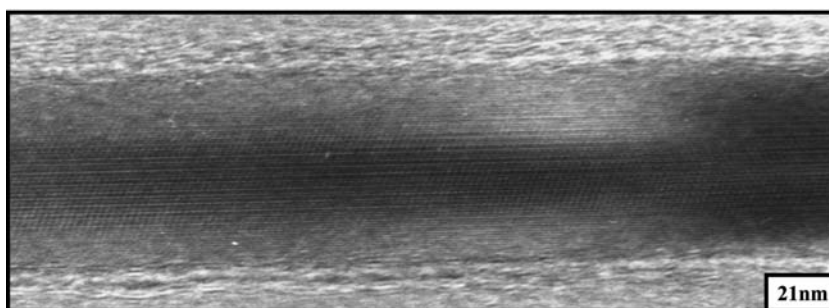
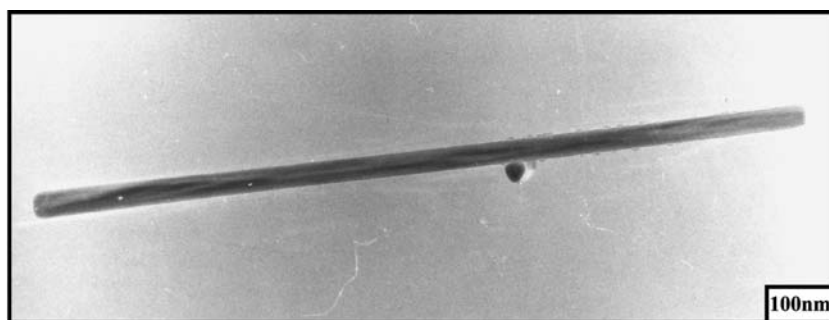


**Fig. 5** TEM patterns at various enhancements of copper nanorods. Hydrazine is added to 0.1 M  $\text{Cu}(\text{AOT})_2$  solubilized in isoctane in the presence of  $10^{-3}$  M NaCl and copper nanorods are produced at the end of the chemical reduction of  $\text{Cu}^{2+}$  by hydrazine.

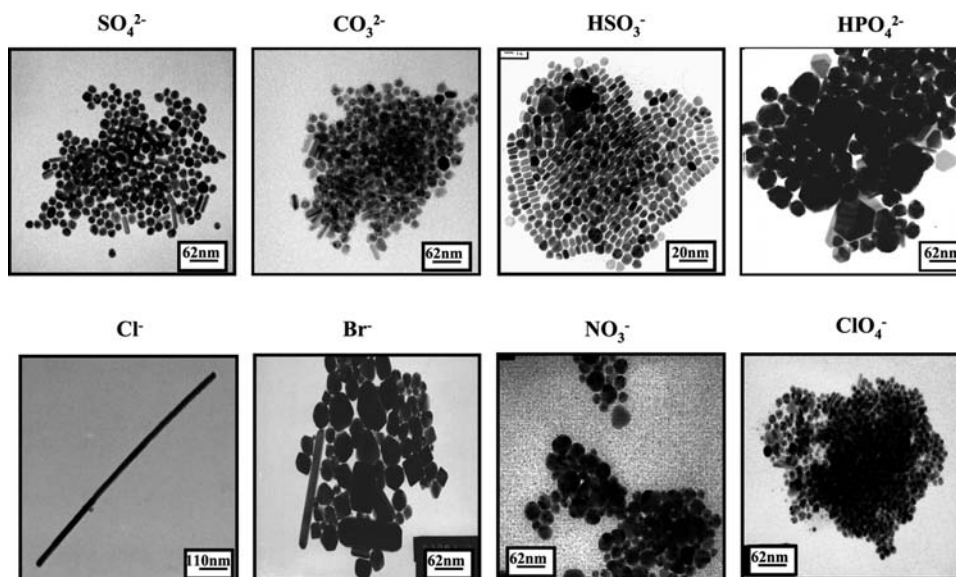


**Fig. 6** Change in the copper nanocrystal shape in the presence of various anions, keeping  $\text{Na}^+$  as the cation,  $[\text{Salt}] = 10^{-3}$  M. The same procedure as described in Fig. 5 is used. NaCl is replaced by  $\text{Na}_2\text{SO}_4$ ,  $\text{Na}_2\text{CO}_3$ ,  $\text{NaHSO}_3$ ,  $\text{Na}_2\text{HPO}_4$ , NaCl, NaBr,  $\text{NaNO}_3$ , and  $\text{NaClO}_4$ .

the role of templates is not as obvious as described above. Adsorption of ions, salts, and molecules has to be taken into account.

#### Influence of adsorption of ions on nanocrystal growth

Let us consider the system described above  $[\text{Cu}(\text{AOT})_2\text{-isooctane-water}]$ . In the region of interconnected cylinders that are in equilibrium with a lamellar phase, small cylinders are obtained. Addition of a small amount of salt to the colloidal solution gives long copper nanorods with a high crystallinity in fivefold symmetry (Fig. 5)<sup>[61]</sup> and an aspect ratio controlled by the concentration of chloride ions in the microphase.<sup>[62,63]</sup> It has been demonstrated that this effect is mainly caused by the chloride ions. This is attributed to selective adsorption of these ions on (001) faces and to the fact that the growth is faster on the (111) faces. Formation of these nanorods is not observed, except with bromide, on replacing chloride by other anions<sup>[64]</sup> (Fig. 6). Note that with bromide anions, a rather large amount of cubic nanocrystals is formed, whereas with most other anions, mainly spherical objects are produced. From this, it is obvious that adsorption of a given anion enables control of the copper nanocrystal shape. These data have to be related to those obtained by Esumi, Matsuhisa, and Torigoe,<sup>[65]</sup> who produced gold nanorods by UV-visible irradiation of a gold salt solubilized in the bulk phase of normal micelles made of CTAC. The authors claim that direct micelles play the role of the template. It is difficult to understand this role: Gold

ions do not interact with the micellar solution and are reduced photochemically. The chloride ions coming from the counterion of the surfactant could play this role, as observed above for copper nanorods produced in the presence of  $\text{Cl}^-$ , and allow the gold crystal growth along the 111 direction. These data can also be related to those published by Jana, Gearheart, and Murphy,<sup>[66,67]</sup> who produced silver and gold nanorods with an aspect ratio controlled by the ratio of seeds and base concentrations in the presence of the CTAC surfactant. As mentioned, cubic  $\text{KMnF}_3$  nanocrystals are formed<sup>[53]</sup> from reverse micelles made from the CTAB surfactant and  $\text{Cu}(\text{AOT})_2\text{-H}_2\text{O-isooctane}$  solution<sup>[63]</sup> in the presence of  $\text{Br}^-$ . Similarly, self-assembled monolayers (SAMs) used as templates and immersed in a solution containing bromide ions produce cubic cadmium sulfide nanoparticles.<sup>[68]</sup> The environments of these various systems totally differ. The only common factor is the presence of bromide ions during the nanocrystal growth. However, it cannot be claimed that the general principle for growing cubes is that bromide ions have to be present during the process. As mentioned, bubbling hydrogen through an aqueous solution containing  $\text{PtCl}_4^{2-}$  produces cubic platinum nanocrystals.<sup>[52]</sup> From this, it can be concluded that cubic nanocrystal growth is more related to the presence of ions that adsorb selectively than the template.

#### Influence of molecule adsorption on the nanocrystal growth

Molecules added to the solution can also play a role in the control of particle shape. Nanodisks<sup>[69]</sup> are

produced in the presence of surfactants that no longer form well-defined templates (aggregates), whereas nanospheres are produced in reverse micelles.<sup>[70]</sup> Nanodisk size depends on the amount of hydrazine present in the solution. Note that this is the first example where it is possible to control nanodisk size, and the color of the colloidal solution containing nanodisks evolves from red to gray<sup>[71]</sup> (Fig. 7). Because the concentration of the surfactant remains unchanged, to explain the disk formation, we have to take into account the adsorption of hydrazine or/and hydrogen, and hydroxyl ions on the faces. Association of molecules used as additives and salts (together) can also play a role in the control of particle shapes. Polymers and salts are needed to produce PbS nanorods<sup>[72]</sup> from functionalized surfactants solubilized in chloroform, whereas spheres are produced in their absence. In the latter case, the surfactants do not self-assemble in chloroform because the head polar group and the alkyl chains are both soluble in this solvent and act as reactants.

From the literature, a general agreement seems to emerge that control of the nanoparticle shape, via inorganic syntheses, needs to involve a mixture of two surfactants.<sup>[73,74]</sup> This has been well demonstrated with various materials such as CdSe, cobalt, and Fe nanorods. The relative ratio of surfactants controls

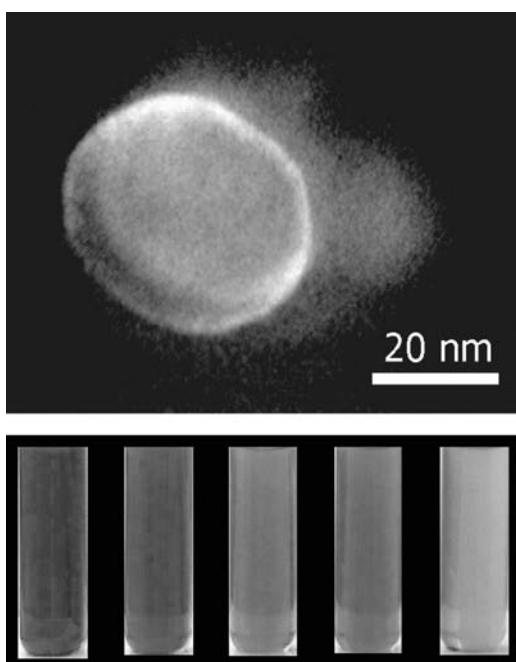


**Fig. 7** Silver nanodisks characterized by various absorption spectra caused by change in the nanodisk size while keeping the same aspect ratio. A large volume of hydrazine added to 0.1 M Ag(AOT) is hexane. The relative amount of hydrazine controls the size of nanocrystals.

their aspect ratio. However, such claims are not always valid. In fact, the presence of a single surfactant is enough to control the dimensions of silver, gold, and copper nanorods. A convincing experiment showing that the selective adsorption of molecules is one of the major parameters in controlling the particle shape is the production of ZnTe and CdTe nanowires<sup>[75,76]</sup> by the solvothermal process. Metals are solubilized in hydrated hydrazine, which is not only an electron transfer medium but also a strong electron donor. These authors claim that in this medium, which is, from my knowledge, a homogeneous solution, hydrazine plays the role of a template.

### NORMAL MICELLES USED TO PRODUCE FERRITE NANOCRYSTALS

Fine magnetic particles, dispersed in a suitable liquid carrier (such as water, kerosene, diester, etc.), form a magnetic fluid. Their magnetic properties<sup>[77,78]</sup> cannot be analyzed without the inclusion of the effects of size, shape, surface, polydispersity, and interactions between particles. For this reason, a method for synthesizing the particles with good control of these parameters is necessary. Recently, we developed a new procedure to make ferrite nanocrystals that allows changing of the nanocrystal size while keeping the same surface area.<sup>[10,79,80]</sup>

Divalent dodecyl sulfate  $[X(DS)_2]$  ( $X = \text{Fe}, \text{Co}, \text{Zn}$ ) is solubilized in aqueous solution and forms mixed oil-in-water micelles. A base is added to the micellar solution, is stirred for 2 hr, and, after centrifugation, the precipitate is washed several times with a solution of 50% water and 50% ethanol to remove the surfactant. Thus the powder obtained consists of ferrite nanocrystals. Depending on the type of ions, X, associated with  $\text{Fe}(DS)_2$  stoichiometric solid solutions of ferrite, is obtained. Hence, various materials such as  $\text{Fe}_3\text{O}_4$ ,<sup>[10,79,80]</sup>  $\gamma\text{-Fe}_2\text{O}_3$ ,<sup>[10,79,80]</sup>  $\text{Co}_x\text{Fe}_y\text{O}_4$ ,<sup>[81]</sup> and  $\text{Co}_x\text{-Zn}_y\text{Fe}_z\text{O}_4$ <sup>[82,83]</sup> were produced and the obtained material depends on the relative concentration of the reactants. Note that  $\text{Fe}_3\text{O}_4$  is the reduced form of  $\gamma\text{-Fe}_2\text{O}_3$ . Immediately after synthesis,  $\text{Fe}_3\text{O}_4$  is produced. After a few hours, the  $\text{Fe}^{2+}$  ions are oxidized to  $\text{Fe}^{3+}$  and  $\gamma\text{-Fe}_2\text{O}_3$  is formed. With this procedure, a large variety of ferrite nanocrystals can be prepared. To obtain an alkaline magnetic fluid, the nanocrystals are dispersed in aqueous solution, whereas for a neutral fluid, the nanocrystals are coated with citrate ions and dispersed in water.<sup>[81,84]</sup> The nanocrystal size distribution is around 20–30%. Changing the surfactant concentration controls the particle size by a factor of 2 or 4. Whatever the fabricated material is, the nanocrystals structure is an inverted spinel. This procedure

drastically differs from syntheses in homogeneous solution.<sup>[85–93]</sup> The major differences are:

1. The reactant concentration is two orders of magnitude lower than that in homogeneous solution.
2. A spinel structure can be obtained in the absence of Fe(III) at the starting point of the reaction, whereas the ratio Fe(II)/Fe(III) must be higher than 0.4 in homogeneous solution. In the latter case, with a high Fe(II) salt concentration and without Fe(III) derivatives,<sup>[94–96]</sup> the formation of Fe<sub>3</sub>O<sub>4</sub> micrometer particles is observed. Their morphology depends critically on parameters similar to those described above (reactant concentrations, pH, ionic strength, etc.). Furthermore, it has been impossible to produce particles in the nanosize range when Fe(II) salt is used for the synthesis.
3. Changing the micellar concentration controls the particle size. In homogeneous solution, it is controlled by changing the type of salt (chlorides, nitrates, perchlorates, etc.), Fe(II)/Fe(III) ratio, pH, and ionic strength of the media. Such drastic changes in experimental conditions induce a large modification in the particle interface (hydroxide formations, etc.) and magnetic properties<sup>[92,93]</sup> of the nanocrystals. Conversely, using colloidal solutions makes it possible to produce nanocrystals with magnetic properties that do not depend on their coating.<sup>[81]</sup>

## CONCLUSION

In the last decade, colloidal solutions were assumed to be very efficient templates for controlling particle size and shape. A large number of groups used reverse micelles to control spherical nanoparticles.<sup>[1,2]</sup> This makes possible determining the various parameters involved in such processes and demonstrates that they can still be considered as efficient nanoreactors with some discrepancies. There are fewer reports concerning the control of the particle shape and it is still rather difficult to determine the key parameters. They depend on the adsorption of salts, molecules, and procedure. Crystal growth on the nanoscale seems to follow behavior similar to that of the bulk phase with a marked dependence on pH. The latter is particularly important when some impurities are present in the growth medium because it influences, for example, the formation either of zwitter-ions or complex ions, the efficiency of which is greater than that of the initial impurity. These elements lead to a decrease in the growth rates of certain crystal faces. Most of the changes are based on the existence of a more or less

epitaxial adsorption layer on the crystal. This layer is composed of solvents, impurities, or salts. Their precise roles are as yet uncertain. The changes are because of the differences between the growth rates of the various crystallographic faces. From this, it can be concluded that the template is not the key parameter in the shape control.

From these comments, we can ask why templates made of surfactants are quite effective in controlling the formation of nanospheres whereas rather large exceptions are observed for anisotropic shapes. This is probably because of the fact that colloidal templates are highly dynamic. The energy needed to produce spherical nanocrystals is less than that for producing anisotropic nanocrystals. A general method for controlling nanocrystal shapes through soft chemistry has not yet been found, but this does not mean that such a method cannot be discovered. To reach a final conclusion, we need more data and we need to compare the fabrication of anisotropic nanocrystals with various types of materials. Probably other approaches, which have yet to be found, are required. This is suggested by the fact that the fabrications of elongated ferrite nanocrystals in biological media and in vitro are completely different. In biological media, the mechanism of crystal growth is not well known. However, to produce similar nanomaterials in vitro, a very high base concentration is needed and the corresponding pH would induce the destruction of the biological media. This means that other ways exist and have to be discovered.

## REFERENCES

1. Pileni, M.P. Reverse micelles as microreactors. *J. Phys. Chem.* **1993**, *97* (27), 6961–6973.
2. Pileni, M.P. Nanosized particles made in colloidal assemblies. *Langmuir* **1997**, *13*, 3266–3276.
3. Vollath, D.; Szabo, D.V.; Taylor, R.D.; Willis, J.O. Synthesis and magnetic properties of nanostructured maghemite. *J. Mater. Res.* **1997**, *12*, 2175–2182.
4. Perez, A.; Melinon, P.; Dupuis, V.; Prevel, B.; Bardotti, L.; Tuallion-Combes, J.; Masenelli, B.; Trilleux, M.; Pellarin, M.; Lerme, J.; Cottancin, E.; Broyer, M.; Jamet, M.; Negrier, M.; Tournus, F.; Gaudry, M. Nanostructured materials from clusters: synthesis and properties. *J. Mater. Trans.* **2001**, *42*, 1460–1470. (Special issue on Nano Metals).
5. Murray, C.B.; Norris, D.J.; Bawendi, M.G. Synthesis and characterization of nearly monodisperse CdE (E = sulfur, selenium, tellurium) semiconductor nanocrystallites. *J. Am. Chem. Soc.* **1993**, *115* (19), 8706–8715.
6. Goya, G.F.; Rechenberg, H.R. Ionic disorder and N<sup>3</sup>el temperature in ZnFe<sub>2</sub>O<sub>4</sub> nanoparticles. *J. Magn. Magn. Mater.* **1999**, *196–197*, 191–192.

7. Shafi, K.V.P.M.; Kolytyn, Y.; Gedanken, A.; Prozorov, R.; Balogh, J.; Lendvai, J.; Felner, I.J. Sonochemical preparation of nanosized amorphous NiFe<sub>2</sub>O<sub>4</sub> particles. *Phys. Chem., B* **1997**, *101* (33), 6409–6414.
8. Sugimoto, T.; Shimotsuma, Y.; Itoh, H. Synthesis of uniform cobalt ferrite particles from a highly condensed suspension of b-FeOOH and b-Co(OH)<sub>2</sub> particles. *Powder Technol.* **1998**, *96*, 85–89.
9. Elmore, W.C. Ferromagnetic colloid for studying magnetic structures. *Phys. Rev.* **1938**, *54*, 309–310.
10. Moumen, N.; Pileni, M.P. Control of the size of cobalt ferrite magnetic fluid. *J. Phys. Chem.* **1996**, *100* (5), 1867–1873.
11. Martin, A. Nanomaterials—a membrane-based synthetic approach. *Science* **1994**, *266*, 1961–1966.
12. van der Zande, B.M.I.; Bohmer, M.R.; Fokkink, L.G.J.; Schonenberger, C. Aqueous gold sols of rod-shaped particles. *J. Phys. Chem., B* **1997**, *1* (6), 852–854.
13. Cepak, V.M.; Martin, C.R. Preparation and stability of template-synthesized metal nanorod sols in organic solvents. *J. Phys. Chem., B* **1998**, *102* (49), 9985–9990.
14. Molares, M.E.T.; Buschmann, V.; Dobrev, D.; Neumann, R.; Scholz, R.; Schuchert, I.U.; Vetter, J. Single-crystalline copper nanowires produced by electrochemical deposition in polymeric ion track membranes. *Adv. Mater.* **2001**, *13*, 62–65.
15. Namatsu, H.; Kurihara, K.; Nagase, M.; Makino, T. Fabrication of 2-nm-wide silicon quantum wires through a combination of a partially-shifted resist pattern and orientation-dependent etching. *Appl. Phys. Lett.* **1997**, *70*, 619–621.
16. Wang, J.; Thompson, D.A.; Robinson, B.J.; Simmons, J.G. Molecular beam epitaxial growth of InGaAs/InGaAsP quantum wires on V-grooved InP substrates with (III) sidewalls. *J. Cryst. Growth* **1997**, *175–176*, 793–798.
17. Nepijko, S.A.; Ievlev, D.N.; Schulze, W.; Urban, J.; Ertl, G. Growth of rodlike Ag nanoparticles by vapor deposition of small clusters. *ChemPhysChem* **2000**, *1*, 140–142.
18. Yu, Y.Y.; Chang, S.S.; Lee, C.L.; Wang, C.R.C. Gold nanorods: electrochemical synthesis and optical properties. *J. Phys. Chem., B* **1997**, *101* (34), 6661–6664.
19. Huang, L.M.; Wang, H.T.; Wang, Z.B.; Mitra, A.; Bozhilov, K.N.; Yan, Y.S. Nanowire arrays electro-deposited from liquid crystalline phases. *Adv. Mater.* **2002**, *14*, 61–64.
20. Wang, Z.L.; Gao, R.P.; Nikoobakht, B.; El-Sayed, M.A. Surface reconstruction of the unstable {110} surface in gold nanorods. *J. Phys. Chem., B* **2000**, *104* (23), 5417–5420.
21. Lisiecki, I.; Pileni, M.P. Synthesis of copper metallic clusters using reverse micelles as microreactors. *J. Am. Chem. Soc.* **1993**, *115* (10), 3887–3896.
22. Tanori, J.; Pileni, M.P. Change in the shape of copper nanoparticles in ordered phases. *Adv. Mater.* **1995**, *7*, 862–864.
23. Mittal, K.; Lindman, B.; Eds. *Surfactant in Solution*; Plenum: New York, 1984.
24. Mittal, K.; Lindman, B.; Eds. *Surfactant in Solution*; Plenum: New York, 1987.
25. Pileni, M.P. *Structure and Reactivity in Reverse Micelles*; Pileni, M.P., Ed.; Elsevier, 1989.
26. Mitchell, D.; Ninham, B. Micelles, vesicles and microemulsions. *J. Chem. Soc., Faraday Trans.* **1981**, *77*, 601–629.
27. Pileni, M.P.; Zemb, T.; Petit, C. Solubilization by reverse micelles: solute localization and structure perturbation. *Chem. Phys. Lett.* **1985**, *118*, 414–420.
28. Robinson, B.H.; Toprakcioglu, C.; Dore, J.C.; Chieux, P. Small-angle neutron-scattering study of microemulsions stabilized by aerosol-OT. *J. Chem. Soc., Faraday Trans.* **1992**, *80*, 13–27.
29. van Dijk, M.A. Dielectric study of percolation phenomena in a microemulsion. *Phys. Rev. Lett.* **1985**, *55* (9), 1003–1005.
30. Huang, J.S. Surfactant interactions in oil continuous microemulsions. *J. Chem. Phys.* **1985**, *82* (1), 480–484.
31. Lemaire, B.; Bothorel, P.; Roux, D. Micellar interactions in water-in-oil microemulsions: 1. calculated interaction potential. *J. Phys. Chem.* **1983**, *87* (6), 1023–1028.
32. Huang, J.S.; Safran, S.A.; Kim, M.W.; Grest, G.S.; Kotlarchyk, M.; Quirke, N. Attractive interactions in micelles and microemulsions. *Phys. Rev. Lett.* **1984**, *53*, 592–595.
33. Jain, T.K.; Cassin, G.; Badiali, J.P.; Pileni, M.P. Relation between exchange process and structure of AOT reverse micellar system. *Langmuir* **1996**, *12* (10), 2408–2411.
34. Fletcher, P.D.I.; Robinson, B.H. Dynamic processes in water in oil microemulsions. *Ber. Bunsenges. Phys. Chem.* **1981**, *85*, 863–867.
35. Petit, C.; Lixon, P.; Pileni, M.P. Structural study of divalent metal bis(2-ethylhexyl) sulfosuccinate aggregates. *Langmuir* **1991**, *7* (11), 2620–2625.
36. Eastoe, J.; Fragneto, G.; Robinson, B.H.; Towey, T.F.; North, A.N.; Leng, K.F.J. Variation of surfactant counterion and its effect on the structure on properties of aerosol-OT based water-in-oil microemulsions. *J. Chem. Soc., Faraday Trans.* **1992**, *88*, 461–471.
37. Eastoe, J.; Steytler, C.; Robinson, B.H.; Heenan, R.K.; North, A.N.; Dore, J.C. Structure of cobalt aerosol-OT reversed micelles studied by small-angle scattering methods. *J. Chem. Soc., Faraday Trans.* **1994**, *90*, 2479–2504.
38. Eastoe, J.; Robinson, B.H.; Heenan, R.K. Water-in-oil microemulsions formed by ammonium and tetrapropylammonium salts of Aerosol OT. *Langmuir* **1993**, *9* (11), 2820–2824.
39. Eastoe, J.; Towey, T.F.; Robinson, B.H.; Williams, J.; Heenan, R.K. Structures of metal bis(2-ethylhexyl)sulfosuccinate) aggregates in cyclohexane. *J. Phys. Chem.* **1993**, *97* (7), 1459–1463.
40. Tanori, J.; Pileni, M.P. Control of the shape of copper metallic particles by using a colloidal system as template. *Langmuir* **1997**, *13* (4), 639–646.
41. Lisiecki, I.; Andre, P.; Filankembo, A.; Petit, C.; Tanori, J.; Gulik-Krzywicki, T.; Ninham, B.W.; Pileni, M.P. Mesostructured fluids: 1. Cu(AOT)<sub>2</sub>-H<sub>2</sub>O-isooctane in oil rich regions. *J. Phys. Chem., B* **1999**, *103* (43), 9168–9175.

42. Lisiecki, I.; Andre, P.; Filankembo, A.; Petit, C.; Tanori, J.; Gulik-Krzywicki, T.; Ninham, B.W.; Pileni, M.P. Mesostuctured fluids: 2. microstructure and supra-aggregation. *J. Phys. Chem., B* **1999**, *103* (43), 9176–9189.
43. André, P.; Filankembo, A.; Lisiecki, I.; Petit, C.; Tanori, J.; Gulik-Krzywicki, T.; Ninham, B.W.; Pileni, M.P. Supra-aggregation: microphase formation in complex fluids. *Adv. Mater.* **2000**, *12*, 119–123.
44. Petit, C.; Pileni, M.P. Synthesis of cadmium sulfide in situ in reverse micelles and in hydrocarbon gels. *J. Phys. Chem.* **1998**, *92* (8), 2282–2286.
45. Pileni, M.P. II–VI Semiconductors made by soft chemistry syntheses and optical properties. *Catal. Today* **2000**, *58*, 151–166.
46. Petit, C.; Lixon, P.; Pileni, M.P. In situ synthesis of silver nanocluster in AOT reverse micelles. *J. Phys. Chem.* **1993**, *97* (49), 12,974–12,983.
47. Motte, L.; Billoudet, F.; Pileni, M.P. Self-assembled monolayer of nanosized particles differing by their sizes. *J. Phys. Chem.* **1995**, *99* (44), 16,425–16,429.
48. Motte, L.; Lisiecki, I.; Pileni, M.P.; Bellisent, M.C.; Dore, J.C. Role of water molecules in the growth of nanosize particles in reverse micelles. In *Hydrogen Bond Networks*; Kluwer Academic Publishers, 1994; 447–454.
49. Duxin, N.; Brun, N.; Bonville, P.; Colliex, C.; Pileni, M.P. Nanosized Fe–Cu–B alloys and composites synthesized in diphasic systems. *J. Phys. Chem., B* **1997**, *101* (44), 8907–8913.
50. Ingert, D.; Pileni, M.P. Limitations in producing nanocrystals using reverse micelles as nanoreactors. *Adv. Funct. Mater.* **2001**, *11*, 136.
51. Pinna, N.; Weiss, K.; Urban, J.; Pileni, M.P. Triangular CdS nanocrystals: structural and optical studies. *Adv. Mater.* **2001**, *13*, 261–264.
52. Henglein, A.; Giersig, M. Reduction of Pt(II) by H<sub>2</sub>: effects of citrate and NaOH and reaction mechanism. *J. Phys. Chem., B* **2000**, *104* (29), 6767–6772.
53. Agnoli, F.; Zhou, W.L.; O'Connor, C.J. Synthesis of cubic antiferromagnetic KMnF<sub>3</sub> nanoparticles using reverse micelles and their self-assembly. *Adv. Mater.* **2001**, *13*, 1697–1699.
54. Li, M.; Schnablegger, H.; Mann, S. Coupled synthesis and self-assembly of nanoparticles to give structures with controlled organization. *Nature* **1999**, *402*, 393–395.
55. Hopwood, J.D.; Mann, S. Synthesis of barium sulfate nanoparticles and nanofilaments in reverse micelles and microemulsions. *Chem. Mater.* **1997**, *9* (8), 1819–1828.
56. Hammond, S.J.R.; Robinson, B.H. Formation and morphology of calcium sulfate nanoparticles and nanowires in water-in-oil microemulsions. *Langmuir* **1999**, *15* (6), 1993–2002.
57. Pileni, M.P. Mesostuctured fluids in oil-rich regions: structural and templating approaches. *Langmuir* **2001**, *17* (24), 7476–7486.
58. Lisiecki, I.; Sack-Kongehl, H.; Weiss, K.; Urban, J.; Pileni, M.P. Annealing process of anisotropic copper nanocrystals. *Langmuir* **2000**, *16* (23), 8802–8808.
59. Tanori, J.; Pileni, M.P. Control of the shape of copper metallic particles by using a colloidal system as template. *Langmuir* **1997**, *13* (4), 639–646.
60. Simmons, B.A.; Li, S.; John, V.T.; McPherson, G.L.; Bose, A.; Zhou, W.; He, J. Morphology of CdS nanocrystals synthesized in a mixed surfactant system. *Nano Lett.* **2000**, *2* (4), 263–268.
61. Lisiecki, I.; Filankembo, A.; Sack-Kongehl, H.; Weiss, K.; Pileni, M.-P.; Urban, J. Structural investigations of copper nanorods by high-resolution TEM. *Phys. Rev., B* **2000**, *61*, 4968–4974.
62. Pileni, M.P.; Tanori, J.; Filankembo, A.; Dedieu, J.D.; Gulik-Krzywicki, T. Template design of microreactors with colloidal assemblies: control the growth of copper metal rods. *Langmuir* **1998**, *14* (26), 7359–7363.
63. Filankembo, A.; Giorgio, S.; Lisiecki, I.; Pileni, M.P. Is the anion major parameter in the shape control of nanocrystal? *J. Phys. Chem., B* **2003**, *107*, 7492–7500.
64. Filankembo, A.; Pileni, M.P. Is the template of self-colloidal assemblies the only factor that controls nanocrystal shapes? *J. Phys. Chem., B* **2000**, *104* (25), 5865–5868.
65. Esumi, K.; Matsuhisa, K.; Torigoe, K. Preparation of rodlike gold particles by UV irradiation using cationic micelles as a template. *Langmuir* **1995**, *11* (9), 3285–3287.
66. Jana, N.R.; Gearheart, L.; Murphy, C.J. Wet chemical synthesis of silver nanorods and nanowires of controllable aspect ratio. *Chem. Commun.* **2001**, (7), 617–618.
67. Jana, N.R.; Gearheart, L.; Murphy, C.J. Wet chemical synthesis of high aspect ratio cylindrical gold nanorods. *J. Phys. Chem., B* **2001**, *105* (19), 4065–4067.
68. Chen, C.-C.; Lin, J.-J. Controlled growth of cubic cadmium sulfide nanoparticles using patterned self-assembled monolayers as a template. *Adv. Mater.* **2001**, *13*, 136–139.
69. Maillard, M.; Giorgio, S.; Pileni, M.P. Silver nanodisks. *Adv. Mater.* **2002**, *14*, 1084.
70. Courty, A.; Lisiecki, I.; Pileni, M.P. TE vibration of self-organized silver nanocrystals. *J. Chem. Phys.* **2002**, *116*, 8074–8078.
71. Maillard, M.; Giorgio, S.; Pileni, M.P. Tuning the size of silver nanodisc with similar aspect ratio: synthesis and optical properties. *J. Phys. Chem., B* **2003**, *107*, 2466–2469.
72. Wang, S.; Yang, S. Preparation and characterization of oriented PbS crystalline nanorods in polymer films. *Langmuir* **2002**, *16* (2), 389–397.
73. Manna, L.; Scher, E.C.; Alivisatos, A.P. Synthesis of soluble and processable rod-, arrow-, teardrop-, and tetrapod-shaped CdSe nanocrystals. *J. Am. Chem. Soc.* **2000**, *122* (51), 12,700–12,706.
74. Puntès, V.F.; Krishnan, K.M.; Alivisatos, A.P. Colloidal nanocrystal shape and size control: the case of cobalt. *Science* **2001**, *291* (5511), 2115–2117.
75. Li, Y.; Ding, Y.; Wang, Z. A novel chemical route to ZnTe semiconductor nanorods. *Adv. Mater.* **1999**, *11*, 847–850.
76. Li, Y.; Liao, H.; Ding, Y.; Fan, Y.; Zhang, Y.; Qian, Y. Solvothermal elemental direct reaction to CdE (E = S, Se, Te) semiconductor nanorod. *Inorg. Chem.* **1999**, *38* (7), 1382–1387.



77. Berkowitz, A.E.; Lahut, J.A.; Jacobs, I.S.; Levinson, L.M.; Forester, D.W. Spin pinning at ferrite-organic interfaces. *Phys. Rev. Lett.* **1975**, *34*, 594–597.
78. Gangopadhyay, S.; Hadjipanayis, G.C.; Sorensen, C.M.; Klabunde, K.J. Effect of particle size and surface chemistry on the interactions among fine metallic particles. *IEEE Trans. Magn.* **1993**, *29*, 2619–2621.
79. Moumen, N.; Bonville, P.; Pileni, M.P. Control of the size of cobalt ferrite magnetic fluids: Mössbauer spectroscopy. *J. Phys. Chem.* **1996**, *100* (34), 14,410–14,416.
80. Feltin, N.; Pileni, M.P. New technique for synthesizing iron ferrite magnetic nanosized particles. *Langmuir* **1997**, *13* (15), 3927–3933.
81. Ngo, A.T.; Bonville, P.; Pileni, M.P. Nanoparticles of  $\text{Co}_x\text{Fe}_{1-x}\text{O}_4$ : Syntheses and properties. *Eur. Phys. J., B* **1999**, *9*, 583–592.
82. Hochepped, J.F.; Bonville, P.; Pileni, M.P. Nonstoichiometric zinc ferrite nanocrystals: syntheses and unusual magnetic properties. *J. Phys. Chem., B* **2000**, *104* (5), 905–912.
83. Hochepped, J.F.; Pileni, M.P. Magnetic properties of mixed cobalt-zinc ferrite nanoparticles. *J. Appl. Phys.* **2000**, *87* (5), 2472–2478.
84. Ngo, A.T.; Bonville, P.; Pileni, M.P. Spin canting and size effects in nanoparticles of nonstoichiometric cobalt ferrite. *J. Appl. Phys.* **2001**, *89* (6), 3370–3376.
85. Jolivet, J.P.; Massart, R.; Fruchart, J.M. Synthèse et étude physicochimique de colloïdes magnetiques non surfactes en milieux aqueux. *Nouv. J. Chim.* **1983**, *7*, 325–331.
86. Rosensweig, R.E.; Kaiser, R.; Miskolczy, G. Viscosity of magnetic fluid in a magnetic field. *J. Colloid Interface Sci.* **1969**, *29*, 680–686.
87. Khalafalla, S.E.; Reimers, G.W. Preparation of dilution-stable aqueous magnetic fluids. *IEEE Trans. Magn. Magn.* **1980**, *16*, 178–183.
88. Sato, T.; Kuroda, C.; Saito, M.; Sugihara, M. *Ferrites: Proceeding of the International Conference*; Hoshino, Y., Ida, S., Sugimoto, M., Eds.; University of Tokyo Press: Tokyo, Japan, 1971; 72 pp.
89. Nakatsuka, K.; Jeyadevan, B. Initial susceptibilities of magnetic fluids dispersing Mn-Zn ferrite and cobalt ferrite particles. *IEEE Trans. Magn. Magn.* **1994**, *16*, 4671–4673.
90. Vandenberghe, R.E.; Vanleerberghe, R.; De Grave, E.; Robbrecht, G. Preparation and magnetic properties of ultra-fine cobalt ferrites. *J. Magn. Magn. Mater.* **1980**, *15*, 1117–1118.
91. Davies, K.J.; Wells, S.; Charles, S.W. The effect of temperature and oleate adsorption on the growth of maghemite particles. *J. Magn. Magn. Mater.* **1993**, *122*, 24–28.
92. Charles, S.W.; Davies, K.J.; Wells, S.; Upadhyay, R.V.; O'Grady, K.; El Hilo, M.; Meaz, T.; Morup, S. The observation of multi-axial anisotropy in ultrafine cobalt ferrite particles used in magnetic fluids. *J. Magn. Magn. Mater.* **1995**, *149*, 14–18.
93. Jolivet, J.P.; Belleville, P.; Tronc, E.; Livage, J. Influence of Fe (II) on the formation of the spines iron oxide in alkaline medium. *Clays Clay Miner.* **1992**, *40*, 531–539.
94. Matijevic, E. Preparation and properties of uniform size colloids. *Chem. Mater.* **1993**, *5* (4), 412–426.
95. Sugimoto, T.; Matijevic, E. Formation of uniform spherical magnetite particles by crystallization from ferrous hydroxide gels. *Colloid Interface Sci.* **1980**, *74*, 227–243.
96. Domingo, C.; Rodriguez-Cemente, R. The pathways to spinel iron oxides by oxidation of iron (II) in basic media. *Mater. Res. Bull.* **1991**, *26*, 47–55.

# Nanocrystalline Magnesia and Alumina: Surface Chemistry

Richard M. Narske

Department of Chemistry, Augustana College, Rock Island, Illinois, U.S.A.

## INTRODUCTION

In recent years the study of the nanocrystalline MgO and Al<sub>2</sub>O<sub>3</sub> has increased because of the potential importance of these methods as catalysts and adsorbents. This research has ranged from preparation of these ultrafine powders with surface areas on the order of 500 to 600 m<sup>2</sup>/g for MgO and 600 to 700 m<sup>2</sup>/g for Al<sub>2</sub>O<sub>3</sub> to the chemistry occurring on the surface of these unique particles. Most of the work on nanocrystalline MgO and Al<sub>2</sub>O<sub>3</sub> has centered on the adsorption and reactions of gases or easily vaporized liquids at elevated temperatures or under high vacuum with very little focusing on the reactions at room temperature with neat liquids or solutions. Very little has been reported on the surface reactions of these particles in slurries with the organic substrate dissolved in the solvent. The purpose of this paper is to introduce recent developments of solvent effects on the surface chemistry of nanoparticle MgO and Al<sub>2</sub>O<sub>3</sub> with organic substrates.

The adsorption and reactions of some organic substrates on aerogel prepared (AP)-MgO and nanocrystalline (NC)-Al<sub>2</sub>O<sub>3</sub> have been reported as vapor reactions, reactions of the neat liquid substrate, and reactions in solvents ranging from pentane to methanol.<sup>[1-6]</sup> These reactions yielded elimination and substitution products. Reactions in pentane showed a greater degree of reactivity on both the AP-MgO and NC-Al<sub>2</sub>O<sub>3</sub> surfaces than reactions involving neat organic substrates. More polar solvents, such as tetrahydrofuran (THF) and methanol, gave results quite different than the hydrocarbon solvent. These studies have also shown that reactivity of AP-MgO and NC-Al<sub>2</sub>O<sub>3</sub> is greater than the reactivity of the bulk materials and is due to more than the surface areas of these nanocrystalline materials.

## SURFACE CHEMISTRY OF MgO NANOPARTICLES

The preparation of nanocrystalline MgO can be accomplished through different methods. Each method produces nanocrystalline MgO. For example, two

methods reported by Ito et al.<sup>[7]</sup> and Stark et al.<sup>[8]</sup> give different size particles of MgO. One method gives particles that have an average size range of 7–15 nm and an average surface area of 250 m<sup>2</sup>/g. These particles, prepared by the conventional preparation (CP), are called CP-MgO particles. In the second method reported by Stark et al.,<sup>[8]</sup> the particles are aerogel prepared, and these particles are 4–7 nm in size and have an average surface area of 500–600 m<sup>2</sup>/g. These nanocrystals of MgO are called CP-MgO or AP-MgO, respectively.

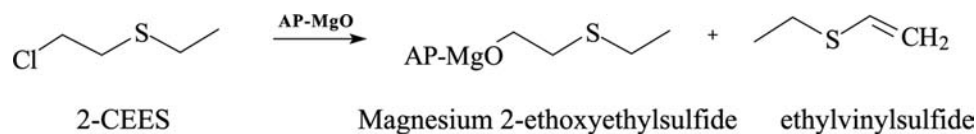
The surface morphology and surface chemistry of these different nanocrystals vary greatly from that of the bulk MgO. Figures 1 and 2<sup>[7-10]</sup> show these differences in the nanocrystal surfaces.

The irregularity of the AP-MgO nanocrystalline surface exposes more edges and corners for reactions to occur than for the CP-MgO nanocrystals. It is believed that many of the –OHs, which make up approximately 30% of the surface of AP-MgO, are exposed on these edges and readily available for reactions. The importance of these –OH groups will be discussed later.

Wagner et al.<sup>[1,2]</sup> reported in 1999 that nanocrystalline metal oxides, such as MgO and CaO, were very effective in decontaminating chemical warfare agents (CWA), such as VX, GD, and HD as well as a CWA mimic, 2-chloroethyl ethyl sulfide (2-CEES). This study was at room temperature using the pure liquid substrate introduced on a column of nanocrystalline oxide. Wagner et al. found that products formed in these reactions over a period of several days. The *t*<sub>1/2</sub> for the reaction of HD on AP-MgO, for example, was 17.8 hr and the kinetic data were still being taken after 1 week into the reaction. 2-Chloroethyl ethyl sulfide was not studied on AP-MgO but was studied on AP-CaO<sup>[2]</sup> (Scheme 1).<sup>[1]</sup>

These reactions were limited by the physical distribution of the agent passing through the column of oxide similar to a mobile phase moving through a column of adsorbent in column chromatography.<sup>[1]</sup> As these compounds studied were very viscous with viscosities of 3.098 cs or greater and surface tensions of 24.5 dynes/cm or greater, the process of moving





Scheme 2

Narske, Klabunde, and Fultz<sup>[4]</sup> also showed the importance of surface  $-\text{OH}$  groups on these reactive sites. These  $-\text{OH}$  groups make up about 30% of the surface of the reactive surface on these particles.<sup>[7]</sup> They showed that the reaction was occurring at the non-H-bonded  $-\text{OH}$  groups on the surface of the AP-MgO by studying what happens to the rate of the reaction when these  $-\text{OH}$  groups are enhanced or hindered. Enhancement was seen by the addition of small amounts of water to the reaction mixture. Small amounts of water were found to increase the reaction rate (Fig. 5).<sup>[4]</sup> To determine what was occurring on these  $-\text{OH}$  groups on the surface, diffuse reflectance FT-IR was utilized to study the surface changes of the AP-MgO. Diffuse reflectance FTIR spectroscopy indicated small amounts of water (below  $10\ \mu\text{L}$ ). This water addition changed the surface of AP-MgO by increasing the non-H-bonded  $-\text{OH}$  groups. Thus the reaction rate increased. As water addition increased (above  $10\ \mu\text{L}$ ), the  $-\text{OH}$  groups became increasingly H-bonded and the rate of decomposition of 2-CEES decreased. Eventually, a monolayer of water covers the surface of the particles and the reaction rate was

slowed to almost zero (see Figs. 6 and 7 for diffuse reflectance FT-IR spectra of the surface of AP-MgO).<sup>[4]</sup> These results indicated that the probable mechanisms needed to explain the reaction products were Sn2 (ethoxyethylsulfide)- and E2 (ethylvinyl sulfide)-type mechanisms involving the  $-\text{OH}$  groups (Scheme 3).

To further indicate the importance of the  $-\text{OH}$  groups in these reactions, capping studies with methoxy trimethylsilane were used. By reacting as many available  $-\text{OH}$  sites with methoxy trimethylsilane, the  $-\text{OH}$  groups would not be available for the reaction. The results of these studies indicated the reaction rate slowed significantly. Rates of 60% of the substrate reacted over 4 hr were observed when the  $-\text{OH}$  groups were available. These rates were reduced to 3–5% of the substrate reacted over the same period of time when the  $-\text{OH}$  groups were not available for the reaction. Thus indicating the importance of free, non-H-bonded  $-\text{OH}$  groups in order for these surface reactions to occur with the 2-CEES substrate in solvents such as pentane<sup>[4]</sup> (see Scheme 4 for the capped  $-\text{OH}$  groups on AP-MgO).

It was also noted in reactions when water was added that the rate of formation of the ethylvinyl sulfide occurred at a slower rate and had lower yield than the alkoxy compound. Scheme 3 shows that there are

**Table 1** Surface area of different AP-MgO preparation batches

Batch <sup>a</sup>	Surface area (m <sup>2</sup> /g)
2	380
3	487
4	581
5	417
6	188
7	336
9	457
10	423
12	499
13	352
14	309
15	642
18	242
CM	77.0
CP	270

<sup>a</sup>Batches 2–18 are all AP-MgO prepared on different days. CM is commercially available MgO and CP is conventionally prepared MgO.

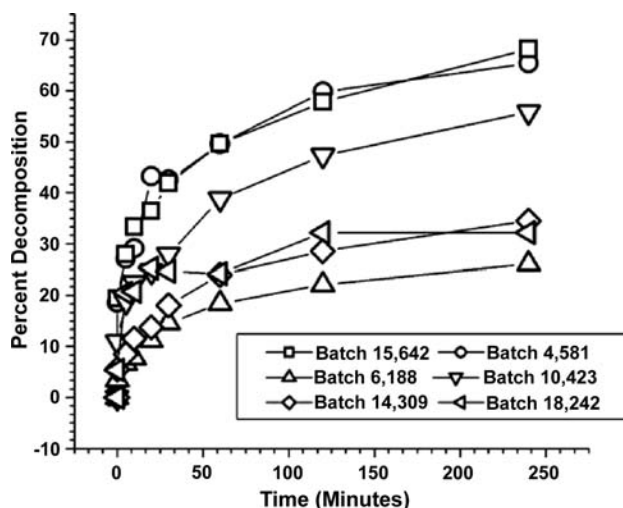


**Fig. 3** Reactions of AP-MgO in pentane: a series of AP-MgO batches of varying surface areas and their heterogeneous reaction with 2-CEES.

**Table 2** Comparison of the rate of consumption of 2-CEES for some representative batches of AP-MgO in molecules/nm<sup>2</sup> min over the first 30 min of the reaction

Time (min)	B4, 581 <sup>a</sup>	B6, 188	B12, 499	B15, 642	CM, 77 <sup>b</sup>	CP, 220 <sup>c</sup>
0.1	-1.7	-0.86	-1.7	-1.6	0	0
5	-0.049	-0.038	-0.048	-0.044	-0.009	-0.026
10	-0.027	-0.021	-0.026	-0.026	-0.0047	-0.015
20	-0.020	-0.016	-0.016	-0.015	-0.0024	-0.0094
30	-0.013	-0.013	-0.012	-0.012	-0.0014	-0.0053

<sup>a</sup>B4, 581 refers to batch 4, surface area = 581 m<sup>2</sup>/g.

<sup>b</sup>Commercially available MgO, surface area = 77 m<sup>2</sup>/g.

<sup>c</sup>Conventionally available MgO, surface area = 220 m<sup>2</sup>/g.

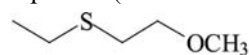
two reaction mechanisms competing on the surface of the AP-MgO, Sn2 and E2. The vinyl compound is being formed by an E2-type mechanism and the alkoxy compound is being formed by a Sn2-type mechanism. The addition of water may make the -OH groups less basic and more nucleophilic, thus slowing the E2-type mechanism.

The alkoxy compound, however, was not able to be isolated during the reaction studies. This compound was found bonded tightly to the surface oxygen on the AP-MgO similar to the results reported by Wagner et al.<sup>[1]</sup> in their work with HD (mustard gas). Diffuse reflectance FT-IR spectroscopy was used to determine that it was present on the surface, as Mawhinney et al. reported in their work with Al<sub>2</sub>O<sub>3</sub><sup>[5]</sup> (Fig. 8).<sup>[4]</sup>

Reactions in more polar solvents, such as THF and methanol, gave much different results than reactions in pentane. The only product observed in the surface reactions of AP-MgO in THF was the vinyl compound. These reaction results indicated that the THF complexes with the surface of the AP-MgO (Scheme 5) and blocks the magnesium sites where the complexation

of the -S- from the 2-CEES substrate occurs. The complexing of THF on the surface of the AP-MgO would not allow the 2-CEES to physi-adsorb on the surface of the AP-MgO and therefore hinders the Sn2 mechanism. Tetrahydrofuran complexation such as this is similar to ethers and thioethers complexing with magnesium in other organomagnesium reactions.<sup>[11]</sup> The THF blocking these sites hinders the Sn2 reaction which forms the alkoxy compound as the mechanism in Scheme 5 shows. The basic -OH groups are now only available for the E2 reaction, which gives the vinyl compound.

Reactions in methanol also gave only one product, the methoxy compound (Structure 1).



**2-methoxyethylethylsulfide**

The methanol is believed to be complexed with the oxygens on the surface of the AP-MgO, thus allowing the methanol groups to act as nucleophiles. A substitution reaction occurs as shown in Scheme 6. Once the methoxy compound is formed it moves from the surface of the MgO and does not bond to the surface of the MgO as the alkoxy product in pentane. This

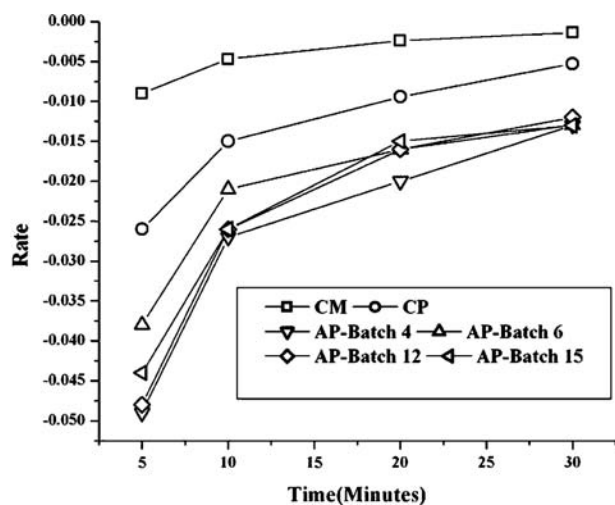


**Fig. 4** Comparison of initial reaction rates for different batches of MgO (rate = molecules/nm<sup>2</sup> min).

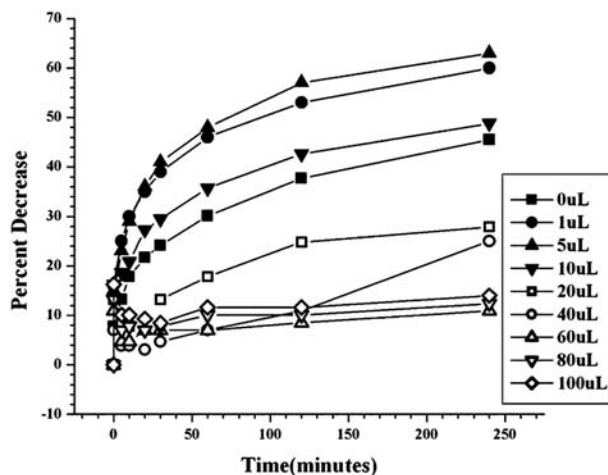


**Fig. 5** Reactions in pentane with water added.



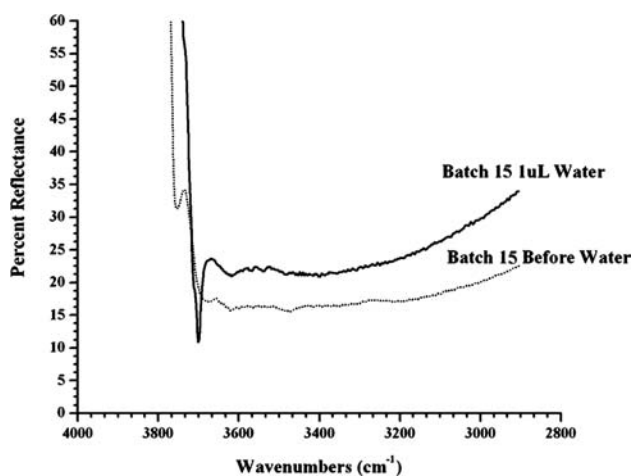


Fig. 6 Diffuse reflectance FT-IR of surface of AP-MgO before and after water was added.

made the product easily analyzed and identified by GC and GC/MS.<sup>[4]</sup>

For surface reactions of AP-MgO, the presence of non-H-bonded –OH groups, the shape or morphology of the crystallite, the surface area and the presence of sites where the molecules become adsorbed on the surface of the crystallite, as well as the distribution of the substrate over the surface are all important for these reactions to occur at a reasonable rate.

## SURFACE CHEMISTRY OF ALUMINUM OXIDE NANOPARTICLES

Because of its importance as a catalyst, the surface chemistry of aluminum oxide,  $\text{Al}_2\text{O}_3$ , has been extensively studied over the years.<sup>[5,6,13–16]</sup> In many of these studies, bulk (non-nanocrystalline)  $\text{Al}_2\text{O}_3$  has been studied.<sup>[13–16]</sup> More recent work has been done on the surface chemistry of nanocrystalline (NC)- $\text{Al}_2\text{O}_3$ .<sup>[5,6,11–17]</sup> Carnes<sup>[17]</sup> has reported a method similar to the preparation of AP-MgO for the preparation of NC- $\text{Al}_2\text{O}_3$ . This again involves aerogel preparation as it did with AP-MgO.<sup>[17]</sup> These nanocrystals typically have surface areas in the range of 700–800  $\text{m}^2/\text{g}$ . The crystallites are on the order of 2–4 nm in size, making them slightly smaller than the AP-MgO crystallites.

The morphology of the surface of NC- $\text{Al}_2\text{O}_3$  is not as well defined as that of AP-MgO. The surface of the NC- $\text{Al}_2\text{O}_3$  seems to be somewhat more amorphous. The crystallites do not seem to form the types of polyhedrons found in AP-MgO, and high resolution TEM studies have not given us much in the way of crystallite structure or surface morphology as it has for AP-MgO. The reactive surfaces, however, are still there, and it has been found that the surface chemistry is slightly

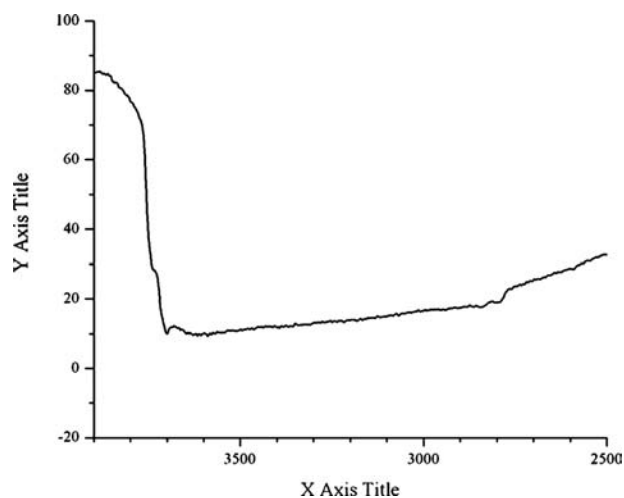
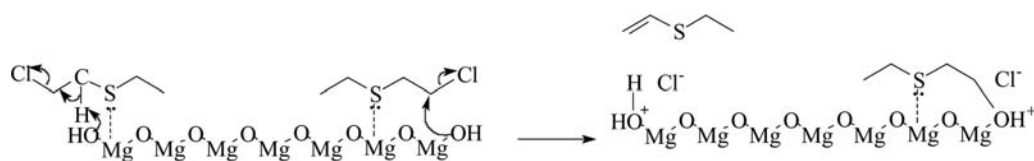


Fig. 7 Diffuse reflectance FT-IR of AP-MgO surface before water was added and before degassing.

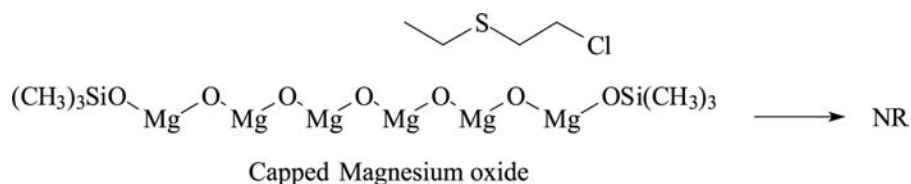
different than that of AP-MgO.<sup>[5,6]</sup> AP-MgO has a basic surface during the initial stages for reactions and changes to an acidic surface as the reaction proceeds toward completion. Fennelonov et al.<sup>[18]</sup> noted this in their work with reactions involving AP-MgO and chlorobutane to form butenes. It was found that the surface changed to  $\text{MgCl}_2$  and thus became acidic. The surface of NC- $\text{Al}_2\text{O}_3$  has –OH groups as well as Lewis acid sites and Lewis base sites. Mawhinney et al.<sup>[5]</sup> found that both were important in the reaction of NC- $\text{Al}_2\text{O}_3$  with 2-CEES in vapor phase surface reactions. They proposed two possible mechanisms for the removal of the chlorogroup in these reactions (Schemes 7 and 8).

Yates found that the optimum reaction conditions were observed when the NC- $\text{Al}_2\text{O}_3$  samples were formed at temperatures of 400–500°C (673–773 K) under vacuum. This activation gave the optimum ratio of unassociated –OH groups on the surface of the oxide. Samples that were activated at these temperatures gave optimum conversion of 2-CEES at reaction temperatures of 70°C to 200°C (303 to 473 K). Samples activated at lower or higher temperatures did not react as well as these. According to Mawhinney et al.,<sup>[5]</sup> the reaction in Scheme 7 is dominant when there are more –OH groups on the surface (activated at lower temperatures), whereas the reaction in Scheme 8 is dominant when the surface has been highly dehydroxylated (activated at higher temperatures). The reactions of Scheme 7 were referred to as hydrolysis reactions and the reactions in Scheme 8 as nucleophilic substitution reactions. To determine the importance of the acid–base pairs of Al–O and the unassociated –OH groups, the surface was reacted with pyridine. The pyridine bonded to the acid–base pairs and not to the –OH groups, therefore hindering the “substitution reaction” of Scheme 8.





Scheme 3



Scheme 4

The reactions at these sites were found to be reduced by 40% while the reaction at the  $-OH$  groups dropped only by 10%. This study showed that both the acid-base pairs and the  $-OH$  were important in this reaction.

Reactions conducted and reported by Martin, Narske, and Klabunde<sup>[19]</sup> in various solvents found results similar to those observed with AP-MgO that were reported by Narske, Klabunde, and Fultz<sup>[4]</sup> and by Mawhinney et al.<sup>[5]</sup> These reactions of NC- $Al_2O_3$  with 2-CEES were studied in pentane, THF, and 3 M HFE-7100<sup>[19]</sup> (methyl perfluorobutyl ether; Structure 2). They found that reactions run in pentane gave the best results. This is similar to what was reported earlier in a previous work done on AP-MgO.<sup>[4]</sup> It was also found that NC- $Al_2O_3$  reacted at a faster rate than did AP-MgO under similar conditions. All reactions studied were with NC- $Al_2O_3$  made in their laboratories and 2-CEES was decomposed completely within 24 hr (Fig. 9).<sup>[19]</sup> Samples from other sources and commercial  $Al_2O_3$  were found not to react as well as

their NC- $Al_2O_3$ . These other samples had smaller surface areas.



HFE-7100

(A methyl perfluorobutyl ether)

Reactions run in HFE-7100, methyl perfluorobutyl ether (Structure 2), preceded as well as reactions run in pentane (Fig. 10).<sup>[19]</sup> Reactions studied in THF showed the same problem that was observed with the MgO reactions reports by Narske, Klabunde, and Fultz<sup>[4]</sup> (Fig. 11).<sup>[19]</sup>

An interesting aspect of this study was the reactions reported with mixed oxide nanocrystals.<sup>[19]</sup> It was found that mixed NC- $Al_2O_3$ /MgO in ratios of 2:1, 1:1, and 1:2 showed reactivities similar to those reported for AP-MgO and NC- $Al_2O_3$  (Fig. 12).<sup>[19]</sup> They also found that the mixed oxides were more influenced by atmospheric water than the pure NC- $Al_2O_3$  samples. The mixed oxide samples were found to lose reactivity when allowed to set on the shelf in sample bottles for a period of time. This is similar to what was found with pure AP-MgO.<sup>[4]</sup> After these samples were heated to 200°C under high vacuum, the reactivity returned. Again these results were similar to what was observed for AP-MgO.

Like the reactions of AP-MgO and the results reported by Mawhinney et al.<sup>[5]</sup> for  $Al_2O_3$ , no ethyl hydroxyethyl sulfide was observed during the reactions. Study of the residual oxides after the reaction with diffuse reflectance FT-IR indicated that the alcohol was bonded to the surface of the  $Al_2O_3$  as the alkoxide (Fig. 13).<sup>[19]</sup> Unlike the reaction of AP-MgO, however, no ethylvinyl sulfide was observed in any of the reactions involving pure NC- $Al_2O_3$ . Some of this compound was observed in reactions involving the

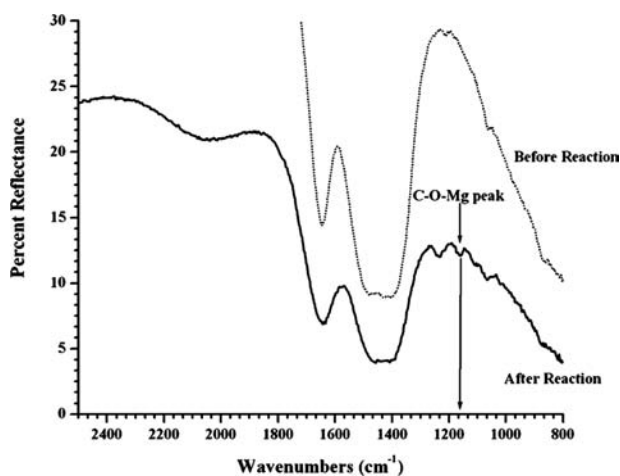
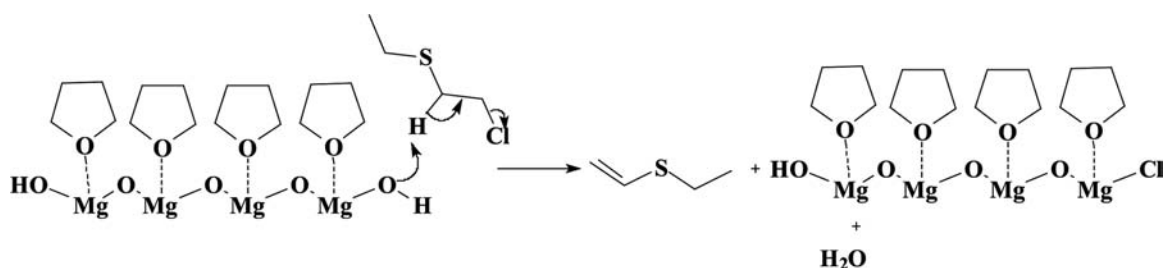
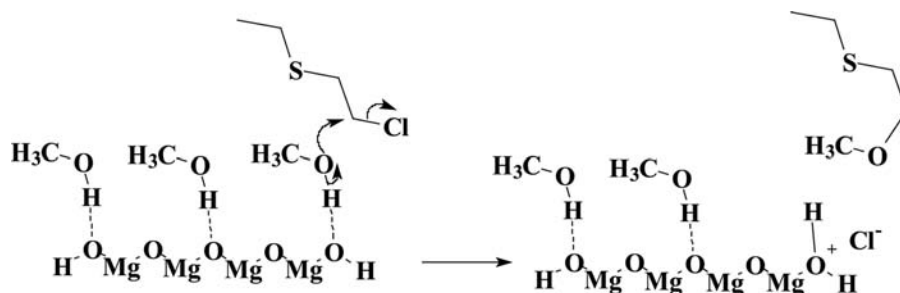


Fig. 8 Diffuse reflectance FT-IR before and after reaction showing the Mg-O- $CH_2$  bonding.



Scheme 5

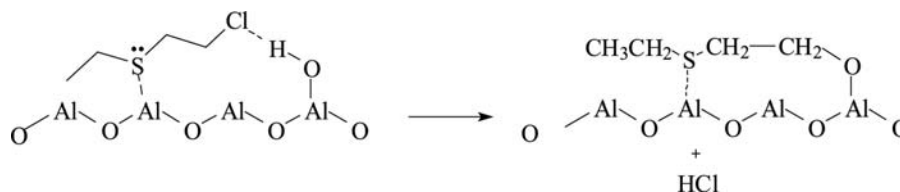


Scheme 6

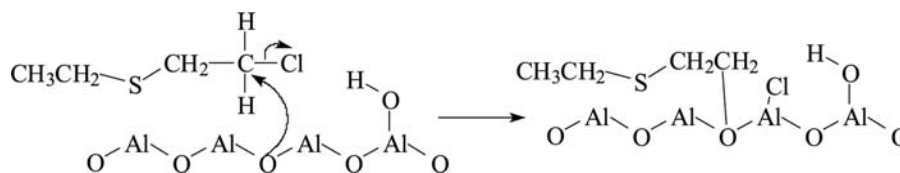
mixed oxides of aluminum/magnesium, but the amounts were barely detectable by GC analysis. Only about 3% of the total conversion product was observed as the vinyl product. This is an indication of a different type of surface on the NC- $\text{Al}_2\text{O}_3$ . The surface of the AP-MgO is a basic surface, thus leading to Sn2/E2-type mechanisms. The surface of the NC- $\text{Al}_2\text{O}_3$  is not as basic as AP-MgO, but it is slightly acidic in nature. The surface of NC- $\text{Al}_2\text{O}_3$  is therefore not conducive to basic attack on the hydrogens of 2-CEES carbons. This type of attack is needed in the E2-type mechanism. Although Mawhinney et al.<sup>[5]</sup> discuss the possibility

of nucleophilic attack by the  $-\text{O}-$  of the Al-O-Al surface, the  $-\text{O}-$  is not basic enough to abstract hydrogen from the carbon to produce the elimination product via an E2-type mechanism. It is, however, nucleophilic enough to substitute for the chloride through a Sn2-type mechanism.

Martin et al.<sup>[19]</sup> agree with the conclusion reported by Mawhinney et al.<sup>[5]</sup> that the probable mechanism on the surface of NC- $\text{Al}_2\text{O}_3$  is twofold. Studies of reactions using only NC- $\text{Al}(\text{OH})_3$  have shown that the decomposition reaction with 2-CEES proceeded at a slightly slower initial rate than the reactions with the



Scheme 7



Scheme 8

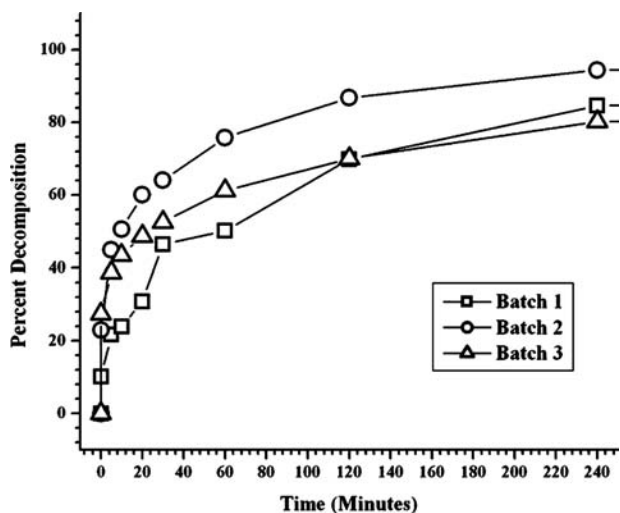


Fig. 9 Comparison of NC-Al<sub>2</sub>O<sub>3</sub> batches 1, 2, and 3 with 2-CEES in pentane.

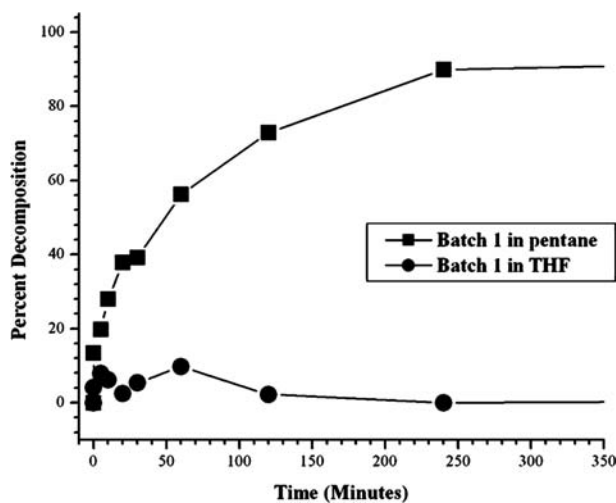


Fig. 11 Comparison of NC-Al<sub>2</sub>O<sub>3</sub> batch 1 in THF and pentane.

NC-Al<sub>2</sub>O<sub>3</sub> (Fig. 14)<sup>[19]</sup> but had decomposed 100% of the 2-CEES within 24 hr. This would seem to indicate that the surface reaction at the -OH is as effective as the reaction at the Al-O-Al surface. Further work is in progress to help confirm this phenomenon and to study this reaction with no available -OH groups. These studies will either confirm or not confirm the presence of two mechanistic pathways on the samples during this reaction.

**CONCLUSION**

The surface chemistry of nanocrystalline AP-MgO and NC-Al<sub>2</sub>O<sub>3</sub> appears similar in nature. Both surfaces

react very rapidly under very mild conditions over similar periods of time in these reactions with 2-CEES. Although NC-Al<sub>2</sub>O<sub>3</sub> does appear to be more reactive than AP-MgO as these reactions are complete within 24 hr, which is not the case for AP-MgO. The differences in reactivity between these two compounds are probably due to differences in crystal size, shape, surface area, and morphology as well as differences in surface acid/base properties. AP-MgO is a basic surface, and NC-Al<sub>2</sub>O<sub>3</sub> is more amphoteric in nature but definitely not basic. As the reaction proceeds on AP-MgO the -OH groups react and the surface changes from basic to acidic<sup>[18]</sup> as the -OH groups are replaced by -Cl groups, thus changing the surface chemistry of the AP-MgO. For NC-Al<sub>2</sub>O<sub>3</sub>, there are two reactive

Nanocrystal - Nanocrystals

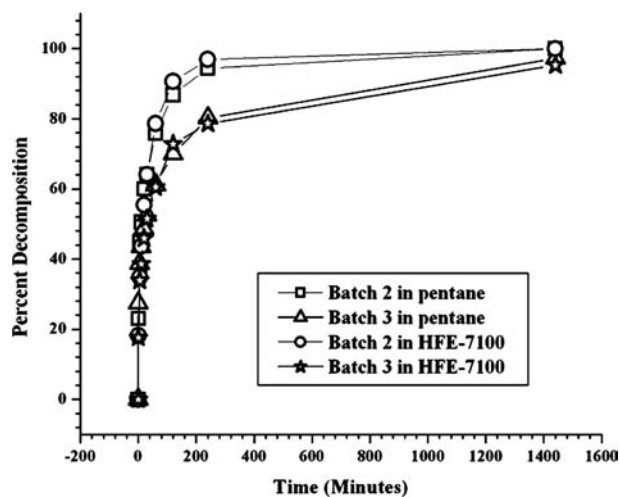


Fig. 10 Comparison of NC-Al<sub>2</sub>O<sub>3</sub> batches 2 and 3 in pentane and HFE-7100.

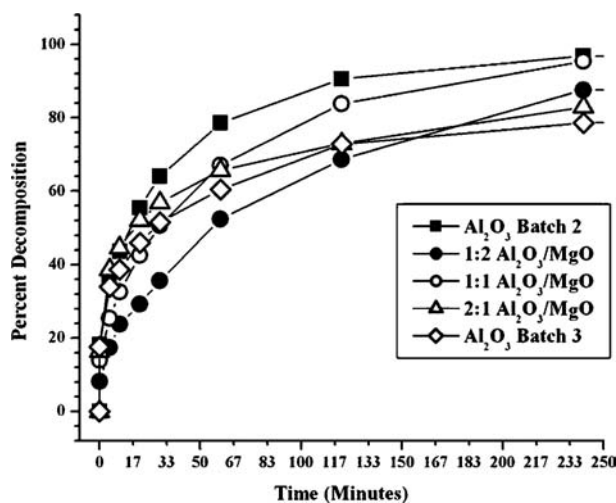


Fig. 12 Comparison of NC-Al<sub>2</sub>O<sub>3</sub> batches 2 and 3 with 1:2, 1:1, and 2:1 Al/Mg mixed oxides in pentane.

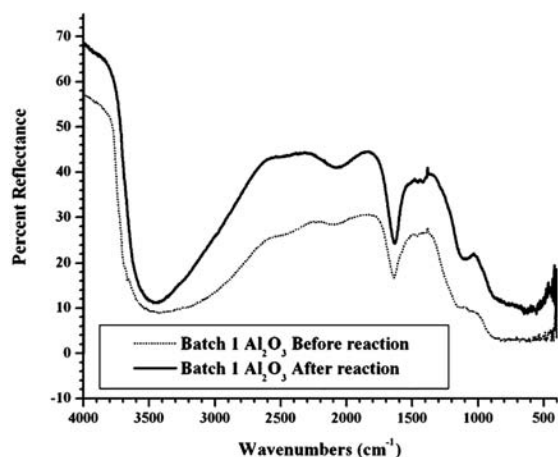


Fig. 13 Diffuse reflectance FT-IR of NC- $\text{Al}_2\text{O}_3$  before and after the reaction with 2-CEES in pentane.

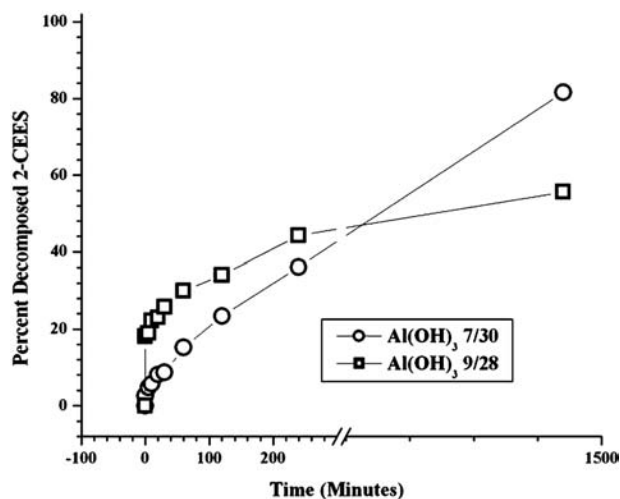


Fig. 14 Comparison of reactions of  $\text{Al}(\text{OH})_3$  with 2-CEES in pentane.

sites, the  $-\text{OH}$  and the  $-\text{O}-$ , on the surface rather than one for AP-MgO, and also the surface does not change as much during the reaction. These are perhaps the reasons why the reactions proceed more rapidly to completion than the AP-MgO. More work is in progress and has to be accomplished in this area in order to further understand these reactions.

## ACKNOWLEDGMENTS

Kansas State University and Dr. Kenneth Klabunde Professor, Kansas State University, for supporting my sabbatical year. ECBE Aberdeen Proving Grounds, Maryland: Phillip Bartram, George Wagner, John Wermaster. Department of Army: Stephen Lee, Augustana College, Rock Island, IL.

## REFERENCES

1. Wagner, G.W.; Bartram, P.W.; Lucas, E.; Decker, S.; Klabunde, K.J. Reactions of VX, GD, and HD with nanosize MgO. *J. Phys. Chem., B* **1999**, *103*, 3225–3228.
2. Wagner, G.W.; Koper, O.; Lucas, E.; Decker, S.; Klabunde, K.J. Reactions of VX, GD, and HD with nanosize CaO: Autocatalytic dehydrohalogenation of HD. *J. Phys. Chem., B* **2000**, *104*, 5118–5123.
3. Lucas, E.M. Studies of Nanocrystalline Magnesium Oxide by Adsorption of Molecular Probes and as a Destructive Adsorbent for Chemical Warfare Agent Mimics. Ph.D. Dissertation. Kansas State University, 2001.
4. Narske, R.M.; Klabunde, K.J.; Fultz, S. Solvent effects on the heterogeneous adsorption and reaction of (2-chloroethyl)ethyl sulfide. *Langmuir* **2002**, *18*, 4819–4825.
5. Mawhinney, D.B.; Rossin, J.A.; Gerhart, K.; Yates, J.T. Adsorption and reaction of 2-chloroethylethyl sulfide with  $\text{Al}_2\text{O}_3$  surfaces. *Langmuir* **1999**, *15*, 4789–4795.
6. Wagner, G.W.; Procell, L.R.; O'Connor, R.J.; Munavalli, S.; Carnes, C.; Kapoor, P.N.; Klabunde, K.J. Reactions of VX, GB, GD, and HD with nanosize  $\text{Al}_2\text{O}_3$ . Formation of aluminosulfonates. *J. Am. Chem. Soc.* **2001**, *123*, 1636–1644.
7. Itoh, H.; Utamapanya, S.; Stark, J.V.; Klabunde, K.J.; Schlup, J.R. Nanoscale metal oxide particles as chemical reagents. Intrinsic effects of particle size on hydroxyl content and on reactivity and acid/base properties of ultra fine magnesium oxide. *Chem. Mater.* **1993**, *5*, 71–77.
8. Stark, J.V.; Park, D.G.; Lagadic, I.; Klabunde, K.J. Nanoscale metal oxide particles/clusters as chemical reagents. Unique surface chemistry on magnesium oxide as shown by enhanced adsorption of acid gases (sulfur dioxide and carbon dioxide) and pressure dependence. *Chem. Mater.* **1996**, *8*, 1904–1912.
9. Klabunde, K.J.; Stark, J.V.; Koper, O.; Mohs, C.; Park, D.G.; Decker, S.; Jiang, Y.; Lagadic, I.; Zhang, D. Nanocrystals as stoichiometric reagents with unique surface chemistry. *J. Phys. Chem.* **1996**, *100*, 12,142–12,153.
10. Klabunde, K.J.; Mohs, C. *Nanoparticles and Nanostructural Materials, Chemistry of Advanced Materials: An Overview*; Interrante, L.V., Hampden-Smith, M.J., Eds.; Wiley-VCH, Inc.: New York, 1998; 271–327.
11. Smith, M.B. *Organic Synthesis*; McGraw-Hill, Inc.: New York, 1994; 686–687.
12. Lambert, J.B.; Shurvell, H.F.; Lightner, D.A.; Cooks, R.G. *Organic Structural Spectroscopy*; Prentice-Hall, Inc.: New Jersey, 1998; 223–226.
13. Tanabe, K. *Solid Acid and Base Catalysts*; Catalysis—Science and Technology; Anderson, J.R., Boudart, M., Eds.; Springer-Verlag: New York, 1981; Vol. 2, 231 pp.

14. Knozinger, H. Specific poisoning and characterization of catalytically active oxide surfaces. *Adv. Catal.* **1976**, *25*, 184.
15. Boehm, H.P.; Knozinger, H. *Nature and Estimation of Functional Groups on Solid Surfaces*; Catalysis—Science and Technology; Anderson, J.R., Boudart, M., Eds.; Springer-Verlag: New York, 1983; 4, 39.
16. Knozinger, H.; Ratnasamy, P. Catalytic aluminas: surface models and characterization of surface sites. *Catal. Rev. Sci. Eng.* **1978**, *17*, 31.
17. Carnes, C. The Chemical and Catalytic Properties of Nanocrystalline Metal Oxides Prepared Through Modified Sol–Gel Synthesis. Ph.D. Dissertation. Kansas State University, 2000.
18. Fennelonov, V.B.; Mel'gunov, M.S.; Mishakov, I.V.; Richards, R.M.; Chesnokov, V.V.; Volodin, A.M.; Klabunde, K.J. Changes in texture and catalytic activity of nanocrystalline MgO during its transformation to MgCl<sub>2</sub> in the reaction with 1-chlorobutane. *J. Phys. Chem., B* **2001**, *105*, 3937–3941.
19. Martin, M.; Narske, R.M.; Klabunde, K.J. Chemistry of Nanocrystalline Metal Oxides. Solvent Effects on the Adsorption and Reaction of 2-Chloroethylethyl Sulfide on AP-Aluminum Oxide and Bimetallic Nanocrystalline Aluminum Oxide/Magnesium Oxide; Abstracts of Papers, 36th Midwest Regional Meeting of the American Chemical Society, Lincoln, NE, Oct. 10–12, 2001; American Chemical Society: Washington, DC, 2001; ORGCHM 182.

# Nanocrystalline Materials: Fatigue

**Alexie Yu. Vinogradov**

*Department of Intelligent Materials Engineering, Osaka City University, Osaka, Japan*

**Sean R. Agnew**

*Department of Materials Science and Engineering, University of Virginia, Charlottesville, Virginia, U.S.A.*

## INTRODUCTION

The processes of damage accumulation and the resulting fracture of materials under cyclic loading at stress levels below the tensile strength are collectively referred to as *fatigue*. These phenomena are quite sensitive to materials structure, including crystal structure grain size, character and distribution of grain boundaries, dislocation density and arrangement, internal stress, texture, surface quality, etc. Additional complexity is introduced by a wide variability of testing and service conditions, including environments. Various factors can be of greater or lesser importance for different aspects of fatigue. However, grain size can be regarded as a key structural factor affecting nearly all aspects of fatigue. This is not surprising because the grain is the elementary structural unit of polycrystalline solids. Furthermore, grain size is known to strongly affect all known mechanisms of inelastic deformation, particularly dislocation slip and deformation twinning. Notably, without plastic deformation mechanisms leading to damage accumulation, there would be no fatigue.

The advent of nanocrystalline materials after the early work by Gleiter<sup>[1]</sup> opened new horizons for the discovery and design of new materials with unusual properties, as well as opportunities for scientific investigation of potentially novel mechanisms heretofore unobserved in classical materials systems. The purpose of the present entry is to review the state-of-the-art within both of these contexts, as investigations of the fatigue behavior of nanocrystalline (NC) materials have been motivated by the possibility that NC materials will have enhanced fatigue resistance, as compared to their coarse-grained counterparts, as well as basic a desire to understand the fundamental mechanisms of deformation and fracture in nanoscale.

Before discussing the fatigue behavior of NC materials, it is useful to briefly outline why the properties, in general, and fatigue response, in particular, of NC materials are considered unique.

1. Nanomaterials are at the “interface” between amorphous and ordinary crystalline solids. Some authors (such as Gleiter)<sup>[1]</sup> have entertained the notion that their structure might be considered a two-phase composite consisting of small perfect crystalline regions of nano-dimensions surrounded by relatively thick glassy-like grain boundaries (Fig. 1). Hence NC materials may inherit some properties from both crystals and glasses, while potentially remaining distinct from both of these extremes.
2. The number of atoms associated with grain boundaries can approach the number of atoms within the grain interior. Another way of stating this is that the volume fraction of grain boundaries can become as large as 50%. Thus the grain boundaries and their specific structure and properties will play a very important role in most, if not all, properties of NC materials.
3. Finally, a grain size of the order 100 nm corresponds to the structural level obtained within severely deformed metals. Specifically, the defects accommodating plastic deformation (dislocations) self-assemble into the collective structures with a characteristic length-scale in tens of nanometers.

A variety of techniques have been developed in the past decade for manufacturing nanomaterials (see Ref.<sup>[2]</sup> for a review). Among these, some of the more important are inert gas condensation, electrodeposition, devitrification from an amorphous precursor obtained by rapid solidification or ball milling, and severe plastic deformation (SPD) (see entry on “Nanocrystalline Substances: Synthesis and Properties”). The present entry emphasizes the latter approach because severe plastic deformation for grain reduction has the advantage of producing of fully dense, bulk ultra-fine grain (UFG) and NC materials with desired purity or target composition. In other words, SPD allows one to produce material suitable for investigation of fatigue behavior using classical testing methods and possessing



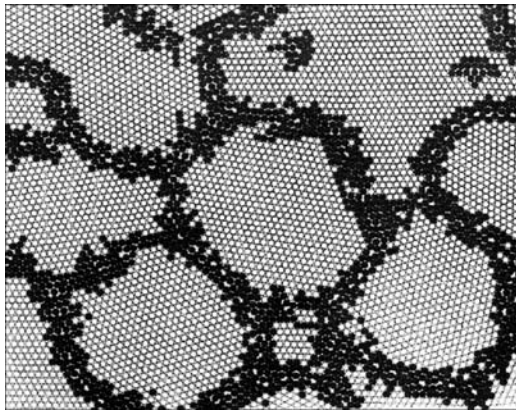


**Fig. 1** Schematic presentation of the atomic structure of nano-materials: two-phase composite structure of crystalline grains and disordered glassy-like grain boundaries. *Source:* From Ref.<sup>[1]</sup>.

dimensions large enough for structural applications, where fatigue properties are of interest. Among SPD techniques, the equal channel-angular pressing (ECAP) technology introduced by Segal<sup>[3]</sup> as a cold (or warm) working technique allows extremely large strains to be imposed on bulk samples without fracture. The technique has proven to be capable of fabricating massive samples with a variety of UFG and nanostructures. As the majority of experimental results concerning fatigue of nanocrystals have been obtained on ECAP materials so far, the present review will primarily be concerned with these materials.

ECAP is performed by passing a billet through two intersecting channels of the same cross section. Severe plastic deformation occurs by simple shear on the plane of intersection between the channels. Because the cross-section geometry does not change during processing, ECA pressing can be repeatedly performed through various routes determined by possible rotations of the billet between subsequent passes. With repeated pressing, the material hardens dramatically so that unusually high strengths can be achieved. Ideally, the resultant strain imposed per ECA pass is controlled by the included angle between channels  $2\theta$  solely (given sharp die channel corners), and the cumulative shear strain  $\Gamma$  after  $N$  passes is  $\Gamma = 2N \cot \theta$ . The effective strain is given by  $\varepsilon_i = 2N \cot \theta / \sqrt{3}$ .<sup>[3]</sup> Thus when the tool angle  $2\theta = 90^\circ$ ,  $\Gamma = 2N$  and the amount of the imposed strain can be substantially higher than is usually attained in standard cold-working procedures, such as rolling.<sup>[3]</sup>

## BACKGROUND

### Fatigue Life Characterization

Total fatigue life of smooth bodies has been conventionally divided into two regions corresponding to

the time required for crack nucleation and propagation.<sup>[4,5]</sup> The resistance to crack initiation naturally requires strength, while the tolerance to the crack advance requires ductility. The most promising feature of SPD materials, which suggests the possibility of obtaining significantly enhanced fatigue properties, is associated with a combination of high strength and good ductility in the nanostructured state.<sup>[2,6,7]</sup> Low-cycle fatigue (LCF) and high-cycle fatigue (HCF) regimes are conventionally distinguished in accord with applied strain amplitude. HCF testing corresponds to probing a material's resistance to crack initiation, whereas LCF testing corresponds to assessing the material's defect tolerance. Combining these two regimes, it is convenient to consider the total strain range  $\Delta\varepsilon_t$  consisting of two components—elastic  $\Delta\varepsilon_{el}$  and plastic  $\Delta\varepsilon_{pl}$ . The empiric Coffin–Manson relationship relates the total fatigue life (number of cycles to failure  $N_f$ ) to  $\Delta\varepsilon_{pl}/2$  as

$$\frac{\Delta\varepsilon_{pl}}{2} = \varepsilon_f'(2N_f)^c \quad (1)$$

where  $\varepsilon_f'$  is the fatigue ductility coefficient (which is often found to be approximately equal to the true fracture ductility  $\varepsilon_f$  in monotonic testing<sup>[4,5]</sup>) and  $c$  is the fatigue ductility exponent. Similarly,  $\Delta\varepsilon_{el}/2$  is related to the number of reversals to failure according to the Basquin law as

$$\frac{\Delta\varepsilon_{el}}{2} = \frac{\sigma_f'}{E}(2N_f)^b \quad (2)$$

where  $E$  is the Young's modulus,  $\sigma_f'$  is the fatigue strength (which is supposed to be related to the yield stress or the ultimate tensile strength of the material), and  $b$  is the Basquin exponent. Hence the fatigue life under a given total strain is expressed in terms of materials constants  $\varepsilon_f'$ ,  $\sigma_f'$ ,  $c$ , and  $b$

$$\frac{\Delta\varepsilon_t}{2} = \frac{\sigma_f'}{E}(2N_f)^b + \varepsilon_f'(2N_f)^c \quad (3)$$

Although a simple equivalence of the pair  $\varepsilon_f'$  and  $\sigma_f'$  to the tensile ductility and  $\sigma_{UTS}$ , respectively, is rarely observed in experiments, the correlation between these pairs of qualities often exists. Eq. (3) is schematically illustrated in Fig. 2 for the fine-grain ECAP AlMgSc alloy. At high strains corresponding to short lives, the plastic strain component is dominant in the total applied strain and the fatigue life is primarily determined by ductility. At long fatigue lives, the elastic strain amplitude is more significant than plastic and fatigue life is dictated by the fracture strength so that the endurance limit increases with strength.<sup>[3,4,8]</sup> Unfortunately, in most cases, ductility is sacrificed as the highest strength levels are achieved. This rule holds

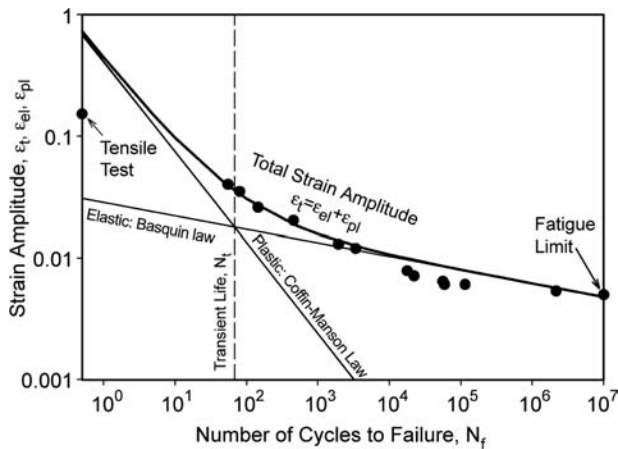


**Fig. 2** Strain-life diagram. Solid line corresponds to Eq. (3) with experimentally obtained parameters of Coffin–Manson and Basquin law for the ECAP Al–4.5Mg–0.2Sc–0.2Zr alloy. Experimental points for this alloy are also plotted.

for most high-strength nanomaterials as well, and those fabricated by inert gas condensation, devitrification from the glassy state, powder compaction, etc. are usually so brittle that their potential is limited. Similarly, the simultaneous enhancement of both HCF and LCF lives is challenging, and inevitably requires a balance between strength and ductility.<sup>[4,8]</sup> It has been shown<sup>[5,6,9]</sup> that nanomaterials manufactured by severe plastic deformation can, in principle, significantly benefit from spectacular improvement of both the strength and ductility.

For a comprehensive assessment of fatigue response, one also needs to evaluate the crack growth rate under a given stress intensity range  $\Delta K$  and loading cycle asymmetry  $R = \sigma_{\max}/\sigma_{\min}$ , where  $\sigma_{\max}$  and  $\sigma_{\min}$  are the maximum and minimum applied stress, respectively. This information is of primary concern for engineering. Furthermore, an in-depth analysis involves characterization of the stress–strain hysteresis loop. In the present review, we briefly address all these issues as they apply to NC materials.

### Effect of Grain Size on Fatigue

To describe the effect of grain size  $d$  on fatigue, it is necessary to specify how the grain size relates to the material's resistance to crack initiation and propagation, i.e., to quantify the effect of  $d$  on fatigue life parameters such as  $\epsilon'_f$ ,  $\sigma'_f$ ,  $c$ ,  $b$ , and the fatigue limit  $\sigma_f$ , defined as the peak cyclic stress below which no fatigue failure occurs prior to  $10^7$  or  $10^8$  cycles. The influence of grain size on the fatigue of conventional polycrystalline materials has been investigated and reviewed on many occasions (see, for example, Refs.<sup>[4,5,10–14]</sup>). Most observations can be summarized in two sentences.

1. The fatigue limit of pure face-centered cubic (f.c.c.) metals is not affected by the grain size.
2. The fatigue strength of materials exhibiting planar slip increases with decreasing grain size and follows the Hall–Petch relationship, shown below, in the same way as the yield stress in conventional polycrystals.

$$\sigma_f = \sigma_{of} + K_f d^{-1/2} \quad (4)$$

where  $\sigma_{of}$  and  $K_f$  empiric materials properties.

It has been concluded that one of the most important fundamental material characteristics governing fatigue is the slip character. During LCF, the wavy-slip materials form a well-defined cell structure, with the cell size being dependent upon the saturation stress and independent of the preliminary strain history.<sup>[4,5,10–12]</sup> Materials with a planar slip do not form a cell structure, and the dislocations are arranged in planar arrays extending across a grain. That grain size has a more pronounced effect on the fatigue behavior of planar slip materials has been convincingly demonstrated by Tomson and Backofen<sup>[11]</sup> by using pure copper (wavy slip) and  $\alpha$ -brass (planar slip). Mughrabi<sup>[14]</sup> suggested extending this standpoint to UFG metals as well.

Indeed, the fatigue limit  $\sigma_f$  of UFG wavy slip aluminum alloys is not improved after multiple ECA pressing despite a remarkable enhancement of their monotonic strength, as will be discussed in more detail below. Results on commercial purity copper vary notably from modest to high  $\sigma_f$  improvement, depending, possibly, on fabrication (number of ECA passes, strain path, etc.). However, the independence of the grain size in coarse-grain wavy slip f.c.c. metals appears to be related to a specific cell structure formed during cycling. Because the typical grain/cell size in the SPD metals of 100–300 nm is smaller than the typical fatigue cell size in coarse-grained metals ( $\sim 500$  nm), exceptions to the classical rules may be anticipated.

A small grain size can result in more homogeneous deformation, which can retard crack nucleation by reducing stress concentrations and ultimately raise the fatigue limit of the material. It has been reported<sup>[15]</sup> that the fatigue limit follows the Hall–Petch relationship with decreasing grain size in the same way as the ultimate tensile strength  $\sigma_{UTS}$  until critical grain size is attained, below which the slope of the  $\sigma - d^{-1/2}$  curve is decreased. Consider NC copper with a grain size  $d = 20$  nm,  $\mu = 45$  GPa, and  $b = 2.5 \times 10^{-10}$  m. An estimate of the stress required for dislocation multiplication (where the source length is assumed to be one-half the grain size,  $d$ )  $\tau \geq 2\mu b/d = 12$  GPa, which is approximately equal to the theoretical strength  $\sigma_{\text{theor}} = E/10$ , where  $E$  is the

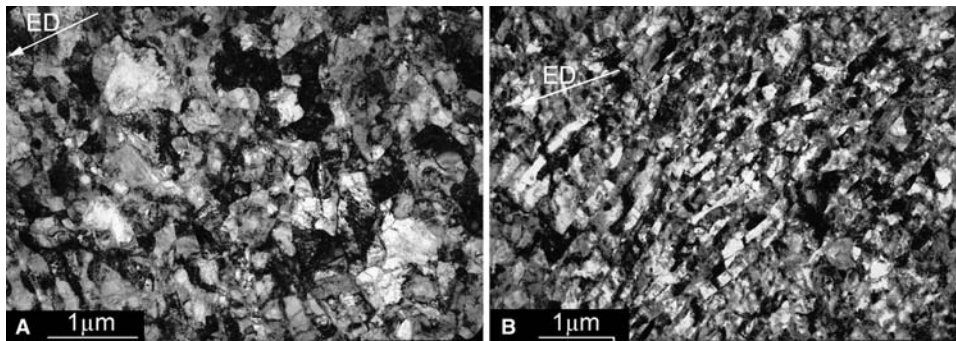


**Fig. 3** Bright-field TEM images illustrating the equiaxed (A) and elongated (B) UFG structures after ECAP (Fe–36Ni Invar alloy after 8 and 12 ECA passes, respectively). Arrows indicate the extrusion direction.

Young's modulus of the material ( $E = 120$  GPa for copper). In other words, dislocation activity within nanocrystalline grains is expected to be extremely difficult, which explains their frequently observed brittleness. On the other hand, there have been suggestions that the plasticity of NC materials may be associated with mechanisms other than perfect dislocation motion. Hence there may be an optimum grain size in the nanoscale region, where the maximum monotonic and cyclic strength is reached. Because the volume fraction of grain boundaries is comparable with the volume of grains, for very small grain sizes, there have been numerous suggestions that the deformation might localize within an amorphous grain boundary region, depicted in Fig. 1. Youngdahl et al.<sup>[17]</sup> concluded that the deformation of nanocrystalline copper with a mean grain size between 30 and 100 nm produced by gas condensation and compaction occurs as a result of dislocation activity. No evidence for grain boundary sliding or rotation was found in their in situ transmission electron microscopy (TEM) experiments.

Experimental results concerning the cyclic behavior are currently available for various UFG SPD metals such as: 1) pure Cu<sup>[18–28]</sup> and Ni<sup>[29]</sup>—the most studied representative wavy-slip materials; 2) single-phase solid solutions—AA5056 Al–Mg alloy<sup>[30,31]</sup> and Fe–36Ni (Invar) alloy,<sup>[32,33]</sup> 3) Ti,<sup>[34,35]</sup> which is a typical example of hexagonal close-packed (h.c.p.) metals exhibiting planar-slip; 4) precipitation hardenable CuCrZr alloy,<sup>[36]</sup> 6061 Al–Mg alloy,<sup>[37]</sup> Al–Mg–Sc alloys,<sup>[38]</sup> and low-carbon steel.<sup>[39]</sup> Brief reviews of the fatigue life of ECAP metals have been reported.<sup>[16,33]</sup> Details of preparation and ECA processing are in the above-cited publications.

## STRUCTURE OF ECAP METALS

Before reviewing the cyclic behavior of UFG materials, it is useful to first observe the microstructure prior to

and after fatigue. A typical UFG structure after ECAP is shown in Fig. 3A. Let us briefly summarize the microstructural features of nanocrystalline materials fabricated by SPD, which are most relevant to fatigue. (See Ref.<sup>[2]</sup> for a comprehensive review.)

1. The average grain size ranges from 100 to 350 nm, depending on the particular metal or alloy. The grain size distribution is often broad, depending on the details of the processing. The largest grains in the grain size distribution can be as large as 1–5  $\mu\text{m}$  after SPD. It is emphasized that the grain boundaries are often hardly visible in TEM bright- or dark-field images.
2. Whether the grains are primarily separated by low- or high-angle boundaries remains an issue of some dispute. Some authors claim high-angle boundaries on the basis of qualitative indications of selected area electron diffraction patterns (SAEDP).<sup>[2]</sup> Others have performed more statistical studies using scanning electron microscopy (SEM)-based electron back scattering diffraction (EBSD), or a similar TEM-based Kikuchi pattern analysis.<sup>[40–42]</sup>
3. Two major structural types can be distinguished by the grain shape: a rather uniform structure with nearly equiaxed grains (Refs.<sup>[1,25]</sup> and references therein) (Fig. 3A), and a kind of fragmented structure with significantly elongated grains (Fig. 3B).
4. There is a great deal of stored energy in these systems associated with dislocations and their structures. Despite the very high average dislocation densities ( $10^{13}$ – $10^{15} \text{ m}^{-2}$ ) commonly observed in these materials by TEM,<sup>[2,43]</sup> it is noted that the interiors of the smaller grains appear to be free of dislocations. Thus it has been surmised that the dislocations may largely be incorporated within the boundaries themselves. These lattice strains associated with these defects are best characterized by using X-ray

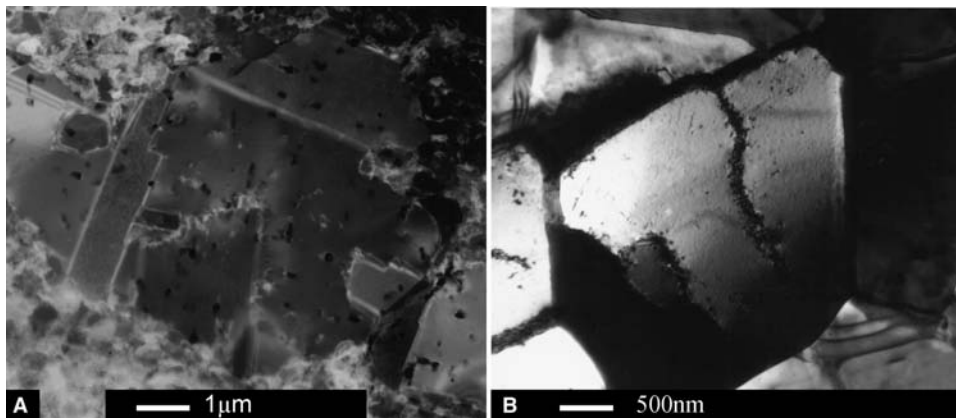


**Fig. 4** Abnormal grain growth in cyclically deformed ECAP copper ( $\Delta\epsilon_{pl}/2 = 5 \times 10^{-3}$ ) (A) and ladder-like dislocation walls formed in the enlarged grains in the course of fatigue (B).

diffraction techniques associated with the broadening of Bragg peaks,<sup>[29]</sup> and frequently identified as root mean squared (rms) strains in that analysis.

5. Because of the large stored energy, microstructural instability is often a hallmark of NC materials. After cyclic deformation, a variety of structural changes have been observed in ECAP metals.
6. The most striking feature of the postfatigue structure pure wavy slip SPD metals is the grain coarsening and abnormal grain growth triggered by cyclic deformation (Fig. 4A). This phenomenon has been noticed in many publications dealing with pure Cu and Ni.<sup>[20–25,29,41]</sup> Recovery, recrystallization, and grain growth can be largely suppressed by limiting the mobility of grain boundaries as well as controlling the ease of relaxation by dislocation climb or cross-glide. Solid solutions and h.c.p. metals are rather stable and no substantial grain growth is observed in the Invar alloy<sup>[24]</sup> (Fig. 5), and Ti after fatigue.<sup>[23]</sup> Grain coarsening in

the 5056 Al–Mg alloy depends on the processing and can be negligible.<sup>[7]</sup>

7. For some materials, the average dislocation density in the central part of the grains may remain unaltered, being of the order of  $10^{12}$ – $10^{15} \text{ m}^{-2}$ . However, the grain boundaries themselves appear more distinct after cycling in all materials examined (e.g., Fig. 5). This seems to be the only noticeable structural change in fatigued Ti, Al–Mg, Cu–0.44Cr–0.2Zr, and Invar alloys, and it may be associated with a reduction in the dislocation density in the immediate vicinity of the grain boundaries.
8. A decrease in the internal stresses during the course of fatigue has been carefully demonstrated by Thiele, Holsten, and Klemm<sup>[29]</sup> for UFG Ni, and by Wang et al.<sup>[25]</sup> for UFG Cu using the X-ray technique. Some of the changes observed by X-ray diffraction may be associated with grain coarsening as well. The evolution of the grain size distribution calculated from the X-ray peak broadening is shown in Fig. 6 for different stages of fatigue of ECAP Cu.

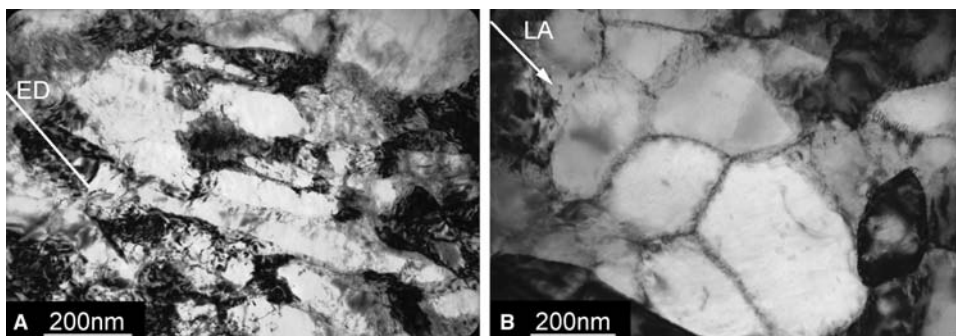


**Fig. 5** TEM photos showing the structure of ECAP Invar alloy (8 ECA pressings, compare Fig. 3A) after fatigue at  $\Delta\epsilon_{pl}/2 = 5 \times 10^{-3}$ . Low dislocation density is observed in some grains (B). Arrows indicate the loading axis that is aligned with extrusion direction.



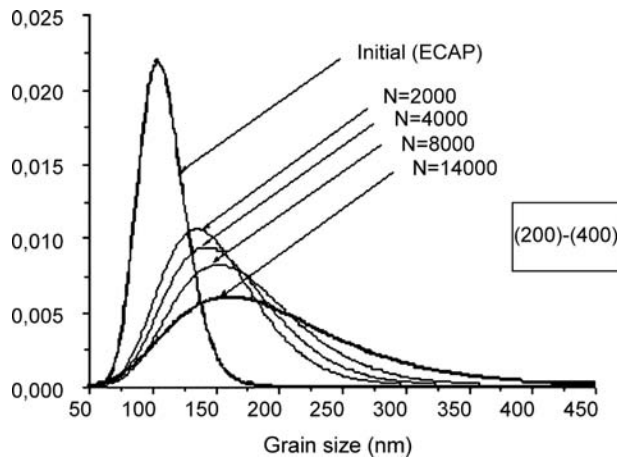


**Fig. 6** Evolution of the grain size distribution in UFG Cu subjected to cyclic deformation with  $\Delta\epsilon/2 = 5 \times 10^{-4}$ ;  $N$ —number of cycles. Source: From Ref.<sup>[25]</sup>.

### HIGH CYCLE FATIGUE BEHAVIOR

Tensile and HCF properties of a variety of ECAP materials are summarized in Table 1. The enhancement

of HCF life in terms of fatigue limit is achieved for most NC materials, as has been expected merely from the improvement of monotonic strength after grain refinement (“Introduction”). The scatter in experimental data obtained by different researchers on UFG Cu is caused by a variety of manufacturing conditions in different laboratories, resulting in a variety of actually imposed strain and resulting microstructures. (Examples of the Wöller plots for two types of ECAP Cu having the equiaxed and elongated grain structure similar to those shown in Fig. 3 are given in Fig. 7A.) As suggested in the section “Background,” a very pronounced improvement of the fatigue limit is observed in a planar slip material, ECAP Ti, processed at elevated temperature (400°C) and then subjected to further strengthening by cold-rolling to 75% area reduction and annealed for structural stabilization at 300°C for 1–2 hr<sup>[35]</sup>. The fatigue limit of 500 MPa in pure SPD titanium is close to that of conventional Ti alloys (Fig. 7B). The impressive improvement of the fatigue strength in the peak-aged ECAP Cu–0.44Cr–0.2Zr alloy<sup>[36]</sup> (Fig. 7A) is also worth noting in comparison with other commercial Cu-based alloys

**Table 1** Grain Size and mechanical properties of SPD alloys

Material	Processing	$\sigma_{0.2}$	(MPa)	$\sigma_{UTS}$ (MPa)	$\delta$ (%)	$\sigma_{f,0}$ (MPa)
Cu 99.96%	CR 75%, HT 550°C, 2 hr	35	140	240	46	65
Cu 99.96%[41]	ECAP, B 8	0.2 eq	390	440	22	80
Cu–0.44Cr–0.2Zr[36]	ECAP Bc, 8, A 500°C, 1 hr	0.16 eq	650	720	1	285
Ti VT1-0	CR	15	380	460	26	240
Ti VT1-0[35]	ECAP Bc, 8 400°C	0.3 eq	640	810	15	380
Ti VT1-0[34]	ECAP Bc, 8 400°C, CR 75%	0.15 el	970	1050	8	420
Fe–36Ni Invar[32]	CR 75%	N/A	275	490	40	137
Fe–36Ni Invar[32]	ECAP Bc 2,	0.30 eq	570	732	47	280
Fe–36Ni Invar[32]	ECAP Bc 8,	0.26 eq	690	790	35	290
Fe–36Ni Invar[32]	ECAP Bc 12,	0.18 el	835	912	52	330
5056 Al alloy	O-temper	25	122	290	43	116
5056 Al alloy	H18	—	407	434	10	152
5056 Al alloy[31]	ECAP C, 4, 150°C	0.35 el	280	340	25	116
5056 Al alloy[31]	ECAP Bc, 8, 110°C	0.22 el	392	442	7	116
6061 Al alloy	O-temper	40–80	150	270	48	40
6061 Al alloy	T6	—	276	310	12	50
6061 Al alloy[37]	ECAP, 1, 125°C	el	310	375	20	80
6061 Al alloy[37]	ECAP, Bc, 4, 125°C	0.4 eq	380	425	20	< 60
Al–4Mg–0.3Sc	Extruded	—	315	415	17	160
Al–1.5Mg–0.2Sc–Zr	ECAP, Bc, 8, 150°C	0.2–0.4	280	280	17	120
Al–3.0Mg–0.2Sc–Zr	ECAP, Bc, 6, 150°C	0.2–0.4	340	360	13	135
Al–4.5Mg–0.2Sc–Zr	ECAP, Bc, 6, 160°C	0.2–0.4	370	400	15	140

$d$  = initial grain size,  $\sigma_{0.2}$  = conventional yield stress,  $\sigma_{UTS}$  = ultimate tensile strength,  $\delta$  = elongation to failure in tension,  $\sigma_{f,0}$  = endurance limit based on  $10^7$  cycles.

CR = cold-rolling, Q = quenching, A = aging, HT = heat treatment; eq and el = equiaxed and elongated grain structure, respectively.

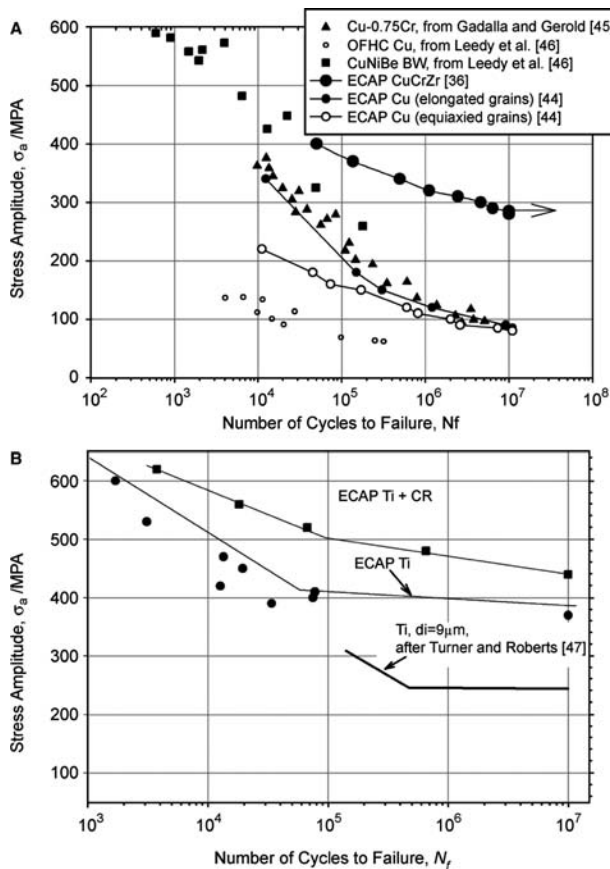


Fig. 7 S-N plots and fatigue limits of ECAP Cu and Cu-0.44Cr-0.2Zr alloy (A) and Ti (B).

and tempers. The combination of affordable electric conductivity, thermal conductivity, and thermal stability with high tensile and fatigue strength make this multifunctional material attractive for a variety of electromechanical applications. The experimental data reveal that the ultimate tensile strength and the fatigue limit of NC SPD metals follow the Hall-Petch relationship<sup>[4]</sup> (Fig. 8). Hence it is concluded that NC materials fabricated by SPD generally demonstrate a great potential for enhancement of high cycle fatigue life, in full agreement with the analysis given in the sections “Introduction” and “Background,” Eq. (6), and Fig. 2.

Markushev and Murashkin<sup>[48]</sup> have reviewed the effect of grain refinement via SPD on the mechanical properties of commercial Al alloys, and concluded that SPD, in general, is not very effective for strength or fatigue improvement of Al alloys. The results of Chung et al.<sup>[37]</sup> on solution treated 6061 Al alloy typify the finding that multiple ECAP does not significantly improve the fatigue limit of Al alloys; however, they demonstrated notable improvement of fatigue limit just after the first pass through the die (note that they did not employ a standard heat treatment for

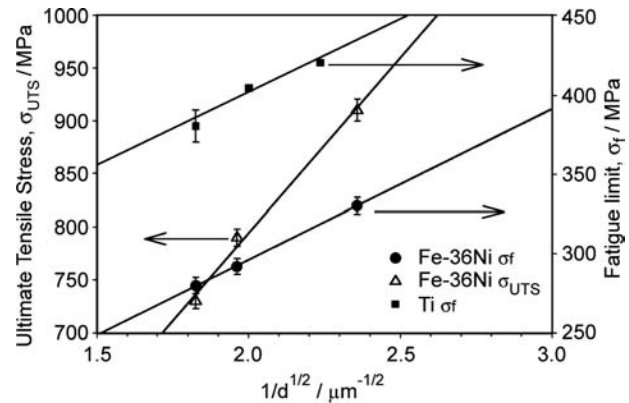


Fig. 8 Hall-Petch behavior of the ultimate tensile strength (for Fe-36Ni alloy) and fatigue limit (for Fe-36Ni and Ti) of ECAP metals.

precipitation hardening). Strengthening via grain refinement by SPD may be masked by other strengthening mechanisms on one hand and, on the other, the redistribution of phases and alloying elements can give rise to grain boundary brittleness and loss of ductility at room temperature. It is noted that grain refinement of Al alloys via SPD has proven extremely valuable for inducing superplasticity at elevated temperatures in a large number of alloy systems.<sup>[49,50]</sup>

## LOW CYCLE FATIGUE BEHAVIOR

At relatively large plastic strain ranges from 10<sup>-4</sup> to 10<sup>-2</sup> and short fatigue lives, the cyclic response of UFG materials is described by the Coffin-Manson law.<sup>[1]</sup> as illustrated in Fig. 9 for UFG Cu and 5056 Al-Mg alloy. Although the data in Fig. 9A are compiled from the results obtained by different researchers on differently processed samples, one can see a reasonable agreement between these results. Samples in the as-received state after ECAP demonstrate notable degradation in low cycle fatigue (LCF) life when compared to the ordinary coarse-grain samples. This is not surprising in view of their lower ductility and poor resistance to macroscopic and microscopic plastic instabilities such as necking, shear banding, cracking, etc. Such behavior is typical of metals with low levels of strain hardening (recall Considères criterion). As will be discussed in detail below, a postprocessing heat treatment can significantly improve the LCF properties. Remarkably, UFG Ti obtained by ECAP did not reveal a significant degradation in low-cyclic fatigue performance in the plastic strain controlled testing, and the Coffin-Manson lines were practically indistinguishable for the samples before and after ECAP<sup>[35]</sup> This result agrees with the general observation in the



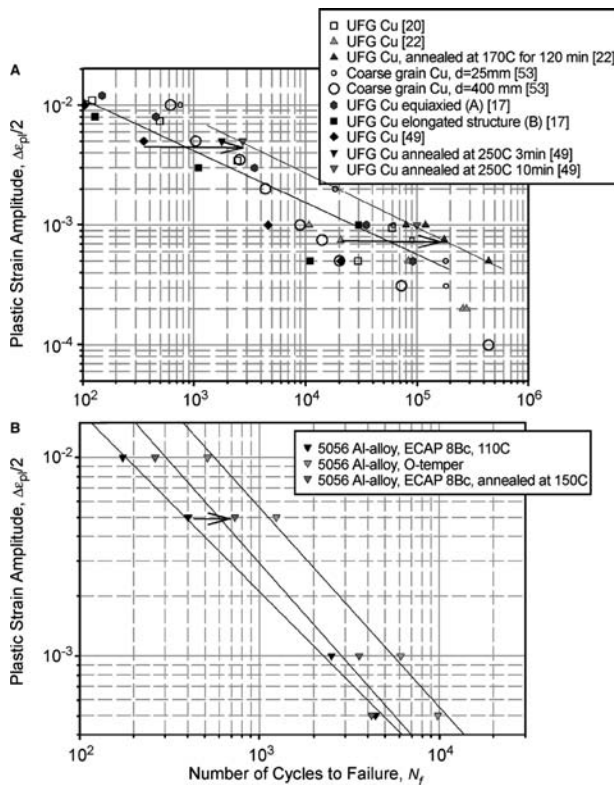


**Fig. 9** Coffin–Manson plots for ultrafine grain Cu (A) and 5056 Al–Mg alloy (B) obtained by SPD (reprinted with permission). Arrows indicate the improvement of fatigue life after post-ECAP heat treatment. *Source:* From Ref.<sup>[30]</sup>.

sections “Introduction” and “Background,” that non-f.c.c. metals can exhibit greater improvement in their fatigue performance if both LCF and HCF regimes is of major concern.

**Cyclic Softening and Hardening**

The cyclic stress–strain curves (CSSC) of NC materials can be represented by a power law in the same way as for other polycrystalline metals (see Refs.<sup>[4,5]</sup> and references therein).

$$\sigma_a = K'_b (\Delta \epsilon_{pl}/2)^{n'_b} \tag{5}$$

This relation is essentially the same as that used to describe the monotonic stress–stress curve

$$\sigma = K \epsilon^n \tag{6}$$

where  $K'_b$ ,  $n'_b$ ,  $K$ , and  $n$  are materials constants, and the subscript index  $b$  stands for the basic CSSC. Fig. 10 summarizes some currently available cyclic stress strain data for ECAP metals. It has been observed in a former communication<sup>[32]</sup> that the slopes of the CSSC in logarithmic scale for the same material

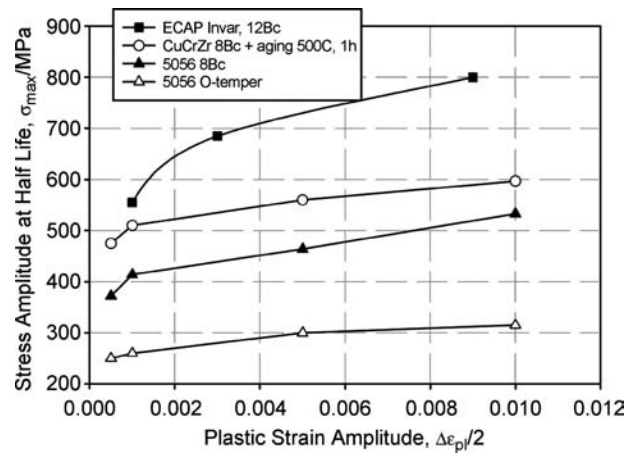


**Fig. 10** Basic cyclic stress–strain curves for several UFG ECAP metals.

(Fe–36 Ni Invar alloy) subjected to different number of ECA pressings between 2 and 12 are approximately the same, i.e., the cyclic strain hardening exponent  $n'_b$  values are nearly equal for all samples regardless of the preimposed strain. Fig. 11 compares the monotonic and CSSC for ECAP Fe–36 Ni Invar alloy (only the initial part of the tensile stress–strain curve is shown). The relative position of the monotonic and cyclic stress–strain curves delivers information on the materials cyclic hardening/softening behavior under different strain amplitudes. In the region of strain amplitudes where the CSSC lies above the monotonic strain–stress curve, the material cyclically hardens.<sup>[5]</sup> On the other hand, in the regions where the CSSC is positioned below the monotonic stress–strain curve, the material cyclically softens. Hence it becomes obvious that the ECAP materials are prone to cyclic softening at any imposed plastic strain amplitude.

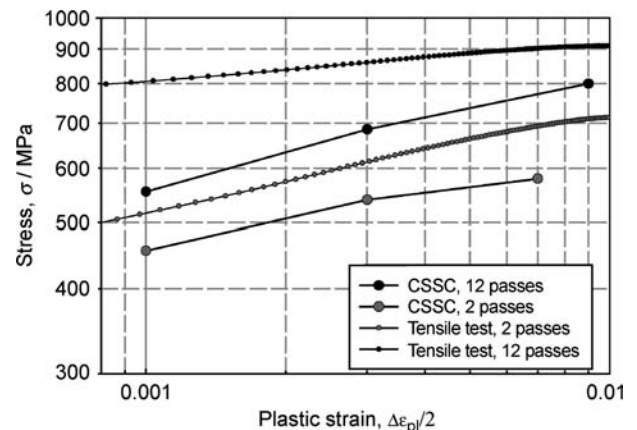


**Fig. 11** Fragments of tensile stress–strain curves and CSSC for ECAP Fe–36Ni Invar alloy after 2 and 12 ECA passes. *Source:* From Ref.<sup>[32]</sup>.

Nanocrystal – Nanocrystals

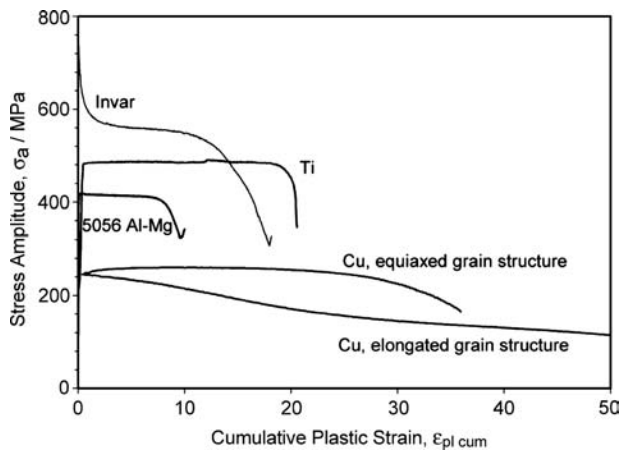


**Fig. 12** Cyclic hardening/softening curves of some selected SPD metals with UFG structures. *Source:* From Ref.<sup>[33]</sup>.

Softening is common for cyclic deformation of pre-strained f.c.c. metals.<sup>[4,5,51]</sup> It has been also clearly observed in many ECAP f.c.c. metals such as copper,<sup>[20–22,26]</sup> Ni,<sup>[29]</sup> single-phase Al–Mg 5056<sup>[30,31]</sup> and Fe–36Ni Invar alloys,<sup>[32]</sup> and precipitation-hardened Cu0.44Cr0.2Zr alloy.<sup>[36]</sup> However, the detailed characteristics of cyclic softening, its phenomenology, and microscopic mechanisms vary broadly depending on the material and processing. Fig. 12 shows the cyclic hardening–softening curves for various NC ECAP metals tested under plastic strain control. The very first investigations of LCF behavior of ECAP materials revealed that the cyclic response strongly depends on processing and the initial UFG structure. Vinogradov et al.<sup>[18]</sup> observed no cyclic softening in ECAP Cu under plastic strain amplitudes  $\Delta\epsilon_{pl}/2 = 5 \times 10^{-4}$  and  $10^{-3}$ . Furthermore, some light hardening was noticed on the early stage of straining (Fig. 12). However, Agnew and Weertman<sup>[20]</sup> observed pronounced cyclic softening in similar UFG Cu produced by ECAP. The degree of softening appears to depend on the temperature, time, and plastic strain amplitude, and can vary from material to material.<sup>[23]</sup> The mechanism of cyclic softening of UFG f.c.c. metal is largely associated with a complex effect of dislocation recovery, cyclically induced dynamic “recrystallization,” and grain coarsening, which is more pronounced at higher strain amplitudes.<sup>[17–21,23,25,27]</sup> Interestingly, cyclic softening and the associated coarsening facilitates the formation of dislocation structures typical for ordinary metals, i.e., cellular and ladder-like dislocation arrangements<sup>[20,23]</sup> (Fig. 4B). Thiele et al.<sup>[29]</sup> performed a detailed structural investigation of the fatigue-induced structures in UFG Ni and the dependence of the grain size. Using X-ray diffraction peak profile analysis, they detected a reduction of internal stresses in the course of cycling. It was demonstrated

that there is a lower threshold grain size  $d_{th}$  of 1  $\mu\text{m}$ , above which dislocation patterning takes place with a length scale ( $\sim 500$  nm) nearly independent of the initial grain size. For materials with  $d < d_{th}$ , the cyclic stress–strain curve obeys the Hall–Petch relation.

Not surprisingly, the SPD structure can be stabilized and the rate of cyclic softening can be reduced by: 1) annealing at an intermediate temperature, i.e., reducing the stored strain energy prior to cyclic loading;<sup>[19,22,26,30,33,44]</sup> 2) using solid solution alloys instead of pure metals;<sup>[31,32]</sup> and 3) precipitation.<sup>[36]</sup> The numerous large-scale shear bands, which are observed in the fatigued ECAP Fe–36Ni alloy, may contribute to the cyclic softening in that alloy. Höppel and Mughrabi,<sup>[55]</sup> using Vickers microhardness measurements, have convincingly shown that the material in the shear band of a cyclically deformed ECAP Cu sample is softer than its surroundings. The values are in line with the concept of cyclically induced dynamic recrystallization and grain growth.<sup>[22,23,26]</sup> Similar measurements have been performed by Vinogradov on the fatigued ECAP Fe–36Ni alloy. It has been demonstrated that the main reason for rapid cyclic softening of the UFG under- or peak-aged CuCrZr alloy (Fig. 12) is related to dislocation cutting of the fine strengthening precipitates.<sup>[36]</sup> The degree of softening is substantially lowered in overaged samples; however, the monotonic mechanical properties (strength and ductility) are degraded in this case.

## FATIGUE DAMAGE AND STRAIN LOCALIZATION

Internal stresses in metals increase during monotonic straining, finally leading to microvoid nucleation or crack initiation as the resources of plastic deformation exhaust in local volumes of the material. Thus it may come as a surprise to some readers that the cyclic deformation of UFG metals fabricated by SPD may reduce the level of internal stress (as indicated by X-ray diffraction measures of rms strains<sup>[29]</sup> and the general cyclic softening behavior referred to above), yet the end result is still a fatigue fracture. The answer, in its general form, is actually trivial: fracture occurs as a result of inhomogeneity in the plastic deformation manifesting itself as strain localization. The gradients of plastic deformation are often connected with grain boundaries, which may serve as barriers to dislocation motion as well as effective sources and sinks of lattice dislocations. These concepts are supported by atomic force microscopy (AFM) observations of fine traces of plastic deformation in UFG copper and nickel where: 1) dislocation activity is particularly visible at the grain boundaries,<sup>[16,33,52]</sup> and 2) dislocation slip is terminated at the grain boundary and is not transferred to an adjacent grain. TEM observations have

also demonstrated some reduction of the dislocation density near the grain boundary during fatigue (compare Fig. 5A and B, for example). Reducing the excess dislocation density around grain boundaries may explain the observed cyclic softening and the decrease of root mean square internal stress levels and, ironically, it may ultimately promote intergranular cracking. Fracture surface analysis and the surface crack morphology shows that failure in the SPD metals indeed occurs intergranularly.<sup>[16,32,35]</sup>

Strain localization in the ECA-processed materials is frequently observed during both monotonic and cyclic deformation.<sup>[10–15,44]</sup> Fig. 13 shows shear bands oriented at 45° to the loading axis in pure Cu after fatigue at  $\Delta\epsilon_{pl}/2 = 5 \times 10^{-3}$  and 5056 Al–Mg alloy after monotonic deformation. These bands commonly appear shortly after yielding in tensile deformation or at the end of saturation in cyclic testing. Fatigue cracks initiate and propagate along this kind of shear band (Fig. 13A).<sup>[25]</sup> Although shear banding is the major form of fatigue damage in wavy-slip UFG materials, these bands play a twofold role in fracture: on one hand, they promote crack nucleation due to strain localization and stress concentration; on the other hand, they reduce the overall elastic stresses, as evidenced by the reduction in stress at the end of saturation in strain controlled tests. Therefore it is unclear if suppression of the susceptibility to shear banding would delay or accelerate fatigue failure because cracking is a likely alternative mechanism for stress relaxation when other plastic mechanisms are exhausted. For instance, in UFG titanium or precipitation-hardened CuCrZr alloy, large-scale shear bands are not observed. However, a large population of surface microcracks is observed on the late stage of fatigue.

The microstructural nature of shear bands has been investigated in detail, at least for UFG Cu. Agnew et al.<sup>[21]</sup> observed that the shear bands in UFG copper appear like ordinary persistent slip bands (PSBs) in coarse-grain poly- and single crystals. For instance, the shear bands were removed by electropolishing, and then they reappeared on the same places during subsequent cyclic loading, indicating materials

softening associated with shear bands. Furthermore, careful structural observations have shown that the shear bands in UFG copper can have essentially the same ladder-like dislocation structure as the PSBs in ordinary crystals. The TEM image shown in Fig. 4B demonstrates the dislocation walls separated by dislocation-free channels in fatigued UFG copper. Höppel et al.<sup>[23]</sup> investigated the microstructural aspects of shear banding in UFG copper, including the dependence of strain amplitude and temperature, and have found that grain coarsening and shear banding are more pronounced at high strain amplitudes, which agrees with the observed faster cyclic softening. Thus pure f.c.c. UFG metals first exhibit relaxation and coarsening during cyclic softening, along with the formation of the low-energy configurations typical of conventional fatigued crystals, i.e., ordinary PSBs may occur. Finally, microcracks appear to initiate on intrusions and then behave similarly to those in conventional metals.

Although a similar scenario is applicable to those UFG metals exhibiting considerable grain coarsening during cycling,<sup>[16,21–23,29]</sup> conflicting observations have been reported by Vinogradov et al.<sup>[54]</sup> and Wu et al.,<sup>[27,28]</sup> who did not observe any gross structural coarsening in fatigued ECAP Cu. Furthermore, using TEM, SEM, and electron channeling contrast imaging (ECCI), it was shown that the dimensions of protrusions on the surface did not match the dimensions of the grains. In fact, numerous questions remain unanswered as to which elements govern the fatigue behavior in the complex UFG microstructure.

There are at least two kinds of plastic instabilities which manifest themselves in various NC metals under various testing conditions: 1) the PSB-like shear bands that appear during fatigue as a result of slow large-scale structural rearrangement involving grain coarsening as a prerequisite for ladder structure formation; and 2) the shear bands that arise both in monotonic and cyclic testing, and phenomenologically (if not structurally) resemble twinning events. Shear bands of the second kind are not crystallographic and are not microscopically straight (Fig. 14A). They emerge

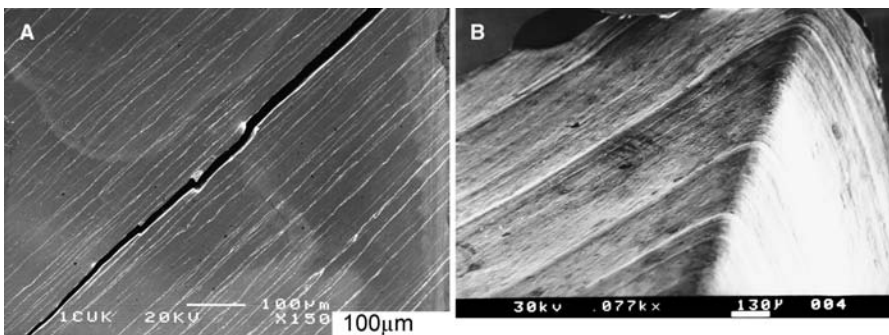


**Fig. 13** SEM micrographs showing the shear bands in fatigued ECAP Cu (A) and in the tensile tested ECAP 5056 Al–Mg alloy (B). Final crack propagating along the shear band is shown in (A).

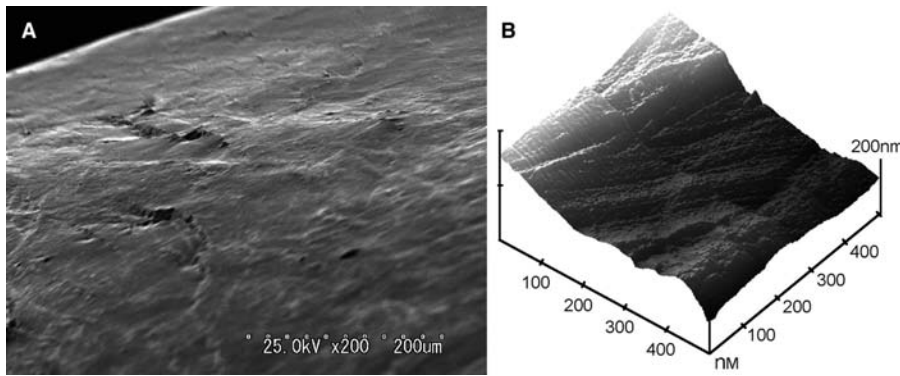


**Fig. 14** SEM image of the shear offset on the surface of fatigued Fe-36Ni ( $\Delta\epsilon_{pl}/2 = 3 \times 10^{-3}$ ) (A). AFM image illustrating the large-scale displacement of adjacent grains along the grain boundary in the shear direction (B). The dislocation slip in the grain interior is clearly visible.

very suddenly at free surfaces along grain boundaries in adiabatic fashion and are accompanied by significant acoustic emissions.<sup>[54,56]</sup> The possibility of grain boundary sliding at ambient temperature in UFG SPD materials has been speculated in the literature<sup>[2,43]</sup> in terms of enhanced diffusion and grain boundary mobility associated with heavily distorted grain boundaries. However, it is of particular importance to note the traces of dislocation slip of 1–10 nm height in the grain interior (Fig. 14B): that the slip lines are confined to a single grain, and the slip does not transfer through the boundary.<sup>[33]</sup> Thus the AFM observations<sup>[16,33,52]</sup> highlight the fact that conventional intragranular dislocation activity cannot be neglected as the most important mechanism of plastic deformation of UFG metals.

Shear bands in NCs may emerge to a free surface in a way similar to the shear bands commonly observed in metallic glasses during inhomogeneous plastic flow,<sup>[57]</sup> which is also accompanied by intensive acoustic emission,<sup>[58]</sup> and the morphology of shear bands in metallic glasses is very similar to that in NCs; however, this similarity may be completely coincidental because the concept of thick amorphous boundaries has not been justified by direct structural observations, particularly for metals fabricated by SPD. Wu et al.<sup>[25,27]</sup> and Vinogradov et al.<sup>[54]</sup> have found that the shear bands tend to align themselves with the plane of simple shear on the last ECA pressing, i.e., these bands are sensitive to the structure and its inhomogeneities formed during the last pass through the die. This leads to a conclusion that the careful control over processing (strain path, temperature, velocity, etc.) may allow control of the material's resistance to shear banding. Indeed, the nanostructure with equiaxed grains is less susceptible to rapid adiabatic shear banding than the structure with the grains (cells, fragments, etc.) elongated in the direction of last shear. Furthermore, UFG copper manufactured using different die sets (with round and rectangular corner) and different processing routes (but the same number of ECA passes and nearly the same grain size) exhibited different

shear banding susceptibility: the softer UFG copper, which saturated at 120 MPa and then cyclically softened at  $\Delta\epsilon_{pl}=1 \times 10^{-3}$ , did not reveal the shear bands during either cyclic or monotonic loading,<sup>[59]</sup> while the stronger copper saturated at 250 MPa and demonstrated many shear band on late stage of fatigue at the same plastic strain amplitude.<sup>[18,54]</sup>

Annealing of as-processed UFG copper at an intermediate temperature for a short time, which does not give rise to substantial grain growth, resulted in the disappearance of adiabatic shear bands and accompanying acoustic emission.<sup>[56]</sup> Despite the considerable difference in the microscopic mechanisms resulting in the two kinds of shear bands, they both appear as precursors of microcracks and serve as a preferred sites of crack nucleation.

## FATIGUE CRACK GROWTH

The fatigue life assessment of smooth bodies delivers only indirect information regarding resistance to flaws either pre-existing or forming in the course of cycling. Comprehensive understanding of fatigue properties requires evaluation of the fatigue crack growth. The attention to fatigue crack growth in NC materials is presently growing with the development of processing techniques capable of producing large enough samples from which to make the standard compact tension (CT) or center-cracked-tension (CCT) specimens. The kinetic diagram showing the crack growth rate  $da/dN$  vs. the stress intensity factor range  $\Delta K$  ( $\Delta K = Y\Delta\sigma\sqrt{\pi a}$ , where  $Y$  is the geometrical factor dependent upon the specimen and crack geometry,  $\Delta\sigma = \sigma_{max} - \sigma_{min}$  is the applied stress range, and  $a$  is the crack length) for a given stress ratio  $R$ , and environment is used commonly to quantify the fatigue crack growth behavior. We should underline that the  $da/dN$  vs.  $\Delta K$  plot for NC materials (Fig. 15) exhibits the same stages of a stable crack propagation as those well known for conventional polycrystals, i.e., a stage of slow crack advance in a near threshold region and



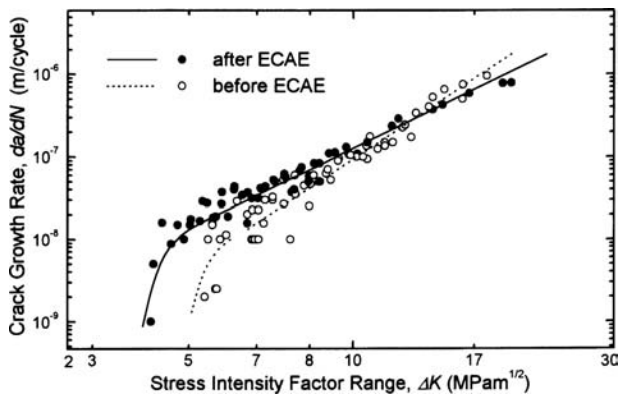


**Fig. 15** Crack growth rate diagram of the fine grain ECAP 5056 Al alloy in comparison with its coarse grain O-temper counterpart. *Source:* From Ref.<sup>[31]</sup>.

an intermediate stage, where the Paris relationship

$$\frac{da}{dN} = C(\Delta K)^m \quad (7)$$

(where  $C$  and  $m$  are materials properties) applies for most materials. Patlan et al.<sup>[30]</sup> found that the fatigue threshold  $\Delta K_{th}$  decreased after ECAP of a non-heat-treatable 5056 Al–Mg alloy (Fig. 15). Chung et al.<sup>[37]</sup> demonstrated very similar results for the UFG 6061 Al alloy and UFG ECAP low carbon steel.<sup>[39]</sup> It has been shown that the crack growth rate in the near threshold region is higher in the UFG state than in the ordinary polycrystalline state; however, the result is reversed at relatively high stress intensity factor increments  $\Delta K$ , i.e.,  $da/dN$  in UFG metals is smaller on the intermediate fatigue stage. Recently, Hanlon, Kwon, and Suresh<sup>[60]</sup> obtained similar results for electrodeposited NC Ni with grain size of 20–40 nm. The lower crack growth resistance in the near threshold regime was attributed to a less tortuous path of the intergranular crack in the UFG structure (Fig. 13A). One can see that the crack propagates nearly perfectly straight on stage I of fatigue and then, as the crack length and the related  $\Delta K$  value increase, the tortuosity of the crack path increases with numerous deflections and attempts to switch from mode II to mode I.

It has long been established in the fracture mechanics approach that the transition from the near-threshold slow crack growth regime to the intermediate fatigue stage is accompanied by a transition in the crack behavior from being strongly structure sensitive to structure insensitive. Such a transition is often observed when the crack tip cyclic plastic zone  $r_{cp}$ , which is estimated as

$$r_{cp} = \lambda \left( \frac{\Delta K}{2\sigma'_y} \right)^2 \quad (8)$$

(where  $\lambda$  is the numerical factor of the order of  $1/\pi$  and  $\sigma'_y$  is the cyclic yield stress determined from the CSSC) becomes of the same order as the grain size  $d$ .<sup>[4,61]</sup> If the stress intensity factor range corresponding to the transition point is denoted as  $\Delta K_T$ , the last equation yields a transition criterion  $r_{cp}(\Delta K_T) \approx d$ . However, estimations of a reverse plastic zone radius  $r_{cp}$  at the transition point return a  $r_{cp}$  value for the materials tested (Cu, 5056, and 6161 Al alloys), which is significantly greater than the average grain size  $d$ . For example, taking for A5056 Al–Mg alloy  $\sigma'_y = 280$  MPa and the threshold  $\Delta K = \Delta K_{th} = 4.3$  MPa  $m^{1/2}$ ,<sup>[31]</sup> one obtains  $r_{cp} = 7$ – $8$   $\mu\text{m}$ —which is considerably larger than  $d = 0.3$ – $0.4$   $\mu\text{m}$ . This suggests that a large number of neighboring grains may be involved into crack tip plasticity, even near threshold. Eq. (8) at the transition point can be simply rearranged as

$$\Delta K_T \sim \sigma'_y \sqrt{d^*} \quad (9)$$

[where  $d^*$  is a characteristic scale of a materials structural unit responsible for fracture (grain size, subgrain or cell size, particle size, etc.)], which predicts  $\Delta K_T$  to increase with  $d$ ; this effect is observed in low-carbon steels (for example, Refs.<sup>[4,61]</sup>). Assuming that threshold  $\Delta K_{th}$  approximately equals  $\Delta K_T$ , the last relationship is often written in a more general, but less-transparent and less-argued form as

$$\Delta K_{th} = A + B\sqrt{d^*} \quad (10)$$

where  $A$  and  $B$  denote materials constants. However, observations reported in Refs.<sup>[30,37,39,60]</sup> show the reduced  $\Delta K_{th}$  in UFG metals processed by SPD and NC metals, in general. If Eq. (9) were valid for these materials, a shift of  $\Delta K_{th}$  to lower magnitudes (1 MPa  $m^{1/2}$  in the 5065 Al alloy, for example) should be expected, which is far below the observed values (of 4–4.5 MPa  $m^{1/2}$  in the same Al alloy). These observations cast some doubt on the general applicability of a simplified plastic zone size concept to explain the fatigue transition behavior of materials. Higo, Pickand, and Knott<sup>[62]</sup> performed a systematic investigation of  $\Delta K_{th}$  and  $da/dN$  dependence on the grain size and the  $\sigma_{0.1}$  yield stress in Cu and Cu–Al alloy with different Al content, i.e., with different stacking fault energy ranged between 5 and 45  $\text{mJ m}^{-2}$  approximately. In contrast with the linear behavior of Eq. (9), they experimentally observed that the propagation rates were slower in the fine-grained materials and  $da/dN$  varied linearly with  $d^{-1/2}$  in the same manner as the  $\sigma_{0.1}$  yield stress, i.e., followed the Hall–Petch relationship, which is the reverse of Eqs. (9) and (10). These effects were pronounced in alloys with higher Al content, i.e., in planar slip metals where (we have stated) a stronger dependence of fatigue life on the grain size

is expected. Thus it is shown that although the fatigue crack growth behavior in NC metals reveals some similarity to that of conventional polycrystals, the quantitative explanation of the fatigue threshold reduction as well as the reduction of the crack growth rate at relatively high  $\Delta K$  is not straightforward. More experimental data are required in the following areas:

1. crack growth rate dependence on  $\Delta K$  at different  $R$  values for different materials (so far, data are only available for Al alloys);
2. precise investigations of fatigue crack closure; and
3. more precise experimental evaluation of the reverse plastic zone are required before the mechanism controlling the fatigue crack behavior will be identified. Despite a somewhat lower tolerance of the NC metals to small and sharp intergranular cracks (at least in Al alloys), these materials demonstrate a better resistance to large cracks, perhaps, because of a smaller plastic zone size, which in turn, according to Eq. (11), appears smaller because of a higher strength and cyclic yield stress.

## FATIGUE MECHANISMS IN UFG MATERIALS

The apparent similarity between the CSSCs in the coarse-grain and NC metals, which we have discussed above, suggests that the major deformation mechanisms are also alike for both kinds of materials. Thus before introducing any complication in the modeling of fatigue behavior of NC metals, one should first determine if it is possible to explain the mechanical properties of SPD metals via ordinary dislocation dynamics.

Many discussions have been put forward in the literature about the particular role of grain boundaries in the properties of UFG materials.<sup>[1,2]</sup> Obviously, the interfacial energy and higher diffusivity of grain boundaries cannot be disregarded for many phenomena (particularly in nanocrystalline materials). In fatigue of SPD metals, for instance, grain boundaries play a significant role. On one hand, the fine-grained structure usually possesses longer fatigue life—at least under stress controlled cycling—than the coarse-grain one. On the other hand, the grain boundaries appear to contribute to the relatively low stability of the UFG structure and the tendency toward recovery and grain coarsening during cycling. Furthermore, grain boundaries appear to play a role in the frequently observed shear banding as well as crack initiation and propagation. Therefore grain boundaries arguably represent the most critical structural element.

## Stress–Strain Response under Cyclic Loading

Despite the complexity of the nanocrystalline structures, the fatigue behavior of NC metals is, in many ways, more easily described than that of ordinary poly- and single crystals. The main reason for simplification is the lack of dislocation patterning in the UFG structures. Vinogradov et al.<sup>[30,35]</sup> have suggested that the shape of a stable hysteresis loop and the cyclic stress–strain curve can be described, at least semiquantitatively, by considering only the kinetics of the average dislocation density within the framework of a simplified one-parameter model first proposed by Essmann and Mughrabi<sup>[63]</sup> for dislocation annihilation. It was assumed that the mobile dislocations initiate at a grain boundary pass through the grain and disappear in the opposite grain boundary. Thus the grain boundaries act as effective sources and sinks for dislocations. Because TEM observations do not reveal any substantial difference between the initial and postfatigued structures, in some UFG metals, it is plausible to suggest that dislocations do not accumulate inside the fine grains during cycling in these cases. Following Essmann and Mughrabi<sup>[63]</sup> and Mughrabi,<sup>[64]</sup> a kinetic equation for dislocation density,  $\rho$ , can be written in its simplest form as

$$\frac{d\rho}{d\gamma} = \frac{2}{bL} - \frac{2}{b}y\rho \quad (11)$$

where  $L$  is the slip path of dislocations with the Burgers vector  $b$  and  $y$  is the so-called annihilation length. The first term on the right-hand side of Eq. (11) describes the rate of dislocation multiplication with the strain increase, while the second term accounts for the strain-induced decrease of dislocation density (dislocation dynamic recovery and annihilation of a general kind). At large enough strains, saturation is attained because of the equilibrium between the dislocation multiplication and annihilation,  $d\rho/d\varepsilon = 0$ .

To describe the stress–strain relationship, we assume that the shear flow stress,  $\tau$ , is controlled by the average total dislocation density as

$$\tau = \tau_0 + \alpha\mu b\sqrt{\rho} \quad (12)$$

where  $\tau_0$  is the friction stress,  $\alpha$  is a geometrical factor of the order of 0.5, and  $\mu$  is the shear modulus. For numerical estimations, one can take  $\tau_0$  as equivalent to the cyclic shear yield stress ( $\sigma_0 \approx 240$  MPa). Combining Eqs. (11) and (12) results in an elementary differential equation, which can be solved analytically assuming  $y$  and  $L$  do not vary with straining. While the assumption concerning the constancy of the annihilation distance seems reasonable, and has been experimentally justified (at least for Cu,<sup>[63]</sup>), the



assumption regarding  $L$  is considerably less obvious. Adopting  $L = \text{const}$  condition for the sake of simplicity one can, however, propose a few arguments in a favor of this suggestion. For the cell structure, which is typical of conventional polycrystals, the slip path has been related to the cell diameter. In UFG materials, the grain size is smaller than the typical cell size, and the grain boundaries form the main barriers for dislocation motion. Therefore it is plausible to relate the dislocation mean free path to the average grain size if the grain size is small enough. Integration of Eq. (14) together with Eq. (12) and  $\tau(0) = \tau_0$  as an initial condition yields

$$\tau = \tau_0 + \alpha\mu b \sqrt{\frac{1 - \exp(-2\gamma\gamma/b)}{Ly}} \quad (13)$$

The saturation stress  $\tau_s$  at sufficiently high strain  $\gamma \gg b/y$  takes the form

$$\tau_s = \tau_0 + \frac{\alpha\mu b}{\sqrt{Ly}} \quad (14)$$

As an example, a typical ascending part of the stable hysteresis loop of the 5056 Al alloy is plotted in Fig. 16 in the so-called relative coordinates<sup>[5]</sup>  $\sigma_r - \varepsilon_{pl,r}$ , where the loop is displaced in such a way that the tip of the compressive half-loop comes to the origin coordinates, and both half-loops are treated as identical. The non-linear curve fit of experimental points by function (13) with two fitting parameters— $L$  and  $y$ —provides a good agreement between the experimental and calculated loops with  $L$  and  $y$  of  $(1.2 \pm 0.6) \times 10^{-7}$  and  $(8.4 \pm 3.0) \times 10^{-9}$  m, respectively (Fig. 16). The ordinary relations between shear and nominal stress–strain characteristics— $\sigma = M\tau$  and  $\varepsilon = \gamma/M$  with  $M \approx 3$  as the geometrical Taylor factor—are adopted. It is worth noting that the mean free pass of dislocations  $L$  appears to be of the order of the half-grain (cell) diam-

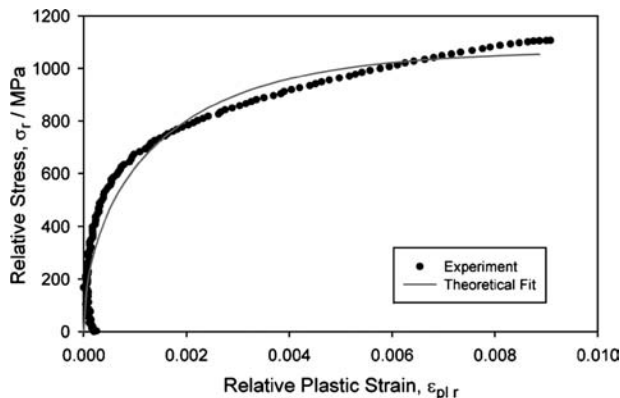


**Fig. 16** Results of modeling of the hysteresis loop shape and CSSC of UFG 5056 Al-alloy within the frames of a single-parametric kinetic dislocation model. *Source:* From Ref.<sup>[30]</sup>.

eter  $d$ , which is in fair agreement with the assumptions made above.

Analogously, by using Eq. (14), one can calculate peak stresses,  $\sigma_s$ , at different plastic strain amplitudes examined, giving an approximation of the cyclic stress–strain curve (Fig. 8).<sup>[30,35]</sup> Because of the simplicity of this one-parameter model, the qualitative agreement between experimental results and calculations achieved is surprising. In the low strain limit, formula (14) can be rewritten as

$$\tau = \tau_0 + \alpha\mu b \sqrt{\frac{2\gamma}{bL}} = \tau_0 + 2\alpha\mu(\gamma b)^{1/2} d^{-1/2} \quad (15)$$

which corresponds to Ashby's expression of the Hall–Petch work-hardening stress  $\tau = \tau_0 + kd^{-1/2}$  [ $\tau_0$  and  $k = k(\gamma)$  are materials properties; compare with Eq. (7)], if  $L = d/2$ . In other words, from Eq. (11), the “ $d^{-1/2}$ ” dependence of the flow stress recovered theoretically agrees with the experimentally observed Hall–Petch behavior of the CSSC and the fatigue limit.

Thus despite oversimplification, this approach is capable of qualitative explaining such experimental results as

1. saturation of the cyclic stress amplitude,
2. high saturation stress,
3. rapid hardening/softening on the early stage of cycling,
4. shape of the cyclic stress–strain curve and
5. Hall–Petch behavior of the fatigue limit.

More precise modeling would require two (or three) kinds of dislocations to be distinguished—mobile and immobile (the former are responsible the intergranular slip and the latter are attracted to the grain boundaries) as has been suggested by Estrin, Braasch, and Brechet<sup>[65]</sup> for ordinary polycrystals.

## Fatigue Life Prediction

The first attempt to model the fatigue life of SPD metal was performed by Ding, Mughrabi, and Höppl<sup>[66]</sup> They considered the NC metal to be a two-phase composite consisting of a soft matrix representing grain interior and “hard” reinforcement representing the heavily distorted nonequilibrium grain boundaries (or the grain boundary affected zone having a characteristic thickness of 5 nm, which they suggested was experimentally supported by TEM and X-ray structural analysis). The authors suggested the dislocation accumulation to be the main strengthening mechanism in UFG metals; however, the grain boundaries also contribute to the resultant strength. The crack growth rate  $da/dN$  was calculated from the fracture mechanics concept assuming  $da/dN$  to be proportional to the

crack tip opening displacement ( $\Delta$ CTOD). The  $\Delta$ CTOD was related to the  $J$ -integral, and the latter was calculated in the cited work with an assumption that within the fatigue damage zone, the local cyclic stress was uniform and equal to the ultimate tensile strength of the UFG material. The empirical Coffin–Manson and Basquin laws were finally derived as

$$\frac{\Delta \varepsilon_{pl}}{2} = \left[ \frac{192C^2}{\lambda \pi^2 F^2} \left( \frac{n'}{n'+1} \right) \left( \frac{\sigma'_y}{K'} \right) \ln \left( \frac{a_f}{a_i} \right) \right]^{\frac{1}{3n'+1}} (2N_f)^{\frac{-1}{3n'+1}}$$

$$\frac{\Delta \sigma}{2} = K' \left[ \frac{192C^2}{\lambda \pi^2 F^2} \left( \frac{n'}{n'+1} \right) \left( \frac{\sigma'_y}{K'} \right) \ln \left( \frac{a_f}{a_i} \right) \right]^{\frac{n'}{3n'+1}} (2N_f)^{\frac{-n'}{3n'+1}} \quad (16)$$

where  $a_i$  and  $a_f$  are the initial and final critical crack length, respectively,  $\lambda$  is a fitting parameter having a sense of the cyclic plastic zone correction factor same as that in Eq. (8), and  $C$  and  $F$  are the so-called GB constraint and GB strengthening factors respectively, which are introduced as:

$$F \equiv \frac{\sigma_{yUFG}}{\sigma_{yO}}$$

$$C \equiv \frac{1}{2} \frac{\Delta \sigma / 2}{\Delta \sigma_{eff} / 2} \quad (17)$$

where  $\sigma_{yUFG}$  and  $\sigma_{yO}$  denote the yield stresses in the UFG and ordinary polycrystalline materials, respectively, and  $\Delta \sigma / 2$  and  $\Delta \sigma_{eff} / 2$  are the average steady-state cyclic flow stress amplitude in the bulk of the material and the effective stress amplitude that contributes to local deformation, respectively. A satisfactory agreement between the calculated from Eqs. (16) fatigue life and experimental data was obtained,<sup>[66]</sup> demonstrating a potential for fatigue life prediction in frames of the proposed phenomenological approach.

## EFFECT OF TEXTURE

It is now understood that crystallographic texture exerts a very strong influence on the cyclic response of polycrystalline metals. For instance, Lukáš and Kunz<sup>[13]</sup> first demonstrated that coarse-grain copper saturates at higher stresses than its small grain analog. Llanes and Laird<sup>[67]</sup> showed that this effect could be attributed to a strong  $\langle 111 \rangle$ – $\langle 100 \rangle$  fiber texture formed in coarse-grain copper during annealing. The SPD processing used to produce most of the materials discussed in this report inevitably results in the formation of at least moderate textures,<sup>[68–70]</sup> which can be important for fatigue because of its effect on dislocation mobility, as well as the relative sensitivity of the material to plastic instabilities. Other methods of producing NC

materials (e.g., film growth or inert gas condensation) may be more or less prone to these textural issues.

## EFFECT OF ENVIRONMENT

It has long been recognized that the environment plays a very important role in fatigue damage, affecting both the crack nucleation and propagation, and a survey of the experimental results concerning the cyclic response of NC materials would not be complete without a few words about environmentally assisted fatigue. Yamasaki et al.<sup>[59]</sup> investigated corrosion fatigue of ECAP copper immersed into 1 M NaNO<sub>2</sub> aqueous solution in terms of cyclic hardening/softening behavior and surface morphology. They found that UFG copper possesses a notably better resistance to environmental attack, including corrosion fatigue, when compared to its coarse-grain counterpart. In contrast with coarse-grain Cu, which shows a transgranular fatigue fracture, corrosion fatigue in UFG specimens occurs intergranularly. Because localized corrosion is the most deleterious, the use of NC materials (having boundaries nearly everywhere) is said to be beneficial in the case where mass loss is the same for both sample types. Further improvement of fatigue properties and corrosion fatigue resistance is possible if the instability problem of SPD materials is resolved.

## EFFECT OF PROCESSING ON FATIGUE AND OPTIMIZATION OF FATIGUE PERFORMANCE

The most influential SPD processing parameter is the amount of strain imposed. Increasing number of ECA pressings results in increasing monotonic strength and fatigue limit.<sup>[32–34,36]</sup> Furthermore, the fatigue properties of UFG metals can be improved by gaining some ductility and reducing constraints for dislocation motion, i.e., by decreasing the tendency for shear banding and strain localization, which is common in many hardened metals. Thus it can be advantageous for fatigue properties to employ materials with a partially recovered structure. The positive effect of heat treatment on LCF has been already revealed in the early fatigue studies of ECAP materials.<sup>[18]</sup> It has been shown, via the acoustic emission technique and microscopic surface observations, that susceptibility to shear banding in ECAP Cu decreases dramatically after a short-term (10 min) annealing at relatively low temperature of 250°C,<sup>[56]</sup> and LCF life can be improved by a factor of 5–10 after a heat treatment that does not result in any grain growth.<sup>[19,21,23]</sup> While ECAP results in considerable reduction of tensile and cyclic ductility, the same materials subjected to a post-ECAP annealing can potentially obtain a higher ductility than its conventional

coarse-grain counterpart,<sup>[23,45]</sup> and shifts the Coffin–Manson line toward higher fatigue lives (Fig. 9).

Because SPD metals retain some ductility after fabrication, their tensile and high cyclic strength can be additionally improved after postprocessing conventional cold rolling with or without intermediate annealing at moderate temperature. This has been shown for several Al–Mg alloys<sup>[31]</sup> and commercial purity Ti<sup>[23,25]</sup> as discussed in the section “High Cycle Fatigue Behavior.”

The effect of precipitation in SPD NC metals is complex. On one hand, it has already been mentioned that precipitates can dramatically increase the thermal stability of SPD metals and, on the other, grain boundaries may recover during aging thereby reducing their susceptibility to strain localization and premature cracking. As an example, it has been shown that optimal aging of ECAP UFG Cu–Cr–Zr alloy results in a high-strength structure with 200 nm grain size, which remains fine after subsequent annealing at temperatures as high as 500°C.<sup>[36]</sup> Kim et al.<sup>[71]</sup> have shown that the one-pass ECA pressing of the solid-solution treated 2024 Al alloy, followed by a low-temperature aging, can impressively enhance both strength and ductility: samples aged at 100°C for 20 hr had the strength  $\sigma_{UTS} = 715$  MPa, and the total elongation to failure  $\delta = 16\%$ . Chung et al.<sup>[37]</sup> have shown that the yield stress and tensile strength of 6061 Al alloy benefit from multiple ECA pressing (four passes) as compared to the one-time-pressed sample (the ECAP of solution treated billets was performed at 125°C and no subsequent heat treatment was applied.) Although the effect of the single ECA pressing of aluminum alloy 6061<sup>[37]</sup> is impressive, it is not clear whether it would be impossible to achieve the same strength and ductility in Al alloys after conventional treatment. Hence two principal competing approaches for enhancement of fatigue properties via SPD can be seen: 1) achievement of compromise between strength and ductility in a minimum number of ECA pressings—one wherever possible, i.e., a cost-effective procedure employing relatively small imposed strains; and 2) achievement of maximum possible strength and high cycle fatigue life. The results of Chung et al.<sup>[37]</sup> show a lack of correlation between the tensile strength and fatigue limit, i.e., the four-pass sample with higher  $\sigma_{UTS}$  has the fatigue limit lower than the one-time pressed sample. In conclusion, there are still great opportunities for the development of optimum processing scheme for desired fatigue properties of SPD materials.

## CONCLUSION

The presently available experimental results concerning the fatigue behavior of NC materials have been reviewed, and the following aspects are highlighted in

retrospect to the available knowledge about the grain size effect on fatigue of conventional materials:

1. The significant enhancement of high cyclic fatigue life has been demonstrated after grain refinement down to submicrocrystalline and nanoscopic size for most materials, depending on the slip mode.
2. Despite the high tensile strength and improved high cyclic fatigue properties on NC and UFG metals, the low cyclic fatigue life appears shorter than that of their coarse-grain counterparts because of some loss in ductility during SPD.
3. Fatigue damage occurs on different scale levels from the intragranular movement of individual dislocations to macroscopic strain localization in the shear bands. The nature of the shear bands on SPD metals has been discussed from the standpoint of the initial ultrafine grain structure and its evolution during cyclic deformation.
4. The susceptibility of the ECAP materials to strain localization and microcracking can be a main factor, which limits their tensile and fatigue ductility and, to a large extent, determines their fatigue performance.
5. Postprocessing annealing has proven to be capable of considerable improvement of LCF performance of SPD metals because of reduction of their susceptibility to strain localization.
6. NC and UFG materials possess lower resistance to crack propagation than their coarse-grain analogs near the threshold.
7. Both grain refinement and dislocation work hardening play an important role in the resultant properties of materials obtained by severe plastic deformation. As a consequence, most of the cyclic properties of NC materials can be rationalized, at least qualitatively, in terms of Hall–Petch and dislocation hardening within a framework of a simple approach involving one- or two-parametric dislocation generation–annihilation kinetics.

The effects of texture, processing, and environment on fatigue life, crack initiation, and propagation in NC materials have been just scarcely studied, and further investigations in this field should be of interest for both potential applications and fundamental issues of fatigue of these materials.

## REFERENCES

1. Gleiter, H. Nanostructured materials—state-of-the-art and perspectives. *Z. Metallk.* **1995**, *86*, 78–83.
2. Valiev, R.Z.; Islamgaliev, R.K.; Alexandrov, I.V. Bulk nanostructured materials from severe plastic deformation. *Prog. Mater. Sci.* **2000**, *45*, 103–185.

3. Segal, V.M. Materials processing by simple shear. *Mater. Sci. Eng., A* **1995**, *197*, 157–164.
4. Suresh, S. *Fatigue of Materials*; Cambridge University Press: Cambridge, United Kingdom, 1991.
5. Polák, J. *Cyclic Plasticity and Low Cycle Fatigue Life of Metals*; Elsevier: The Netherlands, 1991.
6. Valiev, R.Z. Materials science: nanomaterial advantage. *Nature* **2002**, *419*, 887–889.
7. McFadden, S.X.; Mishra, R.S.; Valiev, R.Z.; Zhilyaev, A.P.; Mukherjee, A.K. Low-temperature superplasticity in nanostructured nickel and metal alloys. *Nature* **1999**, *398*, 684.
8. Landgraf, R.W. The resistance of metals to cyclic deformation. In *Achievement of High Fatigue Resistance in Metals and Alloys*; ASTM: Philadelphia, 1970; 3–36. ASTM STP 467.
9. Wang, Y.; Chen, M.; Zhou, F.; Ma, F. High tensile ductility in a nanostructured metal. *Nature* **2002**, *419*, 912–915.
10. Pelloux, R.M. Effect of grain size on fatigue. In *Ultrafine-Grain Metals*; Burke, J.J., Weiss, V., Eds.; Syracuse Univ. Press, 1970; 231 pp.
11. Tompson, A.W.; Backofen, W.A. Effect of grain size on fatigue. *Acta Metall.* **1971**, *19*, 597–606.
12. Plumtree, A.; Abdel-Raouf, H.A. Cyclic stress–strain response and substructure. *Int. J. Fatigue* **2001**, *23*, 177–805.
13. Lukáš, P.; Kunz, L. Effect of grain size on the high cycle fatigue behaviour of polycrystalline copper. *Mater. Sci. Eng.* **1987**, *85*, 67–75.
14. Mughrabi, H. On the grain-size dependence of meta fatigue: outlook on the fatigue of ultrafine-grained metals. In *Investigations and Applications of Severe Plastic Deformation*; NATO Science Series; Lowe, T.C., Valiev, R.Z., Eds.; Kluwer Publishers, 2000; vol. 3/80, 241–253.
15. Li, S.X.; Lu, K.; Guo, F.Q.; Chu, R.; Wang, Z. The strength of amorphous and nanocrystalline FeMoSiB alloys. *Mater. Lett.* **1997**, *30* (4), 305–310.
16. Vinogradov, A.; Hashimoto, S. Multiscale phenomena in fatigue of ultra-fine grain materials—an overview. *Mater. Trans., JIM* **2001**, *42*, 74–84.
17. Youngdahl, C.J.; Weertman, J.R.; Hugo, R.C.; Kung, H.H. Deformation behavior in nanocrystalline copper. *Scr. Mater.* **2001**, *44*, 1475–1478.
18. Vinogradov, A.; Kaneko, Y.; Kitagawa, K.; Hashimoto, S.; Stolyarov, V.; Valiev, R. Cyclic response of ultra-fine grained copper under constant plastic strain amplitude. *Scr. Mater.* **1997**, *36*, 1345–1351.
19. Vinogradov, A.; Patlan, V.; Kitagawa, K. Acoustic emission and strain localization in ultra-fine grained copper produced by equi-channel angular pressing. *Mater. Sci. Forum* **1998**, *312–314*, 607–612.
20. Agnew, S.R.; Weertman, J.R. Low-cycle fatigue behavior of ultrafine grain copper. *Mater. Sci. Eng., A* **1998**, *244*, 145–153.
21. Agnew, S.R.; Vinogradov, A.Yu.; Hashimoto, S.; Weertman, J.R. Overview of fatigue performance of Cu processed by severe plastic deformation. *J. Electron. Mater.* **1999**, *28*, 1038–1044.
22. Mughrabi, H.; Höppel, H.W. Cyclic deformation and fatigue properties of ultrafine grain size materials: current status and some criteria for improvement of the fatigue resistance. In *MRS Proceedings*; 2001; vol. 634, B2.1.
23. Höppel, H.W.; Zhou, Z.M.; Mughrabi, H.; Valiev, R.Z. Microstructural study of the parameters governing coarsening and cyclic softening in fatigued ultrafine-grained copper. *Philos. Mag., A* **2002**, *82*, 1781–1794.
24. Wu, S.D.; Wang, Z.G.; Jiang, C.B.; Li, G.Y. Scanning electron microscopy-electron channelling contrast investigation of recrystallization during cyclic deformation of ultrafine grained copper processed by equal channel angular pressing. *Philos. Mag. Lett.* **2002**, *82*, 559–565.
25. Wang, Z.G.; Wu, S.D.; Jiang, C.B.; Liu, S.M.; Alexandrov, I.V. ECA pressing of copper single crystals and fatigue-induced softening in UFG metals. In *Fatigue 2002*, Proc. of the 8th Int. Fatigue Congress, Stockholm, Sweden, June, 2002; Blom, A.F., Ed.; EMAS: Sweden, 2002; 1541–1547.
26. Höppel, H.W.; Valiev, R.Z. Optimizing fatigue behaviour in ultrafine-grained metals. *Z. Metallkd.* **2002**, *93*, 641–648.
27. Wu, S.D.; Wang, Z.G.; Li, G.Y.; Valiev, R.Z. *Fatigue*; Proc. of the 7th Int. Fatigue Congress, Beijing, P.R. China; Wu, X.R., Wang, Z.G., Eds.; Higher Education Press: P.R. China, 1999; 3, 247–253.
28. Wu, S.D.; Wang, Z.G.; Jiang, C.B.; Li, G.Y.; Alexandrov, I.V.; Valiev, R.Z. The formation of PSB-like shear bands in cyclically deformed ultrafine grained copper processed by ECAP. *Scr. Mater.* **2003**, *48*, 1605–1609.
29. Thiele, E.; Holste, C.; Klemm, R. Influence of size effect on microstructural changes in cyclically deformed polycrystalline nickel. *Z. Metallkd.* **2002**, *93*, 730–736.
30. Patlan, V.; Vinogradov, A.; Higashi, K.; Kitagawa, K. Overview of fatigue properties of fine grain 5056 Al–Mg alloy processed by equal-channel angular pressing. *Mater. Sci. Eng., A* **2001**, *300*, 171–182.
31. Vinogradov, A.; Patlan, V.; Kitagawa, K.; Kawazoe, M. Fatigue properties of 5056 Al–Mg alloy processed by equal-channel angular pressing. *Nanostruct. Mater.* **1999**, *11*, 925–934.
32. Vinogradov, A.; Kopylov, V.; Hashimoto, S. Enhanced strength and fatigue life of ultra-fine grain Fe–36Ni Invar alloy. *Mater. Sci. Eng., A* **2003**, *355*, 277–285.
33. Vinogradov, A.; Hashimoto, S. Fatigue of severely deformed metals. *Adv. Eng. Mater.* **2003**, *5*, 351–358.
34. Stolyarov, V.V.; Alexandrov, I.V.; Kolobov, Yu.R.; Zhu, M.; Zhu, Y.; Lowe, T. *Fatigue'99*; Proc. of the 7th Int. Fatigue Congress, Beijing, P.R. China; Wu, X.R., Wang, Z.G., Eds.; Higher Education Press: P.R. China, 1999; vol. 3, 1345–1351.
35. Vinogradov, A.; Stolyarov, V.V.; Hashimoto, S.; Valiev, R.Z. Cyclic behaviour of ultra-fine grain titanium produced by severe plastic deformation. *Mater. Sci. Eng., A* **2001**, *318*, 163–173.

36. Vinogradov, A.; Suzuki, Y.; Kopylov, V.I.; Patlan, V.; Kitagawa, K. Structure and properties of ultra-fine grain Cu–Cr–Zr alloy produced by equal-channel angular pressing. *Acta Metall.* **2002**, *50*, 1636–1651.
37. Chung, C.S.; Kim, J.K.; Kim, H.K.; Kim, W.J. Improvement of high-cycle fatigue life in a 6061 Al alloy produced by equal channel angular pressing. *Mater. Sci. Eng., A* **2002**, *337*, 39–44.
38. Washikita, A.; Kitagawa, K.; Kopylov, V.I.; Vinogradov, A. Fatigue life of fine-grain Al–Mg–Sc alloys produced by equal-channel angular pressing. *Mater. Sci. Eng., A* **2003**, *349*, 318–326.
39. Kim, H-K.; Choi, M-I.; Chung, C-S.; Shin, D.H. Fatigue properties of ultrafine grained low carbon steel produced by equal channel angular pressing. *Mater. Sci. Eng., A* **2003**, *340*, 243–250.
40. Agnew, S.R.; Kocks, U.F.; Hartwig, K.T.; Weertman, J.R. Texture evolution during equal channel angular forging and dislocation boundary misorientations after severe plastic deformation. In *Proc. 19th Risø Inter. Symp. Mater. Sci.*; Carstensen, J.V., Lefferes, T., Lorentzen, T., Pedersen, O.B., Sørensen, B.F., Winther, G., Eds.; Risø National Laboratory: Roskilde, Denmark, 1998; 201–206.
41. Mishin, O.V.; Gertsman, V.Y.; Valiev, R.Z.; Gottstein, G. Grain boundary distribution and texture in ultrafine-grained copper produced by severe plastic deformation. *Scr. Mater.* **1996**, *35*, 873–878.
42. Terhune, S.D.; Swisher, D.L.; Oh-Ishi, K.; Horita, Z.; Langdon, T.G.; McNelley, T.R. An investigation of microstructure and grain-boundary evolution during ECA pressing of pure aluminium. *Metal. Mater. Trans., A* **2002**, *33* (7), 2173–2184.
43. Valiev, R.Z.; Kozlov, E.V.; Ivanov, Yu.F.; Lian, J.; Nazarov, A.A.; Baudalet, B. Deformation behaviour of ultra-fine-grained copper. *Acta Metall.* **1994**, *42*, 2467–2475.
44. Hashimoto, S.; Vinogradov, A.; Kaneko, Y.; Kitagawa, K.; Valiev, R. On the cyclic behaviour of ultra-fine grained copper produced by equi-channel angular pressing. *Mater. Forum* **1999**, *312–314*, 593–598.
45. Gadalla, A.A.; Gerold, V. The fatigue of copper–chromium alloy. *Ind. J. Pure Appl. Phys.* **1980**, *18* (6), 383–386.
46. Leedy, K.D.; Stubbins, J.F.; Singh, B.N.; Garner, F.A. Fatigue behavior of copper and selected copper alloys for high heat flux applications. *J. Nucl. Mater.* **1996**, *233–237A*, 547–552.
47. Turner, N.G.; Roberts, W.T. Fatigue behavior of titanium. *Trans. AIME* **1968**, *242*, 1223–1230.
48. Markushev, M.V.; Murashkin, M.Yu. Mechanical properties of submicrocrystalline aluminium alloys after severe plastic deformation. *Phys. Met. Metallogr.* **2000**, *90*, 506–515.
49. Komura, S.; Furukawa, M.; Horita, Z.; Nemoto, M.; Langdon, T.G. Optimizing the procedure of equal-channel angular pressing for maximum superplasticity. *Mater. Sci. Eng., A* **2002**, *297*, 111–118.
50. Komura, S.; Horita, Z.; Furukawa, M.; Nemoto, M.; Langdon, T.G. An evaluation of the flow behavior during high strain rate superplasticity in an Al–Mg–Sc alloy. *Metal. Mater. Trans., A* **2001**, *32A*, 707–716.
51. Feltner, C.E.; Laird, C. Cyclic stress–strain response of f.c.c. metals and alloys. *Acta Metall.* **1967**, *15*, 1621–1632.
52. Vinogradov, A.; Hashimoto, S.; Patlan, V.; Kitagawa, K. Atomic force microscopic study of surface morphology of ultra-fine grained materials after tensile testing. *Mater. Sci. Eng., A* **2001**, *319–321*, 862–866.
53. Muhghrabi, H.; Wang, R. Cyclic stress–strain response and high-cyclic fatigue behaviour of copper polycrystals. In *Basic Mechanisms in Fatigue*; Lukáš, P., Polák, J., Eds.; Elsevier: Amsterdam, The Netherlands, 1988; 1–13.
54. Vinogradov, A.; Patlan, V.; Hashimoto, S.; Kitagawa, K. Acoustic emission during cyclic deformation of ultra-fine grain copper processed by severe plastic deformation. *Philos. Mag., A* **2002**, *82*, 317–335.
55. Höppel, H.W.; Mughrabi, H. *Proc. of the Second International Conf. on Severely Deformed Metals*; Wiley VCH: Germany, December, 2003.
56. Vinogradov, A. Acoustic emission in ultra-fine grained copper. *Scr. Mater.* **1998**, *38*, 797–805.
57. Donovan, P.E.; Stobbs, W.M. The structure of shear bands in metallic glasses. *Acta Metall.* **1981**, *29*, 1419–1436.
58. Vinogradov, A. Classification of acoustic emissions in metallic glasses. *J. Acoust. Emiss.* **1999**, *17*, 1–13.
59. Yamasaki, T.; Miyamoto, H.; Mimaki, T.; Vinogradov, A.; Hashimoto, S. Corrosion Fatigue of ultra-fine grain copper fabricated by severe plastic deformation. In *Ultrafine Grain Metals II*; Zhu, Y.T., Langdon, T.G., Mishra, R.S., Semiatin, S.L., Saran, M.J., Lowe, T.C., Eds.; TMS: USA, 2002; 361–370.
60. Hanlon, T.; Kwon, Y.-N.; Suresh, S. Grain size effects on the fatigue response of nanocrystalline metals. *Scr. Mater.* **2003**, *49*, 675–680.
61. Taira, S.; Tanaka, K.; Hoshina, M. Grain size effect on crack nucleation and growth in long-life fatigue of low-carbon steel. In *Fatigue Mechanisms*; Fong, J.T., Ed.; ASTM STP: USA, 1979; vol. 675, 165–173.
62. Higo, Y.; Pickard, A.C.; Knott, J.F. Effect of grain size and stacking fault energy on fatigue-crack-propagation thresholds in Cu–Al aluminium alloys. *Met. Sci.* **1981**, *15* (6), 233–240.
63. Essmann, U.; Mughrabi, H. Annihilation of dislocations during tensile and cyclic deformation and limits of dislocation densities. *Philos. Mag., A* **1979**, *40*, 731–756.
64. Mughrabi, H. Dislocation clustering and long-range internal stresses in monotonically and cyclically deformed metal crystals. *Rev. Phys. Appl.* **1988**, *23*, 367–379.
65. Estrin, Y.; Braasch, H.; Brechet, Y. A dislocation density based constitutive model for cyclic

- deformation. *J. Eng. Mater. Tech. ASME* **1996**, *118* (4), 441–447.
66. Ding, H.Z.; Mughrabi, H.; Höppel, H.W. A low cycle fatigue life prediction model of ultrafine-grained metals. *Fatigue Fract. Eng. Mater. Struct.* **2002**, *25*, 975–984.
  67. Llanes, L.; Laird, C. Effect of grain-size and ramp loading on the low amplitude cyclic stress–strain curve of polycrystalline copper. *Mater. Sci. Eng., A* **1990**, *128* (2), L9–12.
  68. Field, R.D.; Hartwig, K.T.; Necker, C.T.; Bingert, J.F.; Agnew, S.R. Equal-channel angular extrusion of beryllium. *Metall. Mater. Trans., A* **2002**, *23A*, 965–972.
  69. Gholinia, A.; Bate, P.; Prangnell, P.B. Modelling texture development during equal channel angular extrusion of aluminium. *Acta Mater.* **2002**, *50*, 2121–2136.
  70. Agnew, S.R.; Weertman, J.R. The influence of texture on the elastic properties of ultrafine-grain copper. *Mater. Sci. Eng., A* **1998**, *242*, 174–180.
  71. Kim, W.J.; Chung, C.S.; Ma, D.S.; Hong, S.I.; Kim, H.K. Optimization of strength and ductility of 2024 Al by equal channel angular pressing (ECAP) and post-ECAP aging. *Scr. Mater.* **2003**, *49*, 333–338.



# Nanocrystalline Materials: Synthesis and Properties

Alexandr I. Gusev

*Institute of Solid State Chemistry, Ural Division, Russian Academy of Sciences,  
Yekaterinburg, Russia*

## INTRODUCTION

The synthesis of nanocrystalline bulk and powder materials is one of the problems facing the modern materials scientist. In recent decades, the interest paid to this problem has grown remarkably because it was found that the properties of nanocrystalline substances change considerably when the size of crystallites decreases below a threshold value.<sup>[1–8]</sup> Such changes arise when the average size of crystal grains does not exceed 100 nm and are most pronounced when grains are less than 10 nm in size. Ultrafine-grain substances should be studied considering not only their composition and structure, but also particle size distribution. Ultrafine-grain substances with grains 300 to 40 nm in size on the average are usually referred to as submicrocrystalline, while those with grains less than 40 nm in size on the average are called nanocrystalline. The classification of substances by the size  $D$  of their particles (grains) is shown in Fig. 1.

Nanosubstances and nanomaterials may be classified by geometrical shape and the dimensionality of their structural elements. The main types of nanomaterials with respect to the dimensionality include cluster materials, fibrous materials, films and multilayered materials, and also polycrystalline materials whose grains have dimensions comparable in all the three directions (Fig. 2).

The main objective of this entry is to give a general idea about diverse nanocrystalline substances and materials. The chemical composition, the microstructure, the grain size distribution, and, consequently, the properties of nanosubstances largely depend on their production method. It is for this reason that the paper first describes main methods for production of powders and bulk samples in the nanocrystalline state and then considers specific features of the microstructure of nanocrystalline substances. The influence of the nanocrystalline state on properties of various substances and determination of causes of this influence present the objective of the final part of this paper.

## BACKGROUND OF FINE MATERIALS

In December 1959, at his talk at the California Institute of Technology, Feynman<sup>[9]</sup> stressed the problem

of control over the substance in the interval of extremely small dimensions as an insufficiently explored, but very promising field of science. He noted in particular that "...when we have some control of the arrangement of things on a small scale we will get an enormously greater range of possible properties that substances can have, and of different things that we can do... The problems of chemistry... can be greatly helped if our ability to see what we are doing, and to do things on an atomic level, is ultimately developed."

In 1982–1985, Gleiter<sup>[1]</sup> proposed a concept of the nanostructure of solids and was the first to realize a method for production of bulk materials with nanometer-sized grains (crystallites). From that time on, bulk and powder substances, which contained nanometer-sized particles, have been called nanocrystalline. Gleiter's works spurred studies into the synthesis, the structure, and the properties of nanocrystalline substances.

Differences in the properties of fine particles from those of bulk materials have been known and used for a relatively long time. Examples are aerosols, dyeing pigments, and glasses colored with colloidal particles of metals. A very significant field of successful application of fine particles is catalysis of chemical reactions. Multilayered nanostructures are used in electronics. These structures represent a crystal, which has, in addition to the usual lattice of periodically arranged atoms, a superlattice comprising alternating layers of different compositions.

Semiconductor nanoheterostructures, which realize quantum-size effects, are of special interest to electronics. Nanoheterostructures, especially double ones, including quantum wells, wire, and dots, allow controlling basic parameters of semiconductors (the energy spectrum, the forbidden gap width, the effective mass, and the mobility of carriers).

## DISTINCTIVE PROPERTIES

The density of states  $N(E)$  is a continuous function in a three-dimensional (3-D) semiconductor. When the electron gas dimensionality decreases, the energy spectrum

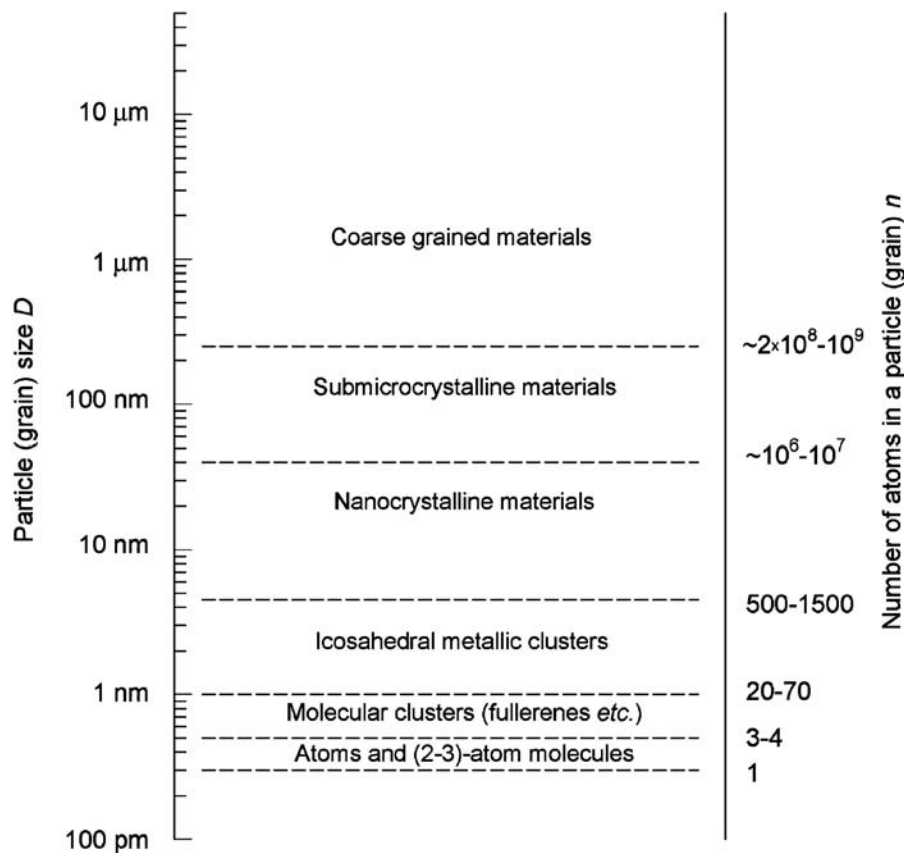


**Fig. 1** Classification of substances and materials by their particle (grain) size  $D$ .

becomes split and discrete (Fig. 3). A quantum well is a two-dimensional structure, in which charge carriers are limited to the direction perpendicular to the layers and can move freely in the layer plane. Charge carriers are limited to two directions in a quantum wire and only move along the wire axis. A quantum dot is a quasi-zero-dimensional (“0”  $D$ ) structure, in which charge carriers are limited in three directions. The electron energy spectrum of an ideal quantum dot is fully discrete

(Fig. 3) and corresponds to the spectrum of a single atom, although a real quantum dot (a “superatom”) can include hundreds of thousands of atoms.

A small size of grains determines a large length of grain boundaries. Also, grains may have various atomic defects (vacancies or their complexes, disclinations, and dislocations), whose number and distribution differ from those in coarse grains 5 to 30  $\mu\text{m}$  in size. If dimensions of a solid in one, two, or three

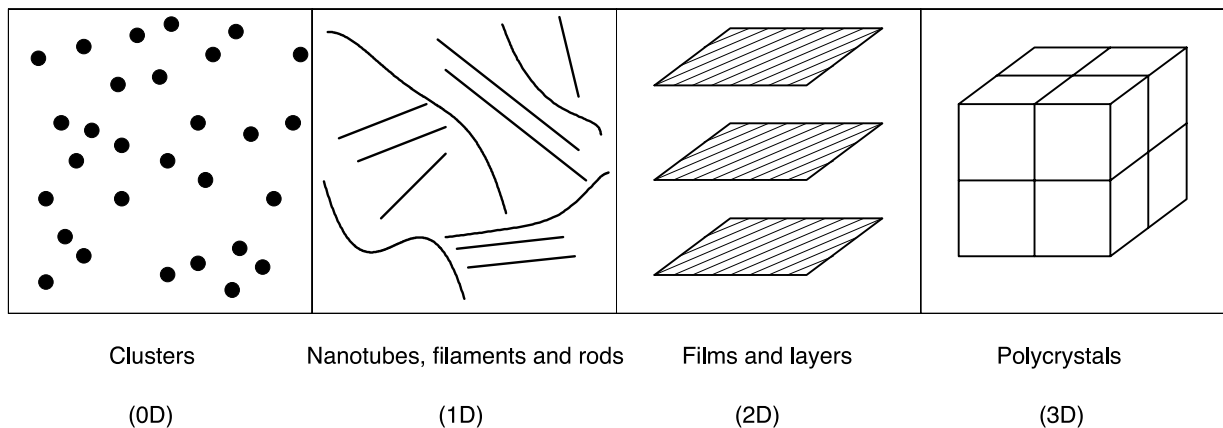


**Fig. 2** Types of nanocrystalline materials: 0-D (zero-dimensional) clusters; 1-D (one-dimensional) nanotubes, filaments, and rods; 2-D (two-dimensional) films and layers; 3-D (three-dimensional) polycrystals.

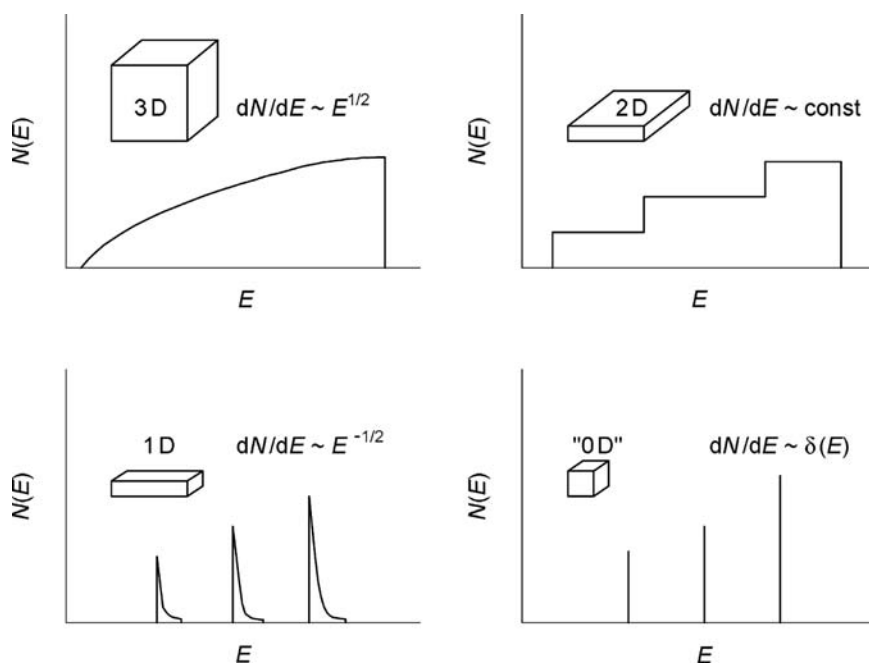


**Fig. 3** Density of states of charge carriers of states  $N(E)$  as a function of the semiconductor dimensionality: (3-D) three-dimensional semiconductor; (2-D) quantum well; (1-D) quantum wire; (0-D) quantum dot.

directions are comparable with characteristic physical parameters having the length dimensionality (the size of magnetic domains, the electron free path, the size of excitons, the de Broglie wavelength, etc.), dimensional effects will be observed for the corresponding properties. Thus dimensional effects imply a set of phenomena connected with changes in properties of substances, which are caused by 1) a change in the particle size, 2) the contribution of interfaces to properties of the system, and 3) comparability of the particle size with physical parameters having the length dimensionality. Specific features of the structure of nanocrystalline substances make their properties differ considerably from those of usual polycrystals. Therefore the decrease in the grain size is viewed as an efficient method for adjustment of properties of solids.

Nanocrystalline substances represent a special state of condensed matter, namely, macroscopic ensembles of superfine particles up to several nanometers in size. Properties of nanosubstances are determined by both specific features of separate particles and their collective behavior, which depends on the interaction between nanoparticles.

## SYNTHESIS OF NANOCRYSTALLINE POWDERS

### Gas Phase Synthesis

Isolated nanoparticles are prepared by the evaporation of a metal, an alloy, or a semiconductor at a controlled temperature in the atmosphere of a low-pressure inert gas and the subsequent condensation of the vapor near

or on a cold surface. The gas phase synthesis provides particles between 2 and several hundreds of nanometers in size. Nanoparticles  $\leq 20$  nm in size have a spherical shape, while coarser particles are faceted.

The metal may be evaporated from a crucible or fed to the evaporation zone as a wire or a powder. A beam of argon ions serves for the metal evaporation. The energy may be injected via direct heating, passage of an electric current, an electric-arc plasma discharge, inductive heating with currents of high and superhigh frequencies, laser radiation, or electron beam heating. A vacuum, a motionless inert gas, a gas flow, or a plasma jet may serve as the working medium. The composition and the size of nanoparticles may be controlled by changing the atmosphere pressure and composition (an inert gas or a reagent gas) and the temperature gradient between the evaporated substance and the surface, on which the vapor condensates.

Properties of isolated nanoparticles largely depend on the contribution of the surface layer. In the case of a spherical particle with the diameter  $D$  and the surface layer thickness  $\delta$ , the fraction of the surface layer in the total volume of the particle is  $\sim 6\delta/D$ . When the surface layer thickness equals 3–4 atomic monolayers (0.5–1.5 nm) and the size of nanoparticles is 10–20 nm, the surface layer accounts for up to 50% of the whole substance.

### Plasmachemical Technique

Low-temperature (4000–8000 K) nitrogen, ammonium, hydrocarbon, or argon plasma of the arc, glow, high-frequency, or superhigh-frequency discharge is used

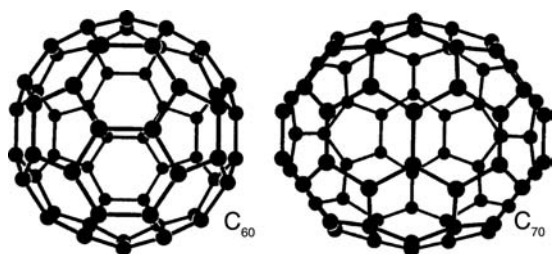


**Fig. 4** Structure of most significant fullerenes  $C_{60}$  and  $C_{70}$ . The  $C_{60}$  molecule is shaped like a soccer-ball and its cage is about 0.7 nm in diameter. All fullerenes exhibit hexagonal and pentagonal rings of carbon atoms.

in the plasmachemical synthesis. Elements, their halogenides, and other compounds serve as the starting material. Particles of plasmachemical powders represent single crystals 10 to 100–200 nm in size. Laser heating provides nanopowders with a narrow particle size distribution. The gas phase synthesis with laser radiation for generation and maintenance of the plasma, in which the chemical reaction takes place, proved to be an efficient method for production of molecular clusters.

Molecular clusters occupy a special place among nanostructured substances. The best known of these structures are the fullerenes,<sup>[10]</sup> representing a new allotropic modification of carbon in addition to graphite and diamond. The  $C_{60}$  and  $C_{70}$  fullerenes are produced by electric arc sputtering of graphite in the helium atmosphere at a pressure of  $\sim 10^4$  Pa. However, electron beam evaporation and laser heating are also used.

A  $C_{60}$  molecule has the structure of a truncated regular icosahedron (Fig. 4), where carbon atoms form a closed hollow spherical surface comprising 5- and 6-member rings. Each atom has its coordination number

equal to 3 and is located at vertices of two hexagons and one pentagon. Crystallization of  $C_{60}$  from a solution or a gas phase leads to appearance of fullerites, which are molecular crystals with a cubic lattice having the constant of 1.417 nm. The  $C_{70}$  fullerene is shaped like a closed spheroid (Fig. 4).

In 1992, a stable  $Ti_8C_{12}^+$  cluster was discovered<sup>[11]</sup> corresponding to a  $Ti_8C_{12}$  molecule in the form of a distorted pentagon dodecahedron (Fig. 5). The  $Ti_8C_{12}$  cluster has the linear dimension of about 0.5 nm.  $Ti_8C_{12}$  clusters were produced by the plasma-chemical gas phase synthesis in a helium atmosphere using hydrocarbons (methane, ethylene, acetylene, propylene, and benzene) and titanium vapors as reagents. Titanium was evaporated under irradiation from a Nd-laser with a 532-nm wavelength. The  $Ti_8C_{12}$  cluster is the first member in the new class of molecular clusters, that is,  $M_8C_{12}$  metallocarbohedrenes, where  $M = Zr, Hf, V, Cr, Mo, \text{ or } Fe$ .

### Precipitation from Colloid Solutions

A standard method for producing nanoparticles from colloid solutions consists of a chemical reaction between the solution components and interruption of this reaction at a certain moment of time. After this, the dispersed system changes from the liquid colloid state to the dispersed solid state. For example, nanocrystalline cadmium sulfide CdS is produced by precipitation from a mixture of  $Cd(ClO_4)_2$  and  $Na_2S$  solutions. The solution pH is increased abruptly to stop the growth of CdS particles.

Mixed-composition nanoparticles, i.e., nanocrystalline heterostructures, are synthesized by precipitation from colloid solutions. The core and the shell of a mixed nanoparticle are made of semiconductor

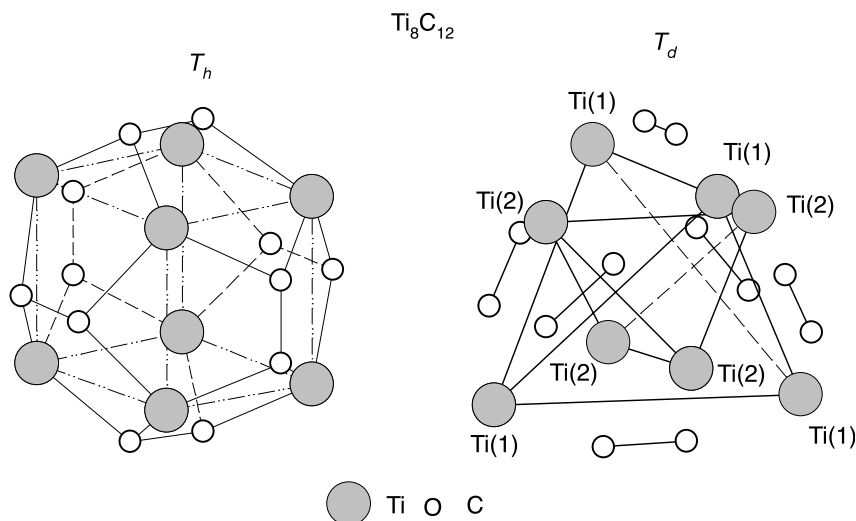


**Fig. 5** Dodecahedral structure of the molecular cluster  $Ti_8C_{12}$  with the symmetries  $T_h$  and  $T_d$  taking into account different length of Ti–C and C–C bonds.

substances having different structures of electronic levels. Heterostructures, such as CdSe/ZnS or ZnS/CdSe, HgS/CdS, ZnS/ZnO, and TiO<sub>2</sub>/SnO<sub>2</sub>, are formed through a controlled precipitation of one type of semiconductor molecules on presynthesized nanoparticles of a semiconductor of another type.

Precipitation from colloid solutions is highly selective and allows producing stabilized nanoclusters with a very narrow particle size distribution.

### Thermal Decomposition and Reduction

Subject to thermal decomposition are elemento- and metallo-organic compounds, carbonyls, formates, oxalates, amides, and imides of metals, which decompose at some temperature and form the synthesized substance. For example, metal powders with particles 100 to 300 nm in size on the average are prepared by pyrolysis of iron, cobalt, nickel, and copper formates in a vacuum or an inert gas at 470–530 K.

Superfine metal powders are also produced by hydrogen reduction of hydroxides, chlorides, nitrates, and carbonates of metals at <500 K. Advantages of this method include a low concentration of impurities and a narrow particle size distribution of powders (Fig. 6).

### Mechanical Synthesis

Mechanical synthesis as a method for producing nanopowders may be divided into two categories: mechanical milling and mechanical alloying. Mechanical milling is used both for grinding and amorphization of the starting material. Mechanical alloying requires grinding, mixing, mass transfer, and chemical interaction of powders of several pure elements, compounds, or alloys. Substances in the crystalline and amorphous states may be prepared by mechanical alloying.

Mechanical synthesis is the most efficient method for large-quantity production of nanopowders.

Grinding and mechanical synthesis are performed in high-energy planetary, ball, or vibrating mills. The average size of powder particles is 200 to 5–10 nm. For example, Fe–Ni and Fe–Al nanocrystalline alloys with grains 5 to 15 nm in size were synthesized by grinding of metal powders in a ball vibrating mill during 300 hr.<sup>[8]</sup>

### Synthesis by Detonation and Electric Explosion

One more type of the mechanical treatment, which provides conditions for synthesis and dispersion of the final product, is a shock wave. Nanocrystalline diamond powders are prepared from mixtures of graphite

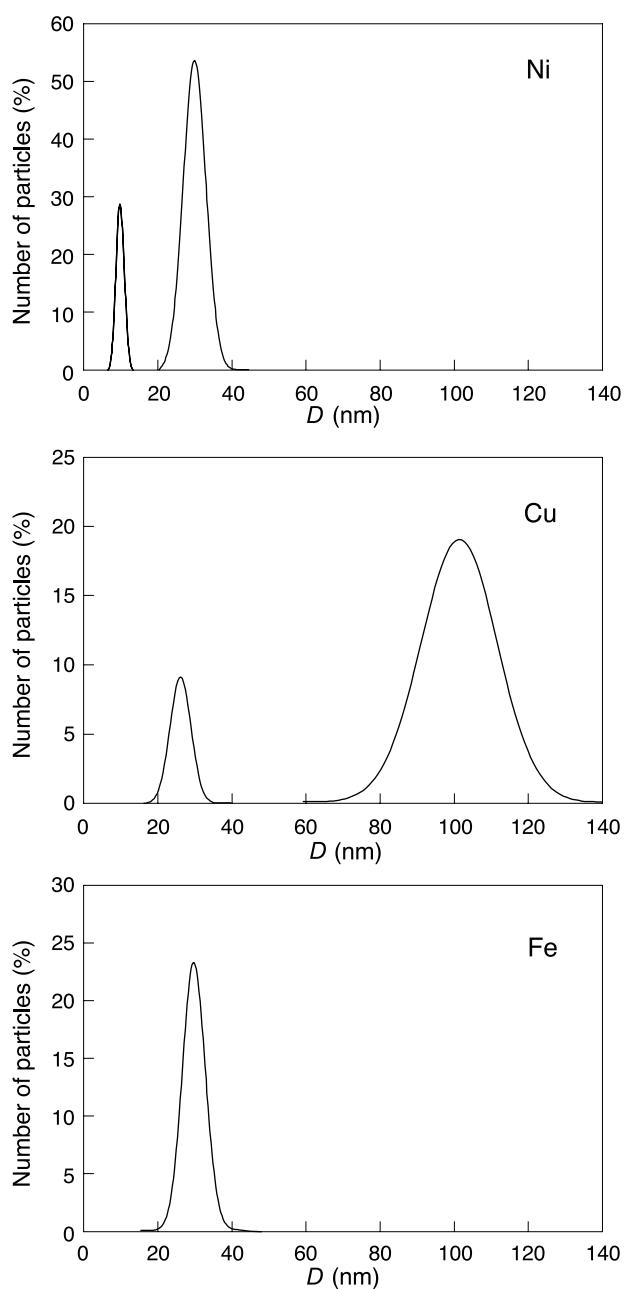


**Fig. 6** Typical distributions of metal particles by their size  $D$ . The particles were synthesized via reduction of metals from compounds in a hydrogen flow.

and metals under the shock wave pressure of a few dozens of gigapascals. Diamond powders may be produced more conveniently by explosion of organic substances with a high concentration of carbon and a low percentage of oxygen.

Detonation of condensed explosives, which decompose with liberation of free carbon, is used for commercial production of diamond nanopowders. The volume of explosion chambers is not less than 2–3 m<sup>3</sup>. Synthesized diamond powders consist of cubic particles about 4 nm in size on the average.

Fine powders with particles up to 50 nm in size are produced by an electric explosion of wire when it passes a strong current pulse,  $10^{-5}$ – $10^{-7}$  sec long, having a density of  $10^4$ – $10^6$  A mm<sup>-2</sup>.<sup>[12]</sup> A wire of diameter 0.1 to 1.0 mm is used. A current pulse quickly heats the metal up to a temperature  $T > 10^4$  K (above the melting point) and the overheated metal is dispersed as in explosion. The average size of particles diminishes as the current density grows and the pulse length shortens. Electric explosion in an inert atmosphere provides powders of metals and alloys. Fine powders of oxides, nitrides, carbides, or their mixtures may be synthesized when reagents (O<sub>2</sub> + He, N<sub>2</sub>, H<sub>2</sub>O, and C<sub>10</sub>H<sub>22</sub>) are added into the reactor.

### Synthesis of Superfine Oxides in Liquid Metals

In this method, molten gallium, lead, or Pb–Bi alloy serve as the working medium. A metal M, whose chemical affinity for oxygen is larger than the oxygen affinity of the molten metal, is dissolved in the melt. Then the dissolved metal M is oxidized by bubbling water vapor or an oxidizing gas mixture (H<sub>2</sub>O + Ar) through the melt. Superfine amorphous oxides of metals are formed as a result of selective oxidation. For example, oxidation of aluminum in molten gallium leads to formation of flocks of amorphous Al<sub>2</sub>O<sub>3</sub> · H<sub>2</sub>O. It consists of fibers 5 to 100 nm in diameter, which are spaced 5 to 400 nm. The synthesized material has a porosity of 97–99 vol.% and a specific surface of 30 to 800 m<sup>2</sup> g<sup>-1</sup>.

Nanostructured oxides SbO<sub>2</sub>, TeO, NiO, GeO<sub>2</sub>, SnO<sub>2</sub>, In<sub>2</sub>O<sub>3</sub>, K<sub>2</sub>O, ZnO, Ga<sub>2</sub>O<sub>3</sub>, Na<sub>2</sub>O, MnO, Li<sub>2</sub>O, Al<sub>2</sub>O<sub>3</sub>, BaO, SrO, MgO, and CaO may be produced via selective oxidation. The method is also applicable to synthesis of superfine nitrides, sulfides, and halogenides. In this case, a mixture of an inert gas and nitrogen N<sub>2</sub>, hydrogen sulfide H<sub>2</sub>S, or gaseous gallium or lead chlorides is passed through the melt with a dissolved metal.

### Self-Propagating High-Temperature Synthesis

Self-propagating high-temperature synthesis (SHS) represents solid-state burning of reagents (metal and carbon for carbides or metal in nitrogen for nitrides) at a temperature of 2500 to 3000 K. Usually, the average size of grains in carbides produced by the SHS method is 5 to 20 μm.

A nanosized powder of titanium carbide was prepared by the SHS method using sodium chloride as an inert dilutant.<sup>[13]</sup> As titanium and carbon are burning, NaCl forms a melt, which insulates the formed carbide particles and prevents their growth. Also, NaCl dissolves well in water and can be easily separated from the synthesized carbide. The size of titanium

carbide particles decreases with growing percentage of NaCl in the initial mixture. The average size of particles is about 100 nm.

### Ordering in Non-stoichiometric Compounds as a Method of Producing a Nanostructure

A nanostructure in non-stoichiometric compounds such as MC<sub>y</sub> cubic carbides is produced through disorder–order transformations, which take place as phase transitions of the first kind with an abrupt change of the volume.<sup>[14]</sup> If a non-stoichiometric compound is cooled quickly from a high temperature, at which the disordered state is at equilibrium, ordering cannot be completed and the compound remains in a metastable disordered state. Because lattice constants of the disordered and ordered phases are different, stresses arise in the sample, leading to the cracking of crystallites at interfaces between the disordered and ordered phases and formation of a nanostructured powder.

The first ordering-induced nanostructure was realized in a non-stoichiometric vanadium carbide.<sup>[15]</sup> The initial powder of the VC<sub>0.875</sub> carbide with grains 1 to 2 μm in size was aged for a long time at 300 K. The aged powder contained agglomerates 5 to 30 μm in size, which were formed by particles measuring about 1 μm. The particles had a complicated structure (Fig. 7). Each entity ~1 μm in size looked like an open rosebud and contained a large number of nanocrystallites in the form of strongly bent plate disks 400 to 600 nm in diameter and 15 to 20 nm thick (Fig. 8). The bulk of the nanocrystallites consisted of the V<sub>8</sub>C<sub>7</sub>-ordered carbide, while the surface layer about 0.7 nm thick included a great number of vacancy agglomerates.

## PREPARATION OF BULK NANOCRYSTALLINE SUBSTANCES

### Disorder–Order Transformations

A nanostructure may be produced not only by ordering of powders, but also bulk non-stoichiometric compounds. Bulk samples of the VC<sub>0.875</sub> carbide were prepared using a hot pressing of a powder of disordered vanadium carbide at a temperature of 2000 K and a pressure of 20–25 MPa.<sup>[16]</sup> The size of grains in sintered samples was 10 to 60 μm. The sintered samples were annealed at 1370 K for 2 hr and then were cooled slowly (at a rate of 100 K hr<sup>-1</sup>) to 300 K or quenched from 1500 to 300 K. The maximum thermal treatment temperature approached the disorder–order transformation temperature  $T_{trans}$  and



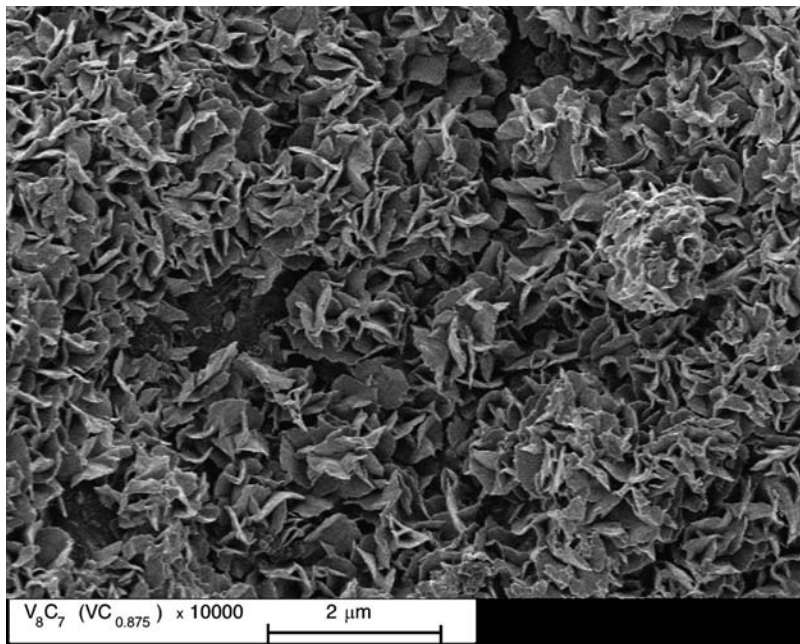


**Fig. 7** Microstructure of a powder of the  $\text{VC}_{0.875}$  vanadium carbide after long-term aging at ambient temperature in an ambient atmosphere ( $\times 10000$  magnification). *Source:* From Ref.<sup>[15]</sup>.

was equal to  $T_{\text{trans}} \pm 100$  K. Along with structural reflections, additional weak reflections corresponding to the  $\text{V}_8\text{C}_7$ -ordered phase appeared in the X-ray diffraction spectrum after both annealing and quenching.

The  $\text{V}_8\text{C}_7$ -ordered phase was formed thanks to the disorder–order transformation. The grain size of the basic phase did not change upon ordering, but superstructural lines widened because of a small size of domains of the ordered phase. Superstructural reflections widened most for the sample, which was quenched from 1500 K. This means that domains of

the ordered phase were smallest in that sample. The size of domains was about 130 nm in annealed samples and  $\sim 20$  nm in samples quenched from 1500 K.

Thus the nanostructure in the bulk non-stoichiometric vanadium carbide represented a set of domains of an ordered phase and was formed thanks to the  $\text{VC}_{0.875} \rightarrow \text{V}_8\text{C}_7$  disorder–order phase transformation.

Ordering is an efficient method for creation of a nanostructure in bulk and powder non-stoichiometric compounds. Disorder–order transformations, which are accompanied by changes of the volume, can

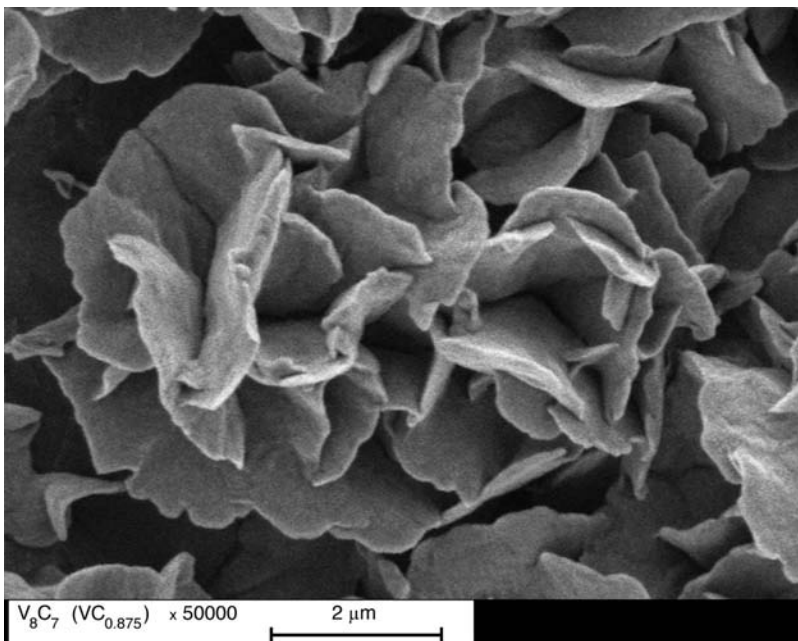


**Fig. 8** Morphology of particles of an aged powder of the  $\text{VC}_{0.875}$  carbide ( $\times 50000$  magnification). *Source:* From Refs.<sup>[15,16]</sup>. Particles about 1  $\mu\text{m}$  in size represent a set of nanocrystallites having the shape of bent plate disks 400 to 600 nm in diameter and about 15–20 nm thick.

be used to produce a nanostructure not only in non-stoichiometric compounds, but also in substitutional solid solutions, including alloys.

### Compaction of Nanopowders

A method for production of bulk nanocrystalline substances, which was proposed by researchers<sup>[17]</sup> in 1981–1986, has been well known. This technology uses the method of evaporation and condensation for production of nanoparticles, which are deposited on the cold surface of a rotating cylinder. Evaporation and condensation are realized in a rarefied inert gas, mostly helium. Particles of the surface condensate are usually faceted. The deposited condensate is removed from the cylinder surface using a special scraper and is placed in a collector. The inert gas is pumped out and the nanocrystalline powder is compacted in a vacuum first at a pressure of  $\sim 1$  GPa and finally at a pressure up to 10 GPa. Bulk nanomaterials prepared by this method contain particles of an average size  $D$  from 1–2 to 80–100 nm and have a relative density of 85–97% depending on evaporation and condensation conditions. The absence of contact with the ambient atmosphere during synthesis and compaction of the nanopowder precludes contamination of the bulk samples. For production of bulk nanocrystalline oxides and nitrides, the metal is evaporated to an oxygen- or nitrogen-containing atmosphere.

Porosity of nanoceramics prepared by compaction of powders is connected with triple junctions of crystallites. It may be decreased and made more uniform by compaction of nanopowders and their sintering at relatively low temperatures  $T \leq 0.5T_m$  ( $T_m$  being the melting point).

The magnetic pulsed method<sup>[18]</sup> is reduced to intensive dry pressing of powders. Pulsed compression waves cause vigorous heating of the powder thanks to the quick release of energy during friction of particles. When the size of particles is small ( $D \leq 0.3 \mu\text{m}$ ), their heating time is shorter than the characteristic length of pulsed compression waves (1–10  $\mu\text{sec}$ ). If compression wave parameters are chosen properly, it is possible to realize dynamic hot pressing of nanopowders thanks to their high surface energy. The magnetic pulsed method provides denser samples than steady-state pressing at nearly equal pressures (Fig. 9). Short-time heating reduces recrystallization caused by high temperatures and helps preserving a small size of particles.

A promising method for compaction of ceramic nanopowders without plasticizers is dry cold ultrasonic pressing.<sup>[19]</sup> Ultrasound decreases interparticle friction, breaks agglomerates and coarse particles, and improves the volume distribution of particles. Therefore the

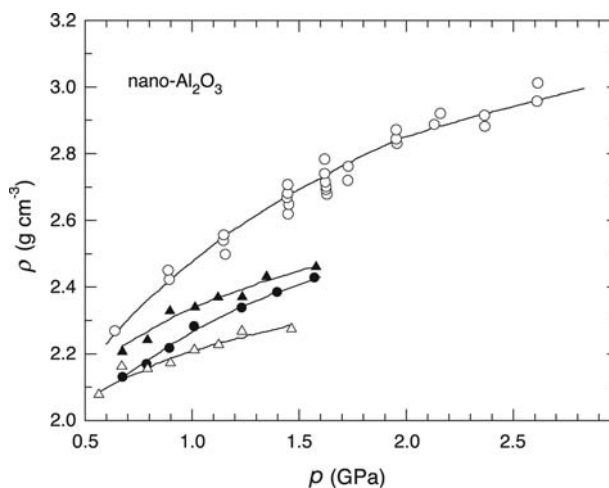


**Fig. 9** Pressure dependence of the density  $\rho$  of the nanocrystalline oxide  $n\text{-Al}_2\text{O}_3$  for steady-state and magnetic pulsed pressing: (1), (2), (3) represent steady-state pressing at temperatures of 300, 620, and 720 K, respectively; (4) represents magnetic pulsed pressing.

density of the compact is enhanced, the growth of grains during sintering is limited, and the nanostructure is preserved. Ultrasonic pressing of nanopowders is especially efficient in the production of intricate articles, such as bushes, gear wheels, and spirals (Fig. 10).

Ceramic nanomaterials are sintered using heating with millimeter-range superhigh frequency (SHF) radiation.<sup>[20]</sup> Volume absorption of the SHF energy ensures one-time uniform heating of the whole sample and provides sintered ceramics having a homogeneous microstructure. The sintering temperature is 1300 to 2300 K. Microwave sintering of compacts, which had a relative density of 70–80% and were made of a  $\text{TiO}_2$  nanopowder with an average size of particles equal to 20–30 nm, allowed producing sinters having a relative density of 97–99% and grains 200 to 220 nm in size on the average.

The existing methods for compaction of nanopowders and sintering of bulk nanomaterials already provide high-density intricate articles. However, it has been so far impossible to maintain the same small size of grains in sintered nanomaterials as in initial nanopowders. To keep the size of grains small, one has to decrease the temperature and duration of sintering and perform the sintering operation under a high pressure.

### Film and Coating Deposition

Deposition on a cold or heated surface of a substrate allows making films and coatings, i.e., continuous layers of a nanocrystalline substance not more than several micrometers thick. Films may have different



**Fig. 10** Ceramic articles synthesized by ultrasonic pressing of nanopowders. *Source:* From Ref.<sup>[19]</sup>.

compositions and the size of their crystallites may change over a wide interval including the amorphous state and multilayer structures (superlattices). Pressing is not necessary because a bulk layer of a nanomaterial is obtained.

Deposition on a substrate may be realized from vapors, plasma, or a colloid solution. In the case of vapor deposition, a metal is evaporated in a vacuum or an oxygen- or nitrogen-containing atmosphere and then vapors of the metal or its compound (an oxide or a nitride) are condensed on a substrate. The size of crystallites in the film may be adjusted by varying the evaporation rate and the substrate temperature. Nanostructured films may be produced by deposition from plasma.

Oxide and sulfide semiconductor films are obtained by deposition on a substrate from colloid solutions. Nanostructured films containing nanoparticles of different semiconductors are prepared by the codeposition method. The methods of chemical and physical deposition from a gaseous phase (CVD and PVD) are traditionally used for producing of films.

### Nanocrystallization of Amorphous Alloys

Non-porous nanostructured materials are produced by crystallization of amorphous metal alloys. Thin bands of amorphous alloys are made by melt spinning, i.e., quick (at a rate  $\geq 10^6 \text{ K sec}^{-1}$ ) cooling of the melt on the surface of a rotating disk. Then the amorphous band is annealed to create a nanostructure.

Considerable study currently devoted to crystallization of amorphous alloys in connection with development of soft magnetic materials in Fe–Cu–M–Si–B

(M = Nb, Ta, W, Mo, or Zr) systems.<sup>[21]</sup> Amorphous alloys of the Fe–Cu–Nb–Si–B system proved to be most successful. Their crystallization at 700–900 K resulted in formation of a uniform nanocrystalline structure. Grains of the  $\alpha$ -Fe(Si) phase  $\sim 10 \text{ nm}$  in size and copper clusters about 1 nm in size were uniformly distributed in the amorphous matrix of the alloy.

Crystallization of quickly solidifying amorphous alloys of the Al–Cr–Ce–M (M = Fe, Co, Ni, or Cu) system, which contained over 92 at.% Al, led to formation of a structure including an amorphous phase and Al-rich icosahedral nanoparticles ( $D \sim 5\text{--}12 \text{ nm}$ ) precipitated in the amorphous phase.<sup>[22]</sup> Alloys with this structure possess a high tensile strength (up to 1340 MPa), which approaches the strength of special steels.

### Severe Plastic Deformation

Severe plastic deformation applies mostly to plastically deformable materials. In addition to the decrease in the average size of grains to 100–200 nm, it allows producing bulk samples with a nearly pore-free structure, which cannot be prepared by compaction of superfine powders.

The main methods, which are used to considerably refine grains without breakage of samples, are high-pressure torsion and equal-channel angular (ECA) pressing (Fig. 11). The ECA pressing method was proposed in Ref.<sup>[23]</sup>. As compared with other methods of plastic deformation, this method provides the most uniform structure of substances. The structure and properties of submicrocrystalline materials, which were produced using severe plastic deformation, are described in Ref.<sup>[24]</sup>.

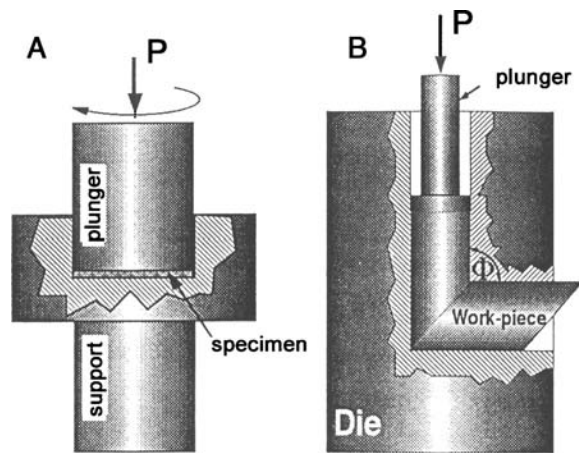


**Fig. 11** Schemes of main methods of severe plastic deformation: *Source:* From Ref.<sup>[24]</sup> (A) high-pressure torsion; (B) equal-channel angular pressing.

The main feature of the structure of submicrocrystalline materials prepared by deformation methods is non-equilibrium grain boundaries, which are a source of strong stresses. Triple junctions of grains represent one more source of stress. Annealing of submicrocrystalline materials causes changes in their microstructure. Initially, when the annealing temperature equals nearly one-third of the melting point, stresses are relaxed, grain boundaries acquire a more equilibrium state, and grains grow insignificantly. The further increase in the annealing temperature and time is followed by collective recrystallization, i.e., coarsening of grains.

The method of severe plastic deformation was used to produce a submicrocrystalline structure in such metals as Cu, Pd, Fe, Ni, and Co, aluminum, magnesium, and titanium alloys, and intermetallics. A bulk nanocrystalline sample with grains  $\sim 30\text{--}40$  nm in size was prepared from a coarse ( $D \sim 2\text{--}5\ \mu\text{m}$ ) powder of a non-stoichiometric  $\text{TiC}_{0.62}$  titanium carbide by the method of high-pressure torsion.<sup>[8]</sup>

## MICROSTRUCTURE OF BULK NANOCRYSTALLINE SUBSTANCES

In the simplest case, a nanocrystalline substance, which comprises atoms of one species, includes two components with different structures: grains (crystallites) 5 to 20 nm in size and intercrystalline boundaries up to 1.0 nm long. Crystallites have a similar structure and differ by their orientations and sizes only. The structure of interatomic interactions is determined by the type of interatomic interactions and the mutual orientation of adjacent crystallites. It was thought originally that the intercrystalline substance is characterized by a random location of atoms and the absence of the long- and short-range order.<sup>[17]</sup> This state

was called a gas-like structure, taking into account the location of atoms only.

Later studies showed that the atomic order on interfaces of nanosubstances approaches the atomic order in coarse-grain polycrystals. An example is a comparative study of the structures of coarse-grain palladium and nanocrystalline palladium n-Pd, which was prepared by evaporation and condensation. This study demonstrated that widening of diffraction reflections for n-Pd was a result of a small size of crystallites and stresses in grains or on interfaces rather than the gas-like structure of the grain-boundary phase or a large number of vacancies in grains.<sup>[25]</sup> Pores were detected only at triple junctions and not on the entire length of the interfaces.<sup>[26]</sup> The atomic density on intercrystalline boundaries proved to be nearly equal to its counterpart in crystallites.

According to Ref.<sup>[27]</sup> the coordination number of the first coordination sphere in an as-prepared n-Pd sample was 5–6% smaller than in coarse-grain palladium. However, almost all atoms were located at lattice sites in n-Pd samples, which were aged at room temperature for several months.<sup>[28]</sup> It was found<sup>[27,28]</sup> that grain boundaries in an as-prepared bulk n-Pd sample were in the equilibrium state with a small short-range order. This state was unstable even at room temperature and the sample acquired a more ordered state during 120–150 days, while the size of crystallites increased from 12 to 25–80 nm.<sup>[29]</sup>

Interfaces in compacted nanocrystalline substances may contain three types of defects:<sup>[2]</sup> separate vacancies, vacancy agglomerates or nanovoids at triple junctions, and large voids instead of missing crystallites (Fig. 12).

The annihilation of positrons<sup>[2,30]</sup> is the most reliable up-to-date method used for the study of free volumes in nanocrystalline substances. It is sensitive to extremely small concentrations of defects in solids, namely, from  $10^{-6}$  to  $10^{-3}$  defects per atom. The capture of positrons by defects allows using the electron-positron annihilation for analysis of interfaces in nanosubstances.

When a positron emitted from a radioactive source gets into a solid, it quickly loses its velocity and energy, which drops to the value corresponding to the crystal temperature. Then the positron diffuses in the substance in the free (delocalized) state and annihilates from this state in the characteristic lifetime  $\tau_f$  of about 100 psec. During the time  $\tau_f$ , the positron may move a distance of about 100 nm in defectless solids. Because the size of grains in a nanosubstance is smaller than the length of the positron diffusion in a defect-free grain, virtually all positrons may reach the grain surface and interfaces. If grains contain defects, which capture positrons, only part of positrons reach the grain boundary. Therefore it is possible to obtain



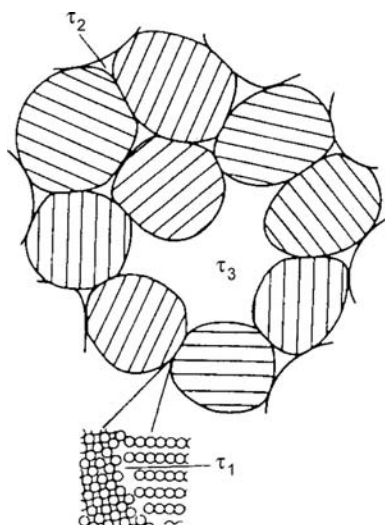


**Fig. 12** Two-dimensional schematic model of a nanocrystalline material with microscopic free volumes as detected by positron lifetime spectroscopy: *Source:* From Ref.<sup>[2]</sup> vacancy-like free volumes (with positron lifetime  $\tau_1$ ) in the interface, nanovoids (agglomerates of about 10 vacancies) at the triple junction of crystallites ( $\tau_2$ ), and a large void ( $\tau_3$ ) of the size of missing crystallites.

information about intragrain defects. After a positron has been captured by a defect, it annihilates from the localized state in a time exceeding  $\tau_f$ . The longer the lifetime of a positron in a defect is, the larger is the free volume.

Schaefer<sup>[2]</sup> and Würschum, Greiner, and Schaefer<sup>[30]</sup> have given considerable study to nanomaterials by the electron-positron annihilation method. Vacancies and nanovoids were detected in nanocrystalline metals Al, Cu, Mo, Pd, Fe, and Ni, nanocrystalline silicon Si and zirconium oxide  $ZrO_2$ , and many other materials. The investigations demonstrated that lifetime spectra of positrons usually contain two strong components and one weak component with intensities  $I_1$ ,  $I_2$ , and  $I_3 = 1 - I_1 - I_2$ , which correspond to the lifetime  $\tau_1$ ,  $\tau_2$ , and  $\tau_3$ , respectively (Fig. 12). In nanocrystalline metals, the lifetime  $\tau_1$  approaches the lifetime of positrons  $\tau_{1V}$  in lattice monovacancies of coarse-grain metals. Therefore  $\tau_1$  is viewed as the lifetime of positrons in vacancy-like free volumes in grain interfaces (interface vacancies). The size of these vacancies corresponds to one or two missing atoms. The positron lifetime  $\tau_2$  characterizes annihilation of positrons in three-dimensional vacancy agglomerates (nanovoids) of the size of about 10 missing atoms. A very long lifetime  $\tau_3$  corresponds to annihilation of positrons in large voids of the size of missing crystallites.

Generally, the positron annihilation revealed the following: 1) the lifetime of positrons in nanocrystalline metals is longer than the lifetime  $\tau_f$  of free

delocalized positrons; 2) positrons are captured by monovacancies, vacancy complexes, and voids, whose size approaches the size of crystallites; and 3) free vacancy volumes, which capture positrons at low temperatures, belong to interfaces and not to crystallites.

The microstructure of submicrocrystalline substances, which are synthesized using severe plastic deformation, differs from the microstructure of compacted nanocrystalline substances. The main feature of the structure of submicrocrystalline substances is the presence of randomly misoriented non-equilibrium grain boundaries. Unannealed submicrocrystalline metals and alloys are characterized by extinction contours along grain boundaries, which point to large elastic stresses. Annealing eliminates dislocations from grains, extinction contours vanish, and a stripe contrast, which is typical of the equilibrium state, appears. The relaxation of interfaces is accompanied by growth of grains during annealing.

## PROPERTIES OF ISOLATED NANOPARTICLES AND NANOCRYSTALLINE POWDERS

The transition from crystals to nanoparticles is followed by changes in the interatomic distances and lattice constants. For example, when the size of Ag and Au particles decreases from 40 to 10 nm, the lattice constant becomes  $\sim 0.1\%$  smaller. When the size of Si particles decreases from 10 to 3 nm, the lattice constant increases by 1.1%. The ambiguity of the dimensional effect may be a result of adsorption of impurities or different chemical compositions of particles. One more possible reason is the structural transformations, which are caused by the decrease in the particle size. Reliable experiments did not reveal shrinkage of the lattice constant as the particle size decreased to 10 nm, whereas shortening of interatomic distances for particles of smaller sizes is real enough as compared with bulk substances.

The most probable reason why the lattice constant of small particles changes as compared with its counterpart in a macroscopic substance consists in uncompensated interatomic bonds of surface atoms and hence the surface relaxation. In the case of nanoparticles, the surface relaxation is a maximum on the surface, decreases toward the center of the particle, and may prove to be oscillating under certain conditions. Thus the lattice constant may either increase or decrease as the size of nanoparticles diminishes.<sup>[7,8]</sup>

The melting temperature  $T_m$  drops non-linearly with decreasing size of small particles of Pb, Sn, Bi, In, Ga, Cu, Ag, Au, and Al. For example, the maximum decrease in the melting temperature of Sn, Ga, and Hg clusters  $\sim 1$  nm in size was 152, 106, and 95 K,

respectively.<sup>[4]</sup> When the radius of CdS colloid nanoparticles was reduced from 4 to 1 nm,  $T_m$  dropped nearly by 800 K.<sup>[31]</sup> According to Refs.<sup>[4]</sup> and <sup>[8]</sup>, melting temperatures of bulk crystals and small particles  $>10$  nm in size differ insignificantly. The melting temperature decreases when the size of nanoparticles becomes less than 10 nm.

Differences in thermodynamic properties of nanoparticles and a bulk substance are a result of changes in the phonon spectrum. The phonon spectrum of small particles contains low-frequency modes, which are absent in spectra of bulk crystals. The phonon spectrum of nanoparticles is limited by some minimum frequency on the side of low-frequency vibrations. No such limitation exists for bulk samples. Specific features of the vibration spectrum of nanoparticles affect the low-temperature heat capacity in the first place.

A theoretical analysis,<sup>[32]</sup> which took into account the quantum-size effect, showed that the low-temperature region ( $T \rightarrow 0$ ) has some temperature  $T_0$ , below which the nanoparticle heat capacity  $C_v(r)$  is smaller than the heat capacity  $C_v$  of a bulk crystal. At  $T > T_0$ , the difference  $\Delta C = C_v(r) - C_v$  becomes positive, reaches a maximum, and, as the temperature rises further, turns to zero. The difference of the heat capacities  $\Delta C = C_v(r) - C_v \rightarrow 0$  with increasing size  $r$  of the particle. These conclusions agree with experimental data.<sup>[33]</sup> The heat capacity of Ag nanoparticles 10 nm in size had the quantum-size effect in a magnetic field with  $B = 6$  T: at  $T < 1$  K and  $T > 1$  K, the heat capacity of Ag nanoparticles was lower and higher than the heat capacity of bulk silver, respectively. In the absence of the magnetic field, the heat capacity of colloid silver nanoparticles was higher than the heat capacity of bulk Ag over the whole temperature interval studied (Fig. 13).

An examination of phonon densities for coarse-grained Ni and a nanocrystalline nickel powder with particles  $\sim 10$  nm in size showed that the density of phonon states increased in n-Ni as compared with coarse-grained Ni at energies lower than 15 meV.<sup>[34]</sup>

Specific features of magnetic properties of nanoparticles are connected with discreteness of electron and phonon states. In particular, the Curie paramagnetism of a nanoparticle can overlap the Pauli paramagnetism at low temperatures. For example, magnetic susceptibility of lithium nanoparticles of diameter 3.2 nm corresponds to the Pauli paramagnetism at high temperatures and obeys the Curie law at low temperatures.<sup>[4]</sup>  $\text{Hg}_{13}$  clusters are weak paramagnetics in a magnetic field of up to 15 kOe independently of temperature. In a field with  $H > 20$  kOe, susceptibility of  $\text{Hg}_{13}$  clusters increases to large paramagnetic values at temperatures below 80 K, although mercury is a diamagnetic.<sup>[4]</sup>

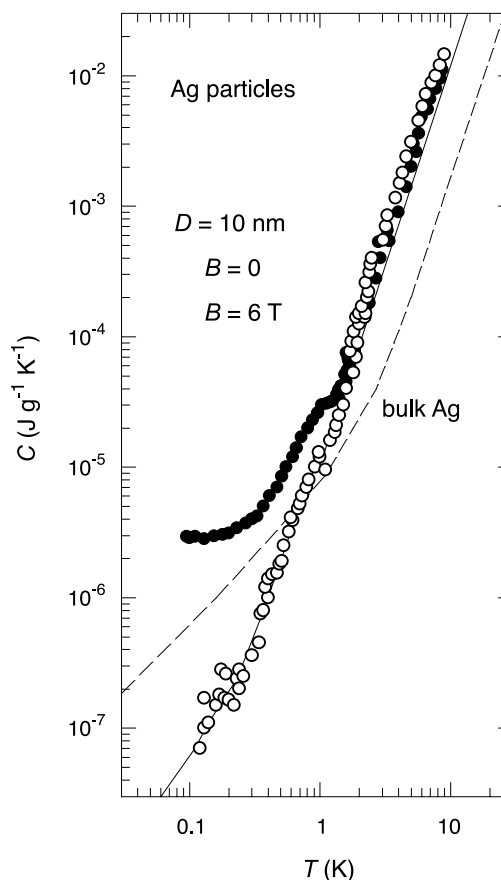


**Fig. 13** Specific heat capacity  $C$  of colloidal Ag with  $D = 10$  nm at  $T \leq 10$  K. Measurements were made in the absence of a magnetic field and in a magnetic field  $B = 6$  T. The dashed line shows the specific heat capacity of bulk coarse-grained silver.

The phenomenon of superparamagnetism is connected with the small size of ferromagnetic particles. When some critical size  $D_c$  is reached, ferromagnetic particles turn to single-domain ones, and, simultaneously, the coercive force  $H_c$  becomes a maximum. As the particle size diminishes further, the coercive force drops abruptly to zero as a result of transition to the superparamagnetic state. Typical ferromagnetics acquire the superparamagnetic state when the particle size is less than 1–10 nm.

When the size of Fe nanoparticles decreases from 80 to 8–10 nm, the coercive force  $H_c$  increases almost three times. The dimension dependence of  $H_c$  for Ni nanoparticles exhibits a maximum corresponding to nanoparticles 15 to 35 nm in diameter. As the particle size diminishes from 15 to 12 nm,  $H_c$  decreases nearly 5 times.<sup>[35]</sup> An analysis of the saturation magnetization  $I_s$  for bulk Ni and a nanocrystalline Ni powder ( $D = 12, 22$  and  $100$  nm)<sup>[36]</sup> showed that refinement of particles to 12 nm caused an almost twofold decrease in the  $I_s$  value as compared with bulk Ni.



Optical dimensional effects show themselves for nanoparticles whose size is smaller than the radiation wavelength and does not exceed 10–15 nm.<sup>[37]</sup> When fine-grain metal films absorb light, the visible part of the spectrum contains peaks, which are absent in the spectra obtained for bulk metals. For example, granulated films of Au particles 4 nm in diameter have a maximum absorption at  $\lambda = 560\text{--}600$  nm. Absorption spectra of Ag, Cu, Mg, In, Li, Na, and K nanoparticles also contain maxima in the optical range.<sup>[4]</sup> Differences in absorption spectra of nanoparticles and bulk metals are explained by the fact that the imaginary part of dielectric permeability is inversely proportional to the particle size. The particle size determines the shape of the low-frequency edge and the absorption bandwidth.

The size of semiconductor nanoparticles is comparable with the Bohr radius of excitons in a macroscopic crystal: the exciton radius changes over broad limits from 0.7 nm for CuCl to 10 nm for GaAs. The decrease in the size of nanoparticles causes displacement of the exciton absorption band to the high-frequency region (“blue” shift). The blue shift is observed for CdS nanoparticles with  $D \leq 10\text{--}12$  nm. When the size of ZnO, ZnS, CdS, and CdSe nanoparticles decreases, their luminescence spectra are displaced to the short-wave region.

### EFFECT OF THE GRAIN SIZE AND INTERFACES ON PROPERTIES OF BULK NANOSUBSTANCES

Properties of bulk nanomaterials depending on the grain size and the state of grain boundaries have been analyzed in reviews.<sup>[6,38,39]</sup>

At 300 K, the microhardness of bulk nanocrystalline substances is usually several times larger than  $H_V$  of coarse-grained substances. The growth of  $H_V$  was observed with decreasing size of n-Fe and n-Ni grains.<sup>[40]</sup> The microhardness  $H_V$  of nanocrystalline n-Cu copper ( $D \sim 16$  nm) is  $\sim 2.5$  times larger than that of copper with grains 5  $\mu\text{m}$  in size. However, as the size of n-Cu grains diminishes from 16 to 8 nm,  $H_V$  decreases by  $\sim 25\%$ . The decrease in  $H_V$  is also observed when n-Pd grains are refined from 13 to 7 nm. The microhardness  $H_V$  of Ni-P, TiAlNb, TiAl, and NbAl<sub>3</sub> nanocrystalline alloys drops as the grain size decreases from 60–100 to 6–10 nm.

In a general case, the microhardness of nanosubstances grows as the grain size decreases to some  $D_c$  value and drops at  $D < D_c$ . Mechanical and elastic properties of nanocrystalline metals are determined not only by a small size of grains, but also by the state of interfaces. Therefore contradictory results on the dimension dependence of the microhardness may be due to different structures of interfaces.

Strength properties of nanosubstances are enhanced with decreasing size of grains. The yield stress of nanocrystalline Pd ( $D = 5\text{--}15$  nm) and Cu ( $D = 25\text{--}50$  nm) is 2–3 times higher than the yield stress of coarse-grained metals.<sup>[41]</sup> The tensile strength of nanocrystalline metals is 1.5–8 times larger than that of coarse-grained metals.<sup>[40,41]</sup>

At temperatures from 150 to 300 K, the heat capacity  $C_p$  of n-Pd ( $D = 6$  nm) and n-Cu ( $D = 8$  nm) is 30–50% and  $\sim 10\%$  higher than the heat capacity of coarse-grained bulk Pd and Cu, respectively. In the interval of 0.06 to 10.0 K, the low-temperature heat capacity of compacted nanocrystalline copper n-Cu with grains 6.0 and 8.5 nm in size proved to be 5–10 times larger than the heat capacity of coarse-grained copper. Measurements of the heat capacity of amorphous, nanocrystalline, and coarse-grained selenium Se over the temperature interval from 220 to 500 K<sup>[42]</sup> revealed a small increase in the heat capacity of bulk nanocrystalline n-Se as compared with coarse-grained Se at  $T < 375$  K. A comparison of the heat capacity of substances in nanocrystalline, amorphous, and coarse-grained states<sup>[43]</sup> showed that the heat capacity of samples prepared by compaction of nanopowders is largely different from the heat capacity of substances in the coarse-grain state (Table 1). Oppositely, this difference does not exceed 2% for samples prepared by crystallization from the amorphous state. One may think that most of the excess heat capacity of compacted nanomaterials is a result of a large surface area of interfaces, structural distortions, and impurities.

The thermal expansion coefficient  $\alpha$  is proportional to the heat capacity. Therefore the coefficient  $\alpha$  of bulk nanosubstances should be higher than  $\alpha$  of coarse-grained polycrystals. Indeed, the coefficient  $\alpha$  of nanocrystalline copper n-Cu with grains 8 nm in size on the average is twice as large as  $\alpha$  of coarse-grained copper.<sup>[44]</sup>

A large surface area of interfaces and a high concentration of defects determine an intensive scattering of charge carriers in nanomaterials. A considerable increase in electroresistivity  $\rho$  of nanocrystalline Cu, Pd, Fe, and Ni and various alloys with decreasing size of grains has been noted by many researchers. For example, at temperatures  $0 < T \leq 275$  K, electroresistivity of n-Cu ( $D = 7$  nm) is 7 to 20 times larger than  $\rho$  of common coarse-grained copper.

The effect of the nanostate on magnetic properties of paramagnetics is well pronounced, e.g., in palladium (Fig. 14).<sup>[8]</sup> At 300 K, susceptibilities of nanocrystalline n-Pd and the initial coarse-grained palladium differ by 8%. According to Ref.<sup>[8]</sup> such a considerable variation of the susceptibility is a result of the presence of intra-grain vacancy complexes in n-Pd, which change the density of electron states at the Fermi level.

**Table 1** Comparison of heat capacity  $C_p$  ( $\text{J mol}^{-1} \text{K}^{-1}$ ) for the nanocrystalline, amorphous, and coarse-grained polycrystalline states of different substances

Material	State					
	Nanocrystalline			Amorphous	Coarse-grained	
	Synthesis method <sup>a</sup>	Crystallite size $D$ (nm)	$C_p$	$C_p$	$C_p$	$T$ (K)
Pd	1	6	37	27	25	250
Cu	1	8	26	—	24	250
Ru	2	15	28	—	23	250
$\text{Ni}_{0.8}\text{P}_{0.2}$	3	6	23.4	23.4	23.2	250
Se	3	10	24.5	24.7	24.1	245

<sup>a</sup>1: Compaction of ultrafine powders prepared by evaporation; 2: ball milling; 3: crystallization from the amorphous state.

Source: From Ref.<sup>[43]</sup>.

The majority of studies into magnetic properties of bulk nanosubstances have dealt with ferromagnetic metals and alloys. A study of submicrocrystalline Ni<sup>[45]</sup> has confirmed that the coercive force of plastically deformed ferromagnetics is several times larger than  $H_c$  of initial metals. However, annealing of submicrocrystalline Ni at  $T \leq 470$  K causes a decrease in the coercive force, while the grain size remains unchanged. Annealing at higher temperatures leads to a decrease in  $H_c$  and an increase in the grain size. Therefore a large

coercive force of submicrocrystalline metals and alloys is equally determined by a non-equilibrium state of interfaces on the one hand and a small size of grains on the other hand. Relaxation of interfaces during annealing and growth of grains cause a decrease in  $H_c$ .

## CONCLUSION

Studies performed in recent decades have considerably improved our understanding of the effects related to the size of grains (crystallites) in solids. For a long time, studies have been focused on small particles (nanoclusters) whose properties are intermediate between properties of isolated atoms and polycrystalline solids. The advent of methods for production of compact materials having an extremely fine-grain structure with nanometer-sized grains provided conditions for the study of the structure and properties of solids in the nanocrystalline state. Each of those methods has its virtues and drawbacks, and neither of them is universal because each is applicable to a certain range of substances. Because of their specific structure, properties of nanocrystalline substances differ considerably from those of usual polycrystals. An analysis of the available experimental data shows that not only the grain size (as in isolated nanoparticles), but also the structure and the state of interfaces (grain boundaries) play a significant role in a nanocrystalline solid. The separation of surface effects (connected with interfaces) and volume effects (related to the size of particles) is very important for the theoretical interpretation of the experimental results obtained for isolated nanoparticles and bulk nanocrystalline materials.

Extensive studies of nanocrystalline substances and materials have led to appearance of new sciences,

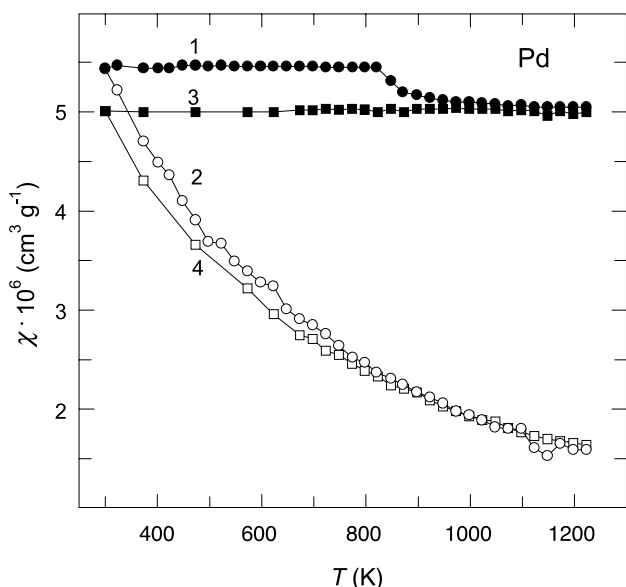


**Fig. 14** Magnetic susceptibility  $\chi$  of nanocrystalline n-Pd and coarse-grained palladium: Source: From Ref.<sup>[8]</sup> (1) annealing  $\chi(300, T)$  and (2) temperature  $\chi(T)$  dependences of the susceptibility for n-Pd; (3) annealing  $\chi(300, T)$  and (4) temperature  $\chi(T)$  dependences of the susceptibility for the initial coarse-grained Pd. The annealing dependences  $\chi(300, T)$  of the susceptibility (curves 1 and 3) were measured at 300 K after annealing at a temperature  $T$  and cooling to 300 K.

namely, nanocrystalline solid-state physics and chemistry. Therefore it is possible to establish tight contacts between nanomaterials and nanotechnologies, which will present the main motive force of the scientific and technological progress in the 21st century.

## REFERENCES

- Gleiter, H. Materials with ultrafine microstructure: Retrospectives and perspectives. *Nanostruct. Mater.* **1992**, *1* (1), 1–19.
- Schaefer, H.-E. Interfaces and Physical Properties of Nanostructured Solids. In *Mechanical Properties and Deformation Behavior of Materials Having Ultrafine Microstructure*; Nastasi, M.A., Parkin, D.M., Gleiter, H., Eds.; Kluwer Academic Press: Dordrecht, Netherlands, 1993; 81–106.
- Siegel, R.W. What do we really know about the atomic-scale structures of nanophase materials?. *J. Phys. Chem. Solids* **1994**, *55* (10), 1097–1106.
- Petrov, Yu.I. *Clusters and Small Particles*; Nauka: Moscow, 1986 (in Russian).
- Andrievskii, R.A. The synthesis and properties of nanocrystalline refractory compounds. *Russ. Chem. Rev.* **1994**, *63* (5), 411–428.
- Gusev, A.I. Effects of the nanocrystalline state in solids. *Phys. Uspekhi* **1998**, *41* (1), 49–76.
- Gusev, A.I. *Nanocrystalline Materials: Preparation and Properties*; Ural Division of the Russ. Acad. Sci.: Yekaterinburg, 1998 (in Russian).
- Gusev, A.I.; Rempel, A.A. *Nanocrystalline Materials*; Nauka-Fizmatlit: Moscow, 2000 (in Russian).
- Feynman, R.P. There is plenty of room at the bottom: An invitation to enter a new field of physics. <http://www.zyvex.com/nanotech/feynman.html>.
- Kroto, H.W.; Heath, J.R.; O'Brien, S.C.; Curl, R.F.; Smalley, R.E. C<sub>60</sub>: Buckminsterfullerene. *Nature* **1985**, *318* (6042), 162–163.
- Guo, B.C.; Kerns, K.P.; Castleman, A.W. Ti<sub>8</sub>C<sub>12</sub><sup>+</sup>-metallo-carbohedrenes: A new class of molecular clusters? *Science* **1992**, *255* (5050), 1411–1413.
- Kotov, Yu.A.; Yavorski, N.A. Study of particles forming at electric explosion of conductors. *Fiz. Him. Obrab. Mater.* **1978**, (4), 24–29 (in Russian).
- Nersisyan, H.H.; Lee, J.H.; Won, C.W. Self-propagating high-temperature synthesis of nano-sized titanium carbide powder. *J. Mater. Res.* **2002**, *17* (11), 2859–2864.
- Gusev, A.I.; Rempel, A.A.; Magerl, A.J. *Disorder and Order in Strongly Nonstoichiometric Compounds: Transition Metal Carbides, Nitrides and Oxides*; Springer: Berlin, 2001.
- Rempel, A.A.; Gusev, A.I. Nanostructure and atomic ordering in vanadium carbide. *JETP Lett.* **1999**, *69* (6), 472–478.
- Gusev, A.I.; Tulin, A.A.; Lipatnikov, V.N.; Rempel, A.A. Nanostructure of dispersed and bulk nonstoichiometric vanadium carbide. *Russ. J. Gen. Chem.* **2002**, *72* (7), 985–993.
- Gleiter, H. Nanocrystalline materials. *Prog. Mater. Sci.* **1989**, *33* (4), 223–315.
- Ivanov, V.V.; Kotov, Yu.A.; Samatov, O.M.; Böhme, R.; Karow, H.U.; Schumacher, G. Synthesis and dynamic compaction of ceramic nanopowders by techniques based on electric pulsed power. *Nanostruct. Mater.* **1995**, *6* (1–4), 287–290.
- Khasanov, O.L.; Dvilis, E.S.; Pokholkov, Yu.P.; Sokolov, V.M. Mechanisms of ultrasonic pressing of ceramic nanopowders. *J. Adv. Mater.* **1999**, *5* (3), 69–75.
- Bykov, Yu.; Ereemeev, A.; Flyagin, V.; Kaurov, V.; Kuftin, A.; Luchinin, A.; Malygin, O.; Plotnikov, I.; Zapevalov, V. The gyrotron system for ceramics sintering. *Ceram. Trans.* **1995**, *59*, 133–140.
- Yoshizawa, Y.; Oguma, S.; Yamauchi, K. New iron-based soft-magnetic alloys composed of ultrafine grain structure. *J. Appl. Phys.* **1988**, *64* (10), 6044–6046.
- Inoue, A. Preparation and novel properties of nanocrystalline and nanoquasicrystalline alloys. *Nanostruct. Mater.* **1995**, *6* (1–4), 53–64.
- Segal, V.M. Materials processing by simple shear. *Mater. Sci. Eng., A* **1995**, *197* (2), 157–164.
- Valiev, R.Z.; Aleksandrov, I.V. *Nanostructured Materials Obtained by Severe Plastic Deformation*; Logos: Moscow, 2000 (in Russian).
- Fitzsimmons, M.; Eastman, J.A.; Müller-Stach, M.; Wallner, G. Structural characterization of nanometer-sized crystalline Pd by X-ray-diffraction techniques. *Phys. Rev., B* **1991**, *44* (6), 2452–2460.
- Ishida, Y.; Ichinose, H.; Kizuka, T.; Suenaga, K. High-resolution electron microscopy of interfaces in nanocrystalline materials. *Nanostruct. Mater.* **1995**, *6* (1–4), 115–124.
- Babanov, Yu.A.; Blaginina, L.A.; Golovshchikova, I.V.; Haubold, T.; Boscherini, F.; Mobilio, S. Defects in nanocrystalline palladium. *Phys. Met. Metallogr.* **1997**, *83* (4), 444–451.
- Löffler, J.; Weissmüller, J.; Gleiter, H. Characterization of nanocrystalline palladium by x-ray atomic density distribution functions. *Nanostruct. Mater.* **1995**, *6* (5–8), 567–570.
- Weissmüller, J.; Löffler, J.; Kleber, M. Atomic structure of nanocrystalline metals studied by diffraction techniques and EXAFS. *Nanostruct. Mater.* **1995**, *6* (1–4), 105–114.
- Würschum, R.; Greiner, W.; Schaefer, H.-E. Preparation and positron lifetime spectroscopy of nanocrystalline metals. *Nanostruct. Mater.* **1993**, *2* (1), 55–62.
- Goldstein, A.N.; Echer, C.M.; Alivisatos, A.P. Melting in semiconductor nanocrystals. *Science* **1992**, *256* (2062), 1425–1427.
- Nonnenmacher, Th.F. Quantum size effect on the specific heat of small particles. *Phys. Lett.* **1975**, *51A* (4), 213–214.
- Goll, G.; Löhneyen, H. Specific heat of nanocrystalline and colloidal noble metals at low temperatures. *Nanostruct. Mater.* **1995**, *6* (5–8), 559–562.
- Trampenau, J.; Bauszus, K.; Petry, W.; Herr, U. Vibrational behaviour of nanocrystalline Ni. *Nanostruct. Mater.* **1995**, *6* (5–8), 551–554.
- Daroczi, L.; Beke, D.I.; Posgay, G.; Kis-Varga, M. Magnetic properties of ball milled nanocrystalline Ni and Fe. *Nanostruct. Mater.* **1995**, *6* (5–8), 981–984.

36. Yao, Y.D.; Chen, Y.Y.; Hsu, C.M.; Lin, H.M.; Tung, C.Y.; Tai, M.F.; Wang, D.H.; Wu, K.T.; Suo, C.T. Thermal and magnetic studies of nanocrystalline Ni. *Nanostruct. Mater.* **1995**, *6* (5–8), 933–936.
37. Bohren, C.F.; Huffman, D.R. *Absorption and Scattering of Light by Small Particles*; Wiley-Interscience: New York, 1998.
38. Andrievskii, R.A.; Glezer, A.M. Size effects in nanocrystalline materials: I. Structure characteristics, thermodynamics, phase equilibria, and transport phenomena. *Fiz. Met. Metalloved.* **1999**, *88* (1), 50–73.
39. Andrievskii, R.A.; Glezer, A.M. Size effects in nanocrystalline materials: II. Mechanical and physical properties. *Fiz. Met. Metalloved.* **2000**, *89* (1), 91–112 (in Russian).
40. Siegel, R.W.; Fougere, G.E. Mechanical properties of nanophase metals. *Nanostruct. Mater.* **1995**, *6* (1–4), 205–216.
41. Neiman, G.W.; Weertman, J.R.; Siegel, R.W. Mechanical behavior of nanocrystalline Cu and Pd. *J. Mater. Res.* **1991**, *6* (5), 1012–1027.
42. Sun, N.X.; Lu, K. Heat capacity comparison among the nanocrystalline, amorphous and coarse-grained polycrystalline states in elemental selenium. *Phys. Rev., B* **1996**, *54* (9), 6058–6061.
43. Rupp, J.; Birringer, R. Enhanced specific-heat-capacity (cp) measurements (150–300 K) of nanometer-sized crystalline materials. *Phys. Rev., B* **1987**, *36* (15), 7888–7890.
44. Birringer, R.; Gleiter, H. Nanocrystalline Materials. In *Encyclopedia of Material Science and Engineering*; Cahn, R.W., Ed.; Pergamon Press: Oxford, 1988; Suppl. 1, 339–349.
45. Mulyukov, Kh.Ya.; Korznikova, G.F.; Abdulov, R.Z.; Valiev, R.Z. Magnetic hysteresis properties of sub-micron grained nickel and their variation upon annealing. *J. Magn. Magn. Mater.* **1990**, *89* (1), 207–213.

# Nanocrystalline Oxides: Surfactant-Assisted Growth

Claudia L. Bianchi  
Silvia Ardizzone  
Giuseppe Cappelletti

*Department of Physical Chemistry and Electrochemistry,  
University of Milan, Milan, Italy*

## INTRODUCTION

Advances in nanoparticle synthesis stem from their fundamental technological importance; numerous research efforts have recently been devoted to the preparation of metal oxide nanostructures with tailored features, because of their unique electronic, optical, and mechanical properties and their widespread potential applications in fields including catalysis, nanoelectronics, optoelectronics, and biotechnology.<sup>[1–4]</sup>

The use of surfactants to control the features of tailored nanoparticles is widespread, and the number of synthetic routes reported in the literature to obtain oxides with controlled features is enormous. The adopted procedures can be complex and composite so that it is not always easy to individuate some common principle in the selection of the stages, conditions, and nature of surfactant molecules. In this article, results will be grouped with reference to three main categories that imply a different philosophy of operation: templated synthesis, microemulsion procedure, and hydrothermal growth.

## TEMPLATED SYNTHESIS

One of the first and main applications of surfactants in the synthesis of metal oxides is as templates or directing agents for the effective control of mesophase structures. In principle, in these syntheses, the morphology of the solid is imposed by the tridimensional mesostructure of a surfactant, which acts as a nucleating agent and which is finally removed after the growth of the inorganic material. By modulating the operation conditions and the surfactant features, the synthesis can be projected toward liquid crystal phases with different tridimensional organization and consequently toward materials having accurately controlled pore network.

Outstanding examples of surfactant templating technique are represented by the synthesis of mesostructured silicates, the M41S family,<sup>[5]</sup> which includes the hexagonal MCM-41, the cubic MCM-48, and the

lamellar MCM-50 phases, obtained in basic media using ionic surfactants as templates. Active debate is present in the literature concerning the actual mechanism of the process, either following the expected liquid crystal templating route or a transformation mechanism from lamellar to hexagonal phase. Vartuli et al.<sup>[6]</sup> found that in the case of MCM41, MCM48, the lamellar, and the cubic octamer, the three-dimensional (3-D) organization of the solid exactly reproduced the behavior of the surfactant in solution; on the other hand, Chen et al.<sup>[7]</sup> used x-ray diffraction (XRD), Si-nuclear magnetic resonance (NMR), and in situ N-NMR, and observed no hexagonal liquid crystalline mesophases either in the synthesis gel or in the surfactant solution used as a template. Stucky and coworkers<sup>[8]</sup> assert a transformation mechanism for the formation of the hexagonal phase where a preformed micellar assembly of a surfactant that is broken up and rearranged upon the addition of the inorganic species to form a new phase, converts to the hexagonal phase upon prolonged ageing. Possibly the formation of these mesophases follows a cooperative self-assembly mechanism, based on the electrostatic interactions between the oppositely charged micellar headgroups and polysilicate species.

Indeed Adachi, Harada, and Harada<sup>[9]</sup> recently proposed a surfactant/oxide interactive mechanism to be controlling the microstructure formation in the growth processes of silica nanotubes by a templating mechanism with cationic surfactants; the important factors leading to the desired morphology are found to be the geometric matching between the occupied area of surfactant and that of silicate molecules at the interface, and the packing parameter of the surfactant/silicate assemblies.

Since the MCM synthesis, the molecular templating technique has been used to synthesize a variety of mesoporous materials<sup>[10]</sup> both for pure oxides and for composites. For example, Chao and Ruckenstein<sup>[11]</sup> recently obtained mesostructured V-Mg oxides by ionic micellar templates by accurately controlling the conditions of charge development at the oxide/surfactant interface.

However, in the case of several oxides (e.g., alumina and titania) where ionic surfactants were used as a template, the nanostructured mesophases collapsed, at least in part, upon surfactant removal.<sup>[12]</sup> The electrostatic surfactant/oxide interactions combined with the fast grain growth of the oxide, which occurs upon calcination of the surfactant-rich precursor, may in fact provoke pore collapse with degradation of the mesostructure.<sup>[12]</sup> Also in our laboratory, the templated synthesis of titanium dioxide by gemini cationic surfactants<sup>[13]</sup> was not fully successful. Mesoporosity induced by the three-dimensional organization of the surfactant could be appreciated by the hysteresis loop of the nitrogen adsorption–desorption isotherm (Fig. 1, curve b), with respect to the reference material prepared without surfactant. However, the promotion of the sample surface area (around 12–13 m<sup>2</sup>/g vs. the reference sample without surfactant, 7–9 m<sup>2</sup>/g) was not relevant owing to sintering between the particles upon heating. The inset to Fig. 1 reports the experimental adsorption isotherms, at the TiO<sub>2</sub>/solution interface, of both the gemini-like and the monomeric pyridinic surfactants. The shape of the two curves, obtained at constant ionic strength and oxide surface potential (solution pH), is markedly different: The monomeric isotherm (curve 2) is S-shaped showing a low adsorbent–adsorbate affinity, in agreement with results by other authors on simple alkylpyridinium salts adsorbed at solid/liquid boundaries. Dodecylpyridinium monomers are reported to be

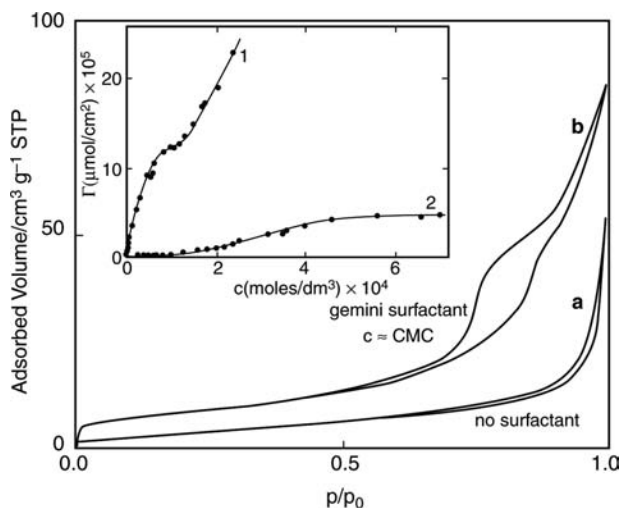


**Fig. 1** N<sub>2</sub> adsorption–desorption isotherms of TiO<sub>2</sub> samples, the reference and the surfactant-assisted one. Inset: linear plot of the surface excess ( $\Gamma$ ) vs. the surfactant equilibrium concentration: 1) dimeric surfactant, 1,10-didodecyl-4,40-bipyridinium chloride; 2) monomeric molecule, 1-dodecyl-4-methylpyridinium chloride. Adsorption of cationic “gemini” surfactants at the TiO<sub>2</sub>/solution interface. *Source:* From Ref.<sup>[13]</sup>.

weakly interacting with rutile.<sup>[14]</sup> The higher affinity of the gemini for the solid appears also from the strikingly larger adsorbed amounts apparent in inset of (Fig. 1, curve 1). Comparing the quasiplateau regions, the gemini adsorbed amounts are about four times larger than for the monomer; however just this high affinity leads to a subsequent collapse of the mesoporous structure during the calcinations step.

Success was achieved, instead, by using neutral surfactants or carboxylic acids as surfactants. In the case of titanium dioxide, for example, very recent results show that the use of tri- or di-block copolymers has led to the formation of stable mesoporous structures.<sup>[15–17,8]</sup> Serrano et al.<sup>[15]</sup> combined the neutral templating route with a crystallization treatment in acid–ethanol mixtures and succeeded in obtaining bimodal micromesoporous anatase TiO<sub>2</sub> (Fig. 2) with a large surface area; hollow titania particles were obtained by using a triblock copolymer (PEO<sub>n</sub>–PPO<sub>m</sub>–PEO<sub>n</sub>).<sup>[16]</sup> In Fig. 2, the nitrogen adsorption isotherm is apparently of type IV, typical of mesoporous materials, although with a remarkable adsorption at low relative pressures, suggesting the presence also of micropores.

By means of neutral templating, other features, besides porosity, could be successfully controlled. Monodisperse titania particles (Fig. 3) of variable sizes could be obtained in the presence of diblock Lutensol (RO(CH<sub>2</sub>CH<sub>2</sub>O)<sub>x</sub>H) and/or triblock-copolymers Pluronic (PEO<sub>n</sub>–PPO<sub>m</sub>–PEO<sub>n</sub>)<sup>[9]</sup> owing to cooperative mechanisms possibly implying steric stabilization. As shown in Fig. 3, highly monodispersed particles are obtained in the presence of Lutensol polymers. In addition, other researchers,<sup>[12]</sup> by simply adjusting the surfactant/solvent ratio, have successfully controlled the size of magnetic nanoparticles ( $\gamma$ -Fe<sub>2</sub>O<sub>3</sub>, Fe), all

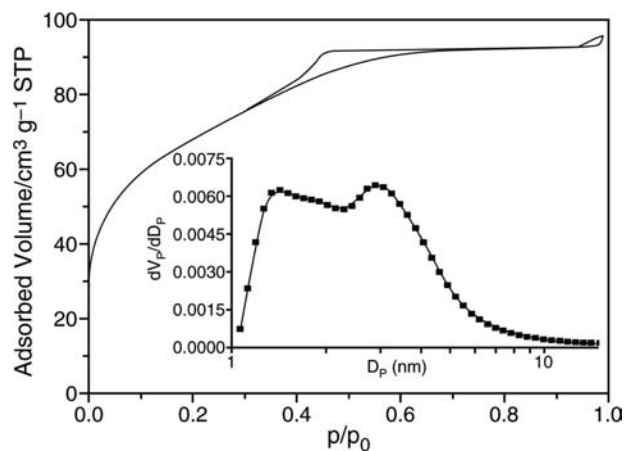


**Fig. 2** N<sub>2</sub> adsorption–desorption isotherm and pore-size distribution of TiO<sub>2</sub> sample after treatment with 1% HCl/EtOH. *Source:* From Ref.<sup>[15]</sup>.



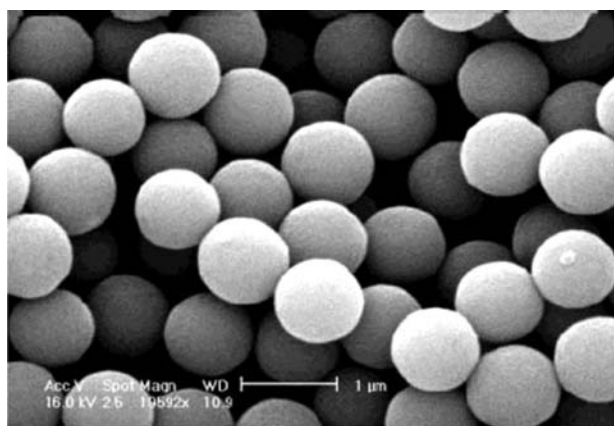


**Fig. 3** SEM pictures of the titania particles synthesized by addition of Lutensol ON 50. *Source:* From Ref.<sup>[16]</sup>.

having spherical shape and uniform size. The phase composition, especially in the case of the possible concomitant formation of different polymorphs, could also be controlled. Luo<sup>[17]</sup> using a triblock copolymer as a structure-directing agent (F-127 or Pluronic P-123) and  $\text{TiCl}_4$  as precursor, by simply varying the solvents, successfully controlled the phase composition and obtained either pure anatase, pure rutile, or bicrystalline compounds (anatase and rutile) or tricrystalline (anatase, rutile, and brookite) with controlled relative enrichment (Table 1). All the samples were calcined at  $380^\circ\text{C}$  for five hours.

## MICROEMULSION TECHNIQUE

A microemulsion is an isotropic and transparent mixture containing oil and water separated by a thin surfactant monolayer. From a particle preparation point of view, the microemulsion system, with an internal structure consisting of small droplets, is the most

interesting. The water-in-oil (w/o) microemulsion is of particular interest because it can be regarded as a collection of tiny compartments made up of the hydrophilic moiety of the surfactant, each filled with water, where the water droplets are in the size range of a few nanometers to 100 nm; they can be used as small microreactors for the product synthesis. The surfactant-stabilized microcavities provide a cage-like effect, which limits particle nucleation, growth, and agglomeration. The size of the final particle will depend much on the size of the droplets in the microemulsion. The droplet size will, in its turn, be influenced by the water-to-surfactant ratio. An increase of this ratio at constant concentration of the surfactant will increase the average diameter of the droplets. When the amount of water and oil is kept at fixed values, an increase in the amount of surfactant will increase the number of droplets. That means that the number of metal ions per droplet will decrease and consequently the size of the particles.<sup>[18]</sup> In the case of a microemulsion-mediated synthesis of acicular  $\gamma\text{-Fe}_2\text{O}_3$  with a spherical diameter of 7–8 nm, Chhabra et al.<sup>[19]</sup> showed that each microemulsion droplet gives birth to a single particle of  $\gamma\text{-Fe}_2\text{O}_3$ .

In the case of  $\text{SnO}_2$ , Chen and Gao<sup>[20]</sup> by combining a simple w/o microemulsion with a hydrothermal process, obtained small single-crystal particles with a narrow size distribution, which could be refined by modulating the ageing conditions. Fig. 4 illustrates the high-resolution transmission electron microscope image of the  $\text{SnO}_2$  nanoparticles. According to the distinct lattice fringes (inset of Fig. 4), the observed nanoparticles are equiaxial single crystals, whose diameters are less than 3.0 nm.

Nanoparticles of either anatase or rutile phases were obtained by the hydrothermal treatment of microemulsions and by only varying the acid (either HCl or  $\text{HNO}_3$ ) during the hydrothermal treatment of the microemulsion. Similarly Yan, Chen, and Zhang<sup>[21]</sup>

**Table 1** Synthetic conditions for mesoporous  $\text{TiO}_2$

Sample	Solvent	Aging time (days)	Phase content <sup>a</sup>	Crystalline size <sup>b</sup> (nm)
Ti-M (F-127)	Methanol	3	Pure A	12
Ti-MH (F-127)	Methanol + $\text{H}_2\text{O}$	3	A (75%) + R (25%)	12 (A)
Ti-E (F-127)	Ethanol	6	A (80%) + R (20%)	16 (A)
Ti-E (P123)	Ethanol	6	A (52%) + R (48%)	17 (A)
Ti-EH (F-127)	Ethanol + $\text{H}_2\text{O}$	6	A (48%) + R (32%) + B (20%)	13 (A)
Ti-HCl (F-127)	Ethanol + HCl	6	Pure R	16
Ti-B (F-127)	1-Butanol	7	A (33%) + R (65%)	14 (R)
Ti-BH (F-127)	1-Butanol + $\text{H}_2\text{O}$	7	Pure R	14
Ti-OH (F-127)	1-Octanol + $\text{H}_2\text{O}$	10	Pure R	20

<sup>a</sup>A, anatase; B, brookite; R, rutile.

<sup>b</sup>Calculated by applying the Scherrer formula on the anatase (1 0 1) or rutile (1 1 0) diffraction peak.

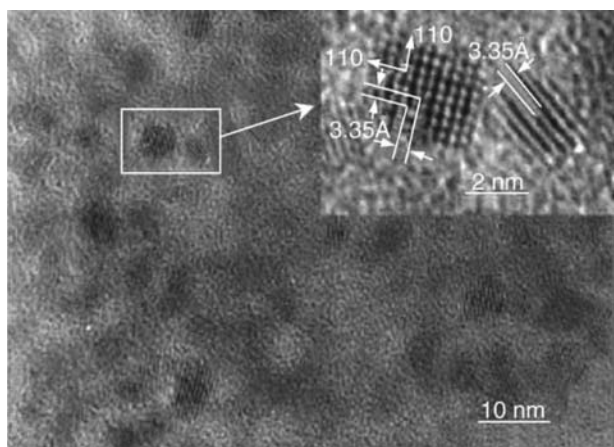


**Fig. 4** HRTEM image of SnO<sub>2</sub> nanoparticles. *Source:* From Ref.<sup>[20]</sup>.

have obtained either anatase or rutile by autoclaving microemulsions and by simply changing the proportion of Cl<sup>-</sup> and SO<sub>4</sub><sup>2-</sup> in the aqueous phase of the microemulsion.

## HYDROTHERMAL GROWTH

In the case of hydrothermal growth of oxides in the presence of surfactants, the nature and extent of the surfactant–oxide interaction are very important because they control the reactions of dissolution–reprecipitation of the solid and, consequently, they potentially impose both morphological and structural aspects. In the case of ionic surfactants, the presence of attractive electrostatic interactions is crucial.

In the preparation of ceria nanorods, Vantomme et al.<sup>[22]</sup> observed that only at pH values above the isoelectric point of the particle attractive interactions with the cationic surfactant cetyltrimethylammonium bromide (CTMA<sup>+</sup>Br<sup>-</sup>) occurred, leading to ion pairs. The ion pairs (Ce–O<sup>-</sup>⋯CTMA<sup>+</sup>) polymerize during micellization and under autoclaving, by interchain attraction, flocculation, or coalescence, which results in the formation of ceria/surfactant bilayers, which in turn drive the orientation growth of ceria nanorods. The positive adsorption of the surfactant at the growing ceria particles is directly observed in the Fourier transform infrared spectroscopy spectrum (Fig. 5A) of the as-synthesized sample, which exhibits absorption bands in the region 2800–2900/cm, attributed to the C–H stretching mode of hydrocarbons and the bands at 1450–1500 and 720/cm assigned to the bending vibration of the C–H band of methylene groups. The presence of the surfactant was appreciable also in the XRD patterns of the as-synthesized sample (Fig. 5B). The peak at the low angle is the result of the

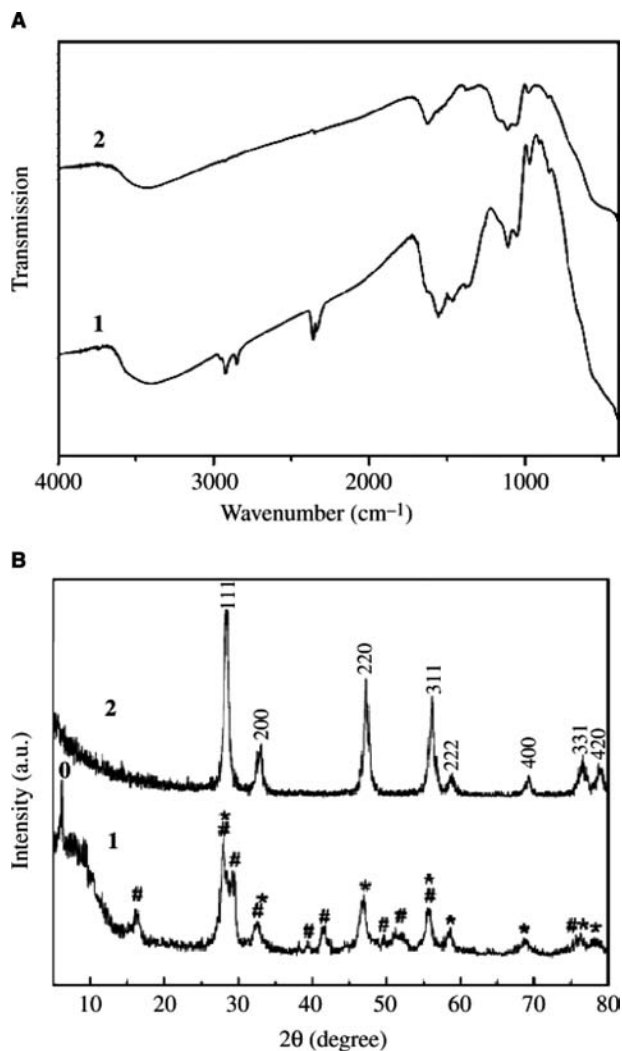


**Fig. 5** Ceria nanorods before (1) and after calcinations (2): (A) FT-IR spectra; (B) x-ray diffraction patterns (\*, reflection of the participating CTMABr species; #, reflections of hexagonal Ce(OH)<sub>3</sub>; \*, reflections of cubic CeO<sub>2</sub>). *Source:* From Ref.<sup>[22]</sup>.

interactions between surfactant and ceria and is similar to an XRD pattern of the surfactant itself (CTMABr).

The analysis of the XPS spectra of carbon 1s of TiO<sub>2</sub>–sodium dodecyl sulfate (SDS) adsorbed samples may allow the obtaining of information concerning the mode of surfactant adsorption. Carbon spectra show the presence of a peak localized at 288.6 eV (Figs. 6A and B). This peak (peak D in the figure) is present in all adsorbates, although its intensity is decreasing with the concentration of the surfactant, while it is not appreciable in the pure salt spectra. In the literature carbon 1s peaks at comparable binding energy are attributed, in the absence of C–O bonds, to carbon species with neighboring electron-attracting species. In the present case it can be suggested that the

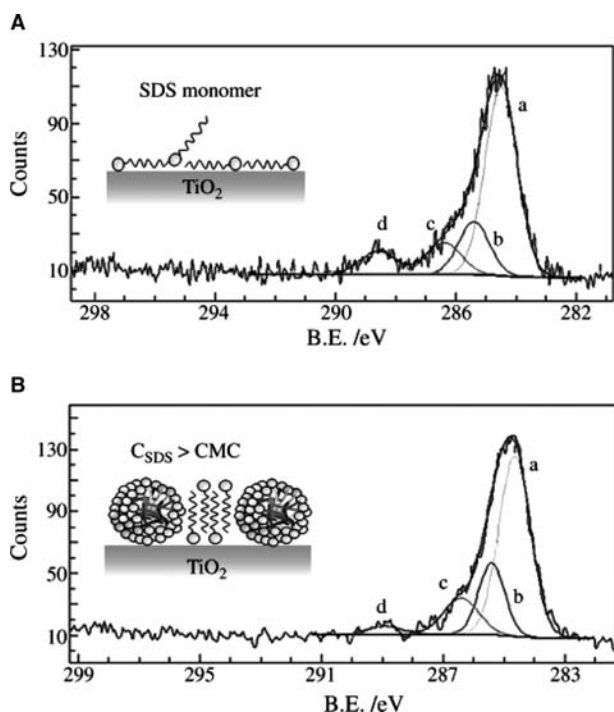


**Fig. 6** XPS C 1s region of  $\text{TiO}_2$  precursor samples hydrothermally grown at  $\text{pH} = 3$ , at increasing surfactant (SDS) concentration (A) monomer; (B) micelles. Components—*a*: 284.6 eV,  $\gamma$  carbons and adventitious; *b*: 285.4 eV,  $\beta$  carbons; *c*: 286.4 eV,  $\alpha$  carbons; and *d*: 288.6 eV. Insets: sketches of the possible surfactant orientations.

peaks at 288.6 eV are the result of local environments produced by the proximity of several sulfate groups on the carbon atoms of the alkyl chain. The observed decreasing intensity of the peak with the surfactant concentration can be related to different orientations assumed by the molecules at the surface. At low surface coverages (monomer adsorption), the molecules can be supposed to be mainly lying flat on the oxide surface (inset Fig. 6A); the carbons in the chain would therefore experience the electron-attractive effects produced by the adsorbed sulfate groups. At higher surfactant concentrations hemimicelles<sup>[13]</sup> start to form and, eventually, micelles also adsorb (inset in Fig. 6B). The alkyl chains in the micelles are shielded from the neighboring interactions with the sulfate groups and the intensity of the 288.6 eV peak decreases progressively.

Also in the case of the hydrothermal growth of  $\text{TiO}_2$  particles, the electrostatic interactions between the oxide surface and ionic surfactants play a central role. Specifically in the case of  $\text{TiO}_2$  crystals, obtained by sol-gel from titanium alkoxide<sup>[23–26]</sup> and subsequently grown in the presence of an anionic surfactant (SDS) the oxide phase composition (Fig. 7) appears to be imposed by the interplay between oxide/surfactant interactions and surfactant self-aggregation processes. At a positive oxide surface charge ( $\text{pH} 3$ ), in the

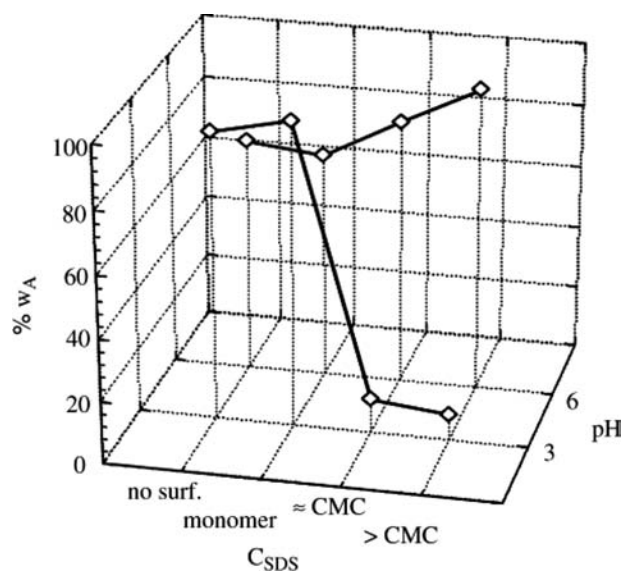


**Fig. 7** Quantitative anatase content by elaboration of x-ray diffractograms of samples calcined at  $600^\circ\text{C}$  as a function of  $\text{pH}$  of the hydrothermal growth. The third axis reports the sequence of the samples obtained for increasing surfactant (SDS) concentration.

absence of surfactant and for the surfactant monomers, anatase is by far the major component, while for surfactant concentrations at the CMC or larger, the anatase content drops dramatically. The situation is opposite in the conditions corresponding to the isoelectric point of the oxide ( $\text{pH} 6$ ). The amount of anatase in the powder increases markedly for the largest surfactant concentration in the hydrothermal treatment.

Conditions of particle-promoted aggregation are reported to favor the growth of rutile crystals and the relative enrichment of the sample in this polymorph, in contrast with the case of anatase. Let us examine now how the conditions adopted during the hydrothermal growth intervene in this process. The most evident case concerns the samples obtained in attractive electrostatic surfactant-oxide conditions ( $\text{pH} 3$ ). When the surface of the precursor particles is the locus of adsorption of surfactant monomers at low degree of coverage with, possibly, a prevailing flat orientation on the surface, the particles do not tend to aggregate, and the formation of anatase is slightly promoted with respect to the sample with no surfactant. At higher concentrations, the micelles are strongly adsorbed and the positively charged oxide acts, at least in part, as the counterion for the organic anion. The presence of strong electrostatic attraction between the micelles and the charged oxide may promote bridging phenomena between different particles. It is even possible that some deposition of soluble  $\text{Ti}(\text{OH})_4$  species may occur in the region with a negative curvature

radius (Fig. 8A) induced by the micelle bridge. For growth processes at the oxide isoelectric point (pH 6) again the monomer at low concentration provokes no important effects, while at higher surfactant concentrations, the micelles much less adsorbed and surrounded by a diffuse double layer of thickness larger than the micelle radius (Fig. 8B), may act as spacers imparting stability to the suspension and, consequently, promoting the growth of the anatase polymorph.

The importance of the effects induced by the presence of a surfactant during the growth of an oxide depends on intrinsic balance between the hydrophilic and hydrophobic surfactant molecule components. Fig. 9 shows the direct comparison between the effects of three ionic surfactants on the  $\text{TiO}_2$  growth, in the respective conditions of attractive electrostatic interactions. It is immediately apparent that the anionic surfactant induces larger effects with respect to the other two molecules in the same conditions, and further that for the same pyridinium head group the longer the alkyl chain the larger the effects. This occurrence is to be traced back to the larger affinity shown

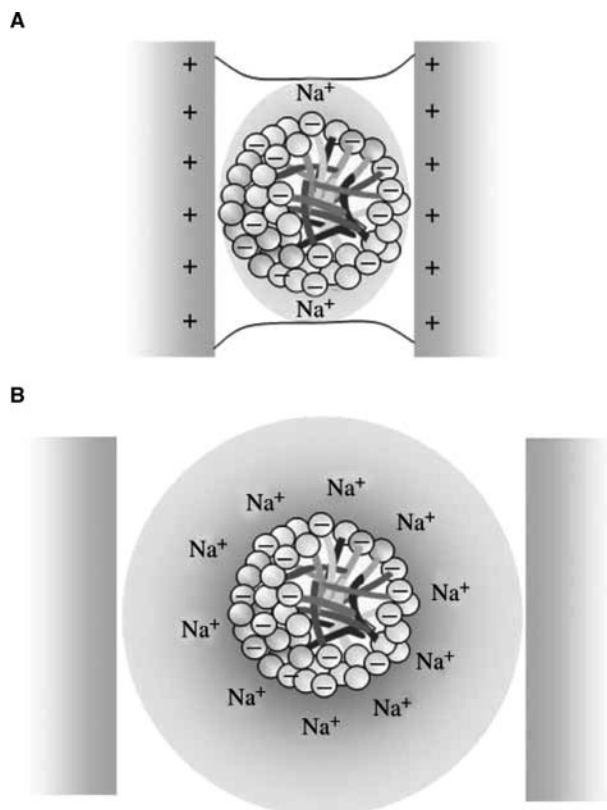


**Fig. 8** Sketches of the possible role played by micelles on the particle attachment, during the growth: (A) in the presence of attractive electrostatic interactions with the  $\text{TiO}_2$  particles (pH 3) and (B) at the particles isoelectric point (pH 6).

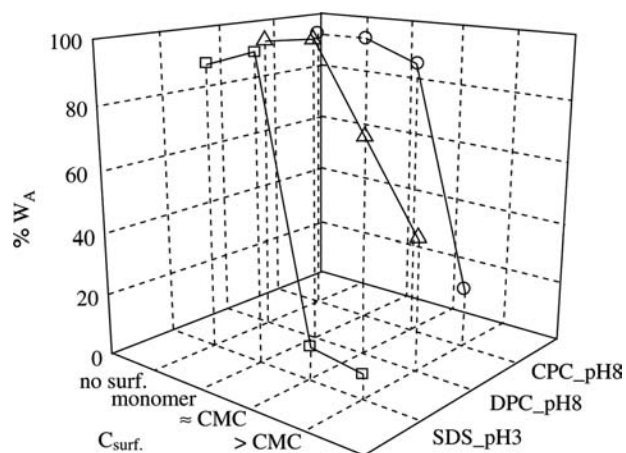


**Fig. 9** Quantitative anatase content of samples calcined at  $600^\circ$  at different surfactant concentrations, in the conditions of attractive oxide–surfactant interactions (SDS, sodium dodecylsulfate; DPC, dodecylpyridinium chloride; CPC, cetylpyridinium chloride).

by SDS toward the  $\text{TiO}_2$  surface, with respect to pyridinium salts.<sup>[27,28]</sup>

In growth processes, surfactants may also act as “shape inducing reagents”,<sup>[29,30]</sup> i.e., as species that, by modulating the surface free energy of the crystal, promote growth along one direction. Numerous recent studies have been focused on the synthesis of one-dimensional (1-D) nanostructures including nanorods and nanowires with their advantages of exceptional anisotropic electronic properties as well as facile applicability for the construction of two-terminal circuit devices. In these cases a careful design of the reaction factors is indispensable for the morphological control of the products. The synthetic approach for 1-D nanocrystals must fulfill the following requirements: the development of a well-defined precursor system that can generate stable monomers, sufficiently high monomer concentration to maintain the kinetically controlled growth regime, and the proper choice of surfactants that can modulate the energy of specific crystal faces. This latter effect can occur either through direct adsorption of the surfactant at the surface of the growing crystallites or be mediated by the formation of complexes or even hydrogen bonding. In the case of the growth of  $\gamma$ -alumina nanofibers, Zhu, Riches, and Barry<sup>[30]</sup> believe that the anisotropic growth of the boehmite precursor is to be related to hydrogen bonding between the oxide groups in the nonionic surfactants and the boehmite surface which reduces the free energy of the crystallites with low dimensions. This will allow the boehmite crystals to grow along one direction.

Sun et al.<sup>[31]</sup> have obtained ZnO single-crystal nanorods by hydrothermal oxidation of a zinc metal

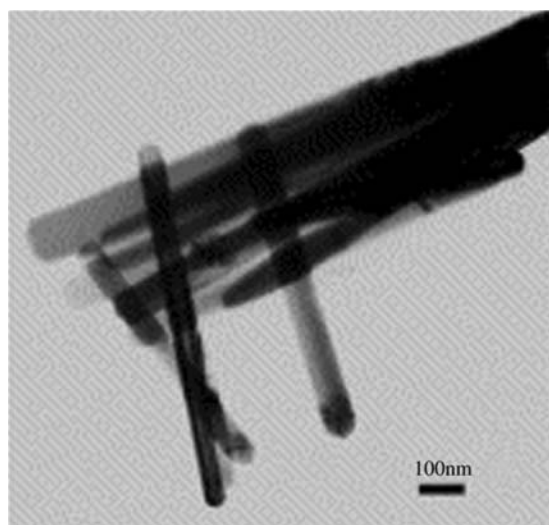


**Fig. 10** TEM micrograph of the ZnO sample obtained in the presence of CTAB with 20 hr of hydrothermal treatment at 180°C. *Source:* From Ref.<sup>[31]</sup>.

powder at 180°C in the presence of cetyltrimethylammonium bromide (CTAB). The typical morphology of the samples obtained in the presence of CTAB with 20 hr of hydrothermal treatment is shown in Fig. 10. The presence of CTAB intervenes in several ways in supporting the oxide growth. On one side the surfactant lowers the surface tension at the ZnO/solution interface so that a lower supersaturation is needed for the solid formation. Further the surfactant acts as a carrier for  $\text{CTA}^+ - \text{Zn}(\text{OH})_4^{2-}$  ion pairs and controls the landing of the growing units onto the (0001) crystal face promoting the preferential growth.

### SURFACTANT-ASSISTED PREPARATION OF NANOPARTICLES FOR APPLICATIONS IN HETEROGENEOUS CATALYSIS

The main advantages of using surfactant-assisted techniques in the preparation of catalytic materials are related to the possibility of controlling properties such as particle size, morphology, and size distribution. Nanosize particles with a narrow size distribution can often be achieved and, therefore, structure-sensitive catalytic reactions can benefit from the preparation procedure. A review by S. Eriksson shows several examples, relative to both metallic particles and oxides, of catalysts prepared by microemulsion technique; they prove to be, in some cases, superior to catalysts prepared by traditional methods, regarding both the catalytic activity and/or selectivity.<sup>[32]</sup> However there may be some drawbacks. For example, in the case of catalysts prepared by microemulsions the scaling-up of the catalyst preparation is still a challenge and in

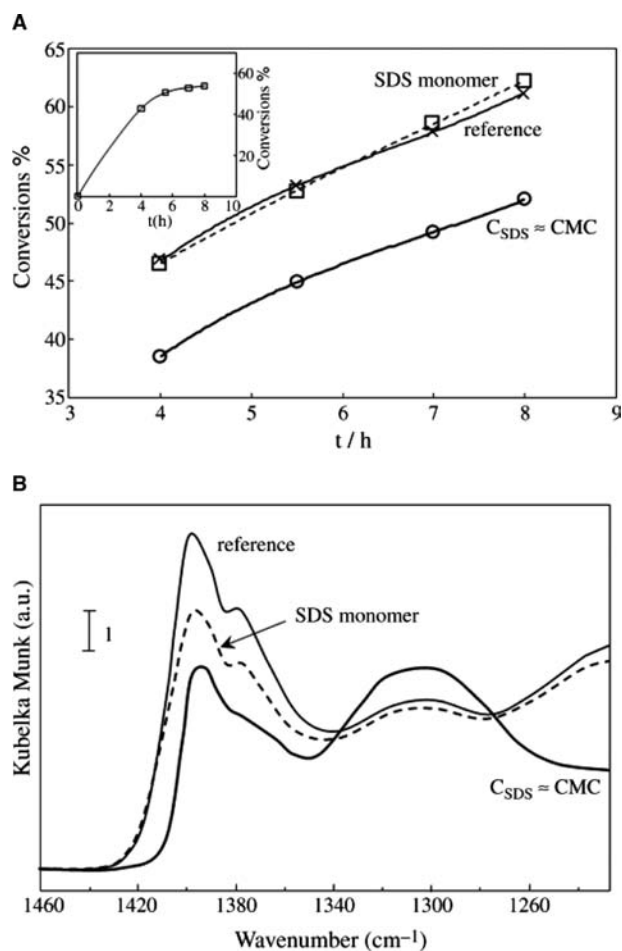


**Fig. 11** (A) Reagents conversion for benzoic acid esterification as a function of the reaction time for  $\text{SO}_4\text{-ZrO}_2$  sample calcined at 620°C. Inset: total reaction profile (conversion vs. time) and (B) DRIFT spectra of the same samples.

some cases the presence of the surfactant in the catalysts preparation may affect the surface structure of the material and, therefore, its catalytic activity. For example the mesosilicates of the M41S family obtained by templating with ionic surfactants proved to be ineffective in several applications, particularly in catalysis, because of the absence of active sites in the siliceous framework. Sulfated zirconia is an excellent solid acid catalyst.<sup>[33–35]</sup> There is abundant catalysis literature in the area of strong zirconia-based solid acids,<sup>[36–38]</sup> such as the isomerization of butane at room temperature<sup>[39]</sup> and hydrocracking and hydroisomerization reactions of molecules in the liquid phase. Conventional preparations of sulfated zirconia lead to microporous material suitable for reactions of small molecules in the vapor phase. If conventional sulfated zirconia is calcined at high temperatures, the micropores collapse and larger pores are formed with wider pore-size distributions.<sup>[40]</sup> To form a catalyst that has shape selectivity for larger molecules, narrow pore-size



distributions need to be created.<sup>[41,42]</sup> However, the synthesis of sulfated zirconia by templating with anionic surfactants produces less active catalysts for the liquid-media reaction of esterification of benzoic acid with methanol. The catalytic conversion (Fig. 11) appreciably decreases in the case of the samples obtained by in situ sol-gel synthesis at the highest concentration of SDS. It is relevant to note that the samples were routinely calcined at 620°C and that no residual surfactant was present in the samples; further the reported decrease in the activity cannot be brought back to morphological effects. Apparently the presence of the surfactant at high concentrations modifies the adsorption of sulfates species at the oxide surface, which creates the acidity of the surface Zr species. The DRIFT spectra of the calcined samples support this hypothesis. The presence of the two intense peaks between 1250 and 1350/cm in the case of the samples obtained at the highest surfactant concentration suggest a different coordination of the sulfate groups bound to zirconia crystallites with respect to the “regular” coordination of sulfates in an active zirconia catalyst.

## CONCLUSIONS

The addition of an amphiphilic molecule in one of the synthetic steps leading to a nanocrystalline material may greatly contribute to controlling the manifold features bearing relevance to the reactivity of the material. The possible choices of operation are numerous and the effects provoked may concern control of the particle size and shape, the relative enrichment in different polymorphs, or the surface state.

The authors believe that the first goal to be reached, in the use of surfactants for the assisted growth of oxides, is the development of a better fundamental understanding concerning the features of the solid-surfactant interactions virtually encompassing all steps in the material evolution. This knowledge, based on general criteria, could be successively used to project a priori the specific conditions to be adopted to obtain the material tailored for the final application.

## REFERENCES

1. Fabregat-Santiago, F.; Mora-Serò, I.; Garcia-Belmonte, G.; Bisquert, J. Cyclic voltammetry studies of nanoporous semiconductors capacitive and reactive properties of nanocrystalline TiO<sub>2</sub> electrodes in aqueous electrolyte. *J. Phys. Chem. B* **2003**, *107* (3), 758–768.
2. Rothschild, A.; Komem, Y. On the relationship between the grain size and gas-sensitivity of chemo-resistive metal-oxide gas sensors with nanosized grains. *J. Electroceram.* **2004**, *13*, 697–701.
3. Vinodgopal, K.; Kamat, P.V. Enhanced rates of photocatalytic degradation of an azo dye using SnO<sub>2</sub>/TiO<sub>2</sub> coupled semiconductor thin films. *Environ. Sci. Technol.* **1995**, *29* (3), 841–845.
4. Nemeth, J.; Dekany, I.; Suvegh, K.; Marek, T.; Klencsar, Z.; Vertes, A.; Fendler, J.H. Preparation and structural properties of tin oxide-montmorillonite nanocomposites. *Langmuir* **2003**, *19*, 3762–3769.
5. Kresge, C.T.; Leonowicz, M.E.; Roth, W.J.; Vartuli, J.C.; Beck, J.S. Ordered mesoporous molecular sieves synthesized by a liquid-crystal template mechanism. *Nature* **1992**, *359* (6397), 710–712.
6. Vartuli, J.C.; Schmitt, C.T.; Kresge, W.J.; Leonowicz, M.E.; McCullen, S.B.; Hellring, S.D.; Beck, J.S.; Schlenker, J.L.; Olson, D.H.; Sheppard, E.W. Effect of surfactant/silica molar ratios on the formation of mesoporous molecular sieves: inorganic mimicry of surfactant liquid-crystal phases and mechanistic implications. *Chem. Mater.* **1994**, *6*, 2317–2326.
7. Chen, C.Y.; Burkett, S.L.; Li, H.X.; Davis, M.E. Studies on mesoporous materials. II. Synthesis mechanism of MCM-41. *Micropor. Mater.* **1993**, *2*, 27–34.
8. Monnier, A.; Schuth, F.; Huo, Q.; Kumar, D.; Margolese, D.; Maxwell, R.S.; Stucky, G.D.; Krishnamurty, M.; Petroff, P.; Firouzi, A.; Janicke, M.; Chmelka, B.F. Cooperative formation of inorganic-organic interfaces in the synthesis of silicate mesostructures. *Science* **1993**, *261* (5126), 1299–1303.
9. Adachi, M.; Harada, T.; Harada, M. Formation Processes of silica nanotubes through a surfactants-assisted templating mechanism in laurylamine hydrochloride/tetraethoxysilane system. *Langmuir* **2000**, *16*, 2376–2384.
10. See the Special issue of *Micropor. Mesopor. Mater.* **1999**, *27* (2 and 3),
11. Chao, Z.S.; Ruckenstein, E. Specific ion and pH effects on supramolecular assembly of mesostructured V-Mg oxides. *Langmuir* **2004**, *20* (18), 7517–7525.
12. Srivastava, D.N.; Perkas, N.; Zaban, A.; Gedanken, A. Sonochemistry as a tool for preparation of porous metal oxides. *Pure Appl. Chem.* **2002**, *74* (9), 1509–1517.
13. Ardizzone, S.; Bianchi, C.L.; Quagliotto, P.; Viscardi, G. Adsorption of cationic “gemini” surfactants at the TiO<sub>2</sub>/solution interface. *Surf. Interf. Anal.* **2002**, *34* (1), 652–656.
14. Koopal, L.K.; Lee, E.M.; Boehmer, M.R. Adsorption of cationic and anionic surfactants on charged metal oxide surfaces. *J. Colloid Interf. Sci.* **1995**, *170* (1), 85–97.
15. Serrano, D.P.; Calleja, G.; Sanz, R.; Pizarro, P. Preparation of bimodal micro-mesoporous TiO<sub>2</sub> with tailored crystalline properties. *Chem. Comm.* **2004**, 1000–1001.
16. Eiden-Assman, S.; Widoniak, J.; Maret, G. Synthesis and characterization of porous and nonporous monodisperse colloidal TiO<sub>2</sub> particles. *Chem. Mater.* **2004**, *16*, 6–11.
17. Luo, H.; Wang, C.; Yan, Y. Synthesis of mesostructured titania with controlled crystalline framework. *Chem. Mater.* **2003**, *15*, 3841–3846.



18. Andersson, M.; Osterlund, L.; Ljungstrom, S.; Palmqvist, A. Preparation of nanosize anatase and rutile TiO<sub>2</sub> by hydrothermal treatment of microemulsion and their activity for photocatalytic wet oxidation of phenol. *J. Phys. Chem. B* **2002**, *106*, 10674–10679.
19. Chhabra, V.; Ayyub, P.; Chattopadhyay, S.; Maitra, A.N. Preparation of acicular  $\gamma$ -Fe<sub>2</sub>O<sub>3</sub> particles from a microemulsion-mediated reaction. *Mater. Lett.* **1996**, *26* (1,2), 21–26.
20. Chen, D.; Gao, L. Novel synthesis of well-dispersed crystalline SnO<sub>2</sub> nanoparticles by water-in-oil microemulsion-assisted hydrothermal process. *J. Coll. Interf. Sci.* **2004**, *279*, 137–142.
21. Yan, M.; Chen, F.; Zhang, J. Synthesis of controllable crystalline nano-TiO<sub>2</sub> at low temperature. *Chem. Lett.* **2004**, *33* (10), 1352–1353.
22. Vantomme, A.; Yuan, Z.Y.; Du, G.; Su, B.L. Surfactant-assisted large-scale preparation of crystalline CeO<sub>2</sub> nanorods. *Langmuir* **2005**, *21* (3), 1132–1135.
23. Cappelletti, G.; Ricci, C.; Ardizzone, S.; Parola, C.; Anedda, A. Aged titania nanoparticles: the simultaneous control of local and long-range properties. *J. Phys. Chem. B* **2005**, *109* (10), 4448–4454.
24. Boiadjeva, T.; Cappelletti, G.; Ardizzone, S.; Rondinini, S.; Vertova, A. The role of surface electrification on the growth and structural features of titania nanoparticles. *Phys. Chem. Chem. Phys.* **2004**, *6* (13), 3535–3539.
25. Boiadjeva, T.; Cappelletti, G.; Ardizzone, S.; Rondinini, S.; Vertova, A. Nanocrystalline titanium oxide by sol-gel method. The role of the solvent removal step. *Phys. Chem. Chem. Phys.* **2003**, *5* (8), 1689–1694.
26. Ionita, M.; Cappelletti, G.; Minguzzi, A.; Ardizzone, S.; Bianchi, C.L.; Rondinini, S.; Vertova, A. Bulk, surface and morphological features of nanostructured tin oxide by a controlled alkoxide-gel path. *J. Nanopart. Res.* *in press*.
27. Ardizzone, S.; Orlandi, M. Adsorption of alkylbenzene-sulfonates at the ZrO<sub>2</sub> solution interface. *J. Electroanal. Chem.* **1995**, *391* (1–2), 181–185.
28. Ardizzone, S.; Grassi, E. Sulphate-modified zirconia catalysts: the role of surface electrification on the features of the sulphate adsorption process. *J. Electroanal. Chem.* **1996**, *417* (1–2), 193–195.
29. Yu, Y.Y.; Chang, S.S.; Lee, C.L.; Wang, C.R.C. Gold nanorods: electrochemical synthesis and optical properties. *J. Phys. Chem. B* **1997**, *101*, 6661–6664.
30. Zhu, H.Y.; Riches, J.D.; Barry, J.C.  $\gamma$ -Alumina nanofibers prepared from aluminum hydrate with poly-(ethylene oxide) surfactant. *Chem. Mater.* **2002**, *14*, 2086–2093.
31. Sun, X.M.; Chen, X.; Deng, Z.X.; Li, Y.D. A CTAB-assisted hydrothermal orientation growth of ZnO nanorods. *Mat. Chem. Phys.* **2002**, *78* (1), 99–104.
32. Eriksson, S.; Nylén, U.; Rojas, S.; Boutonnet, M. Preparation of catalysts from microemulsions and their applications in heterogeneous catalysis. *Appl. Catal. A: Gen.* **2004**, *265* (2), 207–219.
33. Morterra, C.; Cerrato, G.; Ardizzone, S.; Bianchi, C.L.; Signoretto, M.; Pinna, F. Surface features and catalytic activity of sulfated zirconia catalysts from hydrothermal precursors. *Phys. Chem. Chem. Phys.* **2002**, *4* (13), 3136–3145.
34. Melada, S.; Signoretto, M.; Ardizzone, S.; Bianchi, C.L. Physico-chemical features and catalytic activity of sulfated zirconia prepared by sol-gel method. The role of the solvent evaporation step. *Catal. Lett.* **2001**, *75* (3–4), 199–204.
35. Adeeva, V.; de Haan, J.W.; Jaenchen, J.; Lei, G.D.; Schuenemann, V.; van de Ven, L.J.M.; Sachtler, W.M.H.; van Santen, R.A. Acid sites in sulfated and metal-promoted zirconium dioxide catalysts. *J. Catal.* **1995**, *151* (2), 364–372.
36. Ardizzone, S.; Bianchi, C.L.; Cappelletti, G.; Porta, F. Liquid-phase catalytic activity of sulfated zirconia from sol-gel precursors: the role of the surface features. *J. Catal.* **2004**, *227* (2), 470–478.
37. Bianchi, C.L.; Ardizzone, S.; Cappelletti, G. Surface state of sulfated zirconia: the role of the sol-gel reaction parameters. *Surf. Interf. Anal.* **2004**, *36* (8), 745–748.
38. Melada, S.; Ardizzone, S.; Bianchi, C.L. Sulphated zirconia by sol-gel route. The effects of the preparative variables. *Micropor. Mesopor. Mater.* **2004**, *73* (3), 203–209.
39. Song, X.; Sayari, A. Sulfated zirconia-based strong solid-acid catalysts: recent progress. *Catal. Rev.* **1996**, *38* (3), 329–412.
40. Mercera, P.D.L.; Van Ommen, J.G.; Doesburg, E.B.M.; Burggraaf, A.J.; Ross, J.R.H. Zirconia as a support for catalysts: evolution of the texture and structure on calcination in air. *Appl. Catal.* **1990**, *57* (1), 127–148.
41. McIntosh, D.J.; Kydd, R.A. Tailoring the pore size of mesoporous sulfated zirconia. *Micropor. Mesopor. Mater.* **2000**, *37* (3), 281–289.
42. Larsen, G.; Lotero, E.; Nability, M.; Petkovic, L.M.; Shobe, D.S. Surfactant-assisted synthesis of mesoporous zirconia powders with high surface areas. *J. Catal.* **1996**, *164* (1), 246–248.

## BIBLIOGRAPHY

1. Lai, Jr-I.; Shafi, K.V.P.M.; Ulman, A.; Loos, K.; Lee, Y.; Vogt, T.; Lee, W.-L.; Ong, N.P. Controlling the size of magnetic nanoparticles using pluronic block copolymer surfactants. *J. Phys. Chem. B* **2005**, *109* (1), 15–18.

# Nanocrystalline Zeolites

Vicki H. Grassian

Sarah C. Larsen

Department of Chemistry, University of Iowa, Iowa City, Iowa, U.S.A.

## INTRODUCTION

Zeolites are aluminosilicate molecular sieves with pores of molecular dimensions.<sup>[1,2]</sup> Zeolites can be synthesized with a wide range of pore sizes and topologies and are used in applications such as catalysis, chemical separations, and as adsorbents and ion exchangers. The zeolite chemical composition, framework topology, and pore size can be varied to control reactivity and selectivity. Two common zeolites, ZSM-5, and Y, are shown in Fig. 1 with one molecule of adsorbed cyclohexane to show the relative sizes of the pores in these materials. It can be seen that these materials, by their very nature, have dimensions in the nanometer-size regime.

Although the pore dimensions of these materials are in the nanometer-size range, the zeolite crystals prepared through conventional syntheses are typically on the order of micrometers in diameter. Recently, however, there has been a great deal of interest in the synthesis of nanocrystalline zeolites, i.e., zeolites with discrete, uniform crystals with dimensions of less than 100 nm, and their unique properties relative to conventional micrometer-sized zeolite crystals.<sup>[3–16]</sup> For some applications, it would be advantageous to employ much smaller nanometer-sized zeolite crystals in the range 10–100 nm. New synthetic methods have been developed that enable the selective and quantitative formation of small crystallites.

The impact of crystal size on zeolite properties can be profound. For example, Bein<sup>[17]</sup> has studied thin films formed using nanometer-sized zeolites (10–100 nm crystallite size) and has found that “thin films can adsorb and desorb most vapors within a few seconds to minutes, often at room temperature, while the bulk materials usually require substantial heating (ca. 200–300°C) to remove adsorbed vapors.” The facile desorption of products would be a distinct advantage in many gas phase heterogeneous processes involving zeolites, so nanotechnology has the potential to be utilized in many zeolite-based applications. The increased surface area of the small particles also provides these materials with a distinct advantage in heterogeneous catalysis. In addition, these nanometer-sized zeolites can then be assembled into nanostructures, such as thin films, fibers, or

membranes.<sup>[17]</sup> These zeolite nanostructures can potentially be used to control chemical reactivity on molecular length scales. The objectives of this paper are twofold. First, the synthesis of nanocrystalline zeolite particles and the self-assembly of these particles into thin films, fibers, and coatings are discussed. Second, potential applications of nanocrystalline zeolite materials in environmental catalysis are described.

## NANOCRYSTALLINE ZEOLITES MATERIALS: SYNTHESIS AND SELF ASSEMBLY

The synthesis of nanometer-sized zeolites, such as ZSM-5,<sup>[18]</sup> silicalite,<sup>[19]</sup> A,<sup>[20]</sup> Y,<sup>[4,15,21]</sup> Beta,<sup>[3]</sup> L,<sup>[13]</sup> and TS-1<sup>[8]</sup> (the titanium containing analog of ZSM-5), has been reported in the literature. Typically, the particle size distribution is controlled by varying the gel composition or the synthesis temperature and time. Recently, other methods of controlling particle size distribution, such as confined space<sup>[12]</sup> or templating methods,<sup>[16]</sup> have been introduced. In the confined synthesis method, an inert mesoporous support material, such as carbon black, is used to control the particle size in zeolite synthesis. In the templating method, pitch imprinted with colloidal silica<sup>[22]</sup> is used as the crystal template for preparing zeolites with crystal sizes ranging from 13 to 90 nm in size.<sup>[16]</sup> The advantage of these approaches is that a wide range of zeolites can be synthesized by the same general method. In addition, a variety of nanoarchitectures can be constructed using nanocrystalline zeolites as the building blocks. Nanoarchitectures have previously been discussed in the context of multifunctional materials.<sup>[23,24]</sup> A schematic of various possible zeolite nanoarchitectures is shown in Fig. 2. Some examples of specific syntheses and nanoarchitectures are described in more detail below.

## Hydrothermal Synthesis of Nanocrystalline Zeolites X, Y, and ZSM-5

Several methods for the preparation of zeolite Y with nanometer-sized crystals have been reported in the literature.<sup>[4,15,21]</sup> The synthesis of zeolite Y has been

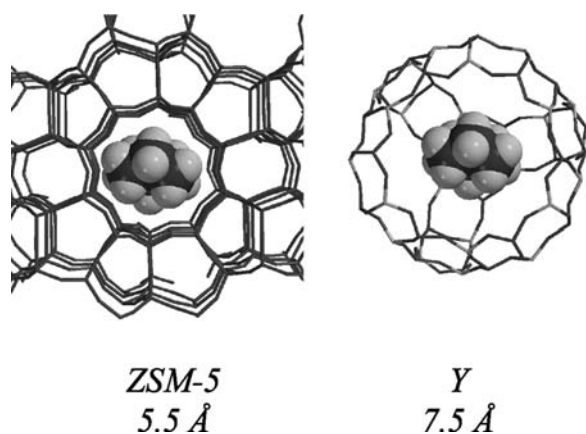


**Fig. 1** Diagram of zeolites ZSM-5 and Y and their relative pore size dimensions.

described by Schoeman, Sterte, and Otterstedt<sup>[21]</sup> and Castagnola and Dutta.<sup>[4]</sup> Typically, this synthetic procedure produces zeolite Y crystals that range in size from 70 to 150 nm with a Si/Al = 1.6. The general features of this synthetic procedure for the synthesis of zeolite Y involve the preparation of a tetramethylammonium hydroxide (TMA)-aluminate solution that is subsequently added to a silica sol to form a homogeneous solution. The solution is then heated at 100°C in a polypropylene bottle with reflux in a poly(ethylene glycol) bath. Recently, Alwy et al.<sup>[25]</sup> reported the synthesis of nanocrystalline zeolite Y with a smaller average crystal size of  $46 \pm 8$  nm and have formed transparent films from this material (vide infra). Fig. 3 shows the scanning electron microscope (SEM) image of the nanocrystalline zeolite Y prepared by Alwy et al. Several other synthetic methods used to prepare zeolite Y and X nanocrystals have been described in the literature.<sup>[5,15,26–29]</sup>

Similar hydrothermal syntheses have been reported for the preparation of nanocrystalline ZSM-5 and silicalite-1 (the purely siliceous form of ZSM-5).<sup>[10,11,19,30–32]</sup> In these studies, ZSM-5 and silicalite were synthesized

with crystal sizes in the range of 10–100 nm. One method involves the hydrothermal crystallization from clear solutions under autogenous pressure,<sup>[32]</sup> and another approach involves using silicalite seed crystals at atmospheric pressure.<sup>[11]</sup> An SEM image of nanocrystalline silicalite synthesized in our laboratory with an average particle size of 39 nm is shown in Fig. 4.

### Templating Methods for the Syntheses of Nanocrystalline Zeolites

Several hydrothermal methods for the synthesis of zeolites Beta and ZSM-5 with nanometer-sized crystals are available in the literature.<sup>[3,14,19,30,33]</sup> In addition, templating methods have been recently reported that rely on the growth of zeolite crystals in a carbon-based template such as carbon black or colloid imprinted carbon (CIC). The advantages of these templating methods are that the zeolite crystal size is controlled by the size of the template and the carbon-based templates reported so far can be easily removed by calcination in air.

The confined space synthesis method described by Jacobsen et al.<sup>[7,12,18]</sup> for the synthesis of zeolites A, X, ZSM-5, and Beta has several distinct advantages over conventional hydrothermal syntheses. The confined space method involves crystallization of a zeolite in the mesopores of an inert porous matrix support. The crystal size distribution is controlled by the size of the mesopores of the inert support and results in a narrow distribution of pore sizes. Carbon black is typically used because it is available with different pore sizes and it can be easily removed by pyrolysis of the carbon.<sup>[7,12,18]</sup> In addition, in the confined space synthesis method, the gel composition and crystallization temperature and time are not as critical in determining the crystal size distributions. Jacobsen et al.<sup>[7,12,18]</sup> reported the synthesis of ZSM-5 with particle sizes ranging from 22 to 45 nm depending on the carbon matrix used in the synthesis. Similarly, they reported the confined space synthesis of zeolites

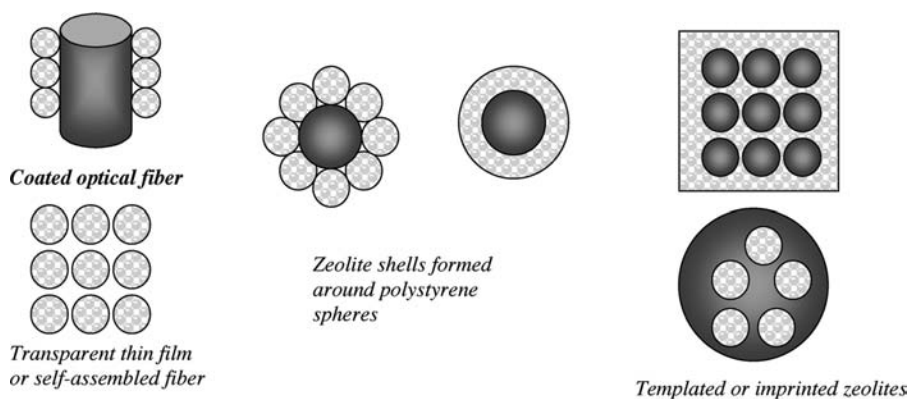


**Fig. 2** Examples of nanoarchitectures that can be formed from nanocrystalline zeolites. The patterned areas represent nanocrystalline zeolite, and the solid shaded areas indicate a support such as polystyrene beads (diameters of ~1–200 nm) or optical fiber.

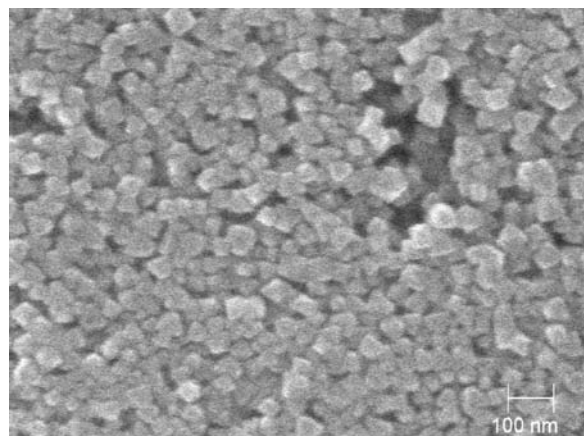


**Fig. 3** Scanning electron microscopic image of the nanocrystalline zeolite Y film.

Beta, Linde Type A (LTA), and Linde Type X (LTX).<sup>[7,12,18]</sup> The disadvantage of the confined space synthesis method is that the size distribution of the resulting zeolites could be quite large because the carbon black template is disordered.

A templating method using colloid imprinted carbons (CIC)<sup>[22]</sup> was recently reported by Kim, Shah, and Pinnavaia<sup>[16]</sup> In this method, colloidal silica is used to imprint mesopores in carbon precursor particles (pitch). In this way, pores of different sizes can be tailored for specific applications.<sup>[22]</sup> Kim, Shah, and Pinnavaia<sup>[16]</sup> prepared CICs with pore diameters of 12, 22, 45, and 85 nm. These CICs were impregnated to incipient wetness with the zeolite precursor solutions for ZSM-5 and then were subjected to hydrothermal synthesis conditions of ~48 hr in an autoclave at 180°C. The CIC was subsequently removed by calcination in air at 570°C. ZSM-5 nanocrystals prepared by this method had average particle sizes of 13, 22, 42, and 90 nm as determined by transmission electron

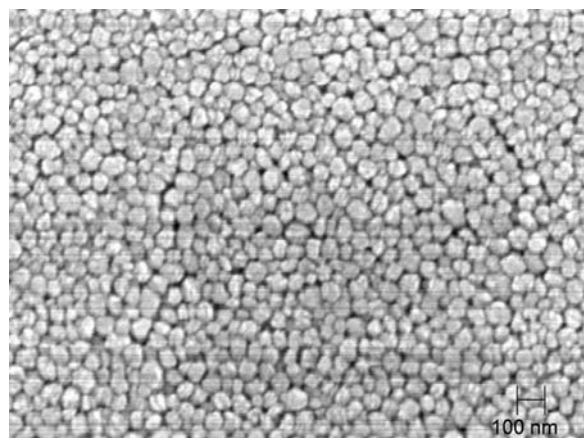


**Fig. 4** Scanning electron microscopic image of silicalite with an average particle size of 39 nm.

microscopy (TEM). One note about the zeolites produced by this method is that the zeolite crystals are intergrown into aggregates because of the nature of the CIC template.

### Assembly of Nanocrystalline Zeolites

Nanometer-sized zeolites can be assembled into zeolite nanostructures, such as fibers or thin films, to optimize their potential for applications in heterogeneous environmental catalysis or perhaps sensor technology. For applications in thermal chemistry, a primary consideration is to increase the surface area of the zeolite and to reduce intracrystalline diffusion effects. For applications in photocatalysis,<sup>[34–36]</sup> the use of optically transparent zeolites would increase the efficiency of the process. The formation of a transparent film of nanocrystalline zeolite Y relative to commercial zeolite Y has been demonstrated by Alwy et al.<sup>[25]</sup> Films of the zeolite Y were prepared by sonication of an aqueous mixture of nanocrystalline zeolite Y for several hours. The resulting hydrosol was pipetted onto a Pyrex slide and dried in ambient air. Films of commercial zeolite Y (Aldrich) were prepared using the same method. Digital images of the zeolite Y films are shown in Fig. 5. In each case, the film was prepared using approximately the same mass of zeolite Y. The film prepared from the nanocrystalline zeolite Y hydrosol is much more uniform than the film prepared from the Aldrich zeolite Y hydrosol. The increased transparency of the films can be observed visually. The “Y” printed on the paper behind the film can be clearly seen through the nanocrystalline zeolite Y film (right) but is much more difficult to see through the Aldrich zeolite Y film (left). To obtain more quantitative information, the percent transmittance (%T) was measured using UV/Vis spectroscopy. The nanocrystalline zeolite Y film had a %T of 70–80 in the 300–700 nm range compared with a %T of 30–40 for the Aldrich Zeolite Y film in the same range.

In considering all the factors to be optimized, zeolite fibers (either coated or hollow)<sup>[37–40]</sup> are potentially very



**Fig. 5** Thin films prepared from hydrosols of Aldrich zeolite Y (left) and nanocrystalline zeolite Y (right).

promising materials. Reactant absorption and product desorption will be facilitated because of the fact that the zeolite layer is very thin.<sup>[17]</sup> For applications involving separations and catalytic reactions, zeolite fibers could be positioned within a tube and reactant gases, or liquids could be flowed over the zeolite fibers. For these applications, a large surface area is desirable and can be achieved using bundles of small-diameter zeolite fibers. A fiber bundle 10 cm in length and 1 cm in diameter containing individual fibers of 100- $\mu\text{m}$  diameter with a packing fraction of 50% has a surface area 1570  $\text{cm}^2$ , compared with a surface area of 31  $\text{cm}^2$  if the inside of a 10-cm-long, 1-cm diameter glass tube was coated directly. For zeolite systems in which optical access is needed for photoexcitation or detection, the zeolite fibers will enable the efficient propagation of light through a long path length of zeolite.

Several methods for the preparation of zeolite coated or hollow fibers have been reported in the literature. Pradhan, Macnaughtan, and Raytery<sup>[39]</sup> reported a method for coating optical fibers with pre-synthesized zeolites via a sol-gel process. Okada et al.<sup>[41]</sup> have reported the coating of zeolite Na-X on glass fibers by a soft solution process, and Deng and Balkus have used laser ablation to coat optical fibers.<sup>[40]</sup> Recently, Ke et al.<sup>[42]</sup> have reported an electrophoretic method for coating carbon fibers. The carbon fibers can then be removed by combustion leaving hollow zeolite fibers. Huang et al.<sup>[6]</sup> reported the self-assembly of zeolite nanocrystals (silicalite, ZSM-5, Beta, A, and faujasite) into films, membranes, and fibers. The self-assembled zeolite fibers that were produced in that study were transparent and approximately 27–33  $\mu\text{m}$  in diameter and  $\sim 1.5$  cm in length.

Nanocrystalline silicalite, a purely siliceous form of ZSM-5, was used to prepare zeolite fibers. An SEM image of the 35-nm particle size silicalite is shown in Fig. 4. From this image, it can be seen that the zeolite

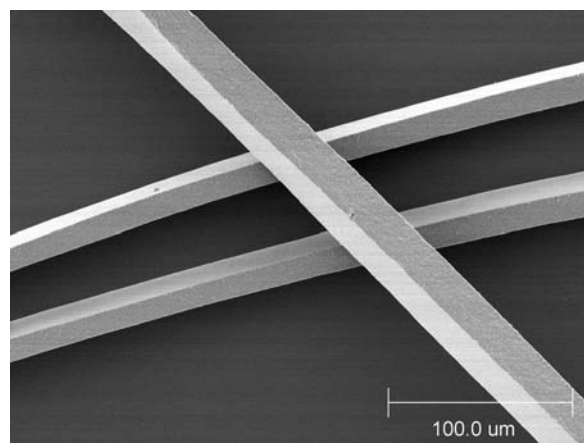


**Fig. 6** Scanning electron microscopic image of free-standing fibers formed from nanocrystalline silicalite (100- $\mu\text{m}$  scale bar).

crystals are uniform in size and are closely packed. The nanocrystalline particles shown in the SEM image in Fig. 4 self-assemble into transparent, rectangular fibers as illustrated in Fig. 6. These films and fibers (Figs. 5 and 6) formed from nanocrystalline zeolites (Figs. 3 and 4) are both examples of zeolite nanoarchitectures.

## NANOCRYSTALLINE ZEOLITE MATERIALS: APPLICATIONS IN ENVIRONMENTAL CATALYSIS

Recently, zeolites have emerged as important materials for applications in environmental catalysis.<sup>[43–46]</sup> Environmental catalysis involves the use of catalysts to solve environmental problems in areas such as emission abatement and environmentally benign synthesis.<sup>[47]</sup> Many new catalysts and catalytic processes have been developed to meet the challenges posed by environmental concerns.<sup>[48]</sup> Besides emissions abatement, the emphasis of environmental catalysis has expanded to include the development of environmentally benign synthetic routes designed to decrease the amount of chemical waste produced.<sup>[46]</sup>

As already noted, nanocrystalline zeolites are promising catalytic materials which have higher external surface areas and reduced diffusion path lengths relative to conventional micrometer-sized zeolites that may be beneficial for catalytic activity and selectivity. For example, nanocrystalline ZSM-5 exhibits increased selectivity and toluene conversion into cresol and decreased coke formation relative to conventional ZSM-5 materials.<sup>[49]</sup> Potential uses of nanocrystalline zeolites as environmental catalysts are described below.

### Environmentally Benign Synthesis: Selective Partial Oxidation Reactions of Hydrocarbons

The partial oxidation of hydrocarbons is significant to chemical industry because the products are used to convert petroleum hydrocarbon feedstocks into chemicals important in the polymer and petrochemical industries. Liquid-phase air oxidations are generally preferred by chemical industry because of the mild reaction conditions. Notable examples<sup>[50]</sup> of liquid phase air oxidation reactions are listed in Table 1. As can be seen from Table 1, the conversions of the oxidation processes are typically very low to maintain high selectivity. This is necessary because the desired partial oxidation products can easily be further oxidized under typical reaction conditions. A major motivation for the development of new oxidation routes is the desire to achieve high selectivities at high conversions.



**Table 1** Examples of liquid-phase oxidation reactions

Reactant	Partial oxidation product	Conversion (selectivity)	Application
Cyclohexane (C <sub>6</sub> H <sub>12</sub> )	Cyclohexyl hydroperoxide, cyclohexanol, cyclohexanone C <sub>6</sub> H <sub>11</sub> OOH, C <sub>6</sub> H <sub>11</sub> OH, C <sub>6</sub> H <sub>10</sub> O	12–13% (>90%)	Nylon-6
Isobutane [CH(CH <sub>3</sub> ) <sub>3</sub> ]	<i>tert</i> -butyl hydroperoxide, <i>tert</i> -butyl alcohol (CH <sub>3</sub> ) <sub>3</sub> COOH, (CH <sub>3</sub> ) <sub>3</sub> COH	10–20%	Propylene oxide

One approach to the partial oxidation of hydrocarbons is to eliminate the use of organic solvents through the use of gas-phase reactants and products. A clean, inexpensive oxidant, molecular oxygen can be used in these reactions. Thus these reactions have the potential to be green processes that use no solvents and minimal energy with catalysts (i.e., zeolites) that have been used in industry for many years. However, several crucial issues related to the application of these processes have emerged. These issues involve improving the efficiency of the photooxidation process and improving the diffusion of product and reactant molecules in the zeolites.<sup>[34,35]</sup>

For the application of zeolites as environmentally benign photooxidation catalysts, a major problem is light scattering by the zeolite. The efficient use of light energy in zeolites requires that light be propagated through a long path length of the zeolite material. However, zeolite crystallites strongly scatter visible light because of their small dimension. Thus only a thin photoreactive zone is obtained regardless of the zeolite bed thickness. In previous photooxidation work, it was determined that yield of photooxidation reactions in zeolites strongly depended on the thickness of the zeolite layer. Using zeolite Y with a crystallite size of approximately 1 μm, product formation for the photooxidation reaction of *p*-xylene (holding irradiation time

and loading constant) was monitored as the sample thickness was varied. The results are shown in Fig. 7 and clearly demonstrate that the effective yield drops drastically as the thickness of the zeolite layer increases. This is because the light is not able to penetrate through more than approximately 100 μm of zeolite and, as stated above, is a problem for applications to photooxidation reactions. Therefore nanocrystalline materials should be better materials for these reactions as they can form optically transparent thin films.

### Environmental Remediation: NO<sub>x</sub> Emissions Abatement

The emission of NO<sub>x</sub> and N<sub>2</sub>O from stationary and automotive sources, such as power plants and lean-burn engines, is a major environmental pollution issue. NO<sub>x</sub> leads to the production of ground-level ozone and acid rain and N<sub>2</sub>O is a greenhouse gas. The catalytic reduction of nitrogen oxides to N<sub>2</sub> is an important environmental challenge for scientists and engineers. Recently, the selective catalytic reduction of NO<sub>x</sub> and N<sub>2</sub>O by hydrocarbons (SCR-HC) over transition-metal exchanged zeolites, particularly in the presence of oxygen, has attracted much interest for emission abatement applications in stationary sources, such as natural gas-fueled power plants.<sup>[43,51–53]</sup> SCR-HC of NO<sub>x</sub> and N<sub>2</sub>O shows promise for applications to lean-burn gasoline and diesel engines where noble-metal three-way catalysts are not effective at reducing NO<sub>x</sub> in the presence of excess oxygen.<sup>[54]</sup> Another aspect of these transition metal-exchanged zeolites that has been reported in the literature is the photocatalytic activity for the direct decomposition of NO<sub>x</sub> and N<sub>2</sub>O<sup>[55–57]</sup> and the SCR-HC of NO<sub>x</sub>.<sup>[58]</sup> The use of zeolite nanostructures would provide some of the same advantages as have been discussed for the oxidation reactions such as more efficient light absorption, reactant diffusion, and increased surface area. Applications for which these materials might be important include transparent objects, such as windows, that could be coated with transparent zeolite thin films. The zeolite thin film would then be activated for NO<sub>x</sub> decomposition by sunlight.

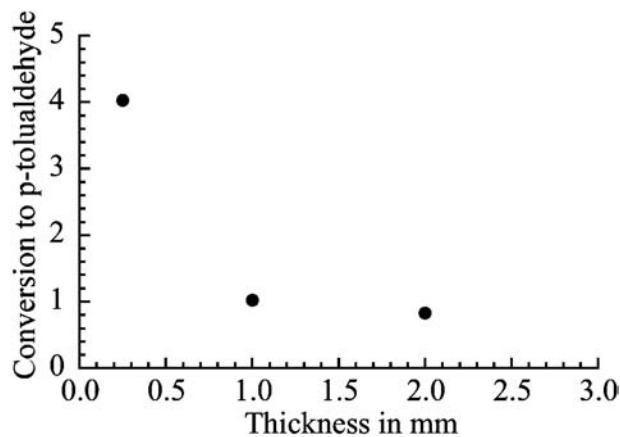


**Fig. 7** Conversion of paraxylene to paratolualdehyde as a function of BaY film thickness.



Another interesting question is whether the catalytic activity of transition-metal exchanged zeolites changes when nanometer-sized zeolites are used instead of conventional zeolites. For example, Zhang, Bao, and Wang<sup>[14]</sup> determined that nanometer-sized HZSM-5 has more Brønsted acid sites on the external surface than conventional HZSM-5. Iron-exchanged zeolites exhibit high activity for the SCR of NO<sub>x</sub> and N<sub>2</sub>O with ammonia or hydrocarbons as the reductant.<sup>[59–67]</sup> In addition, iron-exchanged zeolites are highly resistant to poisoning by water which is a crucial property for potential applications. The catalytic activity of iron-exchanged zeolites is very sensitive to the exchange procedure used to introduce the iron into the zeolite. Therefore it is conceivable that the properties of iron-exchanged nanozeolites could be dramatically affected by the use of nanometer-sized zeolites and have the potential to be more active catalysts.

### Environmental Remediation: Photocatalytic Decomposition of Organic Contaminants

Photocatalysts, such as TiO<sub>2</sub>, can be used to degrade a wide range of organic compounds found in polluted water and air.<sup>[68–70]</sup> Much of the research in the last decade has focused on aqueous solution photocatalysis for the decontamination and purification of water. However, gas phase heterogeneous photocatalysis can be an effective way to remove undesirable organic contaminants from air.<sup>[70–77]</sup> TiO<sub>2</sub> photocatalysts are active at ambient temperatures and pressures in the presence of UV irradiation and oxygen. Potential applications include purifying enclosed atmospheres, such as those found in spacecrafts, offices, industrial plants, and homes. The major pollutants in these applications are oxygenates and aromatics. TiO<sub>2</sub> photocatalysts have been shown to oxidize toluene, trichloroethylene (TCE), methanol/ethanol, and a number of other organic compounds.<sup>[70]</sup> Recently, several groups have considered the use of zeolite TiO<sub>2</sub> composites,<sup>[78–80]</sup> TS-1 (titanium-substituted ZSM-5),<sup>[81]</sup> and nanometer-sized TiO<sub>2</sub>.<sup>[82,83]</sup>

Similar to the problems discussed in the selective oxidation of hydrocarbons, light-scattering problems make these zeolite TiO<sub>2</sub> composite catalysts less than optimal. Zeolite TiO<sub>2</sub> composites prepared using nanometer-sized zeolites may be useful decomposition catalysts. Molecules such as toluene, benzene, and oxygenates, including aldehydes and ketones, are candidates to evaluate the effectiveness of nanometer zeolite TiO<sub>2</sub> composites for the removal of these undesirable organic contaminants from air and water.

### CONCLUSION

The development of nanometer-sized zeolites for applications in heterogeneous catalysis can potentially lead to solutions of several important environmental problems. These problems span from new methodologies in environmentally benign synthesis to new methodologies in environmental remediation of pollutants. The development of new green methodologies for the catalytic syntheses of industrially important compounds is necessary if the production of hazardous waste is to be reduced. The remediation of harmful pollutants using nanometer-sized zeolite catalysts has important implications in the area of emission abatement. NO<sub>x</sub> and volatile organic compounds (VOC) emissions are intimately linked to tropospheric ozone formation in a complex nonlinear way.<sup>[84]</sup>

Because zeolites are also used in sensors and as materials in separation processes, there are other environmental benefits to developing zeolite nanostructured materials that go beyond what has been discussed in this paper. For chemical sensor applications, photoactive molecules can be occluded within the structure of the zeolite.<sup>[17,85,86]</sup> As other molecules enter the pores of the zeolite, they can be expected to influence the electronic structure and therefore the optical spectrum of the occluded chromophores.<sup>[17,86]</sup> Detection of the change in the optical spectrum using a fiber optic would enable the construction of chemical sensors. Zeolites-based sensors could be developed for detection of specific pollutants or perhaps chemical warfare agents. Zeolite thin films could be used in applications to separate hazardous substances from environmentally benign species. These and other applications could result from the further development of the zeolite nanostructures. The studies described in this paper are just a first step in the synthesis and potential uses of nanocrystalline zeolite materials.

### ACKNOWLEDGMENTS

Dr. Russell Larsen, Dr. Weiguo Song, Hassan Alwy, and Gonghu Li are acknowledged for experimental assistance including the synthesis and characterization of nanocrystalline zeolites and zeolite nanoarchitectures. Although some of the research described in this entry has been funded by the EPA through grant R829600 to SCL and VHG, it has not been subjected to the agency's required peer and policy review and therefore does not necessarily reflect the views of the EPA and no official endorsement should be inferred.

## REFERENCES

- Breck, D.W. *Zeolite Molecular Sieves*; Wiley: New York, 1974.
- Davis, M.E. New vistas in zeolite and molecular sieve catalysis. *Acc. Chem. Res.* **1993**, *26*, 111–115.
- Cambor, M.A.; Corma, A.; Mifsud, A.; Perez-Pariente, J.; Valencia, S. Synthesis of nanocrystalline zeolite beta in the absence of alkali metal cations. In *Studies in Surface Science and Catalysis*; Chon, H., Ihm, S.-K., Uh, Y.S., Eds.; Elsevier: Amsterdam, 1997; Vol. 105, 341–348.
- Castagnola, N.B.; Dutta, P.K. Spectroscopic studies of colloidal solutions of nanocrystalline Ru(bpy)<sub>3</sub><sup>2+</sup>-zeolite Y. *J. Phys. Chem., B* **2001**, *105*, 1537–1542.
- Holmberg, B.A.; Wang, H.; Norbeck, J.M.; Yan, Y. Controlling size and yield of zeolite Y nanocrystals using tetramethylammonium bromide. *Microporous Mesoporous Mater.* **2003**, *59*, 13–28.
- Huang, L.; Wang, Z.; Sun, J.; Miao, L.; Li, Q.; Yan, Y.; Zhao, D. Fabrication of ordered porous structures by self-assembly of zeolite nanocrystals. *J. Am. Chem. Soc.* **2000**, *122*, 3530–3531.
- Jacobsen, C.J.H.; Madsen, C.; Janssens, T.V.W.; Jakobsen, H.J.; Skibsted, J. Zeolites by confined space synthesis—characterization of the acid sites in nanosized ZSM-5 by ammonia desorption and <sup>27</sup>Al/<sup>29</sup>Si-MAS NMR spectroscopy. *Microporous Mesoporous Mater.* **2000**, *39*, 393–401.
- Jung, K.T.; Shul, Y.G. Preparation of transparent TS-1 zeolite film by using nanosized TS-1 particles. *Chem. Mater.* **1997**, *9*, 420–422.
- Mintova, S.; Olsen, N.H.; Valtchev, V.; Bein, T. Mechanism of zeolite A nanocrystal growth from colloids at room temperature. *Science* **1999**, *283*, 958–960.
- Mintova, S.; Valtchev, V. Effect of the silica source on the formation of nanosized silicalite-1: an in-situ dynamic light scattering study. *Microporous Mesoporous Mater.* **2002**, *55*, 171–179.
- Reding, G.; Maurer, T.; Kraushaar-Czarnetzki, B. Comparing synthesis routes to nano-crystalline zeolite ZSM-5. *Microporous Mesoporous Mater.* **2003**, *57*, 83–92.
- Schmidt, I.; Madsen, C.; Jacobsen, C.J.H. Confined space synthesis. A novel route to nanosized zeolites. *Inorg. Chem.* **2000**, *39*, 2279–2283.
- Tsapatsis, M.; Lovallo, M.; Okubo, T.; Davis, M.E.; Sadakata, M. Characterization of zeolite L nanoclusters. *Chem. Mater.* **1995**, *7*, 1734–1741.
- Zhang, W.; Bao, X.; Wang, X. A high-resolution solid-state NMR study on nano-structured HZSM-5 zeolite. *Catal. Lett.* **1999**, *60*, 89–94.
- Zhu, G.; Qiu, S.; Yu, J.; Sakamoto, Y.; Xiao, F.; Xu, R.; Terasaki, O. Synthesis and characterization of high-quality zeolite LTA and FAU single nanocrystals. *Chem. Mater.* **1998**, *10*, 1483–1486.
- Kim, S.-S.; Shah, J.; Pinnavaia, T.J. Colloid-imprinted carbons as templates for the nanocasting synthesis of mesoporous ZSM-5 zeolite. *Chem. Mater.* **2003**, *15*, 1664–1668.
- Bein, T. Synthesis and applications of molecular sieve layers and membranes. *Chem. Mater.* **1996**, *8*, 1636–1653.
- Madsen, C.; Jacobsen, C.J.H. Nanosized zeolite crystals—convenient control of crystal sized distribution by confined space synthesis. *Chem. Commun.* **1999**, 673–674.
- Lovallo, M.; Tsapatsis, M. Preferentially oriented submicron silicalite membranes. *AIChE J.* **1996**, *42*, 3020–3029.
- Boudreau, L.C.; Kuck, J.A.; Tsapatsis, M. Deposition of oriented zeolite A films: In situ and secondary growth. *J. Membr. Sci.* **1999**, *152*, 41–59.
- Schoeman, B.J.; Sterte, J.; Otterstedt, J.-E. Colloidal zeolite suspensions. *Zeolites* **1994**, *14*, 110–116.
- Li, Z.; Jaroniec, M. Colloidal imprinting: a novel approach to the synthesis of mesoporous carbons. *J. Am. Chem. Soc.* **2001**, *123*, 9208–9209.
- Wang, X.D.; Yang, Y.L.; Tang, Y.; Wang, Y.J.; Fu, S.K.; Gao, Z. Fabrication of hollow zeolite spheres. *Chem. Commun.* **2000**, 2161–2162.
- Rollison, D. Catalytic nanoarchitectures—the importance of nothing and the unimportance of periodicity. *Science* **2003**, *299*, 1698–1701.
- Alwy, H.; Li, G.; Grassian, V.H.; Larsen, S.C. Development of nanocrystalline zeolites as environmental catalysts. In *Nanotechnology and the Environment*; Alivisatos, P.C., Vicki, B., Karn, B., Masciaglioli, T., Zhang, W.-X., Eds.; American Chemical Society: Washington, DC, *in press*.
- Mintova, S.; Olsen, N.H.; Bein, T. Electron microscopy reveals the nucleation mechanism of zeolite Y from precursor colloids. *Angew. Chem., Int. Ed.* **1999**, *38*, 3201–3204.
- Lassinantti, M.; Hedlund, J.; Sterte, J. Faujasite-type films synthesized by seeding. *Microporous Mesoporous Mater.* **2000**, *38*, 25–34.
- Li, Q.; Creaser, D.; Sterte, J. An investigation of the nucleation/crystallization kinetics of nanosized colloidal faujasite zeolites. *Chem. Mater.* **2002**, *14*, 1319–1324.
- Zhan, B.-Y.; White, M.A.; Lumsden, M.; Mueller-Neuhaus, J.; Robertson, K.N.; Cameron, T.S.; Gharghour, M. Control of particle size and surface properties of crystals of NaX zeolite. *Chem. Mater.* **2002**, *14*, 3636–3642.
- Li, Q.; Creaser, D.; Sterte, J. The nucleation period for TPA-silicalite-1 crystallization determined by two-stage varying-temperature synthesis. *Microporous Mesoporous Mater.* **1999**, *31*, 141–150.
- Schoeman, B.J. A high temperature in situ laser light-scattering study of the initial stage in the crystallization of TPA-silicalite-1. *Zeolites* **1997**, *18*, 97–105.
- Van Grieken, R.; Sotelo, J.L.; Menendez, J.M.; Melero, J.A. Anomalous crystallization mechanism in the synthesis of nanocrystalline ZSM-5. *Microporous Mesoporous Mater.* **2000**, *39*, 135–147.
- Corkery, R.W.; Ninham, B.W. Low-temperature synthesis and characterization of a stable colloidal TPA-silicalite-1 suspension. *Zeolites* **1997**, *18*, 379–386.

34. Blatter, F.; Sun, H.; Vasenkov, H.; Frei, H. Photocatalyzed oxidation in zeolite cages. *Catal. Today* **1998**, *41*, 297–309.
35. Frei, H.; Blatter, F.; Sun, H. Photocatalyzed oxidation of hydrocarbons in zeolite cages. *Chemtech* **1996**, *26*, 24–30.
36. Li, X.; Ramamurthy, V. Selective oxidation of olefins within organic dye cation-exchanged zeolites. *J. Am. Chem. Soc.* **1996**, *118*, 10,666–10,667.
37. Pradhan, A.R.; Macnaughtan, M.A.; Raftery, D. Preparation of zeolites supported on optical fibers. *Chem. Mater.* **2002**, *14*, 3022–3027.
38. Pradhan, A.R.; Uppili, S.; Shailaja, J.; Sivaguru, J.; Ramamurthy, V. Zeolite-coated quartz fibers as media for photochemical and photophysical studies. *Chem. Commun.* **2002**, 596–597.
39. Pradhan, A.R.; Macnaughtan, M.A.; Raftery, D. Zeolite-coated optical microfibers for intrazeolite photocatalysts studied by in situ solid-state NMR. *J. Am. Chem. Soc.* **2000**, *122*, 404–405.
40. Deng, Z.; Balkus, K.J. Pulsed laser deposition of zeolite NaX thin films on silica fibers. *Microporous Mesoporous Mater.* **2002**, *56*, 47–53.
41. Okada, K.; Kuboyama, K.-I.; Takei, T.; Kameshima, Y.; Yasumori, A.; Yoshimura, M. In situ zeolite Na-X coating on glass fibers by soft solution process. *Microporous Mesoporous Mater.* **2000**, *37*, 99–105.
42. Ke, C.; Yang, Y.L.; Ni, Z.; Wang, Y.J.; Tang, Y.; Gu, Y.; Gao, Z. Electrophoretic assembly of nanozeolites: Zeolite coated fibers and hollow zeolite fibers. *Chem. Commun.* **2001**.
43. Marcus, B.M.; Cormier, W.E. Going green with zeolites. *Chem. Eng. Prog.* **1999**, *95*, 47–53.
44. Armor, J.N. Metal-exchanged zeolites as catalysts. *Microporous Mesoporous Mater.* **1998**, *22*, 451–456.
45. Anastas, P.T.; Williamson, T.C. Green chemistry: an overview. In *Green Chemistry: Designing Chemistry for the Environment*; Anastas, P.T., Williamson, T.C., Eds.; American Chemical Society: Washington, DC, 1996; 1–17.
46. Simmons, M. The role of catalysts in environmentally benign synthesis of chemicals. In *Green Chemistry: Designing Chemistry for the Environment*; Anastas, P.T., Williamson, T.C., Eds.; American Chemical Society: Washington, DC, 1996; 1–17.
47. Armor, J.N. Environmental catalysis. *Appl. Catal., B: Environ.* **1992**, *1*, 221–256.
48. Maxwell, I.E.; Naber, J.E.; de Jong, K.P. The pivotal role of catalysis in energy related environmental technology. *Appl. Catal., A* **1994**, *113*, 153–173.
49. Vogel, B.; Schneider, C.; Klemm, E. The synthesis of cresol from toluene and N<sub>2</sub>O on H[Al]ZSM-5: Minimizing the product diffusion by the use of small crystals. *Catal. Lett.* **2002**, *79*, 107–112.
50. Suresh, K.A.; Sharma, M.M.; Sridhar, T. Engineering aspects of industrial liquid-phase air oxidation of hydrocarbons. *Ind. Eng. Chem. Res.* **2000**, *39*, 3958–3997.
51. Iwamoto, M.; Hamada, H. Removal of nitrogen monoxide from exhaust gases through novel catalytic processes. *Catal. Today* **1991**, *10*, 57–71.
52. Iwamoto, M.; Yahiro, H.; Tanda, K.; Mizuno, N.; Mine, Y.; Kagawa, S. Removal of nitrogen monoxide through a novel catalytic process. 1. Decomposition of excessively copper ion exchanged ZSM-5 zeolites. *J. Phys. Chem.* **1991**, *95*, 3727–3730.
53. Shelef, M. Selective catalytic reduction of NO<sub>x</sub> with N-free reductants. *Chem. Rev.* **1995**, *95*, 209–225.
54. Cho, B.K. Nitric oxide reduction by HC over CuZSM-5 monolith catalyst under lean conditions. *J. Catal.* **1993**, *142*, 418.
55. Ebitani, K.; Morokuma, M.; Kim, J.-H.; Morikawa, A. Photocatalytic decomposition of nitrous oxide on Cu ion-containing ZSM-5 catalyst. *J. Catal.* **1993**, *141*, 725–728.
56. Ebitani, K.; Morokuma, M.; Kim, J.-H.; Morikawa, A. Photocatalytic decomposition of dinitrogen oxide on Cu-containing ZSM-5 catalyst. *J. Chem. Soc., Faraday Trans.* **1994**, *90*, 377–381.
57. Anpo, M.; Matsuoka, M.; Shioya, Y.; Yamashita, H.; Giamello, E.; Morterra, C.; Che, M.; Patterson, H.H.; Webber, S.; Ouellette, S.; Fox, M.A. Preparation and characterization of the Cu + /ZSM-5 catalyst and its reaction with NO under UV irradiation at 275 K. In situ photoluminescence, EPR, and FT-IR. *J. Phys. Chem.* **1994**, *98*, 5744–5750.
58. Higashimoto, S.; Matsuoka, M.; Yamashita, H.; Anpo, M.; Kitao, O.; Hidaka, H.; Che, M.; Giamello, E. Effect of Si/Al ratio on the local structure of V/oxide/ZSM-5 catalysts prepared by solid state reaction and their photocatalytic reactivity for the decomposition of NO in the absence and presence of propane. *J. Phys. Chem., B* **2000**, *104*, 10,288–10,292.
59. Long, R.Q.; Yang, R.T. Superior Fe-ZSM-5 catalyst for the selective catalytic reduction of nitric oxide by ammonia. *J. Am. Chem. Soc.* **1999**, *121*, 5595–5596.
60. Long, R.Q.; Yang, R.T. Catalytic performance of Fe-ZSM-5 catalysts for the selective catalytic reduction of nitric oxide by ammonia. *J. Catal.* **1999**, *188*, 332–339.
61. Ma, A.Z.; Grunert, W. Selective catalytic reduction of NO by ammonia over Fe-ZSM-5 catalysts. *Chem. Commun.* **1999**, 71–72.
62. Lobree, L.J.; Hwang, I.; Reimer, J.A.; Bell, A.T. An in situ infrared study of NO reduction by C<sub>3</sub>H<sub>8</sub> over FeZSM-5. *Catal. Lett.* **1999**, *63*, 233–240.
63. Yamada, K.; Pophal, C.; Segawa, K. Selective catalytic reduction of N<sub>2</sub>O by C<sub>3</sub>H<sub>6</sub> over Fe-ZSM-5. *Microporous Mesoporous Mater.* **1998**, *21*, 549–555.
64. Joyner, R.; Stockenhuber, M. Preparation, characterization, and performance of Fe-ZSM-5 catalysts. *J. Phys. Chem., B* **1999**, *103*, 5963–5976.
65. Chen, H.-Y.; Voskoboinikov, T.V.; Sachtler, W.M.H. Reduction of NO<sub>x</sub> over FeZSM-5 catalysts: Adsorption complexes and their reactivity toward hydrocarbons. *J. Catal.* **1998**, *180*, 171–183.
66. Feng, X.; Hall, W.K. Fe-ZSM-5: A durable SCR catalyst for NO<sub>x</sub> removal from combustion streams. *J. Catal.* **1997**, *166*, 368.
67. El-Malki, E.-M.; van Santen, R.A.; Sachtler, W.M.H. Active sites in Fe/MFI catalysts for NO<sub>x</sub> reduction

- and oscillating N<sub>2</sub>O decomposition. *J. Catal.* **2000**, *196*, 212–223.
68. Fox, M.A. Photocatalysis: decontamination with sunlight. *Chemtech* **1992**, *22*, 680–685.
  69. Hoffman, M.R.; Martin, S.T.; Choi, W.; Bahnemann, D.W. Environmental applications of semiconductor photocatalysis. *Chem. Rev.* **1995**, *95*, 69–96.
  70. Linesbiger, A.L.; Lu, G.; Yates, J.T.J. Photocatalysis on TiO<sub>2</sub> surfaces: principles, mechanisms, and selected results. *Chem. Rev.* **1995**, *95*, 735–758.
  71. Peral, J.; Ollis, D.F. Heterogeneous photocatalytic oxidation of gas-phase organics for air purification: acetone, 1-butanol, butyraldehyde, formaldehyde, and m-xylene oxidation. *J. Catal.* **1992**, *136*, 554–565.
  72. Sauer, M.L.; Hale, M.A.; Ollis, D.F. Heterogeneous photocatalytic oxidation of dilute toluene–chlorocarbon mixtures in air. *J. Photochem. Photobiol., A: Chem.* **1995**, *88*, 169–178.
  73. Driessen, M.D.; Goodman, A.L.; Zaharias, G.A.; Grassian, V.H. Gas-phase photooxidation of trichloroethylene on TiO<sub>2</sub> and ZnO. *J. Phys. Chem., B* **1998**, *102*, 549.
  74. El-Maazawi, M.; Finken, A.; Nair, A.; Grassian, V.H. Adsorption and photocatalytic oxidation of acetone on TiO<sub>2</sub>: an in-situ FT-IR study. *J. Catal.* **2000**, *191*, 138–146.
  75. Larson, S.A.; Falconer, J.A. Initial reaction steps in photocatalytic oxidation of aromatics. *Catal. Lett.* **1997**, *44*, 57–65.
  76. Muggli, D.S.; McCue, J.T.; Falconer, J.L. Mechanism of the photocatalytic oxidation of ethanol on TiO<sub>2</sub>. *J. Catal.* **1998**, *173*, 470–483.
  77. Muggli, D.S.; Falconer, J.L. Catalyst design to change selectivity of photocatalytic oxidation. *J. Catal.* **1998**, *175*, 213–219.
  78. Yiming, X.; Langford, C.H. Enhanced photoactivity of a titanium(IV) oxide supported on ZSM5 and zeolite A at low coverage. *J. Phys. Chem.* **1995**, *99*, 11,501–11,507.
  79. Yiming, X.; Langford, C.H. Photoactivity of titanium dioxide supported on MCM41, zeolite X and zeolite Y. *J. Phys. Chem.* **1997**, *101*, 3115–3121.
  80. Takeda, N.; Torimoto, T.; Sampath, S.; Kuwabata, S.; Yoneyama, H. Effect of inert supports for titanium dioxide loading on enhancement of photodecomposition rate of gaseous propionaldehyde. *J. Phys. Chem.* **1995**, *99*, 9986–9991.
  81. Lee, G.D.; Tuan, V.A.; Falconer, J.L. Photocatalytic oxidation and decomposition of acetic acid on titanium silicalite. *Environ. Sci. Technol.* **2001**, *35*, 1252–1258.
  82. Sahle-Demessie, E.; Gonzalez, M. Oxygenation of hydrocarbons Using nanostructured TiO<sub>2</sub> as a photocatalyst: a green alternative. In *Green Chemical Syntheses and Processes*; Anastas, P., Heine, L.G., Williamson, T.C., Eds.; ACS: Washington, DC, 2000; 217–228.
  83. Maira, A.J.; Yeung, K.L.; Soria, J.; Coronado, J.M.; Bolver, C.; Lee, C.Y. Gas-phase photo-oxidation of toluene using nanometer-size TiO<sub>2</sub> catalysts. *Appl. Catal., B: Environ.* **2001**, *29*, 327–336.
  84. Ryerson, T.B.; Trainer, M.; Holloway, J.S.; Parrish, J.S.; Huey, L.G.; Sueper, D.T.; Frost, G.J.; Donnelly, S.G.; Schauffler, S.; Atlas, E.L.; Kuster, W.C.; Goldan, P.D.; Hübler, G.; Meagher, J.F.; Fehsenfeld, F.C. Observations of ozone formation in power plant-plumes and implications for ozone control strategies. *Science* **2001**, *292*, 719.
  85. Meinershagen, J.L.; Bein, T. Optical sensing in nanopores. encapsulation of the solvatochromic dye Nile red in zeolites. *J. Am. Chem. Soc.* **1999**, *121*, 448–449.
  86. Remillard, J.; Jones, J.; Poindexter, B.; Narula, C.; Weber, W. Demonstration of a high temperature fiber-optic gas sensor made with sol-gel process to incorporate a fluorescent indicator. *Appl. Opt.* **1999**, *38*, 5306–5309.

# Nanocrystallization

**John H. Perepezko**

*Materials Science and Engineering, University of Wisconsin, Madison, Wisconsin, U.S.A.*

## INTRODUCTION

This discussion focuses on the development of nanostructured materials through controlled primary crystallization reactions of amorphous alloys. The nanocrystalline state is at the forefront of study in a variety of disciplines involving condensed matter. In broad terms the main activities can be classified into material synthesis strategies, property measurement and evaluation, applications, and computer simulation and modeling. A key attribute of the nanocrystalline state that offers a broad attraction for many disciplines is derived from the nanometer length scale. At this length scale the chemical, biological, physical, mechanical, and structural properties and performance of materials are susceptible to significant changes during synthesis,<sup>[1]</sup> and the current computational capabilities allow for effective simulation and analysis of nanocrystalline assemblies.<sup>[2]</sup>

The principles that govern the kinetics of microstructural evolution apply directly to other devitrification reactions that yield nanostructured intermetallic phases and quasi-crystalline phases that are also promising in terms of their structural and functional performance. Some of the key issues concerning synthesis and stability are illustrated from the observed behavior in specific amorphous alloys, but the discussion also applies to other similar alloy systems.

## OVERVIEW

The nanocrystalline state, where the microstructural size scales are in the 1- to 100-nm range, can be synthesized by a variety of processing routes starting with the vapor, liquid, or solid state.<sup>[1]</sup> Although it may be expected that the final nanocrystalline state is independent of the processing route, in practice this is not the case. For example, for deposition from the vapor at the high rates that promote nanocrystalline grain sizes, residual impurities or entrapped gas can be present in the deposit. Similarly, from an initial solid, the nanocrystalline state is often achieved by the mechanical milling of powders. During subsequent consolidation of powders to a bulk form, it is common to incorporate impurities from the medium used for

milling and to retain a residual porosity.<sup>[3]</sup> The attainment of nanocrystalline structures from the liquid or vapor requires the attainment of a high crystal nucleation rate, which in turn is promoted by a large undercooling before the onset of crystallization. Actually, there are two pathways that may be followed to achieve the high crystal nucleation density.<sup>[4]</sup> If a liquid is rapidly quenched at a rate that happens to coincide with the conditions for a high nucleation rate a nanocrystalline structure is possible by direct quenching.<sup>[5]</sup> However, under most conditions of rapid quenching it is difficult to control the processing and the reproducibility. Instead, a direct cooling to an amorphous state and a subsequent low-temperature crystallization treatment is usually preferred as a method of achieving reproducible nanostructure synthesis including the fabrication of nanostructures in bulk sample volumes.<sup>[6-8]</sup>

The classes of metallic glasses that provide the most effective routes to nanocrystallization are closely related to two important aspects of solidification that involve kinetic competition: 1) avoidance of crystallization upon cooling of the liquid and 2) the control of crystallization upon heating of the glass. Although there are connections between these aspects, including the common underlying important role of melt undercooling as a measure of liquid metastability, in each case the controlling reactions occur under regimes of different kinetic constraints.<sup>[9]</sup> In addition to the closed-system methods involving liquid or vapor quenching, it is recognized that open systems involving continuous deformation<sup>[10]</sup> or irradiation<sup>[11]</sup> can drive a material toward nanocrystallinity and in some cases to an amorphous structure. In this case, the stored energy due to defects, grain refinement, and solute supersaturation is a measure of the level of metastability that is crucial to consider in the analysis of amorphization and the development of nanostructured microstructures.<sup>[12]</sup>

## NANOCRYSTALLIZATION REACTIONS

The crystallization behavior of amorphous materials is of central importance in the synthesis of nanostructured materials. The reaction pathways that are operative

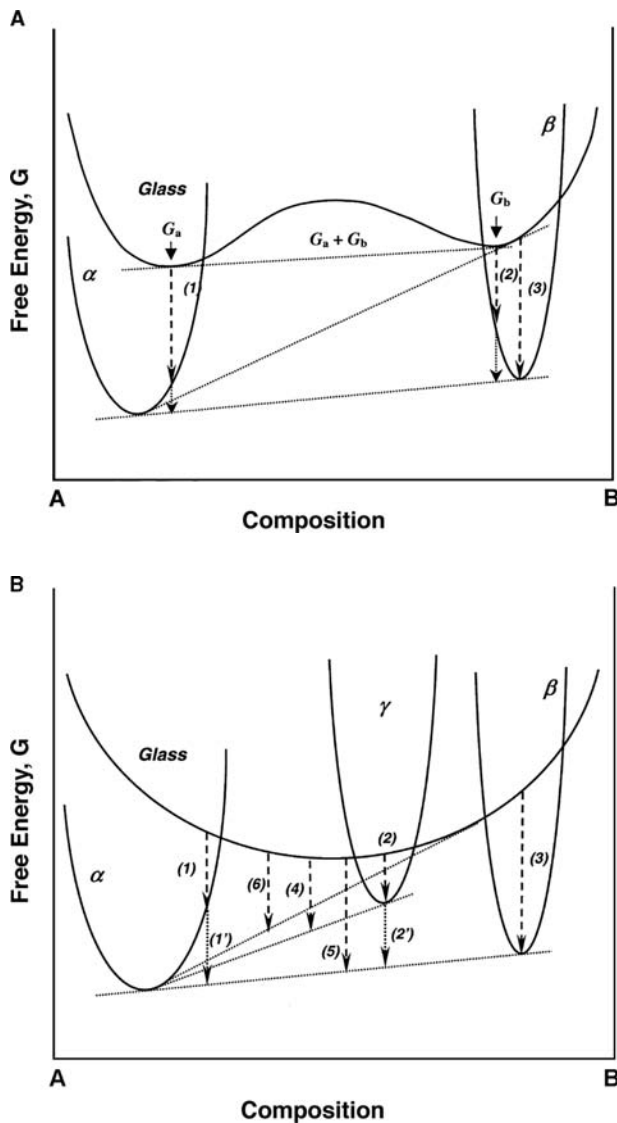


**Fig. 1** Schematic free energy vs. composition diagrams illustrating some of the possible nanocrystallization reactions of an amorphous phase. (A) reaction pathways for an alloy with a negative heat of mixing and a metastable  $\gamma$  phase. (B) reaction pathways for an alloy with a positive heat of mixing.

during crystallization must be identified and controlled to develop successful strategies for the consolidation of amorphous powders or ribbons that can be processed into bulk nanostructured solids. Moreover, the control of the reaction path during crystallization provides for the option to develop nanoscale structures with different phase selection.

The different reaction paths and product selection options are identified in Fig. 1, which illustrates schematically the free energy relationships between an initial amorphous phase that is considered as an undercooled liquid solution and several crystalline product phases that include stable  $\alpha$  and  $\beta$  phases and a metastable  $\gamma$  phase.<sup>[13,14]</sup> Within the alloy composition ranges that

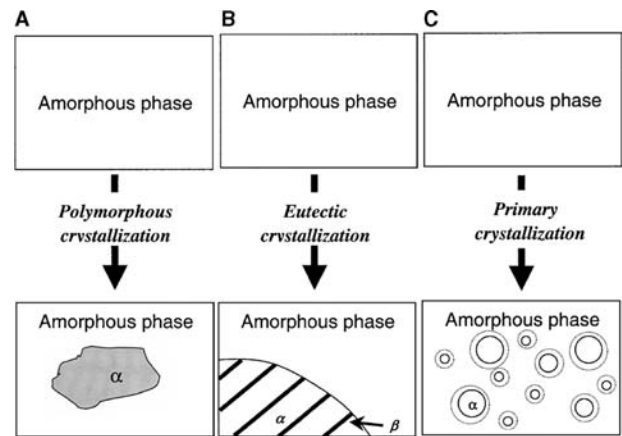


**Fig. 2** Schematic illustration of the characteristic microstructural morphologies that develop during nanocrystallization by (A) polymorphic, (B) eutectic, and (C) primary phase reactions. In (C) the dotted curve around primary phase nanocrystals denotes the extent of the solute diffusion field.

are usually favored for glass formation there are several types of crystallization reactions that can be used to develop nanocrystalline structures during controlled heating or isothermal reaction. One of the simplest reactions is the direct transformation from the glass to a single-phase crystal without composition change as illustrated in Fig. 1A and B by pathways (1) and (2) for either stable or metastable initial product phases. The composition invariant or polymorphic reaction can yield metastable structures such as supersaturated solid solution phases or metastable intermediate phases that can undergo further transformation that is indicated by pathways (1') and (2') in Fig. 1A and B. With primary crystallization, a single phase is the initial product, but the reaction proceeds with a partitioning of solute to yield a solute lean primary crystal and a residual amorphous phase matrix that is enriched in solute.<sup>[6,15–18]</sup> The kinetics of primary crystallization is evidently related to the rate of solute diffusion in the amorphous matrix that is necessary to dissipate the solute that is rejected during primary crystal growth.<sup>[19]</sup> It is also apparent that primary crystallization does not result in a stable equilibrium product structure that is indicated by the compositions  $\alpha_e$  and  $\beta_e$  in Fig. 1A and B. To complete the primary crystallization, a subsequent multiphase crystallization develops either from the nucleation site provided by the primary crystal or directly from the amorphous phase. For example, with eutectic crystallization that is indicated by pathway (3) in Fig. 1A, the product phases (i.e.,  $\alpha$  and  $\beta$ ) often develop by a coupled growth and appear with a lamellar or rod type of regular morphology in a spherulitic pattern.<sup>[8,19]</sup> In this case the synthesis of a nanoscale microstructure requires a high density of  $\alpha$  and  $\beta$  colonies with an ultrafine lamellar spacing. A schematic illustration of the characteristic microstructural morphologies



associated with each of the nanocrystallization reactions is provided in Fig. 2. Often, under high-undercooling conditions metastable phase reactions can develop as a precursor to the formation of stable crystallization products. For example, as indicated in Fig. 1B, the undercooled liquid or amorphous phase can undergo a phase separation reaction leading to the formation of two liquids with different compositions that are indicated by  $G_a$  and  $G_b$  in Fig. 1B. At low temperature or high undercooling, limited atomic mobility will result in a fine scale of phase separation that can extend into the nanoscale regime.<sup>[20]</sup> Moreover, in some cases the interfaces between the different liquid regions can serve as heterogeneous nucleation sites for subsequent crystallization reactions and establish high nucleation product number densities. In addition, there is evidence that in some systems minor impurity levels can promote the development of phase separation reactions.<sup>[14]</sup> Another example of a precursor reaction is the formation of an intermediate phase as a metastable product as illustrated in Fig. 1A for the  $\gamma$  phase.

## KINETICS OF NANOCRYSTALLIZATION

One of the key requirements that must be satisfied for the development of a nanoscale microstructure by a crystallization reaction is the attainment of a very high nucleation product number density. The main features of the steady-state nucleation rate kinetics can be described by

$$J_i^s = \Omega_i \exp\left[-\frac{\Delta G^* f(\theta)}{kT}\right] \quad (1)$$

where  $J_i^s$  is the steady state nucleation rate on a volume ( $i = v$ ) or surface basis ( $i = a$ ).<sup>[12]</sup> Respective values for the prefactor,  $\Omega_i$ , activation barrier,  $\Delta G^*$ , and the contact angle function,  $f(\theta)$ , are used in Eq. (1), and  $kT$  is the thermal energy. The expressions for  $\Omega_i$  involve a product of a nucleation site density on a catalytic surface or volume basis, the number of atoms on a nucleus surface and a jump frequency. For most cases,  $\Omega_v = 10^{30}/\eta \text{ cm}^{-3} \text{ sec}^{-1}$  and  $\Omega_a = 0.10^{22}/\eta \text{ cm}^{-2} \text{ sec}^{-1}$ , with  $\eta$  the liquid shear viscosity (in poise) given by Ref.<sup>[6]</sup> as

$$\eta = 10^{-3.33} \exp\left[\frac{3.34T_L}{T - T_g}\right] \quad (2)$$

in terms of the liquidus temperature,  $T_L$ , and the glass transition,  $T_g$ , and  $\phi$ , the fraction of active catalytic sites. The activation barrier for nucleation is given by

$$\Delta G^* = \frac{b\sigma^3}{\Delta G_v^2} \quad (3)$$

where  $\sigma$  is the liquid–solid interfacial energy,<sup>[21]</sup>  $\Delta G_v$  is the driving free energy for nucleation of a unit volume of product phase, and  $b = 16\pi/3$  for spherical nuclei. With a planar catalytic surface site and spherical nuclei  $f(\theta) = [2 - 3 \cos \theta + \cos^3 \theta]/4$ . Following the establishment of a supersaturation or undercooling, there is an initial time period during which the nucleation cluster population evolves toward the steady-state distribution.<sup>[22]</sup> During this transient period the time-dependent nucleation rate,  $J_i(t)$ , is given by

$$J_i(t) = J_i^s \left[ 1 + 2\Sigma(-1)^n \exp\left(-\frac{n^2 t}{\tau}\right) \right] \quad (4)$$

where  $\tau$  is the time lag or delay time that is estimated by  $(n^{*2}/\pi^2\beta)$ . The critical nucleus size,  $n^*$ , in atoms is obtained from  $n^* = 4\pi r^{*3}/(3V_a)$  where  $V_a$  is the volume per atom and  $r^* = -2\sigma/\Delta G_v$  is the critical nucleus radius. The atomic jump frequency,  $\beta$ , can be estimated by  $D/\lambda^2$ , where  $D$  is the diffusion coefficient in the undercooled phase and  $\lambda$  is the jump distance.<sup>[23,24]</sup>

To achieve a nanocrystalline microstructure (i.e., with a size scale  $\leq 100$  nm) in a fully crystallized volume, the nucleation number density should be at least of the order of  $10^{21} \text{ m}^{-3}$ . Of course, nanocrystallization can be achieved only if there are also restrictions on the kinetics of nanocrystal growth following nucleation.

The kinetic analysis of growth follows different forms that depend on the nature of the solute partitioning associated with phase growth. For example, during polymorphous transformation without solute redistribution, the growth rate,  $V$ , is controlled by interface attachment limited kinetics as represented by

$$V = V_0 \exp\left[-\frac{Q_D}{RT}\right] \left( 1 - \exp\left[-\frac{\Delta G_v}{RT}\right] \right) \quad (5)$$

where  $V_0$  is a prefactor of the order of  $5 \times 10^3 \text{ m/sec}$  and  $Q_D$  is the activation energy for interface jumps.<sup>[19,25]</sup> At low temperature where  $\Delta G_v \gg RT$  growth is diffusion controlled as expressed by

$$V = V_0 \exp\left[-\frac{Q_D}{RT}\right] \quad (6)$$

For the case of eutectic reaction where the solute redistribution is limited to the reaction interface

$$V \cong 4D_1 \frac{\delta}{\lambda^2} \quad (7)$$

where  $D_1$  is the interface diffusivity,  $\delta$  is the thickness of the reaction front, and  $\lambda$  is the lamellar spacing.<sup>[25,26]</sup> With these kinetic modes, the reaction is relatively rapid and a metastable microstructure based on nanocrystals and an amorphous phase with the original

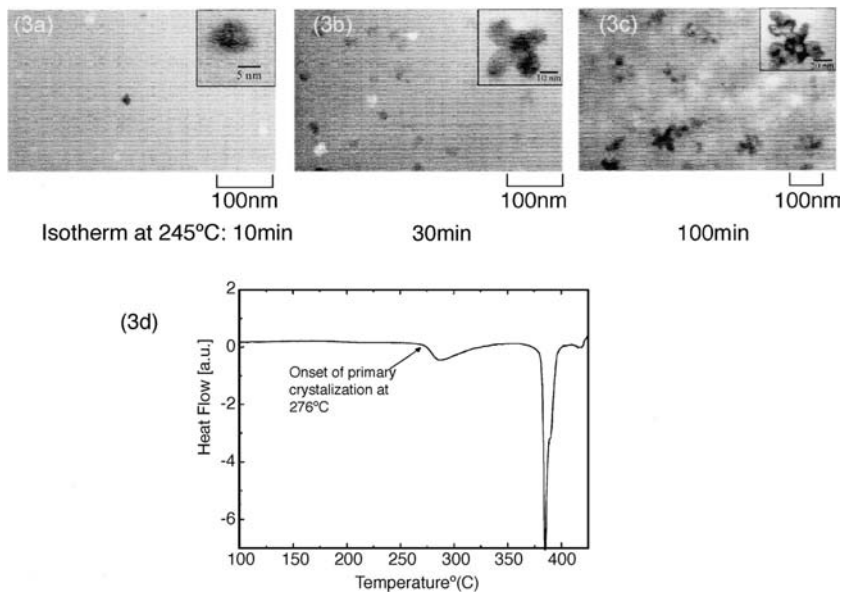


**Fig. 3** TEM bright-field images from an  $\text{Al}_{88}\text{Y}_7\text{Fe}_5$  melt-spun ribbon that was isothermally annealed at  $245^\circ\text{C}$  for (A) 10 min, (B) 30 min, (C) 100 min, and (D) continuous heating differential scanning calorimetry (DSC) trace at 40 K/Min showing a primary crystallization onset at  $276^\circ\text{C}$ .

composition is possible if the kinetics of subsequent decomposition reactions to a more stable phase constitution is sluggish.

When growth requires a redistribution of solute as in primary crystallization, the kinetics are limited by the rate of diffusion of the rejected solute into the amorphous matrix. For evolving nanocrystals that are isolated from each other the growth rate has the following form

$$V = \frac{\alpha}{2} \sqrt{\frac{D}{t}} \quad (8)$$

where  $\alpha$  is a dimensionless factor that is evaluated from the compositions at the particle/matrix interface and the average composition and  $D$  will be controlled by the slowest diffusing solute in a multicomponent alloy.<sup>[26]</sup> However, at high nucleation densities the isolation can be lost as the diffusion fields from neighboring nanocrystals begin to overlap (i.e., soft impingement).<sup>[25]</sup> Under this condition there is a kinetic inhibition to further growth. Concurrent with the growth of nanocrystals, the highly refined sizes indicate that capillarity effects such as Ostwald ripening due to curvature-driven transport (i.e., Gibbs–Thomson effect) can be important.<sup>[25,27]</sup>

## AMORPHIZATION KINETICS AND TRANSITIONS

The kinetic transition between nanocrystalline products and an amorphous phase is a common structural change that occurs during solidification with increasing cooling rate as the liquid undercooling approaches  $T_g$ .

Often, the initiation of the transition is represented by a critical cooling rate and interpreted as a sharp structural change.<sup>[28]</sup> However, there are also many reports of mixed crystal/glass phase structures indicating that the transition occurs over a range of cooling rates reflecting the kinetic competition and the probabilistic nature of nucleation.<sup>[29,30]</sup> It is useful to note that the glass transition is not a phase transformation in a thermodynamic sense, but it is a kinetic manifestation of the slowing of atomic transport in the liquid with cooling. In fact, the calorimetric glass transition signal is due to the large change in heat capacity that occurs when a liquid becomes configurationally frozen. The slowing of atomic transport is also reflected by an increase in liquid viscosity. The time for the liquid structure to relax during cooling is related to the viscosity, and for typical laboratory measurement conditions  $T_g$  corresponds to a viscosity in the range of  $10^{12}$ – $10^{13}$  P ( $10^{11}$ – $10^{12}$  Pa sec).<sup>[31]</sup>

Indeed, following amorphization by rapid melt quenching, many metallic glasses do not exhibit a clear glass transition signal,  $T_g$ , upon reheating. Instead, initial exothermic maxima are observed to develop that indicate a multiple-stage crystallization<sup>[5,32,33]</sup> as shown in Fig. 3 for an amorphous  $\text{Al}_{88}\text{Y}_7\text{Fe}_5$  ribbon after melt spinning and after initial crystallization. The microstructural analysis has established that for many amorphous Al-base alloys that contain transition metal (TM) and rare earth (RE) solutes, the initial crystallization corresponds to primary phase formation (i.e., Al) yielding a sample that contains a high density of nanocrystals within an amorphous matrix.<sup>[5]</sup> This behavior is of importance in understanding the kinetic control of glass formation. The two basic strategies to synthesize amorphous alloys

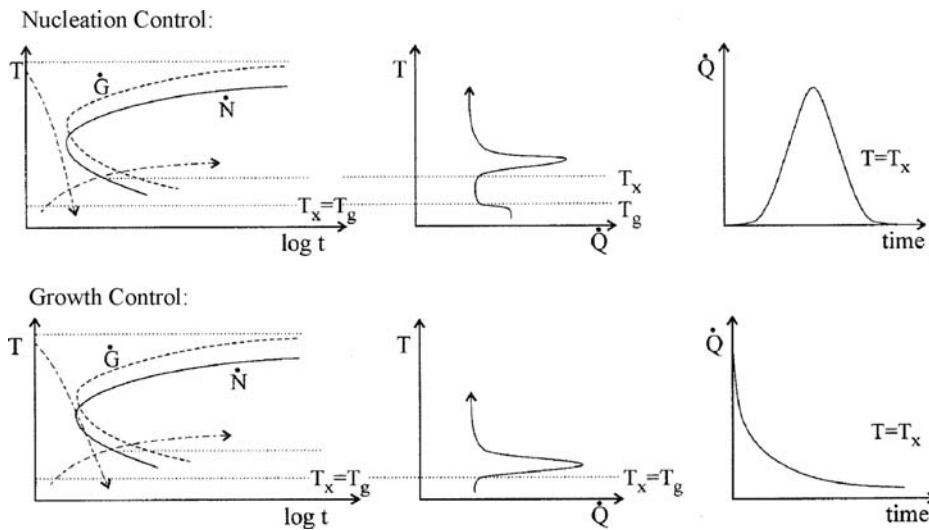


**Fig. 4** The principal forms of kinetic control for metallic glass formation.

are illustrated schematically in Fig. 4. With nucleation control, the undercooling that is achieved during cooling bypasses the nucleation reaction and the nucleation size distribution,<sup>[9]</sup> $C(n)$  that may be retained by the cooling does not overlap with the critical nucleation size,  $n^*$ , at the crystallization temperature,  $T_x$ . As a result, there is no precursor reaction to influence the evolution of crystalline clusters during subsequent thermal treatment. In this way, a clear separation in temperature between the  $T_g$  and  $T_x$  signals can be observed during reheating of a glass. These kinetic conditions are the basis for bulk glass formation during slow cooling. During isothermal annealing at  $T_x$ , the heat evolution rate  $\dot{Q}$  exhibits a clear delay before the onset of the nucleation reaction and a peak maximum associated with the completion of nucleation and continued growth. On the other hand, under growth-controlled conditions the cooling rate is insufficient to bypass the nucleation onset completely so that some small fraction of crystallites may form initially, but the rapidly rising viscosity and falling growth rate with continued cooling near  $T_g$  prevents rapid cluster growth. In addition, the cluster size distribution that is retained overlaps in size with the critical nucleation size at  $T_x$ . In this case, as indicated in Fig. 4, upon reheating a sample with preexisting crystallites (i.e., quenched-in nuclei), rapid crystallization because of the development of quenched-in clusters as well as additional nucleation ensues at  $T_x$ , which will essentially coincide with  $T_g$ .<sup>[34]</sup> Whereas many of the early metallic glass alloys were synthesized under growth-controlled conditions (i.e., marginal glass formers)<sup>[35]</sup> the primary crystallization particle densities in these alloys are of the order of  $10^{18} \text{ m}^{-3}$ . For the class of amorphous Al- and Fe-base glasses, the primary crystallization number densities range from  $10^{21}$  up to almost  $10^{23} \text{ m}^{-3}$ . Both of the

basic mechanisms for glass formation that are outlined in Fig. 3 can yield a high number density of nanocrystals upon devitrification. With nucleation control, nanostructure development can be achieved by controlled reheating, because the maximum in the growth rate typically occurs at a higher temperature than the maximum in the nucleation rate.<sup>[25]</sup> In addition to the two basic synthesis routes outlined in Fig. 4, there is another important distinction between alloys that form bulk glasses and the marginal glass-forming alloys based on the temperature dependence of the liquid viscosity.<sup>[31]</sup> The main features of the viscosity behavior are shown in Fig. 5 where “strong” liquids display an Arrhenius type of temperature dependence. A good example of a strong liquid is  $\text{SiO}_2$ , but the bulk glass-forming alloys also display strong liquid characteristics.<sup>[31]</sup> For the “fragile” liquid behavior shown in

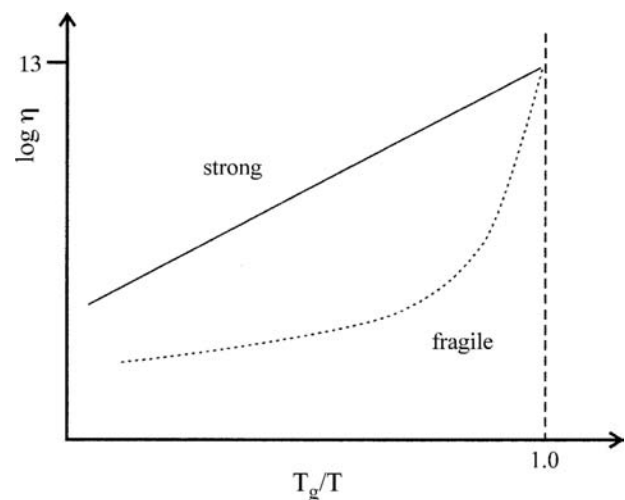


**Fig. 5** A schematic illustration of the liquid viscosity behavior vs.  $T_g/T$  for strong and fragile glasses.

Fig. 5 the viscosity is low even in the undercooled regime, but increases sharply upon approaching the glass transition. It appears that the marginal glass-forming alloys exhibit a fragile type of viscosity behavior. It is evident that the transport behavior will impact both the ease of glass formation and the kinetics of nanocrystal development. The different synthesis routes that are shown in Fig. 4 originate from the relative time scales for the onset of nucleation and melt cooling. The transition from growth control to nucleation control can be achieved either by an increase in the cooling rate or by lengthening the time for onset of nucleation,  $t_n$ . Because  $t_n$  is related to atomic transport in the liquid, strong liquids with high viscosity are favored for bulk glass formation. It is also apparent that  $t_n$  can be lengthened by removing active nucleation sites from the melt. In fact, this is the basis for the effectiveness of melt fluxing, which has been shown to promote bulk glass formation.<sup>[36,37]</sup> The actual mechanism for the development of the ultrahigh number densities of nanocrystals is under active study, and proposals based on homogeneous<sup>[38,39]</sup> and heterogeneous<sup>[35,40]</sup> nucleation and precursor phase separation reactions<sup>[41]</sup> are under examination.

The attainment of nanocrystal dispersions of essentially pure Al with ultrahigh number densities is a critical component of the attractive structural performance, but an equally important characteristic is the high thermal stability. One indication of this stability is the wide temperature range between the primary crystallization and final crystallization of between 75° and 100°C in Fig. 3. Within this range, there is a metastable two-phase coexistence involving the Al nanocrystals and the surrounding amorphous matrix with limited coarsening of the microstructure. The sluggish kinetics is related at least in part to the large differences in component atom sizes and diffusivities<sup>[42–44]</sup> as well as the onset of impingement of the diffusion fields from neighboring nanocrystals.<sup>[40]</sup> Indeed, even at a particle density of  $10^{21} \text{ m}^{-3}$  the average nanocrystal separation is only about 100 nm. It is also evident that for the Al nanocrystals to grow there is a rejection of solute (i.e., TM and RE) as is typical for primary crystallization reactions. The low solute diffusivities, especially for the large RE atom, act to limit the growth,<sup>[45]</sup> and the transport is limited further by the reduced concentration gradient due to impingement as indicated by the asymmetric primary crystallization exotherm in Fig. 3. In fact, because the amorphous matrix composition will also be enriched in TM and RE components, it is possible to use the solute redistribution during primary crystallization to enhance the stability of the amorphous matrix (i.e., raise  $T_g$ ).<sup>[15,46]</sup> This kinetic restriction inhibits further nanocrystal growth and accounts for the asymmetric crystallization peak and the remarkable thermal stability.

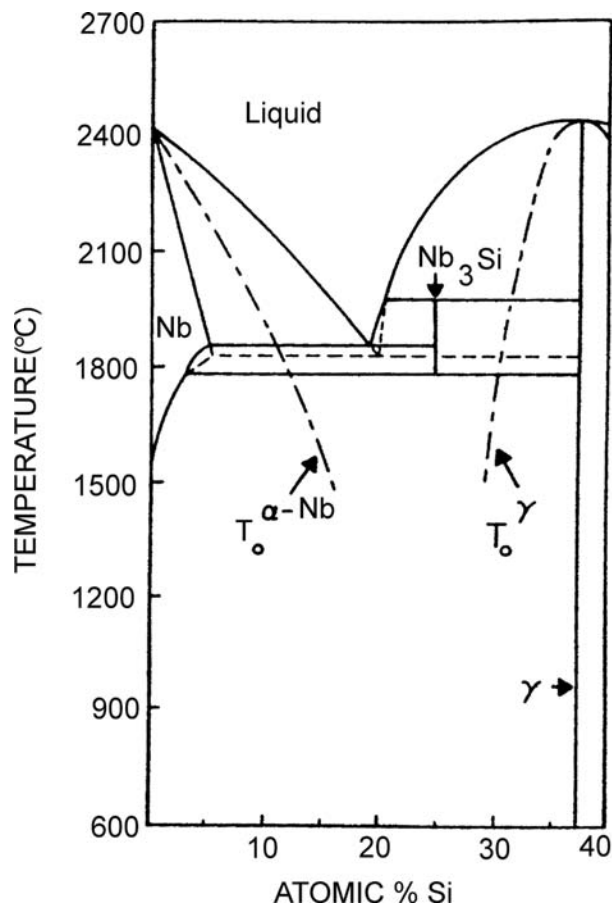
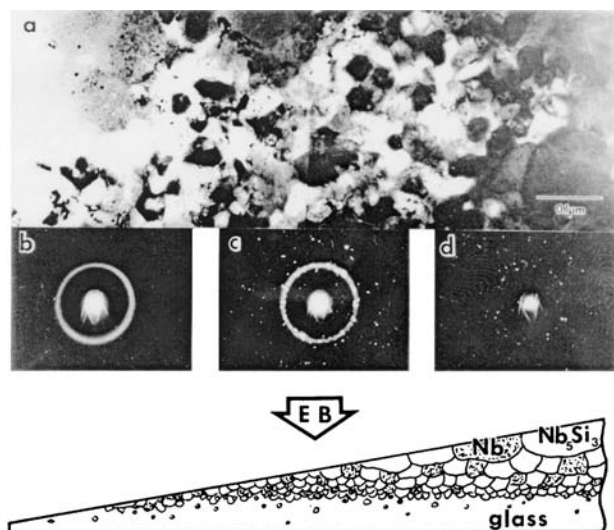


Fig. 6 Phase diagram for the Nb–Si system showing the metastable extension of the  $\text{Nb}_3\text{Si}$  (i.e.,  $\gamma$ ) liquidus to form a metastable eutectic  $L \rightarrow \alpha\text{-Nb} + \text{Nb}_3\text{Si}$ . This extension is relevant when the  $\text{Nb}_3\text{Si}$  phase is absent. Also shown are approximate  $T_0$  curves for the transformation of liquid to  $\alpha\text{-Nb}$  and to  $\gamma$ .

## NANOCRYSTALLIZATION DURING MELT QUENCHING

As noted in Fig. 4, it is possible to encounter conditions that represent the maximum nucleation rate (i.e., the minimum time for the onset of nucleation or the nose of the  $C$  curve) during continuous cooling. One important requirement to achieve a maximum nucleation density is the removal of potent heterogeneous nucleation sites so that the alloy melt may be cooled to the temperature yielding the maximum nucleation rate without prior crystal formation. For homogeneous nucleation the temperature for a maximum nucleation rate is about  $2/3 T_m$ .<sup>[12]</sup> The schematic illustration in Fig. 4 does not provide a perspective on the sensitivity of the microstructural scale to cooling rate at temperatures near the maximum nucleation rate temperature, but this important feature of nanocrystallization can be developed by considering a melt-quenched nanostructure.





**Fig. 7** (A) Microstructure of a Nb–25 at.% Si melt-spun ribbon near the TEM foil edge (the left-hand side of the micrograph) for a specimen polished from one side; (B) SADPs positioned under the areas from which they were taken; (C) a schematic drawing showing the microstructure across the ribbon (EB, electron beam).

For Nb-rich alloys in the Nb–Si system the main solidification reaction is a eutectic yielding Nb + Nb<sub>3</sub>Si as indicated in the phase diagram in Fig. 6.<sup>[47]</sup> The microstructure that is developed following melt spinning is revealed in Fig. 7 for a wedge-shaped sample that was produced by thinning the ribbon of a Nb–25 at.% Si alloy from one side (opposite from the wheel side) the most rapidly cooled region adjacent to the wheel is amorphous. With increasing distance from the chill surface the onset of crystallization is characterized by nanoscale grains with a size of about 15 nm. The fine-grain structure is a mixture of Nb and Nb<sub>5</sub>Si<sub>3</sub>, but the size scale increases to about 100 nm over short distance within the 20- $\mu$ m-thick ribbon before the equiaxed structure evolves into a dendritic morphology.

A common occurrence in the synthesis of nanostructures during rapid solidification is the absence of a phase that according to the equilibrium phase diagram should be present. This occurs when the missing phase is subjected to kinetic limitations in nucleation and/or growth. In the absence of a stable phase, solidification is then governed by a metastable phase diagram. This diagram is constructed from the equilibrium diagram in Fig. 6 where the Nb<sub>3</sub>Si phase is suppressed and where the Nb<sub>5</sub>Si<sub>3</sub> (designated  $\gamma$ ) liquidus extends below the L + Nb<sub>5</sub>Si<sub>3</sub>  $\rightarrow$  Nb<sub>3</sub>Si peritectic isotherm and intersects the Nb liquidus to yield a metastable L  $\rightarrow$  Nb + Nb<sub>5</sub>Si<sub>3</sub> eutectic. For alloys near a peritectic reaction, solidification of the high-temperature phase (in this case, Nb<sub>5</sub>Si<sub>3</sub>) can continue below

the peritectic temperature while the remaining liquid develops only slight undercooling with respect to the low-temperature phase (in this case, Nb<sub>3</sub>Si). Hence, phases that are ordinarily formed by peritectic reactions may often be absent in nanocrystallization reactions.

A useful method for examining the thermodynamic options available to an alloy undergoing nanocrystallization is to examine the  $T_0$  curves for the various liquid-to-crystal transformations in a system. Schematic  $T_0$  curves are included for the Nb and Nb<sub>5</sub>Si<sub>3</sub> ( $\gamma$ ) phases in Fig. 6. The  $T_0$  curves place a bound on temperatures and compositions where partitionless solidification is possible.<sup>[13]</sup> Regardless of the level of undercooling that is achieved during rapid quenching, a range of compositions may exist between adjacent  $T_0$  curves where partitionless solidification is impossible and crystal growth must involve the more difficult process of diffusional solute redistribution into a mixture of solid phases.<sup>[48]</sup> Because of this difficulty, glass formation or nanocrystallization is most likely in this range, which was observed to be centered near Nb<sub>3</sub>Si as indicated in Fig. 6.

The synthesis of a two-phase nanostructure clearly involves copious nucleation. One factor that can increase the opportunity for high nucleation rates is the relatively slow growth for crystals that require solute redistribution. Furthermore, during continuous cooling, the rate of recalescence after the initial nucleation event depends on the crystal growth rate. If it is slow, the melt may be undercooled further, permitting a rapid rise in the nucleation rate.<sup>[12]</sup> Moreover, the two-phase nanostructures that are developed during melt spinning identify an important class of metastable microstructure that is available in the form of very high grain densities of the equilibrium phases that were observed to range from 10<sup>18</sup> to 10<sup>21</sup> m<sup>-3</sup>. A high density of grains for a two-phase mixture is metastable because of a high incoherent interphase boundary area. For example, with a grain size of 0.12  $\mu$ m and an interphase boundary energy in the range of 500–1000 mJ m<sup>-2</sup> that is typical for incoherent interfaces, the excess free energy due to the polycrystalline grain structure is 120–150 J mol<sup>-1</sup>. However, for nanoscale grains with a size of 15 nm the free energy increment increases to the range of 800–1600 J mol<sup>-1</sup>. Thus, with nanostructured grains the level of metastability is comparable with that associated with non-equilibrium crystal structures.<sup>[14]</sup>

The devitrification of an amorphous phase is a fairly well recognized approach to the synthesis of a nanocrystalline grain structure. The attainment of an equiaxed grain structure resulting from an isotropic growth is characteristic of a polymorphic type of crystallization reaction. In this sense the evolution of an equiaxed two-phase nanocrystalline grain structure represents a distinct pattern of non-cooperative growth that does not appear to be readily achieved by continuous heating

or isothermal annealing devitrification treatment. However, the production of a high nucleation density for each phase appears to require a high rate of heat extraction as well as diffusional growth limitations so that the two-phase nanocrystalline structure is limited in spatial extent because of a relatively narrow range of favorable processing conditions.

## NANOCRYSTAL CATALYSIS

The limited experimental information available indicates that the nucleation process during primary crystallization of amorphous alloys is usually heterogeneous in nature, but the origin of the active catalytic sites has not been identified in all cases.<sup>[49]</sup> For example, it has been established that, with several amorphous Fe alloys, the development of a high density of Fe nanocrystals is strongly promoted by the addition of small amounts of certain solutes such as Cu.<sup>[50]</sup> In fact, high-resolution transmission electron microscopy (TEM) and atom probe field ion microscopy (APFIM) observations indicate that Cu solute allows for reactions that act to catalyze Fe nucleation.<sup>[51,52]</sup> In amorphous Al-base alloys it appears that a comparable nucleation catalysis behavior can be observed with both soluble and insoluble additions. For example, the addition of 1 at.% Cu to amorphous Al–Ni–Sm has been reported to yield an Al nanocrystal density approaching  $10^{23} \text{ m}^{-3}$  with diameters of 5–7 nm.<sup>[53]</sup> Similarly, the incorporation of insoluble nanosized Pb crystalline particles in an amorphous matrix is effective in catalyzing the crystallization of Al nanocrystals and yields a significant increase in the total number density of nanocrystals.<sup>[54]</sup> The catalysis behavior highlights the opportunity for the controlled synthesis of bulk alloys with an ultra-high number density of nanoscale dispersoids.

## MECHANICALLY INDUCED CRYSTALLIZATION OF AMORPHOUS PHASES

One consequence of the metastability of nanocrystalline and amorphous phases is that the structure and properties of the materials can depend on the processing pathway. This pathway dependence offers the chance to obtain phases with novel characteristics that cannot be achieved by melt quenching. For example, nanocrystallization reactions during cold rolling occur after continued folding and rolling of initially crystalline or amorphous multilayer samples, as illustrated schematically in Fig. 8. The repeated folding and rolling process can yield a true strain in the multilayer sample of the order of 100.<sup>[55]</sup> The kinetics of this crystallization process appears to be linked to the initial size

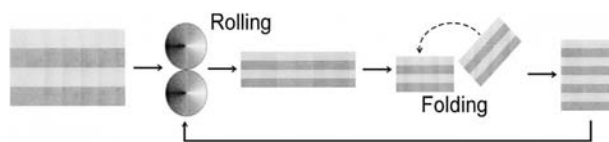


**Fig. 8** A schematic illustration of the cold-roll and fold process. A multilayer of elemental foils with foil thicknesses between 7 and 25  $\mu\text{m}$  is reduced by 50% with each rolling pass.

distribution and density of the quenched-in nuclei in the amorphous matrix. In some cases, for example in melt-spun  $\text{Al}_{92}\text{Sm}_8$ , the sample fully crystallizes during rolling.<sup>[56]</sup> Amorphous alloys that follow the nucleation-controlled solidification pathway and therefore have no significant cluster concentration are considerably more stable against a rolling-induced crystallization reaction.<sup>[57]</sup> The observed primary crystallization of marginal glass formers during initial rolling implies an atomic transport of the constituents through the amorphous matrix. Nanocrystals can also be induced by deformation in bulk glass-forming alloys without any thermal annealing.<sup>[58]</sup> The redistribution of solute atoms during crystallization appears to be characteristic of a driven system where an athermal mechanical process during shear deformation controls the transport.<sup>[59–61]</sup> A more complete understanding of deformation-catalyzed nanocrystallization should also consider the non-equilibrium nature of the rolling process as well as the structural metastability of the amorphous phase. Understanding the nature of shear-induced crystallization is thus not solely a matter of focusing on the processing conditions and their influence on the structural modifications, but necessitates a refined knowledge of the amorphous structure before deformation.

## CONCLUSION

The development of nanostructured materials can be achieved in bulk form by the use of amorphous phases as effective precursors. Indeed, the controlled primary crystallization of amorphous alloys yields essentially a nanophase composite of nanocrystalline primary phase dispersed within an amorphous matrix. It is remarkable that the nanocrystal number density can achieve high levels of  $10^{21}$  to  $10^{23} \text{ m}^{-3}$  at primary phase volume fractions approaching about 30% to yield ultra high strength. An equally remarkable fact is the relative high thermal stability of the nanophase composite. This is truly a novel microstructure that has revealed challenging basic issues on the governing reactions kinetics that control the structure synthesis and performance. At the same time, alternative synthesis routes have been identified based on deformation-induced alloying and glass formation that can be adapted for



processing of bulk glasses. The deformation response of amorphous alloys is sensitive to the processing during synthesis and to the influence of quenched-in crystallites.

## ACKNOWLEDGMENTS

The continued support of the Army Research Office (ARO) and encouragement from Dr. W. Mullins for studies of novel microstructure synthesis during solidification and intense plastic deformation is most gratefully appreciated.

## REFERENCES

- Gleiter, H. Nanocrystalline materials. *Prog. Mater. Sci.* **1989**, *33*, 223–315.
- Yanakov, V.; Wolf, D.; Phillot, S.R.; Mukerjee, A.K.; Gleiter, H. Dislocation processes in the deformation of nanocrystalline aluminium by molecular-dynamics simulation. *Nat. Mater.* **2002**, *1*, 45–48.
- Koch, C.C. The synthesis and structure of nanocrystalline materials produced by mechanical attrition: a review. *Nanostruct. Mater.* **1993**, *2*, 109–129.
- Greer, A.L. Crystallization of amorphous alloys. *Metall. Mater. Trans., A* **1996**, *27A*, 549–555.
- Inoue, A. Amorphous, nanoquasicrystalline and nanocrystalline alloys in Al-based systems. *Prog. Mater. Sci.* **1998**, *43*, 365–520.
- Turnbull, D. Metastable structures in metallurgy. *Metall. Trans., A* **1981**, *12*, 695–708.
- Lu, K. Nanocrystalline metals crystallized from amorphous solids: nanocrystallization, structure and properties. *Mater. Sci. Eng., R Rep.* **1996**, *R16*, 161–221.
- Köster, U.; Schünemann, U. Phase transformations in rapidly solidified alloys. In *Rapidly Solidified Alloys: Processes, Structures, Properties, Applications*; Liebermann, H.H., Ed.; Marcel Dekker, Inc.: New York, 1993; 303–337.
- Perepezko, J.H.; Hebert, R.J. Amorphous aluminum alloys—synthesis and stability. *J. Metall.* **2002**, *54* (3), 34–39.
- Johnson, W.L. Thermodynamic and kinetic aspects of the crystal to glass transformation in metallic materials. *Prog. Mater. Sci.* **1986**, *30*, 81–134.
- Martin, G.; Bellon, P. Driven alloys. *Solid State Phys.* **1996**, *50*, 189–330.
- Boettinger, W.J.; Perepezko, J.H. Fundamentals of solidification at high rates. In *Rapidly Solidified Alloys: Processes, Structures, Properties, Applications*; Liebermann, H.H., Ed.; Marcel Dekker, Inc.: New York, 1993; 17–78.
- Baker, J.C.; Cahn, J.W. Thermodynamics of solidification. In *Solidification*; ASM: Metals Park, OH, 1971; 23–58.
- Perepezko, J.H.; Boettinger, W.J. Use of metastable phase diagrams in rapid solidification. In *Alloy Phase Diagrams*; Bennett, L.H., Massalski, T.B., Giessen, B.C., Eds.; Elsevier: New York, 1983; 223–240.
- Allen, D.R.; Foley, J.C.; Perepezko, J.H. Nanocrystal development during primary crystallization of amorphous alloys. *Acta Mater.* **1998**, *46*, 431–440.
- Clavaguera-Mora, M.T.; Clavaguera, N.; Crespo, D.; Pradell, T. Crystallization kinetics and microstructure development in metallic systems. *Prog. Mater. Sci.* **2002**, *47*, 559–619.
- Tsai, A.P.; Kamiyama, T.; Kawamura, Y.; Inoue, A.; Matsumoto, T. Formation and precipitation mechanism of nanoscale Al particles in Al–Ni base amorphous alloys. *Acta Mater.* **1997**, *45*, 1477–1487.
- Hono, K. Nanoscale microstructural analysis of metallic materials by atom probe field ion microscopy. *Prog. Mater. Sci.* **2002**, *47*, 621–729.
- Porter, D.A.; Easterling, K.E. *Phase Transformations in Metals and Alloys*; Chapman and Hall: New York, 1992.
- Kingery, W.D.; Bowen, H.K.; Uhlmann, D.R. *Introduction to Ceramics*, 2nd Ed.; J. Wiley & Sons: New York, 1976.
- Spaepen, F. Homogeneous nucleation and the temperature dependence of the crystal-melt interfacial tension. *Solid State Phys.* **1994**, *47*, 1–32.
- Russell, K.C. Nucleation in solids: the induction and steady state effects. *Adv. Colloid Interface Sci.* **1980**, *13*, 205–318.
- Kashchiev, D. Solution of the non-steady state problem in nucleation kinetics. *Surf. Sci.* **1969**, *14*, 209–220.
- Kelton, K.F. Crystal nucleation in liquids and glasses. *Solid State Phys.* **1991**, *45*, 75–177.
- Christian, J.W. *The Theory of Transformations in Metals and Alloys*, 2nd Ed.; Pergamon Press: Oxford, UK, 1975.
- Kirkaldy, J.S.; Young, D.J. *Diffusion in the Condensed State*; The Institute of Metals: London, 1987.
- Trivedi, R.K. Theory of capillarity. In *Lectures on the Theory of Phase Transformations*; Aaronson, H.I., Ed.; TMS: Warrendale, PA, 1999; 135–165.
- Clavaguera-Mora, M.T. Glass formation in metallic systems. *Ber. Bunsenges. Phys. Chem.* **1998**, *102*, 1291–1297.
- Perepezko, J.H. Kinetic processes in undercooled melts. *Mater. Sci. Eng., A* **1997**, *226–228*, 374–382.
- Perepezko, J.H.; Uttormark, M.J. Nucleation-controlled solidification kinetics. *Metall. Mater. Trans., A* **1996**, *27*, 533–547.
- Angell, C.A. Formation of glasses from liquids and biopolymers. *Science* **1995**, *267*, 1924–1935.
- Battezzati, L.; Baricco, M.; Schumacher, P.; Shih, W.C.; Greer, A.L. Crystallization behaviour of Al–Sm amorphous alloys. *Mater. Sci. Eng., A* **1994**, *179/180*, 600–604.
- Foley, J.C.; Allen, D.R.; Perepezko, J.H. Analysis of nanocrystal development in Al–Y–Fe and Al–Sm glasses. *Scr. Mater.* **1996**, *35*, 655–660.
- Chen, L.C.; Spaepen, F. Calorimetric evidence for the microcrystalline structure of “amorphous al/transition metal alloys”. *Nature* **1988**, *336*, 366–368.
- Cochrane, R.F.; Schumacher, P.; Greer, A.L. Crystallization of amorphous Al<sub>85</sub>Ni<sub>10</sub>Ce<sub>5</sub> alloy. *Mater. Sci. Eng., A* **1991**, *133*, 367–370.

36. Kui, H.W.; Turnbull, D. The melting of Ni<sub>40</sub>Pd<sub>40</sub>P<sub>20</sub> glass. *Appl. Phys. Lett.* **1985**, *47* (8), 796–797.
37. Drehman, A.J.; Greer, A.L. Kinetics of crystal nucleation and growth in Pd<sub>40</sub>Ni<sub>40</sub>P<sub>20</sub> glass. *Acta Metall.* **1984**, *32*, 323–332.
38. Greer, A.L. Crystallization kinetics of Fe<sub>80</sub>B<sub>20</sub> glass. *Acta Metall.* **1982**, *30*, 171–192.
39. Omata, S.; Tanaka, T.; Ispida, T.; Sato, A.; Inoue, A. Nucleation and growth kinetics of small crystals in amorphous Al<sub>88</sub>Ce<sub>2</sub>Ni<sub>9</sub>Fe. *Philos. Mag., A* **1997**, *76*, 387–412.
40. Perepezko, J.H.; Hebert, R.J.; Tong, W.S. Amorphization and nanostructure synthesis in Al alloys. *Intermetallics* **2002**, *10*, 1079–1088.
41. Gangopadhyay, A.K.; Croat, T.K.; Kelton, K.F. The effect of phase separation on subsequent crystallization in Al<sub>88</sub>Gd<sub>6</sub>La<sub>2</sub>Ni. *Acta Mater.* **2000**, *48*, 4035–4043.
42. Hono, K.; Inoue, A.; Sakurai, T. Atom probe analysis of Fe<sub>73.5</sub>Si<sub>13.5</sub>B<sub>9</sub>Nb<sub>3</sub>Cu<sub>1</sub> nanocrystalline soft magnetic material. *Appl. Phys. Lett.* **1991**, *58*, 2180–2182.
43. Hono, K.; Hiraga, K.; Wang, Q.; Inoue, A.; Sakurai, T. The microstructure evolution of a Fe<sub>73.5</sub>Si<sub>13.5</sub>B<sub>9</sub>Nb<sub>3</sub>Cu<sub>1</sub> nanocrystalline soft magnetic material. *Acta Metall.* **1992**, *40*, 2137–2147.
44. Greer, A.L. Stress effects on interdiffusion in amorphous multilayers. *Defect Diffus. Forum* **1996**, *129/130*, 163–180.
45. Hono, K.; Zhang, Y.; Inoue, A.; Sakurai, T. Atom probe studies of nanocrystalline microstructural evolution in some amorphous alloys. *Mater. Trans., JIM* **1995**, *36*, 909–917.
46. Foley, J.C.; Allen, D.R.; Perepezko, J.H. Strategies for the development of nanocrystalline materials through devitrification. *Mater. Sci. Eng., A* **1997**, *226–228*, 569–573.
47. Bendersky, L.; Biancaniello, F.S.; Boettinger, W.J.; Perepezko, J.H. Microstructural characterization of rapidly solidified Nb–Si alloys. *Mater. Sci. Eng.* **1987**, *89*, 151–159.
48. Boettinger, W.J. Growth Kinetic Limitations During Rapid Solidification. In *Rapidly Solidified Amorphous and Crystalline Alloys*; Kear, B.H., Giessen, B.C., Cohen, M., Eds.; North Holland: Amsterdam, 1982; 15 pp.
49. Wu, R.I.; Wilde, G.; Perepezko, J.H. Glass formation and nanostructure development in Al-based alloys. *Mater. Res. Soc. Symp. Proc.* **2000**, *581*, 101–106.
50. Yoshizawa; Oguma, S.; Yamauchi, K. New Fe-based soft magnetic alloys composed of ultrafine grain structure. *J. Appl. Phys.* **1988**, *64*, 6044–6046.
51. Ayers, J.D.; Harris, V.G.; Sprague, J.A.; Elam, W.T.; Jones, H.N. On the formation of nanocrystals in the soft magnetic alloy Fe<sub>73.5</sub>Nb<sub>3</sub>Cu<sub>1</sub>Si<sub>13.5</sub>B<sub>9</sub>. *Acta Mater.* **1998**, *46*, 1861–1874.
52. Ohkubo, T.; Kai, H.; Ping, D.H.; Hono, K.; Hirotsu, Y. Mechanism of heterogeneous nucleation of alpha-Fe nanocrystals from Fe<sub>89</sub>Zr<sub>7</sub>B<sub>3</sub>Cu<sub>1</sub> amorphous alloy. *Scr. Mater.* **2001**, *44*, 971–976.
53. Hong, S.J.; Warren, P.J.; Chun, B.S. Nanocrystallization behaviour of Al–Y–Ni with Cu additions. *Mater. Sci. Eng., A* **2001**, *304–A306*, 362–366.
54. Perepezko, J.H.; Hebert, R.J.; Wu, R.I.; Wilde, G. Primary crystallization in amorphous Al-based alloys. *J. Non-Cryst. Solids* **2003**, *317*, 52–61.
55. Perepezko, J.H.; Hebert, R.J.; Wu, R.I. Nanostructure synthesis and amorphization during cold rolling. *Mat. Sci. Forum* **2002**, *386–388*, 11–20.
56. Hebert, R.J.; Perepezko, J.H. *Mater. Sci. Eng. in press.*
57. Wilde, G.; Sieber, H.; Perepezko, J.H. Glass formation versus nanocrystallization in an Al<sub>92</sub>Sm<sub>8</sub> alloy. *Scr. Mater.* **1999**, *40*, 779–783.
58. Kim, J.-J.; Choi, Y.; Suresh, S.; Argon, A.S. Nanocrystallization during nanoindentation of a bulk amorphous alloy at room temperature. *Science* **2002**, *295*, 654–657.
59. Sagel, A.; Sieber, H.; Fecht, H.-J.; Perepezko, J.H. Synthesis of an amorphous Zr–Al–Ni–Cu Alloy with large supercooled liquid region by cold rolling of elemental foils. *Acta Mater.* **1998**, *46*, 4233–4241.
60. Hebert, R.J.; Perepezko, J.H. Significance of the heat of mixing for the amorphization of multilayers by deformation processing. *Mat. Sci. Forum.* **2002**, *386–388*, 21–26.
61. Perepezko, J.H.; Hebert, R.J. Alloying reactions in nanostructured multilayers during intense deformation. *Z. Met.kd. in press.*

# Nanocrystals: Size-Dependent Properties and Emerging Applications

G. U. Kulkarni

P. John Thomas

*Chemistry and Physics of Materials Unit, Jawaharlal Nehru Center for Advanced Scientific Research, Bangalore, India*

C.N.R. Rao

*Chemistry and Physics of Materials Unit and CSIR Centre of Excellence in Chemistry, Jawaharlal Nehru Center for Advanced Scientific Research, Bangalore, India*

## INTRODUCTION

Nanocrystals have long been known for their ability to color glasses and catalytic action. New understanding of nanoscale phenomena, especially the changes in the material properties with size are promising to usher in a whole new genre of applications. In this entry, a discussion of the electronic, optical, and magnetic properties of capped nanocrystals, followed by a brief elucidation of select applications is provided.

## ELECTRONIC AND RELATED PROPERTIES

As the size of nanocrystals is varied in the nanometric domain, the electronic structure undergoes various changes. The changes were theoretically addressed as early as the 1960s by Kubo and Frolich.<sup>[4]</sup> Kubo successfully predicted that a gap, now called the Kubo gap ( $\Delta$ ), will emerge as the dimensions are reduced:

$$\Delta = \frac{E_f}{3n} \quad (1)$$

where,  $E_f$  is the bulk Fermi level and  $n$  the number of free electrons in the nanoparticle (a contribution of one electron per atom is usually assumed). A natural consequence of the emergence of Kubo gap is a size-induced metal-insulator transition when the diameter of the particle is decreased to below a few nanometers.<sup>[5-7]</sup> Scanning tunneling spectroscopy (STS) measurements of nanocrystals of various metals have revealed that the nanocrystals of dimensions  $\sim 1 \text{ nm}^3$  exhibit a definitive band gap (up to 70 meV) that decreases gradually as the volume of the nanocrystal increases (see Fig. 1).<sup>[6,8,9]</sup> Photoelectron spectroscopic measurements on mass selected  $\text{Hg}_n$  nanoparticles ( $n = 3-250$ ) in the gas phase reveal that the characteristic HOMO-LUMO (highest occupied molecular orbital-lowest unoccupied molecular orbital) (s-p) energy gap decreases gradually from  $\sim 3.5 \text{ eV}$  for  $n < 3$  to  $\sim 0.2 \text{ eV}$  for  $n < 250$ , as

shown in Fig. 2. The band gap closure is predicted at  $n \sim 400$ . In addition to  $\Delta$ , nanoparticles also possess coulombic energy states that manifest themselves when actual charging and discharging events take place. Experiments have revealed that small nanocrystals possess charging energies ( $U$ ) of the order of hundreds of millielectron Volts. Therefore, in ensembles of nanocrystals, charge transport would be dominated by a hopping mechanism. A large number of studies have addressed charge-transport characteristics of nanocrystalline assemblies. Pellets of monodisperse nanocrystals, obtained by the use of bifunctional ligand that may bind to more than one nanocrystal, or by applying pressure on dried nanocrystalline matter, have been used for electrical transport measurements.<sup>[10-13]</sup> Pellets made of small Au and Pd nanocrystals exhibit non-metallic behavior with specific conductivities in the range of  $10^6 \Omega^{-1} \text{ cm}^{-1}$ .<sup>[10-12]</sup> The conductivity, however, increases dramatically with an increase in the diameter of the nanocrystals. An insulator metal transition has indeed been reported from pellets made of  $\sim 12.5 \text{ nm}$  Au and Ag nanocrystals.<sup>[13]</sup> Electrical transport measurements on layer-by-layer assemblies of nanocrystals on conducting substrates have been carried out by adoption of a sandwich configuration.<sup>[14-16]</sup>

Nanocrystalline films with bulk metallic conductivity have been realized with Au nanocrystals of 5 and 11 nm diameter spaced with ionic and covalent spacers.<sup>[15,16]</sup> The conductivity of monolayered two-dimensional arrays of metal nanocrystals has been studied with patterned electrodes.<sup>[17-22]</sup> Structural disorder and interparticle separation distance are identified as key factors that determine the conductivity of such layers.<sup>[17-20]</sup> The conductivity of such layers can be enhanced by replacing alkane thiol with an aromatic thiol insitu.<sup>[21,22]</sup> That the interaction energy of nanocrystals in such organizations can be continually varied by changing the interparticle distance was exploited by Heath and coworker who prepared a monolayer of Ag ( $\sim 3 \text{ nm}$ ) nanocrystals at air/water interface in a

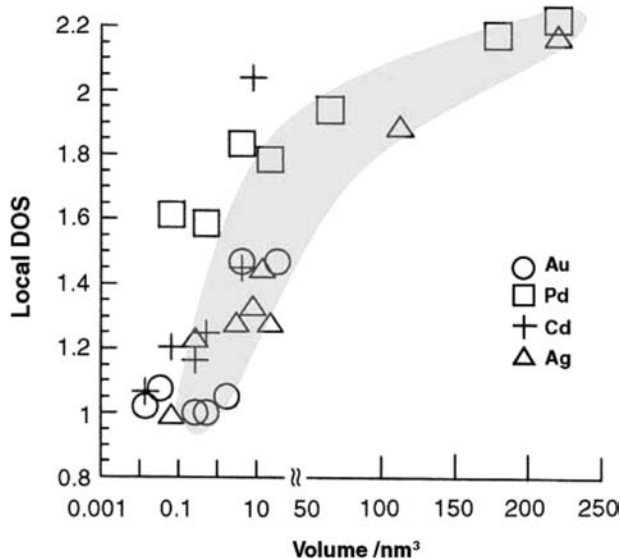


**Fig. 1** Variation of the non-metallic band gap with nanocrystal size in metal nanocrystals. The bandgaps were obtained based on STS measurements. *Source:* From Ref.<sup>[3]</sup>.

Langmuir Blodgett trough and varied the interparticle distance by applying pressure.<sup>[23,24]</sup> A host of measurements including reflectivity and non-linear optical spectroscopic techniques were carried out insitu. This study led to the observation of a reversible Mott–Hubbard

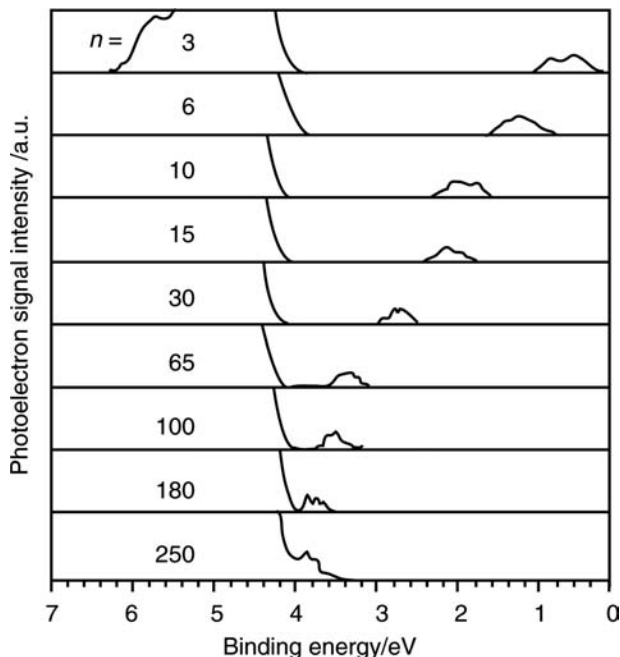


**Fig. 2** Photoelectron spectra of Hg clusters of varying nuclearity. The 6p feature moves gradually toward the Fermi level, emphasizing that the band gap shrinks with increase in cluster size. *Source:* From Ref.<sup>[6]</sup>.

metal–insulator transition in the nanocrystal ensemble wherein the coulomb gap closes at a critical distance between the particles. Tunneling spectroscopic measurements on films of 2.6 nm Ag nanocrystals capped with decanethiol reveal a coulomb blockade behavior attributable to isolated nanocrystals.<sup>[24]</sup> On the other hand, nanocrystals capped with hexane and pentane thiol exhibit characteristics of strong interparticle quantum mechanical exchange (see Fig. 3). Similar behavior was observed in the case of self-assembled two-dimensional arrays of Co nanocrystals and Au nanocrystals.<sup>[25,26]</sup> By varying simple parameters in the synthetic scheme, Rao and coworkers have been able to tune the specific resistivity of a thin film of Au nanocrystals in the range of tens of megaohms to a few ohms (see Fig. 4). Along with the change in conductivity, the nature of the film also undergoes a change from that of an insulator to a metal. Schmid and coworkers as well as Pal et al. have obtained rectifying behavior from

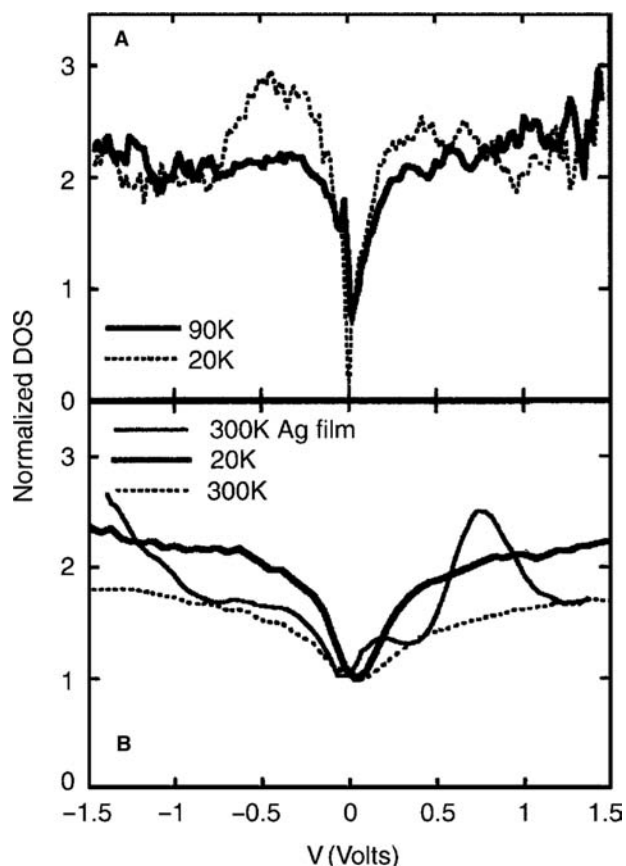


**Fig. 3** Normalized density of states (DOS) measured from arrays of Ag nanocrystals of diameter  $\sim 2.6$  nm capped (A) decanethiol and (B) hexanethiol at various temperatures. The temperature dependence of DOS near 0V for decanethiol capped particles indicates that the films are non-metallic. In the case of hexanethiol capped nanocrystals, the DOS around 0V is temperature independent revealing the metallic nature of the film. *Source:* From Ref.<sup>[21]</sup>.

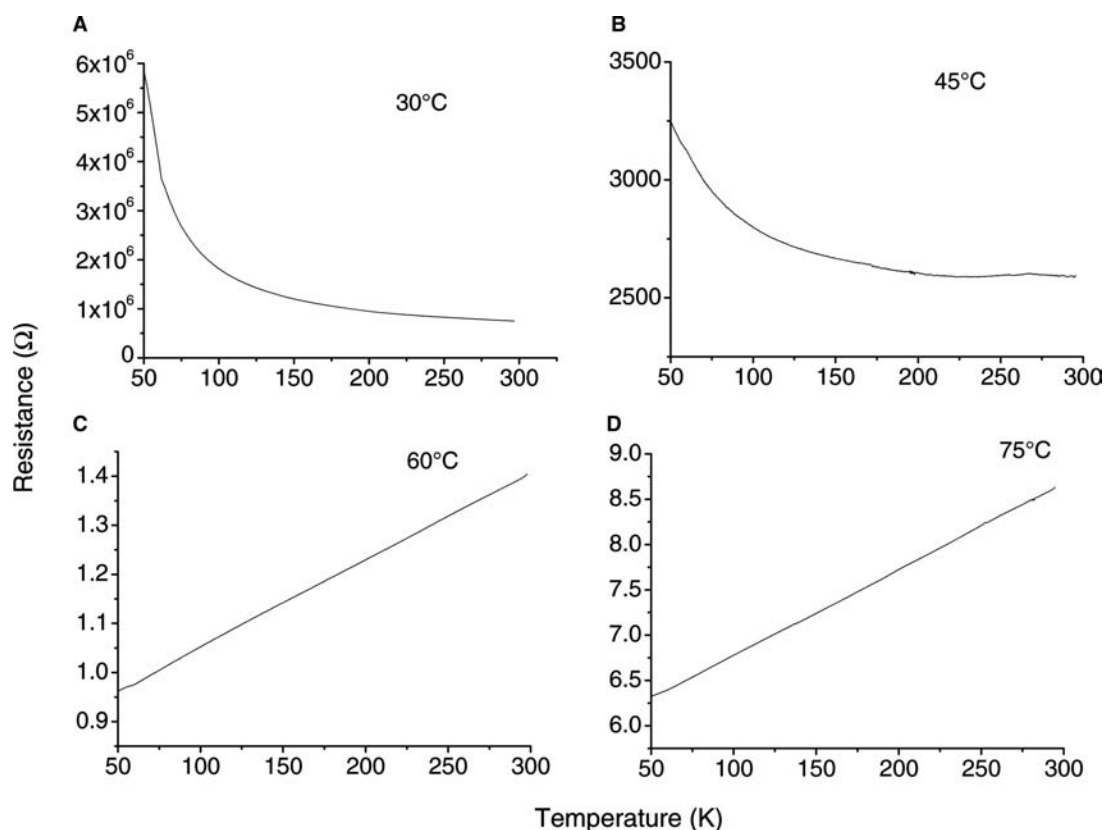


**Fig. 4** The resistance of Au nanocrystal films as a function of temperature. The films (A)–(D) were obtained by carrying out the synthesis at different temperatures: (A) 303 K; (B) 318 K; (C) 333 K; and (D) 348 K.

ensembles of nanocrystals (see Fig. 5).<sup>[27,28]</sup> Although a clear understanding is yet to emerge, it is clear that the observed rectification is related to the high charging energies of the individual nanocrystals.

The capacitance ( $C$ ) of a nanoparticle is related to  $U$  by

$$C = U/2e \quad (2)$$

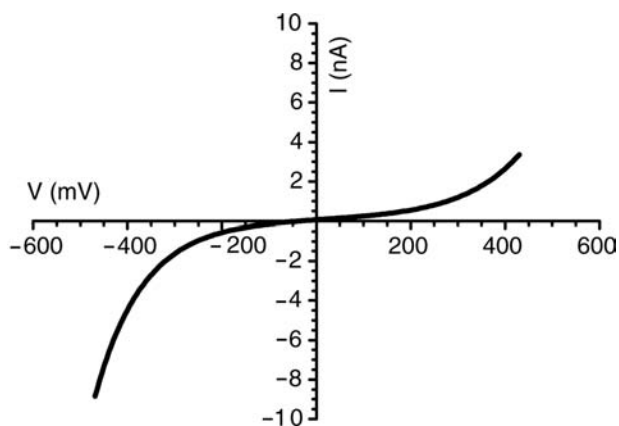


**Fig. 5**  $I$ – $V$  characteristics of dodecanethiol capped Au nanocrystals deposited on an ordered monolayer of gadolinium stearate molecules on a Si substrate.

and is size dependent. Typical values of capacitances of nanocrystals are in the range of  $10^{-18}$  F (aF). At such low capacitances, successive charging events are no longer continuous but are discrete. A measurable change in potential is brought about by varying the charge on the nanocrystal by  $e$ . This is often seen as a coulomb staircase in the  $I$ – $V$  spectra of individual nanocrystals. We have been able to identify the size-dependent changes in the coulomb staircase phenomena in Au and Pd nanocrystals (see Fig. 6).<sup>[29]</sup> It has been proposed that, by using nanocrystals, single-electron devices such as supersensitive electrometers and memory devices could be fabricated. Further, it is supposed that nano-objects could bring a new era in electronics, aptly named nanoelectronics. Proof of concept experiments to test the feasibility of using chemically prepared nanocrystals in single-electron devices have been carried out. For example, Murray and coworkers have found that a single redox reaction taking place at the surface of Au nanocrystals induces a eightfold increase in capacitance.<sup>[30]</sup> Single-electron transistors have been demonstrated with one or a few nanocrystals at the gap between electrodes.<sup>[31]</sup> Schffrin and coworkers have fabricated a nanoswitch based on a layer of Au nanoparticles on a viologen moiety anchored to Au substrate. The  $I$ – $V$  characteristics

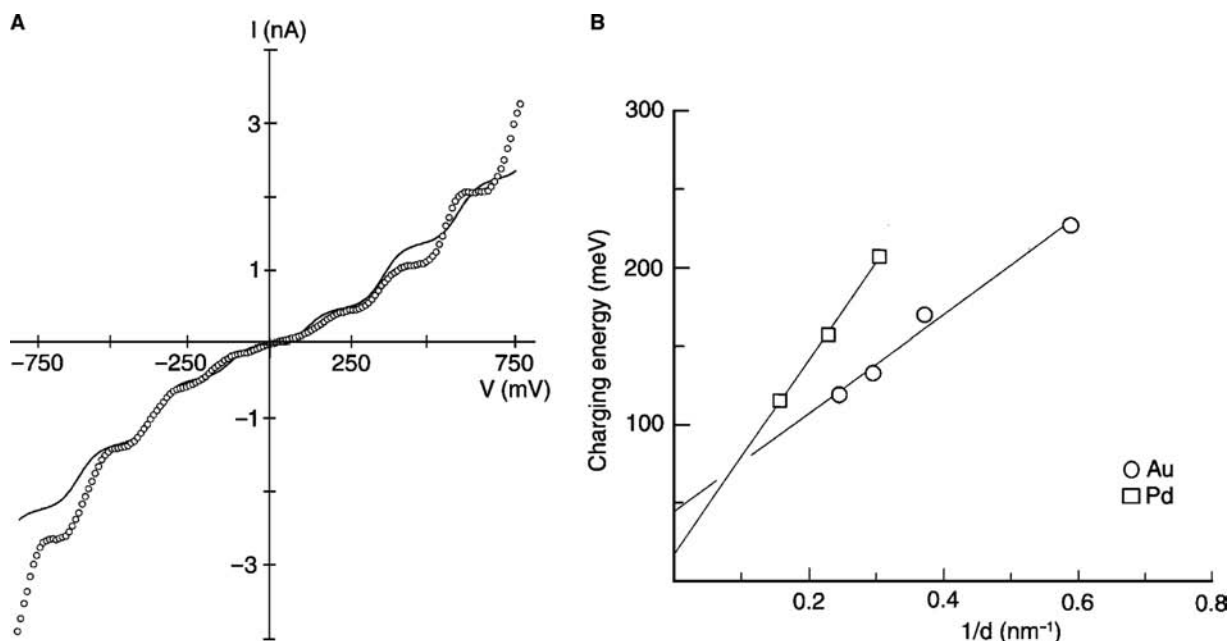


**Fig. 6** (A)  $I$ - $V$  characteristics of an isolated 3.3 nm Pd nanocrystal (dotted line) and the theoretical fit (solid line) obtained at 300 K using a semiclassical model according to which the observed capacitance ( $C$ ) can be resolved into two components  $C_1$  and  $C_2$ , and the resistance ( $R$ ) into  $R_1$  and  $R_2$ , such that  $C = C_1 + C_2$  and  $R = R_1 + R_2$ . For  $C_1 \ll C_2$  and  $R_1 \ll R_2$ , the model predicts steps in the measured current to occur at critical voltages,  $V_c = \frac{n_c e}{C} + \frac{q_0 + e/2}{C}$  where  $q_0$  is the residual charge. (B) Variation of the charging energies of Pd and Au nanocrystals with inverse diameters ( $d$ ). Source: From Ref.<sup>[26]</sup>.

of the Au nanoparticles studied using in situ STS revealed a dependence on the redox state of the viologen groups underneath the nanoparticle. By electrochemically altering the redox state, the conductivity of the circuit could be made high or low.<sup>[32]</sup>

## Nanocomputing

Buoyed by the success of preliminary experiments, it has been supposed that nanoscopic elements could act as ingredients in future computers. Ordered arrays of nanocrystals, in principle, could be thought of as arrays of single-electron transistors (SETs), where the electrostatic interaction between neighboring SETs acts as a means of wireless communication. It has been suggested by Korotkov and Lent that simple logical operations can be performed on a circuitry consisting of arrays of SETs in the form of chains or cells with suitable insulating spacers.<sup>[34,35]</sup> An electric field applied in one direction polarizes the strings into either the 0 or the 1 state. Lent's scheme, named quantum cellular automata, instead uses a square cell consisting of five nanocrystals to denote the state of polarization. Preliminary experiments to evaluate the schemes are currently being pursued. The realization that self-assembly driven fabrication process is not capable of producing defect-free structures has fueled a search

for algorithms that can compute even with defective circuitry. Heath and coworkers have developed TeraMac, a computer that works despite a high concentration of defects in its bank of microprocessors.<sup>[36]</sup> A more radical solution called amorphous computing aims to "engineer pre-specified, coherent behavior from cooperation of large numbers of unreliable parts interconnected in unknown, irregular and time varying ways."<sup>[37-39]</sup>

## Catalysis

Nanocrystals consist of an unusually large fraction of surface atoms. For example, a nanocrystal of size 5 nm has about 80% of its atoms on the surface. This increases the surface area per unit mass and translates to a higher number of active site per unit mass and thereby makes nanocrystals extraordinarily important for catalytic applications such as in autocatalytic converters. In addition to an increased surface area, nanocrystalline metals also possess high reactivity.<sup>[40-42]</sup> When combined with a suitable support, typically a semiconducting oxide surface such as TiO<sub>2</sub> or ZnO, the nanocrystals exhibit an affinity for reactions that have no corresponding bulk analogs. For example, Goodman and coworkers have found that small Au nanocrystals supported on titania catalyze CO



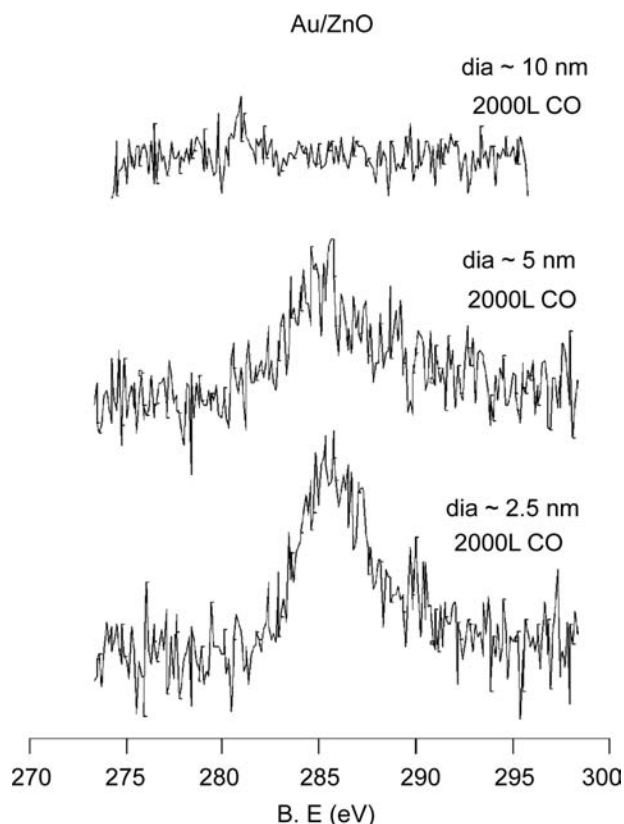


**Fig. 7** C(1s) core-level spectra of CO adsorbed on Au particles supported on a ZnO substrate. The feature at 285 eV corresponds to molecularly adsorbed CO. The diameters have been obtained from the metal coverages. *Source:* From Ref.<sup>[37]</sup>.

oxidation, with the catalytic ability being markedly size dependent.<sup>[43]</sup> Another study has found that Au nanocrystals supported on ZnO exhibit a tendency to adsorb CO.<sup>[44]</sup> The activity is size dependent and is exhibited only by small nanocrystals (diameters <5 nm, see Fig. 7). The increased activity of the small particles is attributable to the charge transfer between the oxide support and the particle. It is supposed that greater understanding of nanoscale charge transfer phenomena would contribute toward understanding of such catalytic processes.

## OPTICAL PROPERTIES

The fluorescent properties of semiconductor nanocrystals have drawn wide attention because of their potential use as labels in fluorescence bioassays.<sup>[45–52]</sup> When compared to dyes currently in use, the emission from fluorescent nanocrystals is brighter and sharper. For example, Nie and coworkers have estimated that CdSe nanocrystals are 20 times brighter and 100 times more stable than a single rhodamine 6G molecule.<sup>[51]</sup> Further, the emission can be brought about by

excitation in a broad range of wavelengths. It is therefore possible to excite nanocrystals of several different sizes simultaneously with a single source and obtain a well-resolved emission at different colors. In order that the nanocrystals are biocompatible, the nanocrystals need to be water soluble and possess pendant groups at the surface, that bind to biomolecules like proteins. These changes can be brought about by tailoring the ligand shell with small DNA fragments or mercapto acids. Several *in vivo* and *in vitro* fluorescence biochemical assays have been carried out with nanocrystalline markers.<sup>[45–47,51]</sup> A few studies have sought to exploit dependence of the plasmon absorption band on the dielectric constant of the surrounding medium in metal nanocrystals to detect binding events taking place at the ligand shell.<sup>[53–55]</sup> Thus, Au nanocrystals could colorimetrically determine the successful hybridization of oligonucleotide strands bound to its surface.<sup>[56,57]</sup> It has been proposed that colorimetric sensing of heavy metal ions could be obtained by the use of carboxylic acid terminated bifunctional thiols bound to metal nanocrystals.<sup>[58,59]</sup> The changes in the electronic absorption spectra of ~5 nm Ag nanocrystals capped with lipoic acid, following the addition of the heavy ions,  $\text{Cu}^{2+}$  and  $\text{Fe}^{2+}$ , is shown in Fig. 8. Such a dampening also brings about a change in color. It is apparent that  $\text{Cu}^{2+}$  ions dampen the plasmon band more effectively than  $\text{Fe}^{2+}$ . It has been suggested that very sensitive detection of nanoparticles could be carried out by measuring the light scattered by the particles.<sup>[61,62]</sup> Yguerabid and coworkers have pioneered the use of large particles ~60 nm for carrying out biochemical assays. In contrast to detection in the liquid state, much progress has been made in surface plasmon based detection of binding events that occur over a bed of nanocrystals. Since 1990, Biacore has been marketing a surface plasmon resonance (SPR) based kit for carrying out immunoassays.<sup>[63]</sup>

Another dimension has been added to the optical properties of nanocrystals by the recognition that the optical properties of a superlattice of nanocrystals could be different from that of the individual nanocrystals owing to interparticle interactions.<sup>[64]</sup> Typical spectra showing such a change in the case of CdSe nanocrystals are shown in Fig. 9. When present in close-packed organization, the absorption spectra of the nanocrystals are broadened and red shifted. This change has been attributed to interparticle dipolar interactions.<sup>[65]</sup> Bawendi and coworkers have studied such changes in the ensemble of CdSe nanocrystals of different diameters and have obtained evidence for long-range resonance transfer of electronic excitation from smaller to bigger nanocrystals owing to dipolar interactions.<sup>[66]</sup> In a noteworthy experiment, Weller and coworkers, prepared drop cast films of giant CdS clusters of the form  $\text{Cd}_{17}\text{S}_4(\text{SCH}_2\text{CH}_2\text{OH})_{26}$  and

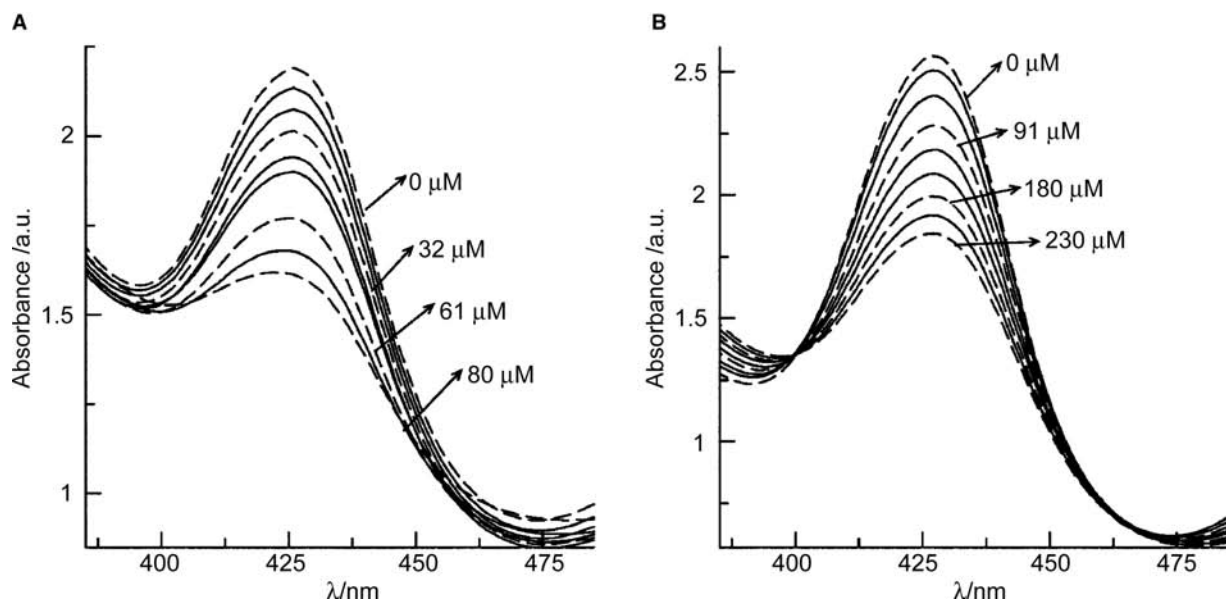


**Fig. 8** Electronic absorption spectra of  $\sim 5$  nm Ag nanoparticles showing changes accompanying the addition of (A)  $\text{Cu}^{2+}$  and (B)  $\text{Fe}^{2+}$  ions. The concentrations of the ions are indicated.

$\text{Cd}_{32}\text{S}_{14}(\text{SCH}_2\text{CH}(\text{CH}_3)\text{OH})_{36}$  with diameters of 1.4 and 1.8 nm, respectively. Further, an integrating sphere was used to collect absorption data, thereby virtually eliminating errors from inhomogeneities and size distributions.<sup>[67]</sup> The experiments due to Weller also support the idea of dipolar interaction leading to the red shift and broadening. Signatures of such interactions have also been seen in the case of CdS multilayer deposits.<sup>[68]</sup> The interparticle interactions, however, could range from weak dipolar interactions to strong exchange interactions based on the interparticle separation. Delocalization of the electronic states of

nanocrystals in ensembles due to exchange interactions have been observed in experiments with CdSe nanocrystals. Gaponenko and coworkers have shown that the optical properties of an ensemble of small ( $\sim 1.6$  nm) CdSe nanocrystals are similar to that of bulk CdSe because of complete delocalization of the electronic states of individual nanocrystals.<sup>[69]</sup> Dipolar coupling interactions in metal nanocrystal assemblies such as in linear rows lead to strong optical anisotropy. The transmitted light depends on whether it is polarized parallel or perpendicular to the rows of nanocrystals. It has been suggested that such material could

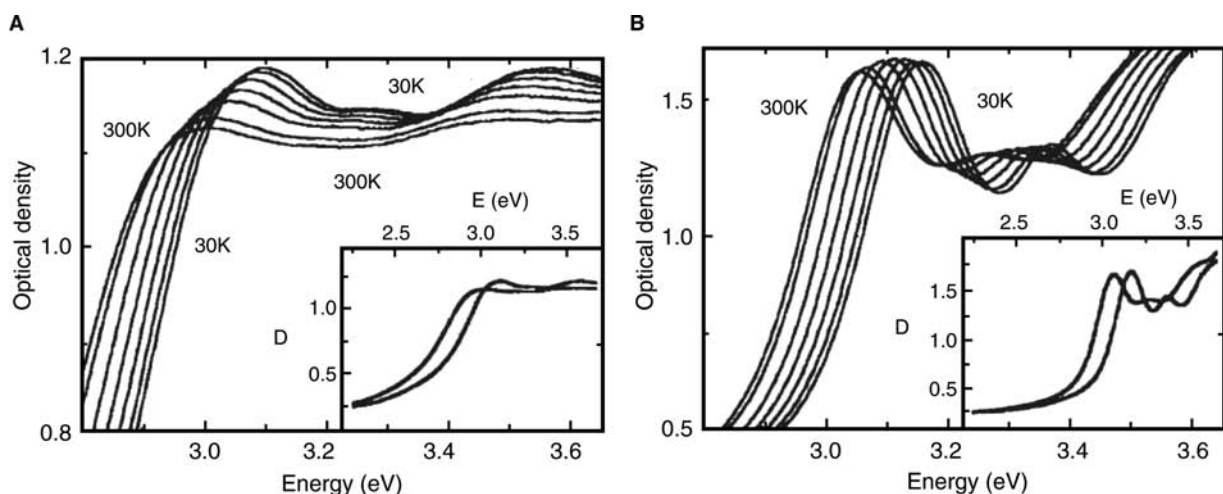


**Fig. 9** Absorption spectra of thin films of close-packed (A) and isolated (B) CdSe nanocrystals at different temperatures (from right to left curves): 30, 80, 130, 180, 230, 280, and 300 K. The insets show the full-range spectrum of optical density  $D$  for the lowest and highest temperatures. A red shift and broadening of the peaks is seen in the case of close-packed films. *Source:* From Ref.<sup>[54]</sup>.

be useful as polarizing filters. Dirix et al. have pioneered a simple method of preparing such assemblies. Their method involved stretching a polyethylene film impregnated with Ag nanocrystals. Dirix et al.<sup>[70]</sup> Atwater and coworkers have suggested that coupled plasmon modes could lead to coherent propagation of electromagnetic energy, i.e., a row of metal nanocrystals could act as a nanoscale waveguide. Using an array generated by means of e-beam lithography, they have provided a proof of concept demonstration.<sup>[71]</sup>

Several polymer/polyelectrolyte-nanocrystal hybrid devices have been fabricated seeking to exploit the electro- and photoluminescent properties of nanocrystalline media.<sup>[72–81]</sup> Device fabrication in all these cases is by low-cost self-assembly based techniques. These devices utilize thin films of these hybrids obtained either by multilayer deposition or drop/spin casting methods. Thus, “solar cells” have been made from poly(2-hexylthiophene)-CdSe nanorod multilayers, lasers from drop cast films of CdSe–titania composites, and infrared emitter from multilayers of HgTe and poly(diallyl dimethyl ammonium chloride) (PDDA). White light electroluminescence is seen in multilayers of CdSe–CdS–poly(phenylenevinylene), CdTe–PDDA. White light emission has also been obtained from drop cast films consisting of a mixture CdSe–ZnS, CdS–ZnS, and poly-laurylmethacrylate. The characteristic of all the above devices can be changed by altering the nanocrystal size.

## MAGNETIC PROPERTIES

It is well known that in the nanometric domain, the coercivity of magnetic nanocrystals tends to zero.<sup>[82,83]</sup> Thus, the nanocrystals behave as superparamagnets with no associated coercivity or retentivity. The blocking

temperature that marks the onset of this superparamagnetism increases with the nanocrystal size. This scenario, however, changes in the case of interacting nanocrystals where the interparticle interaction and, hence, its magnetic properties can be tuned by varying the interparticle distance. Thus, lattices of interacting magnetic nanocrystals are considered important in the future magnetic storage devices. Further, the magnetic moment per atom is seen to increase as the size of a particle decreases.<sup>[87]</sup>

Nanocrystals of Co when organized into two-dimensional arrays exhibit a higher superparamagnetic blocking temperature compared to isolated nanocrystals, i.e., they display a higher resistance to thermal reversal of their spins than when they are isolated.<sup>[88]</sup> Sun et al. report a lattice of nanocrystals each consisting of a Fe core and a Pt shell prepared by heating Fe–Pt alloy nanocrystals.<sup>[89]</sup> Following phase segregation, the interaction between the nanocrystals increased leading to a ferromagnetic film capable of supporting high-density magnetization reversal transitions (see Fig. 10). Exchange spring magnets—nanocomposites that consist of magnetically hard and soft phases interacting via magnetic exchange coupling, have been made by carefully annealing the mixed nanocrystal array consisting of Fe–Pt and Fe<sub>3</sub>O<sub>4</sub>.<sup>[90]</sup> The easy magnetic axis of nanocrystals can be aligned by applying a magnetic field during evaporation of the colloid on a substrate to obtain films with high magnetic anisotropy.<sup>[91–93]</sup> Thus, ferromagnetic films with parallel anisotropy have been made of superparamagnetic  $\gamma$ -Fe<sub>2</sub>O<sub>3</sub> nanocrystals.<sup>[91]</sup> By tuning the substrate–nanocrystal interaction, the films can be made to exhibit perpendicular anisotropy (see Fig. 11).<sup>[92]</sup> Properties such as coercivity, anisotropy can be tuned by altering the size of the nanocrystals, the film

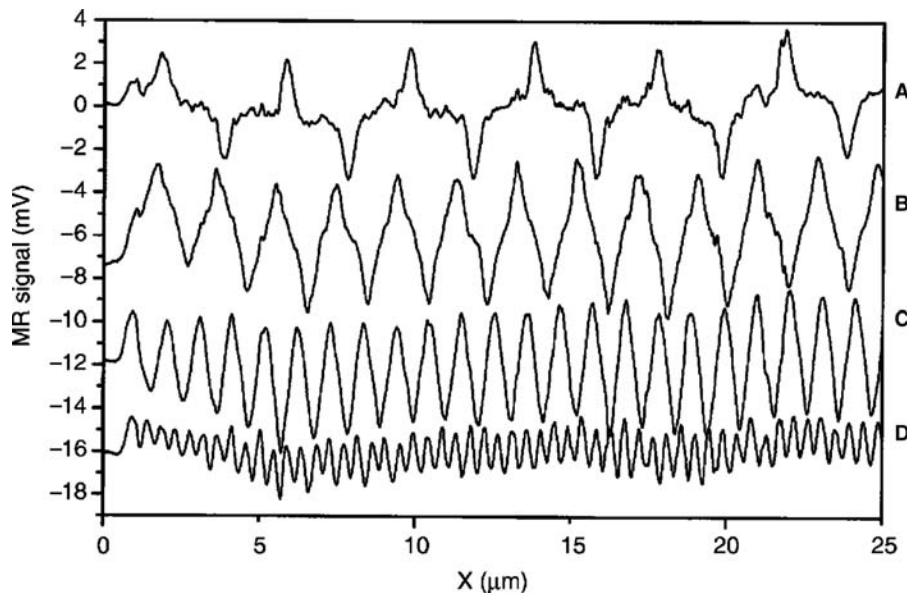


**Fig. 10** Magneto-resistive (MR) read-back signals from written bit transitions in an array of 4-nm-diameter Fe<sub>48</sub>Pt<sub>52</sub> nanocrystals. The line scans reveal magnetization reversal transitions at linear densities of (A) 500; (B) 1040; (C) 2140; and (D) 5000 flux changes per millimeter. Source: From Ref.<sup>[71]</sup>.

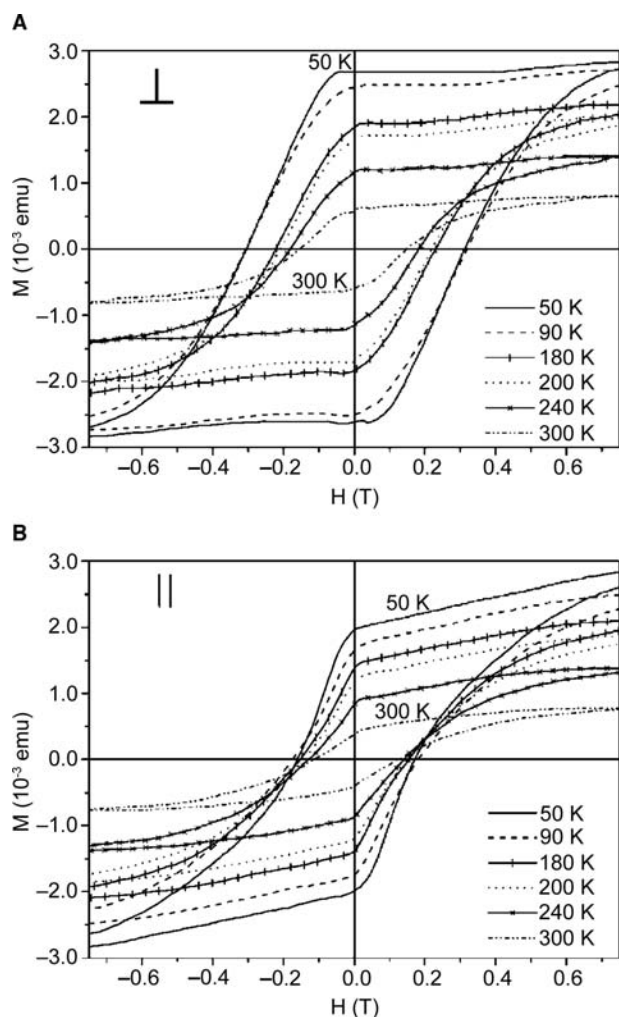


**Fig. 11** Hysteresis loops from a film of  $\gamma\text{-Fe}_2\text{O}_3$  deposited on Si(100) substrates at various temperatures with the substrate held (A) perpendicular and (B) parallel to the applied field direction. The increased coercivity along the perpendicular direction indicates perpendicular anisotropy caused by orientation of the easy magnetic axis of  $\gamma\text{-Fe}_2\text{O}_3$  nanocrystals perpendicular to the substrate. *Source:* From Ref. [78].

thickness or by suitably doping the nanocrystals with magnetic ions.<sup>[91–93]</sup>

### Biomedical Application of Oxide Nanoparticles

Magnetic oxide nanoparticles are considered as biocompatible as they possess no known toxicity. Superparamagnetic oxide nanoparticles have therefore found several biomedical applications.<sup>[94]</sup> By tailoring the ligand shell of magnetic particles to attach to a specific target molecule in a solution containing several different entities and subjecting the liquid to a magnetic field, separation or enhancement in concentration could be achieved. Such aids are rather important in biochemical experiments where very low

concentrations are generally employed. For example, by employing red blood cells labeled with iron oxide nanoparticles, the sensitivity of detection of malarial parasite was shown to be enhanced by Paul et al.<sup>[95]</sup> It has been proposed that hyperthermia—magnetic field induced heating of superparamagnetic particles, could be used to destroy diseased cells and thereby treat cancer. The particles are dispersed in the affected cells and an external AC magnetic field applied to bring about heating of the particles to cause destruction of the cells. Numerous studies have been carried out toward achieving this objective.<sup>[94,96]</sup> Magnetic nanoparticles also find application as magnetic resonance imaging contrast agents. This technology has been commercialized and is widely available.<sup>[94]</sup>

### CONCLUSIONS

Properties of metals and semiconductors become size dependent at the nanoscale because of associated changes in the electronic structure and charge transport. Specifically, electronic, optical, and magnetic properties of nanocrystals have gained importance in view of their potential applications. Small metal nanocrystals with discrete charge states find applications in highly sensitive electrometers and memory devices. Similarly, semiconductor nanocrystals of varying optical gap find applications in photonic materials and fluorescent markers in biochemical assays. Bimetallic and oxide nanocrystals with superparamagnetic domains have demonstrated potential as recording media. The latter especially has gained importance in cancer treatment.

### REFERENCES

1. Silbergliitt, R. Nanomaterials: trends. In *Dekker Encyclopedia of Nanoscience and Nanotechnology*, 2E; Schwarz, J.A., Contescu, C.I., Putyera, K., Eds.; Taylor & Francis: New York, NY, 2009; Vol. 4, 2836–2847.
2. Skandan, G.; Singhal, A. Nanomaterials: Advances in technology and industry. In *Dekker Encyclopedia of Nanoscience and Nanotechnology*, 2E; Schwarz, J.A., Contescu, C.I., Putyera, K., Eds.; Taylor & Francis: New York, NY, 2009; Vol. 4, 2788–2798.
3. Sharma, P.K.; Miao, W.; Giri, A.; Raghunathan, S. Nanomaterials: manufacturing, processing, and applications. In *Dekker Encyclopedia of Nanoscience and Nanotechnology*, 2E; Schwarz, J.A., Contescu, C.I., Putyera, K., Eds.; Taylor & Francis: New York, NY, 2009; Vol. 4, 2799–2814.
4. Kubo, R. Electronic properties of metallic fine particles. 1. *J. Phys. Soc. Jpn.* **1962**, *17*, 975.
5. Edwards, P.P.; Johnston, R.L.; Rao, C.N.R. The size-induced metal-insulator transition in clusters and metal particles. In *Metal Clusters in Chemistry*; Braunstein, P.,

- Oro, G., Raithby, P.R., Eds.; Wiley-VCH: Weinham, 1999.
6. Vinod, C.P.; Kulkarni, G.U.; Rao, C.N.R. Size-dependent changes in the electronic structure of metal clusters as investigated by scanning tunneling spectroscopy. *Chem. Phys. Lett.* **1998**, *289*, 329.
  7. Busani, R.; Folker, M.; Chesnovsky, O. Direct observation of band-gap closure in Mercury clusters. *Phys. Rev. Lett.* **1998**, *81*, 3836.
  8. Miyake, M.; Torimoto, T.; Sakata, T.; Mori, H.; Kuwabata, S.; Yoneyama, H. Characterization of covalently immobilized q-CdS particles on Au(111) by scanning tunneling microscopy and tunneling spectroscopy with high reproducibility. *Langmuir* **1997**, *13*, 742.
  9. Rademann, K.; Rademann, O.D.; Schlauf, M.; Even, V.; Hensel, F. Evolution of surface plasmon resonance absorption in large gas phase clusters of mercury: approaching the bulk. *Phys. Rev. Lett.* **1992**, *69*, 3208.
  10. Brust, M.; Bethell, D.; Schiffrin, D.J.; Kiely, C.J. Novel gold-dithiol nano-networks with non-metallic electronic properties. *Adv. Mater.* **1995**, *7*, 795.
  11. Torma, V.; Schmid, G.; Simon, U. Structure-property relations in Au<sub>55</sub> cluster layers studied by temperature-dependent impedance measurements. *Chem. Phys. Chem.* **2001**, *2*, 321.
  12. Simon, U.; Flesch, R.; Wiggers, H.; Schn, G.; Schmid, G. Chemical tailoring of the charging energy in metal cluster arrangements by use of bifunctional spacer molecules. *J. Mater. Chem.* **1998**, *8*, 517.
  13. Aslam, M.; Mulla, I.S.; Vijayamohan, K. Insulator-metal transition in coulomb blockade nanostructures. *Appl. Phys. Lett.* **2001**, *79*, 689.
  14. Terrill, R.H.; Postlewaite, T.A.; Chen, C.; Poon, C.D.; Terzis, A.; Chen, A.; Hutchinson, J.E.; Clark, M.R.; Wignall, G.; Londono, J.D.; Superfine, R.; Falvo, M.; Johnson, C.S., Jr.; Samulski, E.T.; Murray, R.W. Distance dependence of the low-temperature electron transfer kinetics of (ferrocenylcarboxy)-terminated alkanethiol monolayers. *J. Am. Chem. Soc.* **1995**, *117*, 2896.
  15. Musick, M.D.; Keating, C.D.; Keefe, M.H.; Natan, M.J. Stepwise construction of conductive Au colloid multilayers from solution. *Chem. Mater.* **1997**, *9*, 1499.
  16. Liu, Y.; Wang, Y.; Clauss, R.O. Layer-by-layer ionic self-assembly of Au colloids into multilayer thin-films with bulk metal conductivity. *Chem. Phys. Lett.* **1998**, *298*, 315.
  17. Parthasarathy, R.; Lin, X.-M.; Jaeger, H.A. Electronic transport in metal nanocrystal arrays: the effect of structural disorder on scaling behavior. *Phys. Rev. Lett.* **2001**, *87*, 186807.
  18. Schmelzer, J., Jr.; Brown, S.A.; Wurl, A.; Hyslop, H.; Blaikie, R.J. Finite-size effects in the conductivity of cluster assembled nanostructures. *Phys. Rev. Lett.* **2002**, *88*, 226802.
  19. Doty, R.C.; Yu, H.; Shih, C.K.; Korgel, B.A. Temperature-dependent electron transport through silver nanocrystal superlattices. *J. Phys. Chem.* **2001**, *B105*, 8291.
  20. Ogawa, T.; Kobayashi, K.; Masuda, G.; Takase, T.; Maeda, S. Electronic conductive characteristics of devices fabricated with 1, 10-decanedithiol and gold nanoparticles between 1 micrometer electrode gaps. *Thin Solid Films* **2001**, *393*, 374.
  21. Osifchin, R.G.; Mahoney, W.J.; Bielefeld, J.D.; Andres, R.P.; Henderson, J.I.; Kubiak, C.P. Synthesis of a quantum dot superlattice using molecularly linked metal clusters. *Superlattices Microstruct.* **1995**, *18*, 283.
  22. Osifchin, R.G.; Mahoney, W.J.; Bielefeld, J.D.; Andres, R.P.; Henderson, J.I.; Kubiak, C.P. Electronic conduction through 2d arrays of nanometer diameter metal clusters. *Superlattices Microstruct.* **1995**, *18*, 275.
  23. Markovich, G.; Collier, C.P.; Hendricks, S.E.; Ramacle, F.; Levine, R.D.; Heath, J.R. Architectonic quantum dot solids. *Acc. Chem. Res.* **1999**, *32*, 415.
  24. Medeiros-Ribeiro, G.; Ohlberg, D.A.A.; Williams, R.S.; Heath, J.R. Rehybridization of electronic structure in compressed two-dimensional quantum dot superlattices. *Phys. Rev.* **1999**, *B59*, 1633.
  25. Taleb, A.; Silly, F.; Gusev, A.O.; Charra, F.; Pileni, M.-P. Electron transport properties of nanocrystals: isolated, and supra-crystalline phases. *Adv. Mater.* **2000**, *12*, 633.
  26. Bigioni, T.P.; Harrell, L.E.; Cullen, W.G.; Guthrie, D.K.; Whetten, R.L.; Fist, P.N. Imaging and tunneling spectroscopy of gold nanocrystals and nanocrystal arrays. *Eur. Phys. J.* **1999**, *D6*, 355.
  27. Torma, V.; Reuter, T.; Vidoni, O.; Schumann, M.; Radehaus, C.; Schmid, G. The diode behavior of asymmetrically ordered Au<sub>55</sub> clusters. *Chem. Phys. Chem.* **2001**, *2*, 546.
  28. Pal, S.; John, N.S.; Thomas, P.J.; Kulkarni, G.U.; Sanyal, M.K. Deposition of a metal-organic heterostructure to form magnetic-nonmagnetic bilayer films. *J. Phys. Chem.* **2004**, *108*, 10770.
  29. Thomas, P.J.; Kulkarni, G.U.; Rao, C.N.R. Effect of size on the coulomb staircase phenomenon in metal nanocrystals. *Chem. Phys. Lett.* **2000**, *321*, 163.
  30. Green, S.J.; Stokes, J.I.; Hostetler, M.J.; Peitros, J.; Murray, R.W. Three-dimensional monolayers: nanometer-sized electrodes of alkanethiolate-stabilized gold cluster molecules. *J. Phys. Chem.* **1997**, *B101*, 2663.
  31. Persson, S.H.M.; Olofsson, L.; Hedberg, L. A self-assembled single-electron tunneling transistor. *Appl. Phys. Lett.* **1999**, *74*, 2546.
  32. Gittins, D.L.; Bethell, D.; Schiffrin, D.J.; Nichols, R.J. A nanometer-scale electronic switch consisting of a metal cluster and redox-addressable groups. *Nature* **2000**, *408*, 67.
  33. Benenson, Y.; Shapiro, E. Molecular computing machines. In *Dekker Encyclopedia of Nanoscience and Nanotechnology*, 2E; Schwarz, J.A., Contescu, C.I., Putyera, K., Eds.; Taylor & Francis: New York, NY, 2009; Vol. 4, 2291–2302.
  34. Jortner, J.; Ratner, M. Molecular electronics. In *IUPAC A 'Chemistry For the 21st Century' monograph*; Blackwell Scientific: London, 1997.
  35. Orlov, A.O.; Amlani, I.; Berstein, G.H.; Lent, C.S.; Snider, G.L. Realization of a functional cell for quantum-dot cellular automata. *Science* **1997**, *277*, 928.
  36. Heath, J.R.; Kuekes, P.J.; Snider, G.S.; Williams, R.S. A defect-tolerant computer architecture: opportunities for nanotechnology. *Science* **1998**, *280*, 1716.

37. Abelson, H.; Allen, D.; Coore, D.; Hanson, C.; Homsy, G.; Knoght, T.F., Jr.; Nagpal, R.; Rauch, E.; Sussman, G.J.; Weiss, R. Amorphous Computing, Technical Report A. I. Memo 1665; Massachusetts Institute of Technology, Artificial Intelligence Laboratory Aug, 1999.
38. Coore, D.; Nagpal, R.; Weiss, R. Paradigms for Structure in an Amorphous Computer, Technical Report A. I. Memo 1614; Massachusetts Institute of Technology, Artificial Intelligence Laboratory Oct, 1997.
39. Abelson, H.; Allen, D.; Coore, D.; Hanson, C.; Homsy, G.; Knoght, T.F., Jr.; Nagpal, R.; Rauch, E.; Sussman, G.J.; Weiss, R. Amorphous computing. *Commun. Assoc. Comput. Mach.* **2000**, *43* (5), 74.
40. Mulukutla, R.S. Nanostructured catalysts. In *Dekker Encyclopedia of Nanoscience and Nanotechnology*, 2E; Schwarz, J.A., Contescu, C.I., Putyera, K., Eds.; Taylor & Francis: New York, NY, 2009; Vol. 5, 2967–2973.
41. Zeng, H.C. Nanostructured catalysts: Design and synthesis. In *Dekker Encyclopedia of Nanoscience and Nanotechnology*, 2E; Schwarz, J.A., Contescu, C.I., Putyera, K., Eds.; Taylor & Francis: New York, NY, 2009; Vol. 5, 2974–2985.
42. Goodman, D.W. Catalysis by supported gold nanoclusters. In *Dekker Encyclopedia of Nanoscience and Nanotechnology*, 2E; Schwarz, J.A., Contescu, C.I., Putyera, K., Eds.; Taylor & Francis: New York, NY, 2009; Vol. 1, 744–752.
43. Valden, M.; Lai, X.; Goodman, D.W. Onset of catalytic activity of gold clusters on titania with the appearance of nonmetallic properties. *Science* **1998**, *281*, 1647.
44. Vinod, C.P.; Kulkarni, G.U.; Rao, C.N.R. *Surface Chemistry and Catalysis*; Carley, A., Davies, P., Hutchings, G., Spencer, M., Eds.; Kluwer Academic, **2002**; 191.
45. Sutherland, A.J. Quantum dots as luminescent probes in biological systems. *Curr. Opin. Sol. Stat. Mater. Sci.* **2002**, *6*, 365.
46. Bruchez, M., Jr.; Moronne, M.; Gin, P.; Weiss, S.; Alivisatos, A.P. Semiconductor nanocrystals as fluorescent biological labels. *Science* **1998**, *281*, 2013.
47. Niemeyer, C.M. Nanoparticles, proteins, and nucleic acids: biotechnology meets materials science. *Angew. Chem. Int. Ed.* **2001**, *40*, 4128.
48. Mattoussi, H.; Mauro, J.M.; Goldman, E.R.; Anderson, G.P.; Sundar, V.C.; Mikulec, F.V.; Bawendi, M.G. Self-assembly of CdSe-ZnS quantum dot bioconjugates using an engineered recombinant protein. *J. Am. Chem. Soc.* **2000**, *122*, 12142.
49. Gerion, D.; Pinaud, F.; Williams, S.C.; Parak, W.J.; Zanchet, D.; Weiss, S.; Alivisatos, A.P. Synthesis and properties of biocompatible water-soluble silica-coated CdSe/ZnS semiconductor quantum dots. *J. Phys. Chem.* **2001**, *B105*, 8861.
50. Parak, W.J.; Gerion, D.; Zanchet, D.; Woerz, A.S.; Pellegrino, T.; Micheel, C.; Williams, S.C.; Seitz, M.; Bruehl, R.E.; Bryant, Z.; Bustamante, C.; Bertozzi, C.R.; Alivisatos, A.P. Conjugation of DNA to silanized colloidal semiconductor nanocrystalline quantum dots. *Chem. Mater.* **2002**, *14*, 2113.
51. Chan, W.C.W.; Nie, S. Quantum dot bioconjugates for ultrasensitive nonisotopic detection. *Science* **1998**, *281*, 2016.
52. Li, L.-S.; Alivisatos, A.P. Cadmium selenide quantum rods: Anisotropy. In *Dekker Encyclopedia of Nanoscience and Nanotechnology*, 2E; Schwarz, J.A., Contescu, C.I., Putyera, K., Eds.; Taylor & Francis: New York, NY, 2009; Vol. 1, 487–497.
53. Zangeneh, M.; Terrill, R. Surface plasmon spectra of silver and gold nanoparticle assemblies. In *Dekker Encyclopedia of Nanoscience and Nanotechnology*, 2E; Schwarz, J.A., Contescu, C.I., Putyera, K., Eds.; Taylor & Francis: New York, NY, 2009; Vol. 6, 4271–4282.
54. Schuüller, C. Quantum dots: Inelastic light scattering from electronic excitations. In *Dekker Encyclopedia of Nanoscience and Nanotechnology*, 2E; Schwarz, J.A., Contescu, C.I., Putyera, K., Eds.; Taylor & Francis: New York, NY, 2009; Vol. 5, 3661–3672.
55. Wilcoxon, J.P. Metallic quantum dots. In *Dekker Encyclopedia of Nanoscience and Nanotechnology*, 2E; Schwarz, J.A., Contescu, C.I., Putyera, K., Eds.; Taylor & Francis: New York, NY, 2009; Vol. 3, 2176–2201.
56. Mirkin, C.A.; Letsinger, R.L.; Mucic, R.C.; Storhoff, J.F. A DNA-based method for rationally assembling nanoparticles into macroscopic materials. *Nature* **1996**, *382*, 607.
57. Alivisatos, A.P.; Johnsson, K.P.; Peng, X.; Wilson, T.E.; Loweth, C.J.; Burchez, M.P., Jr.; Schultz, P.G. Organization of nanocrystal molecules using DNA. *Nature* **1996**, *382*, 609.
58. Kim, Y.; Johnson, R.C.; Hupp, J.T. Gold nanoparticle-based sensing of spectroscopically silent heavy metal ions. *Nano Lett.* **2001**, *1*, 165.
59. Berchmans, S.; Thomas, P.J.; Rao, C.N.R. Novel effects of metal ion chelation on the properties of lipoic acid-capped Ag and Au nanoparticles. *J. Phys. Chem.* **2002**, *B106*, 4647.
60. Yguerabide, J.; Yguerabide, E.E. Light-scattering submicroscopic particles as highly fluorescent analogs and their use as tracer labels in clinical and biological applications: II. Experimental characterization. *Anal. Biochem.* **1998**, *262*, 157.
61. Schultz, S.; Smith, D.R.; Mock, J.J.; Schultz, D.A. Single-target molecule detection with nonbleaching multicolor optical immunolabels. *Proc. Natl. Acad. Sci.* **2000**, *97*, 996.
62. <http://www.biocore.com>.
63. Murray, C.B.; Kagan, C.R.; Bawendi, M.G. Synthesis and characterization of monodisperse nanocrystals and close-packed nanocrystal assemblies. *Annu. Rev. Mater. Sci.* **2000**, *30*, 545.
64. Artemyev, M.V.; Woggon, U.; Jaschinski, H.; Gurinovich, L.I.; Gaponenko, S.V. Spectroscopic study of electronic states in an ensemble of close-packed CdSe nanocrystals. *J. Phys. Chem.* **1999**, *B104*, 11617.
65. Kagan, C.R.; Murray, C.B.; Bawendi, M.G. Long-range resonance transfer of electronic excitations in close-packed CdSe quantum-dot solids. *Phys. Rev.* **1996**, *B54*, 8633.



66. Döllefeld, H.; Weller, H.; Eychemüller, A. Semiconductor nanocrystal assemblies: experimental pitfalls and a simple model of particle-particle interaction. *J. Phys. Chem.* **2002**, *B106*, 5604.
67. Samokhvalov, A.; Berfeld, M.; Lahav, M.; Naaman, R.; Rabani, E. Assemblies of CdS quantum particles studied by the attenuated low energy photoelectron spectroscopy. *J. Phys. Chem.* **2000**, *B104*, 8632.
68. Artemyev, M.V.; Bibik, A.I.; Gurinovich, L.I.; Gaponenko, S.V.; Woggon, U. Evolution from individual to collective electron states in a dense quantum dot ensemble. *Phys. Rev.* **1999**, *B60*, 1504.
69. Dirix, Y.; Bastiaansen, C.; Caseri, W.; Smith, P. Oriented pearl-necklace arrays of metallic nanoparticles in polymers: a new route toward polarization-dependent color filters. *Adv. Mater.* **1999**, *11*, 223.
70. Maier, S.A.; Brongersma, M.L.; Kik, P.G.; Meltzer, S.; Requicha, A.A.F.; Koel, B.E.; Atwater, H.A. Plasmonics—a route to nanoscale optical devices. *Adv. Mater.* **2001**, *13*, 1501.
71. Nanda, J.; Narayan, K.S.; Kuruvilla, B.A.; Murthy, G.L.; Sarma, D.D. Sizable photocurrent and emission from solid state devices based on CdS nanoparticles. *Appl. Phys. Lett.* **1998**, *72*, 1335.
72. Colin, V.L.; Schlamp, M.C.; Alivisatos, A.P. Light-emitting diodes made from cadmium selenide nanocrystals and a semiconducting polymer. *Nature* **1994**, *370*, 354.
73. Schlamp, M.C.; Peng, X.; Alivisatos, A.P. Improved efficiencies in light emitting diodes made with CdSe(CdS) core/shell type nanocrystals and a semiconducting polymer. *J. Appl. Phys.* **1997**, *82*, 5837.
74. Dabbousi, B.O.; Bawendi, M.G.; Onitsuka, O.; Rubner, M.F. Electroluminescence from CdSe quantum-dot/polymer composites. *Appl. Phys. Lett.* **1995**, *66*, 1316.
75. Narayan, K.S.; Manoj, A.G.; Nanda, J.; Sarma, D.D. Dual function hybrid polymer-nanoparticle devices. *Appl. Phys. Lett.* **1999**, *74*, 871.
76. Eisler, H.-J.; Sundar, V.C.; Bawendi, M.G.; Ealsh, M.; Smith, H.I.; Klimov, V. Color-selective semiconductor nanocrystal laser. *Appl. Phys. Lett.* **2000**, *80*, 4614.
77. Sundar, V.C.; Eisler, H.-J.; Bawendi, M.G. Room-temperature, tunable gain media from novel II–VI nanocrystal-titania composite matrices. *Adv. Mater.* **2002**, *14*, 739.
78. Huynh, W.U.; Dittmer, J.J.; Alivisatos, A.P. Hybrid nanorod-polymer solar cells. *Science* **2002**, *295*, 2425.
79. Lee, J.; Sundar, V.C.; Heine, J.R.; Bawendi, M.G.; Jensen, K.F. Full color emission from II–VI semiconductor quantum dot-polymer composites. *Adv. Mater.* **2000**, *12*, 1102.
80. Gao, M.; Lesser, C.; Kirstein, S.; Möhwald, H.; Rogach, A.L.; Weller, H. Electroluminescence of different colors from polycation/CdTe nanocrystal self-assembled films. *J. Appl. Phys.* **2000**, *87*, 2297.
81. Sun, S.; Murray, C.B. Synthesis of monodisperse cobalt nanocrystals and their assembly into magnetic superlattices. *J. Appl. Phys.* **1999**, *85*, 4325.
82. Bean, C.P.; Livingston, J.D. Superparamagnetism. *J. Appl. Phys.* **1959**, *30*, 120S.
83. Zhang, D. Magnetic nanomaterials: conventional synthesis and properties. In *Dekker Encyclopedia of Nanoscience and Nanotechnology*, 2E; Schwarz, J.A., Contescu, C.I., Putyera, K., Eds.; Taylor & Francis: New York, NY, 2009; Vol. 3, 1951–1967.
84. Nikles, D.E.; Harrell, J.W. Magnetic nanoparticles for granular recording media. In *Dekker Encyclopedia of Nanoscience and Nanotechnology*, 2E; Schwarz, J.A., Contescu, C.I., Putyera, K., Eds.; Taylor & Francis: New York, NY, 2009; Vol. 3, 2001–2011.
85. Cabuil, V. Magnetic nanoparticles. In *Dekker Encyclopedia of Nanoscience and Nanotechnology*, 2E; Schwarz, J.A., Contescu, C.I., Putyera, K., Eds.; Taylor & Francis: New York, NY, 2009; Vol. 3, 1985–2000.
86. Van de Hear, Milani, P.; Chatelain, A. Magnetic properties of free alkali and transition metal clusters. *Z. Phys. D: Atoms, Mol. Clusters* **1991**, *19*, 241.
87. Russier, V.; Petit, C.; Legrand, J.; Pileni, M.P. Collective magnetic properties of cobalt nanocrystals self-assembled in a hexagonal network: theoretical model supported by experiments. *Phys. Rev.* **2000**, *B62*, 3910.
88. Sun, S.; Murray, C.B.; Weller, D.; Folks, L.; Maser, A. Monodisperse FePt nanoparticles and ferromagnetic FePt nanocrystal superlattices. *Science* **2000**, *287*, 1989.
89. Zeng, H.; Li, J.; Llu, J.P.; Whang, Z.L.; Sun, S. Exchange-coupled nanocomposite magnets by nanoparticle self-assembly. *Nature* **2002**, *420*, 395.
90. Ngo, A.T.; Pileni, M.P. Assemblies of ferrite nanocrystals: partial orientation of the easy magnetic axes. *J. Phys. Chem.* **2001**, *B105*, 53.
91. Thomas, P.J.; Rajamathi, M.; Vanitha, P.V.; Kulkarni, G.U.; Rao, C.N. R. Perpendicular magnetization in self-assembled films of citrate-capped  $\gamma$ -Fe<sub>2</sub>O<sub>3</sub> nanocrystals on Si(100) surfaces. *J. Nanosci. Nanotech* **2005**, *5*, 565.
92. Ngo, A.T.; Pileni, M.P. Nanoparticles of cobalt ferrite: influence of the applied field on the organization of the nanocrystals on a substrate and on their magnetic properties. *Adv. Mater.* **2000**, *12*, 276.
93. Pankhurst, Q.A.; Connolly, J.; Jones, S.K.; Dobson, J. Applications of magnetic nanoparticles in biomedicine. *J. Phys. D: Appl. Phys.* **2003**, *36*, R167.
94. Paul, F.; Melville, D.; Roath, S.; Warhurst, D. A bench top magnetic separator for malarial parasite concentration. *IEEE Trans. Magn. Mag.* **1981**, *17*, 2822.
95. Jordan, A.; Scholz, R.; Wust, P.; Fahling, H.; Felix, R. Magnetic fluid hyperthermia (MFH): cancer treatment with AC magnetic field induced excitation of biocompatible superparamagnetic nanoparticles. *J. Magn. Magn. Mater.* **1999**, *201*, 413.
96. Jordan, A.; Scholz, R.; Maier-Hauff, K.; Johannsen, M.; Wust, P.; Nadobny, J.; Schirra, H.; Schmidt, H.; Deger, S.; Loening, S.; Lanksch, W.; Felix, R. Presentation of a new magnetic field therapy system for the treatment of human solid tumors with magnetic fluid hyperthermia. *J. Magn. Magn. Mater.* **2001**, *225*, 118.

## BIBLIOGRAPHY

1. Yguerabide, J.; Yguerabide, E.E. Light-scattering sub-microscopic particles as highly fluorescent analogs and their use as tracer labels in clinical and biological applications: I. Theory. *Anal. Biochem.* **1998**, *262*, 137.

# Nanocrystals: Synthesis and Mesoscale Organization

G. U. Kulkarni

P. John Thomas

*Chemistry and Physics of Materials Unit, Jawaharlal Nehru Center for Advanced Scientific Research, Bangalore, India*

C.N.R. Rao

*Chemistry and Physics of Materials Unit and CSIR Centre of Excellence in Chemistry, Jawaharlal Nehru Center for Advanced Scientific Research, Bangalore, India*

## Abstract

Organization of metal and semiconductor nanocrystals into mesostructures is an important aspect of nanoscience. New methods of nanocrystal synthesis and functionalization relevant to mesoscopic assembly are described, with emphasis on procedures that deal with monodispersed nanocrystals. Programmed assemblies of nanocrystals in one, two, and three dimensions are discussed.

## INTRODUCTION

A nanocrystal is a tiny chunk of the bulk measuring a few nanometers with a finite number of atoms in it. Nanocrystals in the size range of 1–50 nm are considered important and are obtainable as sols—a dispersion of a solid in a liquid, also called a colloidal sol. Metal sols possess fascinating colors and have long been used as dyes. That such dyes indeed consist of tiny metal chunks was established as early as 1857 by Faraday,<sup>[1]</sup> but a similar realization in the case of semiconducting nanocrystals had to wait for over a century.<sup>[2,3]</sup> Modern techniques of synthesis enable one to obtain sols of metals and semiconductors that can be dried and re-dissolved like watercolors. The colloidal particles display a remarkable tendency to remain single-crystalline and are hence named as nanocrystals. Nanocrystals possess high surface area—a great fraction of the atoms in a nanocrystal is on its surface. A small nanocrystal of 1 nm diameter will have as much as 30% of its atoms on the surface, while a larger nanocrystal of 10 nm ( $\approx 1000$  atoms) will have around 15% of its atoms on the surface.<sup>[4]</sup>

An added dimension to research on nanocrystals is their size-dependent properties. The electronic, magnetic, and optical properties of a nanocrystal depend on its size.<sup>[4]</sup> In small nanocrystals, the electronic energy levels are not continuous as in the bulk but are discrete, owing to the confinement of the electron wave function to the physical dimensions of the particles.<sup>[5]</sup> This phenomenon is called as quantum confinement, and therefore, nanocrystals are also known as quantum dots. In other words, a small nanocrystal could be a very bad conductor although they are tiny silhouettes of the conducting bulk. Likewise, a tiny nanocrystal of a ferromagnet can be paramagnetic in nature. In the case of semiconductors, besides discretization of

levels, the band gap increases due to quantum confinement. In several respects, small nanocrystals behave like molecules. The nanocrystals can be discretely charged with electrons having characteristic charging energies. It means that a nanocrystal carrying an extra electron can exhibit properties different from a neutral species.

The electronic absorption spectrum of metal nanocrystals in the visible region is dominated by the plasmon band. This absorption is due to the collective excitation of the itinerant electron gas on the particle surface and is characteristic of a nanocrystal of a given size. In metal colloids, surface plasmon excitations impart characteristic colors to the metal sols, the beautiful wine-red color of gold sols being well known.<sup>[6–8]</sup> The dependence of the plasmon peak on the dielectric constant of the surrounding medium and the diameter of the nanocrystal was predicted theoretically by Mie and others at the turn of the last century.<sup>[9–12]</sup> The dependence of the absorption band of thiol-capped Au nanocrystals on solvent refractive index was recently verified by Templeton et al.<sup>[13]</sup> Link and El-Sayed<sup>[6]</sup> found that the absorption band splits into longitudinal and transverse bands in Au nano-rods.<sup>[6]</sup>

In contrast to metals, exciton peaks dominate the absorption of semiconductor nanocrystals. Thus, yellowish CdS, exhibits an excitonic absorption around 600 nm, which gradually shifts into the UV region as the nanocrystal diameters are varied below 10 nm. The absorption band can be systematically varied across ranges of a few 100 nm by changing the size of the semiconductor nanocrystal.<sup>[14–17]</sup> Brus and others proposed an independent theory to describe size quantization effects in semiconductor nanocrystals, based on the effective mass approximation<sup>[3,18]</sup> after recognizing the failure of Mie's theory. Since then, theories have grown in sophistication and rigor to include key

effects like surface structure and coupling of electronic states.<sup>[19–21]</sup> However, the understanding of the optical properties of semiconductor nanocrystals is still incomplete and careful experiments on monodisperse nanocrystals are currently being pursued to unravel the mystery.<sup>[22]</sup> In addition to interesting absorption properties, the semiconductor nanocrystals also exhibit luminescent behavior.<sup>[23–26]</sup> The emission from monodisperse semiconductor nanocrystals such as CdSe is intense, narrow, and can be brought about by excitation in a broad range of wavelengths.<sup>[26]</sup> The emission can be tuned by altering the diameter of the nanocrystal (see Fig. 1). Further, control over the emission can be exercised by varying the surface structure and controlling diameter distribution. The above factors have led to the exploration of a wide range of applications for luminescent semiconductor nanocrystals.

The shrinking dimensions of the current microelectronic devices and the realization that current lithographic processes cannot extend to the nanoworld<sup>[27]</sup> have lent tremendous thrust to research aimed at ordering nanocrystals into functional networks.<sup>[28–33]</sup> The nanocrystals akin to covalent systems self-assemble

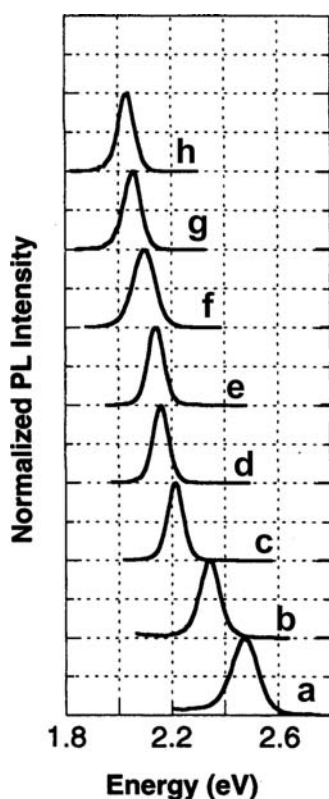


**Fig. 1** The emission spectra of CdSe nanocrystals of different sizes (A) 2.4 nm; (B) 2.5 nm; (C) 2.9 nm; (D) 3.3 nm; (E) 3.9 nm; (F) 4.1 nm; (G) 4.2 nm; (H) 4.4 nm. The change in the emission width is due to decrease in the nanocrystals diameter distribution with increase in diameter. *Source:* Reproduced with permission from Ref.<sup>[26]</sup>.

into ordered arrays in one, two, and three dimensions under the right conditions. Lattices of nanocrystals consist of interacting nanocrystals and may exhibit novel properties arising out of such interactions. The ability to engineer such assemblies, thus, extends the reach of current lithographic techniques and holds promise for a new generation of electronics of the nanoworld.<sup>[28]</sup> In this context, synthesis and programmed assembly of nanocrystals assumes significance.

In this entry, we discuss the structure and stability of mesoscopic organizations of nanocrystals in one, two, and three dimensions obtained by using a variety of surfactants. We also examine certain unusual organizations such as clusters of nanocrystals and microcolloidal crystals.

## SYNTHETIC STRATEGIES

### General Methods

Chemical synthesis of sols of metals and semiconductors results in nanoparticles embedded in a layer of ligands or stabilizing agents that prevent the aggregation of particles. The stabilizing agents employed include surfactants such as long-chain thiols or amines or polymeric ligands such as polyvinylpyrrolidone (PVP). Reduction of metal salts dissolved in appropriate solvents produces small metal particles of varying size distributions.<sup>[34–37]</sup> A variety of reducing agents have been employed for reduction. These include electrides, alcohols, glycols, metal borohydrides, and certain specialized reagents such as tetrakis(hydroxymethyl) phosphonium chloride. Si and Ge nanocrystals can be obtained by reduction of  $\text{GeCl}_4$  or silanes with strong reducing agents such as lithium or sodium naphthalide.<sup>[38–40]</sup>

Kinetic control of precipitation (arrested precipitation) is generally used to obtain semiconductor nanocrystals such as CdS,<sup>[41]</sup> CdSe,<sup>[42]</sup> ZnS, HgTe, PbS, CuS,  $\text{Cu}_2\text{S}$ , AgI, ZnO, AgI, and  $\text{TiO}_2$ .<sup>[43–45]</sup> The nanoparticles so obtained possess a broad distribution in diameters. Thermolysis methods involving the decomposition of organometallic precursors in high boiling organic solvents is used to prepare CdSe,<sup>[46]</sup> CdS,<sup>[46]</sup> PbSe,<sup>[16]</sup> InP,<sup>[17]</sup> ZnSe, GaAs, InSb, GaP nanocrystals.<sup>[44–49]</sup> Reverse micellar methods exploit the “water pools” in water-in-oil mixtures to synthesize nanocrystals and have been successfully utilized in the preparation of Ag, Au, Co, Pt, Co, CdS, CdTe, AgS nanocrystals.<sup>[50,51]</sup> The synthesis of nanocrystals at the air–water interface as in Langmuir–Blodgett films or at a liquid–liquid interface is currently attracting wide attention.<sup>[29,52,53]</sup> CdS, PbS, and MgS nanocrystals have been prepared by exposing Langmuir–Blodgett films of fatty acids to  $\text{H}_2\text{S}$ .<sup>[54]</sup> It has been shown recently that films of metal, semiconductor, and oxide

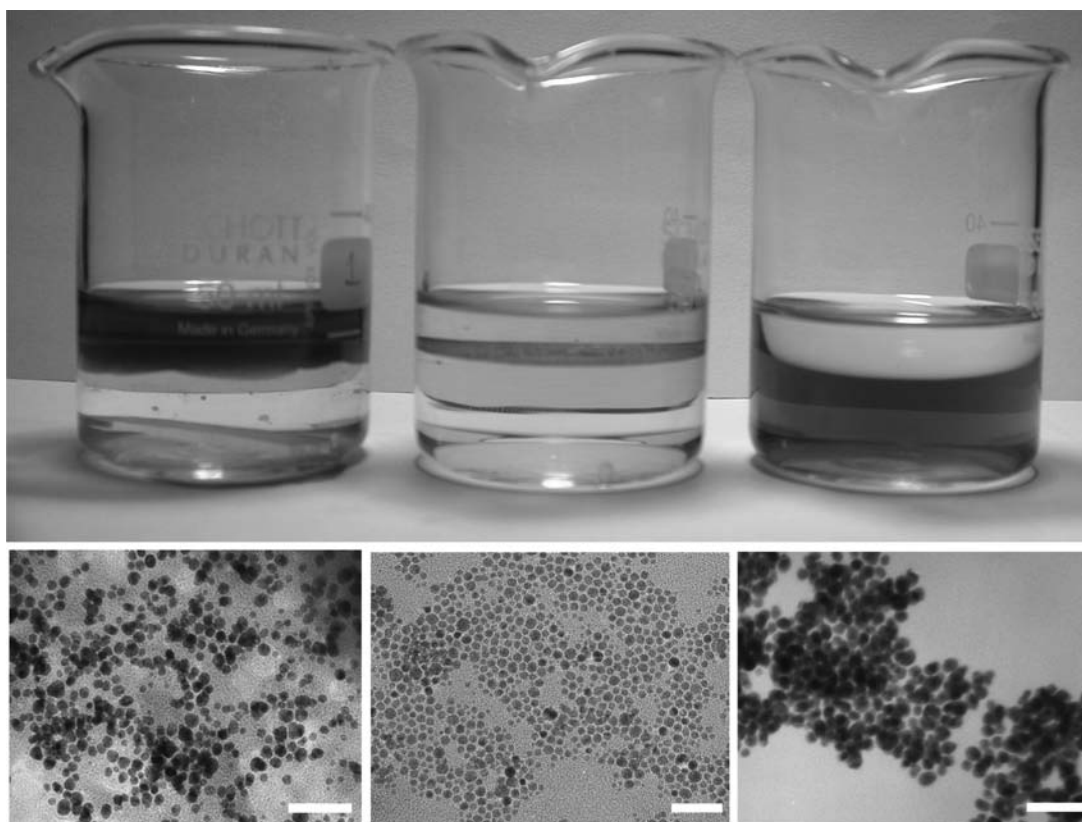


**Fig. 2** Nanocrystalline film of Au formed at the toluene–water interface (middle). Gold is introduced as a toluene solution of  $\text{Au}(\text{PPh}_3)\text{Cl}$  while partially hydrolyzed THPC (tetrakis(hydroxymethyl)phosphoniumchloride) in water acts as a reducing agent. The film is obtained when the two layers are allowed to stand for several hours. When dodecanethiol is added to the toluene layer, the film breaks up forming an organosol (left) while mercaptoundecanoic acid added to water produces a hydrosol (right). Shown below are the corresponding TEM images showing nanocrystals. The scale bars correspond to 50 nm. Films of CdS nanocrystals could also be prepared by adopting the same methods.

nanocrystals can be prepared using a water–toluene interface.<sup>[55,56]</sup> A typical film of Au nanocrystals is shown in Fig. 2. Traditionally, clusters of controlled sizes have been generated by ablation of a metal target in vacuum followed by mass selection of the plume to yield cluster beams.<sup>[57,58]</sup> Such cluster beams could be subject to in situ studies or be directed on to solid substrates. To obtain nanocrystals in solution, Harfenist et al.<sup>[59]</sup> steered a mass-selected Ag cluster beam through a toluene solution of thiol and capped the vacuum prepared particles.

Colloids of alloys have been made by the chemical reduction of the appropriate salt mixture in the solution phase. In the case of semi-conductor nanocrystals, a mixture of salts is subject to controlled precipitation. Thus, Ag–Pd and Cu–Pd colloids of varying composition have been prepared by alcohol reduction of mixtures of silver nitrate or copper oxide with palladium oxide.<sup>[60]</sup> Fe–Pt alloy nanocrystals have been made by thermal decomposition of the Fe and Pt acetylacetonates in high boiling organic solvents.<sup>[61]</sup> Au–Ag alloy nanocrystals have been made by

co-reduction of silver nitrate and chloroauric acid with sodium borohydride.<sup>[62,63]</sup> Semiconductor nanocrystals of the form  $\text{Cd}_x\text{Mn}_{1-x}\text{S}$ ,  $\text{CdS}_x\text{Se}_{1-x}$  have been obtained by the inverted micelle methods as well as in glasses by sol–gel methods.<sup>[22,64]</sup> Alloys of controlled composition are also made by thermal decomposition of carefully chosen precursors, to achieve homogeneity. For example,  $\text{Mn}_2(\mu\text{-SeMe})_2(\text{CO})_8$  was used as selenium source to obtain  $\text{Cd}_{1-x}\text{MnSe}$  nanocrystals.<sup>[65]</sup> Au–Ag alloying and segregation has been brought about by the use of lasers on Au–Ag layered particles.<sup>[66,67]</sup>

### Size Control

The successful synthesis of nanocrystals involves three steps: nucleation, growth, and termination by the capping agent or ligand.<sup>[34–36]</sup> Though the reaction temperature and reagent concentrations provide a rudimentary control of the three steps, it is often impossible to independently control them and so the

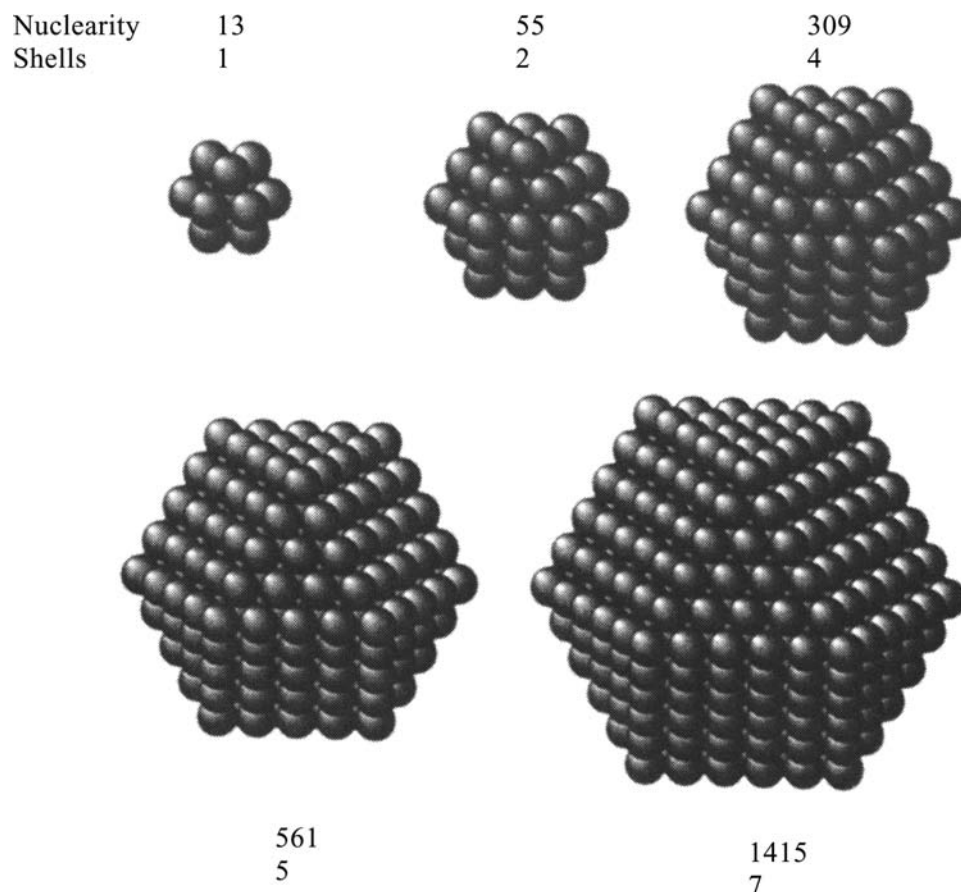


**Fig. 3** Metal nanocrystals in closed-shell configurations with magic number of atoms.

obtained nanocrystals usually exhibit a distribution in size. Typically, the distribution is log-normal with a standard deviation of 10%.<sup>[36]</sup> Given the fact that properties of the nanocrystals are size-dependent, it is significant to be able to synthesize nanocrystals of precise dimensions with minimal size-distributions. This can be accomplished to a limited extent by size selective precipitation either by centrifugation or by use of a miscible solvent–non-solvent liquid mixture to precipitate nanocrystals. However, single crystals of large clusters of semiconducting material such as  $\text{Cu}_{147}\text{Se}_{73}(\text{PET}_3)_{22}$ ,<sup>[68]</sup>  $[\text{Cd}_{10}\text{S}_4(\text{SPh})_{16}]^{4-}$ ,<sup>[69,70]</sup>  $\text{Cd}_{32}\text{S}_{14}(\text{SC}_6\text{H}_5)_{36}\text{DMF}_4$ ,<sup>[69,70]</sup>  $\text{Cd}_{17}\text{S}_4(\text{SCH}_2\text{CH}_2\text{OH})_{26}$ ,<sup>[69,70]</sup>  $\text{Cd}_{32}\text{S}_{14}(\text{SCH}_2\text{CH}(\text{CH}_3)\text{OH})_{36}$ ,<sup>[71]</sup>  $\text{Hg}_{32}\text{Se}_{14}(\text{SeC}_6\text{H}_5)_{36}$ <sup>[72]</sup> have been obtained. Solutions of such clusters possess optical properties similar to those of the sols. Schmid<sup>[73]</sup> and Zamaraev<sup>[74]</sup> succeeded in preparing truly mono-disperse nanocrystals, which they called “cluster compounds.” These cluster compounds are like macromolecules with a core containing metal–metal bonds yet obtainable in definite stoichiometries, typical examples being  $[\text{Pt}_{38}(\text{CO})_{44}\text{H}_2]^{2-}$  and  $\text{Au}_{55}(\text{PPh}_3)_{12}\text{Cl}_6$ . The enhanced stability of  $\text{Au}_{55}$  was recently demonstrated clearly by Boyen et al.<sup>[75]</sup> who exposed a series of  $\text{Au}_n$  nanocrystals to oxidation. These

nanocrystals are bequeathed with special stability because they consist of a magic number of metal atoms, which enables the complete closure of successive shells of atoms in a cubic close-packed arrangement. The magic numbers 13, 55, 147, 309, and 561 correspond to the closure of 1, 2, 3, 4, and 5 shells, respectively.<sup>[76]</sup> A schematic illustration of magic nuclearity nanocrystals is shown in Fig. 3. Since the breakthrough, several magic nuclearity nanocrystals have been prepared including PVP-stabilized  $\text{Pd}_{561}$  nanocrystals.<sup>[77,78]</sup> In Fig. 4 are shown scanning tunnelling and transmission electron microscopic (TEM) images of polymer-protected  $\text{Pd}_{561}$  nanocrystals.

### Shape Control

Since the properties of the nanocrystals follow from the confinement of the electrons to the physical dimensions of the nanocrystals, it would be interesting to vary the shape of the nanocrystals and study the effect of confinement of electrons in such artificial shapes.<sup>[79]</sup> For example, it is predicted that light emitted from a nanorod would be linearly polarized along the growth-axis.<sup>[22]</sup> Such predictions have led to the revival



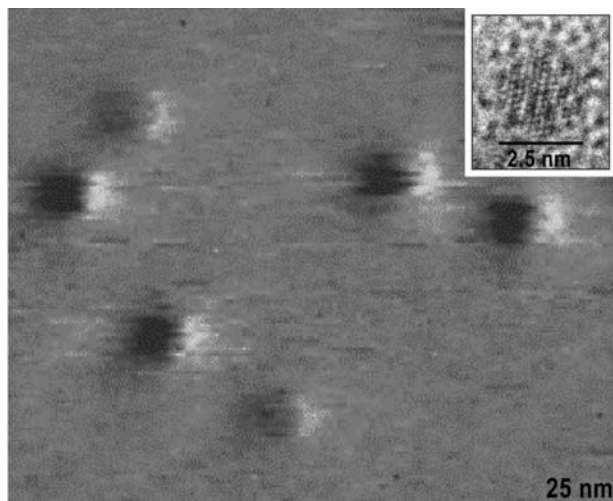


**Fig. 4** Scanning tunneling microscopy image of polymer coated  $\text{Pd}_{561}$  nanocrystals. The nanocrystals are seen as fluffy balls against plane background of the graphite substrate. The inset shows a high-resolution electron micrograph (HRTEM) of an individual nanocrystal. We see the characteristic 11 [111] fringes in the icosahedral shape measuring 2.5 nm. The diameter estimated from STM is  $\approx 3.4$  nm, the difference being due to the ligand shell.

of interest in synthetic strategies yielding non-spherical nanocrystals. Conventional methods such as due to Turkevich<sup>[35]</sup> yield in addition to spherical particles, a mixture of shapes—triangular, teardrop, etc., which

was then thought of as undesirable. Today, smarter synthetic schemes have been designed, which yield selectively nanocrystals in the form of rods, elongated spheres, cubes, and hexagons. CdSe nanocrystals in the form of rods, arrows, teardrops, and tetrapods have been obtained by careful control of thermolysis conditions such as ratio of surfactants and injection volumes.<sup>[22,80]</sup> In Fig. 5 are shown TEM micrographs of soluble CdSe nanorods of various aspect ratios. Triangular CdS nanocrystals have been obtained by inverse micelle methods.<sup>[81]</sup> Big tetrahedral Si nanocrystals as exclusive products have been obtained by careful control of the reducing conditions.<sup>[82]</sup> TEM images of Triangular CdS and Tetrahedral Si nanocrystals are shown in Fig. 6. Some shape control has also been demonstrated in the case of CdS and CdTe nanocrystals.<sup>[83,84]</sup>

### Tailoring the Ligand Shell

Nanocrystals in their native form are dominated by the surface species, the capping agents employed play a role in determining the property of the nanocrystals.<sup>[85]</sup> Hence, in addition to controlling the size and the shape of the nanocrystals, it is also necessary to tailor its surface with the right capping agent. In addition to traditional capping agents that include ions, surfactants, and polymers, a new breed of ligands—dendrimers,

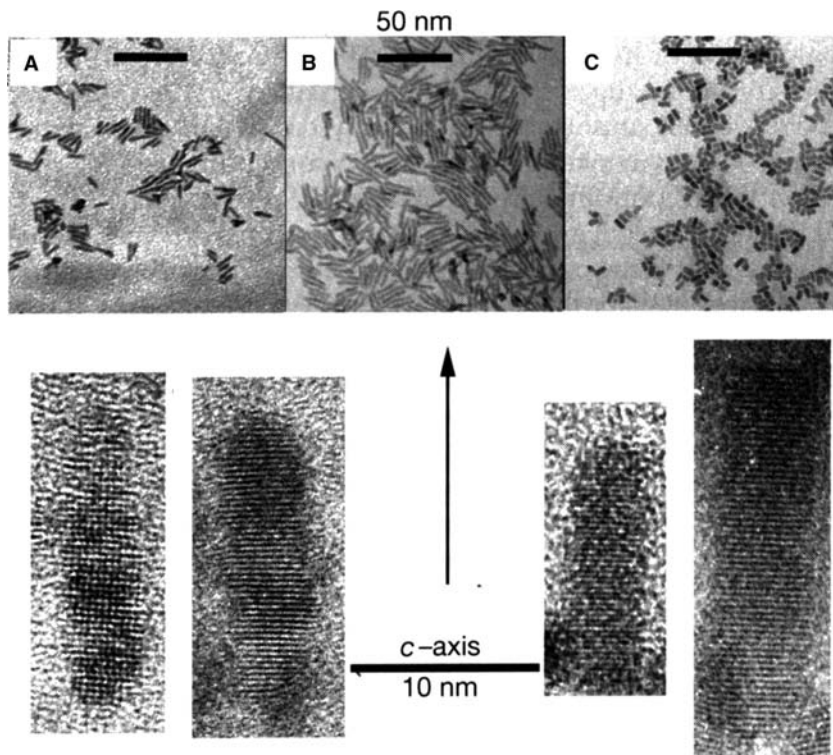


**Fig. 5** (A–C) TEM images of different nanorods of CdSe with different sizes and aspect ratios, high-resolution TEM images of four nanorods are shown below. *Source:* Reproduced with permission from Ref.<sup>[78]</sup>.



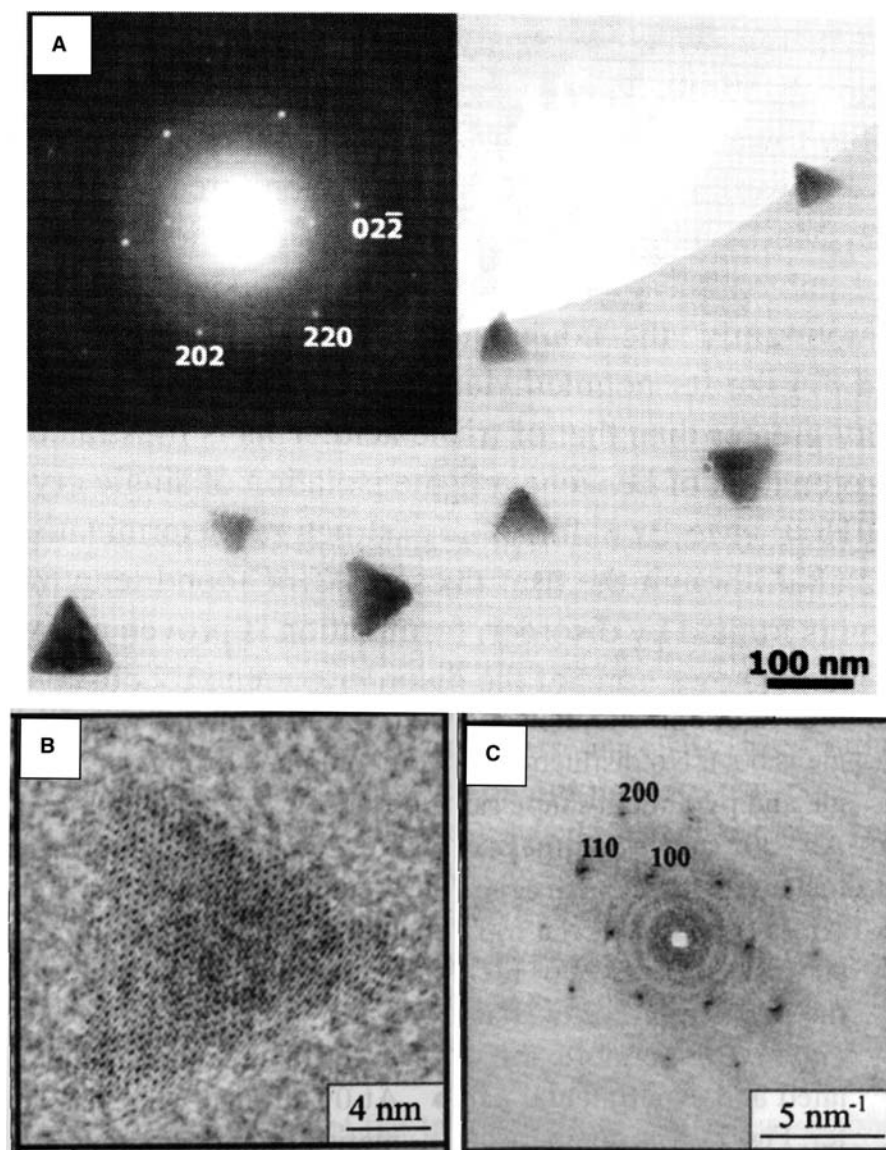


**Fig. 6** (A) TEM micrograph showing tetrahedral Si nanocrystals. The inset shows a selected area electron diffraction pattern typical of a diamond structure. (B) A high-resolution TEM image of a triangular CdS nanocrystal, power spectra is shown alongside. *Source:* Reproduced with permission from Refs.<sup>[79,80]</sup>.

hydrogen bonding fragments of protein, DNA and dyes—with pendant thiol groups as well as silica layers have been used as capping agents.<sup>[86–88]</sup> In some cases, a layer of a noble metal is used as a buffer between the core nanocrystal and the ligand shell.<sup>[89]</sup> Thus, a layer of gold lends special stability to Fe nanocrystals and helps prevent oxidation and in preserving the magnetic properties of Fe (see Fig. 7). Coating of a wider band gap material over a semiconductor nanocrystal aids in lifting the energy of surface states from in between the highest occupied and the lowest unoccupied levels, thereby enhancing the luminescence efficiency.<sup>[14,23]</sup> The lower band gap material acts as a seed for nucleation of the higher band gap material. Thus, core shell nanocrystals such as CdSe–ZnS, Si–SiO<sub>2</sub>, HgS–CdS, PbS–CdS,<sup>[44,45]</sup> ZnS–CdSe,<sup>[90]</sup> ZnSe–CdSe,<sup>[91]</sup> CdTe–HgTe nanocrystals have been obtained.<sup>[92,93]</sup>

Of special interest with regard to tailoring the ligand shells are reactions that enable the total replacement of one set of ligands with another.<sup>[94–98]</sup> These reactions also typically enable the transfer of nanocrystals from one phase to another. A novel method of thiol-derivatizing hydrosols of metal sols has been developed by Sarathy et al.<sup>[95,96]</sup> The procedure involves mixing vigorously a hydrosol containing metal particles of the desired size distribution with a toluene solution of an alkane thiol in the presence of a strong acid or reducing agent. The completion of the derivatization is marked by a vivid interchange of the colors from the aqueous layer to the hydrocarbon layer. The advantage of this method is that well-characterized metal particles can be easily thiol-derivatized in a non-aqueous medium. A variety of hydrosols of Au, Ag, and Pt have been thiolized by this procedure.

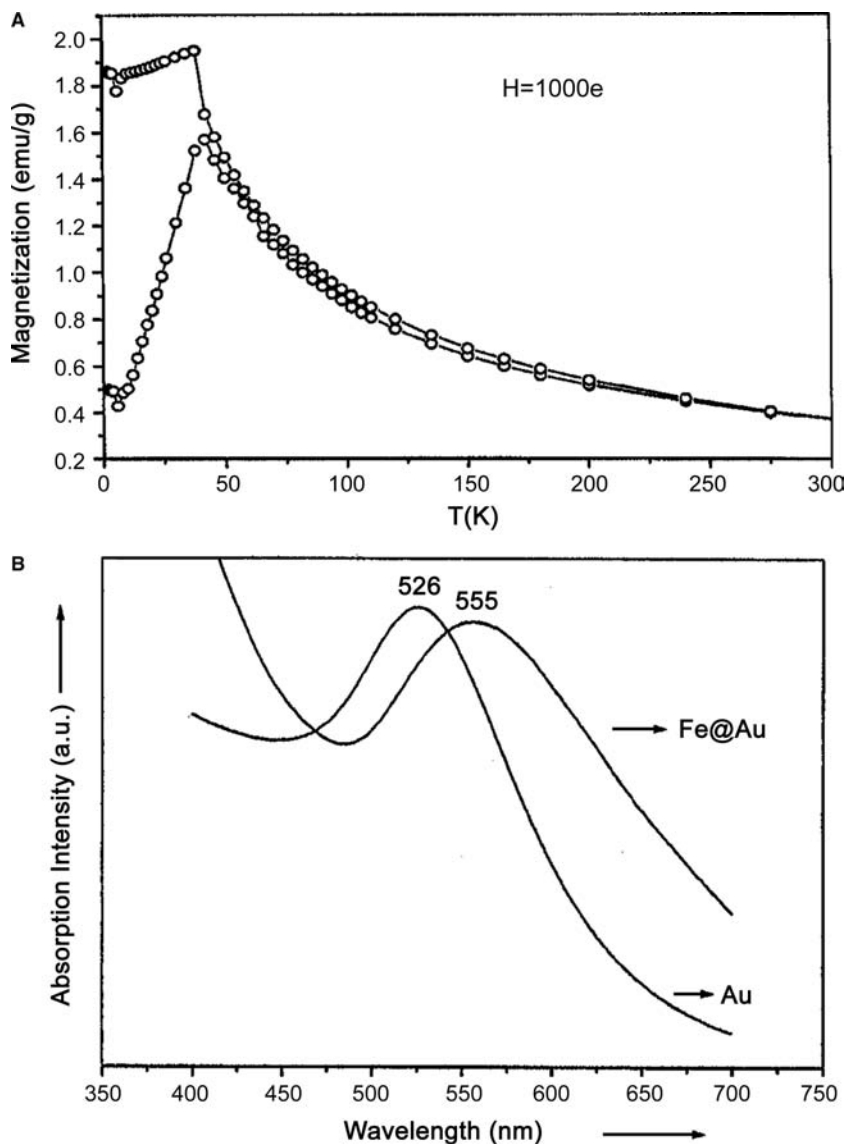


**Fig. 7** (A) Zero field cooled and field cooled magnetization curves for Fe–Au core–shell nanocrystals. The blocking temperature is 42 K. (B) Absorption spectrum showing the Au surface plasmon, shifted due to capping by Fe. For comparison, the spectrum of Au hydrosol is also shown. *Source:* Reproduced with permission from Ref.<sup>[87]</sup>.

A simple modification of this technique is shown to be effective in the case of CdS nanocrystals.<sup>[99]</sup>

### PROGRAMMED ASSEMBLIES

Like molecular systems, nanocrystals capped with suitable ligands spontaneously assemble into ordered aggregates. That such a self-assembly can occur through a variety of weak forces is being recognized. Cooperative assemblies of ligated metal and semiconductor as well as of colloidal polymer spheres seem to occur through the mediation of electrostatic and capillary forces.<sup>[100–102]</sup> The forces that govern the nanocrystal assembly, however, are different in many ways. Surface tension, for example, plays an important role<sup>[36]</sup> because in a nanocrystal, a large fraction of

atoms are present at the surface. Surfactant molecules that self-assemble on solid surfaces have proved to be the best means of obtaining ordered arrays of nanocrystals.<sup>[102]</sup> The way in which the nanocrystals organize themselves depends critically on the core diameter, the nature of the ligand, substrate, and even the dispersive medium used.<sup>[103]</sup> Thiolized metal nanocrystals readily arrange into two-dimensional arrays on removal of the solvent.<sup>[28]</sup> Using suitable methods, they can also be put into one-dimensional organization in the form of strings or assembled in a stepwise fashion in a three-dimensional superlattice (see Fig. 8).

### One-Dimensional Arrangements

Hornayak and coworkers<sup>[104]</sup> used the ordered channels of porous alumina as templates to obtain linear

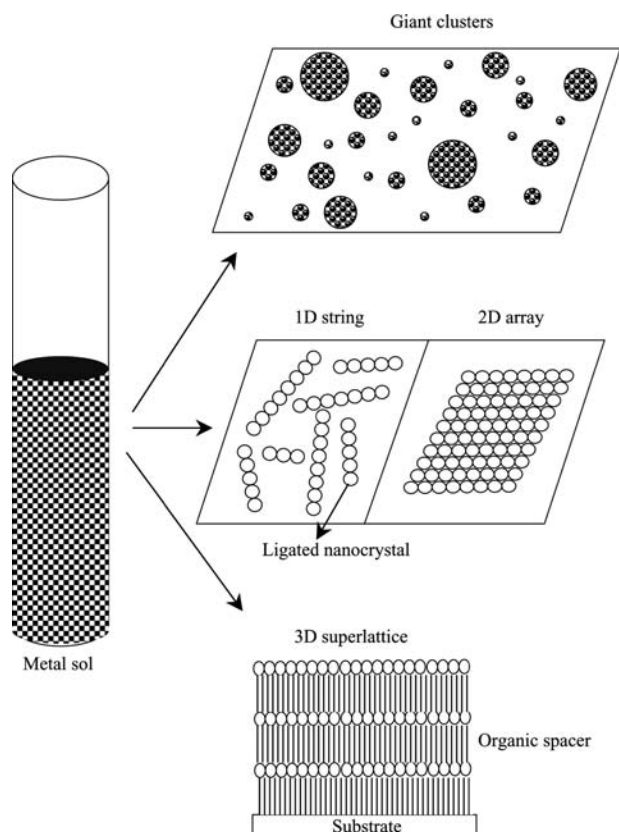


**Fig. 8** Schematic illustration of the various metal nanocrystal organizations.

arrangements of Au nanocrystals. By varying the pore size, the diameter of the nanowire could be controlled. A linear arrangement has also been obtained by coordinating Au particles ( $\approx 1.4$  nm) stabilized with phosphine ligands to single-stranded DNA oligonucleotide of the desired length and specific sequence.<sup>[105,106]</sup> Liquid crystalline phases of a genetically engineered virus–ZnS nanocrystal hybrid material was used as a template to obtain linear arrays of ZnS nanocrystal aggregates.<sup>[107]</sup> Similarly, Pt nanocrystals in the form of ribbons have been obtained using a cholesteric liquid crystalline template.<sup>[108]</sup> Organization of particles in a one-dimensional lattice has met with limited success. Heath and coworkers<sup>[109]</sup> have fabricated wires of Ag nanocrystals by compressing a dispersion of Ag (4.5 nm) nanocrystals in toluene (Fig. 9). The wires were one nanocrystal thick, a few nanocrystals wide, and extended in length from 20 to 300 nm. The interwire separation distance as well as the alignment of the wires could be controlled by compressing the film. Based on preliminary experimental observations, it has been suggested that tobacco mosaic virus tubules could serve as templates for the growth of one-dimensional lattice of quantum dots.<sup>[110]</sup>

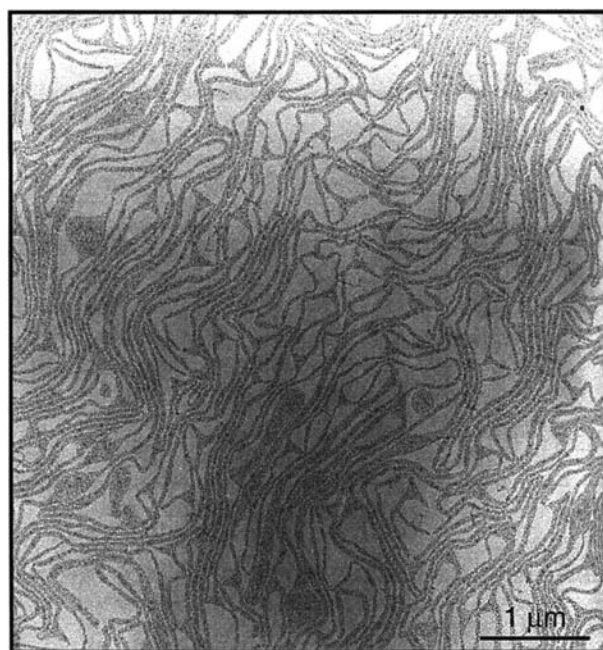


**Fig. 9** TEM image of a continuous stratum structure of compressed LB film of Ag nanocrystals. One-dimensional strings of Ag nanocrystals are clearly seen. *Source:* Reproduced with permission from Ref.<sup>[107]</sup>.

## Two-Dimensional Arrays

Ligands based on long-chain thiols or phosphines have served as good candidates for assembling monodisperse nanocrystals on a flat substrate. Two-dimensional organizations of a variety of nanocrystals can be brought about by simply evaporating a drop of the sol on a flat substrate.

### Arrays of metal nanocrystals

Gold organosols using alkane thiols as surfactants were first prepared by Schiffrin and co-workers<sup>[111]</sup> by phase transferring gold ions and carrying out reduction in the presence of thiols. Several workers have adopted this procedure to obtain thiolized metal nanocrystals.<sup>[112–115]</sup> Whetten et al.<sup>[113]</sup> centrifuged the organosol and separated out fractions containing nanocrystals of different mean sizes, to prepare well-ordered two-dimensional arrays of size-selected Au nanocrystals. Harfenist et al.<sup>[59]</sup> found that Ag nanocrystals prepared by using a cluster beam were stable in air and formed extended two-dimensional arrays. In Fig. 10 is shown a TEM image of two-dimensional array of dodecanethiol covered Ag nanocrystals obtained by Fitzmaurice and coworkers.<sup>[114]</sup> The Ag nanocrystals were prepared following the method of Schiffrin and co-workers.<sup>[111]</sup> Well ordered arrays of



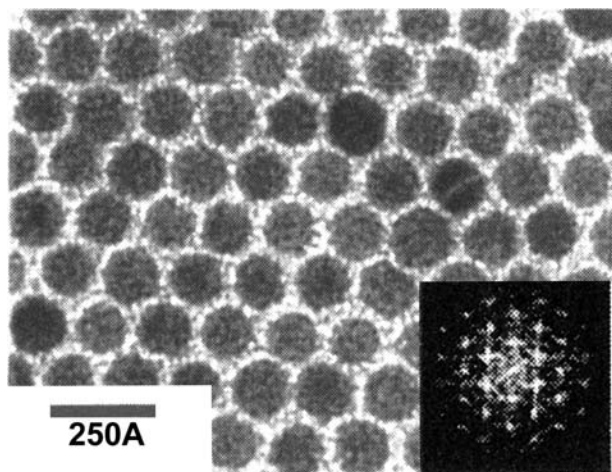


**Fig. 10** Transmission electron micrograph showing hexagonal close-packed Ag nanocrystals (diameter, 7 nm) obtained by evaporating a chloroform dispersion on a carbon substrate. The average interparticle distance is 1.5 nm. Inset shows the 2D power spectrum of the image. *Source:* Reproduced with permission from Ref.<sup>[114]</sup>.

magic nuclearity nanocrystals, Pd<sub>561</sub> and Pd<sub>1415</sub>, have been successfully obtained (see Fig. 11) after replacing their polymer coating by alkanethiols, following the phase transfer method discussed previously.<sup>[116]</sup> Long-chain fatty acids have also been used for ligating and assembling metal nanocrystals. Colloidal dispersion of Co nanocrystals capped with fatty acids were found to self-assemble to yield hexagonally ordered arrays similar to those obtained with alkanethiols.<sup>[117,118]</sup> Similarly, Ag nanocrystals capped with fatty acids of appropriate lengths yield cubic or hexagonal close-packed structures.<sup>[119,120]</sup> Schmid et al.<sup>[121]</sup> have reported an ordered two-dimensional array of small Au<sub>55</sub> nanocrystals (diameter  $\approx$  1.4 nm) on a polymer film (see Fig. 12). At the other end of the size-regime, big Au nanocrystals of 15–90 nm dimensions have also been organized into two-dimensional arrays.<sup>[122]</sup> Arrays of Au–Ag<sup>[62,63]</sup> and Fe–Pt alloy nanocrystals<sup>[61]</sup> have been obtained. Magic nuclearity Pd<sub>561</sub> nanocrystals have been exploited to make Pd–Ni core–shell particles with variable Ni loadings.<sup>[123]</sup> The nanocrystals so obtained possess a core–shell structure, where an Ni layer covers a Pd seed. The magic nuclearity Pd<sub>561</sub> nanocrystals act as high-quality seeds and promote the formation of monodisperse Pd–Ni core–shell nanocrystals. Arrays of Pd<sub>561</sub>Ni<sub>*n*</sub> (*n* upto 10,000 atoms) have been prepared after thiolizing the core–shell nanocrystals as shown in Fig. 13.<sup>[124]</sup> By a simple extension of this technique, arrays of triple layer nanocrystals of the form Pd<sub>561</sub>Ni<sub>3000</sub>Pd<sub>1500</sub> were also obtained. Methods to organize non-spherical metal nanocrystals into two-dimensional arrays have met with very limited success. Thus, hexagonal Pt as well

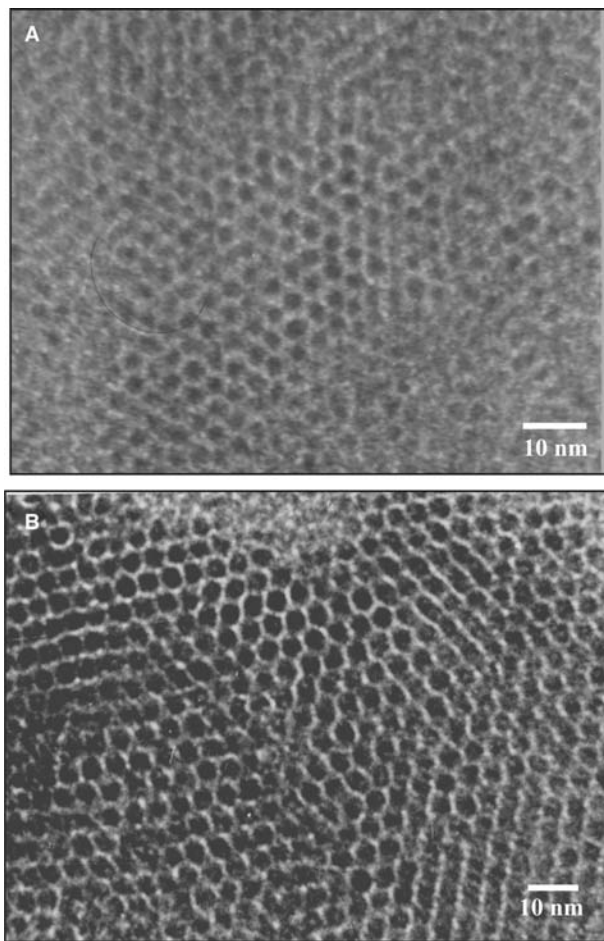


**Fig. 11** TEM micrographs showing hexagonal arrays of thiolized Pd nanocrystals: (A) Pd<sub>561</sub> octanethiol, (B) Pd<sub>1415</sub> octanethiol. Organized arrays of these nanocrystals extend to lengths over several microns.

as elongated silver nanocrystals have been organized into ordered two-dimensional arrays.<sup>[95,125]</sup> Interestingly, ordered two-dimensional lattices containing thiolized spherical Au particles of two different sizes have been reported by Kiely et al. (see Fig. 14),<sup>[115]</sup> who found that the nanocrystals of different radii follow the radius ratio rules formulated for alloying of different metals. Alloy arrays consisting of Au and Ag nanocrystals of different sizes have been made.<sup>[126]</sup>

#### Arrays of semiconductor nanocrystals

Murray, Norris, and Bawendi first made monodisperse CdSe nanocrystals by rapid injection of a tri-*n*-octylphosphine (TOP) solution containing dimethylcadmium and tri-*n*-octylphosphine selenide into a hot solution of TOP and TOP oxide.<sup>[46]</sup> By a simple extension of this technique, CdTe and CdS nanocrystals can also be obtained.<sup>[46]</sup> These nanocrystals could be

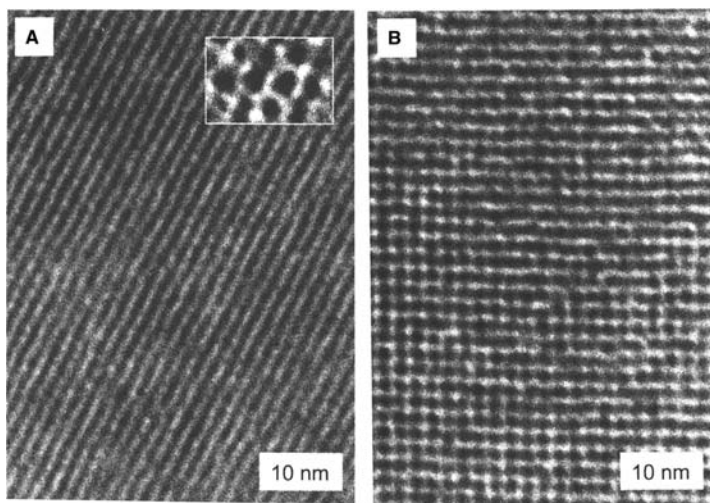


**Fig. 12** TEM images of  $\text{Au}_{55}$  monolayers showing a hexagonal (A) and a cubic (B) structure. The monolayers were prepared on a polyethyleneimine functionalized carbon grid. The magnified inset in (A) shows single clusters in the hexagonal form. Source: Reproduced with permission from Ref.<sup>[136]</sup>.

size-selected to yield monodisperse CdSe nanocrystals.<sup>[127]</sup> Upon drying on a flat substrate, these CdSe nanocrystals assemble into superlattices containing several layers of two-dimensionally ordered nanocrystals. Transmission electron microscopic images showing the different facets of the two-dimensional

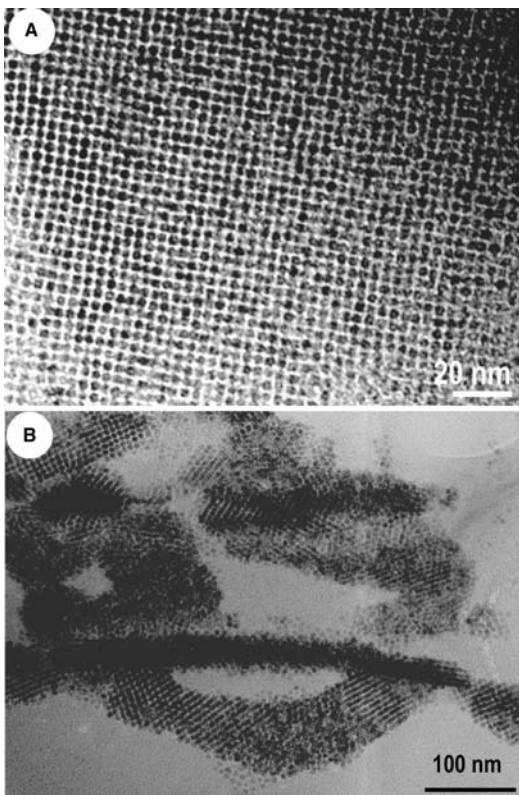


**Fig. 13** TEM image of an ordered array of octanethiol capped (A)  $\text{Pd}_{561}\text{Ni}_{561}$  and (B)  $\text{Pd}_{561}\text{Ni}_{3000}$  nanocrystals. Ni was introduced in the form of its acetate during the reduction process. The nanocrystals were subsequently thiolized.

layers in these superlattices are shown in Fig. 15. Hexanethiol capped PbS nanocrystals, prepared by phase transferring a Pb ion into organic medium using hexanethiol, followed by reaction with  $\text{Na}_2\text{S}$  were also organized into two-dimensional lattices (see Fig. 16).<sup>[128,129]</sup> Motte et al.<sup>[64]</sup> obtained a hexagonally ordered two-dimensional array of  $\text{Ag}_2\text{S}$  nanocrystals synthesized by reverse micelle method. Ordered arrays of InP nanocrystals prepared by the thermolysis method have also been obtained.<sup>[17]</sup>

#### Arrays of oxide nanocrystals

The very first report of two-dimensional arrays was of  $\text{Fe}_3\text{O}_4$  nanocrystals.<sup>[130]</sup> Bentzon et al. observed that the ferrofluid obtained by thermolysis of iron-pentacarbonyl upon drying (over a period of several weeks) yielded well ordered two-dimensional arrays of  $\text{Fe}_3\text{O}_4$  nanocrystals. Since then, easier methods have been devised to obtain arrays of  $\text{Fe}_3\text{O}_4$  nanocrystals.<sup>[131]</sup>

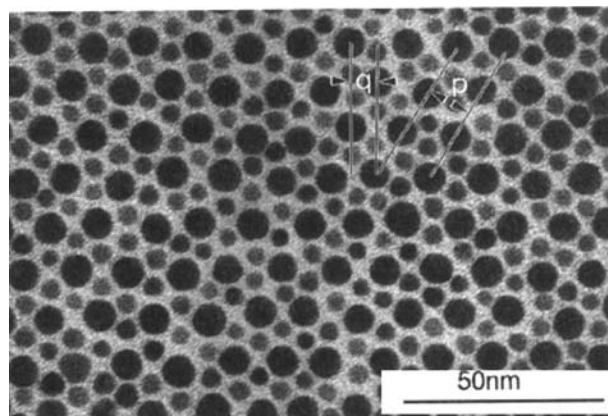


**Fig. 14** A bimodal hexagonal array of Au nanocrystals. The radius ratio of the nanocrystals is 0.58. Source: Reproduced with permission from Ref.<sup>[115]</sup>.



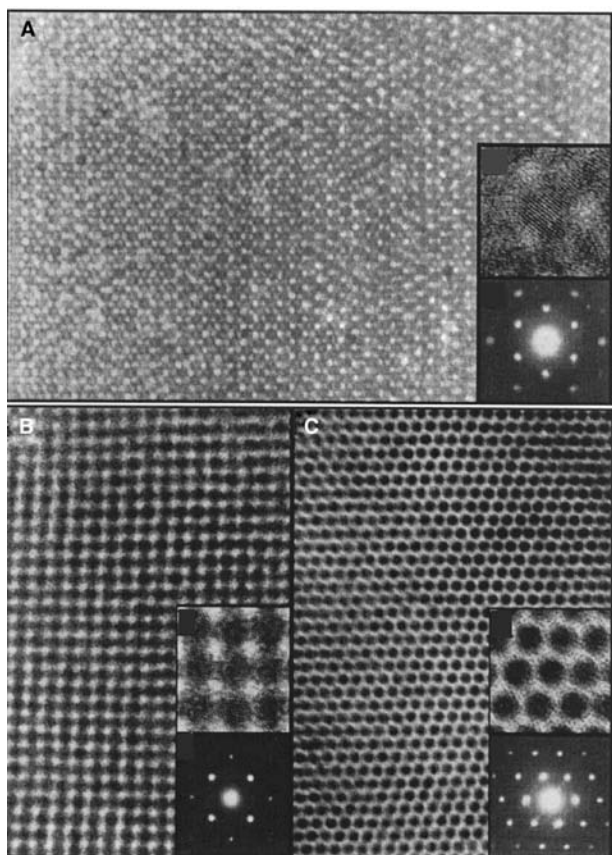


**Fig. 15** Three-dimensional super lattices of 4.8 nm CdSe nanocrystals (A) along  $\langle 100 \rangle$  orientation, (B) along  $\langle 101 \rangle$  orientation, (C) along  $\langle 111 \rangle$  orientation. High-resolution images as well as selected area electron diffraction pattern is shown alongside in each case. *Source:* Reproduced with permission from Ref.<sup>[127]</sup>.

Two-dimensional arrays of amine capped metal oxide nanocrystals such as  $\text{Co}_3\text{O}_4$  have been obtained starting from metal oxide nanocrystals prepared by thermolysis of metal-cupferron complexes.<sup>[132]</sup> In contrast to metal nanocrystals, attempts to organize non-spherical oxide nanocrystals have met with reasonable success. Thus, tetrahedral  $\text{CoO}$  nanocrystals have been organized into extended two-dimensional arrays.<sup>[133]</sup> A rectangular superlattice made of prismatic  $\text{BaCrO}_4$  has been observed.<sup>[134]</sup> More complex arrays such as those consisting of a mixture of nanocrystals of different sizes have been obtained using  $\text{Fe}_3\text{O}_4$  and  $\text{Fe-Pt}$  nanocrystals.<sup>[135]</sup> The mixed arrays were obtained by evaporating a binary mixture of the metal oxide organosols.

#### Other two-dimensional arrangements

It is possible to obtain micrometer-sized rings of monodisperse nanocrystals such as  $\text{Ag}_2\text{S}$ ,  $\text{Ag}$  instead of extended arrays by varying the solvent evaporation

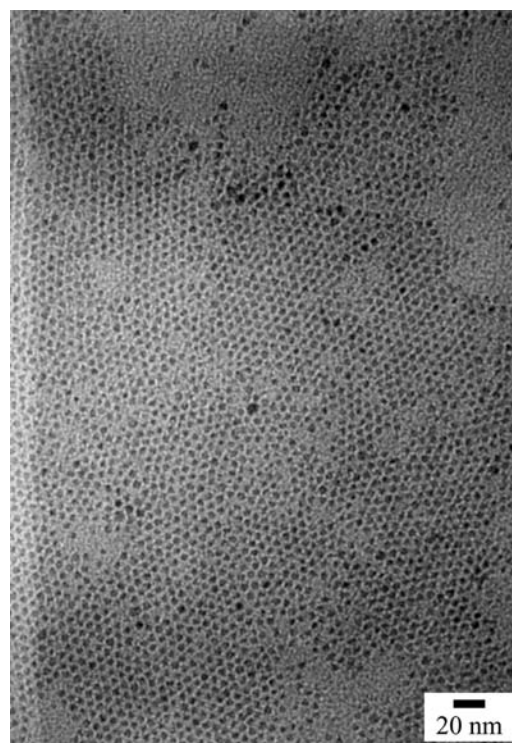


**Fig. 16** TEM micrographs showing hexagonal arrays of hexanethiol capped PbS nanocrystals. *Source:* Unpublished results from our laboratory.

rate and exploiting the resulting fluid instabilities (the marangoni effect) that occurs during evaporation.<sup>[136–140]</sup> Neat Au nanocrystals as well as CdSe–ZnS core-shell nanocrystals of various sizes have been organized into two-dimensional lattices using a protein (chaperonin) template.<sup>[141]</sup>

#### Stability and phase behavior of two-dimensional arrays

The nanocrystal organizations mentioned above are mainly entropy-driven. The two lengths involved, the nanocrystal diameter ( $d$ ) and the ligand chain length ( $l$ ), play an important role in deciding the nature of the organization, i.e., its orderliness. It has been observed experimentally that for a given diameter of the nanocrystal, the packing changes swiftly as the length of the thiol ligand is increased. The stability diagram in terms of  $d$  and  $l$  shown in Fig. 17, which illustrates that extended close-packed organizations of nanocrystals are found for  $d/l$  values  $\sim 2$ . Although entropy-driven, the above cannot be treated as hard sphere organizations. Based on a study of the effect of the solvent polarity on the self-assembly of ligated metal nanocrystals, Korgel et al.<sup>[103,114]</sup> proposed a soft sphere model taking the interparticle interaction into consideration. Accordingly, a ligated nanocrystal



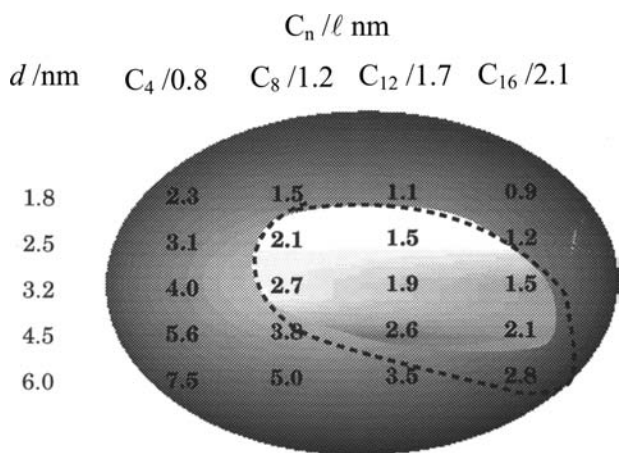


**Fig. 17** The  $d$ - $l$  phase diagram for Pd nanocrystals thiolized with different alkanethiols. The mean diameter,  $d$ , was obtained from the TEM measurements on as-prepared sols. The length of the thiol,  $l$ , is estimated by assuming an all-trans conformation of the alkane chain. The thiol is indicated by the number of carbon atoms,  $C_n$ . The bright area in the middle encompasses systems that form close-packed organizations of nanocrystals. The surrounding darker area includes disordered or low-order arrangements of nanocrystals. The area enclosed by the dashed line is derived from calculations from the soft sphere model. *Source:* Reproduced with permission from Ref.<sup>[116]</sup>.

allows for penetration of the ligand shell up to its hard sphere limit. In this model, the total potential energy,  $E$ , is considered to be a result of two types of forces between the nanocrystals,

$$E = E_{steric} + E_{vdW} \quad (1)$$

$$E_{vdW} = \frac{A}{12} \times \left\{ \frac{d^2}{\tau^2 - d^2} + \frac{d^2}{\tau^2} + 2 \ln \left[ \frac{\tau^2 - d^2}{\tau^2} \right] \right\} \quad (2)$$

$$E_{steric} = \frac{50d/l^2}{(\tau - d)\pi\sigma_a^3} kT e^{-\pi(\tau-d)} \quad (3)$$

The van der Waals interaction due to the polarization of the metal cores constitutes the attractive term, and the steric interaction between the thiol molecules on the two surfaces forms the repulsive term, where  $x$  is the interparticle distance. The Hamaker constant,  $A$ , for Pd nanocrystals, in toluene for instance, has been estimated to be 1.95 eV.<sup>[142]</sup> The calculated diameter of the area occupied by the thiol molecule ( $\sigma_a$ ) on the particle surface is 4.3 Å.<sup>[114]</sup> The total energy is attractive over a range of interparticle distances, the magnitude increasing with fall in distance. There could

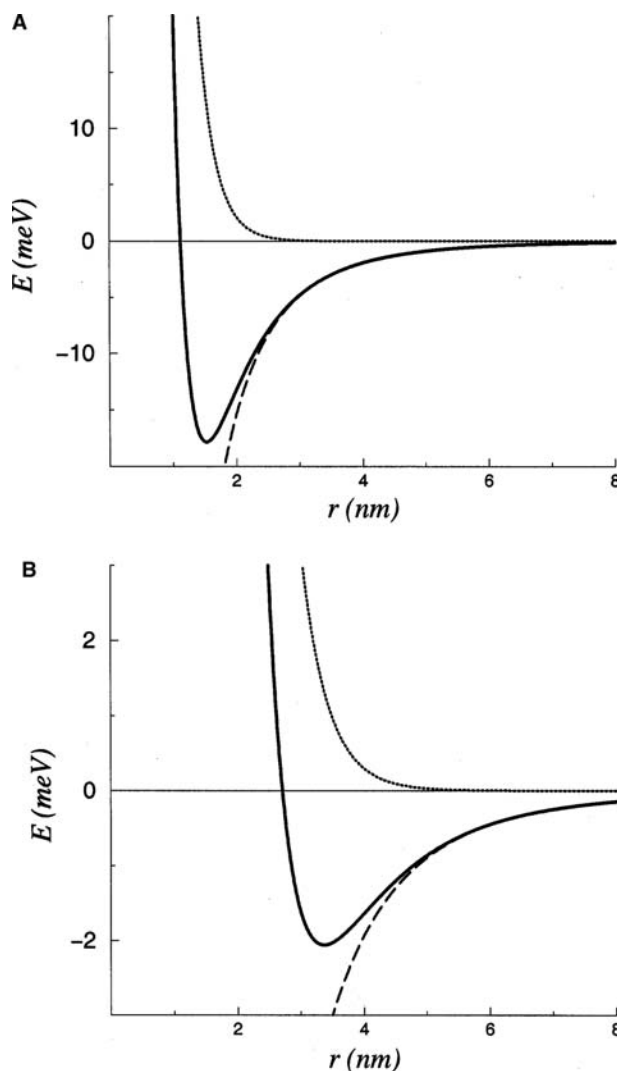


**Fig. 18** Variation of the two components and the total potential energy versus the separation distance between two Pd nanocrystals of 4.5 nm diameter coated with (A) octanethiol (B) dodecanethiol. *Source:* Reproduced with permission from Ref.<sup>[116]</sup>.

be a range of interparticle distances where the attractive energy from the van der Waals term exceeds the repulsive energy owing to the steric factor, giving rise to net stabilization of the two-particle system. This is illustrated in Fig. 18 in the case of 4.5 nm Pd particles. Stabilization energies of 17 and 2 meV are obtained from the calculation for particles coated with octanethiol and dodecanethiol, respectively. When the stabilization energies have moderate values, comparable with the thermal energy of the nanocrystals, ordered organizations can be expected (see the regime shown by dashed line in Fig. 17). If the  $d/l$  and hence the stabilization energy is not favorable, collapsed monolayers of nanocrystals or loosely packed structures are seen. Clearly, the interdigitation of thiol

molecules plays a major role in attributing hardness to the ligated nanocrystal, which in turn decides the nature of the two-dimensional organization. A similar treatment should hold good for other metal and semi-conductor nanocrystals.

### Three-Dimensional Superlattices

Multilayer assemblies using monothiols such as those of CdSe (see Fig. 15) are generally fragile, and are not suited for use in functional devices. One of the means of obtaining robust structures involves multilayer deposition of nanocrystals and has been drawing a great deal of attention over the last few years, since they provide a convenient, low-cost means to prepare ultra-thin films of controlled thicknesses, suited for device applications. In a typical experiment, one end of a monolayer forming bifunctional spacer is tethered to flat substrates such as gold, aluminum, indium tin oxide or glass, leaving the other end free to anchor nanocrystals.<sup>[28,29]</sup> Subsequent layers can be introduced by dipping the substrate sequentially into the respective spacer molecule solution and the nanocrystal dispersion, with intermediate steps involving washing and drying. The formation of the multilayer assembly can be monitored using a variety of spectroscopy and microscopy tools as illustrated in Fig. 19. Thus, employing Au substrates and dithiols as spacers, multilayer assemblies of several nanocrystals such as Au or CdS have been accomplished.<sup>[143]</sup> One such example of layer-by-layer deposition of Pt (5 nm) nanocrystals is shown in Fig. 19. Brust et al.<sup>[144]</sup> have reported the formation of multilayers of Au nanoparticles using dithiols. These workers have confirmed the layer-by-layer deposition of particle arrays by employing UV-Vis spectroscopy and ellipsometry. Multilayers with CdS nanocrystals prepared by the reverse micelle technique and spaced with alkane were made, and measurable photocurrents were generated by these assemblies. Three-dimensional superlattices involving nanocrystals of different metals (e.g. Pt, Au) and of metals and semi-conductors (e.g. Au, CdS) have also been prepared and characterized.<sup>[143]</sup> Such assemblies can be made with polyelectrolytes such as poly(diallyldimethylammonium chloride) (PDDA), polyethyleneimine (PEI),<sup>[145,146]</sup> poly(allylamine hydrochloride) (PAH), polymers such as poly-phenylenevinylene (PPV) as well.<sup>[147,148]</sup> Thus, multilayers such as those of CdTe nanocrystals spaced with PDDA, CdSe spaced with PPV have been prepared.

### Superclusters

It has been proposed that self-similarity in metal nanocrystal organization would manifest in the form of a giant cluster whose shape and size are direct consequences of

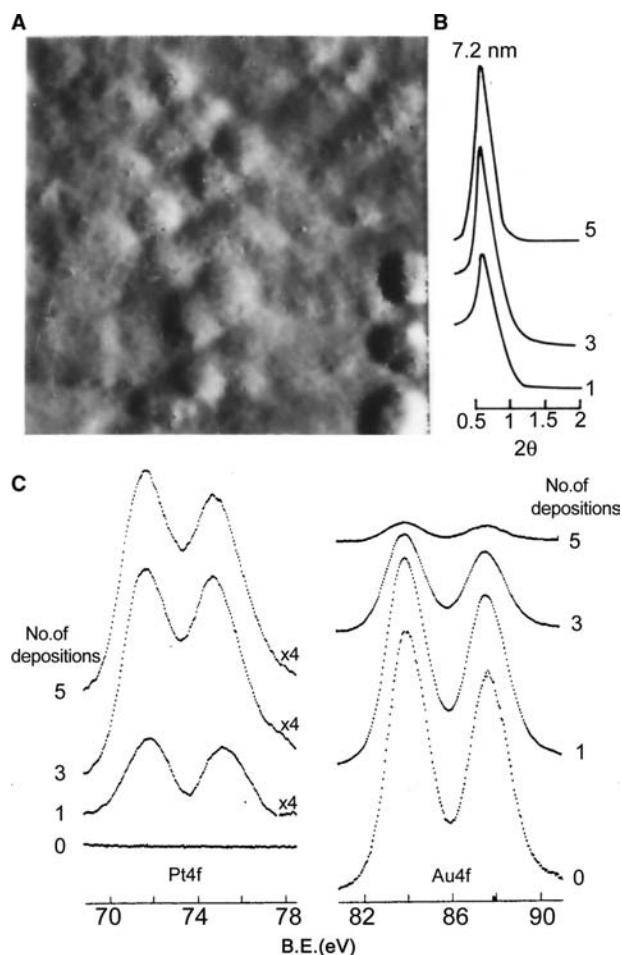


**Fig. 19** Multilayer deposition of Pt (5 nm) nanocrystals on a polycrystalline Au substrate. After each deposition, the structure was characterized by STM, X-ray diffraction as well as by XPS. (A) STM image obtained after the second deposition showing the presence of regular arrays of nanoparticles with an interparticle spacing of 2 nm, extending over 300 nm, corresponding to the size of a typical flat terrace on the substrate, (B) X-ray diffraction pattern of the arrays after the first, third, and fifth depositions exhibiting low-angle reflections with the  $d$ -spacings reflecting the particle diameter and the inter-particle distance. (C) X-ray photoelectron spectra in the Pt(4f) and Au(4f) regions for the 5 nm Pt/Au system. The intensity of the Pt(4f) feature increases with the number of depositions, accompanied by a decrease in the Au(4f) intensity as the substrate gets increasingly shadowed due to the limited escape depth of the photoelectrons.

the nanocrystals themselves.<sup>[149]</sup> The invariance of the shell effects in metal nanocrystals with scaling is shown schematically in Fig. 20. Thus, Pd<sub>561</sub> nanocrystals would be expected to self-aggregate into a giant cluster of the type (Pd<sub>561</sub>)<sub>561</sub> under suitable conditions. The monodisperse nature of the nanocrystals is thought to be important in assisting the self-aggregation process. Formation of such clusters was observed in the mass spectra of magic nuclearity Au<sub>55</sub> nanocrystals. Secondary ion mass

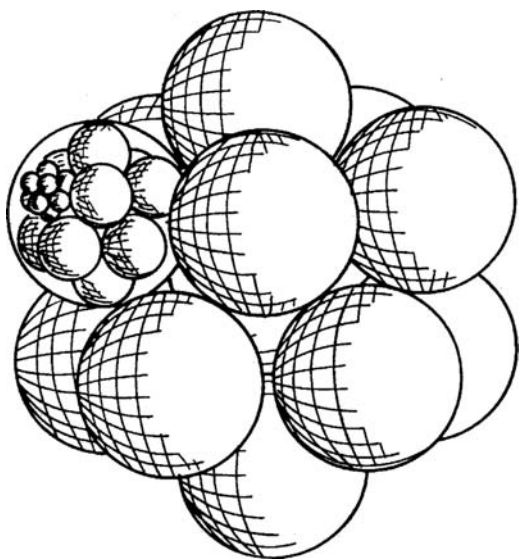


**Fig. 20** Self-similarity: Schematic illustration of the formation of a cluster of metal nanocrystals (supercluster) and a cluster of superclusters. The size effects operating in nanocrystals could be invariant to scaling. *Source:* Reproduced with permission from Ref.<sup>[149]</sup>.

spectrometry indicated the presence of species with large  $m/z$  values and these were attributed to  $(\text{Au}_{13})_{55}$  giant clusters.<sup>[150]</sup> The giant clusters so obtained have, however, not been isolated or imaged. One such observation was made in the case of  $\text{Pd}_{561}$  nanocrystals where the PVP covered nanocrystals aggregated to form giant clusters.<sup>[151]</sup> The TEM image in Fig. 21 is revealing. There are regions where the nanocrystals are densely packed in the form of giant aggregates with estimated nanocrystal nuclearities corresponding to various magic numbers. It is possible that the formation of the giant clusters is facilitated by the polymer shell that encases them. Unlike in case of Pd nanocrystals coated with alkanethiols, which self-assemble to form ordered arrays, the polymer shell effectively magnifies the facets of the metallic core, thereby aiding a giant assembly of the nanocrystals.

### Colloidal Crystals

The tendency of monodisperse nanocrystals to arrange into ordered three-dimensional arrays extending to a few microns has been noticed.<sup>[136]</sup> Careful tuning of crystallization conditions have yielded crystallites of micrometer dimensions consisting of  $\text{Au}_{55}$  nanocrystals and Fe–Pt alloy nanocrystals (4.5 nm) as shown in Fig. 22.<sup>[152,153]</sup> Micron-sized crystals consisting of TOPO capped CdSe nanocrystals have previously been obtained by the groups of Bawendi and Weller.<sup>[127,154]</sup> However, it was observed that the nanocrystal arrangement in all the above crystallites was polymorphous. It is believed that such crystallites, consisting of ordered

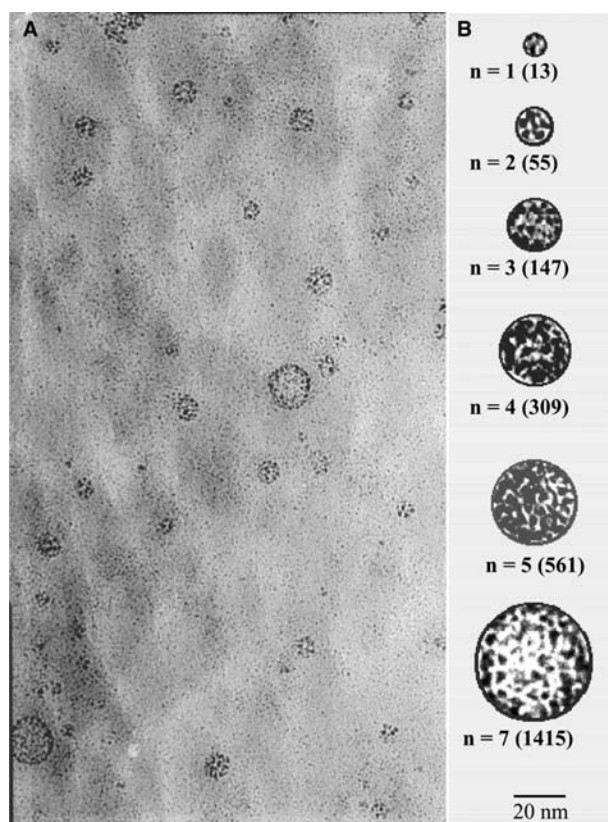


**Fig. 21** TEM micrograph showing the giant clusters comprising  $\text{Pd}_{561}$  nanocrystals. Sample for TEM was prepared by the slow evaporation of a PVP– $\text{Pd}_{561}$  hydrosol. Giant clusters are enclosed in circles whose diameters correspond to magic numbers. The  $n$  and the values in the bracket indicate the number of nanocrystals and closed-shells, respectively.

nanocrystals, could prove to be the best candidates to study the collective properties of an ensemble of nanocrystals.

### Nanocrystal Patterning

Creating patterns of nanocrystals on surfaces has attracted wide attention. Such patterned substrates can act as templates to grow nanowires, etch masks to grow nanopillars and quantum dots.<sup>[155–157]</sup> Other than the layer-by-layer technique mentioned before, simple techniques such as spin coating have been employed to create a nanocrystalline pattern on surfaces.<sup>[158]</sup> In the example shown in Fig. 23, a direct write lithographic technique, dip pen lithography,<sup>[159,160]</sup> which relies on a cantilever used for atomic force microscopy (AFM) to write on a substrate to create patterns of Au nanocrystals on mica substrates. Thus, nanocrystals of metals and semiconductors can be patterned into rectangles of varying aspect ratios.

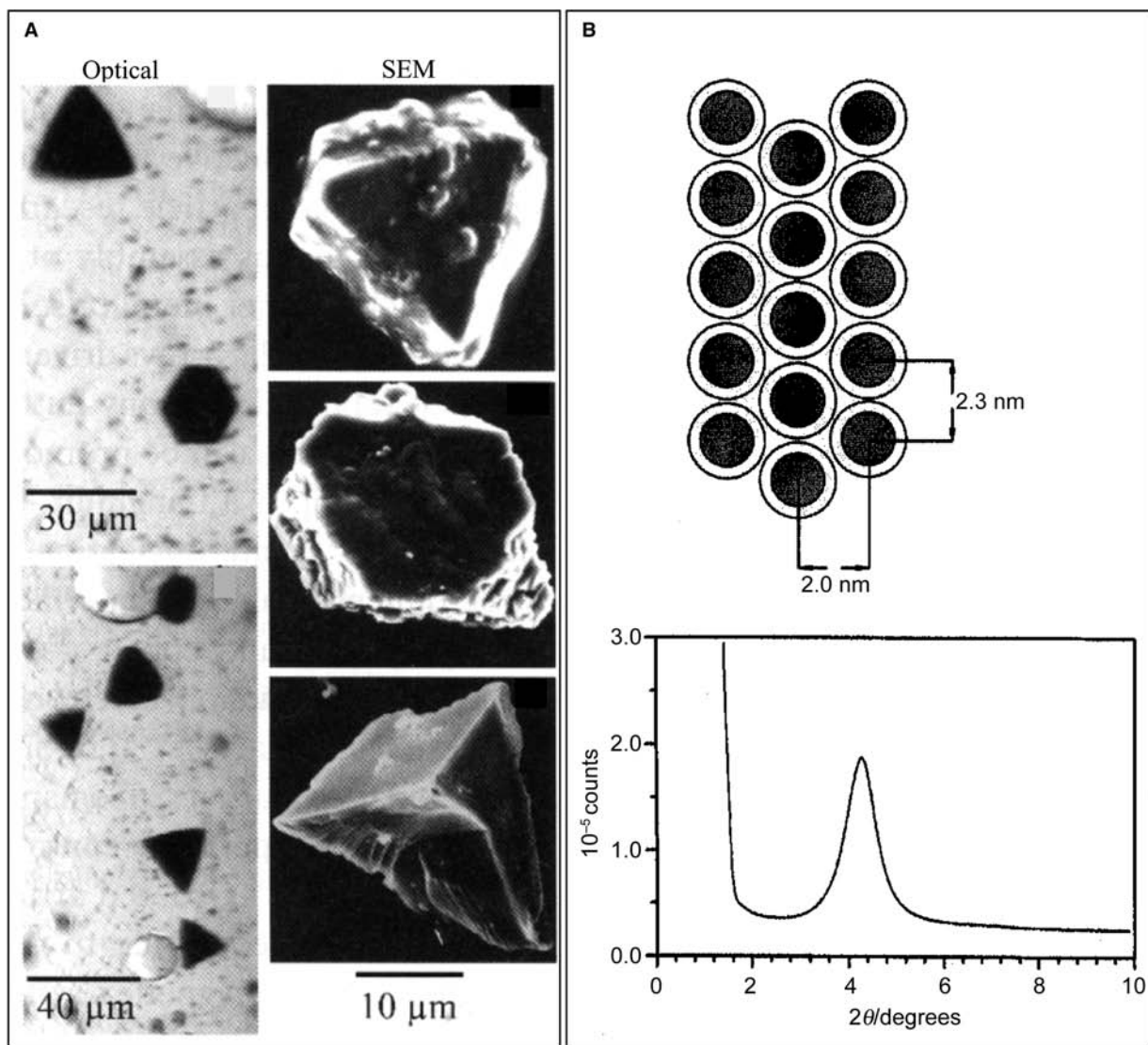


**Fig. 22** Colloidal crystals: (A) from Fe-Pt nanocrystals, (B) Au<sub>55</sub> nanocrystals. A schematic illustration of a Au<sub>55</sub> microcrystal along with the corresponding small angle X-ray diffraction pattern is shown alongside. *Source:* Reproduced with permission from Refs.<sup>[150,151]</sup>

## CONCLUSIONS

Nanocrystals of metal and semiconductors with diameters in the range 1–50 nm form a class of materials with unusual properties that are size-dependent. Excellent electrical conductivity that primarily characterizes a metallic state becomes a rare entity in small nanocrystals (<2 nm) owing to quantum confinement of the electronic states. Similarly, magnetic metals lose much of the coercivity with diminishing size. On the other hand, chemical properties such as reactivity may show up better at smaller sizes owing to more number of surface bonding sites and other electronic effects. Considering the importance of nanocrystals in technological applications, a large number of synthesis methods have evolved in the recent years, which

include reverse micelle and sonochemical methods besides laser ablation. Control over size and shape as well as encasing the nanocrystals with ligands of specialized functionalities have become subjects of urgent inquiry. Semiconductor nanocrystals are being established as practical alternatives to fluorescent dyes. Several exploratory devices whose characteristics are changeable by varying the constituent nanocrystal diameter have been made. While isolated nanocrystals are interesting by themselves, their organizations, of especially those which are capable of self-assembling into well-ordered arrays, have attracted greater attention. Nanocrystals anchored to fragments of DNA or likewise molecules essentially form one-dimensional organizations. When coated with long-chain alkane thiols, nanocrystals exhibit a tendency to assemble into



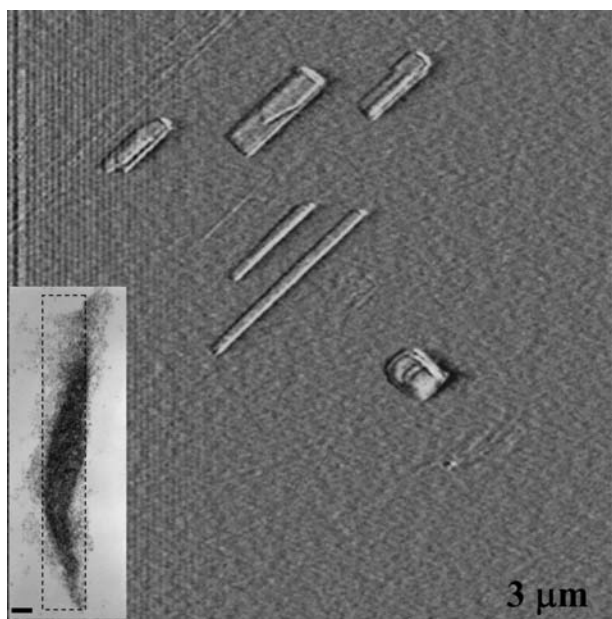


**Fig. 23** Contact AFM scan of a  $9\mu\text{m}^2$  area on mica substrate showing rectangles of various aspect ratios filled with Au nanocrystals. The patterns were obtained by translating an AFM cantilever dipped in a sol across the surface. The inset shows a TEM image of a similar pattern on a holey carbon copper grid, the dotted line bounds the area sought to be filled. The scale bar in the inset corresponds to 50 nm.

hexagonal arrays on flat substrates. The stability of such a two-dimensional organization depends on the diameter of the nanocrystals and the length of the ligand. Multilayers of nanocrystal arrays can also be made in a programmed way by selecting suitable spacer molecules. Patterns of nanocrystals can be tailored on suitable substrates by “dip-pen lithography”, an atomic force microscopy based technique. Another mesoscale aggregation known is the giant clusters of nanocrystals with definite nuclearities. It would be ideal to grow crystals of nanocrystals, but such efforts have met with only a limited success to date, giving micron-sized crystals. Nanocrystal organizations may exhibit properties very different from those of the individual. They are amenable to unprecedented control over the lattice, the size of the nanocrystal and interparticle separation being continuously variable over a range.

## REFERENCES

1. Faraday, M. Experimental relations of gold (and other metals) to light. *Philos. Trans. R. Soc. London* **1857**, *147*, 145.
2. Berry, C.R. Structure and optical absorption of AgI microcrystals. *Phys. Rev.* **1967**, *161*, 848.

3. Brus, L.E. Electron-electron and electron-hole interactions in small semiconductor crystallites: the size dependence of the lowest excited electronic state. *J. Chem. Phys.* **1984**, *80*, 4403.
4. Rao, C.N.R.; Kulkarni, G.U.; Thomas, P.J.; Edwards, P.P. Size-dependent chemistry: properties of nanoparticles. *Chem. Eur. J.* **2002**, *29*, 27.
5. Edwards, P.P.; Johnston, R.L.; Rao, C.N.R. *Metal Clusters in Chemistry*; Braunstein, P., Oro, G., Raithby, P.R., Eds.; Wiley-VCH: Weinheim, 1999.
6. Link, S.; El-Sayed, M.A. Shape and size dependence of radiative, non-radiative and photothermal properties of gold nanocrystals. *Int. Rev. Phys. Chem.* **2001**, *19*, 409.
7. Mulvaney, P. Surface plasmon spectroscopy of nanosized metal particles. *Langmuir* **1996**, *12*, 788.
8. Kamat, P.V. Photophysical, photochemical and photocatalytic aspects of metal nanoparticles. *J. Phys. Chem.* **2002**, *B106*, 7729.
9. Mie, G. Contributions to the optics of turbid media, especially colloidal metal solutions. *Ann. Phys.* **1908**, *25*, 377.
10. Papavassiliou, G.C. Optical properties of small inorganic and inorganic metal particles. *Prog. Solid State Chem.* **1980**, *12*, 185.
11. Gans, R. The form of ultramicroscopic gold particles. *Ann. Phys.* **1912**, *37*, 881.
12. Gans, R. Form of ultramicroscopic particles of silver. *Ann. Phys.* **1915**, *47*, 270.
13. Templeton, A.C.; Pietron, J.J.; Murray, R.W.; Mulvaney, P. Solvent refractive index and core charge influences on the surface plasmon absorbance of alkanethiolate monolayer-protected gold clusters. *J. Phys. Chem. B* **2000**, *104*, 564.
14. Gaponenko, S.V. *Optical Properties of Semiconductor Nanocrystals*; Cambridge University Press: Cambridge, 1998.
15. Vossmeier, T.; Katsikas, L.; Giersig, M.; Popovic, I.G.; Diesner, K.; Chemseddine, A.; Eychmüller, A.; Weller, H. CdS nanoclusters: synthesis, characterization, size-dependent oscillation strength, temperature shift of the electronic transition energy and reversible absorbance shift. *J. Phys. Chem.* **1994**, *98*, 7665.
16. Murray, C.B.; Sun, S.; Gaschler, W.; Doyle, H.; Betley, T.A.; Kagan, C.R. Colloidal synthesis of nanocrystals and nanocrystal superlattices. *IBM J. Res. Dev.* **2001**, *45*, 47.
17. Micic, O.I.; Jones, K.M.; Cahill, A.; Nozik, A.J. Optical, electronic, and structural properties of uncoupled and close-packed arrays of InP quantum dots. *J. Phys. Chem. B* **1998**, *102*, 9791.
18. Brus, L.E. A simple model for the ionization potential, electron affinity, and aqueous redox potentials of small semiconductor crystallites. *J. Chem. Phys.* **1983**, *79*, 5566.
19. Lippens, P.E.; Lannoo, M. Calculation of the band gap for small CdS and ZnS crystallites. *Phys. Rev. B* **1989**, *39*, 10,935.
20. Krishna, M.V.R.; Friesner, R.A. Quantum confinement effects in semiconductor clusters. *J. Chem. Phys.* **1991**, *95*, 8309.

21. Sapra, S.; Shanthi, N.; Sharma, D.D. Realistic tight-binding model for the electronic structure of II-VI semiconductors. *Phys. Rev. B* **2002**, *66*, 205202.
22. Manna, L.; Scher, E.C.; Alivisatos, A.P. Synthesis of soluble and processable rod-, arrow-, teardrop-, and tetrapod-shaped CdSe nanocrystals. *J. Am. Chem. Soc.* **2000**, *122*, 12,700.
23. Trindade, T.; O'Brien, P.; Pickett, N.L. Nanocrystalline semiconductors: synthesis, properties, and perspectives. *Chem. Mater.* **2001**, *13*, 3843.
24. Sutherland, A.J. Quantum dots as luminescent probes in biological systems. *Curr. Opin. Sol. Stat. Mater. Sci.* **2002**, *6*, 365.
25. Bruchez, M., Jr.; Moronne, M.; Gin, P.; Weiss, S.; Alivisatos, A.P. Semiconductor nanocrystals as fluorescent biological labels. *Science* **1998**, *281*, 2013.
26. Peng, X.; Wickham, J.; Alivisatos, A.P. Kinetics of II-VI and III-V colloidal semiconductor nanocrystal growth: Focusing of size distributions. *J. Am. Chem. Soc.* **1998**, *120*, 5343.
27. Service, R.F. Computers: can chip devices keep shrinking? *Science* **1996**, *274*, 1834.
28. Rao, C.N.R.; Kulkarni, G.U.; Thomas, P.J.; Edwards, P.P. Metal nanoparticles and their assemblies. *Chem. Soc. Rev.* **2000**, *29*, 27.
29. Shipway, A.N.; Katz, E.; Willner, I. Nanoparticle arrays on surfaces for electronic, optical, and sensor applications. *Chem. Phys. Chem.* **2000**, *1*, 18.
30. Pileni, M.P. Nanocrystal self-assemblies: fabrication and collective properties. *J. Phys. Chem. B* **2001**, *105*, 3358.
31. Murray, C.B.; Kagan, C.R.; Bawendi, M.G. Synthesis and characterization of monodisperse nanocrystals and close-packed nanocrystal assemblies. *Annu. Rev. Mater. Sci.* **2000**, *30*, 545.
32. Simon, U. Charge transport in nanoparticle arrangements. *Adv. Mater.* **1998**, *10*, 1487.
33. Schmid, G.; Chi, L.F. Metal clusters and colloids. *Adv. Mater.* **1998**, *10*, 515.
34. Schmid, G.; Ed. *Clusters and Colloids: From Theory to Applications*; VCH: Weinheim, 1994.
35. Turkevich, J.; Stevenson, P.C.; Hillier, J. A study of the nucleation and growth processes in the synthesis of colloidal gold. *J. Discuss. Faraday. Soc.* **1951**, *11*, 55.
36. Kirkland, A.I.; Jefferson, D.E.; Duff, D.G.; Edwards, P.P.; Gameson, I.; Johnson, B.F.U.; Smith, D.J. Structural studies of trigonal lamellar particles of gold and silver. *Proc. R. Soc. London A* **1993**, *440*, 589.
37. de Jongh, L.J.; Ed. *Physics and Chemistry of Metal Cluster Compounds*; Kluwer: Dordrecht, 1994.
38. Baldwin, R.K.; Pettigrew, K.A.; Ratai, E.; Augustine, M.P.; Kauzlarich, S.M. Solution reduction synthesis of surface stabilized silicon nanoparticles. *Chem. Commun.* **2002**, 1822.
39. Wilcoxon, J.P.; Samara, G.A.; Provencio, P.N. Optical and electronic properties of Si nanoclusters synthesized in inverse micelles. *Phys. Rev. B* **1999**, *60*, 2704.
40. Koronowski, A.; Giersig, M.; Vogel, M.; Chemseddine, A.; Weller, H. Nanometer sized colloidal germanium particles: wet chemical synthesis, laser induced crystallisation and particle growth. *Adv. Mater.* **1993**, *5*, 634.
41. Rogach, A.L.; Kornowski, A.; Gao, M.; Eychmuller, A.; Weller, H. Synthesis and characterization of a size series of extremely small thiol-stabilized CdSe nanocrystals. *J. Phys. Chem. B* **1999**, *103*, 3065.
42. Herron, N.; Wang, Y.; Eckert, H.S. Synthesis and characterization of surface-capped size-quantized cadmium sulfide clusters. Chemical control of cluster size. *J. Am. Chem. Soc.* **1990**, *112*, 1322.
43. Rossetti, R.; Hull, R.; Gibson, J.M.; Brus, L.E. Excited electronic states and optical spectra of ZnS and CdS crystallites in the 15 to 50 Å size range: evolution from molecular to bulk semiconducting properties. *J. Chem. Phys.* **1985**, *82*, 552.
44. Esteves, A.C.C.; Trindade, T. Synthetic studies on II-VI semiconductor quantum dots. *Curr. Opin. Sol. Stat. Mater. Sci.* **2002**, *6*, 347.
45. Green, M. Solution routes to III-V semiconductor quantum dots. *Curr. Opin. Sol. Stat. Mater. Sci.* **2002**, *6*, 355.
46. Murray, C.B.; Norris, D.J.; Bawendi, M.G. Synthesis and characterization of nearly monodisperse CdE (E = sulfur, selenium, tellurium) semiconductor nanocrystallites. *J. Am. Chem. Soc.* **1993**, *115*, 8706.
47. Cumberland, S.L.; Hanif, K.M.; Javier, A.; Khitrov, G.A.; Strouse, G.F.; Woessner, S.M.; Yun, C.S. Inorganic clusters as single-source precursors for preparation of CdSe, ZnSe, and CdSe/ZnS nanomaterials. *Chem. Mater.* **2002**, *14*, 1576.
48. Gautam, U.K.; Rajamathi, M.; Meldrum, F.; Morgan, P.; Seshadri, R. A solvothermal route to capped CdSe nanoparticles. *Chem. Commun.* **2001**, 629.
49. Guzelian, A.A.; Banin, U.; Kadavanich, A.V.; Peng, X.; Alivisatos, A.P. Colloidal chemical synthesis and characterization of InAs nanocrystal quantum dots. *Appl. Phys. Lett.* **1996**, *69*, 1432.
50. Ahmadi, T.S.; Wang, L.; Henglein, A.; El-Sayed, M.A. Cubic colloidal platinum nanoparticles. *Chem. Mater.* **1996**, *8*, 1161.
51. Pileni, M.P. Reverse micelles as microreactors. *J. Phys. Chem.* **1993**, *97*, 6961.
52. Moriguchi, I.; Shibata, F.; Teraoka, Y.; Kagawa, S. Control of size of CdS formed in organized molecular assembly films by molecular structure and film orderliness. *Chem. Lett.* **1995**, *24*, 761.
53. Platt, M.; Dryfe, R.A.W.; Roberts, E.P.L. Controlled deposition of nanoparticles at the liquid-liquid interface. *Chem. Commun.* **2002**, 2324.
54. Smotkin, E.S.; Lee, C.; Bard, A.J.; Campion, A.; Fox, M.A.; Mallouk, T.E.; Webber, S.I.; White, J.M. Size quantization effects in cadmium sulfide layers formed by a Langmuir-Blodgett technique. *Chem. Phys. Lett.* **1998**, *152*, 265.
55. Rao, C.N.R.; Kulkarni, G.U.; Thomas, P.J.; Agrawal, V.V.; Saravanan, P. Films of metal nanocrystals



- formed at aqueous-organic interfaces. *J. Phys. Chem. B* **2003**, *107*, 7391.
56. Rao, C.N.R.; Kulkarni, G.U.; Thomas, P.J.; Agrawal, V.V.; Gautam, U.K.; Ghosh, M. Nanocrystals of metals, semiconductors and oxides: novel synthesis and applications. *Curr. Sci.* **2003**, *85*, 1041.
  57. Sattler, K.; Mhlback, J.; Recknagel, E. Generation of metal clusters containing from 2 to 500 atoms. *Phys. Rev. Lett.* **1980**, *45*, 821.
  58. Milani, P.; Iannotta, S. *Cluster Beam Synthesis of Nanostructured Materials*; Springer: Berlin, 1999.
  59. Harfenist, S.A.; Wang, Z.L.; Whetten, R.L.; Vezmar, I.; Alvarez, M.M. Three-dimensional hexagonal close-packed superlattice of passivated silver nanocrystals. *Adv. Mater.* **1997**, *9*, 817.
  60. Vasan, H.N.; Rao, C.N.R. Nanoscale Ag-Pd and Cu-Pd alloys. *J. Mater. Chem.* **1995**, *5*, 1755.
  61. Sun, S.; Murray, C.B.; Weller, D.; Folks, L.; Maser, A. Monodisperse FePt nanoparticles and ferromagnetic FePt nanocrystal superlattices. *Science* **2000**, *287*, 1989.
  62. Sandhyarani, N.; Reshmi, M.R.; Unnikrishnan, R.; Vidyasagar, K.; Ma, S.; Antony, M.P.; Selvam, G.P.; Visalakshi, V.; Chandrakumar, N.; Pandian, K.; Tao, Y.T.; Pradeep, T. Monolayer-protected cluster superlattices: structural, spectroscopic, calorimetric, and conductivity studies. *Chem. Mater.* **2000**, *12*, 104.
  63. He, S.T.; Xie, S.S.; Yao, J.N.; Gao, H.J.; Pang, S.J. Self-assembled two-dimensional superlattice of AuAg alloy nanocrystals. *Appl. Phys. Lett.* **2002**, *81*, 150.
  64. Fendler, J.H.; Ed. *Nanoparticles and Nanostructured Films*; Wiley-VCH: Weinheim, 1998.
  65. Mikulec, F.V.; Kuno, M.; Bennati, M.; Hall, D.A.; Griffin, R.; Bawendi, M.G. Organometallic synthesis and spectroscopic characterization of manganese-doped CdSe nanocrystals. *J. Am. Chem. Soc.* **2000**, *122*, 2532.
  66. Chen, Y.H.; Yeh, C.S. A new approach for the formation of alloy nanoparticles: laser synthesis of gold-silver alloy from gold-silver colloidal mixtures. *Chem. Commun.* **2001**, 371.
  67. Abid, J.P.; Girault, H.H.; Brevet, P.F. Selective structure changes of core-shell gold-silver nanoparticles by laser irradiation: homogenisation vs. silver removal. *Chem. Commun.* **2001**, 829.
  68. Herron, N.; Calabrese, J.C.; Farneth, W.E.; Wang, Y. Crystal structure and optical properties of  $\text{Cd}_{32}\text{S}_{14}(\text{SC}_6\text{H}_5)_{36}\text{DMF}_4$ , a cluster with a 15 angstrom CdS core. *Science* **1993**, *259*, 1426.
  69. Zhu, N.; Fenske, D. Novel Cu-Se clusters with Se-layer structures:  $[\text{Cu}_{32}\text{Se}_7(\text{SenBu})_{18}(\text{PiPr}_3)_6]$ ,  $[\text{Cu}_{50}\text{Se}_{20}(\text{SetBu})_{10}(\text{PiPr}_3)_{10}]$ ,  $[\text{Cu}_{73}\text{Se}_{35}(\text{SePh})_3(\text{PiPr}_3)_{21}]$ ,  $[\text{Cu}_{140}\text{Se}_{70}(\text{PEt}_3)_{34}]$  and  $[\text{Cu}_{140}\text{Se}_{70}(\text{PEt}_3)_{36}]$ . *J. Chem. Soc. Dalton Trans.* **1999**, 1067.
  70. Bettenhausen, M.; Eichhofer, A.; Fenske, D.; Semmelmann, M. Synthese und Strukturen neuer selenidound selenolatoverbrckter Kupfercluster:  $[\text{Cu}_{38}\text{Se}_{13}(\text{SePh})_{12}(\text{dppb})_6]$  (1),  $[\text{Cu}(\text{dppp})_2][\text{Cu}_{25}\text{Se}_4(\text{SePh})_{18}(\text{dppp})_2]$  (2),  $[\text{Cu}_{36}\text{Se}_5(\text{SePh})_{26}(\text{dppa})_4]$  (3),  $[\text{Cu}_{58}\text{Se}_{16}(\text{SePh})_{24}(\text{dppa})_6]$  (4) und  $[\text{Cu}_3(\text{SeMes})_3(\text{dppm})]$  (5). *Z. Anorg. Allg. Chem.* **1999**, *625*, 593.
  71. Vossmeier, T.; Reck, G.; Katsikas, L.; Haupt, E.T.K.; Schulz, B.; Weller, H. A double-diamond-superlattice built up of  $\text{Cd}_{17}\text{S}_4(\text{SR})_{26}$  Clusters. *Science* **1995**, *267*, 1476.
  72. Beherens, S.; Bettenhausen, M.; Deveson, A.C.; Eichhofer, A.; Fenske, D.; Lohde, A.; Woggon, U. Synthesis and structure of the nanoclusters  $[\text{Hg}_{32}\text{Se}_{14}(\text{SePh})_{36}]$ ,  $[\text{Cd}_{32}\text{Se}_{14}(\text{SePh})_{36}(\text{PPh}_3)_4]$ ,  $[\text{P}(\text{Et})_2(\text{Ph})\text{C}_4\text{H}_8\text{O}\text{SiMe}_3]^5[\text{Cd}_{18}\text{I}_{17}(\text{PSiMe}_3)_{12}]$ , and  $[\text{N}(\text{Et})_3\text{C}_4\text{H}_8\text{O}\text{SiMe}_3]_5[\text{Cd}_{18}\text{I}_{17}(\text{PSiMe}_3)_{12}]$ . *Angew. Chem. Int. Ed.* **1996**, *35*, 221.
  73. Schmid, G. Hexachlorododecakis (Triphenylphosphine) pentapentacon-taGold  $\text{Au}_{55}[\text{P}(\text{C}_6\text{H}_5)_3]_{12}\text{Cl}_6$ . *Inorg. Synth.* **1990**, *7*, 214.
  74. Vargaftik, M.N.; Zagorodnikov, V.P.; Stolyarov, I.P.; Moiseev, I.I.; Likholobov, V.A.; Kochubey, D.I.; Chuvili, A.L.; Zaikovskiy, V.I.; Zamaraev, K.I.; Timofeeva, G.I. A novel giant palladium cluster. *Chem. Commun.* **1985**, 937.
  75. Boyen, H.G.; Kastle, G.; Weigl, F.; Koslowski, B.; Dietrich, C.; Ziemann, P.; Spatz, J.P.; Riethmuller, S.; Hartmann, C.; Moller, M.; Schmid, G.; Garnier, M.G.; Oelhafen, P. Oxidation-resistant gold-55 clusters. *Science* **2002**, *297*, 1533.
  76. Martin, T.P.; Bergmann, T.; Ghlich, H.; Lange, T. Shell structure of clusters. *J. Phys. Chem.* **1991**, *95*, 6421.
  77. Teranishi, T.; Miyake, M. Size control of palladium nanoparticles and their crystal structures. *Chem. Mater.* **1998**, *10*, 594.
  78. Teranishi, T.; Hori, H.; Miyake, M. ESR study on palladium nanoparticles. *J. Phys. Chem. B* **1997**, *101*, 5774.
  79. Link, S.; Mohamed, M.B.; El-Sayed, M.A. Simulation of the optical absorption spectra of gold nanorods as a function of their aspect ratio and the effect of the medium dielectric constant. *J. Phys. Chem. B* **1999**, *103*, 3073.
  80. Peng, X.; Manna, L.; Yang, W.; Wickham, J.; Scher, E.; Kadavanich, A.; Alivisatos, A.P. Shape control of CdSe nanocrystals. *Nature* **2000**, *404*, 59.
  81. Pinna, N.; Weiss, K.; Sach-Kongehl, H.; Vogel, W.; Urban, J.; Pileni, M.P. Triangular CdS nanocrystals: synthesis, characterization, and stability. *Langmuir* **2001**, *17*, 7982.
  82. Baldwin, R.K.; Pettigrew, K.A.; Garino, J.C.; Power, P.P.; Liu, G.; Kauzlarich, S.M. Room temperature solution synthesis of alkyl-capped tetrahedral shaped silicon nanocrystals. *J. Am. Chem. Soc.* **2002**, *124*, 1150.
  83. Liu, Y.; Zhan, J.; Ren, M.; Tang, K.; Yu, W.; Qian, Y. Hydrothermal synthesis of square thin flake CdS by using surfactants and thiocarbohydrate. *Mater. Res. Bull.* **2001**, *36*, 1231.
  84. Ingert, D.; Pileni, M.P. Limitations in producing nanocrystals using reverse micelles as nanoreactors. *Adv. Mater.* **2001**, *11*, 136.
  85. Zhang, P.; Sham, T.K. Tuning the electronic behavior of Au nanoparticles with capping molecules. *Appl. Phys. Lett.* **2002**, *81*, 736.

86. Niemeyer, C.M. Nanoparticles, proteins, and nucleic acids: biotechnology meets materials science. *Angew. Chem. Int. Ed.* **2001**, *40*, 4128.
87. Chechik, V.; Crooks, R.M. Dendrimer-encapsulated Pd nanoparticles as fluoros phase-soluble catalysts. *J. Am. Chem. Soc.* **2000**, *122*, 1243.
88. Mulvaney, P.; Liz-Marzan, L.M.; Giersig, M.; Long, T. Silica encapsulation of quantum dots and metal clusters. *J. Mater. Chem.* **2002**, *10*, 1259.
89. Lin, J.; Zhou, W.; Kumbhar, A.; Wiemann, J.; Fang, J.; Carpenter, E.E.; O'Connor, C.J. Gold-coated iron (Fe@Au) nanoparticles: synthesis, characterization, and magnetic field-induced self-assembly. *J. Solid. State. Chem.* **2001**, *159*, 26.
90. Fojtik, A.; Henglein, A. Luminescent colloidal silicon particles. *Chem. Phys. Lett.* **1994**, *221*, 363.
91. Kortan, A.R.; Hull, R.; Ophila, R.L.; Bawendi, M.G.; Steigerwald, M.L.; Carroll, P.J.; Brus, L.E. Nucleation and growth of cadmium selenide on zinc sulfide quantum crystallite seeds, and vice versa, in inverse micelle media. *J. Am. Chem. Soc.* **1990**, *112*, 1327.
92. Kershaw, S.V.; Burt, M.; Harrison, M.; Rogach, A.; Weller, H.; Eychmüller, A. Colloidal CdTe/HgTe quantum dots with high photoluminescence quantum efficiency at room temperature. *Appl. Phys. Lett.* **1999**, *75*, 1694.
93. Peng, X.; Schlamp, M.C.; Kadavanich, A.V.; Alivisatos, A.P. Epitaxial growth of highly luminescent CdSe/CdS core/shell nanocrystals with photo-stability and electronic accessibility. *J. Am. Chem. Soc.* **1997**, *119*, 7019.
94. Harai, H.; Aizawa, H.; Shiozaki, H. Preparation of nonaqueous dispersion of colloidal silver by phase transfer. *Chem. Lett.* **1992**, *8*, 1527.
95. Sarathy, K.V.; Raina, G.; Yadav, R.T.; Kulkarni, G.U.; Rao, C.N.R. Thiol-derivatized nanocrystalline arrays of gold, silver and platinum. *J. Phys. Chem. B* **1998**, *101*, 9876.
96. Sarathy, K.V.; Kulkarni, G.U.; Rao, C.N.R. A novel method of preparing thiol derivatised nanoparticles of gold, platinum and silver forming superlattices. *Chem. Commun.* **1997**, 537.
97. Gittins, D.I.; Caruso, F. Spontaneous phase transfer of nanoparticulate metals from organic to aqueous media. *Angew. Chem. Int. Ed.* **2001**, *40*, 3001.
98. Brown, L.O.; Hutchison, J.E. Controlled growth of gold nanoparticles during ligand exchange. *J. Am. Chem. Soc.* **1999**, *121*, 882.
99. Kumar, A.; Mandale, A.B.; Sastry, M. Phase transfer of aqueous CdS nanoparticles by coordination with octadecanethiol molecules present in non-polar organic solvents. *Langmuir* **2000**, *16*, 9299.
100. Terfort, A.; Bowden, N.; Whitesides, G.M. Three-dimensional self-assembly of millimetre-scale components. *Nature* **1997**, *386*, 162.
101. Mirkin, C.A.; Letsinger, R.L.; Mucic, R.C.; Storhoff, J.F. A DNA-based method for rationally assembling nanoparticles into macroscopic materials. *Nature* **1996**, *382*, 607.
102. Collier, C.P.; Vossmeier, T.; Heath, J.R. Nanocrystal superlattices. *Annu. Rev. Phys. Chem.* **1998**, *49*, 371.
103. Korgel, B.A.; Fitzmaurice, D. Condensation of ordered nanocrystal thin films. *Phys. Rev. Lett.* **1998**, *80*, 3531.
104. Hornayak, G.L.; Krill, M.; Pugin, R.; Sawitowski, T.; Schmid, G.; Bovin, J.O.; Karrson, G.; Hofmeister, H.; Hopfe, S. Gold clusters and colloids in alumina nanotubes. *Eur. J. Chem.* **1997**, *3*, 1951.
105. Alivisatos, A.P.; Johnsson, K.P.; Peng, X.; Wilson, T.E.; Loweth, C.J.; Burchez, M.P., Jr.; Schultz, P.G. Organization of nanocrystal molecules using DNA. *Nature* **1996**, *382*, 609.
106. Kumar, A.; Pattarkine, M.; Bhadbhade, M.; Mandale, A.B.; Ganesh, K.N.; Datar, S.S.; Dharmadhikari, C.V.; Sastry, M. Linear superclusters of colloidal gold particles by electrostatic assembly on dna templates. *Adv. Mater.* **2001**, *13*, 341.
107. Mitov, M.; Portet, C.; Bourgerette, C.; Snoeck, E.; Verelst, M. Long-range structuring of nanoparticles by mimicry of a cholesteric liquid crystal. *Nature Mater.* **2002**, *1*, 229.
108. Lee, S.W.; Mao, C.; Flynn, C.E.; Belchar, A.M. Ordering of quantum dots using genetically engineered viruses. *Science* **2002**, *296*, 892.
109. Chung, S.W.; Markovich, G.; Heath, J.R. Fabrication and alignment of wires in two dimensions. *J. Phys. Chem. B* **1998**, *102*, 6685.
110. Dujardin, E.; Peet, C.; Stubbs, G.; Culver, J.N.; Mann, S. Organization of metallic nanoparticles using tobacco mosaic virus templates. *Nano Lett.* **2003**, *3*, 413.
111. Brust, M.; Walker, M.; Bethell, D.; Schiffrin, J.D.; Whyman, R. Synthesis of thiol-derivatized gold nanoparticles in a 2-phase liquid-liquid system. *Chem. Commun.* **1994**, 801.
112. Sandhyarani, N.; Pradeep, T. Crystalline solids of alloy clusters. *Chem. Mater.* **2000**, *12*, 1755.
113. Whetten, R.L.; Khoury, J.T.; Alvarez, M.M.; Murthy, S.; Vezmar, I.; Wang, Z.; Stephens, P.W.; Cleveland, C.H.L.; Luedtke, W.D.; Landman, U. Nanocrystal gold molecules. *Adv. Mater.* **1996**, *8*, 428.
114. Korgel, B.A.; Fullam, S.; Connolly, S.; Fitzmaurice, D. Assembly and self-organization of silver nanocrystal superlattices: ordered soft spheres. *J. Phys. Chem. B* **1998**, *102*, 8379.
115. Kiely, C.J.; Fink, J.; Brust, M.; Bethell, D.; Schiffrin, D.J. Spontaneous ordering of bimodal ensembles of nanoscopic gold clusters. *Nature* **1998**, *396*, 444.
116. Thomas, P.J.; Kulkarni, G.U.; Rao, C.N.R. *J. Phys. Chem. B* **2000**, *104*, 8138.
117. Sun, S.; Murray, C.B. Synthesis of monodisperse cobalt nanocrystals and their assembly into magnetic superlattices. *J. Appl. Phys.* **1999**, *85*, 4325.
118. Petit, C.; Taleb, A.; Pileni, M.P. Cobalt nanosized particles organized in a 2d superlattice: synthesis, characterization, and magnetic properties. *J. Phys. Chem. B* **1999**, *103*, 1805.

119. Pileni, M.P. Optical properties of nanosized particles dispersed in colloidal solutions or arranged in 2D or 3D superlattices. *New. J. Chem.* **1998**, 693.
120. Abe, K.; Hanada, T.; Yoshida, Y.; Tanigaki, N.; Takiguchi, H.; Nagasawa, H.; Nakamoto, M.; Yamaguchi, T.; Yase, K. Two-dimensional array of silver nanoparticles. *Thin Solid Films* **1998**, 327–329, 524.
121. Schmid, G.; Baumle, M.; Beyer, N. Ordered two-dimensional monolayers of Au<sub>55</sub> clusters. *Angew. Chem. Int. Ed.* **2000**, 39, 181.
122. Kim, B.; Tripp, S.L.; Wei, A. Self-organization of large gold nanoparticle arrays. *J. Am. Chem. Soc.* **2001**, 123, 7955.
123. Teranishi, T.; Miyake, M. Novel synthesis of monodispersed Pd/Ni nanoparticles. *Chem. Mater.* **1999**, 11, 3414.
124. Thomas, P.J.; Kulkarni, G.U.; Rao, C.N.R. Mesoscopic assembly of magnetic Pd-Ni nanocrystals into ordered arrays by using alkane thiols. *J. Nanosci. Nanotechnol.* **2001**, 1, 267.
125. Korgel, B.A.; Fitzmaurice, D. Self-assembly of silver nanocrystals into two-dimensional nanowire arrays. *Adv. Mater.* **1998**, 10, 661.
126. Kiely, C.J.; Fink, J.; Zheng, J.G.; Brust, M.; Bethell, D.; Schiffrin, D.J. Ordered colloidal nanoalloys. *Adv. Mater.* **2000**, 12, 640.
127. Murray, C.B.; Kagan, C.R.; Bawendi, M.G. Self-organization of CdSe nanocrystallites into three-dimensional quantum dot superlattices. *Science* **1995**, 270, 1335.
128. Chen, S.; Truax, L.A.; Sommers, J.M. Alkanethiolate-protected PbS nanoclusters: synthesis, spectroscopic and electrochemical studies. *Chem. Mater.* **2002**, 12, 3864.
129. Unpublished results from our laboratory.
130. Bentzon, M.D.; van Wousterghem, J.; Morup, S.; Tholen, A.; Koch, C.J.W. Ordered aggregates of ultra-fine iron oxide particles-supercrystals. *Phil. Mag. B* **1989**, 60, 169.
131. Sun, S.; Zeng, H. Size-controlled synthesis of magnetite nanoparticles. *J. Am. Chem. Soc.* **2002**, 124, 8204.
132. Thomas, P.J.; Saravanan, P.; Kulkarni, G.U.; Rao, C.N.R. Arrays of magnetic nanoparticles capped with alkylamines. *Pramana* **2002**, 58, 371.
133. Yin, J.S.; Wang, Z.L. Ordered self-assembling of tetrahedral oxide nanocrystals. *Phys. Rev. Lett.* **1997**, 79, 2570.
134. Li, M.; Schnablegger, H.; Mann, S. Coupled synthesis and self-assembly of nanoparticles to give structures with controlled organization. *Nature* **1999**, 402, 393.
135. Zheng, H.; Li, J.; Llu, J.P.; Whang, Z.L.; Sun, S. Exchange-coupled nanocomposite magnets by nanoparticle self-assembly. *Nature* **2002**, 420, 395.
136. Maillard, M.; Motte, L.; Ngo, A.T.; Pileni, M.P. Rings and hexagons made of nanocrystals: a marangoni effect. *J. Phys. Chem. B* **2000**, 104, 11,871.
137. Maillard, M.; Motte, L.; Pileni, M.P. Rings and hexagons made of nanocrystals. *Adv. Mater.* **2001**, 16, 200.
138. Ohara, P.C.; Gelbart, W.M. Interplay between hole instability and nanoparticle array formation in ultrathin liquid films. *Langmuir* **1998**, 14, 3418.
139. Vossmeier, T.; Chung, S.W.; Gelbart, W.M.; Heath, J.R. Surprising superstructures: rings. *Adv. Mater.* **1998**, 10, 351.
140. Stowell, C.; Korgel, B.A. Self-assembled honeycomb networks of gold nanocrystals. *Nano Lett.* **2001**, 1, 595.
141. Mcmillan, R.A.; Paavola, C.D.; Howard, J.; Chan, S.L.; Zaluzec, N.J.; Trent, J.D. Ordered nanoparticle arrays formed on engineered chaperonin protein templates. *Nature Mater.* **2002**, 1, 247.
142. Bargeman, D.; Vader, F.V.V. Van der Waals forces between immersed particles. *J. Electroanal. Chem.* **1972**, 37, 45.
143. Sarathy, K.V.; Thomas, P.J.; Kulkarni, G.U.; Rao, C.N.R. Superlattices of metal and metal semiconductor quantum dots obtained by layer-by-layer deposition of nanoparticle arrays. *J. Phys. Chem. B* **1999**, 103, 399.
144. Brust, M.; Bethell, D.; Kiely, C.J.; Schiffrin, D.J. Self-assembled gold nanoparticle thin films with nonmetallic optical and electronic properties. *Langmuir* **1998**, 14, 5425.
145. Blonder, R.; Sheeney, L.; Willner, I. Three-dimensional redox-active layered composites of Au-Au, Ag-Ag and Au-Ag colloids. *Chem. Commun.* **1998**, 1393.
146. Liu, Y.; Wany, Y.; Claus, R.O. Layer-by-layer ionic self-assembly of Au colloids into multilayer thin-films with bulk metal conductivity. *Chem. Phys. Lett.* **1998**, 298, 315.
147. Samokhvalov, A.; Berfeld, M.; Lahav, M.; Naaman, R.; Rabani, E. Assemblies of CdS quantum particles studied by the attenuated low energy photoelectron spectroscopy. *J. Phys. Chem. B* **2000**, 104, 8631.
148. Gao, M.; Richter, B.; Kirstein, S. White-Light electroluminescence from self-assembled Q-CdSe/PPV multilayer structures. *Adv. Mater.* **1997**, 9, 802.
149. Fritsche, H.G.; Muller, H.; Fehrensens, B. Formation of superclusters from metallic clusters. *Z. Phys. Chem.* **1997**, 199, 87.
150. Feld, H.; Leute, A.; Rading, D.; Benninghoven, A.; Schmid, G. Formation of very large gold superclusters (clusters of clusters) as secondary ions up to (Au<sub>13</sub>)<sub>55</sub> by SIMS. *J. Am. Chem. Soc.* **1990**, 112, 8166.
151. Thomas, P.J.; Kulkarni, G.U.; Rao, C.N.R. Magic nuclearity giant clusters of metal nanocrystals formed by mesoscale self-assembly. *J. Phys. Chem. B* **2001**, 105, 2515.
152. Schmid, G.; Pugin, R.; Sawitowski, T.; Simon, U.; Marler, B. Transmission electron microscopic and small angle X-ray diffraction investigations of Au<sub>55</sub>(PPh<sub>3</sub>)<sub>12</sub>Cl<sub>6</sub> microcrystals. *Chem. Commun.* **1999**, 1303.
153. Shevchenko, E.; Talapin, D.; Kornowski, A.; Wiekhorst, F.; Kötzer, J.; Haase, M.; Rogach, A.; Weller, H. Colloidal crystals of monodisperse FePt nanoparticles grown by a three-layer technique of controlled oversaturation. *Adv. Mater.* **2002**, 14, 287.

154. Talapin, D.V.; Shevchenko, E.V.; Kornowski, A.; Gaponik, N.; Haase, M.; Rogach, A.L.; Weller, H. A new approach to crystallization of CdSe nanoparticles into ordered three-dimensional superlattices. *Adv. Mater.* **2001**, *13*, 1868.
155. Ago, H.; Komatsu, T.; Ohshima, S.; Kuriki, Y.; Yumura, M. Dispersion of metal nanoparticles for aligned carbon nanotube arrays. *Appl. Phys. Lett.* **2000**, *77*, 79.
156. Cui, Y.; Lauhon, L.J.; Gudixsen, M.S.; Wang, J.; Lieber, C.M. Diameter-controlled synthesis of single-crystal silicon nanowires. *Appl. Phys. Lett.* **2001**, *78*, 2214.
157. Lewis, P.A.; Ahamed, H.; Sato, T. Silicon nanopillars formed with gold colloidal particle masking. *J. Vac. Sci. Technol. B* **1998**, *16*, 2938.
158. Hong, Y.K.; Kim, H.; Lee, G.; Kim, W.; Park, J.; Cheon, J.; Koo, J.Y. Controlled two-dimensional distribution of nanoparticles by spin-coating method. *Appl. Phys. Lett.* **2002**, *80*, 844.
159. Piner, R.D.; Zhu, J.; Xu, F.; Hong, S.; Mirkin, C.A. Dip-pen nanolithography. *Science* **1999**, *283*, 661.
160. Mirkin, C.A.; Hong, S.; Demers, L. Dippen nanolithography: controlling surface architecture on the sub-100 nanometer length scale. *Chem. Phys. Chem.* **2001**, *2*, 37.

# Nanodiamonds

**Jean-Yves Raty**

*Charge de Recherches du FNRS, University of Liège, Sart-Tilman, Belgium*

**Giulia Galli**

*Lawrence Livermore National Laboratory, Livermore, California, U.S.A.*

## INTRODUCTION

Carbon is everywhere around us. Its stable crystalline phase is graphite, but under some circumstances, it can be converted into its most interesting phase for applications—diamonds. Naturally, a diamond is produced inside the Earth's mantle by a high-pressure–high-temperature phase transformation of graphite. It is metastable and that is the reason why it can be recovered in mines after having migrated toward the most external shells of the Earth.

Its unsurpassed hardness, excellent transport properties, transparency, and inertness make a diamond a material of choice for many industrial applications. Synthetic diamond, produced by a high-pressure–high-temperature treatment of graphite, or by ion bombardment, is now commonly used in industries. But what happens to the carbon phase diagram when the sample size reaches the order of several nanometers?

## OVERVIEW

After the discovery of diamond inclusions (several nanometers in size) in some meteorites that had fallen on Earth, some groups have theoretically studied the relative stability of graphite and diamond as a function of particle size.

The first attempt to understand the stability of diamonds at the nanoscale was published by Badziag et al.<sup>[1]</sup> They computed the binding energy of diamond-like and graphite-like carbon clusters using fixed energy values for carbon–carbon and carbon–hydrogen bonds. They found that below a size of 3–6 nm and a number of 100–21000 carbon atoms, diamond clusters become more stable than their graphitic counterparts. After that precursor study, several groups tried to model the relative diamond-to-graphite stability with more sophisticated models. A charged cluster model was presented by Hwang, Hahn, and Yoon.<sup>[2]</sup> and Jang and Hwang.<sup>[3]</sup> At that time, the crossover between diamond and graphite was predicted to occur for clusters containing 400 atoms. In comparison with

Ref.<sup>[1]</sup>, the model used there was purely electrostatic. Other charge lattice calculations by Gamarnik<sup>[4]</sup> predict the reversal of stability to occur between 4.3 and 10.2 nm, depending on the temperature. It is worth noting that although these models have totally different ingredients and neglect the detailed structure of the clusters, such as specific surface structure or different degrees of hydrogen surface passivation, they reach the same conclusion that a diamond becomes more stable than graphite below 3–10 nm. Indeed, diamonds of several nanometers in diameter have been found or produced in a large variety of environments, as we will discuss in “Nanodiamond Sources.” Then, we will present an overview of the properties of nanodiamonds, both as isolated particles and as assemblies in films, and we will show how promising these carbon nanoparticles are for tomorrow's applications.

## NANODIAMOND SOURCES

### Nanodiamonds in the Sky

Nanoscale diamonds were discovered in 1987 by Lewis et al.<sup>[5]</sup> in meteorites. Not all meteorites contain diamonds. At this time, nanodiamonds have been found in specific types of meteorites, the so-called “carbonaceous chondrites.” Two major sources of nanodiamonds are the “Allende” chondrite (C3V type), which weighed several tons when it fell on Mexico in 1969, and also other types of chondrites, such as the Murchison meteorite (type C2).

The nanodiamonds found in these meteorites have a lognormal size distribution, with a median diameter of 26 Å, corresponding to roughly 1060 atoms. The shape of the distribution has been interpreted to be caused by growth followed by partial conversion of small grains to larger ones. The particles were shown to contain impurities, mainly hydrogen, nitrogen, and oxygen, principally in –COOH groups.<sup>[6]</sup> It is worth noting that in some cases, such as C2-type chondrites, a diamond (in its nanoscale form) is up to five times

more abundant than graphite. Further analysis of meteoritic nanodiamonds by Amarti, Lewis, and Andres.<sup>[7]</sup> revealed the nanodiamond content of the C2 meteorite to be ~400 ppm and attributed the shape of the size distribution to a condensation process.

The major question arising from those discoveries is: How and when were those diamonds produced? Daulton et al.<sup>[8]</sup> performed a detailed high-resolution transmission electron microscopy (HRTEM) study of a large quantity of nanodiamonds coming from meteorites, as well as those produced by means of detonation or chemical vapor deposition (CVD). Their work concludes that meteoritic diamond features (morphology, type of eventual twinning) are much closer to the low-hydrogen-pressure CVD process than to the high-temperature–high-pressure detonation.

These findings are of much interest to the astrophysicists community because chondrites are primitive meteorites that formed *before* the solar system. Their structure and content provide information on nuclear and chemical processes in stars and in the interstellar medium. There still remained some doubts about the fact that the nanodiamonds found in the meteorites are actually presolar.<sup>[9]</sup> Dai et al.<sup>[10]</sup> have studied other nanodiamonds, with structural features similar to the meteoritic samples, which have been found in interplanetary dust particles originating from comets or asteroids. They found that there are very few nanodiamonds in those particles—infinately fewer than in chondrites. Because comets are objects that formed earlier in the solar system than meteorites, this seems to indicate that the nanodiamonds found in the meteorites are not presolar at all.

This hypothesis is corroborated by the discovery of unexpected lines in the infrared spectra of 12 warm supergiants,<sup>[11,12]</sup> which are also carbon-rich protoplanetary nebulae. A broad absorption line centered at 21  $\mu\text{m}$  wavelength was attributed to large polycyclic aromatic hydrocarbon (PAH) molecules or some partially hydrogenated fullerenes,<sup>[13]</sup> before being attributed to nanodiamonds by Hill, Jones, and d'Hendecourt.<sup>[14]</sup> In that study, the observed infrared absorption from the interstellar dust is shown to be comparable to either nitrogen-rich nanodiamonds, or to nanodiamonds containing vacancies and/or interstitial atoms. They also noticed that some absorption features could be explained by the relaxation of part of the nanodiamonds surface toward  $\text{sp}^2$  carbon configuration. By fitting the absorption spectra with those of terrestrial diamonds, they estimate the size of these interstellar nanodiamonds to be around 2.6 and 3 nm, exactly as for meteoritic diamonds.

Other hydrogenated nanodiamond signatures have been indirectly evidenced by Van Kerkhoven, Thielens, and Waelkens.<sup>[15]</sup> around some other types of stars. In those objects, the nanodiamonds are thought to be

hydrogen-terminated, with some surface reconstructions, and could have a size ranging between 1 and 10 nm. The main conclusion of that study is that the nanodiamonds are produced in situ in the disks of stellar objects. Thus they should be present everywhere. The authors suggest that nanodiamonds are indeed present everywhere in space, but remain undetected because of the dehydrogenation of their surface for reconstruction, with the surface carbon getting  $\text{sp}^2$ -bonded.

## Nanodiamonds in Detonation Soots

As one can see, nature seems to favor the appearance of diamond nanoparticles. But it is not only in the cosmos that nanodiamonds can be found.

Indeed, pure trinitrotoluene (TNT) detonation has been shown to produce, among other carbon structures, nanocrystalline (NC) diamonds with diameters of about 10 nm.<sup>[16]</sup> By mixing TNT with some other solids such as RDX (cyclotrimethylene trinitramine— $\text{C}_3\text{H}_6\text{N}_6\text{O}_6$ ), TATB, or NIGU, and by detonating the mixture in an inert gas atmosphere, most spheroidal diamond particles produced were 4 nm in diameter.<sup>[17]</sup> Because of those first studies, the synthesis of nanodiamonds by detonation has been optimized and detonation-produced diamonds are now even commercially available. These nanodiamonds are often called “ultra dispersed diamond” (UDD) because of their very narrow size distribution. A thermodynamic model has been proposed by Vicelli et al.<sup>[18]</sup> in which the nanodiamond formation is produced from nanometric liquid droplets. Aleksenski et al.<sup>[19]</sup> performed a structural study of UDD using X-ray diffraction and small angle X-ray scattering. They evidenced a diamond cluster core of about 43 Å, the surface of which is covered by a mixture of  $\text{sp}^2$ -bonded and  $\text{sp}^3$ -bonded carbons. The authors could explain their small-angle X-ray scattering (SAXS) measurement with a model in which the diamond core is surrounded by onionlike carbon shells and nanosized graphite platelets. The thickness of these surrounding shells seems to be much dependent on the type of detonation synthesis (dry technology–gas cooling, or wet technology–water cooling). Baidakova, Siklitsky, and Vul'.<sup>[20]</sup> further analyzed the fractal dimension of the external shells of nanodiamonds. On annealing, they show that the diamond content of the particles decreases from 1200 K in favor of the formation of graphite flakes on the surface of particles and in favor of onion shells at temperatures 1300 K and higher. Similar transformations occur under electron beam annealing as well. Fig. 1 shows the evolution of the electron energy loss spectroscopy (EELS) of a UDD nanoparticle as a function of exposure time. The spectra rapidly evolve from diamond-like to amorphous-like because of heating produced by the electron beam.



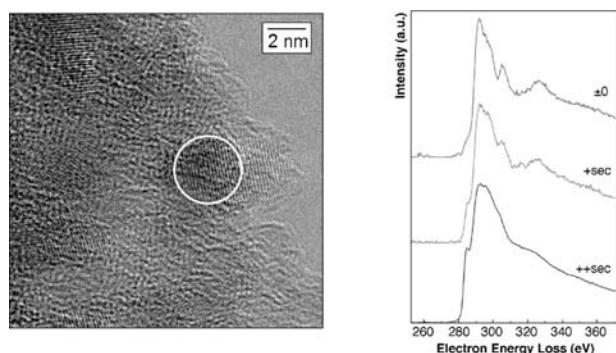


**Fig. 1** Electron energy loss spectroscopy of a single nanodiamond particle. (Courtesy of T. Van Buuren and J. Plitzko.) Left: HRTEM picture of the UDD powder. The particle under study ( $\sim 3$  nm in diameter) is designated by the circle. The reader can notice the enhanced atomic planes. Right: EELS spectra as a function of exposure time.

Other detonation-produced (TNT + RDX) nanodiamonds were analyzed by Chen et al.<sup>[21]</sup> In their study, the particles were almost perfectly spherical and 4–6 nm in diameter, but some larger ( $\sim 15$  nm) spherical particles were also present. The composition analysis evidenced 87–90% carbon, 0.5–1% hydrogen, 1.6–2.5% nitrogen, and 6–10% oxygen. The authors explained the spherical shape of the particles as a consequence of the recrystallization of a liquidlike carbon droplet during the detonation. The structure was shown to be diamond, with a small proportion of  $sp^2$ -bonded carbon atoms.

The small UDD nanocrystals often aggregate in larger conglomerates, as shown in the study of Aleksenskii et al.,<sup>[22]</sup> with small distortion of the initial spherical particle shape (Fig. 2).

The structure and defects of UDD have been extensively studied. In Ref.<sup>[24]</sup>, infrared spectroscopy

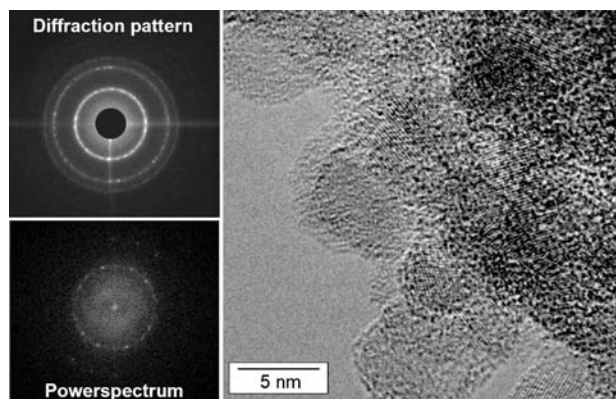


**Fig. 2** Electron diffraction pattern (top left), power spectrum (bottom left), and HRTEM picture of the edge zone of a conglomerate of nanodiamonds (UDD). *Source:* From Ref.<sup>[23]</sup>.

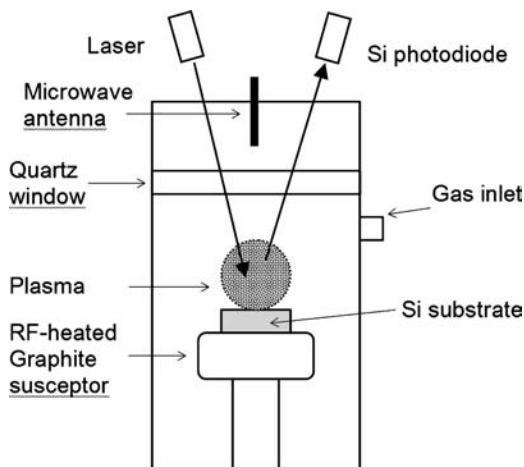


**Fig. 3** Schematic representation of a plasma CVD reactor used in ultrananocrystalline diamond films production. *Source:* From Ref.<sup>[27]</sup>.

evidences O–H, C–H, C=C, C=O, and C–O–C groups. Other surface groups are evidenced by nuclear magnetic resonance (NMR). The electron spin resonance measurement indicates that nitrogen is not present as a substitutional (paramagnetic) site inside the particle's core. However, another group<sup>[25]</sup> has measured a high concentration of paramagnetic centers. These are attributed to dangling C–C bonds located at the interface between the diamond core and the graphene sheets forming the surface. A similar paramagnetism has been observed in Ref.<sup>[26]</sup>.

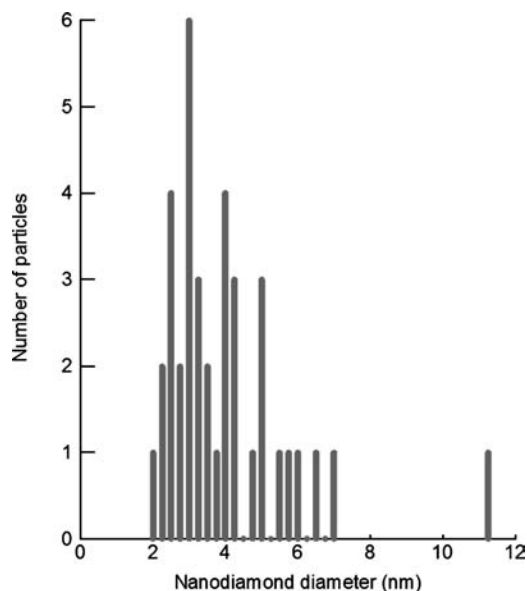


**Fig. 4** Size histogram obtained from the analysis of an HRTEM image of an ultrananocrystalline diamond film where  $C_{60}$  was used as a substitute to  $CH_4$  in the CVD reactor. *Source:* From Ref.<sup>[31]</sup>.

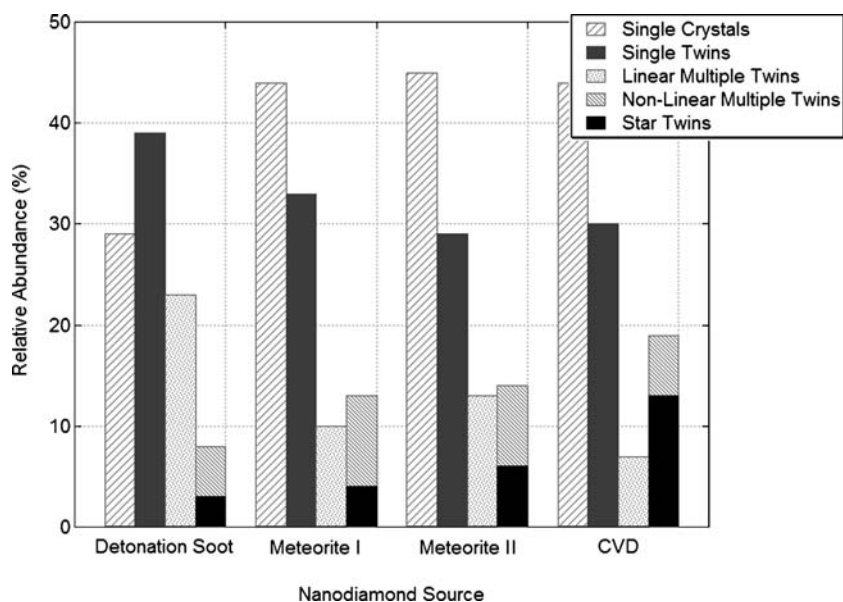


**Fig. 5** Distribution of different twinning types in nanodiamonds from various origins. The meteoritic diamond originated from the Murchison meteorite (I) and the Allende meteorite (II). One can note the similarity in the twinings in meteoritic and CVD nanodiamonds. *Source:* From Ref.<sup>[8]</sup>.

### Nanodiamond CVD Production

In the process of optimizing the CVD technique for the generation of high-quality diamond films, it was shown that, under some conditions, the deposited film was no more a microcrystals assembly, but a smooth film of much smaller diamond particles (Fig. 3).

A typical CVD experiment would involve the injection of a mixture of methane and hydrogen gas in a plasma reactor. The diamond film, with variable morphologies, is deposited on a silicon substrate.<sup>[28]</sup> Under certain conditions of relative CH<sub>4</sub>/H<sub>2</sub> concentrations and substrate temperature, it has been observed that the diamond film consisted of much smaller particles. The CVD-deposited diamonds films are distinguished into three categories: microcrystalline diamonds (0.5–10 μm), nanocrystalline diamonds (50–100 nm), and ultrananocrystalline (UNC) diamonds (2–5 nm). Garcia et al.<sup>[29]</sup> reported diamond particles of 50 nm diameter by applying a negative d.c. bias voltage during the first minutes of the deposition from a mixture of 4% CH<sub>4</sub> in H<sub>2</sub>. The nanometric diamonds appear to be the first stage of diamond growth as long deposition times show them coalesce to form a microcrystalline diamond film. Gruen et al. managed to optimize the gas concentration to generate UNC diamonds.<sup>a</sup> Replacing the major part of hydrogen by argon (typical 1% hydrogen) in the plasma causes the deposition of a smooth film of nanoparticles of only a few nanometers in size (Fig. 4).<sup>[30]</sup> Those UNC films

contain only 2–5% of sp<sup>2</sup>-bonded carbons in grain boundaries and less than 1% hydrogen.

Different plasma CVD techniques are used to produce diamond films. Nanocrystalline diamond crystals with a typical size of 50–100 nm are produced by hollow cathode arc plasma CVD, or direct current glow discharge-assisted CVD, among many other experiments.<sup>[32]</sup> In that last study, a detailed analysis of the proportion of nanodiamonds to graphite shows that up to 75% of carbon is present in the film as sp<sup>3</sup>-bonded carbon in 3- to 5-nm diamond crystals. The remaining sp<sup>2</sup>-bonded atoms are mostly present in the form of a thin graphite layer (150–200 nm) present between the substrate and the UNC diamond, as well as in grain boundaries. This UNC film has been shown to be stable up to 950°C.<sup>[33]</sup>

### NANODIAMOND STRUCTURES

Nanodiamonds that are produced under those very different conditions of atmosphere, temperature, and pressure have similar size distributions. In particular, extraterrestrial nanodiamonds, detonation nanodiamonds, and ultrananocrystalline diamonds have sizes that typically range between 2 and 5 nm (Fig. 4).

The crystallinity of nanodiamonds has been tested by diffraction, but is also directly observable by electron microscopy (enhanced atomic planes in Figs. 1 and 2 transmission electron micrographs). A complete crystallographic study of nanodiamonds produced in the three ways we have described (meteoritic, detonation, and CVD-UNC nanodiamonds) has been performed by Daulton et al.<sup>[8]</sup> in an attempt to determine the origin and synthesis mechanism of meteoritic diamonds. In all those types of nanodiamonds,

<sup>a</sup>A complete review of ultrananocrystalline diamond properties and potential applications can be found in Ref.<sup>[27]</sup>.

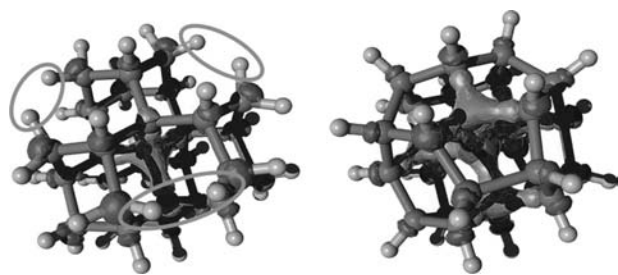


**Fig. 6** Structure of a 0.7-nm 29-carbon atom cluster. Left: The fully hydrogenated cluster. Right: The result of surface reconstruction induced by the removal of six pairs of hydrogen atoms (circled on the left). Carbon atoms are in light grey; hydrogen atoms are in dark grey. The isosurfaces represent the lowest unoccupied molecular orbital (LUMO; here located on the C–H bonds) and the highest occupied molecular orbital (HOMO; here located at the center of the cluster) drawn at 30% of their maximal value.

twinning is often observed, preferentially for the largest particles. Twinning can take different forms, from simple twins, to multiple, to even fivefold star twins. However, the shape of the nanoparticles is globally spherical (Fig. 5).

The structure of the nanodiamond surface is little known.  $sp^2$ -bonded carbon may be present at the surface and in UNC diamond film grain boundaries.<sup>[34]</sup> Hydrogen is present in all three varieties of nanodiamonds, but other impurities have been evidenced in detonation-produced and extraterrestrial nanodiamonds.

Maillard-Schaller et al.<sup>[35]</sup> have measured the impurity content of detonation-produced nanodiamonds by Raman and X-ray photoelectron spectroscopy (XPS). The major impurity is oxygen. The nitrogen content of their samples is 1–2% and traces of N, Fe, S, and Ar are also found.  $H_2$  plasma treatment of the nanodiamonds deposited on a Si substrate by electrophoresis causes oxygen impurities to leave the sample, whereas the nitrogen content remains the same. The  $sp^3/sp^2$  content of the diamonds is unchanged by the high-temperature treatment.

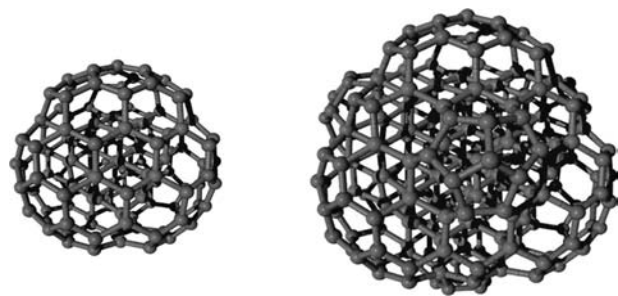


**Fig. 7**  $C_{147}$  and  $C_{275}$  bucky diamonds. The diamond core atoms are represented in light grey. *Source:* From Ref.<sup>[23]</sup>.

## NANODIAMOND PROPERTIES

Very few theoretical studies of single nanodiamonds properties have been performed. Halicioglu<sup>[36]</sup> relaxed spherical nanometric diamond slabs with Brenner potentials. The so-formed structures exhibit inward relaxation from the top surface layers, the interatomic distance between neighboring atoms decreasing from the center of the cluster to the surface. They also noticed significant variations in relative cohesive energy with respect to bulk diamond. Recently, an ab initio molecular dynamics simulation, a parameter-free technique that solves quantum mechanical equations with great accuracy, was used to simulate the structure and to compute the electronic and optical properties of nanodiamonds.<sup>[23]</sup> Contrary to classical treatment, the quantum simulation of nanodiamonds yields an expansion of the cluster volume with respect to bulk diamonds. That tensile stress is at the opposite of what is observed in Si or Ge nanoparticles. The surface reconstruction of nanodiamonds has been shown to strongly affect electronic structure, as shown in Fig. 6.

When the totality of hydrogen is removed from the cluster, the surface is shown to sometime reconstruct in a specific way, forming the so-called “bucky diamonds.” These structures consist of a diamond core the surface of which is reconstructed in a fullerene-like manner (Fig. 7).

The optical properties of nanodiamonds have been studied mostly by X-ray techniques. The X-ray emission and absorption spectra of detonation nanodiamonds are very similar to those of bulk diamonds and are totally different from graphite (Fig. 8).

The differences between bulk diamonds and nanodiamonds are exciton broadening (289.3 eV) and a

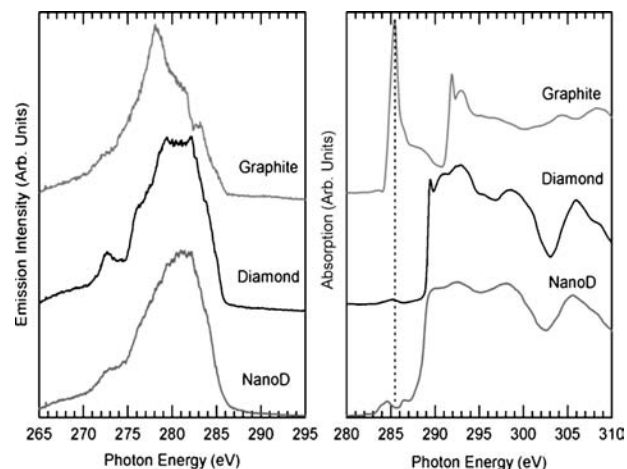


**Fig. 8** X-ray emission (left) and absorption (right) spectra from highly oriented pyrolytic graphite (HOPG), bulk diamonds, and detonation-produced nanodiamonds (4 nm average size). *Source:* From Ref.<sup>[23]</sup>.

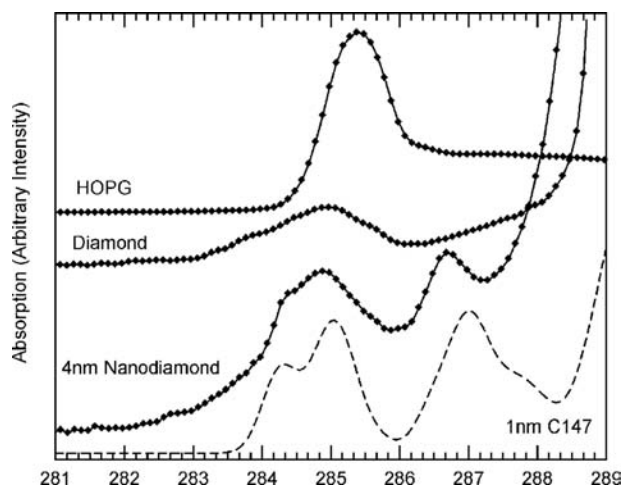


**Fig. 9** Detail of the pre-edge X-ray absorption spectra of HOPG, bulk diamonds, and detonation nanodiamonds vs. the X-ray energy in electron volts. The density of unoccupied states computed ab initio from a  $C_{147}$  bucky diamond is shown for comparison (dashed line). *Source:* From Ref.<sup>[23]</sup>.

shallower secondary minimum (302 eV). However, there are some pre-edge features in the nanodiamond absorption spectrum that are not caused by impurities and are reproducible (Fig. 9). These features could be the signature of specific surface reconstructions such as in bucky diamonds.

Other information can be obtained from Fig. 8: There is no shift in valence and conduction band maximum and minimum in comparison with bulk diamonds. This indicates that quantum confinement does not affect the electronic structure for particles 4 nm and larger. This property can also be observed on computed absorption spectra from Fig. 10.

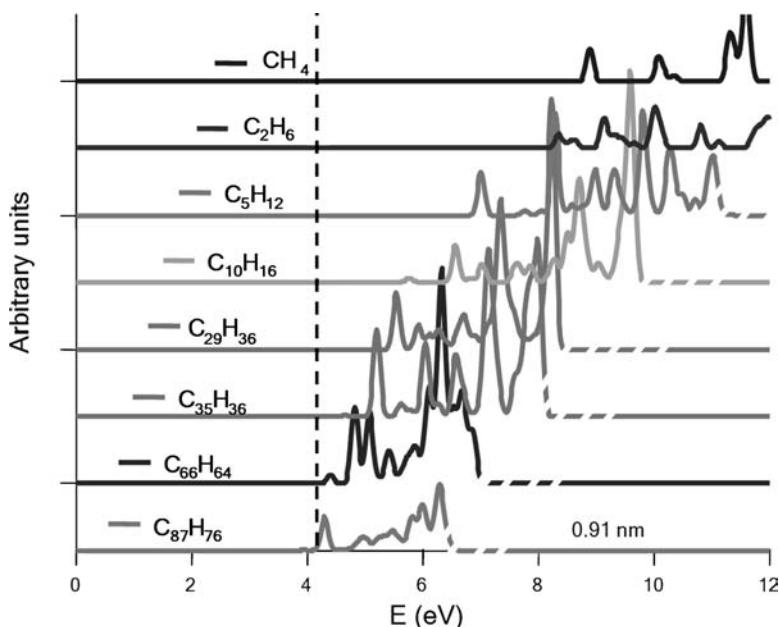


**Fig. 10** Optical spectra of carbon clusters ranging from methane to 1-nm nanodiamonds. The spectra are computed using the time-dependent local density approximation on ab initio-relaxed cluster geometries. The dashed line shows the bulk absorption threshold computed with the same method (4.23 eV for an experimental value of 5.5 eV). *Source:* From Refs.<sup>[38,39]</sup>.

The optical properties of UDD layers have been studied optically and by XPS by Aleksenskii et al.<sup>[37]</sup> The band gap is measured to be 3.5 eV, with many energy levels present in the nanodiamonds band gap and contributing to a broad luminescence band (380–520 nm). The optical absorption of the material is attributed to threefold coordinated atoms on the surface. The unannealed sample contains 8% N and 22% O, mainly under the form of nitrate ions attached to the particle's surface.

The electron transport in ultradisperse diamonds deposited on quartz substrates has been measured by He et al.<sup>[40]</sup> The conductivity of the films is shown to decrease with annealing. Surprisingly, it is semiconducting at high temperature but the temperature dependence of the conductivity is negative at lower temperatures. This behavior is attributed to conduction through surface conduction ( $\pi$ -type because of graphite-like sheets) at low temperature and through diamond core  $\sigma$ -type conduction at higher temperature.

An interesting property of a hydrogenated diamond surface is its “negative electron affinity,” the ability of an electron that is excited in the conduction band to freely leave the material. Nanodiamonds have smaller bandgaps than bulk diamond, and for that reason are excellent candidates for low-threshold electron emission devices. The additional requirement is that the electron affinity is small, or even negative. The electron emission of the UDD film from Ref.<sup>[40]</sup> is strong and has a low field threshold (3.2 V/ $\mu\text{m}$ ). It has been attributed to grain boundaries of nanodiamond films, rather than substrates. A similar field emission study was performed on ultrananocrystalline diamond films by Krauss et al.<sup>[41]</sup> The emission is again attributed to conduction through the grain boundaries–vacuum

interface. With moderate heating (200–300°C), the photoemission yield is increased by a factor of 5.<sup>[42]</sup> When the hydrogenated UNC film is exposed to air, electron affinity is actually shown to become negative. A similar negative electron affinity has been measured after treating a film of deposited nanodiamonds obtained from detonation, but only after treating the film with H<sub>2</sub> plasma, which removes most of the impurities, except nitrogen.<sup>[35]</sup>

## NANODIAMOND NITROGEN N-DOPING

A very promising way to have nanodiamond films incorporated in technological applications is by doping them with nitrogen. The goal is to introduce carrier levels into the diamond gap (this level is located 1.7 eV below the conduction band minimum in bulk diamonds) to increase conductivity and to lower the electron emission voltage threshold. Nitrogen is a major impurity of natural diamond. As we said before, nanodiamonds produced by detonation contain a high percentage (1–2%) of nitrogen. This nitrogen is brought into the diamonds from the trinitrotoluene reactant and cannot be removed from the nanoparti-

cles.<sup>[35]</sup> The precise location of the nitrogen atoms in the nanoparticles is uncertain, but several magnetic studies have been unable to see any trace of substitutional nitrogen (known as P1 center).<sup>[24]</sup> This is surprising as nitrogen is present in N-doped CVD-produced microcrystals as a substitute to core carbon atoms.<sup>[43]</sup> A theoretical study of the grain boundaries of UNC diamonds in the presence of nitrogen impurities has been performed by Zapol et al.<sup>[44]</sup> This tight-binding density functional study shows that nitrogen substitution to carbon in the grain boundary is energetically more favorable than in the crystal's core. The conductivity increase of the N-doped film is then attributed to an increase in threefold coordinated carbon atoms caused by the nitrogen impurity. A recent ab initio molecular dynamics study<sup>[39]</sup> shows that for small diamond clusters, nitrogen is preferentially present as a substitute to surface carbon. The tensile stress evidenced in those nanoparticles<sup>[23]</sup> facilitates nitrogen inclusion in comparison to bulk diamonds, where intentional nitrogen doping has proven to be difficult. Nitrogen incorporation is shown to require more and more energy with increasing particle size (Fig. 11).

Nitrogen doping of UNC films has been studied by Bhattacharyya et al.<sup>[45]</sup> Doping is achieved by introdu-

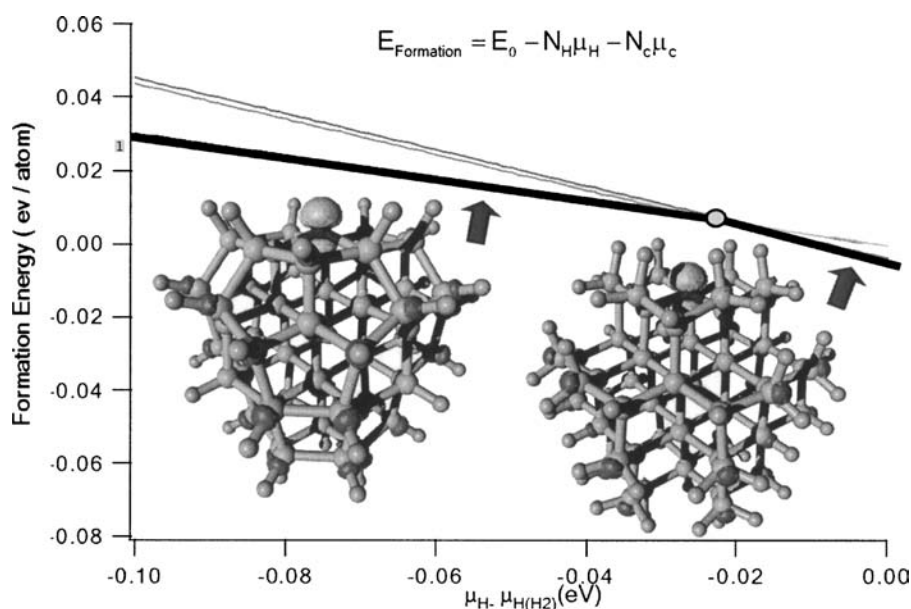


**Fig. 11** Formation energy of 66 carbon atom clusters containing one nitrogen impurity atom as a function of the hydrogen chemical potential  $\mu_{\text{H}}$  (eV). This energy is the difference between the cluster's total energy and the energy the same number of carbon and hydrogen atoms ( $N_{\text{C}}$  and  $N_{\text{H}}$ ) would have in their most stable form (here we consider diamond and the H<sub>2</sub> molecule). The origin of  $\mu_{\text{H}}$  (eV) is taken as the energy of one hydrogen atom in the H<sub>2</sub> molecule. The thick black segments indicate the most stable structures. The stable configurations are the C<sub>65</sub>H<sub>65</sub>N and C<sub>65</sub>H<sub>39</sub>N clusters. In these, the nitrogen atom is substitutional in the particle's surface. Above  $\sim -0.02$  eV, the stable structure is a fully hydrogenated cluster in which the nitrogen atom (in blue) sits on the surface. Below this energy (this would correspond to a higher temperature and/or a lower hydrogen pressure), the stable structure has a partially reconstructed surface in which the nitrogen resides. The C<sub>65</sub>H<sub>66</sub>N and C<sub>65</sub>H<sub>40</sub>N clusters in which the nitrogen atom is substitutional to a core carbon atom are never stable (thin lines). The isosurfaces are drawn at 30% of the maximal value of the HOMO (on the nitrogen atom) and LUMO (on C–H bonds), respectively.



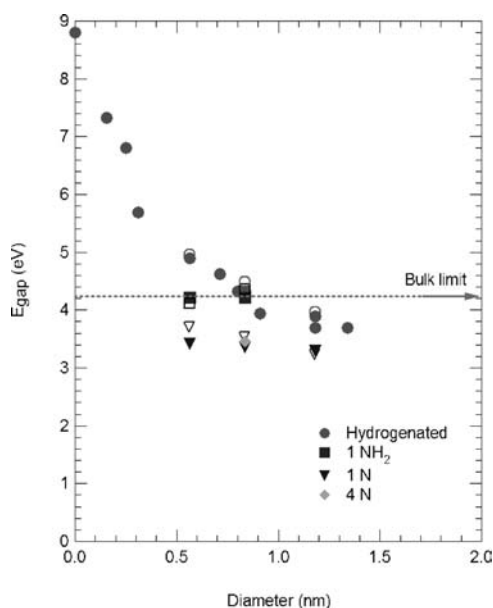


**Fig. 12** Computed HOMO–LUMO energy gaps for various nanodiamonds structures. Red circles: Hydrogenated nanoclusters; black squares: nanodiamonds with a  $\text{NH}_2$  surface group; green triangle: one surface substitutional nitrogen; pink diamond: four surface substitutional nitrogen atoms. The filled symbols represent the nonreconstructed, maximally hydrogenated nanodiamonds; the empty symbols represent (100) reconstructed surfaces.

cing nitrogen gas (1–20%) into the mixture fed to the CVD reactor. They achieved the highest carrier concentration and electrical conductivity ever measured for a phase-pure diamond thin film. The increase of  $\text{N}_2$  gas concentration causes larger grain boundaries and larger grains to be deposited, and increases the conductivity up to  $143 \Omega^{-1} \text{cm}^{-1}$ . This large conductivity is attributed to the large proportion of nitrogen atoms in the grain boundaries. The optical and emission properties of N-doped UNC diamond films are still under investigation. A theoretical study<sup>[39]</sup> has compared the energy gap of hydrogen-terminated nanodiamonds clusters and clusters including various nitrogen impurities on the surface as a function of size. The variation is faster for reconstructed surfaces because of the size evolution of the surface curvature. For nonreconstructed surfaces, the curvature changes little with cluster size and the energy gap remains almost constant and smaller than for H-terminated clusters (Fig. 12).

## NANODIAMONDS FOR THE FUTURE

Nanodiamonds are very promising materials for application, especially under the form of ultrananocrystalline diamond thin films. An extensive review of UNC film properties and potential applications can be found in

Ref.<sup>[27]</sup>. We have cited the perspectives offered in field-induced and light-induced emission by nitrogen-doped UNC films. They could be used to produce bright, low-voltage (cold) cathodes. They may be used in the future as microelectromechanical system (MEMS) materials. Pioneer devices have been successfully produced by Krauss et al.<sup>[46]</sup> The exceptional hardness, fracture strength, and inertness of the films, together with a smooth surface, make UNC a unique material for miniaturized mechanical systems and devices, such as cantilevers, gears, etc. The hydrogen termination of the surface also brings a “natural lubricant” to the moving devices.

UNC diamonds also have potential applications in optoelectronics, as photonic switches, electronic devices (pn junctions), etc. They are on their way to being commercially used as surface acoustic wave devices. Recent experiments have even used UNC films as support to attach ADN.<sup>[47]</sup> These devices have proven to be extremely stable and have opened the way to the integration of biology in electronics.

## CONCLUSION

Nanodiamonds have unique, fascinating properties, as isolated particles or in thin films, but many aspects still have to be understood. The interaction between nanodiamonds is largely unknown. The most intriguing fact is that all types of nanodiamonds have similar features and size distributions (independently of the production type), extreme pressure and temperature, and low-pressure CVD, and are around stars. Indeed, everywhere where scientists have looked for carbon nanostructures with a high-resolution microscope, they found nanodiamonds. Would they not be everywhere around us?

## ACKNOWLEDGMENTS

This work was performed under the auspices of the US Department of Energy at the University of California/Lawrence Livermore National Laboratory under contract no. W-7405-Eng-48. J. Y. R. acknowledges support from the FNRS.

## REFERENCES

1. Badziag, P.; Verwoerd, W.S.; Ellis, W.P.; Greiner, N.R. Nanometre-sized diamonds are more stable than graphite. *Nature* **1990**, *343*, 244–245.
2. Hwang, N.M.; Hahn, J.H.; Yoon, D.Y. Charged cluster model in the low pressure synthesis of diamond. *J. Cryst. Growth* **1996**, *162*, 55–68.



3. Jang, H.M.; Hwang, N.M. Theory of the charged cluster formation in the low pressure synthesis of diamond: part II. Free energy function and thermodynamic stability. *J. Mater. Res.* **1998**, *13*, 3536–3549.
4. Gamarnik, M.Y. Energetical preference of diamond nanoparticles. *Phys. Rev., B* **1996**, *54*, 2150–2156.
5. Lewis, R.S.; Tang, M.; Wacker, J.F.; Anders, E.; Steel, E. Interstellar diamonds in meteorites. *Nature* **1987**, *326*, 160–162.
6. Lewis, R.S.; Anders, E.; Draine, B.T. Properties, detectability and origin of interstellar diamonds in meteorites. *Nature* **1989**, *339*, 117–121.
7. Amarti, S.; Lewis, R.S.; Anders, E. Interstellar grains in meteorites: I. Isolation of SiC, graphite and diamond; size distributions of SiC and graphite. *Geochim. Cosmochim. Acta* **1994**, *58*, 459–470.
8. Daulton, T.L.; Eisenhour, D.D.; Bernatowicz, T.J.; Lewis, R.S.; Buseck, P.R. Genesis of presolar diamonds: comparative high-resolution transmission electron microscopy study of meteoritic and terrestrial nanodiamonds. *Geochim. Cosmochim. Acta* **1996**, *60*, 4853–4872.
9. Koscheev, P.; Gromov, M.D.; Mohapatra, R.K.; Ott, U. History of trace gases in presolar diamonds inferred from ion-implantation experiments. *Nature* **2001**, *412*, 615–617.
10. Dai, Z.R.; Bradley, J.P.; Joswiak, D.J.; Brownlee, D.E.; Hill, H.G.M.; Genge, M.J. Possible in situ formation of meteoritic nanodiamonds in the early solar system. *Nature* **2002**, *418*, 157–159.
11. Buss, R.H.; Cohen, M.; Tielens, A.G.; Werner, M.W.; Bergman, J.D.; Witteborg, F.C.; Rank, D.; Sanford, S.A. Hydrocarbon emission features in the infrared spectra of warm supergiants. *Astrophys. J.* **1990**, *365*, L23–L26.
12. Volk, K.; Kwok, S.; Hrivnak, B.J. High-resolution infrared space observatory spectroscopy of the unidentified 21 micron feature. *Astrophys. J.* **1999**, *516*, L99–L102.
13. Justtanont, K.; Barlow, M.J.; Skinner, C.J.; Roche, P.F.; Aitken, D.K.; Smith, C.H. Mid-infrared spectroscopy of carbon-rich post-AGB objects and detection of the PAH molecule chrysene. *Astron. Astrophys.* **1996**, *309*, 612–628.
14. Hill, H.G.; Jones, A.P.; d'Hendecourt, L.B. Diamonds in carbon-rich proto-planetary nebulae. *Astron. Astrophys.* **1998**, *336*, L41–L44.
15. Van Kerkhoven, C.; Thielens, A.G.; Waelkens, C. Nanodiamonds around HD 97048 and Elias 1. *Astron. Astrophys.* **2002**, *384*, 568–584.
16. Van Thiel, M.; Ree, F.H. Properties of carbon clusters in TNT detonation products: the graphite diamond transition. *J. Appl. Phys.* **1987**, *62*, 1761–1767.
17. Greiner, N.R.; Philips, D.S.; Johnson, J.D.; Volk, F. Diamonds in detonation soots. *Nature* **1998**, *333*, 440–442.
18. Viccelli, A.; Bastea, S.; Glosli, J.N.; Ree, F.H. Phase transformation of nanometer size carbon particles in shocked hydrocarbon and explosives. *J. Chem. Phys.* **2001**, *115*, 2730–2736.
19. Aleksenski, A.E.; Baidakova, M.V.; Vul', A.Ya.; Siklitskiy, V.I. The structure of diamond nanoclusters. *Phys. Solid State* **1999**, *41*, 740–743.
20. Baidakova, M.V.; Siklitskiy, V.I.; Vul', A.Ya. Ultradisperse-diamond nanoclusters. Fractal structure and diamond–graphite phase transition. *Chaos Solitons Fractals* **1999**, *10*, 2153–2163.
21. Chen, P.W.; Ding, Y.S.; Chen, Q.; Huang, F.L.; Yun, S.R. Spherical nanometer-sized diamond obtained from detonation. *Diamond Relat. Mater.* **2000**, *9*, 1722–1725.
22. Aleksenskii, A.E.; Osipov, V.Yu.; Dideikin, A.T.; Vul', A.Ya.; Adriaenssens, G.J.; Afanas'ev, V.V. Ultradisperse diamond cluster aggregation studied by atomic force microscopy. *Tech. Phys. Lett.* **2000**, *26*, 819–821.
23. Raty, J.Y.; Galli, G.; Van Buuren, T.; Bostedt, C.; Terminello, L. Quantum confinement and fullerene-like surface reconstructions in nanodiamonds. *Phys. Rev. Lett.* **2003**, *90*, 037401–037404.
24. Iakoubovskii, K.; Baidakova, M.V.; Wouters, B.H.; Stesmans, A.; Adriaenssens, G.J.; Vul', A.Ya.; Grobet, P.J. Structure and defects of detonation synthesis nanodiamonds. *Diamond Relat. Mater.* **2000**, *9*, 861–865.
25. Shames, A.I.; Panich, A.M.; Kempinski, W.; Alenskii, A.E.; Baidakova, M.V.; Dideikin, A.T.; Osipov, V.Yu.; Siklitskiy, V.I.; Osawa, E.; Osawa, M.; Vul', A.Ya. Defect and impurities in nanodiamonds: EPR, NMR and TEM study. *J. Phys. Chem. Solids* **2002**, *63*, 1993–2001.
26. Belobrov, P.I.; Gordeev, S.K.; Petrakovskaya, E.A.; Falaleev, O.V. Paramagnetic properties of nanodiamonds. *Dokl., Phys.* **2001**, *46*, 459–462.
27. Butler, J.E.; Windischmann, H. Developments in CVD-diamond synthesis during the past decade. *MRS Bulletin* **1998**, *23*, 22–27.
28. Fayette, L.; Marcus, B.; Mermoux, M.; Tourillon, G.; Laffon, K.; Parent, P.; Le Norm, F. Local order in CVD diamond films: comparative Raman, x-ray diffraction and x-ray absorption near-edge studies. *Phys. Rev., B* **1998**, *57*, 14,123–14,132.
29. Garcia, M.M.; Jimenez, I.; Gomez-Aleixandre, C.; Abella, J.M.; Sanchez, O.; Terminello, L.J.; Himpsel, F.J. X-ray absorption spectroscopy and atomic force microscopy study of bias-enhanced nucleation of diamond films. *Appl. Phys. Lett.* **1998**, *72*, 2105–2107.
30. Jiao, S.; Sumant, A.; Kirk, M.A.; Gruen, D.M.; Krauss, A.R.; Auciello, O. Microstructure of ultrananocrystalline diamond films grown by microwave Ar-CH<sub>4</sub> plasma chemical vapor deposition with or without H<sub>2</sub>. *J. Appl. Phys.* **2001**, *90*, 118–122.
31. Qin, L.C.; Zhou, D.; Krauss, A.R.; Gruen, D. TEM characterization of nanodiamonds thin films. *Nanostruct. Mater.* **1998**, *10*, 649–660.
32. Heiman, A.; Gouzman, I.; Christiansen, S.H.; Strunk, H.P.; Comtet, G.; Hellner, L.; Dujardin, G.; Edrei, R.; Hoffman, A. Evolution and properties of nanodiamonds films deposited by direct current glow discharge. *J. Appl. Phys.* **2001**, *89*, 2622–2630.
33. Hoffman, A.; Heiman, A.; Christiansen, S.H. Mechanism of diamond film formation by stress relaxation on a preferentially oriented basal plane graphitic precursor. *J. Appl. Phys.* **2001**, *89*, 5769–5773.
34. Keblinski, P.; Wolf, D.; Phillpot, S.R.; Gleiter, H. Role of bonding and coordination in the atomic structure of

- grain boundaries of diamond and silicon. *J. Mater. Res.* **1998**, *13*, 1077–1099.
35. Maillard-Schaller, E.; Kuettel, O.M.; Diederich, L.; Schlapbach, L.; Zhirnov, V.V.; Belobrov, P.I. Surface properties of nanodiamonds films deposited by electrophoresis on Si(100). *Diamond Relat. Mater.* **1999**, *8*, 805–808.
  36. Halicioglu, T. Properties of diamond and diamond-like clusters in nanometric dimensions. *Phys. Status Solidi, B* **1997**, *199*, 345–350.
  37. Aleksenskii, A.E.; Osipov, V.Yu.; Vul', A.Ya.; Ber, B.Ya.; Smirnov, A.B.; Melekhin, V.G.; Adriaenssens, G.J.; Iakoubovskii, K. Optical properties of nanodiamonds layers. *Phys. Solid State* **2001**, *43*, 145–150.
  38. Gonze, X.; Beuken, J.M.; Caracas, R.; Detraux, F.; Fuchs, M.; Rignanese, G.M.; Sindic, L.; Verstraete, M.; Mikami, M.; Ghosez, P.; Raty, J.Y.; Allan, D.C. First principles computation of material properties: the ABINIT software project. *Comput. Mater. Sci.* **2002**, *25*, 478–492.
  39. Raty, J.Y.; Galli, G.; Hood, R.Q. In press.
  40. He, D.; Shao, L.; Gong, W.; Xie, E.; Xu, K.; Chen, G. Electron transport and electron field emission of nanodiamonds synthesized by explosive detonation. *Diamond Relat. Mater.* **2000**, *9*, 1600–1603.
  41. Krauss, A.R.; Auciello, O.; Ding, M.Q.; Gruen, D.M.; Huang, Y.; Zhirnov, V.V.; Givargizov, E.I.; Breskin, A.; Chechen, R.; Shefer, E.; Konov, V.; Pimetov, S.; Karabutov, A.; Rakhimov, A.; Suetin, N. Electron field emission for ultrananocrystalline diamond film. *J. Appl. Phys.* **2001**, *89*, 2958–2967.
  42. Piantanida, G.; Breskin, A.; Chechik, R.; Katz, O.; Laikhtman, A.; Hoffman, A.; Coluzza, C. Effect of moderate heating on the negative electron affinity and photoyield of air-exposed hydrogen-terminated chemical vapor deposited diamond. *J. Appl. Phys.* **2001**, *89*, 8259–8264.
  43. Nokhrin, S.; Rosa, J.; Vanecek, M.; Badalyan, A.G.; Nesladek, M. EPR study of preferential orientation of crystallites in N-doped high quality CVD diamond. *Diamond Relat. Mater.* **2001**, *10*, 480–484.
  44. Zapol, P.; Sternberg, M.; Curtiss, L.A.; Fraunheim, Th.; Gruen, D.M. Nitrogen impurities in ultrananocrystalline diamond grain boundaries. *Mater. Res. Symp. Proc.* **2000**, *593*, 483–487.
  45. Bhattacharyya, S.; Auciello, O.; Birrel, J.; Carlisle, J.A.; Curtiss, L.A.; Coyette, A.N.; Gruen, D.M.; Krauss, A.R.; Schlueter, J.; Sumant, A.; Zapol, P. Synthesis and characterization of highly conducting nitrogen-doped ultrananocrystalline diamond films. *Appl. Phys. Lett.* **2001**, *79*, 1441–1443.
  46. Krauss, A.R.; Auciello, O.; Gruen, D.M.; Jayatissa, A.; Sumant, A.; Tucek, J.; Mancini, D.C.; Moldovan, N.; Erdemir, A.; Ersoy, D.; Gardos, M.N.; Busmann, H.G.; Meyer, E.M.; Ding, M.Q. Ultrananocrystalline thin films for MEMS and moving mechanical assembly devices. *Diamond Relat. Mater.* **2001**, *10*, 1952–1961.
  47. Yang, W.; Auciello, O.; Butler, J.E.; Cai, W.; Carlisle, J.A.; Gerbi, J.E.; Gruen, D.M.; Knickerbocker, T.; Lasseter, T.L.; Russel, J.N.; Smith, L.M.; Hamers, R.J. DNA modified nanocrystalline diamond thin-films as stable, biologically active substrates. *Nat. Mater.* **2002**, *1*, 253–257.

# Nanoencapsulation of Bioactive Substances

Yury E. Shapiro

Department of Life Sciences, Bar-Ilan University, Ramat-Gan, Israel

## INTRODUCTION

Nanoencapsulation is one of the most important subcategories of controlled-release bionanotechnology. Normally, active substances are encapsulated in submicrometer-sized devices made of barrier materials. These materials are designed to control the rate of release. This concept has been largely inspired by spontaneous assembling of the phospholipid liposomes as a model of biological membranes.<sup>[1]</sup> As in Nature, one has to develop preparations of nanovehicles that allow precise control over their structure and morphology. In this context, the self-assembled superstructures of surfactants (micelles, liposomes)<sup>[2]</sup> and/or polymers (nanoparticles) have proven to be valuable tools.<sup>[3]</sup>

Nanoparticles may be defined as being submicrometer (from 10 to 1000 nm) colloidal systems generally, but not necessarily, made of polymers (biodegradable or not).<sup>[4-6]</sup> Depending on the process used for their preparation, two different types of nanoparticles can be obtained, namely, nanospheres and nanocapsules. Unlike nanospheres (matrix systems where the bioactive substance is dispersed throughout the particles), nanocapsules exhibit a membrane-wall structure with an aqueous or oily core containing the bioactive substance. Thus, nanocapsules may be considered as a “reservoir” or “envelop” system. Because nanoparticles have very high surface areas, the active substance may also be adsorbed or conjugated onto the surface.<sup>[6]</sup> At present, micellar/liposomal systems have also been included under the term “nanoparticles.”

Another type of nanometer-sized carriers is an inclusion complex or clathrate, which can be assembled by inclusion of bioactive substances into molecular cavities of the so-called cavitands,<sup>[7]</sup> or dendrimers.<sup>[8,9]</sup> Natural examples of such internal-cavity-containing molecules are cyclodextrins, which are used widely for preparation of various drug formulations.<sup>[10]</sup> The outer diameter of molecular nanocapsules is in the range of 3–50 nm. The nanometer size ranges of liposomes, nanoparticles, and clathrates offer certain distinct advantages for drug delivery. Because of their subcellular size, they can penetrate deep into tissues through fine capillaries, cross the fenestration present in the epithelial lining (e.g., liver), and generally are taken up efficiently by the cells to perform the so-called

intracellular trafficking.<sup>[6,11,12]</sup> This allows direct delivery of therapeutic agents to target sites in the body followed by the controlled release.<sup>[13]</sup>

## CONTROLLED RELEASE

Controlled-release nanotechnology can solve a variety of problems regarding the effective delivery of a bioactive compound to a target to achieve good local and systemic tolerance during and after application.<sup>[14]</sup> In controlled-release systems, a drug or some other active agent is incorporated into a self-assembled carrier. The main condition of success is to design tissue-friendly and biodegradable accompanying materials.<sup>[4-6]</sup> The delivery carriers are usually required for the following reasons: 1) many effective drugs are characterized by poor aqueous solubility and need to be solubilized; 2) many drugs, such as proteins, are very fragile and need a microenvironment providing protection from hydrolysis or enzymatic degradation; 3) many drugs are highly toxic and require a carrier to shield tissues until the drug release at the targeted tissue occurs; 4) the release itself has to be designed to allow controlling; and 5) targeted delivery of drug can be attained by conjugating a specific vector to the carrier.<sup>[15]</sup>

The rate of releasing the agent depends on the nature of the carrier as well as various environmental factors (such as nature of solvent, osmotic pressure, temperature, pH of media, and so on). The controlled release, depending on rate of releasing, can be classified as triggered, pulsing, or sustained. The rate of delivery of any bioactive substance to a target tissue or reaction site is highly critical. Key advantages to the use of this technology are prolonged activity, fewer doses, fewer undesirable side effects, and reduced toxicity.<sup>[5]</sup>

Three mechanisms of controlled release can be considered: diffusion controlled (through membranes and from matrices), chemically controlled (erosion and cleavage of polymer chain or spacer connecting bioactive agent with carrier, if any), and solvent activated (osmotic pressure and swelling). Each mechanism has certain advantages and must be selected for design of carrier depending on the agent to be released as well as the conditions required to yield favorable release. Recently, significant effort has been devoted to develop

nanotechnology for controlled drug delivery devices because it offers a suitable means of delivering low molecular weight drugs, as well as macromolecules such as peptides, proteins, DNA, or genes by either localized or targeted delivery to the tissue of interest.<sup>[6,11,16,17]</sup>

## LIPOSOMES

Liposomes (or vesicles) are topologically closed nano-sized lamellar aggregates of highly ordered lipid molecules that are normally dispersed in a hydrophilic solvent, typically water. The aggregates may be formed by the combination of both polar and non-polar residues in the same lipid molecule, which is described as amphiphilic. In aqueous medium the amphiphilic molecules arrange the ordered micellar or lamellar structures depending on the concentration, in which the hydrophobic regions are brought into proximity with each other while the polar groups are exposed to water. The amphiphiles are capable of forming a variety of phases due to steric factors such as head group size, variation in the number of acyl chains, or to electrostatic effects arising from attractive or repulsive forces between adjacent polar head groups.<sup>[18]</sup> The different phases can interconvert, either by inward or outward migration of particular amphiphiles changing their shape. Heating, for example, increases the dynamic motion of hydrocarbon chains, effectively broadening the non-polar region. Changes in pH can affect an ionization of polar head groups and so alter their diameter, as can changes in their hydration level.<sup>[19]</sup> Thus, bilayer to nonbilayer transition can take place, resulting in loss of membrane barrier function. These transitions can be exploited to design liposomal carrier systems with preset release properties that are triggered by changes in their microenvironment.<sup>[19]</sup>

Normal micelles, which have only short-range order, form spontaneously when the amphiphiles are added to water. The liquid crystalline phases, which exhibit long-range order, like lamellar (cubic) and normal hexagonal phases, do not disperse spontaneously. When the lamellar phase is diluted with excess aqueous phase, it converts into spherical liposomes (Fig. 1),<sup>[2]</sup> which are widespread carriers for drugs, cosmetics, and many other types of actives.<sup>[19]</sup> Because of the presence of the aqueous core and the hydrophobic lipid bilayers, liposomes can accommodate both hydrophilic and hydrophobic actives. The liposomes can be constructed with widely different physical structures, lipid composition, and surface properties, thus enabling a great deal of control over entrapment and release of their contents.

Three kinds of liposomes are in common use. Large spherical liposomes, each consisting of numerous

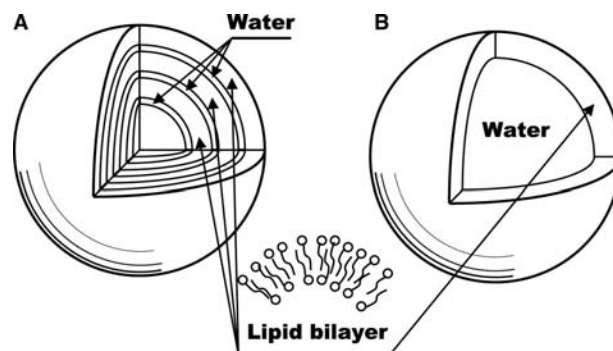


**Fig. 1** Schematic structure of liposomes: (A) multilamellar vesicles, MLV, and (B) small and large unilamellar vesicles, SUV and LUV.

concentric bilayers, alternating with layers of water, are known as multilamellar vesicles (MLVs) (Fig. 1A).<sup>[2]</sup> The MLVs are simple to produce, but the volume available for solute entrapment is limited. By gentle swirling, individual lamellae are able to detach to form large unilamellar vesicles (LUVs) (Fig. 1B).<sup>[20]</sup> Because the interior of LUVs is not occupied by internal lamellae, there is ample space for incorporation of actives. This also means that cells taking up LUVs are less subject to lipid overload. However, LUVs are more fragile than MLVs. In general, MLVs and LUVs vary in their outer diameter, from 100 nm up to 10  $\mu$ m. Their large size range is considered to be a drawback for many medical applications requiring parenteral administration because it leads to rapid clearance from the bloodstream by the cells of the reticuloendothelial system (RES).

Small unilamellar liposomes (SUVs), with outer diameter in the range of 20–100 nm,<sup>[21]</sup> can be obtained by ultrasonication of MLVs.<sup>[18]</sup> Because of their small size, clearance from the systemic circulation is significantly reduced, but SUVs have a much lower capacity for drug entrapment, typically less than 1% of the material available.

## Preparation of Liposomes

### Multilamellar vesicles

Multilamellar vesicles (Fig. 2A) may be prepared from natural or synthetic lipids by suspending them in an aqueous solution maintained at a temperature above the melting point  $T_c$  of the lipid. For unsaturated phospholipids such as egg and soy phosphatidylcholine, which have  $T_c$  values below 0°C, this can be done by stirring in an inert atmosphere of nitrogen or argon to avoid lipid oxidation.<sup>[2]</sup> A small amount of the active solution is entrapped within the interlamellar spaces when lipid is hydrated, followed by the liposome formation. The loaded liposomes can be

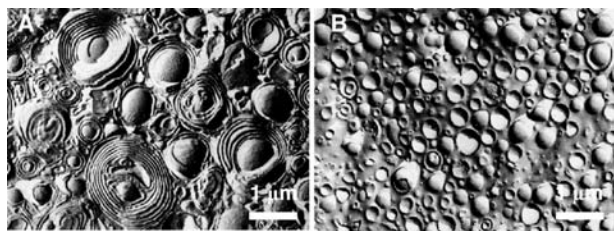


**Fig. 2** Freeze-fracture transmission electron micrographs of liposomes: (A) MLV constituted from 0.1M mixture of tetradecyldimethylaminoxide/tetradecyltrimethyl ammonium bromide/hexanol = 9/1/20, and (B) SUV prepared from 3 wt.% didodecyldimethyl ammonium bromide in water. Source: From Hoffmann, H.; Thunig, C. et al. *Langmuir* 1994, 10 (11), 3972–3981. © 1994, ACS.

separated from non-encapsulated solute using centrifugation or dialysis.

The encapsulation efficiency can be increased by inclusion of a charged amphiphile, such as phosphatidylglycerol or phosphatidic acid, at a molar ratio of 10–20%, or by preliminary freeze-drying of the lipid from an organic solution followed by formation of an expanded foam with an increased surface area, which increases the amount of aqueous phase that can be incorporated.<sup>[22]</sup> The most advanced method, which was designed to achieve high levels of entrapment, particularly of sensitive biomacromolecules such as proteins and nucleic acids, is dehydration/rehydration method.<sup>[23]</sup> It allows a prolongation of exposure of solute to the lipid before its final lamellar structure has been fixed. This may be achieved by preparing MLVs in water followed by converting these to SUVs. Thus, when SUVs are mixed with a solution of the active to be entrapped, most of the amphiphile is directly exposed to the solute. At this stage, water is removed by freeze-drying to produce the vesicles in a metastable state enriched with active. Following the hydration stage, the liposomes are diluted with an isotonic buffer<sup>[23]</sup> to provide an osmotic gradient between the internal and external phases and avoid redistribution of active, and finally washed to remove the nonencapsulated material.

Lipids dissolved in organic solvents can be hydrated in solution without prior solvent removal. If the solvent is water miscible, such as ethanol or propylene glycol, it may be removed at the end of MLV preparation by dialysis or filtration. Water-immiscible solvents such as ether, chloroform, or methylene chloride may also be used, then later removed through evaporation. High-capacity multivesicular liposomes were created in w/o/w double emulsion, containing active in the inner entrapped aqueous phase.<sup>[24]</sup> Composition and conditions are chosen such that each droplet of the organic chloroform–ether disperse phase contains multiple droplets of the initial aqueous

solution of active. The organic solvents are removed under a nitrogen flow, wherein the lipid is deposited around the internal aqueous, drug-containing nanodroplets, which form separate compartments within a single liposome. The method allows encapsulation efficiencies of up to 90%, but requires specialized lipids and rather complex preparation conditions.

Different technology has been applied so far to produce a new solid lipid carrier system, the so-called solid lipid nanoparticles (SLNs).<sup>[25–28]</sup> It is rather effective for encapsulating drugs that are poorly soluble in both aqueous and organic media.<sup>[25]</sup> Solid lipid nanoparticles combine the advantages of both liposomes and polymer nanoparticles. In SLNs the liquid lipid in emulsion is replaced by a solid lipid, e.g., high-melting glycerides (trilaurin, tribehenin) or waxes (cetyl palmitate); the particles are stabilized against aggregation by natural emulsifiers (lecithin), synthetic surfactants (Miranol, Plantaren, Tween 80), or sterically stabilizing polymers (Pluronic F68).<sup>[26,27]</sup> To prepare SLN dispersions, melted lipid mixed with an active was added to a surfactant solution of distilled water at elevated temperature. After stirring, the crude pre-emulsion was homogenized under high pressure between 500 and 1500 bar, applying several homogenization cycles.<sup>[26,27]</sup> Mean particle size of prepared SLNs ranged from 100 to 300 nm.

Within SLNs, actives with a melting point below the melting point of the lipid matrix preferentially distribute to the surface of the particles.<sup>[27]</sup> Wide-angle X-ray scattering investigations suggested that good entrapment efficacy in SLNs can be achieved with lipids of low crystalline order and metastable polymorphs of the  $\beta'$  form.<sup>[28]</sup> This allows optimization of lipid composition in favor of formation of this metastable polymorph.

### Small unilamellar vesicles

Small unilamellar vesicles (Fig. 2B) can be formed easily by high-power probe or bath sonication of MLVs in an inert atmosphere by cooling to dissipate local overheating<sup>[18]</sup> and avoid disruption of lipid molecules. Alternatively, MLVs can be converted into SUVs by use of high-pressure homogenization, such as in the case of SLN, or extrusion. High-pressure extrusion involves forcing MLVs through porous membranes<sup>[29]</sup> at temperatures above  $T_c$ . As a result, lamellar fragments break away and close to form small vesicles of similar diameter to that of the pore. A particular advantage of the method is that the disruptive effects of sonication are avoided. Rapid injection of an ethanol solution of lipid into an aqueous solution also leads to production of vesicles 30 to 110 nm in diameter.<sup>[30]</sup> This method has two disadvantages as compared to sonication: high polydispersity and dilute

suspension of liposomes obtained. Acidic phospholipids such as phosphatidic acid and phosphatidylglycerol are able to form unilamellar liposomes simply by transiently increasing the pH.<sup>[18]</sup> However, this process is critical to ionic strength, presence of other lipid components, and rate of titration.

### Large unilamellar vesicles

Methods for preparing LUVs fall into two categories. The first involves removal of a lipid solubilizing agent, whereas the second applies physical modification of preformed bilayer. In the first case, the lipid is initially dissolved in an aqueous solution of the surfactant (either ionic—cholate, deoxycholate, or non-ionic—Triton 100, octylglucoside) to form mixed lipid–surfactant micelles followed by removal of the surfactant by dialysis, diafiltration, or gel chromatography.<sup>[31]</sup> With another method, a volatile solvent such as diethyl ether, petroleum ether, or dichlorofluoromethane containing dissolved lipid is infused slowly into the aqueous phase, which is maintained at a temperature above the boiling point of the solvent so that bubbles are formed.<sup>[32]</sup> The lipid molecules form a multilayer around the vapor–water interphase, and as the solvents evaporate, uni- and oligolamellar liposomes with the size range of 100–400 nm remain in dispersion. Encapsulation efficiencies up to 46% were reported.

In the more advanced reverse-phase evaporation method, the w/o emulsion containing excess lipid in the organic phase (diethyl ether) is subject to rotary evaporation. At this stage the emulsion inversion takes place. This involves collapse of inverted micelles so that their aqueous contents form the new continuous phase, while their lipid components convert into a vesicular form.<sup>[33]</sup> In the absence of cholesterol, these vesicles have an outer diameter in the range of 50–500 nm, whereas with 50 mol% cholesterol, mean diameter is about 500 nm. High encapsulation efficiencies up to 65% can be achieved using hydrophilic solutes.

Physical modification of existing bilayers involves the above-mentioned extrusion method, which is effective for obtaining both SUVs and LUVs, and exposure of SUVs to alternate cycles of freezing and thawing. These procedures lead to fusion of the SUVs followed by formation of LUVs.<sup>[29]</sup> An elegant method using fusion is based on electrostatic effect. SUVs composed of negatively charged phospholipids are mixed with calcium ions, which cause the vesicles to aggregate and then fuse.<sup>[34]</sup> This results in formation of “cochleate cylinders,” which are rolled-up portions of lipid bilayer. Chelation of Ca<sup>2+</sup> by adding EDTA results in conversion of the cochleates to LUVs.

### Applications of Liposomes

Liposomes have been widely investigated as delivery systems for treatment of cancer, as well as bacterial, fungal, viral, and parasitic diseases.<sup>[35]</sup> Liposome-based gene transfection systems have been promoted as means to achieve the transfection efficacy of viral constructs without any associated risks. Liposomes themselves can serve as immunological adjuvants. They are applied as vehicles to deliver various radioisotopes and contrast agents for use in diagnostic imaging. In general, several beneficial properties of the liposomal form of drugs and the ways of providing their targeted delivery are essential for polymer nanoparticles as well. However, because of the noncovalent interactions responsible for their formation liposomes have only limited stability and are subject to structural changes.<sup>[18]</sup>

Efficiency of both the liposomal forms and nanoparticles depends on the rate of releasing of an active substance and their clearance from the blood. Compounds with low molecular weight release rapidly. Depending on molecular weight and the ability to withstand enzymatic attack, drugs could then act either locally (e.g., hydrolysis of stored sucrose by liposomal fructofuranosidase) or, after diffusion through the lysosomal membrane, in other cell compartments (e.g., inhibition of DNA-directed RNA synthesis by liposomal actinomycin D).<sup>[35]</sup> It was shown that the rate of clearance of injected liposomes from the blood is rather rapid, dose dependent, and biphasic. Neutral MLVs and SUVs exhibit a slower rate of clearance than charged MLVs.<sup>[35]</sup> Understanding of liposomal fate and behavior led to several proposed applications. The most important fact is that liposomes with entrapped material were shown to end up in the fixed macrophages of the RES, mainly in the liver and spleen.<sup>[36]</sup> Fast blood clearance is the principal obstacle to use of liposomes for drug delivery via the parenteral route. Liposome clearance can be substantially reduced by inclusion of monosialoganglioside GM<sub>1</sub>, hydrogenated phosphatidylinositol, or PEG-substituted phosphatidylethanolamine into the bilayer.<sup>[37]</sup> The same effect may be achieved by PEG coating of liposomes—PEGylation.<sup>[38]</sup> This modification hampers detection by the RES, and led to their being called Stealth<sup>TM</sup> liposomes. The long-circulating PEGylated liposomes are considered suitable for targeted drug delivery to tumors and inflammatory foci, as well as for diagnostic imaging applications, e.g., magnetic resonance and scintigraphic imaging.

Two types of targeting are under way: passive and active. Passive targeting is limited in its scope, leads to the rather wide distribution of the drug-filled liposomes in tissues, and depends dramatically on time of circulation. Thus, tremendous efforts are being



directed at present toward the development of control together with modification of the liposome surface with molecules having recognition properties. Typical examples of such modification are antigenic determinants, including various types of membrane receptors, or antibodies (either intact or as active fragments), other proteins, lipoproteins, glycoproteins, and so on, which may associate with bilayers as they do in the living cells. One such way is ligand-coupling strategy, which was originally realized with tumor-specific antibodies, known as immunoliposomes.<sup>[39]</sup> Most of the subsequent studies have used chemical coupling to link a targeting moiety to an amphiphilic molecule inserted into the liposome bilayer. The most widely used approach involves the use of heterobifunctional cross-linking reagents for introducing thiol-ether-based linkages between the lipid anchor and the ligand (e.g., immunoglobulin).<sup>[40]</sup>

The way in which liposomes induce immune responses to antigens associated with them is still not clear, but has been attributed to a depot mechanism and the ability of liposomes and antigen content to migrate to regional lymph nodes. A novel concept, namely, production of the required vaccine antigen by the host cells *in vivo*, promises to alter vaccination, especially where vaccines are either ineffective or unavailable. The concept entails the direct injection of antigen-encoding plasmid DNA, which, after its uptake by cells, finds its path to the nucleus where it transfects the cells.<sup>[41]</sup> Antigen so produced is recognized by the host as foreign and then subjected to pathways leading to protective immunity. Simple mixing of antigen-encoding plasmid DNA or DNA itself and cationic SUV leads to neutralization of polyanionic nucleic acid chain to form a compact nanostructure, known as a lipoplex.<sup>[42]</sup> Each of these nanoparticles carries a small net positive charge, which enables them to interact with the negatively charged cell membranes and gain entry by receptor-mediated endocytosis to perform transfection.

## POLYMER NANOSPHERES

### Manufacture of Nanospheres

The first approaches used to produce polymer nanoparticles were derived from the field of latex engineering. These methods were based on *in situ* polymerization of monomers.<sup>[43,44]</sup> Despite the actual technological advances, polymerization-based methods have some drawbacks and limitations. Thus, alternative methods based on the dispersion of well-characterized preformed polymers or natural biopolymers<sup>[4,5]</sup> have been proposed.<sup>[45]</sup> Together with polymerization-based methods, these new techniques

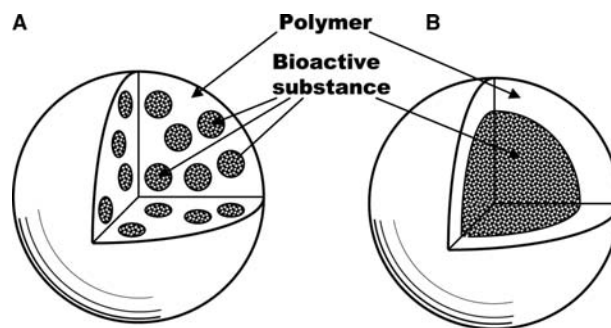


**Fig. 3** Schematic structure of polymer nanoparticles: (A) nanospheres and (B) nanocapsules.

allow the production of both nanospheres and nanocapsules (Fig. 3).

### Polymerization Methods

Two different approaches have been considered for the preparation of nanospheres by polymerization methods, depending on whether a monomer to be polymerized is emulsified in a nonsolvent phase (emulsion polymerization) or dissolved in a solvent that is a nonsolvent for the resulting polymer (dispersion polymerization).<sup>[44]</sup>

In two types of emulsion polymerization, either conventional (o/w emulsion) or inverse (w/o emulsion), the monomer is emulsified in the nonsolvent phase with surfactant, leading to the formation of monomer-swollen micelles and stabilized monomer droplets. The polymerization reaction takes place in the presence of an initiator that creates free reactive monomer radicals. These collide with the unreactive monomers and initiate polymer chain growth, or nucleation.<sup>[44]</sup> The reaction stops when full consumption of monomer or initiator is achieved. The drug to be incorporated to the nanospheres may be present during the polymerization process. Two different mechanisms of nucleation were considered. First, the so-called micellar polymerization mechanism treats the monomer-swollen micelles as the site of nucleation and propagation.<sup>[46,47]</sup> In this case, monomer droplets serve as monomer reservoirs. The monomer molecules reach the micelles by diffusion through the continuous phase. The second mechanism is valid for monomers that are sufficiently soluble in the continuous phase. In this case, homogeneous nucleation followed by propagation can occur directly in this phase, leading to formation of oligomers.<sup>[47]</sup> When the oligomers have reached a certain length, they form primary particles stabilized by surfactant molecules present in the system. In the case of inverse emulsion polymerization, when we deal with w/o system, the water-soluble monomers cannot diffuse from the micelles through the organic phase because of their low partition coefficient.

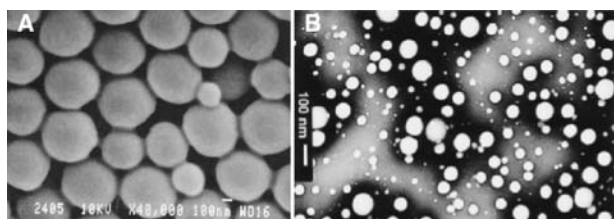


**Fig. 4** (A) Electron scanning micrograph of insulin-loaded poly(ethylcyanoacrylate) nanospheres obtained by a polymerization technique. (B) Transmission electron micrograph of procaine hydrochloride loaded poly(lactide-co-glycolide) nanospheres obtained by precipitation method. *Source:* From Radwan, M.A.; Aboul-Enein, H.Y. J. Microencapsul. **2002**, *19* (2), 225–235. © 2002, Taylor & Francis, Ltd. From Govender, T.; Stolnik, S. et al. J. Control. Release **1999**, *57* (2), 171–185, © 1999, Elsevier.

The resulting nanospheres contain fewer polymer chains and a narrower size distribution as compared to the conventional emulsion polymerization.<sup>[48]</sup>

Both the conventional and inverse emulsion polymerization reactions were applied for the production of biodegradable poly(alkyl cyanoacrylate) (PACA) nanospheres.<sup>[49,50]</sup> In the case of conventional emulsion polymerization, the alkyl cyanoacrylate monomer is added to an aqueous acidic solution of surfactant under vigorous stirring to polymerize it following the anionic mechanism. Drug is dissolved in the polymerization medium either before the addition of monomer or at the end of the polymerization reaction. Nanospheres (Fig. 4A) are sedimented by ultracentrifugation of the obtained suspension. In the case of inverse emulsion polymerization, drug is dissolved in a small amount of water or hydrophilic solvent and emulsified in an organic phase (e.g., isooctane, cyclohexane, and hexane) in the presence of surfactants. Alkyl cyanoacrylate monomers are then added directly or dissolved in an organic solvent to the preformed w/o emulsion under stirring.<sup>[49]</sup> The system becomes milky, and nanospheres with a diameter of 200–300 nm with a narrow polydispersity are formed.

Dispersion polymerization deals with polymerization of monomers dissolved in an aqueous medium that acts as a precipitant for the polymer to be formed. Nucleation is induced in the aqueous monomer solution,<sup>[51]</sup> and the presence of stabilizers or surfactants is not absolutely necessary for the formation of nanospheres.

As mentioned earlier, polymerization methods have significant limitations, especially for formation of nanospheres.<sup>[45]</sup> First, it is very difficult to predict the molecular weight of the resulting material. This is a major drawback because the molecular weight influences the biodistribution and release of the polymer carrier. Second, the presence of free radicals or numerous H<sup>+</sup> ions generated by anionic polymerization

process can inhibit drug activity. Third, the presence of toxic unreacted monomer, initiator, and surfactant molecules requires time-consuming and, sometimes, inefficient procedures for their elimination.

### Dispersion of preformed polymers

Among the numerous synthetic polymers available for the preparation of nanospheres, the most commonly used are polyesters such as poly(lactic acid) (PLA), poly(glycolic acid) (PGA), poly(lactic-co-glycolic acid) (PLGA), poly( $\epsilon$ -caprolactone) (PLG), and poly( $\beta$ -hydroxybutyrate) (PHB).<sup>[4,5]</sup> Under physiological conditions, polyesters are generally degraded by hydrolysis into products that are well tolerated by various tissues.

**Solvent Evaporation Method.** In this method, a polymer is dissolved in an organic solvent (dichloromethane, chloroform, or ethyl acetate).<sup>[52]</sup> A drug is dissolved or dispersed into the polymer solution, and this mixture is then emulsified into an aqueous solution to make an o/w emulsion by using a surfactant such as gelatin, poly(vinyl alcohol) (PVA), polysorbate-80, poloxamer-188, etc. After the formation of emulsion, the organic solvent is evaporated either by heating or continuous stirring.<sup>[53]</sup> The double emulsion method, dealing with w/o/w emulsions, may also be used to prepare nanospheres containing water-soluble drugs.<sup>[54]</sup> Both these methods apply high-speed homogenization or sonication, which are not quite appropriate for large-scale production. In this pursuit, the following approaches have been attempted.

**Spontaneous Emulsification (Solvent Diffusion) Method.** In a modified version of the solvent evaporation method, the water-soluble solvent (acetone or methanol) along with the water-insoluble organic solvent (dichloromethane or chloroform) was used as an oil phase.<sup>[55]</sup> Because of the spontaneous diffusion of the water-soluble solvent, an interfacial turbulence is created between the two phases leading to the formation of smaller particles. As the concentration of water-soluble solvent increases, a considerable decrease in particle size can be achieved.

**Salting-Out Method.** The salting-out technique replaces chlorinated solvents with water-miscible acetone.<sup>[56]</sup> An aqueous phase saturated with electrolytes (e.g., magnesium salts) and containing PVA as a stabilizing and thickening agent is added under stirring to an acetone solution of polymer. The miscibility of both phases is prevented by the saturation of the aqueous phase with electrolytes, according to a salting-out phenomenon. The addition of the aqueous phase is continued until a phase inversion occurs and an o/w

emulsion is formed. Then, a sufficient amount of water is added to disrupt the equilibrium between the two phases and allow complete diffusion of acetone into water followed by polymer precipitation in the form of nanospheres. Other solvents (e.g., tetrahydrofuran) as well as nonelectrolytic salting-out agents (e.g., sucrose) could also be appropriate.<sup>[57]</sup> A variety of polymers can be used with this technique including PLA, methacrylic acid copolymers, and cellulose derivatives.

**Emulsification–Diffusion Method.** This method formally resembles the previous method, but its originality is in using benzyl alcohol as an organic solvent.<sup>[58]</sup> An aqueous phase containing PVA as a stabilizing and thickening agent is added to a solution of polymer in benzyl alcohol under stirring. With an excess of water, an o/w emulsion is obtained because benzyl alcohol has low miscibility with water. The precipitation of the polymer occurs due to the diffusion of benzyl alcohol into water, leading to the formation of nanospheres. By increasing the content of PVA in the external phase, it was possible to produce nanoparticles as small as 70 nm in diameter. The polymers used were PLA, PLGA, PCL, and methacrylic acid copolymers.

**Direct Precipitation Method.** This technique involves the use of polymer solution in an organic solvent that is completely miscible with the aqueous phase (acetone, ethanol, or acetonitrile) and allows nanospheres to be obtained after addition of water (with or without a surfactant) under stirring<sup>[59]</sup> (Fig. 4B). After precipitation of nanoparticles, the solvent is removed by vaporization under vacuum. Applications of this method are limited to drugs that are highly soluble in polar solvents but insoluble in water.

**Supercritical Fluid Technology.** Conventional methods such as in situ polymerization and solvent evaporation often require the use of toxic solvents and surfactants. Supercritical fluids allow attractive alternatives for the nanoencapsulation process because these are environmentally friendly solvents.<sup>[60]</sup> The commonly used methods of supercritical fluid technology are the rapid expansion of supercritical solution (RESS)<sup>[61]</sup> and the supercritical antisolvent (SAS) method.<sup>[62]</sup> A supercritical fluid is a substance that is used in a state above the critical temperature and pressure where gases and liquids can coexist. It is able to penetrate materials such as gas, and to dissolve materials such as liquid. For example, use of carbon dioxide or water in the form of a supercritical fluid allows substitution for an organic solvent.

In the RESS method,<sup>[61]</sup> a polymer is solubilized in a supercritical fluid and the solution is expanded

through a nozzle. Thus, the solvent power of supercritical fluid dramatically decreases and the solute eventually precipitates. A uniform distribution of drug inside the polymer matrix, e.g., PLA nanospheres, can be achieved only for low-molecular-mass (< 10,000) polymers because of the limited solubility of high-molecular-mass polymers in supercritical fluids.<sup>[63]</sup> In the SAS method,<sup>[62]</sup> the solution is charged with the supercritical fluid in the precipitation vessel containing a polymer in an organic solvent. At high pressure, enough antisolvent will enter into the liquid phase so that the solvent power will be lowered and the polymer precipitates. After precipitation, the antisolvent flows through the vessel to strip the residual solvent. When the solvent content has been reduced to the desired level, the vessel is depressured and the solid nanoparticles are collected.

## POLYMER NANOCAPSULES

### Manufacture of Nanocapsules

In general, all the methods for preparation of nanocapsules (Fig. 3B) are based on the self-assembly approach, which resembles aggregation of lipid molecules in aqueous solution into liposomes (Fig. 1).

#### Surface polymerization method

To overcome the instability of liposomes, lipids that are functionalized with polymerizable groups can be polymerized within vesicular structures.<sup>[64]</sup> Because of the polymerization reaction, the individual lipid molecules are interconnected via covalent bonds that stabilize the wall-forming membrane considerably. However, nanocapsules prepared from reactive lipids are rather costly.

In an analogous fashion to the lipids, amphiphilic block copolymers can also aggregate in aqueous solution to vesicular structures.<sup>[65]</sup> Block copolymer liposomes are significantly more stable than those formed from lipids due to the larger size and the lower dynamics of the underlying polymer molecules. Nevertheless, similarly to lipids they are held together solely by noncovalent interactions. Analogously to the reactive lipids, the block copolymer molecules could also be modified with polymerizable groups. Such block-copolymer-based nanocapsules can be expected to possess great potential for encapsulation and controlled release, because the physical properties of their polymer walls can be controlled by the block length or the chemical constitution of the underlying polymer molecules. So far only a few papers dealing with such nanocapsules have appeared.<sup>[66,67]</sup> In one of them the formation of vesicles from poly(isoprene)

*b*-poly-(2 cinnamoyl methacrylate) (PI-PCEMA) diblock copolymer in hexane–tetrahydrofuran mixtures was used as a starting stage.<sup>[66]</sup> The PCEMA blocks were photo-cross-linked and then the PI blocks had to be hydroxylated to make water-soluble nanocapsules. Diameter of the nanocapsules was in the range of 50–60 nm. A rather simple one-step procedure has been used to prepare vesicles of poly(2-methyloxasoline)-*b*-poly(dimethylsiloxane)-*b*-poly(2-methyloxasoline) in aqueous solution.<sup>[67]</sup> The underlying triblock copolymers were modified with methacrylate end groups without disturbing the vesicles in water, which were cross-linked under UV irradiation. Diameter of the obtained nanocapsules could be controlled in the range of 50–500 nm.

A similar concept uses just the geometry of the vesicular aggregates as a template. The interfacial polymerization of monomeric surfactants is an advanced method of this type of technique used for the preparation of nanocapsules.<sup>[68–74]</sup> For example, for the preparation of nanocapsules containing  $\alpha$ -chymotrypsin, the reverse hydrated micelles from *N,N*-diallyl-*N,N*-didodecyl ammonium bromide (DDAB) in cyclohexane entrapping enzyme in the inner aqueous cavities were polymerized by UV irradiation. After precipitation in acetone, these nanocapsules were dispersed in the aqueous medium with the aid of ionic (AOT) or nonionic (Brij-97) surfactants. Nuclear magnetic resonance spectroscopy data suggested that thereby bilayer nanocapsules with an average outer diameter of 20 nm were formed.<sup>[68]</sup> Their inner monolayer was made up of the two-dimensional poly-DDAB network, and the outer monolayer was composed of surfactant molecules.<sup>[69,70]</sup>

Another way used the ability of liposomes to solubilize hydrophobic monomers such as styrene,<sup>[71,72]</sup> acrylates, or alkylmethacrylates<sup>[3,73,74]</sup> within a bilayer. Their subsequent free-radical or UV-initiated polymerization led to the formation of a two-dimensional polymer network entrapped in the interior of the membrane (Fig. 5). The different compartments provided by the self-assembly of the lipid molecules generally serve only as a templates, which, similar to the previous case, control both the size and shape of the resulting nanocapsules. It was shown that the cross-linked polymer nanocapsules formed in vesicular dispersions are able to retain their structure even after isolation from the lipid matrix.<sup>[74]</sup>

Based on the method proposed for preparation of the PACA nanospheres,<sup>[49]</sup> PACA nanocapsules, consisting of a polymer envelope surrounding an oily core, were prepared.<sup>[75]</sup> The monomer molecules located at the surface of the oil nanodroplets, on contact with aqueous hydroxide anions, immediately polymerized at the water–oil interface, followed by the formation of a polymer wall with a mean thickness of about 3 nm.<sup>[75]</sup> It was later shown that the PACA nanocapsule morphology

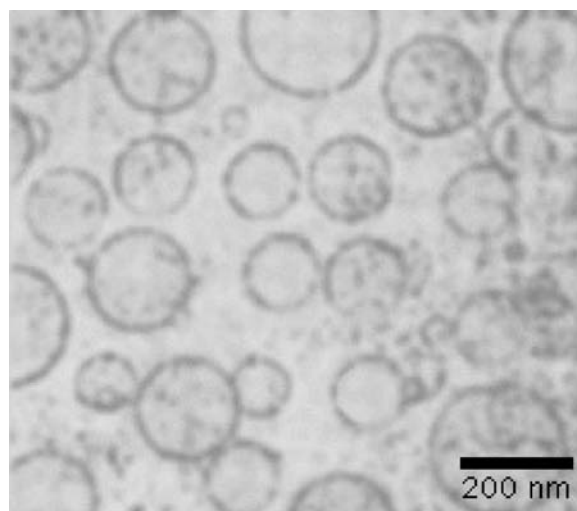


**Fig. 5** Cryotransmission electron micrograph of poly (acrylic acid) hollow nanospheres obtained by polymerization method. (From Sauer, M.; Meier, W. RSC Chem. Commun. 2001, No. 1, 55–56; reproduced by permission of The Royal Society of Chemistry.)

depends on the pH of the aqueous phase, composition of the organic phase, and emulsification conditions.<sup>[76]</sup> This dependence results in formation of a mixture of nanocapsules and nanospheres. When aprotic water-miscible organic solvents such as acetone or acetonitrile were used, only true nanocapsules were obtained.

### Template approach

A similar way for producing polymer nanocapsules is to assemble a preformed polymer wall around a template particle or an oil nanodroplet that can be subsequently removed.<sup>[3]</sup> The most convenient approach is to use an oppositely charged polyelectrolyte self-assembly at charged core surfaces.<sup>[77]</sup> Not all of the ionic groups of the adsorbed polyelectrolyte are consumed by the electrostatic interactions with the surface. As a result, the original surface charge is usually overcompensated by the adsorbed polymer. Hence, the surface charge of the coated particle changes its sign and is now available for the adsorption of a polyelectrolyte of again opposite charge. Such sequential deposition produces ordered polyelectrolyte multilayers. The thickness of the wall is controlled by the number of deposition steps. To avoid a polyelectrolyte-induced particle flocculation, the rather low particle concentrations and the removal of non-adsorbed polyelectrolyte after each step are necessary. Weakly cross-linked melamine formaldehyde particles have been used as template core particles.<sup>[3]</sup> Exposure of the coated particles to an acidic solution of pH < 1.6 dissolves the core without affecting the layered polyelectrolyte wall.

Functionalized polystyrene latex nanoparticles carrying surface charges are also suitable templates for the polyelectrolyte self-assembly technique. Inorganic particles were incorporated into the adsorbed walls by a sequential adsorption of SiO<sub>2</sub> nanoparticles with negative surface charge and cationic poly(*N,N*-diallyl-*N,N*-dimethyl ammonium chloride) (PDDAC).<sup>[78]</sup> Layers with a thickness ranging from tens to hundreds of nanometers could be prepared. Removing the polystyrene core leaves SiO<sub>2</sub>/PDDAC nanocomposite capsules. Nevertheless, the long-term stability of such polyelectrolyte walls in biological fluids (e.g., in blood plasma), or in media of high ionic strength, may be rather limited.

### Coacervation method

This method uses the phenomenon of polymer-polymer incompatibility to form nanocapsules. The wall-forming polymer is dissolved in a solvent and to this solution a second polymer (called the phase inducer) is introduced followed by the formation of a two-phase system. The smartest complex coacervation process uses the interaction of two oppositely charged polyelectrolytes in water to form a polymer-rich coating solution called a coacervate.<sup>[79,80]</sup> If drug nanoparticles or nanodroplets are then added, the phase, rich with the coating polymer, engulfs the drug being encapsulated, thereby forming embryo capsules. Cooling the system causes the coacervate to gel via network formation. Gelatin is a primary polymer component of most coacervation systems.

More rigid nanocapsules can be prepared by a combination of coacervation and emulsion/suspension polymerization approaches. For example, the polymerization of divinylbenzene (DVB) in toluene/DVB swollen polystyrene latex particles or in polystyrene containing toluene droplets leads to the formation of poly-DVB nanocapsules due to limited compatibility of the chemically different polymers in solution followed by a microphase separation and the formation of a poly-DVB wall around a toluene-polystyrene core.<sup>[81]</sup> After evaporation of the internal toluene a cavity remains in the core.

Survival of the polymer walls after removing the solid or liquid core is the general goal of the coacervation method. A rather elegant approach to remove the core under mild conditions has recently been demonstrated.<sup>[82]</sup> First, the core of the particles was formed by a low-molecular-weight poly(dimethylsiloxane) around which a cross-linked organosilicon wall was formed in a second step. The poly(dimethylsiloxane) core was removed quantitatively by ultrafiltration. The remaining organosilicon envelopes obviously had rather high porosity allowing fast releasing the low molecular weight bioactives.

### Applications of Nanoparticles

Nanoparticles used as pharmaceutical forms must satisfy the following conditions: they must be free of any toxic impurities, easy to store and administer, and sterile if parenteral use is expected. One of the most promising applications of nanoparticles is their use as parenteral carriers for anticancer drugs based on their ability to accumulate in a number of tumors.<sup>[83,84]</sup> The encapsulation of a variety of anticancer drugs (e.g., doxorubicin, 5-fluorouracil, dactinomycin, and methotrexate), immunomodulators (muramyl dipeptide-L-alanyl-cholesterol), or antisense oligonucleotides mainly within PACA nanoparticles enhanced their efficacy against experimental tumors in comparison to the free drug.<sup>[84]</sup> A reduction of the general toxicity of anticancer drugs was also achieved. The most effective application of anticancer drug-loaded nanoparticles may be their use in the treatment of hepatic metastases. The incorporation of magnetic subnanoparticles into drug-containing nanoparticles and subsequent electromagnetic guidance has been shown to improve antime-tastatic efficiency by facilitating access to extravascular tumors.<sup>[83]</sup> Two other methods to achieve tumor-specific targeting were by using nanoparticles coated with either monoclonal antibodies, in order to recognize specific cell determinants,<sup>[84]</sup> or with PEG, to increase the blood circulation time of nanoparticles.<sup>[85]</sup>

The nanoparticles of PACA have gained wide popularity recently despite some major drawbacks such as the use of low-pH media and cytotoxicity.<sup>[86]</sup> To overcome these, derivatives of poly(methylidenemalonate) were prepared, i.e., poly(ethyl-2-(ethoxycarbonyl)methyleneoxycarbonyl acrylate)<sup>[87]</sup> and poly(ethyl-2-(ethoxycarbonyl) ethyl methylene malonate-co-ethylene oxide).<sup>[88]</sup> These polymers are associated with both the hydrophilic and hydrophobic functionalities providing long-time circulation of nanoparticles in blood and sustained release.

Intracellular infections are another field of application of nanoparticles. It is known that antibiotics exhibit either poor ability to penetrate the infected cells or decreased activity in intracellular compartments. PACA nanoparticles loaded with ampicillin showed high efficacy against *Listeria monocytigenes* and *Salmonella typhimurium* infections.<sup>[89]</sup> They are suitable for the specific transport of antiviral agents. Recently, PACA nanoparticles loaded with the protease inhibitor saquinavir were shown to be effective in HIV-infected human macrophage cultures.<sup>[90]</sup> The same nanoparticles loaded with primaquine, and even without any drug within, treat parasitic infections such as visceral leishmaniasis.<sup>[89]</sup> The void nanoparticles themselves have immunomodulation activity. This fact opens new prospects in the field of parasitic infections as well as in the treatment of other infections or tumors.

Nanoparticles increase the oral bioavailability of the peptide and protein drugs. For example, enhanced oral bioavailability was reported for insulin (Fig. 4A), dicumarol, and plasmid DNA encapsulated into adhesive nanoparticles made of polyanhydride copolymers of fumaric and sebacic acids.<sup>[6]</sup> The use of nanoparticles is prospective for oral delivery antigens because of their ability to control the release of proteins and to protect them from enzymatic degradation in the gastrointestinal tract. The very slow degradation rate of PMMA nanoparticles is particularly appropriate for vaccine purposes because it provides prolonged contact between the antigen and the immunocompetent cells. At the same time, coating the nanocapsules with monoclonal antibodies is expected to increase the level of absorption of entrapped vaccines and, therefore, the immune response.<sup>[90]</sup> These investigations allow one to create new generations of effective vaccines for oral immunization.

Depending on the rate of desired release, the PACA, PLA, and PLGA nanoparticles can be applied for intramuscular, subcutaneous, and topical administration. For example, the topical use of nanoparticles by the ocular route has been investigated for the treatment of chronic diseases such as glaucoma. Because of their low viscosity in suspensions, these systems can be administered as eye drops providing the sustained drug delivery.<sup>[91]</sup>

## MOLECULAR INCLUSION COMPLEXES

Molecular inclusion complexes of the host–guest type provide unprecedented “molecular nanoencapsulation”

of drugs.<sup>[10]</sup> The most advanced among them are inclusion complexes of  $\alpha$ -,  $\beta$ -, and  $\gamma$ -cyclodextrins<sup>[7]</sup> and dendrimers.<sup>[8,9]</sup>

Cyclodextrins comprise a family of cyclic oligosaccharides. Three major cyclodextrins have a shape of a bracelet built up from glucopyranose units (6 units for  $\alpha$ -, 7 for  $\beta$ -, and 8 for  $\gamma$ -cyclodextrin) (Fig. 6A). The diameter of the inner cavity varies for  $\alpha$ -,  $\beta$ -, and  $\gamma$ -cyclodextrin from 0.5 to 0.8 nm. In an aqueous solution, the slightly apolar cyclodextrin cavity is occupied by water molecules that are energetically unfavored, and therefore may be readily substituted by appropriate “guest” molecules that are less polar than water. One or a few cyclodextrin molecules can entrap one or more “guest” molecules. Most frequently, the host/guest ratio is 1:1; however, 2:1, 1:2, 2:2 (Fig. 6C–E), or even more complicated associations, such as rotoxanes, exist.<sup>[7]</sup> The formerly hydrophobic guest, upon complexation, becomes hydrophilic and effectively protected against any type of reaction, except that with cyclodextrin hydrolysis. The formed inclusion complexes can be isolated as stable crystalline substances.

Natural cyclodextrins, however, have relatively low solubility, both in water and organic solvents, which thus limits their use in pharmaceutical formulations. Recently, various kinds of cyclodextrin derivatives have been prepared to extend the physicochemical properties and inclusion capacity of natural cyclodextrins as novel drug carriers.<sup>[10]</sup> To elongate the actual cyclodextrin cavity or enhance solubility, substituents are attached to the primary or secondary hydroxyl

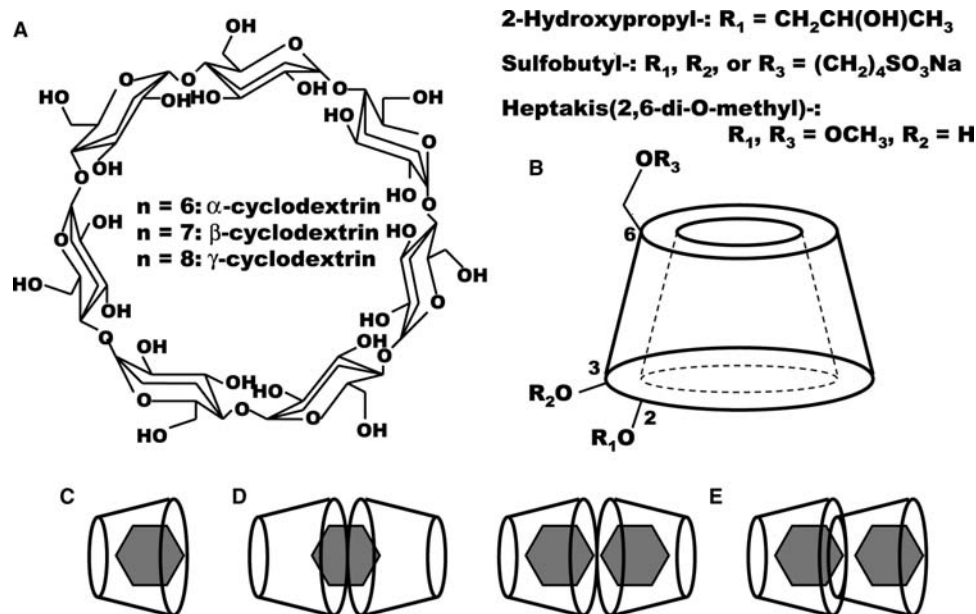


**Fig. 6** Chemical structure of cyclodextrins (A), the schematic representation of their O-derivatives (B), and the possible inclusion complexes 1:1 (C), 2:1 (D), and 2:2 (E).



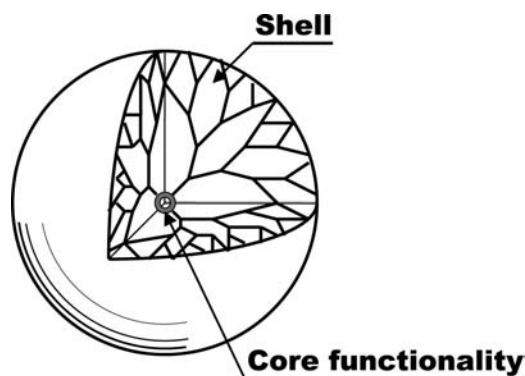


Fig. 7 Schematic structure of a spherical dendrimer of the fifth generation.

groups situated on the two rims of the molecular bracelet. This elongation may be hydrophobic if acyl or hydroxyalkyl groups are attached. At present, the acetylated, hydroxypropylated, and sulfobutylated derivatives, mainly of  $\beta$ - and  $\gamma$ -cyclodextrins, can be considered as drug carriers<sup>[10]</sup> (Fig. 6B).

Dendrimers are highly branched cascade molecules that emanate from a central core through a stepwise, repetitive reaction sequence.<sup>[8]</sup> Such a molecule consists of three topologically different regions: a small initiator core of low density and multiple branching units, the density of which increases with increasing distance from the core, thus eventually leading to a rather densely packed shell (Fig. 7). Dendritic shielding actually amounts to an encapsulation that can create a distinct microenvironment around the core moiety and hence affect its properties. Dendrimers with amphiphilic core-shell structures were shown to look like “unimolecular micelles.”<sup>[92]</sup> Dendrimers that have internal cavities with a dense outer shell may be synthesized by controlling the last step. This has been demonstrated by the preparation of a fifth-generation poly(propyleneimine) dendrimer.<sup>[93]</sup> Because of their outer shell, these molecules can be regarded as dendritic compartments that are capable of retaining guest molecules entrapped during synthesis. If the surface *tert*-butyl groups were removed guest molecules could diffuse out of the compartments. The compact dendrimer topology is promising for both the controlled release<sup>[93]</sup> and confined biochemical nanoreactors.<sup>[8]</sup>

Dendrimers are, generally, not hollow polymer particles. Recently, elegant synthetic protocols have been developed that form the inner cavity directly from dendritic precursors. One of them is based on a polyether dendrimer with a trimesic acid ester core.<sup>[94]</sup> The molecular nanocapsules were formed by selective cross-linking of homoallyl ether groups at the surface of the dendrimer and subsequent degradation of the core region by hydrolysis (Fig. 8). An attractive possibility offered by this method is that the remaining functional

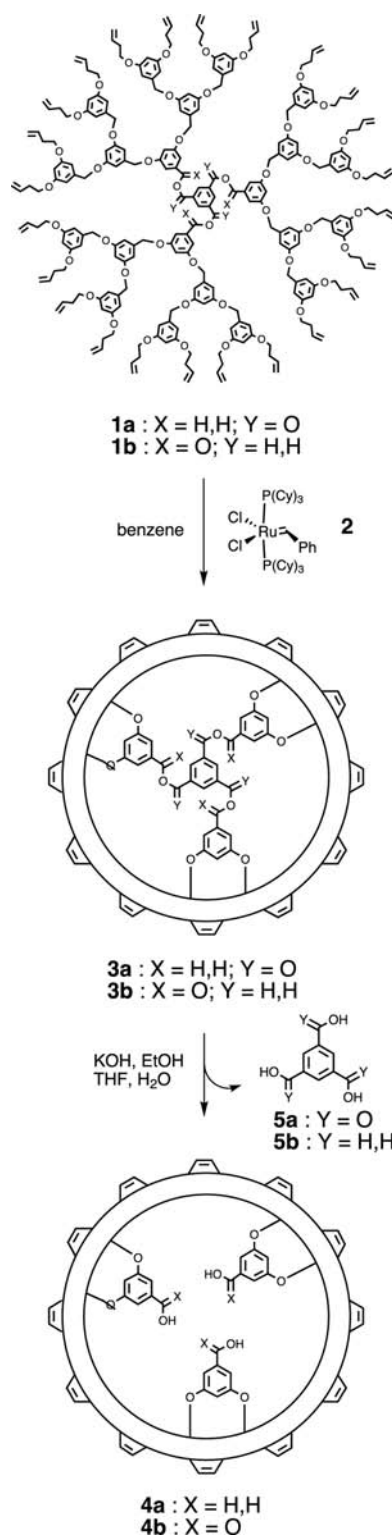


Fig. 8 Preparation of a cored dendrimer. Source: From Ref.<sup>[94]</sup> © 1999, ACS.

groups in the interior of the carrier system could serve as “endoreceptors” available for molecular recognition. This approach allows control over size and geometry of the formed nanocapsules, but preparation

is rather refined. This is still a limiting factor for possible applications of dendrimers as drug carriers.

### Applications of Molecular Inclusion Complexes

The metabolic fate of natural cyclodextrins and their derivatives given orally has been thoroughly investigated and their lack of toxicity has been demonstrated.<sup>[10]</sup> However, the intravenous or intramuscular administration of some  $\beta$ -cyclodextrin derivatives like heptakis(2,6-di-*O*-methyl)- $\beta$ -cyclodextrin in rats and rabbits increased blood urea nitrogen, creatinine, and transaminases, indicating some kidney and liver failure, while those for 2-hydroxypropyl-, 6-*O*-maltosyl- $\beta$ -cyclodextrin, and  $\beta$ -cyclodextrin sulfate at the same dosage remained within normal limits.<sup>[10]</sup> Another drawback of cyclodextrins as drug carriers is their ability to induce human erythrocytes to change their biconcave shape to monoconcave and induce lysis at higher concentrations because cyclodextrins are able to solubilize the biomembrane components. When we deal with the inclusion complex, or when the cyclodextrin cavity is modified by chemical derivatization, the effect on cell membranes can be dramatically mitigated. The above-mentioned 2-hydroxypropyl- and sulfobutyl- $\beta$ -cyclodextrin were generally found to be safe when administered parenterally in animals and humans.<sup>[95]</sup>

One of the most important functions of cyclodextrins is to enhance the aqueous solubility of included drugs. The degree of substitution markedly influences the solubilization. In general, hydroxyalkylated, sulfated, and sulfoalkylated cyclodextrins and their complexes have lower aqueous solubility than parent cyclodextrins.<sup>[10]</sup> When mono- or disaccharides are bounded to one or two primary hydroxyl groups of cyclodextrins through the  $\alpha$ -1,6-glycosidic bond, their solubility in water increases. It is remarkable that the enzymatically prepared branched cyclodextrins have higher affinity to drugs and bioavailability along with weak hemolytic activity.<sup>[96]</sup>

In oral delivery, hydrophilic and hydrophobic cyclodextrin derivatives are useful for immediate- and sustained-release type formulations. The hydrophilic cyclodextrins have been extensively applied to enhance the oral bioavailability of steroids, cardiac glycosides, anti-inflammatory drugs, barbiturates, antiepileptics, neuroleptics, antidiabetics, vasodilators, etc.<sup>[10,96–99]</sup> Recently, highly hydrophilic cyclodextrin derivatives, such as 2-hydroxypropyl-, 6-*O*-maltosyl-, and sulfobutyl- $\beta$ -cyclodextrin have been used to obtain an immediate-release formulation, which is readily dissolved in the gastrointestinal tracts, providing an enhancement of oral bioavailability of poorly water-soluble drugs.<sup>[99]</sup> On the other hand, alkylated and

acylated derivatives are useful as slow-release carriers for water-soluble drugs. Among them heptakis(2,6-di-*O*-ethyl)-, heptakis(2,3,6-tri-*O*-ethyl)-, and heptakis(2,3,6-tri-*O*-butanoyl)- $\beta$ -cyclodextrin were the first slow-release carriers to be used in conjunction with diltiazem, isosorbide dinitrate, and salbutamol.<sup>[10]</sup>

The cyclodextrin vehicles are effective in ophthalmic formulations because they do not irritate the ocular surface resulting in a fast washout of the instilled drug. Hydrophilic 2-hydroxypropyl- and sulfobutyl- $\beta$ -cyclodextrin are nontoxic to the eye and well tolerated in aqueous eye drops with low viscosity. They do not penetrate the corneal barrier, but enhance the ocular bioavailability of included lipophilic drugs like dexamethasone acetate.<sup>[100]</sup>

Cyclodextrins improve the solubility and stability of drugs in topical preparations onto the skin, thus enhancing the transdermal penetration of drugs and sustaining the drug release along with lowering their toxicity.<sup>[10]</sup> In general, hydrophilic cyclodextrins and their complexes penetrate through the skin inefficiently. However, when cyclodextrins are applied under occlusive dressing conditions, they are able to permeate the skin.<sup>[10]</sup> For example, transdermal delivery of prostaglandin E<sub>1</sub>, which is unstable and poorly permeable into the skin, in complex with a penetration enhancer, 1-[2-(decylthio)ethyl]azacyclopentane-2-one, with the aid of 6-*O*-(carboxymethyl)-*O*-ethyl- $\beta$ -cyclodextrin, leads to the treatment of peripheral vascular disorders as an alternative to parenteral injections.<sup>[101]</sup>

Cyclodextrins are effective for providing the targeted drug delivery.<sup>[10]</sup> It is known that the specific delivery of neuropharmaceuticals to the brain is obscured by the presence of the blood-brain barrier. Inclusion complexes with cyclodextrins are able to solve the permeability problem, as it was shown for inclusion complexes of psychotropic agents (phenazepam, gidazepam).<sup>[97,98]</sup> Another example is the conjugate of *N*-leucine-enkephalin and 6-amino-6-deoxy- $\beta$ -cyclodextrin.<sup>[102]</sup> Both types of prodrugs provide brain targeting followed by the sustained release. In general, the substituents introduced at primary hydroxyl groups of cyclodextrins through a spacer of appropriate length are self-included within the cavity. However, the enkephalin conjugate can accommodate other guest molecules (e.g., dothiepine) because the self-inclusion is restricted due to steric hindrance.

### CONCLUSION

It is clear that biology has much to offer nanotechnology in demonstrating how to organize, functionalize, and assemble new molecular and submolecular materials and tools to design nanosize carriers for bioactive substances. From the chemical point of view,

it is important to synthesize newer polymers and surfactants to match the hydrophilic and hydrophobic properties of the bioactive substances. Implementation of cavitands for formation of inclusion complexes can dramatically increase the loading capacity of carriers in combination with polymer nanoparticles and liposomes. Their new amphiphilic derivatives are capable of forming nanospheres and nanocapsules, presenting a high loading capacity toward both hydrophobic and hydrophilic drugs without any polymerization process. In order to provide the targeted delivery and controlled release of the bioactive substance, designing the carriers with tailored surface characteristics based on specific peptide, protein, polynucleotide, or polysaccharide motifs with preordained functions becomes the regular strategy.

## REFERENCES

- Dworkin, J.P.; Deamer, S.A.; Sandford, S.A.; Allamandola, L.J. Self-assembling amphiphilic molecules. *Proc. Natl. Acad. Sci. U. S. A.* **2001**, *98* (3), 815–819.
- Bangham, A.D.; Standish, M.M.; Watkins, J.C. Diffusion of univalent ions across the lamellae of swollen phospholipids. *J. Mol. Biol.* **1965**, *13* (1), 238–252.
- Meyer, W. Polymer nanocapsules. *Chem. Soc. Rev.* **2000**, *29* (5), 295–303.
- Jagur-Grodzinski, J. Biomedical application of functional polymers. *React. Funct. Polym.* **1999**, *39* (2), 99–138.
- Uhrich, K.E.; Cannizzaro, S.M.; Langer, R.S.; Shakesheff, K.M. Polymeric systems for controlled drug release. *Chem. Rev.* **1999**, *99* (11), 3181–3198.
- Panyam, J.; Labhasetwar, V. Biodegradable nanoparticles for drug and gene delivery to cells and tissue. *Adv. Drug Deliv. Rev.* **2003**, *55* (3), 329–347.
- Szejtli, J. Introduction and general overview of cyclodextrins chemistry. *Chem. Rev.* **1998**, *98* (5), 1743–1753.
- Hecht, S.; Fréchet, J.M.J. Dendritic encapsulation of function: applying nature's site isolation principle from biomimetics to material science. *Angew. Chem., Int. Ed.* **2001**, *40* (1), 74–91.
- Gorman, C.B.; Smith, J.C. Structure–property relationship in dendritic encapsulation. *Acc. Chem. Res.* **2001**, *34* (1), 60–71.
- Uekama, K.; Hirayama, F.; Irie, T. Cyclodextrin drug carrier systems. *Chem. Rev.* **1998**, *98* (5), 2045–2076.
- Jung, T.; Kamm, W.; Breitenbach, A.; Kaiserling, E.; Xiao, J.X.; Kissel, T. Biodegradable nanoparticles for oral delivery of peptides. *Eur. J. Pharm. Biopharm.* **2000**, *50* (2), 147–160.
- Song, C.; Labhasetwar, V.; Cui, X.; Underwood, T.; Levi, R.J. Arterial uptake of biodegradable nanoparticles for intravascular local drug delivery. *J. Control. Release* **1998**, *54* (2), 201–211.
- Kreuter, J. Drug targeting with nanoparticles. *Eur. J. Drug Metab. Pharmacokinet.* **1994**, *19* (3), 253–256.
- Wise, D.L.; Ed. *Handbook of Pharmaceutical Controlled Release Technology*; Marcel Dekker, Inc.: New York, 2000.
- Yang, L.; Alexandridis, P. Physicochemical aspects of drug delivery and release from polymer-based colloids. *Curr. Opin. Colloid Interface Sci.* **2000**, *5* (1–2), 132–143.
- Moghimi, S.M.; Hunter, A.C.; Murray, J.C. Long-circulating and target specific nanoparticles: theory to practice. *Pharmacol. Rev.* **2001**, *53* (2), 283–318.
- Carino, G.P.; Jacob, J.S.; Mathiowitz, E. Nanosphere based oral insulin delivery. *J. Control. Release* **2000**, *65* (1–2), 261–269.
- Lasic, D.D. *Liposomes: From Physics to Applications*; Elsevier: Amsterdam, 1993.
- Kirby, C.J.; Gregoriadis, G. Liposomes. In *Encyclopedia of Controlled Drug Delivery*; Mathiowitz, E., Ed.; John Wiley & Sons, Inc.: New York, 1999; Vol. 1, 461–492.
- Reeves, J.P.; Dowben, R.M. Formation and properties of thin-walled phospholipid vesicles. *J. Cell Physiol.* **1969**, *73* (1), 49–60.
- Shapiro, Yu.E. Paramagnetic hydrophilic probing of the colloid systems by NMR spectroscopy. *Russ. Chem. Rev.* **1988**, *57* (8), 717–729.
- New, R.R.C. *Liposomes, A Practical Approach*; Oxford IRL Press: New York, 1990.
- Gregoriadis, G., Ed.; *Liposome Technology*, 2nd; CRC Press: Boca Raton, FL, 1993.
- Kim, S.; Turker, M.S.; Chi, E.Y.; Sela, S.; Martin, G.M. Preparation of multivesicular liposomes. *Biochim. Biophys. Acta* **1983**, *728*, 339–348.
- Müller, R.H.; Jacobs, C.; Kayser, O. Nanosuspensions as particulate drug formulations in therapy. *Adv. Drug Deliv. Rev.* **2001**, *47* (1), 3–19.
- Müller, R.H.; Lucks, J.S. Arzneistoffträger aus festen Lipidteilchen-feste Lipid Nanosphären (SLN). *European Patent 0,605,497*, April 1, 1993.
- Schwarz, C.; Mehnert, W.; Lucks, J.S.; Müller, R.H. Solid lipid nanoparticles (SLN) for controlled drug delivery. *J. Control. Release* **1994**, *30* (1), 83–96.
- Jenning, V.; Gohla, S.H. Encapsulation of retinoids in solid lipid nanoparticles (SLN). *J. Microencapsul.* **2001**, *18* (2), 149–158.
- Szoka, F.; Olson, F.; Health, T.; Vail, W.; Mayhew, E.; Papahadjopoulos, D. Preparation of unilamellar liposomes of intermediate size by a combination of reverse phase evaporation and extrusion through polycarbonate membranes. *Biochim. Biophys. Acta* **1980**, *601*, 559–571.
- Batzri, S.; Korn, E.D. Single bilayer liposomes prepared without sonication. *Biochim. Biophys. Acta* **1973**, *298*, 1015–1019.
- Kagava, Y.; Racker, E. Partial resolution of the enzymes catalyzing oxidative phosphorylation. *J. Biol. Chem.* **1971**, *246* (17), 5477–5487.
- Deamer, D.W.; Bangham, A.D. Large liposomes by an ether vaporization method. *Biochim. Biophys. Acta* **1976**, *443*, 629–634.
- Szoka, F.; Papahadjopoulos, D. Procedure for preparation of liposomes with large internal aqueous space

- and high capture by reverse-phase evaporation. Proc. Natl. Acad. Sci. U. S. A. **1978**, *75* (9), 4194–4198.
34. Papahajopoulos, D.; Vail, W.J.; Jacobson, K.; Poste, G. Cochleate lipid cylinders: Formation by fusion of unilamellar lipid vesicles. *Biochim. Biophys. Acta* **1975**, *394*, 483–491.
  35. Gregoriadis, G.; Ed. *Liposomes as Drug Carriers: Recent Trends and Progress*; John Wiley & Sons: Chichester, U.K., 1988.
  36. Gregoriadis, G.; Ryman, B.E. Liposomal localization of  $\beta$ -fructofuranosidase-containing liposomes injected into rats—some implications in treatment of genetic disorders. *Biochem. J.* **1972**, *129* (1), 123–133.
  37. Gregoriadis, G.; McCormack, B.; Eds. *Targeting of Drugs: Strategies for Stealth Therapeutic Systems*; Plenum Press: New York, 1998.
  38. Klibanov, A.L.; Maruyama, K.; Torchilin, V.P.; Huang, L. Amphipathic PEGs effectively prolong the circulation time of liposomes. *FEBS Lett.* **1990**, *268* (1), 235–237.
  39. Neerunjun, D.; Gregoriadis, G.; Hunt, R. Fate of a liposome-associated agent injected into normal and tumor-bearing rodents. *Life Sci.* **1977**, *21* (3), 357–370.
  40. Wolff, B.; Gregoriadis, G. The use of monoclonal anti-Thy<sub>1</sub> IgG<sub>1</sub> for targeting of liposomes to AKR-A cells. *Biochim. Biophys. Acta* **1984**, *802* (2), 259–273.
  41. Chattergoon, M.; Boyer, J.; Weiner, D.B. Genetic immunization: a new era in vaccines and immune therapeutics. *FASEB J.* **1997**, *11* (10), 753–763.
  42. Felgner, P.L.; Ringold, G.M. Cationic liposome-mediated transfection. *Nature* **1989**, *337*, 387–388.
  43. Durbin, D.P.; El-Aasser, M.S.; Poehlein, G.W.; Vanderhoff, J.W. Influence of monomer pre-emulsification on formation of particles from monomer drops in emulsion polymerization. *J. Appl. Polym. Sci.* **1979**, *24* (3), 703–707.
  44. Lovell, P.A.; Lovell, P.; El-Aasser, M.S. *Emulsion Polymerization and Emulsion Polymers*; John Wiley & Sons, Inc.: New York, 1997.
  45. De Jaeghere, F.; Doelker, E.; Gurny, R. Nanoparticles. In *Encyclopedia of Controlled Drug Delivery*; Mathiowitz, E., Ed.; John Wiley & Sons, Inc.: New York, 1999; Vol. 2, 641–664.
  46. Shapiro, Yu.E.; Dozorova, N.P.; Mironova, N.M.; Balyberdina, T.G. Influence of emulsifier on the microstructure of copolymers of butadiene with methyl methacrylate. *Macromol. Comp. (Russia)* **1981**, *23A* (6), 1374–1380.
  47. Vanderhoff, J.W. Mechanism of emulsion polymerization. *J. Polym. Sci., Polym. Symp.* **1985**, *72*, 161–198.
  48. Carver, M.T.; Hirsch, E.; Wittmann, J.C.; Fitch, R.M.; Candau, F. Percolation and particle nucleation in inverse microemulsion polymerization. *J. Phys. Chem.* **1989**, *93* (12), 4867–4873.
  49. Couvreur, P.; Kante, B.; Roland, M. Possible uses of microdisperse forms as intracellular vehicles. *Pharm. Acta Helv.* **1978**, *53* (12), 341–347.
  50. Krause, H.-J.; Schwarz, A.; Rohdewald, P. Interfacial polymerization, a useful method for the preparation of poly(methylcyanoacrylate) nanoparticles. *Drug Dev. Ind. Pharm.* **1986**, *12* (4), 527–552.
  51. Shen, S.; Sudol, E.D.; El-Aasser, M.S. Dispersion polymerization of methyl methacrylate—mechanism of particle formation. *J. Polym. Sci., A, Polym. Chem.* **1994**, *32* (6), 1087–1100.
  52. Gurny, R.; Peppas, N.A.; Harrington, D.D.; Banker, G.S. Development of biodegradable and injectable lattices for controlled release of potent drugs. *Drug Dev. Ind. Pharm.* **1981**, *7* (1), 1–25.
  53. Scholes, P.D.; Coombes, A.G.A.; Illum, L.; Davis, S.S.; Vert, M.; Davis, M.C. The preparation of sub-500 nm poly(lactide-co-glycolide) microspheres for site-specific drug delivery. *J. Control. Release* **1993**, *25* (1–2), 145–153.
  54. Zambaux, M.F.; Bonneaux, F.; Gref, P.; Maincent, P.; Dellacherie, E.; Alonso, M.J.; Labrude, P.; Vigneron, C. Influence of experimental parameters on the characteristics of poly(lactic acid) nanoparticles prepared by double emulsion method. *J. Control. Release* **1998**, *50* (1–3), 31–40.
  55. Niva, T.; Takeushi, H.; Hino, T.; Kunou, N.; Kawashima, Y. Preparations of biodegradable nanoparticles of water-soluble and insoluble drugs with D,L-lactide/glycolide copolymer by a novel spontaneous emulsification solvent diffusion method and the drug release behavior. *J. Control. Release* **1993**, *25* (1–2), 89–98.
  56. Bindschaedler, C.; Gurny, R.; Doelker, E. Process for Preparing a Powder of Water-Insoluble Polymer Which Can Be Re-dispersed in a Liquid Phase. U.S. Patent 4,968,350, November 6, 1990.
  57. Allemann, E.; Gurny, R.; Doelker, E. Preparation of aqueous polymeric nanodispersions by a reversible salting-out process. *Int. J. Pharm.* **1992**, *87* (1–3), 247–253.
  58. Leroux, J.C.; Allemann, E.; Doelker, E.; Gurny, R. New approach for the preparation of nanoparticles by an emulsification-diffusion method. *Eur. J. Pharm. Biopharm.* **1995**, *41* (1), 14–18.
  59. Couvreur, P.; Roland, M.; Speiser, P. Biodegradable Submicroscopic Particles Containing a Biologically Active Substance. U.S. Patent 4,329,332, May 11, 1982.
  60. Tom, J.W.; Debenedetti, P.G. Particle formation with supercritical fluids. *J. Aerosol Sci.* **1991**, *22* (5), 555–584.
  61. Tom, J.W.; Debenedetti, P.G. Formation of biodegradable polymeric microspheres and microparticles by rapid expansion of supercritical solution. *Biotechnol. Prog.* **1991**, *7* (5), 403–411.
  62. Mawson, S.; Johnston, K.P.; Combes, J.R.; DeSimone, J.M. Formation of poly(1,1,2,2-tetrahydroperfluorodecyl acrylate) submicron fibers and particles from supercritical carbon dioxide solutions. *Macromolecules* **1995**, *28* (9), 3182–3191.
  63. Soppimath, K.S.; Aminabhavi, T.M.; Kulkarni, A.R.; Rudzinski, W.E. Biodegradable polymeric nanoparticles as drug delivery devices. *J. Control. Release* **2001**, *70* (1–2), 1–20.
  64. Ringsdorf, H.; Schlarb, B.; Venzmer, J. Molecular architecture and function of polymeric oriented systems. *Angew. Chem., Int. Ed.* **1988**, *27* (1), 113–158.
  65. Discher, B.M.; Won, Y.-Y.; Ege, D.S.; Lee, J.C.-M.; Bates, F.S.; Discher, D.E.; Hammer, D.A.

- Polymersomes: Tough vesicles made from diblock copolymers. *Science* **1999**, *284*, 1143–1146.
66. Ding, J.; Liu, G. Water-soluble hollow nanospheres as potential drug carriers. *J. Phys. Chem., B* **1998**, *102* (31), 6107–6113.
67. Nardin, C.; Hirt, T.; Leukel, J.; Meier, W. Polymerized ABA triblock copolymer vesicles. *Langmuir* **2000**, *16* (3), 1035–1041.
68. Shapiro, Yu.E.; Pychteeva, E.G.; Fyodorova, G.V. Activity of  $\alpha$ -chymotrypsin immobilized into poly(*N,N*-diallyl-*N,N*-didodecyl ammonium bromide) nanocapsules. *Bioorganic Chem. (Russia)* **1997**, *23* (3), 174–182.
69. Shapiro, Yu.E.; Pykhteeva, E.G.; Levashov, A.V. <sup>1</sup>H NMR self-diffusion in polymer–surfactant nanocapsules and cryogels with enzyme. *J. Colloid Interface Sci.* **1998**, *206* (1), 168–176.
70. Shapiro, Yu.E.; Pykhteeva, E.G. Immobilization of  $\alpha$ -chymotrypsin into the poly(*N,N*-diallyl-*N,N*-didodecyl ammonium bromide)/surfactant nanocapsules. *Appl. Biochem. Biotechnol.* **1998**, *74* (2), 67–84.
71. Kurja, J.; Nolte, R.J.M.; Maxwell, I.A.; German, A.L. Free-radical polymerization of styrene in dioctadecyl-dimethyl ammonium bromide vesicles. *Polymer* **1993**, *34* (10), 2045–2049.
72. Morgan, J.D.; Johnson, C.A.; Kaler, E.W. Polymerization of equilibrium vesicles. *Langmuir* **1997**, *13* (24), 6447–6451.
73. Poulain, N.; Nakache, E.; Pina, A.; Levesque, G. Nanoparticles from vesicle polymerization. *J. Polym. Sci., A, Polym. Chem.* **1996**, *34* (5), 729–737.
74. Hotz, J.; Meier, W. Vesicle-templated polymer hollow spheres. *Langmuir* **1998**, *14* (5), 1031–1036.
75. Al Khouri-Fallouh, N.; Roblot-Treupel, L.; Devissaguet, J.P.; Puiseux, F. Development of new process for the manufacture of polyisobutyrylcyanoacrylate nanocapsules. *Int. J. Pharm.* **1986**, *28* (2–3), 125–135.
76. Puglisi, G.; Fresta, M.; Giammona, G.; Ventura, C.A. Influence of the preparation conditions of poly(ethyl cyanoacrylate) nanocapsule formation. *Int. J. Pharm.* **1995**, *125* (2), 283–287.
77. Donath, E.; Sukhorukov, G.B.; Caruso, F.; Davis, S.A.; Möhwald, H. Novel hollow polymer shells by colloid-templated assembly of polyelectrolytes. *Angew. Chem., Int. Ed.* **1998**, *37* (16), 2201–2205.
78. Caruso, F.; Caruso, R.A.; Möhwald, H. Nanoengineering of inorganic and hybrid hollow spheres by colloidal templating. *Science* **1998**, *282*, 1111–1114.
79. Nihant, N.; Grandfils, C.; Jerome, R.; Teyssie, P. Microencapsulation by coacervation of poly(lactide-co-glycolide). *J. Control. Release* **1995**, *35* (2–3), 117–125.
80. Chan, L.W.; Heng, P.W.S. Effect of poly(vinylpyrrolidone) and ethylcellulose on alginate microspheres prepared by emulsification. *J. Microencapsul.* **1998**, *15* (4), 409–420.
81. Okubo, M.; Konishi, Y.; Minami, H. Production of hollow polymer particles by suspension polymerization. *Colloid Polym. Sci.* **1998**, *276* (7), 638–642.
82. Emmerich, O.; Hugenberg, N.; Schmidt, M.; Sheiko, S.S.; Baumann, F.; Deubzer, B.; Weis, J.; Ebenhoch, J. Molecular boxes based on hollow organosilicon materials. *Adv. Mater.* **1999**, *11* (15), 1299–1300.
83. Couvreur, P.; Grislain, L.; Lenaert, V.; Brasseur, F.; Guiot, P.; Biernacki, A. Biodegradable polymeric nanoparticles as drug carrier for antitumor agents. In *Polymeric Nanoparticles and Microspheres*; Guiot, P., Couvreur, P., Eds.; CRC Press: Boca Raton, FL, 1986; 27–93.
84. Brigger, I.; Dubernet, C.; Couvreur, P. Nanoparticles in cancer therapy and diagnosis. *Adv. Drug Deliv. Rev.* **2002**, *54* (5), 631–651.
85. Allemann, E.; Rousseau, J.; Brasseur, N.; Kudrevich, S.V.; Lewis, K.; van Lier, J.E. Photodynamic therapy of tumors with hexafluoro zinc phthalocyanine formulated in PEG-coated poly(lactic acid) nanoparticles. *Int. J. Cancer* **1996**, *66* (6), 821–824.
86. Lherm, C.; Muller, R.H.; Puiseux, F.; Couvreur, P. Alkylcyanoacrylate drug carriers: II. Cytotoxicity of cyanoacrylate nanoparticles with different alkyl chain length. *Int. J. Pharm.* **1992**, *84* (1), 13–22.
87. Breton, P.; Roy, D.; Marchal-Heussler, L.; Seguin, C.; Couvreur, P.; Lescure, F. New poly(methylidene malonate 2.1.2) nanoparticles: recent developments. In *Targeting of Drugs, Advances in System Constructs*; Gregoriadis, G., McCormack, B., Poste, G., Eds.; Plenum Press: New York, 1994; Vol. 4, 161–172.
88. Bru-Magniez, N.; Larras, V.; Riess, G.; Breton, P.; Couvreur, P.; Roques-Carmes, C. Novel Surfactant Copolymers Based on Methylidene Malonate. *Int. Patent PCT WO 99/38898*, 1999.
89. Kreuter, J. Drug targeting with nanoparticles. In *Colloidal Drug Delivery Systems*; Kreuter, J., Ed.; Marcel Dekker, Inc.: New York, 1994; 219–343.
90. Bender, A.R.; von Briesen, H.; Kreuter, J.; Duncan, I.B.; Rubsamen Waigman, H. Efficiency of nanoparticles as a carrier system for antiviral agents in human immunodeficiency virus-infected human monocytes/macrophages in vitro. *Antimicrob. Agents Chemother.* **1996**, *40* (6), 1467–1471.
91. Le Bourlais, C.A.; Treupelacar, L.; Phodes, C.T.; Sado, P.A.; Leverage, R. New ophthalmic drug delivery system. *Drug Dev. Ind. Pharm.* **1995**, *21* (1), 19–50.
92. Sunder, A.; Krämer, M.; Hanselmann, R.; Mühlaupt, R.; Frey, H. Molecular nanocapsules based on amphiphilic hyperbranched polyglycerols. *Angew. Chem., Int. Ed.* **1999**, *38* (23), 3552–3555.
93. Jansen, J.F.G.A.; Meijer, E.W.; De Brabander van den Berg, E.M.M. The dendritic box: Shape-selective liberation of encapsulated guests. *J. Am. Chem. Soc.* **1995**, *117* (15), 4417–4418.
94. Wendland, M.S.; Zimmerman, S.C. Synthesis of cored dendrimers. *J. Am. Chem. Soc.* **1999**, *121* (6), 1389–1390.
95. Thompson, D.O. Cyclodextrins-enabling excipients: their present and future in pharmaceuticals. *Crit. Rev. Ther. Drug Carr. Syst.* **1997**, *14* (1), 1–104.
96. Yamamoto, M.; Hirayama, F.; Uekama, K. Improvement of stability and dissolution of prostaglandin E<sub>1</sub> by maltosyl- $\beta$ -cyclodextrin in lyophilized formulation. *Chem. Pharm. Bull.* **1992**, *40* (3), 747–751.
97. Andronati, S.A.; Shapiro, Yu.E.; Yakubovskaya, L.N.; Gorbatyuk, V.Ya.; Andronati, K.S.; Krasnoschyokaya,

- S.P. Inclusion compounds of psychotropic agents and cyclodextrins. *J. Incl. Phenom. Mol. Recognit. Chem.* **1996**, *24* (1–2), 175–186.
98. Shapiro, Yu.E.; Gorbatyuk, V.Ya.; Yakubovskaya, L.N.; Andronati, K.S.; Andronati, S.A. Spatial structure of clathrates of the 1,4-benzodiazepine derivatives and  $\beta$ -cyclodextrin. *J. Struct. Chem. (Russia)* **1996**, *37* (5), 847–890.
99. Duchêne, D.; Ed. *New Trends in Cyclodextrins and Derivatives*; Editions de Santé: Paris, 1991.
100. Jarho, P.; Urtti, A.; Pate, D.W.; Suhonen, P.; Järvinen, T. Increase in aqueous solubility, stability and in vitro corneal permeability by hydroxypropyl- $\beta$ -cyclodextrin. *Int. J. Pharm.* **1996**, *137* (2), 209–216.
101. Adachi, H.; Irie, T.; Uekama, K.; Manako, T.; Yano, T.; Saita, M. Combination effects of *O*-carboxymethyl-*O*-ethyl- $\beta$ -cyclodextrin and penetration enhancer HPE-101 on transdermal delivery of prostaglandin E<sub>1</sub> in hairless mice. *Eur. J. Pharm. Sci.* **1993**, *1* (3), 117–123.
102. Djedaini-Pilard, F.; Desalos, J.; Perly, B. Synthesis of a new molecular carrier: *N*-(Leu-enkephalin)yl 6-amido-6-deoxy-cyclomaltoheptaose. *Tetrahedron Lett.* **1993**, *34* (14), 2457–2460.



# Nanofibers and Carbon Nanotubes: Novel Metal Catalyst Supports

Mark A. Keane

Department of Chemistry and Materials Engineering, University of Kentucky,  
Lexington, Kentucky, U.S.A.

## INTRODUCTION

The association of carbon nanofibers and nanotubes with heterogeneous catalysis, the focus of this entry, is twofold. The growth of ordered carbon from metal catalysts has emerged as an economically viable and selective route to a high value graphitic product. The critical catalyst characteristics that have been shown to impact on the dimensions and structure of the carbon product are discussed herein with an evaluation of the growth mechanisms that have been proposed in the literature. The established noncatalytic synthesis methodologies are described and the advantages inherent in a move to a catalytic approach are demonstrated, taking ethylene decomposition over nickel as a model system. The second catalysis/carbon connection deals with the application of nanoscale carbon substrates to disperse a catalytically active metal phase, i.e., preparation of supported metal catalysts. The advantages of carbon nanofibers/nanotubes as metal supports are discussed with an overview of recent literature that describes the catalytic application of metals anchored to structured carbon substrates.

## BACKGROUND

Carbon is unique in that it can bond in different ways to create structures with quite dissimilar properties. The discovery of the  $C_{60}$  closed-cage (nearly) spherical molecule, now commonly known as the “buckyball,”<sup>[1]</sup> multi-/single-walled nanotubes,<sup>[2,3]</sup> carbon nanofibers,<sup>[4,5]</sup> and related materials<sup>[6,7]</sup> has led to a renaissance in the study of carbon-based materials. The selective synthesis of structured carbon materials is now actively pursued and a burgeoning literature on carbon production and characterization has emerged over the past decade. This interest has been fuelled by the unique chemical and physical properties associated with these materials that can be exploited in adsorption,<sup>[8,9]</sup> hydrogen storage,<sup>[10,11]</sup> and electronics applications.<sup>[12]</sup> In addition, the remarkable mechanical properties of structured carbon can be used to good effect as additives for reinforcement purposes,<sup>[13]</sup>

while the associated high aspect ratio and metallic/semiconducting properties can impact on conductivity<sup>[5,14]</sup> in various composites. Although the potential applications are many, widespread utilization requires a low-cost means of fabricating structured carbon that exhibits a high degree of control and reproducibility.

The use of a support to disperse a catalytically active metal phase is not only of economic benefit (lower preparation costs/longer productive lifetime) but the substrate can also influence catalyst performance through electronic interaction(s) and migration effects,<sup>[15]</sup> a phenomenon that has led to the widely applied acronym SMSI,<sup>[16]</sup> i.e., “strong metal support interactions.” The use of carbon nanofibers and nanotubes as catalyst supports is now attracting appreciable research interest; the perceived advantages when compared with activated carbon, as an established metal support, are addressed. This work is still in a formative stage—a compilation of the existing literature is provided with a critical assessment of the trends that have emerged.

## CARBON NANOFIBERS AND NANOTUBES: STRUCTURAL FEATURES

The distinction between carbon nanotubes and nanofibers, as presented in the recent literature, is far from clear. In terms of aspect ratio, length of the major axis divided by width of the minor axis, both nanotubes and nanofibers are characterized by values well in excess (by orders of magnitude) of unity. Nanotube structure can be directly related to the spherical  $C_{60}$  arrangement through a structural elongation that generates a single-walled tube with nanoscale dimensions [Fig. 1(A)]. Graphite, the thermodynamically stable bulk phase of carbon, displays a turbosilicate character, i.e., closed-packed layers that can be mutually displaced in directions normal to the  $c$  axis.<sup>[17]</sup> Where there is a finite number of carbon atoms with a high density of dangling bonds, the structure “closes in” to form more energetically favorable chains, rings, and closed shells.<sup>[18]</sup> The simple single-walled nanotube

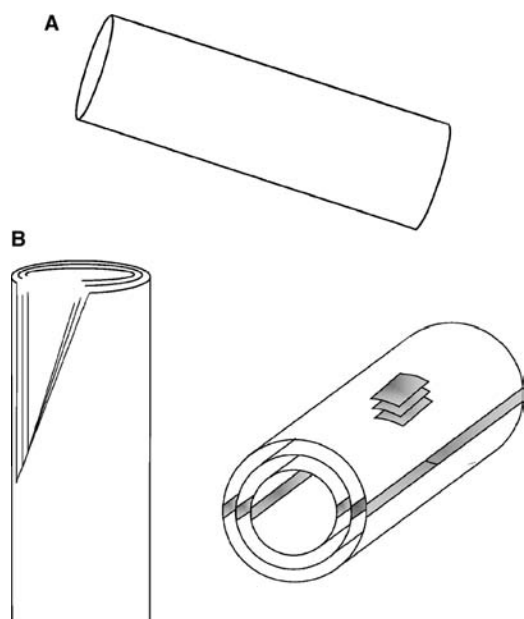


**Fig. 1** Simple schematics showing the three-dimensional structure of (A) SWNT and (B) MWNT.

(SWNT) schematic shown in Fig. 1(A) depicts a long cylinder composed of a hexagonal honeycomb lattice of ( $sp^2$ -hybridized) carbon that is essentially a folded graphene sheet where the open edges match perfectly to form a seamless structure. Closure of these tubes requires curvature to form a convex structure with fragmentation of the hexagonal lattice and incorporation of pentagon rings.<sup>[19]</sup> When produced in the vapor phase, SWNTs are known to self-assemble into larger bundles or ropes that can contain several tens of thousands of individual nanotubes.<sup>[18]</sup> Multiwalled nanotubes (MWNTs) [Fig. 1(B)] are created by the superposition of several concentric cylinders about a common central hollow core in the manner of a “Russian doll.”<sup>[2]</sup> The separation between neighboring tubes is ca. 0.34 nm, close to but typically greater than the interplanar distance of the  $d_{200}$  plane of graphite, due to the constraint induced by the curvature of the graphene planes that form the tube.<sup>[5]</sup> The outer diameter of MWNTs (prepared by an arc-discharge method) generally falls within the range 2–20 nm with an internal diameter ranging from 1 to 3 nm.<sup>[20,21]</sup> The distribution of diameters associated with SWNTs is significantly narrower, ranging from 0.7 to 1.6 nm.<sup>[21,22]</sup>

While there is a tendency in the literature to assign the term “nanotube” as a virtual “catch-all” to describe every nanoscale structured carbon, nanofibers are structurally quite distinct. While they are also graphitic in nature and characterized by a series of ordered parallel graphene layers with again an inter-layer distance of ca. 0.34 nm, the exposed surface

mainly consists of prismatic planes with high surface reactivity when compared with the basal planes of graphite. Two typical lattice arrangements are associated with carbon nanofibers, i.e., the “ribbon” and the “herringbone” orientation.<sup>[5,21,22]</sup> A simple schematic rendering of the ribbon form is given as a visual aid in Fig. 2(A), and this can be compared with the representative transmission electron micrograph (TEM) in Fig. 3(A), where the graphene layers are oriented parallel to the fiber axis. The high aspect ratio associated with carbon nanofibers is immediately evident from the scanning electron micrograph (SEM) given in Fig. 4. The alternative herringbone structure<sup>[5,23]</sup> is illustrated again as a schematic [Fig. 2(B)] accompanied by a TEM image [Fig. 3(B)]—in this instance, the parallel carbon platelets are oriented at an angle to the fiber

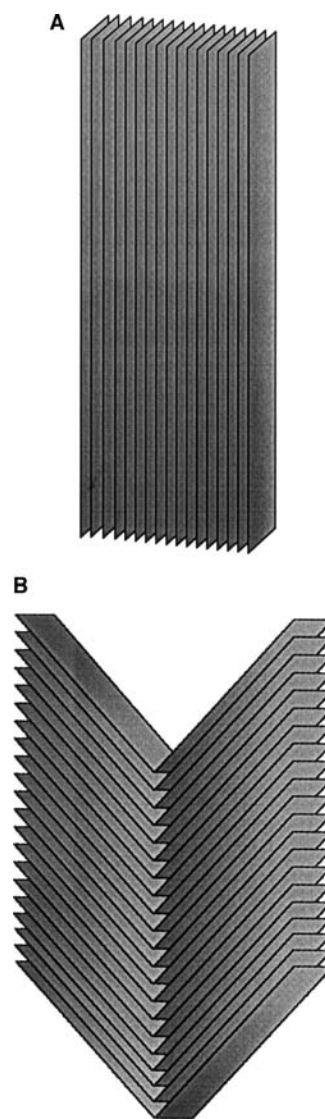


**Fig. 2** Schematic diagram illustrating an idealized rendering of the lattice structure in (A) ribbon and (B) herringbone carbon nanofibers.

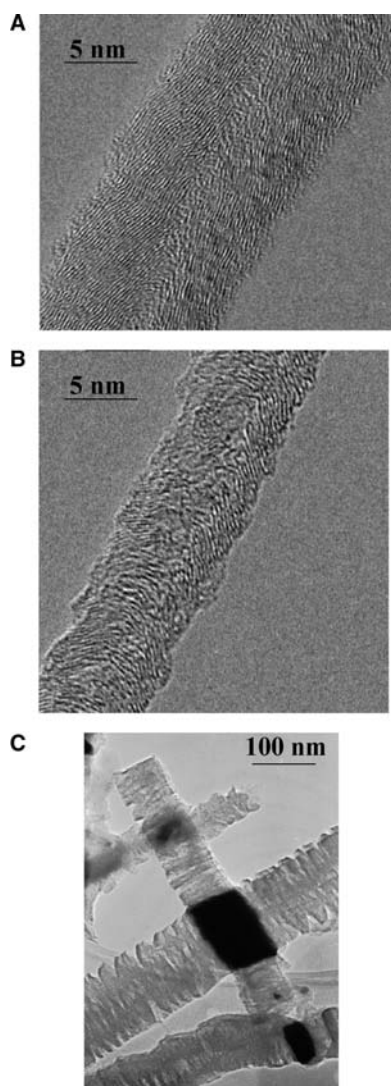


**Fig. 3** Representative TEM images of (A) ribbon, (B) herringbone, and (C) helical carbon nanofibers.

axis. The latter arrangement can lead to deviations in the interlayer spacing toward the outer edges of the graphitic platelets making this particular nanofiber a potential candidate for adsorption applications.<sup>[9]</sup> Nanofibers also exist in the so-called platelet form where the graphene layers are oriented perpendicular to the fiber axis. “Helical” or “ropelike” nanofiber structures have also been reported<sup>[24,25]</sup> where the fibers have a coiled appearance as illustrated by the TEM image in Fig. 3(C). A measurement of the Brunauer–Emmett–Teller (BET) surface area can serve as a useful means of differentiating between carbon nanofibers and nanotubes. The nanofiber has a greater availability of edge sites, whereas the nanotube is characterized by a large exposed exterior basal plane. These features emerge from BET analyses that have yielded typical nanotube surface areas of  $<30 \text{ m}^2 \text{ g}^{-1}$ , appreciably lower than the nanofiber area which can

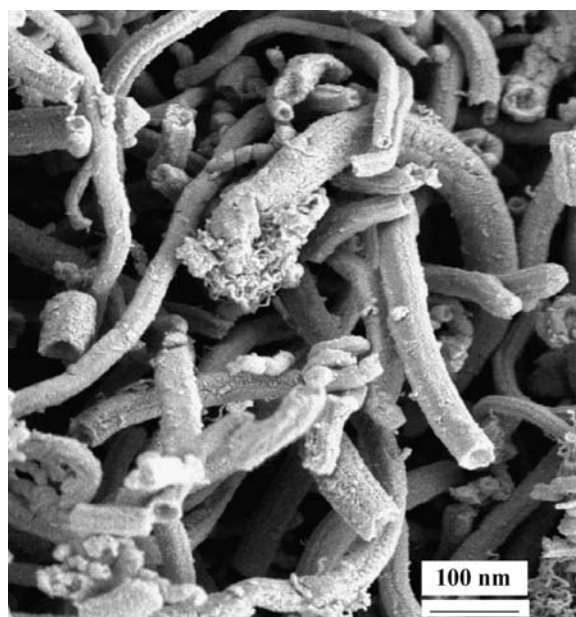


**Fig. 4** Representative SEM image of carbon nanofibers produced via the catalytic decomposition of ethylene.

approach  $200 \text{ m}^2 \text{ g}^{-1}$  depending on the synthesis procedure and post synthesis treatment.<sup>[2,5,26]</sup>

## CARBON NANOFIBER/NANOTUBE SYNTHESIS

The C–C covalent bond that constitutes the graphite planes is one of the strongest in nature, and the perfect lattice alignment endows these materials with high conductivity, enhanced strength, and chemical specificity. The combination of dimension, structure, and topology translates into such a diversity of unique chemical and physical properties that carbon nanofibers/nanotubes are now established as a target high-value product. The established synthesis methodologies can be conveniently divided into noncatalytic and catalytic processes.

### Noncatalytic Approach

The synthesis of graphitic carbon (nanotubes/nanofibers) is now well established by arc discharge<sup>[18,27]</sup> and plasma decomposition.<sup>[27,28]</sup> The arc-discharge technique was developed by Bacon in the early 1960s to produce carbon fibers or “whiskers,”<sup>[29]</sup> and adapted some 30 years later to generate a significant quantity of fullerenes.<sup>[30]</sup> Indeed, Iijima’s landmark reported MWNT synthesis<sup>[2]</sup> was the result of DC arc-discharge evaporation of graphite rods. While such methodologies generate a carbon product of good turbo-static quality, they also produce polyhedron carbon

nanoparticles (low aspect ratio) and an appreciable amorphous carbon component.<sup>[28]</sup> The latter necessitates an additional involved, cumbersome, and costly purification stage in order to extract the desired structured product. In any case, these methodologies are highly energy-demanding batch processes and the amount of material that can be produced is limited. Moreover, carbon structures generated in this fashion exhibit a preponderance of defects, the high temperatures employed can induce sintering and cross-linking of the fiber/tube while the length of the carbon product is typically  $<1\ \mu\text{m}$ .<sup>[21,31]</sup> The separation step can involve a combination of chemical treatment and ultrasound, whereas purification calls for selective oxidation and/or hydrogenation.<sup>[32]</sup> Although structured carbon has been detected in benzene, acetylene, and ethylene flames,<sup>[33]</sup> flame synthesis is not viewed as a viable preparative strategy.

### Catalytic Approach

On the whole, the catalytic route can generate carbon nanofibers/tubes that are largely uniform in diameter, and scale-up of the catalytic process is far more feasible.<sup>[5,21]</sup> In general, catalytic synthesis involves the decomposition of a carbon-containing gas stream typically diluted with an inert (He, Ar) and possibly reactive ( $\text{H}_2$ ) gas flow. The yield and nature (SWNTs and/or MWNTs and/or nanofibers) of the carbon product are determined by the nature of the catalytic metal (with/without a support), the hydrocarbon source, reaction/contact time, and temperature. The fiber/tube diameter appears to be governed by the dimensions of the seed metal particle, whereas the length depends largely on the duration of reaction.<sup>[21,25,34]</sup> Cobalt-, nickel-, and iron-based catalysts have exhibited the highest carbon growth activities<sup>[5]</sup> with the formation of SWNTs requiring very small diameter seed metal particles. Taking nickel-based catalysts as a representative case, the metal has been used in unsupported<sup>[35]</sup> and supported<sup>[24,36,37]</sup> forms and as a bimetallic with copper<sup>[38]</sup> to promote carbon growth from a catalytic decomposition of  $\text{CO}$ <sup>[36,39,40]</sup> and such hydrocarbons as methane,<sup>[36,37,39]</sup> 1-butene,<sup>[8]</sup> 1,3-butadiene,<sup>[8,37]</sup> acetylene,<sup>[40,41]</sup> ethylene,<sup>[8,24,36,41]</sup> *n*-hexane,<sup>[37]</sup> and benzene.<sup>[42]</sup> Hydrogen is not an essential component in these systems, but its presence has been shown to be highly beneficial, not only in initiating the decomposition of the carbon-containing gas<sup>[43]</sup> but also as a means of exerting additional structural control on the growing carbon.<sup>[44]</sup>

The commonly accepted mechanism<sup>[5]</sup> involves reactant (carbon source) decomposition on the top surface of a metal particle followed by a diffusion of carbon atoms into the metal with precipitation at other facets

of the particle to yield the fiber/tube, which continues to grow until the metal particle becomes poisoned or completely encapsulated by carbon. Taking ethylene decomposition over supported Ni as a model system, the simple scheme included in Fig. 5 illustrates the link between the Ni site and the ultimate carbon growth. It has been shown that certain crystallographic orientation(s) of Ni favor(s) reactant decomposition, whereas a different set of faces serves to promote the precipitation of a graphitic carbon product.<sup>[45]</sup> Carbon deposition necessitates a destructive chemisorption of ethylene, i.e., loss of H atoms and C–C bond breakage. The latter is facilitated by a thermodynamically driven multiple bonding of the chemisorbed hydrocarbon with the metal surface that serves to lower the surface free energy.<sup>[21]</sup> Doping Ni catalysts with alkali halides has been shown to increase carbon yield and enhance structural order, effects that are attributed to charge transfer associated with the electronegative/

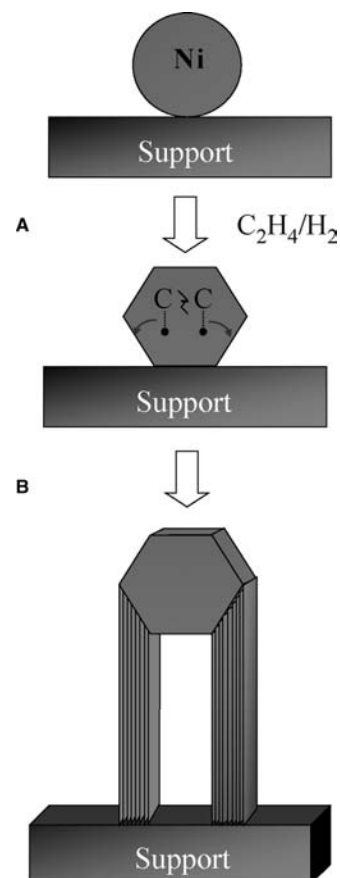


**Fig. 5** Schematic representation of the critical stages associated with the carbon growth via the decomposition of ethylene over supported Ni: (A) destructive adsorption on the Ni surface with dissolution of carbon and diffusion through the restructured metal particle and (B) precipitation of carbon at the rear face of the particle in the form of a graphite platelet with Ni particle extraction from the support.

electropositive halogen/alkali metal.<sup>[21,45]</sup> The rate-determining step is the dissolution and diffusion of carbon through the metal particle where the driving force for diffusion has been ascribed to either a temperature<sup>[46]</sup> or concentration<sup>[47]</sup> gradient. It is believed that the carbon dissolves to form a substoichiometric metal carbide prior to fiber/tube formation.<sup>[48]</sup> The metal carbide is metastable with respect to the metal and graphite and decomposes into graphite that encapsulates the metal particle. The formation of hexagonal Ni<sub>3</sub>C has been proposed as the nucleation species but is not present during steady-state growth.<sup>[24,48]</sup> The involvement of metal carbide remains a supposition where the effect of temperature on the metastable carbide-phase equilibrium must be taken into account, and, in any case, much of the available evidence is indirect and not based on (a problematic) *in situ* analysis. In terms of a concentration gradient process, the carbon concentration in the metal must be greater than that at the metal/graphite interface in order to drive the diffusion forward. Carbon species at the metal/gas interface are known to exhibit a higher solubility than carbon originating from graphite.<sup>[36]</sup> The movement of carbon atoms through the Ni metal lattice necessitates a displacement of Ni atoms as the C atom diameter exceeds the available spacing.<sup>[24]</sup> Rather than an explicit carbide assignment, carbon growth can be considered to result from a stable but fluid supersaturated solution of carbon in the metal. As shown in Fig. 5, carbon growth is accompanied by a reconstruction/faceting of the metal particle.<sup>[38,46,47]</sup> Metal faceting can lead to variations in the surface structure of the carbon which, in turn, affects the mechanical strength, texture, and chemical attributes. Where the metal interaction with the support is relatively weak, the pressure exerted on the metal/support interface due to graphite formation is of sufficient magnitude to extract the metal particle from the support. Once the metal particle is detached from the support, a fresh surface is exposed to ethylene, and growth continues with the Ni particle located on the carbon tip, as depicted in Fig. 5.

The degree of crystalline order of the carbon product is controlled by various factors including the wetting properties of the metal with graphite and the crystallographic orientation of the metal faces that are in contact with the carbon deposit, features that are ultimately reliant upon the choice of catalyst.<sup>[5,22]</sup> The arrangement of the metal atoms at the face where the carbon is deposited ultimately regulates the nature of the precipitated carbon. If the atoms are arranged in such a manner that they are consistent with those of the basal plane structure of graphite then the carbon that dissolves in and diffuses through the particle will be precipitated as an ordered structure. Conversely, if there is little or no match between the atomic

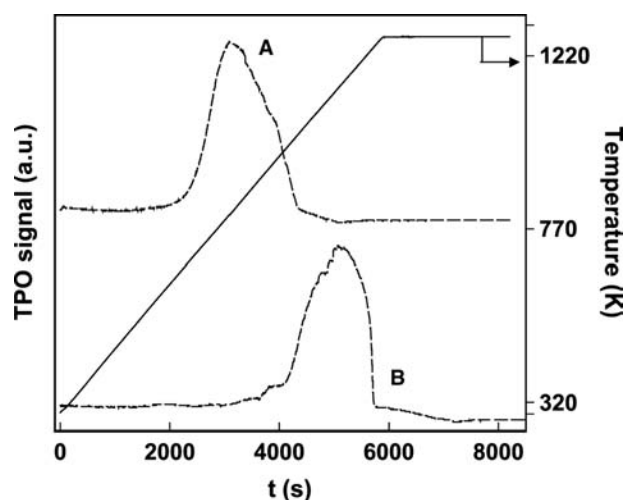


Fig. 6 Temperature-programmed oxidation (TPO) profiles for (A) model amorphous carbon and (B) carbon nanofiber.

arrangements of the depositing face and graphite, a more disordered carbon will be generated. The degree of order in carbon structures can be probed by temperature-programmed oxidation (TPO) where a move from an amorphous to a graphitic structure is accompanied by an elevation of the temperature at which gasification is induced. The TPO profiles of a sample of carbon nanofibers can be assessed against the TPO characteristics of model amorphous carbon in Fig. 6; the fiber is appreciably more resistant to gasification than the unstructured carbon. A hollow central core is evident in the low magnification TEM pictures provided in Fig. 7. This structural feature, also depicted in Fig. 5, has been attributed to a deformation or faceting of the supported metal particle that

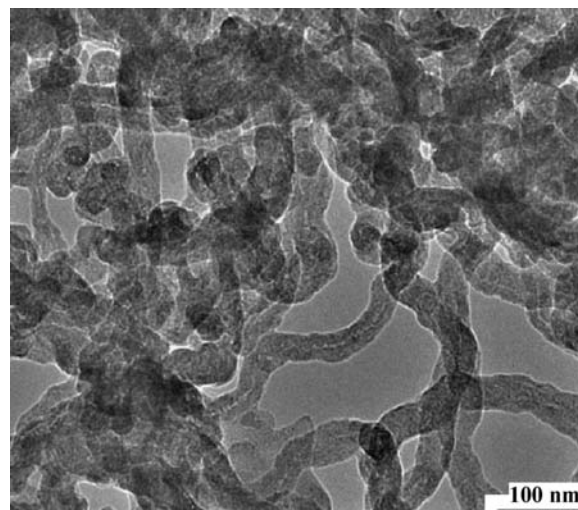


Fig. 7 Representative TEM micrograph showing the nature of carbon nanofiber growth resulting from ethylene decomposition over Ni/SiO<sub>2</sub>.



alters the relative rate of carbon diffusion and fiber nucleation.<sup>[46]</sup>

## CARBON NANOFIBERS/NANOTUBES AS METAL SUPPORTS

Carbon as a support material is well established in heterogeneous catalysis, notably in liquid-phase applications. Activated carbon, usually derived from natural materials (e.g., coal, wood, straw, fruit stones, and shells), has found widespread use because of its high surface area/adsorption capacity coupled with cost effectiveness.<sup>[49]</sup> The high surface area associated with activated carbon (typically  $>600\text{ m}^2\text{ g}^{-1}$ ) is the result of a significant micropore content which can impose physical transport constraints in any catalytic process where the reactants must gain access to metal particles located within these micropores. Graphite is characterized by a low surface area (with limited porosity) which has mitigated against its use as a catalyst support material. Carbon nanofibers (and carbon nanotubes to a lesser extent) possess surface areas well in excess of that associated with graphite with larger pore openings and a consequent alleviation of reactant/product transport constraints. One important aspect of liquid-phase heterogeneous catalytic processes involving carbon-based catalysts is the ease of separation of the solid from solution. The recovery of the carbon nanofibers from aqueous media has been shown to be far more facile (by an order of magnitude) than phase separation involving granular activated carbon powder.<sup>[50]</sup> The nanofibers are extremely robust in nature and do not disintegrate or exhibit any appreciable damage during vigorous agitation unlike the activated carbon, which experiences considerable attrition with prolonged use. In aqueous-phase operation, the intrinsic hydrophobicity of the carbon nanofibers may also serve to aid filtration by repelling water molecules. Moreover, unlike activated carbon, separation of the fibers from solution is not accompanied by any significant loss of (fine) carbon particulates, and catalyst reuse should be greatly facilitated.<sup>[9]</sup>

Any reaction that is promoted by a heterogeneous catalyst proceeds via reactant/catalyst interaction(s) that generate(s) a surface reactive complex. These interactions may be weak, of the “nonbonding” type with the reactant staying intact while sticking to (or absorbing on) the surface. Alternatively, the interactions may involve the formation of new chemical bonds between the surface atoms and the adsorbed molecule (i.e., chemisorption), which necessarily entails extensive reorganization of the bonding within the reactant. The magnitude of the adsorption coefficient depends on the nature of the surface and the chemical identity of the reacting species. Once the reactant is

bound to the surface, it can readily undergo reactions which take place only with difficulty in the gas or liquid phases. This may result from the close proximity of reactant molecules on the surface and/or the changes in bonding consequent upon chemisorption; both are essential features of the catalytic properties of the solid. The choice of a suitable catalyst for a particular reaction depends on the stability of the complexes formed between reactant and catalyst and/or product and catalyst. These must be stable enough to form and provide an alternative pathway to the uncatalyzed reaction, but they must not be too stable as this would lead to an increase in the associated activation with a consequent lowering of reaction rate. The unique electronic, adsorption, and thermal/mechanical properties associated with carbon nanofibers and nanotubes can all play interrelated roles in the design of catalytically efficient supported metal systems. The ability of a substrate to induce electronic perturbations in the supported metal and so impact on chemisorptive and reactivity properties is well established.<sup>[25]</sup> The use of conductive carbon supports, as opposed to activated carbon, to anchor transition metals has been demonstrated to significantly affect the intrinsic metal site activity through charge transfer effects.<sup>[5,51]</sup> The high conductivity/availability of delocalized  $\pi$ -electrons can influence reactant adsorption<sup>[50]</sup> and so the nanofiber/tube can have a synergistic effect in terms of activating the reactant prior to surface reaction. Moreover, given the lower density of carbon fibers relative to amorphous carbon, the pressure required to maintain the same reactant flow through a bed of activated carbon is substantially higher, which can have significant ramifications in terms of energy usage/costs.<sup>[9]</sup> In addition, the enhanced mechanical strength and thermal shock resistance of the structured carbon substrates can also have a bearing in processes that require unavoidable high pressures/temperatures.

## Methodologies for Attaching Metals to Carbonaceous Surfaces

Supported metal catalysts are generally composed of small metal particles (1–100 nm in diameter) dispersed on a high surface area carrier. Modern catalyst formulations often include an “active” metal (Pt, Pd, Ru, etc.) with a secondary component or additive that serves as a promoter where this modification may be directed toward enhancing activity/selectivity, poison resistance, or textural properties. Conventional and commercial metal catalysts are typically prepared via wet impregnation techniques. In this approach, a metal salt precursor (nitrate, halide, etc.) is dissolved in sufficient solvent (normally water) to fill the pores of the support. The water is then evaporated, leaving only



the metal salts on the support that are then activated at elevated temperatures under  $H_2$  (metal salt decomposition with concomitant/subsequent zero valent metal formation) or flowing air (calcination to generate a supported metal oxide) with subsequent reduction in  $H_2$ . The ultimate dispersion of metal on the support is dependent on metal loading, activation temperature, pretreatment (drying/calcination), and the nature of the metal (precursor) and support. Impregnation of graphitic carbon surfaces with metal precursors in aqueous media is, however, problematic as the hydrophobic property of the nanofibers/tubes leads to difficulties with surface wetting that can adversely affect metal dispersion.<sup>[5,52]</sup> This can be circumvented by using organic solvents—the TEM images provided in Fig. 8 illustrate the nature of Pd supported on activated carbon and nanofibers prepared by impregnation of palladium nitrate from butanol. An even dispersion of Pd particles is evident on the carbon nanofibers where the majority of the Pd diameters range from <5 to 30 nm. It is instructive to note that

while the Pd particles supported on activated carbon possess a globular geometry, the metal phase on the nanofibers exhibits a faceting that is characteristic of stronger metal/support interactions. The X-ray diffractogram (XRD) associated with the Pd/nanofiber sample has a strong peak at  $26^\circ$  that is characteristic of highly structured (graphitic) carbon, a response that, as expected, is not present in the profile for Pd/activated carbon (Fig. 9). The representative high-resolution TEM image provided in Fig. 10 illustrates the carbon platelet arrangement in the carbon nanofiber support. The graphite platelets have a parallel alignment with an interplatelet spacing of ca. 0.34 nm, diagnostic of a graphitic species. The Pd phase on both supports displays a cubic geometry with the four XRD peaks at  $40.1^\circ$ ,  $46.7^\circ$ ,  $68.1^\circ$ , and  $82.15^\circ$  corresponding, respectively, to (111), (200), (220), and (311) Pd planes.

There are reports in the literature that describe nanofiber impregnation with Rh,<sup>[53]</sup> Ni,<sup>[54,55]</sup> and Fe-Cu<sup>[56]</sup> from alcohol solutions. Indeed, Pham-Huu

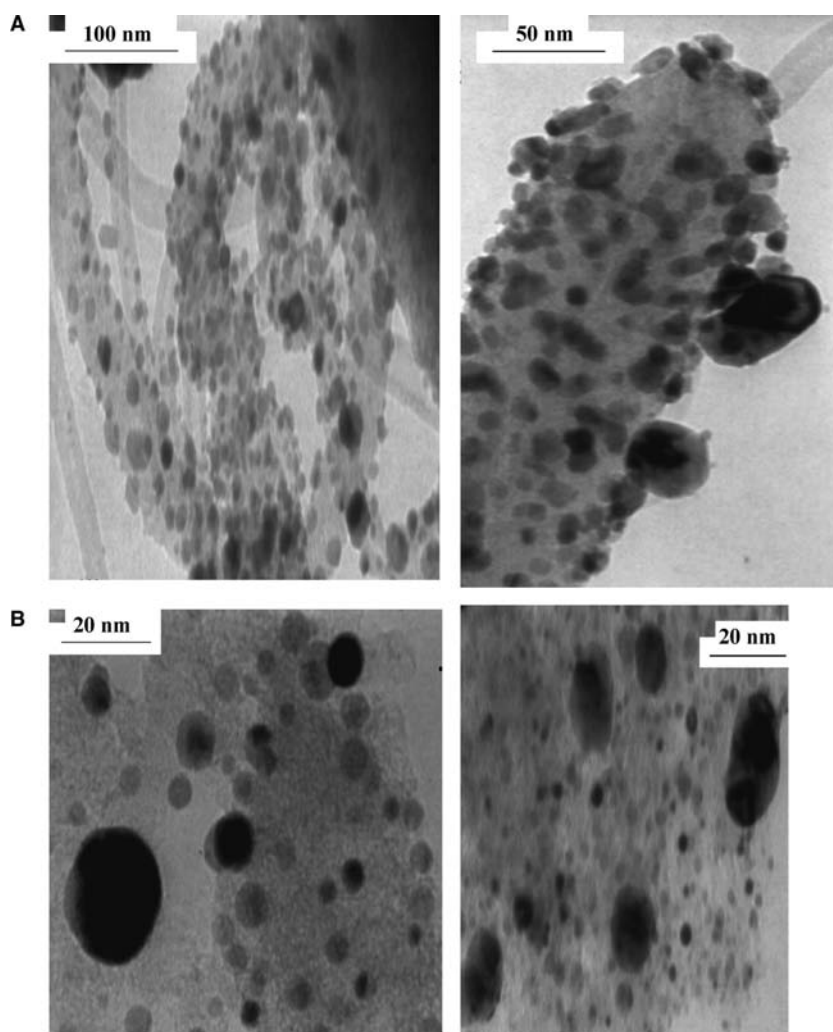


**Fig. 8** Representative TEM images of Pd supported on (A) carbon nanofiber and (B) activated carbon.

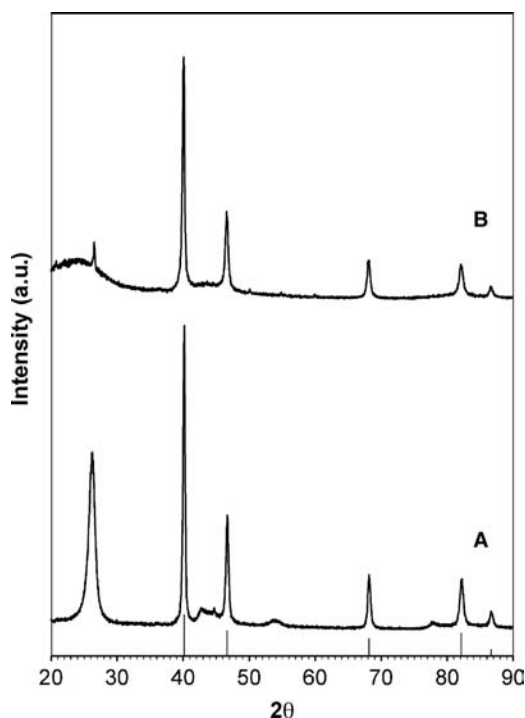


**Fig. 9** XRD patterns for (A) Pd/nanofiber and (B) Pd/activated carbon. The solid lines indicate peak position (with relative intensity) for cubic Pd.

et al.<sup>[48]</sup> and Reshetyenko et al.<sup>[57]</sup> have successfully impregnated graphitic nanofibers with 5% w/w Pd and 15% w/w Ni using aqueous solutions of the metal nitrate and chloride, respectively. In addition, there are

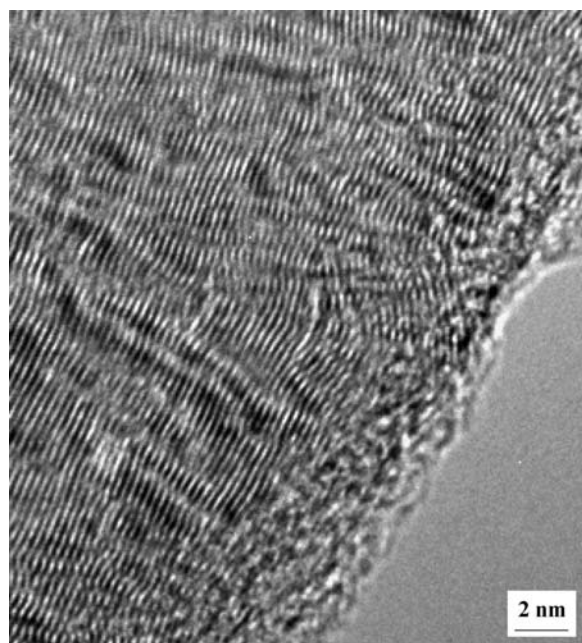


**Fig. 10** Representative high-resolution TEM image showing carbon nanofiber lattice structure.

reported instances (with varying detail) of SWNT and MWNT impregnation with  $\text{Ru}(\text{acac})_3$  in toluene,<sup>[58]</sup>  $\text{H}_2\text{PtCl}_6$  in ethylene glycol,<sup>[59]</sup> and a Pd(II)- $\beta$ -diketone in supercritical  $\text{CO}_2$ <sup>[60]</sup> to deliver metal loadings up to 10% w/w; the metal particle diameters after activation were in the range 2–4 nm. Xue et al.<sup>[61]</sup> have reported the preparation of Pd, Pt, Au, and Ag particles (7–17 nm mean diameter) supported on carbon “nanotubes” (diameter = ca. 20 nm) via thermal decomposition (in  $\text{H}_2$ ) of metal salts impregnated from acetone or water solutions. On the basis of XRD analysis, these authors claimed that the same preparative route but employing conventional graphite or activated carbon supports yielded a wider diameter supported metal phase. The task of assembling the published studies of carbon nanofiber/tube-metal composite synthesis into a database from which common trends/critical variables can be extracted is, as of yet, unfeasible because of the incomplete procedural descriptions that are typically given, notwithstanding the inconsistent nanofiber/nanotube attributions. Nevertheless, the “inertness” of these structured carbon surfaces (as prepared) is a decided issue in determining the capacity for metal uptake and the ultimate metal dispersion. Carbon nanotubes in pristine condition certainly represent an unfavorable surface for metal attachment given the low surface area, absence of functionality, and limited surface defects. This apparent constraint can be circumvented by introducing carboxylic ( $-\text{COOH}$ ), carbonyl ( $-\text{CO}$ ), and hydroxyl ( $-\text{OH}$ ) groups by means of acid treatment and/or mild oxidation.<sup>[5,20,51]</sup> Such pretreatments generate oxygen-containing surface groups which can be acidic, neutral, or basic leading to modification of the point-of-zero charge and can also serve to increase nanotube surface area.<sup>[62]</sup> This facilitates the introduction of a metal phase by ion exchange<sup>[5]</sup> and precipitation,<sup>[62]</sup> preparative routes that are sensitive to solution pH and surface charge. Some final considerations worth flagging with regard to the incorporation of a metal phase onto SWNTs/MWNTs include the possibility of filling the tubes and intercalation of metal layers in the intertube spacing, issues that have been addressed to a limited extent.<sup>[51]</sup>

### Application of Carbon Nanofiber/Nanotube Supported Metal Catalysts

High surface area activated carbon is effective as a metal catalyst support, displaying the following positive attributes:<sup>[63]</sup> 1) structural resistance in acidic and basic media; 2) pore structure that can promote shape selectivity; 3) readily prepared in a variety of physical forms (granules, extrudates, pellets, cloths, etc.); 4) a hydrophobic surface that can be modified

**Table 1** Compilation of recent studies of structured carbon use as metal supports in catalysis applications

Supported metal	Nature of the carbon support	Source/method of carbon support synthesis	Method of metal introduction	Catalytic reaction	Reference
Palladium	Nanofiber	Ethylene decomposition over Ni/Al <sub>2</sub> O <sub>3</sub>	Impregnation	Cinnamaldehyde hydrogenation (liquid phase)	[26],[48]
Palladium	Nanofiber	Ethylene decomposition over unsupported Ni and Ni/Cu	Impregnation	Phenol hydrogenation (gas phase)	[52]
Palladium	Nanotube	Commercial	Impregnation	Cinnamaldehyde hydrogenation (liquid phase)	[64]
Palladium	Filament	Methane decomposition over unsupported Ni and Ni/Cu	Impregnation	1,3-Butadiene hydrogenation (gas phase)	[65]
Platinum	Nanofiber	Hydrocarbon/CO decomposition over unsupported Fe, Ni, and Cu	Impregnation	Fuel cell application	[66]
Platinum	Nanofiber	Acetylene decomposition over unsupported Ni	Electrodeposition	Fuel cell application	[67]
Platinum	Nanofiber	Ethylene/CO decomposition over unsupported Fe	Impregnation	<i>n</i> -Hexane transformation (gas phase)	[68]
Nickel	Nanofiber	Commercial	Impregnation	1-Butene/1,3-butadiene hydrogenation (gas phase)	[69]
Nickel	Nanofiber	Commercial	Impregnation	Ethylene/1-butene/1,3-butadiene hydrogenation (gas phase)	[70]
Nickel	Nanofiber	Ethylene/CO decomposition over unsupported Fe	Impregnation	Ethylene/1-butene hydrogenation (gas phase)	[71]
Nickel	Nanofiber	Ethylene/CO decomposition over unsupported Fe and Fe/Ni	Impregnation	Crotonaldehyde hydrogenation (gas phase)	[55]
Nickel	Filament	Methane decomposition over Ni/Al <sub>2</sub> O <sub>3</sub> , Ni-Cu/Al <sub>2</sub> O <sub>3</sub> , Co/Al <sub>2</sub> O <sub>3</sub> , and Fe-Co/Al <sub>2</sub> O <sub>3</sub>	Impregnation	Methane decomposition (gas phase)	[72]
Nickel	Nanofiber	Methane decomposition over Ni/Al <sub>2</sub> O <sub>3</sub>	Impregnation	Methane decomposition (gas phase)	[73]
Ruthenium	Nanofiber	CO decomposition over Ni/SiO <sub>2</sub>	Deposition/precipitation	Cinnamaldehyde hydrogenation (liquid phase)	[74]
Ruthenium	Nanotube	Commercial	Adsorption	Cinnamaldehyde hydrogenation (liquid phase)	[58]
Ruthenium	Nanotube	Propylene decomposition over Fe/Al <sub>2</sub> O <sub>3</sub>	Impregnation	Ammonia decomposition (gas phase)	[75]

(Continued)

**Table 1** Compilation of recent studies of structured carbon use as metal supports in catalysis applications (*Continued*)

Supported metal	Nature of the carbon support	Source/method of carbon support synthesis	Method of metal introduction	Catalytic reaction	Reference
Rhodium	Nanofiber	Methane decomposition over Ni/Al <sub>2</sub> O <sub>3</sub>	Impregnation/ion exchange	Cyclohexene hydrogenation (liquid phase)	[76]
Rhodium	Nanofiber	Ethylene/CO decomposition over unsupported Fe, Fe/Ni, and Fe/Cu	Impregnation	Ethylene hydroformylation (gas phase)	[53]
Iridium	Nanofiber	Ethane decomposition over Ni/graphite felt	Impregnation	Hydrazine decomposition (gas phase)	[77]
Platinum–ruthenium	Nanofiber	CO decomposition over Ni–Fe/SiO <sub>2</sub>	Deposition	Fuel cell application	[78]
Nickel–aluminum	Nanotube	Propane decomposition over Ni/diatomite	Precipitation	Synthesis of carbon nanotubes (gas phase)	[79]
Ruthenium–barium	Nanofiber	Methane decomposition over Ni	Impregnation	Ammonia synthesis (gas phase)	[80]
Iron–copper	Nanofiber	CO decomposition over unsupported Fe	Impregnation	Ethylene hydrogenation (gas phase)	[56]

chemically to induce varying degrees of hydrophilicity; 5) active (precious metal) phase can be readily recovered from spent catalyst by burning away the carbonaceous support; 6) lower cost of production when compared with oxide supports. Drawbacks to the use of activated carbon as metal support in catalysis include 1) structural breakdown (gasification) at elevated temperatures in a hydrogenating or oxidizing environment; 2) microporosity that can impose transport constraints which lower reaction rate; 3) presence of mineral matter (ash content) that can act as catalyst poison. A move to structured carbon circumvents these shortcomings while retaining the positive traits of carbon as support material. A compilation of published reports of nanofibers/tubes use as catalytic metal supports is provided in Table 1. This list is not presented as definitive but covers those studies where the source of the carbon support (commercial or catalytically produced) and means of metal introduction are clearly stated, and the carbon supported metal has been employed in a catalytic reaction (operated in either gas or liquid phase): these critical process parameters are identified in Table 1. The one seemingly unavoidable ambiguity lies in the nomenclature adopted to categorize the carbon support—the designation adopted in Table 1 is that which is stated in each of the papers. It is, nonetheless, revealing that the BET surface areas associated with the tabulated systems extend from <20<sup>[64]</sup> to >200 m<sup>2</sup> g<sup>-1</sup>.<sup>[53,75]</sup>

To date, the majority of the “metals on structured carbon” studies have dealt with hydrogenation of

either aromatic<sup>[26,48,52,58,64,74]</sup> or aliphatic<sup>[55,56,65,69,70,71]</sup> reactants in the gas<sup>[18,61,62,69,73–75]</sup> or liquid<sup>[19,32,56,68,78]</sup> phase. Carbon nanofibers have apparently found a more widespread application than carbon nanotubes, in part because the larger surface area of the fiber facilitates higher metal loadings. The more instructive studies incorporated “conventional” metal supports as a means of assessing the role of structured carbon in governing the intrinsic activity of the supported metal under directly comparable reaction conditions. With this in mind, it is worth highlighting the examination of gas-phase phenol hydrogenation over supported Pd where the activity delivered by Pd/nanofiber was intermediate between Pd/graphite and Pd/activated carbon (the most active), a response that was attributed to Pd dispersion and metal/support interactions.<sup>[52]</sup> In addition, Pd supported on nanofibers outperformed Pd/charcoal in the liquid-phase hydrogenation of cinnamaldehyde<sup>[26,48]</sup> as a result of the higher surface area associated with the former in tandem with metal/support interactions. Electronic effects were also ascribed to the higher activity of a Ru–Ba bimetallic supported on nanofibers when compared with conventional activated carbon.<sup>[58]</sup> Moreover, gas-phase butene and butadiene hydrogenation activity sequence has been reported<sup>[69,70]</sup> to increase in the order Ni/Al<sub>2</sub>O<sub>3</sub> < Ni/activated carbon < Ni/nanofiber, an effect that was linked to support modifications to the metal particle morphology with possible electronic perturbation to the active sites where B and P doping of the substrate

was shown to influence activity/selectivity.<sup>[70]</sup> The same activity sequence applied to the gas-phase hydrogenation of crotonaldehyde,<sup>[55]</sup> where product (butanal, butanol, and crotyl alcohol) selectivity was found to be influenced by the metal/support interactions that governed the predominant exposed crystallographic face(s). Differences in activity delivered by Fe/Fe–Cu<sup>[56]</sup> and Rh<sup>[53]</sup> supported on nanofiber, activated carbon, and oxide supports in the ethylene hydrogenation and hydroformylation, respectively, were again associated with metal dispersion/morphology and electron transfer with the support. In the liquid-phase hydrogenation of cinnamaldehyde over Pd on carbon nanotubes and activated charcoal, hydrogenation rate was slightly higher over Pd/nanotube, but the selectivity toward C=C bond hydrogenation was significantly increased, a response that was largely attributed to differences in substrate porosity and surface/volume ratio.<sup>[64]</sup>

The presence of oxygen and hydrogen (up to 30 mol% H and 15 mol% O) in surface groups associated with activated carbon has been found to have a significant effect on adsorption properties and, consequently, catalysis.<sup>[9,63]</sup> Carbon–oxygen surface groups can be formed by reaction with oxygen or other oxidizing gases (ozone, nitrogen oxides, carbon oxides, etc.) or with oxidizing solutions (nitric acid, hydrogen peroxide, sodium hypochlorite, etc.). The oxygen-containing carbon nanofiber surface groups have been shown to have a considerable impact on the liquid-phase hydrogenation of cinnamaldehyde over supported Ru<sup>[74]</sup> and Pt,<sup>[81]</sup> where activity was raised by a factor of up to 22 on removing the carbon/oxygen groups and reactant adsorption on the nonpolar fiber surface facilitated hydrogenation. The catalytic use of carbon nanofiber supports in fuel cell applications has largely dealt with “direct-methanol” fuel cells to promote the oxidation of methanol to carbon dioxide and electric current.<sup>[66,67,78]</sup> Indeed, the enhanced electronic conductivity/mechanical strength/thermal-oxidative tolerance demonstrated by carbon nanofibers can translate into wide ranging potential applications in developing fuel cell technology. The tabulated (Table 1) applications that do not entail hydrogenation or oxidation processes include ammonia synthesis,<sup>[80]</sup> methane decomposition,<sup>[72,73]</sup> ammonia decomposition,<sup>[75]</sup> and hydrazine decomposition,<sup>[77]</sup> where the absence of residual impurities on the support, electronic conductivity, and metal dispersion all impacted on catalyst performance.

## CONCLUSION

A closer association of heterogeneous catalysis with structured carbon materials is now developing in terms

of 1) use of solid catalysts to synthesize carbon nanofibers/tubes and 2) subsequent application of the fibers/tubes as catalytic metal supports. Structured carbon materials exhibit unique chemical and physical properties with as of yet untapped potential. A realization of the full potential of these materials requires the development of low-cost methodologies for a controlled (reproducible) fabrication. Flame synthesis and arc discharge/plasma decomposition are very costly/energy demanding, and the yields of carbon are low, necessitating the involvement of exacting separation/purification steps. A catalytic route, employing unsupported and supported metals to decompose a carbon-containing precursor to a structured carbon product, offers a higher degree of control, less severe operating conditions, enhanced product selectivity, and a greater facility for scale-up. While the existing literature is somewhat discordant in the assignment of the term nanotube as opposed to nanofiber as a means of categorizing the carbon product, both forms exhibit a high aspect ratio and electron conducting properties; the higher surface area and enhanced thermal stability of the nanofiber are important considerations in many catalytic applications. Introduction of a metal phase by impregnation from an aqueous solution of the metal salt is problematic given the hydrophobic character of the carbon surface, but this can be alleviated by using organic solvents. Alternatively, the carbon surface can be functionalized by acid treatment and/or mild oxidation that also facilitates the incorporation of a metal phase by ion exchange or precipitation. The catalyst precursor so formed is activated by reduction to generate a supported zero valent metal phase that has been shown to exhibit quite distinct catalytic behavior (most notably in hydrogenation reactions) when compared with conventional activated carbon and oxide supported metal systems. The consensus emerging from the literature suggests that metal particle interactions with nanofibers/tubes are quite distinct as is manifest by modifications to metal particle size, morphology, preferred exposed crystallographic planes, and electronic structure, all critical factors in determining catalytic activity and selectivity. Further catalytic/characterization studies of different carbon supported metal systems with a consideration of promoters/inhibitors as dopants and a wider range of model reactions should lead to a better understanding of the source of what must for now be described as “unique catalytic behavior.”

## ACKNOWLEDGMENTS

The author thanks Dr. Colin Park and Claudia Amorim for their invaluable assistance.

## REFERENCES

- Dravid, V.P.; Lin, X.; Wang, Y.; Lee, A.; Ketterson, J.B.; Chang, R.P.H. Buckytubes and derivatives—their growth and implications for buckyball formation. *Science* **1993**, *259*, 1601–1604.
- Iijima, S. Helical microtubules of graphitic carbon. *Nature* **1991**, *354*, 56–58.
- Terrones, M.; Hsu, W.K.; Kroto, H.W.; Walton, D.R.M. Nanotubes: a revolution in materials science and electronics. *Topics Curr. Chem.* **1999**, *199*, 189–234.
- Rao, C.N.R.; Satishkumar, B.C.; Govindaraj, A.; Nath, M. Nanotubes. *Chem. Phys. Chem.* **2001**, *2*, 78–105.
- de Jong, K.P.; Geus, J.W. Carbon nanofibers: catalytic synthesis and applications. *Catal. Rev. Sci. Eng.* **2000**, *42*, 481–510.
- Iijima, S.; Ichihashi, T.; Ando, Y. Pentagons, heptagons and negative curvature in graphite microtubule growth. *Nature* **1992**, *356*, 776–778.
- Govindaraj, A.; Sen, R.; Nagaraju, B.V.; Rao, C.N.R. Carbon nanospheres and tubules obtained by the pyrolysis of hydrocarbons. *Philos. Mag. Lett.* **1997**, *76*, 363–367.
- Park, C.; Engel, E.S.; Crowe, A.; Gilbert, T.R.; Rodriguez, N.M. Use of carbon nanofibers in the removal of organic solvents from water. *Langmuir* **2000**, *16*, 8050–8056.
- Keane, M.A. Advances in greener separation processes—case study: recovery of chlorinated aromatic compounds. *Green Chem.* **2003**, *5*, 309–317.
- Dillon, A.C.; Jones, K.M.; Bekkedahl, T.A.; Kiang, C.H.; Bethune, D.S.; Heben, M.J. Storage of hydrogen in single-walled carbon nanotubes. *Nature* **1997**, *386*, 377–379.
- Chen, P.; Wu, X.; Lin, J.; Tan, K.L. High H<sub>2</sub> uptake by alkali-doped carbon nanotubes under ambient pressure and moderate temperatures. *Science* **1999**, *285*, 91–93.
- Rao, C.N.R. Novel materials, materials design and synthetic strategies: Recent advances and new directions. *J. Mater. Chem.* **1999**, *9*, 1–14.
- Treacy, M.M.J.; Ebbesen, T.W.; Gibson, J.M. Exceptionally high Young's modulus observed for individual carbon nanotubes. *Nature* **1996**, *381*, 678–680.
- Sandler, J.; Shaffer, M.S.P.; Prasse, T.; Bauhofer, W.; Schulte, K.; Windle, A.H. Development of a dispersion process for carbon nanotubes in an epoxy matrix and the resulting electrical properties. *Polymer* **1999**, *40*, 5967–5971.
- Haller, G.L.; Resasco, D.E. Metal support interaction—group VIII metals and reducible oxides. *Adv. Catal.* **1989**, *36*, 173–235.
- Tauster, S.J.; Fung, S.C.; Baker, R.T.K.; Horsley, J.A. Strong interactions in supported metal catalysts. *Science* **1981**, *211*, 1121–1125.
- Klug, H.P.; Alexander, L.E. *X-Ray Diffraction Procedures*; Wiley: New York, 1974.
- Ajayan, P.M. Nanotubes from carbon. *Chem. Rev.* **1999**, *99*, 1787–1799.
- Ebbesen, T.W. *Carbon Nanotubes, Preparation and Properties*; CRC Press: Boca Raton, FL, 1997.
- Nhut, J.-M.; Pesant, L.; Tessonnier, J.-P.; Winé, G.; Guille, J.; Pham-Huu, C.; Ledoux, M.-J. Mesoporous carbon nanotubes for use as support in catalysis and as nanosized reactors for one-dimensional inorganic material synthesis. *Appl. Catal., A Gen* **2003**, *254*, 345–363.
- Park, C.; Patterson, P.M.; Keane, M.A. Growth of ordered filamentous carbon from the surface of supported metal catalysts. *Curr. Topic. Colloid Interf. Sci.* **2002**, *5*, 93–123.
- Rodriguez, N.M. A review of catalytically grown carbon nanofibers. *J. Mater. Res.* **1993**, *8*, 3233–3250.
- Anderson, P.E.; Rodriguez, N.M. Growth of graphite nanofibers from the decomposition of CO/H<sub>2</sub> over silica-supported iron–nickel particles. *J. Mater. Res.* **1999**, *14*, 2912–2921.
- Zaikovskii, V.I.; Chesnokov, V.V.; Buyanov, R.A. Symmetrical spiral forms of filamentous carbon formed from butadiene-1.3 on the Ni–Cu/MgO catalyst: regularities and mechanism of growth. *Kinet. Catal.* **1999**, *40*, 552–555.
- Park, C.; Keane, M.A. Catalyst support effects in the growth of filamentous carbon from the decomposition of ethylene over nickel. *J. Catal.* **2004**, *221*, 386–399.
- Pham-Huu, C.; Keller, N.; Ehret, G.; Charbonniere, L.J.; Ziessel, R.; Ledoux, M.J. Carbon nanofiber supported palladium catalyst for liquid-phase reactions: an active and selective catalyst for hydrogenation of cinnamaldehyde to hydrocinnamaldehyde. *J. Mol. Catal., A Chem.* **2001**, *170*, 155–163.
- Hatta, N.; Murata, K. Very long graphitic nano-tubules synthesized by plasma decomposition of benzene. *Chem. Phys. Lett.* **1994**, *217*, 398–402.
- Ebbesen, T.W.; Ajayan, P.M. Large scale synthesis of nanotubes. *Nature* **1992**, *358*, 220–222.
- Bacon, R. Growth, structure and properties of graphite whiskers. *J. Appl. Phys.* **1960**, *31*, 284–290.
- Krätsmer, W.; Lamb, L.D.; Fortiropolous, K.; Huffman, D.R. Solid C<sub>60</sub>: a new form of carbon. *Nature* **1990**, *347*, 354–358.
- Terrones, M.; Hsu, W.K.; Kroto, H.W.; Walton, D.R.M. *Fullerenes and Related Structures*; Springer: New York, 1999.
- Colomer, J.-F.; Piedigrosso, P.; Willems, I.; Journet, C.; Bermei, P.; van Tendeloo, G.V.; Fonseca, A.; Nagy, J.B. Purification of catalytically produced multi-wall nanotubes. *J. Chem. Soc., Faraday Trans.* **1998**, *94*, 3753–3758.
- Richter, H.; Hernadi, K.; Caudano, R.; Fonseca, A.; Migeon, H.-N.; Nagy, J.B.; Schneider, S.; Vandooren, J.; Van Tiggelen, P.-J. Formation of nanotubes in low pressure hydrocarbon flames. *Carbon* **1996**, *34*, 427–429.
- Müller, T.E.; Reid, D.G.; Hsu, W.K.; Hare, J.P.; Kroto, H.W.; Walton, D.R.M. Synthesis of nanotubes via catalytic pyrolysis of acetylene: A SEM study. *Carbon* **1997**, *35*, 951–966.
- Figueiredo, J.L.; Bernardo, C.A.; Chludzinski, J.J.; Baker, R.T.K. The reversibility of filamentous carbon growth and gasification. *J. Catal.* **1988**, *110*, 127–138.



36. Kock, A.J.H.M.; de Bokx, P.K.; Boellaard, E.; Klop, W.; Geus, J.W. The formation of filamentous carbon on iron and nickel catalysts: Mechanism. *J. Catal.* **1985**, *96*, 468–480.
37. Chesnakov, V.V.; Zarkovskii, V.I.; Buyanov, R.A.; Molchanov, V.V.; Plyasova, L.M. The formation of morphological structures of carbon from hydrocarbons on nickel-containing catalysts. *Kinet. Catal.* **1994**, *35*, 130–135.
38. Kim, M.S.; Rodriguez, N.M.; Baker, R.T.K. The role of interfacial phenomena on the structure of carbon deposits. *J. Catal.* **1992**, *134*, 253–268.
39. Tomishige, K.; Chen, Y.; Fujimoto, K. Studies on carbon deposition in CO<sub>2</sub> reforming of CH<sub>4</sub> over nickel–magnesia solid solution catalysts. *J. Catal.* **1999**, *181*, 91–103.
40. Park, C.; Baker, R.T.K. Carbon deposition on iron–nickel during interaction with ethylene–hydrogen mixtures. *J. Catal.* **1998**, *179*, 361–374.
41. Willems, I.; Konya, Z.; Colomer, J.-F.; van Tendeloo, G.; Nagarju, N.; Fonseca, A.; Nagy, J.B. Control of the outer diameter of thin carbon nanotubes synthesized by catalytic decomposition of hydrocarbons. *Chem. Phys. Lett.* **2000**, *317*, 71–76.
42. Cherukuri, L.D.; Guang, Y.; Keane, M.A. Catalytic growth of structured carbon via the decomposition of chlorobenzene over Ni/SiO<sub>2</sub>. *Topics Catal.* **2004**, *29*, 119–128.
43. Nolan, P.E.; Lynch, D.C.; Cutler, A.H. Catalytic disproportionation of CO in the absence of hydrogen—encapsulating shell carbon formation. *Carbon* **1994**, *32*, 477–483.
44. Owens, W.T.; Rodriguez, N.M.; Baker, R.T.K. Carbon filament growth on platinum catalysts. *J. Phys. Chem.* **1992**, *96*, 5048–5053.
45. Park, C.; Keane, M.A. Filamentous carbon growth on nickel/silica: potassium and bromine as catalyst promoters. *Chem. Phys. Chem.* **2001**, *2*, 733–741.
46. Yang, R.T.; Chen, J.P. Mechanism of carbon filament growth on metal catalysts. *J. Catal.* **1989**, *115*, 52–64.
47. Alstrup, I. A new model explaining carbon filament growth on nickel, iron and Ni–Cu alloy catalysts. *J. Catal.* **1988**, *109*, 241–251.
48. Pham-Huu, C.; Keller, N.; Charbonniere, L.J.; Ziessel, R.; Ledoux, M.J. Carbon nanofiber supported palladium catalyst for liquid-phase reactions. An active and selective catalyst for hydrogenation of C=C bonds. *J. Chem. Soc., Chem. Commun.* **2000**, *18*, 1871–1872.
49. Keane, M.A. Recovery of chlorinated organic compounds by adsorption on activated carbon and zeolite surfaces. In *Encyclopedia of Surface and Colloid Science*; Hubbard, A.T., Ed.; Marcel Dekker: New York, 2002; 4479–4485.
50. Park, C.; Keane, M.A. Effectiveness of carbon nanofibers in the removal of phenol based organics from aqueous media. In *Interfacial Applications in Environmental Engineering*; Keane, M.A., Ed.; Marcel Dekker: New York, 2003; 165–192.
51. Serp, P.; Corrias, M.; Kalck, P. Carbon nanotubes and nanofibers in catalysis. *Appl. Catal., A Gen.* **2003**, *253*, 337–358.
52. Park, C.; Keane, M.A. Catalyst support effects: gas-phase hydrogenation of phenol over palladium. *J. Colloid Interface Sci.* **2003**, *266*, 183–194.
53. Gao, R.; Tan, C.D.; Baker, R.T.K. Ethylene hydroformylation on graphite nanofiber supported rhodium catalysts. *Catal. Today* **2001**, *65*, 19–29.
54. Park, C.; Baker, R.T.K. Catalytic behavior of graphite nanofiber supported nickel particles: the influence of the nanofiber structure. *J. Phys. Chem. B* **1998**, *102*, 5168–5177.
55. Salman, F.; Park, C.; Baker, R.T.K. Hydrogenation of crotonaldehyde over graphite nanofiber supported nickel. *Catal. Today* **1999**, *53*, 385–394.
56. Rodriguez, N.M.; Kim, M.-S.; Baker, R.T.K. Carbon nanofibers: a unique catalyst support medium. *J. Phys. Chem.* **1994**, *98*, 13108–13111.
57. Reshetenko, T.V.; Avdeeva, L.B.; Ismagilov, Z.R.; Chuvilin, A.L. Catalytic filamentous carbon as supports for nickel catalysts. *Carbon* **2004**, *42*, 143–148.
58. Planeix, J.M.; Coustel, N.; Coq, B.; Brotons, V.; Kumbhar, P.S.; Dutartre, R.; Geneste, P.; Bernier, P.; Ajayan, P.M. Application of carbon nanotubes as supports in heterogeneous catalysis. *J. Am. Chem. Soc.* **1994**, *116*, 7935–7936.
59. Lordi, V.; Yao, N.; Wei, J. Method for supporting platinum on single-walled carbon nanotubes for a selective hydrogenation catalyst. *Chem. Mater.* **2001**, *12*, 733–737.
60. Ye, X.R.; Lin, Y.; Wai, C.M. Decorating catalytic palladium nanoparticles on carbon nanotubes in supercritical carbon dioxide. *J. Chem. Soc., Chem. Commun.* **2003**, *5*, 642–643.
61. Xue, B.; Chen, P.; Hong, Q.; Lin, J.; Tan, K.T. Growth of Pd, Pt, Ag and Au nanoparticles on carbon nanotubes. *J. Mater. Chem.* **2001**, *11*, 2378–2381.
62. Li, C.-H.; Yao, K.-F.; Liang, J. Influence of acid treatments on the activity of carbon nanotube-supported catalysts. *Carbon* **2003**, *41*, 858–860.
63. Rodriguez-Reinoso, F. The role of carbon materials in heterogeneous catalysis. *Carbon* **1998**, *36*, 159–175.
64. Nhut, J.M.; Vieira, R.; Pesant, L.; Tessonnier, J.P.; Keller, N.; Ehret, G.; Pham-Huu, C.; Ledoux, M.J. Synthesis and catalytic uses of carbon and silicon carbide nanostructures. *Catal. Today* **2002**, *76*, 11–32.
65. Chesnokov, V.V.; Prosvirin, I.P.; Zaikovskii, V.I.; Zaitseva, N.A. State of the active component and catalytic properties of Pd/C catalysts on the selective hydrogenation of butadiene-1,3 into butylenes. *Eurasian Chem. Technol. J.* **2003**, *5*, 127–135.
66. Bessel, C.A.; Laubernds, K.; Rodriguez, N.M.; Baker, R.T.K. Graphite nanofibers as an electrode for fuel cell applications. *J. Phys. Chem. B* **2001**, *105*, 1115–1118.
67. Tang, H.; Chen, J.; Nie, L.; Liu, D.; Deng, W.; Kuang, Y.; Yao, K. High dispersion and electrocatalytic properties of platinum nanoparticles on graphitic carbon nanofibers (GCNFs). *J. Colloid Interface Sci.* **2004**, *269*, 26–31.
68. Baker, R.T.K.; Laubernds, K.; Wootsch, A.; Paál, Z. Pt/graphite nanofiber catalyst in *n*-hexane test reaction. *J. Catal.* **2000**, *193*, 165–167.

69. Chambers, A.; Nemes, T.; Rodriguez, N.M.; Baker, R.T.K. Catalytic behavior of graphite nanofiber supported nickel particles: 1. Comparison with other support media. *J. Phys. Chem. B* **1998**, *102*, 2251–2258.
70. Park, C.; Baker, R.T.K. Catalytic behavior of graphite nanofiber supported nickel particles: 2. The influence of the nanofiber structure. *J. Phys. Chem. B* **1998**, *102*, 5168–5177.
71. Park, C.; Baker, R.T.K. Catalytic behavior of graphite nanofiber supported nickel particles: 3. The effect of chemical blocking on the performance of the system. *J. Phys. Chem. B* **1999**, *103*, 2453–2459.
72. Reshetenko, T.V.; Avdeeva, L.B.; Ismagilov, Z.R.; Chuvilin, A.L. Catalytic filamentous carbon as supports for nickel catalysts. *Carbon* **2004**, *42*, 143–148.
73. Shaikhutdinov, Sh.K.; Avdeeva, L.B.; Novgorodov, B.N.; Zaikovskii, V.I.; Kochubey, D.I. Nickel catalysts supported on carbon nanofibers: structure and activity in methane decomposition. *Catal. Lett.* **1997**, *47*, 35–42.
74. Toebes, M.L.; Prinsloo, F.F.; Bitter, J.H.; Dillen, A.J.; Jong, K.P. Influence of oxygen-containing surface groups on the activity and selectivity of carbon nanofiber-supported ruthenium catalysts in the hydrogenation of cinnamaldehyde. *J. Catal.* **2003**, *214*, 78–87.
75. Yin, S.F.; Xu, B.Q.; Ng, C.F.; Au, C.T. Nano Ru/CNTs: A highly active and stable catalyst for the generation of CO<sub>x</sub>-free hydrogen in ammonia decomposition. *Appl. Catal., B Environ.* **2004**, *48*, 237–241.
76. Ros, T.G.; Keller, D.E.; Dillen, A.J.; Geus, J.W.; Koningsberger, D.C. Preparation and activity of small rhodium metal particles on fishbone carbon nanofibers. *J. Catal.* **2002**, *211*, 85–102.
77. Vieira, R.; Pham-Huu, C.; Keller, N.; Ledoux, M.J. New carbon nanofiber/graphite felt composite for use as a catalyst support for hydrazine catalytic decomposition. *J. Chem. Soc., Chem. Commun.* **2002**, *9*, 954–955.
78. Steigerwalt, E.S.; Deluga, G.A.; Cliffl, D.E.; Lukehart, C.M. A Pt–Ru/graphitic carbon nanofiber nanocomposite exhibiting high relative performance as a direct-methanol fuel cell anode catalyst. *J. Phys. Chem. B* **2001**, *105*, 8097–8101.
79. Li, C.; Yao, K.; Liang, J. Study on the features of multi-walled carbon nanotubes supported nickel aluminum mixed oxides. *Appl. Catal., A Gen.* **2004**, *261*, 221–224.
80. Liang, C.; Li, Z.; Qiu, J.; Li, C. Graphitic nanofilaments as novel support of Ru–Ba catalysts for ammonia synthesis. *J. Catal.* **2002**, *211*, 278–282.
81. Toebes, M. Carbon Nanofibers as Catalyst Support for Noble Metals; Ph.D. Thesis; Universiteit Utrecht, 2004.

# Nanofilms in Giant Magnetoresistance Heads

**Edward Grochowski**

*IBM Almaden Research Center, San Jose, California, U.S.A.*

**Robert E. Fontana, Jr.**

*Research Staff Member, IBM Almaden Research Center, San Jose, California, U.S.A.*

## INTRODUCTION

The magnetic hard disk drive has become the foremost data storage device for computer applications based on cost, capacity, performance, and miniature form factor. Although it is a mechanical, rotating disk storage device, power requirements are minimal, usually a few watts; reliability over a wide range of operating environments, from below 0°C to well over 100°C, is excellent; and costs are less than \$0.01 per megabyte. Throughout its 46-year history, hard disk drives have been the recipient of significant technological innovations which have added to the usefulness of this device, and data density on the disk surface, areal density, has increased nearly 35 million times in this period (Fig. 1).<sup>[1]</sup>

The principal magnetic components in a drive are the media or disks, and a recording head that reads and writes data (Fig. 2). These data are recorded in the form of magnetized regions on the media within a deposited thin film of magnetic alloy normally consisting of chromium, cobalt, platinum, and a fourth component as boron. Data are distributed geometrically on a series of concentric rings, or tracks, whose location has been predetermined by a process called formatting. Along these tracks, bits of data are magnetically written by an inductive element in the head, and subsequently sensed or read by the giant magnetoresistive element that is an integral part of the head structure. Fig. 3 is a schematic of the writing process with a projection of the bit length and track width for a 100 Gb/in.<sup>2</sup> areal density. Writing involves a magnetic reorienting of the very small alloy micrograins in the media, and the interface between two magnetized bits is shown in Fig. 3. To maintain an adequate signal-to-noise ratio, a large number of grains are required per bit, nearly 1000 grains. Increasing areal density involves reducing bit dimensions, requiring smaller grain diameters. In the case of 100 Gb/in.<sup>2</sup>, a grain diameter of 5 nm is projected.

Fig. 4 illustrates the history of magnetic recording head design since 1970. The transition from a ferrite, wire-wound inductive head to a thin film head in late

1970s to early 1980s was driven by progressive areal density increases. In both of these early designs, an inductive element performed both read and write functions. As areal density increased beyond 0.10 Gb/in.<sup>2</sup>, this inductive element proved inadequate to maintain an acceptable signal-to-noise ratio in reading and, in addition, the read amplitude was velocity-dependent. A second element was added to recording heads, a simple magnetoresistive (MR) [or anisotropic magnetoresistive (AMR)] sensor that now separated read and inductive write parts of the head, but shared common elements or layers of the structure. The MR element used a nickel-iron (NiFe) ferromagnetic film that consequently changed resistance when experiencing a magnetic field originating from stored bits on the rotating disk media. This modification allowed the write element to be more easily built with fewer copper coil turns than inductive heads that perform both read and write operations.

As areal densities continued to increase beyond 10 Gb/in.<sup>2</sup>, scaling of the MR element to smaller dimensions based on reading submicrometer tracks also reduced signal amplitude. A new read sensor technology was required.<sup>[2,3]</sup>

## GMR HEAD DEFINITION

In 1988, a new magnetoresistive effect was discovered in Germany and France, identified as the giant magnetoresistive (GMR) effect, using multilayers of chromium and iron synthesized by molecular beam epitaxy. When this Cr/Fe structure was tested at liquid helium, cryogenic temperatures in very strong magnetic fields of several thousand Oersteds, or about 100 times greater than what would be obtained from a rotating magnetic media in a disk drive, the result was a resistance change of as much as 50%.<sup>[4]</sup> This newly observed behavior was of great interest to magnetic recording scientists. An application of GMR as a sensor element to magnetic recording would be very valuable at high data densities, where scaling sensor dimensions into the nanometer range could still yield a readable room temperature signal amplitude, or resistance change in

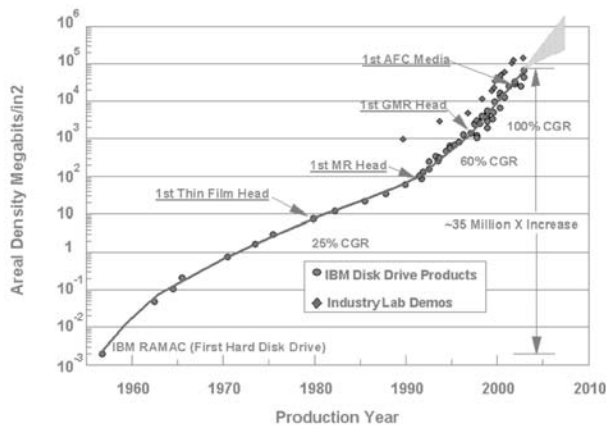


Fig. 1 Hard disk areal density trend.

the presence of a magnetic field of a magnitude experienced with a recorded disk.

Subsequently, IBM researchers demonstrated that the origin of the GMR effect arose from electron spin scattering in ferromagnetic materials. Using conventional vacuum sputtering techniques, unique thin film structures were shown to exhibit the GMR effect at disk drive operating temperatures and in low magnetic fields.<sup>[5]</sup> Whereas in the early investigations, a strong antiparallel (AP) coupling within the Cr/Fe layers was the origin of GMR, IBM researchers found that the interaction of a magnetically fixed or pinned ferromagnetic layer and a magnetically free ferromagnetic layer separated by a highly conductive, non-magnetic spacer also produced the GMR effect. This free layer was free to rotate, responding to external magnetic fields from the disk, while the pinned layer remained magnetically fixed. Control of the spin-dependent current and a valve-like similarity to tunneling between

ferromagnetic layers prompted the label “spin valve” for this structure.<sup>[6]</sup>

The GMR effect varies as the cosine of the angle of magnetizations between pinned and free layers (Fig. 5), varying as

$$\cos(\theta_{\text{free}} - \theta_{\text{pinned}}) = \sin(\theta_{\text{free}}) \quad (1)$$

Considering that  $\theta_{\text{pinned}} = \pi/2$

Therefore the voltage of a spin valve, GMR sensor with width  $W$ , height  $h$ , resistance  $R$ , and a relative term called magnetoresistance  $(\Delta R/R)_{\text{GMR}}$  with current  $I$  passing through the structure is given by:

$$V_{\text{GMR}} = I\{R + (W/2h)(\Delta R/R)\eta \sin \theta_{\text{free}}\} \quad (2)$$

where  $\gamma$  is an efficiency factor which includes any misalignment of the magnetization based on demagnetizing effects.

Fig. 6 shows the read head progress for the transition to giant magnetoresistive heads (GMR) and the accompanying bit pitch and track pitch evolution including projections for future years. These advanced GMR read elements could be composed of multiple films with a total thickness of as small as  $0.01 \mu\text{m}$  with a contact-contact spacing of less than  $0.2 \mu\text{m}$ . These ultrasmall dimensions qualify GMR sensors as nanotechnology devices.

Both MR and GMR read head electrical resistance depends on a magnetic field produced by the recorded information on the disk. In the previous MR heads, this resistance change occurs in a single NiFe film, while in GMR heads, this resistance change occurs in multiple films. Whereas in a conventional NiFe MR film, the resistance change is maintained as a linear response to the disk’s field based on the

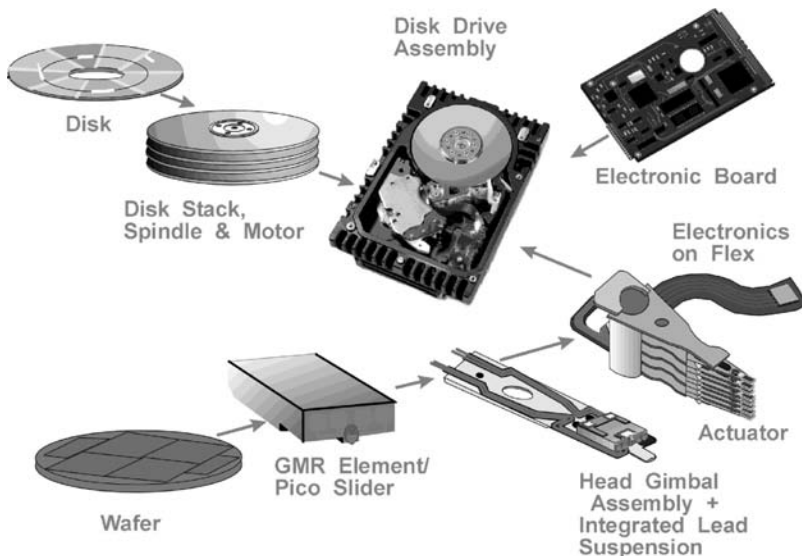


Fig. 2 Magnetic hard disk drive components.

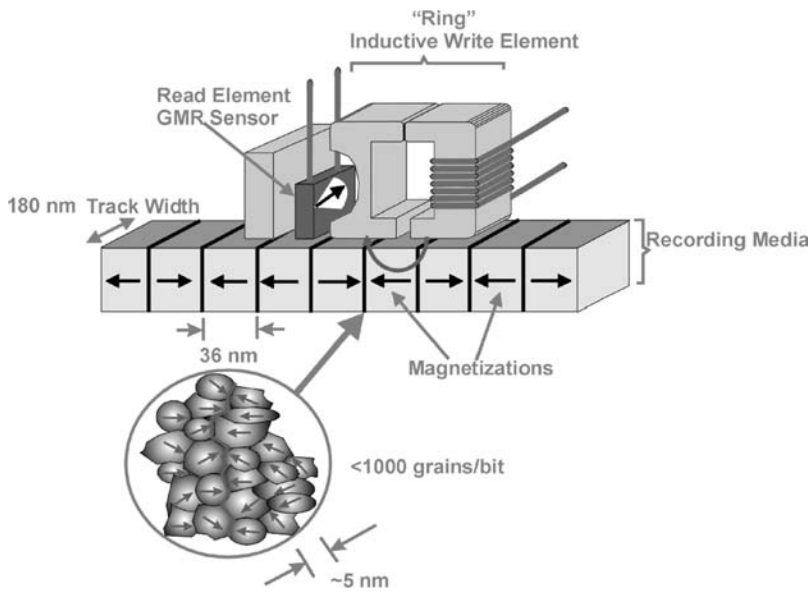


Fig. 3 Magnetic recording basics at 100 Gb/in<sup>2</sup>.

close interaction of a magnetically soft adjacent layer (SAL), and the GMR response is intrinsically linear.<sup>[7]</sup>

There are four fundamental film types in a conventional GMR structure, although some of these films may be comprised of multiple subfilms. Fig. 5 is a cross section of a GMR read sensor and overlying inductive write element through the air bearing surface (ABS). The plane of this figure is parallel with the disk media. A GMR or free film has a variable magnetization that changes under the influence of the disk's magnetic field. The second film is a very thin conducting spacer, usually copper, with a thickness less than the mean free path of electrons. This film allows electrical current to

pass easily to the third film, also a GMR film, which has a fixed or pinned magnetization. The fourth film is a pinning film which maintains the fixed magnetization of the third film through the process of antiferromagnetic exchange coupling. Typical antiferromagnetic exchange films contain the element manganese alloyed with either iridium, platinum, or iron. In contact with both ends of the GMR film stripe is a magnetically hard region, usually composed of an alloy of chromium, platinum, cobalt, and boron. These regions maintain a stability to the GMR sensor by suppressing magnetic domain noise through the use of a longitudinal bias applied to both ends of the GMR multilayer region.

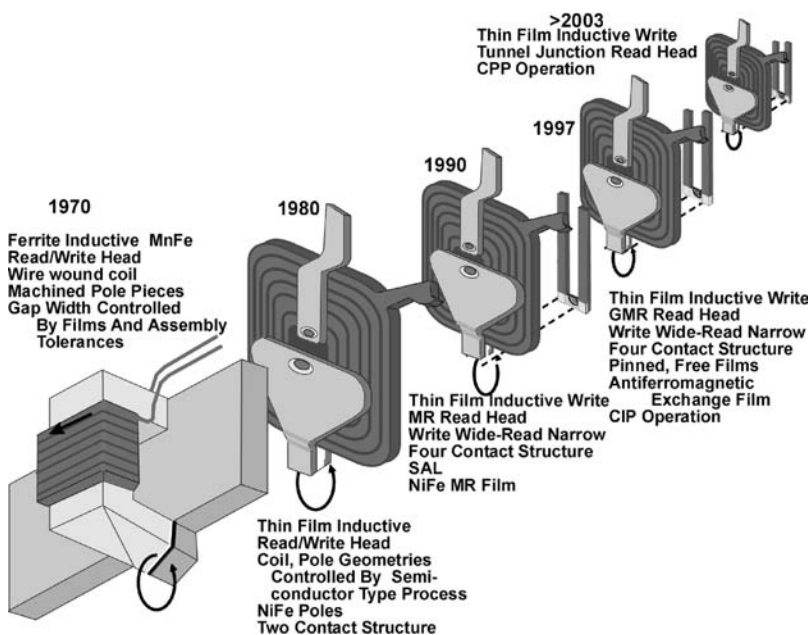


Fig. 4 The evolution of magnetic read/write sensors.

Nanodiamonds -  
Nanolithography

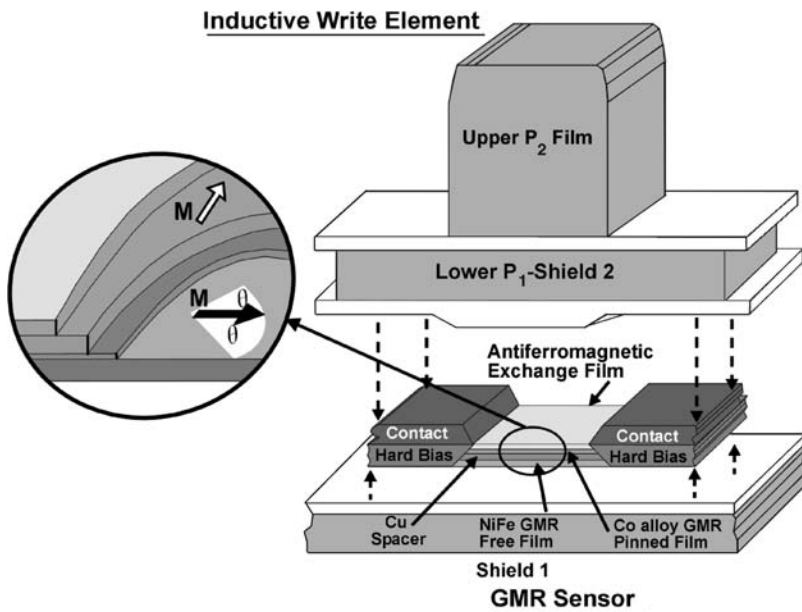


Fig. 5 GMR read sensor with section of inductive write element.

**THE GMR EFFECT**

GMR read sensors exploit the quantum nature of electrons, which have two spins, spin up and spin down. Referring to Fig. 7, a view of a GMR sensor with ABS perpendicular to the plane of the page, the multi-film structure is indicated with antiferromagnetic exchange layer, pinned layer, spacer and GMR free

layer with hard bias, stabilizing end regions, and electrical contacts. The electrical conductivity of this multi-film structure is proportional to the mean free path of electrons and the density of electrons in the films' materials. The mean free path is the distance an electron travels before a scattering event occurs, i.e., the loss of momentum through collisions with phonons or magnons within the material's lattice. Therefore,

Nanodiamonds – Nanolithography

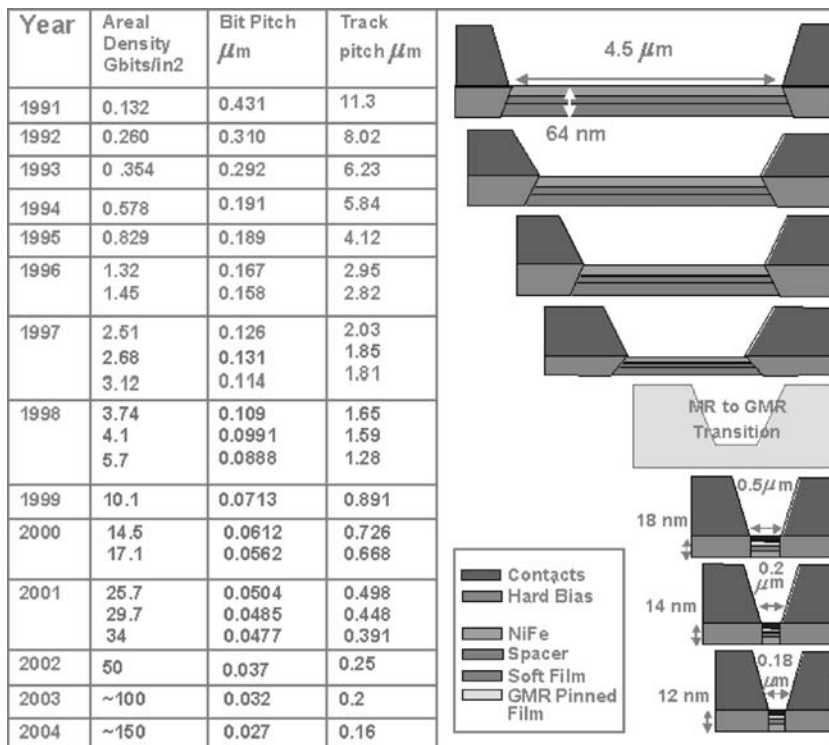


Fig. 6 MR/GMR read head evolution.



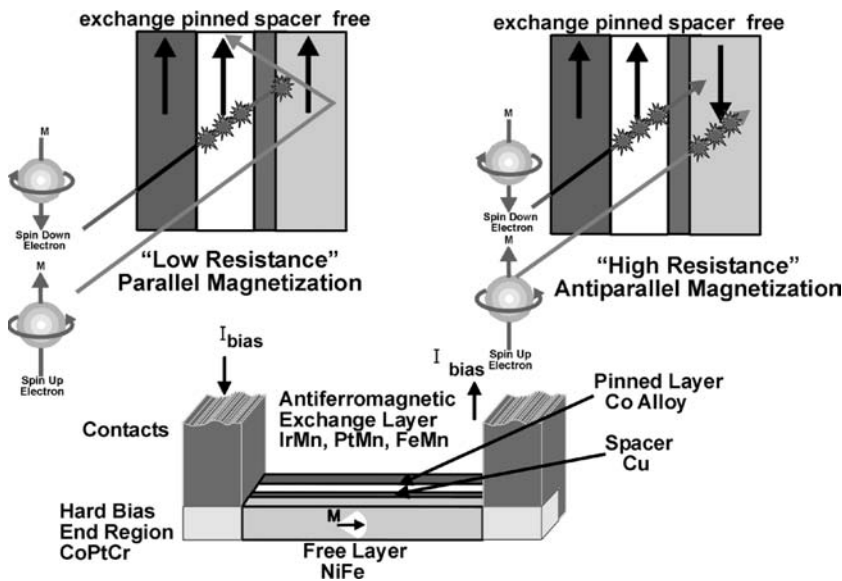


Fig. 7 GMR/spin valve operation. Source: From Ref.[2].

electrical conductivity depends on the amount of electron scattering that occurs within the multifold structure. Electron spin generates a magnetic dipole, analogous to the magnetic dipole originating from electrical current flowing within a loop of conducting wire. Electron scattering can be observed to be more prevalent in films having an opposing magnetization, i.e., mean free paths of electrons are spin-dependent.<sup>[8]</sup>

Conductivity depends on the ability of electrons to traverse the entire multifold structure, without collisions, and both spin up and spin down electron mean free paths are determined by the relative orientations of the magnetizations within each film. In Fig. 7, if these magnetizations are all parallel, as would be the case if the free NiFe layer senses a magnetic field originating from the disk media, the spin up electron's path through the free layer, across the Cu spacer, and penetrating far into the pinned layer results in a low resistance (high conductivity). Spin down electrons undergo collisions in both free and pinned layers and do not add to the conductivity. In fact, spin down electrons would not be able to penetrate far beyond the spacer layer before colliding. If all the magnetizations are antiparallel, as would be the case when no magnetic field from the media is present and the magnetization of the free layer is reversed, the distance of both spin up and spin down electrons is reduced by collisions so that neither can penetrate far beyond the spacer layer. This is the high resistance case. It can be demonstrated that the difference in conductivity between parallel and antiparallel cases for the GMR sensor can be expressed as:

$$\Delta C_{total} = \alpha(\lambda^+ - \lambda^-)^2 \quad (3)$$

where  $C$  is the sensor conductivity,  $\alpha$  is a proportionality constant,  $\lambda^+$  is the mean free path of electrons with spin parallel to the magnetization, and  $\lambda^-$  is the mean free path antiparallel. Typical GMR sensors exhibit conductivity changes of 10% from antiparallel to parallel states, although values larger than 20% have been reported in the laboratory.<sup>[9]</sup>

### INTERNAL MAGNETIC FIELDS IN GMR STRUCTURES

Fig. 8 demonstrates a GMR/spin valve linear voltage response to a changing external disk media magnetic field, which is the read process in magnetic recording. To design an efficient GMR read structure, the full linear portion of this curve is the operating response region, and is obtained by matching the free layer

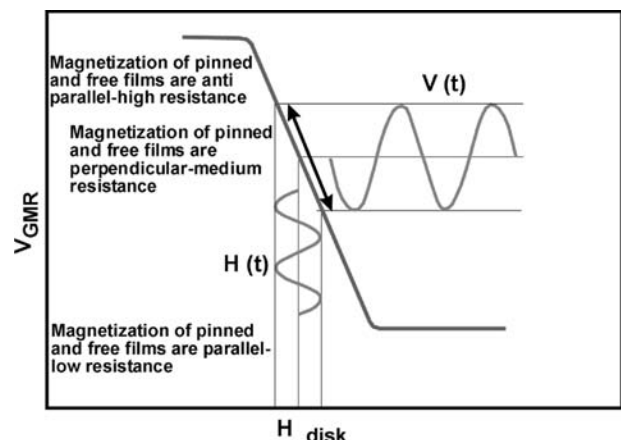


Fig. 8 Spin valve response to disk magnetic field.

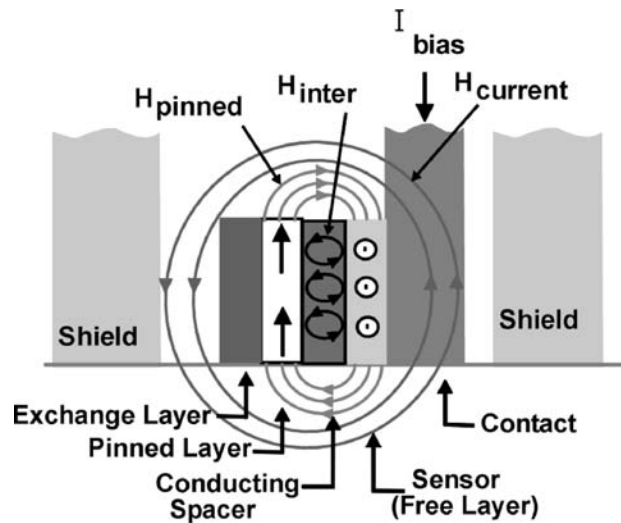
magnetic moment with the magnetic flux originating from the disk media.

$$M_{st} \sim M_r d \tag{4}$$

where  $M_s$  is the magnetization and  $t$  is thickness of the GMR free layer and, conversely,  $M_r$  and  $d$  are the magnetization and the thickness of the disk media layer. The GMR voltage, and therefore  $\sin \theta_{free}$ , is proportional to the time-varying disk field  $H(t)$  applied along the structure's transverse direction. The free layer magnetization is normally oriented  $90^\circ$  to this field, along the longitudinal direction of the sensor when no disk field is present, previously shown in Fig. 5. For this magnetic field "balancing" between GMR and disk moments to be effective, the net of all other magnetic forces within the GMR free layer must be zero, as shown in Fig. 9. This design objective is often referred to as the "proper bias" of the GMR read head, so that

$$H_{pinned} + H_{inter} + H_{elect} = 0 \tag{5}$$

where  $H_{pinned}$  is the magnetostatic field arising from the pinned layer,  $H_{inter}$  is the spacer coupled field between pinned and free layers, and  $H_{elect}$  is the normal induced field arising from electrical sense current flowing within the free layer. Also shown in Fig. 9 are the shield structures that function to isolate the GMR sensor from adjacent disk media magnetic fields, assuring that only one specific magnetized region of transition is read at a time. In many GMR designs, the overlying



$$H_{pinned} + H_{inter} + H_{current} = 0$$

Key: Electrons shared between layers

Fig. 9 Spin valve head (GMR) internal magnetic fields.

inductive head  $P_1$  element also serves as one side of the shield structure (Fig. 5).

### GMR STABILIZATION

Figs. 5–7 show a magnetic hard bias region contiguous to the GMR element which adds a longitudinal magnetic bias to the structure. As in MR read heads, complex multidomain regions within the NiFe free layer must be prevented from forming within the thin film. These regions would promote Barkhausen induced noise effects in the GMR sensor read back signal. Unlike the prior MR read head structures, in GMR read heads, only the free layer must make contact with the hard bias end regions because the pinned and exchange regions have a fixed magnetization in a direction perpendicular to the current flow (transverse direction). During processing, the pinned and exchange layer's magnetization is oriented by heating beyond the "blocking temperature," i.e., the temperature above which magnetization reverts to a very low value (Fig. 10). A cooling cycle in a transverse magnetic field determines the final pinned layer's magnetic orientation. As the hard bias end regions are also magnetically oriented, but in the longitudinal direction, the alloy selection for this film as well as the pinned layer is critical, based on blocking temperatures. Usually, an alloy of CoPtCr is selected for the hard bias region because its longitudinal magnetization is not affected by the thermal cycle required to set the pinned layer's transverse orientation. In addition, the pinned layer's blocking temperature must still be high enough to remain stable during heat cycling in subsequent process operations. Table 1 shows the blocking

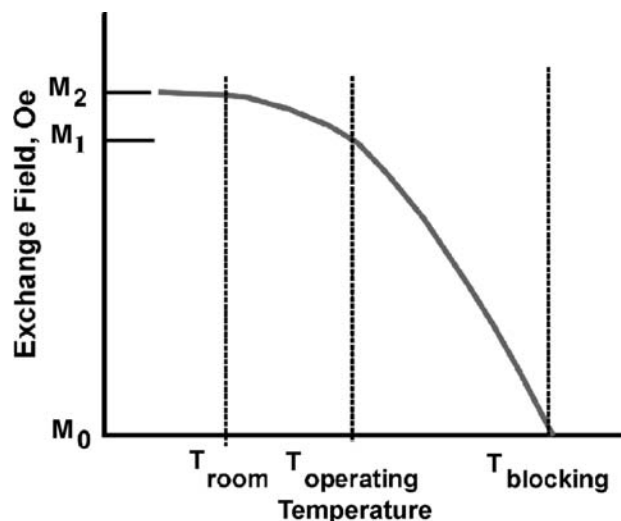


Fig. 10 The blocking temperature.

**Table 1** Comparison of antiferromagnets for GMR/spin valves

Antiferromagnet	Blocking temperature [°C]	Exchange energy [erg/cm <sup>2</sup> ]	Critical thickness [Å]
Ni <sub>45</sub> Mn <sub>55</sub>	375	0.24	300
Ni <sub>49</sub> Mn <sub>51</sub>	340	0.20	300
$\alpha$ -Fe <sub>2</sub> O <sub>3</sub>	320	0.10	<500
Cr <sub>40</sub> Mn <sub>40</sub> Pt <sub>20</sub>	300	0.12	250
Pt <sub>20</sub> Pd <sub>30</sub> Mn <sub>50</sub>	300	0.12	250
Ir <sub>20</sub> Mn <sub>80</sub>	280	0.15	80
Ru <sub>12</sub> Rh <sub>8</sub> Mn <sub>80</sub>	225	0.17	100
Ni <sub>50</sub> O <sub>50</sub>	210	0.12	350
Fe <sub>50</sub> Mn <sub>50</sub>	180	0.11	110

Source: From Ref.<sup>[1]</sup>.

temperature for some common antiferromagnetic alloys used in GMR heads.

### ANTIFERROMAGNETIC EXCHANGE COUPLING

Exchange coupling is a principal mechanism that determines GMR head operation, and it may be considered as the interaction between a ferromagnet (NiFe in this case) in contact with an antiferromagnet, with sample compositions as shown in Table 1. Referring to Fig. 11, a ferromagnetic material is defined as one in which all atomic dipole moments line up in the same direction; whereas in antiferromagnetic materials, the

moments of adjacent atoms line up in opposite directions. In the former material, there is a net magnetic moment while in the latter there is no net macroscopic moment. Exchange may be defined as the tendency for neighboring atomic dipoles to line parallel or antiparallel to each other, and it results from the overlap of orbiting electrons in neighboring atoms. Exchange may occur within the same material or in two different adjacent materials. In the latter case, because exchange principally occurs across distances between atoms in a solid, it can be considered a near-neighbor phenomenon and is critically dependent on the quality and purity of the interface.

If an antiferromagnetic film is deposited onto a ferromagnetic film by vacuum sputtering, a clean, contaminant-free interface results, and the atoms align themselves by exchange so that a permanent biasing layer is created, which maintains the ferromagnet oriented in a constant direction. The B/H hysteresis loop of a ferromagnet/antiferromagnet structure is shifted by an amount  $H_x$  and is a direct measure of the amount of exchange coupling occurring across the interface. The ideal antiferromagnetic material would basically be an insulator with a high exchange energy, a high blocking temperature for process stability with a narrow blocking temperature range and distribution, and with a small critical thickness.<sup>[6]</sup>

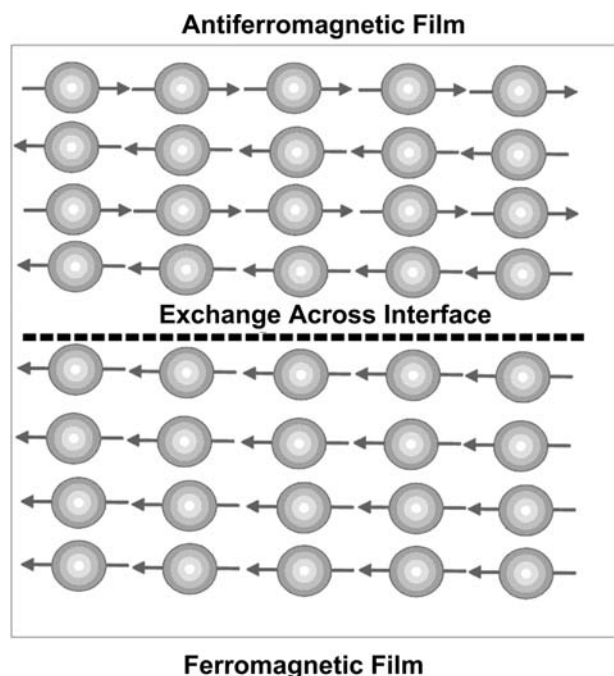


**Fig. 11** Ferromagnetic/antiferromagnetic interface structure. Source: From Ref.<sup>[11]</sup>.

### MORE COMPLEX GMR STRUCTURES

In a nanolayer GMR structure, thin (as small as a monolayer) films of Co or Fe are added to NiFe free layer / Cu spacer interface, resulting in an increase in the GMR signal amplitude up to 50%. These nanolayer films are believed to reduce the spin-dependent scattering at the interface by improving the interfacial purity of the NiFe, which could be lost by mixing with Cu during the sputtering process. The nanolayers may be

added to the NiFe free layer, or the pinned layer, or both, and many GMR read head structures attain higher GMR amplitudes through the use of nanolayers.

In a dual spin valve or dual GMR structure, the NiFe free layer is surrounded with two Cu spacers, as well as two pinned and antiferromagnetic exchange layers in an almost symmetrical configuration. This can be considered as a combination of two simple GMR structures, back-to-back and sharing a common free layer. In this case, a majority of electrons originating from this free layer can now reach a pinned layer, eliminating any electrons from these layers that do not participate in the GMR effect. It is estimated that an increase in the GMR amplitude reaches up to 33% for the dual structure. In addition, because the GMR structures are mirror images of each other, the current induced field is effectively cancelled so that proper biasing may occur independent of applied current. Conversely, because more films are involved in the dual GMR structure, the resulting resistance of the structure is lower, and this may lead to a lower overall GMR signal.

Depositing an additional layer of ruthenium or rhodium within the pinned layer was shown to stabilize the magnetization of this film and enhance the exchange field. This could allow the use of many more antiferromagnets, which previously did not have adequate fields, but had other beneficial characteristics such as higher blocking temperatures or better insulation properties. Based on the phenomenon of antiparallel (AP) coupling, the pinned layer now consists of two ferromagnetic films separated by the AP-spacer layer. This increased stabilization can also be the result of decreasing the demagnetizing field in the pinned layer, thereby reducing any rotation of the magnetization. It is estimated that a 25- to 100-times improvement in pinned layer stabilization results from AP pinning and, as areal density increases necessitate narrower and shorter GMR structures, this technique is expected to become more prevalent in read heads.

The use of a thin interposed layer of a non-magnetic metal, such as ruthenium, to create a coupling effect between two ferromagnetic layers to retain opposite magnetic orientations was recently extended to the magnetic disk structure.<sup>[11,12]</sup> This media structure, termed antiferromagnetic coupled (AFC) media, was demonstrated to exhibit good magnetic stability as areal density increases beyond 30 Gb/in.<sup>2</sup>, thereby delaying the effects of superparamagnetism. The latter phenomenon occurs when metal grains within the media become so small that the energy required to create or erase the bits of magnetically stored information is the thermal energy ( $kT$ ), where  $k$  is the Boltzmann constant and  $T$  is the operating temperature of the disk

drive) of the environment.<sup>[13]</sup> Ruthenium thicknesses of 6C( about three atomic layers) are commonly used because coupling strength oscillates with film thickness. It was found that at a thickness of maximum strength, electron waves in this ruthenium spacer constructively interfere and allow the magnetically polarized energy from one interface through to the other ferromagnetic layer. The AFC medium is projected to find application in magnetic storage for many years to come.

## GMR PROCESSING–LITHOGRAPHY

Fig. 1 indicated a 100% growth rate in areal density for magnetic recording since 1997, based on the use of GMR read sensors, in effect doubling this parameter every year. This density increase in magnetic recording originates from a shrinking in the bit cell area, which results from lithographic and processing improvements. This is in contrast to the integrated circuit (IC) field in which the transistor count in an IC device doubles every 1.5 years (roughly 60% growth rate). In the latter case, only about one-third of this increase originates from a transistor cell area or lithographic improvements. This is shown in Fig. 12, where historical IC, general IC, and IC gate features are compared with historical magnetic recording head, inductive write head width, and GMR element length. The critical head dimensions, P2w (or write width) determines the track width and GMRw, the read width for the track.<sup>[14]</sup>

It is convenient to describe the fundamentals of processing for both inductive write element and GMR read sensor, which are both integrated into a single read/write structure. The actual head processing is similar to thin film integrated circuit processing, and consists of a sequence of patterning by application of

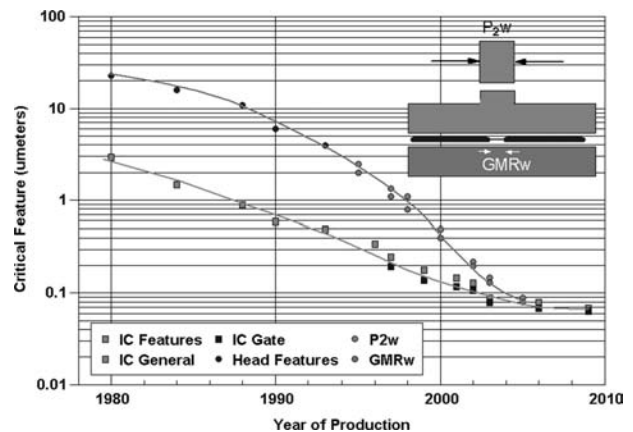


Fig. 12 Lithographic critical feature roadmap for GMR heads and semiconductor IC.

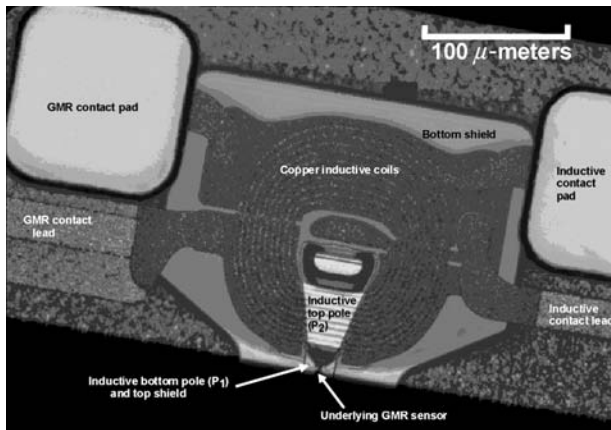


Fig. 13 Partial microphotograph of inductive write, GMR read head.

photoresist, masking and exposure operations (lithography), film deposition, and localized material removal by etching to create the various layers and structures. In addition, the use of lift-off operations, as well as highly directional etching as special techniques for the control of vertical and horizontal dimensions of critical features, is required at these feature sizes and topographies. Fig. 13 is a top view microphotograph of the head structure and Fig. 14 identifies the principal parts as seen from this view. It can be seen that only the overlying inductive write element is visible. In Fig. 15, the actual vertical structure is indicated, in which the GMR sensor is first formed by successive depositions followed by a series of insulators and metal films which comprise the inductive element. The total device structure consists of the order of 20 layers, ranging in thickness from as thin as 1–2 nm in the GMR sensor to 3–4 μm for the pole tip of the inductive write element. Progressively higher areal densities were achieved by reducing both critical

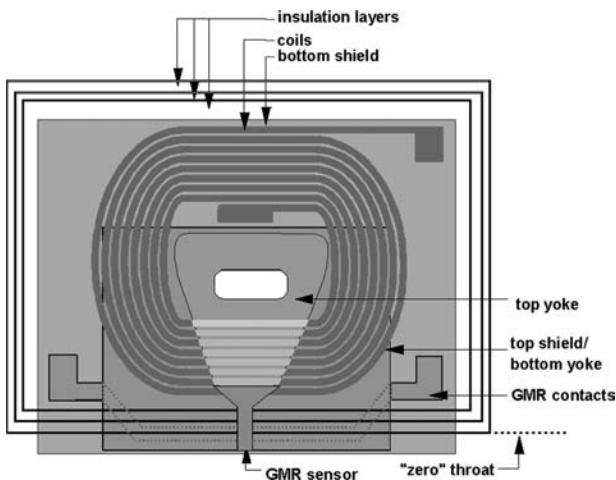


Fig. 14 Thin film head, top view.

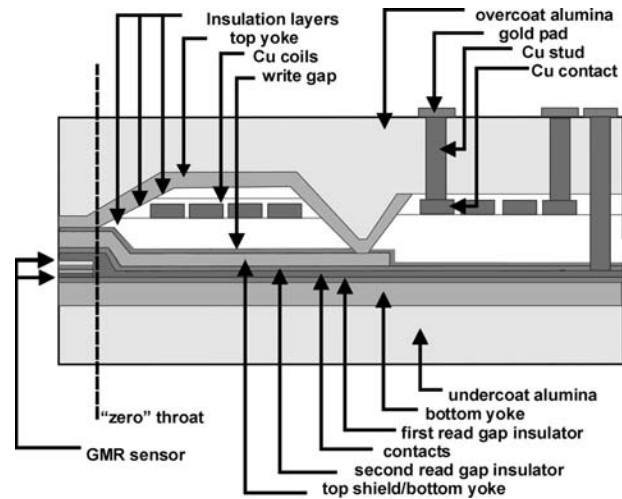


Fig. 15 Thin film head, side-section view.

thicknesses and horizontal dimensions of the head structure in a process referred to as scaling. Over the past 10 years, areal density has increased by a factor of 400, which has required a GMR sensor thickness decrease of a factor of 10–15, the sensor width MRw decreased by a similar factor, and the inductive pole tip width P2w scaled down also by a similar factor. It can be projected that further areal densities increases, which are expected as the norm in magnetic recording although probably not retaining the previous 100% growth, will involve continual decreases in these critical dimensions well into the subnanometer range for vertical GMR dimensions, and into the submicrometer range for the horizontal dimension of P2w.

An outline of typical processing operations for both inductive and GMR structures for the read/write head is shown in Fig. 16. There are four fundamental, generic operations which involve specific equipment and processes, and these are very similar to those employed in IC processes. Photo, involving the application of a

Ph = Photo Pl = Plating Dp = Deposition Pa = Patterning	
Bottom Yoke or Shield	$2Ph + Pl + 2Dp + 1Pa = 6$
Gap(s)	$Ph + 3Dp + Pa = 5$
Top Shield	$2Ph + Pl + 2Dp + 1Pa = 6$
Sensor/Stabilization/Contacts	$2Ph + 6Dp + 2Pa = 10$
Coil(s) + Insulators	$4Ph + Pl + 2Dp = 7$
Top Yoke	$2Ph + Pl + 2Dp + 1Pa = 6$
Contacts, Studs, Pads	$3Ph + 3Pl + 6Dp = 12$
Overcoat	$1Dp + Pa = 2$
Total Processes	54

Fig. 16 Inductive write/GMR read process operations.



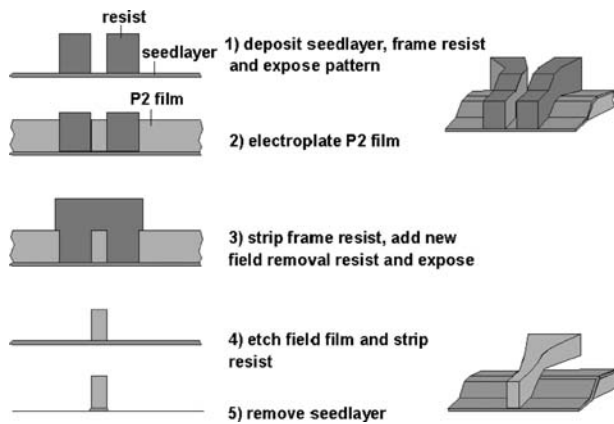


Fig. 17 Inductive head P2w processing.

photosensitive resist film and its subsequent exposure by a photo mask and UV light source; plating, or electroplating, the formation of a relatively thick metal film by an electrolytic process (this operation usually requires the preformation of a metal seed film to complete the electric circuit prior to plating); deposition, usually referring to a vacuum sputtering operation in which very thin metal films are accurately formed with precise control of composition, magnetic orientation, and crystallographic structure; and finally, patterning, which denotes the formation of elements of the head by either subtractive etching or “a lift-off” process. The latter can be illustrated by an example of the formation of the inductive pole structure, or P2w, as shown in Fig. 17. This material removal technique is applied to maintain tight control of vertical walls of a very small horizontal pattern, which is usually of the order of  $\mu\text{m}$  thick, i.e., has a high aspect ratio of as much as 10:1. As soon as the seed layer is applied and resist pattern formed in Fig. 17, the thick P2 NiFe film is electroplated. The center region is protected with a new field removal resist and exposed.

After stripping this resist and etching both field film and seedlayer, the final pole region remains. The particular topography of this P2 film originates from the requirement that the inductive yokes must encircle the copper coils and insulator layers, as shown in Fig. 15. This yoke topography for the head conforms to the multiple layers of polymers and coils, and the resulting head topography can be greater than  $10\ \mu\text{m}$ . “Zero throat” in this figure refers to the point at which the inductive throat begins and is defined by the edge of one of the polymer insulators.

## GMR PROCESS

For the formation of a GMR sensor, referring to Fig. 15, the GMR gap consists of two dielectric layers which electrically isolate the contacts and sensor from

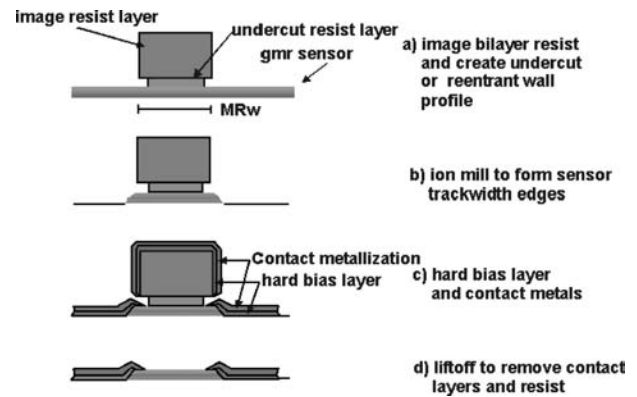


Fig. 18 GMR head MRw processing.

the surrounding shield and inductive element. Furthermore, these electrical contacts and sensor are connected via a contiguous junction process in which a degree of geometric overlapping results. The horizontal dimensions for MRw, as well as the previous example of frame plating for P2w, require a fine-line lithographic equipment and process to form the images. These sensor dimensions define a trackwidth capability on the disk and, as areal density evolves to increased levels, these dimensions become progressively smaller. The contiguous junction process uses a critical lithography step with about  $1\ \mu\text{m}$  thick resist to form this trackwidth by a similar process to P2w—the use of a resist mask to protect the active GMR region during the subtractive removal of sensor material to define the GMR dimensions. This etching process, shown in Fig. 18, is a resist structure which exhibits a reentrant or negative wall angle and, therefore, subsequent depositions of contact metal and hard bias stabilization films do not completely seal the resist edges. This allows the resist “stencil” to be removed in this lift-off process based on the exposure of the undercut region by the dissolving in the appropriate solvent. The stencil is actually floated away in this solvent, leaving the GMR sensor defined by this structure. Subsequent processing and layers form the inductive write element.

## FUTURE SCALING OF GMR NANOLAYER SENSORS

As was previously indicated, areal density increases require further reduction in MRw by scaling of MRw in an evolutionary trend described in Fig. 6. The process challenge is to create submicrometer openings with a controlled undercut in the resist images. For example, if a future trackwidth is  $0.3\ \mu\text{m}$ , this would result in a  $0.1\text{-}\mu\text{m}$  undercut, which also would be the base dimension of the resist structure overhang, a dimension that could reduce the structural integrity



of this resist structure at its base. In addition, this overhang also determines the amount of contact to sensor overlap at the junction region, inferring that the read sensor trackwidth is fixed by both the image resist as well as control of the undercut. Future GMR sensor processing must address both image size in the resist, as determined by the exposure tool and process, as well as image profile in the resist.

The above discussion addresses track density, but another important factor for future GMR structures is scaling of thickness of the GMR sensor to higher linear (bit) densities. The GMR sensor layer thickness must be decreased to allow it to be saturated by progressively smaller magnetic transitions originating from the disk. In addition, the shield separation above and below the GMR sensor is determined by two dielectric thicknesses—top and bottom. At today's areal densities of 40 Gb/in.<sup>2</sup>, shield separations are approximately 70 nm; and the films that comprise a GMR sensor, the NiFe free layer, spacer layer, pinned layer, and antiferromagnetic exchange layer are about 2, 2, 2, and 15 nm, respectively. The latter would not be expected to scale to a smaller thickness because this value is determined by antiferromagnetic coupling to the pinned layer. Future areal density increases require that top and bottom insulating layers must be reduced to less than 25 nm, and that GMR free, spacer, and pinned films must all be less than 2 nm. It will be a challenge to demonstrate insulating layers with a high degree of electrical integrity. It does seem reasonable that this challenge will be met.

## POTENTIAL DESIGN CHANGES IN GMR SENSORS

As future scaling requirements reduce the vertical dimensions of GMR sensors, a reduction in the width of this element can also be expected. It is proposed that there is a critical width dimension, as well as a critical NiFe thickness, where the GMR effect is reduced to a very low value, i.e., the  $\Delta R/R$  of the sensor approaches a value where the resulting signal-to-noise ratio does not permit accurate reading of the data. One solution to this reduced GMR effect is to pass the sense electrical current normal to the sensor as opposed to a longitudinal direction, along the long axis of the element. This type of device, known as current perpendicular to the sensor's plane (CPP), is a significant excursion for today's current in-plane (CIP) GMR devices, and is being studied in many laboratories. A variation of this concept is to replace the metallic spacer with a very thin insulator, of the order of a few angstroms in thickness. In this structure, known as a tunnel valve or tunnel junction device, current carriers are able to tunnel through the thin insulator film

when magnetizations on either side are parallel, and are prevented from tunneling in the antiparallel case. Preparing a very thin insulator that is pin hole-free is a significant process challenge. The CPP read device may become important as areal densities increase well beyond 100 Gb/in.<sup>2</sup>.

## CONCLUSION

The GMR nanotechnology was shown to enable large areal density increases in magnetic hard disk drives, which have occurred rapidly in the past 5–10 years.<sup>[13,16]</sup> Based on the importance of magnetic storage to the computer age, a significant research-and-development effort is being maintained on a worldwide basis to enhance the read capability of GMR technology for higher areal densities, and this involves the exploration of new magnetic materials, scaling down sensor horizontal and vertical dimensions, and finally, considering alternative structures based on today's GMR sensors.

## ACKNOWLEDGMENT

The authors would like to express their appreciation to Bruce Gurney, of the IBM Almaden Research Center, for his scientific contributions to this manuscript and for his review of the final document, and for the research efforts of Dr. Gurney and many other IBM Almaden colleagues for their contributions to GMR. Additionally, the graphics and document support of Michael Xu, also of Almaden, is acknowledged.

## REFERENCES

1. <http://www.storage.ibm.com/hdd/technolo/grochows/grocho01.htm> (accessed November 2002).
2. Gurney, B.; Grochowski, E. Spin valve sensors take up where MR heads leave off. *Data Storage* **1998**, 5 (10), 59
3. Grochowski, E. Magnetoresistive head technology and areal density growth. *Insight* **1995**, 8 (4), 4
4. Baibich, M.; Broto, J.; Fert, A.; Van Dau, F.; Petroff, F.; Eitenne, P.; Creuzet, G.; Friederich, A.; Chazelas, J. Giant magnetoresistance of (001) Fe/(001) Cr magnetic superlattices. *Phys. Rev. Lett.* **1988**, 61 (21), 2472
5. Parkin, S.; More, N.; Roche, K. Oscillations in exchange coupling and magnetoresistance in metallic superlattice structures: Co/Ru, Co/Cr and Fe/Cr. *Phys. Rev. Lett.* **1990**, 64 (19), 2304
6. Gurney, B.; Carey, M.; Tsang, C.; Williams, M.; Parkin, S.; Fontana, R., Jr.; Grochowski, E.; Pinarbasi, M.; Lin, T.; Mauri, D. Spin Valve Giant Magnetoresistive Sensor Materials for Hard Disk Drives. In *Datatech*, 4th Ed. Ed.; 2000; 87pp.

7. Gurney, B.; Speriosu, V.; Wilhoit, D.; Lefakis, H.; Fontana, R., Jr.; Heim, D.; Dovek, M. Can spin valves be reliably deposited for magnetic recording applications?. *J. Appl. Phys.* **1998**, *81* (8), 3998
8. Gurney, B.; Speriosu, V.; Lefakis, H.; Wilhoit, D.; Need, O. Direct measurement of spin-dependent conduction-electron mean free paths in ferromagnetic metals. *Phys. Rev. Lett.* **1993**, *71* (24), 4023
9. Speriosu, V.; Herman, D., Jr.; Sanders, I.; Yogi, T. Magnetic thin films in recording technology. *IBM J. Res. Develop.* **1990**, *34* (6), 884
10. Lin, T.; Mauri, D. Field-anneal effects on magnetic and magnetoresistive properties of Fe–Mn, Ir–Mn and NiO spin valves. *IEEE Trans. Magn.* **1999**, *35* (5), 2607
11. Margulies, D.; Fullerton, E.; Schabes, M.; Do, H.; Grochowski, E.; Carey, M.; Gurney, B.; Moser, A.; Best, M.; Rubin, K.; Rosen, H.; Doerner, M.; Mirzamaani, M.; Tang, K. Antiferromagnetically Coupled Magnetic-Medium Structure Extends Areal Density for Hard Disk Drives. In *Datatech*, 7th Ed.; 2001; 9pp.
12. Fullerton, E.; Margulies, D.; Schabes, M.; Carey, M.; Gurney, B.; Moser, A.; Best, M.; Zeltzer, G.; Rubin, K.; Rosen, H. Antiferromagnetically coupled magnetic media layers for thermally stable high density recording. *Appl. Phys. Lett.* **2000**, *77* (23), 3806
13. Charap, S.; Lu, P.; He, Y. Thermal stability of recorded information at high densities. *IEEE Trans. Magn.* **1997**, *33* (1), 978
14. Fontana, R., Jr.; MacDonald, S.; Santini, H.; Tsang, C. Process considerations for critical features in areal density thin film magnetoresistive heads: A review. *IEEE Trans. Magn.* **1999**, *35* (2), 806
15. Thompson, D.; Best, J. The future of magnetic data storage technology. *IBM J. Res. Develop.* **2000**, *44* (3), 311
16. Grochowski, E.; Thompson, D. Outlook for maintaining areal density growth in magnetic recording. *IEEE Trans. Magn.* **1994**, *30* (6), 3797

## BIBLIOGRAPHY

1. Gurney, B.; Wilhoit, D.; Speriosu, V.; Sanders, I. Influence of Au and Ag at the interface of sputtered giant magnetoresistance Fe/Cr multi-layers. *IEEE Trans. Magn.* **1990**, *26* (5), 2747
2. Tsang, C.; Fontana, R., Jr.; Lin, T.; Heim, D.; Gurney, B.; Williams, M. Design, fabrication, and performance of spin valve read heads for magnetic recording applications. *IBM J. Res. Develop.* **1998**, *42* (1), 103
3. Dieny, B.; Speriosu, V.; Parkin, S.; Gurney, B.; Wilhoit, D.; Mauri, D. Giant magnetoresistance in soft ferromagnetic multi-layers. *Phys. Rev., B* **1991**, *43* (1), 1297
4. Ashar, K. *Magnetic Disk Drive Technology*; IEEE Press: New York, NY, 1997.

# Nanofiltration Separations

Eric M.V. Hoek

Anna Jawor

Department of Chemical and Environmental Engineering, University of California–Riverside, Riverside, California, U.S.A.

## INTRODUCTION

The term “nanofiltration” (NF) generally refers to a class of pressure-driven membrane separation processes whereby nanometer- or larger-sized substances may be selectively removed from a carrier fluid. The name “nanofiltration” is derived from two phrases. The prefix “nano” means 1 billionth. Hence, 1 nm has a value of  $10^{-9}$  m or 10 Å. The suffix “filtration” refers to a process whereby solutes are physically separated from a solvent by passing the solution through a semipermeable barrier or medium.<sup>[1]</sup> The review that follows intends to introduce the reader to the basic concepts of nanofiltration separations, the material properties of NF membranes, the common applications of NF separations, the theory and models describing NF separation performance, and some performance limitations.

## NANOFILTRATION BASICS

Membrane processes are advanced filtration processes, which utilize separation properties of finely porous polymeric or inorganic films and are used in a wide range of industrial processes to separate biological macromolecules, colloids, ions, solvents, and gases. The development and application of membrane separation processes is one of the most significant recent advances in chemical, environmental, and biological process engineering. Membrane processes are commonly distinguished based on the main driving force, which is applied to accomplish the separation. An overview of the driving forces and related membrane separation processes is given in Table 1.<sup>[2]</sup>

Nanofiltration falls into the category of pressure-driven membrane processes, and it fills an important gap between ultrafiltration (UF) and reverse osmosis (RO). Ultrafiltration processes are intended to remove all particles, colloids, and large macromolecules, while passing small macromolecules and dissolved substances. Reverse osmosis membranes are designed to separate all dissolved solutes from their carrier solvent down to monovalent ions, dissolved metals, and

organics above a few hundred daltons (Da). Nanofiltration was originally conceived to perform water softening (i.e., removal of divalent ions in water production), but more generally intends to remove, selectively, a particular solute (e.g., divalent ion) while allowing another solute (e.g., monovalent ion) to pass with the solvent through the membrane. Fig. 1 provides another perspective of various pressure-driven filtration processes and the substances they are intended to remove.

In nanofiltration processes, a selective separation takes place across a semipermeable separation layer, which is formed over the top of a porous support. The driving force of the separation process is the pressure difference between the feed (retentate) and the filtrate (permeate) side of the separation layer of the membrane. The size of NF membrane pores in combination with the surface electrical properties allows divalent ions and uncharged solutes larger than a few thousand daltons to be highly retained, while monovalent ions and low-molecular weight organics are reasonably well transmitted. The nominal *molecular weight cutoff* for many commercially available nanofiltration membranes ranges from a few hundred to a few thousand daltons.<sup>[3]</sup> These characteristics make NF membranes extremely useful in the fractionation and selective removal of many dissolved solutes from complex process streams. Other advantages include high flux and low energy consumption (because of low operating pressure requirement), as well as reduced environmental impact compared with conventional processes such as evaporation and extraction.<sup>[4]</sup>

## MATERIALS

Nanofiltration membranes are characterized by pore diameters of about 5 Å to 5 nm and operating pressure between 5 and 40 bars. Because they significantly reject many ions, NF membranes are often wrongly categorized as “loose RO” membranes. The most notable difference between RO and NF is the ability of NF to highly reject multivalent ions, while significantly passing monovalent ions. Another distinctive feature of NF membranes is their ability to reject uncharged,

**Table 1** Driving forces and their related membrane separation processes

Driving force	Membrane process
Pressure difference	Microfiltration, ultrafiltration, nanofiltration, reverse osmosis
Chemical potential difference	Pervaporation, dialysis, gas separation, liquid membranes
Electrical potential difference	Electrodialysis, membrane electrolysis
Temperature difference	Membrane distillation

dissolved materials and positively charged ions according to the size and shape of the molecule in question. These selective separation capabilities are directly related to the membrane material properties.

It is widely known that retained organic and colloidal matter may adhere strongly to polymeric surfaces through non-covalent interactions—such as those arising from van der Waals, electrostatic, and acid–base properties of the polymer materials—and cause severe performance decline.<sup>[5–12]</sup> Nanofiltration membranes often become “fouled” by dissolved organic and colloidal matter, which is ubiquitous in many natural and industrial waters. Hence one of the challenges from a materials perspective is to create a membrane with optimal pore size, surface charge, and hydrophilic nature to effect a highly selective separation with low energy consumption, while minimizing the adhesion for fouling materials.

The array of membrane materials to select from includes polysulfone, polyethersulfone, sulfonated polyethersulfone, cellulose acetate and its derivatives, polyethylene, polypropylene, polyvinyl alcohol derivative, polyamide, polyacrylonitrile, polyvinylidene fluoride, organo-mineral complexes, ceramic, alumina, and other metal oxides.<sup>[13–18]</sup> The polysulfone materials dominate UF/MF applications for water and wastewater treatment, while contemporary RO/NF membrane usage is almost entirely limited to polyamide-based thin-film composites. Although cellulose acetate (CA) technology predates other membrane types and remains relatively inexpensive to purchase and install, the use of cellulose acetate membranes has largely been displaced by polyamide thin-film composite membranes today. Across the range of possible materials, there are two basic material types: integrally skinned asymmetric layers and thin-film composites.

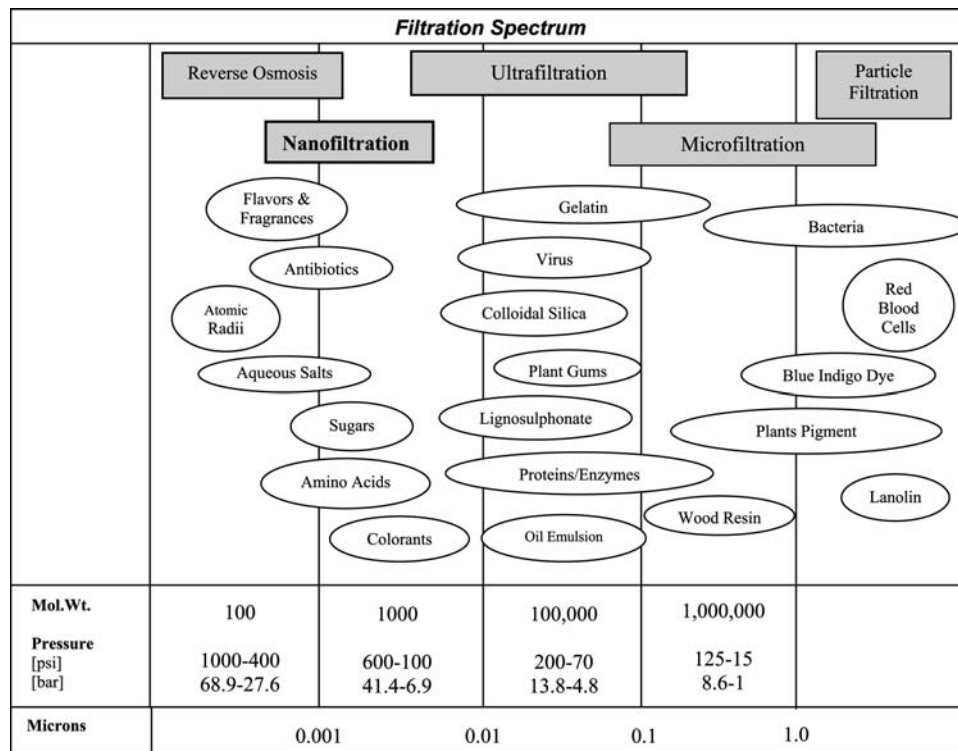


**Fig. 1** Diagram known as the “filtration spectrum,” indicating schematically the place of nanofiltration among other common pressure-driven filtration processes.

## Integrally Skinned Asymmetric Membranes

Polymeric asymmetric membranes may be prepared through a phase inversion technique. Phase inversion is a process whereby a polymer is transformed in a controlled manner from a liquid to a solid state.<sup>[16]</sup> The cross section of an integrally skinned, asymmetric phase-inversion membrane is schematically illustrated in Fig. 2(A). The most popular phase-inversion membranes may be constructed from cellulose acetate (CA), cellulose diacetate (CD), regenerated cellulose (RC), polysulfone (PS), polyethersulfone (PES), sulfonated PS or PES, polyacrylonitrile (PAN), or polyvinylidene fluoride (PVDF). Scanning electron microscope (SEM) images of PAN and PS membrane cross sections are presented in Fig. 2(B) and (C), respectively.

Polysulfone membranes formed by phase inversion are used as microfiltration or ultrafiltration membranes, or as the support layer upon which a thin-film composite RO or NF membrane is formed. However, because we have defined nanofiltration as a process by which nanometer-sized or larger-sized substances are removed from a liquid feed, any material used to perform such a separation may be considered a “nanofiltration membrane.” A characteristic of the PS membranes is that an increasing degree of sulfonation correlates with increasing water permeability and salt rejection.<sup>[19,20]</sup> Dense-skinned phase inversion membranes composed of cellulosic materials typically function as reverse osmosis membranes.

## Organic Thin-Film Composite Membranes

In 1978, efforts to improve the performance of “poly” membranes by Cadotte et al.<sup>[21]</sup> yielded composite membranes having excellent combinations of high salt rejection and water permeability. Cadotte et al.’s ideas were developed at FilmTec Corporation into a reverse osmosis/nanofiltration membrane product designated as “FT30.” The FT30 membrane is a thin-film composite membrane consisting of three layers: a polyester support web, a microporous (polysulfone) interlayer, and an ultrathin polyamide barrier (skin layer) on top. Fig. 3(A) provides a schematic illustration of a generic thin-film composite (TFC) membrane construction resembling that of FT30.

There are several clones of the FT30 membrane that are now commercially available; some are made under license from FilmTec and others are made by other proprietary synthetic routes. The skin layer of NF membranes may be as thin as 50 nm in cross section up to several hundred nanometers. The composite structure of two commercial NF membranes can be seen in the field emission SEM images of Fig. 3(B) and (C). The surface properties of TFC membranes have been studied extensively, largely in efforts to understand the role of surface properties on separation performance and fouling. In particular, studies focusing on surface charge/potential, hydrophobicity, and roughness dominate the literature (see “Membrane Properties and Performance”).

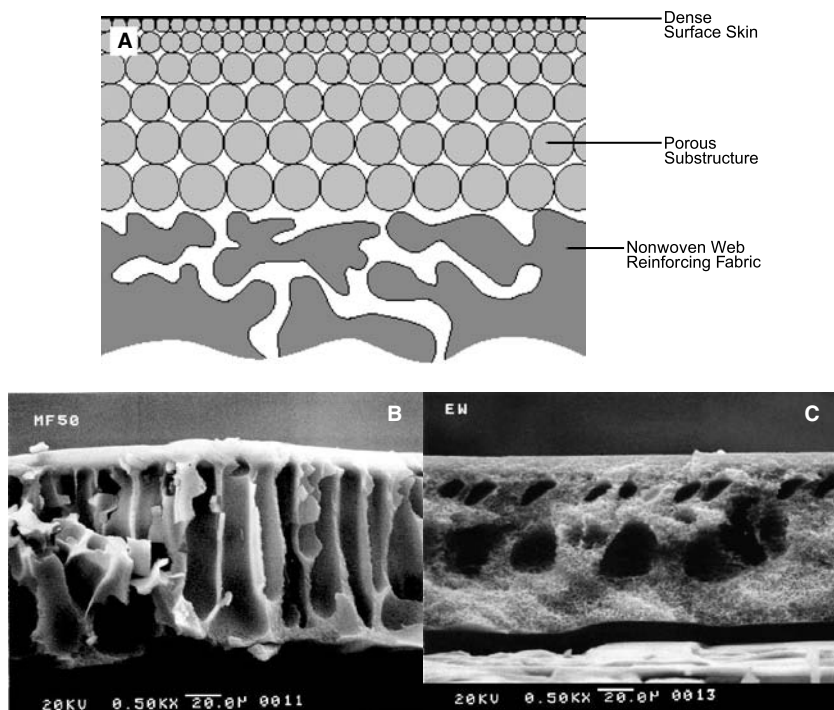


**Fig. 2** Cross-section illustration of (A) an integrally skinned asymmetric membrane, plus SEM cross sections of dense-skinned (B) polyacrylonitrile and (C) polysulfone membranes manufactured by GE-Osmotics Inc. *Source:* Illustration in (A) was adapted from Ref.<sup>[60]</sup>.

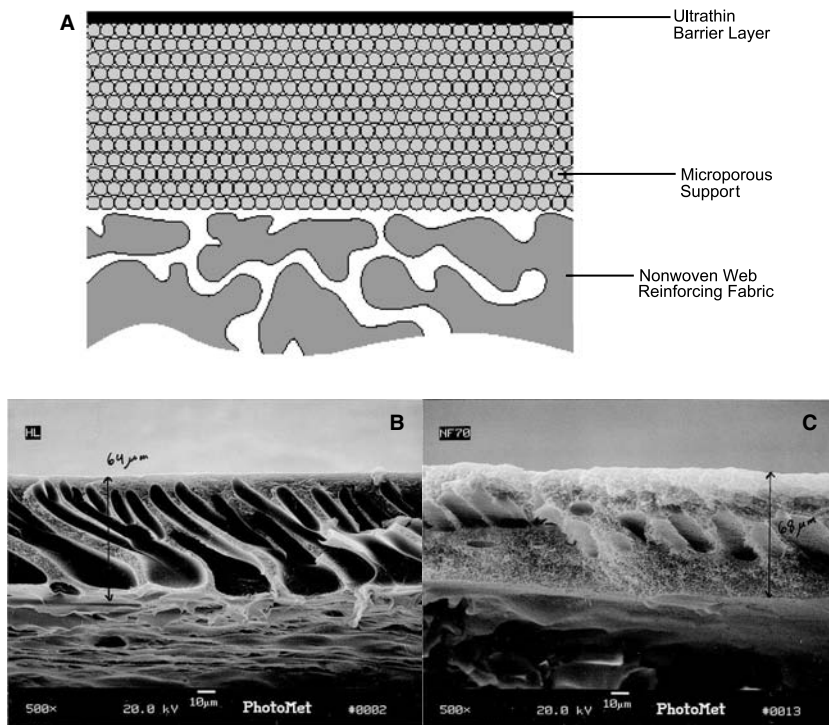


**Fig. 3** Cross-section illustration of (A) thin-film composite membrane, plus SEM cross sections of two commercially available polyamide membranes manufactured by (B) GE-Osmonics Inc. and (C) Dow-FilmTec. *Source:* illustration in (A) was adapted from Ref.<sup>[60]</sup>.

### Inorganic Thin-Film Composite Membranes

Ceramic composite membranes have been used in a number of industrial separations. They are synthesized from dispersions of silica, titania, or other metal oxide nanoparticles that are forced to agglomerate on the surface of a similar metal oxide microparticle layer. After initial formation, the material is usually sintered at high temperature to form a continuous layer. The base material of construction makes ceramic membranes particularly well suited for treating high-temperature or acidic/caustic wastewaters, as well as for high-fouling industrial streams. The extreme heat tolerance and chemical resistance of ceramics allows repeated cycles of use, cleaning with harsh physical or chemical treatments, and reuse that are unachievable with polymeric membrane materials. However, to date, ceramic membranes are much too expensive to be used in applications requiring large membrane surface area (such as water production or municipal wastewater treatment), so their use has been limited to specialty industrial separations.<sup>[22,23]</sup>

In principle, the cross-sectional structure of ceramic nanofiltration membranes has much the same look as organic TFC membranes. Fig. 4 is an SEM photo of an experimental thin-film composite ceramic membrane (courtesy of Marc Anderson of the University of Wisconsin). There are three distinct layers. A thin film comprised of small titanium dioxide ( $\text{TiO}_2$ ) nanoparticles, a middle support layer made

from larger  $\text{TiO}_2$  nanoparticles, and a structural base formed from much larger  $\text{TiO}_2$  particles. One of the current goals in ceramic membrane material research and development is to create a membrane with UF-like permeability, but NF-like selectivity. This may be achieved by taking advantage of nanoparticles with high surface charge density sintered to maintain more open pore structures than the pores in polymeric NF membranes.

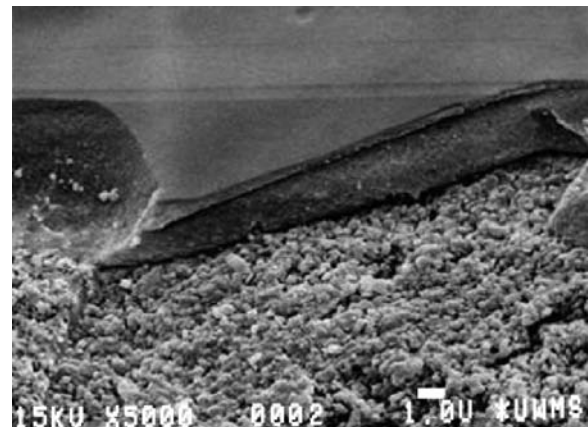


**Fig. 4** Scanning electron microscope image of ceramic composite membrane showing three distinct layers of  $\text{TiO}_2$  nanoparticle construction: dense skin layer over top of nanoporous support and microporous structural support layers.



## Nanofiltration Element Design

Membrane modules are available in spiral-wound, plate-and-frame, hollow-fiber, and tubular configurations as depicted in Fig. 5. Almost all NF membranes used today employ the spiral-wound configuration. In a spiral-wound element (SWE), the membrane leaves are sealed and wrapped around a permeate collection tube. An open mesh spacer separates the active layers of membrane material on the feed side, while a similar spacer lies between the backsides of the membranes and serves as a channel for the treated water to travel to the permeate collection tube. A significant amount of research was performed in the past to optimize the design of feed spacers used in SWEs, and the currently available elements perform quite well. Generally, a thicker feed spacer is used for high fouling waters to prevent clogging of the channel cross section, which can result in a significant tangential pressure drop.

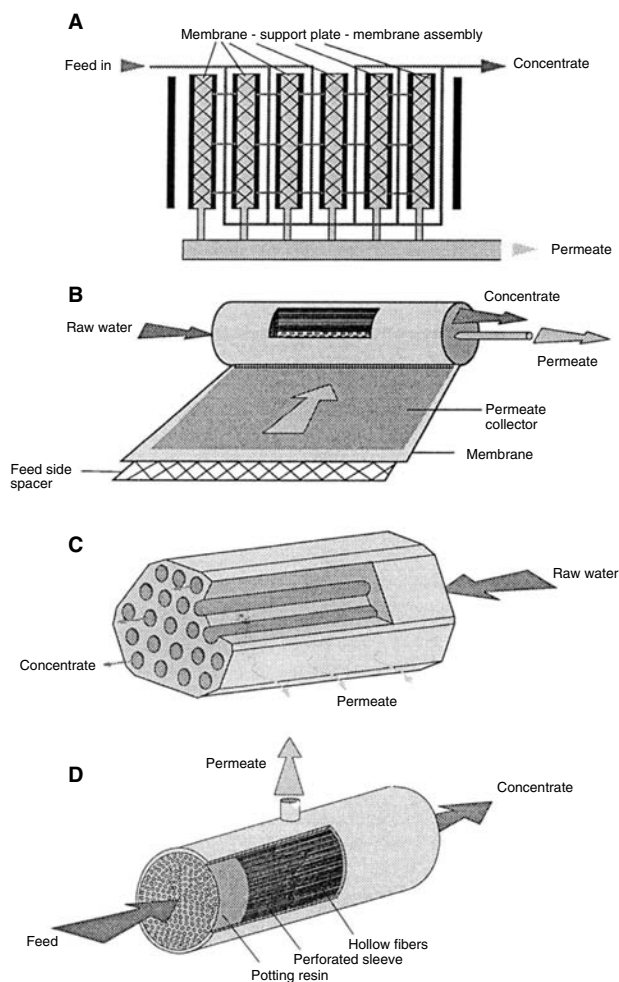


**Fig. 5** Schematic representation of the four principle membrane modules: (A) plate-and-frame; (B) spiral-wound; (C) tubular; (D) hollow-fiber. *Source:* From Ref.<sup>[61]</sup>.

## APPLICATIONS

Currently, the reduction of hardness (i.e.,  $\text{Ca}^{2+}$  and  $\text{Mg}^{2+}$ ) and dissolved organics from water are among the most important applications for nanofiltration membranes. However, the selective properties of NF membranes make them suitable for a wide array of unconventional applications. An important example is recovery of heavy metals (e.g., Ni, Fe, Cu, Zn, etc.) and reclamation of wastewaters from metalworking plants and textile mills. More recently, NF membranes have been adopted for use in the biotechnology and pharmaceutical industries for purification of small bioactive organic molecules such as antibiotics or separation of small organic components from biological liquids (e.g., lactic acid separation from fermentation broths, amino acid removal from protein hydrolysates, or removal of organics from municipal wastewater).<sup>[2]</sup> Timmer<sup>[2]</sup> provided a concise summary of the various applications for nanofiltration membranes that have been reported to date. This summary has been reproduced in Table 2.

## PERFORMANCE

The performance of nanofiltration membranes is defined by solvent and solute permeability, as well as fouling resistance. The summary that follows considers the roles of membrane material properties, operating conditions, and fouling, but begins by defining NF performance and the fundamental mechanisms governing NF membrane separations. Finally, mechanisms of NF membrane fouling are discussed and the role of membrane material properties on separation performance and fouling is reviewed.

### Defining NF Separation Performance

When an external pressure is imposed on a liquid adjacent to a nanofiltration membrane, the liquid will flow through the membrane in proportion to the applied pressure. Liquid flow through a NF membrane is described as a solvent flux ( $J_v$ ), which is given by a Darcy-type relation such as

$$J_v = \frac{\Delta p_{\text{eff}}}{\mu R_{\text{tot}}} \quad (1)$$

in which  $\Delta p_{\text{eff}}$  is the effective trans-membrane pressure,  $\mu$  is the permeate viscosity, and  $R_{\text{tot}}$  is the total hydraulic resistance toward solvent flow.

Dissolved solutes also flow toward the membrane by the convective flow of their carrier solvent. If the membrane inhibits transport of the solute, it will

**Table 2** Overview of nanofiltration applications in various industries

Industry	Application
Water production	Recovery of LiOH during treatment of battery waste
	Removal of degreasing agents from water
	Removal of precursors of disinfection byproducts
	Hardness removal
	Removal of natural organic matter (a.o. color)
	Removal of pesticides
	Removal of heavy metals (As, Pb), Fe, Cu, Zn, and silica
Food	Treatment of brackish water
	Demineralization of whey
	Demineralization of sugar solutions
	Recycle of nutrients in fermentation processes
	Separation of sunflower oil from solvent
	Recovery of cleaning-in-place solutions
Textile and paper	Recovery of regeneration liquid from decoloring resins in sugar industry
	Effluent treatment
	Purification of organic acids
	Removal of dyes from wastewater
	Removal of amino acids
	Recovery of water and salts from wastewater
Chemical	Recovery and reuse of chromium(III) and chromium(II)
	Recovery of water from wastewater or wastewater treatment effluent
	Recovery of bleaching solution
	Sulfate removal preceding chlorine and NaOH production
	CO <sub>2</sub> removal from process gasses
	Preparation of bromide
	Recovery of caustic solutions in cellulose and viscose production CaSO <sub>4</sub> precipitation
	Separation of heavy metals from acid solutions
	Removal of metal sulfates from wastewater
	Cleaning of machine rinsing solutions
Agriculture	Removal of nickel
	Recovery of Cu-ions from ore extraction liquids
	Al <sup>3+</sup> removal from canning industry wastewater
	Removal of phosphate, sulfate, nitrate, and fluoride
	Removal of algal toxins
	Purification of landfill leachate
	Removal of selenium from drainage water

Source: From Ref.<sup>[2]</sup>

be retained at the feed side of the membrane. The distribution of a noncharged solute at the membrane/solution interface is determined by steric exclusion. Because of its size, a solute only has access to a fraction of the total surface area of a pore, and a separation between multiple solutes can only be accomplished if the solutes are different in size.<sup>[2,14,24]</sup>

For charged solutes, two additional distribution mechanisms contribute to the separation. First,

Donnan exclusion has a pronounced effect on the separation of charged solutes by NF membranes. Because of the slightly charged nature of the membrane, solutes with an opposite charge compared with the membrane (counterions) are attracted, while solutes with a similar charge (co-ions) are repelled. At the membrane surface, a distribution of co-ions and counterions will occur, thereby causing an additional separation. Second, because of the charge of the membrane and the dipole

momentum of water, water molecules may exhibit polarization in the pore.<sup>[25]</sup> This polarization results in a decrease of the dielectric constant inside the pore, thereby making it less favorable for a charged solute to enter. However, even in a situation that the dielectric constant inside the pore is equal to that of water, a change in electrostatic free energy of the ion occurs when the ion is transferred from the bulk into the pore,<sup>[26]</sup> which can also cause ion exclusion.

After the solute distributes at the membrane/solution interface, it is transported through the membrane by convection and diffusion. At the permeate side, a second distribution process occurs, which determines the permeate concentration. The actual, or intrinsic, rejection by a nanofiltration membrane is given by

$$R_s = 1 - \frac{C_p}{C_m} \quad (2a)$$

where  $C_p$  is the permeate solute concentration and  $C_m$  is the membrane surface solute concentration. However, there is no accurate method of determining the actual membrane surface solute concentration. Because the feed and permeate solute concentrations can be measured, the solute retention is typically described by

$$R_o = 1 - \frac{C_p}{C_b} \quad (2b)$$

where  $R_o$  represents the observed solute retention and  $C_b$  represents the bulk salt concentration. Retained solutes accumulate at the membrane surface in a concentrated layer and thus diffuse back into the bulk in proportion to the concentration gradient, and hence a concentration profile develops. This phenomenon is called concentration polarization.

The performance of NF membranes has been studied extensively in terms of membrane properties, operating conditions, module geometry, and treatment train configuration. Of considerable importance are the influences of membrane filter geometry and crossflow hydrodynamics on concentration polarization (CP). Concentration polarization influences nanofiltration performance via two mechanisms. First, CP enhances the passage of retained solutes by increasing the chemical potential gradient driving diffusive transport through the membrane, and second, elevated salt concentrations at the membrane surface reduce electrostatic forces that originate from the membrane surface charge and which tend to reduce foulant deposition. Accumulation of a fouling deposit layer on the membrane surface creates an additional hydraulic resistance to permeation (over that of the membrane alone) and enhances concentration polarization.<sup>[27,28]</sup>

## Solute Transport Model

Determining the significance of various solute transport mechanisms—diffusion, convection, and electromigration—on NF membrane performance is most rigorously accomplished by coupling a model of solute transport through the membrane based on the extended Nernst–Planck (NP) equation with a CP model based on the convective–diffusion equation.<sup>[29]</sup> However, knowledge of the actual charge density of the membrane pores is required to make appropriate use of the NP model, and this is rather difficult to determine for real membranes. In addition, a cumbersome numerical scheme is required to solve the set of equations that result from coupling the local NP model with a local CP model based on the solution of the convection–diffusion equation. Coupling the solution–diffusion model and a simple mass transfer model (film theory) provides a reasonable and analytical solute transport and CP model.<sup>[30–32]</sup> While the application of a stagnant film model to membrane separations may be debated, the model provides quite reasonable prediction of NF separation performance.

The starting point for the mathematical description of NF membrane performance is the solution–diffusion model. The model assumes that solute permeation is driven by the gradient in chemical potential of the solute across the membrane.<sup>[30]</sup> Thus the flux ( $J$ ) of an individual component ( $i$ ) is represented mathematically by

$$J_i = -L_i \frac{d\mu_i}{dx} \quad (3)$$

where  $d\mu_i/dx$  is the gradient in chemical potential of component  $i$  and  $L_i$  is a coefficient of proportionality linking this chemical potential driving force with flux. The chemical potential is written as

$$d\mu_i = RTd \ln(\gamma_i c_i) + v_i dp \quad (4)$$

where  $c_i$  is the molar concentration of component  $i$ ,  $\gamma_i$  is the activity coefficient linking concentration with activity,  $p$  is the pressure, and  $v_i$  is the molar volume of component  $i$ . Following the applicable assumptions for reverse osmosis, the combination of Eqs. (3) and (4) leads to a Fick's law type of relation that is ultimately reduced to

$$J_i = B \Delta C_w = B C_w R_i \quad (5)$$

where  $B$  is the solute permeability of the membrane.<sup>[30]</sup> When the transport equation is expressed in terms of solvent flux ( $J_v$ ), the equation is generally written as

$$J_v = A(\Delta P - \Delta \pi_m) \quad (6)$$

where  $\Delta P$  is the applied pressure and  $\Delta\pi_m$  is the osmotic pressure at the membrane surface because of concentration of rejected ionic species at the surface of the membrane. The parameter  $A$  is the pure solvent permeability of the membrane, which is the inverse of the intrinsic membrane resistance,  $R_m$ .

### Solute Concentration Polarization Model

The buildup in concentration of rejected solutes at the membrane–liquid interface results in the formation of a concentrated mass boundary (“film”) layer, called the *salt concentration polarization layer*. At steady state, the solute flux through the film is constant and is related to the solvent flux through the membrane ( $J_v$ ) via the following one-dimensional, steady-state mass balance within the film layer:

$$-J_v C - D \frac{dC}{dy} = J_v C_p \quad (7)$$

where  $C$  is the local solute concentration,  $D$  is the solute diffusivity,  $C_p$  is the solute permeate concentration, and  $y$  is the distance normal to the membrane surface.<sup>[31]</sup> Integrating over the solute concentration polarization layer thickness ( $\delta_s$ ) with the appropriate boundary conditions ( $y = 0$ ,  $C = C_m$ ;  $y = \delta_s$ ,  $C = C_b$ ) results in the classic film theory equation,

$$J_v = \frac{D}{\delta_s} \ln\left(\frac{C_m - C_p}{C_b - C_p}\right) = k \ln\left(\frac{C_m - C_p}{C_b - C_p}\right) \quad (8)$$

where  $C_m$  is the membrane surface solute concentration,  $C_b$  is the bulk solute concentration,  $C_p$  is the permeate solute concentration, and the ratio of solute diffusivity ( $D$ ) to the solute concentration polarization layer thickness ( $\delta_s$ ) is set equal to the solute mass transfer coefficient ( $k$ ). This expression can be rearranged to provide a direct calculation of the concentration polarization factor ( $C_m/C_b$ ) as

$$\frac{C_m}{C_b} = (1 - R_0) + R_0 \exp\left(\frac{J_v}{k}\right) \quad (9)$$

For laminar flow in a thin rectangular channel, the mass transfer coefficient is often related to a Sherwood number ( $Sh$ ) through a relationship such as

$$k = Sh \frac{D}{d_h} = 1.85 \left( Re Sc \frac{d_h}{L} \right)^{1/3} \frac{D}{d_h} \quad (10)$$

where  $Re$  is the Reynolds number,  $Sc$  is the Schmidt number,  $d_h$  is the channel hydrodynamic diameter, and  $L$  is the channel length.<sup>[30–32]</sup> By expanding the

individual components,

$$Re = \frac{\rho u d_h}{\mu}; Sc = \frac{\mu}{\rho D}; d_h \cong 2H \quad (11)$$

Eq. (10) can be rearranged to reveal the mass transfer coefficient's dependence on flow rate, channel geometry, and solute type via

$$k = 0.808 \left( \frac{\gamma_0 D^2}{L} \right)^{1/3} \quad (12a)$$

Here  $\gamma_0$  indicates the wall shear rate, which is defined by  $\gamma_0 = 6Q/WH^2$ , where  $Q$  is the volumetric feed flow rate,  $W$  is the crossflow channel width, and  $H$  is the channel height.<sup>[32]</sup> From Eq. (12a), it becomes clear that the mass transfer coefficient represents the velocity with which a solute migrates away from the membrane surface (back into the bulk) as a function of solute diffusivity, tangential convection, and filter geometry. This explains the enhanced performance obtained from optimizing channel geometry and cross-flow hydrodynamics.

An alternative solute mass transfer coefficient has been derived for laminar flow through thin-rectangular channel with a turbulence promoting feed spacer, such as is used in a nanofiltration spiral-wound element, the mass transfer coefficient may be written as

$$k = 0.31 \left( \frac{\gamma_0 D^4}{\nu^{1/3}} \right)^{1/2}, \quad (12b)$$

where  $\nu$  is the kinematic solution viscosity. Rearranging the film theory equation provides an estimation of the *trans*-membrane osmotic pressure. The resulting expression is

$$\Delta\pi_m = C_b R T R_o \exp\left(\frac{J_v}{k}\right) \quad (13)$$

Thus osmotic pressure is directly proportional to bulk solute concentration, solute rejection, solvent flux, and solute mass transfer. More importantly,  $\Delta\pi_m$ ,  $R_o$ ,  $C_b$ , and  $J$  can be measured experimentally, so the effective mass transfer coefficient can easily be determined and compared with prediction by Eq. (13).

### Fouling and Nanofiltration Performance

Most municipal, industrial, and natural waters contain complex mixtures of dissolved, macromolecular colloidal, and particulate matter. Conventional processes used to pretreat NF feed waters fail to remove sub-micron colloids, macromolecules and dissolved matter.

This matter accumulates at the membrane surface and results in severe performance decline—a phenomenon known as *fouling*. Fouling of NF membranes may result in loss of both *solvent flux and solute retention*. A review of fouling studies reveals that the foulants of greatest concern for nanofiltration (NF) separations are colloidal matter consisting of organics, silica, clays, metal oxides (specifically iron and manganese), and microorganisms.<sup>[33–42]</sup> Fouling may be further categorized into *reversible* and *irreversible* fouling. Flux and solute retention may decline because of solution chemistry effects, concentration polarization, or colloid cake layer formation. The original membrane performance may be recovered by simply flushing the membrane with clean water, and hence these types of fouling are considered reversible. Irreversible fouling is defined as a decline in performance that can only be recovered through harsh chemical cleaning, but often only partially recovered. Frequent chemical cleaning of membranes degrades polymeric thin films, and hence reduces the life span of membranes in many applications. Furthermore, it decreases process efficiency because of the reduced flux and enhanced solute passage, requiring higher applied pressures and larger membrane area. This makes fouling a very important parameter in process design.

### Fouling Mechanisms and Models

Interactions between accumulated dissolved and colloidal matter at a NF membrane surface result in several potential fouling mechanisms. Fouling by dissolved organics and sparingly soluble salts is difficult to describe quantitatively, but colloidal fouling is better understood. Because colloids fall within the approximate size range of 10 nm to 10 μm and NF membrane “pores” are no more than a few nanometers in diameter, pore-blocking mechanisms are considered negligible. Thus the major fouling mechanisms discussed below include the hydraulic pressure drop across the foulant deposit (cake) layer and enhanced osmotic pressure effects, which were recently shown to be the predominant fouling mechanism for RO and NF membranes.<sup>[28]</sup> Most practical nanofiltration processes operate with a constant flux, so this convention will be used to describe fouling mechanisms. The objective is to be able to describe the transient applied pressure required to maintain a constant flux in light of the various transient mechanisms of fouling.

The total system pressure is a combination of the trans-membrane hydraulic ( $\Delta p_m$ ), the trans-membrane osmotic ( $\Delta \pi_m$ ), and the trans-cake hydraulic ( $\Delta p_c$ ) pressure drops and may be expressed mathematically as

$$\Delta P_{\text{total}} = \Delta p_m + \Delta \pi_m + \Delta p_c \quad (14)$$

The *trans*-membrane hydraulic pressure drop is determined by rearranging Eq. (1) to obtain

$$\Delta p_m = J_v \mu R_m \quad (15)$$

Hence by analogy, the trans-cake hydraulic pressure drop may be described from

$$\Delta p_c = J_v \mu R_c, \quad (16)$$

where  $R_c$  is the hydraulic resistance offered by the cake layer to the pure solvent.

The cake resistance may be described through the Carman–Kozeny equation, as a function of specific cake resistance (per unit thickness) and cake layer thickness,

$$R_c = r_c \delta_c = \frac{180(1 - \varepsilon)^2}{d_f^2 \varepsilon^3} \delta_c \quad (17a)$$

or specific cake resistance (per unit mass) and cake layer mass per unit membrane area,

$$R_c = \alpha_c M_c = \frac{180(1 - \varepsilon)}{\rho_f d_f^2 \varepsilon^3} M_c \quad (17b)$$

Here  $\varepsilon$  is the cake layer porosity,  $d_f$  represents the nominal foulant diameter, and  $\rho_f$  is the nominal foulant particle density. In most existing models, it is assumed that the specific cake resistance is constant in time and across the cake layer thickness and only the foulant layer thickness (or mass) changes with time.

It was recently experimentally demonstrated that diffusion of rejected salt ions was hindered within colloid deposit layers formed over nanofiltration membranes.<sup>[28,43]</sup> In addition, it was suggested that tangential flow may be hindered within a foulant deposit layer, further reducing solute mass transfer within the deposit layer. The result was elucidation of a single mechanism—“cake-enhanced concentration polarization”—capable of describing the majority of observed flux decline, as well as the observed decline in salt rejection because of colloidal fouling of NF (and RO) membranes.

The overall mass transfer coefficient was considered the sum of two mass transfer coefficients, one describing salt back-diffusion from the membrane surface through the cake layer, and one through the remainder of the salt CP layer. Incorporating the hindered mass transfer coefficient into Eq. (13) yields

$$\Delta \pi_m^* = f_{os} C_b R_o \exp \left[ \frac{J_v}{k} + J_v \delta_c \left( \frac{1 - \ln(\varepsilon^2)}{D_{\infty} \varepsilon} - \frac{1}{D_{\infty}} \right) \right] \quad (18)$$

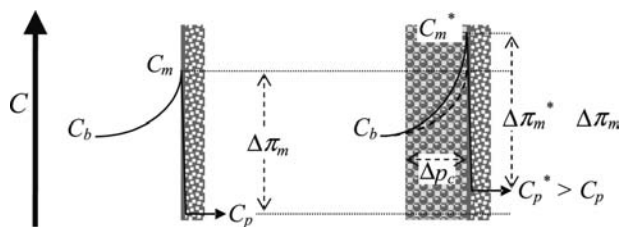


**Fig. 6** Conceptual illustration of enhanced concentration polarization because of foulant accumulation in crossflow nanofiltration. The bulk tangential flow velocity,  $U_0$ , and the salt ion diffusion coefficient are critical parameters in determining mass transfer in the salt concentration polarization layer. Tangential flow and salt ion back-diffusion may be locally hindered in the presence of a foulant deposit layer, thus enhancing the membrane surface salt concentration and trans-membrane osmotic pressure.

where  $\Delta\pi_m^*$  is termed the “cake-enhanced osmotic pressure.”

The term in parentheses in Eq. (18) is derived by considering a thin cake layer, in which the tangential flow field is stagnant within the cake, and it represents diffusion through the cake and into the bulk.<sup>[44]</sup> This concept is illustrated in Fig. 6. The reduced salt diffusivity in the cake layer is expressed as  $\varepsilon D_\infty / \tau$ , with the tortuosity,  $\tau$ , being approximated as  $1 - \ln(\varepsilon^2)$ .<sup>[45–47]</sup> Note that in the absence of a foulant deposit layer, Eq. (18) reduces to Eq. (13) as the term in brackets reduces to  $J_v/k$ .

Combining the trans-membrane hydraulic, trans-cake hydraulic, and (cake-enhanced) trans-membrane osmotic pressure drops allows direct estimation of the total applied pressure needed to maintain a constant flux as a function of increasing deposit thickness. Of course, a priori knowledge of potential foulants is not always possible, which makes rigorous prediction of fouling phenomena difficult without some experimentation or pilot testing. Furthermore, physical or chemical polydispersity of foulants in many NF applications makes prediction of fouling behavior practically impossible. Perhaps the most important implication of enhanced concentration polarization is that an elevated solute concentration at the membrane surface may enhance solute transport through the membrane. Therefore, fouling can have severe consequences for NF separations subject to permeate water quality regulation if the separation is not designed with consideration of fouling.

## Membrane Properties and Performance

Nanofiltration membranes may be constructed of any number of polymeric organic or inorganic materials, but they most commonly appear as polyamide

thin-film composites. Commercially available polyamide NF membranes have charged, reasonably hydrophilic surfaces, which naturally repel co-ions, and to maintain electroneutrality at the membrane / solution interface, counterions are also prevented from passing through the membrane. The degree of ion exclusion increases with increasing co-ion valence because of increased electrostatic repulsion by the membrane. However, the degree of ion exclusion also decreases with increasing counterion valence because high valence counterions tend to screen out membrane surface charge. Moreover, high electrolyte concentrations cause the membrane charge to be more effectively shielded by the counterions, thus reducing the selectivity of the membrane.<sup>[48]</sup> The rejection of sodium chloride with NF varies from 0% to 50% according to the feed concentration and electrolyte composition.

Hirose, Ito, and Kamiyama<sup>[49]</sup> suggested an approximately linear relationship between membrane surface roughness and permeate flux for cross-linked aromatic polyamide TFC membranes, where permeability increased with increasing surface roughness. The linear relationship was attributed to surface unevenness of the TFC membrane skin layer, which resulted in enlargement of the effective membrane area. This is the explanation offered by most membrane manufacturers. However, Kwak et al.<sup>[15]</sup> showed that substitution of bisphenol biphenyl rings with either methyl or halogen strongly influenced rejection and permeability of aromatic polyester TFC membranes. Higher flux and lower rejection were associated with the smoother membrane surfaces obtained from methyl substitution, while lower flux and higher rejection were associated with the rougher membrane surfaces resulting from halogen substitution.

Additional work by Kwak and Ihm,<sup>[50]</sup> coupling nuclear magnetic resonance (NMR) spectroscopy and atomic force microscopy (AFM), showed an important relationship between proton spin-lattice relaxation times and permeability, regardless of surface morphological features. This indicates that membrane morphology (especially the increased surface area because of roughness) is not solely responsible for the low-pressure, high-flux performance of polyamide membranes. In fact, it suggests that the structure and thickness of the thin-film polymer network determine membrane permeability.

## Membrane Properties and Fouling

Physical and chemical properties of NF membranes (i.e., permeability, salt retention, “pore” size, etc.) control the rate and extent of colloidal fouling.<sup>[18,28,43,44]</sup> The high hydraulic resistance of NF membranes enables substantial foulant deposit layers to form



before fouling is detected, and rejection of ionic solutes exacerbates fouling by screening electrostatic interactions.<sup>[43]</sup> Other recent studies suggest that membrane surface properties also influence fouling resistance of NF membranes.<sup>[6,10,12,13,15,16,49–51]</sup> Several investigations of NF membrane fouling have explored the roles of membrane pore size, surface roughness, electrokinetic surface properties, membrane hydrophobicity/hydrophilicity, and specific chemical functionality.<sup>[51–53]</sup> Various analytical techniques have been employed for evaluating specific physical and chemical surface properties of membranes, including Raman spectroscopy (structure),<sup>[13]</sup> electron spin resonance (solute mobility in membrane polymer matrix and pores),<sup>[13]</sup> AFM, SEM, and TEM (surface morphology, structure, and pore size),<sup>[10,13,15,16,50,54,55]</sup> streaming potential (membrane surface zeta potential),<sup>[56,57]</sup> NMR spectroscopy (permeability),<sup>[50]</sup> (hydrophobicity) contact angle,<sup>[18]</sup> and X-ray photoelectron

spectroscopy (XPS, surface chemical functional groups).<sup>[58,59]</sup>

Field-emission scanning electron microscope (FESEM) images of two commercially available nanofiltration membranes are shown in Fig. 7. The two membranes exhibit RMS roughness values of (A) 12.8 and (B) 56.5 nm (taken from Ref.<sup>[43]</sup>). Additional properties of membranes (A) and (B) include zeta potentials of  $-18$  and  $-25$  mV (at 10 mM and pH 7), pure water contact angles of 51.9 and 51.7, hydraulic resistances of  $3.26 \times 10^{10}$  and  $3.13 \times 10^{10}$  Pa s/m, and salt rejections of 35% and 83% (at 30 gfd and 10 mM NaCl), respectively. Field-emission scanning electron microscope images in Fig. 7(C) and (D) are of the membranes from (A) and (B), respectively, after filtration of identical 200 mg/L suspensions of 100-nm spherical silica colloids in a 10 mM NaCl solution. Different masses of colloidal foulants accumulate on the membrane

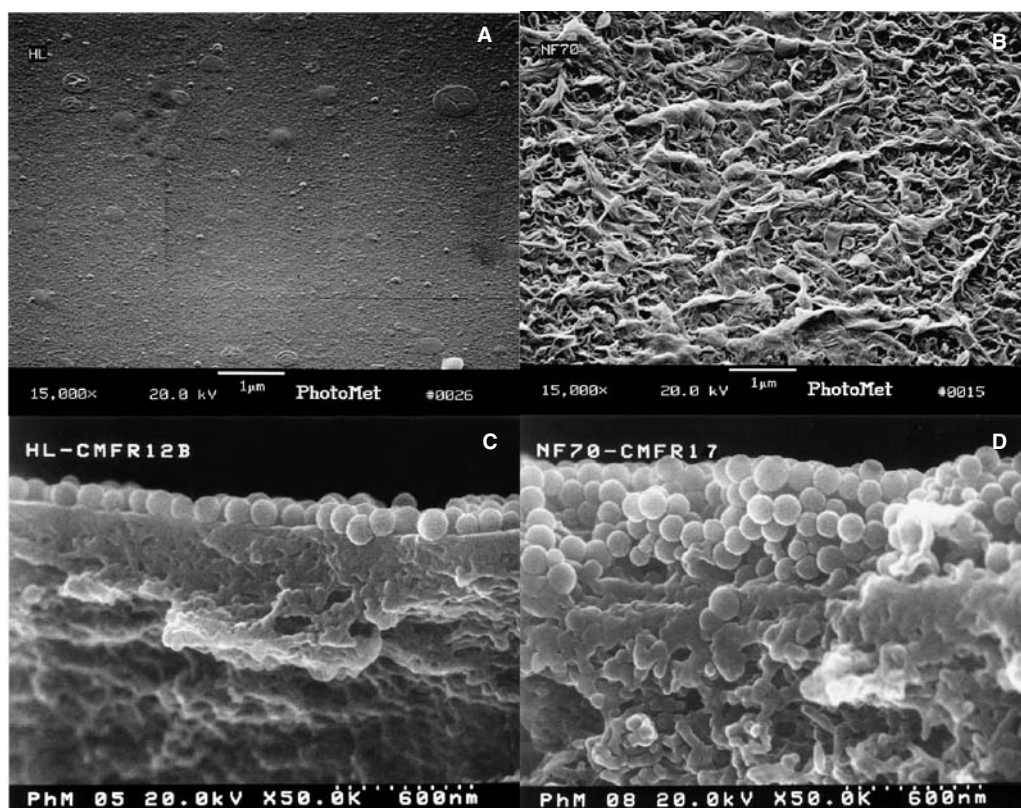


**Fig. 7** Field-emission scanning electron microscope (FESEM) images of two commercially available nanofiltration membranes with RMS roughness values of (A) 12.8 nm and (B) 56.5 nm taken from Ref.<sup>[43]</sup>. Additional (A) and (B) membrane properties include zeta potentials of  $-18$  and  $-25$  mV (at 10 mM and pH 7), pure water contact angles of 51.9 and 51.7, hydraulic resistances of  $3.26 \times 10^{10}$  and  $3.13 \times 10^{10}$  Pa s/m, and salt rejections of 35% and 83% (at 30 gallons per square foot of membrane per day, gfd, and 10 mM NaCl), respectively. Field-emission scanning electron microscope images of fouled NF membranes in (C) and (D) show the membranes from (A) and (B), respectively, accumulate different amounts of colloidal foulants when the same feed suspension was filtered through the membranes under identical operating conditions. The membrane in (B) with significantly rougher and more negatively charged surface appears to attract a thicker deposit layer of 100 nm silica colloids than the smoother membrane in (A).

surfaces even when operating conditions (i.e., flux, crossflow, temperature, etc.) were constant.

It is not entirely clear why these membranes attract different amounts of the colloidal foulant. It has been suggested that subtle differences in physico-chemical surface properties and salt rejections may control the initial rate of deposition.<sup>[10]</sup> Differing salt rejections will yield different membrane surface salt concentrations (all other conditions being equal), and thus repulsive electrostatic interactions are suppressed creating more favorable conditions for foulant deposition. In this case, the membrane in (B) and (D) had higher salt rejection, which may have countered the slightly greater membrane zeta potential. It has also been suggested that membrane surface roughness may decrease electrostatic repulsive interactions, further enhancing colloidal foulant deposition.

## CONCLUSION

Nanofiltration separations are performed in many industries and for many applications. The key material properties of nanofiltration membranes are their selectivity, which may derive from various combinations of size, charge, and dielectric exclusion. The most common nanofiltration membranes are comprised of a thin, dense polymer film polymerized over the top of a porous membrane cast on a fabric support. The most common nanofiltration module type is the flat-sheet, spiral-wound element design. The performance of NF separations is defined by the solvent permeability and the difference between various solute permeabilities. Fouling is a major concern in most industrial and water treatment applications of nanofiltration separations because it leads to higher operating costs, deterioration of NF thin films, and decreased selectivity. Overall, nanofiltration separations offer low-cost, environmentally friendly, semiselective separation capability for a host of applications and are a promising nanotechnology.

## REFERENCES

- Cheremisinoff, N.P. *Liquid Filtration*; Butterworth-Heinemann, 1998, USA.
- Timmer, J.M.K. Doctoral Dissertation; Technische Universiteit Eindhoven: Eindhoven, Netherlands, 2001.
- Meadows, D.M.; Wadley, S.; Buckley, C.A. Evaluation of nanofiltration for recovery of brine from sugar liquor decolourising resin regeneration waste. *Water Sci. Technol.* **1992**, *25*, 339–350.
- Lu, X.; Bian, X.; Shi, L. Preparation and characterization of NF composite membrane. *J. Membr. Sci.* **2002**, *210*, 3–11.
- Bowen, W.R.; Hilal, N.; Lovitt, R.W.; Wright, C.J. Direct measurement of interactions between adsorbed protein layers using an atomic force microscope. *J. Colloid Interface Sci.* **1998**, *197*, 348–352.
- Bowen, W.R.; Doneva, T.A. Atomic force microscopy studies of membranes: effect of surface roughness on double-layer interactions and particle adhesion. *J. Colloid Interface Sci.* **2000**, *229*, 544–549.
- Brant, J.A.; Childress, A.E. Assessing short-range membrane–colloid interactions using surface energetics. *J. Membr. Sci.* **2002**, *203*, 257–273.
- Brant, J.A.; Childress, A.E. Membrane–colloid interactions: comparison of extended DLVO predictions with AFM force measurements. *Environ. Eng. Sci.* **2002**, *19*, 413–427.
- Hoek, E.M.V.; Bhattacharjee, S.; Elimelech, M. Effect of surface roughness on colloid–membrane DLVO interactions. *Langmuir* **2003**, *19*, 4836–4847.
- Vrijenhoek, E.M.; Elimelech, M.; Hong, S. Influence of membrane surface properties on initial rate of colloidal fouling of reverse osmosis and nanofiltration membranes. *J. Membr. Sci.* **2001**, *188*, 115–128.
- Zhu, X.H.; Elimelech, M. Fouling of reverse-osmosis membranes by aluminum-oxide colloids. *J. Environ. Eng.-ASCE* **1995**, *121*, 884–892.
- Zhu, X.; Elimelech, M. Colloidal fouling of reverse osmosis membranes: measurements and fouling mechanisms. *Environ. Sci. Technol.* **1997**, *31*, 3654–3662.
- Khulbe, K.C.; Matsuura, T. Characterization of synthetic membranes by Raman spectroscopy, electron spin resonance, and atomic force microscopy: a review. *Polymer* **2000**, *41*, 1917–1935.
- Mulder, M. *Basic Principles of Membrane Technology*, 2nd Ed.; Kluwer Academic Publishers: Dordrecht, NL, 1996.
- Kwak, S.Y.; Yeom, M.O.; Roh, I.J.; Kim, D.Y.; Kim, J.J. Correlations of chemical structure, atomic force microscopy (AFM) morphology, and reverse osmosis (RO) characteristics in aromatic polyester high-flux RO membranes. *J. Membr. Sci.* **1997**, *132*, 183–191.
- Kim, J.Y.; Lee, H.K.; Kim, S.C. Surface structure and phase separation mechanism of polysulfone membranes by atomic force microscopy. *J. Membr. Sci.* **1999**, *163*, 159–166.
- Petersen, R.J. Composite reverse osmosis and nanofiltration membranes. *J. Membr. Sci.* **1993**, *83*, 81–150.
- Combe, C.; Molis, E.; Lucas, P.; Riley, R.; Clark, M.M. The effect of CA membrane properties on adsorptive fouling by humic acid. *J. Membr. Sci.* **1999**, *154*, 73–87.
- Bowen, W.R.; Doneva, T.A.; Yin, H.B. Polysulfone-sulfonated poly(ether ether) ketone blend membranes: Systematic synthesis and characterisation. *J. Membr. Sci.* **2001**, *181*, 253–263.
- Bowen, W.R.; Doneva, T.A.; Yin, H.B. The effect of sulfonated poly(ether ether ketone) additives on membrane formation and performance. *Desalination* **2002**, *145*, 39–45.
- Cadotte, J.; Forester, R.; Kim, M.; Petersen, R.; Stocker, T. Nanofiltration membranes broaden the use of membrane separation technology. *Desalination* **1988**, *70*, 77–88.

22. Faibish, R.S.; Cohen, Y. Fouling-resistant ceramic-supported polymer membranes for ultrafiltration of oil-in-water microemulsions. *J. Membr. Sci.* **2001**, *185*, 129–143.
23. Faibish, R.S.; Cohen, Y. Fouling and rejection behavior of ceramic and polymer-modified ceramic membranes for ultrafiltration of oil-in-water emulsions and microemulsions. *Colloids Surf., A* **2001**, *191*, 27–40.
24. Cheryan, M. *Ultrafiltration and microfiltration handbook*; Technomic, 1998.
25. Bontha, J.R.; Pintauro, P.N. Water orientation and ion solvation effects during multicomponent salt partitioning in a nafion cation exchange membrane. *Chem. Eng. Sci.* **1994**, *49*, 3835–3851.
26. Glueckauf, E. The distribution of electrolytes between cellulose acetate membranes and aqueous solution. *Desalination* **1976**, *18*, 155–172.
27. Carter, J.W.; Hoyland, G.; Hasting, A.P.M. Concentration polarisation in reverse osmosis flow systems under laminar conditions. Effect of surface roughness and fouling. *Chem. Eng. Sci.* **1974**, *29*, 1651–1658.
28. Hoek, E.M.V.; Kim, A.S.; Elimelech, M. Influence of crossflow membrane filter geometry and shear rate on colloidal fouling in reverse osmosis and nanofiltration separations. *Environ. Eng. Sci.* **2002**, *19*, 357–372.
29. Bhattacharjee, S.; Kim, A.S.; Elimelech, M. Concentration polarization of interacting solute particles in cross-flow membrane filtration. *J. Colloid Interface Sci.* **1999**, *212*, 81–99.
30. Wijmans, J.G.; Nakao, S.; Van Den Berg, F.R.; Troelstra, F.R.; Smolders, C.A. Hydrodynamic resistance of concentration polarization boundary layers in ultrafiltration. *J. Membr. Sci.* **1985**, *22*, 117–134.
31. Zydney, A.L.; Colton, C.K. A concentration polarization model for the filtrate flux in cross-flow microfiltration of particulate suspensions. *Chem. Eng. Commun.* **1986**, *47*, 1–21.
32. Blatt, W.F.; Dravid, A.; Michaels, A.S.; Nelson, L. Solute polarization and cake formation in membrane ultrafiltration: causes, consequences, and control techniques. In *Membrane Science and Technology: Industrial, Biological, and Waste Treatment Processes*; Flinn, J.E., Ed.; Plenum Press: Columbus, OH, 1970.
33. Porter, J.J. Recovery of polyvinyl alcohol and hot water from the textile wastewater using thermally stable membranes. *J. Membr. Sci.* **1998**, *151*, 45–53.
34. Liew, M.K.H.; Fane, A.G.; Rogers, P.L. Fouling of microfiltration membranes by broth-free antifoam agents. *Biotechnol. Bioeng.* **1997**, *56*, 89–98.
35. Kelley, S.T.; Zydney, A.L. Protein fouling during microfiltration: comparative behavior of different model proteins. *Biotechnol. Bioeng.* **1997**, *55*, 91–100.
36. Hagen, K. Removal of particles, bacteria and parasites with ultrafiltration for drinking water treatment. *Desalination* **1998**, *119*, 85–91.
37. Fu, L.T.; Dempsey, B.A. Optimizing membrane operations with enhanced coagulation of toc for drinking water treatment. In *Optimizing Membrane Operations with Enhanced Coagulation of toc for Drinking Water Treatment*; Abstracts of Papers of the American Chemical Society; American Chemical Society: ENVR, 1996; 13 pp.
38. Potts, D.E.; Ahlert, R.C.; Wang, S.S. A critical review of fouling of reverse osmosis membranes. *Desalination* **1981**, *35*, 235–264.
39. Tchobanoglous, G.; Darby, J.; Bourgeois, K.; Mcardle, J.; Genest, P.; Tylla, M. Ultrafiltration as an advanced tertiary treatment process for municipal wastewater. *Desalination* **1998**, *119*, 315–321.
40. Van Houtte, E.; Verbauwhede, J.; Vanlerberghe, F.; Demunter, S.; Cabooter, J. Treating different types of raw water with micro- and ultrafiltration for further desalination using reverse osmosis. *Desalination* **1998**, *117*, 49–60.
41. Vera, L.; Villarroel-Lopez, R.; Delgado, S.; Elmaleh, S. Cross-flow microfiltration of biologically treated wastewater. *Desalination* **1997**, *114*, 65–75.
42. Hong, S.K.; Elimelech, M. Chemical and physical aspects of natural organic matter (NOM) fouling of nanofiltration membranes. *J. Membr. Sci.* **1997**, *132*, 159–181.
43. Hoek, E.M.V. Ph.D. Dissertation; Yale University: New Haven, CT, 2002.
44. Hoek, E.M.V.; Elimelech, M. Cake-enhanced concentration polarization: a new fouling mechanism for salt rejecting membranes. *Environ. Sci. Technol.* **2003**, *17*, 5581–5588.
45. Maxwell, J.C. *Treatise on Electricity and Magnetism*; Clarendon Press, 1881.
46. Cussler, E.L. *Diffusion: Mass transfer in Fluid Systems*, 2nd Ed.; Cambridge University Press: Cambridge, UK, 1984.
47. Boudreau, B.P. The diffusive tortuosity of fine-grained un lithified sediments. *Geochim. Cosmochim. Acta* **1996**, *60*, 3139–3142.
48. Mickley, M.C. A charged ultrafiltration membrane for water softening. *IDA J.* **1985**, *1*, 1–13.
49. Hirose, M.; Ito, H.; Kamiyama, Y. Effect of skin layer surface structures on the flux behaviour of RO membranes. *J. Membr. Sci.* **1996**, *121*, 209–215.
50. Kwak, S.Y.; Ihm, D.W. Use of atomic force microscopy and solid-state NMR spectroscopy to characterize structure–property–performance correlation in high-flux reverse osmosis (RO) membranes. *J. Membr. Sci.* **1999**, *158*, 143–153.
51. Elimelech, M.; Zhu, X.; Childress, A.E.; Hong, S. Role of membrane surface morphology in colloidal fouling of cellulose acetate and composite aromatic polyamide reverse osmosis membranes. *J. Membr. Sci.* **1997**, *127*, 101–109.
52. Zhu, X.H.; Elimelech, M. Colloidal fouling of reverse osmosis membranes—measurements and fouling mechanisms. *Environ. Sci. Technol.* **1997**, *31*, 3654–3662.
53. Riedl, K.; Girard, B.; Lencki, R.W. Influence of membrane structure on fouling layer morphology during apple juice clarification. *J. Membr. Sci.* **1998**, *139*, 155–166.
54. Knoell, T.; Safarik, J.; Cormack, T.; Riley, R.; Lin, S.W.; Ridgway, H. Biofouling potentials of

- microporous polysulfone membranes containing a sulfonated polyether–ethersulfone/polyethersulfone block copolymer: correlation of membrane surface properties with bacterial attachment. *J. Membr. Sci.* **1999**, *157*, 117–138.
55. Bowen, W.R.; Doneva, T.A. Atomic force microscopy studies of membranes: effect of surface roughness on double-layer interactions and particle adhesion. *J. Membr. Sci.* **2000**, *229*, 544–549.
  56. Childress, A.E.; Elimelech, M. Effect of solution chemistry on the surface charge of polymeric reverse osmosis and nanofiltration membranes. *J. Membr. Sci.* **1996**, *119*, 253–268.
  57. Childress, A.E.; Elimelech, M. Relating nanofiltration membrane performance to membrane charge (electrokinetic) characteristics. *Environ. Sci. Technol.* **2000**, *34*, 3710–3716.
  58. Ferjani, E.; Mejdoub, M.; Roudesli, M.S.; Chehimi, M.M.; Picard, D.; Delamar, M. Xps characterization of poly(methylhydrosiloxane)-modified cellulose diacetate membranes. *J. Membr. Sci.* **2000**, *165*, 125–133.
  59. Beverly, S.; Seal, S.; Hong, S. Identification of surface chemical functional groups correlated to failure of reverse osmosis polymeric membranes. *J. Vac. Sci. Technol.* **2000**, *18*, 1107–1113.
  60. Filmtec. *Why Filmtec Thin-Film Composite RO Membranes Outperform Cellulose Acetate Membranes in Water Purification Service*: Filmtec Corporation. Dow FilmTech website; <http://www.pacificro.com/DeFilmWh.pdf>, (accessed July 1998).
  61. Mallevalle, J., Odendaal, P.E., Wiesner, M.R., Eds.; *Water Treatment Membrane Processes*. McGraw Hill: New York, NY, 1996.

# Nanofriction and Nanowear of Sliding Systems: Simulations

W.C.D. Cheong

Materials Science and Characterisation Laboratory, Institute of Materials Research and Engineering, Singapore, Singapore

## INTRODUCTION

The macroscopic behavior of coatings has been well documented and studied, using continuum mechanics. Failure under common tribological situations can occur not only due to coating wear but also by the debonding of the coating from the substrate. However, there are to date relatively few studies on nanometer scale characteristics of coating systems. Deformation mechanisms have been shown to be very different on the nanometer scale.<sup>[1–4]</sup> A full understanding of the mechanical behavior of diamond coating on the nanometer scale is an essential issue if coatings on the nanometer scale are to be used like its macroscale counterparts in the various applications mentioned before.

Various failure mechanisms of the substrate/coating composite on the nanometer scale are studied in this entry using molecular dynamics simulation through a parametric elastic–plastic analysis, for common nanomechanical processes. The nanomechanical processes that will be discussed are uniaxial compression, biaxial compression, indentation, and sliding.

## BACKGROUND

It has been shown that the mechanisms of friction and wear on the nanometer scale can be absolutely different from their micrometer or larger scale counterparts. It was found that friction stress is constant and of the order of the theoretical shear strength, when a sliding contact size is small. However, at a critical contact size, there is a transition beyond which the frictional stress decreases with increasing contact size, until it reaches a second transition where the friction stress gradually becomes independent of the contact size. Hence, the mechanisms of slip are size-dependent, or in other words, there exists a scale effect. This phenomenon is not observed in larger scale contacts.<sup>[5,6]</sup>

Making use of such understanding of tribology on the nanometer scale, recent developments in nanotechnology have revealed wondrous potential in modifying

surfaces on the nanometer scale. By observing lizard's feet, researchers have proven that clusters of nanometer scale contacts can provide strong adhesion just like the spatula at the ends of the hairs on a lizard's feet that allow them to walk on walls and ceilings.<sup>[7]</sup> On the other hand, based on nanostructures of the surfaces of lotus leaves, engineered surfaces with the right surface energy and nanoscopic bumps can ensure that dust particles do not stick to the surface easily, hence resulting in self-cleansing capabilities.<sup>[8]</sup>

Hard coatings such as diamond-like carbon layers are widely used as protective coatings on metal substrates, such as steel. Recently, the passivating of silicon surfaces within micro-electromechanical systems using carbon films has been proposed to prevent stiction and to reduce friction. Coatings have industrial applications in many engineering components. Both soft and hard coatings can inhibit adhesion between the substrate and the counterface resulting in decreased wear. They may also make surface defects less harmful by moving crack initiation sites from the surface down to subsurface regions, thus improving the performance of the substrate.

Various techniques such as chemical vapor deposition (CVD) and pulse laser deposition are being used to deposit carbon on to silicon.<sup>[9]</sup> Depending on the technique and conditions, either amorphous carbon films or diamond-like carbon films can be produced, of which the latter exhibit high density, extreme hardness, high thermal conductivity, chemical inertness, and infrared transparency. However, the films often suffer from adhesion problems—partially or totally delaminated at the interface or in the substrate due to high compressive stresses.<sup>[10–21]</sup> For example, Freller et al.<sup>[11]</sup> showed that when the compressive stress in a film exceeds the ultimate tensile strength of the substrate, failure occurs in the substrate. Zehnder et al.<sup>[12]</sup> reported that a film deposited at 20°C showed no evidence of failure in the bulk, but delaminated at the interface, all over the sample. On the other hand, a film grown at 500°C would adhere very well to the silicon substrate, but would delaminate when its thickness exceeds 600 nm. Som et al.<sup>[13]</sup> studied the delamination

of CVD diamond films deposited on silicon and estimated that the biaxial compressive stress to initiate the film buckling was 1.19 GPa.

## DISCUSSION

### Uniaxial and Biaxial Compression of Diamond-Coated Silicon

Buckling delamination of a coating is unwanted in industrial applications. Thus, a fundamental understanding of the stress relief patterns or buckling modes and the stress levels at which buckling occurs is necessary. Some very interesting buckling patterns such as telephone-cord, sinusoidal wave, sinusoidal shape with extra branches, and a strings-of-beads pattern have been reported in Refs.<sup>[15,17,18]</sup>. Gioia and Ortiz<sup>[10]</sup> have compiled most of these patterns in their paper on delamination of compressed thin films. However, the studies to date have been mainly using experimental techniques and continuum mechanics. Although Pailthorpe, Mitchell, and Bordes<sup>[1]</sup>, McKenzie, Muller, and Pailthorpe<sup>[2]</sup>, and Rosenblum et al.<sup>[3]</sup> used atomistic simulation in their studies on coating, they concentrated mainly on the energy diffusion, the structure of films, and the mismatch-induced residual thermal stresses in film substrate systems.

The buckling of a thin film is caused by local compressive stresses on the film, introduced by the coating process. Thornton<sup>[4]</sup> pictured this process as follows: first the incident atoms transfer kinetic energy to the substrate and become loosely bonded “ad atoms.” They then diffuse over the surface exchanging energy with the substrate until they are either desorbed or trapped at low energy sites of the substrate. Thus, the initial kinetic energy transfer to the substrate can induce a tensile stress on the substrate. When the atoms diffuse over the surface, a compressive stress can be induced back to the coated atoms.

In the present molecular dynamics simulation, for convenience but still capturing the nature of the residual stress generation, we apply the tensile stresses on the substrate before placing the coating and then release the stress with the coating on, so that the film will undergo compressions as experienced in experiment. We focus on the deformation of a diamond carbon coating on silicon under various stress levels with different ratios of compressive stresses in two perpendicular directions,  $X$  and  $Y$ , as shown in Fig. 1. A piece of diamond cubic silicon (1 0 0) with the control volume of  $10.3 \times 10.3 \times 3.8 \text{ nm}^3$  (i.e., 19 unit cells  $\times$  19 unit cells  $\times$  7 unit cells), containing 21,516 atoms, was used as a substrate. The outermost layer of the substrate atoms with the exception of the top (1 0 0) surface was thermostated to 300 K. The tensile stresses

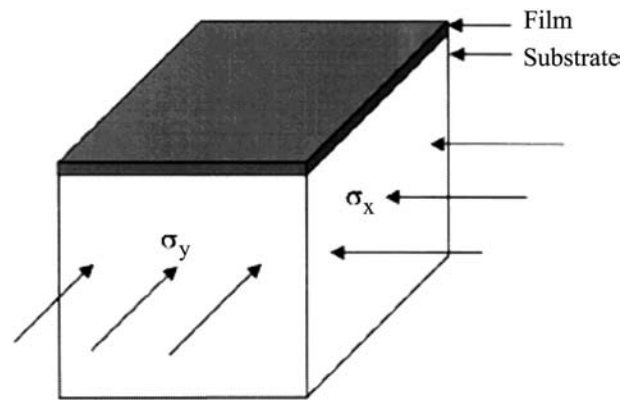


**Fig. 1** The simulation model for compression of diamond-coated silicon.

were applied by forced atomic displacements at the boundary of the control volume in the following distinct ways to uncover the effect of stress variation in the film plane: (i) uniaxially (along the  $X$ -direction), i.e. the stress externally applied in  $Y$ -direction would be zero and hence the stress ratio is  $\sigma_y/\sigma_x = 0$ , (ii) biaxially with less displacement along  $Y$ -direction to give the stress ratio of  $\sigma_y/\sigma_x \approx 0.5$ , and (iii) biaxially with equal displacements along both  $X$ - and  $Y$ -directions to give the stress ratio of  $\sigma_y/\sigma_x \approx 1$ . Three atomic layers of diamond coating with dimensions  $9.987 \times 9.987 \times 0.1783 \text{ nm}^3$  having 4817 atoms were placed on the stressed substrate. The coating and substrate were relaxed together for 5Ps and then the stresses on the substrate were released gradually. A three-body Tersoff potential,<sup>[22,23]</sup> which has been used in many successful MD simulation studies,<sup>[24–28]</sup> was used for Si–Si and C–C interactions. A two-body Morse potential was used for C–Si interactions. This potential has been proved to be reliable in describing C–Si, C–Cu, and C–Al interactions.<sup>[27–32]</sup> Since the purpose of this study is to explore the deformation patterns of the film, to facilitate the observation of the buckling deformation, we apply sufficiently large stresses, much higher than the critical buckling stress measured in relevant experiments,<sup>[13,15]</sup> provided that they are within the elastic limit of silicon.

#### Substrate under uniaxial stress ( $\sigma_y/\sigma_x = 0$ )

When subjected to a uniaxial stress  $\sigma_x$ , we find that the substrate of monocrystalline silicon deforms plastically at a Cauchy stress (also known as true stress and defined as force/current area) of 16.0 GPa. Hence, in the present study, the coating was placed on the substrate pretensioned to 12.5 GPa at which the silicon substrate still deforms elastically. Fig. 2A shows a cross-section of part of the substrate and film after releasing the stress on the substrate. The film buckled



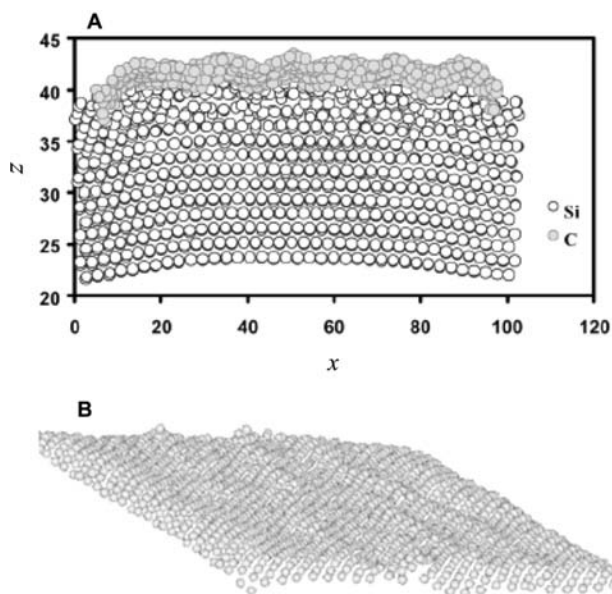


**Fig. 2** (A) A cross-section of portion of the film and substrate. (B) Sinusoidal buckling pattern of the top layer of the film in  $X$ -direction, after releasing the uniaxial stress ( $\sigma_y/\sigma_x = 0$ ).

and slightly delaminated in some places at the film–substrate interface. The top layer of the film viewed from the top, at a tilted angle, is shown in Fig. 2B. This presents an interesting buckling pattern with sinusoidal wrinkles mainly in  $X$ -direction along which the stress is applied.

#### Substrate under biaxially unequal stresses ( $\sigma_y/\sigma_x = 0.5$ )

In this case, the substance deforms plastically at a Cauchy stress of 18.32 GPa in the  $X$ -direction and 9.72 GPa in the  $Y$ -direction. Coating was placed on the substrate having the same strain along  $X$  as in case (i) with  $\sigma_x = 15.10$  GPa and  $\sigma_y = 8.86$  GPa, which were well below the above critical stress values. Fig. 3A shows a cross-section of part of the substrate and film after releasing the stress on the substrate. The film buckled and delaminated, but the delamination occurred only at certain places at the interface. The deformation in the topmost layer of the film is shown in Fig. 3B. It is clear that the size of the wrinkles is bigger than that of case (i), but the buckling mode in the present case is no longer uniaxially sinusoidal. The application of  $\sigma_y$  created the wave in  $Y$ -direction as well.

#### Substrate under biaxially equal stresses ( $\sigma_y/\sigma_x = 1$ )

Now the substrate starts to deform plastically at a Cauchy stress of 13.8 GPa in both  $X$ - and  $Y$ -directions.

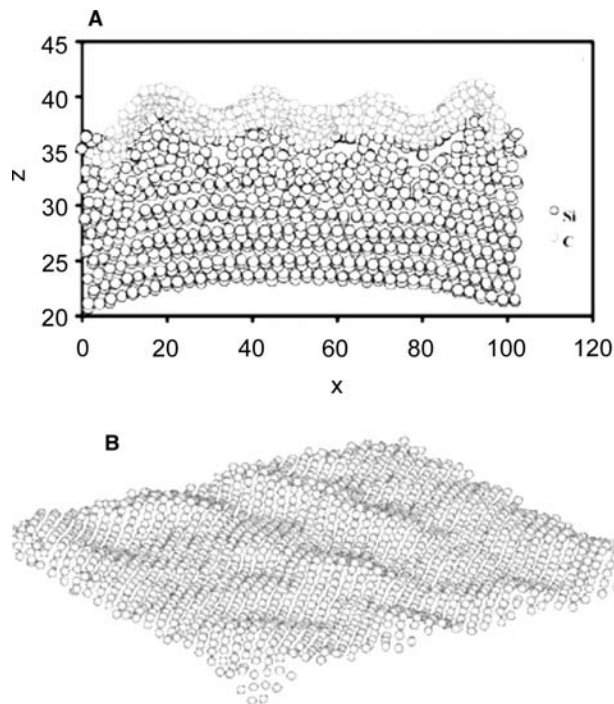


**Fig. 3** (A) A cross-section of portion of the film and substrate. (B) Wavy buckling pattern of the top layer of the film, after releasing the biaxial stresses ( $\sigma_y/\sigma_x = 0.5$ ).

The coating was placed on the substrate having the same strain along  $X$  as in case (i) with both  $\sigma_x$  and  $\sigma_y = 13.4$  GPa, which were below the above critical values. Again on releasing the stress, the film buckled and delaminated. A cross-section of part of the film and substrate is shown in Fig. 4A and the topmost layer of the film is shown in Fig. 4B. Now, it is interesting to note that the size of the wrinkles becomes larger than those in both cases and the overall buckling pattern approaches a telephone-cord-like structure as observed in many experiments.

In all the three cases, although the delamination occurs at the interface, the film tends to attract a layer of Si atoms. This is because both the C–C interaction ( $348 \text{ kJ mol}^{-1}$ ) and the C–Si interaction ( $285 \text{ kJ mol}^{-1}$ ) are greater than the Si–Si interaction ( $176 \text{ kJ mol}^{-1}$ ),<sup>[38]</sup> so that the Si atoms are attracted toward the C-film when the film possesses a considerable bending rigidity. The results show that within each case, the buckling mode and the size of the wrinkles did not change significantly, but the pattern became more pronounced, on completely releasing the stress. On the other hand, the buckling mode did vary with the  $\sigma_y/\sigma_x$  ratio, from mainly a sinusoidal mode with  $\sigma_y/\sigma_x = 0$  to a telephone-cord-like structure  $\sigma_y/\sigma_x = 1$ .

Thin film buckling does occur on the atomic scale when the compressive stresses in a film are sufficiently high. The buckling mode varies with  $\sigma_y/\sigma_x$ , indicating that the stress ratio is an important factor that

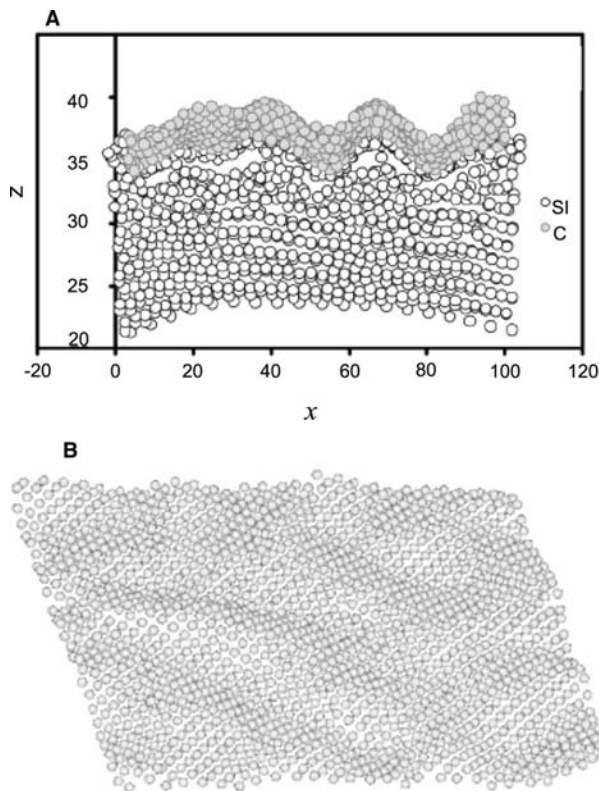


**Fig. 4** (A) A cross-section of portion of the film and substrate. (B) Telephone-cord-like buckling pattern of the top layer of the film, after releasing the biaxial stresses ( $\sigma_y/\sigma_x = 1$ ).

influences the nature of the buckling patterns. It is interesting to note that the pattern of atomic scale buckling of a thin film is similar to that observed in microscale experiments.

## MOLECULAR DYNAMICS SIMULATIONS

Two particular situations are analyzed by molecular dynamics calculations, showing the variations of atomic structures in coating layers and substrate during the indentation and sliding of diamond-coated silicon.

### Indentation of Diamond-Coated Silicon

Simulations of the deformation of diamond carbon-coated silicon under indentation with different coating thicknesses are carried out in this entry. A piece of diamond cubic silicon (1 0 0) with control volume size of  $10.3 \times 10.3 \times 5.5 \text{ nm}^3$ , containing 30 411 atoms, was used as a substrate. The outermost layer of the substrate atoms with the exception of the top (1 0 0) surface was maintained at 300 K by scaling the

velocities of the thermostat atoms. Various atomic layers of diamond carbon coating with top surface area  $9.987 \times 9.987 \text{ nm}^2$  were placed on the substrate. The coating and substrate were then indented with a rigid spherical indenter and the results of the indentation were analyzed. The indentation speed is 300 m/s and the indenter radius is 2 nm.

A three-body Tersoff potential was used for Si–Si and C–C interactions. A two-body Morse potential was used for C–Si interactions.

In a micrometer scale study of indentation of diamond-like carbon coating on steel, Michler and Blank<sup>[33]</sup> found that if the coating thickness is larger than radius of indenter, the coating deforms with increasing indentation load before the substrate experiences plastic deformation. For the cases when coating thickness is comparable with radius of indenter or smaller, coating fracture occurs after plastic deformation of substrate. Five different modes of coating/substrate failure were investigated by Michler and Blank<sup>[33]</sup> by varying the coating thickness and indenter radius ratio ( $h/R$ ). (a) When  $h/R \geq 33$  (infinite coating thickness), the coating layers were found to deform before substrate experiences plastic deformation. Also, circumferential cone cracks are formed close to the contact edge of indenter and top coating layer. In addition, if the contact radius is of the order of the indenter radius subsurface, cracks are also possible. (b) When  $h/R = 3.3$ , coating layer deforms plastically before cracking occurs. It is found that plastic zone extension is slightly larger than the layer thickness. (c) When  $h/R = 0.33$ , the extension of plastic zone in substrate reaches twice the contact radius, approximately. The cracks that nucleate at the interface below the indenter are the dominant failure mechanism. (d) When  $h/R = 0.033$ , the plastic zone extension is found to be identical to the case when  $h/R = 0.33$  and approaches the case of an elastic, fully plastic indentation into a homogeneous unlayered steel solid. Moreover, the layer bent around indentation edge. (e) When  $h/R = 0.0033$  (very thin coating layer), the bending of coating layer is low due to the low bending stiffness of coating layer. Radial and circumferential cracks under the indenter were probable.

Summarizing, three locations for preferential crack initiations were identified with decreasing ratio of layer thickness to indenter radius: (a) at the surface outside the contact area; (b) at the interface close to the symmetry axis; and (c) within the contact area at the surface or interface.<sup>[33]</sup>

On the nanometer scale, plastic deformation of silicon can occur by means of phase transformation and plastic flow without the formation of cracks or dislocations as reported in previous studies.<sup>[34–36]</sup> As such the mechanisms of coating/substrate deformation are very different from its micrometer counterparts.

It is found in this entry that the indentation of diamond carbon-coated silicon also leads to plastic deformation in both the diamond carbon-coating and silicon substrate owing to phase transformation and plastic flow. There is no observable formation of dislocation or cracks. The initiation of plastic deformation and the location of plastic deformation, however, vary with the thickness of the diamond coating.

Four distinct failure mechanisms of coating and substrate due to nanoindentation are observed: (i) When the ratio of thickness of coating to indenter radius  $t^*$  ( $=t/R$ ) is 0.35. It is found that the deformation of substrate is almost identical to that in silicon owing to indentation without the carbon coating. (ii) When  $t^* = 0.7$ , it is found that the substrate requires higher indentation load to yield when compared with the case without coating owing to the thicker coating. The substrate experiences plastic deformation before there is any plastic deformation in the coating.

(iii) When  $t^* = 1.4$ , it is found that the coating experiences plastic deformation before the substrate. The substrate also experiences plastic deformation when the indenter is further loaded. (iv) When  $t^* = 2.8$ , it is found that there is no plastic deformation in silicon substrate. The mechanism of plastic deformation for the carbon-coating is similar to the plastic deformation of carbon specimen owing to nanoindentation.

Further elaboration of the four distinct mechanisms of coating–substrate plastic deformation owing to nanoindentation will be given in the following section. The results of molecular simulation calculations demonstrate the variation in deformation mechanism during nanoindentation with different coating thicknesses to asperity radius ratio.

a. Thin coating layer ( $t^* = 0.35$ )

Fig. 5A–C show the deformation of the carbon coating and silicon substrate at various time

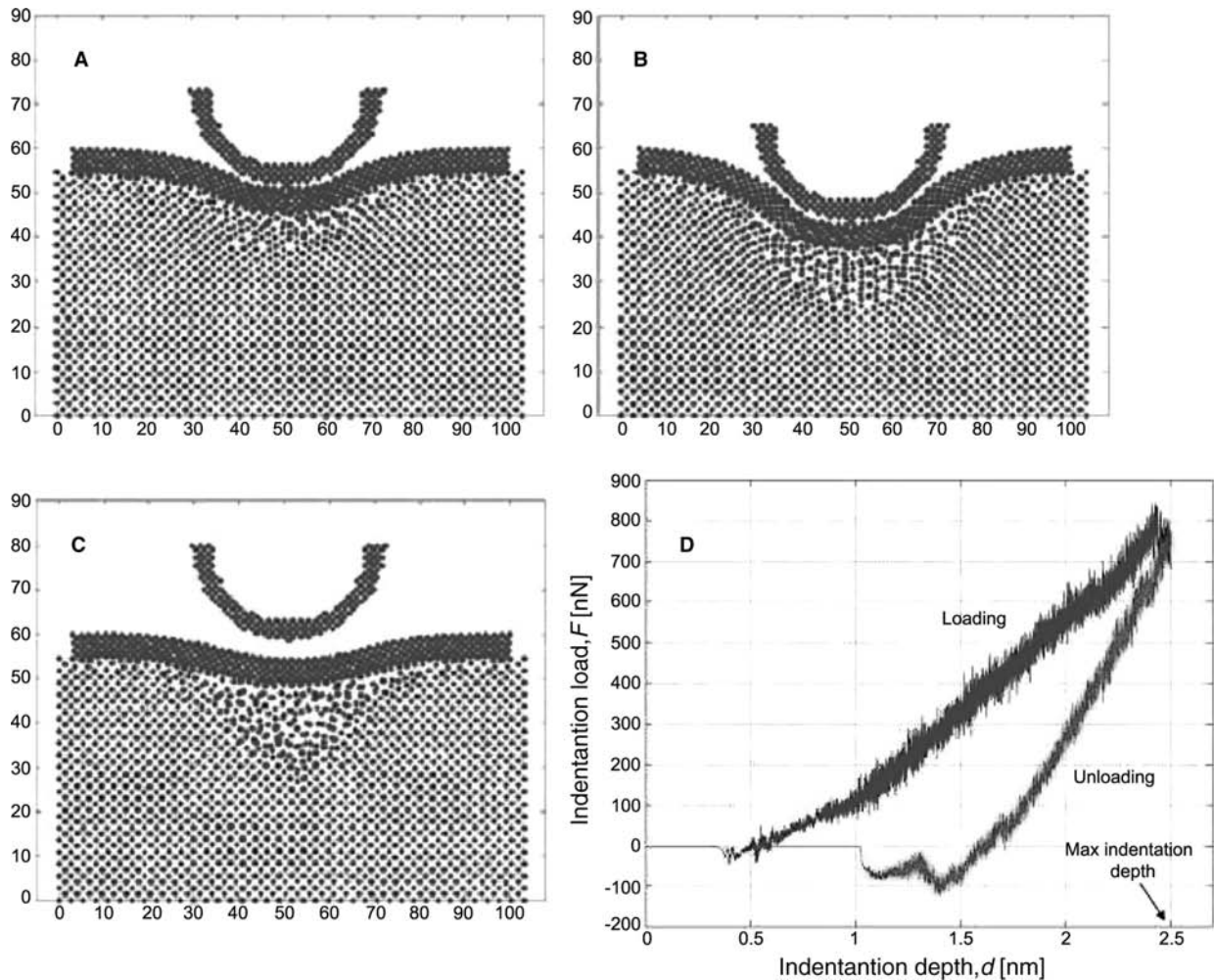


**Fig. 5** Indentation of diamond-coated silicon in case of thin coating layer when compared with the indenter radius ( $t^* = 0.35$ ). Cross-sectional views at different stages for loading and unloading during the indentation (A–C) and load versus displacement curve for indentation (D).

steps when  $t^* = 0.35$ . It is clearly shown that there is no plastic deformation in the coating and the coating recovers in an elastic manner when the indenter is unloaded. Plastic deformation, however, is evident in the silicon substrate even though the coating is intact. The mechanism of plastic deformation for the silicon substrate is similar to that of the plastic deformation of silicon due to indentation without the carbon coating.<sup>[29]</sup> The silicon substrate deforms plastically due to phase transformation and plastic flow. The resultant transformed zone is amorphous. The residual damage zone extends deep below the interface of the coating and the substrate. As a result of plastic deformation in the substrate and elastic recovery in the coating, the substrate delaminates from the coating at the substrate-coating interface below the indenter. Fig. 5D shows the

load-displacement diagram of the indenter due to the indentation. As expected, the load-displacement diagram is similar to the load-displacement diagram due to the direct indentation of silicon with a rigid indenter.<sup>[29]</sup> The main difference is the greater stiffness of the diamond-coated silicon when compared with the silicon specimen without coating.

b. Medium thickness coating layer ( $t^* = 0.7$ )

Fig. 6A–C show the deformation of the carbon coating and silicon substrate at various time steps when  $t^* = 0.7$ . It is clear that plastic deformation occurs in both the carbon coating and the silicon substrate. The damaged zone in the silicon substrate is noticeably smaller when compared with the case when  $t^* = 0.35$ . Plastic deformation of the silicon substrate is confined to the coating-substrate interface directly under the indenter. In addition, plastic deformation of

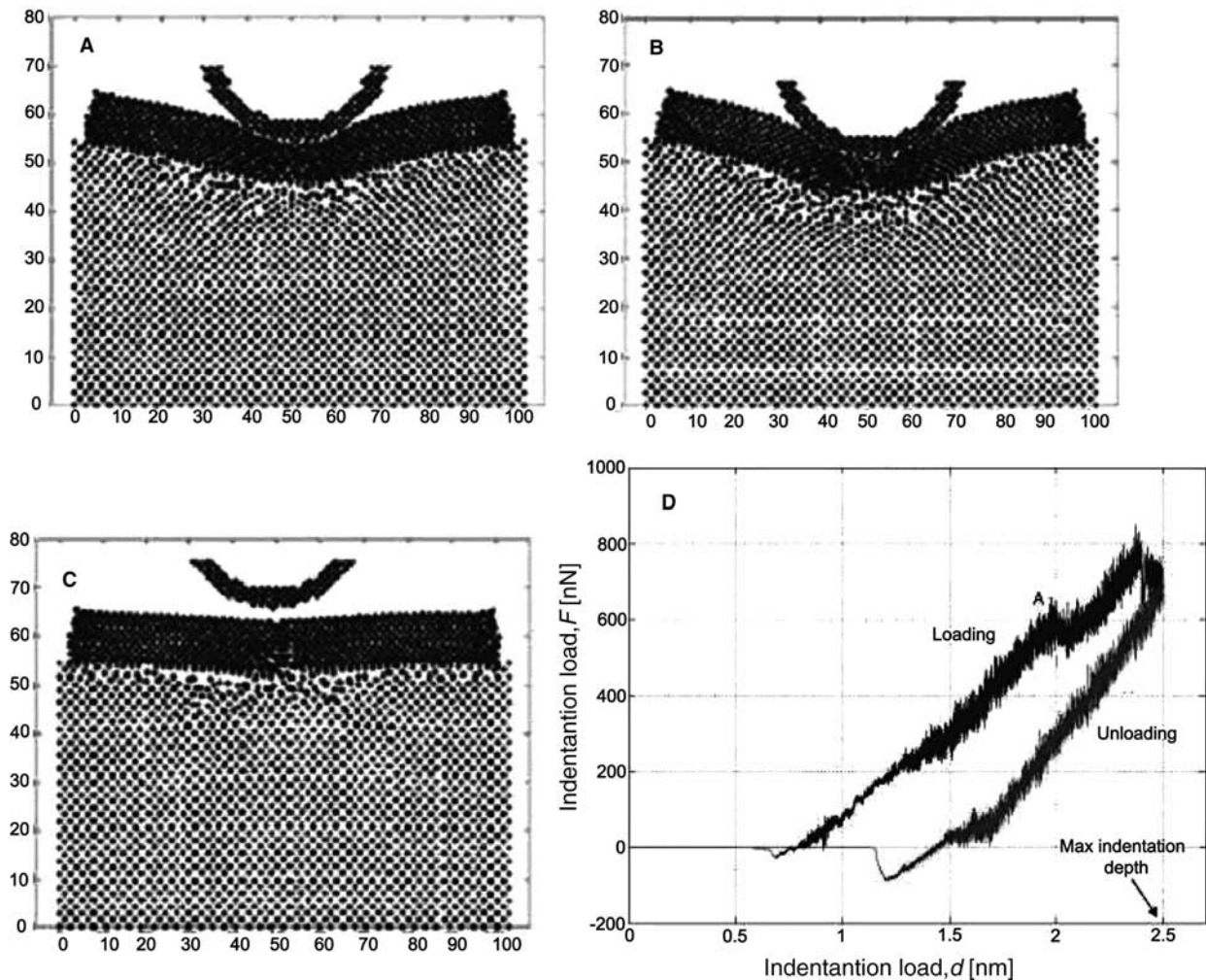


**Fig. 6** Indentation of diamond-coated silicon in case of medium thickness of coating layer when compared with the indenter radius ( $t^* = 0.70$ ). Cross-sectional views at different stages for loading and unloading during the indentation (A–C) and load versus displacement curve for indentation (D).



the substrate occurs before plastic deformation of the carbon coating. Delamination between substrate and coating due to plastic deformation of substrate is observed. Fig. 6D shows the force–displacement diagram of the rigid indenter. It can be seen that there is a significant drop of the indenter force at point A. This can be explained by the plastic deformation of the carbon coating. For thickness  $t^* = 0.7$ , the plastic deformation of the coating occurs throughout the entire thickness of the coating in the region directly under the indenter. The substrate experiences plastic deformation when the loading force is 400 nN. On further indentation, the coating also experiences plastic deformation when the loading force reaches 600 nN. From Fig. 6, it is obvious that plastic deformation in the diamond coating initiates from interface of the coating and the substrate

directly beneath the indenter owing to tensile stresses at the bottom surface of the carbon coating. The carbon changes from diamond cubic structure to a disordered amorphous graphitic form as discovered in experiments.<sup>[37]</sup>

c. Thick coating layer ( $t^* = 1.4$ )

Fig. 7A–C show the deformation of the carbon coating and silicon substrate at various time steps when  $t^* = 1.4$ . It can be seen that plastic deformation also occurs in both the carbon coating and the silicon substrate. The damaged zone in the silicon substrate is once again much localized and is confined to the coating–substrate interface directly beneath the indenter. The plastic deformation of the coating when  $t^* = 1.4$ , however, occurs before the plastic deformation of the substrate. Fig. 7D shows the force–displacement diagram of the indenter. The two significant drops in loading force

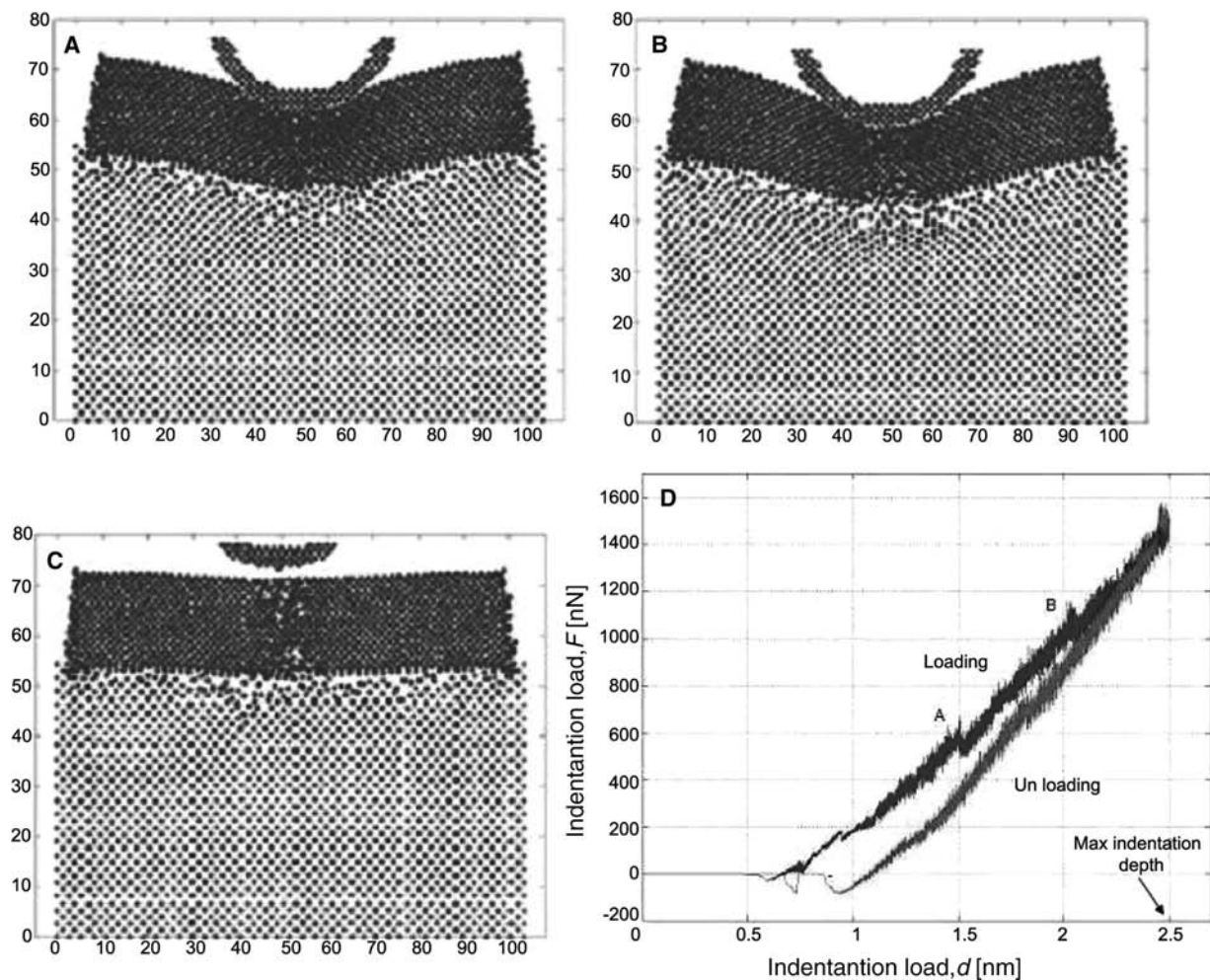


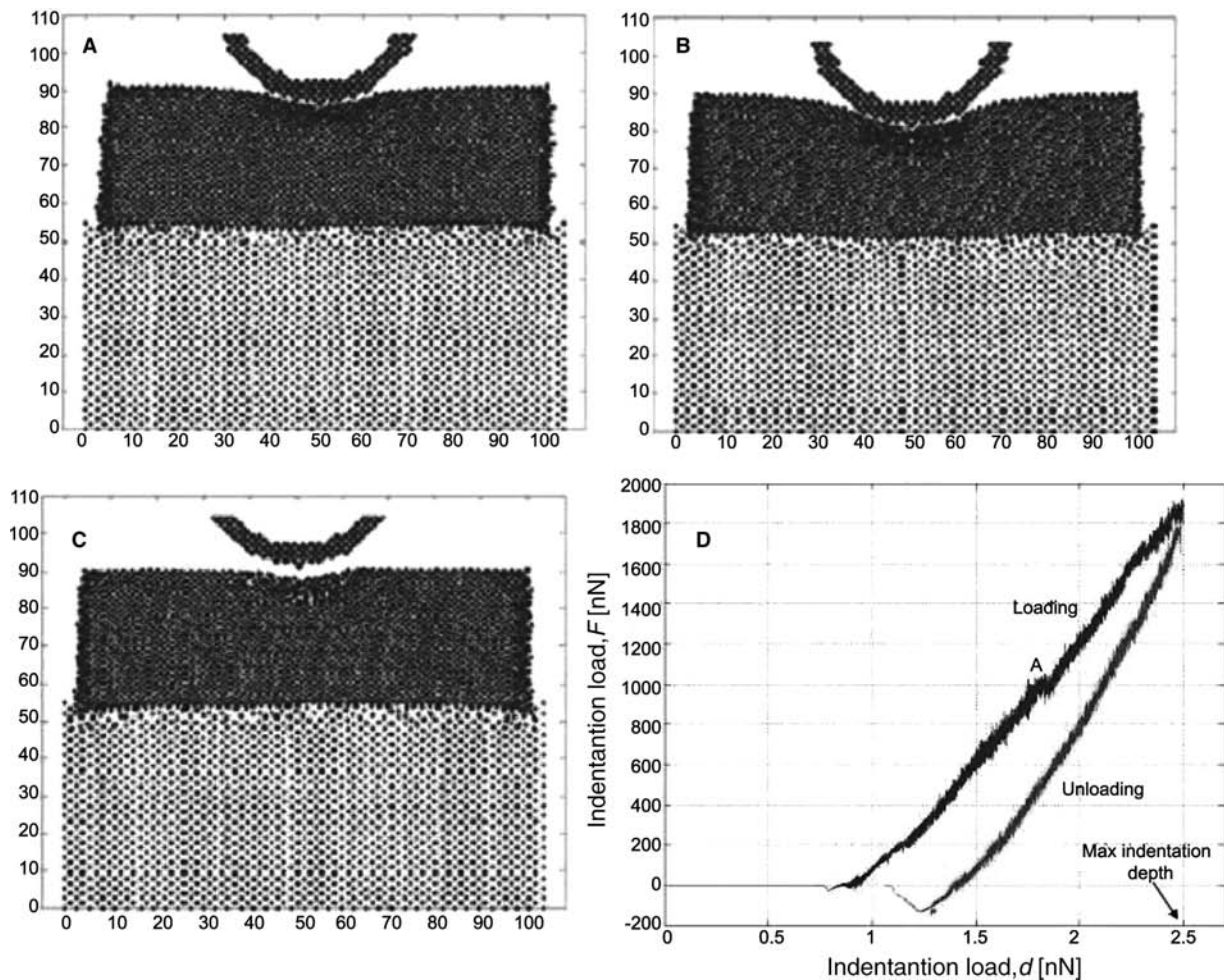
**Fig. 7** Indentation of diamond-coated silicon in case of thick coating layer when compared with the indenter radius ( $t^* = 1.4$ ). Cross-sectional views at different stages for loading and unloading during the indentation (A–C) and load versus displacement curve for indentation (D).

marked A and B are explained by the plastic deformation of the coating first at the top surface of the coating followed by plastic deformation of the coating initiating from the bottom surface of the coating when the force reaches 600 nN. The initial plastic deformation in the carbon is a result of direct contact with the indenter. Phase transformation to a graphitic amorphous phase occurs due to the stresses generated when the indenter indents the coating. The second plastic deformation in the carbon coating occurs due to the significant bending experienced by the coating during indentation. Tensile stresses generated on the bottom surface of the carbon coating due to bending of the coating layer induces a phase transformation of tetrahedral carbon to an amorphous graphitic phase leading to the plastic deformation. This occurs when the loading force reaches 1100 nN. The silicon substrate only experiences plastic

deformation when the loading force reaches 800 nN.

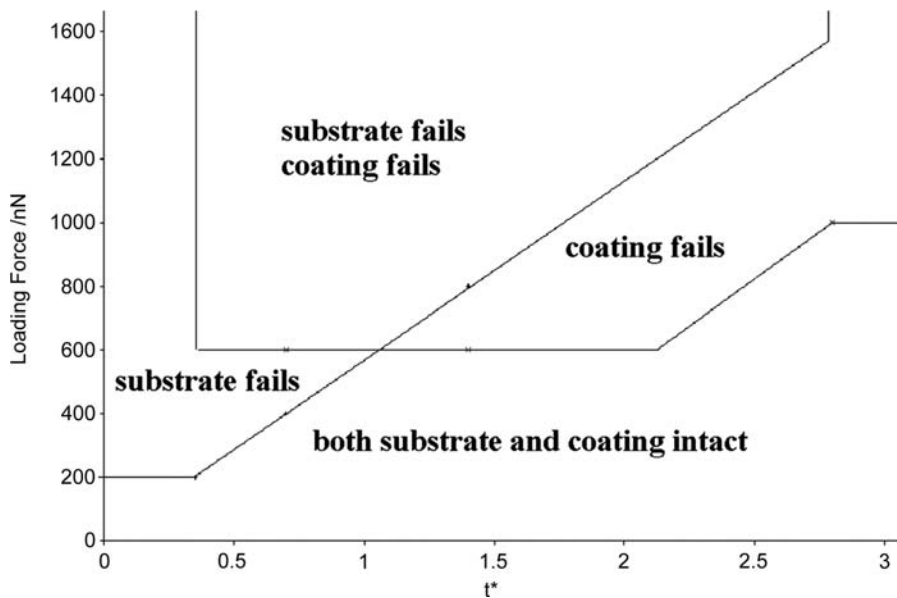
d. Very thick coating layer ( $t^* = 2.8$ )

Fig. 8A–C show the deformation of the carbon coating and silicon substrate at various time steps when  $t^* = 2.8$ . It can be seen that in this case, plastic deformation only occurs in the carbon coating. No observable plastic deformation is seen in the silicon substrate throughout the entire indentation process. The mechanism of plastic deformation in carbon coating is the same as that observed in direct indentation of a carbon specimen with a rigid indenter. Fig. 8D shows the force–displacement diagram of the indenter. Instead of having two drops in the force as in the previous case ( $t^* = 1.4$ ), there is only one drop in the force (pt A). This is consistent with the plastic deformation on the top surface of the carbon coating when the loading force reaches 1000 nN.



**Fig. 8** Indentation of diamond-coated silicon in case of very thick coating layer when compared with the indenter radius ( $t^* = 2.8$ ). Cross-sectional views at different stages for loading and unloading during the indentation (A–C) and load versus displacement curve for indentation (D).





**Fig. 9** Failure map of carbon-coated silicon system owing to nanoindentation.

Noting the force at which the coating and substrate experience plastic deformation, a failure map can be plotted. Fig. 9 shows a plot of the failure map of a carbon-coated monocrystalline silicon obtained using molecular dynamics simulation. Hence, the plastic deformation of a diamond-coated silicon system can

be defined using the failure map, provided the scale of analysis is small enough to ensure that crack formation and dislocations are not initiated.

Hence as a conclusion, no observable formation of dislocations is found throughout the indentations in this present study. The occurrence of plastic

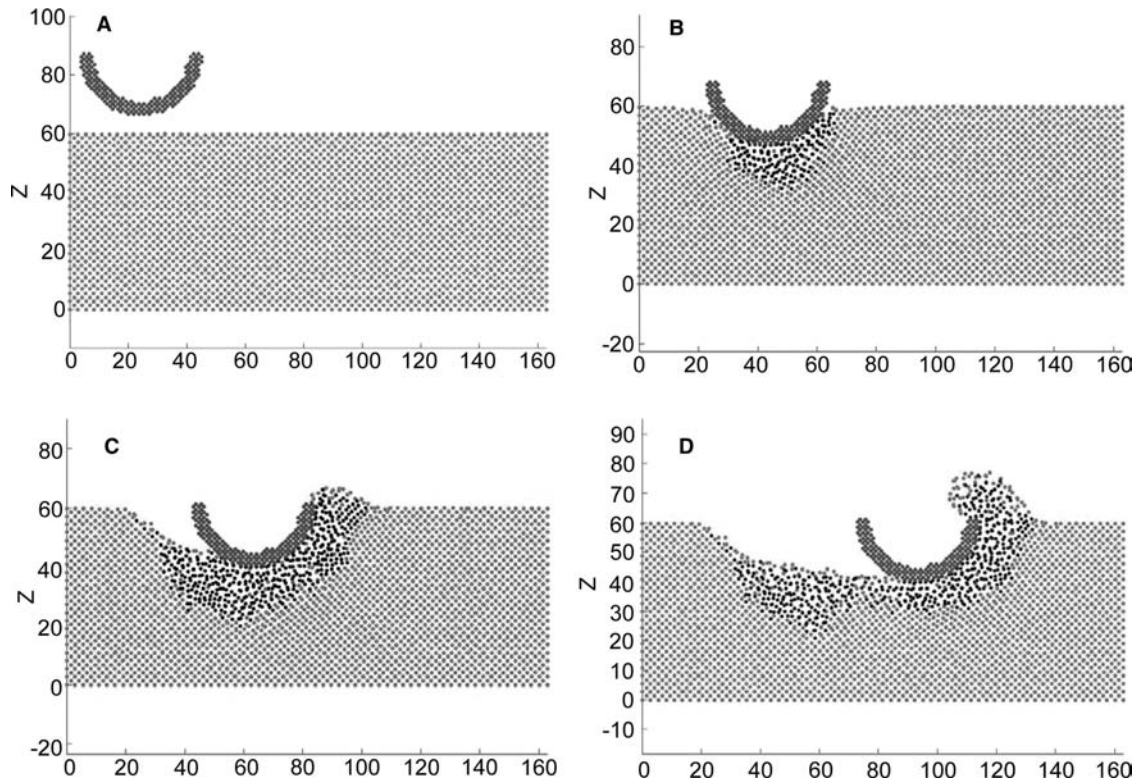


**Fig. 10** Cross-sectional views at different stages for sliding without coating ( $r^* = 0$ ). (A) Snapshot of sliding simulation at 0 time step; (B) Snapshot of sliding simulation at 20,000 time steps; (C) Snapshot of sliding simulation at 40,000 time steps; (D) Snapshot of sliding simulation at 60,000 time steps.

deformation in carbon coating and silicon substrate is solely due to amorphous phase transformation and plastic flow. As observed, the size of residual amorphous zone formed at the end of indentation decreases with the thickness of carbon coating. The initiation and location of plastics deformation, however, varies with the thickness of the carbon coating.

### Sliding of Diamond-Coated Silicon

The simulations of sliding on diamond-coated silicon are discussed in this section. The diamond asperity used is hemispherical and has a radius of 2.14 nm, consists of 1818 atoms with 0.357 nm bond length. The silicon substrate consists of 46,993 atoms, each separated away by 0.543 nm, and the dimension is  $(120 \times 68 \times 44)$  atoms, or  $(16.29 \times 9.23 \times 5.97)$  nm<sup>3</sup>. Four variations of coating thicknesses are used.

The carbon asperity is sliding and subsequent cutting into the diamond-coated silicon substrate is at a sliding speed of 100 m/s and maximum depth of cut 2 nm.

Figs. 10–14 are cross-sections of the four simulations of sliding with four different coating thicknesses.

For the same examples, Fig. 15A–D show the variation of sliding force versus time and Fig. 16A–E show the variation of normal force versus time.

In all four cases of different coating thicknesses, there were no signs of dislocations within the substrate. The inelastic deformation observed under the tool tip and along the sliding path is caused by viscous flow in the amorphous region rather than other failure mechanisms such as dislocations. Such a transformation mechanism is similar to that of nanoindentation.<sup>[29]</sup> Silicon in diamond cubic structure first transforms into a metallic body centered  $\beta$ -silicon, and upon removal of stresses,  $\beta$ -silicon further transforms into amorphous silicon.

The following examples demonstrate the variations in deformation mechanism in nanosliding with different coating thicknesses to asperity radius ratio.

#### a. No coating ( $t^* = 0$ )

The non-coated system shows similar general wear mechanisms as those described by Zhang and Tanaka.<sup>[30]</sup> As the depth of cut of the asperity increases, the mechanism of wear progresses from no-wear to adhering, ploughing,

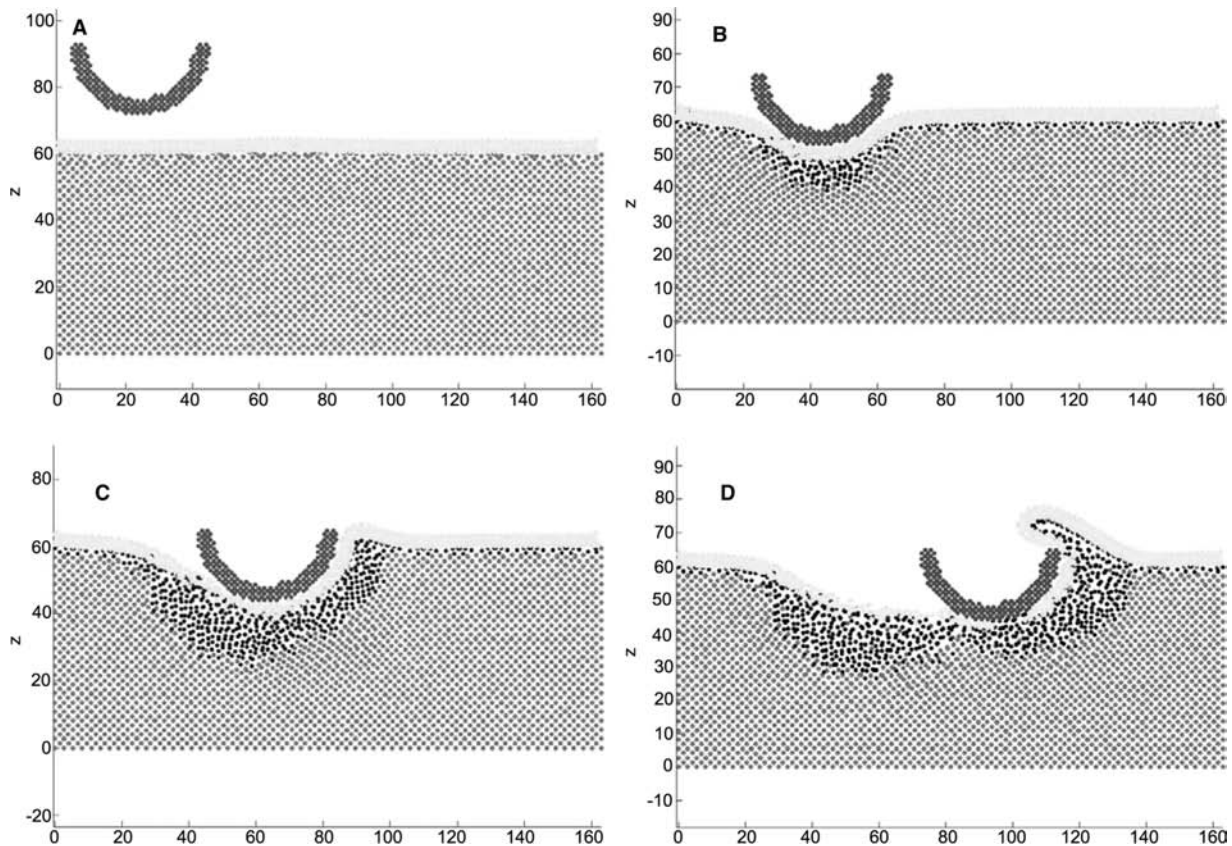


**Fig. 11** Cross-sectional views at different stages for sliding with very thin coating ( $t^* = 0.17$ ). (A) Snapshot of sliding simulation at 0 time step; (B) Snapshot of sliding simulation at 20,000 time steps; (C) Snapshot of sliding simulation at 40,000 time steps; (D) Snapshot of sliding simulation at 60,000 time steps.

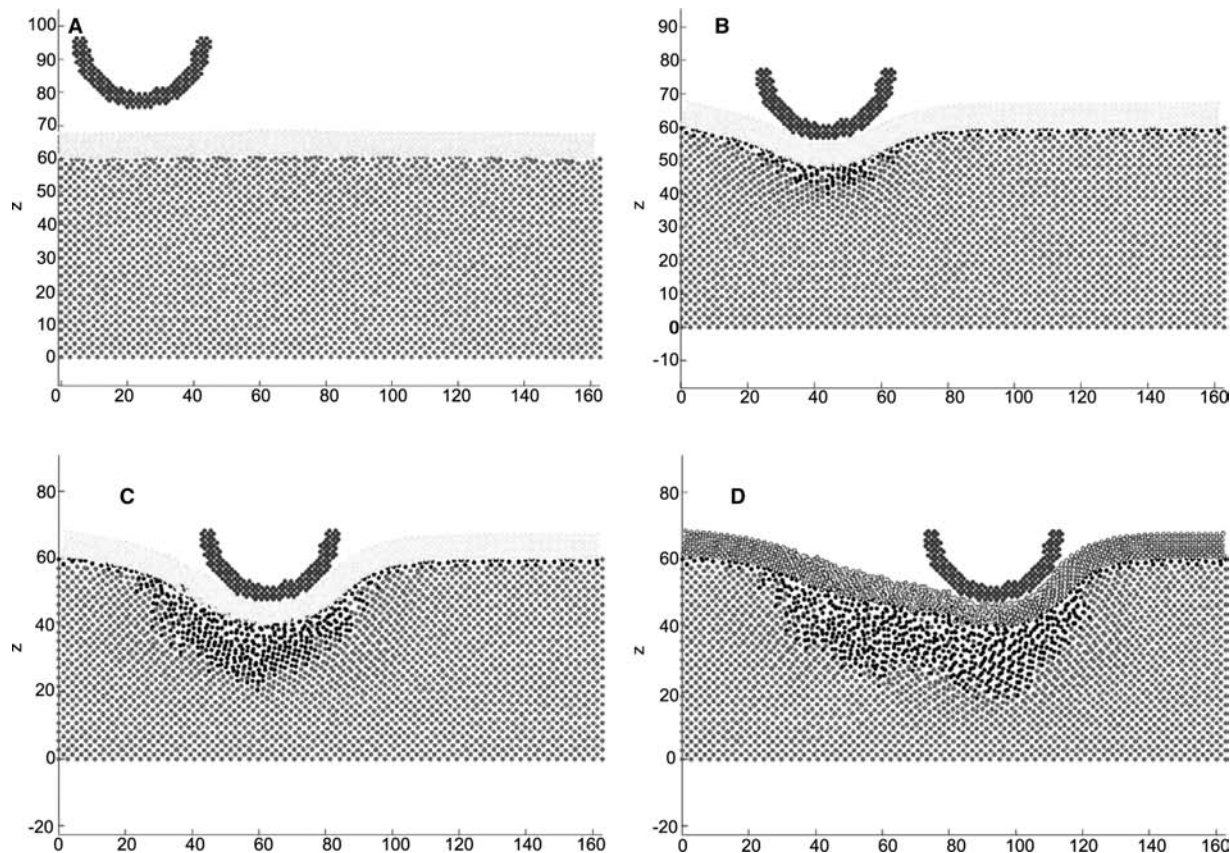


**Fig. 12** Cross-sectional views at different stages for sliding with thin coating ( $t^* = 0.35$ ). (A) Snapshot of sliding simulation at 0 time step; (B) Snapshot of sliding simulation at 20,000 time steps; (C) Snapshot of sliding simulation at 40,000 time steps; (D) Snapshot of sliding simulation at 60,000 time steps.

and finally cutting. Formation of chip is observed when the asperity is cutting the substrate (see Fig. 10).

The sliding force increases linearly from 0 to 0.03 nN as the depth of cut of the asperity increases to and remains constant at that value as the asperity ploughs through it (see Fig. 15A). Observing the normal force on the asperity (see Fig. 16A), it is found that the asperity experiences an initial attractive force when the asperity is first in contact with the silicon surface. The normal force increases linearly to 0.04 nN as the depth of cut of the asperity increases. As the asperity ploughs through the silicon causing the formation of a chip, the normal force stabilizes at 0.02 nN.

b. Very thin coating ( $t^* = 0.17$ )

The plastic deformation mechanism in this case is very similar to that of sliding without coating. The presence of the very thin coating does not change the depth of phase transformation in the silicon substrate. The coating experiences plastic deformation through plastic flow and the silicon substrate experiences plastic

deformation as in the case of sliding without coating. As the asperity slides over the carbon-coated silicon substrate, it begins to plough into the substrate forming a chip (see Fig. 11). The main difference between sliding with coating of this thickness and sliding without coating is the thinner chip formed in the case of sliding with coating. The coating contains the chips formed and hence the chip formed is thinner than that of sliding without coating. The coating fails as the asperity slides over it ploughing into the substrate. No delamination is observed.

Initially, the sliding force remains constant because the contact area is small (Hurtado and Kim). The sliding force increases as the depth of cut increases to 0.06 nN. Stick-slip phenomena are observed as the asperity slides over the coating. However, the stick-slip pattern is irregular because of the damage to the carbon coating as the asperity slides over it. The ploughing force 0.06 nN is much higher in this case than in sliding without coating because the coated chips provide more resistance to the



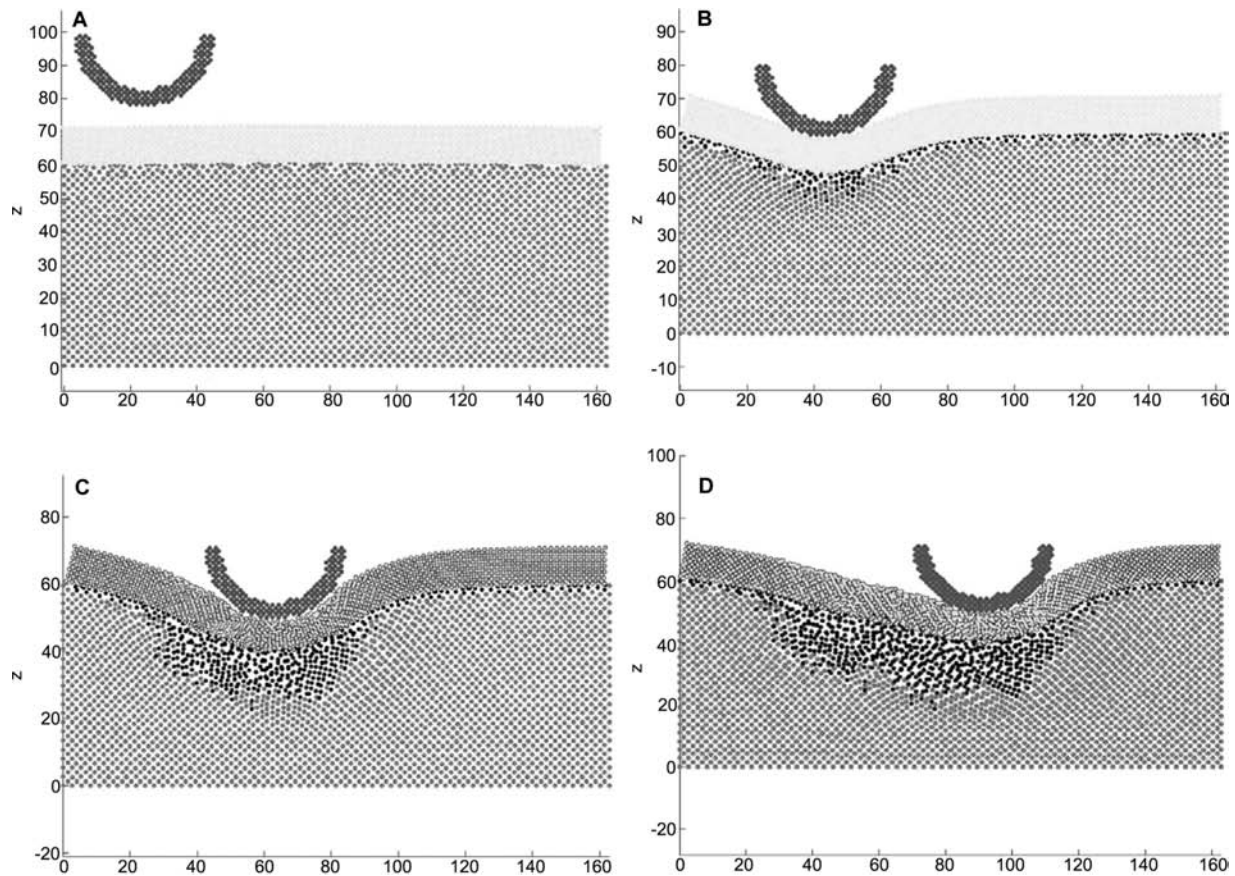


**Fig. 13** Cross-sectional views at different stages for sliding with medium thickness coating ( $t^* = 0.70$ ). (A) Snapshot of sliding simulation at 0 time step; (B) Snapshot of sliding simulation at 20,000 time steps; (C) Snapshot of sliding simulation at 40,000 time steps; (D) Snapshot of sliding simulation at 60,000 time steps.

asperity. Fig. 15B shows the asperity sliding force versus time steps plot.

The maximum normal force is much higher at 0.07 nN owing to the carbon coating on top

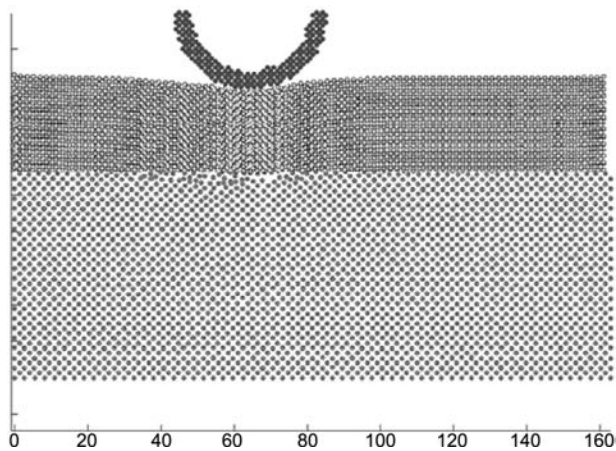


**Fig. 14** Cross-sectional view for sliding with thick coating ( $t^* = 1.4$ ).

of the silicon substrate. There is a large drop in the normal force experienced by the asperity due to failure and tearing of the carbon coating indicated by the point Q in the figure. The normal stress stabilizes at 0.01 nN because the chips formed are still contained by the carbon coating and hence do not exert that much a normal force on the asperity as in the case of sliding with coating. Fig. 16B shows the asperity normal force versus time steps plot.

c. Thin coating ( $t^* = 0.35$ )

As the thickness is increased, no ploughing is observed at the same depth of cut. Contrary to what is expected with a thicker coating, the size of the amorphous region of the substrate is surprisingly larger when  $t^* = 0.35$ , where there is no ploughing, than in the case when  $t^* = 0.17$ , when ploughing occurs. This could be due to the absence of chip formation. In the case of  $t^* = 0.17$ , the formation of chips allows the amorphous silicon to flow out of the substrate, thereby relieving the stresses

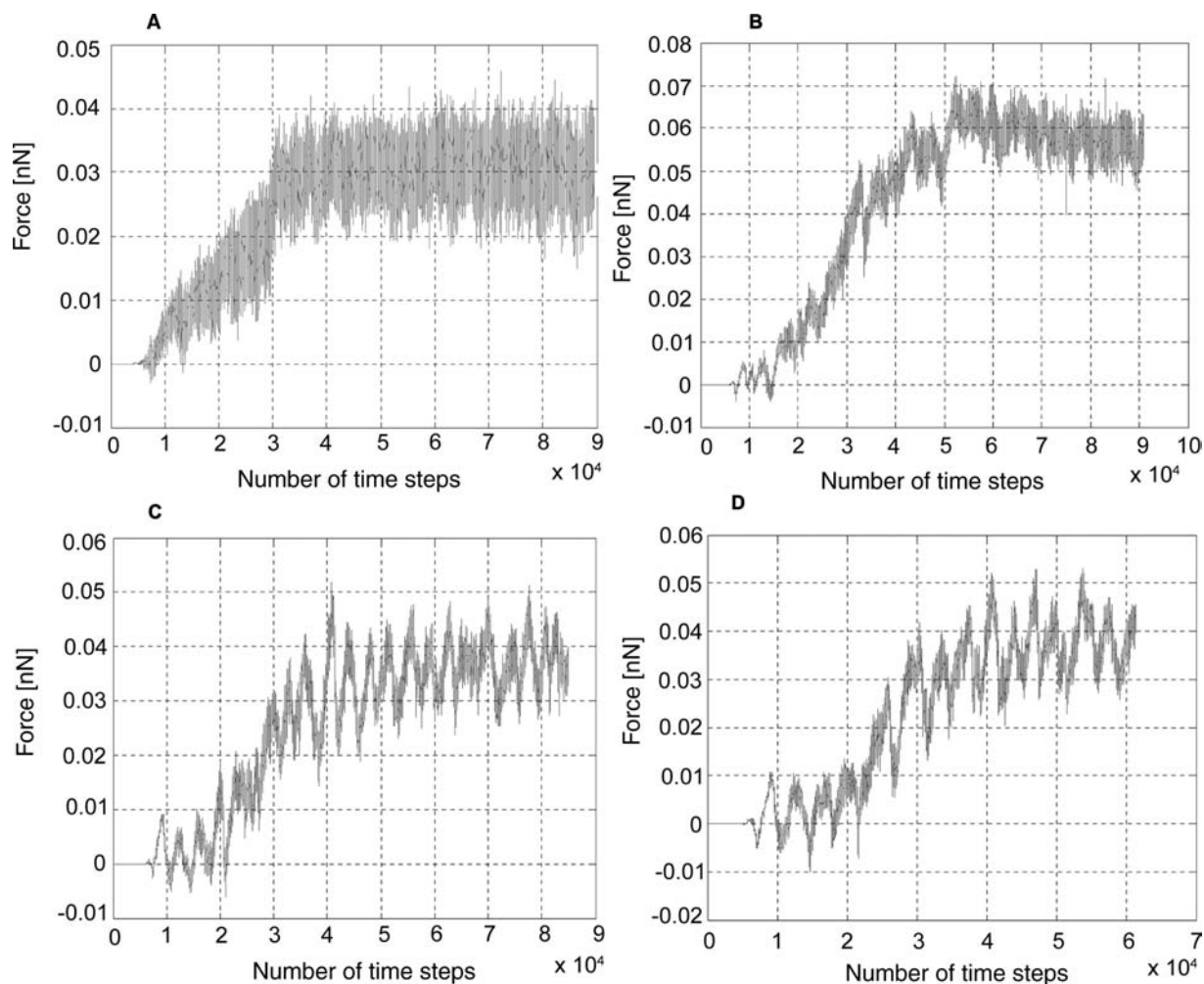


**Fig. 15** Sliding force versus number of time steps for coatings of various thicknesses: (A) no coating; (B) very thin coating ( $t^* = 0.17$ ); (C) thin coating ( $t^* = 0.35$ ); (D) moderate thickness coating ( $t^* = 0.7$ ).

under the asperity. However, in the case of  $t^* = 0.35$ , the thicker coating prevents the formation of chips and hence the higher stresses lead to the formation of a deeper amorphous region under the asperity. Though the coating undergoes plastic deformation, it adheres to the amorphous silicon without tearing or debonding. Fig. 12 shows snap shots of the plastic deformation of diamond-coated silicon due to sliding with  $t^* = 0.35$  at various time steps. The initial sliding force is once again constant because of the initial small contact area in no-wear sliding. The sliding force increases from 0 to 0.03 nN as the depth of cut of the asperity increases. The final sliding force is much lower than the case of coating thickness owing to the absence of ploughing and chipping. The stick-slip pattern is regular because the coating remains intact throughout the entire no-wear sliding process. Fig. 15C

shows the asperity sliding force versus time steps plot.

The maximum normal force reaches 0.1 nN, which is higher than the case of thin coating. This implies that the maximum normal force on the asperity increases with coating thickness. There is little drop in normal force as no chipping occurs and the normal force can be explained by the plastic deformation experienced by the silicon substrate beneath the coating. Fig. 16C shows the asperity normal force versus time steps plot.

d. Medium thickness coating ( $t^* = 0.7$ )

As the thickness is increased further, the thicker coating takes more of the load of the sliding asperity. This results in a smaller amorphous zone in the silicon substrate. There is no plastic deformation in the coating as the coating recovers elastically as the asperity passes. In both this case and the previous one, the silicon

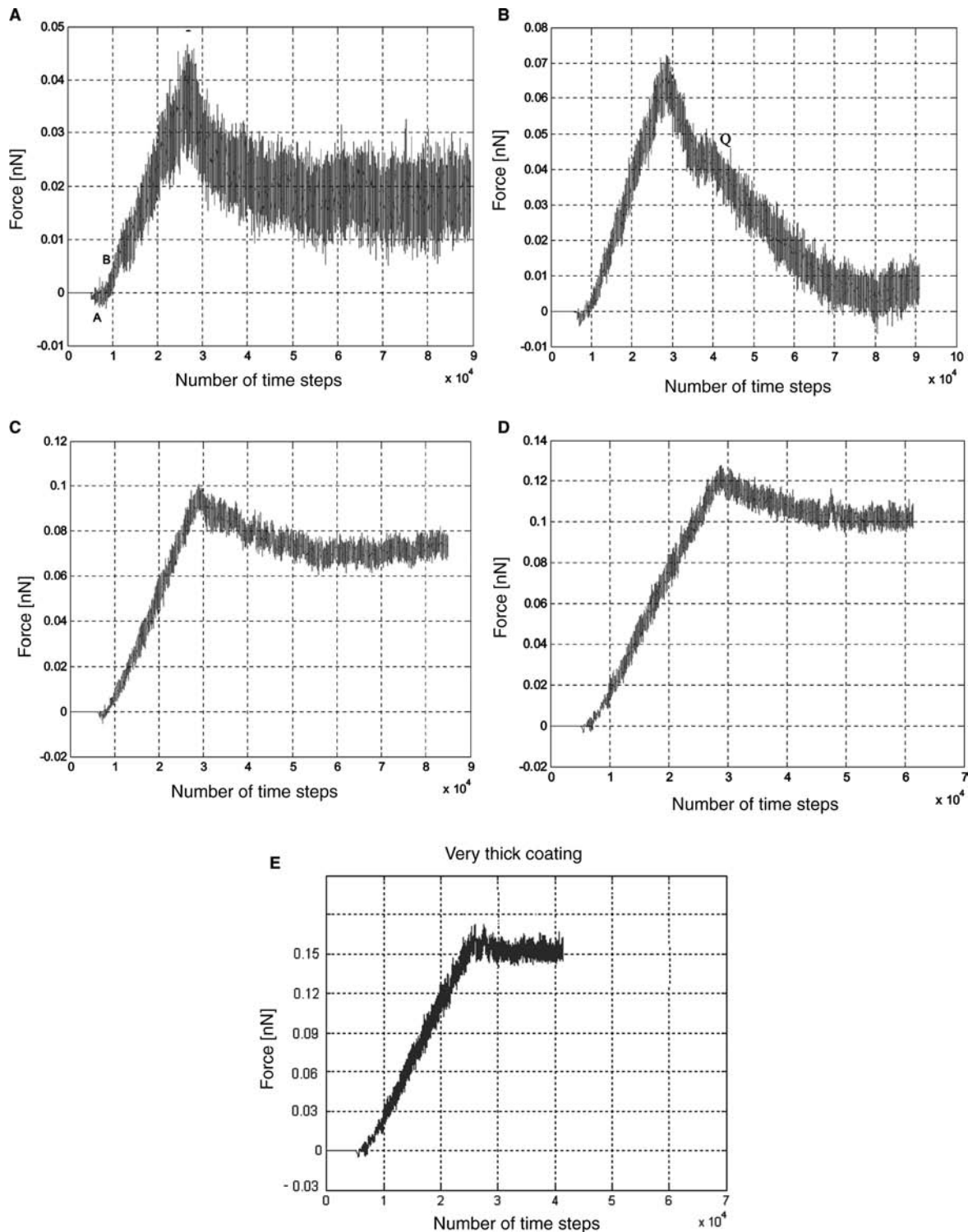


**Fig. 16** Normal force versus number of time steps for coatings of various thicknesses: (A) no coating; (B) very thin coating ( $t^* = 0.17$ ); (C) thin coating ( $t^* = 0.35$ ); (D) moderate thickness coating ( $t^* = 0.7$ ); (E) thick coating ( $t^* = 1.4$ ).

substrate fails before coating. Fig. 13 shows snapshots of the plastic deformation of diamond-coated silicon due to sliding with  $t^* = 0.7$  at various time steps.

It can be seen from the figure that further increases to the coating thickness do not change the sliding force plot. Fig. 15D shows the asperity sliding force versus time steps plot.



The maximum normal force reaches 0.12 nN, which is even higher than the case of thick coating. This is consistent with the observation that the maximum normal force on the asperity increases with coating thickness. This might be explained by the increase in rigidity of the coating with increasing thickness. There is little drop in normal force as no chipping occurs and the normal force stabilizes at 0.1 nN as the asperity slides over the carbon coating. The drop in the normal force can be explained by the plastic deformation experienced by the silicon substrate beneath the coating. Fig. 16D shows the asperity normal force versus time steps plot.

e. Thick coating ( $t^* = 1.4$ )

When  $t^* = 1.4$ , there is no observable plastic deformation in the silicon substrate except for the coating–substrate interface (see Fig. 14). Plastic deformation of the carbon coating occurs in a way similar to that of sliding on a diamond substrate. The sliding force versus time plot is no different from when  $t^* = 0.7$  and  $t^* = 0.35$ , as no chips were formed during sliding.

The normal force stabilizes at the maximum value after the linear increase owing to the increasing depth of cut. There is no drop in the normal force because there is no observable plastic deformation in the substrate (see Fig. 16E).

## CONCLUSIONS

It is very difficult to study the effects of carbon coating on silicon substrate on the nanometer scale experimentally. In this entry, it is shown that molecular dynamics simulation can be used to study the effects of the carbon coating on such scales. The simulation results have shown that thin film buckling does occur on the atomic scale when the compressive stresses in a film are sufficiently high. The buckling mode varies with  $\sigma_y/\sigma_x$ , indicating that the stress ratio is an important factor that influences the nature of the buckling patterns. It is interesting to note that the pattern of atomic scale buckling of a thin film is similar to that observed in microscale experiments.

In the case of indentation on diamond-coated silicon, no observable formation of dislocations is found throughout the indentations or sliding. The occurrence of plastic deformation in carbon coating and silicon substrate is solely due to amorphous phase transformation and plastic flow. As observed, the size of residual amorphous zone formed at the end of indentation decreases with the thickness of carbon coating. The

initiation and location of plastic deformation, however, varies with the thickness of the carbon coating. In the case of sliding, however, even though the occurrence of plastic deformation in carbon coating and silicon substrate is also due to amorphous phase transformation and plastic flow, the size of the residual amorphous zone in the silicon does not necessarily decrease with increasing coating thickness. As discussed in the previous section, a thicker coating restricts the formation of chips and hence inhibits stress relief because of chip formation in the deformation zone, leading to a larger residual amorphous zone.

Hence, using the molecular dynamics simulation, it is possible to observe in real-time, the effects of carbon coating on silicon substrate deformation owing to compression, indentation, and sliding. The results show that the effects of coating on a nanometer scale differ considerably from their larger micrometer scale counterparts.

## ACKNOWLEDGMENTS

The author is grateful to Prof. L. C. Zhang and Dr. Kausala Mylvaganam of the University of Sydney for their contribution and support to this work.

## REFERENCES

1. Pailthorpe, B.A.; Mitchell, D.; Bordes, N.S. Thermal diffusion in molecular dynamics simulations of thin film diamond deposition. *Thin Solid Films* **1998**, *332*, 109.
2. McKenzie, D.R.; Muller, D.; Pailthorpe, B.A. Compressive-stress-induced formation of thin-film tetrahedral amorphous carbon. *Phys. Rev. Lett.* **1991**, *67*, 773.
3. Rosenblum, I.; Adler, J.; Brandon, S.; Hoffman, A. Molecular-dynamics simulation of thermal stress at the (100) diamond/substrate interface: effect of film continuity. *Phys. Rev. B* **2000**, *62*, 2920.
4. Thornton, J.A. High rate thick film growth. *Annu. Rev. Mater. Sci.* **1977**, *7*, 239.
5. Hurtado, J.A.; Kim, K.S. Scale effects in friction of single-asperity contacts. *Proc. R. Soc. London A* **1999**, *455*, 3363–3400.
6. Zhang, L.C.; Johnson, K.L.; Cheong, W.C.D. A molecular dynamics study of scale effects on the friction of single-asperity contacts. *Tribol. Lett.* **2001**, *10*, 1–2.
7. Geim, A.K.; Dubonos, S.V.; Grigorieva, I.V.; Novoselov, K.S.; Zhukov, A.A.; Shapova, S.Yu. Microfabricated adhesive mimicking gecko foot-hair. *Nature Mater.* **2003**, *2*, 461–463.
8. Blossey, R. Self-cleaning surfaces—virtual realities. *Nature Mater.* **2003**, *2*, 301–306.

9. Ohring, M. *Materials Science of Thin Films*; Academic Press: San Diego, 2002.
10. Gioia, G.; Ortiz, M. Delamination of compressed thin films. *Adv. Appl. Mech.* **1997**, *33*, 120.
11. Freller, H.; Hempel, A.; Lilge, J.; Lorenz, H.P. Influence of intermediate layers and base materials on adhesion of amorphous carbon and metal-carbon coatings. *Diamond Relat. Mater.* **1992**, *1*, 563.
12. Zehnder, T.; Balmer, J.; Luthy, W.; Weber, H.P. Determination of limits in deposition of adhering a-C films on silicon produced by pulsed laser deposition. *Thin Solid Films* **1995**, *263*, 198.
13. Som, T.; Bhargava, S.; Malhotra, M.; Bist, H.D.; Kulkarni, V.N.; Kumar, S. MeV He<sup>+</sup> ion induced delamination of diamond films. *Appl. Phys. Lett.* **1998**, *72*, 3014.
14. Peng, X.L.; Clyne, T.W. Mechanical stability of DLC films on metallic substrates: Part I—Film structure and residual stress levels. *Thin Solid Films* **1998**, *312*, 207.
15. Iyer, S.B.; Harshavardhan, K.S.; Kumar, V. Structural studies of reactively sputtered carbon nitride thin films. *Thin Solid Films* **1995**, *256*, 94.
16. Ager, J.W., III; Drory, M.D. Quantitative measurement of residual biaxial stress by Raman spectroscopy in diamond grown on a Ti alloy by chemical vapor deposition. *Phys. Rev. B* **1993**, *48*, 2601.
17. Gille, G.; Rau, B. Buckling instability and adhesion of carbon layers. *Thin Solid Films* **1984**, *120*, 109.
18. Nir, D. Stress relief forms of diamond-like carbon thin films under internal compressive stress. *Thin Solid Films* **1984**, *112*, 41.
19. Audoly, B. Stability of straight delamination blisters. *Phys. Rev. Lett.* **1999**, *83*, 4124.
20. Crosby, K.M.; Bradley, R.M. Pattern formation during delamination and buckling of thin films. *Phys. Rev. E* **1999**, *59*, 2542.
21. Peyla, P. Undulated blistering during thin film delamination. *Phys. Rev. E* **2000**, *62*, 1501.
22. Tersoff, J. Modeling solid-state chemistry: interatomic potentials for multicomponent systems. *Phys. Rev. B* **1989**, *39*, 5566.
23. Tersoff, J. New empirical model for the structural properties of silicon. *Phys. Rev. Lett.* **1986**, *56*, 632.
24. Belak, J.; Boercker, D.B.; Stowers, I.F. Simulation of nanometer-scale deformation of metallic and ceramic surfaces. *Mater. Res. Soc. Bull.* **1993**, *18*, 55.
25. Inamura, T.; Shimada, S.; Takezawa, N.; Ikawa, N. Crack initiation in machining monocrystalline silicon. *Ann. CIRP* **1999**, *48*, 81.
26. Shimada, S.; Ikawa, N.; Inamura, T.; Ohmori, H.; Sata, T. Brittle-ductile transition phenomena in micro-indentation and micromachining. *Ann. CIRP* **1995**, *44*, 523.
27. Komanduri, R.; Chandrasekaran, N.; Raff, L.M. Molecular dynamics simulation of nanometric cutting of silicon. *Philos. Mag. B* **2001**, *81*, 1989.
28. Zhang, L.C.; Tanaka, H. On the mechanics and physics in the nano-indentation of silicon mono-crystals. *JSME Int. J. Ser. A* **1999**, *42*, 546.
29. Cheong, W.C.D.; Zhang, L.C. Molecular dynamics simulation of phase transformation in silicon mono-crystals due to nano-indentation. *Nanotechnology* **2000**, *11*, 1.
30. Zhang, L.C.; Tanaka, H. A molecular dynamics study of scale effects on the friction of single-asperity contacts. *Tribol. Int.* **1998**, *31*, 425.
31. Komanduri, R.; Chandrasekaran, N.; Raff, L.M. MD simulation of nanometric cutting of single crystal aluminum—effect of crystal orientation and direction of cutting. *Wear* **2000**, *242*, 60.
32. Komanduri, R.; Chandrasekaran, N.; Raff, L.M. MD simulation of indentation and scratching of single crystal aluminium. *Wear* **2000**, *240*, 113.
33. Michler, J.; Blank, E. Analysis of coating fracture and substrate plasticity induced by spherical indentors: diamond and diamond-like carbon layers on steel substrates. *Thin Solid Films* **2001**, *381*, 119.
34. Zhang, L.C.; Tanaka, H. On the mechanics and physics in the nano-indentation of silicon monocrystals. *JSME Int. J. Ser. A: Solid Mechanics Material Eng.* **1999**, *14*, 546.
35. Zhang, L.C.; Tanaka, H. Towards a deeper understanding of wear and friction on the atomic scale—a molecular dynamics analysis. *Wear* **1997**, *211*, 44.
36. Cheong, W.C.D.; Zhang, L.C. A stress criterion for the  $\beta$ -Sn transformation in silicon under indentation and uniaxial compression. *Key Eng. Mater.* **2003**, *603*, 233.
37. Gogotsi, Y.G.; Kailer, A.; Nickel, K.G. Materials: transformation of diamond to graphite. *Nature* **1999**, *401*, 663.
38. Lide, D.R. *CRC Handbook of Chemistry and Physics*; Chemical Rubber Company Press: Boca Raton, FL, 2000–2001.

# Nanolithography: Length Scale Limitations

Takashi Ito

Akiruno Technology Center, Fujitsu Ltd., Tokyo, Japan

## INTRODUCTION

Lithography is one of the fundamental technologies by which nanoscale patterns required for the fabrication and integration of nanodevices are generated. Lithographic requirements are becoming increasingly severe. In the semiconductor industry, the past three decades have seen the critical length-scales of component devices decrease by several orders of magnitude, from 15  $\mu\text{m}$  in the case of the first integrated circuit, to less than 130 nm routinely obtained today. The phenomenal rate of decrease in size seems to reach the limitation of conventional optical lithography. The exposure wavelength, photoresist performance, and equipment determine the lithography limitation. The size of the constituent atoms imposes a fundamental limit on the minimum length scale that can be ultimately attained. This entry first provides an overview of the fundamentals of optical lithography. It is shown how minimum attainable device dimensions are intimately related to the wavelength of light used. Then, several techniques under investigation for further enhancing the resolution of this workhorse of the microelectronics industry are described. As the options available to industry are not all “optical,” the discussions cover the various non-optical lithographic techniques currently being explored.

## TECHNOLOGY OVERVIEW OF LITHOGRAPHY

Fig. 1 illustrates how the lithographic options vary as the critical device dimension decreases, and provides estimates of the timescales on which decisions may need to be made regarding which options to adopt.<sup>[1]</sup> Optical lithography technology has been traditionally used by reducing wavelengths of light sources from mercury lamps to excimer lasers such as KrF and ArF excimer lasers, and probably F<sub>2</sub> and Ar<sub>2</sub> lasers in the future. Phase shift masks (PSM) and immersion configuration can extend the resolution limit for each optical lithography. Extreme ultraviolet (EUV) of wavelengths ranging from 11 to 14 nm is used as extension of the optical method. Non-optical lithography with proximity X-ray

(PXL), electron beam (EBL), and ion beam (IPL) have a potential for finer patterns (as opposed to those produced via optical methods) because of their shorter wavelengths. Electron-beam projection lithography (EPL), which uses mask projection technique, projects to be most promising. However, electron beam direct writing (EBDW) has a drawback on its throughput. Nanoimprint is a simple technique just like paper printing. A shift by the microelectronics industry to any non-optical lithographic technique will require the introduction of a new infrastructure of tools, materials, and processing technologies, resulting in huge research and development costs.

## PROJECTION OPTICAL LITHOGRAPHY

Key elements of a practical lithographic system are essentially the same for all technologies—optical and non-optical. As shown in Fig. 2, they include the following: 1) A set of “masks” containing the patterns of components to be fabricated in and/or on the substrate, the tools for making the masks, and the metrology for ensuring precise dimensions and pattern overlay. 2) An energy source (e.g., a light source) for transferring the pattern from a mask to the substrate. 3) A medium—known as a “photoresist” or “resist”—for recording the pattern on the substrate following exposure to the source, and which allows subsequent processing of material in and/or on the underlying substrate. 4) Procedures for reliable detection of pattern defects, which clearly becomes more challenging as the critical dimensions decrease. The lithographic process—especially projection optical lithography—is closely related to the developing process in print photography, where the photographic negative plays the role of the mask, and the photographic emulsion on the print is the resist.

## Resolution Limits

The resolution limit in conventional projection optical lithography is largely determined by the well-known Rayleigh’s equation. The resolution (minimum resolvable feature)  $R$  and the corresponding depth of focus

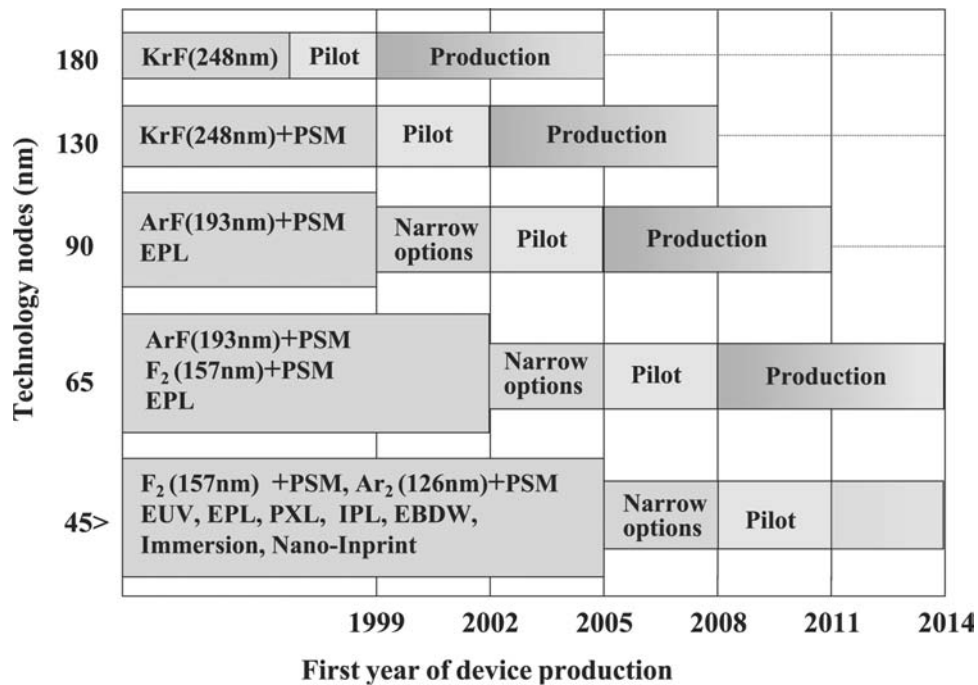


Fig. 1 Technology options of lithography.

(DOF) are given by the following:<sup>[2]</sup>

$$R = k_1 \lambda / NA$$

$$DOF = k_2 \lambda / NA^2$$

Here  $\lambda$  is the exposure wavelength, NA is the numerical aperture of the optical system, and  $k_1$  and  $k_2$  are

constants that depend on the specific resist material, process technology, and image-formation technique used. Fig. 3 shows the evolution of projection optical lithography. It compares the required minimum feature size and the wavelength of the exposure light. At the beginning of the introduction of the projection system, the required minimum feature size was relatively large compared to

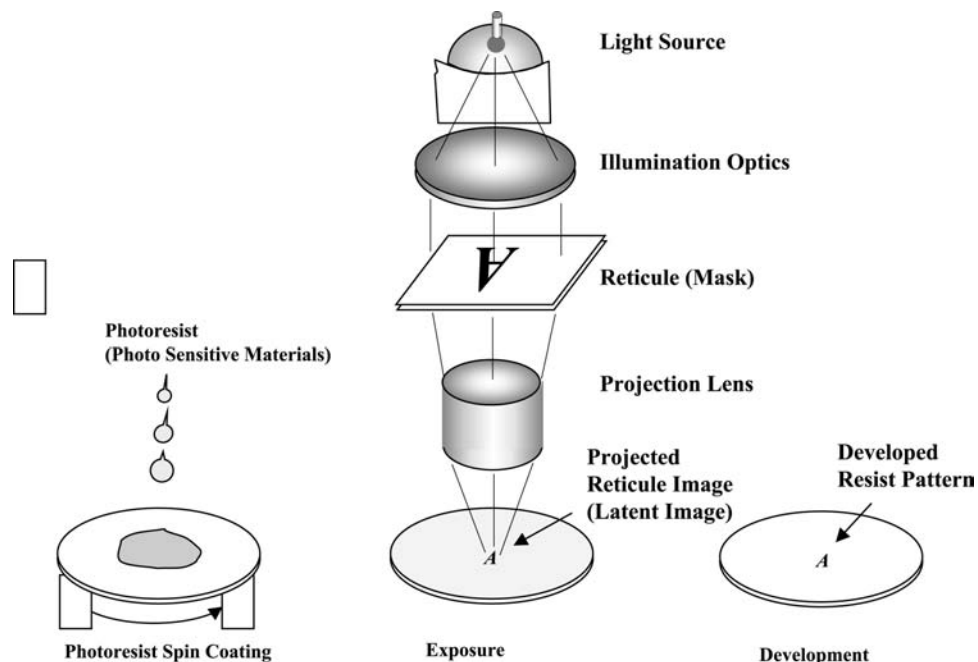
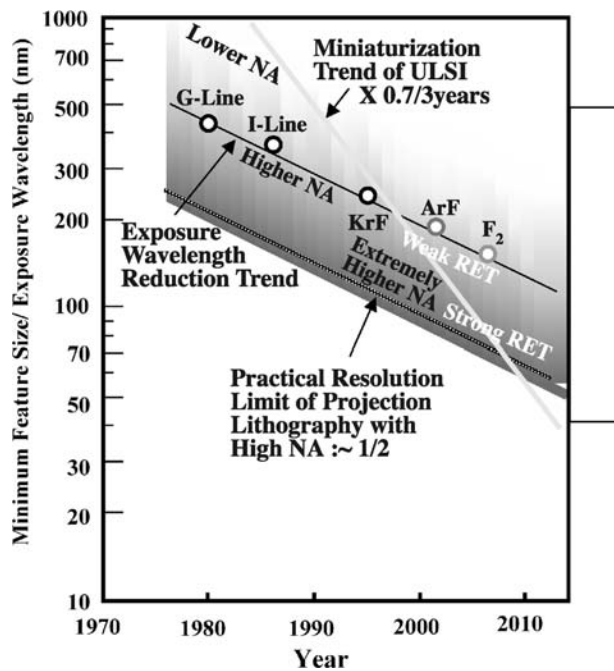


Fig. 2 Principle of lithography.



**Fig. 3** Trend minimum feature size and exposure wavelength of optical lithography. Practical resolution limit is reduced to approximately half of wavelength with extremely higher NA and resolution enhancement techniques. Miniaturization exceeds the wavelength reduction trend for ULSI manufacturing.

the wavelength of the exposure light. Then low-NA lens system was used. However, as the miniaturization requirement of the semiconductor devices is faster than the reduction rate of the wavelength of exposure light, higher resolution was required. Therefore, to obtain higher resolutions, shorter-wavelength light and lens systems with larger numerical apertures are required. In general, the minimum feature size that can be obtained is almost the same as (or slightly smaller than) the wavelength of light used for the exposure, for which one needs a relatively large numerical aperture (typically  $\geq 0.5$ ). In such high-NA lens systems, the depth of focus becomes very small, and so the exposure process becomes sensitive to slight variations in the thickness and absolute position of the resist layer.<sup>[3]</sup> The smaller the depth of focus, the more rapidly a focused beam diverges on moving away from the focal point. With the recent introduction of a “chemical mechanical polishing” technology, the topographic variations of substrate surfaces have been reduced, making it possible to use extremely large NA systems; however, the margin for error becomes extremely small under such high-NA exposure conditions.

## Resolution Enhancement

To improve the resolution of an optical lithography system without introducing other impractical

constraints (on, e.g., wafer smoothness), several resolution-enhancement strategies were proposed.<sup>[4–6]</sup> Fig. 4 shows a schematic view of a typical projection optical-exposure system. Such a system consists of several subsystems, and resolution-enhancement ideas can be applied at various points. These may take the form of modified illumination at the light source, phase shifting of the wave front in the mask plane, and/or filtering with an aperture (pupil) at the projection lens. Some basic ideas of resolution enhancement are illustrated in Fig. 5, which compares image formation in: a) the conventional setup with b) phase shifting and c) modified illumination.

Consider the case when the image on the mask is a simple grating. In the conventional system (a), several diffracted light rays are generated by the grating. Zero-th order light proceeds straight through the system, and several rays of higher order are generated with diffraction angles of  $\theta$  (first order),  $2\theta$  (second order),  $3\theta$  (third order) and so on, with  $\theta \sim \lambda/a$  for small  $\theta$  (where  $a$  is the grating periodicity). Near the resolution limit, only the zero-th order and first-order rays pass through the lens pupil. Now consider case (b), where the phase of the light passing through the grating mask is modified to have a periodicity twice that of the grating itself. (Phase shifting also requires a higher degree of coherency in the source light compared to the conventional case.) The transmitted wave front is in turn modified, such that the zero-th order light is canceled out and the diffraction angle of the first-order rays halved to  $0.5\theta$ . As a result, the spatial frequency of the patterns that can be imaged is doubled (or, put in another way, the resolvable grating periodicity is halved). Although both the opaque pattern and the phase modifications on a real mask will be considerably more complex than a simple grating, this example nevertheless serves to illustrate the substantial improvement in resolution that can be achieved by this approach. Fig. 6 shows an example of resist patterns formed by using KrF (248 nm) light and a phase shift mask: structures having half the wavelength of the exposure light are clearly visible.

Next, we consider oblique (or off-axis) illumination, as shown in (c). Zero-th order light no longer passes through the center of the pupil, but at an angle to the vertical. The first-order rays again emerge at angles of  $\pm\theta$  with respect to the zero-th order ray. And at the resolution limit, one of these passes through the side of the lens pupil opposite to that of the zero-th order ray, while the other diffracted ray is blocked. Therefore the result is geometrically equivalent to the phase-shifted case (b), and again leads to a doubling of the spatial frequency of the images that can be resolved. At present, the most advanced mass-produced LSI circuits have a critical dimension of 90 nm. This is achieved by using partially coherent light from ArF excimer laser

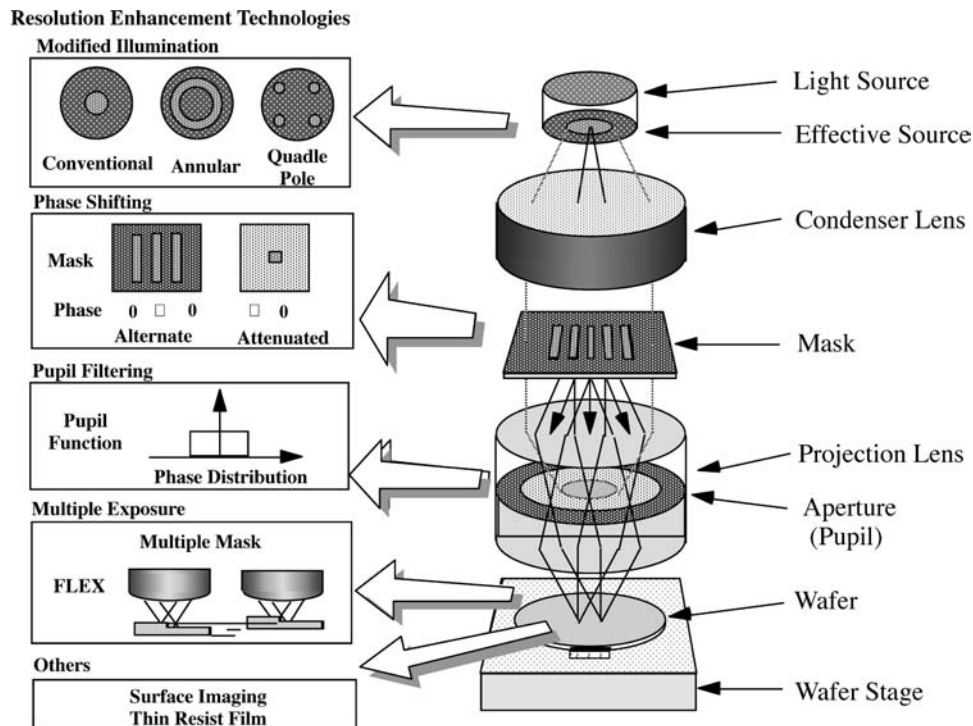


Fig. 4 Schematic view of exposure optical system and various resolution enhancement technologies for each stage of the system.

with a wavelength of 193 nm, in combination with some resolution-enhancement techniques such as off-axis illumination, phase shift mask, and optical proximity correction, as well as advanced resist systems. To further reduce the critical dimension, wavelength reduction is being actively pursued using F<sub>2</sub> and Ar<sub>2</sub> excimer lasers (wavelengths of 157 and 126 nm, respectively). The combination of shorter-wavelength light and resolution-enhancement techniques may ensure optical lithography's position as the most productive lithographic technology for nanofabrication of length-scale of even less than 50 nm.

### ELECTRON BEAM LITHOGRAPHY

Electron beam lithography—in which a beam of electrons, rather than photons, is used as the exposure source—has extremely high-resolution capabilities combined with a large depth of focus. To date, it has been mainly used in the production of masks and reticles for optical lithography. But it has also been used in the fabrication of very fine-scale devices for fundamental and device-verification studies, and also in the small-scale production of the specialized very high frequency devices. However, in the context of mass-produced

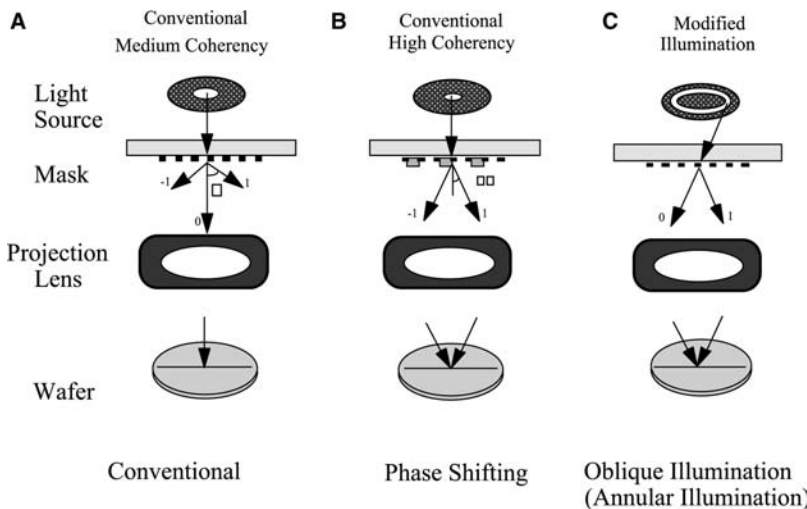
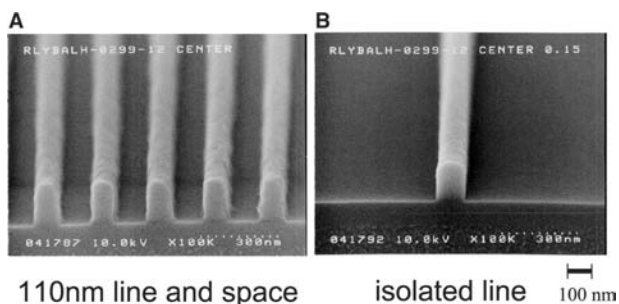


Fig. 5 Grating pattern image formation.





**Fig. 6** An example of resolution enhancement technology and the effect of phase shifting technology.

integration circuitry, the greatest problem of electron beam lithography is the low throughput capability of the system. While using a finely focused electron beam makes it possible to delineate extraordinarily fine patterns, writing of chip-scale patterns with a single electron beam is a slow process. According to the pattern complexity, the exposure time for the mask writing also becomes very long. Accordingly, there has been considerable interest in developing techniques to expand the throughput of electron beam lithography, and these have generally involved finding ways to enlarge and make the electron beam parallel. Fig. 7 shows various electron-beam writing procedures.

The electron projection lithography (EPL), such as cell projection or chip projection, is one such approach that makes use of parallel exposure. Specifically, in a conventional variable-shaped beam system, the maximum size of the electron beam is sufficient to encompass a mask containing the pattern of several memory cells, which have a repetitive structure. So if such a mask is used in place of the second aperture of the shaped beam system, the pattern can be projected on the substrate in a single exposure. Fig. 8

shows a resist pattern produced by this approach: the periodically arrayed patterns at the top are produced by exposure using a cell-projection aperture, whereas the random wiring patterns at the bottom were written by using a variable-shape aperture. But even with this system, throughput remains a critical issue.

A more promising approach to improve throughput is to use a projection optical setup, geometrically equivalent to that used in optical lithography: an image of the desired pattern is projected from a mask. Most notable of the recent attempts to utilize projection are scattering angular limited projection electron beam lithography (SCALPEL), developed by Bell Laboratories; projection reduction exposure with variable axis immersion lenses (PREVAIL), developed by IBM; and low-energy electron beam proximity projection lithography (LEEPL) (see Refs.<sup>[7]</sup> and<sup>[8]</sup>). These approaches will be used in conjunction with optical lithography.

**PROXIMITY X-RAY LITHOGRAPHY**

Proximity X-ray lithography is essentially a form of “shadow printing”—a mask is held in close proximity to the substrate surface, and the image is simply produced on exposure by the shadow of the mask on the surface. Proximity techniques were used in the early days of optical lithography, but have long since been superseded by projection techniques: the former are more susceptible to resolution-limiting diffraction effects. Resolution is less of an issue with proximity printing using X-rays, as the wavelengths used are so much smaller.

The exposure system of the PXL is shown in Fig. 9. A synchrotron is used as the source of X-ray radiation; recently, sources of synchrotron radiation have been developed that can store currents as high as 500 mA

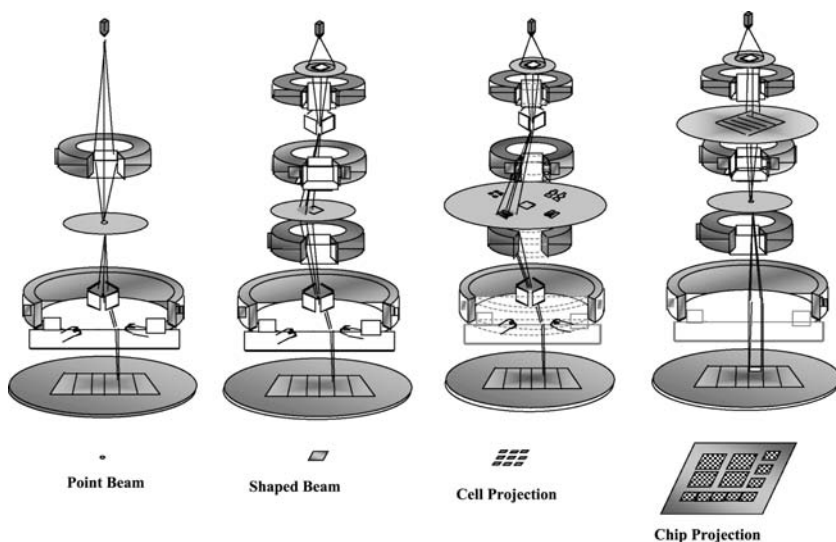


**Fig. 7** Various electron beam writing systems; simple point electron beam, shaped electron beam, patterned cell projection, and chip pattern projection.

Nanodiamonds – Nanolithography

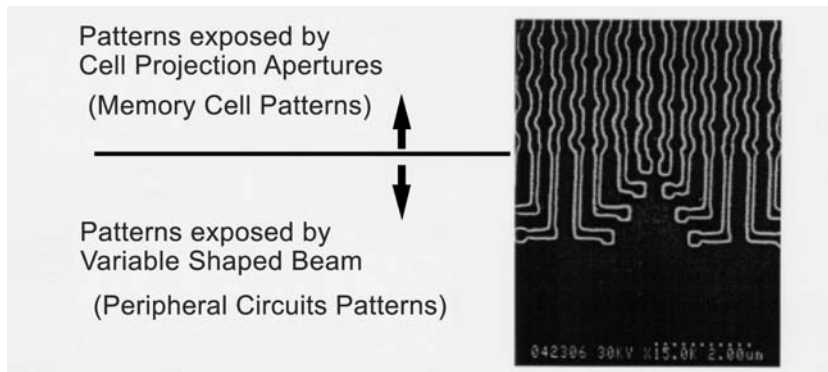


**Fig. 8** Resist patterns delineated by cell projection system.

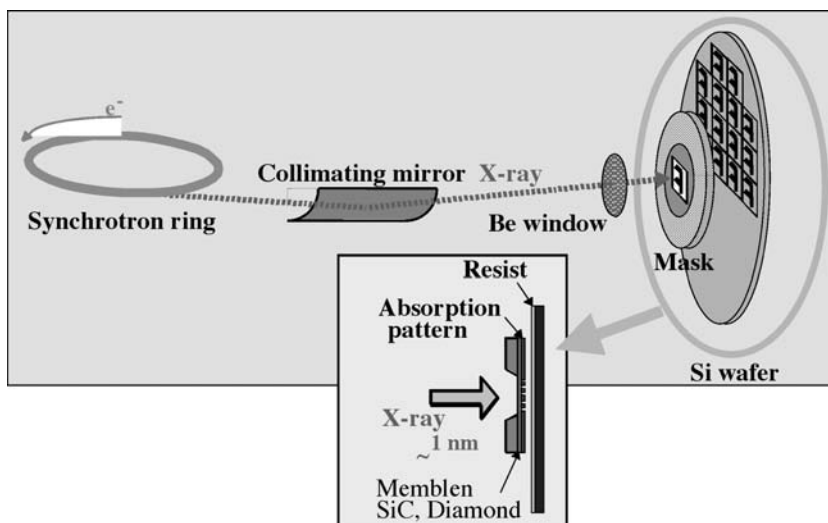
with electron folding lifetimes longer than 10 hr, which should be stable enough for practical usage. The X-ray is first collimated by using a silicon carbide mirror, before passing through a transparent window of beryllium into a chamber containing the mask and wafer. Alignment of the sample uses a vertical X–Y stage, in contrast to the horizontal stages used in most other lithographic techniques. The X-ray used has a wavelength of about 1 nm. The mask is prepared on a membrane of silicon carbide or diamond, and a layer of Ta (patterned by direct-write electron beam lithography) serves to absorb the X-rays and so generate the shadow on the semiconductor wafer. The final image exposed by PXL is limited by the electron-beam-made mask.

Fig. 10 shows a series of typical patterns produced in the resist layer following X-ray exposure and subsequent development.<sup>[9]</sup> The patterns shown were formed on stepped substrates, and exhibited critical dimensions as small as 150 nm with a distribution of less than 10 nm ( $3\sigma$ ). Fig. 11 shows poly silicon patterns transferred from resist patterns with PXL. Dry etching technique was inevitably used to transfer the resist patterns to poly silicon ones.

## EXTREME ULTRAVIOLET LITHOGRAPHY

Extreme ultraviolet (EUVL) lithography is a promising candidate for achieving critical dimensions of 50 nm and below.<sup>[10]</sup> This approach utilizes the same principle of conventional optical projection lithography and also obeys Rayleigh's equation (shown earlier). But now, the exposure wavelength is in the range 11–13 nm, which introduces its own problems. Fig. 12 shows the concept of EUV optics. First, as the absorption of light in this short-wavelength regime is very strong, lens-based refractive optics cannot be used in this lithographic system: an all-reflective optic system must therefore be employed. A second difficulty relates to the mirrors themselves. A conventional mirror surface cannot be used at these wavelengths, so one must resort to multilayer structures that rely on interference effects to achieve reflectivity. And even then, the resulting reflectivities are rather low, typically 60–70% at 13 nm. Accordingly, the number of mirror surfaces in the system needs to be kept as low as possible—6 or fewer—to avoid significant reductions in the light intensity level.

In the case of multilayer mirror optics, the requirement of fewer optical elements means that aspherical



**Fig. 9** System of proximity X-ray lithography. X-ray is generated from a synchrotron ring, reflects on a collimating mirror, and irradiates a wafer through a mask. The mask is made of SiC membrane or diamond and absorption pattern.

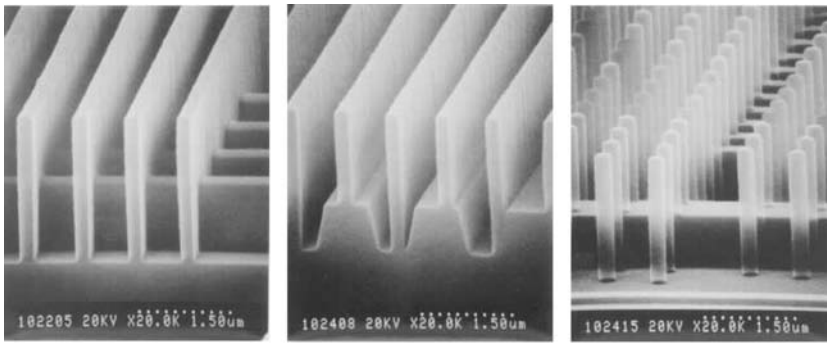


Fig. 10 Resist patterns on different substrates. Source: NTT-AT.

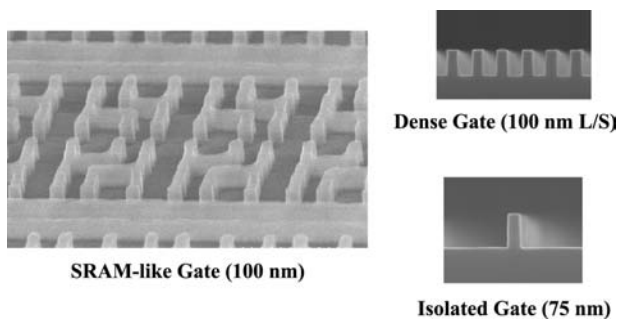


Fig. 11 Examples of polysilicon patterns transferred with X-ray lithography. SRAM-like gate, dense gate, and isolated gate patterns are shown.

mirrors must be introduced to achieve such capabilities. Such aspherical mirrors need to be extremely precise, with figure errors and surface roughness less than 0.1–0.2 nm. As such, an extremely high precision metrology system needs to be developed if this approach to lithography is to become viable.

The source of EUV light is another problematic issue.<sup>[11]</sup> At present, the best candidate is a laser-produced plasma of xenon gas. But the energy

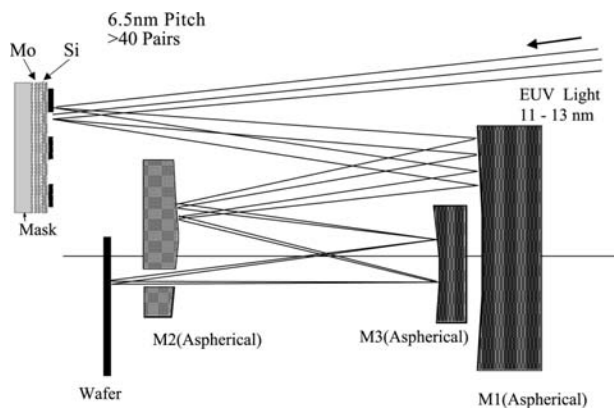


Fig. 12 Concept of EUVL optics.

conversion ratio of laser light (from a YAG laser) to EUV light is so small that lasers of enormous power are required to achieve practical EUV exposure intensities. Therefore, different strategies, such as the use of electrical discharge lamps, are being explored for providing practical light sources for EUV lithography.<sup>[12]</sup> Fig. 13 shows an example of resist line-space patterns of 40 nm delineated by an experimental EUV exposure system. The result features its promising lithographic candidate for nanofabrication.

### EMERGING TECHNOLOGIES

Several other approaches are proposed for delineating patterns below 100 nm. The configuration of the ion beam projection lithography (IPL) is schematically shown in Fig. 14. The ion beam can be used to avoid deep penetration of the incident ions because of their

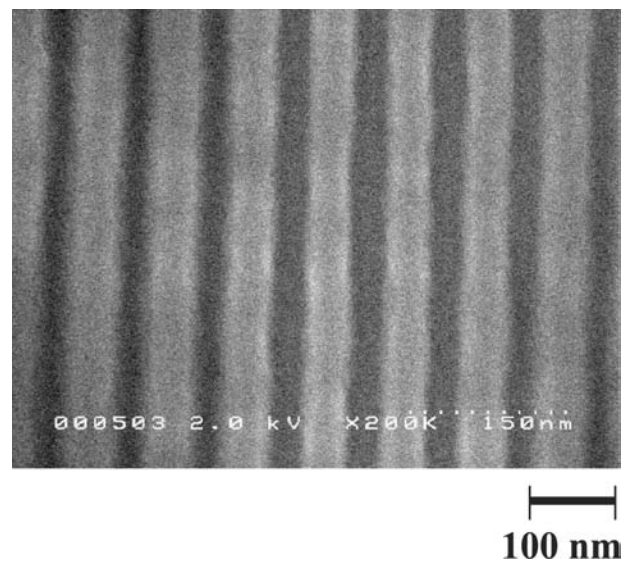


Fig. 13 40-nm line-and-space resist patterns delineated by EUV exposure system.

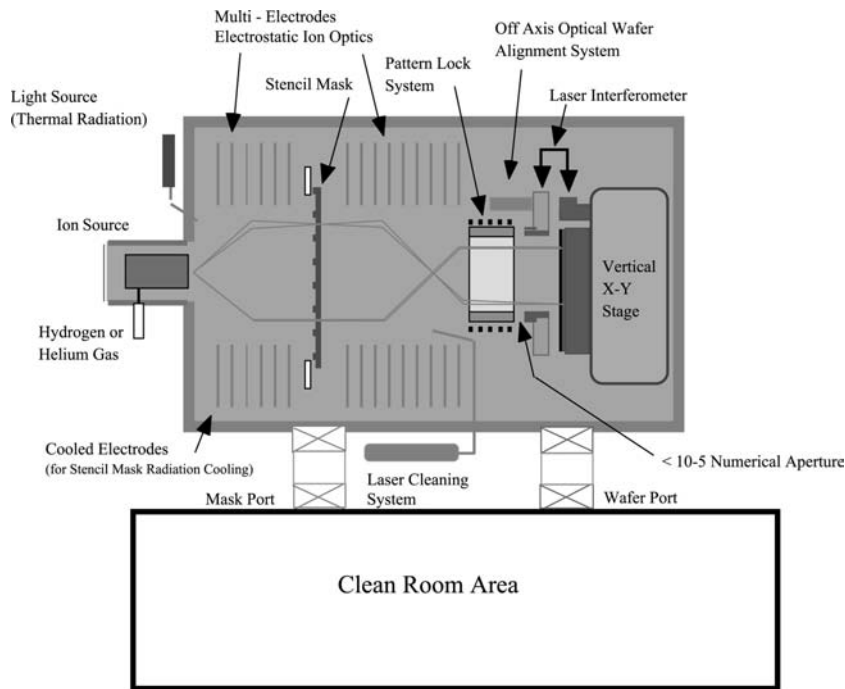


Fig. 14 Schematic top view of ion projection lithography system.

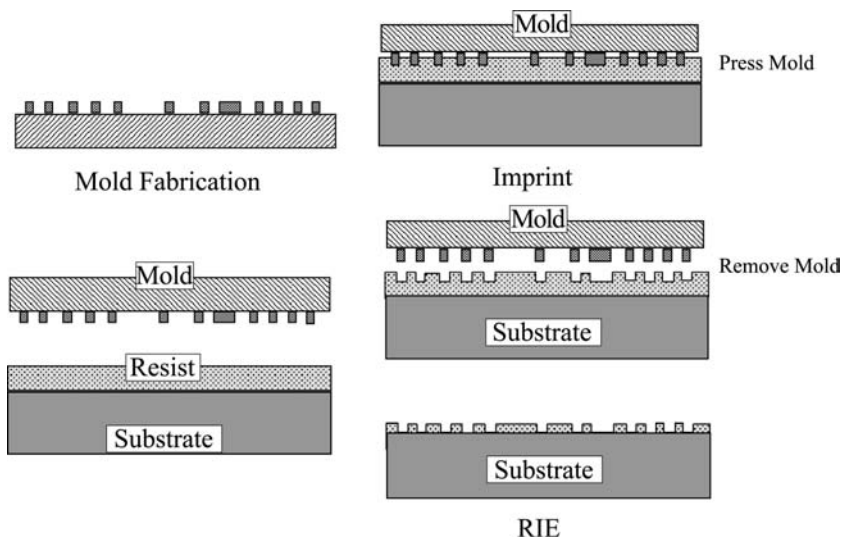


Fig. 15 Process of nanoimprint lithography.

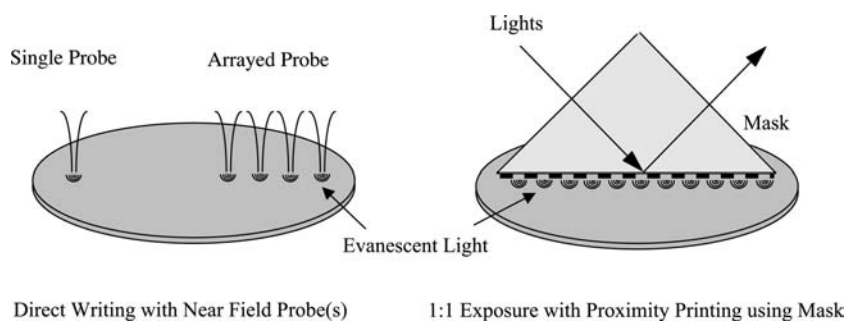


Fig. 16 Concept of near field optical lithography using evanescent light. Direct writing on the left side and proximity printing on the right side.

Nanodiamonds – Nanolithography

weight compared to electrons. The principle of the nanoimprint lithography is schematically shown in Fig. 15. It is just a printing of patterns. The near-field optical lithography recently appearing is shown in Fig. 16. The technique uses evanescent light. Direct writing with a near-field probe and exposure with proximity printing with a mask are realized to limited applications. Limitations of those technologies to fine patterns are currently under investigation. IPL is one of the candidates of the next-generation lithography for production. Whereas the latter two approaches are good techniques to delineate nanostructures for the investigation of nanometer devices.

## CONCLUSION

Optical lithography is a fundamental process in the manufacture of highly integrated microelectronic circuitry. But with the relentless commercial drive for ever smaller, faster, and cheaper components, the existing technology are rapidly being pushed to their limits. However, optical lithography has far from reached the end of the road, and will continue to be used for some years, adopting light sources of smaller wavelengths (such as F<sub>2</sub> or Ar<sub>2</sub> excimer lasers) and optical techniques for further enhancing resolution. Depending on requirements for images and costs, possible next-generation lithographic technologies using non-optical sources are being actively explored. Whether the future of lithography lies with X-rays, electron beams or extreme ultraviolet light is far from clear at present. Critical issues remain to be solved with all of these alternative approaches. It is the time of length-scale limitation when those developments are abandoned. The requirement of nanoscale patterning will make those emerging technologies practical ones.

## ACKNOWLEDGMENT

The author would like to thank Dr. S. Okazaki, Association of Super-Advanced Electronics Technologies for discussions and supplying data.

## REFERENCES

1. Inter. SEMATECH; Ed. *International Technology Roadmap for Semiconductors*, 1999 Ed.; Semiconductor Industry Association (SIA): New York, USA.
2. Klein, M.V.; Furtak, T.E. *OPTICS*; John Wiley & Sons: New York, USA, 1986; 398 pp.
3. Okazaki, S. Resolution limits of optical lithography. *J. Vac. Sci. Technol.* **1991**, *B9* (6), 2829–2833.
4. Levenson, M.D. et al. Improving resolution in photolithography with a phase-shifting mask. *IEEE Trans.* **1982**, *ED-29*, 10, 1828–1836.
5. Terasawa, T. et al. 0.3 μm optical lithography using a phase shifting mask. *Proc. SPIE* **1989**, *1088*, 25–33.
6. Matsuo, K. et al. High resolution optical lithography system using oblique incidence illumination. *Technol. Dig. IEDM '91* **1991**, 970–972.
7. Berger, S.D. et al. Projection electron beam lithography: a new approach. *J. Vac. Sci. Technol.* **1991**, *B9* (6), 2996–2999.
8. Utsumi, T. Low-energy E-beam proximity lithography (LEEPL). *Jpn. J. Appl. Phys.* **1999**, *38* (12B), 7046–7051.
9. Deguchi, K. et al. Patterning characteristics of a chemically-amplified negative resist in synchrotron radiation lithography. *Jpn. J. Appl. Phys.* **1992**, *31*, 2954–2958.
10. Kinoshita, H. et al. Soft x-ray reduction lithography using multilayer mirrors. *J. Vac. Sci. Technol.* **1989**, *B7* (6), 1648–1651.
11. Kubiak, G.D. et al. High power extreme-ultraviolet source based on gas jets. *Proc. SPIE* **1998**, *3331*, 81–89.
12. Silfvast, W.T. et al. High power plasma discharge source at 13.5 nm and 11.4 nm for EUV lithography. *Proc. SPIE* **1999**, *3676*, 272.



# Nanomaterials: Advances in Technology and Industry

Ganesh Skandan

Amit Singhal

NEI Corporation, Piscataway, New Jersey, U.S.A.

## INTRODUCTION

The emerging field of Nanotechnology, including nanomaterials, nanoscale devices, and nanobiotechnology, has been purported to impact every aspect of our life in the decades to come. The race to capitalize on Nanotechnology, “the next big thing,” began in the wake of the abating Internet mania in the year 2000, although basic and applied research on various aspects of this field has been intensely pursued since the early 1990s. For a comprehensive review of scientific advances in this field during the 1990s, the reader is referred to the World Technology Evaluation Center Report.<sup>[1]</sup> We should all remember that studies in catalysis and small metal particles began more than a century ago and represents one of the most significant applications of nanomaterials to date. In many instances, Nanotechnology has been referred to as a “disruptive technology,” the elegant and pithy phrase coined by Harvard professor, Clayton Christensen.<sup>[2]</sup> With the rapid influx of venture capital into the up-and-coming Nanotechnology industry (although it is a far cry from the investment activity that was seen in the mid-1990s with the then emerging internet industry), start-ups are realizing the need for sustainable competitive advantage in what is now becoming a crowded space. Given the scientific evidence so far, the potential for Nanotechnology to beneficially impact various aspects of our life and society exists, but attempting to predict them all at this stage is futile.

To put this field in perspective to the uninitiated, it has often been mentioned that Nanotechnology today is in the same state computers were in the 1960s.<sup>[1]</sup> Perhaps, a more apt comparison should be to the Industrial Revolution that began in the late eighteenth century. The Industrial Revolution enabled products that were already in use to be made cheaper, faster, and of uniform and of predictable quality.<sup>[3,4]</sup> The Nanotechnology Revolution underway has the potential to impact the performance of existing products, but not so much in terms of cost. At the same time, Nanotechnology has the potential to make possible new products that would otherwise not be possible. All of this has spawned the growth of Nanotechnology

as an industrial sector, while in reality it is an aggregate of several different industries brought together in ways never seen before. Accordingly, it is helpful to compare this new industrial sector to the several industries that came into existence during and after the Industrial Revolution: railroad, automobile, commercial aviation, and most recently, internet. Several hundreds of companies came into existence in the initial stages of each of these industries: there was a time when there was a large number of companies with *motor works* being the common suffix for a majority of them.<sup>[4]</sup> This is much the same today with the word *nano* being the prefix in the name of the company. Based on information garnered by market research entities such as CMP Cientifica,<sup>[5]</sup> Business Communication Company,<sup>[6]</sup> and Nanobusiness Alliance,<sup>[7]</sup> the number of companies worldwide that are active in nanotechnology at the present time can be estimated to be in excess of 400. As it has happened in all of these industries, the initial flurry of activity fades in a few years as the companies come to grips with the realities of the market forces. The start-ups burn through the invested capital, and either close shop or morph into a company with a different objective. The stage had been set by the year 2001 for this story line to be repeated in the Nanotechnology industry, except that the financial climate has been dismal since that time, with investment capital becoming a scarce commodity.

Just as it is said that beauty lies in the eyes of the beholder, an objective definition for Nanotechnology depends on the aspect of the field that the person is involved with. To an oncologist working with nanotechnology, it could mean targeted drug delivery to cure certain specific types of cancer, while to a scientist involved with computing, Nanotechnology could refer to molecular switches. The purpose of this entry is to look at technological and commercial advances made to date in the area of Nanomaterials either enabling new products or improving existing products. The focus is on products having the potential to beneficially impact present markets, as opposed to a number of markets that may emerge in the future. Moreover, special emphasis is given on applications where the presence of nanoscale features adds certain



functionality, instead of simply providing a high-surface-area template.

## OVERVIEW

In a broad sense, Nanomaterials include nanoscale particles (metal/ceramic/metalloid/organic particles or composites thereof, nanotubes, and buckyballs), nanoparticles dispersed (or suspended) in a liquid, or nanoparticles dispersed in a polymeric material, either as a coating or a bulk material. A distinction between functional and non-functional nanoscale features needs to be drawn: by nonfunctional nanoscale features, we mean that the nanoparticle simply acts as a high surface area support for a second-phase material, and does not possess any intrinsic functionality. A good example is a ceramic catalyst support, such as a honeycomb structure, in which catalytically active metallic nanoparticles are embedded in the high-surface-area ceramic material. As alluded to earlier, such high-surface-area materials have been in existence for decades. On the other hand, functional nanoparticles are those where the nanoparticles themselves perform a certain function, as a result of their particular crystalline structure, or the lack thereof; e.g., particles having gas sensing capabilities because of their ability to undergo redox reactions.

A few nanomaterials companies made rapid progress (measured in terms of the ability to raise capital and build substantial manufacturing capability) in the mid- to late 1990s, with the anticipation that they will be ready if and when the market emerges. Most of them have found out that either the anticipated markets never materialized, or the products they envisioned did not meet the cost requirement of the targeted industry. A case in point was a company that was initially funded by a U.S. government small business innovative research (SBIR) initiative. The company's manufacturing technology was unique, and the nanopowder product had a sufficient number of distinguishing features from the state-of-the-art, especially with respect to performance. The company attracted investment (initially backed by venture capital and later by large corporations in the same market sector), and a full-scale production facility was commissioned within 5 years of obtaining seed capital. However, the well-funded company failed to make any impact on the market because the market was driven by cost, and not by performance. The company's product was superior and more expensive, but the market had no need for a better product, as the available product at that time more than met what the majority of customers desired. The metrics of comparison had shifted from performance to cost. It was too late by the time management realized the market forces

in play, and the company had to close down its production facility by the start of the new millennium, and abandon its forays into nanomaterials, at least for the moment. The lesson here is that while nanotechnology can lead to a better product, it may not necessarily lead to a "business" because the mass market is not ready to pay a higher price for an improved product. To extend this thought further, it may so happen that, while a particular product developed by a company is superior in performance to an existing product, the sales volume generated may be too small to support a large-scale manufacturing infrastructure. It appears that the maximum potential exists for products that are just not improved, but enabled solely by the use of nanomaterials.

The initial part of this article will describe advances made by small and large corporations in producing a variety of nanopowders, because nanopowders provide the all-important building block for forming nanostructured materials. The discussion will be limited to technologies that were successfully developed into, at least, a quasi-commercial operation. As it turns out, the roots of a vast number of nanopowder synthesis processes are either a university or some other research laboratory. However, synthesis processes that are still practiced only in a research environment are excluded from the discussion. Furthermore, the discussion will be restricted to ceramic and metal nanoparticles. Carbon-based materials (e.g., fullerenes/bucky balls, single-wall carbon nanotubes, and multiwall carbon nanotubes) and chalcogenide nanotubes, and organic nanoparticles are beyond the scope of the present discussion.

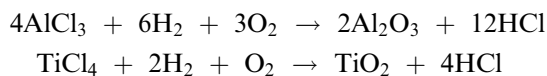
The second part will describe the activities of companies involved in commercializing nanomaterials for specific applications, where substantial value is added to nanoparticles by way of surface treatment or incorporation into a host matrix. Also included are work performed at corporations that purchase nanoparticles from the open market and incorporate them into an end product. This section will also detail the activities of a few companies that are vertically integrated, i.e., they synthesize their own raw nanomaterials and integrate them into a component or a device. However, such vertical integration is not common in the materials industry.

The final section is a reflection on the past decade of nanomaterials development, and a prognosis of where things are likely to be by the end of the decade.

## PART I: NANOPOWDER PRODUCTION

Two of the pioneers in production of nanopowders of single-phase oxides (e.g.,  $\text{SiO}_2$ ,  $\text{TiO}_2$ ,  $\text{Al}_2\text{O}_3$ ,  $\text{Fe}_2\text{O}_3$ , and  $\text{ZrO}_2$ ) are located on either side of the Atlantic

Ocean: Degussa Corporation, headquartered in Europe, and Cabot Corporation in the United States. Both companies have been in production of nanopowders for several decades now, accounting for much of the “nanopowder sales” figures quoted in reports by some market research analysts. Over the years, Degussa and Cabot have steadily made incremental improvements in particle characteristics, such as reduction in aggregate size and altering surface characteristics to suit specific applications. The Degussa Process, called the AEROSIL<sup>®</sup> process,<sup>[8]</sup> involves hydrolysis of gaseous metallic chlorides under the influence of water, which develops during the oxyhydrogen reaction, which, in turn, leads to a high-temperature reaction zone. Example reactions are as follows:



Nanoparticles of titanium dioxide, produced by Degussa, are sold as Degussa P25, and are an extremely well characterized nanopowder. The powder has a surface area of  $\sim 50 \text{ m}^2/\text{g}$ , with a primary particle size of 21 nm. Fig. 1 shows a transmission electron microscopic (TEM) image of  $\text{TiO}_2$  nanopowders. The purity of the oxides is in general  $>99\%$ , and in some cases, the purity is in excess of 99.9%. The reason for the high purity is that the chloride byproduct is cleaned relatively well through distillation. These nanopowders are used in a number of commercial applications, some of which are: aluminum oxide used in Ink jet papers (smoothing and sealing), cable insulation (improvement in dielectric strength), photo resists for production of integrated circuits (ICs) (rheology); titanium dioxide in ultraviolet (UV) protecting gels (transparent, yet 100% UV protection); zirconium oxide in IC substrate boards (higher resolution), battery separators (filler), and polystyrene (free flow aid).

High-surface-area  $\text{SiO}_2$  has been the flagship product of Cabot Corporation (in addition to carbon black, which itself is a nanostructured powder, given the high surface area of the powder particles). Cab-o-sil<sup>®</sup> is the trade name of Cabot's  $\text{SiO}_2$

nanopowders, an electron micrograph of which is shown in Fig. 2.<sup>[9]</sup> Nanoparticles of  $\text{SiO}_2$  are produced by a flame process, which substantially resembles the Degussa process described above. An experimental grade of aluminum oxide is also produced by Cabot using the same process, with a surface area of  $\sim 55 \text{ m}^2/\text{g}$ . The reported average aggregate length, which is different from the aggregate size measured by a typical instrument, such as Coulter N4 plus or a Horiba LA 920, is 150–170 nm.

Interestingly enough, unlike conventional materials development—where a unique material is often developed in response to either an actual or a perceived need—the above-described oxide nanopowders have largely found use in new markets as soon as they became available in large quantities. For example, the production process for synthesis of nanoparticles of aluminum oxide was developed well before the powders began to be used in inkjet papers. Moreover, nanopowders of aluminum oxide, titanium oxide, and silicon dioxide have been commoditized over the years by the two industry giants mentioned above, thereby leaving little room for nanopowder-producing neophytes to use their approach to penetrate well-established markets. A further discussion on the barrier to entry is presented in the final section of the entry.

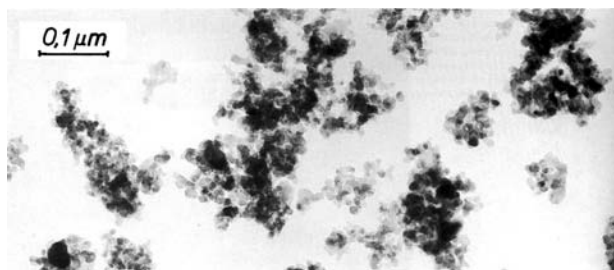


**Fig. 1** TEM image of Degussa's P25 titanium dioxide powder.

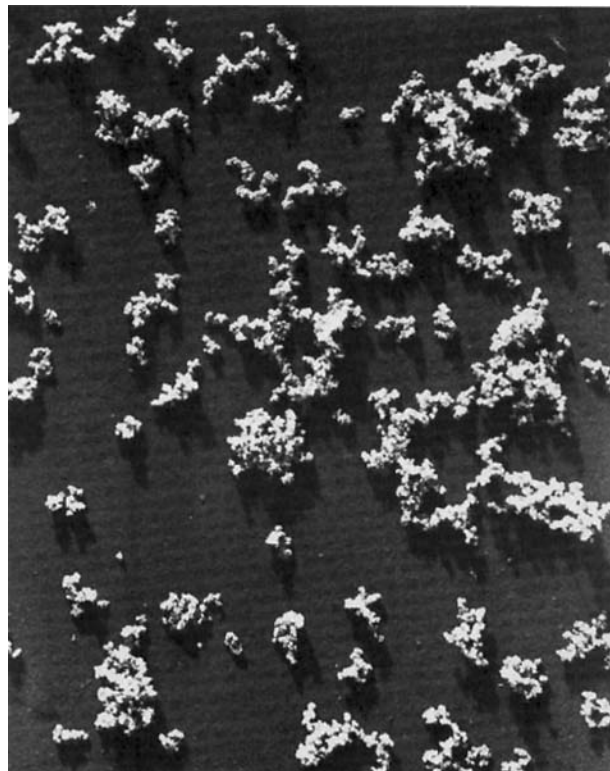


**Fig. 2** Electron micrograph of nanoparticles of  $\text{SiO}_2$ , produced by Cabot Corporation.

Baikowski International,<sup>[10]</sup> a company based in France with operations in the United States as well as in Japan, also provides nanoparticles of aluminum oxide with exceptional purity:  $\geq 99.99\%$  (in addition to micron- and submicron-size particles). The powders have a high surface area,  $\sim 120 \text{ m}^2/\text{g}$ . Some grades of such high-surface-area powders have an aggregate size as small as  $\sim 0.3\text{--}0.4 \mu\text{m}$ . The company exclusively produces aluminum oxide, and caters largely to the lighting (for producing translucent ceramics) and polishing (chemical mechanical polishing) industries.

The perceived need for spherical nanoparticles, and with a lower degree of aggregation than what was commercially available, prompted extensive research into new synthesis processes at universities and national laboratories. As soon as a basic research showed promise, the technologies were transferred to a private entity [usually with the aid of federal funds in the form of either SBIRs, or its sister program, small business technology transfer (STTRs)], often located near the originating research institution. The start-ups were the so-called “spin-off” nanomaterial companies. Two such companies in the early days of the Nanotechnology industry were Nanophase Technologies Inc. in Illinois, and Nanodyne Inc. in New Brunswick, although Nanophase Technologies Inc. was funded by equity investment very early on in the life of the company. Nanophase Technologies (NASDAQ: NANX), which evolved from research activity at Argonne National Laboratory in the outskirts of Chicago, focused on the production of oxide nanoparticles, including such commonly used oxides as aluminum oxide, titanium dioxide, and zinc oxide, as well as a number of not so commonly used materials, such as yttrium oxide, copper oxide, and cerium oxide. The synthesis process, schematically shown in Fig. 3, is based on high rate evaporation of metals followed by oxidation in the gas phase.<sup>[11]</sup> The process yields nanoparticles on a commercial scale with a spherical morphology (in many cases) and with minimal

aggregation, which was different from the nanopowders available at that time, although the surface areas were comparable. As of the writing of this entry, all of the compositions mentioned above are available in tonnage quantities. The strategy to market these products appears to be to sell the nanopowders to larger chemical manufacturers, as opposed to directly providing it to the end user; e.g., the biggest customer of Nanophase Technologies is BASF.<sup>[12]</sup>

Nanodyne Inc. was a spin-off from Rutgers—The State University of New Jersey, the basis for the technology being intellectual property and prior research that was carried out at Exxon Corporation. The hallmark of the Nanodyne synthesis approach, shown schematically in Fig. 4, was that existing and commercially available processing technologies (e.g., fluidized bed and rotary furnaces) were used to produce nanostructured materials that were protected by a structure of matter patent. The sole focus of the company was to produce ultrafine grained powders of WC/Co. Research had shown that fine-grained WC/Co materials possessed improved hardness without the usual accompanying loss in toughness, and this provided the impetus to commercialize ultrafine grained WC/Co for tool bits.<sup>[13]</sup> A pilot plant was first built in New Brunswick, NJ, with investment from venture capitalists (Ampersand and CMEA). Later, Union Miniere (now Umicore) bought out the interests of all the shareholders, and a semifull-scale production plant was constructed in North Carolina. Unfortunately, the plant was shut down not too long after it was commissioned,<sup>[14]</sup> and Nanodyne Inc. went into the history books as one of the first casualties of the Nanotechnology industry.

Just about the time that nanopowders were coming in vogue in the United States, a company called Advanced Powder Technology (APT) was founded in Australia.<sup>[15]</sup> Unlike the vapor-phase approaches that were being championed by many companies in the United States, APT developed a patented solid state

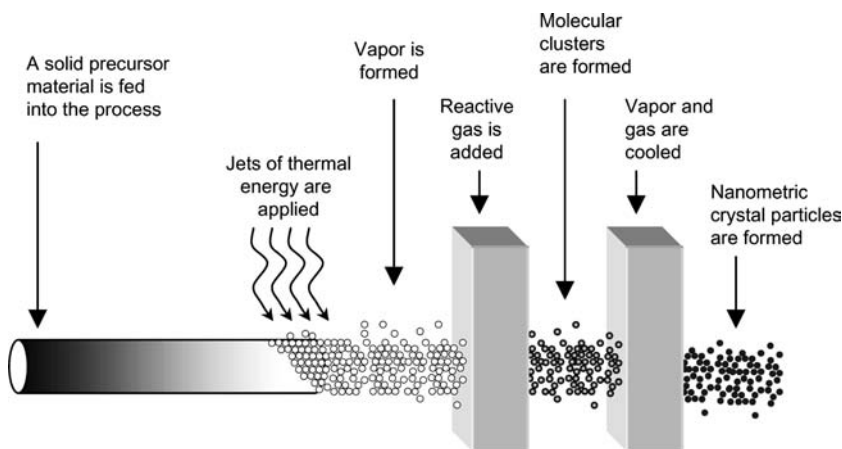


Fig. 3 Schematic showing the vapor-phase process practiced at Nanophase Corporation.

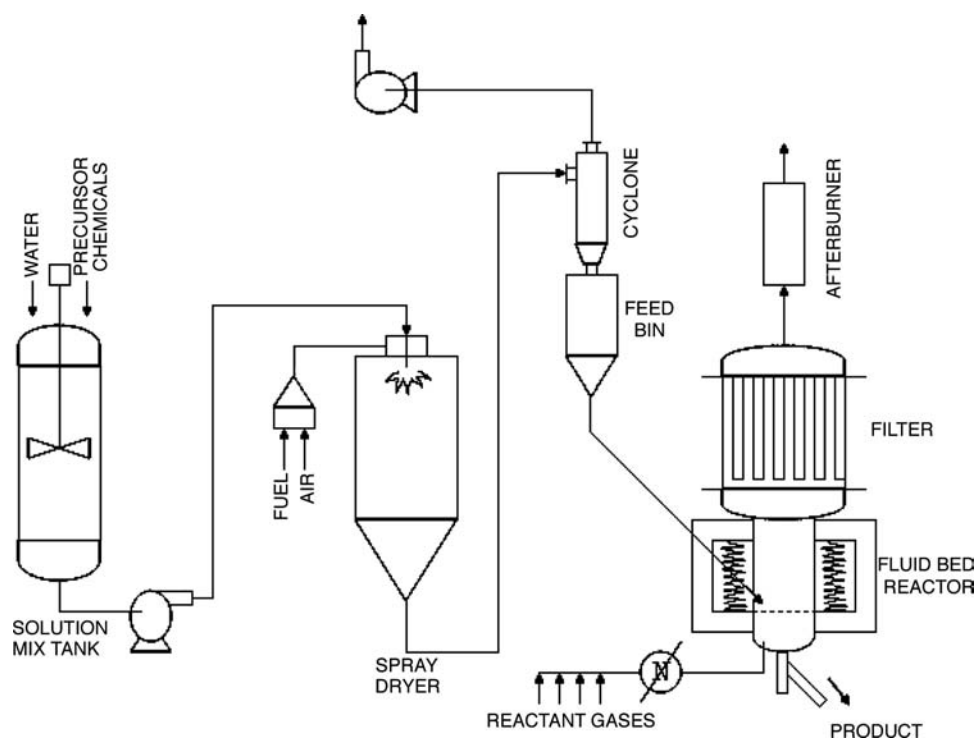


Fig. 4 Schematic of the spray conversion process, developed by Nanodyne Inc.

process that combined a milling operation. Dry milling was used to induce chemical reactions through ball-powder collisions that resulted in nanoparticles forming within a salt matrix. Particle size is defined by the chemistry of the reactant mix, milling, and heat treatment condition. Particle agglomeration is minimized by the salt matrix, which is then removed by a simple washing procedure. While reducing the size of particles by milling had been known for a very long time, APT was among the first to reduce the particle size to the nanoscale. A joint venture with Samsung Corporation was announced in 2001. One of the major products was cerium oxide, which has generally been an expensive material and was scarcely available in a nanopowder form. The technology has also been extended to other compositions, such as zinc oxide.

During the mid- to late 1990s, alternative vapor-phase technologies to what was practiced at Nanophase Technologies was developed by a number of companies, including NEI Corporation, the company that the authors work for. At NEI, a process called combustion flame-chemical vapor condensation (CF-CVC) was developed to produce oxide nanoparticles,<sup>[16]</sup> the origins of which were in a process invented at Rutgers University.<sup>[17,18]</sup> The CF-CVC process, shown schematically in Fig. 5, utilized a flat flame in a reduced pressure environment as the heat source for pyrolyzing vapors of metalorganic precursors. The geometry of the flame insured that the

pyrolysis was uniform, and the condensation of the pyrolyzed species into nanoparticles was rapid. The end result was the formation of high-surface-area nanoparticles with a narrow primary particle size distribution, combined with one of the smallest aggregate sizes among nanopowders available in the market. For example, titanium dioxide nanopowders had a surface area of  $\sim 65\text{--}75\text{ m}^2/\text{g}$  with an aggregate size (as measured by Coulter N4 Plus) of  $\sim 0.1\text{--}0.12\text{ }\mu\text{m}$ . Aluminum oxide nanopowders had a surface area of  $\sim 120\text{ m}^2/\text{g}$  with an aggregate size of only  $\sim 0.125\text{ }\mu\text{m}$ .<sup>[19,20]</sup>

Significant progress in developing new methods of nanopowder synthesis was made at Nanomaterials Research Corporation (NRC) toward the late 1990s. The production system was based on a patented process<sup>[21]</sup> utilizing ultrarapid thermal quenching of high-temperature vapors through a boundary layer converging-diverging nozzle. A suspension of precursor material, which was, for the most part, generated from a fluidized bed of micron size metal particles, was continuously fed to a thermal reaction zone and vaporized under conditions that minimized superheating and favored nucleation of the resulting vapor. The expansion ahead of the nozzle led to rapid condensation, and minimization of nanoparticle coalescence. The process produced metals, intermetallics, single-phase and multicomponent oxides, and even some non-oxides. Subsequently, NRC, which was mostly funded through a number of SBIR programs until

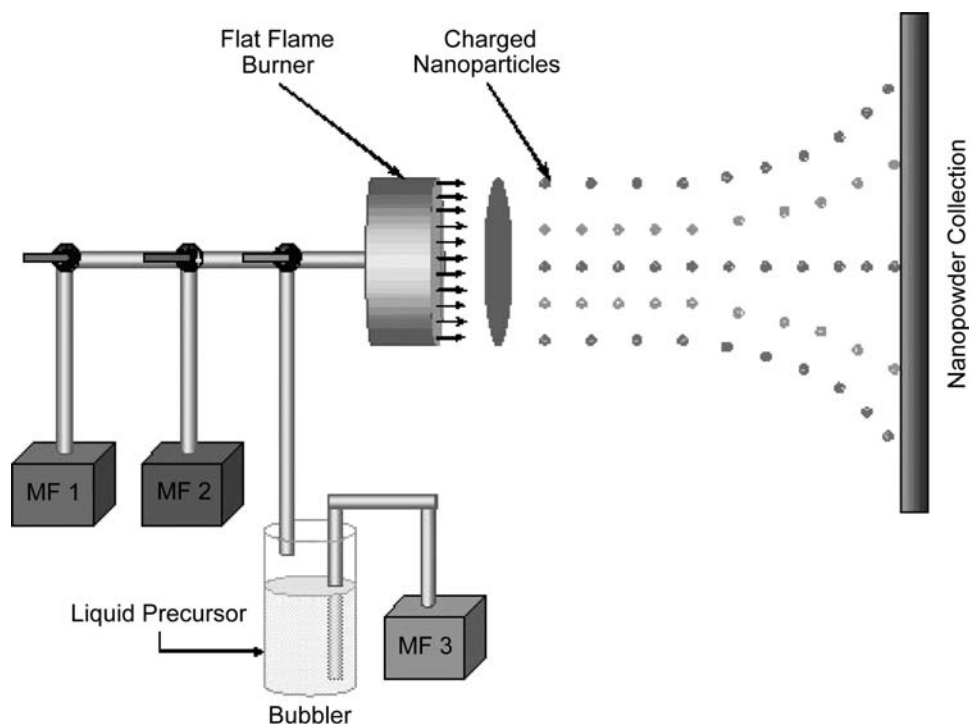


Fig. 5 Schematic layout of the CF-CVC process, developed at NEI Corporation.

then, spun off a separate entity called NanoProducts Inc. A partnership with a major Japanese powder equipment company, Hosokawa Micron Corp., was announced in 2001 for scale-up of the nanopowder synthesis process.<sup>[22]</sup> Production is said to be commencing in Japan, as well as in the United States. NRC has also developed other gas-phase nanopowder synthesis processes, similar to the one described above, some of them utilizing chemical precursors such as acetates and nitrates.

Meanwhile, through the 1990s, the process of spinning off nanopowder- and nanomaterial-producing companies from universities continued in the United States. One such company that came into existence in the mid-1990s was TAL Materials, located in Michigan, which focused on a process based on combustion of precursors in a flame.<sup>[23]</sup> However, unlike many of the processes described above, the TAL Materials technology did not require the precursors to be vaporized. The precursors were pyrolyzed in a tubular reactor, and high-surface-area nanopowders were collected downstream.<sup>[24]</sup> The company, which was still in its infancy at the time this entry was being written, has focused on multicomponent oxide particles for value-added applications in lasers, and of the like.<sup>[25]</sup>

Nanoscale Materials Inc.<sup>[26]</sup> (formerly known as Nantek Inc.), which started operating in 1995, was spun out of Kansas State University—the first commercial spin-off from this university. The company

sells an array of oxide nanoparticles, mostly single phase, under the trade name NanoActive™. The powders are characterized by an extremely small feature size, resulting in enormously high surface areas. Accordingly, applications that can benefit from a very high surface area are ideal users of NanoActive™. According to the company, their oxide powders have shown utility in a variety of applications, including destructive adsorption, purification of air and water, scrubbing of acid gases, and sequestering of odors and toxic gases.

Unlike many of its competitors, which emerged from transitioning of a research activity into a business in nanomaterials, Altair Nanomaterials evolved from being a leaseholder on titanium ore mines in the Tennessee Valley to a manufacturer of oxide (and some nonoxide) nanoparticles, titanium dioxide in particular.<sup>[27]</sup> The Altair process is a solution-based process, wherein particles are precipitated and milled to be reduced to a smaller size while in suspension.<sup>[28]</sup> As of the writing of this entry, initial sales into the thermal spray market had been reported, along with success in animal trials of a phosphate powder for treatment of a kidney disease. Altair is a publicly traded company (NASDAQ: ALTI), and the total sales volume of nanopowders appears to be in the tens of thousands of dollars per quarter.

Nanotechnologies, Inc.,<sup>[29]</sup> based in Texas, and Technanogy<sup>[30]</sup> in California (both backed by venture capital funding), were relative newcomers to the

business of producing nanopowders. Both companies championed vapor phase processes, where a plasma source was used to vaporize metallic materials. The initial emphasis for both companies was on aluminum nanoparticles, with the objective of using them as rocket fuel, and as a component in the primer for bullets. Neither of these two applications seems to have held up to their initial promise, presumably because of cost considerations. Nanotechnologies Inc. has also initiated the development of oxide nanoparticles, and recently announced collaboration with AirProducts Inc. and Essilor, a manufacturer of eyeglasses.

Argonide Corporation<sup>[31]</sup> came into existence in the early 1990s, after transferring nanopowder production technology from Russia. A wire of the desired material is exploded in a continuous manner within a controlled atmosphere. A variety of metals including tungsten, aluminum, and oxide nanopowders are produced by the process.<sup>[32]</sup>

The path followed by a majority of companies has been somewhat self-directed, as opposed to being directed by the needs of the customer. As a result, considerable emphasis has been placed on the production of single-phase oxide nanopowders, such as aluminum oxide, titanium oxide, zinc oxide, and cerium oxide. This has been driven more by what their individual technologies can offer, and less by what the specific needs of an application are. Accordingly, an additional step of converting the single-phase oxide nanopowders into a useful form has become necessary, which reduces the importance of the starting material, which in turn requires it to be relatively inexpensive. Many nanopowder-producing companies have an eventual price target of ~\$10/lb; it remains to be seen if such a low price is attainable, and even if so, to what extent it remains a viable business for small companies.

In contrast to passive or non-functional nanoparticles, i.e., where the internal crystal structure does not contribute to a particular physical phenomenon, functional nanoparticles present significant opportunities for enhancing the properties of a product. Three prominent examples include: 1) multicomponent nanoparticles of electronic oxide ceramics; 2) nanocomposite electrodes for lithium-ion batteries; and 3) active materials for chemical gas sensors and biochemical activity. Processing of these materials is particularly challenging, given the complexity of the material systems, thus it is not surprising that there are very few companies active in these areas, although the market opportunity is immense.

Barium titanate, and variations thereof, is perhaps the most widely used electronic ceramic material. As such, this has prompted the nanomaterials community to investigate the potential benefits of nanostructured barium titanate. It is most commonly used as a sintered high dielectric material (both thick films and bulk).

Accordingly, many companies have made several attempts in developing fine particles of barium titanate. One of the most widely practiced synthesis methods has been the hydrothermal process, where precursors are allowed to react at relatively low temperatures, but at well above ambient pressures. TPL Inc. (Albuquerque, NM) has reportedly scaled a process for producing tonnage quantities of ultrafine multicomponent oxide powders belonging to the titanate family.<sup>[33]</sup>

NEI Corp. has developed processes for producing nanostructured powders of compositions used as electrodes in rechargeable lithium-ion batteries, and related energy storage devices.<sup>[34–36]</sup> Rechargeable lithium-ion batteries present a market opportunity for nanomaterials as three aspects of this class of energy storage device need improvement: energy density, rate capability, and cost. The ability to stabilize structures that are intrinsically of high energy density (example shown below) in a nanoparticle has the potential of inducing improvements in energy density. The rate capabilities of rechargeable batteries can be enhanced by reducing the particle size of electrode materials, because it is well established that the rate capabilities of lithium-ion batteries are limited by solid-state diffusion of lithium ions within the electrode materials.<sup>[37]</sup> Furthermore, compositions that utilize relatively inexpensive compositions (i.e., based on iron rather than cobalt) become viable cathode materials when the particle size is reduced to the nanoscale.

Macrocrystalline layered lithium manganese oxide, which has a theoretical energy density twice that of the presently used lithium cobalt oxide, suffers from structural instability during electrochemical cycling, and as a result, exhibits significant capacity decline. Moreover, the rate capability is less than desirable. NEI Corp. is developing nanostructured and doped layered lithium manganese oxide. Fig. 6 shows the charge/discharge curves of the sample under a low current density. The first charge capacity and discharge capacity were within 15% of the theoretical value. When the current density was raised to 22.5 mA/g during charge and discharge, the discharge capacity dropped, but did not show any capacity fade. Furthermore, development work is underway to increase the discharge capacity at high current densities.

Sensing an opportunity in gas detection instruments needed for industrial health and safety, environmental monitoring, and process control, Nanomaterials Research Corporation spent considerable effort in producing single-phase and doped oxide nanoparticles and integrating them into gas sensors.<sup>[38]</sup> Fig. 7 shows a comparison of the sensitivity of coarse-grained and nanostructured powders. NEI Corp. made initial forays into this market using its low-pressure flame deposition (LPFD) process, which is a high rate



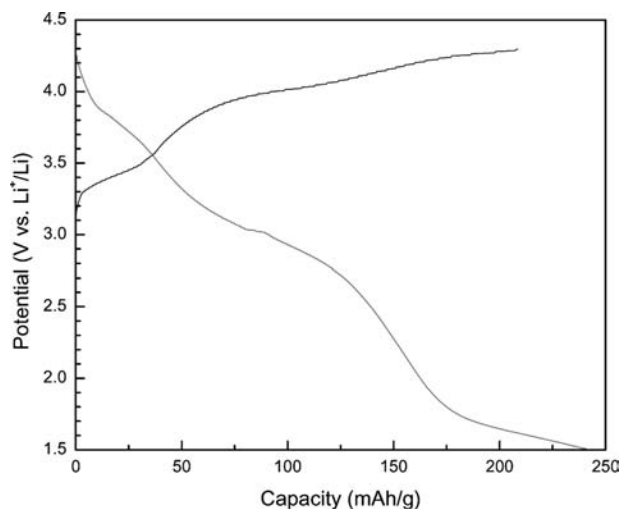


**Fig. 6** A charge/discharge curve of a nano- $\text{LiMn}_x\text{M}_{1-x}\text{O}_2$  cathodes in a Li-test cell at a current density of 2.7 mA/g.

process for depositing and sintering nanoparticles in situ on a substrate.<sup>[39,40]</sup> The process leads to a porous nanoparticulate thick film structure, which is a desired morphology for gas sensor applications. However, the company did not obtain sufficient traction from the end users of such a technology, and has subsequently shelved the process.

## PART II: VALUE-ADDED NANOMATERIALS AND NANOMATERIALS-ENABLED PRODUCTS

In the materials business, the idea of not just producing nanopowders, but also integrating in-house synthesized nanoparticles into a final end product is generally believed to be a good strategy. The argument is that, although nanoparticles have properties that are uniquely distinct from their coarser counterparts, they are still a “raw material,” and so do not carry much more value than a commodity. NanoGram was

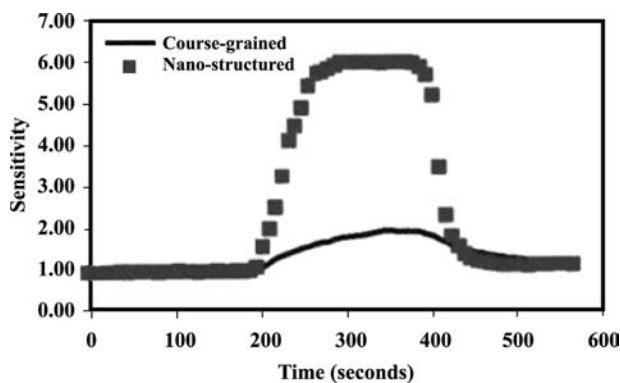


**Fig. 7** Data showing the difference in the sensitivity between coarse grained and nanostructured materials.

perhaps the first company to build a business on this concept, and have taken it to the extreme. The company, which was founded in the early 1990s with venture capital backing, concentrated on a laser pyrolysis process as the predominant nanopowder synthesis method. A substantial amount of intellectual property was created in the “use” of nanoparticles for a host of applications, including lithium batteries and chemical mechanical polishing. For example, NanoGram was the first to patent the use of nanoparticles of vanadium oxide as cathode materials for a lithium battery,<sup>[41]</sup> although sol-gel derived vanadium oxide xerogels (which are, by definition, nanostructured materials) have been shown to possess significantly higher capacity than coarse particles of vanadium oxide.<sup>[42]</sup> The laser nanoparticle synthesis process was subsequently modified to directly deposit nanostructured films at high rates on substrates.<sup>[43]</sup> Using this and other nanocomposite technologies, forays were made into the optical waveguide business at the turn of the millennium. The company appears to be deft at changing course as the market evolves. Recently, a new spin-off called NanoGram Devices Corporation has been formed to commercialize energy storage devices for the medical industry.

Another example of a vertically integrated company is Photon-X (Malvern, PA).<sup>[44]</sup> The company was established through a sizable venture capital investment. Among the first products envisioned were optical amplifier modules that support high capacity systems, but consume considerably less power with a smaller footprint than conventional products. These amplifier modules were based on new waveguide materials utilizing optical polymers and their nanocomposites. The company has combined materials innovations with new and improved optical designs that enable a reduction in the number of pump lasers for amplifiers. Reducing the number of pump lasers significantly reduces the electrical power consumption. Right from the start, the company’s goal was to be the provider of amplifier modules, made from building blocks that are all developed and fabricated in-house.

InMat Inc., a New Jersey-based start-up, is among a handful of companies that have released their products in the commercial market.<sup>[45]</sup> The technology and some of the principals of InMat originated from Hoechst Research, which had ceased operations in New Jersey in the mid-1990s. The basic technology is a composite formulation consisting of butyl rubber with a dispersion of exfoliated clay particles. The exfoliated layers of clay have nanometer dimensions along the *c* axis, and hence the material is a nanocomposite, which has the unique feature of reducing permeability of air by as much as 200%, while maintaining the flexibility of butyl rubber. As an example, a coating of the nanocomposite is applied to a tennis ball,<sup>[46]</sup> thereby

increasing its life span. The company is working on establishing its presence into the tire industry and chemically protective gloves, both of which can benefit from rubbers that are less permeable.

Along similar lines, at NEI Corporation, efforts are underway to commercialize transparent polymer nanocomposite coatings that are also hard and scratch-resistant. Innovations have centered on increasing the refractive index, altering the thickness of the coating between 1 and 25  $\mu\text{m}$  (as required by the application), and introducing additional functionalities such as electrical conductivity.<sup>[47]</sup>

There are also several examples of companies where nanomaterials form an integral part of the final product. For example, Konarka Technologies,<sup>[48]</sup> based in Massachusetts, has built upon dye-sensitized solar cells invented by Grätzel more than 10 years ago.<sup>[49]</sup> The core of the dye-sensitized technology consists of nanometer-scale crystals of titanium dioxide semiconductor coated with a monolayer of light-absorbing dye and embedded in an electrolyte between the front and back electrical contacts. The dye absorbs the photon in light. The company claims to be using low-cost raw materials and an inexpensive manufacturing technology to bring this nanomaterial-enabled photovoltaic technology to market.

NanoMagnetics<sup>[50]</sup> (UK) has used nanoparticulate magnetic films to produce a data-recording density of  $\sim 6$  Gbit/in.<sup>2</sup> According to the company, this should eventually lead to a density of several Tbits per square inch. NanoMagnetics realized the importance of a uniform grain size in the film, and has used a protein molecule called ferritin as the cage in which a cobalt-platinum metal alloy is deposited. The advantage in using a protein molecule is that they are always of the same size: a 12-nm-diameter cage with an 8-nm cavity. This way, the size of the alloy nanoparticle is limited to the size of the cavity.

There are also instances where nanomaterials constitute a critical component of the process. A case in point is Reactive Nanotechnologies Inc., which is building upon intellectual property generated at University of Maryland, and claims to have developed a new method of joining that replaces current processes of soldering and brazing, as well as opens up new applications in the areas of metal-to-ceramic joining.<sup>[51]</sup> The principle of joining employed by Reactive Nanotechnologies Inc. is based on a self-propagating exothermic reaction. Two dissimilar components are sandwiched with a stack of alternating layers of elements (with a thickness of several hundred nanometers)—say aluminum and nickel—that undergo an exothermic reaction. The reaction between the two metals is initiated at one end, and propagates rapidly through to the other end. The advantage of the approach is that the components being bonded are

not sensitive to the high temperature. The company envisions opportunities in the microelectronics market for application of its technology. A similar (but not competing) technology has been developed by SusTech Darmstadt in Germany.<sup>[52]</sup> The microwave curable adhesive system works on the principle that nanoparticulate ferrites pick up energy from electromagnetic AC fields, convert it into heat, and pass to the immediate surrounding.

A noticeable trend has emerged, in which large corporations are buying out (or exclusively licensing the intellectual property) small companies that have forayed into areas of interest to the large corporations, although there may not be any significant sales.<sup>[53]</sup> One notable example is the purchase by DuPont Titanium Technologies, a wholly owned subsidiary of DuPont, of a fledging company called NanoSource Technologies in July 2002. NanoSource Technologies Inc., which was founded in 1999, entered into an exclusive licensing agreement with Tekna Plasma Systems Inc. (Sherbrooke, Quebec, Canada) to produce nanoparticles of titanium dioxide. Moreover, the company had announced in January 2001 that it had developed a first-of-its-kind polymer coating for the surface of titanium dioxide nanoparticles that would make it usable in cosmetic applications.<sup>[54]</sup>

### PART III: FUTURE PERSPECTIVES

Given the recent flurry of activity in nanomaterials both in the academia and the industry, one can only conclude that there is still plenty of ground to cover. With the federal governments of advanced and developing nations apportioning increasingly large sums of money each year for research in nanomaterials and nanotechnology, we are most likely still away from seeing the peak in research output. In fact, in our judgment, the biggest breakthroughs are yet to come. In just the past few years, nanomaterials have already penetrated the consumer market, even if the sales volume in dollar terms is only in the tens of millions of dollars. Higher-volume applications requiring larger quantities of nanomaterials take a longer amount of time to be qualified for use, and we can expect to see them incorporated in products over the next several years. At the same time, it is quite difficult to clearly predict where the greatest commercial advances are going to be, and how they will manifest themselves in products. While significant advances in nanotechnology are routinely announced in technical and trade journals, transferring them into applications requires overcoming a number of barriers. Most notable among them are the lack of reproducibility of results reported from various laboratories, and the fact that results are often obtained from non-standardized tests, making

real-life comparisons difficult. To add to all of this, progress in nanomaterials is often at odds with the human nature of inflating what is achievable in the near term, but not envisioning what can be achieved in the distant future.

Interest in specialized nanomaterials and functionalized complex nanoparticles is growing. However, the demand for single-phase and multicomponent oxide powders of commonly used compositions is, at best, tepid. This is because oxide nanopowders, even with excellent particle characteristics such as small primary particle size and small amount of aggregation, do not possess sufficient distinguishing features from the powders that have been available since the latest blitz in this field. In other words, the market has been commoditized, and so does not present new opportunities. Therefore, it is exceptionally difficult for a small company to make much progress as a profitable enterprise.

Another likely scenario is that nanomaterials will be used in a large number of products, where the addition of a relatively small quantity leads to a major change in the properties and performance of the end product. The value-added nanomaterial with functionalized surfaces is likely to possess a unique functionality. Because the additive will impact a large enough market, it will justify the investment in the process technology. The challenge at the hands of companies, particularly the smaller companies in this field, is to identify such applications and team up with the right partners so that it becomes a win-win situation for both parties.

## CONCLUSION

Although the number of small nanomaterials companies throughout the world is quite large, each at various stages of commercialization, only a handful of companies are likely to withstand the test of time 10 years from now. Those without sustainable competitive advantage will lose the support of their investors (including federal sources of funding) and cease to exist. On the other hand, those that are wildly successful in certain segments of the market are likely to become takeover targets of large companies dominating that particular niche of the industry.

The companies cited in this article do not represent ALL the companies working in this area, but to the authors' knowledge, they represent examples of the transition from science to technology.

## REFERENCES

1. Workshop Report on R & D Status and Trends in Nanoparticles, Nanostructured Materials and Nanodevices in the United States. In *Proc. of the May 8–9, 1997 Workshop*.
2. Christensen, C.M. *The Innovator's Dilemma*, 1st Ed.; HarperBusiness: New York, NY.
3. Drucker, P.F. *Innovation and Entrepreneurship*, 1st Ed.; HarperBusiness: New York, NY, 2000.
4. Drucker, P.F. *Managing in the Next Society*, 1st Ed.; St. Martin's Press: New York, NY, 2002.
5. [www.CMP-cientifica.com](http://www.CMP-cientifica.com).
6. [www.bccresearch.com](http://www.bccresearch.com).
7. [www.nanobusiness.org](http://www.nanobusiness.org).
8. *Technical Literature*; Degussa Corporation: Germany.
9. *Technical Literature, Cab-o-Sil<sup>®</sup> Untreated Fumed USA Silica: Properties and Function*; Cabot Corporation: USA.
10. [www.baikowski.com](http://www.baikowski.com).
11. Ford, Q. *Ceram. Ind.* **1998**, 31.
12. Lu, S. *Proc. of the American Ceramic Society, Annual Meeting*; 2003, in press.
13. McCandlish, L.; Kear, B. Chemical processing and properties of nanostructured WC-Co materials. *Nanostruct. Mater.* **1993**, 3, 19.
14. Rittner, M., Ed. *Nanoparticle News*.
15. [www.aptpowders.com](http://www.aptpowders.com).
16. Glumac, N.; Chen, Y.-J.; Skandan, G.; Kear, B.H. Scalable high-rate production of non agglomerated nanopowder in low pressure flames. *Mater. Lett.* **1998**, 34, 148–153.
17. US Patent No. 5,514,356.
18. US Patent No. 5,876,683.
19. [www.neicorporation.com](http://www.neicorporation.com).
20. Skandan, G.; Singhal, A. *Met. Powder Rep.* **1999**, 54 (5), 18.
21. US patent number 5,788,738.
22. [www.ceramicbulletin.org/newsarchive.asp](http://www.ceramicbulletin.org/newsarchive.asp).
23. [www.talmaterials.com](http://www.talmaterials.com).
24. Bickmore, C.; Walder, K.; Baranwal, R.; Hinklin, T.; Treadwall, D.; Laine, R. J. *Eur. Ceram. Soc.* **1998**, 18, 287.
25. Laine, R. *Proc. of the Nanoparticle 2002 Conference, New York*.
26. [www.nanoscalematerials.com](http://www.nanoscalematerials.com).
27. [www.altairnanomaterials.com](http://www.altairnanomaterials.com).
28. Sabacky, B. *Proc. of the Nanoparticle 2000 Conference*.
29. [www.nanoscale.com](http://www.nanoscale.com).
30. [www.technanogy.net](http://www.technanogy.net).
31. [www.argonide.com](http://www.argonide.com).
32. Tepper, F. Nanosize powders produced by electro-explosion of wire and their potential applications. *Powder Metall.* **2000**, 43 (4), 320.
33. [www.tplinc.com](http://www.tplinc.com).
34. Singhal, A.; Skandan, G.; Amatucci, A.; Pereira, N. In *Nanostructured Electrodes for Rechargeable Li Rechargeable*, Proceedings Volume of Electrochemical Society—Workshop on Interfaces, Phenomena and Nanostructures in Lithium Batteries, Argonne, Dec. 11–13, 2000.
35. *Nanoparticle News*; Business Communications Company.
36. Singhal, A.; Skandan, G. *Proc. of the Conference on Rechargeable Batteries, France. In press*.

37. Sides, C.R.; Li, N.; Patrissi, C.J.; Scrosati, B.; Martin, C.R. Nanoscale materials for Li-ion batteries. *MRS Bull.* **2002**, *27* (8), 604.
38. Hooker, S. *Proc. of the Nanoparticle 2000 Conference*.
39. Skandan, G.; Glumac, N.; Chen, Y.-J.; Cosandey, F.; Heims, E.; Kear, B. Low pressure flame deposition of nanostructured oxide films. *J. Am. Ceram. Soc.* **1998**, *81*, 2753.
40. Skandan, G.; Singhal, A. *Mater. Technol.* **1998**, *13* (4), 149.
41. US Patent of Nanogram.
42. Sol-gel paper on vanadium oxide, take from Hosokawa Micron file.
43. Kambe, N. *Proc. of the Nanoparticle 2002 Conference*.
44. [www.photon-X.net](http://www.photon-X.net).
45. [www.inmat.com](http://www.inmat.com).
46. [http://www.smalltimes.com/document\\_display.cfm?document\\_id=2997](http://www.smalltimes.com/document_display.cfm?document_id=2997).
47. [http://www.smalltimes.com/document\\_display.cfm?document\\_id=5884](http://www.smalltimes.com/document_display.cfm?document_id=5884).
48. [www.konarkatech.com](http://www.konarkatech.com).
49. Graetzel patents.
50. [www.nanomagnetics.com](http://www.nanomagnetics.com).
51. [www.reactivenanotech.com](http://www.reactivenanotech.com).
52. [www.sustech.de](http://www.sustech.de).
53. [http://www.smalltimes.com/document\\_display.cfm?document\\_id=4173](http://www.smalltimes.com/document_display.cfm?document_id=4173).
54. [www.nanosource.com](http://www.nanosource.com).

# Nanomaterials: Manufacturing, Processing, and Applications

Pramod K. Sharma

Weifang Miao

Anit Giri

Srikanth Raghunathan

*Nanomat, Inc., North Huntingdon, Pennsylvania, U.S.A.*

## INTRODUCTION

The particles with small size in the range from a few to several tens of nanometers are called quasi zero-dimensional mesoscopic system, quantum dots, quantized or Q-particles, etc.<sup>[1]</sup> The reason that nanoscale materials and structures are so interesting is that size constraints often produce qualitatively new behavior. Nanotechnology arises from the exploitation of new properties, phenomena, processes, and functionalities that matter exhibits at intermediate sizes between isolated atoms or molecules ( $\sim 1$  nm) and bulk materials (over 100 nm). As opposed to the microscale, the nanoscale is not just another step toward miniaturization, but is a qualitatively new scale. Hence quantum and size phenomena are allowed to manifest themselves either at a purely quantum level or in a certain admixture of quantum and classical components. At the foundation of nanosystems lie the quantum manifestations of matter that become relevant. Consequently, instead of being a limitation or an elusive frontier, quantum phenomena have become the crucial enabling tool for nanotechnology. Extensive research on semiconductor quantum dots has shown that these particles have properties halfway between macroscopic (bulk) and microscopic (molecular-like) substances and have recently aroused great interest in laser, photochemistry, and non-linear optics.<sup>[2–4]</sup> Bawendi et al.<sup>[3]</sup> have observed a number of discrete electronic transitions and LO-phonon progression which were cleanly resolved for the first time in nanometer-scale cluster in CdSe. Jungnickel and Henneberger<sup>[5]</sup> have described the luminescence properties of semiconductor nanocrystals and the carrier processes that are relevant for the light emission. Their study was concentrated on nanocrystal of size  $\approx 5$  nm, and hence observed strong carrier confinement. A size dependence in the luminescence efficiency of ZnS:Mn nanocrystals has also been observed by Bargava et. al.<sup>[6]</sup> and stated that the  $Mn^{2+}$  ion d-electron states act as efficient luminescent centers while interacting with s-p electronic

states of the host nanocrystals. They showed that this electronic interaction provides an effective energy transfer path and leads to high luminescent efficiencies at room temperature and hence suggested that nanocrystals doped with optically active luminescent centers may create new opportunities in the study and application of nanoscale material structures.

Because nanomaterials possess unique, beneficial chemical, physical, and mechanical properties, they can be used for a wide variety of applications. This review primarily focuses on the synthesis, properties, and applications of nanomaterials. It has been proven that the particles at the nanometer level have improved quality with respect to their potential application that include, but are not limited to, various structural, optical, electrical, mechanical, and catalytic activity, biomedical, next-generation computer chips, kinetic energy (KE) penetrators with enhanced lethality, better insulation materials, low-cost flat-panel displays, elimination of pollutants, tougher and harder cutting tools, high-sensitivity sensors, high-power magnets, future weapon platforms, aerospace, large lasting satellites, longer-lasting medical implants, corrosion resistance, etc. [Figure 1](#) shows the improvements in the final properties of the nanomaterials.

## SYNTHESIS OF NANOMATERIALS

There are several methods that can be used to synthesize solids. Solids can be also prepared in various forms as fibers, films, foams, ceramics, powders, single crystals, and nanoparticles. However, those solids, which are not thermodynamically stable, may be much more difficult to prepare and may require special methods. The oldest and widely used method is the solid-state routing of synthesizing metal oxides. In this traditional technique, the powder reactants are mixed together, pressed into pellets or some other shape, and then heated in a furnace for prolonged periods. However,

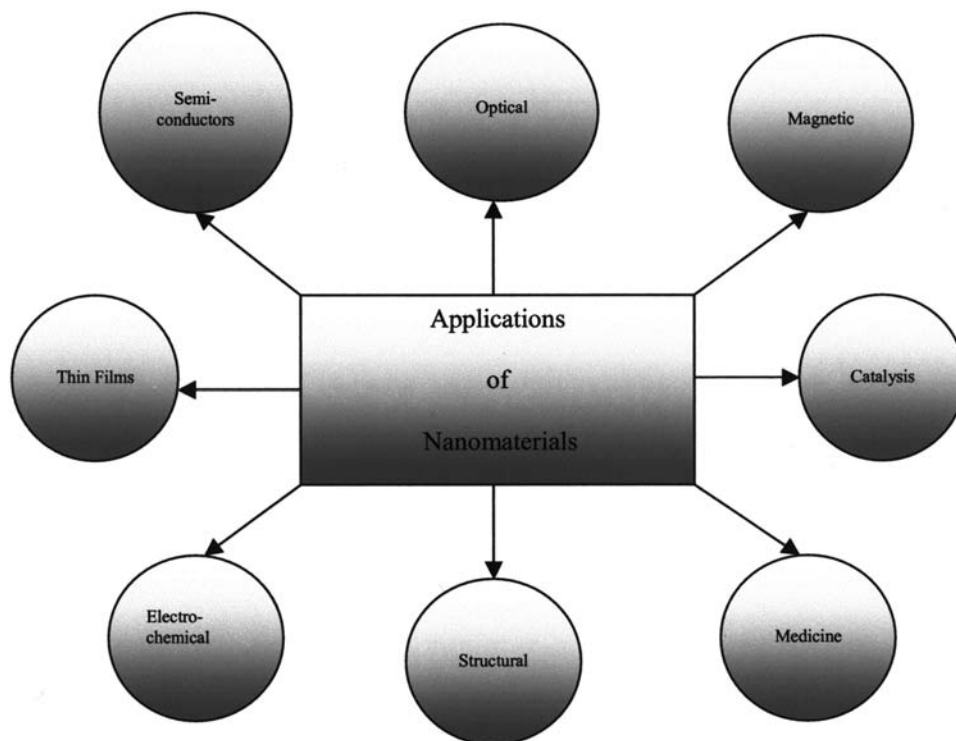


Fig. 1 Applications of nanomaterials.

this method is not very sophisticated because of the following reasons:

- It requires a high temperature to react the reactants.
- Slow diffusion of ions.
- Unhomogenized reaction mixtures.
- Impure final product because of unreacted reactants.
- Large particle size and bimodal particle size distribution.
- Defects, e.g., points/line/twinning.
- Metal oxides with unusual oxidation states cannot be prepared, e.g., vanadates and tungstates.
- Low surface area.

Solids with nanosize particle size cannot be prepared by traditional method simply because the reactants are not mixed on the atomic scale. All the alternative methods, e.g., hydrothermal, sol-gel, Pechini, CVD, and microwave, described in the rest of this section address this problem by achieving atomic scale mixing of reactants, in gas, liquid, or even solid phases. Most of these are low-temperature methods, although finally firing may be required at high temperatures especially for ceramic-type products. These methods enable the final product with the following characteristics:

- Nanosize particles.
- Narrow particle size distribution.

- High surface area.
- Homogenous.
- Pure.
- Improved properties.

### Hydrothermal Synthesis

Hydrothermal methods are becoming a popular technique to precipitate mixed metal oxides directly from either homogeneous or heterogeneous solution. Hydrothermal method utilizes water under pressure and at temperatures above its normal boiling point as a means of speeding up the reactions between solids.<sup>[7]</sup> Water is an excellent solvent because of its high dielectric constant. This decreases with rising temperature and increases with rising pressure, with temperature effect predominating. In addition, the high dielectric constant of water is confirmed to a region of low temperature and high densities (pressure). This property is mainly responsible for increasing the solubility of many sparingly soluble compounds under hydrothermal conditions leading to many useful chemical reactions such as hydrolysis, precipitation, coprecipitation, and crystal growth.

Hydrothermal reactions are usually performed in closed vessels. The pressure-temperature relations of water at constant volume are shown in Fig. 2. The reactants are either dissolved or suspended in a known



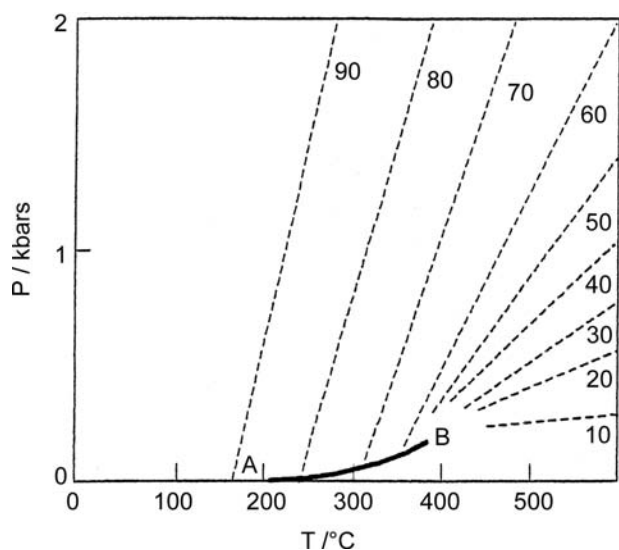


**Fig. 2** Pressure–temperature relations for water at constant volume. *Source:* From Basic Solid State Chemistry by A. R. West, John Wiley and Sons, Ltd, NY, 1999.

amount of water and are transferred to acid digestion reactors or autoclaves (Fig. 3). Under hydrothermal conditions, reactants otherwise difficult to dissolve can go into solution and reprecipitate.

Hydrothermal reaction is a single-step process for preparing several oxides and phosphates.<sup>[7–9]</sup> Oguri, Rimen, and Bowen<sup>[10]</sup> obtained narrow size distribution of spherical submicron titanium hydrous oxide, which could be readily transformed into polycrystalline anhydrous anatase with spherical morphology. Fine particles of ferroelectric lead titanate with high Curie temperature were prepared via hydrothermal technique.<sup>[11]</sup> Kutty and Balachandran synthesized

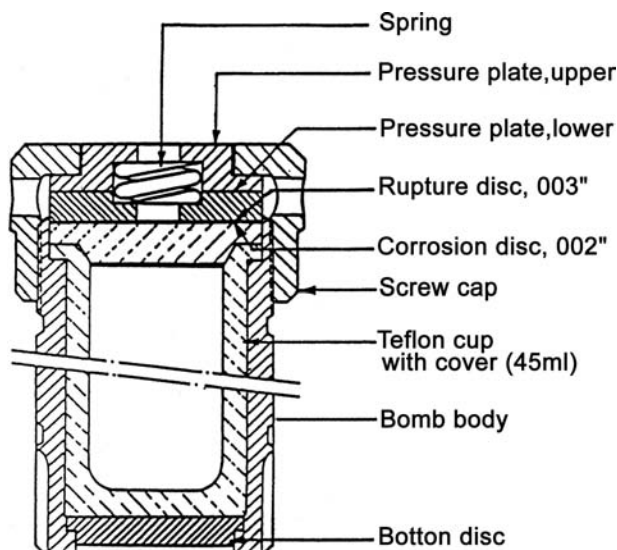


**Fig. 3** Schematic diagram of an autoclave.

lead zirconate titanate (PZT) in better compositional homogeneity and sinterability. This technique was further used for the fabrication of nanocrystalline metal oxides. Sharma et al.<sup>[12]</sup> have synthesized nanosize  $\alpha$ -alumina using hydrothermal method with particle size of 10 nm. Quantum size particles ( $< 10$  nm) of  $Y_2O_3$  could also be achieved by this technique at  $170^\circ C$  using seeds<sup>[12]</sup> and are shown in Fig. 4. This method was further employed for the fabrication of several other metal oxides, e.g., ZnO,  $TiO_2$ , and  $ZrO_2$ , with nanosize particles.<sup>[12–15]</sup>

### Sol–Gel Synthesis

In sol–gel synthesis, the precursors, which are essentially the starting compounds for the preparation of a colloid, consist of a metal or metalloid element surrounded by various links called ligands. These ligands do not include another metal or metalloid atom, but may be inorganic, such as aluminum nitrate [ $Al(NO_3)_3$ ], or organic, such as aluminum butoxide [ $Al(OC_4H_9)_3$ ]. Metal alkoxides are more widely used than any other precursors because metal alkoxides react readily with water. However, for some non-silicates, especially for transition-metal-oxide gels, inorganic precursors are used. The transition-metal-oxide gels are also used for obtaining thin-film ferroelectric materials such as barium titanate, electrochromic  $WO_3$  films, and semiconducting  $V_2O_5$  films.<sup>[16–20]</sup> Fig. 5 is the high-resolution transmission electron microscopy (HRTEM) of  $\alpha$ - $Al_2O_3$  derived by sol–gel method.

A gel can be classified as aquagel, alcogel, xerogel, and aerogel depending on the nature of the medium that is contained within the gel's three-dimensional network of particles. An aquagel is a gel wherein water

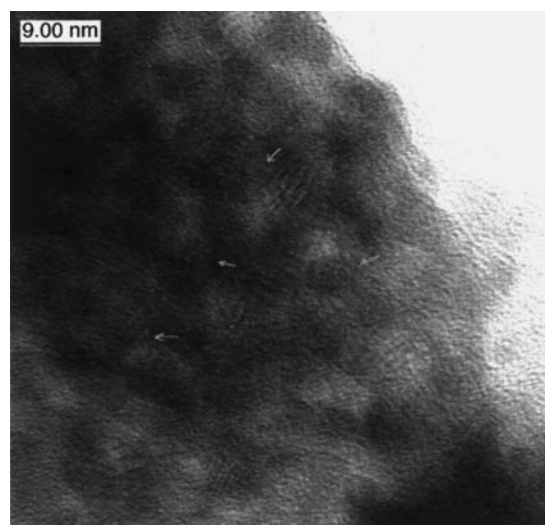


**Fig. 4** Hydrothermally prepared nanosize yttria.

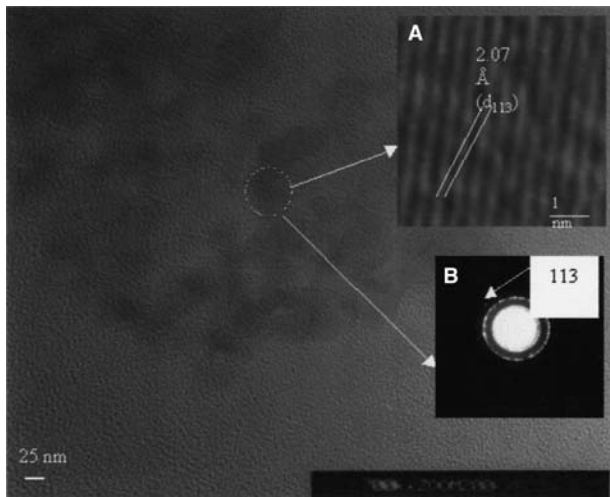


**Fig. 5** High-resolution transmission electron microscopy of  $\alpha$ -alumina synthesized by sol-gel process. Source: From Ref.<sup>[29]</sup>.

is contained within its interstices. An alcogel is a gel in which the water is replaced by alcohol substitution. When the gel is in as-dried condition, it is called a xerogel. If the gel is supercritically dried (a drying process in which a medium is replaced, by another medium, under controlled conditions so that the gel structure does not collapse), then the resulting gel is termed an aerogel, where the fluid trapped in the gel interstices is air. The techniques used to preserve the gel structure include freeze-drying. This apparatus is called the freeze-dryer and is used commercially to preserve food-stuffs such as instant coffee powders, dry milk powder, and non-dairy coffee creamer, has been used to synthesize materials, and is available in large sizes. This method has also been used to synthesize dispersion-strengthened alloy and composite systems.<sup>[18]</sup> The rationale behind the preservation of the open structure of the aquagel or alcogel is to facilitate the accelerated expulsion of the fluid trapped at the interstices of the gel, which is made of a continuous, three-dimensional network of nanocrystalline particles, during the metal deposition process in a fluidized-bed reactor. The open structure (greater grain boundary area) of the aerogel lends itself to processing at very low temperatures unlike its commercial counterparts. This method is also useful in the hydrogen reduction, carburization, nitridation, and a host of other surface treatment processes. A schematic of the aerogel is depicted in Fig. 6.

The specific advantages of the sol-gel synthesis technique are as follows:

- Sol-gel synthesis is a very viable alternative method to produce nanocrystalline elemental, alloy, and composite powders in an efficient and cost-effective manner.

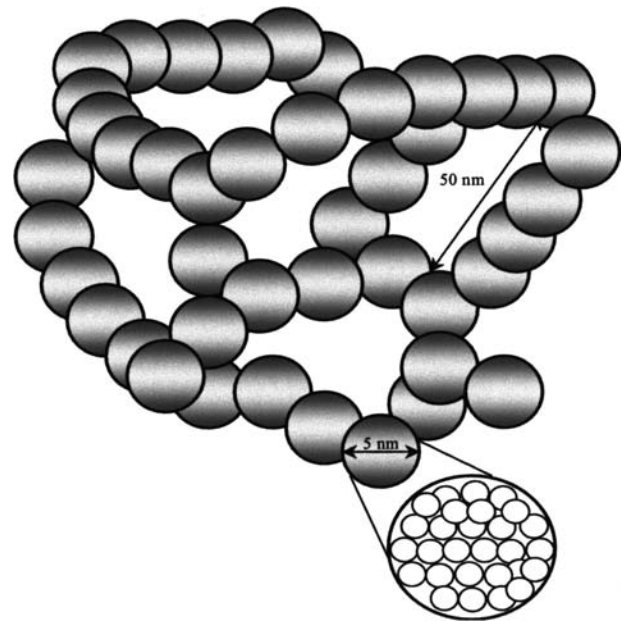


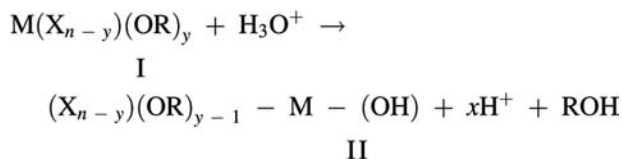
**Fig. 6** A schematic of an aerogel structure.

- Almost any combination of materials could be synthesized at very low temperatures.
- Greater control of material chemistry and homogeneity is possible.
- Sol-gel synthesized powders could be processed, such as for coating, carburization, and nitridation, at substantially lower temperatures.
- Nanocrystalline powders could be consolidated at much lower pressures and temperatures.
- Enhanced densification of high-temperature materials without the low-temperature binders, which are detrimental to their performance under extreme conditions, is also possible via sol-gel synthesis of nanocrystalline materials.
- Thermomechanical processing of the components could be accomplished at significantly lower processing conditions.
- Processes, such as infiltration, could be carried out uniformly because of the continuous, three-dimensional network of nanocrystalline particles.

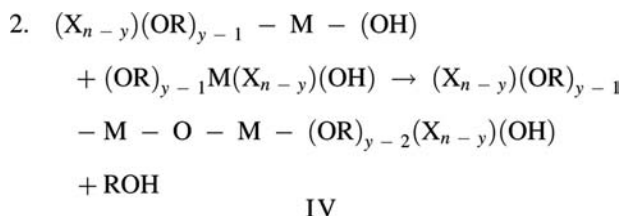
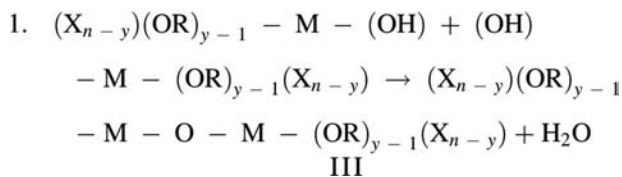
However, there are several factors that affect the sol-gel chemistry, but among them, the pH of the aqueous solution plays important roles in the particle morphology, stability, and the particle size of the final reaction products. During the polymerization process, the three-dimensional networks of particles serve as nuclei for further growth. This growth proceeds by a mechanism called Ostwald ripening whereby particles dissolve and reprecipitate on larger, less-soluble nuclei. Ostwald ripening ceases to exist when the difference in solubility between the smallest and largest particles

becomes negligible. Nevertheless, this growth continues to larger sizes at higher temperatures. Europium-doped yttrium oxide (Eu:Y<sub>2</sub>O<sub>3</sub>) was synthesized by a sol-gel method in the presence of Tween-80 and ε-caprolactam in pH range 4–10. It has been observed that the variation in surface area, pore size, and pore volume of the final product was strongly dependent on the initial pH of the solution. The powder with a large surface area (~230 m<sup>2</sup>/g) and low pore diameter (~16 nm) was obtained when the powder was processed at pH ~ 4. The crystallite sizes of the powders processed at pH ~ 4 and 10 were found to be 35 and 198 nm, respectively.

At low pH, the reaction rate of the hydrolysis is governed by the hydronium ion in solution (H<sub>2</sub>O + H<sup>+</sup> → H<sub>3</sub>O<sup>+</sup>) and is also observed by Sakka and Kamiya<sup>[21]</sup> (described below). In this reaction, the amount of water is small because of the rapid formation of H<sub>3</sub>O<sup>+</sup>. Cagle and Keefer have stated that the hydrolysis/condensation in low pH condition is relatively controlled and selective, thus generating relatively more linear polymers of metal.<sup>[22–24]</sup> Hydrolysis can be represented by the following equation



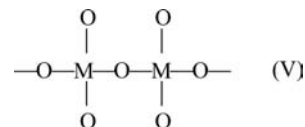
Condensation can take place by any of the following two equations:



The linear polymerization can be explained by a simple steric argument: monomers (II) are more readily hydrolyzed than dimers (III or IV), which are, in turn, more readily hydrolyzed than middle groups in chains. Therefore the reaction polymerization at low pH is expected to be a linear chain (III or IV) with

low cross-links and is also suggested by Pope and Mackenzie.<sup>[25]</sup>

At high pH, the reaction is governed by the hydroxyl ions (OH<sup>-</sup>). Although the initial growth leads to linear chains, because of the high concentration of OH<sup>-</sup> ions, it results in the cyclization because the probability of intermolecular reaction is higher than intramolecular reaction.<sup>[26]</sup> At high pH value, hydrolysis/condensation is uncontrolled and unselective, which leads to highly branched polymers. It also generates larger interconnected particles.<sup>[26–28]</sup> The polymeric chain at high pH is larger than the one at low pH. At high pH, the most probable metal-oxygen polymeric network formed in the chain is the structure V as shown in Fig. 7. Nevertheless, the larger interstices at pH > 7 result in larger grains, as shown in Fig. 7. Thus the crystallite size of the powder at pH > 7 (198 nm at pH ~ 10) was smaller than the powder at pH < 7 (35 nm at pH ~ 4). At pH ~ 10, a cube-like morphology of the particles is seen in Fig. 8. In contrast, the morphology at pH ~ 4 has totally changed into polygonal shape with size of 40 nm (shown in Fig. 8).



#### Modified sol-gel synthesis: microemulsions as microreactors

Microemulsion-based sol-gel synthesis is a versatile technique to prepare materials with novel microstructures, in particular, ultrafine (nanosize) powders, e.g., TiO<sub>2</sub>, Al<sub>2</sub>O<sub>3</sub>, ZrO<sub>2</sub>, etc.<sup>[30–32]</sup> A microemulsion may be defined as a thermodynamically stable, optically isotropic solution of two immiscible liquids (e.g., water and oil) consisting of microdomains of one or both liquids stabilized by an interfacial film of surfactants.<sup>[33,34]</sup> The surfactant molecule generally has a polar (hydrophilic) head group and a long chained aliphatic (hydrophobic) tail. Such molecules

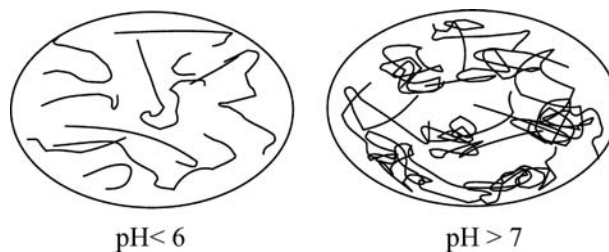
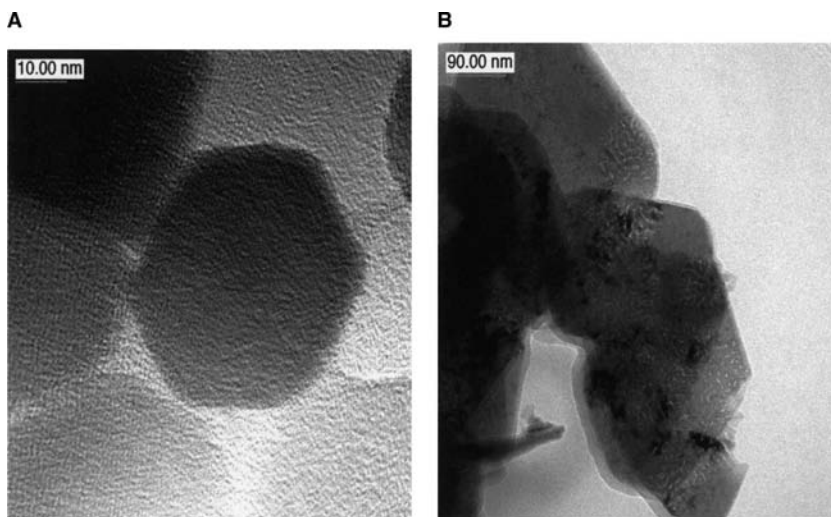


Fig. 7 Schematic diagram of polymeric network in different pH range.



**Fig. 8** High-resolution transmission electron microscopy of Eu-doped yttria at pH (A) 4 and (B) 10.

optimize their interactions by residing at the oil / water interface, thereby considerably reducing the interfacial tension. In water-in-oil microemulsion, the aqueous phase is dispersed as microdroplets (typically 10–25 nm in size) surrounded by a monolayer of surfactant molecules in the continuous hydrocarbon phase. The aqueous cores of microemulsions containing soluble metal salts are used as microreactors for the synthesis of nanoparticles. Because of the dynamic nature of the microdroplets, the exchange mechanism involves coalescence and fusion of the droplets upon collision, which then disintegrate into droplets, and this process occurs continuously in the microemulsion.<sup>[35]</sup> If two reactants, A and B, are dissolved in the aqueous core of two identical water-in-oil microemulsions, upon mixing, they will form a precipitate, AB. The growth of these particles in microemulsion is suggested to involve interdrop exchange and nuclei aggregation.<sup>[36,37]</sup> Recently, this method has been applied for the fabrication of cubic BaTiO<sub>3</sub> (please refer to Fig. 9).

### Polymerized Complex Method

Wet chemical method using polymeric precursor based on the Pechini process has been employed to prepare a wide variety of ceramics oxides.<sup>[38]</sup> The process offers several advantages for processing ceramic powders such as direct and precise control of stoichiometry, uniform mixing of multicomponents on a molecular scale, and homogeneity. In this process, an alpha hydroxycarboxylic acid, preferentially citric acid, is used to chelate various cations by forming a polybasic acid. In the presence of a polyhydroxy alcohol, normally ethylene glycol, these chelates react with the alcohol to form ester and water by-products. When the mixture is heated, polyesterification occurs in the

liquid solution and results in a homogenous sol, in which metal ions are uniformly distributed throughout the organic polymeric matrix. When excess solvents are removed, an intermediate resin is formed. This resin gives metal oxides on burning. All the organic matter removes on heat treatment.

In polymerized complex method, several metal ions in a solution could be first chelated to form metal complexes and then polymerized to form a gel, which seems to be one of the most suitable among several other chemical solution processes of nanocrystalline particles because rigidly fixed cations are homogeneously

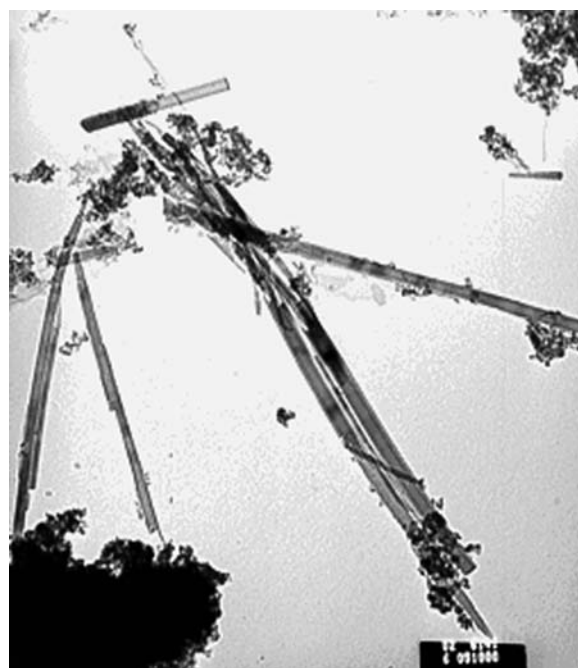


**Fig. 9** Nanosize metal oxides synthesized by microemulsion-mediated sol-gel.



dispersed in the polymer network and have few chances to segregate even during pyrolysis. This method has been already successfully applied to prepared highly pure samples of various double oxides such as  $\text{BaTiO}_3$ ,<sup>[39]</sup>  $\text{Y}_6\text{WO}_{12}$ ,<sup>[40]</sup> mixed-cation oxides,<sup>[41]</sup> and even for various superconductors<sup>[42]</sup> with multiple cationic compositions.

### Chemical Vapor Deposition

Chemical vapor deposition (CVD) may be defined as the deposition of a solid on a heated surface from a chemical reaction in the vapor phase. It is a versatile process suitable for the manufacturing of coatings, powders, fibers, and monolithic components. It is possible to produce most metals, metal oxides, and non-metallic elements such as carbon and silicon as a large number of compounds including carbides, nitrides, oxides, intermetallics, and many others. The main advantage of CVD is that the deposition rate is high and thick coatings or nanoparticles can be readily obtained. The process is generally competitive and, in some cases, more economical than the physical vapor deposition (PVD). Additionally, it is not restricted to a line of sight deposition, which is a general characteristic of sputtering, evaporation, and other PVD processes. However, two major areas of applications of CVD have rapidly developed the last 20 years or so, namely, in the semiconductor industry and in the metallurgical coating industry which includes cutting tool fabrication. Very recently, the CVD process has been given enormous attention owing to the possibility of mass production of monodisperse nanoscale powders; however, the mechanism of powder synthesis kinetics is still not clear.<sup>[43–46]</sup> Kim, Yu, and Lee<sup>[46]</sup> have synthesized nanosize  $\text{TiO}_2$  powders using CVD. Carbon nanotubes have also synthesized by CVD method using Fe–Mo nanoparticles.<sup>[47]</sup>

### Microwave Synthesis

Recently, there has been a growing interest in heating and sintering of ceramics by the microwave energy.<sup>[48,49]</sup> The interest in the use of microwave processing spans a number of fields from food processing to medical applications to chemical applications. A major area of research in microwave processing of ceramics includes microwave material interaction, dielectric measurement, microwave equipment design, new material development, sintering, joining, and modeling. Therefore the microwave processing of ceramics has emerged as a successful alternative to conventional processing. Nevertheless, microwave method not only offers the advantages of a uniform heating at lower temperature and time than the conventional method, but also provides an economic method of processing. The microwave energy has been already successively utilized in the fabrication of ceramics as well as carbon fibers at low temperature and time. Varadan et al.<sup>[50]</sup> and Sharma, Varadan, and Varadan<sup>[51]</sup> have synthesized various electroceramics such as barium strontium titanate (BST) and lead zirconate titanate (PZT) by microwave. Fig. 10 shows the schematic diagram of a typical domestic microwave unit used by Sharma, Varadan, and Varadan. These materials are observed to have improved mechanical, electrical, and electronic properties. Until recently, microcoiled carbon fibers with large surface area have also been fabricated by using microwave aid.<sup>[52]</sup>

Fig. 11 shows a schematic diagram of a microwave chemical deposition unit used for the fabrication of carbon nanotubes and coils. It consists of microwave magnetron, circulator, four-stub tuner, waveguide, cavity, etc. The microwave power can be adjusted from 0 to 3000 W at a frequency of 2.45 GHz. The function of circulator was to prevent power reflected by the load, thus preventing overheating of the magnetron. The forward and reflected powers were determined

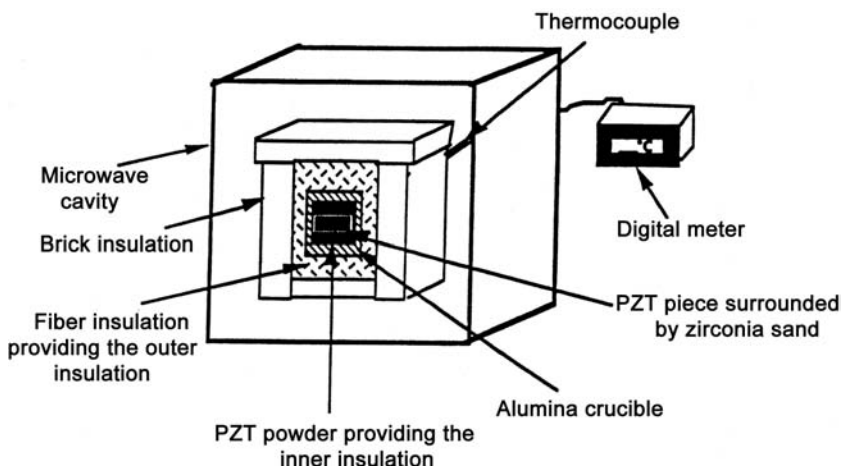


Fig. 10 Schematic diagram of microwave used for the powder.

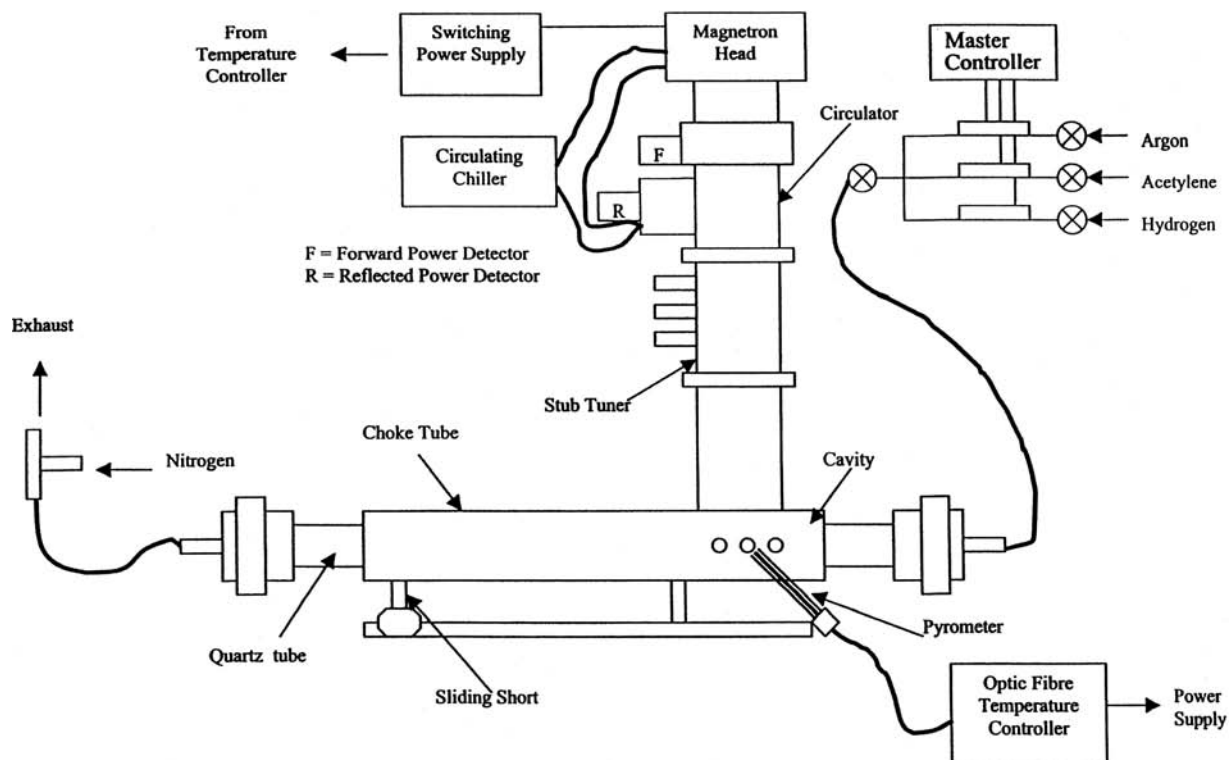


Fig. 11 Schematic diagram of the microwave chemical vapor deposition of carbon nanotubes.

by a power meter that is helpful in determining impedance matching. The four-stub tuner, consisting four threaded stubs spaced at  $3/8$  wavelength apart, was another part to optimize impedance matching. These stubs were adjusted properly, and the four-stub tuner became a matching network which maximized the power transmitted to the load by matching the source impedance to that of the load. As an important part of cavity, sliding short was used to adjust the length of the cavity such that it could resonate at 2.45 GHz. High field intensities could be attained when the cavity resonates. A quartz tube, which was the reaction chamber, passed through the cavity. Reaction gases were introduced from one end of the quartz tube and exhausted at the other end. The flow rates were controlled by a set of flow controller. In this microwave CVD system, SiC was chosen as substrate because of its high loss tangent; thus it could absorb microwave energy effectively. A fibrous morphology with a hollow tube inside was obtained. The diameter of these Multi-wall nanotubes (MWNT) ranges from 20 to 30 nm as shown in Figs. 12–14.

### High-Energy Ball Milling Processes

Ball milling has been utilized in various industries to perform size reduction for a long time. Recently, materials with novel microstructures and properties have

been synthesized successfully via high-energy ball milling processes.<sup>[53,54]</sup> Although different terms have been used to describe the high-energy ball milling processes, three terms are generally used to distinguish powder particle behavior during milling: mechanical alloying (MA), mechanical milling (MM), and mechanochemical synthesis (MS). Mechanical alloying

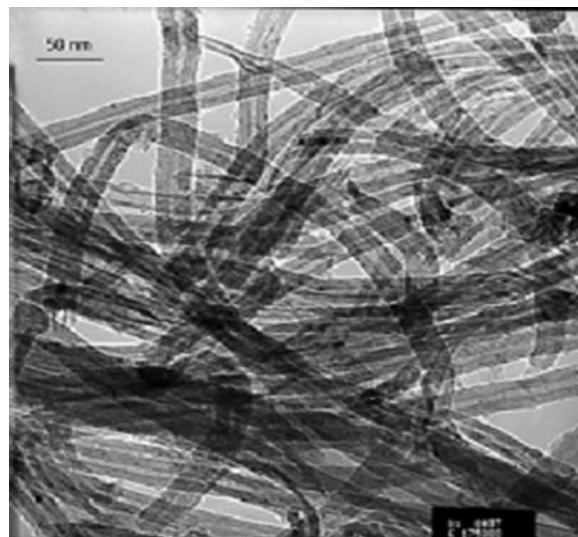
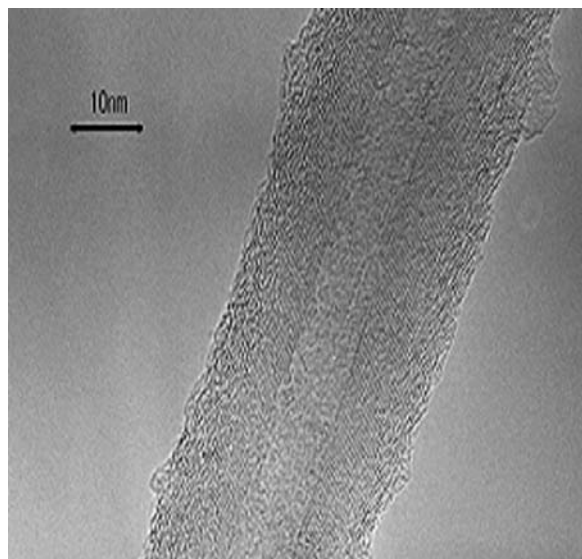


Fig. 12 Transmission electron microscopy of the CNTs obtained from microwave.





**Fig. 13** High-resolution transmission electron microscopy of MWCNT from microwave CVD.

is referred to when mixtures of powders are milled together. In this case, material transfer is involved to obtain a homogeneous alloy. Mechanical milling describes a milling process when no material transfer is involved; that is, only powder with uniform composition is milled. Mechanochemical synthesis, on the other hand, is a special MA process where chemical reactions between the powders take place during milling. The unique feature of the MS process is that grain refinement and chemical reactions take place at low temperatures under far-from-equilibrium conditions.

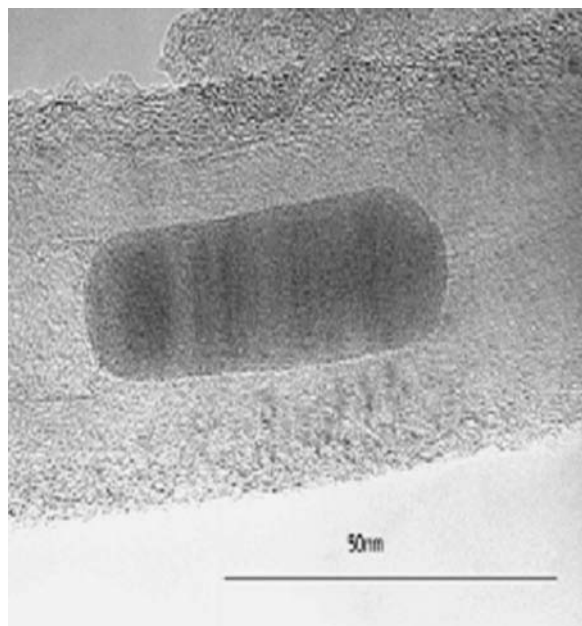
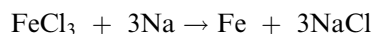


**Fig. 14** High-resolution transmission electron microscopy of MWNTs with Encapsulated Co.

A wide variety of nanostructure (grain size in the range of 1–100 nm) materials have been synthesized via MA and MM techniques.<sup>[53–55]</sup> However, MA and MM are not capable of synthesizing nanoscale powders primarily because of cold welding and agglomeration during milling. In other words, individual powders synthesized by MA and MM usually contain many nanosize grains and may show rather low specific surface area values.

It has been shown more recently that the nanocomposite mixtures formed during mechanochemical reactions can be further processed into nanoscale particles.<sup>[56–58]</sup> For instance, nanocomposite of Fe and NaCl was obtained by milling FeCl<sub>3</sub> and sodium metal according to the following reaction:



On dissolution of the soluble NaCl phase by a simple washing process after milling, Fe nanoparticles with relatively narrow particle size distribution can be obtained.<sup>[56]</sup> The synthesis of ultrafine oxide powders with particle size of 10–50 nm has also been reported.<sup>[59,60]</sup>

There are some inherent advantages in processing nanomaterials via high-energy ball milling techniques, such as excellent versatility, scalability, and cost-effectiveness. Therefore high-energy ball milling techniques are well suited for manufacturing large quantity of nanomaterials. A major concern of ball milling techniques is the powder contamination. While the contamination is mainly caused by the wear of milling media and container, the level of contamination depends on factors such as milling time, milling intensity, and milling atmosphere. Attempts have been made in recent years to minimize the powder contamination during ball milling. For example, using the same material for the container and grinding media as the powder being milled will help reduce the contamination.

## PROPERTIES OF NANOMATERIALS

### Optical Properties

It is well known that the yttrium oxide (Y<sub>2</sub>O<sub>3</sub>) has its application in the lighting industry for Eu:Y<sub>2</sub>O<sub>3</sub>, the red phosphor of the trichromatic fluorescent lamps.<sup>[61]</sup> Because of a <sup>5</sup>D<sub>0</sub>→<sup>7</sup>F<sub>2</sub> transition within europium, Eu:Y<sub>2</sub>O<sub>3</sub> shows luminescence properties and emits red light with a wavelength of 611 nm.<sup>[62]</sup> The rare earth ions, such as Eu<sup>3+</sup> and Nd<sup>3+</sup>, show sharp emissions based on electron transitions within the 4f manifold. Furthermore, their emission is found to be highly dependent on the local environment of rare earth ions.

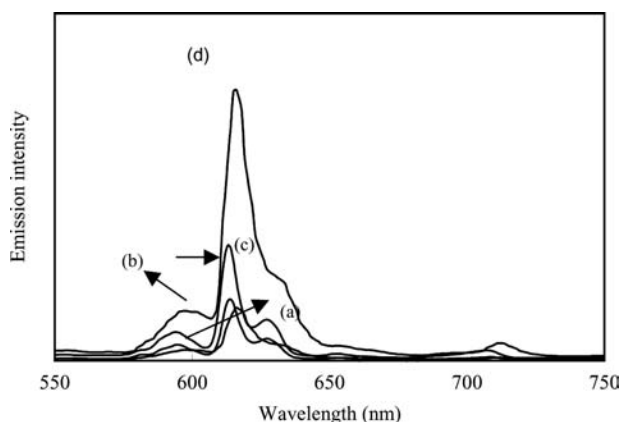


**Fig. 15** Emission spectra of powder with the particle size (A) 6  $\mu\text{m}$ , (B) 1  $\mu\text{m}$ , (C) 0.2  $\mu\text{m}$ , and (D) 0.01  $\mu\text{m}$ .

Therefore the fluorescence of  $\text{Eu}^{3+}$  ions can be used as a probe to investigate the local surrounding in the host, e.g., yttria, alumina, and mullite.

Effect of particle size on fluorescence behavior ( ${}^5\text{D}_0 \rightarrow {}^7\text{F}_2$  transition) of  $\text{Eu}^{3+}$  in the yttria powder was studied by Sharma et al.<sup>[63]</sup> The most noteworthy feature of Fig. 15 is the sensitivity of  ${}^5\text{D}_0 \rightarrow {}^7\text{F}_2$  peak (614 nm) with the particle size. It has been observed that the peak emission intensity of  ${}^5\text{D}_0 \rightarrow {}^7\text{F}_2$  transition increases approximately fivefold as the average particle size decreases from 6  $\mu\text{m}$  to 10 nm. This suggests that the emission intensity of fluorescence varies inversely as the particles size increases. Its behavior was expected from the quantum-confinement model as described by Bawendi et al.<sup>[64]</sup> and Alivisatos et al.<sup>[65]</sup> Goldburt et al.<sup>[66]</sup> have observed high efficiency in Tb-doped  $\text{Y}_2\text{O}_3$  nanocrystals which was measured at 18% as compared with 16% in the bulk and stated that the non-radiative contribution decreases with decrease in particle size. The size dependence of the fluorescence emission intensity can also be demonstrated in terms of number of particles per unit area facing toward the incident light as described by Iwasaki, Ida, and Kimura.<sup>[67]</sup> Increasing surface area of smaller particles (refer Table 1) leads to enhancement in the fluorescence intensity.<sup>[67]</sup> All spectral features were found to be unchanged except the intensity of the peak centered at 395 nm, which was found to be enhanced and shifted to lower wavelength (higher energy level) as the par-

tle size decreased. This shift in excitation spectra with particle size is the evidence of quantum confinement. Gallagher et al.<sup>[68]</sup> have reported a shift of 60 nm in the excitation peak at the maximum emission from  $\text{Mn}^{2+}$  doped in ZnS nanocrystals to shorter wavelength with decrease in particle size because of quantum-confined ZnS.

### Electrochromic devices

An electrochromic device consists of materials in which an optical absorption band can be introduced or an existing band can be altered by the passage of current through the materials or by the application of an electric field. Nanocrystalline materials, such as tungstic oxide ( $\text{WO}_3 \cdot \text{H}_2\text{O}$ ) gel, are used in very large electrochromic display devices. The reaction governing electrochromism (a reversible coloration process under the influence of an electric field) is the double injection of ions (of protons,  $\text{H}^+$ ) and electrons, which combine with the nanocrystalline tungstic acid to form a tungsten bronze. These devices are primarily used in public billboards and ticker boards to convey information. Electrochromic devices are similar to liquid-crystal display (LCD) commonly used in calculators and watches. However, electrochromic devices display information by changing color when a voltage is applied. When the polarity is reversed, the color is bleached. The resolution, brightness, and contrast of these devices greatly depend on the tungstic acid gel's grain size. Hence nanomaterials are being explored for this purpose. Using nanostructure materials, color change will be faster and uniform. Additionally, the number of cycles of coloration and bleaching can be enhanced. Recently, Ntera Inc. has developed an electrochromic display technology called NanoChromics<sup>TM</sup> using nanostructure film electrodes. The nanostructure films are derived from sol-gel precursors and formulated to suit the particular coating application method.

### Catalytic Properties

Some of \$10 trillion worth of chemicals and materials are produced each year through catalytic processes,

**Table 1** Comparison of  $\text{Li-MO}_2$  in microparticle and nanoparticle size

Properties	$\text{LiNiO}_2$ <sup>[74]</sup>		$\text{LiMnO}_2$ <sup>[75]</sup>		$\text{LiCoO}_2$ <sup>[77]</sup>		$\text{Li}[\text{Cu}_{1-x}\text{Fe}_x]\text{O}_2$	
	Micro	Nano	Micro	Nano	Micro	Nano	Micro	Nano
Crystallite size	830 nm	300 nm	$\approx$ microns	5–50 nm <sup>[75]</sup>	1.67 $\mu\text{m}$ <sup>[74]</sup>	60 nm	$\approx$ microns	< 50 nm <sup>[80]</sup>
Capacity (mAh/g)	90 <sup>[1]</sup>	205 <sup>[1]</sup>	130 <sup>[76]</sup>	250	87 <sup>[1]</sup> 140 <sup>[78]</sup> ; 126 <sup>[79]</sup> ;	167 <sup>[1]</sup>	140 <sup>[1]</sup>	230 <sup>[1]</sup>
Potential (V)	4.2	4.2	4.1	3.8	4.1 <sup>[78]</sup> ; 3.9 <sup>[79]</sup>	4.2	4.1	4.2

according to industry estimates and published in Chemical and Engineering News. Most of these processing deal with the microscopic size of the particle with diameters measuring no more than a few billionths of a meter. In catalysis, the goal is to design catalysts with certain features that help boost catalytic performance. It is anticipated that this goal will be more closely approached through tailoring a catalyst particle via nanoparticle synthesis and assembly, so that it performs only specific chemical conversions, performs at high yield, and does so with greater energy efficiency. It has been established that the nanostructures have higher surface area than do conventional materials. The high surface areas can be attained either by fabricating small particles or clusters where the surface-to-volume ratio of each particle is high (category I) or by creating materials where the void surface area (pores) is high compared with the amount of bulk support materials (category II). Materials such as highly dispersed supported metal catalysts and gas phase clusters fall into the first category, and microporous (nanometer-pored) materials such as zeolites, high surface area metal oxides, porous carbon, and amorphous silica fall into category II. The nanostructure approach to high surface area materials may have significant impact in petrochemical process, biosensors, gas sensors, absorption and adsorption phenomena, gas storage, energy storage, battery performance, biological reactions, etc.

### Electrochemical Properties

Lithium-based rechargeable batteries have been proposed for a wide variety of extremely demanding applications. These applications include, but are not limited to, electric vehicle (EV), start-light-ignition (SLI), portable electronics, and personal communications devices. The lithium battery technology can be generally classified as cathode, anode, and electrolyte technology (liquid-electrolyte and solid-electrolyte types). Although variation in cathode materials for lithium has been recognized as a highly flexible and versatile technological approach for the production of high-energy density batteries, none of the existing battery technology is capable of satisfying the energy- and power-density requirements in the aforementioned applications. The widespread use of battery is severely hampered by poor performance of cathode materials of Li-ion battery because of the following characteristics:

- Micron-size particles.
- Small surface area.
- Unstable structure during cycling.
- Inadequate mechanical strength.
- Costly precursors, high-temperature stability.

Furthermore, the aforementioned characteristics are the primary factors that deprive the overall performance of the battery, which include the following

- Inferior electrochemical stability.
- Inferior mechanical properties.
- Greater toxicity.
- Low power-to-energy ratio.
- High costs.
- Low cycle life.
- Low calendar life.
- Poor thermal management capabilities.
- Inferior manufacturability.
- Potential hazards, especially of the liquid electrolytes, because of leakage, deposition, and explosion.

To obviate the aforementioned deficiencies associated with cathode materials, researchers have developed a new class of material using nanoparticles of different cathode materials based on metal oxides, which will exceed, or meet, the above performance requirements.

Furthermore, it is now well established that the limitations in the rate capabilities of Li-ion batteries are caused by slow solid-state diffusion of Li within the electrode materials.<sup>[69–72]</sup> As a result, there is tremendous interest in the development of *nanostructure* Li-ion battery cathode electrodes. These batteries can store two to three times more energy per unit weight and volume than the one with micron-particle-size electrode.<sup>[73]</sup> Table 1 represents the improvement in the Li-ion battery.

### Energy Storage

Recent interest in the use of hydrogen as a multi-purpose fuel has emphasized the necessity of reliable storage system for this element. LaNi<sub>5</sub> alloy stores up to 1.6%, while FeTi stores up to 1 wt.% of hydrogen in the form of metal hydride. The hydrogen capacity in these host materials was quite low, and hence research was focused on the storage of hydrogen in molecular sieves especially in natural and synthetic zeolites.<sup>[81]</sup> CsA-zeolite was found to have hydrogen storage capacity of ~6 wt.%. On the other hand, it is also well known that the carbon nanotubes (CNTs) have the capacity of hydrogen storage.<sup>[81–83]</sup> Dillon et al.<sup>[82]</sup> reported that the SWNTs with low purity could adsorb 5 wt.% of H<sub>2</sub> at 133 K and 0.040 MPa. This value of hydrogen storage was enhanced to 8 wt.% for highly pure Single wall nano tubes (SWNT) in the studies of Ye et al.<sup>[81]</sup> However, temperature was reduced to 80 K and pressure was increased to 7.18 MPa. At room temperature, the hydrogen capacity was only 4 wt.% at 10 MPa.

## Biomedical

Biomolecule/inorganic interactions can be used to produce ceramics with increased toughness. Fundamental studies of biomineralization, in which an organic substance (usually protein or peptide or lipid) interacts with an inorganic phase (e.g., calcium carbonate or hydroxyapatite), have led to the bioinspired synthesis of composite materials. Hydroxyapatite (HAp), a major inorganic component of bone, has been used extensively for biomedical implant applications and bone regeneration because of its bioactive, biodegradable, and osteoconductive properties. However, the application of pure HAp is very limited because of its brittleness. Because the natural bone is a composite mainly consisting of nanosized needlelike HAp crystals and collagen fibers, many efforts have been made to modify by polymers such as polylactic acid, collagen, chitosen, and polyethylene and have received much attention in the field of medical applications because of their excellent biocompatibility and biodegradability.<sup>[84]</sup> Additionally, the following materials are used in various applications of biomedical, biotechnical, and bioengineering.

### Nano-ZnO

1. Biosensor: Nanoparticles of ZnO can sense the toxic and hazardous gas such as H<sub>2</sub>, SF<sub>6</sub>, and gasoline in shorter time because of high surface area.
2. Neutralizes biochemical use in biological weapons because high surface area of nanostructured ZnO is highly reactive and able to degrade toxic biochemical (e.g., naphthalene, anthracene, phenol, chlorophenol, and polyaromatic hydrocarbons) use in biological weapons.

### Nano-MgO and nano-TiO<sub>2</sub>

Nano-MgO and nano-TiO<sub>2</sub> neutralize the biological immune buildings, e.g., bacteria and virus, which are used as biological warfare agents.

### Magnetic nanoparticles of iron

Magnetic particles coated with biocompatible polymers dispersed in water could be used as

- Site-specific drug delivery after being attached with drug molecules to the magnetic particles.
- Magnetic tourniquet. In this case, a person with blood loss because of injury could be injected with the magnetic particles dispersed in water. Then a magnet could be placed on the injury site. The

magnetic particles will agglomerate there and hence would prevent the blood from flowing out.

### Biodegradable nanosilica

Biodegradable nanosilica can be used for drug delivery. It is important for an inorganic material to be used as a drug delivery agent; it should be biodegradable, nanosized, porous, and non-toxic. Nanostructured silica can be a good candidate for a drug delivery agent, which can easily degrade and would not provide any side effect. This kind of drug delivery system will be extremely valuable for the instant wound therapy of any injured person.

### Protein tagging using nanoluminescent particles

Protein tagging is an experimental strategy in which a tag such as a probe (luminescent lanthanides, e.g., Eu, Sm, etc.) is attached to primary sequence of a protein. The size of the tag used for attachment to the loops of a protein must be extremely small.

This strategy can also be used in:

- Cancer therapy: to block interactions such as enzyme substrate interactions or interaction of a toxin with a specific cell or a component of a cell.
- Drug delivery: for delivery of protein drugs to cells.

### CdS and ZnS semiconductor quantum dots

Immunosensor, bioanalytical, and biolabels: Semiconductor quantum dots are highly light-absorbing luminescent nanoparticles, whose absorbance onset and emission maximum shift to higher energy with decreasing particle size because of quantum confinement effect.

Quantum dots can conjugate with antibodies using an engineered adapter protein and are new types of reagents for immunosensors and bioanalytical applications.

### Nanogold particles

1. Labeling of target molecules, especially protein with nanogold particles, has revolutionized the visualization of cellular or tissue components by electron microscopy or atomic force microscopy.
2. As a bioconjugate: with DNA, it can detect the active site of DNA and can be used in disease diagnostics.

### Nanoparticles in gene therapy

Nanoparticles are now also being used as a delivery mechanism in gene therapy. Nanoparticles can be

employed to insert good DNA into specific sites to replace faulty genes in such disorders as cystic fibrosis.

## Textile

Another huge industry that will be impacted by nanotechnology is the textiles industry. Companies are working on “smart” fabrics that can change their physical properties according to surrounding conditions or even monitor vital signs. The incorporation of nanoparticles and capsules in clothing offers some promise, and nanotubes would make extremely light and durable materials. Fabrics are already being marketed that are highly resistant to water, stains, and wrinkling.

## Magnetic Properties

Ferromagnetic nanomaterials have potential advantages over existing materials in numerous applications in soft magnets,<sup>[85]</sup> hard magnets,<sup>[86]</sup> magnetic recording,<sup>[87,88]</sup> etc. The study and exploitation of magnetism at the nanometer scale have been exceptionally active research areas over the past two decades. Ferromagnetic nanoparticles (usually referred to as magnetic nanoparticles) have generated great interest because of their size-dependent magnetic properties. The ferromagnetic interaction leads to parallel spins on adjacent atoms. However, the exchange forces responsible are short range, and magneto static forces dominate at great distances. Magnetic domains arise spontaneously in bulk ferromagnets to minimize their overall energy. The typical sizes of the domains are in nanometer-size range. Below a certain size, which is in the nanometer range, it is energetically favorable for a particle to be monodomain.

The coercivity of magnetic materials has a striking dependence on their size. It increases with the reduction of particle size in the nanometer range going through a maximum at the single domain size, and then decreases again for very small particles because of thermal effects and becomes zero at the superparamagnetic particle size. Iron, which is a soft magnetic material with coercivity about 20 Oe at room temperature, could be made “hard” with a coercivity of 540 Oe when the particle size is reduced to about 12 nm.<sup>[89]</sup> Remarkably low coercivity of the order of a few millioersteds along with high saturation magnetization and permeability has been achieved in  $\text{Fe}_{74}\text{Si}_{15}\text{B}_7\text{Cu}_1\text{Nb}_3$  nanocrystalline magnetic alloy where  $\alpha$ -Fe(Si) nanocrystallites of size  $\sim 10$  nm are embedded in an amorphous matrix.<sup>[90]</sup> These materials were synthesized

by melt spinning followed by annealing. The nanocrystallites, whose dimension is less than the exchange length, are exchange-coupled with randomly oriented easy axes of magnetization. The combination of random orientation and averaging over multiple grains makes the preference for magnetization in a particular direction, and therefore the effective magnetic anisotropy and hence coercivity are small.<sup>[91,92]</sup> Several other nanocrystalline soft magnetic alloys based on Fe(Co)–Si–B have been studied.<sup>[93]</sup>

R–Fe–B (R = Nd, Pr, Dy, Pr) alloys, prepared using melt-spinning, exhibited very high coercivity in the range 10–100 kOe.<sup>[86]</sup> In these permanent or hard magnets, the large coercivity is a result of the highly anisotropic tetragonal  $\text{R}_2\text{Fe}_{14}\text{B}$  phase, which were produced in the nanoscale size during melt spinning or subsequent crystallization. Several other permanent magnets, e.g.,  $\text{SmCo}_5$ ,  $\text{Sm}_2\text{Co}_{17}$ ,  $\text{Sm}_2\text{Fe}_{17}\text{N}_{2.6}$ , etc., with high coercivity have been made with nanosized microstructure.<sup>[86]</sup> Another class of hard magnetic material is called nanocomposite permanent magnet or exchange-coupled magnet where the nanocomposite consisting of a hard magnetic material such as  $\text{Nd}_2\text{Fe}_{14}\text{B}$  and a soft magnetic phase such as  $\alpha$ -Fe are coupled through exchange interaction.<sup>[94,95]</sup> This leads to high coercivity and high remanence to saturation magnetization ratio and hence high maximum energy product values. In these magnets, the crystallite size needs to be less than 20 nm for exchange coupling to occur. Most of these nanocomposite magnets have been prepared by melt spinning and mechanical alloying.<sup>[96,97]</sup> Recently, a chemical synthesis has been proposed with the potential for making three-dimensional magnets with high maximum energy product.<sup>[98]</sup> First,  $\text{Fe}_{58}\text{Pt}_{42}$  and  $\text{Fe}_3\text{O}_4$  nanoparticles of 4-nm size are mixed and allowed to self-assemble. When it was heated and chemically reduced, FePt (hard)– $\text{Fe}_3\text{Pt}$  (soft) nanocomposite is formed. The particles are 5 nm in size. The maximum energy product is 20.1 MGOe compared with 13 MGOe for FePt alone. This is an exciting new development that shows promise for making strong magnets.<sup>[99]</sup> Moreover, 4-nm particles of  $\text{Fe}_{52}\text{Pt}_{48}$  (synthesized by very similar chemical route) that self-assembled into arrays when annealed exhibited a coercivity of 1800 Oe.<sup>[100]</sup> These  $\text{Fe}_{52}\text{Pt}_4$  nanocrystal assemblies are smooth ferromagnetic films, and initial magnetic recording experiments suggested that it could support high-density magnetization reversal transitions or bits. A key requirement for magnetic recording at areal density in the terabits per square inch regime is a medium with nanometer-size, magnetically isolated grains with moderately high writable coercivity.<sup>[87,88]</sup> With these 4-nm  $\text{Fe}_{52}\text{Pt}_{48}$  self-assembled particles, it might be possible to achieve magnetic recording at areal density in the terabits per square inch range.

## CONCLUSION

This review highlighted on the fabrication of nanomaterials by various methods e.g. chemical, physical and mechanophysical. The various properties e.g. chemical, physical, mechanical, magnetic, optical and electrical, of nanomaterials have discussed in detail. Nanostructured materials exhibit novel and technologically attractive properties, which can be exploited for a variety of applications which include, but are not limited to the biomedical, energy, displays, insulations, elimination of pollutants, catalysis, microelectronics, high power magnets, sensors, aerospace, weapons, automobiles etc.

## REFERENCES

1. Khairutdinov, R.F.; Rubtsora, N.A.; Costa, S.M.B. Size effect in steady-state and time-resolved luminescence of quantized MoS<sub>2</sub> particle colloidal solutions. *J. Lumin.* **1996**, *68*, 299.
2. Kortan, A.A.; Hull, R.; Opila, R.L.; Bawendi, M.G.; Steigerwald, M.L.; Carrol, P.J.; Bruce, L.E. Nucleation and growth of cadmium selenide on zinc sulfide quantum crystallite seeds, and vice versa, in inverse micelle media. *J. Am. Chem. Soc.* **1990**, *112*, 1327.
3. Bawendi, M.G.; Wilson, W.L.; Rothberg, L.; Carroll, P.J.; Jedju, T.M. Electronic structure and photoexcited-carrier dynamics in nanometer-size CdSe clusters. *Phys. Rev. Lett.* **1990**, *65*, 1623.
4. Alivisatos, A.P.; Harris, A.L.; Lennos, N.J.; Steigerwald, M.L.; Bruce, L.E. Electronic states of semiconductor clusters: homogeneous and inhomogeneous broadening of the optical. *J. Chem. Phys.* **1988**, *89*, 4001.
5. Jungnickel, V.; Henneberger, F. Luminescence related processes in semiconductor nanocrystals—the strong confinement regime. *J. Lumin.* **1996**, *70*, 238.
6. Bargava, R.N.; Gallagher, D.; Hong, X.; Nurmikko, A. Optical properties of manganese-doped nanocrystals of ZnS. *Phys. Rev. Lett.* **1994**, *72*, 416.
7. Rabenau, A. *Chem. Intl. Ed. Eng.* **1985**, *24*, 1026.
8. Clearfield, A. Hydrothermal synthesis of selected phosphates and molybdates. *Prog. Cryst. Growth Charact.* **1991**, *21*, 1.
9. Haushalter, R.C.; Mundi, L.A. Reduced molybdenum phosphates: octahedral-tetrahedral framework solids with tunnels, cages, and micropores. *Chem. Mater.* **1992**, *4*, 31.
10. Oguri, Y.; Riman, R.E.; Bowen, H.K. Processing of anatase prepared from hydrothermally treated alkoxy-derived hydrous titania. *J. Mater. Sci.* **1988**, *23*, 2897.
11. Cheng, H.; Ma, J.; Qiang, D. Hydrothermal synthesis of PbTiO<sub>3</sub> from PbO and TiO<sub>2</sub>. *J. Mater. Sci. Lett.* **1996**, *15*, 1245.
12. Sharma, P.K.; Jilavi, M.H.; Nass, R.; Schmidt, H. Seeding effect in hydrothermal synthesis of nanosize yttria. *J. Mater. Sci. Lett.* **1998**, *17*, 883.
13. Sharma, P.K.; Jilavi, M.H.B.; Nass, R.; Schmidt, H. Hydrothermal synthesis of nanosize alpha-Al<sub>2</sub>O<sub>3</sub> from seeded aluminum hydroxide. *J. Am. Ceram. Soc.* **1998**, *10*, 883.
14. Kimel, R.A. *Thesis*; The Pennsylvania State University, 2002; 8.
15. Yang, J.; Mei, S.; Ferreira, J.M.F. Hydrothermal synthesis of nanosized titania powders: influence of peptization and peptizing agents on the crystalline phases and phase transitions. *J. Am. Ceram. Soc.* **2000**, *83*, 1361.
16. Raghunathan, S.; Bourell, D.L. Synthesis and evaluation of advanced nanocrystalline tungsten-based materials. *P/M Sci. Technol. Briefs* **1999**, *1*, 9.
17. Raghunathan, S. Tungsten and Tungsten-Based Alloys and Composites for High Heat Flux Duty, Proceedings of the APMI/MPIF PM<sup>2</sup>TEC Conference, Nashville, TN, May, 16–19, 1993.
18. Raghunathan, S. Synthesis, Consolidation, and High-Temperature Deformation Characteristics of Nanocrystalline Tungsten and Tungsten-Based Alloy and Composite Powders. Ph.D. Dissertation. The University of Texas at Austin, October, 1991.
19. Raghunathan, S.; Persad, C.; Bourell, D.L.; Marcus, H.L. *Mater. Sci. Eng.* **1991**, *A131*, 243.
20. Persad, C.; Raghunathan, S. *Mater. Res. Soc. Symp. Proc.* **1988**, *120*, 23.
21. Sakka, S.; Kamiya, K. The sol-gel transition in the hydrolysis of metal alkoxides in relation to the formation of glass fibers and films. *J. Non-Cryst. Solids* **1992**, *48*, 31.
22. Cagle, P.C.; Klemperer, W.G.; Simmons, C. A Molecular architecture and its role in silica sol-gel polymerization. In *Better Ceramics Through Chemistry III*; Mater. Res. Soc. Symp. Proc.; Zelinski, B.J.J., Brinker, C.J., Clark, D.E., Ulrich, D.R., Eds.; 1990; Vol. 180, 29 pp. Pittsburgh, PA.
23. Keefer, K.D. *Silicon-Based Polymer Science; A Comprehensive Resource*; Adv. Chem. Ser.; Zeigler, J.M., Gordon, F.W., Eds.; Am. Chem. Soc.: Washington, DC, 1990; Vol. 224, 228.
24. Kelts, L.W.; Effinger, N.J.; Melpoder, S.M. Sol-gel chemistry studied by <sup>1</sup>H and <sup>29</sup>Si nuclear magnetic resonance. *J. Non-Cryst. Solids* **1996**, *83*, 353.
25. Pope, E.J.A.; Mackenzie, J.D. Sol-gel processing of silica II. The role of the catalyst. *J. Non-Cryst. Solids* **1986**, *87*, 185.
26. Klemperer, W.G.; Ramamurthi, S.D. Molecular growth pathways in silica sol-gel polymerization. In *Better Ceramics Through Chemistry III*; Mater. Res. Soc. Symp. Proc.; Brinker, C.J., Clark, D.E., Ulrich, D.R., Eds.; 1988; Vol. 121, 1 pp. Pittsburgh, PA.
27. Chen, Y-W.; Yen, T-M.; Li, C. Preparation of alumina-zirconia materials by the sol-gel method from metal alkoxides. *J. Non-Cryst. Solids* **1995**, *185*, 49.
28. Liu, C.; Zhong, H.; Komarnani, S.; Pantano, C.G. *J. Sol-Gel Sci. Technol.* **1994**, *1*, 141.
29. Sharma, P.K.; Varadan, V.V.; Varadan, V.K. Effect of tween-80 on the control of particle size and shrinkage properties of nanoscale-alumina synthesized by sol-gel processing. *J. Am. Ceram. Soc.* **2002**, *85*, 2584.



30. Scolan, E.; Sanchez, C. Synthesis and characterization of surface-protected nanocrystalline titania particles. *Chem. Mater.* **1998**, *10*, 3217.
31. Lin, C.P.; Wen, S.B. Variations in a boehmite gel and oleic acid emulsion under calcinations. *J. Am. Ceram. Soc.* **2002**, *85*, 1467.
32. Ramamurthi, S.D.; Xu, Z.; Pyne, D.A. Nanometer-sized  $ZrO_2$  particles prepared by a sol-emulsion-gel method. *J. Am. Ceram. Soc.* **1990**, *73*, 2760.
33. De Gennes, P.G.; Taupin, C. Microemulsions and the flexibility of oil/water interfaces. *J. Phys. Chem.* **1982**, *86*, 2294.
34. Leung, R.; Hou, M.J.; Manohar, C.; Shah, D.O.; Chun, P.W. *Macro- and Microemulsions*; Shah, D.O., Ed.; American Chemical Society: Washington, DC, 1981; 325 pp.
35. Eicke, H.F.; Shepherd, J.C.W.; Steinemann, A. *J. Colloid Interface Sci.* **1976**, *56*, 168.
36. Fendler, J.H. Atomic and molecular clusters in membrane mimetic chemistry. *Chem. Rev.* **1987**, *87*, 877.
37. Sugimoto, T. Preparation of monodispersed colloidal particles. *Adv. Colloid Interface Sci.* **1987**, *28*, 65.
38. Pechini, M.P. US Pat. No 3,33,0697, July 11, 1967
39. Kumar, S.; Messing, G.L.; White, W.B. *J. Am. Ceram. Soc.* **1993**, *76*, 617.
40. Yoshimura, M.; Ma, J.; Kakihana, M. Low-temperature synthesis of cubic and rhombohedral  $Y_6WO_{12}$  by a polymerized complex method. *J. Am. Ceram. Soc.* **1998**, *81*, 2721.
41. Lessing, P.A. *Am. Ceram. Soc. Bull.* **1989**, *68*, 1002.
42. Kakihara, M.; Yoshimura, M.; Mazaki, H.; Yasuoka, H.; Borjesson, L. *J. Appl. Phys.* **1992**, 3904.
43. Cheng, W.; Skendan, G.; Denforth, S.C.; Kear, B.H.; Hahn, H. Chemical vapor processing and applications for nanostructured ceramic powders and whiskers. *Nanostruct. Mater.* **1994**, *4*, 507.
44. Ennis, B.J.; Green, J.; Davis, R. *Chem. Eng. Process.* **1994**, 34.
45. Kear, B.H.; Skandan, G. Thermal spray processing of nanoscale materials: Davos, Switzerland, August 4–8, 1997. *Nanostruct. Mater.* **1997**, *8*, 765.
46. Kim, S.Y.; Yu, J.H.; Lee, J.S. The characteristics of nanosized  $TiO_2$  powders synthesized by chemical vapor condensation. *Nanostruct. Mater.* **1999**, *12*, 471.
47. Li, Y.; Liu, J.; Wang, Y.; Wang, Z.L. Preparation of monodispersed Fe–Mo nanoparticles as the catalyst for CVD synthesis of carbon nanotubes. *Chem. Mater.* **2001**, *13*, 1008.
48. Krage, M.K. Microwave sintering of ferrites. *Am. Ceram. Soc. Bull.* **1981**, *60*, 1232.
49. Roy, R.; Komarneni, S.; Yang, L.J. Controlled microwave heating and melting of gels. *J. Am. Ceram. Soc.* **1985**, *68*, 392.
50. Selmi, F.; Komarneni, S.; Varadan, V.K.; Varadan, V.V. Microwave sintering of Sb-doped  $SnO_2$ . *Mater. Lett.* **1990**, *10*, 235.
51. Sharma, P.K.; Varadan, V.V.; Varadan, V.K. Dielectric and piezoelectric properties of microwave sintered PZT. *Smart Struct. Mater.* **2001**, *10*, 878.
52. Xi, J.; Sharma, P.K.; Varadan, V.V.; Varadan, V.K.; Pradhan, B.K.; Eser, S. *Mater.* thermal, Raman and surface area studies of microcoiled carbon fiber synthesized by CVD microwave system. *J. Phys. Chem.* **2002**, *76*, 217.
53. Koch, C.C.; Smith, A.P.; Bai, C.; Spontak, R.J.; Balik, C.M. Nonequilibrium processing of polymer materials by mechanical attrition. *Mater. Sci. Forum* **1992**, *88*, 49.
54. Suryanarayana, C. Mechanical alloying and milling. *Prog. Mater. Sci.* **2001**, *46*, 1.
55. Miao, W.F.; Ding, J.; McCormick, P.G.; Street, R. A comparative study of mechanically alloyed and mechanically milled  $Nd_{10}Fe_{84}B_6$ . *J. Appl. Phys.* **1996**, *79*, 2079.
56. Ding, J.; Miao, W.F.; McCormick, P.G.; Street, R. Mechanochemical synthesis of ultrafine Fe powder. *Appl. Phys. Lett.* **1995**, *67*, 3804.
57. McCormick, P.G. Application of mechanical alloying to chemical refining (Overview). *Mater. Trans., JIM* **1995**, *36*, 161.
58. McCormick, P.G.; Froes, F.H. The Fundamentals of mechanochemical processing. *J. Metallurg.* **1998**, *50*, 61.
59. Ding, J.; Tsuzuki, T.; McCormick, P.G. Ultrafine alumina particles prepared by mechanochemical/thermal processing. *J. Am. Ceram. Soc.* **1996**, *79*, 2956.
60. Gopalan, S.; Singhal, S.C. Mechanochemical synthesis of nano-sized  $CeO_2$ . *Sci. Mater.* **2000**, *42*, 993.
61. Mishra, K.C.; Berkowitz, J.K.; Johnson, K.H.; Schmidt, P.C. Electronic structure and optical properties of europium activated yttrium oxide phosphor. *Phys. Rev., B* **1992**, *45*, 10,902.
62. Wickersheim, A.; Lefever, R.A. *J. Electrochem. Soc.* **1964**, *111*, 47.
63. Sharma, P.K.; Jilavi, M.H.; Nass, R.; Schmidt, H. Effect of solvent, host precursor, dopant concentration and crystallite size on the fluorescence properties of Eu(III) doped yttria. *Opt. Mater.* **1998**, *10*, 161.
64. Bawendi, M.G.; Kortan, A.R.; Steigerwald, M.L.; Bruce, L.E. X-ray structural characterization of larger CdSe semiconductor clusters. *J. Chem. Phys.* **1989**, *91*, 7282.
65. Alivisatos, A.P.; Harris, A.L.; Carroll, M.L.; Steigerwald, M.L.; Bruce, L.E. Electron–vibration coupling in semiconductor clusters studied by resonance Raman spectroscopy. *J. Chem. Phys.* **1989**, *90*, 3463.
66. Goldburt, E.T.; Kulkarni, B.; Bhargava, R.N.; Taylor, J.; Liberta, M. Size dependent efficiency in Tb doped  $Y_2O_3$  nanocrystalline phosphor. *J. Lumin.* **1997**, *72–74*, 190.
67. Iwasaki, S.; Ida, T.; Kimura, K. Blue-Green photoluminescence from ultrafine colloidal Si particles in 2-propanol. *Jpn. J. Appl. Phys.* **1996**, *35*, L-551.
68. Gallagher, D.; Heady, W.E.; Racz, J.M.; Bhargava, R.N. Homogeneous precipitation of doped zinc sulfide nanocrystals for photonic applications. *J. Mater. Res.* **1995**, *10*, 870.
69. Bruce, P.G. Solid-state chemistry of lithium power sources. *Chem. Commun.* **1997**, *19*, 1817.
70. Che, G.; Jirage, K.B.; Fisher, E.R.; Martin, C.R.; Yoneyama, H. Chemical-vapor deposition-based template synthesis of microtubular  $TiS_2$  battery electrodes. *J. Electrochem. Soc.* **1997**, *144*, 4296.

71. Whittingham, M.S. U.S. Patent 4,009,052, 1973
72. Whittingham, M.S. *Science* **1976**, *192*, 1126.
73. Ching, S.; Petrovay, D.J.; Jorgensen, M.L.; Suib, S.L. Sol-gel synthesis of layered birnessite-type manganese oxides. *Inorg. Chem.* **1997**, *36*, 883.
74. Chang, C.C.; Kim, J.Y.; Kumta, P.N. Influence of crystallite size on the electrochemical properties of chemically synthesized stoichiometric LiNiO<sub>2</sub>. *J. Electrochem. Soc.* **2002**, *149*, A1114.
75. Im, D.; Manthiram, A. Nanostructured lithium manganese oxide cathodes obtained by reducing lithium permanganate with methanol. *J. Electrochem. Soc.* **2002**, *149*, A1001.
76. Bruce, P.G.; Armstrong, A.R.; Gitzendanner, R.L. *J. Electrochem. Soc.* **1999**, *9*, 193.
77. Liu, J.; Wen, Z.; Gu, Z.; Wu, M.; Lin, Z. Synthesis by an EDTA-based soft-chemistry route and characterization of nanosized LiCoO<sub>2</sub> cathode materials. *J. Electrochem. Soc.* **2002**, *149*, A1405.
78. Cho, J.; Kim, Y.J.; Park, B. LiCoO<sub>2</sub> Cathode material that does not show a phase transition from hexagonal to monoclinic phase. *J. Electrochem. Soc.* **2001**, *148*, A1110.
79. Lu, C.H.; Yeh, P.Y. Surfactant effects on the microstructure and electrochemical properties of emulsion-derived lithium cobalt oxide powders. *Mater. Sci. Eng.* **2001**, *B84*, 243.
80. Kim, J.; Manthiram, A. Synthesis and lithium intercalation properties of nanocrystalline lithium iron oxides. *J. Electrochem. Soc.* **1999**, *146*, 4371.
81. Ye, Y.; Ahn, C.C.; Witham, C.; Fultz, B.; Liu, J.; Rinzier, A.G.; Colbert, D.; Smith, K.A.; Smalley, R.E. Hydrogen adsorption and cohesive energy of single-walled carbon nanotubes. *App. Phys. Lett.* **1999**, *74*, 2307.
82. Dillon, A.C.; Jones, K.M.; Bekkedahl, T.A.; Kiang, C.H.; Bethune, D.S.; Heben, M.J. Storage of hydrogen in single-walled carbon nanotubes. *Nature* **1997**, *386*, 377.
83. Liu, C.; Fan, Y.Y.; Liu, M.; Cong, H.T.; Cheng, H.M.; Dresselhaus, M.S. Hydrogen storage in single walled carbon nanotubes at room temperature. *Science* **1999**, *286*, 1127.
84. Chen, F.; Wang, Z.C.; Lin, C.J. Preparation and characterization of nano-sized hydroxyapatite particles and hydroxyapatite/chitosan nano-composite for use in biomedical materials. *Mater. Lett.* **2002**, *57*, 858.
85. Herzer, G. Nanocrystalline soft magnetic materials. *J. Magn. Magn. Mater.* **1996**, *157/158*, 133.
86. Hadjipanayis, G.C. Nanophase hard magnets. *J. Magn. Magn. Mater.* **1999**, *200*, 373.
87. Weller, D.; Doerner, M.F. Extremely high-density longitudinal magnetic recording media. *Annu. Rev. Mater. Sci.* **2000**, *30*, 611.
88. Bate, G. Magnetic recording materials since 1975. *J. Magn. Magn. Mater.* **1991**, *100*, 413.
89. Giri, A.K.; Julian, C.; Gonzalez, J.M. Coercivity of Fe-SiO<sub>2</sub> nanocomposite materials prepared by ball milling. *J. Appl. Phys.* **1994**, *76*, 6573.
90. Yoshizawa, Y.; Oguma, S.; Yamauchi, K. New Fe-based soft magnetic alloys composed of ultrafine grain structure. *J. Appl. Phys.* **1988**, *64*, 6044.
91. Herzer, G. Grain structure and magnetism of nanocrystalline ferromagnets. *IEEE Trans. Magn.* **1989**, *25*, 3327.
92. Herzer, G. Grain size dependence of coercivity and permeability in nanocrystalline ferromagnets. *IEEE Trans. Magn.* **1990**, *26*, 1397.
93. Yoshizawa, Y. Magnetic properties and microstructure of nanocrystalline Fe-based alloys. *Mater. Sci. Forum* **1999**, *307*, 51.
94. Kneller, E.F.; Hawig, R. The exchange-spring magnet: A new material principle for permanent magnets. *IEEE Trans. Magn.* **1991**, *27*, 3588.
95. Skomski, R.; Coey, J.M.D. Giant energy product in nanostructured two-phase magnets. *Phys. Rev., B* **1993**, *48*, 15,812.
96. McCormic, P.G.; Miao, W.F.; Smith, P.A.I.; Ding, J.; Street, R. Mechanically alloyed nanocomposite magnets. *J. Appl. Phys.* **1998**, *83*, 6256.
97. Coey, J.M.D. Permanent magnetism. *Solid State Commun.* **1997**, *102*, 101.
98. Zeng, H.; Li, J.; Liu, J.P.; Wang, Z.L.; Sun, S. Exchange-coupled nanocomposite magnets by nanoparticles self-assembly. *Nature* **2002**, *420*, 395.
99. Sellmyer, D.J. Strong magnets by self-assembly. *Nature* **2002**, *420*, 374.
100. Sun, S.; Murray, C.B.; Weller, D.; Folks, L.; Moser, A. Monodisperse FePt nanoparticles and ferromagnetic FePt nanocrystal superlattices. *Science* **2000**, *287*, 1989.

# Nanomaterials and Molecular Devices: De Novo Design Theory

Kwang S. Kim  
P. Tarakeshwar  
Han Myoung Lee

*Department of Chemistry, Pohang University of Science and Technology,  
Pohang, South Korea*

## INTRODUCTION

The immense potential of functional nanomaterials in the fields of communication, information storage, materials, and biological sciences has heightened the quest to obtain them. In this quest, the “bottoms-up” approach, with its emphasis on chemical methods, has proven to be of more value than the classical “top-down” approach. Design strategies based on quantum theoretical methods are particularly suited to accelerate the “bottoms-up” approach, because of their ability to predict the properties of these nanomaterials to a high degree of accuracy. In the course of this entry, we show how the pursuit for small, fast, and powerful nanoelectronic and nanomechanical devices, chemical/biochemical sensors/monitors, DNA chips, etc. can be vastly facilitated using an approach based on de novo theoretical design.

The first step in this process is to obtain a detailed insight of intermolecular interactions prevailing in these nanomaterials. This is because most physical phenomena, such as molecular recognition,<sup>[1]</sup> nanorecognition,<sup>[2]</sup> molecular clustering/aggregation,<sup>[2]</sup> self-assembly,<sup>[3,4]</sup> and self-synthesis,<sup>[5]</sup> are the result of competitive and cooperative effects of several types of interatomic, intramolecular, and intermolecular interactions.<sup>[6,7]</sup>

Based on a thorough understanding of various interaction forces and mechanisms, one can design molecular clusters, inorganic/metal clusters, endo-/exo-hedral fullerenes/nanotubes, non-linear optical materials, ionophores/receptors/sensors, polypeptides/membranes/enzymes, organic nanotubes/nanowires, photo/electro-nanodevices, and nanomechanical molecular devices. In the course of this entry, we show how the above strategy helped design novel and experimentally viable ionophores,<sup>[8–12]</sup> organic nanotubes,<sup>[4–6]</sup> nanowires,<sup>[5]</sup> molecular flippers,<sup>[13]</sup> and molecular switches,<sup>[14]</sup> etc.

## INTERMOLECULAR FORCES

The intricacies of most intermolecular interactions can be obtained from the study of molecular clusters.<sup>[15–18]</sup> These diverse intermolecular interactions can broadly be classified as: 1) H-bonding, 2) ionic interactions, 3) intermolecular interactions involving  $\pi$  systems, 4) metallic interactions, and 5) interactions involving quantum species.

## DESIGN AND DEVELOPMENT OF FUNCTIONAL MOLECULES, NANOMATERIALS, AND NANODEVICES

In the following account, we discuss the strategies employed to design nanoclusters, nanowires, ionophores, receptors, sensors, carbon-based nanomaterials, organic nanotubes, encapsulated nanowires, non-linear optical switches, and nanomechanical devices.

### Nanoclusters and Nanowires

Clusters, in addition to offering several ways of making new materials, are a fundamental subject for understanding the intrinsic nature of materials.<sup>[15,16]</sup> The investigation of H-bonded clusters,<sup>[18–22]</sup> metal clusters,<sup>[23–25]</sup> and clusters containing  $\pi$  systems<sup>[26–29]</sup> not only provides the necessary information for nanomaterial design but also highlights some of the important similarities and differences in their structures and properties. In this discussion, we focus our attention on noble metal clusters and metal nanowires. Theoretical investigations of these noble metal clusters, to a large extent, depend on the ability of the theoretical method to describe metallic interactions. In particular, the ability of the method to accurately describe relativistic effects is vital to the success of the design

strategy. Small noble metal clusters<sup>[23–25,30–33]</sup> are of particular interest because the dominance of quantum effects in such small dimensions alludes to the emergence of several interesting characteristics, such as their catalytic properties, etc. While most studies were concentrated on pure metallic clusters, it has recently been realized that mixed metallic clusters exhibit unique electronic, magnetic, optical, and mechanical properties. For example, mixed clusters of gold and silver have been found to exhibit enhanced optical non-linearity over the corresponding bulk metals. Another advantage of studying these mixed clusters is that they help understand the mechanism of alloying. A recent example of the utility of theoretical methods is illustrated in the case of gold–tungsten clusters, wherein theoretical calculations were able to accurately predict the structures and properties, before they were experimentally identified.<sup>[24,25]</sup>

One of the highlights of neutral and anionic gold and silver clusters is that they exhibit an even–odd oscillation in their stability and electronic properties.<sup>[23]</sup> Owing to the spin pairing, the clusters having an even number of atoms tend to be more stable in the neutral state, while those having an odd number of atoms tend to be more stable in the anionic state. Since the 6s orbital energy of Au is almost as low as 5d orbitals due to the relativistic effect, the strong s–d hybridization in Au favors one-dimensional and two-dimensional structures in the case of the gold clusters. This explains the ductility of small gold clusters. In contrast, silver clusters exhibit a strong preference to exist as three-dimensional structures with spherical coordination because the valence orbitals are predominantly of the s-type. A similar argument can also be employed to explain the low coordination number of the Au atom in the gold clusters as compared to the Ag atom in the silver clusters. This preference in coordination reflects

itself in the location of the Au and Ag atoms in the corresponding binary clusters of gold and silver, with the Au atoms being located on the boundary, while Ag atoms are generally located in the inner side (Fig. 1). In the anionic systems of both pure and mixed clusters, there is a marked tendency to adopt low-dimensional conformations as compared to the corresponding neutral clusters. However, in the mixed clusters, the conformational preferences are strongly correlated to the number of Au and Ag atoms in the cluster. Given the higher energy of the Ag 5s as compared to the Au 6s orbital, electron transfers from Ag to Au atoms are found in the mixed clusters. This together with the predilection for Au atoms to be located on the boundary indicates that the core of the mixed clusters is positively charged, while the surface is negatively charged. The easy formation of the mixed gold–silver clusters and as a consequence their alloys is due to the significant electrostatic stabilization accruing from the charge transfer from Au to Ag atoms.

In order to obtain more insight into the role of dimensionality, we extend the clusters to nanowires, thin-films, and the bulk systems.<sup>[34]</sup> Toward low-dimensional structures, there is a strong sharpening of the d bands, which vastly enhances the corresponding density of states and raises the band edges. This strong preference for lower-dimensional structures is in consonance with the experimental observation that the interatomic interactions progressively become stronger in low-coordinated systems. In our discussion of gold clusters, the presence of an excess charge promotes linearity.<sup>[23]</sup> Interestingly, it was experimentally noted that a wire of at least four gold atoms suspended between two gold electrodes is linear.<sup>[35,36]</sup> However, theoretical calculations of a free-standing, one-dimensional gold wire indicate that a two-dimensional structure is more stable.<sup>[37]</sup> Therefore a subject of

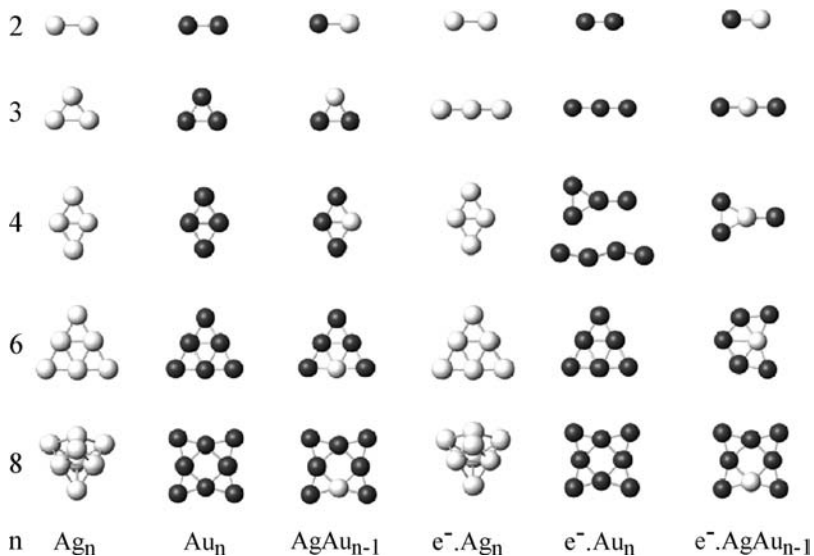


**Fig. 1** Predicted lowest-energy conformers of neutral and anionic clusters of pure silver ( $\text{Ag}_{2-4,6,8}$ ), pure gold ( $\text{Au}_{2-4,6,8}$ ), and gold–silver alloys ( $\text{AgAu}_{1-3,5,7}$ ).

intense interest in the recent past is on methods to obtain one-dimensional gold nanowires. It would be useful to modulate the charge transfer in gold alloy nanowires by injecting *s* electrons into gold wire without distorting its band structure.<sup>[38]</sup> The *s* band of the alloying metal should therefore possess similar energy levels as the 6*s* orbital of gold. Of all the *s* band metals, beryllium, magnesium, zinc, cadmium, and mercury have their valence energy levels closest to that of the 6*s* orbital of gold, and hence can form alloys with gold. Then, density functional calculations were carried out on free-standing, infinite monoatomic gold wires alloyed with both magnesium and zinc. In the alloy chains, the locations of the gold and zinc (or magnesium) atoms were alternated and investigated as both one- and two-dimensional structures. In sharp contrast to pure gold nanowires, the one- and two-dimensional structures of both gold–magnesium and gold–zinc alloys exhibit distinct minima in the plots of the cohesive energy, indicating that both forms are energetically accessible. We note that both zinc 4*s* and magnesium 3*s* bands display *p* character near the Fermi energy. This *sp* hybridization, which is absent in pure gold nanowires, favors a linear structure in the case of these alloyed nanowires.

### Ionophores, Receptors, and Chemical Sensors

The design and synthesis of receptors capable of binding anionic or cationic guests are of crucial importance because of their potential applications in environmental and biological processes. Unlike nanoclusters and nanowires, the theoretical challenge in these systems is to

describe the interactions of an organic system with a charged metal, or another organic cation. Furthermore, one has to take into account the role of the environment in modulating the binding characteristics. The environment could either be solvents, molecules, or other ions.

We begin our discussion of ionophore/receptor design with one of the seemingly intractable problems of contemporary biochemistry: the selective recognition of the ammonium cation ( $\text{NH}_4^+$ ).<sup>[8,39]</sup> Much of the problem is due to the nearly equivalent sizes of  $\text{NH}_4^+$  and the potassium cation ( $\text{K}^+$ ).<sup>[40]</sup> In the following account, we show on how we circumvent the problem and were successful in identifying a series of receptors with improved selectivity and affinity for  $\text{NH}_4^+$ .<sup>[8]</sup> The first step in the receptor design was that high selectivity for  $\text{NH}_4^+$  could be achieved with cation– $\pi$  interactions,<sup>[40–42]</sup> if the receptors have an optimal space to capture  $\text{NH}_4^+$  and exhibit strong interactions toward  $\text{NH}_4^+$ . However, the ionic radius of  $\text{K}^+$  is nearly similar to that of  $\text{NH}_4^+$ , so spatial differentiation is not useful. Therefore we take advantage of the differences in coordination numbers.  $\text{K}^+$  favors a coordination number of six, while  $\text{NH}_4^+$  favors only four. Furthermore, one has also to take into account the directional H-bonds involving  $\text{NH}_4^+$  cations, to describe the higher selectivity for  $\text{NH}_4^+$  over  $\text{K}^+$ . Our initial calculations indicated that a benzene-based tripod system with imidazoline arms (Fig. 2A) possesses vacant sites for the interaction with only one solvent molecule, while the  $\text{K}^+$  ion has three vacant sites for three solvent molecules. In order to maximize the affinity and selectivity of these receptors for  $\text{NH}_4^+$ , it becomes important to maximize the  $\pi$ -electron density of the receptor. Indeed, receptors with enhanced

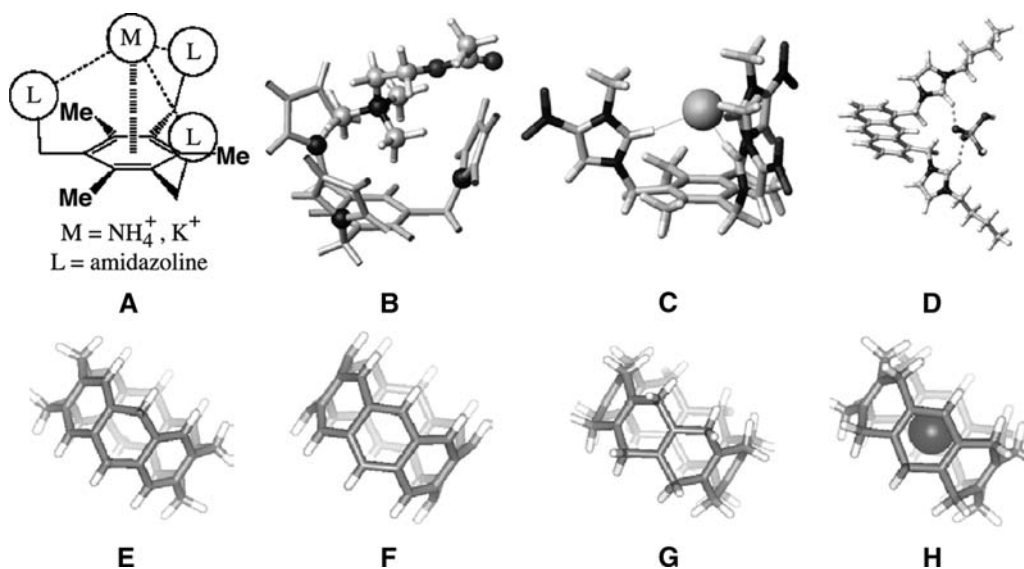


**Fig. 2** Receptors for  $\text{NH}_4^+$  (A), acetylcholine (B),  $\text{Cl}^-$  (C),  $\text{H}_2\text{PO}_4^-$  (D), and structures of collarenes (E), cyclacenes (F), beltene (G), and  $\text{Rb}^+$ -complexed [8]beltene (H).

$\pi$ -electron density by trimethylated phenyl ring with the strong proton-withdrawing subunits exhibit much higher affinities and selectivities.

Given this background, an extended concept has been applied to the receptor design for a biologically important molecule, acetylcholine.<sup>[9]</sup> The receptor should have higher affinity and selectivity for acetylcholine over  $\text{NH}_4^+$ . This requires enhanced dispersion interactions and diminished ionic interactions, which is met by replacing the imidazole arms of the  $\text{NH}_4^+$  receptors with pyrrole (Fig. 2B). These theoretical inferences were confirmed by experiments.

Interactions involving anions are very different from those of cations. As anions are more polarizable and hence more susceptible to polar solvents than cations, it becomes important to take into account solvent effects. Based on molecular dynamics simulations combined with ab initio calculations, highly selective anionophores have been designed.<sup>[10–12]</sup> Enhanced dipole moments (Fig. 2C) were employed by attaching a strategically placed electron-withdrawing group.<sup>[10]</sup> This approach would also aid in the design of novel functional molecular systems and biologically important chemosensors. Utilizing the  $\text{CH}^+ \dots \text{X}^-$  H-bonds, fluorescent photoinduced electron transfer chemosensors for the recognition of  $\text{H}_2\text{PO}_4^-$  have also been designed and synthesized (Fig. 2D). In addition, we have also been successful in designing cyclopeptides as amphi-ionophores.<sup>[43,44]</sup>

It would be appealing to explore the possibility of carbon-based materials being used as ionophores.<sup>[45–47]</sup> Belt-shape carbocyclic-conjugated systems (annulenes, beltene, cyclacenes, and collarenes) are closely related

to other carbon-based systems containing curved surfaces. These include fullerenes and carbon nanotubes. The ion binding characteristics of these carbon materials have been unraveled through ab initio calculations, Monte Carlo, and molecular dynamics simulations of collarenes (benzene rings linked by methylene linkages), cyclacenes (composed only of benzene rings), and beltene (ethene groups linked by methylene linkages), and their complexes with various cations (alkali, alkaline-earth metal, and organic cations) in both the gas and aqueous phases (Fig. 2E–H). Additionally, suitable substituents could also enhance their binding affinities and selectivities. In particular, the designed molecules could be modified to be soluble in polar solvents by adding hydrophilic groups on the edges of the molecules.

### Carbon-Based Nanomaterials

Since the discovery of fullerenes and carbon nanotubes, much effort has gone into the discovery of other interesting allotropes of carbon with unusual structural characteristics and novel physical properties.<sup>[48–50]</sup> Toward this end, the geometries, electronic structures, and energetics of small carbon nanotori were investigated employing both tight-binding and semiempirical quantum chemical methods.<sup>[51]</sup> It should be mentioned here that the very large size of these carbon-based materials precludes the use of high-level quantum methods. One therefore has to take recourse to the use of semiempirical or tight-binding methods. As can be seen from Fig. 3, the structures and electronic

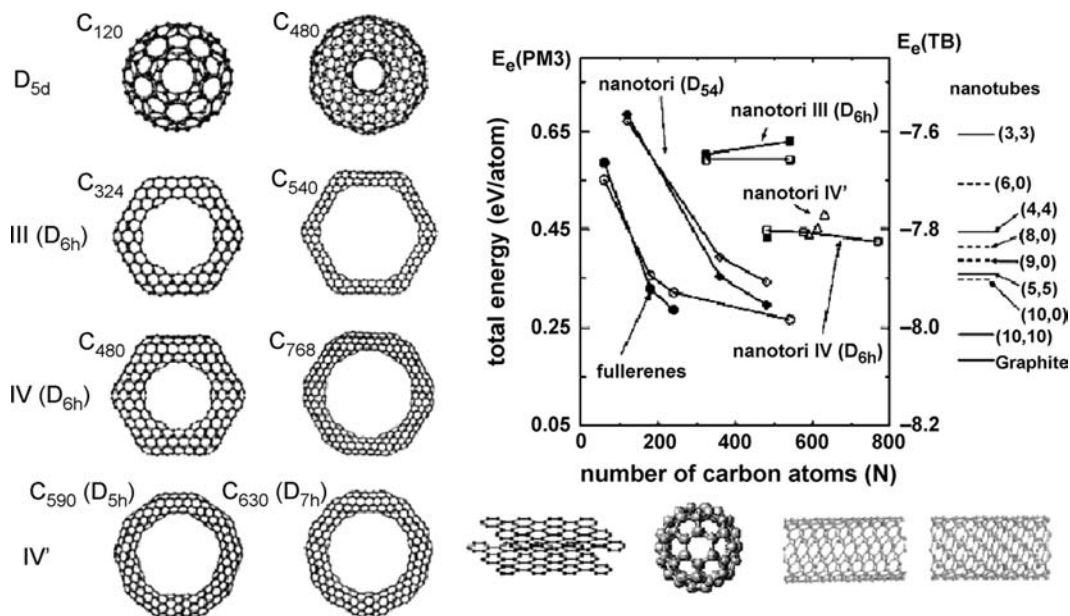


**Fig. 3** Optimized structures of various types of carbon nanotube tori and their stability compared with grapheme, fullerene, and nanotubes. Source: From Ref.<sup>[51]</sup>.



properties of the smallest nanotori exhibit interesting metal, semiconductor, and insulator characteristics depending on nanotube building blocks.

An interesting offshoot in the context of carbon-based nanomaterials is the role of external perturbations in modulating their physical and chemical characteristics. These perturbations can include cations or neutral atoms. In this context, we examined the magnetic properties of exohedral fullerenes of alkali-metal fullerenes ( $A_xC_{60}$ ,  $A = \text{Na, K, Rb, Cs}$ )<sup>[52,53]</sup> and the spin properties of endohedral fullerenes ( $A-C_{60}$ ,  $A = \text{N, P, As, O, S}$ )<sup>[54-57]</sup> (Fig. 4). The most interesting aspect of the experimental investigation of endohedral fullerenes was the fact that the encapsulated nitrogen, which possesses three unpaired electrons and is paramagnetic in nature, is totally inert within  $C_{60}$ . Our calculations, however, indicated that the interaction observed in the case of  $N-C_{60}$  is predominantly dispersive in nature. These systems are interesting because endohedral fullerenes containing paramagnetic atoms could be utilized to design quantum computers.<sup>[58]</sup>

## Organic Nanotubes

There are several advantages in using hydrogen bonds to design nanomaterials,<sup>[4-6,59]</sup> and in particular nanotubes, because these nanotubes have potential applications as artificial biological channels, drug delivery, nanochemical reactors, etc.<sup>[60-63]</sup> One of the spectacular aspects of a recent report on the self-assembly of an organic nanotube from non-tubular units of calix[4]hydroquinone (CHQ) was that the theoretical design preceded the actual experiment of synthesis and investigation of the X-ray structure.<sup>[4-6]</sup> Apart from highlighting the robustness of the theoretical approach, this study also provided several insights into the mechanism of self-assembly of CHQ nanotubes.

In the absence of water, for each CHQ monomer, the number of dangling H atoms is 4, while in the presence of water, these dangling H atoms of CHQs form chains  $HQ-(\text{water}-HQ-HQ)_n\text{water}$ . Although the strength of one-dimensional short H-bonding interaction ( $\sim 10$  kcal/mol) is similar to or slightly stronger

than the strength of the  $\pi-\pi$  stacking interaction, the assembly along the one-dimensional short H-bonds relay should be much more favorable because the number of H-bonds is three times the number of  $\pi-\pi$  stacks. Indeed, in experiments with water, CHQs are assembled to form long tubular structures with four infinitely long, short strong H-bond arrays. The CHQ tubes assemble to form long tubular structures in the presence of water, which in turn, form bundles with intertubular  $\pi-\pi$  stacking interactions (Fig. 5), resulting in crystals with well-ordered two-dimensional arrays of pores. The structures of these pores were utilized for the synthesis of encapsulated nanowires,<sup>[5]</sup> which would be described in the next section. A needle-like nanotube bundle exhibits the infinitely long one-dimensional H-bonding network between hydroxyl groups of CHQs and water molecules and well-ordered intertubular  $\pi-\pi$  stacking pairs (Fig. 5). The geometries of the calculated  $\pi-\pi$  stacks are very close to the  $\pi-\pi$  stacks in the X-ray structure.

## Encapsulated Metallic Nanowires

As was mentioned earlier, CHQ nanotubes arrays can be utilized in promising templates for nanosynthesis. Redox reaction of the nanotube in the presence of silver nitrate leads to the formation of a silver nanowire arrays in the pores (pore size of  $8 \times 8 \text{ \AA}^2$ ) of the CHQ nanotube. The wires exist as uniformly oriented three-dimensional arrays of ultrahigh density. The driving force for the formation of these nanowires is the free energy gain due to the reduction-oxidation process.<sup>[64,65]</sup> The resulting nanowire is composed of four dumbbells, each of which contains two silver atoms, superimposed on one another and crisscrossed in their length.

The theoretical characterization of the reduced form of the CHQ nanotube was carried out using plane-wave pseudopotential methods.<sup>[66]</sup> Our calculations indicated that upon reduction with silver nitrate, the CHQ nanotubes get transformed to the corresponding calix[4]quinone-hydroquinone (CQHQ) nanotubes, whose band gaps of 0.3 eV indicate that they are semiconducting in nature. The gross structural feature

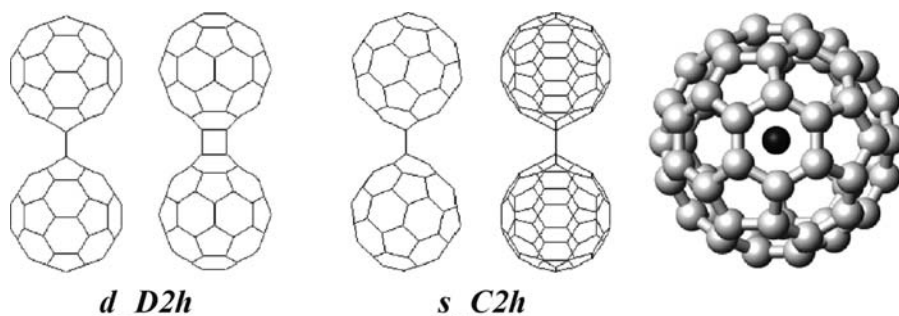


**Fig. 4** Ground triplet ( $d_{D_{2h}}$ ) and excited singlet ( $s_{C_{2h}}$ ) states of  $(C_{60})_2^{2-}$  with two views (for the alkali cation-doped exohedral fullerenes), and N-containing endohedral fullerene.

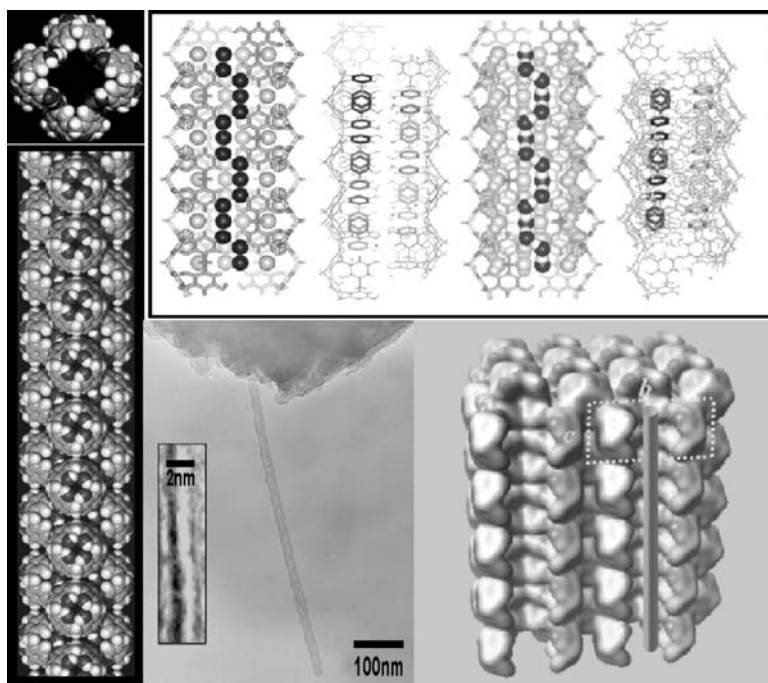


**Fig. 5** Calix[4]hydroquinone nanotubes: structure, longitudinal one-dimensional H-bond relay vs. intertubular  $\pi$ - $\pi$  stacking, the HREM image of a single nanotube, and the water-accessible surface of the tubes. Each tube has four pillar frames of short H-bonds, and the pore size is  $8 \times 8 \text{ \AA}^2$ . The unit cell is drawn by the dashed lines. *Source:* From Ref.<sup>[4]</sup>.

of CQHQ nanotubes is similar to that of CHQ nanotubes, with well-ordered H-bond arrays and intertubular  $\pi$ - $\pi$  stacking pairs. In the CQHQ nanotubes, there are only two infinitely long one-dimensional H-bond arrays per nanotube because two hydroxyl groups are transformed to the corresponding reduced forms. Simultaneously, silver cations get transformed to metallic silver. Upon reduction of the CHQ nanotubes, the silver atoms are located within the reduced CQHQ nanotube (Fig. 6). In the case of 2/2 nanowire, the predicted cohesive energy is 2.4 eV, which is 0.9 eV smaller than the bulk value. The encapsulation of a silver nanowire within the

CQHQ nanotube leads to several additional states in the band gap region, which are similar to that of an isolated silver nanowire. In this case two  $s$  channels cross the Fermi energy level, which indicates the existence of quantum conductance.

### Non-linear Optical Switches and Right-/Left-Handed Helices of Polypeptides

We had talked about harnessing the interaction of photons, electrons, protons, or charged species with

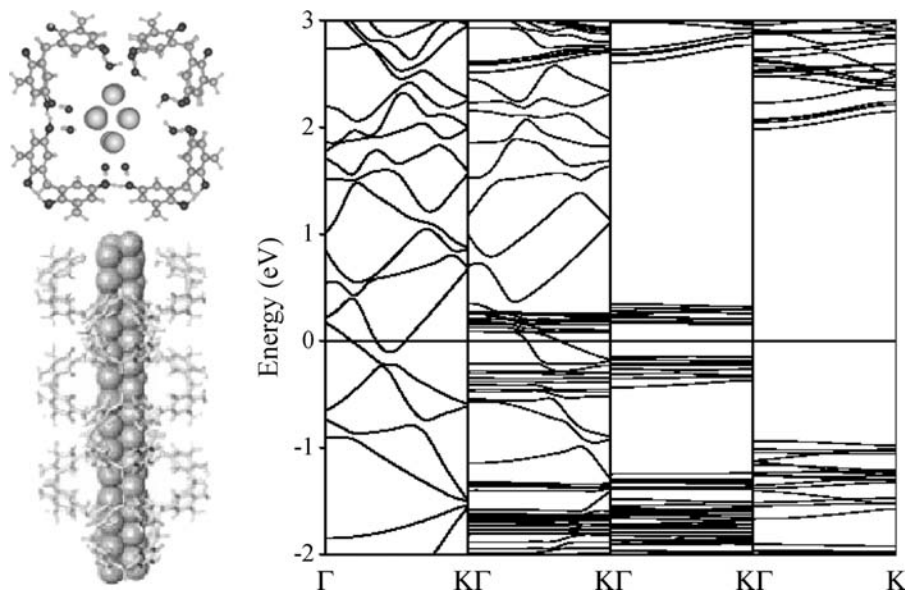


**Fig. 6** Top and side views of a silver nanowire inside a calix[4]quinone-hydroquinone (CQHQ) nanotubes (left figures), and the band structures of an isolated silver nanowire (left—first on the right figure), a silver nanowire encapsulated in a CQHQ nanotube (second), a CQHQ nanotube (third), and a calix[4]hydroquinone (CHQ) nanotube (last). *Source:* From Ref.<sup>[66]</sup>.

molecular systems in the design of new nanodevices. While photochemical and electrochemical switching devices have been extensively investigated, most of the photochemical switching devices are limited to the linear regime. However, it would be of interest to use non-linear optical properties for an efficient memory device. In investigations of the interaction of photons with matter, it is essential that the employed theoretical method should be capable of characterizing both open-shells and excited states. The theoretical investigations of 1,2-bis-(3-thienyl)-ethene derivatives indicate that after photoswitching, the resulting  $\pi$ -conjugated closed forms exhibit highly non-linear optical properties.<sup>[67]</sup> The substitution of suitable donors and acceptors on certain strategic positions of these ethene derivatives, however, makes the closed form non-linear optically active and the resulting molecular system behaves as an efficient non-linear optical switch. It should be noted that the above discussion on non-linear optical devices involves the breaking and formation of bonds. It is interesting to explore the possibility of devices, which rely entirely on conformational or enantiomeric changes.

Peptides are well-known biological systems, whose conformational characteristics are well understood. To date, the conventional wisdom was that a polypeptide can exist only as right-handed helix. However, calculations reveal the feasibility of a left-handed helix.<sup>[68]</sup> Most of these calculations on these peptide systems were carried out using molecular dynamic simulations based on empirical potentials. The calculations indicate that the diameter of the left-handed helix is larger than the conventional right-handed helix. The left-handed helix is stabilized when the terminal residues are charged, because the dipole moments of carbonyl groups for the former are aligned opposite to those of the latter. Thus a molecular dynamics simulation of a poly-alanine peptide capped with neutral amino and methyl groups ( $\text{CH}_3\text{-(Ala)}_n\text{-NH}_2$ ) under neutral charge conditions yielded a right-handed  $\alpha$ -helix pattern, in about  $\sim 1.8$  nsec. However, when the terminals are charged ( $\text{NH}_3^+\text{-(Ala)}_{30}\text{-COO}^-$ ), a left-handed  $\lambda$ -helix is formed in about  $\sim 4.0$  nsec. During the formation of the left-handed  $\lambda$ -helix, helix-nucleation first occurs at the terminal sites (in particular, near the N-terminus in the case of the left-handed  $\lambda$ -helix) and it promotes the propagation of the helix pattern along the segment. It should be noted that in both the molecular dynamics simulations, only the terminal composition is different. Therefore the handedness of the final conformation is related to the terminal charge conditions. The propagation of the helix pattern along the segment clearly shows that sequential local interactions determine the nascent folding patterns of the protein. The initial folding in the left-handed  $\lambda$ -helix arises from the electrostatic interactions of the positively charged  $\text{NH}_3^+$  group with

the adjacent carbonyl dipole moiety, followed by the dipole-dipole interactions between two adjacent carbonyl moieties. These results were further confirmed with more accurate calculations using a density functional approach. The preceding discussion implies that a transition between left-handed and right-handed helix motifs can be triggered by the presence of charged species near the end of the helix terminals. Such a possibility holds immense promise in the development of novel chiral switches.

## Nanodevices

Up to now, our discussion was only centered on static systems. However, the quest for nanodevices implies that one has to induce motion in a system using external or internal means. The external means could include changes in pH, radiation, etc. We discuss one such device (a molecular flipper), which has been designed, synthesized, and characterized.<sup>[13]</sup> The flipping/flapping motion, in the case of designed device, is due to the changes in edge-to-face and face-to-face aromatic interactions.<sup>[69,70]</sup> It is interesting to note that this conformational change can be electrochemically controlled by reduction/oxidation of the quinone moiety in the molecular system.

The strategy for the design of nanodevices is to harness the subtle changes in the  $\pi$ -electron densities of a quinone moiety as results of changes in the electronic environment.<sup>[70,71]</sup> Quinones are particularly suited for this endeavor because their electronic characteristics can be electrochemically or photochemically controlled. Based on a theoretical investigation of the conformational characteristics of *p*-benzoquinone-benzene complexes, we found that the energy difference between the

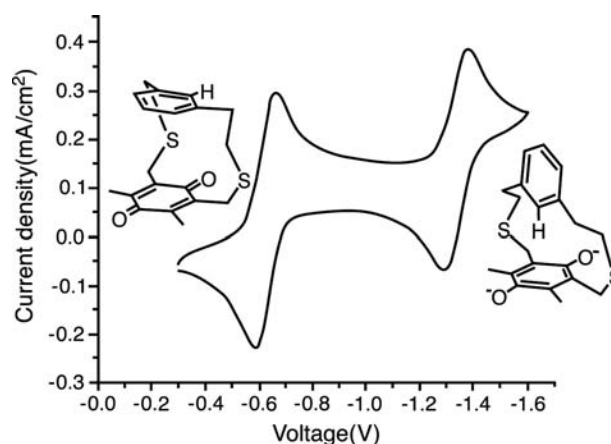


**Fig. 7** Cyclic voltammogram of MHQC(left)/MQC(right) (1 mM) in acetonitrile with tetrabutylammonium dihydrogen phosphate (0.1 M) at 25°C (scan rate 100 mV/sec). *Source:* From Ref.<sup>[13]</sup>.

stacked and edge-to-face conformations of cyclophane molecules (Fig. 7) is substantial. Thus if one could subtly control the conformational characteristics of 2,11-dithio[4,4]metametaquinocyclophane (MQC) (stacked conformer is 7 kcal/mol more stable than the edge-to-face conformer) and 2,11-dithio[4,4]metametahydroquinocyclophane (MHQC) (edge-to-face is 9 kcal/mol more stable than the edge-to-face conformer) by electrochemical and/or photochemical means, we can have a very interesting model of a potential molecular device. The cyclic voltammograms of MQC exhibit two clear reversible redox reactions (Fig. 7). In aprotic media, quinones exhibit two reduction peaks separated by 0.7 V, which corresponds to the formation of a radical anion species and a dianion species of quinones, respectively. This is in agreement with the reduction characteristics of MQC. Two well-separated reduced states of MQC are formed in the aprotic solvent of acetonitrile upon reduction. Therefore the electronic states of MQC and MHQC can be easily transformed into each other by simple electrochemical control of the redox reaction, which results in large conformational flapping motions due to a preference for the stable conformation caused by the change in the electronic state of the quinone moiety.

Thus a cyclophane system composed of quinone and benzene rings exhibits a flapping motion involving squeezing and thrusting motions in the presence of solvent molecules by electrochemical redox process. This case illustrates a promising pathway of harnessing the differences in the relative magnitudes of different kinds of intermolecular interactions to design a nanomechanical device. The large flapping/flipping motion from the edge-to-face and stacked conformations and vice versa is a first step toward a propelling molecular vessel or a molecular flipper that can be electrochemically or photochemically controlled. It could be applied to design molecular hinges, molecular switches, and eventually to design mobile nanomechanical devices.

## CONCLUSION

In the course of this entry, we have illustrated using several examples from our work that knowledge of interaction forces, together with a judicious choice of theoretical methods, can be employed in the de novo design of functional nanomaterials and nanodevices. The knowledge of interaction forces could also be utilized for the development of novel functional molecular systems having the capacity of controlled assembly. We have discussed the design and synthesis of several functional molecular systems such as nanowires/nanotubes, ionophores/receptors/sensors, electron/proton/molecular tweezers, molecular vehicles, and molecular-robots/bio-nanorobots. We expect that

some of the ideas gleaned from our work would find utility in the search for molecular nanoelectronic/mechanical devices, quantum computing devices, biomolecular sensors, and nanosurgery. Although this research field is still in the embryonic stage, the advent of fast computers and extremely powerful programs should revolutionize the design and development of nanomaterials and nanodevices in the near future. One of the advantages of the present work is that it also helps obtain an enhanced understanding of the processes in the macroscopic world.

## ACKNOWLEDGMENTS

This work was supported by the Korean Ministry of Science and Technology under the Creative Research Initiatives Program.

## REFERENCES

1. Atwood, J.L.; Davis, J.E.D.; MacNicol, D.D.; Vögtle, F.; Lehn, J.-M., Eds.; *Comprehensive Supramolecular Chemistry*; Elsevier: Amsterdam, 1996, Vols. 1–11.
2. Tarakeshwar, P.; Kim, K.S. Nanorecognition. In *Encyclopedia of Nanoscience and Nanotechnology*; Nalwa, H.S., Ed.; American Scientific Publishers: California, 2003.
3. Kuhn, H.; Försterling, H.-D. *Principles of Physical Chemistry: Understanding Molecules, Molecular Assemblies and Supramolecular Machines*; John Wiley & Sons Inc.: New York, 1999.
4. Hong, B.H.; Lee, J.Y.; Lee, C.-W.; Kim, J.C.; Bae, S.C.; Kim, K.S. Self-assembled organic nanotube arrays with infinitely long one-dimensional H-bonds. *J. Am. Chem. Soc.* **2001**, *123* (43), 10748–10749.
5. Hong, B.H.; Bae, S.C.; Lee, C.-W.; Jeong, S.; Kim, K.S. Ultrathin single-crystalline silver nanowire arrays formed in an ambient solution phase. *Science* **2001**, *294* (5541), 348–351.
6. Kim, K.S.; Suh, S.B.; Kim, J.C.; Hong, B.H.; Lee, E.C.; Yun, S.; Tarakeshwar, P.; Lee, J.Y.; Kim, Y.; Ihm, H.; Kim, H.G.; Lee, J.W.; Kim, J.K.; Lee, H.M.; Kim, D.; Cui, C.; Youn, S.J.; Chung, H.Y.; Choi, H.S.; Lee, C.-W.; Cho, S.J.; Jeong, S.; Cho, J.-H. Assembling phenomena of calix[4]hydroquinone nanotube bundles by one-dimensional short hydrogen bonding and displaced  $\pi$ - $\pi$  stacking. *J. Am. Chem. Soc.* **2002**, *124* (47), 14268–14279.
7. Braga, D.; Grepioni, F. Intermolecular interactions in nonorganic crystal engineering. *Acc. Chem. Res.* **2000**, *33* (9), 601–608.
8. Oh, K.S.; Lee, C.-W.; Choi, H.S.; Lee, S.J.; Kim, K.S. Origin of the high affinity and selectivity of novel receptors for  $\text{NH}_4^+$  over  $\text{K}^+$ : Charged hydrogen bonds vs. cation- $\pi$  interaction. *Org. Lett.* **2000**, *2* (17), 2679–2681.
9. Yun, S.; Ihm, H.; Kim, H.G.; Lee, C.-W.; Banyopadhyay, I.; Oh, K.S.; Gong, Y.J.; Lee, J.W.;

- Yoon, J.; Lee, H.C.; Kim, K.S. Molecular recognition of fluoride anion: Benzene-based tripodal imidazolium receptor. *J. Org. Chem.* **2003**, *68* (6), 2467–2470.
10. Yun, S.; Kim, Y.-O.; Kim, D.; Kim, H.G.; Ihm, H.; Kim, J.K.; Lee, C.-W.; Lee, W.J.; Yoon, J.; Oh, K.S.; Yoon, J.; Park, S.-M.; Kim, K.S. Rational design of biologically important chemosensors: A novel receptor for selective recognition of acetylcholine over ammonium cations. *Org. Lett.* **2003**, *5* (4), 471–474.
  11. Ihm, H.; Yun, S.; Kim, H.G.; Kim, J.K.; Kim, K.S. Tripodal nitro-imidazolium receptor for anion binding driven by (C–H)<sup>+</sup>–X<sup>–</sup> hydrogen bonds. *Org. Lett.* **2002**, *4* (17), 2897–2900.
  12. Kim, S.K.; Singh, N.J.; Kim, S.J.; Kim, H.G.; Kim, J.K.; Lee, J.W.; Kim, K.S.; Yoon, J. A new fluorescent photo-induced electron transfer chemosensor for the recognition of H<sub>2</sub>PO<sub>4</sub><sup>–</sup>. *Org. Lett.* **2003**, *5* (12), 2083–2086.
  13. Kim, H.G.; Lee, C.-W.; Yun, S.; Hong, B.H.; Kim, Y.-O.; Kim, D.; Ihm, H.; Lee, J.W.; Lee, E.C.; Tarakeshwar, P.; Park, S.-M.; Kim, K.S. An electrochemically controllable nanomechanical molecular system utilizing edge-to-face and face-to-face aromatic interactions. *Org. Lett.* **2002**, *4* (22), 3971–3974.
  14. Majumdar, D.; Lee, H.M.; Kim, J.; Kim, K.S. Photo-switch and nonlinear optical switch: Theoretical studies on 1,2-bis-(3-thienyl)-ethene derivatives. *J. Chem. Phys.* **1999**, *111* (13), 5866–5872.
  15. Kim, K.S.; Tarakeshwar, P.; Lee, J.Y. Molecular clusters of  $\pi$ -systems: Theoretical studies of structures, spectra and origin of interaction energies. *Chem. Rev.* **2000**, *100* (11), 4145–4185.
  16. Haberland, H., Ed.; *Clusters of Atoms and Molecules*; Springer-Verlag: Berlin, 1994.
  17. Castleman, A.W., Jr.; Bowen, K.H., Jr. Clusters: Structure, energetics, and dynamics of intermediate states of matter. *J. Phys. Chem.* **1996**, *100* (31), 12911–12944.
  18. Tarakeshwar, P.; Lee, H.M.; Kim, K.S. Insights from Theoretical Investigations of Aqueous Clusters. In *Reviews of Modern Quantum Chemistry*; Sen, K.D., Ed.; World Scientific: Singapore, 2002; 1642–1683.
  19. Lee, H.M.; Suh, S.B.; Lee, J.Y.; Tarakeshwar, P.; Kim, K.S. Structures, energies, vibrational spectra, and electronic properties of water monomer to decamer. *J. Chem. Phys.* **2000**, *112* (22), 9759–9772.
  20. Lee, H.M.; Suh, S.B.; Lee, J.Y.; Tarakeshwar, P.; Kim, K.S. Structures, energies, vibrational spectra, and electronic properties of water monomer to decamer. *J. Chem. Phys.* **2001**, *114* (7), 3343.
  21. Lee, H.M.; Suh, S.B.; Kim, K.S. Structures, energies, and vibrational spectra of water undecamer and dodecamer: Ab initio study. *J. Chem. Phys.* **2001**, *114* (24), 10749–10756.
  22. Lee, H.M.; Suh, S.B.; Kim, K.S. Structures, energies, and vibrational spectra of water undecamer and dodecamer: Ab initio study. *J. Chem. Phys.* **2001**, *115* (15), 7331.
  23. Lee, H.M.; Maofa, G.; Sahu, B.R.; Tarakeshwar, P.; Kim, K.S. Geometrical and electronic structures of gold, silver, and gold–silver binary clusters: Origins of ductility of gold and gold–silver alloy formation. *J. Phys. Chem., B* **2003**, *107* (37), 9994–10005.
  24. Pyykkö, P.; Runeberg, N. Icosahedral W–Au<sub>12</sub>: A predicted closed-shell species, stabilized by aurophilic attraction and relativity and in accord with the 18-electron rule. *Angew. Chem. Int. Ed.* **2002**, *41* (12), 2174–2176.
  25. Li, X.; Kiran, B.; Li, J.; Zhai, H.-J.; Wang, L.-S. Experimental observation and confirmation of icosahedral W–Au<sub>12</sub> and Mo–Au<sub>12</sub> molecules. *Angew. Chem. Int. Ed.* **2002**, *41* (24), 4786–4789.
  26. Brutschy, B. The structure of microsolvated benzene derivatives and the role of aromatic substituents. *Chem. Rev.* **2000**, *100* (11), 3891–3920.
  27. Muller-Dethlefs, K.; Hobza, P. Noncovalent interactions: A challenge for experiment and theory. *Chem. Rev.* **2000**, *100* (1), 143–168.
  28. Tarakeshwar, P.; Choi, H.S.; Kim, K.S. Olefinic vs. aromatic  $\pi$ –H interaction: A theoretical investigation of the nature of interaction of first-row hydrides with ethene and benzene. *J. Am. Chem. Soc.* **2001**, *123* (14), 3323–3331.
  29. Manojkumar, T.K.; Choi, H.S.; Tarakeshwar, P.; Kim, K.S. Ab-initio studies of neutral and anionic *p*-benzoquinone–water clusters. *J. Chem. Phys.* **2003**, *118* (19), 8681–8686.
  30. Schwerdtfeger, P. Gold goes nano—From small clusters to low-dimensional assemblies. *Angew. Chem. Int. Ed.* **2003**, *42* (17), 1892–1895.
  31. Yoon, J.; Kim, K.S.; Baek, K.K. Ab initio study of the low-lying electronic states of Ag<sub>3</sub><sup>–</sup>, Ag<sub>3</sub>, and Ag<sub>3</sub><sup>+</sup>: A coupled-cluster approach. *J. Chem. Phys.* **2000**, *112* (21), 9335–9342.
  32. Häkkinen, H.; Moseler, M.; Landman, U. Bonding in Cu, Ag, and Au clusters: Relativistic effects, trends, and surprises. *Phys. Rev. Lett.* **2002**, *89* (3), 033401(1–4).
  33. Negishi, Y.; Nakamura, Y.; Nakajima, A.; Kaya, K. Photoelectron spectroscopy of gold–silver binary cluster anions (Au<sub>n</sub>Ag<sub>m</sub>; 2 ≤ n + m ≤ 4). *J. Chem. Phys.* **2001**, *115* (8), 3657–3663.
  34. Nautiyal, T.; Youn, S.J.; Kim, K.S. Effect of dimensionality on the electronic structure of Cu, Ag, and Au. *Phys. Rev., B* **2003**, *68* (4), 033407(1–4).
  35. Ohnishi, H.; Kondo, V.; Takayanagi, K. Quantized conductance through individual rows of suspended gold atoms. *Nature* **1998**, *395* (6704), 780–783.
  36. Yanson, A.I.; Bollinger, G.R.; van den Brom, H.E.; Agrait, N.; van Ruitenbeek, J.M. Formation and manipulation of a metallic wire of single gold atoms. *Nature* **1998**, *395* (6704), 783–785.
  37. Rodrigues, V.; Fuhrer, T.; Ugarte, D. Signature of atomic structure in the quantum conductance of gold nanowires. *Phys. Rev. Lett.* **2000**, *85* (19), 4124–4127.
  38. Geng, W.-T.; Kim, K.S. Linear monatomic wires stabilized by alloying: Ab initio density functional calculations. *Phys. Rev., B* **2003**, *67* (4), 233403(1–4).
  39. Bühlmann, P.; Pretsch, E.; Bakker, E. Carrier-based ion-selective electrodes and bulk optodes: 2. Ionophores for potentiometric and optical sensors. *Chem. Rev.* **1998**, *98* (4), 1593–1688.
  40. Kim, D.; Hu, S.; Tarakeshwar, P.; Kim, K.S.; Lisy, J.M. Cation– $\pi$  interactions: A theoretical investigation of the

- interaction of metallic and organic cations with alkenes, arenes, and heteroarenes. *J. Phys. Chem., A* **2003**, *107* (8), 1228–1238.
41. Kim, K.S.; Lee, J.Y.; Lee, S.J.; Ha, T.-K.; Kim, D.H. On binding forces between aromatic ring and quaternary ammonium compound. *J. Am. Chem. Soc.* **1994**, *116* (16), 7399–7400.
  42. Ma, J.C.; Dougherty, D.A. The cation– $\pi$  interaction. *Chem. Rev.* **1997**, *97* (5), 1303–1324.
  43. Cui, C.; Cho, S.J.; Kim, K.S. Cation affinities of [16]starand model—Comparison with 12-crown-4: Crucial role of dipolar moiety orientations. *J. Phys. Chem., A* **1998**, *102* (7), 1119–1123.
  44. Suh, S.B.; Cui, C.; Son, H.S.; U., J.S.; Won, Y.; Kim, K.S. Novel amphi-ionophore in aqueous solution: Cyclohexaaryl. *J. Phys. Chem., B* **2002**, *106* (8), 2061–2064.
  45. Choi, H.S.; Suh, S.B.; Cho, S.J.; Kim, K.S. Ionophores and receptors using cation– $\pi$  interactions: Collarenes. *Proc. Natl. Acad. Sci. U. S. A.* **1998**, *95* (21), 12094–12099.
  46. Choi, H.S.; Kim, K.S. Structures, magnetic properties, and aromaticity of cyclacenes. *Angew. Chem. Int. Ed.* **1999**, *38* (15), 2256–2258.
  47. Choi, H.S.; Kim, D.; Tarakeshwar, P.; Suh, S.B.; Kim, K.S. A new type of ionophore family utilizing the cation–olefin  $\pi$  interaction: Theoretical study of [n] beltene. *J. Org. Chem.* **2002**, *67* (6), 1848–1851.
  48. Dresselhaus, M.S.; Dresselhaus, G.; Eklund, P.C. *Science of Fullerenes and Carbon Nanotubes*; Academic Press: San Diego, 1996.
  49. Dunlap, B.I. Connecting carbon tubules. *Phys. Rev., B* **1992**, *46* (3), 1933–1936.
  50. Itoh, S.; Ihara, S.; Kitakami, J. Toroidal form of carbon C<sub>360</sub>. *J. Phys. Rev., B* **1993**, *47* (3), 1703–1704.
  51. Oh, D.-H.; Park, J.M.; Kim, K.S. Structures and electronic properties of small carbon nanotube tori. *Phys. Rev., B* **2000**, *62* (3), 1600–1603.
  52. Kim, K.S.; Park, J.M.; Kim, J.; Suh, S.B.; Tarakeshwar, P.; Lee, K.H.; Park, S.S. Dimer to monomer phase transition in alkali–metal fullerenes: Magnetic susceptibility changes. *Phys. Rev. Lett.* **2000**, *84* (11), 2425–2428.
  53. Oszlányi, G.; Bortel, G.; Faigel, G.; Tegze, M.; Gránásky, L.; Pekker, S.; Stephens, P.W.; Bendele, G.; Dinnebier, R.; Mihály, G.; Jánossy, A.; Chauvet, O.; Forró, L. Dimerization in KC<sub>60</sub> and RbC<sub>60</sub>. *Phys. Rev., B* **1995**, *51* (18), 12228–12232.
  54. Park, J.M.; Tarakeshwar, P.; Kim, K.S.; Clark, T. Nature of the interaction of paramagnetic atoms (A = <sup>4</sup>N, <sup>4</sup>P, <sup>3</sup>O, <sup>3</sup>S) with  $\pi$  systems and endohedral fullerenes A–C<sub>60</sub>. *J. Chem. Phys.* **2002**, *116* (24), 10684–10691.
  55. Almeida Murphy, T.; Pawlik, Th.; Weidinger, A.; Höhne, M.; Alcalá, R.; Spaeth, J.-M. Observation of atomlike nitrogen in nitrogen-implanted solid C<sub>60</sub>. *Phys. Rev. Lett.* **1996**, *77* (6), 1075–1078.
  56. Mauser, H.; van Eikema Hommes, N.J.R.; Clark, T.; Hirsch, A.; Pietzak, B.; Weidinger, A.; Dunsch, L. Stabilization of atomic nitrogen inside C<sub>60</sub>. *Angew. Chem. Int. Ed.* **1997**, *36* (24), 2835–2838.
  57. Lu, J.; Zhang, Z.; Zhao, X. Electronic structures of endohedral N–C<sub>60</sub>, O–C<sub>60</sub> and F–C<sub>60</sub>. *Chem. Phys. Lett.* **1999**, *312* (2–4), 85–90.
  58. Ardavan, A.; Austwick, M.; Benjamin, S.C.; Briggs, G.A.D.; Dennis, T.J.S.; Ferguson, A.; Hasko, D.G.; Kanai, M.; Khlobystov, A.N.; Lovett, B.W.; Morley, G.W.; Oliver, R.A.; Pettifor, D.G.; Porfyrikis, K.; Reina, J.H.; Rice, J.H.; Smith, J.D.; Taylor, R.A.; Williams, D.A.; Adelman, C.; Mariette, H.; Hamers, R.J. Nanoscale solid-state quantum computing. *Philos. Trans. R. Soc., Math. Phys. Eng. Sci.* **2003**, *361* (1808), 1473–1485.
  59. Chin, D.N.; Zerkowski, J.A.; MacDonald, J.C.; Whitesides, G.M. *Organized Molecular Assemblies in the Solid State*; Whitesell, J.K., Ed.; John Wiley & Sons Inc.: New York, 1999; 185 pp.
  60. Bong, D.T.; Clark, T.D.; Granja, J.R.; Ghadiri, M.R. Self-assembling organic nanotubes. *Angew. Chem. Int. Ed.* **2001**, *40* (6), 988–1011.
  61. Muchado, V.G.; Baxter, P.N.W.; Lehn, J.-M. Self-assembly in self-organized inorganic systems: A view of programmed metallosupramolecular architectures. *J. Braz. Chem. Soc.* **2001**, *12* (4), 431–462.
  62. Prins, L.G.; Reinhoudt, D.N.; Timmerman, P. Non-covalent synthesis using hydrogen bonding. *Angew. Chem. Int. Ed.* **2001**, *40* (13), 2382–2426.
  63. Hof, F.; Craig, S.L.; Nuckolls, C.; Rebek, J. Molecular encapsulation. *Angew. Chem. Int. Ed.* **2002**, *41* (9), 1488–1508.
  64. Braun, E.; Eichen, Y.; Sivan, U.; Ben-Yoseph, G. DNA-templated assembly and electrode attachment of a conducting silver wire. *Nature* **1998**, *391* (6669), 775–778.
  65. Taton, T.A.; Mirkin, C.A.; Letsinger, R.L. Scanometric DNA array detection with nanoparticle probes. *Science* **2000**, *289* (5485), 1757–1760.
  66. Suh, S.B.; Hong, B.H.; Tarakeshwar, P.; Youn, S.J.; Jeong, S.; Kim, K.S. Electronic structure of silver subnanowires in self-assembled organic nanotubes: Density functional calculations. *Phys. Rev., B (Rapid Commun.)* **2003**, *67* (24), 241402(1–4).
  67. Majumdar, D.; Lee, H.M.; Kim, J.; Kim, K.S. Photo-switch and nonlinear optical switch: Theoretical studies on 1,2-bis-(3-thienyl)-ethene derivatives. *J. Chem. Phys.* **1999**, *111* (13), 5866–5872.
  68. Son, H.S.; Hong, B.H.; Lee, C.-W.; Yun, S.; Kim, K.S. A new type of helix pattern in poly-alanine peptide. A new type of helix pattern in polyalanine peptide. *J. Am. Chem. Soc.* **2001**, *123* (3), 514–515.
  69. Hong, B.H.; Lee, J.Y.; Cho, S.J.; Yun, S.; Kim, K.S. Theoretical study of the conformations and strain energies of [n,n]metaparacyclophanes: Indication of stable edge-to-face and displaced face-to-face conformers for n = 4. *J. Org. Chem.* **1999**, *64* (15), 5661–5665.
  70. Lee, J.Y.; Kim, K.S.; Mhin, B.J. Intramolecular charge transfer of pi-conjugated push–pull systems in terms of polarizability and electronegativity. *J. Chem. Phys.* **2001**, *115* (20), 9484–9489.
  71. Lee, J.Y.; Mhin, B.J.; Kim, K.S. New quantum chemical parameter for the substituent effect in benzene based on charge flux. *J. Phys. Chem., A* **2003**, *107* (19), 3577–3579.



# Nanomaterials and Nanodevices: Ion-Beam Technology

**Dmitri Litvinov**

*Center for Nanomagnetic Systems, University of Houston, Houston, Texas, U.S.A.*

**Sakhrat Khizroev**

*Electrical and Computer Engineering, Florida International University,  
Miami, Florida, U.S.A.*

## INTRODUCTION

The development of semiconductor integrated circuits (IC) and mass-data acquisition and storage systems set in motion the transformation of the human enterprise that will continue shaping world economies as well as political and social systems for at least the next half-century.<sup>[1,2]</sup> However, the end of the technology road map for semiconductors is rapidly approaching, and new technologies will be needed to cross over to a new era in integrated electronic systems.<sup>[3]</sup> Many highly innovative materials and device ideas have been proposed to help the transition, driven by various nanotechnology initiatives.<sup>[4–9]</sup> The realization of these ideas is subject to the availability of cost-efficient materials synthesis and device fabrication capabilities. While new nanofabrication technologies are constantly emerging, the economic reality calls for the adaptation of the vast IC fabrication tool set developed over the past several decades to fabrication at nanoscale.

Ion-beam technologies based on wide-area ion beams, focused ion beams (FIB), and shaped multiple ion beams have generated substantial interest in applications in nanostructured materials and nanodevice fabrication and prototyping.<sup>[10–16]</sup> In this entry, the utilization of ion beams for nanomaterials synthesis and fabrication of nanoscale devices is reviewed. Special emphasis is paid to FIB processing of nanoscale magnetic devices<sup>[17]</sup> because FIB has played a critical role in the successful development of magnetic recording at areal densities beyond 100 Gbit/in<sup>2</sup>, which is one of the very few examples of a fully functional nanotechnology with a significant economical impact.

## ION-BEAM SYNTHESIS OF NANOSTRUCTURED MATERIALS

Ion-beam implantation has been one of the key IC manufacturing tools for controlled incorporation of

impurities (dopants) into predefined regions on semiconductor wafers (matrix).<sup>[18]</sup> A remarkable feature of ion implantation is that nearly any element from the periodic table can be implanted into any matrix, making the technology highly versatile. Well-known examples include implantation of group V elements such as phosphorus or arsenic into silicon used for defining n-type Si regions and implantation of group III elements such as boron used for p-type Si regions. Ion bombardment is used for hardening of steels via formation of nitrides at the metal surface. Energetic processes based on ion-assisted deposition and ion-beam deposition have been used for the synthesis of metastable phases of various materials (e.g., diamond or cubic boron nitride).<sup>[19–21]</sup>

In the applications mentioned above, ion-beam implantation is used for the synthesis of homogenous materials where implanted species form chemical bonds with the host material. Ion implantation is typically followed by the annealing step to heal the ion-induced damage of the crystalline structure of the matrix and to activate the implanted species.

If the dose of ion implant exceeds the miscibility limit in the host materials or if the ion species and the host material are immiscible, the annealing step leads to the precipitation of a new phase in the form of clusters (or nanoclusters) as illustrated in Fig. 1. Such precipitates/nanoclusters can lead to significant modification of the electrical, mechanical, magnetic, and optical properties of the host material. Formation of nanoclusters, which is often referred to as ion-beam synthesis, has been documented for a large variety of ion species and host materials. The examples include elemental metal and semiconductor nanocrystals in inert hosts, compound nanocrystals formed as a result of chemical reaction between the ion implant and the matrix, metal alloys and compound semiconductors (II–VI, III–V, and IV–VI) formed by coimplantation of multiple reactive ion species into the host.<sup>[22–31]</sup>

Among potential applications of nanomaterials formed by ion-beam synthesis are all-optical switching

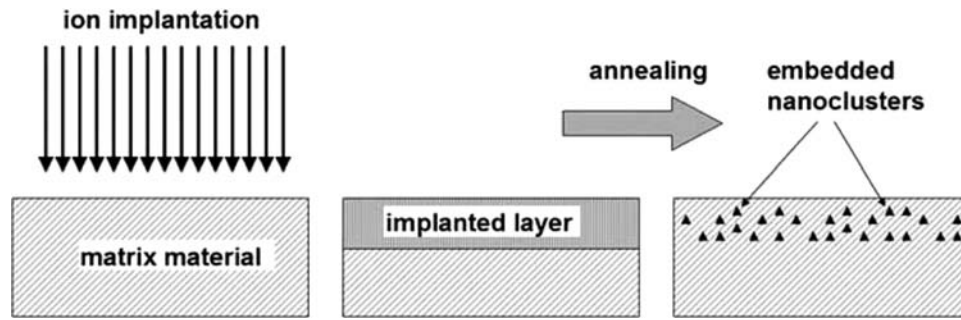


Fig. 1 A schematic of ion-beam synthesis process flow.

that utilizes highly non-linear optical response of metal nanoclusters embedded into non-conducting matrix, opto-electronic devices based on the unique optical response of semiconducting quantum dots, non-volatile memory, spintronics, and single-electron transistor devices.<sup>[32–38]</sup>

### FOCUSED ION-BEAM FOR RAPID PROTOTYPING OF NANOSCALE DEVICES

The principle of operation of an FIB system is similar to the principle of operation of a typical electron-beam (e-beam) system used in electron microscopy (SEM, TEM) or e-beam lithography. The key difference is the source: FIB systems use a liquid metal ion source (LMIS). In such an ion source, a reservoir of liquid metal is in contact with the dull end of a sharp needle (usually made of tungsten). Metal from the melt flows toward the sharp tip of the needle biased at a relatively high voltage ( $\sim 10$  kV) with respect to the extractor electrode. The source is designed such that the high electric field between the extractor electrode and the needle tip is sufficient for field ion emission. Extracted metal ions travel through the beam shaping/focusing column, which is similar to a typical e-beam column with the main difference being the polarity of the voltages applied to accelerating and focusing components. A typical LMIS uses gallium (Ga), which melts at  $29.78^\circ\text{C}$  (slightly above room temperature); this significantly simplifies the design and reliability issues.

The resolution limits of an FIB system are defined mainly by the tool design (such as finite penumbra due to finite source size and the precision of the beam shaping column) and not by diffraction limits, which are in deep subangstrom range.<sup>[39]</sup> The utilization of ions adds great versatility as compared to e-beam systems:

1. Focused ion beams can be used for direct etching of device patterns on a wafer using physical

sputtering of materials with heavy energetic Ga ions.

2. Focused ion beams can also be used for highly localized material deposition where the ion beam is used as a material carrier. In this application, a vapor source (either gaseous or near-the-melting point solid) is inserted into the ion-beam path.
3. Focused ion beams can be effective for local ion implantation and ion mixing.
4. As in e-beam lithography, a pattern can be written into resist using secondary electrons for resist exposure.
5. An important feature of a typical FIB system is that it allows high-resolution imaging using either secondary electrons or ions.

Owing to the direct write capability, FIB is an ideal fabrication tool for the rapid prototyping of nanoscale devices. For example, with FIB, even in the academic environment, one complete iteration necessary for making a magnetic recording transducer (write/read head) with sub-100 nm features takes less than 1 hr.<sup>[40]</sup> For comparison, with e-beam lithography in the streamlined industrial environment, it takes months to go through one iteration cycle. In practice, it usually takes several iterations to complete the design of a next-generation recording head. Such tremendous time and resource savings with FIB is a critical advantage for prototyping at nanoscale.

An additional advantage resulting from larger ion mass, as compared to the mass of an electron, is the fact that the FIB is much less influenced by stray fields. For example, in the magnetic data storage industry, one of the main obstacles in implementing e-beam lithography in the fabrication of magnetic recording heads suitable for areal densities above  $100\text{ Gbit/in}^2$  is the frequent occurrence of the physical shift in patterned features due to the interaction between the e-beam and magnetic thin films.<sup>[41]</sup> This shift, depending on the properties of a thin film, could be as large as 100 nm (for  $\text{Ni}_{45}/\text{Fe}_{55}$ ). For comparison with FIB, at

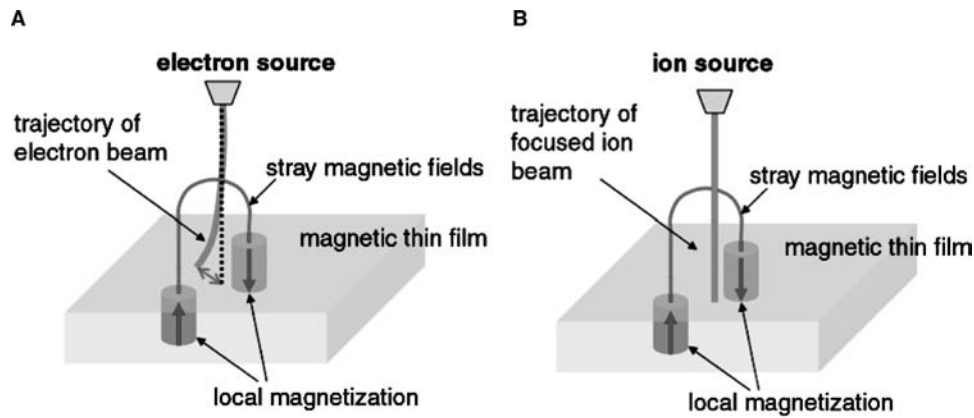


Fig. 2 Schematic diagrams showing trajectories of focused (A) electron and (B) ion beams.

equal conditions, this shift could be reduced to an unnoticeable level, as shown in schematic diagrams in Figs. 2A and B, respectively.

The FIB-based fabrication not only has the advantage of using fewer steps than lithography-based processing but also has the potential to pattern magnetic materials with higher resolution than what is achievable with e-beam lithography. The study on magnetic devices at Seagate showed that with 50% reproducibility, e-beam and FIB are capable of feature sizes of 30 and 10 nm, respectively, with individual devices made with FIB in sub-10 nm feature size range.

The FIB is especially attractive for a small research laboratory/an academic environment. Patterns with nanoscale features can be defined without using complex and expensive fabrication facilities. With the FIB's direct etch/write capability (no mask-based lithography is necessary), a university just needs to have one FIB system available to trim relatively large devices into nanoscale devices of different geometries for further experimentation and testing. The ability to rapidly fabricate at nanoscale for further characterization and optimization makes FIB an indispensable

tool for the rapid development of emerging technologies in the field of nanotechnology.

## ION-BEAM LITHOGRAPHY

Proximity and projection ion-beam lithographies (IBL) can be thought of as an extension of the FIB technology discussed above in that multiple ion beams are used to simultaneously write the pattern into resist.<sup>[42,43]</sup> Note, IBL is typically not used for the direct etching of the device patterns. In proximity IBL, illustrated in Fig. 3, a stencil mask is illuminated by a broad beam of energetic ions (e.g., helium) and the transmitted beamlets transfer the mask pattern to resist on a substrate. The theoretical resolution limit imposed by the range of secondary electrons and atom scattering within the resist is 1–2 nm (R. Kubena, unpublished data).<sup>[44–46]</sup> Using a small (a few micrometers) mask-to-wafer gap overcomes the practical limitations of diffraction and penumbra (due to a finite source size). Ion-beam lithography is on a fast track to practical application in the sub-10 nm domain by

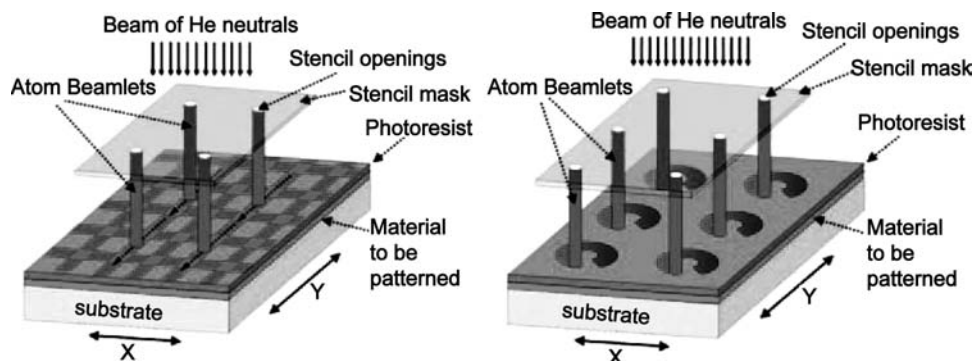
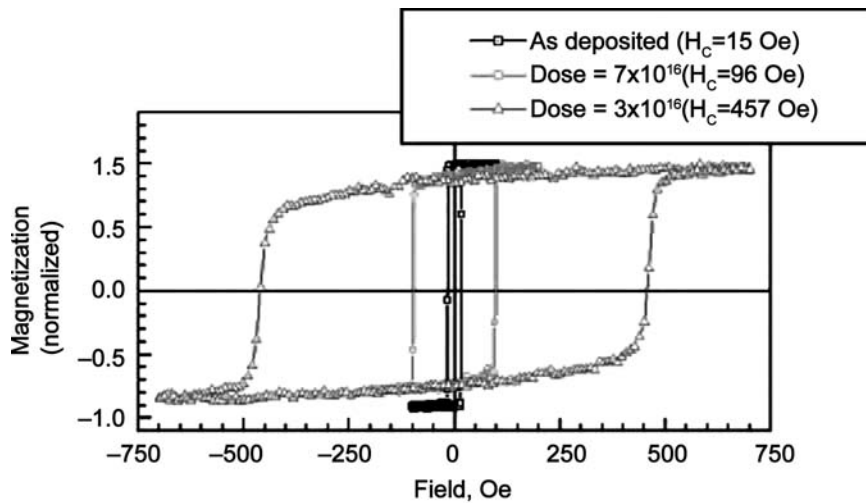


Fig. 3 A schematic of IBL: beamlets formed by an aperture plate write a periodic pattern in resist on a scanned substrate.



**Fig. 4**  $M$ - $H$  loops for 50 nm Co films with different Ga<sup>+</sup> implantation doses: as-deposited Co film;  $7 \times 10^{15}$  ions/cm<sup>2</sup>;  $3 \times 10^{16}$  ions/cm<sup>2</sup>.

leveraging the many important developments of membrane mask technology in the proximity x-ray and projection ion and electron programs of the past two decades. It should be noted that it is also possible to generate a beam of neutrals that allows elimination of the negative effects of stray fields onto the beam.

A variation of IBL is projection IBL, which eliminates the need for stencil masks with ultrafine features. In projection IBL, the initial set of relatively wide beams is focused onto a substrate to achieve fine features.<sup>[47,48]</sup>

## ION-BEAM APPLICATIONS IN MAGNETIC DATA STORAGE

### Ion-Beam Modification of Magnetic Materials

Recently, there has been substantial interest in capitalizing on existing semiconductor processing technologies for magnetic thin film device fabrication. For example, e-beam lithography and chemical-mechanical polishing have been firmly accepted as next-generation tools for advanced magnetic recording applications.<sup>[49,50]</sup> Similarly, ion implantation and FIB processing, which are widely used in the semiconductor industry, are steadily gaining ground in magnetic thin film materials processing.<sup>[12,51]</sup> To enable wide commercialization of these techniques in magnetic recording applications, a detailed study of these powerful fabrication tools with respect to their application to magnetic materials processing is necessary.<sup>[52-54]</sup> In this section, the effects of Ga<sup>+</sup> ion implantation on magnetic properties of magnetic thin films and the application of FIB implantation for tailoring of magnetic properties at nanoscale are presented.<sup>[55]</sup>

Fig. 4 compares the  $M$ - $H$  loops of an as-deposited Co film and two Co films with implant doses of  $7 \times 10^{15}$  ions/cm<sup>2</sup> and  $3 \times 10^{16}$  ions/cm<sup>2</sup>. Note, if all Ga<sup>+</sup> ions were implanted into the film,  $7 \times 10^{15}$  ions/cm<sup>2</sup> and  $3 \times 10^{16}$  ions/cm<sup>2</sup> doses would correspond to  $\sim 1.5\%$  (atomic %) and  $\sim 6.6\%$  (atomic %), respectively. Substantial modifications to the magnetic properties can be observed. The coercivity of Ga<sup>+</sup> implanted films increased by factors of 6 and 30 for  $7 \times 10^{15}$  ions/cm<sup>2</sup> and  $3 \times 10^{16}$  ions/cm<sup>2</sup> implant doses, respectively. Also, the  $M$ - $H$  loop squareness,  $S$ , defined as the ratio of the remanent magnetization,  $M_r$ , to the saturation magnetization,  $M_s$ , changed from a perfectly square loop in the case of as-deposited Co film with  $S = 1$  to  $S < 0.9$  in the case of the higher implant dose. Reduced squareness and shearing of the hysteresis loop indicate a reduction in exchange coupling in the Ga<sup>+</sup> ion implanted films. It should be noted that exchange coupling is one of the key parameters controlled during the development of the magnetic recording medium.

Fig. 5 compares atomic force microscopy (AFM) and magnetic force microscopy (MFM) images of the Co film implanted with a Ga dose of  $7 \times 10^{15}$  ions/cm<sup>2</sup>. Magnetization patterns in MFM images can be clearly tracked to the grain structure observed in AFM images. This suggests that ion implantation results in reduced intergranular exchange coupling. This is consistent with the observed shearing of magnetization loops (see Fig. 4). These data are similar to previously reported observations on permalloy thin films where an increase in coercivity was attributed to the introduction of extended defects.<sup>[56]</sup> In the present study such extended effects are represented by Ga-rich grain boundaries.

Local ion implantation can be achieved using FIB. Figs. 6A and B show MFM images of an as-deposited

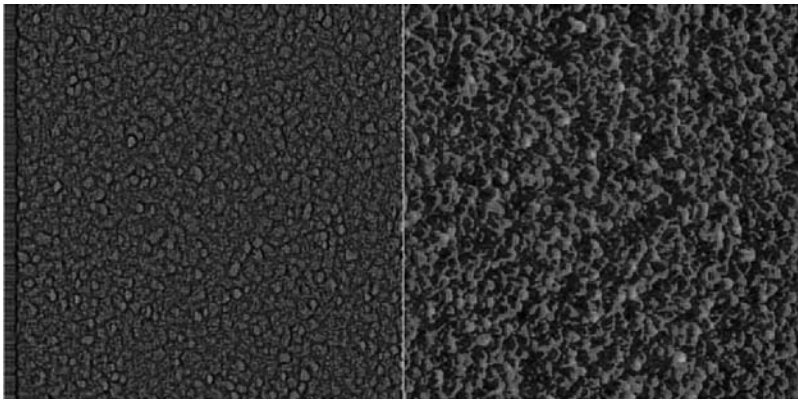


**Fig. 5** AFM (left)/MFM (right) scans ( $3\ \mu\text{m} \times 3\ \mu\text{m}$ ) of Co films implanted at  $3 \times 10^{16}$  ions/cm<sup>2</sup>.

Co film and a Co film implanted with 50 keV Ga<sup>+</sup> ions at  $1 \times 10^{16}$  ions/cm<sup>2</sup> using FIB implantation, respectively. Similar to the above observations, a clear split of the film into a magnetic multidomain state can be observed in Fig. 6B. At the same time, using AFM, no measurable modification of the film topography could be observed (RMS roughness in both cases was 0.9 nm). As discussed above, a dramatic change in magnetic domain patterns may be attributed to the diffusion of the implanted Ga<sup>+</sup> ions to the intergranular boundaries, thus reducing the exchange coupling between the individual magnetic grains.

Fig. 7 compares the MFM image of four  $300 \times 300$  nm structures defined by FIB etching of the as-deposited Co film and of an intentionally ion implanted material. A transition to a magnetic multiple domain state attributed to ion implantation can be clearly observed.

In summary, ion implantation can be used for the modification of the properties of magnetic materials. For example, Ga ion implantation leads to the reduction of exchange coupling between magnetic grains and the formation of extended domain wall pinning defects. Implantation can be also achieved locally using FIB technology.

## Nanofabrication of Magnetic Transducers

### Magnetic recording heads

Magnetic recording has had very high areal bit density growth rates for the past 10–12 yr.<sup>[57]</sup> The resultant dramatic reduction of the bit size has led to the rapid scaling of the characteristic grain size and to the corresponding shrinkage of the thermal activation volume in conventional polycrystalline media. This, in turn, has led to challenging issues related to long-term data stability. Medium magnetic stability is controlled by the ratio of the magnetic anisotropy energy,  $K_U V$ , to the energy of thermal fluctuations,  $k_B T$ , where  $K_U$  is the recording layer magnetic anisotropy energy density, and  $V$  is the thermal activation volume, which approximately corresponds to the volume of a single grain in a polycrystalline medium. The ratio  $K_U V / k_B T$  is kept at a value of 40–60 to ensure 10–15 yr data stability.<sup>[58]</sup> At the superparamagnetic limit, the scaling of the grain size necessary to maintain the adequate SNR can no longer be compensated by increasing  $K_U$  because of the limited write fields achievable with conventional write heads.<sup>[59,60]</sup> It has been predicted that the superparamagnetic limit for conventional

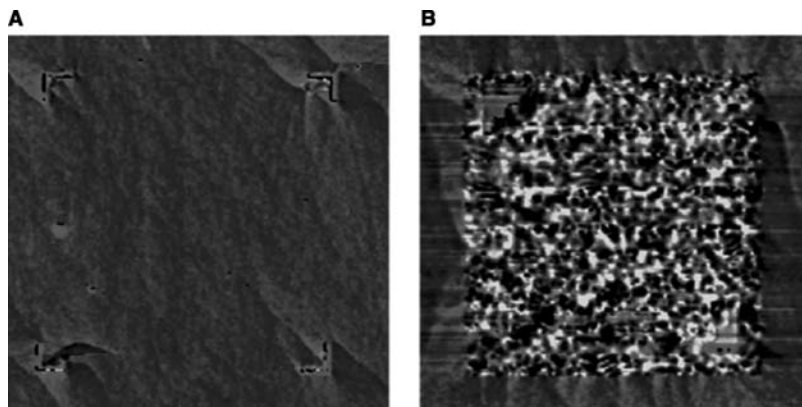


**Fig. 6** Magnetic force microscopy image of (A) as-deposited Co film and (B) Ga<sup>+</sup> ion implanted section in the Co film.



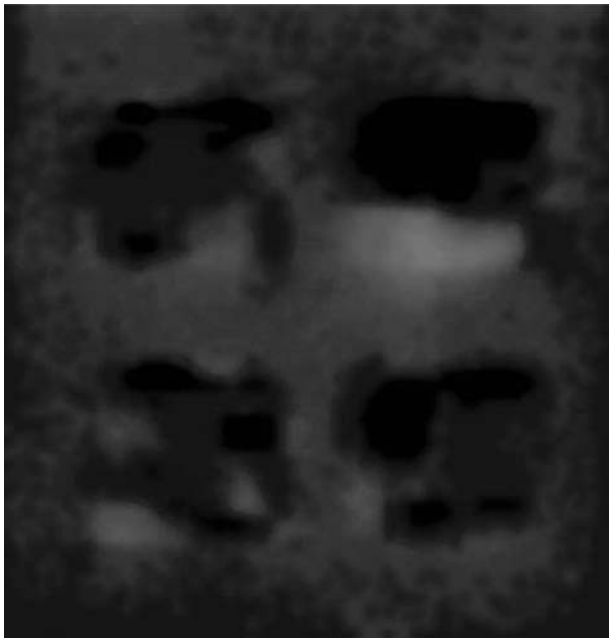


**Fig. 7** Magnetic force microscopy images of four  $300\text{ nm} \times 300\text{ nm}$  Co squares formed by FIB etching in hcp Co film. Top left square is as-deposited Co; the remaining three squares are locally implanted with a  $\sim 1 \times 10^{16}$  ions/cm<sup>2</sup> dose using a 50 keV beam.

longitudinal recording is an areal bit density of  $\sim 150\text{ Gbit/in}^2$ .<sup>[61]</sup>

A schematic of the conventional (longitudinal) recording paradigm is shown in Fig. 8A. During writing, the magnetic field generated by a write head aligns the magnetization along the track in either a positive or a negative direction. A magnetoresistive sensor detects the bit boundaries during playback. The lateral dimensions of a bit define the areal bit density that such a drive supports. As shown in Fig. 8B, the recording medium has a polycrystalline alloy structure where, to reduce noise, a bit is represented

by the average magnetic moment of 50–100 grains. The SNR is typically 14–16 dB, measured with the autocorrelation SNR of a repetitive pseudorandom bit sequence. The 32-fold increase in bit density over the past 5 yr has been achieved by reducing grain size, while holding the number of grains per bit approximately constant.

A solution to extend the superparamagnetic limit was recently introduced in the form of perpendicular recording, where larger write fields enable the enhancement of the thermal stability ratio.<sup>[62,63]</sup> A schematic diagram of a typical perpendicular recording system is shown in Fig. 8C.<sup>[40]</sup> In this technology, the magnetization of the media is oriented normal to the disk surface and the use of a single-pole write head, mirrored in a soft underlayer, effectively doubles the available write field compared to longitudinal recording.

It should be noted that the transition of a highly competitive multibillion dollar industry such as the magnetic data storage industry to a different technology is not easy. Early demonstrations of ultra-high-density magnetic recording using an FIB fabricated magnetic recording head have played a key role in the process. An FIB image of a nanoscale trackwidth perpendicular magnetic thin film head fabricated of relatively wide (about  $1\ \mu\text{m}$ ) longitudinal ring-type heads using FIB trimming from the air-bearing surface (ABS) is shown in Fig. 9A. As mentioned above, it takes approximately 1 hr to trim one head into the nanoscale dimensions. It would have taken more than several months to make similar changes to the design using conventional lithography-based methods. An MFM image of two 65 nm-wide adjacent tracks recorded with an FIB-made single-pole perpendicular head with a trackwidth of 60 nm is shown in Fig. 9B. At a 4:1 bit cell aspect ratio, such a narrow track corresponds to an areal density of the order of 1 Tbit/in<sup>2</sup>. With a series of follow-up

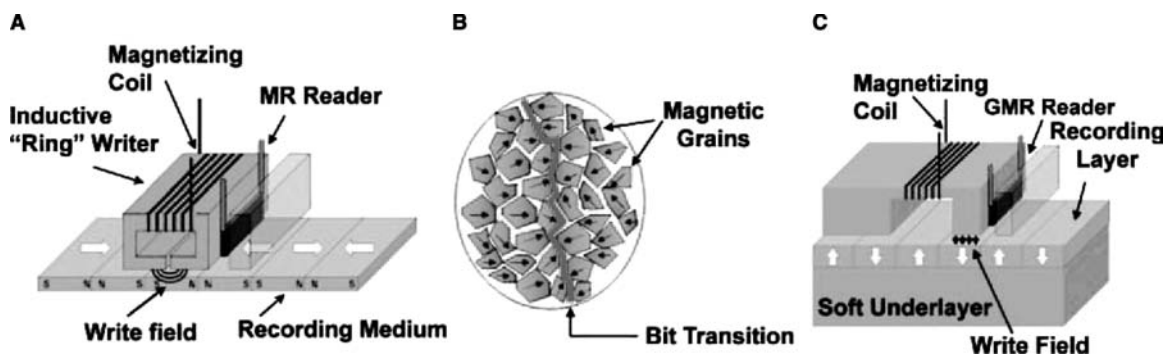


**Fig. 8** (A) A schematic of a conventional longitudinal recording scheme employed in today's hard drives. (B) A schematic of a single-bit transition in a polycrystalline medium. (C) A schematic of a perpendicular recording system. The soft magnetic underlayer acts as a magnetic mirror, doubling the amplitude of the write field.



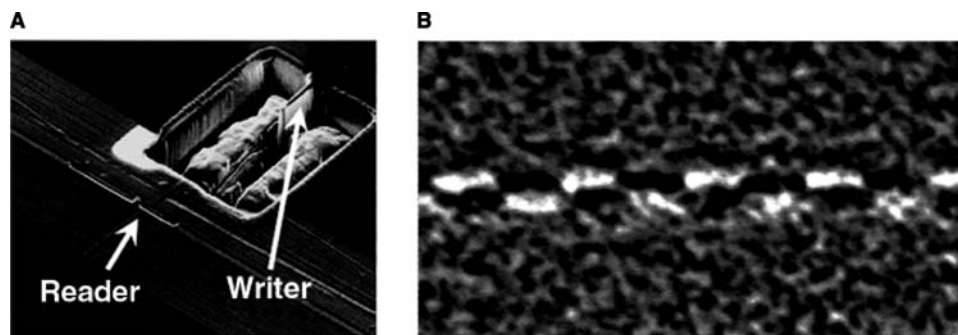


**Fig. 9** (A) Micrograph of an FIB-made perpendicular write head with a 60 nm wide write pole. (B) Magnetic force microscopy image of two adjacent 65 nm-wide tracks recorded into Co/Pd multilayer medium using FIB writer.

experiments, this demonstration has resulted in a major shift to perpendicular recording in the entire multibillion dollar magnetic data storage industry today.<sup>[64]</sup>

#### Ultra-high-resolution MFM

As we step into the world of nanodimensions, the importance of high-precision microscopy is evident.<sup>[65]</sup> Scanning probe microscopy (SPM) is generally recognized as one of the most critical and unique techniques utilized for imaging with nanoscale resolution.<sup>[66]</sup> Many important discoveries of the last two decades would have been impossible without SPM. Some examples are carbon nanotube-based applications, new-generation magnetic media for data storage, detection of magnetic flux quanta in superconductors, and others.<sup>[67,68]</sup> With so many important discoveries resulting from the ability to directly see nanoscale objects, innovations for improving the resolution of SPM even further are critical.<sup>[69]</sup>

This section discusses MFM, which is used for measuring a magnetic field emanating from an object with sub-100 nm resolution.<sup>[70]</sup> Today, MFM, unlike some other more popular modes of SPM, such as AFM and scanning tunneling microscopy, does not provide spatial resolution sufficient for study of the intergranular effects in different media. Most of these effects are caused by the quantum-mechanical exchange coupling with the characteristic length of interaction of the order of 1 nm. The best MFM system today provides resolution only of the order of 30–50 nm. Such a relative low resolution is attributed to the long-range magnetostatic interaction between a probe and a sample. However, it is believed that the resolution of MFM can be substantially improved with more advanced nanoscale fabrication methods with more flexible control of the probe geometry at the nanoscale (see Fig. 10). Recently, it was reported how FIB can be used to fabricate MFM probe tips that would provide not only improved resolution but also directional

information about the magnetic field emanating from a sample.<sup>[71]</sup>

#### Magnetic nanotubes

The process and control of the magnetization switching in nanoscale magnetic probes is of critical importance for a number of emerging technologies, including magnetic random access memory (MRAM), magnetic nanoelectromechanical systems (NEMS), magnetic recording at densities beyond 1 Tbit/in<sup>2</sup>, and others. In this case, considering that the magnetic domain wall width in a typical “soft” magnetic material is of the order of 100 nm, controllable switching of the magnetization becomes an issue with the reduction of the characteristic pole tip dimensions into the sub-100 nm range.

In recognition of earlier theoretical conclusions, a rectangular probe with a magnetic void (tube-like structure of the probe tip) at the ABS in the form

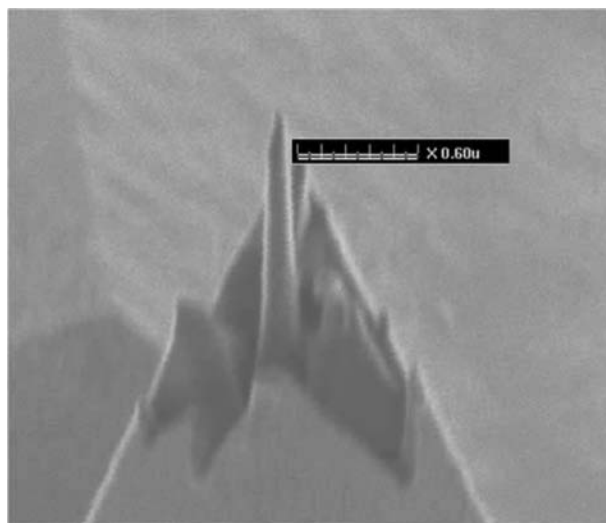


**Fig. 10** Electron image of an FIB-made nanoscale probe with a 40 nm × 40 nm × 10 nm apex.

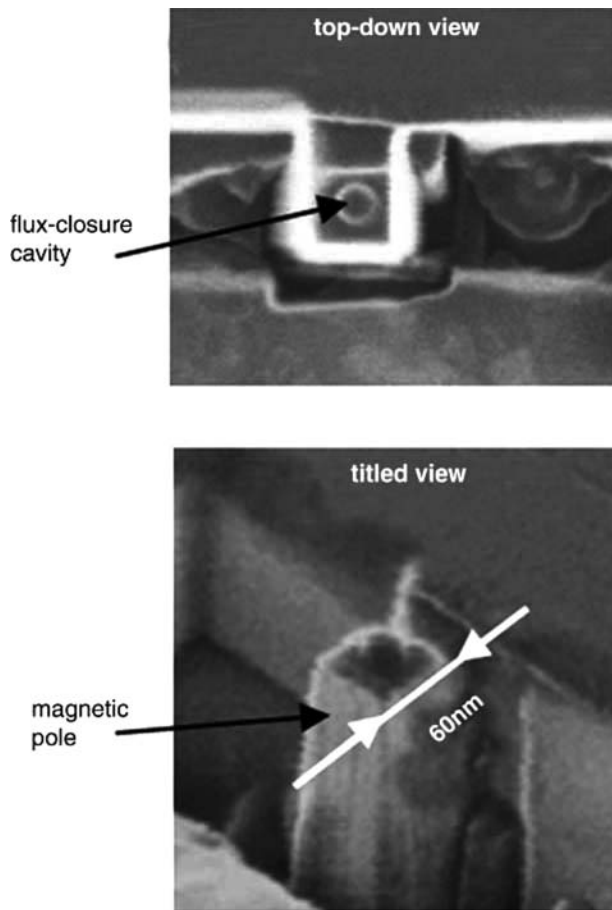


**Fig. 11** Micrographs of a 60 nm × 60 nm magnetic nanotube with a 40 nm flux cavity fabricated using FIB etching of a magnetic recording head.

of a physical cavity, as shown in Fig. 11, was fabricated.<sup>[72]</sup> Magnetic nanoprobes with a rectangular cross section of 60 × 60 nm<sup>2</sup> and a probe length (throat height) that varied in the range of 100–1000 nm were fabricated using FIB trimming of regular magnetic recording heads. Each magnetic nanotube had a 40 nm-deep cavity with a 40 nm diameter created at the ABS of the probe tip via FIB, as shown in Fig. 11. The FIB-made nanotubes were composed of a Ni/Fe (45/55) alloy with saturation magnetization of 1.6 T and with an anisotropy field of approximately 20 Oe. Also, it is clear that the shape of the nanotubes can be easily varied with FIB. These FIB-made nanotubes are perfect prototype devices to study the physics of magnetization switching in different types of MRAM and other magnetic devices.

### Nanomanufacturing of Patterned Magnetic Recording Media

It should be noted that the perpendicular recording discussed above has its own superparamagnetic

limit and is expected to top out of steam at 500–1000 Gbit/in<sup>2</sup>. If no alternative technology is developed to further extend the superparamagnetic limit, the high-areal density growth rate in magnetic recording technology will come to a halt in 2006–2007. Currently, there are two possible approaches to meeting the superparamagnetic challenge. One is thermally assisted recording on high-anisotropy media where local heating is used to temporarily reduce the magnetic anisotropy during writing.<sup>[73]</sup> The other is nanoscale-patterned medium recording (N-PMR), a single-grain-per-bit recording paradigm, where SNR is maintained by eliminating the randomness of the recording medium through lithographic patterning or self-assembly methods. The N-PMR would face a superparamagnetic limit for a bit size of 3–4 nm or a bit density of 20–50 Tbits/in<sup>2</sup>.<sup>[74]</sup>

One of the promising approaches to N-PMR fabrication and prototyping is IBL, which is under development by the team of the University of Houston, Seagate, the National Institute of Standards and Technology, and Lawrence Berkeley National Lab. A stencil mask with an array of open apertures is used to produce trillions of parallel atom beams. These beams create an N-PMR medium pattern as the substrate is scanned across the unit cell. Because the openings of the aperture array are widely spaced, the ultimate resolution of e-beam lithography necessary for writing these masks is in the 5–8 nm range, not the 20–30 nm that would apply for patterning dense media directly.<sup>[75]</sup> The relatively low (e.g., 1%) pattern density on the stencil mask means the mask will be extremely durable and suffer minimal distortion.

## CONCLUSIONS

In summary, ion-beam technologies represent a versatile tool for next generations of material systems and nanoscale devices. Ion beams can be used for synthesis of various nanocomposite materials, materials properties modifications at nanoscale, and fabrication of record setting functional nanometer scale devices.

## REFERENCES

1. Feder, B.J. In the world of the very small, companies make big plans. *The New York Times* **2002**, Dec 16.
2. Greenspan, A. Productivity, In *the U.S. Department of Labor and American Enterprise Institute Conference*, Washington, DC, Oct 23, 2002.
3. International Technology Roadmap for Semiconductors; <http://public.itrs.net/>.
4. Collier, C.P.; Wong, E.W.; Belohradsky, M.; Raymo, F.M.; Stoddart, J.F.; Kuekes, P.J.; Williams, R.S.;

- Heath, J.R. Electronically configurable molecular-based logic gates. *Science* **1999**, *285*, 391–394.
5. Meindl, J.D.; Chen, Q.; Davis, J.A. Limits on silicon nanoelectronics for terascale integration. *Science* **2001**, *293*, 2044–2049.
  6. Bachtold, A.; Hadley, P.; Nakanishi, T.; Dekker, C. Logic circuits with carbon nanotube transistors. *Science* **2001**, *294*, 1317–1320.
  7. Heinrich, A.J.; Lutz, C.P.; Gupta, J.A.; Eigler, D.M. Molecule cascades. *Science* **2002**, *298*, 1381–1387.
  8. Service, R.F. Small clusters hit the big time. *Science* **1996**, *271*, 920–922.
  9. Nirmal, M.; Dabbousi, B.O.; Bawendi, M.G.; Macklin, J.J.; Trautman, J.K.; Harris, T.D.; Brus, L.E. Fluorescence intermittency in single cadmium selenide nanocrystals. *Nature* **1996**, *383*, 802–804.
  10. Li, J.; Stein, D.; McMullan, C.; Branton, D.; Aziz, M.J.; Golovchenko, J.A. Ion-beam sculpting at nanometre length scales. *Nature* **2001**, *412*, 166–169.
  11. Budai, J.D.; White, C.W.; Withrow, S.P.; Chisholm, M.F.; Zhu, J.; Zuhr, R.A. Controlling the size, structures and orientation of semiconductor nanocrystals using metastable phase recrystallization. *Nature* **1997**, *390*, 384–386.
  12. Khizroev, S.; Bain, J.A.; Litvinov, D. Fabrication of nanomagnetic probes via focused ion beam etching and deposition. *Nanotechnology* **2002**, *13*, 619–622.
  13. Weller, D.; Baglin, J.E.E.; Kellock, A.J.; Hannial, K.A.; Toney, M.; Kusinski, G.; Lang, S.; Best, M.E.; Terris, B.D. Ion induced magnetization reorientation on Co/Pt multilayers for patterned media. *J. Appl. Phys.* **2000**, *87*, 5768–5770.
  14. Chen, C.W. *Magnetism and Metallurgy of Soft Magnetic Materials*; North-Holland: Amsterdam, 1977.
  15. Ozkaya, D.; Langford, R.M.; Chan, W.L.; Petford-Long, A.K. Effect of Ga implantation on the magnetic properties of permalloy thin films. *J. Appl. Phys.* **2002**, *91*, 9937–9942.
  16. Devolder, T.; Viue, C.; Harry, B.; Ferre, J.; Chappert, C.; Gierak, J.; Jamet, J.-P.; Aign, T.; Meyer, P.; Chen, Y.; Rousseaux, F.; Mathet, V.; Launois, H.; Kaitasov, O. Ion beam-induced magnetic patterning at the sub-0.1  $\mu\text{m}$  level. *Comp. Rend. Acad. Sci. Ser. II Fasc. B—Mec. Phys. Astron. Paris* **1999**, *327*, 915–923.
  17. Litvinov, D.; Khizroev, S. Focused ion beam (FIB) in future probe storage industry. *Nanotechnology* **2002**, *13*, 179–184.
  18. Poate, J.M.; Saadatmand, K. Ion beam technologies in the semiconductor world. *Rev. Sci. Instrum.* **2002**, *73*, 868–872.
  19. Lifshitz, Y.; Kohler, T.; Frauenheim, T.; Guzman, I.; Hoffman, A.; Zhang, R.Q.; Zhou, X.T.; Lee, S.T. The mechanism of diamond nucleation from energetic species. *Science* **2002**, *297*, 1531–1533.
  20. Khizroev, S.; Litvinov, D. On the mechanism of the cubic phase formation in the boron nitride thin-film systems. *Appl. Phys. Lett.* **2001**, *79*, 353–355.
  21. Rabalais, J.W.; Kasi, S. Growth of thin chemically bonded diamondlike films by ion-beam deposition. *Science* **1998**, *239*, 623–625.
  22. Garhards, I.; Ronning, C.; Hofsass, H.; Seibt, M.; Gibhardt, H. Ion beam synthesis of diamond-like carbon thin films containing copper nanocrystals. *J. Appl. Phys.* **2003**, *93*, 1203–1207.
  23. Muller, T.; Heining, K.-H.; Moller, W.; Bonafos, C.; Coffin, H.; Cherkashin, N.; Assayag, G.B.; Schamm, S.; Zanchi, G.; Claverie, A. multi-dot floating-gates for non-volatile semiconductor memories: their ion beam synthesis and morphology. *Appl. Phys. Lett.* **2004**, *85*, 2373–2375.
  24. Klimenkov, M.; von Borany, J.; Matz, W.; Grotzschel, R.; Herrmann, F. Formation of a single interface-near, delta-like Ge nanocluster band in thin  $\text{SiO}_2$  films using ion-beam synthesis. *J. Appl. Phys.* **2002**, *91*, 10062–10067.
  25. Mantl, S. Ion beam synthesis of epitaxial silicides: fabrication, characterization and applications. *Mater. Sci. Rep.* **1992**, *8* (1–2), 1–95.
  26. Zuhr, R.A.; Magruder, R.H., III; Anderson, T.A.; Wittig, J.E. Nanosize metal alloy particle formation in Ag and Cu sequentially implanted silica. *Mater. Res. Soc. Symp. Proc.* **1994**, *316*, 457.
  27. White, C.W.; Withrow, S.P.; Williams, J.M.; Budai, J.D.; Meldrum, A.; Sorge, K.D.; Thompson, J.R.; Boatner, L.A. FePt nanoparticles formed in  $\text{Al}_2\text{O}_3$  by ion beam synthesis: annealing environment effects. *J. Appl. Phys.* **2004**, *95*, 8160–8166.
  28. Zhu, J.G.; White, C.W.; Budai, J.D.; Withrow, S.P.; Chen, Y. Growth of Ge, Si, and SiGe nanocrystals in  $\text{SiO}_2$  matrices. *J. Appl. Phys.* **1995**, *78*, 4386–4389.
  29. Okamoto, S.; Kanemitsu, Y.; Min, K.S.; Atwater, H.A. Photoluminescence from GaAs nanocrystals fabricated by Ga<sup>+</sup> and As<sup>+</sup> co-implantation in  $\text{SiO}_2$  matrices. *Appl. Phys. Lett.* **1998**, *73*, 1829–1831.
  30. Bonafos, C.; Garrido, B.; Lopez, M.; Romano-Rodriguez, A.; Gonzalez-Varona, O.; Perez-Rodriguez, A.; Morante, J.R. Ion-beam synthesis and structural characterization of ZnS nanocrystals in  $\text{SiO}_2$ . *Appl. Phys. Lett.* **1998**, *72* (26), 3488–3490.
  31. Matsuura, D.; Kanemitsu, Y.; Kushida, T.; White, C.W.; Budai, J.D.; Meldrum, A. Optical characterization of CdS nanocrystals in  $\text{Al}_2\text{O}_3$  matrices fabricated by ion-beam synthesis. *Appl. Phys. Lett.* **2000**, *77*, 2289–2291.
  32. Magruder, R.H., III; Haglund, R.F., Jr.; Yang, L.; Wittig, J.E.; Zuhr, R.A. Physical and optical properties of Cu nanoclusters fabricated by ion implantation in fused silica. *J. Appl. Phys.* **1994**, *76*, 708.
  33. Flytzanis, C.; Hache, F.; Klein, M.C.; Ricard, D.; Roussignol, P. Semiconductor and metal crystallites in dielectrics. In *Progress in Optics XXIX*; Wolf, E., Ed.; Elsevier, 1991; 321 pp.
  34. von Borany, J.; Grotzschel, R.; Heining, K.-H.; Markwitz, A.; Matz, W.; Schmidt, B.; Skorupa, W. Multimodal impurity redistribution and nanocluster formation in Ge implanted silicon dioxide films. *Appl. Phys. Lett.* **1997**, *71*, 3215–3217.
  35. Brongersma, M.F.; Polman, A.; Min, K.S.; Boer, E.; Tambo, T.; Atwater, H.A. Tuning the emission wavelength of Si nanocrystals in  $\text{SiO}_2$  by oxidation. *Appl. Phys. Lett.* **1998**, *72*, 2577–2579.

36. Kapetanakis, E.; Normand, P.; Tsoukalas, D.; Beltsios, K. Room-temperature single-electron charging phenomena in large-area nanocrystal memory obtained by low-energy ion beam synthesis. *Appl. Phys. Lett.* **2002**, *80*, 2794–2796.
37. Shi, J.; Gider, S.; Babcock, K.; Awschalom, D.D. Magnetic clusters in molecular beams, metals, and semiconductors. *Science* **1996**, *271*, 937–941.
38. Klein, D.L.; Roth, R.; Lim, A.K.L.; Alivisatos, A.P.; McEuen, P.L. A single-electron transistor made from a cadmium selenide nanocrystals. *Nature* **1997**, *389*, 699.
39. Orloff, J. High-resolution focused ion beams. *Rev. Sci. Instrum.* **1993**, *64* (5), 1105.
40. Khizroev, S.; Kryder, M.H.; Ikeda, Y.; Rubin, K.; Arnett, P.; Best, M.; Thompson, D.A. Recording heads with trackwidths suitable for 100 Gbit/in<sup>2</sup> density. *IEEE Trans. Magn.* **1999**, *35* (5), 2544–2546.
41. The Feynman Lectures on Physics: Electromagnetism; Addison-Wesley Publishing, 1970; Vol. 2, Chap. 26-2.
42. Wolfe, J.C.; Pendharkar, S.V.; Ruchhoeft, P. A proximity ion beam lithography process for high density nanostructures. *J. Vac. Sci. Technol. B.* **1996**, *14*, 3896.
43. Melngailis, J.; Mondelli, A.A.; Berry, I.L.; Mohondro, R. A review of ion projection lithography. *J. Vac. Sci. Technol. B.* **1998**, *16*, 927.
44. Wolfe, J.C.; Ruchhoeft, P. Atom beam lithography: non-contact beam technology for the sub-10nm domain, Plenary Talk. EIPBN Conference, Tampa, May 27, 2003.
45. Kaesmaier, R.; Löschner, H.; Stengl, G.; Wolfe, J.C.; Ruchhoeft, P. Ion Projection Lithography: International Development Program. *J. Vac. Sci. Technol. B.* **1999**, *17*, 3091–3097.
46. Ruchhoeft, P.; Wolfe, J.C. Determination of resist exposure parameters in helium ion beam lithography: absorbed energy gradient, contrast, and critical dose. *J. Vac. Sci. Technol. B.* **2000**, *18*, 3177–3180.
47. Kaesmaier, R.; Loschner, H. Overview of the Ion Projection Lithography European MEDEA and International Program, SPIE Conference on Microlithography, Santa Clara, CA, Feb 2000.
48. Bruenger, W.H.; Torkler, M.; Leung, K.N.; Lee, Y.; Williams, M.D.; Loeschner, H.; Stengl, G.; Fallmann, W.; Paschke, F.; Stangl, G.; Rangelow, I.W.; Hudek, P. Resolution improvement of ion projector with a low energy spread multicusp ion source. *Microelectron. Eng.* **1999**, *46*, 477.
49. Fontana, R.E.; Katine, J.; Rooks, M.; Viswanathan, R.; Lille, J.; MacDonald, S.; Kratschmer, E.; Tsang, C.; Nguyen, S.; Robertson, N.; Kasiraj, P. E-beam writing: a next-generation lithography approach for thin-film head critical structures. *IEEE Trans. Magn.* **2002**, *38*, 95–100.
50. Johns, E.; Tran, U.; Jayashankar, J.; Eckert, A.; Batra, S.; Rottmayer, R. Magnetic recording heads, 2002nd Meeting of The Electrochemical Society, Salt Lake City, 2002, 256 pp.
51. Weller, D.; Baglin, J.E.E.; Kellock, A.J.; Hannial, K.A.; Toney, M.; Kusinski, G.; Lang, S.; Best, M.E.; Terris, B.D. Ion induced magnetization reorientation in Co/Pt multilayers for patterned media. *J. Appl. Phys.* **2000**, *87*, 5768.
52. Chen, C.W. *Magnetism and Metallurgy of Soft Magnetic Materials*; North-Holland: Amsterdam, 1977; Chap. 7.
53. Ozkaya, D.; Langford, R.M.; Chan, W.L.; Petford-Long, A.K. *J. Appl. Phys.* **2002**, *91*, 9937.
54. Ferre, J.; Chappert, C.; Bernas, H.; Jamet, J.P.; Meyer, P.; Kaitasov, O.; Lemerle, S.; Mathet, V.; Rousseaux, F.; Launois, H. Irradiation induced effects on magnetic properties of Pt/Co/Pt ultrathin films. *J. Magn. Magn. Mater.* **1999**, *199*, 191.
55. Litvinov, D.; Wolfe, J.C.; Svedberg, E.B.; Ambrose, T.; Howard, K.; Chen, F.; Schlesinger, T.E.; Khizroev, S. Ion implantation of magnetic thin films and nanostructures. *J. Magn. Magn. Mater.* **2004**, *283*, 128.
56. Baglin, J.E.E.; Tabacniks, M.H.; Fontana, R.; Kellock, A.J.; Bardin, T. Effects of ion irradiation on ferromagnetic thin films. *Mater. Sci. Forum* **1997**, *248*, 87–93.
57. Moore, F. Storage technologies—the long view. *Comput. Technol. Rev.* **2003**, Jul. ([http://www.findarticles.com/p/articles/mi\\_m0BRZ/is\\_7\\_23/ai\\_108112601](http://www.findarticles.com/p/articles/mi_m0BRZ/is_7_23/ai_108112601)).
58. Charap, S.H.; Lu, P.L.; He, Y.J. Thermal stability of recording information at high densities. *IEEE Trans. Magn.* **1997**, *33* (1), 978–983.
59. Litvinov, D.; Kryder, M.H.; Khizroev, S. Recording physics of perpendicular media: hard layers. *J. Magn. Magn. Mater.* **2002**, *241*, 453–465.
60. Plumer, M.L.; van Ek, J.; Weller, D. *The Physics of Ultra-High-Density Magnetic Recording*; Springer: Berlin, 2001.
61. Bertram, N.H.; Williams, M. SNR and density limit estimates: a comparison of longitudinal and perpendicular recording. *IEEE Trans. Magn.* **2000**, *36* (1), 4–9.
62. Iwasaki, S.; Takemura, K. An analysis for the circular mode of magnetization in short wavelength recording. *IEEE Trans. Magn.* **1975**, *11*, 1173.
63. Cain, W.; Payne, A.; Baldwinson, M.; Hempstead, R. Challenges in the practical implementation of perpendicular magnetic recording. *IEEE Trans. Magn.* **1996**, *32* (1), 97–102.
64. Khizroev, S.; Crue, B.W.; Litvinov, D. Method for Forming a Perpendicular Recording Read/Write Head. U.S. patent 6,513,228, Feb 4, 2003.
65. Hobbs, P.C.D.; Abraham, D.W.; Wickramasinghe, H.K. Magnetic force microscopy with 25nm resolution. *Appl. Phys. Lett.* **1989**, *55*, 2357.
66. Martin, Y.; Wickramasinghe, H.K. Magnetic imaging by “force microscopy” with 1000Å resolution. *Appl. Phys. Lett.* **1987**, *50*, 1455.
67. Avouris, Ph.; Hertel, T.; Martel, R.; Schmidt, T.; Shea, H.R.; Walkup, R.E. Carbon nanotubes: nanomechanics, manipulation, and electronics devices. *Appl. Surf. Sci.* **1999**, *14*, 201–209.
68. Khizroev, S.; Zuo, F.; Alexandrakis, G.C.; Schlueter, J.A.; Geiser, U.; Williams, J.M. Vortex pinning in layered organic superconductors:  $\kappa$ -(BEDT-TTF)<sub>2</sub>-Cu[N(CN)<sub>2</sub>]Br. *J. Appl. Phys.* **1996**, *79* (8), 6586–6588.
69. Skidmore, G.D.; Dahlberg, E.D. Improved spatial resolution in magnetic force microscopy. *Appl. Phys. Lett.* **1997**, *71*, 3293.
70. Khizroev, S.; Jayasekara, W.; Bain, J.A.; Jones, R.E., Jr.; Kryder, M.H. MFM quantification of magnetic

- fields generated by ultra-small single pole perpendicular heads. *IEEE Trans. Magn.* **1998**, *34* (4), 2030–2032.
71. Litvinov, D.; Khizroev, S. Orientation-sensitive magnetic force microscopy in future probe storage applications. *Appl. Phys. Lett.* **2002**, *81* (10), 1878–1880.
  72. Slonczewski, J.C. Magnetic theory of very small devices. *J. Appl. Phys.* **1990**, *67* (9), 5341.
  73. McDaniel, T.W.; Challener, W.A.; Sendur, K. Issues in heat-assisted perpendicular recording. *IEEE Trans. Magn.* **2003**, *39* (4), 1972.
  74. Rettner, C.T.; Anders, S.; Thompson, T.; Albrecht, M.; Ikeda, Y.; Best, M.E.; Terris, B.D. Magnetic characterization and recording properties of nanopatterned  $\text{Co}_{70}\text{Cr}_{18}\text{Pt}_{12}$  perpendicular media. *IEEE Trans. Magn.* **2002**, *38* (4), 1725.
  75. Wind, S.J.; Appenzeller, J.; Martel, R.; Derycke, V.; Avouris, P. Fabrication and electrical characterization of top gate single-wall carbon nanotube field-effect transistors. *J. Vac. Sci. Technol. B.* **2002**, *20*, 2798.

# Nanomaterials: Trends

Richard Silbergliitt

RAND Corporation, Arlington, Virginia, U.S.A.

## INTRODUCTION

This entry reviews recent trends in the development and characterization of nanomaterials, which we define as materials with a nanoscale component or structure that exerts a significant influence on properties or function. The trends that we discuss are part of a larger trend in technological development toward integration of disciplines such as physics, chemistry, materials science and engineering, and biology, as well as toward the development of multifunctional materials compatible with increasingly complex environments.<sup>[1]</sup> We identify three principal trends that provide the organizational framework for the entry:

1. Integration of organic and biological materials with nanoscale inorganic and polymeric materials (*bionanomaterials*).
2. Incorporation of nanoscale components into materials to improve functionality (*nanocomposites*).
3. Use of “top-down” (e.g., lithography) and “bottom-up” (e.g., self-assembly) processing approaches, sometimes in combination, to produce novel nanoscale structures (*functional-nanostructures*).

Each of these trends is discussed in a separate section, with references to the recent (e.g., since 2000) literature. Considering the continuing rapid evolution of this research area, the references are intended to be illustrative rather than comprehensive. The discussed trends are aimed at developing materials to be used in new devices, components, and products, so while a detailed discussion of these items is outside the scope of this entry, we do examine the possible implications of trends in nanomaterials for applications with potential societal effects.<sup>[2]</sup> Specifically, we examine possible high-growth and low-growth developments and drivers and barriers to achieving each, as well as the possible synergistic influences that these developments might exhibit. In this discussion, we follow the approach described in Ref.<sup>[1]</sup>.

## BIONANOMATERIALS

Fig. 1 schematically illustrates the domain of bionanomaterials. This is the intersection of nanomaterials, which introduces scale effects to influence materials function, and biomaterials, which introduces biology into materials function at a variety of scales. It incorporates concepts, methods, raw materials, and instrumentation from nanoscience and nanotechnology as well as biology and bioengineering to develop new functional materials at the nanoscale. In some cases, the design and assembly of these materials is based on approaches that imitate or build upon phenomena or mechanisms that occur in nature, which is indicated in Fig. 1 by the inverted arrow labeled “biomimetic design/assembly.” These biomimetic approaches are sometimes aimed at developing materials with biological function and application, e.g., an encapsulant for targeted drug delivery. But biomimetics can also be applied to the design and assembly of nanoscale materials for non-biological applications, e.g., electronic or optoelectronic materials, or catalysts.

### Biomimetic Approaches

Recent use of biomimetic approaches includes the use of motor proteins to shuttle molecules along bioengineered tracks,<sup>[3]</sup> the use of “sticky-ended” cohesion of complementary DNA molecules to assemble nanostructures,<sup>[4]</sup> the use of block copolymers of polypeptides to form ordered silica structures,<sup>[5]</sup> and the design of self-assembling synthetic substitutes for the collagen proteins that form templates for bone growth.<sup>[6]</sup> A number of recent reviews describe biologically motivated materials design and assembly approaches with a broad range of applications including catalysis, drug design and delivery, tissue engineering, energy collection, storage, conversion and transport, sensing and actuation, bioassays, chemical and biological agent detection, and electronics.<sup>[7–9]</sup>

### Supramolecular Materials

Supramolecular materials (assemblies of molecules that are built up through molecular, non-covalent,



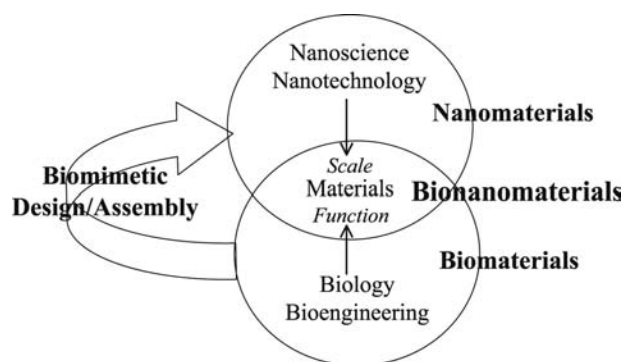


**Fig. 1** Schematic illustration of the domain of bionanomaterials.

forces) have emerged as a key ingredient in achieving function at the nanoscale.<sup>[10]</sup> These materials can be self-assembled into nanoscale structures such as disks, strips, cylinders, and ribbons to which biologically active materials can be attached.<sup>[11]</sup> Selective cleaving of the self-assembling ends can also be used to obtain functionalized nanoporous materials.<sup>[12]</sup> The biological self-assembly process itself has also been adapted for non-biological materials assembly, as molecules based on short peptide sequences taken from fibrinogen (an active ingredient in coagulation) have been used to direct the self-assembly of polyethylene glycol.<sup>[13]</sup> In efforts to link biologically driven assembly to electronic devices, peptides with highly specific binding properties to semiconductor heterostructures have been experimentally demonstrated<sup>[14]</sup> and designed using computational algorithms.<sup>[15]</sup>

Dendrimers (supramolecular materials with a branched tree structure) are being developed and tailored as vehicles for encapsulating drugs for targeted delivery or even strands of DNA for gene therapy, as well as to “harvest” sunlight and transfer the energy into the center of the molecule where it might be used in optoelectronic or photovoltaic applications.<sup>[16]</sup> Dendrimers based on liquid crystals have also been proposed for optoelectronic applications,<sup>[17]</sup> and a liquid crystal phase with a very large unit cell, containing 30 dendrimers, has recently been demonstrated.<sup>[18]</sup>

A possible alternative to dendrimers for encapsulation is afforded by nanocompartments formed from lipid bilayer membranes<sup>[19]</sup> or vesicles formed from copolymers containing hydrophobic and hydrophilic blocks.<sup>[20]</sup> Complexes of closed lipid bilayer membranes and DNA show promise for gene delivery without use of viruses, although much remains to be learned about the relationship between the supramolecular structures formed by these complexes and their efficiency of gene transfer and expression.<sup>[21]</sup>

## Biomaterialization

Living organisms form mineralized crystals of many types, often containing complex multifunctional structures (e.g., mollusk shell, sea urchin skeleton, biogenic silica), sometimes with features that have not been incorporated in synthetic materials.<sup>[22]</sup> The development of such biomaterialized crystals has been shown to depend on both stereochemical recognition of surface step edges by amino acids and resultant changes in free energy of the growing crystal surface,<sup>[23]</sup> linking biological, physical, and chemical interactions in the formation of biomaterials with varied asymmetric structures.<sup>[24]</sup> Biomaterialization principles have recently been used to fabricate a large micropatterned single crystal of calcite from a patterned amorphous calcium carbonate template, with oriented nucleation induced by a self-assembled monolayer of alkanethiol on gold or silver.<sup>[25]</sup>

## Nanoparticle Probes

One of the first successful applications of bionanomaterials is the use of DNA-tagged nanoparticles for bioassays and biosensors. This has been accomplished through the observation of electrical changes due to binding of the target species to oligonucleotides functionalized with gold nanoparticles<sup>[26]</sup> and through the fluorescence of semiconductor nanocrystals linked to oligonucleotides.<sup>[27]</sup>

## Biomedical Applications

Recent bionanomaterials studies aimed at biomedical applications include the development of nanomaterials linking radioactive atoms to monoclonal antibodies for tumor-specific radiation therapy<sup>[28]</sup> and the incorporation of nanoparticles into cement used for orthopedic implants to reduce inflammatory reaction.<sup>[29]</sup> Several university centers in the United States and Europe are focused on biomedical applications such as diagnostics, drug delivery, and implants and prostheses,<sup>[30]</sup> including work on dendrimers, nanomembranes, and biologically driven motors.<sup>[31]</sup> A recent very thoughtful review argues that it is the research effort itself in areas related to nanomedicine that will produce useful results in the near term, rather than the achievement of specific biomedical application objectives.<sup>[32]</sup>

Whether the bionanomaterials trends highlighted above will lead to revolutionary advances in technology or merely to continued incremental improvements is impossible to predict. **Fig. 2** schematically illustrates two possible paths—a high-growth path under which nanomaterials pervasively affect biology

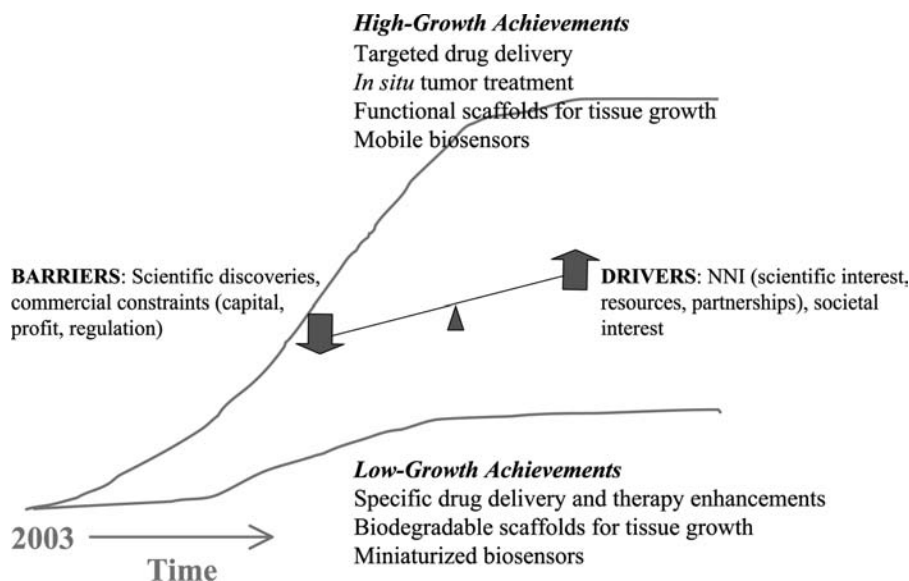


Fig. 2 Possible growth paths for bionanomaterials applications.

and medicine and a low-growth path under which the continued integration of biology, materials, and nanoscience leads to technological advances in specific areas of opportunity. There are currently strong drivers toward the high-growth path, in particular the high level of scientific interest and available resources, including partnerships between academic, governmental, and commercial institutions, resulting from the U.S. National Nanotechnology Initiative (NNI) and similar initiatives in Europe and Japan, as well as strong societal interest in and fascination with nanoscience and nanotechnology. However, there are also strong barriers that, if not overcome, will push toward the low-growth path, in particular the need for major scientific discoveries and commercial constraints such as the availability of capital, the need to show profit, and regulatory requirements.

The following are some of the significant scientific questions that need to be addressed to progress along either path:

- Can integration of functional biological materials into nanoscale materials systems be reproducibly scaled?
- Can biological function be sufficiently retained in synthetic bionanomaterials to allow high-accuracy molecular recognition and targeting?
- Can encapsulation schemes for bionanomaterials be implemented on a cost-effective commercial scale?
- Can short-term or long-term compatibility of synthetic bionanomaterials in the human body be demonstrated?
- Can effective methods for determining unintended side effects of bionanomaterials be developed and implemented?

The rate at which progress is made in addressing these questions will determine the timescale in Fig. 2, in addition to whether progress is toward the high-growth or the low-growth path.

## NANOCOMPOSITES

The incorporation of nanoscale components into materials to improve function is perhaps currently the most advanced area of nanomaterials. A growing number of commercial entities already produce nanoparticles with an estimated world market near \$500 million in 2000 and growth projected in applications such as conductive and magnetic coatings, optical fibers, phosphors, biological labels, orthopedic materials, sunscreens, catalysts, and scratch-resistant coatings.<sup>[33,34]</sup> From the perspective of the chemical industry, nanocomposites can be separated into those that incorporate nanoscale clays, nanoscale oxides or metals, and carbon nanotubes.<sup>[35]</sup> We will adopt a slight generalization of this approach and organize the following discussion around polymer nanocomposites (based on nanoscale silicates including clays); composites incorporating metal, oxide, and semiconductor nanoparticles and nanocrystals; nanoscale coatings and films based on these; and composites incorporating carbon nanotubes or semiconductor nanowires.

### Polymer Nanocomposites

The interest in polymer nanocomposites stems from the fact that the dispersion of a relatively small amount (e.g., <5%) of a layered silicate such as clay can provide significantly improved properties, including strength,

barrier properties, reduced water absorption, and reduced flammability, so long as the clay is exfoliated or intercalated into layers of nanoscale thickness.<sup>[36–38]</sup> Recent experimental work<sup>[39]</sup> demonstrates the positive influence of dispersed silicate nanolayers on both the crystalline morphology and mechanical properties of the nanocomposite, and recent theoretical work<sup>[40]</sup> suggests that the toughening mechanisms may be similar to those postulated for biological structural materials such as spider silk and abalone adhesive. Silicate-based nanocomposites have also been made from aerospace epoxy material and demonstrated both to have improved mechanical properties and appropriate viscosity and cure kinetics to remain suitable for standard composite molding techniques such as resin transfer molding.<sup>[41]</sup>

### Nanoparticle and Nanocrystal Composites

Advances in and approaches to the characterization of the electrical, magnetic, optical, and chemical properties of isolated and assembled nanoscale particles and crystals and attempts to use them to improve materials and device function are described in a recent series of articles.<sup>[42]</sup> Nanomaterials investigated include Co, Ni, Fe, and magnetic alloy nanoparticles for magnetic device applications;<sup>[43]</sup> CdSe<sup>[44]</sup> and Mn-doped ZnS<sup>[45]</sup> nanocrystals for optical and laser applications; nanoscale Au and Ag for optoelectronic applications;<sup>[46]</sup> and nanoparticles capped with organic materials for electronic applications.<sup>[47]</sup>

An alternative approach to incorporating functional Fe nanoparticles into electronic devices consists of introducing Fe<sub>2</sub>O<sub>3</sub> nanoparticles externally produced onto a Si wafer and annealing in ultrahigh vacuum.<sup>[48]</sup> Glass ceramics consisting of SnO<sub>2</sub> nanocrystals dispersed in SiO<sub>2</sub> have also been studied as potential non-linear materials for all-optical switching devices.<sup>[49]</sup>

Mulvaney<sup>[46]</sup> shows that optical properties of Au and Ag nanoparticles depend on shape. Both size and geometric shape of Au and Ag nanoparticles have been shown to be controllable through solution-phase chemistry, yielding Ag nanocubes and Au nanoboxes with a truncated cubic shape.<sup>[50]</sup>

With respect to catalytic applications, capped metallic nanoparticles have been demonstrated to avoid aggregation on electrode surfaces and show catalytic activity on both metal and Pt-doped polymer substrates,<sup>[51]</sup> while semiconductor nanoclusters have been demonstrated to enable the photooxidation of the toxic aromatic organic material pentachlorophenol.<sup>[52]</sup> A novel synthesis route to a porous composite nanostructure including catalytic metal oxide nanoparticles uses aqueous solutions of metal salts together with an aqueous dispersion of synthetic clay and surfactants.<sup>[53]</sup>

### Nanoscale Coatings and Films

All of the nanoparticle and nanocrystal material types mentioned in the previous section have been implemented as nanoscale coatings or films. FePt nanoparticles were synthesized and self-assembled into nanocrystal superlattices and annealed into ferromagnetic films that are mechanically robust and support high-density magnetization reversal transitions required for magnetic data storage.<sup>[54]</sup> Ni nanoparticles were also epitaxially grown on a TiN thin-film matrix and exhibited significantly higher coercivity than randomly oriented Ni particles.<sup>[55]</sup> A quantum-dot light-emitting diode was fabricated by sandwiching a monolayer of CdSe (ZnS) nanocrystals between two organic thin films, using phase separation between these films and the organic materials capping the nanocrystals.<sup>[56]</sup> Films of Au nanoparticles functionalized with aromatic molecules were spin coated onto interdigitated electrode structures and used as vapor sensors.<sup>[57]</sup>

Nanoscale coatings and films have been demonstrated to produce enhancements of a variety of technologically important properties. Nanoporous films of PbZr<sub>x</sub>Ti<sub>1-x</sub>O<sub>3</sub> (PZT) allow tailoring of dielectric properties to increase the figure of merit for piezoelectric applications.<sup>[58]</sup> Thin films of optical polymers with nanoscale corrugated surfaces provide an alternative approach to antireflection coatings.<sup>[59]</sup> Nanostructured hydroxyapatite coatings provide improved adhesion and corrosion resistance for medical implants.<sup>[60]</sup> Nanocrystalline Al<sub>2</sub>O<sub>3</sub> coatings on glass substrates provide increased hardness with no degradation of optical properties.<sup>[61]</sup> Nanoscale coatings also provide the possibility of controlled gradients in mechanical properties that may provide new design options for damage-resistant materials surfaces.<sup>[62]</sup>

### Nanotube and Nanowire Composites

Carbon nanotubes are exceedingly interesting materials both from a scientific viewpoint and because their unique combination of properties (high conductivity, high tensile strength, high temperature capability, plus nanoscale dimensionality) make them suitable, in principle, for many important commercial applications. As described in a recent review,<sup>[63]</sup> carbon nanotubes are already in use as an additive to graphite in a majority of the lithium ion batteries found in cell phones and laptop computers; are anticipated to enter the commercial flat-panel display market as field emitters in 2003; have many additional potential applications including conductive plastics, high-performance fibers for composite materials, and flexible sensors for gas detection; and could be enabling materials for new nanoelectronic technologies. In this entry, we will constrain

our discussion to aspects of nanotube research related to the formation of composite materials in which the nanotubes improve functionality.

The simplest version of the carbon nanotube, a cylindrically rolled sheet of hexagonally arrayed carbon atoms, or single-walled carbon nanotube (SWNT), has been produced in strands of macroscopic length,<sup>[64]</sup> and micrometer-long crystals consisting of ordered arrays of aligned SWNTs have also been produced.<sup>[65]</sup> Composite materials with a nanocrystalline  $\text{Al}_2\text{O}_3$  matrix and reinforcement by ropes of SWNTs that form a network at the grain boundaries have recently been fabricated<sup>[66]</sup> by ball-milling to mix the  $\text{Al}_2\text{O}_3$  powders and nanotubes, followed by consolidation using the low-temperature spark plasma sintering process. The best of these composites, fully dense with 10 vol.% SWNTs, had a fracture toughness of  $9.7 \text{ MPa m}^{1/2}$ , almost three times that of pure  $\text{Al}_2\text{O}_3$  of the same grain size. Peigney<sup>[67]</sup> suggests that the high toughness of these  $\text{Al}_2\text{O}_3$ -carbon nanotube composites results from the combination of high-quality starting materials, homogeneous dispersion without damaging the nanotubes, and the relatively short time and low temperature required for spark plasma sintering. This work demonstrates that carbon nanotubes can be used as reinforcement for ceramic matrix composites. The next steps toward application will include investigation of larger specimens than the  $19 \times 2\text{--}4 \text{ mm}$  disks reported in Ref.<sup>[66]</sup>.

Another type of composite material that can be formed from nanotubes involves the incorporation of fullerenes (e.g.,  $\text{C}_{60}$ ) inside the nanotube<sup>[68]</sup> to form the so-called peapods. It has been demonstrated<sup>[69]</sup> that fullerenes containing metal atoms inside the cage of

carbon atoms that make up the fullerene molecule can also be encapsulated inside single-walled carbon nanotubes in a one-dimensional array of “peapods.” Such an arrangement with Gd atoms inside  $\text{C}_{82}$  molecules, which are then encapsulated inside single-wall carbon nanotubes, has been shown to behave as an array of quantum dots, with proposed potential application for quantum well-based electronic and optoelectronic devices.<sup>[70]</sup> Another composite nanotube material with potential application is a column of liquid Ga inside a carbon nanotube, which is proposed as a nanothermometer based on the increase in height of the Ga meniscus with increasing temperature.<sup>[71]</sup>

Semiconductor nanowires are actively being developed as an alternative to carbon nanotubes for nanoelectronic device applications.<sup>[72]</sup> Superlattice structures have been developed in nanowires, in which the semiconductor material changes along the long axis of the nanowire, allowing designed changes in the electronic properties. Such composite nanomaterials have been produced using GaP, GaAs, and InP;<sup>[73]</sup> Si and SiGe;<sup>[74]</sup> and InAs and InP.<sup>[75]</sup> These materials are proposed for applications including nanobarcodes, LEDs, and thermoelectric devices.

Whether the nanocomposites trends highlighted above will lead to revolutionary advances in technology or merely to continued incremental improvements is impossible to predict. Fig. 3 schematically illustrates two possible paths—a high-growth path under which nanocomposite materials are pervasively applied throughout society and a low-growth path under which the use of nanocomposites leads to incremental improvements in specific technology areas. There are currently strong drivers toward the

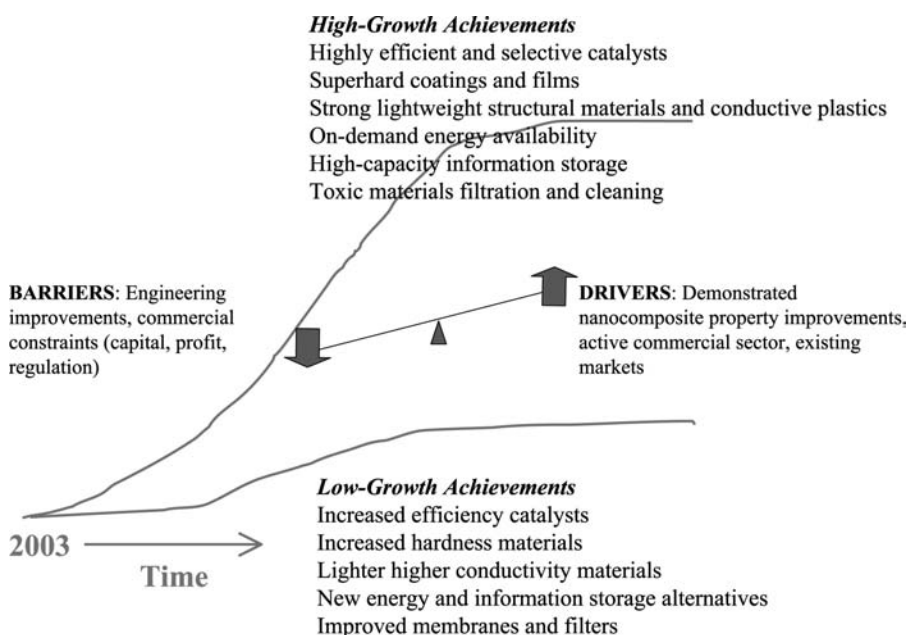


Fig. 3 Possible growth paths for nanocomposites applications.

high-growth path, in particular the demonstrated property improvements already achieved with nanoparticle composites in such areas as catalysis and surface strengthening, as well as the presence of an active commercial sector and existing markets. However, there are also barriers that, if not overcome, will push toward the low-growth path, in particular the need for continuing engineering improvements and commercial constraints such as the availability of capital, the need to show profit, and regulatory requirements.

The following are some of the significant technical issues that need to be addressed to progress along either path:

- Functionalization of nanoscale components and maintenance of that function in the composite material.
- Design and implementation of effective interfaces between the nanoscale components and the composite matrix.
- Demonstration of reproducible composite behavior and long-term stability.
- Scaling up the nanocomposite for cost-effective production while retaining the property improvements.

The rate at which progress is made in addressing these issues will determine the timescale in Fig. 3, in addition to whether progress is toward the high-growth or the low-growth path.

## FUNCTIONAL NANOSTRUCTURES

Perhaps the most fundamental type of functional nanostructure is a microscopic composite with multiple phases formed in situ during processing. As discussed by Ma,<sup>[76]</sup> metal alloys with nanoscale grain size typically have increased strength, but lack plasticity necessary for forming or to avoid catastrophic failure in load-bearing applications, and several different approaches to increasing ductility and toughness in such alloys employ a non-uniform or composite microstructure. He et al.<sup>[77]</sup> described an alloy design and solidification process leading to as-cast Ti-based alloys with an in situ composite microstructure consisting of a nanocrystalline matrix and a ductile dendritic phase. The presence of the dendritic phase is shown to increase the plasticity of the material by preventing the propagation of bands of shear stress that, if allowed to grow, could cause catastrophic failure. Thus this type of microscopic composite combines the increased strength of the nanoscale grain size with good ductility and a high elastic-strain limit, and was produced with conventional casting methods, suggesting that the approach may have more general potential

for strong, yet tough, metal alloys. The combination of nanoscale grains with microscale dendrites in this material emphasizes the fact that useful nanomaterials do not have to be exclusively nanoscale.

## Nanofabrication Methods

A variety of different approaches to fabricate nanostructured materials are described in a recent set of articles,<sup>[78]</sup> including the use of lithographic patterns to induce or guide a self-assembly process,<sup>[79]</sup> applications of lithography using “soft” materials such as organic elastomers,<sup>[80]</sup> and the use of an atomic force microscope tip to “write” nanostructures onto a gold substrate with alkanethiol “ink”, namely, dip-pen nanolithography.<sup>[81]</sup> Another nanofabrication method uses metallic mask membranes fabricated from nanochannel glass (a glass matrix with uniform arrays of hollow channels as small as 20 nm) to produce regular arrays of magnetic dots for magnetic storage application.<sup>[82]</sup> A recent study compared ferroelectric nanostructures fabricated via self-assembly of dispersed nanoparticles synthesized from a microemulsion and via electron beam lithography of a polymer precursor layer,<sup>[83]</sup> with the self-assembly approach producing droplets in the 50–60 nm range (which the authors argued was several times too large for self-assembly), while the lithographic approach produced arrays of 60–70 nm particles with spacing down to 150 nm.

The stability of fabricated nanostructures under application conditions can be an important issue. Nanoscale features produced on a Cu crystal by ion sputtering under ultrahigh vacuum were demonstrated to be stabilized at room temperature in air for a week or more (far longer than needed to serve as a useful process step) by an oxidation treatment.<sup>[84]</sup> The authors noted that without the oxidation treatment, the stability of such nanoscale features is limited by thermally activated diffusion to about 200 K. Feedback-controlled ion beam sputtering has been used to “sculpt” a 5-nm pore in a Si<sub>3</sub>N<sub>4</sub> membrane, which was then used as a detector for a single DNA molecule.<sup>[85]</sup> The authors suggest that this nanofabrication method could be used to fabricate slits, trenches, crosses, and other structures for nanoscale semiconductor devices.

## Nanofabrication via Self-Assembly

Self-assembly phenomena have been used both to form templates for fabricating nanostructures and to assemble the nanostructure itself. Dynospheres (latex particles 0.5 μm in diameter suspended in water) were self-assembled into regular arrays that were used as a mask to deposit arrays of Ni nanoparticles.<sup>[86]</sup>

Polymethylmethacrylate (PMMA) spheres were self-assembled in trenches in Si wafers to form a three-dimensional photonic crystal.<sup>[87]</sup> Nanowires of single-crystal Si that self-align to form a structure suitable for photoemission applications were grown from a thermally evaporated Ni film subjected to magnetron sputtering of Si.<sup>[88]</sup> An Al film deposited on a Si or SiO<sub>2</sub> substrate was anodized to produce a hexagonally ordered nanoporous Al<sub>2</sub>O<sub>3</sub> structure.<sup>[89]</sup> A large variety of topological structures have been produced in mesoporous SiO<sub>2</sub> by combining sol gel and emulsion chemistry with molecular self-assembly.<sup>[90]</sup>

Self-assembled nanostructured films have been shown to possess useful chemical and optical properties. A self-assembled monolayer of hexadecanethiol on a gold surface was shown to block the interaction of the surface with neutral molecules such as water and volatile sulfuric compounds, enhancing its effect as a selective detector of mercury vapor.<sup>[91]</sup> Self-assembled multilayer superlattice films containing chromophoric organic molecules were shown to be useful for optical switching based on their large second-order non-linear optical response.<sup>[92]</sup>

### Self-Assembly with Diblock Copolymers

Films of copolymers consisting of two distinct blocks [e.g., polystyrene (PS) and PMMA] spontaneously assemble into ordered domains with morphology principally depending on the molecular weight ratio of the constituent polymers, allowing the formation of nanoscale tailored polymer dot arrays via chemical removal of one of the blocks. These polymer dot arrays can then be used as templates or masks to form nanoscale dot arrays of metals or insulators on silicon and other

substrates.<sup>[93]</sup> Incorporation of metal nanoclusters synthesized in situ from decomposition of precursors within one of the copolymer blocks was demonstrated to produce patterned structures with selective phase separation and particle confinement.<sup>[94]</sup> Arrays of Co nanowires with application as ultrahigh-density magnetic data storage media have also been fabricated using nanoporous films derived from diblock copolymers.<sup>[95]</sup> Combining a diblock copolymer of polystyrene and polyethylene oxide with a dilute homogeneous solution of a silica precursor leads to a mesostructured silica film that can be calcined to produce closed-cell mesoporous silica films with potential application as low dielectric constant insulators.<sup>[96]</sup> Control of optical energy transfer was demonstrated by embedding semiconducting polymers into the pores of such a silica film, suggesting their potential application in optoelectronics as well.<sup>[97]</sup>

Whether the functional nanostructures trends highlighted above will lead to revolutionary advances in technology or merely to continued incremental improvements is impossible to predict. Fig. 4 schematically illustrates two possible paths—a high-growth path under which advances in functional nanostructure fabrication lead to a broad range of new materials and devices and a low-growth path under which functional nanosystems penetrate existing markets in an incremental fashion. There are currently strong drivers toward the high-growth path, in particular the continuing integration of top-down and bottom-up fabrication approaches and the increasingly interdisciplinary nature of research in this area. However, there are also strong barriers that, if not overcome, will push toward the low-growth path, in particular the need for continuing scientific advances, the need to address

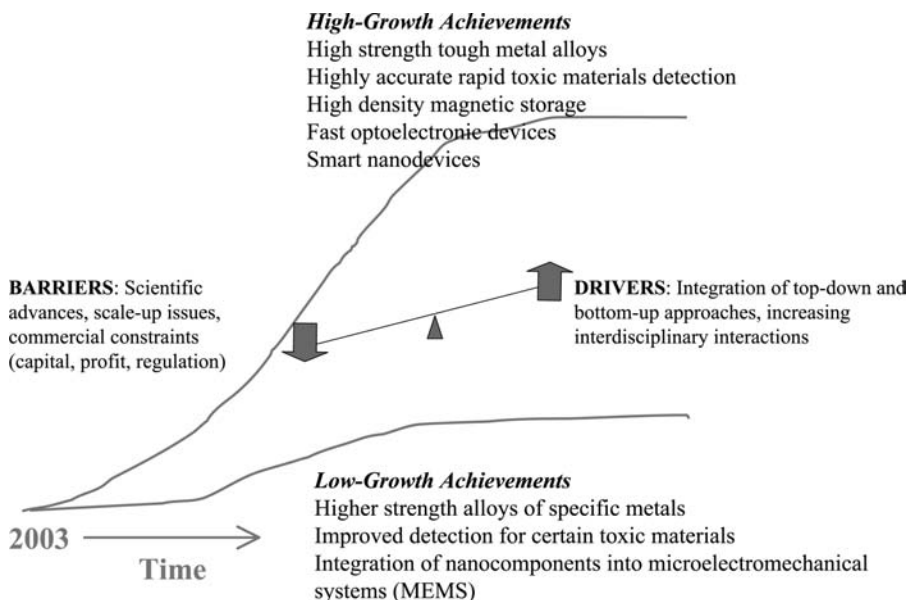


Fig. 4 Possible growth paths for functional nanostructure applications.



**Table 1** Synergisms between nanomaterials applications

	Targeted drug delivery	In situ tumor treatment	Mobile biosensors	Super membranes and catalysts	Superhard coatings and films	Cheap energy storage	High-strength tough metal alloys	Fast precise toxic materials detection	Smart nanodevices
Targeted drug delivery		Facilitates	Spur development	–	–	–	–	Counter chemical and bio agents	Smart drug delivery
In situ tumor treatment	–		Spur development	–	–	–	–	–	–
Mobile biosensors	Facilitates	Facilitates		Blood filters	–	–	–	–	Smart biosensors
Super membranes and catalysts	–	–	Blood filters		–	Improved energy conversion	–	Counter chemical and bio agents	Improved chemical processes
Superhard coatings and films	–	–	Facilitates	–		Facilitates	Long-life structural materials	–	–
Cheap energy storage	–	Facilitates	Facilitates	Improved energy conversion	Spur development		–	Counter chemical and bio agents	Portable power
High-strength tough metal alloys	–	–	–	–	Long-life structural materials	Facilitates		Facilitates	Facilitates
Fast precise toxic materials detection	Counter chemical and bio agents	–	Facilitates	Counter chemical and bio agents	–	Counter chemical and bio agents	–		Counter chemical and bio agents
Smart nanodevices	Smart drug delivery	Facilitates	Smart biosensors	Improved chemical processes	–	Portable power	Facilitates	Counter chemical and bio agents	

scale-up issues, and commercial constraints such as the availability of capital, the need to show profit, and regulatory requirements.

The following are some of the significant scientific issues that need to be addressed to progress along either path:

- Retention of microscopic nanostructures under application conditions.
- Reproducible, scalable, cost-effective fabrication of designed nanostructures.
- Demonstration of nanostructure function in macroscopic materials and devices.
- Demonstration of long-term nanostructure functional stability.

The rate at which progress is made in addressing these issues will determine the timescale in Fig. 4, in addition to whether progress is toward the high-growth or the low-growth path.

## SYNERGISTIC INFLUENCES

The development of certain nanomaterials trends will in some cases exert a synergistic influence on the development of other trends. Table 1 illustrates some of these potential effects for possible high-growth applications of the nanomaterials trends discussed above. Three application developments are considered for each nanomaterials area. Targeted drug delivery, in situ tumor treatment, and mobile biosensors are the bionanomaterials developments considered. Super membranes and catalysts, superhard coatings and films, and cheap energy storage are the nanocomposites developments considered. High-strength tough alloys, fast precise toxic materials detection, and smart nanodevices are the functional nanostructures developments considered. Where the presence of one development could facilitate the other development, e.g., targeted drug delivery and in situ tumor treatment, the word “facilitates” is shown in the appropriate box. This effect is not always symmetric. For example, the presence of in situ tumor treatment would not facilitate targeted drug delivery. In some cases, synergism between the two developments would improve function, e.g., smart nanodevices together with super membranes and catalysts would lead to improved chemical processes. In other cases, the synergism might lead to an entirely new capability, as for example targeted drug delivery and smart nanodevices would enable smart drug delivery. For the purposes of this analysis, we assumed that the synergisms leading to improved function or new capabilities were symmetric. The boxes in Table 1 with dashes indicate no synergism between the two developments.

The following paragraphs briefly summarize the synergisms listed in Table 1 (symmetric synergisms are only discussed once).

*Targeted drug delivery:* facilitates in situ tumor treatment by providing a mechanism; spurs development of mobile biosensors by providing an application; together with fast precise toxic materials detection could provide detection coupled with treatment for chemical or biological (CB) agents; together with smart nanodevices could provide smart drug delivery.

*In situ tumor treatment:* spurs development of mobile biosensors by providing an application.

*Mobile biosensors:* facilitate targeted drug delivery and in situ tumor treatment by providing locations; together with super membranes and catalysts could provide the basis for blood filters; together with smart nanodevices could provide smart biosensing.

*Super membranes and catalysts:* together with cheap energy storage could provide a means for improved energy conversion; together with fast precise toxic materials detection could provide both for detection and filtering or destruction of CB agents; together with smart nanodevices could provide a means for improving the selectivity and yield of chemical processes that involve separations or catalysis.

*Superhard coatings and films:* could facilitate mobile biosensors and cheap energy storage by providing protection from damaging materials or hostile environments; together with high-strength tough metal alloys could provide long-life structural materials.

*Cheap energy storage:* could facilitate in situ tumor treatment and mobile biosensors by providing cost-effective power sources; could spur development of superhard coatings and films by providing an application; together with fast precise toxic materials detection could provide a means for detection and destruction of CB agents; together with smart nanodevices could provide on-demand portable power sources.

*High-strength tough metal alloys:* can facilitate cheap energy storage, fast precise toxic materials detection, and smart nanodevices by providing functional structural materials.

*Fast precise toxic materials detection:* facilitates mobile biosensors by providing the mechanism for the biosensor.

*Smart nanodevices:* facilitate in situ tumor treatment by providing a means for treatment delivery to the tumor site; facilitate high-strength tough metal alloys by providing a possible means for fabrication.

## ACKNOWLEDGMENTS

The author is extremely grateful to Frank Gac, John Gilman, Eric Landree, Parry Norling, Fyl Pincus,

Stephen Rattien, Ulrich Strom, and Julia Warner for providing reference materials for this entry, and to Philip Antón and Fyl Pincus for their insightful reviews of the draft and several useful suggestions that were incorporated into the final version. The author also acknowledges the financial support of the Rand Corporation for the development of this work.

## REFERENCES

1. Antón, P.S.; Silberglitt, R.; Schneider, J. *The Global Technology Revolution: Bio/Nano/Materials Trends and Their Synergies with Information Technology by 2015*; 2001. RAND MR-1307-NIC, available to the public at <http://www.rand.org/publications/MR/MR1307>.
2. National Science and Technology Council (NSTC)/Subcommittee on Nanoscale Science, Engineering and Technology (NSET) *Societal Implications of Nanoscience and Nanotechnology*; Roco, M.C., Bainbridge, W.S., Eds.; 2001. Available to the public at <http://www.nano.gov> or <http://itri.loyola.edu/nano/NSET.Societal.Implications/>.
3. Vogel, V. Reverse engineering: Learning from proteins how to enhance the performance of synthetic nanosystems. *MRS Bull.* **2002**, *27* (2), 972–978.
4. Seeman, N.C.; Belcher, A.M. Emulating biology: Building nanostructures from the bottom up. *PNAS* **2002**, *99* (Suppl. 2), 6451–6455.
5. Cha, J.N.; Stucky, G.D.; Morse, D.E.; Deming, T.J. Biomimetic synthesis of ordered silica structures mediated by block copolypeptides. *Nature* **2000**, *403*, 289–292.
6. Taton, T.A. Boning up on biology. *Nature* **2001**, *412*, 491–492.
7. Ball, P. Natural strategies for the molecular engineer. *Nanotechnology* **2002**, *13*, R15–R18.
8. Bashir, R. DNA-mediated artificial nanobiostucture: State of the art and future directions. *Superlattices Microstruct.* **2001**, *29* (1).
9. Asefa, T.; Coombs, N.; Grondy, H.; Jaroniec, M.; Kruk, M.; MacLachlan, M.J.; Ozin, G.A. Bio-inspired nanocomposites: From synthesis toward potential applications. *Mater. Res. Symp. Proc.* **2002**, *707*, AA5.5.1/HH5.5.1–AA5.5.12/HH5.5.12.
10. Supramolecular materials. *MRS Bull.* **2000**, *25* (4), 26–58. Moore, J.S., Ed.
11. Stupp, S.I.; Pralle, M.U.; Tew, G.N.; Li, L.; Sayar, M.; Zubarev, E.R. Self-assembly of organic nano-objects into functional materials. *MRS Bull.* **2000**, *25* (4), 42–48.
12. Ikkala, O.; ten Brinke, G. Functional materials based on self-assembly of polymeric supramolecules. *Science* **2002**, *295*, 2407–2409.
13. Seal, B.L.; Panitch, A. Biologically-based self-assembling hydrogels. *Mater. Res. Soc. Symp. Proc.* **2002**, *724*, N3.2.1–N3.2.6.
14. Whaley, S.R.; English, D.S.; Hu, E.L.; Barbara, P.F.; Belcher, A.M. Selection of peptides with semiconductor binding specificity for directed nanocrystal assembly. *Nature* **2000**, *405*, 665–668.
15. Lustig, S.R.; Jagota, A. Selectivity of polypeptide binding to nanoscale substrates. *Mater. Res. Soc. Symp. Proc.* **2002**, *724*, N4.6.1–N4.6.6.
16. Fréchet, J.M.J. Nanostructure Synthesis: Functional Polymers and Dendrimers. In *Nanoscience and Nanotechnology: Shaping Biomedical Research*; NIH Bioengineering Consortium (BECON) Symposium Report; 2000, accessed on Feb. 5, 2003 at [http://www.becon1.nih.gov/becon\\_symposia.htm](http://www.becon1.nih.gov/becon_symposia.htm).
17. Percec, V.; Glodde, M.; Bera, T.K.; Miura, Y.; Shlyanovskaya, I.; Singer, K.D.; Balagurusamy, V.S.K.; Helney, P.A.; Schnell, I.; Rapp, A.; Spless, H.-W.; Hudson, S.D.; Duan, H. Self-organization of supramolecular helical dendrimers into complex electronic materials. *Nature* **2002**, *417*, 384–387.
18. Ungar, G.; Liu, Y.; Zeng, X.; Percec, V.; Cho, W.-D. Giant supramolecular liquid crystal lattice. *Science* **2003**, *299*, 1208–1211.
19. Kisak, E.T.; Coldren, B.; Zasadzinski, J.A. Nanocompartments enclosing vesicles, colloids, and macromolecules via interdigitated lipid bilayers. *Langmuir* **2002**, *18*, 284–288.
20. Gravano, S.M.; Borden, M.; von Werne, T.; Doerffler, E.M.; Salazar, G.; Chen, A.; Kisak, E.; Zasadzinski, J.A.; Patten, T.E.; Longo, M.L. Poly(4-(aminomethyl)-styrene)-*b*-polystyrene: Synthesis and unilamellar vesicle formation. *Langmuir* **2002**, *18*, 1938–1941.
21. Safinya, C.R. Structures of lipid–DNA complexes: Supramolecular assembly and gene delivery. *Curr. Opin. Struct. Biol.* **2001**, *11*, 440–448.
22. Weiner, S.; Addadi, L.; Wagner, H.D. Materials design in biology. *Mater. Sci. Eng., C* **2000**, *11*, 1–8.
23. Orme, C.A.; Noy, A.; Wierzbicki, A.; McBride, M.T.; Grantham, M.; Teng, H.H.; Dove, P.M.; DeYoreo, J.J. Formation of chiral morphologies through selective binding of amino acids to calcite surface steps. *Nature* **2001**, *411*, 775–779.
24. Addadi, L.; Weiner, S. Crystals, asymmetry and life. *Nature* **2001**, *411*, 753–755.
25. Aizenberg, J.; Muller, D.A.; Grazul, J.L.; Hamann, D.R. Direct fabrication of large micropatterned single crystals. *Science* **2003**, *299*, 1205–1208.
26. Park, S.-J.; Taton, T.A.; Mirkin, C. Array-based electrical detection of DNA with nanoparticle probes. *Science* **2002**, *295*, 1503–1506.
27. Gerion, D.; Parak, W.J.; Williams, S.C.; Zanchet, D.; Micheel, C.M.; Alivisatos, A.P. Sorting fluorescent nanocrystals with DNA. *J. Am. Chem. Soc.* **2002**, *124*, 7070–7074.
28. McDevitt, M.R.; Ma, D.; Lai, L.T.; Simon, J.; Borchardt, P.; Frank, R.K.; Wu, K.; Pellegrini, V.; Curcio, M.J.; Miederer, M.; Bander, N.H.; Scheinberg, D.A. Tumor therapy with targeted atomic nanogenerators. *Science* **2001**, *294*, 1537–1540.
29. Shortkroff, S.; Turell, M.B.; Rice, K.; Thornhill, T.S. Cellular response to nanoparticles. *Mater. Res. Symp. Proc.* **2002**, *704*, W11.5.1–W11.5.6.
30. Malsch, I. Biomedical applications of nanotechnology. *Ind. Phys.* **June/July 2002**, *8* (3), 15–17.

31. Voss, D. Nanomedicine nears the clinic. *Technol. Rev. January/February 2000*, *103* (1), 60–64.
32. Haberzettl, C.A. Nanomedicine: Destination or journey? *Nanotechnology 2002*, *13*, R9–R13.
33. Rittner, M.N. Nanostructured materials. *Am. Ceram. Soc. Bull. March 2002*, *81* (3), 33–36.
34. Thayer, A.M. Nanotech offers some there, there. *Chem. Eng. News November 26 2001*, *79* (48), 13–16.
35. Wood, A.; Scott, A. Nanomaterials a big market potential. *Chem. Week October 16 2002*, 17–21.
36. Vaia, R.A.; Giannelis, E.P. Polymer nanocomposites: Status and opportunities. *MRS Bull. 2001*, *26* (5), 394–401.
37. Alexandre, M.; Beyer, G.; Henrist, C.; Cloots, R.; Rulmont, A.; Jérôme, R.; Dubois, P. “One-pot” preparation of polymer/clay nanocomposites starting from Na<sup>+</sup> montmorillonite. 1. Melt intercalation of ethylene-vinyl acetate copolymer. *Chem. Mater. 2001*, *13*, 3830–3832.
38. VanderHart, D.L.; Asano, A.; Gilman, J.W. NMR measurements related to clay-dispersion quality and organic-modifier stability in nylon-6/clay nanocomposites. *Macromolecules 2001*, *34* (12), 3819–3822.
39. Reynaud, E.; Shah, D.; Giannelis, E.P. Correlation between nanostructure and crystalline morphology and mechanical response in nylon 6 nanocomposites. *Mater. Res. Soc. Symp. Proc. 2003*, *734*, B5.10.1–B5.10.9.
40. Gersappe, D. Molecular mechanisms of failure in polymer nanocomposites. *Phys. Rev. Lett. 29 July 2002*, *89* (5), 058301-1–058301-4.
41. Chen, C.; Curliss, D. Processing, dynamic studies and properties of exfoliated aerospace epoxy-organoclay nanocomposites. *Mater. Res. Soc. Symp. Proc. 2002*, *703*, V1.2.1–V1.2.6.
42. Liz-Marzán, L.M.; Norris, D.J., Eds. New aspects of nanocrystal research. *MRS Bull. 2001*, *26* (12), 981–1019. Edited by L.M. Liz-Marzán, and D.J. Norris.
43. Murray, C.B.; Sun, S.; Doyle, H.; Betley, T. Monodisperse 3d transition-metal (Co, Ni, Fe) nanoparticles and their assembly into nanoparticle superlattices. *MRS Bull. 2001*, *26* (12), 985–991.
44. Klimov, V.I.; Bawendi, M.G. Ultrafast carrier dynamics, optical amplification, and lasing in nanocrystal quantum dots. *MRS Bull. 2001*, *26* (12), 998–1004.
45. Shim, M.; Wang, C.; Norris, D.J.; Guyot-Sionnest, P. Doping and charging in colloidal semiconductor nanocrystals. *MRS Bull. 2001*, *26* (12), 1005–1008.
46. Mulvaney, P. Not all that’s gold does glitter. *MRS Bull. 2001*, *26* (12), 1009–1014.
47. Schiffrin, D.J. Capped nanoparticles as potential electronic components with nanoscale dimensions. *MRS Bull. 2001*, *26* (12), 1015–1019.
48. Prabhakaran, K.; Shafi, K.V.P.M.; Ulman, A.; Ogino, T. Multi-functionalization of silicon by nanoparticles through “plug and play” approach. *Mater. Res. Soc. Symp. Proc. 2002*, *703*, V3.17.1–V3.17.6.
49. Chiodini, N.; Paleari, A.; DiMartino, D.; Spinolo, G. SnO<sub>2</sub> nanocrystals in SiO<sub>2</sub>: A wide-band-gap quantum-dot system. *Appl. Phys. Lett. 2002*, *81* (9), 1702–1704.
50. Sun, Y.; Xia, Y. Shape-controlled synthesis of gold and silver nanoparticles. *Science 2002*, *298*, 2176–2179.
51. Maye, M.M.; Luo, J.; Lou, Y.; Ly, N.K.; Chan, W.-B.; Phillip, E.; Helpel, M.; Zhong, C.J. Investigating catalytic properties of composite nanoparticle assemblies. *Mater. Res. Soc. Symp. Proc. 2002*, *703*, V10.6.1–V10.6.6.
52. Wilcoxon, J.P. Catalytic photooxidation of pentachlorophenol using semiconductor nanoclusters. *J. Phys. Chem., B 2000*, *104*, 7334–7343.
53. Zhu, H.Y.; Lu, G.Q. Molecular engineered porous nanocomposites of metal oxide and clay using surfactants. *Mater. Res. Soc. Symp. Proc. 2002*, *703*, V1.5.1–V1.5.10.
54. Sun, S.; Murray, C.B.; Weller, D.; Folks, L.; Moser, A. Monodisperse FePt nanoparticles and ferromagnetic FePt nanocrystal superlattices. *Science 2000*, *287*, 1902–1903.
55. Zhou, H.; Kvit, A.; Kumar, D.; Narayan, J. Nickel nanocomposite thin films. *Mater. Res. Soc. Symp. Proc. 2002*, *703*, V9.12.1–V9.12.6.
56. Coe, S.; Woo, W.-K.; Bawendi, M.; Bulović, V. Electroluminescence from single monolayers of nanocrystals in molecular organic devices. *Nature 2002*, *420*, 800–803.
57. Zhang, H.-L.; Evans, S.D.; Henderson, J.R.; Miles, R.E.; Shen, T.-H. Vapour sensing using surface functionalized gold nanoparticles. *Nanotechnology 2002*, *13*, 439–444.
58. Suyal, G.; Seifert, A.; Setter, N. Pyroelectric nanoporous films: Synthesis and properties. *Appl. Phys. Lett. 2002*, *81* (6), 1059–1061.
59. Ibn-Elhaj, M.; Schadt, M. Optical polymer thin films with isotropic and anisotropic nano-corrugated surface topologies. *Nature 2001*, *410*, 796–799.
60. Zhang, Z.; Dunn, M.F.; Xiao, T.S.; Tomsia, A.P.; Saiz, E. Nanostructured hydroxyapatite coatings for improved adhesion and corrosion resistance for medical implants. *Mater. Res. Soc. Symp. Proc. 2002*, *703*, V7.5.1–V7.5.6.
61. Cayton, R.H.; Brotzman, R.W., Jr. Nanocomposite coatings—applications and properties. *Mater. Res. Soc. Symp. Proc. 2002*, *703*, V8.1.1–V8.1.6.
62. Suresh, S. Graded materials for resistance to contact deformation and damage. *Science 2001*, *292*, 2447–2451.
63. Ouellette, J. Building the nanofuture with carbon tubes. *Ind. Phys. December 2002/January 2003*, *8* (6), 18–21.
64. Zhu, H.W.; Xu, C.L.; Wu, D.H.; Wei, B.Q.; Vajtai, R.; Ajayan, P.M. Direct synthesis of long single-walled carbon nanotube strands. *Science 2002*, *296*, 884–886.
65. Schlittler, R.R.; Seo, J.W.; Gimzewski, J.K.; Durkan, C.; Saifullah, M.S.M.; Welland, M.E. Single crystals of single-walled carbon nanotubes formed by self-assembly. *Science 2001*, *292*, 1136–1139.
66. Zhan, G.-D.; Kuntz, J.D.; Wan, J.; Mukherjee, A.K. Single-wall carbon nanotubes as attractive toughening agents in alumina-based nanocomposites. *Nat. Mater. 2003*, *2*, 38–42.
67. Peigney, A. Tougher ceramics with nanotubes. *Nat. Mater. 2003*, *2*, 15–16.
68. Smith, B.W.; Monthieux, M.; Luzzi, D.E. Encapsulated C<sub>60</sub> in carbon nanotubes. *Nature 1998*, *396*, 323–324.

69. Hirahara, K.; Suenaga, K.; Bandow, S.; Kato, H.; Okazaki, T.; Shinohara, H.; Iijima, S. One-dimensional metallofullerene crystal generated inside single-walled carbon nanotubes. *Phys. Rev. Lett.* **2000**, *85*, 5384–5387.
70. Lee, J.; Kim, H.; Kahng, S.-J.; Kim, G.; Son, Y.-W.; Ihm, J.; Kato, H.; Wang, Z.W.; Okazaki, T.; Shinohara, H.; Kuk, Y. Bandgap modulation of carbon nanotubes by encapsulated metallofullerenes. *Nature* **2002**, *415*, 1005–1008.
71. Gao, Y.; Bando, Y. Carbon nanothermometer containing gallium. *Nature* **2002**, *415*, 599.
72. Appell, D. Wired for success. *Nature* **2002**, *419*, 553–555.
73. Gudiksen, M.S.; Lauhon, L.J.; Wang, J.; Smith, D.C.; Lieber, C.M. Growth of nanowire superlattice structures for nanoscale photonics and electronics. *Nature* **2002**, *415*, 617–620.
74. Wu, Y.; Fan, R.; Yang, P. Block-by-block growth of single-crystalline Si/SiGe superlattice nanowires. *Nano Lett.* **2002**, *2* (2), 83–86.
75. Björk, M.T.; Ohlsson, B.J.; Sass, T.; Persson, A.I.; Thelander, C.; Magnusson, M.H.; Deppert, K.; Wallenberg, L.R.; Samuelson, L. One-dimensional steeplechase for electrons realized. *Nano Lett.* **2002**, *2* (2), 87–89.
76. Ma, E. Controlling plastic instability. *Nat. Mater.* **2003**, *2*, 7–8.
77. He, G.; Eckert, J.; Löser, W.; Schultz, L. Novel Ti-base nanostructure-dendrite composite with enhanced plasticity. *Nat. Mater.* **2003**, *2*, 33–37.
78. Emerging methods for micro- and nanofabrication. *MRS Bull.* **2001**, *26* (7), 506–546. Edited by C.A. Mirkin and J.A. Rogers.
79. Chou, S.Y. Nanoimprint lithography and lithographically induced self-assembly. *MRS Bull.* **2001**, *26* (7), 512–517.
80. Love, J.C.; Anderson, J.R.; Whitesides, G.M. Fabrication of three-dimensional microfluidic systems by soft lithography. *MRS Bull.* **2001**, *26* (7), 523–528.
81. Mirkin, C.A. Dip-pen nanolithography: Automated fabrication of custom multicomponent, sub-100-nanometer surface architectures. *MRS Bull.* **2001**, *26* (7), 535–538.
82. Cheng, B.; Yang, K.; Justus, B.L.; Yeh, W.J. Regular array of magnetic nano-dots prepared by nanochannel glass replica masks. *Mater. Res. Soc. Symp. Proc.* **2002**, *721*, E5.6.1–E5.6.5.
83. Bhattacharyya, S.; Chattopadhyay, S.; Alexe, M. Fabrication of isolated ferroelectric nanostructures. *Mater. Res. Soc. Symp. Proc.* **2003**, *740*, I10.3.1–I10.3.6.
84. Sekiba, D.; Bertero, S.; Buzio, R.; de Mongeot, F.B.; Boragno, C.; Valbusa, U. Fabrication of stable nanopatterns on metals. *Appl. Phys. Lett.* **2002**, *81* (14), 2632–2634.
85. Li, J.; Stein, D.; McMullan, C.; Branton, D.; Aziz, M.J.; Golovchenko, J.A. Ion-beam sculpting at nanometre length scales. *Nature* **2001**, *412*, 166–169.
86. Ng, V.; Lee, Y.V.; Chen, B.T.; Adeyeye, A.O. Nanostructure array fabrication with temperature-controlled self-assembly techniques. *Nanotechnology* **2002**, *13*, 554–558.
87. Ferrand, P.; Egen, M.; Griesebock, B.; Ahopelto, J.; Müller, M.; Zentel, R.; Romanov, S.G.; Sotomayor Torres, C.M. Self-assembly of three-dimensional photonic crystals on structured silicon wafers. *Appl. Phys. Lett.* **2002**, *81* (15), 2689–2691.
88. Ji, C.; Guliyants, E.A.; Abeysinghe, D.; Anderson, W.A. Self-organized Si nanowires with room-temperature photo-emission. *Mater. Res. Soc. Symp. Proc.* **2002**, *728*, S3.34.1–S3.34.6.
89. Cai, A.; Zhang, H.; Hua, H.; Zhang, Z. Direct formation of self-assembled nanoporous aluminum oxide on SiO<sub>2</sub> and Si substrates. *Nanotechnology* **2002**, *13*, 627–630.
90. Zhao, D.; Yang, P.; Huo, Q.; Chmelka, B.F.; Stucky, G.D. Topological construction of mesoporous materials. *Curr. Opin. Solid State Mater. Sci.* **1998**, *3*, 111–121.
91. Mirsky, V.M.; Vasjari, M.; Novotny, I.; Rehacek, V.; Tvarozek, V.; Wolfbeis, O.S. Self-assembled monolayers as selective filters for chemical sensors. *Nanotechnology* **2002**, *13*, 175–178.
92. Wang, G.; Zhu, P.; Marks, T.J.; Ketterson, J.B. Ultrafast frequency-selective optical switching based on thin self-assembled organic chromophoric films with a large second-order nonlinear response. *Appl. Phys. Lett.* **2002**, *81* (12), 2169–2171.
93. Black, C.T.; Guarini, K.W.; Sandstrom, R.L.; Yeung, S.; Zhang, Y. Formation of nanometer-scale dot arrays from diblock copolymer templates. *Mater. Res. Soc. Symp. Proc.* **2002**, *728*, S4.9.1–S4.9.8.
94. Tadd, E.H.; Bradley, J.; Goldberg, E.P.; Tannenbaum, R. Self-assembly of metal nanoclusters in block copolymers. *Mater. Res. Soc. Symp. Proc.* **2002**, *703*, V2.1.1–V2.1.10.
95. Ursache, A.; Bal, M.; Goldbach, J.T.; Sandstrom, R.L.; Black, C.T.; Russell, T.P.; Tuominen, M.T. Terabit density cobalt nanowire arrays with tunable magnetic properties. *Mater. Res. Soc. Symp. Proc.* **2002**, *721*, E3.3.1–E3.3.6.
96. Yu, K.; Smarsly, B.; Brinker, J. Closed-cell mesostructured porous silica films templated by PS-*b*-PEO without additional microporosity. *Mater. Res. Soc. Symp. Proc.* **2002**, *728*, S1.9.1–S1.9.7.
97. Nguyen, T.-Q.; Wu, J.; Doan, V.; Schwartz, B.J.; Tolbert, S.H. Control of energy transfer in oriented conjugated polymer-mesoporous silica composites. *Science* **2000**, *288*, 652–656.

# Nanomechanical Resonant Devices: Surface Chemistry

Joshua A. Henry  
Debodhonyaa Sengupta  
Melissa A. Hines

Department of Chemistry, Cornell University, Ithaca, New York, U.S.A.

## INTRODUCTION

The sensitivity of nanomechanical resonant sensors to the applied mass or force is determined in part by their quality factor or  $Q$ —a dimensionless quantity that is inversely proportional to the rate of mechanical energy dissipation in the sensor. The  $Q$  of megahertz-range silicon resonators is shown to be surprisingly sensitive to surface chemistry; by changing one monolayer on the surface of a 250 nm-thick device, the rate of mechanical energy dissipation can be increased by at least a factor of 2. The chemical dependence of this effect and possible mechanisms are discussed.

## RESONANT SENSORS AND MECHANICAL ENERGY DISSIPATION: THE ROLE OF $Q$

High-performance nanomechanical sensors based on resonant mechanical motion have been proposed for a wide variety of applications, including mass spectrometry, calorimetry, scanned probe microscopy, electrometry, biological sensing, and, perhaps, even cellular telephony.<sup>[1–6]</sup> By virtue of their small size, nanomechanical structures, such as cantilevers and resonators, are inherently more sensitive to applied forces than their macroscopic counterparts. Importantly, this increased sensitivity is not accompanied by increased fragility. In fact, the opposite is observed. The strength of macroscopic devices is typically limited by bulk defects (e.g., dislocations), not by intrinsic materials properties. In contrast, nanomechanical devices are typically much smaller than the average distance between defects; they are strong, robust, and failure resistant. Having their roots in the microelectronics industry, these devices are also economically viable—they can be mass fabricated and integrated into complex architectures.

At what point, though, will this simple scaling break down? At what length scale will the properties of nanomechanical devices begin to diverge from their macroscopic counterparts? In the following, we show

that the mechanical properties of *micron-scale* devices are sensitive to submonolayer-level changes in surface chemistry. This sensitivity is both exciting and troubling. On the one hand, the increased sensitivity invariably opens up new opportunities in both science and technology. On the other hand, this sensitivity implies that submonolayer control of surface chemistry may be necessary for the production of high-performance devices—a challenge for real-world applications.

In a resonant sensor, a change in mass, temperature, charge, or other applied force induces a small shift in the resonant frequency of a vibrating element. For example, the frequency of a cantilever-based mass sensor will decrease in response to the adsorption of mass. Although many different detection techniques are possible, resonant detectors are all limited by the same fundamental problem—the frequency shift,  $\Delta f$ , induced by the applied force must be detectable. In principle, a frequency shift can be measured with arbitrary precision by simply counting oscillations with respect to a stable time base. In practice, all mechanical devices dissipate energy, and these losses limit the measurement time-scale, and thus the accuracy of the measurement.

To illustrate this process, Fig. 1A compares the displacement of a free resonant structure to one loaded with an applied mass. The applied mass slightly lowers the resonant frequency of the free cantilever,  $f_0$ , to  $f$ , leading to the gradual development of a phase lag,  $\Delta\phi(t)$ , with time, which is given by

$$\Delta\phi = (f - f_0)t \quad (1)$$

In Fig. 1A, the phase lag is readily visible in spite of the slow exponential decay of the vibration because of mechanical energy losses. The Fourier transform of this displacement, which is conveniently measured with a spectrum analyzer in the laboratory, is shown at right. In the frequency domain, the frequency shift,  $\Delta f$ , is directly measured.

The data in Fig. 1B illustrate the deleterious effects of mechanical energy dissipation on resonant sensors. In Fig. 1A and B, the resonant frequencies of the



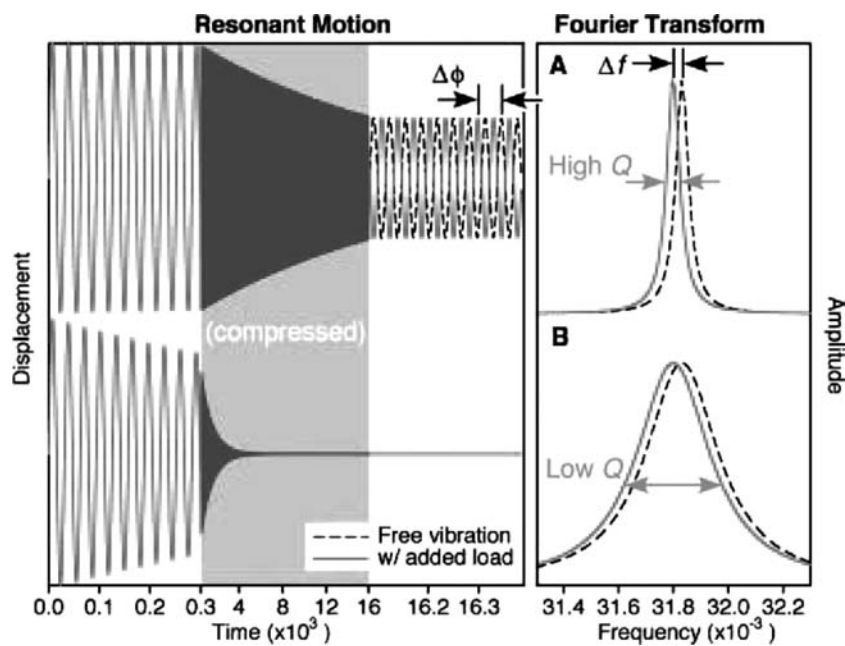


**Fig. 1** Performance of a mass detector based on a resonant cantilever. (A) A detector with high  $Q$  (low inherent mechanical energy dissipation). The accumulated phase shift,  $\Delta\phi$ , is readily detected, and the narrow line width of the frequency spectrum enables sensitive detection of the frequency shift,  $\Delta f$ . (B) The effects of increased mechanical energy dissipation (low  $Q$ ). Mechanical energy losses prevent long-time measurements; however, the frequency shift is still observable in the Fourier transformed signal. In both, the shaded region indicates a compressed timescale.

loaded and unloaded device,  $f$  and  $f_0$ , are identical; the only difference between the simulations is the rate of mechanical energy dissipation. The resonator in Fig. 1B is more highly damped, making the accumulated phase lag difficult to visualize at long times. In this noise-free (although finite) simulation, the frequency shift remains visible in the frequency domain and neither increases nor decreases in magnitude.

Importantly, the width of the resonance in the frequency domain is determined by the rate of mechanical energy dissipation; this quantity determines the minimum detectable frequency shift. The rate of mechanical energy dissipation in a resonant structure is parametrized by the *quality factor* or  $Q$  of the resonator, a dimensionless quantity. Qualitatively,  $Q$  is the number of free oscillations a device will undergo after an impulsive excitation. For example, a typical musical tuning fork has  $Q \sim 10,000$  ( $= \pi \times 440 \text{ Hz} \times 10 \text{ sec}$ ). Mathematically,

$$Q = \frac{2\pi E}{\delta E} = \frac{f}{\delta f} \quad (2)$$

where  $E$  is the energy stored in the resonator,  $\delta E$  is the energy dissipated per cycle, and  $\delta f$  is the half-power frequency width of the resonator. A detailed analysis of the factors limiting the sensitivity of resonant detectors has been presented by Ekinici, Yang, and Roukes.<sup>[7]</sup> In general, the bottom line is simple: high-sensitivity detectors demand high- $Q$  (low mechanical loss) resonators.

### PUZZLING QUALITY FACTORS IN NANOMECHANICAL DEVICES

As the push towards the development of high-sensitivity nanomechanical structures intensified in the late 1990s,

many researchers began to note a puzzling anticorrelation between resonator size and quality factor and hypothesized that these effects were surface related.<sup>[8–11]</sup> This behavior is exemplified by the performance of the 50 nm-wide, 100–200 nm-thick, metal-coated silicon wires with vibrational frequencies in the 100–400 MHz range, displayed in Fig. 2.<sup>[9]</sup> In this case, the rate of mechanical energy dissipation ( $Q^{-1}$ ) had a near-linear dependence on the surface-to-volume ratio of the wires, which strongly suggests that dissipation is occurring at the surface or in the near-surface region.

Studies of scaling behavior are a powerful probe of the fundamental origins of mechanical energy dissipation, because these studies can isolate the effects of different loss mechanisms. For example, the quality factors of macroscopic resonators are often limited by coupling to the supporting structure (so-called clamping losses). In contrast, viscous-drag-induced losses limit the performance of micromechanical devices operated in air or liquid.<sup>[12]</sup> (For this reason, nanomechanical resonators are almost exclusively operated in vacuum.) Mathematically,

$$\frac{1}{Q_{\text{total}}} = \frac{1}{Q_{\text{clamping}}} + \frac{1}{Q_{\text{drag}}} + \frac{1}{Q_{\text{bulk}}} + \dots \quad (3)$$

where each term in the summation represents a distinct energy loss channel.

Importantly, Eq. (3) implies that the performance of mechanical resonators is fundamentally limited by the bulk properties of the resonator material. In insulators, thermoelastic (th) and phonon–phonon scattering (ph) processes lead to intrinsic upper bounds for the  $fQ$

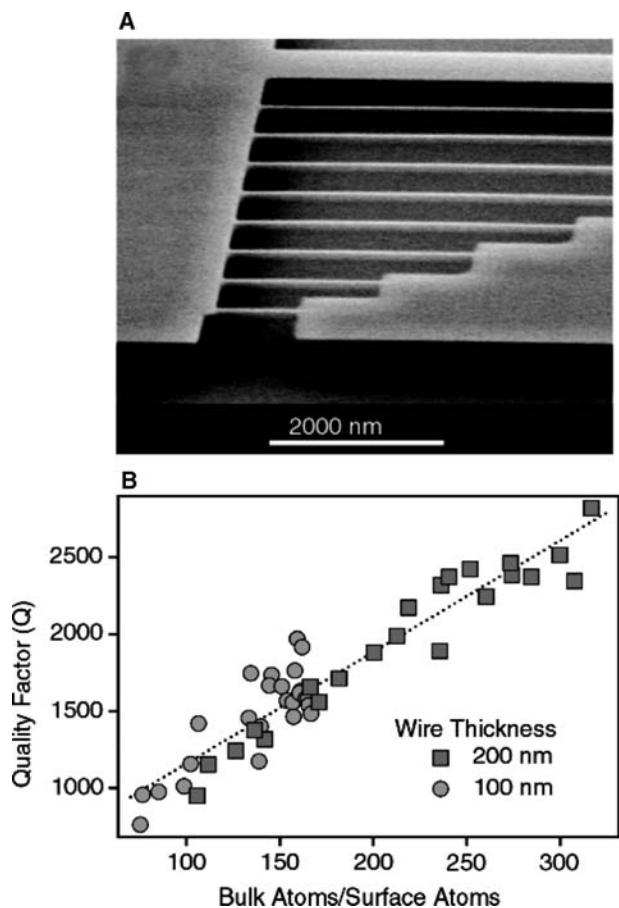


**Fig. 2** The performance of metal-coated, 100–400 MHz silicon nanoresonators. (A) Scanning electron microscopy image of typical nanoresonators. (B) The quality factor displays a near-linear scaling dependence on the volume-to-surface area ratio. *Source:* From Ref.<sup>[9]</sup>.

product of a resonator,<sup>[13]</sup>

$$fQ|_{\text{th}} = 9C^2/\kappa T\alpha^2\rho \quad \text{and} \quad (4)$$

$$fQ|_{\text{ph}} = \rho v^2(1 + f^2\tau^2)/\tau\gamma^2CT$$

respectively, where  $\tau$  is the phonon scattering time, and the other parameters are materials properties.<sup>a</sup> At room temperature, the quality factor of a 1 GHz silicon oscillator is limited to  $\leq 10^5$ . Quartz (and other insulators) should have similar limitations, whereas electronic losses in metals will lead to much poorer intrinsic performance. The performance of today's nanomechanical resonators remains far from this fundamental limit. For example, the  $fQ$  product of our best oscillators is  $8.7 \times 10^{11}$ , one of the highest

<sup>a</sup> $\kappa$  is the thermal conductivity,  $\alpha$  is the thermal expansion coefficient,  $\rho$  is the mass density,  $C$  is the specific heat,  $\gamma$  is the Gruneisen parameter, and  $v$  is the velocity of sound.

reported at room temperature but still two orders of magnitude below the fundamental limit.

The scaling behavior observed by many different groups worldwide have a clear implication—a significant amount of mechanical energy is being dissipated at the surface (or in the near-surface region) of nanomechanical resonators. But is this effect truly surface chemical? Or does it reflect the existence of a damaged or stressed surface layer—an artifact of the processing environment?

The dramatic effect of surface chemistry was conclusively demonstrated and isolated by studying the quality factor of identical micromechanical resonators with chemically controlled surfaces, as shown in Fig. 3A. By replacing 1.3 nm of silicon oxide on the resonator surface with a single atomic layer of H atoms, the quality factor of the functionalized resonators was uniformly increased, as shown by the relative quality factors plotted in Fig. 3B.<sup>[14]</sup> Interestingly, surface chemistry has a much more dramatic effect on large resonators than on small ones—a counterintuitive result. In all cases, H-terminated resonators dissipated significantly less energy than oxide-terminated

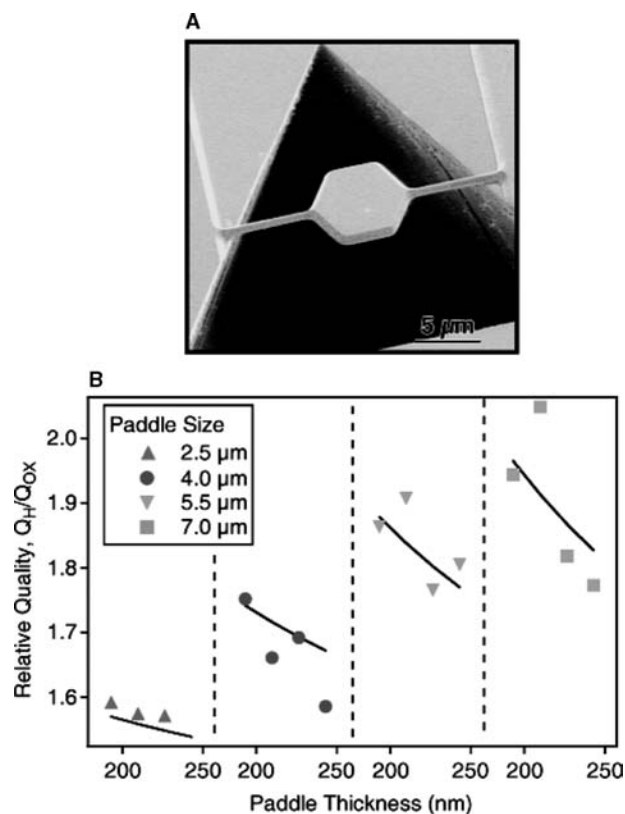


**Fig. 3** The effect of oxidation on suspended silicon torsional resonators. (A) Scanning electron micrograph of 5 μm resonator. (B) Relative quality factors of H- and oxide-terminated paddles (points) and best two-parameter global fit (lines) to Eq. (5). The oxide termination was 13 Å thick. *Source:* From Ref.<sup>[14]</sup>.

resonators. More importantly, the observed scaling behavior could be explained by three independent sources of mechanical energy dissipation—dissipation to the supporting structure (which should be constant across the series), dissipation in the bulk silicon of the resonator (which should be proportional to the resonator volume,  $V$ ), and dissipation in the surface oxide layer (which should be proportional to the surface area of the resonator,  $A$ ). From Eq. (3), these mechanisms should lead to scaling behavior of the form

$$\frac{Q^H}{Q^{\text{ox}}} = 1 + \frac{aA}{V + b} \quad (5)$$

where  $a$  and  $b$  are size-independent constants. (In this analysis, possible chemical losses introduced by the H-terminated surface were neglected because of their relatively small contribution).<sup>[14]</sup> The solid lines in Fig. 3B represent the best global fit to this simple model.

Importantly, the fit in Fig. 3B implies that over 50% of the losses in a 7  $\mu\text{m}$ -wide, 190 nm-thick paddle resonator are directly attributable to surface chemistry. In other words, more than half of the mechanical energy dissipation is controlled by less than 1% of the resonator! Moreover, the scaling of Eq. (5) implies that surface-induced mechanical energy losses will become increasingly more severe as we enter the realm of true nanomechanical devices. Why are surface-induced losses dominant? And can these losses be chemically controlled?

## CHEMICAL CONTROL OF MECHANICAL ENERGY DISSIPATION

Although H-terminated resonators have relatively high quality factors, these devices have little commercial promise because of their relative instability. For example, Fig. 4 follows a single H-terminated resonator over the course of 1 week in high vacuum ( $10^{-8}$  Torr). Two changes during this time are readily apparent. First, adsorption from the gas phase slowly shifted the resonant frequency downward by 0.07%. This shift can be used to accurately quantify the total mass of the adsorbate (but not its identity). As shown in Fig. 4, 1 week in vacuum produced a frequency shift equivalent to that expected from the adsorption of only 1.5 monolayers of  $\text{H}_2\text{O}$ , illustrating the impressive sensitivity of even relatively large resonators. Unfortunately, Fig. 4 also shows that this adsorption led to increased mechanical energy dissipation, as evidenced by the steady increase in linewidth with time. Over this period, mechanical energy dissipation increased by 90%.

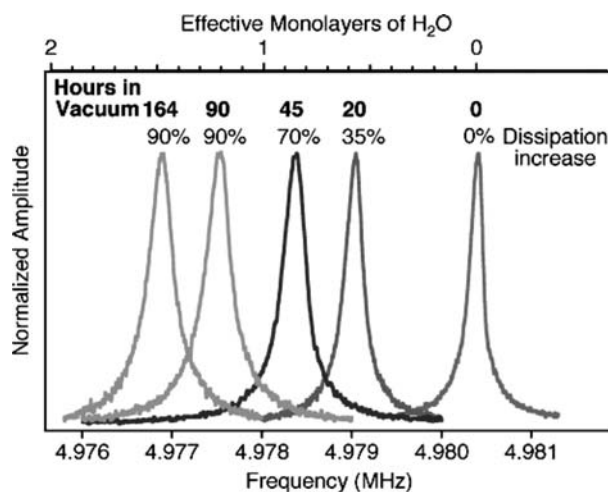


**Fig. 4** The response function of a single H-terminated resonator as a function of time in a  $10^{-8}$  Torr vacuum chamber. The frequency shift is attributed to slow adsorption from the gas phase. The increase in mechanical energy dissipation is calculated from the changes in  $Q$ .

These data suggest that a chemically resistant, hydrogen-like monolayer that is directly bonded to the silicon surface (i.e., with no intervening oxide layer) will have improved performance. From a chemical standpoint, the logical choice is a simple alkyl ( $-\text{C}_n\text{H}_{2n+1}$ ) monolayer, which is both dense and exceptionally stable.<sup>[15,16]</sup> These monolayers can be prepared by immersing H-terminated devices in the appropriate pure 1-alkene at an elevated temperature ( $\sim 200^\circ\text{C}$ ). From a mechanical standpoint, though, this choice is highly questionable. Solid hydrocarbons are waxes—highly dissipative materials completely unsuited for resonant applications. (Imagine the behavior of a wax tuning fork!) If surface-induced dissipation is dominant, will alkyl monolayers not exacerbate the problem?

These expectations are seemingly borne out by the data in Fig. 5. Resonators terminated with a dodecyl ( $-\text{C}_{12}\text{H}_{25}$ ) monolayer have significantly poorer performance (i.e., lower  $Q$ ) than freshly H-terminated resonators.<sup>[17]</sup> After approximately 2 days in vacuum ( $10^{-8}$  Torr), though, this ordering reverses because of the poor stability of the H-terminated resonators. Even after 1 week in vacuum, the frequencies and quality factors of the dodecyl-terminated resonators are essentially unchanged, showing that the alkyl-terminated resonators are indeed highly adsorption resistant.<sup>[17]</sup>

The observed stability of dodecyl-terminated resonators is consistent with the known reactivity of alkyl-terminated Si(111) surfaces. Linford and coworkers showed that silicon surfaces protected by alkyl monolayers bonded directly to the surface are remarkably stable to chemical attack.<sup>[15]</sup>  $\text{C}_{18}\text{H}_{37}$ -monolayers not only remain bound to the surface after

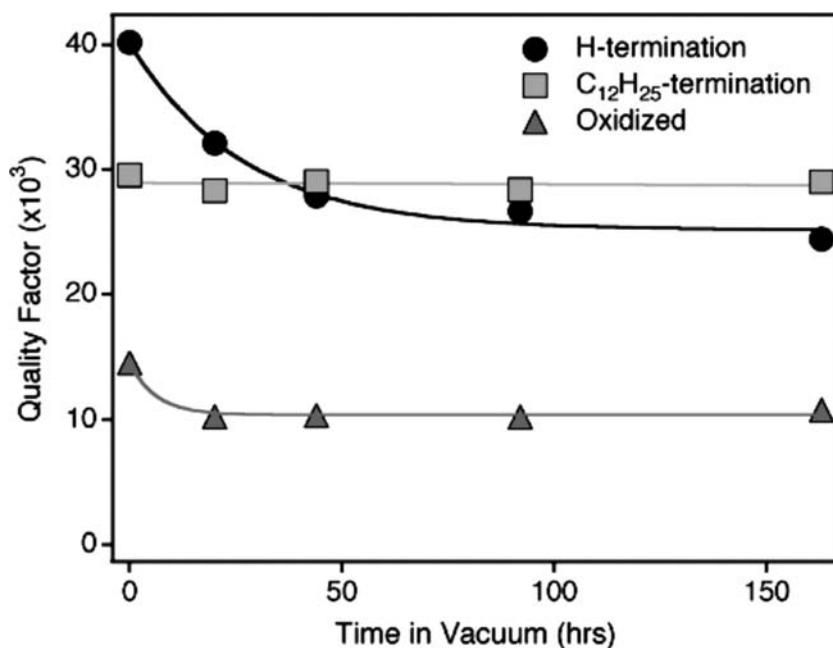


**Fig. 5** Decay of the quality factors of resonators with three different surface terminations held in a  $10^{-8}$  Torr vacuum with time. The solid lines represent the best exponential fits. *Source:* From Ref.<sup>[17]</sup>.

extended exposure to boiling strong acids and bases, but XPS measurements showed little oxidation of the underlying surface after weeks of exposure to laboratory air.<sup>[16]</sup>

To test the hypothesis that the intrinsically poor mechanical properties of waxes affect the quality factors of alkyl-terminated resonators, monolayers of varying chain lengths were studied (J. A. Henry, D. Sengupta, and M. A. Hines, in preparation).<sup>[18]</sup> Because chain length has little effect on monolayer packing and density over the range from  $-C_2H_5$  to  $-C_{18}H_{37}$ , chain length is an experimentally tractable

means of controlling monolayer thickness. If intrinsic mechanical energy dissipation in the monolayer dominates, the quality factors of alkyl-terminated resonators should decrease with increasing chain length. In fact, the opposite is observed. As shown by Fig. 6, resonators terminated with  $C_{18}$ -monolayers have nearly identical performance to those terminated by  $C_{12}$ -monolayers.<sup>[17,18]</sup> Similar results were obtained for ethyl-terminated resonators (J. A. Henry, D. Sengupta, and M. A. Hines, in preparation). The conclusion is inescapable—intrinsic dissipation in the monolayer appears to have little effect on the mechanical energy

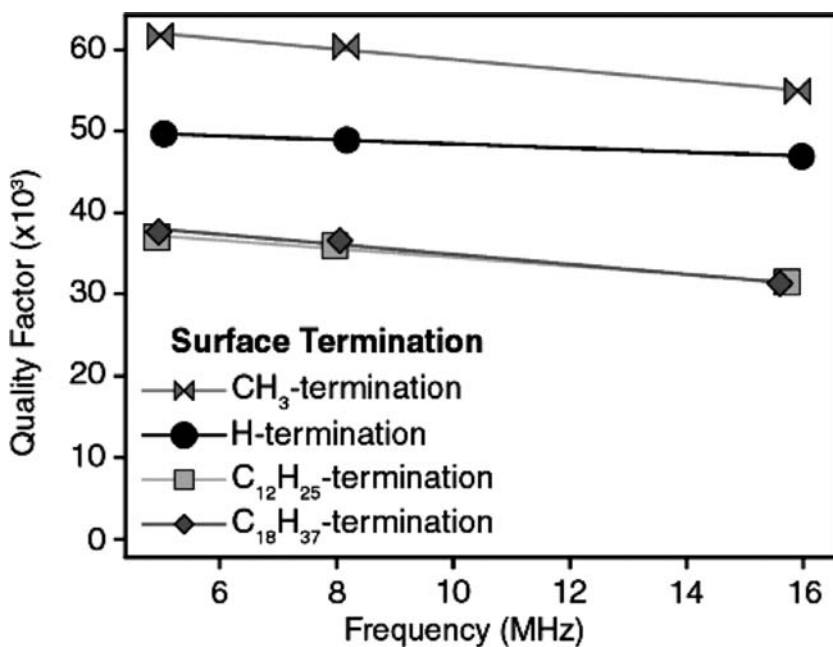


**Fig. 6** The effect of surface termination on the quality factors of three different sizes of micromechanical silicon torsional resonators. The solid lines are meant to guide the eye. *Source:* From Ref.<sup>[18]</sup>.

dissipation, at least in the relatively large (7  $\mu\text{m}$  wide, 250 nm thick) resonators examined in this study.

Why, then, do H-terminated resonators have significantly better performance than these long-chain alkyl-terminated devices? In this system, long-chain alkyl groups are not a perfect analog of hydrogen, as their 0.42 nm diameter is significantly larger than the 0.38 nm spacing between binding sites on the Si(111) surface. Because of this, only 50% of the surface sites can be alkyl-terminated.<sup>[19]</sup> Presumably, the remaining sites remain H-terminated. There is one exception to this rule—the 0.21 nm diameter of methyl groups allows for complete alkyl termination.

Unfortunately, the simple alkene-based synthesis used for long-chain monolayers cannot be used for methyl termination. Instead, a two-step synthesis is required. First, the surface of a H-terminated resonator must be completely chlorinated, either by immersion in a  $\text{PCl}_5$ -saturated solution using benzoyl peroxide as a radical initiator or by exposure to  $\text{Cl}_2(\text{g})$  during UV illumination.<sup>[20,21]</sup> The latter procedure is clearly preferred for this application, as  $\text{PCl}_5$  severely etches the silicon and structurally damages micromechanical devices.<sup>[18]</sup> After chlorination, the devices are methylated by immersion in a boiling solution of methyl magnesium chloride ( $\text{CH}_3\text{MgCl}$ , methyl Grignard reagent).<sup>[20,21]</sup>

As shown in Fig. 6, methyl-terminated resonators have significantly higher quality factors than either H-terminated or long-chain-alkyl-terminated resonators.<sup>[18]</sup> In contrast to H-terminated devices, methyl-terminated resonators are stable in vacuum. Interestingly, the methyl-terminated resonators are equally stable in air, even at 100% humidity, as long as they are stored in a sealed container (e.g., belljar). If left unprotected in the laboratory, though, a slow degradation of  $Q$  is observed. This degradation is tentatively ascribed to a low flux of reactive species (e.g., radicals) in laboratory air. Importantly, this result shows that methyl-terminated resonators may be suitable for technological applications with suitable packaging.

The difference in the quality factors of methyl-terminated and long-chain-alkyl-terminated resonators cannot be ascribed to differences in the synthetic approach (i.e., alkene-based vs. Grignard-reagent-based), as dodecyl- and octadecyl-terminated resonators prepared by both the approaches showed nearly identical performance (J. A. Henry, D. Sengupta, and M. A. Hines, in preparation). Instead, the differences between  $\text{C}_1$ - and  $\text{C}_n$ -terminated resonators are attributed to differences in monolayer packing density. Resonators terminated by a full monolayer of alkyl groups have higher performance than those terminated by a half monolayer.

Not all alkyl monolayers give equally high performance. For example, chlorosilane-based chemistries

have been successfully used to prepare antistiction coatings on micromechanical devices.<sup>[22,23]</sup> In this case, the alkyl monolayer is not bound directly to the silicon surface; instead, it is bound to a thin chemical oxide on the silicon surface. The oxide layer increases mechanical energy dissipation significantly, as resonators functionalized with the chlorosilane-based syntheses have worse performance than even the oxide-coated resonators discussed earlier.<sup>[17]</sup> Indeed, these resonators have the worst performance of any functionalized resonators tested to date.

In summary, methyl-terminated resonators have the highest quality factors and best stabilities to date. At least for silicon devices, high performance appears to be correlated with two characteristics. First and foremost, the performance of a coating appears to be directly correlated with its ability to resist surface oxidation. Oxidized resonators have uniformly poor performance, even when protected by subsequent alkyl functionalization. Second, a coating that functionalizes every surface site yields better performance than a lower-density coating. Interestingly, the mechanical properties of the surface monolayer have no apparent effect on the performance of the resonator, suggesting that this source of dissipation is too small to be observed in the megahertz-range resonators studied here.

These observations bode well for the production of functionalized resonators of controlled surface chemistry for sensor applications. The past decade has seen tremendous advances in the field of organosilicon surface chemistry, and many different strategies for silicon functionalization have been reported.<sup>[24]</sup> Nevertheless, more research is clearly needed to fully understand the correlation between surface chemistry and mechanical energy dissipation.

### The Mechanism of Surface-Induced Mechanical Energy Dissipation

The coupling of macroscopic mechanical deformations to atomic-scale surface chemistry is at first surprising; however, defect-induced mechanical energy dissipation in *bulk materials* has been understood in a general sense for at least half a century. It is likely, although not proven, that a similar mechanism accounts for the dissipation in micromechanical structures.

When a periodic macroscopic stress is applied to a (imperfect) material, the chemical bonds surrounding the defects will be stressed, usually anisotropically. If the stress puts the defects in a non-equilibrium configuration, the defects will relax to their ground state configuration with a finite relaxation time,  $\tau^*$ . If this relaxation time is much faster or much slower than the vibrational period (i.e., if relaxation is

instantaneous or adiabatic), the defects will have little effect on mechanical energy dissipation. On the other hand, if the relaxation time is comparable to the vibrational period, the material will be anelastic, and relaxation will occur with a significant phase lag to the applied stress. This phase lag inevitably leads to mechanical energy dissipation and “internal friction.”<sup>b</sup> As first discussed by Zener, the quality factor of an anelastic material will obey the relationship<sup>[25]</sup>

$$\frac{1}{Q} = \frac{E_u - E_r}{\bar{E}} \frac{\omega\tau^*}{1 + (\omega\tau^*)^2} \quad (6)$$

where  $E_u$  and  $E_r$  describe the elastic response (Young's modulus) of the solid to instantaneous and adiabatic perturbations, respectively.  $\bar{E}$  is the geometric mean of  $E_u$  and  $E_r$ , and  $\omega$  is the radial frequency of oscillation. Defects are not necessary for dissipation, though. Akhiezer showed that a similar effect occurs when vibrational modes (e.g., phonons) interact with stress fields.<sup>[26]</sup>

Chemically induced mechanical energy dissipation in *bulk* silicon was demonstrated by Mihailovich and Parpia.<sup>[27]</sup> In this case, the quality factors of macroscopic, kilohertz-range silicon resonators were found to be strongly dependent on boron doping density (over the range of  $6 \times 10^{13}$  to  $6 \times 10^{16}$  dopants/cm<sup>3</sup>). Mechanical energy dissipation was therefore attributed to stress-induced shifts of electronic holes occupying energy-split ground states.

The density of surface electronic defect states can be estimated from the charge carrier lifetime. Interestingly, the quality factors and charge carrier lifetimes of functionalized silicon surfaces follow the same (qualitative) trend in initial performance (CH<sub>3</sub> > H > long-chain alkyl monolayers) and relative stability (CH<sub>3</sub> > long-chain alkyl > H-monolayers).<sup>[28,29]</sup>

What is surprising, then, is not the existence of a surface-mediated dissipation channel, but the relative magnitude of the dissipation. For example, by changing a *single monolayer of molecules* on the surface of a 7 μm-wide, 250 nm-thick Si resonator from -C<sub>2</sub>H<sub>5</sub>/H to -CH<sub>3</sub>, less than 0.07% of the total mass, the quality factor of the device can be improved by 95% (J. A. Henry, D. Sengupta, and M. A. Hines, in preparation). Moreover, there is increasing evidence that surface-induced dissipation is primarily related to surface defects (e.g., a small degree of oxidation) and not to the majority sites on the surface.<sup>[17]</sup>

To date, most of the research on chemically induced micromechanical energy losses has focused on silicon

resonators, primarily because of their prevalence. Nevertheless, there is no reason to believe that silicon is the ultimate material in terms of dissipation. Indeed, Eq. (4) predicts that many semiconductors and insulators (e.g., silicon, diamond, and carbon nanotubes) will have comparable intrinsic losses. For this reason, resonators fabricated from materials with relatively unreactive surfaces, such as diamond or carbon nanotubes, may have superior performance.<sup>[30]</sup>

## CONCLUSIONS

The rate of mechanical energy dissipation in micro-mechanical silicon resonators is exquisitely sensitive to the chemical state of the surface. Changes at the monolayer level can increase the rate of dissipation in 250 nm-thick, megahertz-range resonators by at least a factor of 2. This magnitude of surface-induced losses increases as the size (i.e., volume-to-surface ratio) of the resonator decreases, suggesting that submonolayer control of surface chemistry will be necessary for the production of the high-performance nanoscale mechanical resonators necessary for the proposed sensor applications.

## ACKNOWLEDGMENT

This work was supported by the Cornell Center for Materials Research, a Materials Research Science and Engineering Center of the National Science Foundation (DMR-0079992), and performed in part at the Cornell Nanoscale Science and Technology Facility (ECS-9731293).

## REFERENCES

1. Thundat, T.; Wachter, E.A.; Sharp, S.L.; Warmack, R.J. Detection of mercury vapor using resonating micro-cantilevers. *Appl. Phys. Lett.* **1995**, *66*, 1695–1697.
2. Nakagawa, Y.; Schafer, R.; Güntherodt, H.J. Picojoule and submillisecond calorimetry with micromechanical probes. *Appl. Phys. Lett.* **1998**, *73*, 2296–2298.
3. Stowe, T.D.; Yasumura, K.; Kenny, T.W.; Botkin, D.; Wago, K.; Rugar, D. Attonewton force detection using ultrathin silicon cantilevers. *Appl. Phys. Lett.* **1997**, *71*, 288–290.
4. Cleland, A.N.; Roukes, M.L. A nanometre-scale mechanical electrometer. *Nature* **1998**, *392*, 160–162.
5. Ilic, B.; Craighead, H.G.; Krylov, S.; Senaratne, W.; Ober, C.; Neuzil, P. Attogram detection using nanoelectromechanical oscillators. *J. Appl. Phys.* **2004**, *95*, 2694–2703.

<sup>b</sup>For simplicity, we consider the case of a single, well-defined type of defect. These arguments are readily extended to the case of multiple defect types.



6. Nguyen, C.T.-C. Frequency-selective MEMS for miniaturized low-power communication devices. *IEEE Trans. Microw. Theory Tech.* **1999**, *47*, 1486–1503.
7. Ekinici, K.L.; Yang, Y.T.; Roukes, M.L. Ultimate limits to inertial mass sensing based upon nanoelectromechanical systems. *J. Appl. Phys.* **2004**, *95*, 2682–2689.
8. Mihailovich, R.E.; MacDonald, N.C. Dissipation measurements of vacuum-operated single-crystal silicon microresonators. *Sens. Actuators* **1995**, *50*, 199–207.
9. Carr, D.W.; Evoy, S.; Sekaric, L.; Parpia, J.M.; Craighead, H.G. Measurement of mechanical resonances and losses in nanometer-scale silicon wires. *Appl. Phys. Lett.* **1999**, *75*, 920–922.
10. Yang, J.; Ono, T.; Esashi, M. Surface effects and high quality factors in ultrathin single-crystal silicon cantilevers. *Appl. Phys. Lett.* **2000**, *77*, 3860–3863.
11. Yang, J.; Ono, T.; Esashi, M. Investigating surface stress: surface loss in ultrathin single-crystal silicon cantilevers. *J. Vac. Sci. Technol. B.* **2001**, *19*, 551–556.
12. Bhiladvala, R.B.; Wang, Z.J. Effects of fluids on the Q factor and resonance frequency of oscillating micrometer and nanometer scale beams. *Phys. Rev. E.* **2004**, *69*, 036307(1)–036307(5).
13. Braginsky, V.B.; Mitranov, V.P.; Panov, V.I. *Systems with Small Dissipation*; University of Chicago Press: Chicago, 1985; Chapter 2.
14. Wang, Y.; Henry, J.A.; Zehnder, A.T.; Hines, M.A. Surface chemical control of mechanical energy dissipation in micromachined silicon devices. *J. Phys. Chem. B.* **2003**, *107*, 14,270–14,277.
15. Linford, M.R.; Fenter, P.; Eisenberger, P.M.; Chidsey, C.E.D. Alkyl monolayers on silicon prepared from 1-alkenes and hydrogen-terminated silicon. *J. Am. Chem. Soc.* **1995**, *117*, 3145–3155.
16. Terry, J.; Linford, M.R.; Wigren, C.; Cao, R.; Pianetta, P.; Chidsey, C.E.D. Alkyl-terminated Si(111) surfaces: a high-resolution, core level photoelectron spectroscopy study. *J. Appl. Phys.* **1999**, *85*, 213–221.
17. Henry, J.A.; Wang, Y.; Hines, M.A. Controlling energy dissipation and stability of micro mechanical silicon resonators with self-assembled monolayers. *Appl. Phys. Lett.* **2004**, *84*, 1765–177.
18. Wang, Y.; Henry, J.A.; Sengupta, D.; Hines, M.A. Methyl monolayers suppress mechanical energy dissipation in micromechanical silicon resonators. *Appl. Phys. Lett.* **2004**, *85*, 5736–5738.
19. Sieval, A.B.; van den Hout, B.; Zuilhof, H.; Sudhölter, E.J.R. Molecular modeling of alkyl monolayers on the Si(111) surface. *Langmuir* **2000**, *16*, 2987–2990.
20. Bansal, A.; Li, X.; Lauermann, X.; Lewis, N.S.; Yi, S.I.; Weinberg, W.H. Alkylation of Si surfaces using a two-step halogenation/Grignard route. *J. Am. Chem. Soc.* **1996**, *118*, 7225–7226.
21. Terry, J.; Linford, M.R.; Wigren, C.; Cao, R.; Pianetta, P.; Chidsey, C.E.D. Determination of the bonding of alkyl monolayers to the Si(111) surface using chemical-shift, scanned-energy photoelectron diffraction. *Appl. Phys. Lett.* **1997**, *71*, 1056–1058.
22. Parikh, A.N.; Allara, D.L.; Azouz, I.B.; Rondelez, F. Intrinsic relationship between molecular structure in self-assembled n-alkylsiloxane monolayers and deposition temperature. *J. Phys. Chem.* **1994**, *98*, 7577–7590.
23. Mauboudian, R.; Carraro, C. Surface chemistry and tribology of MEMS. *Ann. Rev. Phys. Chem.* **2004**, *55*, 35–54.
24. Buriak, J.M. Organometallic chemistry on silicon and germanium surfaces. *Chem. Rev.* **2002**, *102*, 1271–1308.
25. Zener, C. *Elasticity and Anelasticity of Metals*; University of Chicago Press: Chicago, 1948.
26. Akhiezer, A. *Zh. Eksp. Teor. Fiz.* **1938**, *8*, 1318.
27. Mihailovich, R.E.; Parpia, J.M. Low temperature mechanical properties of boron-doped silicon. *Phys. Rev. Lett.* **1992**, *68*, 3052–3055.
28. Royea, W.J.; Juang, A.; Lewis, N.S. Preparation of air-stable, low recombination velocity Si(111) surfaces through alkyl termination. *Appl. Phys. Lett.* **2000**, *77*, 1988–1990.
29. Webb, L.J.; Lewis, N.S. Comparison of the electrical properties and chemical stability of crystalline Si(111) surfaces alkylated using Grignard reagents or olefins with Lewis-acid catalysts. *J. Phys. Chem. B* **2003**, *107*, 5404–5412.
30. Sazonova, V.; Yaish, Y.; Ustunel, H.; Roundy, D.; Arias, T.A.; McEuen, P.L. A tunable carbon nanotube electromechanical oscillator. *Nature* **2004**, *431*, 284–287.

# Nanoparticle Arrays: Optical and Electronic Applications

Ilona Kretzschmar

Mark A. Reed

*Department of Electrical Engineering, Yale University,  
New Haven, Connecticut, U.S.A.*

## INTRODUCTION

The need for increasing miniaturization of circuitry, as described by Moore's law, requires the reduction of feature size for electronic components, decreasing by an order of magnitude every 10 years. With contemporary minimum feature sizes of  $\sim 0.1 \mu\text{m}$ , circuits with dimensions on the atomic length scale will need to be achieved within the next 30 years<sup>[1]</sup> for this progress to continue.

There are two possible routes to smaller feature sizes: 1) the traditional "top-down" approach, where feature size is simply reduced by scaling of presently used devices; and 2) the more recent "bottom-up" approach based on enlargement, where the self-assembly of macromolecular and colloidal building blocks is used to create larger, functional devices. "Top-down" fabrication processes presently experience a bottleneck because most common lithographic techniques used for the creation of small features are limited to a spatial resolution in the upper nanometer range.<sup>[2]</sup> Feature sizes down to 10 nm have been realized by special techniques, but the small-area and low-throughput properties of these processes are economically challenging. Thus new avenues toward smaller-scale and more densely packed structures need to be explored, and new fabrication methods using the bottom-up approach need to be developed. Two-dimensional and three-dimensional structures can be self-assembled using nanometer-sized objects with the control of feature size in the nanometers to hundreds of nanometer range, bridging the gap between atomic manipulation and modern lithography. The simplicity and low processing costs connected with it make methods based on self-assembly economically interesting. Nanoparticles present ideal building blocks for self-assembly because: 1) they can be synthesized with narrow size distributions ( $\sigma \leq 5\%$ ) from a variety of materials; 2) they come in many different shapes; and 3) their small dimensions lead to a wide functional diversity with respect to their electronic, optical, and catalytic properties, which is usually very different from bulk materials.

This entry reviews recent accomplishments in the fabrication of two-dimensional and three-dimensional

nanoparticle structures using self-assembly, which may be used in electronic applications. Synthetic approaches to monodisperse metallic, semiconducting, insulating, and core-shell structured nanoparticles are briefly reviewed. The basic principles behind two-dimensional and three-dimensional nanoparticle assembly from solutions, by templating and by networking with organic and biological molecules, are presented. Some interesting properties of various nanoparticle arrays and their possible applications in optical and electronic devices are discussed. Finally, recent developments in the self-assembly of nanobuilding blocks other than nanoparticles are briefly mentioned.

## NANOPARTICLE SYNTHESIS

The underlying concept of nanosized particle synthesis is to stabilize small particles by surface derivatization while they are formed in a solution to prevent their coalescence or aggregation.<sup>[3-5]</sup> For most applications, monodisperse nanoparticle solutions with size distributions of  $\sigma \leq 5\%$  are desirable. Nanoparticles are divided into three classes based on their conduction properties: 1) metallic nanoparticles; 2) semiconductor nanoparticles, often referred to as nanocrystallites because of their well-formed crystalline cores and controlled surface chemistry; and 3) nonmetallic nanoparticles. A new class of nanoparticles with core-shell structures, comprising a combination of any of the above, has lately received attention because of their applications in photonic crystals.<sup>[6]</sup>

### Metallic Nanoparticles

Metallic nanoparticles are generally synthesized via the addition of a reducing agent (e.g., sodium citrate) to an aqueous solution of a metal salt under reflux conditions.<sup>[3,7]</sup> Using citrates, nanoparticles with size distributions of  $10 < \sigma < 15\%$  are obtained. Size distribution cannot be narrowed further because of the tendency of nanoparticles to flocculate. The latter can be circumvented by the performance of a two-phase reduction process, which involves the transfer

of metal salt into an organic phase using long-chain alkylammonium surfactants in the first step and the subsequent reduction of the salt in the presence of capping ligands. Monolayer-protected cluster (MPC) molecules in the range of 1–7 nm have been synthesized with size distributions of  $\sigma \sim 5\%$ .<sup>[8]</sup> The advantage of MPCs is that they can be repeatedly isolated from, and redissolved in, common organic solvents without irreversible aggregation and decomposition.<sup>[8]</sup> The gas-phase synthesis of gold MPCs with diameters as small as  $1.9 \pm 0.6$  nm has been reported.<sup>[9]</sup> These clusters are melted and recrystallized in the gas phase prior to deposition, thus yielding clusters that are single face-centered cubic (fcc) crystals. More recent research has focused on controlled production of nanoparticles with shapes other than spherical. For example, disk-shaped cobalt nanoparticles have been synthesized by employing the rapid decomposition of  $\text{Co}_2(\text{CO})_8$  in hot organic solvents in the presence of linear amines and trioctylphosphine oxide (TOPO).<sup>[10]</sup> Anisotropy in growth is induced by TOPO acting as a selective adsorber, altering the relative growth rates of different crystal faces. The effect is enhanced in the presence of linear amines. The disks have average diameters of  $2 \times 4$ ,  $4 \times 35$ , and  $4 \times 90$  nm. They represent high surface area crystals and are also expected to be single magnetic domains (breakup into single magnetic domains occurs at 70–100 nm for cobalt spheres). Furthermore, triangular gold–silver alloy nanoframes<sup>[11]</sup> are obtained when compact silver nanoprisms are etched in  $\text{HAuCl}_4$ . Although these differently shaped particles do not yet exhibit the desirable size distribution of  $\leq 5\%$ , they allow a glimpse at what kind of shape control is possible.

### Semiconductor Nanoparticles

Compound semiconductor nanoparticles, such as CdS, CdSe, PbS, InAs, and ZnSe, can be synthesized by: 1) arrested precipitation in a solution; 2) precipitation in nanostructured templates; or 3) use of molecular precursors.<sup>[3,4]</sup> Arrested precipitation provides a cheap route to many different semiconductor nanoparticles, but because it is performed at low temperatures, the trapping of defects formed during early stages of preparation may cause low crystallinity in the nanoparticles. In contrast, the method based on molecular precursors [e.g.,  $(\text{CH}_3)_2\text{Cd}$  and tri-*n*-octylphosphine selenide (TOPSe)], which are injected into a hot organic ligand such as TOPO, yields organic ligand-capped nanocrystallites (e.g., CdSe) with a size distribution of about 5%. The second advantage of method 3 is that it yields grams of materials. Fig. 1 shows transmission electron microscopy (TEM) images and a small-angle electron diffraction pattern of the  $\langle 101 \rangle_{\text{SL}}$  projection through a three-dimensional superlattice of 4.8-nm CdSe nanocrystals.

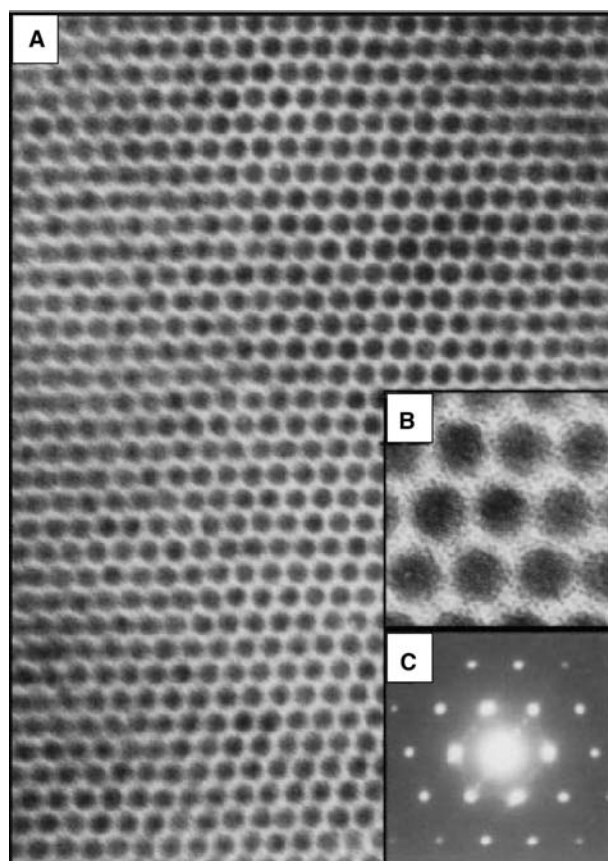


**Fig. 1** (A) TEM image showing the  $\langle 101 \rangle_{\text{SL}}$  projection of a superlattice of 4.8-nm CdSe nanocrystals. (B) High magnification shows the lattice imaging of individual nanocrystals. (C) Small-angle electron diffraction demonstrates the perfection of the  $\langle 101 \rangle_{\text{SL}}$  projection of the fcc superlattice. *Source:* From Ref.<sup>[3]</sup>. With permission from the Annual Review of Materials Science, Volume 30. © 2000 by Annual Reviews.

### Non-metallic Nanoparticles

Catalyzed hydrolysis and condensation of an alkoxy-metal precursor in a solution are used to prepare monodispersed metal oxide particles.<sup>[5]</sup> In particular, silicon dioxide spheres are usually prepared by the so-called Stöber method, which involves hydrolyzing tetraethyl orthosilicate with ammonium hydroxide in ethanol.<sup>[12]</sup>

### Core–Shell Nanoparticles

Core–shell nanoparticles are synthesized by the coating of nanoparticles with a second material.<sup>[6]</sup> There are four requirements that need to be fulfilled for successful coating: 1) the core particle must be stable under conditions used for the coating step; 2) heterogeneous nucleation (i.e., coating material on core) must be more likely than homogeneous nucleation; 3) the coating and core material should not interdiffuse under coating conditions; and 4) the coating of particles should not lead to

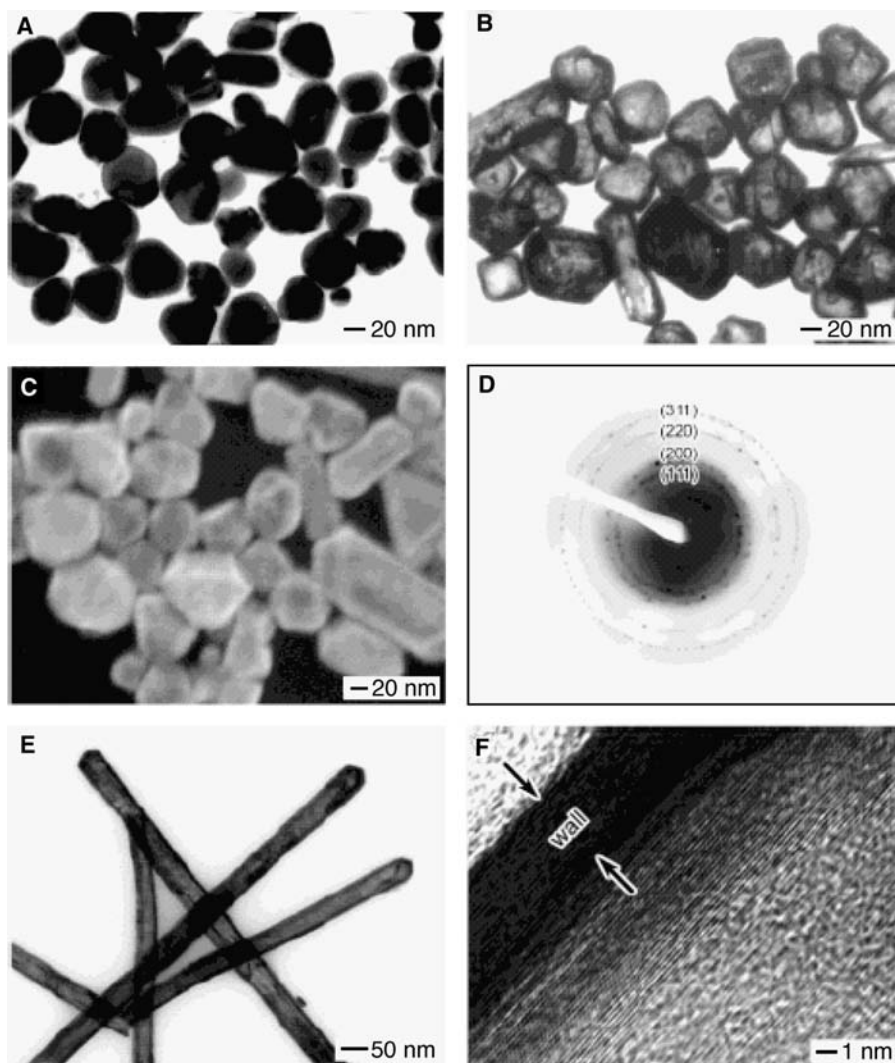


**Fig. 2** (A) A TEM image of silver nanoparticles synthesized using a polyol process. (B, C) Transmission electron microscopy and SEM images of gold nanoshells formed by reacting these silver nanoparticles with an aqueous  $\text{HAuCl}_4$  solution. (D) Selected area electron diffraction (SAED) pattern obtained by focusing the electron beam on a random assembly of gold nanoshells. (E) A TEM image of gold nanotubes formed by reacting silver nanowires with an aqueous  $\text{HAuCl}_4$  solution. (F) High-resolution transmission electron microscopy (HRTEM) image of the edge of an individual gold nanotube, indicating its uniform wall thickness and single crystalline structure. *Source:* From Ref.<sup>[14]</sup>; ©American Chemical Society, 2003.

aggregation of newly formed core-shell particles. The additional surface shell stabilizes the particles toward coalescence, increases their dispersibility, and also allows the tuning of electrical and optical properties.

A subclass of core-shell particles is produced when the core is dissolved after (while) the shell has been (is being) formed.<sup>[13]</sup> For example, hollow, crystalline gold nanoparticles (Fig. 2)<sup>[14]</sup> are produced when crystalline silver templates are exposed to  $\text{HAuCl}_4$ . Owing to the higher standard reduction potential of the  $\text{AuCl}_4^-/\text{Au}$  pair compared to the  $\text{Ag}^+/\text{Ag}$  pair, gold is plated while the silver core dissolves. The procedure is versatile and can be extended to any metal that can be reduced by the template metal.

### NANOPARTICLE ASSEMBLY INTO ORDERED TWO-DIMENSIONAL AND THREE-DIMENSIONAL ARRAYS

The assembly of nanoparticles into functional two-dimensional and three-dimensional arrays requires

excellent control of interparticle as well as particle-surface interactions.<sup>[15–17]</sup> One general prerequisite for the formation of crystalline arrays is a very uniform nanoparticle size distribution. Forces governing self-assembly are static and dynamic in nature. Assuming that nanoparticles act as hard spheres with electrically neutral surfaces, their interaction potential consists of two terms: short-range steric repulsion, and short-range attractive van der Waals force. An additional long-range electrostatic Coulomb repulsion is present in systems with charged particle surfaces. All three potentials are combined in the Derjaguin–Landau–Verwey–Overbeck (DLVO)<sup>[18]</sup> theory. Dynamic forces are at work when particles move through (hydrodynamic) solutions and with respect to each other (steric repulsion). We have divided the assembly methods into three groups: 1) self-assembly of nanoparticles onto planar substrates; 2) self-assembly into structured templates; and 3) self-assembly by coordination with organic and biological linkers. Nanoparticle assembly using the Langmuir–Blodgett (LB) technique is not

included, although close-packed two-dimensional films can be obtained and transferred to solid substrates with the LB technique.<sup>[19,20]</sup>

### Self-Assembly onto Planar Substrates

Convective self-assembly of nanoparticles from solutions onto planar substrates occurs in two stages: 1) onset of array growth (nucleation phase), and 2) array growth. A prerequisite for nucleation is that the nanoparticle suspension forms a wetting film on the substrate. The thickness of the wetting film influences both the nucleation and the growth of the array. The particles move toward each other because of hydrodynamic pressure caused by solvent flux from the bulk suspension toward the drying array (hydrodynamic forces). As the particles start to protrude through the surface of the evaporating film, they experience attractive, lateral capillary immersion forces, which leads to close packing of particles.<sup>[21,22]</sup> In the case of two-dimensional films, the evaporation rate influences the formation of two-dimensional arrays because of competition between solvent dewetting and superlattice formation.

Excessively high rates of evaporation (i.e., when pure solvents are used) lead to dewetting (film thinning) prior to superlattice formation. Particles move away from holes in the wetting film, whereas the convective flow inside wetting droplets drives particles toward the rim of droplets, leading to the formation of ring structures.<sup>[23]</sup> The addition of a nonvolatile liquid to the evaporating solution (e.g., dodecanethiol) reduces the evaporation rate, whereas it increases the time for particle assembly, resulting in better long-range order on the micrometer scale.<sup>[24]</sup> Fig. 3 shows a TEM image of a two-dimensional 5.5-nm gold nanoparticle array with excellent long-range order. Multilayer formation can be induced by higher nanoparticle concentrations because interparticle interactions become more frequent. Murray, Kagan, and Bawendi<sup>[3]</sup> showed that three-dimensional nanocrystal superlattices coherent over hundreds of micrometers are produced when CdSe nanocrystallites capped with long-chain alkyl tail groups are deposited from a low-boiling alkane/high-boiling alcohol mixture. Sedimentation because of gravitational forces can be neglected for very small nanoparticles (<300 nm) because thermal agitation compensates for gravitational forces.

Interestingly, the formation of ordered, stable particles comprising nanoparticles (270–630 nm) was recently reported to occur when an aqueous colloidal suspension was added to fluorinated oil.<sup>[25]</sup> Using mixtures of nanoparticles with largely differing sizes (40 vs. 270 nm) led to an assembly of 40-nm gold nanoparticles in a ring structure on the side of the array in contact with air (Fig. 4).

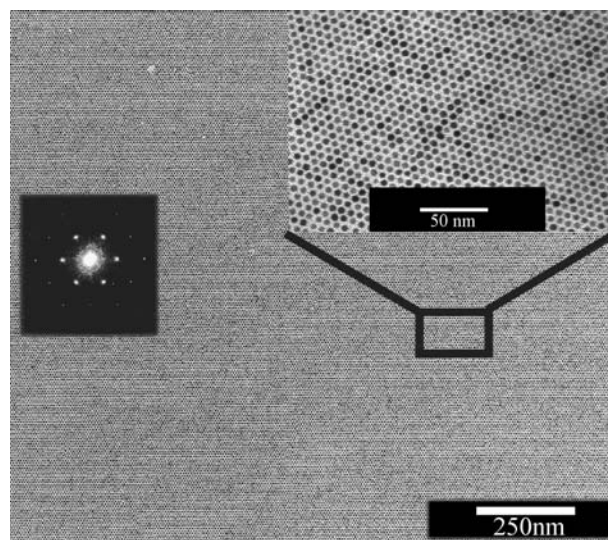


**Fig. 3** Long-range ordered nanocrystal monolayer formed by 10  $\mu\text{L}$  of colloid in the toluene dodecanethiol mixture, with a thiol volume fraction of  $6.3 \times 10^{-3}$  and a particle concentration of  $1.2 \times 10^{13} \text{ mL}^{-1}$ . Source: From Ref.<sup>[24]</sup>; ©American Chemical Society, 2003.

One disadvantage of the convective assembly described above is that it gives no control over the place of assembly. Therefore it is desirable to develop techniques that allow array positioning using electric fields. Giersing and Mulvaney<sup>[26]</sup> first observed that citrate-stabilized and alkanethiol-stabilized gold colloids (14.1 nm) electrophoretically deposited onto carbon-coated copper grids when a positive voltage was applied (50 mV). Monolayers formed exhibit small domains of hexagonally ordered, close-packed particles. Solomentsev, Böhmer, and Anderson<sup>[27]</sup> developed an electrohydrodynamic (EHD) theory describing the electroosmotic flow around charged particles attached to an electrode leading to clustering of particles. Electrophoresis is also used for the assembly of opals (i.e., highly periodic, ordered arrays of silica spheres with diameters between 300 and 550 nm), which are used as photonic bandgap crystals (see below).<sup>[28]</sup> Dielectrophoresis,<sup>[29]</sup> the a.c. variant of electrophoresis, can be used to create one-dimensional, two-dimensional, and free-standing three-dimensional assemblies of micron-sized particles in between planar electrodes. Electrode shapes and dimensions determine the structure of the final array, but particle type and operating conditions also play a role. The application of a.c. currents to electrodes immersed in metallic nanoparticle suspensions (15–30 nm) leads to the growth of metallic nanoparticle wires between electrodes.<sup>[30]</sup> Interestingly, the wires self-repair after burnout because of high voltage. If a mixture of metallic nanoparticles and polystyrene (PS) spheres is used, conducting wires with a PS shell form. Assembly into a planar

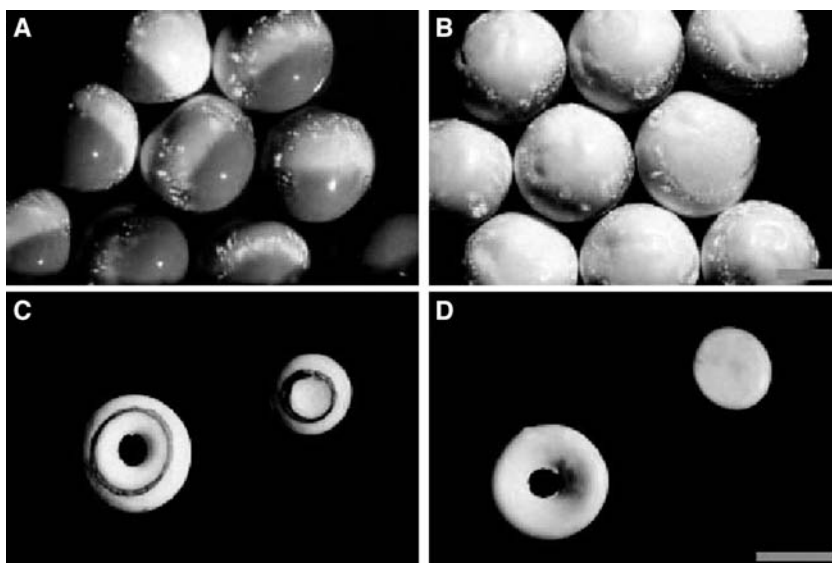


**Fig. 4** Examples of anisotropic particles. (A) Unoriented spherical assemblies incorporating regular (white) and magnetic (brown) latexes. (B) In the presence of a magnetic field originating from below, these particles immediately form an array with the white halves oriented up. If the magnetic field gradient is reversed, the particles flip to form an array with the brown side up. (C, D) Two assemblies of complex shape obtained in the presence of small gold particles, as viewed from opposite faces. A metallic ring is deposited only on the side of the particle that was originally exposed to air. *Source:* Reproduced with permission from Ref.<sup>[25]</sup>. © 2003 American Association for the Advancement of Science.

superlattice is observed when binary colloidal suspensions are exposed to an a.c. electric field.<sup>[31]</sup> The lattice shape is controlled by particle concentration, size, and a.c. frequency. At low frequencies, induced dipole interaction and attractive EHD flow govern superlattice formation, whereas at high frequencies, EHD flow is negligible because dipole–dipole interactions between particles become attractive. Magnetic fields can also be used to improve the monolayer packing of diamagnetic materials (e.g., silver nanoparticles; 6.5 nm).<sup>[32]</sup> Because of interactions with the magnetic field, particles are pulled up in a positive field and pulled down in a negative field. The coating of non-magnetic Al<sub>2</sub>O<sub>3</sub> spheres (47 μm) with a 2- to 3-μm-thick Ni layer by electroless plating yields magnetic microspheres that can be manipulated into two-dimensional and three-dimensional arrays by means of magnetic force from an electromagnet.<sup>[33]</sup>

### Assembly Using Structured Templates

Many applications require particle arrays with more complex patterns than close-packed two-dimensional and three-dimensional arrays obtained by the planar assemblies described above. A very promising approach to complex nanoparticle arrays is the direction and confinement of nanoparticle assembly by substrate structure. For example, two-dimensional particle arrays (300–800 nm) can be obtained using substrates with one-dimensional grating patterns.<sup>[34]</sup> Striped structures as well as hexagonal and centered rectangular lattices with varying lattice spacings are produced by the variation of particle size and grating spacing. The main driving forces for assembly formation are capillary forces and self-shadowing effects.

For three-dimensional arrays, the patterning of surfaces with micrometer features is commonly achieved

by soft lithography.<sup>[35]</sup> The term summarizes a group of microfabrication techniques, which use patterned elastomers as stamps, molds, or masks to generate micropatterns and microstructures. Direct evaporation-induced self-assembly (DEISA)<sup>[36]</sup> of silica nanoparticles (100–500 nm) leads to fcc, close-packed opal crystal architectures. Depending on the substrate pattern, complex forms that offer optical functionality and quality can be obtained. The assembly is directed by colloidal interactions, capillary forces, and surface tension forces between spheres and wall materials. For larger particles (700–2500 nm), sedimentation because of gravitational forces interferes with the assembly and can be circumvented by stirring of the solution during assembly. An interesting variant combines soft lithography and nanoparticle assembly (i.e., a surface pattern is created using one type of nanoparticles, and subsequently filled with nanoparticles of a second type).<sup>[37]</sup>

A very interesting, relatively new three-dimensional nanoparticle structure, the so-called inverse opal,<sup>[28]</sup> is obtained by the infiltration of close-packed three-dimensional microparticle arrays with smaller nanoparticles of a higher refractive index material. The smaller nanoparticles completely occupy the void space of the microparticle array, thereby creating a lattice that is retained when the host microparticles are removed (dissolved). This leaves a collection of micrometric spherical cavities surrounded by a high refractive index nanoparticle material, in which both the cavities and the high refractive material are connected throughout the structure. Inverse opals show even better bandgap properties than opals; however, it is necessary that the photonic properties appear in the transparent region of the material that forms the inverse structure. Defect densities in opals depend on particle monodispersity and size; the more



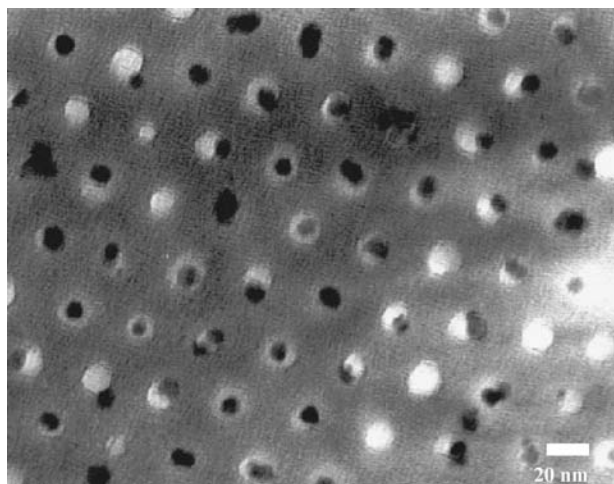


**Fig. 5** Nanoparticles  $\sim 10$  nm in diameter are deposited into the polymer template. The larger size limits the number of nanoparticles per nanopore. *Source:* Reprinted with permission from Ref.<sup>[39]</sup>.

monodisperse and the smaller the particles are, the lower is the number of defects.

Instead of elastomeric stamps, self-organizing diblock copolymers<sup>[38]</sup> can be employed. They are of great interest to industries because of their compatibility with standard silicon technology. Diblock copolymers consist of two polymers [e.g., PS and poly(methylmethacrylate) (PMMA)], which, under certain conditions, spontaneously self-assemble into patterned structures because of phase separation. Misner et al.<sup>[39]</sup> deposited monolayer-protected nanoparticles ( $\sim 10$  nm) into a mask (Fig. 5) made from a PS/PMMA diblock copolymer by a simple dipping process, allowing the creation of arrays of isolated nanoparticles.

### Assembly Using Organic Linkers and Biological Templates

The third method utilizes organic and biological molecules as linkers and templates for the assembly of nanoparticles into ordered two-dimensional and three-dimensional structures. The assembly is directed by specific interactions of functional groups on the linker molecule or template. For example, a hydrogen bonding network is suggested as the origin of the crystallization of mercaptosuccinic acid-capped gold nanoparticles ( $3.7 \pm 0.5$  nm) into hexagonal closed-packed, colloidal gold crystals from an aqueous solution<sup>[40]</sup> (i.e., mercaptosuccinic acid functions as capping ligand and linker). Furthermore, highly ordered hexagonal and cubic monolayers of Au<sub>55</sub> MPCs have been formed on polymer-coated substrates.<sup>[41]</sup> Double end-functionalized organic linker molecules have been employed in the creation of well-ordered two-dimensional nanoparticle arrays,<sup>[42]</sup>

which are extremely important for molecular electronics applications.<sup>[43]</sup>

Biomolecules, with their typical size dimensions in the range of 5–200 nm, are perfectly suited for nanoparticle assembly.<sup>[44]</sup> The utilization of, for example, nucleic acids and proteins as programmable recognition units can modify and improve assembly capacities of nanoparticles and thus allow nanostructured and mesoscopic supramolecular hybrid architectures. The tremendous recognition capabilities of biomolecules and their potential to be addressed through biochemical procedures provide the basis for entirely novel routes to construct advanced materials rationally.<sup>[44]</sup> Recently,<sup>[45]</sup> for example, protein linker units were generated, which directly recognized distinct surfaces of semiconductor materials, whereby no previous functionalization of the linkers was necessary. Thus peptides with semiconductor binding specificity could be used for the controlled placement of structurally related materials in close proximity and the assembly of a variety of practically important materials. Repetitive nanocluster materials can be generated using DNA hybridization. Regular two-dimensional lattices of bacterial cell surface proteins, nanometer-sized and micrometer-sized nucleic acid components, as well as hollow biological compartments have been employed as templates for nanoparticle architectures (e.g., engineered chaperonin proteins<sup>[46]</sup> and hollow tobacco mosaic virus:  $300 \times 18$  nm, inner diameter = 4 nm).<sup>[47]</sup>

The synthesis of hollow three-dimensional arrays of interconnected titania nanospheres<sup>[48]</sup> is achieved by the covering of a mixed latex bead/virus array with an ultrathin layer of titanium alkoxide (Fig. 6). The templates are removed by oxygen plasma, which also converts the titanium alkoxide to titania. In contrast to the infiltration of three-dimensional particle arrays described above, this process leads to a positive copy of the array structure. Biological linkers can also be used in the synthesis of nanoparticles (e.g., immobilized histidine-rich peptide mineralizes gold nanocrystals on template nanotubes with uniform size distribution). Nanocrystal size and packing density are controlled by the adjustment of pH, temperature, and ion concentration.<sup>[49]</sup>

### PROPERTIES AND APPLICATION OF NANOPARTICLE ASSEMBLIES

Ordered colloidal systems<sup>[50]</sup> have lattice spacings ranging from nanometers to micrometers. Their resulting ability to diffract ultraviolet, visible, and near-infrared light makes them useful for sensors, narrow-band optical filters, optical switches, photonic bandgap materials, waveguides, and other types of optical and electrooptical devices.

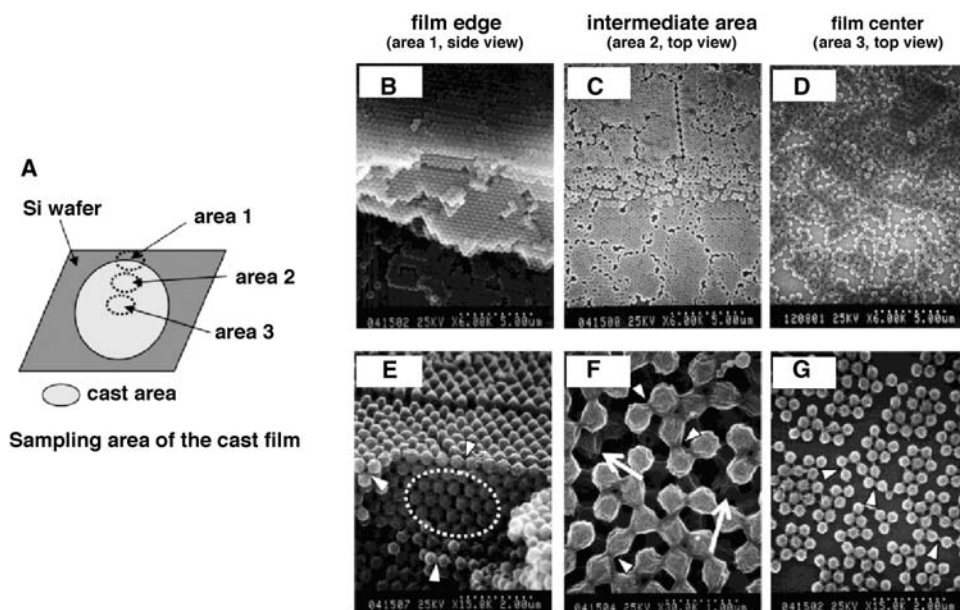


**Fig. 6** Scanning electron microscopy images of titania-coated multilayers of latex particles. (A) Schematic representation of the sampling area. The series of parts B–D and E–G were obtained before and after the oxygen plasma process, respectively. Images in parts B and E are obtained at the edge of the cast area (area 1). Images in parts C and F are obtained around the intermediate cast area (area 2). Images in parts D and G are obtained in the center of cast area (area 3). *Source:* From Ref.<sup>[48]</sup>; ©American Chemical Society, 2003.

However, the arrangement of metallic nanoparticles (a few nanometers in size) in close-packed structures with  $\sim 1$  nm interparticle spacing leads to the formation of tunneling junctions, which have electrical capacitance values of about  $10^{-19}$  F. Such small capacitances allow single-electron tunneling (i.e., controlled charge transport) at room temperature. This ability has been recognized as a fundamental concept for ultimate miniaturization in electronics.<sup>[51]</sup> Single-electron devices based on single nanoparticles trapped between two electrodes<sup>[52]</sup> and nanoparticles immersed in a polymer matrix<sup>[53]</sup> have been reviewed elsewhere and are therefore not discussed in the following.

### Charge Transfer in Two-Dimensional Nanoparticle Arrays

Langmuir films of hydrocarbon-functionalized silver quantum dots (2–5 nm) show transition from classical behavior to quantum-mechanical coupling when the interparticle distance is reduced to below  $12 \text{ \AA}$ .<sup>[19]</sup> Reversible insulator-to-metal transitions occur when interparticle spacing is decreased to  $< 5 \text{ \AA}$ .<sup>[19]</sup> This tuning capability shows that the electronic band structure of a solid made of quantum dots can be tailored by the adjustment of wave function overlap of adjacent particles. Recently, a theoretical description supporting bandgap modulation by interparticle spacing was

published.<sup>[54]</sup> Compressed hexagonal, closed-packed Langmuir films are transferable to any kind of substrate as Langmuir–Schaeffer films, thus permitting the parallel fabrication of single-electron, solid-state capacitance devices, which show Coulomb blockade as well as step structures reminiscent of Coulomb staircase.<sup>[20]</sup>

One major problem of nanoparticle array formation is the finite distribution of particle sizes in the array, leading to disorder, which in turn affects the charge transport through the arrays.<sup>[55]</sup> Beverly et al. found that the transition temperature between different transport regimes (mobility and hopping) in two-dimensional arrays depends on array disorder. As a result of their study, they predict that a metal–insulator transition will be observed with size distributions  $< 3\%$ . Three types of disorder that can be found in nanoparticle arrays are: 1) global structural disorder; 2) local structural disorder (i.e., interparticle coupling); and 3) charge disorder. Parthasarathy, Lin, and Jaeger<sup>[56]</sup> show that current–voltage characteristics of arrays with long-range order are well fit by single-power law, whereas a sufficiently large amount of disorder leads to distinct deviations from single-power law.

### Nanoparticle Arrays in Photonic Devices

Photonic crystals are spatially periodic arrays of particles arranged within a medium of different dielectric

constants. Their effect on propagation of electromagnetic waves can be compared to that of electrons in semiconductors. They combine the quantum confinement of electronic states with simultaneous phonon confinement in the same structure. Photonic bandgap structures (PBS) were originally proposed in 1993 by Yablonovitch.<sup>[57]</sup> The development of PBS was initiated by the need of a photonic bandgap in quantum optics. The realization of photonic bandgap crystals could lead to miniaturization and high-speed performance of optical integrated circuits. They also have profound applications in telecommunications, lasers, fiber optics, data processing, and display technologies. The size of the photonic gap is determined by: 1) refractive index contrast (refractive index of material vs. surrounding substance), and 2) filling fraction (percentage of volume that is occupied by voids). Wang et al.<sup>[58]</sup> theoretically predict that metal nanoparticles self-assembled into three-dimensional structures could be used as photonic bandgap crystals because of a complete gap below the plasma frequency.

Fig. 7 displays an inverse silicon opal with a complete three-dimensional bandgap near  $1.5\ \mu\text{m}$ .<sup>[59]</sup> Controlling the interactions of light and materials for photonic device application at nanoscale dimensions requires structures that guide electromagnetic energy with a lateral mode confinement at below the diffraction limit of light, the so-called waveguides. Closely spaced silver nanorods have been employed in a plasmon waveguide, which shows electromagnetic energy transport from a source to a detector over distances of  $0.5\ \mu\text{m}$ .<sup>[60]</sup> Numerous applications are possible for light-guiding and light-focusing elements operating below the diffraction limit. A regular gold nanoparticle array deposited on a dielectric waveguide could be utilized for the design of two-dimensional photonic devices in the visible and the infrared (IR), which are relevant for optical communication and microlasers.<sup>[61]</sup>

### Data Storage Media

Magnetic nanoparticle arrays<sup>[62]</sup> can serve as high-density data storage devices, magnetoelectronic devices, and patterned media. Each nanoparticle could store one bit of data, implying densities in the  $150\ \text{Gbit cm}^{-2}$  range for particles in the few nanometers size range. Magnetic logic gates can be realized by manipulation of data through magnetostatic interactions between chains of magnetic elements.

### CONCLUSION

Two-dimensional and three-dimensional arrays of nanoparticles represent a new class of electronic materials with promising properties necessary for their

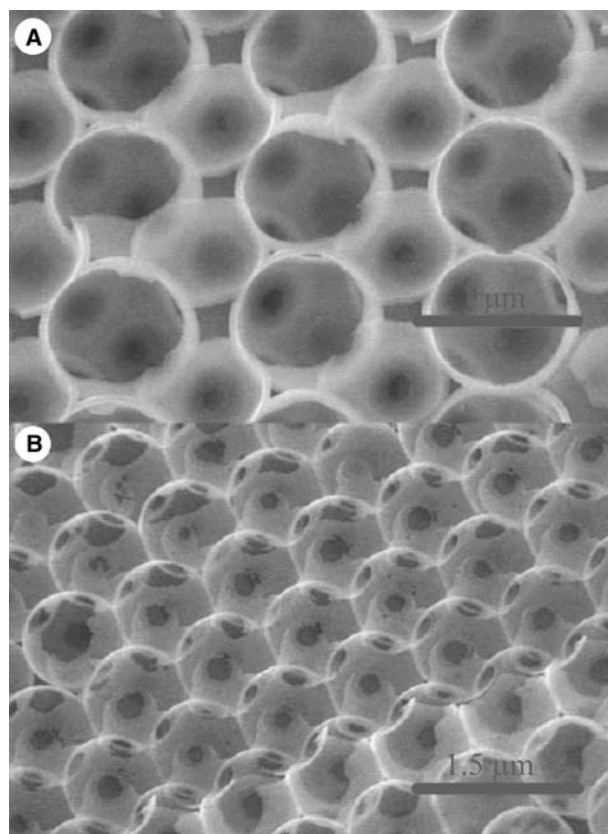


**Fig. 7** Scanning electron microscopy images of internal facets of silicon inverse opal: (A) [110] facet; (B) [111] facet. *Source:* Reprinted with permission from Ref.<sup>[59]</sup>. ©2000 Nature.

application in small-scale electronic devices. In particular, the fact that their band structures can be engineered by simply changing: 1) the size of nanoparticles comprising the array; 2) the capping and/or spacer ligands in between particles; or 3) the packing order in the array makes them suitable candidates. Despite the fact that considerable research focuses on nanoparticle synthesis and assembly, there are still remaining significant open tasks and questions. One major task emerges—it is desirable to develop new, or to improve existing, syntheses toward even smaller size distributions ( $\sigma \leq 3\%$ ).

Metal nanowires are envisioned as another class of useful building blocks for electronic circuits.<sup>[63]</sup> Their assembly employs the distinct surface chemistry of differently derivatized wires with planar surfaces (Fig. 8, top). The same principle is utilized to interconnect two nanowires in a perpendicular fashion by binding them selectively with bifunctionalized spacers, which opens up the opportunity to construct three-dimensional circuits. High-voltage, anodized, porous aluminum oxide membranes are used as templates to grow wires with sections of alternating materials (i.e., metals, insulators, semiconductors, and/or molecules).

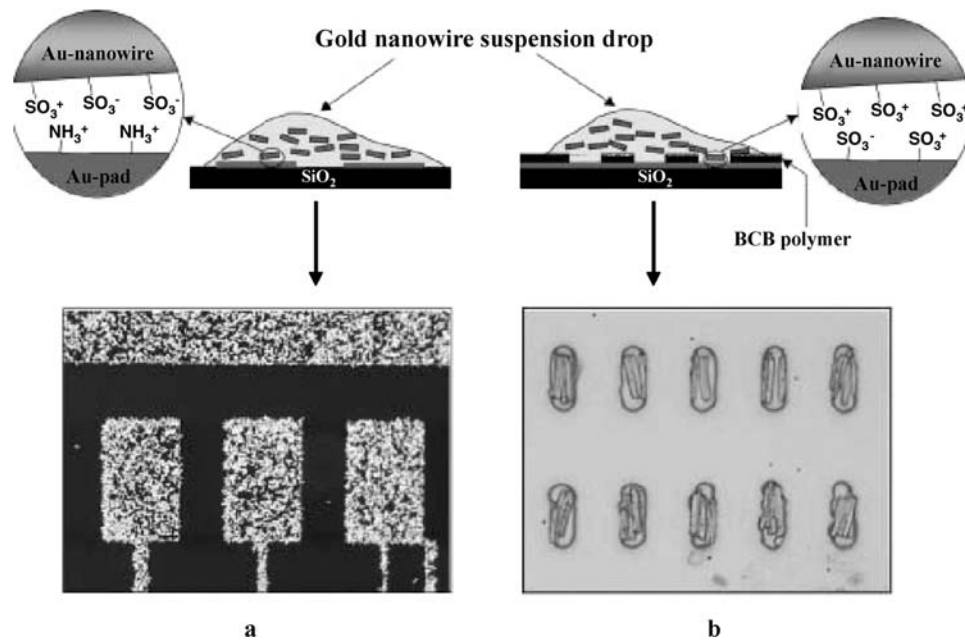


**Fig. 8** Top: Scheme showing the selective adhesion and alignment of negatively charged gold nanowires on lithographically patterned surfaces. Bottom: (A) Dark field optical micrograph ( $500\times$  magnification) of gold nanowires on '2-mercaptoethylamine derivatized gold pads patterned on a  $\text{SiO}_2/\text{Si}$  wafer. (B) Bright field optical micrograph ( $1000\times$  magnification) of gold wires in long wells ( $4\mu\text{m} \times 8\mu\text{m} \times 600\text{nm}$  deep) chemically etched in a divinylsiloxanebis(benzocyclobutene) (BCB) polymer layer on Au. The Au metal at the bottom of the wells is derivatized with '2-mercaptoethanesulfonic acid. Source: Reprinted with permission from Ref.<sup>[63]</sup>.

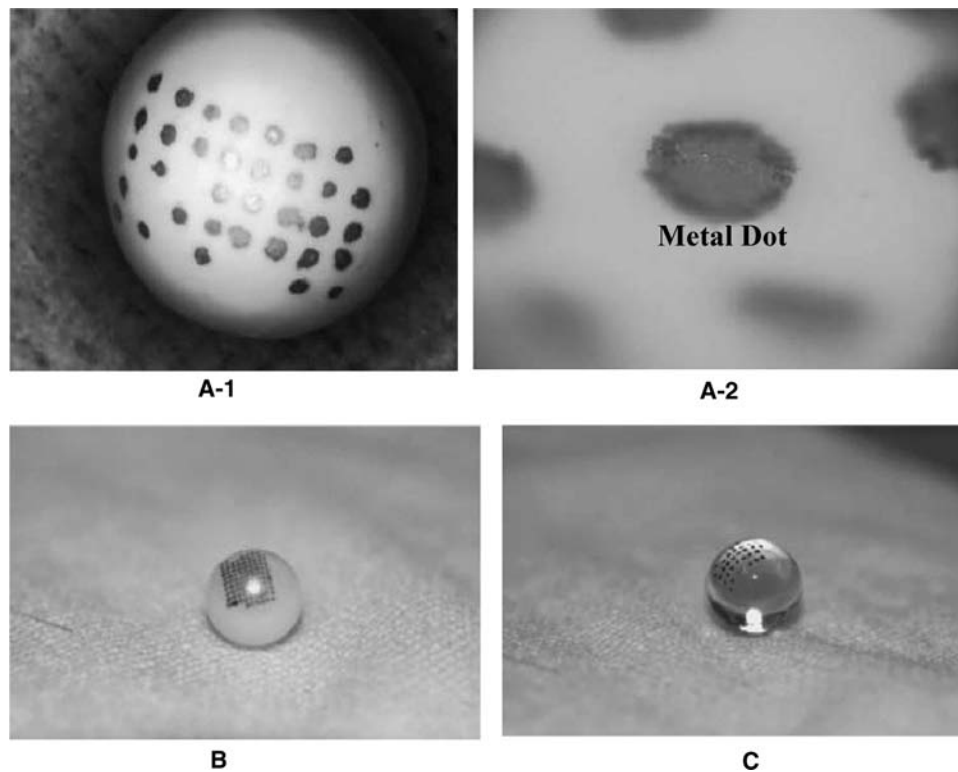


**Fig. 9** Metal dot grid array on various spheres. (A-1) Metal dot grid array on  $\text{Al}_2\text{O}_3$  sphere ( $\phi^3$ , 10 mm). (a-2) Magnified view of (a-1). (B) Metal dot grid array on nylon sphere ( $\phi^3$ , 9.5 mm). (C) Metal dot grid array on glass sphere ( $\phi^3$ , 12 mm). Source: Reprinted from Ref.<sup>[65]</sup> with permission from Elsevier.



Wires are released by the chemical etching of the membrane and the bottom electrode. The  $\text{Al}_2\text{O}_3$  membrane can also be removed independently of the bottom electrode, resulting in anchored, free-standing wires, which in a second process step can be coated with additional materials. Silica-coated silver wires with core diameters of 30–40 nm, controlled sheath thicknesses in the range of 2–100 nm, and lengths from 2 to  $\sim 50 \mu\text{m}$  could find use as interconnects in fabricating nanoelectric devices.<sup>[64]</sup>  $\text{SiO}_2/\text{Ag}$  wires form well-dispersed solutions in water, alcohol, and acetone without the need for additional surfactants and their cores can be readily removed by immersion into an aqueous solution of ammonia with  $\text{pH} \sim 11$ . The combination of nanowires, nanoparticles, and nanoparticle arrays presents a powerful tool for circuitry with three-dimensional architectures.

Plating technology allows selective plating of metals where a seed material has been drawn.<sup>[65]</sup> The process is divided into three steps: 1) drawing of amino–silane coupler as seed material; 2) activation of the catalyst; and 3) electroless metal plating. Multilayer circuits with interconnections can be fabricated using this approach. The method can easily be applied to the transfer of structures onto three-dimensional objects such as spheres, enabling the so-called ball semiconductor technology (Fig. 9).

A discovery by Weismüller et al.<sup>[66]</sup> reveals another intriguing area of application for nanoparticles in an area other than electronics or optics. They found that commercially available black Pt with 6 nm grain size sintered into a nanoporous sample displayed charge-induced reversible strain. On application of a voltage, the porous metal composite experienced an unprecedented maximum volume change of  $\sim 0.45\%$ , which is large enough to do mechanical work. Baughman<sup>[67]</sup> suggests using such materials as artificial muscles, and emphasizes that observed volume changes correspond to negative pressure, something that is not easily realized otherwise.

Nanoparticles are versatile building blocks, which can be self-assembled into two-dimensional and three-dimensional structures. Their size-dependent electronic properties make them unique candidates for future electronics and optics applications.

## REFERENCES

1. Takahashi, Y.; Ono, Y.; Fujiwara, A.; Inokawa, H. Silicon single-electron devices. *J. Phys., Condens. Matter* **2002**, *14*, R995.
2. Chen, Y.; Pepin, A. Nanofabrication: Conventional and nonconventional methods. *Electrophoresis* **2001**, *22*, 187.
3. Murray, C.B.; Kagan, C.R.; Bawendi, M.G. Synthesis and characterization of monodisperse nanocrystals and close-packed nanocrystal assemblies. *Annu. Rev. Mater. Sci.* **2000**, *30*, 545.
4. Trindade, T.; O'Brien, P.; Pickett, N.L. Nanocrystalline semiconductors: Synthesis, properties and perspective. *Chem. Mater.* **2001**, *13*, 3843.
5. Xia, Y.; Gates, B.; Yin, Y.; Lu, Y. Monodispersed colloid spheres: Old materials with new applications. *Adv. Mater.* **2000**, *12*, 693.
6. Caruso, F. Nanoengineering of particle surfaces. *Adv. Mater.* **2001**, *13*, 11.
7. Goia, D.V.; Matijević, E. Preparation of monodispersed metal particles. *New J. Chem.* **1998**, *22*, 1203.
8. Templeton, A.C.; Wuelfing, W.P.; Murray, R.W. Monolayer-protected cluster molecules. *Acc. Chem. Res.* **2000**, *33*, 27.
9. Dorogi, M.; Gomez, J.; Osifchin, R.; Andres, R.P.; Reifengerger, R. Room-temperature Coulomb blockade from a self-assembled molecular nanostructure. *Phys. Rev., B* **1995**, *52*, 9071.
10. Puentes, V.F.; Zachnet, D.; Erdonmez, C.K.; Alivisatos, A.P. Synthesis of hcp-Co nanodisks. *J. Am. Chem. Soc.* **2002**, *124*, 12874.
11. Métraux, G.S.; Cao, Y.C.; Jin, R.; Mirkin, C.A. Triangular nanoframes made of gold and silver. *Nano Lett.* **2003**, *3*, 519.
12. Stöber, W.; Fink, A.; Bohn, E. Controlled growth of monodispersed silica spheres in micron size range. *J. Colloid Interface Sci.* **1968**, *26*, 62–69.
13. Caruso, F. Hollow capsule processing through colloidal templating and self-assembly. *Chem. Eur. J.* **2000**, *6*, 413.
14. Sun, Y.; Mayers, B.T.; Xia, Y. Template-engaged replacement reaction: A one-step approach to the large-scale synthesis of metal nanostructures with interiors. *Nano Lett.* **2002**, *2*, 481.
15. Shipway, A.N.; Katz, E.; Willner, I. Nanoparticle arrays on surfaces for electronic, optical, and sensor applications. *ChemPhysChem* **2000**, *1*, 18–52.
16. Radloff, C.; Moran, C.E.; Jackson, J.B.; Halas, N.J. Nanoparticles: Building Blocks for Functional Nanostructures. In *Molecular Electronics*; Reed, M.A., Lee, T., Eds.; American Scientific Publishers: Stevenson Ranch, 2003; 229–262.
17. Fendler, J.H. Chemical self-assembly for electronic application. *Chem. Mater.* **2001**, *13*, 3196.
18. Quesada-Perez, M.; Callejas-Fernandez, J.; Hildalgo-Alvarez, R. Interaction potentials, structural ordering and effective charges in dispersions of charged colloidal particles. *Adv. Colloid Interface Sci.* **2002**, *95*, 295.
19. Collier, C.P.; Saykally, R.J.; Shiang, J.J.; Henrichs, S.E.; Heath, J.R. Reversible tuning of silver quantum dot monolayers through the metal–insulator transition. *Science* **1997**, *277*, 1978.
20. Markovich, G.; Leff, D.V.; Chung, S.-W.; Soye, H.M.; Dunn, B.; Heath, J.R. Parallel fabrication and single-electron charging of devices based on ordered, two-dimensional phases of originally functionalized metal nanocrystals. *Appl. Phys. Lett.* **1997**, *70*, 3107.
21. Dimitrov, A.S.; Nagayama, K. Steady-state unidirectional convective assembling of fine particles into two-dimensional arrays. *Chem. Phys. Lett.* **1995**, *243*, 462.

22. Dushkin, C.D.; Lazarov, G.S.; Kotsev, S.N.; Yoshimura, H.; Nagayama, K. Effect of growth conditions on the structure of two-dimensional latex crystals: Experiment. *Colloid Polym. Sci.* **1999**, *277*, 914.
23. Deegan, R.D.; Bakajin, O.; Dupont, T.F.; Huber, G.; Nagel, S.R.; Witten, T.A. Contact line deposits in an evaporating drop. *Phys. Rev., E* **2000**, *62*, 756.
24. Lin, X.M.; Jaeger, H.M.; Sorensen, C.M.; Klabunde, K.J. Formation of long-range-ordered nanocrystal superlattices on silicon nitride substrates. *J. Phys. Chem., B* **2001**, *105*, 3353.
25. Velev, O.D.; Lenhoff, A.M.; Kaler, E.W. A class of microstructured particles through colloidal crystallization. *Science* **2000**, *287*, 2240.
26. Giersing, M.; Mulvaney, P. Preparation of ordered colloid monolayers by electrophoretic deposition. *Langmuir* **1993**, *9*, 3408.
27. Solomentsev, Y.; Böhmer, M.; Anderson, J.L. Particle clustering and pattern formation during electrophoretic deposition: A hydrodynamic model. *Langmuir* **1997**, *13*, 6058.
28. Meseguer, F.; Blanco, A.; Míguez, H.; Gracia-Santamaría, F.; Ibasate, M.; López, C. Synthesis of inverse opals. *Colloids Surf., A* **2002**, *202*, 281.
29. Docoslis, A.; Alexandridis, P. One-, two-, and three-dimensional organization of colloidal particles using nonuniform alternating current electric fields. *Electrophoresis* **2002**, *23*, 2174.
30. Hermanson, K.D.; Lumsdon, S.O.; Williams, J.P.; Kaler, E.W.; Velev, O.D. Dielectrophoretic assembly of electrically functional microwires from nanoparticle suspensions. *Science* **2001**, *294*, 1082.
31. Ristenpart, W.D.; Aksay, I.A.; Saville, D.A. Electrically guided assembly of planar superlattices in binary colloidal suspensions. *Phys. Rev. Lett.* **2003**, *90*, 128303.
32. Nawa, M.; Baba, R.; Nakabayashi, S.; Dushkin, C. Ordering effect of high magnetic field on silver nanoparticle arrays for electron transfer devices. *Nano Lett.* **2003**, *3*, 293.
33. Wen, W.; Wang, N.; Zheng, D.W.; Chen, C.; Tu, K.N. Two- and three-dimensional arrays of magnetic microspheres. *J. Mater. Res.* **1999**, *14*, 1186.
34. Ye, Y.-H.; Badilescu, S.; Truong, V.-V.; Rochon, P.; Natansohn, A. Self-assembly of colloidal spheres on patterned substrates. *Appl. Phys. Lett.* **2001**, *79*, 872.
35. Xia, Y.; Whitesides, G.M. Soft lithography. *Annu. Rev. Mater. Sci.* **1998**, *28*, 153.
36. Yang, S.M.; Míguez, H.; Ozin, G.A. Opal circuits of light-planarized microphotonic crystal chips. *Adv. Funct. Mater.* **2002**, *12*, 425.
37. Hua, F.; Shi, J.; Lvov, Y.; Cui, T. Patterning of layer-by-layer self-assembled multiple types of nanoparticle thin films by lithographic technique. *Nano Lett.* **2002**, *2*, 1219.
38. Spatz, J.P. Nano- and micropatterning by organic-inorganic templating of hierarchical self-assembled structures. *Angew. Chem., Int. Ed.* **2002**, *41*, 3359.
39. Misner, M.J.; Skaff, H.; Emrick, T.; Russell, T.P. Direct deposition of nanoparticles using diblock copolymer templates. *Adv. Mater.* **2003**, *15*, 221.
40. Wang, S.; Sato, S.; Kimura, K. Preparation of hexagonal-closed-packed colloidal crystals of hydrophilic monodisperse gold nanoparticles in bulk aqueous solution. *Chem. Mater.* **2003**, *15*, 2445.
41. Schmid, G.; Bäuml, M.; Beyer, N. Ordered two-dimensional monolayers of Au<sub>55</sub> clusters. *Angew. Chem., Int. Ed.* **2000**, *39*, 181.
42. Andres, R.P.; Bielefeld, J.D.; Henderson, J.I.; Janes, D.B.; Kolagunta, V.R.; Kubiak, C.P.; Mahoney, W.J.; Osifchin, R.G. Self-assembly of a two-dimensional superlattice of molecularly linked metal clusters. *Science* **1996**, *273*, 1690.
43. Andres, R.P.; Datta, S.; Janes, D.B.; Kubiak, C.P.; Reifenberger, R. The Design, Fabrication and Electronic Properties of Self-Assembled Molecular Nanostructures. In *Handbook of Nanostructured Materials and Nanotechnology*; Nalwa, H.S., Ed.; American Press: San Diego, 2000; *3*, 179–231.
44. Niemeyer, C.M. Nanoparticles, proteins, and nucleic acids: Biotechnology meets materials science. *Angew. Chem., Int. Ed.* **2001**, *40*, 4128.
45. Whaley, S.R.; English, D.S.; Hu, E.L.; Barbara, P.F.; Belcher, A.M. Selection of peptides with semiconductor binding specificity for directed nanocrystal assembly. *Nature* **2000**, *405*, 665.
46. McMillan, R.A.; Paavola, C.D.; Howard, J.; Chan, S.L.; Zaluzec, N.J.; Trent, J.D. Ordered nanoparticle arrays formed on engineered Chaperonin protein templates. *Nat. Mater.* **2002**, *1*, 247.
47. Dujardin, E.; Peet, C.; Stubbs, G.; Culver, J.N.; Mann, S. Organization of metallic nanoparticles using tobacco mosaic virus templates. *Nano Lett.* **2003**, *3*, 413.
48. Fujikawa, S.; Kunitake, T. Surface fabrication of hollow nanoarchitectures of ultrathin titania layers from assembled latex particles and tobacco mosaic viruses as templates. *Langmuir* **2003**, *19*, 6545.
49. Djalali, R.; Chen, Y.-F.; Matsui, H. Au nanocrystal growth on nanotubes controlled by conformations and charges of sequenced peptide templates. *J. Am. Chem. Soc.* **2003**.
50. Gong, T.; Marr, D.W.M. Electrically switchable colloidal ordering in confined geometries. *Langmuir* **2001**, *17*, 2301.
51. Simon, U. Charge transport in nanoparticle arrangements. *Adv. Mater.* **1998**, *10*, 1487.
52. Feldheim, D.L.; Keating, C.D. Self-assembly of single electron transistors and related devices. *Chem. Soc. Rev.* **1998**, *27*, 1.
53. Godovsky, D.Y. Device applications of polymer-nanocomposites. *Adv. Polym. Sci.* **2000**, *153*, 163.
54. Remacle, F.; Levine, R.D. Quantum dots as chemical building blocks: Elementary theoretical considerations. *ChemPhysChem* **2001**, *2*, 20.
55. Beverly, K.C.; Sampaio, J.F.; Heath, J.R. Effects of size dispersion disorder on the charge transport in self-assembled 2-D Ag nanoparticle arrays. *J. Phys. Chem., B* **2002**, *106*, 2131.
56. Parthasarathy, R.; Lin, X.-M.; Jaeger, H.M. Electronic transport in metal nanocrystal arrays: The effect of structural disorder on scaling behavior. *Phys. Rev. Lett.* **2001**, *87*, 186807.



57. Yablonovitch, E. Photonic band-gap structures. *J. Opt. Soc. Am., B* **1993**, *10*, 283.
58. Wang, Z.; Chan, C.T.; Zhang, W.; Ming, N.; Sheng, P. Three-dimensional Self-assembly of metal nanoparticles: Possible photonic crystal with a complete gap below the plasma frequency. *Phys. Rev., B* **2001**, *64*, 113108.
59. Blanco, A.; Chomski, E.; Grabtchak, S.; Ibisate, M.; John, S.; Loenard, S.W.; Lopez, C.; Meseguer, F.; Miguez, H.; Mondia, J.P.; Ozin, G.A.; Toader, O.; van Driel, H.M. Large-scale synthesis of a silicon photonic crystal with a complete three-dimensional bandgap near 1.5 micrometers. *Nature* **2000**, *405*, 437.
60. Maier, S.A.; Kik, P.G.; Atwater, H.A.; Meltzer, S.; Harel, E.; Koel, B.E.; Requicha, A.A.G. Local detection of electromagnetic energy transport below the diffraction limit in metal nanoparticle plasmon waveguides. *Nat. Mater.* **2003**, *2*, 229.
61. Linden, S.; Kuhl, J.; Giessen, H. Controlling the interaction between light and gold nanoparticles: Selective suppression of extinction. *Phys. Rev. Lett.* **2001**, *86*, 4688.
62. Ross, C.A. Patterned magnetic recording media. *Annu. Rev. Mater. Res.* **2001**, *31*, 203.
63. Kovtyukhova, N.I.; Mallouk, T.E. Nanowires as building blocks for self-assembling logic and memory circuits. *Chem. Eur. J.* **2002**, *8*, 4355.
64. Yin, Y.; Lu, Y.; Sun, Y.; Xia, Y. Silver nanowires can be directly coated with amorphous silica to generate well-controlled coaxial nanocables of silver/silica. *Nano Lett.* **2002**, *2*, 427.
65. Konishi, S.; Honsho, K.; Yanada, M.; Minami, I.; Kimura, Y.; Ikeda, S. Direct drawing method for micro-fabrication based on selective metal plating technology. *Sens. Actuators, A* **2003**, *103*, 135.
66. Weismüller, J.; Viswanath, R.N.; Kramer, D.; Zimmer, P.; Würschum, R.; Gleiter, H. Charge-induced reversible strain in metal. *Science* **2003**, *300*, 312.
67. Baughman, R.H. Muscles made from metal. *Science* **2003**, *300*, 268.

# Nanoparticle Assemblies: Magnetic Properties

Xiangcheng Sun

Center for Materials for Information Technology, University of Alabama,  
Tuscaloosa, Alabama, U.S.A.

## INTRODUCTION

Studies on system of magnetic nanoparticles with sizes in the nanometer scale have been the object of intensive research because of their many technological applications and unique magnetic properties that differ considerably from those of bulk materials.<sup>[1–3]</sup> Nanometer magnetic particles exhibit specific properties such as superparamagnetism<sup>[4]</sup> because of their very small sizes and fundamental change in the coordination, symmetry, and confinement.<sup>[1–3]</sup> Superparamagnetism is regarded as a unique feature of magnetic nanoparticles and has great relevance to modern potential technologies including magnetic resonance imaging contrast agents, data lifetime in high-density information storage, and ferrofluid technology.<sup>[5,6]</sup> However, because of the various contributions (i.e., magnetocrystalline, surface, shape, and dipolar anisotropy), the transition from superparamagnetic state to collective magnetic excitations (i.e., spin-glass) could occur in the interacting magnetic nanoparticles systems.<sup>[7,8]</sup> The study on the mechanism of superparamagnetic properties in the system of fine magnetic particles will facilitate the control of superparamagnetic behavior and be favorable for their technological applications.<sup>[9]</sup>

## OVERVIEW

Following the discovery of the method for the preparation of fullerenes in macroscopic quantities by the so-called Kratschmer–Huffman carbon-arc method,<sup>[10]</sup> some novel magnetic system of carbon-coated ferromagnetic materials, e.g., Fe, Co, and Ni, had successfully been obtained.<sup>[1,4]</sup> Interest was paid not only to the properties of the encapsulated particles, in particular, to those involving novel magnetic properties of ferromagnetic materials.

As an alternative magnetic nanoparticles system, carbon-encapsulated ferromagnetic materials should be considered good candidates for studying the effect of particle size on crystalline structure, magnetization process, magnetic interparticle interaction effect,<sup>[11–14]</sup> superparamagnetism,<sup>[3,4,15]</sup> and quantum relaxation of magnetization.<sup>[16]</sup>

We herein use the modified arc-discharge (carbon-arc) method to generate two types of nickel nanoparticles [Ni(C) and Ni(O)] and iron nanoparticles [Fe(C) and Fe(O)] in methane and in a mixture of H<sub>2</sub> and Ar atmospheres. High-resolution transmission electron microscopy (HRTEM), nanoscale electron diffraction (SAED), and X-ray diffraction (XRD) were used to investigate the remarkable microstructure. Moreover, various magnetic measurements were performed by superconducting quantum interference device magnetometer (SQUID) and Mössbauer magnetometer at different temperature and magnetic fields. Typical and modified superparamagnetic behaviors have been evidenced. The relationships between the microstructure and novel magnetic behavior have also been established.

## EXPERIMENTAL PROCEDURE

The detailed experimental apparatus (modified arc discharge) was fully illustrated elsewhere.<sup>[17]</sup> The pure material (bulk Ni and Fe) to be evaporated was laid on a water-cooled copper stage, which served as the anode. A copper arm that was also water-cooled supports the upper carbon rod, which served as the cathode. After the chamber was evacuated, the desired gas of methane or a mixture of H<sub>2</sub> and Ar were back-filled as a reactant gas to reach the desired pressure; the distance between the two electrodes can be adjusted from outside the chamber, so that the arc can be started and controlled during a continuous operation.

A JEOL-2010EX high-resolution transmission electron microscope (HRTEM) operated at 200 keV was used to reveal the internal structure and morphology of the particle. It also allowed us to record selected area diffraction (SAED) analysis information. X-ray diffraction (XRD) was conducted using CuK $\alpha$  radiation in a Siemens X-ray diffractometer to identify the different nanophases and the crystal structure of nanoparticles.

Mössbauer spectra were recorded at room temperature using an Austin Science Associates Model S-600 spectrometer with a <sup>57</sup>Co/Rh source. The absorption spectra were fitted by using the *NORMOS* program that

used the input parameters as a first approximation to fit the experimental curve.

The magnetization (d.c. susceptibility) measurements were carried out using a quantum design superconducting quantum interference device (SQUID) magnetometer in the temperature range from 2 to 300 K at different applied magnetic fields. For the zero-field-cooled (ZFC) magnetization measurements, the sample was first cooled down to 2 K without the applied field, after which the magnetic field was applied. The sample was then slowly warmed up to 300 K for subsequent measurements of the magnetic moments (ZFC). Thereafter, for the field-cooled (FC) magnetization measurement, the sample was cooled down to 2 K without turning the magnetic field off; measurements of magnetic moment could be obtained at each intermediate temperature (FC). The magnetization as a function of temperature [ $M(T)$ ] reveals some of the main features of a superparamagnetic system. The average blocking temperature ( $T_B$ ), below which the particle moments are blocked, is usually considered an important parameter when characterizing the magnetic behavior of a magnetic nanoparticles system. In general,  $T_B$  can be obtained by analyzing the zero-field-cooled and field-cooled (ZFC/FC) magnetization vs. temperature curve. Above  $T_B$ , thermal fluctuations can flip the direction of the magnetic moment; in addition, no hysteresis is observed in the  $M(H)$  measurement. When the particles interact, magnetic dipole–dipole interactions become significant (stronger). This dipole interaction may be either ferromagnetic or antiferromagnetic depending upon the dipole orientations. In those cases, the superparamagnetic

relaxation process becomes highly blocked and the magnetic dipole–dipole interactions may become important in determining the magnetic state of the nanoparticle system. Thus a system of nanometer particles with disordered magnetic moments may exhibit spin-glass behavior (collective behavior), such as that observed in the  $\gamma$ - $\text{Fe}_2\text{O}_3$  magnetic particle systems.<sup>[18]</sup> In such systems, the irreversible temperature,  $T_{\text{irr}}$ , is defined by the point where the ZFC and FC branches of  $M(T)$  curves separate.

## RESULTS AND DISCUSSION

### The Assemblies of Ni(C) and Ni(O) Particle Systems

Powder X-ray diffraction profiles of Fig. 1A clearly show the presence of a majority of fcc Ni, with a small amount of hexagonal  $\text{Ni}_3\text{C}$  present from carbon-encapsulated Ni nanoparticles. Additionally, that the hexagonal  $\text{Ni}_3\text{C}$  phase is detectable using XRD suggests that the hexagonal  $\text{Ni}_3\text{C}$  most likely is one single phase along with majority of fcc Ni phase in these assemblies of Ni(C) nanoparticles. However, the main reflection peaks of XRD (Fig. 1B) for pure Ni nanoparticles coated with NiO layers are similar to those of the pure fcc Ni phase, except that the peaks are broader. One can infer from such a XRD study that the concentration of NiO oxide on the surface of Ni(O) nanoparticles should be less than a few percent. This is quite similar to the results reported before.<sup>[13]</sup> The average grain size estimated from the XRD

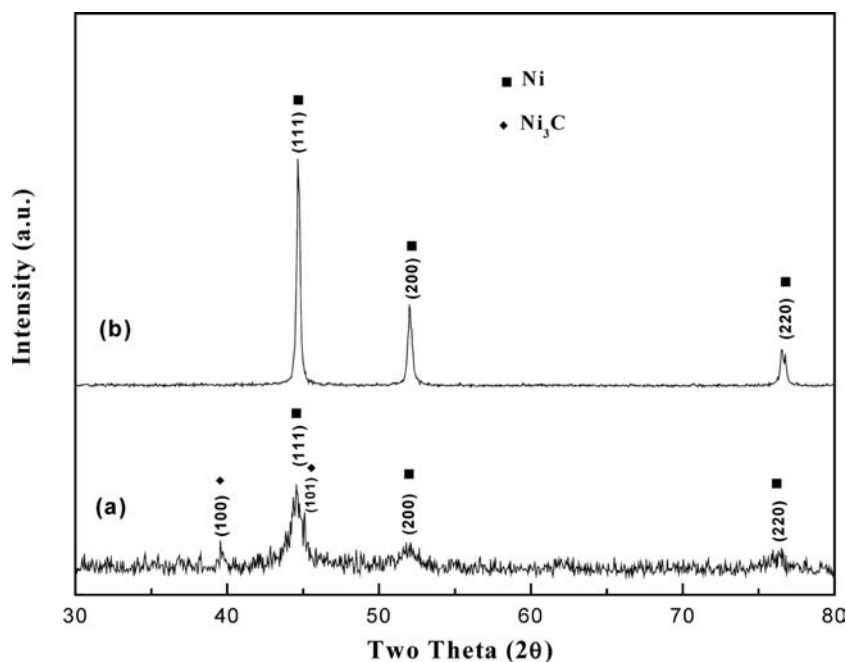


**Fig. 1** Powder X-ray diffraction patterns of Ni(C) (A) and Ni(O) (B) nanoparticles at room temperature. *Source:* From Ref.<sup>[24]</sup>.

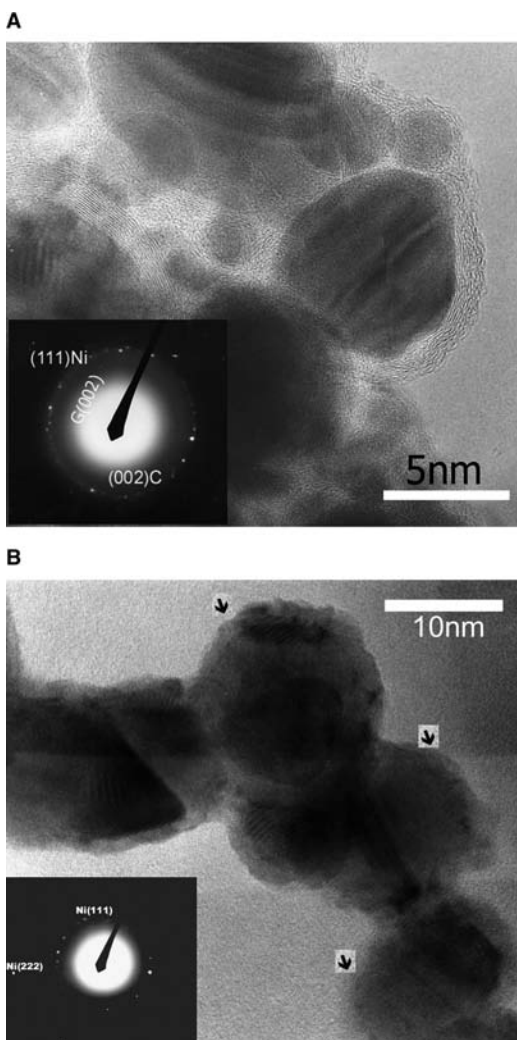


**Fig. 2** (A) HRTEM image and corresponding SAED patterns of Ni(C) nanoparticles. Note that arrows indicate the carbon layers; G symbol is carbon phase; C symbol is Ni<sub>3</sub>C phase. (B) HRTEM image and corresponding SAED patterns of Ni(O) nanoparticles. The arrows indicate NiO oxide layers. *Source:* From Ref.<sup>[24]</sup>.

patterns using the Scherrer formula shows that these two kinds of Ni nanoparticles have an average grain size of 10–15 nm, which is consistent with the corresponding HRTEM images (Fig. 2).

High-resolution transmission electron microscopy images and SAED patterns (Fig. 2A and B) also indicate that most of particles are spherical in shape and do not show any well-developed facets. It is worth noting from Fig. 2A that several carbon layers encapsulating the Ni lattice planes are quite visible. The contiguous carbon fringes around the Ni nanocrystal are good evidence for completed encapsulation by carbon layers. Both fcc-Ni (111) and hexagonal Ni<sub>3</sub>C (101) phases are clearly observed from SAED patterns of Ni(C) particles. In addition, the (002) reflection is

also present from those encapsulated carbon layers. However, only fcc-Ni and NiO phases are verified from SAED patterns of Ni(O) particles (Fig. 2B). Nano-energy dispersive spectroscopy (EDS) analysis can further confirm the presence of Ni, O, and carbon phases in these two-kind Ni particles. Those results are in good agreement with the XRD analysis and HRTEM observations.

One significant morphological characteristic to note, from the HRTEM images (Fig. 2A), is that neither gaps nor intermediate phases are observed between the outer carbon layer and the core materials in the Ni(C) carbon cages. These characteristics typically reflect a growth history of these nanoencapsulated Ni particles, in which carbon atoms dissolve into a molten or solid carbon–metal alloy and then graphite precipitate at the surface during carbon-arc discharge plasma process.<sup>[19]</sup> However, Fig. 2B shows some polycrystalline discontinuities in the layers of the Ni(O) nanoparticles.

Fig. 3 shows the magnetization vs. field plots ( $M$  vs.  $H$  hysteresis loops) at 300 K (Fig. 3A) and 2 K (Fig. 3B) for the assemblies of Ni(C) nanoparticles. Figure 3A indicates a rapid increase with increasing applied magnetic field without saturation because of the superparamagnetic relaxation and the noncollinear moment of the surface spins in the smaller particle assembly.<sup>[20]</sup> Hysteresis is absent with a little remanence and coercivity ( $H_C$ ), which suggests the presence of a long-range magnetic dipole–dipole interaction among the assemblies of superparamagnetic Ni(C) particles. With decreasing temperature, the magnetization of the samples increases and exhibits a symmetric hysteresis loop under both ZFC and FC at 2 K, indicating a transition from superparamagnetic to ferromagnetic behavior. Specifically, the temperature dependence of

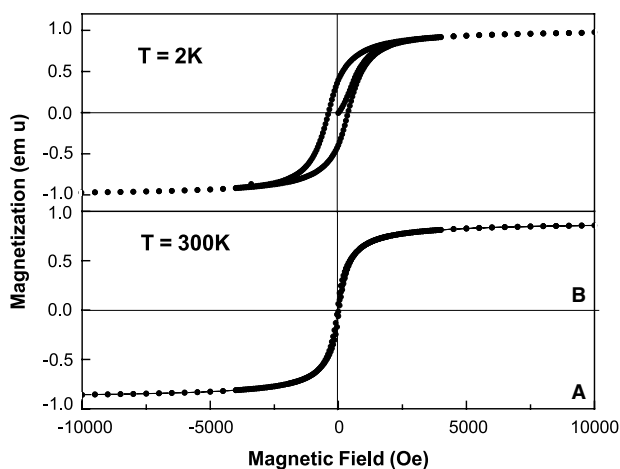


**Fig. 3** (A–B) Field dependence of magnetization for the assemblies of Ni(C) nanoparticles at 2 and 300 K, respectively. *Source:* From Ref.<sup>[24]</sup>.

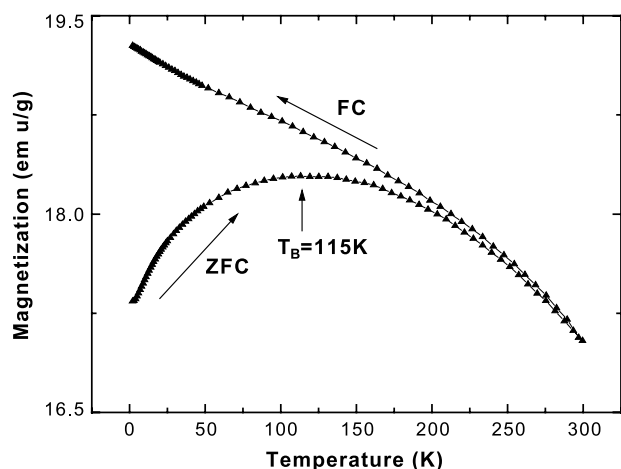


**Fig. 4** Temperature dependence of magnetization for the assemblies of Ni(C) nanoparticles at applied field of 1000 Oe; the blocking temperature is about 115 K. *Source:* From Ref.<sup>[24]</sup>.

the magnetization under the ZFC ( $M_{ZFC}$ ) and FC ( $M_{FC}$ ) conditions gives further confirmation of superparamagnetism in the assemblies of Ni(C) nanoparticles, as shown in Fig. 4.

An important feature to note from Fig. 4 is the temperature at which the  $M_{ZFC}$  curve exhibits a cusp that defines as the blocking temperature ( $T_B$ ). Below  $T_B$ , the superparamagnetic transition is blocked; in other words, the magnetization cannot relax during the time of the measurements. In particular, the well-defined  $T_B$  of the  $M_{ZFC}$  at 115 K and broad blocking temperature ranges are consistent with the particle size distribution as observed from HRTEM images. Furthermore, the continued increase of the  $M_{ZFC}$  and the irreversibility occurring below 225 K are also consistent with the presence of superparamagnetic particles.<sup>[20]</sup>

Therefore for the assemblies of Ni(C) nanoparticles above  $T_B$ , the magnetization could be free to align with the fields during the measurement time, and the curves of magnetization vs. applied field should exhibit no hysteresis loop (Fig. 3A). In such a superparamagnetic state, the relative magnetization  $M/M_s$  can be described by the standard Langevin function,<sup>[21–23]</sup>  $L$ , using the relation:

$$M/M_s(T = 0) = \coth(\mu H/kT) - kT/\mu H$$

where  $M_s(T = 0)$  is the 0 K saturation magnetization of the sample, and  $\mu$  is the particle moment given by  $M_s(V)$  where  $M_s$  is the saturation magnetization of the bulk phase and  $\langle V \rangle$  is the average particle volume.

Fig. 5 shows good agreement with Langevin function of the observed magnetization  $M/M_s$  curves as a function of the applied magnetic fields at room temperature for the assemblies of Ni(C) particles.

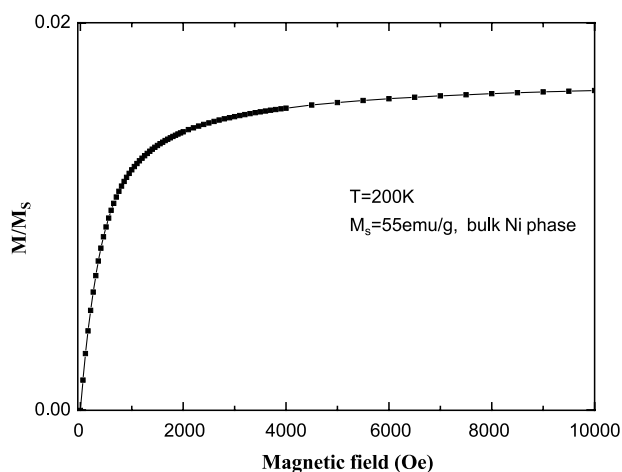


**Fig. 5** Experimental curves of relative magnetization as a function of applied fields at 300 K for the assemblies of Ni(C) nanoparticles. *Source:* From Ref.<sup>[24]</sup>.

Consequently, below the  $T_B$ , a hysteresis loop response is observed (Fig. 3B) because thermal energy is not enough to allow the alignment of particle moments with the applied fields. Consistent with the theory of superparamagnetism,<sup>[15,24,25]</sup> the coercivity,  $H_C$ , has the temperature dependence of  $H_C = H_{C0}[1 - (T/T_B)^{1/2}]$  at lower temperatures.

Fig. 6 shows the variation of the coercivity with temperature for the assemblies of Ni(C) particles. It is evident from this figure that the coercivity ( $H_C$ ) vs. temperature ( $T$ ) data can be fit to the above expression. It is interesting to note, from Fig. 6, that the zero temperature coercivity ( $H_{C0}$ ) is determined to be  $\sim 425$  Oe and the blocking temperature  $T_B$  is determined to be  $\sim 120$  K. Note that this  $T_B$  value is very close to the one that inferred from the sharp maximum of  $M_{ZFC}$  curves.

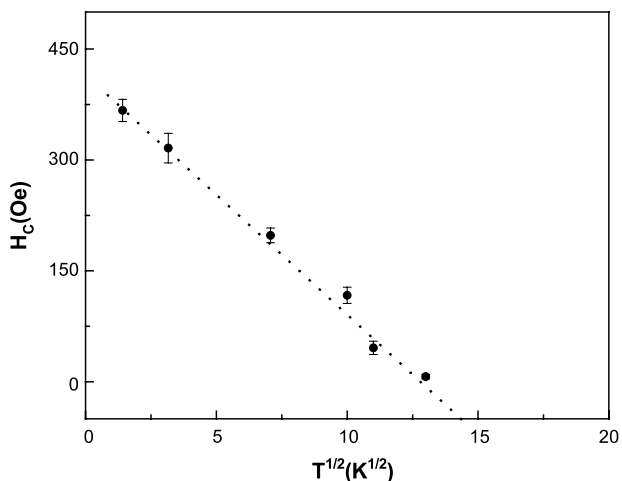


**Fig. 6** Plot of  $H_C(T)$  vs.  $T^{1/2}$  for the assemblies of Ni(C) nanoparticles. The  $T_B$  is near 120 K. *Source:* From Ref.<sup>[24]</sup>.

It is known that a small magnetic particle becomes single domain below some critical size because of the interplay between the energy of dipole fields and domain wall creation.<sup>[26]</sup> Consequently, Ni(C) nanoparticles, with an average size of about 10.5 nm, may be considered as having a single magnetic domain, the origin of its magnetic hysteresis being spin rotation. Thus the magnetic behavior is size-dependent and should be considered in conjunction with thermal energy and surface anisotropy aspects.<sup>[27]</sup> In particular, single-domain particles below a certain critical diameter are greatly affected by temperature fluctuations. From Table 1, at 300 K, it is clear that the  $M_r$  and  $H_C$  values of the assemblies of Ni(C) particles are significantly lower than that of microcrystalline Ni. Compared with 300 K, the assemblies of Ni(C) particles show much larger remanent magnetization ( $M_r$ ) and coercivity ( $H_C$ ) at 2 K. This implies that the thermal energy for demagnetizing becomes dominant over spontaneous magnetization at 300 K for the assemblies of Ni(C) nanoparticles. At 2 K, however, the thermal energy effects decrease significantly, so that the interparticle dipole–dipole interaction and surface anisotropy energy may play a significant role in determining the magnetic behavior.<sup>[27]</sup> It can be supposed that such Ni(C) superparamagnetic particle assemblies exhibit modified superparamagnetic behavior. The larger decrease of remanent magnetization ( $M_r$ ) and coercivity ( $H_C$ ) at  $T > T_B$  for the assemblies of Ni(C) particles is a unique characteristic that associated with modified superparamagnetism.

In addition, from Table 1, the saturation magnetization ( $M_s$ ) of the assemblies of Ni(C) nanoparticle is suppressed in magnitude compared to that of the bulk Ni from microstructural analysis (HRTEM) results. We contribute this result to a small amount of carbon solubility in Ni particles. Hwang et al.<sup>[27]</sup> suggest that the decrease in  $M_s$  is a result of the nonmagnetic or weakly magnetic interface that leads to a decrease in the effective magnetic moment per unit mass. So the possibility is that some carbon (which is diamagnetic)

may have remained inside the Ni nanocrystals as a metastable solid solution, thereby reducing the contribution of the effective magnetic moment during magnetization process.<sup>[27]</sup>

On the other hand, one may suggest that the existence of the small amount of metastable hexagonal Ni<sub>3</sub>C phase in the assemblies of Ni(C) nanoparticles has also affected the magnetization process. The metastability Ni<sub>3</sub>C is generally attributed to the low maximum solubility of carbon in nickel (2.7 at.% at 1600 K). The metastable hexagonal Ni<sub>3</sub>C phase, in particular, is expected to be nonferromagnetic because of strong hybridization between Ni and C orbital except that it remains in a disordered state.<sup>[28]</sup> Therefore the saturation magnetization ( $M_s$ ) from the minority of metastable Ni<sub>3</sub>C phase effect should be ruled out of this study. Thus the gradual decrease in  $M_s$  could be attributed to the nanocrystalline nature of the encapsulated particles, coupled with possible carbon solution in Ni nanoparticle.<sup>[27]</sup>

Magnetization vs. temperature measurements at different magnetic fields ( $H = 100, 1000, \text{ and } 10,000 \text{ Oe}$ ), for the assemblies of Ni(O) nanoparticles, are shown in Fig. 7A–C. It seems that this is typical ferromagnetic nanocluster glass behavior (collective behavior) for the assemblies of nanoparticles.<sup>[29,30]</sup> Note the deviation between the zero-field cooling (ZFC) and field cooling (FC) magnetization below the irreversibility temperature ( $T_{irr}$ ). This strong irreversibility is very dependent on the strength of applied magnetic fields. This behavior may be attributed to the random distribution of stronger magnetic dipole–dipole interactions and surface anisotropy effects among those Ni(O) nanoparticles. High-resolution transmission electron microscopy images of Fig. 2B confirm that those Ni(O) nanoparticles are well connected. It is possible that the dipole interaction energy among those Ni(O) nanoparticles is strong to be on the same order of magnitude as the anisotropy energy, kV. Furthermore, it is interesting to observe that the strong irreversibility in curves of Fig. 7A and B disappears when magnetic fields reach 10,000 Oe in Fig. 7C. This means that  $T_{irr}$  decreases with increasing applied fields. This occurred while the anisotropy field and dipole–dipole interaction effects among these Ni(O) nanoparticles are surpassed. In other words, this collective behavior is expected for energy barriers that are reduced by the external field, allowing reorientation of the moments by the thermal fluctuations at lower temperatures. Actually, the above observed magnetic phenomena suggest that those ferromagnetic Ni(O) nanoparticle assemblies can exhibit nanocluster glass behavior depending on external applied fields.<sup>[31–35]</sup>

From a magnetic point of view, the Ni(O) particles are an assembly of nanoclusters together with stronger interparticle interactions. The magnetic dipole interactions in

**Table 1** Comparison of saturation magnetization ( $M_s$ ), remanent magnetization ( $M_r$ ), and coercivity ( $H_C$ ) values for carbon-encapsulated Ni nanocrystals and Ni in bulk

	$T$ (K)	$M_s$ (emu/g)	$M_r$ (emu/g)	$H_C$ (Oe)	$d$ (nm)
Ni(C)	300	22.5	1.37	7	$10 \pm 0.2$
Ni(C)	200	23.9	2.11	46	$10 \pm 0.2$
Ni(C)	100	24.9	2.70	117	$10 \pm 0.2$
Ni(C)	50	25.2	7.08	198	$10 \pm 0.2$
Ni(C)	10	25.2	7.37	316	$10 \pm 0.2$
Ni(C)	2	25.2	10.55	367	$10 \pm 0.2$
Bulk Ni	300	55.0	2.70	100	2–3 $\mu\text{m}$

Source: Ref.<sup>[24]</sup>.



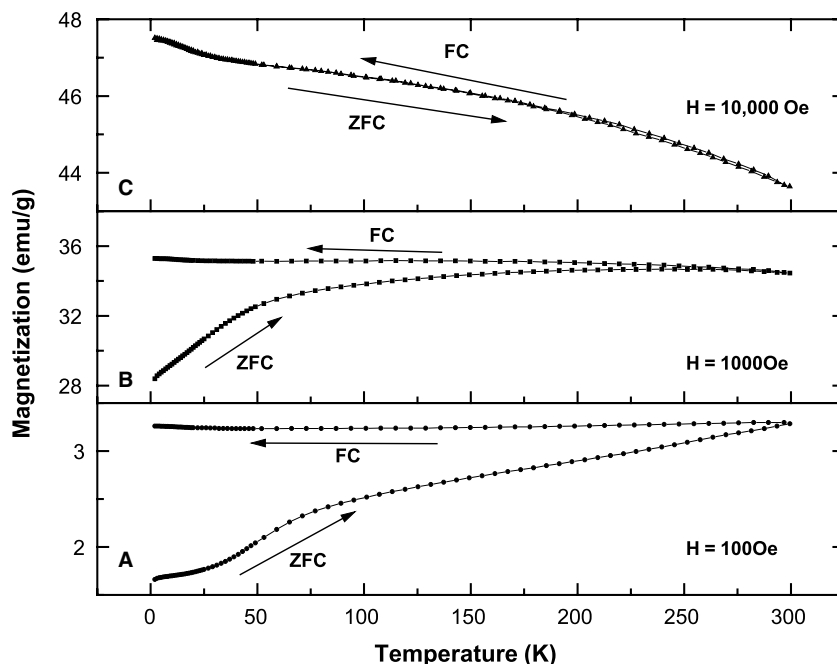


**Fig. 7** Temperature dependence of magnetization for the assemblies of Ni(O) nanoparticles at different applied magnetic fields; (A) 100 Oe, (B) 1000 Oe, and (C) 10,000 Oe. Source: From Ref.<sup>[24]</sup>.

the overall particle, which, in turn, lead to the magnetic ordered state, resemble cluster glass behavior (collective behavior). Consequently, the  $T_{irr}$  vanishes when the applied field is strong enough to flip the overall cluster moments and destroy the blocking of the interaction behavior.<sup>[31–35]</sup>

Table 2 shows that the assemblies of Ni(O) nanoparticles possess a larger coercivity and remanence magnetization from RT to 2 K compared with the bulk Ni and the assemblies of Ni(C) nanoparticles. These phenomena could be explained by the exchange anisotropy interaction and the spin flip behavior near the interface of the Ni(O) nanoparticles and their oxide layer on the particle surface.<sup>[13]</sup> It is also consistent with the studies of the ordering of the nanocluster magnetic moments in the case of stronger dipole–dipole interaction that cause aggregation and subsequent ferromagnetic-like ordering of the nanoparticles.<sup>[34–36]</sup> This suggests that this magnetic

**Table 2** Comparison of saturation magnetization ( $M_s$ ), remanent magnetization ( $M_r$ ), and coercivity ( $H_C$ ) values for pure Ni nanocrystals coated with NiO oxide and Ni in bulk

$T$ (K)	$M_s$ (emu/g)	$M_r$ (emu/g)	$H_C$ (Oe)	$d$ (nm)
Ni(O) 300	43.66	16.85	265	$24 \pm 0.2$
Ni(O) 200	45.49	18.02	265	$24 \pm 0.2$
Ni(O) 100	46.01	19.44	372	$24 \pm 0.2$
Ni(O) 50	46.76	20.00	382	$24 \pm 0.2$
Ni(O) 10	46.76	20.52	500	$24 \pm 0.2$
Ni(O) 2	47.18	21.12	547	$24 \pm 0.2$
Bulk Ni 300	55.00	2.70	100	2–3 $\mu\text{m}$

Source: Ref.<sup>[24]</sup>.

phenomenon can be interpreted in terms of ordering of the ferromagnetic Ni moments in the ferromagnetic nanocluster glass state below  $T_{irr}$ .<sup>[18,29]</sup>

### The Assemblies of Fe(C) and Fe(O) Particle Systems

Powder X-ray diffraction patterns of both Fe(C) and Fe(O) nanoparticles are shown in Fig. 8A and B, respectively. It is very apparent to reveal that  $\alpha$ -Fe (bcc),  $\gamma$ -Fe (fcc), and  $\text{Fe}_3\text{C}$  (orthorhombic) nanophases are detected from the assemblies of Fe(C) nanoparticles; these three phases are usually found in similarly prepared Fe–C nanocomposites.<sup>[19]</sup> However, dominant  $\alpha$ -Fe nanophases and a small amount of  $\text{Fe}_3\text{O}_4$  phases are examined from the assemblies of Fe(O) nanoparticles. As revealed by high-resolution images (HRTEM) of Figs. 9A,B and 10A,B, these Fe(C) nanoparticles ( $\alpha$ -Fe,  $\gamma$ -Fe, and carbide  $\text{Fe}_3\text{C}$ ) are typically spherical in core-shell shape and completely encapsulated by the wrapping shell carbon layers, which thickness is uniform over the surface of each particle. The size of three core nanocrystals is generally 10 to 15 nm, and note that each core nanocrystal is tightly covered by 10 to 40 carbon layers rather than a single carbon layer only.<sup>[19,37]</sup> Meanwhile, electron diffraction (SAED) patterns of Figs. 9 and 10 further confirm the presence of  $\alpha$ -Fe,  $\gamma$ -Fe, and carbide  $\text{Fe}_3\text{C}$  nanophases that were covered with carbon layers. Especially, X-ray diffraction (XRD) and electron diffraction (SAED) patterns indicate that no intermediate phases are observed between the wrapping carbon

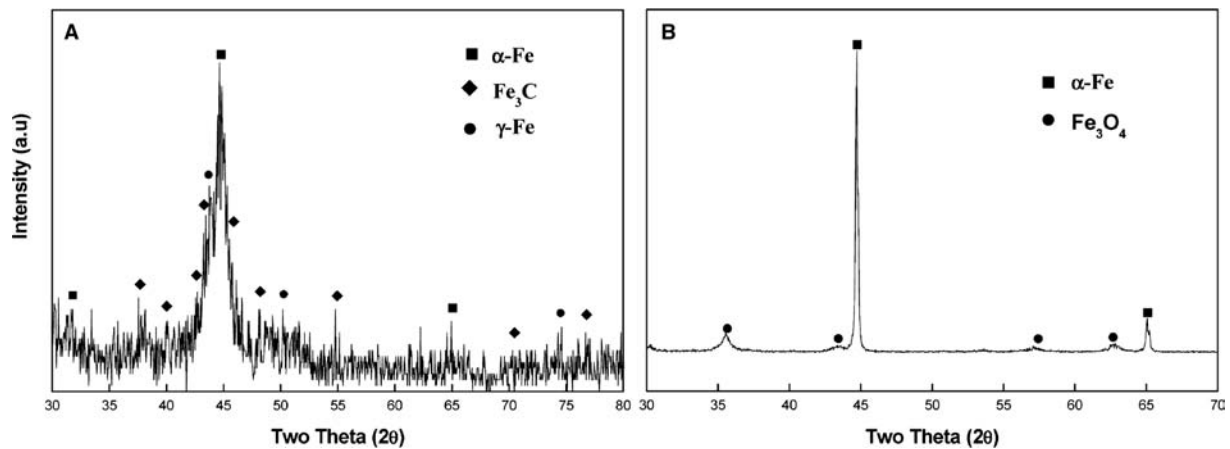


**Fig. 8** (A–B) XRD patterns for Fe(C) nanoparticles (A) and Fe(O) nanoparticles (B). *Source:* From Ref.<sup>[11]</sup>.

layers and three core nanocrystals.<sup>[12]</sup> These striking structural properties are in well agreement with our previous work of other carbon-coated transition metal particles.<sup>[12,15,17,24,25]</sup>

On the other hand, HRTEM images of Fe(O) nanoparticles in Fig. 11 show that the particles are roughly spherical with many structure defects and slight distortion inside the particle's core. The particle size is about

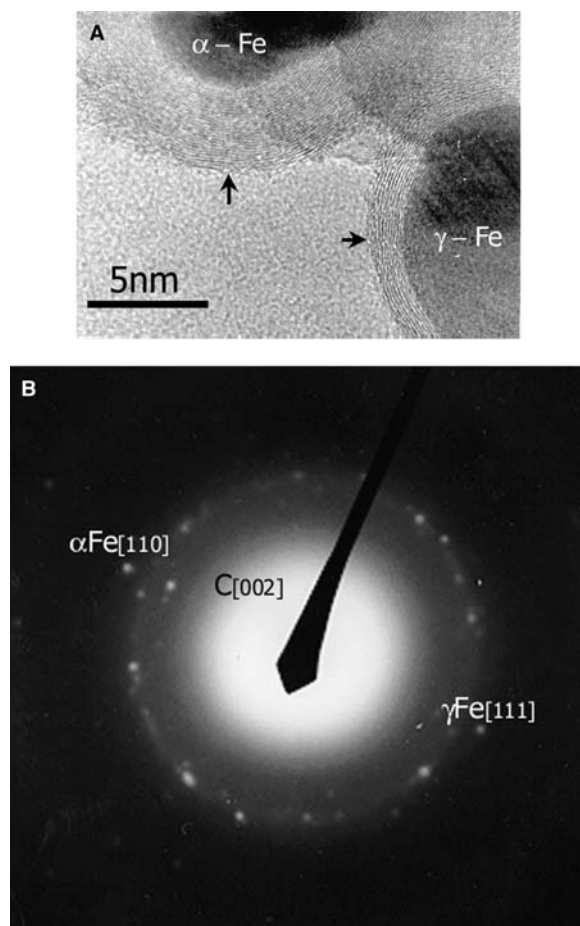


**Fig. 9** (A–B) HRTEM image (A) and SAED patterns (B) for  $\alpha$ -Fe(C) and  $\gamma$ -Fe(C) nanoparticles. Note that arrows indicate the carbon layers. *Source:* From Ref.<sup>[11]</sup>.

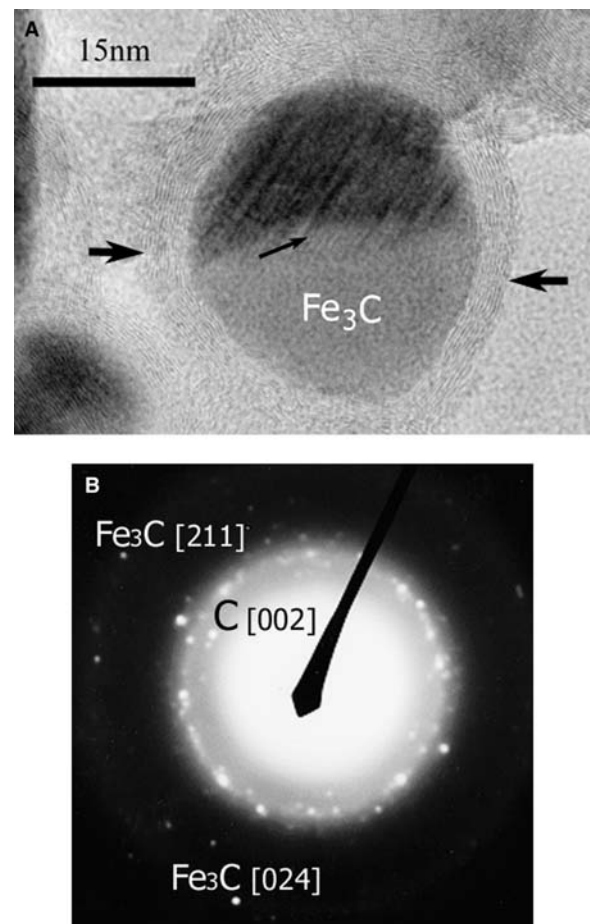


**Fig. 10** (A–B) HRTEM image (A) and SAED patterns (B) for  $\text{Fe}_3\text{C}$  phases in Fe(C) nanoparticles. Note that arrows indicate the carbon layers and structure defects. *Source:* From Ref.<sup>[11]</sup>.

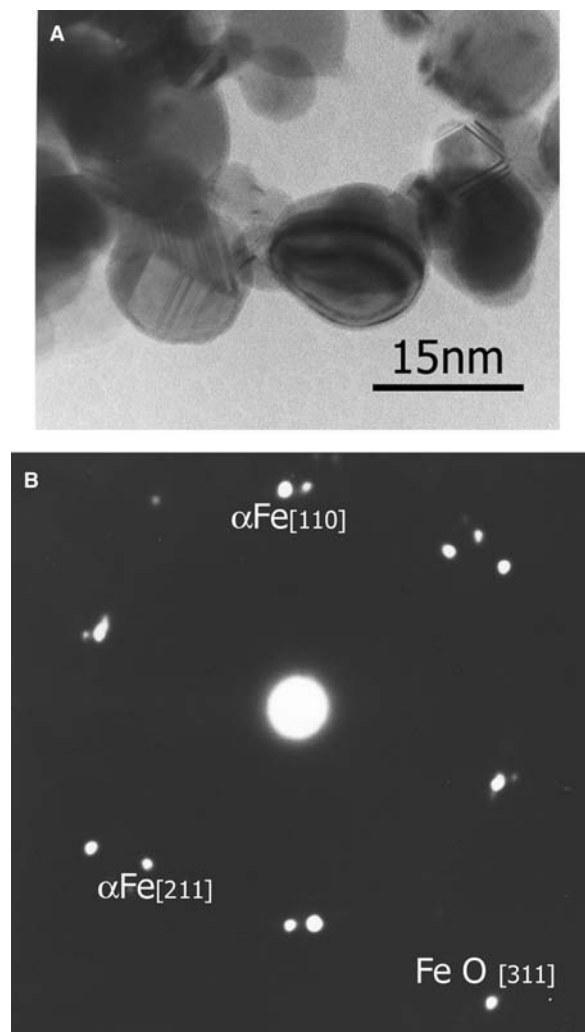


**Fig. 11** (A–B) HRTEM image (A) and SAED patterns (B) for Fe(O) nanoparticles. *Source:* From Ref.<sup>[11]</sup>.

15–20 nm. Electron diffraction patterns (SAED) in Fig. 11 reveal the existence of  $\alpha$ -Fe and  $\text{Fe}_3\text{O}_4$  nanophases; moreover, additional diffuse SAED line patterns could be attributed to a few of spinel-type  $\text{Fe}_3\text{O}_4$  oxide that, surrounding on the surface of these Fe(O) particles, also reflect the presence of structure defect inside the particles.

Typical Mössbauer spectra and hyperfine fields of the assemblies of Fe(C) and Fe(O) nanoparticles at room temperature are shown in Fig. 12A–D. Spectra of Fig. 12A and C are fitted into the following components: the three sextets whose magnetic hyperfine field ( $H_{\text{hyp}}$ ) values of 335, 271, and 200 kOe are assigned to  $\alpha$ -Fe and two carbide  $\text{Fe}_3\text{C}$  nanophases, respectively,<sup>[38–40]</sup> also, the singlet near zero velocity with an isomer shift ( $\text{IS}$ ) =  $-0.126$  mm/sec is assigned to  $\gamma$ -Fe. On the other hand, Fig. 12B and D is decomposed into two phases: the two external sextets of low intensity with a magnetic field of 477 and 444 kOe are

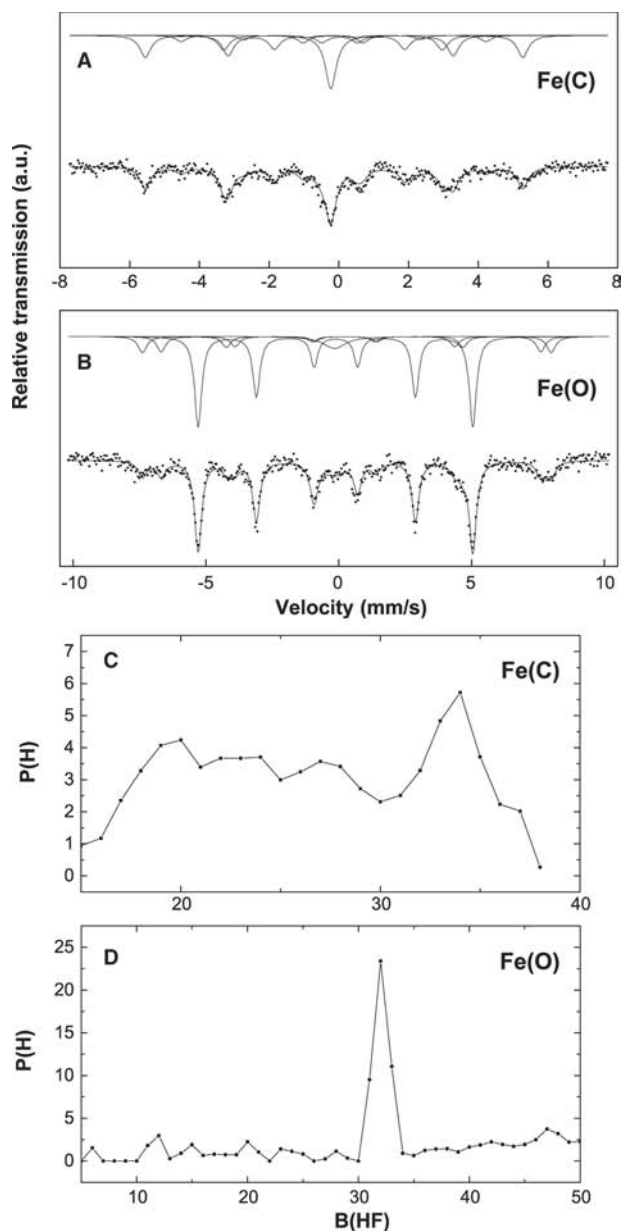


**Fig. 12** (A–D) Mössbauer spectra and hyperfine field distributions for Fe(C) and Fe(O) nanoparticles. *Source:* From Ref.<sup>[11]</sup>.

assigned to the  $\text{Fe}_3\text{O}_4$  structure; the next internal intense sextet with a magnetic field of 320 kOe is assigned to  $\alpha$ -Fe.<sup>[41,42]</sup> Generally speaking, Mössbauer spectra results at room temperature are in well agreement with that of above XRD analysis and HRTEM observations, which confirm these distinct nanophases in both Fe nanoparticles. In addition, the evidence of modified superparamagnetic absorption peaks could be observed at room temperature from Fig. 12A. However, such superparamagnetism can be blocked by interparticle dipole interactions because of the fact that the encapsulated particles are in contact with each other, which suggests that the assemblies of Fe(C)

nanoparticles display modified superparamagnetic relaxation at room temperature.<sup>[39]</sup> Whereas, from Fig. 12B, it can be seen that ferromagnetic properties at room temperature appear in the assemblies of Fe(O) nanoparticles because of the increased magnetocrystalline anisotropy that originated from structure defects and the coupling effects between ferromagnetic  $\alpha$ -Fe core and antiferromagnetic oxide ( $\text{Fe}_3\text{O}_4$ ) shell layer in each particles.<sup>[7,12]</sup> As we know, from the HRTEM images of Fig. 11, these Fe(O) nanoparticles are combined with the aligned necklace structure; thus the magnetic moment of these particles couples with that of adjacent larger particles and becomes stable under thermal fluctuation. Therefore it should not be surprising that the assemblies of Fe(O) nanoparticles display ferromagnetic properties at room temperature.

## CONCLUSION

In summary, two types of nickel (Ni) and iron (Fe) nanoparticles, carbon-coated Ni and Fe nanoparticles [Ni(C) and Fe(C)], as well as pure fcc Ni and  $\alpha$ -Fe nanoparticles that coated with oxide layers [Ni(O) and Fe(O)] have been successfully synthesized using modified graphite arc-discharge method. High-resolution transmission electron microscopy (HRTEM), electron diffraction (SAED), and X-ray diffraction (XRD) analyses have been used to characterize these distinct structural morphologies of Ni and Fe nanoparticles. The presence of the majority of carbon-encapsulated fcc Ni and the minority of  $\text{Ni}_3\text{C}$  phases is confirmed in these Ni(C) particles; meanwhile, the evidence of pure Ni nanocrystal coated with NiO layer is observed from these Ni(O) particles. On the other hand, the presence of carbon-encapsulated  $\alpha$ -Fe,  $\gamma$ -Fe, and  $\text{Fe}_3\text{C}$  phases is also identified in those Fe(C) particles; the evidence of pure  $\alpha$ -Fe surrounded by an Fe oxide layer composed of  $\text{Fe}_3\text{O}_4$  is examined from those Fe(O) particles.

Magnetization measurements [ $M(T)$  and  $M(H)$  curves] for the assemblies of Ni nanoparticles indicate that typical ferromagnetic nanocluster glass behavior (collective behavior) has been observed because of stronger ferromagnetic dipole-dipole interaction effects among the assemblies of Ni(O) particles. However, modified superparamagnetic properties at  $T > T_B$  have been found in the assemblies of Ni(C) particles. The blocking temperature,  $T_B$ , is determined to be near 115 K under a certain applied field. Moreover, a gradual decrease in saturation magnetization ( $M_s$ ) is observed, which is attributed to the nanocrystalline nature of the encapsulated particles, coupled with possible carbon solution in Ni nanocrystals.

Mössbauer spectra and hyperfine magnetic fields at room temperature for the assemblies of Fe(C) and

Fe(O) nanoparticles confirm their distinct nanophases that were detected by XRD analysis and HRTEM observation. Especially, the assemblies of Fe(O) nanoparticles exhibit ferromagnetic properties at room temperature because of the stronger interparticle interaction and bigger magnetocrystalline anisotropy effects among these Fe(O) nanoparticles. Furthermore, modified superparamagnetic relaxation is observed in the assemblies of Fe(C) nanoparticles, which is attributed to the nanocrystalline nature of the carbon-coated nanoparticles. As a matter of fact, it is necessary to perform further studies on magnetization measurements and confirm these specific magnetic properties.

## REFERENCES

1. Dravid, V.P.; Host, J.J.; Teng, M.H.; Elliott, B.; Hwang, J.; Johnson, D.L.; Mason, T.O.; Weertman, J.R. Controlled-size nanocapsules. *Nature* **1995**, *374* (6523), 602.
2. Dormann, J.L.; Fiorani, D. *Magnetic Properties of Fine Nanoparticles*; North-Holland: Amsterdam, 1992.
3. Leslie-Pelecky, D.L.; Rieke, R.D. Magnetic properties of nanostructured materials. *Chem. Mater.* **1996**, *8* (8), 1770–1783.
4. McHenry, M.E.; Majetich, S.A.; Artman, J.O.; Degraef, M.; Staley, S.W. Superparamagnetism in carbon-coated Co particles produced by the Kratschmer carbon arc process. *Phys. Rev., B* **1994**, *49* (16), 11,358–11,363.
5. Popplewell, J.; Sakhnini, L. The dependence of the physical and magnetic properties of magnetic fluids on particle size. *J. Magn. Magn. Mater.* **1995**, *149* (1–2), 72–78.
6. Raj, K.; Moskowitz, B.; Casciari, R. Advances in ferrofluid technology. *J. Magn. Magn. Mater.* **1995**, *149* (1–2), 174–180.
7. Jonsson, T.; Svedlindh, P.; Hansen, M.F. Static scaling on an interacting magnetic nanoparticle system. *Phys. Rev. Lett.* **1998**, *81* (18), 3976–3979.
8. Zhang, J.; Boyd, C.; Luo, W. Two mechanisms and a scaling relation for dynamics in ferrofluids. *Phys. Rev. Lett.* **1996**, *77* (2), 390–393.
9. Rondinone, A.J.; Samia, A.C.S.; Zhang, Z.J. Superparamagnetic relaxation and magnetic anisotropy energy distribution in  $\text{CoFe}_2\text{O}_4$  spinel ferrite nanocrystallites. *J. Phys. Chem., B* **1999**, *103* (33), 6876–6880.
10. Kratschmer, W.; Lamb, L.D.; Fostirpoulos, K.; Huffman, D.R. Solid  $\text{C}_{60}$ : a new form of carbon. *Nature* **1990**, *347* (6290), 354–358.
11. Sun, X.C.; Nava, N. Microstructure and magnetic properties of Fe(C) and Fe(O) nanoparticles. *Nano Lett.* **2002**, *2* (7), 765–769.
12. Sun, X.C.; Gutierrez, A.; Yacaman, M.J.; Dong, X.L.; Jin, S.R. Investigations on magnetic properties and structure for carbon encapsulated nanoparticles of Fe, Co, Ni. *Mater. Sci. Eng., A* **2000**, *286* (1), 157–160.
13. Yao, Y.D.; Chen, Y.Y.; Tai, M.F.; Wang, D.H.; Lin, H.M. Magnetic anisotropy effects in nano-cluster nickel particles. *Mater. Sci. Eng., A* **1996**, *217/218*, 281–285.

14. Dormann, J.L.; Fiorani, D.; Tronc, E. On the models for interparticle interactions in nanoparticle assemblies: comparison with experimental results. *J. Magn. Magn. Mater.* **1999**, *202* (1), 251–267.
15. Sun, X.C.; Dong, X.L.; Toledo, J.A. Superparamagnetic properties of carbon encapsulated Ni nanoparticle assemblies. *J. Nanosci. Nanotechnol.* **2001**, *1* (3), 291–294.
16. Tejada, J.; Ziolo, R.F.; Zhang, X.X. Quantum tunneling of magnetization in nanostructured materials. *Chem. Mater.* **1996**, *8* (8), 1784–1792.
17. Dong, X.L.; Xiao, Q.F.; Zhao, X.G.; Chuang, Y.C.; Jin, S.R.; Sun, W.M. Characterization of ultrafine  $\gamma$ -Fe(C),  $\alpha$ -Fe(C) and Fe<sub>3</sub>C particles synthesized by arc-discharge in methane. *J. Mater. Sci.* **1998**, *33* (7), 1915–1919.
18. Fiorani, D.; Dormann, J.L.; Cherkaoui, R.; Tronc, E.; Lucari, F.; D’Orazio, F.; Spinu, L.; Nogues, M.; Garcia, A.; Testa, A.M. Collective magnetic state in nanoparticles systems. *J. Magn. Magn. Mater.* **1999**, *196–197*, 143–147.
19. Saito, Y.; Yoshikawa, T.; Okuda, M.; Fujimoto, N.; Suzuki, K.; Kasuya, A.; Nishina, Y. Carbon nanocapsules encaging metals and carbides. *J. Phys. Chem. Solids* **1993**, *54* (12), 1849–1860.
20. Zhang, L.; Ziolo, R.F.; Ying, J.Y. Novel  $\gamma$ -Fe<sub>2</sub>O<sub>3</sub>/SiO<sub>2</sub> magnetic nanocomposites via sol-gel matrix-mediated synthesis. *Nanostruct. Mater.* **1997**, *9* (1–8), 185–188.
21. Charles, S.W.; Popplewell, J. *Ferromagnetic Materials*; Wolhfarth, E.P., Ed.; North-Holland: Amsterdam, 1982.
22. Jacobs, I.S.; Bean, C.P. *Magnetism*; Rado, G.T., Suhl, H., Eds.; Academic Press: New York, 1963.
23. Bean, C.P.; Livingston, J.D. Superparamagnetism. *J. Appl. Phys.* **1959**, *30*, 120S–129S.
24. Sun, X.C.; Dong, X.L. Magnetic properties and microstructure of carbon encapsulated Ni nanoparticles and pure Ni nanoparticles coated with NiO layer. *Mater. Res. Bull.* **2002**, *37* (5), 991–1004.
25. Sun, X.C. Microstructure characterization and magnetic properties of nanomaterials. *Mol. Phys.* **2002**, *100* (19), 3059–3063.
26. Kang, Y.S.; Risbud, S.; Rabolt, J.F.; Stroeve, P. Synthesis and characterization of nanometer-size Fe<sub>3</sub>O<sub>4</sub> and  $\gamma$ -Fe<sub>2</sub>O<sub>3</sub> particles. *Chem. Mater.* **1996**, *8* (8), 2209–2211.
27. Hwang, J.H.; Dravid, V.P.; Teng, M.H.; Host, J.J.; Elliott, B.R.; Johnson, D.L.; Mason, T.Q. Magnetic properties of graphically encapsulated nickel nanocrystals. *J. Mater. Res.* **1997**, *12* (4), 1076–1082.
28. Yue, L.P.; Sabiryanov, R.; Kirkpatrick, M.E.; Leslie-Pelecky, D.L. Magnetic properties of disordered Ni<sub>3</sub>C. *Phys. Rev., B* **2000**, *62* (13), 8969–8975.
29. Morup, S.; Bodker, F.; Hendriksen, P.V.; Linderroth, S. Spin-glass-like ordering of the magnetic moments of interacting nanosized maghemite particles. *Phys. Rev., B* **1995**, *52* (1), 287–294.
30. Garcia del Muro, A.; Battle, X.; Labarta, A. Erasing the glassy state in magnetic fine particles. *Phys. Rev., B* **1999**, *59* (21), 13,584–13,587.
31. Giguere, A.; Foldeaki, M.; Dunlap, R.A.; Chahine, R. Magnetic properties of Dy–Zr nanocomposites. *Phys. Rev., B* **1999**, *59* (1), 431–435.
32. Luo, W.L.; Nagel, S.R.; Rosenbaum, T.F.; Rosensweig, R.E. Dipole interactions with random anisotropy in a frozen ferrofluid. *Phys. Rev. Lett.* **1991**, *67* (19), 2721–2724.
33. Detoro, J.A.; Lopez de la Torre, M.A.; Riveiro, J.M.; Puche, A.S.; Herrero, A.G.; Otero-Diaz, L.C. Spin-glass-like behavior in mechanically alloyed nanocrystalline Fe–Al–Cu. *Phys. Rev., B* **1999**, *60* (18), 12,918–12,923.
34. Dormann, J.L.; D’Orazio, F.; Lucari, F.; Tronc, E.; Prene, P.; Jolivet, J.P.; Fiorani, D.; Cherkaoui, R.; Nogues, M. Thermal variation of the relaxation time of the magnetic moment of  $\gamma$ -Fe<sub>2</sub>O<sub>3</sub> nanoparticles with interparticle interactions of various strengths. *Phys. Rev., B* **1996**, *53* (21), 14,291–14,297.
35. Lu, J.J.; Deng, H.Y.; Huang, H.L. Thermal relaxation of interacting fine magnetic particles—field-cooled and zero-field-cooled magnetization variation. *J. Magn. Magn. Mater.* **2000**, *209* (1–3), 37–41.
36. Bonetti, E.; Del Bianco, L.; Fiorani, D.; Rinaldi, D.; Caciuffo, R.; Herando, A. Disordered magnetism at the grain boundary of pure nanocrystalline iron. *Phys. Rev. Lett.* **1999**, *83* (14), 2829–2832.
37. Saito, Y.; Yoshikawa, T.; Okuda, M.; Fujimoto, N.; Yamamuro, S.; Wakoh, K.; Sumiyama, K.; Suzuki, K.; Kasuya, A.; Nishina, Y. Iron particles nesting in carbon cages grown by arc discharge. *Chem. Phys. Lett.* **1993**, *212* (3–4), 379–383.
38. Bi, X.X.; Ganguly, B.; Huffman, G.P.; Huggins, F.E.; Endo, M.; Eklund, P.C. Nanocrystalline  $\alpha$ -Fe, Fe<sub>3</sub>C and Fe<sub>7</sub>C<sub>3</sub> produced by CO<sub>2</sub> laser pyrolysis. *J. Mater. Res.* **1993**, *8* (7), 1666–1674.
39. Zhang, H. The Mössbauer spectra of graphite-encapsulated iron and iron compound nanocrystals prepared in carbon arc method. *J. Phys. Chem. Solids* **1999**, *60* (11), 1845–1847.
40. Rechenberg, H.R.; Coaquira, J.A.H.; Marquina, C.; Landa, B.G.; Ibarra, M.R.; Benito, A.M.; Naser, W.; Munoz, E.; Martinez, M.T. Mössbauer and magnetic characterisation of carbon-coated small iron particles. *J. Magn. Magn. Mater.* **2001**, *226–230*, 1930–1932.
41. Varanda, L.C.; Jafelici, M.J.; Goya, G.F. Magnetic properties of spindle-type iron fine particles obtained from hematite. *J. Magn. Magn. Mater.* **2001**, *226–230*, 1933–1935.
42. Vijayakumar, R.; Koltypin, Y.; Felner, I.; Gedanken, A. Sonochemical synthesis and characterization of pure nanometer-sized Fe<sub>3</sub>O<sub>4</sub> particles. *Mater. Sci. Eng., A* **2000**, *286* (1), 101–105.

# Nanoparticle Suspensions: Phase Behavior

Subramanian Ramakrishnan

Charles F. Zukoski

*Department of Chemical and Biomolecular Engineering, University of Illinois at Urbana-Champaign, Urbana, Illinois, U.S.A.*

## INTRODUCTION

The assembly of nanoparticles into interesting and useful structures requires the manipulation of particle interactions at the level of a few times the average thermal energy in the system such that the particles can sample an ensemble of states. When allowed to reach equilibrium, colloidal suspensions display phase behavior similar to that seen in molecular systems. The phases observed can be manipulated through alterations in particle density and particle surface chemistry. The richness of the phase diagram can be expanded by introducing anisotropic interactions, or by working with mixtures of particles. Under some conditions, as the strength of attraction or particle concentration is increased, suspensions fall out of equilibrium and glasses or gels are observed. Here we review links that have been recently made between experimental observations and statistical mechanics of suspension phase behavior and suggest where advances will be made in the future.

## BACKGROUND

Colloidal suspensions display phase behavior similar to that of molecular systems.<sup>[1]</sup> Order/disorder transitions are referred to as fluid/crystal transitions. Suspension phases separate out into dilute and concentrated phases in equilibrium with each other, thus displaying gas/fluid transitions. Dense suspensions form glasses. Although in single-component molecular systems, the thermodynamic variables used to describe phase transitions are density, temperature, and pressure, in colloidal systems, the variables are density, temperature, osmotic pressure, and strength of interaction. The last variable distinguishes colloidal suspensions most strongly from molecular systems. For example, because the strength of interaction can be tuned by solution properties, at fixed temperature, one can map out an entire phase diagram.<sup>[1]</sup>

The connection between descriptions of phase transitions in molecular systems and colloidal systems is based on the use of the effective potential where

solvent-mediated interactions are ascribed to the particle interaction energy. The basis of this mapping goes back to McMillan and Mayer,<sup>[2]</sup> and the treatment of colloidal suspensions containing one type of particle as a pseudo-one-component system has been extensively tested. As the range and strength of attractions and repulsions can be varied over an enormous range with colloidal particles, suspensions of nanoparticles offer a unique test bed for treatments of molecular phase behavior.

The phase behavior of repulsive systems has been extensively studied.<sup>[1,3]</sup> For monotonic repulsive interactions, only order/disorder and glass transitions are observed. The effects of attractions have seen less investigations because of the limited number of experimental systems where the strength of attraction can be varied systematically over a range around the average thermal energy in the system. The limited number of model systems where weak attractions can be modulated arises from the ubiquitous nature of van der Waals interactions and the large magnitudes of these attractions at contact for particles half a micron or larger in size. Realization that the strength of van der Waals forces at contact is limited by the granularity of matter (which limits the distance of closest approach) leads one to conclude that nanoparticles will experience only weak attractions. Indeed, this realization has led to startling connections between the phase behavior of nanoparticles or large molecules, and the simulations and analytical models for the phase behavior of particles experiencing weak, short-range attractions.<sup>[4-6]</sup>

Suspensions containing nanoparticles are widely used in the production of ceramics, consumer products, paints and inks, and quantum dots for optical applications. Nanoparticles are used because of their optical properties, the fact that the electronic states of nanoparticles are altered from their states in the bulk, and because they offer unique chemical and physical properties to the suspensions. Of growing interest in the assembly of nanoparticles are the factors that control the states into which nanoparticles assemble. Key examples can be found in biochemistry, where biological systems are controlled by the



interactions and assembly of nanoparticles whereas the structure of globular macromolecules is often determined by X-ray diffraction derived from crystals. Thus advances in the use of nanoparticles and an understanding of complex biological systems will be tied to a greater understanding of particle interactions and how these alter the state of nanoparticle aggregation.

The fact that many systems of interest interact weakly where the strength of attractions lies on the order of a few times the average thermal energy in the system means that many nanoparticle systems sample an ensemble of states and are subject to undergoing phase transitions. Progress toward unraveling the effects of particle shape, anisotropy of interaction, and details of the spatial extent of the particle interaction as well as the kinetics of the self-assembly process is being made through investigations of systems containing nanoparticle spheres with centrosymmetric interactions. In this entry, we focus attention on these advances while returning to more complex systems at the end as an indication of the opportunities for advancement that lead into the future.

As discussed above, a key feature of suspensions as opposed to pure molecular systems lies in the fact that particle interactions can be tuned based on the composition of the continuous phase. Thus, as a result, small changes in solution variables such as pH, ionic type or composition, and polymer concentration or molecular weight or temperature can give rise to dramatic changes in the state of particle aggregation and the mechanical properties of the suspension.<sup>[1,3]</sup> As a specific example, suspensions of silica particles stabilized with octadecyl chains grafted to their surface and suspended in a near-index matching fluid can be crystallized, gelled, made to separate into two liquid phases, or separated into three equilibrium phases, depending on the amount and size of added non-adsorbing polymer.<sup>[7,8]</sup> The literature abounds in the number of examples in which interactions between various kinds of particles are manipulated to place them into useful structures. Although the details of how these structures are achieved will vary with the chemistry of the solid and fluid phases of interest, the underlying physical chemistry of the colloidal state will be common between different materials, thus offering general guidelines on how to achieve the desired properties.

The complexity of describing the interactions and phase behavior of colloidal suspensions is simplified to a certain extent by treating the suspension as an effective one-component system with the interactions between the particles mediated by the solvent and various additives. This allows the extensive literature developed in the field of molecular thermodynamics to be harvested to advantage. Of key concern to these systems is the particle interaction energy. Here we will

focus on particles with hard cores (i.e., the particles cannot interpenetrate) that experience attractions or repulsions.

## HARD SPHERE BEHAVIOR

Hard spheres represent a model system that contains much of the essential physics for describing behavior in dense systems and has been extensively studied in the thermodynamics and statistical mechanics literature.<sup>[1]</sup> The development of suspensions where particles interact very nearly as hard spheres has advanced the understanding of both fields. A significant advancement was made when links between the order/disorder phase transition in charged stabilized latex particles and computer simulations of the interactions of hard spheres were established. Since this initial connection, advances have been made in understanding the microstructure, thermodynamics, and nonequilibrium behavior of dilute and dense systems of hard spheres.

Hard spheres interact with each other only when they touch with an infinite repulsion at contact representing their impenetrable physical volume. Thus entropy changes because of different packings control suspension equilibrium microstructures. Fig. 1 is the plot of the experimentally measured static structure factor for hard sphere suspensions at different volume fractions.<sup>[9]</sup> The structure factor is an equilibrium property that is indicative of the average spacing between the hard sphere particles and can be determined experimentally by scattering techniques. At a volume fraction ( $\phi$ ) of 0.495, suspensions of Brownian hard spheres arrange in an ordered lattice such that their entropy is maximized. The onset of freezing produces a solid at a volume fraction of 0.545 and the crystal can be further compressed to the closest packing density of 0.74. This phenomenon was first discovered through computer simulations and these predictions were first experimentally tested with colloidal suspensions.<sup>[1,10]</sup> Computer simulations demonstrate that face-centered cubic (FCC) microstructures have the lowest energy, but ground-based experiments and those done under microgravity conditions<sup>[11]</sup> (to reduce the effects of density mismatches) indicate that the particles tend to crystallize as randomly stacked hexagonal close-packed (HCP) structures, although an FCC microstructure slowly emerges if the crystals are allowed to age.

Nucleation rates, crystal growth velocities, and induction times for crystallization in hard sphere suspensions have been the subject of numerous computer simulations and experimental studies (commonly used techniques include light scattering and microscopy). Although the equilibrium states of the suspensions are not impacted by the particles being suspended in

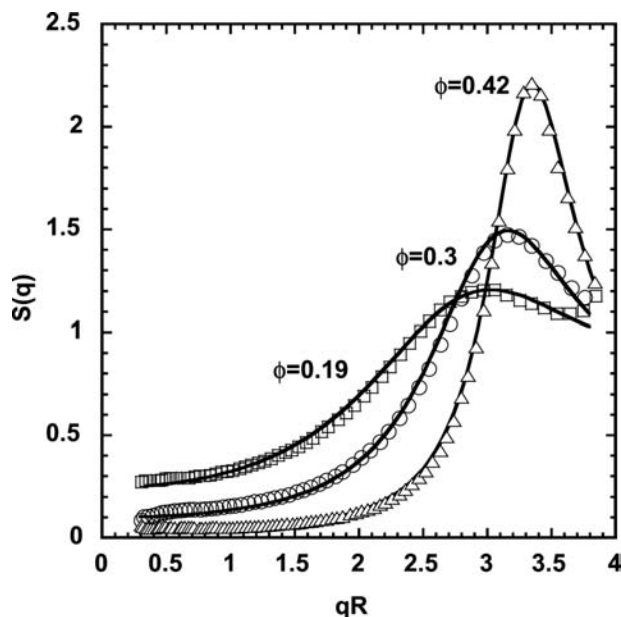


**Fig. 1** Static structure  $S(q)$  of hard sphere colloidal suspensions plotted as a function of the dimensionless wave vector  $qR$ . Here  $R$  is the sphere radius and  $q$  is the scattering vector [ $q = 4\pi/\lambda_1 \sin(\theta/2)$ , where  $\lambda_1$  is the wavelength of incident radiation and  $\theta$  is the scattering angle]. The solid lines are Percus–Yevick calculations of  $S(q)$  for hard spheres. The open symbols are the experimental points as measured by small-angle X-ray scattering on the octadecyl-coated hard sphere silica system. The height of the first peak in the structure factor is indicative of the coherence of the first cage of particles and increases with increasing volume fraction. *Source:* From Ref.<sup>[9]</sup>.

a dissipative continuous phase, all rate processes are influenced to greater or lesser degrees by this continuous phase. Accounting for these hydrodynamic interactions is essential in understanding the mechanical behavior in the low to intermediate volume fraction regime.

At elevated volume fractions approaching the glass transition ( $\phi \sim 0.58$ ), suspension mechanics appears dominated by long-time self-diffusivities, which, once scaled on the infinite solution diffusivity, begin to be well described by models dominated by cage dynamics and cooperative rearrangements where hydrodynamic interactions are less important.<sup>[12]</sup> The approach of the glass transition results in the long-time self-diffusivity dropping to zero and a divergence in the zero shear rate suspension viscosity. Thus a complete description of suspension dynamic behavior requires a transition from regions where suspension mechanics is dominated by hydrodynamic interactions at low  $\phi$  to one where cage dynamics dominates at elevated  $\phi$ .<sup>[13]</sup>

Studies on the crystallization of hard spheres show a characteristic maximum in crystal nucleation rate as volume fraction is raised above 0.495 (Fig. 2).<sup>[14]</sup>

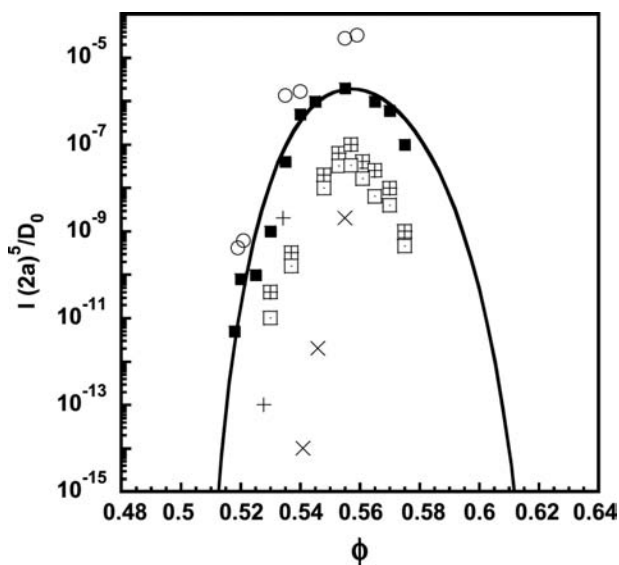


**Fig. 2** Comparisons of predicted (solid line) and literature values of hard sphere nucleation rates as a function of particle volume fraction. The calculations are based on the kinetic model of Dixit and Zukoski. A maximum in the nucleation rate is observed at a volume fraction of 0.56. This is attributed to the competing effects of reduced particle diffusion and the increase in the thermodynamic driving force at elevated volume fractions. *Source:* From Ref.<sup>[14]</sup>.

To understand these observations, two different models have been developed: 1) the application of classical nucleation theory, which employs the combination of thermodynamic and kinetic descriptions that account for changes in self-diffusivity with volume fraction;<sup>[15]</sup> and 2) a completely kinetic description of nucleation,<sup>[16]</sup> which differs significantly from classical theories by making no reference to the solid–liquid surface tension. Both of the approaches predict a maximum in nucleation rate at  $\phi \sim 0.56$ , as measured by experiments. In the classical model, just above  $\phi = 0.495$ , the thermodynamic driving force increases rapidly with volume fraction. The flux of particles to a cluster surface is determined by self-diffusion. As self-diffusivities decrease rapidly as  $\phi$  approaches the glass transition near 0.58, the rate flux of particles to the nucleus surface drops to zero with increasing volume fraction. The competition between these two effects results in a maximum in nucleation rate. In the kinetic model, the flux of particles to a cluster surface is controlled by gradient diffusion. Just above  $\phi = 0.495$ , the flux of particles to a cluster surface increases simply because the bulk concentration increases, whereas the concentration at the cluster surface changes slowly. However, as  $\phi$  further increases, the concentration difference between the bulk and the surface decreases, with the nucleation rate passing through a maximum. In this model, the flux to the surface is governed by

gradient diffusion that has a much weaker dependence on volume fraction than self-diffusivity. A difference in the predictions of these two models lies in the volume fraction dependence of the size of a critical nucleus. Although the kinetic model predicts a minimum in critical nucleus size with increasing volume fraction, the classical approach predicts a monotonic decrease in critical cluster size with increasing volume fraction. There are two experimental data sets reporting volume fraction dependence of the critical nucleus size. In one, the critical nucleus size monotonically decreases, whereas in the second, a minimum in critical nucleus size is reported. Consequently, the differences in these descriptions of hard sphere crystal nucleation will require further experimental and modeling work.

### SOFT REPULSIONS

The addition of “soft” or long-range repulsions to colloidal particles can overcome the attractive van der Waals attraction to render them stable against aggregation. The most common method of electrostatic stabilization is the adsorption of charged species or dissociation of bound surface groups. The range of electrostatic repulsion is characterized by the Debye length ( $\kappa^{-1}$ ) and can be regulated by adding salt to the system.<sup>[1]</sup> The Debye length scales inversely with the square root of the ionic strength of the suspension. Charged particles exhibit an order/disorder phase transition (Fig. 3)<sup>[17]</sup> similar to those seen in hard

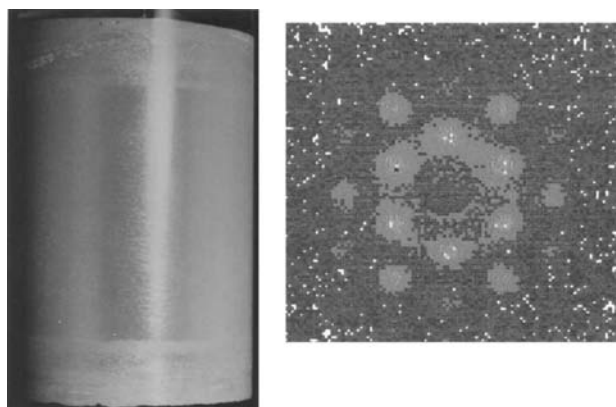


**Fig. 3** Optical visualization of 229-nm (diameter) latex particle suspensions at a volume fraction of 0.53 at rest in a transparent shear cell and the resulting small-angle neutron scattering result. The observed iridescence is because of the crystalline packing of the latex particles. The small-angle neutron scattering pattern for the above suspension is given in the form of an isointensity plot where the highest intensity is represented by the lightest color. The spots are indicative of a microstructure with long-range orientational order consisting of HCP planes. *Source:* From Ref.<sup>[17]</sup>.

sphere systems, but at quite low volume fractions. The phase transition can be achieved by two means: by increasing the particle volume fraction, or by increasing the range of repulsion (decreasing the ionic strength). The FCC-ordered phase prevails at higher concentrations, or with shorter-range repulsions. As the range of repulsion is increased (say, by the removal of screening species in solution, thereby increasing the Debye length), a lower-density, body-centered cubic (BCC) packing forms the lowest free-energy ordered phase. BCC and FCC phases coexist under certain conditions in charged colloids as observed by the experiments of Chaikin et al.<sup>[18]</sup> The BCC–FCC–liquid triple point occurs when the interparticle spacing is 4.9 times the Debye length.

The equilibrium thermodynamics of the phase transitions in electrostatically stabilized suspensions is well captured by treating the particles as effective hard spheres where the effective hard sphere diameter is determined by the range and strength of the repulsion through self-consistent ways. More sophisticated approaches use one-component plasma and mean spherical approximation solutions of the pair distribution function or perturbation theory predictions of the suspension osmotic pressure and location of the phase boundaries (Fig. 4).<sup>[17,19,20]</sup> These models agree well with experimental observations when the particle surface charge is taken as the adjustable parameter.

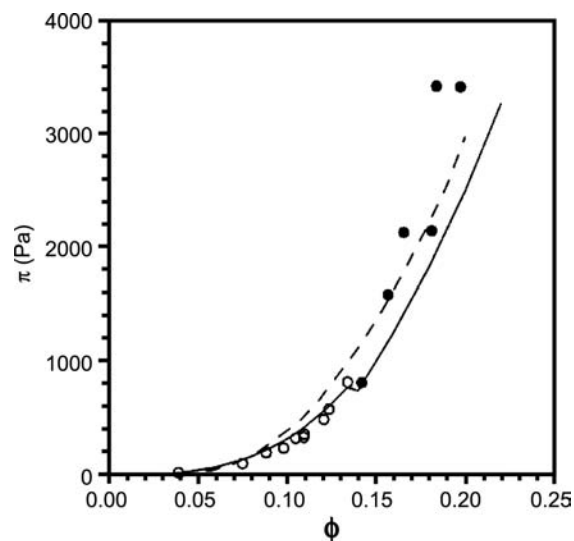


**Fig. 4** Osmotic pressure as a function of volume fraction for suspensions of charged 35-nm (diameter) latex particles. The open circles represent the liquid phase (or the disordered state), whereas the solid phase of the suspension is shown in closed circles. The solid line is the prediction of perturbation theory and the dashed line is that of the cell model. The latex particles are highly charged and undergo a fluid/crystal transition at a low volume fraction of 0.14. *Source:* From Ref.<sup>[17]</sup>.

Good agreement is found for osmotic pressure through the disorder/order phase transition using these models.<sup>[18–21]</sup>

In very low ionic strength media, the ions that have dissociated from the particles provide a significant addition to screening of the electrostatic repulsions. Consequently, over extremely wide ranges of volume fractions, suspensions can sit on the edge of order/disorder transitions. Each time the particle concentration is increased, the resulting addition of counterions decreases the range of the interparticle repulsion such that the effective volume fraction lies below 0.495 and the ordered phase remains unstable relative to the liquid phase.<sup>[22,23]</sup>

Encouraged by the accuracy of the effective hard sphere models in capturing the location of the phase boundary, attempts have been made to describe the kinetics of crystallization in charged sphere systems. A one-to-one mapping is complicated by different interpretations of how the diffusivity of the particle changes with the strength of repulsion. Recent experiments, simulations, and modeling efforts reveal the weaknesses of this approach. The location of the maximum in the nucleation rate, which occurs at a  $\phi$  of 0.56 in hard spheres, depends sensitively on the strength and range of repulsions and is often not observed experimentally. In addition, depending on the strength and range of repulsions, drastically different nucleation rates are predicted at similar supersaturations, suggesting that a simple mapping of particle charge and Debye parameter into an effective particle size does not capture the subtleties of the kinetics of phase changes in systems with soft repulsions.<sup>[24,25]</sup>

## WEAKLY ATTRACTIVE SUSPENSIONS

Investigations of the phase behavior of weakly attractive suspensions have seen relatively less work due primarily to a lack of model experimental systems, and/or methods independently characterizing the strength and range of the attractive forces. In the classical colloids literature, the goal has long been to control the state of aggregation that results when van der Waals attractions overwhelm repulsive forces. Van der Waals attractive potentials have contact values of  $\sim AR/12\delta$ , where  $A \sim 1-10kT$  is the material-dependent Hamaker coefficient,  $R$  is the sphere radius,  $kT$  is the product of Boltzmann's constant and the absolute temperature, and  $\delta$  is the distance of closest separation. Values for  $\delta$  will depend on the material used and the morphology of the particles. However, several studies have suggested that  $\delta \sim 0.65$  nm represents a minimum for liquid and molecularly smooth surfaces.<sup>[26]</sup> The study of the phase behavior of attractive colloidal systems has been

limited by the large magnitude of this contact force when  $R$  is larger than  $\sim 50$  nm. Up to a few years ago, most studies of attractive colloidal systems were based on understanding the rates of irreversible aggregation and the morphologies of the resulting aggregates.

Progress in controlling the magnitude of the attractive forces has been made by driving  $A$  to very small values by matching the index of refraction of the particle to that of the solvent, but even here, the number of model systems remains very small. More recently, there has been the realization that when  $R$  is small, the van der Waals attractions are small and the strength of attraction can be modulated in the range of a few  $kT$ .<sup>[6]</sup> Under these conditions, aggregation is reversible and suspensions can undergo phase transitions. This opens the door for connecting discussions of the thermodynamics of solutions and solute/solvent interactions with the language of suspensions, not surprisingly demonstrating the smooth transition in physical behavior as particle size grows from the molecular to the colloidal.

The two best studied systems of attractive colloidal suspensions are based on suppressing van der Waals attractions by index matching the particles while further suppressing attractions by coating the particles with short hydrocarbon chains that act as steric stabilizers. Silica particles coated with octadecyl hydrocarbon chains or trimethoxysilane materials, and polymethylmethacrylate particles stabilized by a layer of polyhydroxyesteric acid suspended in a number of solvents have been used as model hard sphere systems. Attractions are generated in one of three ways. The first two involve changing the state of the coating/solvent interactions by altering the composition of the continuous phase, or by changing suspension temperature. Both methods drive the unfavorable stabilizing hair/solvent interactions, resulting in attractive interactions.

The third method of altering the strength of attraction involves addition of a nonadsorbing polymer. In a solution containing a nonadsorbing polymer, when two colloidal particles approach each other, the polymer is excluded from the gap between the particles. This exclusion leads to an imbalance in osmotic pressure of the polymer solution between the gap and in bulk solution. The imbalance drives the particles together and the resulting attraction is called "depletion" attraction. The strength of attraction is proportional to the polymer concentration, and the range of attraction is determined by the size ratio of polymer to colloid.<sup>[27,28]</sup> Depletion systems have the added advantage of providing a means of independently controlling both the strength and the range of attraction. The disadvantage of using depletion interactions as models of weakly attractive colloidal

suspensions is that the suspension becomes a three-component system and the application of standard pseudo-one-component interaction potentials fails to describe the suspension thermodynamic behavior. Nevertheless, a great deal has been learned through experimental and modeling efforts focusing on depletion systems.

A third system for studying the phase behavior of weakly attractive suspensions involves native nanoparticles. As mentioned above, for these systems, van der Waals attractions are sufficiently small that suspensions become thermodynamically stable without steric coatings or index matching. The strength of the attraction can be modulated through changes in temperature, pH, ionic strength, or concentration of the nonadsorbing polymer.

For all of these systems, one of the keys to understanding phase behavior lies in developing methods to characterize the strength and range of the attractive interaction. One of the advantages of the depletion system is that analytical models are available for characterizing the strength of attraction in the limit of dilute particles. As the particle volume fraction increases, these models fail quantitatively and, in some cases, qualitatively.<sup>[7]</sup> However, the effects of the control variables (i.e., the concentration and molecular weight of the polymer) are captured in these models. Unfortunately, for the development of model systems, there are no a priori methods of knowing how changes in control parameters alter the strength or range of attraction in the octadecyl silica system as solvent composition or temperature is altered, or in nanoparticle suspensions with changes in continuous phase composition. However, it is the sensitivity of the interactions to the chemistry of the particles and solvent that offers the richness of the observed behavior and technological applications of many colloidal systems. As a result, there is growing attention being placed on developing methods for characterizing the effects of continuous

phase composition on the strength of attraction of nanoparticles.

Attractive systems are expected to show disorder/order as well as gas/liquid phase transitions. In the colloidal field, the first models to capture this were those on depletion systems as described by Gast, Hall, and Russel,<sup>[28]</sup> where they demonstrated that when the range of the attraction was on the order of  $0.3R$  or larger, a phase diagram similar to that expected for molecules would be observed. This phase diagram in a space where the inverse of the dimensionless strength of attraction is plotted as a function of particle concentration has a critical point and a triple point expected for systems showing liquid/liquid and liquid/solid phases. As the range of the attraction is reduced, the critical point drops below the triple point and there are only two stable phases predicted: fluids and crystals. Despite having a finite size potential and an attractive potential, thermodynamically stable gas/liquid transition is lost. The critical point lies below the fluid/solid phase boundary. The spinodal for this fluid/fluid phase boundary can be probed when the system is quenched rapidly, at which point the system spontaneously decomposes into a dilute and a concentrated colloidal suspension. A common interaction potential used to describe attractions is the Yukawa potential. The interaction energy  $u(r)$  for Yukawa systems is given by:

$$u(r) = \left\{ \begin{array}{ll} \infty & r < 2R \\ -\frac{\varepsilon}{kT} \frac{e^{(R/\lambda)(1-r/2R)}}{r/2R} & r \geq 2R \end{array} \right\}$$

where  $\lambda/R$  is the range of attraction and  $\varepsilon/kT$  is the strength of attraction. The phase diagram of Yukawa fluids is given in Fig. 5<sup>[29]</sup> for different values of  $\lambda/R$  and, as mentioned above, the critical point begins to drop below the fluid/solid phase boundary for  $\lambda/R = 0.29$ .

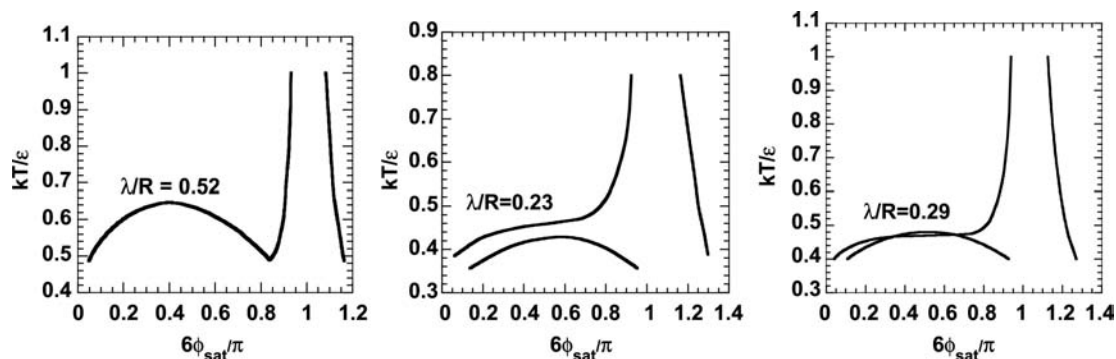


**Fig. 5** Phase diagram calculations of the Yukawa potential using the perturbation theory for different ranges of attraction  $\lambda/R$ . When  $\lambda/R < 0.29$  (small ranges of attraction), the critical point begins to move below the fluid/solid phase boundary. The phase diagram of  $\lambda/R = 0.23$  is what is typically seen in a number of protein solutions and in solutions of inorganic nanoparticles. Source: From Ref.<sup>[29]</sup>.

Understanding of the influence of the extent of the attractive well on phase behavior was advanced by understanding the phase behavior of fullerenes ( $C_{60}$ ),<sup>[4]</sup> where detailed calculations showed that no liquid phase would be stable, and protein suspensions, where the existence of a metastable fluid/fluid phase transition was revealed.<sup>[30,31]</sup>

In the limit of very-short-range attractions between particles, the simplest model for the interparticle interaction is the adhesive hard sphere (AHS) potential.<sup>[1]</sup> The AHS potential is a two-parameter potential with  $\Gamma_{\text{AHS}}$  characterizing the strength of interactions and  $R$  the particle radius. Extensive simulations and density functional theory calculations have identified the phase boundary associated with the liquid/liquid transition, percolation, and liquid/solid transition. However, the AHS system contains certain limitations, and predictions of the phase boundary for all values of  $\Gamma_{\text{AHS}}$  are not possible.<sup>[32]</sup> However, as the range of attraction is decreased, the AHS, square well, and Yukawa interactions begin to converge if normalized by a common measure of the strength of attraction.<sup>[6]</sup> The general phase diagram resembles that of a very-short-ranged square well fluid or Yukawa fluid, with the liquid/liquid phase transition lying below the liquid/solid phase transition. Experimentally, this is seen in a number of protein solutions and in solutions of inorganic nanoparticles.

The utility of the square well interaction models in the limit of very narrow wells (i.e., approaching the AHS potential) for describing the thermodynamics of nanoparticle suspensions (proteins and inorganic silicotungstic acid) and in locating crystallization conditions has been repeatedly demonstrated.<sup>[6,23]</sup> Because of the inherent complexity in characterizing all the interaction forces (electrostatic, van der Waals, depletion, solvation and structural forces, hydrogen bonding, and salt bridges) between two nanoparticles in suspension, indirect measures of the overall interactions must be used. The experimental variables suggested for characterizing the interactions have been the inverse osmotic compressibility  $(d\Pi/d\rho)_{\text{sat}}$  at the solubility point, the second virial coefficient ( $B_2$ ), the relative solution viscosity ( $\eta/\eta_c$ ), and the solubility  $\phi_{\text{sat}}$ . Various techniques have been developed for extracting these parameters for model-free representations of phase behavior that become important for testing different interaction potentials. These studies demonstrated the universal nature of the solubility curve when the measured second virial coefficient ( $B_2/16\pi R^3/3$ ) characterizing pair interactions was plotted against the solubility  $\phi_{\text{sat}}$  (Fig. 6).<sup>[23]</sup> Agreement between theory and experiment is excellent. These results suggest that the crystallization boundaries of nanoparticle suspensions are relatively insensitive to the details of the interaction potential and that if two

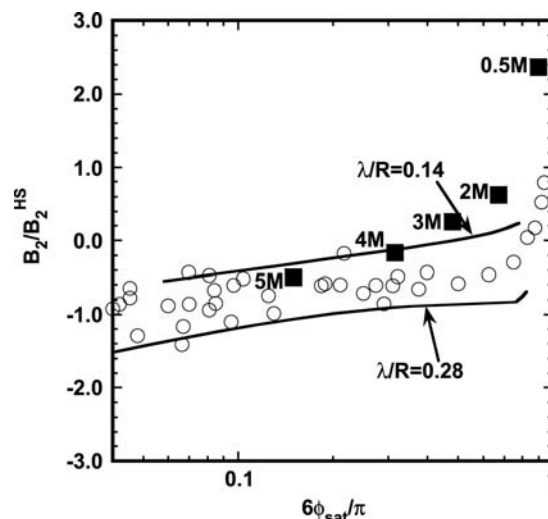


**Fig. 6** Measured second virial coefficients of STA (solid squares) in different background salt concentrations compared with data on a number of proteins (lysozyme; Bovine Pancreatic Trypsin Inhibitor (BPTI) open circles) in different buffer solutions. The second virial coefficients are non-dimensionalized with the hard sphere value and plotted against the solubility (volume fraction  $\phi_{\text{sat}}$ ) of the respective species. The solid lines are calculations of the attractive Yukawa potential with two different ranges of attractions  $\lambda/R$  of 0.14 and 0.28. The values of 0.14 and 0.28 indicate that attractions between the particles are short-ranged. The experimental data for silicotungstic acid (STA) (at high salt concentrations) and proteins collapse within the narrow range of attractions, which are only a fraction of the particle diameter. The collapse also indicates that proteins and STA are thermodynamically similar; if two suspensions have the same  $B_2$ , then they have the same solubility. This plot also provides an opportunity to extract interaction potential parameters for a given experimental system in a model-independent manner. *Source:* From Ref.<sup>[23]</sup>

suspensions have the same  $B_2/(16\pi R^3/3)$ , then they will have the same solubility. These results have applications in the location of solution conditions giving rise to protein crystals.

Rates of nanoparticle crystallization have been the subject of controversy. In the first place, these crystals often nucleate slowly (Fig. 7).<sup>[33]</sup> Without this being the case, it would not be possible to probe the existence of the metastable liquid/liquid spinodal. Numerous studies have applied classical nucleation theory to extract solid/liquid surface tensions that are in broad agreement with experiments. Kulkarni and Zukoski<sup>[34]</sup> demonstrated that these surface tensions were in good agreement with predictions based on pair interaction models that are capable of predicting the location of the solubility boundary. The influence of the location of metastable liquid/liquid spinodal relative to the solubility curve on the rate of nucleation has been explored. Simulations and analytical models indicate



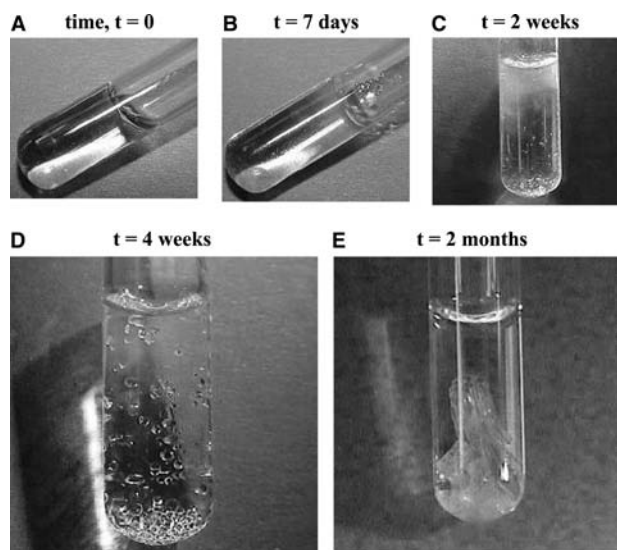


**Fig. 7** Lysozyme solution in 0.6 M sodium phosphate buffer, pH 7.0, at an initial concentration of 100 mg/mL at 10°C. The solution starts fluidlike (A) and gels over a period of 1 week (B). Crystallites appear to nucleate within the gel (C), which grow (D) and finally form large ordered crystals (E), in equilibrium with a fluid of low protein concentration. A detailed study of the solubility and crystal nucleation kinetics revealed that these phenomena are largely controlled by the strength of attraction and that if two proteins have the same  $B_2$ , then they have the same kinetics of nucleation. Source: From Ref.<sup>[33]</sup>.

that the enhanced compressibility of the suspension near the critical point will greatly enhance the rate of crystal nucleation.<sup>[35,36]</sup> Thus modeling efforts suggest that high-quality crystals can be grown near the critical point of the phase boundary. However, experimental verifications of these observations are difficult because of the high concentrations of proteins at the critical point ( $\sim 400$  mg/mL). There have been a number of experimental studies in measuring the nucleation rates of proteins under a variety of conditions.<sup>[37–39]</sup> Kinetic models of nucleation consistently overpredict experimental estimates. Dixit and Zukoski<sup>[36]</sup> attribute this to the use of simple centrosymmetric potentials in describing the kinetics of nucleation. More sophisticated patchy interactions that better approximate protein interactions with resulting modifications in the nucleation mechanism might provide an answer.

Connections between absolute rates of crystal nucleation and theoretical predictions have led to some controversies. Although many studies confirm that classical nucleation theory captures the supersaturation dependence on the nucleation rate, the absolute rate is very poorly described by these models. As with molecular systems, measuring the rate of nucleation and linking what can be measured to what is predicted by extant models remain at the heart of

this controversy. A significant conclusion is that we have a poor understanding of what it is that controls the rates of crystal formation in supersaturated nanoparticle suspensions.<sup>[37–39]</sup>

As mentioned earlier, control over the strength and range of attractions can be achieved by the addition of non-adsorbing polymers to colloidal suspensions. The important variables in these systems are the polymer concentration ( $c_p$ ), which determines the strength of attraction, and the size ratio of polymer to colloid ( $R_g/R$ ), which determines the range of attraction. Recent experiments performed on silica<sup>[7,8]</sup> and polymethylmethacrylate model systems<sup>[27,40]</sup> characterize phase behavior as a function of particle volume fraction,  $R_g/R$  and  $c_p$ . In addition, osmotic compressibility and microstructures have been measured for the octadecylsilica suspensions suspended in decalin in the presence of polystyrene over a wide range of molecular weights.<sup>[8,9]</sup> A variety of phases are observed depending on the value of  $R_g/R$  and polymer concentration (Fig. 8).<sup>[8]</sup> Even though standard theories could predict the  $R_g/R$  value of 0.3 below which crystallization occurred, the predictions of solution miscibility with

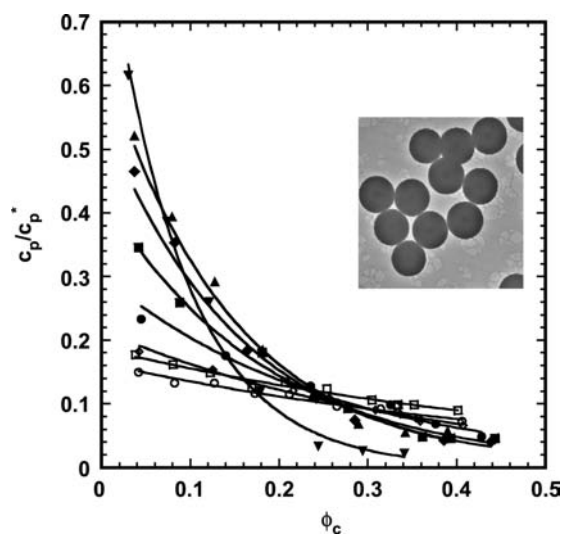


**Fig. 8** Phase diagram of 100-nm (diameter) octadecanol-coated silica particles (inset figure) suspended in decalin in the presence of nonadsorbing polystyrene. The molecular weight of polystyrene is varied to achieve eight different size ratios of polymer to colloid ( $R_g/R$ ) and the phase diagram determined for each  $R_g/R$ . Open symbols represent gel boundaries for  $R_g/R = 0.025$  (circles), 0.061 (squares), and 0.09 (diamonds). Filled symbols represent binodals for fluid–solid [ $R_g/R = 0.243$  (circles)] and fluid–fluid [ $R_g/R = 0.525$  (squares), 0.802 (diamonds), 1.10 (triangles), and 1.74 (reverse triangles)] phase separation. The solid lines (phase boundaries) are drawn to guide the eye. The colloidal silica suspensions are stable below the solid line. As more polymer is added and as one crosses the phase boundary, phase separation/gelation occurs depending on  $R_g/R$ . Source: From Ref.<sup>[8]</sup>.

$R_g/R$  at fixed colloid volume fraction are in direct contradiction to what is observed experimentally. Experimentally, solution miscibility improves as  $R_g/R$  increases at fixed  $\phi$ , whereas standard theories predict the opposite trend. Comparisons with recently developed Polymer Reference Interaction Site Model (PRISM)<sup>[41,42]</sup> led to qualitative agreements with experimental data. PRISM is a three-component model (particles, polymer, and solvent) that treats the polymers as flexible chains of monomer units that have both conformational and translational entropy, which needs to be taken into account in describing the thermodynamics of colloid–polymer mixtures. The theory takes into account particle–particle, polymer–polymer, and polymer–particle interactions and qualitatively captures the right trends in phase behavior.

In addition to crystallization and liquid–liquid phase separation, suspensions experiencing very-short-range attractions are observed to gel when  $R_g/R < 0.1$ .<sup>[7,8]</sup> Gelation is a phenomenon in which particles aggregate, forming a space-spanning structure that has a finite elastic modulus and yield stress. As mentioned before, gelation is a kinetic phenomenon and hence cannot be described by standard thermodynamic models. A dynamic model, which captures the arrest of particles with increasing polymer concentration and hence predicts the gelation boundary, is needed. The recently developed mode coupling theory (MCT), combined with PRISM (for colloid polymer mixtures), is capable of predicting gel boundaries.<sup>[43,44]</sup> MCT views the gel as particles trapped by a network of bonds that hinders the particle motion, resulting in a nonergodic state. Thus gelation (according to MCT) is caused by formation of long-lived cages. Gelation occurs at the point where the long-range self-diffusivity drops to zero. MCT is capable of predicting density autocorrelation functions as are measured by dynamic light scattering and has been applied to hard sphere systems where it captures many of the details of the colloidal hard sphere glass transition. It has also been applied to attractive suspensions where the gel line and dependence on  $R_g/R$  have been explored and the theory qualitatively captures the observed trends, particularly for  $\phi$  above 0.2.

MCT is also successful in predicting another interesting phenomenon observed when increasing amounts of polymer are added to glassy hard sphere suspensions (i.e.,  $\phi > 0.58$ ). The experimental observation is that, on addition of polymer (or when turning on a weak attraction), particles, on average, move closer together, but the coherence of the first shell of particles is disrupted. The result is that particles that are trapped by their nearest neighbors in the glassy state are now free to diffuse and the glass melts. However, on adding more polymer, the coherence of the first shell of particles is reestablished, the ability of particles to

diffuse freely is diminished, and, with a sufficiently large polymer concentration, the suspensions gel. MCT is able to explain the observed phenomena based on the “cage” effect.<sup>[44]</sup> Thus, by introducing attractions in the system, one can go from glasses to liquids to gels. Recent studies on the dynamics of these systems demonstrate that the internal dynamics of gels is different from those of glasses. In particular, in glasses, the root mean square (RMS) displacement scales on the particle diameter, whereas in the gels, the RMS displacement of the particles scales on the localization length that is determined by the extent of the interparticle attraction and the particle volume fraction.

Of particular interest is the suggestion that suspensions of particles experiencing extents of attraction less than about  $0.1R$  will not display thermodynamically stable phase transitions. Instead, with increasing volume fraction or with increasing strength of attraction, these suspensions gel or form irreversible aggregates. Thus the fractal flocs formed in irreversible aggregation (such as when salt is added to dilute latex suspensions) may result from short-range attractions rather than from strong attractions. This phenomenon can be circumvented in some cases. For example, if uniform suspensions are made up below the gel line in depletion systems and the particles are allowed to settle, crystals will form even when  $R_g/R < 0.1$ . This observation indicates that understanding of the dynamics of attractive colloidal suspensions remains a fruitful area of research.

## CONCLUSION

Suspensions of nanoparticles display a wide range of phase behavior—glasses, gels, crystals, and even separation into two liquid phases. The key variables that control the phase behavior are the range and strength of particle interactions. These variables can, in turn, be tuned in a number of different ways: by adding salt and polymer, by changing temperature, etc. Progress has been made in understanding the physics behind the phase separation process by working with well-characterized suspensions where the particles are spherical and interact with centrosymmetric potentials. This work has provided a basis for understanding the effects of particle anisotropy of interactions on phase behavior and the kinetics of the assembly process. As we look into the future, the challenges lie in extending the concepts and tools developed on simple systems to systems that are more complex, including anisotropic (rods and biological systems such as DNA) particles, and to mixtures of different kinds of particles (e.g., rods and spheres). Questions that must be answered include how interactions in such complex systems can be tuned to make them assemble into

useful structures. For example, most studies of order/disorder phase transitions have focused on systems that produce cubic crystals. However, proteins are known to crystallize into a wealth of space groups. Is it possible to engineer the space group into which particles assemble by designing particle shape or surface chemistry? Similar questions can be asked about gels: Is it possible to alter the nature of the particle interactions to create gels with the desired volume fraction and flow properties by engineering particle size and shape? Answering these questions requires advances in descriptions of phase behavior and kinetics of phase transitions as well as new synthetic approaches that result in particles of controlled surface chemistry. As an indication of the opportunities that are developing, we conclude this section by giving below a few examples involving systems with more complex interactions that lead to interesting phase behavior.

Tohver et al.<sup>[45,46]</sup> recently described a new mechanism for stabilizing colloidal particles. They noticed that when small amounts of charged nanoparticles were added to a gelled colloidal microsphere suspension (gelation occurs because of the attractive van der Waals forces), the gel melts and the suspension flows. However, increasing the amount of the nanoparticles flocculates the suspension. The initial stabilization mechanism is attributed to the segregation of the nanospheres on the surface of the microsphere colloidal particles because of their highly repulsive coulombic interactions in solution. This haloing effect results in a dense cloud of nanoparticles around each large particle such that when two large particles approach, they feel repulsive osmotic forces similar to that developed by overlapping double layers. This reduces the long-range van der Waals interactions between the colloidal spheres, thereby stabilizing the suspension. Increasing the amount of the nanospheres increases depletion attractions between spheres, thereby flocculating them at higher concentrations.

Polyelectrolytes (DNA, F-actin, and viruses) are complex molecules (in size and shape) that have a charge distribution on their surface, which is quite different from the uniform charge distribution on spheres that we dealt with in “Weakly Attractive Suspensions.” In solution, charged polyelectrolytes repel each other (DNA in water) in the presence of monovalent ions, which is what is expected because like charges always repel. However, in the presence of multivalent ions, like charge attractions have been observed in a number of polyelectrolyte systems. Butler et al.<sup>[47]</sup> studied polyelectrolyte condensation using anionic rodlike M13 virus and a series of “tunable” divalent cations with the aim of understanding the role of ion multivalence and geometry in the phase change process. Using the experimental system, they were able to construct a multivalent ion–polyelectrolyte phase

diagram and developed an experimentally motivated criterion for like-charge attraction based on the ion valence, ion size, and the Gouy–Chapman length. The phase diagram defines regions between disordered rods and regions where the rods have condensed into an aligned structure. This phase behavior is of interest because it demonstrates the ability of multivalent ions to produce a lowest free-energy state for electrostatically repulsive rods and provides insights into novel methods for organizing anisotropic particles.

Adams et al.<sup>[48]</sup> describe a rich phase diagram for mixtures of colloidal rods (filamentous bacteriophage fd virus) and spheres (polystyrene latex, polyethylene oxide, and polyethylene glycol). The phases they observed include: bulk demixing into rod-rich and rod-poor phases, and microphase separation into a variety of morphologies. One microphase consists of layers of rods alternating with layers of spheres; in another microphase, the spheres reversibly assemble into columns, which in turn pack into a crystalline array. Using the concepts of depletion attractions, they were able to predict the majority of the experimentally observed phases. The spheres and rods were modeled as hard objects, and the work done on the phase behavior of just pure hard spheres and hard rods aided in the development of a theory for the mixtures. However, the simple theory is unable to predict the existence of the columnar phase—the description of which remains a theoretical challenge.

The above cases were chosen to exemplify opportunities that exist for manipulating the states of aggregation of colloidal suspensions. Clearly, by working with strengths of attraction and repulsion on the order of a few times the average thermal energy of the system and by manipulating the degree of anisotropy of particle interactions, a wide range of structures can be built. This field will continue to require attention as the assembly of nanostructures continues to be of scientific and technological significance.

## ACKNOWLEDGMENTS

This work was supported by the Nanoscale Science and Engineering Initiative of the National Science Foundation under NSF Award number DMR-0117792.

## REFERENCES

1. Russel, W.B.; Saville, D.A.; Schowalter, W.R. *Colloidal Dispersions*; Cambridge University Press: Cambridge, 1989.
2. McQuarrie, D.A. *Statistical Mechanics*; Harper Collins: New York, 1976.

3. Hunter, R.J. *Foundations of Colloid Science*; Clarendon Press: Oxford, 1987; Vol. 1.
4. Hagen, M.H.J.; Meijer, E.J.; Mooij, G.; Frenkel, D.; Lekkerkerker, H.N.W. Does C-60 have a liquid-phase?. *Nature* **1993**, *365* (6445), 425–426.
5. Hagen, M.H.J.; Frenkel, D. Determination of phase diagrams for the hard-core attractive Yukawa system. *J. Chem. Phys.* **1994**, *101* (5), 4093–4097.
6. Rosenbaum, D.; Zamora, P.C.; Zukoski, C.F. Phase behavior of small attractive colloidal particles. *Phys. Rev. Lett.* **1996**, *76* (1), 150–153.
7. Ramakrishnan, S.; Fuchs, M.; Schweizer, K.S.; Zukoski, C.F. Entropy driven phase transitions in colloid-polymer suspensions: Tests of depletion theories. *J. Chem. Phys.* **2002**, *116* (5), 2201–2213.
8. Shah, S.A.; Chen, Y.L.; Schweizer, K.S.; Zukoski, C.F. Phase behavior and concentration fluctuations in suspensions of hard spheres and nearly ideal polymers. *J. Chem. Phys.* **2003**, *118* (7), 3350–3361.
9. Shah, S.A.; Chen, Y.L.; Ramakrishnan, S.; Schweizer, K.S.; Zukoski, C.F. Microstructure of dense colloid-polymer suspensions and gels. *J. Phys., Condens. Matter* **2003**, *15* (27), 4751–4778.
10. Hachisu, S.; Kobayashi, Y. Kirkwood–Alder transition in monodisperse latexes: II. Aqueous latexes at high electrolyte concentration. *J. Colloid Interface Sci.* **1974**, *46*, 470–476.
11. Zhu, J.X.; Li, M.; Rogers, R.; Meyer, W.; Ottewill, R.H.; Russell, W.B.; Chaikin, P.M. Crystallization of hard-sphere colloids in microgravity. *Nature* **1997**, *387* (6636), 883–885.
12. Pusey, P.N. Colloidal suspensions. In *Liquids, Freezing and Glass Transition*; Hansen, J.P., Levesque, D., Zinn-Justin, J., Eds.; Elsevier: Amsterdam, 1991; 763–942. Part II.
13. Fuchs, M.; Cates, M.E. Theory of nonlinear rheology and yielding of dense colloidal suspensions. *Phys. Rev. Lett.* **2002**, *89* (24), 248304 (1–4).
14. Dixit, N.M.; Zukoski, C.F. Kinetics of crystallization in hard-sphere colloidal suspensions. *Phys. Rev., E* **2001**, *64* (041604), 1–10.
15. Russel, W.B. On the dynamics of the disorder order transition. *Phase Transitions* **1990**, *21* (2–4), 127–137.
16. Dixit, N.M.; Zukoski, C.F. Kinetics of crystallization in hard-sphere colloidal suspensions. *Phys. Rev., E* **2001**, *6404* (4), 1–10.
17. Chen, L.B. *The Dynamic Properties of Concentrated Charge Stabilized Suspensions*; Ph.D. Thesis; University of Illinois at Urbana-Champaign: Urbana, 1991.
18. Chaikin, P.M.; Pincus, P.; Alexander, S.; Hone, D. Bcc–Fcc, melting and reentrant transitions in colloidal crystals. *J. Colloid Interface Sci.* **1982**, *89* (2), 555–562.
19. Voegtli, L.P.; Zukoski, C.F. Adsorption of ionic species to the surface of polystyrene latexes. *J. Colloid Interface Sci.* **1991**, *141* (1), 92–108.
20. Voegtli, L.P.; Zukoski, C.F. A perturbation treatment of the order–disorder phase-transition in colloidal suspensions. *J. Colloid Interface Sci.* **1991**, *141* (1), 79–91.
21. Hone, D.; Alexander, S.; Chaikin, P.M.; Pincus, P. The phase-diagram of charged colloidal suspensions. *J. Chem. Phys.* **1983**, *79* (3), 1474–1479.
22. Beresfordsmith, B.; Chan, D.Y.C. Highly asymmetric electrolytes—a model for strongly interacting colloidal systems. *Chem. Phys. Lett.* **1982**, *92* (5), 474–478.
23. Ramakrishnan, S.; Zukoski, C.F. Characterizing nanoparticle interactions: linking models to experiments. *J. Chem. Phys.* **2000**, *113* (3), 1237–1249.
24. Dixit, N.M.; Zukoski, C.F. Pseudo-steady rates of crystal nucleation in suspensions of charged colloidal particles. *J. Phys., Condens. Matter* **2003**, *15* (10), 1531–1552.
25. Palberg, T. Crystallization kinetics of repulsive colloidal spheres. *J. Phys., Condens. Matter* **1999**, *11* (28), R323–R360.
26. Israelachvili, J.N. *Intermolecular and Surface Forces*; Academic Press: London, 1991.
27. Lekkerkerker, H.N.W.; Poon, W.C.K.; Pusey, P.N.; Stroobants, A.; Warren, P.B. Phase-behavior of colloid plus polymer mixtures. *Europhys. Lett.* **1992**, *20* (6), 559–564.
28. Gast, A.P.; Hall, C.K.; Russel, W.B. Phase separations induced in aqueous colloidal suspensions by dissolved polymer. *Faraday Discuss.* **1983**, *76*, 189–201.
29. Ramakrishnan, S. *Thermodynamics and Phase Behavior of Nanoparticles*; M.S. Thesis; University of Illinois at Urbana-Champaign: Urbana, 1998.
30. Lomakin, A.; Asherie, N.; Benedek, G.B. Monte Carlo study of phase separation in aqueous protein solutions. *J. Chem. Phys.* **1996**, *104* (4), 1646–1656.
31. Asherie, N.; Lomakin, A.; Benedek, G.B. Phase diagram of colloidal solutions. *Phys. Rev. Lett.* **1996**, *77* (23), 4832–4835.
32. Stell, G. Sticky spheres and related systems. *J. Stat. Phys.* **1991**, *63* (5–6), 1203–1220.
33. Kulkarni, A.M. *An Investigation of Phase Behavior and Crystal Nucleation Kinetics in Solution of Globular Protein*; Ph.D. Thesis; University of Illinois at Urbana-Champaign: Urbana, 2001.
34. Kulkarni, A.M.; Zukoski, C.F. Nanoparticle crystal nucleation: Influence of solution conditions. *Langmuir* **2002**, *18* (8), 3090–3099.
35. ten Wolde, P.R.; Frenkel, D. Enhancement of protein crystal nucleation by critical density fluctuations. *Science* **1997**, *277* (5334), 1975–1978.
36. Dixit, N.M.; Zukoski, C.F. Crystal nucleation rates for particles experiencing short-range attractions: applications to proteins. *J. Colloid Interface Sci.* **2000**, *228* (2), 359–371.
37. Dixit, N.M.; Kulkarni, A.M.; Zukoski, C.F. Comparison of experimental estimates and model predictions of protein crystal nucleation rates. *Colloids Surf., A Physicochem. Eng. Asp.* **2001**, *190* (1), 47–60.
38. Galkin, O.; Vekilov, P.G. Direct determination of the nucleation rates of protein crystals. *J. Phys. Chem., B* **1999**, *103* (49), 10,965–10,971.
39. Galkin, O.; Vekilov, P.G. Control of protein crystal nucleation around the metastable liquid–liquid phase boundary. *Proc. Natl. Acad. Sci.* **2000**, *97* (12), 6277–6281.
40. Ilett, S.M.; Orrock, A.; Poon, W.C.K.; Pusey, P.N. Phase-behavior of a model colloid–polymer mixture. *Phys. Rev., E* **1995**, *51* (2), 1344–1352.

41. Fuchs, M.; Schweizer, K.S. Structure of colloid-polymer suspensions. *J. Phys., Condens. Matter* **2002**, *14* (12), R239–R269.
42. Fuchs, M.; Schweizer, K.S. Structure and thermodynamics of colloid-polymer mixtures: a macromolecular approach. *Europhys. Lett.* **2000**, *51* (6), 621–627.
43. Bergenholtz, J.; Fuchs, M. Gel transitions in colloidal suspensions. *J. Phys., Condens. Matter* **1999**, *11* (50), 10,171–10,182.
44. Bergenholtz, J.; Poon, W.C.K.; Fuchs, M. Gelation in model colloid-polymer mixtures. *Langmuir* **2003**, *19* (10), 4493–4503.
45. Tohver, V.; Smay, J.E.; Braem, A.; Braun, P.V.; Lewis, J.A. Nanoparticle halos: a new colloid stabilization mechanism. *Proc. Natl. Acad. Sci.* **2001**, *98* (16), 8950–8954.
46. Tohver, V.; Chan, A.; Sakurada, O.; Lewis, J.A. Nanoparticle engineering of complex fluid behavior. *Langmuir* **2001**, *17* (26), 8414–8421.
47. Butler, J.C.; Angelini, T.; Tang, J.X.; Wong, G.C.L. Ion multivalence and like-charge polyelectrolyte attraction. *Phys. Rev. Lett.* **2003**, *91* (2), 028301 (1–4).
48. Adams, M.; Dogic, Z.; Keller, S.L.; Fraden, S. Entropically driven microphase transitions in mixtures of colloidal rods and spheres. *Nature* **1998**, *393* (6683), 349–352.

# Nanoparticle Synthesis: Biological Path

**Kenji Iwahori**

*CREST, Japan Science and Technology Agency (JST), Kawaguchi, Japan*

**Ichiro Yamashita**

*Graduate School of Material Science, Nara Institute of Science and Technology (NAIST), Ikoma, Japan*

## INTRODUCTION

A variety of nanoparticles (NPs) have been synthesized using the cage protein apoferritin and *Listeria* ferritin. Metal oxide NPs (Co, Ni, and Cr) and semiconductor NPs (CdSe and ZnSe) were described to be made by using apoferritin with a 7 nm diameter inner cavity. The synthesized NPs show small-size dispersion, which is ideal for use as a nanoelectronic device component. There are many kinds of protein cages suitable as biotemplates, and researchers have been searching for new biotemplates with an inner cavity. Larger or smaller cage-shaped proteins have been used as biotemplates and the mechanism of biomineralization has been studied. Recent works concerning the synthesis of NPs using supramolecular protein cages are reviewed. The applications of NPs made using biotemplates are also introduced.

## BACKGROUND

Nanotechnology includes a very wide range of research fields, ranging from biology to semiconductor engineering. This emerging technology has the potential to answer many difficult, so far unsolved problems by means of nanometric approaches. There are many materials being used in nanotechnology, but it is not an exaggeration to say that NPs are the fundamental component of nanotechnology. Various NPs are used or expected to be used in many applications such as magnetic recording materials, catalytic materials, fluorescent markers, drug delivery systems, and quantum electronics. Especially, conductive or semiconductor NPs are anticipated to be good quantum electronics device components. They are also used to make the nanostructures using bottom-up technology.

There are a number of methods for making NPs and they are classified into three categories: physical methods, chemical methods, and biological methods. Physical methods include grinding, laser abrasion, and ion injection. Chemical methods include the sol-gel method and the tri-*n*-octylphosphine oxide (TOPO) method. Biological methods include using proteins and biomineralization using a nanometric inner cavity

or outer surface of biosupramolecules for synthesizing NPs. There are advantages and disadvantages in each of the three methods, and researchers synthesize NPs using the method that most closely matches their needs.

Miniaturization of electronic device components to nanoscale dimensions is one of the most intensively studied research areas in nanotechnology. It is clear that the conventional fine-process technology based on photolithography cannot produce nanometer-size structures. To overcome this challenging problem, Yamashita et al. proposed a method utilizing the NPs or nanowires (NWs) synthesized using a biotemplate. The biotemplate technique is one of the most suitable methods to synthesize uniform NPs and NWs, when the inner cavity of a protein shell is used as a spatially restricted synthesis chamber. Because electron energy levels are strongly dependent on the NP or NW size, the homogeneity in size is ideal for an electronics device component. This is also true for photoluminescence. Biological methods offering uniform particle sizes are, therefore, well suited for synthesizing NPs for nanoelectronic devices.

NPs synthesis using the cavities of biotemplate molecules is currently a hot research area. Researchers are synthesizing a variety of uniform, high-quality NPs using several kinds of cage-shaped proteins such as CCMV, *Listeria* ferritin, DPS, HSP, and ferritin. Yamashita group mainly uses the cage-shaped protein, ferritin, to synthesize metal and semiconductor NPs and is elucidating the biomineralization mechanism of NPs in the cavity. In this entry, the recent proceedings and the latest research results of NP synthesis using a biotemplate are described.

## SYNTHESIS OF METAL COMPLEXES AND METAL OXIDE MATERIAL NPs IN THE APOFERRITIN PROTEIN

Ferritin is a major cellular iron-storage protein. Ferritin protein exists widely in many biological species and plays an important role in the homeostasis of ferrous



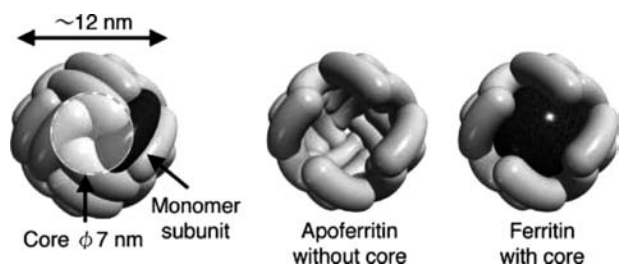


**Fig. 1** Schematic drawing of the cage-shaped protein—apoferritin without core and ferritin with core.

ion levels in the body. The ferrihydrite cores in ferritin can be removed fairly easily by dialysis against a solution containing a reducing agent.<sup>[1]</sup> Ferritin without a ferrihydrite core is called apoferritin. Fig. 1 shows schematic drawing of the apoferritin molecule. The outer and inner diameters are approximately 12 and 7 nm, respectively. There are narrow channels along the threefold axis connecting the cavity and outside, through which iron ions pass into the cavity. The native apoferritin consists of 24 polypeptide subunits, and there are two types of subunits, the light-chain subunit (L-subunit) and the heavy-chain subunit (H-subunit). H-subunit has a ferroxidase center that oxidizes ferrous iron to ferric iron. L-subunits play an important role in the self-assembly of ferritin molecules into a two-dimensional (2-D) crystal at the air–water interface via a salt-bridge interaction.

There are many previous works describing how metal complexes and inorganic materials are sequestered in the native apoferritin cavity.<sup>[2–12]</sup> Okuda et al.<sup>[7]</sup> also fabricated nickel hydroxide NPs in the horse spleen apoferritin (HsAFr) cavity by incubating ammonium nickel sulfate solution with HsAFr. The Ni core was imaged by transmission electron microscopy (TEM) after staining with 1% aurothioglucose. Aurothioglucose is too big to go through the channels and cannot stain the cavity, which makes it possible to investigate core formation. The optimized conditions for nickel core formation were 0.3 mg/ml HsAFr and 5 mM ammonium nickel sulfate in water containing dissolved carbon dioxide. The pH was maintained at pH 8.6 using two buffer solutions of 4-(2-hydroxyethyl) piperazine-1-ethanesulfonic acid) and 3-(Cyclohexylamino)-2-hydroxy-1-propanesulfonic acid (HEPES-CAPSO) with 20 mM ammonia. Ammonium ions were supplied to suppress bulk precipitation. Interestingly, the nickel oxide core did not form in a degassed reaction solution. It was also shown that the absence of carbonate ions leads to no nickel hydroxide core formation. The existence of carbonate ions is indispensable for nickel hydroxide core formation. The core formation ratio (CFR) of nickel hydroxide in the apoferritin cavity is nearly 100% (Fig. 2). The CFR was calculated using TEM images, dividing the

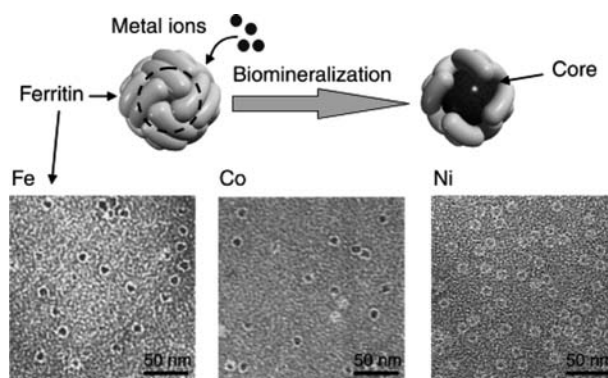


**Fig. 2** Typical TEM images of cobalt, nickel, and chromium NPs synthesized in the HsAFr cavity. NPs were observed by TEM with 1% aurothioglucose staining. The TEM image negatively stained shows many dots surrounded by ferritin protein shells. As aurothioglucose is too big to penetrate through narrow channels, the dots are attributed to individual metal cores.

number of ferritins with core by the total number of ferritin molecules. The synthesized nickel complexes NPs were characterized by energy dispersive X-ray spectrometry (EDS) and two EDS peaks specific to nickel (7.5 keV and 0.9 keV) were observed. Judging from the synthesis conditions and EDS measurements, it was concluded that the core is nickel hydroxide.

Okuda et al.<sup>[7]</sup> also synthesized chromium NPs in the HsAFr cavity. Chromium cores formed in about 80% of apoferritin cavities (Fig. 2). The formation of chromium cores needed carbonated ions or carbon dioxide bubbling in the reaction solution, as is the case for nickel hydroxide NP synthesis. The role of carbonate ions in the chemistry of the core formation reaction remains unknown, but they may coordinate nickel and chromium ions and stabilize them in the bulk solution or accelerate the hydroxylation in the apoferritin cavity compared to the bulk solution outside.

The above experiments used native ferritin molecules. Native apoferritin is a heteroassembly of L-subunit and H-subunits. The stoichiometry of L- and H-subunits varies from molecule to molecule, which is undesirable from an application point of view. Therefore, Takeda et al. produced recombinant apoferritin and investigated the difference between native ferritin and homogeneous recombinant ferritin,<sup>[13]</sup> and Iwahori produced several kinds of recombinant ferritins. In this entry, two important recombinant ferritins will be introduced.

1. Fer-0 recombinant ferritin: all L-subunits.
2. Fer-8 recombinant ferritin: all L-subunits lacking the first eight amino acids.

Nickel core formation by Fer-8 was studied. 0.3 mg/ml recombinant apoferritin Fer-8 was incubated in the

reaction solution with 5 mM ammonia nickel sulfate, 150 mM HEPES, CAPSO, and 20 mM ammonia water around pH 8.7 for 24 hr at room temperature. After the core formation process, the solution was centrifuged at low speed to discard precipitates and the supernatant was observed by TEM. TEM image revealed that nearly 100% of Fer-8 formed nickel cores. A similar result was obtained with HsAFr. Nickel hydroxide cores can be formed in the native and recombinant ferritin and the nickel hydroxide core formation needs carbonate ions.

Douglas and Stark<sup>[6]</sup> synthesized cobalt oxide NPs in the HsAFr cavity and *Listeria* ferritin by oxidizing Co(II) with H<sub>2</sub>O<sub>2</sub> while the reaction solution was dynamically titrated at pH 8.5 using NaOH. Tsukamoto et al. also successfully formed a metal complex core using cobalt oxide (Co<sub>3</sub>O<sub>4</sub>) in HsAFr and Fer-8.<sup>[12]</sup> In this case, a one-pot synthesis method was employed. The one-pot synthesis using buffer solution is more suitable for mass production, because the pH control using a buffer agent is very simple. The effect of the buffer reagents on the stability of cobalt ions and cobalt complex ions, which affects the cobalt core biomineralization, was studied. A thorough survey of the optimum conditions for the one-pot Co<sub>3</sub>O<sub>4</sub> core synthesis revealed that the optimum conditions consist of mixing 3 mM Co(II) ion with 0.5 mg/ml apoferritin in 100 mM HEPES pH 8.3 buffer solution followed by the oxidation of Co (II) ion by the addition of hydrogen peroxide (H<sub>2</sub>O<sub>2</sub>) at 50°C. Under these conditions, Co<sub>3</sub>O<sub>4</sub> cores were formed in over 90% of apoferritin cavities. The synthesized core analysis by X-ray photoemission spectroscopy (XPS) and electron energy-loss spectroscopy proved that they contained cobalt atoms, and the X-ray powder diffraction (XRD) structure analysis confirmed the core structure as Co<sub>3</sub>O<sub>4</sub>, which was consistent with the results obtained from lattice images of the cores by high-resolution TEM observations.

### SYNTHESIS OF SEMICONDUCTOR NPs IN THE APOFERRITIN CAVITY

Reports of inorganic NP synthesis in the apoferritin cavity have so far mostly been of metal complexes. It is of great interest to explore the possibility of synthesizing compound semiconductor NPs in the apoferritin cavity. Because the electron energy levels of the semiconductor NPs depend on their size and shape, semiconductor NPs can be a quantum dot or photofluorescence marker and are very attractive for nanoelectronics. However, the introduction of oppositely charged ions is very difficult and there are only a few reports of II–VI compound semiconductor NP synthesis. Kim and Mann<sup>[14]</sup> reported small cadmium

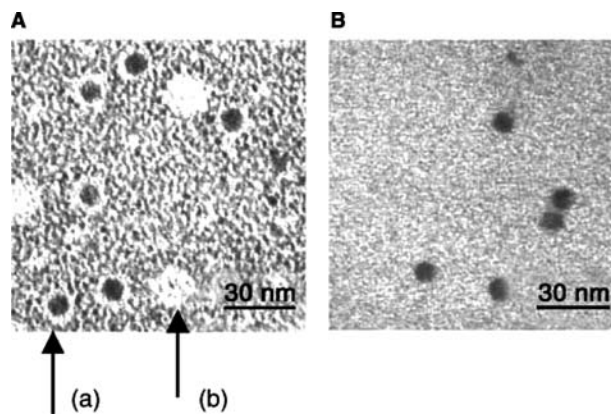


**Fig. 3** TEM images of CdSe NPs synthesized in the HsAFr cavity. The images are stained by 1% aurothioglucose. (A) Cores are surrounded by white rings, which are negatively stained protein shells. The arrowhead (a) shows the apoferritin with CdSe core and the arrowhead (b) shows the apoferritin without CdSe core. (B) TEM image of synthesized CdSe-ferritin molecule without stain. Homogenous dots from CdSe NPs were observed.

sulfide (CdS) core formation in the apoferritin cavity,<sup>[14]</sup> and Yamashita, and Hara reported synthesis of homogenous cadmium selenide (CdSe)<sup>[15]</sup> and Iwahori reported that of zinc selenide (ZnSe)<sup>[16]</sup> semiconductor NPs.

For the synthesis of CdSe NPs in the apoferritin cavity (Fig. 3), Yamashita et al. developed a new chemical reaction system. In aqueous solution, which is the fundamental solution for the biotemplate NPs synthesis, the chemical reaction between Cd<sup>2+</sup> and Se<sup>2-</sup> is very fast and induces CdSe aggregation very quickly. Therefore, Yamashita et al. designed a slow chemical reaction system where Cd<sup>2+</sup> is stabilized by excess ammonia and forms positively charged tetra-aminocadmium ions (Cd(NH<sub>3</sub>)<sub>4</sub><sup>2+</sup>). Se<sup>2-</sup> ions are supplied by selenourea. Selenourea is comparatively unstable in aqueous solution and slowly degrades to release Se<sup>2-</sup>. This slow chemical reaction of tetra-aminocadmium ions and selenium ions leads to suppression of the bulk precipitation in the reaction solution. CdSe nuclei are produced very slowly in the bulk solution, but in the apoferritin cavity, where the Cd<sup>2+</sup> ions are concentrated by the electrostatic potential made by the inner negative amino acid residues, nuclei are formed quickly. Once the nuclei are made, the CdSe surface works in a self-catalytic way so that homogenous CdSe semiconductor NPs are synthesized in the apoferritin cavity. The consumption of Cd<sup>2+</sup> and Se<sup>2-</sup> by the crystal growth in the cavity further lowers the possibility of a nucleus appearing in the bulk solution. Therefore, this slow chemical reaction system can produce fully developed CdSe semiconductor NPs selectively in the apoferritin cavity.

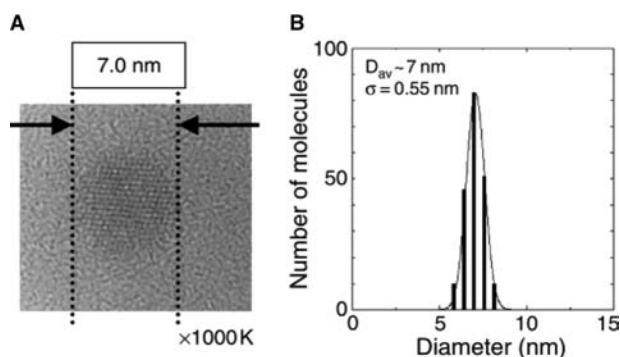


**Fig. 4** High-resolution TEM image of CdSe NPs in the apoferritin cavity. (A) A single crystal of CdSe. The diameter of CdSe NPs is 7 nm. (B) Diameter distribution of synthesized CdSe NPs.

XPS data of the synthesized CdSe-ferritin revealed that the cores are composed of Cd and Se. After heat treatment at 500°C to remove the protein shell, a set of fairly sharp XRD peaks was observed and the core structure was determined to be a cubic phase (zinc blend) CdSe with a little hexagonal phase (wurtzite). The average diameter of the obtained CdSe cores using TEM images was 7 nm, which is the same as that of the apoferritin cavity. The dispersion of diameters was small, and the standard deviation of the diameter was less than 10% of the average diameter (Fig. 4).

Following the CdSe NP synthesis, Iwahori et al. reported the successful synthesis of homogenous ZnSe NPs in the apoferritin cavity. ZnSe is also a promising material for n-type semiconductors. ZnSe NPs could be used as a quantum label for biological use, because its fluorescent light does not quench easily. The slow chemical reaction synthesis process was slightly modified for ZnSe NPs, and the optimum reaction conditions for ZnSe NPs was determined.<sup>[16]</sup> The CFR for ZnSe NPs reached more than 90% using the determined optimal conditions. The characterization of the synthesized ZnSe NPs in the apoferritin cavity by XRD and EDS revealed that they were a collection of cubic ZnSe polycrystals (Fig. 5).

To study the mechanism of ZnSe NP synthesis in the apoferritin cavity, Iwahori et al.<sup>[16]</sup> constructed three recombinant apoferritins, which differ in the electric charge of the threefold channel and the inner surface of apoferritin cavity.

1. Fer-8—the recombinant apoferritins that are composed of only L-subunit and lack the first eight amino acid residues from N-terminal.
2. 8A—the recombinant apoferritin derived from Fer-8 in which the Asp-131 and Glu-134 amino acids at the threefold channel were replaced by neutral alanine amino acid residues.

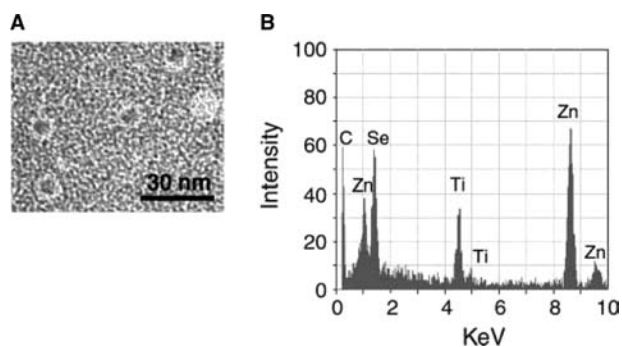


**Fig. 5** TEM image of ZnSe NPs and the EDS analysis of ZnSe synthesized in the apoferritin cavity. The images were stained by 1% aurothioglucose. (A) Cores are surrounded by white rings, which are negatively stained protein shells. (B) An EDS spectra of synthesized ZnSe NPs. The C and Ti peaks are ascribable to the TEM grid.

3. 8AK—the recombinant apoferritin derived from 8A, which has the Glu-58, Glu-61, and Glu-64 replaced by positively charged lysines.

ZnSe NPs were synthesized in the cavities using these three purified recombinant apoferritins. ZnSe CFR of three recombinant apoferritins depended on the amino acid residues of the threefold channel and inner cavity.<sup>[16]</sup> Three factors are found to be important to ZnSe NP synthesis in the apoferritin cavity.

1. Zn ion transformation through the threefold channel, which selectively introduces Zn ion into the apoferritin cavity.
2. Zn ion accumulation in the apoferritin cavity by the internal positive potential made by glutamic acid residues.
3. ZnSe nuclei formation at a nucleation site inside the cavity.

These results are potentially useful for the synthesis of a variety of compound semiconductor NPs in the apoferritin cavity.

## FABRICATION OF BIOTEMPLATE NPs IN CAGE-SHAPED PROTEINS

NP synthesis using the biotemplate, apoferritin, has been described above. Other kinds of biosupramolecules have also been used as biotemplates to synthesize NPs. Such biotemplates include mammalian protein cages, small protein cages from bacteria, and viral protein cages. Choosing the protein cages from nature, the researcher can fabricate a variety of NPs of different size and materials.

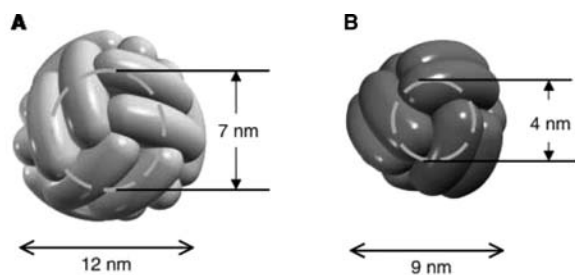
Viral protein cages have a wide variety of shapes and sizes and, hence, are good templates to produce various sizes of NPs. The adenovirus has a diameter of close to 100 nm, and the cowpea mosaic virus (CPMV) has an inner cavity with a diameter of 30 nm. Cowpea chlorotic mottle virus (CCMV) has an inner cavity with a diameter of 28 nm, and the average diameter of the brome mosaic virus (BMV) particle is 26 nm and the inner cavity is only 8 nm.<sup>[17]</sup>

CCMV undergoes a reversible pH-dependent swelling that results in a 10% increase in virus size. This transition is the result of an expansion at the pseudo threefold axis of the virus particle, which causes the formation of 60 separate openings (each 0.2 nm in diameter) in the protein shell. Douglas and Young<sup>[18]</sup> utilized this character and synthesized paratungstate and decavanadate in the CCMV using the pH-dependent reversible gating system. The synthesized NPs showed a diffraction pattern consistent with the ammonium salt of paradodecatungstate ion,  $(\text{NH}_4)_{10}\text{H}_2\text{W}_{12}\text{O}_{42}\cdot 4\text{H}_2\text{O}$ . A similar approach was used to constrain the mineralization of a vanadate species in the cavity of CCMV. This synthesis also results in the formation of monodisperse vanadate NPs with essentially the same size distribution as that seen for the paratungstate. These crystals showed XRD consistent with a mixture of  $\text{Na}_6\text{V}_{10}\text{O}_{28}\cdot 18\text{H}_2\text{O}$  and  $(\text{NH}_4)_6\text{V}_{10}\text{O}_{28}\cdot 18\text{H}_2\text{O}$ .

Considering the smaller cages, which are more attractive from nanoelectronic point of view, there is *Listeria* ferritin (LisFr). This ferritin-like protein from the bacteria *Listeria innocua* has been shown to form a twelve-subunit cage structure making as 4 nm diameter interior cavity (Fig. 6).<sup>[19,20]</sup> This small cage structure

has the capacity to hold 500 Fe atoms as a ferric oxyhydroxide.<sup>[21,22]</sup> Allen et al.<sup>[23]</sup> have cloned the LisFr into an *E. coli* expression system and purified recombinant apoL-FLP (raLisFr), which does not have Fe atoms in the cavity. They investigated the Fe mineralization in raLisFr under non-physiological conditions. In the reaction solution at 65°C and pH 6.5, raLisFr mineralizes Fe NP in the cavity. The analysis revealed that the cores are ferromagnetic  $\gamma\text{-Fe}_2\text{O}_3$ .<sup>[23]</sup> Douglas and coworkers have also been able to form cobalt NPs in raLisFr. They synthesized two types of cobalt NPs,  $\text{Co}(\text{O})\text{OH}$  at 23°C and  $\text{Co}_3\text{O}_4$  at 65°C. Both cobalt NPs were 5 nm in diameter, which is the same as the cavity size of raLisFr.<sup>[24]</sup>

An old technique was renewed by Belcher et al., when the phage display method was used to select peptides with specific affinity against the semiconductor surface, GaAs.<sup>[25]</sup> Now, as a result of researchers' efforts, many such target-specific peptides are available. Kramer et al. recently reported that silver NPs (Ag-NPs) were synthesized in the apoferritin cavity. They used genetically engineered human L-subunit ferritin (HLCF) with a silver-binding peptide, AG4. AG4 is a dodecapeptide (Asn-Pro-Ser-Ser-Lue-Phe-Arg-Tyr-Leu-Pro-Ser-Asp) selected by a phage peptide display library. This dodecapeptide was shown to be able to reduce the silver ions to metallic silver at neutral pH and synthesize Ag NPs.<sup>[26-28]</sup> They constructed chimera protein, AG4 peptide sequence fused to the C-terminal of L-chain ferritin sequences, and this chimera protein makes a 24-mer cage-shaped protein with the AG4 peptide displayed on the inner cavity surface. When the LCF-AG4 protein cages were incubated in the presence of 0.4 mM  $\text{AgNO}_3$ , the Ag NPs with an average diameter of 5 nm was synthesized in the cavity of LCF-AG4. Recently, many kinds of metal target-specific peptides have been isolated by the phage display method. If the most suitable metal-binding peptide for the purpose was selected and the fusion-protein cage was made, the NP suitable for various applications could be synthesized.



	Ferritin	<i>Listeria</i> ferritin
Diameter	12 nm	9 nm
Diameter of cavity	7 nm	4 nm
Molecular weight	450 kDa	240 kDa
No. of subunits	24	12

**Fig. 6** Schematic drawing of HsAfr (A) and apoferritin from *Listeria innocua* (B). The spherical hollow shell of ferritin is composed of 24 polypeptide subunits. The *Listeria* ferritin is composed of 12 polypeptide subunits. The inner and outer diameters of the protein shell are about 7 nm and 12 nm for ferritin and about 4 nm and 9 nm for *Listeria* ferritin.

## APPLICATION OF BIOTEMPLATE NPs

Yamashita group used ferritin to make a 2-D array of nanodots for a floating nanodot gate memory (FNGM). FNGM has a similar structure to metal-oxide semiconductor field-effect transistor (MOSFET), but has a nanodot array embedded in the silicon dioxide layer just above the channel. Electrons are stored in the nanodot array, usually one electron per dot, and shut off the channel current by electrostatic potential. The storage of electrons is controlled by the gate electrode. For this FNGM, a well-ordered array having nanodots of the same size (less than 10 nm) is

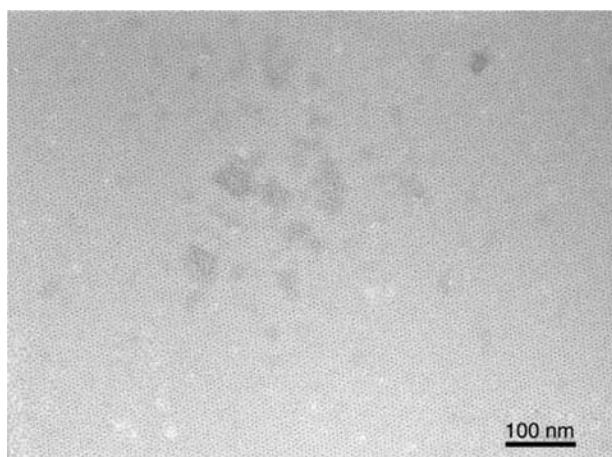


**Fig. 7** TEM image of the 2-D array of apoferritin stained by uranyl acetate on the TEM grid coated with carbon. The TEM grid was treated with ion coater to make a hydrophilic layer before use. The black dots represent the apoferritin cores stained with uranyl acetate. The surrounding white parts represent the apoferritin protein shells. A well-ordered 2-D array is clearly visible.

necessary. It is very difficult for conventional semiconductor technology to fulfill this target. Yamashita et al. employed ferritin molecules to overcome this problem.

The first step is to make a ferritin monolayer with a high density. Yoshimura<sup>[29]</sup> demonstrated that in the presence of 2% glucose, a well-ordered 2-D array of ferritin molecules could be made beneath a denatured polypeptide film at the air–water interface (Fig. 7). Furuno, Sasabe, and Ulmer can make this 2-D array of ferritin molecules on the artificial polypeptide, poly-1-benzyl-L-histidine (PBLH), membrane.<sup>[30]</sup> A ferritin molecule has a divalent cation-binding site at the two-fold axis surface, which promotes 2-D crystallization. The ferritin 2-D crystal has a density near to  $10^{12}$  dots/cm<sup>2</sup>. Furuno, Sasabe, and Ulmer further transferred the ferritin-nanodot array onto a hydrophobic Si substrate. Negatively stained TEM images showed almost perfect hexagonally close-packed arrays. High-resolution SEM visualized the iron oxide cores held within the protein shells. A clear hexagonally packed array of distinct white dots is observed. Because the ferritin should be placed at the designed area, some method for placing the ferritin monolayer on the target area is necessary. Yoshii et al. modified the silicon substrate with aminosilane. Aminosilane is positively charged and ferritin is negatively charged at neutral pH. Therefore, the aminosilane layer attracts ferritin, and ferritin adheres to the modified aminosilane. This method can also produce a ferritin monolayer with high density, around  $10^{12}$  dots/cm<sup>2</sup>.<sup>[31]</sup>

The second step is to eliminate the protein moiety from the protein array. For use in electronic devices,

the protein shell must be removed from the ferritin array. It was anticipated that heat treatment would eliminate the protein shell of the ferritin molecule. A 500°C heat treatment for 1 hr under nitrogen gas was experimentally proven to eliminate the protein shell from the ferritin molecule. Yamashita et al. confirmed the removal of the protein shell from the ferritin molecule by atomic force microscopy (AFM) observation in contact mode, Fourier transform IR spectroscopy (FTIR), and weight-loss measurement.<sup>[32,33]</sup> Detailed experiments confirmed that the ferritin protein shells were eliminated by the heat treatment at around 450°C for 1 hr under nitrogen. Recently, Yoshii et al. demonstrated that the proteins could be eliminated completely by 500°C heat treatment in a rapid thermal annealing (RTA) furnace for 10 min under oxygen. XPS measurement showed that the spectrum peak from nitrogen atom completely disappeared after RTA heat treatment. In this case, ferritin was adsorbed on the aminosilane layer, and the RTA treatment eliminated the aminosilane layer too.<sup>[31]</sup> Hikono et al. also demonstrated that UV/ozone treatment for 45 min at 115°C eliminates the protein moiety of the ferritin array.<sup>[33]</sup> The obtained nanodot array has a density of about  $10^{12}$  dots/cm<sup>2</sup>,<sup>[32]</sup> which is dense enough to be used for a floating nanodots gate.

The third step is embedding the nanodots in the silicon dioxide layer. Before embedding, the iron oxide nanodots have to be reduced. This was carried out using the ammonia plasma treatment. Now, Hikono et al. are currently studying electron storage by this nanodots array. We can fabricate a 2-D array of iron NPs on the Si substrate by bionanoprocess. This array of nanodots with homogenous size has a high density ( $10^{12}$  NPs/cm<sup>3</sup>), which is difficult to be achieved by conventional methods. The fabrication of the key component of the FNGM is just one example (Fig. 8). The method of making key components based on biomineralization, self-assembly, and elimination of the

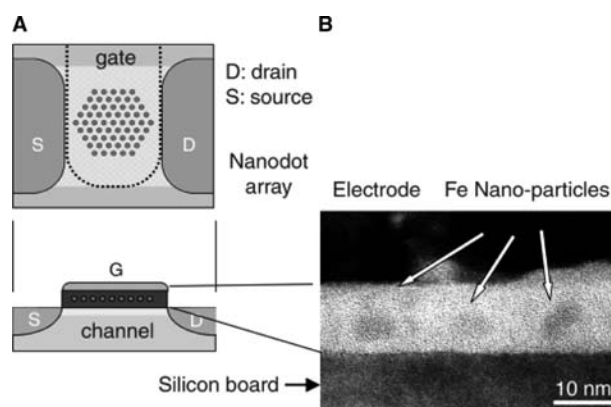


**Fig. 8** Schematic drawing of the floating gate memory (A) and a cross section TEM image of a nanodevice (B).

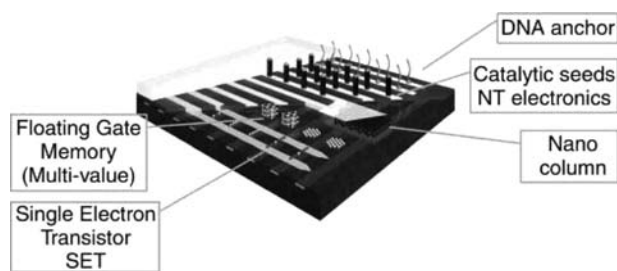


Fig. 9 Some applications of the “bionanoprocess.”

cage protein can be extended to many other applications. Fig. 9 shows some examples of Yamashita group's other targets.

## CONCLUSIONS

Researchers can make many types of NPs including metal oxide and semiconductor NPs in the cage-shaped protein, apoferritin. The synthesized NPs have some advantages compared to chemically synthesized NPs. The semiconductor-ferritin could be used as a photochemical reagent for sensing, a drug delivery system, a biomarker, a photo device, and so on. The number of the kinds of NPs that can be formed using the bio-temple method is increasing and we can expect to see useful products addressing specific problems soon. The proposal by Yamashita, Hayashi and Hara to make electronic components using the heterocomplex consisting of the inner NP and outer protein shell provides a unique solution for nanofabrication.

There are many kinds of biosupramolecules usable as biotemplates for the biomineralization of inorganic materials. These molecules could be employed to produce many kinds of heterocomplexes consisting of an inner inorganic material portion and an outer protein sheath of various shapes and sizes. These complexes can be used as self-assembling nanoblocks for fabricating nanostructures. By closely studying nature, we can open up a new biological pathway for nanofabrication using protein supramolecules.

## ACKNOWLEDGMENTS

We thank Mr. H. Furusho of Nara Institute Science and Technology for the high-resolution TEM observation and Dr. M. Okuda, Matsushita Electric Industrial Co., Ltd., for the valuable TEM images. We also thank Dr. M. Muraoka of CREST, Japan Science and Technology Agency, for the valuable discussions and Ms. R. Tsukamoto for the TEM image of cobalt oxide NPs.

## REFERENCES

- Douglas, T.; Dickson, D.P.E.; Betteridge, S.; Charnock, J.; Garner, C.D.; Mann, S. Synthesis and structure of an Iron (III) sulfide-ferritin bioinorganic nanocomposite. *Science* **1995**, *269*, 54–57.
- Meldrum, F.C.; Wade, V.J.; Nimmo, D.L.; Heywood, B.R.; Mann, S. Synthesis of inorganic nanophase materials in supramolecular protein cages. *Nature* **1991**, *349*, 684–687.
- Meldrum, F.C.; Heywood, B.R.; Mann, S. Magnetoferritin; In vitro synthesis of a novel magnetic protein. *Science* **1992**, *257*, 522–523.
- Mann, S. Molecular tectonics in biomineralization and biomimetic materials chemistry. *Nature* **1993**, *365*, 499–505.
- Meldrum, F.C.; Douglas, T.; Levi, S.; Arosio, P.; Mann, S. Reconstitution of manganese oxide cores in horse spleen and recombinant ferritins. *J. Inorg. Biochem.* **1995**, *58*, 59–64.
- Douglas, T.; Stark, V.T. Nanophase cobalt oxyhydroxide mineral synthesized within the protein cage of ferritin. *Inorg. Chem.* **2000**, *39*, 1828–1830.
- Okuda, M.; Iwahori, K.; Yamashita, I.; Yoshimura, H. Fabrication of nickel and chromium nanoparticles using the protein cage of apoferritin. *Biotech. Bioeng.* **2003**, *84*, 187–194.
- Wong, K.K.W.; Mann, S. Biomimetic synthesis of cadmium sulfide-ferritin nanocomposites. *Adv. Mater.* **1996**, *8*, 928–932.
- Ueno, T.; Suzuki, M.; Goto, T.; Matsumoto, T.; Nagayama, K.; Watanabe, Y. Size-selective olefin hydrogenation by a Pd nanocluster provided an apo-ferritin cage. *Angew. Chem. Int. ed.* **2004**, *43*, 2527–2530.
- Kramer, M.R.; Li, C.; Carter, C.D.; Stone, O.M.; Naik, R.R. Engineered protein cages for nanomaterial synthesis. *J. Am. Chem. Soc.* **2004**, *126*, 13,282–13,286.
- Dominguez-Vera, J.M.; Colacio, E. Nanoparticles of Prussian blue ferritin: a new route for obtaining nanomaterials. *Inorg. Chem.* **2003**, *42*, 6983–6985.
- Tsukamoto, R.; Iwahori, K.; Muraoka, M.; Yamashita, I. Co<sub>3</sub>O<sub>4</sub> nanoparticle synthesis using cage-shaped protein cavity. *Bull. Chem. Soc. Jpn. in press.*
- Takeda, S.; Ohta, M.; Ebina, S.; Nagayama, K. Cloning, expression and characterization of horse L-ferritin in *Escherichia coli*. *Biochim. Biophys. Acta.* **1993**, *1174*, 218–220.
- Kim, K.W.W.; Mann, S. Biomimetic synthesis of cadmium sulfide ferritin nanocomposites. *Adv. Mater.* **1996**, *8*, 928–932.
- Yamashita, I.; Hayashi, J.; Hara, H. Bio-temple synthesis of uniform CdSe nanoparticles using cage-shaped protein, Apoferritin. *Chem. Lett.* **2005**, *33*, 1158–1159.
- Iwahori, K.; Yoshizawa, K.; Muraoka, M.; Yamashita, I. Fabrication of ZnSe nano-particles in the apoferritin cavity by designing a slow chemical reaction system. *Inorg. Chem. in press.*
- Lane, L.C. The bromoviruses. *Adv. Virus Res.* **1974**, *19*, 151–220.



18. Douglas, T.; Young, M. Host-guest encapsulation of materials by assembled virus protein cages. *Nature* **1998**, *393*, 152–155.
19. Bozzi, M.; Mignogna, G.; Stefanini, S.; Bara, D.; Longhi, C.; Valenti, P.; Chiancone, E. Iron-binding Ferritin Related to the DNA-binding Proteins of the Dps Family in *Listeria innocua*. *J. Biol. Chem.* **1997**, *272*, 3259–3265.
20. Ilari, A.; Stefanini, S.; Chiancone, E., et al. The dodecameric ferritin from *Listeria innocua* contains a novel intersubunit iron-binding site. *Nature Struct. Biol.* **2000**, *7*, 38–43.
21. Stefanini, S.; Cavallo, S.; Montagnini, B., et al. Incorporation of iron by the unusual dodecameric ferritin from *Listeria innocua*. *Biochem. J.* **1999**, *338*, 71–75.
22. Yang, X.; Chiancone, E.; Stefanini, S.; Ilari, A.; Chasteen, N.D. Iron oxidation and hydrolysis of a novel ferritin from *Listeria innocua*. *Biochem. J.* **2000**, *349*, 783–786.
23. Allen, M.; Willits, D.; Mosolf, J.; Young, M.; Douglas, T. Protein cage constrained synthesis of ferrimagnetic iron oxide nanoparticles. *Adv. Mater.* **2002**, *14* (21), 1562–1565.
24. Allen, M.; Willits, D.; Young, M.; Douglas, T. Constrained synthesis of cobalt oxide nanomaterials in the 12-subunit protein cage from *Listeria innocua*. *Inorg. Chem.* **2003**, *42*, 6300–6305.
25. Lee, S.; Mao, C.; Flynn, C.E.; Belcher, A.M. Ordering of quantum dots using generically engineered viruses. *Science* **2002**, *296*, 892–895.
26. Naik, R.R.; Stringer, J.S.; Agarwal, G.; Morley, O.S.; Jones, S.E.; Stone, M.O. Biomimetic synthesis and patterning of silver nanoparticles, *Nature Mat.* **2002**, *1*, 169–172.
27. Yu, L.; Banerjee, I.A.; Matsui, H. Direct growth of shape-controlled nanocrystals on nanotubes via biological recognition. *J. Am. Chem. Soc.* **2003**, *125* (48), 14,837–14,840.
28. Naik, R.R.; Jones, S.E.; Murray, C.J.; McAuliffe, J.C.; Vaia, R.A.; Stone, M.O. Peptide templates for nanoparticle synthesis derived from polymerase chain reaction-driven phage display. *Adv. Funct. Mater.* **2004**, *14*, 25–30.
29. Yoshimura, H. Two-dimensional crystals of apoferritin. *Adv. Biophys.* **1997**, *34*, 93–107.
30. Furuno, T.; Sasabe, H.; Ulmer, K.M. Binding of ferritin molecules to a charged polypeptide layer of poly-1-benzyl-L-histidine. *Thin Solid Films* **1989**, *180*, 23–30.
31. Yoshii, S.; Yamada, K.; Matsukawa, N.; Yamashita, I. Making monolayer of inorganic nanoparticles on silicon substrate. *Jpn. J. Appl. Phys.* **2005**, *44*, 1518–1523.
32. Yamashita, I. Fabrication of a two-dimensional array of nano-particles using ferritin molecule. *Thin Solid Films* **2001**, *393*, 12–18.
33. Hikono, T.; Uraoka, Y.; Fuyuki, T.; Yamashita, I. Novel method for making nanodot arrays using a cage-like protein. *Jpn. J. Appl. Phys.* **2003**, *42*, 398–399.

# Nanoparticles: Generation, Functionalization, and Ion Sensing

Jason J. Davis

Paul D. Beer

*Inorganic Chemistry Laboratory, Department of Chemistry,  
University of Oxford, Oxford, U.K.*

## INTRODUCTION

During the past decade or so, considerable interest has grown in the potential commercial and technological exploitation of nanoscale materials in analytical chemistry.<sup>[1]</sup> A particular focus of this interest has been the utilization of specific size-dependent electronic, optical, or magnetic properties. Nanoparticles are crystalline clusters (metallic, semiconducting, or insulating) composed of a few hundred to a few thousand atoms and are, characteristically, of nanometer dimension. One consequence of this size is that many of their properties are dominated by their surface rather than by the bulk volume<sup>[2]</sup> and, indeed, this fact alone can make these structures very amenable to chemical or environmental influence, or “tuning.” Their nanometer diameter is also the same order of magnitude as the de Broglie wavelength of electrons/holes at room temperature and this, then, can lead to a quantization of electronic/hole energy levels, a phenomenon that has led to the term “quantum dots” (QD). The energy-level spacings are related to particle size.<sup>[3]</sup> Although the term “nanoparticles” has been coined only at a time when advances in microscopy have allowed us to resolve them as such, nanoparticles have been in use for many years; for example, Faraday carried out pioneering work with gold nanoparticles, and some of the intense colors evident in stained glass arise from the presence of nanometer-sized oxide clusters.

Gold nanoparticles received substantial attention during the past decade or so. The potential technical importance of monolayer-protected metal nanoparticles in developing nanoscale optoelectronic devices, (bio)chemical sensors, corrosion-resistant materials, and new catalysts has made them one of the primary targets of highly intensive, nanoparticle-based research activity. To date, for example, both single electron and nonlinear optical devices have been constructed from these materials.<sup>[4–6]</sup> In addition to utilizing the optical and electronic properties inherent in metallic structures, the magnetic characteristics of suitable particles have also been of some interest, particularly in

consideration of separation technologies. For example, nanoparticles of iron oxide ( $\text{Fe}_3\text{O}_4$ ) can be suitably modified with a biological moiety of interest, e.g., a cell and their “superparamagnetic” properties used in magnetic field modulated manipulations/separation.<sup>[7]</sup> The possible use of magnetic nanoparticles as contrast agents in magnetic resonance imaging has also been cited.<sup>[8]</sup> Through suitable surface chemical modification, it should be possible to generate magnetic nanoparticles with a propensity to concentrate in particular tissue (or cellular) regions allowing, e.g., enhanced image contrast generation between diseased or cancerous cells and healthy cells. To date, these have both been shown to be more effective than conventional magnetic resonance imaging (MRI) agents (such as gadolinium complexes) and capable of allowing in vivo cellular tracking.<sup>[9]</sup>

This report will aim to outline the general properties of metallic and semiconducting nanoparticles, their modification and possible application in high-sensitivity, selective ion sensing. There is no universally adopted definition as to what constitutes a nanoparticle, but we will be concerned here with the properties and utilization of particles <100 nm in diameter. Although more progress has been made in the functionalization of metallic (notably gold and silver) particles, the properties and potential utilization of semiconducting particles will also be discussed.

## METALLIC NANOPARTICLES

Although metal colloids have been known since the mid-18th century, only during the past decade or so has it been possible to controllably generate homogeneous samples and to subsequently scrutinize them at levels of resolution comparable to particle size.<sup>[10,11]</sup> Although much of the seminal (and applied) work in this field has been carried out with gold, nanometer-sized metal particles of silver,<sup>[12]</sup> platinum,<sup>[13]</sup> iridium, and palladium<sup>[14]</sup> have also been prepared. Although recent work has recognized that nanoparticle shape (in addition to size) greatly influences physical and

chemical properties,<sup>[15,16]</sup> this topic will not be discussed here.

## Synthesis and Characterization

Metal nanoparticles can be formed through laser vaporization of metallic rods. However, this method is not generally amenable to either scaling up or subsequent chemical modification strategies. Interestingly, with particles prepared under such conditions, certain “magic numbers” of constituent atoms are evident,<sup>[17]</sup> an observation consistent with nonbulk, “atomistic” character. Perhaps the most practical and flexible means of nanoparticle generation is by chemically reductive routes in solution. As “bare” metallic nanoparticles are typically unstable in solution controlled surface functionalization (either during or after synthesis—see below) has been key. Aqueous phase citrate reduction of HAuCl<sub>4</sub> has been, perhaps, the major workhorse in this area; subsequently, surface-bound citrate moieties can be readily displaced by thiolated organics in the formation of monolayer-protected metallic clusters (MPCs). A breakthrough in this field was the demonstration by Brust and coworkers<sup>[11]</sup> of a solvent-based, high-concentration, monodisperse synthesis through a surfactant catalyst-based phase transfer of chloroaurate ions (typically with subsequent reduction by a borohydride). Most conveniently, chloroaurate reduction is carried out in the presence of alkanethiols,<sup>[11]</sup> and, to a large extent, it is possible to control nanoparticle size through the relative ratios of tetrachloroaurate and thiol. In essence, these capped nanoparticles behave like large organic molecules, in that they can be separated from solution in powdered form, redissolved in solvent, and recrystallized as required. The surface functionalization afforded by these preparative methods stabilizes the particles to aggregation and further allows their properties to be influenced by the structure of the monolayer-forming molecules. In addition, this functionalization can be utilized in mediating surface-confinement (e.g., self-assembly of the nanoparticle itself onto an underlying solid support). Analogous chemistry can be used in the formation of other particles—chloroplatinate reduction yields, for example, platinum nanoparticles.

## Properties

Metal nanoparticles have extraordinary size-dependent optical properties, not present in the bulk metal. Specifically, nanoparticles of silver, gold, and copper show distinct and well-defined plasmon absorption in the visible spectrum, an absorption characterized by

an extremely large molar adsorption coefficient. These unique optical, electrical, and surface chemical characteristics are controllable through both particle size and aggregation,<sup>[18,19]</sup> and can also be “tuned” to a degree by the nature of the surface functionalization.<sup>[20–22]</sup> Interestingly, the effect that the size-dependent electrical characteristics of nanoparticles can have on the properties of surface-confined molecules has recently been resolved in a <sup>13</sup>C NMR study.<sup>[23]</sup>

Although diffraction analyses have shown that nanoparticles adopt the same crystal structure as the bulk metal, this appears to be less the norm as the particle size falls. For example, gold nanoparticles can adopt an icosahedral structure quite different to the bulk face-centered cubic arrangement. The valence and conduction band density of states (DOS) of these particles undergo significant variance with size; specifically, the initially continuous DOS is progressively replaced by discrete energy levels, the spacing of which increases with decreasing particle size (Fig. 1). As this spacing exceeds thermal energy, a “band gap” effectively opens up in the metal. At smaller sizes still, discrete, energetically separated, quanta are resolvable. These size effects are observable in both metallic and semiconducting particles, although, in the latter, “quantum dot” behavior can be observed at comparatively large (tens of nanometers) particle size.

From the perspective of developing derived electro-analytical devices, the redox properties of nanoparticles have been of some interest. The redox behavior of MPCs has been probed both diffusively in solution<sup>[24,25]</sup> and in surface-confined mono- or multilayer films.<sup>[26–30]</sup> Again, as soon as nanoparticles fall below a finite size (<1 nm), available electronic states become quantized and, electrochemically, this has the effect of the particle behaving, in essence, as a multivalent redox species.<sup>[31]</sup> The specific electrostatic charging of the metallic core of monolayer protected nanoparticles has also been referred to as quantized double layer charging.<sup>[20]</sup> The ability of these films to mediate current flow is of obvious application to the development of sensors.

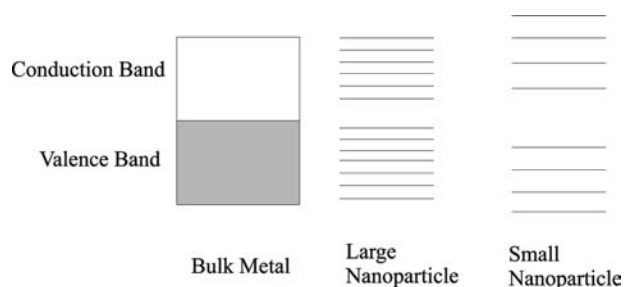


**Fig. 1** Schematic layout showing the progression from metallic band structure to quantized electronic structure as nanoparticle dimensions fall.

## Postsynthesis Nanoparticle Functionalization

Although it is commonly advantageous to modify nanoparticles as they are created, the covalent attachment of molecules to the surface of a nanoparticle is, generally, a dynamic process in which the surface-confined molecules are in dynamic equilibrium with those in the surrounding solution. Because of this, it is possible to displace surface bound molecules with those for which surface-confinement is more thermodynamically favorable—for example, it is possible to displace short chain alkane thiols with those of longer chain.<sup>[32]</sup> The use of terminally functionalized alkanethiols facilitates the controlled introduction of surface chemistry into generated nanoparticles—they can be rendered anionic, cationic, hydrophobic and/or suitable for coupling to other molecules or surfaces.

## Biomodification

Although the electron scattering propensity of metallic nanoparticles makes them useful biotagging markers,<sup>[33,34]</sup> the association of nanoparticles with biomolecules further brings with it the possibility of using them in highly sensitive optical or electrical bioassays. To date, methods have been developed where protein, antibodies, and oligonucleotides can be robustly anchored to particles. Nanoparticles heavily functionalized with oligonucleotides have been used as probes in a variety of DNA detection methods and as elemental building blocks in materials synthesis schemes based upon the sequence-specific hybridization properties of DNA.<sup>[35–37]</sup> Typically, the direct adsorption of protein or enzyme onto bare metallic surfaces is accompanied by gross change in protein fold (denaturation) and loss of biological activity. Interestingly, several recent studies have indicated biostability at colloidal metal surfaces.<sup>[38]</sup>

## SEMICONDUCTING NANOPARTICLES

Much excitement has recently surrounded the potential optical utilization of spherical semiconducting nanocrystals (typically 15–120 Å in diameter),<sup>[39,40]</sup> such as those composed of cadmium sulfide,<sup>[40]</sup> cadmium selenide, or gallium arsenide.<sup>[41]</sup> As with metallic nanoparticles, the dimensions lead to very interesting optical and electronic properties arising from the confinement of excitons (electron/hole pairs) within the particle, and their subsequent quantized behavior. These properties have led to novel research activity associated with the development of quantum computers, laser diodes, and solar cell technology. The semiconducting band gap associated with these particles is tunable through diameter control at the point of synthesis—the smaller the particle, the greater the energy level spacing

between quantized levels; in the case of fluorescence, the absorption and emission peaks shift to longer wavelengths with increasing particle size.<sup>[36]</sup>—2.5 nm CdSe particles, for example, fluoresce in the green, while 7-nm equivalents fluoresce in the red.<sup>[36]</sup> The potential use of these structures as fluorescent labels has been a core focus during the past 2–3 years; the advantages they hold over more traditional organic fluorophore labels are marked. The fact that equally sized quantum dots made of different materials give rise to different emission/absorption frequencies means that quantum dots are tunable fluorophores. They have wider excitation and narrower emission spectra than conventional organic dye molecules; the former is desirable because several probes with different emission peaks can be excited with a single source, decreasing the number of equipment that might be needed to perform imaging (in fact, QDs can be excited efficiently at any wavelength shorter than that of their emission peak<sup>[36]</sup>). A narrow emission spectra reduces spectral cross-talk between different detection channels; in other words, fluorophores of differing emission peaks appear clearer and more distinct from each other. Additionally, these dots also suffer considerably less from the problems of photobleaching inherent in organic dyes and have an associated higher quantum yield (thus they appear “brighter”).<sup>[42]</sup> These quantum yields can be further increased by surrounding the dot with an epitaxially grown layer of larger band gap semiconducting material. For example, cadmium selenide dots can be capped with zinc sulfide. These so-called, “core-shell nanocrystals” have associated quantum yields that can be as high as 80%.<sup>[43]</sup>

## Synthesis

Semiconducting dots are typically synthesized in organic solvent at high temperature from metallic salt and insulator precursors (e.g., a cadmium salt with powdered selenium) in the presence of a stabilizing surface-active agent. As a direct result of this method of forming (stabilized and solubilized) quantum dots, freshly made particles are generated with a surface coating, commonly trioctyl phosphine oxide (TOPO). As with metallic nanoparticles, it appears that the electrical properties of particles are strongly affected by geometry as well as size.<sup>[44]</sup> Likewise, as properties are size-dependent, it is clearly advantageous to ensure that size distributions are as narrow as possible in any sample.

## Functionalization

Commonly, quantum dots (and nanoparticles in general) are functionalized by utilizing capping molecules with thiol groups. These capping molecules attach to

the surface of the quantum dot by binding at the sulfur atom. This is simple to achieve experimentally: normal procedure involves adding the cap to a colloidal dispersion of quantum dots in an organic solvent and then heating.<sup>[45]</sup> Monodentate binding leads to stable isolable products, but bidentate binding has also been used<sup>[46]</sup> and, theoretically, gives a more stable cap/surface interaction. To utilize the fluorescent characteristics of these structures in biological media they must, of course, be made water-soluble, and capping with a hydrophilic thiol is one means of achieving this (Fig. 2). A more involved (but ultimately more stable) method of aqueous solubilization is achievable through surface silanization.<sup>[42]</sup> As well as allowing solubility refinements, these surface functionalization methodologies can, subsequently, also be used in either coupling of the quantum dots to other molecules (biomolecules, for example) or their surface assembly.<sup>[47]</sup>

### THE SURFACE-ASSEMBLY OF NANOPARTICLES

To make use of the intrinsic physiochemical properties of these particles in the development of novel

electronic and/or optical devices, methods must be established whereby controlled (many of the potentially useful properties are strongly perturbed on aggregation) assembly on solid surfaces can be achieved.<sup>[48,49]</sup> In recent years, a variety of methods have been reported whereby mono (two-dimensional) and multilayers (three-dimensional) of both metallic<sup>[31,50,51]</sup> and semiconducting<sup>[52–54]</sup> particles have been generated (with various degrees of control and homogeneity) and characterized. The “new physics” associated with these surfaces has opened up tremendous opportunities for both fundamental research and new applications.<sup>[32,55–58]</sup> Although many groups have utilized physical methods of depositing particles, covalent,<sup>[59,60]</sup> or ionic<sup>[61,62]</sup> assembly offers more control<sup>[63–69]</sup> (Fig. 3). The assembly of nanoparticle films can also be electrochemically modulated in cases where the particles are initially decorated with redox-active moieties.<sup>[70]</sup> A number of biomolecule-mediated nanoparticle assembly strategies have also been proposed for both metallic and semiconducting particles.<sup>[37,45,71]</sup>

Because the most useful quantum dot surfaces are those generated from closely packed (although not physically in contact) colloids, considerable efforts

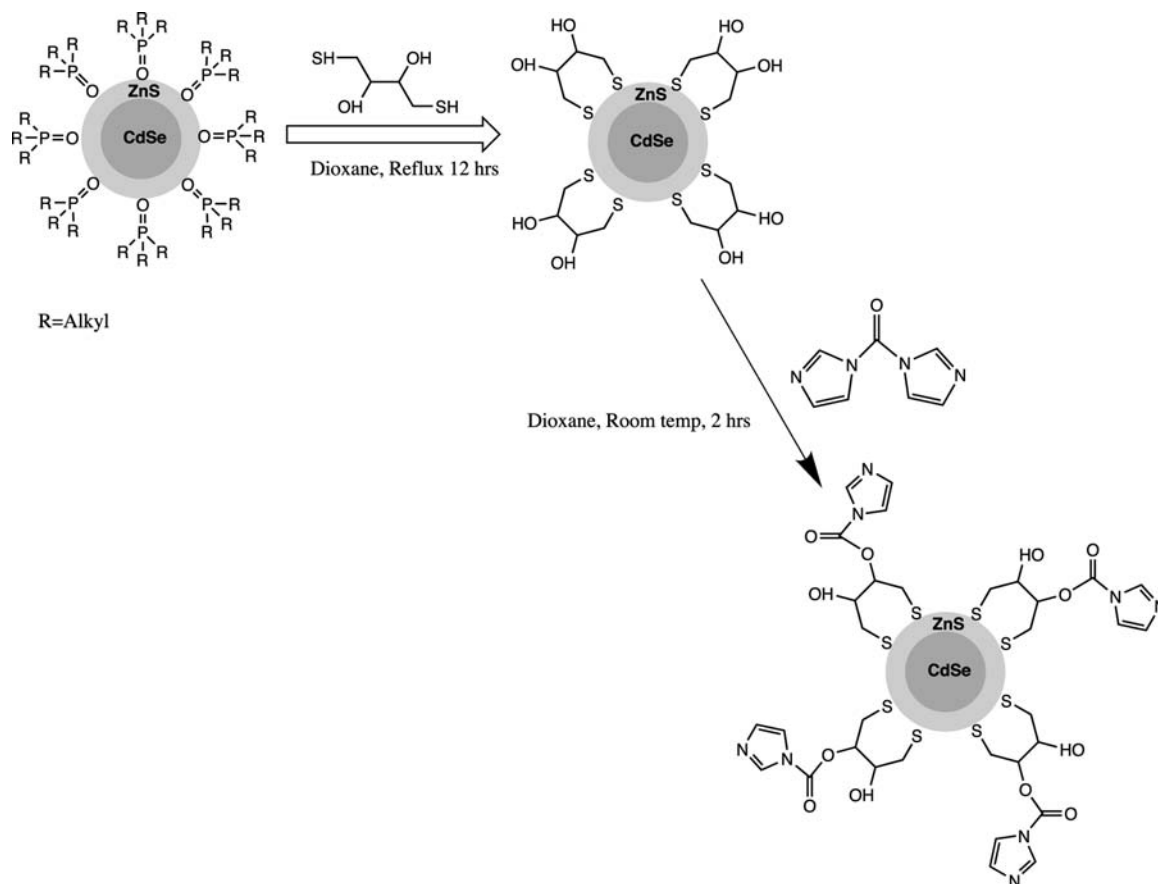


**Fig. 2** Functional self-assembly on the surface of semiconducting quantum dots can be used to render them both water soluble and amenable to subsequent (bio)chemical functionalization.

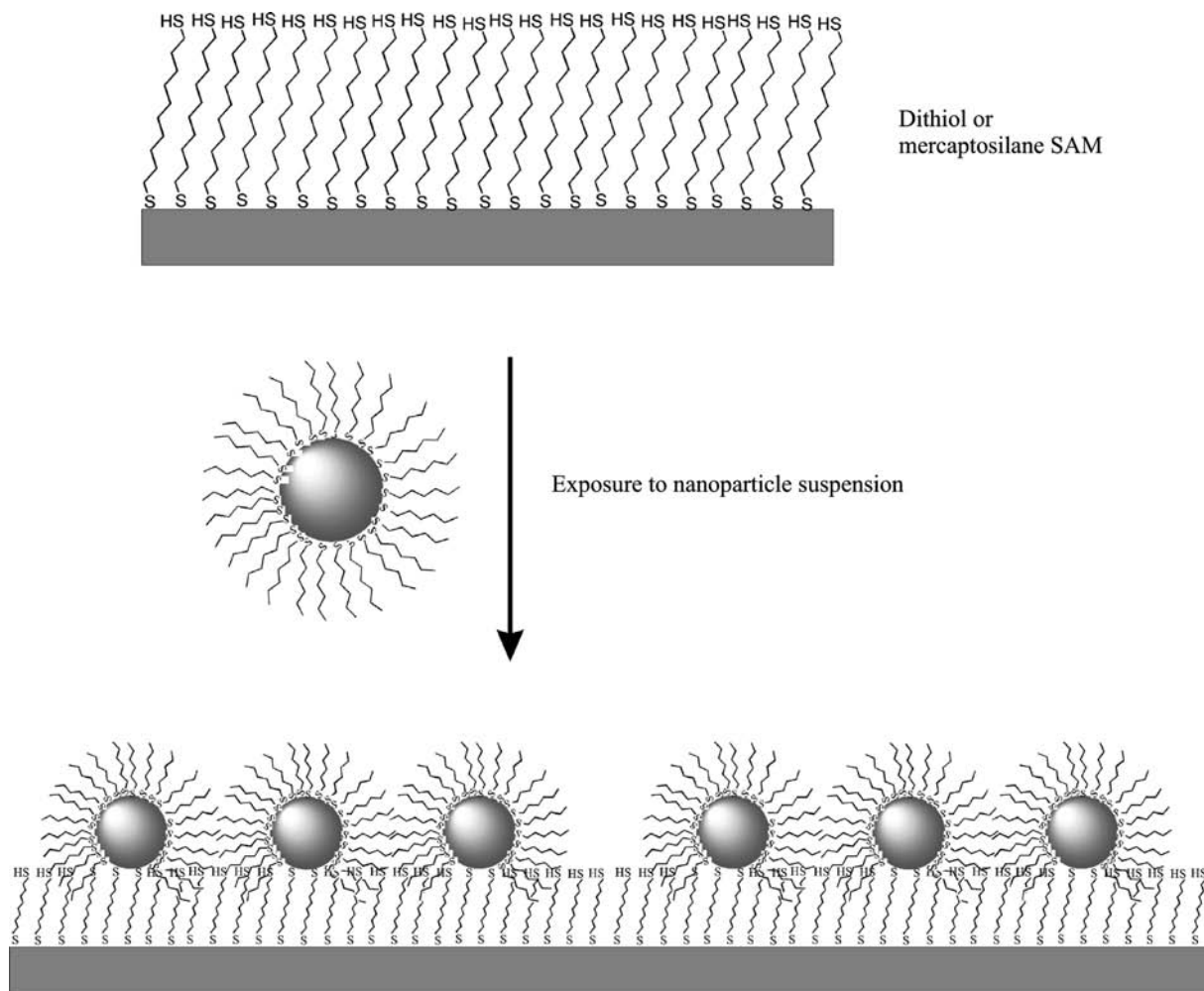


**Fig. 3** Schematic representation of a covalent surface assembly protocol for the immobilization of monolayer-capped gold nanoparticles on a functionalized gold electrode surface.

have been expended in attempts to control this, something which is easiest to achieve if particle–surface interactions are maximized (ideally at the expense of particle–particle interactions).<sup>[72]</sup> In a typical, well-packed 10-nm nanoparticle adlayer, there are  $1 \times 10^{10}$ – $1 \times 10^{11}$  colloids/cm<sup>2</sup>, depending on edge-to-edge distance. These assembled adlayers are conveniently analyzed at angstrom levels of resolution, by electron microscopy or scanning probe microscopy.

The immobilization of colloidal nanoparticles onto optically transparent electrode surfaces [such as indium tin oxide (ITO)], on which optoelectrochemical analyses can be performed, has also been demonstrated.<sup>[73]</sup> Electrochemical studies have resolved electron transfer rate constants between nanoparticles and underlying electrode surfaces of the order of  $100 \text{ sec}^{-1}$ <sup>[74]</sup> and, predictably, this shows significant dependence on the alkanethiol modification of the particles.<sup>[75]</sup> Uosaki et al.<sup>[62]</sup> demonstrated that, in addition to the strong electronic coupling between

surface-confined nanoparticles and their underlying support, fast electron transfer is possible from redox-active moieties attached to gold particles and the underlying electrode. Even in multilayer films, (thermally activated hopping) electron transfer is effectively “channeled” to/from the underlying support via intervening particles. The sensitivity of these electrochemical characteristics to environment is of direct relevance to the generation of derived sensing systems.

### ION SENSING AT NANOPARTICLE SURFACES

The development of molecular receptors designed to selectively recognize and sense charged or neutral guest species of biological and environmental importance is a highly topical research field. The “reporting” of recognition may be through “physical change,” such as an interfacial mass change associated with bonding (detectable through piezoelectric devices). One may



imagine that the “interaction” (binding) and “signaling” regions of a sensor are distinct, and that the monitored signal—be it optical, electrochemical, or otherwise in nature—is reliably and reproducibly perturbed by specific interactions occurring at the neighboring binding site. With electrochemical sensors, perturbation of a voltammetrically monitored electron transfer process, achieved by localization of a redox-active group (e.g., ferrocene) in the vicinity of the receptor, may be achieved by one or a combination of through-space and through-bond interactions. Optical sensing can be achieved through perturbation of an optical signal, typically by equivalent mechanisms. We will focus here on optical and electrochemical transduction where specific molecular association is accompanied by a change in the monitored optical or electrochemical signals derived from the sensor. Such changes can facilitate qualitative or quantitative analyte determination.

Supramolecular chemistry may be defined as the investigation of molecular systems in which the components are reversibly associated by noncovalent intermolecular interaction. From a sensing perspective, such systems may be loosely described as comprising of a “host” sensor and a “guest” analyte species, the latter being neutral, cationic, or anionic. The binding intermolecular forces include electrostatics (ion–ion, ion–dipole, and dipole–dipole), hydrogen bonding,  $\pi$ – $\pi$  stacking interactions, dispersion and induction forces (van der Waals), and hydrophobic or solvophobic effects. Individually, these interactions are relatively weak, but in combination they lead to thermodynamically stable complexes, the formation of which can be utilized in the generation of ion sensors.

### Cation Sensing

The binding of a cation at a receptor site can be achieved through electrostatic ion–ion or ion–dipole interactions. In general, it is advantageous to utilize polydentate receptor sites that, for well-known thermodynamic reasons (chelate and macrocyclic effects), exhibit increased cation binding affinity. Oxygen-containing crown ethers were the first macrocyclic ligands synthesized which bound alkali metal cations with high selectivity (tunable through structure/geometry). Cryptand and spherand receptor molecules are more highly organized and can accordingly associate very strongly with specific s-block cationic analytes. Through the incorporation of redox-active moieties into these receptors, sensory systems electrochemically responsive to, e.g., lithium,<sup>[76]</sup> sodium,<sup>[77]</sup> and potassium,<sup>[78]</sup> as well as larger cations (some of considerable environmental concern), such as rubidium and cesium,<sup>[79]</sup> has also been achieved.

### Anion Sensing

The physiological and environmental importance of inorganic anions has fuelled a considerable amount of interest in anion recognition and sensing.<sup>[80]</sup> For example, nitrates and phosphates are present in low concentrations in wastewater, but high levels are a contributing factor to eutrophication and, accordingly, are of environmental significance. Although substantial progress has been made in the development of specific, sensitive, cation receptors, similar work with anions has been hindered by their characteristic small charge density (relative to isoelectronic cations) and, subsequently, general low binding affinity. The additional effects of competitive solvation mean that aqueous-phase anion recognition remains a considerable challenge. The design and construction of receptors that can selectively recognize and sense anionic guest species via a macroscopic physical response is thus a current area of chemical sensor technology receiving considerable attention.<sup>[81]</sup> Anions are excellent electron pair donors, so they will strongly interact with suitable electron pair acceptors, the simplest of these being an electropositive hydrogen atom capable of forming a hydrogen bond. The directionality of hydrogen bonds introduces the possibility of designing receptors with specific shapes, capable of differentiating between anionic guests of different geometry. Again, by combining a binding site with redox-active moiety, electroanalytical methods can be applied to anion sensing. In recent work, the redox-active ferrocene moiety was used in the electrochemical sensing of anions, both in organic and aqueous media.<sup>[81,82]</sup> Transduction of anion binding is achieved by through-space and through-bond stabilization of the higher ( $\text{Fe}^{\text{III}}$  in the case of ferrocenium) oxidation state and, in voltammetric experiments, this is observable through a cathodic shift in the ferrocene/ferrocenium electrochemical half-wave potential. Acyclic, macrocyclic, and calixarene amide-functionalized ferrocene derivatives have all been subsequently shown to undergo substantial cathodic perturbations of the respective metallocene redox couple in the presence of a variety of anions of biological and environmental importance. These molecular sensors are capable of detecting  $\text{Cl}^-$ ,  $\text{Br}^-$ ,  $\text{H}_2\text{PO}_4^-$ ,  $\text{ReO}_4^-$ , and  $\text{CH}_3\text{CO}_2^-$  (down to low micromolar levels) with, in some cases, the strength of binding correlating with basicity of the anionic guest.

### Surface-Confined Chemical Sensors

Self-assembled monolayers (SAMs) can be formed from the exposure of a pristine metallic surface to suitably functionalized molecules, which subsequently form ordered, two-dimensional crystalline arrays; the

degree of ordering being dependent on molecular structure and size, substrate morphology, coverage, temperature, and solvent. By combining molecular-scale recognition with such assembly, it is possible to develop a powerful means of generating interfaces capable of analyte detection under a variety of conditions. The “surface tethering” of receptors yields a number of specific additional advantages; efficiency, in terms of quantity of material required, is high; the sensor can be portable, robust, and capable of being used in a variety of environments. In addition to this, and as discussed below, the preorganization of molecular receptors at a surface enhances the thermodynamic driving force associated with receptor/analyte binding and, therefore, both binding affinity and detection limits.<sup>[83]</sup>

Recent work has shown that the introduction of a surface-anchoring thiol moiety into a redox-active anion sensor allows the generation of robust sensing molecular arrays capable of analyte detection in a variety of polar and nonpolar environments. Specifically, by incorporating hydrogen bond donor amide groups and directly linking these functionalities to a redox-active ferrocene unit, hydrogen-bond mediated anion recognition is accompanied by a significant perturbation in the electrochemical characteristics of the monolayer. Strikingly, the anion binding affinities associated with such SAMs are, in some cases, orders-of-magnitude greater than those associated with the same receptors free in solution. This “surface amplification,” which can lead to the development of highly effective sensors, is attributable to two

things: 1) The “macrocyclic effect” is the entropy- and enthalpy-driven increased thermodynamic stability of a complex formed between an ion (usually cationic) and a multidentate macrocyclic ligand in comparison to the equivalent complex formed with open chain (noncyclic) ligands. By “preorganizing” the host pseudo macrocycle on a surface, and thereby restricting its vibrational and rotational degrees of freedom, the entropic driving force accompanying complex formation is further increased. 2) The comparatively low dielectric constant of the SAM receptor binding site is also likely to significantly enhance anion binding efficacy. The ability to tune both geometry and binding affinity of the host molecular receptor allows one to achieve highly selective sensing. For example, the SAMs shown in Fig. 4 are able to sense dihydrogen phosphate in the presence of more than a 10,000-fold molar excess of halide in solvent. Functional surfaces of this type are able to detect low levels of perrhenate anion (a model for pertechnetate, an environmentally important radioactive waste product of the nuclear and radiopharmaceutical industries) in *aqueous* solution. By increasing both receptor binding affinity and electroanalytical detection sensitivity, it should be possible to extend this aqueous sensing to more basic anions.

### Nanoparticle Sensors

The optical and/or electrical/electrochemical properties of metallic or semiconducting nanoparticles and

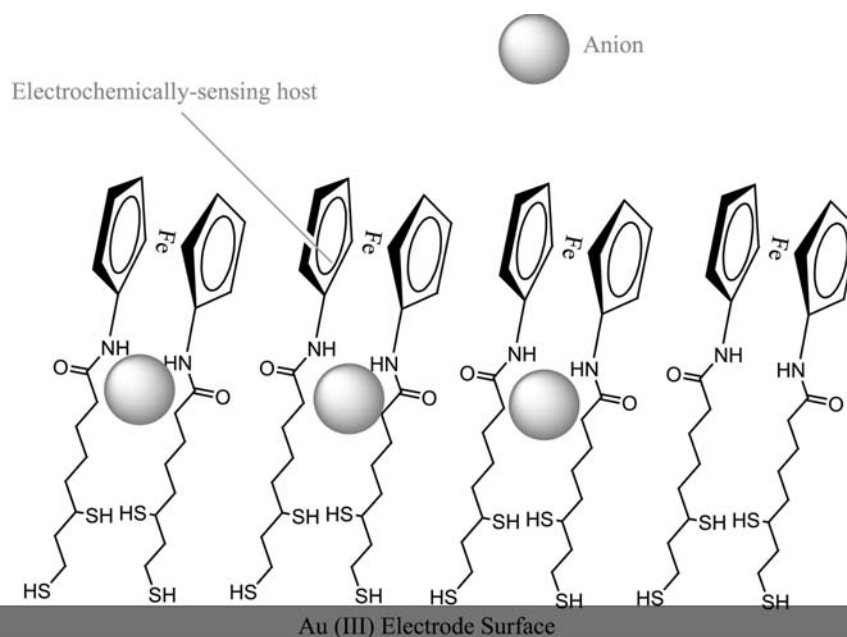


**Fig. 4** Schematic representation of a self-assembling, hydrogen-bonding ferrocene amide capable of electroanalytical anion sensing. With the specific receptors shown, hydrogen phosphate anion recognition cathodic shifts in the ferrocene half-wave potential are  $>290$  mV in magnitude—greater, to our knowledge, than anything reported to date. *Source:* From Ref.<sup>[81]</sup>.

their arrays can be applied to molecular sensing in a variety of ways. One can envisage the role of the nanoparticles being one or combinations of the following:

1. Acting as structural template to preorganize the binding site/receptors—in this case, transduction is not from the particle itself.
2. Utilizing the nanoparticle optical properties (plasmon absorption or fluorescence) in transduction—the optical properties of gold nanoparticles (both in solution and surface-confined), for example, are highly sensitive to both the dielectric properties of the intermediate environment and aggregation.
3. Making use of nanoparticle conductance in either the electrochemical sensing of molecular binding at mono- or multilayer films, or in recognition-mediated change in film conductance.

Perhaps the least technically challenging, but nonetheless demonstrably powerful, use of nanoparticles in sensing lies with colorimetric assays. Additionally, nanoparticle arrays have considerable potential in vapor-phase analyte detection, Raman, and optical or electrochemical recognition.

### Colorimetric sensing

As mentioned earlier, gold nanoparticles exhibit characteristic plasmon absorptions that typically give their solutions a pink coloration. The sensitivity of this visible absorption (note: stable nanoparticle suspensions do not appreciably scatter visible light) to aggregation can be utilized in the nanoparticle equivalent of the latex agglutination test,<sup>[84]</sup> in which analyte-mediated color change is readily detectable through the use of standard UV–visible spectroscopy. Perhaps the best example of this has been recently demonstrated by Mirkin and coworkers in high-sensitivity colorimetric detection of DNA.<sup>[85]</sup> In this work, gold nanoparticles were surface-functionalized with thiolated single-stranded DNA. In the presence of *femtomolar* levels of the complementary DNA, subsequent hybridization-mediated agglutination leads to a visible red-to-purple color change. Colorimetric immunoassays have also been developed based on either antibody or antigen nanoparticle functionalization.<sup>[86]</sup> Related colorimetric titrations have recently been extended to the generation of ion-sensing systems. Specifically, by self-assembly of appropriately functionalized receptors on nanoparticles, cation- or anion-mediated linking or aggregation can be spectroscopically monitored (Fig. 5). In using self-assembling thiolated crown ethers, Lin et al.<sup>[87]</sup> were able to

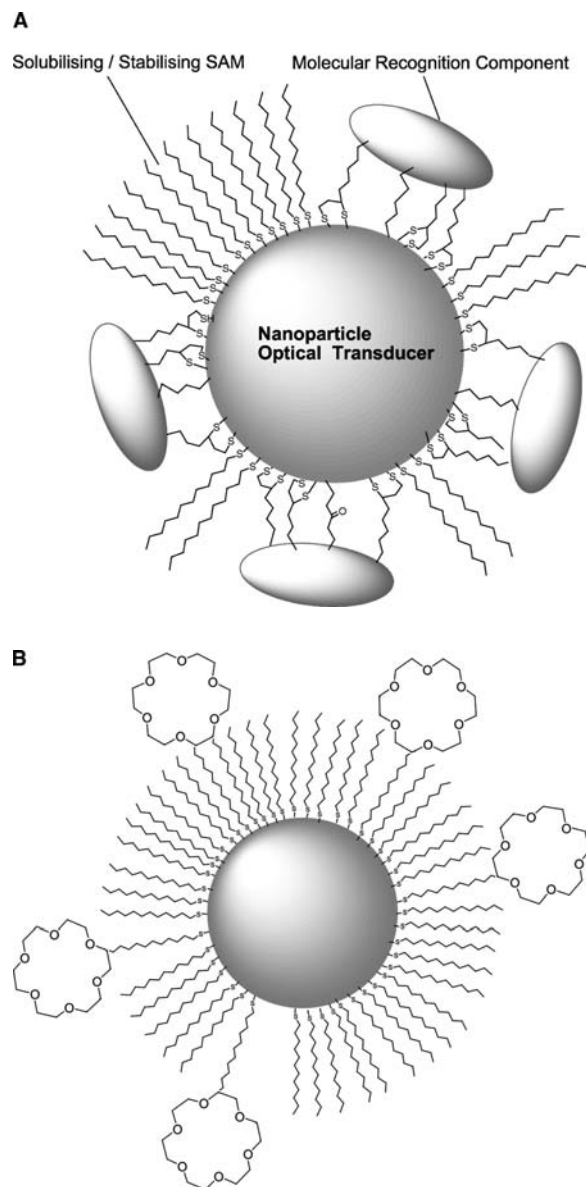


**Fig. 5** A) Diagrammatic representation of a nanoparticle appropriately functionalized such that its properties are stable, it is soluble in an appropriate environment, and labeled with a molecular receptor/chemical or biochemical recognition agent. The latter may be a coordination site, oligonucleotide or antibody, for example. B) Place exchange of solubilizing alkyl thiols with a thiolated crown ether produces nanoparticle species that are sensitive to cations; 18-crown-6 and 15-crown-5 ether modified nanoparticles are sensitive to low levels of potassium. Thiolated carboxylic acid modified colloids are sensitive to the presence of heavy metal cations. *Source:* From Refs.<sup>[87]</sup> and<sup>[88]</sup>.

construct colorimetric assays, based on standard, proximity-linked, coupling of plasmons, for potassium, with detection limits down to low micromolar level. Similarly, cadmium-, mercury-, and lead-responsive assays have been developed.<sup>[88]</sup>

## Vapor phase sensing

The initially Ohmic, thermally activated, conductance properties of MPC films are sensitively dependent on the separation of, and intervening medium between, the particles. The “intercalation” of organic vapor into such films leads to a detectable decrease in the conductance. Although this phenomenon appears to be highly dependent on the structural aspects of the nanoparticle film, it may be applicable to the generation of highly robust sensors.<sup>[89]</sup> To date, several research groups have demonstrated fast, reversible, and highly sensitive (<5 ppm in some cases) responses to a variety of solvent vapors.<sup>[90]</sup> Although the mechanisms of vapor sensitivity are poorly understood, the phenomenon has been qualitatively considered in terms of both film swelling and dielectric change.<sup>[91,92]</sup>

## SERS—Raman sensing at surfaces

The Raman scattering attainable from an adsorbate on a rough metal surface is greatly enhanced over the attainable rate on flat substrates. This enhancement, observable on “active metals,” is greatest when the surface roughness is of the order of tens of nanometers and, although not fully understood, is associated with the ability of such surfaces to enhance/focus electromagnetic radiation. Although it is nearly 20 years since the discovery of surface-enhanced Raman scattering of molecules adsorbed at suitable roughened metallic interfaces,<sup>[93,94]</sup> where up to  $10^6$ -fold enhancements over the adsorbate natural Raman scattering can be observed, the generation of suitable roughened surfaces by etching or deposition methods suffers from reproducibility issues. Through the surface-confinement of nanoparticles, homogeneous surfaces of precisely appropriate roughness can be reproducibly fabricated. Furthermore, the plasmon characteristics of colloids appear to further magnify signal enhancement.<sup>[48]</sup> The use of colloidal gold or silver nanoparticles in enhancing the spectroscopic data attainable from interfaces has been demonstrated,<sup>[95,96]</sup> where million-fold enhancements leading, in some cases, to attomolar sensitivity, have been observed.<sup>[97]</sup>

## Electroanalytical sensing

Through the functionalization of colloidal gold nanoparticles with self-assembling amidoferrocenes, Astruc et al.<sup>[98,99]</sup> were able to demonstrate the establishment of an effective redox probe for dihydrogen phosphate and hydrogen sulfate in an organic solvent medium. This work makes use of the diffusive nature of solubilized nanoparticles, the facile access of anions to the hydrogen-bonding receptor site, and the reliable

electrochemical communication with redox-active units confined to the particle surface. Although additional preorganizational effects were noted in these studies, they pave the way to others in which the controlled assembly of redox-active molecular or ionic receptors on nanoparticles (free in solution or assembled in arrays on a surface) may lead to highly effective electroanalytical devices.

## Plasmon and optical sensing

Plasmon resonance sensors are ubiquitous in the study of interfacial (bio)molecular interactions and function by detecting changes in local refractive index with high sensitivity.<sup>[100]</sup> The collective oscillation of electrons responsible for the characteristic plasmon absorption of metallic nanoparticles is highly sensitive to changes in local (surface) refractive index.<sup>[101,102]</sup> In view of the associated local enhancement of electromagnetic field, one may propose that such a surface can act as an “antenna” for interfacial processes such as molecular recognition. By utilizing the environmental sensitivity of appropriately functionalized nanoparticles, one might envisage the development of related SPR sensors of nanometer (“molecular level”) dimension. Because we have observed that it is possible to modify nanoparticles surfaces with SAMs, the terminal functionality of which is flexible, it is possible to generate stable colloids which are sensitive to/reactive to different species<sup>[103]</sup> (Fig. 5). In pursuit of this and related optical goals, several groups have recently generated nanoparticles functionalized with molecular recognition moieties.<sup>[20,82,99,104]</sup>

As a specific example, and with the aim of producing optical and redox-active nanoparticle anion sensors, the synthesis of a new amide–disulfide functionalized zinc metalloporphyrin has been reported.<sup>[82]</sup> This compound can be self-assembled on to gold nanoparticles to produce a novel anion-selective optical sensing system (Fig. 6). In this work, the nanoparticle itself is utilized as a diffusive “template” on which the receptor is “preorganized.” The zinc Lewis acid and hydrogen bond-mediated recognition of halide, nitrate, or dihydrogen phosphate by the zinc metalloporphyrin center is associated with a perturbation of the porphyrin optical spectrum. What makes this particularly striking is the ability of the nanoparticle to generate a solution-phase, but preorganized, receptor of high analyte binding affinity. As discussed in the previous section, the combined enthalpic and entropic factors associated with the monolayer-based, receptor site and its surrounding low dielectric are such that binding constants are enhanced by more than 2 orders of magnitude in comparison to the nonparticle-confined receptor (Table 1). Significantly, this enhanced binding affinity is such that anion recognition in a

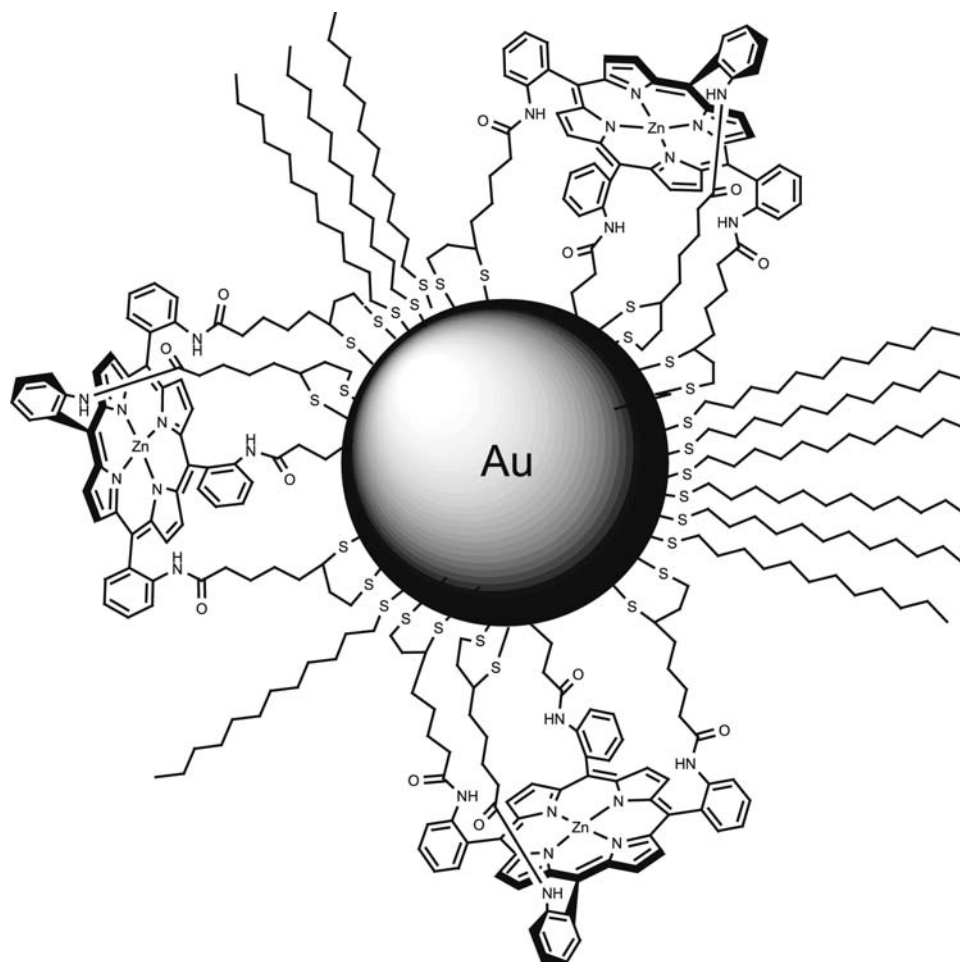


**Fig. 6** Schematic of an anion-sensing zinc porphyrin nanoparticle. The tetrapodal porphyrin is anchored to the nanoparticle surface through disulfide moieties. Note, for reasons of clarity, that the relative sizes of nanoparticle and porphyrin are false. *Source:* From Ref.<sup>[82]</sup>.

mixed aqueous/solvent system, a challenging situation because of the competitive solvation of the anion, is possible. By further tailoring the receptor site chemical and geometric properties, it should be possible to

generate yet more powerful sensing systems. Because functionalized SAMs can be similarly generated on semiconducting nanoparticles, sensing systems based on, e.g., a recognition-based perturbation of fluorescence may be feasible.

**Table 1** Association constant ( $\log K$ ) data for anion binding by Zn porphyrin receptor both assembled on the surface of a nanoparticle and free in solution

Anion	Particle free Zn porphyrin	Particle bound Zn porphyrin
$\text{Cl}^-$	>6	>6
$\text{Br}^-$	4.12	4.97
$\text{I}^-$	3.21	4.00
$\text{NO}_3^-$	2.41	3.22
$\text{H}_2\text{PO}_4^-$	>6	>6
$\text{ClO}_4^-$	0	0
* $\text{Cl}^-$	<2	4.3
* $\text{H}_2\text{PO}_4^-$	2.5	4.1

\*Data obtained in DMSO at 298 K.

## CONCLUSION

The potential impact of nanoscale science and technology on our lives is considerable. In recent years, much progress has been made in both generating and analyzing nanoscale material. To exploit some of the striking properties observed in matters of such dimensions, methods must be developed where homogeneous samples of material can be produced in useful quantities and incorporated into functional devices. In this article, we have attempted to summarize recent progress made in characterizing and utilizing the size-dependent properties of nanoparticles and quantum dots. Specifically, we have outlined and demonstrated

methods by which the environmental sensitivities inherent in these structures can be used in sensing technologies. Although interest in generating smaller analytical devices for been around for some time, only in recent years has it been possible to make use of the specific functional properties that are apparent at the nanometer scale. The ability to selectively and sensitively detect ions is of considerable environmental, clinical, and chemical importance. Through designed functionalization of nanoparticles with receptor moieties, it is possible to construct derived optical or electroanalytical assays. We have specifically introduced methodologies whereby nanoparticle-based ion assays can be developed. Through further refinement of nanoparticle functionalization, manipulation, and interrogation, the creation of a vast number of novel and highly responsive sensory devices seems feasible.

## ACKNOWLEDGMENTS

The authors wish to acknowledge support from the Engineering and Physical Sciences Research Council (EPSRC) and The Royal Society.

## REFERENCES

- Martin, C. Membrane-based synthesis of nanomaterials. *Chem. Mater.* **1996**, *8*, 1739.
- Alivisatos, A. Semiconductor clusters, nanocrystals, and quantum dots. *Science* **1996**, *271*, 933.
- Bawendi, M.; Steigerwald, M.; Brus, L. The quantum mechanics of larger semiconductor clusters ("quantum dots"). *Annu. Rev. Phys. Chem.* **1990**, *41*, 477.
- Klein, D.; Roth, R.; Lim, A.; Alivisatos, A.; McEuen, P. A single-electron transistor made from a cadmium selenide nanocrystal. *Nature* **1997**, *389*, 699.
- Wang, B.; Wang, H.; Li, H.; Zeng, C.; Hou, J.; Xiao, X. Tunable single-electron tunneling behavior of ligand-stabilized gold particles on self-assembled monolayers. *Phys. Rev.*, **B 2001**, *63*, 6303.
- Novak, J.; Brousseau, L.; Vance, F.; Johnson, R.; Lemon, B.; Hupp, J.; Feldheim, D. Nonlinear optical properties of molecularly bridged gold nanoparticle arrays. *J. Am. Chem. Soc.* **2000**, *122*, 12029.
- Miltenyi, S.; Muller, W.; Weichel, W.; Radbruch, A. High gradient magnetic cell separation with MACS. *Cytometry* **1990**, *11*, 231.
- Hahn, P.; Stark, D.; Lewis, J.; Saini, S.; Elizondo, G.; Weissleder, R.; Fretz, C.; Ferrucci, J. First clinical trial of a new superparamagnetic iron oxide for use as an oral gastrointestinal contrast agent in MR imaging. *Radiology* **1990**, *175*, 695.
- Yeh, T.; Zhang, W.; Ildstad, S. In vivo dynamic MRI tracking of rat T-cells labeled with superparamagnetic iron-oxide particles. *Magn. Reson. Med.* **1995**, *33*, 200.
- Sato, T.; Ahmed, H.; Brown, D.; Johnson, B.F.G. Single electron transistor using a molecularly linked gold colloidal particle chain. *J. Appl. Phys.* **1997**, *82*, 696.
- Brust, M.; Fink, J.; Bethell, D.; Schiffrin, D.J.; Kiely, C.J. Synthesis and reactions of functionalized gold nanoparticles. *J. Chem. Soc., Chem. Commun.* **1995**, *16*, 1655.
- Murthy, S.; Bigioni, T.P.; Wang, Z.L.; Khoury, J.T.; Whetten, R.L. Liquid-phase synthesis of thiol-derivatized silver nanocrystals. *Mater. Lett.* **1997**, *12*, 321.
- Yee, C.; Scotti, M.; Ulman, A.; White, H.; Rafailovich, M.; Sokolov, J. One-phase synthesis of thiol-functionalized platinum nanoparticles. *Langmuir* **1999**, *15*, 4314.
- Yee, C.K.; Jordan, R.; Ulman, A.; White, H.; King, A.; Rafailovich, M.; Sokolov, J. Novel one-phase synthesis of thiol-functionalized gold, palladium, and iridium nanoparticles using superhydride. *Langmuir* **1999**, *15*, 3486.
- Jin, R.; Cao, Y.; Mirkin, C.; Kelly, K.; Schatz, G.; Zheng, J. Photoinduced conversion of silver nanospheres to nanoprisms. *Science* **2001**, *294*, 1901.
- Huang, T.; Murray, R. Visible luminescence of water-soluble monolayer-protected gold clusters. *J. Phys. Chem., B* **2001**, *105*, 12498.
- Duncan, M.; Rouvray, D. Microclusters. *Sci. Am.* **1989**, *261*, 110.
- Henglein, A.; Lilie, J. Storage of electrons in aqueous solution: The rates of chemical charging and discharging the colloidal silver microelectrode. *J. Am. Chem. Soc.* **1981**, *103*, 1059.
- Kopple, K.; Meyerstein, D.; Meisel, D. Mechanism of the catalytic hydrogen production by gold sols. Hydrogen/deuterium isotope effect studies. *J. Phys. Chem.* **1980**, *84*, 870.
- Templeton, A.; Wuelfing, W.P.; Murray, R.W. Monolayer-protected cluster molecules. *Acc. Chem. Res.* **2000**, *33*, 27.
- Markovich, G.; Collier, C.P.; Henrichs, S.E.; Remacle, F.; Levine, R.D.; Heath, J.R. Architectonic quantum dot solids. *Acc. Chem. Res.* **1999**, *32*, 415.
- Chen, S.; Ingram, R.S.; Hostetler, M.J.; Pietron, J.J.; Murray, R.W.; Schaaff, T.G.; Khoury, J.T.; Alvarez, M.M.; Whetten, R.L. Gold nanoelectrodes of varied size: Transition to molecule-like charging. *Science* **1998**, *280*, 2098.
- Zelakiewicz, B.; Dios, A.d.; Tong, Y. <sup>13</sup>C NMR spectroscopy of <sup>13</sup>Cl-labeled octanethiol-protected Au nanoparticles: Shifts, relaxations, and particle-size effect. *J. Am. Chem. Soc.* **2003**, *125*, 18.
- Hicks, J.F.; Templeton, C.A.; Chen, S.; Sheran, K.M.; Jasti, R.; Murray, R.W.; Debord, J.; Schaaff, T.G.; Whetten, R.L. The monolayer thickness dependence of quantized double-layer capacitances of monolayer-protected gold clusters. *Anal. Chem.* **1999**, *71*, 3703.
- Quinn, B.M.; Liljeroth, P.; Kontturi, K. Interfacial reactivity of monolayer-protected clusters studied by scanning electrochemical microscopy. *J. Am. Chem. Soc.* **2002**, *124*, 12915.



26. Gittins, D.I.; Bethell, D.; Nichols, R.J.; Schiffrin, D.J. Redox-connected multilayers of discrete gold particles: A novel electroactive nanomaterial. *Adv. Mater.* **1999**, *11*, 737.
27. Chen, S. Self-assembling of monolayer-protected gold nanoparticles. *J. Phys. Chem., B* **2000**, *104*, 663.
28. Hicks, J.F.; Zamborini, F.P.; Osisek, A.J.; Murray, R.W. The dynamics of electron self-exchange between nanoparticles. *J. Am. Chem. Soc.* **2001**, *123*, 7048.
29. Chen, S. Electrochemical studies of Langmuir-Blodgett thin films of electroactive nanoparticles. *Langmuir* **2001**, *17*, 6664.
30. Jhaveri, S.D.; Lowy, D.A.; Foos, E.E.; Snow, A.W.; Ancona, M.G.; Tneder, L.M. Self-assembling monolayer formation of glucose oxidase covalently attached on 11-aminoundecanethiol monolayers on gold. *J. Chem. Soc., Chem. Commun.* **2002**, *14*, 1544.
31. Chen, S.; Murray, R.W.; Feldberg, S.W. Quantized capacitance charging of monolayer-protected Au clusters. *J. Phys. Chem., B* **1998**, *102*, 9898.
32. Ingram, R.; Hostetler, M.; Murray, R. Polyhetero-functionalized alkanethiolate-stabilized gold cluster compounds. *J. Am. Chem. Soc.* **1997**, *119*, 9175.
33. Schultz, S.; Smith, D.R.; Mock, J.J.; Schultz, D.A. Single-target molecule detection with nonbleaching multicolor optical immunolabels. *Proc. Natl. Acad. Sci. U. S. A.* **2000**, *97*, 996.
34. Moller, R.; Csaki, A.; Kohler, J.M.; Fritzsche, W. Electrical classification of the concentration of bioconjugated metal colloids after surface adsorption and silver enhancement. *Langmuir* **2000**, *17*, 5426.
35. Mirkin, C.; Letsinger, R.; Mucic, R.; Storhoff, J. A DNA-based method for rationally assembling nanoparticles into macroscopic materials. *Nature* **1996**, *382*, 607.
36. Bruchez, M.; Moronne, M.; Gin, P.; Weiss, S.; Alivisatos, A. Semiconductor nanocrystals as fluorescent biological labels. *Science* **1998**, *281*, 2013.
37. Taton, T.; Mucic, R.; Mirkin, C.; Letsinger, R. The DNA-mediated formation of supramolecular mono- and multilayered nanoparticle structures. *J. Am. Chem. Soc.* **2000**, *122*, 6305.
38. Brown, K.; Fox, A.; Natan, M. Morphology-dependent electrochemistry of cytochrome *c* at Au colloid-modified SnO<sub>2</sub> electrodes. *J. Am. Chem. Soc.* **1996**, *118*, 1154.
39. Mattoussi, H. et al. Properties of CdSe nanocrystal dispersions in the dilute regime: Structure and interparticle interactions. *Phys. Rev., B* **1998**, *58*, 7850.
40. Murray, C.; Norris, D.; Bawendi, M. Synthesis and characterization of nearly monodisperse CdE (E = sulfur, selenium, tellurium) semiconductor nanocrystallites. *J. Am. Chem. Soc.* **1993**, *115*, 8706.
41. Olshavsky, M.; Goldstein, A.; Alivisatos, A. Organometallic synthesis of gallium-arsenide crystallites, exhibiting quantum confinement. *J. Am. Chem. Soc.* **1990**, *112*, 9438.
42. Gerion, D.; Pinaud, F.; Williams, S.; Weiss, S.; Alivisatos, A. Synthesis and properties of biocompatible water-soluble silica-coated CdSe/ZnS semiconductor quantum dots. *J. Phys. Chem., B* **2001**, *105*, 8861.
43. Peng, X.; Schlamp, M.; Kadanavich, A.; Alivisatos, A. Epitaxial growth of highly luminescent CdSe/CdS core/shell nanocrystals with photostability and electronic accessibility. *J. Am. Chem. Soc.* **1997**, *119*, 7019.
44. Hu, J.; Li, L.; Yang, W.; Manna, L.; Wang, L.; Alivisatos, A. Linearly polarized emission from colloidal semiconductor quantum rods. *Science* **2001**, *292*, 2060.
45. Mitchell, G.; Mirkin, C.A.; Letsinger, R.L. Programmed assembly of DNA functionalized quantum dots. *J. Am. Chem. Soc.* **1999**, *121*, 8122.
46. Mattoussi, H.; Mauro, J.; Goldman, E.; Anderson, G.; Sundar, V.; Mikulec, F.; Bawendi, M. Self-assembly of CdSe-ZnS quantum dot bioconjugates using an engineered recombinant protein. *J. Am. Chem. Soc.* **2000**, *122*, 12142.
47. Zanchet, D.; Micheel, C.; Parak, W.; Gerion, D.; Alivisatos, A. Electrophoretic isolation of discrete Au nanocrystal/DNA conjugates. *Nano Lett.* **2001**, *1*, 32.
48. Shipway, A.; Katz, E.; Willner, I. Nanoparticle arrays on surfaces for electronic, optical, and sensor applications. *ChemPhysChem* **2000**, *1*, 18.
49. Gudiksen, M.; Leuhon, L.; Wang, J.; Smith, D.; Leiber, C. Growth of nanowire superlattice structures for nanoscale photonics and electronics. *Nature* **2002**, *415*, 617.
50. Zamborini, F.; Hicks, J.; Murray, R. Quantised double layer charging of nanoparticle films assembled using carboxylate/(Cu<sup>2+</sup> or Zn<sup>2+</sup>)/carboxylate bridges. *J. Am. Chem. Soc.* **2000**, *122*, 4514.
51. Templeton, A.; Zamborini, F.; Wuelfing, W.; Murray, R. Controlled and reversible formation of nanoparticle aggregates and films using Cu<sup>2+</sup>-carboxylate chemistry. *Langmuir* **2000**, *16*, 6682.
52. Ogawa, S.; Hu, K.; Fan, F.; Bard, A. Photoelectrochemistry of films of quantum size lead sulfide particles incorporated in self-assembled monolayers on gold. *J. Phys. Chem., B* **1997**, *101*, 5707.
53. Nakanishi, T.; Ohtani, B.; Shimazu, K.; Uosaki, K. Layer-by-layer self-assembly of composite films of CdS nanoparticle and alkanedithiol on gold: An x-ray photoelectron spectroscopic characterization. *Chem. Phys. Lett.* **1997**, *278*, 233.
54. Nakanishi, T.; Ohtani, B.; Uosaki, K. Fabrication and characterization of CdS-nanoparticle mono- and multilayers on a self-assembled monolayer of alkanedithiols on gold. *J. Phys. Chem., B* **1998**, *102*, 1571.
55. Yamada, M.; Quiros, I.; Mizutani, J.; Kubo, K.; Nishihara, H. Preparation of palladium nanoparticles functionalized with biferrocene thiol derivatives and their electro-oxidative deposition. *Phys. Chem. Chem. Phys.* **2001**, *3*, 3377.
56. Quiros, I.; Yamada, M.; Mizutani, J.; Kubo, K.; Kurihara, M.; Nishihara, H. Preparation of alkanethiolate-protected palladium nanoparticles and their size dependence on synthetic conditions. *Langmuir* **2002**, *18*, 1413.
57. Yamada, M.; Nishihara, H.J. Electrochemical construction of an alternating multi-layered structure of palladium and gold nanoparticles attached with biferrocene moieties. *J. Chem. Soc., Chem. Commun.* **2002**, *21*, 2578.

58. Murata, M.; Yamada, M.; Fujita, T.; Kojima, K.; Kurihara, M.; Kubo, K.; Kobayashi, Y.; Nishihara, H. Structural conversion and spin separation in bis(ferrocenylethynyl)anthraquinones triggered by proton-coupled intramolecular electron transfer. *J. Am. Chem. Soc.* **2001**, *123*, 12903.
59. Bakkers, E.; Marsman, A.; Jennekens, L.; Vanmaekelbergh, D. Distance-dependent electron transfer in Au/spacer/Q-CdSe assemblies. *Angew. Chem., Int. Ed. Engl.* **2000**, *39*, 2297.
60. Pethkar, S.; Aslam, M.; Mulla, I.; Ganeshan, P.; Vijayamohan, K. Preparation and characterisation of silver quantum dot superlattice using self-assembled monolayers of pentanedithiol. *J. Mater. Chem.* **2001**, *11*, 1710.
61. Sagara, T.; Kato, N.; Kakashima, N. Electroreflectance study of gold nanoparticles immobilized on an aminoalkanethiol monolayer coated on a polycrystalline gold electrode surface. *J. Phys. Chem., B* **2002**, *106*, 1205.
62. Uosaki, K.; Kondo, T.; Okamura, M.; Song, W. Electron and ion transfer through multilayers of gold nanoclusters covered by self-assembled monolayers of alkythiols with various functional groups. *Faraday Discuss.* **2002**, *121*, 373.
63. Kiely, C.J.; Fink, J.; Brust, M.; Bethell, D.; Schiffrin, D.J. Spontaneous ordering of bimodal ensembles of nanoscopic gold clusters. *Nature* **1998**, *396*, 444.
64. Sun, S.H.; Murray, C.B.; Weller, D.; Folks, L.; Moser, A. Monodisperse FePt nanoparticles and ferromagnetic FePt nanocrystal superlattices. *Science* **2000**, *287*, 1989.
65. Jin, J.; Iyoda, T.; Cao, C.S.; Song, Y.L.; Jiang, L.; Li, T.J.; Zhu, D.B. Self-assembly of uniform spherical aggregates of magnetic nanoparticles through—Interactions. *Angew. Chem., Int. Ed. Engl.* **2001**, *40*, 2135.
66. Gittins, D.I.; Bethell, D.; Nichols, R.J.; Schiffrin, D.J. Diode-like electron transfer across nanostructured films containing a redox ligand. *J. Mater. Chem.* **2000**, *10*, 79.
67. Caruso, F.; Mohwald, H. Preparation and characterization of ordered nanoparticle and polymer composite multilayers on colloids. *Langmuir* **1999**, *15*, 8276.
68. Pardo-Yissar, V.; Katz, E.; Lioubashevski, O.; Willner, I. Layered polyelectrolyte films on Au electrodes: Characterization of electron-transfer features at the charged polymer interface and application for selective redox reactions. *Langmuir* **2001**, *17*, 1110.
69. Caruso, F.; Spasova, M.; Saigueirino-Maceira, V.; Liz-Marzan, L.M. Multilayer assemblies of silica-encapsulated gold nanoparticles on decomposable colloid templates. *Adv. Mater.* **2001**, *13*, 1090.
70. Yamada, M.; Tadera, T.; Kubo, K.; Nishihara, H. Electrochemical deposition of biferrocene derivative-attached gold nanoparticles and the morphology of the formed film. *J. Phys. Chem., B* **2003**, *107*, 3703.
71. Gerion, D.; Parak, W.; Williams, S.; Zanchet, D.; Micheel, C.; Alivisatos, A. Sorting fluorescent nanocrystals with DNA. *J. Am. Chem. Soc.* **2002**, *124*, 7070.
72. Chu, L.; Yang, S. Contributions of r-1, r-2, r-3 terms of the full dipole fields associated with Raman scattering enhancement from CN molecules adsorbed on a 2-D array of Ag spheroids. *J. Appl. Phys.* **1985**, *57*, 453.
73. Doron, A.; Katz, E.; Willner, I. Organization of Au colloids as monolayer films onto ITO glass surfaces: Application of the metal colloid films as base interfaces to construct redox-active monolayers. *Langmuir* **1995**, *11*, 1313.
74. Hicks, J.; Zamborini, F.; Murray, R. Dynamics of electron transfers between electrodes and monolayers of nanoparticles. *J. Phys. Chem., B* **2002**, *106*, 7751.
75. Chen, S.; Pei, R. Ion-induced rectification of nanoparticle quantized capacitance charging in aqueous solutions. *J. Am. Chem. Soc.* **2001**, *123*, 10607.
76. Plenio, H.; Diodone, R. Complexation of Na<sup>+</sup> in redox-active ferrocene crown ethers, a structural investigation, and an unexpected case of Li<sup>+</sup> selectivity. *Inorg. Chem.* **1995**, *34*, 3964.
77. Shephard, D.; Johnson, B.; Matters, J.; Parson, S. Novel redox-active ruthenium cluster crown compounds capable of host-guest chemistry. *J. Chem. Soc. Dalton Trans.* **1998**, *14*, 2289.
78. Beer, P.; Gale, P.; Chen, Z.; Drew, M.; Powell, H. New ionophoric calix[4]diquinones: Coordination chemistry, electrochemistry, and x-ray crystal structures. *Inorg. Chem.* **1997**, *36*, 5880.
79. Webber, P.; Beer, P.; Chen, G.; Felix, V.; Drew, M. Bis(calix[4]diquinone) receptors: Cesium- and rubidium-selective redox-active ionophores. *J. Am. Chem. Soc.* **2003**, *125*, 5774.
80. Beer, P.; Gale, P. Anion recognition and sensing: The state of the art and future perspectives. *Angew. Chem., Int. Ed. Engl.* **2001**, *40*, 486.
81. Beer, P.; Davis, J.; Drillsma-Milgrom, D.; Szemes, F. Anion recognition and redox sensing amplification by self-assembled monolayers of 1,1-bis(alkyl-N-amido)ferrocene. *J. Chem. Soc., Chem. Commun.* **2002**, *16*, 1716.
82. Beer, P.D.; Cormode, D.P.; Davis, J.J. Porphyrin-functionalised nanoparticle anion sensors **2008**, *18*, 32–40.
83. Davis, J.J.; Beer, P.D.; Szemes, F.S.; Drillsma-Milgrom, D. *J. Chem. Soc., Chem. Commun.* **2002**, 1716.
84. Bangs, L.B. New developments in particle-based immunoassays: Introduction. *Pure Appl. Chem.* **1996**, *68*, 1873.
85. Elghanian, R.; Storhoff, J.; Mucic, R.; Letsinger, R.; Mirkin, C. Selective colorimetric detection of polynucleotides based on the distance-dependent optical properties of gold nanoparticles. *Science* **1997**, *277*, 1078.
86. Erp, R.V.; Gribnau, T.C.J.; Van Sommeren, A.P.G. Application of a sol particle immunoassay to the determination of affinity constants of monoclonal antibodies. *J. Immunoass.* **1991**, *12*, 425.
87. Lin, S.; Liu, S.; Lin, C.; Chen, C. Recognition of potassium ion in water by 15-crown-5 functionalized gold nanoparticles. *Anal. Chem.* **2002**, *74*, 330.
88. Kim, Y.; Johnson, R.; Hupp, J. Gold nanoparticle-based sensing of “spectroscopically silent” heavy metal ions. *Nano Lett.* **2001**, *1*, 165.

89. Zamborini, F.; Leopold, M.; Hicks, J.; Kulesza, P.; Malik, M.; Murray, R. Electron hopping conductivity and vapor sensing properties of flexible network polymer films of metal nanoparticles. *J. Am. Chem. Soc.* **2002**, *124*, 8958.
90. Vossmeier, T.; Guse, B.; Besnard, I.; Bauer, R.; Mullen, K.; Yasuda, A. Gold nanoparticle/polyphenylene dendrimer composite films: Preparation and vapor-sensing properties. *Adv. Mater.* **2002**, *14*, 238.
91. Zhang, H.; Evans, S.; Henderson, J.; Miles, R.; Shen, T. Vapour sensing using surface functionalized gold nanoparticles. *Nano Technol.* **2002**, *13*, 439.
92. Evans, S.; Johnson, S.; Cheng, Y.; Shen, T. Vapour sensing using hybrid organic-inorganic nanostructured materials. *J. Mater. Chem.* **2000**, *10*, 183.
93. Blatchford, C.G.; Campbell, J.R.; Creighton, J.A. Plasma resonance-enhanced Raman scattering by absorbates on gold colloids: The effects of aggregation. *Surf. Sci.* **1982**, *120*, 435.
94. Tran, C.D. Subnanogram detection of dyes on filter paper by surface-enhanced Raman scattering spectrometry. *Anal. Chem.* **1984**, *56*, 824.
95. Soper, S.A.; Ratzhlaff, K.L.; Kuwana, T. Surface-enhanced resonance Raman spectroscopy of liquid chromatographic analytes on thin-layer chromatographic plates. *Anal. Chem.* **1990**, *62*, 1438.
96. Grabar, C.C.; Griffith-Freeman, R.; Hommer, M.B.; Natan, M.J. Preparation and characterization of Au colloid monolayers. *Anal. Chem.* **1995**, *67*, 735.
97. Duyne, R.P.v.; Haller, K.L.; Altkorn, R.I. Spatially resolved surface enhanced Raman spectroscopy: Feasibility, intensity dependence on sampling area and attomole mass sensitivity. *Chem. Phys. Lett.* **1986**, *126*, 190.
98. Labande, C.; Astruc, D. Colloids as redox sensors: Recognition of  $\text{H}_2\text{PO}_4^-$  and  $\text{HSO}_4^-$  by amidoferrocenylalkylthiol-gold nanoparticles. *J. Chem. Soc., Chem. Commun.* **2000**, *12*, 1007.
99. Labande, A.; Ruiz, J.; Astruc, D. Supramolecular gold nanoparticles for the redox recognition of oxoanions: Syntheses, titrations, stereoelectronic effects, and selectivity. *J. Am. Chem. Soc.* **2002**, *124*, 1782.
100. Brochman, J.; Nelson, B.; Corn, R. Surface plasmon resonance imaging measurements of ultrathin organic films. *Annu. Rev. Phys. Chem.* **2000**, *51*, 41.
101. Malinsky, M.; Kelly, K.; Schatz, G.; Duyne, R.v. Chain length dependence and sensing capabilities of the localized surface plasmon resonance of silver nanoparticles chemically modified with alkanethiol self-assembled monolayers. *J. Am. Chem. Soc.* **2000**, *123*, 1471.
102. Bright, R.; Musick, M.; Natan, M. Preparation and characterization of Ag colloid monolayers. *Langmuir* **1998**, *14*, 5695.
103. Weisbecker, C.S.; Merritt, M.V.; Whitesides, G.M. Molecular self-assembly of aliphatic thiols on gold colloids. *Langmuir* **1996**, *12*, 3763.
104. Jensen, T.R.; Malinsky, M.D.; Haynes, C.L.; Van Duyne, R.P. Nanosphere lithography: Tunable localized surface plasmon resonance spectra of silver nanoparticles. *J. Phys. Chem., B* **2000**, *104*, 10549.

# Nanoparticles: Synthesis in Polymer Substrates

**Bai Yang**

*College of Chemistry, Jilin University, Changchun, China*

**Junhu Zhang**

*Department of Chemistry, Jilin University, Changchun, China*

## INTRODUCTION

Advanced materials composed of inorganic nanoparticles are currently one of the most dynamic areas of scientific research. These particles represent significant fundamental and commercial interest with a wide range of applications including the next generation of optics, electronics, catalysts, and sensors. In the past 20 years, with the increasing developments in nanotechnology, nanoelectronics, and nanobioelectronics, functional building blocks with which to construct microstructures and devices are under intensive investigation. Increasing attention has been paid to metal or semiconductor nanoparticles, which have also been called nanocrystals, nanoclusters, quantum dots, and Q particles.

Nanoparticles are in the size range of 1–100 nm, which lies between single atoms or molecules and bulk materials, and their chemical and physical properties differ markedly from those of the bulk solids. The reasons for these properties can be attributed to high surface area and quantum size effect, which is caused by the reduced size in three dimensions. One typical example is that the melting temperature of nanoparticles strongly depends on the particle size and is substantially lower than the bulk melting temperature. The melting point of 2.5-nm Au nanoparticles is ~40% lower than that of bulk gold. Similar behavior has been observed for CdS nanoparticles. At the same time, with the decrease in the number of atoms in the particles, their electronic properties also start to change. This is the so-called quantum size effect, which can be observed as a blue shift in the optical band gap or exciton energy. When the size of particles is reduced to nanometer scale, the number of atoms at the surfaces or grain boundaries of the crystalline regions is comparable to the number of those that are in the crystalline lattice itself. Physical and chemical properties, which are usually determined by the molecular structure of the bulk lattice, become increasingly dominated by the defect structure of the surface. During the preparation of nanoparticles, engineering of the size and surface structure is of both theoretical and practical

importance, because it leads to mechanical, chemical, electrical, optical, magnetic, electro-optical, and magneto-optical properties that are substantially different from those observed for the corresponding bulk materials. Chemists, biologists, and materials scientists have studied and reviewed the preparation and characterization of metal and semiconductor nanoparticles in detail, focusing on their physical and chemical properties.<sup>[1–24]</sup>

Nanoparticles can be synthesized from a variety of materials with controllable sizes, shapes, and structures, but because of their high specific surface area and low surface energy, nanoparticles are not stable in ambient circumstances, and they must be incorporated in certain kinds of materials. Materials such as reverse micelles and surfactant vesicles,<sup>[25]</sup> glass,<sup>[26,27]</sup> zeolites,<sup>[28,29]</sup> and polymers<sup>[30–34]</sup> have been used as the substrate to prepare composite materials containing nanoparticles. During the preparation of such materials, the substrate not only can prevent the nanoparticles from aggregation, but also can accurately control their size and surface structure. In addition, in applications for optical, electrical, and magnetic devices, nanoparticles are mostly used in the form of thin films. Currently, such films can be made by spin coating,<sup>[35–37]</sup> spraying,<sup>[38,39]</sup> chemical deposition,<sup>[40–42]</sup> electrical deposition,<sup>[43–46]</sup> Langmuir–Blodgett (LB) technique,<sup>[47–51]</sup> and layer-by-layer self-assembly (LBL) method.<sup>[51–57]</sup>

In this entry, we will focus on the preparation of nanoparticles in polymer matrices and the assembly of nanoparticles at interfaces.

## PREPARATION OF NANOPARTICLES IN POLYMER MATRICES

Polymers have been considered one of the most important matrix materials for the preparation and application of nanoparticles because of their mechanical, optical, electrical, and thermal properties.<sup>[30–34]</sup> In polymer networks, movements of nanometer-sized particles are restricted by the polymer chains, so aggregation is avoided and the nanoparticles are stabilized

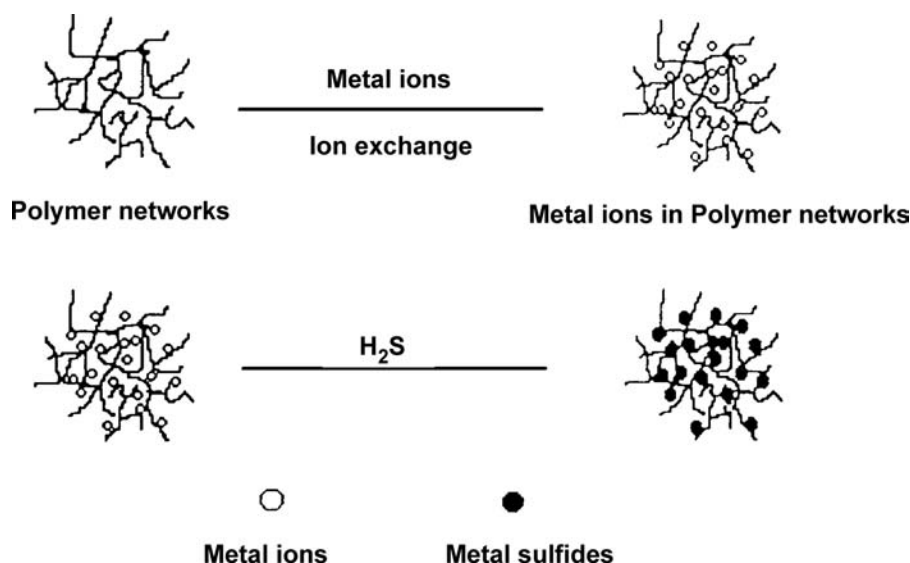


**Fig. 1** Scheme for the assembly of metal sulfide nanoparticles in polymer networks. *Source:* From Ref.<sup>[64]</sup>.

by the polymer networks. The size and size distribution of the particles can also be controlled by the concentration and density of metal ions. In order to prepare nanoparticles in polymer networks, the metal ions should be previously dispersed in the polymer networks. There have been two methods for the incorporation of metal ions into polymer networks.

The first method involves the introduction of metal ions into polymer networks by a metal-ion-containing monomer. PbS nanoparticles with an average size of 4.0 nm have been prepared in polymer networks by H<sub>2</sub>S treatment of a copolymer of styrene and lead methylacrylate.<sup>[58,59]</sup> The concentration of the metal ions could be controlled by altering the relative proportion of the two monomers. Infrared (IR) measurements and the variations of the molecular weight of the copolymer before and after reacting with H<sub>2</sub>S implied that there exist Pb–OOC bonds on the surface of the nanoparticles. PbS nanoparticles act as cross-linking agents, and the interaction of the polymer with the nanoparticles gives a surface chemical modification of the PbS nanoparticles, which strongly affects the optical properties of the nanoparticles.

The second method involves the introduction of metal ions into polymer networks by ion-exchange adsorption.<sup>[60–65]</sup> As shown in Fig. 1,<sup>[64]</sup> cross-linked polymer networks were formed by polymerization of styrene with a cross-linking agent. Then the polymerizate was sulfonated by sulfuric acid, and the product could be immersed in an aqueous solution that contained metal salts to adsorb metal ions into the polymer networks by exchange with H<sup>+</sup> of –SO<sub>3</sub>H. By varying the duration of the ion exchange and the concentration of the metal salt solution, we can control the concentration of the metal ions. The metal-ion-containing polymer networks could be dissolved in

an organic solvent and then treated with H<sub>2</sub>S gas, after which the solution turns yellow but without precipitation, which shows the formation of CdS nanoparticles. The resulting nanoparticles had a narrow particle size distribution. By this method, CdS, Cu-doped ZnS, and Cu<sub>2</sub>S/CdS/ZnS nanoparticles could also be prepared. All these results indicated that the polymer networks could effectively prevent the particles from growing and aggregating.

Metal or semiconductor nanoparticles may also be prepared in situ in the microdomain space formed in block copolymers.<sup>[66–71]</sup> Block copolymers exhibit phase separation, which may help isolate the nanoparticles as they form. When a copolymer is used as the matrix for nanoparticles, the particle size is controlled by the composition of the copolymer and the concentration of metal ions. Nafion film, which is a type of ionic polymer and can adsorb metal ions by ion exchange, has also been used to prepare nanoparticles.<sup>[72–75]</sup> Similarly, the size of the nanoparticles can be controlled by the initial metal ion concentration and subsequent thermal annealing treatment.

## THIN FILMS OF NANOPARTICLES

### Nanoparticles in LB Films

Transferring a well-packed monolayer from aqueous solution surfaces to solid substrates was demonstrated about 60 years ago by the Langmuir–Blodgett (LB) technique. Surfactant structures have also been used for direct assembly of metallic, semiconducting, and magnetic nanoparticles. This organization can be accomplished by adsorbing particles electrostatically to charged surfactant headgroups or by in situ

generation of particles beneath monolayers at the air–water interface.<sup>[47–51,76–83]</sup> Surfactant monolayers with attached nanoparticles can be transferred to solid supports using standard LB techniques.

Monolayers of surfactants have proven to be versatile as templates for the in situ growth of thin nanoparticle films. These monolayers are formed from a range of naturally occurring and synthetic surfactants or from a mixture of suitable surfactants, and their two-dimensional phase behavior and structure are well understood. Fendler and Meldrum have described the formation of sulfide semiconductor nanoparticulate films under a Langmuir monolayer of surfactants as follows:<sup>[51]</sup> After the spreading of surfactant monolayer on the air–water interface of the metal ion solution with an atmosphere of H<sub>2</sub>S, metal sulfide bonds formed at a large number of sites at the monolayer–aqueous interface. Well-separated nanoparticles of metal sulfide then formed and coalesced into interconnected arrays of semiconductor nanoparticles and a porous semiconductor particulate film composed of particles 20–40 Å thick and 30–80 Å in diameter. Once the first layer of semiconductor nanoparticulate film formed, subsequent layers were deposited up to a plateau thickness beyond which the film cannot grow. The presence of a monolayer with an appropriate surface charge is essential to the formation of the sulfide semiconductor nanoparticulate film. In the absence of a monolayer, infusion of H<sub>2</sub>S over an aqueous metal ion solution resulted in the formation of large, irregular, and polydispersed metal sulfide particles, which precipitated in the bulk solution before settling to the bottom of the trough. Furthermore, the nanoparticulate film could not form under positively charged monolayers.

Thin films of nanoparticles can also be fabricated by spreading surfactant-stabilized nanoparticles on aqueous solutions and then transferring them to solid substrates by the LB technique. The technique can be regarded as analogous to monolayer formation from simple surfactants. Nanoparticulate films were formed at the air–water interface by dispersing surfactant-stabilized nanoparticles on an aqueous subphase, which was contained in a Langmuir trough. There are many intrinsic benefits to this method. The nanoparticles are prepared before the incorporation into the films, allowing one to control their dimensions, physical properties, and the particle size and distribution. Gao et al. have reported the fabrication of Fe<sub>2</sub>O<sub>3</sub>/polymer composite film using the LB method.<sup>[77]</sup> Methacrylic acid was used as the surfactant to prepare Fe<sub>2</sub>O<sub>3</sub> nanoparticles by the microemulsion method in a system of water–toluene. After a cross-linking agent together with an initiator were added into the organosol and reacted under ultrasonic stirring, an organic–inorganic composite microgel was obtained. This composite

microgel showed good amphiphilic properties and could be transferred onto solid substrates from a pure water interface using the LB technique. Infrared and UV–visible (UV–vis) spectra of the film showed the presence of some residual vinyl groups, which means that the microgel could be further polymerized. Polymerization of surfactant in the composite films improved the stability of the LB film.

### Assembly of Nanoparticle Monolayers

Solution-based approaches to surface assembly of metal and semiconductor nanoparticles typically involve electrostatic or covalent binding of the particle to a surface-bound molecular or polymeric thin film.<sup>[84–90]</sup> Self-assembly of metal nanoparticle monolayers on polymer-coated substrates yields macroscopic surfaces that are highly active for surface-enhanced Raman scattering (SERS).<sup>[85–87]</sup> Nanoparticles are bound to the substrate through multiple bonds between the colloidal metal and functional groups on the polymer such as cyanide (CN), amine (NH<sub>2</sub>), and thiol (SH). Self-assembly of nanoparticles onto the oppositely charged substrate surface is governed by a delicate balance of the adsorption and desorption equilibria. The efficient adsorption of one monolayer of nanoparticles onto the oppositely charged substrate surface is the objective of the immersion step. Preventing the desorption of the nanoparticles during the rinsing process is of equal importance. The optimization of the self-assembly in terms of maximizing the adsorption of nanoparticles from their dispersions and minimizing their desorption upon rinsing requires the correct selection of stabilizers and the careful control of the kinetics of the processes.

The deposition process may also be performed on a substrate modified by an LB film, which may give a charged surface. As we have reported,<sup>[91]</sup> one monolayer of PbI<sub>2</sub> nanoparticles can be adsorbed on a substrate modified by LB films through electrostatic interactions. First, we transferred two layers of Y-type LB film of stearic acid onto some hydrophilic substrates, which allowed one layer of bipolar pyridinium to be adsorbed onto the carboxylic surface of the LB film. Finally, we deposited one layer of anionic PbI<sub>2</sub> after the bipolar pyridinium. The structure of the self-assembled monolayer film is shown in Fig. 2. Substrates such as Si, CaF<sub>2</sub>, quartz, glass, Ag, and Au are widely used for LB processes, so LB film-covered slides can provide a wide range of substrates for a self-assembled monolayer of nanoparticles. In order to observe the PbI<sub>2</sub> nanoparticles monolayer in the self-assembled film with transmission electron microscopy (TEM), a copper grid covered with a very thin layer of formvar was used as the LB film substrate. A TEM



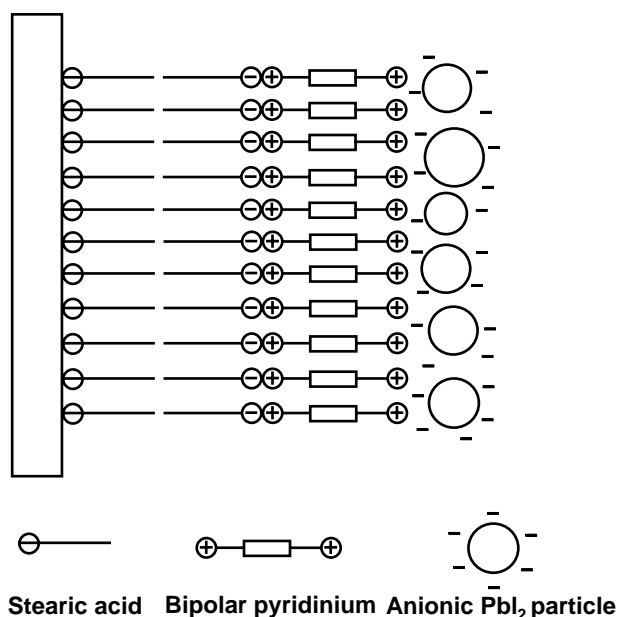


**Fig. 2** Scheme for one monolayer of  $\text{PbI}_2$  nanoparticles in the stearic acid–bipolar pyridinium– $\text{PbI}_2$  four layer structure. Source: From Ref.<sup>[91]</sup>.

photograph of the self-assembly film shows that all the  $\text{PbI}_2$  nanoparticles are round and closely packed, but without any large aggregates. As a comparison, one droplet of the  $\text{PbI}_2$  solution was dropped onto the grid and blown dry with  $\text{N}_2$ . TEM measurements showed that the small particles had aggregated into large ones during the evaporation in the sample preparation. This contrast proves that the bipolar pyridinium film interacts with the nanoparticles strongly and can effectively keep the small particles from aggregating.

Covalent attachment strategies often take advantage of the reactivity of the outer shell atoms in the nanoparticles. Many metallic and semiconductor nanoparticles (Au, Ag, CdS, CdSe) have a high affinity for amine and/or thiol moieties.<sup>[54]</sup> For example, Colvin et al. have covalently attached CdS nanoparticles to Au and Al substrates using bifunctional cross-linkers.<sup>[84]</sup> Natan and coworkers have assembled Au and Ag nanoparticles on  $-\text{NH}_2$  and  $-\text{SH}$  terminated organosilane polymers on silica substrates.<sup>[85,87]</sup> The kinetics of this surface-assembly reaction have been investigated in some detail, affording control over the number of particles on the surface.

Alternatively, close-packed monolayers of alkanethiol-stabilized nanoparticles have been formed by solvent evaporation.<sup>[17,18]</sup> Self-assembled arrays involve self-organization of size-selected nanoparticles encapsulated in protective, compact organic coatings into monolayers, thin films, and superlattices. A key step in this process is the fabrication of size- and shape-controlled nanoparticle superlattices that can grow large

enough for technological applications. In this case, the length of the organic ligand defines the distance between particles. This distance has a pronounced effect on the electronic properties of the resulting structure. Particles that can be self-assembled are usually smaller than 10 nm in size, and it is in this size range that many exciting and unusual physical properties are enhanced.

### Layer-by-Layer Assembly of Nanoparticles

The LBL method developed by G. Decher is one of the most promising new methods of thin film deposition, and it is often used for oppositely charged polymers.<sup>[92–94]</sup> Recently, it has also been successfully applied to thin films of nanoparticles and other inorganic materials,<sup>[51–57]</sup> such as Au,<sup>[95–97]</sup> Ag,<sup>[98–101]</sup> CdS,<sup>[102]</sup> PbS,<sup>[103]</sup>  $\text{Fe}_3\text{O}_4$ ,<sup>[104–106]</sup> CdSe,<sup>[107–109]</sup> HgTe,<sup>[110]</sup>  $\text{TiO}_2$ ,<sup>[111]</sup>  $\text{SiO}_2$ ,<sup>[112–114]</sup> and others.<sup>[115–119]</sup> Its simplicity and universality combined with the resulting high quality of coatings and uniform distribution of nanoparticles open broad perspectives for this technique both in research and in industry. Compared with other techniques for the fabrication of thin films of nanoparticles, the LBL method has two main advantages: 1) simplicity (the relative ease of preparation and versatility have contributed to the rapid development of this method), 2) universality (tolerance of the substrate shapes and materials and the dual, organic–inorganic nature of the coating).

The LBL assembly of nanoparticles can be described as the sequential adsorption of monolayers of nanoparticles on positively charged layers of a polyelectrolyte. Interestingly, purely inorganic LBL films were described more than 30 years ago.<sup>[120]</sup> The deposition of the films can be performed in a cyclic manner, which is made possible by the overcompensation of surface charge, which often takes place when polyelectrolytes and other high molecular weight species are adsorbed onto a solid–liquid interface. The construction of an LBL film of nanoparticles requires four simple steps.<sup>[52]</sup> 1) prime a cleaned substrate by absorbing a layer of surfactant or polyelectrolyte onto its surface; 2) immerse the primed substrate in a dilute aqueous solution of a cationic or anionic polyelectrolyte for the optimized length of time for adsorption of a monolayer; 3) rinse and dry the substrate; 4) immerse the polyelectrolyte monolayer covered substrate in a dilute dispersion of oppositely charged semiconductor nanoparticles, also for the optimized length of time for adsorption of a monolayer of nanoparticles. These four operations complete the self-assembly of one polyelectrolyte–nanoparticle bilayer, and by repeating them, multilayered self-assembly films of polyelectrolyte and nanoparticles can be fabricated. The electrostatic attraction between semiconductor colloids

and a layer of polyelectrolytes ensures the facile adsorption. At the same time, the electrostatic repulsion between similarly charged species in solution limits the thickness of the newly formed thin layer of nanoparticles.

Our group has reported several kinds of LBL films of nanoparticles,<sup>[121–131]</sup> among which we have also fabricated a CdS nanoparticle/cationic polyelectrolyte multilayer film based on electrostatic interactions.<sup>[122]</sup> An aqueous solution of CdS nanoparticles was prepared by the addition of mercaptoacetic acid as a stabilizer agent. Infrared measurements imply that mercaptoacetic acid was chemically modified on the surface of CdS nanoparticles through thiol groups, with carboxylic acid groups pointing to the solvent, and the carboxylic acid group was in a state of  $\text{COO}^-$ , which made it possible to use the surface-modified CdS nanoparticles as the negatively charged species in the LBL assembly process. A quartz substrate covered with aminopropylsilane was prepared by treating with the vapor of 3-aminopropyltriethoxysilane and then reacted with HCl solution to become positively charged. Then, using the LBL method, negatively charged nanoparticles and positively charged polyelectrolyte could be alternatively deposited on the substrate. The structure of the LBL film is shown in Fig. 3. UV-vis absorption spectroscopy was used to monitor the LBL assembly process, and the similarity of the absorption spectra of the alternating films to that of the CdS nanoparticles in the visible region implies that the CdS nanoparticles were successfully assembled in the alternating film. In the UV-vis spectra (Fig. 4) of multilayer films with different numbers of layers, a linear increase of the absorbance of CdS

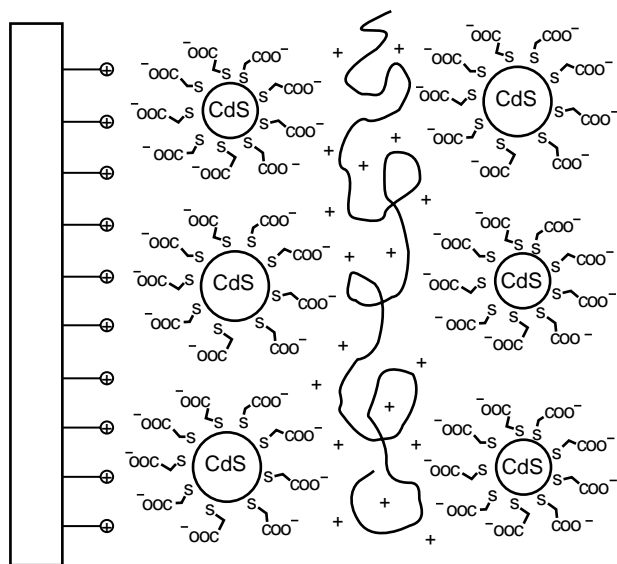


**Fig. 3** Scheme for the assembly of CdS nanoparticles in LBL films. *Source:* From Ref.<sup>[122]</sup>.

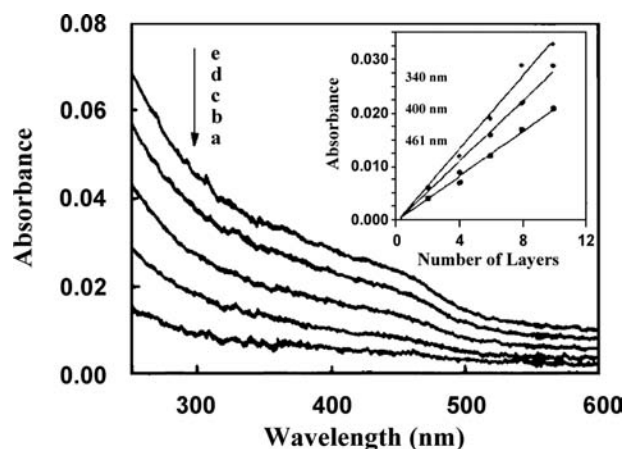


**Fig. 4** UV-vis absorption spectra of the LBL films of CdS nanoparticles and a cationic polyelectrolyte with different numbers of layers. Inset: absorbance vs. number of layers at 340, 400, and 461 nm. *Source:* From Ref.<sup>[122]</sup>.

nanoparticles could be observed, which indicates that the oppositely charged species were deposited equivalently in different steps during the LBL process. The deposition process was also monitored by quartz crystal microbalance (QCM), which can detect the adsorption of the charged species in the LBL films. The QCM results of the LBL film in different steps also show a uniform deposition process.

The driving force of the LBL process of nanoparticles could be not only electrostatic interactions, but also coordinative interactions<sup>[132,133]</sup> or hydrogen bonds.<sup>[134,135]</sup> As is well known, there exist typical coordinate complexations between pyridine and some transition metals. Based on coordinative bonds, CdS nanoparticles with general Cd-rich surfaces could be assembled in LBL films by alternating deposition with poly(4-vinylpyridine) (PVP). The construction of CdS/PVP multilayer film is shown in Fig. 5. The substrate was modified first to create a surface covered with pyridine groups. The resulting substrate was then dipped into a colloidal CdS solution to adsorb one layer of CdS nanoparticles. After being washed, the substrate was transferred to the PVP solution to absorb one PVP layer. The CdS/PVP multilayer films were prepared by repeating the above steps. UV-vis spectra were used to monitor the self-assembly process, confirming a stepwise and uniform assembly process. The driving force for the CdS/PVP multilayer film was identified by IR spectroscopy. By comparing IR spectra of pure PVP and the multilayer film (Fig. 6), a new peak at  $1610\text{ cm}^{-1}$  appeared in the spectrum of the multilayer film. Since the coordinate complexation between pyridine groups and metal ions usually exhibits this band because of the formation of coordination bonds, we considered that CdS nanoparticles were assembled into the multilayer film based on the

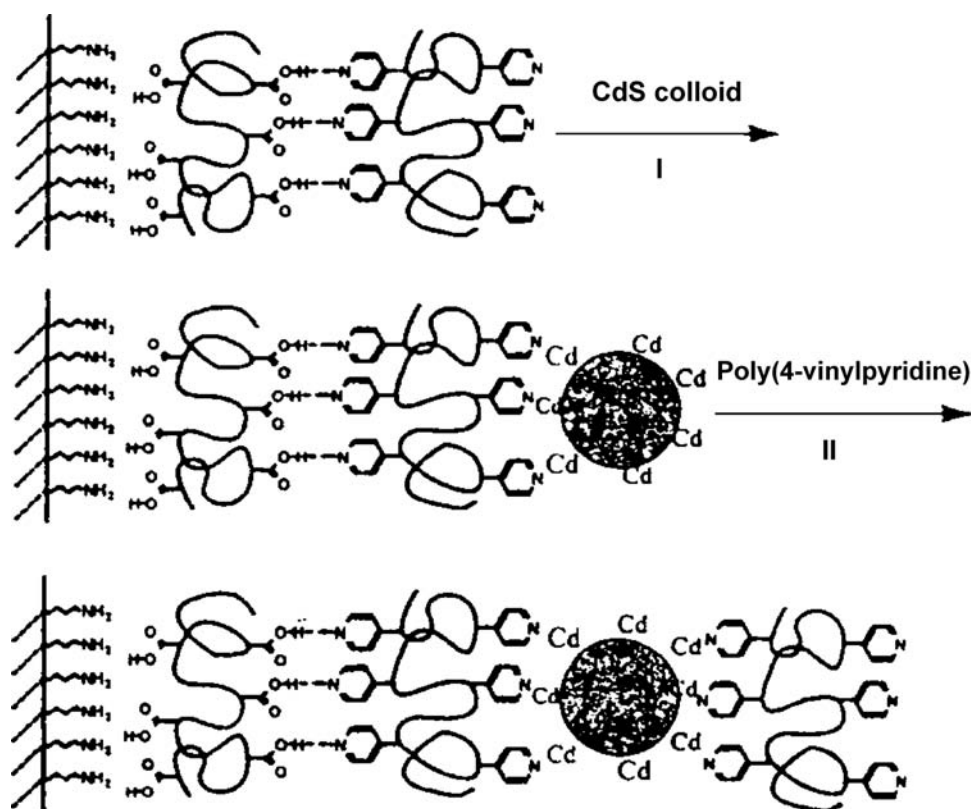


Fig. 5 Scheme for the build-up of alternating films of PVP/CdS nanoparticles based on coordinative bonds. *Source:* From Ref.<sup>[134]</sup>.

formation of coordinative bonds between the surface Cd atoms of CdS nanoparticles and the pyridine groups of PVP. We also found that CdS nanoparticles that have S-rich surfaces could not be assembled with PVP, which ensures the driving force to be coordinative bonds.

It has recently been reported that nanoparticles could also be formed in situ in LBL films of polyelectrolytes.<sup>[136–139]</sup> Silver nanoparticles were prepared in situ within poly(acrylic acid) (PAA) and poly(allylamine hydrochloride) (PAH) multilayer films. Carboxylic acid groups in the PAH/PAA-based multilayers bind silver cations by ion exchange with the acid protons. Subsequent reduction forms metallic nanoparticles. Because PAA has a pH-dependent degree of ionization, the multilayer film can be fabricated with different concentrations of free acid groups that are available to bind silver cations depending on the multilayer assembly pH. The nanoparticle size and silver concentration can be controllably increased by reducing the assembly pH of PAH/PAA-based multilayers. Furthermore, because the metal-binding carboxylic acid groups are reprotonated upon nanoparticle formation, the synthesis methodology can be repeatedly cycled to incorporate more silver cations, which increases the size and concentration of silver nanoparticles.

Recently, the LBL process has been applied to the surface modification of colloidal microspheres, which represent attractive building blocks from which to create ordered and complex materials. Möhwald and co-workers have demonstrated the LBL assembly of polyelectrolytes on the surface of colloidal latex spheres.<sup>[140,141]</sup> The main advantage of this LBL process is that the film thickness on the colloidal spheres could be fine-tuned by altering the number of layers deposited and the solution conditions from which the polymers are adsorbed. More recently, nanoparticles of SiO<sub>2</sub>, Ag, and Au have also been assembled on the surface of colloidal microspheres.<sup>[24,142–148]</sup> Assembly of nanoparticles on the surface of colloidal microspheres resulted in the formation of nanoparticle-coated microspheres. By removing the colloidal microspheres template through calcination or dissolution, hollow spheres of metal or silica were formed, which may find applications in catalysis, sensing, optics, and separations.

## CONCLUSION

With the development of nanoscience and nanotechnology, nanosized building blocks as nanoparticles will attract more and more attention. In both bulk and film

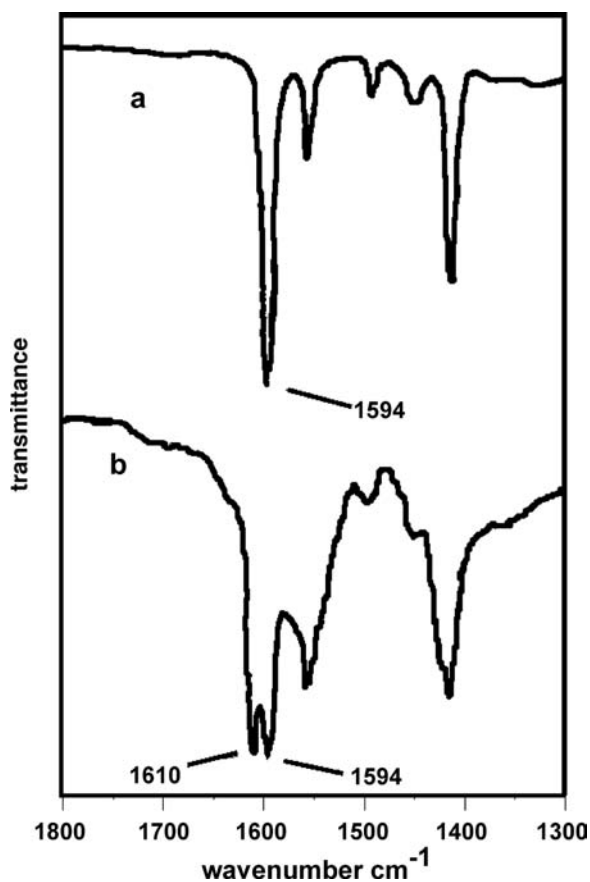


**Fig. 6** Infrared spectra of (A) pure PVP and (B) PVP/CdS multilayers. Source: From Ref.<sup>[134]</sup>.

structures, nanoparticles can be stabilized and assembled. We have introduced the incorporation of polymers as the substrates for nanoparticles and the assembly of nanoparticles in thin film structures such as LB films, self-assembled monolayers, and LBL multilayers, which have proved to have potential applications in optics, electronics, magnetism, catalysis, and sensors. Research will now focus on controlling the size, shape, and surface structure of nanoparticles, as well as fabricating new nanostructured materials and looking for new applications. The assembly of nanoparticles on microscale substrates such as patterned surfaces or microspheres, and the physical and chemical properties of single nanoparticles continue to invite our scrutiny.

## REFERENCES

1. Kayanuma, Y. Quantum-size effects of interacting electrons and holes in semiconductor microcrystals with spherical shape. *Phys. Rev., B* **1988**, *38* (14), 9797–9805.
2. Bard, A.J. Semiconductor particles and arrays for the photoelectrochemical utilization of solar energy. *Ber. Bunsenges. Phys. Chem.* **1988**, *92* (11), 1187–1194.

3. Steigerwald, M.L.; Brus, L.E. Synthesis, stabilization, and electronic structure of quantum semiconductor nanoclusters. *Annu. Rev. Mater. Sci.* **1989**, *19*, 471–495.
4. Henglein, A. Small-particle research: Physicochemical properties of extremely small colloidal metal and semiconductor particles. *Chem. Rev.* **1989**, *89* (8), 1861–1873.
5. Steigerwald, M.L.; Brus, L.E. Semiconductor crystallites: A class of large molecules. *Acc. Chem. Res.* **1990**, *23* (6), 183–188.
6. Wang, Y. Nonlinear optical properties of nanometer-sized semiconductor clusters. *Acc. Chem. Res.* **1991**, *24* (5), 133–139.
7. Wang, Y.; Herron, N. Nanometer-sized semiconductor clusters: Materials synthesis, quantum size effects, and photophysical properties. *J. Phys. Chem.* **1991**, *95* (2), 525–532.
8. Nair, S.V.; Ramaiah, L.M.; Rustagi, K.C. Electron states in a quantum dot in an effective-bond-orbital model. *Phys. Rev., B* **1992**, *45* (11), 5969–5979.
9. Schmid, G. Large clusters and colloids: Metals in the embryonic state. *Chem. Rev.* **1992**, *92* (8), 1709–1727.
10. Weller, H. Quantized semiconductor particles: A novel state of matter for materials science. *Adv. Mater.* **1993**, *5* (2), 88–95.
11. Weller, H. Colloidal semiconductor Q-particles—Chemistry in the transition region between solid-state and molecules. *Angew. Chem., Int. Ed.* **1993**, *32* (1), 41–53.
12. Linsebigler, A.L.; Lu, G.Q.; Yates, Y.T., Jr. Photocatalysis on TiO<sub>2</sub> surfaces: Principles, mechanisms, and selected results. *Chem. Rev.* **1995**, *95* (3), 735–758.
13. Henglein, A. Electronics of colloidal nanometer particles. *Ber. Bunsenges. Phys. Chem.* **1995**, *99* (7), 903–913.
14. Alivisatos, A.P. Semiconductor cluster, nanocrystals, and quantum dots. *Science* **1996**, *271*, 933–937.
15. Alivisatos, A.P. Perspectives on the physical chemistry of semiconductor nanocrystals. *J. Phys. Chem.* **1996**, *100* (31), 13226–13239.
16. Henglein, A. Nanoclusters of semiconductors and metals, colloidal nano-particles of semiconductors and metals: Electronic structure and processes. *Ber. Bunsenges. Phys. Chem.* **1997**, *101* (11), 1562–1572.
17. Wang, Z.L. Structural analysis of self-assembling nanocrystal superlattices. *Adv. Mater.* **1998**, *10* (1), 13–30.
18. Wang, Z.L. Transmission electron microscopy of shape-controlled nanocrystals and their assemblies. *J. Phys. Chem., B* **2000**, *104* (6), 1153–1175.
19. Templeton, A.C.; Wuelfing, W.P.; Murray, R.W. Monolayer-protected cluster molecules. *Acc. Chem. Res.* **2000**, *33* (1), 27–36.
20. Link, S.; El-Sayed, M.A. Spectral properties and relaxation dynamics of surface plasmon electronic oscillations in gold and silver nanodots and nanorods. *J. Phys. Chem., B* **1999**, *103* (40), 8410–8426.
21. El-Sayed, M.A. Some interesting properties of metals confined in time and nanometer space of different shapes. *Acc. Chem. Res.* **2001**, *34* (4), 257–264.
22. Gehr, R.J.; Boyd, R.W. Optical properties of nanostructured optical materials. *Chem. Mater.* **1996**, *8* (8), 1807–1819.
23. Schärfl, W. Crosslinked spherical nanoparticles with core-shell topology. *Adv. Mater.* **2000**, *12* (24), 1899–1908.

24. Caruso, F. Nanoengineering of particle surfaces. *Adv. Mater.* **2001**, *13* (1), 11–22.
25. Fendler, J.H. Atomic and molecular clusters in membrane mimetic chemistry. *Chem. Rev.* **1987**, *87* (5), 877–899.
26. Ekimov, A.I.; Efros, A.L.; Onushchenko, A.A. Quantum size effect in semiconductor microcrystals. *Solid State Commun.* **1985**, *56* (11), 921–924.
27. Jain, R.K.; Lind, R.C. Degenerate 4-wave mixing in semiconductor-doped glasses. *J. Opt. Soc. Am.* **1983**, *73* (5), 647–653.
28. Wang, Y.; Herron, N.J. Optical-properties of CdS and PbS clusters encapsulated in zeolites. *J. Phys. Chem.* **1987**, *91* (2), 257–260.
29. Moller, K.; Bein, T.; Herron, N.; Mahler, W.; Wang, Y. Encapsulation of lead sulfide molecular clusters into solid matrices. Structural analysis with X-ray absorption spectroscopy. *Inorg. Chem.* **1989**, *28* (15), 2914–2919.
30. Wang, Y.; Suna, A.; Mahler, W.; Kasowski, R. PbS in polymers. From molecules to bulk solids. *J. Chem. Phys.* **1987**, *87* (12), 7315–7322.
31. Ziolo, R.F.; Giannelis, E.P.; Weinstein, B.A.; O'Horo, M.P.; Ganguly, B.N.; Mehrotra, V.; Russell, M.W.; Huffman, D.R. Matrix-mediated synthesis of nanocrystalline  $\gamma$ -Fe<sub>2</sub>O<sub>3</sub>: A new optically transparent magnetic material. *Science* **1992**, *257*, 219–222.
32. Cahn, R.W. Nanostructures come of age. *Nature* **1992**, *359*, 591–592.
33. Moffitt, M.; Eisenberg, A. Size control of nanoparticles in semiconductor–polymer composites. 1. Control via multiplet aggregation numbers in styrene-based random ionomers. *Chem. Mater.* **1995**, *7* (6), 1178–1184.
34. Beecroft, L.L.; Ober, C.K. Nanocomposite materials for optical applications. *Chem. Mater.* **1997**, *9* (6), 1302–1317.
35. De, G.T. Sol–gel synthesis of metal nanoclusters–silica composite films. *J. Sol–Gel Sci. Technol.* **1998**, *11* (3), 289–298.
36. Fan, H.Y.; Zhou, Y.Q.; Lopez, G.P. Stepwise assembly in three dimensions: Preparation and characterization of layered gold nanoparticles in porous silica matrices. *Adv. Mater.* **1997**, *9* (9), 728–731.
37. Barnes, K.A.; Karim, A.; Douglas, J.F.; Nakatani, A.I.; Gruell, H.; Amis, E.J. Suppression of dewetting in nanoparticle-filled polymer films. *Macromolecules* **2000**, *33* (11), 4177–4185.
38. Salata, O.V.; Dobson, P.J.; Hull, P.J.; Hutchison, J.L. Fabrication of PbS nanoparticles embedded in a polymer film by a gas–aerosol reactive electrostatic deposition technique. *Adv. Mater.* **1994**, *6* (10), 772–775.
39. Schulz, D.L.; Pehnt, M.; Rose, D.H.; Urgiles, E.; Cahill, A.F.; Niles, D.W.; Jones, K.M.; Ellingson, R.J.; Curtis, C.J.; Ginley, D.S. CdTe thin films from nanoparticle precursors by spray deposition. *Chem. Mater.* **1997**, *9* (4), 889–900.
40. Gorer, S.; Hodes, G. Nanostructure and Size Quantization in Chemical Solution Deposited Semiconductor Films. In *Studies in Surface Science and Catalysis: Semiconductor Nanoclusters—Physical, Chemical, and Catalytic Aspects*; Kamat, P.V., Meisel, D., Eds.; Elsevier Science B.V.: Netherlands, 1997; 103, 297–320.
41. Gorer, S.; Albuayaron, A.; Hodes, G. Chemical solution deposition of lead selenide films—A mechanistic and structural study. *Chem. Mater.* **1995**, *7* (6), 1243–1256.
42. Pastoriza-Santos, I.; Serra-Rodríguez, C.; Liz-Marzán, L.M. Self-assembly of silver particle monolayers on glass from Ag<sup>+</sup> solution in DMF. *J. Colloid Interface Sci.* **2000**, *221*, 236–241.
43. Rajeshwar, K.; Tacconi, N.R. Electrodeposition and Characterization of Nanocrystalline Semiconductor Films. In *Studies in Surface Science and Catalysis: Semiconductor Nanoclusters—Physical, Chemical, and Catalytic Aspects*; Kamat, P.V., Meisel, D., Eds.; Elsevier Science B.V.: Netherlands, 1997; Vol. 103, 321–351.
44. Zoval, J.V.; Stiger, R.M.; Biernacki, P.R.; Penner, R.M. Electrochemical deposition of silver nanocrystallites on the atomically smooth graphite basal plane. *J. Phys. Chem.* **1996**, *100* (2), 837–844.
45. Zoval, J.V.; Biernacki, P.R.; Penner, R.M. Implementation of electrochemically synthesized silver nanocrystallites for the preferential SERS enhancement of defect modes on thermally etched graphite surfaces. *Anal. Chem.* **1996**, *68* (9), 1585–1592.
46. El-Kouedi, M.; Sandrock, M.L.; Seugling, C.J.; Foss, C.A. Electrochemical synthesis of asymmetric gold–silver iodide nanoparticle composite films. *Chem. Mater.* **1998**, *10* (11), 3287–3289.
47. Zhao, X.K.; Yuan, Y.X.; Fendler, J.H. Size-quantized semiconductor particles formed at monolayer surfaces. *J. Chem. Soc., Chem. Commun.* **1990**, 1248–1252.
48. Zhao, X.K.; Xu, S.Q.; Fendler, J.H. Ultrasmall magnetic particles in Langmuir–Blodgett films. *J. Phys. Chem.* **1990**, *94* (6), 2573–2581.
49. Zhao, X.K.; Fendler, J.H. Size quantization in semiconductor particulate films. *J. Phys. Chem.* **1991**, *95* (9), 3716–3723.
50. Zhao, X.K.; Fendler, J.H. Semiconductor particles formed at monolayer surfaces. *Langmuir* **1991**, *7* (3), 520–524.
51. Fendler, J.H.; Meldrum, F.C. The colloid chemical approach to nanostructured materials. *Adv. Mater.* **1995**, *7* (7), 607–632.
52. Fendler, J.H. Self-assembled nanostructured materials. *Chem. Mater.* **1996**, *8* (8), 1616–1624.
53. Schmid, G.; Chi, L.F. Metal clusters and colloids. *Adv. Mater.* **1998**, *10* (7), 515–526.
54. Feldheim, D.L.; Keating, C.D. Self-assembly of single electron transistors and related devices. *Chem. Soc. Rev.* **1998**, *27* (1), 1–12.
55. Shipway, A.N.; Katz, E.; Willner, I. Nanoparticle arrays on surfaces for electronic, optical, and sensor applications. *Chem., Phys. Chem.* **2000**, *1* (1), 18–52.
56. Shipway, A.N.; Willner, I. Nanoparticles as structural functional units in surface-confined architectures. *Chem. Commun.* **2001**, 2035–2045.
57. Fendler, J.H. Chemical self-assembly for electronic applications. *Chem. Mater.* **2001**, *13* (10), 3196–3210.
58. Gao, M.Y.; Yang, Y.; Yang, B.; Bian, F.L.; Shen, J.C. Synthesis of PbS nanoparticles in polymer matrices. *Chem. Commun.* **1994**, 2779–2780.

59. Gao, M.Y.; Yang, Y.; Yang, B.; Shen, J.C. Effect of the surface chemical modification on the optical properties of polymer-stabilized PbS nanoparticles. *Faraday Discuss.* **1995**, *91* (22), 4121–4125.
60. Huang, J.M.; Yang, Y.; Yang, B.; Liu, S.Y.; Shen, J.C. Synthesis of the CdS nanoparticles in polymer networks. *Polym. Bull.* **1996**, *36* (3), 337–340.
61. Huang, J.M.; Yang, Y.; Yang, B.; Liu, S.Y.; Shen, J.C. Preparation and characterization of Cu<sub>2</sub>S/CdS/ZnS nanocomposite in polymeric networks. *Polym. Bull.* **1996**, *37* (5), 679–682.
62. Huang, J.M.; Yang, Y.; Xue, S.H.; Yang, B.; Liu, S.Y.; Shen, J.C. Photoluminescence and electroluminescence of ZnS:Cu nanocrystals in polymeric networks. *Appl. Phys. Lett.* **1997**, *70* (18), 2335–2337.
63. Yang, Y.; Huang, J.M.; Yang, B.; Liu, S.Y.; Shen, J.C. Electroluminescence from ZnS/CdS nanocrystals/polymer composite. *Synth. Met.* **1997**, *91* (1–3), 347–349.
64. Huang, J.M.; Yang, Y.; Yang, B.; Liu, S.Y.; Shen, J.C. Assembly and applications of the inorganic nanocrystals in polymer networks. *Thin Solid Films* **1998**, *327–329*, 536–540.
65. Yang, Y.; Huang, J.M.; Liu, S.Y.; Shen, J.C. Preparation, characterization and electroluminescence of ZnS nanocrystals in a polymer matrix. *J. Mater. Chem.* **1997**, *7* (1), 131–133.
66. Moffitt, M.; McMahon, L.; Pessel, V.; Eisenberg, A. Size control of nanoparticles in semiconductor–polymer composites. 2. Control via sizes of spherical ionic microdomains in styrene-based diblock ionomers. *Chem. Mater.* **1995**, *7* (6), 1185–1192.
67. Sankaran, V.; Cummins, C.C.; Schrock, R.R.; Cohen, R.E.; Silbey, R.J. Small PbS clusters prepared via ROMP block copolymer technology. *J. Am. Chem. Soc.* **1990**, *112* (19), 6858–6859.
68. Sankaran, V.; Yue, J.; Cohen, R.E.; Schrock, R.R.; Silbey, R.J. Synthesis of zinc sulfide clusters and zinc particles within microphase-separated domains of organometallic block copolymers. *Chem. Mater.* **1993**, *5* (8), 1133–1142.
69. Selvan, S.T.; Spatz, J.P.; Klok, H.A.; Möller, M. Gold–polypyrrole core–shell particles in diblock copolymer micelles. *Adv. Mater.* **1998**, *10* (2), 132–134.
70. Bronstein, L.M.; Sidorov, S.N.; Valetsky, P.M.; Hartmann, J.; Cölfen, H.; Antonietti, M. Induced micellization by interaction of poly(2-vinylpyridine)-block-poly(ethylene oxide) with metal compounds. Micelle characteristics and metal nanoparticle formation. *Langmuir* **1999**, *15* (19), 6256–6262.
71. Hashimoto, T.; Harada, M.; Sakamoto, N. Incorporation of metal nanoparticles into block copolymer nanodomains via in-situ reduction of metal ions in microdomain space. *Macromolecules* **1999**, *32* (20), 6867–6870.
72. Hilinski, E.F.; Lucas, P.A. A picosecond bleaching study of quantum-confined cadmium sulfide microcrystallites in a polymer film. *J. Chem. Phys.* **1988**, *89* (6), 3435–3441.
73. Kuczynski, J.P.; Milosavljevic, B.H.; Thomas, J.K. Photophysical properties of cadmium sulfide in nafion film. *J. Phys. Chem.* **1984**, *88* (5), 980–984.
74. Kakuta, N.; White, J.M.; Campion, A.; Bard, A.J.; Fox, M.A.; Webber, S.E. Surface analysis of semiconductor-incorporated polymer systems. 1. Nafion and CdS–nafion. *J. Phys. Chem.* **1985**, *89* (1), 48–52.
75. Wang, Y.; Suna, A.; McHugh, J. Optical transient bleaching of quantum-confined CdS clusters: The effects of surface-trapped electron–hole pairs. *J. Chem. Phys.* **1990**, *92* (11), 6927–6939.
76. Peng, X.G.; Zhang, Y.; Yang, J.; Zou, B.S.; Xiao, L.Z.; Li, T.J. Formation of Nanoparticulate Fe<sub>2</sub>O<sub>3</sub>–stearate multilayer through the Langmuir–Blodgett method. *J. Phys. Chem.* **1992**, *96* (8), 3412–3415.
77. Gao, M.Y.; Peng, X.G.; Shen, J.C. Polymer Langmuir–Blodgett film of organic–inorganic (Fe<sub>2</sub>O<sub>3</sub>) composite microgel. *Thin Solid Films* **1994**, *248*, 106–109.
78. Peng, X.G.; Lu, R.; Zhao, Y.Y.; Qu, L.H.; Chen, H.Y.; Li, T.J. Control of distance and size of inorganic nanoparticles by organic matrices in ordered LB monolayers. *J. Phys. Chem.* **1994**, *98* (28), 7052–7055.
79. Nakaya, T.; Li, Y.J.; Shibata, K. Preparation of ultra-fine particle multilayers using the Langmuir–Blodgett technique. *J. Mater. Chem.* **1996**, *6* (5), 691–697.
80. Kang, Y.S.; Risbud, S.; Rabolt, J.; Stroeve, P. Brewster angle microscopy study of a magnetic nanoparticle/polymer complex at the air/water interface. *Langmuir* **1996**, *12* (18), 4345–4349.
81. Nabok, A.V.; Richardson, T. Cadmium sulfide nanoparticles in Langmuir–Blodgett films of calixarenes. *Langmuir* **1997**, *13* (12), 3198–3210.
82. Li, L.S.; Qu, L.H.; Wang, L.J.; Lu, R.; Peng, X.G.; Zhao, Y.Y.; Li, T.J. Preparation and characterization of quantum-sized PbS grown in amphiphilic oligomer Langmuir–Blodgett monolayers. *Langmuir* **1997**, *13* (23), 6183–6187.
83. Lefebure, S.; Ménager, C.; Cabuil, V.; Assenheimer, M.; Gallet, F.; Flament, C. Langmuir monolayers of monodispersed magnetic nanoparticles coated with a surfactant. *J. Phys. Chem., B* **1998**, *102* (15), 2733–2738.
84. Colvin, V.L.; Goldstein, A.N.; Alivisatos, A.P. Semiconductor nanocrystals covalently bound to metal surfaces with self-assembled monolayers. *J. Am. Chem. Soc.* **1992**, *114* (13), 5221–5230.
85. Freeman, R.G.; Grabar, K.C.; Allison, K.J.; Bright, R.M.; Davis, J.A.; Guthrie, A.P.; Hommer, M.B.; Jackson, M.A.; Smith, P.C.; Walter, D.G.; Natan, M.J. Self-assembled metal colloid monolayers: An approach to SERS substrates. *Science* **1995**, *267*, 1629–1632.
86. Chumanov, G.; Sokolov, K.; Gregory, B.W.; Cotton, T.M. Colloidal metal films as a substrate for surface-enhanced spectroscopy. *J. Phys. Chem.* **1995**, *99* (23), 9466–9471.
87. Bright, R.M.; Musick, M.D.; Natan, M.J. Preparation and characterization of Ag colloid monolayers. *Langmuir* **1998**, *14* (20), 5695–5701.
88. Bandyopadhyay, K.; Patil, V.; Vijayamohan, K.; Sastry, M. Adsorption of silver colloidal particles through covalent linkage to self-assembled monolayers. *Langmuir* **1997**, *13* (20), 5244–5248.
89. Patil, V.; Mayya, K.S.; Sastry, M. Long-term stability of self-assembled monolayers of an aromatic bifunctional molecule during adsorption of silver colloidal particles. *Langmuir* **1999**, *15* (19), 6587–6590.



90. Patolsky, F.; Ranjit, K.T.; Lichtenstein, A.; Willner, I. Dendritic amplification of DNA analysis by oligonucleotide-functionalized Au-nanoparticles. *Chem. Commun.* **2000**, 1025–1026.
91. Gao, M.Y.; Zhang, X.; Yang, B.; Shen, J.C. A monolayer of PbI<sub>2</sub> nanoparticles adsorbed on MD-LB film. *Chem. Commun.* **1994**, 2229–2230.
92. Decher, G. Fuzzy nanoassembly: Toward layered polymeric multicomposites. *Science* **1997**, *277*, 1232–1237.
93. Bertrand, P.; Jonas, A.; Laschewsky, A.; Legras, R. Ultrathin polymer coatings by complexation of polyelectrolytes at interfaces: Suitable materials, structure and properties. *Macromol. Rapid Commun.* **2000**, *21* (7), 319–348.
94. Hammond, P.T. Recent explorations in electrostatic multilayer thin film assembly. *Curr. Opin. Colloid Interface Sci.* **2000**, *4* (6), 430–442.
95. Schmitt, J.; Decher, G.; Dressick, W.J.; Brandow, S.L.; Geer, R.E.; Shashidhar, R.; Calvert, J.M.; Schmitt, J. Metal nanoparticle/polymer superlattice films: Fabrication and control of layer structure. *Adv. Mater.* **1997**, *9* (1), 61–65.
96. Blonder, R.; Sheeney, L.; Willner, I. Three-dimensional redox-active layered composites of Au–Au, Ag–Ag and Au–Ag colloids. *Chem. Commun.* **1998**, 1393–1394.
97. Musick, M.D.; Keating, C.D.; Lyon, L.A.; Botsko, S.L.; Peña, D.J.; Holliway, W.D.; McEvoy, T.M.; Richardson, J.N.; Natan, M.J. Metal films prepared by stepwise assembly. 2. Construction and characterization of colloidal Au and Ag multilayers. *Chem. Mater.* **2000**, *12* (10), 2869–2881.
98. Cassagneau, T.; Fendler, J.H. Preparation and layer-by-layer self-assembly of silver nanoparticles capped by graphite oxide nanosheets. *J. Phys. Chem., B* **1999**, *103* (11), 1789–1793.
99. Pastoriza-Santos, I.; Koktysh, D.S.; Mamedov, A.A.; Giersig, M.; Kotov, N.A.; Liz-Marzán, L.M. One-pot synthesis of Ag@TiO<sub>2</sub> core-shell nanoparticles and their layer-by-layer assembly. *Langmuir* **2000**, *16* (6), 2731–2735.
100. Kometani, N.; Tsubonishi, M.; Fujita, T.; Asami, K.; Yonezawa, Y. Preparation and optical absorption spectra of dye-coated Au, Ag, and Au/Ag colloidal nanoparticles in aqueous solutions and in alternate assemblies. *Langmuir* **2001**, *17* (3), 578–580.
101. Malynych, S.; Luzinov, I.; Chumanov, G. Poly(vinyl pyridine) as a universal surface modifier for immobilization of nanoparticles. *J. Phys. Chem., B* **2002**, *106* (6), 1280–1285.
102. Hu, K.; Brust, M.; Bard, A.J. Characterization and surface charge measurement of self-assembled CdS nanoparticle films. *Chem. Mater.* **1998**, *10* (4), 1160–1165.
103. Kotov, N.A.; Dékány, I.; Fendler, J.H. Layer-by-layer self-assembly of polyelectrolyte–semiconductor nanoparticle composite films. *J. Phys. Chem.* **1995**, *99* (35), 13065–13069.
104. Liu, Y.J.; Wang, A.B.; Claus, R.O. Layer-by-layer electrostatic self-assembly of nanoscale Fe<sub>3</sub>O<sub>4</sub> particles and polyimide precursor on silicon and silica surfaces. *Appl. Phys. Lett.* **1997**, *71* (16), 2265–2267.
105. Aliev, F.G.; Correa-Duarte, M.A.; Mamedov, A.; Ostrander, J.W.; Giersig, M.; Liz-Marzán, L.M.; Kotov, N.A. Layer-by-layer assembly of core-shell magnetite nanoparticles: Effect of silica coating on interparticle interactions and magnetic properties. *Adv. Mater.* **1999**, *11* (12), 1006–1010.
106. Mamedov, A.A.; Kotov, N.A. Free-standing layer-by-layer assembled films of magnetite nanoparticles. *Langmuir* **2000**, *16* (13), 5530–5533.
107. Gao, M.Y.; Richter, B.; Kirstein, S. White-light electroluminescence from self-assembled Q-CdSe/PPV multi-layer structures. *Adv. Mater.* **1997**, *9* (10), 802–805.
108. Gao, M.Y.; Richter, B.; Kirstein, S.; Möhwald, H. Electroluminescence studies on self-assembled films of PPV and CdSe nanoparticles. *J. Phys. Chem., B* **1998**, *102* (21), 4096–4103.
109. Cassagneau, T.; Mallouk, T.E.; Fendler, J.H. Layer-by-layer assembly of thin film zener diodes from conducting polymers and CdSe nanoparticles. *J. Am. Chem. Soc.* **1998**, *120* (31), 7848–7859.
110. Rogach, A.L.; Koktysh, D.S.; Harrison, M.; Kotov, N.A. Layer-by-layer assembled films of HgTe nanocrystals with strong infrared emission. *Chem. Mater.* **2000**, *12* (6), 1526–1528.
111. Liu, Y.J.; Wang, A.B.; Claus, R. Molecular self-assembly of TiO<sub>2</sub>/polymer nanocomposite films. *J. Phys. Chem., B* **1997**, *101* (8), 1385–1388.
112. Ariga, K.; Lvov, Y.; Onda, M.; Ichinose, I.; Kunitake, T. Alternately assembled ultrathin film of silica nanoparticles and linear polycations. *Chem. Lett.* **1997**, 125–126.
113. Lvov, Y.M.; Rusling, J.F.; Thomsen, D.L.; Papadimitrakopoulos, F.; Kawakami, T.; Kunitake, T. High-speed multilayer film assembly by alternate adsorption of silica nanoparticles and linear polycation. *Chem. Commun.* **1998**, 1229–1230.
114. Hattori, H. Anti-reflection surface with particle coating deposited by electrostatic attraction. *Adv. Mater.* **2001**, *13* (1), 51–54.
115. Keller, S.W.; Kim, H.N.; Mallouk, T.E. Layer-by-Layer assembly of intercalation compounds and heterostructures on surfaces: Toward molecular “beaker” epitaxy. *J. Am. Chem. Soc.* **1994**, *116* (19), 8817–8818.
116. Kleinfeld, E.R.; Ferguson, G.S. Stepwise formation of multilayered nanostructural films from macromolecular precursors. *Science* **1994**, *265*, 370–373.
117. Lvov, Y.; Ariga, K.; Ichinose, I.; Kunitake, T. Assembly of multicomponent protein films by means of electrostatic layer-by-layer adsorption. *J. Am. Chem. Soc.* **1995**, *117* (22), 6117–6123.
118. Rosidian, A.; Liu, Y.J.; Claus, R.O. Ionic self-assembly of ultrahard ZrO<sub>2</sub>/polymer nanocomposite thin films. *Adv. Mater.* **1998**, *10* (14), 1087–1091.
119. Ostrander, J.W.; Mamedov, A.A.; Kotov, N.A. Two modes of linear layer-by-layer growth of nanoparticle–polyelectrolyte multilayers and different interactions in the layer-by-layer deposition. *J. Am. Chem. Soc.* **2001**, *123* (6), 1101–1110.
120. Iler, R.K. Multilayers of colloidal particles. *J. Colloid Interface Sci.* **1966**, *21*, 569–594.
121. Gao, M.Y.; Gao, M.Y.; Zhang, X.; Yang, Y.; Yang, B.; Shen, J.C. Constructing PbI<sub>2</sub> nanoparticles into a multilayer structure using the molecular deposition (MD) method. *Chem. Commun.* **1994**, 2777–2778.

122. Gao, M.Y.; Zhang, X.; Yang, B.; Li, F.; Shen, J.C. Assembly of modified CdS particles/ cationic polymer based on electrostatic interactions. *Thin Solid Films* **1996**, *284–285*, 242–245.
123. Sun, Y.P.; Hao, E.C.; Zhang, X.; Yang, B.; Gao, M.Y.; Shen, J.C. Monolayer of TiO<sub>2</sub>/PbS coupled semiconductor nanoparticles. *Chem. Commun.* **1996**, 2381–2382.
124. Hao, E.C.; Yang, B.; Yu, S.; Gao, M.Y.; Shen, J.C. Formation of orderly organized cubic PbS nanoparticles domain in the presence of TiO<sub>2</sub>. *Chem. Mater.* **1997**, *9* (7), 1598–1600.
125. Sun, Y.P.; Hao, E.C.; Zhang, X.; Yang, B.; Shen, J.C.; Chi, L.F.; Fuchs, H. Buildup of composite films containing TiO<sub>2</sub>/PbS nanoparticles and polyelectrolytes based on electrostatic interaction. *Langmuir* **1997**, *13* (19), 5168–5174.
126. Hao, E.C.; Yang, B.; Zhang, J.H.; Zhang, X.; Sun, J.Q.; Shen, J.C. Assembly of alternating TiO<sub>2</sub>/CdS nanoparticle composite films. *J. Mater. Chem.* **1998**, *8* (6), 1327–1328.
127. Hao, E.C.; Sun, Y.P.; Yang, B.; Zhang, X.; Liu, J.M.; Shen, J.C. Synthesis and photophysical properties of ZnS colloidal particles doped with silver. *J. Colloid Interface Sci.* **1998**, *204* (2), 369–373.
128. Sun, J.Q.; Hao, E.C.; Sun, Y.P.; Zhang, X.; Yang, B.; Zou, S.; Shen, J.C.; Wang, S.B. Multilayer assemblies of colloidal ZnS doped with silver and polyelectrolytes based on electrostatic interaction. *Thin Solid Films* **1998**, *327–329*, 528–531.
129. Hao, E.C.; Sun, H.P.; Zhou, Z.; Liu, J.Q.; Yang, B.; Shen, J.C. Synthesis and optical properties of CdSe and CdSe/CdS nanoparticles. *Chem. Mater.* **1999**, *11* (11), 3096–3102.
130. Hao, E.C.; Qian, X.M.; Yang, B.; Wang, D.J.; Shen, J.C. Assembly and photoelectrochemical studies of TiO<sub>2</sub>/CdS nanocomposite film. *Mol. Cryst. Liq. Cryst.* **1999**, *337*, 181–184.
131. Hao, E.C.; Yang, B.; Ren, H.; Qian, X.M.; Xie, T.F.; Shen, J.C.; Li, D.M. Fabrication of composite film comprising TiO<sub>2</sub>/CdS and polyelectrolytes based on ionic attraction. *Mater. Sci. Eng., C* **1999**, *10*, 119–122.
132. Hao, E.C.; Wang, L.Y.; Zhang, J.H.; Yang, B.; Zhang, X.; Shen, J.C. Fabrication of polymer/inorganic nanoparticles composite films based on coordinative bonds. *Chem. Lett.* **1999**, 5–6.
133. Xiong, H.M.; Cheng, M.H.; Zhou, Z.; Zhang, X.; Shen, J.C. A new approach to the fabrication of a self-organizing film of heterostructured polymer/Cu<sub>2</sub>S nanoparticles. *Adv. Mater.* **1998**, *10* (7), 529–532.
134. Hao, E.C.; Lian, T.Q. Layer-by-layer assembly of CdSe nanoparticles based on hydrogen bonding. *Langmuir* **2000**, *16* (21), 7879–7881.
135. Hao, E.C.; Lian, T.Q. Buildup of polymer/Au nanoparticle multilayer thin films based on hydrogen bonding. *Chem. Mater.* **2000**, *12* (11), 3392–3396.
136. Dante, S.; Hou, Z.Z.; Risbud, S.; Stroeve, P. Nucleation of iron oxy-hydroxide nanoparticles by layer-by-layer polyionic assemblies. *Langmuir* **1999**, *15* (6), 2176–2182.
137. Joly, S.; Kane, R.; Radzilowski, L.; Wang, T.; Wu, A.; Cohen, R.E.; Thomas, E.L.; Rubner, M.F. Multilayer nanoreactors for metallic and semiconducting particles. *Langmuir* **2000**, *16* (3), 1354–1359.
138. Dai, J.H.; Bruening, M.L. Catalytic nanoparticles formed by reduction of metal ions in multilayered polyelectrolyte films. *Nano Lett.* **2002**, *2* (5), 497–501.
139. Wang, T.C.; Rubner, M.F.; Cohen, R.E. Polyelectrolyte multiplayer nanoreactors for preparing silver nanoparticle composites: Controlling metal concentration and nanoparticle size. *Langmuir* **2002**, *18* (8), 3370–3375.
140. Donath, E.; Sukhorukov, G.B.; Caruso, F.; Davis, S.A.; Möhwald, H. Novel hollow polymer shells by colloid-templated assembly of polyelectrolytes. *Angew. Chem. Int. Ed.* **1998**, *37* (16), 2202–2205.
141. Sukhorukov, G.B.; Donath, E.; Davis, S.; Lichtenfeld, H.; Knippel, E.; Knippel, M.; Budde, A.; Möhwald, H. Layer-by-layer self assembly of polyelectrolytes on colloidal particles. *Colloids Surf. A* **1998**, *137*, 253–266.
142. Caruso, F.; Lichtenfeld, H.; Giersig, M.; Möhwald, H. Electrostatic self-assembly of silica nanoparticle–polyelectrolyte multilayers on polystyrene latex particles. *J. Am. Chem. Soc.* **1998**, *120*, 8523–8524.
143. Caruso, F.; Caruso, R.A.; Möhwald, H. Nanoengineering of inorganic and hybrid hollow spheres by colloidal templating. *Science* **1998**, *282*, 1111–1114.
144. Caruso, F.; Möhwald, H. Preparation and characterization of ordered nanoparticle and polymer composite multilayers on colloids. *Langmuir* **1999**, *15* (23), 8276–8281.
145. Caruso, R.A.; Susha, A.S.; Caruso, F. Multilayered titania, silica, and laponite nanoparticle coatings on polystyrene colloidal templates and resulting inorganic hollow spheres. *Chem. Mater.* **2001**, *13* (2), 400–409.
146. Gittins, D.I.; Susha, A.S.; Schoeler, B.; Caruso, F. Dense nanoparticulate thin films via gold nanoparticle self-assembly. *Adv. Mater.* **2002**, *14* (7), 508–512.
147. Cassagneau, T.; Caruso, F. Contiguous silver nanoparticle coatings on dielectric spheres. *Adv. Mater.* **2002**, *14* (10), 732–736.
148. Dong, A.G.; Wang, Y.J.; Tang, Y.; Ren, N.; Yang, W.L.; Gao, Z. Fabrication of compact silver nanoshells on polystyrene spheres through electrostatic attraction. *Chem. Commun.* **2002**, 350–351.

## BIBLIOGRAPHY

1. Hao, E.C.; Zhang, H.; Yang, B.; Ren, H.; Shen, J.C. Preparation of luminescent polyelectrolyte/Cu-doped ZnSe nanoparticle multilayer composite films. *J. Colloid Interface Sci.* **2001**, *238* (2), 285–290.
2. Zhang, H.; Yang, B.; Wang, R.B.; Zhang, G.; Hou, X.L.; Wu, L.X. Fabrication of a covalently attached self-assembly multilayer film based on CdTe nanoparticles. *J. Colloid Interface Sci.* **2002**, *247* (2), 361–365.

*Encyclopedia of*

# Nanoscience and Nanotechnology

*Second Edition*

## Volume V

*Pages 2923 through 3708*

*Nanophase – Risk*

Nanophase –  
Nanostructured  
Composites

Nanostructured  
Materials –  
Nanostructures

Nanotube – Noble

Nonlinear – Oxide

Palladium –  
Platinum

Polyelectrolyte –  
Polymer

Polypropylene –  
Proteins

Quantum – Risk

# Nanophase Powders: Mechanosynthesis

F. Miani

F. Maurigh

Department of Engineering, DIEGM University of Udine, Udine, Italy

F. Delogu

Department of Chemical Engineering and Materials, University of Cagliari, Cagliari, Italy

## Abstract

This entry considers mechanosynthesis of nanophase powders, i.e., the production of nanophase compounds by mechanochemical action starting from elemental powders. The paper focuses on the operating principles of the most common devices employed for the process, along with some kinematic aspects, some specific mechanical considerations, thermodynamic and kinetic issues, atomistic of mechanically induced phase transformations, and a detailed example in kinetics. The entry ends with current applications and industrial trends of mechanosynthesized powders.

## INTRODUCTION

Among the different processes that are able to produce nanocrystalline powders in bulk quantities, mechanosynthesis, i.e., the synthesis of nanograined powders by means of mechanical activation, is one of the most interesting from an industrial point of view. Mechanosynthesis of nanophase powders is one of the less sophisticated technologies—and in such a sense also the most inexpensive—to produce nanophase powders; in fact it exploits devices and processes that have many aspects in common with mixing, fine grinding, and comminution of materials. However, it does have interest for applications, as in principle this is a very low-cost process and its potential for industrial applications is very significant. This entry describes the basis of the process, some possible applications and perspectives of mechanosynthesized nanophase powders and some simple ideas that are able to depict part of the process, with a specific mind to the mechanosynthesis of nanocrystalline materials starting from elemental powder precursors. Mechanosynthesis belongs to the family of process technologies known as mechanical alloying, which are basically using the same or very similar apparatuses, i.e. milling or size reduction devices, which could be generally described as ball mills. A recent thorough analysis by Suranarayana<sup>[1]</sup> of the processes related to mechanical alloying defines mechanosynthesis as a mechanochemical synthesis, attributing most of the research work in this field of mechanical alloying to McCormick,<sup>[2]</sup> Takacs,<sup>[3]</sup> and Matteazzi,<sup>[4]</sup> it is also necessary to quote the fundamental and pioneering work of Butyagin<sup>[5]</sup> and Boldyrev<sup>[6]</sup> and some important developments by Calka.<sup>[7]</sup> Although, owing to many different process parameters and conditions, a complete modelling of the mechanical alloying process and mechanosynthesis

of nanophase materials would be an aim very difficult to reach, it is useful to identify the *operating principle of the most common devices* employed for the process, along with some *kinematic aspects, some specific mechanical considerations, and thermodynamic and kinetic* issues of the process as well. Finally, current production of mechanosynthesized powders and perspectives will be briefly discussed.

## THE MECHANOSYNTHESIS PROCESS

The concept of the mechanosynthesis process is very simple: to seal in a vial some—usually powdered—materials along with grinding media, which are usually balls, and to reduce the size of the materials by mechanical action, providing in the same time an intimate mixing of the different materials introduced, so close that diffusion and chemical reactivity are greatly enhanced. For clarity, one could consider a mixture of elemental powders—for simplicity, we could limit to powders of element *A* and element *B*—introduced in a cylindrical container, the jar of a vibrating mill, with repeated and prolonged impacts imposed by mechanical energy imparted to grinding media (Fig. 1).

Depending on the nature of the reactants, different intermixing mechanisms are possible; generally speaking, the ductile phase tends to incorporate—if such a phase is present—a more brittle phase, with a tendency to form particles that are microscopically (to a scale of  $\mu\text{m}$ ) folded.

With prolonged milling, the crystal size of both reactants decreases in an exponential way, following a decreasing trend with the processing time  $t$  of the type:<sup>[8,9]</sup>

$$d = d_f + (d_i - d_f)e^{-c_1 t} \quad (1)$$

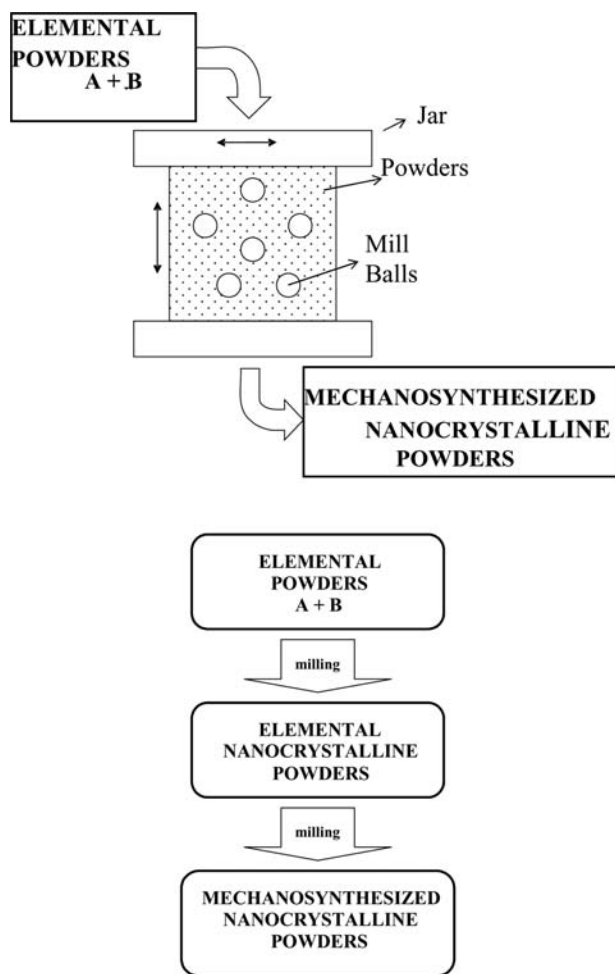
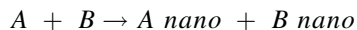


Fig. 1 Mechanochemical synthesis schematic process and steps.

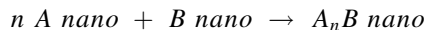
where  $d$  should be considered representative of the crystal size, being  $d_i$  the initial,  $d_f$  the steady state crystal size and  $c_1$  an empirical constant depending on the process parameter. Other possible trends of the crystal size evolution with milling time are discussed in the next paragraph, especially if exothermic effects of the reaction  $A + B \rightarrow A_xB_y$  are to be taken into account.

The gradual transformation of the milled powders from a rather coarse to a nanocrystalline grain size could be simply depicted as a formal reaction:



Fecht<sup>[10]</sup> has been considering mechanical milling—i.e. the reduction of metal powders of elements and intermetallic compounds to nanocrystalline powders by grinding—and he has proposed empirical estimates for the enthalpy stored. These estimates could be a base for an evaluation of the mechanochemical energy transfer imparted to the powders. In mechanochemical processing, as time is increasing, along with the energy imparted to the materials, new phases/compounds

tend to appear. It has been generally recognized, by different authors, that the generic reaction path linking the time evolution of the reactants with time is sigmoidal.<sup>[8–10]</sup> We shall come back to this point dealing with the process kinetics. Here, we could depict the second step of the reaction as:



This is an oversimplification, as the mechanochemical synthesis process occurs continuously. However, it may be useful to evaluate, for instance, energetic aspects.

## KINEMATIC AND MECHANICAL ASPECTS

Milling devices are of different nature: vibrating mills, planetary mills, attritor mills, and tumbling mills—with efficiencies in the process that are decreasing from vibrating to tumbling—have been employed successfully. The different devices employed for research purposes are described in Koch;<sup>[11]</sup> there has been a tendency of different research groups<sup>[5,12,13]</sup> to develop ad hoc mills for the synthesis by milling of nanophase materials. Figure 2 describes a mill developed in the University of Udine, which has been scaled-up to be industrially employed.

The most important physical parameters involved are well described in a series of papers by Cocco and Delogu,<sup>[8,9,14]</sup> in an attempt to propose a quantitative understanding of the mechanical alloying processes. These authors have underlined the importance of relating basic and phenomenological aspects, suggesting that the framework of solid-state chemistry and chemical kinetics should be the most fruitful to interpret results and develop new trends. For the sake of simplicity, considering a mill with just one ball, and adopting the terminology of Butyagin,<sup>[5]</sup> one of the pioneers in the field of mechanochemistry, they propose: where  $m_b$  and  $m_p$  are the mass of the ball and of the powder. With such a situation, it could be interesting to adopt the quantitative techniques used in engineering the deformation processes, as it has been proposed earlier by Maurice and Courtney.<sup>[15]</sup> In any case, with the aid of simple kinetic trends, the milling time should be related to the energy dose, not only for device scale up but also for process control. This could help, for instance, to control exothermic mechanochemical reactions where combustion appears, imparting the completion of a mechanochemical synthesis of nanocrystalline materials.

A possible new design for a jar for laboratory milling is the one presented above (Fig. 3), together with its constructional details. The purpose of the experimental jar is to use a diathermic oil to monitor heat release during processing. The jar has been produced with integral

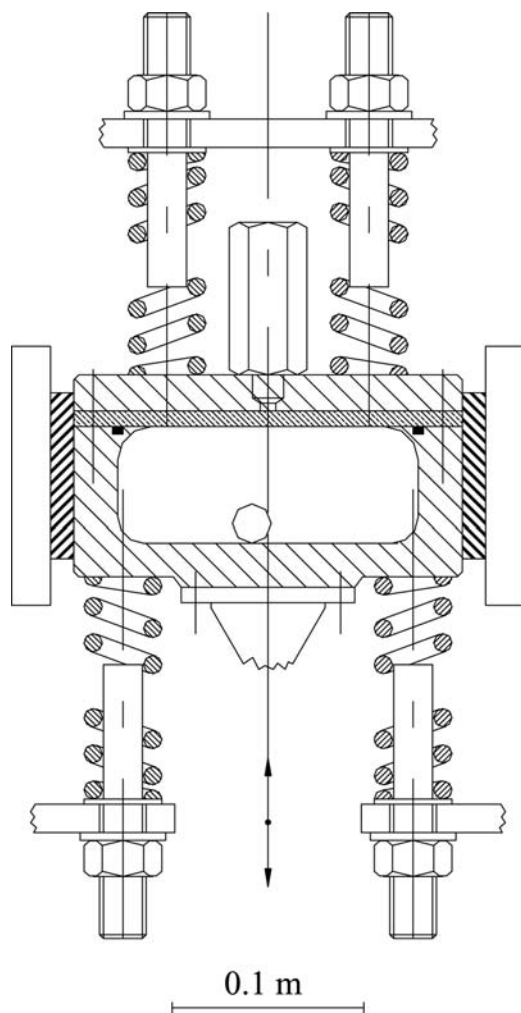


**Fig. 2** Experimental vibrating mill for the synthesis of nanophase materials in significant quantities. *Source:* From Ref.<sup>[12]</sup>.

internal channels by means of selective laser sintering<sup>[16]</sup> and it is available for experimentation on SPEX 8000 mills; typical dimensions of the main cylinder are 75 mm in height, 60 mm in outside diameter.

## THERMODYNAMICS

Mechanochemistry is a technique involving far from equilibrium processing; so, in principle, thermodynamics arguments should not be of help; however, it is possible to conceive the most simple reaction in the mechanochemistry of nanocrystalline materials—the one involving elemental powders *A* and *B*—as a two-step process: the first could be thought as a reduction of the crystal domains, the second as the formation of a nanophase compound or alloy. Fecht's extrapolation may be employed for the first step, Miedema model for the second step, assuming that the enthalpy of alloy formation is the same also in the nanocrystalline status.<sup>[10]</sup>

This approach is able to give order of magnitude correct results, as could be checked comparing these semi-empirical calculations<sup>[10]</sup> to the actual heat release.<sup>[17]</sup>

Fecht proposed an empirical regression with an analysis by means of DSC (differential scanning calorimetry) data on nanocrystalline metals and intermetallic compounds obtained by 24 hr ball milling by SPEX milling. Scanning up to 870 K with 20 K/min, he got the results listed in Table 3.

These data allow to estimate the excess enthalpy stored:

$$\Delta H/\Delta H_f = 8.5 \cdot 10^{-5} T_m \quad (2)$$

where  $\Delta H_f$  is the enthalpy of melting.

## KINETICS

For what concerns kinetic evolution, the situation is very complex. We have different and contrasting phenomena. Dealing with the mechanochemistry of nanophase materials, we are interested to obtain a crystal size of the order of tens of nanometers, which is usually considered an effective value for applications. The crystal size evolution with time could be depicted with equations of the type (1) reported here. More in detail, a phenomenological modeling approach to size refinement of metal crystallites under mechanical processing could be described as the following. In the framework of what we have previously described, the processing of powder in ball mills is characterized by three fundamental features. First, the transfer of energy to powders takes place at impact events involving both powders and milling tools. Second, only small powder amounts are trapped between milling tool surfaces at impact. Third, the granular flow inside the reactor allows an efficient redistribution and homogenization of powders after each impact.<sup>[18]</sup> Having all powder particles roughly the same, probability of being involved in collisions, mechanical processing can be regarded as a discrete process with statistical character.

A statistical description of the progressive decrease of the domains of coherent diffraction as a function of the number of collisions in a given sequence can be hardly based on the total number of powder particles. In fact, this is continuously modified during the course of mechanical treatment as a consequence of fracturing and coalescence processes.<sup>[1]</sup> A suitable quantity to consider is instead the volume of powder trapped at collision. Depending on the size of milling tools, their relative impact velocity and the total amount of powder inside the reactor,<sup>[19,20]</sup> it keeps approximately constant during the whole time of mechanical treatment.



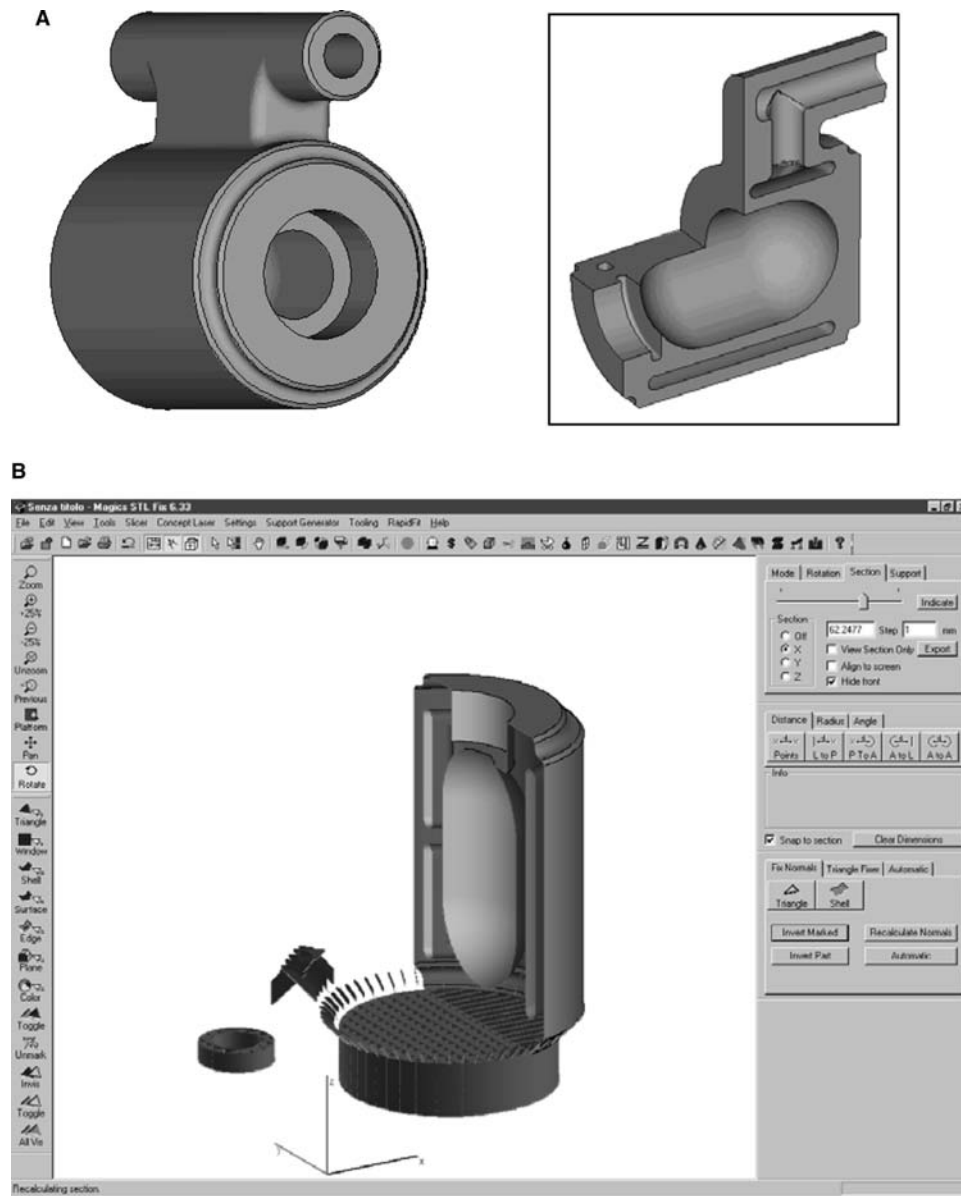


**Fig. 3** (A) Prototype vial for the Spex 8000 Mill, along with a section view of internal channels. (B) Prototype vial for the Spex 8000 Mill: constructional details for the direct metal selective laser sintering processing.

A statistical modeling of ball milling must necessarily address a few fundamental questions concerning the relationships between processing parameters and rate of crystallite size decrease. How large is the powder amount involved at impact in deformation processes severe enough to result in a crystallite size decrease? How many impacts are necessary to attain a given average crystallite size? Being the powder amount trapped at collisions, only a small fraction of the total powder charge inside the reactor, which is the relationship between the total number of impacts and the number of collisions undergone by a given fraction of powder?

Approximate answers to such questions can be found by developing a simple phenomenological model referred to the case of mechanical processing carried out by employing a single milling ball. Under the assumption that the volume  $v_{\text{imp}}$  and the average density  $\rho$  of powders trapped at collision keep constant during the processing, the mass  $m_{\text{imp}} = v_{\text{imp}} \rho$  of powder involved on the average in individual collisions is also constant. The rate of crystallite size decreases is proportional to the volume fraction  $x_{\text{imp}} = v_{\text{imp}}/v_p$  of powder worked at impact,  $v_p$  being the total volume of powder inside the reactor. However, it is generally believed that the fraction of trapped powder must

**Table 1** Butyagin terminology for an elementary mechanochemical process: ball milling with one ball, after Cocco<sup>[14]</sup>

Physical quantity	Expression	Units
Impact energy	$E = \frac{1}{2} m_b v_{imp}^2$	J
Impact frequency	$N$	hit/s
Milling intensity	$I = NE = \frac{1}{2} Nm_b v_{imp}^2$	W
Energy dose	$D = It = NEt = \frac{1}{2} Nm_b v_{imp}^2 t$	J
Specific dose	$D_m = \frac{NEt}{m_p}$	J/kg

experience critical loading conditions (CLCs) to undergo microstructural refinement. Correspondingly, the crystallite size will decrease only in the fraction of powder that would have been subjected to a mechanical stress  $\sigma$  higher than a given threshold value  $\sigma_0$ . The volume fraction  $k$  of powder experiencing CLCs at impact is then expected to be smaller than  $x_{imp}$ . Under the assumption that the powder charge keeps perfectly homogeneous after each impact, all the volume fractions  $k$  in which it can be ideally subdivided have the same probability of being involved in a collision. These assumptions allow an analytical description of the kinetics of mechanically induced processes on a statistical basis.

Let  $\chi_0$  be the volume fraction of powder never subjected to CLCs. Of course,  $\chi_0$  is equal to 1 as far as no impact occurs. At the first collision, a volume fraction  $\chi_1(1) = k$  of powder has undergone for the first time CLCs. The fraction of powder charge never subjected to CLCs is then equal to  $\chi_0(1) = 1 - k$ . After the second impact, the fraction of powder never subjected to CLCs becomes equal to  $\chi_0(2) = (1 - k)^2$ . The fractions of powder subjected to CLCs one and two

**Table 2** Fecht's data<sup>[10]</sup> for the empirical extrapolation of the excess enthalpy stored in mechanically milled nanocrystalline powders

Material	Structure	$T_m$ (K)	$d$ (nm)	$\Delta H$ (kJ/mol)
Fe	bcc	1809	8	2.1
Cr	bcc	2148	9	4.2
Nb	bcc	2741	9	2.1
W	bcc	3683	9	4.6
Co	hcp	1768	14	1.0
Zr	hcp	2125	13	3.4
Hf	hcp	2495	13	2.2
Ru	hcp	2773	13	7.2
NiTi	CsCl	1583	5	5
CuEr	CsCl	1753	12	6.8
SiRu	CsCl	2073	7	10.1
AlRu	CsCl	2300	8	5.2

**Table 3** Iron conversion ratio  $\alpha$  in the mechanochemical synthesis of nanophase iron carbides, using a SPEX 8000 mill

Milling time (h)	Fe conversion ratio $\alpha$
0.25	12.2
0.5	12.7
0.75	14.8
1	13.6
1.25	14.1
1.5	13.2
1.75	13.9
2	16.6
2.5	26.2
3	26.9
3.5	32.4
5	51.8
7.5	68.4
10	82.1
15	91.0

times are instead, respectively,  $\chi_1(2) = 2k(1 - k)$  and  $\chi_2(2) = k^2$ . The fraction of powder  $\chi_0(n)$  that never experienced CLCs can only decrease as the number  $n$  of collisions increases according to the following equation:

$$\chi_0(n + 1) = \chi_0(n) - k\chi_0(n). \quad (3)$$

The amount of powder subjected to CLCs for  $i$  times after  $n$  impacts depends instead on two contributions. The first one is quantified by the fraction  $k\chi_i(n)$ , which at the  $n^{\text{th}}$  collision is subjected to CLCs for the  $(i + 1)$ -th time and becomes part of the fraction  $\chi_{i+1}(n)$ . The second contribution is due to the fraction  $k\chi_{i-1}(n)$ , which, experiencing CLCs for the  $i^{\text{th}}$  time at the  $n^{\text{th}}$  collision, becomes part of the fraction  $\chi_i(n)$ . It then follows that

$$\chi_i(n + 1) = \chi_i(n) - k\chi_i(n) + k\chi_{i-1}(n). \quad (4)$$

The experimental evidence that a large number  $n$  of collisions is generally required to observe a significant decrease of the average crystallite size  $L$  suggests that the fraction  $k$  of powder subjected to CLCs at impact is small.<sup>[1,20]</sup> Under such circumstances, Eqs. (3) and (4) can be written in continuous form. Correspondingly,

$$d\chi_0(n) = -k\chi_0(n)dn \quad (5)$$

and

$$d\chi_i(n) = -k\chi_i(n)dn + k\chi_{i-1}(n)dn. \quad (6)$$

Equations (5) and (6) can be readily solved, the solutions being, respectively,

$$\chi_0(n) = e^{-kn}, \tag{7}$$

and<sup>[21]</sup>

$$\chi_i(n) = \frac{(kn)^i}{i!} e^{-kn}. \tag{8}$$

Being the total amount of powder inside the vial constant,  $\sum_{i=0}^{\infty} \chi_i(n) = 1$ .

The set of mathematical functions defined by Eqs. (7) and (8) can be used to roughly describe the kinetics of crystallite size refinement process under the assumption that the powder subjected to CLCs for  $i$  times has a characteristic average crystallite size  $L_i$ . The crystallite size  $L$  averaged over the whole powder charge inside the reactor is then equal to

$$L = \sum_{i=0}^n \chi_i(n) L_i = \left[ L_0 + knL_1 + \frac{(kn)^2}{2} L_2 + \dots \right] e^{-kn}. \tag{9}$$

It can be seen that  $k$  represents the apparent rate constant of the process. The crystallite size decrease is expected to be progressive and then  $L_0 > L_1 > L_2 > \dots > L_i > \dots$ . The connection between successive  $L_0, L_1, L_2, \dots, L_i, \dots$  values is, however, completely lacking, experimental evidences indicating only that a final asymptotic value  $L_f$  is attained. Yet, the relationship between the  $L_0, L_1, L_2, \dots, L_i, \dots, L_f$  values represents one of the outstanding questions regarding the process of crystallite size decrease. What is the  $L_i$  value attained by powder fraction  $\chi_i(n)$  subjected  $i$  times to CLCs? How many times CLCs must be undergone by a given volume fraction of powder to attain the final asymptotic  $L_f$  value of crystallite size?

According to Eq. (9), the gradual decrease of the average crystallite size  $L$  can be completely characterized only when all the  $L_0, L_1, L_2, \dots, L_i, \dots, L_f$  values are estimated. Although possible in principle, such result is not obtainable by currently available experimental methods. The comparison between experimental data and theoretical curves can, however, still provide useful insight provided that some possible relationships between the  $L_0, L_1, L_2, \dots, L_i, \dots, L_f$  values are considered. In the simplest case, the final asymptotic  $L_f$  value is attained already after the first critical loading event. Under such circumstances,  $L_0 \neq L_1 = L_2 = \dots = L_i = \dots = L_f$  and Eq. (9)

can be re-written as

$$L = L_0 e^{-kn} + L_f (1 - e^{-kn}). \tag{10}$$

When the final asymptotic  $L_f$  value is attained after two critical loading events  $L_0 \neq L_1 \neq L_2 = \dots = L_i = \dots = L_f$ . Correspondingly,

$$L = L_0 e^{-kn} + L_1 kn e^{-kn} + L_f [1 - (1 + kn)e^{-kn}]. \tag{11}$$

Along the same line, when the final asymptotic  $L_f$  value is attained after three critical loading events  $L_0 \neq L_1 \neq L_2 \neq L_3 = \dots = L_i = \dots = L_f$  and

$$L = L_0 e^{-kn} + L_1 kn e^{-kn} + \frac{(kn)^2}{2} e^{-kn} + L_f \left[ 1 - \left( 1 + kn + \frac{(kn)^2}{2} \right) e^{-kn} \right]. \tag{12}$$

Equations (10)–(12) and analogous ones obtainable under different assumptions can be adjusted to express the Neperian logarithm of the ratio between  $(L - L_f)$  and  $(L_0 - L_f)$ . Accordingly, in the first case considered

$$\ln \frac{(L - L_f)}{(L_0 - L_f)} = -kn, \tag{13}$$

in the second case

$$\ln \frac{(L - L_f)}{(L_0 - L_f)} = -kn + \ln \left[ 1 + \frac{(L_1 - L_f)}{(L_0 - L_f)} kn \right] \tag{14}$$

and in the third one

$$\ln \frac{(L - L_f)}{(L_0 - L_f)} = -kn + \ln \left[ 1 + \frac{(L_1 - L_f)}{(L_0 - L_f)} kn + \frac{(L_2 - L_f)}{(L_0 - L_f)} \frac{(kn)^2}{2} \right]. \tag{15}$$

A detailed characterization of experimental curves of crystallite size decrease as a function of the number  $n$  of collisions and a proper fitting procedure can thus provide indications on the crystallite size  $L_0, L_1, L_2, \dots, L_i, \dots$  values as well as on the apparent rate constant  $k$ .

The feasibility of such a comparison between experimental data and theoretical curves is shown for Cu powders with nominal purity level of 99.99%. The reader interested in details is kindly addressed to original papers.<sup>[22,23]</sup> Powder processing was carried out in a commercial Spex/Mixer Mill mod. 8000 equipped with a variable speed electrical motor controlled by a

frequency inverter.<sup>[22,23]</sup> The mill was operated at about 25, 28, and 43 Hz. Amounts of powder equal to 8 g were treated under Ar atmosphere in a stainless steel vial with a single ball at impact energies roughly equal to 0.03, 0.10, and 0.25 J. The lowest impact energy at the lowest mill frequency was obtained by using a SiN ball with diameter and mass of about 14 mm and 4.5 g, respectively. In all the other cases, a stainless steel ball with the same diameter but a mass of 12 g was used. Undesired effects due to different powder amounts trapped at impacts are thus avoided.

The decrease in the average crystallite size was quantified by X-ray diffraction (XRD) analyses on powders sampled at given milling times. A Rigaku Diffractometer D/Max equipped with a Cu-K $\alpha$  radiation tube and a graphite monochromator in the diffracted beam was used. Crystalline peak profiles were analyzed with the Rietveld method.<sup>[22,23]</sup> The average size  $L$  of coherent diffraction domains and the strain content  $\varepsilon$  were estimated according to the Williamson–Hall method.<sup>[22,23]</sup>

Experimental data obtained at the aforementioned impact energies are quoted in Figs. 4A–C as a function of the number  $n$  of collisions. It can be seen that the average crystallite size  $L$  undergoes a monotonic decrease at rates increasing with the impact energy  $E$ . The initial crystallite size  $L_0$  is the same for all the curves, but different final values  $L_f$  are found. In particular,  $L_f$  decreases as  $E$  increases.

Although trends in Fig. 4A–C have apparently the same shape, significant differences become evident when the Neperian logarithm of  $(L - L_f)/(L_0 - L_f)$  is quoted as a function of the number  $n$  of collisions as in Fig. 5A–C. Data in Fig. 5A are best-fitted by Eq. (15), apparent rate constant  $k$  and crystallite sizes  $L_1$  and  $L_2$  being the fitting parameters. The initial and final  $L_0$  and  $L_f$  values are indeed known. Three critical loading events are then necessary at an impact energy of 0.03 J to decrease the crystallite size roughly from 58 to 20 nm. Data reported in Fig. 5B and obtained at the intermediate impact energy of about 0.10 J are best-fitted by Eq. (14). In this case, the fitting parameters are  $k$  and  $L_1$ . The kinetic model suggests, therefore, that two critical loading events are necessary to decrease the crystallite size roughly from 58 to 17 nm at about 0.10 J. Finally, the linear plot in Fig. 5C obtained at about 0.25 J is best-fitted by Eq. (13), where  $k$  is the only fitting parameter. Accordingly, a single critical loading event is sufficient for the crystallite size to decrease from about 58 to 15 nm.

The different  $L_i$  values worked out by best-fitting procedures are reported in Fig. 6 as a function of the number  $i$  of critical loading events. Such data provide a first rough insight into the kinetics of crystallite size decrease under mechanical processing by relating the

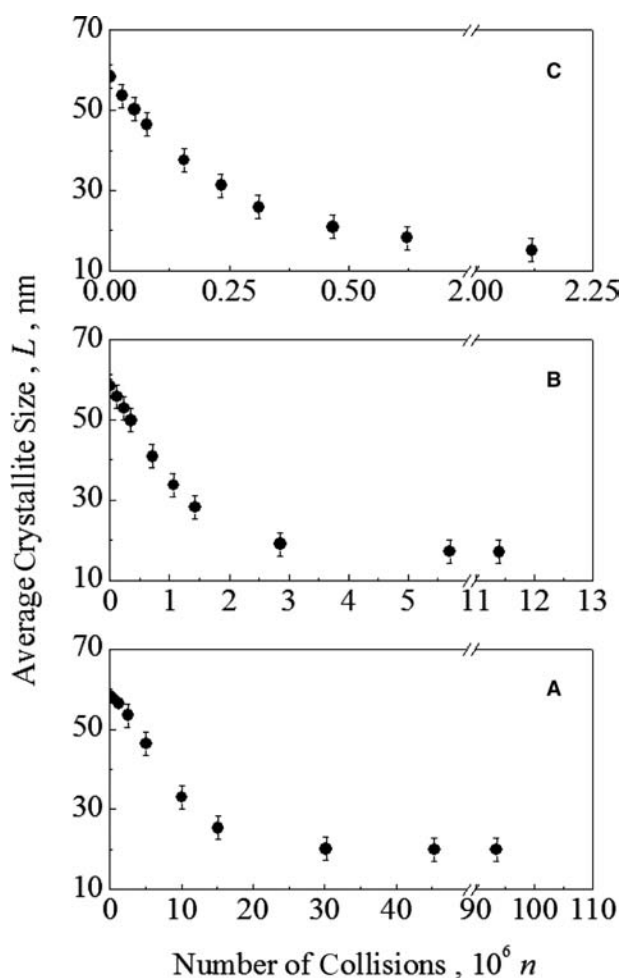


**Fig. 4** The average crystallite size  $L$  as a function of the number  $n$  of collisions for experimental trials performed at  $E$  values equal to (A) 0.03, (B) 0.10, and (C) 0.25 J. Error bars are included. The bars of the first points in (A) have been eliminated for the sake of clarity.

average impact energy  $E$  to the number of critical loading events necessary to decrease the crystallite size of a given powder volume from the initial to the final value. It appears that at high impact energy, the high mechanical stress attained induces a sudden drop of crystallite size from the initial value to the lowest one possible under such loading conditions. The crystallite size decrease becomes, however, as more gradual as impact energy and impact loading becomes lower.

If thermal effects are present, i.e. if the enthalpy of reaction  $A + B$  is high enough to increase temperature, we should introduce a term:

$$\frac{\partial}{\partial t} d(t, T) = f(t) + g(t) e^{-\frac{E}{RT}} \quad (16)$$

where  $E$  is an activation energy,  $R$  is the gas constant, and  $T$  the absolute temperature. This leads to an

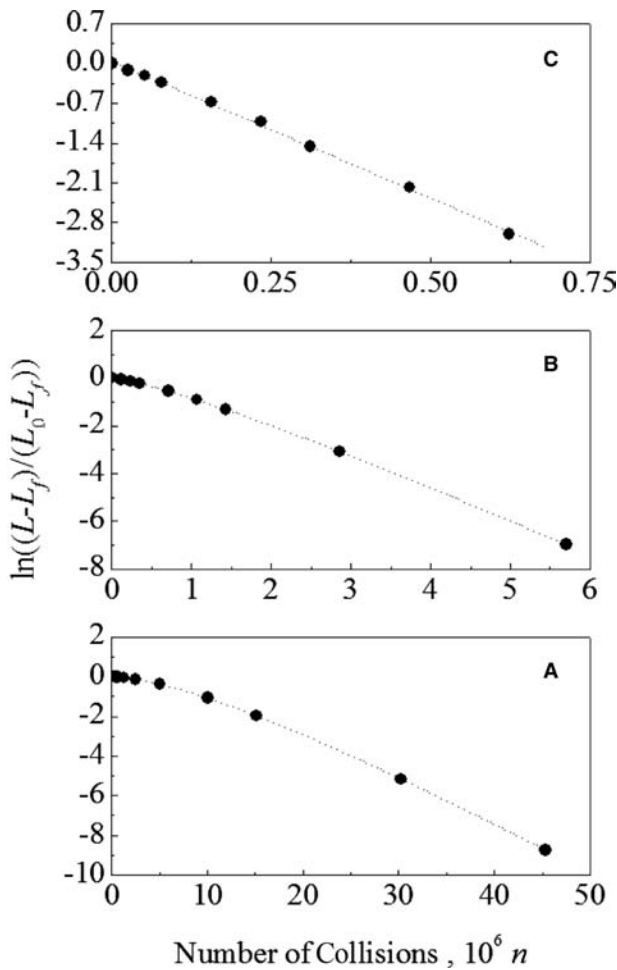


**Fig. 5** The Neperian logarithm of the ratio  $(L - L_f)/(L_0 - L_f)$  as a function of the number  $n$  of collisions for experimental trials performed at  $E$  values equal to (A) 0.03, (B) 0.10, and (C) 0.25 J. Best-fitted curves are also shown.

integrated form of the type:

$$d(t) = \int_0^t f(u) + g(u) e^{-\frac{u}{\tau}} du + d_0 \quad (17)$$

where  $d_0$  is the initial grain size. Even though this is a hypothesis that neglects chemistry and assumes the existence of just one chemical species or compound, this equation is too general to be exploited on a practical ground; however, it does take into account the mechanism of grain reduction due to milling action in the term  $f(t)$  and the grain growth in the second term. If the reaction  $A + B$  is exothermic enough, adiabatic temperature  $T$ , for the sake of simplicity, may be evaluated considering a simple first principle calculation. In the case the temperature is low enough, the integral equation will coincide with Eq. (1). Avvakumov<sup>[24]</sup> has proposed a kinetic equation for

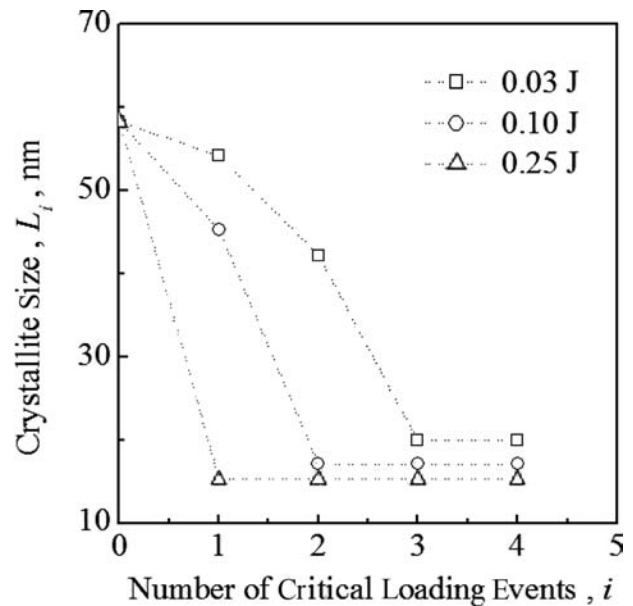
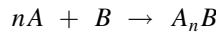


**Fig. 6** The crystallite size  $L_i$  of powders subjected to CLCs for  $i$  times. Impact energies are indicated.

mechanochemical synthesis, Cocco, Delogu<sup>[8,9,14]</sup> and others have validated it in some applications of mechanical alloying. One should consider the elements  $A$  and  $B$  that react to form the compound  $A_nB$  at the initial ratio of the  $A$  on  $B$  reactant in the reaction:



By considering  $\alpha$  as the degree of reaction, atoms reacted on the initial atoms,  $n$  as the stoichiometric number,  $m$  as the initial atomic ratio of  $A$  atoms on  $B$  atoms and  $\varepsilon$  as  $n/m$  ratio, a generalized Avvakumov equation is proposed here:

$$\frac{\partial}{\partial t} \alpha(t) = (1 - \alpha(t))(1 - \varepsilon \alpha(t))f(t) \quad (18)$$

With the initial condition  $\alpha(t = 0) = 0$ , it is possible to integrate then the equation to:

$$\alpha(t) = \frac{e^{\left(-\int_0^t f(u) du + \int_0^t f(u) du \varepsilon\right)} - 1}{-1 + \varepsilon e^{\left(-\int_0^t f(u) du + \int_0^t f(u) du \varepsilon\right)}} \quad (19)$$

which is still a complicate expression. More insight could be given if the elemental powders are introduced in the vial with an initial ratio  $m$  of  $A$  on  $B$  species equal to the stoichiometric ratio of the formed compound  $A_nB$ ,  $n$ . In such a case  $\varepsilon = n/m = 1$  and the

equation simplifies to:

$$\frac{\partial}{\partial t} \alpha(t) = (1 - \alpha(t))^2 f(t) \quad (20)$$

which may be integrated as:

$$\alpha(t) = \frac{\int_0^t f(u) du}{\int_0^t f(u) du + 1} \quad (21)$$

Now it is possible to make the position

$$F = \int_0^t f(u) du \quad (22)$$

and formally calculate  $\alpha$  as a function of  $F$ .

$$\alpha = \frac{F}{F + 1} \quad (23A)$$

It is possible to invert such a relationship to estimate the unknown function  $f(t)$  on the basis of experimental evolution.

$$F = \frac{\alpha}{1 - \alpha} \quad (23B)$$

Coming back to the general solution, one could consider equation (19) as a function of  $F$  as:

$$\alpha_\varepsilon = \frac{e^{(F(\varepsilon-1))} - 1}{\varepsilon e^{(F(\varepsilon-1))} - 1} \quad (24)$$

In general, the two  $F$  functions will be different; however, it is quite likely that the  $f(t)$  function does not depend strongly on composition, as it physically takes into account the mechanical response at a microstructural level of the mixture to the repeated impacts of the balls. This is equivalent to assume that the crystal size evolution does not change too much with slight variations of composition. It is then possible, by algebraic substitution, to link the more simple kinetics, described by Eq. (19) at initial stoichiometric ratio, to the general described by Eq. (18) in such a way:

$$\alpha_\varepsilon = \frac{e^{\left(\frac{\alpha(\varepsilon-1)}{1-\alpha}\right)} - 1}{\varepsilon e^{\left(\frac{\alpha(\varepsilon-1)}{1-\alpha}\right)} - 1} \quad (25)$$

where  $\alpha$  may be computed using the values of the mixture at initial stoichiometric composition.

## ATOMISTIC MECHANISM OF MECHANICALLY INDUCED PHASE TRANSFORMATIONS

The nature of atomistic processes underlying physical and chemical transformations induced by mechanical processing is a long-standing problem. Far from being satisfactorily solved, it is the focus of a lively debate constantly stimulated by the development of conceptual frameworks alternative to the defect-enhanced thermal diffusion scenarios initially proposed.<sup>[25–30]</sup> These latter represent a generalization of the mechanisms based on thermal diffusion developed to rationalize solid state amorphization reactions in binary diffusion couples.<sup>[25]</sup> The analogy between layered arrangements used in diffusion couples and lamellar microstructures observed during the initial stages of mechanical treatment suggested that their underlying mechanisms could be similar.<sup>[25–30]</sup> Phase transformations taking place under mechanical processing conditions were thus interpreted in terms of diffusion processes with a rate enhanced by structural defects accumulated in the solid.<sup>[25–30]</sup> The hypothesis that mechanochemical transformations proceed via thermal diffusion implies, however, severe limitations to its applicability and suffers eventually of an incapability to explain fine thermodynamic and kinetic features. Most difficulties originate from the evidence that chemical processes governed by diffusion must be governed by a suitable driving force. Accordingly, mechanically induced phase transformations could take place only in chemical systems characterized by a negative enthalpy of mixing.<sup>[25–30]</sup> In spite of this, solid state reactions are also observed in the case of immiscible systems with positive enthalpy of mixing and of pure intermetallic phases.<sup>[1]</sup> However, the obtainment of crystalline solid solutions and disordered solids implies in principle a raise of free energy and then the generation of a thermodynamic driving force opposed to mixing and disordering.

The evident shortcomings mentioned here are to a large extent avoided by different approaches laying emphasis on the capability of mechanical forces to induce atomic-scale mixing phenomena independent of thermal contributions.<sup>[31–48]</sup> Theoretically predicted or numerically inferred atomic-scale mechanisms are based on interface roughening<sup>[32]</sup> and shear-induced disordering processes.<sup>[34]</sup> Within these conceptual frameworks, thermal diffusion is not rejected or excluded in principle, but the key role is played by atomic displacements resulting from the action of shear stresses.<sup>[31–38]</sup> The fundamental motivations underlying aforementioned mechanistic hypotheses originate from the evidence that severe mechanical loads produce a series of local shear events on the microscopic scale,<sup>[1]</sup> with consequent localization of considerable amounts of energy in relatively small regions of solid phase.<sup>[31–48]</sup>



The shear induced rearrangements of atomic species results in turn in the generation of complex aggregates of atoms with defective coordination.<sup>[43,45–48]</sup> During the time period of mechanical loading, such rearrangements mediate mass transport and chemical mixing.<sup>[43,45–48]</sup> Once the load is removed, shear events are interrupted and transient defective structures relax and to a large extent disappear as a consequence of thermal equilibration.<sup>[46–48]</sup> These evidences suggest therefore a strong coupling between thermally and mechanically induced mechanisms of mass transport, establishing a connection between the conventional thermal diffusion scenarios and more recent approaches. As a result, mechanochemical phase transformations can be thought to originate from the competition of so-called ballistic displacements and thermal effects.<sup>[31–48]</sup>

Despite the considerable efforts operated, the intimate mechanisms governing mechanically induced processes are, however, still a matter of debate and the role of localized mechanical stresses as well as of related excited states need suitable clarification. In light of the complicated nature of mechanochemical transformations, governed by intertwined hierarchies of atomistic events, numerical simulations are expected to play an increasingly important role in the definition of detailed mechanistic scenarios. A clear example of the potential of such methods when applied to shear induced transformations is given by their capability of satisfactorily addressing the questions related to the dissolution of nanometer-sized precipitates into crystalline matrices in binary immiscible systems.<sup>[45]</sup> Numerical findings clearly showed that shear induced mass transport is connected in this case with the motion of dislocations generated during plastic deformation.<sup>[45]</sup> A mechanistic regime resembling the one observed in turbulent flow mixing was accordingly observed.<sup>[45]</sup> Another striking feature of shear induced processes becomes evident when interface mixing is studied.<sup>[34,46,47]</sup> Molecular dynamics calculations have indeed shown that the mutual dissolution of chemical species at plane interfaces, illustrated in Fig. 7 for the case of an amorphizing Ni–Zr system,<sup>[46,47]</sup> produces a power-law dependence of the intermixed layer thickness analogous to that characteristic of thermal diffusion.<sup>[34,46,47]</sup> Correspondingly, the square of layer thickness increases linearly with time, even though the atomic-scale mechanism governing mixing is completely different from the vacancy-mediated one underlying thermal activation. Similar results are found in studies concerning the impact of rough surfaces.<sup>[48]</sup>

It follows that the simple time dependence of the number of atoms intermixed is not able to univocally define the transformation mechanism and that numerical investigations, though limited by the availability of suitable computational resources, represent the most

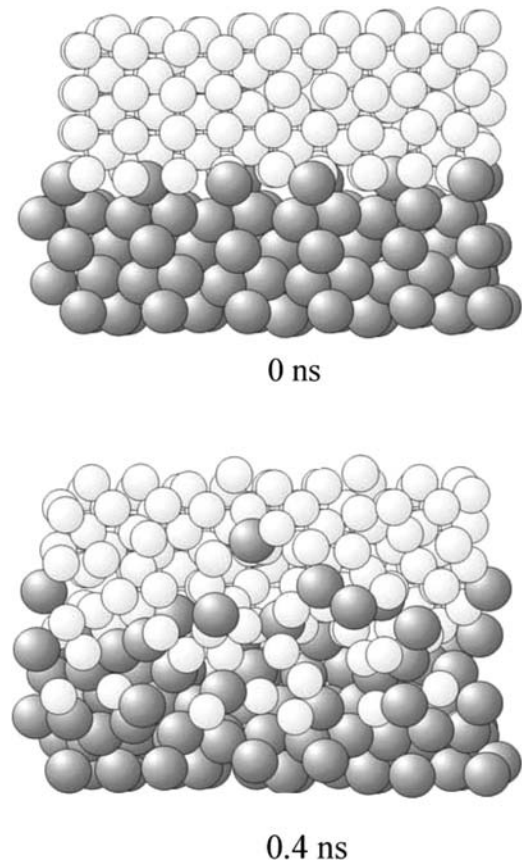


**Fig. 7** The effects of shear on a smooth Ni–Zr interface. Shearing is carried out by moving the upper Ni semi-crystal (light gray atoms) to the right and the bottom Zr semi-crystal (dark gray atoms) to the left. Configurations refer to the times quoted. The whole system consisted of 18,000 Ni atoms arranged in a stacking sequence of 20 (111) face-centered cubic *cF4* planes and 18750 Zr atoms arranged in a stacking sequence of 30 (100) hexagonal close-packed *hP2* planes. Simulation details can be found elsewhere. *Source:* From Refs.<sup>[46,47]</sup>.

promising method to shed light on the details of mechanochemical transformations.

### AN EXAMPLE IN THE MECHANOSYNTHESIS OF Fe<sub>3</sub>C

Kinetic quantitative studies are not very common in mechanochemistry of nanophase materials. A set of experiments was performed several years ago, and results were published in Ref.<sup>[49]</sup>. In such a system,<sup>[50,51]</sup> experimental results suggest that fracturing of graphite crystal progresses by steps: fracturing along the hexagonal plane and subsequent fracturing of the hexagonal networks. Most of the experiments were performed at a fixed initial stoichiometric composition, 3 Fe 1 C; this composition corresponds to that of cementite Fe<sub>3</sub>C.

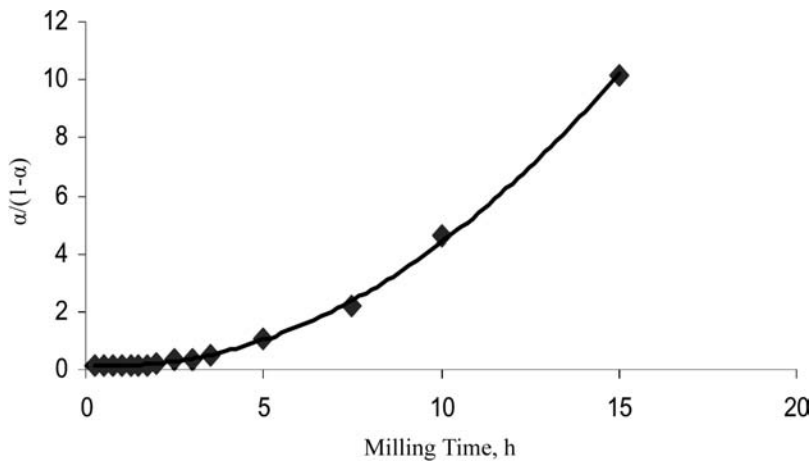


**Fig. 8** Mechano-synthesis of nanocrystalline iron carbides: plot of equation (23B) suggests a possible parabolic trend of  $F(t)$  function; squares are experimental data.

In such conditions, in the modified Avvakumov equation (18) reported earlier,  $\varepsilon = 1$  holds, and it is possible to consider the simpler equation (19) and its solution (20). Using a Spex 8000 vibrating laboratory mill, with 6 g of powder charge and a ball to powder weight ratio 10 to 1, it was possible to identify by appropriate microstructural analysis—Mossbauer spectroscopy and X-ray diffraction—several phases, Fe, C, a low carbon martensite like alloy and three main types of carbides. If we simplify the kinetic trend considering  $\text{Fe}_3\text{C}$ , cementite, as the unique carbide present, and we neglect the martensite-like alloy, we have to take into account just three chemical species: Fe, C, and  $\text{Fe}_3\text{C}$ . In such a way, the real kinetic evolution is simplified; experimental results are reported for iron in Table 3.

The  $F(t)$  function presented above is as in Fig. 8.

The  $R^2$  value for a quadratic fit is high indeed and a good correlation is found linking  $(\alpha/(1-\alpha))$  to  $F(t)$ . The almost parabolic trend of  $F(t)$  means that the derivative of the  $F(T)$  function,  $f(t)$ , could be linear. It is possible that an approach decoupling the two main contributions to reaction rates in mechano-synthesis would be found in the future, linking  $f(t)$  to the crystal size evolution. Considering such a hypothesis, Eq. (20) could become:

$$\frac{\partial}{\partial t} \alpha(t) = \frac{c(1 - \alpha(t))^2}{d} \quad (26)$$

which one may solve as:

$$\alpha(t) = \frac{\int_0^t \frac{1}{d(u)} du}{\int_0^t \frac{1}{d(u)} du + \frac{1}{c}} \quad (27)$$

The crystal size evolution  $d(t)$  may be evaluated by means of X-ray diffraction line broadening;

experimental results for this specific system are presented in Table 4.

One might check that the crystal size evolution could be assumed as a simple reciprocal function of time. In this case  $1/d_{\text{Fe}} = 0.0259t + 0.0111$  and  $1/d_{\text{C}} = 0.0682t + 0.0189$ , where  $d_{\text{Fe}}$  and  $d_{\text{C}}$  are the iron and carbon crystal size. The reciprocal of the grain size  $d$  could be assumed as<sup>[10]</sup>  $1/d = 1/d_{\text{Fe}} + 1/d_{\text{C}}$  and in this case, by summing  $1/d_{\text{Fe}}$  and  $1/d_{\text{C}}$  contribution, as  $1/d = 0.0941t + 0.03$ . Substituting this expression in Eq. (26) and integrating as in Eq. (27), one could obtain:

$$\alpha(t) = \frac{ct(941.t + 600.)}{941.ct^2 + 600.ct + 20000.} \quad (28)$$

where  $c$  should be evaluated by data fitting. With the choice  $c = 0.81$ , the data fitting is excellent, apart from the first three or four points of the kinetics; this could be due to an erroneous attribution of the

**Table 4** Iron and carbon crystal size evolution in the mechano-synthesis of nanophase iron carbides with a laboratory SPEX 8000 mill

Milling time (h)	Fe crystal size (nm)	C crystal size (nm)
0.25	38	24.6
0.5	32.5	20.4
0.75	34.2	15.7
1	31.3	10.8
1.25	27.9	
1.5	23.6	
1.75	18.1	
2.5	11.6	
3	13.4	
3.5	8.8	
5	9.3	

hyperfine field distribution in the Mossbauer spectra at early milling times.

The agreement with the  $F(t)$  function is also excellent, as reported in Fig. 9.

## INDUSTRIAL TRENDS AND RESULTS

At the moment of writing this entry, there are two companies that are exploiting successfully the mechanochemical synthesis of nanocrystalline powders: Advanced Powder Technology Pty Ltd<sup>[52]</sup> of Perth, Western Australia, and M.B.N., Italy.<sup>[53]</sup> Both companies have strong connections with the university field and could be considered as spin-offs of the research group of Matteazzi<sup>[5]</sup> and McCormick.<sup>[2]</sup> Matteazzi has pioneered the works in the mechanochemical synthesis of nanophase powders and, along with Le Caer, he was the first to employ the terminology “mechanochemical synthesis” in obtaining nanocrystalline carbides and silicides<sup>[54]</sup> and aluminides.<sup>[55]</sup> These compounds, and especially carbides, have remarkable industrial applications in the field of cutting tool materials. Matteazzi chose the  $Fe-C$  system as a model for the mechanochemical synthesis of nanocrystalline carbides for the availability of a powerful tool in microstructural analysis, Mossbauer spectroscopy,<sup>[56]</sup> which is applicable to Fe-containing systems. Subsequently, he studied alumina-based nanocomposites<sup>[57]</sup> and the solid state reduction of oxides such as the transformation of haematite to nanocrystalline wustite.<sup>[58]</sup> Further works

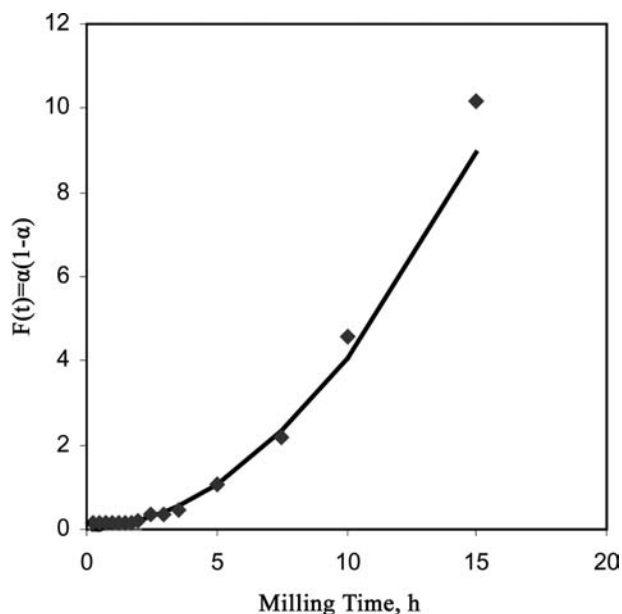


**Fig. 9** Experimental results (in squares) in mechanochemical synthesis of iron carbide compared with values calculated according to real crystal size evolution [(Eq. 28)].

include the first reported applications of mechanochemical synthesized materials to catalysis<sup>[59,60]</sup> and the development of a vibrating mill<sup>[12,13]</sup> scaling up the possibilities of mechanochemical synthesis of the SPEX 8000 mill. Latest developments include the study of grain growth and of consolidation by means of CIP (cold isostatic pressing) and HIP (hot isostatic pressing).<sup>[61]</sup> The Italian company M.B.N.<sup>[53]</sup> has now developed and scaled-up, with an industrial production capacity of 200 t/years of materials, several of the earlier work by Matteazzi. The company is now focusing on the Mechanomade<sup>®</sup>, which is basically a mechanochemical synthesis technique, and on consolidation technologies such as forging and extrusion with the processes of Mechanoforge<sup>®</sup> and Mechano XT<sup>®</sup>. These techniques have led, for instance, to the production of an  $Al_2O_3$  doped copper alloy (99% Cu, 1%  $Al_2O_3$ ), which has outstanding mechanical properties (Yield strength 800 MPa, Ultimate Tensile Strength 900 MPa).

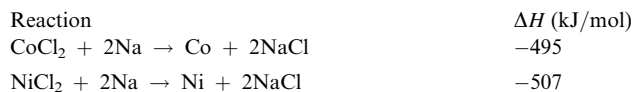
McCormick has obtained the most interesting results in the field of mechanochemical synthesis of nanocrystalline materials. With different coauthors and collaborators, along the years, he has started studying the Mechanical Alloying process, considering further some constructional details of vibrating mills. He has recently exploited some results in the field of displacement mechanochemical reactions, which are interesting for the industrial field to patent a specific process—now property of an industrial spin-off of the University of Western Australia, Advanced Powder Technology Pty Ltd<sup>[52]</sup>—that has been called mechanochemical processing MCP<sup>®</sup>. Mechanochemical processing consists of solid-state displacement mechanochemical reactions caused by collisions between particles and balls inside mills. At the end of the reactions nanocrystalline powders (grain size  $\sim 10$  nm) within a soluble salt matrix are obtained. Thermal treatments, at low or intermediate temperatures, are typically performed depending on the specific nanocrystalline powders to be obtained. The final step is washing the salt matrix with appropriate solvents, allowing to get separated nanoparticles.

The use of a diluent phase may be necessary to:

1. Avoid combustion reactions during milling
2. Reduce the volume fraction of nanoparticles (in this way it is possible to avoid nanoparticles being agglomerated).
3. Control the particle size distribution.

Comparing it with the more simple mechanochemical reaction, which has been presented in previous paragraphs, it is harder to model the physicochemical process. McCormick has obtained main results by using single ( $A + BC \rightarrow AB + C$ ) or double ( $AB + CD \rightarrow AD + BC$ ) displacement reactions.

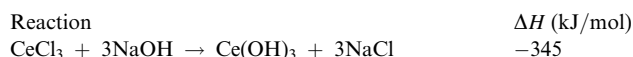
For instance, in the production of ultrafine Co and Ni particles<sup>[62]</sup> with a narrow particle size distribution of 10–20 nm, the reactions:



were obtained by SPEX 8000 processing with a ball-to-powder ratio 3 : 1 and with typical processing times of the order of 24 hr. Here and in other previous works, a remarkable effect of the diluent phase NaCl was observed on the influence of the mean particle size, being of the order of nanometers in case 25–50% wt diluent, and increasing it to the micron range when not present.

Further examples include the synthesis of metal sulfide nanoparticles<sup>[63]</sup> reaction of the type:  $\text{ZnCl}_2 + \text{CaS} \rightarrow \text{ZnS} + \text{CaCl}_2$ , with a mean particle size, observed by TEM, of 12 nm.

The synthesis of metal-oxide nanoparticles was described in Ref.<sup>[64]</sup>. A representative reaction is:



Finally, one should also consider the activities of the Institute of Solid State Chemistry and Mechanochemistry of Novosibirsk, RUS,<sup>[65]</sup> which have a research experience in the field of mechanochemistry dating back to 1970s. Several applications, which span from the metal industry to the field of medicine and cosmetics, are now directed to the mechanochemical synthesis of ceramic powders such as, for instance, nanocrystalline  $\text{Al}_2\text{O}_3$ .<sup>[66]</sup>

## CONCLUSIONS

This entry has presented some aspects of mechanochemical synthesis of nanophase powders, with an elementary modeling of the process<sup>[67]</sup> and a general perspective on the results in the field. Mechanochemistry is one of the most appealing technologies for the synthesis of nanophase materials and, at an industrial and commercial level, it is already exploited for sintered products,<sup>[53]</sup> abrasive processing,<sup>[52]</sup> catalysis,<sup>[52,53]</sup> medical,<sup>[53]</sup> cosmetic,<sup>[53,65]</sup> and even cleaning applications. Among different mechanochemical processes, MCP® process—which combines mechanochemical synthesis with appropriate thermal post-treatments—appears the most interesting for its capability to obtain nanocrystalline powders of the order of 10–20 nm of many different materials.

Possible research activities, related to applications in the field, would most likely include the study of the influence of diluents in mechanochemical reactions and techniques for engineering, controlling, and sizing particles, which have dimensions two order of magnitude less than the finest powders used in metal powder technologies.

More details of the technologies of nanostructured material synthesis by mechanical attrition, in which mechanochemistry should be inserted, are described in the entry by Koch<sup>[68]</sup> in this Encyclopedia; the reader is referred there not only for a more thorough description of these technologies, but also to appreciate shortcomings of this methodology, mainly represented by powder contamination during milling, which have not been discussed here.

## ACKNOWLEDGMENTS

The authors thank Dr. Nicola Zampa for technical help in CAD drawings; Fabio Miani appreciates fruitful discussion and communication with Prof. Carl Koch.

## REFERENCES

1. Suranarayana, C. Mechanical alloying and milling. *Prog. Mater. Sci.* **2001**, *46*, 1–184.
2. Dodd, A.C.; McCormick, P.G. Factors affecting the particle size of powders synthesised by mechanochemical processing. *J. Metastable Nanocryst. Mater.* **2003**, *15–16*, 545–552.
3. Takacs, L. Self-sustaining reactions induced by ball milling. *Prog. Mater. Sci.* **2002**, *47*, 355–414.
4. Matteazzi, P.; Basset, D.; Miani, F. Mechanochemistry of nanophase materials. *Nanostruct. Mater.* **1993**, *2*, 217–229.
5. Butyagin, P. Rehbinders' predictions and advances in mechanochemistry. *Colloids Surf. A: Physicochem. Eng. Aspects* **1999**, *160*, 107–115.
6. Urakaev, F.Kh.; Boldyrev, V.V. Mechanism and kinetics of mechanochemical processes in comminuting devices. *Powder Technol.* **2000**, *107*, 93–107.
7. Calka, D.; Wexler, D. Mechanical milling assisted by electrical discharge. *Nature* **2002**, *419*, 147–151.
8. Delogu, F.; Monagheddu, M.; Mulas, G.; Schiffini, L.; Cocco, G. Some kinetic features of mechanical alloying transformations processes. *J. Non-Cryst. Solids* **1998**, *232–234*, 383–389.
9. Delogu, F.; Cocco, G. Impact-induced disordering of intermetallic phases during mechanical processing. *Mater. Sci. Eng.* **2003**, *A343*, 314–317.
10. Miani, F.; Fecht, H.J. Evaluating the mechanochemical power transfer in the mechanochemistry of nanophase

- Fe-C and Fe-Cu powders. *Int. J. Refractory Metals Hard Mater.* **1999**, *17*, 133–139.
11. Koch, C.C. Top-down synthesis of nanostructured materials: mechanical and thermal processing methods. *Rev. Adv. Mater. Sci.* **2003**, *5*, 91–99.
  12. Basset, D.; Matteazzi, P.; Miani, F. Designing a high energy mill for the synthesis of nanophase materials in large quantities. *Mater. Sci. Eng.* **1993**, *A168*, 149–152.
  13. Basset, D.; Matteazzi, P.; Miani, F. Measuring the impact velocities of balls in high energy mills. *Mater. Sci. Eng.* **1994**, *A174*, 71–74.
  14. Cocco, G.; Delogu, F.; Schiffrini, L. Toward a quantitative understanding of the mechanical alloying process. *J. Mater. Syn. Processing* **2000**, *8*, 167–180.
  15. Courtney, T.H.; Maurice, D. Process modelling of the mechanism of mechanical alloying. *Scripta Materialia* **1996**, *34* (1), 5–11.
  16. Bourell, D.L.; Marcus, H.L.; Barlow, J.W.; Beaman, J.J. Selective laser sintering of metals and ceramics. *Int. J. Powder Metall.* **1992**, *28* (4), 369–381.
  17. Umemoto, M.; Liu, Z.G.; Takaoka, H.; Sawakami, M.; Tsuchiya, K.; Masuyama, K. Production of bulk cementite and its characterization. *Metall. Mater. Trans.* **2001**, *32A*, 2127–2131.
  18. Manai, G.; Delogu, F.; Schiffrini, L.; Cocco, G. Mechanically induced self-propagating combustions: experimental findings and numerical simulation results. *J. Mater. Sci.* **2004**, *39*, 5319–5325.
  19. Courtney, T.H. Process modelling of mechanical alloying. *Mater. Trans., JIM* **1995**, *36*, 110–122.
  20. Maurice, D.R.; Courtney, T.H. Milling dynamics: Part II. Dynamics of a Spex mill and a one-dimensional mill. *Metall. Mater. Trans. A* **1996**, *27*, 1973–1979.
  21. Szabò, Z.G. Kinetic characterization of complex reaction systems. In *Comprehensive Chemical Kinetics: The Theory of Kinetics*; Bamford, C.H., Tipper, C.F.H., Eds.; Elsevier Science Publishers: Oxford, 1969; *2*, 1–80.
  22. Delogu, F.; Cocco, G. Crystallite size refinement in elemental species under mechanical processing conditions. *Mater. Sci. Eng. A* **2006**, *422*, 198–204.
  23. Delogu, F.; Cocco, G. The size refinement of Cu crystallites under mechanical processing conditions: a phenomenological modelling approach. *J. Mater. Sci.* **2007**, *42*, 4356–4364.
  24. Avvakumov, E.; Senna, M.; Kosova, N. Some theoretical aspects of mechanochemical reactions. In *Soft Mechanochemical Synthesis: A Basis for New Chemical Technologies*; Kluwer Academic Publisher: New York, Boston, Dordrecht, London, Moscow, 2002; 39–46.
  25. Johnson, W.L. Thermodynamic and kinetic aspects of the crystal to glass transformation in metallic materials. *Prog. Mater. Sci.* **1986**, *30*, 8–134.
  26. Meng, W.J.; Nieh, C.W.; Johnson, W.L. Maximum thickness of amorphous NiZr interlayers formed by a solid-state reaction technique. *Appl. Phys. Lett.* **1987**, *51*, 1693–1695.
  27. Gosele, U.; Tu, K.N. Critical thickness of amorphous phase formation in binary diffusion couples. *J. Appl. Phys.* **1989**, *66*, 2619–2626.
  28. Highmore, R.J. Nucleation issues in solid-state amorphisation. *Phil. Mag.* **1990**, *B62*, 455–467.
  29. Greer, L. Transformation of metastable phases. *Phil. Mag.* **1990**, *B61*, 525–538.
  30. Yavari, R.; Desrè, P.J. Thermodynamics and kinetics of amorphisation during mechanical alloying. *Mater. Sci. Forum* **1992**, *43*, 88–90.
  31. Butyagin, P.Yu. Mechanochemical synthesis: mechanical and chemical factors. *J. Mater. Syn. Proc.* **2000**, 205–211.
  32. Bellon, P.; Averbach, R.S. Nonequilibrium roughening of interfaces in crystal under shear: application to ball milling. *Phys. Rev. Lett.* **1995**, *74*, 1819–1822.
  33. Hammerberg, J.E.; Holian, B.L.; Roder, J.; Bishop, A.R.; Zhou, S. Nonlinear dynamics and the problem of slip at material interfaces. *J. Physica* **1998**, *D123*, 330–340.
  34. Fu, X.Y.; Falk, M.L.; Rigney, D.A. Sliding behaviour of metallic glass part II. Computer simulations. *Wear* **2001**, *250*, 420–430.
  35. Martin, G. Phase stability under irradiation: ballistic effects. *Phys. Rev.* **1984**, *B30*, 1424–1436.
  36. Xu, J.; Collins, G.S.; Peng, L.S.J.; Atzmon, M. Deformation-assisted decomposition of unstable Fe<sub>50</sub>Cu<sub>50</sub> solid solution during low-energy ball milling. *Acta Mater.* **1999**, *47*, 1241–1253.
  37. Bellon, P.; Averbach, R.S.; Odonuga, S.; Li, Y.; Krasnochtchekov, P. Crossover from superdiffusive mixing in plastically deformed solids. *Phys. Rev. Lett.* **2007**, *99*, 110602.
  38. Hoagland, R.G.; Baskes, M.I. An atomistic study of the effects of stress and hydrogen on a dislocation lock in nickel. *Scripta Mater.* **1998**, *39*, 417.
  39. Bulatov, V.; Abraham, F.F.; Kubin, L.; Devincere, B.; Yip, S. Connecting atomistic and mesoscale simulations of crystal plasticity. *Nature* **1998**, *391*, 669–672.
  40. Ovid'ko, I.A.; Rezis, A.B. Effect of elastic distortions on solid-state amorphization at grain boundaries and dislocations. *J. Phys. D: Appl. Phys.* **1999**, *32*, 2833–2840.
  41. Horstemeyer, M.F.; Baskes, M.I.; Plimpton, S.J. Length scale and time scale effects on the plastic flow of fcc metals. *Acta Mater.* **2001**, *49*, 4363–4374.
  42. Kadau, K.; Germann, T.C.; Lomdahl, P.S.; Holian, B.L. Microscopic view of structural phase transitions induced by shock waves. *Science* **2002**, *296*, 1681–1684.
  43. Lund, A.C.; Schuh, C.A. Driven alloys in the athermal limit. *Appl. Phys. Lett.* **2003**, *82*, 2017–2021.
  44. Levitas, V.I. High-pressure mechanochemistry: conceptual multiscale theory and interpretation of experiments. *Phys. Rev.* **2004**, *B70*, 184118.
  45. Odonuga, S.; Li, Y.; Krasnochtchekov, P.; Bellon, P.; Averbach, R.S. Forced chemical mixing in alloys driven by plastic deformation. *Phys. Rev. Lett.* **2005**, *95*, 045901.
  46. Delogu, F.; Cocco, G. Molecular dynamics investigation on the role of sliding interfaces and friction in the formation of amorphous phases. *Phys. Rev. B* **2005**, *71*, 144108.

47. Delogu, F.; Cocco, G. Numerical simulations of structural modifications at a Ni-Zr sliding interface. *Phys. Rev. B* **2005**, *72*, 014124.
48. Delogu, F.; Cocco, G. Numerical simulations of atomic-scale disordering processes at impact between two rough crystalline surfaces. *Phys. Rev. B* **2006**, *74*, 035406.
49. Miani, F.; Matteazzi, P.; Basset, D. Mechanochemistry of iron carbides at composition  $Fe_{75}C_{25}$ : modelling of the process kinetics. *J. Alloys Comp.* **1994**, *204*, 151–156.
50. Yelsukov, E.P.; Dorofeev, G.A.; Konygin, G.N.; Fomin, V.M.; Zagainov, Comparative analysis of the mechanisms and kinetics of mechanical alloying in systems  $Fe(75)X(25)$  ( $X = Si, C$ ). *Phys. Metals Metallography* **2002**, *93* (3), 278–288.
51. Yelsukov, E.P.; Dorofeev, G.A.; Fomin, V.M.; Konygin, G.N.; Zagainov, A.V.; Maratkanova, A.N. Mechanically alloyed  $Fe(100-x)C(x)$  powders: i. structure, phase composition and temperature stability. *Phys. Metals Metallography* **2002**, *94* (4), 356–366.
52. <http://www.advancednanotechnology.com> (accessed December 2007).
53. <http://www.mbn.it> (accessed December 2007).
54. Le Caer, G.; Bauer-Grosse, E.; Pianelli, A.; Bouzy, E.; Matteazzi, P. Mechanically driven syntheses of carbides and silicides. *J. Mater. Sci.* **1990**, *25*, 4726–4731.
55. Matteazzi, P.; Miani, F.; Le Caer, G.; Bauer Grosse, E. Mechanochemistry of intermetallic compounds. *Proceedings of the 2nd EUROMAT*, Cambridge, U.K.; The Institute of Materials: London, 1991; Vol. 2, 359–365.
56. Matteazzi, P.; Miani, F.; Le Caer, G. Kinetics of cementite mechanochemistry. *Hyperfine Interactions* **1991**, *68*, 173–176.
57. Matteazzi, P.; Le Caer, G. Synthesis of nanocrystalline alumina-metal composites by room-temperature ball milling of metal oxides and aluminium. *J. Am. Ceramic Soc.* **1992**, *75*, 1–7.
58. Matteazzi, P.; Le Caer, G. Reduction of haematite with carbon by room temperature ball milling. *Mater. Sci. Eng. A* **1991**, *A149*, 135–142.
59. Trovarelli, A.; Matteazzi, P.; Dolcetti, G.; Lutman, A.; Miani, F. Nanophase iron carbides as catalysts for carbon dioxide hydrogenation. *Appl. Catal. A* **1993**, *94*, L9–L13.
60. Miani, F.; Matteazzi, P.; Dolcetti, G.; Lutman, A.; Trovarelli, A. Catalytic properties of mechanochemically synthesized nanophase iron carbides. *Mater. Sci. Eng.* **1993**, *A168*, 153–155.
61. Matteazzi, P.; Wolf, F. Mechanochemistry of high speed steel AISI M2: powder consolidation. *Mater. Sci. Eng. A* **1998**, *248*, 19–34.
62. Ding, J.; Tsuzuki, T.; McCormick, P.G.; Street, R. Ultrafine Co and Ni particles prepared by mechanochemical processing. *J. Phys. D: Appl. Phys.* **1996**, *29*, 2365–2369.
63. Tsuzuki, T.; McCormick, P.G. Mechanochemical synthesis of metal sulphide nanoparticles. *Nanostruct. Mater.* **1999**, *12*, 75–78.
64. Tsuzuki, T.; McCormick, P.G. Synthesis of metal-oxide nanoparticles by mechanochemical processing. *Mater. Sci. Forum* **2000**, *343–346*, 383–388.
65. <http://www.solid.nsc.ru/eng/> (accessed December 2007).
66. Karagedov, G.R.; Lyakhov, N.Z. Preparation and sintering of  $Al_2O_3$  nanosized powder. *Nanostruct. Mater.* **1999**, *11*, 559–572.
67. Vasconcelos, I.; de Figueiredo, R.S. Transformation kinetics on mechanical alloying. *J. Phys. Chem. B* **2003**, *107*, 3761–3767.
68. Koch, C.C. Nanostructured materials: Synthesis by mechanical attrition. In *Dekker Encyclopedia of Nanoscience and Nanotechnology*, 2E; Schwarz, J.A., Contescu, C.I., Putyera, K., Eds.; Taylor & Francis: New York, NY, 2009; Vol. 4, 3019–3029.



# Nanoporosity Evolution on Dealloying

Jonah Erlebacher

Department of Materials Science and Engineering, Johns Hopkins University,  
Baltimore, Maryland, U.S.A.

## INTRODUCTION

Nanoporous metals (NPMs) are materials formed during selective chemical or electrochemical dissolution of one or more components out of a homogenous alloy. This process is known as *dealloying* or *selective dissolution*. Dealloying transforms initially dense alloys into materials with a uniform, open porosity, with ligament widths and spacings tunable between just a few nanometers to many hundreds of nanometers, and usually employing only the simplest electrochemical processing. This entry reviews the physical characteristics of NPMs, the experimental variables that can be fruitfully varied in their fabrication, and the theoretical models that attempt to explain nanoporosity evolution during dealloying.

Historically, selective dissolution has been primarily studied in those technologically important systems for which the formation of nanoporosity is undesirable. For instance, Zn can be selectively dissolved from brass (Cu/Zn alloys) and can lead to stress corrosion cracking.<sup>[1]</sup> The dealloying of strength-hardening S-phase precipitates in the important aviation alloy Al-2024 can lead to pitting corrosion and, ultimately, materials failure;<sup>[2]</sup> even stainless steels may be dealloyed of iron if the chromium content is too small.<sup>[3]</sup> Within the context of corrosion, dealloying is obviously problematical, and a significant amount of effort has been made in its avoidance.

## NANOPOROUS METALS FORMED BY DEALLOYING

However, for some systems, dealloying yields nanoporous materials with remarkable properties. For example, the dealloying of silver from silver/gold alloys<sup>[4–6]</sup> or copper from copper/gold alloys<sup>[7]</sup> results in the formation of nanoporous gold (NPG). This material has highly positive characteristics: 1) a uniform open porosity; 2) a very high surface area (greater than 5 m<sup>2</sup>/g);<sup>[8]</sup> 3) a conductive bicontinuous network with characteristic length tunable between 5 and 1000 nm;<sup>[9]</sup> and 4) a biocompatible surface to which can be attached all sorts of functionalized biomolecules

via thiol endgroup chemistry. In this light, NPG is an attractive catalyst support material, with vast applicability in sensor designs of all kinds. Furthermore, NPG can be formed in a variety of useful forms, including bulk, thin film, and, recently, nanowires.<sup>[8]</sup> For these reasons, NPG represents the prototypical example of an NPM, but is only one example of a number of different alloys that can be rendered nanoporous by dealloying. An incomplete list of alloys that have been dealloyed includes (Ag, Cu)/Au,<sup>[4–6]</sup> (Ag, Ni, Cu)/Pd,<sup>[10,11]</sup> Al/(Cu, Ni),<sup>[12]</sup> and Mn/Cu,<sup>[13]</sup> where the first element(s) in the couple is the element(s) selectively dissolved, leaving behind the second element(s) porous.

Fig. 1 shows a plan view scanning electron microscopy (SEM) micrograph of a thin film with nominal composition Ag<sub>65</sub>Au<sub>35</sub> (at.%) dealloyed in nitric acid under free corrosion (i.e., simply immersed in concentrated nitric acid). Silver is readily soluble in nitric acid, whereas gold is not. After approximately 5 min in nitric acid, the entire film has been dealloyed of silver, and the result is that the initially dense film has been transformed into a nanoporous film with ligaments approximately 20 nm in diameter and with spacing also of approximately 20 nm. Silver and gold are completely miscible across the entire composition range and thus the alloy has not phase-separated prior to dealloying. This is the key point underlying the physics of nanoporosity evolution during dealloying—the nanoporous structure observed is simply not an “excavated” one. Rather, porosity forms dynamically during selective dissolution via mass transport of the gold atoms from their original lattice sites to sites along the nanoporous backbone. Such a conclusion is borne out by a number of experimental observations involving X-ray and neutron diffraction that fail to probe any preexisting structure prior to dealloying.<sup>[14]</sup> The anodic dissolution of silver from silver/gold alloys has yielded pores as small as 5 nm.<sup>[6]</sup> Such a diffusion of the noble alloy components from their “bulk” lattice positions to the porous skeleton *during* dissolution is a characteristic feature of all systems that can be dealloyed.

For the purposes of this entry, we restrict the definition of NPMs to include only those materials created by selective dissolution at room temperature. Open,

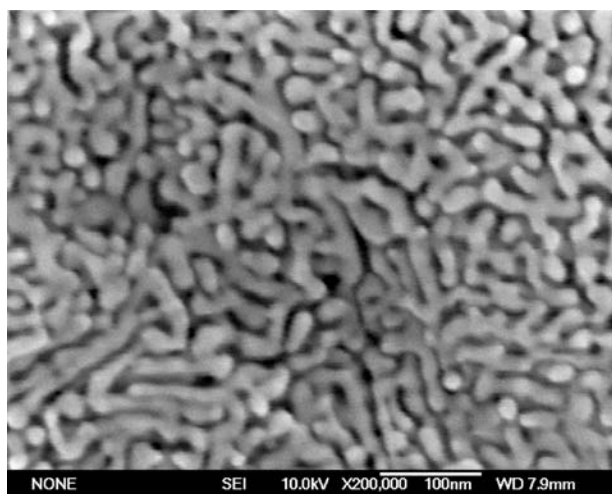


**Fig. 1** Plan view SEM micrograph ( $\times 200,000$ ) of a nanoporous gold film with nominal predealloying composition  $\text{Ag}_{65}\text{Au}_{35}$  (at.%), dealloyed in nitric acid under free corrosion.

porous metals have been made by other methods, including electrochemical plating through colloidal or liquid crystal templates,<sup>[15,16]</sup> reduction of metal oxides,<sup>[17,18]</sup> etc. A related class of NPMs formed by selective dissolution that has found wide applicability for the catalysis of hydrogenation is the Raney<sup>®</sup> catalyst.<sup>a</sup> These materials are made by a selective dissolution of Al from Al (at.%)–rich Al/Ni or Al/Cu alloys in hot NaOH solution.<sup>[12]</sup> The morphology of Raney catalysts typically is nanoporous Ni or Cu with pore diameters  $< 5$  nm; however, the alloy usually falls apart during dissolution, with the ultimate result that the Raney catalysts are also typically nanoparticulate. We speculate that the reasons for this disintegration may be because of the complex phase diagram of Al/Ni and the presence of intermetallics with widely different lattice parameters, or, it may be because of a lack of mobility of the remaining Ni atoms under conditions of selective dissolution.

### Physical Characteristics of Alloys That May Be Dealloyed

A significant collection of evidence has led to the identification of a number of general physical characteristics required of the alloys that may lead to nanoporosity on dealloying. The four most important characteristics are:

- a. *The difference in dissolution potentials  $\Delta E$  of the alloy components or soluble complexes of*

*the alloy components must be sufficiently large.* If so, a potential can be applied across an electrochemical cell at a magnitude where the less noble alloy components dissolve into electrolytes, but the more noble components do not. A difference in the dissolution potentials of the alloy components of several hundred millivolts is usually adequate as a general benchmark.

- b. *The composition of the alloy must be neither too rich nor too poor in the more noble species.* As discussed below, if the alloy is too rich in the noble species, no dealloying will occur. Conversely, if there is too little noble species, porosity evolution cannot be maintained and one is usually left with a mass of distinct nanoparticles collected in the bottom of a beaker.
- c. *Surface diffusion of the more noble species must be sufficiently fast in electrolytes.* Given that the more noble element species must move from their original lattice sites and agglomerate into the backbone of the nanoporous sponge, at the very least, they must move fast enough. As discussed below, a benchmark of  $10^{-14} \text{ cm}^2 \text{ sec}^{-1}$  seems reasonable as a minimal diffusivity for which one may observe dealloying.
- d. *The alloy must be sufficiently homogenous and ideally stress-free.* Good uniform porosity is not observed even in such lattice-matched alloys as Ag/Au when residual stresses or inhomogeneities exist. Such factors manifest themselves in insidious ways: in vapor-deposited thin films, there are often residual stresses because of mechanical interactions between the film and the substrate, which can lead to cracking at grain boundaries during dealloying; in bulk materials, there can be segregation of one component to the grain boundary during annealing cycles, and this, too, can lead to cracking at grain boundaries.

### Physics of Nanoporosity Evolution during Dealloying: The Fundamental Problem

The central issue that any model for nanoporosity evolution during dealloying must address is the fact that the atoms of the more noble species in the alloy must physically move from the lattice sites they occupied in the unattacked alloy and reposition themselves in the backbone of a highly porous skeleton during selective dissolution. The fundamental problem associated with this movement is that the driving force for such rearrangement is counterintuitive. Usually,

<sup>a</sup>Raney<sup>®</sup> is a registered trademark of W. R. Grace and Co.

the driving force for atomic diffusion follows a concentration gradient, or follows a direction so as to lower overall surface area; but in nanoporosity evolution, this does not occur. Given the fact of movement of the noble alloy component, it might be thought that, optimally, the noble atoms might arrange themselves on the surface to form a dense monolayer, protecting the bulk of the alloy from further dissolution (a process called *passivation*). Because typical alloy compositions are a few tens of percent noble elements, passivation should occur only after a few tens of monolayers have been dissolved. For sufficiently low applied potential, this in fact does occur, but for applied potentials over a critical potential  $E_c$ , it does not. Despite some kind of atomic mobility, the noble atoms move in such a way as both to agglomerate (moving against a concentration gradient as they diffuse from the base of pits, where there exists a surface with locally bulk alloy composition to the noble element-rich walls of the porous skeleton) and also to increase dramatically the surface area of the material as it becomes nanoporous.

An early suggestion to account for the observed enrichment of noble atoms in the porous skeleton is based on the observation that as porosity evolves, the near-surface region becomes depleted of the less noble species. This will create a concentration gradient perpendicular to the average alloy/electrolyte interface position, driving bulk diffusion of the less noble species to the surface where they can be dissolved away.<sup>[19]</sup> However, early on, it was recognized that volume diffusion in the unattacked alloy is quite slow, with diffusion coefficients extrapolated to room temperature typically significantly less than  $10^{-30} \text{ cm}^2 \text{ sec}^{-1}$ .<sup>[20]</sup> A “back-of-the-envelope” calculation shows that this diffusion rate is too small, and yields an estimate of the required magnitude: Typical velocities of the interface between the porous region and the unattacked bulk alloy are on the order of one monolayer per sec (we have measured this rate for  $\text{Ag}_{65}\text{Au}_{35}$  alloys), with corresponding characteristic widths of 5–10 nm. If surface diffusion is operative, noble atoms on the surface must agglomerate by diffusing a distance on the order of 1 nm (less than half of a pore diameter) in about 1 sec, suggesting the required benchmark surface diffusion coefficient to be minimally on the order of  $10^{-14} \text{ cm}^2 \text{ sec}^{-1}$ .

Until recently, it also could have been argued that surface diffusion was also too slow. At the time the bulk diffusion mechanism was proposed, only a few measurements of the surface self-diffusion coefficient for many of the materials in porosity-evolving alloys had been measured, and only in vacuum. Even now, there are few such measurements, and such non-electrolyte measurements typically yield diffusion coefficients (extrapolated to room temperature) orders

of magnitude slower than the benchmark;<sup>b</sup> for this reason, a consideration of bulk diffusion necessarily required invoking the formation of faster-moving esoteric pointlike defects such as divacancies in order for mass transport to be consistent with the observed etch rates.<sup>[19]</sup>

Thus it is quite remarkable that the surface diffusivity of fcc metal adatoms was discovered to be, in fact, many orders of magnitude faster in electrolytes than in air or vacuum, typically greatly exceeding the proposed threshold value. The first indication of such behavior was seen during in situ electrochemical scanning tunneling microscopy (STM) of alloy dissolution in which islanding of the noble species was observed at room temperature.<sup>[22,23]</sup> A global measurement of surface diffusion on Au and Pt surfaces shows a strong dependence of diffusivity on applied potential, and both are much faster in electrolytes than in any other environment for which a measurement of surface diffusivity has been made (for details, see below). Bulk diffusion likely plays little, if any, role except perhaps in dealloying of very low melting temperature alloys such as In/Sn.<sup>[24]</sup>

### Model of Nanoporosity Evolution during Dealloying

Of course, just because noble species *can* move out of growing pits does not mean they will necessarily do so. The reason they do is schematically illustrated in Fig. 2, and has to do with the particular way in which pits penetrate into the bulk alloy, coupling the kinetics of etching with the thermodynamics of the alloy/electrolyte interface.<sup>[4]</sup> Consider one of the pits at the interface between nanoporous material and unattacked alloy; the sidewalls of the pit are connected to the already-formed porosity, so they have nominally pure noble species composition whereas the base of the pit is comprised of pure alloy. To propagate the pit further, a less noble atom is first pulled out of the base of the pit, leaving behind a vacancy coordinated primarily with less noble atoms (as required of percolation; see below). The etch front spreads laterally, then pulls out all less noble atoms in the base of the pit within the next monolayer of dissolution. The noble atoms that are left behind could stay in place as adatoms,

<sup>b</sup>Relevant extrapolation relies on large area mass transfer diffusion measurements, and not the diffusivities of particular species observed atomistically using scanning probe or field ion microscopy (for typical surface diffusion coefficients, see Ref.<sup>[21]</sup> and references therein). The surface mass transfer self-diffusion coefficients of Pt, Au, and Cu in vacuum, extrapolated to room temperature, are  $4.6 \times 10^{-22}$ ,  $2.7 \times 10^{-19}$ , and  $1.2 \times 10^{-14} \text{ cm}^2 \text{ sec}^{-1}$ , respectively.

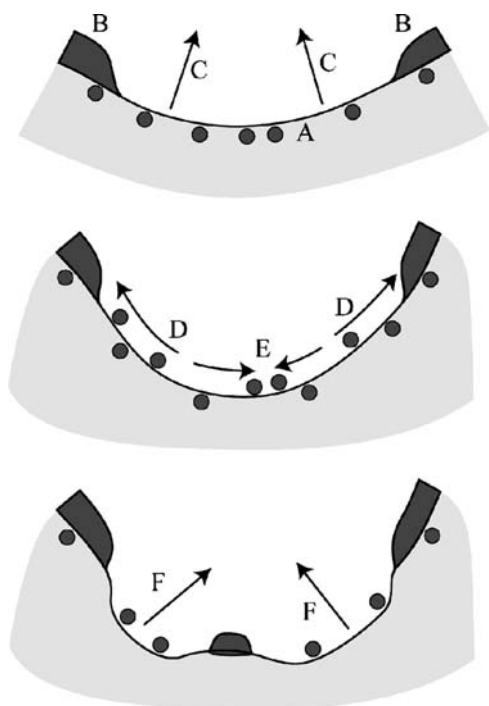


**Fig. 2** Schematic illustrating how porosity evolves during selective dissolution. 1) In the base of a pit, the alloy surface (A) is exposed between regions of accumulated noble component (B) at the base of any already-formed nanoporous skeleton. Atoms of the less noble alloy component in the exposed alloy surface are dissolved into the electrolyte (C). 2) As the interface dissolves, the surface area increases, and noble adatoms are released onto the surface. These adatoms condense onto already-agglomerated noble atom clusters (D), or nucleate new clusters (E) when noble atom ligaments (B) are too far away. 3) The less noble element in the exposed alloy surface dissolves into the electrolyte (F), and the cycle of increasing pore area and noble element agglomeration repeats.

populating the base of the pit and slowing down further dissolution, but the thermodynamics of the alloy/electrolyte interface (see below) predicts that such a condition would place the surface far out of equilibrium, thus the adatoms will tend to agglomerate and coarsen. The nearest places to agglomerate are the sidewalls of the pit, where the pit connects to the noble element-rich porous skeleton, so it is to there that they diffuse. This diffusion either occurs after the lateral etch front that penetrated a monolayer into the bulk has consumed all the less noble atoms in that monolayer (in which case the noble species really are left as adatoms), or the noble atoms are swept along with the lateral etch front as it etches out of the pit. Which particular mechanism is chosen likely depends on the applied potential (i.e., the etch rate), but in either case, the noble atoms have swept themselves out of the base

of the pit, which continues to penetrate further into the bulk of the alloy.

This scenario, our current “working model” of alloy dissolution, predicts that the length scale of porosity is set very early in the dissolution process, basically within the first monolayer of dissolution, for this is the only point in time at which the noble atoms agglomerate into two-dimensional islands without the presence of preexisting pore walls. The particular island spacing chosen  $\lambda$  will depend on the etch rate, the density of nucleated islands, and also on how long the islands have to coarsen before the next layer of alloy is attacked. Whatever spacing the system chooses,  $\lambda$  becomes characteristic of the dealloyed microstructure. If the diameter of a pit is equal to or less than  $\lambda$ , then noble atoms will always have time to get to the pore sidewalls. If the diameter of a pit is greater than  $\lambda$ , the noble atoms will nucleate a new passivating cluster and the pit will bifurcate.

It is important to realize that as a pit grows into the bulk, its time-averaged radius of curvature always increases. In a continuum picture, we may say that the local velocity of the pit is always normal to its surface. Atomistically, the pit radius increases because of the undercutting of its sidewalls. This is perhaps best seen by a consideration of the early stages of porosity evolution. Let a (111) facet of the bulk fcc alloy be exposed to electrolyte. Initially, the less noble component is etched out of the topmost monolayer, and the noble elements agglomerate into clusters with spacing  $\lambda$ , as discussed above. When the second monolayer gets attacked, the bases of the noble atom islands get fed with more noble atoms, forming noble element-rich mounds. As the alloy gets etched further, the bases of these mounds are fed by noble atoms released from the alloy in between them. But the circumferences of the mounds are growing at the same time that the area of fresh alloy surface is diminishing. This means that the bases of the mounds are becoming noble element-poor, thus susceptible to undercutting. These coupled processes lead to a model in which a pit radius of curvature effectively increases as it penetrates into the bulk. Eventually, these pore radii become greater than  $\lambda/2$ , a new cluster nucleates, the pit bifurcates, and the process continues ad infinitum.

The particular value of  $\lambda$  that a system will choose to take depends on a wide variety of parameters including: 1) etch rate (which depends on the choice of electrolytes, applied potentials, and the concentration of less noble constituents predissolved in the electrolyte); 2) surface diffusivity (which depends on the choice of materials, but also the variation in diffusivity with applied potential); and 3) the thermodynamics and composition of the alloy itself (what phases exist).

## CLASSICAL CHARACTERIZATION OF DEALLOYING

### The Parting Limit

Empirically, it is observed that if the noble alloy constituent is of sufficiently high concentration in the alloy, no selective dissolution can occur. This composition is referred to as the *parting limit*, a reference from the gold purification industry, which, for a long time, has used selective dissolution to “part” silver from gold. The parting limit varies widely for the alloys known to exhibit nanoporosity evolution, but typically sits between 20 and 60 at.%.<sup>[25]</sup>

The origin of the parting limit is likely because of a combination of geometrical percolation and surface diffusion, as suggested by Sieradzki, Corderman, and Shukla<sup>[26]</sup> and demonstrated through atomistic simulation. Geometrical percolation of the less noble component becomes the baseline criterion for dissolution. If the less noble atoms are not sufficiently percolating through the structure, there is no chance for dissolution to proceed past atoms near the surface. For example, in the fcc lattice, the geometrical site percolation threshold is 0.198.<sup>[27]</sup> Thus in principle, no dissolution should occur for compositions richer than approximately 80% in the noble component. This criterion does not work well for the silver/gold alloys. To account for the difference, copious surface diffusion of gold may be invoked; for sufficiently high gold fraction (over about 50 at.%), the silver atoms are connected by only single-digit wide chains, which are quickly plugged up by gold atoms diffusing into terrace defects left by silver atoms, blocking further dissolution and functionally suppressing the parting limit for the system compared with geometrical site percolation.

### The Critical Potential

When the potential applied to a dealloy system is sufficiently positive, copious dissolution of the less noble element occurs. In fact, dissolution rates can be quite high (hundreds of milliamperes per square centimeter), and it is in this regime that porosity evolution occurs. If the voltage is sufficiently small, a current decay is observed and the surface enriches in the more noble component, passivating it from further dissolution. By “sufficiently large” is meant a qualitative measure—a voltage higher than the dissolution overpotential for the pure less noble component, but still lower than the potential required for dissolution of the more noble component. Similarly, a “sufficiently small” voltage is still larger than the dissolution overpotential for the pure less noble component, but less than the sufficiently large voltage leading to porosity evolution.

The cutoff potential  $E_c$  between the potential regime leading to passivation and the regime leading to nanoporosity evolution is called the *critical potential*.<sup>[25]</sup> Although central to nanoporosity evolution, the critical potential is the least understood of the basic phenomena associated with dealloying. Usually, the critical potential is introduced in the context of a potential sweep, a measure of the anodic dissolution of current vs. applied potential as the potential is ramped more positively at a fixed rate. A generalized polarization curve obtained this way is illustrated in Fig. 3. At low potentials, the dissolution current is usually small but constant; on reaching the critical potential, the dissolution current rises exponentially. The critical potential depends quite sensitively on alloy composition. For the range of compositions for which Au/Ag alloys exhibit dealloying behavior (up to 50 at.% Au), the critical potential spans a 500-mV range.<sup>[28]</sup>

The critical potential is essentially empirical. An arbitrary current threshold is established (e.g., 1 mA/cm<sup>2</sup>), and the critical potential for a particular alloy composition is identified when, during a potential sweep, the dissolution current rises above this threshold.<sup>[28]</sup> Microscopically, it seems that the critical potential is the dividing potential between a potential regime in which surface diffusion driven by capillarity (surface energy reduction) wins over roughening and leads to passivation, and a potential regime in which capillarity is too slow to prevent porosity evolution.

Seen in the context of the working model (see above), the microscopical evolution of the surface during a potential sweep is as follows: The small current associated with passivation is associated with the removal of the less noble species from the first few monolayers of materials. The noble species remaining has plenty of time to agglomerate into islands, and even coarsen. Within this time, the surface remains

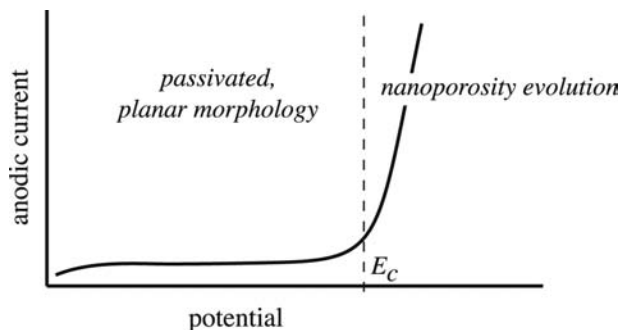


**Fig. 3** Typical shape of anodic polarization curves for systems exhibiting dealloying. At low potentials, the alloy remains flat and partially passivated with the noble alloy components. Above the critical potential, nanoporosity may evolve.

basically flat. Scanning tunneling microscopy observations of flat surfaces populated with islands have been seen in a number of systems, including Ag/Au and Cu/Au alloys.<sup>[22,29,30]</sup> By the time that the potential has risen to  $E_c$ , a significant fraction of the surface may be covered with the more noble species, and this will inhibit the onset of copious pitting. This suggests that the empirically measured critical potential as defined via a current threshold may be significantly higher than a “fundamental” critical potential truly separating passivation from porosity evolution. At the very least, the critical potential should be sweep rate-dependent, decreasing with increasing sweep rate, and, in fact, this observation has been recently made.<sup>[28]</sup>

## DETAILS OF MICROSCOPICAL PHYSICAL PROCESSES INVOLVED IN DEALLOYING

### Multiscale Description of Dealloying

Fig. 4 illustrates all of the various processes occurring simultaneously during the selective dissolution of an alloy and the formation of a nanoporous material. The range of scales associated with the various microscopical processes is large. An incomplete list includes: 1) solution-phase transport of cations through the nanochannels into the bulk of the electrolyte and the development of solution side concentration gradients (scale: microns); 2) the range of mechanical interaction between the nanoporous overlayer and the unattacked material (scale: millimeters); and 3) length scales associated with the agglomeration of the more noble element into clusters (scale: nanometers). In this section, we examine how various intrinsic aspects of dealloying may affect nanoporosity evolution.

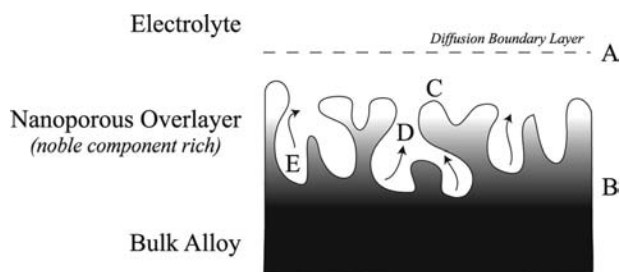


**Fig. 4** Typical physical processes occurring on different length scales during dealloying. (A) Transport and concentration gradients in electrolytes (micrometers to centimeters); (B) mechanical interaction between the unetched bulk alloy and the growing nanoporous overlayer (nanometers to millimeters); (C) surface diffusion at the alloy/electrolyte interface (nm); (D) transport of dissolved cations through nanochannels (nanometers laterally, millimeters in extent); and (E) chemical dissolution kinetics (nanometers).

### Solution-Phase Transport during Dealloying

It has long been recognized that the rate-limiting step during porosity evolution cannot be the solution side transport of the cations from alloys. A diffusion-limited condition in the electrolyte would result in a condition akin to that of electropolishing,<sup>[31]</sup> and the interface would only stabilize, regardless of any effect of selective dissolution. This can be seen through a perturbation analysis, the fundamental notion of which is that a protuberance on the alloy/electrolyte interface will etch faster than a pit because the tip of the protuberance is slightly closer to the edge of the diffusion barrier layer. Thus the only effect a diffusion-limited condition may have on porosity evolution is to slow etching from pits (at the bottom of which exists exposed alloy), and this will tend to stabilize the evolving structure.<sup>[32]</sup>

### Mechanical Properties of Nanoporous Overlayers

Although not central to the issue of what materials may be selectively etched to form nanoporosity, it is still quite important to keep in mind that as a porous region forms, there is a reasonably sharp boundary between the porous overlayer and the unattacked alloy. If the porous overlayer and the bulk alloy have different mechanical properties, or if a significant stress in the overlayer develops (as may be the case if the lattice parameter of the overlayer is different from the bulk alloy), then this gradient in stress and mechanical properties may lead to cracking and other undesirable materials failure. Such issues have been of central importance in the field of *stress corrosion cracking*.<sup>[1]</sup>

### Surface Diffusion

Measurement of the surface diffusion coefficient of the noble atom species at the alloy/electrolyte interface is central to a detailed understanding of how nanoporosity evolves during selective dissolution. This quantity is, in general, very difficult to measure, but enough data have been gathered to show conclusively a generally large enhancement of the surface diffusion rate for a few of the metals typically involved in dealloying (Au and Pt) over their diffusivities in air or vacuum (typically four to five orders of magnitude faster).

Good measurements of surface diffusivity can be made by observations of the morphological evolution of initially rough surfaces. The method is based on the classical theory of morphological relaxation developed by Mullins<sup>[33]</sup> and Herring,<sup>[34]</sup> the essence of which is that, in the absence of other factors, a non-flat surface will evolve toward planarity to reduce



its overall surface energy at a rate related to the diffusivity of the species involved in surface mass transport. Such measurements give an average measure of surface diffusion coefficients typically averaged over a range of orientations, and may be performed in a variety of environments, including air, vacuum, or electrolytes under potential control.

Therefore the measurement method uses an initially rough surface, and tracks its surface area with time. Surface area may be measured by a variety of methods including integrated charge passed when forming a monolayer of hydride or oxide,<sup>[16]</sup> or tracking of the time evolution of the charge of the double layer.<sup>[35]</sup> Measurements of surface diffusivity made using these methods have been made for Au and Pt: For Au, at potentials near critical potentials (approximately 400 mV vs. SCE for  $\text{Ag}_{80}\text{Au}_{20}$ ), surface diffusivity is on the order of  $10^{-14} \text{ cm}^2 \text{ sec}^{-1}$  in  $\text{H}_2\text{SO}_4$ , reaching the abovesuggested benchmark required for dealloying, and rises further with increasing potential.<sup>[36]</sup> In contrast, platinum does not have surface diffusivity more than the order of  $10^{-18} \text{ cm}^2 \text{ sec}^{-1}$  at moderate applied potentials in a variety of electrolytes.<sup>[37,38]</sup> Although significantly faster than its value in vacuum,<sup>[21]</sup> the surface self-diffusion rate of Pt seems to be too slow to allow porosity evolution to occur by the mechanism of the working model. In fact, this observation may explain why Pt alloys, although satisfying the homogeneity and nobility requirements for dealloyable materials, have, to date, not yielded an alloy that can be rendered nanoporous by selective dissolution.

### Postdealloying morphological evolution

The suggestion that surface diffusion is rapid for fcc metals in electrolytes is confirmed by postdealloying morphological evolution experiments in which a fully dealloyed material with a nanoporous microstructure remains immersed in electrolytes for extended periods. With copious surface diffusion, the surface area is expected to diminish with time because mass transport is driven by surface energy reduction. If the geometry of the material remains self-similar (i.e., stays porous but with larger and larger ligaments), then the characteristic length scale of the porosity  $l$  should grow as  $l \sim t^{1/4}$ .

Neutron scattering experiments have confirmed that this scaling behavior indeed is observed for NPG remaining immersed in nitric acid, and diffusion studies in other electrolytes suggest that a variety of electrolytes may be used.<sup>[14]</sup> Fig. 5 shows a plan view SEM of the real-space time evolution of a fully dealloyed and nanoporous thin film (originally 32 at.% Au) immersed in nitric acid at room temperature. The length scale of the porosity ranges from 10 nm at the smallest, as-formed end of the time scale, to nearly 50 nm after immersion in nitric acid for a day at room temperature. The time scale for coarsening is generally much greater than the time scale for porosity evolution in the first place (in Fig. 5, the film was fully porous after 12 min). This suggests an advantageous feature for nanomanufacturing—it should be possible to make whatever size porosity is desired, quench the

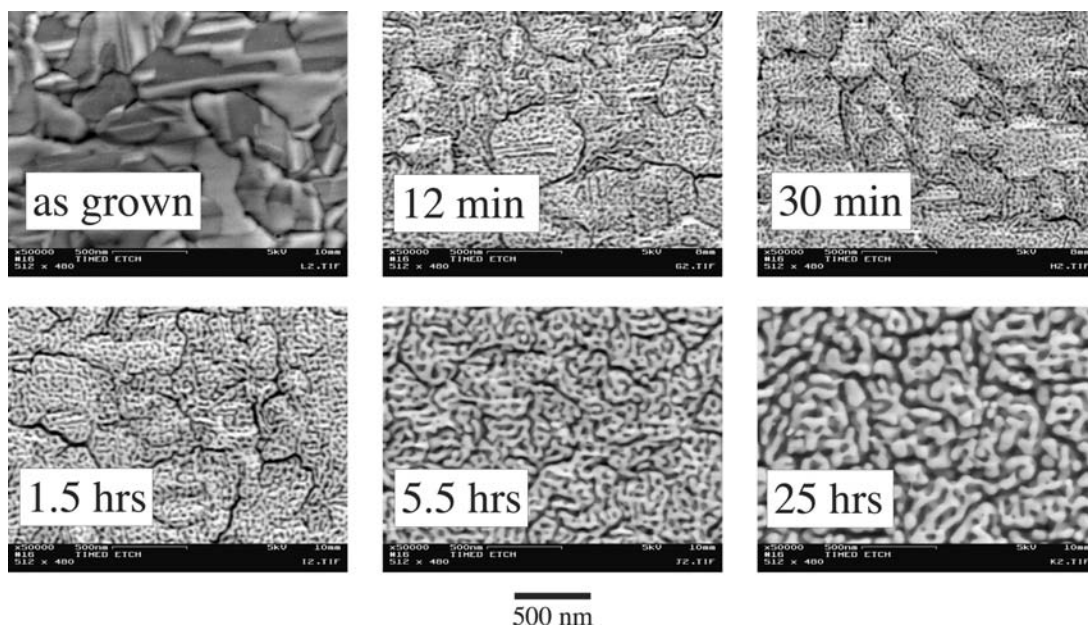


**Fig. 5** Coarsening of dealloyed structures by continued immersion in electrolytes at room temperature. Illustrated are plan view SEM micrographs of a film of  $\text{Ag}_{65}\text{Au}_{35}$  (at.%) immersed in nitric acid for various intervals. The film is completely dealloyed of silver by 12 min, and continues to coarsen at room temperature because of enhanced gold surface self-diffusion in the electrolyte.

system in air or water (quench in the sense of putting into an environment where the kinetics of surface diffusion turns off), and then coarsen the material to the desired porous length scale simply by a timed immersion in the proper electrolyte. A similar coarsening behavior is also observed for thermal cycling, but here it is generally required to anneal at elevated temperatures.<sup>[9]</sup>

### Thermodynamics and Adatom Kinetics of the Alloy/Electrolyte Interface

To get a sense of the equilibrium concentration of noble component adatoms on the surface of the alloy, a regular solution model may be used for the alloy/electrolyte interface.<sup>[4]</sup> The components of the solution are not the constituents of the alloy; rather, the components of the solution are adatoms (and really only adatoms of the noble alloy constituent), and “nothing” (more realistically, lattice positions occupied by adsorbed anions). Such a model gives the interface free energy  $f$  as a function of adatom surface fraction  $c$ , depending on an ideal entropy of mixing, and an enthalpy of mixing, depending only on bond energies and the average coordination of each species. For reasonable values of the bond energies, the model yields a minimum in  $f$  vs.  $c$  at approximately  $c_{\text{eq}} \sim 10^{-8}$  per site. This number represents the fraction of adatoms of the noble element one might find at the alloy/electrolyte interface where the alloy is not dissolved away and is extremely low. Therefore, when the acid attacks the alloy and quickly removes the less noble atoms from the base of the pit, the noble adatoms left behind are in a highly non-equilibrium state. This provides the driving force for transport out of the pits.

The kinetics of the surface diffusion of noble adatoms cannot be adequately described by simple Fickian diffusion because the concentration gradient of noble atoms rises, moving out of the pit; this is to be expected because of the highly non-equilibrium state of the adatoms on the surface. A model that adequately describes noble atom diffusion must incorporate at least two phenomena: 1) if the noble atom concentration is supersaturated, noble atoms should tend to agglomerate, diffusing against a concentration gradient as they form clusters; and 2) if the local noble concentration is nearly dense, no diffusion should occur. It has been shown that the Cahn–Hilliard diffusion equation incorporating concentration-dependent mobility demonstrates these characteristics, and a continuum model for the evolution of the alloy/electrolyte interface based on this model reproduces many of the characteristics of nanoporosity evolution.<sup>[4]</sup>

### CONCLUSION

Nanoporosity formed from the selective dissolution of alloys containing functionally more and less noble elements is a general method to form high surface area materials out of monolithic dense starting structures. For this reason, this class of materials holds particular promise for development into technologically important nanostructured materials. Thin films of starting alloy materials may be deposited and subsequently dealloyed. Thus nanoporous materials should be easily integrated into conventional microelectronics or microfluidics. Their high surface area may be functionalized with different chemisorbed or electrodeposited materials, making them useful in sensor applications or other applications where high conductivity nanoporous materials are desired. Furthermore, the characteristics of nanoporous materials may be straightforwardly tuned using a minimal set of parameters—in particular, length scales of porosity are smaller when dealloyed at higher applied potential, and larger length scale porosity may be made simply by postdealloying heat treatment or immersion into the proper electrolyte.

Within a greater nanotechnological context, the utility of very high room temperature surface diffusivities in electrochemical environments has yet to be fully exploited. Nanostructures placed in particular electrochemical environments may be susceptible to morphological decay over very short time periods, which may be advantageous to smoothen out undesirable roughness. In addition, the electrochemical environment may be simply adjusted in a variety of different ways, from the applied potential to the dissolution/deposition rate. The competition between roughening effects because of selective dissolution, noble atom agglomeration, and the smoothening effects of capillarity will certainly yield many kinds of interesting non-equilibrium pattern formation phenomena of which nanoporosity evolution is just one example.

### ACKNOWLEDGMENTS

The author expresses gratitude to the National Science Foundation for the continuing support of research into nanoporosity evolution during dealloying.

### REFERENCES

1. Sieradzki, K.; Kim, J.S.; Cole, A.T.; Newman, R.C. The relationship between dealloying and transgranular stress-corrosion cracking of Cu–Zn and Cu–Al alloys. *J. Electrochem. Soc.* **1987**, *143*, 1635–1639.

2. Vukmirovic, M.B.; Dimitrov, N.; Sieradzki, K. Dealloying and corrosion of Al alloy 2024-T3. *J. Electrochem. Soc.* **2002**, *149*, B428–B439.
3. Williams, D.E.; Newman, R.C.; Song, Q.; Kelly, R.G. Passivity breakdown and pitting corrosion of binary alloys. *Nature* **1991**, *350*, 216–219.
4. Erlebacher, J.; Aziz, M.J.; Karma, A.; Dimitrov, N.; Sieradzki, K. Evolution of nanoporosity in dealloying. *Nature* **2001**, *410*, 450–453.
5. Forty, A.J. Corrosion micromorphology of noble metal alloys and depletion gilding. *Nature* **1979**, *282*, 597–598.
6. Forty, A.J. Selective Dissolution and De-alloying of Silver–Gold and Similar Alloys. In *Sir Charles Frank: An 80th Birthday Tribute*; Chamber, R.B., Ed.; Adam Hilger: Bristol, 1991; 164–187.
7. Fritz, J.D.; Pickering, H.W. Selective anodic dissolution of Cu–Au alloys: TEM and current transient study. *J. Electrochem. Soc.* **1991**, *138*, 3209–3218.
8. Ji, C.; Searson, P.C. Fabrication of nanoporous gold nanowires. *Appl. Phys. Lett.* **2002**, *81*, 4437–4439.
9. Li, R.; Sieradzki, K. Ductile–brittle transition in random porous Au. *Phys. Rev. Lett.* **1992**, *68*, 1168–1171.
10. Rambert, S.; Landolt, D. Anodic dissolution of binary single phase alloys: I. Surface composition changes on AgPd studied by Auger electron spectroscopy. *Electrochim. Acta* **1986**, *31*, 1421–1431.
11. Rambert, S.; Landolt, D. Anodic dissolution of binary single phase alloys: II. Behavior of CuPd, NiPd and AgAu in LiCl. *Electrochim. Acta* **1986**, *31*, 1433–1441.
12. Smith, A.J.; Tran, T.; Wainwright, M.S. Kinetics and mechanism of the preparation of Raney<sup>®</sup> copper. *J. Appl. Electrochem.* **1999**, *29*, 1085–1094.
13. Min, U.-S.; Li, J.C.M. The microstructure and dealloying kinetics of a Cu–Mn alloy. *J. Mater. Res.* **1994**, *9*, 2878–2883.
14. Aziz, M.J.; Corcoran, S.G.; Erlebacher, J.; Newman, R.C.; Sieradzki, K. Alloy corrosion. *MRS Bull.* **1999**, *24*, 24–28.
15. Jiang, P.; Cizeron, J.; Bertone, J.F.; Colvin, V.L. Preparation of macroporous metal films from colloidal crystals. *J. Am. Chem. Soc.* **1999**, *121*, 7957–7958.
16. Attard, G.S.; Bartlett, P.N.; Coleman, N.R.B.; Elliott, J.M.; Owen, J.R.; Wang, J.H. Mesoporous platinum films from lyotropic liquid crystalline phases. *Science* **1997**, *278*, 838–840.
17. Chen, G.Z.; Fray, D.J.; Farthing, T.W. Direct electrochemical reduction of titanium dioxide to titanium in molten calcium chloride. *Nature* **2000**, *407*, 361–364.
18. Maya, L.; Brown, G.M.; Thundat, T. Porous platinum electrodes derived from the reduction of sputtered platinum dioxide films. *J. Appl. Electrochem.* **1999**, *29*, 883–888.
19. Pickering, H.W.; Wagner, C. Electrolytic dissolution of binary alloys containing a noble metal. *J. Electrochem. Soc.* **1967**, *114*, 698–706.
20. Haasen, P. *Physical Metallurgy*; Cambridge University Press, 1992.
21. Seebauer, E.G.; Allen, C.E. Estimating surface diffusion coefficients. *Prof. Surf. Sci.* **1995**, *49*, 265–330.
22. Oppenheim, I.C.; Trevor, D.J.; Chidsey, C.E.D.; Trevor, P.L.; Sieradzki, K. In situ scanning tunneling microscopy of corrosion of silver–gold alloys. *Science* **1991**, *254*, 687–689.
23. Moffat, T.P.; Fan, F.F.; Bard, A.J. Electrochemical and scanning tunneling microscopic study of dealloying of Cu<sub>3</sub>Au. *J. Electrochem. Soc.* **1991**, *138*, 3224–3235.
24. Kaiser, H. Selective dissolution of high and low diffusivity alloys—A comparison of kinetical and micromorphological aspects. *Corros. Sci.* **1993**, *34*, 683–699.
25. Pickering, H.W. Characteristic features of alloy polarization curves. *Corros. Sci.* **1983**, *23*, 1107–1120.
26. Sieradzki, K.; Corderman, R.R.; Shukla, K. Computer simulations of corrosion: Selective dissolution of binary alloys. *Philos. Mag., A* **1989**, *59*, 713–746.
27. Stauffer, D. *Introduction to Percolation Theory*; Taylor and Francis: London, 1985.
28. Sieradzki, K.; Dimitrov, N.; Movrin, D.; McCall, C.; Vasiljevic, N.; Erlebacher, J. The dealloying critical potential. *J. Electrochem. Soc.* **2002**, *149*, B370–B377.
29. Wagner, K.; Brankovic, S.R.; Dimitrov, N.; Sieradzki, K. Dealloying below the critical potential. *J. Electrochem. Soc.* **1997**, *144*, 3545–3555.
30. Ateya, B.G.; Pickering, H.W. The effects of potential and kinetic parameters on the formation of passivating noble metal rich surface layers during the selective dissolution of binary alloys. *Corros. Sci.* **1996**, *38*, 1245–1267.
31. Wagner, C. Contribution to the theory of electropolishing. *J. Electrochem. Soc.* **1954**, *101*, 225–228.
32. Sieradzki, K. Curvature effects in alloy dissolution. *J. Electrochem. Soc.* **1993**, *140*, 2868–2872. A sign error in this reference leads to the referred-to conclusion, as discussed in Ref. [28].
33. Mullins, R.R. Flattening of a nearly plane solid surface due to capillarity. *J. Appl. Phys.* **1959**, *30*, 77–83.
34. Herring, C. Surface Tension as a Motivation for Sintering. In *Structure and Properties of Solid Surfaces*; Gomer, R., Smith, C.S., Eds.; University of Chicago Press, 1953.
35. Gonzalez Velasco, J. Residual currents associated with surface reorganization processes for solid metal electrodes in contact with electrolytes. *J. Electrochem. Soc.* **1997**, *144*, 4142–4145.
36. Dona, J.M.; Gonzalez Velasco, J. Mechanism of surface diffusion of gold adatoms in contact with an electrolytic solution. *J. Phys. Chem.* **1993**, *97*, 4714–4719.
37. Martinez Jubrias, J.J.; Hidalgo, M.; Marcos, M.L.; Gonzalez Velasco, J. On the surface diffusion of Pt adatoms in acidic solutions. *Surf. Sci.* **1996**, *266*, 239–250.
38. Hidalgo, M.; Marcos, M.L.; Gonzalez Velasco, J. Electrochemically induced changes in the surface diffusion in polycrystalline platinum electrodes. *Appl. Phys. Lett.* **1995**, *67*, 1486–1488.

# Nanoporous Anodic Alumina: Structural and Optical Anisotropy

**E. Stefan Kooij**

*Faculty of Science and Technology, Department of Solid State Physics,  
University of Twente, Enschede, The Netherlands*

**Aurelian C. Gâlcă**

*University of Twente, Enschede, The Netherlands*

**Herbert Wormeester**

*Faculty of Science and Technology, University of Twente, Enschede, The Netherlands*

**Bene Poelsema**

*Faculty of Applied Physics, University of Twente, Enschede, The Netherlands*

## INTRODUCTION

Porous aluminum oxide has stimulated considerable interest as a nanostructural template, primarily because of the self-organized formation of extremely well-aligned cylindrical pores.<sup>[1–13]</sup> One of the fascinating aspects is the tunability of the interpore distance and pore diameter by simple variation of the anodization parameters<sup>[1,2,4,6,9,11,13]</sup> such as voltage and electrolyte solution composition. Apart from the application of aluminum oxide films as filtration membranes,<sup>[14]</sup> they are frequently used to fabricate nanowires with large aspect ratios.<sup>[13,15–20]</sup> Many different materials, such as metals, both magnetic<sup>[21–29]</sup> and nonmagnetic,<sup>[30–36]</sup> semiconductors,<sup>[37–44]</sup> nanotubes,<sup>[45–48]</sup> and even heterostructures,<sup>[49]</sup> have been grown in the porous membranes using primarily electrodeposition. Furthermore, porous aluminum oxide membranes have also been used as humidity sensors,<sup>[50,51]</sup> or as cathodes for organic light-emitting diodes.<sup>[52]</sup>

To control and optimize the formation of the aluminum oxide structure as well as the deposition of material within this porous matrix, in situ characterization techniques will certainly be required. Optical reflection techniques provide a nondestructive method to in situ monitor processes such as the anodization and the growth of nanowires. A major advantage of these techniques is their full compatibility with electrochemical or vacuum environments. Several spectroscopic ellipsometry studies of porous aluminum oxide structures, obtained under different anodization conditions, have been published.<sup>[53–56]</sup> These investigations were performed on aluminum oxide films, formed by anodizing bulk aluminum samples. Different optical models have been proposed, which take into account

the porosity of the film itself, but also include the barrier layer structure between the oxide matrix and the bulk substrate. In these models, the number of parameters is often large due to a proper description of the barrier layer. Determination of the properties of the anodized film in terms of actual physical quantities is not straight forward.

To avoid the aforementioned problems related to the barrier layer, and also to enable an accurate determination of the film thickness, a thin-film sample geometry is employed. The aluminum layer has a well-defined thickness, which can be determined by ex situ techniques, such as electron microscopy. Moreover, full anodization of the aluminum layer allows a smaller number of model parameters, as no bulk aluminum remains and the aforementioned barrier layer is practically absent. In this work, we show that scanning electron microscopy (SEM) enables accurate ex situ characterization of the film thickness and the pore structure after anodization. Ellipsometry spectra are analyzed using an optical model, which takes into account the anisotropy of the porous structure arising from the randomly distributed, aligned pores within the oxide. Based on the original work by Bruggeman<sup>[57]</sup> and Wien,<sup>[58]</sup> expressions are given for the parallel and perpendicular components of the dielectric functions, in terms of the cylinder fraction and a nanoporosity of the aluminum oxide matrix. The resulting fit parameters are quantitatively compared with the sample structure determined from electron microscopy images. Furthermore, chemical etching in phosphoric acid solutions enables controlled widening of the pores, and therewith provides a means to test the accuracy of our model. Moreover, we show that ellipsometric experiments on samples etched under different

conditions allow identification of the etch process in terms of the order of the etch reaction and the corresponding rate constant.

## ANODIZATION OF ALUMINUM THIN-FILM SAMPLES

Thin-film aluminum samples are grown by conventional sputtering on a silicon wafer (Philips Research Laboratories, Eindhoven). Prior to aluminum sputtering, a 75-nm platinum layer is deposited on a 10-nm titanium adhesion layer. The aluminum layer grown on top of this structure is approximately 1- $\mu\text{m}$  thick. Scanning electron microscopy (SEM) indicates that the actual thickness amounts to  $920 \pm 5$  nm, while the titanium and platinum layers have a combined thickness of  $85 \pm 5$  nm. Wafers are cut into  $14 \times 14$  mm samples to enable mounting in the anodization cell, which is schematically illustrated in Fig. 1. After mounting of the sample using an O-ring, a circular area with a diameter of 7.5 mm is exposed to the electrolyte.

Porous aluminum oxide is obtained by anodization of the aluminum film in a two-electrode configuration at a constant voltage of 15 V in 15 vol.%  $\text{H}_2\text{SO}_4$  at room temperature with continuous stirring. The

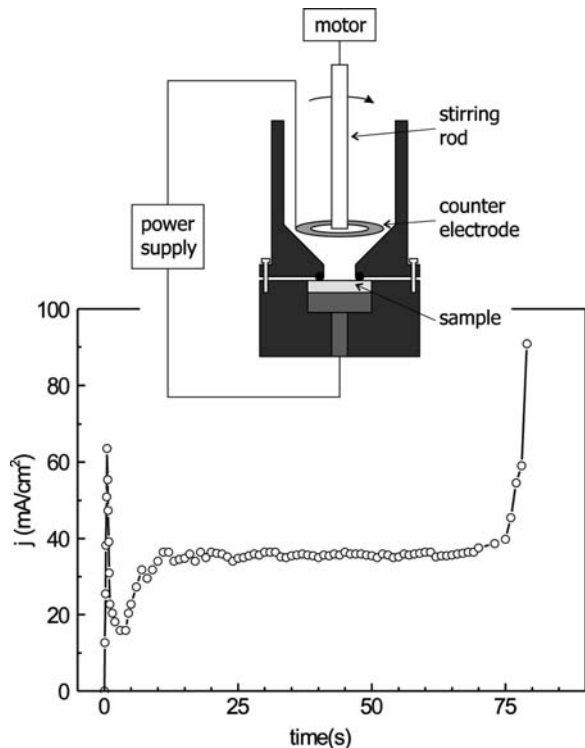


**Fig. 1** Schematic representation of the anodization cell used in the experiments. Also shown is the time evolution of the anodization current during the anodic oxidation at 15 V in 15 vol.%  $\text{H}_2\text{SO}_4$  aqueous solution.

procedure is identical to that described by Van der Zande et al.<sup>[31]</sup> A typical anodization transient is shown in Fig. 1. An initial current peak is observed as a result of double-layer charging, followed by a current plateau corresponding to a constant anodization of the aluminum. After approximately 70 sec, the current rapidly increases, indicating that the pore fronts have reached the platinum substrate. For longer times, oxidation of water gives rise to oxygen gas evolution, which leads to bubble formation.

## STRUCTURAL CHARACTERIZATION OF THE NANOPOROUS STRUCTURE

To enable accurate quantitative modeling of our optical results, the structural properties of the aluminum films before and after anodization have been characterized. Scanning electron microscopy provides information on the film thickness, pore distribution, and the pore diameter, while X-ray diffraction is used to characterize the crystallographic structure of the films in the pristine and as-anodized state.

### Scanning Electron Microscopy

Scanning electron microscope measurements are performed with a LEO Gemini 1550 FEG-SEM, equipped with a field emission gun plus Thermo Noran Vantage EDX system and Thermo Noran MAXray parallel beam spectrometer. The electron acceleration voltage can be set between 200 V and 30 kV; owing to this low voltage, deposition of a thin metal (gold) film is not required. This lateral resolution is approximately 2 nm.

A typical top-view SEM image of the as-anodized samples is shown in Fig. 2A. An approximately random distribution of pores in the aluminum oxide film is observed after anodic oxidation. Despite the apparent absence of azimuthal order, there is a preferred lateral distance separating adjacent pores. To quantify this, we used Scion Image software (Beta 4.0.2, Scion Corporation) to calculate the radial distribution function by radial integration of the autocorrelation image such as that shown in Fig. 2B; the result is shown in Fig. 2C. A single peak is observed at a distance of 33.5 nm, corresponding to the average interpore distance. The absence of peaks at larger distances indicates that there is no long-range organization of the pores in the film. Close examination of the autocorrelation image in Fig. 2B indicates that there is some azimuthal order in a sixfold symmetry. The pore density, as determined from the top-view images, amounts to  $950 \mu\text{m}^{-2}$ . With the interpore distance as determined above from the radial distribution function, we calculate that the pore density for a perfect hexagonal

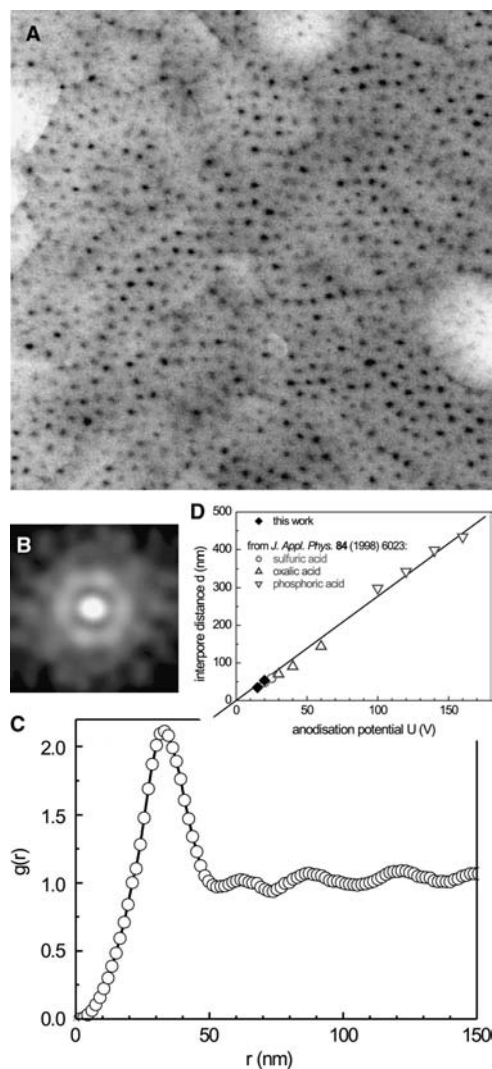


**Fig. 2** (A) Top-view SEM image of as-anodized porous aluminum oxide. The image size is  $1\ \mu\text{m} \times 1\ \mu\text{m}$ . (B) The autocorrelation image calculated from the SEM image, from which the radial distribution function in (C) is obtained by radial integration. In (D), the average inter-pore distances obtained from the radial distribution functions for our samples are compared to literature values.

arrangement amounts to  $1029\ \mu\text{m}^{-2}$ . Because of a certain degree of azimuthal disorder exhibited by the ring structure in the insert in Fig. 2B, the actual density obtained by counting the pores is slightly lower. In Fig. 2D, the average inter-pore distances, determined for our samples anodized at 15 and 20 V, are compared to results in literature,<sup>[6]</sup> spanning a much larger range of anodization potentials. Clearly visible is the linear relation between the inter-pore distance and the applied voltage.

Cross-section SEM images are identical to what has been described in the literature, and clearly show the parallel alignment of the pores, with the same average inter-pore distance as determined from the top-view

images. The pores initiate at the surface and extend all the way down to the platinum layer. For the as-anodized aluminum oxide, the average pore diameter of 11.5 nm is the same throughout the film thickness. The thickness of the aluminum film prior to anodization, as determined from SEM images, amounts to approximately 920 nm. Upon anodization, the film considerably expands to approximately 1400 nm. The expansion by 50% is anomalously large. When we neglect the porosity and only consider the film thickness and the densities of aluminum and aluminum oxide, a maximum thickness increase of 30% is to be expected. The aforementioned 50% expansion can only be explained by taking into account the 10% mesoporosity due to the cylindrical pores [as determined from images such as those in Fig. 2A] and an additional 33% nanoporosity of the aluminum oxide matrix, which will be discussed later. The latter porosity arises from defects and nanosized voids resulting from the considerable deformation upon anodization and the corresponding material transport away from the substrate. More quantitatively, the charge involved in the anodization procedure (obtained by integration of the curve in Fig. 1) can be related to the aluminum density. From this, we conclude that practically all aluminum atoms are oxidized to trivalent  $\text{Al}^{3+}$ .

## X-Ray Diffraction

High-angle X-ray scattering measurements are performed using a single-crystal diffractometer (CAD4, Enraf Nonius) employing a rotating anode Cu-K $\alpha$  source ( $\lambda_{\text{CuK}\alpha} = 1.542\ \text{\AA}$ ). The instrumental broadening for this system is estimated to be  $0.2^\circ$ . Scans are performed in the  $\theta$ - $2\theta$  configuration.

The X-ray diffraction experiments show that the platinum and aluminum layers before anodization are polycrystalline. A part of the X-ray spectra for samples before and after anodization are shown in Fig. 3. The high-intensity Si 004 peak corresponding to the substrate is observed at  $69.2^\circ$ . We designate the first peak at  $2\theta = 33.3^\circ$  as the interface Si 002 peak as the corresponding volume peak is “forbidden”; the intensity ratio of the Si 004 and Si 002 peaks is indeed more than  $10^4$ . The two peaks for the sample prior to anodization in Fig. 3 at  $2\theta = 38.6^\circ$  and  $2\theta = 40.0^\circ$  correspond to Al 111 and Pt 111, respectively. Very small, but still discernable, are the Al 002 and Pt 002 contributions. The diffraction peak positions are in perfect agreement with the lattice constants  $a = 4.05\ \text{\AA}$  and  $a = 3.92\ \text{\AA}$  for fcc aluminum and platinum, respectively.

After anodization, the Pt 111 peak is still present, but the Al 111 peak is no longer observed. From the height of the Al 111 peak prior to anodization and



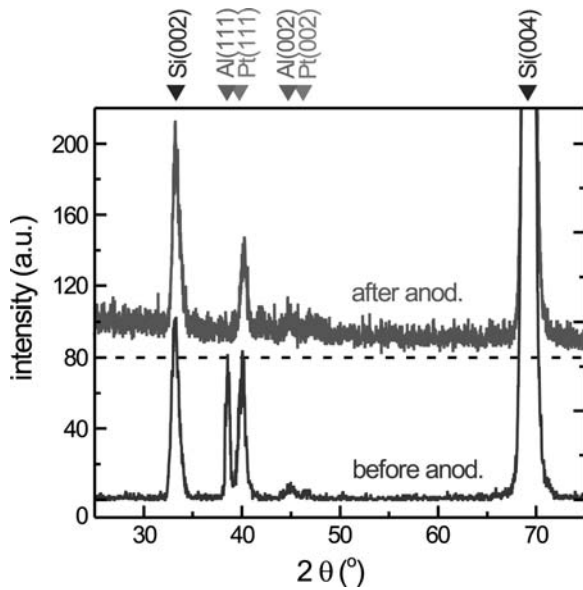


**Fig. 3** X-ray diffraction spectrum before and after anodization of the aluminum film. The diffraction peak positions for silicon, aluminum, and platinum are indicated.

the noise level in spectrum, we estimate that more than 95% of the aluminum has been transformed into aluminum oxide. This is in good agreement with the conclusion in the previous section based on the quantitative analysis of the anodization experiment. Also, in contrast to the original sample, the X-ray spectrum of the anodized sample in Fig. 3 exhibits broad background intensity. We attribute this background signal to the amorphous aluminum oxide formed upon anodization. The amorphous nature of the aluminum oxide is also supported by the absence of any peaks related to crystalline alumina.

### OPTICAL CHARACTERIZATION BY SPECTROSCOPIC ELLIPSOMETRY

The optical properties of our samples prior to anodization and after formation of porous aluminum oxide are characterized using spectroscopic ellipsometry. Also, the effect of pore widening by chemical etching is investigated. In ellipsometry, the change of the polarization state of linearly polarized light is measured upon reflection at the surface. The complex reflection coefficient  $\rho$  is defined as

$$\rho = \frac{r^p}{r^s} = \tan(\Psi)e^{i\Delta} \quad (1)$$

where  $r^p$  and  $r^s$  are the reflection coefficients for the parallel and perpendicular polarizations, respectively. For a single interface,  $r^p$  and  $r^s$  represent the Fresnel

reflection coefficients. Historically, the quantity  $\rho$  is expressed in the two angles,  $\Psi$  and  $\Delta$ . Although the actual ellipsometry measurement is relatively simple, the analysis of the results is often complicated. An accurate model is required for the system under consideration, which enables simulation or fitting of the results.

The optical response of a multilayered structure with known dielectric functions can be calculated using the Abeles matrix algorithm. Details of the original method are described by Azzam and Bashara.<sup>[59]</sup> Two types of matrices are used. One describes the transition from medium  $m$  to medium  $m + 1$

$$\mathbf{I}_{m,m+1} = \frac{1}{t_{m,m+1}} \begin{pmatrix} 1 & r_{m,m+1} \\ r_{m,m+1} & 1 \end{pmatrix} \quad (2)$$

where  $r_{m,m+1}$  and  $t_{m,m+1}$  are the Fresnel reflection and transmission coefficients, respectively. Another matrix describes the light passage through the medium and involves the phase factors

$$\mathbf{L}_{m,m+1} = \begin{pmatrix} e^{-i\Delta_m} & 1 \\ 1 & e^{i\Delta_m} \end{pmatrix} \quad (3)$$

where  $\Delta_m = (2\pi/\lambda) d_m n_m \cos(\theta_m)$  with  $\lambda$  being the wavelength of the light in vacuum (in nm),  $d_m$  the thickness of layer  $m$  (in nm),  $\theta_m$  the angle of the light, and  $n_m$  the refractive index of medium  $m$ . The angles in the various media are related through Snell's law:

$$n_m \sin(\theta_m) = n_{m+1} \sin(\theta_{m+1}) \quad (4)$$

For our system consisting of an anodic aluminum oxide layer ( $m = 2$ ), a platinum layer ( $m = 3$ ), and a titanium layer ( $m = 4$ ) on a silicon substrate ( $m = 5$ ), in contact with the ambient (air;  $m = 1$ ), a matrix product is defined

$$\mathbf{A} = \mathbf{I}_{1,2} \mathbf{L}_{2,3} \mathbf{I}_{3,4} \mathbf{L}_{4,5} \quad (5)$$

and the overall reflection coefficient is calculated from  $r = \mathbf{A}_{21}/\mathbf{A}_{11}$ . For both the parallel and perpendicular polarizations, the reflection coefficients  $r^p$  and  $r^s$  can be obtained by inserting the appropriate Fresnel coefficients in Eq. (2) and the ellipsometric quantity in Eq. (1) can be calculated.

In the case of a film with uniaxial anisotropy, i.e., with an out-of-plane dielectric function  $\epsilon_{ex}$  (the extraordinary direction) different from the dielectric function  $\epsilon_{or}$  parallel to the substrate surface (the ordinary direction), the same matrix formalism can be used.<sup>[59]</sup> For our films, in which the cylindrical pores give rise to such uniaxial anisotropy, this is schematically represented in Fig. 4. Obviously, the optical response for the  $s$ -polarization remains unchanged and is completely

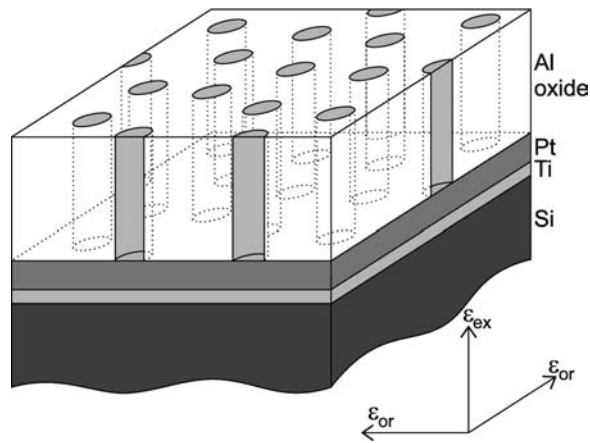


**Fig. 4** Schematic representation of the geometry and structural anisotropy of an anodized thin-film aluminum sample, indicating the ordinary and extraordinary directions referred to in the text.

described by the ordinary dielectric function  $\epsilon_{or}$ . For the  $p$ -polarization, a modified propagation angle is calculated by inserting the extraordinary refractive index  $n_{ex} = (\epsilon_{ex})^{1/2}$  into Eq. (4). For the rest of the calculation, only the ordinary dielectric function  $\epsilon_{or}$  of the anisotropic medium has to be taken into account.

### Anisotropic Model for Porous Anodic Aluminum Oxide

As is evident from the previous section, the samples have a clear structural anisotropy. However, several studies on the optical characterization of anodic aluminum oxide templates on bulk aluminum substrates did not take this into consideration.<sup>[53–55]</sup> Results obtained on films, formed on bulk aluminum by anodization in sulfuric acid, indicated that there was no apparent optical anisotropy. Because of the small dimension of the pores, conventional effective medium approximations yielded adequate results. Ellipsometry measurements on our samples, which consist of a fully oxidized aluminum thin film with a well-determined thickness, indicate that optical anisotropy needs to be taken into account. Especially upon widening of the pores by chemical etching, the anisotropy becomes more pronounced as the pore sizes substantially increase. To obtain adequate, unambiguous fit results, we incorporated the optical anisotropy in a model that contains a minimum number of three parameters: 1) a film thickness; 2) a mesoporosity, related to the cylindrical void fraction; and 3) a nanoporosity of the aluminum oxide matrix.

As described in a previous section in relation to the thickness increase of the film during anodization, the aluminum oxide matrix is highly amorphous and presumably consists of a highly porous, noncrystalline

structure containing voids with sizes in the low-nanometer range. In the work by Palibroda, Farcas, and Lupsan<sup>[60]</sup> the structure of the oxide was reported to be gel-like, containing a large number of “bubbles,” formed during the anodization procedure. The effective dielectric function of the nanoporous aluminum oxide, with porosity  $f_p$ , is modeled using the conventional effective medium approximation established by Bruggeman<sup>[57]</sup>

$$0 = (1 - f_p) \frac{\epsilon_{Al_2O_3} - \epsilon_p}{\epsilon_{Al_2O_3} + 2\epsilon_p} + f_p \frac{\epsilon_a - \epsilon_p}{\epsilon_a + 2\epsilon_p} \quad (6)$$

where  $\epsilon_a$  and  $\epsilon_{Al_2O_3}$  represent the dielectric functions of the ambient (air in all cases presented here;  $\epsilon_a = 1$ ) and that of the aluminum oxide structure (we use the value of crystalline  $Al_2O_3$ ), respectively.

The system with uniaxial anisotropy, formed by the almost perfectly aligned cylindrical pores in the oxide matrix, is described by two different dielectric functions  $\epsilon_{ex}$  and  $\epsilon_{or}$  (Fig. 4). The extraordinary component describes the optical response of the film for electric field vectors parallel to the long axis of the cylindrical pores. Owing to the relatively small difference in dielectric constants of the oxide and the ambient, screening effects can be neglected. Therefore we can interpret the system of parallel pores as a set of parallel plates, and use the corresponding Wiener bound<sup>[58]</sup> to describe the dielectric function  $\epsilon_{ex}$

$$\epsilon_{ex} = (1 - f_{cyl})\epsilon_p + f_{cyl}\epsilon_a \quad (7)$$

where  $f_{cyl}$  represents the overall pore volume fraction.

For the ordinary component, we consider a cross section through the film parallel to the interface. The effective dielectric function  $\epsilon_{or}$  of this two-dimensional system of randomly distributed circles (with  $\epsilon_a$ ) in the oxide matrix (with  $\epsilon_p$ ) is modeled using an adaptation from the original work of Bruggeman,<sup>[57]</sup> which will be briefly outlined. Bruggeman provides expressions for the dielectric function  $\epsilon'$  of small spherical inclusions of fraction  $\delta'$ , with dielectric function  $\epsilon_i$ , in a host matrix with  $\epsilon_h$ , for both the two- and three-dimensional cases. These equations, referred to as the Rayleigh formulas, can be summarized in a generalized expression

$$\frac{\epsilon' - \epsilon_h}{\epsilon' + (n-1)\epsilon_h} = \delta' \frac{\epsilon_i - \epsilon_h}{\epsilon_i + (n-1)\epsilon_h} \quad (8)$$

with  $n = 2, 3$  as the system dimension. Rewriting yields an expression for the effective dielectric function

$$\epsilon' = \epsilon_h \frac{1 + \delta'(n-1) \frac{\epsilon_i - \epsilon_h}{\epsilon_i + (n-1)\epsilon_h}}{1 - \delta' \frac{\epsilon_i - \epsilon_h}{\epsilon_i + (n-1)\epsilon_h}} \quad (9)$$

As  $\delta'$  is small, we may neglect higher-order terms to obtain

$$\epsilon' \approx \epsilon_h \left( 1 + \delta' n \frac{\epsilon_i - \epsilon_h}{\epsilon_i + (n-1)\epsilon_h} \right) \quad (10)$$

The above is only valid for infinitely small inclusions. Bruggeman extended this to an arbitrary concentration  $f$  of one medium dispersed in the host material. Consider a first inclusion  $\delta'$  of medium with  $\epsilon_i$  in the host with  $\epsilon_h$ ; this will result in a dielectric function  $\epsilon'$  of this quasi-homogeneous medium, as given by Eq. (10). A second inclusion  $\delta''$  will give rise to an effective dielectric function

$$\epsilon'' \approx \epsilon' \left( 1 + \delta'' n \frac{\epsilon_i - \epsilon'}{\epsilon_i + (n-1)\epsilon'} \right) \quad (11)$$

where  $\epsilon'$  is the dielectric function of the quasi-homogeneous material before adding  $\delta''$ . In general, to obtain an increase  $d\delta_1$  of material with dielectric function  $\epsilon_i$ , in case of an already present fraction  $\delta_1$ , an amount  $\delta' = d\delta_1 / (1 - \delta_1)$  needs to be added. This can be explained as follows: A fraction  $\delta_1$  of the amount  $\delta'$  is distributed in the already-present quantity  $\delta_1$ , while only a fraction  $1 - \delta_1$  of  $\delta'$  leads to an increase of  $\delta_1$ . From Eq. (11), we find

$$\frac{d\epsilon}{n\epsilon} = \frac{d\delta_1}{1 - \delta_1} \frac{\epsilon_i - \epsilon}{\epsilon_i + (n-1)\epsilon} \quad (12)$$

which can be rewritten to yield

$$\left( \frac{1}{\epsilon_i - \epsilon} + \frac{1}{n\epsilon} \right) d\epsilon = \frac{d\delta_1}{1 - \delta_1} \quad (13)$$

The right-hand side is integrated from  $\delta_1 = 0$  to  $\delta_1 = f$ , while on the left we integrate from  $\epsilon = \epsilon_h$  (initially at  $\delta_1 = 0$ , there are no inclusions) to  $\epsilon = \epsilon_{or}$  (the final effective dielectric function of a fraction  $f$  of the medium with dielectric function  $\epsilon_i$  in the host matrix with  $\epsilon_h$ ):

$$\int_{\epsilon_h}^{\epsilon_{or}} \left( \frac{1}{\epsilon_i - \epsilon} + \frac{1}{n\epsilon} \right) d\epsilon = \int_0^f \frac{d\delta_1}{1 - \delta_1} \quad (14)$$

We obtain

$$1 - f = \frac{\epsilon_i - \epsilon_{or}}{\epsilon_i - \epsilon_h} \sqrt{\frac{\epsilon_h}{\epsilon_{or}}} \quad (15)$$

which, for our two-dimensional system ( $n = 2$ ) with

$\epsilon_i = \epsilon_a$  and  $\epsilon_h = \epsilon_p$ , yields

$$1 - f = \frac{\epsilon_a - \epsilon_{or}}{\epsilon_a - \epsilon_p} \sqrt{\frac{\epsilon_p}{\epsilon_{or}}} \quad (16)$$

### Ellipsometry Spectra of As-Anodized Porous Aluminum Oxide Films

For optical characterization, we use a rotating polarizer spectroscopic ellipsometer equipped with a Xe lamp and a scanning monochromator. Measurements are performed in the visible and near-UV region of the spectrum at wavelengths between 300 and 800 nm at a fixed angle of incidence. The angle of incidence can be set between 45° and 70°.

In Fig. 5, a typical ellipsometry spectrum is shown for an anodized film. As already described in the previous sections, anodic oxidation leads to a highly porous oxide structure of approximately 1400-nm thickness, which is essentially transparent for visible light. This explains the oscillations observed in both  $\cos(\Delta)$  and  $\tan(\Psi)$  in Fig. 5, which arise from interference of light reflected at the platinum/aluminum oxide interface and at the aluminum oxide/air interface.

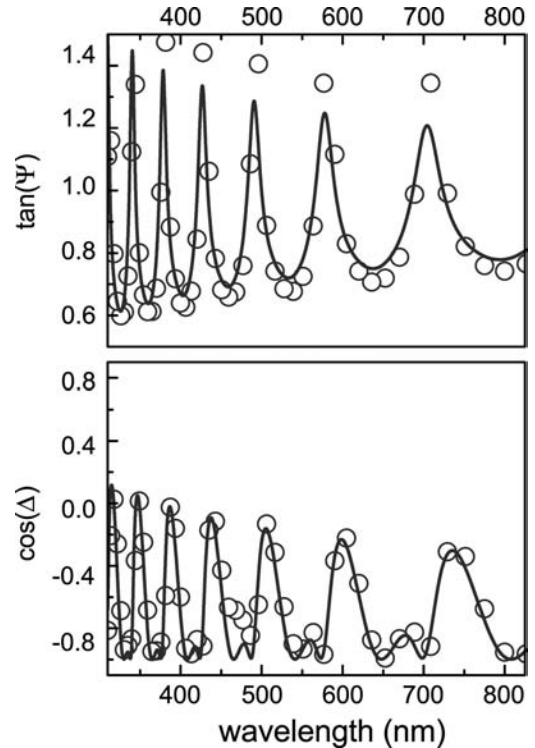


**Fig. 5** Ellipsometry spectrum for an as-anodized porous aluminum oxide film. The open circles represent experimental data obtained at an incident angle of 60°. The solid lines result from the fitting procedure as described in the text.

The solid lines in Fig. 5 represent the result of a fitting procedure using the Abeles matrix algorithm and the optical model described in preceding sections, using bulk dielectric functions taken from literature. The aforementioned three parameters are varied, leading to a thickness of 1400 nm, a cylinder fraction  $f_{\text{cyl}} = 9.9\%$ , and a nanoporosity  $f_p = 28\%$ . The numerical fit errors in all cases amount to approximately 3%, 3%, and 10%, for the thickness, the cylinder fraction, and the nanoporosity, respectively. These results are in good, quantitative agreement with what we concluded from analysis of the SEM images on identical samples.

To verify the accuracy of our model, we also performed measurements at different incident angles. Although the absolute values of both  $\cos(\Delta)$  and  $\tan(\Psi)$  are different, oscillations similar to those in Fig. 5 are observed. Comparison of the experimental results at different angles to calculations of the optical response using the parameters obtained from the fitting procedure as described in relation to Fig. 5 yields perfect correlation between the calculation and the measurements, supporting the validity of our model.

Despite the convincing results presented above, one might argue that, even after prolonged drying under ambient conditions, some aqueous solution may still be present in the porous structure. Especially for nanoporous oxide materials, it has been reported that water, incorporated during the preparation, is still present within the nanovoids.<sup>[61]</sup> This would have a pronounced influence on the analysis of the optical response in terms of (Eqs. (6), (7) and (16)). To obtain an indication if there is any water present in as-anodized samples after drying in air, we performed ellipsometry measurements on such a sample before and after heating to approximately 200°C under moderate vacuum conditions. All optical spectra, both before and after heating in vacuum, were identical, indicating the absence of water within the porous structure of the as-anodized samples. This indicates that either there is indeed no water present within the nanoporous matrix, or that the water is contained in such small volumes that capillary forces prevent evaporation of the aqueous solvent even at elevated temperature. However, the latter explanation may be dismissed. As we will show in the next section, chemical etching does not affect the nanoporous structure, presumably because of the fact that aqueous solution is not able to penetrate into the (sub)nanometer-sized voids.

### Tunable Pore Sizes by Chemical Etching

Chemical etching in aqueous phosphoric acid solutions leads to controlled, homogeneous widening of the pores along their entire length. Apparently, diffusion

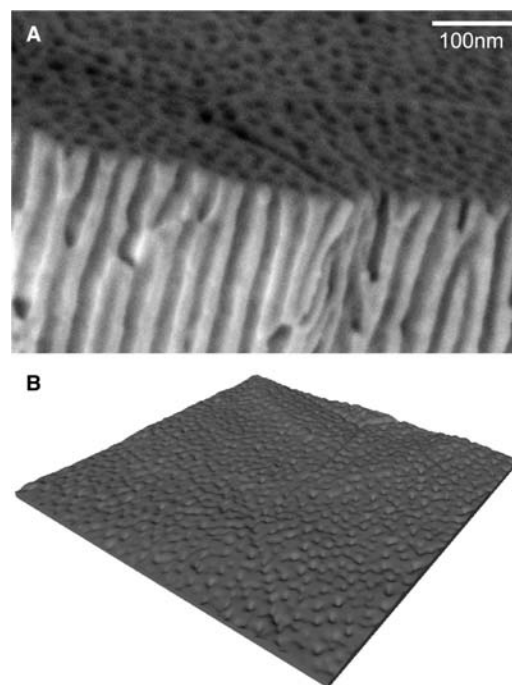


**Fig. 6** (A) Scanning electron microscope and (B) atomic force microscope images of a porous aluminum oxide sample after chemical etching for 10 min in a 2 vol.%  $\text{H}_3\text{PO}_4$  aqueous solution. Scan size in the AFM image is  $1 \mu\text{m} \times 1 \mu\text{m}$ .

of the etchant or etch products is not rate limiting. The average pore diameter in Fig. 6A after immersion of the as-anodized sample in 2 vol.%  $\text{H}_3\text{PO}_4$  solution for 10 min increases from 11.5 nm to approximately 22 nm. Upon prolonged etching and/or using a higher concentration of phosphoric acid, the pores become wider. Furthermore, the enlargement of the pores now also enables the study of these membranes using atomic force microscopy (AFM) as shown in Fig. 6B. Atomic force microscopy measurements are performed using a PicoScan (Molecular Imaging) operated in a.c. mode, using silicon cantilevers (Nanosensors). The pore size of as-anodized samples is too small compared to the tip radius; the tip cannot reach into the pores to obtain a good image. After sufficient pore widening, the pores can be imaged, but they appear markedly smaller than their actual size.

We studied the effect of chemical etching using spectroscopic ellipsometry, with a twofold objective: 1) The use of a noninvasive technique allows a fast characterization of the time evolution of the porous system; and 2) the controlled etching of the pores allows us to verify the validity and assess the accuracy of our optical model as it has been described in the previous section.

In Fig. 7, the ellipsometry spectrum of a sample after chemical etching for 10 min in 3 vol.%  $\text{H}_3\text{PO}_4$  is shown. Comparison with the results in Fig. 5 indicates that the number of oscillations has decreased. This can

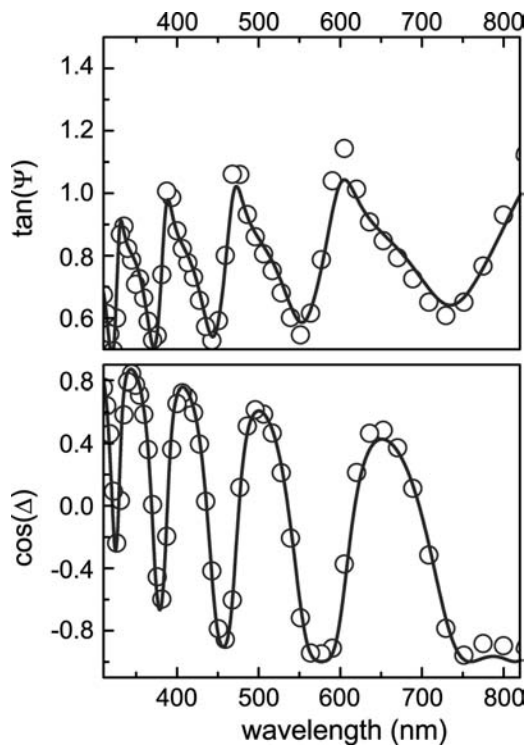


**Fig. 7** Ellipsometry spectrum for a porous aluminum oxide film after chemical etching for 10 min in 3 vol.% H<sub>3</sub>PO<sub>4</sub> aqueous solution. The open circles represent experimental data obtained at an incident angle of 60°. The solid lines result from the fitting procedure as described in the text.

be qualitatively understood by the fact that, owing to the higher cylinder fraction, the refractive index and thus the optical thickness is reduced, which gives rise to a change of the interference. Also, with decreasing wavelength, the amplitude of the oscillations in both  $\cos(\Delta)$  and  $\tan(\Psi)$  decreases. This is direct evidence for the contribution of anisotropy to the optical response. In the absence of anisotropy, the amplitude of the oscillations will be identical over the entire energy range, as long as the substrate (platinum in our case) has a slowly varying dielectric function. The solid lines in Fig. 7 are obtained by fitting the results to our optical model, as described in the previous sections. Clearly, the calculated lines are in perfect agreement with the measured data, therewith supporting our model. The fit results indicate a thickness of 1395 nm, a cylinder void fraction  $f_{cyl} = 46\%$ , and a nanoporosity  $f_p = 34\%$ . When we compare these results with that obtained for the as-anodized sample, chemical etching leads to a significant increase of the cylinder fraction. It may be expected that chemical etching leads to a decrease of the film thickness, but the change is within the error of the fitting procedure. The same holds for the negligible increase of the nanoporosity during chemical etching.

The cylinder fraction is related to the average pore radius  $r$  through

$$f_{cyl} = \rho_{cyl} \pi r^2 \tag{17}$$

where  $\rho_{cyl}$  is the pore density as determined from SEM images, such as those in Figs. 2 and 6. Comparison of the radii determined from SEM images to those obtained from analysis of ellipsometry spectra show that there is good agreement over the entire range of cylinder fractions. This provides valuable evidence for our anisotropic optical model.

The etch rate, and therewith the pore widening process, depends on the concentration of the phosphoric acid solution. This is shown by the solid symbols in Fig. 8, in which the cylinder fraction is plotted as a function of etch time for different etchant concentrations. With an increasing amount of H<sub>3</sub>PO<sub>4</sub> in solution, the etch rate, and thus the rate with which the pores are widened, rises.

A simple model is used to analyze the results in Fig. 8. If we assume a linear etch rate  $\nu(c) = dr/dt$ , which only depends on the acid concentration  $c$ , the linear increase of the pore radius  $r$  with time  $t$  is given by

$$r = r_0 + \nu t \tag{18}$$

where  $r_0 = 5.75$  nm is the initial pore radius after anodization prior to chemical etching. The time dependence of the cylinder fraction is obtained by taking

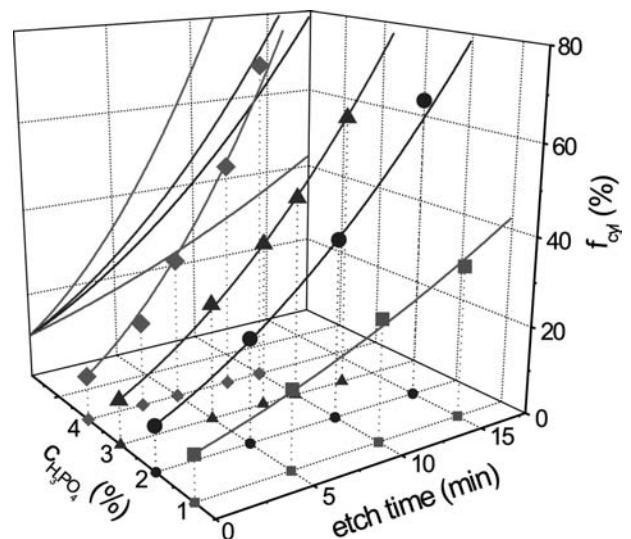


**Fig. 8** Three-dimensional representation of the cylinder fraction  $f_{cyl}$  obtained from ellipsometry measurements, as a function of etching time in different H<sub>3</sub>PO<sub>4</sub> solutions. The solid lines represent fit results as described in the text.



the derivative of Eq. (17)

$$\frac{df_{\text{cyl}}}{dt} = \frac{df_{\text{cyl}}}{dr} \frac{dr}{dt} = \rho_{\text{cyl}} 2\pi r \nu \quad (19)$$

where  $dr/dt = \nu$ . After substitution of the time dependence of the pore radius, the above expression is integrated to yield

$$f_{\text{cyl}} = f_0 + \pi \rho_{\text{cyl}} (2r_0 \nu t + \nu^2 t^2) \quad (20)$$

where  $f_0 = \rho_{\text{cyl}} \pi r^2$  is the initial cylinder fraction before chemical etching. With the linear etch rate  $\nu(c)$  being the only parameter, we fitted the data in Fig. 8. The etch rate  $\nu(c)$  as a function of the  $\text{H}_3\text{PO}_4$  concentration  $c$  is described by  $\nu(c) = kc^n$ , with the order  $n = 2/3$  and a rate constant  $k = 1.7 \times 10^{13} \text{ m}^3 \text{ s}^{-1} \text{ mol}^{-2/3}$ .

Finally, analysis of ellipsometry spectra using the aforementioned model also yields values for the nanoporosity  $f_p$ . Although there appears to be a relatively small increase of  $f_p$  in the initial stages of the etch procedure, it is much less pronounced than the increase of the cylinder fraction  $f_{\text{cyl}}$ . In fact, the variation of  $f_p$  is almost within the numerical fitting errors. Furthermore, there is no discernible difference for high and low  $\text{H}_3\text{PO}_4$  concentrations. Apparently, owing to their very small size, the voids within the nanoporous structure are not accessible to the solvent that inhibits chemical etching in these (sub)nanometer voids. This is not unlikely, as the considerable deformations during the anodic oxide formation give rise to a large number of defects, such as dislocations and vacancies.<sup>[60,62,63]</sup> Obviously, these small “voids” in the amorphous oxide matrix are not accessible to the relatively large water molecules. The average nanoporosity amounts to approximately 36%. This is in good agreement with the value we indirectly deduced on the basis of the film thickness increase upon anodization of the aluminum, as determined from SEM images.

## CONCLUSION

We have presented a detailed characterization study of porous aluminum oxide formed through anodization of thin-film aluminum samples with a well-defined geometry. Prior to anodization, the thickness of the aluminum film was determined using scanning electron microscopy. X-ray diffraction experiments yield powder-like spectra, indicating that the aluminum layer is polycrystalline.

Electron microscopy clearly shows the formation of randomly distributed, but almost perfectly aligned, cylindrical pores with their long axis perpendicular to the film/substrate interface. Additionally, comparison

of X-ray diffraction spectra obtained before and after anodization show a nearly complete transformation of aluminum to aluminum oxide.

Ellipsometry spectra, obtained after anodization, were analyzed in terms of a newly developed model, which contains only three physically relevant parameters: the film thickness, the cylindrical pore fraction, and a nanoporosity of the remaining aluminum oxide matrix. The model accurately reproduces the experimentally observed features, and the absolute values of the fitting parameters are in perfect agreement with that observed in electron microscopy images.

Chemical etching of the porous structure in diluted phosphoric acid solution gives rise to a homogeneous widening of the pores over their entire length. This provides us with an ideal system to verify the accuracy of our optical model. The increase of the cylinder fraction with increasing etching time and etchant concentration, as determined from ellipsometry spectra, is again in perfect agreement with electron microscopy images. In contrast to the cylinder fraction, the nanoporosity of the aluminum oxide remains unchanged, presumably because of the inaccessibility of the small defect-like voids in the amorphous oxide to the etch solution.

## ACKNOWLEDGMENTS

Philips Research (Eindhoven) is gratefully acknowledged for supplying the samples. This work is part of the research program of the Stichting voor Fundamenteel Onderzoek der Materie (FOM), financially supported by the Nederlandse Organisatie voor Wetenschappelijk Onderzoek (NWO) and Philips Research.

## REFERENCES

1. Keller, F.; Hunter, M.S.; Robinson, D.L. Structural features of oxide coatings on aluminum. *J. Electrochem. Soc.* **1953**, *100* (9), 411–419.
2. Masuda, H.; Hasegawa, F.; Ono, S. Self-ordering in cell arrangement of anodic porous alumina formed in sulfuric acid solution. *J. Electrochem. Soc.* **1997**, *144* (5), L127–L129.
3. Thompson, G.E. Porous anodic alumina: Fabrication, characterization and applications. *Thin Solid Films* **1997**, *297*, 192–201.
4. Masuda, H.; Yamada, H.; Satoh, M.; Asoh, H.; Nakao, M.; Tamamura, T. Highly ordered nanochannel-array architecture in anodic alumina. *Appl. Phys. Lett.* **1997**, *71* (19), 2770–2772.
5. Jessensky, O.; Müller, F.; Gösele, U. Self-organized formation of hexagonal pore arrays in anodic alumina. *Appl. Phys. Lett.* **1998**, *72* (10), 1173–1175.
6. Li, A.P.; Müller, F.; Bimer, A.; Nielsch, K.; Gösele, U. Hexagonal pore arrays with a 50–420 nm interpore



- distance formed by self-organization in anodic alumina. *J. Appl. Phys.* **1998**, *18* (11), 6023–6026.
- Li, A.P.; Müller, F.; Birner, A.; Nielsch, K.; Gösele, U. Fabrication and microstructure of hexagonally ordered two-dimensional nanopore arrays in anodic alumina. *Adv. Mater.* **1999**, *11* (6), 483–487.
  - Li, A.P.; Müller, F.; Birner, A.; Nielsch, K.; Gösele, U. Polycrystalline nanopore arrays with hexagonal ordering in aluminum. *J. Vac. Sci. Technol., A* **1999**, *17* (4), 1428–1431.
  - Li, A.P.; Müller, F.; Gösele, U. Polycrystalline and monocrystalline pore arrays with large interpore distance in anodic alumina. *Electrochem. Solid-State Lett.* **2000**, *3* (3), 131–134.
  - Crouse, D.; Lo, Y.H.; Miller, A.E.; Crouse, M. Self-ordered pore structure of anodized aluminum on silicon and pattern transfer. *Appl. Phys. Lett.* **2000**, *76* (1), 49–51.
  - Sulka, G.D.; Stroobants, S.; Moshchalkov, V.; Borghs, G.; Celis, J.P. Synthesis of well-ordered nanopores by anodic aluminum foils in sulfuric acid. *J. Electrochem. Soc.* **2002**, *149* (7), D97–D103.
  - Yuan, Z.; Huang, H.; Fan, S. Regular alumina nanopillar arrays. *Adv. Mater.* **2002**, *14* (4), 303–306.
  - Gao, T.; Meng, G.; Zhang, J.; Sun, S.; Zhang, L. Template synthesis of Y-junction metal nanowires. *Appl. Phys., A* **2002**, *74*, 403–406.
  - Anodisc<sup>®</sup> Whatman; <http://www.whatman.co.uk>.
  - Hulteen, J.C.; Martin, C.R. A general template-based method for the preparation of nanomaterials. *J. Mater. Chem.* **1997**, *7* (7), 1075–1087.
  - Hanaoka, T.A.; Heilmann, A.; Kröll, M.; Kormann, H.P.; Sawitowski, T.; Schmid, G.; Jutzi, P.; Klipp, A.; Kreibitz, U.; Neuendorf, R. Alumina membranes—Templates for novel nanocomposites. *Appl. Organomet. Chem.* **1998**, *12*, 367–373.
  - Ihle, G.; Junges, B.; Junges, U.; Laeri, F.; Schüth, F.; Vietze, U. Ordered porous materials as media for the organization of matter on the nanoscale. *Appl. Organomet. Chem.* **1998**, *12*, 305–314.
  - Schwarzacher, W.; Kasyutich, O.I.; Evans, P.R.; Darbyshire, M.G.; Yi, G.; Fedosyuk, V.M.; Rousseaux, F.; Cambril, E.; Decanini, D. Metal nanostructures prepared by template electrodeposition. *J. Magn. Magn. Mater.* **1999**, *198–199*, 185–190.
  - Zhang, X.Y.; Zhang, L.D.; Chen, W.; Meng, G.W.; Zheng, M.J.; Zhao, L.X. Electrochemical fabrication of highly ordered semiconductor and metallic nanowire arrays. *Chem. Mater.* **2001**, *13*, 2511–2515.
  - Schmid, G. Materials in nanoporous alumina. *J. Mater. Chem.* **2002**, *12*, 1231–1238.
  - Ferré, R.; Ounadjela, K.; George, J.M.; Piroux, L.; Dubois, S. Magnetization processes in nickel and cobalt electrodeposited nanowires. *Phys. Rev., B* **1997**, *56* (21), 14066–14075.
  - Strijkers, G.J.; Dalderop, J.H.J.; Broeksteeg, M.A.A.; Swagten, H.J.M.; De Jonge, W.J.M. Structure and magnetization of arrays of electrodeposited Co wires in anodic alumina. *J. Appl. Phys.* **1999**, *86* (9), 5141–5145.
  - Metzger, R.M.; Konovalov, V.V.; Sun, M.; Xu, T.; Zangari, G.; Xu, B.; Benakli, M.; Doyle, W.D. Magnetic nanowires in hexagonally ordered pores of alumina. *IEEE Trans. Magn.* **2000**, *36* (1), 30–35.
  - Zheng, M.; Menon, L.; Liu, Y.; Bandyopadhyay, S.; Kirbt, R.D.; Sellmeyer, D.J. Magnetic properties of Ni nanowires in self-assembled arrays. *Phys. Rev., B* **2000**, *62* (18), 12282–12286.
  - Nielsch, K.; Wehrspohn, R.B.; Barthel, J.; Kirschner, J.; Gösele, U.; Fischer, S.; Kronmüller, H. Hexagonally ordered 100 nm period nickel nanowire arrays. *Appl. Phys. Lett.* **2001**, *79* (9), 1360–1362.
  - Wang, Y.W.; Zhang, L.D.; Meng, G.W.; Peng, X.S.; Jin, Y.X.; Zhang, J. Fabrication of ordered ferromagnetic–nonmagnetic alloy nanowire arrays and their magnetic property dependence on annealing temperature. *J. Phys. Chem., B* **2002**, *106*, 2502–2507.
  - Zhan, Q.; Chen, Z.; Xue, D.; Li, F.; Kunkel, H.; Zhou, X.; Roshko, R.; Williams, G. Structure and magnetic properties of Fe–Co nanowires in self-assembled arrays. *Phys. Rev., B* **2002**, *66*, 134436.
  - Sorop, T.G.; Untiedt, C.; Luis, F.; Kröll, M.; Raşa, M.; De Jongh, L.J. Magnetization reversal of ferromagnetic nanowires studied by magnetic force microscopy. *Phys. Rev., B* **2003**, *67*, 014402.
  - Han, G.C.; Zhong, B.Y.; Luo, P.; Wu, Y.H. Angular dependence of the coercivity and remanence of ferromagnetic nanowire arrays. *J. Appl. Phys.* **2003**, *93* (11), 9202–9207.
  - Hornyak, G.L.; Patrissi, C.J.; Martin, C.R. Fabrication, characterization and optical properties of gold nanoparticle/porous alumina composites: The nonscattering Maxwell–Garnett limit. *J. Phys. Chem., B* **1997**, *101* (9), 1548–1555.
  - Van der Zande, B.M.I.; Böhmer, M.R.; Fokink, L.G.J.; Schönenberger, C. Colloidal dispersions of gold rods: Synthesis and optical properties. *Langmuir* **2000**, *16*, 451–458.
  - Itoh, N.; Tomura, N.; Tsuji, T.; Hongo, M. Deposition of palladium inside straight mesopores of anodic alumina tube and its hydrogen permeability. *Microporous Mesoporous Mater.* **2000**, *39*, 103–111.
  - Black, M.R.; Padi, M.; Cronin, S.B.; Rabin, O.; McGlure, T.; Dresselhaus, G.; Hagelstein, P.L.; Dresselhaus, M.S. Intersubband transitions in bismuth nanowires. *Appl. Phys. Lett.* **2000**, *77* (25), 4142–4144.
  - Wang, Z.; Su, Y.K.; Li, H.L. AFM study of gold nanowire array electrodeposited within anodic aluminum oxide template. *Appl. Phys., A* **2002**, *74*, 563–565.
  - Pang, Y.T.; Meng, G.W.; Shan, W.J.; Zhang, L.D.; Gao, Y.K.; Zhao, A.W.; Mao, Y.Q. Arrays of ordered Ag nanowires with different diameters in different areas embedded in one piece of anodic alumina membrane. *Appl. Phys., A* **2003**, *77* (5), 717–720.
  - Zhang, J.; Wang, X.; Peng, X.; Zhang, L. Fabrication, morphology and structural characterization of ordered single-crystal Ag nanowires. *Appl. Phys., A* **2002**, *75*, 485–488.
  - Zelenski, C.M.; Hornyak, G.L.; Dorhout, P.K. Synthesis and characterization of CdS particles within a nanoporous aluminum oxide template. *Nanostruct. Mater.* **1997**, *9*, 173–176.

38. Xu, D.; Shi, X.; Gui, L.; Tang, Y. Electrochemical preparation of CdSe nanowire arrays. *J. Phys. Chem., B* **2000**, *104*, 5061–5063.
39. Peng, X.S.; Zhang, J.; Wang, X.F.; Wang, Y.W.; Zhao, L.X.; Meng, G.W.; Zhang, L.D. Synthesis of highly ordered CdSe nanowire arrays embedded in anodic alumina membrane by electrodeposition in ammonia alkaline solution. *Chem. Phys. Lett.* **2001**, *343*, 470–474.
40. Zheng, M.; Li, G.; Zhang, X.; Hunag, S.; Lei, Y.; Zhang, L. Fabrication and structural characterization of large-scale uniform SnO<sub>2</sub> nanowire array embedded in anodic alumina membrane. *Chem. Mater.* **2001**, *13*, 3859–3861.
41. Wang, Y.C.; Leu, I.C.; Hon, M.H. Preparation of nano-sized ZnO arrays by electrophoretic deposition. *Electrochem. Solid-State Lett.* **2002**, *5* (4), C53–C55.
42. Wang, Z.; Li, H.L. Highly ordered zinc oxide nanotubules synthesized within the anodic aluminum oxide template. *Appl. Phys., A* **2002**, *74*, 201–203.
43. Kouklin, N.; Menon, L.; Bandyopadhyay, S. Room-temperature single-electron charging in electrochemically synthesized semiconductor quantum dot and wire arrays. *Appl. Phys. Lett.* **2002**, *80* (9), 1649–1651.
44. Sander, M.S.; Gronsky, R.; Sands, T.; Stacy, A.M. Structure of bismuth telluride nanowire arrays fabricated by electrodeposition into porous anodic alumina template. *Chem. Mater.* **2003**, *15*, 335–339.
45. Iwasaki, T.; Motoi, T.; Den, T. Multiwalled carbon nanotubes growth in anodic alumina nanoholes. *Appl. Phys. Lett.* **1999**, *75* (14), 2044–2046.
46. Jeong, S.H.; Hwang, H.Y.; Lee, K.H.; Jeong, Y. Template-based carbon nanotubes and their application to a field emitter. *Appl. Phys. Lett.* **2001**, *78* (14), 2052–2054.
47. Hu, W.; Gong, D.; Chen, Z.; Yuan, L.; Saito, K.; Grimes, C.A.; Kichambare, P. Growth of well-aligned carbon nanotube arrays on silicon substrates using porous alumina film as a nanotemplate. *Appl. Phys. Lett.* **2001**, *79* (19), 3083–3085.
48. Steinhart, M.; Wendroff, J.H.; Greiner, A.; Wehrspohn, R.B.; Nielsch, K.; Schilling, J.; Choi, J.; Gösele, U. Polymer nanotubes by wetting of ordered porous templates. *Science* **2002**, *296*, 1997.
49. Peña, D.J.; Mbindyo, J.K.N.; Carado, A.J.; Mallouk, T.E.; Keating, C.D.; Razavi, B.; Mayer, T.S. Template growth of photoconductive metal–CdSe–metal nanowires. *J. Phys. Chem., B* **2002**, *106*, 7458–7462.
50. Sberveglieri, G.; Murri, R.; Pinto, N. Characterization of porous Al<sub>2</sub>O<sub>3</sub>–SiO<sub>2</sub>/Si sensor for low and medium humidity ranges. *Sens. Actuators, B* **1995**, *23*, 177–180.
51. Nahar, R.K.; Khanna, V.K. Ionic doping and inversion of the characteristic of thin film porous Al<sub>2</sub>O<sub>3</sub> humidity sensor. *Sens. Actuators, B* **1998**, *46*, 35–41.
52. Kukhta, A.V.; Gorokh, G.G.; Kolesnik, E.E.; Mitkovets, A.I.; Taoubi, M.I.; Koshin, Y.A.; Mozalev, A.M. Nanostructured alumina as a cathode of organic light-emitting devices. *Surf. Sci.* **2002**, *507–510*, 593–597.
53. De Laet, J.; Vanhellemont, J.; Terryn, H.; Vereecken, J. Characterization of various aluminum oxide layers by means of spectroscopic ellipsometry. *Appl. Phys., A* **1992**, *54*, 72–78.
54. De Laet, J.; Vanhellemont, J.; Terryn, H.; Vereecken, J. Characterization of different conversion coatings on aluminum with spectroscopic ellipsometry. *Thin Solid Films* **1993**, *233*, 58–62.
55. De Laet, J.; Terryn, H.; Vereecken, J. Development of an optical model for steady state porous anodic films on aluminum formed in phosphoric acid. *Thin Solid Films* **1998**, *320*, 241–252.
56. Stein, N.; Rommelfangen, M.; Hody, V.; Johann, L.; Lecuire, J.M. In situ spectroscopic ellipsometric study of porous alumina film dissolution. *Electrochim. Acta* **2002**, *47*, 1811–1817.
57. Bruggeman, D.A.G. Berechnung verschiedener physikalischer konstanten von heterogenen substanzen. *Ann. Phys.* **1935**, *24*, 636–664.
58. Wien, O. Lamellare doppelbrechung. *Phys. Z* **1904**, *12*, 332.
59. Azzam, R.M.A.; Bashara, N.H. *Ellipsometry and Polarized Light*; North Holland: Amsterdam, 1987.
60. Palibroda, E.; Farcas, T.; Lupsan, A. A new image of porous aluminum oxide. *Mater. Sci. Eng., B* **1995**, *32*, 1–5.
61. Benes, N.; Spijksma, G.; Verweij, H.; Wormeester, H.; Poelsema, B. CO<sub>2</sub> sorption of a thin silica layer determined by spectroscopic ellipsometry. *AIChE J.* **2001**, *47*, 1212–1218.
62. Du, Y.; Cai, W.L.; Mo, C.M.; Chen, J.; Zhang, L.D.; Zhu, X.G. Preparation and photoluminescence of alumina membranes with ordered pore arrays. *Appl. Phys. Lett.* **1999**, *74* (20), 2951–2953.
63. Huang, G.S.; Wu, X.L.; Mei, Y.F.; Shao, X.F.; Siu, G.G. Strong blue emission from anodic alumina membranes with ordered nanopore array. *J. Appl. Phys.* **2003**, *93* (1), 582–585.

# Nanostructured Alloys: Cryomilling Synthesis and Behavior

**David Witkin**

*Department of Chemical Engineering and Materials Science,  
University of California–Irvine, Irvine, California, U.S.A.*

**Piers Newbery**

**Bing Q. Han**

**Enrique J. Lavernia**

*Department of Chemical Engineering and Materials Science,  
University of California–Davis, Davis, California, U.S.A.*

## INTRODUCTION

In this entry, the cryomilling process and its products are covered, including the formation of nanostructured powders and their thermal stability. The microstructural changes that occur during consolidation and secondary processing are also considered. Finally, the mechanical properties of the bulk product will be discussed. The discussion focuses on metals, with particular attention paid to aluminum alloys, and their potential as high-strength structural materials.

## BACKGROUND

Cryomilling is a mechanical attrition technique in which powders are milled in a slurry with milling balls and a cryogenic liquid, originally developed to produce dispersion strengthened metal powders.<sup>[1–3]</sup> Because cryomilling relies on severe plastic deformation, the formation of nanostructures within the powder particles can be compared to other ball milling methods, as well as to microstructural refinement of bulk materials attained via equal channel angular pressing (ECAP), friction stir processing, and cold working. As a powder metallurgy technique, it requires a consolidation step, and changes in microstructure and properties during consolidation can be compared with those for consolidated or compacted nanoparticles and traditional ball-milled powders.

The possible advantages to using a cryogenic liquid, usually nitrogen, rather than carrying out the milling at room temperature, are that the low temperature suppresses the annihilation of dislocations, a larger dislocation density is possible, and the development of the nanostructure is obtained in a shorter time.<sup>[3]</sup> The extent to which these advantages are realized in practice differs between material systems and have not been explored to the fullest. For softer metals, like

aluminum, the particular advantage of the cryogenic temperature is that it prevents substantial agglomeration of the powder during milling. For reactive metals, it can reduce the amount of contamination, oxygen in titanium, for example.

## STRUCTURAL EVOLUTION DURING CRYOMILLING

The processing parameters for cryomilling are very similar to ball milling, i.e., the time of milling, the ball-to-powder mass ratio, the size of the mill, and the milling media (material and ball diameter) can significantly influence the end product. Modified ball-milling attritors are used, connected to a liquid nitrogen feed, with an inserted thermocouple to ensure that the liquid nitrogen in the milling chamber is kept at a constant level. Typical parameters for cryomilling are a ball-to-powder mass ratio of 36:1, 6 mm diameter chrome steel balls, an attritor rotation speed of 180 rpm, and a milling time of 8 hr. A small amount (~0.25 wt%) of stearic acid is added to the slurry to prevent powder agglomeration. The powder used for cryomilling usually has a preferred size of about 50  $\mu\text{m}$ , which is not changed significantly after milling has been completed. As of now, there has been little investigation of the effect of cryomilling parameters on the structure and properties of the final, consolidated material.

## Formation of Nanocrystalline Structure

A basic empirical description of the development of nanostructures during mechanical milling, which cryomilling is likely to follow, has been presented by Fecht.<sup>[4]</sup> This comprises a three-stage process of grain refinement, starting with the localization of deformation into shear bands with high dislocation density,

which is followed by annihilation and recombination of dislocations, forming nanometer-scale subgrains. This subgrain structure extends throughout the sample during continued milling. The final stage is the transformation of the subgrain boundary structure to randomly oriented high-angle grain boundaries.<sup>[4]</sup>

The minimum grain size achievable by ball milling,  $d_{\min}$ , has been related to several physical properties for elemental metals. In the case of melting temperature ( $T_m$ ), there is an inverse relation for  $d_{\min}$  for lower melting point fcc metals. For hcp, bcc, and higher melting point fcc metals (above that of Pd at 1555°C),  $d_{\min}$  is constant with respect to  $T_m$ , where the value of  $d_{\min}$  is ranked fcc < bcc < hcp.<sup>[5,6]</sup> However, if  $d_{\min}$  is normalized by the magnitude of the respective Burgers vector,  $b$ , metals of all three crystal systems, including some alloys, can be represented by an equation of the form

$$\frac{d_{\min}}{b} = A \exp[-cT_m] \quad (1)$$

where  $A$  and  $c$  are constants.<sup>[7]</sup> For fcc metals, an inverse relationship has also been found between  $d_{\min}$  and bulk modulus, and a direct relationship between  $d_{\min}$  and the minimum equilibrium distance between two unstressed edge dislocations.<sup>[6]</sup> More recently, Mohamed was able to support Fecht's empirical model with a demonstration of the relationship between  $d_{\min}$  and the activation energy for recovery, which in turn can be related to melting temperature and bulk modulus.<sup>[7]</sup> One consequence of these correlations, especially pertinent to a discussion of cryomilling, is the prediction that milling at lower temperatures will not reduce  $d_{\min}$  appreciably in metals with lower self-diffusion activation energies, such as Al.

Another factor to consider in the grain refinement process is microstructural inhomogeneity. The empirical model cited previously describes deformation localized

into shear bands that ultimately comprise the entire sample.<sup>[4]</sup> It would not be surprising, therefore, to find microstructural features that manifest different relative degrees of deformation, and not simple log-normal distributions of randomly oriented equiaxed grains.

For cryomilled Al–7.5Mg, two distinctive components of the microstructure were observed after cryomilling for 8 hr: A random distribution of equiaxed grains between 10 and 30 nm in diameter and, less frequently, elongated grains measuring 100–200 nm long by 30 nm wide as shown in Fig. 1.<sup>[2,8]</sup> A similar microstructure was observed in cryomilled commercial purity Al.<sup>[9]</sup> Transmission electron microscopy (TEM) investigation of cryomilled Al–7.5Mg–0.3Sc revealed that the mean width of the elongated regions in cryomilled powder was essentially equal to the average grain size of equiaxed grains.<sup>[10]</sup> These elongated grains were compared to the lamellar structures that arise during cold rolling of wrought Al to high strains, with continued deformation taking place within the individual lamellae, producing subgrains that are roughly equiaxed.<sup>[9,11,12]</sup> This microstructure is thus consistent with the empirical model, but the appearance of high-angle grain boundaries separating elongated regions is not necessarily anticipated.<sup>[4]</sup> The implication for the cryomilled Al–Mg, though not stated, is that these microstructures are evidence of insufficient milling time. Elongated grains of similar dimensions were also reported as a transient feature in cryomilled Inconel 625, present in samples milled for 4 and 6 hr, but not in powder milled for 8 hr.<sup>[13]</sup>

A high dislocation density and microtwins have been observed in cryomilled Al alloys, as shown in Fig. 2, where high-resolution electron microscopy (HREM) investigation revealed a density of dislocations of  $1.3 \times 10^{17} \text{ m}^{-2}$  in the elongated grains described above.<sup>[2]</sup> In comparison, for cold rolled Al–Mg alloys

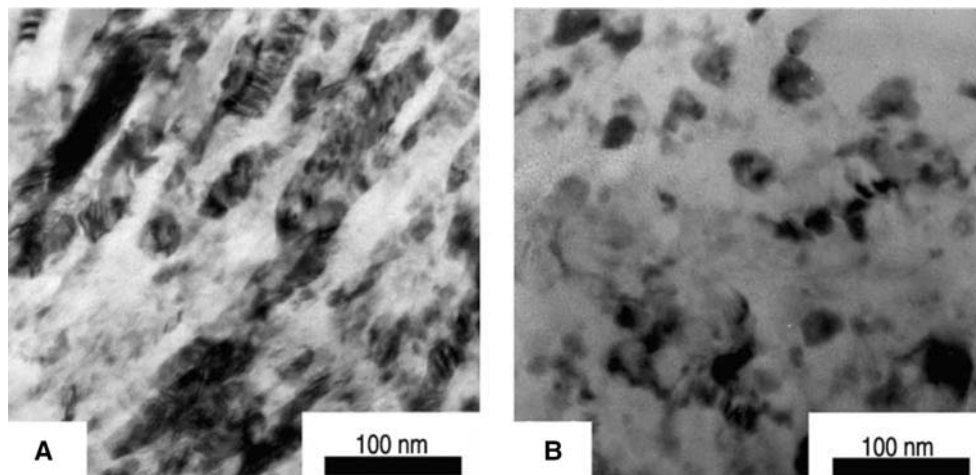


**Fig. 1** Transmission electron microscopy images showing the two different microstructures present in as-cryomilled Al–7.5Mg powder: (A) elongated grains and (B) equiaxed grains. *Source:* From Ref.<sup>[2]</sup>.

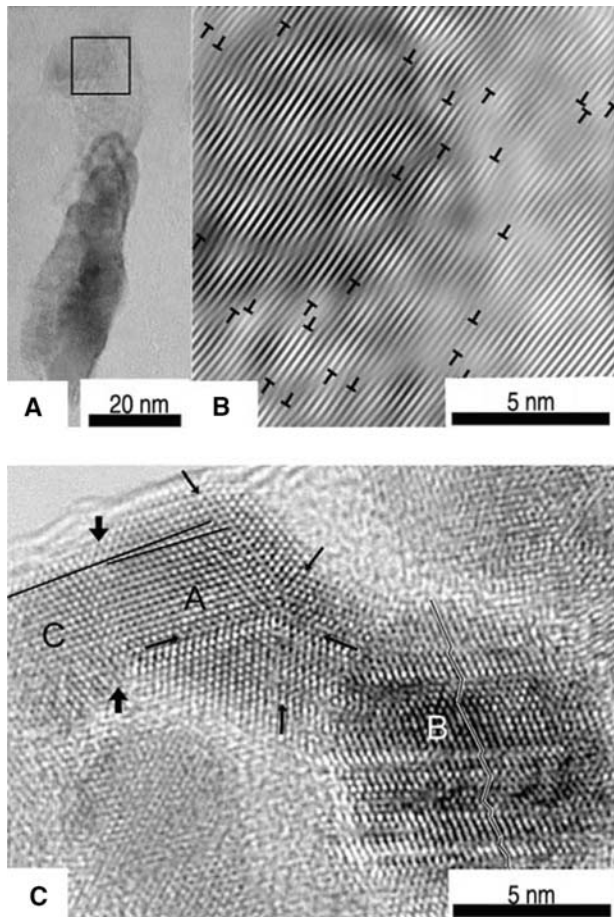


**Fig. 2** High-resolution electron microscopy images showing the microstructure of cryomilled Al-7.5Mg. (A) Typical elongated grain. (B) An enlarged Fourier-filtered image of the area marked with a black square in (A) imaged using (000) and a {111} pair. Dislocations are indicated with a “T”. (C) Equiaxed grains where grain A contains a five-fold twin, marked with smaller arrows, and grain B contains microtwins and stacking faults. There is a 5° small-angle grain boundary between grains A and C marked with two larger arrows. *Source:* From Ref.<sup>[2]</sup>.

the dislocation density was  $5 \times 10^{15} \text{ m}^{-2}$  at a strain of 3.5. Many of the cryomilled dislocations existed as dipoles, which are often present in heavily deformed metals. Within the equiaxed grains, few dislocations were seen. However, twins were frequently observed in grains with dimensions less than 10 nm, as shown in Fig. 2(C). It is worthwhile to note that the occurrence of twins is not common in Al and its alloys. In addition, the HREM investigations also found some nonequilibrium grain boundaries in the as-milled powder.

A significant aspect of the cryomilled microstructure to consider is the presence of nanoscale dispersoids. While  $\text{Al}_2\text{O}_3$  or carbide particles may be present in Al-bearing alloys, as in mechanically alloyed materials, the additional formation of AlN is the result of milling in the liquid nitrogen environment. Examples of

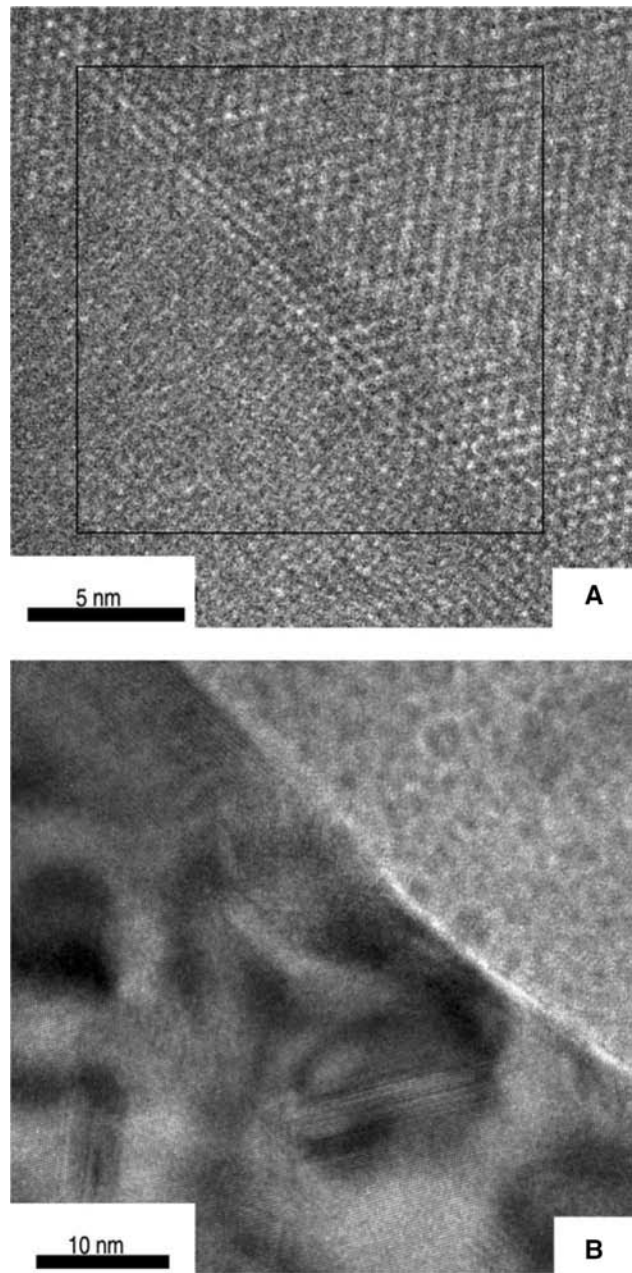


**Fig. 3** High-resolution electron microscopy images of AlN dispersoids in extruded cryomilled Al-10Ti-2Cu: (A) higher magnification image of a single dispersoid and (B) multiple dispersoids adjacent to a grain boundary. *Source:* From Ref.<sup>[14]</sup>.

dispersoids with a length of approximately 10 nm in extruded cryomilled Al-10Ti-2Cu are shown in Fig. 3.<sup>[14]</sup> There have been some differences reported in the size and nature of the nitrogen-containing dispersoids: While a cryomilled Al- $\text{Al}_2\text{O}_3$  composite contained platelets about 10 nm and separated by 80 nm, in NiAl the dispersoids ranged in size from 5 to 100 nm, and were distributed inhomogeneously after consolidation.<sup>[1,15-17]</sup> However, it must be mentioned

that reported values for the dispersoid particle spacing come from materials consolidated and processed by different means, using widely varying temperatures, so they likely do not represent the as-milled distribution for each of the systems.

### Thermal Stability of Cryomilled Powders

Nanocrystalline materials for structural application produced via cryomilling or mechanical milling require the consolidation of the powders, which has often been evaluated a priori by isothermal annealing experiments to assess the thermal stability of the microstructure. It must be noted that these studies do not include grain growth that could arise due to the application of both temperature and stress, for example, as experienced during hot isostatic pressing.

On the basis of the available data for cryomilled alloys presented graphically in Fig. 4, cryomilled Al, or alloys containing Al, would appear to be more thermally stable than Ni or Fe. Fe-2.6Al, for example, exhibits much greater thermal stability than Fe without Al.<sup>[18-23]</sup> Although the incorporation of the oxide layer on the premilled Al powders probably adds resistance to grain growth, as has been described for milled Al, the presence of nitride dispersoids in the structure is likely to be of paramount importance in stabilizing the grain size. AlN has a higher stability compared to Fe and Ni nitrides. Ni<sub>3</sub>N, for example, decomposes above 500°C.<sup>[19,24]</sup> The importance of N-containing dispersoids was emphasized when NiAl was cryomilled in liquid Ar, so that no AlN or Al(ON) could form, and the grain growth of this material during isothermal annealing led to grain sizes roughly an order of magnitude larger than when the NiAl was milled in liquid nitrogen.<sup>[25]</sup>

Inconel 625 departs from the usual behavior of increasing grain size above 700°C, as shown in Fig. 4,

since annealing at 900°C actually led to a smaller grain size. This was attributed to the precipitation of two niobium-bearing phases, Ni<sub>3</sub>Nb and NbC, and their stabilizing effect.<sup>[23]</sup>

Investigation of both mechanically milled Fe and cryomilled Al has indicated two different values of activation energy for grain growth, depending on the annealing time and temperature.<sup>[22,26]</sup> In both cases, lower temperature data gave a better fit to the parabolic grain growth relationship given by

$$D^{1/n} - D_0^{1/n} = kt \quad (2)$$

where  $D_0$  and  $D$  are the grain size initially and at time  $t$ , respectively, and  $k$  is an Arrhenius-type rate constant that includes the activation energy for grain growth. The denominator of the exponent,  $n$ , would be 0.5 in the ideal case where the only driving force on the grain boundary results from its curvature. Deviations from this value, which are the norm, are attributed to pinning of the grain boundaries.<sup>[27]</sup> The higher temperature data were fitted to a model that accounts for pinning forces on a migrating grain boundary. Both Fe and Al relied on Burke's equation:

$$\frac{D_0 - D}{D_m - D} + \ln\left(\frac{D_m - D_0}{D_m - D}\right) = kt \quad (3)$$

where  $D_m$  refers to the maximum grain size that would arise purely from the pinning force.

### CONSOLIDATION OF CRYOMILLED POWDERS

Typically, prior to consolidation, the cryomilled powder is transferred to Al cans fitted with hollow stems and valves for hot vacuum degassing, to remove

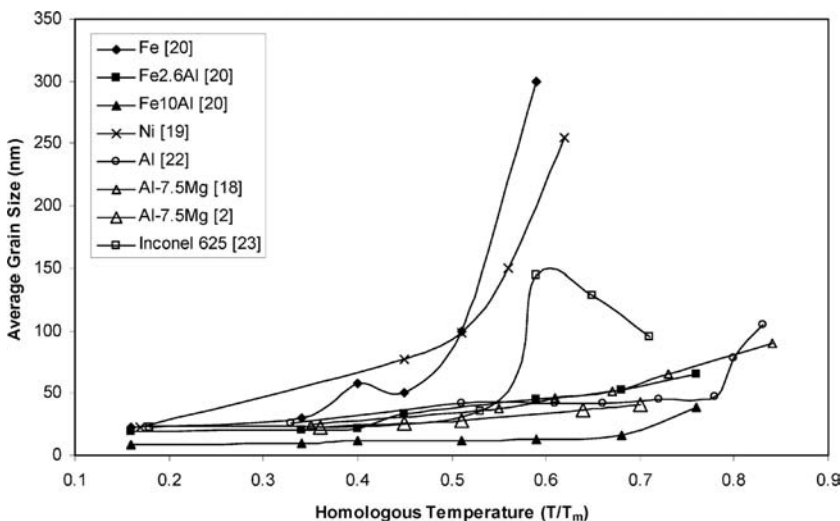


Fig. 4 Graph showing the variation of grain size with isothermal annealing temperature of various cryomilled powders.



gaseous impurities such as H, the presence of which would severely embrittle the material. The temperatures and times used for degassing can significantly increase the grain size of the powder above that for the as-milled condition. For Al, annealing data suggests grain growth at the degassing temperature from about 25 to about 65 nm, based on x-ray diffraction and TEM measurements.<sup>[18]</sup> Once the degassing cycle is completed, the can is then sealed at the stem to preserve the vacuum.

### Hot Isostatic Pressing

Beginning with the earliest work, the most common primary consolidation route has been hot isostatic pressing (HIPping). In this case, cryomilled Al was HIPped at approximately  $0.84T_m$ , but the as-HIPped microstructure was not described with nearly the same detail as the as-milled powders.<sup>[1]</sup>

Like the milling process itself, where the evolution of particle size and morphology is paralleled by grain size refinement, the HIP consolidation process also takes place at two length scales. Modeling of the HIP process typically focuses on the densification of the powders, and not the transformations taking place within the powders.<sup>[28]</sup> The densification has been described as a three-step process, beginning with loose packing of powder in the can, elimination of connected porosity due to the growth of necks at contact points between adjacent particles, and reduction of the size of individual pores.<sup>[29]</sup> The growth of necks and filling in of pores at each stage is accomplished by a combination of plastic deformation of the powder particles, power-law creep, and mass diffusion to the remaining free surfaces.

The consequence of the HIP densification is that the material filling the pores is different from that originating directly from the cryomilled powder. This is clearly seen in Fig. 5, which shows the microstructure of cryomilled Al 5083 that had been HIPped at a temperature of  $300^\circ\text{C}$  ( $0.67T_m$ ) and a pressure of 172 MPa.<sup>[30]</sup> In Fig 5(A), an optical micrograph of the as-HIPped material shows contrast between the lighter-colored material surrounding the milled particles and the particles themselves. Additionally, Fig. 5(B) presents a TEM image of a shared particle boundary which illustrates the difference in grain size between the particles, for which the grain size averages less than 100 nm, and the surrounding interparticle regions, for which the grain sizes range between 1 and  $3\mu\text{m}$ .<sup>[30]</sup> Based on the optical image in Fig. 5(A), these coarse-grained regions represent about 10–20% of the sample. Not only are the interparticle regions coarser grained, they are probably free of the dispersoids that give the cryomilled material high thermal stability. It is therefore

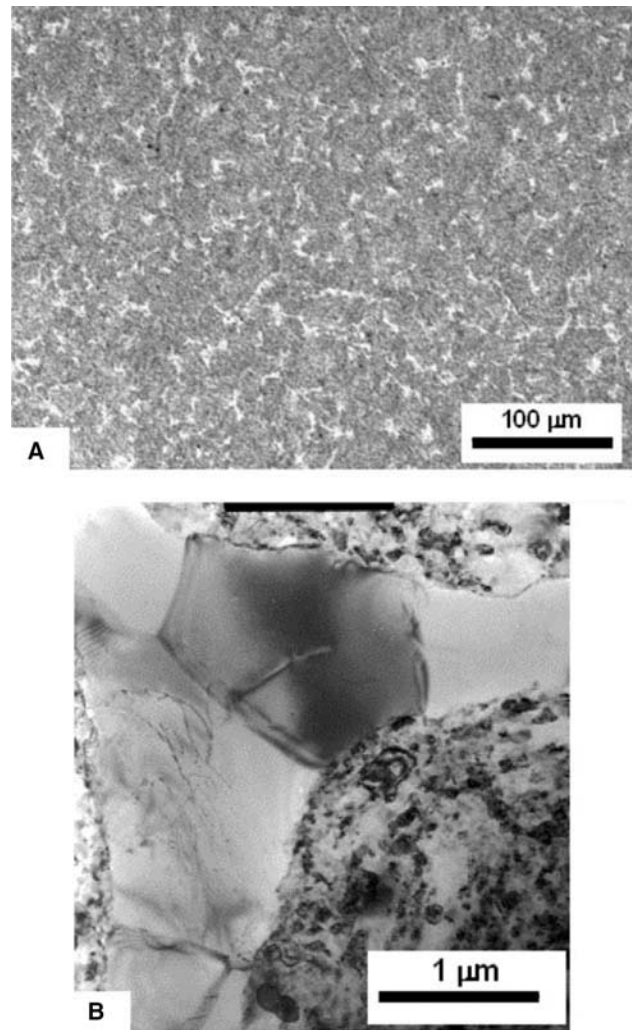


**Fig. 5** Micrographs of as-HIPped Al 5083: (A) optical showing cryomilled material surrounded by lighter interparticle material arising from densification and (B) TEM showing the coarser grained interparticle region between the fine grained material originating from the cryomilled powder. *Source:* From Ref.<sup>[30]</sup>.

likely that the interparticle regions will increase in relative grain size upon further thermo-mechanical processing. A higher HIP temperature has been correlated with a larger number of relatively coarse grains (300–1000 nm) and a lower strength.<sup>[31]</sup>

### Extrusion

Powder metallurgy products must be fabricated in such a way as to break up prior particle boundaries, homogenize the material, and close remaining pores to eliminate possible stress concentration points that can serve to initiate cracks or lead to failure by interface debonding. As illustrated in Fig. 5, HIPping does not necessarily homogenize the material completely,

and it may not be entirely sufficient to remove residual porosity, necessitating additional processing. The favored method until now has been extrusion. The first reported cryomilling of Al (with  $\text{Al}_2\text{O}_3$ ) used a combination of HIP and extrusion, while an initial effort to cryomill NiAl with 0.5 wt%  $\text{Y}_2\text{O}_3$  used HIPping or extrusion of canned powders at three different reduction ratios.<sup>[16,17]</sup>

During extrusion, it has been found for cryomilled Al 5083 that the average grain size increases by 130–250%.<sup>[32]</sup> However, in general, there has not been a lot of reported research on the comparison of extruded microstructures with that obtained directly from HIPping. The increase in grain size during extrusion depends on the relative effect of the dispersoids and the solute atoms, which in turn would depend on their distribution throughout the grains. If a network of dispersoids exists at the grain boundaries, the grain boundaries must break free, or the dispersoids themselves might migrate during extrusion. Alternatively, if the dispersoids are generally found in the grain centers, the presence of Mg at the grain boundaries of cryomilled Al 5083 could be important. However, high Mg mobility in Al at the extrusion temperatures used (150–250°C) would allow grain boundaries to migrate and lead to grain growth. In this case, the final extruded grain size would reflect the distribution of the dispersoids.

Ongoing research activities regarding the processing of cryomilled powders include alternative primary consolidation methods, such as cold isostatic pressing (CIPping) and secondary processing, including different types of extrusion, forging, hot pressing, and rolling.

## MECHANICAL PROPERTIES OF CRYOMILLED MATERIALS

Consolidated cryomilled materials have exhibited much increased strength over conventionally processed material, usually at the expense of ductility. For the Al alloy 5083, the yield strength ( $\sigma_y$ ) and ultimate tensile stress (UTS) of cryomilled material has been measured to be around 450 and 500 MPa, compared to 120 and 275 MPa for relatively coarse (grain size  $\sim 200 \mu\text{m}$ ) 5083. The cryomilled Al 5083 also had greater strength than ECAP material, which had a UTS of  $\sim 350$  MPa. However, whereas the ECAP Al 5083 had a similar strain at fracture to the conventional material, the elongation of the cryomilled Al 5083 was about half.<sup>[33]</sup> Cryomilled Al–7.5Mg was also found to have a  $\sigma_y$  and a UTS about 30% above those of the strongest commercially available form of Al 5083, but in this case there was no apparent decrease in ductility.<sup>[34]</sup> This was attributed to the presence of ductile, crack blunting micrometer-size grains that had developed in the HIPped and extruded structure. It is possible that the

large grains may have developed out of the HIP structure discussed previously.

Cryomilled Al–Mg–Sc alloy and Al–Mg alloys were consolidated and processed to have a grain size of about 200 and 300 nm, respectively. The Al–Mg–Sc alloy exhibited a  $\sigma_y$  of 630 MPa, a UTS of 730 MPa, and an elongation-to-failure of approximately 2.7%.<sup>[35]</sup> The material consolidated from cryomilled Al–Mg powder also had a high strength, having a  $\sigma_y$  and UTS of 642 and 847 MPa, respectively, and it failed in the strain-hardening region, with a similar low ductility of 1.4%.<sup>[36]</sup> Inspection of the stress–strain curves revealed a brief strain-hardening region after yielding and a low strain-hardening region. In addition, localized shear (Lüders) bands and macroscopic necking have been observed in cryomilled Al–Mg alloys.<sup>[37]</sup>

The fundamental reason for the increased strength of cryomilled structural alloys, in comparison to those processed conventionally, is probably the increase in  $\sigma_y$  due to a reduction in the mean grain size ( $d$ ) based on the Hall–Petch relationship:

$$\sigma_y = \sigma_0 + k_y d^{-1/2} \quad (4)$$

where  $\sigma_0$  is the lattice friction stress, and  $k_y$  is the Hall–Petch slope. Two cryomilled systems for which grain size variation has been achieved by changing the HIP temperature are commercial purity Al and Al 5083. The average grain sizes for cryomilled extrusions were in the range 100–200 nm for the Al and 150–300 nm for the Al 5083, and their Hall–Petch plots are shown in Fig. 6.<sup>[30,31]</sup> The calculated  $k_y$  values were 0.09 and 0.28  $\text{MPa} \sqrt{\text{m}}$  for the cryomilled Al and Al 5083, respectively.

It has been found that extruded cryomilled Al alloys have a yield stress roughly 15% higher than mechanically alloyed Al at a similar fraction of dispersoid particles.<sup>[24]</sup> Establishing the precise reason for the difference is complicated by the presence of AlN and a smaller grain size for the cryomilled alloys. Both strengthening contributions are considered additive, but the grain size distribution and uneven particle spacing may well complicate the extent to which separate contributions can be determined.<sup>[38]</sup> Two other sources of strengthening may also need to be taken into account: that due to differences in the concentration and the distribution of solute atoms and dislocations.

Stress–strain curves for two extrusions of cryomilled commercial purity Al with average grain sizes of 116 and 179 nm are shown in Fig. 7.<sup>[39]</sup> The larger grain size, obtained by using a higher HIP temperature, resulted in an increase in the ductility at the expense of a drop in the strength. The curves in Fig. 7 show only the extent of uniform plastic deformation. After

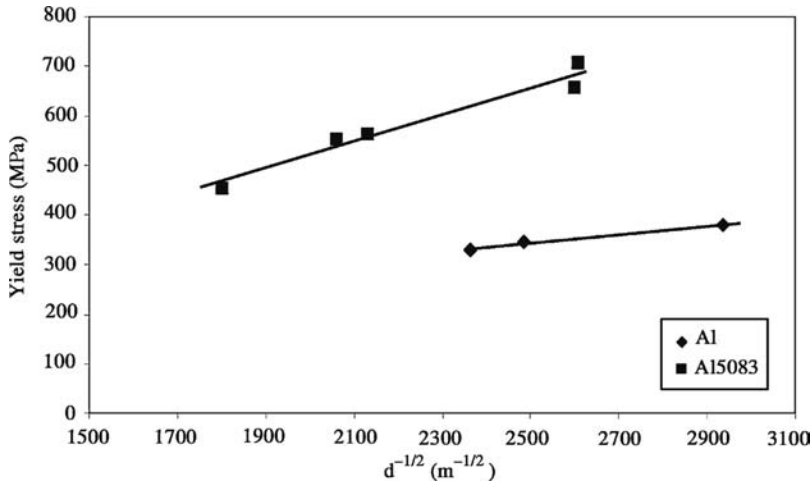


**Fig. 6** Hall-Petch plots relating yield stress to the mean grain size for extrusions of cryomilled Al and Al 5083. *Source:* From Refs.<sup>[30,31]</sup>.

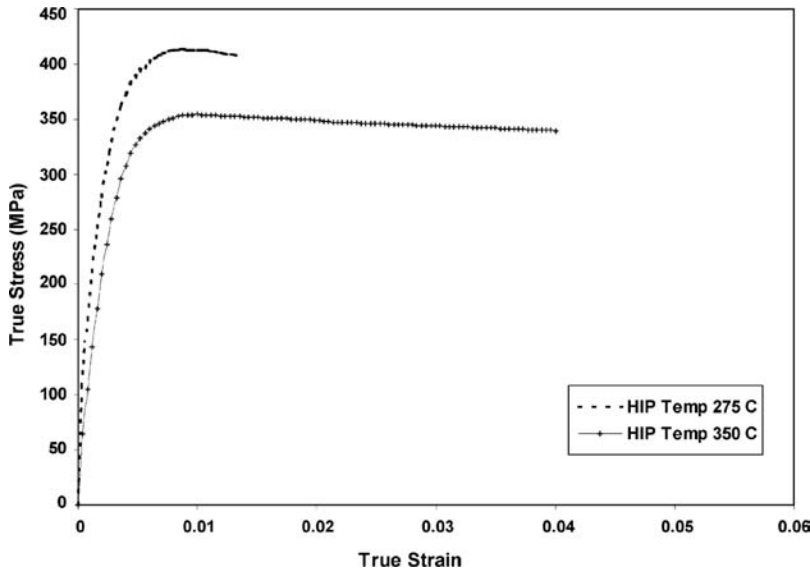


**Fig. 7** Room temperature stress-strain curves (strain rate of  $10^{-3} \text{ sec}^{-1}$ ) for extrusions of cryomilled Al HIPped at different temperatures. The data are displayed to the extent of uniform plastic strain. *Source:* From Ref.<sup>[39]</sup>.

the onset of necking, reductions in area were more than 20% and 50%, respectively, hinting that greater elongations can be achieved if flow localization can be prevented.<sup>[31]</sup>

Alloys with a bimodal grain size distribution have been investigated as a means to enhance ductility through the blending of cryomilled powder with a fraction of unmilled powder of the same chemical composition.<sup>[36]</sup> The nanostructured regions of bimodal Al-7.5Mg alloy had grain sizes of 100–300 nm. In the consolidated material, there were also larger grained bands, originating from the unmilled powder, which had a grain size of  $\sim 1 \mu\text{m}$ . There was a trend of decreasing strength and increasing elongation with an increasing fraction of micrometer-grain material, as shown in Fig. 8. A good combination of strength and ductility was obtained in the cryomilled Al-7.5Mg with 30% added unmilled powder.<sup>[36]</sup>

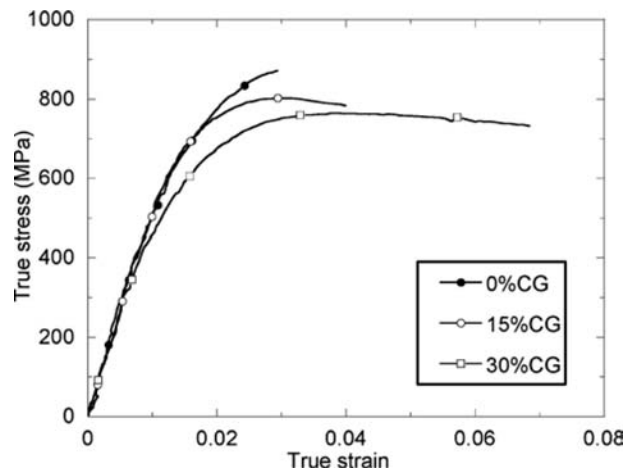


**Fig. 8** Room temperature stress-strain curves for extrusions of cryomilled Al-7.5%Mg containing from 0% to 30% unmilled coarse grained (CG) powder. *Source:* From Ref.<sup>[36]</sup>.

## CONCLUSIONS

The properties of cryomilled materials indicate both their promise and areas where additional work is necessary. In the powder form, the cryomilled materials exhibit grain sizes that are comparable to the minimum grain sizes achieved in mechanical milling. The thermal stability of cryomilled Fe is similar to that of mechanically milled Fe, but can be increased dramatically by the addition of Al. In the case of cryomilled Al-bearing alloys, their relative thermal stability exceeds that of Fe and Ni, probably due to the presence of Al nitrides that form during milling. Once consolidated, cryomilled materials typically possess considerable strength compared to both conventional and fine-grained materials processed by other methods.

The consolidation history has a significant effect on the mechanical properties of nanostructured materials. The microstructures of the consolidated materials are fairly complex, and a full understanding of the mechanical behavior remains tentative. Despite the complexity of the microstructure, existing data on cryomilled Al indicate that the Hall–Petch relationship describes the mechanical properties to a reasonable degree. This in turn suggests that dislocation interactions at grain boundaries are responsible for the plastic deformation, and not alternative mechanisms such as grain boundary sliding. The observation that coarse grains within the fine-grained matrix improve ductility has prompted an effort to increase fracture toughness by blending relatively coarse-grained unmilled powder with the cryomilled powder prior to consolidation and secondary processing.

## ACKNOWLEDGMENT

Support from the Office of Naval Research under Contract N00014-03-C-0163 is gratefully acknowledged.

## REFERENCES

- Luton, M.J.; Jayanth, C.S.; Disko, M.M.; Matras, S.; Vallone, J. Cryomilling of nano-phase dispersion strengthened aluminum. *Mater. Res. Soc. Symp. Proc.* **1989**, *132*, 79–86.
- Zhou, F.; Liao, X.Z.; Zhu, Y.T.; Dallek, S.; Lavernia, E.J. Microstructural evolution during recovery and recrystallization of a nanocrystalline Al–Mg alloy prepared by cryogenic ball milling. *Acta Mater.* **2003**, *51*, 2777–2791.
- Petkovic-Luton, R.; Vallone, J. Method for producing dispersion strengthened metal powders. U.S. Patent 4,647,304, Mar 3, 1987.
- Fecht, H.-J. Nanostructure formation by mechanical attrition. *Nanostruct. Mater.* **1995**, *6*, 33–42.
- Koch, C.C. Synthesis of nanostructured materials by mechanical milling: problems and opportunities. *Nanostruct. Mater.* **1997**, *9*, 13–22.
- Eckert, J.; Holzer, J.C.; Krill III, C.E.; Johnson, W.L. Structural and thermodynamic properties of nanocrystalline fcc metals prepared by mechanical attrition. *J. Mater. Res.* **1992**, *7*, 1751–1761.
- Mohamed, F.A. A dislocation model for the minimum grain size obtainable by milling. *Acta Mater.* **2003**, *51*, 4107–4119.
- Liao, X.Z.; Huang, J.Y.; Zhu, Y.T.; Zhou, F.; Lavernia, E.J. Nanostructures and deformation mechanisms in a cryogenically ball-milled Al–Mg alloy. *Philos. Mag.* **2003**, *83*, 3065–3075.
- Zhou, F.; Witkin, D.; Nutt, S.R.; Lavernia, E.J. On the mechanisms of nanostructure formation in Al produced by a low-energy ball milling at cryogenic temperature. *Mater. Sci. Eng. A.* **2004**, *375–377*, 917–921.
- Zhou, F.; Nutt, S.R.; Bampton, C.C.; Lavernia, E.J. Nanostructure in an Al–Mg–Sc alloy processed by low-energy ball milling at cryogenic temperature. *Metall. Mater. Trans. A.* **2003**, *34*, 1985–1992.
- Hansen, N. New discoveries in deformed metals. *Metall. Mater. Trans. A.* **2001**, *32*, 2917–2935.
- Hughes, D.A.; Hansen, N. High angle boundaries formed by grain subdivision mechanisms. *Acta Mater.* **1997**, *45*, 3871–3886.
- He, J.; Lavernia, E.J. Development of nanocrystalline structure during cryomilling of Inconel 625. *J. Mater. Res.* **2001**, *16*, 2724–2732.
- Hayes, R.W.; Berbon, P.B.; Mishra, R.S. Microstructure characterization and creep deformation of an Al-10wt%Ti-2wt%Cu nanocomposite. *Metall. Mater. Trans. A.* **2004**, *35*, 3855–3861.
- Aikin, B.J.M.; Dickerson, R.M.; Jayne, D.T.; Farmer, S.; Whittenberger, J.D. Formation of aluminum nitride during cryomilling of NiAl. *Scripta. Metall. Mater.* **1994**, *30*, 119–122.
- Whittenberger, J.D.; Arzt, E.; Luton, M.J. Preliminary investigation of a NiAl composite prepared by cryomilling. *J. Mater. Res.* **1990**, *5*, 271–277.
- Whittenberger, J.D.; Arzt, E.; Luton, M.J. 1300 K compressive properties of a reaction milled NiAl–AlN composite. *J. Mater. Res.* **1990**, *5*, 2819–2827.
- Zhou, F.; Rodriguez, R.; Lavernia, E.J. Thermally stable nanocrystalline Al–Mg alloys powders produced by cryomilling. *Mater. Sci. Forum* **2002**, *386–388*, 409–414.
- Lee, J.; Zhou, F.; Chung, K.H.; Kim, N.J.; Lavernia, E.J. Grain growth of nanocrystalline Ni powders prepared by cryomilling. *Metall. Mater. Trans. A.* **2001**, *32*, 3109–3115.
- Perez, R.J. Synthesis and stability of nanocrystalline Fe alloys produced by high energy ball milling. Ph.D. Thesis, University of California, Irvine, 1997.
- Perez, R.J.; Jiang, H.G.; Dogan, C.P.; Lavernia, E.J. Grain growth of nanocrystalline cryomilled Fe–Al powders. *Metall. Mater. Trans. A.* **1998**, *29*, 2469–2475.
- Zhou, F.; Lee, J.; Dallek, S.; Lavernia, E.J. High grain size stability of nanocrystalline Al prepared by mechanical attrition. *J. Mater. Res.* **2001**, *16*, 3451–3458.

23. Chung, K.H.; Lee, J.; Rodriguez, R.; Lavernia, E.J. Grain growth behavior of cryomilled INCONEL 625 powder during isothermal heat treatment. *Metall. Mater. Trans. A.* **2002**, *33*, 125–134.
24. Benjamin, J.S.; Bomford, M.J. Dispersion strengthened aluminum made by mechanical alloying. *Metall. Trans. A.* **1977**, *8*, 1301–1305.
25. Huang, B.; Vallone, J.; Luton, M.J. The effect of nitrogen and oxygen on the synthesis of B2 NiAl by cryomilling. *Nanostruct. Mater.* **1995**, *5*, 631–642.
26. Malow, T.R.; Koch, C.C. Grain growth in nanocrystalline iron prepared by mechanical attrition. *Acta Mater.* **1997**, *45*, 2177–2186.
27. Humphreys, F.J.; Hatherly, M. *Recrystallization and Related Annealing Phenomena*; Elsevier Scientific: Oxford, 1996.
28. Atkinson, H.V.; Davies, S. Fundamental aspects of hot isostatic pressing: an overview. *Metall. Mater. Trans. A.* **2000**, *31*, 2981–3000.
29. Ashby, M.F. Sintering and hot isostatic pressing diagrams. In *Powder Metallurgy: An Overview*; Jenkins, I., Wood, J.V., Eds.; The Institute of Metals: London, 1991; 144–166.
30. Witkin, D.; Lavernia, E.J. Processing controlled mechanical properties and microstructures of bulk cryomilled Al–Mg alloys. In *Processing and Properties of Structural Nanomaterials*; Shaw, L.L., Suryanarayana, C., Mishra, R.S., Eds.; TMS: Chicago, 2003; 117–124.
31. Hayes, R.W.; Witkin, D.; Zhou, F.; Lavernia, E.J. Deformation and activation volumes for cryomilled ultrafine-grained aluminum. *Acta Mater.* **2004**, *52*, 4259–4271.
32. Witkin, D.; Han, B.Q.; Lavernia, E.J. Microstructural evolution of an ultrafine-grained cryomilled Al 5083 during thermomechanical processing. *J. Mater. Res. in press*.
33. Han, B.Q.; Mohamed, F.A.; Lavernia, E.J. Tensile behavior of bulk nanostructured and ultrafine grained aluminum alloys. *J. Mater. Sci.* **2003**, *38*, 3319–3324.
34. Tellkamp, V.L.; Melmed, A.; Lavernia, E.J. Mechanical behavior and microstructure of a thermally stable bulk nanostructured Al alloy. *Metall. Mater. Trans. A.* **2001**, *32*, 2335–2343.
35. Han, B.Q.; Lavernia, E.J.; Mohamed, F.A. Mechanical behavior of a cryomilled near-nanostructured Al–Mg–Sc alloy. *Metall. Mater. Trans. A.* **2005**, *36*, 345–355.
36. Witkin, D.; Lee, Z.; Rodriguez, R.; Nutt, S.R.; Lavernia, E.J. Al–Mg alloy engineering with bimodal grain size for high strength and increased ductility. *Scripta Mater.* **2003**, *49*, 297–302.
37. Han, B.Q.; Lee, Z.; Witkin, D.; Nutt, S.R.; Lavernia, E.J. Deformation behavior of bimodal nanostructured 5083 Al alloys. *Metall. Mater. Trans. A.* **2005**, *36* (4), 957–965.
38. Hansen, N. Strengthening of aluminum by a three-dimensional network of aluminum-oxide particles. *Acta Metall.* **1969**, *17*, 637–642.
39. Witkin, D. Microstructural evolution and mechanical properties of nanostructured Al and Al alloys. Ph.D. Thesis, University of California, Irvine, 2005.

## BIBLIOGRAPHY

1. Gusev, A.I. Nanocrystalline materials: synthesis and properties. In *Dekker Encyclopedia of Nanoscience and Nanotechnology, 2E*; Schwarz, J.A., Contescu, C.I., Putyera, K., Eds.; Taylor & Francis: New York, NY, 2009; Vol. 4, 2621–2636.
2. Fecht, H.-J. Nanostructured materials: synthesis by mechanical means. In *Dekker Encyclopedia of Nanoscience and Nanotechnology, 2E*; Schwarz, J.A., Contescu, C.I., Putyera, K., Eds.; Taylor & Francis: New York, NY, 2009; Vol. 5, 3030–3039.
3. Koch, C.C. Nanostructured materials: synthesis by mechanical attrition. In *Dekker Encyclopedia of Nanoscience and Nanotechnology, 2E*; Schwarz, J.A., Contescu, C.I., Putyera, K., Eds.; Taylor & Francis: New York, NY, 2009; Vol. 5, 3019–3029.
4. Miani, F.; Maurigh, F.; Delogu, F. Nanophase powders: mechanosynthesis. In *Dekker Encyclopedia of Nanoscience and Nanotechnology, 2E*; Schwarz, J.A., Contescu, C.I., Putyera, K., Eds.; Taylor & Francis: New York, NY, 2009; Vol. 5, 2923–2937.

# Nanostructured Catalysts

Ravichandra S. Mulukutla

Nanoscale Materials, Inc., Manhattan, Kansas, U.S.A.

## INTRODUCTION

Practicing green chemistry has become more important over the last decade, reflecting the design, development, and implementation of chemical products and processes to reduce or eliminate the use and generation of substances hazardous to human health and the environment. Some of the principles of green chemistry<sup>[1]</sup> are as follows: 1) It is better to prevent waste than to treat or clean up waste after it has been created. 2) Synthetic methods should be designed to maximize the incorporation of all materials used in the process into the final product. 3) The use of auxiliary substances, solvents, separation agents, and others should be avoided; when used these substances should be innocuous. 4) Employ catalysts or catalytic reagents as selective as possible and that are superior to stoichiometric reagents. Hence, the application of catalysts in chemical reactions and more so the impact of nanostructured catalysts is the scope of this article; a few examples will be discussed pertaining to the topic. A catalyst is considered to be active in any given chemical process if it shows high conversion, is selective to the desired products, is stable for a prolonged period of time, and has good mechanical strength. Out of all the concerns, conversion and selectivity dictate the fate of the catalyst in a larger way as it can significantly change the economics of the process. High conversion can be achieved in general if the catalyst species is not sintered during the reaction and selectivity is achieved from the specific crystal structure of the catalytic active metal or the metal oxide precursor. Hence, controlling the catalyst species at molecular level is possible if catalysts were fabricated at nanometer scale. From the definition, particles of between 1 and 10 nm in size have definite crystal structure at nanometer level, and hence the application of nanostructured materials as catalysts can drastically change the conversion and selectivity in the chemical processes. This article describes in detail how nanostructured catalysts affect the catalytic process in comparison to bulk catalysts. More examples can be found in the book chapter written by Klabunde and Mulukutla.<sup>[2]</sup>

## NANOSTRUCTURED CATALYSTS FOR SELECTIVE PROCESSES

Selectivity in a chemical reaction is defined as the production of one molecule out of many other thermodynamically feasible product molecules. There is an enormous opportunity, for to understand selectivity is very important, and it is less understood than activity.<sup>[3]</sup> On the nanometer scale, bifunctional catalysis has been documented as playing a major role in selectivity. On nanostructured catalysts reactant molecules undergo chemical change to produce intermediates. These reaction intermediates will then diffuse a certain distance to other sites where they undergo further rearrangements to produce the final product, which then desorbs. In this case, selectivity changes markedly with conversion. As can be seen from Fig. 1, nanostructured catalysts can be divided into two classes: the first category is composed of nanoparticles of metals supported on metal oxides or molecular sieves and the second includes high-surface-area nanocrystalline metal oxides themselves as catalysts or catalyst supports. Examples for each category are shown and will be described in detail in the following sections.

## NANOPARTICLE SUPPORTED CATALYSTS

Nanoparticle catalysts can be designed and synthesized from various methodologies.<sup>[4]</sup> The most attractive and appropriate methods involve nanoparticles of metals or metal oxides supported on inert oxides, molecular sieves, and polymers.

### Gold Nanoparticle Catalysts

Gold nanoparticle catalysts have attracted wide attention because of their wide applications in CO oxidation, epoxidation of propylene, water-gas-shift reaction, hydrogenation of unsaturated hydrocarbons, and liquid phase selective oxidation.<sup>[5]</sup> It is well known that gold is a poor catalyst in the bulk form,



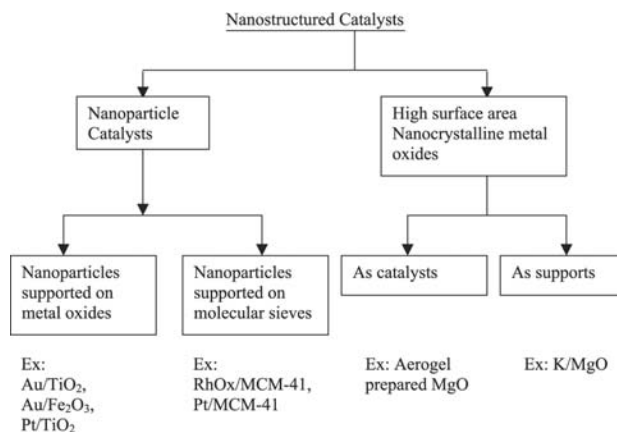


**Fig. 1** Classification of nanostructured catalysts.

whereas gold nanoparticles supported on oxides exhibit high catalytic activity. A schematic representation of gold nanoparticles supported on oxides is shown in Fig. 2A.

Zhong and Maye<sup>[4]</sup> demonstrated a novel approach involving monolayer-encapsulated metal nanoparticles in a core-shell nanostructured assembly as shown in Fig. 2B. The core-shell assembled nanostructure undergoes structural or morphological changes during catalytic activation and reaction within both the individual core-shell structure and the collective network environment. The monolayer encapsulation imparts the nanoparticles with shell reactivity and processibility dictated by functional groups in a three-dimensional framework.

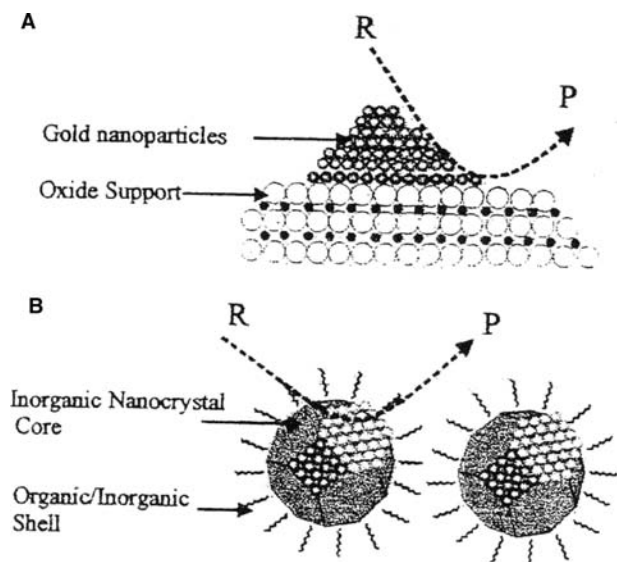


**Fig. 2** Schematic representation of nanoparticle catalysts.<sup>[2]</sup> (A) Oxide-supported nanoparticle catalyst, (B) core-shell nanoparticle catalyst. *Source:* Reprinted with permission from Ref.<sup>[4]</sup>. Wiley-VCH Verlag GmbH.

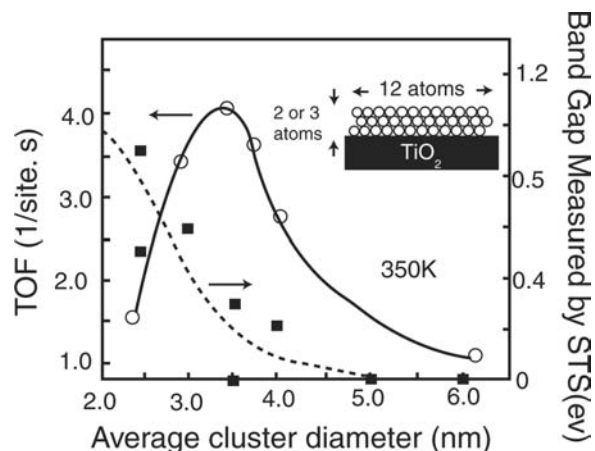


**Fig. 3** Turnover frequencies and bandgaps measured by STM as a function of the diameter of Au islands deposited on TiO<sub>2</sub>. *Source:* Reprinted with permission from Ref.<sup>[5]</sup>. Elsevier Science B.V. © 2001.

Valden et al. reported Au/TiO<sub>2</sub> catalyst<sup>[6]</sup> and demonstrated the change in turnover frequency (TOF) of CO oxidation with the change in the diameter of Au islands. As can be seen from Fig. 3, the CO oxidation reaches a maximum at an Au cluster diameter of 3.5 nm, where Au partially loses its metallic nature. They have suggested that this transition might be correlated to the high catalytic activity.

Hayashi and coworkers<sup>[7]</sup> found that Au supported on TiO<sub>2</sub> could catalyze epoxidation of propylene in the gas phase containing O<sub>2</sub> and H<sub>2</sub>. There are several factors that influence the catalytic activity of the reaction. The most important is the method of preparation, as shown in Fig. 4. The Au/TiO<sub>2</sub> was prepared by either an impregnation method or a deposition precipitation method. The impregnation method did not result in selective oxidation, but instead complete oxidation to H<sub>2</sub>O and CO<sub>2</sub>, whereas the direct precipitation method led to epoxidation with selectivities above 90%. The difference in the structure of the catalysts prepared by the different methods influences the selectivity. The impregnation method produces large, spherical Au particles with sizes of about several tens of nanometers in diameter, whereas the direct precipitation method results in small hemispherical Au particles strongly contacted with TiO<sub>2</sub> support. This is a very interesting example of how structure and size of the nanoparticles affects the selectivity of the reaction.

**Platinum Nanoparticle/MCM-41 Catalysts**

Over the last three decades, there have been considerable efforts to synthesize platinum nanoparticle supported catalysts and attempts to study the selectivity

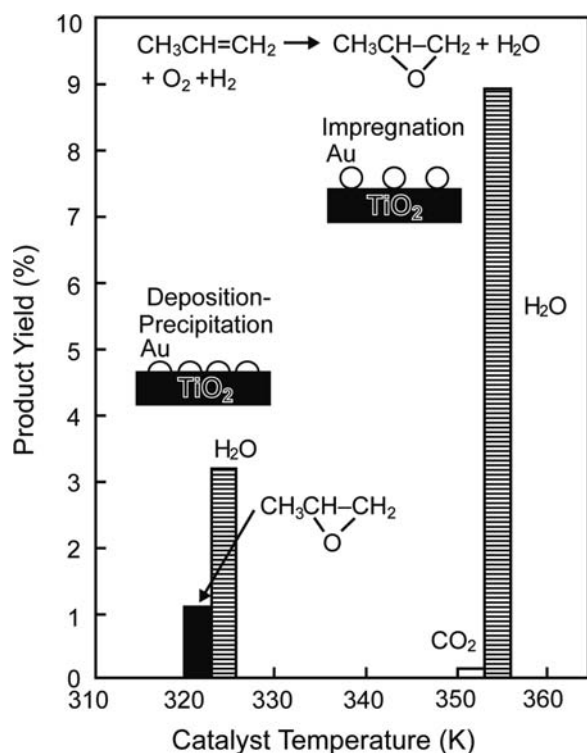


**Fig. 4** Epoxidation of propylene over Au/TiO<sub>2</sub> prepared by different methods. *Source:* Reprinted with permission from Ref.<sup>[5]</sup>. Elsevier Science B.V. © 2001.

in various organic reactions. A classical example is the work of Junges et al.,<sup>[8]</sup> who prepared Pt nanoparticles on MCM-41 and applied the catalyst for low-temperature carbon monoxide oxidation. In this work, three methods were employed to synthesize Pt-MCM-41: 1) incipient wetness, 2) ion exchange, and 3) in situ methods. The Pt particle sizes obtained with the three preparation methods varied substantially. For the in situ loading the final average particle size was around 4–6 nm, and TEM observation revealed that the 4-nm-sized particles are located in the pore channels of the MCM-41, while the larger particles might be present on the external surface of MCM-41. The samples synthesized by ion exchange method resulted in 10-nm-sized particles. The incipient wetness impregnation resulted in 2-nm-sized Pt particles with total Pt loading up to 2% mass. All three catalysts were evaluated for CO oxidation with air in an open flow reactor at gas hourly space velocity 25,000 hr<sup>-1</sup>. The synthetic methods, which resulted in different sizes of Pt particle, had a strong influence on the catalytic performance. The best performance was observed on the samples prepared by incipient wetness, where 50% conversion was achieved at a temperature of 85°C due to the Pt nanoparticles around 2 nm, which resulted in high conversion. The other two catalysts showed 50% conversion between 110° and 130°C.

The work on Pt nanoparticle catalysts provided ample evidence that nanoparticles of Pt can exhibit high rates for CO conversion.

### RhOx Nanoparticle/MCM-41

Mulukutla et al.<sup>[9–12]</sup> synthesized RhOx nanoparticles in the MCM-41 molecular sieve via a sol-gel method. As shown in Fig. 5, assorted sizes of RhOx nanoparticles were prepared by changing the conditions of the

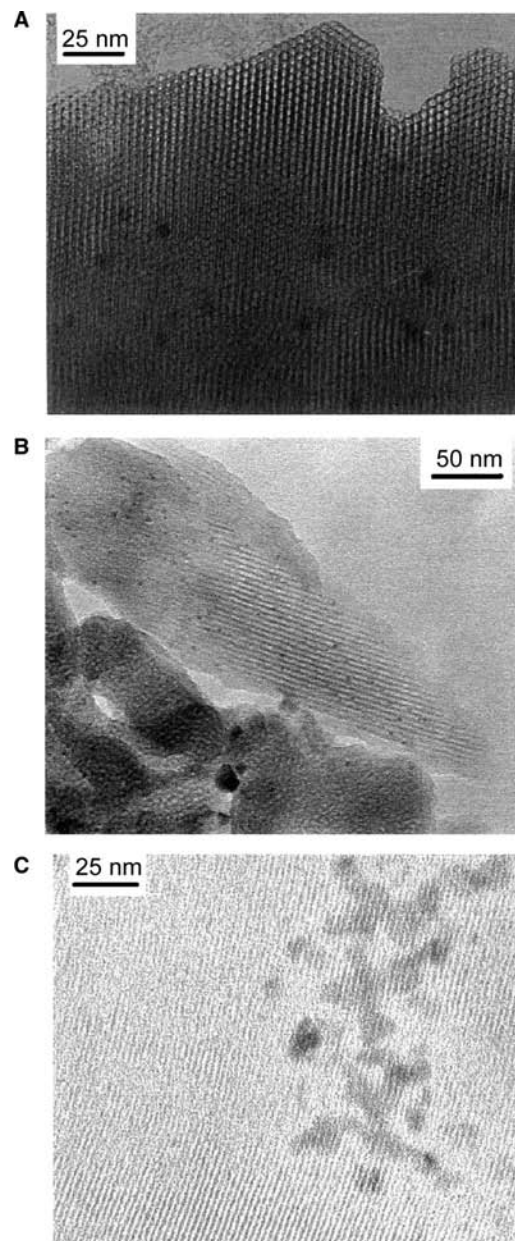


**Fig. 5** TEM photographs of (A) Rh-MCM-41-A-200; (B) Rh-MCM-41-B-200, and (C) Rh-su-MCM-41-200. *Source:* Reprinted with permission from Ref.<sup>[12]</sup>. Elsevier Science B.V. © 2002.

synthesis. The size and location of the resulting rhodium oxide particles varied with the hydrothermal synthesis conditions as shown in TEM photographs in Fig. 5. The RhOx nanoparticles in Rh-MCM-41-A with Si/Rh = 200 (Fig. 5A) grew to 6- to 8-nm RhOx particles and they seemed to be located in the bulk of MCM-41. The local structure of MCM-41 might have been destroyed because the particle sizes were larger than the MCM-41 pore diameter (3.2 nm). The argument for RhOx on the surface has been ruled out from the comparison with the MCM-41 supported RhOx sample (Fig. 5C) with a similar Rh loading. Furthermore, the RhOx particles in Rh-MCM-41-A (Fig. 5A) were orthorhombic, whereas the RhOx particles supported on the MCM-41 surface were hexagonal, demonstrating the different locations between the two samples.

The Rh-MCM-41-B with Si/Rh = 200 (Fig. 5B) possessed <3-nm-sized RhOx particles, which were smaller than the MCM-41 with pore diameter of 3.4 nm. TEM photograph of Fig. 5B depicts that the RhOx particles are located in the pore channels of MCM-41. Fig 5C is a TEM photograph of the Rh-su-MCM-41 having Si/Rh = 200, where rhodium oxides are observed as aggregates of about 10-nm size, while the MCM-41 pore channels are clearly visible.

RhOx nanoparticles in the MCM-41 with different particle sizes, structures, and locations in the MCM-41 were used as catalysts for NO-CO reactions. The NO reduction with CO was performed in the presence and absence of O<sub>2</sub>. On the Rh-MCM-41-B catalyst, the NO conversion to N<sub>2</sub> and N<sub>2</sub>O in the absence of O<sub>2</sub> began between 275° and 300°C as shown in Fig. 6. The conversion to N<sub>2</sub>O reached a maximum of 30% at 325°C. The selectivity to N<sub>2</sub> increased with

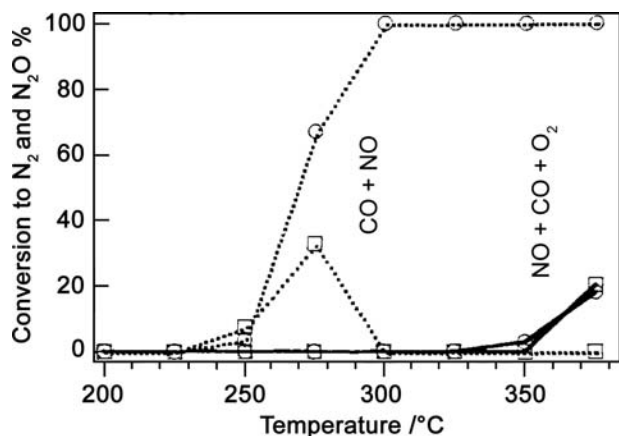


**Fig. 6** The NO conversion to N<sub>2</sub> and N<sub>2</sub>O against reaction temperature on the Rh-MCM-41-B catalyst; (O) N<sub>2</sub>, (□) N<sub>2</sub>O, (—) NO + CO + O<sub>2</sub>, (---) CO + NO. Source: Reprinted with permission from Ref.<sup>[11]</sup> Acta Materialia Inc. Published by Elsevier Science Ltd. © 2001.

temperature and reached 92% at 375°C. Excess oxygen (4%) was added to the stream of NO and CO, which resulted in unexpected promotion of the NO conversion to N<sub>2</sub> and N<sub>2</sub>O as shown in Fig. 6. The reaction in the presence of O<sub>2</sub> proceeded at 250°C, whereas it did not proceed below 275°C in the absence of O<sub>2</sub>. The promotion phenomenon by excess O<sub>2</sub> is of interest and it may be attributed to the nanosized rhodium oxide precursors in the pore channels of MCM-41. The excess O<sub>2</sub> usually poisons the Rh catalysis since O<sub>2</sub> oxidizes CO to CO<sub>2</sub> very rapidly. It was concluded that under the reaction conditions NO conversion was promoted in the NO-CO reaction in the presence of excess O<sub>2</sub> on the Rh-MCM-41-B catalyst.

Fig. 7 depicts the NO conversion to N<sub>2</sub> and N<sub>2</sub>O on the Rh-MCM-41-A catalyst with and without O<sub>2</sub>. At 275°C there was about 75% conversion to N<sub>2</sub> and the rest was N<sub>2</sub>O, and at the higher temperatures the selectivity toward N<sub>2</sub> was 100%. However, the presence of O<sub>2</sub> in the stream dramatically suppressed the conversion of NO, and the NO conversion to N<sub>2</sub> and N<sub>2</sub>O began above 375°C. Thus, the Rh-MCM-41-A catalyst, which had RhOx particles of the size of 6–8 nm exhibited a negative effect of excess O<sub>2</sub> on the NO conversion. These results are entirely different from those observed with the Rh-MCM-41-B catalyst. NO conversion to N<sub>2</sub> and N<sub>2</sub>O in the NO-CO reaction on the RhOx supported on MCM-41 (Rh-su-MCM-41) catalyst exhibited a negative effect by excess O<sub>2</sub>. This feature resembles that observed with the Rh-MCM-41-A catalyst. This observation on the nanostructured RhOx-MCM-41 is emphasized to show that the active sites in different locations and particles sizes play a significant role in the catalytic reaction of NO-CO in presence of O<sub>2</sub>.

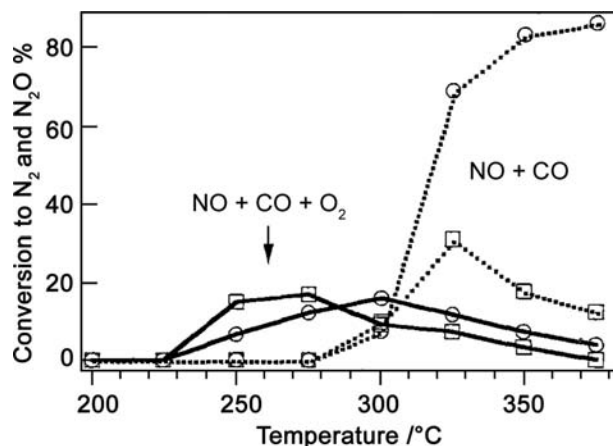


**Fig. 7** The NO conversion to N<sub>2</sub> and N<sub>2</sub>O against reaction temperature on the Rh-MCM-41-A catalyst; (O) N<sub>2</sub>, (□) N<sub>2</sub>O, (—) NO + CO + O<sub>2</sub>, (---) CO + NO. Source: Reprinted with permission from Ref.<sup>[11]</sup> Acta Materialia Inc. Published by Elsevier Science Ltd © 2001.

## NANOCRYSTALLINE METAL OXIDE AS CATALYSTS/CATALYST SUPPORTS

Synthesis of high-surface-area nanocrystalline alkaline metal oxides has drawn much attention because of their high surface area and adsorption capacity compared to their commercial analogues. Some examples are MgO, CaO, TiO<sub>2</sub>, and Al<sub>2</sub>O<sub>3</sub>. The extraordinary properties of these nanocrystalline oxides are due to the morphological features of the small crystallites possessing higher populations of reactive surface sites such as edges, corners, and ion vacancies. It has been proposed that some of these nanocrystalline metal oxides, because of their defective sites, might have catalytic properties and that they can be used as catalyst supports because they have high surface area. The following are some examples where nanocrystalline MgO exhibited catalytic properties. In addition, it has been used as support for synthesizing superbase catalysts.

### Aerogel-Prepared MgO

Utamapanya, Klabunde, and Schlup<sup>[13]</sup> prepared nanocrystalline MgO through an aerogel method using supercritical drying and were successful in obtaining high surface areas in the range of 400–500 m<sup>2</sup>/g with crystallite sizes of about 3 nm. The nanocrystalline MgO obtained is referred to as AP-MgO.

### Chlorination of Hydrocarbons with Aerogel-Prepared MgO

Aerogel-prepared MgO, when exposed to Cl<sub>2</sub> gas at atmospheric pressure and room temperature, exothermally formed an extremely reactive AP-MgO-Cl<sub>2</sub> adduct; 15% Cl<sub>2</sub> by weight was adsorbed on the surface.<sup>[14]</sup> The chlorine adduct was able to chlorinate hydrocarbons in a batch reactor. The normal forms of MgO did not react with Cl<sub>2</sub> gas. Richards, Mulukutla, and Mishakov<sup>[15]</sup> performed further investigation on the characterization of the AP-MgO-Cl<sub>2</sub> adduct, conducting pulse reactions and demonstrating the catalytic behavior of AP-MgO in the chlorination of hydrocarbons. The XPS characterization of AP-MgO-Cl<sub>2</sub> indicated that the binding energy for Cl 2p is 198.2 eV and this value corresponds to monochloro compounds similar to NaCl and KCl. Hence, the chlorinated species on the surface of AP-MgO is not MgCl<sub>2</sub>. As shown in Fig. 8A, the chlorination of propane conducted over AP-MgO at temperatures from 0° to 200°C proceeded in normal light. The expected products were 1-chloropropane, 2-chloropropane, and 1,2-dichloropropane. Fig. 8B shows the reaction data conducted without AP-MgO where the reaction

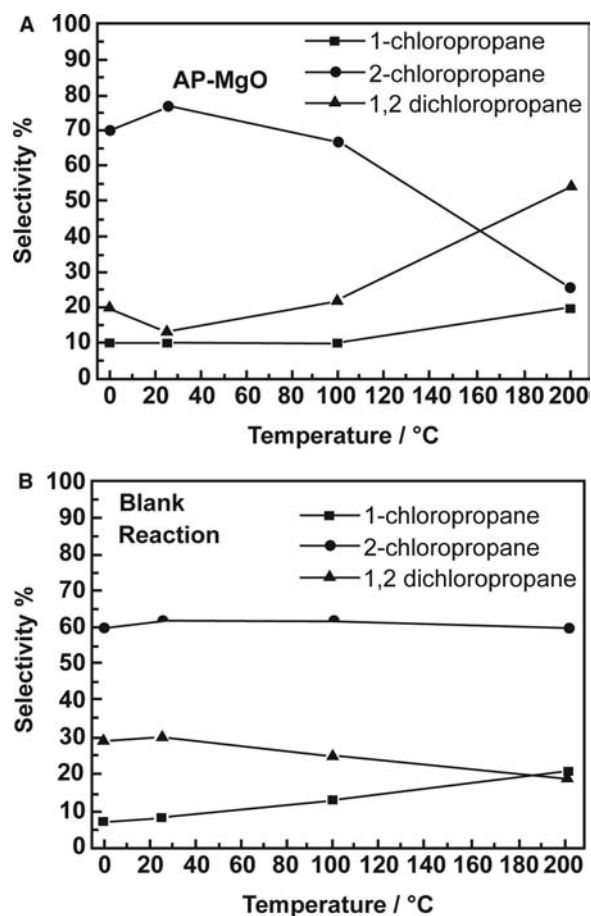


**Fig. 8** Chlorination of propane (A) with AP-MgO catalyst. (B) Blank reaction. *Source:* Reprinted with the permission from Ref.<sup>[13]</sup>. Acta Materialia Inc. Published by Elsevier Science Ltd © 2001.

proceeded with the help of normal light. As noted, the selectivity to 1,2-dichloropropane up to 60% was observed when the reaction was conducted at 200°C with AP-MgO, with simultaneous decrease of the 2-chloropropane. The selectivity was not affected in the case of a blank reaction.

### Dehydrochlorination of 1-Chlorobutane with Aerogel-Prepared MgO

Mishakov et al.<sup>[16]</sup> and Fenelonov et al.<sup>[17]</sup> evaluated nanocrystalline MgO for dehydrochlorination of 1-chlorobutane. Exposure of AP-MgO to 1-chlorobutane at 200–350°C resulted in both stoichiometric and catalytic dehydrochlorination to form isomers of butene and simultaneous topochemical conversion of MgO to MgCl<sub>2</sub>. The resulting MgCl<sub>2</sub> was believed to be an active catalyst for the dehydrochlorination reaction. As shown in Fig. 9, the

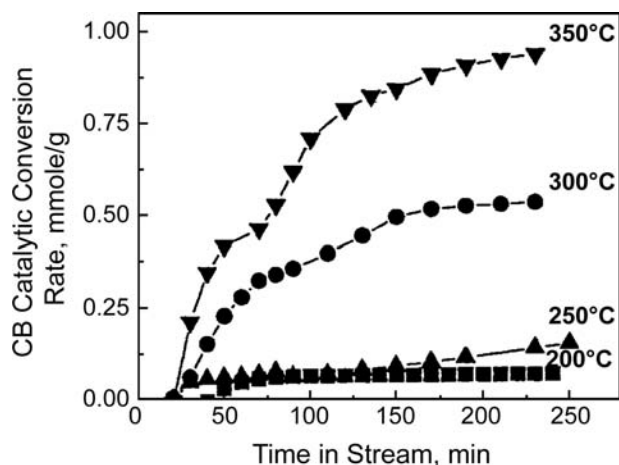


**Fig. 9** Kinetics of chlorobutane conversion at different temperatures. *Source:* Reprinted with permission from Ref.<sup>[17]</sup>. American Chemical Society © 2001.

conversion of chlorobutane at different temperatures over time established the formation of active  $\text{MgCl}_2$  from AP-MgO. The formation of such an active catalyst species on the surface of nanocrystalline MgO was possible only with AP-MgO. Hence, this work is a striking example of how a high-surface-area catalytic species such as  $\text{MgCl}_2$  can be formed from a nanocrystalline MgO.

### Potassium/Aerogel-Prepared MgO

The high surface area of AP-MgO in the range of  $350\text{--}500\text{ m}^2/\text{g}$  can be used as a support. Sun and Klabunde<sup>[18]</sup> prepared potassium metal-doped nanocrystalline MgO, which exhibited high activity in base-catalyzed isomerization and alkylation. It was established that 10 wt.% of K-doped AP-MgO showed 100% conversion to isomerized products from 2,3-dimethyl-1-butene at room temperature in 30 min. However, the use of commercial analogues and lower-surface-area MgO did not result in such high conversions. The edges/corners on the polyhedral crystallites of high-surface-area MgO are responsible for creating superbasic sites to obtain a highly active isomerization catalysts.

### CONCLUSION

This entry demonstrates that nanostructured catalysts can be designed by several methods. The prominent ways are synthesizing metal nanoparticles supported on metal oxides and sol-gel method of generating

metal/metal oxide nanoparticles in MCM-41 molecular sieves. Nanocrystalline metal oxides with high surface area, which were prepared from aerogel methods, can be used as catalysts or catalyst supports. The examples show that nanostructured catalysts have a significant influence on the conversion and selectivity of the chemical reactions. Control and understanding of particle size and structure of the catalytic active species is the most important factor in achieving the difference between the catalytic property of nanostructured catalysts vs. bulk catalysts.

### REFERENCES

1. Anastas, P.T.; Warner, J.C. *Green Chemistry: Theory and Practice*; Oxford University Press: New York, 1998.
2. Klabunde, K.J.; Mulukutla, R.S. Chemical and Catalytic Aspects of Nanocrystals. In *Nanoscale Materials in Chemistry*; Klabunde, K.J., Ed.; John Wiley & Sons, Inc., 2001; 223–261, Chap. 7.
3. Somorjai, G.A.; Borodko, Y.G. Research in nanosciences—Great opportunity for catalysis science. *Catal. Letters* **2001**, *76* (1–2), 1–5.
4. Zhong, C.-J.; Maye, M.M. Core-shell assembled nanoparticles as catalysts. *Adv. Mater.* **2001**, *13*, 1507–1511.
5. Haruta, M.; Date, M. Advances in the catalysis of Au nanoparticles. *Appl. Catal.* **2001**, *222*, 427–437.
6. Valden, M.; Lai, X.; Goodman, D.W. *Science* **1998**, *281*, 1647.
7. Hayashi, T.; Tanaka, K.; Haruta, M. *J. Catal.* **1998**, *78*, 566.
8. Junges, U.; Jacobs, W.; Voigt-Martin, I.; Krutzsch, B.; Schuth, F. MCM-41 as a support for small platinum particles: A catalyst for low-temperature carbon monoxide oxidation. *J. Chem. Soc., Chem. Commun.* **1995**, 2283–2284.
9. Mulukutla, R.S.; Asakura, K.; Namba, S.; Iwasawa, Y. Nanosized rhodium oxide particles in the MCM-41 mesoporous molecular sieve. *Chem. Commun.* **1998**, 1425–1426.
10. Mulukutla, R.S.; Asakura, K.; Kogure, T.; Namba, S.; Iwasawa, Y. Synthesis and characterization of rhodium oxide nanoparticles in mesoporous MCM-41. *Phys. Chem., Chem. Phys.* **1999**, *1*, 2027–2032.
11. Mulukutla, R.S.; Shido, T.; Asakura, K.; Iwasawa, Y. Nanoparticles of  $\text{RhO}_x$  in the MCM-41: A novel catalyst for NO–CO reaction in excess  $\text{O}_2$ . *Scr. Mater.* **2001**, *44*, 1695–1698.
12. Mulukutla, R.S.; Shido, T.; Asakura, K.; Kogure, T.; Iwasawa, Y. Characterization of rhodium oxide nanoparticles in MCM-41 and their catalytic performances for NO–CO reactions in excess  $\text{O}_2$ . *Appl. Catal., A Gen.* **2002**, *228*, 305–314.
13. Utamapanya, S.; Klabunde, K.J.; Schlup, J.R. Nano-scale metal oxide particles/clusters as chemical reagents.



- Synthesis and properties of ultrahigh surface area magnesium hydroxide and magnesium oxide. *Chem. Mater.* **1991**, *3*, 175–181.
14. Sun, N.; Klabunde, K.J. Nanocrystal metal oxide–chlorine adducts: Selective catalysts of chlorination of alkanes. *J. Am. Chem. Soc.* **1999**, *121*, 5587–5588.
  15. Richards, R.; Mulukutla, R.S.; Mishakov, I.; Chesnokov, V.; Volodin, A.; Zaikovski, V.; Sun, N.; Klabunde, K.J. Nanocrystalline ultra high surface area magnesium oxide as a selective base catalyst. *Scr. Mater.* **2001**, *44*, 1663–1666.
  16. Mishakov, I.; Bedilo, A.; Richards, R.; Chesnokov, V.; Volodin, A.; Zaikovskii, V.; Buyanov, R.A.; Klabunde, K.J. Nanocrystalline MgO as a dehydrohalogenation catalyst. *J. Catal.* **2002**, *206*, 40–48.
  17. Fenelonov, V.B.; Melgunov, M.S.; Mishakov, I.V.; Richards, R.M.; Chesnokov, V.V.; Volodin, A.M.; Klabunde, K.J. Changes in texture and catalytic activity of nanocrystalline MgO during its transformation to MgCl<sub>2</sub> in the reaction with 1-chlorobutane. *J. Phys. Chem., B* **2001**, *105*, 3937–3941.
  18. Sun, N.; Klabunde, K.J. High activity solid super base catalysts employing nanocrystals of metal oxides: Isomerization and alkylation catalysis, including conversion of propylene–ethylene mixtures to pentenes and heptenes. *J. Catal.* **1999**, *185*, 506–512.



# Nanostructured Catalysts: Design and Synthesis

Hua Chun Zeng

Department of Chemical and Environmental Engineering,  
National University of Singapore, Singapore, Singapore

## INTRODUCTION

Natural and manmade catalytic materials are among the oldest “nanostructured materials” known long before the era of nanoscience and nanotechnology. The classic heterogeneous catalysts consist of active nanoscale metal component(s) and solid carriers,<sup>[1]</sup> namely, “inert” oxide supports such as alumina, silicates, or magnesium oxide, to increase the reaction surface area and metal utilization. Conventional processing techniques for fabrication of supported catalysts contain one or more of the following steps: impregnation, precipitation, coating, rewashing, ion-exchange, pulverization, dyeing, and calcination, etc.<sup>[2]</sup> Nanoscale metal clusters or particles can be thus formed on the oxide carriers after these processes. It is now well known that the particle size, local composition, and structure (shape) of nanoscale catalysts determine the ultimate catalytic activity and selectivity. For example, it has been demonstrated that the activity of TiO<sub>2</sub>-supported gold particles is very sensitive to their size (2 to 3 nm) in the CO oxidation reaction with oxygen at ambient conditions.<sup>[3]</sup> It is also well known that the structure and composition of nanocatalysts may change under the reaction conditions, and thus their performance could be time-dependent. Nonetheless, prevailing catalyst preparation still remains largely as a technological art rather than a science, although surface science has significantly deepened our general understanding of heterogeneous catalysis using single-crystal model catalysts.<sup>[4]</sup>

Over the past 15 to 20 years, we have witnessed exciting advances in the design and synthesis of low-dimensional nanostructured materials, ranging from fullerenes, carbon nanotubes, supramolecular assemblies, mesoporous structures, to various organic-inorganic hybrid materials. Taking advantage of the rapid development in nanoscience and nanotechnology, a wide range of synthetic techniques are now in place. For example, nanostructured materials can be prepared with constrained or unconstrained synthetic methods, in which inorganic or organic templates (e.g., porous oxides, organic ligands, well-oriented crystal planes, and supramolecule-directing agents) are commonly employed. With these newer approaches

and knowledge, a huge variety of nanostructured catalytic materials have been designed and synthesized, which will be the main review topic of the present entry. With the emphasis on catalytic prospect, the objective of this entry thus aims at introducing various design and synthesis strategies for this new class of materials. Future challenges and research directions in this area will also be addressed.

## DESIGN AND SYNTHESIS OF NANOSTRUCTURED CATALYTIC MATERIALS

Because of the advances in nanostructured catalytic materials and assembling methodologies, we may have to reexamine the roles of each component in the traditional heterogeneous catalysts and redevelop the technology. In fact, a practical solid catalyst is normally not a simple chemical compound, but a highly organized multicomponent materials system (e.g., active components and carrier). In this regard, a modern view of solid catalysts is different from the traditional one. An organized assembly of catalytic materials can be considered as a “catalyst device”,<sup>[5]</sup> and the ways of chemical and structural organizations in the device will give profound impacts on its ultimate performance. In the foreseeable future, a transformation from the traditional catalyst preparation to a more sophisticated “assembly” technology is anticipated in view of the rapid progress of this field. As the first steps toward this end, nonetheless, various nanocomponents with desired chemical and structural properties and organization programmability must be fabricated and investigated for the constitution of a nanocatalyst “toolbox.” In the following sections, we will look into the current trends of research in this important area.

### Architectures of Porous Materials

Many significant progresses in porous materials have been made over the past two decades, which extends the commonly known zeolites (chemical formula  $M_{x/n}^{n+}[(AlO_2)_x(SiO_2)_y]^{x-} \cdot zH_2O$ , where  $M^{n+}$  represents

a metal cation; pore diameter <1 nm) from microporous regime (pore diameter <2 nm) to mesopores (2–10 nm),<sup>[6]</sup> large mesopores (>10 nm), and macropores (>50 nm). In particular, crystalline VPI-5 with uniform pores larger than 1.0 nm had been synthesized for the first time in 1988, as illustrated in Fig. 1.<sup>[7]</sup> Subsequently, periodic mesoporous solids were discovered by Mobil researchers in 1992.<sup>[8]</sup> These ordered porous materials with large pore openings had significantly enhanced our ability in utilizing intrapore chemical reactivity and space confinement for catalytic reactions, sorption processes, ion exchange, as well as materials synthesis, including architectures for growth and organization of functional nanomaterials. For example, hexagonal MCM-41 and cubic MCM-48 (Mobil codes) can be prepared with cationic surfactants under basic conditions. These mesoporous silicates together with various modifications (i.e., with metal cations via ion exchange, complexation, and direct “planting”)<sup>[9]</sup> allow us to tailor chemical and thermal properties to meet different working environments. For instance, isomorphous substitution and post-synthesis incorporation of active metal species are the two major methods for metal introduction to mesoporous silica.<sup>[10]</sup> Furthermore, surface functionalization with organic groups will change the chemical properties of the surfaces, forming hybrid inorganic–organic

mesoporous silicates. In the latter cases, the mesopores of the prepared solids can be viewed as nanoscopic reactors, separators, or host templates for chemical processes and nanostructured materials fabrication.

Various methods have been developed to introduce organic surface groups onto the mesoporous hosts, on the basis of chemical reactions between the hydroxyl-covered surfaces and reactive silane coupling agents. For example, covalent grafting, coating, and co-condensation reactions are common methods to tailor surface properties these days.<sup>[11]</sup> In grafting processes, surface modification with organic ligands and functional groups is normally carried out by silylation that takes place on free and geminal silanol groups [i.e.,  $\equiv\text{Si}-\text{OH}$  and  $=\text{Si}(\text{OH})_2$ ] under dry conditions. On the other hand, coating provides a means to introduce organics onto hydrated pore surfaces where a monolayer of water is present to form organosilanes. Compared to the above two methods, the co-condensation process is a more direct method. The surface organic functional groups can be anchored together with the formation of mesoporous silicates under so-called “one pot” synthetic conditions.<sup>[12]</sup> These organic–inorganic hybrids possess a number of advantages for catalytic applications that organic polymers and amorphous/nonporous silica counterparts do not have.<sup>[11]</sup> In many cases, space confinement and

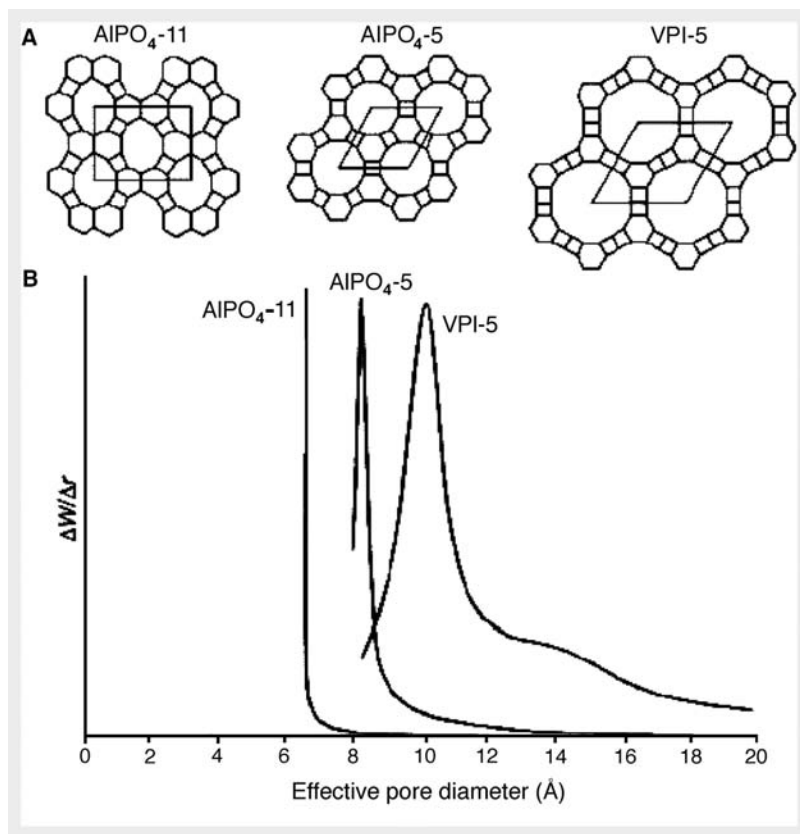


**Fig. 1** (A) Pore characteristics in some representative aluminophosphates  $\text{AlPO}_4\text{-11}$ ,  $\text{AlPO}_4\text{-5}$ , and VPI-5. (B) Measured pore sizes by argon adsorption techniques, noting that the VPI-5 shows a pore diameter greater than 1.0 nm. *Source:* From Ref.<sup>[7]</sup>.

stabilization of the catalyst in the mesoporous solid can be attributed to the observed enhancement of catalytic activity. These materials have demonstrated utility as catalysts in acid/base catalysis, oxidations, reductions, enantioselective catalysis, stereospecific polymerizations, and fine chemicals synthesis.<sup>[11]</sup> Rich inclusion chemistry of this class of materials with guest species in the internal space had been reviewed recently.<sup>[9]</sup>

Over the past decade, increasing research activities have been shown in the fabrication of hierarchical porous structures that possess ordered pores ranging from micro- to macroscale. There have been a number of techniques developed.<sup>[7]</sup> For example, microporous colloidal particles have been used for shape-, film-casting to prepare a range of hierarchical porous structures. On the other hand, bulk dissolution and restructuring of preexisting oxides have been used to fabricate shaped hierarchical structures of zeolite. Furthermore, structures with mesoporosity can be prepared by using surfactants as structuring directing agents.<sup>[7]</sup> In addition to these approaches, new film formation methods allow us to fabricate various zeolite and molecular sieve layers and membranes. In recent years, pore sizes of ordered mesoporous oxides have been extended up to 10 nm with the use of block copolymers, and from 100 nm to 1  $\mu\text{m}$  with Latex spheres as templating structures.<sup>[13,14]</sup> For example, non-ionic polyethylene oxide surfactants were used to prepare wormhole-like, MSU-type SBA-n and CMI-1 mesoporous materials. With decaoxyethylene-cetyl-ether or polyoxyethylene(6)tridecyl-ether surfactants, hierarchical macroporous metal oxides had been synthesized without using polymeric sphere template.<sup>[13]</sup> It is believed that the macro-mesostructured metal oxides were formed through an intermediate phase of supermicelles (the length in the micrometer range and the diameter in the submicrometer range) and mesostructured nanoparticles of metal oxides. The removal of the organic components resulted in the formation of hierarchical mesoporous-macroporous structures.<sup>[13]</sup> The approach had been successfully applied to  $\text{ZrO}_2$ ,  $\text{Nb}_2\text{O}_5$ ,  $\text{Ta}_2\text{O}_5$ ,  $\text{Al}_2\text{O}_3$ , and  $\text{CeO}_2$  oxide systems, and the networks of the pores can be preserved at elevated temperatures to meet catalytic applications. Very recently, hierarchical and self-similar growth of self-assembled mesophase crystals in micrometer size had been investigated with the assistance of glass substrate. Ordered octahedral crystal building units can be assembled into various high-ordered stack structures via edge-sharing. It is found that the large structures are formed through stepwise nucleation from the edges of the previous crystals.<sup>[15]</sup>

In addition to the general interest in the synthesis and design of micro-, meso-, and macroporous materials, there are interests in the preparation of single-site molecular receptors in silica matrix for specific

adsorption and catalysis applications. Using molecular imprinting techniques, both microporosity and chemical functionality have been achieved for this new class of organic-inorganic hybrid materials. Typically, bulk-imprinted silica with hydrophilic framework can be prepared via copolymerization of the imprint organosilane(s) with a silica source (normally, silicon alkoxides such as tetraethyl orthosilicate, TEOS), followed by a mild thermal treatment.<sup>[16]</sup> Fig. 2 shows a flowchart of this type of synthesis, where organic functional groups (such as amines) can be immobilized into the silica matrix possessing high specific surface area. The imprinted silicas can act as shape-selective base catalysts,<sup>[17]</sup> and the hydrophilic framework prepared in this way offers an interesting potential to stabilize polar reactive intermediates and transition states at the active sites.<sup>[16]</sup>

Finally, it should be mentioned that the mesoporous materials can be used as traditional high-surface-area catalytic supports for active metal loading. On the other hand, nanostructured metallic catalysts encapsulated can nucleate the expansion of the mesopore channels. For example, prefabricated gold and platinum nanoparticles had been investigated to tune the pore size of the mesoporous silica (SBA-15) that are grown around them (e.g., in the range of 9.2 to 11.6 nm).<sup>[18]</sup>

Other important applications of the porous materials include template synthesis of nanostructured catalytic materials used as either individual (freestanding) catalysts or basic building blocks for self-assembly, as will be discussed in subsequent sections.

## Designs of Layered Organic-Inorganic Nanohybrids

In recent years, layered organic-inorganic materials have attracted increasing research attention not only because of the fundamental interest in general supramolecular chemistry, but also because of their potential usage as precursors for catalytic nanomaterials processing. There are two basic types of clay materials: cationic and anionic clays. The cationic clays, which have been investigated extensively over the past decades, were conventional catalysts used in oil cracking before the replacement of zeolites in 1964.<sup>[19]</sup> They have been used in many industrial chemical processes such as isomerization, liquid refining, and Friedel-Crafts alkylation, including some emerging environmental technologies (such as cation exchange and waste carriers).<sup>[19]</sup> In this class of materials, cations are located in the lamellar space (interlayer space) formed by negatively charged alumino-silicate layers. As they are generally prepared starting from the natural minerals, these clays and modified clay catalysts promise widespread industrial applications in the future owing to

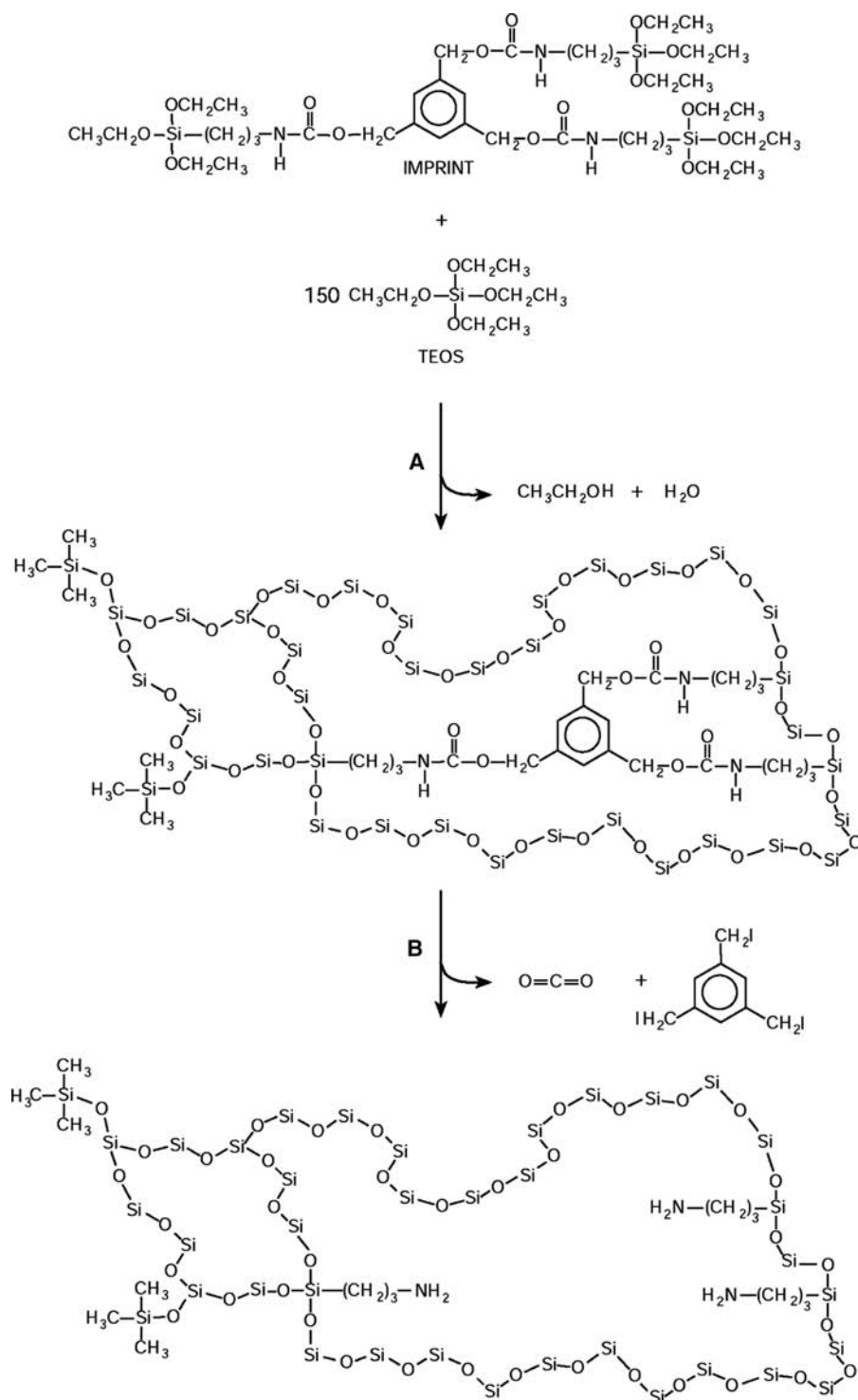


**Fig. 2** Process of molecular imprinting in bulk silica. (A) Sol-gel hydrolysis and condensation catalyzed by HCl. (B) Removal of the aromatic core and creation of a cavity with spatially organized aminopropyl groups covalently anchored to the pore surfaces. Source: From Ref.<sup>[17]</sup>.

the low cost. Similar to cationic clays, anionic clays also have alternate lamellar structures, but with an opposite charge arrangement. Anionic clays are mainly synthetic. The preparation is relatively simple and inexpensive; they can be synthesized primarily with coprecipitation, anion exchange, and structure reconstruction methods. Hydrotalcite-like compounds (HTlcs), for example, have been investigated

extensively over the past decade, and they have been widely used as catalysts, flame retardants, molecular sieves, anion adsorbents, ion-exchangers, and medicine stabilizers.<sup>[20]</sup> The sheet-like structure containing cations can be derived from layered Mg(OH)<sub>2</sub> (brucite) structure. When divalent cations are partially substituted by trivalent ones, positive charges will be built-up within the octahedron sheets. For solid charge

neutrality, anions have to be intercalated into the interlayer space, as illustrated in Fig. 3. The HTlcs have a chemical formula of  $[M_{1-x}^{II}M_x^{III}(\text{OH})_2]^{x+}(\text{A}_{x/n}^{n-}) \cdot m\text{H}_2\text{O}$  (where M = metal, A = interlayer anions),<sup>[20]</sup> whose properties can be tuned with variations of cationic brucite-like sheets and anionic interlayer species. For example, organics- and polymer-containing HTlcs should be viewed as supramolecular assemblies or nanocomposites composed of organic parts (anionic) and inorganic molecular sheets (cationic).<sup>[21]</sup> It is important to realize that the intercalative ability in these alternately arranged layers is based on electrostatic interaction, and the inorganic parts are dissolvable in acidic environment while the organic parts are removable by ionic exchange or oxidation at elevated temperatures. Furthermore, layer charge density can be tuned with the content of  $M^{III}$  cations in the synthesis. The basal spacing (the distance between two brucite-like sheets) depends on the size of the intercalants. For instance, large-sized biomolecular anions (up to several nanometers), such as nucleoside monophosphates and deoxyribonucleic acid (DNA), have been intercalated into the interlayer space of  $\text{Mg}_{0.68}\text{Al}_{0.32}(\text{OH})_2(\text{NO}_3)_{0.32} \cdot 1.2\text{H}_2\text{O}$  (a pristine HTlc).<sup>[22]</sup> Because of their synthetic versatility in compositional tailoring, this class of organic-inorganic hybrids has been used as precursor compounds for the synthesis of functionalized metal-oxide nanomaterials and nanocomposites after the thermal removal or conversion of polymeric intercalants.<sup>[23]</sup> The chemical nature of the intercalated anions, such as oxidative or non-oxidative, had been investigated with respect to thermal reactions, in which nanostructured  $\text{Co}_3\text{O}_4$  spinel oxides were formed from  $\text{Co}^{II}\text{Co}^{III}$ -HTlc precursors.<sup>[24]</sup> Nanocrystalline  $\text{Co}_{3-x}\text{Al}_x\text{O}_4$  can also be incorporated into the  $\gamma\text{-Al}_2\text{O}_3$  matrix via the simultaneous formation of catalyst and support from the  $\text{Co}^{II}\text{Co}^{III}$ -HTlc and alumina xerogel.<sup>[25]</sup>

In addition to the above bulk materials preparations, organic-inorganic hybrid materials can also be prepared into thin films to meet new applications. The major synthetic methods employed in this area



**Fig. 3** The hydrotalcite-like anionic-clays have a layered structure similar to that of brucite  $[\text{Mg}(\text{OH})_2]$  but with some positive charges. To maintain the electrical neutrality for the solid, intercalation of anions (e.g., nitrate and carbonate or even DNA) into the interbrucite layers (i.e., interlayer space) occurs, which leads to a hydrotalcite-like structure.

are sol-gel-based techniques, intercalation reactions, layer-by-layer assembly (e.g., Langmuir-Blodgett technique and electrostatic self-assembly), and evaporation techniques, as exemplified in Fig. 4.<sup>[26]</sup> Although the primary objective of these film-fabrication developments is for organic-inorganic electronics, it is believed the hybrid structures prepared can be extended to catalytic applications, including chemical sensors, in the near future.

Very recently, single-crystal bulk organic-inorganic hybrids had been investigated for the fabrication of catalytic nanocomposites and large-scale organization of catalysts under high-temperature environments.<sup>[27,28]</sup> In particular, individual  $\text{MoS}_2$  (used in hydrodesulfurization) layers can be converted from direct sulfidation of single-molecular sheets of  $\text{MoO}_3$  supported with organic “pillars” in the interlamellar layers. As there has been a large variety of metal-oxide-organic hybrids available nowadays, this method provides a new means for the indirect synthesis of lamellar organic-inorganic catalytic hybrid materials consisting of building units of transition metal dichalcogenides.<sup>[27]</sup> To make the catalytic materials usable in high-temperature environments, large-scale organization of metal-oxide nanostructures in a controllable manner at elevated temperatures is highly desirable but particularly challenging, because of the difficulties in controlling the interconnectivity among individual crystallites due to random nucleation and grain growth upon heating. An organized condensation of single-molecular  $\text{MoO}_3$  sheets can be achieved with a controlled removal of the organic intercalants.<sup>[28]</sup> This

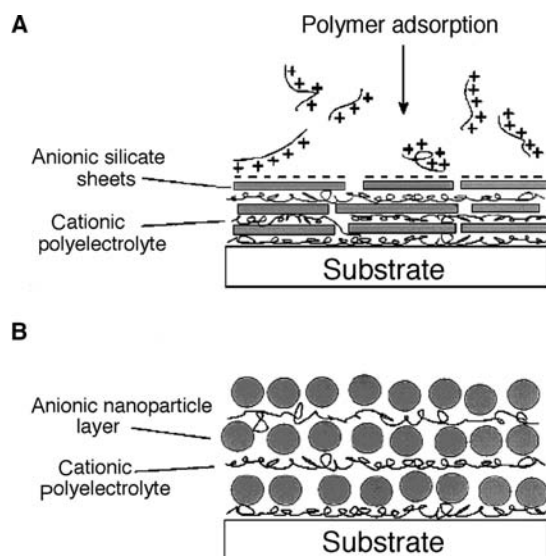


**Fig. 4** (A) Electrostatic assembly of anionic inorganic layers and cationic organic layers. (B) A similar assembly of (A) but with negatively charged layers formed from nanoparticles (e.g., CdSe or CdS). *Source:* From Ref.<sup>[26]</sup>.

controlled condensation takes place within the space provided by the pristine organic–inorganic hybrid single-crystals. In this sense, the role of precursor crystal can be viewed as a microscopic “green compact” analogous to the macroscopic one in ceramic processing.<sup>[28]</sup> These new types of catalyst organization may be useful for microreactor systems where fluid stream stability is crucial, because the stacking of nanostructured catalysts can be controlled to reduce flow resistance.

In addition to the above chemical conversion and organization of nanostructured catalytic materials, organic–inorganic hybrids have also been used in the preparation of freestanding nanostructured materials. For example, catalytically important materials such as tungsten oxide nanowires, tungsten disulfide nanotubes, and VO<sub>x</sub>-nanotubes had also been prepared from organic–inorganic hybrid precursors that were preorganized in the forms of lamellar mesostructures.<sup>[29–31]</sup> The final nanostructures are formed either with high-temperature processing or with hydrothermal treatment. These synthesized individual inorganic nanostructures will be the subject of the next section.

### Nanobuilding Blocks and Mesoscale Self-Organizations

The research in low-dimensional catalytic materials has blossomed in many new directions since Iijima’s discovery of carbon nanotubes in 1991.<sup>[32]</sup> For example, syntheses of low-dimensional catalytic nanostructures of MoS<sub>2</sub>, WS<sub>2</sub>, MoO<sub>3</sub>, TiO<sub>2</sub>, V<sub>2</sub>O<sub>5</sub>, ZrO<sub>2</sub>, Co<sub>3</sub>O<sub>4</sub>, ZnO, etc. have been carried out,<sup>[33–41]</sup> together with fabrications of nanostructured catalyst carriers such as MgO, Al<sub>2</sub>O<sub>3</sub>, and SiO<sub>2</sub>.<sup>[42–44]</sup> While many significant breakthroughs have been made for the metal oxides and chalcogenides, the search for new types of nanostructures and self-assemblies continues, aiming at complementary functionalities and performances. Technologically, many known catalytic materials are expected to gain better utilizations, because of their new properties and possible high catalytic activities in the nanometer regime (quantum confinement effect).<sup>[39]</sup> Discrete, freestanding nanostructures can be viewed as basic structural units or construction building blocks; they can be used individually or collectively (after a proper organization/assembly, will be addressed soon) in heterogeneous catalysis and chemical-sensing applications.

Many synthetic strategies have been developed for the fabrication of nanostructures. For example, metal oxide nanoparticles (zero-dimension, 0-D) can be prepared rather routinely via sol–gel methods<sup>[45]</sup> and direct precipitation.<sup>[46]</sup> A great variety of core-shell nanostructures (0-D) have also been prepared via

sol–gel and other coating methods (e.g., layer-by-layer deposition) with the assistance of removable inner-core supports.<sup>[47]</sup> On the other hand, one-dimensional (1-D) nanomaterials can be fabricated with the following techniques. 1) Utilizing intrinsic structural anisotropy: Inorganic materials with low structural symmetries can be prepared into 1-D morphology along certain crystallographic axes.<sup>[37,40]</sup> The unidirectional growths can be further manipulated with the assistance of inorganic salts or ionic/nonionic organic surfactants present in the solution synthesis.<sup>[48]</sup> 2) Template-directed growth: In addition to the soft templates (such as self-assembled molecular structures, e.g., micelles discussed in the previous sections), this method utilizes solid templates for growth depositions or chemical insertions. For example, non-porous single-crystalline NaCl substrate and porous supports such as zeolites, MCM-41, and anodic alumina membranes (with parallel 1-D channels) have been used in the synthesis of 1-D nanostructures,<sup>[49]</sup> including semiconductor metallic barcodes (Fig. 5).<sup>[50]</sup> The resultant nanostructures can be harvested by template-removal. In certain cases, however, the template can become a part of the resulting 1-D nanostructures. These latter cases had recently been demonstrated in the synthesis of 1-D bimorph composites of TiO<sub>2</sub>–SnO<sub>2</sub> and Co<sub>0.05</sub>Ti<sub>0.95</sub>O<sub>2</sub>–SnO<sub>2</sub>,<sup>[51]</sup> and in the preparation of Ag/MoO<sub>3</sub> catalytic nanostructures.<sup>[52]</sup> 3) Surfactant-assisted synthesis: Preferred electrostatic and chemical interactions between organic surfactants and certain crystallographic

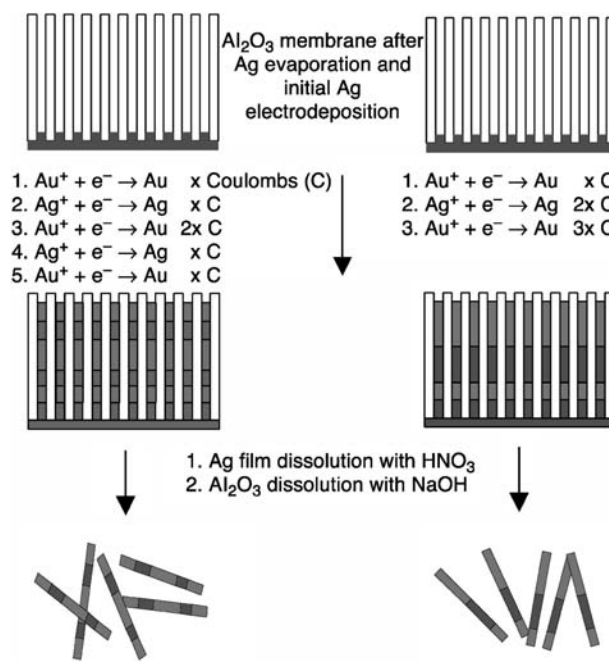


**Fig. 5** Synthesis of barcoded 1-D materials with alumina membrane template where 1-D channels are parallel to each other. *Source:* From Ref.<sup>[50]</sup>.



surfaces will restrict the growth along certain directions, resulting in the kinetic control of the growth anisotropy. This method had been investigated extensively for metals (e.g., Au) and semiconductor nano-materials such as CdSe, ZnSe, CdS, and ZnS in recent years.<sup>[53,54]</sup> 4) Oriented attachment: This growth mechanism had recently been investigated for the synthesis of 1-D materials such as ZnO nanorods and  $\beta$ -Co(OH)<sub>2</sub> nanoplatelets, respectively, from smaller building blocks.<sup>[55,56]</sup>

Individual nanostructure units can be used as model catalysts or chemical-sensing devices. For example, a gas sensor for NO<sub>2</sub> detection had been developed with a single nanoribbon of SnO<sub>2</sub>. In the illuminated state (UV light), photo-generated holes recombine with trapped electrons at the SnO<sub>2</sub> surface, desorbing NO<sub>2</sub> and increasing the sensing current.<sup>[57]</sup> The general advantages of nanodevices are small size, fast response, and high sensitivity. If required, 2-D- or even 3-D nanostructures can be further constructed from starting 0-D- or 1-D subunits via mesoscale self-assembly processes. There have been numerous investigations in this area using organic surfactants.<sup>[40,41]</sup> As illustrated in Fig. 6, direct crystallite coupling via oriented attachment process provides another possible means to serve this purpose.<sup>[58]</sup> More examples in this area can be found in the literatures.<sup>[55,59]</sup> Unlike the layered nanostructures (2-D), self-assembled 2-D

nanostructures must possess different properties, because of the presence of discrete low-dimensional subunits and organic capping molecules within the assemblies. The retention or removal of these organizing agents is an important issue in catalytic applications, as the presence of organic components will change the inorganic nature of catalysts (hybridization). Future detailed comparisons for different design strategies are urgently needed.

In addition to the ordered organic–inorganic assemblies, nanoarchitectures of multifunctional catalysts can be further achieved by introducing dispersible organic-capped inorganic nanostructures into 3-D gel matrixes, which will also create the necessary chemical functionality and porosity in addition to the better material utilization. In particular, structurally shaped (or faceted) nanocatalysts may provide predesigned active catalytic sites for the desired chemical reactions, although they may appear to be random in the composite matrixes.

### Interfacial Engineering and Self-Assembly

Our understanding of the catalyst carrier has now gone beyond its supporting role; various levels of participation of carriers in catalytic reactions have been known in atomic and molecular scales.<sup>[60]</sup> As mentioned earlier, the surface functionalities of catalytic materials (in either planar or spherical form) can be further modified with the guide of nanochemistry principles<sup>[61]</sup> and a wide range of surface-engineering processes available.<sup>[47]</sup> In addition to metal single-crystal surfaces that have been investigated extensively over the past three decades, the synergetic effects of catalyst–carrier systems have been investigated with model catalysts, which may be closer to the reality of a heterogeneous catalytic reaction environment. Taking advantage of the electron beam lithography technique, for example, metal nanoparticles have been arrayed on silicon surface at predesignated locations.<sup>[62]</sup> Pt and Ag nanoparticle arrays were prepared at different interparticle distances. By varying the particle size and distances between particles, the structural factors responsible for the selectivity and activity in diverse catalytic reactions had been investigated.<sup>[62]</sup> Other versions of model catalysts on oxidized silicon wafers have also been fabricated by spin-coating technique in recent years.<sup>[63]</sup> These wafer-supported catalytic metal and metal-oxide thin films have been tested under catalytic reaction conditions and investigated with state-of-the-art surface analytical techniques. Various catalyst systems have been studied over the past few years.<sup>[63]</sup> In view of its versatility, this evaluation approach is expected to be suitable for the characterization of various nanostructured

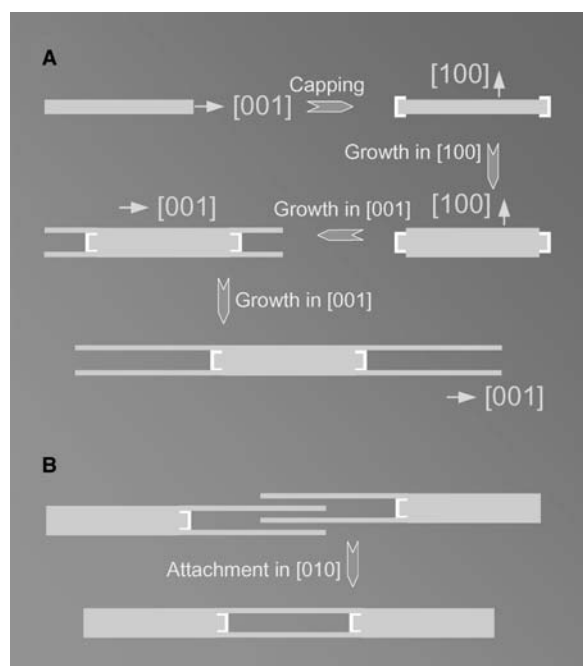


**Fig. 6** (A) Flowchart of synthesis of forklike  $\alpha$ -MoO<sub>3</sub> nanostructures via manipulating growth directions with TiO<sub>2</sub> capping. (B) Oriented attachment between two forklike nanostructures along the [010] direction (perpendicular to the paper). *Source:* From Ref.<sup>[58]</sup>.

catalytic materials that can be prepared into colloidal suspensions for spin-coating.

Apart from electron/ion beam lithography techniques, nanoelectrochemical patterning process and photolithography methods have also been widely used in the fabrication of substrate patterns for the deposition of nanostructured materials. These processes have been conducted in both vapor-phase (e.g., chemical vapor deposition) and liquid phase (e.g., solution growth), producing various patterned 2-D nanostructures on the supports. For example, the hierarchical self-assembly of gold nanoparticles onto an organic bilayer template pattern on silicon had been demonstrated.<sup>[64]</sup> Furthermore, ordered porous structures had been fabricated by self-assembly of zeolite nanocrystals on micropatterned silicate film surfaces.<sup>[65]</sup> Without demanding pretreatments, single-crystal surfaces have recently been proven to be suitable for nanoparticle self-aligned growth. In particular, a hexagonal superlattice of anatase TiO<sub>2</sub> nanospheres has been arranged on  $\alpha$ -MoO<sub>3</sub> (010) surface without any surfactants and surface patterns,<sup>[66]</sup> noting that both TiO<sub>2</sub> and  $\alpha$ -MoO<sub>3</sub> are important catalysts in this material combination. With well-developed surface science techniques, in-depth investigations of supported nanostructured catalysts can be further pursued. Elegant examples in this area have been reported in the literature, as shown in Figs. 7 and 8

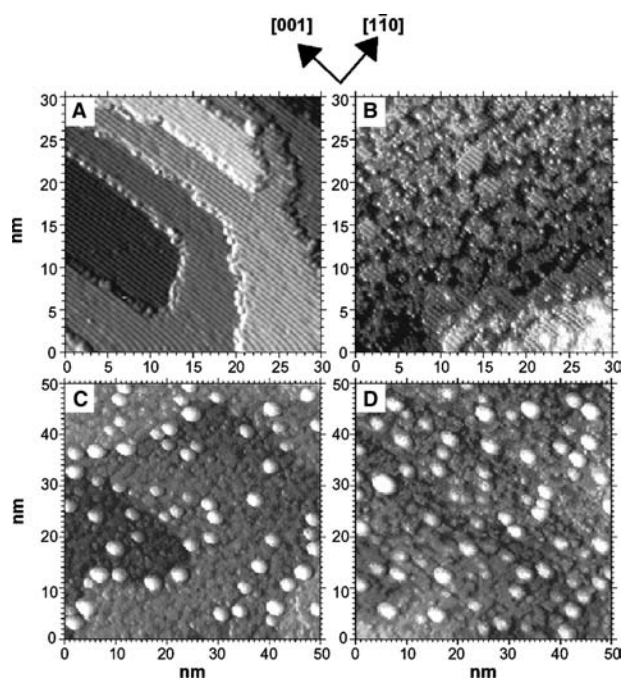


**Fig. 7** Scanning tunneling microscopic images of TiO<sub>2</sub>(110)-(1 × 1): (A) clean surface before oxygen exposure, and (B) after oxygen exposure at 650 K. Scanning tunneling microscopic images of Au/TiO<sub>2</sub>(110)-(1 × 1): (C) before CO:O<sub>2</sub> exposure, and (D) after CO:O<sub>2</sub> exposure at 300 K. *Source:* From Ref.<sup>[3]</sup>.

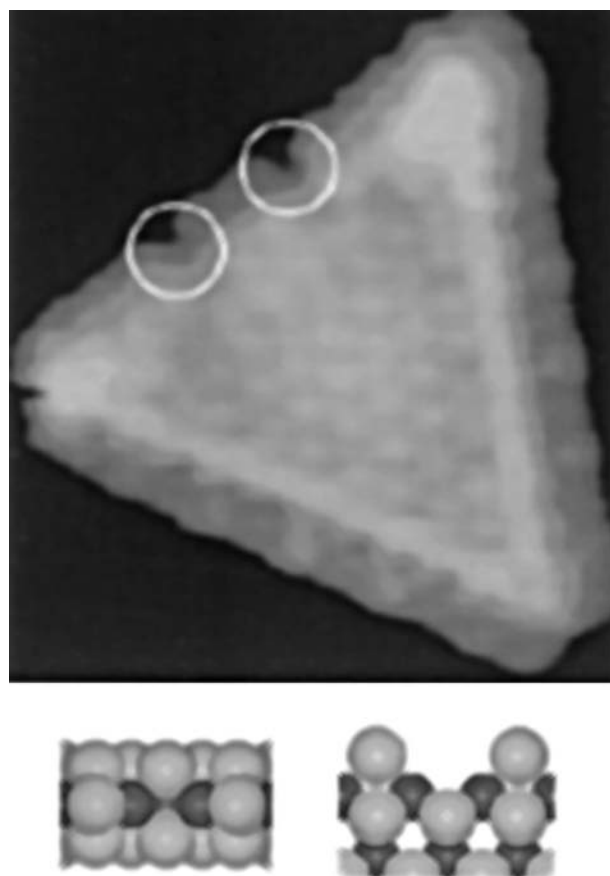


**Fig. 8** A scanning tunneling microscopic image of a MoS<sub>2</sub> nanocluster exposed to atomic hydrogen at 600 K, which resulted in the formation of S vacancies (circled). Models below: side and top views of S vacancies. *Source:* From Ref.<sup>[67]</sup>.

for the investigations on CO oxidation and hydrodesulfurization.<sup>[3,67]</sup> On the (110) surface of TiO<sub>2</sub>, Au particles show high activity at 2–3 nm for CO oxidation. However, Au particles in the Au–TiO<sub>2</sub> composite aerogel retain high activity for the same reaction at a size of 6 nm, because of an increase in the interfacial contact area of the gold with multiple domains of TiO<sub>2</sub> in the aerogel matrix.<sup>[68]</sup> The catalytic bifunctionality of an active composite can thus be explored when the support and catalyst have comparable sizes (within a factor of 2).<sup>[68]</sup>

Similar to vertical arrays of carbon nanotubes, catalytic materials have also been prepared into 2-D arrays, but with an extruding direction perpendicular to the surface. Recently, ZnO nanorods and GaN nanotubes had been prepared with gold nanoparticle catalysts in the vapor phase and with a subsequent thermal treatment to remove inner templates (e.g., in the synthesis of GaN nanotubes, ZnO nanorods were used as templates);<sup>[69]</sup> the diameter of the prepared 1-D nanostructures is proportional to the size of metal catalysts in the synthesis. This method is now widely used in

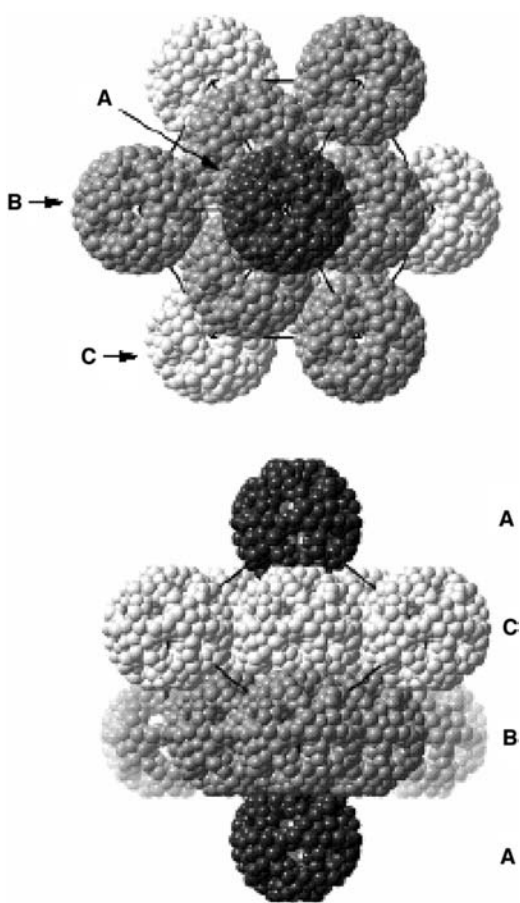


**Fig. 9** Packing of ball-like anions  $\{[\text{Mo}_2\text{O}_4(\text{CH}_3\text{COO})]_{30} \{(\text{Mo})\text{Mo}_5\text{O}_{21}(\text{H}_2\text{O})_6\}_{12}\}^{42-}$  in the crystal lattice (space filling model viewed along  $[111]$  (top) and perpendicular to  $[111]$  (bottom)). *Source:* From Ref.<sup>[70]</sup>.

the synthesis of 1-D-nanostructures, including the control of periodic chemical component variation along a nanostructure.

### Superpolyhedral Clusters and Their Organizational Forms

Compared with the nanobuilding blocks discussed above, inorganic super fullerene and polyhedral clusters, which have been synthesized in recent years, are

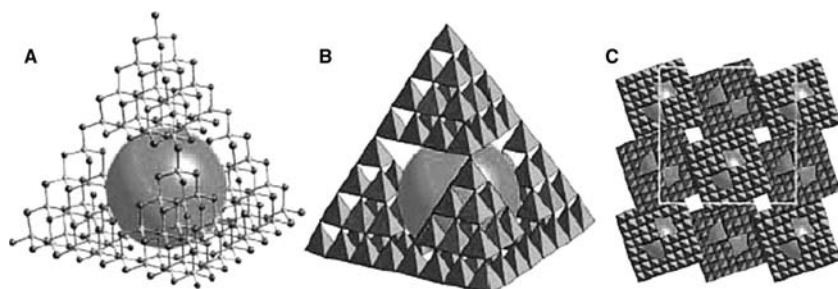


**Fig. 10** Models of the  $[\text{Cd}_{16}\text{In}_{64}\text{S}_{134}]^{44-}$  anionic clusters: (A) a ball-and-stick model, (B) the same view as (A) shown as metal-centered tetrahedra, and (C) crystal packing of the clusters, viewed along the  $c$  axis (the unit cell is framed). The large sphere indicates the central cavity. *Source:* From Ref.<sup>[71]</sup>.

generally much smaller but with more distinct geometrical features. This class of materials is formed from even smaller metal–ligand polyhedra, such as tetrahedrons, octahedrons through edge-, corner-sharing, etc. On the other hand, these super inorganic “molecules” can be further packed into repeated arrangements, giving away larger crystallites. Fig. 9 shows a representative packing of this type of superclusters.<sup>[70]</sup> Instead of oxygen in zeolites, basic units of tetrahedrons can now be extended to sulfur, noting that the ionic radius of  $\text{S}^{2-}$  is much larger than that of  $\text{O}^{2-}$ . For example, metal sulfides can now be prepared into supertetrahedral clusters with a large cavity, as shown in Fig. 10 for  $[\text{Cd}_{16}\text{In}_{64}\text{S}_{134}]^{44-}$  (3.1 nm in edge length).<sup>[71]</sup> A great variety of this type of superpolyhedral clusters and molecules has been prepared nowadays and has been reviewed recently.<sup>[72]</sup> One common feature in these superpolyhedral clusters is their inner cavity. If treated as nanobuilding blocks in their further architectures, the superclusters with inner space will create even more complex structures in addition to their chemical complexity in nanoconfinement regime. Many of these solids show a semiconducting character.<sup>[72]</sup> Apart from the assembly shown in Fig. 9, there have existed a great number of organization schemes of inorganic clusters with organic counterparts.<sup>[45]</sup> These tailor-made organic–inorganic nanocomposites could be potential candidates for future heterogeneous catalysis applications.

### CONCLUSION

We have examined various design and synthesis strategies for the fabrication of nanostructured catalytic materials. Generally speaking, nanostructured “kits-and-parts” as well as their organization methodologies have been available to constitute a nanocatalyst toolbox, i.e., they are ready for direct usage or further assembly. To transform “catalytic materials” to real custom “catalysts”, however, a large research endeavor is needed, and this includes systematic investigations on multicomponent assemblies and resultant chemico-physical properties, including hierarchical pore structures. It is noted that the catalytic

performance of these materials remains largely untested, despite the significant progress in materials research. While traditional methods will still dominate the industrial-scale catalyst processing at the present time, we are beginning to see nanostructured catalytic materials in practical applications of “chemical plant/laboratory-on-a-chip” and chemical-sensing technology where the amount of catalysts required is small, and supported type catalysts may not be needed. For larger-scale industrial chemical processes, for instance, it is believed that the traditional “metal ions impregnation” can be replaced with “nanostructures impregnation,” as the nanobuilding blocks can be prepared into colloidal suspensions for metal loading on general catalyst supports. Furthermore, nanoarchitectures of these building units can be achieved with the well-developed sol–gel technology. Perhaps, simultaneous formation of nanobuilding blocks and supporting oxide matrix should be considered as a next level of architectures, where the catalyst and support could be better integrated in the new-generation catalysts.

## REFERENCES

- Bell, A.T. The impact of nanoscience on heterogeneous catalysis. *Science* **2003**, *299*, 1688–1691.
- Stiles, A.B.; Koch, T.A. *Catalyst Manufacture*, 2nd Ed.; Marcel Dekker: New York, USA, 1995.
- Valden, M.; Lai, X.; Goodman, D.W. Onset of catalytic activity of gold clusters on titania with the appearance of nonmetallic properties. *Science* **1998**, *281*, 1647–1650.
- Somorjai, G.A. From surface materials to surface technology. *MRS Bull.* **1998**, *23*, 11–29.
- de Jong, K.P. Assembly of solid catalysts. *Cat. Technol.* **1998**, *2*, 87–95.
- Férey, G. Microporous solids: from organically templated inorganic skeletons to hybrid frameworks... ecumenism in chemistry. *Chem. Mater.* **2001**, *13*, 3084–3098.
- Davis, M.E. Ordered porous materials for emerging applications. *Nature* **2002**, *417*, 813–821.
- Kresge, C.T.; Leonowicz, M.E.; Roth, W.J.; Vartuli, J.C.; Beck, J.S. Ordered mesoporous molecular sieves synthesized by a liquid-crystal template mechanism. *Nature* **1992**, *359*, 710–712.
- Moller, K.; Bein, T. Inclusion chemistry in periodic mesoporous hosts. *Chem. Mater.* **1998**, *10*, 2950–2963.
- Morey, M.S.; Stucky, G.D.; Schwarz, S.; Fröba, M. Isomorphic substitution and postsynthesis incorporation of zirconium into MCM-48 mesoporous silica. *J. Phys. Chem., B* **1999**, *103*, 2037–2041.
- Stein, A.; Melde, B.J.; Schrodin, R.C. Hybrid inorganic–organic mesoporous silicates—nanoscopic reactors coming of age. *Adv. Mater.* **2000**, *12*, 1403–1419.
- Sayari, A.; Hamoudi, S. Periodic mesoporous silica-based organic–inorganic nanocomposite materials. *Chem. Mater.* **2001**, *13*, 3151–3168.
- Blin, J.-L.; Léonard, A.; Yuan, Z.-Y.; Gigot, L.; Vantomme, A.; Cheetham, A.K.; Su, B.-L. Hierarchically mesoporous/macroporous metal oxides templated from polyethylene oxide surfactant assemblies. *Angew. Chem., Int. Ed.* **2003**, *42*, 2872–2875.
- Yi, G.-R.; Moon, J.H.; Manoharan, V.N.; Pine, D.J.; Yang, S.-M. Packings of uniform microspheres with ordered macropores fabricated by double templating. *J. Am. Chem. Soc.* **2002**, *124*, 13354–13355.
- Tian, Z.R.; Liu, J.; Voigt, J.A.; McKenzie, B.; Xu, H. Hierarchical and self-similar growth of self-assembled crystals. *Angew. Chem., Int. Ed.* **2003**, *42*, 414–417.
- Bass, J.D.; Katz, A. Thermolytic synthesis of imprinted amines in bulk silica. *Chem. Mater.* **2003**, *15*, 2757–2763.
- Katz, A.; Davis, M.E. Molecular imprinting of bulk, microporous silica. *Nature* **2000**, *403*, 286–289.
- Kónya, Z.; Puentes, V.F.; Kiricsi, I.; Zhu, J.; Alivisatos, A.P.; Somorjai, G.A. Nanocrystal templating of silica mesopores with tunable pore sizes. *Nano Lett.* **2002**, *2*, 907–910.
- Vaccari, A. Preparation of catalytic properties of cationic and anionic clays. *Catal. Today* **1998**, *41*, 53–71.
- Cavani, F.; Trifirò, F.; Vaccari, A. Hydrotalcite-type anionic clays: preparation, properties and applications. *Catal. Today* **1991**, *11*, 173–301.
- Leroux, F.; Besse, J.-P. Polymer interleaved layered double hydroxides: a new emerging class of nanocomposites. *Chem. Mater.* **2001**, *13*, 3507–3515.
- Choy, J.H.; Kwak, S.Y.; Jeong, Y.J.; Park, J.S. Inorganic layered double hydroxides as nonviral vectors. *Angew. Chem., Int. Ed.* **2000**, *39*, 4042–4045.
- Xu, Z.P.; Xu, R.; Zeng, H.C. Sulfate-functionalized carbon/metal-oxide nanocomposites from hydrotalcite-like compounds. *Nano Lett.* **2001**, *1*, 703–706.
- Xu, R.; Zeng, H.C. Mechanistic investigation on self-redox decomposition of cobalt–hydroxide–nitrate compounds with different nitrate anion configurations in interlayer space. *Chem. Mater.* **2003**, *15*, 2040–2048.
- Sampanthar, J.T.; Zeng, H.C. Synthesis of Co<sup>II</sup>Co<sup>III</sup>Al<sub>x</sub>O<sub>4</sub>–Al<sub>2</sub>O<sub>3</sub> nanocomposites via decomposition of Co<sub>0.73</sub>Co<sub>0.27</sub>(OH)<sub>2.00</sub>(NO<sub>3</sub>)<sub>0.23</sub>(CO<sub>3</sub>)<sub>0.02</sub>·0.5 H<sub>2</sub>O in sol–gel derived  $\gamma$ -Al<sub>2</sub>O<sub>3</sub> matrix. *Chem. Mater.* **2001**, *13*, 4722–4730.
- Mitzi, D.B. Thin-film deposition of organic–inorganic hybrid materials. *Chem. Mater.* **2001**, *13*, 3283–3298.
- Wei, X.M.; Zeng, H.C. Sulfidation of single molecular sheets of MoO<sub>3</sub> pillared by bipyridine in nano-hybrid MoO<sub>3</sub>(4,4'-bipyridyl)<sub>0.5</sub>. *Chem. Mater.* **2003**, *15*, 433–442.
- Wei, X.M.; Zeng, H.C. Large-scale organizations of MoO<sub>3</sub> nanoplatelets with single-crystalline MoO<sub>3</sub>(4,4'-bipyridyl)<sub>0.5</sub>. *J. Phys. Chem., B* **2003**, *107*, 2619–2622.
- Li, X.-L.; Liu, J.-F.; Li, Y.-D. Large-scale synthesis of tungsten oxide nanowires with high aspect ratio. *Inorg. Chem.* **2003**, *42*, 921–924.

30. Li, Y.D.; Li, X.L.; He, R.R.; Zhu, J.; Deng, Z.X. Artificial lamellar mesostructures to WS<sub>2</sub> nanotubes. *J. Am. Chem. Soc.* **2001**, *124*, 1411–1416.
31. Krumeich, F.; Muhr, H.-J.; Niederberger, M.; Bieri, F.; Schnyder, B.; Nesper, R. Morphology and topochemical reactions of novel vanadium oxide nanotubes. *J. Am. Chem. Soc.* **1999**, *121*, 8324–8331.
32. Iijima, S. Helical microtubules of graphitic carbon. *Nature* **1991**, *354*, 56–58.
33. Tenne, R.; Margulis, L.; Genut, M.; Hodes, G. Polyhedral and cylindrical structures of tungsten disulfide. *Nature* **1992**, *360*, 444–446.
34. Tenne, R.; Homyonfer, M.; Feldman, Y. Nanoparticles of layered compounds with hollow cage structures. *Chem. Mater.* **1998**, *10*, 3225–3238.
35. Che, G.L.; Lakshmi, B.B.; Fisher, E.R.; Martin, C.R. Carbon nanotubule membranes for electrochemical energy storage and production. *Nature* **1998**, *393*, 346–349.
36. Rao, C.N.R.; Cheetham, A.K. Science and technology of nanomaterials: current status and future prospects. *J. Mater. Chem.* **2001**, *11*, 2887–2894.
37. Patzke, G.R.; Krumeich, F.; Nesper, R. Oxidic nanotubes and nanorods—anisotropic modules for a future nanotechnology. *Angew. Chem., Int. Ed.* **2002**, *41*, 2446–2461.
38. Kovtyukhova, N.I.; Mallouk, T.E. Nanowires as building blocks for self-assembling logic and memory circuits. *Chem. Eur. J.* **2002**, *8*, 4355–4363.
39. Rao, C.N.R.; Kulkarni, G.U.; Thomas, P.J.; Edwards, P.P. Size-dependent chemistry: properties of nanocrystals. *Chem. Eur. J.* **2002**, *8*, 29–35.
40. Xia, Y.; Yang, P.; Sun, Y.; Wu, Y.; Mayers, B.; Gates, B.; Yin, Y.; Kim, F.; Yan, H. One-dimensional nanostructures: synthesis, characterization, and applications. *Adv. Mater.* **2003**, *15*, 353–389.
41. Cölfen, H.; Mann, S. Higher-order organization by mesoscale self-assembly and transformation of hybrid nanostructures. *Angew. Chem., Int. Ed.* **2003**, *42*, 2350–2365.
42. Tang, C.; Bando, Y.; Sato, T. Oxide-assisted catalytic growth of MgO nanowires with uniform diameter distribution. *J. Phys. Chem., B* **2002**, *106*, 7449–7452.
43. Pu, L.; Bao, X.; Zou, J.; Feng, D. Individual alumina nanotubes. *Angew. Chem., Int. Ed.* **2001**, *40*, 1490–1493.
44. Jung, J.H.; Ono, Y.; Hanabusa, K.; Shinkai, S. Creation of both right-handed and left-handed silica structures by sol-gel transcription of organogel fibers comprised of chiral diaminocyclohexane derivatives. *J. Am. Chem. Soc.* **2000**, *122*, 5008–5009.
45. Sanchez, C.; Soler-Illia, G.J. de A.A.; Ribot, F.; Lalot, T.; Mayer, C.R.; Cabuil, V. Designed hybrid organic-inorganic nanocomposites from functional nanobuilding blocks. *Chem. Mater.* **2001**, *13*, 3061–3083.
46. Feng, J.; Zeng, H.C. Size-controlled growth of Co<sub>3</sub>O<sub>4</sub> nanocubes. *Chem. Mater.* **2003**, *15*, 2829–2835.
47. Caruso, F. Nanoengineering of particle surfaces. *Adv. Mater.* **2001**, *13*, 11–22.
48. Lou, X.W.; Zeng, H.C. Hydrothermal synthesis of  $\alpha$ -MoO<sub>3</sub> nanorods via acidification of ammonium-heptamolybdate-tetrahydrate. *Chem. Mater.* **2002**, *14*, 4781–4789.
49. Lakshmi, B.B.; Patrissi, C.J.; Martin, C.R. Sol-gel template synthesis of semiconductor oxide micro- and nanostructures. *Chem. Mater.* **1997**, *9*, 2544–2550.
50. Nicewarner-Peña, S.R.; Freeman, R.G.; Reiss, B.D.; He, L.; Peña, D.J.; Walton, I.D.; Cromer, R.; Keating, C.D.; Natan, M.J. Submicrometer metallic barcodes. *Science* **2001**, *294*, 137–141.
51. He, R.; Law, M.; Fan, R.; Kim, F.; Yang, P. Functional bimorph composite nanotapes. *Nano Lett.* **2002**, *2*, 1109–1112.
52. Dong, W.; Feng, S.; Shi, Z.; Li, L.; Xu, Y. A well-confined redox route to silver nanoparticles on the surface of MoO<sub>3</sub>. *Chem. Mater.* **2003**, *15*, 1941–1943.
53. Wang, Z.L.; Gan, R.P.; Nikoobakht, B.; El-Sayed, M.A. Surface reconstruction of unstable {110} surface in gold nanorods. *J. Phys. Chem., B* **2000**, *104*, 5417–5420.
54. Trindade, T.; O'Brien, P.O.; Pickett, N.L. Nanocrystalline semiconductors: synthesis, properties, and perspectives. *Chem. Mater.* **2001**, *13*, 3843–3858.
55. Pacholski, C.; Korowski, A.; Weller, H. Self-assembly of ZnO from nanodots to nanorods. *Angew. Chem., Int. Ed.* **2002**, *41*, 1188–1191.
56. Sampanthar, J.T.; Zeng, H.C. Arresting butterfly-like intermediate nanocrystals of  $\beta$ -Co(OH)<sub>2</sub> via ethylenediamine-mediated synthesis. *J. Am. Chem. Soc.* **2002**, *124*, 6668–6675.
57. Law, M.; Kind, H.; Messer, B.; Kim, F.; Yang, P. Photochemical sensing of NO<sub>2</sub> with SnO<sub>2</sub> nanoribbon nanosensors at room temperature. *Angew. Chem., Int. Ed.* **2002**, *41*, 2405–2408.
58. Lou, X.W.; Zeng, H.C. Complex  $\alpha$ -MoO<sub>3</sub> nanostructures with external bonding capacity for self-assembly. *J. Am. Chem. Soc.* **2003**, *125*, 2697–2704.
59. Liu, B.; Zeng, H.C. Hydrothermal synthesis of ZnO nanorods in the diameter regime of 50 nm. *J. Am. Chem. Soc.* **2003**, *125*, 4430–4431.
60. Campbell, C.T.; Parker, S.C.; Starr, D.E. The effect of size-dependent nanoparticle energetics on catalyst sintering. *Science* **2002**, *298*, 811–814.
61. Ozin, G.A. Nanochemistry: synthesis in diminishing dimensions. *Adv. Mater.* **1992**, *4*, 612–649.
62. Somorjai, G.A. The development of molecular surface science and the surface science of catalysis: berkeley contribution. *J. Phys. Chem., B* **2000**, *104*, 2969–2979.
63. Loos, J.; Thune, P.C.; Niemantsverdriet, J.W.; Lemstra, P.J. Polymerization and crystallization of polyethylene on a flat model catalyst. *Macromolecules* **1999**, *32*, 8910–8913.
64. Hoepfener, S.; Maoz, R.; Cohen, S.R.; Chi, L.; Fuchs, H.; Sagiv, J. Metal nanoparticles, nanowires, and contact electrodes self-assembled patterned monolayer templates—a bottom-up chemical approach. *Angew. Chem., Int. Ed.* **2002**, *41*, 1036–1040.
65. Huang, L.; Wang, Z.; Sun, J.; Miao, L.; Li, Q.; Yan, Y.; Zhao, D. Fabrication of ordered porous structures by self-assembly of zeolite nanocrystals. *J. Am. Chem. Soc.* **2000**, *122*, 3530–3531.

66. Yang, H.G.; Zeng, H.C. Self-aligned growth of hexagonal TiO<sub>2</sub> nanosphere arrays on  $\alpha$ -MoO<sub>3</sub> (010) surface. *Chem. Mater.* **2003**, *15*, 3113–3120.
67. Helveg, S.; Lauritsen, J.V.; Lægsgaard, E.; Stensgaard, I.; Nørskov, J.K.; Clausen, B.S.; Topsøe, H.; Besenbacher, F. Atomic-scale structure of single-layer MoS<sub>2</sub> nanoclusters. *Phys. Rev. Lett.* **2000**, *84*, 951–954.
68. Rolison, D.R. Catalytic nanoarchitectures—the importance of nothing and the unimportance of periodicity. *Science* **2003**, *299*, 1698–1701.
69. Goldberger, J.; He, R.R.; Zhang, Y.F.; Lee, S.W.; Yan, H.Q.; Choi, H.J.; Yang, P.D. Single-crystal gallium nitride nanotubes. *Nature* **2003**, *422*, 599–602.
70. Müller, A.; Krickemeyer, E.; Bögge, H.; Schmidtman, M.; Peters, F. Organizational forms of matter: an inorganic super fullerene and Keplerate based on molybdenum oxide. *Angew. Chem., Int. Ed.* **1998**, *37*, 3360–3363.
71. Li, H.; Kim, J.; O’Keeffe, M.; Yaghi, O.M. [Cd<sub>16</sub>In<sub>64</sub>S<sub>134</sub>]<sup>44-</sup>: 31-Å tetrahedron with a large cavity. *Angew. Chem., Int. Ed.* **2003**, *42*, 1819–1821.
72. Férey, G. Supertetrahedra in sulfides: matter against mathematical series? *Angew. Chem., Int. Ed.* **2003**, *42*, 2576–2579.



# Nanostructured Composites: Carbon-Derived Fibers

Peter M.A. Sherwood

*Department of Chemistry, Kansas State University,  
Manhattan, Kansas, U.S.A.*

## INTRODUCTION

This entry discusses the importance of nanostructure and especially interfacial chemical interactions in the formation of composites where an appropriate matrix material is strengthened by a carbon fiber. Such composites have mechanical and other properties that are especially dependent upon the surface chemistry of the fibers; in other words, the nanostructure of the surface region has a dramatic impact on these properties. The focus of the entry will be upon the types of fiber currently used in composite production, with an emphasis upon the surface chemistry of carbon fibers determined by X-ray photoelectron spectroscopy (XPS) in the core and valence band region.

## CARBON FIBERS

Fibers find a number of important practical applications. Fibers themselves may be woven into a structure that can be one-, two-, or three-dimensional. The surface chemistry of the fibers is important when the fibers are used to generate a fabric, which may require treatment such as dyeing. This entry will focus on carbon fibers. Carbon fibers are light and strong fibers, which consist of largely graphitic character. The microstructure of the fibers can vary considerably depending upon their production, although on a nanoscale dimension the untreated fibers consist largely of graphite. The principal use for these fibers is to employ them to construct a composite which involves a matrix which is often an epoxy resin or plastic.

The remarkable feature of composites composed of a fiber and a matrix is that the surface chemistry of the fiber has a dramatic impact on the mechanical and other properties of the composite. For example, in carbon fiber composites with an epoxy resin matrix the load that can be sustained without fracture for the same fiber and matrix can be increased by a factor of three by changing the surface chemistry of the outer 5 to 10 Å of the carbon fiber surface.

Carbon is known in three principal allotropic forms, graphite, diamond, and fullerenes. Graphite materials have extensive applications associated with their high

thermal and electrical conductivity and their negligible thermal expansion. In addition, they are one of the lightest refractory materials known and possess bio-compatible characteristics.

Perfect graphite has continuous planar hexagonal sheets of carbon atoms with six-member carbon rings with each sheet separated by 3.354 Å from the adjoining sheets. Many less-ordered forms of carbon are known such as pyrolytic carbon where the hexagonal sheets have only short-range order, with intersheet separations that differ from those of perfect graphite.

Carbon fibers were first made in the form of carbon filaments by heating cellulose fibers, an approach used by Thomas Edison.<sup>[1]</sup> Carbon fibers of the type of such value today are high modulus fibers. These fibers were developed independently by Bacon,<sup>[2,3]</sup> Shindo,<sup>[4]</sup> and Watt,<sup>[5]</sup> who all used a process of continual stretching of the precursor material as it was carbonized during heat treatment.

Commercial carbon fibers are derived from two principal sources. The first source is based upon textile fibers, especially polyacrylonitrile. The second source is based upon mesophase pitch. In both cases an initial fiber is heated and stretched leading to decomposition to form carbon in a form which may be more or less graphitic-like. Residual molecules of the precursor may be left; for example, the fiber may contain nitrogen if the precursor was polyacrylonitrile. Carbon fiber manufacturers can vary the stretching and heating conditions to yield a fiber with the desired properties (such as the fiber modulus). A third source of carbon fiber has been less well used and is based upon fibers produced when hydrocarbon gas mixtures pass over a catalyst at high temperatures. These fibers have potential, but there are production difficulties associated with the formation of continuous fiber lengths (referred to as a “tow”) and reproducible fiber diameters. Fibers formed from the two principal sources are generally sold with particular “tow” sizes (such as 3000 fibers and 12,000 fibers) and very substantial lengths.

It has long been recognized that carbon fibers must be surface treated in order that they can be used for composite production. Early attempts to use untreated fibers led to composites with very disappointing

composite properties. Various, commercially confidential, methods were developed for surface treating the fibers. These methods are nearly always made an integral part of the carbon fiber production process, the treatment plant being included in the carbon fiber production line. Most manufacturers sell fibers with surface treatment “tuned” to the matrix application. Thus a particular type of treatment is recommended for epoxy matrices, and a different treatment for phenolic matrices. The particular treatment methods are not reported. In addition to surface treatment, fibers are generally subjected to a thin coating of a polymeric material known as a “size.” This practice is conducted so that the fiber “tows” are easier to handle. In fact, the extent to which fiber surface treatment and sizing impacts the final composite properties is not well understood. The so-called “tuning” of surface treatment to a particular matrix is frequently not based upon a complete understanding of the factors involved. It is the purpose of this entry to address this matter in more detail.

A very full discussion of the synthesis and other important details of carbon fibers can be found elsewhere (e.g., Ref.<sup>[6]</sup>).

### CARBON FIBER SURFACE CHEMISTRY AND TOPOGRAPHY

Carbon fibers can be produced with a range of surface chemistry and topography. Most commercial carbon fibers, with the exception of those specially prepared for high absorption characteristics, have a relatively low surface area. This is deliberate and a feature of the production process, which may lead to grooves on the fibers resulting from the original production process for the fibers, which involves the extrusion of a polymer (such as polyacrylonitrile) or a pitch to produce the fiber.

When a fiber is placed in a matrix material such as a polymer or resin, the initial first step is the wetting of the fiber by the matrix material. This wetting is assisted if there is some chemical or physical interaction between the fiber and the matrix material. The first key step in the process is thus the wetting of the fiber that allows the fiber to come into contact with the matrix, and then the possible chemical interaction between the fiber and the matrix. Interaction between the fiber and the matrix can involve both chemical and physical interaction.

Carbon fibers are surface treated by processes that nearly always lead to the oxidation of the carbon fiber surface. These processes may involve gas-phase oxidants such as ozone, liquid oxidants such as sodium hypochlorite, and electrochemical oxidation in various electrolytes. Plasma oxidation may also be conducted,

although in practice it presents practical problems as a result of the need to pass the fibers without damage into a very low pressure region with the plasma gas. These surface treatments result in two major changes on the carbon fiber surfaces, namely, a change in the fiber surface chemistry and a change in the fiber surface topography. Unfortunately, it is not possible to separate these two factors in a simple way. This is because the surface treatment methods change both the surface chemistry and topography at the same time. Fig. 1 illustrates this situation for a high-modulus carbon fiber based upon pitch.<sup>[7]</sup> The atomic force microscope (AFM) data for this fiber change substantially as one compares the AFM data (A) for the carbon fiber (which was neither surface treated nor sized by the manufacturer) before treatment with the fiber after treatment. Before treatment the fiber shows a smooth surface with striations, which are associated with the production of the mesophase pitch fibers, used in the production process. When the fiber is subjected to surface treatment resulting from the galvanostatic electrochemical oxidation of the fiber in 1 M nitric acid at 0.5 A for 10 sec, the surface topography clearly changes. Some pitting of the surface can be observed, but the original surface striations from the production process are clearly visible. When the galvanostatic oxidation is conducted for 1 min rather than 10 sec the surface topography changes substantially, with all the original surface striations being lost.

The changes in surface topography produced by the surface treatment are quite clear, and in fact it is clear from the AFM image that the topographical features show differences on a nanoscale dimension.

It is interesting to examine whether there are any changes that arise in the surface chemistry, and not surprisingly one finds that the surface is oxidized by the electrochemical treatment. There are many ways to examine the changes that arise in surface chemistry (for a review, see, for example, Refs.<sup>[8,9]</sup>). One especially powerful method is the use of XPS. This entry will focus on this technique for the following reasons. The technique is normally non-destructive, the information comes from the outer 10–100 Å of the surface, is atomic (i.e., the atomic numbers of the elements in the surface region can be identified), and provides chemical details. It will be shown below that the topographical changes seen in Fig. 1 are also associated with chemical changes, and these chemical changes can be identified by XPS.

### X-RAY PHOTOELECTRON SPECTROSCOPY

X-ray photoelectron spectroscopy [which is sometimes referred to as electron spectroscopy for chemical analysis (ESCA)] is a mature surface analytical probe that is

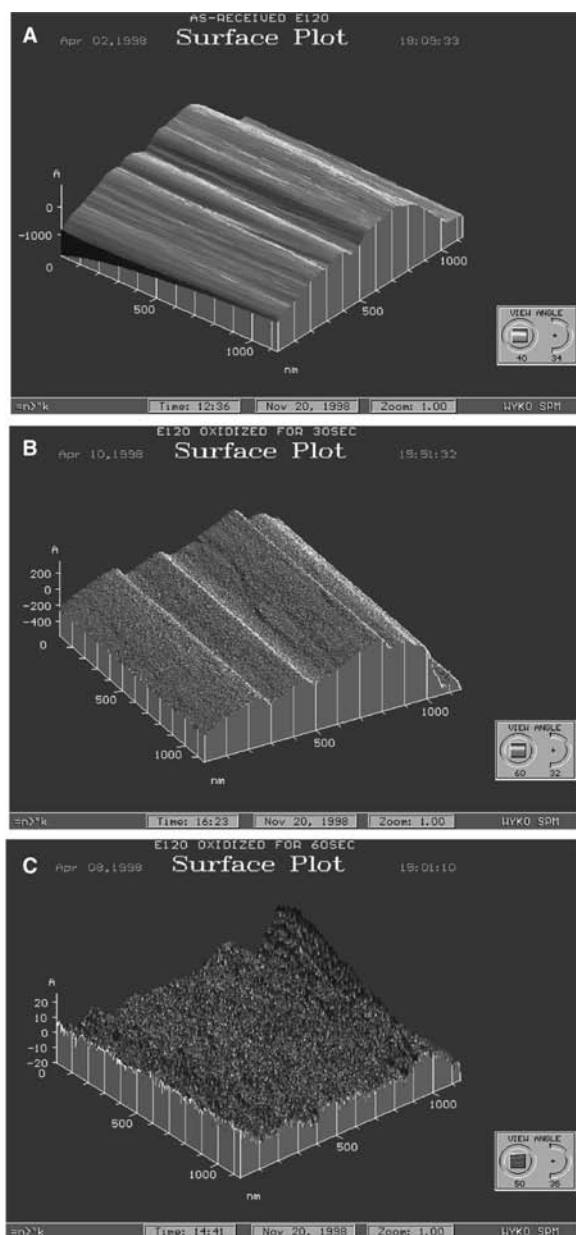


**Fig. 1** Atomic force microscope images of (A) a high-modulus pitch-based carbon fiber that was neither surface treated nor sized, (B) the same carbon fibers after electrochemical oxidation in 1 M nitric acid at 0.5 A for 10 sec, and (C) same as (B) but oxidized for 1 min.

one of a number of ultra-high vacuum surface analysis techniques. The experiment involves placing the sample of interest in an ultra-high vacuum ( $10^{-9}$  to  $10^{-10}$  Torr) and then exposing the surface to soft X-rays. This leads to the emission of photoelectrons from both the core and valence band region. The X-ray light used is normally a soft X-ray, typically Mg  $K\alpha$  (1253.6 eV) or Al  $K\alpha$  (1486.6 eV), the latter source having the advantage that it can be obtained in monochromatic form using a range of commercial X-ray

monochromators. As the energy of the photon is known and the energy of the photoelectron measured, the binding energy that holds the electron into the material is simply obtained by the difference in the photon and photoelectron energy with suitable corrections for sample work function and any charging effects. The core region readily provides information about the type of atom present because core electrons normally come at very distinct binding energies, and an examination of an overall spectrum (i.e., a spectrum collected over a wide energy range, typically 1000 or more electron volts) leads to the easy identification of the elements present. Closer examination of the core region obtained by obtaining photoelectron data over a narrow energy range (typically around 15 eV) allows energy shifts that are characteristic of chemical differences to be identified. It took about 60 years from the first photoelectron spectroscopy experiments before it was realized that core electrons, which take no part in chemical bonding, do in fact give rise to a chemical shift. The reason for this shift is that while the core electrons are strongly attracted to the positively charged atomic nucleus, they are also repelled by the outer valence electrons (the electrons that take part in chemical bonding), leading to a small but readily detectable chemical shift. When the author first started in this field in 1972 it was hoped that chemical shifts might be quite substantial, allowing subtle chemical differences to be determined. It became clear over the past 30 years that these shifts, while very useful, are sometimes small and it is not uncommon for compounds with different chemistry to exhibit similar chemical shifts as a result of a “canceling out” of the principal factors that determine the chemical shift. In fact, the main factors are the charge on the atom from which the photoelectron is ejected, the charge on the surrounding atoms, and the difference in extra atomic relaxation energy between different compounds containing the atom of interest. Atomic charge is a useful but very subjective quantity, because while the nuclear charge (the number of protons in the nucleus) is known exactly, the electronic charge is not clearly defined when it comes to the valence electrons because these electrons are shared between different atoms involved in chemical bonding. Nevertheless, simple models based upon atomic charge have proved very useful for the prediction of core chemical shifts in XPS (see, for example, Ref.<sup>[10]</sup>).

Fig. 2 illustrates the type of information that can be obtained for a simple carbon compound, and how a simple calculation can explain the spectrum. The experimental data are for the compound *N*-methyl-2-pyrrolidinone (NMP), frozen as a solid from the gas phase by forming the solid on a liquid-nitrogen-cooled plate.<sup>[11]</sup> Two peaks can readily be seen in the C1s region, the peak at higher binding

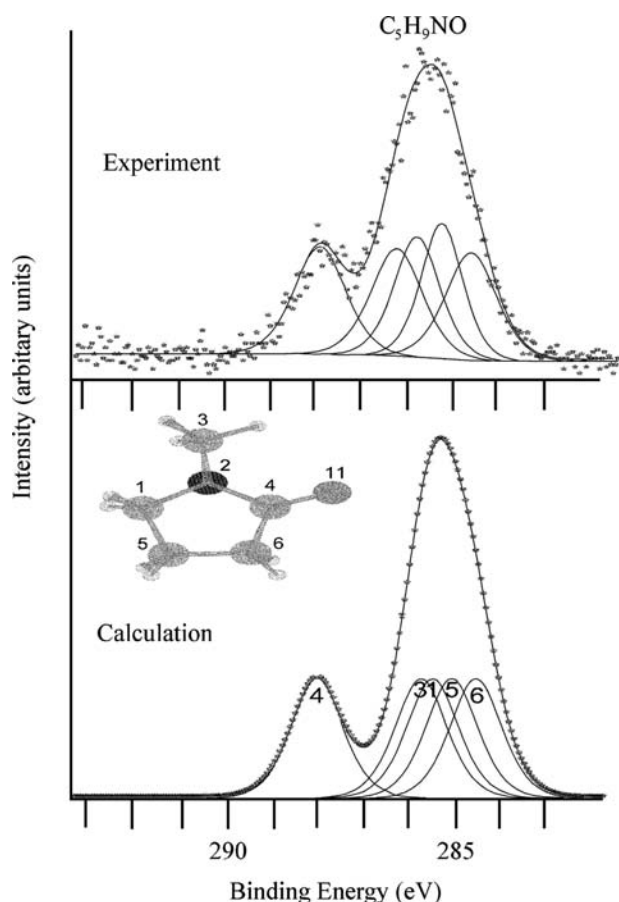


**Fig. 2** X-ray photoelectron spectrum of frozen NMP in the C1s region showing the experimental and calculated spectrum. The calculated spectrum shows the component peak positions obtained from a molecular orbital cluster calculation, with the peak areas obtained by adjusting the number of electrons associated with each atomic orbital type by the orbital's photoelectron cross section.

energy being due to the carbon atom (No. 4) associated with the C=O (where No. 11 is the oxygen atom) group in the molecule. The spectrum can be understood by examination of the calculated spectrum obtained using the relaxation potential model, which suggests that the four remaining carbon atoms form the low binding energy peak around 285 eV. In fact, the observed shift of around 3–3.5 eV from the C–H carbons is typical for the carbon atom of the >C=O group in a wide range of carbon compounds. Fig. 2 indicates that it is expected that the shift between some inequivalent atoms will be small (such as between carbon atoms 1, 3, 5, and 6). The experimental data have been fitted to a number of component peaks. The curve fitting of XPS data is an important approach to the analysis of core XPS data, and the method has proved a valuable method for extracting chemical information in a wide range of systems. Of course, any curve fitting

process is approximate, and there is never a unique answer. The best approach is to use a combination of well-developed fitting procedures, where the understanding of the peak shape and position is good, and combine this approach with a situation where the chemical environment changes and the fitted spectra have to be conducted in a consistent manner.

It is useful at this stage to return to the carbon fiber sample discussed in the previous section. The X-ray photoelectron spectrum observed in this case shows the significant *chemical* changes that accompany the *topographical* changes discussed above. Fig. 3 shows the core and valence band region observed<sup>[7]</sup> for the three samples indicated by (A), (B), and (C) in Fig. 1.

The overall XPS spectrum shows that the surface is practically entirely carbon, which is expected for an untreated and unsized fiber. The detailed O1s region can be seen to be of very low intensity. The detailed C1s region shows some very small amounts of surface functionality that can be seen from the curve fitted features at high binding energy of the principal C1s graphitic peak around 285 eV. In fact, the width and fine details of this peak can be associated with not only residual surface functionality, but also the degree of graphitic character of the carbon fiber.<sup>[12,13]</sup> The 10-sec electrochemical treatment gives the spectra shown in (B). Now a dramatic increase can be seen in the amount of oxygen with respect to carbon. The detailed C1s region now shows an additional peak shifted by about 2 eV from the graphitic peak at

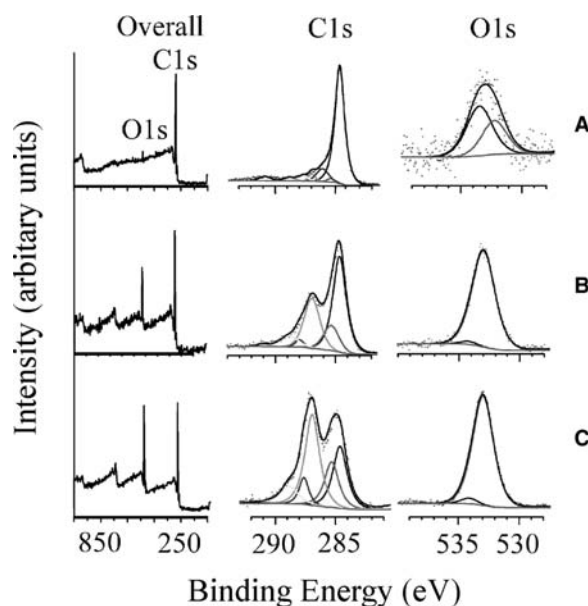


**Fig. 3** X-ray photoelectron spectra of the fibers described in Fig. 1. The overall region identifies the O1s and C1s features which are expanded and curve fitted in the separate C1s and O1s regions.



around 285 eV. In addition, other features can be fitted to the C1s region. The O1s region shows a single intense peak. The 60-sec treatment shown in (C) shows a significant increase in the amount of oxygen, with the detailed C1s region showing the peak at 287 eV now showing the greatest intensity.

These results can be understood in terms of the oxidation of the carbon fiber at the edge sites to form a C/O functionality that lies between a  $>C=O$  and a  $>C-OH$  functionality. This grouping, which will be referred to as the “bridged structure,” can be represented as shown in Fig. 4.

The C–O groups can be seen to have the intermediate functionality described above. The “main peak” is represented by the carbon atoms attached to the oxygen atoms, and this is the peak that corresponds to the feature at 287 eV. The  $\beta$ -carbon peak arises at about 0.7 eV to higher binding energy of the principal graphitic feature around 284.6 eV. It is interesting to note that the principal form of oxidized carbon is the bridged structure of Fig. 4. A number of authors suggest that oxidized carbon forms a stable carboxylic acid surface functionality, but the author finds that while this type of functionality is formed in certain cases it never is very intense, and this type of functionality frequently decomposes with the loss of carbon dioxide. The author has conducted extensive studies of the surface chemistry of these systems, and in nearly all cases the types of functionality described above are found.<sup>[8]</sup>

Core XPS is a very valuable approach to the study of the chemistry of carbon fiber surface, but the approach is not always able to distinguish between different surface functionalities. For example, it is not possible to distinguish between  $>C-OH$  and  $>C-O-C<$  functionality. As noted above the “chemical shifts” obtained with XPS are dependent upon electrostatic effects. The valence band region contains electrons whose energy is determined by the mixing of atomic orbitals to give molecular orbitals that are involved in the chemical bonding of the materials under study. This region gives “shifts” whose position

depends upon the chemical bonding and thus depends upon factors different from those that give rise to the core shifts. The author has found that this region complements the core region and can often distinguish between subtle chemical differences. For example, it is possible to distinguish between  $>C-OH$  and  $>C-O-C<$  functionality. In oxidized carbon systems the C2s and O2s atomic orbitals strongly mix to give molecular orbitals when C/O functionality is present, with shifts that are the reverse to those found in the core region. For example  $>C-OH$  functionality occurs at higher binding energy to  $>C=O$  functionality in the core O1s region, but the reverse is true in the principally O2s valence band region around 25 eV finding energy. Using model calculations it is possible to predict the changes in the valence band region that would arise when different surface functionalities are present. Fig. 5 shows the predicted valence band XPS spectra for a series of oxidized carbon species that are represented by a  $D_{6h}$ -symmetry-substituted coronene structure with different functionalities with the molecular orbitals calculated by multiple scattered wave  $X\alpha$  calculations.<sup>[14,15]</sup> The calculations predict a different separation between the principally O2s region around 25 eV and the principally C2s region around 18 eV. Note how this separation is predicted to be significantly larger for the  $-C-O-C-$  functionality than for the  $-C-OH$  functionality. This has allowed the author to distinguish between these two groups experimentally.<sup>[16]</sup> It should also be noted that the calculations predict that the  $-COOH$  carboxylic acid functionality should give rise to two separated peaks in the valence band region.

### The Effect of Size and Initial Surface Treatment

Most carbon fibers used in practical applications have a surface that is sized and initially surface treated by the manufacturer. The presence of this initial surface treatment and size can have a significant impact on the interaction of the fiber with a matrix. To illustrate

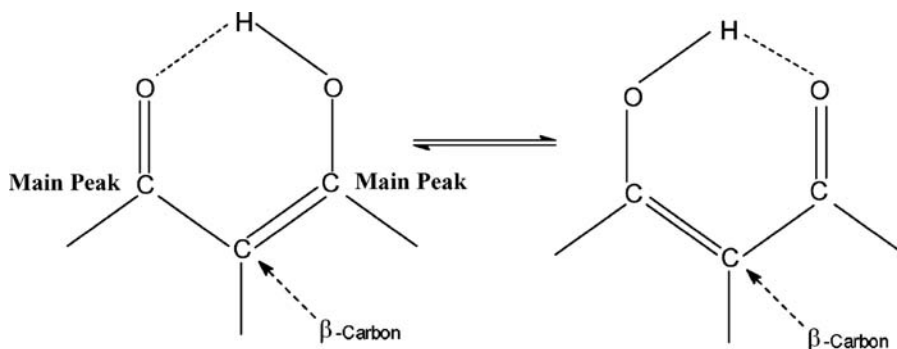
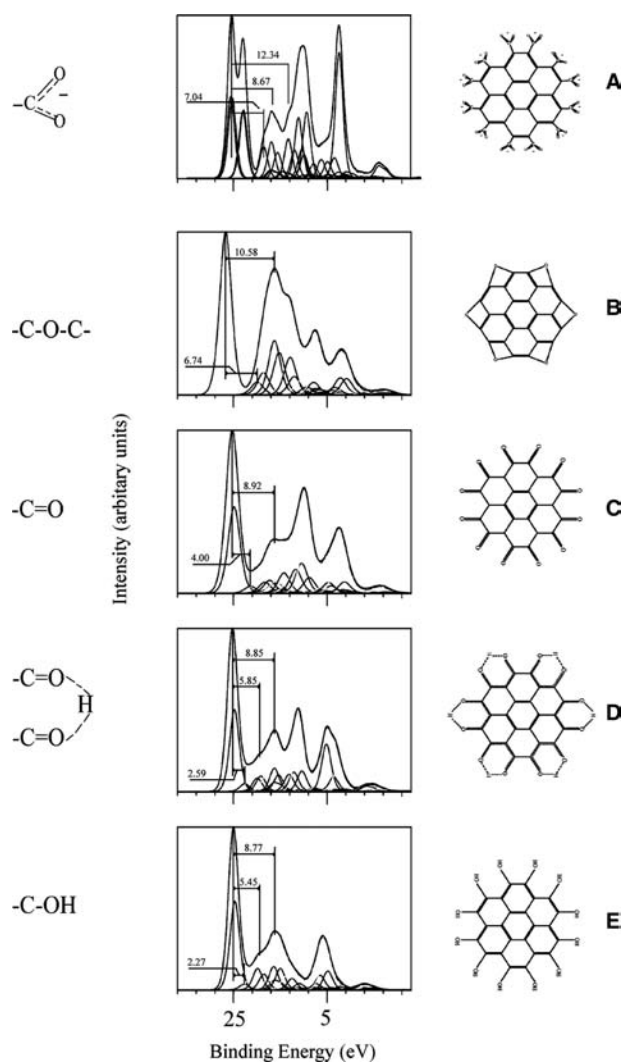


Fig. 4 Representation of the hydrogen-bridged oxide structure (HBS) unit showing the location of the “ $\beta$ ” and “main” carbon atoms.



**Fig. 5** Calculated X-ray photoelectron valence band spectra of model compounds used to represent typical oxidized carbon fiber surfaces. (A) carboxyl, (B) epoxide, (C) carbonyl, (D) bridged, and (E) hydroxide functional groups.

this point consider taking a commercially surface-treated fiber and the same fiber with the commercial surface treatment removed. Let us now apply an oxidative surface treatment to both fibers, which involves potentiostatic treatment in 1 M nitric acid for 20 min.<sup>[17]</sup> The C1s XPS data for both experiments are shown in Fig. 6, where “untreated” refers to the commercially surface-treated fiber with the surface treatment removed.

The fiber with no surface treatment can be seen to exhibit steadily increasing C/O functionality with the “bridged structure” of Fig. 4 appearing as a separate peak at higher binding energy (286.7 eV) than the C1s graphitic peak at 284.6 eV. Note how the corresponding “beta” peak of Fig. 4 is shown with half the intensity as the “bridged structure” at 285.3 eV.

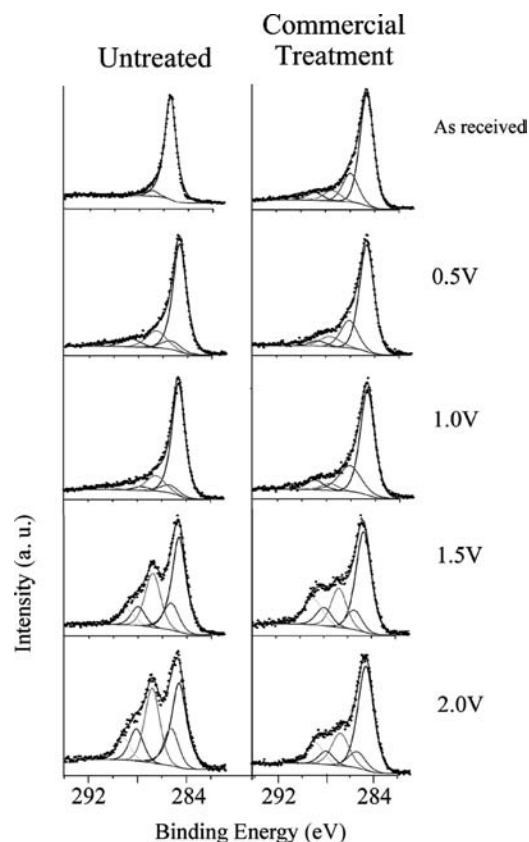


**Fig. 6** X-ray photoelectron spectra of the C1s region of an IM7 commercially surface-treated carbon fiber before and after electrochemical oxidation under potentiostatic conditions in 1 M nitric acid for 20 min. The voltages shown are with respect to the saturated calomel electrode. The “untreated” sample is the IM7 commercially surface-treated sample with the surface treatment removed by heating. Source: From Ref.<sup>[17]</sup>.

At 1.5 and 2.0 V, additional features at 288.1 eV can be seen due to  $>C=O$  surface functionality and 288.8 eV due to  $-CO_2H$  functionality. Note how the curve fitting includes the non-linear background in the fit, and note also how the fit has to be consistent over the whole range of spectra, an illustration of the curve fitting approach discussed above.

In contrast, the spectra for the commercially treated sample show marked differences on electrochemical oxidation from the untreated fiber. The differences are particularly striking at 1.5 and 2.0 V; in fact, the amount of oxidation at 2.0 V seems to be less than that at 3.0 V.

The principal lesson that one can learn from these results is the importance of a well-defined and untreated surface as a precursor for chemical interaction.

The presence of size on a carbon fiber surface might seem to be a simple matter to remove before the fiber was used to form a composite. Solvent extraction



would seem the appropriate approach, but in fact while the size is generally applied in a solvent solution, the removal of the size by solvent is not straightforward. In fact, the surface chemistry is dominated by the size, and solvent extraction does not remove all the size, with significant interaction occurring between the size and the underlying surface treatment. The higher the level of surface treatment the more difficult it is to remove the size.<sup>[7,18]</sup>

## MONITORING THE BURIED FIBER-MATRIX INTERFACE

The purpose of surface treatment of carbon fibers is to increase the wetting of the fiber by the matrix and to allow chemical and physical interaction with the matrix material. The interfacial chemistry that occurs between the fiber and the matrix, which has seen to be based on a nanoscale topography on the fiber surface, will be very important in final composite performance.

The author has approached the challenge of examination of this buried interface by developing a technique where photoelectron spectroscopy can be used to probe this interface by placing a very thin layer of the matrix onto the fiber. The matrix layer is so thin that the interfacial region can be probed by XPS. The outer surface region can also be examined and ultraviolet photoelectron spectroscopy (UPS) can be used for this purpose. Fig. 7 illustrates this approach by showing the valence band spectra for a thin film of polyvinyl alcohol placed on an oxide-free orthophosphate coating on metallic aluminum.<sup>[19]</sup> The coating is so thin that the underlying aluminum can be seen, the Al2p region showing two features one because of metallic aluminum and the other because of aluminum orthophosphate, suggesting a film thickness for the phosphate film of about 20 Å. Fig. 7(A) shows the valence band region using X-ray light and UV light. The spectrum in (A) is identical to that in (B), which is for a sample of polyvinyl alcohol when He(II) UV light is used. This confirms that the outer film region is polyvinyl alcohol because the photoelectrons generated by UV light have a much smaller escape depth than those generated by X-ray light. The valence band region in Fig. 7(A) for X-ray light is quite different from that of polyvinyl alcohol shown in Fig. 7(B) and that of aluminum orthophosphate (Fig. 7(A)).<sup>[1]</sup> If the valence band spectrum of polyvinyl alcohol is added to that of the aluminum orthophosphate film, the spectra do not superimpose and this can be demonstrated by using difference spectra.<sup>[19]</sup> Also, an additional peak is seen in the C1s region for the PVA-coated phosphate film.

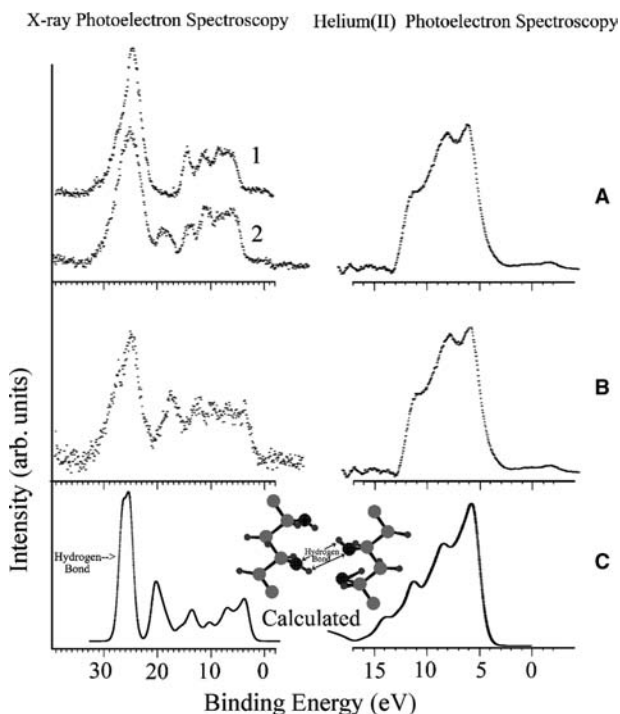


**Fig. 7** Valence band photoelectron spectra using X-ray and UV radiation. (A) shows the valence band region for a sample of aluminum with an oxide-free phosphate film, coated with a very thin film of polyvinyl alcohol (PVA). In the X-ray photoelectron spectra for (A), “1” is the valence band spectrum for the orthophosphate film on aluminum without any overlying PVA, and “2” the spectrum with the PVA film. (B) shows the valence band region for polyvinyl alcohol. (C) shows the calculated valence band region for polyvinyl alcohol generated from a band structure calculation. *Source:* From Ref.<sup>[19]</sup>.

In a carbon fiber system this buried interface can be probed using this approach. For example, the polyimide matrix material K3B is valuable as a matrix that can withstand higher temperatures than a typical epoxy resin matrix. Unfortunately, it is not easy to obtain a chemical interaction between the carbon fibers and this matrix. It is possible to see chemical interaction when a particular surface oxidation is conducted on the carbon fibers. Fig. 8 shows the C1s core region for an untreated IM7 carbon fiber, for K3B, and for a thin film of K3B on this fiber. The difference spectrum (Fig. 8(E) and 8(F)) between the spectrum with the thin K3B film (thin enough to probe the interface region) and the sum of the carbon fiber and K3B spectrum shows no significant difference. In other words, there has been no chemical interaction at the interface. When the untreated IM7 carbon fibers are electrochemically oxidized under galvanostatic conditions at 0.5 A in 1 M nitric acid for 40 sec, and the process repeated, then the corresponding difference spectrum does indeed show a difference, indicating a chemical

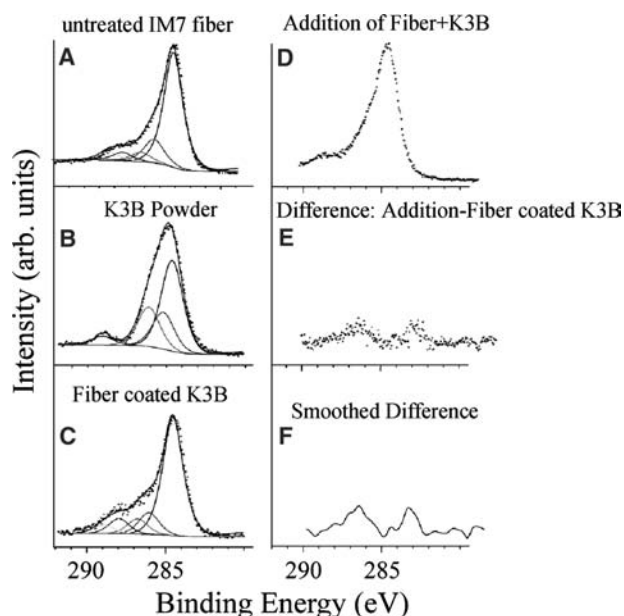


**Fig. 8** X-ray photoelectron spectra of the C1s region for (A) as-received IM7 fibers; (B) K3B powder; (C) fibers in part (A) dip-coated with K3B solution; (D) addition of parts (A) and (B); (E) difference of parts (D) and (C); (F) smoothed version of part (E). The intensity scales for parts (D)–(F) are the same.

reaction between the carbon fiber surface and the K3B (Fig. 9).

When a carbon fiber surface does not chemically react with the matrix material, then a “coupling agent”—another molecule that reacts with both the carbon fiber surface and the matrix—can be used. X-ray photoelectron spectroscopy can be used to monitor the effectiveness of this approach. For example, one can use a titanium alkoxide coupling agent (tetrakis(2-ethylhexyl) titanate, TOT) to couple a surface-treated carbon fiber to a phenolic resin. Fig. 10 shows the way in which the coupling agent acts.

The valence band XPS spectrum can be used to show that the interface between the coupling agent and the fiber and matrix is as suggested. Fig. 11 shows the difference spectrum for the difference between the XPS spectrum of a thin film of a phenolic resin on an E-120 pitch-based carbon fiber electrochemically oxidized in 1 M orthophosphoric acid, and the same situation but with TOT added to the resin. The surface treatment in this case leads to the formation of  $-C-OH$  functionality on the fiber surface. Hence the reaction scheme in Fig. 10. The smoothed difference spectrum in Fig. 11 was obtained using the background-subtracted spectra. It can be seen that the difference spectrum gives good agreement with the spectrum calculated for the  $Ti(OCH_3)_4$  molecule based upon a multiple scattered wave  $X\alpha$  calculation.<sup>[20]</sup> The five features identified in the outer valence band region are in

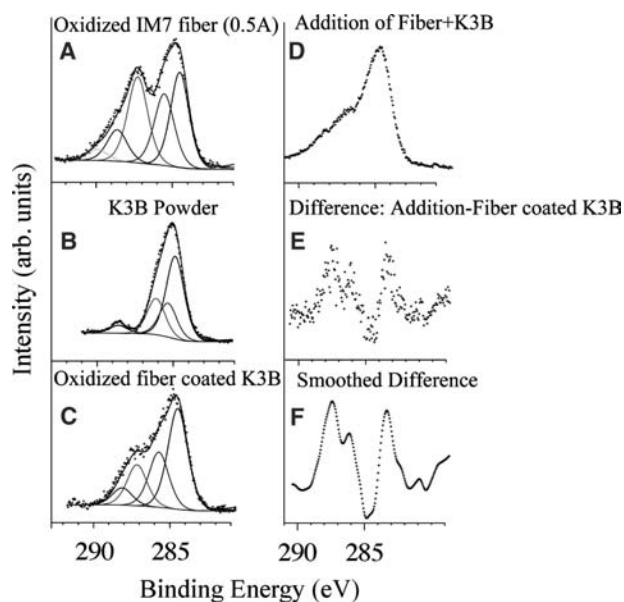


**Fig. 9** X-ray photoelectron spectra of the C1s region for (A) IM7 fibers galvanostatically oxidized in 1 M nitric acid at 0.5 A for 40 sec; (B) K3B powder; (C) fibers in part (A) dip-coated with K3B solution; (D) addition of parts (A) and (B); (E) difference of parts (D) and (C); (F) smoothed version of part (E). The intensity scales for parts (D)–(F) are the same. *Source:* From Ref.<sup>[11]</sup>.

good agreement with the difference spectrum. The difference spectrum also gives evidence of the presence of oxidized titanium ( $TiO_2$ ). This can be seen when one considers that the calculated spectrum for  $TiO_2$  (based upon a multiple scattered wave  $X\alpha$  calculation on the  $TiO_6^{8-}$  cluster) suggests that the peak identified as “2” in this calculation would fill the valley between peaks 1 and 2 and 3–5 in the calculated spectrum of  $Ti(OCH_3)_4$ . Thus the presence of  $TiO_2$  is consistent with the features observed in the valence band spectrum.

## NANOTUBES AND COMPOSITES

Carbon nanotubes have considerable potential for composite fabrication. In recent years there have been an enormous number of important developments in this area. There are many recent reviews and books on this area (e.g., Ref.<sup>[21]</sup>). The interest in nanotubes as the “ultimate carbon fiber” arises from the very desirable mechanical properties with the potential for a very high Young’s modulus which can be close to that of the in-plane value for perfect graphite, some 10 to 100 times greater than currently available carbon fibers. Single-wall nanotubes have good flexibility unlike carbon fibers, and thus composites with such nanotubes would be unlikely to fracture when exposed

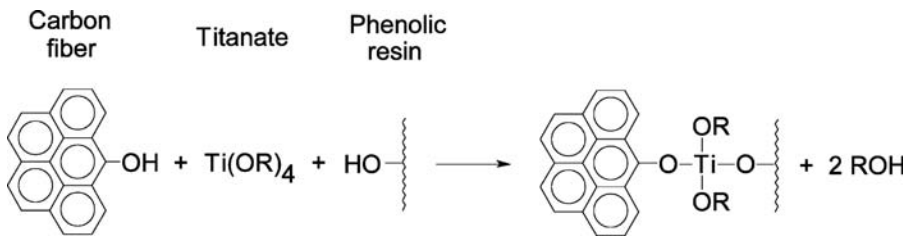


**Fig. 10** Reaction scheme between tetrakis(2-ethylhexyl) titanate (TOT) and an oxidized carbon fiber surface.

to compressive stress along the axis of the fiber, in contrast to carbon fibers reinforced composites.

There has been little success so far in replacing carbon fibers with carbon nanotubes in composite fabrication. The principal problem is the difficulty of getting good interaction between the carbon nanotube and the matrix. This entry has focused strongly on this issue, because it is so important in the development of practical composites. We have seen how this interaction can be studied and achieved in this entry. Further discussion of this issue can be found elsewhere (e.g., Ref.<sup>[21]</sup>). It is likely that the interfacial interaction issues, and other issues associated with the differences between carbon fibers and nanotubes such as the tendency of the latter to aggregate, will limit the use of nanotubes in composite applications.

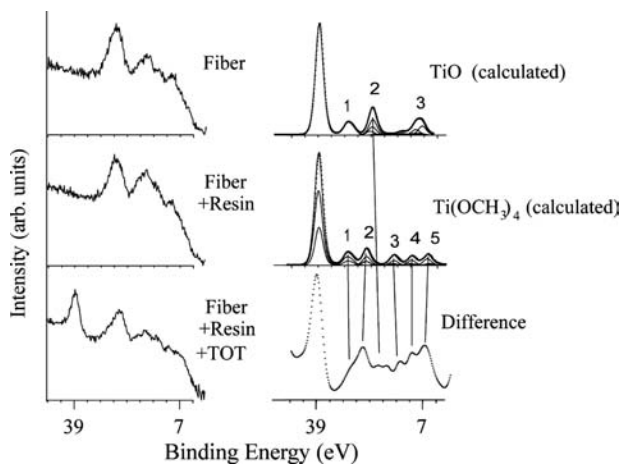


**Fig. 11** X-ray photoelectron spectra in the valence band region for E-120 pitch-based carbon fibers. The experimental valence band spectra of the fiber which was surface treated by galvanostatic oxidation in 1 M orthophosphoric acid at 0.5 A for 30 sec is shown (indicated as “fiber”), together with the fiber with a very thin coating of a phenol-formaldehyde resin (indicated as “fiber + resin”), and a fiber where the resin coating contains tetrakis(2-ethylhexyl) titanate (TOT) (indicated as “fiber + resin + TOT”). The difference spectra between “fiber + resin + TOT” and “fiber + resin” are shown where a non-linear background was removed from both the spectra and the difference spectra were smoothed. The difference spectra are compared with the calculated valence band spectrum for  $\text{Ti(OCH}_3)_4$  and  $\text{TiO}_2$  calculated by multiple scattered wave  $X\alpha$  calculations.

## CONCLUSION

The surface chemistry associated with the buried interface between a carbon fiber (or carbon nanotube) and the matrix plays a very important role in determining the practical performance of the chosen composite. The surface treatment methods available change both the nanostructure and the chemistry at the interface. Surface science methods, especially XPS, have a very valuable role to play in probing and understanding this interaction.

## ACKNOWLEDGMENTS

This material is based upon work supported by the National Science Foundation under grant No. CHE-0137502. The U.S. Government has certain rights in this material.

## REFERENCES

- Edison, T.A. Electric Lamp. U.S. Patent 223,898, January 27, 1880.
- Bacon, R. Growth, structure, and properties of graphite whiskers. *J. Appl. Phys.* **1960**, *31* (2), 283–290.
- Bacon, R.; Tang, M.M. Carbonization of cellulose fibers: II. Physical property study. *Carbon* **1964**, *2* (3), 220–221.
- Shindo, A. *Graphite Fiber*, Osaka Kogyo Gijutsu Shikensho Hokoku No. 317, 1961, Government Industrial Research Institute, Osaka, Japan, 1–317.
- Watt, W. Carbon work at the royal aircraft establishment. *Carbon* **1972**, *10* (2), 121–143.
- Dresselhaus, M.S.; Dresselhaus, G.; Sugihara, K.; Spain, I.L.; Goldberg, H.A. *Graphite Fibers and Filaments*; Springer Series in Materials Science; Springer-Verlag: Berlin, 1988; Vol. 5.
- Wang, Y.-Q.; Zhang, F.-Q.; Sherwood, P.M.A. X-ray photoelectron spectroscopic study of carbon fiber surfaces: 23. Interfacial interactions between polyvinyl alcohol and carbon fibers electrochemically oxidized in nitric acid solution. *Chem. Mater.* **1999**, *11* (9), 2573–2583.
- Sherwood, P.M.A. Surface analysis of carbon and carbon fibers for composites. *J. Electron Spectrosc. Relat. Phenom.* **1996**, *81* (8), 319–342.

9. Drzal, L.T. The surface composition and energetics of type A graphite fibers. *Carbon* **1977**, *15* (4), 129–138.
10. Sherwood, P.M.A. Analysis of the x-ray photoelectron spectra of transition metal compounds using approximate molecular orbital theories. *J. Chem. Soc., Faraday Trans. II* **1976**, *72* (10), 1791–1804.
11. Viswanathan, H.; Wang, Y.-Q.; Audi, A.A.; Allen, P.J.; Sherwood, P.M.A. X-ray photoelectron spectroscopic studies of carbon fiber surfaces: 24. Interfacial interactions between polyimide resin and electrochemically oxidized PAN-based carbon fibers. *Chem. Mater.* **2001**, *13* (5), 1647–1655.
12. Viswanathan, H.; Rooke, M.A.; Sherwood, P.M.A. X-ray photoelectron spectroscopic studies of carbon-fiber surfaces: 21. Comparison of carbon fibers electrochemically oxidized in acid using achromatic and monochromatic XPS. *Surf. Interface Anal.* **1997**, *25* (6), 409–417.
13. Xie, Y.; Sherwood, P.M.A. X-ray photoelectron spectroscopic studies of carbon fiber surfaces: 11. Differences in the surface chemistry and bulk structure of different carbon fibers based on poly(acrylonitrile) and pitch and comparison with various graphite samples. *Chem. Mater.* **1990**, *2* (3), 293–299.
14. Xie, Y.; Sherwood, P.M.A. X-ray photoelectron spectroscopic studies of carbon fiber surfaces: 13. Valence-band studies of oxidized fibers interpreted by Xa calculations. *Chem. Mater.* **1991**, *3* (1), 164–168.
15. Weitzsacker, C.L.; Sherwood, P.M.A. X-ray photoelectron spectroscopic studies of carbon-fiber surfaces: 19. Surface chemical changes during electrochemical oxidation in base. *Surf. Interface Anal.* **1995**, *23* (7&8), 531–538.
16. Xie, Y.; Wang, T.; Franklin, O.; Sherwood, P.M.A. X-ray photoelectron spectroscopic studies of carbon fiber surfaces: Part XVI. Core-level and valence-band studies of pitch-based fibers electrochemically treated in ammonium carbonate solution. *Appl. Spectrosc.* **1992**, *46* (4), 645–651.
17. Wang, Y.-Q.; Viswanathan, H.; Audi, A.A.; Sherwood, P.M.A. X-ray photoelectron spectroscopic studies of carbon fiber surfaces: 22. Comparison between surface treatment of untreated and previously surface-treated fibers. *Chem. Mater.* **2000**, *12* (4), 1100–1107.
18. Weitzsacker, C.L.; Bellamy, M.; Sherwood, P.M.A. Studies of the effect of size on carbon fiber surfaces. *J. Vac. Sci. Technol., A* **1994**, *12* (4, part 2), 2392–2397.
19. Wang, Y.-Q.; Sherwood, P.M.A. Interfacial interactions of polymer coatings with oxide-free phosphate films on metal surfaces. *J. Vac. Sci. Technol., A* **2003**, *21* (4), 1120–1125.
20. Wang, T.; Sherwood, P.M.A. X-ray photoelectron spectroscopic studies of carbon fiber surfaces: 20. Interfacial interactions between phenolic resin and electrochemically oxidized carbon fibers using titanium alkoxide coupling agents and their effect on oxidation behavior. *Chem. Mater.* **1995**, *7* (5), 1031–1040.
21. Dresselhaus, M.S.; Dresselhaus, G.; Avouris, P. *Carbon Nanotubes Synthesis, Structure, Properties and Applications*; Topics in Applied Physics, Springer-Verlag: Berlin, 2001; Vol. 80.

# Nanostructured Composites: Titanium-Based Alloys

Jürgen Eckert  
Jayanta Das  
Ki Buem Kim

*FG Physikalische Metallkunde, Technische Universität Darmstadt,  
Darmstadt, Germany*

## INTRODUCTION

Metastable materials with microstructural features, i.e., particles or grain sizes, layer thicknesses, or domain sizes, in the nanometer range (typically less than 100 nm at least in one dimension) have unique features, such as an appreciable fraction of their atoms in defect environments at the grain–interface boundaries, leading to a significant impact on their mechanical, physical, and chemical properties, which significantly differ from those of their conventional coarse-grained counterparts.<sup>[1–5]</sup> Normally, nanostructured materials (NsM) with an average grain size of 5 nm have about 50% of their atoms within the first two nearest-neighbor planes of the grain boundaries, in which distinct atomic displacements from the normal lattice sites occur.<sup>[2,5]</sup> Obviously, this has a strong impact on the properties of the material.

In 1959, Feynman at Caltech, U.S.A., has proposed<sup>[4]</sup> the idea of obtaining an enormously greater range of possible properties of condensed matter by control over the structure in the range of extremely small dimensions (nanometer scale). Later (1982–1985), Gleiter<sup>[1]</sup> was the first to realize a method for the production of such materials with nanometer-sized grains (crystallites). These materials have been categorized by Gleiter<sup>[5,6]</sup> as follows: 1) the dimensions/size of the materials/devices itself are on a nanometer scale,<sup>[6,7]</sup> 2) bulk materials/devices in which a thin surface region has a nanometer-sized microstructure,<sup>[6,8]</sup> or 3) building blocks (grains) of a bulk solid having a nanometer length scale.<sup>[5,6,9]</sup> The technological applications of the above mentioned materials are 1) catalysts and semiconductor devices and 2) surfaces with enhanced corrosion resistance, hardness, wear resistance or protective coatings, and quantum dots. The third category of materials with homogeneous nanometer-sized building blocks is often called “NsM” or nanophase materials, nanocrystalline materials, or supermolecular solids.<sup>[5]</sup> These metastable materials can be synthesized in both metallic<sup>[3,6,10]</sup> and non-metallic/polymeric<sup>[11]</sup> systems. The attempts

on controlled processing, microstructural, mechanical, and specific property characterization to find the applicability of such NsM of either single or multiple phases with layered, rod-shaped, or equiaxed crystallites with/without tailored grain boundary composition or homogeneous dispersion in a second phase matrix are a part of the emerging and rapidly growing field of nanotechnology.<sup>[5]</sup>

## BACKGROUND

It is well known that the mechanical behavior of polycrystalline metals and alloys depends on the grain size,  $d$ . The well-known empirical Hall–Petch relation<sup>[12,13]</sup> relates the yield strength,  $\sigma_y$ , to the average grain size,  $d$ , according to the following equation

$$\sigma_y = \sigma_0 + kd^{-1/2} \quad (1)$$

where  $\sigma_0$  is the friction stress and  $k$  is a constant. This relation yields a linear increase of yield strength with decrease in grain size. However, most measurements<sup>[10,14]</sup> seem to indicate that the strength of polycrystalline metals/alloys drops below the values predicted by extrapolation of Eq. (1) for a grain size of about 8–10 nm. This phenomenon is known as “inverse Hall–Petch relationship.”<sup>[14]</sup> So, it seems that a critical grain size determines the dominant deformation mode, which is governed either by dislocation mechanisms or by grain boundary processes.<sup>[14]</sup> In the lower grain size regime (<10 nm), grain boundary sliding and/or Coble creep apparently constitute the dominant deformation modes.<sup>[14]</sup> However, the determination of the Hall–Petch relationship (strength = hardness/3) is mainly based on hardness measurements. Recent studies<sup>[15–23]</sup> to explore the plastic deformation mechanisms of this class of materials suggest that nanocrystalline materials can also deform by twinning<sup>[15,16]</sup> and rotational movement of grain boundary disclinations triggering grain body

rotation.<sup>[17]</sup> In the former case indentation techniques were used to deform the nanometer-scale grains locally to evaluate the mode of strain accommodation under constrained conditions.<sup>[15,16]</sup> In contrast, it was observed recently that the deformation of bulk consolidated nanocrystalline specimens (grain size <100 nm) proceeds through a shear banding mechanism.<sup>[22,23]</sup> Usually, the strength of bulk nanocrystalline materials is 5–10 times higher than that of the corresponding coarse-grained counterparts.<sup>[24,25]</sup> On the other hand, the ductility of NsM at room temperature has not lived up to the expected level and is often disappointingly low.<sup>[25]</sup> The major limitations of ductility for nanocrystalline materials have been identified<sup>[25]</sup> as: 1) artifacts from processing; 2) force instability; and 3) crack nucleation and propagation instability.

## DEVELOPMENT AND PROCESSING OF NsM AND COMPOSITES

A variety of laboratory-scale processing techniques have been employed in the past decade to synthesize NsM. These can be broadly classified as: 1) rapid solidification;<sup>[26,27]</sup> 2) mechanical alloying and compaction;<sup>[28–31]</sup> 3) severe plastic deformation methods<sup>[32]</sup> including equal channel angular pressing (ECAP)<sup>[33]</sup> and high pressure torsion;<sup>[34]</sup> 4) surface mechanical attrition treatment (SMAT);<sup>[35]</sup> 5) cold working and recrystallization;<sup>[36]</sup> 6) gas-phase condensation of particulates and consolidation;<sup>[1,37,38]</sup> 7) electrodeposition;<sup>[39–41]</sup> 8) controlled annealing treatment;<sup>[42–45]</sup> severe mechanical deformation;<sup>[46,47]</sup> or high pressure torsion<sup>[48]</sup> of as-prepared bulk metallic glasses (BMGs)/amorphous precursors.

Among the above-mentioned techniques, electro- and vapor deposition methods are capable of producing thin films with mean grain sizes, i.e., order of tens of nanometers.<sup>[39–41]</sup> For example, dense single-phase 100- $\mu\text{m}$  thin sheets have been produced in pure (Ni, Co, Cu) and binary alloys (Ni–Fe, Ni–W) with grain sizes of 20–40 nm<sup>[39–41,49,50]</sup> by pulsed electrodeposition techniques. The limitations in these cases are not only the pick-up of impurities like sulfur or carbon, but also hydrogen filled nanobubbles/voids in the material. The other methods are able to produce nano/ultrafine-grained bulk materials. Gas-phase or inert gas condensation methods<sup>[1,37,38]</sup> are mostly used for the production of pure metals, such as Cu, Ni, and Pd, with equiaxed grain sizes in the range of 5–50 nm. The problems associated with this process are limited specimen volume, material yield, and rather high impurity level at the particle boundaries resulting in incomplete densification as well as retaining the nanoscale grain size during consolidation.<sup>[28]</sup> Ball milling or mechanical alloying is one of the efficient

techniques for the production of nanocrystalline materials because of its simplicity and processability to obtain a variety of metastable phases and alloys,<sup>[28–31,51–61]</sup> for example, Ni<sub>60</sub>Nb<sub>40</sub>,<sup>[51]</sup> Fe–Cu,<sup>[54]</sup> Ni<sub>60</sub>Mo<sub>40</sub>, and Ni<sub>85</sub>Mo<sub>15</sub><sup>[55]</sup> solid solutions with largely extended solubility ranges. The production of not only pure nanostructured body centered cubic (bcc), hexagonally close packed (hcp),<sup>[55]</sup> and face centered cubic metals,<sup>[53]</sup> as well as binary Fe–Cu<sup>[54]</sup> and Ni–Mo<sup>[56]</sup> and a variety of other nanostructured alloys,<sup>[57,58]</sup> but also multicomponent alloys<sup>[28,59–61]</sup> has been reported. Specifically, cryomilling in a liquid nitrogen medium has been shown<sup>[30,31]</sup> to produce ultrafine-grained aluminum alloys, and the resulting powder has been consolidated at elevated temperatures to nearly full density with insignificant grain growth. But the principal disadvantages of this processing route include the inability to control the purity of the material, to retain the nanocrystalline grain size, and to obtain full density upon consolidation.<sup>[30,31]</sup> Nanocrystalline metals and alloys with lower impurity contents have been prepared in recent years by severe plastic deformation/SMAT/ECAP including Al alloy–01420, Cu, Ni, Ti, and Ti–6Al–4V, steels, and intermetallic compounds as well as Al–Mg alloys.<sup>[32–38]</sup> In this entry, we will report on structural nanocrystalline/ultrafine-grained Ti-base alloys prepared by metal mold casting. This single-step fabrication procedure is relatively simple and allows easy control of the contamination level.

To improve the ductility of NsM, different composite materials have been developed. These can be broadly categorized according to their microstructures: 1) two phase homogeneous nanostructures (minimum of two constituent phases with nanometer length scale)<sup>[61]</sup> and 2) heterostructures consisting of micro- and nanocrystalline phase mixtures (single/multiple phases with different length scale).<sup>[62–64]</sup> It is quite obvious that the factors governing the strengthening and toughening mechanisms in multiphase composite microstructures include the properties of the reinforcing phases, such as their elastic properties, yield strength, and ductility, as well as the properties of the interface between the different phases in terms of its strength and crystallographic orientation, together with the volume fraction, size, and morphology of the second phase.<sup>[65,66]</sup> The idea behind this composite approach is to avoid catastrophic failure in nanostructured/glassy material by controlling the plastic instability via generation and interaction of multiple shear bands (SBs). In this aspect, Leng and Courtney<sup>[67]</sup> demonstrated the possibility of SB confinement under tension by fabricating laminated composite specimens consisting of a layer of metallic glass bonded between two ductile metal layers. The first category of nanocomposites has been discussed in detail in Ref.<sup>[61]</sup>. The latter category preferably contains a bimodal grain size



distribution, as it was demonstrated for pure Cu,<sup>[62]</sup> or Ti-<sup>[63]</sup> and Zr-<sup>[64,68]</sup> base multicomponent alloys. Ma<sup>[69]</sup> summarized the strategies that were used to improve the ductility of nanocrystalline materials by backing up the grain size (sacrificing some strength owing to a mixture of micro/nanometer-sized grains) for materials prepared by cold working and annealing (for inducing abnormal grain growth) as well as for specimens where a non-uniform grain structure is obtained by introducing a micrometer-sized dendritic phase in a nanocrystalline/ultrafine matrix upon solidification.<sup>[63,64,68]</sup> The basic idea<sup>[70,71]</sup> of preparing such “in situ composite microstructures” was shown to be feasible in improving the ductility of bulk NsM and BMGs,<sup>[64,70–74]</sup> even though a few BMGs show enhanced ductility recently.<sup>[75,76]</sup>

### SYNTHESIS, MICROSTRUCTURE AND MECHANICAL PROPERTIES

The synthesis of the nanostructured composites discussed in this entry is mainly based on arc-melting and/or Cu mold casting. It is well known that BMGs are usually obtained near deep (stable/metastable) eutectics in multicomponent systems.<sup>[77]</sup> However, for the available eutectic reactions in any alloy system, most of them may not be sufficiently deep to allow bulk glass formation at relatively low cooling rates (100–500 K/sec) by casting in metallic molds. In these cases, the nucleation of crystalline phases is expected through eutectic reactions. The cooling rates are very high ( $10^4$ – $10^5$  K/sec) for very thin/smaller diameter samples (100  $\mu\text{m}$ –1 mm).<sup>[78]</sup> Hence, a glassy structure can be formed in this case. On the other hand, the competing eutectic nucleation of crystals cannot be suppressed in larger diameter/thick samples.<sup>[73,78]</sup> However, by obtaining a high degree of undercooling under a range of casting conditions, the growth of these eutectic crystallization products can be restricted to the nanometer scale ( $\sim 100$  nm).<sup>[74,78,79]</sup> Additionally, by adopting multicomponent recipes,<sup>[74,80]</sup> such nanoeutectic structures can be promoted, making them readily accessible upon solidification.<sup>[74,79]</sup>

The microstructure formation of Ti-base nanostructured/glassy alloys can be schematically illustrated with the help of a pseudo-ternary phase diagram (Fig. 1) considering three different groups of constituent elements: 1) Ti (base element); 2) Nb/Ta/Zr/Mo (bcc  $\beta$ -phase isomorphous stabilizers) + Sn; and 3) Cu/Ni/Fe (eutectic matrix formers). The phase fields are plotted on the basis of the microstructural evolution at slow cooling rate of  $10^1$ – $10^2$  K/sec and metastable phase formation on different length scale. There are three (partly) overlapping phase fields that can be distinguished: a glassy region, an eutectic region

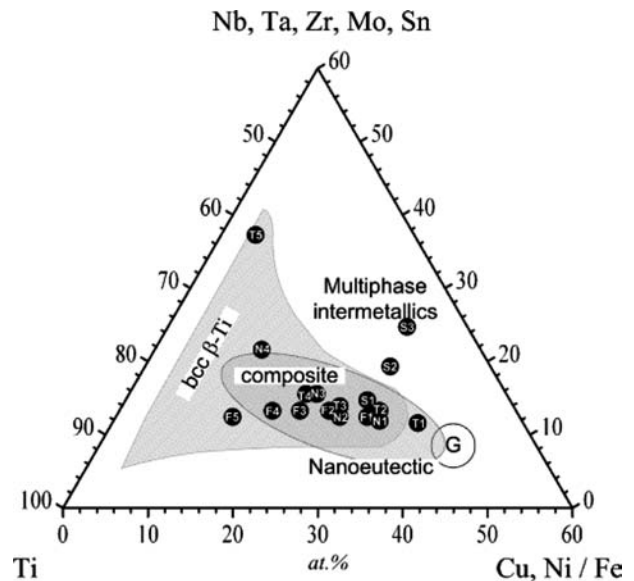
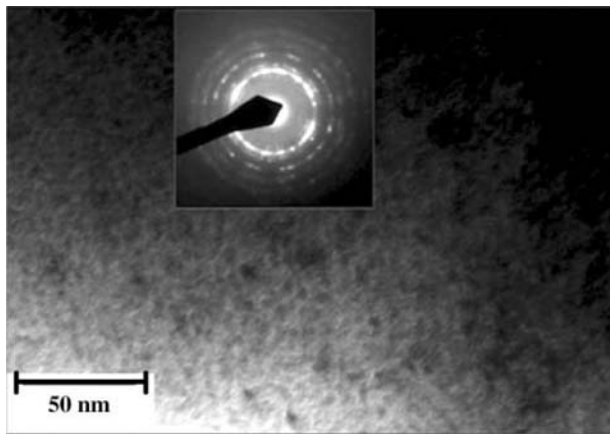


Fig. 1 Pseudo-ternary phase formation diagram for the Ti-(Nb, Ta, Zr, Mo, Sn)-(Cu, Ni/Fe) system.

(nanometer length scale), and finally a region where a bcc  $\beta$ -Ti-type solid solution forms, which sometimes coexists with other crystalline phase rather than bcc or nanoeutectic phases (marked as multiphase intermetallics). The overlapping of these regions produces composite microstructures with different length scale.

The glass-forming alloy composition is marked by a circle (G) in Fig. 1. In recent years, bulk glass formation was observed first in  $\text{Ti}_{50}\text{Cu}_{25}\text{Ni}_{20}\text{Sn}_5$ ,<sup>[81]</sup> and subsequently quite a large number of BMGs have been reported, e.g., for Ti-Cu-Ni-Si-B,<sup>[82]</sup> Ti-Cu-Ni-Sn-Be,<sup>[83]</sup> Ti-Cu-Ni-Sn-Be-Zr,<sup>[84]</sup> or Cu-rich Ti-Cu-Ni-Zr<sup>[85]</sup> alloys. These compositions are close to the circle marked as G. However, the glass-forming ability (GFA) of the Ti-base multicomponent alloys<sup>[81–84]</sup> is rather poor in comparison to Zr-base multicomponent alloys,<sup>[86]</sup> and the GFA abruptly decreases for higher Ti + Zr contents in the alloys.<sup>[85]</sup> Moving to the area with higher Ti + Sn content located in the upper left of the glassy region in the phase formation diagram yields nanostructured/glassy composites with submicron-sized hcp Ti particles, e.g., for a  $\text{Ti}_{50}\text{Cu}_{23}\text{Ni}_{20}\text{Sn}_7$  alloy cast to a thickness of 3 mm in diameter.<sup>[73]</sup> A typical microstructure of this type of alloy is presented in Fig. 2. The selected area diffraction pattern clearly confirms the existence of nanocrystalline particles in a glassy matrix. Modification of the glass-forming alloy composition and higher Ti + Nb contents in a  $\text{Ti}_{50}\text{Cu}_{20}\text{Ni}_{20}\text{Nb}_{10}$  alloy<sup>[79]</sup> lead to the formation of a nanoeutectic microstructure in 2–3-mm diameter cast rods.

On the other hand, the formation of micrometer-sized bcc  $\beta$ -Ti phase primary precipitates along with



**Fig. 2** A bright field TEM image of the matrix microstructure of  $\text{Ti}_{50}\text{Cu}_{23}\text{Ni}_{20}\text{Sn}_7$ . The inset shows a selected area electron diffraction (SAED) pattern taken from the matrix confirming the formation of nanocrystalline phase(s). *Source:* From Refs.<sup>[63,73]</sup>

a nanoeutectic microstructure has been observed in a wide range of cooling rates of  $10\text{--}10^3\text{ K/sec}$ .<sup>[80]</sup> The composition of these alloys lies in the “composite” region marked in Fig. 1. Moreover, a broad region of fully bcc beta-Ti phase alloys exists near to the left axis of Ti-(Nb/Ta/Mo/Zr), which can be easily understood when considering the respective binary alloy phase diagrams.<sup>[87]</sup> The composite microstructure formation and their effect on mechanical properties have been investigated by manipulating the compositions in a series of Ti-Cu-X-Sn-M alloy ( $X = \text{Ni, Fe, Cr, Co}$ ;  $M = \text{Nb, Ta, Mo, Zr}$ ).

### Effect of Ta

The variation in the Ti + Ta content of the alloys such as, for example, (T1)  $\text{Ti}_{52.0}\text{Cu}_{19.6}\text{Ni}_{16.8}\text{Sn}_{5.6}\text{Ta}_{6.0}$ , (T2)  $\text{Ti}_{56.0}\text{Cu}_{16.8}\text{Ni}_{14.4}\text{Sn}_{4.8}\text{Ta}_{8.0}$ , (T3)  $\text{Ti}_{60.0}\text{Cu}_{14.0}\text{Ni}_{12.0}\text{Sn}_{4.0}\text{Ta}_{10}$ , (T4)  $\text{Ti}_{64.0}\text{Cu}_{11.2}\text{Ni}_{9.6}\text{Sn}_{3.2}\text{Ta}_{12.0}$ , and (T5)  $\text{Ti}_{58.8}\text{Cu}_{1.1}\text{Ni}_{3.2}\text{Sn}_{5.0}\text{Ta}_{31.9}$  has been investigated systematically.<sup>[88,89]</sup> The compositions are marked in Fig. 1 as T1–T5. It can be seen that these compositions lie near to the glassy region and are shifted toward the left axis of the phase formation diagram. The microstructure of alloy T1 (2-mm $\phi$  rods solidified at  $10^2\text{--}10^3\text{ K/sec}$ ) exhibits mixed amorphous regions and nano/ultrafine-grained matrix. This composition lies in the “nanoeutectic region” in Fig. 1. The presence of a submicron-sized  $\beta$ -Ti phase was revealed from scanning electron microscopy (SEM) and x-ray diffraction (XRD) investigations.<sup>[88]</sup>

With increase of the Ti + Ta content in alloy T3 (3-mm $\phi$  rods) the existence of a micrometer-sized

$\beta$ -Ti phase with dendritic morphology can be observed<sup>[88]</sup> that is homogeneously distributed in a nanostructured matrix, as depicted in Fig. 3A. The XRD pattern [inset to Fig. 3A] clearly shows the presence of strong reflections from the  $\beta$ -Ti phase and broad diffuse peaks from the matrix phase (detailed investigations will be discussed later). The details of the nanostructured matrix revealed by SEM are presented in Fig. 3B, showing the eutectic morphology of the phases. The mechanical properties under uniaxial compression at an initial strain rate of  $10^{-4}/\text{sec}$  of the dendritic phase-reinforced nanostructured eutectic composites of alloys (T1, T2, T3; 2–3 mm $\phi$  as-cast rods) are listed in Table 1. The improvement of the mechanical properties (strength and room temperature plastic deformability) for alloy T3 compared to alloy T1 and other Ti-base bulk glassy alloys<sup>[81]</sup> can be clearly deduced from Table 1. This improvement is because of the presence of the micrometer-sized toughening phase ( $\beta$ -Ti).<sup>[63,88]</sup>

Slowly cooled ( $10\text{--}100\text{ K/sec}$ ) arc-melted ingots of different alloy composition (T2–T5) show a wide variation in the volume fraction of the  $\beta$ -Ti dendrites, whose values are about 20, 35, 65 and 95 vol.%, for alloys T2–T5, respectively.<sup>[88]</sup> A representative microstructure of alloy T3 as observed by SEM and a bright field transmission electron microscopic (TEM) image from the matrix are presented in Figs. 3C and 3D, respectively. The size of the dendritic phase in the arc-melted ingot [Fig. 3C] is larger than that of the 3-mm $\phi$  rods [Fig. 3A] owing to the lower cooling rate of arc-melting. Also the eutectic phases in the matrix are coarser than those in the faster cooled as-cast rods. The eutectic matrix mainly consists of  $\beta$ -Ti- and  $\gamma$ -CuTi-type phases (Fig. 3D) in alloy T3, as reported earlier.<sup>[80]</sup> The arc-melted alloys (T2–T5) with different compositions possess lower yield strength than the as-cast rods (Table 1) because of their coarser microstructural features.

Fig. 4 shows the variation in the mechanical properties of arc-melted ingots owing to different Ti + Ta addition, which ultimately changes the volume fraction of the toughening phase because of the shift of the alloy composition across the composite phase field from right to left, as depicted in Fig. 1. It seems that the yield strength and the plastic deformation for alloys T2–T5 are insensitive to the volume fraction of the dendritic phase. The increase in the elastic modulus for composites T2–T5 is because of the decrease in the volume fraction of the nanostructured matrix phase. Energy dispersive x-ray spectroscopy analyses suggest that there is no significant change in the composition of the dendritic phase, which varies only between 55 and 60 at.% Ti, 2 and 4 at.% Cu, 3 and 4 at.% Ni,  $\sim 5$  at.% Sn, and 26 and 33 at.% Ta.<sup>[88]</sup> However, the near beta alloy (alloy T5, in the single bcc phase field

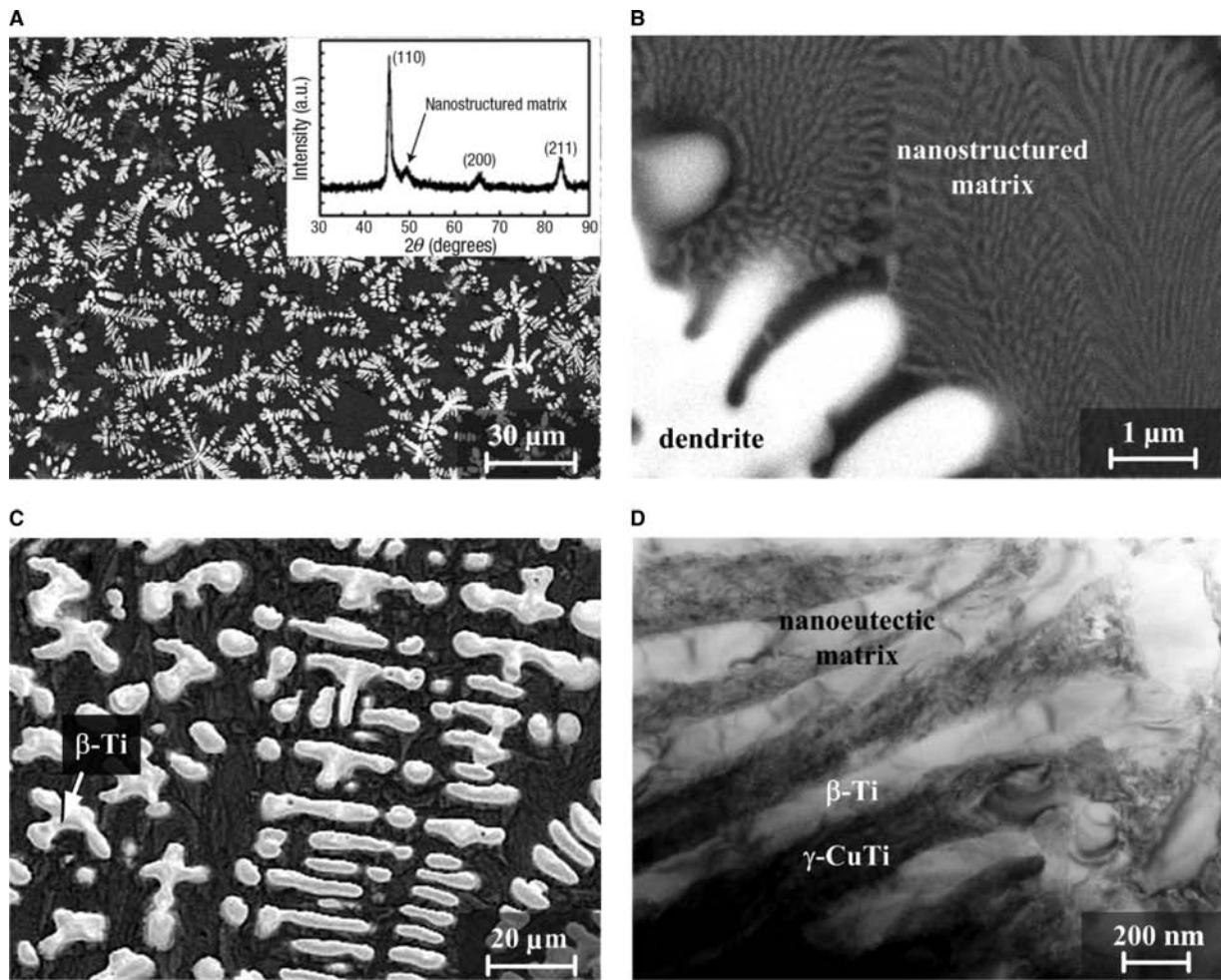


**Fig. 3** An SEM backscattered electron (BSE) image of as-cast  $\text{Ti}_{60.0}\text{Cu}_{14.0}\text{Ni}_{12.0}\text{Sn}_{4.0}\text{Ta}_{10}$  3-mm $\phi$  rod showing (A) in situ formed dendrites ( $\beta$ -Ti phase) in a dark matrix (inset: XRD pattern showing the dendrites to be a bcc phase and weak intensity from the matrix); (B) Magnified image of the dark matrix (a) showing the fine nanoeutectic microstructure; (C) SEM BSE image of an arc-melted  $\text{Ti}_{60.0}\text{Cu}_{14.0}\text{Ni}_{12.0}\text{Sn}_{4.0}\text{Ta}_{10}$  alloy showing a coarse dendritic microstructure; and (D) TEM bright field image of the nanoeutectic matrix. *Source:* From Refs.<sup>[80,88]</sup>

**Table 1** Room temperature compression test results of Ti-Cu-Ni-Sn-Ta alloys: Young's modulus,  $E$ , yield stress,  $\sigma_y$ , yield strain,  $\epsilon_y$ , fracture stress,  $\sigma_f$ , and plastic strain,  $\epsilon_p$

Alloy	Cast details	$E$	$\sigma_y$	$\epsilon_y$	$\sigma_f$	$\epsilon_p$
T1	$\phi$ 2 mm	63	1800	3.1	2251	1.4
	$\phi$ 3 mm	52	1516	3.1	1732	0.8
T2	Arc melted	49	941	2.1	2468	19.2
T3	$\phi$ 2 mm	69	1755	2.8	2440	4.7
	$\phi$ 3 mm	73	1525	2.3	2282	6.0
	Arc melted	71	1037	1.7	2196	16.5
T4	Arc melted	89	1073	1.4	2214	17.9
T5	Arc melted	43	894	2.3	4027	62.5 <sup>a</sup>

<sup>a</sup>Specimen without failure.

*Source:* From Ref.<sup>[88]</sup>.

of Fig. 1) with fully  $\beta$ -Ti microstructure shows a drop in the elastic modulus to 43 GPa (Fig. 4, Table 1) and superplastic-like room temperature compressibility of 62.5% plastic strain without failure.<sup>[88]</sup> The composition of the  $\beta$ -Ti phase was estimated to be  $\text{Ti}_{43.6}\text{Cu}_{0.}\text{Ni}_{1.6}\text{Sn}_{2.0}\text{Ta}_{52.8}$ .<sup>[88]</sup> Probably, a high amount of Ta (~50 at.%) significantly promotes the formation of  $\alpha'$  and  $\alpha''$  martensite in the  $\beta$ -Ti phase.<sup>[90]</sup> This drastically decreases the elastic modulus and increases Poisson's ratio. It has recently been suggested that the deformation mechanism and the pronounced cold workability of near beta Ti(Nb,Ta) alloys are also linked to the formation of deformation twins on a nanometer length scale (Eckert, J.; Das, J.; He, G.; Calin, M.; Kim, K.B. Ti-base bulk nanostructure-dendrite composites: microstructure and deformation. Mater. Sci. Eng. A. Submitted).



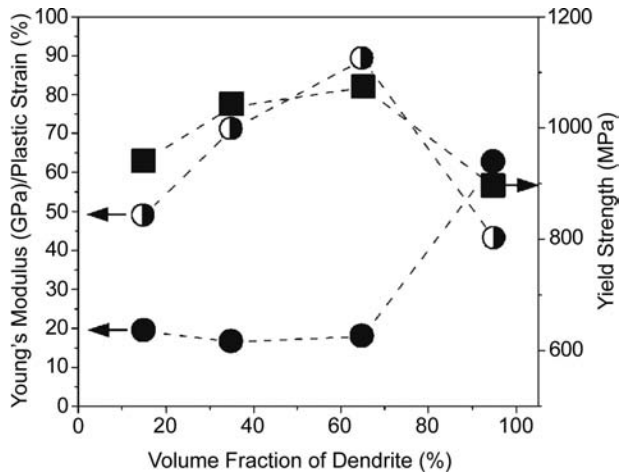


**Fig. 4** Effect of composition dependent dendritic volume fraction on Young's modulus (○), plastic strain (●) and yield strength (■).

### Effect of Nb

A large number of alloys with varying Ti + Nb content have been investigated<sup>[91]</sup> by mixing  $Ti_{80}Nb_{20}$  and  $Ti_{40}Cu_{28}Ni_{24}Sn_8$  with different portions to obtain

(N1)  $Ti_{56.0}Cu_{16.8}Ni_{14.4}Sn_{4.8}Nb_{8.0}$ , (N2)  $Ti_{60.0}Cu_{14.0}Ni_{12.0}Sn_{4.0}Nb_{10.0}$ , (N3)  $Ti_{64.0}Cu_{11.2}Ni_{9.6}Sn_{3.2}Nb_{12.0}$ , and (N4)  $Ti_{66.1}Cu_{8.0}Ni_{4.8}Sn_{7.2}Nb_{13.9}$  alloys. The alloys have been prepared by arc-melting and were solidified in the shape of 60 mm × 15 mm × 12 mm bars. The compositions of these alloys are indicated as N1–N4 in the phase formation diagram (Fig. 1) and lie right to left in the diagram according to their chemical composition. The changes in the microstructure with composition are clearly shown in Fig. 5. Alloy N1 contains a relatively fine dendritic phase with distinct epitaxial features, indicating a strong tendency for preferential growth of the dendritic bcc  $\beta$ -Ti phase.<sup>[91]</sup> The volume fraction of the dendrites is evaluated to be about 20 vol.%. It is revealed by TEM that the matrix contains a complex eutectic structure with grain sizes of about 30–200 nm.<sup>[91]</sup> In contrast, alloy N2 (Fig. 5A) contains “lopstick”-like dendrites, which are isolated by the matrix phase. The volume fraction of the dendrites in alloy N2 is about 40 vol.%.<sup>[91]</sup> The matrix exhibits a typical eutectic structure with an interlamellar spacing of about 50–150 nm, as shown in Fig. 5B. The high resolution TEM image from such a fine eutectic structure mainly consists of moiré fringes.<sup>[91]</sup> In case of alloys N3 and N4, both the

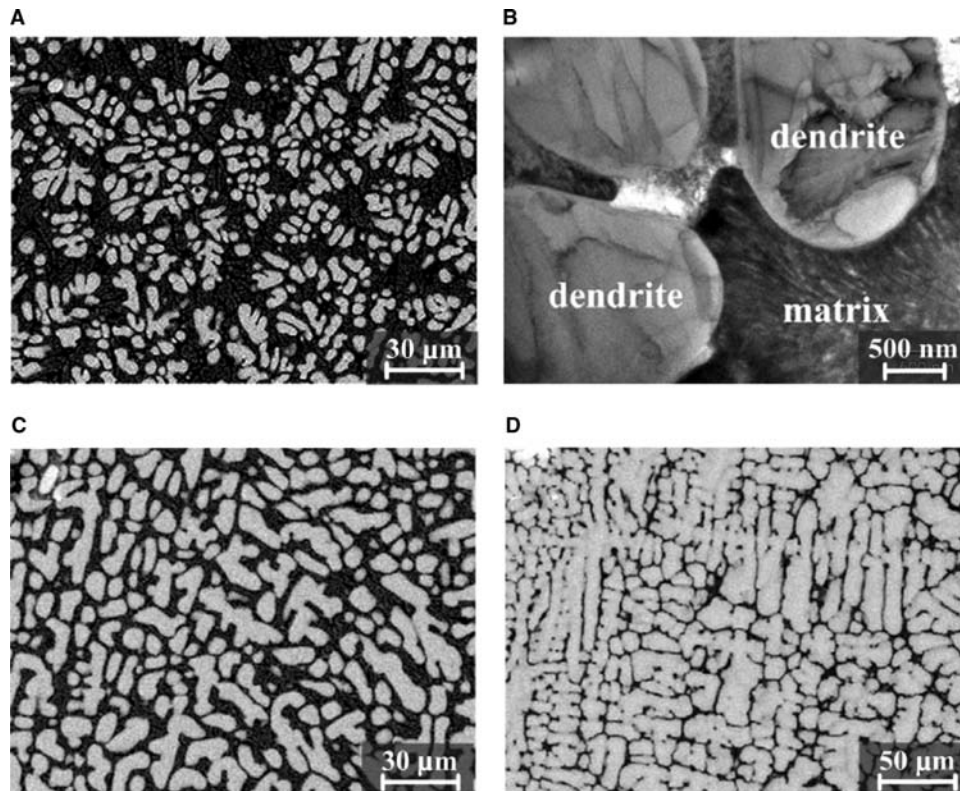


**Fig. 5** A BSE image of arc-melted  $Ti_{60.0}Cu_{14.0}Ni_{12.0}Sn_{4.0}Nb_{10}$  showing (A) in situ formed dendrites ( $\beta$ -Ti phase) in a dark matrix; (B) TEM bright field image showing the micrometer-sized dendrites dispersed in a nanoeutectic matrix. BSE images showing an increase in the volume fraction of dendritic phase with increase in Ti + Ta + Sn content in; (C)  $Ti_{64.0}Cu_{11.2}Ni_{9.6}Sn_{3.2}Nb_{12.0}$ ; and (D)  $Ti_{66.0}Cu_{8.0}Ni_{4.8}Sn_{7.2}Nb_{14}$  arc-melted ingots. Source: From Ref.<sup>[91]</sup>.

dendritic phase and the eutectic matrix exhibit a coarser morphology (Figs. 5C and 5D) than that observed for the former alloys N1 and N2. The volume fraction of the  $\beta$ -Ti dendrites is about 60 and 95 vol.% for alloys N3 and N4, respectively.<sup>[91]</sup> Except for alloy N1 (dendrite composition:  $Ti_{55.8}Cu_{1.4}Ni_{1.0}Sn_{20.1}Ta_{21.7}$ ), there is only an insignificant change in the composition of the dendrites for alloys N2–N4, which was estimated to vary from 65 to 67 at.% Ti, 3.5 to 4.5 at.% Cu, 2 to 3 at.% Ni, 5.5 to 9.5 at.% Sn, and 19.5 to 20 at.% Nb.

The mechanical properties of these Ti–Cu–Ni–Sn–Nb alloys have been investigated under compression.<sup>[91]</sup> All four alloys exhibit elastic deformation and pronounced yielding followed by plastic deformation with significant work-hardening. It can be clearly seen from Fig. 6 that there is an increase in the plastic deformability and a decrease in the yield strength with increasing volume fraction of dendrites in the different alloys. The important phenomenon noticed in these alloys is a significant change in the transition behavior from elastic to plastic deformation.<sup>[91]</sup> A higher volume fraction of nano/ultrafine-sized matrix (alloy N1) yields a gradual elastic–plastic transition, whereas alloy N4 with fully coarse  $\beta$ -Ti phase shows a sharp transition. Very similar mechanical properties were also observed when substituting Nb by Mo.<sup>[91]</sup>

### Effect of Sn

The evolution of the microstructure has also been studied for  $Ti_{57-x}Cu_{15}Ni_{14}Sn_{4+x}Nb_{10}$  ( $0 \leq x \leq 10$ ) alloys.<sup>[92]</sup> These alloys (S1:  $x = 0$ , S2:  $x = 5$ , S3:  $x = 10$ ) are located in the pseudo-ternary phase formation diagram (Fig. 1) from the bottom to the top

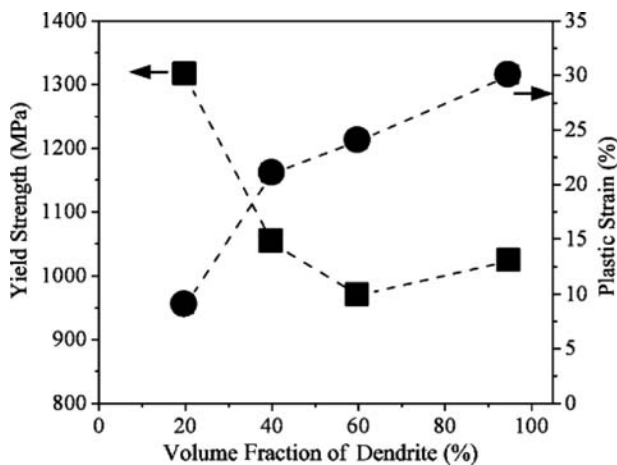


**Fig. 6** Effect of composition dependent dendritic volume fraction on plastic strain plastic strain (●) and yield strength (■).

with increase in the Sn content. All the alloys were cast as 5-mm diameter cylindrical rods. The microstructures of these alloys reveal that the phase field moves with increasing Sn content from a dendrite + nanoeutectic (hypoeutectic) morphology toward multiphase intermetallics in the hypereutectic region. Fig. 7A shows XRD patterns for alloys S1–S3 with different Sn content. It can be clearly seen that more unknown intermetallics appear with increasing amount of Sn in the alloy composition, which is also confirmed by microstructural observations (Fig. 7D). The existence of the dendritic  $\beta$ -Ti phase together with a nanoeutectic matrix (Fig. 7B) in alloy S1 represents a hypoeutectic microstructure resulting in a yield strength of 1226 MPa with 2.5% plastic strain.<sup>[92]</sup> Increasing the Sn content from 4 to 9 at.% shifts the alloy composition from a hypo- to a hypereutectic microstructure, as depicted in Fig. 7C. This can also be visualized by considering the Ti–Sn(Nb) pseudo-binary phase diagram.<sup>[87]</sup> Alloy S2 has a yield strength of 758 MPa but shows a poor ductility of only about 1%.<sup>[92]</sup> For 14 at.% Sn (S3), the composition of the alloy completely shifts to the intermetallic area, yielding different intermetallics in the as-solidified microstructure (Fig. 7D), as also revealed by XRD (Fig. 7A). S3 exhibits only elastic deformation and fails at only 300 MPa fracture stress.<sup>[92]</sup>

### Effect of Fe, Cr, and Co

To prepare “biocompatible” nanostructure–dendrite composites, He and Hagiwara<sup>[93,94]</sup> substituted Ni in

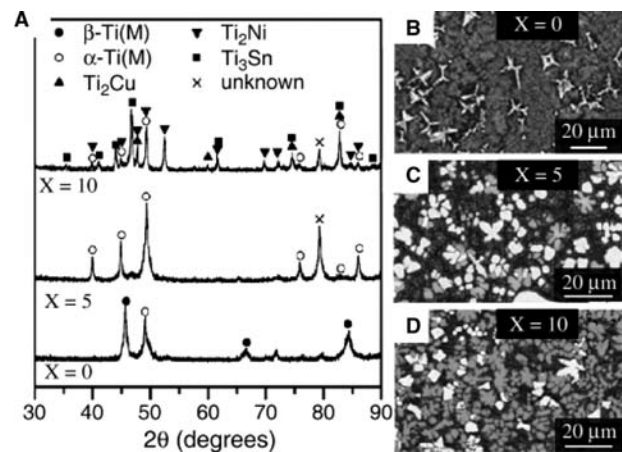


**Fig. 7** (A) The XRD pattern of as-cast 5 mm $\phi$ ,  $Ti_{57-x}Cu_{15}Ni_{14}Sn_{4+x}Nb_{10}$  ( $x = 0, 5, 10$  at.%) alloys showing the formation of multiphase intermetallics with increase in Sn content. The SEM images of  $Ti_{57-x}Cu_{15}Ni_{14}Sn_{4+x}Nb_{10}$ ; (B)  $x = 0$ ; (C)  $x = 5$ ; and (D)  $x = 10$ . Source: From Ref.<sup>[92]</sup>.

the alloy composition by Fe, Co, and Cr. As Ti-base alloys have been paid a lot of attention in recent years owing to their excellent biocompatibility, low density, excellent corrosion resistance, and good balance of mechanical properties,<sup>[95,96]</sup> this alloy design approach is highly interesting. The Young modulus of the so far available commercial biocompatible Ti-base alloys is very high (110 GPa) compared with that of bone (15–25 GPa).<sup>[97]</sup> This rather high value is detrimental, as a low rigidity of the implants is considered to be effective for promoting bone healing and remodeling.<sup>[96]</sup> Accordingly, it is highly desirable to develop advanced Ti-base alloys, which could imitate the elastic modulus of cortical bone.<sup>[98]</sup>

Along this line the microstructure and mechanical properties of  $\text{Ti}_{60}\text{Cu}_{14}\text{Ni}(\text{Fe},\text{Cr},\text{Co})_{12}\text{Sn}_4\text{Ta}(\text{Nb})_{10}$  alloys<sup>[93,94]</sup> have been investigated. All these alloys were prepared by arc-melting under slow cooling conditions (10–100 K/sec) and reshaped into 60 mm × 15 mm × 12 mm bars. In general there was no change in the microstructural constituents of these alloys observed compared to the earlier discussed nanoeutectic–dendrite composites. Fig. 8A exemplifies the characteristic micrometer-scale bright  $\beta$ -Ti phase in an ultrafine eutectic matrix for  $\text{Ti}_{60}\text{Cu}_{14}\text{Fe}_{12}\text{Sn}_4\text{Nb}_{10}$ .<sup>[93]</sup> The composition of the dendrites was estimated to be  $\text{Ti}_{64.36}\text{Cu}_{9.34}\text{Fe}_{7.61}\text{Sn}_{6.99}\text{Nb}_{11.7}$ ,<sup>[93]</sup> indicating an enrichment with Ti, Nb, and Sn compared to the nominal composition of the alloy. In contrast, the matrix is enriched with Cu and Fe.<sup>[93]</sup> XRD analysis reveals the presence of the bcc  $\beta$ -Ti phase and a hcp  $\alpha$ -Ti phase.<sup>[93]</sup> An increase in the Ti + Sn content without altering the Nb content in the alloy composition was observed to increase the volume fraction of the dendritic phase.<sup>[93]</sup> The compositions of this type of alloys are indicated in Fig. 1 as F1–F5. The increase in the volume fraction of the nanoeutectic structure from <2 to 75 vol.% increases the yield strength from 1050 to 1515 MPa and decreases the plastic strain from 20% to 3.7%.<sup>[93]</sup> Addition of Cr or Co instead of Fe in the alloy gives similar microstructural features as shown in Fig. 8B.

The Co-containing ( $\text{Ti}_{60}\text{Cu}_{14}\text{Co}_{12}\text{Sn}_4\text{Nb}_{10}$ ) (Fig. 8B) and Fe-containing ( $\text{Ti}_{74}\text{Cu}_8\text{Fe}_6\text{Sn}_2\text{Nb}_{10}$ ) alloys exhibit low elastic moduli ( $E$ ) of 67 and 54 GPa, respectively, similar to  $E = 55$  GPa for the well-known Ti–35Nb–7Zr–5Ta (wt.%) alloy.<sup>[95]</sup> However, Ti–35Nb–7Zr–5Ta also has a very low yield strength ( $\sigma_y = 530$  MPa) compared to the novel Ti-base nanostructured composites with biocompatible elements ( $\sigma_y = 1051$  MPa for  $\text{Ti}_{74}\text{Cu}_8\text{Fe}_6\text{Sn}_2\text{Nb}_{10}$ , and  $\sigma_y = 1050$  MPa for  $\text{Ti}_{60}\text{Cu}_{14}\text{Co}_{12}\text{Sn}_4\text{Nb}_{10}$ ).<sup>[94]</sup> This is a significant achievement, as this type of nanostructured composite material<sup>[93,94,99]</sup> combines low modulus and twice higher yield strength compared to conventional Ti-base microcrystalline near beta alloys used so far for biomedical purposes.<sup>[99]</sup>

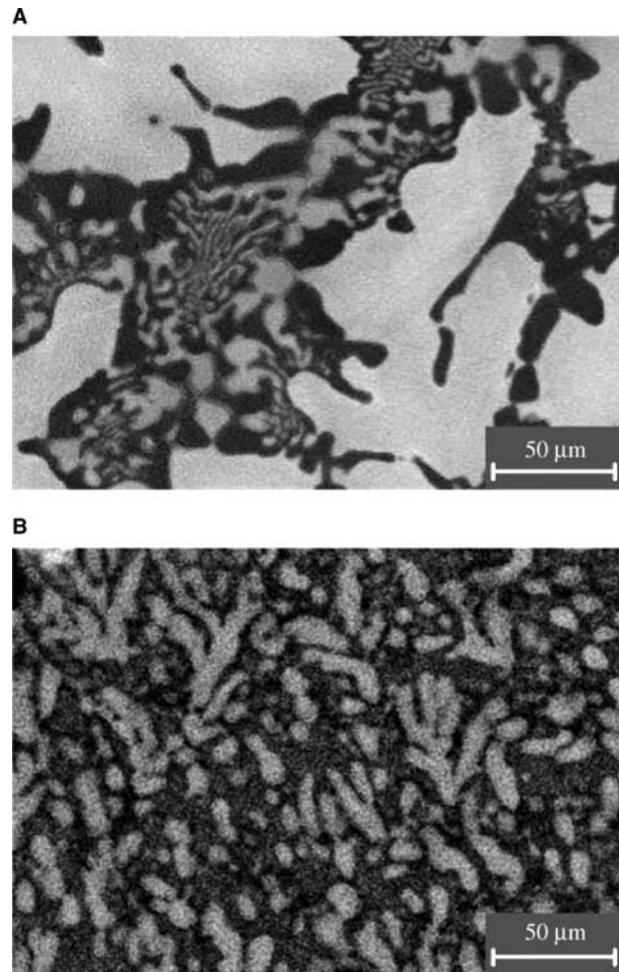


**Fig. 8** Images [SEM (BSE)] of  $\text{Ti}_{60.0}\text{Cu}_{14.0}\text{X}_{12.0}\text{Sn}_{4.0}\text{Nb}_{10}$  arc-melted ingots (A)  $X = \text{Fe}$  and (B)  $X = \text{Cr}$  showing dendrites in a nano/ultrafine microstructure. *Source:* From Refs.<sup>[93,94]</sup>.

## SOLIDIFICATION MECHANISM

To clarify the solidification mechanism of nanoeutectic matrix–dendritic phase composites,  $\text{Ti}_{60}\text{Cu}_{14}\text{Ni}_{12}\text{Sn}_4\text{Ta}_{10}$  and  $\text{Ti}_{74}\text{Cu}_{14}\text{Ni}_{12}$  alloy were selected for detailed investigations.<sup>[100]</sup> The composition of the latter Ti–Cu–Ni alloy is analogous to the former nanostructure–dendrite  $(\text{Ti} + \text{Sn} + \text{Nb})_{74}\text{Cu}_{14}\text{Ni}_{12}$  alloy composition.<sup>[88]</sup> Both alloys were solidified into 3-mm diameter rods in a Cu mold at a cooling rate of about 250 K/sec.<sup>[74,78]</sup> The as-cast microstructure of the Ti–Cu–Ni–Sn–Ta multicomponent alloy shows similar features<sup>[63]</sup> as described above for the alloys containing a dendritic phase dispersed in a nanoeutectic matrix. The matrix exhibits a two-phase eutectic microstructure with 65–95-nm interlamellar spacing, as shown in Fig. 9A. The eutectic rods are identified as bcc phase (Im3m) with composition  $\text{Ti}_{57.0}\text{Cu}_{7.6}\text{Ni}_{3.1}\text{Sn}_{10.8}\text{Ta}_{21.5}$  corresponding to a  $\beta$ -Ti phase. An indexed nanobeam



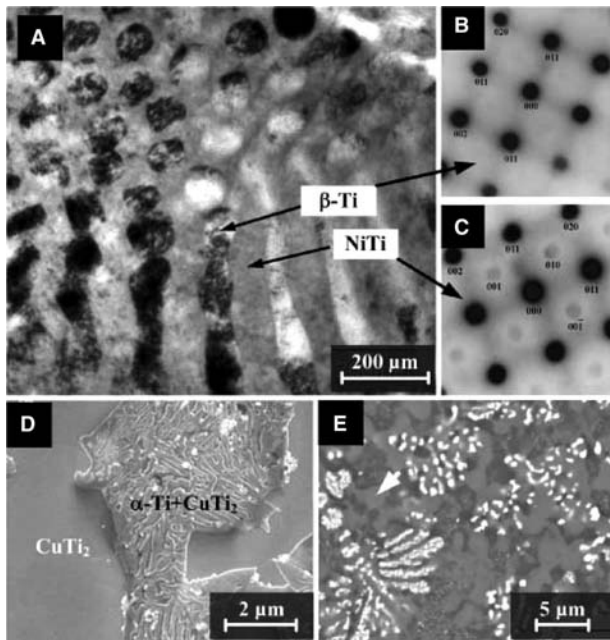


**Fig. 9** (A) A TEM bright field image of  $\text{Ti}_{60.0}\text{Cu}_{14.0}\text{Ni}_{12.0}\text{Sn}_{4.0}\text{Ta}_{10}$  (3-mm $\phi$  rod) showing the existence of  $\beta$ -Ti and NiTi phases; (B,C) SAED patterns from the corresponding phases; (D) SEM image of a  $\text{Ti}_{74}\text{Cu}_{14}\text{Ni}_{12}$  alloy showing the eutectoid  $\text{CuTi}_2$  and  $\alpha$ -Ti phases decomposed from the  $\beta$ -Ti phase in a  $\text{CuTi}_2$  matrix formed after peritectic reaction; and (E) An SEM image of  $\text{Ti}_{60.0}\text{Cu}_{14.0}\text{Ni}_{12.0}\text{Sn}_{4.0}\text{Ta}_{10}$  after heat treatment at 1073 K showing formation of the  $\text{CuTi}_2$  equilibrium phase (marked by an arrow). Source: From Ref.<sup>[100]</sup>.

diffraction pattern of this phase is shown in Fig. 9B. The second phase of the nanoeutectic is enriched with Ni and Cu, having a composition of  $\text{Ti}_{49.5}\text{Cu}_{24.5}\text{Ni}_{22.1}\text{Sn}_{1.2}\text{Ta}_{2.7}$ .<sup>[100]</sup> This phase is identified as a NiTi phase (B2) (Fig. 9C) even though it contains a high amount of Cu. Interestingly, the NiTi phase possesses a B19 structure in some regions of the specimen, which is possibly because of the presence of the high amount of Cu in the NiTi phase (>15 at.%), which suppresses the B2  $\rightarrow$  B19 transformation at room temperature.<sup>[100–102]</sup>

The microstructure of the ternary Ti–Cu–Ni alloy reveals dendritic eutectoid colonies consisting of  $\alpha$ -Ti and  $\text{CuTi}_2$  phases in a  $\text{CuTi}_2$  matrix.<sup>[100]</sup> Overall compositional analysis suggests the formation of a primary  $\beta$ -Ti phase, which finally undergoes eutectoid decomposition into the  $\alpha$ -Ti and  $\text{CuTi}_2$  phases.<sup>[100]</sup> There is a peritectic reaction between the primary  $\beta$ -Ti phase and the remaining liquid leading to the formation of the  $\text{CuTi}_2$  matrix,<sup>[100]</sup> which can be understood from the Cu–Ti binary phase diagram.<sup>[87]</sup> Annealing  $\text{Ti}_{60}\text{Cu}_{14}\text{Ni}_{12}\text{Sn}_4\text{Ta}_{10}$  at 1073 K induces the formation of the stable  $\text{CuTi}_2$  phase in the microstructure (Fig. 9E, marked by an arrow).

These investigations clearly suggest that the solidification behavior of  $\text{Ti}_{60}\text{Cu}_{14}\text{Ni}_{12}\text{Sn}_4\text{Ta}_{10}$  can be understood by considering it as a pseudo-ternary (Ti + Sn + Ta)<sub>74</sub> $\text{Cu}_{14}\text{Ni}_{12}$  alloy and by comparing it with an analogous composition in the Ti–Cu–Ni ternary system. After the formation of the  $\beta$ -Ti dendrites in  $\text{Ti}_{60}\text{Cu}_{14}\text{Ni}_{12}\text{Sn}_4\text{Ta}_{10}$ , the  $\text{CuTi}_2$  equilibrium phase is kinetically excluded because of sluggish diffusion in the melt, in the multicomponent recipe, in the higher cooling rate, and in the presence of Nb and Sn, which suppresses the eutectoid decomposition and stabilizes the  $\beta$ -Ti phase.<sup>[88,91,100]</sup> The peritectic formation of  $\text{CuTi}_2$  in the matrix is replaced by a metastable equilibrium between  $\beta$ -Ti and NiTi, which results in eutectic solidification of the remaining liquid even when the alloy is solidified at a low cooling rate of 10–100 K/sec. The metastability of this equilibrium is demonstrated by the recovery of the equilibrium phase ( $\text{CuTi}_2$ ) upon heat treatment of as-cast samples.<sup>[100]</sup>

## DEFORMATION AND FRACTURE MECHANISMS

The fracture surfaces after compression and the slip traces evolved on the specimen surface were widely investigated for Ti–Cu–(Ni,Fe,Co,Cr)–Sn–(Ta,Nb,Mo,Zr) alloys.<sup>[63,88,91,92,103]</sup> Most fractographic observations reveal regions on the fracture surface that are covered by melting features and strong light emission at the moment of fracture.<sup>[104]</sup> Evidence of “liquid droplets” on the fracture surface of dendritic phase-reinforced Ti–Cu–Ni–Sn–X (X = Ta, Nb, Mo) alloys has also been reported.<sup>[104]</sup> It was noticed that these nanostructured composite materials can store a high amount of elastic energy of up to 46 MJ/m<sup>3</sup>.<sup>[104]</sup> This significantly affects their fracture behavior, as conventional Al- and Mg-base alloys, stainless steel, and superalloys<sup>[105–107]</sup> have a resilience of <10 MJ/m<sup>3</sup>. The high stored elastic energy in these nanocomposites is released into a small volume in a narrow SB, leading to a sharp temperature increase within a thin layer during the fast propagation of the shear crack,<sup>[108]</sup> which finally appears as a melting or a vein-like pattern.<sup>[109]</sup>

Even though some of the as-cast alloys crumble into multiple pieces and show a distensile fracture mode of fracture,<sup>[110]</sup> on a macroscopic length scale a correlation between the shear fracture angle and the plastic deformability holds good<sup>[111]</sup> for a series of Ti–Cu–Ni–Sn–Nb nanostructured composites. Table 2 reveals that the macroscopic shear fracture angle ( $\theta_C^E$ ) increases from 46° to 51° in the order of the alloys N1  $\rightarrow$  N4, i.e., with the increase in the volume fraction of dendrites in the alloy (see section “Effect of Nb”). This feature is contradictory to the previous results for BMGs<sup>[112]</sup> and the Mohr–Coulomb criterion,<sup>[113]</sup> which is suitable for monolithic BMGs

**Table 2** Alloy composition, plastic strain,  $\epsilon_p$ , and shear fracture angles,  $\theta_C^F$ , of the investigated alloys

Alloy composition	Plastic strain, $\epsilon_p$ (%)	Final fracture angle, $\theta_C^F$ (°)	Initial SB angle, $\theta_C^O$ (°)	Rotation, $\theta_C^F - \theta_C^O$ (°)
(N1) Ti <sub>56</sub> Cu <sub>16.8</sub> Ni <sub>14.4</sub> Sn <sub>4.8</sub> Nb <sub>8</sub>	9	46	43.5	2.5
(N2) Ti <sub>60</sub> Cu <sub>14</sub> Ni <sub>12</sub> Sn <sub>4</sub> Nb <sub>10</sub>	21	48	41.4	6.6
(N3) Ti <sub>64</sub> Cu <sub>11.2</sub> Ni <sub>9.6</sub> Sn <sub>3.2</sub> Nb <sub>12</sub>	24	50	41.9	8.1
(N4) Ti <sub>66</sub> Cu <sub>8</sub> Ni <sub>4.8</sub> Sn <sub>7.2</sub> Nb <sub>14</sub>	30	51	40.5	10.5

Source: From Refs.<sup>[91,111]</sup>.

and BMG composites.<sup>[109,112,114,115]</sup> The surfaces of all the specimens are full of dense SBs, and they are aligned to both directions ( $\pm\theta_C^F$ ) with the compressive stress axis, i.e., parallel (primary SBs) and perpendicular (secondary SBs) to the final fracture plane. At a low magnification (50 $\times$ ) the SB spacing was measured to be 150  $\mu\text{m}$ .<sup>[116]</sup> For all the alloys, the SBs on the specimen surface display a bended morphology, which is observed from the macro- to the micrometer scale.<sup>[117]</sup>

From these observations it is suggested that the bending or rotation of the SBs is correlated with the high compressive ductility (up to 20–30%) of the four alloys. Therefore, a compressive specimen before and after deformation can be schematically illustrated as in Fig. 10A. Assuming that the original dimension of the specimen is  $a_0 \times a_0 \times l_0$ , the initial shear angle of the SBs is  $\theta_C^O$  and the length of the primary SBs is  $l_{SB}$ . After compression up to a plastic strain,  $\epsilon_p$ , the dimension of the specimen is changed to  $a \times a \times l$ . The angle between the primary shear plane and the stress axis is now  $\theta_C^F$ , owing to a strong rotation. Therefore, if it is assumed that the volume  $V$  of the specimen and the length  $l_{SB}$  of the primary SB remain nearly constant before and after deformation, the following relationships can be proposed<sup>[111]</sup>

$$V = a_0 \times a_0 \times l_0 = a \times a \times l \quad (2)$$

$$l_{SB} = a_0 / \sin(\theta_C^O) = a / \sin(\theta_C^F) \quad (3)$$

For a compressive specimen, the plastic strain  $\epsilon_p$  can be expressed as

$$\epsilon_p = (l_0 - l) / l_0 \quad (4)$$

From Eqs. (2)–(4), one can get the relationship between  $\theta_C^O$ ,  $\theta_C^F$ , and the plastic strain  $\epsilon_p$  as

$$\sin(\theta_C^O) = \sqrt{1 - \epsilon_p} \sin(\theta_C^F) \quad (5)$$

The initial shear angle  $\theta_C^O$  of the SBs can be calculated from Eq. (5) if the compressive plastic strain  $\epsilon_p$  and the final shear fracture angle  $\theta_C^F$  (Table 2) are known. The initial shear angle  $\theta_C^O$  of the primary SBs with respect to the stress axis is in the range of 40.5–43.5° for the four Ti-base alloys.<sup>[91,111]</sup> Taking the

average value of  $\theta_C^O = 41.8 \pm 0.9^\circ$  and Eq. (5) into account, the possible final fracture angle  $\theta_C^F$  can be calculated. The difference ( $\theta_C^F - \theta_C^O$ ) between the two shear fracture angles before and after fracture, that corresponds to the rotation angle ( $\theta_C^F - \theta_C^O$ ), increases from 2.5° to 10.5° when the compressive plastic strain increases from 8.9% to 30%.<sup>[91,111]</sup>

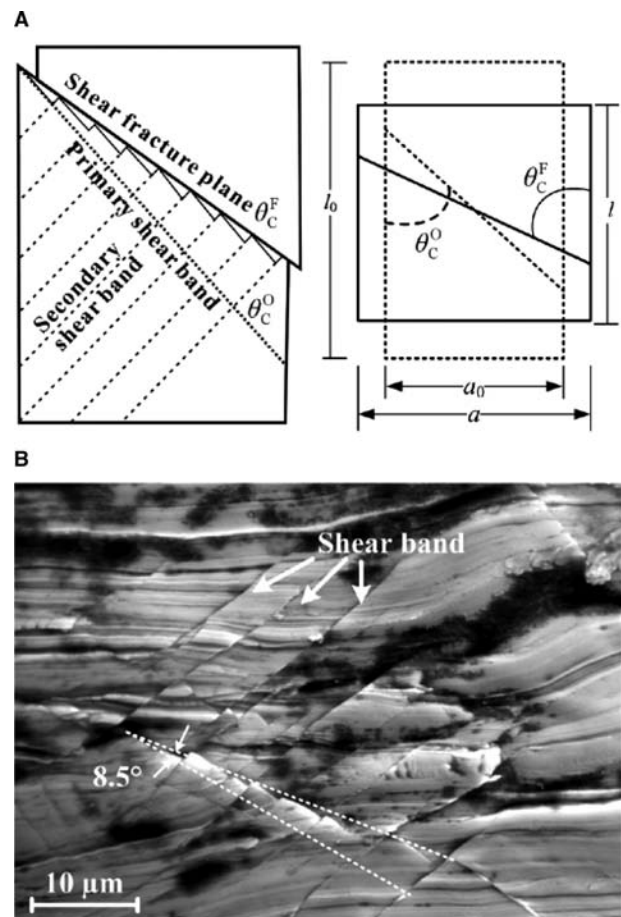


**Fig. 10** (A) Schematic illustration of the rotation of the primary shear plane because of SB impingement and (B) SEM image (secondary electron contrast) of the intersection and impingement between the two sets of SBs introducing a rotation of 8.5° of the shear plane on a microscopic scale for Ti<sub>66</sub>Cu<sub>8.0</sub>Ni<sub>4.8</sub>Sn<sub>7.2</sub>Ta<sub>14</sub> specimen after 25% plastic deformation. Source: From Refs.<sup>[111,118]</sup>.

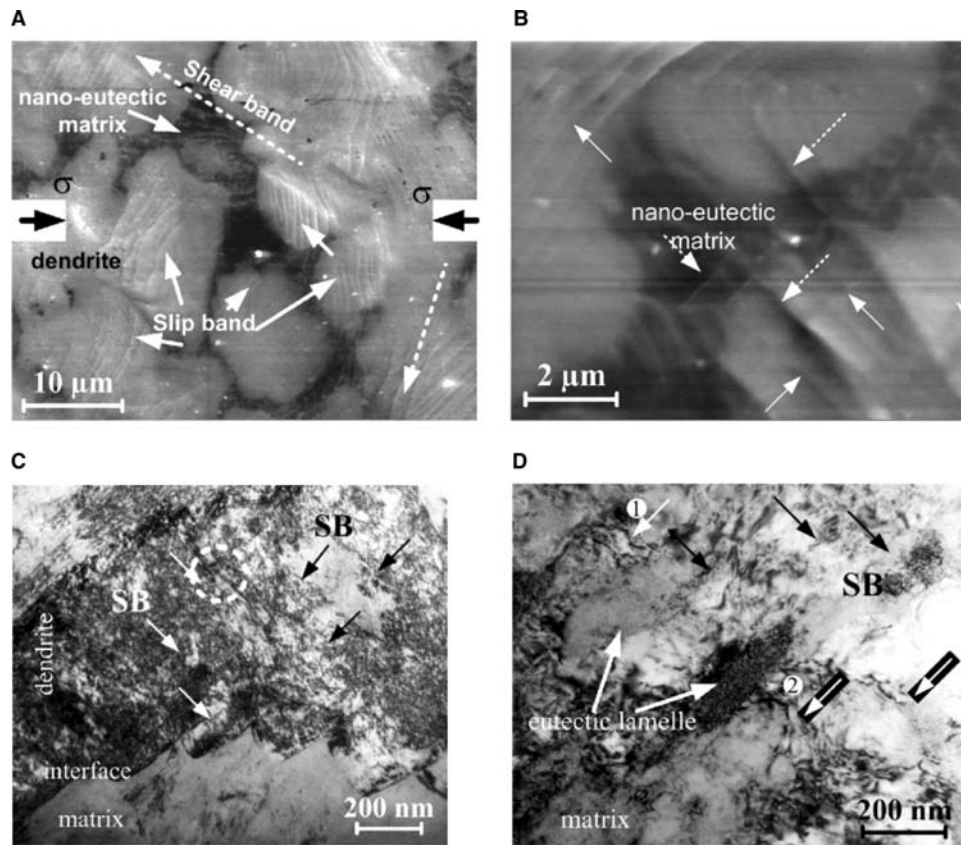


**Fig. 11** Microstructural features of the  $Ti_{66}Cu_{8.0}Ni_{4.8}Sn_{7.2}Ta_{14}$  specimen deformed up to ( $\epsilon_p = 8.1\%$ ): (A) formation of slip bands (small arrows) in the dendrites; (B) nucleation and passing of SBs at the dendrite–nanoeutectic matrix interface (dotted arrows); (C) A TEM bright field image of a 25% deformed alloy  $Ti_{66}Cu_{8.0}Ni_{4.8}Sn_{7.2}Ta_{14}$  specimen showing the intersection of SBs in the dendrites and a stepped morphology at the dendrite–matrix interface; and (D) passing of the SBs through the nano-eutectic structure indicating a set of SBs (black arrows) aligned parallel to the interface of eutectic lamellae and restricted propagation (at point 1) of another set of SBs (white arrows) in perpendicular direction, which are further regenerated at point 2. *Source:* From Refs.<sup>[118]</sup>, Eckert, J.; Das, J.; Kim, K.B.; Baier, F.; Löser, W.; Calin, M.; Zhang, Z.F.; Gebert, A. Deformation behavior of a  $Ti_{66}Cu_8Ni_{4.8}Sn_{7.2}Nb_{14}$  nanostructured composite containing ductile dendrites. *J. Alloy. Comp.* Submitted.

To get a clear view on the microscopic length scale, alloy N4 was deformed up to 25% plastic strain.<sup>[116]</sup> A large number of impingement and intersection events of the SBs under primary and secondary direction are observed on the specimen surface, as depicted in Fig. 3A. The SB spacing is on the order of 5–10  $\mu m$  measured at 2000  $\times$  magnification. The intersection of the SBs creates a morphology, which is similar to the surface of a “pineapple.” During plastic deformation of the composite, a set of SBs (primary direction) is activated, and it interacts with the SBs moving to the other direction (secondary direction). Additional deformation enforces the secondary SBs to cut through the primary SBs (Fig. 3D), yielding steps at the intersection points. However, with further deformation shear occurs in both directions (primary and secondary) and creates steps in both primary and secondary SBs to accommodate the applied strain. This finally appears as the structure depicted in

Fig. 10B. The change in the macroscopic fracture angle can be correlated with the impingement of the SBs on the microscopic scale, as illustrated in Fig. 10B by the dotted lines. The initial SB angle rotates by  $8.5^\circ$  after 25% deformation in alloy N4 (Table 2). The activation of two different sets of SBs along two different directions ( $\pm\theta_C^\circ$ ) is quite similar to a dislocation slip mechanism initiated through conjugated slip systems.<sup>[113]</sup>

To reveal the evolution of SBs in nanostructured composites,  $Ti_{66}Cu_8Ni_{4.8}Sn_{7.2}Nb_{14}$  (N4) was deformed up to different amounts of plastic strain (8% and 25%) without failure (Eckert, J.; Das, J.; Kim, K.B.; Baier, F.; Löser, W.; Calin, M.; Zhang, Z.F.; Gebert, A. Deformation behavior of a  $Ti_{66}Cu_8Ni_{4.8}Sn_{7.2}Nb_{14}$  nanostructured composite containing ductile dendrites. *J. Alloy. Comp.* Submitted). A large number of deformation bands were observed on the 8% plastically deformed specimen. The density of these bands is very

high, and their growth is restricted within the dendrites. Because the composite shows a work-hardening behavior, these bands must be “slip bands” that form because of dislocation movement in the dendrites. Typical features of such fine profuse slip bands are presented in Fig. 11A and are marked by small white arrows. The thick black arrows indicate the direction of the applied stress. In most regions the dendrites show “wrinkle”-like features along with a high density of slip bands at the center of the specimen. This indicates that the initiation of the localized deformation is related to both the high-strength nanostructured matrix and the ductile dendrites.<sup>[117]</sup> At this stage it is anticipated that some of the grains in the nanoeutectic matrix may contribute to the strain via dislocation movement. Interestingly, in a region close to the “wrinkled” dendrites, a few SBs are observed to pass through the dendrites, as indicated by a dotted white arrow in Fig. 11A. However, the majority of the area on the specimen surface does not display this feature. These bands are relatively sharper than the slip bands and have different contrast. The overall features suggest that there might be a preferred orientation with the applied stress axis. Because the strain distribution is not completely homogenous in the material,<sup>[116]</sup> these observations validate that the initial deformation originates from dislocation movement and the formation of slip bands inside the dendrites and proceeds through shear banding.<sup>[116]</sup> A magnified image of a set of parallel SBs passing through the interface between the nanoeutectic matrix and the dendrites is shown in Fig. 11B. This observation is very similar to the findings for a  $\text{Ti}_{62}\text{Cu}_{14}\text{Ni}_{12}\text{Sn}_4\text{Nb}_8$  nanocomposite with different volume fraction of dendrites.<sup>[117]</sup> The surface of the 24.5% deformed specimen (alloy N4) shows remarkably different features in comparison to the specimen subjected to only 8% plastic strain. The strongly deformed sample is buckled and barreled. In addition, the formation of highly dense SBs on the specimen surface is observed throughout the sample. A large number of impingement and intersection events<sup>[117]</sup> of the SBs under primary and secondary direction occur on the specimen surface, similar to the one depicted in Fig. 10B. The SB spacing is on the order of 5–10  $\mu\text{m}$ .<sup>[116]</sup>

Further analyses<sup>[118,119]</sup> based on TEM investigations on the nanometer length scale of the 24.5% deformed  $\text{Ti}_{66}\text{Cu}_8\text{Ni}_{4.8}\text{Sn}_{7.2}\text{Nb}_{14}$  specimen revealed a stepped morphology at the interface between the dendrites and the nanoeutectic matrix [Fig. 11C]. The slip transfer from the nanostructured matrix to the dendrites is believed to initiate such a stepped morphology owing to the passing of SBs without generating cracks (Eckert, J.; Das, J.; Kim, K.B.; Baier, F.; Löser, W.; Calin, M.; Zhang, Z.F.; Gebert, A. Deformation behavior of a  $\text{Ti}_{66}\text{Cu}_8\text{Ni}_{4.8}\text{Sn}_{7.2}\text{Nb}_{14}$  nanostructured

composite containing ductile dendrites. *J. Alloy. Comp.* Submitted).<sup>[118]</sup> The SB spacing is only 150–250 nm, as shown in Fig. 11C, although it appears to be 5–10  $\mu\text{m}$  at lower magnification under SEM conditions [Fig. 10B]. A triangle-shape contrast is often observed around the intersection regions between the SBs aligned to two directions inside the dendrites. A high resolution TEM study from the apex of a SB inside a dendrite revealed the existence of amorphous-like and distorted/disordered lattice fringes owing to extensive local lattice distortion in highly strained areas within the dendrites in regions as the one marked by a circle in Fig. 11C.<sup>[119]</sup> On the other hand, passing of SBs (primary and secondary) through the nanoeutectic matrix has also been clearly observed.<sup>[118]</sup> Fig. 11D shows the existence of SBs, which are aligned perpendicular to each other in the nanoeutectic matrix, as marked by the white and black arrows. The passing of the SBs into the matrix becomes easier when propagating under a direction almost parallel with the nanoscale rods (marked by the white arrows).<sup>[116]</sup> On the other hand, the nanoscale eutectic lamellae hinder the propagation of the SBs when they are aligned perpendicularly, as evidenced in Fig. 5B (marked by black arrows). Fig. 11D shows that the SBs (white arrows) are significantly deflected at the interfaces of the eutectic lamellae (at point 1). After a few layers of the eutectic rods the SB regenerates (at point 2) and propagates through the nanoeutectic matrix. This indicates that the nucleation and restricted propagation of SBs are also controlled by the nanometer scale eutectic matrix.

## CONCLUSIONS

A new class of high strength and ductile composites has been developed by tailoring Ti-base BMG-forming alloy compositions by simple in situ processing methods. The nanostructured composites are toughened by choosing the proper composition and by designing the microstructure to a bimodal grain size distribution of micrometer-scale dendrites embedded in a nano/ultrafine eutectic matrix. The evolution of such a metastable nano-heterostructure with different length scale of constituent phases is realized by inexpensive processing for a wide range of cooling rates ( $10^1$ – $10^3$  K/sec). This is a significant achievement to prepare cast nanostructured composites at such a low cooling rate in bulk form (60 mm  $\times$  15 mm  $\times$  12 mm).

The combination of appreciable ductility (up to 61%) and strength (>1800 MPa) together with high elastic strain ( $\epsilon_y \approx 3\%$ ) for these alloys is believed to be promising for several engineering applications such as high-performance springs, microgears, medical devices, sports equipment, wear resistant materials,



etc. Synthesizing such a composite microstructure has paved the way to develop advanced composites by manipulating the microstructures as a function of both composition and casting conditions/cooling rate. Designing new nanostructured alloys with biocompatible elements (Cr, Co, and Fe) that combine both high strength and low elastic modulus (54 GPa) is promising for a wide range of biomedical applications. It is also anticipated that composites having a nanostructured matrix with micrometer-sized ductile dendrites can be widely used to toughen other Ti-, Mg-, La-, Pd-, Fe- and Cu-base NsM.

## ACKNOWLEDGMENTS

The authors are grateful to M. Frey, H. Grahl, R. Günther, H. Kempe, U. Kunz, H. Lehmann, H.G. Lindenkreuz, H.J. Klauss, C. Mickel, and C. Wasmund for technical assistance and to F. Baier, M.D. Baró, M. Calin, A. Concustell, E. Fleury, A. Gebert, A.L. Greer, A. Güth, G. He, M. Heilmaier, A. Inoue, W.L. Johnson, D.H. Kim, U. Kühn, W. Löser, N. Mattern, C. Müller, S.K. Roy, D.J. Sordelet, L. Schultz, S. Scudino, M. Stoica, S. Venkataraman, T.G. Woodcock, L.Q. Xing, W. Xu, A.R. Yavari, P. Yu, and Z.F. Zhang for stimulating discussions. Financial support provided by EU within the framework of the research and training networks on Bulk Metallic Glasses (HPRN-CT-2000-00033) and Ductile BMG Composites (MRTN-CT-2003-504692) as well as by the Deutscher Akademischer Austauschdienst (DAAD) and the Deutsche Forschungsgemeinschaft (DFG) (Grants No. EC 111/10 and EC 111/12) are gratefully acknowledged.

## REFERENCES

- Gleiter, H. Nanocrystalline materials. *Prog. Mater. Sci.* **1989**, *33* (4), 223–315.
- Siegel, R.W.; Fougere, G.E. Mechanical properties of nanophase metals. *Nanostruct. Mater.* **1995**, *6* (1–4), 205–216.
- Edelstein, A.S.; Cammarata, R.C. *Nanomaterials: Synthesis, Properties and Applications*; IOP Publishing: Bristol, 1996.
- Feynman, R.P. There's plenty of room at the bottom. In *Engineering and Science*; California Institute of Technology: Pasadena, U.S.A., 1960; Vol. XXIII (5), 22–36.
- Gleiter, H. Nanostructured materials: basic concepts and microstructure. *Acta Mater.* **2000**, *48* (1), 1–29.
- Gleiter, H. Nanostructured materials: state of the art and perspectives. *Nanostruct. Mater.* **1995**, *6* (1–4), 3–14.
- Gossard, A.C. GaAs/AlAs layered films. *Thin Sol. Films* **1979**, *57* (1), 3–13.

- Nötzel, R.; Fukui, T.; Hasegawa, H.; Temmyo, J.; Kozen, A.; Tamamura, T. Self-organized microstructure growth. *Chem. Vapor Depos.* **1995**, *1* (3), 81–88.
- Suryanarayana, C. Nanocrystalline materials. *Inter. Mater. Rev.* **1995**, *40* (2), 41–64.
- Koch, C.C. *Nanostructured Materials: Processing Properties and Applications*; Noyes Publishing/William Andrew Publishing: Norwich, NY, 2002.
- Lieberwirth, I.; Katzenberg, F.; Petermann, J. Nanostructured polymer films by electron-beam irradiation and selective metallization. *Adv. Mater.* **1991**, *10* (13), 997–1001.
- Hall, E.O. The deformation and ageing of mild steel: III discussion of results. *Proc. Phys. Soc. London B* **1951**, *64* (9), 747–752.
- Petch, N.J. The cleavage strength of polycrystals. *J. Iron Steel Inst.* **1953**, *174*, 25–28.
- Chokshi, A.H.; Rosen, A.; Karch, J.; Gleiter, H. On the validity of the Hall-Petch relationship in nanocrystalline materials. *Scripta Metall.* **1989**, *23* (10), 1679–1683.
- Chen, M.; Ma, E.; Hemker, K.J.; Sheng, H.; Wang, Y.; Cheng, X. Deformation twinning in nanocrystalline aluminum. *Science* **2003**, *300* (5623), 1275–1277.
- Yamakov, V.; Wolf, D.; Phillpot, S.R.; Mukherjee, A.K.; Gleiter, H. Dislocation processes in the deformation of nanocrystalline aluminum by molecular-dynamics simulation. *Nat. Mater.* **2002**, *1* (1), 45–48.
- Ovid'ko, I.A. Materials science—deformation of nanostructures. *Science* **2002**, *295* (5564), 2386–2386.
- Carsley, J.E.; Fisher, A.; Milligan, W.W.; Aifantis, E.C. Mechanical behavior of a bulk nanostructured iron alloy. *Metall. Mater. Trans. A* **1998**, *29* (9), 2261–2271.
- Koch, C.C.; Morris, D.G.; Lu, K.; Inoue, A. Ductility of nanostructured materials. *MRS Bull.* **1999**, *24* (2), 54–58.
- Malow, T.R.; Koch, C.C. Mechanical properties in tension of mechanically attrited nanocrystalline iron by the use of the miniaturized disk bend test. *Acta Mater.* **1998**, *46* (18), 6459–6473.
- Kumar, K.S.; Swygenhoven, H.V.; Suresh, S. Mechanical behavior of nanocrystalline metals and alloys. *Acta Mater.* **2003**, *51* (19), 5743–5774.
- Jia, D.; Ramesh, K.T.; Ma, E. Effects of nanocrystalline and ultrafine grain sizes on constitutive behavior and shear bands in iron. *Acta Mater.* **2003**, *51* (12), 3495–3509.
- Wei, Q.; Jia, D.; Ramesh, K.T.; Ma, E. Evolution and microstructure of shear bands in nanostructured Fe. *Appl. Phys. Lett.* **2002**, *81* (7), 1240–1242.
- Weertman, J.R. Mechanical behavior of nanocrystalline metals. In *Nanostructured Materials: Processing, Properties and Applications*; Koch, C.C., Ed.; William Andrews Publishing: Norwich, NY, 2002; 397–421.
- Koch, C.C. Ductility in nanostructured and ultra fine-grained materials: recent evidence for optimism. *J. Metastable Nanocryst. Mater.* **2003**, *18*, 9–19.
- Inoue, A. Fabrication and novel properties of nanostructured Al base alloys. *Mater. Sci. Eng. A* **1994**, *179*, 57–61.
- Kim, Y.H.; Inoue, A.; Masumoto, T. Increase in mechanical strength of Al-Y-Ni amorphous-alloys by

- dispersion of nanoscale fcc-Al particles. *Mater. Trans. JIM* **1991**, *32* (4), 331–338.
28. Koch, C.C. Synthesis of nanostructured materials by mechanical milling: problems and opportunities. *Nanostruct. Mater.* **1997**, *9* (1–8), 13–22.
  29. Zhang, X.; Wang, H.; Scattergood, R.O.; Narayan, J.; Koch, C.C. Evolution of microstructure and mechanical properties of in situ consolidated bulk ultra-fine-grained and nanocrystalline Zn prepared by ball milling. *Mater. Sci. Eng. A* **2003**, *344* (1–2), 175–181.
  30. Tellkamp, V.L.; Melmed, A.; Lavernia, E.J. Mechanical behavior and microstructure of a thermally stable bulk nanostructured Al alloy. *Metall. Mater. Trans. A* **2001**, *32* (9), 2335–2343.
  31. Zhou, F.; Liao, X.Z.; Zhu, Y.T.; Dallek, S.; Lavernia, E.J. Microstructural evolution during recovery and recrystallization of a nanocrystalline Al-Mg alloy prepared by cryogenic ball milling. *Acta Mater.* **2003**, *51* (10), 2777–2791.
  32. Valiev, R.Z.; Islamgaliev, R.K.; Alexandrov, I.V. Bulk nanostructured materials from severe plastic deformation. *Prog. Mater. Sci.* **2000**, *45* (2), 103–189.
  33. Muñoz-Morris, M.A.; Oca, C.G.; Gonzalez-Doncel, G.; Morris, D.G. Microstructural evolution of dilute Al-Mg alloys during processing by equal channel angular pressing and during subsequent annealing. *Mater. Sci. Eng. A* **2004**, *375*, 835–856.
  34. Valiev, R.Z.; Ivanisenko, Y.V.; Rauch, E.F.; Baudelet, B. Structure and deformation behaviour of armco iron subjected to severe plastic deformation. *Acta Mater.* **1996**, *44* (12), 4705–4712.
  35. Tao, N.R.; Wang, Z.B.; Tong, W.P.; Sui, M.L.; Lu, J.; Lu, K. An investigation of surface nanocrystallization mechanism in Fe induced by surface mechanical attrition treatment. *Acta Mater.* **2002**, *50* (18), 4603–4616.
  36. Wang, Y.M.; Chen, M.W.; Sheng, H.W.; Ma, E. Nanocrystalline grain structures developed in commercial purity Cu by low-temperature cold rolling. *J. Mater. Res.* **2002**, *17* (12), 3004–3007.
  37. Sanders, P.G.; Fougere, G.E.; Thompson, L.J.; Eastman, J.A.; Weertman, J.R. Improvements in the synthesis and compaction of nanocrystalline materials. *Nanostruct. Mater.* **1997**, *8* (3), 243–252.
  38. Sanders, P.G.; Eastman, J.A.; Weertman, J.R. Elastic and tensile behavior of nanocrystalline copper and palladium. *Acta Mater.* **1997**, *45* (10), 4019–4025.
  39. Hughes, R.O.; Smith, S.D.; Pande, C.S.; Johnson, H.R.; Armstrong, R.W. Hall-Petch strengthening for the microhardness of 12 nanometer grain diameter electrodeposited nickel. *Scripta Metall.* **1986**, *20* (1), 93–97.
  40. El-Sharik, A.M.; Erb, U.; Palumbo, G.; Aust, K.T. Deviations from Hall-Petch behavior in as-prepared nanocrystalline nickel. *Scripta Metall. Mater.* **1992**, *27* (9), 1185–1188.
  41. Ebrahimi, F.; Zhai, Q.; Kong, D. Deformation and fracture of electrodeposited copper. *Scripta Mater.* **1998**, *39* (9), 315–321.
  42. Inoue, A.; Zhang, T.; Masumoto, T. Zr-Al-Ni amorphous-alloys with high glass-transition temperature and significant supercooled liquid region. *Mater. Trans. JIM* **1990**, *31* (3), 177–183.
  43. Leonhard, A.; Xing, L.Q.; Heilmair, M.; Gebert, A.; Eckert, J.; Schultz, L. Effect of crystalline precipitations on the mechanical behavior of bulk glass forming Zr-based alloys. *Nanostruct. Mater.* **1998**, *10* (5), 805–817.
  44. Fan, C.; Takeuchi, A.; Inoue, A. Preparation and mechanical properties of Zr-based bulk nanocrystalline alloys containing compound and amorphous phases. *Mater. Trans. JIM* **1999**, *40* (1), 42–51.
  45. Fan, C.; Li, C.F.; Inoue, A. Nanocrystal composites in Zr-Nb-Cu-Al metallic glasses. *J. Non-Cryst. Solids* **2000**, *270* (1–3), 28–33.
  46. He, Y.; Poon, S.J.; Shiflet, G.J. Synthesis and properties of metallic glasses that contain aluminum. *Science* **1988**, *241* (4873), 1640–1642.
  47. Kim, J.J.; Choi, Y.; Suresh, S.; Argon, A.S. Nanocrystallization during nanoindentation of a bulk amorphous metal alloy at room temperature. *Science* **2002**, *295* (5555), 654–657.
  48. Valiev, R.Z.; Gunderov, D.V.; Zhilyaev, A.P.; Popov, A.G.; Pushin, V.G. Nanocrystallization induced by severe plastic deformation of amorphous alloys. *J. Metastable Nanocryst. Mater.* **2004**, *22*, 21–26.
  49. Schuh, C.; Nieh, T.G.; Yamasaki, T. Hall-Petch breakdown manifested in abrasive wear resistance of nanocrystalline nickel. *Scripta Mater.* **2002**, *46* (10), 735–740.
  50. Lu, L.; Li, S.X.; Lu, K. An abnormal strain rate effect on tensile behavior in nanocrystalline copper. *Scripta Mater.* **2001**, *45* (10), 1163–1169.
  51. Koch, C.C.; Cavin, O.B.; McKamey, C.G.; Scarbrough, J.O. Preparation of amorphous Ni<sub>60</sub>Nb<sub>40</sub> by mechanical alloying. *Appl. Phys. Lett.* **1983**, *43* (11), 1017–1019.
  52. Koch, C.C. The synthesis and structure of nanocrystalline materials produced by mechanical attrition: a review. *Nanostruct. Mater.* **1993**, *2* (2), 109–129.
  53. Eckert, J.; Holzer, J.C.; Krill, C.E., III; Johnson, W.L. Structural and thermodynamic properties of nanocrystalline fcc metals prepared by mechanical attrition. *J. Mater. Res.* **1992**, *7* (7), 1751–1761.
  54. Eckert, J.; Holzer, J.C.; Johnson, W.L. Influence of microstructure and composition on the grain-size of nanocrystalline Fe-Cu alloys. *Scripta Metall. Mater.* **1992**, *27* (9), 1105–1110.
  55. Fecht, H.J.; Hellstern, E.; Fu, Z.; Johnson, W.L. Nanocrystalline metals prepared by high-energy ball milling. *Metall. Trans. A* **1990**, *21* (9), 2333–2337.
  56. Trudeau, M.L.; Schultz, R. High-resolution electron-microscopy study of Ni-Mo nanocrystals prepared by high-energy mechanical alloying. *Mater. Sci. Eng. A* **1991**, *134*, 1361–1367.
  57. Murty, B.S.; Ranganathan, S. Novel materials synthesis by mechanical alloying/milling. *Int. Mater. Rev.* **1998**, *43* (3), 101–141.
  58. Zaluska, A.; Zaluski, L.; Strom-Olsen, J.O. Nanocrystalline magnesium for hydrogen storage. *J. Alloy Comp.* **1999**, *288* (1–2), 217–225.
  59. Seidel, M.; Eckert, J.; Schultz, L. Formation of amorphous Zr-Al-Cu-Ni with a large supercooled



- liquid region mechanical alloying. *J. Appl. Phys.* **1995**, *77* (10), 5446–5448.
60. Eckert, J.; Kubler, A.; Schultz, L. Mechanically alloyed  $Zr_{55}Al_{10}Cu_{30}Ni_5$  metallic glass composites containing nanocrystalline W particles. *J. Appl. Phys.* **1999**, *85* (10), 7112–7119.
61. Eckert, J. Mechanical behavior of nanocrystalline metals. In *Nanostructured Materials: Processing, Properties and Applications*; Koch, C.C., Eds.; William Andrews Publishing: Norwich, NY, 2002; 423–525.
62. Wang, Y.; Chen, M.; Zhou, F.; Ma, E. High tensile ductility in a nanostructured metal. *Nature* **2002**, *419* (6910), 912–915.
63. He, G.; Eckert, J.; Löser, W.; Schultz, L. Novel Ti-base nanostructure-dendrite composite with enhanced plasticity. *Nat. Mater.* **2003**, *2* (1), 33–37.
64. Das, J.; Löser, W.; Kühn, U.; Eckert, J.; Roy, S.K.; Schultz, L. High-strength Zr-Nb-(Cu,Ni,Al) composites with enhanced plasticity. *Appl. Phys. Lett.* **2003**, *82* (26), 4690–4692.
65. Odette, G.R.; Chao, B.L.; Shekherd, J.W.; Lucas, G.E. Ductile phase toughening mechanisms in a TiAl-TiNb laminate composite. *Acta Metall. Mater.* **1992**, *40* (9), 2381–2389.
66. Hull, D. *An Introduction to Composite Materials*; Cambridge University Press: Cambridge, U.K., 1981.
67. Leng, Y.; Courtney, T.H. Fracture-behavior of laminated metal metallic-glass composites. *Metall. Trans. A* **1990**, *21* (8), 2159–2168.
68. Eckert, J.; Kühn, U.; Mattern, N.; He, G.; Gebert, A. Structural bulk metallic glasses with different length-scale of constituent phases. *Intermetallics* **2002**, *10* (11–12), 1183–1190.
69. Ma, E. Instabilities and ductility of nanocrystalline and ultrafine-grained metals. *Scripta Mater.* **2003**, *49* (7), 663–668.
70. Hays, C.C.; Kim, C.P.; Johnson, W.L. Microstructure controlled shear band pattern formation and enhanced plasticity of bulk metallic glasses containing in situ formed ductile phase dendrite dispersions. *Phys. Rev. Lett.* **2000**, *84* (13), 2901–2904.
71. Kühn, U.; Eckert, J.; Mattern, N.; Schultz, L. ZrNbCuNiAl bulk metallic glass matrix composites containing dendritic bcc phase precipitates. *Appl. Phys. Lett.* **2002**, *80* (14), 2478–2480.
72. Szuecs, F.; Kim, C.P.; Johnson, W.L. Mechanical properties of  $Zr_{56.2}Ti_{13.8}Nb_{5.0}Cu_{6.9}Ni_{5.6}Be_{12.5}$  ductile phase reinforced bulk metallic glass composite. *Acta Mater.* **2001**, *49* (9), 1507–1513.
73. He, G.; Löser, W.; Eckert, J.; Schultz, L. Enhanced plasticity in a Ti-based bulk metallic glass-forming alloy by in situ formation of a composite microstructure. *J. Mater. Res.* **2002**, *17* (12), 3015–3018.
74. Das, J.; Güth, A.; Klauss, H.J.; Mickel, C.; Löser, W.; Eckert, J.; Roy, S.K.; Schultz, L. Effect of casting conditions on microstructure and mechanical properties of high-strength  $Zr_{73.5}Nb_9Cu_7Ni_1Al_{9.5}$  in situ composites. *Scripta Mater.* **2003**, *49* (12), 1189–1195.
75. Das, J.; Tang, M.B.; Kim, K.B.; Theissmann, R.; Baier, F.; Wang, W.H.; Eckert, J. “Work-hardenable” ductile bulk metallic glass. *Phys. Rev. Lett.* **2005**, *94* (20), 205501 (1–4).
76. Schroers, J.; Johnson, W.L. Ductile bulk metallic glass. *Phys. Rev. Lett.* **2004**, *93* (25), 255506 (1–4).
77. Johnson, W.L. Bulk glass-forming metallic alloys: science and technology. *MRS Bull.* **1999**, *24* (10), 42–56.
78. Srivastava, R.M.; Eckert, J.; Löser, W.; Dhindaw, B.K.; Schultz, L. Cooling rate evaluation for bulk amorphous alloys from eutectic microstructures in casting processes. *Mater. Trans.* **2002**, *43* (7), 1670–1675.
79. Louzguine, D.V.; Kato, H.; Inoue, A. High strength and ductile bulk Ti-Ni-Cu-Nb alloy with submicron-size structure units obtained by arc-melting. *J. Alloy Comp.* **2004**, *375* (1–2), 171–174.
80. Dai, Q.L.; Sun, B.B.; Sui, M.L.; He, G.; Li, Y.; Eckert, J.; Luo, W.K.; Ma, E. High-performance bulk Ti-Cu-Ni-Sn-Ta nanocomposites based on a dendrite-eutectic microstructure. *J. Mater. Res.* **2004**, *19* (9), 2557–2566.
81. Zhang, T.; Inoue, A. Thermal and mechanical properties of Ti-Ni-Cu-Sn amorphous alloys with a wide supercooled liquid region before crystallization. *Mater. Trans. JIM* **1998**, *39* (10), 1001–1006.
82. Zhang, T.; Inoue, A. Preparation of Ti-Cu-Ni-Si-B amorphous alloys with a large supercooled liquid region. *Mater. Trans. JIM* **1999**, *40* (4), 301–306.
83. Kim, Y.C.; Kim, W.T.; Kim, D.H. Glass forming ability and crystallization behavior in amorphous  $Ti_{50}Cu_{32-x}Ni_{15}Sn_3Be_x$  ( $x = 0, 1, 3, 7$ ) alloys. *Mater. Trans. JIM* **2002**, *43* (5), 1243–1246.
84. Kim, Y.C.; Kim, W.T.; Kim, D.H. A development of Ti-based bulk metallic glass. *Mater. Sci. Eng. A* **2004**, *375*, 127–135.
85. Hays, C.C.; Glade, S.C. Thermophysical properties and glass forming ability in the alloy series  $(Ti_{100-x}Zr_x)_{45}(Ni_{14.5}Cu_{85.5})_{55}$ . *Appl. Phys. Lett.* **2002**, *80* (17), 3096–3098.
86. Peker, A.; Johnson, W.L. A highly processable metallic-glass— $Zr_{41.2}Ti_{13.8}Cu_{12.5}Ni_{10.0}Be_{22.5}$ . *Appl. Phys. Lett.* **1993**, *63* (17), 2342–2344.
87. Massalski, T.B.; Okamoto, H.; Subramanian, P.R.; Kasperzak, L. *Binary Alloy Phase Diagrams*, 2nd Ed.; ASM International: Ohio, U.S.A., 1992.
88. He, G.; Löser, W.; Eckert, J. In situ formed Ti-Cu-Ni-Sn-Ta nanostructure-dendrite composite with large plasticity. *Acta Mater.* **2003**, *51* (17), 5223–5234.
89. Eckert, J.; He, G.; Das, J.; Löser, W. Nanostructured composites in multicomponent alloy systems. *Mater. Trans. JIM* **2003**, *44* (10), 1999–2006.
90. Jeong, H.W.; Kim, S.E.; Hyun, Y.T.; Lee, Y.T.; Park, J.K. Microstructures and elastic moduli of binary titanium alloys containing biocompatible alloying elements. *Mater. Sci. Forum* **2005**, *475–479*, 2291–2294.
91. He, G.; Eckert, J.; Löser, W.; Hagiwara, M. Composition dependence of the microstructure and the mechanical properties of nano/ultrafine-structured Ti-Cu-Ni-Sn-Nb alloys. *Acta Mater.* **2004**, *52* (10), 3035–3046.
92. He, G.; Eckert, J.; Hagiwara, M. Effect of Sn on microstructure and mechanical properties of Ti-base

- dendrite/ultrafine-structured multicomponent alloys. *Metall. Mater. Trans. A* **2004**, *35* (11), 3605–3612.
93. He, G.; Hagiwara, M. Effect of composition on microstructure and compressive mechanical properties in Ti-Cu-Fe-Sn-Nb alloys. *Mater. Trans. JIM* **2004**, *45* (5), 1555–1560.
  94. He, G.; Hagiwara, M. Ti-Cu-M(Fe,Cr,Co)-Sn-Ta(Nb) alloys with potential for biomedical applications. *Mater. Trans. JIM* **2004**, *45* (4), 1120–1123.
  95. Long, M.; Rack, H.J. Titanium alloys in total joint replacement—a materials science perspective. *Biomaterials* **1998**, *19* (18), 1621–1639.
  96. Niinomi, M. Recent metallic materials for biomedical applications. *Metall. Mater. Trans. A* **2002**, *33* (3), 477–486.
  97. Rho, J.Y.; Roy, M.E.; Tsui, T.Y.; Pharr, G.M. Elastic properties of microstructural components of human bone tissue as measured by nanoindentation. *J. Biomed. Mater. Res.* **1999**, *45* (1), 48–54.
  98. Niinomi, M. Fatigue performance and cyto-toxicity of low rigidity titanium alloy, Ti-29Nb-13Ta-4.6Zr. *Biomaterials* **2003**, *24* (16), 2673–2683.
  99. He, G.; Eckert, J.; Dai, Q.L.; Sui, M.L.; Löser, W.; Hagiwara, M.; Ma, E. Nanostructured Ti-based multi-component alloys with potential for biomedical applications. *Biomaterials* **2003**, *24* (28), 5115–5120.
  100. Woodcock, T.G.; Kusy, M.; Mato, S.; Alcalá, G.; Thomas, J.; Löser, W.; Gebert, A.; Eckert, J.; Schultz, L. Formation of a metastable eutectic during the solidification of the alloy  $\text{Ti}_{60}\text{Cu}_{14}\text{Ni}_{12}\text{Sn}_4\text{Ta}_{10}$ . *Acta Mater.* **2005**, *53* (29), 5141–5149.
  101. Santamarta, R.; Schryvers, D. Twinned b.c.c. spherical particles in a partially crystallized  $\text{Ti}_{50}\text{Ni}_{25}\text{Cu}_{25}$  melt-spun ribbon. *Intermetallics* **2004**, *12* (3), 341–348.
  102. Tang, W.; Sandström, R.; Miyazaki, S. Phase equilibria in the pseudobinary  $\text{Ti}_{0.5}\text{Ni}_{0.5}\text{-Ti}_{0.5}\text{Cu}_{0.5}$  system. *J. Phase Equilib.* **2000**, *21* (3), 227–234.
  103. He, G.; Eckert, J.; Löser, W.; Hagiwara, M. Processing dependence of Young's modulus of Ti-base nanostructured alloys. *Solid State Commun.* **2004**, *129* (11), 711–715.
  104. Eckert, J.; He, G.; Zhang, Z.F.; Löser, W. Fracture-induced melting in glassy and nanostructured composite materials. *J. Metastable Nanocryst. Mater.* **2004**, *20–21*, 357–365.
  105. Truman, J.E. Constitution and properties of steels. In *Materials Science and Technology*; Cahn, R.W., Haasen, P., Kramer, E.J., Eds.; VCH: Cambridge, 1993; Vol. 8, 530 pp.
  106. Murakami, Y. Aluminum-based alloys. In *Materials Science and Technology*; Cahn, R.W., Haasen, P., Kramer, E.J., Eds.; VCH: Cambridge, 1993; Vol. 8, 217 pp.
  107. Neite, G.; Kubota, K.; Higashi, K.; Hehmann, F. Magnesium-based alloys. In *Materials Science and Technology*; Cahn, R.W., Haasen, P., Kramer, E.J., Eds.; VCH: Cambridge, 1993; Vol. 8, 117 pp.
  108. Abraham, F.F.; Gao, H. How fast can cracks propagate. *Phys. Rev. Lett.* **2000**, *84* (14), 3113–3116.
  109. Zhang, Z.F.; Eckert, J.; Schultz, L. Difference in compressive and tensile fracture mechanisms of  $\text{Zr}_{59}\text{Cu}_{20}\text{Al}_{10}\text{Ni}_8\text{Ti}_3$  bulk metallic glass. *Acta Mater.* **2003**, *51* (4), 1167–1179.
  110. Zhang, Z.F.; He, G.; Eckert, J. Shear and distensile fracture behaviour of Ti-based composites with ductile dendrites. *Philos. Mag.* **2005**, *85* (9), 897–915.
  111. Zhang, Z.F.; He, G.; Zhang, H.; Eckert, J. Rotation mechanism of shear fracture induced by high plasticity in Ti-based nano-structured composites containing ductile dendrites. *Scripta Mater.* **2005**, *52* (9), 945–949.
  112. Zhang, Z.F.; He, G.; Eckert, J.; Schultz, L. Fracture mechanisms in bulk metallic glassy materials. *Phys. Rev. Lett.* **2003**, *91* (4), 045505 (1–4).
  113. Dieter, G.E. *Mechanical Metallurgy*, 3rd Ed.; McGraw-Hill Book Company: London, 1988.
  114. Zhang, Z.F.; Eckert, J.; Schultz, L. Fatigue and fracture behavior of bulk metallic glass. *Metall. Mater. Trans.* **2004**, *35A* (11), 3489–3498.
  115. Lewandowski, J.J.; Lowhaphandu, P. Effects of hydrostatic pressure on the flow and fracture of a bulk amorphous metal. *Philos. Mag.* **2002**, *82* (17–18), 3427–3441.
  116. Kim, K.B.; Das, J.; Baier, F.; Eckert, J. Heterogeneous distribution of shear strains in deformed  $\text{Ti}_{66.1}\text{Cu}_8\text{Ni}_{4.8}\text{Sn}_{7.2}\text{Nb}_{13.9}$  nanostructure-dendrite composite. *Phys. Stat. Sol. A* **2005**, *202* (13), 2405–2412.
  117. Zhang, H.; Pan, X.F.; Zhang, Z.F.; Das, J.; Kim, K.B.; Muller, C.; Baier, F.; Kusy, M.; Gebert, A.; He, G.; Eckert, J. Toughening mechanisms of a Ti-based nanostructured composite containing ductile dendrites. *Z. Metallkunde* **2005**, *96* (6), 675–680.
  118. Kim, K.B.; Das, J.; Baier, F.; Eckert, J. Propagation of shear bands in  $\text{Ti}_{66.1}\text{Cu}_8\text{Ni}_{4.8}\text{Sn}_{7.2}\text{Nb}_{13.9}$  nanostructure-dendrite composite during deformation. *Appl. Phys. Lett.* **2005**, *86* (17), 171909.
  119. Kim, K.B.; Das, J.; Baier, F.; Eckert, J. Lattice distortion/disordering and local amorphization in the dendrites of a  $\text{Ti}_{66.1}\text{Cu}_8\text{Ni}_{4.8}\text{Sn}_{7.2}\text{Nb}_{13.9}$  nanostructure-dendrite composite during intersection of shear bands. *Appl. Phys. Lett.* **2005**, *86* (20), 201909.

# Nanostuctured Materials: Metals on Microtubule Supports

Silke Behrens

*Forschungszentrum Karlsruhe, Institute of Technical Chemistry, Karlsruhe, Germany*

Eberhard Unger

*Institute of Molecular Biotechnology, Jena, Germany*

## INTRODUCTION

Compared to bulk materials, nanoscale materials, with their large surface areas and possible quantum confinement effects, possess distinct electronic, optical, and chemical properties.<sup>[1–3]</sup> Therefore the synthesis of defined nanostructures is of potential interest in various fields including catalysis or microelectronics. In catalysis, for example, interesting applications for metal nanoparticles emerge from an enhanced activity, good selectivity (controllable by surface modifiers), and synergistic effects in bimetallic catalysts.<sup>[4,5]</sup> In electronics, a fundamental concept for miniaturization is the handling of single charges by means of single electron tunneling (SET) in ordered one-, two-, or three-dimensional arrangements of metal or semiconductor clusters.<sup>[6]</sup> Inspired by the unique physical and chemical properties, much effort has been made to tailor defined one-, two-, or three-dimensional nanostructures ranging from ordered nanoparticle arrays to nanowires.<sup>[7,8]</sup>

In biology, nanostructures are familiar objects. Biological components exhibit size dimensions from the nanometer to the micrometer size range together with exceptional molecular recognition capabilities and functionalities for distinct biochemical transformations and translocations. However, many of these biomolecules do not possess the required physical or chemical properties. DNA, for example, has the appropriate recognition capabilities, but poor electric characteristics prevent its direct use in electric circuits.<sup>[9]</sup> On the other hand, inorganic materials such as metals or semiconductors display, for example, the desired electric or optical properties, but their controlled deposition into defined nanostructures is difficult by conventional methods. Recently, the unique features of biological systems have been explored as building blocks for bottom-up assembly or controlled deposition of novel inorganic materials and devices with advanced structures and functionalities.<sup>[10–12]</sup> For example, the specific recognition properties of oligonucleotides<sup>[13,14]</sup> or antibodies<sup>[15]</sup> have been exploited for assembling metal

nanoparticles into well-ordered three-dimensional aggregates. The protein cages of viruses have been used as a template for a controlled deposition and organization of metallic nanoparticles.<sup>[16]</sup> Motivated by future electronic applications, researchers used DNA to control the deposition of metals<sup>[17]</sup> and create conductive nanowires consisting of silver,<sup>[18]</sup> gold,<sup>[19]</sup> palladium,<sup>[20]</sup> platinum,<sup>[21]</sup> and copper.<sup>[22]</sup>

In this entry we address the template-directed deposition of metals on microtubule supports for fabricating metal nanostructures ranging from regular arrays of nanoclusters to continuous nanowires.

## GENERATING NANOSTRUCTURES ON BIOLOGICAL SUPPORTS

Biotemplating strategies take advantage of the characteristic dimensions of biological support, ranging from a few nanometers up to several micrometers. The structure of these biostructures is well defined for a controlled deposition of inorganic materials. Moreover, the surface of these biomolecular components reveals specific patterns of surface functionalities, e.g., amino acid residues or the bases of nucleic acids that are able to bind metal ions or nanoparticles by formation of metal–ligand complexes or electrostatic interaction. In this approach, the biostructure serves as a functionalized scaffold where the metal is generated in situ and shaped into a nanostructure with its morphology dependent on that of the biotemplate.

The basic concept of a surface-controlled, heterogeneous metallization of a biotemplate consists essentially of several steps: First, appropriate metal ions are bound to the biomolecule, creating reactive sites and thus providing activation of defined sites at the biotemplate. Second, the metal ion/biomolecule adducts are treated with a reducing agent establishing metal nuclei attached to the biostructure. In another strategy, nanoparticles that were previously obtained by a homogeneous nucleation process in solution are attached to the surface functionalities of the

biotemplate. Once small metal seeds cover the biotemplate, the metal growth proceeds autocatalytically by consuming the educt feedstock from solution. The final metal coating does not necessarily have to consist of the same metal as the first formed metal nuclei or bound metal seeds, as has been shown by several groups.<sup>[19,23–25]</sup> Within this concept, homogeneous cluster nucleation or heterogeneous background metalization—if the reduction is carried out on a substrate—should be suppressed as much as possible as it leads to unspecific deposition of the metal. Many metal deposition techniques require special reaction conditions influenced by various parameters including applied temperature, educt concentration, the reduction potential of the reducing agent, and, in general, the presence of non-native chemicals. As a consequence, the biomolecular structure used needs to exhibit a sufficient physical and chemical stability toward these non-native conditions for metal deposition.

### STRUCTURAL FEATURES AND PROPERTIES OF MICROTUBULE TEMPLATES

Microtubules, ubiquitously present in eukaryotic cells, are proteinaceous filaments with a diameter of about 25 nm and several micrometers in length.<sup>[26]</sup> As part of the cytoskeleton, microtubules are involved in a variety of cellular functions including maintenance of the cellular shape, segregation of the genetic material during mitosis and meiosis, intracellular transport of organelles as well as cell motility. The repeating unit of these polymeric structures is the  $\alpha\beta$ -tubulin heterodimer, 4–5 nm in diameter and 8 nm in length, and a  $M_w$  of approximately 55,000 each. Microtubules assembled *in vitro* are typically composed of 12 to 14 protofilaments consisting of longitudinally connected heterodimers with a strict  $\alpha\beta$ -alternation. Neighboring heterodimers are tilted by approximately 1 nm with respect to the long axis of the microtubule resulting in a helical array of tubulin subunits. *In vitro*, microtubules can be assembled from tubulin at physiological temperature, pH, and ionic strength in the presence of the cofactors guanosine-5'-triphosphate and magnesium ions. The assembly of microtubules is reversible. At 0°C microtubules depolymerize into the heterodimers, a feature actually exploited to purify microtubule protein from porcine brain by applying several temperature-dependent centrifugation cycles. Even at the assembly–disassembly steady state where the average length of microtubules in solution is constant, microtubules are highly dynamic. They constantly polymerize and depolymerize, both *in vivo* and *in vitro*. Application of such protein assemblies as template or support for inorganic materials, however, requires a certain stability regarding the dynamic

structural properties and the exposure of the biomolecules to non-physiological conditions such as metal ion precursors or elevated temperatures. Therefore we used taxol which suppresses the dynamic instability of microtubules or glutaric dialdehyde which cross-links the tubulin subunits. Treatment with glutaric dialdehyde results in stabilized microtubules remaining intact in the presence of metal ion precursors and up to temperatures of approximately 90°C.

Microtubules are very promising as biotemplates because of their favorable geometric aspect ratio (with a thickness of 25 nm and lengths up to several micrometers) and the variety of potential metal-binding sites at their surface. Moreover, depending on the assembly conditions, tubulin is able to form not only microtubules but also various other polymorphic assemblies with different geometries, among them sheets, ribbons, spirals, or rings.<sup>[27]</sup>

### CONTROL OF METAL NANOSTRUCTURES BY MICROTUBULE SUPPORTS

It is possible to conjugate Au nanoparticles to biological components and, eventually, control their arrangement into one- to three-dimensional structures with interesting physical properties. Conjugation of Au nanoparticles to biological reporter molecules such as antibodies has long been known to be connected with electron-dense tags for biological samples in transmission electron microscopy (TEM).<sup>[28,29]</sup> Mirkin and coworkers prepared three-dimensional Au colloid aggregates revealing, for example, unusual optical<sup>[13,30]</sup> and electric<sup>[31]</sup> properties.

We examined the surface of microtubules as a template to guide the assembly of Au nanoparticles into tube-like superstructures. The Au particles could easily be connected to microtubule supports by simply incubating the Au nanoparticles with the protein assembly. By this method, the microtubule surface was densely decorated by Au nanoparticles. The particles, however, were not arranged in a geometrically regular pattern but were randomly distributed over the whole surface of the biomolecular support. Fig. 1 shows Au particles, ~5 nm in size, arranged along the backbone of a single microtubule. The conjugation of Au particles to protein surfaces may depend upon several phenomena: It is well known that Au atoms bind to proteinaceous surfaces via a covalent bond to S atoms occurring, e.g., in amino acid side chains of methionine or cysteine.<sup>[32]</sup> Cysteine or methionine residues, however, are not located in freely accessible parts of the tubulin molecule on the outside surface of a microtubule. Besides this, at pH 6.8, often used for assembly of microtubules, the surface of a microtubule (isoelectric point: pI 4.2<sup>[33]</sup>) displays a net negative charge which

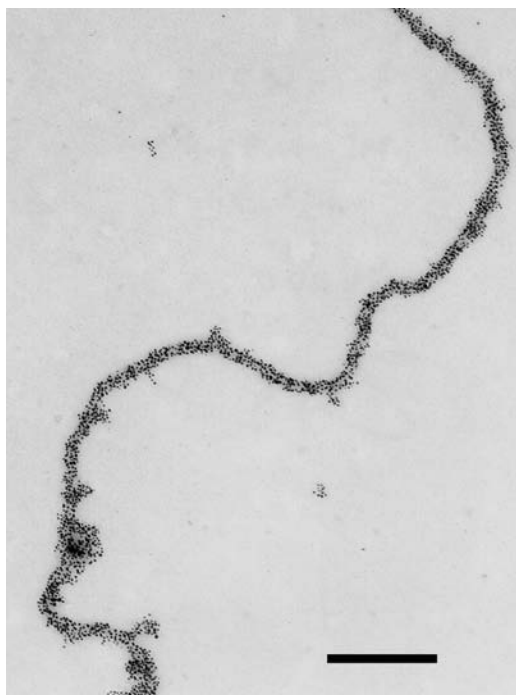


**Fig. 1** Transmission electron micrograph of Au particles, 5 nm in size, bound to a single microtubule filament by simple mixing of the biostructure with the preformed Au nanoparticles (scale bar, 250 nm). The particles are randomly distributed over the microtubule surface.

should result in the repulsion of the likewise negatively charged Au particles. However, non-specific electrostatic binding could occur at domains positively charged at this pH, e.g., lysine residues which could cause a random distribution of particles over the surface of the biomolecule.<sup>[34]</sup> By another strategy, ~2-nm Au particles attached to microtubule backbones were directly nucleated in situ from  $\text{HAuCl}_4$  in the presence of microtubule templates. As a result, the microtubule surface got densely covered by small, 2.3-nm Au particles. The distribution of particles over the microtubule surface, however, was not completely random, but bore some resemblance to the helical arrangement of the tubulin subunits within the protein assembly (Fig. 2), a feature pronounced in a higher gear for nucleation of palladium on microtubules (see below; Fig. 3).

Metal properties, e.g., catalytic activity and selectivity, and optical and electric properties can be altered by combination with a second metal.<sup>[35]</sup> Bimetallic Au/Pd particles in the size range of 3 to 60 nm have been synthesized by a seed-growth mechanism and stabilized by microtubule supports: In a first step, the Au nanoparticles were linked to the protein surface and, in a second step, these Au seeds were covered with Pd by reduction of  $\text{Na}_2\text{PdCl}_4$  with trisodium citrate at 70°C.<sup>[8]</sup> The formation of the bimetallic Pd/Au

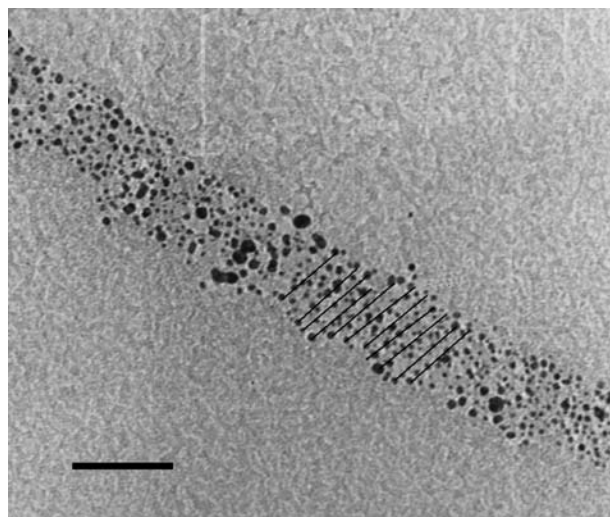


**Fig. 2** Transmission electron micrograph of a single microtubule densely covered by Au nanoparticles, 2.3 nm in size. The particles were directly nucleated in situ with sodium borohydride in the presence of the microtubule template (scale bar, 150 nm).

particles was confirmed by energy dispersive X-ray analysis (EDX). The product of a typical synthesis contained both bimetallic Pd/Au particles and a few Pd particles nucleated directly on the Au-free parts of the protein surface. Examining the catalytic activity by hydrogenation of crotonic acid as a test reaction, we found that the obtained microtubule-supported Au/Pd particles revealed a high catalytic activity under very mild reaction conditions (atmospheric pressure and 25°C) in aqueous reaction medium. Within the size range of the particles investigated (particle diameter, 3.8 to 61.8 nm), an increase in catalytic activity with decreasing particle diameter was observed.

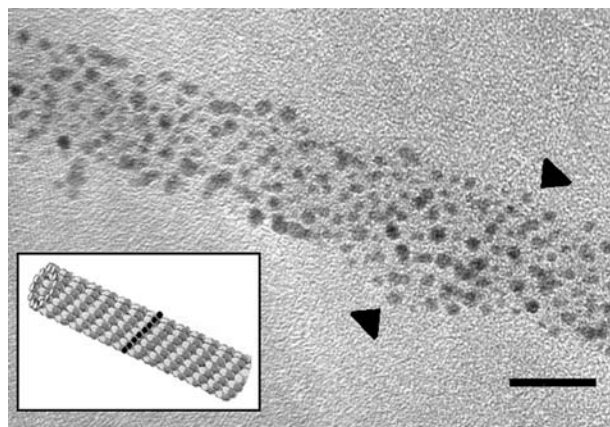


**Fig. 3** Transmission electron micrograph of Pd particles, 3.1 nm in size, nucleated on the surface of a microtubule (scale bar, 20 nm). The particles reflect the arrangement of the helical template. *Source:* From Ref.<sup>[36]</sup>. © 2002, Wiley-VCH.

Microtubules also promote directly the in situ formation of regular nanoparticle arrays with defined patterns when coupled with an appropriate chemical reaction and, as a support, provide some stabilization of the attached particles. Small monometallic Pd nanoparticles were nucleated in situ after incubation with a Pd ion precursor.<sup>[36]</sup> After incubation, the adsorbed metal ions could be subsequently reduced to form ordered arrays of Pd nanoparticles along the backbone of the microtubule reflecting the tubulin pattern in an isomolecular fashion. Depending on the kind of reducing agent used, particles with different sizes were obtained. Reduction with trisodium citrate at 90°C yielded particles having 1.9 nm in diameter. Applying a dimethylamine reduction bath at room temperature allowed the synthesis of slightly larger Pd particles with a mean particle diameter of 3.1 nm. Fig. 3 shows Pd particles on a microtubule obtained by reduction with dimethylamine borane. The particles were mainly attached to the surface of the biotemplate resulting in densely covered microtubule filaments. High-resolution TEM revealed the crystalline character of the particles. Lattice spacings were consistent with a pure metallic palladium phase, which was further confirmed by EDX. Interestingly, the obtained Pd particle arrays resembled closely the helical arrangement of the

tubulin subunits in the protein assembly. The preferential Pd deposition on the biotemplate suggests that in this case specific molecular interactions between functional groups on the protein surface and the Pd in solution were important for the formation of the superlattice arrays. We assume that, firstly, precursor Pd (II) ions were bound to the protein surface, followed by a heterogeneous surface-controlled nucleation process, and, finally, yielding nanosized particles attached to the protein template. The surface of a microtubule consists of defined patterns of amino acid residues providing various active sites for metal ion binding and particle nucleation. The question, however, arises which of these amino acid residues are actually involved in metal ion binding and the process of particle formation. According to the hard acids and bases (HSAB) principle after Parr and Pearson, Pd<sup>II</sup> is a soft metal ion and, thus, is expected to bind to soft donor ligands such as to the N or S atoms in the side chains of tryptophan, histidine, cysteine, and methionine. Some of the amino acids, e.g., lysine and arginine, are protonated at the applied pH, so that they are excluded as donor ligands. Fig. 4A shows a schematic diagram of the  $\alpha\beta$ -tubulin as seen from the outside of a microtubule. It displays the selected amino acids tryptophan, histidine, cysteine, and methionine at the

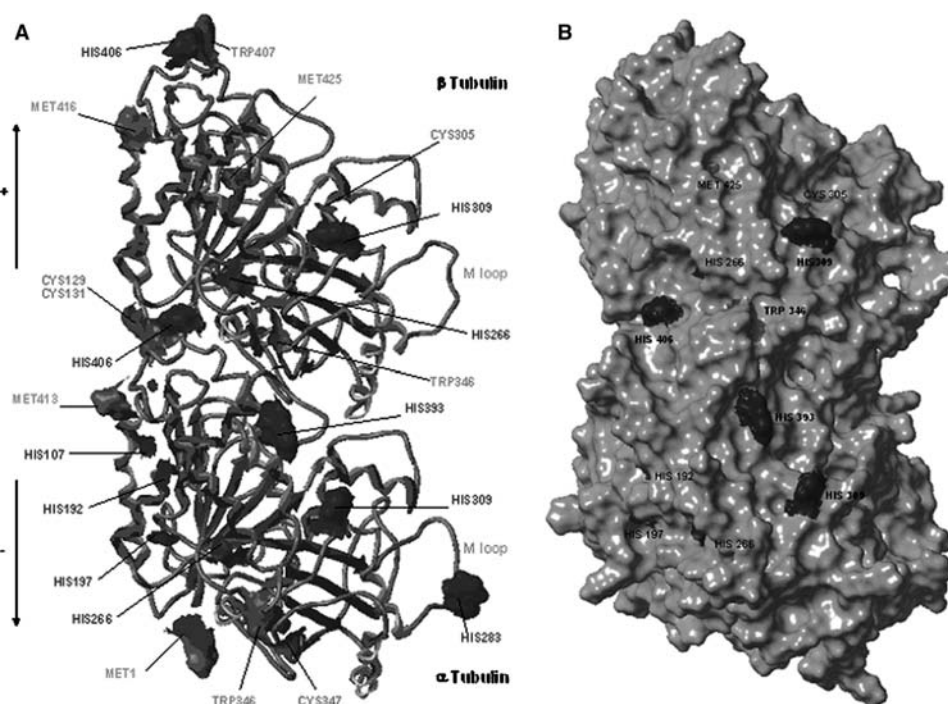


**Fig. 4** A) Ribbon diagram of  $\alpha\beta$ -tubulin as seen from the outside of a microtubule for selected N and S containing amino acids (cysteine: red; methionine: blue, histidine: green; and tryptophan: orange). B) The solvent accessible surfaces (Connolly surface) for the whole tubulin molecule (gray) and for the selected amino acids remaining freely accessible on the outer surface after assembly into microtubules. The histidine residues ( $\alpha$ : 309, 393, and 406;  $\beta$ : 309) are centrally positioned and easily accessible. These histidine residues should be the preferred sites for Pd<sup>II</sup> binding and particle nucleation. *Source*: From Ref.<sup>[36]</sup>. © 2002, Wiley-VCH.



microtubule outside surface. Tubulin assembly into microtubules involves two types of contacts: head-to-tail binding forming the protofilaments and lateral contacts between the protofilaments. As a consequence, some of the amino acids located in the periphery of the tubulin molecule will be covered after tubulin assembly. Fig. 4B shows the solvent accessible surfaces (Connolly surface) for the remaining amino acids. Some of the shown amino acids are located in channels or only parts of them are exposed to the surface of the molecule. As a result, only four histidine residues are actually centrally positioned on both  $\alpha$ - and  $\beta$ -tubulin at the microtubule's outer surface, and should be freely accessible. We therefore suggest that these histidine residues are potential sites for the binding of Pd ions and Pd particle nucleation. In fact, histidine is a typical metal-binding residue in peptides due to the deprotonated N3 atom in the imidazole ring.<sup>[37–39]</sup> By varying, the experimental conditions it was possible to control the Pd coating of the template. If the reservoir of metal ions present was increased, the Pd clusters on the template grew and were further connected to generate a quasi-continuous coverage of the microtubule surface with palladium aggregates.

The assumption that these metal clusters were heterogeneously grown in situ, after binding of Pd(II) ions selectively at the histidine sites, was supported by theoretical simulations of Ciacchi and coworkers.<sup>[40]</sup> They investigated the heterogeneous nucleation of Pt clusters on DNA and proteins by means of first principles molecular dynamics simulations. They found that Pt dimers formed from a Pt<sup>II</sup> complex, covalently bound to a biopolymer, and a free Pt<sup>II</sup> complex after a single reduction step. The imidazole ring, which is a structural feature of both histidine and the purine bases guanine and adenine, was a key residue at the biopolymer surface to induce the formation of these platinum dimers. The formation of Pt dimers was only possible in the presence of strong donor ligands such as purine DNA bases or histidine amino acids, and appeared to be forbidden in the homogeneous dimer formation reaction leading to a weaker Pt–Pt bond. Because of the delocalized electronic states on the heterocyclic ligands, the biopolymer-bound Pt atoms and dimers accepted reducing electrons more easily than the free complexes or dimers in solution and, moreover, the initially formed Pt–Pt bonds were stabilized. Thus the presence of these ligand systems contributed to enhancing the reaction rate of the heterogeneous cluster nucleation channel. The first-formed Pt nuclei developed then into bigger particles consuming the feedstock of metal complexes in solution and hindering the homogeneous formation of metal particles. As a result, the kinetics of the reduction and deposition process was locally enhanced at the surface of the biopolymer. Thus such a preferential heterogeneous

particle growth on an activated biotemplate permits a certain degree of control over the metallization process.

In addition to Au and Pd, other noble metals such as Rh, Ru, and Ag have been used in material synthesis with this type of microtubule template. Fig. 4 displays small Rh nanoparticles on a microtubule obtained by in situ reduction with NaN<sub>3</sub>. For electroless metal plating with Ni or Co, the surface of the template had to be previously activated with noble metal atoms or clusters. Kirsch and coworkers deposited about 10-nm-thick Ni or Co coats on microtubule templates, which yielded magnetic nanowires with an outer diameter of 50 to 60 nm.<sup>[24,25]</sup> In a first step, the microtubule surface was activated by adsorption of a molecular Pd catalyst. In a second step, Ni or Co was deposited onto the activated microtubules by applying an electroless metallization bath with dimethylamine borane as reducing agent. In their experiments they found clear evidence that nucleation of Ni crystallites started exclusively at the catalytic surface of the Pd catalyst.

## CONCLUSION

The interdisciplinary field emerging between biotechnology and materials science for the production of nanoscale materials is a rapidly growing field. Our results illustrate the potential of protein assemblies as biological components with their unique chemical and topological features for the controlled deposition of metals into well-defined, protein-supported nanostructures. In the interplay, the biological and inorganic components provide structure-directing properties and, furthermore, the biological support stabilizes the resulting nanostructure. Au colloids, for example, have been pursued as building blocks for the formation of wire-like structures through manipulation by microtubule templates. When coupled with an appropriate chemical reaction, microtubules promote the in situ formation of ordered arrays of metal nanoparticles resembling the arrangement of the protein molecules within the assembly. Preferential heterogeneous particle growth on the biotemplate permits control over the metallization process on the nanometer scale. Depending on the reaction conditions, the composites formed range from the isomolecular decoration of every protein molecule with one nanoparticle to the complete coating of the whole protein assembly. Although many examples exist where metallic nanoparticles and materials have successfully been deposited on biomolecules,<sup>[10,11]</sup> there still remains a great demand for new, mild, and selective chemical deposition techniques. One of the major advantages associated with this type of protein assemblies as biological template is that it will enable the future design

of various patterns of nanomaterials, e.g., ring structures exploiting the great diversity in size and shape of biomolecular tools, e.g., the polymorphic tubulin assemblies. A variety of technical obstacles still have to be solved ranging from the currently limited availability of large amounts of the biological building blocks to the improvement of analytical techniques. Because of the very low amount of material used in single nanodevices, the costs of the protein components should normally not limit application. A decrease in production costs will be required, however, for scale-up of both purification techniques and artificial syntheses. Biomolecular structures modified by genetic engineering and combined with an appropriate metal deposition technique will allow producing advanced materials on the nanometer scale with, for example, novel electronic, optical, magnetic, or catalytic properties.

## REFERENCES

- Weller, H. Quantized semiconductor particles: A novel state of matter for materials science. *Adv. Mater.* **1993**, *5* (2), 88–95.
- Murray, C.B.; Norris, D.J.; Bawendi, M.G. Synthesis and characterization of nearly monodisperse CdE (E=S, Se, Te) semiconductor nanocrystallites. *J. Am. Chem. Soc.* **1993**, *115*, 8706–8715.
- Henglein, A. Small-particle research: Physicochemical properties of extremely small colloidal metal and semiconductor particles. *Chem. Rev.* **1989**, *89*, 1861–1873.
- Bönnemann, H.; Brijioux, W. Potential applications of nanostructured metal colloids. *Metal Clusters in Chemistry*; Braunstein, P., Oro, L.A., Raithby, P.R., Eds.; Wiley-VCH: Weinheim, Germany, 1999; Vol. 2, 913–931.
- Schmid, G.; Maihack, V.; Lantermann, F.; Peschel, S. Ligand-stabilized metal clusters and colloids: Properties and applications. *J. Chem. Soc., Dalton Trans.* **1996**, 589–595.
- Simon, U. Charge transport in nanoparticle arrangements. *Adv. Mater.* **1998**, *10* (17), 1487–1492.
- Xia, Y.; Yang, P.; Sun, Y.; Wu, Y.; Mayers, B.; Gates, B.; Yin, Y.; Kim, F.; Yan, H. One-dimensional nanostructures: Synthesis, characterization, and applications. *Adv. Mater.* **2003**, *15* (5), 353–389.
- Behrens, S.; Rahn, K.; Habicht, W.; Böhm, K.J.; Rösner, H.; Dinjus, E.; Unger, E. Nanoscale particle arrays induced by highly ordered protein assemblies. *Adv. Mater.* **2002**, *14* (22), 1621–1625.
- Dekker, C.; Ratner, M. Electronic properties of DNA. *Phys. World* **2001**, *14*, 29–33.
- Niemeyer, C.M. Biomolecules meet nanoparticles. *Angew. Chem., Int. Ed.* **2001**, *40*, 4128–4158.
- Dujardin, E.; Mann, S. Bio-inspired materials chemistry. *Adv. Mater.* **2002**, *14*, 775–788.
- Storhoff, J.J.; Mirkin, C.A. Programmed material synthesis with DNA. *Chem. Rev.* **1999**, *99*, 1849–1862.
- Mirkin, C.; Letsinger, R.; Mucic, R.; Storhoff, J. A DNA-based method for rationally assembling nanoparticles into macroscopic materials. *Nature* **1996**, *382*, 607–608.
- Cao, Y.; Jin, R.; Mirkin, C.J. DNA-modified core-shell Ag/Au nanoparticles. *Am. Chem. Soc.* **2001**, *123*, 7961–7962.
- Connolly, S.; Fitzmaurice, D. Programmed assembly of gold nanocrystals in aqueous solution. *Adv. Mater.* **1999**, *11*, 1202–1205.
- Dujardin, E.; Peet, C.; Stubbs, G.; Cluver, J.N.; Mann, S. Organization of metallic nanoparticles using tobacco mosaic virus templates. *Nano Lett.* **2003**, *3* (3), 413–417.
- Richter, J. Metallization of DNA. *Physica, E* **2003**, *16*, 157–173.
- Braun, E.; Eichen, Y.; Sivan, U.; Ben-Yoseph, G. DNA-templated assembly and electrode attachment of a conducting silver wire. *Nature* **1998**, *391*, 775–778.
- Keren, K.; Krueger, M.; Gilad, R.; Ben-Yoseph, G.; Sivan, U.; Braun, E. Sequence-specific molecular lithography on single DNA molecules. *Science* **2002**, *297*, 72–75.
- Richter, J.; Seidel, R.; Kirsch, R.; Mertig, M.; Pompe, W.; Plaschke, J.; Schackert, H.K. Nanoscale palladium metallization of DNA. *Adv. Mater.* **2000**, *12*, 507–510.
- Mertig, M.; Ciacchi, L.C.; Seidel, R.; Pompe, W. DNA as a selective metallization template. *Nano Lett.* **2002**, *2*, 841–844.
- Monson, C.F.; Wolley, A.T. DNA-templated construction of copper nanowires. *Nano Lett.* **2003**, *3*, 359–363.
- Ford, W.; Harnack, O.; Yasuda, A.; Wessels, J. Platinated DNA as precursors to templated chains of metal nanoparticles. *Adv. Mater.* **2001**, *13*, 1793–1797.
- Kirsch, R.; Mertig, M.; Pompe, W.; Wahl, R.; Sadowski, G.; Böhm, K.J.; Unger, E. Three-dimensional metallization of microtubules. *Thin Solid Films* **1997**, *305*, 248–253.
- Mertig, M.; Kirsch, R.; Pompe, W. Biomolecular approach to nanotube fabrication. *Appl. Phys., A* **66**, 723–727.
- Nogales, E. Structural insights into microtubule function. *Ann. Rev. Biochem.* **2000**, *69*, 277–302.
- Unger, E.; Böhm, K.J.; Vater, W. Structural diversity and dynamics of microtubules and polymorphic tubulin assemblies. *Electron Microsc. Rev.* **1990**, *3*, 355–395.
- Roth, J. The silver anniversary of gold: 25 years of the colloidal gold marker system for immunocytochemistry and histochemistry. *Histochem. Cell Biol.* **1996**, *106*, 1–8.
- Hermann, R.; Walther, P.; Müller, M. Immunogold labeling in scanning electron microscopy. *Histochem. Cell Biol.* **1996**, *106*, 31–39.
- Storhoff, J.; Lazarides, A.; Mucic, R.; Mirkin, C.A.; Letsinger, R.; Schatz, G. What controls the optical properties of DANN-linked gold nanoparticle assemblies? *J. Am. Chem. Soc.* **2000**, *122*, 4640–4650.
- Park, S.; Lazarides, A.; Mirkin, C.; Brazis, P.; Kannewurf, C.; Letsinger, R. The electrical properties of gold nanoparticle assemblies linked by DNA. *Angew. Chem., Int. Ed.* **2000**, *39*, 3845–3848.
- Gole, A.; Dash, C.; Ramakrishnan, V.; Sainkar, S.R.; Mandale, A.B.; Rao, M.; Sastry, M. Pepsin-gold conjugates: Preparation, characterization, and enzymatic activity. *Langmuir* **2001**, *17*, 1674–1679.

33. Stracke, R.; Böhm, K.J.; Wollweber, L.; Tuszyński, J.A.; Unger, E. Analysis of the migration behaviour of single microtubules in electric fields. *Biochem. Biophys. Res. Commun.* **2002**, *293*, 602–609.
34. Keating, C.; Kovaleski, K.; Natan, M. Heightened electromagnetic fields between nanoparticles: Surface enhanced Raman scattering from metal–cytochrome c–metal sandwiches. *J. Phys. Chem., B* **1998**, *102*, 9414–9425.
35. Lee, A.F.; Baddeley, C.J.; Hardacre, C.; Ormerod, R.M.; Lambert, R.M. Structural and catalytic properties of novel Au/Pd bimetallic colloid particles: EXAFS, XRD, and acetylene coupling. *J. Phys. Chem.* **1995**, *99*, 6096–6102.
36. Behrens, S.; Rahn, K.; Habicht, W.; Böhm, K.J.; Rösner, H.; Dinjus, E.; Unger, E. Nanoscale particle arrays induced by highly ordered protein assemblies. *Adv. Mater.* **2002**, *14* (22), 1621–1625.
37. Djuran, M.I.; Milinković, S.U. Hydrolysis of amide bond in histidine-containing peptides promoted by chelated amino acid palladium (II) complexes: Dependence of hydrolytic pathway on the coordination modes of the peptides. *Polyhedron* **1999**, *18*, 3611–3616.
38. Appelton, T.G.; Pesch, F.J.; Wienken, M.; Menzer, S.; Lippert, B. Linkage isomerism in square–planar complexes of platinum and palladium with histidine and derivatives. *Inorg. Chem.* **1992**, *31* (21), 4410–4419.
39. Parac, T.N.; Kostić, N.M. Effects of linkage isomerism and acid–base equilibria on reactivity and catalytic turnover in hydrolytic cleavage of histidyl peptides coordinated to palladium (II). Identification of the active complex between palladium (II) and the histidyl residue. *J. Am. Chem. Soc.* **1996**, *118*, 5946–5951.
40. Ciachi, L.C.; Mertig, M.; Seidel, R.; Pompe, W.; De Vita, A. Nucleation of platinum clusters on biopolymers: A first principles study of the molecular mechanisms. *Nanotechnology* **2003**, *14*, 840–848.

# Nanostructured Materials: Synthesis by Mechanical Attrition

Carl C. Koch

*Department of Materials Science and Engineering, North Carolina State University,  
Raleigh, North Carolina, U.S.A.*

## INTRODUCTION

A wide variety of techniques are being used to synthesize nanostructured materials including inert gas condensation, rapid solidification, electrodeposition, sputtering, crystallization of amorphous phases, and chemical processing.<sup>[1]</sup> Mechanical attrition—ball milling of powders—is a technique that has also been used widely for preparation of nanostructured materials.<sup>[2,3]</sup> The term “mechanical attrition” can be subdivided into “mechanical milling,” which is the milling of single composition powders, often elements, and “mechanical alloying,” which involves milling of dissimilar powders such that material transfer occurs during milling. Unlike many of the methods for synthesis of nanostructured materials, mechanical attrition produces its nanostructures not by cluster assembly, but by the structural decomposition of coarser-grained structures as the result of severe plastic deformation. This has become a popular method to fabricate nanocrystalline materials because of several factors: the simplicity of the process, the relatively inexpensive equipment (on the laboratory scale) needed, and the applicability to essentially all classes of materials. A major advantage of mechanical attrition is the possibility for easily scaling up to tonnage quantities of material for various applications. The disadvantages that are often cited are contamination from the milling media and/or atmosphere, and the need, for many applications, to consolidate the powder product without coarsening the nanocrystalline microstructure.

A number of reviews concerned with the synthesis of nanostructured materials by mechanical attrition have been published in recent years, e.g., those of Koch,<sup>[2,4]</sup> Fecht,<sup>[5]</sup> Suryanarayana and Koch,<sup>[1]</sup> and Fecht.<sup>[3]</sup> This article will serve to update these previous reports. The details of the mechanical attrition processes, equipment used, etc. has been covered in a number of reviews (e.g., Ref.<sup>[4]</sup>), and will not be repeated here. The phenomenology of the development of nanoscale microstructures by mechanical attrition will be reviewed for the various classes of materials including single-phase metals, metallic alloys, brittle materials, and multiphase materials. Several mechanisms proposed for the development of a nanoscale

microstructure will then be described with reference to recent experimental observations. Finally, a brief discussion of the problems associated with mechanical attrition as a processing method will be presented. These are powder contamination and the need to consolidate the powders into bulk form without coarsening the nanoscale microstructure.

## PHENOMENOLOGY—EXPERIMENTAL OBSERVATIONS

### Single-Phase Elements—Mechanical Milling

Mechanical attrition has been found to refine grain size of all solid elements studied to the nanoscale. However, the minimum grain size achieved is dependent on a number of process variables as well as properties of the element. The minimum grain size obtainable by milling has been attributed to a balance between the defect/dislocation structure introduced by the plastic deformation of milling and its recovery by thermal processes.<sup>[6]</sup> It has been found that the minimum grain size induced by milling scales inversely with the melting temperature of the group of fcc structure metals studied.<sup>[6]</sup> These data are plotted in Fig. 1, along with data for other metals and carbon (graphite).<sup>[2]</sup> For these data, only the lower melting point metals show a clear inverse dependence of minimum grain size on melting temperature. The minimum grain size for elements with higher melting temperatures (larger than melting temperature for Ni) exhibits essentially constant values with melting temperature for given crystal structure classes. For these elements, it appears that  $d_{\min}$  is in the order: fcc < bcc < hcp. However, before explanations for the above based on the strain hardening response, twinning, or other fundamental differences in deformation behavior for the various metallic crystal structures can be considered, it should be pointed out that a number of variables can influence the values of the minimum grain size attained by ball milling. First of all, most of the measurements reported in Fig. 1 are based on the analysis of X-ray line broadening measurements. It is now well established that such measurements are subject to difficulty in terms of

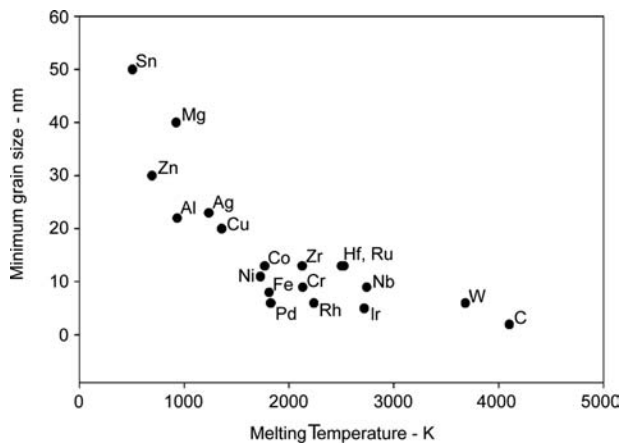


**Fig. 1** Minimum nanocrystalline grain size for ball milled elements vs. their melting temperature. *Source:* From Refs.<sup>[2,6–8]</sup>.

absolute quantitative values for grain sizes. Variability among analysis techniques for X-ray line broadening, as well as comparisons between these X-ray line broadening results and those from transmission electron microscopy (TEM) measurements, can be significant. However, most of the data in Fig. 1 are obtained from the Cal Tech group, Professor W. L. Johnson and coworkers,<sup>[6,7]</sup> or from Oleszak and Shingu.<sup>[8]</sup> Both of these groups used the approach of Williamson and Hall<sup>[9]</sup> to estimate the crystallite size and root-mean-square (rms) strain from the X-ray line broadening. Although the mill energies and contamination levels were very different in these studies, remarkable agreement for minimum grain size,  $d$ , is found for Al, Cu, Ni, and Fe. Oleszak and Shingu<sup>[8]</sup> found a lower  $d$  value for W (5.5 nm) than the value (9 nm) obtained by Fecht et al.<sup>[7]</sup> The Cal Tech group used a high-energy shaker mill (Spex 8000), while Oleszak and Shingu used a conventional horizontal low-energy ball mill. The metallic impurity level (Fe) from the shaker mill is much larger ( $\sim 2$  at.% Fe) than that from the conventional ball mill ( $< 0.1\%$  Fe). Conversely, the reported oxygen concentrations were about 4 times higher for powders milled in the conventional mill than for those from the shaker mill. The observation that the minimum nanocrystalline grain sizes for a number of elements milled in a low-energy mill are comparable to those milled in a high-energy mill is contrary to the conclusions previously reported after milling TiNi in a high-energy Spex shaker mill and a lower-energy vibratory mill.<sup>[10]</sup> After about 10 h in the Spex mill, the grain size (determined by both TEM and X-ray line broadening analysis) decreased to about 4–5 nm. At longer milling times, an amorphous structure was observed. Milling for 100 h in the vibratory mill resulted in a grain size of about 15 nm. It was originally assumed that this value represented a saturation to the minimum grain size obtainable in the lower energy mill.

However, in the light of the work of Oleszak and Shingu, it is likely that the  $d_{\min}$  was not obtained at 100 h in the lower-energy mill, and that continued milling may have further reduced the grain size. These results suggest that total strain, rather than milling energy or ball–powder–ball collision frequency, is responsible for determining the minimum nanocrystalline grain size. This is different from ball milling-induced amorphization or disordering, where it appears that the energy and frequency of ball–powder–ball collisions determine the final structures formed in “driven systems.” However, it is consistent with observations of nanocrystallites formed by high strain values using other non-cyclic deformation methods.<sup>[11]</sup> These results suggest that mill energy per se is not critical to the final microstructure, although, naturally, the kinetics of the process are dependent on the energy, and times for attaining the same microstructure can be several orders of magnitude longer in the low-energy mills than in high-energy mills.

Milling temperature has been observed to affect the rate at which the nanocrystalline structure develops. The milling time at which a given grain size was attained in a TiNi intermetallic compound was a function of milling temperature.<sup>[10]</sup> In this case, amorphization occurred at a “critical” grain size of about 4–5 nm, thus the final nanocrystalline grain size at each milling temperature could not be determined. Shen and Koch<sup>[12]</sup> also observed smaller nanocrystalline grain sizes in both Cu and Ni milled at  $-85^{\circ}\text{C}$  compared with samples milled at room temperature. For example, for Cu,  $d = 26 \pm 3$  nm for room temperature milling and  $d = 17 \pm 2$  nm for milling at  $-85^{\circ}\text{C}$ . Evidence for smaller nanocrystalline grain sizes formed by milling at low temperatures have now been observed in a number of materials including the intermetallic compound  $\text{CoZr}$ <sup>[13]</sup> and elemental Zn.<sup>[14]</sup>

### Metallic Alloys—Mechanical Alloying

While the majority of studies of nanocrystalline materials synthesized by ball milling have been on single-composition materials—i.e., either elemental metals, intermetallic compounds, or metal alloys—there have been a number of studies on mechanical alloying of dissimilar powders that result in nanoscale microstructures. First, the alloy effect on nanocrystalline grain size on nanocrystalline alloys will be discussed. These include both alloys made by mechanical alloying of dissimilar powders or milling of alloy powders. It has been suggested that the ultimate grain size achievable by milling is determined by the minimum grain size that can sustain a dislocation pileup within a grain and by the rate of recovery

during milling.<sup>[6]</sup> To estimate the composition dependence of grain size after milling, one may use the formula suggested by Nieh and Wadsworth.<sup>[15]</sup> The minimum distance,  $L$ , between dislocations is given by  $L = 3Gb/\pi(1 - \nu)h$ , where  $G$  is shear modulus,  $b$  is Burgers vector,  $\nu$  is Poisson ratio, and  $h$  is hardness. Indeed, if this is related to the formation of a minimum nanocrystalline grain size, then this nanocrystalline grain size is inversely proportional to hardness, and therefore, in most cases, to composition. In fact, a decreasing nanocrystalline grain size with solute concentration is observed in nanocrystalline alloy systems exhibiting solid solution hardening, such as Cu (Fe), Ti (Cu), Nb (Cu), Cu (Ni), and Cu (Co).<sup>[16]</sup> Also consistent with this is the essentially constant nanocrystalline grain size in Ni (Co), where hardness does not change significantly with composition<sup>[12]</sup> and the increased grain size in nanocrystalline Ni (Cu), Fe (Cu), and Cr (Cu), which exhibit an apparent solid solution softening effect.<sup>[16]</sup> However, the influence of alloying elements on the hardness of the nanocrystalline solid solutions is different from that in conventional polycrystalline solid solutions. The hardness of nanocrystalline solid solutions depends on both solid solution hardening and grain boundary hardening, while the latter makes the major contribution to total hardness. The increase in hardness resulting from the solid solution hardness effect in nanocrystalline alloys is of the same magnitude as that in conventional grain size polycrystalline alloys. However, the addition of alloying elements into the matrix for nanocrystalline alloys may have a strong influence on the grain boundary energy and grain boundary diffusion coefficient and thus on the deformation and recovery mechanisms of the nanocrystalline alloys formed by mechanical attrition. The different deformation and recovery behaviors are responsible for the various grain sizes obtained by milling and thus for the decreased or increased grain boundary hardening effects for the various nanocrystalline solid solutions.

Nanocrystalline grains are observed during the mechanical alloying of dissimilar component powders. Klassen, Oehring, and Bormann<sup>[17]</sup> followed the phase formation and microstructural development during the mechanical alloying of Ti and Al powder blends of overall composition  $Ti_{25}Al_{75}$ . TEM revealed nanocrystalline grains of partially ordered  $L1_2$  phase with a crystallite size of 10–30 nm in the alloy layers at the interface between the pure Ti and Al lamellae at the very early stages of the milling process. The alloy phase that develops between the pure powder components consists of nanocrystalline grains, presumably because of the multiple nucleation events and the slow growth occurring at the relatively low temperatures (100–200°C above ambient) during milling. Trudeau et al.<sup>[18]</sup>

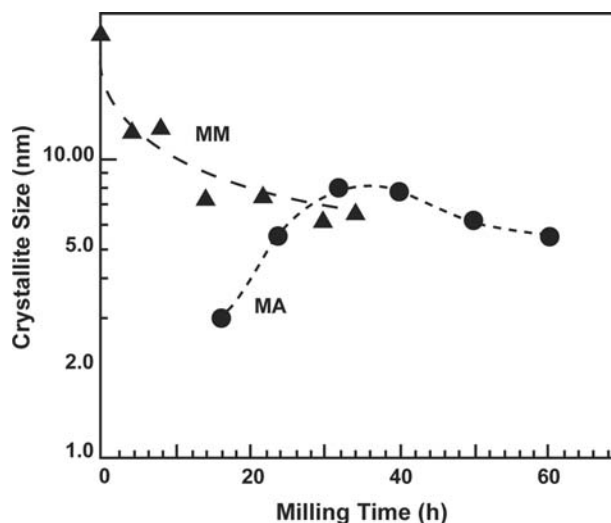


**Fig. 2** Crystallite size for FeTi intermetallic phase for low-energy (●) mechanical alloying of Fe and Ti powders, and (▲) mechanical milling of the FeTi compound powders. Source: From Ref.<sup>[18]</sup>.

prepared nanocrystalline FeTi by both low milling energy mechanical alloying (MA) of elemental Fe and Ti powders and mechanical milling (MM) of FeTi compound powders. Higher mill energies resulted in amorphization. The grain size of the MM Fe/Ti steadily decreases with milling time, while that for the MA Fe/Ti initially increases and then decreases to values essentially identical to those for the milled samples. This effect is illustrated in Fig. 2.

### Brittle Materials

The first materials subjected to mechanical alloying were combinations of ductile metals and brittle oxide powders, or with both components ductile metals. It was not clear that, if both components were brittle, the welding of the dissimilar powders believed to be required for the alloying to occur would take place. It might be expected that brittle components would simply fracture during milling and be reduced in size to the limit of comminution observed in the grinding of brittle mineral powders. However, it has been found that ball milling of nominally brittle materials can lead to alloying of brittle components, e.g., Si and Ge,<sup>[19]</sup> and the introduction of significant plastic deformation and high dislocation densities in brittle compounds, e.g.,  $Nb_3Sn$ .<sup>[20]</sup> Si and Ge are completely brittle at room temperature, and yet complete solid solutions of Si–Ge alloys were obtained across the binary phase diagram. Thus alloying on the atomic scale was observed by mechanical alloying of brittle components.  $Nb_3Sn$  is an extremely brittle intermetallic compound that elastically fractures until tested at temperatures



above about 1400°C. However, ball milling Nb<sub>3</sub>Sn can produce large amounts of plastic deformation, as observed by TEM of the milled powder. The dislocations so produced then induce a nanocrystalline grain structure similar to that formed in milled ductile metals. It is not yet clear how ball milling can produce large plastic deformation in materials that are very brittle under uniaxial stress conditions. It is suggested that the high hydrostatic stress component, which may exist in the powders during milling, can favor plastic deformation over fracture and allow a large dislocation density to be generated.<sup>[20]</sup> Mechanical attrition was also found to induce nanocrystalline microstructures in brittle ceramics, such as ZrO<sub>2</sub>, and ceramic powder mixtures, such as Fe<sub>2</sub>O<sub>3</sub>/Cr<sub>2</sub>O<sub>3</sub> and ZrO<sub>2</sub>/Y<sub>2</sub>O<sub>3</sub>.<sup>[3]</sup>

### Polymer Blends

The application of mechanical attrition to polymeric materials was initiated by Shaw.<sup>[21]</sup> To fracture the polymer particulates, and on the microscopic level the polymer chains, milling was conducted at temperatures below the glass transition temperature of the given polymer. Shaw's group has studied a number of homopolymers such as polyamide, polyethylene, acrylonitrile-butadiene-styrene, polypropylene, and polystyrene. Refinement of the microstructure typically occurred and milling-induced structural and property changes were noted that were very material-specific. Subsequently, others have studied milling-induced changes in the structure of several semicrystalline and amorphous homopolymers.<sup>[22]</sup> For example, in poly(ethylene terephthalate) (PET), milling promotes an oriented amorphous morphology in both high- and low-crystallinity PET. Molecular weight, glass transition temperature, and impact strength have been used to probe the milling-time-dependent molecular and property evolution of several homopolymers, e.g., poly(methylmethacrylate) (PMMA) and polyisoprene (PI). Milling of PMMA resulted in monotonic decreases in molecular weight and glass transition temperature, reflecting the milling-induced scission of the polymer chains. PI exhibited much different behavior in that the decrease in glass transition temperature,  $T_g$ , given by  $\Delta T_g = T_{g,0} - T_g(t_m)$ , where  $T_{g,0}$  is the glass transition temperature of the unmilled polymer, first increased and then decreased, as illustrated in Fig. 3. In this case, cryomilled PI does not exhibit a monotonic increase in  $\Delta T_g$ , but instead shows a sharp maximum at relatively short milling times (2 h), followed by a drop to almost zero before again increasing slightly for longer milling times. This unusual, but reproducible, behavior strongly suggests that the PI chains undergo chemical crosslinking during

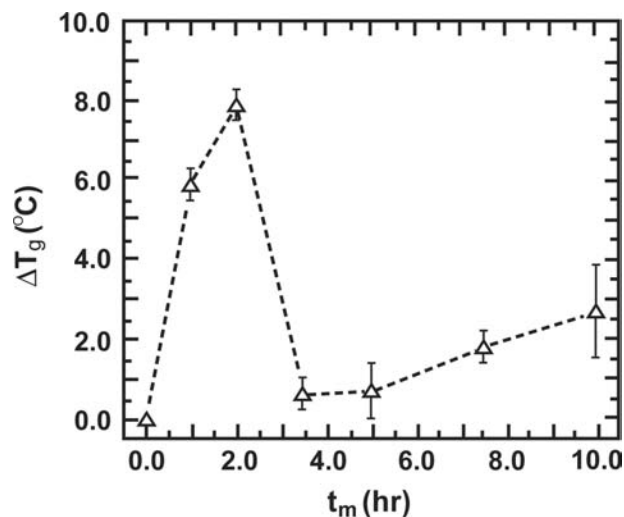


Fig. 3 Dependence of  $\Delta T_g$  on milling time,  $t_m$ , for cryomilled polyisoprene. Source: From Ref.<sup>[22]</sup>.

cryomilling. In such a case, we imagine a dynamic competition between chains breaking (causing a decrease in molecular weight) and crosslinking (promoting an increase in molecular weight) under the non-equilibrium conditions of milling. Sol-gel analysis and Fourier transform infrared (FTIR) spectroscopy yielded further evidence for milling-induced crosslinking in PI. Mechanical attrition was also performed at cryogenic temperatures to incorporate PI into PMMA.<sup>[23]</sup> A number of experimental techniques were used to study the structure of these normally immiscible polymer mixtures. TEM clearly showed that the solid-state blending by mechanical attrition of polymeric materials can yield nanoscale dispersions of immiscible polymers. The strong evidence for free radical formation and crosslinking induced by milling suggests many possibilities for the design of novel new polymeric materials with nanoscale microstructures. Incorporation of inorganic dispersoids in polymeric materials at the nanoscale by mechanical attrition is an area of research not yet fully explored.

### Nanocomposites

Nanoscale precipitates or dispersoids used to strengthen structural materials have been commonly used for about a century. However, the combination of nanoscale second phases in a nanocrystalline matrix are new microstructures and mechanical attrition is a particularly suited synthesis method for such materials. Because equilibrium solid solubility limits can be significantly enhanced by mechanical attrition of systems of limited mutable solubilities<sup>[24]</sup> to form nanocomposites, the immiscible nature of the component phases must be strong. Metals with very different atomic sizes

such as Pb and Al can form nanocomposites<sup>[25]</sup> as well as covalently or ionic bonded compounds in metallic matrices, such as  $\gamma$ -Al<sub>2</sub>O<sub>3</sub> and AlN in Fe.<sup>[26]</sup>

Metalloid second phases in nanocrystalline grain size matrices have been produced via the method of cryomilling. This technique of reactive milling of metals in liquid nitrogen was first developed by Huang, Vallone, and Luton<sup>[27]</sup> for Al, and has since been applied to several other metallic materials. The cryomilling of elemental Al and Ni powders in liquid nitrogen resulted in a nanoscale grain size for the Ni-base matrix of about 6 to 11 nm. Continued cryomilling in nitrogen resulted in a reaction between N, O, and the Al, which depleted the Al content of the matrix until, at long cryomilling times (170 h), the structure consisted of nanocrystalline Ni with AlN and  $\gamma$ -Al<sub>2</sub>O<sub>3</sub> nanoscale dispersions. Similar to the results they obtained from their work on Al, the presence of the nanoscale dispersoids resulted in a marked inhibition of grain growth even on annealing at high temperatures. The Ni-based nanocrystalline grain size containing the nitride and oxide dispersoids maintained a nanoscale grain structure with limited grain growth (grain size distribution of mostly about 11 nm, with some grains up to 300 nm) after annealing at 1373 K. The same material milled in argon was found to have extensive grain growth to about 1  $\mu$ m grain size after annealing at this temperature. These results demonstrated the effectiveness of nanoscale second phases in a nanoscale matrix to impede grain growth.

## MECHANISMS FOR NANOCRYSTAL SYNTHESIS BY MECHANICAL ATTRITION

### Single-Phase Metals by Mechanical Attrition

The first description of the evolution of a nanoscale grain structure during mechanical milling of elemental metals was given by Fecht and coworkers and summarized, for example, in Ref.<sup>[5]</sup> The basis of this first model was a study of the nanocrystallization of AlRu and Ru by mechanical attrition.<sup>[28]</sup> The structure/microstructure of AlRu as a function of milling time was followed by analysis of X-ray line broadening to estimate average grain size and lattice strain and TEM and high-resolution TEM (HRTEM) to directly observe the microstructural development. The TEM and HRTEM studies showed that, at the early stages of milling, the deformation was localized within shear bands that are approximately 0.5–1  $\mu$ m wide. The shear bands contain a high dislocation density. At a given strain, these dislocations begin to annihilate and recombine to small-angle grain boundaries separating individual cells or grains. Small grains, 8–12 nm in diameter, observed within the shear bands and electron

diffraction patterns suggest that the misorientation angles between the grains are relatively small. At longer milling times, the grain size steadily decreased, consistent with the X-ray results, and the shear bands coalesced. The small-angle boundaries were replaced by higher-angle boundaries, implying grain rotation, as reflected by the disappearance of texture in the electron diffraction patterns, as well as the random orientation of the grains observed from the lattice fringes in HRTEM. Fecht summarized the observed phenomenology of nanocrystallization by mechanical attrition into the following three stages:

- Stage 1. Deformation localization in shear bands containing a high dislocation density.
- Stage 2. Dislocation annihilation/recombination/rearrangement to form a cell/subgrain structure with nanoscale dimensions—further milling extends this structure throughout the sample.
- Stage 3. The orientation of the grains becomes random, that is, low angle grain boundaries disappear as high angle grain boundaries replace them, by presumably grain boundary sliding, rotation.

From evidence of the atomic-level lattice strain and the stored enthalpy as a function of reciprocal grain size (or milling time), it was concluded that two different regimes can be distinguished, i.e., dislocation vs. grain boundary deformation mechanisms.<sup>[5]</sup> The lattice strain in the fcc elements studied by Eckert et al.,<sup>[6]</sup> milled in a high-energy shaker mill, was found to increase continuously with decreasing grain size, and reach a maximum value at the smallest grain size. This is in contrast to the earlier observation on Ru and AlRu, which indicated a maximum in strain vs.  $1/d$ ,<sup>[29]</sup> and the more recent study of Oleszak and Shingu<sup>[8]</sup> on a low-energy mill, which also shows a broad maximum in strain vs.  $1/d$  for a number of elements including several fcc elements. The lattice strain values available from the literature are plotted against reciprocal grain size,  $1/d$ , in Fig. 4. With the exception of Ru, the data increased lattice strain with  $1/d$  appear to fall on a common relatively narrow band before decreasing from the maximum strain values. However, these data are obtained from several groups using mills with various energy levels and possible differences in milling temperature. It has been demonstrated<sup>[12]</sup> that lower milling temperature resulted in larger values for lattice strain for Cu and Ni. However, the data from the low-energy mill<sup>[8]</sup> should be self-consistent and exhibit interesting behavior. That is, the strain rises with decreasing grain size, reaches a maximum, and then decreases to low values for the smallest nanocrystalline grain sizes. A maximum in strain with  $1/d$  was previously explained by either a change in deformation mechanism from dislocation generation and

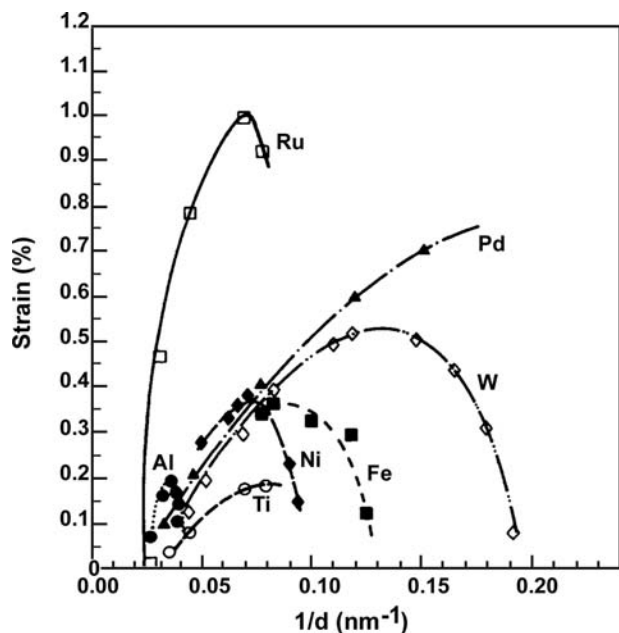


Fig. 4 Lattice strain vs. reciprocal grain size. Source: From Ref.<sup>[2]</sup>.

movement to grain boundary sliding, grain rotation,<sup>[28]</sup> or, in brittle intermetallics to fracture after the strain maximum is reached.<sup>[18]</sup> A problem with the first mechanism is that the nanocrystalline grain size continues to decrease after the strain maximum is reached, and grain boundary sliding and rotation presumably cannot result in grain size reduction. There is no clear evidence at present in the elements for the fracture mechanism, which would also presumably result in a finer particulate distribution.

Additional information to help explain the mechanism of nanocrystalline formation comes from measurements of stored enthalpy. Maxima in stored enthalpy vs.  $1/d$  are typically observed.<sup>[6,8,29]</sup> However, the maximum in stored enthalpy is often found at smaller grain sizes than the strain maximum, as illustrated in Fig. 5 for W.<sup>[8]</sup> Here the maximum in strain occurs at  $d = 8.3$  nm, while the maximum in stored enthalpy is at  $d = 5.5$  nm. Several suggestions have been offered to explain the maxima in stored enthalpy with  $1/d$ , including decreasing strain<sup>[8,29]</sup> or impurity pickup during milling.<sup>[29]</sup> The latter is an unlikely explanation for samples obtained by low-energy milling,<sup>[8]</sup> where metallic impurity contamination is negligible. It is stated that the stored enthalpy comes mainly from grain boundaries<sup>[28,29]</sup> and grain boundary strains. Stress relaxation may be responsible for the maxima,<sup>[8]</sup> but, as noted above, the strain and stored enthalpy maxima do not necessarily coincide.

While the general concepts described above for synthesis of elemental metal nanocrystalline structures by mechanical attrition are likely to have some validity,

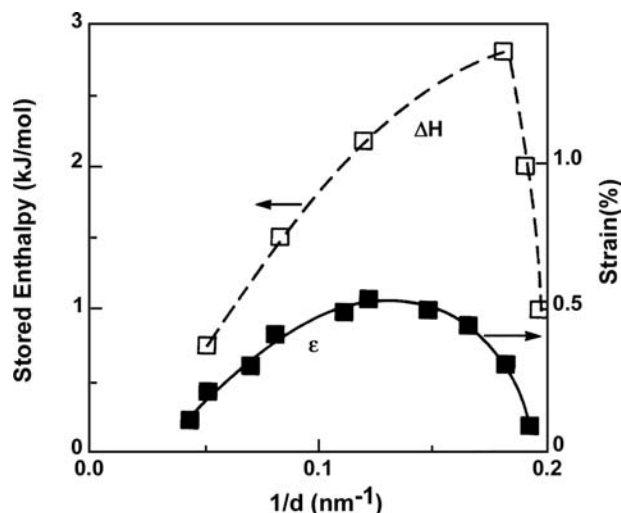


Fig. 5 Stored enthalpy ( $\Delta H$ ) and lattice strain ( $\epsilon$ ) vs. reciprocal grain size for W. Source: From Refs.<sup>[2,8]</sup>.

questions still remain especially regarding the maxima in lattice strain and stored enthalpy, and the mechanism of grain refinement. Several recent experimental studies as well as suggested alternate mechanisms will now be discussed.

Recent studies of the synthesis of nanocrystalline Zn by milling at liquid nitrogen temperatures (cryomilling) have provided evidence for an alternate mechanism for making nanoscale grains.<sup>[30,31]</sup> In most previous studies, the progress of nanocrystallization as a function of milling time was followed by X-ray diffraction line broadening analysis, which gives an average grain size. The grain size so determined typically exhibits monotonically decreasing values with milling time. This is also the case for cryomilled Zn, as illustrated in Fig. 6. This average grain size decreases rapidly for the early milling times, and then saturates to a value of about 20 nm for the longer times.

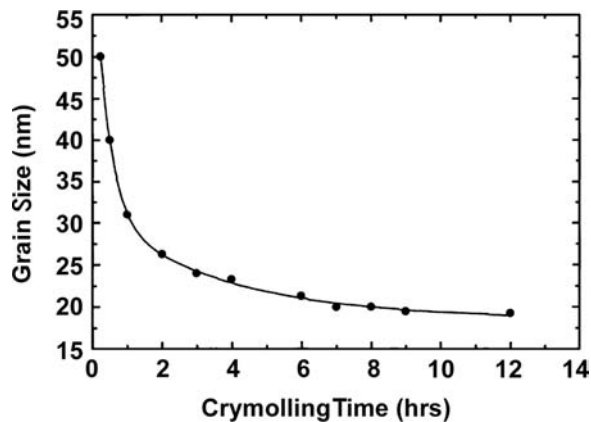
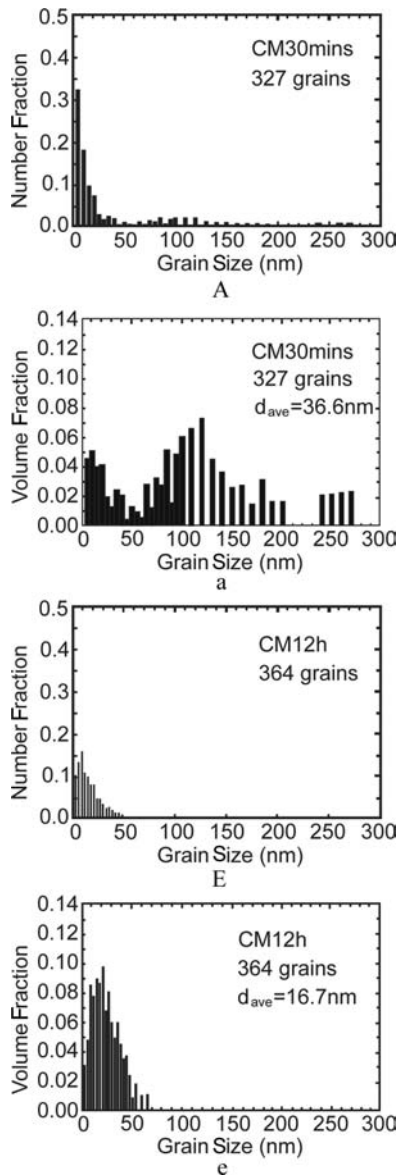
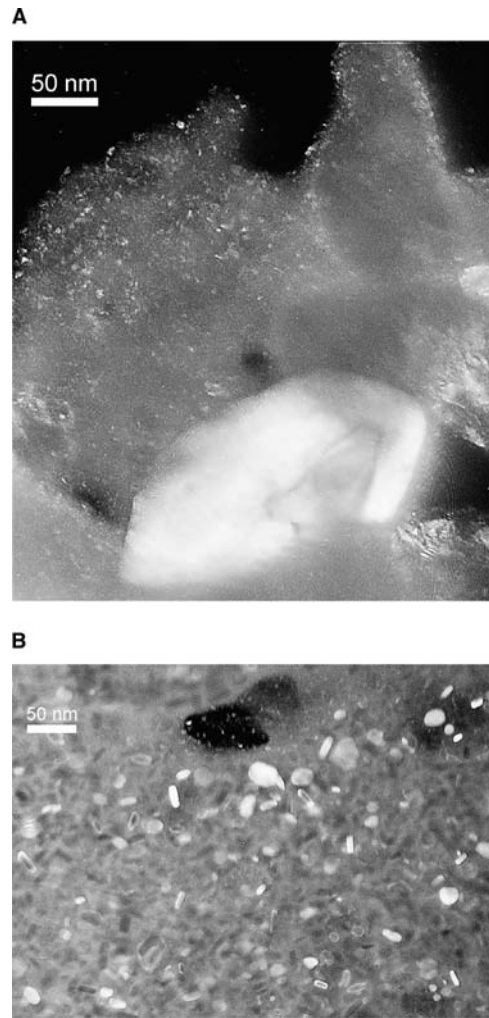


Fig. 6 Average grain size for cryomilled Zn vs. milling time. Source: From Ref.<sup>[30]</sup>.

with milling time, an extensive study using TEM was carried out.<sup>[30]</sup> It was surprising to observe a large fraction of very small grain sizes (less than 5 nm) even in the very early stages (e.g., 0.5 h) of cryomilling. The grain size distribution was found to be essentially bimodal for the shorter milling times, as shown in Fig. 7A and a for 0.5 h of milling, and then collapsed to one peak at longer milling times, and finally narrowed to a tighter distribution at the longest times, as seen in Fig. 7E and e for a milling time of 12 h. These distributions were determined from dark-field TEM micrographs, as shown in Fig. 8A and B for the samples milled 0.5 and 12 h, respectively. From Figs. 7 and 8, it is observed that at short milling times,



**Fig. 7** The number fraction and volume fraction of grain size at cryomilling times: 30 min (A, a) and 12 h (E, e). *Source:* From Ref.<sup>[30]</sup>.



**Fig. 8** (A) TEM dark field image for Zn cryomilled for 30 min. (B) TEM dark field image for Zn cryomilled for 12 h. *Source:* From Ref.<sup>[30]</sup>.

grains of about 250 nm size exist together with small grains of less than 10 nm. It was suggested that the very small grains formed at the early milling times might have been caused by a dynamic recrystallization (DRX) phenomenon. Dynamic recrystallization refers to the occurrence of crystallization during deformation. The mechanisms and transformation kinetics for both static and dynamic recrystallization have been reviewed by Doherty et al.<sup>[32]</sup> It appears that DRX can occur as a nucleation and growth process, or as a recovery process. Many issues related to the transformation kinetics for DRX remain unresolved, and the underlying mechanisms are not well understood. However, it is assumed that the high dislocation densities possible by deformation at low temperatures and the nucleation sites probably provided by shear banding are consistent with cryogenic temperature milling of, e.g., Zn, in the high strain, high strain rate deformation which occurs. Evidence for the possibility of dynamic

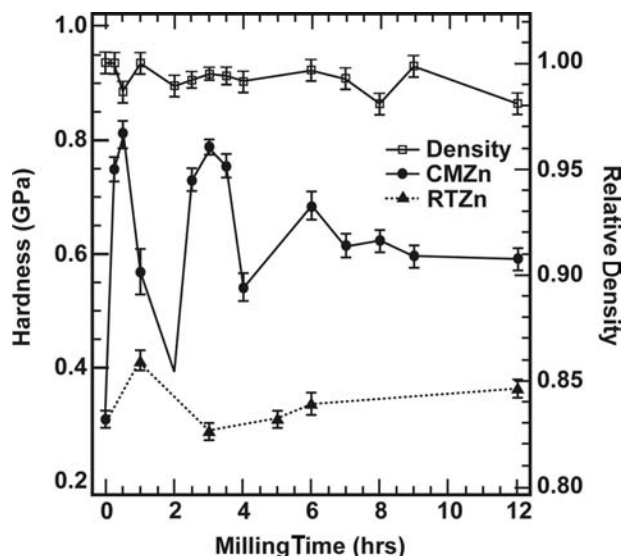


**Fig. 9** Hardness vs. milling time for Zn milled at 100 K (solid circles) and at room temperature (solid triangles). The relative densities for the cryomilled samples are indicated by open squares. *Source:* From Ref.<sup>[33]</sup>.

recrystallization playing a role in the synthesis of nanocrystalline grain sizes in metals is dramatically observed in the oscillatory hardness behavior with cryomilling time in Zn.<sup>[33]</sup> This oscillatory hardness behavior is illustrated in Fig. 9. The dramatic oscillatory hardness changes with milling times at cryogenic temperatures are not reflected in the hardness data for samples milled at room temperature. They are also not related to any artifact, such as porosity, as shown by the essentially constant, and nearly theoretical, density of the samples. Transmission electron microscopy showed that large variations in the dislocation density and grain-size distribution occurred during cryomilling. The observations suggest that dynamic recrystallization takes place in larger grains (>50 nm), when the dislocation density due to strain hardening reaches a critical level to nucleate DRX. A reaction-rate model was developed which accounts for the DRX effect and the observed oscillations in hardness. Good agreement was obtained with the experimental data. These results imply that in special circumstances, i.e., where conditions are right to nucleate DRX, the dynamic recrystallization reaction may also contribute to the synthesis of a nanoscale grain microstructure. In analogy to “continuous recrystallization,”<sup>[32]</sup> the mechanism proposed by Fecht and coworkers, in which dislocation structures continuously rearrange themselves during deformation in a recovery-like fashion that ends in high-angle boundaries, nanocrystalline grains, can sometimes be also formed by a “discontinuous” DRX process.

He and Lavernia<sup>[34]</sup> offered an alternative explanation for the synthesis of nanoscale microstructures

in cryomilled Inconel 625 alloy. This Ni-base alloy was milled in liquid nitrogen to form a nanocrystalline grain structure. TEM observations indicated that grains in the cryomilled powder were deformed into elongated grains containing a high density of deformation faults. With continued milling, the elongated grains fractured into small nanoscale fragments. The occurrence of the elongated grains and their subsequent fragmentation were attributed to repeated strain fatigue and fracture caused by the cyclic impact loading in random directions, along with cold welding. A high density of mechanical nanoscale twins was also observed.

While most of the studies on the development of nanocrystalline grain structures by mechanical attrition have involved observing the microstructure as a function of milling time, and presumably, total average strain, Tao et al.<sup>[35]</sup> recently investigated the microstructure of a pure Fe plate that had been subjected to surface mechanical attrition. In this case, the milling balls were impacted on the surface of the Fe plate by vibratory motion, such that the surface layer was subjected to high-strain-rate plastic deformation. The degree of plastic deformation was highest at the surface of the plate and decreased, eventually to zero, as distance from the surface into the plate increased. The structure and microstructure of the deformed Fe was then studied by X-ray diffraction line broadening analysis as the plate was progressively etched, layer by layer, and by scanning electron microscopy (SEM), TEM, and HRTEM observations of the cross sections of the surface layers. X-ray diffraction results showed that the grain size was a minimum at the surface and increased with depth, while the microstrain was a maximum at the surface and dropped to about zero at a depth of 60  $\mu\text{m}$ . From the electron microscopy, the surface-treated layer could be subdivided into several sections in terms of grain (or cell) size. From the top surface these were:

- Section 1. Nanostructured regime:  $\sim 0\text{--}15\ \mu\text{m}$ ;
- Section 2. Submicron-sized regime:  $\sim 15\text{--}40\ \mu\text{m}$ ;
- Section 3. Micron-sized regime:  $\sim 40\text{--}60\ \mu\text{m}$ .

Beyond a depth of 60  $\mu\text{m}$ , the original Fe matrix showed some evidence of plastic deformation but no grain refinement. At the regions adjacent to the strain-free matrix, homogeneously distributed dislocation lines are observed, and the dislocation density increases as the distance from the surface decreases. In addition, dense dislocation walls (DDWs) are observed, with spacing in the micron range and parallel to each other along  $\{110\}$  planes. Dislocation tangles are also observed and in some regions the dislocation density is high. With decreasing depth, into Section 3, most original grains are subdivided into micron-sized

cells, which are either roughly equiaxed or lamellar. The misorientation of these cells of DDWs are small, typically less than  $1^\circ$ . At still smaller depths, that is in Section 2, the cell sizes are found to decrease with elongated cells several microns long and about 200–400 nm thick. Some equiaxed cells are also seen that are  $\sim 200$ – $500$  nm in size. Finally, near the surface, where the deformation strain and strain rates are maximum, nanocrystalline microstructures are observed. Equiaxed nanocrystalline grains are observed near the surface, while at the bottom of Section 1, lamellar nanoscale grains are observed. However, inside the lamellar grains, smaller equiaxed grains are also present. Based on these extensive microstructural observations, the sequence of nanocrystalline formation was summarized as follows. Formation of DDWs and dislocation tangles (DTs) first occur, then the DDWs and DTs transform into subboundaries with small misorientations. Finally, the subboundaries and subgrains evolve into nanocrystalline grains with large misorientation angles between them. It was suggested that, for the synthesis of nanocrystalline grains during plastic deformation, high strain rates were necessary as well as large strains. This suggestion is consistent with observations of plastic-deformation-induced grain refinement at high strains, while lower strain rates such as equal channel angular pressing or cold rolling typically produce grain sizes no smaller than about 100–200 nm. However, it may be at variance with the results of low-energy milling experiment, where similar minimum grain sizes have been observed to those produced by high-energy milling.<sup>[8]</sup> More studies along the lines of the above are needed to clarify the mechanism for synthesis of nanocrystalline metals by mechanical attrition.

### Nanocrystallization Mechanisms for Milling of Dissimilar Elements

The proposed mechanism for nanocrystallization on milling of dissimilar elements that form an intermediate phase, e.g., TiAl from Ti and Al powders,<sup>[17]</sup> was the biasing of nucleation vs. growth of the new phase at the relatively low temperatures of milling, as described earlier in this paper. However, milling of dissimilar metals that do not form intermediate phases can also form nanoscale microstructures and the mechanism must be different. Zghal et al.<sup>[36]</sup> reported the results of milling the normally immiscible Cu–Ag and Ni–Ag systems. The Cu–Ag microstructure after milling at lower temperatures exhibits a pronounced texture and a complex microstructure. Milling at higher temperature produced small equiaxed nanoscale grains, which were the result of dynamic recrystallization. In the case of Ni–Ag, which has a larger positive

heat of mixing than Cu–Ag, complete mixing was not possible, and a nanocomposite was formed. It was suggested that, as texture was not observed in the Ni-rich phase, which featured smaller grain size (5–10 nm), full mixing of the components cannot take place because of the differences in their mechanical properties.

More studies are needed to clarify the diverse possible mechanisms for nanocrystallization by mechanical attrition of dissimilar powders.

### PROBLEMS: CONTAMINATION AND POWDER CONSOLIDATION

A serious problem with the milling of fine powders is the potential for significant contamination from the milling media (balls and vial) or atmosphere. If steel balls and containers are used, iron contamination can be a problem. It poses a most serious risk for the highly energetic mills, e.g., the Spex shaker mill, and depends on the mechanical behavior of the powder being milled, as well as its chemical affinity for the milling media. For example, milling Ni to attain the minimum grain size in a Spex mill resulted in Fe contamination of 13 at.%, while the Fe contamination in nanocrystalline Cu similarly milled was only  $\leq 1$  at.%.<sup>[16]</sup> Lower-energy mills result in substantially less, often negligible, Fe contamination. Other milling media, such as tungsten carbide or ceramics, can be used, but contamination from such media is also possible. Interstitial element (oxygen, nitrogen) contamination can be controlled by milling and subsequent powder handling in a pure inert gas atmosphere, with care taken that the milling vial is leak-free during processing.

Powder consolidation to theoretical density of nanocrystalline materials prepared by mechanical attrition without significant coarsening is necessary for many property measurements, e.g., mechanical behavior, and for applications requiring bulk materials. There is no room in this paper to adequately review the escalating efforts in this important field. However, a number of successes have been documented by both conventional and innovative methods and are reviewed by Groza.<sup>[37]</sup> For the special case of very ductile, relatively low melting temperature metals such as Zn and Al, it has been found that, in the absence of a process control agent during milling, cold welding can dominate the process and the powders can be “consolidated” into spherical-shaped balls that can be up to 6–8 mm in diameter.<sup>[38]</sup> Thus in situ consolidation can be attained in these cases during milling. Disks can be formed from the spherical samples via compression. Such disks are suitable for mechanical tests such as miniaturized disk bend tests or small-size tensile samples.



## CONCLUSION

Mechanical attrition of powders is a simple and versatile method to prepare nanocrystalline microstructures in a variety of materials including metals, ceramics, polymers, intermetallics, and composites. The mechanism for formation of nanoscale grains by severe plastic deformation induced by ball milling, in general, involves the competition between defect production and defect recovery by thermal processes. The details by which this occurs are still not completely defined. In most cases, a continuous buildup of dislocation density and the rearrangement of dislocations into first cells, and then small equiaxed grains, occur. In some cases, there is evidence for discontinuous dynamic recrystallization. More systematic TEM studies on a variety of materials are needed to confirm the mechanism. Problems of powder contamination during processing must be considered, but can be minimized. Consolidation of the powders with nanoscale microstructures into bulk structures is a topic that requires further attention.

## ACKNOWLEDGMENTS

The author's research on nanocrystalline materials has been supported over the years by the U.S. National Science Foundation under grants number DMR-9203479, DMR-9508797, DMR-9871980, and DMR-201474.

## REFERENCES

- Suryanarayana, C.; Koch, C.C. Nanostruct. Mater. In *Non-Equilibrium Processing of Materials*; Suryanarayana, C., Ed.; Pergamon, Elsevier Science Ltd.: Oxford, UK, 1999; 313 pp.
- Koch, C.C. Synthesis of nanostructured materials by mechanical milling: problems and opportunities. *Nanostruct. Mater.* **1997**, *9*, 13.
- Fecht, H.J. Nanostructured materials and composites prepared by solid state processing. In *Nanostructured Materials: Processing, Properties, and Applications*; Koch, C.C., Ed.; William Andrew Publishing: Norwich, NY, 2002; 73 pp.
- Koch, C.C. The synthesis and structure of nanocrystalline materials produced by mechanical attrition: a review. *Nanostruct. Mater.* **1993**, *2*, 109.
- Fecht, H.J. Nanostructure formation by mechanical attrition. *Nanostruct. Mater.* **1995**, *6*, 33.
- Eckert, J.; Holzer, J.C.; Krill, C.E., III; Johnson, W.L. Structural and thermodynamic properties of nanocrystalline fcc metals prepared by mechanical attrition. *J. Mater. Res.* **1992**, *7*, 1751.
- Fecht, H.J.; Hellstern, E.; Fu, Z.; Johnson, W.L. Nanocrystalline metals prepared by high-energy ball milling. *Metall. Trans., A* **1990**, *21A*, 2333.
- Olesak, D.; Shingu, P.H. Nanocrystalline metals prepared by low energy ball milling. *J. Appl. Phys.* **1996**, *79*, 2975.
- Williamson, G.K.; Hall, W.H. X-ray line broadening from filed aluminum and wolfram. *Acta Metall.* **1953**, *1*, 22.
- Yamada, K.; Koch, C.C. The influence of mill energy and temperature on the structure of the TiNi intermetallic after mechanical attrition. *J. Mater. Res.* **1993**, *8*, 1317.
- Lowe, T.C.; Valiev, R.Z. Producing nanoscale microstructures through severe plastic deformation. *JOM* **2000**, *52*, 27.
- Shen, T.D.; Koch, C.C. The influence of dislocation structure on formation of nanocrystals by mechanical attrition. *Mater. Sci. Forum* **1995**, *179-181*, 17-24.
- Pathak, D.K. Effect of Milling Temperature on the Amorphization of Intermetallic Compounds by Mechanical Milling. Ph.D. Dissertation. North Carolina State University: Raleigh, NC, 1995.
- Zhang, X. Synthesis and Characterization of Nanocrystalline Zn. Ph.D. Dissertation. North Carolina State University: Raleigh, NC, 2001.
- Nieh, T.G.; Wadsworth, J. Hall-Petch relation in nanocrystalline solids. *Scr. Metall. Mater.* **1991**, *25*, 955.
- Shen, T.D.; Koch, C.C. Formation, solid solution hardening and softening of nanocrystalline solid solutions prepared by mechanical attrition. *Acta Mater.* **1996**, *44*, 753.
- Klassen, T.; Oehring, M.; Bormann, R. The early stages of phase formation during mechanical alloying of Ti-Al. *J. Mater. Res.* **1994**, *9*, 47.
- Trudeau, M.L.; Schultz, R.; Zaluski, L.; Hosatte, S.; Ryan, D.H.; Doner, C.B.; Tessier, P.; Strom-Olsen, J.O.; Van Neste, A. Nanocrystalline iron-titanium alloys prepared by high energy mechanical deformation. *Mater. Sci. Forum* **1992**, *21*, 305.
- Davis, R.M.; Koch, C.C. Mechanical alloying of brittle components: silicon and germanium. *Scr. Metall.* **1987**, *21*, 305.
- Cho, Y.S.; Koch, C.C. Structural evolution in Nb<sub>3</sub>Sn during mechanical attrition. *Mater. Sci. Eng., A* **1991**, *A141*, 139.
- Shaw, W.J.D. Current understanding of mechanically alloyed polymers. *Mater. Sci. Forum* **1998**, *19*, 269-272.
- Koch, C.C.; Smith, A.P.; Bai, C.; Spontak, R.J.; Balik, C.M. Nonequilibrium processing of polymeric materials by mechanical attrition. *Mater. Sci. Forum* **2000**, *49*, 343-346.
- Smith, A.P.; Ade, H.; Balik, C.M.; Koch, C.C.; Smith, S.D.; Spontak, R.J. Cryogenic mechanical alloying of poly(methyl methacrylate) with polyisoprene and poly(ethylene-alt-propylene). *Macromolecules* **2000**, *33*, 2595.
- Suryanarayana, C. Mechanical Alloying. In *Non-Equilibrium Processing of Materials*; Suryanarayana, C., Ed.; Pergamon, Elsevier Science Ltd.: Oxford, UK, 1999; 49 pp.
- Zhu, M.; Li, B.L.; Gao, Y.; Li, L.; Luo, K.C.; Sui, H.X.; Li, Z.X. Microstructure characteristics of nanophase

- composite synthesized by mechanical alloying of immiscible Pb–Al and Fe–Cu systems. *Scr. Mater.* **1997**, *36*, 447.
26. Perez, R.J.; Huang, B.; Lavernia, E.J. Effect of in-situ formation of nanoscale  $\gamma$ -Al<sub>2</sub>O<sub>3</sub> and AlN on thermal stability of cryomilled nanocrystalline Fe. In *Metastable Phases and Microstructure*; MRS Symp. Proc.; Bormann, R., Mazzone, G., Shull, R.D., Averback, R.S., Ziolo, R.F., Eds.; Materials Research Society: Warrendale, Pennsylvania, USA, 1996; 400, 31 pp.
  27. Huang, B.; Vallone, J.; Luton, M.J. The effect of nitrogen and oxygen on the synthesis of B2 NiAl by cryomilling. *Nanostruct. Mater.* **1995**, *6*, 631.
  28. Hellstern, E.; Fecht, H.-J.; Garland, C.; Johnson, W.L. Mechanism of achieving nanocrystalline AlRu by ball milling. *Mater. Res. Soc. Symp. Proc.* **1989**, *132*, 137.
  29. Hellstern, E.; Fecht, H.-J.; Fu, Z.; Johnson, W.L. Structural and thermodynamic properties of heavily mechanically deformed Ru and AlRu. *J. Appl. Phys.* **1989**, *65*, 305.
  30. Zhang, X.; Wang, H.; Narayan, J.; Koch, C.C. Evidence for the formation mechanism of nanoscale microstructures in cryomilled Zn powder. *Acta Mater.* **2001**, *49*, 1319.
  31. Zhang, X.; Wang, H.; Kassem, M.; Narayan, J.; Koch, C.C. Origins of stored enthalpy in cryomilled nanocrystalline Zn. *J. Mater. Res.* **2001**, *16*, 3485.
  32. Doherty, R.D.; Hughes, D.A.; Humphries, F.J.; Jonas, J.J.; Jensen, D.J.; Kassner, M.E.; King, W.E.; McNelley, T.R.; McQueen, H.J.; Rollett, A.D. Current issues in recrystallization: a review. *Mater. Sci. Eng., A* **1997**, *A238*, 219.
  33. Zhang, X.; Wang, H.; Scattergood, R.O.; Narayan, J.; Koch, C.C. Modulated oscillatory hardening and dynamic recrystallization in cryomilled nanocrystalline Zn. *Acta Mater.* **2002**, 3995.
  34. He, J.; Lavernia, E.J. Development of nanocrystalline structure during cryomilling of Inconel 625. *J. Mater. Res.* **2001**, *16*, 2724.
  35. Tao, N.R.; Wang, Z.B.; Tong, W.P.; Sui, M.L.; Lu, J.; Lu, K. An investigation of surface nanocrystallization mechanism in Fe induced by surface mechanical attrition treatment. *Acta Mater.* **2002**, 4603.
  36. Zghal, S.; Bhattacharya, P.; Twesten, R.; Wu, F.; Bellon, P. Structural and chemical characterization of Cu–Ag and Ni–Ag nanocomposites synthesized by high energy ball milling. *J. Metastable Nanocryst. Mater.* **2002**, *13*, 165.
  37. Groza, J.R. Nanocrystalline powder consolidation methods. In *Nanostruct. Mater.: Processing, Properties, and Applications*; Koch, C.C., Ed.; William Andrew Publishing: Norwich, NY, 2002; 115 pp.
  38. Zhang, X.; Wang, H.; Kassem, M.; Narayan, J.; Koch, C.C. Preparation of bulk ultrafine-grained and nanostructured Zn, Al, and their alloys by in situ consolidation of powders during mechanical attrition. *Scr. Mater.* **2002**, *46*, 661.

# Nanostructured Materials: Synthesis by Mechanical Means

H.-J. Fecht

Materials Division, University of Ulm, Ulm, Germany

## INTRODUCTION

Internal interfaces in materials are extended defects, such as grain boundaries and interphase boundaries, which can be found in almost every natural or artificially produced material or man-made structure.<sup>[1]</sup> In general, the correlation between the atomic structure and the energy of interfaces can be described by their respective excess free volume,<sup>[2]</sup> which can be minimized by the formation of closely packed structural units of atoms so that interfaces with low index planes and low index atomic rows are parallel to each other.<sup>[3,4]</sup> However, the experimental evidence concerning structure–energy correlations of internal interfaces, in particular under thermodynamic equilibrium conditions where entropic effects should be taken into account, remains unclear because of the inherent experimental difficulties and the generally small interface-to-volume ratio in conventional polycrystals.

Decreasing the grain size of a material to a few nanometers leads to a drastic increase of the number of grain boundaries (or other internal interfaces) reaching typical densities up to  $10^{19}$  interfaces per cubic centimeter. The large number of atoms located in these interfaces in comparison with the crystalline part scales roughly with the reciprocal grain size and corresponds approximately to  $3 \delta/d$ ,  $\delta$  being the width of the interface, typically 0.8–1.2 nm.<sup>[5]</sup> For example, for a material with a grain or domain size of 5 nm, about 50% of the overall atoms deviate from ideal lattice site positions and become influenced by the grain boundaries. At the same time, the energy (and other properties) of the material is being increased in proportion to the level of atomic disorder of the material, i.e., in proportion to the overall grain boundary area. Nanostructured materials have therefore attracted considerable scientific interest for more than a decade because of their unusual and sometimes unexpected physical (electronic, magnetic, mechanical, optical) and chemical (catalytic) properties.<sup>[6]</sup>

Besides the synthesis of clusters, thin films, multilayers, and coatings from the gas or liquid phase, chemical methods such as sol–gel processes and electrodeposition are common methods of synthesizing

nanostructured materials. As a versatile alternative, however, mechanical methods have been developed which allow to fabricate nanostructured materials in large quantities with a broad range of chemical compositions and atomic structural arrangements.<sup>[7,8]</sup> These methods can, for example, be applied to powder samples, thin-foil sandwiches, and to the surface of bulk samples in order to produce nanostructures at surfaces as discussed below. As a result, a wide range of metals, alloys, intermetallics, ceramics, and composites can be prepared in an amorphous, nanocrystalline, or quasicrystalline state. Because of the broad range of possible atomic structures very different properties in comparison with conventional materials are obtained. For example, nanostructured particles prepared by mechanical attrition can exhibit unusually high values in hardness,<sup>[9,10]</sup> enhanced hydrogen solubility,<sup>[11]</sup> giant-magneto-resistance effects,<sup>[12]</sup> magnetic spin-glass behavior,<sup>[13]</sup> etc.

## EXPERIMENTAL

A variety of mechanical milling devices have been developed for different purposes.<sup>[14]</sup> The basic process of mechanical attrition is illustrated in Fig. 1. Powder particles with typical particle diameters of about 20–100  $\mu\text{m}$  are placed together with a number of hardened steel or WC-coated balls in a sealed container, which is shaken violently. Consequently, plastic deformation at high strain rates ( $\sim 10^3$ – $10^4 \text{ sec}^{-1}$ ) occurs within the particles and the average grain size can be reduced to a few nanometers after extended milling. The temperature rise during this process is modest and is generally estimated to be  $\leq 100$  to  $200^\circ\text{C}$ . The collision time corresponds to typically 2 msec.

High-energy milling forces can be obtained by using high frequencies and small amplitudes of vibration. Ball mills (e.g., SPEX model 8000), which are preferable for small batches of powder, i.e.,  $\approx 10 \text{ cm}^3$ , are sufficient for research purposes. As the kinetic energy of the balls is a function of their mass and velocity, dense materials (steel or tungsten carbide) are preferable to ceramic balls. During mechanical attrition contamination by

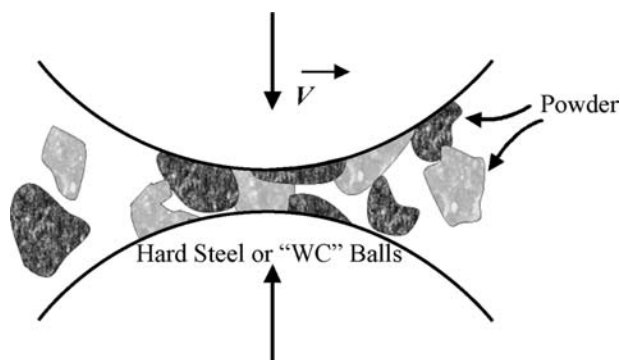


Fig. 1 Schematic sketch of the process of mechanical attrition and the corresponding shear action of metal powders.

the milling tools (Fe) and atmosphere (trace elements of  $O_2$ ,  $N_2$  in rare gas) can be problematic. By minimizing the milling time and using the purest metal powders available, a thin coating of the milling tools by the respective powder material is generally obtained, which reduces Fe-contamination levels of less than typically 1 at.%. Atmospheric contamination can be minimized or eliminated by sealing the vial with a flexible “O”-ring after the powder has been loaded in an inert gas glove box. Small experimental ball mills can also be enclosed completely in an inert gas glove box. As a consequence, oxygen and nitrogen contamination can be limited to less than 300 ppm. In this respect, the nanoscaled powder material obtained has often a higher purity than materials synthesized by alternative methods, such as chemical processes or inert gas evaporation and condensation. In addition, the structural contributions of small pores occurring during compaction of small clusters can be safely neglected.<sup>[15]</sup>

An alternate route to producing samples with high levels of both plastic deformation and interfacial area is cold rolling of layered elemental sheets.<sup>[16]</sup> Each deformation cycle consists typically of rolling the multilayered sandwich to a thickness of approximately 80  $\mu\text{m}$  and subsequent folding as shown in Fig. 2. Here the large increase in interfacial area is created internally with absolutely negligible contamination at ambient temperature.

As a further example of more technical relevance, the development of high-speed ICE trains reaching velocities of more than 300 km/hr is also a materials challenge concerning the mechanical integrity and safety required for the railway tracks (high-strength steel with composition Fe–0.8 at.% C–1.3 at.% Mn).<sup>[17]</sup> In particular, the interaction and slip between wheel and rail has to be optimized and is controlled by sophisticated electronics. On the steel surface where the local pressure typically is exceeding 1.0–1.5 GPa, solid-state transformations have been observed which are caused by friction-induced shear forces and have strong similarities with mechanical attrition of powder samples.

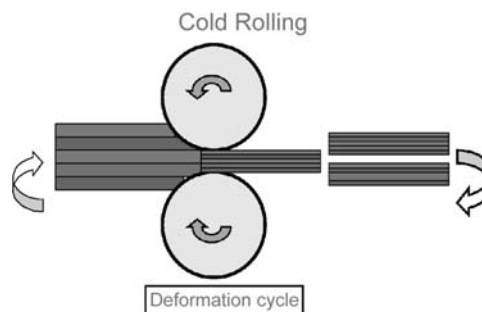


Fig. 2 Schematic sketch of the process of cold rolling of elemental foils.

## EXPERIMENTAL RESULTS

### Nanostructure Formation

During mechanical milling or attrition the metal powder particles are subjected to severe plastic deformation from collisions with the milling tools. Consequently, plastic deformation at high strain rates ( $\sim 10^3$ – $10^4 \text{ sec}^{-1}$ ) occurs within the particles and the average grain size can be reduced to a few nanometers after extended milling. As such, the metal particle is plastically deformed with most of the mechanical energy expended in the deformation process being converted into heat, but the remainder being stored in the metals, thereby raising its internal energy.<sup>[18,19]</sup>

The microstructural changes as a result of mechanical attrition can be followed by X-ray diffraction methods averaged over the sample volume. The X-ray diffraction patterns exhibit an increasing broadening of the crystalline peaks as a function of milling time. The peak broadening is caused by size as well as internal strain effects.<sup>[20,21]</sup> The average coherently diffracting domain size (grain or crystal size) and the microstrain as a function of milling time are obtained from the integral peak widths assuming Gaussian peak shapes. Based on the method of X-ray analysis applied (Scherrer formula,<sup>[22]</sup> Williamson and Hall method at full width at half maximum, or integral peak width at half maximum,<sup>[23]</sup> Warren–Averbach analysis,<sup>[24]</sup> etc.) the weighting of the grain size distribution is different and therefore the average grain size can vary by a factor of two. Further evaluation by TEM and small angle X-ray or neutron diffraction improves the accuracy of the data.

After corrections for  $K_z$  and instrumental broadening, the line broadening due to the small crystal size is constant in  $K$ -space and is given by  $\Delta K = 0.9 (2\pi/d)$ , where  $d$  is the average domain or grain diameter. The strain broadening corresponds to  $\Delta K = A \langle e^2 \rangle^{1/2} K$  with  $A$  being a constant depending on the strain distribution ( $A \approx 1$  for a random distribution of dislocations<sup>[25]</sup> and  $\langle e^2 \rangle^{1/2}$  being the rms strain). Additional defects which might contribute to the peak broadening,

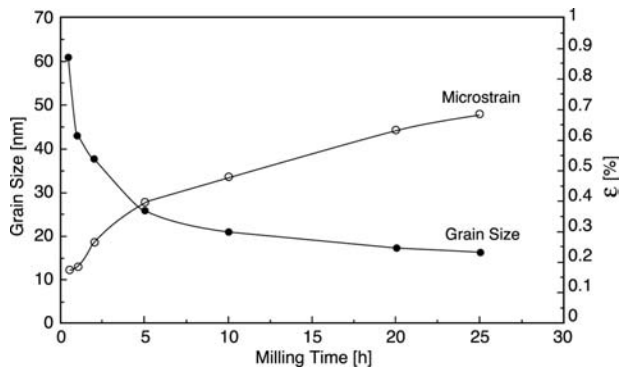


**Fig. 3** The average grain size and microstrains as a function of milling time for iron powder determined from X-ray line broadening.

such as stacking faults, can be safely neglected in all cases discussed here. However, for some metals with very small stacking fault energies, e.g., Co, the contribution of stacking faults to the peak broadening can be considerable, but is clearly the exception.

As a result, it is generally found that in the very beginning mechanical attrition leads to a fast decrease of the average grain size to 40–50 nm. Further refinement occurs slowly to about 10–15 nm after extended milling. The average atomic level strain is reaching values up to 0.7% as shown in Fig. 3 for the milling of Fe powders.

From a combination of X-ray, electron, and neutron diffraction, the elemental processes leading to the grain size refinement include three basic stages:<sup>[26]</sup>

- i. Initially, the deformation is localized in shear bands consisting of an array of dislocations with high density (up to  $10^{16}$  per  $m^2$ ). Here the dislocation cell size dimensions are basically a function of the acting shear stress  $\tau$  resulting in an average cell size dimension  $L$  of  $L = 10Gb/\tau$  with  $G$  being the shear modulus and  $b$  the Burgers vector.
- ii. At a certain strain level, these dislocations annihilate and recombine to small angle grain boundaries separating the individual grains. The subgrains formed via this route are already in the nanometer-size range.
- iii. The orientations of the single-crystalline grains with respect to their neighboring grains become completely random. Thus the microstructure becomes identical with the microstructure of samples produced by the noble gas condensation and compaction and exhibiting a largely reduced number of internal pores.

### Extended Solid Solutions and Metallic-Glass Formation

Extended solid solutions far beyond the thermodynamic equilibrium have generally been noted in the

course of mechanical milling of alloys. In addition, for phase mixtures with negative enthalpies of mixing and large (>15%) atomic size mismatch solid-state amorphization is observed. During this process long-range solute diffusion and solute partitioning are suppressed and therefore highly metastable amorphous and nanocrystalline states become accessible.

For example, during mechanical alloying of 75 at.% Zr and 25 at.% Al the formation of a supersaturated hcp ( $\alpha$ -Zr) solid solution was observed prior to the solid-state-amorphization reaction.<sup>[27]</sup> However, in all cases of binary alloys it remained unclear whether indeed a metallic glass has been formed or just a material with “X-ray amorphous structure”. More recently, a similar phase transformation sequence has been investigated in a mechanically alloyed multicomponent elemental  $Zr_{60}Al_{10}Ni_9Cu_{18}Co_3$  powder mixture with an alloy composition that is known to form a bulk metallic glass when cooled from the liquid state.<sup>[28]</sup> These multicomponent alloys are considerably more stable than binary alloys and can be heated above the glass transition temperature before crystallization sets in. The X-ray spectra at different stages of the milling process are characterized by the successive disappearance of the elemental Al, Co, Cu, and Ni peaks and a simultaneous shift of the Zr peaks to higher scattering angles, corresponding to a decrease in the lattice constant of the hcp-Zr as a result of the rapid dissolution of the smaller atoms, such as Cu, Ni, Co, and Al in the ( $\alpha$ -Zr) matrix<sup>[29]</sup> as shown in Fig. 4.

An alternate route to producing samples with high levels of both plastic deformation and interfacial area is by cold rolling of layered elemental sheets in an inert gas atmosphere with subsequent folding between each deformation cycle. In this case, the large increase in interfacial area is created internally with negligible contamination.

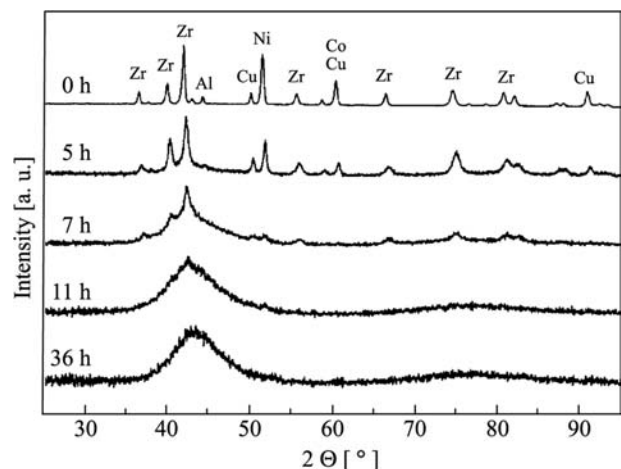


**Fig. 4** X-ray spectra for mechanically alloyed  $Zr_{60}Al_{10}Ni_9Cu_{18}Co_3$  powder samples exhibiting the transformation from the initially crystalline powder mixture to an amorphous glass-like structure.

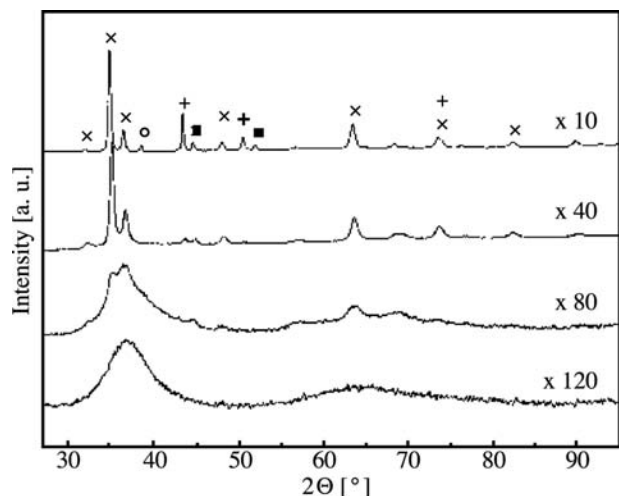


**Fig. 5** XRD profiles showing development of a metallic glass by cold rolling of elemental foils of Zr, Al, Cu, and Ni (x: Zr, o: Al, +: Cu, ◆: Ni).

In contrast to mechanical alloying of powder samples the uncertainty in the temperature during processing is removed as the sample is in firm contact with the massive rolls and deformation can be performed at a low strain rate in order to maintain ambient temperatures.

This approach has been used to examine amorphous phase formation in several binary alloys such as Zr–Ni and Cu–Er.<sup>[30,31]</sup> In the prior work on amorphous phase formation, deformation rates in excess of  $1 \text{ sec}^{-1}$  were employed and some annealing was needed to complete the amorphization reaction.<sup>[32]</sup> In contrast, fully amorphous foils of a multicomponent  $\text{Zr}_{65}\text{Al}_{7.5}\text{Cu}_{17.5}\text{Ni}_{10}$  alloy have been synthesized at ambient temperatures from a layered array of individual elemental sheets by repeated low strain rate ( $0.1 \text{ sec}^{-1}$ ). Fig. 5 exhibits the X-ray diffraction patterns from the Zr–Al–Ni–Cu foils taken after 10, 40, 80, and 120 deformation cycles. High resolution TEM analysis exhibits further evidence that a true amorphous phase has been formed when some nanocrystallites of Zr are still present after 80 cycles as shown in Fig. 6A. The sample becomes fully amorphous after 120 cycles (Fig. 6B). However, structural features and corresponding contrast variations of the order of about 2 nm (Fig. 6B) are apparent and typical for a small-scale phase separation.

### Thermal Stability

As a result of the cold work considerable energy has been stored in the powder particles. Therefore thermodynamically these materials are far removed from their equilibrium configuration and a large driving force toward equilibrium exists. The stored energy is released during heating to elevated temperatures due to recovery, relaxation processes within the grain boundaries, and grain

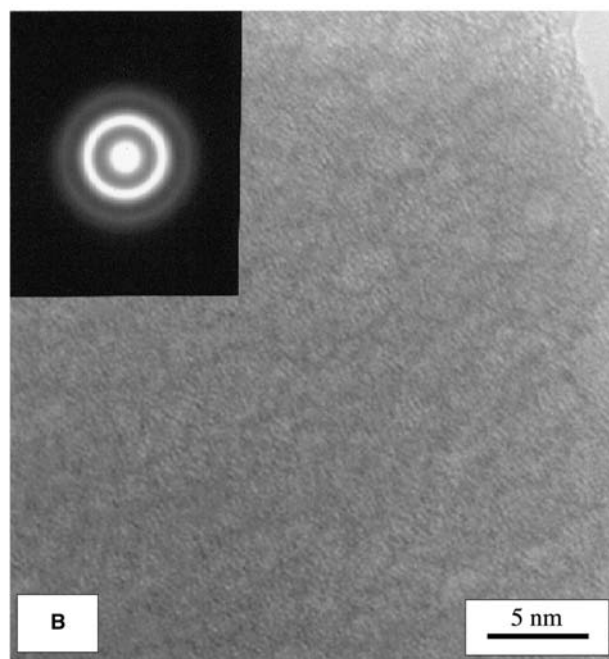
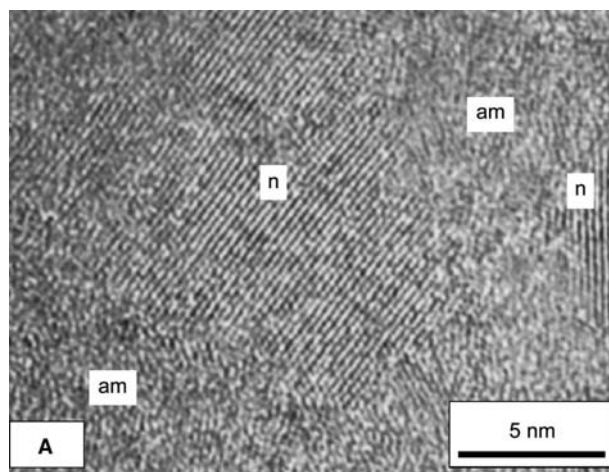


**Fig. 6** High-resolution TEM micrograph of a cold-rolled multilayered sample exhibiting a remaining nanocrystalline Zr-rich crystallite surrounded by an amorphous matrix (A) after 80 cycles of deformation and (B) a fully amorphous sample after 120 cycles.

growth. As a consequence, during annealing at elevated temperatures, relaxation and grain-growth processes will occur leading to a concomitant increase of the grain size.

This behavior has been investigated for a number of materials and presented here in detail for iron. For extended periods of milling time a fast decrease of the average grain size to nanometer dimensions is observed with a stationary average grain size  $d = 15 \text{ nm}$  and 0.7% microstrain as mentioned above. The enthalpy release during differential scanning calorimetry (DSC) heating experiments spreads over the entire temperature range of the scan as shown in Fig. 7. The very broad



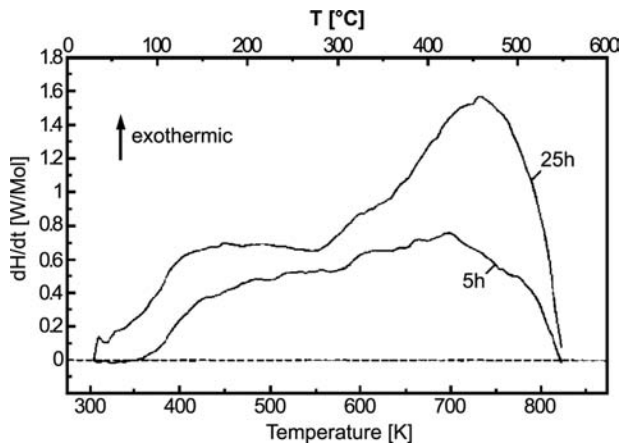


**Fig. 7** Exothermal DSC heating scan at 10 K/min of iron powder after mechanical attrition for 5 and 25 hr showing two stages of heat release (below and above ca. 550 K).

signal does not exhibit any distinct peaks but a further increase of the exothermic signal for  $T > 550$  K.

X-ray diffraction of powder samples annealed for 80 min at each temperature revealed the evolution of grain size and strain as a function of annealing temperature as shown in Fig. 8. The microstrain is decreasing rapidly below 550 K whereas the grain size remains nearly constant in this range. As such, the enthalpy release during the first exotherm in Fig. 7 is only related to relaxation and not to grain growth. Grain growth starts to become significant above about 570 K. Furthermore, it has been found that after a fast increase at early times the average grain size  $d$  changes from 15 to about 30–40 nm. The average grain size remains constant for  $t \geq 2400$  sec and reaches values of 100–200 nm at temperatures about 870 K.

As such, two regimes with and without grain growth can be clearly distinguished. As the influence of lattice point defects and lattice dislocations is negligible, the enthalpy release can be clearly assigned to the existence

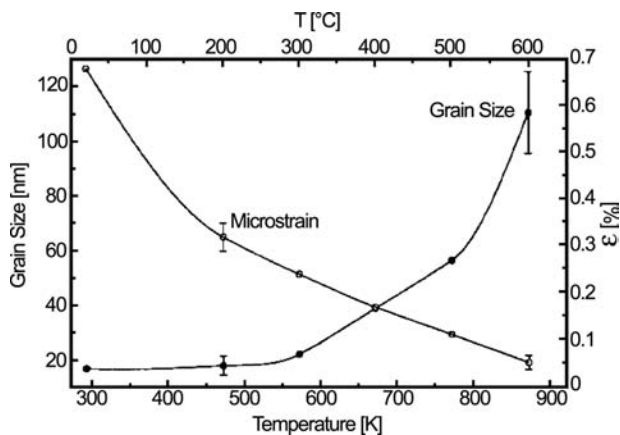


**Fig. 8** Dependence of the stationary grain size and microstrain of (initially) nanocrystalline Fe-powder milled for 25 hr on annealing as a function of temperature.

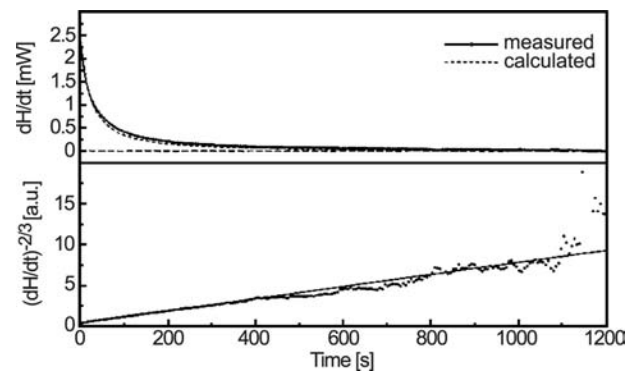


**Fig. 9** Isothermal exothermic DSC curve at 500°C of nanocrystalline iron (upper part) and plot of  $(dH/dt)^{-2/3}$  vs. time (lower part).

of grain boundaries. The reduction of the microstrains is probably caused by grain boundary relaxation and annihilation of secondary grain boundary dislocations. Based on elastic theory it is estimated that this contribution to the overall energy is less than about 10%.

Further isothermal DSC measurements allow to analyze the grain-growth processes in nanocrystalline Fe. For example, the isothermal DSC curve shown in the upper part of Fig. 9 was measured at 770 K after annealing the sample at 670 K and heating to 770 K at a rate of 50 K/min. A monotonically decreasing signal typical for grain growth is observed. Similar signals are observed at 470, 570, and 670 K and clearly differ from those measured in isothermal recrystallization processes controlled by nucleation and growth in conventional polycrystalline metals which are described by Johnson–Mehl–Avrami-type models.<sup>[33]</sup> Fig. 9 does not exhibit the expected maximum related to an incubation time for nucleation, but shows only a decrease in the signal.

Furthermore,  $(dH/dt)^{-2/3}$  should scale linearly with time when normal parabolic grain-growth behavior is assumed.<sup>[34]</sup> This assumption is well approximated for  $t < 1200$  sec as shown in the lower part of Fig. 9. The upper part of Fig. 9 includes a fit to the measured DSC signal assuming parabolic grain growth and a grain boundary energy of  $1.2 \text{ J/m}^2$  in agreement with theoretical estimates for fully relaxed large-angle grain boundaries in bcc-Fe.<sup>[35]</sup>

## DISCUSSION

### Elemental Metals

The energies finally stored during mechanical attrition largely exceed those resulting from conventional cold working of metals and alloys (cold rolling, wire drawing, extrusion, etc.). During conventional deformation, the excess energy is rarely found to exceed

1–2 kJ/mol and therefore is never more than a small fraction of the enthalpy of fusion  $\Delta H_f$ . In the case of mechanical attrition, however, the energy determined can reach values typical for crystallization enthalpies of metallic glasses corresponding to about 40%  $\Delta H_f$ .<sup>[36]</sup>

A simple estimate demonstrates that these energy levels cannot be achieved by the incorporation of defects which are found during conventional processing. In the case of pure metals, the contribution of point defects (vacancies, interstitial) can be safely neglected because of the high recovery rate at the actual processing temperature. Even taking nonequilibrium vacancies into account which can form as a consequence of dislocation annihilation up to concentrations of  $10^{-3}$ , such contributions are energetically negligible in comparison.

The maximum dislocation densities that can be reached in heavily deformed metals are less than  $10^{16} \text{ m}^{-2}$  which would correspond to an energy of less than 1 kJ/mol. Therefore it is assumed that the major energy contribution is stored in the form of grain boundaries and related strains within the nanocrystalline grains which are induced through grain boundary stresses.

Other detailed studies are obtained from cold rolling and torsion,<sup>[37]</sup> wire drawing,<sup>[38]</sup> and cyclic deformation<sup>[39]</sup> processes resulting in an asymptotic saturation of the flow stresses. This is considered as a result of the simultaneous occurrence of dislocation multiplication and annihilation leading to a saturation of the dislocation density. In particular, under cyclic deformation slip becomes highly localized in so-called persistent slip bands (shear bands). These lie parallel to the primary glide plane and are separated by regions containing the original matrix structure. These bands consist of dense walls of dislocations, largely screw dislocations having a density  $\sim 10^{13} \text{ m}^{-2}$ . The closest spacing between screw dislocations of opposite sign is  $\sim 50 \text{ nm}$ , the minimum distance before annihilation occurs. For edge dislocations which are more relevant for the deformation of fcc crystals this critical annihilation length is found to be 1.6 nm for Cu. As such, it has been concluded that the annihilation of dislocations can set a natural limit to the dislocation densities which can be achieved by plastic deformation (typically less than  $10^{13} \text{ m}^{-2}$  for screw dislocations and  $10^{16} \text{ m}^{-2}$  for edge dislocations).<sup>[7]</sup> Steady-state deformation is observed when the dislocation multiplication rate is balanced by the annihilation rate.

It is expected that the shear modulus of the grain boundary regions is lowered by about 40% when the “volume-fraction” of the grain boundaries becomes comparable to that of the crystals.<sup>[1,38,39]</sup> Localized deformation then proceeds by the dilatation of the grain-boundary layers similar to superplastic behavior<sup>[40]</sup> with the undeformed crystallites moving in a “sea” of dilated grain boundaries.

## Extended Solid Solutions

Mechanical attrition has also gained much attention as a nonequilibrium process resulting in solid-state alloying reactions beyond the equilibrium solubility limit for a broad range of alloys, intermetallics, ceramics, and composites.<sup>[41,42]</sup> In the case of mechanical attrition of a binary powder mixture, amorphous phase formation can occur by intermixing of the atomic species on an atomic scale, thus driving the crystalline solid solution outside of its stability range against “melting” resulting in solid-state amorphization.<sup>[43]</sup> This process is considered as a result of both mechanical alloying<sup>[44]</sup> and the incorporation of lattice defects into the crystal lattice.<sup>[45]</sup>

The formation of extended solid solutions during mechanical attrition of systems with negative heat of mixing can be explained in terms of milling-induced interdiffusion reactions.<sup>[46]</sup> In this regard the action of deformation (i.e., “driven system”) and especially shearing processes in causing atomic-scale mixing has been clarified recently.<sup>[47]</sup> This can be considered as an athermal process that yields a high level of homogenization of the component atoms provided that sufficient deformation is applied. In fact, Monte Carlo simulations indicate that deformation can yield a solid solution even in alloy systems with a positive enthalpy of mixing. In this case, the driven system action, characterized by a “forcing parameter” as the frequency ratio between forced and thermally activated jumps, results in a behavior that is similar to that resulting from an enhanced diffusivity characteristic of a high-temperature, high-entropy state with extended solubilities.

An alternate route to producing samples with high levels of both plastic deformation and interfacial area is by cold rolling of layered elemental sheets which are folded between each deformation cycle. In this case, the large increase in interfacial area is created internally with absolutely negligible contamination. Similarly, in contrast to mechanical attrition the uncertainty in the temperature during processing is removed as the sample is in firm contact with the massive rolls and deformation can be performed at a low strain rate to maintain ambient temperatures. This approach has been used to examine amorphous-phase formation in several binary alloys such as Zr–Ni,<sup>[48]</sup> Cu–Er,<sup>[49]</sup> and Al–Pt<sup>[50]</sup> and also for the preparation of bulk Fe/Ag nanomultilayers with giant magnetoresistance.<sup>[51]</sup>

In the prior work on amorphous-phase formation, deformation rates in excess of  $1 \text{ sec}^{-1}$  were employed and some annealing was needed to complete the amorphization reaction. Fully amorphous foils of a multicomponent  $\text{Zr}_{65}\text{Al}_{17.5}\text{Cu}_{17.5}\text{Ni}_{10}$  alloy have been synthesized at ambient temperatures from a layered array of individual elemental sheets by repeated low-strain-rate ( $0.1 \text{ sec}^{-1}$ ) cold rolling.<sup>[52]</sup> Fig. 5 shows

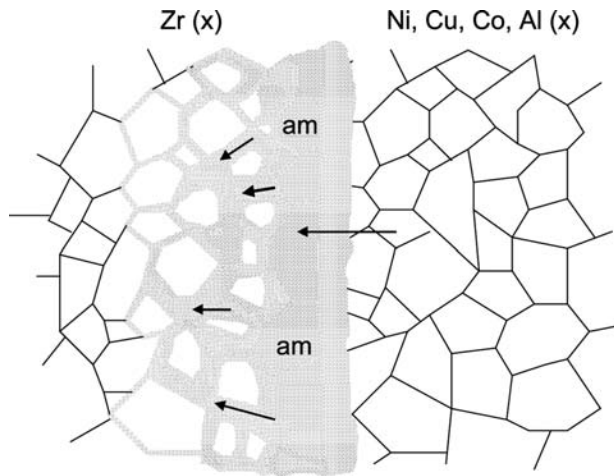


**Fig. 10** Schematics of solid-state amorphization reaction at an intermediate stage.

X-ray diffraction patterns from the Zr–Al–Ni–Cu foils taken after 10 (A), 80 (B), and 120 (C) deformation cycles. High-resolution TEM analysis exhibits further evidence that a true amorphous phase has been formed as shown in Fig. 6.

The detailed X-ray and electron diffraction experiments revealed that the crystal-to-glass transition was preceded by a rapid solution of smaller atoms such as Cu, Ni, Co, and Al in the  $\alpha$ -Zr matrix to supersaturation levels with a concomitant reduction in grain size to values below 30 nm as schematically shown in Fig. 10.

As a final product, a fully amorphous Zr–Al–Ni–Cu–Co samples were obtained with structural and thermal properties identical to a metallic glass of the same composition produced by liquid undercooling. Fig. 11 exhibits a high-resolution TEM image of a fully amorphous, metallic glass with identical composition produced from the liquid state. Whereas structural features on the scale of 2 nm have been observed in the amorphous phase formed in the solid state (Fig. 6B), such contrast variations typical for small-scale phase separation have not been observed by cooling from the liquid phase. This structurally homogeneous state is thermodynamically closer to the equilibrium, albeit metastable.

Surprisingly, thermal analysis of cold-rolled amorphous samples and amorphous powder samples prepared by mechanical alloying also reveals a distinct glass transition at  $T_g = 647$  K and about 620 K, respectively, as shown in Fig. 12 (followed by a sharp exothermic crystallization peak at 745 K which is not shown here). As such, it is worthy to note that very similar to amorphization reactions observed in mechanically alloyed Zr-based powder mixtures of similar composition the initial stage of cold rolling is characterized by the dissolution of solute into Zr along

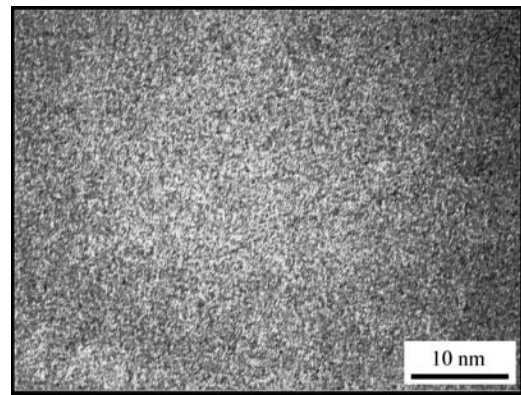


**Fig. 11** High-resolution TEM micrograph of a glassy  $Zr_{60}Al_{10}Ni_9Cu_{18}Co_3$  alloy slowly (10 K/sec) cooled from the liquid state.

with a reduction in grain size to about 30 nm before the onset of the crystal-to-glass transition. The formation of similar amorphous phases from two inherently different initial states, i.e., the solid and the liquid state, suggests that compositionally induced static disorder in a mechanically driven system can lead to the same final glassy state which is conventionally derived from freezing the dynamic disorder of a liquid out to a glass.

### Nanocrystallization of Surfaces

Many microscopic processes occurring during mechanical attrition and mechanical alloying of powder particles exhibit common features with processes relevant in tribology and wear. For example, the effects of work hardening, material transfer, and erosion during wear

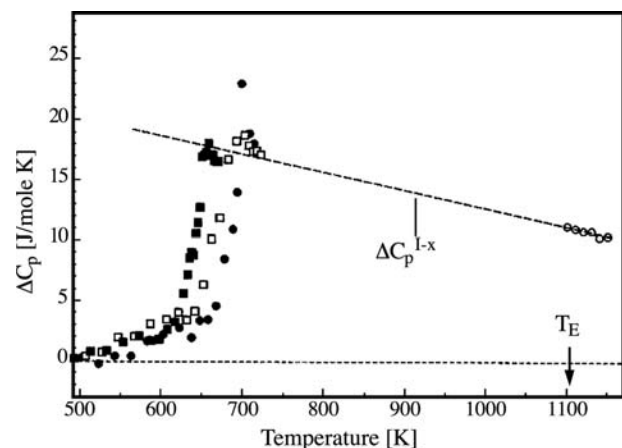


**Fig. 12** Thermal analysis exhibiting the difference in heat capacity of the sample material  $Zr_{60}Al_{10}Ni_9Cu_{18}Co_3$  in comparison with the thermodynamically stable crystalline configuration for amorphous mechanically alloyed powder, bulk metallic glass, and foil stacks (black squares: mechanically alloyed powder, open circles: liquid cooling, closed circles: cold rolling).

situations result in similar microstructures of the wear surface as observed during mechanical attrition.<sup>[53,54]</sup> In particular, during sliding wear, large plastic strains and strain gradients are created near the surface. Typical plastic shear strain rates can correspond here to several  $10^3 \text{ sec}^{-1}$ .

Close to the surface of wear scars as well as in the wear debris of Cu, nanocrystalline structures have been observed by high-resolution electron microscopy with an average grain size of 4–5 nm.<sup>[55]</sup> Within the interior of the grains no defects were observed suggesting that most of the defects are absorbed by the grain boundaries because of their proximity. However, this type of plastic deformation at high strain rates does not seem to be limited to metals and alloys,<sup>[56]</sup> but has been observed in ceramics<sup>[57]</sup> and diamond<sup>[58]</sup> as well.

During sliding wear a special tribo layer develops on the surface of a sliding component being subjected to large plastic strains. This surface layer often is called the Beilby layer which, for a long time, was thought to be amorphous because its microstructure could not be resolved with the instruments commonly used.<sup>[59]</sup> There are indeed some systems in which truly amorphous layers are produced by sliding,<sup>[60]</sup> but in most cases the subsurface layer with a thickness of several micrometers has a nanocrystalline structure.

Corresponding X-ray diffraction and TEM results indicate that the average grain size of the extremely deformed surface layer corresponds to about 20 nm,

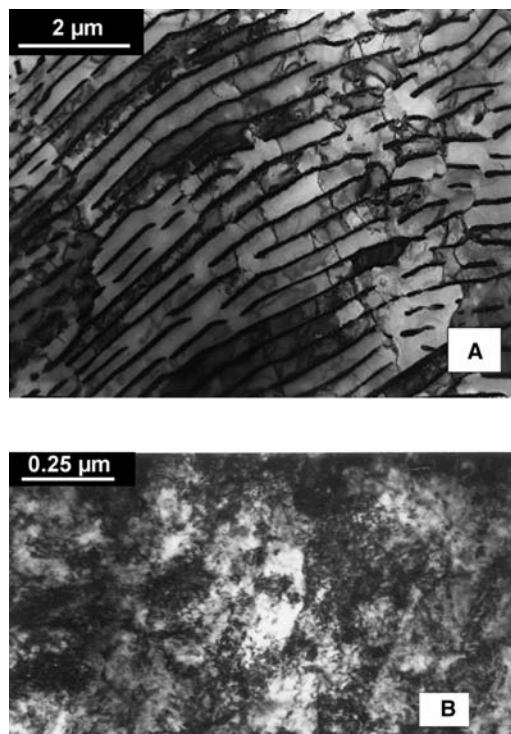


**Fig. 13** TEM bright field images (A) of the nanostructured surface layer and (B) the initial pearlitic steel sample.

whereas a gradient in grain size is observed further away from the surface reaching values up to 200 nm.<sup>[61]</sup> For example, Fig. 13 exhibits TEM micrographs and the corresponding diffraction patterns of the initial pearlitic structure (A) in comparison with the nanocrystalline layer near the surface (B).

Corresponding X-ray diffraction and TEM results indicate that the average grain size of the extremely deformed surface layer is decreased to about 20 nm, whereas a gradient in grain size is observed further away from the surface where values up to 200 nm are reached.<sup>[62,63]</sup> As a consequence, hardness measurements have been performed by nanoindentation and conventional methods as shown in Fig. 14A and B as a function of deformation and also temperature. This remarkable increase in hardness and mechanical strength of regions near the surface by a factor of 4–5 is clearly related to the fact that the average grain size is drastically decreased by the continuous deformation process as found by TEM analysis and X-ray diffraction. The apparent hysteresis seen in Fig. 14B is an indication that the microstructure is drastically changed during thermal annealing resulting in considerable grain growth and (re-) precipitation of Fe-carbides and concomitant mechanical softening.<sup>[64]</sup>

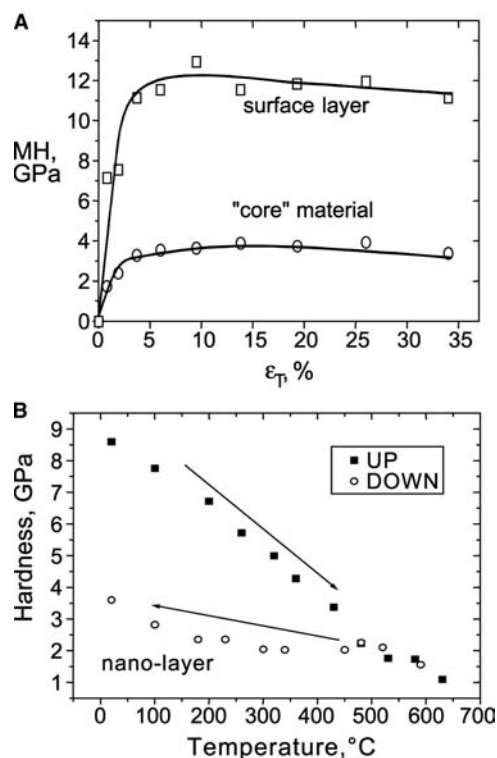


**Fig. 14** Microhardness of the nanostructured surface layer of a high-speed railway track and the pearlitic material (core) as a function of total deformation during measurements with indenters of (A) variable pyramid angle and (B) “in situ” as a function of temperature. *Source:* Courtesy of Y. Millman.

## CONCLUSION

Severe plastic deformation, which can be achieved by a number of different methods, leads to a refinement of the microstructure to a nanometer scale. The correlation of structural and thermal analysis reveals that the defect structure after long milling times is composed of a network of large angle grain boundaries. These grain boundaries are formed by reorganization of dislocations produced in the initial step of the deformation process. Because of the high density of grain boundaries and the large amounts of stored enthalpy, relaxation processes of the heavily deformed structure and grain growth start at rather low temperatures. In some cases with large chemical driving force (large negative enthalpies of mixing, "deep eutectics") the formation of a glass-like state with a distinct glass transition temperature is observed. However, this state obtained by solid-state processing exhibits a distinct underlying disordering on the scale of 2 nm not observed in glassy alloys with identical composition produced from the liquid.

Furthermore, many microscopic processes occurring during mechanical attrition and mechanical alloying of powder particles exhibit common features with processes relevant in tribology and wear. For example, the effects of work hardening, material transfer, and erosion during wear situations result in similar nanostructured layers of a wear surface as observed during mechanical attrition. Typical plastic shear strain rates can correspond here to several  $10^3$ . As such, the study of extreme plastic deformation processes not only is opening new processing routes for a variety of advanced nanostructured materials but also improves the understanding of technologically relevant deformation processes, e.g., surface wear, on a nanoscopic level which often limit the lifetime of technical components.

## ACKNOWLEDGMENTS

The financial support by the Deutsche Forschungsgemeinschaft (G.W. Leibniz program, grant Fe 313/11-1; Network "Funktionelle Nanostrukturen," project B6) and the collaboration with W.L. Johnson, J.H. Perepezko, A. Sagel, R. Wunderlich and I. Manna are gratefully acknowledged.

## REFERENCES

- Lojkowski, W.; Fecht, H.-J. The structure of intercrystalline interfaces. *Prog. Mater. Sci.* **2000**, *45*, 339.
- Fecht, H.-J. Intrinsic instability and entropy stabilization of grain boundaries. *Phys. Rev. Lett.* **1990**, *65*, 610.
- Fecht, H.-J.; Gleiter, H. A lock-in model for the atomic structure of interphase boundaries between metals and ionic crystals. *Acta Metall.* **1985**, *33* (4), 557.
- Gleiter, H. *Physical Metallurgy*; Cahn, R.W., Haasen, P., Eds.; Elsevier: Amsterdam, 1983; 650.
- Kuwano, H.; Ouyang, H.; Fultz, B. A Mössbauer spectrometry study of nanophase Cr-Fe synthesized by mechanical alloying: A measurement of grain boundary width. *Nanostruct. Mater.* **1992**, *1*, 143.
- Gleiter, H. Nanocrystalline materials. *Prog. Mater. Sci.* **1989**, *33*, 223.
- Fecht, H.-J. *Nanomaterial Synthesis, Properties and Applications*; Edelstein, A., Camarata, B., Eds.; Institute of Physics Publishing: Bristol, 1996; 89 pp.
- Fecht, H.-J. Nanostructured materials and composites prepared by solid state processing. In *Nanostructured Materials*; Koch, C.C., Ed.; Noyes Publications: New York, USA, 2002; 73 pp.
- Koch, C.C. The synthesis and structure of nanocrystalline materials produced by mechanical attrition: A review. *Nanostruct. Mater.* **1993**, *2*, 109.
- Kehrel, A.; Moelle, C.; Fecht, H.J. *Nanophase Materials*; Hadjipanayis, G.C., Siegel, R.W., Eds.; Kluwer Academic Publishers: Dordrecht, Basten, London, 1994; 287pp.
- Moelle, C.; Fecht, H.J. Thermodynamic properties and phase stability of nanocrystalline metals and hydrides. *Nanostruct. Mater.* **1993**, *3*, 93.
- Yasuna, K.; Terauchi, M.; Otsuki, A.; Ishihara, K.N.; Shingu, P.H. Bulk metallic multilayers produced by repeated press-rolling and their perpendicular magnetoresistance. *J. Appl. Phys.* **1997**, *82*, 2435.
- Zhou, G.F.; Bakker, H. Spin-glass behavior of amorphous  $\text{Co}_2\text{Ge}$  synthesized by mechanical milling. *Phys. Rev. Lett.* **1994**, *72*, 2290.
- Kuhn, W.E.; Friedmann, I.L.; Summers, W.; Szegvari, A. *ASM Metals Handbook*; Powder Metallurgy, Metals Park: Ohio, 1985; Vol. 7, 56.
- Schaefer, H.-E.; Würschum, R.; Gessmann, T.; Stöckl, G.; Scharwaechter, P.; Frank, W.; Valiev, R.Z.; Fecht, H.-J.; Moelle, C. Diffusion and free volumes in nanocrystalline Pd. *Nanostruct. Mater.* **1995**, *6*, 869.
- Johnson, W.L. Thermodynamic and kinetic aspects of the crystal to glass transformation in metallic materials. *Prog. Mater. Sci.* **1986**, *30*, 81.
- Baumann, G.; Fecht, H.-J.; Liebelt, S. Formation of white-etching layers on rail treads. *Wear* **1996**, *191*, 133.
- Fecht, H.-J.; Hellstern, E.; Fu, Z.; Johnson, W.L. Nanocrystalline metals prepared by high-energy ball milling. *Metall. Trans.* **1990**, *21A*, 2333.
- Miani, F.; Fecht, H.-J. Evaluating the mechanochemical power transfer in the mechanosynthesis of nanophase Fe-C and Fe-Cu powders. *Int. J. Refract. Met. Hard Mater.* **1999**, *17*, 133.
- Williamson, G.K.; Hall, W.H. X-ray line broadening from filed aluminium and wolfram. *Acta Metall.* **1953**, *1* (1), 22.
- Wagner, C.N.J.; Boldrick, M.S. The structure of amorphous and nanocrystalline metals and alloys. *J. Mater. Sci. Eng.* **1991**, *A133*, 26.
- Guinier, A. *X-Ray Diffraction*; W.H. Freeman and Company: San Francisco, 1963; 121 pp.
- Fecht, H.-J.; Moelle, C. Properties of nanophase materials synthesized by mechanical attrition. *Mater. Res. Soc. Symp. Proc., Nanophase Nanocomposite Mater. II* **1997**, *457*, 113.

24. Warren, B.E.; Averbach, B.L. The effect of cold-work distortion on X-ray diffraction. *J. Appl. Phys.* **1950**, *21*, 595.
25. Friedel, J. *Dislocations*; Pergamon Press: Oxford, 1964; 418.
26. Fecht, H.-J.; Han, G.; Fu, Z.; Johnson, W.L. Metastable phase formation in the Zr–Al binary system induced by mechanical alloying. *J. Appl. Phys.* **1990**, *67*, 1744.
27. Sagel, A.; Wunderlich, R.K.; Perepezko, J.H.; Fecht, H.-J. Glass formation in a multicomponent Zr-based alloy by mechanical attrition and liquid undercooling. *Appl. Phys. Lett.* **1997**, *70*, 580.
28. Sagel, A.; Wanderka, N.; Wunderlich, R.K.; Schubert-Bischoff, N.; Fecht, H.-J. Early stages of solid-state amorphization reaction during mechanical alloying of a multicomponent Zr-powder mixture. *Scripta Mater.* **1998**, *38*, 163.
29. Samwer, K.; Fecht, H.-J.; Johnson, W.L. *Glassy Metals III*; Topics in Applied Physics; Beck/Güntherodt, Springer Verlag: Berlin, 1994; Vol. 72, 6.
30. Atzmon, M.; Unruh, K.M.; Johnson, W.L. Formation and characterization of amorphous erbium-based alloys prepared by near-isothermal cold-rolling of elemental composites. *J. Appl. Phys.* **1985**, *58*, 3865.
31. Bourdeaux, F.; Yavari, A.R. Amorphization by solid-state reaction of crystalline aluminum and platinum multilayers prepared by cold rolling. *J. Appl. Phys.* **1990**, *67*, 2385.
32. Chen, L.C.; Spaepen, F. Analysis of calorimetric measurements of grain growth. *J. Appl. Phys.* **1991**, *69*, 679.
33. Tschöpe, A.; Birringer, R.; Gleiter, H. Calorimetric measurements of the thermal relaxation in nanocrystalline platinum. *J. Appl. Phys.* **1992**, *71*, 5391.
34. Wolf, D. Atomic structure and energy of twist boundaries in fcc-metals. *Philos. Mag.* **1990**, *A62*, 447.
35. Haessner, F.; Hemminger, W. Recrystallization of highly textured materials. *Z. Metallk.* **1978**, *69*, 553.
36. Lloyd, D.J.; Kenny, D. The stress-strain behavior of copper over a large strain range. *Scripta Metall.* **1978**, *12* (10), 903.
37. Grosskreutz, J.C.; Mughrabi, H. *Constitutive Equations in Plasticity*; Argon, A.S., Ed.; MIT Press: Cambridge, MA, 1971; 251 pp.
38. Gilman, J.J. Mechanical behavior of metallic glasses. *J. Appl. Phys.* **1975**, *46*, 1625.
39. Donovan, P.E.; Stobbs, W.M. The shear band deformation process in microcrystalline Pd<sub>80</sub>Si<sub>20</sub>. *Acta Metall.* **1983**, *31*, 1.
40. Hatherly, M.; Malin, A.S. Shear bands in deformed metals. *Scripta Metall.* **1984**, *18*, 449.
41. Schwarz, R.B.; Johnson, W.L. Solid state amorphization transformation. *J. Less-Common Met.* **1988**, *140*, 1.
42. Shingu, P.H. Mechanical alloying. *Mat. Sci. Forum* **1992**, *188-189*, 88.
43. Fecht, H.-J.; Fu, Z.; Johnson, W.L. Specific-heat anomaly during vitrification of hydrided Fe<sub>2</sub>Er single crystals. *Phys. Rev. Lett.* **1990**, *64*, 1753.
44. Fecht, H.J.; Johnson, W.L. Entropy and enthalpy catastrophe as a stability limit for crystalline material. *Nature* **1988**, *334*, 50.
45. Fecht, H.J. Defect-induced melting and solid-state amorphization. *Nature* **1992**, *356*, 133.
46. Koch, C.C. *Materials Science and Technology*; Cahn, R.W., Haasen, P., Kramer, E.J., Eds.; VCH: Weinheim, 1991; Vol. 15, 193.
47. Bellon, P.; Averback, R.S. Nonequilibrium roughening of interfaces in crystals under shear: Application to ball milling. *Phys. Rev. Lett.* **1995**, *74*, 1819.
48. Atzmon, M.; Verhoeven, J.D.; Gibson, E.D.; Johnson, W.L. Formation and growth of amorphous phases by solid-state reaction in elemental composites prepared by cold working. *Appl. Phys. Lett.* **1984**, *45*, 1052.
49. Atzmon, M.; Unruh, K.M.; Johnson, W.L. Formation and characterization of amorphous erbium-based alloys prepared by near-isothermal cold-rolling of elemental composites. *J. Appl. Phys.* **1985**, *58*, 3865.
50. Bourdeaux, F.; Yavari, A.R. Amorphization by solid-state reaction of crystalline aluminum and platinum multilayers prepared by cold rolling. *J. Appl. Phys.* **1990**, *67*, 2385.
51. Yasuna, K.; Terauchi, M.; Otsuki, A.; Ishihara, K.N.; Shingu, P.H. Magnetic effects in multilayered structures. *Appl. Phys. Lett.* **1997**, *82*, 2435.
52. Sagel, A.; Sieber, H.; Fecht, H.J.; Perepezko, J.H. Amorphization of Zr–Al–Ni–Cu during cold rolling of elemental foils at ambient temperatures. *Philos. Mag. Lett.* **1998**, *77*, 109.
53. Ivanisenko, Y.V.; Baumann, G.; Fecht, H.-J.; Safarov, I.M.; Korznikov, A.V.; Valiev, R.Z. Nanostructured and hardness of white layer at the surface of railroad rails. *Phys. Met. Metallogr.* **1997**, *83*, 303.
54. Fecht, H.-J. Nanostructure formation by mechanical attrition. *Nanostruct. Mater.* **1995**, *6*, 33.
55. Ganapathi, S.K.; Rigney, D.A. An HREM study of the nanocrystalline material produced by sliding wear processes. *Scripta Metall.* **1990**, *24*, 1675.
56. Doyle, F.D.; Aghan, R.L. *Metall. Trans.*, **B 1975**, *6*, 143.
57. Porat, R.; Berger, S.; Rosen, A. Sintering behaviour and mechanical properties of nanocrystalline WC/Co. *Mat. Sci. Forum* **1996**, *225-227*, 629.
58. Humble, P.; Hannink, R.H.-J. *Nature* **1978**, *273*, 37.
59. Beilby, G. *Aggregation and Flow of Solids*; Macmillan: London, 1921.
60. Askenazy, P. Deformation-Induced Amorphization of Cu–Ti Intermetallics. Ph.D. Thesis. California Institute of Technology, 1992.
61. Bürkle, G. Ph.D. Thesis; University of Ulm, 2003.
62. Lojkowski, W.; Djahanbakhsh, M.; Bürkle, G.; Gierlotka, S.; Zielinski, W.; Fecht, H.-J. Nanostructure formation on the surface of railway tracks. *J. Mater. Sci. Eng., A* **2001**, *303*, 197.
63. Milman, Yu.V.; Chugunova, S.I.; Goncharova, I.V.; Djahanbakhsh, M.; Bürkle, G.; Lojkowski, W.; Fecht, H.-J. The mechanical properties of the nanocrystalline layer on the surface of railway tracks. *J. Mater. Sci. Eng., A* **2001**, *303*, 209.
64. Ivanisenko, Y.; Valiev, R.Z.; Fecht, H.-J. *Scripta Mater.* **2003**, *in press*.



# Nanostructured Materials: Synthesis in Supercritical Fluids

Yuehe Lin

*Pacific Northwest National Laboratory, Richland, Washington, U.S.A.*

Xiang-Rong Ye

Chien M. Wai

*Department of Chemistry, University of Idaho, Moscow, Idaho, U.S.A.*

## INTRODUCTION

Supercritical fluid (SCF) approach is a novel and emerging technology to generate nanomaterials in small areas, high-aspect-ratio structures, complicated surfaces, and poorly wettable substrates with high uniformity, high homogeneity, and minimum environmental problems.

Through hydrogen reduction of metal- $\beta$ -diketone complexes in supercritical CO<sub>2</sub>, a rapid, convenient, and environmentally benign approach has been developed to synthesize a variety of nanostructured materials: 1) metal (Pd, Ni, and Cu) nanowires and nanorods sheathed within multiwalled carbon nanotube (MWCNT) templates; 2) nanoparticles of palladium, rhodium, and ruthenium decorated onto functionalized MWCNTs. These highly dispersed nanoparticles are expected to exhibit promising catalytic properties for a variety of chemical or electrochemical reactions; 3) Cu, Pd, or Cu-Pd nanocrystals deposited onto SiO<sub>2</sub> or SiC nanowires (NWs). Different types of nanostructures were achieved, including nanocrystal-NW, spherical aggregation-NW, shell-NW composites, and “mesoporous” metals supported by the framework of NWs.

## BACKGROUND

Supercritical fluid synthesis and processing of nanostructured materials have attracted an increased attention during the past decade.<sup>[1–6]</sup> SCFs exhibit a novel hybrid of liquid-like and gas-like properties. They have appreciable densities and can dissolve solid compounds like liquid solvents yet they have low viscosities, low surface tension, and high diffusivities like gases. As a result of their high compressibility, SCFs offer a convenient means of accessing a wide range of solvent properties without physically changing the

solvent. Because of these unusual properties, the synthesis and processing of nanostructured materials using SCFs show significant advantages over conventional processes: 1) SCFs facilitate permeation, diffusion, and penetration to small areas, high-aspect-ratio structures, complicated surfaces, and poorly wettable substrates to attain high uniformity and homogeneity, therefore being capable of fabricating nanostructured materials which are difficult to accomplish through traditional methods; 2) SCFs allow higher concentrations of starting materials than chemical vapor deposition (CVD) does and provide diffusivities higher than liquid solvents do, therefore SCF synthesis and processing could be very fast; 3) the solvent strength of a SCF can be varied by manipulation of fluid temperature and pressure, thus allowing a degree of control and rapid separation of products which is not possible using conventional solvents; and 4) some SCFs, such as supercritical CO<sub>2</sub> (scCO<sub>2</sub>), leave no solvent residues and are recyclable, thus being environmentally benign. Furthermore, unreacted materials, by-products, and contaminants in SCFs can be easily removed from the system; therefore products of high purity can be obtained. The synthesis and processing of nanostructured materials such as nanoparticles, nanowires, nanorods, nanotubes, nanocomposites, and thin solid films with nanoscale thickness have been achieved through a number of SCF physical and chemical transformations in which a SCF can act as a medium either for transporting solute species or for chemical reactions, or both. In some cases, the SCF itself can also take part in the reactions. Table 1 summarizes the typical SCF approaches to a variety of nanostructured materials.<sup>[1–6]</sup> The aim of this entry is to show how to use SCFs in the synthesis and processing of nanostructured materials templated by MWCNTs and nanowires (NWs).

**Table 1** Typical SCF approaches to nanostructured materials

	Nanoparticles, nanowires, nanorods nanotubes, nanocomposites	Thin films
Physical transformation	Rapid expansion of supercritical solutions (RESS)	Physical RESS deposition
	Supercritical-assisted nebulization and atomization	Physical deposition in SCFs
	Physical impregnation in SCFs without expansion	
	Supercritical antisolvent precipitation	
	Supercritical drying processes	
	Size-selective supercritical dispersion and dissolution	
	Physical deposition processes in SCFs	
Chemical transformation	RESS into liquid solvents	SCF transport and chemical deposition
	Hydrothermal reactions	SCF transport chemical vapor deposition
	Water-in-SCF microemulsion reactions	SCF immersion deposition
	Arrested precipitation in SCFs	SCF chemical deposition
	SCF-liquid-solid approach	Chemical fluid deposition
		SCF Deposition of Self-Assembled Monolayers
		Electrodeposition in SCFs
	Hydrothermal leaching	

Because of their exceptional electrical and mechanical properties caused by quantum confinement effects, one-dimensional carbon nanotubes (CNTs) and NWs have stimulated a growing interest over the past decade for their application potential as interconnects and building blocks for functional nanodevices.<sup>[7–10]</sup> CNTs also have other possible uses including storage of hydrogen and other gases, membrane materials for batteries and fuel cells, anodes for Li-ion batteries, capacitors, and chemical filters.<sup>[11–13]</sup> Modification of CNTs and NWs to produce nanocomposites provides an attractive strategy to expand, improve, or alter their properties and functions as well as their promising applications.<sup>[14–25]</sup>

Because of their small size, high chemical stability, high-aspect-ratio cavities, and large surface-area-to-volume ratio, CNTs have been considered as templates for confining and directing the growth of metallic nanowires, nanorods or tubular structures, or as supports for metal nanoparticles which can be impregnated in the cavities or attached to the external walls of the CNTs.<sup>[26–36]</sup> The produced metal/CNT composites can be used as catalysts, sensors, semiconductor devices, data storage, and processing devices, contrast agents in magnetic resonance imaging, new reinforced metal-nanofiber materials, and in xerography.<sup>[26,27,35,37–41]</sup> Metal impregnation in the hollow interiors of the CNTs can be achieved in situ during

CNT growth by incorporating the metals or metal precursors along with the carbon source. Although Fe, Co, Ni, Ti, Cu, and certain lanthanide and transition-metal carbides have been successfully trapped in CNTs using this method, harsh conditions such as high temperature or arc evaporation are usually required, and impurities could be produced as encapsulated carbon clusters and soot.<sup>[42–44]</sup> Capillary drawing of low-melting metals into cavities of CNTs provides a simple approach for metal loading,<sup>[28,45]</sup> however, CNTs are not wetted by liquids with surface tensions higher than 100–200 mN m<sup>-1</sup>, thereby excluding most metals and other elements in the periodic table.<sup>[46]</sup> The most promising and flexible approach to metal loading is then to deposit metals into the cavities or onto the external walls of CNTs through a chemical reaction such as CVD or wet chemical process.<sup>[13,15,26,29–32,35,36,47–55]</sup> However, by virtue of the small inner diameter and the extremely high aspect ratio of CNTs, this approach requires high temperatures or extensive reaction times for filling metals into the inner cavities of CNTs, and, consequently, the percentage of filled CNTs often is low. The CVD procedure may suffer from the limited volatility of metal precursors and the resulting low-vapor-phase concentration and mass-transfer-limited reactions, in addition to the high temperature for the decomposition or reduction of metal precursors. In the case of wet

chemical procedures, a hindrance could be the slow process for concentrating and impregnating reactants into the cavity of CNTs. As the pristine surface of the CNTs is rather inert and poorly hydrophilic, this approach also results in unsatisfactory adhesion and coverage control of metal nanoparticles coated onto the outer walls of CNTs, and metal agglomeration into fewer larger particles as well.<sup>[53,54]</sup> For most of the catalytic applications, catalyst particles loaded on the exterior of the CNTs are preferred because they are more accessible to the reactant molecules than those encapsulated inside the internal channels. In order to obtain a specific nucleation of metals on the outer surface with good adhesion and control, functionalization of CNTs before metal deposition is required and can be accomplished by chemical treatments using a myriad of oxidants, such as HNO<sub>3</sub>, KMnO<sub>4</sub>, OsO<sub>4</sub>, HNO<sub>3</sub>/H<sub>2</sub>SO<sub>4</sub>, and RuO<sub>4</sub> to generate -COOH, -OH, and other functional groups on the external walls of CNTs.<sup>[15,31,32,36,55,56]</sup> Also, one-step or two-step sensitization-activation methods have been used for introducing catalytic nuclei (often Pd-Sn alloys or Pd nuclei) to the otherwise non-catalytic CNT surface to achieve a better metal loading through electroless deposition.<sup>[13,30]</sup> However, the known wet chemical processes usually involve tedious and time-consuming treatment of CNTs and generate aqueous wastes.

Considerable efforts have also been spent to the modification of NWs to produce hybrid nanocomposites, in which NWs were decorated with nanoparticles, or sheathed by thin films, shells, and molecular layers, and most methods for modifying are solution-based.<sup>[17-25]</sup>

Based on hydrogen reduction of metal- $\beta$ -diketone complexes in supercritical CO<sub>2</sub>, we have developed a rapid, direct, and clean approach for the modification of MWCNTs and NWs to achieve nanocomposites as follows: metal nanowires or nanorods sheathed within MWCNT templates, MWCNTs decorated with catalytic metal nanoparticles, NWs decorated with metal nanocrystals, spherical aggregations of metal nanocrystals strung up by NWs, NWs wrapped by metallic shells, and "mesoporous" metals supported by the framework of NWs.<sup>[57-59]</sup>

### HYDROGEN REDUCTION OF METAL- $\beta$ -DIKETONE COMPLEXES IN SCCO<sub>2</sub>

Hydrogen reduction of metal precursors such as metal- $\beta$ -diketone complexes in scCO<sub>2</sub> has proven to be one of the most successful approaches for synthesizing sterically stabilized metal nanocrystals.<sup>[60,61]</sup> ScCO<sub>2</sub> reactions and particle nucleation occur in the presence of organic capping ligands, which bind to the surface of the agglomerates to form monolayers and quench further growth, providing size control and nanocrystal

stabilization. Moreover, the steric stabilization of nanocrystals in scCO<sub>2</sub> varies with the tunable density and solvation power of scCO<sub>2</sub>, enabling reversible stabilization and destabilization of colloidal dispersion, which could improve many aspects of nanocrystal processing, such as size-selective separation, synthesis, and self-assembly. Robust, highly crystallized, relatively size-monodisperse, and sterically stabilized silver, iridium, and platinum nanocrystals ranging in diameter from 20 to 120 Å were synthesized in scCO<sub>2</sub> by reducing metal- $\beta$ -diketone complexes with H<sub>2</sub> in the presence of fluorinated thiol ligands.

Hydrogen reduction of metal- $\beta$ -diketone complexes in scCO<sub>2</sub> has also been demonstrated as an effective method to deposit metal films into high-aspect-ratio structures of inorganic and polymer substrates as well as into mesoporous solids.<sup>[62-67]</sup> Herein a metal- $\beta$ -diketone complex is dissolved into scCO<sub>2</sub> and a heated substrate (or mesoporous solid) is exposed to the solution. H<sub>2</sub> is then mixed into the solution and initiates a chemical reaction involving the precursor, thereby yielding metal films onto the substrate.

Likewise, hydrogen reduction of metal- $\beta$ -diketone complexes in scCO<sub>2</sub> can be applied to the modification of MWCNTs and NWs using a typical experimental set-up shown in Fig. 1.<sup>[57-59]</sup> The MWCNTs have diameters of about 20–30 nm and lengths of about 2–3  $\mu$ m. Two types of NWs, SiO<sub>2</sub>, and SiC NWs, 40 to 110 nm in diameter, several tens of micrometers in length, and randomly oriented on silicon substrates, were subjected to modification. MWCNTs, SiO<sub>2</sub>, or SiC NWs on silicon substrates were loaded in a 3.47-mL high-pressure stainless steel reactor along with a metal- $\beta$ -diketone complex. Following precursor loading, valve V<sub>1</sub> was closed while valves V<sub>2</sub>, V<sub>3</sub>, and V<sub>4</sub> were opened and H<sub>2</sub> at 3 atm was allowed to flow through the reactor for 5 min to expel the air inside. Valves V<sub>2</sub>, V<sub>3</sub>, and V<sub>4</sub> were then closed, and V<sub>1</sub> was opened to charge the H<sub>2</sub>-CO<sub>2</sub> mixer with 80 atm

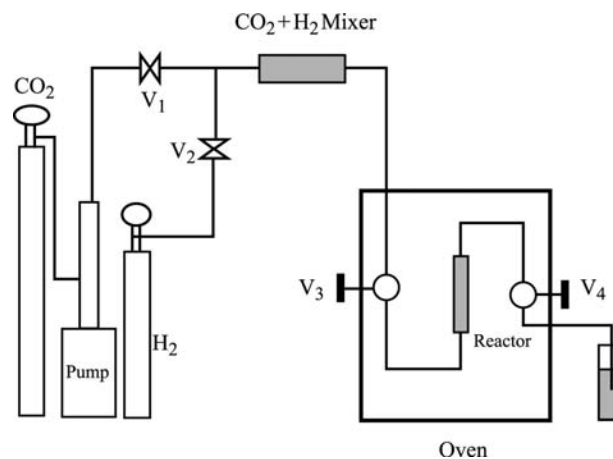
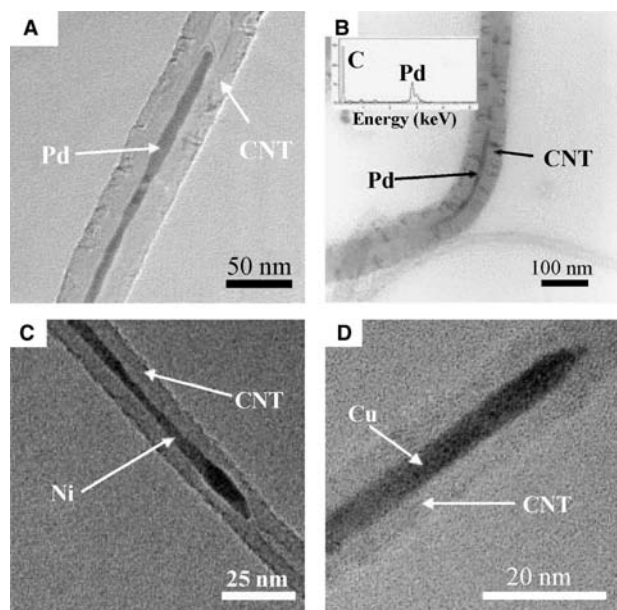


Fig. 1 Schematic drawing of the experimental apparatus.

of CO<sub>2</sub>. After mixing of H<sub>2</sub> and CO<sub>2</sub>, valve V<sub>3</sub> was opened forcing the mixture into the reactor. Valves V<sub>1</sub> and V<sub>3</sub> were then closed for the dissolution of the precursor in the CO<sub>2</sub> solution. To ensure complete dissolution, the reactor was left undisturbed for 30 min. After that, the reactor was heated gradually to the desired temperature and kept at this constant temperature for 5–10 min. After the reaction, the reactor was cooled to 35°C and vented slowly by opening V<sub>4</sub>. Neat CO<sub>2</sub> flow was used to flush the reactor twice to remove the possible unreacted species and by-products. The reactor was then opened to recover the modified MWCNTs or NWs.

## METAL NANOWIRES AND NANORODS SHEATHED WITHIN MWCNTS

Unfunctionalized MWCNTs were used as the templates for confining and directing the growth of metal nanowires and nanorods caused by the hydrogen reduction of metal- $\beta$ -diketone complexes in scCO<sub>2</sub>. The metal- $\beta$ -diketone complexes used were M(hfa)<sub>2</sub>·xH<sub>2</sub>O (M=Pd, Ni, and Cu; hfa=hexafluoroacetylacetonate), and the temperatures of hydrogen reduction were 80–150°C, 250°C, and 250°C for filling palladium, nickel, and copper into MWCNTs, respectively. Transmission electron microscopy (TEM) observation of many different views of the product revealed several forms of foreign materials inside the MWCNTs. The amount of filled MWCNT out of the total number of nanotubes is estimated at about 10%. Fig. 2A and B shows the TEM images of



**Fig. 2** TEM images of metal nanowires or nanorods impregnated in MWCNT templates. (A,B) Palladium. (C) Nickel. (D) Copper. *Source:* From Ref.<sup>[57]</sup>.

nanowires or nanorods sheathed within carbon nanotubes. The nanowires are 7–9 nm in diameter and can be more than 200 nm in full length. The diameter of nanowires corresponds to the inner diameter of the MWCNTs and varies along the wires due to the fluctuation in the MWCNT diameter. The nanowires can be straight or curved, depending upon the curvature of the CNT wrapping. Fig. 2B also shows several segments of nanowires or nanorods that have been filled into the MWCNT. A typical energy dispersive X-ray spectrum (EDS) conducted on an individual nanowire or nanorod in the TEM is shown as an inset in Fig. 2B. It confirms that the nanowires and nanorods were made purely of palladium. Similarly, nanowires and nanorods of nickel or copper can also be developed within the channels of MWCNT templates, as shown in Fig. 2C and D.

Fig. 3A shows a high-resolution transmission electron microscopy (HRTEM) image of a Pd nanorod sheathed by a MWCNT, revealing that the Pd nanorod is composed of segments of single crystals. The region marked by a dashed square in Fig. 3A was further enlarged and is shown in Fig. 3B. Fourier transform and Fourier filtered HRTEM image are shown as insets in Fig. 3B. The HRTEM image processing indicates that this segment of Pd nanorod possesses the face centered cubic (fcc) structure with a measured lattice constant of 0.38 nm, which is comparable with the reported lattice constant of 0.3887 nm.

Similar to CVD and some wet chemical processes for MWCNT decoration, nucleation of metals as nanoparticles on the outside of MWCNTs occurred unavoidably in supercritical CO<sub>2</sub> along with metal filling. As has been reported, the defects in the MWCNT structure can provide favored sites for nucleation and growth of particles. Therefore besides the pure nanowire (or nanorod)/MWCNT composites, nanowire (or nanorod)/MWCNT/nanoparticle composites are also observed. As shown in Fig. 3A, a couple of palladium nanoparticles were attached to the exterior surface of the MWCNT sheathing the nanowire. Based on our experiment, we can somehow adjust the outside or inside loading preference of a metal by functionalization of MWCNTs. Metal deposition occurs only on the external walls of functionalized MWCNTs.

## MWCNTS DECORATED WITH CATALYTIC METAL NANOPARTICLES

### Functionalization of MWCNTs

The functionalization of MWCNTs was performed by dispersing and refluxing 0.5 g of MWCNTs in 40 mL of concentrated H<sub>2</sub>SO<sub>4</sub>–HNO<sub>3</sub> mixture (1:1 v/v ratio) for 6 hr to form a dark-brown suspension. The reaction

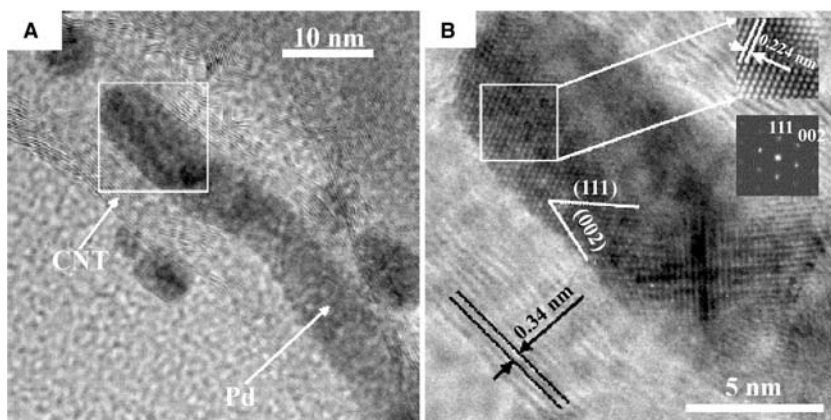


**Fig. 3** (A) HRTEM images of a Pd nanorod sheathed within a MWCNT, revealing that the Pd nanorod is crystalline with a fcc structure, (B) enlarged section of (A) showing that the imaging zone axis is [110]. *Source:* From Ref.<sup>[57]</sup>.

mixture was then diluted with distilled water to 200 mL and stirred for several hours, cooled down to room temperature, and filtered. The recovered black solid was washed several times with distilled water and finally dried at room temperature in vacuum. Previous X-ray photoelectron spectroscopy (XPS) and diffraction reflectance infrared Fourier transform (DRIFT) studies revealed that the surfaces of functionalized MWCNTs become covered with carboxylic ( $-\text{COOH}$ ), Carbonyl ( $>\text{C}=\text{O}$ ), and hydroxyl ( $-\text{COH}$ ) groups.<sup>[31,32,68]</sup> These functional groups have been demonstrated to provide favorite nucleation sites for metal nanoparticle growth and to stabilize the nanoparticles by increasing the nanoparticle–CNT interaction.

### Functionalized MWCNTs Decorated with Catalytic Palladium Nanoparticles

Modification of 10 mg of functionalized MWCNTs was carried out through hydrogen reduction of  $\text{Pd}(\text{hfa})_2 \cdot x\text{H}_2\text{O}$  at  $80^\circ\text{C}$ . A bright field TEM micrograph of the MWCNTs after  $\text{scCO}_2$  deposition using 10 mg of  $\text{Pd}(\text{hfa})_2 \cdot x\text{H}_2\text{O}$  is shown in Fig. 4A. Well-dispersed, spherical particles were anchored onto the external walls of MWCNTs, and the size range of these particles was about 5–10 nm. A selected area electron diffraction (SAED) pattern on a nanoparticle is shown as an inset in Fig. 4A, and the bright rings with occasional bright spots signify the crystalline nature

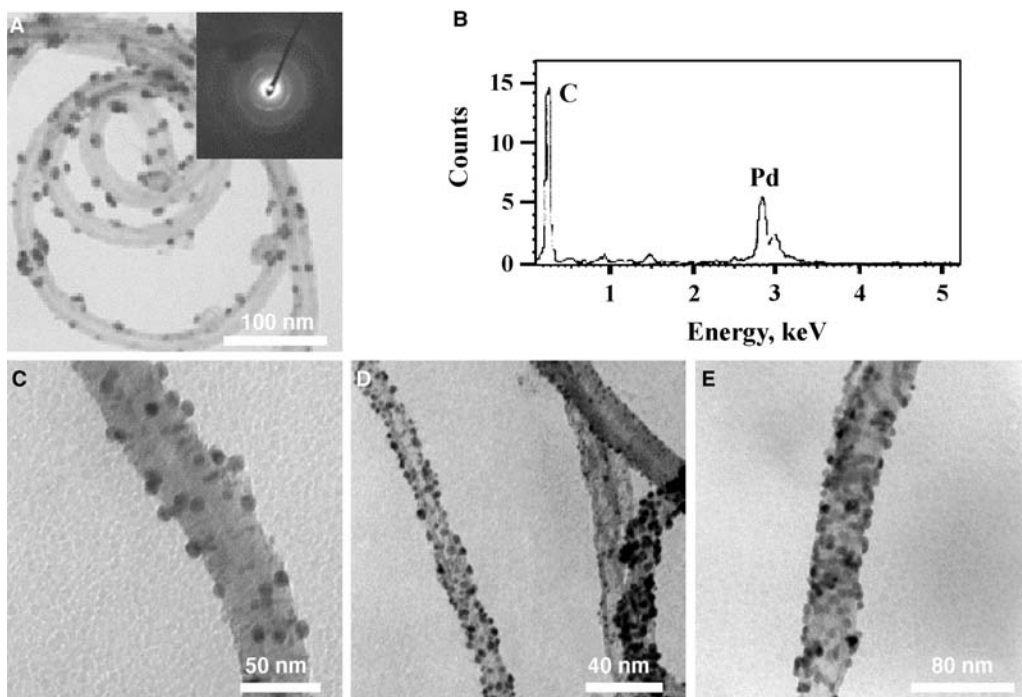


**Fig. 4** TEM images and EDX spectroscopy of MWCNTs decorated with Pd nanoparticles after hydrogen reduction of (A) 10 mg, (C) 20 mg, (D) 30 mg and (E) 50 mg  $\text{Pd}(\text{hfa})_2$ . *Source:* From Ref.<sup>[58]</sup>.



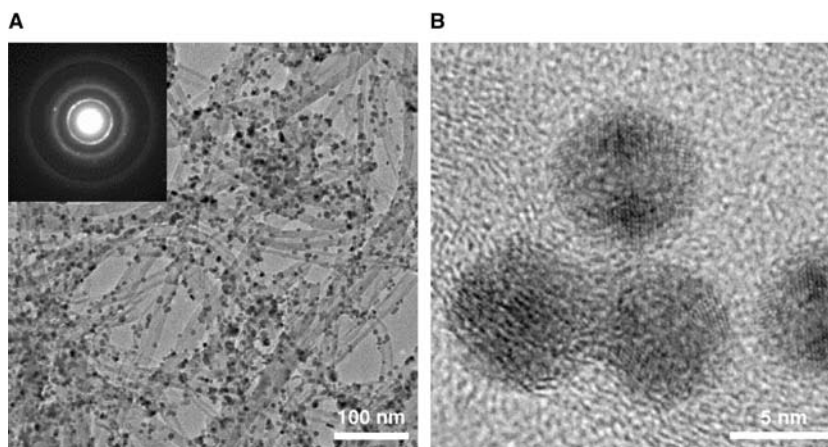


**Fig. 5** (A) TEM and (B) HRTEM images of MWCNTs decorated with Rh nanoparticles.

of the nanoparticle. EDS examination confirmed the presence of Pd in the nanoparticles decorating MWCNTs (Fig. 4B). For comparison, a commercial Pd on activated carbon catalyst sample was also examined by TEM, and the results showed numerous very large Pd particles irregularly distributed on carbon surfaces. The MWCNT appears to provide a unique template for decoration of nanometer-sized Pd metal particles on the carbon surfaces. By increasing the amount of Pd(hfa)<sub>2</sub> precursor, the loading density of Pd nanoparticles on the outer walls of CNTs can be increased (Fig. 4C to E).

#### Functionalized MWCNTs Decorated with Catalytic Rhodium Nanoparticles

Rh(acac)<sub>2</sub>·xH<sub>2</sub>O (acac=acetylacetonate) was used as the metal precursor in the hydrogen reduction reaction for loading Rh nanoparticles onto functionalized MWCNTs. The adopted temperature for the reduction was 250°C. A representative TEM image of MWCNTs decorated with Rh nanoparticles is displayed in Fig. 5A. A high and homogeneous dispersion of nanoparticles with a uniform distribution of particle sizes centered around 3–5 nm can be distinguished. The nanoparticles are comparable in size to the diameter of MWCNTs and are crystalline in nature as indicated by the SAED pattern given as an inset in Fig. 5A. The HRTEM image shown in Fig. 5B verifies that Rh nanoparticles are crystallites with visible lattice fringes.

#### Functionalized MWCNTs Decorated with Catalytic Ruthenium Nanoparticles

Decoration of Ru nanoparticles onto functionalized MWCNTs was performed by using Ru(acac)<sub>3</sub>·xH<sub>2</sub>O as the metal precursor for hydrogen reduction at 250°C. Fig. 6 presents the TEM images of highly dispersed Ru nanoparticles attached on MWCNTs, with

very tiny diameters around 1 nm and a uniform distribution throughout the full length of MWCNTs. The SAED pattern exhibits a set of diffraction rings from Ru metal. The diffraction did not appear as clear spots, but as concentric rings, each of which consists of a large number of very small spots, suggesting that the nanoparticles are composed of many fine crystallites. EDS spectrum of the nanocomposite shows emission from Ru, indicating the chemical identity of nanoparticles as Ru containing.

#### Chemical States of Metal Nanoparticles Decorated onto Functionalized MWCNTs

The chemical composition of the nanoparticles deposited onto functionalized MWCNTs was analyzed by XPS. Survey XPS spectra of the decorated MWCNTs provide results similar to those from EDS. In addition to peaks of C, O, and Si resulting from the MWCNTs and background (MWCNTs were dispersed onto silicon substrates for XPS analysis), each survey XPS spectrum shows strong peaks of Pd,

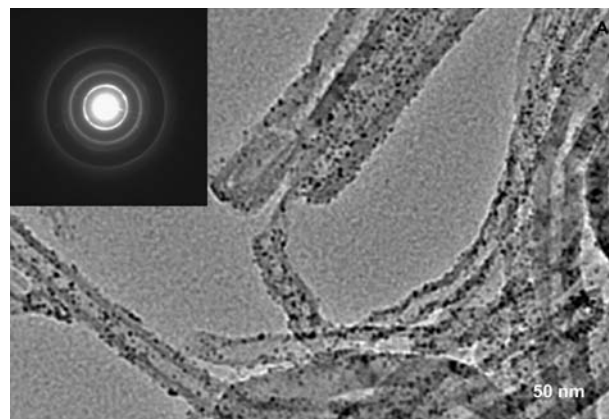


**Fig. 6** TEM image of highly dispersed Ru nanoparticles attached on MWCNTs.



Rh, or Ru. No other heterolement including fluorine was detected, implying no byproducts or unreacted precursors are present in the nanocomposites.

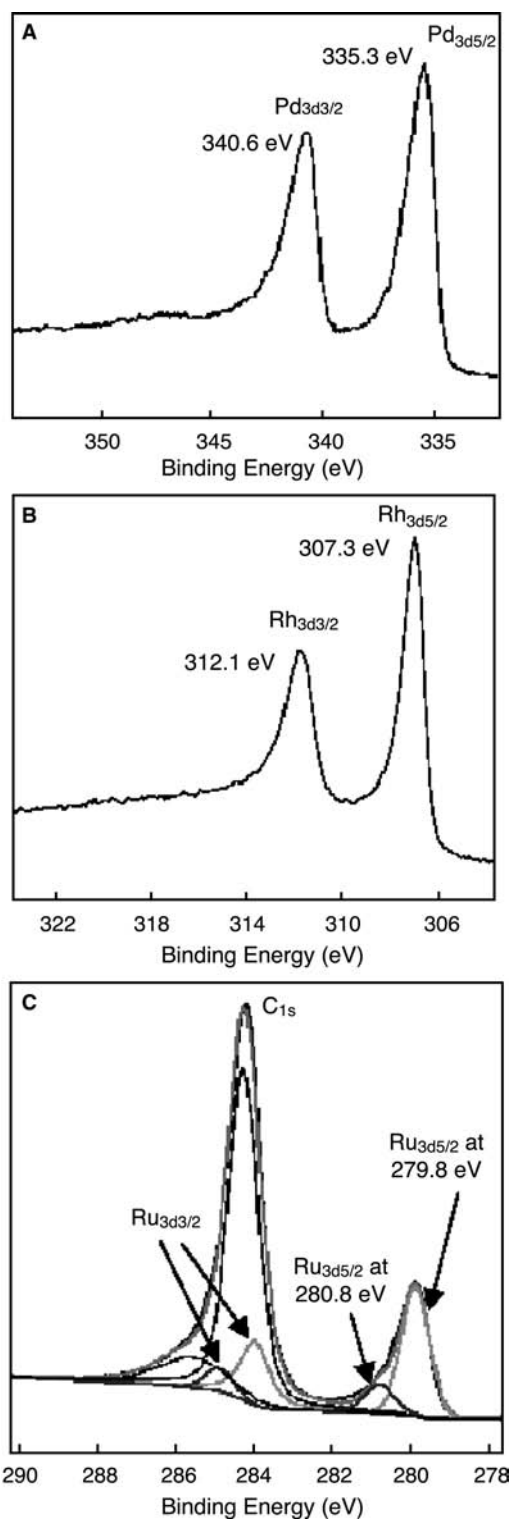
The states of MWCNT-supported palladium, rhodium, and ruthenium nanoparticles can be more clearly identified through high-resolution XPS analysis. A typical high-resolution Pd<sub>3d</sub> XPS spectrum of the Pd-decorated MWCNTs is shown in Fig. 7A. The binding energies, 335.3 eV for Pd<sub>3d5/2</sub> peak and 340.6 eV for Pd<sub>3d3/2</sub> peak, are in accordance with those reported for Pd<sup>0</sup>.<sup>[69]</sup> Furthermore, the peaks are asymmetric, having a line shape typical of metallic Pd.<sup>[69]</sup> All these imply that the palladium in the nanoparticles is zero-valent. No significant changes were observed in the binding energies or intensities of the Pd<sub>3d</sub> XPS core levels after exposing the palladium-decorated MWCNTs to air for 1 month, which demonstrates the stability of the palladium nanoparticles.

Fig. 7B displays the high-resolution Rh<sub>3d</sub> core level XPS spectrum of MWCNTs coated with Rh nanoparticles. The spectrum shows a low-energy band Rh<sub>3d5/2</sub> at 307.3 eV, and a high-energy band Rh<sub>3d3/2</sub> centering at 312.1 eV. As the Rh<sub>3d5/2</sub> and Rh<sub>3d3/2</sub> peaks for rhodium metal lie at 307.2 and 312.0 eV, respectively,<sup>[69]</sup> this indicates that Rh is also in the zero-valent state in Rh nanoparticle-MWCNT composites.

For MWCNTs decorated with ruthenium nanoparticles, the high-resolution Ru<sub>3d</sub> XPS spectrum has been obscured by the C<sub>1s</sub> spectrum. The deconvoluted spectrum shown in Fig. 7C gives broad bands that can be curve-fitted into two pairs of Ru<sub>3d</sub> peaks, therefore two chemically different Ru entities can be identified: the dominant pair with a Ru<sub>3d5/2</sub> peak at 279.8 eV corresponds well with the 3d5/2 and 3d3/2 lines of element Ru<sup>0</sup>, indicating that the majority of ruthenium loaded on MWCNTs is present as metallic Ru; the minor pair showing a Ru<sub>3d5/2</sub> peak at 280.8 eV can be assigned to Ru oxides. The presence of Ru oxides is responsible for the strong interaction between highly dispersed Ru nanoparticles and oxygen-containing groups on the functionalized MWCNTs and could also be resulted from the slight oxidation of Ru nanoparticles upon exposure of samples to ambient air.

### Promising Applications of the Metal-MWCNT Nanocomposites in Catalysis

Chemistry in ecologically benign solvents is of increasing interest in recent years. Most solvents used in organic syntheses for heterogeneous or homogeneous catalysis are coming under close scrutiny because of their toxicity and waste generation. There is a great push in industry today to replace these solvents with environmentally friendly solvents such as liquid or supercritical CO<sub>2</sub>. We have recently reported that

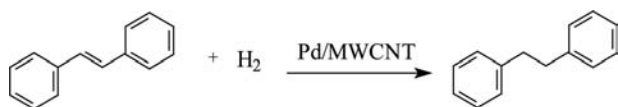


**Fig. 7** High-resolution (A) Pd<sub>3d</sub>, (B) Rh<sub>3d</sub>, and (C) Ru<sub>3d</sub> XPS spectra of MWCNTs decorated with Pd, Rh, or Ru nanoparticles.

palladium nanoparticles dispersed by a water-in-CO<sub>2</sub> microemulsion are very effective catalysts for hydrogenation of a number of olefins.<sup>[70]</sup> However,

separation of products from the surfactants and reuse of the catalyst are potential technical difficulties associated with the microemulsion technique. Developing effective heterogeneous catalysts that can be reused for chemical synthesis in liquid or supercritical CO<sub>2</sub> is currently of great interest to the chemical industry. The Pd nanoparticle–MWCNT composite may provide an effective catalyst for chemical synthesis in a green solvent that allows easy separation of products and minimizes waste solvent generation.

The catalytic capability of the Pd–MWCNT composite was tested for hydrogenation of a CO<sub>2</sub>-soluble olefin *trans*-stilbene in liquid CO<sub>2</sub>:



In this test, stilbene was dissolved in a mixture of 5 atm H<sub>2</sub> and 100 atm of CO<sub>2</sub> to make a 0.033 mol/L solution. The solution was pumped into a 6.94-mL stainless steel vessel loaded with 5 mg of the Pd–MWCNT composite (reported in Fig. 4C) at room temperature (23°C). Ultrasonication was applied to the vessel for 10 sec to disperse the catalyst. The product was trapped in CDCl<sub>3</sub> at different times and analyzed by proton NMR (Bruker, AMX 300). According to our NMR results, conversion of stilbene to 1,2-diphenylethane was about 80% and 96% after 5 and 10 min of reaction, respectively.

A number of noble metal–carbon fiber or metal porphyrin–graphite composites have been demonstrated to catalyze electrochemical reactions significantly.<sup>[13,71,72]</sup> The Pd–MWCNT nanocomposite was also tested for its electrocatalytic activity in oxygen reduction that is

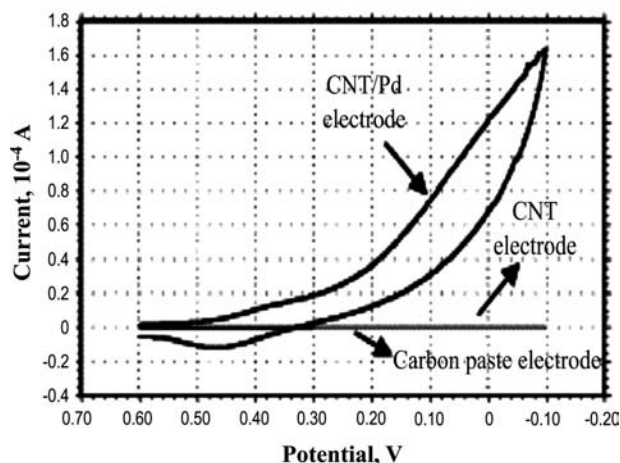


**Fig. 8** Cyclic voltammograms of oxygen reduction in 1.0 M H<sub>2</sub>SO<sub>4</sub>. Source: From Ref.<sup>[58]</sup>.

important in fuel cell applications. For comparison, graphite powder, MWCNTs, and Pd–MWCNT (Fig. 4C) were mixed individually with mineral oil to make three different carbon paste working electrodes. Cyclic voltammetry measurements were conducted at room temperature in a three-compartment electrochemical cell. The electrolyte was 1.0 M H<sub>2</sub>SO<sub>4</sub> saturated with oxygen. The potential was cycled between +0.60 and -0.10 V at 40 mV/sec. As shown in Fig. 8, essentially no O<sub>2</sub> reduction was observed over the potential window for the carbon paste electrodes of bare MWCNT and graphite powder. In contrast, for the Pd–MWCNT electrode, a very large O<sub>2</sub> reduction wave was observed at potentials characteristic for Pd electrocatalysis. The enhancement of the cathodic current indicates a high electrocatalytic activity of the Pd–MWCNT electrode for the reduction of oxygen.

The highly dispersed Rh and Ru nanoparticles on MWCNTs are also expected to be potential catalysts for a variety of reactions.<sup>[26,73]</sup> As a catalyst for the hydrogenation of *trans*-cinnamaldehyde and the hydroformylation of hex-1-ene in the liquid phase, Rh-supported MWCNTs were found to be very selective toward C=C double-bond hydrogenation and the production of linear and branched aldehydes, respectively.<sup>[73]</sup> However, Ru nanoparticles anchoring on MWCNTs showed an unexpected increase in selectivity (up to 92%) for cinnamyl alcohol in liquid-phase hydrogenation of cinnamaldehyde.<sup>[26]</sup>

## METAL–NW NANOCOMPOSITES

### Metal–SiO<sub>2</sub> NW Composites

Modification of SiO<sub>2</sub> NWs was performed by hydrogen reduction of Cu(hfa)<sub>2</sub>·xH<sub>2</sub>O in scCO<sub>2</sub> at 250°C and 80°C, respectively. Typical SEM images of SiO<sub>2</sub> NWs after copper deposition are shown in Fig. 9, and three types of nanostructures are clearly visible. When a lower precursor concentration (2.0 × 10<sup>-3</sup> mol/L) was used in the experiment, discrete Cu nanoparticles were found to randomly anchor to the SiO<sub>2</sub> NWs (inset of Fig. 9A). As the concentration of the precursor increased to 2.7 × 10<sup>-2</sup> mol/L, the NWs became thicker after coating, wrapped by shells of densely packed Cu nanoparticles. The average outside diameter of the wire-shell composite structures can be up to 400 nm, indicating that the shells were composed of multilayers of Cu nanoparticles. The rough surfaces of the composites suggested that the copper coating was polycrystalline. We believe that the Cu nanoparticles were nucleated in the SCF medium and then deposited onto the SiO<sub>2</sub> NW surfaces to form the coated layer. Noticeable from the SEM images is also the aggregation of the Cu nanocrystals to form larger structures, most of which were sphere-like

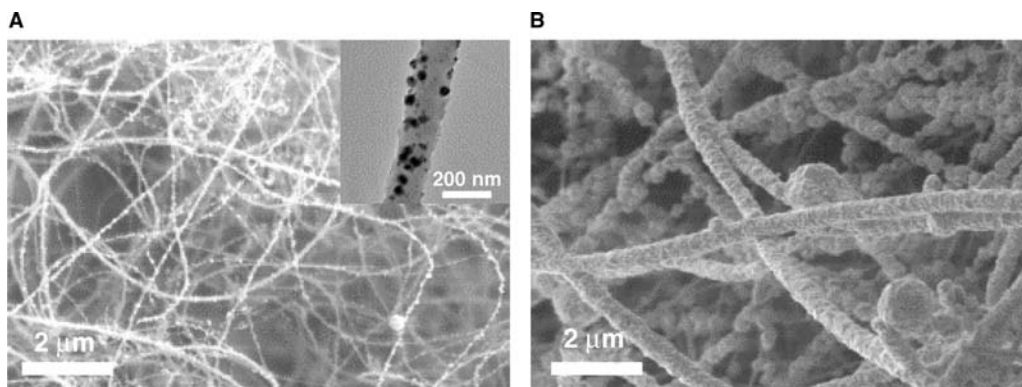


**Fig. 9** SEM images of SiO<sub>2</sub> NWs after copper deposition from supercritical CO<sub>2</sub> solutions of (A)  $2.0 \times 10^{-3}$  (B)  $2.7 \times 10^{-2}$  mol/L Cu(hfa)<sub>2</sub>. Source: From Ref.<sup>[59]</sup>.

and “strung” up by the NWs. The inset in Fig. 9A shows a TEM image of a nanoparticle-decorated NW. Cu nanoparticles with different sizes, ranging from several to 50 nm in diameter, strung onto the SiO<sub>2</sub> NWs.

### Metal Alloy–SiC NW Composites

In principle, a number of metal precursors can be used as starting materials as long as they are soluble in CO<sub>2</sub>, and metals other than palladium and copper, or metal alloys can be coated on the SiO<sub>2</sub> NWs to form nanocomposites. Furthermore, NWs suitable for the SCF fabrication process are not limited to SiO<sub>2</sub>. Such hydrogen reduction of metal precursors in supercritical CO<sub>2</sub> may provide a general and clean process to modify NWs with metallic nanoparticles. Fig. 10 describes Cu–Pd alloy nanoparticles attached to SiC NWs through hydrogen reduction of a mixture of Cu(hfa)<sub>2</sub>·xH<sub>2</sub>O (95%) and Pd(hfa)<sub>2</sub>·xH<sub>2</sub>O (5%) in scCO<sub>2</sub> at 80°C. Some aggregated balls of metals are also observed.

### CONCLUSION

SCF approach is a novel and emerging technology to generate nanomaterials in small areas, high-aspect-ratio

structures, complicated surfaces, and poorly wettable substrates with high uniformity, high homogeneity, and minimum environmental problems.

Through hydrogen reduction of metal-β-diketone complexes in supercritical CO<sub>2</sub>, a rapid, convenient, and environmentally benign approach has been developed to synthesize a variety of nanostructured materials: 1) metal (Pd, Ni, and Cu) NWs and nanorods sheathed within MWCNT templates; 2) nanoparticles of palladium, rhodium, and ruthenium decorated onto functionalized MWCNTs. These highly dispersed nanoparticles are expected to exhibit promising catalytic properties for a variety of chemical or electrochemical reactions; 3) Cu or Cu–Pd nanocrystals deposited onto SiO<sub>2</sub> or SiC NWs. Different types of nanostructures were achieved, including nanocrystal-NW, spherical aggregation-NW, shell-NW composites, and “mesoporous” metals supported by the framework of NWs.

### ACKNOWLEDGMENTS

This work was supported by a LDRD program at Pacific Northwest National Laboratory (PNNL) and the Idaho-NSF-EPSCoR and ARO-DEPSCoR

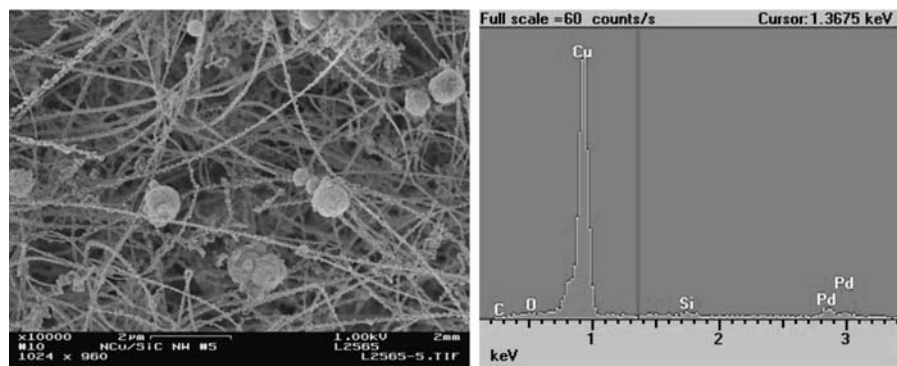


**Fig. 10** Cu–Pd–SiC nanocomposites. (A) SEM image of Cu–Pd nanocrystals supported by SiC NWs, (B) EDS of the nanocomposites.

programs. Ye also acknowledges a PNNL fellowship to work at PNNL. The work was partially performed at the Environmental Molecular Sciences Laboratory, a national scientific user facility sponsored by the U.S. DOE's Office of Biological and Environmental Research and located at PNNL. PNNL is operated for the Department of Energy by Battelle.

## REFERENCES

1. Darr, J.A.; Poliakoff, M. New directions in inorganic and metal-organic coordination chemistry in supercritical fluids. *Chem. Rev.* **1999**, *99*, 495–541.
2. Cansell, F.; Chevalier, B.; Demourgues, A.; Etourneau, J.; Even, C.; Garrabos, Y.; Pessey, V.; Petit, S.; Tressaud, A.; Weill, F. Supercritical fluid processing: a new route for materials synthesis. *J. Mater. Chem.* **1999**, *9*, 67–75.
3. Cooper, A.I. Recent developments in materials synthesis and processing using supercritical CO<sub>2</sub>. *Adv. Mater.* **2001**, *13*, 1111–1114.
4. Cooper, A.I. Materials HIPE-creating nanostructures using SCFs. *Mater. World* **2002**, *10* (1), 24–26.
5. Schiffrin, D.J. Capped nanoparticles as potential electronic components with nanoscale dimensions. *MRS Bull.* **2001**, *26*, 1015–1019.
6. Ye, X.R.; Wai, C.M. Making nanomaterials in supercritical fluids: a review. *J. Chem. Educ.* **2003**, *80*, 198–204.
7. Ajayan, P.M. Nanotubes from carbon. *Chem. Rev.* **1999**, *99*, 1787–1800.
8. Hu, J.; Odom, T.W.; Lieber, C.M. Chemistry and physics in one dimension: synthesis and properties of nanowires and nanotubes. *Acc. Chem. Res.* **1999**, *32*, 435.
9. Lieber, C.M. The incredible shrinking circuit. *Sci. Am.* **2001**, *285* (3), 59.
10. Cobden, D.H. Molecular electronics: nanowires begin to shine. *Nature* **2001**, *409*, 32–33.
11. Saito, S. Carbon nanotubes for next-generation electronics devices. *Science* **1997**, *278*, 77–78.
12. Baum, R.M. Nurturing nanotubes. *Chem. Eng. News.* **1997**, *75* (26), 39.
13. Liu, Z.L.; Lin, X.H.; Lee, J.Y.; Zhang, W.D.; Han, M.; Gan, L.M. Preparation and characterization of platinum-based electrocatalysts on multiwalled carbon nanotubes for proton exchange membrane fuel cells. *Langmuir* **2002**, *18*, 4054–4060.
14. Lin, Y.; Rao, A.M.; Sadanadan, B.; Kenik, E.A.; Sun, Y.P. Functionalizing multiple-walled carbon nanotubes with aminopolymers. *J. Phys. Chem., B* **2002**, *106*, 1294–1298.
15. Tsang, S.C.; Chen, Y.K.; Harris, P.J.F.; Green, M.L.H. A simple chemical method of opening and filling carbon nanotubes. *Nature* **1994**, *372*, 159–162.
16. Banerjee, S.; Wong, S.S. Synthesis and characterization of carbon nanotube-nanocrystal heterostructures. *Nano Lett.* **2002**, *2*, 195–200.
17. Osterloh, F.E.; Martino, J.S.; Hiramatsu, H.; Hewitt, D.P. Stringing up the pearls: self-assembly, optical and electronic properties of CdSe- and Au-LiMo<sub>3</sub>Se<sub>3</sub> nanoparticle-nanowire composites. *Nano Lett.* **2003**, *3*, 125–129.
18. Sun, X.H.; Sammynaiken, R.; Naftel, S.J.; Tang, Y.H.; Zhang, P.; Kim, P.S.; Sham, T.K.; Fan, X.H.; Zhang, Y.F.; Lee, C.S.; Lee, S.T.; Wong, N.B.; Hu, Y.F.; Tan, K.H. Ag nanostructures on a silicon nanowire template: preparation and X-ray absorption fine structure study at the Si K-edge and Ag L<sub>3,2</sub>-edge. *Chem. Mater.* **2002**, *14*, 2519–2526.
19. Sun, X.H.; Li, C.P.; Wong, N.B.; Lee, C.S.; Lee, S.T.; Teo, B.K. Reductive growth of nanosized ligated metal clusters on silicon nanowires. *Inorg. Chem.* **2002**, *41*, 4331–4336.
20. Wen, X.G.; Yang, S.H. Cu<sub>2</sub>S/Au core/sheath nanowires prepared by a simple redox deposition method. *Nano Lett.* **2002**, *2*, 451–454.
21. Yin, Y.D.; Lu, Y.; Sun, Y.G.; Xia, Y.N. Silver nanowires can be directly coated with amorphous silica to generate well-controlled coaxial nanocables of silver/silica. *Nano Lett.* **2002**, *2*, 427–430.
22. Kovtyukhova, N.T.; Martin, B.R.; Mbindyo, J.K.N.; Smith, P.A.; Razavi, B.; Mayer, T.S.; Mallouk, T.E. Layer-by-layer assembly of rectifying junctions in and on metal nanowires. *J. Phys. Chem., B* **2001**, *105*, 8762–8769.
23. Duan, X.F.; Huang, Y.; Lieber, C.M. Nonvolatile memory and programmable logic from molecule-gated nanowires. *Nano Lett.* **2002**, *2*, 487–490.
24. Li, C.P.; Sun, X.H.; Wong, N.B.; Lee, C.S.; Lee, S.T.; Teo, B.K. Silicon nanowires wrapped with Au film. *J. Phys. Chem., B* **2002**, *106*, 6980–6984.
25. Li, C.Z.; Sha, H.; Tao, N.J. Adsorbate effect on conductance quantization in metallic nanowires. *Phys. Rev., B* **1998**, *58*, 6775–6778.
26. Planeix, J.M.; Coustel, N.; Coq, B.; Brotons, V.; Kumbhar, P.S.; Dutartre, R.; Geneste, P.; Bernier, P.; Ajayan, P.M. Application of carbon nanotubes as supports in heterogeneous catalysis. *J. Am. Chem. Soc.* **1994**, *116*, 7935–7936.
27. Calvert, P. Strength in disunity. *Nature* **1992**, *357*, 365.
28. Ajayan, P.M.; Iijima, S. Capillarity-induced filling of carbon nanotubes. *Nature* **1993**, *361*, 333–334.
29. Li, J.; Moskovits, M.; Haslett, T.L. Nanoscale electroless metal deposition in aligned carbon nanotubes. *Chem. Mater.* **1998**, *10*, 1963–1967.
30. Ang, L.M.; Hor, T.S.A.; Xu, G.Q.; Tung, C.H.; Zhao, S.; Wang, J.L.S. Electroless plating of metals onto carbon nanotubes activated by a single-step activation method. *Chem. Mater.* **1999**, *11*, 2115–2118.
31. Yu, R.; Chen, L.; Liu, Q.; Lin, J.; Tan, K.L.; Ng, S.C.; Chan, H.S.O.; Xu, G.Q.; Hor, T.S.A. Platinum deposition on carbon nanotubes via chemical modification. *Chem. Mater.* **1998**, *10*, 718–722.
32. Ebbesen, T.W.; Hiura, H.; Bisher, M.E.; Treacy, M.M.J.; Shreeve-Keyer, J.L.; Haushalter, R.C. Decoration of carbon nanotubes. *Adv. Mater.* **1996**, *8*, 155–157.
33. Pradhan, B.K.; Toba, T.; Kyotani, T.; Tomita, A. Inclusion of crystalline iron oxide nanoparticles in uniform carbon nanotubes prepared by a template carbonization method. *Chem. Mater.* **1998**, *10*, 2510–2515.

34. Kyotani, T.; Tsai, L.; Tomita, A. Formation of platinum nanorods and nanoparticles in uniform carbon nanotubes prepared by a template carbonization method. *Chem. Commun.* **1997**, 701–702.
35. Che, G.; Lakshmi, B.B.; Martin, C.R.; Fisher, E.R. Metal-nanocluster-filled carbon nanotubes: catalytic properties and possible applications in electrochemical energy storage and production. *Langmuir* **1999**, *15*, 750–758.
36. Lordi, V.; Yao, N.; Wei, J. Method for supporting platinum on single-walled carbon nanotubes for a selective hydrogenation catalyst. *Chem. Mater.* **2001**, *13*, 733–737.
37. Freemantle, M. Filled carbon nanotubes could lead to improved catalysts and biosensors. *Chem. Eng. News* **1996**, *74* (29), 62.
38. Cook, J.; Sloan, J.; Green, M.L.H. Carbon nanotube chemistry. *Chem. Ind.* **1996**, *16*, 600–603.
39. Ebbesen, T.W. Carbon nanotubes. *Phys. Today* **1996**, *49* (6), 26–32.
40. Kong, J.; Franklin, N.R.; Zhou, C.W.; Chapline, M.G.; Peng, S.; Cho, K.J.; Dai, H.J. Nanotube molecular wires as chemical sensors. *Science* **2000**, *287*, 622–625.
41. Kong, J.; Chapline, M.G.; Dai, H.J. Functionalized carbon nanotubes for molecular hydrogen sensors. *Adv. Mater.* **2001**, *13*, 1384–1386.
42. Sen, R.; Govindaraj, A.; Rao, C.N.R. Metal-filled and hollow carbon nanotubes obtained by the decomposition of metal-containing free precursor molecules. *Chem. Mater.* **1997**, *9*, 2078–2081.
43. Guerret-Piecourt, C.; Le Bouar, Y.; Loiseau, A.; Pascard, H. Relation between metal electronic structure and morphology of metal compounds inside carbon nanotubes. *Nature* **1994**, *372*, 761–765.
44. Liu, S.W.; Zhu, J.J.; Mastai, Y.; Felner, I.; Gedanken, A. Preparation and characteristics of carbon nanotubes filled with cobalt. *Chem. Mater.* **2000**, *12*, 2205–2211.
45. Ugarte, U.; Chatelain, A.; de Heer, W.A. Nanocapillarity and chemistry in carbon nanotubes. *Science* **1996**, *274*, 1897–1899.
46. Dujardin, E.; Ebbesen, T.W.; Hiura, H.; Tanigaki, K. Capillarity and wetting of carbon nanotubes. *Science* **1994**, *265*, 1850.
47. Chu, A.; Cook, J.; Heeson, R.J.R.; Hutchison, J.L.; Green, M.L.H.; Sloan, J. Filling of carbon nanotubes with silver, gold, and gold chloride. *Chem. Mater.* **1996**, *8*, 2751–2754.
48. Matsui, K.; Pradhan, B.K.; Kyotani, T.; Tomita, A. Formation of nickel oxide nanoribbons in the cavity of carbon nanotubes. *J. Phys. Chem., B* **2001**, *105*, 5682–5688.
49. Che, G.L.; Lakshmi, B.; Fisher, E.R.; Martin, C.R. Carbon nanotubule membranes for electrochemical energy storage and production. *Nature* **1998**, *393*, 346–349.
50. Hsu, W.K.; Trasobares, S.; Terrones, H.; Terrones, M.; Grobert, N.; Zhu, Y.Q.; Li, W.Z.; Escudero, R.; Hare, J.P.; Kroto, H.W.; Walton, D.R.M. Electrolytic formation of carbon-sheathed mixed Sn–Pb nanowires. *Chem. Mater.* **1999**, *11*, 1747–1751.
51. Govindaraj, A.; Satishkumar, B.C.; Nath, M.; Rao, C.N.R. Metal nanowires and intercalated metal layers in single-walled carbon nanotube bundles. *Chem. Mater.* **2000**, *12*, 202–205.
52. Hsin, Y.L.; Hwang, K.C.; Chen, F.R.; Kai, J.J. Production and in-situ metal filling of carbon nanotubes in water. *Adv. Mater.* **2001**, *13*, 830–833.
53. Xue, B.; Chen, P.; Hong, Q.; Lin, J.; Tan, K.L. Growth of Pd, Pt, Ag and Au nanoparticles on carbon nanotubes. *J. Mater. Chem.* **2001**, *11*, 2378–2381.
54. Chen, P.; Wu, X.; Lin, J.; Tan, K.L. Synthesis of Cu nanoparticles and microsized fibers by using carbon nanotubes as a template. *J. Phys. Chem., B* **1999**, *103*, 4559–4561.
55. Lago, R.M.; Tsang, S.C.; Lu, K.L.; Chen, Y.K.; Green, M.L.H. Filling carbon nanotubes with small palladium metal crystallites: the effect of surface acid groups. *J. Chem. Soc., Chem. Commun.* **1995**, 1355–1356.
56. Hwang, K.C. Efficient cleavage of carbon graphene layers by oxidants. *J. Chem. Soc., Chem. Commun.* **1995**, 173–174.
57. Ye, X.R.; Lin, Y.; Wang, C.M.; Wai, C.M. Supercritical fluid fabrication of metal nanowires and nanorods templated by multi-walled carbon nanotubes. *Adv. Mater.* **2003**, *15*, 316–319.
58. Ye, X.R.; Lin, Y.; Wai, C.M. Decorating catalytic palladium nanoparticles on multi-walled carbon nanotubes in supercritical CO<sub>2</sub>. *Chem. Commun.* **2003**, 642–643.
59. Ye, X.R.; Zhang, H.F.; Lin, Y.; Wang, L.S.; Wai, C.M. Modification of SiO<sub>2</sub> nanowires with metallic nanocrystals from supercritical CO<sub>2</sub>. *J. Nanosci. Nanotech.* **2004**, *4*, 62–65.
60. Shah, P.S.; Husain, S.; Johnston, K.P.; Korgel, B.A. Nanocrystal arrested precipitation in supercritical carbon dioxide. *J. Phys. Chem., B* **2001**, *105*, 9433–9440.
61. Shah, P.S.; Husain, S.; Johnston, K.P.; Korgel, B.A. Role of steric stabilization on the arrested growth of silver nanocrystals in supercritical carbon dioxide. *J. Phys. Chem., B* **2002**, *106*, 12178–12185.
62. Watkins, J.J.; Blackburn, J.M.; McCarthy, T.J. Chemical fluid deposition: reactive deposition of platinum metal from carbon dioxide solution. *Chem. Mater.* **1999**, *11*, 213–215.
63. Long, D.P.; Blackburn, J.M.; Watkins, J.J. Chemical fluid deposition: a hybrid technique for low-temperature metallization. *Adv. Mater.* **2000**, *12*, 913–915.
64. Blackburn, T.M.; Long, D.P.; Watkins, J.J. Reactive deposition of conformal palladium films from supercritical carbon dioxide solution. *Chem. Mater.* **2000**, *12*, 2625–2631.
65. Blackburn, J.M.; Long, D.P.; Cabanas, A.; Watkins, J.J. Deposition of conformal copper and nickel films from supercritical carbon dioxide. *Science* **2001**, *294*, 141–145.
66. Fernandes, N.E.; Fisher, S.M.; Poshusta, J.C.; Vlachos, D.G.; Tsapatsis, M.; Watkins, J.J. Reactive deposition of metal thin films within porous supports from supercritical fluids. *Chem. Mater.* **2001**, *13*, 2023–2031.
67. Cabanas, A.; Blackburn, J.M.; Watkins, J.J. Deposition of Cu films from supercritical fluids using

- Cu(I)- $\beta$ -diketonate precursors. *Microelectron. Eng.* **2002**, *64*, 53–61.
68. Dai, L.; Griesser, H.J.; Mau, A.W.H. Surface modification by plasma etching and plasma patterning. *J. Phys. Chem., B* **1997**, *101*, 9548–9554.
69. Moulder, J.F.; Stickle, W.F.; Sobol, P.E.; Bomben, K.D. *Hand Book of X-ray Photoelectron Spectroscopy*; Chastain, J., Ed.; Perkin-Elmer: Eden Prairie, MN, 1992.
70. Ohde, H.; Wai, C.M.; Kim, H.; Kim, J.; Ohde, M. Hydrogenation of olefins in supercritical CO<sub>2</sub> catalyzed by palladium nanoparticles in a water-in-CO<sub>2</sub> microemulsion. *J. Am. Chem. Soc.* **2002**, *124*, 4540–4541.
71. Steigerwalt, E.S.; Deluga, G.A.; Lukehart, C.M. Pt–Ru/carbon fiber nanocomposites: synthesis, characterization, and performance as anode catalysts of direct methanol fuel cells. A search for exceptional performance. *J. Phys. Chem., B* **2002**, *106*, 760–766.
72. Collman, J.P.; Chng, L.L.; Tyvoll, D.A. Electrocatalytic reduction of dioxygen to water by iridium porphyrins adsorbed on edge plane graphite electrodes. *Inorg. Chem.* **1995**, *34*, 1311–1324.
73. Giordano, R.; Serp, P.; Kalck, P.; Kihn, Y.; Schreiber, J.; Marhic, C.; Duvail, J.-L. Preparation of rhodium catalysts supported on carbon nanotubes by a surface mediated organometallic reaction. *Eur. J. Inorg. Chem.* **2003**, 610–617.



# Nanostuctured Multilayers: Applications in X-Ray Optics

## Michael Störmer

*Department of Nanotechnology, Institute of Materials Research, GKSS Research Centre GmbH, Geesthacht, Schleswig-Holstein, Germany*

## Carsten Michaelsen

### Jörg Wiesmann

*Incoatec GmbH, Geesthacht, Schleswig-Holstein, Germany*

## Paulo Ricardo

*Department of Nanotechnology, Institute of Materials Research, GKSS Research Centre GmbH, Geesthacht, Schleswig-Holstein, Germany*

## Rüdiger Bormann

*Institute of Materials Research, GKSS Research Centre GmbH, Geesthacht, Schleswig-Holstein, Germany*

## INTRODUCTION

The discovery of X-rays in 1895 by W.C. Röntgen gave materials science and engineering a powerful research tool. Investigations with X-rays are non-destructive and often very fast, which explains their widespread use. There are mainly two fields of application, namely chemical analysis by means of X-ray fluorescence spectrometry (XRF) and structure determination by means of X-ray diffractometry (XRD). The first field deals with the use of multilayer mirrors for the detection of even very small amounts of an element in a specimen. In the second field, multilayer mirrors are employed to obtain structural information, e.g., on the crystal structure, the texture of materials, or phase formation. Diffractometry is also used to determine the crystal lattice spacing of a structure, to estimate the grain size in nanocrystalline materials, to observe structural transformations, to measure the internal strain in materials, or to identify new structures, e.g., in protein crystallography. X-ray investigations can be improved by using state-of-the-art X-ray optics. There are various types of X-ray optical elements, e.g., crystals, mono-/multilayer mirrors, zone plates, capillaries, or X-ray lenses. Here, multilayer mirrors will be presented as powerful X-ray optics for XRF and XRD, especially X-ray reflectometry (XRR). State-of-the-art physical vapor deposition technologies enable us to produce very precise and accurate multilayer mirrors. They consist of alternating layers of

high-Z and low-Z (heavy and light elements) materials with a double-layer thickness or period  $d$  in the nanometer range. In the field of X-ray optics, multilayer mirrors are competitive elements to improve the performance of complete X-ray optical systems by collimation, beam shaping, beam guidance, and monochromatization.

## OVERVIEW

In the electromagnetic spectrum, X-rays occupy the region between gamma and ultraviolet rays, ranging from hard X-rays via soft X-rays to extreme ultraviolet radiation (EUV). In this region the wavelength  $\lambda$  of X-rays is expressed in nanometers, e.g.,  $1 \text{ nm} = 10^{-9} \text{ m} = 10 \text{ \AA}$ .<sup>[1]</sup> To convert wavelengths into photon energy  $E$ , the relationship  $\hbar\omega\lambda = 1239.842 \text{ eV nm}$  can be applied.<sup>[2]</sup> Since the discovery of X-ray diffraction in 1912, it has been possible to investigate the structure of materials with atomic resolution.<sup>[3]</sup> The success of X-ray investigations depends on the properties of the optical system; this fact has driven forward the development of various sources, optics, and detectors. During the last 30 years, new X-ray sources such as synchrotron facilities have been built to achieve sufficient intensity and collimation. For these sources, now various X-ray optics are available, e.g., crystals, grazing-incidence mirrors, zone plates, X-ray lenses, and multilayer mirrors. The use of the state-of-the-art

X-ray optics can dramatically improve the outgoing X-ray beam,<sup>[4]</sup> and it can open up totally new methods for the investigation of materials.<sup>[5]</sup> Here, multilayer mirrors will be introduced and discussed as powerful X-ray optical elements in chemical analysis and structure determination. A multilayer consists of alternating layers of high-Z and low-Z materials with a double-layer thickness or period  $d$  in the order of nanometers (2–10 nm). In XRF, multilayer mirrors<sup>[6]</sup> have been used as analyzer crystals to measure the elemental composition of a material, especially to detect light elements by means of wavelength-dispersive XRF.<sup>[7]</sup> They work as a filter for a distinct emission line of the stimulated fluorescence radiation of a specimen. Because of the low atomic number of light elements, the fluorescence yield is poor.<sup>[8]</sup> Some improvements are still possible because of advanced deposition techniques, which make more exotic materials available as thin films. Furthermore, not only the peak reflectivity but also the background suppression originating from the matrix elements plays an important role in reducing the measuring time. Their optimization leads to an improved lower limit of detection (LLD). In this section, improvements for the detection of boron, carbon, and aluminum will be presented and discussed. In XRD, laterally graded multilayers on figured substrates for beam conditioning were introduced by Göbel and Schuster.<sup>[9–12]</sup> The layer thickness gradient fulfills Bragg's law for the X-ray wavelength of interest across the whole mirror length. Therefore, such a graded multilayer acts both as a monochromator and as a beam shaper for X-rays. A divergent "white" beam from an X-ray source is converted into a parallel monochromatic beam by a parabolically curved, laterally graded multilayer mirror ("Göbel-Mirror"). These multilayer mirrors combine the advantages of perfect single crystals (with large incidence angle but low acceptance angle) and total-reflection mirrors (with high reflectivity but small incidence angle). The use of high-precision prefigured optical substrates has led to a new generation of curved graded multilayer mirrors that achieve peak reflectivities higher than 70% at Bragg angles between 0.5° and 3°. Therefore, multilayer mirrors have attained an important and preferential role as optical elements for X-ray laboratory equipment.

## XRF

### La/B<sub>4</sub>C Multilayer for the Detection of Boron (B-K $\alpha$ : $E = 183 \text{ eV}/\lambda = 6.775 \text{ nm}$ )

To fabricate multilayer mirrors, alternating stacks of two different materials are deposited by magnetron sputtering onto a substrate in a vacuum system at an

Ar working pressure of 0.1–0.5 Pa. The as-deposited La/B<sub>4</sub>C multilayers (Fig. 1) are of good structural quality: Each of the 50 double layers is smooth, and the double-layer thickness (approximately 10 nm) is uniform over the whole stack. The small-angle Bragg peaks (inset of Fig. 1) indicate that the layer roughness is less than 0.5 nm. At higher magnification, the interdiffusion appears to be broader at the B<sub>4</sub>C-on-La interface than at the La-on-B<sub>4</sub>C interface. These results are consistent with the XRR data, which show that the small-angle Bragg peaks are less intense than expected. This could be explained by the chemical interdiffusion at each interface. Furthermore, the electron diffraction of a small area indicates that both layers are amorphous.

Figure 2 shows a comparison of the measured reflectivities of the Mo/B<sub>4</sub>C multilayer previously used for B detection<sup>[14,15]</sup> and the newly developed La/B<sub>4</sub>C multilayer. For this comparison, s-polarized radiation with photon energies of 50–250 eV at a fixed incidence angle of 24.5° was used at a synchrotron reflectometer (Beamline G1 at HASYLAB, DESY in Hamburg).<sup>[16]</sup> Both multilayers consist of 40 pairs each, with a period of approximately 8.5 nm. Fig. 2 shows the reflectance vs. photon energy of 50–250 eV at a fixed incidence

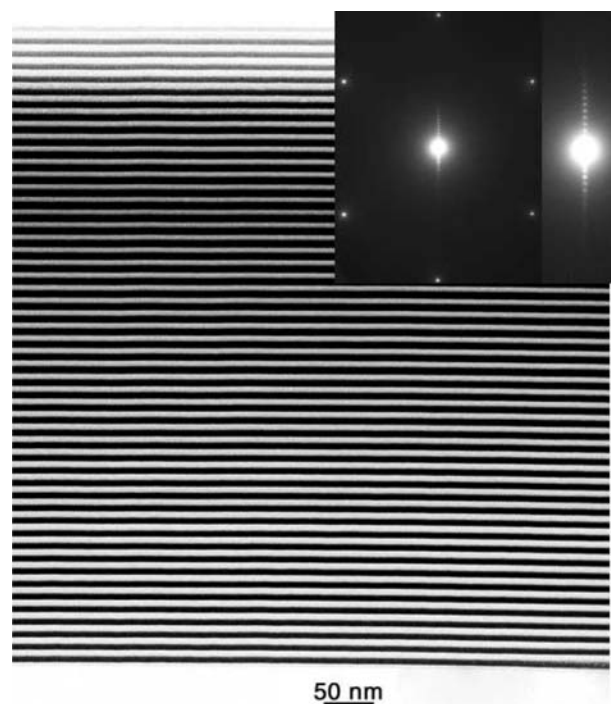


**Fig. 1** Cross-section TEM image of a La/B<sub>4</sub>C multilayer, 50 double layers are visible with a period of approximately 10 nm. La layers: dark; B<sub>4</sub>C layers: bright. Two different electron diffraction patterns with different magnification are shown in the inset. The surrounding spots of the Si substrate can be seen on the left inset. *Source:* For experimental details, see Ref.<sup>[13]</sup>.

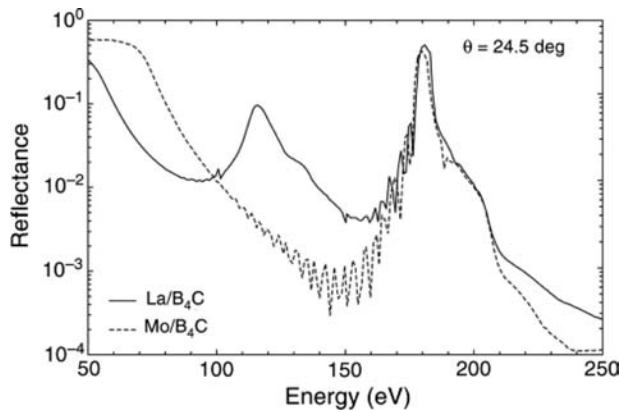


**Fig. 2** Experimental reflectivity vs. photon energy at a fixed incidence angle of 24.5°: comparison of La/B<sub>4</sub>C and Mo/B<sub>4</sub>C multilayers, using synchrotron radiation. Source: For experimental details see Ref.<sup>[13]</sup>.

angle of 24.5°. The first-order Bragg peak of both multilayers is determined at 183 eV, but the reflectivities obtainable at this energy are different. The higher peak intensity of 53% occurred for the La/B<sub>4</sub>C multilayer whereas the reflectivity for the Mo/B<sub>4</sub>C multilayer was only 38%. Moreover, it is remarkable that the La/B<sub>4</sub>C multilayer showed less reflectivity in the range below 100 eV, which is important for Si-L radiation at 90 eV. So, the improved suppression of unwanted Si fluorescence radiation in the case of the La/B<sub>4</sub>C multilayer is a clear advantage because it decreases the background in the XRF measurement of boron within a silicon matrix. This is crucial for applications in the semiconductor industry. Furthermore, La/B<sub>4</sub>C showed a superior suppression of O-K fluorescence radiation.<sup>[17]</sup> The latter experiments reveal that over the whole angular range (0°–30°) the reflectivity at 525 eV is lower for La/B<sub>4</sub>C than for Mo/B<sub>4</sub>C. The better suppression of fluorescence radiation of oxygen and silicon leads to the assumption that La/B<sub>4</sub>C should be the superior boron analyzer for samples consisting of these elements. On the other hand, Fig. 2 shows another peak at 115 eV, which is because of the lanthanum absorption edge, which in turn leads to an enhanced XRF background if the investigated sample emits radiation at this energy. This enhanced background may occur if the sample contains phosphorus (L emission line at 120 eV).

The patented<sup>[18]</sup> La/B<sub>4</sub>C multilayer mirror is particularly suited for the detection of boron. Fig. 3 illustrates its performance by means of the XRF spectra of a sample with a high boron content (B<sub>4</sub>C plate) using the La/B<sub>4</sub>C and Mo/B<sub>4</sub>C multilayers as analyzers. Fig. 4 demonstrates the superiority of this mirror with respect to samples having a low boron content. A 707-nm thick borophosphosilicate glass (BPSG) film containing 5% B and 2.95% P was used

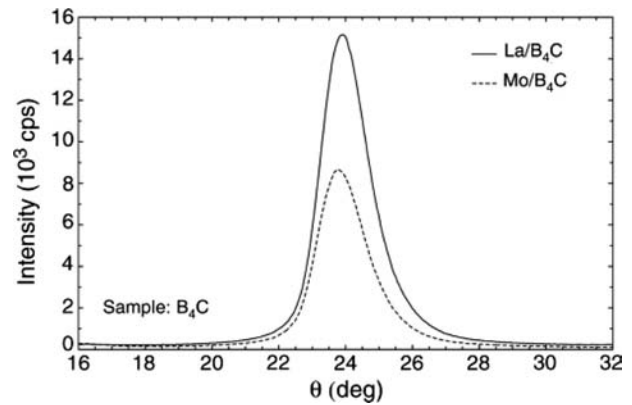


**Fig. 3** X-ray fluorescence measurements of a B<sub>4</sub>C specimen (high boron concentration) using La/B<sub>4</sub>C and Mo/B<sub>4</sub>C multilayers as analyzers. Performed by means of wavelength-dispersive XRF. The boron peak at approximately 24.5° is increased for the new multilayer. Source: From Ref.<sup>[13]</sup>.

as a sample. BPSG is important in semiconductor manufacturing; it is used in the process of wafer-flattening.<sup>[19]</sup> Consequently, the new La/B<sub>4</sub>C multilayer mirror offers a clear improvement in the detection of boron, irrespective of its concentration.

To quantify the improvement achieved in XRF applications, the LLD is determined using the following formula:  $LLD = 3 \cdot c(B) / (p - b) \cdot \sqrt{b} / 100s$ , where  $c(B)$  is the boron content, and  $p$  and  $b$  are the intensities of the peak and background, in counts per second. Table 1 shows the results for both test samples with different analyzers. The determination of the LLD reveals that there is an improvement of approximately 29% for the La/B<sub>4</sub>C multilayer as well as for the sample with a low boron content and a significant phosphorus content.

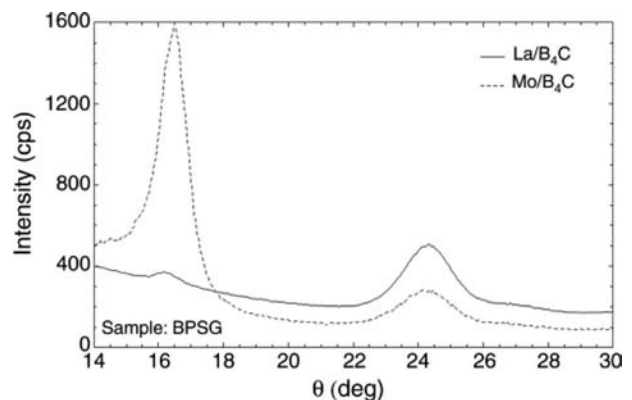


**Fig. 4** XRF measurements of a BPSG specimen (low boron concentration) using La/B<sub>4</sub>C and Mo/B<sub>4</sub>C multilayers as analyzers. Performed by means of wavelength-dispersive XRF. The boron peak at approximately 24.5° is increased for the new multilayer. Source: From Ref.<sup>[13]</sup>.

**Table 1** LLD of Mo/B<sub>4</sub>C and La/B<sub>4</sub>C multilayers using B<sub>4</sub>C and BPSG as test samples with high and low boron content, respectively

Analyzer	B <sub>4</sub> C LLD (ppm)	BPSG LLD (ppm)
Mo/B <sub>4</sub> C	344	896
La/B <sub>4</sub> C	243	634

LLD =  $3 \cdot c(B) / (p - b) \cdot \sqrt{b/100s}$ , where  $c(B)$  is the boron content, and  $p$  and  $b$  are the intensities of the peak and the background, in counts per second. The unit of the LLD is ppm.

Source: From Ref.<sup>[13]</sup>.

To summarize, the higher peak reflectivity and the better suppression of unwanted radiation lead to this improvement of boron detection. Thus, La/B<sub>4</sub>C has replaced Mo/B<sub>4</sub>C in multilayer mirrors used in X-ray optical applications below 190 eV. Further XRR investigations have shown that the La/B<sub>4</sub>C multilayers remain stable after 30 min of annealing at 150°C and their X-ray optical properties do not change. After annealing at 780°C for 30 min, the reflectivity of the multilayer stack is reduced. However, the existence of many Bragg orders shows that the multilayered structure of the whole stack is still present but slightly rougher. Moreover, transmission electron microscopy (TEM) investigations show that crystallization of the layers and grain coarsening take place. This thermal stability makes the La/B<sub>4</sub>C multilayers promising for synchrotron applications. The use of La/B<sub>4</sub>C multilayers for normal-incidence applications at X-ray wavelengths above the boron edge would be interesting for future EUV lithography, bearing in mind that the calculated normal-incidence reflectivity of an ideal La/B<sub>4</sub>C multilayer mirror would be 80% at a wavelength of 6.6 nm.

### Multilayers for the Detection of Carbon (C-K $\alpha$ : $E = 277 \text{ eV}/\lambda = 4.476 \text{ nm}$ )

For the detection of carbon at photon energy of 277 eV, various multilayer combinations have been developed and investigated. Previously, V/C and Ti/C had been considered for this energy. As shown by theoretical calculations, it is possible to improve the reflectivity at this photon energy by replacing the V or Ti layer with one of their alloys. The best results are achieved with oxides and nitrides (Table 2). This procedure promises an improved

**Table 2** Calculated reflectivity of various ideal multilayers with a  $d$ -spacing of 6 nm and a thickness ratio of  $\Gamma = 0.4$  at a photon energy of 277 eV

Multilayer	V/C	VC/C	VN/C	VO/C	Ti/C	TiC/C	TiN/C	TiO <sub>2</sub> /C
Reflectivity (%)	41.3	40.6	48.7	48.5	39.2	39.8	49.4	51.2

Source: From Ref.<sup>[20]</sup>.

absorption-to-dispersion ratio because the use of alloys reduces the density. Furthermore, the absorption edge of N and O is close, but not too close, to the C edge.

Figure 5 shows the energy scans of some of the multilayers (Table 2), which were deposited by magnetron sputtering and examined by synchrotron radiation. The peak reflectivities measured at 277 eV are 29.4% and 37.1% for the V/C and the TiO<sub>2</sub>/C multilayers, respectively. These results are lower than the calculated values for ideal multilayers. However, the expected advantage of the oxides shown is confirmed experimentally. The energy scans in Fig. 5 also reveal the differences between the two multilayers at energies of 450–525 eV. The V/C multilayer has an enhanced reflectivity at around 525 eV, which is because of the V-L edge. This reflectivity is undesired because it may lead to unwanted background radiation in samples containing oxygen (525 eV). Therefore, it can be concluded that V as a multilayer material is unfavorable if the sample contains oxygen. For the promising TiO<sub>2</sub>/C multilayer, the Ti-L edge is located at about 450 eV, which is sufficiently far away from the O-K emission line at 525 eV. Note that the difference in reflectivity between the two multilayers at 525 eV is more than one order of magnitude. Therefore, in the case of the Ti-based multilayer a lower background is expected. A second effect leading to an improved background is the reduction in density and absorption of the oxide or nitride multilayers. To check the performance of various carbon analyzers, XRF measurements with a graphite sample have been carried out and confirmed the above assumptions. The TiO<sub>2</sub>/C multilayer clearly has the best background suppression (Fig. 6). Consequently, compared to the carbon detection limit for V/C (181 ppm), the improvement for TiO<sub>2</sub>/C (128 ppm) is about 29% and that for TiN/C (146 ppm) about 19%.

### Multilayers for the Detection of Aluminum (Al-K $\alpha$ : $E = 1487 \text{ eV}/\lambda = 0.834 \text{ nm}$ )

The improvement of the detection limit of Al in samples with high Si contents is again of relevance for the semiconductor industry. Because Si (1740 eV) is a neighbor of Al in the periodic table of elements, their emission lines are not so well separated. Besides, a high Si content in the specimen causes an enhanced XRF background around the Al emission line. Usually, in

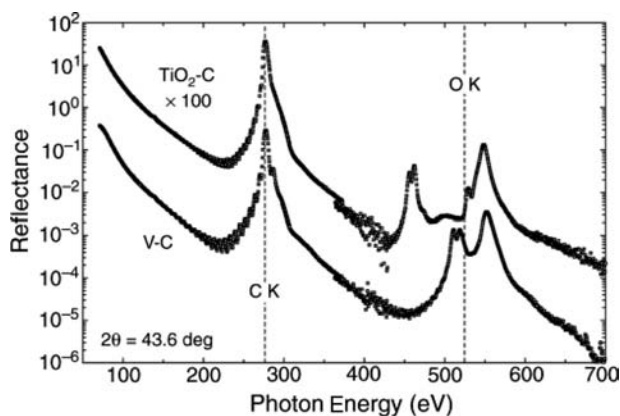


**Fig. 5** Experimental reflectivity vs. photon energy at a fixed incidence angle of  $21.5^\circ$ : comparison of  $\text{TiO}_2/\text{C}$  and  $\text{V}/\text{C}$  multilayers. *Source:* From Ref.<sup>[20]</sup>.

XRF spectrometers the  $\text{W}/\text{Si}$  multilayer is employed for this energy range. The multilayer exhibits rather broad Bragg peaks, which result in relatively poor background suppression. The first attempt to reduce the background was the replacement of the reflector  $\text{W}$  with the lighter compound  $\text{WSi}_2$ . The lower density of  $\text{WSi}_2$  ( $9.8 \text{ g/cm}^3$ ) compared to that of  $\text{W}$  ( $19.3 \text{ g/cm}^3$ ) gave rise to lower absorption and narrower Bragg peaks. The theoretical reflectivities given in Fig. 7 confirm these considerations, although the  $\text{Al}$ -peak reflectivity is reduced. In a second attempt,  $\text{W}$  was replaced with  $\text{Ta}$  ( $16.6 \text{ g/cm}^3$ ). As  $\text{Ta}$  has a suitable absorption edge close to  $1740 \text{ eV}$ , the calculated reflectivity of  $\text{Ta}/\text{Si}$  is even more reduced around the  $\text{Si}$  emission line. The  $\text{Al}$ -peak reflectivity is only reduced slightly. The XRF measurements (Fig. 8) have been carried out with a  $12\text{-nm}$   $\text{Al}$  film on a  $\text{Si}$  wafer, using  $\text{W}/\text{Si}$ ,  $\text{WSi}_2/\text{Si}$ , and  $\text{Ta}/\text{Si}$  multilayer analyzers. As expected, the reflectivities of the  $\text{WSi}_2/\text{Si}$  and  $\text{Ta}/\text{Si}$  multilayers at the  $\text{Si}$  emission line have been reduced compared

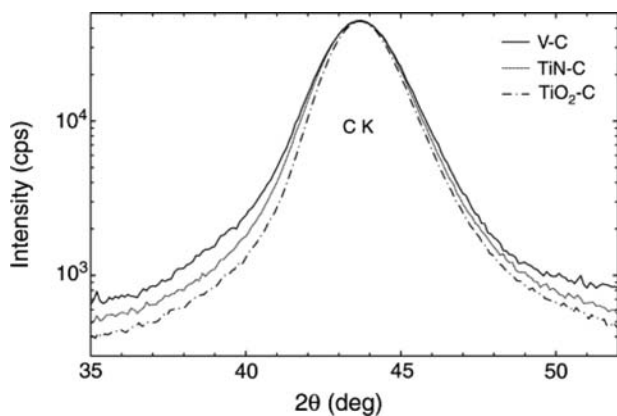


**Fig. 6** XRF measurements of a graphite sample using  $\text{V}/\text{C}$ ,  $\text{TiN}/\text{C}$ , and  $\text{TiO}_2/\text{C}$  multilayers as analyzers. *Source:* From Ref.<sup>[20]</sup>.

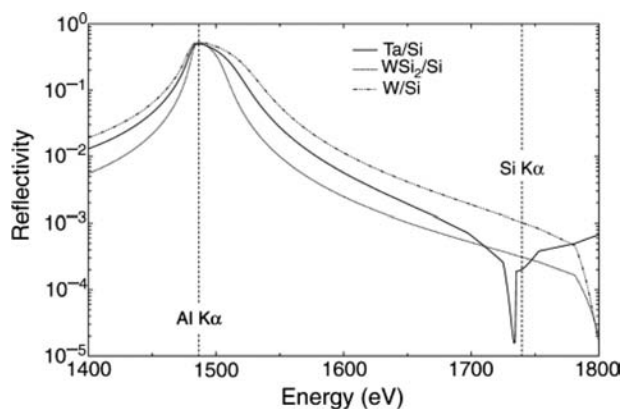


**Fig. 7** Theoretical reflectivity vs. photon energy for the three multilayers,  $\text{Ta}/\text{Si}$ ,  $\text{WSi}_2/\text{Si}$ , and  $\text{W}/\text{Si}$ , each of them with  $4\text{-nm}$  double-layer spacing, calculated using Henke's optical constants. *Source:* From Ref.<sup>[20]</sup>.

to those of  $\text{W}/\text{Si}$ , and additionally, the signal-to-background ratio around the  $\text{Al}$  line has been improved. The  $\text{Al}$  detection limits of  $\text{W}/\text{Si}_2$  and  $\text{Ta}/\text{Si}$  are improved by  $42\%$  and  $60\%$ , respectively, compared to those of  $\text{W}/\text{Si}$ .<sup>[21]</sup> These results confirm the assumption that the neighboring  $\text{Si}$  radiation contributes to the background at the  $\text{Al}$  line. Finally, for the measurement of low  $\text{Al}$  concentrations in  $\text{Si}$ -rich specimens,  $\text{Ta}/\text{Si}$  provides the best performance because of the decisive signal-to-background ratio around the  $\text{Al}$  emission line.

## XRD

In this entry, the applications of multilayer mirrors in XRD will be reviewed in a more general way. Today, multilayer mirrors are available for almost all X-ray sources. The percentage of multilayer mirrors for the

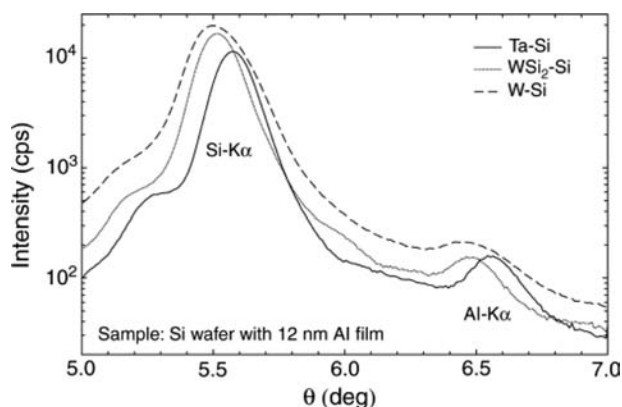


**Fig. 8** X-ray fluorescence measurements of a  $12\text{-nm}$  thick  $\text{Al}$  coating on silicon wafer, using  $\text{Ta}/\text{Si}$ ,  $\text{WSi}_2/\text{Si}$ , and  $\text{W}/\text{Si}$  multilayers as analyzers. The different peak positions are because of slightly different double-layer spacings. *Source:* From Ref.<sup>[20]</sup>.

Cu-K $\alpha$  wavelength ( $\lambda = 0.1541 \text{ nm}/E = 8048 \text{ eV}$ ) is approximately 85% of the whole market. Mo, Co, and Cr multilayer mirrors have market shares of 5%, 6%, and 4%, respectively. Thus, a lot of work has been devoted to the improvement of the peak reflectivity and spectral resolution of X-ray optics using copper radiation. However, most multilayer mirrors share a large number of important properties. First, we will report on the design, substrate specifications, and requirements for X-ray optics. Additionally, the optimization will be described, especially the selection of materials. Then, the characterization of curved graded multilayer mirrors will be presented. Finally, we will look at various applications of this state-of-the-art technology.

### Multilayer Mirrors for XRD

The design of laterally graded multilayer mirrors is described in detail by Schuster et al.<sup>[22]</sup> To summarize briefly, there are three major mirror types for the use in XRD: parabolic, elliptic, and planar. As mentioned above, a parabolic mirror collects the divergent beam from a source (located at the focus of the parabola), and then it generates parallel beams (Fig. 9). A concave elliptic mirror converts a divergent beam from a source into a convergent beam. When the source is positioned at the first focus, the outgoing beam is directed into the second focus of the ellipse. A planar mirror is the simplest optical system, because its reflecting surface does not change the inclination laterally. However, provided the multilayer period and its gradient fit perfectly to the shape of the mirror, a high peak reflectivity can be achieved.

### Substrate Specifications for Figured Multilayer Mirrors for Use in XRD

For the fabrication of X-ray mirrors various substrate materials are used, for instance single-crystalline pure silicon, fused silica, and quartz. Before deposition, it is important to have a surface with low roughness,

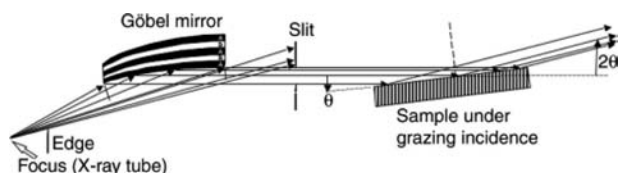


**Fig. 9** Parabolically curved and laterally graded multilayer mirror (known as Göbel mirror) attached to an X-ray tube. The divergent beam from the X-ray tube is converted into a parallel beam. The resulted beam in the sample direction is also monochromatic.

small slope errors, and a good long-term stability. There are different methods to achieve such a substrate surface and a figured X-ray optics. With the first method, the multilayers are deposited on flat and smooth substrates. These are often silicon wafers that are commercially available at a reasonable price and have an excellent surface quality. The rms roughness is below 3 Å. To reach the desired shape, the wafer with the multilayer on top is pressed onto a negative form. This curvature of the mirror is fixed with a glued backing plate. The advantage of this technique is the low risk involved. Typical slope errors are 15 arcsec rms. A second method for the fabrication of multilayers is possible provided the deposition process is stable and reproducible: Before deposition, prefigured fused quartz substrates are processed by mechanical and ion-beam polishing to achieve the desired shape. Their surface roughness is below 2.5 Å, and the typical slope error of these substrates is below 1.7 arcsec rms. This is by about a factor of 10 better than with the first method.

### XRD Multilayer Requirements

The multilayer mirrors for XRD are designed to achieve high reflectivity, good beam uniformity, low divergence, and high spectral purity.<sup>[23]</sup> Here, we will consider the requirements for parabolically figured multilayer mirrors. Such a mirror is able to convert a divergent beam from a source into a parallel beam. Therefore, the multilayer period  $d$  has to fulfil the dispersion-corrected multilayer Bragg equation:

$$d = \frac{\lambda}{2 \left( 1 - \frac{\delta}{\sin^2 \Theta} \right) \sin \Theta}$$

where  $\delta$  ( $< 10^{-4}$ ) is the mean decrement of the refractive index of the multilayer, and  $\Theta$  is the parabola-dependent Bragg angle of the multilayer;  $p$  is the parabola parameter, and  $x$  is the coordinate extending from the vertex along the parabola symmetry axis. After including the parabola equation, the angle of incidence is given by  $\Theta(x) = \text{arccot} \sqrt{2x/p}$ . Please note that there is now a clear dependence between the multilayer period  $d$  and position  $x$ , which is an important issue concerning the quality of a parallel beam X-ray optics. The requirements for elliptical and planar multilayer mirrors are given in Ref.<sup>[22]</sup>.

### Optimization of Multilayer Mirrors (Selection of Materials)

The performance of a multilayer mirror depends on the selection of the two materials (spacer with low  $Z$  and



reflector with high  $Z$ ), as discussed by Spiller.<sup>[23]</sup> Ideally, a pair with a high X-ray optical contrast  $\Delta\delta$  and small absorption coefficients is chosen. However, the measured performance is often lower than that expected from the theory; this may be because of errors in layer thickness, uncertainties in the optical constants, contamination, and interdiffusion or intermixing at the interface of the materials. Simulations are useful to find the best combination of materials. Atomic scattering factors for all elements<sup>[24]</sup> and their optical constants are available on the Internet at [http://www-cxro.lbl.gov/optical\\_constants/](http://www-cxro.lbl.gov/optical_constants/) for energies up to 30 keV and at <http://physics.nist.gov/PhysRefData/Xcom/Text/XCOM.html> for energies up to 100 GeV. With IMD (software for modeling the optical properties of multilayer films)<sup>[25]</sup> it is also possible to simulate the theoretical reflectivity of a multilayer mirror (Fig. 7). Intensities of specular reflected X-rays can be computed based on the Fresnel equations including interfacial roughness and/or diffuseness.<sup>[26–28]</sup> With these simulations, the quality of multilayers can be checked, and therefore, thin film growth can be controlled to achieve atomic sharp interfaces and high reflectivity. For instance, a promising combination should have a small transition zone and low roughness between the materials. Furthermore, TEM investigations are carried out to explain the microstructure at the interface of various magnetron sputtered multilayers.<sup>[29,30]</sup> To reduce the interdiffusion at the interfaces, barrier layers are incorporated, e.g., in Mo/Si multilayers for EUV applications.<sup>[31,32]</sup>

### Characterization of Multilayer Mirrors for XRD

Reflectivity measurements are the first step to determine double-layer spacing (or period), roughness, and density of each layer of the multilayer. In Fig. 10, a parabolic mirror designed for Cr- $K\alpha$  radiation is shown. In this energy range, absorption and dispersion are higher; so the number of periods is reduced to 70 layer pairs. The reflectivity curves are measured at three positions (or focal distances) of a graded Cr/C multilayer. The average peak reflectivity is about 74%, which is a high value for Cr- $K\alpha$  radiation, and enables many applications.

Figure 11 shows a typical variation in double-layer spacing  $d$  across a parabolically curved graded W/Si multilayer measured by XRR. The solid line gives the ideal curve with a period of 4.88 nm at 150 mm and a gradient of  $1.95 \times 10^{-8}$ . So the high accuracy and high precision are evident. The applied magnetron sputtering process is highly reproducible; therefore, it allows the fabrication of multilayers with a period within a 1% tolerance range around the desired values.

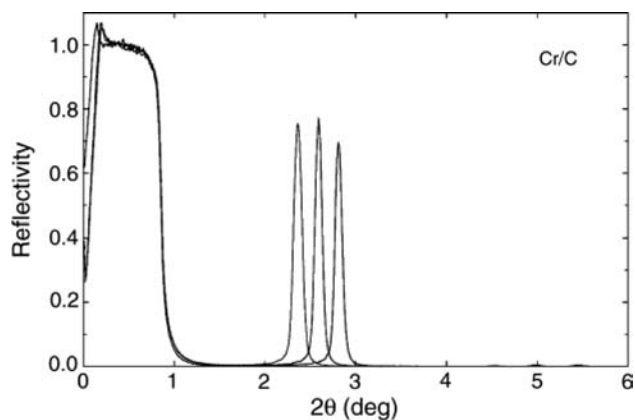


**Fig. 10** Reflectivity vs. incidence angle across a Cr/C multilayer at different focal distances,  $f = 75, 90,$  and  $105$  mm. The  $d$ -spacings are 4.88, 5.34, and 5.90 nm, measured with Cr- $K\alpha$  radiation by means of XRR. The multilayer has 70 Cr/C pairs and a thickness ratio of  $\Gamma = 0.5$ . Source: From Ref.<sup>[22]</sup>.

Please note that the difference in  $d$ -spacing over a distance of about 10 mm equals one atom.

The beam uniformity was checked by coupling the parallel beams to a channel-cut monochromator (for experimental details, see Refs.<sup>[33–35]</sup>). Because of the extremely small acceptance angle of the monochromator, the quality and also the imperfections of the mirrors are obvious. The typical width of the parallel beam after a multilayer mirror is approximately 1 mm. The intensity deviation over the beam width is less than 20% because of the small period error of the multilayer and small slope error of the curved mirror. The beam divergence can be measured with a rocking curve on the Si(004) reflection. The typical full

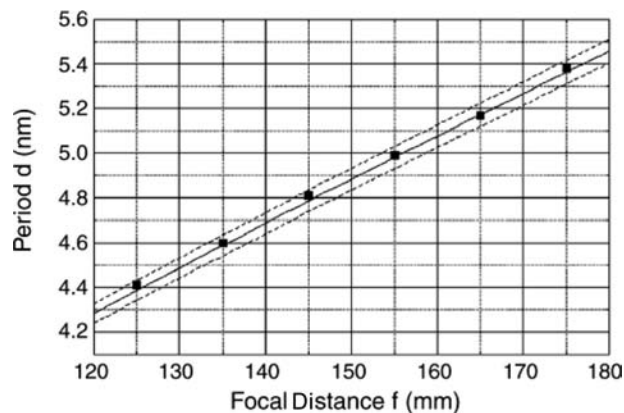


**Fig. 11** Double-layer spacing  $d$  vs. focal distance  $f$  across a parabolically curved graded W/Si multilayer measured by means of XRR (full squares). The solid line gives the ideal period based on the focal distance. To guide the eye, the two sidelines indicate a tolerance band of  $\pm 1\%$  around the ideal curve. Source: From Ref.<sup>[33]</sup>.

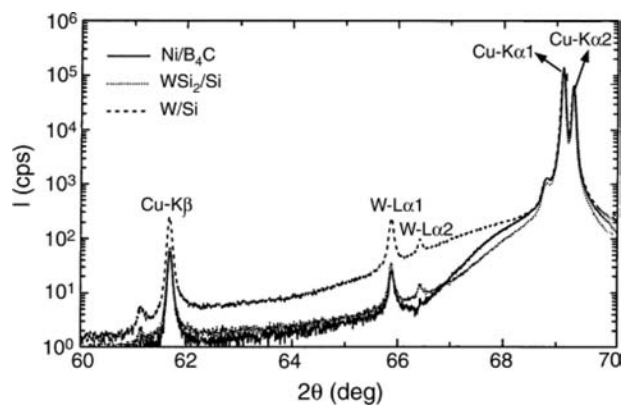


**Fig. 12** Suppression of Cu-K $\beta$  radiation: diffraction measurements around Si(004) carried out with various parabolic multilayers (Ni/B<sub>4</sub>C, WSi<sub>2</sub>/Si, and W/Si) in the incident beam path. *Source:* From Ref.<sup>[36]</sup>.

width at half maximum (FWHM) of a rocking curve is about 0.03° for WSi<sub>2</sub>/Si and Ni/B<sub>4</sub>C multilayer mirrors.

With many XRD applications, monochromatic radiation is required for the investigation of a specimen. Therefore, K $\beta$  radiation and Bremsstrahlung should be suppressed. The K $\beta$  suppression was examined by measuring a  $\theta$ -2 $\theta$  scan around the Si(004) reflection from a single-crystalline Si wafer. As shown in Fig. 12, W/Si multilayer mirrors have a relatively poor suppression of Cu-K $\beta$  and W-L $\beta$  lines, whereas WSi<sub>2</sub>/Si and Ni/B<sub>4</sub>C multilayer mirrors offer an improved spectral purity. Furthermore, the thermal stability of WSi<sub>2</sub>/Si multilayers is superior to that of W/Si multilayers.<sup>[37]</sup> Consequently, the K $\beta$ -to-K $\alpha$ 1 intensity ratio achieved (or suppression factor) is better than 1:2000. The normalized K $\beta$ -to-K $\alpha$ 1 intensity ratios for the W/Si, WSi<sub>2</sub>/Si, and Ni/B<sub>4</sub>C multilayers are about 1:0.28:0.21. An additional check of the monochromatization by means of a quartz powder specimen confirmed this result.<sup>[33]</sup>

Table 3 summarizes the intensity gain factors obtained from various parabolically curved graded multilayer mirrors by coupling the parallel beam to a channel-cut monochromator. The details of the

**Table 3** Intensity gain factors (mirror length 60 mm, focal distance from the center of each mirror 150 mm, thickness ratio of  $\Gamma = 0.5$ , 50 layer pairs for W/Si, and 100 layer pairs for the other material combinations)

Year	Multilayer	Intensity gain factors
1995	W/Si	6
1997	W/Si	11
1997	WSi <sub>2</sub> /Si	12
1999	Ni/B <sub>4</sub> C	16

*Source:* From Ref.<sup>[33]</sup>.

experimental setup are described in Ref.<sup>[34]</sup>. The parallel beams lead to a considerable increase in the throughput when coupled to these low-acceptance channel-cut monochromators. Compared to a configuration without a multilayer mirror, an intensity gain factor of 6 has been achieved using a bent and glued multilayer mirror. Please note that the small acceptance angle of the channel-cut monochromator leads to a conservative gain factor. In diffraction experiments, the gain factor is expected to be higher because of the larger acceptance angle. As can be seen in Table 3, the use of prefabricated quartz substrates can improve the intensity gain factor from 6 to 11 when W/Si multilayer mirrors have been used. This setup also allows a comparison between various multilayer materials. WSi<sub>2</sub>/Si multilayer mirrors show an intensity gain factor of about 12. A further intensity improvement has been obtained applying Ni-based multilayer mirrors, which have a gain factor of approximately 16. The theoretical limit is in the range of 20–25, depending on the multilayer materials.<sup>[38]</sup> The photon flux of these parallel beam X-ray optics is approximately  $3 \times 10^9$  cps for Cu-K $\alpha$  radiation at a source-to-detector distance of 435 cm and with an X-ray generator operated at 40 kV and 40 mA.

### Applications of Multilayer Mirrors in XRD

The previously mentioned features of multilayer mirrors namely high reflectivity, good beam uniformity, low divergence, and good spectral purity are the basis for their success in the market and numerous applications. Today, approximately 50% of all XRD instruments are equipped with graded multilayer mirrors, and this number is still increasing. The above mentioned gain factor of more than one order of magnitude can be displayed in XRR. The upper reflection curve in Fig. 13 was measured with an incident beam Göbel mirror for Cu-K $\alpha$  radiation and the lower curve without the Göbel mirror but with a graphite diffracted beam monochromator to suppress the influence of Cu-K $\beta$  radiation. The measurements were carried out with a Bruker AXS D8 Advance Diffractometer equipped with a reflectometry stage with a knife-edge collimator. The distance between the knife-edge and the specimen was 10  $\mu$ m. All other measurement conditions were identical. The specimen was a V/C multilayer with 40 pairs and a period of 6.5 nm. The two measurements were plotted without normalizing in units of counts per second. Please note that the primary intensity provided by the Göbel mirror is more than one order of magnitude. Consequently, it is possible to investigate more Bragg orders. In another measurement, a dynamic range of nine orders of magnitude was achieved by measuring the native oxide

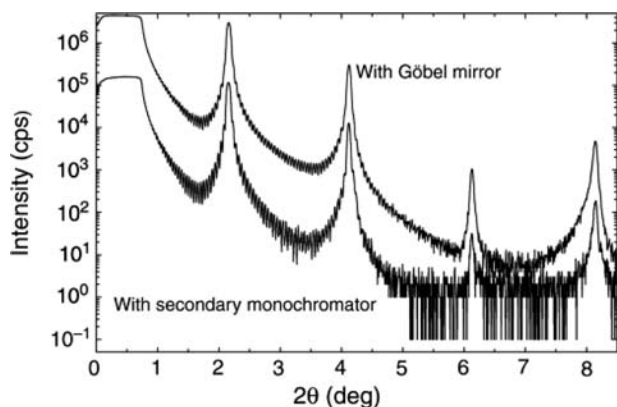


**Fig. 13** Cu-K $\alpha$  reflectivity curves of a V/C-multilayer film, 6.5-nm  $d$ -spacing and 40 pairs, measured with an incident beam Göbel mirror and with a secondary monochromator, respectively. *Source:* From Ref.<sup>[39]</sup>.

layer on top of a silicon wafer. Such a dynamic range is not achievable with conventional diffractometers, only at synchrotron sources and nowadays in the laboratory with Göbel mirrors. The high intensity also allows diffuse XRR (cf. Ref.<sup>[20]</sup>). Here, we also describe a comparison between conventional Bragg–Brentano geometry and parallel beam geometry with respect to the effect of peak broadening. In the first case, the position of the specimen with reference to the center of the diffractometer has to be adjusted very accurately; otherwise, the measured peaks of the diffraction pattern will be influenced, showing peak broadening with increasing deviation. The peak width plays an important role in considering the grain size in powder measurements or the internal stress of a coating. The use of parallel beams allows to avoid these problems. There is no sensitivity to sample displacement, which leads to peak broadening and to peak shifts because of defocusing.<sup>[20,40]</sup> Therefore, it is possible to do measurements with variable-temperature attachments and to investigate samples with low absorption (e.g., plastics) or with irregularly shaped surfaces, for example, an ancient statue.<sup>[10]</sup>

The resolution of XRR measurements can be improved by the use of a different wavelength, as shown in Fig. 14. The reflectivity of a V/C multilayer is measured with Cu and Cr radiation. For each measurement a Göbel mirror that has been optimized for the selected wavelength is used. In the measurement using Cr-K $\alpha$  radiation ( $E = 5415 \text{ eV}/\lambda = 0.2290 \text{ nm}$ ) the Kiessig fringes are clearly resolved between the main order reflections from the multilayer; when employing Cu radiation, they are not resolved. The Kiessig fringes are because of the total film thickness of about 260 nm. Their number between the main order reflections equals the number of bilayers minus 2. Thus, it is possible to determine the number of bilayers

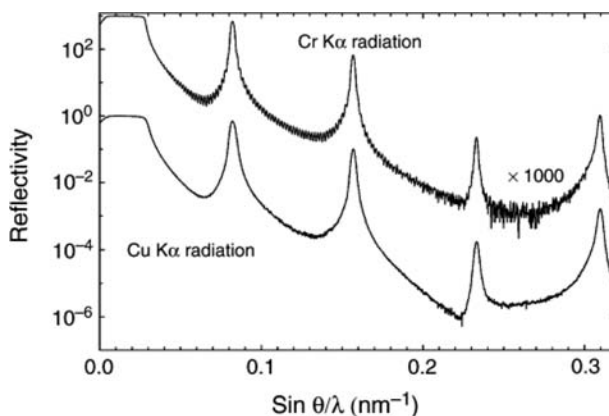


**Fig. 14** Reflectivity measurements of a V/C-multilayer film, 6.5-nm  $d$ -spacing and 40 pairs, obtained with Cu-K $\alpha$  (40 kV, 40 mA) and Cr-K $\alpha$  (35 kV, 35 mA) radiation, respectively, and using Göbel mirrors optimized for these wavelengths ( $2\theta$  step size:  $0.004^\circ$ , scan speed: 1 step/s, total measurement time: 35 min 25 s). *Source:* From Ref.<sup>[39]</sup>.

( $N = 40$ ). This example demonstrates the higher resolution that is achievable with a change to another wavelength.

## CONCLUSIONS

In the field of XRF, nanostructured multilayer mirrors are applied in the detection of light elements. The recently developed multilayer mirrors for the detection of boron, carbon, and aluminum presented and discussed here achieve a much lower and consequently better LLD. This improvement is not only because of higher reflectivity but also because of lower background. In the field of XRD, significant progress has been made in the design and fabrication of curved graded multilayer mirrors that are employed to achieve high reflectivity, good beam uniformity, low divergence, and high spectral purity. A typical XRD multilayer mirror displays the following properties, depending on the materials used: reflectivity  $>70\%$ , Bragg angle:  $0.8^\circ$ – $2^\circ$ , Bragg peak width:  $0.03^\circ$ – $0.06^\circ$ , rms slope error  $<0.01^\circ$ , total divergence  $<0.033^\circ$ . The application of X-ray multilayer mirrors is currently expanding in new fields where the X-ray intensities are weak.<sup>[41–43]</sup> Today, the characterization of thin films and layer stackings is also possible using specular XRR at Cr wavelength. Moreover, measurements with diffuse XRR can be performed with a quality previously confined to synchrotron radiation sources. In protein crystallography and life sciences, very small crystals, large unit cells, and anisotropic structures can be investigated by means of XRD. In addition, these powerful multilayer mirrors coupled to low-power X-ray tubes can lead to the development of

new, small, and transportable instruments with significant X-ray intensity. Finally, the recent developments and applications in X-ray optics should be mentioned here. In protein crystallography, elliptically bent focusing multilayer mirrors are employed, especially in single crystal diffraction. Two-dimensional focusing is possible when two mirrors are combined in a Montel scheme.<sup>[20]</sup> Larger X-ray optics are required for beam alignment, beam guidance, and monochromatization in the soft X-ray range at free electron lasers. For this application (50–200 eV), amorphous carbon coatings are used as a 500-mm long total-reflection mirror. These monolayers exhibit a uniformity of better than 2% in thickness over the whole length.<sup>[44,45]</sup> Depth-graded multilayer mirrors used as optical elements at synchrotrons provide a broad and well-defined reflectivity profile.<sup>[46]</sup> Thus, the use of nanostructured multilayer mirrors for X-ray optical applications is still growing in many directions.

## ACKNOWLEDGMENTS

We would like to thank W. Jäger, C. Dieker, and S. Hollensteiner (Christian-Albrechts University of Kiel, Germany) and J. Feldhaus, J. Schneider, C. Nowak, and B. Steeg (HASYLAB/DESY, Hamburg, Germany) for the collaboration. Special thanks to H. Göbel and M. Schuster (Siemens, Munich, Germany) and L. Brügemann (Bruker AXS, Karlsruhe, Germany).

## REFERENCES

- Cullity, B.D. *Elements of X-ray Diffraction*; Addison-Wesley: Reading, Massachusetts, USA, 1978.
- Attwood, D. *Soft X-rays and Extreme Ultraviolet Radiation*; Cambridge University Press: Cambridge, 2000.
- Sweet, R.M. X-ray crystallography. In *Encyclopedia of Optical Engineering*, 1st Ed.; Driggers, R.G., Ed.; Marcel Dekker, Inc.: New York, 2000; 3, 3022–3028.
- Spiller, E. X-ray optics. In *Encyclopedia of Optical Engineering*, 1st Ed.; Driggers, R.G., Ed.; Marcel Dekker, Inc.: New York, 2003; 3, 3042–3049.
- Michette, A. X-ray microscopy. In *Encyclopedia of Optical Engineering*, 1st Ed.; Driggers, R.G., Ed.; Marcel Dekker, Inc.: New York, 2003; 3, 3029–3041.
- Underwood, J.H.; Barbee, T.W., Jr. Layered synthetic microstructures as Bragg diffractors for X-rays and extreme ultraviolet: theory and predicted performance. *Appl. Opt.* **1981**, *20* (17), 3027–3034.
- Jenkins, R. *X-ray Fluorescence Spectrometry. In Chemical Analysis Series*; Wiley: New York, 1988; Vol. 152.
- Chattarji, D. *The Theory of Auger Transitions*; Academic: London, 1976; 60–62.
- Göbel, H.E. High-temperature XRPD for sealed-off capillary specimen, Talk I01, Abstracts (ISSN 0569-4221), Annual Meeting of the American Crystallographic Association, USA, Aug 9–14, 1992.
- Göbel, H.E. A new parallel-beam diffractometer system using a tailored multilayer optic. Abstracts of Papers. *Adv. X-ray Anal.* **1995**, *38*; 43rd Annual Denver X-ray Conference, Steamboat Springs, Colorado, USA, Aug 1–5, 1994.
- Schuster, M.; Göbel, H. Application of graded multilayer optics in X-ray diffraction. *Adv. X-ray Anal.* **1997**, *39*, 57–71.
- Göbel, H. Röntgen-Analysegerät. German Patent Application P 44 07 278.3, March 4, 1994.
- Michaelsen, C.; Wiesmann, J.; Bormann, R.; Nowak, C.; Dieker, C.; Hollensteiner, S.; Jäger, W. La/B<sub>4</sub>C multilayer mirrors for X-rays below 190 eV. *Proc. SPIE* **2001**, *4501*, 135–141.
- Schuster, M.; Mueller, L.; Mauser, K.E.; Straub, R. Quantitative X-ray fluorescence analysis of boron in thin films of borophosphosilicate glasses. *Thin Solid Films* **1988**, *157* (2), 325–336.
- Wood, J.L.; Hart, K.L. Reflectivity and Resolution X-ray Dispersive and Reflective Structures for Carbon, Beryllium, Boron Analysis. US Patent 4,785,470, November 15, 1988.
- Birken, H.G.; Blessing, C.; Kunz, C.; Wolf, R. Investigations on the consistency of optical constants in the XUV determined by different methods. *Rev. Sci. Instrum.* **1989**, *60*, 2223–2226.
- Michaelsen, C.; Wiesmann, J.; Bormann, R.; Nowak, C.; Dieker, C.; Hollensteiner, S.; Jäger, W. Multilayer mirror for X-rays below 190 eV. *Opt. Lett.* **2001**, *26* (11), 792–794.
- Michaelsen, C.; Bormann, R. Device and Method for Analyzing Atomic and/or Molecular Elements by Means of Wavelength Dispersive X-ray Spectrometric Devices, . US Patent 6,628,748 B2, Sept 30, 2003.
- Levy, R.A.; Nassau, K. Viscous behavior of phosphosilicate and borophosphosilicate glasses in VLSI processing. *Solid State Technol.* **1986**, *29* (10), 123–140.
- Michaelsen, C.; Wiesmann, J.; Hoffmann, C.; Wulf, K.; Brügemann, L.; Storm, A. Recent developments of multilayer mirror optics for laboratory X-ray instrumentation. *Proc. SPIE* **2002**, *4782*, 143–151.
- Ricardo, P.; Wiesmann, J.; Novak, C.; Michaelsen, C.; Bormann, R. Improved analyser multilayers for aluminium and boron detection with X-ray fluorescence. *Appl. Optics* **2001**, *40* (16), 2747–2754.
- Schuster, M.; Göbel, H.; Brügemann, L.; Bahr, D.; Burgäzy, F.; Michaelsen, C.; Störmer, M.; Ricardo, P.; Dietsch, R.; Holz, T.; Mai, H. Laterally graded multilayer optics for X-ray analysis. *Proc. SPIE* **1999**, *3767*, 183–198.
- Spiller, E. *Soft X-ray Optics*; SPIE The International Society of Optical Engineering: Bellingham, USA, 1994.
- Henke, B.L.; Gullikson, E.M.; Davis, J.C. X-ray interactions: photoabsorption scattering, transmission and reflection at  $E = 50\text{--}30,000\text{ eV}$ ,  $Z = 1\text{--}92$ . *At. Data Nucl. Data Tables* **1993**, *54*, 181–342.
- Windt, D. IMD: software for modeling the optical properties of multilayer films. *Comput. Phys.* **1998**, *12*, 360–370.

26. Born, M.; Wolf, E. *Principles of Optics*; 7th Ed.; Cambridge University Press: Cambridge, 2003.
27. Stearns, D.G. The scattering of X-rays from nonideal multilayer structures. *J. Appl. Phys.* **1989**, *65* (21), 491–506.
28. Nevot, L.; Croce, P. Characterisation des surface par reflexion rasante de rayons X. Application a l'etude du polissage de quelques verres silicates. *Rev. Phys. Appl.* **1980**, *15*, 761–779.
29. Borchers, C.; Ricardo, P.; Michaelsen, C. Interfacial wetting and percolation threshold in ultrathin Ni/C multilayer films. *Philos. Mag.* **2000**, *A80* (7), 1669–1679.
30. Borchers, C.; Michaelsen, C. Ultrathin metal/light material multilayer films: thermodynamics and microstructure. *Philos. Mag.* **2002**, *A82* (6), 1195–1205.
31. Braun, S.; Mai, H.; Moss, M.; Scholz, R.; Leson, A. Mo/Si multilayers with different barrier layers for applications as extreme ultraviolet mirrors. *Jpn. J. Appl. Phys., Part 1: Regular Papers Short Notes Rev. Papers* **2002**, *41* (6B), 4074–4081.
32. Bajt, S.; Alameda, J.B.; Barbee, T.W., Jr.; Clift, W.M.; Folta, J.A.; Kauffmann, B.; Spiller, E.A. Improved reflectance and stability of Mo/Si multilayers. *Proc. SPIE* **2001**, *4506*, 65–75.
33. Michaelsen, C.; Ricardo, P.; Anders, D.; Schuster, M.; Schilling, J.; Göbel, H. Improved graded multilayer mirrors for XRD applications. *Adv. X-ray Anal.* **2000**, *42*, 308–320.
34. Schuster, M.; Göbel, H. Parallel-beam coupling into channel-cut monochromators using curved graded multilayers. *J. Phys. D: Appl. Phys.* **1995**, *28*, A270–A275.
35. Schuster, M.; Göbel, H. Calculation of improvement to HRXRD system through-put using curved graded multilayers. *J. Phys. D: Appl. Phys.* **1996**, *29* (6), 1677–1679.
36. Ricardo, P. *Entwicklung von Multilagen für Anwendungen in der Röntgenanalytik*; Ph.D. dissertation; Technical University Hamburg-Harburg, Germany: Fortschritt-Berichte VDI Reihe 8, No. 1065, Düsseldorf; 99; VDI Verlag 2005.
37. Senderak, R.; Jergel, M.; Luby, S.; Majkova, E.; Holy, V.; Haindl, G.; Hamelmann, F.; Kleineberg, U.; Heinzmann, U. Thermal stability of  $W_{1-x}Si_x/Si$  multilayers under rapid thermal annealing. *J. Appl. Phys.* **1997**, *81* (5), 2229–2235.
38. Gutman, G.; Vermon, B. Calculation of improvement to HRXRD system through-put using curved graded multilayers. *J. Phys. D: Appl. Phys.* **1996**, *29* (6), 1675–1676.
39. Michaelsen, C.; Störmer, M.; Brügemann, L. Cr-K $\alpha$  Göbel Mirrors for improved resolution in X-ray reflectometry investigations. Lab Report XRD 30, Bruker-AXS, Order-No. L88-E00030, 1999. Available at: <http://www.brukerxs.de>
40. Stömmer, R.; Martin, A.R.; Hub, W.; Göbel, H.; Pietsch, U. X-ray scattering from silicon surfaces: a tool for quality control. *Microelectron. Eng.* **1999**, *45* (2), 257–263.
41. Michaelsen, C.; Wiesmann, J.; Hoffmann, C.; Wulf, K.; Brügemann, L.; Storm, A. Optimized performance of graded multilayer optics for X-ray single crystal diffraction. *Proc. SPIE* **2004**, *5193*, 211–219.
42. Storm, A.B.; Michaelsen, C.; Oehr, A.; Hoffmann, C. Multilayer optics for Mo radiation based crystallography. *Proc. SPIE* **2004**, *5537*, 177–181.
43. Akhsakhalyan, A.A.; Akhsakhalyan, A.D.; Kharitonov, A.I.; Klunokov, E.B.; Murav'ev, V.A.; Salashchenko, N.N. Quadrelliptical reflector based on multilayer structures for the hard X-ray rang. *Nucl. Instrum. Methods Phys. Res.* **2005**, *A543* (1), 346–349.
44. Steeg, B.; Juha, L.; Feldhaus, J.; Jacobi, S.; Sobierajski, S.; Michaelsen, C.; Andrejczuk, A.; Krzywinski, J. Total reflection amorphous carbon mirrors for vacuum ultraviolet free electron lasers. *Appl. Phys. Lett.* **2004**, *84* (5), 657–659.
45. Störmer, M.; Liard-Cloup, A.; Felten, F.; Jacobi, S.; Steeg, B.; Feldhaus, J.; Bormann, R. Investigations of large X-ray optics for free electron lasers. *Proc. SPIE* **2004**, *5533*, 58–65.
46. Morawe, Ch.; Peffen, J.-Ch.; Kozhevnikov, I.V. Depth-graded multilayers. *J. Phys.* **2003**, *IV: JP 104*, 239–242.

# Nanostructured Silica and Silica-Derived Materials

Ho-Cheol Kim  
Geraud Dubois

IBM Almaden Research Center, San Jose, California, U.S.A.

## INTRODUCTION

Silicates are the most commonly found minerals as they are compounds of silicon and oxygen, which together make up almost 75% of the earth's crust. Consequently, silicates are a basic building block of various natural or artificial structures. With emerging interests in nanoscale science and technology, silicate materials containing nanometer-sized structures have been studied and their new and interesting physical, chemical, and biological phenomena are begun to be understood. The control of silica material structures at a nanoscopic level attracts a great deal of interest among the scientific community in the last decade and remains an ongoing challenge. While various kinds of silica polymeric materials have been known for years, new morphologies have recently appeared, such as spherical hollow spheres, transparent films, mesoporous materials with narrow pore size distribution, and nanoporous thin films. In this entry, we discuss some old and new aspects of the synthesis of silica polymeric nanostructures, as well as their use in emerging technologies.

## SILICA NANOPARTICLES

In 1968, Stöber and Fink<sup>[1]</sup> hydrolyzed a dilute solution of tetraethylorthosilicate (TEOS) in ethanol at high pH and obtained uniform spheres of amorphous silica whose sizes could be varied from 10 nm to 2  $\mu$ m simply by changing the concentrations of the reactants. Examples of dense silica nanoparticles synthesized according to the Stöber process are depicted in Fig. 1.

This method was later improved by many others and appears to be the simplest and most effective route to monodispersed silica spheres.<sup>[2]</sup> Two types of reactions occur in the formation of silica particles: silanol groups are formed by hydrolysis of alkoxy silane groups and siloxane bridges are formed by a condensation polymerization reaction.

Recent mechanistic studies suggest that several types of micrometer-sized colloidal particles prepared by the precipitation method are in fact, the result of

aggregation of much smaller subunits, or nanometer-sized primary particles, rather than continuous growth by diffusion of species from the solution to the nucleating surfaces.<sup>[3]</sup> In some cases, a broad range of size distribution was observed during the period of growth, indicating the occurrence of multiple nucleation events.<sup>[4]</sup> The uniformity of size in the final product may be achieved through a self-sharpening growth process during which small particles grew more rapidly than larger ones.

The surfaces of these silica colloids are typically terminated with three silanol types: free or isolated silanols, hydrogen-bonded or vicinal silanols, and geminal silanols (Scheme 1).

Silica nanoparticle surfaces can be rendered non-polar by post-treatment with hexamethyldisilazane (commonly used in industry for the manufacture of hydrophobic fumed silica), alkoxy silanes, or alcohols (esterification).<sup>[5–7]</sup> The treated silica nanoparticles can then be dispersed in various non-alcoholic solvents, such as methyl isobutyl ketone, cyclohexane, n-octane, or diethyl ether. Protected and unprotected monodispersed silica colloidal spheres are commercially available in large quantities from Nissan Chemical Industries, a company that has produced silica colloids for many years and whose monodispersed products are marketed under the trade name Snowtex<sup>®</sup>. Those readers with interest in the applications of monodispersed colloidal silica spheres can find a recent survey by Xia et al.<sup>[8]</sup>

Whereas dense silica particles have been known since 1956, spherical silica materials with hollow interiors have drawn interest in recent years because of their potential uses as low-density capsules for controlled-release drugs, dyes and inks, development of artificial cells, protection of proteins, or enzymes, and catalysis.<sup>[9]</sup> Many procedures for the generation of hollow silica spheres exist, including layer-by-layer deposition on (sub)micrometer-sized latex particles,<sup>[10]</sup> interfacial synthesis,<sup>[11]</sup> the use of hybrid polystyrene/siloxane latex particles,<sup>[12,13]</sup> and more recently, the controlled precipitation of silicic acid on functionalized polystyrene latexes<sup>[14]</sup> or the liquid phase deposition of silica onto fullerene surfaces.<sup>[15]</sup> Two major requirements



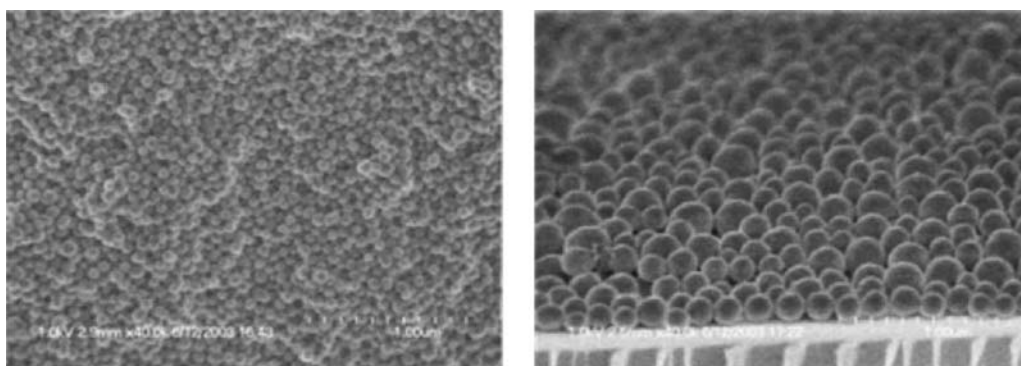
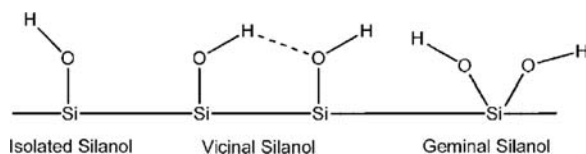


**Fig. 1** Scanning electron microscope pictures of dense silica nanoparticles (left: 50 nm diameter; right: 150 and 200 nm diameter).



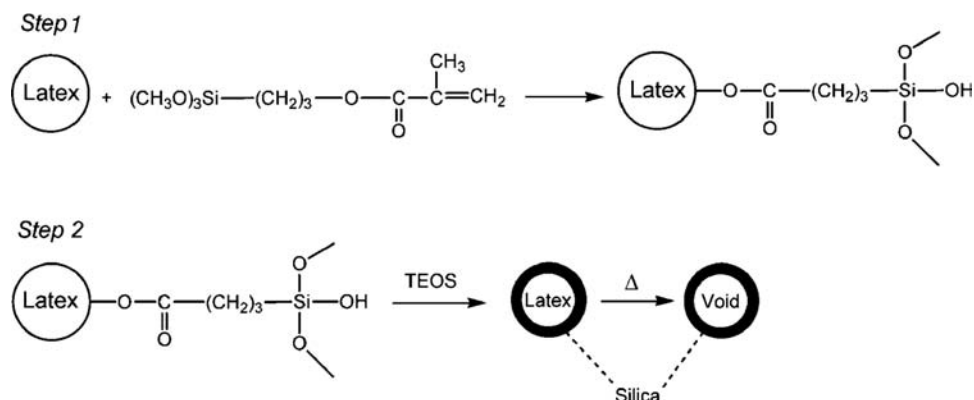
**Scheme 1** Surface silanol types.

of any of these synthetic methods are to ensure a homogeneous deposition of silica and to prevent multiparticle aggregation. Hereafter we describe two of the aforementioned strategies as examples for the synthesis of spherical silica particles with hollow interiors. The first approach is divided in two steps as shown in Scheme 2. First, 3-(trimethoxysilyl) propyl methacrylate (MPS) is covalently attached to the surface of polystyrene latex particles leading to silanol-functionalized particles. Then, the silanols are used to nucleate the deposition of a silica layer onto the hybrid particles' surface by reaction with TEOS in aqueous basic alcoholic suspensions. Using this process, stable non-aggregated suspensions of hollow silica nanoparticles with 20 nm thick shells are produced as illustrated by the transmission electron microscope (TEM) images in Fig. 2. It is notable that

dense silica particles are not detected, indicating that the polycondensation reaction only takes place at the seed surface.

The second approach involves the slow controlled precipitation of silica from a sodium silicate solution onto polystyrene latexes bearing amine functionalities or amine and carboxylate groups (zwitterionic surface). Control of the sodium silicate solution pH is critical. A pH of 9.7 ensures a homogeneous coating of the latex particles in 24 hr and minimizes the non-templated precipitation of silica particles (Scheme 3). Interestingly for this approach, deposition of the coated particles on a surface from aqueous solution by slow evaporation leads to highly organized hexagonal lattices. The voids between adjacent spheres are still open, indicating that the organized array is indeed formed by the stacking of silica coated spheres (Fig. 3).

For both strategies, the latex core is removed by calcination in a final step leading to the formation of hollow silica spheres with theoretically closed central pores, the pore size being dictated by the size of the starting polymeric core. While closed cell porosity is advantageous in the case of hollow silica nanoparticles for the applications mentioned previously, other applications benefit more from open porosity and high



**Scheme 2** Formation of hollow silica beads.

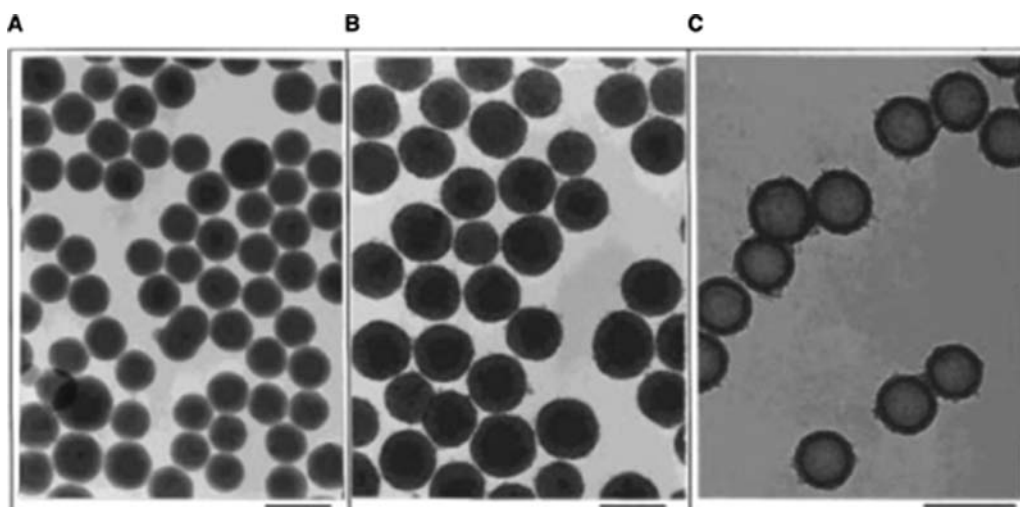


**Fig. 2** Transmission electron microscope micrographs of (A) SiOH-functionalized latex particles, (B) silica-coated latex particles, and (C) hollow silica nanoparticles.

surface area. These include ion exchange, gas adsorption, heterogeneous catalysis, hydrogen and or methane storage, and many others.

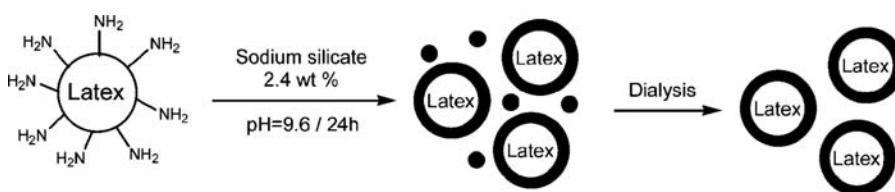
## NANOPOROUS MEDIA

Porous media are very useful in numerous applications for every day life. When the pore size reaches several nanometers, they can find potential applications in state-of-the-art technologies including electronics, optics, biotechnology, and so on. Porous materials may be fully crystalline (zeolites), ordered on a mesoscopic length scale but amorphous on an atomic length scale (surfactant-templated materials), or fully disordered (silica gels).<sup>[16,17]</sup> While the engineering of micro structure has been achieved in the case of zeolites for more than 50 years, precise control of the pore size distribution and the shape and volume of the void spaces for mesoporous silicates only emerged in the early 1990s with the synthesis of the so-called M41S periodic mesoporous silica.<sup>[18]</sup> In the synthesis of this material (Scheme 4), the hydrolysis and polycondensation of the silica precursor was templated by micelles preformed from a surfactant, an amphiphilic molecule that self-organizes in aqueous media into supramolecular arrays due to polarity differences between the lyophobic head group and lyophilic tail. While a

structure-directing agent (surfactant) is used for the synthesis of both zeolites and M41S materials, only in the latter case is a true template mechanism operative as a direct correlation of the surfactant array size and shape to final pore size and geometry is observed. The pores of these solids are classified according to size: pores size below 2 nm are called micropores, those in the range 2–50 nm are denoted mesopores, and those above 50 nm are macropores.<sup>[19,20]</sup>

Depending upon the nature of the surfactant (e.g., cationic, anionic, neutral, zwitterionic, bolaamphiphile, Gemini, divalent, and commercially available polymers), different mesophases are obtained: MCM-41 (hexagonal), MCM-48 (cubic), MCM-50 (lamellar), SBA-1, SBA-6, HMS, MSU-n, MSU-V, and many others.<sup>[21]</sup> When a charged surfactant is used, calcination of the as-synthesized material is mandatory to fully remove the template, whereas in the case of a neutral surfactant washing is sufficient. This neutral templating route allows the direct synthesis of hybrid organic–inorganic mesoporous materials where an organic molecule can be incorporated either in the channels or inside the walls.<sup>[22,23]</sup> These organically functionalized silicas present a very high surface area and tightly controlled porosity with a loading of organic groups that can be varied over a large range.

In the semiconductor industry, scientists have recently drawn inspiration from the molecular templated



**Scheme 3** Silica coating of amino-functionalized latex particles.

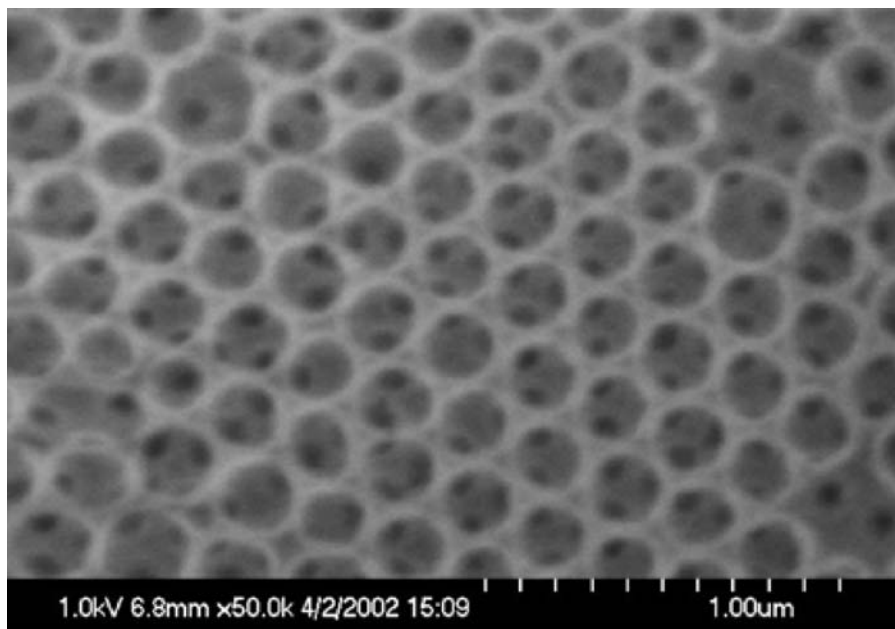
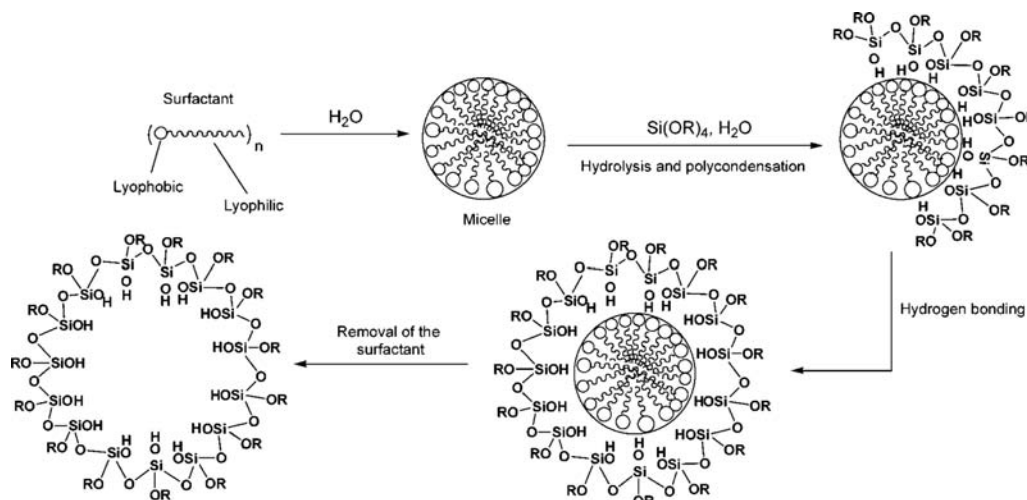


**Fig. 3** Scanning electron microscope image of an organized multilayer of 200-nm-sized coated spheres after calcinations. With the chosen acceleration voltage, the complete coating is not visible in this case.

synthesis of mesoporous solids to develop materials with low dielectric constant (low  $k$ ) for advanced microelectronics. As electronic devices get smaller and smaller, improvements in back end of the line (BEOL) interconnect performance require the reduction of resistance and capacitance, hence, new insulating materials having lower dielectric constant are needed.<sup>[24]</sup> Fig. 4 represents a typical BEOL structure containing multilayers of hard mask, dielectrics, etch stop, and cap coating. For over 30 years, silicon dioxide ( $\text{SiO}_2$ ) has been the dielectric insulator of choice for the semiconductor industry due to its excellent dielectric breakdown strength, a high modulus, good thermal conductivity, and excellent adhesion to other materials. However,  $\text{SiO}_2$  is being replaced with materials

possessing lower permittivity to achieve reduced capacitance for next technology generations. For example, at the 65 nm technology generation, the target effective dielectric constant ( $k_{\text{eff}}$ ) according to the 2001 International Technology Roadmap for Semiconductors is 2.3–2.6.<sup>[25]</sup> The  $k_{\text{eff}}$  is a composite value comprised of the dielectric, hard mask, barrier cap layer, and etch stop layer as schematically shown in Fig. 4. To achieve this ultra low dielectric constant, materials with  $k < 2.2$  will be required. Porous structure is unavoidable choice for dielectric material in order to attain sufficiently low dielectric constants.

The incorporation of nanosized pores into a matrix structure leads to a significant decrease in the dielectric constant of the bulk material since the dielectric



**Scheme 4** General mechanism for the formation of M41S materials.

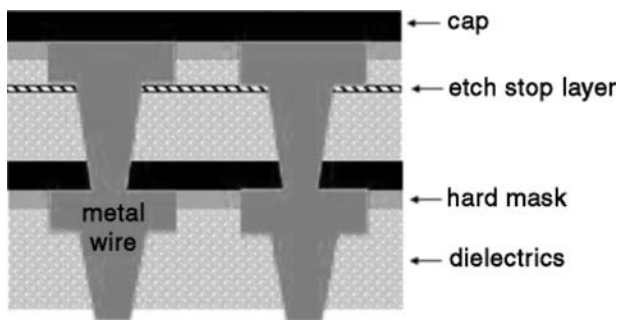


Fig. 4 A typical structure of multilayered BEOL.

constant of air is about one. The dielectric constant of the material can therefore be adjusted by simply varying the level of nanoporosity. Among a variety of method to generate nanoporosity in organic or inorganic films, an approach developed in IBM, known as the so-called *sacrificial porogen approach*, has been recognized as a simple and effective route to thin films containing nanometer sized pores.<sup>[26–31]</sup> It utilizes phase separation of two component systems where one component (e.g., organosilicates matrix) crosslinks into a network effectively limiting domain growth and coarsening of the porogen phase (an organic, labile polymeric component) that is ultimately expelled from

the film by thermal decomposition. Fig. 5 depicts the schematics of pore generating process. The morphology of nanohybrid, where the phase separated porogen domain is entrapped within crosslinked organosilicate matrix, and hence the pore morphology is strongly dependent on the interaction between porogen and matrix material, and molecular weight, molecular architecture, and loading level of the porogen.

This process is able to generate various morphology and dimensions of the pores. Two distinctive pore morphologies could be observed depending on the phase separation kinetics. As shown in the right side of Fig. 5, when the porogen and matrix undergo the liquid–solid phase separation caused by the crosslinking of the matrix material, which is a typical nucleation and growth (NG) process, random shapes of pores with broad size distribution are obtained. Porogens of homopolymers or copolymers with linear or branched molecular architectures show NG type phase behavior. In contrast, well-defined, quite-ordered pore structure with narrow size distribution is obtained when preassembled porogens template the porous structure.<sup>[32]</sup> By the definition of templating (TP), the procedure involves a preassembled mould with the specific morphology that can be transferred to the final porous structure. As shown by the cross-sectional TEM images in Fig. 6, microstructures of pores

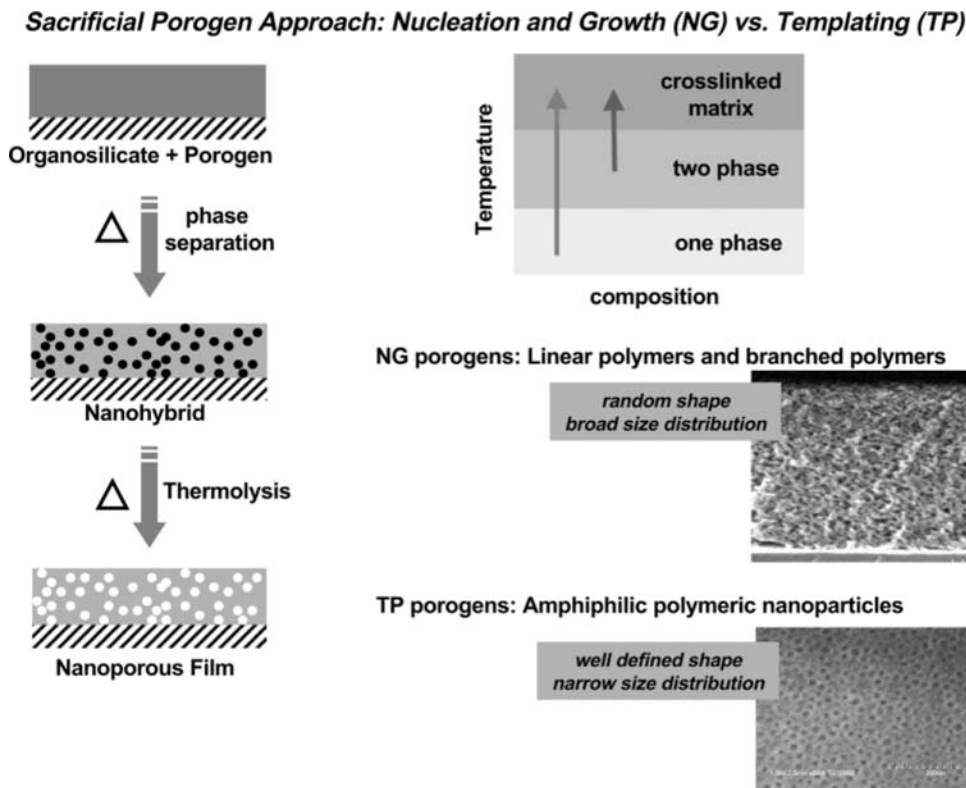
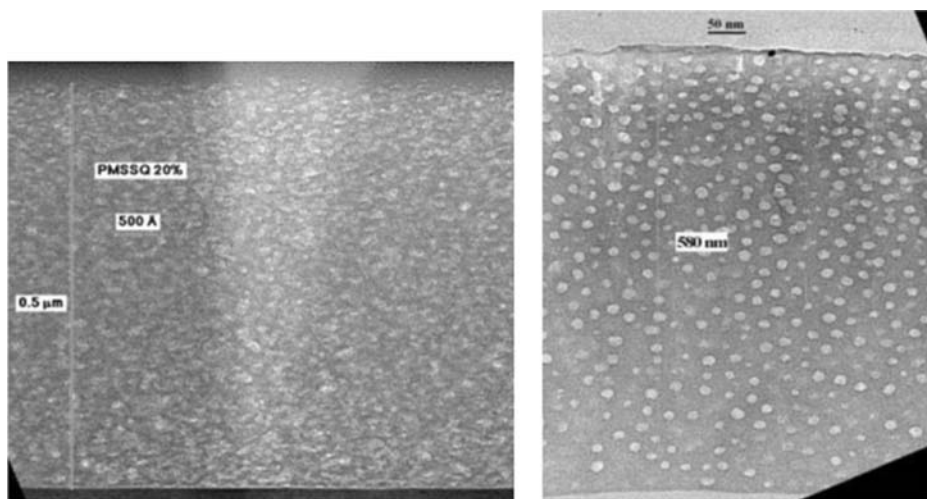


Fig. 5 Schematics of the sacrificial porogen approach to nanoporous organosilicates. Two distinct microstructures of pores are observed with different molecular architectures of porogens as shown in the right side.





**Fig. 6** Transmission electron microscope images of porous thin films generated by two different routes. Left: NG; Right: TP.

generated by two routes are very different. TP process (right-side image of Fig. 6) provides well-defined regular pore structures while NG process (left-side image of Fig. 6) gives random structures of pores.

In addition to the low dielectric constant, the nanoporous organosilicate thin films have a number of interesting properties which make them very attractive for many potential applications including optical components, catalyst supports, separation media, high density biosubstrates, and so on. Due to the nanoscopic dimensions of pores, these materials are optically homogeneous within visible wavelength of light. As shown in Fig. 7, for example, the refractive index of thin films of organosilicates also can be easily controlled over broad ranges (1.16–1.35 for this example) by simply varying the amount of porogen loadings.

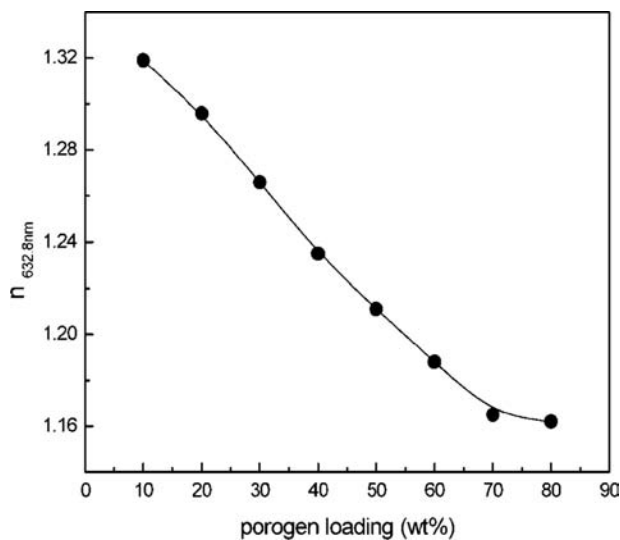


**Fig. 7** Refractive index of porous organosilicate thin films as a function of porosity.

One simple application of this controllable refractive index is optical coating on glass to enhance transmission of light (i.e., antireflection effect).<sup>[33,34]</sup> With a single layer of homogeneous dielectric material coating on a substrate, antireflection effect can be achieved if  $n_2^2 = n_1 n_3$  and  $h = \lambda/4$ , where  $h$  is coating thickness,  $\lambda$  is the wavelength of incident light,  $n_1$ ,  $n_2$ , and  $n_3$  are the refractive indices of substrate, dielectric material, and air, respectively. A dielectric material of  $n_2 = 1.22$  is required for glass substrate ( $n_1 \sim 1.5$ ,  $n_3 \sim 1$ ), which is not attainable with pure solid dielectric materials as the lowest  $n_2$  of dielectric materials is about 1.35 (cryolite,  $n_2 = 1.38$  for  $\text{MgF}_2$ ).<sup>[35]</sup> Fig. 8 shows the optical transmission spectra of glass slides coated with  $\sim 60$  nm of nanoporous poly(methylsilsesquioxane) (PMSSQ) generated from 50 wt% porogen loading ( $n \sim 1.22$ ). Compared to the uncoated glass, single and double sided nanoporous coatings increase the optical transmission through the glass from  $\sim 91.7\%$  to  $\sim 94.4\%$  and  $\sim 98.2\%$ , respectively. In addition, thin films of the nanoporous film with optical thickness ranging within visible wavelength are found to be robust.

Due to the nanoscopic dimension of pores and intrinsic hydrophobicity of PMSSQ, the porous PMSSQ films show very selective sorption behavior. A quartz crystal microbalance (QCM) combined with reflectance infrared spectroscopy (IR) study revealed this selectivity.<sup>[36]</sup> With organic liquids having surface tension below the critical value (38–48 dyne/cm), the extent of sorption increased with porosity of PMSSQ films. Extremely low amounts of sorption were measured with the liquids having a surface tension higher than the critical value. The selective sorption behavior can be interpreted by capillary condensation resulting from the lowered vapor pressure in the nanoscopic pores and the experimental data are in good agreement with calculations using the Kelvin equation.

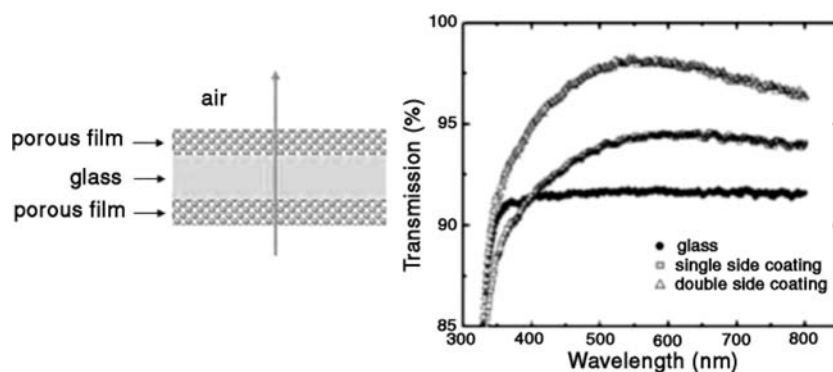


Fig. 8 Antireflection effect of nanoporous thin films coated on a glass slide.

The nanoporous PMSSQ thin films show potentials as biosubstrates when the hydrophilicity is controlled. A wide range of surface hydrophilicity can be obtained by a simple UV/ozone treatment on nanoporous PMSSQ films. Although the precise mechanism of UV/ozone treatment has remained unclear in literature, it has been widely used for a variety of etching/cleaning applications in the microelectronics industry. It is known that ozone is dissociated by absorption of 253.7 nm radiation or thermal heating into atomic oxygen which is postulated to be the predominant etchant species. Over the temperature range from room temperature to  $\sim 300^{\circ}\text{C}$ , organic materials are broken down into simple volatile oxidation products such as carbon dioxide, water, etc.<sup>[37,38]</sup> Fig. 9 shows water contact angles on dense PMSSQ surface as a function of UV/ozone treatment time at  $30^{\circ}\text{C}$ . The treatment gives surfaces having water contact angles ranging from  $105^{\circ}$  to  $25^{\circ}$  with increasing treatment time.

Since biosystems are based on aqueous environment, controlled hydrophilicity of solid surface is very useful for numerous applications in biotechnology including microarrays, affinity separation channels, etc. The ability to control surface hydrophilicity is applicable for pattern generation by limiting the area of UV/ozone treatment using a mask. Hydrophilic patterns in hydrophobic matrix can be obtained since only the area exposed both to UV and ozone becomes hydrophilic while masked areas remain as hydrophobic. Fig. 10 shows the patterning process and an optical micrograph of a patterned surface where hydrophilic area (diameter =  $250\ \mu\text{m}$ ) is decorated with a fluorescent dye (6-FAM amidite). Due to the porous, three-dimensional structure of the matrix, the patterned substrate has higher number density of functional groups than flat surface, which results in ten times higher fluorescence intensity than the corresponding flat silicon wafer surface. The arrays

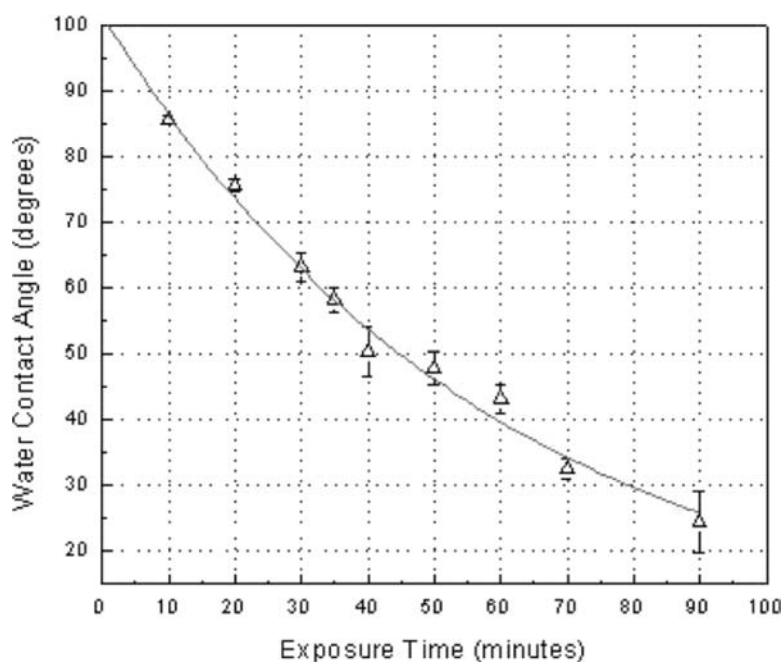
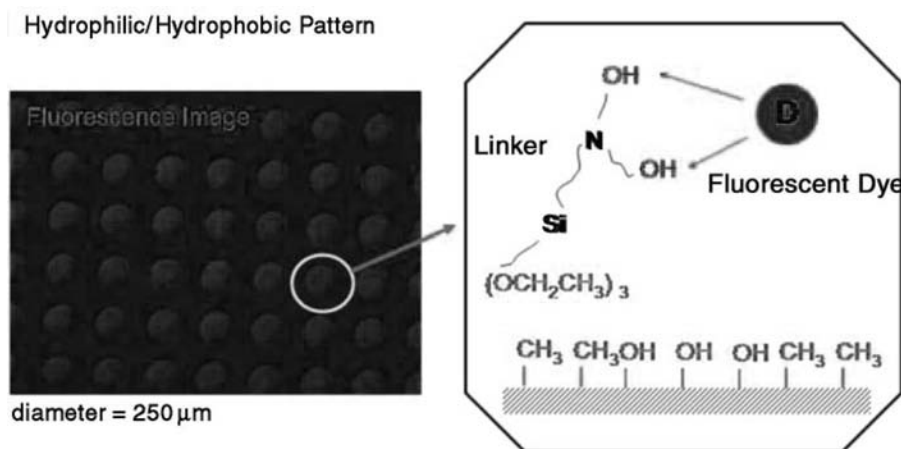


Fig. 9 Water contact angles of dense PMSSQ surface as a function of UV/ozone treatment time at  $30^{\circ}\text{C}$ .





**Fig. 10** Nanoporous PMSSQ surface with hydrophilicity-contrasted patterns.

of patterns containing high surface area are desirable to reduce the overall size of an array while maximizing the number of reaction sites within the pattern and minimizing the required reagent and sample volume.<sup>[39–41]</sup>

## CONCLUSIONS

Silicates with controlled nanoscopic structures are very attractive for a variety of potential applications due to their novel and interesting physical, chemical, and biological properties. Effort continues to explore new nanostructures, to optimize properties, and to utilize them for numerous end-uses, including optical components, electronics, separation media, catalysis, and biotechnology.

## REFERENCES

1. Stöber, W.; Fink, A. Controlled growth of monodisperse silica spheres in the micron size range. *J. Colloid Interface Sci.* **1968**, *26*, 62.
2. Iler, R.K. *The Chemistry of Silica*; Wiley: New York, 1979.
3. Ocana, M.; Rodriguez-Clemente, R.; Serna, C.J. Uniform colloidal particles in solution: formation mechanisms. *Adv. Mater.* **1995**, *7*, 212.
4. Bogush, G.H.; Tracy, M.A.; Zukowski, C.F. IV. Preparation of monodisperse silica particles: control of size and mass fraction. *J. Non-Cryst. Solids* **1988**, *104*, 95.
5. Van Helden, A.K.; Jansen, J.W.; Vrij, A. Preparation and characterization of spherical monodisperse silica dispersions in non-aqueous solvents. *J. Colloid Interface Sci.* **1981**, *81*, 354.
6. Badley, R.D.; Ford, W.T.; McEnroe, F.J.; Assink, R.A. Surface modification of colloidal silica. *Langmuir* **1990**, *6*, 792.
7. Suratwala, T.I.; Hanna, M.L.; Miller, E.L.; Whitman, P.K.; Thomas, I.M.; Ehrmann, P.R.; Maxwell, R.S.; Burnham, A.K. Surface chemistry and trimethylsilyl functionalization of stober silica sols. *J. Non-Cryst. Solids* **2003**, *2–3*, 349.
8. Xia, Y.; Gates, B.; Yin, Y.; Lu, Y. Monodispersed colloidal spheres: old materials with new applications. *Adv. Mater.* **2000**, *12*, 693.
9. Caruso, F. Nanoengineering of particle surfaces. *Adv. Mater.* **2001**, *13*, 11.
10. Caruso, F. Hollow capsule processing through colloidal templating and self-assembly. *Chem. Eur. J.* **2000**, *6*, 413.
11. Hubert, D.H.W.; Jung, M.; German, A.L. Vesicle templating. *Adv. Mater.* **2000**, *12*, 1291 (References cited).
12. Tissot, I.; Novat, C.; Lefebvre, F.; Bourgeat-Lami, E. Hybrid latex particles coated with silica. *Macromolecules* **2001**, *34*, 5737.
13. Tissot, I.; Reymond, J.P.; Lefebvre, F.; Bourgeat-Lami, E. SiOH-functionalized polystyrene latexes. A step toward the synthesis of hollow silica nanoparticles. *Chem Mater.* **2002**, *14*, 1325.
14. Cornelissen, J.J.; Connor, E.F.; Kim, H.-C.; Lee, V.Y.; Magbitang, T.; Rice, P.M.; Volksen, W.; Sundberg, L.K.; Miller, R.D. Versatile synthesis of nanometer sized hollow silica spheres. *Chem. Commun.* **2003**, (8), 1010.
15. Whitsitt, E.A.; Barron, A.R. Silica coated fullerenols: seeded growth of silica spheres under acidic conditions. *Chem. Commun.* **2003**, (9), 1042.
16. Hüsing, N.; Schubert, U. Aerogels-airy materials: chemistry, structure, and properties. *Angew. Chem. Int. Ed.* **1998**, *37*, 22.
17. Schüth, F. Endo- and exotemplating to create high-surface-area inorganic materials. *Angew. Chem. Int. Ed.* **2003**, *42*, 3604.
18. Kresge, C.T.; Leonowicz, M.E.; Roth, W.J.; Vartuli, J.C.; Beck, J.C. Ordered mesoporous molecular-sieves by a liquid-crystal template mechanism. *Nature* **1992**, *359*, 710.
19. Rouquerol, J.; Avnir, D.; Fairbridge, W.; Everett, D.H.; Haynes, J.H.; Pernicone, N.; Ramsay, J.D.; Sing, K.S.W.; Unger, K.K. Recommendations for the characterization of porous solids. *Pure Appl. Chem.* **1994**, *66*, 1739.
20. Sing, K.S.W.; Everett, D.H.; Haul, R.A.W.; Moscou, L.; Pierotti, A.; Rouquerol, J.; Siemieniewska, T. Reporting physisorption data for gas solid systems with special

- reference to the determination of surface area and porosity. *Pure Appl. Chem.* **1985**, *57*, 603.
21. Ying, J.Y.; Mehnert, C.P.; Wong, M.S. Synthesis and applications of supramolecular-templated mesoporous materials. *Angew. Chem. Int. Ed.* **1999**, *38*, 59.
  22. Mercier, L.; Pinnavaia, T.J. Direct synthesis of hybrid organic-inorganic nanoporous silica by a neutral amine assembly route: structure-function control by stoichiometric incorporation of organosiloxane molecules. *Chem. Mater.* **2000**, *12*, 188.
  23. MacLachlan, M.J.; Asefa, T.; Ozin, G.A. Writing on the wall with a new synthetic quill. *Chem. Eur. J.* **2000**, *6*, 2507.
  24. Miller, R.D. In search of low-*k* dielectrics. *Science* **1999**, *286*, 412.
  25. *The National Technology Roadmap for Semiconductors*; Semiconductor Industry Association: San Jose, CA, 2001.
  26. Miller, R.D.; Hedrick, J.L.; Yoon, D.Y.; Cook, R.F.; Hummel, J.P. Phase-separated inorganic-organic hybrids for microelectronic applications. *MRS Bull.* **1997**, *22*, 44.
  27. Hedrick, J.L.; Miller, R.D.; Hawker, C.J.; Carter, K.R.; Volksen, W.; Yoon, D.Y.; Trollsas, M. Templating nanoporosity in thin-film dielectric insulators. *Adv. Mater.* **1998**, *10*, 1049.
  28. Nguyen, C.V.; Carter, K.R.; Hawker, C.J.; Hedrick, J.L.; Jaffe, R.L.; Miller, R.D.; Remenar, J.F.; Rhee, H.-W.; Rice, P.M.; Toney, M.F.; Trollsas, M.; Yoon, D.Y. Low-dielectric, nanoporous organosilicate films prepared via inorganic/organic polymer hybrid templates. *Chem. Mater.* **1999**, *11*, 3080.
  29. Hawker, C.J.; Hedrick, J.L.; Miller, R.D.; Volksen, W. Supramolecular approaches to nanoscale dielectric foams for advanced microelectronic devices. *MRS Bull.* **2000**, *25*, 54.
  30. Nguyen, C.; Hawker, C.J.; Miller, R.D.; Huang, E.; Hedrick, J.L.; Gauderon, R.; Hilborn, J.G. Hyperbranched polyesters as nanoporosity templating agents for organosilicates. *Macromolecules* **2000**, *33*, 4281.
  31. Heise, A.; Nguyen, C.; Malek, R.; Hedrick, J.L.; Frank, C.W.; Miller, R.D. Starlike polymeric architectures by atom transfer radical polymerization: templates for the production of low dielectric constant thin films. *Macromolecules* **2000**, *33*, 2346.
  32. Connor, E.F.; Sundberg, L.K.; Kim, H.-C.; Cornelissen, J.J.; Magbitang, T.; Rice, P.M.; Lee, V.Y.; Hawker, C.J.; Volksen, W.; Hedrick, J.L.; Miller, R.D. Templating of silsesquioxane crosslinking using unimolecular self organizing polymers. *Angew. Chem. Int. Ed.* **2003**, *42*, 3785.
  33. Walheim, S.; Schäffer, E.; Mlynek, J.; Steiner, U. Nanophase separated polymer films as high-performance antireflection coatings. *Science* **1999**, *283*, 520.
  34. Kim, H.-C.; Wilds, J.B.; Kreller, C.R.; Volksen, W.; Brock, P.J.; Lee, V.Y.; Magbitang, T.; Hedrick, J.L.; Hawker, C.J.; Miller, R.D. Fabrication of multilayer poly(methylsilsesquioxane) thin films. *Adv. Mater.* **2002**, *14*, 1637.
  35. Born, M.; Wolf, E. *Principles of Optics*; Pergamon Press: New York, 1959.
  36. Kim, H.-C.; Wilds, J.B.; Hinsberg, W.D.; Johnson, L.R.; Volksen, W.; Magbitang, T.; Lee, V.; Hedrick, J.L.; Hawker, C.J.; Miller, R.D. Selective sorption of nanoporous poly(methylsilsesquioxane). *Chem. Mater.* **2002**, *14*, 4628.
  37. Wood, P.C.; Wydeven, T.; Tsuji, O. Critical process variables for UV-ozone etching of photoresist. *Mat. Res. Soc. Symp. Proc.* **1993**, *315*, 237.
  38. Keene, M.T.J.; Denoyl, R.; Llewellyn, P.L. Ozone treatment for the removal of surfactant to form MCM-41 type materials. *Chem. Commun.* **1998**, *20*, 2203.
  39. Niemeyer, C.M.; Blohm, D. DNA microarray. *Angew. Chem. Int. Ed.* **1999**, *38*, 2865.
  40. Pirrung, M.C. How to make a DNA chip. *Angew. Chem. Int. Ed.* **2002**, *41*, 1276.
  41. MacBeath, G.; Schreiber, S.L. Printing proteins as microarrays for high-throughput function determination. *Science* **2000**, *289*, 1760.

# Nanostuctured Ultrastrong Materials

**Nicholas A. Kotov**

*Department of Chemical Engineering, University of Michigan,  
Ann Arbor, Michigan, U.S.A.*

**Arif A. Mamedov**

*Oklahoma State University and Nomadics, Inc., Stillwater, Oklahoma, U.S.A.*

**Dirk M. Guldi**

*Radiation Laboratory, University of Notre Dame, Notre Dame, Indiana, U.S.A.*

**Zhiyong Tang**

*Department of Chemical Engineering, University of Michigan,  
Ann Arbor, Michigan, U.S.A.*

**Maurizio Prato**

*Dipartimento di Scienze Farmaceutiche, Università di Trieste, Trieste, Italy*

**James Wicksted**

*Department of Physics, Oklahoma State University,  
Stillwater, Oklahoma, U.S.A.*

**Andreas Hirsch**

*Institut für Organische Chemie, Universität Erlangen-Nürnberg,  
Erlangen, Germany*

## INTRODUCTION

The mass–strength ratio is of exceptional importance for different applications. Critical parts of various moving vehicles from satellites to aircrafts to cars depend on strength and toughness of the materials they are made of, while strict limitations on the weight of the different components are placed by the launch technology. Single-walled carbon nanotubes (SWNT) present significant potential as the basic material for space applications. The exceptional mechanical properties of SWNTs<sup>[1–6]</sup> have prompted intensive studies of their composites. These qualities can also be used in a variety of other technologies from automotive to military and medical. However, the present composites have shown only a moderate strength enhancement when compared to other hybrid materials.<sup>[7–9]</sup> Although substantial advances have been made,<sup>[10]</sup> the mechanical characteristics of SWNT-doped polymers are noticeably below their highly anticipated potential. Pristine SWNTs are well known for poor solubilization, which leads to phase segregation of composites. Severe structural inhomogeneities

result in the premature failure of the hybrid SWNT–polymer materials. The connectivity with and uniform distribution within the matrix are essential structural requirements for the strong SWNT composites.<sup>[11–13]</sup> Here we show that a new processing approach based on sequential layering of chemically modified nanotubes and polyelectrolytes can greatly diminish the phase segregation and render SWNT composite highly homogeneous. Combined with chemical cross-linking, this processing leads to drastically improved mechanical properties. The tensile strength of the composites is several times higher than that of SWNT composites made via mixing; it approaches values seen for hard ceramics. The universality of the layering approach applicable to a wide range of functional materials makes possible successful incorporation of SWNT into a variety of composites, imparting them required mechanical properties.

The thin-film membranes that are obtained as a result of the layer-by-layer process can be used as an intermediate or as a component of ultrastrong laminates. At the same time, the prepared membranes can also be utilized in the as-prepared form for space and

biomedical technologies because of the combined strength and multiple functionalities of the SWNT membranes.

## RESULTS AND DISCUSSION

Single-walled carbon nanotube composites are typically prepared by blending, in situ polymerization, and extrusion. After extensive surface modification, such as grafting or polymer wrapping,<sup>[12–14]</sup> the phase segregation from a macromolecular matrix is smaller than for pristine SWNT, but still remains high owing to vastly different molecular mobilities of both components. Very intense research on appropriate surface modification of SWNT is currently under way in many groups around the world. Nevertheless, most common loadings of nanotubes in the polymer matrix are within the 1–15 wt.% range, whereas more than 50% of the SWNT content is needed for materials with special mechanical performance without compromising the homogeneity of the composite at the nanometer level. This high loading of the nanotubes is particularly important when both electrical and mechanical qualities of the nanotubes are going to be utilized.

The phase segregation between dissimilar materials can be circumvented by applying a new deposition technique often called layer-by-layer assembly (LBL).<sup>[15]</sup> It is based on the alternating adsorption of monolayers of individual components attracted to each other by electrostatic and van der Waals interactions and can be carried out with a variety of polyelectrolytes and other compounds with high molecular weight. The immobilization of the macromolecular compounds and strong interdigitation of the nanometer-thick film allows for the close-to-perfect molecular blending of the components.<sup>[16,17]</sup>

The SWNT–polyelectrolyte composites produced in this study were assembled onto a solid support via alternate dipping of a solid substrate (glass slides, Si wafers) into dispersions of SWNT and polyelectrolyte solutions.<sup>[18–20]</sup> The individual assembly steps, i.e., adsorption of SWNT and polyelectrolyte monolayers, were interlaced by rinsing steps to remove the excess of assembling materials. When the LBL procedure was complete, the multilayer films were lifted off the substrate to obtain uniform freestanding membranes, which can be handled as regular composites.<sup>[21]</sup> Such films make possible straightforward testing of their mechanical properties. It is important to note that large-area membranes for space telescopes and similar applications can similarly be made by deposition on the substrates of appropriate size.

Single-walled carbon nanotubes were produced by laser ablation and subsequently purified via acid treatment. They were manufactured by laser vaporization

of carbon rods doped with Co, Ni, and FeS in an atmosphere of Ar:H<sub>2</sub>. It needs to be pointed out that the standard SWNT products made by HiPCO and other methods contain significant amount of soot, graphite flakes, and remnants of the catalyst, which need to be removed before the assembly. The quality of the dispersion directly affects the mechanical performance of the resulting composite.

A suspension of SWNT raw material was refluxed in 65% HNO<sub>3</sub> and subsequently purified by centrifugation. Supplemented by sonication, this treatment results in the partial oxidation of ca. 5% of the total number of carbon atoms both in caps and walls of SWNT.<sup>[22]</sup> A similar type of dispersion can also be made following other methods, such as polymer wrapping the nanotubes and chemical derivatization. Optimization of the aqueous nanotube dispersions should be considered as one of the most critical direction of the optimization of the carbon nanotube composites and speed and quality of their processing in the composites.

The presence of carboxylic acid groups affords the preparation of metastable SWNT dispersions after 1-min sonication in deionized water without any additional surfactant. Thus-prepared, negatively charged SWNT with a zeta potential of  $-0.08$  V can be layer-by-layer assembled with positively charged polyelectrolyte, such as branched poly(ethyleneimine) (PEI; Mw = 70,000) (Fig. 1). Because the overall negative charge of the SWNT used here was fairly small, a layer of SWNT was replaced with a layer of poly(acrylic acid) (PAA; Mw = 450,000) after every fifth deposition cycle (Fig. 1). These additional layers improve the linearity of the deposition process and present a convenient chemical anchor for subsequent chemical modification. For the same reasons, a single PEI/PAA bilayer was deposited on a bare glass or Si

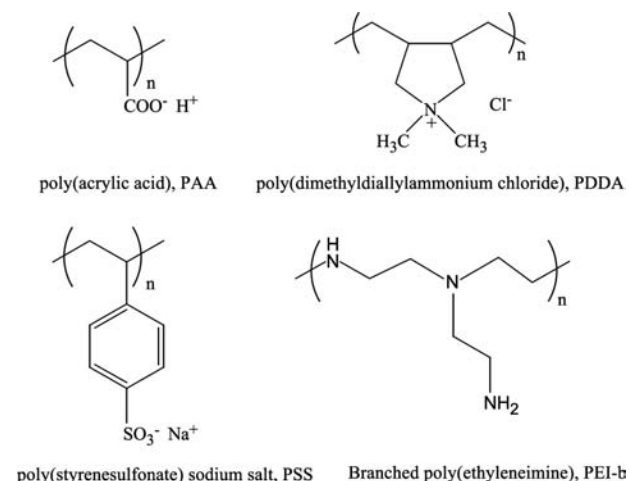


**Fig. 1** Common polyelectrolytes used for LBL process.

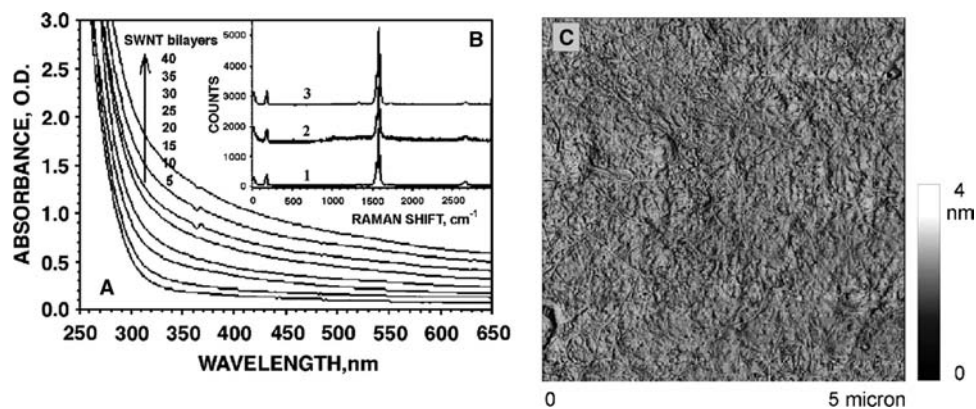


**Fig. 2** Structural characterization of SWNT multilayers. (A) Sequential UV-vis spectra of a glass substrate in the course of the LBL deposition of SWNT. The spectra were taken for a total number of (PEI/SWNT) bilayers indicated in the graph. (B) Raman scattering spectra of SWNT dispersion (1), LBL film on a glass substrate (2), and freestanding film (3). (C) Tapping mode AFM image (DI, Multimode IIIA) of a Si wafer bearing (PEI/PAA)(PEI/SWNT)<sub>5</sub>. *Source:* From Refs.<sup>[18,19]</sup>

substrate before the SWNT assembly. The assembly conditions of the entire procedure (pH, ionic strength, concentrations, etc.) were optimized so that the dipping cycles can be repeated as many times as needed with linear growth of the multilayers (Fig. 2A). This enables the preparation of films with any desirable thickness and architecture tailored to different applications. The ionic conditions of LBL assembly were the following: 1% solution of PEI at pH 8.5; 1% PAA at pH 6 (pH 3 for wafer coating); SWNT at pH 6.8. All solutions were made in 18 MΩ deionized (DI) water without addition of any extra salt or other low molecular weight electrolyte. Deionized water was also used for rinsing at pH 8.5, adjusted by NaOH. Wafers and glass slides were cleaned in piranha solution, rinsed with DI water, sonicated for 15 min, and again thoroughly rinsed with DI water. After that, they were coated with a precursor layer: PEI (10 min) + PAA (15 min, pH 3), followed by the deposition of (PEI/SWNT)<sub>5</sub>. The layer sequence of (PEI/PAA)-(PEI/SWNT)<sub>5</sub> was repeated until the desirable thickness was obtained. Exposure times of 10 and 60 min was used for polyelectrolytes and SWNT baths, respectively.<sup>[18,19]</sup>

Multilayer stacks with a cumulative structure of [(PEI/PAA)(PEI/SWNT)<sub>5</sub>]<sub>6</sub> and [(PEI/PAA)(PEI/SWNT)<sub>5</sub>]<sub>8</sub> containing 30 and 40 (PEI/SWNT) bilayers, respectively, were typically used in this study.

We are currently investigating other methods of SWNT dispersion in water to avoid excessive damage to the SWNT wall, for example, wrapping the nanotubes with copolymers, which can work equally well on the SWNT and multiwalled carbon nanotubes (MWNT). For some applications, MWNTs can be the preferred materials because of their lower cost.

Similarly to other polyelectrolyte LBL systems,<sup>[15]</sup> a submonolayer of SWNT is deposited in each

deposition cycle. The final morphology of the multilayers can be described as a mixture of individual carbon nanotubes and their 4–9-nm bundles intricately interwoven together in a fine fabric (Fig. 2C). Two important structural characteristics should be pointed out. Single-walled carbon nanotubes uniformly cover the entire surface of the substrate without any evidence of phase separation. Also, the presence of oxidized flat graphite sheets and other forms of carbon colloids in our experiments was very small. Both these factors contributed to the mechanical properties of the composites. The quality of the nanotube material was also assessed by Raman spectroscopy. (Raman measurements were performed in a backscattering configuration with 50 mW of 514.5-nm laser light incident on the samples). The characteristic Raman peaks for SWNTs, e.g., the radial breathing mode at  $\sim 182 \text{ cm}^{-1}$  and the tangential C–C stretching modes located at  $\sim 1560 \text{ cm}^{-1}$  (G1 mode) and  $\sim 1583 \text{ cm}^{-1}$  (G2 mode), were very sharp and narrow, indicating the high uniformity of the SWNT and low level of impurities present in the films. A barely visible peak at  $\sim 1340 \text{ cm}^{-1}$  (D mode) revealed the presence of residual amounts of disordered carbon structures. Using the correlation between the frequency of the radial breathing mode,  $\nu$ , and the SWNT diameter,  $d$ , expressed as  $d = 223.75/\nu$ ,<sup>[23]</sup> a value of  $d = 1.2 \text{ nm}$  is obtained, which is in a good agreement with the SWNT diameters obtained from atomic force microscopy (AFM) images of many individual nanotubes. From these images, the length of the nanotubes was estimated to be 2–7  $\mu\text{m}$ .

Poly(ethyleneimine) was utilized as the LBL partner of SWNT because of the terminal -NH<sub>2</sub> and backbone -NH- groups in the main chain and branches suitable for the subsequent chemical modification of the composite.<sup>[24]</sup> The PEI chains can be cross-linked 1) with

each other and 2) with carboxyl groups on SWNT and PAA. Chemical stitching increases the connectivity of the polyelectrolyte matrix with SWNT, and therefore, the load transfer in the composite.<sup>[13]</sup> We used here the combination of both modification pathways. Partial covalent SWNT-PEI-PAA cross-linking was achieved by heating the films to 130°C after the deposition of each layer, resulting in amide bonds between a variety of protonated and non-protonated functional groups of PEI, PAA, and SWNT complementing the intrinsic ionic cross-linking of the LBL films.<sup>[25]</sup> Subsequently, the film was exposed to glutaraldehyde at room temperature. The sample was cross-linked in 0.5% glutaraldehyde solution in phosphonate buffer (0.054 M Na<sub>2</sub>HPO<sub>4</sub>, 0.013 M NaH<sub>2</sub>PO<sub>4</sub>, pH 7.4) for 1 hr at room temperature. To remove unreacted glutaraldehyde, the film was rinsed with tap water for 3 × 10 min and then with DI water the same number of times. This reaction produces a tight network of polymeric chains and nanotubes connected by dialdehyde linkages. It was found that if only 1% of all carbon atoms of SWNT are chemically bonded to the polymer matrix, such cross-linking drastically increases the shear between them by an order of magnitude.<sup>[13]</sup> Therefore a 5% density of -COOH groups on the SWNT surface cited above should be sufficient to obtain good connectivity with the polyelectrolyte matrix. Note that these groups are not completely utilized at the moment because of the relatively low temperature of the amide bond cross-linking step.

The mechanical properties of the LBL-assembled SWNT thin films were studied in their freestanding form prepared by the chemical delamination from the substrate.<sup>[21]</sup> Multilayers of SWNT were separated from the silicon wafers by immersion into 0.5% aqueous HF for 3 min. The Raman scattering spectrum of the separated film is almost identical to that of the supported film and original nanotubes (Fig. 2B), demonstrating that the structure of SWNT remains mostly unaltered during cross-linking and delamination.

The breathing mode frequency shifts from 185 cm<sup>-1</sup> in the assembled film to 182 cm<sup>-1</sup> in the cross-linked, self-standing films, indicating a small expansion of the tube diameters.<sup>[18,19]</sup>

The delaminated thin films (Fig. 3A) can be easily handled in a variety of ways. They can be made of any desirable size or shape determined only by the dimensions of the substrate. The films that we routinely prepare in this study were ca. 1 × 3 cm. Assemblies with a structure of [(PEI/PAA)(PEI/SWNT)<sub>5</sub>]<sub>6</sub> and [(PEI/PAA)(PEI/SWNT)<sub>5</sub>]<sub>8</sub> displayed an SWNT content of 50 ± 5 wt.% as calculated from carbon and nitrogen energy-dispersive X-ray analysis (EDAX) peak integrals. Previously reported composites made with modified SWNT revealed strong inhomogeneities even at SWNT loadings as low as 6–8%.<sup>[8,9]</sup> The cross-sectional image of the freestanding film (Fig. 4A,B) clearly demonstrates the absence of micron-scale inhomogeneities although the occasional inclusion of round 30–60 nm particles can be seen (possibly dust). The slight variations in the gray-scale contrast between different strata show the actual variations in SWNT distribution within the sample. They originate from small deviations in SWNT adsorption conditions, such as dispersion concentration and pH, during the buildup procedure. In scanning electron microscopy (SEM) (Fig. 3A), the surface of the sample also appears smooth and continuous. Typically, the separation of single-walled or multiwalled carbon nanotubes and their bundles in mixed polymer composites can be observed as whiskers clearly visible in transmission electron microscopy (TEM) and SEM images.<sup>[4,26]</sup> The TEM examination of the initial stages of rupturing showed that virtually no fiber pullout occurs in the LBL multilayers (Fig. 3B). This can be contrasted by extensive nanotube pullout reported before by several groups.<sup>[4,26]</sup> For many TEM images obtained in different areas of the self-standing films, we were able to observe only one SWNT bundle bridging the break region (Fig. 3C). The same image also shows two

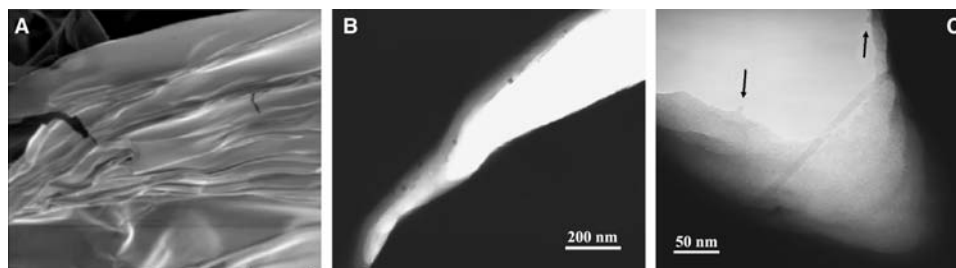


**Fig. 3** Electron microscopy of the rupture region in SWNT multilayers. (A) Scanning electron microscopic image of the surface and broken edges of [(PEI/PAA)(PEI/SWNT)<sub>5</sub>]<sub>8</sub>. (B, C) Transmission electron microscopic images of ruptured areas of the freestanding films. The arrows indicate the likely stubs of the broken nanotube bundles. They were identified as such because 1) their diameters are both equal to that of the actual SWNT bundle bridging the gap and 2) their mutual positioning presents a virtually perfect match with the expected location of the ends of a bundle broken during gap opening.



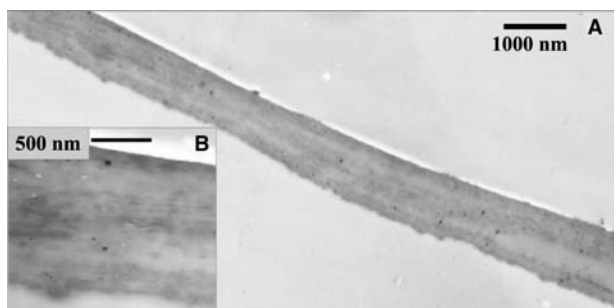


**Fig. 4** Transmission electron microscopic examination of the homogeneity of the SWNT LBL film. Survey (A) and close-up (B) TEM images of SWNT film cross sections. The top and bottom sides of the film are slightly different in roughness: The one that was adjacent to the flat substrate is smoother than the “growth” surface of the film. *Source:* From Refs.<sup>[18,19]</sup>

broken carbon fiber stubs embedded in the walls of the crack (marked by arrows in Fig. 3C). In total, the microscopy results indicate the efficient load transfer in the LBL composite. Similar films are currently prepared from the multiwalled carbon nanotubes utilizing the polymer wrapping (Fig. 5).

The mechanical properties of the layered composites were tested on a custom-made thin-film, tensile-strength tester (McAllister Inc.) recording the displacement and applied force by using pieces cut from [(PEI/PAA)(PEI/SWNT)<sub>5</sub>]<sub>6</sub> and [(PEI/PAA)(PEI/SWNT)<sub>5</sub>]<sub>8</sub> freestanding films. The tester was calibrated on similar pieces made from cellulose acetate membranes and Nylon threads. [(PEI/PAA)(PEI/SWNT)<sub>5</sub>]<sub>6</sub> and [(PEI/PAA)(PEI/SWNT)<sub>5</sub>]<sub>8</sub> samples had an average TEM thickness of 0.75 and 1.0 μm, respectively. Their typical stress ( $\sigma$ ) vs. strain ( $\epsilon$ ) curves differed quite markedly from stretching curves previously seen for SWNT composites<sup>[10]</sup> and for LBL films solely made from polyelectrolytes, (PEI/PAA)<sub>40</sub>, obtained by the same

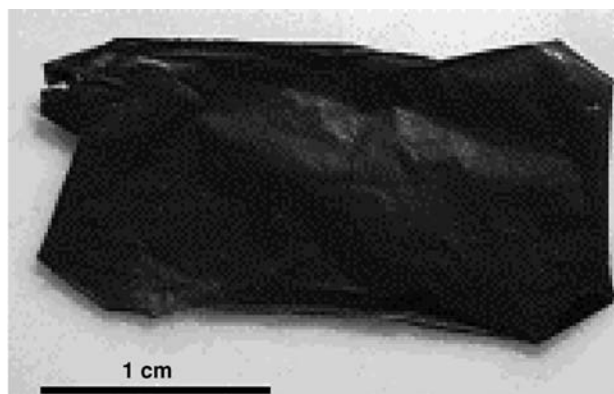


**Fig. 5** Optical photograph of the free-standing LBL films made from multiwalled carbon nanotubes.

assembly procedure (Fig. 6B). They displayed a characteristic wave-like pattern, gradual increase of  $d\sigma/d\epsilon$  derivative, and the complete absence of the plateau region for high strains corresponding to plastic deformations (Fig. 6A). The latter correlates well with the enhanced connectivity of SWNT with the polymer matrix (Fig. 3). Other mentioned stretching features indicate the reorganization of the layered composite under stress. A process similar to the sequential breakage of cross-linked parts of coiled molecules (see AFM image in Fig. 2) observed in natural nanocomposites, such as seashells and bones,<sup>[27,28]</sup> is likely to be responsible for the wave-like pattern and the increase of the stretching curve slope. This statement can be substantiated by the AFM investigation of the single molecules of a polyelectrolyte adsorbed to the substrate (Fig. 7). Atomic force microscopy images of poly(diallyldimethylammonium) chloride (PDDA) (Fig. 7) polycation adsorbed to silicates revealed the actual conformation of macromolecules at the organic–inorganic interface. Similarly to PEI, this polyelectrolyte has a positive charge when adsorbed to silica or glass. Coiling of PEI is expected to be even stronger than that of PDDA because the latter has intrinsically strong propensity to form a rod-like structure because of its greater charge. The intentionally rarified submonolayers of polycation were made from  $2 \times 10^{-7}$  wt.% solutions to resolve single chains (Fig. 7A). These are intricately entangled to form a continuous film at higher concentrations. Adsorbed polyelectrolyte were found to be present in the film in different conformational states: extended (Fig. 7C),

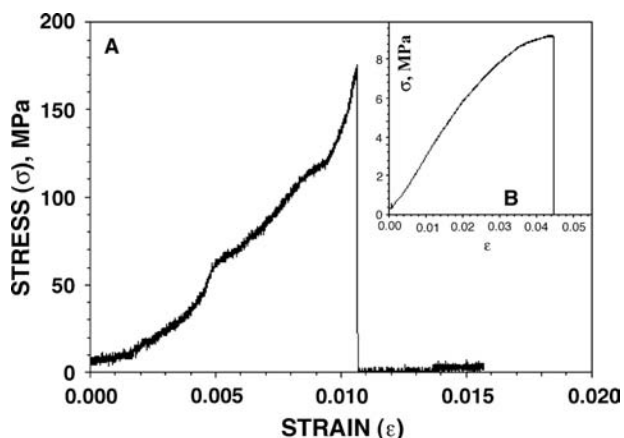


**Fig. 6** Typical tensile-strength curves of the SWNT LBL films. Stress–strain dependence for (A) [(PEI/PAA)(PEI/SWNT)<sub>5</sub>]<sub>8</sub> and (B) a similar free-standing multilayer film solely made from polyelectrolytes. The dependence of the mechanical properties of the cross-linked LBL composites on humidity was tested in the range of relative humidity of 30–100%,  $T = 298^\circ\text{C}$ , and was found to be negligible. *Source:* From Refs.<sup>[18,19]</sup>

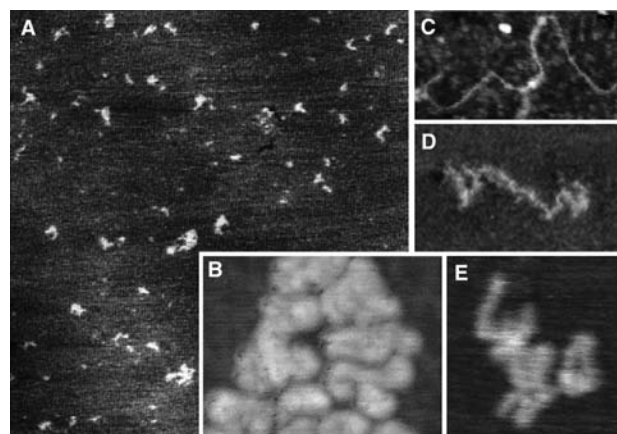


**Fig. 7** Atomic force microscopy of rarified PDDA films. (A) Overview of adsorbed PDDA molecules ( $2 \times 2 \mu\text{m}$ , mica). (B) Cluster of PDDA molecules ( $360 \times 230 \text{ nm}$ , Si wafer). (C) Fully extended PDDA chain ( $350 \times 170 \text{ nm}$ ). (D) Partially coiled PDDA chain ( $160 \times 80 \text{ nm}$ , mica). (E) Typical highly coiled conformation of PDDA chain ( $100 \times 110 \text{ nm}$ ). Source: From Ref.<sup>[29]</sup>.

partially coiled (Fig. 7D), and tightly coiled (Fig. 7E). The length of the macromolecules in extended conformation, 350–400 nm (Fig. 7C), coincides with that expected for poly(diallyldimethylammonium) chloride with  $M_w=200,000$ . As can be seen from Fig. 7A, most of the molecules (>75%) are present in the tightly coiled conformation. Moreover, the AFM examination of the clusters of the macromolecules molecules (Fig. 7B) demonstrates that this is apparently the preferential conformation of the polyelectrolyte in densely packed films made at higher concentrations used for multilayer preparation.<sup>[29]</sup>

Considering the complexity of the deformation process, the assessment of elastic and inelastic behavior in each part of the curve will be carried out upon detailed microscopic investigation. Meanwhile, the values of  $d\sigma/d\varepsilon$  exceeding 50 GPa should be noted.

The comparison with stretching curves of polyelectrolytes (Fig. 6B) shows that the incorporation of nanotubes in the LBL structure resulted in the transfer of the SWNT strength to the entire assembly. The stretching curves of the SWNT multilayers display a clear break point. The ultimate tensile strength,  $T$ , was found to be  $220 \pm 40 \text{ MPa}$  with some readings being as high as 325 MPa. This is several times to an order of magnitude greater than the tensile strength of strong industrial plastics with  $T = 20\text{--}66 \text{ MPa}$ .<sup>[30]</sup> It is also substantially higher than the tensile strength of carbon fiber composites made by mixing: Polypropylene filled with 50 vol.% carbon fibers has  $T = 53 \text{ MPa}$ .<sup>[31]</sup> A recent study on SWNT–poly(vinylalcohol) ribbons with axially aligned nanotubes reported a

tensile strength of 150 MPa.<sup>[10]</sup> The  $T$  values obtained for SWNT LBL films are in fact close to those of ultrahard ceramics and cermets such as tungsten monocarbide ( $T = 340 \text{ MPa}$ ), silicon monocarbide ( $T = 300 \text{ MPa}$ ), and tantalum monocarbide ( $T = 290 \text{ MPa}$ ).<sup>[30]</sup> Such strength and failure strain greater than in cermets (ca. > 1% in SWNT LBL vs. 0.2–0.6% in carbides) displayed by an organic composite is quite remarkable.

The tensile strength of single carbon nanotubes was experimentally determined to be between 13 and 50 GPa.<sup>[26,32]</sup> The lower values obtained for the SWNT multilayers should be mainly attributed to the contribution of polyelectrolytes and some uncertainty in the actual cross-section area at the break point and a degree of cross-linking. The mixing law predicts that polyelectrolyte matrix with  $T = 9 \text{ MPa}$  makes negligible contribution to the strength of the composite while taking about 50% of its volume fraction. [SWNT is  $d = 1.14 \text{ g/cm}^3$ . Because the density of the polyelectrolytes used for the preparation of the multilayers (i.e., PDDA  $d = 1.04 \text{ g/cm}^3$ ; PAA  $d = 1.14 \text{ g/cm}^3$ ) is almost the same, the volume fraction of SWNT in the composite can be considered to be equal to the mass fraction.] Additionally, the decrease of the mechanical strength of the nanotubes in the process of ionic functionalization (estimate 15%)<sup>[33]</sup> should also be considered as a factor affecting the strength of these composites. These issues are pointed out as means of further optimization of the multilayers. Tuning of their molecular structure and composition should lead to vast improvement of their mechanical properties that could possibly approach those of pristine carbon nanotubes.

It is also interesting to compare the  $T$  values for SWNT composite films to those obtained for other LBL films made with other inorganic components such as montmorillonite platelets, M, and nanoparticles, NP, for instance 8–10-nm magnetite nanoparticles. The freestanding films (PDDA/NP)<sub>40</sub> and (PDDA/NP/PDDA/M)<sub>40</sub> made according to Ref.<sup>[21]</sup> revealed  $T$  equal to 40 and 72 MPa, respectively. In conjunction with the tensile strength data (see above), it can be concluded that inorganic or SWNT components act as a molecular armor in the layered composites significantly reinforcing them. The molecular organization of the material made possible the transfer of a part of their strength to the entire assembly.

## CONCLUSION

The technology of the preparation of nanocomposites described above should be considered as an effective

tool in developing new ultrastrong materials. High structural homogeneity and interconnectivity of the structural components of the LBL films combined with high SWNT loading leads to significant increase of the strength of nanocomposites, being somewhat weaker than some other organic and carbon fiber materials but at the same time being far beyond their potential as ultrastrong composites. The described technique minimizes the structural defects originating from phase segregation and opens a possibility for the molecular design of layered hybrid structural materials from different polymers and other nanoscale building blocks. The prepared freestanding membranes can serve as a unique component for a variety of technologies. One of its great advantages over other technologies is the ability to prepare ultrathin ultrastrong membranes with minimal heterogeneity. We expect these composite materials to be used initially in high-value applications, most possibly as a critical part of a space or biomedical device. Once the carbon nanotubes become less expensive and the LBL processing becomes a routine operation, the same composites can be utilized in more high-volume products such as building construction materials and car components. At the same time, the less-expensive alternatives to the ultrastrong composites with comparable performance can be developed from carbon- or ceramics-based nanomaterials.

## REFERENCES

- Wong, E.W.; Sheehan, P.E.; Lieber, C.M. Nanobeam mechanics: Elasticity, strength, and toughness of nanorods and nanotubes. *Science (Washington DC)* **1997**, *277*, 1971–1975.
- Popov, V.N.; Van Doren, V.E.; Balkanski, M. Elastic properties of single-walled carbon nanotubes. *Phys. Rev., B* **2000**, *61*, 3078–3084.
- Baughman, R.H. et al. Carbon nanotube actuators. *Science (Washington DC)* **1999**, *284*, 1340–1344.
- Qian, D.; Dickey, E.C.; Andrews, R.; Rantell, T. Load transfer and deformation mechanisms in carbon nanotube-polystyrene composites. *Appl. Phys. Lett.* **2000**, *76*, 2868–2870.
- Yu, M.F.; Lourie, O.; Dyer, M.J.; Moloni, K.; Kelly, T.F.; Ruoff, R.S. Strength and breaking mechanism of multiwalled carbon nanotubes under tensile load. *Science (Washington DC)* **2000**, *287*, 637–640.
- Salvetat, J.P.; Kulik, A.J.; Bonard, J.-M.; Briggs, G.A.D.; Stöckli, T.; Méténier, K.; Bonnamy, S.; Béguin, F.; Burnham, N.A.; Forró, L. Elastic modulus of ordered and disordered multiwalled carbon nanotubes. *Adv. Mater. (Weinheim, Germany)* **1999**, *11*, 161–165.
- Shaffer, M.S.P.; Windle, A.H. Fabrication and characterization of carbon nanotube/poly(vinyl alcohol) composites. *Adv. Mater. (Weinheim, Germany)* **1999**, *11*, 937–941.
- Haggenmueller, R.; Gommans, H.H.; Rinzler, A.G.; Fischer, J.E.; Winey, K.I. Aligned single-wall carbon nanotubes in composites by melt processing methods. *Chem. Phys. Lett.* **2000**, *330*, 219–225.
- Watts, P.C.P.; Hsu, W.K.; Chen, G.Z.; Fray, D.J.; Kroto, H.W.; David, R.M. A low resistance boron-doped carbon nanotube-polystyrene composite. *J. Mater. Chem.* **2001**, *11*, 2482–2488.
- Vigolo, B.; Pénicaud, A.; Coulon, C.; Sauder, C.; Pailler, R.; Journet, C.; Bernier, P.; Poulin, P. Macroscopic fibers and ribbons of oriented carbon nanotubes. *Science* **290**, 1331–1334.
- Salvetat, J.P.; Andrew, G.; Briggs, D.; Bonard, J.M.; Bacsá, R.R.; Kulik, A.J.; Stöckli, T.; Burnham, N.A.; Forró, L. Elastic and shear moduli of single-walled carbon nanotube ropes. *Phys. Rev. Lett.* **1999**, *82*, 944–947.
- Chen, J.; Rao, A.M.; Lyuksyutov, S.; Itkis, M.E.; Hamon, M.A.; Hu, H.; Cohn, R.W.; Eklund, P.C.; Colbert, D.T.; Smalley, R.E.; Haddon, R.C. Dissolution of full-length single-walled carbon nanotubes. *J. Phys. Chem., B* **2001**, *105*, 2525–2528.
- Frankland, S.J.V.; Caglar, A.; Brenner, D.W.; Griebel, M. Molecular simulation of the influence of chemical cross-links on the shear strength of carbon nanotube-polymer interfaces. *J. Phys. Chem., B* **2002**, *106*, 3046–3048.
- Star, A.; Stoddart, J.F.; Steuerman, D.; Diehl, M.; Boukai, A.; Wong, E.W.; Yang, X.; Chung, S.W.; Choi, H.; Heath, J.R. Preparation and properties of polymer-wrapped single-walled carbon nanotubes. *Angew. Chem., Int. Ed.* **2001**, *40*, 1721–1725.
- Decher, G. Fuzzy nanoassemblies toward layered polymeric multicomposites. *Science* **1997**, *277*, 1232–1237.
- Wu, A.; Yoo, D.; Lee, J.K.; Rubner, M.F. Solid-state light-emitting devices based on the tris-chelated ruthenium(II) complex: 3. High efficiency devices via a layer-by-layer molecular-level blending approach. *J. Am. Chem. Soc.* **1999**, *121*, 4883–4891.
- Mamedov, A.A.; Belov, A.; Giersig, M.; Mamedova, N.N.; Kotov, N.A. Nanorainbows. Graded semiconductor films from quantum dots. *J. Am. Chem. Soc.* **2001**, *123*, 7738–7739.
- Mamedov, A.A.; Kotov, N.A.; Prato, M.; Guldi, D.; Wicksted, J.P.; Hirsch, A. Molecular design of strong SWNT/polyelectrolyte multilayers composites. *Nat. Mater.* **2002**, *1*, 190–194.
- Mamedov, A.A.; Guldi, D.M.; Prato, M.; Kotov, N.A. Layer-by-Layer Assembly of Carbon Nanotubes. In *Abstracts of Papers*, 223rd ACS National Meeting, Orlando, FL, United States, April 7–11, 2002.
- Rouse, J.H.; Ounaies, Z.; Lellehei, P.T.; Siochi, E.J. Incorporation of Carbon Nanotubes Within Stepwise Assembled Polyelectrolyte Films. In *Abstracts of Papers*, 223rd ACS National Meeting, Orlando, FL, United States, April 7–11, **2002**.
- Mamedov, A.A.; Kotov, N.A. Free-standing layer-by-layer assembled films of magnetite nanoparticles. *Langmuir* **2000**, *16*, 5530–5533.
- Mawhinney, D.B.; Naumenko, V.; Kuznetsova, A.; Yates, J.T., Jr.; Liu, J.; Smalley, R.E. Surface defect site

- density on single walled carbon nanotubes by titration. *Chem. Phys. Lett.* **2000**, *324*, 213–216.
23. Rols, S.; Righi, A.; Alvarez, L.; Anglaret, E.; Almairac, R.; Journet, C.; Bernier, P.; Sauvajol, J.L.; Benito, A.M.; Maser, W.K.; Muñoz, E.; Martinez, M.T.; de laFuente, G.F.; Girard, A.; Ameline, J.C. Diameter distribution of single wall carbon nanotubes in nanobundles. *Eur. Phys. J., B* **2000**, *18*, 201–205.
  24. Westenhoff, S.; Kotov, N.A. Quantum dot on a rope. *J. Am. Chem. Soc.* **2002**, *124*, 2448–2449.
  25. Sullivan, D.M.; Bruening, M.L. Ultrathin, ion-selective polyimide membranes prepared from layered poly-electrolytes. *J. Am. Chem. Soc.* **2001**, *123*, 11805–11806.
  26. Li, F.; Cheng, H.M.; Bai, S.; Su, G.; Dresselhaus, M.S. Tensile strength of single-walled carbon nanotubes directly measured from their macroscopic ropes. *Appl. Phys. Lett.* **2000**, *77*, 3161–3163.
  27. Thompson, J.B.; Kindt, J.H.; Drake, B.; Hansma, H.G.; Morse, D.E.; Hansma, P.K. Bone indentation recovery time correlates with bond reforming time. *Nature (London)* **2001**, *414*, 773–776.
  28. Smith, B.L.; Schäffer, T.E.; Viani, M.; Thompson, J.B.; Frederick, N.A.; Kindt, J.; Belcher, A.; Stucky, G.D.; Morse, D.E.; Hansma, P.K. Molecular mechanistic origin of the toughness of natural adhesives, fibers and composites. *Nature (London)* **1999**, *399*, 761–763.
  29. *CRC Materials Science and Engineering Handbook*; CRC: Boca Raton, FL, 1992.
  30. Fu, S.Y.; Lauke, B.; Mäder, E.; Yue, C.Y.; Hu, X.; Mai, Y.W. Hybrid effects on tensile properties of hybrid short-glass-fiber- and short-carbon-fiber-reinforced polypropylene composites. *J. Mater. Sci.* **2001**, *36*, 1243–1251.
  31. Yu, M.F.; Files, B.S.; Arepalli, S.; Ruoff, R.S. Tensile loading of ropes of single wall carbon nanotubes and their mechanical properties. *Phys. Rev. Lett.* **2000**, *84*, 5552–5555.
  32. Garg, A.; Sinnott, S.B. Effect of chemical functionalization on the mechanical properties of carbon nanotubes. *Chem. Phys. Lett.* **1998**, *295*, 273–278.
  33. Tang, Z.; Kotov, N.A.; Magonov, S.; Ozturk, B. *Nat. Mater.* **2003**, *2* (6), 413–418.

# Nanostructures Based on Layered Transition-Metal Chalcogenides

**Russell R. Chianelli**

*Chemistry Department, University of Texas at El Paso,  
El Paso, Texas, U.S.A.*

**Myriam Perez de la Rosa**

*Materials Research and Technology Institute, University of Texas at El Paso,  
El Paso, Texas, U.S.A.*

## INTRODUCTION

The discovery of carbon nanotubes by Ijima<sup>[1]</sup> initiated a new area of materials science. Following Ijima's discovery, Tenne et al.<sup>[2]</sup> later found layered sulfides (MoS<sub>2</sub> and WS<sub>2</sub>) to form nanotubes and other fullerene-type structures. Nanoparticles based on layered transition metal sulfides (LTMS) are of special interest because of their diverse applications. Layered transition metal sulfides have been extensively studied because of their crucial role in the petroleum and chemical industry. MoS<sub>2</sub>-based and WS<sub>2</sub>-based catalysts have been used for sulfur and nitrogen removal from petroleum feedstock.<sup>[3]</sup> In addition, MoS<sub>2</sub> is used as a lubricant additive.<sup>[4]</sup> Related compounds of TiS<sub>2</sub>, as well as MoS<sub>2</sub>, can work as cathodes in lithium nonaqueous batteries<sup>[5,6]</sup> and possess interesting and useful intercalation chemistry.<sup>[7]</sup> WS<sub>2</sub>, WSe<sub>2</sub>, TiS<sub>2</sub>, MoS<sub>2</sub>, MoSe<sub>2</sub>, and MoTe<sub>2</sub> are all semiconductors with unusual properties and potential electronic applications.<sup>[8]</sup>

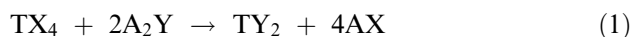
The structure of MoS<sub>2</sub>, WS<sub>2</sub>, and ReS<sub>2</sub> consists of a two-dimensional layered closed-packed sulfur arrangement with a transition metal sandwiched between each layer. Weak van der Waals interlayer forces occur between stacked "sandwiches" that allow easy, low-strength shearing.<sup>[9,10]</sup> These materials are highly folded and distorted in nature, forming commonly known "rag" and "tubular" structures. Layered transition metal sulfide materials appear as morphological analogs of fullerenes exhibiting structures described as inorganic fullerenes (IFs), single sheets, folded sheets, nanocrystals, and nested IFs, also known as "onion crystals" or "Russian dolls."

Fullerene-related nanoparticles of MoS<sub>2</sub> can be obtained by electron beam irradiation,<sup>[11]</sup> laser ablation<sup>[12]</sup> of MoS<sub>2</sub> bulk powder, and arc discharge.<sup>[13]</sup> Scanning tunneling microscope electrical pulses over amorphous MoS<sub>3</sub> nanoparticles lead to the formation of closed MoS<sub>2</sub> shell IF (a few layers thick) and amorphous MoS<sub>3</sub>.<sup>[14]</sup> Inorganic fullerene nanoparticles have been synthesized recently by a variety of methods. Others

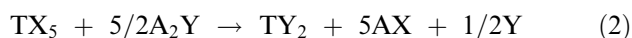
have reported the gas-phase synthesis of fullerene-like structures of WS<sub>2</sub><sup>[2]</sup> and MoS<sub>2</sub><sup>[15]</sup> and nested fullerenes of MoS<sub>2</sub>.<sup>[16]</sup> Complex WS<sub>2</sub> nanostructures have been obtained by template growth by Whitby et al.<sup>[17]</sup> The preparation and optical characterization of crystalline nanoparticles prepared by intercalation and ultrasonic fragmentation of bulk crystals have also been studied.<sup>[18–20]</sup> Divigalpitiya, Frindt, and Morrison<sup>[21–23]</sup> have reported the synthesis and preliminary characterization of composites based on single sheets of MoS<sub>2</sub>. Wilcoxon, Samara, and Newcomes<sup>[24]</sup> Wilcoxon and Samara,<sup>[25]</sup> and Parsapour et al.<sup>[26]</sup> have reported the growth of MoS<sub>2</sub> nanoparticles using micelle techniques.

## SYNTHESIS OF LAYERED TRANSITION METAL SULFIDES

A variety of methods have been used to synthesize LTMS. In general, poorly crystalline dichalcogenides are prepared by heating under hydrogen sulfide flow. The highly folded material is prepared by heating several grams of amorphous MoS<sub>2</sub> for 2 hr at 400°C in a stream of H<sub>2</sub> mixed with 15% H<sub>2</sub>S. As a result, the structure denoted as "poorly crystalline" and "raglike" LTMS is obtained.<sup>[27–29]</sup> The "rag" structure consists of stacked but highly folded and disordered MoS<sub>2</sub> layers (Fig. 1). The number of stacks and the dimensions of the layers can vary by changing the preparation conditions. The general reaction scheme of low-temperature metaphorical reaction in a solution is:



where T = transitional metal, X = salt anion (Cl, carboxylate, etc.), A = alkali-like cation (Li<sup>+</sup>, Na<sup>+</sup>, NH<sub>4</sub><sup>+</sup>, etc.), and Y = chalcogenides anion. Redox reactions tend to occur because the transition metal ions and the chalcogenides exist in several oxidation states:





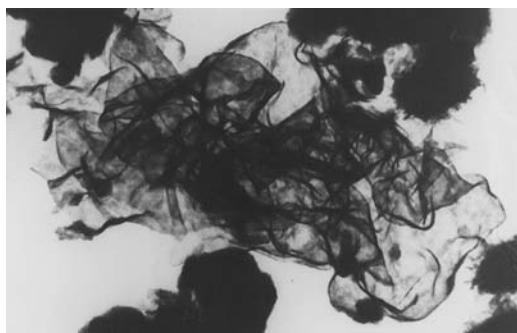
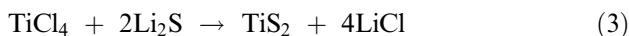


**Fig. 1** Folded and disorder sheets of MoS<sub>2</sub>. *Source:* From Ref.<sup>[28]</sup>.

The great stability that the oxides and hydroxides lend to the transition metal salt eliminates the need for an aqueous environment. Moreover, hydroxylic solvents, in general, are very reactive and can serve as solvents for TX<sub>4</sub> or TX<sub>5</sub>. Poor reaction between hydrogen sulfide and the transition metal salt does not allow for direct synthesis of TY<sub>2</sub> species. This is why alkali chalcogenides must be used. Even in the absence of oxygen in air or water, the reaction of TiCl<sub>4</sub> with H<sub>2</sub>S is unfavorable at temperatures lower than 400°C. These are highly reactive ionic sources of chalcogenides and the reaction readily proceeds at room temperature. Lithium sulfide was found to be the most convenient source of sulfide ion:



For precipitation at room temperature, tetrahydrofuran and ethyl acetate are suitable solvents. Dark precipitates are obtained and easily filtered. Repeated washings with the solvent completely remove LiCl excess. To obtain crystalline TiS<sub>2</sub>, further heating at 400–600°C is required in a sealed quartz tube under an inert atmosphere. This example illustrates the synthesis of TiS<sub>2</sub> but it can be applied to any other transition metal sulfide.

WS<sub>2</sub>, ReS<sub>2</sub>, and OsS<sub>2</sub> can be prepared by heating amorphous sulfides at 400°C in a stream of H<sub>2</sub> mixed with 15% H<sub>2</sub>S. The structure of the ReS<sub>2</sub> poorly crystalline structure is the most likely material for the production of large amounts of nanotubes and fullerene-like materials. Recently, tetraalkylammonium thiomolybdates have been used to incorporate carbon into the extremely disordered materials and it is believed that this impurity increases the ability of the MoS<sub>2</sub> to fold.<sup>[30–32]</sup>

### NESTED INORGANIC FULLERENE ONION-LIKE STRUCTURE

Carbon fullerene Onion-like structures have been obtained under high electron irradiation using



**Fig. 2** Onion-like structures in MoS<sub>2</sub>. *Source:* From Ref.<sup>[11]</sup>.

transmission electron microscopy (TEM).<sup>[33]</sup> Tenne et al.<sup>[2]</sup> and Margulis et al.<sup>[34]</sup> have also observed fullerene Onion-like structures in layered materials including WS<sub>2</sub> and MoS<sub>2</sub>. Electron-irradiated MoS<sub>2</sub> crystals at 0.5 MeV energy were studied by Yacaman et al. using high-resolution electron microscopy. The irradiated MoS<sub>2</sub> crystals presented two main features: onion layers with fullerene-like structures, and others with their planes rotated with respect to each other by well-defined angles.<sup>[11]</sup> In the case of carbon, Onion-like structures tend to be rounded.<sup>[33]</sup> However, the layered materials Onion-like structures are faceted near the center and rounded at the edges, as illustrated in Fig. 2. MoS<sub>2</sub> layers in Onion-like structures are not evenly spaced (Fig. 3). Another interesting feature of these structures is illustrated in Fig. 4, where a relative



**Fig. 3** High-resolution transmission electron microscopy image of MoS<sub>2</sub> Onion-like structure. Fourier transform of the structure is shown in the inset. *Source:* From Ref.<sup>[11]</sup>.



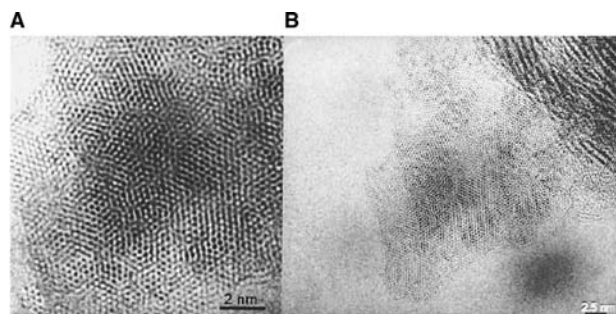


**Fig. 4** Irradiated MoS<sub>2</sub> that illustrated a relative rotation of 10° by the layers on MoS<sub>2</sub> around an axis perpendicular to the image: (A) low magnification; and (B) high magnification. Source: From Ref.<sup>[11]</sup>.

rotation of the MoS<sub>2</sub> layers around an axis perpendicular to the basal plane can be clearly seen.

In a different approach, IFs such as IF-MoS<sub>2</sub> have also been synthesized using high-temperature methods that occur above 650°C. These methods involve such techniques as growth from the gas phase in which MoO<sub>3</sub> in the vapor phase is reacted with H<sub>2</sub>S in a carrier gas (Fig. 5). The gas-phase reactor synthesis has achieved great control over the nanoparticles growth parameters. This process consists of MoO<sub>3</sub> powder placed in the inner part of the reactor, (a) which is heated to 780°C. Molecular clusters (MoO<sub>3</sub>)<sub>3</sub> are formed and carried down through the reactor by N<sub>2</sub> gas. Hydrogen gas diffuses through the nozzles (c) from the outer reactor (b) and starts to react with the molecular clusters. The mild reduction conditions yield reduced MoO<sub>3-x</sub> clusters, which are less volatile and form MoO<sub>3-x</sub> nanosize particles at the low part of (a). The suboxide nanoparticles reach a size less than 5 nm before the sulfidization step. The coated oxide nanoparticles are swept by the carrier gas outside the reactor (a). Because the nanoparticles are surface-passivated, they land on the ceramic filter (d) and the oxide-to-sulfide conversion continues within the core without coalescence of the nanoparticles. The gas-phase reactor synthesis process generates pure IF-MoS<sub>2</sub> phase and the control over the size and shape of the nanoparticles is quite good.<sup>[35]</sup> A characteristic image of three IF nanoparticles produced in the gas-phase reactor is illustrated in Fig. 6.

MoS<sub>2</sub> fullerene-like nanoparticles can also be produced by a combination of sonochemistry and electrochemistry, recently termed sonoelectrochemistry. Sonoelectrochemical formation of nanoscale metal powders has been achieved by applying an electric current pulse to nucleate the electrodeposit, followed by a burst of ultrasonic energy that removes the metal particles from the sonic probe cathode.<sup>[36]</sup> Mastai et al. used the known process for cathodic electrodeposition of MoS<sub>2</sub> from solutions of thiomolybdate ions.

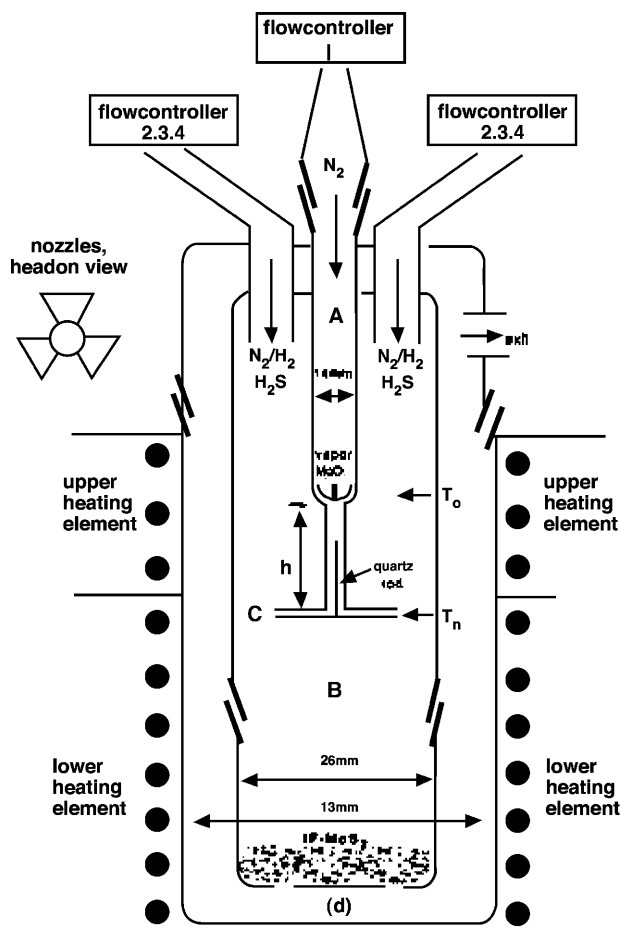


**Fig. 5** (A) Vertical gas-phase reactor for synthesis of MoS<sub>2</sub> fullerene-like nanoparticles: (a) inner tube; (b) middle tube; (c) nozzles; (d) external tube. (B) Closer look at the inner reactor (a). Source: From Ref.<sup>[35]</sup>.

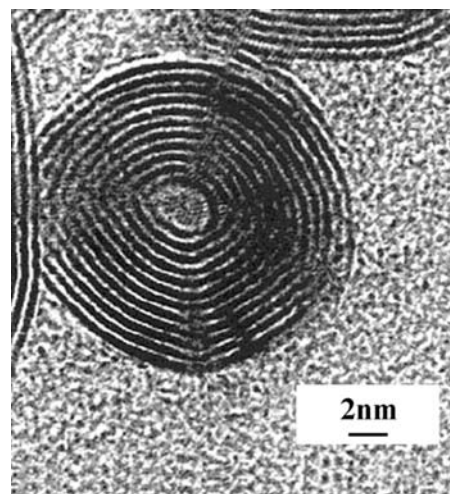


**Fig. 6** "Russian doll" structures obtained by gas-phase synthesis. Source: From Ref.<sup>[15]</sup>.

Normally amorphous MoS<sub>2</sub> is deposited and becomes crystalline after heat treatment, forming a highly textured film.<sup>[36]</sup> Fig. 7 illustrates TEM images of the sonoelectrochemically prepared MoS<sub>2</sub> particles at different orientations with respect to the electron beam. The curved and closed nature of the structures can be observed at different angles. The authors could not state if the structures are made up of MoS<sub>2</sub> sheets entirely, are hollow, or contain a core of another material (i.e., MoO<sub>2</sub>, amorphous MoS<sub>2</sub>). However, the presence of MoS<sub>2</sub> planes inside the closed structures, but oriented in various directions (Fig. 7C),

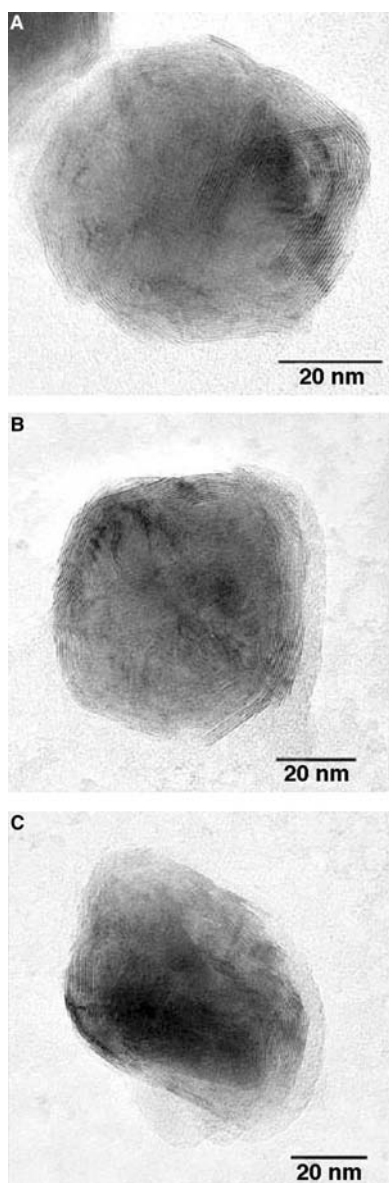


**Fig. 7** Transmission electron microscopy images of the same MoS<sub>2</sub> particles taken with the sample rotated in the sample rotated in the direction of the electron beam at an angle of (A) +45°; (B) 0°; and (C) -45°. *Source:* From Ref.<sup>[36]</sup>.

suggests that the structures are hollow to some extent, as stated by Mastai et al.

They suggested an interesting mechanism to explain the closed curved structure. Amorphous MoS<sub>2</sub> is suspected to be formed by electrodepositing onto the sonic probe cathode. The deposit is then removed from the probe surface by a sonic shock wave. The deposit could be found in a spheroid or planar structure because nucleating electrodeposits are often nanoparticulates. The effect of the shock wave is not enough to crystallize the deposit according to the authors. They concluded that the cause of the crystallization, and possibly bending, which normally require high temperatures, is the collapse of cavitation bubbles. Cavitation bubble nucleation is favored at a surface, either of the sonic probe itself or of MoS<sub>2</sub>, which was previously removed from the probe surface. The bubble can then grow with the MoS<sub>2</sub> attached to it. During collapse, the high temperature at the surface of the bubble can cause crystallization.<sup>[36]</sup> The authors presented two cases to describe the crystallization of the particle. If the original amorphous particle was spheroidal, then the final crystallized particle is likely to maintain a related morphology. If the original particle, as removed from the probe, is closer to two-dimensional, curvatures and closures may occur around the collapsing bubble (the bubble then determines the shape of the structure), or the temperature from the bubble surface into the solution should cause a temperature gradient across the particle, which could also cause curvature. The closure is energetically preferred because of bond energy released by removing reactive edges. The less common nanotube formation could occur if the nucleated deposit were filamentary, or, more likely, if the bubble collapse occurred at the electrodeposit that was still on the electrode surface.<sup>[36]</sup> In that case, the effect of the bubble collapse is asymmetric, which could lead to an asymmetric-shaped structure of the final product. Sonochemical reactions that take place inside the collapsing bubble result always in amorphous products because of fast cooling rates ( $>10^{10}$  K/sec).<sup>[36]</sup>

On the other hand, amorphous or crystalline materials are produced by aqueous ionic reactions that take place in the 2000-nm ring surrounding the collapsing bubble. When operated separately, electrochemistry or sonochemistry yields amorphous MoS<sub>2</sub>. The proposed mechanism, involving the collapse of the cavitation bubble, logically explains the crystallization of this amorphous compound and (bending and closure) considers that the amorphous particle is not already related to the final shape and size.

Ultrasonic radiation not only induces crystallization and shape control reactions, but it can also induce chemical reactions. The combination of electrochemical and sonic processes provides many experimental

variables, which allow to control particle size and shape distribution, and will probably be applicable to the formation of closed structures of other layered compounds that can be prepared by electrochemical techniques.<sup>[36]</sup>

## MOS<sub>2</sub> NANOTUBES

Microtubes of MoS<sub>2</sub> have been grown by Remskar et al.<sup>[37]</sup> MoS<sub>2</sub> nanotubes produced using a template have been reported by Zelenski and Dorhout.<sup>[38]</sup> A low-temperature method developed by Prasad, Diemann, and Muller<sup>[39]</sup> produced MoS<sub>2</sub> from solution-phase precursors within the porous membrane of electrochemically generated Al<sub>2</sub>O<sub>3</sub>. MoS<sub>2</sub> nanotubes were obtained using Prasad, Diemann, and Muller method and characterized by high-resolution electron microscopy (HREM) and electron diffraction by Chianelli et al.<sup>[40]</sup> MoS<sub>2</sub> nanotubes were prepared using non-porous alumina templates produced by ionization of aluminum. To obtain the nanotubes, a solution-phase precursor of (NH<sub>4</sub>)<sub>2</sub>MoS<sub>4</sub> in dimethylformide (DMF) was prepared. Small pieces of alumina template were immersed into the solution for a few seconds. The templates were dried at 70°C on a hot plate until the solvent evaporated. The samples were loaded into a quartz tube, which was placed into a furnace and treated with a mixture of 10% H<sub>2</sub>/N<sub>2</sub> at 450°C. The MoS<sub>2</sub> nanotubes were then removed from the templates and characterized by high-resolution transmission electron microscopy (HRTEM). Computational calculations were carried out to study the properties of the MoS<sub>2</sub> nanotubes. A minimum diameter was determined to indicate the structural stability of the MoS<sub>2</sub> nanotubes.<sup>[40]</sup>

In Fig. 8A and B, two images of the Al<sub>2</sub>O<sub>3</sub> template used to produce the MoS<sub>2</sub> nanotubes are illustrated. The figure shows low-magnification and high-magnification scanning electron microscopy (SEM) pictures of the surface and the cross section of the template. The cross-section band structure illustrates pores of 25 nm in diameter in uniform distribution (Fig. 8A). The pore length was about 25 μm wide and 250 μm long, as observed in Fig. 8B. The MoS<sub>2</sub> nanotubes were grown in the pores of the templates. A characteristic high-resolution image of a nanotube is illustrated in Fig. 9. The nanotube shown is approximately 260 nm long. An interplanar average distance of about 6.25 Å and an interplanar distance of about 2.74 Å (100 plane) were determined by measuring the (002) planes of the MoS<sub>2</sub> structure at the border of the tubes using higher-magnification micrographs.<sup>[40]</sup> This value is larger than the 6.16 Å expected for crystalline MoS<sub>2</sub>. It should be noted that the (002) planes are not seen in the interior part of the tube indicating normal contrast for a tubular structure.

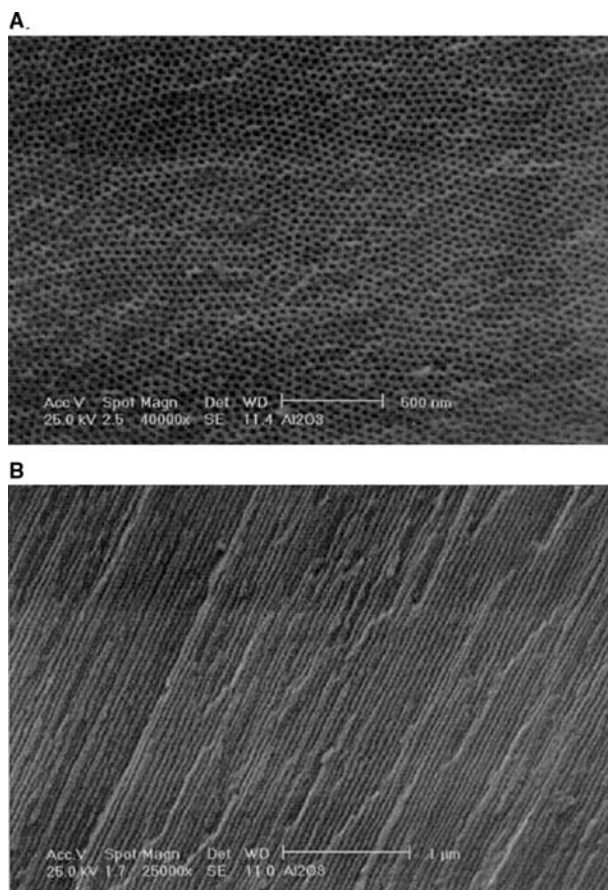


**Fig. 8** Scanning electron microscopy images of the surface of electrochemically produced Al<sub>2</sub>O<sub>3</sub>. (A) Low-magnification picture of the cross-section band structure. (B) High-magnification picture of the pores. *Source:* From Ref.<sup>[40]</sup>.

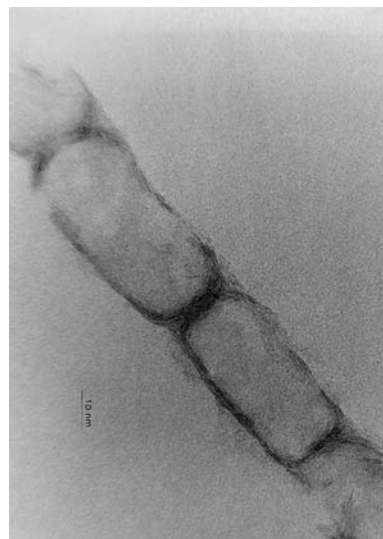


**Fig. 9** High-resolution transmission electron microscopy image of a section of a MoS<sub>2</sub> tube. *Source:* From Ref.<sup>[40]</sup>.

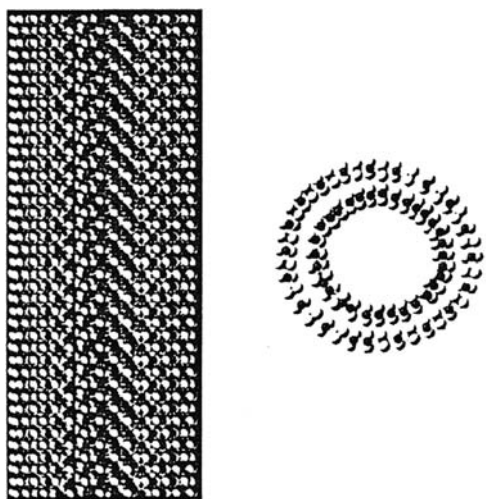


**Fig. 10** Molecular model (Cerius<sup>2</sup>) of MoS<sub>2</sub> nanotube formed by two layers. *Source:* From Ref.<sup>[40]</sup>.

A 2H-MoS<sub>2</sub> nanotube structure was determined by electron diffraction. The (002) reflection also showed an expansion to 6.22 Å of the lattice parameter as already mentioned. It was noted that the tube is not continuous, but it is split in several sections, each one with a diameter from 15 to 30 nm and a length between 150 and 500 nm. Commonly, the sections of the tube are ellipsoidal. However, in some cases, the shape is distorted as in the last section of the long tube (Fig. 9). The planes of the nanotubes are bent in a similar fashion as the bending of carbon nanotubes previously reported.<sup>[41]</sup> A computer-generated model of a MoS<sub>2</sub> nanotube including two layers built using Cerius<sup>2</sup> (molecular simulation program, ACCELRY S Corporation) is shown in Fig. 10. The MoS<sub>2</sub> in trigonal prismatic coordination was used as a starting model. As the minimum energy configurations were searched, stable configurations for cylinders of different sizes were calculated. Analyzing the Mo–S distances, two groups of measurements were reported. One group contains the interior Mo–S distances [Mo–S (int)] and the other contains the exterior Mo–S distances [Mo–S (ext)]. The mean distance for the Mo–S interior bond is 2.65 Å and the mean distance for the exterior bond is 2.75 Å. The calculation implied that MoS<sub>2</sub> nanotubes of this diameter are not stable because bending to form a tube of this diameter requires stretching of the Mo–S bonds well beyond their normal length of 2.41 Å.<sup>[40]</sup> The mean distance for six tubes between 20 and 120 Å was also calculated and plotted in Fig. 11.<sup>[40]</sup> The mean values of both the interior and the exterior Mo–S bonds approach the single crystal value of 2.41 Å. Chianelli et al. stated that below a value of approximately 120 Å, the tubes might be highly unstable because of bond strain. They have reported MoS<sub>2</sub> nanotubes

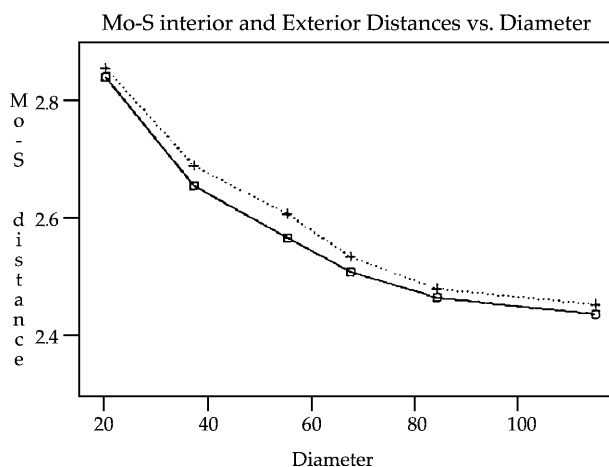


**Fig. 11** Interior and exterior distances as a function of tube diameter. *Source:* From Ref.<sup>[40]</sup>.

containing bending zones that, in the case of MoS<sub>2</sub> crystals, are often observed on the edges of the surface.<sup>[20]</sup> Hence “bent zones” are important to understanding the behavior of MoS<sub>2</sub> sheets. Fig. 12A and B presents the model of a bent sheet of MoS<sub>2</sub> comprised of four layers of MoS<sub>2</sub>. Examination of the values of the S–S and Mo–Mo distances shows a very large distortion that clearly appears in the bending zone. In comparison with the distances in the straight sections of the sheet, an increase of 20% in the distance between neighboring atoms is observed. This strongly emphasizes the instability of bent layers as the radius of curvature is reduced.

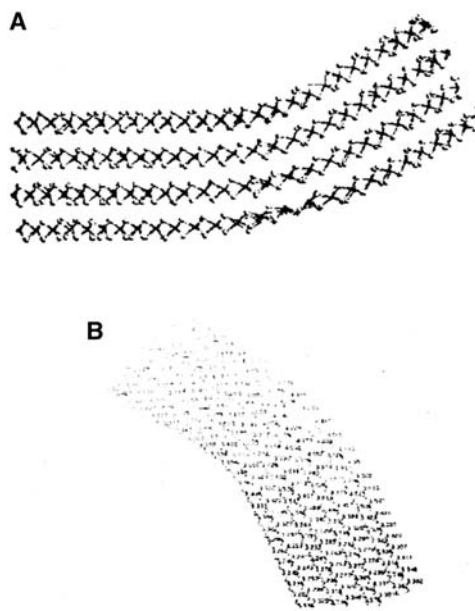


**Fig. 12** (A) Model of a bent sheet (30°) of MoS<sub>2</sub> (with four layers). (B) Atoms' position measurements for a similar sheet. *Source:* From Ref.<sup>[40]</sup>.



Synthetic nanotubes, lubricants, and catalysts all exhibit similar bending phenomena. Yacaman et al. reported that even in the case of MoS<sub>2</sub> crystals, a bending effect is often observed at the edges of the crystal surface. Their study showed that although large MoS<sub>2</sub> nanotubes can be synthesized, their minimum size is limited by the strain induced by stretched Mo–S bonds that are required to close tubes with diameters less than approximately 10 nm. Tenne et al.<sup>[42]</sup> earlier reported the synthesis of WS<sub>2</sub> nanotubes with diameters in the range of 10 nm. However, a close examination of their published micrographs reveals that the “nanotubes” become broken and discontinuous as the diameter becomes smaller, in agreement with Yacaman et al.’s study. This is in contrast to nanotubes of carbon that can exist down to very small diameters because of the change in carbon bonding, which is natural in fullerene-based materials. Layered materials such as MoS<sub>2</sub> and WS<sub>2</sub> cannot be formed into small nanotubes unless a change in Mo–S bond occurs. A change from six coordinates to a lower metal coordination might result in smaller-diameter nanotubes; however, this phenomenon has not yet been reported, but is possibly based on the known chemistry of Mo and S. Furthermore, the nanotubes made by the template method are not infinitely long but break into sections, giving the shape of a “Spanish chorizo,” a term coined by Yacaman et al. Calculations indicate that, in principle, there is no structural energetic reason for a nanotube not to grow infinitely. The total energy of the nanotube will be minimized by the distortion from the edge to the center described in “Nested Inorganic Fullerene Onion-like Structure.” Nevertheless, HRTEM images clearly show that two sections of the tube are in contact, but each one is preserving its corresponding layers. Therefore it is very likely that the sections are produced as a result of growth kinetics.

MoS<sub>2</sub> single-wall nanotubes (SWNTs) were grown by a catalyzed transport reaction involving C<sub>60</sub> as a growth promoter.<sup>[42]</sup> Remskar et al. show that the MoS<sub>2</sub> nanotubes grow in twisted chiral bundles of identically structured molecules stacked together with interstitial iodine. The nanotubes were found to vary in length but not in diameter. The chemical composition of the bundles was determined by energy-dispersive x-ray spectroscopy (EDX) and x-ray fluorescence spectrometry to be (MoS<sub>2</sub>)–I<sub>x</sub> with  $x \sim 1/3$ . However, the authors did not find C<sub>60</sub> incorporated into the structure using energy electron loss spectrometer (EELS). The bundles possess a hexagonal close-packed structure of identical nanotubes along the longitudinal direction revealed by HRTEM. The center-to-center distance between two tubes was found to be 0.961(1) nm, as seen in Fig. 13. A complex electron diffraction pattern shows a slightly distorted hexagonal symmetry, as illustrated in Fig. 14C.

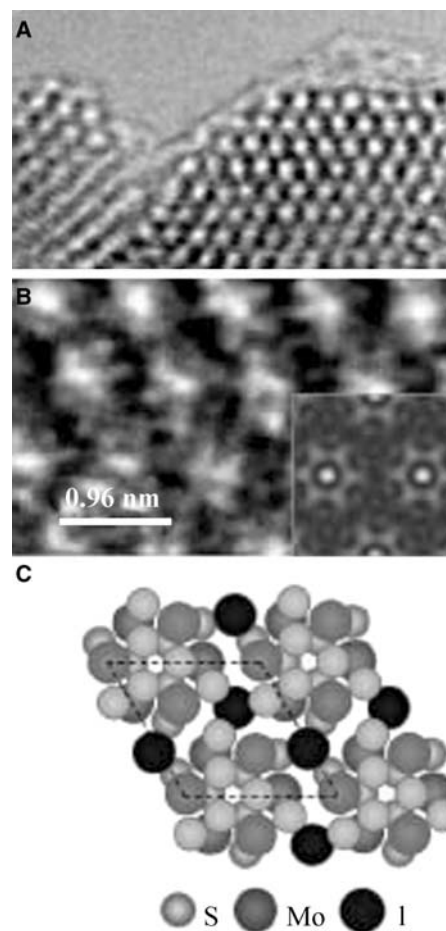


**Fig. 13** The cross section of a (MoS<sub>2</sub>)–I<sub>x</sub> TEM image of (A) hexagonal structure of the tubes. (B) High-resolution view of the structure. The insert shows an image simulation for zone [001]. (C) A model structure perpendicular to the nanotube axis (gray, S; dark gray, Mo; black, I). *Source:* From Ref.<sup>[42]</sup>.

Perpendicular to the bundle axis, a period of 0.83 nm is dominant.<sup>[42]</sup> The period is equal with regard to the period 0.27 nm belonging to the hexagonal pattern. Another strong peak located close to the (030) spot is caused by a period of 0.30(1) nm. Two strong periods of 0.20(1) and 0.30(1) nm are present along the axis. The transition electron diffraction (TED) data were confirmed by x-ray diffraction where intense peaks were found corresponding to interlayer distances of 0.832(1), 0.351(1), 0.314(1), 0.308(1), 0.279(1), and 0.20(1) nm.<sup>[42]</sup> Remskar et al. proposed a model (3,3) armchair nanotube structure illustrated in Figs. 13C and 14B. The distance between sulfur and molybdenum atoms in the nanotube is nearly of the same distance in platelike MoS<sub>2</sub>. The close position of molybdenum and sulfur atoms in neighboring layers perpendicular to the nanotube axis requires at least 25% extension of the unit cell along the tube axis to avoid overlap of the covalent radii.<sup>[42]</sup> The distance

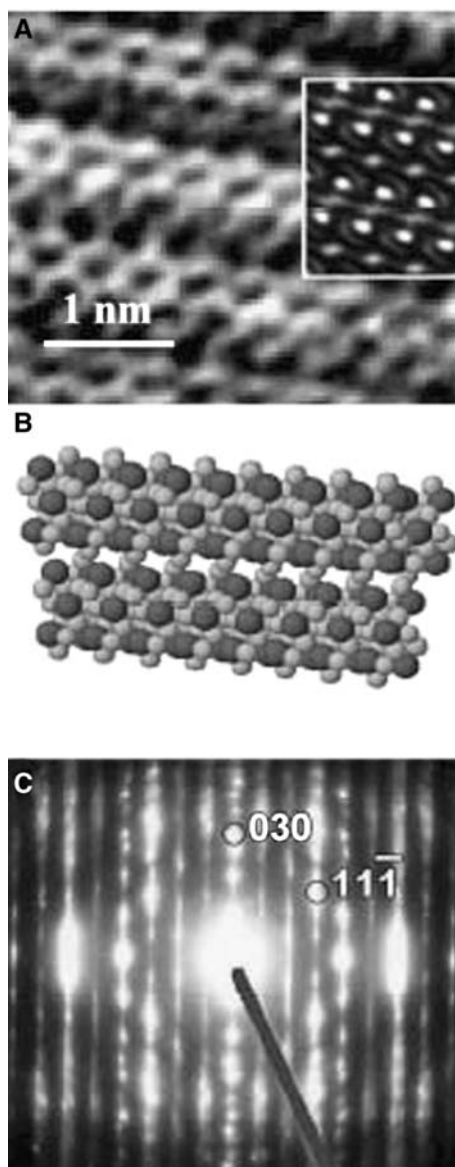


**Fig. 14** The  $(\text{MoS}_2)\text{-I}_x$  TEM image and electron diffraction in zone [101]. (A) High-resolution image with image simulation revealing ordered stacking of nanotubes; bright spots correspond to the positions of molybdenum atoms. (B) Model structure of the tubes. (C) Corresponding electron diffraction pattern indexed in accordance with the model structure. *Source:* From Ref.<sup>[42]</sup>.

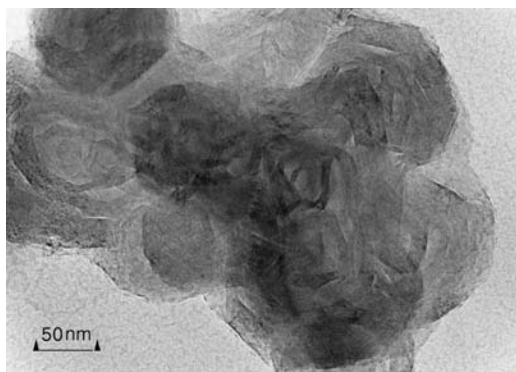
between the layers was determined to be 0.20 nm by diffraction patterns. The unit cell of the hexagonal close-packed nanotubes within a bundle was found to be 0.40 nm along the bundle axis and 0.96 nm perpendicular to the bundle axis. Their van der Waals diameter corresponds approximately to the distance between the closest sulfur atoms on adjacent nanotubes [0.35(1) nm]. Iodine atoms are inserted in interstitial trigonal voids between the nanotubes, creating one-dimensional rows along the bundle axis.

The periodicity of possible sites for iodine position along the bundle is 0.40 nm, which is slightly less than the van der Waals distance for iodine (0.43 nm). The observed HRTEM images are in agreement with their simulations using the symmetry operations of group  $P6_3 (C_6)$ .<sup>[42]</sup> The authors found  $C_{60}$  to be essential in the growth process, but a detail mechanism is not clear at the moment.

## ZRSE<sub>2</sub> AND SNS<sub>2</sub> FILAMENT-LIKE NANOPARTICLES

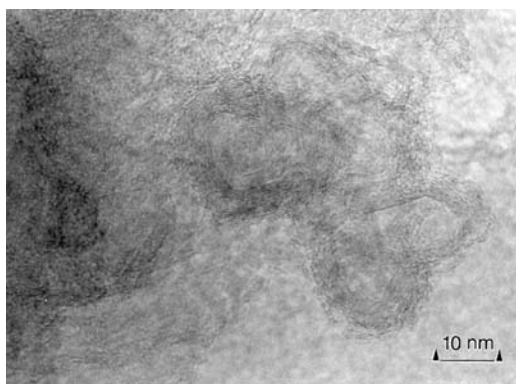
Filament-like nanoparticles of  $\text{ZrSe}_2$  and  $\text{SnS}_2$  were obtained by microwave plasma process.<sup>[43]</sup> Synthesis is performed using microwaves with a frequency of 0.915 or 2.45 GHz.<sup>[44]</sup> The reaction takes place inside a quartz tube passing a monomode microwave cavity.<sup>[45]</sup> The precursor compounds are vaporized outside of the reaction zone and introduced to the reaction gas in front of the plasma zone, where the nanoparticles are formed. The reaction gas is preheated to avoid the precipitation of the precursor. The reaction was preformed under a pressure of 30 mbar using 0.915-GHz plasma. The reaction temperature was set at 260°C or 580°C. The flow rate of the gas was adjusted to obtain a residence time of the particles of about 8 msec in the reaction zone at a temperature of 580°C, and about 4 msec at 260°C. Further reduction of the reaction temperature is obtained by using 2.45-GHz microwaves. Vollath et al. were able to perform the reaction at a temperature as low as 160°C. Gas pressure was set to 10 mbar. The residence time of the particles in the reaction zone was about 2 msec. The reaction temperature was determined directly after the reaction zone. Because microwave plasma was a nonequilibrium system, the true temperature of the particles during the formation was different. The reaction products were collected on cooled surfaces. Sulfide synthesis used  $\text{H}_2\text{S}$  as a carrier. The metals were introduced in the form of  $\text{SnCl}_4$ . Elemental sulfur was obtained along with the nanoparticles. To evaporate the sulfur excess, the reaction product was heated up to 120–140°C in a vacuum. The selenide samples were prepared using argon 4 vol.%  $\text{H}_2$  as plasma gas. Selenium was introduced in the form of  $\text{SeCl}_4$ . Fine particles of selenides are extremely sensitive to humidity; therefore the specimens were handled under argon gas prior to electron microscopy data collection. Filament-like morphology is a characteristic example of  $\text{ZrSe}_2$  small particles, as illustrated in Fig. 15. The filaments are randomly bent and knotted together. At higher magnifications, the lattice planes clearly show the same bends and twists as the particles (Fig. 16). The fringes in the micrograph represent the  $\text{Se-Zr-Se}$  {0002} layers with a distance of 0.36 nm close to the





**Fig. 15** Filament-like zirconium selenide particles. *Source:* From Ref.<sup>[43]</sup>.

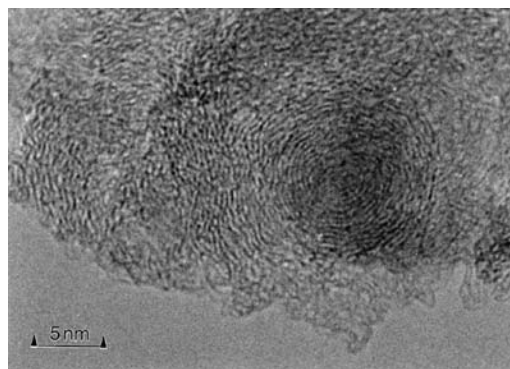
reported value of 0.3095 nm.<sup>[46]</sup> This filament-like structure is not unique for  $ZrSe_2$  and also appears in the case of  $SnS_2$  structures (Fig. 17). The distance of the lattice fringes for  $SnS_2$  is 0.56 nm, which corresponds to the  $\{0001\}$  planes (JCPDS value, 0.589 nm).<sup>[47]</sup> The reduced number of dislocation-like structures is the main difference between the  $SnS_2$  and  $ZrSe_2$  structures. In addition to these filament-like structures,  $ZrSe_2$  exhibited Onion-like crystal structures with varying distances between the lattice planes, as shown in Fig. 18. The distance between the lattice fringes was determined to be 0.34 nm. The lattice images (Figs. 17 and 19) show layered structures containing defects and varying distances between the planes.  $ZrSe_2$  tends to recrystallize in the electron microscope; therefore it cannot be completely ruled out that the particles are crystallized under the electron beam of the microscope. The electron diffraction pattern obtained from the  $SnSe_2$  samples shows a pattern similar to  $SnS_2$ <sup>[47,48]</sup> with a 1.5% expansion from 0.589 to 0.598 nm for the  $\{0001\}$  spacing, whereas the lattice parameter in the  $a$ -direction shows no expansion.



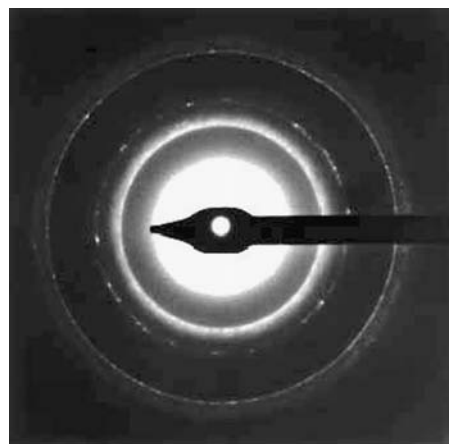
**Fig. 16** Filament-like structures of zirconium selenide particles at higher magnification. The lattice fringes distance is 0.36 nm. *Source:* From Ref.<sup>[43]</sup>.



**Fig. 17**  $SnS_2$  filaments, synthesized at 200°C. The lattice fringes distance is 0.56 nm, corresponding to the  $\{0002\}$  planes. The filaments have a length of around 30 nm and a width of 3–4 nm. *Source:* From Ref.<sup>[43]</sup>.



**Fig. 18** Onion-like zirconium selenide particle formed under electron microscope observation. *Source:* From Ref.<sup>[43]</sup>.



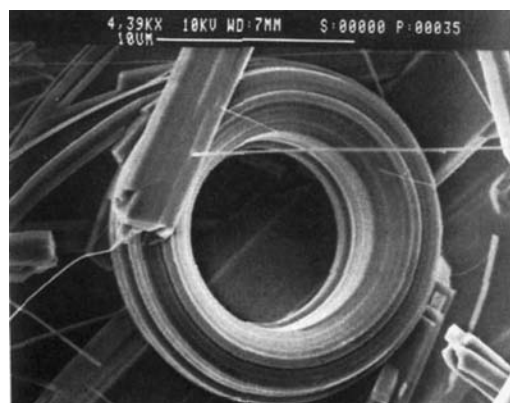
**Fig. 19** Zirconium selenide electron diffraction. *Source:* From Ref.<sup>[43]</sup>.

Table 1 compares the diffraction patterns for the two  $\text{SnS}_2$  phases according to JCPDS tables with experimental values. The first diffraction line of the (00*i*) type shows a maximum intensity at 0.589 nm, corresponding to the  $\beta$ - $\text{SnS}_2$  structure. However, the diffraction line observed at 0.306 nm is not allowed for  $\beta$ - $\text{SnS}_2$ . This line is allowed for the ordered polytype of the  $\beta$ -structure. Considering these observations, the authors may be tempted to conclude that the nanoparticles synthesized within this study represent a structural transition from the  $\beta$ - $\text{SnS}_2$  structure to its ordered polytype.

The  $\text{ZrSe}_2$  nanoparticle structures are not so subtle. The material has obviously a layered structure but the diffraction pattern, shown in Fig. 19, does not agree with  $\text{ZrSe}_2$  and  $\text{ZrSe}_3$  of the selenide phases with layered structures. The electron diffraction pattern indicates a broad distribution of the distances between the lattice planes. Assuming an expanded *c*-axis of 0.676 nm instead of 0.619 nm, the diffraction patterns disagree significantly with the hexagonal  $\text{ZrSe}_2$  structure.<sup>[46]</sup> The second zirconium–selenium phase with layered structure is  $\text{Zr}_2\text{Se}_3$ ,<sup>[49]</sup> given that a *c*-axis expansion from the JCPDS value of 1.251–1.351 nm has to be assumed. Furthermore, this assumed expansion in the *c*-axis still does not match the actual diffraction pattern with the published pattern. Assuming an 8% or 9% expansion in the van der Waals bond, the *c*-axis may still be reasonable. If a similar expansion is also assumed in the *a*-direction, the diffraction pattern obtained with the nanosized particles fits relatively well with the published diffraction pattern for  $\text{ZrSe}_2$  or  $\text{Zr}_2\text{Se}_3$ . Undoubtedly, this may not be a valid description of the actual structure because expanding in the *a*-direction means an elongation of the covalent bonds. Table 2 summarizes the results of measured *d*-values and shows the possible calculated indices, based on a *c*-axis and *a*-axis expansion.

### POTENTIAL USE OF LAYERED TRANSITION METAL CHALCOGENIDES AS MICROMACHINE COMPONENTS

Recently, transition metal trichalcogenides have been synthesized at high temperatures in a variety of shapes. Trichalcogenides such as  $\text{NbSe}_3$ ,  $\text{TiS}_3$ , and others have layered as well as chainlike structures.<sup>[50]</sup> These objects exhibit unusual morphologies larger than atomic scales; Fig. 20 shows an example. Morphologies observed include “wheels,” “tubes,” “rods,” and numerous other shapes. The ability to synthesize shapes such as these from materials that can be metals, magnets, semiconductors, and insulators has led to speculations regarding the construction of micromachines. For example, the “wheel,” if magnetic,



**Fig. 20** Structure of trichalcogenide– $\text{NbSe}_3$  shown. *Source:* From Ref.<sup>[50]</sup>.

might be incorporated into a microelectric motor. In another example, a microbattery might be constructed based on the intercalating abilities of the LTCM. Fabrication seems feasible, but reproducible synthesis in large uniform quantities remains a problem; however, possibilities for micromachine devices seem extensive.

### NANOPARTICULATE HETEROGENEOUS CATALYSIS

Heterogeneous catalysis used in the petroleum refining and chemical industries is an obvious example of widely applied nanoparticles. Traditionally, the industries have relied successfully on empirical methods for synthesizing these materials, but have not applied the understanding of nanoparticles to make further improvements.  $\text{MoS}_2$  may be used as an example to show how understanding of nanoparticles leads to improvements in catalytic activity and selectivity.

Catalysts based on  $\text{MoS}_2$  have been widely used in the petroleum refining industry since World War II. Usually the  $\text{MoS}_2$  is mixed with a second component such as Co or Ni to improve activity.<sup>[3]</sup> These very successful catalysts were largely discovered and developed empirically. Recently, much progress has been made in understanding their catalytic properties from a nanoparticulate point of view.<sup>[51]</sup>

Several issues have become clear and are probably applicable to other heterogeneous catalysts:

1. Commercial catalysts, because they are made at relatively low temperatures, appear in a highly folded and disordered form such as that described above. This is disadvantageous because maximum activity is obtained on catalysts that are well crystallized, and a major unrealized challenge is to cheaply make

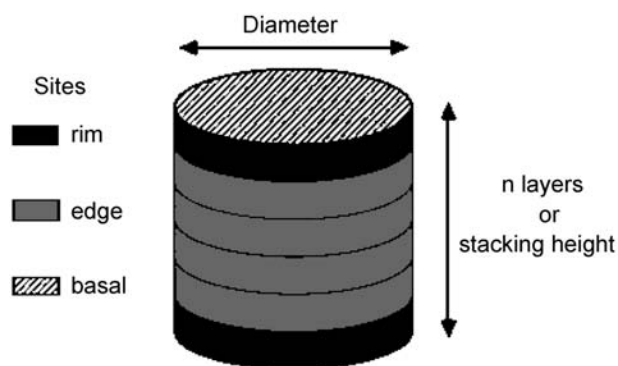
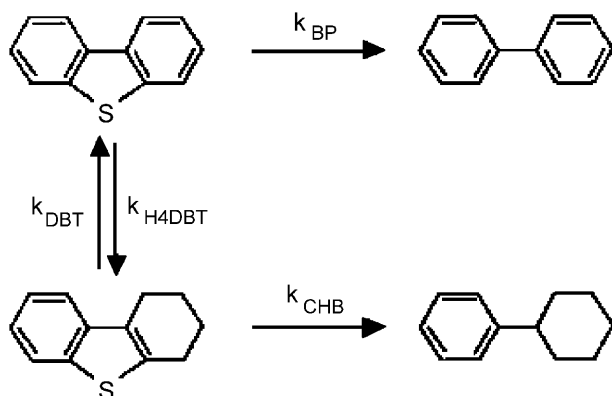


Fig. 21 "Rim/edge" model. Source: From Ref.<sup>[51]</sup>.

nanocrystals of these commercial catalysts in large quantities in a supported form.

- In the case of  $\text{MoS}_2$ , the selectivity of the reaction is determined by the "stack height" of the crystallites, as indicated in Fig. 21. The industrially important hydrodesulfurization (HDS) reaction, indicated in Scheme 1, occurs along two pathways that take place on different parts of the crystal. The first pathway leading to cyclohexylbenzene occurs only on the "rim" sites, and the second pathway leading to biphenyl occurs on the "rim" and "edge" sites. Thus the aspect ratio of the nanoparticles must be controlled to positively affect the selectivity of the reaction, and the diameter of the crystallite must be made as small as possible to maximize the activity. All these must be accomplished with as much crystalline order as can possibly be retained.
- Working catalysts are "promoted" with a second metal such as Co or Ni. This metal usually occurs as a second component, such as  $\text{Co}_9\text{S}_8$  that interacts at the  $\text{MoS}_2$  edge plane and can form an interface with it. It is at this interface that the promotion effect occurs by



Scheme 1

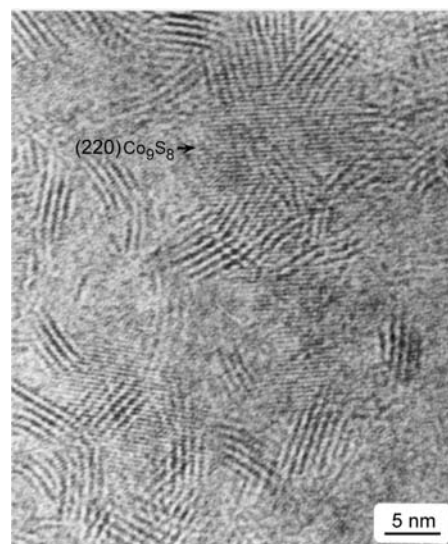


Fig. 22 High resolution electron micrograph showing the interface between  $\text{Co}_9\text{S}_8$  inclusions and the  $\text{MoS}_2$  edge plane. Source: from "Hydrodesulfurization catalysts prepared by two methods analysed by transmission electron microscopy, J. Catal. Sec Ref.<sup>[52]</sup>.

setting up an interaction at the junction of the two materials. A high-resolution electron micrograph of such an interaction is shown in Fig. 22.<sup>[52]</sup> It is a further challenge to synthesize these complex nanophase materials in an optimum form in commercial quantities.

### THE STRUCTURE AND POTENTIAL ROLE OF ATMOSPHERIC NANOPARTICLES IN PHOTOCATALYTIC AND THERMAL PRODUCTION AND ATMOSPHERIC POLLUTANTS

Nanoparticles are now being recognized as playing a potentially important role in the complex physical and chemical process that occurs above heavily polluted cities.<sup>[53]</sup> Atmospheric aerosols occurring in these areas are found to be complex materials that have the potential to accelerate important ozone-forming reactions both photocatalytically and thermocatalytically. In addition, because the particles are small enough to inhale, they represent a considerable health hazard. The aerosols consist of two intermixed components: the first consists of amorphous carbonaceous materials of variable composition with "fullerene-like" materials dispersed throughout; the second is an inorganic material consisting of nanoparticles of oxides and sulfides "supported" on clay minerals. These inorganic components have all of the characteristics of an airborne photocatalyst. Nanoparticles of  $\text{Fe}_2\text{O}_3$ ,  $\text{MnO}_2$ ,

and FeS<sub>2</sub> have demonstrated catalytic properties, particularly when occurring in the nanoparticles range as they do in the subject aerosol materials. These materials have band gaps that occur in the broad solar spectrum, enhancing the photocatalytic adsorption of solar radiation beyond that of the wider band gap aluminosilicate and titanate materials that also occur in aerosols. In addition, the materials are acidic and probably are coated with moisture when suspended in air, further enhancing the catalytic ability to crack hydrocarbons and create free radicals. Although this area is still being studied, nanoparticulates appear to play an important, but as yet undetermined, environmental role.

## CONCLUSION

The layered transition metal sulfur structure encloses the significance of the fundamental and applied chemistry of molybdenum disulfide. Their properties and crucial catalytic uses of unpromoted and promoted systems are strongly dependent both on the weak van der Waals interlayer interactions and on the nature of the sites defined by its layered structure. Complete understanding of the catalytic properties of MoS<sub>2</sub> requires more information on the edge planes that terminate the anisotropic layers, which are the location of catalytically active sites. Further progress in developing this understanding will enhance the ability to improve the catalysts' effectiveness for HDS processes. The combination of chemical synthesis and physical processes provides many experimental variables that allow control of particle size and shaping distribution, and will probably be applicable to the formation of closed structures of other layered compounds. It is a further challenge to synthesize these complex nanophase materials in an optimum form in commercial quantities.

## ACKNOWLEDGMENTS

The authors would like to thank the U.S. Department of Energy (DOE) Gateway Initiatives, United States.

## REFERENCES

- Ijima, S. Single-shell carbon nanotubes of 1-nm diameter. *Nature* **1993**, *363* (6430), 603–605.
- Tenne, R.; Margulis, L.; Genut, M.; Hodes, G. Polyhedral and cylindrical structures of tungsten disulfide. *Nature* **1992**, *360* (6403), 444–446.
- Weiser, O.; Landa, S. *Sulfide Catalysts: Their Properties and Applications*; Oxford, 1973.
- Hilton, M.R.; Fleischauer, P.D. On the use of a Brale indenter to evaluate the cross-sectional morphology of sputter-deposited molybdenum disulfide solid lubricant films. *Thin Solid Films* **1989**, *172* (2), L81–L83.
- Whittingham, M.S. Electrical energy storage and intercalation chemistry. *Science* **1976**, *192* (4244), 1126–1127.
- Tributsch, H. Photoelectrochemical behavior of layer-type transition metal dichalcogenides. *Faraday Discuss. Chem. Soc.* **1981**, *70*, 190–200.
- Whittingham, M.S.; Jacobson, A.J.; Eds.; *Intercalation Chemistry*; Academic Press: New York, 1982.
- Wilson, J.A.; Yoffe, A.D. Transition metal dichalcogenides. Discussion and interpretation of the observed optical, electrical, and structural properties. *Adv. Phys.* **1969**, *18* (73), 193–335.
- Singer, I.L. *Fundamentals of Friction: Macroscopic and Microscopic Processes*; Singer, I.L., Pollock, H.M., Eds.; Kluwer: Dordrecht, 1992; 237 pp.
- Bowden, F.P.; Tabor, D. *Friction: An Introduction to Tribology 91*; Anchor: Garden City, NY, 1973.
- Yacaman, M.J.; Lopez, H.; Santiago, P.; Galvan, D.H.; Garzon, I.L.; Reyes, A. Studies of MoS<sub>2</sub> structures produced by electron irradiation. *Appl. Phys. Lett.* **1996**, *69* (8), 1065.
- Parrilla, P.A.; Dillion, A.C.; Jones, K.M.; Riker, G.D.; Shultz, L.; Ginley, D.S.; Heben, M.J. The first true inorganic fullerenes? *Nature* **1999**, *397* (6715), 114.
- Dresselhaus, M.D.; Dresselhaus, G.; Eklund, P.C. *Science of Fullerenes and Carbon Nanotubes*; Academic Press, Inc.: New York, 1996; 1–6; 110–116.
- Homyonfer, M.; Mastai, Y.; Hershinkel, M.; Volterra, V.; Hutchison, J.L.; Tenne, R. Scanning tunneling microscope induced crystallization of fullerene-like MoS<sub>2</sub>. *J. Am. Chem. Soc.* **1996**, *118* (33), 7804–7808.
- Zak, A.; Feldman, Y.; Alperovich, V.; Rosentsveig, R.; Tenne, R. Growth mechanism of MoS<sub>2</sub> fullerene-like nanoparticles by gas-phase synthesis. *J. Am. Chem. Soc.* **2000**, *122* (45), 11,108–11,116.
- Feldman, Y.; Wasserman, E.; Srolovitz, D.J.; Tenne, R. High-rate, gas-phase growth of MoS<sub>2</sub> nested inorganic fullerenes and nanotubes. *Science* **1995**, *267* (5195), 222–225.
- Whitby, R.L.D.; Hsu, W.K.; Boothroyd, C.B.; Kroto, H.W.; Walton, D.R.M. Tungsten disulphide coated multi-walled carbon nanotubes. *Chem. Phys. Lett.* **2002**, *359* (1, 2), 121–126.
- Lu, E.; Persans, P.D.; Ruppert, A.F.; Chianelli, R.R. Preparation and characterization of molybdenum disulfide microcrystals in colloidal dispersion. *Mater. Res. Soc. Symp. Proc.* **1990**, *164*, 153–158. (*Mater. Issues Microcryst. Semicond.*)
- Roxlo, C.B.; Deckman, H.W.; Dunsmuir, J.H.; Ruppert, A.F.; Chianelli, R.R. Surface disorder and exfoliation in lithographically textured molybdenum disulfide. *Mater. Res. Soc. Symp. Proc.* **1987**, *82*, 481–485. (*Charact. Def. Mater.*)
- Chianelli, R.R.; Ruppert, A.F.; Yacaman, M.J.; Vazquez-Zavala, A. HREM studies of layered transition metal sulfide catalytic materials. *Catal. Today* **1995**, *23* (3), 269–281.

21. Divigalpitiya, W.M.R.; Frindt, R.F.; Morrison, S.R. Inclusion systems of organic molecules in restacked single-layer molybdenum disulfide. *Science* **1989**, *246* (4928), 369–371.
22. Divigalpitiya, W.M.R.; Frindt, R.F.; Morrison, S.R. Oriented films of molybdenum trioxide. *Thin Solid Films* **1990**, *188* (1), 173–179.
23. Divigalpitiya, W.M.R.; Frindt, R.F.; Morrison, S.R. Molecular composite films of molybdenum disulfide and styrene. *J. Mater. Res.* **1991**, *6* (5), 1103–1107.
24. Wilcoxon, J.P.; Samara, G.; Newcomer, P. Optical features of nanosize iron and molybdenum sulfide clusters. *Mater. Res. Soc. Symp. Proc.* **1995**, *358*, 277–281. (Microcryst. Nanocryst. Semicond.).
25. Wilcoxon, J.P.; Samara, G.A. Strong quantum-size effects in a layered semiconductor: MoS<sub>2</sub> nanoclusters. *Phys. Rev., B Condens. Matter* **1995**, *51* (11), 7299–7302.
26. Parsapour, F.; Kelley, D.F.; Craft, S.; Wilcoxon, J.P. Electron transfer dynamics in MoS<sub>2</sub> nanoclusters: normal and inverted behavior. *J. Chem. Phys.* **1996**, *104* (13), 4978–4987.
27. Chianelli, R.R.; Prestridge, E.B.; Pecoraro, T.A.; DeNeufville, J.P. Molybdenum disulfide in the poorly crystalline “rag” structure. *Science* **1979**, *203* (4385), 1105–1107.
28. Chianelli, R.R. Amorphous and poorly crystalline transition metal chalcogenides. *Int. Rev. Phys. Chem.* **1982**, *2* (2), 127–165.
29. Chianelli, R.R. Fundamental studies of transition metal sulfide hydrodesulfurization catalysts. *Catal. Rev., Sci. Eng.* **1984**, *26* (3–4), 361–393.
30. Chianelli, R.R.; Ruppert, A.F.; Behal, S.K.; Kear, B.H.; Wold, A.; Kershaw, R. The reactivity of molybdenum disulfide single crystal edge planes. *J. Catal.* **1985**, *92* (1), 56–63.
31. Passaretti, J.D.; Chianelli, R.R.; Wold, A.; Dwight, K.; Covino, J. Preparation and properties of the systems cobalt rhodium sulfide (Co<sub>1-x</sub>Rh<sub>x</sub>S<sub>2</sub>), cobalt ruthenium sulfide (Co<sub>1-x</sub>Ru<sub>x</sub>S<sub>2</sub>), and rhodium ruthenium sulfide (Rh<sub>1-x</sub>Ru<sub>x</sub>S<sub>2</sub>). *J. Solid State Chem.* **1986**, *64* (3), 365–371.
32. Chianelli, R.R.; Pecoraro, T.A. U.S. Patent 42,884,422, 1981.
33. Ugarte, D. Curling and closure of graphitic networks under electron-beam irradiation. *Nature* **1992**, *359* (6397), 707–709.
34. Margulis, L.; Salitra, G.; Tenne, R.; Tallanker, M. Nested fullerene-like structures. *Nature* **1993**, *365* (6442), 113–114.
35. Tenne, R. Fullerene-like materials and nanotubes from inorganic compounds with a layered (2-D) structure. *Colloids Surf., A Physicochem. Eng. Asp.* **2002**, *208* (1–3), 83–92.
36. Mastai, Y.; Homyonfer, M.; Gedenken, A.; Hodes, G. Room temperature sonochemical synthesis of molybdenum sulfide fullerene-like nanoparticles. *Adv. Mater.* **1999**, *11* (12), 1012.
37. Remskar, M.; Skraba, Z.; Cleton, F.; Sanjines, R.; Levy, F. MoS<sub>2</sub> as microtubes. *Appl. Phys. Lett.* **1996**, *69* (3), 351–353.
38. Zelenski, C.M.; Dorhout, P.K. Template synthesis of near-monodisperse microscale nanofibers and nanotubes of MoS<sub>2</sub>. *J. Am. Chem. Soc.* **1998**, *120* (4), 734–742.
39. Prasad, T.P.; Diemann, E.; Muller, A. Thermal decomposition of ammonium dithiomolybdate, ammonium tetrathiomolybdate, ammonium dithiotungstate, and ammonium tetrathiotungstate. *J. Inorg. Nucl. Chem.* **1973**, *35* (6), 1895–1904.
40. Chianelli, R.R.; Berhault, G.; Santiago, P.; Mendoza, D.; Espinosa, A.; Ascencio, J.A.; Yacaman, M.J. Synthesis, fundamental properties and applications of nanocrystals, sheets, nanotubes and cylinders based on layered transition metal chalcogenides. *Mater. Technol. (Poulton-le-Fylde, UK)* **2000**, *15* (1), 54–61.
41. Curl, R.F.; Kroto, H.W.; Smalley, R.E. The 1996 Nobel prizes in science. *Sci. Am.* **1997**, *276* (1), 14–16; 18.
42. Remskar, R.; Mrzel, A.; Skraba, Z.; Jesih, A.; Ceh, M.; Demsar, J.; Stadelmann, P.; Levy, F.; Mihailovic, D. Self-assembly of subnanometer-diameter single-wall MoS<sub>2</sub> nanotubes. *Science* **2001**, 292.
43. Vollath, D.; Seith, B.; Szabo, D.V. Nanoparticles from compounds with layered structures. *Acta Mater.* **2002**, *48*, 953–967.
44. Vollath, D.; Seith, B.; Szabo, D.V. German Patent application P 196 28 357.4, 1996.
45. Vollath, D.; Mobius, A. First World Congress on Microwave Processing, Florida, 1987. paper XVII-4.
46. van Arkel, A.E. *Physica* **1924**, pp. 4, 300 (JCPDS 3-1189).
47. NBS Monogr. **1971**, pp. 9, 25 (JCPDS 23-677).
48. Guenter, J.R.; Oswald, H.R. *Naturwissenschaften* **1968**, pp. 55, 177 (JCPDS 21-1231).
49. Salomons, W.; Wiegers, G.A. *Recl. Trav. Chim.* **1968**, pp. 87, 1339 (JCPDS 37-1492).
50. Trumbore, F.A.; Ter Haar, L.W. Unusual crystal growth morphologies in the niobium-selenium system. *Chem. Mater.* **1989**, *1* (5), 490–492.
51. Chianelli, R.R.; Daage, M.; Ledoux, M.J. Fundamental studies of transition metal sulfide catalytic materials. *Adv. Catal.* **1994**, *40*, 177–232.
52. Cruz-Reyes, J.; Avalos-Borja, M.; Farias, M.H.; Fuentes, S. Hydrodesulfurization catalysts prepared by two methods analyzed by transmission electron microscopy. *J. Catal.* **1992**, *137* (1), 232–242.
53. Yacaman, M.J.; Chianelli, R.R. The Structure and Potential Role of Atmospheric Nanoparticles, Proceedings of the WERC/HSRC Meeting, Albuquerque, NM, April 23–25, 1997.

# Nanostructures Derived from Phase-Separated Polymers

Michael R. Bockstaller

Edwin L. Thomas

Massachusetts Institute of Technology, Cambridge, Massachusetts, U.S.A.

## INTRODUCTION

The field of polymer-based materials continues its enormous growth covering a wide range of products from disposable coffee cups to car bumpers to biomedical devices. The increased emphasis on enhancement of properties via materials with structures of components engineered on the nanoscale has opened up many new opportunities. For example, blending different polymers while retaining their individual properties in the composite is an effective way of engineering new nano- and microstructural materials from a limited palette of commodity polymers. At present five major reasons for the technological importance of polymer multicomponent systems can be identified: 1) improvements in material performance via synergistic interactions (e.g., temperature resistance, modulus, adhesion); 2) realizing desired processing conditions (e.g., melt viscosity, softening point, solvent resistance); 3) recycling industrial or municipal scrap polymers; 4) adjusting product composition to customer specifications by mixing of different batches; and 5) dilution of high-performance polymers for cost reduction.

Despite their great industrial relevance, there exists no formally accepted nomenclature for multicomponent polymer systems. A possible classification scheme is provided in [Scheme 1](#). Understanding and controlling the mechanisms of phase separation and nanostructure formation in polymer systems allows one to tailor the performance of these materials to a manifold of applications. For example, co-continuous blends of high- and low-melting point polymers where the low-melting point component is the majority component facilitate to dramatically increase thermal and mechanical properties such as toughness, stress at break, or high-temperature creep resistance while retaining ease of processability. Recent research suggests possible future applications of multicomponent polymer systems that are more far-reaching. Nanostructures based on block copolymer-homopolymer blends are currently studied as a platform for photonic materials with possible use in integrated optics or in thin films as non-lithographic route toward controlled patterning

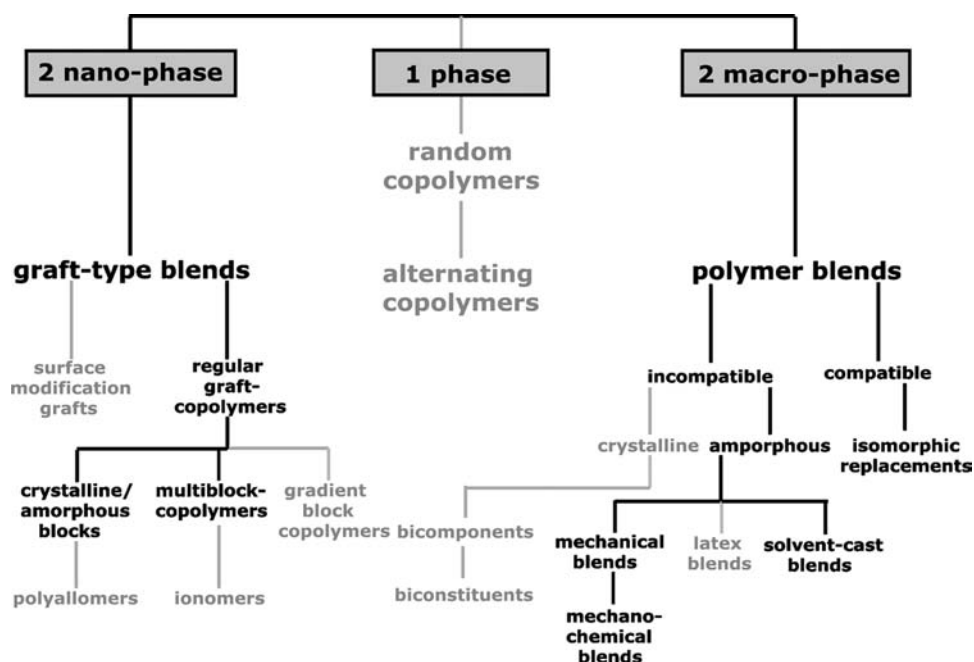
of 100-nm feature sizes. The future technological impact of the latter type of applications will crucially depend on the ability to control structure formation on multiple length scales by strategic design of chemical groups as well as integrating synthetic design with specific processing pathways that increase the likelihood of attaining a targeted structure.

This article reviews polymer phase behavior and nanostructure formation beginning with a discussion of molecular architecture, equilibrium thermodynamics, and phase separation dynamics. The second part describes recent achievements to control the structure formation processes over macroscopic dimensions. The interplay of relevant balancing forces in self-organization processes is discussed aiming to give the reader some intuition about how molecular details and processing conditions can be used in order to control structure formation. In the third part, new research areas will be presented in which polymer-based nanostructures are likely to have major technological impact. Throughout, examples will focus on synthetic polymers that either are of high industrial interest or that suitably represent characteristics of a broad range of macromolecules but leaving out the complex structure formation processes found in natural biopolymers.

## MOLECULAR ARCHITECTURE AND PHASE DIAGRAM

The term *polymer* means “many units” and designates a large molecule made up of smaller repeating units, the number of which determines the degree of polymerization  $N$ . Other basic quantities characterizing a polymer chain are the molecular weight  $M = Nm$ , with  $m$  being the molecular weight of a single repeat unit, and its radius of gyration  $R_G$  which scales as  $N^{1/2}$  for flexible chains in their melt state. As a rule of thumb, molecular weights of common-type flexible polymers of  $M \sim 10^5$  g/mol correspond to an effective size of the polymer chain of  $R_G \sim 10$  nm. The inherent length scale in the nanometer range renders polymer materials





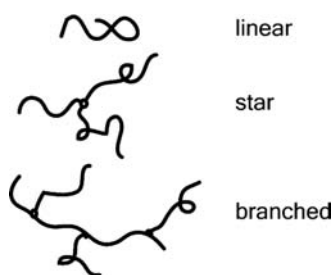
**Scheme 1** Multicomponent polymer system classification scheme. The types of polymer systems relevant to this text are marked in black.

naturally attractive for nanoengineering purposes. Depending on the synthetic procedure, the repeating unit of a linear polymer may comprise a single identifiable precursor such as in poly(styrene) (PS) or might be composed of the residues of several smaller molecules as in poly(hexamethylene-adipamide) (Nylon-6,6). Table 1 shows the chemical structures of a small selection of polymers relevant to this article. Next to

the linear chain architecture, synthetic strategies have been developed to also obtain well-defined star- or branched molecular structures. For a detailed discussion of methods for polymer synthesis the reader is referred to Refs.<sup>[1]</sup> and<sup>[2]</sup>. A small subset of the wealth of architectures is shown in Scheme 2. Depending on molecular architecture, degree of polymerization, and temperature, the physical state of polymeric

**Table 1** Structure and nomenclature of selected polymers

Structure	Monomer	Nomenclature (abbreviation)
		Poly(styrene) (PS)
		Poly(isoprene) (PI)
		Poly(methylmethacrylate) (PMMA)
		Poly(hexamethylene adipamide) (Nylon-6,6)



**Scheme 2** Selection of homopolymer architectures.

materials can vary between viscous liquid, glassy, semi-crystalline, or liquid crystalline. Crystallization processes, which require a highly regular stereochemistry of the polymer, and the associated hierarchy of structures are beyond the scope of this article and will only be briefly mentioned.

## Homopolymer Blends

The equilibrium phase behavior of a mixture of two linear polymers A and B was first derived by Flory<sup>[3]</sup> and Huggins.<sup>[4]</sup> According to the Flory–Huggins theory, the change in free energy upon mixing  $\Delta G_m$  for a binary polymer blend is given by

$$\frac{\Delta G_m}{k_B T} = \frac{\phi_A}{N_A} \ln \phi_A + \frac{\phi_B}{N_B} \ln \phi_B + \phi_A \phi_B \chi \quad (1)$$

with  $k_B$  denoting the Boltzmann constant,  $T$  the temperature,  $N_{A/B}$  the degree of polymerization (the number of mers of A and B),  $\phi_{A/B}$  the volume fraction of polymers A and B, and  $\chi$  the Flory–Huggins segment–segment interaction parameter. As large chains assume fewer mixed configurational states, the entropic contribution (first two terms in Eq. (1)) decreases with increasing molecular weight of the polymers. The phase behavior of binary polymer blends is then largely determined by the value of  $\chi$  that is fixed by the particular choice of the repeating units of polymers A and B.  $\chi$  parameters can often be expressed as a linear function of  $1/T$ , i.e.,  $\chi(T) = \alpha + \beta/T$ ; values for  $\alpha$  and  $\beta$  have been tabulated for a variety of monomers.<sup>[5]</sup> Given a binary polymer mixture, the phase behavior can be predicted by the calculation of the spinodal and binodal that are given by the criteria of stability (Eq. (2)) and thermodynamic equilibrium (Eq. (3)), respectively.

$$\frac{\partial^2}{\partial \phi_A^2} \Delta G_m = 0 \quad (2)$$

$$\frac{\partial}{\partial \phi_A} \Delta G_m(\phi_A)^{\text{phase 1}} = \frac{\partial}{\partial \phi_A} \Delta G_m(\phi_A)^{\text{phase 2}} \quad (3)$$

The binodal and spinodal curves meet in the critical point that is given for a symmetric polymer blend with equal molecular volumes ( $N_A v_A = N_B v_B$ ,  $v_i$  denoting the volume of monomer  $i$ ) by  $\phi_c = 1/2$  and  $\chi_c = 2/N$ . A typical phase diagram for a binary mixture of symmetric linear homopolymers is shown in Fig. 1. Depending on the sign and temperature dependence of  $\chi$ , different types of phase behavior can be distinguished, the most important are referred to as: upper critical solution temperature (UCST, mixing upon heating), which is found for positive  $\chi$  and  $d\chi/d(1/T) > 0$ , as well as lower critical solution temperature (LCST, mixing upon cooling), which is found for negative  $\chi$  and  $d\chi/d(1/T) < 0$ . In a few experimental systems, closed-loop behavior has been observed, i.e., low-temperature LCST and high-temperature UCST.<sup>[6]</sup> Table 2 shows a list of some homopolymers that are frequently found in industrial applications and their mixing behavior.

## Mechanisms of phase separation in homopolymer blends

There are two major mechanisms of phase separation that have been identified and that occur in different

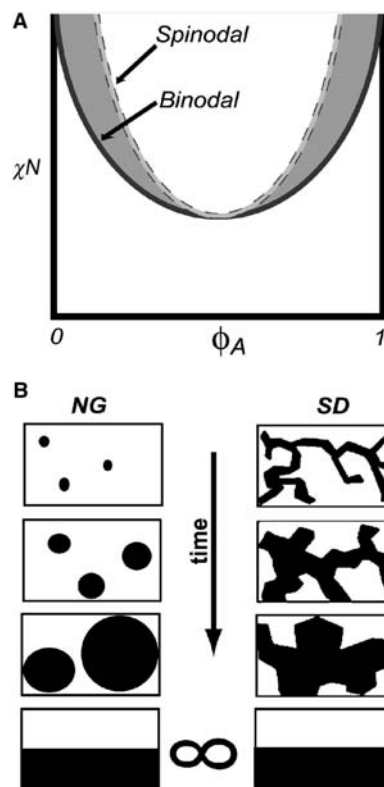


**Fig. 1** (A) Phase diagram of a symmetric homopolymer blend ( $N_A = N_B$ ). Shaded area indicates metastable region. (B) Schematic of the mechanism of phase separation in the metastable (nucleation and growth, NG) and unstable (spinodal decomposition, SD) region of the phase diagram.

**Table 2** Mixing behavior of selected homopolymer blends

Polymer 1	Polymer 2	Miscibility
Poly(styrene)	Poly(butadiene)	no
Poly(styrene)	Poly(methyl methacrylate)	no
Poly(styrene)	Poly(dimethyl siloxane)	no
Nylon-6,6	Poly(ethylene-propylene)	no
Poly(propylene)	Poly(ethylene)	no
Poly(styrene)	Poly(vinyl methylether)	yes
Poly(styrene)	Poly(dimethyl phenyleneoxide)	yes
Poly(ethylene oxide)	Poly(acrylic acid)	yes
Poly(vinylchloride)	Poly(butylene terephthalate)	yes
Poly(methyl methacrylate)	Poly(vinylidene fluoride)	yes

parts of the phase diagram as shown in Fig. 1: nucleation and growth (NG) and spinodal decomposition (SD). NG occurs in the metastable region of the phase diagram (the area between binodal and spinodal) and is characterized by the following steps: 1) initial formation of spherical fragments of the more stable phase (requires activation barrier); 2) growth of nuclei by first diffusion of material from the supersaturated continuum followed by droplet–droplet coalescence and Ostwald-ripening. Spinodal decomposition, which is the commonly observed mechanism for phase separation in homopolymer blends, occurs in the unstable region of the phase diagram and is characterized by initial small-amplitude composition fluctuations that increase with time and result in interconnected phase morphologies at intermediate stages of phase separation. Co-continuous polymer blends have been the subject of intense research as they generally exhibit superior mechanical properties. Co-continuous interconnected morphologies are commonly induced either by arresting SD or by mechanical mixing of polymer mixtures. Such systems often suffer the problem that they tend to move toward the equilibrium macrophase-separated structure. Blending of homopolymers in the presence of appropriately chosen graft copolymers has been shown to be a versatile alternative to mechanical mixing, facilitating the stabilization of co-continuous blends by increasing the thermodynamic stability and flexibility of the interface.<sup>[7]</sup> Figure 2 shows the microstructure of a poly(ethylene)/poly(amide) co-continuous blend

and the associated enhancement of elastic and tensile properties. Note that the elastic modulus increases by order of magnitudes in the case of the co-continuous blend with regard to its phase separated counterpart.

## Block Copolymers

Block copolymers consist of two distinct polymer chains that are covalently linked together to form a chain. The large variety of block configurations that can be constructed using modern synthetic methods can be classified based on the number of chemically distinct blocks as well as linear vs. branched connectivity of the blocks within a copolymer as indicated in Scheme 3. As structure formation processes of most of these systems are still under discussion, this article will focus on the current understanding of the simplest and most studied system—linear amorphous diblock copolymers. For excellent review articles in this field we refer the reader to Refs.<sup>[8–10]</sup>

Because block copolymers are single-component systems, they cannot macrophase separate in the melt like a pair of linear homopolymers does. Instead, block copolymers segregate on a local scale. The decrease of A–B segment contacts by local segregation is often referred to as microphase separation. The enthalpy gain obtained by the local segregation process is counterbalanced by an associated loss in system entropy that results from the localization of the block joints at the intermaterial dividing surface (IMDS) and the necessary stretching of the polymer chains away from the IMDS in order to maintain uniform density. As the entropic contribution can be shown to scale as  $N^{-1}$  with  $N = N_A + N_B$ , it is again the product  $\chi N$  that dictates the microphase-separation process. Three different limiting regimes exist for diblock copolymer melts: 1) the disordered state with unperturbed Gaussian chain statistics ( $R_G \sim N^{1/2}$ ) which is found for  $\chi N \ll 1$ ; 2) the ordered state in the weak segregation limit ( $\chi N \sim 10$ ) with sinusoidal composition fluctuations representing a periodic microstructure; and 3) the ordered state in the strong segregation limit ( $\chi N \gg 10$ ) where strong repulsive forces between segments of A and B result in sharp interfaces separating nearly pure A and B domains with pronounced stretching of the block chains ( $R_G \sim N^{2/3}$ ). Below the order–disorder transition temperature, enthalpic effects become more influential and the block copolymer microphase separates. The product  $\chi N$  and the compositional parameter  $f = N_A/(N_A + N_B)$  determine one of seven phases that represent free-energy minima for the ensemble of molecular configurations. The following sequence of phases has been observed

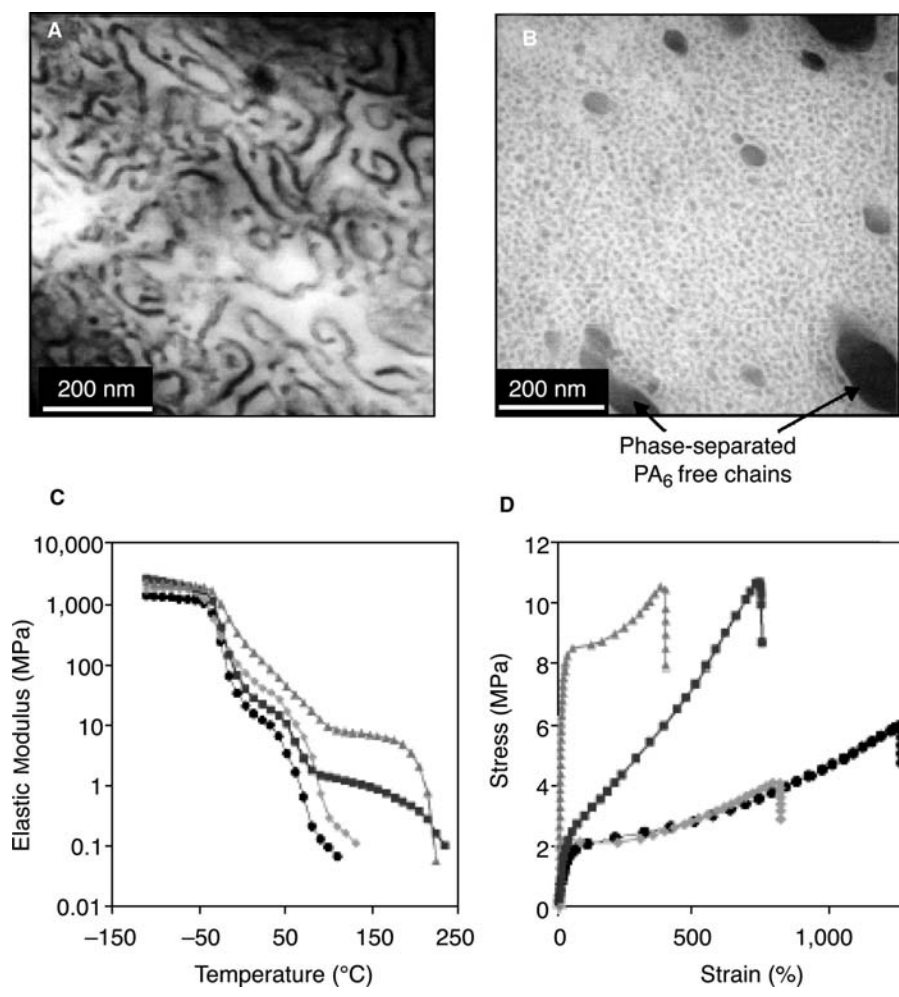
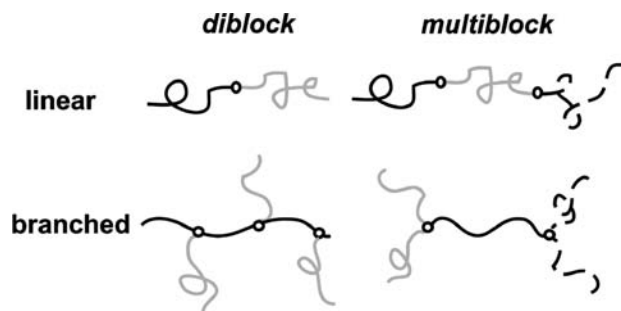


**Fig. 2** Transmission electron micrographs of (A) co-continuous nanostructured blend (80/20 ratio poly(ethylene)/Nylon-6,6); (B) phase separated blend. (C) and (D) show the increase of elastic modulus and stress–strain properties for co-continuous phase formation. Triangles: co-continuous (80/20), squares: micellar blend (80/20), diamonds: macrophase separated blend, circles: poly(ethylene). *Source:* From Ref.<sup>[8]</sup>. © 2002, Macmillan Publishers Ltd.

for PS–PI diblocks:  $f_{PS} < 0.17$ , body-centered cubic (BCC);  $0.17 < f_{PS} < 0.28$ , hexagonal;  $0.28 < f_{PS} < 0.34$ , bicontinuous (double gyroid);  $0.34 < f_{PS} < 0.62$ , lamellar;  $0.62 < f_{PS} < 0.66$ , inverse double gyroid;  $0.66 < f_{PS} < 0.77$  inverse hexagonal;  $f_{PS} > 0.77$ , inverse BCC. Depending on the packing frustration self-consistent field calculations also suggested the formation of a double diamond and a perforated lamellar

structure between the well-established lamellar and cylinder phases, but these microdomain geometries are considered to be only metastable and will not be discussed here. A phase diagram along with a schematic of the different periodic microstructures found as a function of  $\chi N$  and  $f$  for a typical diblock copolymer is shown in Fig. 3. Fig. 4 demonstrates the observation of the above mentioned morphologies via electron micrographs of PS–PI diblock copolymers.



**Scheme 3** Selection of di- and multiblock copolymer architectures.

### Block copolymer–homopolymer blends

A natural continuation of the research mentioned above is the study of block copolymer/homopolymer blends. Structure formation in blends of homopolymers and block copolymers is determined by the interplay of macrophase separation of the homopolymer and the microphase separation of the block copolymer. Which effect predominates depends on the relative lengths of the respective polymers and on the composition of the blend. In binary blends, low-molecular weight homopolymer is solubilized within



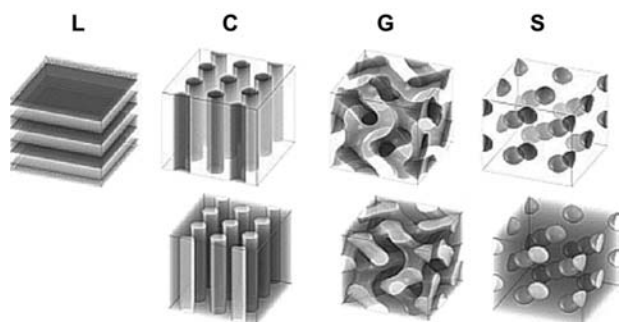
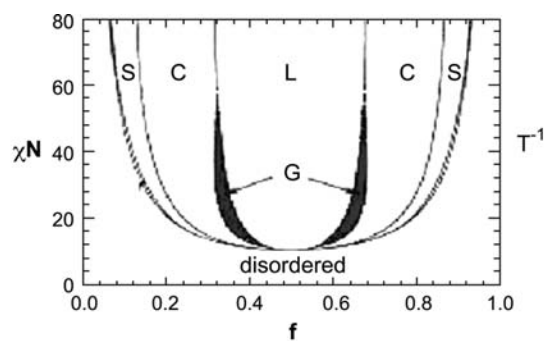


**Fig. 3** Phase diagram of a symmetric block copolymer ( $N_A = N_B$ ). L: lamellar phase, C: cylindrical phase, G: gyroid phase, S: spherical phase (cubic body centered). (More information about minimal surfaces: <http://www.msri.org/publications/sgp/jim/images/stills/mini/index.html>.)

a microphase-separated block copolymer structure at low concentrations. Increasing the molecular weight of the homopolymer such that it approaches that of the block copolymer leads to an increasing tendency for segregation of the homopolymer to the center of the domain. If the molecular weight of the homopolymer exceeds the one of the block copolymer, macrophase separation tends to predominate.<sup>[11]</sup>

### Binary block copolymer blends

Binary block copolymer blends offer another route toward nanoscale structures. Binary blends of triblock (ABC) and diblock (ac) copolymers, with the upper and lower case characters distinguishing the chemical composition and molecular weight of the respective blocks, were extensively studied because of their potential to microphase separate into *non-centrosymmetrical* morphologies. These nanostructures are of high technological interest, as the absence of centrosymmetry implies macroscopic polarization that is associated with many useful properties such as piezo- and pyroelectricity and second-order non-linear optical activity. Theoretical studies on the formation of non-centrosymmetric morphologies were performed for the case of lamellar structure and suggest that non-centrosymmetrical

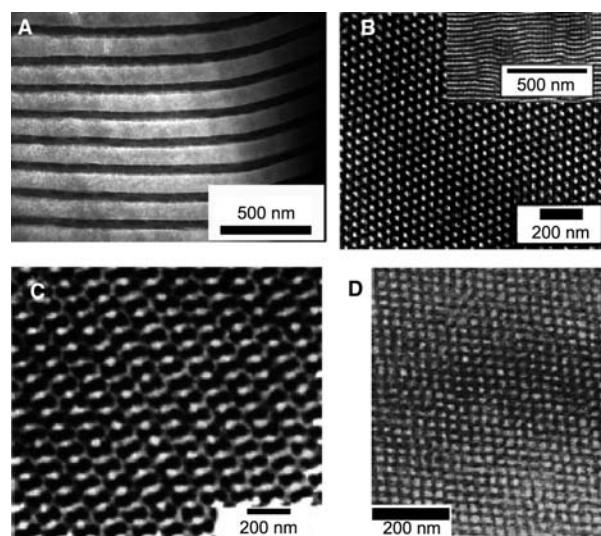


**Fig. 4** Transmission electron micrographs of (A) lamellar; (B) hexagonal cylindrical viewing direction along cylinder axis, inset: viewing direction perpendicular to cylinder axis; (C) gyroid [view direction along (110)] and (D) BCC spherical phase of poly(styrene-*b*-isoprene) copolymer [along (100)]. For all micrographs, the isoprene block was stained with Osmiumtetroxide to enhance contrast.

morphologies require sufficient asymmetry between the Aa and Cc domains. Fig. 5 shows a schematic of possible lamellar morphologies in blends of ABC and ac block copolymers along with an excellent electron micrograph providing non-centrosymmetrical lamellar structure obtained by blending a poly(styrene-*b*-butadiene-*b*-*tert*-butylmethacrylate) triblock copolymer with poly(styrene-*b*-*tert*-butylmethacrylate) diblock copolymer.<sup>[12]</sup>

### STRATEGIES FOR CONTROLLING THE SELF-ORGANIZATION PROCESSES

Mechanical behavior can be readily tuned when, e.g., glassy mesostructures are formed in a rubbery matrix, and indeed, glassy-rubbery block copolymers are used for various applications as advanced engineering materials. However, the possible impact of block copolymer nanostructures that are envisioned is much more far-ranged. The emerging challenges that have to be resolved involve the extension of hierarchically ordered structures to larger length scales and the development of new processing technologies that allow to control the ordering process at various length scales. In the following sections, several approaches will be presented that address these challenges. 1) Strategic design of the molecular architecture, e.g., by introducing anisotropic groups that introduce configurational

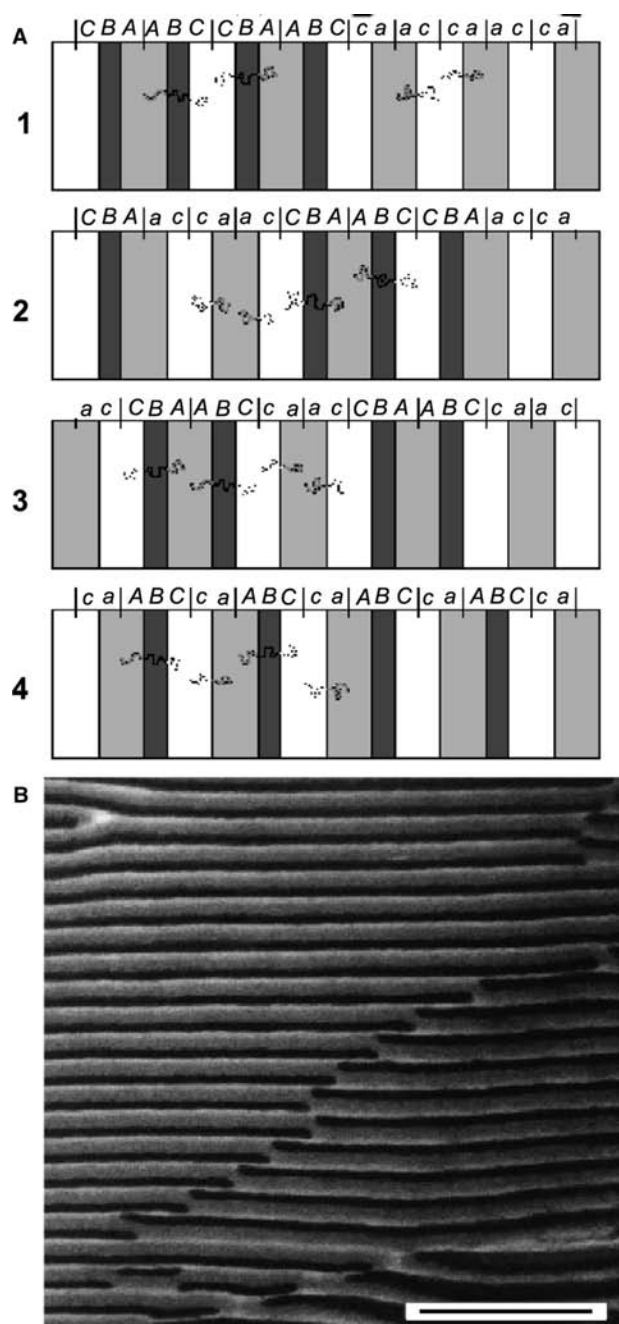


**Fig. 5** (A) Diagram of the possible lamellar morphologies of ABC/ac block copolymer blends. 1: Macrophase separation, 2: random sequence, 3: centrosymmetric sequence, 4: non-centrosymmetric sequence. (B) Transmission electron micrograph of the non-centrosymmetric blend. Scale bar: 250 nm. Source: From Ref.<sup>[13]</sup>. © 1999, Macmillan Publishers Ltd.

constraints to the self-assembling process; 2) by exploiting the effect of external fields on the self-assembly process; or 3) by using surface energetics and selective polymer–substrate interactions to guide the system to the desirable global geometries.

## Techniques Involving Molecular Architecture

### Structure formation in rod–coil block copolymer systems

If one block in a coil–coil block copolymer is substituted by a polymer type that exhibits highly restricted conformational freedom, a rod–coil block copolymer is obtained. The interest in rod–coil block copolymers is fueled by the extraordinary wealth of morphologies that are found in rod–coil systems, which can result in novel functional materials with intriguing optical or electronic properties. This spectrum of domain morphologies is due to the delicate interplay between liquid crystallinity of the rod block combined with the phase separated microdomain morphologies. Rod–coil block copolymers also provide an excellent example of *designer nanoscale materials* as the rod blocks represent active sites that can be addressed by external fields (flow, electric, magnetic), providing a means to guide the system into well-defined macroscopically ordered states. A rod-like conformation of a polymer is induced either by stepwise coupling of rigid mesogenic units to form low-molecular weight oligomeric rods or in macromolecular systems by creating a rigid polymer backbone with alternating conjugation, by steric hindrance of side groups attached to each repeating unit or by the formation of helical secondary structures. The asymmetry in the rigidity of the respective rod vs. coil blocks significantly increases the Flory–interaction parameter  $\chi$ , such that rod–coil block copolymers microphase separate already at low weight fractions of the rod component. The hierarchical order from the nano- to the microscale results as a consequence of the mutual repulsion of the dissimilar blocks and the packing constraints that are imposed by the connectivity as well as the tendency toward orientational ordering of the rod block.

Currently, there exists no general theoretical framework that can account for the complex phase behavior thus observed in rod–coil copolymer systems. Three examples will be provided that represent some of the new morphologies that are encountered in rod–coil block copolymer systems. For excellent review articles of this field we refer the reader to Refs.<sup>[13]</sup> and<sup>[14]</sup>.

Stupp et al. reported the formation of large, well-organized supramolecular structures ( $10^2$  kDa) by self-assembly of rod–coil *oligomers* consisting of an elongated mesogenic rods with volume filling fractions ranging from 0.19 to 0.36 and a coil-like poly(isoprene) (PI) part.<sup>[15]</sup> Depending on the rod filling fraction, the formation of a strip morphology ( $f_{\text{rod}} = 0.36$ ) or a hexagonal superlattice structure ( $f_{\text{rod}} = 0.25$ ) was observed. Substituting the poly(isoprene) coil block by a (styrene)<sub>9</sub>-*b*-(isoprene)<sub>9</sub> oligomer was reported to result in the formation of mushroom-like assemblies



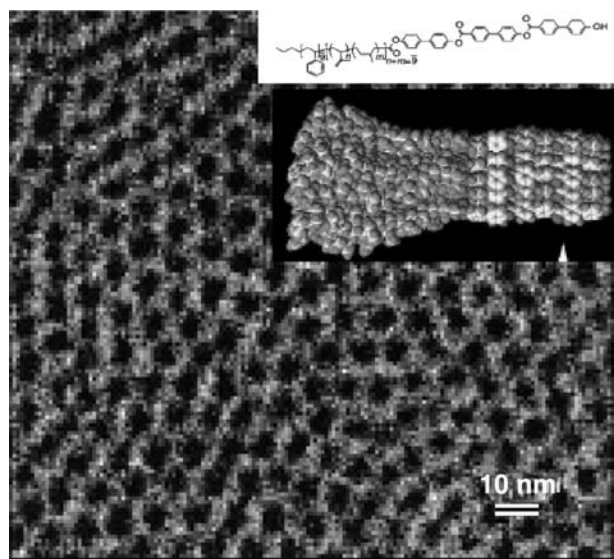


**Fig. 6** Transmission electron micrograph revealing superlattice of regularly shaped aggregates. Inset: Suggested mushroom-like morphology of the aggregate. *Source:* From Ref.<sup>[16]</sup>. © 2001, American Association for the Advancement of Science.

containing about  $N = 100$  rod-coil oligomers that self-organize into superlattice domains. A schematic of the proposed structure is given in Fig. 6.

Chen et al. investigated the structures formed in *high-molecular* rod-coil block copolymer systems consisting of poly(hexylisocyanate) with  $N = 900$  as the rod block and poly(styrene) with  $N = 300$  as the coil block.<sup>[16]</sup> Depending on the volume fraction of rod component, the formation of three different morphologies was reported. These were explained to occur as the result of microphase separation of the blocks and crystallization of the rods during solvent evaporation. For a volume filling fraction of the rod component  $f_{\text{rod}} = 0.42$ , the formation of a wavy lamellar structure was observed, in which the rod blocks are tilted

with respect to the layer normal by about  $60^\circ$ . For  $f_{\text{rod}} = 0.73$  a novel “zigzag” morphology was observed in which the rod and coil blocks are arranged in a zigzag fashion and the rod blocks are tilted with respect to the layer normal by  $45^\circ$ . For even higher rod filling fractions ( $f_{\text{rod}} > 0.96$ ) an “arrowhead-like” pattern formation was observed. Fig. 7 shows electron micrographs of the observed morphologies. The complexity of the structure formation process in rod-coil systems is indicated by the pronounced effect of solvent on the structures depicted in Fig. 7. Well-oriented zigzag patterns were observed only when toluene was used, whereas the use of chloroform as a solvent resulted in more disordered arrangement of the zigzags. The observed difference can be understood as the quality of the solvent determines the onset of microphase separation of the blocks as well as the onset of liquid crystallization of the rod blocks. As a consequence, rod-coil morphologies often do not represent equilibrium structures but rather kinetically trapped states. Park and Thomas have continued the study of microstructure formation in rod-coil block copolymers and demonstrated the formation of long-range periodic domain walls yielding a hierarchical morphology with order on multiple length scales consisting of interchain crystals of the rod blocks (1.5 nm), block copolymer microdomains (55 nm), and periodic Neel domain walls ( $\sim 1 \mu\text{m}$ ).<sup>[17]</sup> This study is remarkable for two reasons. First, the block copolymer-poly(3-(triethoxysilyl)propylisocyanate-*b*-styrene) (PIC-PS) employed in their study contains reactive groups as part of the isocyanate rod blocks. These entities allow the polymer to be covalently tethered to inorganic substrates after microstructure formation. Second, by directional solvent evaporation, the authors demonstrated unidirectional alignment of domain wall patterns on the centimeter length scale while maintaining interchain and microdomain ordering. A pair of atomic force micrographs of the observed hierarchical rod-coil structure are shown in Fig. 8.

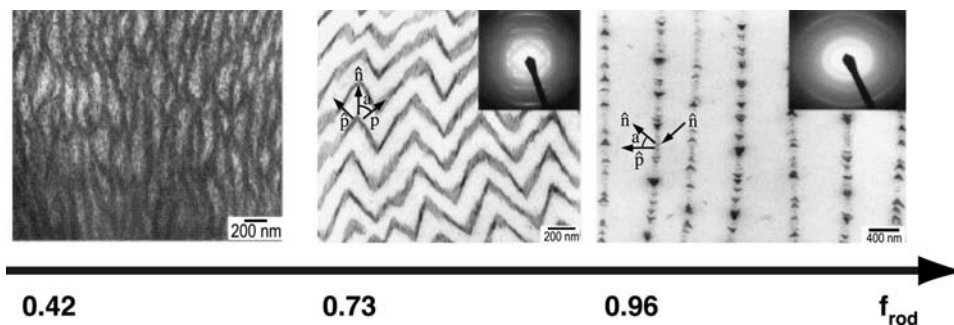


**Fig. 7** Transmission electron micrographs of the morphologies of the PHIC-PS rod-coil block copolymer: wavy-lamellar ( $f_{\text{PHIC}} = 0.42$ ), zigzag ( $f_{\text{PHIC}} = 0.89$ ) and bilayer arrowhead ( $f_{\text{PHIC}} = 0.96$ ). The dark regions correspond to PS (stained with Rutheniumoxide). *Source:* From Ref.<sup>[17]</sup>. © 2001, American Association for the Advancement of Science.

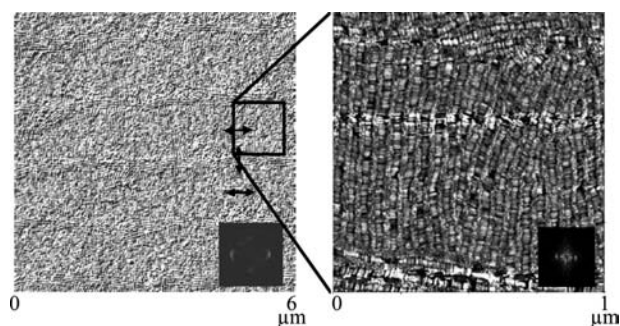


**Fig. 8** Tapping mode atomic force micrographs of the hierarchical structure formation of PS-PIHC thin films after casting on silica substrate. The insets show Fourier-transformed images.

### Effect of Mechanical and Electric Fields

Polymeric materials can undergo dramatic changes in their structure in response to external fields. This provides opportunities to direct distinct alignments of polymeric nanostructures through processing. Polymer engineers have long exploited processing to increase properties (e.g., fiber production) through increase of crystallinity and chain orientation. For many envisioned applications of polymer-based nanostructures, it is of special importance to be able to produce functional macroscopic materials with uniform large-scale orientation. In general, self-assembly processes alone do not result in globally ordered structures but rather heterogeneous morphologies consisting of randomly oriented grains within which the domains have homogeneous alignment. The possibility to induce global order in block copolymer microstructures by flow field alignment was pioneered by Keller, Pendemonte, and Willmouth in extruded polymer materials and a variety of other flow methods have been developed, such as roll-casting and extensional flow.<sup>[18–20]</sup> Kornfield et al. studied the influence of oscillatory shear on the alignment of lamellar morphology forming block copolymers by in situ rheo-optical methods that allow monitoring the alignment of the lamellae as a function of applied shear rate and amplitude.<sup>[19]</sup> It was argued that with increasing shear rate three different microstructure regimes can be distinguished for layered microstructured block copolymers in which the polymer domains have dissimilar viscoelastic properties. Two characteristic frequencies that determine the effect of oscillatory shear on the alignment of lamellar samples were identified: a lower frequency limit  $\omega_d$  that is associated with the lifetime of fluctuations on a layered structure and a higher frequency limit  $\omega_c$  that reflects the dynamics of conformational distortions of single polymer chains. It was found that oscillatory strain shearing induces parallel alignment with respect to the shear direction for  $\omega < \omega_d$ , perpendicular

alignment for  $\omega_d < \omega < \omega_c$ , and parallel alignment for  $\omega_c < \omega$ .

For cylindrical microdomain forming coil-coil block copolymers subjected to steady or oscillatory shear, parallel orientation, i.e., the cylinder axes are aligned along the flow direction, was found to be the usual orientational state. However, by anchoring liquid crystalline side groups to a coil-coil block copolymer, Osuji et al. could demonstrate that the strong interaction of the mesogens with the applied flow field can force the cylindrical microdomains to align *transverse* to the flow direction.<sup>[21]</sup> In their study of the effect of oscillatory mechanical shear on the microstructure formation of a PS-PI block copolymer in which each isoprene block was functionalized with a mesogenic group, the authors concluded that the invariant homogeneous anchoring of the mesogens with respect to the IMDS results in the transverse cylindrical orientation under shear. A schematic of the proposed structural model of perpendicular smectic layers and transverse cylindrical microdomains is given in Fig. 9.

Amundson et al.<sup>[22]</sup> presented a detailed mechanistic study of the effect of electrical fields on the structure evolution in lamellar block copolymer systems. By applying electrical fields of 1.8 MV/m to a symmetric PS-PMMA diblock copolymer while heating the polymer above glass transition temperature, a significant increase in orientation of the lamellae along the electric field direction could be observed. The ordering effect of the electric field could be explained by the orientational dependence of the systems free-energy in the presence of the external field. The situation is similar to the effect of an oscillatory shear-field when  $\omega < \omega_d$ . The external field raises the free-energy associated with lamellar compression or splay and hence causes movement and annihilation of defect walls and disclination lines. A schematic of the defect movement along with electron micrographs of the films with and without electric field alignment is shown in Fig. 10. Recently, Thurn-Albrecht et al. applied a similar procedure to align cylindrical PS-PMMA block copolymers using electric field strengths of 40 MV/m.<sup>[23]</sup>

### Thin Film Morphologies

Whereas bulk morphologies of microphase-separated block copolymers are often typified by grains of ordered domains that are randomly oriented with respect to each other, thin films can sometimes exhibit highly ordered domains. This orientation can be understood as a direct result of the surface and interfacial energy minimization. The possible applications of block copolymer thin films have been widely recognized and constitute a very active current field of

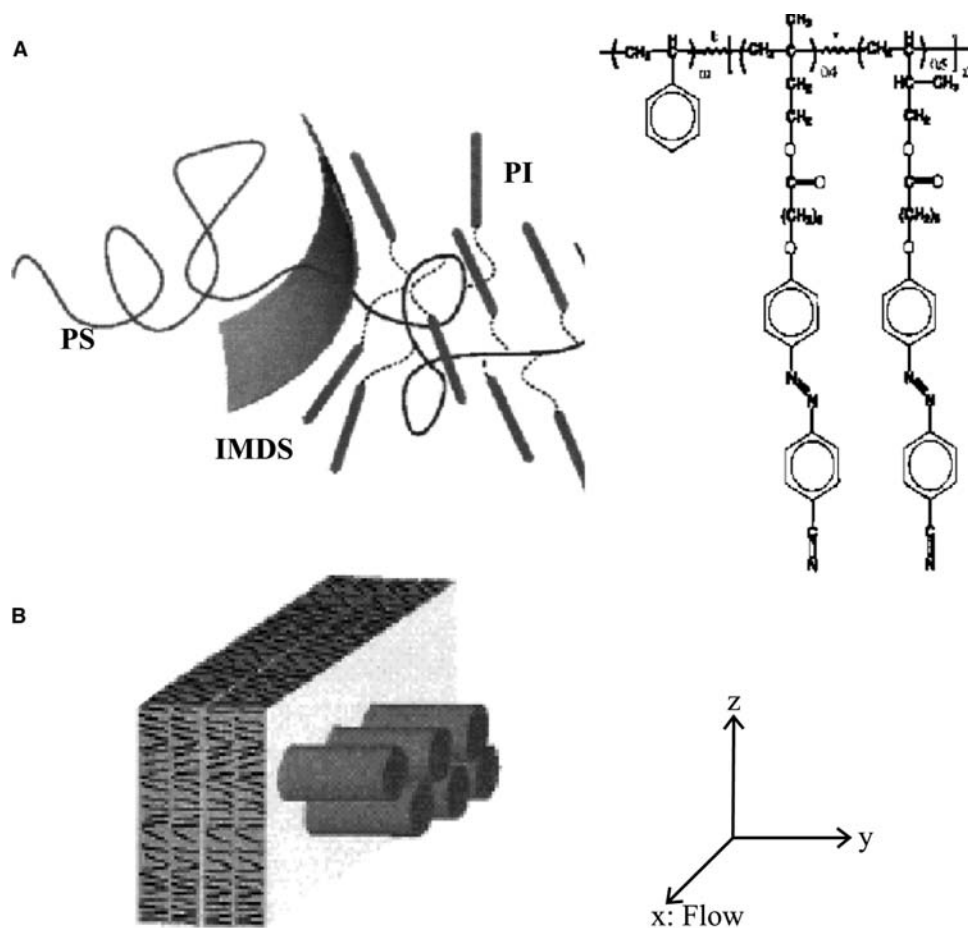


**Fig. 9** Schematic structural model of the transverse alignment of cylindrical microdomains and smectic layers. Flow is along  $x$ - and vorticity is along  $y$  direction. The model represents a compromise structure in which cylinders are transverse and smectic layers are perpendicular, but the boundary condition for the mesogens are maintained homogeneous. *Source:* From Ref.<sup>[22]</sup>.

research. An excellent introduction to the field is the recent review article by Fasolka and Mayes.<sup>[24]</sup> Of the various microdomain types, the most investigated is the lamellar. Most theoretical work regarding the physics of thin film morphology was done for the case of symmetrical boundary conditions that is realized, e.g., when the film is located in between two identical substrates. It was found that for films with thickness greater than the lamellar thickness,  $t > L$ , the lamellae orient parallel to the substrate surface. As a result of the surface substrate boundary conditions the most energetically compatible block is expressed at each of the surfaces. Depending on which block wets the respective surface, one distinguishes between symmetric (same block wets each surface) and antisymmetric (different blocks wet the two surfaces) wetting. The equilibrium conditions for stability of symmetric films are then given as  $t = nL$ , with  $n$  being an integer, and  $t = (n + 1/2)L$  for antisymmetric wetting. It was proposed that the entropic penalty that is imposed on chains when surface-parallel lamellae are constrained to film thicknesses incommensurate with

integer multiples of  $L$  can induce the perpendicular lamellar orientation if the entropic penalty exceeds the enthalpic gain from preferential wetting. A summary of possible thin film morphologies is given in Fig. 11.

Although the assumption of symmetric boundary conditions simplifies the analysis, many practical thin film situations exhibit asymmetric boundary conditions, e.g., supported film systems. In supported film systems, the polymer-substrate interfacial energy of a given type of monomer can differ from its surface energy by an order of magnitude. The presence of asymmetric boundary conditions can therefore result in new morphological trends not found in the symmetric case, e.g., the formation of hybrid structures involving parallel as well as perpendicular alignment. At the time of writing no theoretical model has been developed that could accurately account for many of the experimental observations. This is in part due to the finite roughness and deformability of most surfaces on the molecular scale that represents a major problem in the application of the theoretical models mentioned above to real supported films.



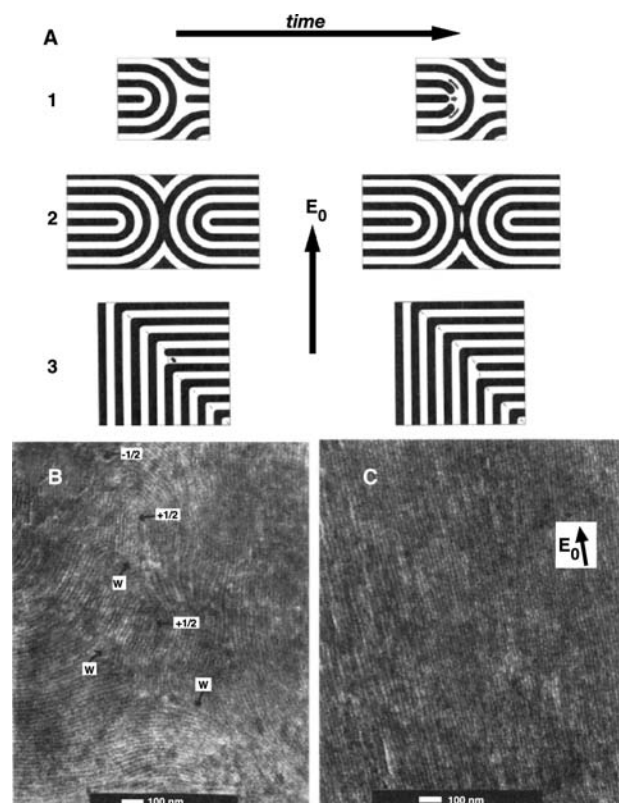


**Fig. 10** (A) Movement of the disclination lines and wall defects occurring by glide and climb of edge dislocations and creation of pores. 1: Disclination lines approach by perforation of layer; 2: focal conic loop forms island that grows by climb motion along the disclination loop; 3: through combination of climb and glide motion an edge dislocation propagates along a wall defect. (B) Transmission electron micrographs of PS-PMMA perpendicular to field direction and (C) parallel to field direction. *Source:* From Ref.<sup>[23]</sup>.

### Epitaxial crystallization of block copolymer thin films

Epitaxy denotes the oriented overgrowth of one crystalline material upon the surface of another. In general, this process requires an approximate agreement in lattice spacings of the two components. Epitaxy is a traditional method of material science used to control registration and orientation. Block copolymers that contain one crystallizable block are of great interest as the crystallization provides an additional driving force for the microphase separation. The resulting morphology is the result of the interplay between segregation and crystallization process and is therefore process-path dependent, resulting in new opportunities to control the structure formation process by directing the crystallization process. Epitaxial methods were shown to be particularly interesting in controlling the orientation of microphase-separated block copolymer domains over large areas. De Rosa et al. recognized

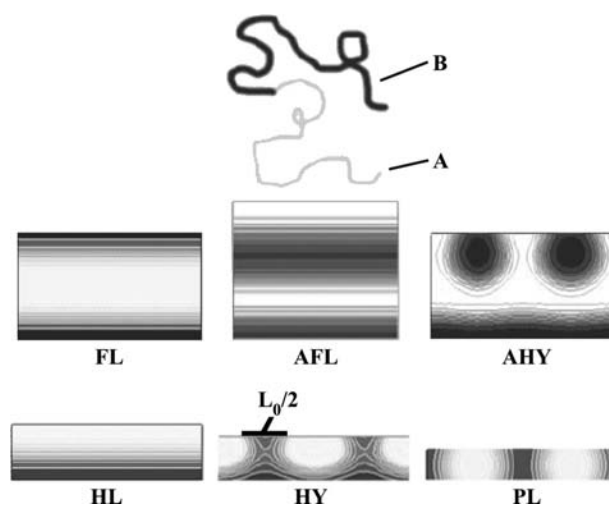


**Fig. 11** Diblock copolymer thin film morphologies as a function of boundary conditions. A-block is gray, B-block is black.  $L_0$ : film thickness, FL: symmetric surface-parallel full lamellae, AFL: antisymmetric surface-parallel lamellae, AHY: antisymmetric hybrid structure, HL: half-lamellae, HY: symmetric hybrid structure, PL: surface-perpendicular lamellae. *Source:* From Ref.<sup>[24]</sup>. © 2001, Annual Reviews.

that because of crystallographic matching of poly(ethylene) and benzoic acid crystals, the poly(ethylene) blocks of a semicrystalline poly(ethylene-*b*-ethylene-propylene-*b*-ethylene) triblock copolymer can be epitaxially crystallized onto crystals of benzoic acid thereby directing the microphase separation process.<sup>[25]</sup> Electron micrographs depicting the microstructure of the block copolymer thin film with and without epitaxial direction are shown in Fig. 12. Epitaxial control over the microphase separation process continues to attract much attention as it opens a new dimension to the control of nanostructure formation: crystal orientation on the 1–10-nm length scale as well as microstructure orientation on the 10–100-nm length scale.

### TRENDS IN EXPLOITING POLYMER-BASED NANOSTRUCTURES

Recent advances in understanding the formation of nanostructures based on self-assembled microphase separated block copolymers and the external parameters that afford global ordering of these structures have resulted in applications that capitalize on the specific structural characteristics rather than on a volume averaged behavior. Microphase separated block copolymers have been studied extensively as an alternative approach to conventional lithographic techniques to produce highly ordered nanostructures with possible

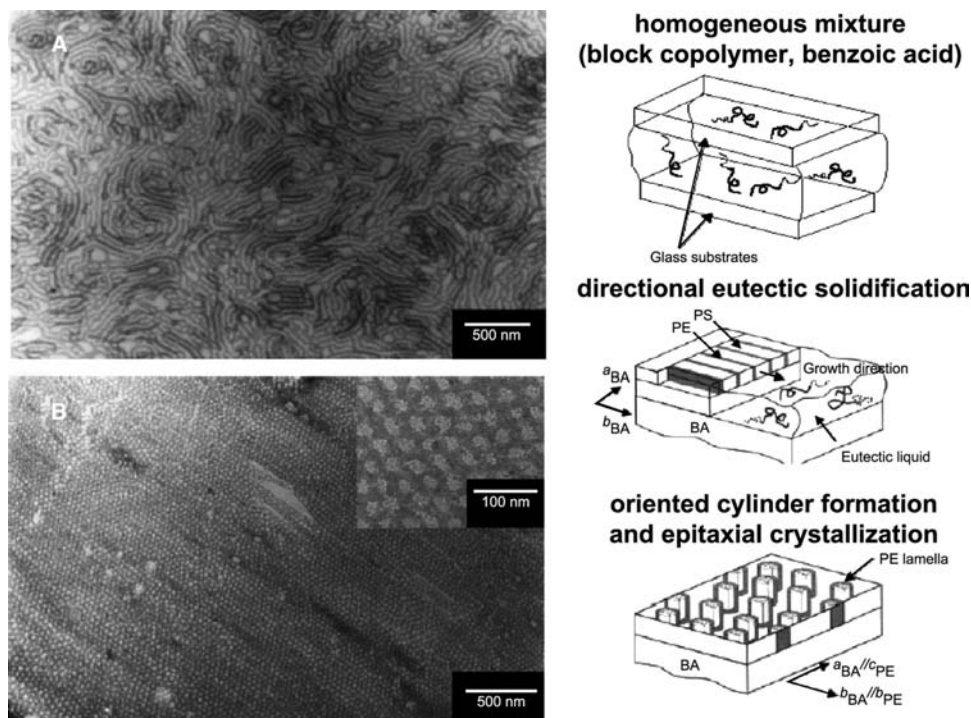


**Fig. 12** Transmission electron micrographs of (A) solvent-cast and (B) directionally solidified/epitaxially crystallized PS-PE copolymer. PE domains form pseudo-hexagonal lattice of perpendicular-oriented cylinders. The styrene blocks have been stained with Rutheniumtetroxide for contrast enhancement. The inset in B shows magnified region demonstrating the non-circular shape of the PS-PE interface resulting from the 15% smaller domain spacing of benzoic acid in *b* direction. *Source:* From Ref.<sup>[25]</sup>. © 2000, Macmillan Publishers Ltd.

applications such as a high-density magnetic recording device or a photonic band-gap material. In the following we present some examples of the new directions in this area of research.

### Block Copolymers as Photonic Band Gap Materials

As block copolymers self-assemble into periodic one-, two-, or three-dimensional equilibrium structures, optical effects such as photonic band gaps can be obtained when the molecular weight of the block copolymer is high enough such that the domain spacing is of the order of the wavelength of light (typically  $M \sim 10^6$  g/mol). Photonic band gaps denote frequency regions in which light of certain polarization and propagation direction cannot propagate through the material.<sup>[26]</sup> As the synthesis and processing of high molecular weight polymers is delicate, the first observation of a self-assembled polymer-based photonic material was not published until 1999.<sup>[27]</sup> Various techniques have been developed in order to solve the eminent problem of the inherently low dielectric contrast between typical polymers. Methods such as selective deposition of high index nanocrystals within the polymer scaffold<sup>[28]</sup> or selective etching of one of the

domains<sup>[29]</sup> can raise the dielectric contrast. It could be shown that even for high molecular weight copolymers the double gyroid microdomain morphology can be obtained, indicating pathways to three-dimensional photonic crystals that combine a full photonic band gap with the advantageous mechanical properties of polymeric materials and the ease of self-assembly. Fig. 13B shows a scanning electron micrograph of a double gyroid obtained from high molecular weight PS-PI after selective etching of the PI matrix using UV/ozone.<sup>[29]</sup>

### Block Copolymer Lithography

The typical length scale of microphase separation, 10–100 nm, is particularly interesting as it provides a versatile alternative to conventional photolithographic techniques for surface structuring. Possible applications for regular texturing of a surface at the 10-nm length scale are the fabrication of high-storage magnetic recording media, DNA electrophoresis membranes or microoptical elements. Of particular interest is the combination of the controlled structure formation on the nanometer length scale with the distinct chemical nature of the respective blocks. Lopes and Jaeger demonstrated the selective decoration of the

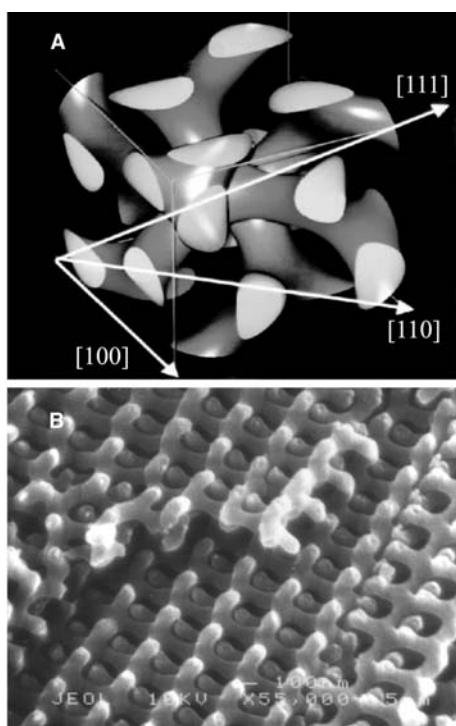


**Fig. 13** (A) Schematic model of the double-gyroid morphology showing two interpenetrating networks (here: PS) embedded in the matrix material (here: air). (B) Scanning electron micrograph of a free-standing interconnected PS network obtained from a high molecular weight double-gyroid PS-PI block copolymer after selective UV/ozone etching of the PI domain.

PS domains of a cylindrical microstructure forming PS-PMMA diblock copolymer by evaporation of gold on top of the spin-casted polymer thin film.<sup>[30]</sup> The dense packing of gold nanocrystals on the PS domains allowed for the formation of a regular pattern of conducting nanowires 50 nm in width which are of great interest as interconnects, gratings, or for biosensor applications. A schematic of the described structure formation process along with electron micrographs of the resulting structures is shown in Fig. 14. Block copolymer lithography has also been studied as possible alternative to conventional lithographic techniques for the fabrication of high-density magnetic storage media. For example, Cheng et al. demonstrated that single-domain ferromagnetic cobalt dots can be fabricated using self-assembled block copolymer lithography.<sup>[31]</sup> In their study, the authors took advantage from the significantly different etching rates of organic-inorganic block copolymers when exposed to a reactive ion beam, allowing the selective etching of one component from the microstructure while converting the inorganic-containing block to a ceramic. A thin film of spherical microdomain morphology forming poly(styrene-*b*-ferrocenyldimethylsilane) (PS-PFS) block

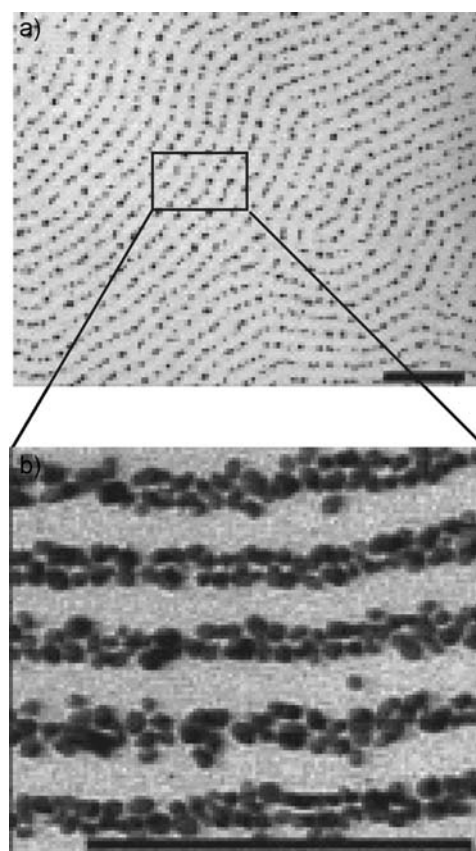


**Fig. 14** (A) Metal nanochain and nanowire formation after vapor-deposition of Au onto a thin film of cylindrical PS-PMMA block copolymer and annealing for 1 min at 180°C under Ar atmosphere. Au highly selectively decorates the PS domain. (B) Magnification of A demonstrating individual nanocrystal array formation. Scale bars: 200 nm. *Source:* From Ref.<sup>[30]</sup>. © 2001, Macmillan Publishers Ltd.

copolymer was cast on a layered cobalt-tungsten-silica substrate and the PFS domains used as a mask for subsequent reactive ion etching. A schematic of the procedure as well as a scanning electron micrograph of the obtained nanodot arrays is shown in Fig. 15.

### Inorganic-Organic Mesostructures from Block Copolymer Phases

At present, great attention is being paid to the preparation of complex inorganic-organic hybrid materials with long-range order that could find possible applications in catalysis, membrane, and separation technology. Two major synthetic approaches can be distinguished: 1) the in situ synthesis of inorganic particles within a block copolymer domain that has been loaded with a suitable precursor reagent and 2) the simultaneous self-assembly of the block copolymer in the presence



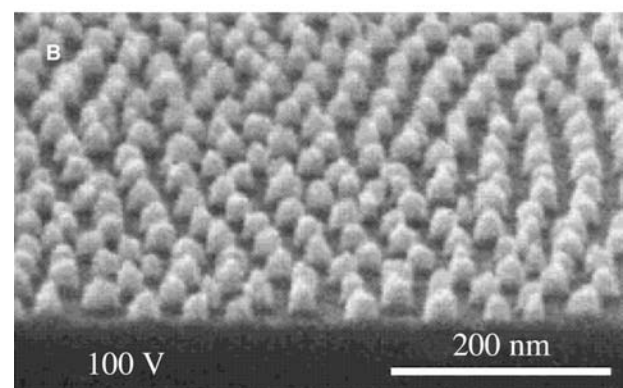
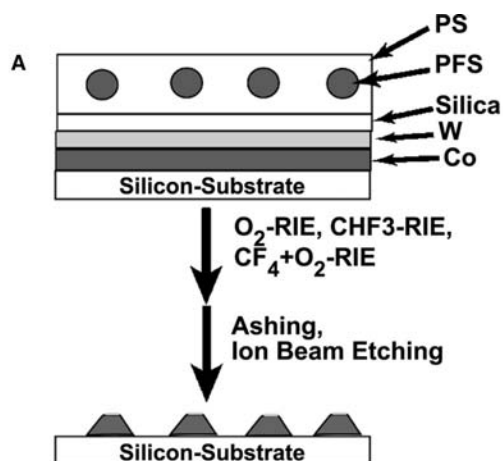


**Fig. 15** (A) Schematic of the sequential reactive ion etch process (see text for details). (B) Tilted scanning electron micrograph showing Co-nanodot arrays obtained after complete etching of the PS-PFS block copolymer. *Source:* From Ref.<sup>[31]</sup>. © 2001, Wiley Interscience.

of ex situ synthesized nanoparticles that are surface-tailored in order to allow preferential sequestration within a target domain. Whereas the first approach facilitates higher volume filling fractions of the inorganic material, the second approach allows better control of the structural characteristics of the sequestered component. Micropatterned solid particles in a block copolymer matrix were produced by Bootongkong and Cohen in a nanoreactor scheme, in which the hydrophilic domain of a poly(styrene-*b*-acrylic acid) block copolymer is pre-loaded with a metal salt that is reduced in a second reaction step.<sup>[32]</sup> The procedure is outlined in Fig. 16. The authors demonstrated that the block copolymer nanoreactor scheme might be applied to a wide variety of metal (Pd, Cu, Au, Ag) as well as semiconductor (PbS) nanocrystals. Whereas the block copolymer nanoreactor scheme results in the formation of discrete or interconnected nanocrystals dispersed within the respective block copolymer domain, Templin et al. demonstrated that by swelling of the poly(ethylene oxide) domain of a poly(ethylene oxide-*b*-isoprene) block copolymer with an inorganic

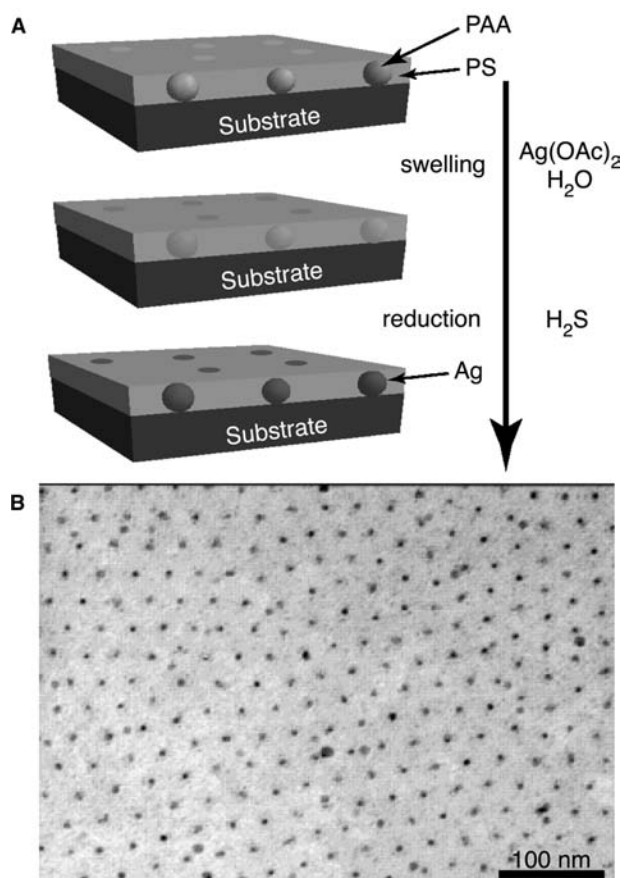


**Fig. 16** (A) Schematic of the nanoreactor approach. 1: Thin film cast of spherical PS-PAA; 2: selective swelling of PAA spheres with metal precursor; 3: formation of metal nanocrystals by reduction of metal precursor. (B) Transmission electron micrograph of thin film demonstrating hexagonal array of Ag nanodots within PS matrix. *Source:* From Ref.<sup>[32]</sup>. © 2002, American Chemical Society.

precursor followed by hydrolysis and calcination, continuous inorganic nanorelief structures can be obtained.<sup>[33]</sup> The authors also described the formation of the “plumber’s nightmare” morphology for the hybrid material, which is an uncommon bicontinuous morphology for block copolymers and which was explained by subtle differences in the phase behavior of hybrid vs. neat block copolymer structures. In contrast to the abovementioned in situ approaches, ex situ methodologies become advantageous when precise control of the structural features of the inorganic component becomes relevant to the desired function of the hybrid material or the geometrical characteristics of the inorganic component cannot be obtained through in situ synthesis. For example, Ha and Thomas studied the incorporation of “two-dimensional” clay sheets into lamellar PS-PI block copolymer microstructures.<sup>[34]</sup> The authors demonstrated that by decorating the mineral’s surface with poly(styrene),

individual clay sheets can be preferentially sequestered within the polystyrene domain of the block copolymer. The resulting nanocomposite materials exhibit highly anisotropic mechanical and permeability properties. An electron micrograph of the nanocomposite material revealing single-layer clay sheets sequestered within the poly(styrene) domains is shown in Fig. 17. The development of surface decoration techniques that allow for molecular level dispersion of the inorganic component within the polymer matrix represents a major advancement in the field as the inclusion of single-sheet (exfoliated) mineral layers permits to downscale the amount of inorganic component by an order of magnitude (only 2 wt.% inorganic is needed) while providing the advantageous material properties.

The control of the composites' architecture on the nanometer scale is of special importance for future research in this area as it facilitates to dramatically decrease the switching speed in these materials which is diffusion limited, scaling as the square of the feature size. At present, research focus is on the development of next-generation actuator materials that capitalize from both the mechanical and optical characteristics of the sequestered component as well as the rapid dynamic response to external stimulus that results from the architectural control on the molecular level.

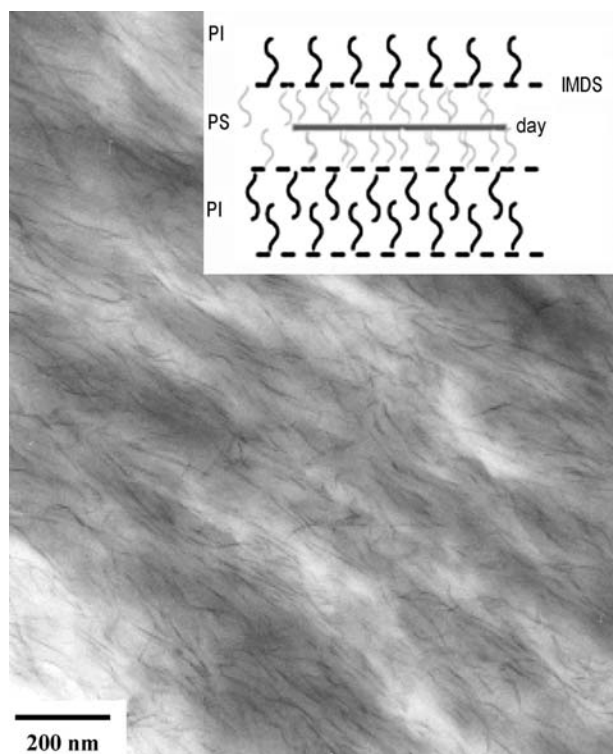


**Fig. 17** Transmission electron micrograph of exfoliated clay-PS-PI nanocomposite (no stain). Individual PS-decorated clay sheets are sequestered within PS layers. Inset: Schematic of the composite structure.

## ACKNOWLEDGMENTS

This material is based upon work supported by, or in part by, the Alexander von Humboldt Foundation (Feodor-Lynen program) as well as the U.S. Army Research Laboratory and the U.S. Army Research Office under Contract DAAD-19-02-0002. We thank Dr. J.-W. Park, A.M. Urbas, and Y.-H. Ha for their contribution of electron and atomic force micrographs to this work.

## REFERENCES

1. Hiemenz, P.C. *Polymer Chemistry: The Basic Concepts*; Marcel Dekker: New York, 1984.
2. Hadjichristidis, N.; Pitsikalis, M.; Pispas, S.; Iatrou, H. Polymers with complex architecture by living anionic polymerization. *Chem. Rev.* **2001**, *101*, 3747–3792.
3. Flory, P.J.J. Thermodynamics of high polymer solutions. *Chem. Phys.* **1941**, *9*, 660.
4. Huggins, M.L.J. Solutions of long chain compounds. *Chem. Phys.* **1941**, *9*, 440.
5. Balsara, N.P.; Fetters, L.J.; Hadjichristidis, N. Thermodynamic interactions in model polyolefin blends obtained by small-angle neutron scattering. *Macromolecules* **1992**, *25* (23), 6137.
6. Ryu, D.Y.; Jeong, U.; Kim, J.K.; Russel, T.P. Closed-loop phase behavior in block copolymers. *Nat. Mater.* **2002**, *1*, 114–117.
7. Pernot, H.; Baumert, M.; Court, F.; Leibler, L. Design and properties of co-continuous nanostructured polymers by reactive blending. *Nat. Mater.* **2002**, *1*, 54–58.
8. Bates, F.S. Polymer-polymer phase behavior. *Science* **1991**, *251*, 898–905.
9. Bates, F.S.; Fredrickson, G.H. Block copolymer thermodynamics. *Annu. Rev. Phys.* **1990**, *41*, 525–557.
10. Hamley, I.W. *The Physics of Block Copolymers*; Oxford University Press: New York, 1998.
11. Winey, K.I.; Thomas, E.L.; Fetters, L. Swelling a lamellar diblock copolymer with homopolymer—Influences of homopolymer concentration and molecular weight. *Macromolecules* **1991**, *24* (23), 6182–6188.
12. Goldacker, T.; Abetz, V.; Stadler, R.; Eruhimovich, I.; Leibler, L. Non-centrosymmetric superlattices in block copolymer blends. *Nature* **1999**, *398*, 137–139.
13. Lee, M.; Cho, B.-K.; Zin, W.-C. Supramolecular structures from rod-coil block copolymers. *Chem. Rev.* **2001**, *101*, 3869–3892.
14. Klok, H.-A.; Lecommandoux, S. Supramolecular materials via block copolymer self-assembly. *Adv. Mater.* **2001**, *13* (16), 1217–1229.
15. Stupp, S.I.; LeBonheur, V.; Walker, K.; Li, L.S.; Huggins, K.E.; Keser, M.; Amstutz, A. Supramolecular materials: self-organized nanostructures. *Science* **1997**, *276*, 384–389.
16. Chen, J.T.; Thomas, E.L.; Ober, C.K.; Mao, G.P. Self-assembled smectic phases in rod-coil block copolymers. *Science* **1996**, *276*, 343–346.

17. Park, J.-W.; Thomas, E.L. Multiple ordering transitions: hierarchical self-assembly of rod-coil block copolymers. *Adv. Mater.* **2003**, *15* (7–8), 585–588.
18. Honeker, C.C.; Thomas, E.L. Perpendicular deformation of a near-single-crystal triblock copolymer with a cylindrical morphology. *Macromolecules* **2000**, *33* (25), 9407–9417.
19. Chen, Z.-R.; Kornfield, J.A.; Smith, S.D.; Grothaus, J.T.; Satkowski, M.M. Pathways to macroscale order in nanostructured block copolymers. *Science* **1997**, *277*, 1248–1253.
20. Keller, A.; Pedemonte, E.; Willmouth, F.M. Macro lattice from segregated amorphous phases of a three block copolymer. *Colloid Polym. Sci.* **1970**, *238*, 385–389.
21. Osuji, C.; Zhang, Y.; Mao, G.; Ober, C.K.; Thomas, E.L. Transverse cylindrical microdomain orientation in a LC diblock copolymer under oscillatory shear. *Macromolecules* **1999**, *32*, 7703–7706.
22. Amundson, K.; Helfand, E.; Quan, X.; Smith, S.D. Alignment of block copolymer microstructures. *Macromolecules* **1994**, *27* (22), 6559–6570.
23. Thurn-Albrecht, T.; Schotter, J.; Kastle, G.A.; Emley, N.; Shibauchi, T.; Krusin-Elbaum, L.; Guarini, K.; Black, C.T.; Tuominen, M.T.; Russell, T.P. Ultrahigh-density nanowire arrays grown in self-assembled diblock copolymer templates. *Science* **2000**, *290*, 2126–2129.
24. Fasolka, M.J.; Mayes, A.M. Block copolymer thin films: physics and applications. *Annu. Rev. Mater. Res.* **2001**, *31*, 323–355.
25. De Rosa, C.; Park, C.; Thomas, E.L.; Lotz, B. Microdomain patterns from directional eutectic solidification and epitaxy. *Nature* **2000**, *405*, 433–437.
26. Joannopoulos, J.D.; Meade, R.D.; Winn, J.N. *Photonic Crystals*; Princeton University Press: New Jersey, 1995.
27. Fink, Y.; Urbas, A.M.; Bawendi, M.G.; Joannopoulos, J.D.; Thomas, E.L. Block copolymers as photonic bandgap materials. *J. Lightwave Technol.* **1999**, *17* (11), 1963–1969.
28. Bockstaller, M.R.; Kolb, R.; Thomas, E.L. Metallodielectric photonic crystals based on diblock copolymers. *Adv. Mater.* **2001**, *13* (23), 1783–1786.
29. Urbas, A.M.; Maldovan, M.; Thomas, E.L. Bicontinuous cubic photonic crystal in a block copolymer system. *Adv. Mater.* **2002**, *14* (24), 1850–1853.
30. Lopes, W.A.; Jaeger, H.M. Hierarchical self-assembly of metal nanostructures on diblock copolymer scaffolds. *Nature* **2001**, *414*, 735–738.
31. Cheng, J.Y.; Ross, C.; Chan, V.Z.-H.; Thomas, E.L.; Lammertink, R.G.H.; Vansco, G.J. Formation of cobalt magnetic dot array via block copolymer lithography. *Adv. Mater.* **2001**, *13* (15), 1174–1178.
32. Boontongkong, Y.; Cohen, R.E. Cavitated block copolymer micellar thin films: Lateral arrays of open nanoreactors. *Macromolecules* **2002**, *35* (9), 3647–3652.
33. Templin, M.; Franck, A.; Du Chesne, A.; Leist, H.; Zhang, Y.; Ulrich, R.; Schaedler, V.; Wiesner, U. Organically modified aluminosilicate mesostructures from block copolymer phases. *Science* **1997**, *278*, 1795–1798.
34. Ha, Y.H.; Thomas, E.L. Deformation behavior of roll-cast layered silicate/triblock copolymer nanocomposites. *Macromolecules* **2002**, *35* (11), 4419–4428.

# Nanotube Sensors

**Marc Wirtz**

*PPG Industries, Inc., Monroeville, Pennsylvania, U.S.A.*

**Charles R. Martin**

*Department of Chemistry, University of Florida,  
Gainesville, Florida, U.S.A.*

## INTRODUCTION

We have been exploring the transport and electrochemical properties of nanotube membranes prepared by the template method,<sup>[1–3]</sup> a general approach for preparing nanomaterials. This method entails synthesis or deposition of the desired material within the cylindrical and monodisperse pores of a nanopore membrane or other solid. We have used polycarbonate filters, prepared via the “track-etch” method,<sup>[4]</sup> and nanopore aluminas, electrochemically prepared from Al foil,<sup>[5]</sup> as our template materials. Cylindrical nanostructures with monodisperse diameters and lengths are obtained, and depending on the membrane and synthetic method used, these may be solid nanowires or hollow nanotubes. We and others have used this method to prepare nanowires and tubes composed of metals,<sup>[5–12]</sup> polymers,<sup>[13–15]</sup> semiconductors,<sup>[16,17]</sup> carbons,<sup>[18,19]</sup> and Li<sup>+</sup> intercalation materials.<sup>[20–22]</sup> It is also possible to prepare composite nanostructures, both concentric tubular composites, where an outer tube of one material surrounds an inner tube of another,<sup>[23,24]</sup> and segmented composite nanowires.<sup>[25]</sup>

One application for these nanotube membranes is in electroanalytical chemistry where the membrane is used to sense analyte species.<sup>[26,27]</sup> In that work, membranes containing gold nanotubes with inside diameters that approached molecular dimensions (1–4 nm) were used.<sup>[26]</sup> The Au nanotube membrane was placed between two salt solutions and a constant transmembrane potential was applied. The resulting transmembrane current, associated with migration of ions through the nanotubes, was measured. When an analyte molecule whose diameter was comparable to the inside diameter of the nanotubes was added to one salt solution, this molecule partitioned into the nanotubes and partially occluded the pathway for ion transport. This resulted in a decrease in the transmembrane ion current, and the magnitude of the drop in current was found to be proportional to the concentration of the analyte.<sup>[26]</sup>

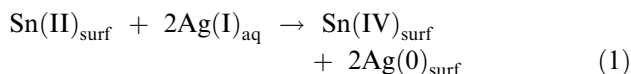
In the experiment discussed above, a baseline transmembrane ion current was established, and the analyte molecule, in essence, turned off this current. It occurred to us that there might be an advantage in doing the opposite, i.e., starting with an ideally zero current situation and having the analyte molecule switch on the ion current. In other words, we would like to make a synthetic membrane that mimics the function of a ligand-gated ion channel. An example is the acetylcholine-gated ion channel,<sup>[28]</sup> which is closed (“off” state) in the absence of acetylcholine but opens (and supports an ion current, “on” state) when acetylcholine binds to the channel. To accomplish this, the off state was obtained by making gold and alumina membranes hydrophobic, and the on state was obtained by introducing ions and electrolyte into the membrane.<sup>[29]</sup> Ions were introduced by either partitioning a hydrophobic ionic species (e.g., a drug or a surfactant) into the membrane.

## MEMBRANE PREPARATION AND ANALYSIS

Commercially available track-etched polycarbonate filters are used as the templates to prepare the Au nanotubes. The track-etch process<sup>[4]</sup> entails bombarding a solid material (in this case a ~10- $\mu$ m-thick polycarbonate film) with a collimated beam of high-energy nuclear fission fragments to create parallel damage tracks in the film. The damage tracks are then etched into monodisperse cylindrical pores by exposing the film to a concentrated solution of aqueous base. The diameter of the pores is determined by the etch time and the etch-solution temperature. Membranes with pore diameters ranging from as small as 10 nm to as large as ~10  $\mu$ m are commercially available. The membranes used for these studies had nominal pore diameters of 30 nm and contained  $6 \times 10^8$  pores per square centimeter of membrane surface area.

The electroless plating method is used to deposit the Au nanotubes<sup>[7,30]</sup> within the pores of these

membranes. Briefly, the template membrane is first “sensitized” by immersion into a  $\text{SnCl}_2$  solution, which results in deposition of  $\text{Sn(II)}$  onto all of the membrane’s surfaces (pore walls and membrane faces). The sensitized membrane is then immersed into a  $\text{AgNO}_3$  solution, and a surface redox reaction occurs [Eq. (1)], which yields nanoscopic metallic  $\text{Ag}$  particles on the membrane surfaces.



(The subscripts surf and aq denote species adsorbed to the membrane surfaces and species dissolved in solution, respectively.) The membrane is then immersed into a commercial gold plating solution and a second surface redox reaction occurs, which yields  $\text{Au}$  nanoparticles on the surfaces [Eq. (2)].



These surface-bound  $\text{Au}$  nanoparticles are good autocatalysts for the reduction of  $\text{Au(I)}$  to  $\text{Au(0)}$  using formaldehyde as the reducing agent. As a result,  $\text{Au}$  deposition begins at the pore walls, and  $\text{Au}$  tubes are obtained within the pores.<sup>[7,9,30,31]</sup>

### ESTIMATION OF THE NANOTUBE INSIDE DIAMETER

We used a gas-transport method to obtain an estimate of the inside diameter (i.d.) of the template-synthesized  $\text{Au}$  nanotubes.<sup>[7]</sup> Briefly, the tube-containing membrane is placed in a gas-permeation cell, and the upper and lower half-cells are evacuated. The upper half-cell is then pressurized, typically to 20 psi (138 kPa) with  $\text{H}_2$ , and the pressure–time transient associated with leakage of  $\text{H}_2$  through the nanotubes is measured using a pressure transducer in the lower half-cell. The pressure–time transient is converted to gas flux ( $Q$ ,  $\text{mol s}^{-1}$ ), which is related to the radius of the nanotubes ( $r$ , cm) via.<sup>[7]</sup>

$$Q = 4/3(2\pi/MRT)^{1/2}(nr^3\Delta P/l) \quad (3)$$

where  $\Delta P$  is the pressure difference across the membrane ( $\text{dyn cm}^{-2}$ ;  $1 \text{ dyn} = 10^{-5} \text{ N}$ ),  $M$  is the molecular weight of the gas,  $R$  is the gas constant ( $\text{erg K}^{-1} \text{ mol}^{-1}$ ;  $1 \text{ erg} = 10^{-7} \text{ J}$ ),  $n$  is the number of nanotubes in the membrane sample,  $l$  is the membrane thickness (cm), and  $T$  is the temperature (K). At long plating times, membranes containing nanotubes with i.d.’s of molecular dimensions are obtained (Fig. 1).

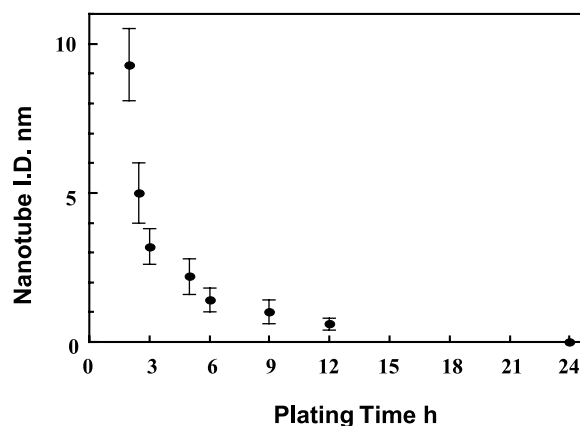


Fig. 1 Variation of the nanotube effective inside diameter with plating time.

### CHEMICAL SENSING WITH THE Au NANOTUBE MEMBRANES

These  $\text{Au}$  nanotube membranes have been used as sensors for the determination of ultratrace concentrations of ions and molecules.<sup>[26,27]</sup> In this case, the nanotube membrane was allowed to separate two salt solutions, a constant transmembrane potential was applied, and the resulting transmembrane current was measured. When an analyte of comparable dimensions to the inside diameter of the nanotubes was added to one of the salt solutions, a decrease in transmembrane current was observed. The magnitude of this drop in transmembrane current ( $\Delta i$ ) is proportional to the analyte concentration.

### CALIBRATION CURVES AND DETECTION LIMITS

As in the transport experiments, a U-tube cell was assembled with the nanotube membrane separating the two halves of the cell. The two half-cells were filled with the desired electrolyte and an electrode was placed into each half-cell. Three different sets of electrodes and electrolytes were used. The first set consisted of two Pt plate electrodes, and the electrolyte used in both half-cells was 0.1 M  $\text{KF}$ . The second set consisted of two  $\text{Ag/AgCl}$  wires, and the electrolyte used in both half-cells was 0.1 M  $\text{KCl}$ . The third set consisted of two  $\text{Ag/AgI}$  wires immersed in 0.1 M  $\text{KI}$ .

As noted above, the experimental protocol used with these cells was to immerse the electrodes into the appropriate electrolyte and apply a constant potential between the electrodes. The resulting transmembrane current was measured and recorded on an  $X-t$  recorder. After obtaining this baseline current, the

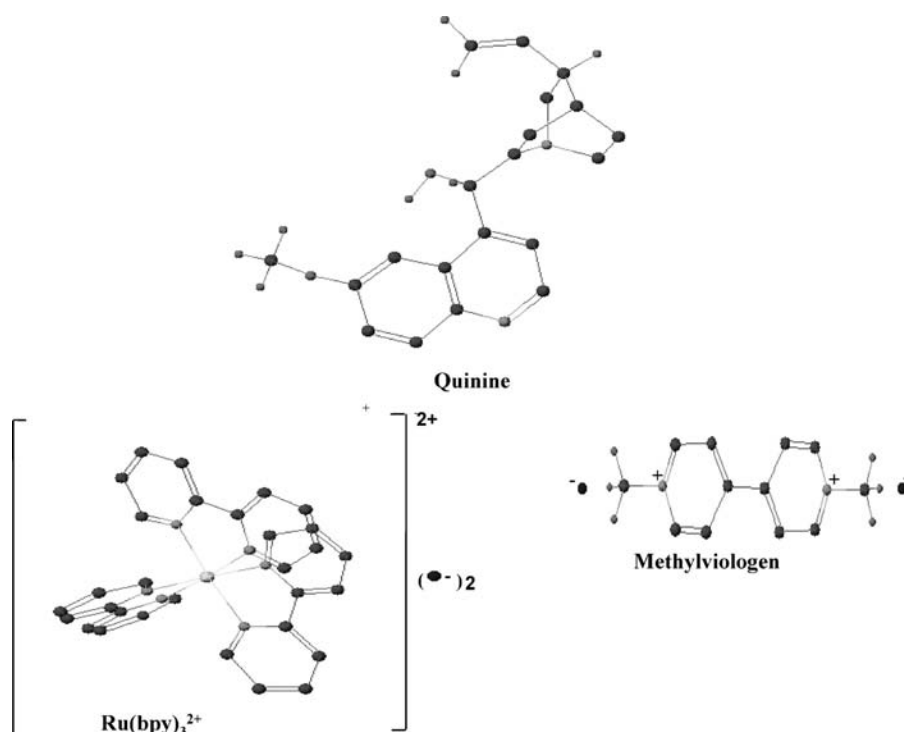


**Fig. 2** Chemical structures and approximate relative sizes of the three “big molecule/small molecule” pairs used in the molecular filtration experiments. Quinine, MV<sup>2+</sup>, and Ru(bpy)<sub>3</sub><sup>2+</sup> were also used as analytes in the sensor work.

anode half-cell was spiked with a known quantity of the desired analyte (Fig. 2). This resulted in a change in the transmembrane current,  $\Delta i$  (Fig. 3). A potentiostat was used to apply the potential between the electrodes and measure the transmembrane current. The transmembrane potential used was on the order of 0.5 V.<sup>[26,27]</sup>

Plots of  $\log \Delta i$  vs.  $\log[\text{analyte}]$  for the analytes Ru(bpy)<sub>3</sub><sup>2+</sup>, MV<sup>2+</sup>, and quinine (Fig. 2) were obtained using Ag/AgCl electrodes and 0.1 M KCl as the

electrolyte in both half-cells (Fig. 4). For these experiments, a membrane with 2.8-nm i.d. Au nanotubes was used. A log–log format is used for these “calibration curves” because of the large dynamic range (spanning as much as 5 orders of magnitude in analyte concentration) obtained with this cell. Analogous calibration curves were obtained for the other electrode/electrolyte systems investigated. The detection limits<sup>[26]</sup> obtained are shown in Table 1. For the divalent cationic electrolytes, the detection limits were lowest (best) in the Ag/AgI/KI cell and worst in the Pt/KF cell. The detection limit for quinine was

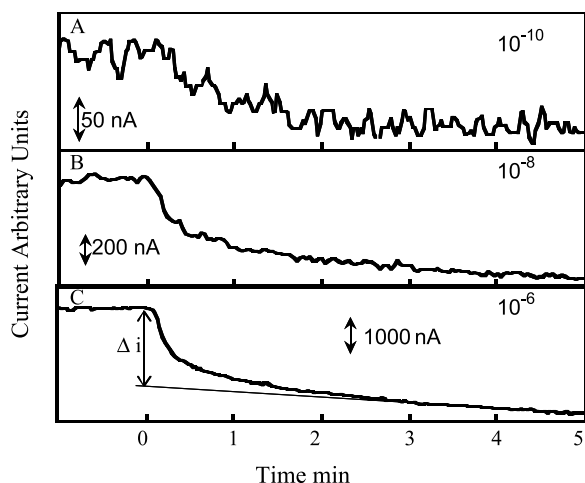


**Fig. 3** Nanotube membrane sensor current–time transients associated with spiking the anode half cell with the indicated concentrations of Ru(bpy)<sub>3</sub><sup>2+</sup>. Tube i.d. = 2.8 nm; Ag/AgCl/KCl cell;  $\Delta i$  determined as shown in C.

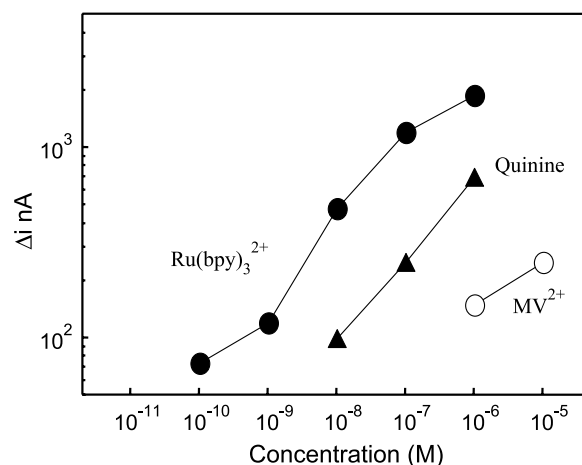


**Fig. 4** Calibrations curves for the indicated analytes. Membrane and cell are as described in Fig. 3.



**Table 1** Detection limits obtained for the three different electrode/electrolyte systems studied (nanotubule i.d.)

Cell	Analyte	Detection limit (M)
Pt/KF	Ru (bpy) <sub>3</sub> <sup>2+</sup>	10 <sup>-9</sup>
Ag/AgCl/KCl	Ru (bpy) <sub>3</sub> <sup>2+</sup>	10 <sup>-10</sup>
	Quinine	10 <sup>-8</sup>
	MV <sup>2+</sup>	10 <sup>-6</sup>
	2-naphthol	10 <sup>-6</sup>
Ag/AgI/KI	Ru (bpy) <sub>3</sub> <sup>2+</sup>	10 <sup>-11</sup>
	Quinine	10 <sup>-8</sup>
	MV <sup>2+</sup>	10 <sup>-7</sup>
	2-naphthol	10 <sup>-6</sup>

the same in both the Ag/AgI/KI and Ag/AgCl/KCl cells. In general, the detection limit decreases as the size of the analyte molecule increases (Fig. 2). Finally, the detection limits obtained (down to 10<sup>-11</sup> M) are extraordinary and compete with even the most sensitive of modern analytical methods.

The majority of the quinine in both the KCl and KI solutions is present as the monoprotonated (monocationic) form. Perhaps the reason the detection limits for Ru(bpy)<sub>3</sub><sup>2+</sup> and MV<sup>2+</sup> are lower in the Ag/AgI/KI cell while the detection limit for quinine is the same in both this cell and the Ag/AgCl/KCl cell has to do with the difference in charge of these analytes (predominantly monocationic vs. dicationic). To explore this point, the detection limits for a neutral analyte, 2-naphthol, were obtained in both the Ag/AgI/KI and Ag/AgCl/KCl cells. Like quinine, the detection limit for this neutral analyte was the same in both cells (10<sup>-6</sup> M) (Table 1).

In the membrane transport studies, it was shown that Ru(bpy)<sub>3</sub><sup>2+</sup> and MV<sup>2+</sup> come across such membranes as the ion multiples Ru(bpy)<sub>3</sub><sup>2+</sup>(X<sup>-</sup>)<sub>2</sub> and MV<sup>2+</sup>(X<sup>-</sup>)<sub>2</sub> (X<sup>-</sup> = anion).<sup>[7]</sup> In the KI cell, the ion multiple contains two larger (relative to chloride) iodide anions. Perhaps the larger size of the iodide ion multiple accounts for the lower detection limit in the KI-containing cell. If this is true, then the difference between the quinine cation paired with one I<sup>-</sup> vs. this cation paired with one Cl<sup>-</sup> is not great enough to cause the detection limit for this predominantly monovalent analyte to be significantly different in the Ag/AgI/KI vs. the Ag/AgCl/KCl cells (Table 1).

The final variable to be investigated is the effect of nanotube inside diameter on detection limit. To explore this parameter, membranes with nanotube inside diameters of approximately of 3.8, 2.8, 2.2, 1.8, and 1.4 nm were prepared and used in the Ag/AgI/KI cell.<sup>[26]</sup> Calibration curves for the analytes Ru(bpy)<sub>3</sub><sup>2+</sup>, MV<sup>2+</sup>, and quinine were generated as

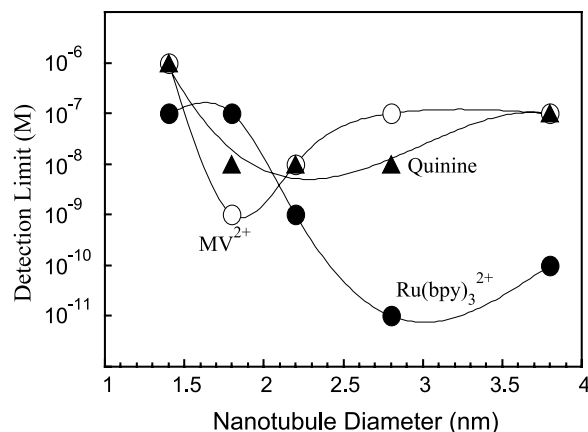
before, and detection limits were obtained from these calibration curves. Fig. 5 shows plots of detection limits for these three different analytes vs. the nanotube inside diameter in the membrane used. A minimum in this plot is observed for each of the three analytes.

The nanotube membrane that produces the minimum (best) detection limit depends on the size of the analyte. These molecules decrease in size in the order Ru(bpy)<sub>3</sub><sup>2+</sup> > quinine > MV<sup>2+</sup>. The nanotube membrane that yields the lowest detection limit follows this size order; that is, the nanotube diameters that produce the lowest detection limit for Ru(bpy)<sub>3</sub><sup>2+</sup>, quinine, and MV<sup>2+</sup> are 2.8, 2.2, and 1.8 nm, respectively. For the roughly spherical analytes, the optimal tube diameter is a little over twice the diameter of the molecule.

### MOLECULAR-SIZE-BASED SELECTIVITY

The data presented above show a strong correlation between detection limit and the relative sizes of the nanotube and the analyte molecule (Fig. 5). This indicates that this device should show molecular-size-based selectivity. This is not surprising given the transport studies previously discussed. To explore size-based selectivity, a series of solutions were prepared containing decreasing concentrations of the analyte species, but containing a constant (higher) concentration of an interfering species. The interfering species was smaller than the analyte species. The response of the nanotube membrane (nanotube diameter = 2.8 nm) to these solutions was then measured starting from lowest to highest concentration of the analyte species.

The small pyridine molecule was used as the first interfering species. When present at a concentration of 10<sup>-4</sup> M, pyridine offered very little interference for any of the analytes Ru(bpy)<sub>3</sub><sup>2+</sup>, MV<sup>2+</sup>, or quinine.

**Fig. 5** Detection limits for MV<sup>2+</sup>, quinine, and Ru(bpy)<sub>3</sub><sup>2+</sup> vs. i.d. of the nanotubes used in the sensor.

The detection limits in the presence of  $10^{-4}$  M pyridine were  $10^{-10}$  M for  $\text{Ru}(\text{bpy})_3^{2+}$ ,  $10^{-6}$  M for  $\text{MV}^{2+}$ , and  $10^{-7}$  M for quinine, within an order of magnitude of the detection limit with no added interfering species (Table 1). In other words, this nanotube membrane sensor can detect  $10^{-10}$  M  $\text{Ru}(\text{bpy})_3^{2+}$  in the presence of 6 orders of magnitude higher pyridine concentration.

A second set of experiments was performed using the larger  $\text{MV}^{2+}$  as the interfering species. Now at low concentrations of analyte, there is a region where the device produces a constant response as a result of the constant concentration ( $10^{-4}$  M) of this interfering species; that is, the much higher concentration of the  $\text{MV}^{2+}$  swamps the response of the device. However, as the concentration of  $\text{Ru}(\text{bpy})_3^{2+}$  increases, there is a concentration range where the device responds to this analyte species without interference from the  $\text{MV}^{2+}$ . This concentration range begins at concentrations of  $\text{Ru}(\text{bpy})_3^{2+}$  above  $10^{-8}$  M. That is, the size-based selectivity is such that the larger analyte species,  $\text{Ru}(\text{bpy})_3^{2+}$ , can be detected down to  $10^{-8}$  M in the presence of 4 orders of magnitude higher concentration of the smaller interfering species,  $\text{MV}^{2+}$ .

## SYNTHETIC ION CHANNEL PORES

We have conducted experiments that provide proof of the basic concept that an analyte molecule can switch on an ion current in a synthetic membrane-based ion-channel mimic.<sup>[29]</sup> The membrane used for most experiments was a commercially available microporous alumina filter. The pores in this membrane were made hydrophobic by reaction with an 18-carbon ( $\text{C}_{18}$ ) alkyl silane. When placed between two salt solutions, the pores in this  $\text{C}_{18}$ -derivatized membrane are not wetted by water, yielding the off state of the membrane. When exposed to a solution containing a sufficiently high concentration of a long-chain ionic surfactant (the analyte), the surfactant molecules partition into the hydrophobic membrane, and ultimately cause the pores to flood with water and electrolyte. As a result, the membrane will now support an ion current, and the ion channel-mimetic membrane is switched to its on state. Cationic drug molecules can also switch this membrane from the off to the on state.

## MEMBRANE PREPARATION AND A.C. IMPEDANCE EXPERIMENTS WITH 1-DODECANESULFONIC ACID ANALYTE

The alumina membranes were Anopore<sup>®</sup> (Whatman Inc., Clifton, New Jersey) that had nominally

200-nm-diameter pores and were 60- $\mu\text{m}$  thick. The alumina membranes were modified with octadecyltrimethoxysilane.<sup>[29]</sup> The membrane assembly was mounted between the halves of a U-tube permeation cell, and both half-cells were filled with  $\sim 20$  mL of 0.1 M KCl. A Ag/AgCl working electrode was immersed into one half-cell solution, and a Pt counter electrode and a Ag/AgCl reference electrode were placed in the other half-cell.<sup>[32,33]</sup>

Alternating current impedance measurements proved to be a useful way to demonstrate the analyte-induced switching of the membrane between the off and on states. The uppermost curve in Fig. 6 is the Nyquist plot for a  $\text{C}_{18}$ -modified alumina membrane with 0.1 M KCl solutions, and no analyte (1-dodecanesulfonic acid, DBS) on either side of the membrane. As per prior investigations of ion-channel and ion-channel-mimetic membranes,<sup>[34,35]</sup> the impedance data were interpreted in terms of the equivalent circuit shown in the inset of Fig. 6, where  $R_s$  is the solution resistance,  $R_m$  is the membrane resistance, and  $C$  is the membrane capacitance. The dashed curve is the best fit to the experimental data, from which the  $R_m$  (Fig. 7) and  $C$  values were obtained. Also shown in Fig. 6 are impedance data after spiking the half-cell electrolyte solutions to the indicated concentrations with the analyte (DBS).

In the absence of DBS, the membrane resistance is very large,  $>50$  M $\Omega$  as opposed to  $\sim 5$   $\Omega$  for the

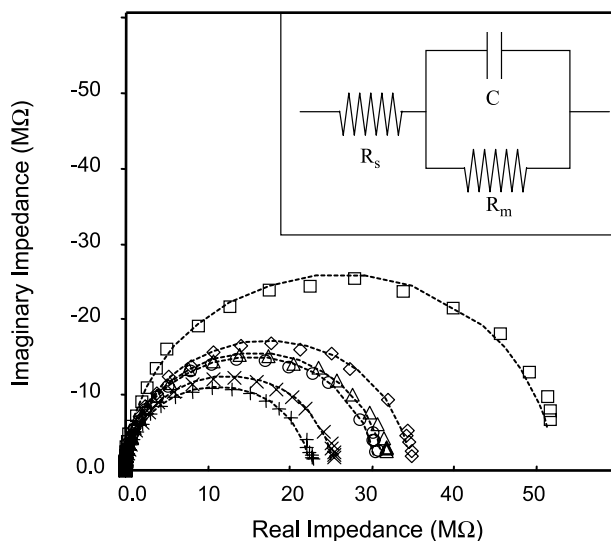


**Fig. 6** Nyquist plots for a  $\text{C}_{18}$ -modified alumina membrane upon exposure to increasing concentrations of DBS in 0.1 M KCl. The points are the experimental data. The lines are calculated data obtained using the equivalent circuit shown in the inset. Concentrations of DBS were as follows:  $\square$  = 0 nM;  $\blacklozenge$  = 1.4 nM;  $\triangle$  = 3 nM;  $\circ$  = 10 nM;  $\times$  = 40 nM;  $+$  = 100 nM.

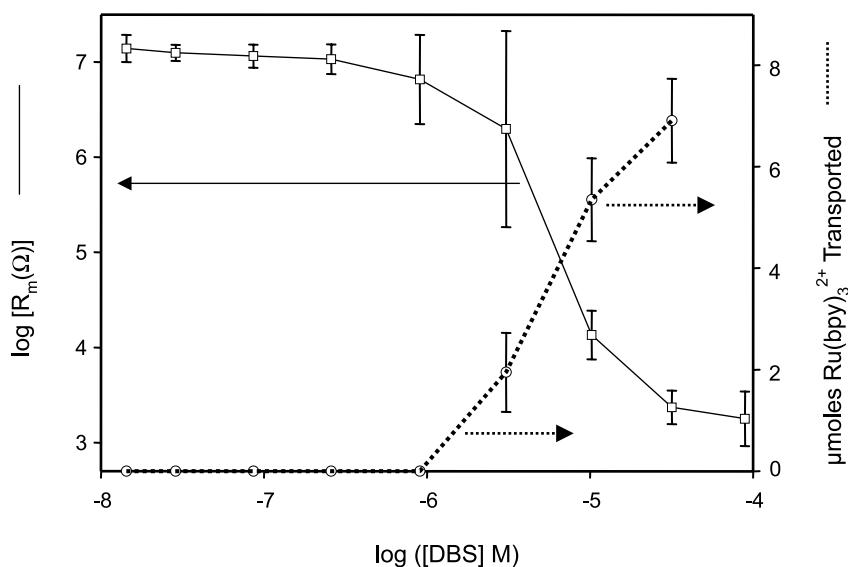


**Fig. 7** Plots of log membrane resistance (left y axis) and micromoles  $\text{Ru}(\text{bpy})_3^{2+}$  transported across the membrane (right y axis) vs.  $\log[\text{DBS}]$  for a  $\text{C}_{18}$ -modified alumina membrane. The error bars represent the standard deviation of three separate experiments.

alumina membrane before modification with the  $\text{C}_{18}$  silane. Transport experiments (vide infra) show that this is because the very hydrophobic  $\text{C}_{18}$ -modified pores are not wetted by water. This is supported by contact angle measurements on the membrane surface, where a water contact angle of  $130(+8)^\circ$  was obtained for the  $\text{C}_{18}$ -treated alumina membrane as opposed to  $\sim 8(+1)^\circ$  for the untreated membrane.

While over the concentration range  $10^{-9}$  to  $10^{-7}$  M, there is some drop in membrane resistance with increasing DBS concentration (Fig. 8),  $R_m$  remains very large ( $>20$  MΩ). However, over the DBS concentration range between  $10^{-6}$  and  $10^{-5}$  M, there is a precipitous, 4-order-of-magnitude, drop in  $R_m$  (Fig. 7). This drop signals the analyte-induced switching of the membrane from the off to the on states.

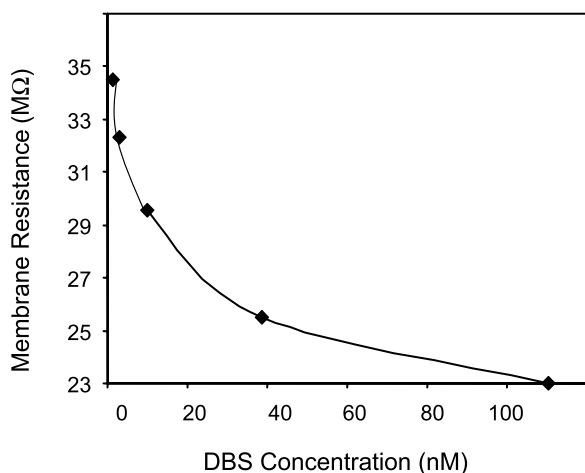


**Fig. 8** Plot of membrane resistance vs. DBS concentration.

## TRANSPORT EXPERIMENTS

These were conducted by mounting the membrane between the two halves of a U-tube permeation cell and adding 0.1 M KCl to each half-cell. The feed half-cell was also  $50 \mu\text{M}$  in either  $\text{Ru}(\text{bpy})_3^{2+}$  or naphthalene disulfonate ( $\text{NDS}^{2-}$ ), the permeate ions. An increment of the analyte surfactant (for these experiments DBS) was added to both the feed and permeate half-cells and permeation was allowed to occur for 24 hr. After this time, the permeate half-cell was sampled and the UV absorbance was used to determine the moles of the permeate ion transported. The permeate solution was then returned to the permeate half-cell and a second increment of DBS was added. Permeation was again allowed to occur for 24 hr and the amount of permeate ion transport was again determined. This process was repeated for various DBS concentrations over the range from  $10^{-8}$  to  $10^{-4}$  M.

The data obtained for  $\text{Ru}(\text{bpy})_3^{2+}$  transport are shown in Fig. 7. At DBS concentrations below  $10^{-6}$  M, there is no detectable  $\text{Ru}(\text{bpy})_3^{2+}$  in the permeate solution. It is important to emphasize that each permeation data point in Fig. 7 corresponds to an additional 24 hr of permeation time. Hence by the time the DBS concentration was increased to  $9 \times 10^{-7}$  M, the total permeation time was 5 days. The inability to detect  $\text{Ru}(\text{bpy})_3^{2+}$  in the permeate solution after 5 days of permeation shows that over the DBS concentration range 0 to  $\sim 10^{-6}$  M, the pores in the  $\text{C}_{18}$  membrane are not wetted by water, making the rate of  $\text{Ru}(\text{bpy})_3^{2+}$  transport immeasurably small. These data again show that at DBS concentrations below  $10^{-6}$  M, the membrane is in the off state.

At DBS concentrations above  $10^{-6}$  M,  $\text{Ru}(\text{bpy})_3^{2+}$  transport is switched on, and flux increases with concentration of DBS for concentrations above this value. The impedance and transport data tell a consistent story about the effect of DBS on the  $\text{C}_{18}$ -derivatized membrane (Fig. 7). At low DBS concentrations ( $<10^{-6}$  M) where the membrane resistance is in the  $10^7 \Omega$  range,  $\text{Ru}(\text{bpy})_3^{2+}$  is not transported. The sudden drop in  $R_m$  at DBS concentrations above  $\sim 10^{-6}$  M is seen in the transport experiments as an abrupt switching on of  $\text{Ru}(\text{bpy})_3^{2+}$  transport across the membrane.

## X-RAY PHOTOELECTRON SPECTROSCOPY

X-ray photoelectron spectroscopy (XPS) was used to show that the prototypical analyte dodecylbenzene sulfonate (DBS) is present on the  $\text{C}_{18}$ -modified alumina surface after exposure of the membrane to DBS solution. However, the XPS cross section for S from the DBS proved too weak to obtain unambiguous evidence; furthermore, O, C, and  $\text{Na}^+$  (the counterion for the DBS) are ubiquitous, and therefore not useful as probes to prove that DBS is present on the surface. For this reason, we used a surface ion-exchange reaction to replace  $\text{Na}^+$  with  $\text{Cs}^+$  as the counterion for the surface-bound DBS. We then used XPS to look for the presence of  $\text{Cs}^+$  on the  $\text{C}_{18}$ -modified surface that had been treated with DBS, using an identical surface that was exposed to the  $\text{Cs}^+$  solution but not to DBS as the control.

Figure 9 shows XPS data for a  $\text{C}_{18}$ -modified membrane that had been exposed to an aqueous 2.0 mM solution of  $\text{Na}^+$ -DBS, rinsed, exposed to a 100 mM aqueous solution of  $\text{CsNO}_3$ , and then extensively rinsed again. The Cs 3d peaks at 724 and 738 eV are clearly evident.<sup>[36]</sup> This may be contrasted to the

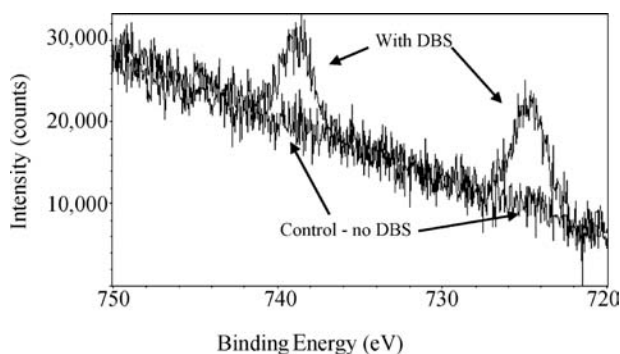


**Fig. 9** X-ray photoelectron spectroscopy data for a  $\text{C}_{18}$ -modified alumina-membrane surface that was exposed to a DBS solution and then to a  $\text{Cs}^+$  solution and for an identical surface that was exposed to  $\text{Cs}^+$  but not to DBS.

control surface—a  $\text{C}_{18}$ -modified alumina membrane that was exposed to the  $\text{Cs}^+$  solution but not to DBS—where no Cs signal is seen (Fig. 9). These data show that exposure of the membrane to DBS results in partitioning of this analyte species onto the  $\text{C}_{18}$ -modified surface.

## MEASUREMENTS OF ION CURRENT

While the transport experiments show that the analyte DBS can switch on ion (e.g.,  $\text{Ru}(\text{bpy})_3^{2+}$  and  $\text{NDS}^{2-}$ ) transport across the membrane, we also wanted to obtain a direct measure of the ion current. To do this, a constant transmembrane potential of 1.5 V was applied and the resulting transmembrane ion current was measured. The current was monitored for 30 min and then the half-cell solutions were spiked with DBS to a total concentration of  $10^{-9}$  M. The current was again measured for 30 min and the half-cells were spiked again with DBS. This process was repeated for various DBS concentrations over the range from  $10^{-9}$  to  $10^{-3.5}$  M.

Figure 10 shows the measured ion current vs. time data; at the indicated times, the electrolyte solutions were spiked to the indicated concentrations with DBS. The ion-current data show the same general trend as both the impedance and transport data—at concentrations below  $\sim 10^{-6}$  M, the ion current is at a very low baseline value and at concentrations above  $\sim 10^{-6}$  M, the ion current abruptly switches on. In addition, the  $10^{-5.5}$  M datum shows that the transition from the low-current to the high-current state very abruptly occurs.

Both the impedance and ion-current data show that when the membrane is in the off state, some small baseline current does flow across the membrane. It is important to note that the resistance value for the off state obtained by the impedance and ion current measurements are essentially identical. As shown in Fig. 6, the impedance measurement yields a value of  $\sim 10^7 \Omega$ . The ion current in the off state is  $\sim 1.5 \times 10^{-7}$  A, which for a 1.5 V transmembrane potential yields a membrane resistance of  $\sim 10^7 \Omega$ . However, the issue left to resolve is—what is supporting this baseline ion current when the membrane is in the off state? At this point, we cannot say other than to suggest that this current results from some surface conduction process that occurs along the pore walls when the pores are devoid of water. In the absence of DBS, this surface conduction process may involve residual surface hydroxyl sites. The impedance data (Fig. 6) indicate that in the presence of DBS, the surfactant itself is involved in the conduction process.

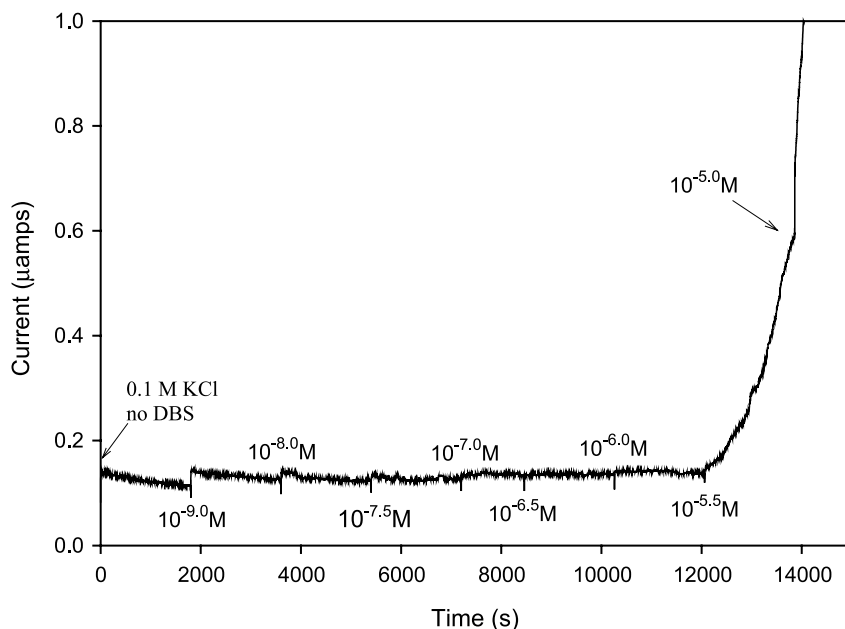


**Fig. 10** Ion current through a  $C_{18}$ -modified alumina membrane vs. time. The contacting solution phases were spiked with the indicated concentrations of DBS at the indicated times. The electrolyte was 0.1 M KCl. A constant transmembrane potential of 1.5 V was applied.

## DETECTION OF DRUG MOLECULES

To explore the role of the hydrophobic effect in driving the analyte species into the  $C_{18}$ -derivatized alumina membrane, we investigated the effect of hydrophobic cationic drug molecules on the membrane resistance. The molecules and their molecular weights are amiodarone ( $645 \text{ g mol}^{-1}$ ), amitriptyline ( $278 \text{ g mol}^{-1}$ ), and bupivacaine ( $288 \text{ g mol}^{-1}$ ) (Fig. 11). Because its molecular weight is more than double those of the other drugs and because it contains very hydrophobic iodo substituents, amiodarone is by far the most hydrophobic of these molecules. If the hydrophobic effect is responsible for driving molecules into the  $C_{18}$ -derivatized membrane, then the transition from the off to the on state would occur at lowest concentrations for amiodarone, and this is what is experimentally

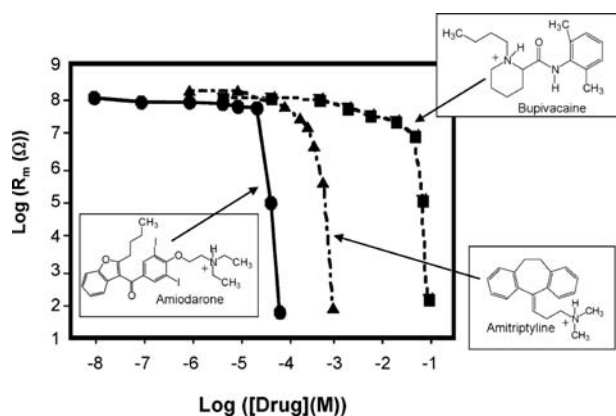


**Fig. 11** Plots of log membrane resistance vs. log[Drug] for the indicated drugs and a  $C_{18}$ -modified alumina membrane.

observed (Fig. 11). There is only a 3% difference in the molecular weights of amitriptyline and bupivacaine; however, bupivacaine presents two additional opportunities for hydrogen bonding with water—the lone pairs on the carbonyl group and the lone pair of the nonprotonated nitrogen. For this reason, bupivacaine is much more hydrophilic, and it would be expected to be the mostly poorly detected of the three drugs; Fig. 11 shows that this is also experimentally observed.

## CONCLUSION

We have described a highly sensitive method of electroanalysis based on Au nanotube membranes. In addition, we have also shown that synthetic micropore and nanotube membranes can mimic the function of ligand-gated ion channels; that is, they can be switched from an off state to an on state in response to the presence of a chemical stimulus. This concept of ion-channel mimetic sensing, as originally proposed by Umezawa's group,<sup>[32]</sup> has been of considerable interest in analytical chemistry.<sup>[37–40]</sup> There is also considerable appeal in using naturally occurring and genetically engineered protein channels as sensors (Ref.<sup>[41]</sup>, and references therein). Such research at the bio/nano interface is of great current interest in our group.

## ACKNOWLEDGMENT

Aspects of this work were supported by the Office of Naval Research and the National Science Foundation.

## REFERENCES

1. Martin, C.R. Nanomaterials—a membrane-based synthetic approach. *Science* **1994**, *266*, 1961–1966.
2. Hulteen, J.C.; Martin, C.R. A general template-based method for the preparation of nanomaterials. *J. Mater. Chem.* **1997**, *7* (7), 1075–1087.
3. Martin, C.R.; Mitchell, D.T. Nanomaterials in analytical chemistry. *Anal. Chem.* **1998**, *70*, 322A–327A.
4. Fleischer, R.L.; Price, P.B.; Walker, R.M. *Nuclear Tracks in Solids*; University of California Press: Berkeley, CA, 1975.
5. Hornyak, G.L.; Patrissi, C.J.; Martin, C.R. Fabrication, characterization and optical properties of gold-nanoparticle/porous-alumina composites: the non-scattering Maxwell–Garnett limit. *J. Phys. Chem., B* **1997**, *101*, 1548–1555.
6. Nishizawa, M.; Menon, V.P.; Martin, C.R. Metal nanotubule membranes with electrochemically switchable ion-transport selectivity. *Science* **1995**, *268*, 700–702.
7. Jirage, K.B.; Hulteen, J.C.; Martin, C.R. Nanotubule-based molecular-filtration membranes. *Science* **1997**, *278*, 655–658.
8. Hulteen, J.C.; Martin, C.R. Introducing chemical transport selectivity into gold nanotubule membranes. *J. Am. Chem. Soc.* **1998**, *120*, 6603–6604.
9. Jirage, K.B.; Hulteen, J.C.; Martin, C.R. Effects of thiol chemisorption on the transport properties of gold nanotubule membranes. *Anal. Chem.* **1999**, *71*, 4913–4918.
10. Hou, Z.; Abbott, N.L.; Stroeve, P. Self-assembled monolayers on electroless gold impart pH-responsive transport of ions in porous membranes. *Langmuir* **2000**, *16*, 2401–2404.
11. Tourillon, G.; Pontinnier, L.; Levy, J.P.; Langlais, V. Electrochemically synthesized Co and Fe nanowires and nanotubes. *Electrochem. Solid-State Lett.* **2000**, *3*, 20–23.
12. Schonenberger, C.; van der Zande, B.M.I.; Fokkink, L.G.J.; Henry, M.; Schmid, C.; Kruger, M.; Bachtold, A.; Huber, R.; Birk, H.; Stauer, U. Template synthesis of nanowires in porous polycarbonate membranes: electrochemistry and morphology. *J. Phys. Chem., B* **1997**, *101*, 5497–5505.
13. Martin, C.R. *Handbook of Conducting Polymers*, 2nd Ed.; Reynolds, J.R., Skotheim, T., Elsebaumer, R., Eds.; Marcel Dekker, Inc., 1997; 409–421.
14. Demoustier-Champagne, S.; Stavaux, P.-Y. Effect of electrolyte concentration and nature on the morphology and the electrical properties of electropolymerized polypyrrole nanotubules. *Chem. Mater.* **1999**, *11*, 829–834.
15. Sukeerthi, S.; Contractor, Q. Molecular sensors and sensor arrays based on polyaniline microtubules. *Anal. Chem.* **1999**, *71*, 2231–2236.
16. Lakshmi, B.B.; Patrissi, C.J.; Martin, C.R. Sol–gel template synthesis of semiconductor oxide micro- and nanostructures. *Chem. Mater.* **1997**, *9*, 2544–2550.
17. Lakshmi, B.B.; Dorhout, P.K.; Martin, C.R. Sol–gel template synthesis of semiconductor nanostructures. *Chem. Mater.* **1997**, *9*, 857–862.
18. Che, G.; Lakshmi, B.B.; Martin, C.R.; Fisher, E.R. Metal nanocluster-filled carbon nanotubules: catalytic properties and possible applications in electrochemical energy storage and production. *Langmuir* **1999**, *15*, 750–758.
19. Che, G.; Fisher, E.R.; Martin, C.R. Carbon nanotubule membranes for electrochemical energy storage and production. *Nature* **1998**, *393*, 346–349.
20. Patrissi, C.J.; Martin, C.R. Sol–gel-based template synthesis and Li-insertion rate performance of nanostructured vanadium pentoxide. *J. Electrochem. Soc.* **1999**, *146*, 3176–3180.
21. Li, N.; Patrissi, C.J.; Martin, C.R. Rate capabilities of nanostructured LiMn<sub>2</sub>O<sub>4</sub> electrodes in aqueous electrolyte. *J. Electrochem. Soc.* **2000**, *147*, 2044–2049.
22. Che, G.; Jirage, K.B.; Fisher, E.R.; Martin, C.R.; Yoneyama, H. Chemical-vapor deposition-based template synthesis of microtubular TiS<sub>2</sub> battery electrodes. *J. Electrochem. Soc.* **1997**, *144*, 4296–4302.
23. Cepak, V.M.; Hulteen, J.C.; Che, G.; Jirage, K.B.; Lakshmi, B.B.; Fisher, E.R.; Martin, C.R. Fabrication and characterization of concentric tubular composite micro- and nanostructures using the template synthesis method. *J. Mater. Res.* **1998**, *13*, 3070–3080.
24. Cepak, V.M.; Hulteen, J.C.; Che, G.; Jirage, K.B.; Lakshmi, B.B.; Fisher, E.R.; Martin, C.R. Chemical strategies for template syntheses of composite micro and nanostructures. *Chem. Mater.* **1997**, *9*, 1065–1067.
25. Martin, B.R.; Dermody, D.J.; Reiss, B.D.; Fang, M.; Lyon, L.A.; Natan, M.J.; Mallouk, T.E. Orthogonal self-assembly on colloidal gold–platinum nanorods. *Adv. Mater.* **1999**, *11*, 1021–1025.
26. Kobayashi, Y.; Martin, C.R. Highly-sensitive methods for electroanalytical chemistry based on nanotubule membranes. *Anal. Chem.* **1999**, *71*, 3665–3672.
27. Kobayashi, Y.; Martin, C.R. Toward a molecular coulter counter. *J. Electroanal. Chem.* **1997**, *431*, 29–33.
28. Voet, D.; Voet, J.G. *Biochemistry*, 2nd Ed.; Wiley: New York, 1995; 1297–1298.
29. Steinle, E.D.; Mitchell, D.T.; Wirtz, M.; Lee, S.B.; Young, V.Y.; Martin, C.R. Ion channel mimetic micropore and nanotube membrane sensors. *Anal. Chem.* **2002**, *74*, 2416–2422.
30. Menon, V.P.; Martin, C.R. Fabrication and evaluation of nanoelectrode ensembles. *Anal. Chem.* **1995**, *67*, 1920–1928.
31. Kang, M.; Martin, C.R. Investigations of potential-dependent fluxes of ionic permeates in gold nanotubule membranes prepared via the template method. *Langmuir* **2001**, *17*, 2753–2759.
32. Armstrong, R.D.; Covington, A.K.; Evans, G.P. Mechanistic studies of the valinomycin-based potassium-selective electrode using ac impedance methods. *J. Electroanal. Chem.* **1983**, *159*, 33–40.
33. Xie, S.-L.; Cammann, K. Apparent ion-exchange current densities at valinomycin based potassium ion-selective PVC membranes obtained with an AC-impedance method. *J. Electroanal. Chem.* **1987**, *229*, 249–263.



34. Zhang, W.; Spichiger, U.E. An impedance study of  $Mg^{2+}$ -selective membranes. *Electrochim. Acta* **2000**, *45*, 2259–2266.
35. Ding, L.; Li, J.; Dong, S.; Wang, E. Supported phospholipid membranes: comparison among different deposition methods for a phospholipid monolayer. *J. Electroanal. Chem.* **1996**, *416*, 105–112.
36. Muilenberg, G.E., Ed.; *Handbook of X-Ray Photoelectron Spectroscopy*; Perkin-Elmer Corporation: Eden Prairie, 1978.
37. Sugawara, M.; Kojima, K.; Sazawa, H.; Umezawa, Y. Ion-channel sensors. *Anal. Chem.* **1987**, *59*, 2842–2846.
38. Xiao, K.P.; Bühlmann, P.; Umezawa, Y. Ion-channel-mimetic sensing of hydrophilic anions based on monolayers of a hydrogen bond-forming receptor. *Anal. Chem.* **1999**, *71*, 1183–1187.
39. Wu, Z.; Tang, J.; Cheng, Z.; Yang, X.; Wang, E. Ion channel behavior of supported bilayer lipid membranes on a glassy carbon electrode. *Anal. Chem.* **2000**, *72*, 6030–6033.
40. Katayama, Y.; Ohuchi, Y.; Yang, X.; Wang, E. The design of cyclic AMP recognizing oligopeptides and evaluation of its capability for cyclic AMP recognition using an electrochemical system. *Anal. Chem.* **2000**, *72* (19), 4671–4674.
41. Bayley, H.; Martin, C.R. Resistive-pulse sensing from microbes to molecules. *Chem. Rev., Sens. Them. Issue* **2000**, *100*, 2575–2594.

# Nanotubes: Functionalization

## Stanislaus S. Wong

Materials and Chemical Sciences Department, Brookhaven National Laboratory, Upton, New York, U.S.A., and Department of Chemistry, State University of New York at Stony Brook, Stony Brook, New York, U.S.A.

## Sarbajit Banerjee

Department of Chemistry, State University of New York at Stony Brook, Stony Brook, New York, U.S.A.

## INTRODUCTION

Carbon is one of the most prevalent elements in nature, and is critical to a number of important biological and geological structures. Of importance to chemistry, it can form  $sp$ -,  $sp^2$ -, and  $sp^3$ -hybridized bonds permitting the production of a wide range of geometries and hence, compounds. Graphite, albeit a key component of pencils, has one of the largest in-plane elastic moduli of any material, because of the extended sheets of  $sp^2$ -hybridized carbon arranged in a honeycomb mesh of hexagons. Diamond is the gem of choice, although it is simply a thermodynamically metastable form of carbon with the largest hardness of any material; it has the highest thermal conductivity and melting point of any solid. Fullerenes,<sup>[1–3]</sup> discovered by Kroto et al. in 1985, were produced by using laser vaporization techniques in the gas phase and were initially serendipitously detected using a molecular beam apparatus. They now have been reported to occur naturally in some forms of carbon soot<sup>[4]</sup> and have been produced by resistive heating of carbon rods in a vacuum,<sup>[5]</sup> in plasma discharges between carbon electrodes in He, and by oxidative combustion of gasoline/benzene/argon gas mixtures.<sup>[6]</sup> These molecules, essentially truncated icosahedrons, can be viewed as graphite sheets wrapped into closed carbon cages, consisting of 60 atoms shaped into a soccer ball with pentagons that can then accommodate curvature in the system.<sup>[2]</sup>

Another potentially more useful class of materials has arisen from the generation of fullerenes, that is essentially a nanometer-scale self-assembled structure of carbon. This time, however, we are not referring to cake and sandwich structures but rather to graphitic carbon, forming seamless cylindrical shells,<sup>[7]</sup> the carbon nanotubes. Of an intrinsic structural beauty,<sup>[8,9]</sup> these tubes consist of shells of  $sp^2$ -hybridized (trivalent) carbon atoms forming a hexagonal network that is itself arranged helically within the tubular motif (Fig. 1). Nanotubes are observed in two distinct

structural forms (which can be controlled by growth conditions): multiwall nanotubes (MWNTs), which are made by coaxially nesting successively larger nanotubes<sup>[10]</sup> separated roughly by the interplanar graphite spacing of  $\sim 0.34$  Å, and single-wall nanotubes (SWNTs), which consist of a single graphene sheet rolled into a seamless tube.<sup>[11–14]</sup>

## OVERVIEW

The diameter and helicity of a defect-free SWNT can be uniquely characterized by the roll-up vector,  $c_h = na + mb \equiv (n, m)$ , connecting crystallographically equivalent sites on a two-dimensional (2-D) graphene sheet, where  $a$  and  $b$  are the graphene lattice unit vectors, and  $n$  and  $m$  are integers. Each pair of integers  $(n, m)$  defines a different way of rolling up the graphene sheet to form a carbon nanotube. Electronic band structure calculations predict that the  $(n, m)$  indices will determine whether a SWNT will be a metal or a semiconductor.<sup>[11–15]</sup>

To first order,  $(n, 0)$  or zigzag SWNTs will exhibit two distinct types of behavior. The nanotubes will be metallic when  $n/3$  is an integer, but otherwise semiconducting. So as  $c_h$  rotates away from  $(n, 0)$ , chiral  $(n, m)$  SWNTs are possible with similar electronic properties to zigzag tubes. When  $(2n + m)/3$  is an integer, the tubes are metallic; otherwise, they are semiconducting. If  $c_h$  is rotated  $30^\circ$  relative to  $(n, 0)$ ,  $m = n$ . These  $(n, n)$  or armchair tubes are metallic. Zigzag and armchair tubes with wrapping angles of  $0^\circ$  or  $30^\circ$  are called achiral tubes. Single-walled nanotubes with intermediate wrapping angles are referred to as chiral tubes. Both  $(n, 0)$  and  $(n, n)$  nanotubes have especially high symmetry and exhibit a mirror symmetry plane normal to the tubule axis.<sup>[9]</sup> In other words, their structure determines their electronic behavior.

Because of their seamless cylindrical graphitic shells, carbon nanotubes<sup>[16]</sup> might be stiffer and stronger than

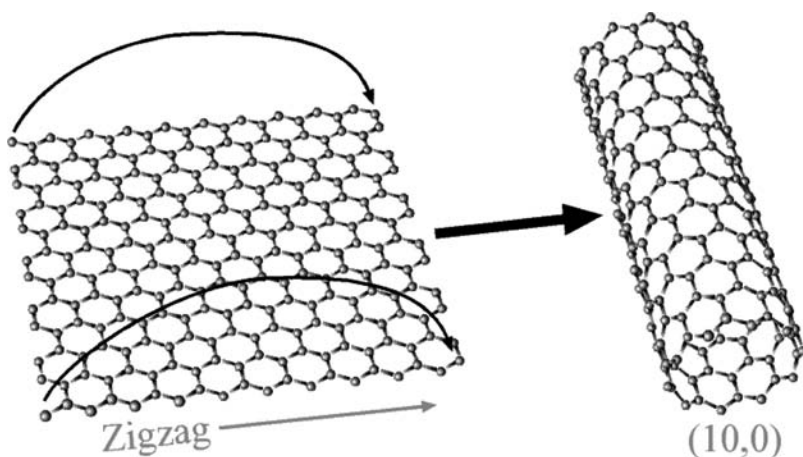


**Fig. 1** A single-wall carbon nanotube (SWNT) may be visualized as a sheet of graphite rolled up to form a seamless cylinder that is 1 atom in thickness. The roll-up vector or direction determines whether the tube is metallic or semi-conducting, and tubes are accordingly classified as either zigzag, armchair, or chiral. *Source:* Dr. Elton Graugnard, University of Illinois.

potentially any other known material with implications for the design of composite materials, as well as nanometer-scale devices.<sup>[17]</sup> In fact, mechanical measurements have shown that multiwalled nanotubes have a very high stiffness and, in fact, a high Young's modulus in the TPa range, at least as large if not higher than the in-plane modulus of graphite.<sup>[18]</sup> By measuring the amplitude of the intrinsic thermal vibrations of MWNTs, one group has shown that the Young's modulus of elasticity (the ratio of the force per unit area applied to the nanotube to the deformation thereby produced) is about  $1 \times 10^{12}$  Pa or  $1 \times 10^{12}$  N/m<sup>2</sup>, which is among the highest of any known material. Furthermore, bending and buckling experiments<sup>[19]</sup> indicate that MWNTs can be repeatedly bent through large angles without undergoing catastrophic failure, and that they can sustain forces that will deform a local area of the nanotube by as much as 16% without irreversible damage. Thus not only do these tubes possess extremely desirable mechanical properties of strength and flexibility,<sup>[20]</sup> but also, as has been noted, at least some are metallic in character.<sup>[21]</sup>

Indeed, the fundamental importance and uniqueness of SWNTs, relative to other types of fibrous materials such as Kevlar, arises from their molecularly "perfect" structure; there are no or relatively few imperfections within the length of the material that would cause weakness or instability. Furthermore, no surface passivation is required of these seamless cylinders. They are thought to have a host of wide-ranging, potential applications including catalyst supports in heterogeneous catalysis, field emitters, high-strength engineering fibers, sensors, actuators, tips for scanning probe microscopy, gas storage media, and as molecular wires for the next generation of electronics devices.<sup>[22–30]</sup>

Understanding the chemistry of SWNTs thus becomes critical to rational manipulation of their properties. In fact, the ability to disperse and solubilize carbon nanotubes would open up new prospects in aligning and forming molecular devices and allow for

the development of a reproducible chemistry of these materials to take place. Nonetheless, this objective necessitates controlled chemical functionalization of tubes, a relatively unexplored area of research.

In this entry, we will explore existing strategies of nanotube functionalization, ending with recent efforts to treating nanotubes as chemical reagents (be it inorganic or organic) in their own right or in understanding chemical reactivity involving tubes from a structural perspective, which would expand the breadth and types of reactions SWNTs can undergo in solution phase. Indeed, from their inherent structure, one can view nanotubes as sterically bulky,  $\pi$ -conjugated ligands or conversely, as electron-deficient alkenes. Moreover, controllable chemical functionalization suggests that these unique electronic and mechanical properties can be tailored in a determinable manner. For instance, it has been predicted<sup>[31]</sup> that covalent chemical attachments can decrease the maximum buckling force by about 15% regardless of tubular helical structure or radius. Prevailing themes in nanotube functionalization have been involved with dissolution of tubes, enabling more precise manipulation and fractionation of these materials, as well as predictable functionalization of nanotube surfaces, at the ends (Fig. 2) as well as the sidewalls (Fig. 3). Indeed, controllable derivatization is essential for advanced functionalized material applications, as well as for the efficient generation of SWNT nanocomposites.

## SIDEWALL FUNCTIONALIZATION OF SWNTS

The sidewalls of purified SWNTs have been non-covalently functionalized<sup>[32]</sup> with a bifunctional molecule, namely 1-pyrenebutanoic acid, succinimidyl ester, which  $\pi$  stacks onto the graphene sidewalls; amide groups on proteins then react with the anchored ester to form amide bonds for protein immobilization. In an analogous fashion, ferritin, streptavidin, and

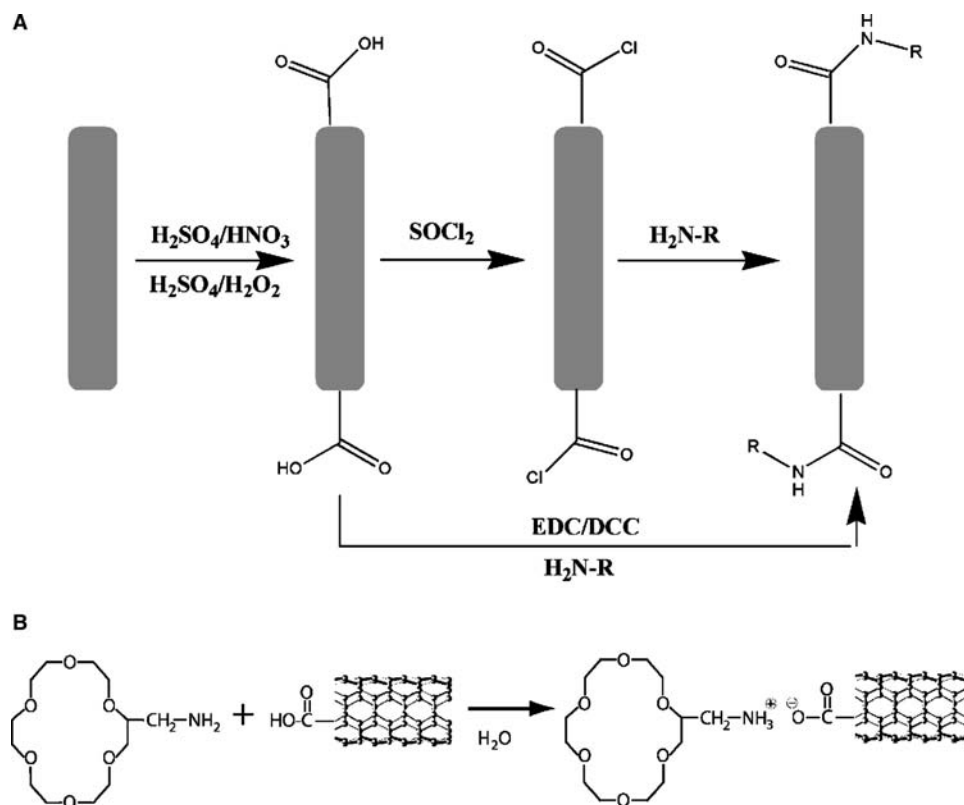


**Fig. 2** (A) Schematic of a common functionalization route, used to derivatize SWNTs at ends and defect sites. SWNTs are acid-treated to generate carboxylic acid groups at the ends and defect sites. These acidic functionalities are then linked to amines either by an initial reaction with  $\text{SOCl}_2$  and subsequently with an amine, or through carbodiimide-mediated amide bond formation with amines. An alternative route to functionalization is through zwitterionic interactions between carboxylic acid and amine groups. Panel (B) shows an example where oxidized SWNTs were linked to an amino-derivatized crown ether moiety.

biotin have been similarly localized on nanotube surfaces with high specificity and efficiency. In another approach to immobilizing proteins on the nanotube surface, SWNTs have been functionalized with bovine serum albumin (BSA) proteins via a diimide-activated amidation under ambient conditions. Based on data such as atomic force microscopy (AFM), thermal gravimetric analysis, Raman spectroscopy, and gel electrophoresis, the resultant nanotube–BSA conjugates are structurally interlinked, highly water-soluble, and bioactive, forming dark-colored aqueous solutions.<sup>[33]</sup>

It turns out that Raman spectroscopy, in particular, is notably effective at denoting the presence and extent of functionalization as well as for understanding vibrational and electronic properties of nanotubes and fullerenes. Whereas the radial breathing modes (RBM)<sup>[34,35]</sup> near  $200\text{ cm}^{-1}$  depend sensitively on tube diameter, the high-frequency tangential displacement G modes<sup>[36]</sup> near  $\sim 1590\text{ cm}^{-1}$  and the second-order G' bands<sup>[37]</sup> near  $2600\text{ cm}^{-1}$  are sensitive to the charge exchanged between nanotubes and guest atoms that have intercalated into the interstitial channels in the tube bundles. Indeed, the line shapes of the G band allow

for differentiation between semiconducting and metallic tubes. Semiconducting tubes are characterized by sharp Lorentzians while metallic tubes show Breit–Wigner–Fano line broadening. Importantly, in the context of this review, the shape and intensity of a weak disorder mode peak at  $1290\text{--}1320\text{ cm}^{-1}$  has been correlated with the extent of nanotube sidewall functionalization.<sup>[38]</sup>

Much effort has been involved with fluorinating tubes. High-temperature (over  $500^\circ\text{C}$  for several hours) reactions using pure fluorine gas destroyed nanotube structure, whereas at room temperature, transmission electron microscopy (TEM), X-ray diffraction, and Fourier transform-infrared (FT-IR) spectroscopy showed that fluorine–SWNT intercalation compounds could be formed.<sup>[39]</sup> Similarly, MWNTs<sup>[40]</sup> can be fluorinated at room temperature by using a gaseous mixture of  $\text{BrF}_3$  and  $\text{Br}_2$ . SWNTs fluorinated at temperatures ranging from  $150$  to  $325^\circ\text{C}$  survived the fluorination process. Two major diagnostic features<sup>[41]</sup> in the Raman spectra of the fluorinated tubes are 1) a decrease in intensity of the radial breathing mode near  $200\text{ cm}^{-1}$  and 2) an increase in the intensity of the disorder D band at  $\sim 1320\text{ cm}^{-1}$ , which are attributable to

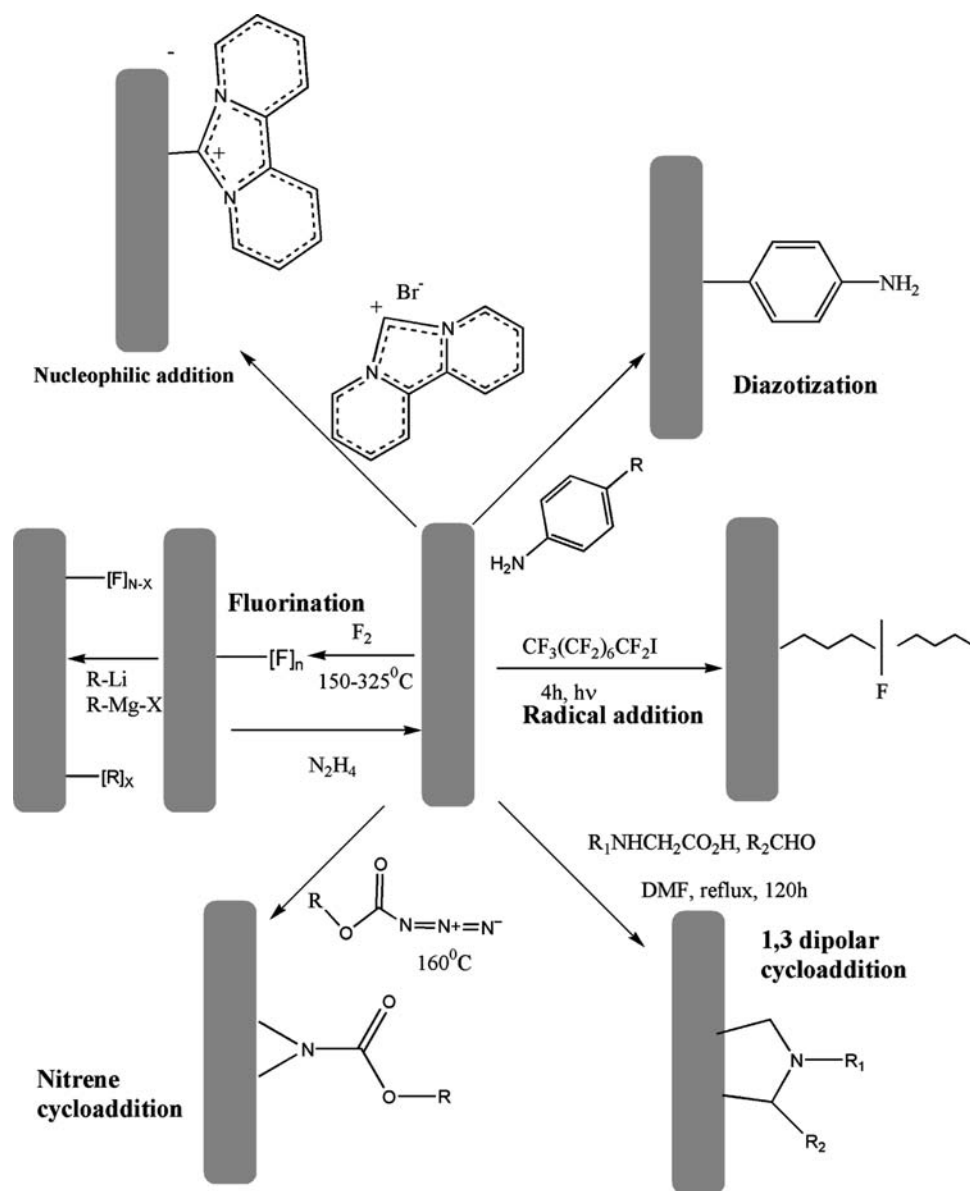


Fig. 3 Schematic demonstrating various sidewall functionalization reactions of SWNTs.

the destruction of the intrinsic  $sp^2$ -hybridized structure as C–F bonds are created and sidewall carbons become  $sp^3$ -hybridized. These fluorinated tubes can also be solubilized in various alcohol solvents via ultrasonication. Scanning tunneling microscopy (STM) images (Fig. 4) of fluorinated tubes reveals a dramatic banded structure indicating broad continuous regions of fluorination terminating abruptly in bands orthogonal to the tube axis. These results suggest that the fluorine adds more favorably around the circumference of the tube, backed up by semiempirical AM1 calculations.<sup>[42]</sup> Further calculations show that the F atoms tend to bond next to each other.<sup>[43]</sup>

Sidewall-fluorinated nanotubes can be further modified by reacting them with alkyl magnesium

bromides in a Grignard synthesis or by reaction with alkyllithium precursors to yield sidewall-alkylated nanotubes, via a concerted, allylic displacement mechanism.<sup>[44]</sup> These routes render SWNTs soluble in various organic solvents such as chloroform, methylene chloride, and tetrahydrofuran. Covalent attachment to the sidewalls was confirmed by ultraviolet (UV)–visible (vis)–near IR spectroscopy, in which optical features originating from transitions between the van Hove singularities in the 1-D electron density of states of the tube disappear as the electronic structure becomes perturbed.

Oxidizing these alkylated nanotubes in air allows for recovery of pristine nanotubes. As for fluorinated tubes, it was found that hydrazine could be used to

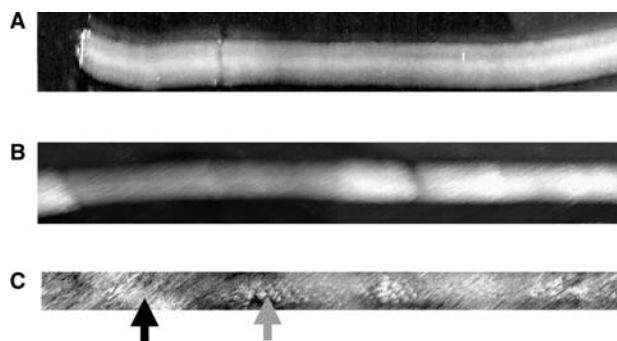


**Fig. 4** Scanning tunneling microscopy (STM) images. (A) An image of a SWNT fluorinated at 250°C for 12 hr. The approximate carbon-to-fluorine ratio by microprobe analysis is 2:1. (B) An image of a SWNT fluorinated at 150°C for 5 hr. The corresponding carbon-to-fluorine ratio, in this case, by microprobe analysis is 3.7:1. The darker area on the left side of the image appears to be a less-fluorinated area. (C) A high-resolution image of a carbon nanotube fluorinated at 250°C for 1 hr, obtained by using a C<sub>60</sub> functionalized STM tip. *Source:* Professors Kevin Kelly and Naomi Halas, Rice University.

regenerate the unfluorinated starting material;<sup>[45]</sup> a procedure was also established to “tune” the fluorine content of the tubes by first fluorinating heterogeneously, solvating in alcohol, and then defluorinating with substoichiometric quantities of hydrazine to generate tubes with different fluorine contents.<sup>[46]</sup> Heating at 100°C in noble gases of fluorinated tubes can also lead to recovery of pristine tubes, as determined by a decrease in the IR intensity of C–F stretch bands at 1207 cm<sup>-1</sup>, reappearance of bands for the A<sub>2u</sub> mode at 867 cm<sup>-1</sup> and E<sub>1u</sub> mode at 1579 cm<sup>-1</sup>, as well as the reduced resistance of nanotubes samples.<sup>[47]</sup>

There are a number of other sidewall functionalization strategies. Single-walled nanotubes have been chemically functionalized in situ by a thermally induced reaction with diazonium compounds, generated by action of isoamyl nitrite on aniline derivatives<sup>[48]</sup> (Fig. 3). Tetra-*tert*-butylphthalocyanines have been immobilized on SWNTs through a  $\pi$ - $\pi$  interaction.<sup>[49]</sup> Direct addition to the unsaturated  $\pi$ -electron systems of SWNTs can occur through the following: 1) a [2 + 1] cycloaddition of nitrenes; 2) the addition of nucleophilic carbenes; and 3) the addition of radicals (through the photoinduced addition of perfluorinated alkyl radicals).<sup>[50]</sup> Tubes functionalized in these ways enable a large variety of functional groups to be introduced onto nanotube surfaces with implications for nanocomposite formation (Fig. 3).

Recently, our group was involved with developing<sup>[51]</sup> an ozonolysis protocol (Fig. 5) involving treatment of tubes at -78°C, followed by reaction with various reagents, in independent runs, to generate a higher proportion of carboxylic acid/ester, ketone/

aldehyde, and alcohol groups, respectively, on the nanotube surface. This “one-pot” oxidative methodology has three major consequences: first, the purification of as-prepared SWNTs to obtain a high-quality product; second, the chemical functionalization of nanotube sidewalls; and third, a systematic procedure to select for particular distributions of oxygenated functional groups in the resultant purified SWNTs.

Significantly, this work bears out the theoretical prediction that 1,3 dipolar cycloaddition to the SWNT sidewalls is experimentally achievable. In fact, these experiments indicate that a certain degree of control over the presence of particular functional groups on the surfaces of these SWNTs can be obtained by judicious choice of the appropriate cleaving agent, all of which can be achieved with minimal sample loss. More importantly, this protocol presents a nondestructive, low-temperature method of introducing oxygenated functionalities directly onto the sidewalls and not simply at the end caps of SWNTs. Thus molecular species, which can be currently tethered to the ends of the nanotubes, can now be chemically dispersed along the sidewalls as well, with implications for the design of nanotube-based optoelectronic devices and well-dispersed nanocomposites.

## INORGANIC INTERFACES TO SWNTS

While nanotubes have been treated with dichlorocarbene and Birch reduction conditions (i.e., lithium in 1, 2-diaminoethane),<sup>[52]</sup> recent efforts have been involved with generating more controllable derivatization of SWNTs, both spatially and structurally. One of the ideas pursued by our group was to derivatize SWNTs with relatively bulky inorganic complexes, which not only yields a novel metal-based molecular coordination complex but also offers the possibility of tailorable solubility in a variety of solvents, through mechanisms such as charge-mediated stabilization along the length of the tube and ligand exchange, without completely disrupting the tube’s electronic structure. In addition, these generated adducts can be used in a number of different catalytic processes, including homogeneous catalysis, upon which the expensive metal-support assembly can be readily recovered from solution. As another example of the utility of metal complexation, nanotubes, functionalized with a ruthenium complex, for example, have been utilized to create interconnects showing multiple T- and Y-junctions.<sup>[53]</sup>

Specifically, both oxidized nanotubes and raw, unfunctionalized SWNTs have been reacted with Vaska’s compound, *trans*-IrCl(CO)(PPh<sub>3</sub>)<sub>2</sub>, to form covalent nanotube–metal complexes.<sup>[54]</sup> Moreover, the complexes of oxidized SWNTs with Vaska’s



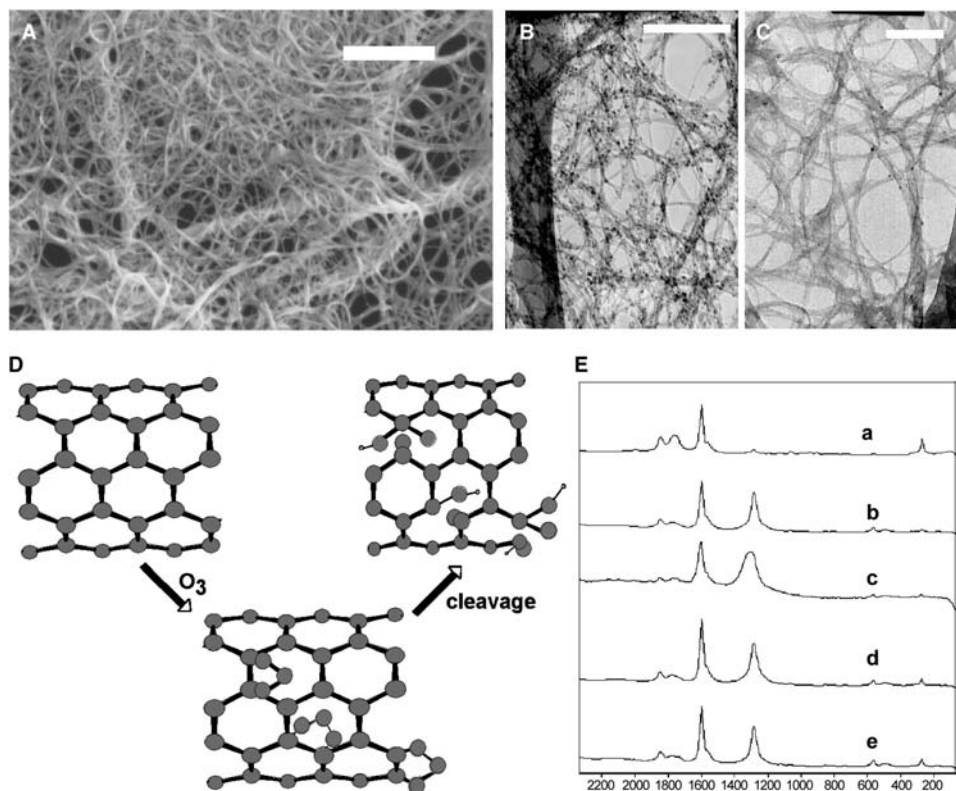


**Fig. 5** (A) Scanning electron micrograph (SEM) of ozonized tubes. Scale bar is 1  $\mu\text{m}$ . (B) Transmission electron micrograph (TEM) of as-prepared HiPco tubes. (C) TEM of ozone purified HiPco tubes. Scale bars in panels (B) and (C) are 130 and 140 nm, respectively. (D) Proposed reaction scheme for ozonation. The primary ozonide that is initially formed is cleaved to yield functional groups on the sidewalls. (E) Raman spectra show an increase of the D band upon ozonation, implying sidewall functionalization and considerable perturbation of the electronic structure.

compound are much more soluble in dimethylformamide (DMF) than raw tubes, a finding that should facilitate the chemical manipulation as well as photo-physical analyses of these materials. In fact, the solubility of oxidized tubes varied with the concentration of Vaska's complex added, suggesting that dissolution was chemically induced. The solubility of a typical adduct sample in DMF at room temperature was  $\sim 250$  mg/L, about 1 order-of-magnitude improvement over that found for unmodified tubes.<sup>[55]</sup> Analogously, the SWNT adduct with Wilkinson's complex<sup>[56]</sup> (Fig. 6) shows a relatively high degree of solubility in dimethylsulfoxide (DMSO), reproducibly  $> 150$  mg/L, and roughly 30% of that value in DMF and tetrahydrofuran (THF). Our results with oxidized nanotubes, but otherwise unmodified with any of these metal complexes, showed a solubility of  $\sim 25$  to 35 mg/L in DMF and 4–10 mg/L in THF. Conceptually, the novelty of this derivatization is that the nanotube can be considered as a primary ligand, as a functional moiety like any other, with respect to the central metal atom, Ir. Results were confirmed by  $^{31}\text{P}$  nuclear magnetic resonance (NMR) spectroscopy, FT-IR spectroscopy, electron ionization mass spectroscopy, as well as data

from transmission electron microscopy (TEM) and energy-dispersive X-ray analysis (EDX).

To summarize, Vaska's compound complexes to raw nanotubes by  $\eta^2$  coordination across the graphene double bonds. In effect, ligand binding is an associative process with the formation of a  $\pi$  complex and is expected to be similar to that observed<sup>[57,58]</sup> in (TCNE)IrBr(CO)(PPh<sub>3</sub>)<sub>2</sub> or in the fullerene adduct.<sup>[59]</sup> This type of reaction, in which the ligand acts as a weak base toward the metal complex, has been referred to as a "reductive addition" (with respect to the metal).<sup>[60]</sup> For the adduct formed with the oxidized SWNTs, coordination through the oxygen atoms seems a more likely possibility, in other words, through an oxidative addition to form a hexacoordinate structure. Oxidative additions to form 18e<sup>-</sup> "coordinatively saturated" compounds are well known for Vaska's compound and other related d<sup>8</sup> complexes and have been extensively studied.<sup>[61,62]</sup> Thus it is postulated that the oxidized nanotubes coordinate to the compound via oxidative addition to form an Ir(III) complex. These conclusions are in general agreement with theoretical predictions, based on a cluster model approach and a density functional theory study.<sup>[63]</sup>

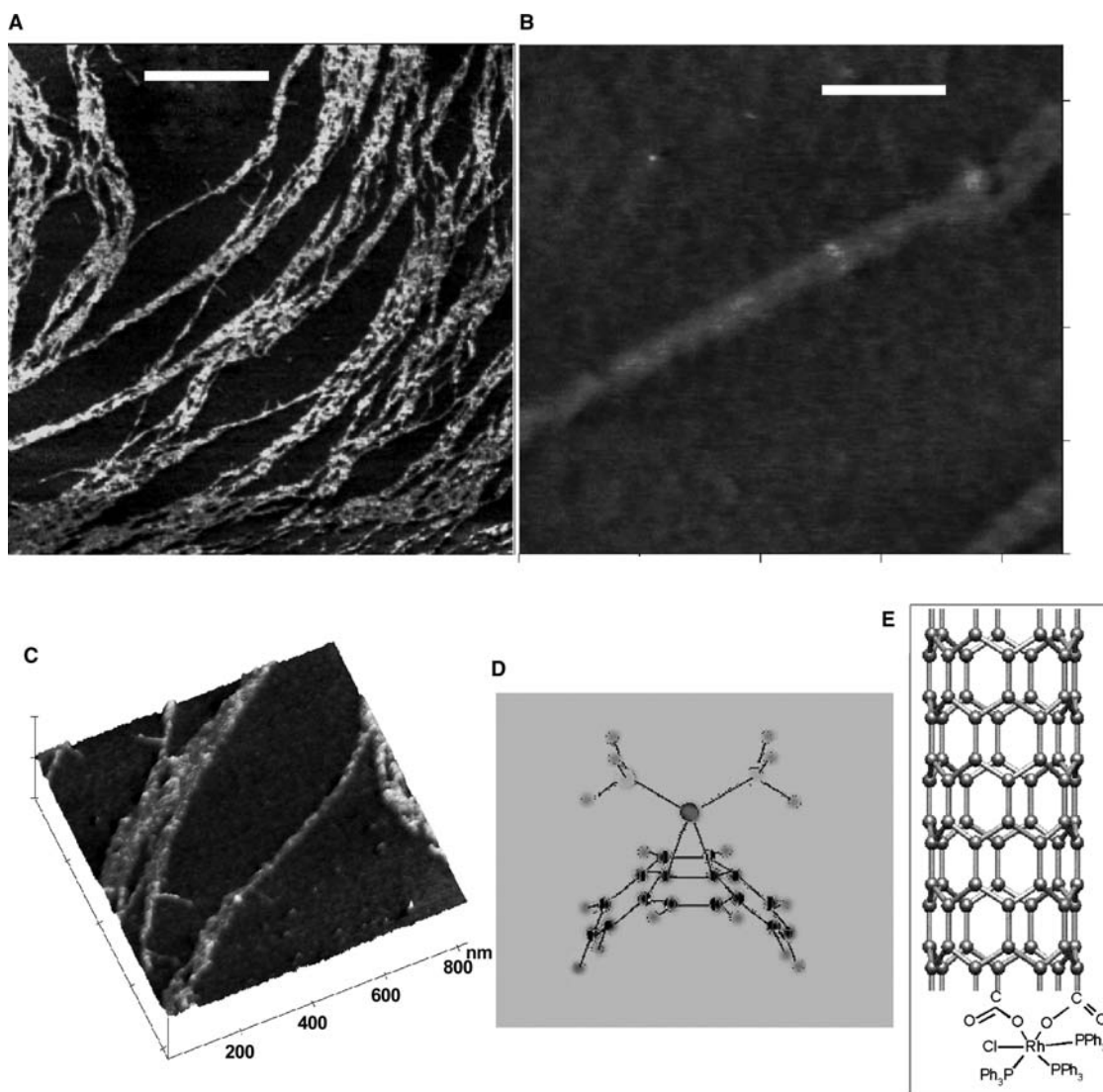


**Fig. 6** Atomic force microscopy (AFM) height images of functionalized nanotube adducts. Scale bars are (A) 500 nm, (B) 100 nm, and (C) 200 nm. (A) A high density of tubes has been deposited from solution. Aggregates of tubes appear to be exfoliating into smaller bundles. (B) Image of a single bundle roughly 15 nm in diameter. (C) A 3-D view of exfoliating tubes. The bundles are relatively clean and free of nanoparticulate impurities. (D) Optimized geometry of  $M(PH_3)_2$  coordinated in an  $\eta^2$  fashion to SWNT sidewalls. (E) Proposed structure of SWNT–Wilkinson's adduct. Panel (D) is based on a schematic provided by Professor Antonio Sgamellotti (Universita di Perugia).

The reactivity of SWNTs toward metal complexes is substantially different from that of fullerenes, although both possess a non-planar  $sp^2$  configuration. Curvature effects and different degrees of local strain between the two structures likely account for the observed differences in behavior. Specifically, the presence of five-membered cyclopentadienyl-like rings in  $C_{60}$  substantially enhances the affinity of (6,6) bonds in coordinating metal complexes and allows for strong back donation in the resulting adducts, thereby promoting their stability. However, theoretical calculations on molecular fragments replicating SWNT surface curvature indicate that, unlike in the

case of fullerenes, five-membered rings are not present to stabilize  $\pi^*$  ligand orbitals and hence, back-bonding interactions are much weaker in these systems.<sup>[63]</sup> This would rationalize the preference for oxidative addition, when that should become a possibility.

Single-wall nanotubes have also been used as substrates for the deposition of metals by electron-beam evaporation, resulting, in the case of Au, Al, Pb, and Fe, in the formation of discrete particles on nanotubes due to a weak interaction between metals and nanotubes.<sup>[64]</sup> Acid groups on treated SWNTs can act as nucleation sites for a well-dispersed deposition of Pt

clusters.<sup>[65]</sup> With Ti, Ni, and Pd, quasi-continuous coatings are possible, resulting in the formation of nanotube-supported metal nanowire structures.<sup>[66]</sup> Zinc oxide nanowires have been grown on the surfaces of MWNTs without the presence of catalyst through a thermal treatment.<sup>[67]</sup>

Our group has been involved with the generation of nanotube heterostructures as well, involving the creation of nanotube–nanocrystal adducts. Indeed, a novel strategy of altering the electronic properties of nanotubes is to chemically functionalize them with a moiety or structure whose intrinsic properties are electronically configurable. One such structure is the family of semiconductor nanocrystals,<sup>[68]</sup> such as CdS and CdSe, alternately known as quantum dots, which exhibit strongly size-dependent optical and electrical properties. The high luminescence yield of these materials<sup>[69]</sup> as well as the potential of adjusting emission and absorption wavelengths by selecting for nanocrystal size make quantum dots attractive for constructing optoelectronic devices, for instance, with tailored properties. In fact, the electronic structure of semiconductor nanocrystallites exhibits distinctive quantum effects;<sup>[70]</sup> the bandgap of these materials increases with decreasing particle size.

We have reported<sup>[71]</sup> the synthesis and characterization of SWNTs covalently joined to CdSe and TiO<sub>2</sub> semiconductor nanocrystals by short chain organic molecule linkers (Fig. 7). In each case, purified, oxidized nanotubes were reacted with nanocrystals, derivatized with either amine or acid terminal groups in a reaction mediated by a carbodiimide reagent. By judiciously varying the nature of the organic capping groups on the nanocrystal surface and the organic bifunctional linkers, we can modulate interactions between the nanotubes and the nanocrystals, with implications for self-assembly. Such composites are expected to be useful for applications as diverse as molecular electronics, photocatalysis, solar energy conversion, and as probes for scanning force microscopy.

TEM examination (Fig. 8) showed nanocrystals linked to the oxidized SWNTs, forming discrete nanocomposites. The nanocrystals tend to be concentrated at the open caps and the “ends,” where there is the largest concentration of carboxylic groups<sup>[72,73]</sup> and thus, the highest probability of amide bond formation.<sup>[74]</sup> A commonly observed structure was a cluster of nanoparticles, especially in the case of CdSe, localized at the outer edges of the tubes (Fig. 8D). In other cases, especially with individual tubes, numbers of nanocrystals tended to disperse along the sidewalls, presumably attaching to defect sites on the oxidized nanotube surface (Fig. 8C). The TiO<sub>2</sub> system showed substantially greater coverage of the tubes with the nanoparticles (Fig. 8D). Carboxyl groups adsorb strongly onto bare titanium dioxide surfaces.<sup>[75]</sup> Hence, larger numbers of

these particles can interact with nanotubes and in effect, amide bond formation may not be required for an underivatized, uncapped TiO<sub>2</sub>–SWNT adduct to be directly produced. Indeed, we postulate that this is the reason for the enhanced coverage with TiO<sub>2</sub> particles. Energy-dispersive X-ray analysis on both nanocomposite systems was consistent with the presence of appropriately functionalized nanocrystals attached to nanotubes as proposed. These patterns of nanocrystal clustering on the nanotubes were not observed in control experiments, without the use of carbodiimide linking agents, where the tubes themselves were found to remain totally separate from the nanocrystals.

## SOLUBILIZATION OF NANOTUBES

Whereas fluorination tends to derivatize tubes and disrupt band structure of SWNTs, most experiments involving solubilization of nanotubes aim for the retention of important photophysical properties. Moreover, solubilization facilitates the placement of a huge array of functional groups onto SWNT surfaces for composite formation.

By visual inspection and quantification using UV–visible absorption spectroscopy, small-diameter SWNTs (ca. 0.7 nm), grown by a gas-phase catalytic process,<sup>[76]</sup> were found to be somewhat soluble in a number of organic solvents such as 1,2-dichlorobenzene, chloroform, 1-methylnaphthalene, dimethylformamide (DMF), and tetrahydrofuran (THF).<sup>[55]</sup> Laser-oven produced SWNTs (with diameters of about 1.2 nm) can be dissolved to some extent in DMF, *N*-methylpyrrolidinone, and hexamethylphosphoramide.<sup>[77]</sup> Many strategies aimed at improving the solubility behavior of nanotubes involve the oxidation and purification of nanotubes; reports<sup>[78,79]</sup> have placed the total percentage of acidic sites, generated by such processing, in full-length SWNTs at a range of 1–3% and defect sites in the 5% range. Examples of defects in nanotubes include pentagon/heptagon Stone–Wales-type defects, associated with a rotation of a bond in the SWNT atom network, vacancies in the nanotube lattice, the presence of adatoms or carbon dimers on the sidewalls, the occurrence of sp<sup>3</sup>-hybridized carbons, and pentagon-terminated caps.<sup>[80–82]</sup>

Indeed, metallic and semiconducting SWNTs were initially derivatized in organic solutions, such as chloroform, dichloromethane, aromatic solvents (including benzene, toluene, and chlorobenzene), and CS<sub>2</sub>, by converting acid-terminated, purified nanotubes with thionylchloride to generate acylchloride groups that could then be reacted with amines such as octadecylamine.<sup>[83]</sup> This work was later extended to amide formation from alkyl–aryl amines such as 4-dodecylaniline.<sup>[84]</sup> NMR spectra of the soluble SWNTs exhibited peaks because of the aliphatic and aromatic

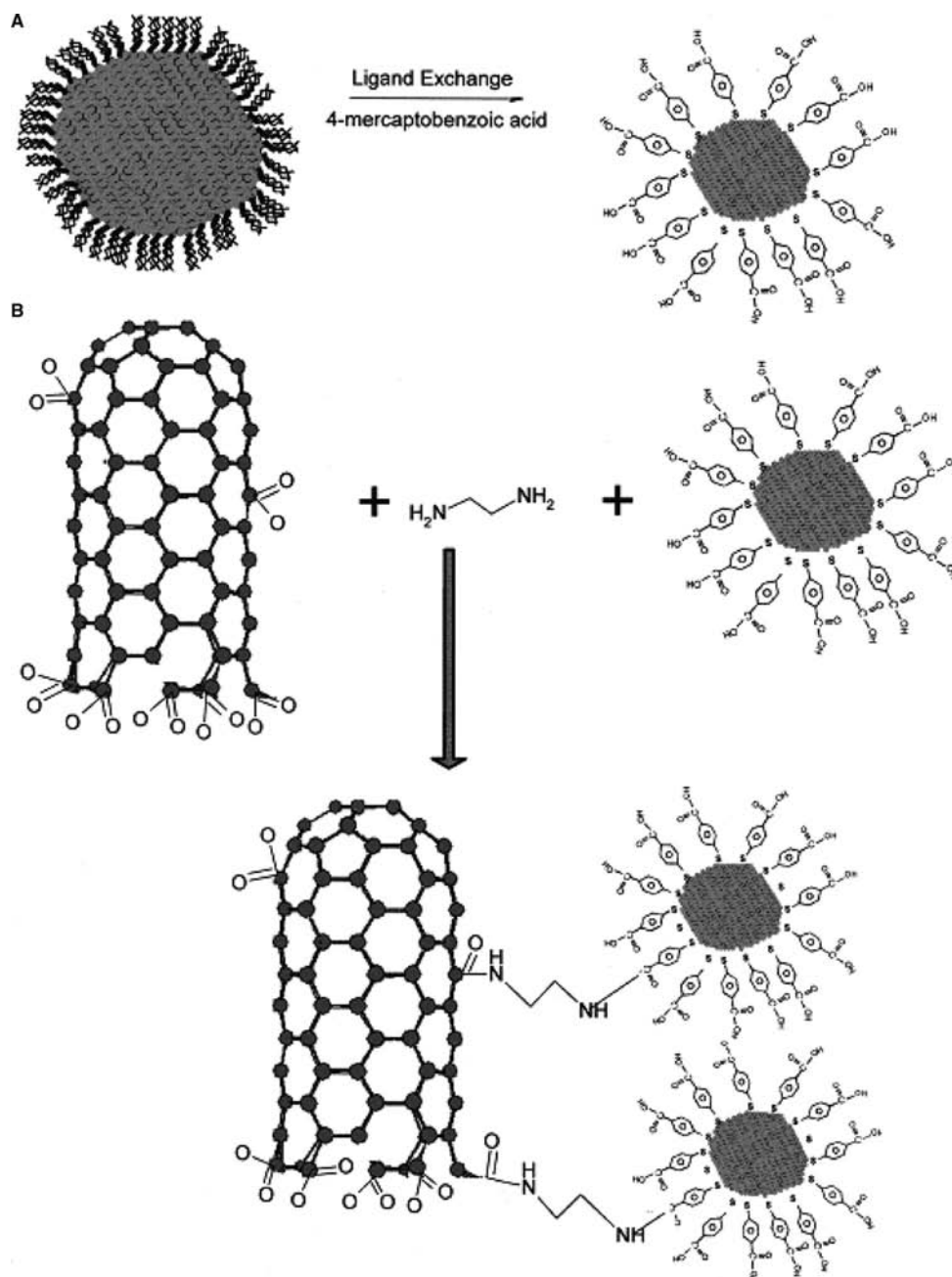


**Fig. 7** Schematic of the addition of derivatized CdSe nanocrystals to oxidized SWNTs. Trioctylphosphine oxide (TOPO)-capped nanocrystals were prepared by established methods using organometallic precursors. (A) TOPO capping was substituted for a thiol ligand to form a carboxylic acid terminated CdSe nanocrystal. Substituted thiocarboxylic acids used included *p*-mercaptobenzoic acid, thioglycolic acid, and 3-mercaptopropionic acid. (B) The nanocrystals prepared in panel (A) were linked to oxidized SWNTs by an ethylenediamine linker in the presence of N-ethyl-N'-(3-dimethylaminopropyl)carbodiimide (EDC).

moieties, respectively. Raman spectroscopy indicated that nanotube structure was likely preserved. Solution-phase mid-IR analysis<sup>[85]</sup> shows that, for the reaction with octadecylamine, the weight percentage of the octadecylamino functionality is about 50%, at defect sites as well as the ends of SWNTs. Full-length dissolution<sup>[86]</sup> of purified SWNTs (containing

carboxylic acid groups) was also achieved through an acid–base reaction by forming an octadecylammonium, SWNT-carboxylate zwitterion. AFM showed that the majority of the SWNT ropes were exfoliated into small ropes (2–5 nm in diameter) and individual nanotubes with lengths of several microns during the dissolution process.

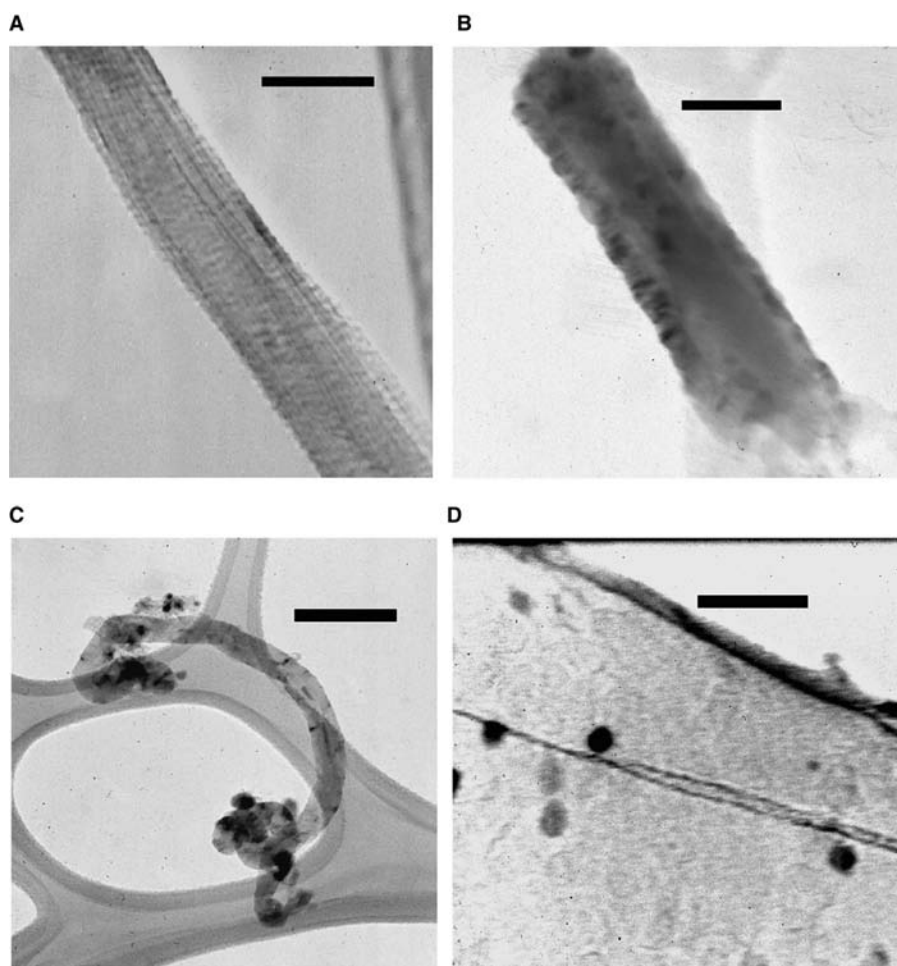


**Fig. 8** TEMs of (A) a purified single-walled carbon nanotube bundle. Scale bar denotes 30 nm. (B) Oxidized SWNT bundle circumscribed by capped  $\text{TiO}_2$  particles. Scale bar is 45 nm. (C) Oxidized tubes linked to CdSe nanocrystals capped with 4-mercaptopropionic acid. The crystallites are concentrated at the functionalized open ends, with some coverage on the sidewalls, likely on defect sites. Scale bar is 150 nm. (D) Oxidized nanotube linked to CdSe nanoparticles capped with 3-mercaptopropionic acid. Image at high magnification shows prolate nanocrystals scattered along the length of the tube. Scale bar represents 20 nm.

Single-wall nanotubes, functionalized with esters<sup>[87]</sup> at defect sites [i.e.,  $\text{SWNT-COO}(\text{CH}_2)_{17}\text{CH}_3$ ], have been prepared, as determined by Raman and IR bands, leading to improved solubilization in solvents such as THF and  $\text{CHCl}_3$ . Strong attachment of deuterium<sup>[88]</sup> to SWNTs in solution has been observed when deuterated ethanol is used as a coreactant in esterification reactions; results were obtained from  $^2\text{H}$  NMR and FT-IR measurements. Derivatization based on 1,3-dipolar cycloaddition of azomethine ylides, generated by the condensation of an  $\alpha$ -amino acid and an aldehyde, has been used to solubilize tubes in most organic solvents.<sup>[89]</sup> Evidence of functionalization was further supported by observation of fluorescence in the adducts, as was also noted in SWNT–aniline systems.<sup>[90]</sup> SWNTs have also been functionalized with derivatized pyrene, via a similar reaction, namely the esterification of nanotube-bound carboxylic acids, to create adducts soluble in chloroform, THF, and toluene.<sup>[91]</sup> Fluorescence and fluorescence excitation results suggest that the tethered pyrenes form “intramolecular” (intrananotube) excimers. The pyrene monomer and excimer excitations are quenched by the SWNTs in a mechanism whereby the nanotubes serve as

acceptors for excited-state energy transfers from the tethered pyrene moieties.

It has been proposed, for instance, that large organic groups assist in solubility by exfoliation of the bundles into individual tubes through the formation of intervening moieties that can overcome the intrinsic van der Waals forces<sup>[92]</sup> between these tubes. It is not surprising, given this improved solubility, that recent work has been performed on separating soluble SWNTs and zwitterion-functionalized shortened SWNTs by length, diameter, and chirality from THF using high-performance liquid chromatography (HPLC) and gas chromatography techniques.<sup>[93,94]</sup> In addition, this body of solubilization work in stable, organic solvents has allowed Raman and near-IR spectroscopies to be used for the detection and identification of different species (i.e., diameters and metallicity) of SWNTs based on their Raman frequencies and vis–near IR electronic transitions.<sup>[95]</sup>

In water, a stable dispersion of full-length, well-separated individual tubes has been formed upon stabilization in gum arabic,<sup>[96]</sup> a water-soluble polysaccharide; adsorption is presumed to disrupt the intertube interactions in the crystalline ropes. Aqueous solubilization

(in the range of 0.1 to 0.3 mg/mL) was also achieved by functionalizing SWNTs with glucosamine. In this case, grafting of the glucosamine to the tubes was achieved by reacting the amine with acyl chloride groups created on the SWNT surface.<sup>[97]</sup> Treatment of nanotubes with a 9:1 mixture of sulfuric acid and hydrogen peroxide for 30 min followed by sonication for varying lengths of time allows for the creation of carboxylate groups on defect sites and tube ends, which render the SWNTs water-soluble in different pH buffers. Electronic structure is maintained, as evidenced by absorption spectra, where the van Hove singularities are maintained.<sup>[28]</sup> There has also been a claim that SWNTs, sonicated and dispersed in 1% sodium dodecylsulfate buffer and glycerol, can be distributed to a certain extent by diameter and length simply by the application of an electric field, again implying that solubilization has consequences for rational manipulation of nanotubes.<sup>[98]</sup> Molecular dynamics simulations indicate that in water, polar functional groups attached to SWNTs are likely to be more energetically stable in extended configurations, whereas non-polar functional groups will prefer to remain folded.<sup>[99]</sup>

To generalize and broaden the potential of functionalization, in our group, we have also solubilized oxidized SWNTs through the attachment of organic moieties in a large number of solvents of varying polarity.<sup>[100]</sup> In this case, we grafted a functionalized organic crown ether, namely 2-aminomethyl-18-crown-6, onto our SWNTs. The resultant, synthesized adduct yielded concentrations of dissolved nanotubes on the order of  $\sim 1$  g/L in water as well as in methanol, according to optical measurements. These values are dramatic improvements over conventional dissolution behavior of unfunctionalized nanotubes. The nanotube-crown ether adduct can be readily redissolved in a number of different organic solvents, such as ethanol, 2-propanol, acetone, *o*-dichlorobenzene (ODCB), dimethylformamide (DMF), tetrahydrofuran (THF), dimethylsulfoxide (DMSO), ethyl acetate, and benzene, at substantially high concentrations. One implication of these results lies in further exploitation of the solution chemistry of these tubes for photophysical analyses in a number of previously untested solvents as well as for the generation of novel nanoscale architectures.

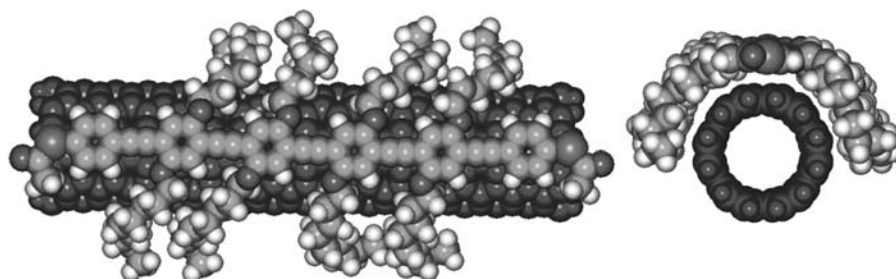


**Fig. 9** Molecular model of a (6,6) SWNT complex with poly(aryleneethynylene)s (PPE), showing interaction of the polymer backbone with the SWNT sidewall through  $\pi$  stacking. *Source:* Dr. Jian Chen, Zyvex Corporation.

## SWNT-POLYMER COMPOSITES

Single-wall nanotubes can also be solubilized in water by non-covalently associating them with linear polymers such as polyvinyl pyrrolidone and polystyrene sulfonate. In this case, the polymers rigidly and uniformly associate with the sides of nanotube, disrupting the hydrophobic interface with water and the intertube interactions within the tubular aggregates (Fig. 9). Nanotubes can then be “unwrapped” by changing the solvent system.<sup>[101]</sup> In another study, wrapping of polymer ropes (modified poly(*p*-phenylenevinylene) around the tube lattice occurs in a well-ordered periodic fashion, arising from a van der Waals interaction between the phenyl rings of the polymer and the hexagonal lattice of the nanotube; solutions of the polymer in toluene are thought to be able to suspend nanotubes “indefinitely.”<sup>[102]</sup> Based on Raman and absorption data, it is thought that the polymer interacts preferentially with nanotubes of certain diameters or a range of diameters. The attachment<sup>[103]</sup> of lipophilic and hydrophilic dendra, which are terminated with long alkyl chains and oligomeric poly(ethylene glycol) moieties, respectively, via amidation and esterification reactions, can render SWNTs and MWNTs soluble in common organic solvents, such as hexane and chloroform as well as water, to form colored homogeneous solutions. These functionalized tubes can be defunctionalized in homogeneous solutions under base- and acid-catalyzed hydrolysis reaction conditions.<sup>[104]</sup> These functional polymer-nanotube composites may have unique, favorable properties; for instance, SWNT-poly(metaphenylenevinylene) composites have nearly eightfold increase in electrical conductivity compared with just the polymer and have favorable photo- and electroluminescence properties as well.<sup>[105]</sup>

## ADDITIONAL CHEMICAL FUNCTIONALIZATION STRATEGIES

Single-wall nanotubes can also be modified by a number of other methodologies. Sonication of tubes in a monochlorobenzene solution of poly(methyl



methacrylate) (PMMA) created SWNTs with many defects in the sidewalls when burned in oxygen.<sup>[106]</sup> Using radio frequency glow-discharge plasma activation,<sup>[107]</sup> amino-dextran chains have been immobilized onto acetaldehyde-treated aligned SWNTs through a Schiff-base formation and reductive stabilization with sodium cyanoborohydride, while periodate-oxidized dextran-fluorescein isothiocyanate (FITC) chains have been chemically grafted onto ethylenediamine-derivatized SWNTs via the same reaction. SWNTs can also be derivatized by bombardment<sup>[108,109]</sup> with  $\text{CH}_3$  and  $\text{CF}_3$  radicals impacting with incident energies of 10, 45, and 80 eV, as was confirmed by X-ray photoelectron spectroscopy and scanning electron microscopy.

Chemical functionalization of SWNTs attached to conventional atomic force microscopy (AFM) probes was also demonstrated as a methodology yielding high-resolution, chemically sensitive images on samples containing multiple chemical domains.<sup>[10,74,110]</sup> Moreover, when these probes were derivatized with amine, carboxy, and biotin groups at their ends with domains of similarly defined functional groups localized on the surface, they could be used to measure specific and definable interactions in a variety of solvent media (Fig. 10).

## MANIPULATION OF TUBES

Although it appears that oxidized SWNTs have a tendency to stack and form larger aggregates,<sup>[111]</sup>

interesting nanoscale architectures can be created by judicious manipulation of the chemistry of these tubes. For instance, lightly etched SWNTs have been chemically reacted<sup>[112]</sup> to form rings, with an average diameter of 540 nm (Fig. 11). The same research group created a hollow spherical ring made of nested SWNTs.<sup>[113]</sup> To accomplish this geometry, SWNTs were first adsorbed onto amine-terminated silica gels in solution, a step that determined the nature of the nested network. Subsequent drying and reabsorption cycles were used to grow the nest layer-by-layer through nanotube–nanotube interactions. Ultimately, the silica gels were etched away to give hollow cages.

Carboxy-terminated SWNTs have been assembled onto amino-terminated gold surfaces via electrostatic interactions, with the aid of dicyclohexylcarbodiimide condensation agents.<sup>[114]</sup> Similar chemical strategies were employed to adsorb SWNTs onto silver surfaces.<sup>[115]</sup> Work has also been completed on depositing tubes on chemically functionalized nanolithographic patterns. Creation of these assemblies is critical because these strategies allow for precise positioning of nanotubes in specific locations and orientations; consequently, there is now the potential of creating simple nanostructures with SWNTs and of connecting these to other structures. This is crucial to the fabrication and development of simple electrical circuits with tubes and hence, provides for a means of measuring electron transport characteristics in these systems.<sup>[116]</sup> Recently, it has also been found<sup>[117]</sup> that ozonized SWNTs can be assembled onto amine-terminated self-assembled

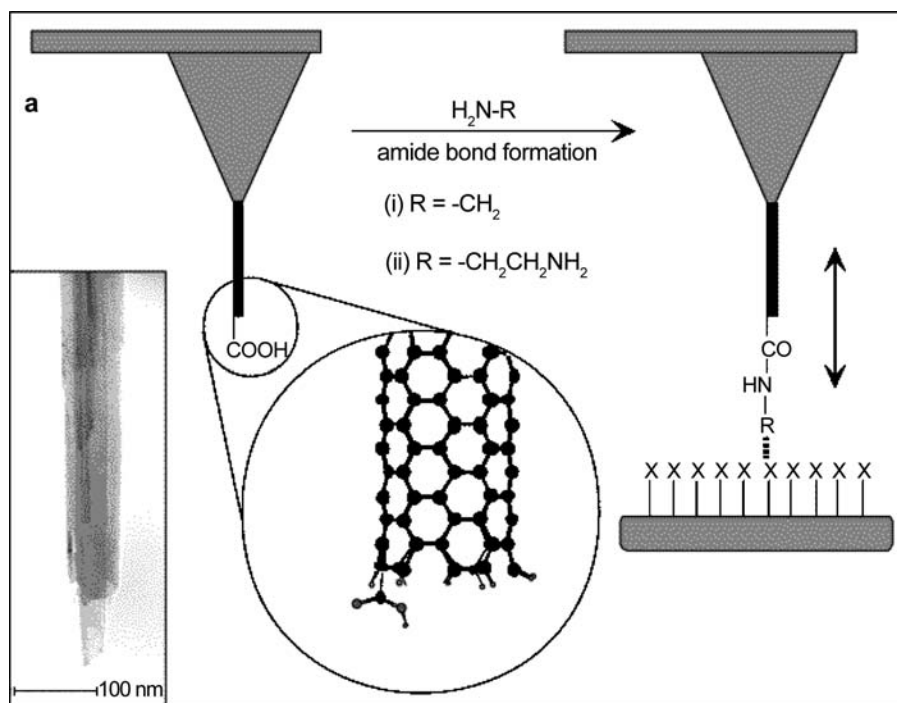


**Fig. 10** Preparation of functionalized carbon nanotube tips. Diagram illustrating the modification of a nanotube tip by coupling an amine to a pendant carboxyl group, and the application of this probe to sense specific interactions with functional groups (X) of a substrate. The circular inset is a molecular model of a single nanotube wall with one carboxyl group at the tip end. Inset: TEM image showing the open end of a shortened nanotube tip.

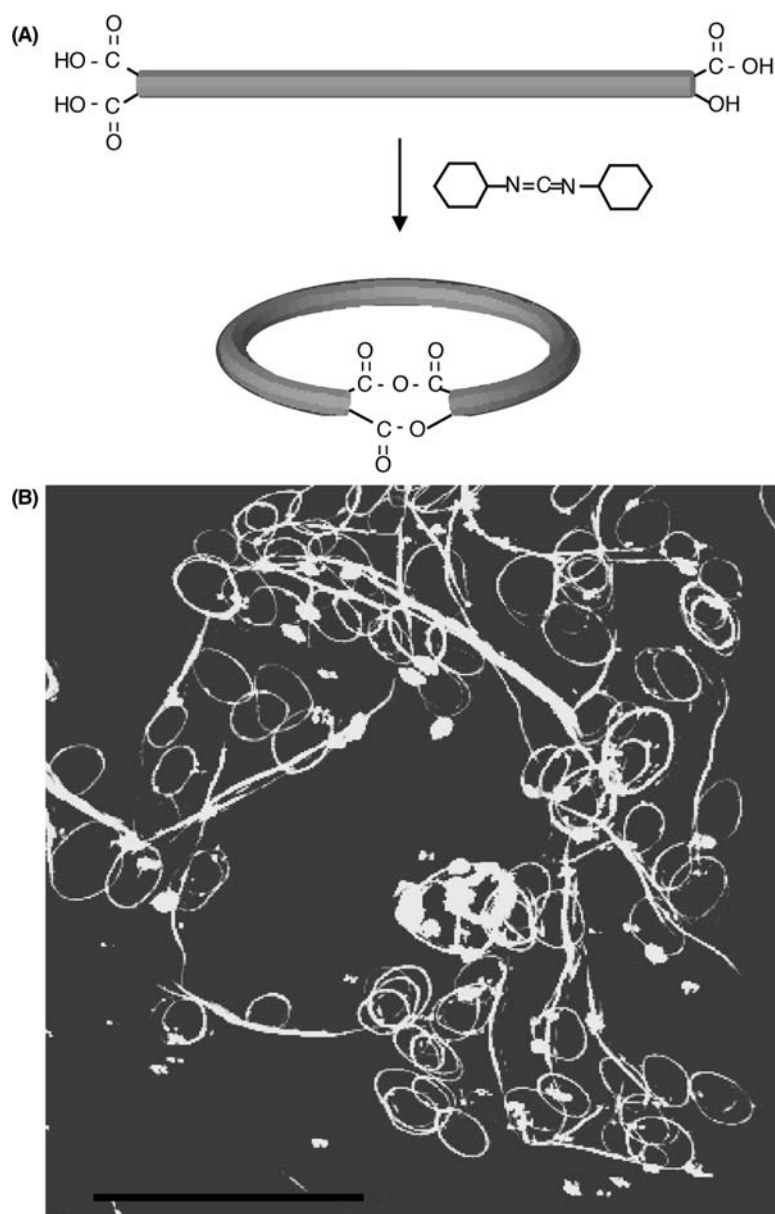


**Fig. 11** (A) A possible scheme for nanotube ring closure with *N,N'*-dicyclohexylcarbodiimide (DCC). (B) AFM images of closed ring systems. The scale bar is 2  $\mu\text{m}$ . *Source*: Professor Masahito Sano, Yamagata University.

monolayers (SAMs) as well as physically adsorbed via layer-by-layer deposition with bridging of metal cations, i.e.,  $\text{Fe}^{+3}$  on carboxylate-terminated SAMs or  $\text{Cu}^{+2}$  on thiol-terminated SAMs. A further advance has come from a report of room-temperature assembly of directional SWNT strings across polymer microchannels.<sup>[118]</sup>

## CONCLUSION

Rational nanotube functionalization provides for the potential of the manipulation of nanoscale properties in a predictive manner. In many cases, it may also render tubes soluble and stable in aqueous and organic

solution, thereby enabling further exploitation of their wet chemistry and investigation of their photophysical properties. In addition, derivatization allows for a number of site-selective nanochemistry applications such as the possibility of self-assembly of nanotubes with tailorable electronic properties, important for advances in molecular electronics. Other derivatized nanotube adducts also show the potential for novel charge transfer characteristics, the development and understanding of which have implications for photocatalysis as well as for scanning probe microscopy with functionalized tips. Finally, chemical manipulation of SWNTs is critical for hierarchical build-up of these nanomaterials into novel architectures, such

as nanocomposites and nanocircuits, with unique structural properties.

## REFERENCES

- Curl, R.F.; Smalley, R.E. Fullerenes. *Sci. Am.* **1991**, *265*, 32.
- Kroto, H.W.; Heath, J.R.; O'Brien, S.C.; Curl, R.F.; Smalley, R.E. C<sub>60</sub>: buckminsterfullerene. *Nature* **1985**, *318*, 162.
- Smalley, R.E.; Yakobson, B.I. The future of the fullerenes. *Solid State Commun.* **1998**, *107* (11), 597.
- McKinnon, J.T.; Bell, W.L.; Barkley, R.M. Combustion synthesis of fullerenes. *Combust. Flame* **1992**, *88*, 102.
- Kratschmer, W.; Lamb, L.D.; Fostiropoulos, K.; Huffman, D.R. Solid C<sub>60</sub>: a new form of carbon. *Nature* **1990**, *347*, 354.
- Yosida, Y. Scanning electron microscope images of fullerene (C<sub>60</sub>) whiskers. *Jpn. J. Appl. Phys.* **1992**, *31*, L505.
- Ebbesen, T.W. Carbon nanotubes. *Phys. Today* **1996**, *49*, 26.
- Yakobson, B.I.; Smalley, R.E. Fullerene nanotubes: C-1000000 and beyond. *Am. Sci.* **1997**, *85*, 324.
- Dresselhaus, M.S.; Dresselhaus, G.; Eklund, P.C. *Science of Fullerenes and Carbon Nanotubes*; Academic Press: New York, 1996.
- Wong, S.S.; Joselevich, E.; Woolley, A.T.; Cheung, C.L.; Lieber, C.M. Covalently functionalized nanotubes as nanometer-sized probes in chemistry and biology. *Nature* **1998**, *394*, 52.
- Mintmire, J.W.; Dunlap, B.I.; White, C.T. Are fullerene tubules metallic? *Phys. Rev. Lett.* **1992**, *68*, 631.
- Hamada, N.; Sawada, S.; Oshiyama, A. New one-dimensional conductors: graphitic microtubules. *Phys. Rev. Lett.* **1992**, *68*, 1579.
- Saito, R.; Fujita, M.; Dresselhaus, G.; Dresselhaus, M.S. Electronic structure of graphene tubules based on C<sub>60</sub> fullerene. *Phys. Rev., B* **1992**, *46*, 1804.
- White, C.T.; Robertson, D.H.; Mintmire, J.W. Helical and rotational symmetries of nanoscale graphitic tubules. *Phys. Rev., B* **1993**, *47*, 5485.
- Saito, R.; Dresselhaus, G.; Dresselhaus, M.S. Electronic structure of chiral graphene tubules. *Appl. Phys. Lett.* **1992**, *60*, 2204.
- Dresselhaus, M.S.; Dresselhaus, G.; Avouris, P. *Carbon Nanotubes: Synthesis, Structure, Properties, and Applications*; Springer Verlag: Berlin, 2001.
- Sawada, S.; Hamada, N. Energetics of carbon nanotubes. *Solid State Commun.* **1992**, *83*, 917.
- Yakobson, B.I.; Brabec, C.J.; Bernholc, J. Nanomechanics of carbon tubes: instabilities beyond linear response. *Phys. Rev. Lett.* **1996**, *76*, 2511.
- Falvo, M.R.; Clary, G.J.; Taylor, R.M.I.; Chi, V.; Brooks, F.P.J.; Washburn, S.; Superfine, R. Bending and buckling of carbon nanotubes under large strain. *Nature* **1997**, *389*, 582.
- Yakobson, B.I. Mechanical relaxation and "intramolecular plasticity" in carbon nanotubes. *Appl. Phys. Lett.* **1998**, *72*, 918.
- Fischer, J.E.; Dai, H.; Thess, A.; Lee, R.; Hanjani, N.M.; Dehaas, D.L.; Smalley, R.E. Metallic resistivity in crystalline ropes of single-wall carbon nanotubes. *Phys. Rev., B* **1997**, *55*, R4921.
- Bachtold, A.; Hadley, P.; Nakanshi, T.; Dekker, C. Logic circuits with carbon nanotube transistors. *Science* **2001**, *294*, 1317.
- Lordi, V.; Yao, N.; Wei, J. Method for supporting platinum on single-walled carbon nanotubes for a selective hydrogenation catalyst. *Chem. Mater.* **2001**, *13*, 733.
- Planeix, J.M.; Coustel, N.; Coq, B.; Brotons, V.; Kumbhar, P.S.; Dutartre, R.; Geneste, P.; Bernier, P.; Ajayan, P.M. Application of carbon nanotubes as supports in heterogeneous catalysis. *J. Am. Chem. Soc.* **1994**, *116*, 7935.
- Baughman, R.H.; Cui, C.; Zakhidov, A.A.; Iqbal, Z.; Barisci, J.N.; Spinks, G.M.; Wallace, G.G.; Mazzoldi, A.; De Rossi, D.; Rinzler, A.G.; Jachinski, O.; Roth, S.; Kertesz, M. Carbon nanotube actuators. *Science* **1999**, *284*, 1340.
- Baughman, R.H.; Zakhidov, A.A.; de Heer, W.A. Carbon nanotubes—the route toward applications. *Science* **2002**, *297*, 787.
- Fan, S.; Chapline, M.G.; Franklin, N.R.; Tomblor, T.W.; Cassell, A.M.; Dai, H. Self-oriented regular arrays of carbon nanotubes and their field emission properties. *Science* **1999**, *283*, 512.
- Zhao, W.; Song, C.; Pehrsson, P.E. Water-soluble and optically pH-sensitive single-walled carbon nanotubes from surface modification. *J. Am. Chem. Soc.* **2002**, *124*, 12,418.
- Kong, J.; Franklin, N.R.; Zhou, C.; Chapline, M.G.; Peng, S.; Cho, K.; Dai, H. Nanotube molecular wires as chemical sensors. *Science* **2000**, *287*, 622.
- Yang, C.-M.; Kanoh, H.; Kaneko, K.; Yudasaka, M.; Iijima, S. Adsorption behaviors of HiPco single-walled carbon nanotube aggregates for alcohol vapors. *J. Phys. Chem., B* **2002**, *106*, 8994.
- Garg, A.; Sinnott, S.B. Effect of chemical functionalization on the mechanical properties of carbon nanotubes. *Chem. Phys. Lett.* **1998**, *295*, 273.
- Chen, R.J.; Zhang, Y.; Wang, D.; Dai, H. Noncovalent sidewall functionalization of single-walled carbon nanotubes for protein immobilization. *J. Am. Chem. Soc.* **2001**, *123*, 3838.
- Huang, W.; Taylor, S.; Fu, K.; Lin, Y.; Zhang, D.; Hanks, T.W.; Rao, A.M.; Sun, Y.-P. Attaching proteins to carbon nanotubes via diimide-activated amidation. *Nano Lett.* **2002**, *2*, 311.
- Yu, Z.; Brus, L.E. Rayleigh and Raman scattering from individual carbon nanotube bundles. *J. Phys. Chem., B* **2001**, *105*, 1123.
- Yu, Z.; Brus, L.E. (*n,m*) Structural assignments and chirality dependence in single-wall carbon nanotube Raman scattering. *J. Phys. Chem., B* **2001**, *105*, 6831.
- Rao, A.M.; Richter, E.; Bandow, S.; Chase, B.; Eklund, P.C.; Williams, K.A.; Fang, S.; Subbaswamy, K.R.; Menon, M.; Thess, A.; Smalley, R.E.; Dresselhaus, G.; Dresselhaus, M.S. Diameter-selective Raman scattering from vibrational modes in carbon nanotubes. *Science* **1997**, *275*, 187.

37. Corio, P.; Brown, S.D.M.; Marucci, A.; Pimenta, M.A.; Kneipp, K.; Dresselhaus, G.; Dresselhaus, M.S. Surface-enhanced resonant Raman spectroscopy of single-wall carbon nanotubes adsorbed on silver and gold surfaces. *Phys. Rev., B* **2000**, *61*, 13,202.
38. Bahr, J.; Tour, J.M. Covalent chemistry of single-wall carbon nanotubes. *J. Mater. Chem.* **2002**, *12*, 195.
39. Hamwi, A.; Alvergnat, H.; Bonnamy, S.; Beguin, F. Fluorination of carbon nanotube. *Carbon* **1997**, *35*, 723.
40. Yudanov, N.F.; Okotrub, A.V.; Shubin, Y.V.; Yudanov, L.I.; Bulusheva, L.G. Fluorination of arc-produced carbon material containing multiwall nanotubes. *Chem. Mater.* **2002**, *14*, 1472.
41. Marcoux, P.R.; Schreiber, J.; Batail, P.; Lefrant, S.; Renouard, J.; Jacob, G.; Albertini, D.; Mevellec, J.-V. A spectroscopic study of the fluorination and defluorination reactions on single-walled carbon nanotubes. *Phys. Chem., Chem. Phys.* **2002**, *4*, 2278.
42. Kelly, K.F.; Chiang, I.W.; Mickelson, E.T.; Hauge, R.H.; Margrave, J.L.; Wang, X.; Scuseria, G.E.; Radloff, C.; Halas, N.J. Insight into the mechanism of sidewall functionalization of single-walled nanotubes: an STM study. *Chem. Phys. Lett.* **1999**, *313*, 445.
43. Bauschlicher, C.W. Hydrogen and fluorine binding to the sidewalls of a (10,0) carbon nanotube. *Chem. Phys. Lett.* **2000**, *322*, 237.
44. Boul, P.J.; Liu, J.; Mickelson, E.T.; Huffman, C.B.; Ericson, L.M.; Chiang, I.W.; Smith, K.A.; Colbert, D.T.; Margrave, J.L.; Smalley, R.E. Reversible sidewall functionalization of buckytubes. *Chem. Phys. Lett.* **1999**, *310*, 367.
45. Mickelson, E.T.; Huffman, C.B.; Rinzler, A.G.; Smalley, R.E.; Hauge, R.H.; Margrave, J.L. Fluorination of single-walled carbon nanotubes. *Chem. Phys. Lett.* **1998**, *296*, 188.
46. Mickelson, E.T.; Chiang, I.W.; Zimmerman, J.L.; Boul, P.J.; Lozano, J.; Liu, J.; Smalley, R.E.; Hauge, R.H.; Margrave, J.L. Solvation of fluorinated single-wall carbon nanotubes in alcohol solvents. *J. Phys. Chem., B* **1999**, *103*, 4318.
47. Zhao, W.; Song, C.; Zheng, B.; Liu, J.; Viswanathan, T. Thermal recovery behavior of fluorinated single-walled carbon nanotubes. *J. Phys. Chem., B* **2002**, *106*, 293.
48. Bahr, J.L.; Tour, J.M. Highly functionalized carbon nanotubes using in situ generated diazonium compounds. *Chem. Mater.* **2001**, *13*, 3823.
49. Wang, X.; Liu, Y.; Qiu, W.; Zhu, D. Immobilization of tetra-*tert*-butylphthalocyanines on carbon nanotubes: a first step towards the development of new nanomaterials. *J. Mater. Chem.* **2002**, *12*, 1636.
50. Holzinger, M.; Vostrowsky, O.; Hirsch, A.J.; Hennrich, F.; Kappes, M.; Weiss, R.; Jellen, F. Sidewall functionalization of carbon nanotubes. *Angew. Chem., Int. Ed.* **2001**, *40*, 4002.
51. Banerjee, S.; Wong, S.S. Rational sidewall functionalization and purification of single-walled carbon nanotubes by solution-phase ozonolysis. *J. Phys. Chem., B* **2002**, *106*, 12,144.
52. Chen, Y.; Haddon, R.C.; Fang, S.; Rao, A.M.; Eklund, P.C.; Lee, W.H.; Dickey, E.C.; Grulke, E.A.; Pendergrass, J.C.; Chavan, A.; Haley, B.E.; Smalley, R.E. Chemical attachment of organic functional groups to single-walled carbon nanotube material. *J. Mater. Res.* **1998**, *13*, 2423.
53. Frehill, F.; Vos, J.G.; Benrezzak, S.; Koos, A.A.; Konya, Z.; Ruther, M.G.; Blau, W.J.; Fonseca, A.; Nagy, J.B.; Biro, L.P.; Minett, A.I.; in het Panhuis, M. Interconnecting carbon nanotubes with an inorganic metal complex. *J. Am. Chem. Soc.* **2002**, *124*, 13,694.
54. Banerjee, S.; Wong, S.S. Functionalization of carbon nanotubes with a metal-containing molecular complex. *Nano Lett.* **2002**, *2*, 49.
55. Bahr, J.L.; Mickelson, E.T.; Bronikowski, M.J.; Smalley, R.E.; Tour, J.M. Dissolution of small diameter single-walled carbon nanotubes in organic solvents. *Chem. Commun.* **2001**, 193.
56. Banerjee, S.; Wong, S.S. Structural characterization, optical properties, and improved solubility of carbon nanotubes functionalized with Wilkinson's catalyst. *J. Am. Chem. Soc.* **2002**, *124*, 8940.
57. McGinnety, F.; Ibers, J.A. Structure and bonding in  $[\text{Ir}(\text{O}_2)(\text{Ph}_2\text{PCH}_2 \cdot \text{CH}_2 \cdot \text{PPh}_2)_2][\text{PF}_6]$  and in  $\text{IrBr}(\text{CO})(\text{PPh}_3)_2\text{C}_2(\text{CN})_4$ . *Chem. Soc. Chem. Commun.* **1968**, (5), 235.
58. Manojlovic-Muir, L.; Muir, K.W.; Ibers, J.A. Geometries of transition metal complexes containing simple alkenes. *Discuss. Faraday Soc.* **1969**, *47*, 84.
59. Balch, A.J.; Catalano, V.J.; Lee, J.W. Accumulating evidence for the selective reactivity of the 6–6 ring fusion of  $\text{C}_{60}$ . Preparation and structure of  $(n^2\text{-C}_{60})\text{Ir}(\text{CO})\text{Cl}(\text{PPh}_3)_2 \cdot 5\text{C}_6\text{H}_6$ . *Inorg. Chem.* **1991**, *30*, 3980.
60. Vaska, L. Reversible activation of covalent molecules by transitional metal complexes. The role of the covalent molecule. *Acc. Chem. Res.* **1968**, *1*, 335.
61. Cotton, F.A.; Wilkinson, G.; Murillo, C.A.; Bochmann, M. *Advanced Inorganic Chemistry*; John Wiley and Sons: New York, 1999.
62. McAuliffe, C.A.; Levason, W. *Phosphine, Arsine, and Stilbene Complexes of the Transition Elements*; Elsevier Scientific: New York, 1979.
63. Nunzi, F.; Mercuri, F.; Sgamellotti, A.; Re, N. The coordination chemistry of carbon nanotubes: a density functional study through a cluster model approach. *J. Phys. Chem., B* **2002**, *106*, 10,622.
64. Zhang, Y.; Dai, H. Formation of metal nanowires on suspended single-walled carbon nanotubes. *Appl. Phys. Lett.* **2000**, *77*, 3015.
65. Yu, R.; Chen, L.; Liu, Q.; Lin, J.; Tan, K.-L.; Ng, S.C.; Chan, H.S.O.; Xu, G.-Q.; Hor, T.S.A. Platinum deposition on carbon nanotubes via chemical modification. *Chem. Mater.* **1998**, *10*, 718.
66. Zhang, Y.; Franklin, N.W.; Chen, R.J.; Dai, H. Metal coating on suspended carbon nanotubes and its implication to metal–tube interaction. *Chem. Phys. Lett.* **2000**, *331*, 35.
67. Kim, H.; Sigmund, W. Zinc oxide nanowires on carbon nanotubes. *Appl. Phys. Lett.* **2002**, *81*, 2085.

68. Brus, L.E. Quantum crystallites and nonlinear optics. *Appl. Phys., A* **1991**, *53*, 463.
69. Dabbousi, B.O.; Rodriguez-Viejo, J.; Mikulec, F.V.; Heine, J.R.; Mattoussi, H.; Ober, R.; Jensen, K.F.; Bawendi, M.G. (CdSe)ZnS Core-shell quantum dots: synthesis and characterization of a size series of highly luminescent nanocrystallites. *J. Phys. Chem., B* **1997**, *101*, 9463.
70. Alivisatos, A.P. Perspectives on the physical chemistry of semiconductor nanocrystals. *J. Phys. Chem., B* **1996**, *100*, 13,226.
71. Banerjee, S.; Wong, S.S. Synthesis and characterization of carbon nanotube-nanocrystal heterostructures. *Nano Lett.* **2002**, *2* (3), 195.
72. Ajayan, P.M.; Ebbesen, T.W.; Ichihashi, T.; Iijima, S.; Tanigaki, K.; Hiura, H. Opening carbon nanotubes with oxygen and implications for filling. *Nature* **1993**, *361*, 333.
73. Liu, J.; Rinzler, A.G.; Dai, H.; Hafner, J.H.; Bradley, R.K.; Boul, P.J.; Lu, A.; Iverson, T.; Shelimov, K.; Huffman, C.B.; Rodriguez-Macias, F.; Shon, Y.S.; Lee, T.R.; Colbert, D.T.; Smalley, R.E. Fullerene pipes. *Science* **1998**, *280*, 1253.
74. Wong, S.S.; Woolley, A.T.; Joselevich, E.; Cheung, C.L.; Lieber, C.M. Covalently-functionalized single-walled carbon nanotube probe tips for chemical force microscopy. *J. Am. Chem. Soc.* **1998**, *120*, 8557.
75. Lawless, D.; Kapoor, S.; Meisel, D. Bifunctional capping of CdS nanoparticles and bridging to titanium dioxide. *J. Phys. Chem.* **1995**, *99*, 10,329.
76. Nikolaev, P.; Bronikowski, M.J.; Bradley, R.K.; Rohmund, F.; Colbert, D.T.; Smith, K.A.; Smalley, R.E. Gas-phase catalytic growth of single-walled carbon nanotubes from carbon monoxide. *Chem. Phys. Lett.* **1999**, *313*, 91.
77. Ausman, K.D.; Piner, R.; Lourie, O.; Ruoff, R.S.; Korobov, M. Organic solvent dispersions of single-walled carbon nanotubes: toward solutions of pristine nanotubes. *J. Phys. Chem., B* **2000**, *104*, 8911.
78. Hu, H.; Bhowmik, P.; Zhao, B.; Hamon, M.A.; Itkis, M.E.; Haddon, R.C. Determination of the acidic sites of purified single-walled carbon nanotubes by acid-base titration. *Chem. Phys. Lett.* **2001**, *345*, 25.
79. Mawhinney, D.B.; Naumenko, V.; Kuznetsova, A.; Yates, J.T., Jr.; Liu, J.; Smalley, R.E. Surface defect site density on single walled carbon nanotubes by titration. *Chem. Phys. Lett.* **2000**, *324*, 213.
80. Stone, A.J.; Wales, D.J. Theoretical studies of icosahedral footballene sixty-carbon-atom molecules and some related species. *Chem. Phys. Lett.* **1986**, *128*, 501.
81. Orlikowski, D.; Nardelli, M.B.; Bernholc, J.; Roland, C. Theoretical STM signatures and transport properties of native defects in carbon nanotubes. *Phys. Rev., B* **2000**, *61*, 14,194.
82. Xia, Y.; Ma, Y.; Xing, Y.; Mu, Y.; Tan, C.; Mei, L. Growth and defect formation of single-wall carbon nanotubes. *Phys. Rev., B* **2000**, *61*, 11,088.
83. Chen, J.; Hamon, M.A.; Hu, H.; Chen, Y.; Rao, A.M.; Eklund, P.C.; Haddon, R.C. Solution properties of single-walled carbon nanotubes. *Science* **1998**, *282*, 95.
84. Hamon, M.A.; Chen, J.; Hu, H.; Chen, Y.; Itkis, M.E.; Rao, A.M.; Eklund, P.C.; Haddon, R.C. Dissolution of single-walled carbon nanotubes. *Adv. Mater.* **1999**, *11*, 834.
85. Hamon, M.A.; Hu, H.; Bhowmik, P.; Niyogi, S.; Zhao, B.; Itkis, M.E.; Haddon, R.C. End-group and defect analysis of soluble single-walled carbon nanotubes. *Chem. Phys. Lett.* **2001**, *347*, 8.
86. Chen, J.; Rao, A.M.; Lyuksyutov, S.; Itkis, M.E.; Hamon, M.A.; Hu, H.; Cohn, R.W.; Eklund, P.C.; Colbert, D.T.; Smalley, R.E.; Haddon, R.C. Dissolution of full-length single-walled carbon nanotubes. *J. Phys. Chem., B* **2001**, *105*, 2525.
87. Hamon, M.A.; Hui, H.; Bhowmik, P.; Itkis, H.M.E.; Haddon, R.C. Ester-functionalized soluble single-walled carbon nanotubes. *Appl. Phys., A* **2002**, *74*, 333.
88. Fu, K.; Kitaygorodskiy, A.; Rao, A.M.; Sun, Y.-P. Deuterium attachment to carbon nanotubes in solution. *Nano Lett.* **2002**, *2*, 1165.
89. Georgakilas, V.; Kordatos, K.; Prato, M.; Guldi, D.M.; Holzinger, M.; Hirsch, A. Organic functionalization of carbon nanotubes. *J. Am. Chem. Soc.* **2002**, *124*, 760.
90. Sun, Y.; Wilson, S.R.; Schuster, D.I. High dissolution and strong light emission of carbon nanotubes in aromatic amine solvents. *J. Am. Chem. Soc.* **2001**, *123*, 5348.
91. Qu, L.; Martin, R.B.; Huang, W.; Fu, K.; Zweifel, D.; Lin, Y.; Sun, Y.-P. Interactions of functionalized carbon nanotubes with tethered pyrenes in solution. *J. Chem. Phys.* **2002**, *117*, 8089.
92. Bahr, J.L.; Yang, J.; Kosynkin, D.V.; Bronikowski, M.J.; Smalley, R.E.; Tour, J.M. Functionalization of carbon nanotubes by electrochemical reduction of aryl diazonium salts: a bucky paper electrode. *J. Am. Chem. Soc.* **2001**, *123*, 6536.
93. Zhao, B.; Hu, H.; Niyogi, S.; Itkis, M.E.; Hamon, M.A.; Bhowmik, P.; Meir, M.S.; Haddon, R.C. Chromatographic purification and properties of soluble single-walled carbon nanotubes. *J. Am. Chem. Soc.* **2001**, *123*, 11,673.
94. Chattopadhyay, D.; Lastella, S.; Kim, S.; Papadimitrakopoulos, F. Length separation of zwitterion-functionalized single wall carbon nanotubes by GPC. *J. Am. Chem. Soc.* **2002**, *124*, 728.
95. Hamon, M.A.; Itkis, M.E.; Niyogi, S.; Alvaraez, T.; Kuper, C.; Menon, M.; Haddon, R.C. Effect of rehybridization on the electronic structure of single-walled carbon nanotubes. *J. Am. Chem. Soc.* **2001**, *123*, 11,292.
96. Bandyopadhyaya, R.; Nativ-Roth, E.; Regev, O.; Yerushalmi-Rozen, R. Stabilization of individual carbon nanotubes in aqueous solutions. *Nano Lett.* **2002**, *2*, 25.
97. Pompeo, F.; Resasco, D.E. Water solubilization of single-walled carbon nanotubes by functionalization with glucosamine. *Nano Lett.* **2002**, *2*, 369.
98. Umek, P.; Mihailovic, D. Separation of SWNTs by diffusion. *Synth. Met.* **2001**, *121*, 1211.
99. Halicioglu, T.; Jaffe, R.L. Solvent effect on functional groups attached to edges of carbon nanotubes. *Nano Lett.* **2002**, *2*, 573.

100. Kahn, M.G.C.; Banerjee, S.; Wong, S.S. Solubilization of oxidized single-walled carbon nanotubes in organic and aqueous solvents through organic derivatization. *Nano Lett.* **2002**, *2*, 1215.
101. O'Connell, M.; Boul, P.; Ericson, L.M.; Huffman, C.; Wang, Y.; Haroz, E.; Kuper, C.; Tour, J.; Ausman, K.D.; Smalley, R.E. Reversible water-solubilization of single-walled carbon nanotubes by polymer wrapping. *Chem. Phys. Lett.* **2001**, *342*, 265.
102. Dalton, A.B.; Stephan, C.; Coleman, J.N.; McCarthy, B.; Ajayan, P.M.; Lefrant, S.; Bernier, P.; Blau, W.J.; Byrne, H.J. Selective interaction of a semiconjugated organic polymer with single-wall nanotubes. *J. Phys. Chem., B* **2000**, *104*, 10,012.
103. Sun, Y.-P.; Huang, W.; Lin, Y.; Fu, K.; Kitaygorodskiy, A.; Riddle, L.A.; Yu, Y.J.; Carroll, D.L. Soluble dendron-functionalized carbon nanotubes: preparation, characterization, and properties. *Chem. Mater.* **2001**, *13*, 2864.
104. Fu, K.; Huang, W.; Lin, Y.; Riddle, L.A.; Carroll, D.L.; Sun, Y.-P. Defunctionalization of functionalized carbon nanotubes. *Nano Lett.* **2001**, *1*, 439.
105. Star, A.; Stoddart, J.F.; Steurman, D.; Diehl, M.; Boukai, A.; Wong, E.W.; Yang, X.; Chung, S.-W.; Choi, H.; Heath, J.R. Preparation and properties of polymer-wrapped single-walled carbon nanotubes. *Angew. Chem., Int. Ed.* **2001**, *40*, 1721.
106. Koshio, A.; Yudasaka, M.; Zhang, M.; Iijima, S. A simple way to chemically react single-walled carbon nanotubes with organic materials using ultrasonication. *Nano Lett.* **2001**, *1*, 361.
107. Chen, Q.; Dai, L.; Gao, M.; Hunag, S.; Mau, A. Plasma activation of carbon nanotubes for chemical modification. *J. Phys. Chem., B* **2001**, *105*, 618.
108. Ni, B.; Sinnott, S.B. Chemical functionalization of carbon nanotubes through energetic radical collisions. *Phys. Rev., B* **2000**, *61*, R16343.
109. Ni, B.; Andrews, R.; Jacques, D.; Qian, D.; Wijesundra, M.B.J.; Choi, Y.; Hanley, L.; Sinnott, S.B. A combined computational and experimental study of ion-beam modification of carbon nanotube bundles. *J. Phys. Chem., B* **2001**, *105*, 12,719.
110. Yang, Y.; Zhang, J.; Nan, X.; Liu, Z. Toward the chemistry of carboxylic single-walled carbon nanotubes by chemical force microscopy. *J. Phys. Chem., B* **2002**, *106*, 4139.
111. Kukovec, A.; Kramberger, C.; Holzinger, M.; Kuzmany, H.; Schalko, J.; Mannsberger, M.; Hirsch, A. On the stacking behavior of functionalized single-wall carbon nanotubes. *J. Phys. Chem., B* **2002**, *106*, 6374.
112. Sano, M.; Kamino, A.; Okamura, J.; Shinkai, S. Ring closure of carbon nanotubes. *Science* **2001**, *293*, 1299.
113. Sano, M.; Kamino, A.; Okamura, J.; Shinkai, S. Noncovalent self-assembly of carbon nanotubes for construction of "cages". *Nano Lett.* **2002**, *2*, 531.
114. Liu, Z.; Shen, Z.; Zhu, T.; Hou, S.; Ying, L.; Shi, Z.; Gu, Z. Organizing single-walled carbon nanotubes on gold using a wet chemical self-assembling technique. *Langmuir* **2000**, *16*, 3569.
115. Wu, B.; Zhang, J.; Wei, Z.; Cai, S.; Liu, Z. Chemical alignment of oxidatively shortened single-walled carbon nanotubes on silver surface. *J. Phys. Chem., B* **2001**, *105*, 5075.
116. Liu, J.; Casavant, M.; Cox, M.; Walters, D.A.; Boul, P.; Lu, W.; Rimberg, A.J.; Smith, K.A.; Colbert, D.T.; Smalley, R.E. Controlled deposition of individual single-walled carbon nanotubes on chemically functionalized templates. *Chem. Phys. Lett.* **1999**, *303*, 125.
117. Cai, L.; Bahr, J.L.; Yao, Y.; Tour, J.M. Ozonation of single-walled carbon nanotubes and their assemblies on rigid self-assembled monolayers. *Chem. Mater.* **2002**, *14*, 4235.
118. Chen, J.; Haiying, L.; Weimer, W.S.; Halls, M.D.; Waldeck, D.H.; Walker, G.C. Noncovalent engineering of carbon nanotube surfaces by rigid, functional conjugated polymers. *J. Am. Chem. Soc.* **2002**, *124*, 9034.



# Nanowires: Molecular Assembly

Tomoyuki Akutagawa

Takayoshi Nakamura

Research Institute for Electronic Science, Hokkaido University, Sapporo, Japan

Jan Becher

Department of Chemistry, University of Southern Denmark, Odense, Denmark

## INTRODUCTION

Fabrication of one-dimensional (1-D) fundamental nanoscale structures from molecular systems through bottom-up approach should be one of the most important steps to realize nanoscale electronic devices.<sup>[1–3]</sup> Because 1-D systems are the structures with the lowest dimension that permit efficient electron transport, the nanowires are expected to be critical to functionalize and integrate the nanoscale electronic devices. Nanowires are important units in constructing electronic circuits, particularly in electrical conducting; thus a variety of nanowires have been the focus of extensive studies aimed toward nanoscale electronic systems.<sup>[1–4]</sup> At present, a wide range of compounds from inorganic metals, semiconductors, and carbon nanotubes have been employed as nanowires (Fig. 1).<sup>a</sup> The diameter, length, and electronic structure of these nanowires varied significantly. The electronic properties of nanowires range from insulating, semiconducting, metallic, to superconducting. Electrical conduction within nanowires is dominated by the carriers at around Fermi level of the band structure, just as in bulk metals and semiconductors (Fig. 1).<sup>[5]</sup> Although the electronic density of states along the short axis of nanowire has a discrete character because of the restricted lattice translation, that along the wire direction is approximately represented as the band structure.<sup>[6]</sup> The doped polymers, single-walled carbon nanotubes (SWCNTs), semiconductor, and metal nanowires may have Fermi surfaces. On the other hand, DNAs are the insulator with large band gap. Semiconductor nanowires are more important than metal nanowires from the viewpoint of device application.<sup>[7]</sup>

Although only a few examples are reported for the preparation of nanowires of molecular assemblies,<sup>[8–10]</sup> we consider that these molecular nanowires should have

an important role in the complete bottom-up manufacture of the molecular electronics. Such nanowires can be assembled from  $\pi$ -molecules through molecule-by-molecule  $\pi$ -stacking. The researches in the field of “molecular conductors” will offer a guiding principle in constructing electrical conducting molecular nanowires.<sup>[11–15]</sup> The anisotropic charge-transfer (CT) interaction in molecular conductors is advantageous to form the 1-D  $\pi - \pi$  stacking nanowire structure. In addition, “supramolecular chemistry” will offer powerful tools to fabricate molecular nanowires through the self-assembly process.<sup>[16–18]</sup> Appropriate design of molecule to orient and integrate the molecular-assembly nanowires on the substrate surface should be effective to realize molecular-assembly electronic devices. Furthermore, the techniques of “Langmuir–Blodgett (LB) Films” are very useful methods to fabricate nanoscale molecular-assembly structures on a variety of substrate surfaces.<sup>[19–21]</sup> To realize molecular-assembly nanoscale devices through bottom-up chemical approach, three types of scientific concepts—molecular conductor, supramolecular chemistry, and surface science—should be linked together.

## Molecular Conductors

A large number of molecular conductors, ranging from semiconductors to metals and superconductors, was prepared.<sup>[11–15]</sup> In general, a stable organic molecule has a closed-shell electronic structure without conduction carriers, thereby making molecular solids highly insulating. Conduction carriers can be generated via the intermolecular CT interaction between the highest occupied molecular orbital (HOMO) of the electron donor (D) and the lowest occupied molecular orbital (LUMO) of the electron acceptor (A) molecules. Figure 2A shows the molecular structures of typical D and A molecules utilized in the field of molecular conductors. Among them, tetrathiafulvalene (TTF) and 7,7,8,8-tetracyano-*p*-quinodimethane (TCNQ) are the well-known D and A molecules, respectively, which gave the first molecular metal of (TTF<sup>+0.59</sup>)(TCNQ<sup>-0.59</sup>). The degree of CT ( $\delta$ ) in the

<sup>a</sup>Recent progress in nanowires. See special issue of nanowires in Ref.<sup>[4]</sup>.

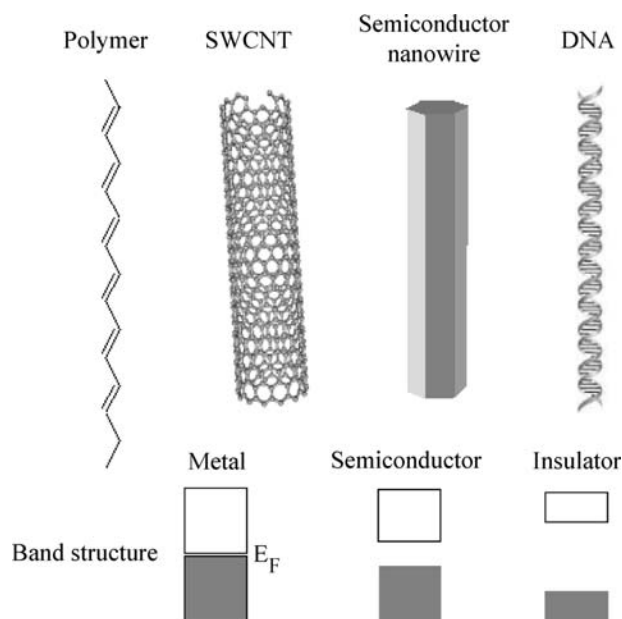


**Fig. 1** Nanowires constructed from doped-polymer, SWCNT, semiconductor, and DNA. The electronic band structures of these are illustrated below.

binary  $(D^{+\delta})(A^{-\delta})_x$  CT complex depends on the ionization potential of D and electron affinity of A molecules. The planar  $\pi$ -conjugated D and A molecules have a tendency to form the 1-D columnar structure through the  $\pi - \pi$  stacking interaction, which also formed 1-D  $\pi$ -band structure (Fig. 2B). Because the  $\pi$ -orbitals exist orthogonal to the molecular plane, the direction of  $\pi - \pi$  interaction is highly anisotropic. Therefore, the 1-D  $\pi - \pi$  interaction in the molecular conductors is suitable for obtaining molecular nanowires.

### Langmuir–Blodgett Technique

Langmuir–Blodgett (LB) method is one of the conventional fabrication techniques of nanoscale thin-film structures utilizing the air–water interface.<sup>[19–21]</sup> Figure 3 illustrates typical procedures to obtain Langmuir monolayer at the air–water interface and the film-forming processes of LB multilayers on substrate. Amphiphilic molecules having hydrophilic and hydrophobic moieties are dissolved into conventional organic solvents, which were spread at the air–water interface. The monolayer with a thickness of molecular scale can form a variety of molecular-assembly structures such as gas-, liquid-, and solid-like short- and long-range orders through the control of surface pressure ( $F$ ,  $\text{mN m}^{-1}$ ). Increase in the  $F$  enhances the magnitude of intermolecular interactions between the molecules. The chemical designs of hydrophilicity and hydrophobicity of the component molecules are

important to obtain stable monolayer at the air–water interface.

Stable monolayers at the air–water interface can be transferred onto hydrophilic or hydrophobic substrates via dipping of the substrate. Glass, quartz,  $\text{CaF}_2$ , Si, and mica are utilized as typical hydrophilic substrates. The surface wetting of these substrates largely influences the surface morphologies of the transferred LB films. Another conventional deposition technique is the horizontal-lifting method, which directly transfers the monolayer at the air–water interface onto the hydrophobic substrate.

Electrically active thin films have been fabricated by the LB techniques.<sup>[22–24]</sup> For example, metallic and semiconducting LB films have been obtained from amphiphilic molecular conductors based on TTF and TCNQ derivatives.<sup>[22–24]</sup> Although the LB films possess a periodicity along the film-forming direction, random distribution of two-dimensional crystalline domains on the substrate surface dispels bulk periodicity within the substrate surface. To realize nanoscale electronic devices through bottom–up self-assembly approach, the orientation and size control of these electrical active domains within the substrate surface are two of the important problems that need to be overcome.

### Supramolecular Chemistry

The term of supramolecular chemistry is a last key science to realize the bottom–up self-assembly approach.<sup>[16–18]</sup> Supramolecule is defined as an entity composed of several or large numbers of molecules, which are connected to each other through the non-covalent weak intermolecular interactions such as van der Waals (dipole–dipole, dipole-induced dipole and dispersion interactions), charge–transfer, hydrogen-bonding interactions, etc. The design of these intermolecular interactions is essential to obtain self-assembly molecular nanowires. Self-assembled supramolecules bearing the desired structure can be achieved by using programmed molecules that are appropriately designed. From the flexibility in supramolecular designs together with the rich physics in molecular conductors, electrical active molecular nanowires are considered as very promising candidates for constructing future nanoscale devices.

A large number of complex supramolecular assemblies have already been constructed.<sup>[16–18]</sup> A simple complex between cation and crown ether is one of the typical model systems of supramolecules<sup>[25,26]</sup> (Fig. 4). Crown ethers such as 12-crown-4, 15-crown-5, and 18-crown-6 have hydrophilic cavity to bind cation through metal–oxygen interatomic interactions. According to the size of hydrophilic cavity, cations can be selectively included into the cavity.

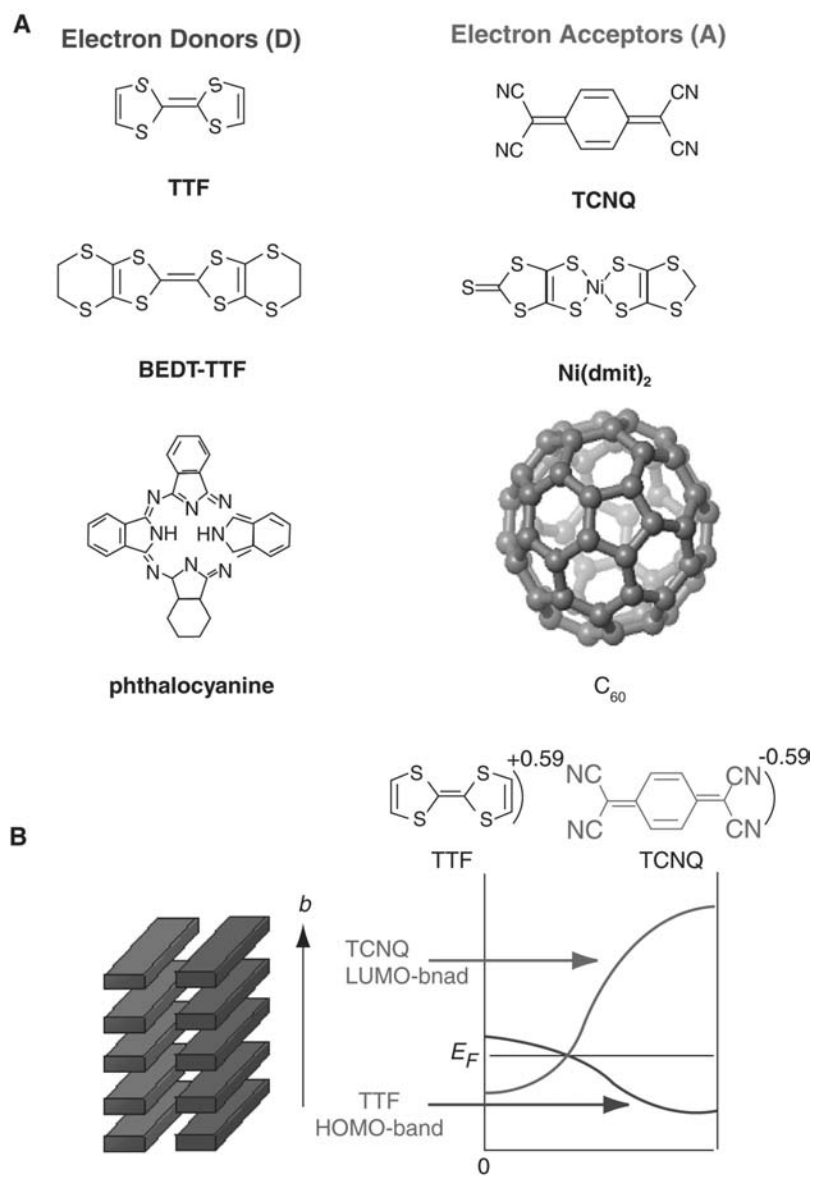


**Fig. 2** Molecular structures of typical (A) electron donor (D) and acceptor (A) molecules employed in molecular conductors. (B) The 1-D columnar structure through the  $\pi - \pi$  stacking interaction in crystals (left) and metallic 1-D  $\pi$ -band structure of (TTF)(TCNQ) (right).

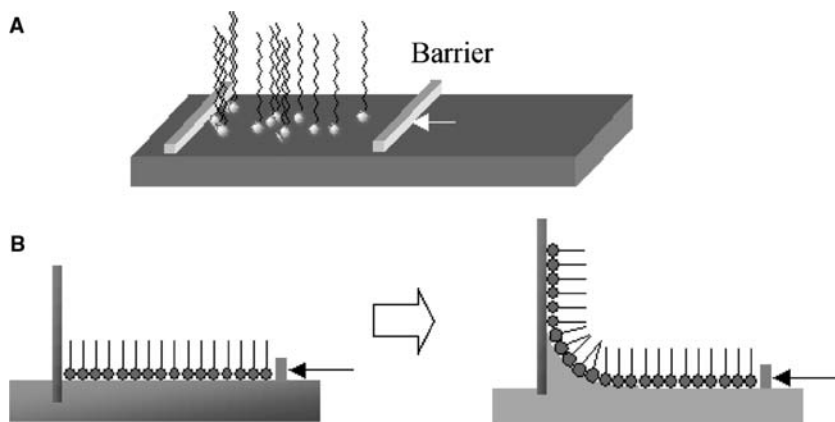


**Fig. 3** Langmuir-Blodgett technique to fabricate nanoscale thin-film structures. (A) Langmuir monolayer at the air-water interface. Amphiphilic molecule has hydrophilic (red head) and hydrophobic tail. Surface pressure ( $F$ ,  $\text{mN m}^{-1}$ ) can be controlled by moving barriers. (B) Transfer process of Langmuir monolayer onto substrate surface.

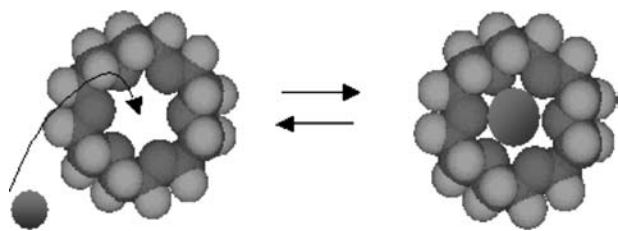


**Fig. 4** Supramolecular complex between the cation and crown ether. Cations are complexed into the crown ether cavity through cation–oxygen interactions.

For example, 15-crown-5 and 18-crown-6 molecules show high  $\text{Na}^+$  and  $\text{K}^+$  affinity, respectively. We already introduced two design concepts of molecular conductors and LB technique to fabricate molecular-assembly nanowires. For an effective design of molecular nanowires, we further introduced the supramolecular approach to obtain nanowire orientation on the substrate surface.

## RESULTS AND DISCUSSION

### Design of Molecules for Fabricating Molecular-Assembly Nanowires

Amphiphilic bis(tetrathiafulvalene) [bis(TTF)] macrocycle **1** was designed from the concepts of molecular conductors, Langmuir–Blodgett films, and supramolecular chemistry.<sup>[27,28]</sup> The molecule has two redox-active TTF units that are linked via a [24]crown-8 macrocycle and two long hydrophobic decylthio-chains (Fig. 5). Two TTF units within the molecule **1** can act as electron donor for realizing intermolecular CT interaction with electron acceptors,

which forms electrically conducting 1-D  $\pi$ - $\pi$  stacks. The second structural point is the introduction of two hydrophobic chains ( $-\text{SC}_{10}\text{H}_{21}$ ), which were introduced into one side of the TTF unit. By introducing these hydrophobic chains, the molecule has amphiphilic character to apply the LB technique. The last designing point is carried out via the supramolecular approach—the introduction of ion-recognizing crown ether moiety into the molecule. The ion-recognizing property can be employed to fabricate oriented molecular-assembly nanowires on the substrate surface.

Compound **1** was synthesized by the cyanoethyl protected TTF building block.<sup>[29,30]</sup> Stepwise deprotection/alkylation procedure was performed by  $\text{CsOH} \cdot \text{H}_2\text{O}/2,6\text{-bis}(2\text{-iodoethoxy})\text{ethane}$ . Because a TTF molecule possesses a two-step redox process ( $\text{TTF} \rightarrow \text{TTF}^+$  and  $\text{TTF}^+ \rightarrow \text{TTF}^{2+}$ ),<sup>[11–15]</sup> donor **1** possesses a four-step redox process. The cyclic voltammetry (CV) diagram of donor **1** in 1,2-dichloroethane ( $\text{C}_2\text{H}_4\text{Cl}_2$ ) vs. SCE showed the two-step, two-electron oxidation waves at 0.56 and 0.90 V, respectively.<sup>[27,28]</sup> The two TTF units in donor **1**, linked via [24]crown-8 unit, independently exhibited redox reaction.

The CT complex between one molecule of donor **1** and two molecules of 2,3,5,6-tetrafluoro-7,7,8-tetracyano-*p*-quinodimethane ( $\text{F}_4\text{-TCNQ}$ ),  $(\text{1})(\text{F}_4\text{-TCNQ})_2$  was prepared to fabricate oriented molecular-assembly nanowires. The electronic ground state of the CT complexes can be discussed in terms of the differences between the redox potentials,  $\Delta E = E_{1/2}(\text{donor}) - E_{1/2}(\text{F}_4\text{-TCNQ})$ , for electron donor **1** and  $\text{F}_4\text{-TCNQ}$ .<sup>[31,32]</sup> Partial CT states,  $(\text{D}^{+\delta})(\text{A}^{-\delta})$  with  $0.5 < \delta < 1$ , are necessary for the formation of metallic CT complexes having a segregated-stack structure, which is achieved when  $\Delta E$  has a value between  $-0.02$  and  $0.34$  V.<sup>[31,32]</sup> Fully ionic  $(\text{D}^+)(\text{A}^-)$  and neutral  $(\text{D}^0)(\text{A}^0)$  CT complexes are typically observed when  $\Delta E < -0.02$  V

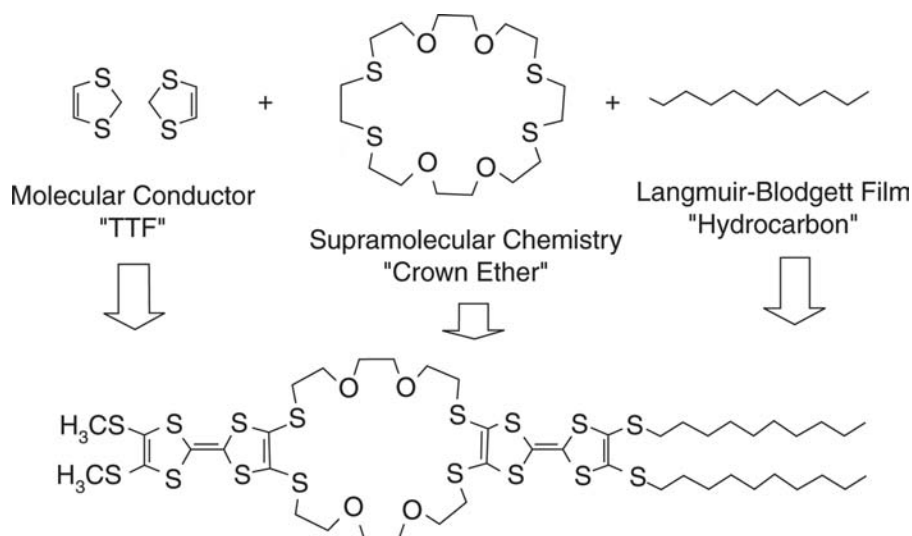


**Fig. 5** Molecular design of amphiphilic bis(tetrathiafulvalene) [bis(TTF)] macrocycle **1** from the viewpoints of molecular conductor (TTF), supramolecular chemistry (crown ether), and Langmuir–Blodgett films (hydrocarbons).

and  $\Delta E > 0.34$  V, respectively. In the case of donor **1** and F<sub>4</sub>-TCNQ ( $E_{1/2}(\mathbf{1}) = 0.73$  V), the  $\Delta E$  values of CT complex of  $(\mathbf{1})(\text{F}_4\text{-TCNQ})_2$  was  $-0.17$  V. Because these values were far from the conditions of partial CT complexes, fully ionic ground state  $(\mathbf{1}^{2+})(\text{F}_4\text{-TCNQ}^-)_2$  was expected for the molecular nanowires.

### Monolayer of Charge–Transfer Complexes at the Air–Water Interface

The CT complex  $(\mathbf{1})(\text{F}_4\text{-TCNQ})_2$  was prepared in situ by mixing donor **1** and two equivalent of F<sub>4</sub>-TCNQ in CHCl<sub>3</sub>/CH<sub>3</sub>CN (9:1, v/v). Concentration of the spreading solution was fixed at 1 mM with respect to  $(\mathbf{1})(\text{F}_4\text{-TCNQ})_2$ . Surface pressure ( $F$ )–area per molecule ( $A$ ) isotherms were recorded at 291.5 K with a barrier speed of 50 cm<sup>2</sup> min<sup>-1</sup>. The LB monolayers were transferred onto freshly cleaved mica surfaces by a single up-stroke drawing. Because the macrocyclic moiety may recognize ions introduced into the subphase upon the formation and deposition of the monolayers, the K<sup>+</sup> ions were introduced into the subphase for realizing ion recognition at first.

The  $F$ – $A$  isotherms of the floating monolayers of the CT complex of  $(\mathbf{1})(\text{F}_4\text{-TCNQ})_2$  on pure water and aqueous 0.01 M KCl subphase are shown in Fig. 6. The surface areas of CT complexes extrapolated at 0 mN m<sup>-1</sup> on pure water and 0.01 M KCl subphase

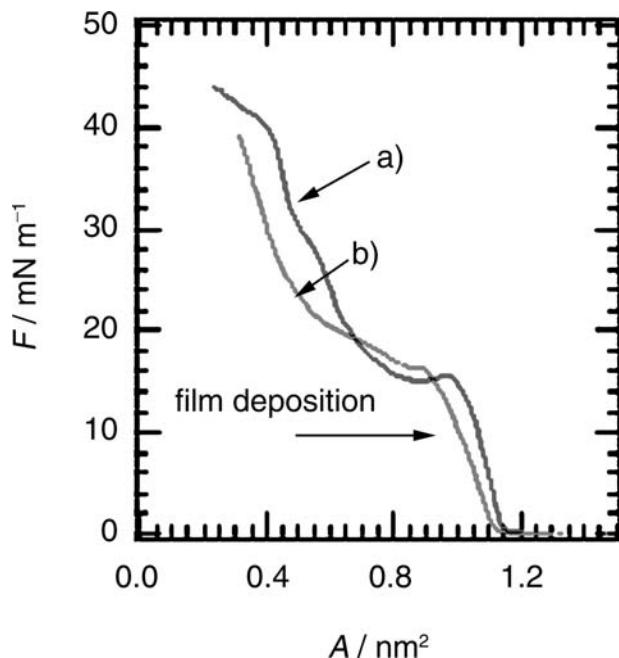


**Fig. 6**  $F$ – $A$  isotherms of CT complex of  $(\mathbf{1})(\text{F}_4\text{-TCNQ})_2$  on A) pure water and B) 0.01 M KCl subphase. The films were transferred at 10 mN m<sup>-1</sup>.

are almost consistent with each other ( $A_0 \sim 1.2$  nm<sup>2</sup>). Because these values are larger than that of neutral **1** ( $A_0 = 0.6$  nm<sup>2</sup>), the formation of CT complex causes much expansion of the surface area. The films were deposited under a controlled surface pressure of 10 mN m<sup>-1</sup>, at which point the surface areas of  $(\mathbf{1})(\text{F}_4\text{-TCNQ})_2$  on pure water and 0.01 M KCl ( $A_{10} \sim 1.1$  nm<sup>2</sup>) were almost identical to each other.

### Molecular-Assembly Nanowires on Mica Surface

Figure 7 shows the surface morphologies of the CT complex of  $(\mathbf{1})(\text{F}_4\text{-TCNQ})_2$  that transferred onto freshly cleaved mica by a single withdrawal from monolayer on A) pure water and B) 0.01 M KCl subphase. Although both films showed the formation of molecular-assembly nanowires, significant difference about the nanowire orientation was confirmed between them. Both nanowires had typical width of 50 nm and height of  $\sim 2.5$  nm. By introducing 0.01 M KCl into the subphase, the nanowire orientation appeared as network structure connecting the well-developed nanowires to each other. Almost all the nanowires on the mica surface formed an angle of 60° to each other.

Because the  $F$ – $A$  isotherm of  $(\mathbf{1})(\text{F}_4\text{-TCNQ})_2$  between pure water and 0.01 M KCl subphase was almost consistent with each other, the CT complex may not recognize K<sup>+</sup> ion at the air–water interface. Therefore the orientation of nanowire should occur during the film deposition processes because the orientation direction of the nanowires was consistent with the crystal lattice of mica.<sup>[33,34]</sup> The morphology of nanowires on mica surface strongly depended on the cation species that were introduced into the subphase (Fig. 8). When we introduced Li<sup>+</sup> (ion radius  $r_i = 0.6$  Å) or Na<sup>+</sup> ( $r_i = 0.95$  Å) into the subphase, although the formation of nanowires were confirmed, the nanowire orientation completely disappeared. Much larger cation of Cs<sup>+</sup> ( $r_i = 1.69$  Å) yielded the

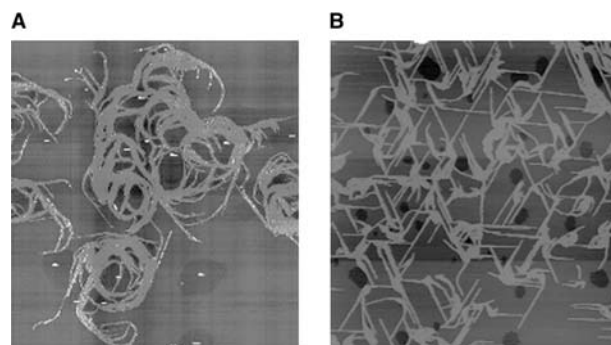


**Fig. 7** Surface morphology of transferred nanowires of  $(\mathbf{1})(\text{F}_4\text{-TCNQ})_2$  from A) pure water and B) 0.01 M KCl. The scales of AFM images are  $10 \times 10 \mu\text{m}^2$ .



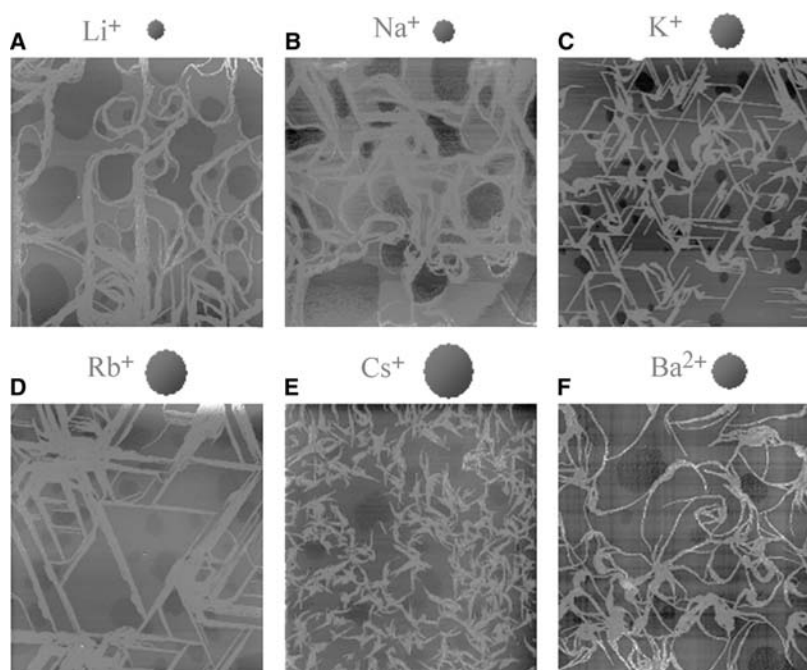


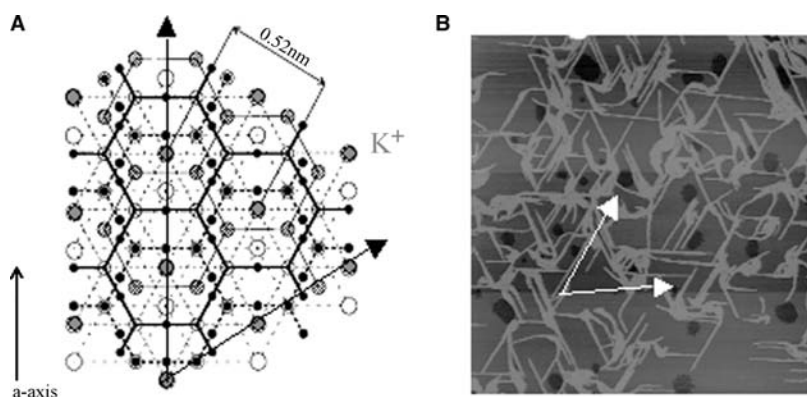
**Fig. 8** Surface morphology of transferred nanowires of (1)(F<sub>4</sub>-TCNQ)<sub>2</sub> on mica from A) LiCl, B) NaCl, C) KCl, D) RbCl, E) CsCl, and F) BaCl<sub>2</sub> containing subphase. The concentration of ions in the subphase was fixed at 0.01 M. The scales of AFM images are 10 × 10 μm<sup>2</sup>.

ill-developed molecular nanowires with maximum length of less than ~1 μm. In the case of Rb<sup>+</sup> ( $r_i = 1.48 \text{ \AA}$ ), well-developed oriented nanowires were observed at a typical length of above 2 μm. The most densely developed oriented nanowires were confirmed by the introduction of K<sup>+</sup> ( $r_i = 1.33 \text{ \AA}$ ) into the subphase, which resulted in a typical nanowire dimension of  $2.5 \times 50 \times \sim 2000 \text{ nm}^3$ . Although Ba<sup>2+</sup> ( $r_i = 1.35 \text{ \AA}$ ) has almost similar ionic radius to that of K<sup>+</sup>, the nanowire orientation completely disappeared on the mica surface.

The difference of the nanowire orientation according to the ions is related with the surface property of mica rather than the ion radius. Mica has a typical composition of KAl<sub>3</sub>Si<sub>3</sub>O<sub>10</sub>(OH)<sub>2</sub>, and vacant potassium sites of sixfold symmetry appear by the cleavage (Fig. 9).<sup>[33,34]</sup> These K<sup>+</sup> sites should be negatively charged and attract cations when the mica substrates are immersed in the K<sup>+</sup>-containing subphase. The

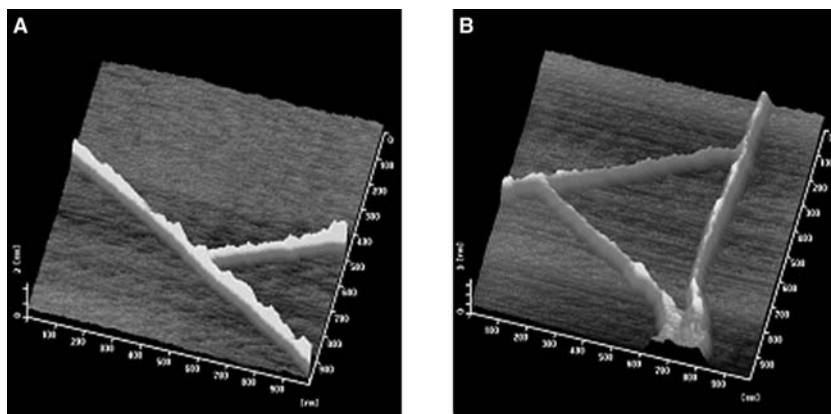
nanowire orientation may occur by matching of the surface potential of mica surface and that of the nanowires, rather than by ion recognition of individual molecules. The anionic species of F<sub>4</sub>-TCNQ anion radical should be embedded on K<sup>+</sup>, and nanowires may orient in an epitaxial way through the lattice matching between mica and nanowires. Such recognition mechanism is the most probable explanation for the nanowire orientation. Although the dimension of nanowires is much larger than the unit cell of hexagonal array of K<sup>+</sup> on mica surface, the nanowire orientation was affected by the K<sup>+</sup> array on mica surface.

Figure 10 shows selected AFM images (1 × 1 μm<sup>2</sup>) of oriented molecular-assembly nanowires on mica. As previously mentioned, the nanowires oriented 60° to each other, which provided interesting nanoscale structures such as nanowire tree and triangles. The six-folded connecting modes of each nanowire form novel nanoscale junction structures, which can



**Fig. 9** (A) Crystal structure of mica surface. Hexagonal arrays of K<sup>+</sup> sites are indicated by red closed circles. (B) Atomic force microscopy (AFM) image of oriented nanowires on mica surface deposited from 0.01 M KCl subphase. The white arrows correspond to hexagonal lattice of K<sup>+</sup> site on mica, showing the relation between the nanowire orientation and K<sup>+</sup> array.





**Fig. 10** Selected AFM images of oriented molecular-assembly nanowires. (A) Nanowire tree and (B) nanowire triangles. Scale of AFM images are  $1 \times 1 \mu\text{m}^2$ .

apply for constructing the integrated nanoscale electronic circuits.

### Molecular-Assembly Structures within Nanowire

The single crystal of  $(2)(\text{F}_4\text{-TCNQ})_2$  were obtained, and here donor **2** is the four-alkyl chain derivative of compound **1**. Assuming a similar molecular packing structure of CT complex between  $(2)(\text{F}_4\text{-TCNQ})_2$  and  $(1)(\text{F}_4\text{-TCNQ})_2$ , we can discuss the molecular-assembly structure in the nanowires based on the crystal structure of  $(2)(\text{F}_4\text{-TCNQ})_2$ .<sup>[35]</sup> Figure 11 shows the unit cell of  $(2)(\text{F}_4\text{-TCNQ})_2$  viewed along the  $b$  axis. Donor **2** formed an intramolecular  $\pi$ - $\pi$  dimer through folding of the flexible 24-crown-8 moiety, in which the  $\pi$ -planes of the two TTF units overlapped at their inner  $\text{C}_3\text{S}_5$  rings. Along the  $c$  axis, the D-A layers are separated by the hydrophobic decylthio chains; moreover, the hydrophilic and hydrophobic layers are alternately arranged. The crystal structure suggests that the direction normal to the substrate surface in the LB film is consistent with the  $c$  axis ( $c = 1.72 \text{ nm}$ ). As indicated in Fig. 11, which shows the  $\pi$ - $\pi$  stacking structure within the  $ab$  plane, the  $\pi$ - $\pi$  dimer structure of

$\text{F}_4\text{-TCNQ}$  stacked alternately with the intramolecular TTF dimer along the  $-a+b$  axis. The  $\pi$ - $\pi$  stacking sequence between donor **2** and  $\text{F}_4\text{-TCNQ}$  was  $-\text{D}-\text{A}-\text{A}-\text{D}-$ , forming a 1-D mixed-stack structure.

The molecular orientation within the LB films was evaluated by using the polarized ultraviolet-visible-near infrared (UV-vis-NIR) spectra.<sup>[19-21]</sup> The polarized UV-vis-NIR spectra of the LB film of  $(1)(\text{F}_4\text{-TCNQ})_2$  did not indicate any in-plane anisotropy with the normal incidence, indicating the isotropic distribution of molecular orientation within the substrate surface. Two sharp absorptions (B bands) were assigned to the intramolecular transition of the  $\text{F}_4\text{-TCNQ}^-$  anion radical,<sup>[36]</sup> while the C and D bands were assigned to the intramolecular transitions of  $\text{TTF}^+$  and  $\text{F}_4\text{-TCNQ}^-$ , respectively.<sup>[37]</sup> The broad A bands were assigned to the intramolecular transition of bis(TTF)-macrocycles,<sup>[38-40]</sup> which overlapped with the B bands. With  $45^\circ$  incidences (Fig. 12A), the absorption intensity for the s-polarization was larger than that for the p-polarization. Because the intramolecular transition moments of donor **1** and  $\text{F}_4\text{-TCNQ}$  lie along the long axes of TTF and  $\text{F}_4\text{-TCNQ}$  molecules, the long axes of donor **1** and  $\text{F}_4\text{-TCNQ}$  were relatively parallel to the substrate surface.

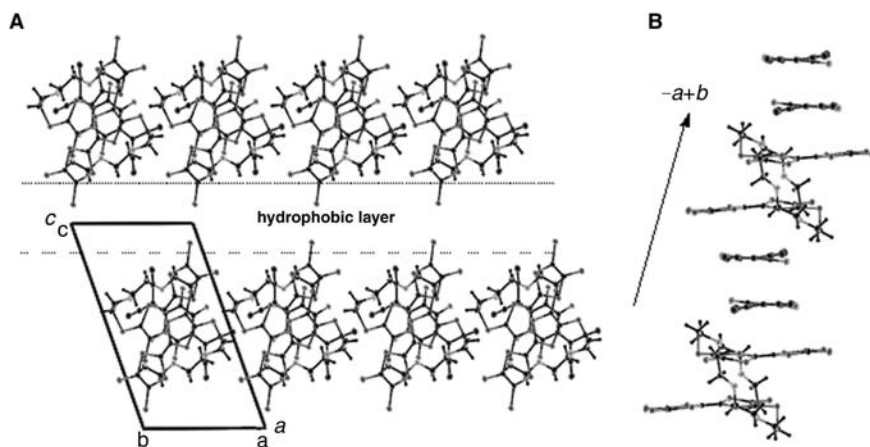


**Fig. 11** Crystal structure of CT complex  $(2)(\text{F}_4\text{-TCNQ})_2$ . (A) Unit cell viewed along the  $b$  axis. (B) Alternate  $\pi$ - $\pi$  stacking structure between donor **2** and  $\text{F}_4\text{-TCNQ}$  dimer along the  $-a+b$  axis. Alkyl chains are omitted.

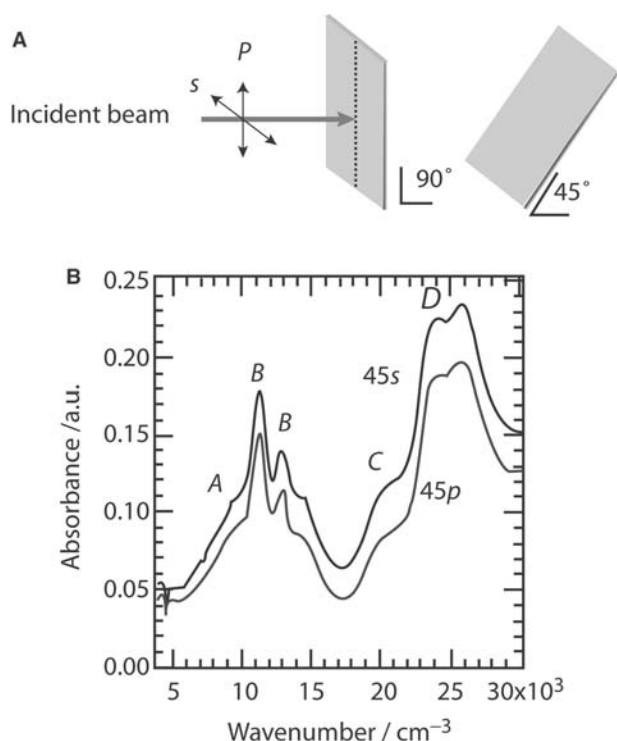


**Fig. 12** Polarized UV-vis-NIR spectra of the LB film of  $(1)(F_4\text{-TCNQ})_3$ . A) Optical arrangements of the substrates to measure the polarized UV-vis-NIR spectra at  $90^\circ$  and  $45^\circ$  incidence. B) Polarized UV-vis-NIR spectra of  $45^\circ$  incidence with p- and s-polarization.

From the results of X-ray structural analysis and polarized UV-vis-NIR spectra, we constructed the schematic molecular packing model within the nanowire (Fig. 13).<sup>[27,28]</sup> The nanowires transferred from  $K^+$  containing subphase had typical dimensions of  $2.5 \times 50 \times \sim 1000 \text{ nm}^3$ . Considering the molecular size of donor **1**, the nanowire should be composed of 1–2 molecular layers in the height direction and 20–30 molecules in the width direction. Assuming that the nanowire has a local structure similar to that of crystal structure of  $(2)(F_4\text{-TCNQ})_2$ , the longitudinal direction of the nanowire should correspond to the  $\pi$ - $\pi$  stacking direction of TTF units and/or  $F_4\text{-TCNQ}$  molecules. Therefore, a few thousand molecules are

necessary to form over 1- $\mu\text{m}$ -long nanowire, taking into account that the standard  $\pi$ - $\pi$  stacking distance is around 0.35 nm.

### Electrical Conductivity and Magnetic Properties

To estimate the electrical conductivity of nanowires, the temperature-dependent electrical conductivity and paramagnetic susceptibility were measured in the form of the LB film. Figure 14 shows the temperature-dependent electrical conductivity (right scale) and paramagnetic susceptibility (left scale) of LB film of  $(1)(F_4\text{-TCNQ})_2$ . The room-temperature electrical conductivity ( $\sigma_{RT}$ ) was  $1.5 \times 10^{-3} \text{ S cm}^{-1}$  with an activation energy of 0.17 eV. The semiconducting temperature dependence was consistent with that of the mixed-stack arrangement of donor and  $F_4\text{-TCNQ}$  dimer. Although the accumulated film should be composed of piles of nanowires and monolayers of  $(1)(F_4\text{-TCNQ})_2$ , each nanowire may have the same order of electrical conductivity.

The temperature-dependent paramagnetic susceptibility ( $\chi$ ) of the LB films of  $(1)(F_4\text{-TCNQ})_2$  was measured via electron spin resonance (ESR). As shown in Fig. 14,  $\chi$  increased monotonically with decreasing temperatures, which followed the Curie-Weiss law. The line-shape of the ESR signals could be fitted using Lorentzian. Line width around 0.5 mT did not show anomaly within the measured temperature range. Because  $g$ -values for  $\text{BEDT-TTF}^+$  cation and  $F_4\text{-TCNQ}^-$  anion radicals have been typically observed at 2.0074 and 2.0025, respectively,<sup>[11–15]</sup> the  $g$ -values ( $\sim 2.004$ ) of the LB films for  $(1)(F_4\text{-TCNQ})_2$  were observed in the intermediate range between  $\text{BEDT-TTF}$  and  $F_4\text{-TCNQ}$ , which indicated that both the cation and the anion radical species contribute to the paramagnetic susceptibility of the LB films.

### CONCLUSION

We constructed oriented molecular-assembly nanowires, which are important parts for the fabrication

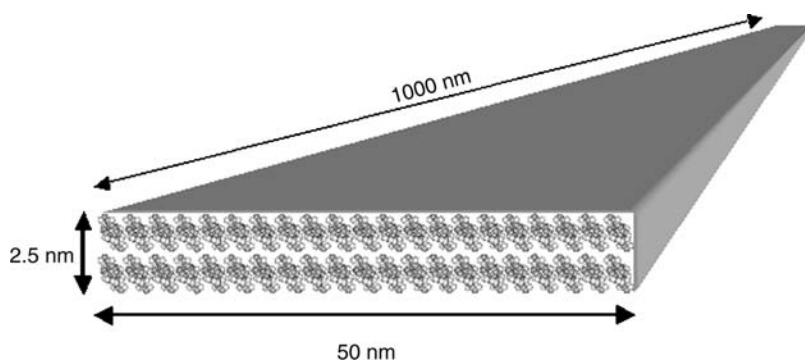


**Fig. 13** Possible molecular arrangements within a nanowire.

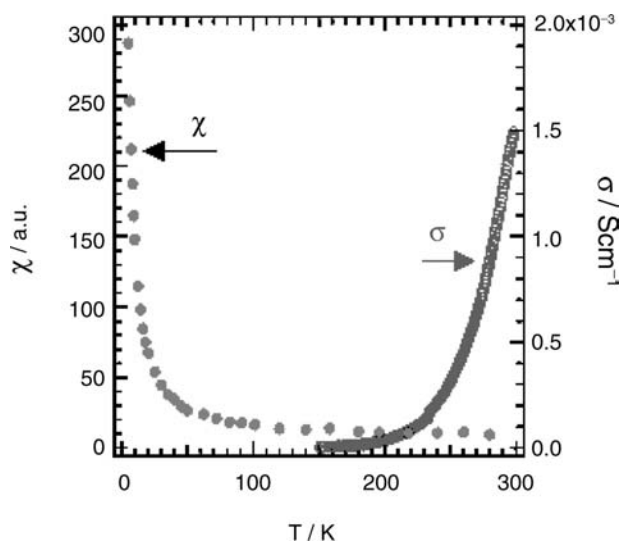


Fig. 14 Temperature-dependent electrical conductivity (right scale) and paramagnetic susceptibility (left scale) of the LB film of (1)(F<sub>4</sub>-TCNQ)<sub>2</sub>.

of nanoscale electronic devices. Molecular-assembly nanowires have a potential to fabricate nanoscale electronics in all self-assembly chemical processes. Amphiphilic bis(TTF) macrocycle derivative is one such example, forming self-assembly nanowires oriented on mica surface. This molecule was designed from the viewpoints of: 1) molecular conductor; 2) Langmuir–Blodgett films; and 3) supramolecular chemistry. Designs from the concepts of molecular conductor and Langmuir–Blodgett film are necessary to construct nanoscale electrical conducting, one-dimensional structure. Furthermore, the design of weak intermolecular interactions (ion recognition) from the supramolecular approach should be a key methodology to construct oriented molecular-assembly nanowires. Control of electronic structures of the nanowires may be achieved through careful design of the charge–transfer interactions (electronic dimensionality, bandwidth, carrier concentration, etc.), while a variety of nanoscale structures such as zero-dimensional nanodots and nanowires should be obtainable from the designs of supramolecular chemistry.

## REFERENCES

- Akutagawa, T.; Nakamura, T. *Semiconductor and Molecular-Assembly Nanowires, Chemistry of Nano-Molecular Systems—Toward the Realization of Molecular Devices*; Sugiura, K., Matsumoto, T., Tada, H., Nakamura, T., Eds.; Springer-Verlag: Berlin, 2002; 122–147.
- Joachim, C.; Gimzewski, J.K.; Aviram, A. Electronic using hybrid-molecular and mono-molecular devices. *Nature* **2000**, *408*, 541–548.
- Heath, J.R.; Kuekes, P.J.; Snider, G.S.; Williams, R.S. A defect-tolerant computer architecture: opportunities for nanotechnology. *Science* **1998**, *280*, 1716–1721.
- Adv. Mater.* **2003**, *15* (5).
- Kittel, C. *Introduction to Solid State Physics*, 6th Ed.; John Wiley: New York, 1986.
- Ferry, D.K.; Goodnick, S.M. *Transport in Nanostructures*; Ahmed, H., Pepper, M., Broers, A., Eds.; Cambridge Univ. Press: Cambridge, 1997.
- Hu, J.; Odom, T.W.; Lieber, C.M. Chemistry and physics in one dimension: synthesis and properties of nanowires and nanotubes. *Acc. Chem. Res.* **1999**, *32*, 435–445.
- Favier, F.; Liu, H.; Penner, R.M. Size-selective growth of nanoscale tetrathiafulvalene bromide crystallites on platinum particles. *Adv. Mater.* **2001**, *13*, 1567–1570.
- Nostrum, C.F.; Picken, S.J.; Schouten, A.-J.; Nolte, R.J.M. Synthesis and supramolecular chemistry of novel liquid crystalline crown ether-substituted phthalocyanines: toward molecular wires and molecular ionoelectronics. *J. Am. Chem. Soc.* **1995**, *117*, 9957–9965.
- Nostrum, C.F. Self-assembly wires and channels. *Adv. Mater.* **1996**, *8*, 1027–1030.
- Cowan, D.O. *New Aspects of Organic Chemistry*; Yoshida, Z., Shiba, T., Oshiro, Y., Eds.; Kodansha: Tokyo, 1989.
- Farges, J.-P.; Ed. *Organic Conductors*. Marcel Dekker: New York, 1994.
- Nalwa, H.S.; Ed.; *Handbook of Organic Conductive Molecules and Polymers*; Wiley: Stuttgart, 1997; Vol. 1.
- Williams, J.M.; Ferraro, J.R.; Thorn, R.J.; Carlson, K.D.; Geiser, U.; Wang, H.; Kini, A.M.; Whangbo, M.-H. *Organic Superconductors*; Prentice-Hall: New Jersey, 1992.
- Ishiguro, T.; Yamaji, K.; Saito, G. *Organic Superconductors*, 2nd Ed.; Springer: New York, 1998.
- Lehn, J.-M. *Supramolecular Chemistry*; VCH: Weinheim, 1995.
- Vögtle, F. *Supramolecular Chemistry*; Wiley: Tokyo, 1995.
- Steed, J.W.; Atwood, J.L. *Supramolecular Chemistry*; Wiley: Chichester, 2000.
- Roberts, G.; Ed.; *Langmuir–Blodgett Films*; Plenum Press: New York, 1990.
- Ulman, A. *An Introduction to Ultrathin Organic Films*; Academic Press: San Diego, CA, 1991.
- Petty, M.C. *Langmuir–Blodgett Films. An Introduction*; Cambridge University Press: Cambridge, 1996.
- Nakamura, T. *Handbook of Organic Conductive Molecules and Polymers. Vol. 1 Charge–Transfer Salts, Fullerenes and Photoconductors*. Nalwa, H.S., Ed.; Wiley: Stuttgart, 1997; 728–780.
- Bryce, M.R.; Petty, M.C. Electrical conductive Langmuir–Blodgett films of charge–transfer materials. *Nature* **1995**, *374*, 771–776.
- Metzger, R.M. Electrical rectification by a molecule: the advent of unimolecular electronic devices. *Acc. Chem. Res.* **1999**, *32*, 950–957.
- Weber, E.; Toner, J.L.; Goldberg, I.; Vögtle, F.; Laidler, D.A.; Stoddart, J.F.; Bartsch, R.A.; Liotta, C.L. *Crown*

- Ethers and Analogs*; Patai, S., Rappoport, Z., Eds.; John Wiley & Sons: New York, 1989.
26. Gokel, G.W. *Crown Ethers and Cryptands*; Stoddart, J.F., Ed.; RSC: Cambridge, 1994.
  27. Akutagawa, T.; Ohta, T.; Hasegawa, T.; Nakamura, T.; Christensen, C.A.; Becher, J. Formation of oriented molecular nanowires on mica surface. *Proc. Nat. Acad. Sci. U. S. A.* **2002**, *99*, 5028–5033.
  28. Nakamura, T.; Ohta, T.; Tatewaki, Y.; Wakahara, K.; Akutagawa, T.; Hasegawa, T.; Christensen, C.A.; Becher, J. submitted for publication.
  29. Nielsen, M.B.; Lomholt, C.; Becher, J. Tetrathiafulvalenes as building blocks in supramolecular chemistry II. *Chem. Soc. Rev.* **2000**, *29*, 153–164.
  30. Simonsen, K.B.; Svenstrup, N.; Lan, J.; Simonsen, O.; Mørk, P.; Kristensen, C.J.; Becher, J. Sequential functionalisation of bis-protected tetrathiafulvalene-dithiolates. *Synthesis* **1996**, 407–418.
  31. Torrance, J.B.; Vazquez, J.E.; Mayerle, J.J.; Lee, V.Y. Discovery of a neutral-to-ionic phase transition in organic materials. *Phys. Rev. Lett.* **1981**, *46*, 253–257.
  32. Saito, G.; Ferraris, J.P. Requirements for an “organic metal”. *Bull. Chem. Soc. Jpn* **1980**, *53*, 2142–2145.
  33. Wyckoff, R.W.G. *Crystal Structures*; Wiley: New York, 1960; Vol. 4.
  34. Lima-de-Faria, J. *Structural Mineralogy. An Introduction*; Kluwer: Dordrecht, 1994.
  35. Akutagawa, T.; Kakiuchi, K.; Hasegawa, T.; Nakamura, T.; Becher, J. submitted for publication.
  36. Torrance, J.B.; Mayerle, J.J.; Bechgaard, K. Comparison of two isostructural organic compounds, one metallic and the other insulating. *Phys. Rev., B* **1980**, *22*, 4960–4965.
  37. Jacobsen, C.S. *Optical Properties in Semiconductor and Semimetals. High Conducting Quasi-One-Dimensional Organic Crystals*; Conwell, E., Ed.; Academic Press: New York, 1988; 293–384.
  38. Akutagawa, T.; Abe, Y.; Nezu, Y.; Nakamura, T.; Kataoka, M.; Yamanaka, A.; Inoue, K.; Inabe, T.; Christensen, C.A.; Becher, J. Linear pentaiodide in the radical cation salt of a tetrathiafulvalene bisannulated macrocycle. *Inorg. Chem.* **1998**, *37*, 2330–2331.
  39. Akutagawa, T.; Abe, Y.; Hasegawa, T.; Nakamura, T.; Inabe, T.; Christensen, C.A.; Becher, J. Tuning of intramolecular  $\pi$ - $\pi$  overlap mode of tetrathiafulvalene bisannulated macrocycles in the open-shell electronic state. *Chem. Lett.* **2000**, 132–133.
  40. Abe, Y.; Akutagawa, T.; Hasegawa, T.; Nakamura, T.; Sugiura, K.; Sakata, Y.; Inabe, T.; Christensen, C.A.; Becher, J. Structures and electronic properties of TTF bisannulated 24-crown-8 charge transfer complexes. *Synth. Met.* **1999**, *102*, 1599–1600.

# Nanowires and Nanobelts: Mechanical Properties

Zhong Lin Wang

Center for Nanoscience and Nanotechnology, Georgia Institute of Technology,  
Atlanta, Georgia, U.S.A.

## INTRODUCTION

Because of the high size and structure selectivity of nanomaterials, their physical properties could be quite diverse, depending on their atomic-scale structure, size, and chemistry.<sup>[1]</sup> To maintain and utilize the basic and technological advantages offered by the size specificity and selectivity of the nanomaterials, there are three key challenges that we need to overcome for the future technological applications of nanomaterials. First, synthesis of size, morphology and structurally controlled nanomaterials, which are likely to have the precisely designed and controlled properties. Secondly, novel techniques for characterizing the properties of individual nanostructures and their collective properties.<sup>[2]</sup> This is essential for understanding the characteristics of the nanostructures. Finally, integration of nanomaterials with the existing technology is the most important step for their applications, especially in nanoscale electronics and optoelectronics.

Characterizing the mechanical properties of individual nanotubes/nanowires/nanobelt [called one-dimensional (1-D) nanostructure] is a challenge to many existing testing and measuring techniques because of the following constraints. First, the size (diameter and length) is rather small, prohibiting the applications of the well-established testing techniques. Tensile and creep testing require that the size of the sample be sufficiently large to be clamped rigidly by the sample holder without sliding. This is impossible for 1-D nanomaterials using conventional means. Secondly, the small size of the nanostructure makes their manipulation rather difficult, and specialized techniques are needed for picking up and installing individual nanostructure. Therefore new methods and methodologies must be developed to quantify the properties of individual nanostructure. The objective of this entry is to introduce the theory and techniques that have developed for characterizing the mechanical properties of individual nanotubes/nanowires/nanobelt using in situ transmission electron microscopy (TEM).

## DYNAMIC BENDING MODULUS BY ELECTRIC FIELD-INDUCED MECHANICAL RESONANCE

The main challenge for characterizing the mechanical behavior of a single nanostructure is its ultrasmall size that prohibits the application of conventional techniques. We first have to see the nanostructure and then measure its properties. TEM is a powerful tool for characterizing the atomic-scale structures of solid materials. A modern TEM is a versatile machine that not only can provide a real space resolution better than 0.2 nm but also can give a quantitative chemical and electronic analysis from a region as small as 1 nm. It is feasible to receive a full structure characterization from TEM. A powerful and unique approach could be developed if we can integrate the structural information of a nanostructure provided by TEM with the properties measured in situ from the same nanostructure.<sup>[3–5]</sup> This is a powerful technique that not only can provide the properties of an individual nanotube but also can give the structure of the nanotube through electron imaging and diffraction, providing an ideal technique for understanding the property–structure relationship. The objective of this section is to introduce this technique and its applications.

## Experimental Method

To carry out the property measurement of a 1-D nanostructure, a specimen holder for a TEM was built for applying a voltage across a 1-D nanostructure and its counter electrode (Fig. 1).<sup>[4,6]</sup> In the area that is loading specimen in conventional TEM, an electromechanical system is built that allows not only the lateral movement of the tip, but also applying a voltage across the 1-D nanostructure with the counter electrode. This setup is similar to the integration of scanning probe technique with TEM. The static and dynamic properties of the 1-D nanostructures can be obtained by applying a controllable static and alternating electric field. The microstructure of the measured object can be fully characterized by electron imaging, diffraction, and chemical analysis techniques.

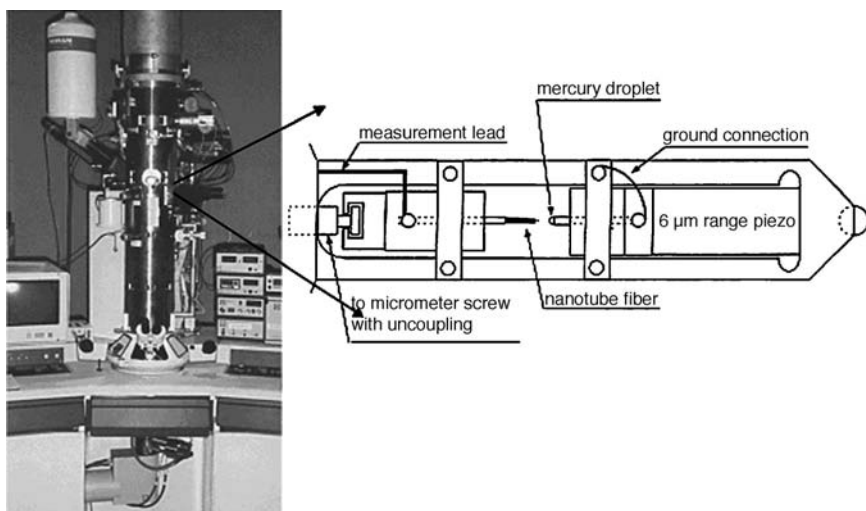


**Fig. 1** A transmission electron microscope and a schematic diagram of a specimen holder for in situ measurements.

The 1-D nanostructure to be used for property measurements is directly imaged under TEM (Fig. 2), and electron diffraction patterns and images can be recorded from the 1-D nanostructure. The information provided by TEM directly reveals both the surface and the intrinsic structure of the 1-D nanostructure. This is a unique advantage over the SPM techniques. The distance from the 1-D nanostructure to the counter electrode is controllable. The typical dimensions of

the 1-D nanostructures are 5–100 nm in diameter/width and lengths of 1–20  $\mu\text{m}$ . The counter electrode is typically an Au ball of diameter  $\sim 0.25$  mm.

### The Fundamental Resonance Frequency and Non-linear Effect

Our first measurements were carried out for multi-walled carbon nanotubes produced by an arc-discharge technique. Because of the sharp needle shape of a carbon nanotube, it can be charged by an externally applied voltage; the induced charge is distributed mostly at the tip of the carbon nanotube and the electrostatic force results in the deflection of the nanotube. Alternatively, if an applied voltage is an alternating voltage, the charge on the tip of the nanotube is also oscillating, so is the force. If the applied frequency matches the natural resonance frequency of the nanotube, mechanical resonance is induced. By tuning the applied frequency, the first and the second harmonic resonances can be observed (Fig. 3). The analysis of the information provided by the resonance experiments relies on the theoretical model for the system. The most established theory for modeling mechanical systems is the continuous elasticity theory, which is valid for large-size objects. For atomic scale mechanics, we may have to rely on molecular dynamics. The diameter of the nanotube is between the continuous model and the atomistic model; thus we need to examine the validity of applying the classical elasticity theory for the data analysis.

We have compared the following three characteristics between the results predicted by the elasticity theory and the experimental results shown in Fig. 3. First, the theoretical node for the second harmonic resonance occurs at  $0.8L$ , and the experiment showed  $\sim 0.76L$ . Secondly, the frequency ratio between the second to the first mode is  $\nu_2/\nu_1 = 6.27$  theoretically, while

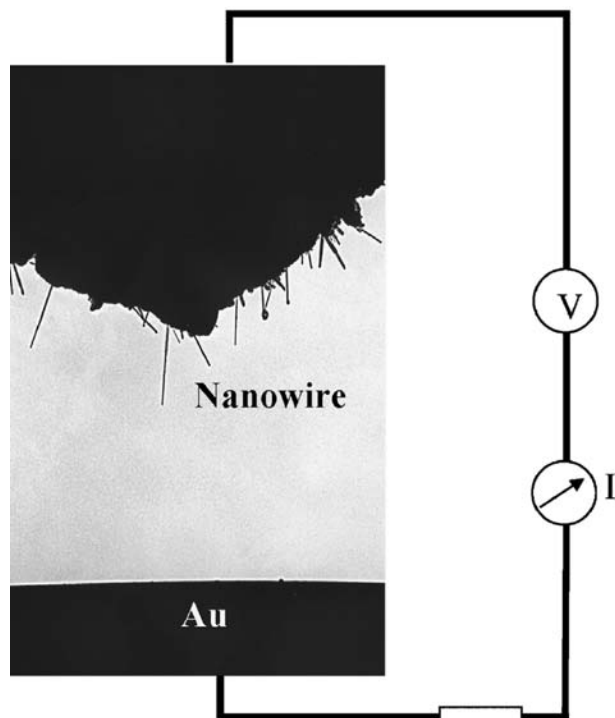


**Fig. 2** TEM image showing one-dimensional nanostructures at the end of the electrode and the other counter electrode. A constant or alternating voltage can be applied to the two electrodes to induce electrostatic deflection or mechanical resonance.



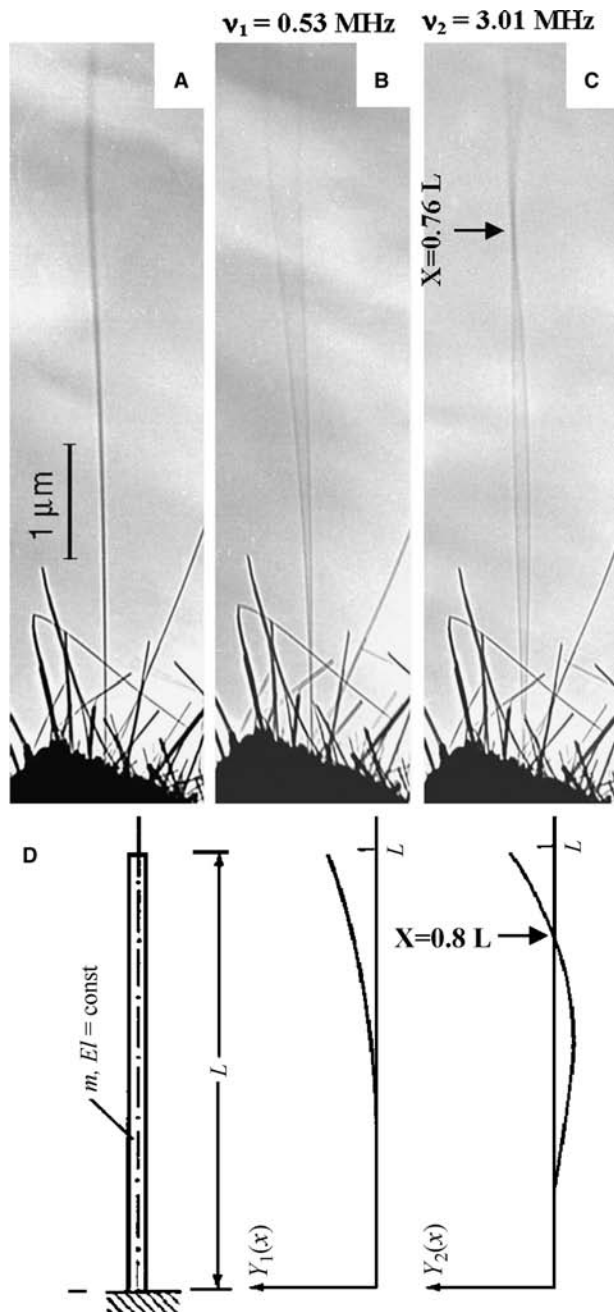


**Fig. 3** A selected carbon nanotube at (A) stationary, (B) the first harmonic resonance ( $\nu_1 = 1.21$  MHz), and (C) the second harmonic resonance ( $\nu_2 = 5.06$  MHz). (D) The traces of a uniform one-end fixed elastic beam at the first two resonance modes, as predicted by the continuous elasticity theory.

the observed one is  $\nu_2/\nu_1 = 5.7$ . The agreement is reasonably well if one looks into the assumptions made in the theoretical model: the nanotube is a uniform and homogeneous beam, and the root of the clamping side is rigid. The latter, however, may not be realistic in practical experiment. Finally, the shape of the nanotube during resonance has been compared quantitatively with the shape calculated by the elasticity theory, and the

agreement is excellent. Therefore we can still use the elasticity theory for the data analysis.

If the nanotube is approximated as a uniform solid bar with one end fixed on a substrate, from classical elasticity theory, the resonance frequency is given by<sup>[7]</sup>

$$\nu_i = \frac{\beta_i^2}{8\pi} \frac{1}{L^2} \sqrt{\frac{(D^2 + D_i^2)E_b}{\rho}} \quad (1)$$

where  $D$  is the tube outer diameter,  $D_i$  the inner diameter,  $L$  the length,  $\rho$  the density, and  $E_b$  the bending modulus. It must be pointed out that the bending modulus is different from Young's modulus, because bending modulus depends on the geometrical shape of the object. The resonance frequency is nanotube selective and it is a specific value of a nanotube.

The correlation between the applied frequency and the resonance frequency of the nanotube is not trivial. From Fig. 2 we know that there are some electrostatic charges built on the tip of the carbon nanotube. With consideration of the difference between the surface work functions between the carbon nanotube and the counter electrode (Au), a static charge exists even when the applied voltage is withdrawn. Therefore under an applied field the induced charge on the carbon nanotube can be represented by  $Q = Q_0 + \alpha V_0 \cos \omega t$ , where  $Q_0$  represents the charge on the tip to balance the difference in surface work functions,  $\alpha$  is a geometrical factor, and  $V_0$  is the amplitude of the applied voltage. The force acting on the carbon nanotube is

$$\begin{aligned} F &= \beta(Q_0 + \alpha V_0 \cos \omega t)V_0 \cos \omega t \\ &= \alpha\beta V_0^2/2 + \beta Q_0 V_0 \cos \omega t + \alpha\beta V_0^2/2 \cos 2\omega t \end{aligned} \quad (2)$$

where  $\beta$  is a proportional constant. Thus resonance can be induced at  $\omega$  and  $2\omega$  at vibration amplitudes proportional to  $V_0$  and  $V_0^2$ , respectively. The former is a linear term in which the resonance frequency equals to the applied frequency, while the latter is a non-linear term and the resonance frequency is twice of the applied frequency. In practical experiments, the linear and non-linear terms can be distinguished by observing the dependence of the vibration amplitude on the magnitude of the voltage  $V_0$ . This is an important process to ensure the detection of the linear term.

Another factor that one needs to consider is to identify the true fundamental resonance frequency. From Eq. (1), the frequency ratio between the first two modes is 6.27. In practice, if resonance occurs at  $\omega$ , resonance could occur also at  $2\omega$ , which is the double harmonic. To identify the fundamental frequency, one needs to examine the resonance at a frequency that is half or close to half of the observed resonance frequency; if no resonance occurs, the observed frequency is the true fundamental frequency.

The diameters of the tube can be directly determined from TEM images at a high accuracy. The determination of length has to consider the 2-D projection effect of the tube. It is essential to tilt the tube and to catch its maximum length in TEM, which is likely to be the true length. This requires a TEM that gives a tilting angle as large as  $\pm 60^\circ$ . Also, the operation voltage of the TEM is important to minimize radiation damage. The 100-kV TEM used in our experiments showed almost no detectable damage to a carbon nanotube, while a 200-kV electron could quickly damage a nanotube. The threshold for radiation damage of carbon nanotubes is  $\sim 150$  kV.

To trace the sensitivity of resonance frequency on beam illumination and radiation damage at 100 kV, a carbon nanotube was resonanced for more than 30 min. The resonance frequency showed an increase of  $\sim 1.4\%$  over the entire period of experiment, but no dependence on the electron dose was found. The FWHM for the resonance peak was measured to be  $\Delta\nu/\nu = 0.6\%$  in a vacuum of  $10^{-4}$ – $10^{-5}$  Torr. A slight increase in the resonance frequency could be related to the change of carbon structure under the electron beam, but such an effect has a negligible effect on the measurement of the bending modulus.

The Young's modulus is a quantity that is defined to characterize the interatomic interaction force, and it is the double differential of the bonding energy curve between the two atoms. The ideal case is that it is an intrinsic property at the atomic level and is independent of the sample geometry. For the nanotube case, the bending of a nanotube is determined not only by the Young's modulus, but also by the geometrical shape of the nanotube, such as the wall thickness and tube diameter. What we have measured by the in situ

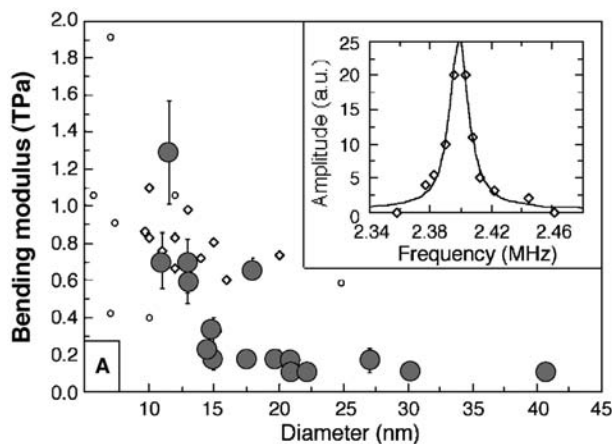


**Fig. 4** Bending modulus of the multiwalled carbon nanotube produced by arc-discharge as a function of the outer diameter of the nanotube. The inner diameter of the nanotubes is  $\sim 5$  nm, independent of the outer diameter. The FWHM of the resonance peak is inserted.

TEM experiments is the bending modulus. Fig. 4 shows a group of experimentally measured bending modulus of multiwalled carbon nanotubes. It is apparent that the smaller-size nanotubes have a bending modulus approaching the Young's modulus, while the modulus for the larger-size ones is much smaller. This size-dependent property is related to the elastic deformation of the carbon nanotubes.

To explore the intrinsic meaning of the measured  $\Delta\nu/\nu_1$  value, we consider a 1-D harmonic oscillator with an intrinsic resonance frequency  $\nu_1$ . If a viscosity (or friction) force is acting on the particle and the force is proportional to the instantaneous speed of the particle, the damping of the vibration amplitude is given by  $\exp(-t/\tau_0)$ , where  $\tau_0$  is the life decay constant of the oscillator. This decay constant is related to  $\Delta\nu/\nu_1$  by  $\Delta\nu/\nu_1 \ll 1$  by

$$\tau_0 = [(\Delta\nu/\nu_1)\pi\nu_1/1.732]^{-1} \quad (3)$$

For  $\Delta\nu/\nu_1 = 0.65\%$ ,  $\nu_1 = 1.0$  MHz, the lifetime is  $\tau_0 = 85$   $\mu$ sec. From the definition of  $\tau_0$ , the viscosity/friction coefficient  $\eta = 2M/\tau_0$ , where  $M$  is the mass of the particle; thus the time decay constant depends mainly on the viscosity coefficient of the nanotube in vacuum ( $10^{-4}$  Torr) under which the measurement was made, and it is almost independent of the intrinsic structure of the carbon nanotube. This agrees with our experimental observation and Eq. (1) can also be used to explain the larger value of  $\Delta\nu/\nu_1$  obtained in air than that in vacuum given that the atmosphere should have a higher viscosity (friction) coefficient.

Theoretical investigation by Liu, Zheng, and Jiang<sup>[8]</sup> suggests that the Eq. (1) used for the analysis is based on the linear analysis, which is valid for a small amplitude of vibration; for large vibration amplitude, the nonlinear analysis may have to be used. Based on the nonlinear elasticity theory, they have successfully explained the rippling effect observed experimentally by Wang, Poncharal, and de Heer.<sup>[4]</sup> In practical experiments, the resonance frequency shows no drift as the vibration increases to as large as  $30^\circ$ , suggesting that the frequency measured can still be quantified using the linear analysis.

## BENDING MODULUS OF COMPOSITE NANOWIRES

The technique demonstrated for carbon nanotubes applies to any nanowire shape object regardless of its conductivity.<sup>[9]</sup> Here we use composite silicon carbide–silica nanowires synthesized by a solid–vapor process as an example. The as-synthesized materials are grouped into three basic nanowire structures: pure  $\text{SiO}_x$  nanowires, coaxially  $\text{SiO}_x$  sheathed  $\beta$ -SiC

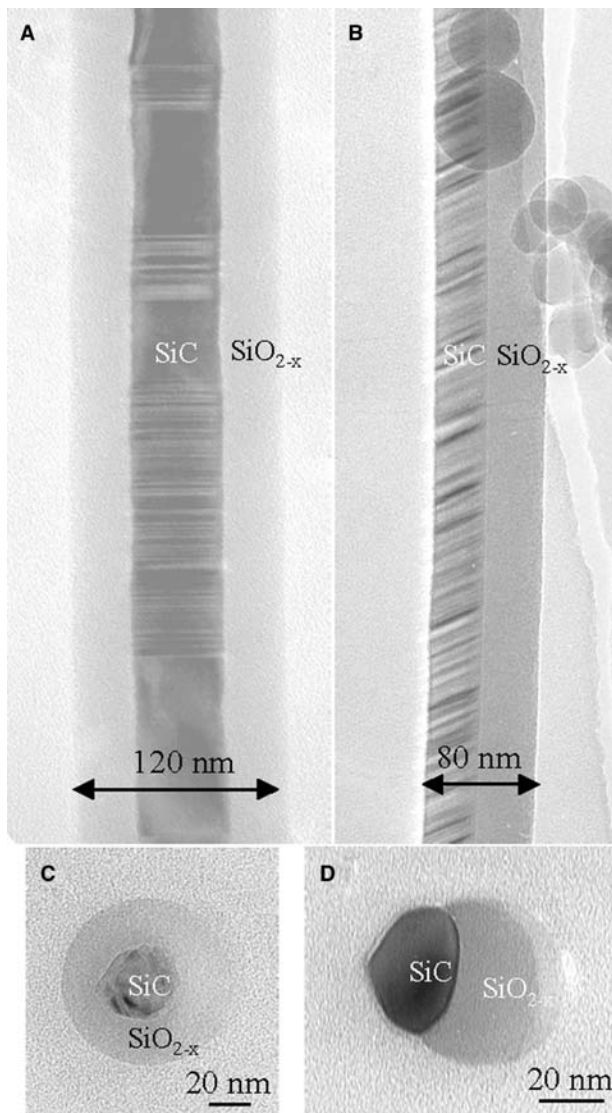


**Fig. 5** (A,B) TEM images of the coaxial and biaxial structured SiC-SiO<sub>x</sub> nanowires, and (C,D) the cross-sectional TEM images, respectively.

nanowires, and biaxial  $\beta$ -SiC-SiO<sub>x</sub> nanowires. Fig. 5 depicts the TEM images of the nanowires and their cross-section images, showing the coaxial and biaxial structures. The nanowires are uniform with a diameter of 50–80 nm, and a length that can be as long as 100  $\mu$ m. The coaxial SiC-SiO<sub>x</sub> nanowires have been extensively studied and have a  $\langle 111 \rangle$  growth direction with a high density of twins and stacking faults perpendicular to the growth direction.

For a beam with one end hinged and the other free, the resonance frequency is given by:<sup>[7]</sup>

$$\nu_0 = (\beta^2/2\pi)(EI/m)^{1/2}/L^2 \quad (4)$$

where  $\nu_0$  is the fundamental resonance frequency,  $\beta = 1.875$ ,  $EI$  is the flexural rigidity (or bending stiffness),  $E$  is the Young's modulus,  $I$  is the moment of inertia about a particular axis of the rod,  $L$  is the length of the beam, and  $m$  is its mass per unit length. For a uniform solid beam with a coaxial cable structured nanowire whose core material density is  $\rho_c$  and diameter is  $D_c$  and a sheath material density that is  $\rho_s$  with outer diameter  $D_s$ , the average density of the nanowire is given by

$$\rho_e = \rho_c(D_c^2/D_s^2) + \rho_s(1 - D_c^2/D_s^2) \quad (5)$$

The effective Young's modulus of the composite nanowire,  $E_{\text{eff}}$ , is

$$E_{\text{eff}} = \rho_e[8\pi f_0 L^2/\beta^2 D_s]^2 \quad (6)$$

The bending modulus for the coaxial cable structured SiC-SiO<sub>x</sub> nanowires results in combination from SiC and SiO<sub>x</sub>, where the contribution from the sheath layer of SiO<sub>x</sub> is more than that from the SiC core because of its larger flexural rigidity (or bending stiffness). The bending modulus increases as the diameter of the nanowire increases (Table 1), consistent with the theoretically expected values of  $E_{\text{eff}} = \alpha E_{\text{SiC}} + (1 - \alpha)E_{\text{SiO}_x}$ , where  $\alpha = (D_c/D_s)^4$ . The data match well to the calculated values for larger diameter nanowires.

From the cross-sectional TEM image of a biaxially structured nanowire, the outermost contour of the cross section of the nanowire can be approximated to be elliptical. Thus the effective Young's modulus of the nanowire can be calculated using Eq. (6) with the introduction of an effective moment of inertia and density. For an elliptical cross section of half long-axis  $a$  and half short-axis  $b$ , the moments of inertia are  $I_x = \pi ab^3/4$ , and  $I_y = \pi ba^3/4$ , where  $a$  and  $b$  can be calculated from the widths of the composite nanowire. With consideration of the equal probability of resonance with respect to the  $x$  and  $y$  axes, the effective moment of inertia introduced in the calculation is

**Table 1** Measured Young's modulus of coaxial cable structured SiC-SiO<sub>x</sub> nanowires (SiC is the core, and silica is the sheath) ( $\rho_{\text{Silica}} = 2.2 \times 10^3 \text{ kg/m}^3$ ;  $\rho_{\text{SiC}} = 3.2 \times 10^3 \text{ kg/m}^3$ ). The Young's moduli of the bulk materials are  $E_{\text{SiC}} = 466 \text{ GPa}$  and  $E_{\text{SiO}_2} = 73 \text{ GPa}$

$D_s$ (nm) ( $\pm 2$ nm)	$D_c$ (nm) ( $\pm 1$ nm)	$L$ ( $\mu$ m) ( $\pm 0.2$ $\mu$ m)	$f_0$ (MHz)	$E_{\text{eff}}$ (GPa) experimental	$E_{\text{eff}}$ (GPa) theoretical
51	12.5	6.8	0.693	46 $\pm$ 9.0	73
74	26	7.3	0.953	56 $\pm$ 9.2	78
83	33	7.2	1.044	52 $\pm$ 8.2	82
132	48	13.5	0.588	78 $\pm$ 7.0	79
190	105	19.0	0.419	81 $\pm$ 5.1	109

**Table 2** Measured Young's modulus of biaxially structured SiC–SiO<sub>x</sub> nanowires.  $D_{\text{wire}}$  and  $D_{\text{SiC}}$  are the widths across the entire nanowire and across the SiC subnanowire, respectively

$D_{\text{wire}}$ (nm) (±2 nm)	$D_{\text{SiC}}$ (nm) (±1 nm)	$L$ (μm) (±0.2 μm)	$f_o$ (MHz)	$E_{\text{eff}}$ (GPa) experimental
58	24	4.3	1.833	54 ± 24.1
70	36	7.9	0.629	53 ± 8.4
83	41	4.3	2.707	61 ± 13.8
92	47	5.7	1.750	64 ± 14.3

taken to be approximately  $I = (I_x + I_y)/2$ , and the density per unit length is  $m_{\text{eff}} = A_{\text{SiC}}\rho_{\text{SiC}} + A_{\text{Silica}}\rho_{\text{Silica}}$ , where  $A_{\text{SiC}}$  and  $A_{\text{Silica}}$  are the cross sectional areas of the SiC and SiO<sub>x</sub> sides, respectively. The experimentally measured Young's modulus is given in Table 2.

## BENDING MODULUS OF OXIDE NANOBELTS

### Nanobelts—Structurally Controlled Nanowires

In the literature, there are a few names being used for describing 1-D elongated structures, such as nanorod, nanowire, nanoribbon, nanofiber, and nanobelts. When we named the nanostructures to be “nanobelts”,<sup>[10]</sup> we mean that the nanostructure has specific growth direction, the top/bottom surfaces and side surfaces are well-defined crystallographic facets. The requirements for nanowires are less restrictive than for nanobelts because a wire has a specific growth direction, but its side surfaces may not be well defined, and its cross section may not be uniform nor have a specific shape. Therefore, *we believe that nanobelts are more structurally controlled objects than nanowires, or simply a nanobelt is a nanowire that has well-defined side surfaces.* It is well known that the physical property of a carbon nanotube is determined by the helical angle at which the graphite layer was rolled up. It is expected that, for thin nanobelts and nanowires, their physical

and chemical properties will depend on the nature of the side surfaces.

The most typical nanobelt is ZnO (Fig. 6A), which has a distinct cross section from the nanotubes or nanowires.<sup>[10]</sup> Each nanobelt has a uniform width along its entire length, and the typical widths of the nanobelts are in the range of 50 to 300 nm. A ripple-like contrast appearing in the TEM image is due to the strain resulting from the bending of the belt. High-resolution TEM (HRTEM) and electron diffraction studies show that the ZnO nanobelts are structurally uniform, single crystalline, and dislocation free (Fig. 6B).

There are a few kinds of nanobelts that have been reported in the literature. Table 3 summarizes the nanobelt structures of function oxides.<sup>[10–14]</sup> Each type of nanobelts is defined by its crystallographic structure, the growth direction, top surfaces, and side surfaces. Some of the materials can grow along two directions, but they can be controlled experimentally. Although these materials belong to different crystallographic families, they do have a common faceted structure, which is the nanobelt structure. In addition, nanobelts of Cu(OH)<sub>2</sub>,<sup>[15]</sup> MoO<sub>3</sub>,<sup>[16,17]</sup> MgO,<sup>[18,19]</sup> and CuO.<sup>[20]</sup>

### Dual-Mode Resonance of Nanobelts

Because of the mirror symmetry and rectangular cross section of the nanobelt (Fig. 7A), there are two distinct fundamental resonance frequencies corresponding to the vibration in the thickness and width directions, which are given from the classical elasticity theory as.<sup>[21]</sup>

$$\nu_x = \frac{\beta_1^2 T}{4\pi L^2} \sqrt{\frac{E_x}{3\rho}} \quad (7)$$

$$\nu_y = \frac{\beta_1^2 W}{4\pi L^2} \sqrt{\frac{E_y}{3\rho}} \quad (8)$$

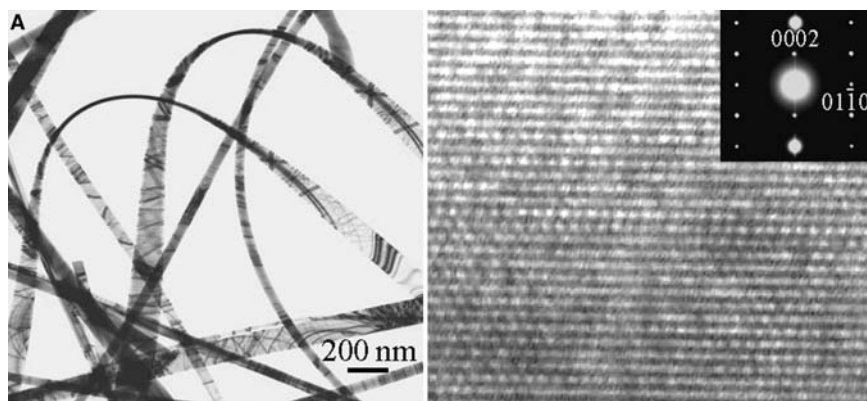


**Fig. 6** (A) TEM image of ZnO nanobelts synthesized by a solid–vapor phase technique. (B) High-resolution TEM image of a ZnO nanobelt with incident electron beam direction along  $[2\bar{1}\bar{1}0]$ . The nanobelt grows along  $[0001]$ , with top/bottom surfaces  $(2\bar{1}\bar{1}0)$  and side surfaces  $(01\bar{1}0)$ .

**Table 3** Crystallographic geometry of functional oxide nanobelts

Nanobelt	Crystal structure	Growth direction	Top surface	Side surface
ZnO	Wurtzite	[0001] or [01 $\bar{1}$ 0]	$\pm(2\bar{1}\bar{1}0)$ or $\pm(2\bar{1}\bar{1}0)$	$\pm(01\bar{1}0)$ or $\pm(0001)$
Ga <sub>2</sub> O <sub>3</sub>	Monoclinic	[001] or [010]	$\pm(100)$ or $\pm(100)$	$\pm(010)$ or $\pm(10\bar{1})$
<i>t</i> -SnO <sub>2</sub>	Rutile	[101]	$\pm(10\bar{1})$	$\pm(010)$
<i>o</i> -SnO <sub>2</sub> wire	Orthorhombic	[010]	$\pm(100)$	$\pm(001)$
In <sub>2</sub> O <sub>3</sub>	C-Rare earth	[001]	$\pm(100)$	$\pm(010)$
CdO	NaCl	[001]	$\pm(100)$	$\pm(010)$
PbO <sub>2</sub>	Rutile	[010]	$\pm(201)$	$\pm(10\bar{1})$

where  $\beta_1 = 1.875$ ;  $E_x$  and  $E_y$  are the bending modulus if the vibration is along the  $x$  axis (thickness direction) and  $y$  direction (width direction), respectively;  $\rho$  is the density,  $L$  is the length,  $W$  is the width, and  $T$  is the thickness of the nanobelt. The two modes are decoupled and they can be observed separately in experiments.

Changing the frequency of the applied voltage, we found two fundamental frequencies in two orthogonal directions transverse to the nanobelt.<sup>[21]</sup> Fig. 7C and D shows the harmonic resonance with the vibration planes nearly perpendicular and parallel to the viewing direction, respectively. For calculating the bending modulus, it is critical to accurately measure the fundamental resonance frequency ( $\nu_1$ ) and the dimensional sizes ( $L$ , and  $T$  and  $W$ ) of the investigated ZnO nanobelts. To determine  $\nu_1$ , we have checked the stability of the resonance frequency to ensure that one end of the nanobelt is tightly fixed, and the resonant excitation has been carefully checked around the half value of the resonance frequency.

ZnO nanobelts can be used as a force sensor. Fig. 8A shows a selected ZnO nanobelt with a hooked end, which is equivalent to a cantilever with an integrated tip. Because of the two transverse vibration modes of the nanobelt, resonance along two orthogonal directions has been observed (Fig. 8B and C). The two resonance modes just correspond to the two modes of the tip operation when the nanobelt-base cantilever is used as a force sensor: one is the tapping mode and the other is the noncontact mode. Thus the force sensor fabricated using the ZnO nanobelts is versatile for applications on hard and soft surfaces.

### Bending Modulus of Nanobelt

The geometrical parameters are the key for derivation of the mechanical property from the measured resonance frequencies. The specimen holder is rotated about its axis so that the nanobelt is aligned perpendicular to the electron beam; thus the real length ( $L$ ) of the

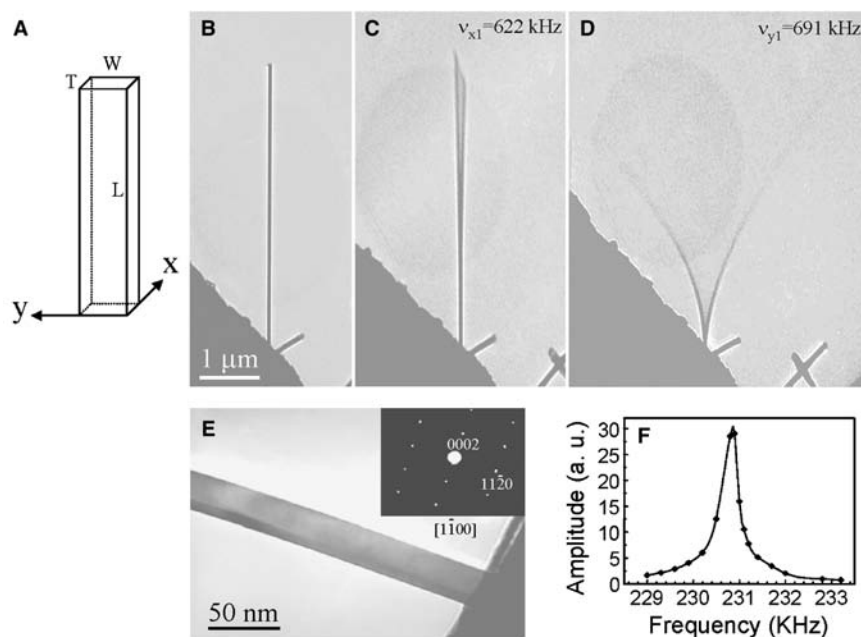


**Fig. 7** A selected ZnO nanobelt at (A,B) stationary, (C) the first harmonic resonance in the  $x$  direction,  $\nu_{x1} = 622$  kHz, and (D) the first harmonic resonance in the  $y$  direction,  $\nu_{y1} = 691$  kHz. (E) An enlarged image of the nanobelt and its electron diffraction pattern (inset). The projected shape of the nanobelt is apparent. (F) The FWHM of the resonance peak measured from another ZnO nanobelt. The resonance occurs at 230.9 kHz.



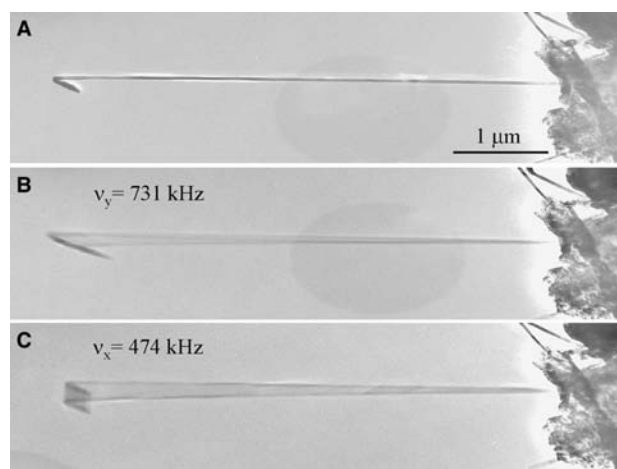


**Fig. 8** A selected ZnO nanobelt with a hooked end at (A) stationary, (B) resonance at 731 kHz in the plane almost parallel to the viewing direction, and (C) resonance at 474 kHz in the plane closely perpendicular to the viewing direction.

nanobelt can be obtained. The normal direction of the wide facet of the nanobelt could be firstly determined by electron diffraction pattern, which was  $[2\bar{1}\bar{1}0]$  for the ZnO nanobelt. Then the nanobelt was tilted from its normal direction by rotating the specimen holder, and the tilting direction and angle were determined by the corresponding electron diffraction pattern. As shown in the inset of Fig. 7E, the electron beam direction is  $[1\bar{1}00]$ . The angle between  $[1\bar{1}00]$  and  $[2\bar{1}\bar{1}0]$  is  $30^\circ$ , i.e., the normal direction of the wide facet of this nanobelt is  $30^\circ$  tilted from the direction of the electron beam. Using the projected dimension measured from the TEM image (Fig. 7E), the geometrical parameters of this nanobelt are determined to be  $W = 28$  nm and  $T = 19$  nm. Based on the experimentally measured data, the bending modulus of the ZnO nanobelts is calculated using Eqs. (7) and (8). The experimental results are summarized in Table 4.<sup>[21]</sup> The bending modulus of the ZnO nanobelts was  $\sim 52$  GPa. This value represents the modulus that includes the scaling effect and geometrical shape, and it cannot be directly compared to the Young's modulus of ZnO ( $c_{33} = 210$  GPa,  $c_{13} = 104$  GPa),<sup>[22]</sup> because

the shape of the nanobelt and the anisotropic structure of ZnO are convoluted in the measurement. The bending modulus measured by the resonance technique, however, has excellent agreement with the elastic modulus measured by nanoindentation for the same type of nanobelts.<sup>[23]</sup>

Although nanobelts of different sizes may have a slight difference in bending modulus, there is no obvious difference if the calculation was done using either Eq. (7) or Eq. (8). The ratio of two fundamental frequencies  $\nu_{y1}/\nu_{x1}$  is consistent with the aspect ratio  $W/T$ , as expected from Eqs. (7) and (8), because there is no significant difference between  $E_x$  and  $E_y$ .

The resonance technique demonstrated here is very sensitive to the structure of a nanowire. Fig. 9A and B shows a silicon nanowire that has a Au tip, but the Au particle is off the symmetric axis of the nanowire. This asymmetric structure results in two distinct resonance along two perpendicular directions (Fig. 9C and D). The difference between the two resonance frequencies is related to the mass of the Au particle.

## THE HARDNESS OF A NANOBELT BY NANOINDENTATION

Nanoscale mechanical properties of individual zinc oxide nanobelts were characterized by Nanoscope IIIa atomic force microscope (AFM) (Fig. 10A) and Hysitron TriboScope with homemade side-view CCD camera.<sup>[23]</sup> The prepared nanobelt sample was investigated by two means: one is by tapping mode of Nanoscope IIIa, using a diamond indenter tip with a radius of  $<25$  nm. The other is by STM mode of Hysitron TriboScope, an add-on force transducer from Hysitron Inc., using a diamond cubic corner tip with a radius of  $<40$  nm. In either case, individual nanobelts were imaged, and then nanoindentations were made on the nanobelt using varied loads (Fig. 10B and C). After indentation, the indent was imaged in situ using the image mode of the AFM. For nanoindentations, the hardness is normally defined as the maximum load divided by the projected area of the indenter in contact

**Table 4** Bending modulus of the ZnO nanobelts.  $E_x$  and  $E_y$  represents the bending modulus corresponding to the resonance along the thickness and width directions, respectively

Nanobelt	Length $L$ ( $\mu\text{m}$ ) ( $\pm 0.05$ )	Width $W$ (nm) ( $\pm 1$ )	Thickness $T$ (nm) ( $\pm 1$ )	Fundamental frequency (kHz)			Bending modulus (GPa)		
				$W/T$	$\nu_{x1}$	$\nu_{y1}$	$\nu_{y1}/\nu_{x1}$	$E_x$	$E_y$
1	8.25	55	33	1.7	232	373	1.6	$46.6 \pm 0.6$	$50.1 \pm 0.6$
2	4.73	28	19	1.5	396	576	1.4	$44.3 \pm 1.3$	$45.5 \pm 2.9$
3	4.07	31	20	1.6	662	958	1.4	$56.3 \pm 0.9$	$64.6 \pm 2.3$
4	8.90	44	39	1.1	210	231	1.1	$37.9 \pm 0.6$	$39.9 \pm 1.2$



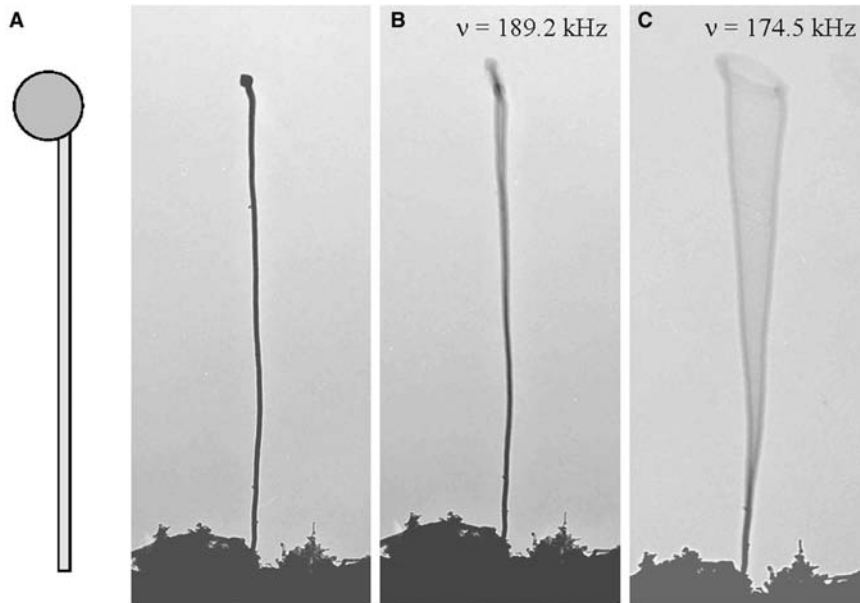


**Fig. 9** (A) A silicon nanowire with a gold particle at the tip, showing (B,C) two independent resonance along two perpendicular directions.

with the sample at the maximum load. Thus,

$$H = \frac{P_{MAX}}{A_C} \quad (9)$$

where  $H$ ,  $P_{MAX}$ , and  $A_C$  are the hardness, maximum applied load, and projected contact area at the maximum applied load, respectively. Because the indenter tip is not rigid during indentation, the elastic modulus cannot be directly determined from the load vs. the displacement curve. However, the reduced elastic modulus can be determined from the unloading

portion of the curve by the relation:

$$E_r = \frac{\sqrt{\pi}}{2} \cdot \frac{dP}{dh} \cdot \frac{1}{\sqrt{A_c}} \quad (10)$$

where  $E_r$  and  $dP/dh$  are the reduced modulus and experimentally measured stiffness, respectively.

Based on Eq. (9), using load vs. deflection curves during nanoindentation, the hardness of ZnO and SnO<sub>2</sub> nanobelts was calculated as a function of indentation penetration, and the result is summarized in Fig. 10D. The hardness of ZnO is lower than that in the SnO<sub>2</sub>

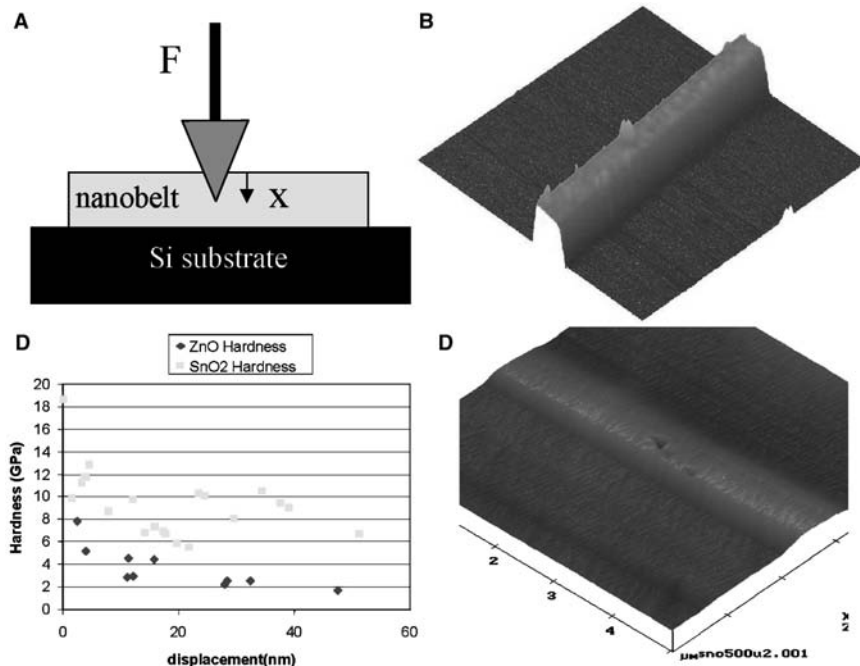


**Fig. 10** (A) Schematic of nanoindentation on ZnO by AFM tip. (B,C) AFM image of a nanobelt before and after being indented, showing plastic deformation on the surfaces. (D) Hardness of ZnO and SnO<sub>2</sub> nanobelts as a function of penetration during nanoindentation.

nanobelt. Also, it can be seen that the lower the penetration of the nanoindentation, the higher the hardness of the nanobelt, which is attributed to the strain gradient effect (size effect) during nanoindentation for most materials.<sup>[24]</sup> The effective elastic modulus can also be derived from the force–displacement curve and the result is  $E = 45$  GPa for ZnO, in good agreement with that from the resonance technique.<sup>[21]</sup>

## NANOBELTS AS NANOCANTILEVERS

The cantilever-based scanning probe microscopy (SPM) technique is one of the most powerful approaches in imaging, manipulating, and measuring nanoscale properties and phenomena. The most conventional cantilever used for SPM is based on silicon,  $\text{Si}_3\text{N}_4$  or SiC, which is fabricated by e-beam or optical lithography technique and typically has a dimension of thickness of  $\sim 100$  nm, width of  $\sim 5$   $\mu\text{m}$ , and length of  $\sim 50$   $\mu\text{m}$ . Utilization of nanowire- and nanotube-based cantilevers can have several advantages for SPM. Carbon nanotubes can be grown on the tip of a conventional cantilever and be used for imaging surfaces with a large degree of abrupt variation in surface morphology.<sup>[25,26]</sup> We demonstrate here the manipulation of nanobelts by AFM and its potential as nanocantilevers.<sup>[27]</sup>

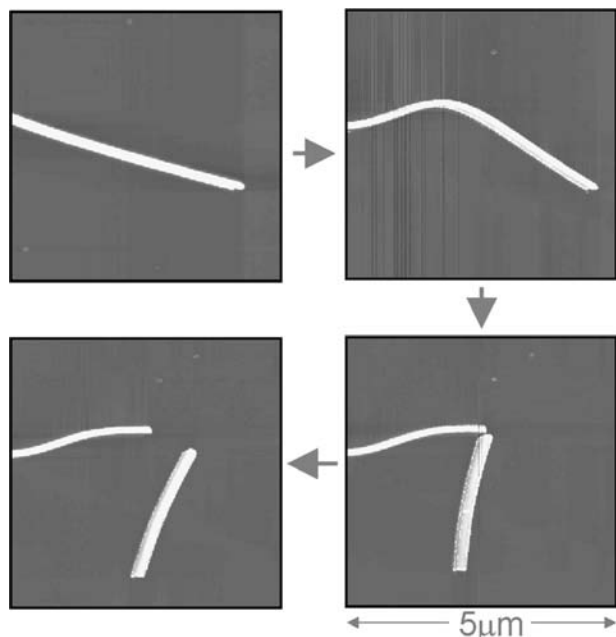


**Fig. 11** A series of shape of a ZnO nanobelt created by manipulation using an AFM tip, showing deformation and break-up. *Source:* Image courtesy of M.S. Arnold, Ph. Avouris.

Manipulation of nanobelts is important for integrating this structurally controlled nanomaterial with microelectrical mechanical system (MEMS). Using an AFM tip, a nanobelt can be manipulated into different shapes (Fig. 11). A ZnO nanobelt of 56 nm in width can be bent for over  $60^\circ$  without breaking, demonstrating extremely high mechanical flexibility. Further bending bent the nanobelt into two segments. This is a technique for cutting a nanobelt into specific length.

Combining MEMS technology with self-assembled nanobelts, we are able to produce cost-effective cantilevers with much heightened sensitivity for a range of devices and applications. Force, pressure, mass, thermal, biological, and chemical sensors are all prospective devices. Semiconducting nanobelts are ideal candidates for cantilever applications. Structurally, they are defect-free single crystals, providing excellent mechanical properties. The reduced dimensions of nanobelt cantilevers offer a significant increase in cantilever sensitivity. The cantilevers under consideration are simple in design and practice. Using a Dimension 3000 SPM in tapping mode, we have successfully lifted ZnO nanobelts from a silicon substrate. Capillary forces are responsible for the adhesion strength between the AFM probe and the ZnO nanobelts. Combining the aforementioned techniques with micromanipulation has led to the alignment of individual ZnO nanobelts onto silicon chips (Fig. 12). The aligned ZnO cantilevers were manipulated to have a range of lengths. This exemplifies our ability to tune the resonance frequency of each cantilever and thus modify cantilevers for different applications such as tapping and contact mode AFM. The nanobelt-based nanocantilever is  $\sim 50$ – $1000$  times smaller than the conventional cantilever. Decreased size in microoptical mechanical devices corresponds to increased sensitivity. Combining the aforementioned techniques with micromanipulation has led to the horizontal alignment of individual ZnO nanobelts onto silicon chips (Fig. 12). This exemplifies our ability to tune the resonance frequency of each cantilever and thus modify cantilevers for different applications such as contact, noncontact, and tapping mode AFM.

## THE WORK FUNCTION AT THE TIP OF A NANOBELT BY RESONANCE TECHNIQUE

The field-emission property for well-aligned ZnO nanowire arrays has been reported,<sup>[28]</sup> demonstrating a promising application of semiconductor nanowires as field emitters for flat panel display. Following the Fowler–Nordheim (F–N) theory,<sup>[29]</sup> an important physical quantity in electron field emission is the surface work function, which is well documented for elemental materials. For the emitters such as ZnO

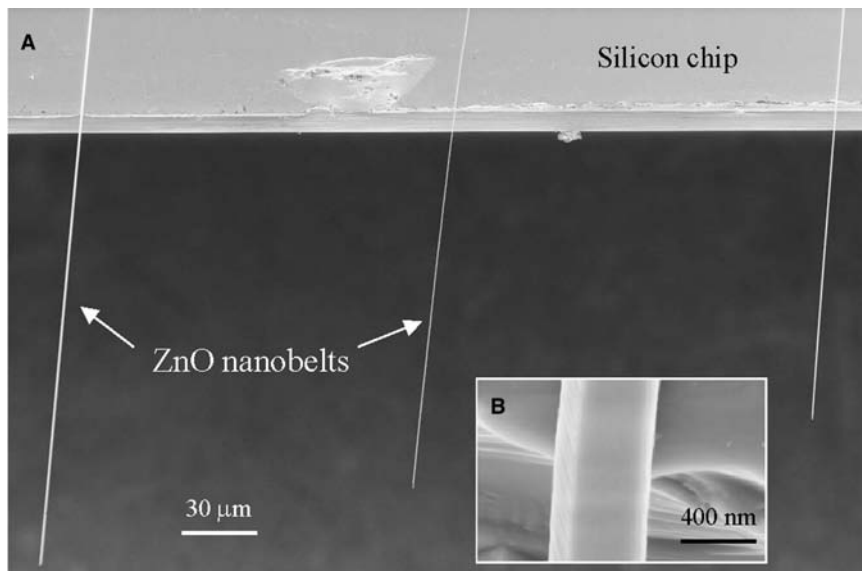


**Fig. 12** Site-specific placement and alignment of ZnO nanobelts onto a silicon chip, forming nanocantilever arrays. The inset is an enlarged SEM image of the third nanocantilever showing its shape; the width of the cantilever was measured to be 525 nm.

nanowire arrays, most of the electrons are emitted from tips of the nanowires, and it is the local work function that matters to the properties of the field emission. However, the work function measured based on the F-N theory is an average over the large scale of emitting materials. So it is necessary to measure the local work function at the tip of an individual emitter. Gao, Pan, and Wang<sup>[30]</sup> have measured the work function at the tips of carbon nanotubes by an in situ TEM technique. The measurement relies on the mechanical resonance of the carbon nanotube induced by an externally applied oscillating voltage with tunable frequency.

The measurement of the work function at the tip of a single ZnO nanobelt was carried out in situ at 200 kV in a Hitachi HF-2000 FEG TEM. A specimen holder was built for applying a voltage across a nanobelt

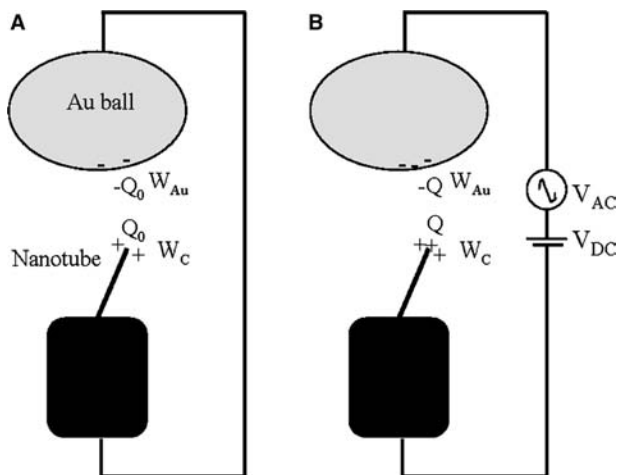


**Fig. 13** Experimental set-up for measuring the work function at the tip of a ZnO nanobelt.

and its counter gold electrode. The nanobelts to be used for measurements are directly imaged under TEM. Fig. 13 is a setup for work function measurement. One end of the nanobelt was electrically attached to a gold wire, and the other end faces directly against the gold ball. Because of the difference in the surface work function between the ZnO nanobelt and the counter Au ball, a static charge  $Q_0$  exists at the tip of the nanobelt to balance this potential difference.<sup>[31]</sup> The magnitude of  $Q_0$  is proportional to the difference between the work function of the nanobelt tip (NBT) and the Au electrode,  $Q_0 = \alpha (\phi_{Au} - \phi_{NBT})$ , where  $\alpha$  is related to the geometry and distance between the nanobelt and the electrode.

The measurement is based on the mechanical resonance of the nanobelt induced by an externally alternative electric field. Experimentally, a constant voltage  $V_{d.c.}$  and an oscillating voltage  $V_{a.c.} \cos 2\pi ft$  are applied onto the nanobelt (Fig. 13A), where  $f$  is the frequency and  $V_{a.c.}$  is the amplitude. Thus the total induced charge on the nanobelt is

$$Q = Q_0 + \alpha e(V_{d.c.} + V_{a.c.} \cos 2\pi ft) \quad (11)$$

The force acting on the nanobelt is proportional to the square of the total charge on the nanobelt

$$\begin{aligned} F &= \beta [Q_0 + \alpha e(V_{d.c.} + V_{a.c.} \cos 2\pi ft)]^2 \\ &= \alpha^2 \beta \{ (\phi_{Au} - \phi_{NBT} + eV_{d.c.})^2 + e^2 V_{a.c.}^2 / 2 \\ &\quad + 2eV_{a.c.} (\phi_{Au} - \phi_{NBT} + eV_{d.c.}) \\ &\quad \times \cos 2\pi ft + e^2 V_{a.c.}^2 / 2 \cos 4\pi ft \} \end{aligned} \quad (12)$$

where  $\beta$  is a proportional constant. In Eq. (12), the first term is constant and it causes a static deflection of the ZnO nanobelt. The second term is a linear term,

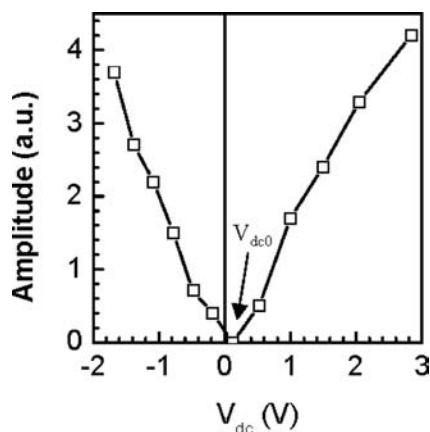


**Fig. 14** A plot of vibration amplitude of a ZnO nanobelt as a function of the applied direct current voltage, from which the offset voltage  $V_{dc0} = 0.12$  V.

and the resonance occurs if the applied frequency  $f$  is tuned to the intrinsic mechanical resonance frequency  $f_0$  of the ZnO nanobelt. The most important result of Eq. (12) is that, for the linear term, the resonance amplitude  $A$  of the nanobelt is proportional to  $V_{a.c.}(\phi_{Au} - \phi_{NBT} + eV_{d.c.})$ .

The principle of the measurement is as follows. We first set  $V_{d.c.} = 0$  and tune the frequency  $f$  to get the mechanical resonance induced by the applied oscillating field. Second, under the resonance condition of keeping  $f = f_0$  and  $V_{a.c.}$  constant, slowly change the magnitude of  $V_{d.c.}$  from zero to a value  $V_{d.c.0}$  that satisfies  $\phi_{Au} - \phi_{NBT} + eV_{d.c.0} = 0$ . At this moment, the resonance amplitude  $A$  becomes zero although the external a.c. voltage is still in effect. Therefore the work function at the tip of the ZnO nanobelt is  $\phi_{NBT} = \phi_{Au} + eV_{d.c.0}$ , while  $\phi_{Au} = 5.1$  eV. Fig. 14 is a plot of the vibration amplitude  $A$  of the nanobelt as a function of the applied direct current voltage  $V_{d.c.}$ , from which the value for  $V_{d.c.0}$  is determined. The work function of the ZnO nanobelts is  $\sim 5.2$  eV.<sup>[32]</sup>

## CONCLUSION

The property characterization of nanomaterials is challenged by their small-size structures because of the difficulties in manipulation. A typical example is the mechanical properties of individual 1-D nanostructures, such as nanotubes, nanowires, and nanobelts. This entry reviews the experimental methods for measuring the mechanical properties of 1-D nanostructures using a resonance technique in TEM. The static and dynamic properties of the 1-D nanostructures can be obtained by applying controllable static and alternating electric fields. The resonance of carbon nanotubes

can be induced by tuning the frequency of the applied voltage. The technique is powerful in such a way that it can directly correlate the atomic-scale microstructure of the carbon nanotube with its physical properties, providing a one-to-one correspondence in structure-property characterization.

Because of the rectangular cross section of the nanobelt, two fundamental resonance modes have been observed corresponding to two orthogonal transverse vibration directions, showing the versatile applications of nanobelts as nanocantilevers and nanoresonators. The bending modulus of the ZnO nanobelts was measured to be  $\sim 52$  GPa. Nanobelts have also been demonstrated as ultrasmall nanocantilevers for sensor and possibly imaging applications in AFM.

## ACKNOWLEDGMENTS

The results reviewed in this paper were partially contributed from my group members and collaborators: Ruiping Gao, Xuedong Bai, Scott Mao, William Hughes, and Enge Wang, to whom I am very grateful. Research supported by NSF, NASA, and NSFC.

## REFERENCES

1. Wang, Z.L.; Liu, Y.; Zhang, Z. *Handbook of Nanophase and Nanostructured Materials*; Tsinghua University Press: Beijing, 2002; I-IV Kluwer Academic Publisher: New York.
2. Wang, Z.L.; Hui, C. *Electron Microscopy of Nanotubes*; Kluwer Academic Publisher: New York, 2003.
3. Poncharal, P.; Wang, Z.L.; Ugarte, D.; de Heer, W.A. Electrostatic deflections and electromechanical resonances of carbon nanotubes. *Science* **1999**, *283*, 1513–1516.
4. Wang, Z.L.; Poncharal, P.; de Heer, W.A. Nanomeasurements of individual carbon nanotubes by in-situ TEM. *Pure Appl. Chem.* **2000**, *72*, 209–219.
5. Gao, R.P.; Wang, Z.L.; Bai, Z.G.; de Heer, W.A.; Dai, L.M.; Gao, M. Nanomechanics of aligned carbon nanotube arrays. *Phys. Rev. Lett.* **2000**, *85*, 622–635.
6. Wang, Z.L.; Poncharal, P.; de Heer, W.A. Measuring physical and mechanical properties of individual carbon nanotubes by in-situ TEM. *J. Phys. Chem. Solids* **2000**, *61*, 1025–1030.
7. Meirovich, L. *Elements of Vibration Analysis*; McGraw-Hill: New York, 1986.
8. Liu, J.Z.; Zheng, Q.S.; Jiang, Q. Effect of ripping mode on resonances of carbon nanotubes. *Phys. Rev. Lett.* **2001**, *86*, 4843–4846.
9. Wang, Z.L.; Dai, Z.R.; Bai, Z.G.; Gao, R.P.; Gole, J.L. Side-by-side silicon carbide-silica biaxial nanowires: synthesis, structure and mechanical properties. *Appl. Phys. Lett.* **2000**, *77*, 3349–3351.

10. Pan, Z.W.; Dai, Z.R.; Wang, Z.L. Nanobelts of semi-conducting oxides. *Science* **2001**, *291*, 1947–1949.
11. Wang, Z.L.; Pan, Z.W.; Dai, Z.R. Semiconducting Oxide Nanostructures. US Patent No. 6,586,095, July 1, 2003.
12. Dai, Z.R.; Pan, Z.W.; Wang, Z.L. Gallium oxide nanoribbons and nanosheets. *J. Phys. Chem., B* **2002**, *106*, 902–904.
13. Dai, Z.R.; Pan, Z.W.; Wang, Z.L. Growth and structure evolution of novel tin oxide diskettes. *J. Am. Chem. Soc.* **2002**, *124*, 8673–8680.
14. Kong, X.Y.; Wang, Z.L. Spontaneous polarization and helical nanosprings of piezoelectric nanobelts. *Nano Lett.* **2003**, *in press*.
15. Wen, X.G.; Zhang, W.X.; Yang, S.H.; Dai, Z.R.; Wang, Z.L. Solution phase synthesis of Cu(OH)<sub>2</sub>/nanoribbons by coordination self-assembly using Cu/sub 2/S nanowires as precursors. *Nano Lett.* **2002**, *2* (12), 1397–1401.
16. Li, Y.B.; Bando, Y.; Golberg, D.; Kurashima, K. Field emission from MoO<sub>3</sub>/nanobelts. *Appl. Phys. Lett.* **2002**, *81* (26), 5048–5050.
17. Zhou, J.; Xu, N.S.; Deng, S.Z.; Chen, J.; She, J.C.; Wang, Z.L. Large-area nanowire arrays of molybdenum and molybdenum oxides: Synthesis and field emission properties. *Adv. Mater.* **2003**, *in press*.
18. Li, Y.B.; Bando, Y.; Sato, T. Preparation of network-like MgO nanobelts on Si substrate. *Chem. Phys. Lett.* **2002**, *359* (1–2), 141–145.
19. Liu, J.; Cai, J.; Son, Y.C.; Gao, Q.M.; Suib, S.L.; Aindow, M. Magnesium manganese oxide nanoribbons: synthesis, characterization, and catalytic application. *J. Phys. Chem., B* **2002**, *106* (38), 9761.
20. Wen, X.G.; Zhang, W.X.; Yang, S.H. Synthesis of Cu(OH)<sub>2</sub> and CuO nanoribbon arrays on a copper surface. *Langmuir* **2003**, *19*, 5898–5903.
21. Bai, X.D.; Wang, E.G.; Gao, P.X.; Wang, Z.L. Dual-mode mechanical resonance of individual ZnO nanobelts. *Appl. Phys. Lett.* **2003**, *82*, 4806–4808.
22. Carlotti, G.; Socino, G.; Petri, A.; Verona, E. Acoustic investigation of the elastic properties of ZnO films. *Appl. Phys. Lett.* **1987**, *51*, 1889–1891.
23. Mao, S.X.; Zhao, M.H.; Wang, Z.L. Probing nano-scale mechanical properties of individual semiconducting nanobelt. *Appl. Phys. Lett.* **2002**, *83*, 993–995.
24. Duan, D.M.; Wu, N.; Slaughter, W.S.; Mao, S.X. Length scale effect on mechanical behavior due to strain gradient plasticity. *Mater. Sci. Eng., A* **2001**, *A303* (1–2), 241–249.
25. Yenilmez, E.; Wang, Q.; Chen, R.J.; Wang, D.; Dai, H.J. Wafer scale production of carbon nanotube scanning probe tips for atomic force microscopy. *Appl. Phys. Lett.* **2002**, *80* (12), 2225–2227.
26. Dai, H.J.; Hafner, J.H.; Rinzler, A.G.; Colbert, D.T.; Smalley, R.E. Nanotubes as nanoprobe in scanning probe microscopy. *Nature* **1996**, *384*, 147–150.
27. Hughes, W.; Wang, Z.L. Nanobelt as nanocantilever. *Appl. Phys. Lett.* **2003**, *82*, 2886–2888.
28. Lee, C.J.; Lee, T.J.; Lyu, S.C.; Zhang, Y.; Ruh, H.; Lee, H.J. Field emission from well-aligned zinc oxide nanowires grown at low temperature. *Appl. Phys. Lett.* **2002**, *81* (19), 3648–3650.
29. Fowler, R.H.; Nordheim, L.W. Electron emission in intense electric fields. *Proc. R. Soc., Lond., A* **1928**, *119* (781), 173.
30. Gao, R.P.; Pan, Z.W.; Wang, Z.L. Work function at the tips of multi-walled carbon nanotubes. *Appl. Phys. Lett.* **2001**, *78*, 1757–1759.
31. Kelvin, L. *Philos. Mag.* **1898**, *46*, 82.
32. Bai, X.D.; Wang, E.G.; Gao, P.X.; Wang, Z.L. Measuring the work function at a nanobelt tip and at a nanoparticle surface. *Nano Lett.* **2003**, *3*, 1147–1150.

# Near-Field Microscopy

**Björn T. Rosner**

*NanoInk Inc., Chicago, Illinois, U.S.A.*

**Daniel W. van der Weide**

*Department of Electrical and Computer Engineering, University of Wisconsin, Madison, Wisconsin, U.S.A.*

## INTRODUCTION

While force interactions are most commonly employed for probing, manipulation, and addressing of nanoscale features, dielectric contrast mechanisms are also potentially useful means of probing nanostructures. Optical absorption or emission, dielectric contrast in the infrared (IR), far-infrared (FIR), or microwave regime are all part of a rich pool of phenomena observable with electromagnetic interactions, with applications in nanoelectronics, spintronics, and biotechnology being developed. To attain the highest resolution, it is necessary to confine the area in which the probing field interacts with the sample to subwavelength dimensions. This is accomplished by fabricating probes with subwavelength-sized features and scanning such near-field probes very close to the sample. This article summarizes such near-field techniques in the visible, IR, and microwave regime and relates them to current and future applications.

## HISTORICAL OVERVIEW

Doing microscopy with electromagnetic waves usually implies using visible light. This is because Abbe's<sup>[1]</sup> much-cited criterion limits resolving power to  $\sim \lambda/2$  (where  $\lambda$  is the wavelength), so using millimeter wave and infrared frequencies would result in unattractively low resolution. While this criterion is correct for far-field microscopy, it is not limiting when near-field interactions are taken into account. Theoretical considerations were first published by Synge<sup>[2]</sup> in 1928 and Bethe<sup>[3]</sup> in 1944. The first practical implementation of near-field microscopy was developed for radio frequency applications by Frait<sup>[4]</sup> (1959) and Soohoo<sup>[5]</sup> (1962). Further important milestones were the first use of a coaxial waveguiding probe to localize microwave fields for measuring material properties by Bryant and Gunn<sup>[6]</sup> in 1965 and  $\lambda/60$  wavelength-relative resolution

achieved by Ash and Nichols<sup>[7]</sup> in 1972 using a subwavelength aperture. The advent of scanning tunneling microscopy (STM)<sup>[8]</sup> and subsequent scanning probe techniques provided a means by which accurate nanoscale tip-sample distance control became possible for the first optical near-field microscopes.<sup>[9,10]</sup> Finally, the advent of scanning force microscopy (SFM) in 1986<sup>[11]</sup> allowed for near-field scanning optical microscopy (NSOM or SNOM) instruments relying on (shear-) force feedback<sup>[12]</sup> in 1992. From that point, near-field microscopy has spread through a wealth of techniques and applications to form a diverse and very active field of research.

## SCANNING NEAR-FIELD OPTICAL MICROSCOPY

### Fiber Probes

For visible wavelengths, the most common probe type today uses tapered optical fibers that are coated with an opaque metal layer except at the apex where a small opening defines the optical output (Fig. 1). The shear-force feedback signal is commonly electronically detected using tuning fork feedback.<sup>[14]</sup> In comparison to SFM probes, straight SNOM fibers are much stiffer and more fragile, leading to slower scan speeds and difficulties in establishing reliable feedback, particularly on soft samples. Another major concern for optical near-field microscopy is the low-power throughput of NSOM fibers because they act as cutoff waveguides for light near the apex. To improve transmission over that of the common technique of pulling heated fibers, meniscus etching<sup>[15]</sup> and double-tapered probes have been used.<sup>[16]</sup> Tube etching, a technique where the polymer coating of the fiber is not removed prior to etching, has been introduced.<sup>[17]</sup> Typical applications for fiber-NSOM instruments are found in chemistry, biology, material science, and integrated optics, e.g.,



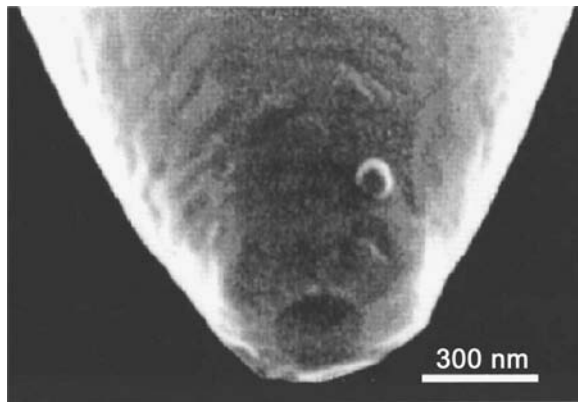


**Fig. 1** A scanning electron micrograph of a typical tapered aluminum-coated optical fiber tip. *Source:* From Ref.<sup>[13]</sup>. © 1995 American Institute of Physics.

single molecule spectroscopy,<sup>[18]</sup> cell membrane structure<sup>[19]</sup> analysis, and optical waveguide mapping<sup>[20]</sup> (Fig. 2). Another field of activity is to use NSOM as a means for high-density optical data storage.<sup>[21]</sup> Further information regarding aperture NSOM can be found in two review articles by Hecht et al.<sup>[22]</sup> and Dunn.<sup>[23]</sup>

### Apertureless Probes

Apertureless SNOM is the complement to aperture SNOM. Apertureless SNOM includes a wide variety of related approaches, including the use of surface plasmons and scattering-type SNOM (s-SNOM). While the use of plasmon-guiding effects to localize light is still in its infancy, considerable interest in this field exists<sup>[24]</sup> because light throughput might be increased by orders of magnitude, e.g., through the use of a tetrahedral tip with an integrated surface-plasmon guide as a scanning probe.<sup>[25]</sup>

The s-SNOM technique is a prime example of apertureless SNOM.<sup>[26]</sup> Here a sharp probe, typically an STM or SFM probe, is scanned over an illuminated surface (Fig. 3). The optical contrast of s-SNOM arises from the dipole-dipole interaction between the sharp tip and the sample, leading to characteristic local scattering [more about the theory can be found in the section about infrared (IR) near-field microscopy]. The main advantage of s-SNOM is that the resolution is not limited by an aperture or the skin depth of metal, but rather by the sharpness of the probing tip, potentially leading to better resolution. This advantage has been used to localize polymerization of commercial photoresists in an effort to push the resolution of optical lithography. Resolutions down to 70 nm were recently reported using this technique.<sup>[28]</sup> An s-SNOM setup was also used to simultaneously record optical amplitude and phase contrast on a subwavelength scale.<sup>[29]</sup>

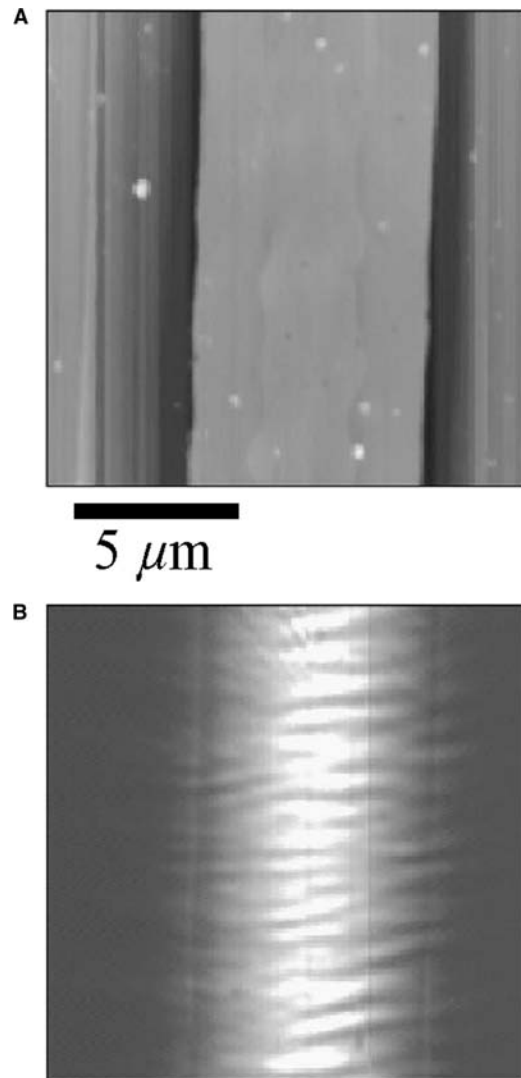


**Fig. 2** Topography (A) and optical intensity map (B) of the TM mode in a Ti:LiNbO<sub>3</sub> waveguide, taken using a typical fiber NSOM setup. *Source:* From Ref.<sup>[20]</sup>. © 2002 American Institute of Physics.

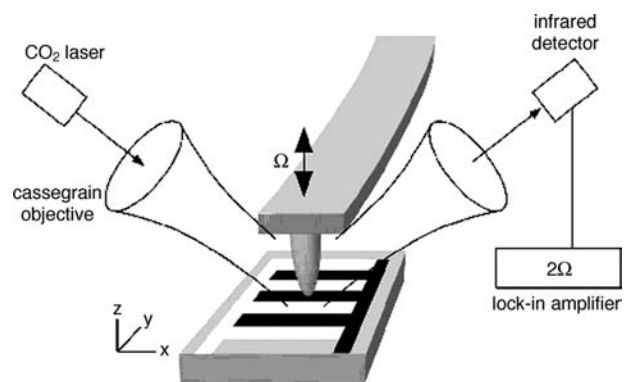


**Fig. 3** Sketch of a scattering-type near-field optical microscope using higher-order modulation for background suppression. *Source:* From Ref.<sup>[27]</sup>. © 2000 American Institute of Physics.

## Integrated Probes

Finally, researchers have been microfabricating SNOM probes that could be applied in the same fashion as cantilevered SFM probes, with minor instrumental changes. Some of the proposed concepts are passive, such as metal-coated probes with circular<sup>[30]</sup> apertures and solid immersion lenses on cantilevers<sup>[31]</sup> (strictly speaking a far-field technique). Initial efforts have been made to fabricate active devices in GaAs that include integrated light sources.<sup>[32]</sup> Considerably more research has been performed to produce photodetectors integrated close to the probe<sup>[33,34]</sup> or right at the apex of the sharp tip,<sup>[35]</sup> preferably integrated with the cantilever and chip body.<sup>[36]</sup>

## SCANNING NEAR-FIELD INFRARED AND FAR-INFRARED MICROSCOPY

Because of the wealth of chemical information available through vibrational band spectroscopy, many traditional infrared techniques such as Fourier-transform infrared spectroscopy (FTIR), thermal probing, and Raman scattering have become cornerstones of chemical characterization. In recent years, characterization of optoelectronic devices in the IR also gained importance for probing integrated-circuit lasers. Proximal probes offer a way to combine IR imaging with subwavelength resolution. Fiber-based aperture scanning near-field infrared microscopy (SNIM) setups, similar to optical fiber NSOM instruments, have been developed, based on special infrared transmissive fibers and etching techniques.<sup>[37]</sup>

The far-infrared (FIR) spectrum ( $10 \mu\text{m} < \lambda < 1 \text{mm}$ ) is of particular interest because it is part of the molecular fingerprint regime. Here characteristic molecular rotational or vibrational absorption spectra offer the promise of chemical microscopy. Biological membrane absorption and conductive or dielectric properties of materials, e.g., superconductors and quantum dots, offer additional applications for FIR near-field microscopy. Little work has been performed in this frequency regime, mostly because high-power FIR sources and sensitive FIR detection are not yet readily available.

### Aperture Techniques

One practical FIR technique is to use a three-dimensional funnel or tapered cylindrical waveguide to confine radiation in an aperture approach. This geometry was employed<sup>[38]</sup> to overcome the imperfect focusing capabilities of traditional FIR optics. Power transmittance in the

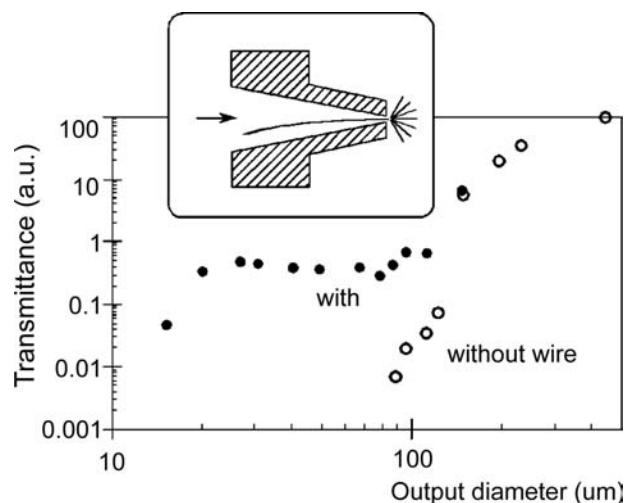


**Fig. 4** The relative transmittance at a wavelength of  $\lambda = 392 \mu\text{m}$  of focusing cones with different output apertures is investigated. Adding a central, coaxial wire prevents cutoff reflection at  $d < \lambda/2$ . Source: From Ref.<sup>[39]</sup>. © 1995 Elsevier Science.

cutoff region is

$$T = e^{-4\pi\sqrt{f_c^2 - f^2}t}$$

where  $t$  is the penetration depth into the cutoff region, and  $f$  and  $f_c$  are the frequency of the radiation and the cutoff frequency, respectively. In practice, a sharp cutoff in transmitted intensity was found at an aperture size of about  $\lambda/2$ . This setup was then applied for far-infrared near-field spectroscopy of two-dimensional electron systems.<sup>[38]</sup> Aperture confinement of FIR radiation has been one of the leading techniques to date<sup>[39,40]</sup> because of its straightforward implementation. Keilmann et al. showed that by introducing a center conductor into the tapered hollow guide and creating an in situ coaxial waveguide, the aperture size can be decreased by almost an order of magnitude without losing transmitted power (Fig. 4). It was also found that the transmitted power varies with a period of  $\lambda/2$  as the length of wire protruding from the aperture is extended because it acts as a resonant antenna.

### Apertureless Techniques

Using apertureless (scattering) SNIM (Fig. 3) in the IR and FIR has even better prospects than in the visible regime. For one, because the resolution depends on the scattering tip, not the wavelength, the wavelength-specific resolution is far better. Far-infrared microscopy with nanometer resolution is possible and has been demonstrated.<sup>[41,42]</sup> Furthermore, because the wavelength is much longer than the occasional

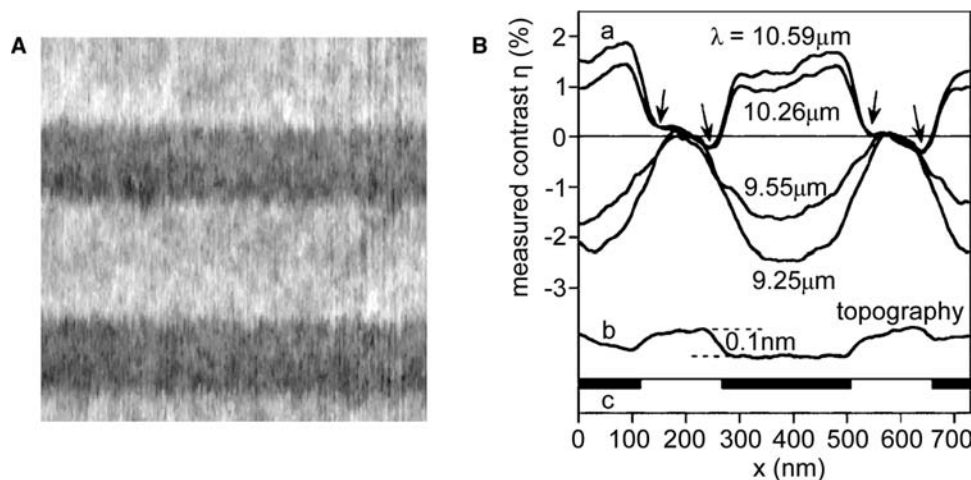


**Fig. 5** (A) Infrared s-SNOM image of a flat Si sample with subsurface doping (bright), taken at  $\lambda = 10.59 \mu\text{m}$ . (B) Line scans taken across doping stripes, measured at four different wavelengths, demonstrating 30-nm spatial resolution and a contrast reversal when the infrared wavelength tunes through the induced plasmon resonance, here at about  $\lambda = 10 \mu\text{m}$ . Source: From Ref.<sup>[27]</sup>. © 2000 American Institute of Physics.

distance variations between tip and sample, optical interference effects play less of a role, reducing the risk of topographical artifacts in the optical data. In scattering-type instruments, it is also possible to eliminate topography contrast and record pure optical contrast.<sup>[42,43]</sup> Here when applying noncontact SFM, the nonlinear dipole–dipole interaction between the tip and sample leads to (purely optical) higher modulation harmonics in the scattered signal, which can be used for lock-in detection. Following one argument,<sup>[42]</sup> image contrast arises from the interaction between the polarizable probe (modeled as a sphere with polarizability  $\alpha$  and radius  $a$ ) and the dielectric or metallic sample with complex dielectric number  $\epsilon$ . This results in an effective polarizability of the coupled system

$$\alpha_{\perp}^{\text{eff}} = \frac{\alpha(1 + \beta)}{1 - \frac{\alpha\beta}{16\pi(z+a)^3}}$$

where  $\beta = (\epsilon - 1)/(\epsilon + 1)$ . This formula shows both strong enhancement at short probe–sample separation  $z$  and the existence of amplitude and phase effects because  $\alpha$  and  $\beta$  are complex. Thus the scattered far field  $E_{\text{sca}} = \alpha^{\text{eff}}E$  reports the phase and amplitude of the complex near-field interaction. With this technique, Knoll and Keilmann<sup>[27]</sup> have mapped conductivity of a silicon sample with nanometer resolution using a scattering-type near-field microscope and 10.6- $\mu\text{m}$  radiation as shown in Fig. 5. The same researchers<sup>[44]</sup> reported contrast between polystyrene (PS) and polymethylmethacrylate (PMMA) on the nanometer scale using the same instrument and two wavelengths around 10  $\mu\text{m}$  (Fig. 6). Hillenbrand et al.<sup>[45]</sup> applied this instrument to probe the local interaction with an

SiC sample and found phonon-enhanced near-field coupling that is extremely sensitive to the chemical and structural composition of polar materials.

### Additional Techniques

Another promising approach is to use antenna structures as near-field sources.<sup>[46,47]</sup> While any coaxial open-ended waveguide can be considered an antenna, guiding radiation at visible or infrared wavelengths is

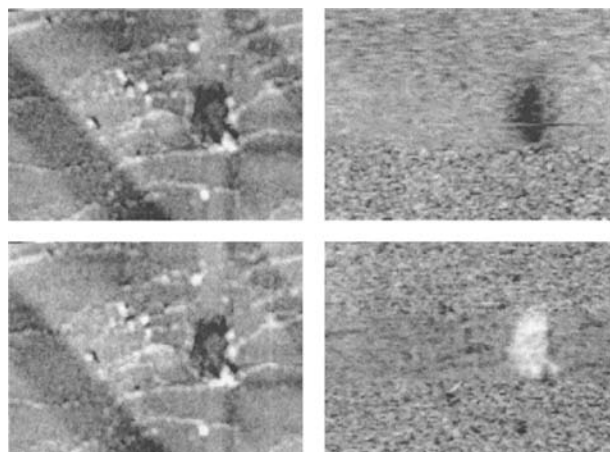


**Fig. 6** Simultaneously acquired topography (left) and infrared images (right) of PS embedded in PMMA using an s-SNOM. The upper row is recorded with an illumination wavelength of  $\lambda = 9.68 \mu\text{m}$ , where PS has an absorption maximum. The lower row shows the same spot, illuminated at the PMMA absorption maximum wavelength of  $\lambda = 10.17 \mu\text{m}$ . The field of view is  $3.5 \times 2.5 \mu\text{m}$ . Source: From Ref.<sup>[44]</sup>. © 1999 Nature.

not yet technologically feasible. However, by using antennas that collect far-field radiation and channel it to near-field tips for exciting the sample, antenna concepts can be very effective. Other approaches for FIR near-field microscopy include THz time domain spectroscopy (TDS) using photoconductive THz emitters<sup>[40]</sup> pumped by femtosecond optical lasers and all-electronic generation of THz radiation with nonlinear transmission lines (NLTL).<sup>[48]</sup>

Aperture probes, scattering probes, and coaxial tips form the main body of research on near-field microscopy as it is applied in NSOM. An entirely different approach to infrared microscopy lies in the use of photothermal signals for near-field spectroscopy.

Here a thermal probe in temperature-sensing mode directly measures absorption of incident IR radiation by sensing the induced heating of the sample. This heating can either be directly measured for each wavelength in the dispersive approach<sup>[49]</sup> or a Fourier-transform absorption spectrum can be acquired when using intensity-modulated illumination.<sup>[50]</sup> Many other thermal techniques exist, e.g., scanning thermal microscopy (SThM) where the tip is used to heat the sample and sense heat flow out of the probe. More about localized thermal imaging can be found in a review by Kölzer et al.<sup>[51]</sup> Reviews of near-field infrared microscopy and near-field vibrational spectroscopy have been written by Dragnea and Leone<sup>[52]</sup> and by Pollock and Smith.<sup>[53]</sup>

## SCANNING NEAR-FIELD MICROWAVE MICROSCOPY

Unlike in the visible or infrared regime, metals are good conductors for microwave frequencies. Metal waveguides are an efficient means of transmitting

microwave power and can be subwavelength sized in cross section. Microwave near-field probes are either broadband or resonant, which can make them more sensitive, but also more limited in the frequency range in which they can be operated.

## Coaxial Waveguides

An advantageous waveguide design is to use tapered coaxial waveguide probes that increase resolution and provide high throughput. For the highest resolution, a sharpened center helps concentrate the fringing fields emanating from the probe apex (lightning rod effect) and thus confines the interaction area between the probe and sample. Proof-of-principle experiments with a sample between two such sharpened coaxial transmission line tips by Keilmann et al.<sup>[54]</sup> resulted in  $\lambda/10^6$  wavelength-relative resolution. Integrating coaxial structures with cantilevered SFMs enables microscale probing of passive or active samples in reflection or transmission mode, respectively. Initial probes by van der Weide et al.<sup>[55]</sup> were made by coating a commercial silicon SFM probe with photoresist and gold, then opening the coaxial structure by gently rubbing the tip on a substrate while in feedback. These probes allowed for local measurements of waveforms on fast integrated circuits. Microfabricated probes (Fig. 7)<sup>[36]</sup> have various advantages, among them higher resolution and batch fabrication. Probes made from GaAs report superior signal transfer.<sup>[57]</sup>

## Scanning Tunneling Microscopy-Based Microwave Microscopy

Just as with SFM, STM can offer a tip-sample distance feedback system for microwave near-field

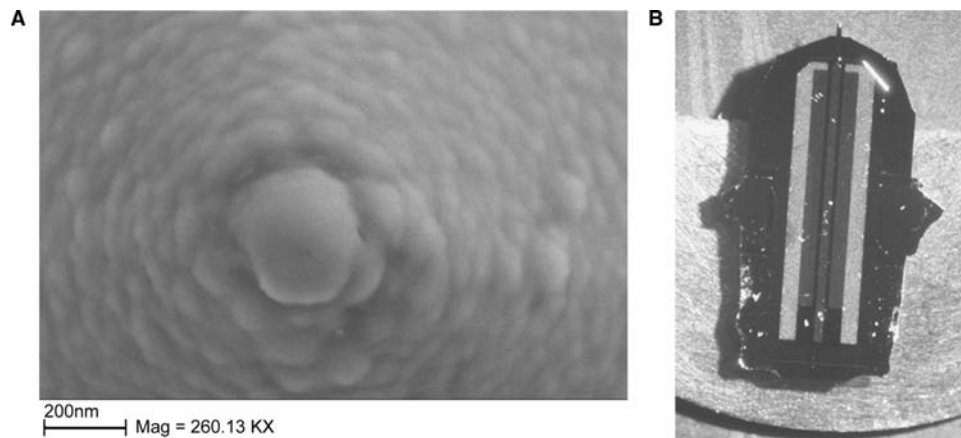


**Fig. 7** (A) Scanning electron micrograph of a nanometer-scale Schottky diode at the apex of an SFM tip. (B) This SNOM detector is integrated on a cantilever and chip body that contains waveguides for straightforward connection to macroscopic instrumentation. *Source:* From Ref.<sup>[56]</sup>. © 2002 American Institute of Physics.

microscopy while providing a sharp conducting tip to localize high-frequency electromagnetic interaction. One such system was developed by Kramer et al.<sup>[58]</sup> Here higher harmonic signals are generated because of tunnel junction nonlinearities. Because the higher-harmonic generation strongly depends on the electronic properties of the surface, it is possible to differentiate different chemical species. McCarty and Weiss<sup>[59]</sup> and Michel et al.<sup>[60]</sup> have explored this possibility in a number of publications. These instruments have been applied from d.c. to 20 GHz, recording linear or nonlinear (higher-harmonic)<sup>[61]</sup> microwave spectra. Usually, topography has been controlled using conventional STM while simultaneously recording millimeter wave amplitude in transmission or reflection mode.

### Apertureless Approaches

Scattering of incident far-field microwave radiation from a conducting tip in close proximity to a sample is analogous to s-SNOM in the visible, IR, or FIR regions. Thus numerical and theoretical treatments of s-SNOM can be applied to the microwave regime if certain material constants, such as indices of refraction, are revised. Surprisingly, although the resolution of such a microscope is defined by the sharpness of the tip and can lie in the nanometer range, little research has been carried out in this field. Keilmann et al.<sup>[62]</sup> described the coaxial setup specified above<sup>[58]</sup> as essentially equivalent to an s-SNOM setup for the microwave regime. Instead of using far-field optics to focus the radiation, they use coaxial cables to direct the fields, which is much more convenient for microwave frequencies. They point out that the resolution achieved is already an order of magnitude higher than the microwave penetration depth of the tip material, indicating that no intrinsic physical mechanism seems to exist that would limit the resolution achievable.

### Ultrafast Scanning Tunneling Microscopy

Ultrafast scanning tunneling microscopy (USTM) was independently invented by Weiss et al.<sup>[63]</sup> and Nunes and Freeman<sup>[64]</sup> in 1993. Both techniques rely on pump and probe experiments for highest temporal resolution. Using femtosecond lasers that repetitively illuminate photoconductive (PC) switches ensures high temporal resolution, while using a sharp tip gives the additional benefit of high spatial resolution. The nonlinear current vs. voltage tunneling characteristics are employed to measure the picosecond cross-correlation. In the setup of Nunes, pump and probe travel along one transmission line while Weiss employs the more common setup of pumping the sample and probing the tunneling tip as shown in Fig. 8.

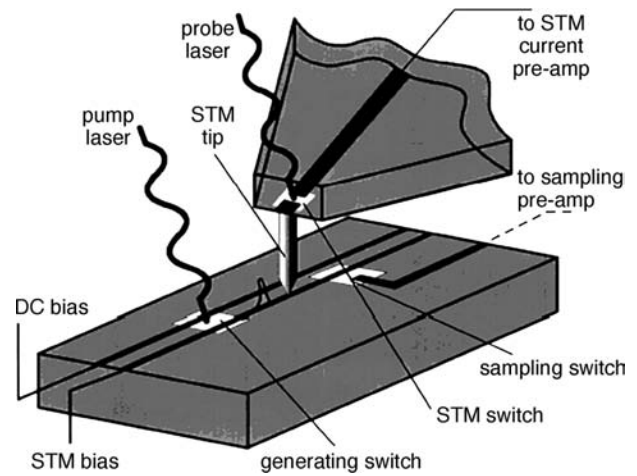


**Fig. 8** Localized pump and probe setup that uses photoconductive switches to trigger a pulse on the DUT and to probe the instantaneous voltage on the DUT through the tip. *Source:* (From Ref.<sup>[65]</sup>. © 1996 American Institute of Physics.

A related pump-probe technique was introduced by Kim et al.<sup>[66]</sup> that relies on direct conduction through a tip. They brought a probe with Ti tip, PC switch, and electric lead into contact with a transmission line. The convolution between pump pulse and probe pulse could be mapped out by probing the instantaneous electric field at the tip position by opening the PC switch and collecting the signal transmitted through the tip. Takeuchi and Mizuhara<sup>[67]</sup> improved on this concept by using an LT-GaAs tip and employing SFM feedback. A propagating pulse on a metal strip was mapped in 2-D and observed in sequential images with 0.8-psec time intervals.

Oesterschulze et al.<sup>[68]</sup> have also reported on an SFM setup with Lt-GaAs probe and PC switches. Here contact and noncontact images of a voltage pulse on a coplanar stripline were presented with picosecond temporal resolution.

### Resonant Probes

Resonant structures are superior in that they allow localization of high field areas and are often more sensitive. However, most resonant techniques do not allow for resolution on the single micrometer scale or below. Among those larger-scale probes are narrow resonant slots in a rectangular hollow waveguide<sup>[69,70]</sup> and open resonant coaxial resonators.<sup>[71]</sup>

For higher resolution, Tabib-Azar et al.<sup>[72]</sup> have used a tapered stripline resonator for near-field microwave microscopy in a series of publications. The resonator is designed by capacitively coupling to the stripline, and a sharpened stainless steel wire was used as a probe tip. Because the strong distance

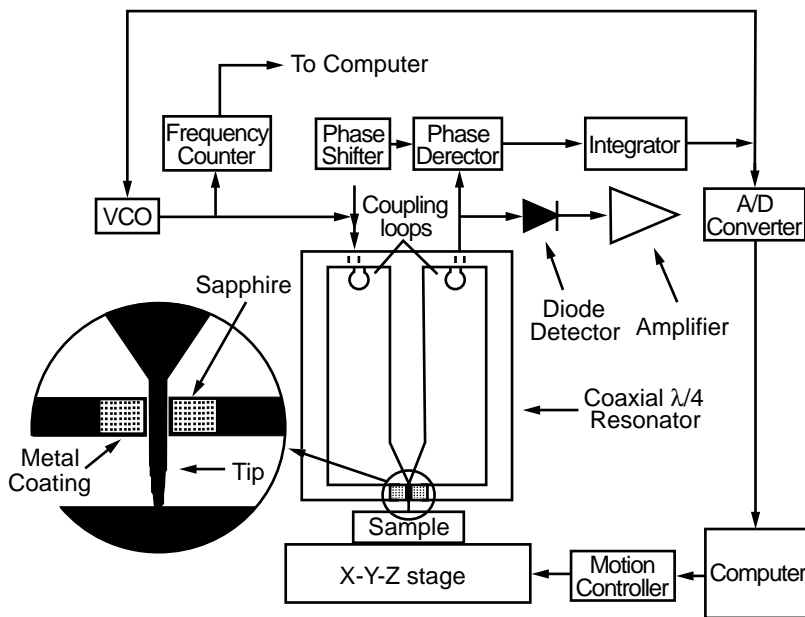


**Fig. 9** Resonant SNMM setup using a coaxial cavity. *Source:* From Ref.<sup>[73]</sup>. © 1997 American Institute of Physics.

dependence of the reflected signal is also present in this resonant setup, an independent distance control was employed. The researchers used a reflectance-compensated fiber optic distance sensor next to the tip and maintained the probe-sample separation with an accuracy of  $0.4\ \mu\text{m}$ . The researchers claim  $0.4\ \mu\text{m}$  spatial resolution at 1 GHz for this instrument.

High-resolution microwave near-field probes incorporating  $\lambda/4$  coaxial resonators have been produced by the group of Xiang<sup>[73]</sup> using an STM-like tip as a point-like field emitter, protruding from a small aperture (Fig. 9). The sharp tip results from tapering the center conductor of the coaxial cavity. The instrument achieves a spatial resolution of 100 nm and was used to image dielectric-constant profiles and ferroelectric domains.<sup>[74]</sup> Ferroelectric domains can be imaged using microwave fields by taking advantage of the nonlinear components in the dielectric constant for these materials. The contrast mechanism is based on a low-frequency oscillating voltage between sample and substrate that modulates the effective dielectric constant of the sample. The slight shift of the resonance frequency in the coaxial resonator probe could be related to this variation in dielectric constant, allowing for quantitative mapping of the third-order dielectric constant in a ferroelectric domain structure as seen in Fig. 10. To decrease tip damage resulting from excessive forces on the tip, and to be able to image unprepared conducting samples, Duewer et al.<sup>[75]</sup> introduced a tip-sample feedback scheme based on regulating the resonance frequency of the cavity to maintain a constant separation. In this experiment, conductivity was simultaneously measured via the amplitude of the cavity resonance. The principle for resistivity microscopy is

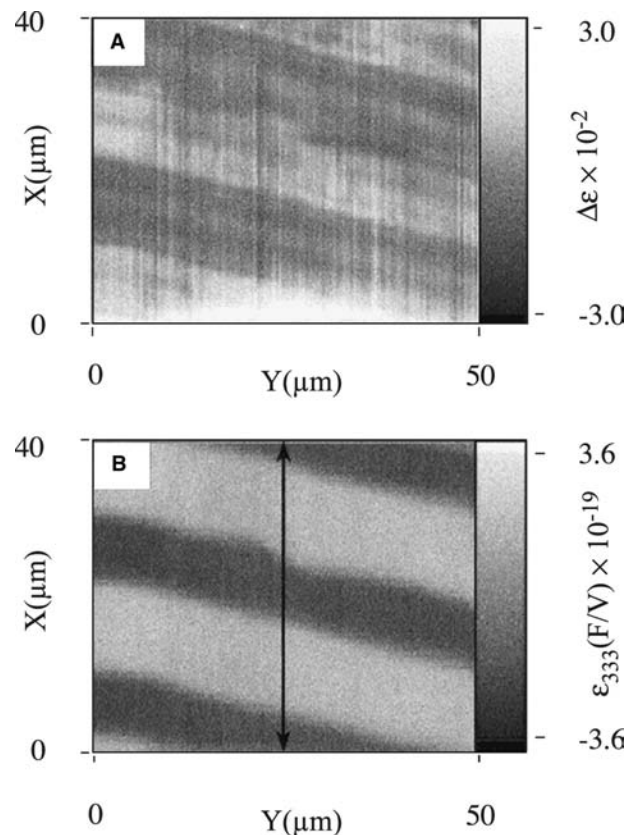


**Fig. 10** Linear dielectric constant image (A) and nonlinear third-order dielectric constant image (B) of the same area of a  $\text{LiNbO}_3$  single crystal with periodically polarized ferroelectric domains, recorded using a coaxial resonator SNMM. *Source:* From Ref.<sup>[74]</sup>. © 1998 American Institute of Physics.



based on the fact that the reflection of electromagnetic waves from conducting surfaces is determined by their resistivity. Therefore measuring the reflected amplitude and phase of a near-field probe yields a resistivity map. The reflection coefficient of a plane wave from a conducting surface is

$$\Gamma = \left( \frac{Z_s - Z_0}{Z_s + Z_0} \right)$$

where  $Z_0$  is the characteristic impedance of the line and  $Z_s$  is the surface impedance, which is directly connected to the conductivity:

$$Z_s = \sqrt{\frac{i\omega\mu_0}{\sigma + i\omega\epsilon}}$$

where  $\omega$  is the radial frequency,  $\mu_0$  is the permeability of free space, and  $\epsilon$  is the dielectric constant. For thick conducting layers, much thicker than the skin depth, surface impedance is measured while thin layers yield sheet resistance. Another important application of evanescent microwave probing is to measure spatially resolved surface impedance of high-temperature superconductor films. By finding superconducting and normally conducting features on superconducting thin films, it is possible to localize defects and evaluate film quality. The contrast mechanism is based on variations in microwave absorption when keeping the sample close to the critical temperature.<sup>[76]</sup> Others employ room temperature normal-state measurements<sup>[77]</sup> and relate them to the film's superconducting properties.

Tabib-Azar et al.<sup>[78]</sup> have used evanescent microwave probes for several nontraditional probing applications. These include transient and steady state thermography on semiconducting materials with 0.01 K thermal and 1  $\mu$ s temporal resolution. We recently published a review of near-field microscopy in the microwave and infrared regime.<sup>[56]</sup>

## CONCLUSION

We have summarized recent and current trends in optical, infrared, and microwave near-field microscopy incorporating surface force feedback. In the visible regime, the most common techniques are fiber-based aperture microscopes and scattering-type setups using AFM tips. On the other side of the spectrum in the microwave regime, metallic waveguide geometries play a dominant role. Future developments will enable combined probing of topography and field at the nanometer scale. The development of tools and instruments for mechanical manipulation of structures at nanometer length scales has driven progress in

nanoscale science and technology. At these scales, the doors to new worlds in biology, chemistry, and physics begin to open, enabling new applications such as real-time protein structure identification, molecular electronics, and quantum computation. However, to approach these ambitious applications, a great instrumental challenge must be surmounted: Tools must not only be able to touch, hold, and move molecular-scale objects, but must also be able to identify and control molecules and molecular-scale objects such as nanowires based on their chemical species or function. Near-field probes that combine access to dielectric contrast mechanisms at the nanometer scale hold out this promise.

## REFERENCES

1. Abbe, E. Beiträge zur Theorie des Mikroskops und der mikroskopischen Wahrnehmung. *Arch. Mikrosk. Anat. Entwickl.mech.* **1873**, *9*, 413–468.
2. Syngé, E.H. A suggested method for extending microscopic resolution into the ultra-microscopic region. *Philos. Mag.* **1928**, *6*, 356–362.
3. Bethe, H.A. Theory of diffraction by small holes. *Phys. Rev.* **1944**, *66* (7–8), 163–182.
4. Frait, Z. The use of high-frequency modulation in studying ferromagnetic resonances. *Czechoslov. J. Phys.* **1959**, *9*, 403–404.
5. Soohoo, R.F. A microwave magnetic microscope. *J. Appl. Phys.* **1962**, *33* (3), 1276–1277.
6. Bryant, C.A.; Gunn, J.B. Noncontact technique for the measurement of semiconductor resistivity. *Rev. Sci. Instrum.* **1965**, *36* (11), 1614–1617.
7. Ash, E.A.; Nicholls, G. Super-resolution aperture scanning microscope. *Nature* **1972**, *237* (5357), 510–512.
8. Binnig, G.; Rohrer, H. Scanning tunneling microscopy. *Helv. Phys. Acta* **1982**, *55* (6), 726–735.
9. Pohl, D.; Denk, W.; Lanz, M. Optical stethoscopy: Image recording with resolution  $\lambda/20$ . *Appl. Phys. Lett.* **1984**, *44* (7), 651–653.
10. Betzig, E.; Lewis, A.; Harootunian, A.; Isaacson, M.; Kratschmer, E. Near-field scanning optical microscopy (NSOM). *Biophys. J.* **1986**, *49*, 269
11. Binnig, G.; Quate, C.F.; Gerber, C. Atomic force microscope. *Phys. Rev. Lett.* **1986**, *56* (9), 930–933.
12. Toledo-Crow, R.; Yang, P.C.; Chen, Y.; Vaez-Iravani, M. Near-field differential scanning optical microscope with atomic force regulation. *Appl. Phys. Lett.* **1992**, *60* (24), 2957–2959.
13. Obermüller, C.; Karrai, K. Far field characterization of diffracting circular apertures. *Appl. Phys. Lett.* **1995**, *67* (23), 3408–3410.
14. Karrai, K.; Grober, R.D. Piezo-electric tuning fork tip-sample distance control for near field optical microscopes. *Ultramicroscopy* **1995**, *61*, 197–205.
15. Hoffmann, P.; Dutoit, B.; Salathe, R.P. Comparison of mechanically drawn and protection layer chemically etched optical fiber tips. *Ultramicroscopy* **1995**, *61* (1–4), 165–170.

16. Saiki, T.; Mononobe, S.; Ohtsu, M.; Saito, N.; Kusano, J. Tailoring a high-transmission fiber probe for photon scanning tunneling microscope. *Appl. Phys. Lett.* **1996**, *68* (19), 2612–2614.
17. Stöckle, R.M.; Fokas, C.; Deckert, V.; Zenobi, R.; Sick, B.; Hecht, B.; Wild, U.P. High-quality near-field optical probes by tube etching. *Appl. Phys. Lett.* **1999**, *75* (2), 160–162.
18. Xie, S.; Lu, P.; Bian, R.; Sanchez, E.; Leung, P. Near-Field Single Molecule Spectroscopy, Quantum Electronics and Laser Science Conference, Anaheim, CA, , 1996, 256–257.
19. Hulst, N.F.v.; Moers, M.H.P. Biological applications of near-field optical microscopy. *IEEE Eng. Med. Biol.* **1996**, *15* (1), 51–58.
20. Campillo, A.L.; Hsu, J.W.P.; White, C.A.; Jones, C.D.W. Direct measurement of the guided modes in LiNbO<sub>3</sub> waveguides. *Appl. Phys. Lett.* **2002**, *80* (13), 2239–2241.
21. Minh, P.N.; Ono, T.; Tanaka, S.; Goto, K.; Esashi, M. Near-field recording with high optical throughput aperture array. *Sens. Actuators, A* **2002**, *95* (2–3), 168–174.
22. Hecht, B.; Sick, B.; Wild, U.P.; Deckert, V.; Zenobi, R.; Martin, O.J.F.; Pohl, D. Scanning near-field optical microscopy with aperture probes: Fundamentals and applications. *J. Chem. Phys.* **2000**, *112* (18), 7761–7774.
23. Dunn, R.C. Near-field scanning optical microscopy. *Chem. Rev.* **1999**, *99*, 2891–2927.
24. Fischer, U.C. Microscopic Electromagnetic Radiation Transmitter or Detector. US Patent #5,770,855, 1998
25. Heimel, J.; Fischer, U.C.; Fuchs, H. SNOM/STM using a tetrahedral tip and a sensitive current-to-voltage converter. *J. Microsc.* **2001**, *202* (1), 53–59.
26. Zenhausern, F.; O'Boyle, M.P.; Wickramasinghe, H.K. Apertureless near-field optical microscope. *Appl. Phys. Lett.* **1994**, *65* (13), 1623–1625.
27. Knoll, B.; Keilmann, F. Infrared conductivity mapping for nanoelectronics. *Appl. Phys. Lett.* **2000**, *77* (24), 3980–3982.
28. Yin, X.; Fang, N.; Zang, X.; Martini, I.B.; Schwartz, B.J. Near-field two-photon nanolithography using an apertureless optical probe. *Appl. Phys. Lett.* **2002**, *81* (19), 3663–3665.
29. Hillenbrand, R.; Keilmann, F. Complex optical constants on a subwavelength scale. *Phys. Rev. Lett.* **2000**, *85* (14), 3029–3032.
30. Drews, D.; Ehrfeld, W.; Lacher, M.; Mayr, K.; Noell, W.; Schmitt, S.; Abraham, M. Nanostructured probes for scanning near-field optical microscopy. *Nanotechnology* **1999**, *10*, 61–64.
31. Belier, B.; Santos, A.; Bonnafé, J.; Nicu, L.; Temple-Boyer, P.; Bergaud, C. Micro-optomechanical sensor for optical connection in the near field. *Appl. Phys. Lett.* **2000**, *77* (12), 1768–1770.
32. Heisig, S.; Rudow, O.; Oesterschulze, E. Optical active gallium arsenide cantilever probes for combined scanning near-field optical microscopy and scanning force microscopy. *J. Vac. Sci. Technol., B* **2000**, *18* (3), 1134–1137.
33. Danzebrink, H.U.; Ohlsson, O.; Wilkening, G. Fabrication and characterization of optoelectronic near-field probes based on an SFM cantilever design. *Ultramicroscopy* **1995**, *61*, 131–138.
34. Tanaka, Y.; Fukuzawa, K.; Kuwano, H. Microfabrication of microtip on photocantilever for near-field scanning microscopy and investigation of effect of microtip shape on spatial resolution. *J. Appl. Phys.* **1998**, *83* (7), 3547–3551.
35. Davis, R.C.; Williams, C.C. Nanometer-scale absorption spectroscopy by near-field photodetection optical microscopy. *Appl. Phys. Lett.* **1996**, *69* (9), 1179–1181.
36. Rosner, B.; Bork, T.; Agrawal, V.; van der Weide, D.W. Microfabricated silicon coaxial field sensors for near-field scanning optical and microwave microscopy. *Sens. Actuators, A* **2002**, *102*, 185–194.
37. Dragnea, B.; Preusser, J.; Szarko, J.M.; Leone, S.R.; Hinsberg, W.D. Pattern characterization of deep-ultraviolet photoresists by near-field infrared microscopy. *J. Vac. Sci. Technol., B* **2001**, *19* (1), 142–152.
38. Keilmann, F.; Merz, R. Far-infrared Near-field Spectroscopy of Two-dimensional Electron Systems. In *Near Field Optics*; Kluwer Academic Publishers: Dordrecht, 1993; 317–324.
39. Keilmann, F. FIR microscopy. *Infrared Phys. Technol.* **1995**, *36* (1), 217–224.
40. Hunsche, S.; Koch, M.; Brener, I.; Nuss, M.C. THz near-field imaging. *Opt. Commun.* **1998**, *150*, 22–26.
41. Lahrech, A.; Bachelot, R.; Gleyzes, P.; Boccara, A.C. Infrared-reflection-mode near-field microscopy using an apertureless probe with a resolution of 600. *Opt. Lett.* **1996**, *21* (17), 1315–1317.
42. Hillenbrand, R.; Knoll, B.; Keilmann, F. Pure optical contrast in scattering-type scanning near-field microscopy. *J. Microsc.* **2001**, *202* (1), 77–83.
43. Labardi, M.; Patane, S.; Allegrini, M. Artifact-free near-field optical imaging by apertureless microscopy. *Appl. Phys. Lett.* **2000**, *77* (5), 621–623.
44. Knoll, B.; Keilmann, F. Near-field probing of vibrational absorption for chemical microscopy. *Nature* **1999**, *399*, 134–137.
45. Hillenbrand, R.; Taubner, T.; Keilmann, F. Phonon-enhanced light-matter interaction at the nanometre scale. *Nature* **2002**, *418*, 159–162.
46. Grober, R.D. High Efficiency Near-Field Electromagnetic Probe Having a Bowtie Antenna Structure. US Patent #5,696,372, . 1997.
47. Rosner, B.; Peck, J.; van der Weide, D.W. Near field antennas integrated with scanning probes for THz to visible microscopy: Scale modeling and limitations on performance. *IEEE Trans. Antennas Propag.* **2002**, *50*, 670–675.
48. van der Weide, D.W.; Keilmann, F. Coherent Periodically Pulsed Radiation Spectrometer. US Patent #5,748,309, 1998
49. Bozec, L.; Hammiche, A.; Pollock, H.M.; Conroy, M.; Chalmers, J.M.; Overall, N.J.; Turin, L. Localized photothermal infrared spectroscopy using a proximal probe. *J. Appl. Phys.* **2001**, *90*, 5159–5165.
50. Hammiche, A.; Pollock, H.M.; Reading, M.; Claybourn, M.; Turner, P.; Jewkes, K. Photothermal FTIR spectroscopy: A step towards FT-IR microscopy at a resolution better than the diffraction limit. *Appl. Spectrosc.* **1999**, *53* (7), 810–815.

51. Kölzer, J.; Oesterschulze, E.; Deboy, G. Thermal imaging and measurement techniques for electronic materials and devices. *Microelectron. Eng.* **1996**, *31*, 251–270.
52. Dragnea, B.; Leone, S.R. Advances in submicron infrared vibrational band chemical imaging. *Int. Rev. Phys. Chem.* **2001**, *20* (1), 59–92.
53. Pollock, H.M.; Smith, D.A. The Use of Near-Field Probes for Vibrational Spectroscopy and Photothermal Imaging. In *Handbook of Vibrational Spectroscopy*; John Wiley & Sons: Indianapolis, 2002.
54. Keilmann, F.; Weide, D.W.v.d.; Eickelkamp, T.; Merz, R.; Stöckle, D. Extreme sub-wavelength resolution with a scanning radio-frequency transmission microscope. *Opt. Commun.* **1996**, *129*, 15–18.
55. van der Weide, D.W. Localized picosecond resolution with a near-field microwave/scanning-force microscope. *Appl. Phys. Lett.* **1997**, *70* (6), 677–679.
56. Rosner, B.T.; van der Weide, D.W. High-frequency near-field microscopy. *Rev. Sci. Instrum.* **2002**, *73* (7), 2505–2525.
57. Heisig, S.; Oesterschulze, E. Gallium arsenide probes for scanning near-field probe microscopy. *Appl. Phys., A* **1998**, *66*, S385–S390.
58. Kramer, A.; Keilmann, F.; Knoll, B.; Guckenberger, R. The coaxial tip as a nano-antenna for scanning near-field microwave transmission microscopy. *Micron* **1996**, *27* (6), 413–417.
59. McCarty, G.S.; Weiss, P.S. Scanning probe studies of single nanostructures. *Chem. Rev.* **1999**, *99* (7), 1983–1990.
60. Michel, B.; Mizutani, W.; Schierle, R.; Jarosch, A.; Knop, W.; Benedickter, H.; Bächthold, W.; Rohrer, H. Scanning surface harmonic microscopy: Scanning probe microscopy based on microwave field-induced harmonic generation. *Rev. Sci. Instrum.* **1992**, *63*, 4080–4085.
61. Stranick, S.J.; Bumm, L.A.; Kamna, M.M.; Weiss, P.S. Linear and Nonlinear Spectroscopy with The Tunable AC Scanning Tunneling Microscope. In *Photons and Local Probes*; Kluwer Academic Publishers: Dordrecht, 1995; 221–233.
62. Keilmann, F.; Knoll, B.; Kramer, A. Long-wave-infrared near-field microscopy. *Phys. Status Solidi, B* **1999**, *215*, 849–854.
63. Weiss, S.; Ogletree, D.F.; Botkin, D.; Salmeron, M.; Chemla, D.S. Ultrafast scanning probe microscopy. *Appl. Phys. Lett.* **1993**, *63* (18), 2567–2569.
64. Nunes, G.; Freeman, M.R. Picosecond resolution in scanning tunneling microscopy. *Science* **1993**, *262*, 1029–1032.
65. Botkin, D.; Glass, J.; Chemla, D.S.; Ogletree, D.F.; Salmeron, M.; Weiss, S. Advances in ultrafast scanning tunneling microscopy. *Appl. Phys. Lett.* **1996**, *69* (9), 1321–1323.
66. Kim, J.; Williamson, S.; Nees, J.; Wakana, S.; Whitaker, J. Photoconductive sampling probe with 2.3-ps temporal resolution and 4V sensitivity. *Appl. Phys. Lett.* **1993**, *62* (18), 2268–2270.
67. Takeuchi, K.; Mizuhara, A. Image observation of picosecond electrical pulse by scanning force optoelectronic microscope. *IEEE MTT-S Int. Microw. Symp. Dig.* **1997**, *3*, 1643–1646.
68. Oesterschulze, E.; Heisig, S.; Steffens, W.M. Cantilever probes for spatio-temporal imaging of voltage pulses with an ultrafast scanning probe microscope. *J. Vac. Sci. Technol., B* **2001**, *19* (1), 107–110.
69. Golosovsky, M.; Davidov, D. Novel millimeter-wave near-field resistivity microscope. *Appl. Phys. Lett.* **1996**, *68* (11), 1579–1581.
70. Abu-Teir, M.; Golosovsky, M.; Davidov, D.; Frenkel, A.; Goldberger, H. Near-field scanning microwave probe based on a dielectric resonator. *Rev. Sci. Instrum.* **2001**, *72* (4), 2073–2079.
71. Steinhauer, D.E.; Vlahacos, C.P.; Dutta, S.; Wellstood, F.C.; Anlage, S.M. Surface resistance imaging with a scanning near-field microwave microscope. *Appl. Phys. Lett.* **1997**, *71* (12), 1736–1738.
72. Tabib-Azar, M.; Su, D.P.; Pohar, A.; LeClair, S.R.; Ponchak, G. 0.4  $\mu\text{m}$  spatial resolution with 1 GHz ( $\lambda = 30$  cm) evanescent microwave probe. *Rev. Sci. Instrum.* **1999**, *70* (3), 1725–1729.
73. Gao, C.; Wei, T.; Duewer, F.; Lu, Y.; Xiang, X.D. High spatial resolution quantitative microwave impedance microscopy by a scanning tip microwave near-field microscope. *Appl. Phys. Lett.* **1997**, *71* (13), 1872–1874.
74. Gao, C.; Duewer, F.; Lu, Y.; Xiang, X.D. Quantitative nonlinear dielectric microscopy of periodically polarized ferroelectric domains. *Appl. Phys. Lett.* **1998**, *73* (8), 1146–1148.
75. Duewer, F.; Gao, C.; Takeuchi, I.; Xiang, X.D. Tip-sample distance feedback control in a scanning evanescent microwave microscope. *Appl. Phys. Lett.* **1999**, *74* (18), 2696–2698.
76. Takeuchi, I.; Wei, T.; Duewer, F.; Yoo, Y.K.; Xiang, X.D.; Talyansky, V.; Pai, S.P.; Chen, G.J.; Venkatesan, T. Low temperature scanning-tip microwave near-field microscopy of  $\text{YBa}_2\text{Cu}_3\text{O}_{7-x}$  films. *Appl. Phys. Lett.* **1997**, *71* (14), 2026–2028.
77. Golosovsky, M.; Galkin, A.; Davidov, D. High-spatial resolution resistivity mapping of large-area YBCO films by a near-field millimeter-wave microscope. *IEEE Trans. Microw. Theor. Tech.* **1996**, *44* (7), 1390–1392.
78. Tabib-Azar, M.; Ciocan, R.; Ponchak, G.; LeClair, S.R. Transient thermography using evanescent microwave microscope. *Rev. Sci. Instrum.* **1999**, *70* (8), 3387–3390.

# Near-Field Raman Spectroscopy

Eric Ayars

*Department of Physics, California State University–Chico,  
Chico, California, U.S.A.*

## INTRODUCTION

Near-field Raman Spectroscopy (NFRS) combines the chemical-information-gathering power of Raman spectroscopy with the spatial resolution of the atomic force microscope (AFM). In addition, it allows the researcher to correlate topographic and optical data in ways impossible via other techniques. This entry presents an overview of the methods used in NFRS, a brief history of the field, and a tour of some recent achievements in this rapidly evolving field. As with any other field at this stage of development, there are still unanswered questions in NFRS; some of these will be addressed as well.

## NEAR-FIELD SCANNING OPTICAL MICROSCOPY

Microscopy is one of the most powerful tools available in modern science. Much of our basic understanding of the world comes from our ability to see the details of how things operate. Until recently, however, the available resolution for optical microscopes has been limited by diffraction effects arising from the wave nature of light. Near-field scanning optical microscopy (NSOM) provides a means of surpassing those limits, thus bringing to the researcher a variety of research tools available in visible-light optics at resolutions previously unattainable at those wavelengths. Because near-field Raman microscopy (NSRM) obtains both its resolution and its enhancement effects from the characteristics of light in the near field, it is necessary to begin any discussion of NSRM with an overview of NSOM.

### Resolution Limits to Conventional Microscopy

The fundamental limit to resolution of conventional optical microscopes arises from the nature of light. Because light is a wave, it diffracts on interaction with the sample being studied. The diffraction angle depends on the light frequency and the spatial frequency of the features on the sample. In order to resolve an object, it is necessary to collect not only

the central zeroth-order diffracted light, but some of the higher orders as well.<sup>[1]</sup> These higher-order diffraction maxima contain the spatial information.

As an example, consider a one-dimensional sample with some contrast mechanism having two distinct spatial frequencies (Fig. 1). Here, the contrast is represented as height; it could be contrast in color, refractive index, reflectivity, optical density, fluorescence, or anything else observable with light. The lens shown in Fig. 1 has sufficient numeric aperture (NA) to capture the light diffracted from the larger features, but light diffracted from the smaller features is not collected. Thus, the image formed does not include the components with higher spatial frequency. A lens with a higher NA could collect the light from these smaller features, but there is a practical limit to how far this sort of improvement can go. The highest NA obtainable with oil-immersion lenses is just over 1.4, resulting in a minimum resolution of roughly 250 nm for visible light.

### How to Avoid Resolution Limits

NSOM allows higher resolution than would be allowed by the Abbe limit. It does this by utilizing the continuity of the fields near an aperture or sharpened conductor. The illumination pattern cannot change instantaneously from subwavelength source spot to broad far-field spot. In the far field, defined as distances greater than a few tip radii from the source, light is diffracted at extremely high angles and illuminates a broad region. At the tip, the light is constrained to a region near the tip.<sup>[2]</sup> Close to the tip, in the near field, the light is still limited to a relatively small region, on the order of the tip radius. By holding the sample within this near-field region, the illuminated area on the sample is kept small—smaller than would be allowed by the Abbe limit. Light interacting with the sample can be collected in the far field with conventional optics. Although the collection optics are incapable of resolving that illuminated region, the light collected is known to have originated from a well-defined small spot; by scanning the aperture over the sample one can form a rasterized image with optical resolution approximately equal to that spot size.

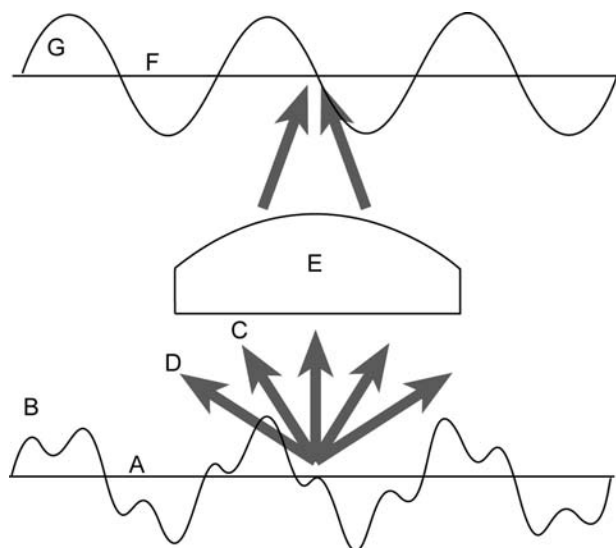


**Fig. 1** The origin of the resolution limit in conventional microscopy. Object (A) has a contrast profile (B) with two distinct spatial frequencies. Light from the sample is diffracted by the larger features at angle (C), and by the smaller features at angle (D). The lens (E) collects only the light diffracted by the larger features, so the resulting image (F) contains information about only the larger features (G). Increasing the magnification would create a larger image of (G), with no increase in information content.

In the region near the tip, often called the near-field enhancement region, the electric field decreases exponentially with distance. This is of particular importance in Raman applications, where the enhanced electric field in the near field can result in significantly increased Raman signal and may be responsible for other effects as well.

The earliest NSOM systems used a sharpened optical fiber as a tip. This was prepared by either heating and pulling or boundary-layer chemical etching<sup>[3]</sup> and then was coated with metal to constrain the electric field to the interior of the tip. An aperture at the end of this tip is formed by focused ion-beam machining or, more commonly, by holding the tip at an angle during the metal-coating process so that the end was shadowed and not coated. This subwavelength aperture is held close to the sample and acts as a light source or detector, or both, depending on the experimental configuration. More recent systems have used a sharpened metallic tip or metal-coated AFM tip as a scattering source. This “apertureless” tip is held near the sample as before, and then illuminated externally.

### Behavior of Light Near a Tip

The problem of diffraction through a subwavelength aperture was first solved by Bethe<sup>[4]</sup> and later improved

by Bouwkamp.<sup>[5]</sup> Their solution assumes a circular aperture in an infinitely thin, flat, perfect conductor. Other work has been done, e.g., with numeric calculations of the field components near a two-dimensional tip (a slit) with a more realistic tip profile made of real materials<sup>[6]</sup> and apertureless NSOM.<sup>[7–9]</sup> All of these calculations show the same basic characteristics in the resulting fields: very strong distance dependence, evanescent fields near the tip, and dependence on polarization.

The square of the electric field for light emerging from a tip aperture with the original polarization (Bethe–Bouwkamp model) is shown in Fig. 2. Here the aperture radius is one-fifth the wavelength of the light, and the electric field magnitude is calculated at a distance of one-tenth the aperture radius. Some light emerging from the aperture is polarized at 90° to the incident light; this profile (with the same tip parameters) is shown in Fig. 3. There is also a relatively strong component of the emerging light that is polarized in the direction of propagation, which is shown in Fig. 4. All of these fields, with the exception of the central component of the first, die out rapidly with increasing distance from the tip. Fig. 5 shows the field profile at increasing distance from the tip for the first case, corresponding to Fig. 2.

For apertureless tips, there is a similar enhancement region near the tip. Typically, the tip is modeled as a conical metal probe with a spherical apex. The enhancement region extends over a region approximately the size of the diameter of the tip apex, and only the component of the light polarized in the direction of the tip axis is strongly enhanced. This enhancement occurs for both metallic and dielectric probes, but for metallic probes there is additional enhancement because of surface plasmon–polaritons at the apex of the tip.<sup>[9]</sup> One significant advantage to apertureless tips

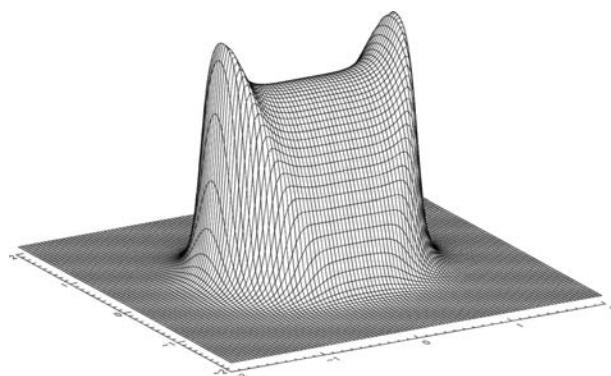


**Fig. 2** Near-field enhancement. Graph height represents the intensity of the light emerging from a circular subwavelength aperture with the incident ( $x$ ) polarization, with an aperture size  $a$  equal to one-fifth the wavelength, at a distance of one-tenth  $a$ .



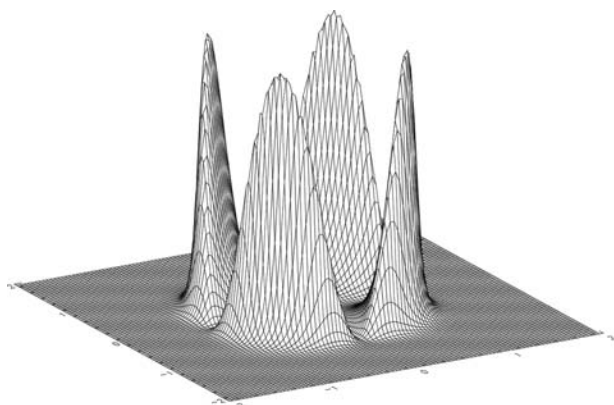


**Fig. 3** Near-field enhancement, showing the component of the light intensity polarized at  $90^\circ$  ( $y$ ) to the incident light. The aperture parameters are the same as in Fig. 2.

is that the incident light intensity is not subject to the limitations<sup>[10]</sup> imposed by the threat of thermal breakdown of the reflective coating on a fiber optic tip. Ordinary lenses are used to focus the light on the tip, either from the side or through the sample from below with a high-NA lens.<sup>[11]</sup> The illuminated region is much larger than the tip; but the signal from the enhancement region at the tip is by far the dominant component of the collected signal.

### Tip–Sample Distance Regulation

For either aperture or apertureless NSOM and NSRM, it is necessary to hold the tip at a close and well-regulated distance from the sample. The feedback mechanism responsible for maintaining this near-field distance is central to any microscope head design and depends on the type of tip used. Frequently, tips are formed by coating commercial cantilever AFM tips

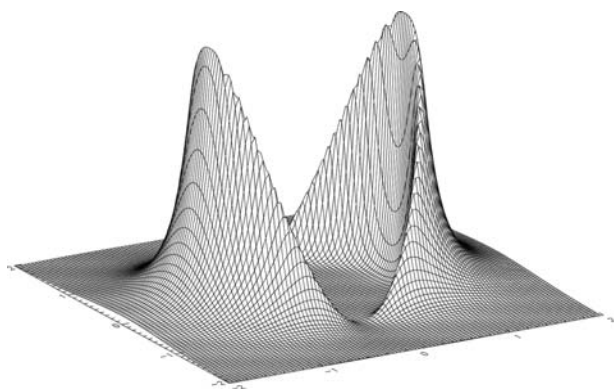


**Fig. 4** Near-field enhancement, showing the component of the light intensity polarized in the direction of the incident light ( $z$ ). The aperture parameters are the same as in Fig. 2.

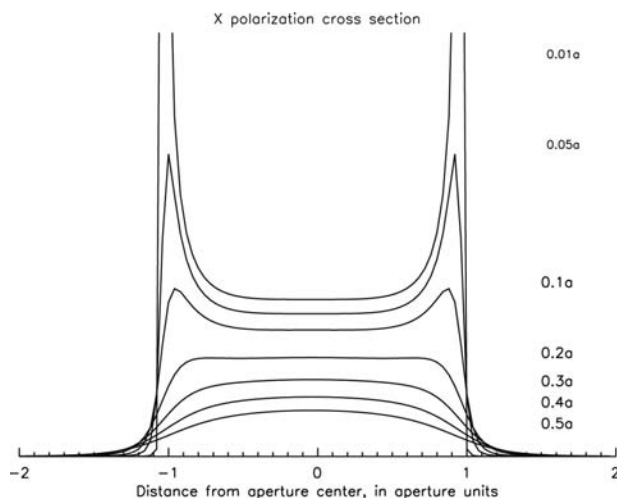


**Fig. 5** Line cuts showing distance dependence of near-field enhancement. The line at  $0.1a$  is a cut through the center of Fig. 2; the others show how that enhancement changes with distance.

with metal. If this is the case, it is simplest to use standard AFM feedback methods, described elsewhere. If the tips used are formed from optical fibers or etched metal wires, or if it is desirable to control the tip–sample distance more precisely than is possible with relatively flexible cantilever AFM tips, then shear-force feedback must be used. In shear-force feedback, the tip is shaken, at or near its resonance, in a plane perpendicular to the plane of the sample. Some measurement of the tip oscillation amplitude is made, and as the tip approaches the sample this amplitude decreases. The feedback electronics keep the tip positioned via piezoelectric actuators so that the amplitude remains at some intermediate value between its free-oscillation value and zero. By recording the adjustment necessary to maintain a constant tip–sample distance, it is possible to map the topographic features of the sample. This topographic detail can then be correlated to the optical information for a better understanding of the phenomena being observed.

The earliest method of shear-force tip–sample distance control was optical feedback. In an optical feedback system, a laser beam is focused on the oscillating fiber near the tip. The diffraction pattern “shadow” of the tip falls on an edge-masked detector. The signal from this detector serves as a measurement of the tip oscillation amplitude, and thus provides a shear-force feedback signal.

In recent years, optical feedback has been largely superseded by tuning-fork feedback.<sup>[12]</sup> In the tuning-fork method for distance regulation, the optical fiber or wire, with the subwavelength aperture or tip at the end, is glued to the side of a small quartz tuning fork. The fork/tip assembly is shaken at or near its



resonance, and the piezoelectric tuning fork provides an electric signal proportional to the amplitude of oscillation of the tip. The tuning-fork method offers considerable advantages over the optical feedback method. It eliminates the difficulty of aligning and focusing the feedback laser with the fiber and edge mask. With optical feedback, any drift in feedback laser power or alignment of the feedback optics can be misinterpreted as a change in feedback level, causing problems in low-light experiments requiring long integration times. Tuning-fork feedback provides a feedback signal that is much more stable on long scans. Finally, tuning-fork feedback does not require a second laser beam, thus eliminating one more source of noise in spectroscopic or fluorescence applications.

## RAMAN SPECTROSCOPY

Raman spectroscopy, discovered in 1928 by Chandrasekhara Venkata Raman, is the spectroscopy of vibrational transitions measured by the inelastic scattering of light. The energy of vibrational levels typically corresponds to wave numbers of  $10^2$  to  $10^4 \text{ cm}^{-1}$ , compared with the  $10^4$  to  $10^6 \text{ cm}^{-1}$  of valence electron transitions seen with visible and UV spectroscopy. The light wavelength required for absorption spectroscopy in this energy range is in the infrared to far-infrared range. This range of wavelengths is inconvenient to work with: appropriate optical materials for this entire range of wavelengths are scarce or non-existent, requiring different gratings and detectors for different portions of the region, entirely reflective optics, and relatively large sample volumes. By measuring these transitions with inelastic scattering, it is possible to cover the entire vibrational spectrum with a single recording using easily managed visible light. In addition, the selection rules for IR spectroscopy and for Raman spectroscopy are markedly different. Some vibrations are strongly IR active but weak or non-existent in Raman; others are strongly Raman active but weak in IR. The two tools should be regarded as complementary: For a complete understanding of the vibrational levels of the material, it is often necessary to study both IR and Raman spectra.

Raman spectroscopy has advantages over IR spectroscopy. The primary advantage is the ability to do the spectroscopy with visible light. The benefits of using conventional optics, readily available light sources, and visible-light alignment are not to be underestimated. Another advantage is the ability to work with small sample volumes. Micro-Raman systems typically can work with a sample region of about 1- $\mu\text{m}$  diameter on a surface, whereas IR spectroscopy,

as an absorptive phenomenon, requires a larger volume of material to have a significant effect. Water is a strong absorber of IR light, so it is difficult to do IR spectroscopy of compounds in aqueous solution, but water is a weak Raman scatterer, making it ideal for the study of biological materials in solution.

In the classical one-dimensional derivation of the Raman effect,<sup>[13]</sup> the polarization  $P$  of the material depends on the polarizability  $\alpha$  of the material and on the incident electric field  $E$ , which is provided by the incident light at frequency  $\nu_o$ :

$$P = \alpha E_o \cos(2\pi\nu_o t) \quad (1)$$

The electric field magnitude  $E_o$  is presumed to be constant over the dimensions of the oscillation. This is an excellent approximation for visible light in the far field. Charges in the material may oscillate at some frequency  $\nu_m$  about their equilibrium positions:

$$q = q_o \cos(2\pi\nu_m t) \quad (2)$$

This oscillation may induce a change in the polarizability of the material, which can be approximated by a Taylor expansion of  $\alpha$ :

$$\alpha \approx \alpha_o + \left(\frac{\partial\alpha}{\partial q}\right) q_o + \dots \quad (3)$$

Combining these and simplifying gives, to first order in  $q$ :

$$P \approx \alpha_o E_o \cos(2\pi\nu_o t) + \frac{1}{2} q_o \left(\frac{\partial\alpha}{\partial q}\right)_o E_o [\cos\{2\pi(\nu_o - \nu_m)t\} + \cos\{2\pi(\nu_o + \nu_m)t\}] + \dots \quad (4)$$

The first of these terms is the Rayleigh scattering, which is unshifted in frequency. The second is the Raman scattering, at the characteristic Stokes (–) and anti-Stokes (+) frequencies. The existence of Raman-scattered light depends on the Raman activity,  $\partial\alpha/\partial q$ : if there is no change in the polarizability for a given vibrational transition,  $\partial\alpha/\partial q = 0$  and the transition is not Raman active.

In three dimensions, the equations become tensorial, but other than that the derivation is essentially unchanged. Change in the polarizability tensor  $\alpha$ , which is symmetric for conventional Raman scattering, still determines the activity, but now the vibration is Raman active if any one of the polarizability tensor components is changed during the vibration. Additionally, the three-dimensional form of the derivation brings to light the polarization dependence of the

Raman activity. It is possible, in crystalline materials, e.g., to have normal modes of vibration that are excited only by certain polarization states of the incident light. This is a great advantage in solid-state studies, because it allows investigation of anisotropic bonds for a more complete understanding of the material.

The primary experimental difficulty with Raman spectroscopy is signal-to-noise ratio. The quantum efficiency of Raman spectroscopy is typically on the order of  $10^{-6}$ : for every million photons that strike the sample, one might be Raman shifted. This low signal level is exacerbated by the close proximity, spectrally, of the Rayleigh-scattered light. The spectrometer must be designed to minimize internal scattering of this unshifted light, as even slight scattering will overwhelm the small Raman signal. A double spectrometer has long been the accepted minimum for Raman work, and triple spectrometers are not unusual. These cut the amount of light that reaches the detector, but they cut the amount of scattered light that reaches the detector even more. In recent years, the development of holographic notch filters has allowed researchers to block the unshifted light before it reaches the spectrometer.<sup>[14–16]</sup> This allows use of single spectrometers and lessens the signal losses associated with double and triple spectrometers. Use of a holographic notch filter and single spectrometer also allows one to collect the final signal with a charge-coupled device (CCD). This permits collection of an entire spectrum at once, rather than one point at a time, which is a great advantage when—as in NSRM—long integration times are necessary.

## NEAR-FIELD RAMAN SPECTROSCOPY

The primary difficulty with Raman spectroscopy is also the primary weakness of near-field scanning optical microscopy: low signal levels. The amount of light that can be sent through a subwavelength probe aperture is severely limited by the shape and material of the probe.<sup>[17]</sup> The combination of this low excitation power and the low cross section for Raman scattering necessitates long integration times. In order to image the sample, this long integration time must be applied at each point in the scan.

The first NSOM image successfully taken on a Raman line was achieved in 1995.<sup>[18]</sup> The image, a  $4\text{-}\mu\text{m}^2$  square area on a sample of Rb-doped potassium titanyl phosphate (KTP), used the difference in Raman spectra between the pure and the doped regions as a contrast mechanism. It used a tapered fiber probe, had a resolution of approximately 250 nm, and took over 10 hr to complete.

Apertureless probes offer much higher illumination power, and may offer greater near-field enhancement

as well.<sup>a</sup> The resolution of an NSOM image is dependent on the size of the probe, so the smaller tip size for an apertureless probe also offers a resolution advantage. The highest-resolution NSRM images published to date, with spatial resolution of less than 25 nm, have been produced using silver apertureless probes<sup>[19]</sup> (Fig. 6). The data represented by Fig. 6 took approximately 40 min to collect.

The significant decrease in the time it takes to obtain an NSRM image with apertureless probes has resulted in their almost universal adoption. It has also sparked a surge in research applications. Recent uses of NSRM include measurement of residual stress in a damaged silicon wafer,<sup>[20]</sup> imaging of organic molecules,<sup>[21]</sup> and measurement of variation in Raman spectra along single-walled nanotubes<sup>[19]</sup> as well as many others.

## Differences Between NSRM and Micro-Raman

It is tempting to view NSOM-Raman spectroscopy as merely the next resolution increase in a well-understood chain of improvements. Micro-Raman spectroscopy increased the spatial resolution of Raman studies far beyond that of ordinary Raman work,<sup>[22]</sup> and on a superficial level, NSOM-Raman is seen as the next step in resolution enhancement. This is not entirely the case: there are aspects of NSRM that are fundamentally different from micro-Raman.

The differences between NSRM and other Raman spectroscopies originate with the nature of light in the near field. As discussed above, the electric field components near an NSOM tip are not uniform in either space or polarization. For an apertured tip, with  $x$ -polarized incident light, the transmitted light has  $x$ ,  $y$ , and  $z$  components. With apertureless tips, there is a similarly strong enhancement of the polarization component along the tip axis. The total intensity of the radiation varies strongly with distance from the tip. This variation is due to the presence, in the near field, of evanescent (non-propagating) modes, which exist for each of the three polarization states.

The first of the effects in near-field Raman spectroscopy is due to the overall enhancement of the light intensity near the probe aperture. This enhancement does not extend to the far field, and thus does not contribute to measurements of the total radiation emitted from the probe. Because this total intensity near the probe tip includes the evanescent modes, which do not contribute to any far-field intensity measurements, there is actually more light available for Raman

<sup>a</sup>The magnitude of the enhancement is inversely related to the radius of curvature of the probe. Apertureless probes are typically much sharper than tapered fiber probes, although the geometry of the two is different enough that a direct comparison is difficult.

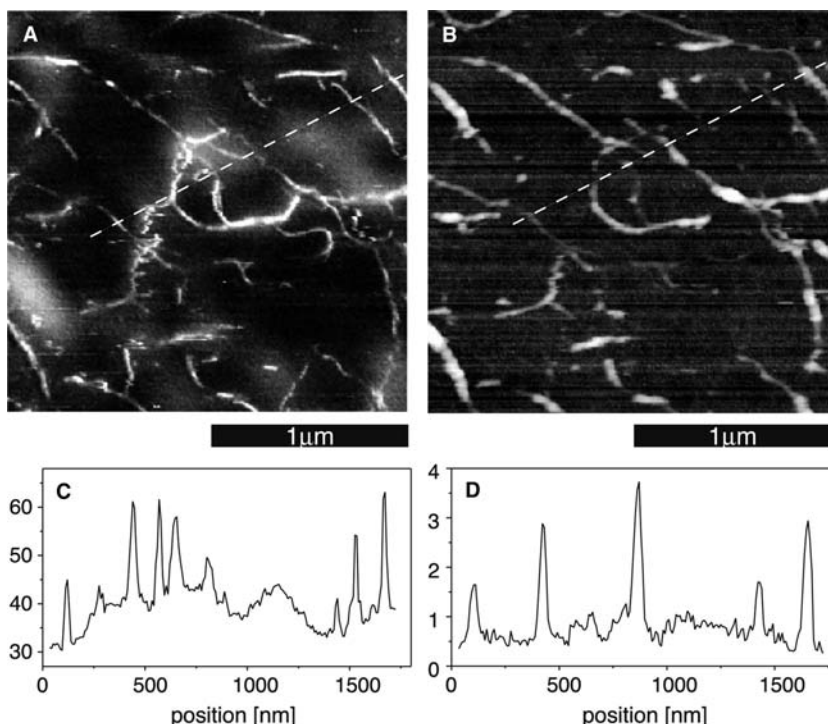


**Fig. 6** Raman image of carbon nanotubes (A) together with simultaneously acquired topography (B). Line scans (C) and (D) are taken along the dotted lines in (A) and (B), and have vertical scales of kcts/sec and nm, respectively. *Source:* Courtesy of Achim Hartschuh, Physikalische Chemie, Universität Siegen.

excitation in the near field than one would expect. This effect has proven useful in measuring the Raman spectra of extremely thin films: in the far field, there is no observed Raman signal from the film, but when a tip is in the near field there is a strong signal from the film.<sup>[23]</sup> The same effect may be useful for measurements of surface states on solids.

The  $z$  polarization component of the light near the probe also leads to unusual near-field Raman effects.<sup>[24]</sup> In conventional Raman spectroscopy, vibrational modes with  $x$  or  $y$  components are excited by the incident light, which is necessarily polarized in the  $xy$  plane. Modes with purely  $z$  components require an electric field in the  $z$  direction for excitation. In liquid- or gas-phase Raman work, this is not a limitation, likewise in amorphous materials or polycrystalline materials with domain size less than the minimum spot size. In single-crystal work, the  $z$  modes are usually measured by reorienting the crystal so that the incident light has a polarization component along the desired axis. In near-field Raman, there is a  $z$  component of the field that provides excitation of these modes without reorientation of the crystal. This effect can be effectively “turned off” by moving the tip out of the near field. Comparison of near-field and far-field spectra allows the researcher to determine the polarization dependence of the material.

The third of the effects possible in NSRM is due to the strong gradient in the near-field electric fields.<sup>[25]</sup> In the standard derivation of the Raman effect (Eqs. (1)–(4)) it is assumed that the electric field

magnitude remains constant over the entire extent of the oscillation. For conventional Raman techniques, this is true. Even for confocal Raman spectroscopy, this is an excellent approximation; the intensity of the traveling wave is not going to change measurably over molecular distances. With NSRM, however, the approximation no longer holds. The traveling-wave component of the transmitted radiation is only part of the oscillating field present in NSOM: the evanescent modes also contribute to the total electric field and to the Raman excitation.

The effect of the field gradient can be explored by taking a Taylor expansion of the electric field.

$$E \approx E_0 + \left( \frac{\partial E}{\partial q} \right)_0 q + \dots \quad (5)$$

Inserting that expansion in place of  $E_0$  in the derivation given in Eqs. (1)–(4) gives:

$$\begin{aligned} P \approx & \alpha_0 E_0 \cos(2\pi\nu_0 t) \\ & + \frac{1}{2} q_0 \left( \frac{\partial \alpha}{\partial q} \right)_0 E_0 [\cos\{2\pi(\nu_0 - \nu_m)t\} \\ & + \cos\{2\pi(\nu_0 + \nu_m)t\}] \\ & + \frac{1}{2} q_0 \left( \frac{\partial E}{\partial q} \right)_0 \alpha_0 [\cos\{2\pi(\nu_0 - \nu_m)t\} \\ & + \cos\{2\pi(\nu_0 + \nu_m)t\}] + \dots \quad (6) \end{aligned}$$

The first two terms of Eq. (6) are the same as before. The third describes a scattering with the same Stokes

and anti-Stokes frequency shifts as the Raman lines, but no dependence on the Raman activity  $\partial\alpha/\partial q$ . Instead, this scattering term is dependent on the field gradient and the polarizability. Selection rules for this term depend on the characteristics of  $\alpha$ , and so would have activity similar to IR absorption spectroscopy. The net result would be the observation of transitions that are normally seen in IR absorption spectroscopy but are not Raman active.

The effect of a strong electric field gradient on Raman spectra has been discussed previously as a mechanism for some of the observed spectral lines in surface-enhanced Raman spectroscopy (SERS).<sup>[26]</sup> Because there is no good, controllable method of regulating distance or field gradient in SERS, NFRS offers the first opportunity to test the distance dependence of this effect. The effect was also predicted as an effect in the Raman spectra of microparticles suspended in laser traps.<sup>[27]</sup> This prediction was tested at the time, but for the gradients available in that experimental configuration the strength of the effect was calculated to be four orders of magnitude lower than the Raman effect and no lines were observed. There has been at least one possible sighting of this field-gradient effect in NFRS<sup>[28]</sup> although some other researchers who have looked for it have not seen it.<sup>[19]</sup>

## CONCLUSION

Near-field Raman spectroscopy allows researchers to make measurements of chemical bonds and vibrational transitions with spatial resolution unavailable via conventional optical methods. These high-resolution spectroscopic data come with corresponding topographic information, allowing better understanding of how nanoscale features affect the nanoscale spectroscopic data. The enhancement region near the tip falls off very rapidly, so NSRM can be used for Raman measurements of thin films and surface effects that would otherwise be either too small to observe or washed out by the bulk signal.

The primary difficulties in NSRM are low signal level and correspondingly long integration times. The development and use of apertureless tips has greatly increased the signal strength available, decreased the time required for image collection, and increased the resolution as well. These improvements have brought NSRM to the point where it is possible to obtain detailed high-resolution images, with separate topographic and Raman data, in well under an hour.

NSRM is not simply the next resolution step beyond micro-Raman. The presence of the metallic probe near the sample causes changes in intensity and polarization of the incident light, resulting in effects similar to surface-enhanced Raman spectroscopy. It is also

possible, although not yet entirely certain, that the strong field gradients created by the tip may make visible some lines that are not normally Raman active.

## REFERENCES

1. Abbe, E. Beiträge zur Theorie des Mikroskops und der mikroskopischen Wahrnehmung. *Arch. Mikrosk. Anat.* **1873**, *9*, 413–468.
2. Betzig, E.; Trautman, J.K. Near-field optics: Microscopy, spectroscopy, and surface modification beyond the diffraction limit. *Science* **1992**, *257*, 189–195.
3. Hoffmann, P.; Dutoit, B.; Salathé, R.P. Comparison of mechanically drawn and protection layer chemically etched optical fiber tips. *Ultramicroscopy* **1995**, *61*, 165–170.
4. Bethe, H.A. Theory of diffraction by small holes. *Phys. Rev.* **1944**, *66* (7), 163–182.
5. Bouwkamp, C.J. On the diffraction of electromagnetic wave by circular disks and holes. *Phillips Res. Rep.* **1950**, *5*, 401–522.
6. Novotny, L.; Pohl, D.W.; Regli, P. Light propagation through nanometer-sized structures: The two-dimensional-aperture scanning near-field optical microscope. *J. Opt. Soc. Am., A* **1994**, *11* (6), 1768–1778.
7. Jersch, J.; Demming, F.; Hildenhagen, L.J.; Dickmann, K. Field enhancement of optical radiation in the near-field of scanning probe microscope tips. *Appl. Phys., A* **1998**, *66* (1), 29–34.
8. Milner, R.G.; Richards, D. The role of tip plasmons in near-field Raman microscopy. *J. Microsc.* **2001**, *202*, 66–71.
9. Furukawa, H.; Kawata, S. Local field enhancement with an apertureless near-field-microscope probe. *Opt. Commun.* **1998**, *148*, 221–224.
10. La Rosa, A.H.; Jakobson, B.I.; Hallen, H.D. Origins and effects of thermal processes on near-field optical probes. *Appl. Phys. Lett.* **1995**, *67* (18), 2597–2599.
11. Hayazawa, N.; Tarun, A.; Inouye, Y.; Kawata, S. Near-field enhanced Raman spectroscopy using side illumination optics. *J. Appl. Phys.* **2002**, *92* (12), 6983–6986.
12. Karrai, K.; Grober, R.D. Piezoelectric tip-sample distance control for near-field optical microscopes. *Appl. Phys. Lett.* **1995**, *66* (14), 1842–1844.
13. Ferraro, J.R.; Nakamoto, K. Basic Theory. In *Introductory Raman Spectroscopy*; Academic Press, Inc.: San Diego, 1994; 13–17.
14. Carrabba, M.; Spencer, K.; Rich, C.; Rauh, D. The utilization of a holographic Bragg diffraction filter for Rayleigh line rejection in Raman spectroscopy. *Appl. Spectrosc.* **1990**, *44* (9), 1558–1561.
15. Pelletier, M.J.; Reeder, R.C. Characterization of holographic band-reject filters designed for Raman spectroscopy. *Appl. Spectrosc.* **1991**, *45* (5), 765–770.
16. Sharma, S.K.; Schoen, C.L.; Helsley, C.E.; Owen, H. Performance of a holographic supernotch filter. *Appl. Spectrosc.* **1993**, *47* (3), 305–308.
17. Paesler, M.A.; Moyer, P.J. The Tapered Optical Fiber and Other Sensing Elements. In *Near-Field Optics*:

- Theory, Instrumentation, and Applications*; John Wiley & Sons, Inc.: New York, 1996; 46–53.
18. Jahncke, C.L.; Paesler, M.A.; Hallen, H.D. Raman imaging with near-field scanning optical microscopy. *Appl. Phys. Lett.* **1995**, *67* (17), 2483–2485.
  19. Hartschuh, A.; Sánchez, E.J.; Xie, X.S.; Novotny, L. High-resolution near-field Raman microscopy of single-walled carbon nanotubes. *Phys. Rev. Lett.* **2003**, *90* (9), 95503.
  20. Webster, S.; Batchelder, D.N.; Smith, D.A. Submicron resolution measurement of stress on silicon by near-field Raman spectroscopy. *Appl. Phys. Lett.* **1998**, *72* (12), 1478–1480.
  21. Hayazawa, N.; Inouye, Y.; Sekkat, Z.; Kawata, S. Near-field Raman imaging of organic molecules by an apertureless metallic probe scanning optical microscope. *J. Chem. Phys.* **2002**, *117* (3), 1296–1301.
  22. Delhaye, M.; Dhamelincourt, P. Raman microprobe and microscope with laser excitation. *J. Raman Spectrosc.* **1975**, *3*, 33–43.
  23. Anderson, M.S. Locally enhanced Raman spectroscopy with an atomic force microscope. *Appl. Phys. Lett.* **2000**, *76* (21), 3130–3132.
  24. Ayars, E.J.; Hallen, H.D. Surface enhancement in near-field Raman spectroscopy. *Appl. Phys. Lett.* **2000**, *76* (26), 3911–3914.
  25. Ayars, E.J.; Hallen, H.D.; Jahncke, C.L. Electric field gradient effects in Raman spectroscopy. *Phys. Rev. Lett.* **2000**, *85* (19), 4180–4183.
  26. Sass, J.K.; Neff, H.; Moskovits, M.; Holloway, S. Electric field gradient effects on the spectroscopy of adsorbed molecules. *J. Phys. Chem.* **1981**, *85*, 621–623.
  27. Knoll, P.; Marchl, M.; Kiefer, W. Raman spectroscopy of microparticles in laser light traps. *Indian J. Pure Appl. Phys.* **1988**, *26*, 268–277.
  28. Ayars, E.J.; Jahncke, C.L.; Paesler, M.A.; Hallen, H.D. Fundamental differences between micro- and nano-Raman spectroscopy. *J. Microsc.* **2001**, *202* (1), 142–147.

# Near-Field Raman Spectroscopy: Resolution Enhancement

Satoshi Kawata

*Department of Applied Physics, Osaka University, Osaka, Japan*

Yasushi Inouye

*Osaka University, Osaka, Japan*

## INTRODUCTION

Optical microscopy is a well-established technology of microanalysis for material science, biology, pathological diagnostics, industry, and so on. However, the smallest analyzing dimension of the sample resolvable with a conventional optical microscope is a half wavelength of light or several hundreds of nanometers in visible region because of the nature of the light wave. This is a so-called diffraction limit of light, which is not small enough to observe the structures of interest in the current advanced sciences and technologies, including protein molecules, quantum nanodevices, and self-assembled molecules. Near-field optical microscopy is a tool to overcome the barrier of wavelength by confining photons in nanoscale volume.

A combination of the state-of-the-art near-field technology with the conventional optical measurements enables us to explore the nanoworld with visible light.<sup>[1,2]</sup> Especially, near-field Raman spectroscopy makes it possible to assign molecules, to analyze chemical behavior of molecules, and to observe molecular dynamics at nanometric or molecular scale.<sup>[3,4]</sup> Lasers and detectors of visible region are available in Raman spectroscopy, and quenching phenomenon<sup>[5]</sup> and photobleaching could be avoided; hence near-field Raman spectroscopy is suitable for molecular sensing with a nanometric spatial resolution. Because the cross section of Raman scattering is much smaller than fluorescence and infrared absorption cross section, it is necessary to enhance Raman cross section for its accurate measurement. This can be performed by using a metallic tip that also works as one of a near-field probe for detection. In this article, we present how the metallic tip works as a near-field probe at first and then show the current progress in near-field Raman spectroscopy using a metallic tip.

## LOCAL FIELD ENHANCEMENT AT A METALLIC TIP

A small metallic structure with size smaller than the probing wavelength scatters light field and enhances the electric field intensely because of the strong interaction between the light field and the metal structure when the light is incident on such a structure. The reason for such an enhancement of the light field is that collective oscillation of free electrons in the metal resonates with the light field. This phenomenon is known as localized surface plasmon polaritons (SPPs). The electric field, which is coupled with the localized SPPs at the metallic structure, comprises evanescent field. Because the evanescent field is localized around the structure, the superresolving capability is attained by detecting the field for observation, measurement, and so on. Such a scheme of near-field scanning optical microscopy (NSOM) with a metallic probe of which the tip enhances electric field locally and strongly was first proposed in 1994.<sup>[6]</sup> The NSOM is called as an apertureless NSOM,<sup>[7,8]</sup> and the resolution is determined by the radius of the tip.

An apex of a metallic probe, such as a tip of a scanning tunneling microscopy (STM), works as a scatterer for enhancing electric field locally.<sup>[9]</sup> Fig. 1A shows intensity distribution of the light field scattered at the tip that is obtained using a numerical analysis.<sup>[1]</sup> Fig. 1B shows a schematic model for calculation. In this model, it is considered that a silver metallic tip with radius 20 nm is placed in contact on a glass substrate (refractive index: 1.5). The silver tip is illuminated with plane wave traveling in the substrate. Wavelength of the incident field is 488 nm, and its polarization is TM mode (i.e., p-polarization). Incident angle is 45°. Evanescent field is generated over surface of the glass substrate because the incident angle meets the



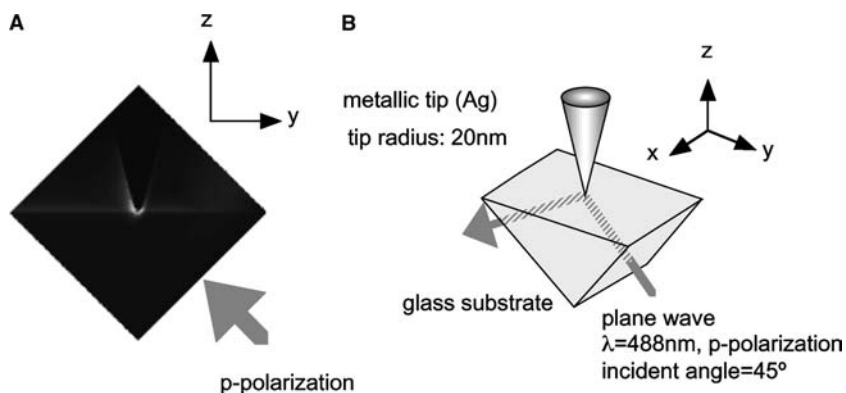


**Fig. 1** Field enhancement effect induced by a metallic tip. (A) Intensity distribution of electric field locally enhanced at a silver probe tip calculated by the FDTD method. (B) Schematic of the calculation model for the analysis.

condition of total internal reflection. Finite-difference time-domain (FDTD) method was used in the calculation.<sup>[10,11]</sup> Localized and enhanced field spot is observed in the proximity of the tip apex of Fig. 1A. The size of the small spot is around 30 nm, while approximately corresponds to the radius of the tip. Maximum intensity of the small spot was calculated to be 80 times as large as intensity of the incident field. Considering the tip to be a glass probe having the same tip radius of 20 nm, enhancement factor of the glass tip was calculated to be 7 when illuminating with TM mode. No enhancement of electric field was estimated at the metallic tip when TE mode (i.e., s-polarization) is used for illumination light in the calculation. These analyses show that strong enhancement of the localized field requires the use of a metallic tip and TM mode illumination in an apertureless probe, and that the small light field spot strongly enhanced at the tip is caused by excitation of the localized SPPs.

## NEAR-FIELD RAMAN SPECTROSCOPY AND MICROSCOPY

Fig. 2 shows illustrations of (a) near-field excitation of Raman scattering and (b) conventional Raman

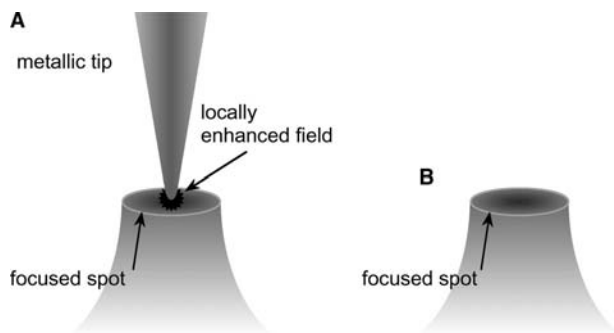


**Fig. 2** Schematic illustration of illumination for (A) near-field Raman spectroscopy using a locally enhanced field, (B) conventional micro-Raman spectroscopy.

microspectroscopy (far-field detection). For near-field Raman spectroscopy, a metallic tip is placed in the vicinity of the specimen and local electric field is generated at the tip apex. Raman scattering of molecules, which are just below the enhanced electric field at the metallic tip, is selectively enhanced and detected with a sufficiently high spatial resolution.

An optical setup of near-field Raman microscopy is shown in Fig. 3.<sup>[3,4,12,13]</sup> An expanded and collimated light field from a laser enters into the epi-illumination inverted microscope. A circular mask is inserted in the optical path of the illumination light and located at the conjugate plane of the pupil of the objective lens with numerical aperture (NA) equal to 1.4. Because the mask rejects part of the beam corresponding to focusing angles that are less than  $\text{NA} = 1.0$ , the transmitted light forms a focused spot that produces an evanescent field on the sample surface.<sup>[14]</sup> As the metallic tip approaches to the focused spot, a locally enhanced electric field is observed to be generated at the tip apex. Fig. 4 shows CCD images of the scattering of the evanescent field at the metallic tip that were observed from the side of the tip. In Fig. 4A, the tip

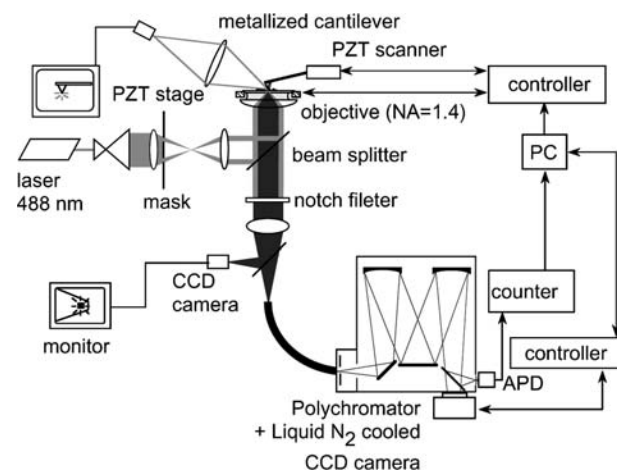


**Fig. 3** Optical setup of near-field Raman spectroscopy using a metallic tip.

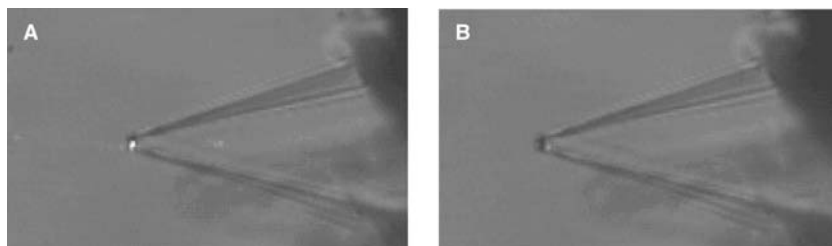


**Fig. 4** (A) Photograph of a metallized cantilever tip shining in the focused evanescent field. (B) Photograph of a metallized tip which is retracted 500 nm from the sample.

is in contact with the sample surface placed on the focused spot, which corresponds to Fig. 2A. Strong Rayleigh scattering of the evanescent field at the tip apex is seen in the figure. In Fig. 4A and 4, the tip is 0 and 500 nm away from the sample surface, respectively. No scattering of the evanescent field is observed because the tip is out of the skin depth of the evanescent field, while only very weak Rayleigh scattering light at the focused spot is observed because of the sample roughness. The electric field enhanced locally at the tip is scattered inelastically by Raman active molecules, which corresponds to near-field Raman scattering. Raman scattering is collected by the same objective lens and is directed to the spectrophotometer (focal length = 300 mm, 1200 lines/mm) that is equipped with a liquid-nitrogen-cooled CCD camera ( $1340 \times 400$  channels) for Raman spectra measurement and with an avalanche photodiode (APD) for Raman imaging. The APD is located after the exit slit of the spectrophotometer so that a specific Stokes-shifted line can be detected. Excitation light or Rayleigh scattering is sufficiently rejected by a notch filter. The metallic tip is a silicon cantilever that is coated with a 40-nm-thick silver film by a thermal evaporation process. The evaporation is performed at a relatively slow rate of  $0.3 \text{ \AA}$  per second to avoid undesirable bending of the silicon lever. Fig. 5 shows a scanning electron micrograph of a metallized tip. Diameter of the silver-coated tip apex is around

40 nm. The distance between the sample and the cantilever is regulated in contact-mode AFM operation, and the sample is scanned with piezoelectric transducers (PZT) in the  $X$ - $Y$  plane. Near-field Raman images are reconstructed by detecting near-field Raman signal at a specific Stokes-shifted line with the APD while scanning the PZT stage on the sample.

Raman spectra of Rhodamine 6G obtained with the near-field Raman microscope are shown in Fig. 6. Spectrum (A) is obtained with a silver-coated cantilever, and spectrum (B) is obtained without it. Intensity of spectrum (A) is higher than that of (B) because of the local field enhancement at the silver tip. Several Stokes-shifted Raman lines are observed in the spectrum. Acquisition time of the spectrum was 5 sec, and no accumulation was performed. The sample was made by casting the solution of Rhodamine 6G ( $6.0 \times 10^{-4}$  wt) onto the 8-nm silver island-coated coverslip and depositing Rhodamine 6G because of evaporation of the solution. Raman scattering is hence doubly enhanced because of surface-enhanced Raman scattering (SERS) both with the metallized tip and silver island film coated on substrate.

The Raman spectrum of Fig. 6A includes not only near-field component, but also far-field component. Near-field spectrum is obtained by subtracting the far-field spectrum of Fig. 6 obtained without the tip from the spectrum shown in Fig. 6A. Fig. 7 shows

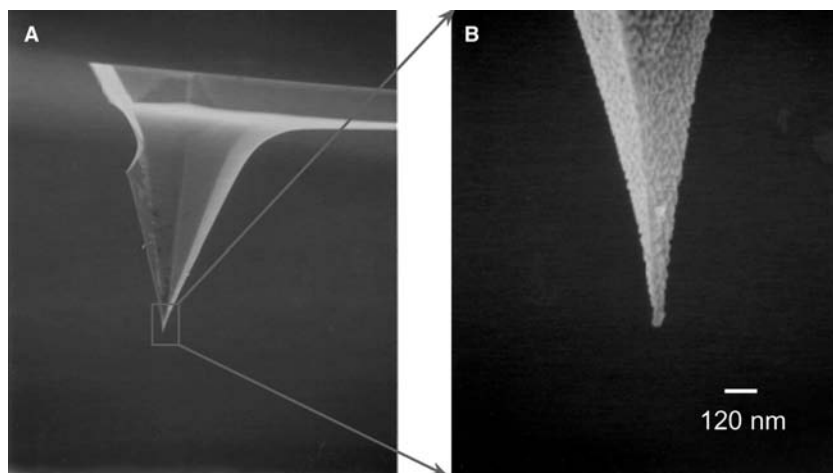


**Fig. 5** Scanning electron microscopy images of the metallized cantilever tip. (A) Whole image of the tip. (B) Expanded image of the apex.

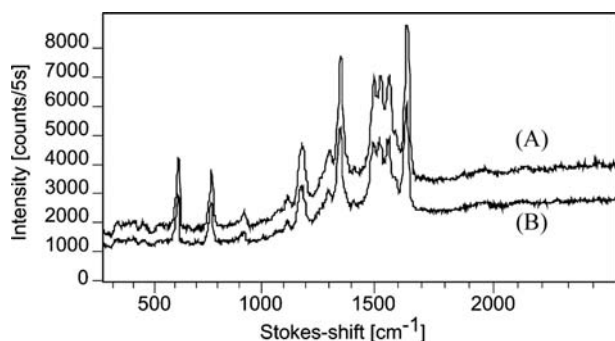


**Fig. 6** Raman spectra of Rhodamine 6G. (A) Spectrum obtained with locally enhanced field. (B) Spectrum of conventional micro-Raman measurement.

the result of subtraction of a near-field Raman spectrum of Rhodamine 6G. Each of Stokes-shifted peaks can be assigned to vibrational mode, such as peaks at 1359, 1503, 1570, and 1647  $\text{cm}^{-1}$  which correspond to the aromatic C–C stretching vibrational modes, a peak at 1269  $\text{cm}^{-1}$  which corresponds to the asymmetric vibrational mode of C–O–C bonding, a peak at 1120  $\text{cm}^{-1}$  which corresponds to the in-plane bending mode of C–H bonding, and a peak at 766  $\text{cm}^{-1}$  which corresponds to the out-of-plane bending mode of C–H bonding. Assignment of all Stokes-shifted peaks observed in Fig. 7 is shown in Table 1. When a silicon cantilever was used for near-field Raman detection, no enhancement is observed.<sup>[4]</sup>

Fig. 8 shows the Raman spectra of crystal violet molecules. Spectra (A) and (B) have been obtained with and without the metallic tip, respectively. The peaks at 1383, 1537, 1586, and 1617  $\text{cm}^{-1}$  are assigned to the C–C stretching vibrational mode of the aromatic ring; the peak at 1363  $\text{cm}^{-1}$  is assigned to the *N*-phenyl vibrational mode; the peak at 1172  $\text{cm}^{-1}$  is assigned to the C–H in-plane bending vibrational mode; the peaks

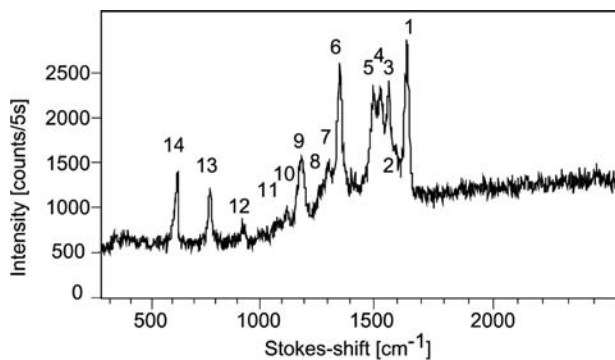


**Fig. 7** Near-field Raman spectrum of Rhodamine 6G obtained by subtracting the spectrum of Fig. 6B from that of Fig. 6A.

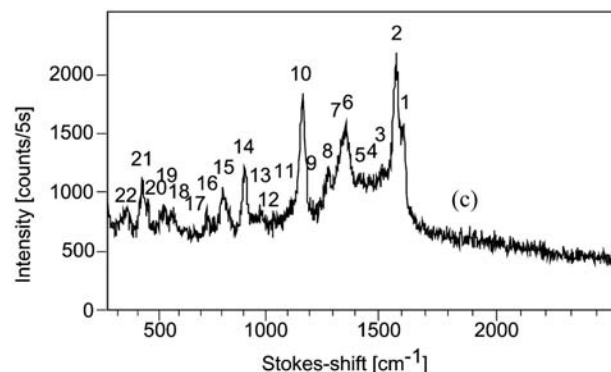
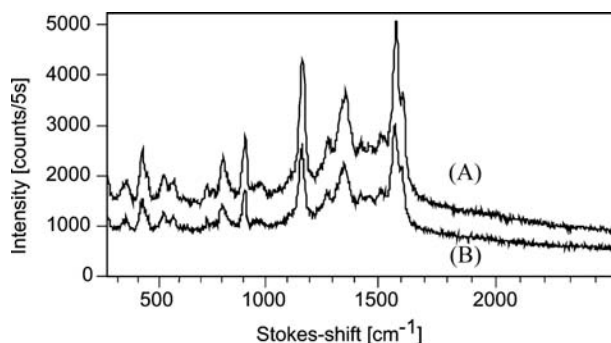


**Fig. 8** Raman spectra of crystal violet. (A) Spectrum obtained with locally enhanced field. (B) Spectrum of conventional micro-Raman measurement. (C) Near-field Raman spectrum of crystal violet obtained by subtracting the spectrum of (B) from that of (A).

at 908 and 798  $\text{cm}^{-1}$  are assigned to the C–H out-of-plane bending vibrational mode; the peak at 414  $\text{cm}^{-1}$  is assigned to the C–C–C out-of-plane bending vibrational mode; and the peak at 332  $\text{cm}^{-1}$  is

**Table 1** Assignment of rhodamine 6G molecules

	Stokes shift ( $\text{cm}^{-1}$ )	Assignment
1	1647	arom C–C str
2	1596	
3	1570	arom C–C str
4	1532	
5	1503	arom C–C str
6	1359	arom C–C str
7	1308	
8	1269	C–O–C
9	1185	
10	1120	C–H ip bend
11	1084	
12	919	
13	766	C–H op bend
14	608	C–C–C ip bend

arom: aromatic; bend: bending; str: stretching; ip: in-plane; op: out-of-plane.

**Table 2** Assignment of crystal violet molecules

	Stokes shift ( $\text{cm}^{-1}$ )	Assignment
1	1617	arom C–C str
2	1586	arom C–C str
3	1537	arom C–C str
4	1475	arom C–C str
5	1440	arom C–C str
6	1383	arom C–C str
7	1363	<i>N</i> -phenyl
8	1290	
9	1211	
10	1173	C–H ip bend
11	1115	
12	980	
13	937	
14	908	C–H op bend
15	798	C–H op bend
16	757	
17	724	
18	557	
19	520	
20	435	
21	414	C–C–C op bend
22	332	Ph–C–Ph

arom: aromatic; bend: bending; str: stretching; ip: in-plane; op: out-of-plane.

assigned to the phenyl–C–phenyl vibrational mode. These peaks are in good agreement with the results of other authors.<sup>[15–17]</sup> The peak at  $2050\text{ cm}^{-1}$  is a ghost line, which arises from the laser diode that was used as feedback in AFM operation. The exposure time of the liquid-nitrogen-cooled CCD camera was 1 sec with  $230\text{-}\mu\text{W}$  laser power at the entrance of the inverted microscope. Fig. 8C shows near-field Raman spectrum of crystal violet which is obtained by subtracting the spectrum of Fig. 8B from that of Fig. 8A. Assignment of all Stokes-shifted peaks observed in Fig. 8 is shown in Table 2.

## NEAR-FIELD RAMAN IMAGING

Molecular identification at nanometric scale is possible in two dimensions by detecting near-field Raman signal at a specific Stokes line with a monochromator and a point detector while scanning the sample laterally. A metallic tip reduces measurement time for Raman imaging drastically because of the amplification of near-field Raman scattering with locally enhanced field. Consequently, spatial distribution of molecules can be

imaged at nanometric scale during reasonable acquisition time.<sup>[13]</sup> Near-field Raman imaging enables us to attain direct and sensitive observation of many kinds of molecules and their local distributions as well as biological cells without labeling with dye.

In this section, we show such an example of molecular imaging. Mixed aggregates of Rhodamine 6G and crystal violet molecules are used as samples for near-field Raman imaging. The sample is prepared by casting ethanol solution of Rhodamine 6G and crystal violet on a coverslip coated with an 8-nm-thick silver film and drying the solution. The distribution of molecules for

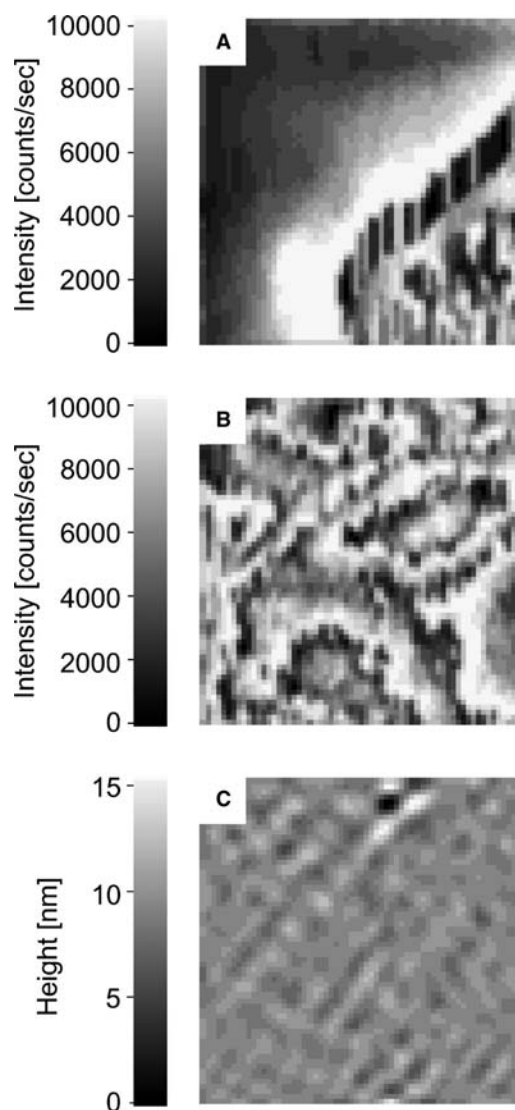


**Fig. 9** Near-field Raman images obtained at (A)  $607\text{ cm}^{-1}$ ; C–C–C in-plane bending mode of Rhodamine 6G and (B)  $908\text{ cm}^{-1}$ ; C–H out-of-plane bending mode of crystal violet; (C) the corresponding topographic image of the scanned area. It took 10 min to obtain one image where  $1 \times 1\text{ }\mu\text{m}$  scanning area consisted of  $64 \times 64$  pixels.

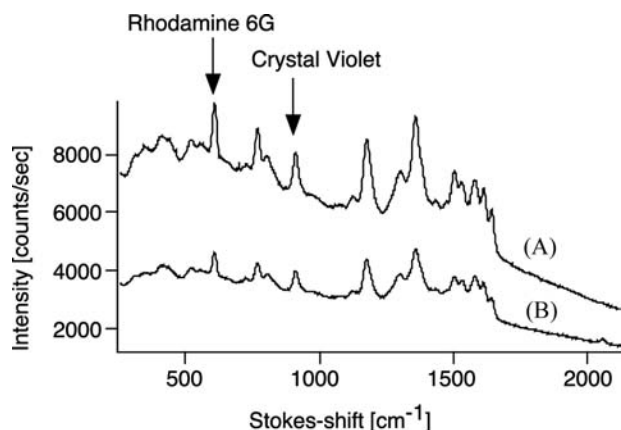


**Fig. 10** Typical Raman spectra of the aggregated sample used in Fig. 9, (A) with and (B) without a metallic tip. Stokes-shifted-lines of Rhodamine 6G and crystal violet are observed. Arrows indicate the Stokes-shifted-lines used for near-field Raman imaging in Fig. 9.

both samples is fairly inhomogeneous and is set to have a 1-nm average thickness of the layer of molecules.

Fig. 9A–C shows near-field Raman images from the same area of the sample, where the concentrations of Rhodamine 6G and crystal violet are  $1.25 \times 10^{-3}$  and  $1.25 \times 10^{-2}$  wt.%, respectively. These concentrations resulted in a comparable Raman scattering intensity from Rhodamine 6G and crystal violet because Rhodamine 6G yields higher scattering cross section than that of crystal violet molecules. Fig. 9A shows an image corresponding to the peak at  $607 \text{ cm}^{-1}$ , which comes from the Stokes-shifted C–C–C in-plane bending vibrational mode of Rhodamine 6G. Fig. 9B is obtained at  $908 \text{ cm}^{-1}$  of which peak corresponds to the Stokes-shifted line of the C–H out-of-plane bending vibrational mode of crystal violet. Fig. 9C shows a corresponding topographic image obtained simultaneously with Fig. 9A in AFM operation. The dimension of all the images comprising  $64 \times 64$  pixels

was  $1 \times 1 \mu\text{m}$ . The scanning rate used for each line was 0.1 Hz. At this rate, a single image can be achieved in only 10 min. Fig. 10 shows the Raman spectra of the mixed sample, which exhibits the Stokes-shifted lines of both Rhodamine 6G and crystal violet molecules. The arrows depicted in Fig. 10 point to the Stokes-shifted lines used for the near-field Raman imaging in Fig. 9. We can selectively obtain the distributions of each vibrational mode that we cannot distinguish in the topographic image. The distributions of each vibrational mode are quite different and show complicated structures corresponding to the inhomogeneous distributions of both molecules. According to Fig. 9A, Rhodamine 6G molecules are mainly localized at the lower right position of the figure; on the other hand, Fig. 9B shows that crystal violet molecules are randomly dispersed in the scanned area. In Fig. 9C, the island structures of the silver film are observed in the topographic image because the average thickness of the aggregated molecular layer is estimated to be 1 nm which is much thinner than the silver film (average thickness: 8 nm). Accordingly, the distributions of both molecules are not clearly seen in the topographic image that reflects the pancake structure of the silver grains (30–50 nm in diameter and 8 nm in thickness). Note that without a metallic tip (far-field detection), we could not obtain such high-resolution images because the far-field signal is averaged out within the focused spot [Fig. 2B]. Fig. 9 shows that the near-field Raman images attain the molecular vibrational distributions with a high sensitivity, even if the thickness of the molecular layer is 1 nm. In the experiment, organic dye molecules adsorbed on silver films were used. While the silver films are required for dye molecules to quench the strong fluorescence, near-field Raman spectroscopy and imaging by an apertureless metallic probe scanning optical microscope are applicable not only to organic, but also to inorganic sample even without the support of the silver films. Single molecule detection can be performed after optimizing

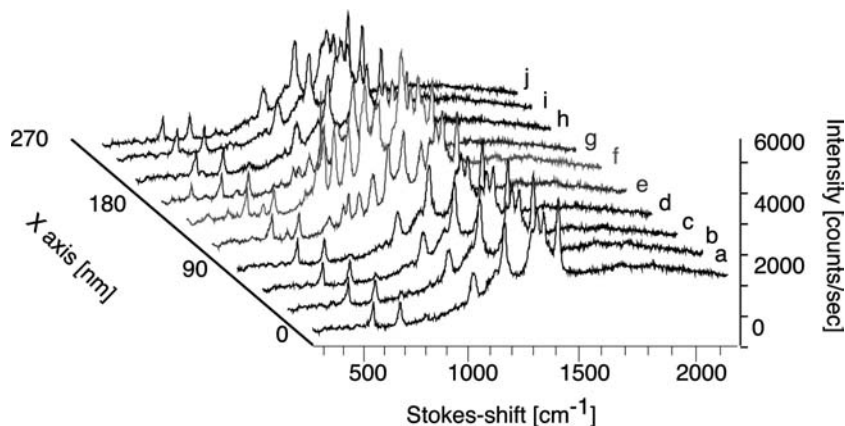


**Fig. 11** Near-field Raman spectra mapping at several positions.



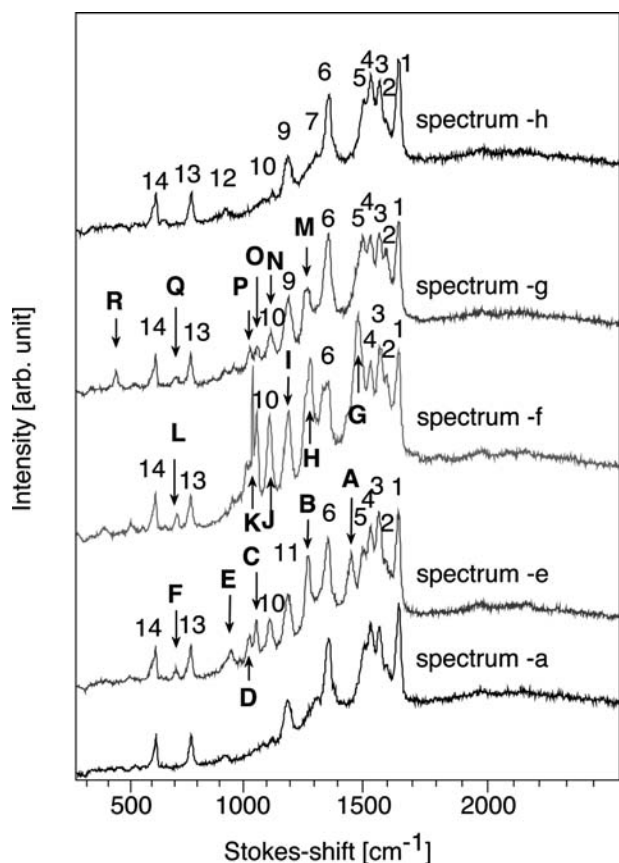


**Fig. 12** Some features in the near-field region can be seen and the remarkable near-field characteristic Raman spectra -e, -f, -g in Fig. 11 are plotted. For comparison, spectrum -a and -h are also shown. The numbers correspond to the same assignments as shown in Fig. 7 and remarkable features are pointed out by arrows with capital alphabets (A ~ R).

the tip material, shape,<sup>[18]</sup> and illumination method<sup>[19]</sup> because the enhancement factor is very sensitive to the tip and the polarization of the light.

### SPECTRAL CHANGE OF NEAR-FIELD RAMAN SPECTRUM

Because near-field Raman spectroscopy using a metallic tip realizes surface-enhanced Raman scattering singly on its apex, chemical enhancement of Raman scattering can be expected besides physically electromagnetic enhancement as mentioned above. Fig. 11 shows a one-dimensional near-field image of the Rhodamine 6G distribution at spatial steps of 30 nm. At each position, the near-field Raman spectrum is detected. The spectra in Fig. 11 are all enhanced by the tip apex, while some of them, e.g., spectra -e, -f, and -g, exhibit remarkable features which are quite different from others or from far-field spectrum.

The distinguishable near-field features in those spectra replotted in Fig. 12 are marked with capital alphabetic letters, and the numbers in different spectra correspond to the same assignments as in Fig. 7. Some peaks are slightly shifted and their relative intensities are quite different from those of the far-field spectrum. Furthermore, some additional peaks, which are not observed in the far-field, appear.

For the aromatic C–C stretching vibrational mode, the peaks between 1350 and 1650  $\text{cm}^{-1}$  are heavily modified. New shifted peaks, e.g., A: 1457  $\text{cm}^{-1}$  in spectrum -e, G: 1483  $\text{cm}^{-1}$  in spectrum -f, appeared. For the C–H out-of-plane bending vibrational mode (number 13), peak intensities are constant throughout the scanning, while for the in-plane bending (number 11), weak peaks are strongly enhanced and slightly shifted (see, e.g., J: 1112  $\text{cm}^{-1}$ ). For the C–O–C bending vibrational mode, the new Stokes-shifted peaks appear and those are largely enhanced (see peaks, e.g., B: 1278  $\text{cm}^{-1}$ , H: 1286  $\text{cm}^{-1}$ , and M: 1275  $\text{cm}^{-1}$ ). Furthermore, other new peaks which have not been assigned yet also appear in the spectra (see, e.g., C: 1054  $\text{cm}^{-1}$ , D: 1027  $\text{cm}^{-1}$ , E: 946  $\text{cm}^{-1}$ , F: 902  $\text{cm}^{-1}$ , K: 1040  $\text{cm}^{-1}$ , L: 705  $\text{cm}^{-1}$ , O: 1057  $\text{cm}^{-1}$ , P: 1027  $\text{cm}^{-1}$ , Q, 700  $\text{cm}^{-1}$ , and R: 425  $\text{cm}^{-1}$ ). Some of the peaks can be identified as the same vibrational modes (e.g., C, K, and O; D and P; L and Q). While some of Stokes-shifted peaks are strongly enhanced, the fluorescence intensity is constant throughout the positions. This can be explained by the chemical mechanism of surface-enhanced Raman scattering because of the charge transfer excitation between molecules and metal.<sup>[20]</sup>

### CONCLUSION

Application of near-field optics to Raman spectroscopy brings microanalysis of most of materials to their nano-identifications. For example, molecules can be assigned, observed, and detected directly at the nanometric or molecular scale by using this technique without the need for staining a specimen with a dye. Low cross section of Raman scattering is amplified to detectable level by the locally enhanced field at a metallic tip. Near-field Raman signal is also enhanced by the chemical interaction between molecules and metallic tip. The nanoscale chemical phenomenon has a potential for determination of molecular orientation. Raman spectroscopy coupled with locally enhanced electromagnetic field, which may contribute to nonlinear spectroscopy such as multiphoton processes, second harmonic generation, and coherent anti-Stokes Raman scattering, will be one of the main topics of microspectroscopic or nanospectroscopic research in the next decade.



## REFERENCES

1. Kawata, S., Ed.; *Near-Field Optics and Surface Plasmon Polaritons*; Springer-Verlag: Berlin, Germany, 2001.
2. Kawata, S., Ohtsu, M., Irie, M., Eds.; *Nano-Optics*; Springer-Verlag: Berlin, Germany, 2002.
3. Inouye, Y.; Hayazawa, N.; Hayashi, K.; Sekkat, Z.; Kawata, S. Near-field scanning optical microscope using a metallized cantilever tip for nanospectroscopy. *Proc. Soc. Photo-Opt. Instrum. Eng.* **1999**, *3791*, 40–48.
4. Hayazawa, N.; Inouye, Y.; Sekkat, Z.; Kawata, S. Metallized tip amplification of near-field Raman scattering. *Opt. Commun.* **2000**, *183*, 333–336.
5. Bian, R.X.; Dunn, R.C.; Xie, X.S. Single molecule emission characteristics in near-field microscopy. *Phys. Rev. Lett.* **1995**, *75*, 4772–4775.
6. Inouye, Y.; Kawata, S. Near-field scanning optical microscope using a metallic probe tip. *Opt. Lett.* **1994**, *19*, 159–161.
7. Zenhausem, F.; O'Boyle, M.P.; Wickramasinghe, H.K. Apertureless near-field optical microscopy. *Appl. Phys. Lett.* **1994**, *65*, 1623–1625.
8. Bachelot, R.; Gleyzes, P.; Boccara, A.C. Near-field optical microscope based on local perturbation of a diffraction spot. *Opt. Lett.* **1995**, *20*, 1924–1926.
9. Inouye, Y.; Kawata, S. A scanning near-field optical microscope having scanning electron tunnelling microscope capability using a single metallic probe tip. *J. Microsc.* **1995**, *178*, 14–19.
10. Furukawa, H.; Kawata, S. Analysis of image formation in a near-field scanning optical microscope: Effects of multiple scattering. *Opt. Commun.* **1996**, *132*, 170–178.
11. Furukawa, H.; Kawata, S. Local field enhancement with an apertureless near-field-microscope probe. *Opt. Commun.* **1998**, *148*, 221–224.
12. Hayazawa, N.; Inouye, Y.; Sekkat, Z.; Kawata, S. Near-field Raman scattering enhanced by a metallized tip. *Chem. Phys. Lett.* **2001**, *335*, 369–374.
13. Hayazawa, N.; Inouye, Y.; Sekkat, Z.; Kawata, S. Near-field Raman imaging of organic molecules by an apertureless metallic probe scanning optical microscope. *J. Chem. Phys.* **2002**, *117*, 1296–1301.
14. Hayazawa, N.; Inouye, Y.; Kawata, S. Evanescent field excitation and measurement of dye fluorescence using a high N.A. objective lens in a metallic probe near-field scanning optical microscopy. *J. Microsc.* **1999**, *194*, 472–476.
15. Gicquel, J.; Carles, M.; Bodot, H. Resonance Raman investigation of charge-transfer complexes between a trityl cation (crystal violet) and sulfonated azo derivatives. *J. Phys. Chem.* **1979**, *83*, 699–706.
16. Sunder, S.; Bernstein, H.J. Resonance Raman-spectrum of a deuterated crystal violet— $[P(CH_3)_2N \cdot C_6D_4]_3 C^+Cl^-$ . *Can. J. Chem.* **1981**, *59*, 964–967.
17. Watanabe, T.; Pettinger, B. Surface-enhanced Raman scattering from crystal violet adsorbed on a silver electrode. *Chem. Phys. Lett.* **1982**, *89*, 501–507.
18. Krug, J.T., II; Sanchez, E.J.; Xie, X.S. Design of near-field optical probes with optimal field enhancement by finite difference time domain electromagnetic simulation. *J. Chem. Phys.* **2002**, *116*, 10895–10901.
19. Novotny, L.; Sanchez, E.J.; Xie, X. Near-field optical imaging using metal tips illuminated by higher-order Hermite–Gaussian beams. *Ultramicroscopy* **1998**, *71*, 21–29.
20. Otto, A.; Mrozek, I.; Grabhorn, H.; Akemann, W. Surface-enhanced Raman-scattering. *J. Phys. Condens. Matter* **1992**, *4*, 1143–1212.

# Near-Field Scanning Optical Microscopy: Chemical Imaging

**Bogdan Dragnea**

*Department of Chemistry, Indiana University,  
Bloomington, Indiana, U.S.A.*

## INTRODUCTION

Chemical near-field microscopy is a promising optical technique, which transcends the diffraction limit of classical optical microscopy while maintaining its spectroscopic capabilities and sharing the benefit of topographic contrast from proximal probe microscopies. Several techniques and sources of chemical contrast are discussed, from the time-resolved mapping of electric field-induced molecular reorientation in polymer films to the vibrational Raman spectrum of single-carbon nanotubes with 28 nm spatial resolution in the optical image.

## BEYOND THE DIFFRACTION LIMIT

With the advent of scanning probe microscopies, the past 20 years or so have witnessed an explosion of analytical tools to explore materials at a nanometer scale. Advances in the understanding of physical and chemical phenomena at these length scales are expected to have a strong impact on microbiology, materials science, and microelectronics. At present, modified viruses are explored as nanobeakers for controlled chemical reactions in confined environments.<sup>[1]</sup> New materials having exotic optical and electronic properties have been synthesized.<sup>[2,3]</sup> Novel polymeric resists for sub-100 nm photolithography<sup>[4]</sup> and alternative schemes for electronic component integration are intensely explored.<sup>[5]</sup> As a general feature, systems representative of these domains often possess a complex hierarchical organization, which requires the ability to map chemical phenomena on a certain range of length scales.<sup>[6]</sup> Such studies, more often than not, involve some type of direct imaging technique, which is non-intrusive, has chemical specificity, and has adequate space and time resolution.

Vibrational spectroscopy, encompassing infrared (IR), near-IR, Raman, inelastic neutron scattering, electron energy loss, and cavity ring-down spectroscopy, has exquisite chemical specificity. The positions and intensities of vibrational absorption bands

can be used to confirm or identify the presence of a particular group, whereas spectral correlations can be used to access structural and environmental information on selected groups.<sup>[7]</sup> IR and Raman spectroscopies are particularly non-intrusive, require a small amount of sample, and can be easily coupled with microscopy to provide for spatial resolution.<sup>[8,9]</sup> The importance of these qualities is reflected in the available range of commercial Raman and Fourier transform infrared (FTIR) microscopes, and in the multitude of applications ranging from materials science to forensics and identification of cultural artifacts. For basic research applications (usually concerning molecular relaxation phenomena), pulsed lasers and fast detectors provide for temporal resolution down to a few femtoseconds.

Classical microscopes achieve a maximum spatial resolution of about 10–20  $\mu\text{m}$  in mid-IR (for wavelengths between 2 and 10  $\mu\text{m}$ ), whereas Raman microscopes approach the 1- $\mu\text{m}$  limit. The current spatial resolution limitation in mid-IR is because of the lack of suitable dielectrics to build aberration-corrected lenses.<sup>[10]</sup> Even if perfect materials were available, there is still a fundamental limitation of imaging instruments based on spherical lenses or mirrors. This fundamental spatial resolution limit is known as the Abbe diffraction limit.<sup>[11]</sup> Following Abbe's explanation, every object behaves as a superposition of diffraction gratings. In any classical imaging instrument, the front lens is placed, for practical reasons, at least several wavelengths from the object from which the scattered light is collected. The smaller the details of the object are, the higher are the diffraction orders or spatial frequencies of the scattered light. Not all the spatial frequencies will make their way into the lens; there is a cutoff spatial frequency necessarily connected to the geometry of the collection optics. Moreover, the highest spatial frequencies decay exponentially along the object normal.<sup>[12]</sup> Thus the geometry of the lens and the distance to the sample limit the achievable spatial resolution at:  $\Delta x = \lambda / (2\pi\text{NA})$ , where  $\lambda$  is the wavelength and NA is the numerical aperture of the lens.

Many problems studied by vibrational microspectroscopy would gain from better spatial resolution. Some of these problems are reviewed later in the section “Applications of Optical Near-Field Microscopy in Chemistry” of this entry. Although the Abbe resolution limit of classical microscopes continues to be pushed in small steps, especially for visible wavelengths, by using special geometries of illumination<sup>[13]</sup> or non-linear optical effects,<sup>[14,15]</sup> two other conceptually different approaches currently hold the promise of a major breakthrough in ultramicroscopy. The first is the near-field approach, an idea credited to Synge,<sup>[16]</sup> who proposed the use of a subwavelength source of light such as a tiny hole in a metal screen illuminated by bright light or a gold particle, scattering light from a location very close to the sample surface in a dark-field illumination configuration (Fig. 1). A key element of Synge’s approach is the location of the light source very close to the sample surface. As a consequence of the probe proximity, sampling of the evanescent waves bound to the surface occurs. Because in modern instruments based on Synge’s idea, the subwavelength light source is scanned across the sample surface by maintaining a constant gap between the surface and the probe to sequentially map the near-field optical interaction, such a microscope is called a near-field scanning optical microscope (NSOM or SNOM),<sup>[17]</sup> as opposed to far-field instruments, which deal with propagating waves only. The second approach is the negative refraction concept upon which Pendry<sup>[18]</sup> built his idea of a superlens. Such a lens may overcome the evanescent wave decay and therefore should focus light to considerably smaller areas than that allowed by the Abbe diffraction limit. Although numerous experimental realizations of Synge’s proposal have broken the diffraction limit barrier by more than one order of magnitude, the more recent solution based on the Pendry superlens remains in the stage of theoretical concept.

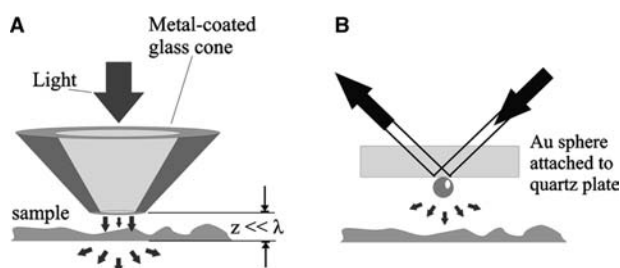


**Fig. 1** Synge’s proposal for an ultrahigh resolution optical microscope to overcome the diffraction limit. The subwavelength source of light may be (A) a microscopic aperture defined in a metal screen, at the tip of a sharp dielectric cone, and (B) a nanoparticle with large optical polarizability. The proximity of the probe to the surface is an essential element in near-field microscopy.

We are concerned here with those techniques and applications of the NSOM principles that have been applied to chemical problems. A number of alternative non-optical techniques, capable of nanoscale mapping with chemical specificity, will be also mentioned with the goal of situating the near-field optical microspectroscopy within the broader context of chemical mapping methodologies.

## APERTURE, APERTURELESS, AND TIPLESS NSOM

Three approaches have been used to date to generate near-field optical images with spatial resolution superior to the diffraction limit. The first approach, and the most often utilized at present, is the one based on a subwavelength optical aperture at the apex of a tapered transparent optical fiber, which has been metal-coated<sup>[19]</sup> (Fig. 1). The spatial resolution is limited by the size of the aperture and the electromagnetic skin depth of the metal coating. The second method is based on an apertureless sharp tip, usually metallic, which is acting as a scattering probe, converting surface sample-bound evanescent waves into propagating waves (Fig. 2). The spatial resolution attainable with this method is determined by the tip radius, rather than the electromagnetic skin depth of the metal.<sup>[20]</sup> The third proposal does not use a tip. The probe in this case can be a nanoparticle, which is manipulated by optical tweezers to scan the sample surface.<sup>[21]</sup> The theory of this microscope, including the excitation of particle eigenmodes, has been worked out by Lester, Arias-Gonzalez, and Niefo-Vesperinas<sup>[22]</sup> Tischer et al. have demonstrated a related nanoparticle-based technique that is able to provide topological three-dimensional (3-D) images of nanoscopic cavities

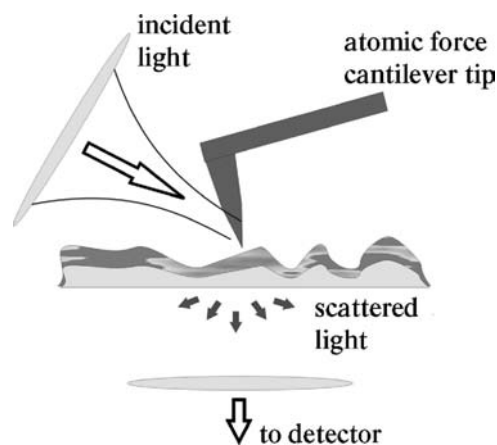


**Fig. 2** Schematic of the optical probe region in an apertureless NSOM with grazing illumination.

accessible to the particle with 20-nm spatial resolution normal to the immersed surfaces and  $\sim 200$ -nm lateral resolution. The accessible volumes are reconstructed from the histogram of thermal position fluctuations of the particle, hence the name of the technique—3-D thermal noise imaging.<sup>[23]</sup> The 3-D thermal noise imaging has not been used yet in conjunction with near-field measurements. Palanker et al.<sup>[24]</sup> have used a localized non-equilibrium plasma concentration on a semiconductor surface photoinduced by a tightly focused laser beam operating at visible wavelengths as a scanning local probe for near-field IR reflectivity measurements.

Among the three near-field optical schemes, only the optical fiber NSOM and the apertureless NSOM have been applied to the spatial mapping of chemical properties. Nevertheless, the nanoparticle approach holds a special appeal because of intrinsic field enhancements at the particle surface,<sup>[25]</sup> which may provide for 3-D surface-enhanced Raman or IR microspectroscopy of fluid-immersed interfaces in the future.<sup>[26]</sup> Several comprehensive reviews on the theory and applications of the optical fiber NSOM and the apertureless NSOM, especially in the visible range of the spectrum, have been published to date.<sup>[27–30]</sup> Particularities and chemical applications of the mid-IR NSOM have been reviewed by Dragnea and Leone<sup>[31]</sup> and Keilman.<sup>[32]</sup> The far-IR and the microwave region have been covered by Rosner and van der Weide.<sup>[33]</sup>

Choosing an apertureless or a fiber optic aperture NSOM for chemical characterization depends on the type of application. The fiber-based instrument is closer to a scanning confocal microscope, which, instead of the NSOM aperture, would use the real image of a pinhole formed through a lens system. Therefore contrast formation is arguably more intuitive. An important advantage of the aperture scheme is negligible background. For a perfect metal coating, the only light comes from the subwavelength aperture. As a consequence, sensitive detection schemes such as photon counting can be used. Bringing the light close to the sample through a fiber may represent a very important feature, which makes the aperture NSOM unique for certain applications dealing with samples immersed in an absorbing fluid. For example, Hong et al.<sup>[34]</sup> have succeeded to image living cells in water using an IR near-field microscope. Such studies are not possible in far field or with an apertureless NSOM because of the strong attenuation of the incident beam caused by water absorption bands associated with H–O–H bending, which overlap with the protein amide bands at  $\sim 1650\text{ cm}^{-1}$ . However, in aperture NSOM, because the gap between the fiber probe aperture and the cell membrane (sample surface) is of a few nanometers, most of the signal comes from absorption by the cellular protein and not by the water layers

between the probe and the sample surface. A disadvantage of the optical fiber approach is low transmission ( $10^{-4}$ – $10^{-6}$ , depending on the wavelength and on the fiber taper profile), combined with a limit on the incident light power dictated by the damage threshold of the metal coating ( $\sim 10\text{ mW}$  for Al-coated fibers). The throughput problem is a challenge in particular at longer wavelengths because the cutoff diameter for guided propagation occurs earlier along the taper than for shorter wavelengths, and the light has to propagate evanescently over longer distances until it reaches the aperture. At IR wavelengths, one usually has to reach a compromise between spatial resolution, determined by the aperture diameter, and sensitivity. The fiber probe fabrication remains, at present, the main challenge and a key element for further improvements of the aperture NSOM, at least at IR wavelengths.

The apertureless NSOM has four advantages on its side, with respect to the aperture NSOM. 1) The attainable optical resolution exceeds that of the aperture-based microscopes. This is because of the fact that, for a suitable incident field polarization, field enhancement occurs in a very localized area of the size of the tip radius.<sup>[35]</sup> 2) The problem of the strong attenuation in the fiber taper is alleviated in the apertureless scheme because the light is focused from the far field directly on the tip, without loss. This is why the apertureless NSOM has, until now, dominated microspectroscopy applications in the mid-IR and far-IR ranges, where the losses within the fiber taper are the largest. 3) The tip fabrication step can be avoided altogether because a large selection of commercial atomic force microscopy (AFM) tips is available. Apertureless tips are more robust and their fabrication is more reproducible than that of coated optical fiber tips. 4) The range of usable wavelengths is not limited, such as in the case of fiber-based NSOMs by material properties. The main disadvantage of the apertureless NSOM comes from strong scattered light in areas of the tip shaft, far from the sample, which creates a strong background for the detector. Furthermore, the background usually varies during scanning because of the  $z$ -motion of the tip in constant force scanning mode, hence the strong possibility of topographic artifacts. Great care has to be taken to decouple the topographic artifacts, which often adds complexity to the experimental setup. However, several strategies have been found to eliminate this problem from apertureless NSOM images.<sup>[20,36]</sup>

Whether an apertureless or a fiber optic aperture NSOM is chosen, two issues have to be considered while interpreting the data: one is the mechanism of contrast generation; the other is scanning probe imaging artifacts.<sup>[37]</sup> The electromagnetic field distribution around a nanoscopic object is extremely sensitive to both physical characteristics of the object and

the illumination mode. A rigorous description of the interaction optical between the probe and the field close to the surface is necessary to properly describe the image formation. Numerous simulation schemes for numerically solving Maxwell's equations have been used. The practical difference between these schemes lies in how the challenge of sharp corners and edges, much smaller than the wavelength, is handled.<sup>[38]</sup> Palanker et al.<sup>[39]</sup> have provided an approximate phenomenological model for contrast formation in aperture IR-NSOM. The model relies on a photon tunneling picture in which the size of the barrier representing the tip/gap/surface system is determined experimentally from tip-surface approach curves. The model correctly reproduces the observed differences between near-field and far-field IR absorption spectra

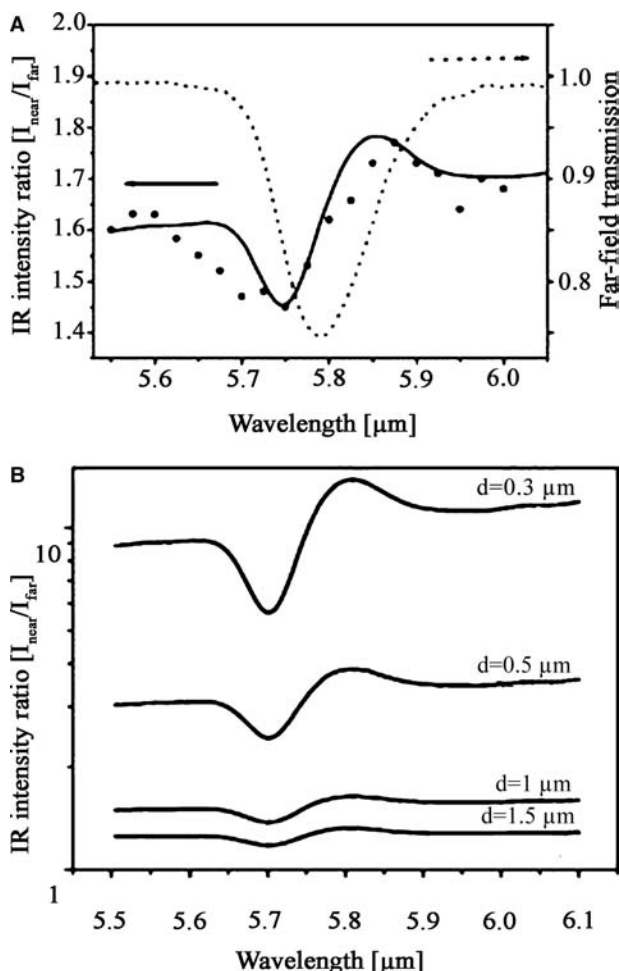


**Fig. 3** (A) Differences between experimental infrared near-field (symbols) and far-field (dashed line) spectra. The continuous line represents a fit generated from a phenomenological model based on the photon tunneling picture. (B) Calculated spectra for tip diameters ranging from 0.3 to 1.5 μm. The amplitude of the near-field modulation is inversely proportional to the aperture diameter. *Source:* From Ref.<sup>[39]</sup>, with permission.

obtained experimentally (Fig. 3). An analytical approximation for the scattered field in the apertureless case has been proposed by Hillenbrand, Knoll, and Keilmann.<sup>[36]</sup>

To avoid *z*-motion crosstalk in the optical images, the safest way is to turn off the force feedback on the *z*-piezo and scan at constant height. However, if constant gap scanning is required to be certain that the near-field optical images are not merely topographic artifacts, according Hecht et al.,<sup>[37]</sup> at least one of the following conditions should be satisfied:

- Near-field images and topographic images are uncorrelated. This means that often the best way to use a near-field microscope is on samples that are flat, but have heterogeneities with strong optical contrast.
- When correlations between the topographic image and the optical image are apparent, they should be displaced by a constant amount.
- The spatial resolution of the optical image is different from that of the topographic image.

## APPLICATIONS OF OPTICAL NEAR-FIELD MICROSCOPY IN CHEMISTRY

In a few NSOM applications, which take advantage of the presence of narrow absorption bands of the sample and tunable light sources, such as in the case of vibrational microspectroscopy or the fluorescence emission properties of the sample, the near-field image contrast formation can be at least qualitatively understood in a more straightforward way than by numerically solving the Maxwell equations. A few examples from this category are described below.

### Fluorescence NSOM

In fluorescence NSOM, the chemical contrast is achieved by measuring the local fluorescence spectroscopy of the sample. Because the fluorescence wavelengths of many organic materials lie in the visible range, this method has been extensively applied to organic materials. The visible wavelength range has the benefit of sensitive detectors, optimized optics, and powerful and relatively low-cost laser sources. These features, plus the fact that the strong excitation background can be easily filtered out, made fluorescence NSOM reach single-molecule sensitivity at room temperature.<sup>[40]</sup> Fluorescence NSOM has been used to directly identify molecular aggregations in amorphous conjugated polymer films of approximately 100 nm, which were detrimental to the photoluminescent and

electronic properties of the film.<sup>[41]</sup> Such studies have clearly shown that the NSOM technique can contribute to a better understanding of the technologically important thin organic films. Barbara, Adams, and O'Connor<sup>[42]</sup> have reviewed the characterization of complex organic thin film materials by time-resolved and wavelength-resolved near-field microspectroscopy. In organic materials for electronic devices, the device fabrication processes induce morphological changes at length scales for which NSOM became the method

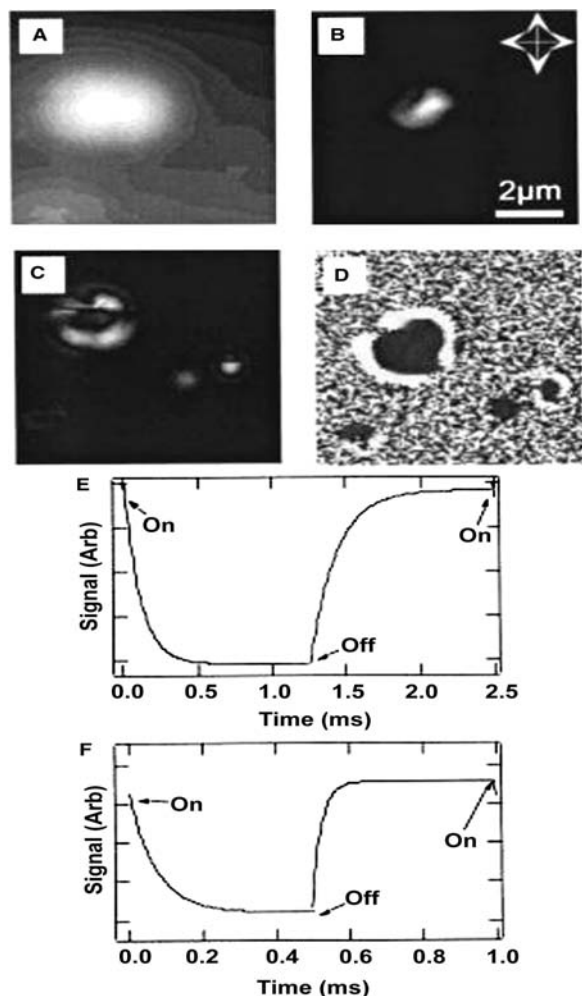


**Fig. 4** Measuring the local field-induced reorientation in molecular films. A sinusoidal electric bias is applied between the Al coating of the fiber probe and the transparent support electrode on which a polymer-dispersed liquid crystal film is deposited. Frame (A) represents the shear-force topographic image acquired simultaneously with near-field optical images (B–D). Frames represent the modulated optical signal as a function of the applied voltage. (D) A map of the phase lag of the optical modulation signal with respect to the applied bias. Frames (E) and (F) represent time-dependent variations in the transmitted optical signal from central and edge probe locations. The relaxation rate is faster in the edge region. Source: From Ref.<sup>[42]</sup>.

of choice. More recently, fluorescence NSOM investigations have proven instrumental in the direct observation of the influence of device operating conditions on local organic material morphology.<sup>[43]</sup> Fig. 4 is an illustration of how the dynamics of field-induced local reorientation of polymer-dispersed liquid crystal films can be measured using fluorescence NSOM.

## Raman Near-Field Microscopy

When chemical identification is required, few methods can be as specific as vibrational spectroscopy. In vibrational Raman spectroscopy, the chemical contrast comes from a non-linear effect: the molecule polarizability is modulated, depending on the molecular symmetry, by vibrational interactions. Because of its non-linear origin, the Raman scattering has a much smaller molecular cross section ( $10^{-31}$ – $10^{-29}$  cm<sup>2</sup>) when compared with typical IR absorption cross sections ( $10^{-17}$ – $10^{-16}$  cm<sup>2</sup>). However, when a molecule is placed in close vicinity to a rough metal surface, the Raman scattering may be enhanced by an average factor of  $10^6$ . The surface enhancement is thought to be of both chemical and electromagnetic origin; however, the separation of contributions from these two effects continues to be elusive.<sup>[25]</sup> An additional enhancement for surface-enhanced Raman scattering (SERS) of approximately  $10^5$  occurs when there is resonance between the pump wavelength and a molecular electronic transition. Even when combining these enhancements, the resulting cross section seems to be too small to be used to generate aperture NSOM contrast, if one takes into consideration the limit imposed by fiber damage threshold on the pump power,  $\sim 10$  mW. However, Emory and Nie<sup>[44]</sup> and Kneipp et al.<sup>[45]</sup> showed that the aforementioned enhancements represent only ensemble-averaged values, and that selected silver colloidal particles may exhibit individual Raman enhancement factors of  $10^{14}$ – $10^{15}$ , or effective molecular cross sections for Raman scattering comparable with linear IR absorption. The discovery boosted the interest in the possibility of using the surface enhancement to build near-field Raman scattering probes. The apertureless NSOM approach has been the method of choice in this endeavor. In this case, the nanostructure generating SERS enhancement is the tip itself. To establish a strong electromagnetic local enhancement, the electric field polarization of the pump laser beam has to be oriented along the tip axis.<sup>[35]</sup> Two experimental apertureless schemes have been implemented, different in respect to the way in which this condition is accomplished (Fig. 5). The first approach has been to use the side illumination of the tip.<sup>[46]</sup> Its advantage is that opaque samples can be



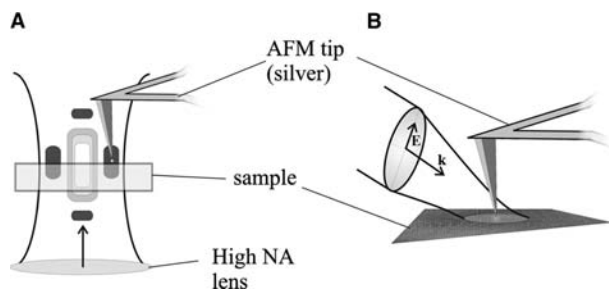


**Fig. 5** Apertureless Raman NSOM approaches. (A) On-axis illumination. The contour lines in the center of the focused beam represent schematically the distribution of regions of equal intensity. (B) Grazing incidence illumination.

imaged. The disadvantage is that long working distance Raman objectives have to be used, which limits the collection efficiency. An alternative illumination technique is to use on-axis illumination by strongly focused light, with the tip displaced from the center of the beam in the direction of polarization in one of the side lobes of the focal region.<sup>[47]</sup> An impressive optical 25-nm spatial resolution and a photon rate of a few thousands of photons per second have been obtained on isolated single-walled carbon nanotubes using this approach by Hartschuh, Anderson, and Novotny. Because of the large Raman signal, acquisition of simultaneous near-field Raman and topographic images is possible. In this work, local variations in the Raman spectrum along a carbon nanotube have been found (Fig. 6). A clear proof of the near-field origin of the Raman enhancement has been made through tip-sample distance measurements.<sup>[47]</sup> The Raman spectrum local variations reflect changes in the molecular structure, which can be caused by defects, the presence of catalyst particles, or variations in the tube lattice, clearly demonstrating the promise that SERS-NSOM hold for experimental investigations of individual nanostructures, perhaps down to the single macromolecule level.

### Infrared Near-Field Microscopy

The impressive chemical sensitivity and spatial resolution of the Raman NSOM are based on the local enhancement of the field very close to the tip. The decrease in enhancement is predicted to vary as  $(a + H)^{-12}$ , with the distance  $H$  from the tip, where  $a$  is the radius of the tip.<sup>[25]</sup> This means that apertureless Raman SERS is essentially a surface technique, which probes a 1- to 2-nm-thick layer. In the case of aperture NSOM, the axial length of the probing region roughly corresponds to the diameter of the aperture. For a 100-nm aperture, one may probe a  $\sim$ 100-nm film without loss in lateral resolution. However, the

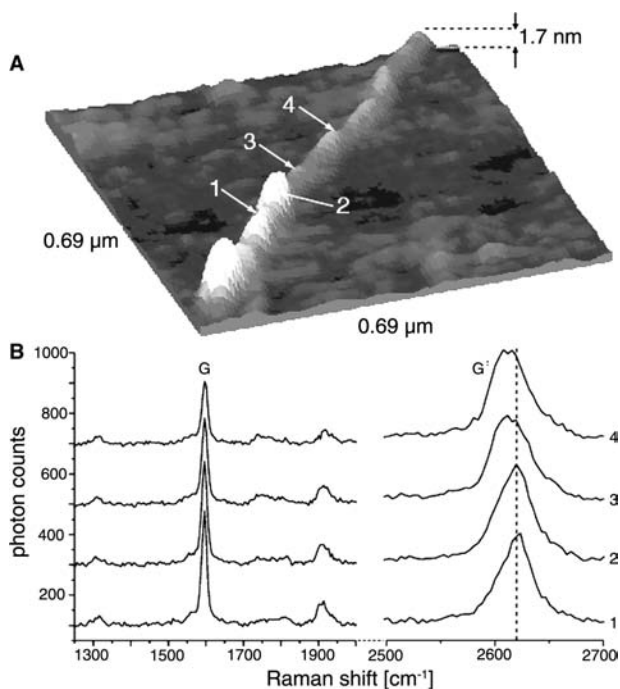


**Fig. 6** (A) Topographic image of a single-wall nanotube on glass. (B) Near-field Raman spectra detected at the marked positions 1–4 in (A). The three bumps in the topographic image are probably metal catalyst nanoparticles. *Source:* From Ref.<sup>[47]</sup>.

aperture scheme has not made the same progress as the apertureless NSOM in Raman microscopy because of the absence of surface enhancement. An alternative is IR near-field microscopy.

Mapping the chemical composition of thin films by transmission IR-NSOM has proven particularly useful in the characterization of polymeric resists for deep ultraviolet (DUV) nanolithography.<sup>[48]</sup> In this example, IR absorption near-field spectroscopy has been employed by taking advantage of the “fingerprint” region of the molecular spectra of different compounds resulting from the DUV-patterned exposure of the resist. The goal of this work was the characterization of the latent image formation during the technological steps of proximity mask-assisted DUV patterning and postexposure bake. Two polymeric species were present: poly(methacrylic acid) in the exposed regions and poly(*tert*-butylmethacrylate) in the unexposed regions, which is a photoresist from the acrylate family showing promise for DUV lithography. The most prominent differences in the IR spectra of the two polymers reside in the 2500–3500  $\text{cm}^{-1}$  region, because of the hydroxyl absorption of the poly(methacrylic acid), and in the 800–1500  $\text{cm}^{-1}$  region, because of the loss of the *t*-butoxy group (Fig. 7A). Tuning the wavelength of the color center laser source on and off, the OH stretch absorption

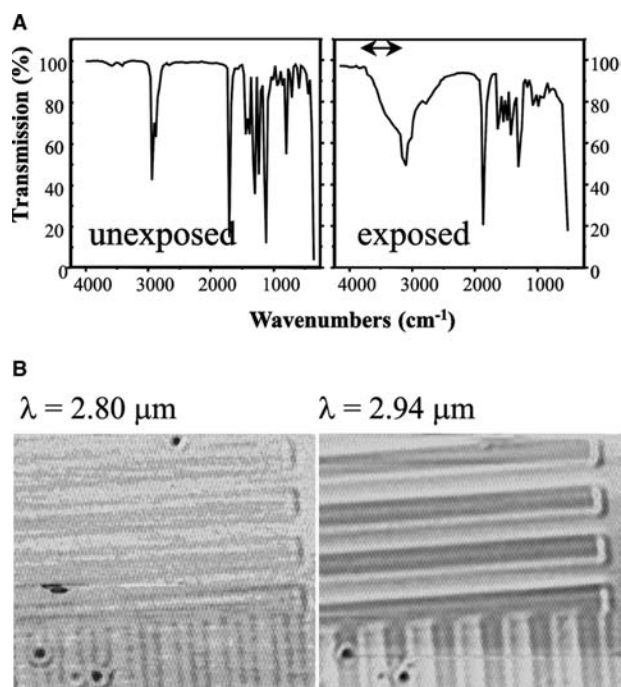


**Fig. 7** (A) Infrared spectra of as-coated (left) and irradiated and postexposure baked polymeric resist films (right). The horizontal double arrow represents the tunable wavelength range of the IR color center laser. (B) IR-NSOM mapping of 8  $\mu\text{m}/8 \mu\text{m}$  line/space pattern latent images written by DUV exposure on a 1- $\mu\text{m}$ -thick chemically amplified photoresist film. The images are taken at wavelengths outside (2.80  $\mu\text{m}$ ) and within (2.94  $\mu\text{m}$ ) the OH stretch absorption band of the exposed polymer, in constant height mode (shear-force coupling with the sample disabled).

band resulted in generating chemical contrast in near-field images of the latent pattern (Fig. 7B). The attained optical resolution was approximately 280 nm for a 3- $\mu\text{m}$  wavelength. McDonough et al.<sup>[49]</sup> have extended this work in a promising direction by measuring the water vapor uptake in photolithographic polymers in a controlled environment.

Although the IR fingerprint region offers a very convenient way for chemical identification, there are three main experimental challenges to consider when working with IR-NSOM. The first is the limited availability of tunable laser sources in IR. The closest to the ideal source from the point of view of spectral brightness, tunability, and collimation is the free electron laser,<sup>[50]</sup> which has the best chances at present to support the realization of an IR near-field microspectroscopic instrument that would surpass the spatial resolution of an FTIR microscope, while covering the same spectral range. Another possible approach is to use a tabletop ultrafast broadband laser source. By difference frequency mixing, the signal and the idler beams in a nonlinear crystal tunable IR radiation

between 2.5 and 12  $\mu\text{m}$  can be obtained at reasonable average powers (around 10 mW).<sup>[51]</sup> Another popular choice, especially for apertureless IR-NSOMs, are CO<sub>2</sub> lasers. Knoll and Keilmann<sup>[52]</sup> used a tunable CO<sub>2</sub> laser coupled with such a microscope to demonstrate vibrational band contrast around  $\lambda = 10 \mu\text{m}$  on polystyrene particles embedded in polymethyl methacrylate. On the biological applications side, Akhremitchev et al. reported on monolayer-sensitive imaging of DNA hexadecanethiol stripes, using a similar instrument. In this case, chemical contrast was achieved because of absorption by phosphate stretching band of DNA.<sup>[53]</sup> Interestingly, the measured infrared contrast, free of topographic artifacts, was significantly greater than the calculated one in both examples. This result was interpreted as evidence for surface-enhanced IR absorption.<sup>[54]</sup>

Besides the light source challenge, other experimental issues to be aware of when dealing with IR-NSOM are: probe optimization, to increase coupling with the near-field; and improved detection, because the detectivity of available detectors for IR is approximately four orders of magnitude less than in the visible. Moreover, vibrational absorptions in IR are a few orders of magnitude weaker than the average electronic absorptions in the visible. These aspects have been considered in detail by Dragnea and Leone<sup>[31]</sup> in their review of submicron infrared vibrational band chemical imaging.

### Nonlinear Near-Field Spectroscopy

The various field enhancements present in the near field make possible the observation and use of coherent non-linear effects for near-field imaging. Non-linear techniques are appealing because: 1) the signal wavelength is shifted with respect to the pump wavelength. As a consequence, these techniques have low background and, sometimes, the signal wavelength is situated in a spectral region where detectors have higher sensitivity (such as in the IR-visible sum frequency generation, a vibrational spectroscopy where the measurements are done in the visible although molecular vibrational bands are probed). 2) Based on same principles as SERS, resonant enhancements may boost the non-linear optical response by orders of magnitude. It follows that in certain situations, the non-linear optical contrast will be significantly enhanced with respect to linear absorption microspectroscopy. 3) Within the dipole approximation, depending on the symmetry of the sample and the order of the non-linear effect in use, interfacial or bulk selectivity can be obtained. Techniques and applications of non-linear chemical imaging microspectroscopy have been reviewed by Schaller et al.<sup>[55]</sup>

## OTHER TECHNIQUES OF CHEMICAL MICROSCOPY

The resolution range of near-field optical microscopy covers length scales between a single molecule and a few microns. At the smallest scales, it overlaps with scanning tunneling microscopy (STM), from the same family of scanning probe techniques. The single-molecule chemistry, imaging, and manipulation by STM have been described in detail in a recent review by Ho.<sup>[56]</sup> An alternative scanning probe technique with chemical specificity is chemical force microscopy (CFM), a variant of AFM.<sup>[57]</sup> CFM overcomes the chemical non-specificity of AFM by covering the tips with well-defined layers of molecular groups having specific interactions with the surface species to be studied.<sup>[57]</sup> CFM is a complementary technique to chemical NSOM in several respects: first, it is a surface technique, which probes only the topmost atomic layers of the sample; second, chemical identification of unknown compounds is not possible—a priori knowledge of the sample is necessary; third, transient species cannot be studied by CFM, which is essentially a static method; and, fourth, the contrast mechanism arises from different molecular forces between the tip and the surface, whereas in optical microscopy, chemical information is usually gathered using molecular vibrational or electronic transitions.

## CONCLUSION

Instrumental advances in chemical near-field optical microscopy have been the focus of the majority of articles published in the past decade in this area. However, at present, the field starts to emerge from the stage of method development. The selected examples mentioned above have been chosen to provide an illustration of notable concepts, which already have begun to shape the research areas where they have been applied, rather than to faithfully illustrate the breath of this rapidly emerging field. At present, these applications mostly span topics in molecular materials, where interesting property variations occur at submicron length scales. Although the potential of the chemical near-field microscopy for biological sciences has been demonstrated with high-resolution Raman, IR near-field, and non-linear optical spectroscopy, significant contributions to solving problems in this area are still to come.

## REFERENCES

- Douglas, T.; Young, M. Host-guest encapsulation of materials by assembled virus protein cages. *Nature* **1998**, *393* (6681), 152–155.
- Alivisatos, A.P.; Barbara, P.F.; Castleman, A.W.; Chang, J.; Dixon, D.A.; Klein, M.L.; McLendon, G.L.; Miller, J.S.; Ratner, M.A.; Rossky, P.J.; Stupp, S.I.; Thompson, M.E. From molecules to materials: current trends and future directions. *Adv. Mater.* **1998**, *10* (16), 1297–1336.
- Markovich, G.; Collier, C.P.; Henrichs, S.E.; Remacle, F.; Levine, R.D.; Heath, J.R. Architectonic quantum dot solids. *Acc. Chem. Res.* **1999**, *32* (5), 415–423.
- Wallraff, G.M.; Hinsberg, W.D. Lithographic imaging techniques for the formation of nanoscopic features. *Chem. Rev.* **1999**, *99* (3), 1801–1821.
- Nealey, P.F.; Black, A.J.; Wilbur, J.L.; Whitesides, G.M. Micro- and nanofabrication techniques based on self-assembled monolayers. In *Molecular Electronics*; Jortner, J., Ratner, M., Eds.; Blackwell Science: Osney Mead, Oxford, 1997.
- Whitesides, G.M.; Boncheva, M. Beyond molecules: self-assembly of mesoscopic and macroscopic components. *Proc. Natl. Acad. Sci. U. S. A.* **2002**, *99* (8), 4769–4774.
- Chalmers, J.M.; Griffiths, P.R. *Handbook of Vibrational Spectroscopy*; John Wiley and Sons: New York, 2002.
- Wetzel, D.L.; LeVine, S.M. Microspectroscopy—imaging molecular chemistry with infrared microscopy. *Science* **1999**, *285* (5431), 1224–1225.
- Fujii, G. To fuse or not to fuse: The effects of electrostatic interactions, hydrophobic forces, and structural amphiphilicity on protein-mediated membrane destabilization. *Adv. Drug Deliv. Rev.* **1999**, *38* (3), 257–277.
- Humecki, H.J. *Practical Guide to Infrared Microspectroscopy*; Marcel Dekker: New York, 1995.
- Born, M.; Wolf, E. *Principles of Optics*, 6th Ed.; Cambridge University Press: Cambridge, 1980.
- Goodman, J.W. *Introduction to Fourier Optics, Physical and Quantum Electronics*; McGraw-Hill: New York, 1968.
- Schrader, M.; Bahlmann, K.; Giese, G.; Hell, S.W. 4Pi-confocal imaging in fixed biological specimens. *Biophys. J.* **1998**, *75* (4), 1659–1668.
- Klar, T.A.; Jakobs, S.; Dyba, M.; Egner, A.; Hell, S.W. Fluorescence microscopy with diffraction resolution barrier broken by stimulated emission. *Proc. Natl. Acad. Sci. U. S. A.* **2000**, *97* (15), 8206–8210.
- Williams, R.M.; Zipfel, W.R.; Webb, W.W. Multiphoton microscopy in biological research. *Curr. Opin. Chem. Biol.* **2001**, *5* (5), 603–608.
- Syngé, E.H. Suggested method for extending microscopic resolution into the ultra-microscopic region. *Philos. Mag.* **1928**, *6* (2), 356–362.
- Courjon, D. *Near-Field Microscopy and Near-Field Optics, 1*; Imperial College Press: London, 2003.
- Pendry, J.B. Negative refraction makes a perfect lens. *Phys. Rev. Lett.* **2000**, *85* (18), 3966–3969.
- Betzig, E.; Isaacson, M.; Lewis, A. Collection mode near-field scanning optical microscopy. *Appl. Phys. Lett.* **1987**, *51* (25), 2088–2090.
- Zenhausern, F.; Martin, Y.; Wickramasinghe, H.K. Scanning interferometric apertureless microscopy—optical

- imaging at 10 Angstrom resolution. *Science* **1995**, *269* (5227), 1083–1085.
21. Sugiura, T.; Okada, T.; Inouye, Y.; Nakamura, O.; Kawata, S. Gold-bead scanning near-field optical microscope with laser-force position control. *Opt. Lett.* **1997**, *22* (22), 1663–1665.
  22. Lester, M.; Arias-Gonzalez, J.R.; Nieto-Vesperinas, M. Fundamentals and model of photonic-force microscopy. *Opt. Lett.* **2001**, *26* (10), 707–709.
  23. Tischer, C.; Altmann, S.; Fisinger, S.; Horber, J.K.H.; Stelzer, E.H.K.; Florin, E.L. Three-dimensional thermal noise imaging. *Appl. Phys. Lett.* **2001**, *79* (23), 3878–3880.
  24. Palanker, D.V.; Knippels, G.M.H.; Smith, T.I.; Schwettman, H.A. IR microscopy with a transient photo-induced near-field probe (tipless near-field microscopy). *Opt. Commun.* **1998**, *148* (4–6), 215–220.
  25. Moskovits, M. Surface-enhanced spectroscopy. *Rev. Mod. Phys.* **1985**, *57* (3), 783–826.
  26. Kneipp, K.; Kneipp, H.; Itzkan, I.; Dasari, R.R.; Feld, M.S. Surface-enhanced Raman scattering and biophysics. *J. Phys., Condens. Matter* **2002**, *14* (18), R597–R624.
  27. Pohl, D.W.; Bach, H.; Bopp, M.A.; Deckert, V.; Descouts, P.; Eckert, R.; Guntherodt, H.J.; Hafner, C.; Hecht, B.; Heinzlmann, H.; Huser, T.; Jobin, M.; Keller, U.; Lacoste, T.; Lambelet, P.; MarquisWeible, F.; Martin, O.J.F.; Meixner, A.J.; Nechay, B.; Novotny, L.; Pfeiffer, M.; Philipona, C.; Plakhotnik, T.; Renn, A.; Sayah, A.; Segura, J.M.; Sick, B.; Siegner, U.; Tarrach, G.; Vahldieck, R.; Wild, U.P.; Zeisel, D.; Zenobi, R. Optical microscopy in the nano-world. *Chimia* **1997**, *51* (10), 760–767.
  28. Hecht, B.; Sick, B.; Wild, U.P.; Deckert, V.; Zenobi, R.; Martin, O.J.F.; Pohl, D.W. Scanning near-field optical microscopy with aperture probes: fundamentals and applications. *J. Chem. Phys.* **2000**, *112* (18), 7761–7774.
  29. Dunn, R.C. Near-field scanning optical microscopy. *Chem. Rev.* **1999**, *99* (10), 2891.
  30. Dereux, A.; Girard, C.; Weeber, J.C. Theoretical principles of near-field optical microscopies and spectroscopies. *J. Chem. Phys.* **2000**, *112* (18), 7775–7789.
  31. Dragnea, B.; Leone, S.R. Advances in submicron infrared vibrational band chemical imaging. *Int. Rev. Phys. Chem.* **2001**, *20* (1), 59–92.
  32. Keilmann, F. Vibrational-infrared near-field microscopy. *Vib. Spectrosc.* **2002**, *29* (1–2), 109–114.
  33. Rosner, B.T.; van der Weide, D.W. High-frequency near-field microscopy. *Rev. Sci. Instrum.* **2002**, *73* (7), 2505–2525.
  34. Hong, M.K.; Jeung, A.G.; Dokholyan, N.V.; Smith, T.I.; Schwettman, H.A.; Huie, P.; Erramilli, S. Imaging single living cells with a scanning near-field infrared microscope based on a free electron laser. *Nucl. Instrum. Methods Phys. Res., B Beam Interact. Mater. Atoms* **1998**, *144* (1–4), 246–255.
  35. Wessel, J. Surface-enhanced optical microscopy. *J. Opt. Soc. Am., B, Opt. Phys.* **1985**, *2* (9), 1538–1541.
  36. Hillenbrand, R.; Knoll, B.; Keilmann, F. Pure optical contrast in scattering-type scanning near-field microscopy. *J. Microsc. Oxf.* **2001**, *202* (77–83).
  37. Hecht, B.; Bielefeldt, H.; Inouye, Y.; Pohl, D.W.; Novotny, L. Facts and artifacts in near-field optical microscopy. *J. Appl. Phys.* **1997**, *81* (6), 2492–2498.
  38. Girard, C.; Joachim, C.; Gauthier, S. The physics of near-field. *Rep. Prog. Phys.* **2000**, *63* (893–938).
  39. Palanker, D.V.; Simanovskii, D.M.; Huie, P.; Smith, T.I. On contrast parameters and topographic artifacts in near-field infrared microscopy. *J. Appl. Phys.* **2000**, *88* (11), 6808–6814.
  40. Trautman, J.K.; Macklin, J.J.; Brus, L.E.; Betzig, E. Near-field spectroscopy of single molecules at room-temperature. *Nature* **1994**, *369* (6475), 40–42.
  41. DeAro, J.A.; Weston, K.D.; Buratto, S.K.; Lemmer, U. Mesoscale optical properties of conjugated polymers probed by near-field scanning optical microscopy. *Chem. Phys. Lett.* **1997**, *277* (5–6), 532–538.
  42. Barbara, P.F.; Adams, D.M.; O'Connor, D.B. Characterization of organic thin film materials with near-field scanning optical microscopy (NSOM). *Annu. Rev. Mater. Sci.* **1999**, *29* (433).
  43. McNeill, J.D.; O'Connor, D.B.; Barbara, P.F. Imaging organic device function with near-field scanning optical microscopy. *J. Chem. Phys.* **2000**, *112* (18), 7811–7821.
  44. Emory, S.R.; Nie, S.M. Near-field surface-enhanced Raman spectroscopy on single silver nanoparticles. *Anal. Chem.* **1997**, *69* (14), 2631–2635.
  45. Kneipp, K.; Wang, Y.; Kneipp, H.; Perelman, L.T.; Itzkan, I.; Dasari, R.; Feld, M.S. Single molecule detection using surface-enhanced Raman scattering (SERS). *Phys. Rev. Lett.* **1997**, *78* (9), 1667–1670.
  46. Anderson, M.S.; Pike, W.T. A Raman-atomic force microscope for apertureless—Near-field spectroscopy and optical trapping. *Rev. Sci. Instrum.* **2002**, *73* (3), 1198–1203.
  47. Hartschuh, A.; Anderson, N.; Novotny, L. Near-field Raman spectroscopy using a sharp metal tip. *J. Microsc. Oxf.* **2003**, *210* (234–240).
  48. Dragnea, B.; Preusser, J.; Szarko, J.M.; Leone, S.R.; Hinsberg, W.D. Pattern characterization of deep-ultraviolet photoresists by near-field infrared microscopy. *J. Vac. Sci. Technol., B* **2001**, *19* (1), 142–152.
  49. McDonough, L.A.; Dragnea, B.; Preusser, J.; Leone, S.R.; Hinsberg, W.D. Water vapor uptake in photolithographic polymers observed by infrared near-field scanning optical microscopy in a controlled environment. *J. Phys. Chem., B* **2003**, *107* (21), 4951–4954.
  50. Cricenti, A.; Generosi, R.; Luce, M.; Perfetti, P.; Margaritondo, G.; Talley, D.; Sanghera, J.S.; Aggarwal, I.D.; Tolk, N.H. Very high resolution near-field chemical imaging using an infrared free electron laser. *Phys. Chem. Chem. Phys.* **2002**, *4* (12), 2738–2741.
  51. Michaels, C.A.; Stranick, S.J.; Richter, L.J.; Cavanagh, R.R. Scanning near-field infrared microscopy and spectroscopy with a broadband laser source. *J. Appl. Phys.* **2000**, *88* (8), 4832–4839.

52. Knoll, B.; Keilmann, F. Near-field probing of vibrational absorption for chemical microscopy. *Nature* **1999**, *399* (6732), 134–137.
53. Akhremitchev, B.B.; Sun, Y.J.; Stebounova, L.; Walker, G.C. Monolayer-sensitive infrared imaging of DNA stripes using apertureless near-field microscopy. *Langmuir* **2002**, *18* (14), 5325–5328.
54. Osawa, M. Surface-Enhanced Infrared Absorption. In *81 Near-Field Optics and Surface Plasmon Polaritons*; Springer-Verlag, 2001.
55. Schaller, R.D.; Johnson, J.C.; Wilson, K.R.; Lee, L.F.; Haber, L.H.; Saykally, R.J. Nonlinear chemical imaging nanomicroscopy: from second and third harmonic generation to multiplex (broad-bandwidth) sum frequency generation near-field scanning optical microscopy. *J. Phys. Chem., B* **2002**, *106* (20), 5143–5154.
56. Ho, W. Single-molecule chemistry. *J. Chem. Phys.* **2002**, *117* (24), 11,033–11,061.
57. Noy, A.; Sanders, C.H.; Vezenov, D.V.; Wong, S.S.; Lieber, C.M. Chemically-sensitive imaging in tapping mode by chemical force microscopy: relationship between phase lag and adhesion. *Langmuir* **1998**, *14* (7), 1508–1511.

# Noble Metal Nanoparticles on Carbon Fibers

Dmitri A. Bulushev

Igor Yuranov

Swiss Federal Institute of Technology,  
Lausanne, Switzerland

## INTRODUCTION

Today, noble metal nanoparticles find many applications in different fields of human activity. To increase the stability of nanoparticles, a deposition over another material (support) is often performed. The surface chemistry of the support determines the size and structure of the formed metal particles. Among different types of materials used as supports, carbons attract great interest due to their specific characteristics: 1) chemical resistance to acids and bases; 2) opportunity to tailor both physical and chemical surface properties; and 3) easy recovery of precious metals by support burning.<sup>[1–4]</sup> Being in the form of microfibers, carbonaceous materials offer a number of additional advantages.<sup>[5]</sup> Carbon fibers (CFs) are flexible and exhibit the highest specific strength of all reinforcing fibers.<sup>[6]</sup> They have good electrical and thermal conductivity, and low linear coefficient of thermal expansion and abrasion.<sup>[1]</sup> The fibers are also favored, because of the ease in handling when they are used in felt or woven forms.<sup>[7,8]</sup> Activated carbon fibers (ACFs), which are usually utilized as metal nanoparticle supports, assure better reactant transport properties as compared with granular or powdered activated carbons (AC). The unique physical and chemical properties of novel forms of fibrous carbon–carbon nanofibers (CNFs) and carbon nanotubes (CNTs) offer also impressive opportunities for supporting metal nanoparticles.<sup>[9–13]</sup>

The scope of this entry is to review the current status of research of noble metal nanoparticles supported on carbon micro- and nanofibrous materials. Special attention is given to the role of the support surface chemistry and morphology in the formation and properties of metal nanoparticles. Application fields for these promising nanostructured materials are considered.

## ACTIVATED CARBON FIBERS

Activated carbon fibers are produced from polymeric microfibers through processes of carbonization and activation. They exhibit a superhigh specific surface area, normally in the range of 1500–3000 m<sup>2</sup>/g. This originates from uniform split-shaped micropores (<2 nm) that are believed to open directly to the outer fiber surface.<sup>[8]</sup> The chemical reactivity of carbon surface is primarily due to the existence of unsaturated valences (active sites) at the edges of graphitelike hexagonal crystallites (graphene layers). Heteroatoms (mainly oxygen, hydrogen, and nitrogen) form functional groups on these active sites (Fig. 1). In high surface area carbons, surface oxygen may be responsible for more than 20% of their mass. The polar functional groups make the carbon surface more accessible to the metal precursor during impregnation from aqueous solutions. Acidic properties of a carbon material are caused by the presence of carboxylic, phenolic, lactone, and lactol groups. Carbons treated with liquid oxidants (H<sub>2</sub>O<sub>2</sub>, HNO<sub>3</sub>, KMnO<sub>4</sub>, etc.) usually contain more carboxylic groups than O<sub>2</sub>-oxidized samples.<sup>[2,14]</sup> Upon heat treatment, carboxylic groups evolve CO<sub>2</sub> at relatively low temperatures (below 573 K); however, other groups are thermally more stable. At elevated temperatures, less acidic groups provide an interaction of metal precursors or nanoparticles with the support and thus minimize the metal sintering.<sup>[4]</sup> Pyrones are considered to be the most important basic functionalities at the edges of graphene layers.<sup>[14,15]</sup> Nitrogen-containing groups and inorganic impurities can also play a non-negligible role.

Depending on pH, either negatively or positively charged functional groups may exist on a carbon surface in aqueous solutions. A net overall surface charge is zero at the isoelectric point (pH<sub>IEP</sub>). The surface attracts cations at pH > pH<sub>IEP</sub>, and anions



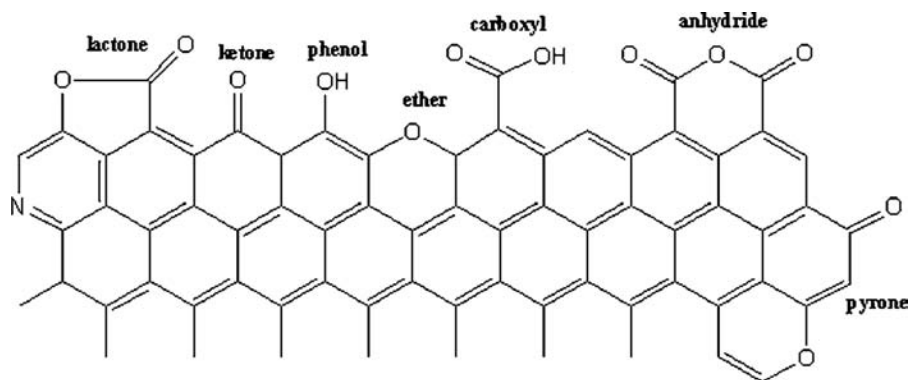


Fig. 1 Functional groups on carbon surface.

at  $\text{pH} < \text{pH}_{\text{IEP}}$ .<sup>[2]</sup> When preparing metal nanoparticles, the support surface should have a suitable charge. Otherwise, electrostatic repulsion forces may be stronger than nonspecific dispersion forces of attraction, and upon drying, the benefits of having a large support surface would be lost with subsequent loss of metal dispersion.

## CARBON NANOFIBERS AND NANOTUBES

Since their discovery,<sup>[9]</sup> CNFs (nanotubes) have captured attention of researchers worldwide.<sup>[10–13,16]</sup> Potentially, CNFs have unique properties for use as a support: with diameters in the range of 1–100 nm and lengths of 0.1–1000  $\mu\text{m}$ , they have a high specific surface area of 10–500  $\text{m}^2/\text{g}$ , being free of micropores and impurities. The materials exhibit an outstanding mechanical stability. Carbon nanofibers are conductive or semiconductive along fibrils and quantized cross-fibrils. This offers opportunities of novel applications that are dependent on the electron conductivities in terms of nanofiber diameters and surface properties.

The manufacturing processes of CNFs now include different methods of graphite vaporization and thermal or plasma-enhanced chemical vapor deposition (CVD).<sup>[17]</sup> Catalytic growth of CNFs by CVD has a great potential for scaled-up material synthesis. Depending on the synthesis conditions and catalyst used, the fibers of different morphologies (tubular, fishbone, platelet, ribbon types, etc.) can be produced (Fig. 2). The tubular type fibers (CNTs) have a hollow core. The fiber surface exposes only basal planes of graphite, while only graphite plane edges are exposed on the surface of the fishbone and platelet type fibers. Another strategy of CNF fabrication involves a template synthesis using anodic nanoporous alumina and ordered mesoporous silicas.<sup>[18–23]</sup>

Due to the peculiar structure, as-produced CNTs [multiwalled (MWNTs) and single-walled (SWNTs)] do not possess a high amount of functional groups on the surface (basal planes of graphite), and mainly surface defects can be considered as anchoring sites for metals. Special pretreatment procedures are needed in this case to achieve optimal interaction between the support and metal precursor. At the same time, CNFs

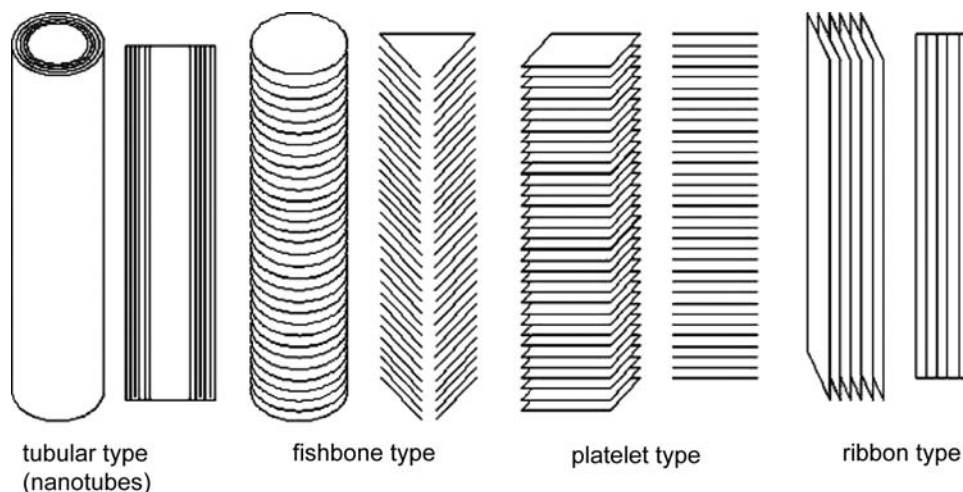


Fig. 2 Types of carbon nanofibers.

can be used as a support without any pretreatment. Fishbone and platelet structures present potentially reactive groups on the graphene platelet edges. The nature and concentration of the groups are modified by chemical or thermal treatments. Nitric acid treatment is effective for the creation of oxygen-containing groups on the fiber surface. An estimation of the amount of carboxylic/phenolic groups formed on CNTs after  $\text{HNO}_3$  treatment gave  $\sim 10^{21}$  sites per gram.<sup>[24]</sup> Similar value was obtained for the  $\text{HNO}_3$ -treated ACFs.<sup>[25]</sup>

## SUPPORTED METAL NANOPARTICLES

It is well known that mechanical, physical, and chemical properties of nanoparticles may differ considerably from those of bulk substances. Physical properties of unsupported nanoparticles are thoroughly reviewed.<sup>[26]</sup> The deposition over support often endows particles with novel or improved properties. These changes are provided by the change of electronic and structural properties, strong interaction with the support, and increase of the particle/support interface length taking place with metal dispersion. These factors are closely interrelated and determine, for example, the number of catalytically active sites and adsorption energies during catalytic reactions. Thus, the dispersion of a supported metal can be extremely high, making almost every metal atom accessible to reactants. Advantages of metal dispersing over support widely used for catalytic applications are also applicable for different fields of nanotechnology.

Among the noble metals, the most fascinating example of the change of catalytic properties, because of the metal dispersion change, is gold. Noble properties of bulk gold are known for centuries. However, when decreasing the Au particle size up to 3–10 nm, gold becomes a very active catalyst for low-temperature CO oxidation, water gas-shift reaction, NO reduction, diol oxidation, and other reactions.<sup>[27]</sup> An analysis of the activity of gold catalysts in CO oxidation allowed to conclude that the most important reason of the improved activity of finely dispersed gold is the increase of the concentration of low co-ordinated surface Au atoms.<sup>[28]</sup> The effects of the support nature may contribute, but to a lower extent.<sup>[28]</sup>

## NOBLE METAL NANOPARTICLES SUPPORTED ON CARBON FIBERS

Different methods such as incipient-wetness impregnation, ion exchange, organometallic grafting, electron beam evaporation, and deposition/precipitation

followed by reduction are used to prepare noble metal nanoparticles supported on carbon fibrous materials. In all cases, a delicate optimization of carbon surface chemistry is needed to achieve optimal interaction between the support and metal precursor.

## Noble Metals on Carbon Microfibers

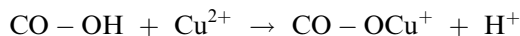
The effectiveness of gold and silver adsorption by AC and ACFs from solutions is dependent on the type of the metal precursor, conditions and properties of the carbon surface.<sup>[29–31]</sup> It was found that up to 3 g of metallic gold could be collected on 1 g of ACFs from an  $\text{Au}^{3+}$ -containing solution.<sup>[32]</sup> A decrease of the surface carboxylic groups content was observed after gold adsorption/reduction.<sup>[25]</sup> The reduction capacity was larger than the amount of carbon dioxide released, but approximately equal to the amount of protons produced.<sup>[33]</sup> At the same time, Jia et al.<sup>[34]</sup> report that the oxygen functionality on AC does not have an effect on adsorption of Au and Ag cyanide anionic forms  $[\text{M}(\text{CN})_2]^{n-}$ , while total pore volume is important. They indicated that the graphene layers on carbon are the main adsorption sites of cyanide anions.

Bulushev et al.<sup>[25]</sup> tried to apply aqueous  $\text{HAuCl}_4$  to obtain gold nanoparticles on ACFs. However, utilization of this Au precursor resulted in fast metallization of the external fiber surface independent of the support pretreatment. The obtained material was almost not active in CO oxidation at room temperature, confirming that only big particles of gold are formed on the ACF surface. In contrast, adsorption of ethylenediamine (en) complex  $[\text{Au}(\text{en})_2]\text{Cl}_3$  led to nanosized gold deposition. Interaction took place via ion exchange of  $[\text{Au}(\text{en})_2]^{3+}$  with the surface carboxylic and phenolic groups.  $\text{Au}^{3+}$  exchanged with protons of phenolic groups could be reduced to metallic state by hydrogen (573–773 K) forming nanoparticles of 3–5 nm size, which are extremely active in CO oxidation at room temperature. Ion exchange of the precursor with carboxylic groups was accompanied by spontaneous reduction of  $\text{Au}^{3+}$  to metallic gold nanoparticles of  $\sim 2$  nm size, which served as nucleation sites of bigger particle ( $>9$  nm) formation during  $\text{H}_2$  reduction. Such particles were less active in CO oxidation. The regulation of the carboxylic/phenolic group ratio performed by thermal treatment of ACFs in inert atmosphere allowed controlling the Au particle size. Thus, the treatment at 973 K led to the removal of carboxylic groups, while phenolic groups were still stable. The Au nanoparticles prepared on such a support exhibited the highest activity in CO oxidation. The complete removal of oxygen-containing surface groups at 1273 K resulted in a carbon support, which did not interact with  $[\text{Au}(\text{en})_2]^{3+}$ . It was also found that prior

precipitation–deposition of iron hydroxide on the ACF surface removed mainly carboxylic groups, keeping the phenolic groups intact. This led to the formation of very active Au nanoparticles (3–5 nm) non-contacting with Fe<sub>2</sub>O<sub>3</sub> nanoparticles (Fig. 3).

The importance of the phenolic groups for the interaction of Au nanoparticles with the support was claimed for the Au/AC catalysts prepared using metal sols.<sup>[35]</sup> Among the catalysts with the same average Au particle size (~12 nm), the catalysts based on AC with higher concentration of phenolic groups were more active in liquid phase oxidation of ethylene glycol.<sup>[35]</sup>

Interaction of copper precursors with the carbon surface was also shown<sup>[36,37]</sup> to be dependent on the presence of oxygen-containing surface groups. It was noted that pretreatment of carbon materials in HNO<sub>3</sub> significantly increased copper adsorption. This gives evidence that the following reaction may play an important role for copper adsorption:



Nitrogen-containing groups (pyridinic surface groups) incorporated by ammonia treatment at high temperature may also act as surface co-ordination sites adsorbing Cu<sup>2+</sup> ions from the solution.<sup>[38]</sup>

Baker and coworkers<sup>[39,40]</sup> deposited Cu nanoparticles on different allotropic forms of carbon: AC, diamond, and graphitized microfibers. Activated carbon contains small domains of disordered graphitic

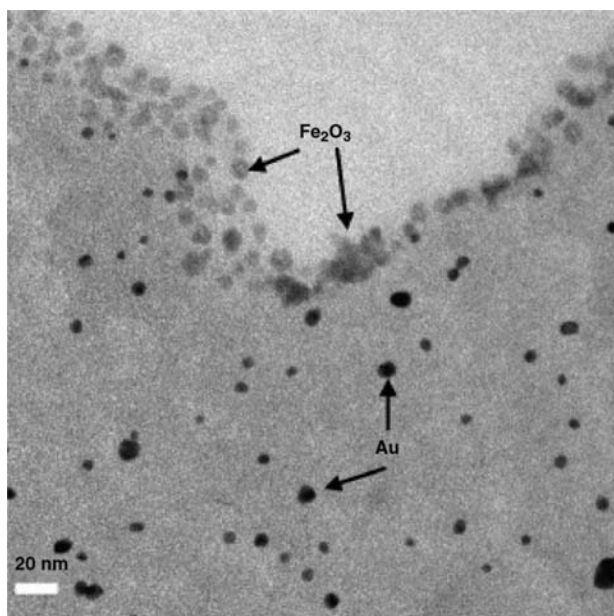


**Fig. 3** Gold nanoparticles on activated carbon microfibers: HRTEM image of the 1.3 wt.% Au/4.5 wt.% FeO<sub>x</sub>/ACFs (elementary filament cut). *Source:* From Ref.<sup>[25]</sup>. © Elsevier, 2004.

structures and has lower electronic and thermal conductivities. Graphite is the most stable form of carbon and possesses excellent thermal and electronic properties. Diamond is an electrical insulator, but it exhibits excellent thermal conductivity. Weakly acidic and non-acidic groups were presented on graphitized CFs and diamond, contrary to AC treated in HNO<sub>3</sub>, which contained strongly and weakly acidic groups. Reduction of Cu<sup>2+</sup> to metallic copper by H<sub>2</sub> was found to be dependent on the nature of carbon support. It was proposed that epitaxial interaction existed between copper and diamond surfaces, which facilitated the copper reduction on that material. The most difficult was the reduction of Cu<sup>2+</sup> on AC, since the strongly acidic carboxylic groups formed copper-carboxylate species on the surface. A higher Cu dispersion was obtained via wet impregnation on diamond as compared with graphitized CFs. It was assigned to stabilization of copper through “dangling” bonds on the diamond surface. Cu dispersed by ion exchange was stabilized on graphitized CFs in aggregates of globular particles deposited on top of graphitic basal planes and smaller crystallites at the edges of defects within these planes. Such distribution of copper affected its reducibility. The shape of supported Cu particles was also found to depend on the carbon support. Thus, following the reduction in H<sub>2</sub> at 373 K, Cu particles on AC and graphitized fibers adopted a toroidal (or “donut”) geometry. For diamond-supported copper, a hexagonal-shaped form was found. The latter geometry was predominant for all supports when the reduction temperature was increased to 573 K. After 24 hr of reduction, the following mean size of the Cu particles was obtained on AC, graphitized fibers, and diamond: 11–20, 8–12, and 7–15 nm, respectively.<sup>[39,40]</sup>

Highly dispersed palladium (3–6 nm)<sup>[41,42]</sup> and platinum<sup>[43]</sup> were supported on ACFs via impregnation followed by reduction. It was mentioned that a large amount of surface functional groups on ACFs made the reduction of platinum precursor to metallic state difficult.<sup>[43]</sup>

### Noble Metals on Carbon Nanofibers and Nanotubes

Due to their unique nature, CNTs and nanofibers are considered as exciting supports for noble metal nanoparticles. Indeed, hollow nanotube cavities can be used to control a particle size and shape. High metal dispersion was obtained on CNTs even if the specific surface area of the support was only 25 m<sup>2</sup>/g.<sup>[44]</sup> Nanotubes can be filled by metals during the arc-discharge synthesis in the presence of metals or through opening and filling the tubes by a metal precursor followed by reduction. It is also possible to remove unwanted metal

particles from outside surface of CNTs. An example of Pd nanoparticles inside the CNTs is shown in Fig. 4.<sup>[45]</sup>

Bera et al.<sup>[46]</sup> deposited Pd nanoparticles (3 nm) inside the CNTs during one-step synthesis using an arc-discharge in solution. The process took place via reduction of  $[\text{PdCl}_4]^{2-}$  anions and simultaneous encapsulation of Pd nanoparticles in CNTs during rolling of graphene sheets from the anode.

Satishkumar et al.<sup>[47]</sup> managed to fill CNTs by Au, Ag, Pd, and Pt nanoparticles. They opened the ends of nanotubes using a variety of oxidants, treated nanotubes with acid solutions containing noble metal ions, reduced the samples in liquid phase, and closed the ends of the filled CNTs by heating in a benzene/hydrogen gas mixture. Encapsulated metal particles of 1–17 nm size were obtained.

An example of Pt nanoparticles located on the external surface of CNTs is shown in Fig. 5.<sup>[48]</sup> The sample was prepared through the treatment of CNTs in an ethylene glycol solution of  $\text{H}_2\text{PtCl}_6 \cdot \text{aq}$  at 313 K followed by washing with diluted  $\text{HNO}_3$ .

Xue et al.<sup>[49]</sup> synthesized Au, Ag, Pd, and Pt particles with the average size of 8, 17, 7, and 8 nm, respectively, on the outer surface of CNTs by impregnation from a metal salt solution, evaporation of the solvent, and reduction in  $\text{H}_2$  at 973 K. It was noticed that the

particle size corresponded to the size of nanotubes used as a support. By comparison, much bigger particles of Pd were obtained on graphite and AC using the same preparation method. The adhesion of nanoparticles to CNTs was not strong. However, stabilization of the particles using different coupling compounds could be achieved.<sup>[50–52]</sup> Thus, alkanethiolate-capped Au nanoparticles (2 and 5 nm) were assembled on the surface of  $\text{HNO}_3$ -treated MWNTs in the presence of bifunctional linking agents.<sup>[52]</sup> The chemistry involved in the assembly is a combination of the hydrophobic interaction between the alkyl chains of the capping molecules and the hydrophobic backbones of nanotubes as well as of the hydrogen-bonding interaction between carboxylic groups of linking molecules and the functional groups of the nanotubes' surface. The organic shells could be removed by thermal treatment. The morphology and packing density for the nanoparticle assembly depended on the relative concentrations of nanoparticles, linking molecules and nanotubes.

It is important to note that Au,<sup>[50]</sup> Pd,<sup>[50,53,54]</sup> and Rh<sup>[55]</sup> could not be attached to CNTs and CNFs without functionalization of the support. However, Au, Pt, and Ag nanoparticles with size of 1–7 nm were successfully obtained on  $\text{HNO}_3$ -pretreated CNTs.<sup>[24]</sup>

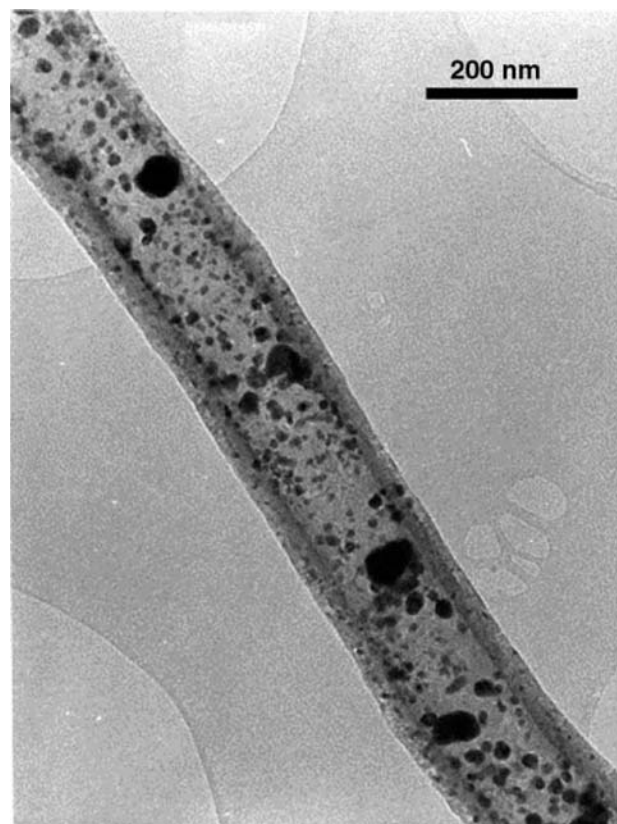


**Fig. 4** HRTEM image of Pd nanoparticles inside carbon nanotubes. *Source:* From Ref.<sup>[45]</sup>. © Elsevier, 2003.

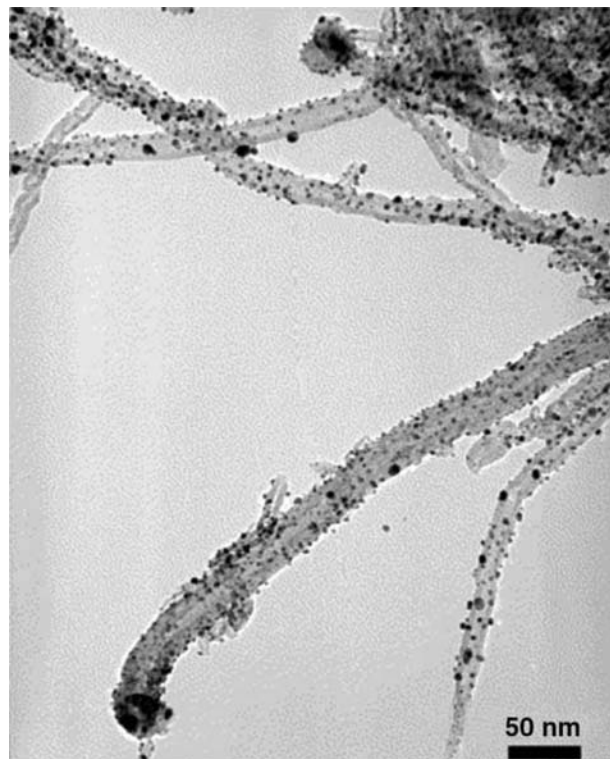


**Fig. 5** HRTEM image of Pt nanoparticles on the external surface of carbon nanotubes. *Source:* From Ref.<sup>[48]</sup>. © Elsevier, 2004.

Ye, Lin, and Wai<sup>[56]</sup> decorated MWNTs with Pd particles by reduction of Pd  $\beta$ -diketone precursor in supercritical CO<sub>2</sub>. The authors obtained well-dispersed particles of 5–10 nm size anchored to the external walls of the support.

Hoogenraad et al.<sup>[53,54]</sup> used tubular and fishbone type CNFs as supports for Pd nanoparticles. Pd was deposited from the ammine complex [Pd(NH<sub>3</sub>)<sub>4</sub>]Cl<sub>2</sub>. It was essential to keep air-free conditions during drying of impregnated material in order to escape big Pd particle formation. The hemispherical Pd particles with the size of 1.5–4 nm were observed by HRTEM (high-resolution transmission electron microscopy) after reduction.

Chesnokov et al.<sup>[57]</sup> used three types of CNFs for Pd deposition from PdCl<sub>2</sub>. They showed that Pd nanoparticles exhibited a strong interaction with the butt ends of graphite (0 0 2) layers. This interaction probably resulted in electron transfer from the metal to the support and stabilization of nanoparticles.

Ma et al.<sup>[58]</sup> studied Cu particles supported on different (fishbone, platelet, ribbon, and tubular) types of CNFs. Copper was deposited from aqueous salt solutions. If Cu nanoparticles were located on the edge sites of nanofibers, they adopted a thin faceted morphology indicating a strong metal–support interaction. The particles formed in such a way were very stable with respect to sintering. However, the particles tended to acquire a globular geometry if the copper was supported on AC or the basal planes of graphite, showing a very weak interaction with the support. Thus, the fishbone and platelet CNFs were the best supports to provide small particles with a narrow size distribution. A precursor salt and carbon surface functionality turned out to also affect the particle size distribution and stability.

Supported Cu nanoparticles (<10 nm) were prepared using CNFs with a diameter ranging from 100 nm.<sup>[59]</sup> Carbon nanofibers were impregnated with a copper salt solution, dried and treated by H<sub>2</sub> (773 K). The electronic properties of the nanoparticles differed considerably from those of bulk copper. It was noticed that the size of Cu particles was dependent on the size of CNFs: the smaller the fiber diameter, the smaller the Cu nanoparticle size obtained. However, the nanoparticles were not strongly attached to the support and could be detached by ultrasonic treatment.

Up to 10 wt.% of platinum loading on SWNTs was achieved by Lordi, Yao, and Wei<sup>[60]</sup> using K<sub>2</sub>PtCl<sub>4</sub> as a metal precursor and reduction by ethylene glycol. The average size of supported Pt nanoparticles was 1–2 nm. These particles were located on bundles of CNTs but never on isolated tubes. The authors pointed out that a strong agitation could remove weakly bound Pt particles from the support. Therefore, the nanotubes were

pretreated in diluted HNO<sub>3</sub> in order to create surface functional groups able to stabilize Pt nanoparticles. Similarly, it was noted that functional groups may provide not only effective interaction of the Rh precursor with carbon, but also stabilization of the resulting Rh nanoparticles.<sup>[61]</sup>

Extremely small stable Pt nanoparticles were synthesized on the nanostructured carbon by incipient-wetness impregnation from an H<sub>2</sub>PtCl<sub>6</sub>/acetone solution followed by drying and H<sub>2</sub> reduction.<sup>[22]</sup> In this case the carbon structure was composed of ordered nanotubes, which were originally formed inside the cylindrical nanochannels of the SBA-15 template. Even after the template had been removed, the nanotubes were rigidly interconnected into a hexagonal array by carbon spacers, which were formed inside the complementary micropores between the SBA-15 nanochannels. When the Pt loading was 2 wt.%, the Pt nanoparticles were less than 1.3 nm in diameter. A narrow particle size distribution (~2.5 nm) was observed at 50 wt.% Pt loading.

## APPLICATIONS OF NOBLE METAL NANOPARTICLES SUPPORTED ON CARBON FIBROUS MATERIALS

Decoration of CFs by metal nanoparticles endows the materials with new valuable properties. Up to now, noble metal nanoparticles supported on carbon fibrous materials have been mostly applied as heterogeneous catalysts. However, other applications are intensively developing.

### Catalytic Applications of Noble Metals on Carbon Microfibers

Gold nanoparticles on ACFs possess the catalytic activity in room-temperature CO oxidation comparable with the best reported catalysts (Au/TiO<sub>2</sub>, Au/Fe<sub>2</sub>O<sub>3</sub>).<sup>[62]</sup> The activity increases in the presence of water vapor and hydrogen. Application fields of Au nanoparticles on CFs could be extended to other catalytic reactions, since Au on the conventional activated carbon is shown to be an effective catalyst, for example, for liquid phase selective oxidation of alcohols and aldehydes.<sup>[35,63,64]</sup>

Copper catalysts supported on AC, graphitized carbon microfibers, and diamond powder were studied in crotonaldehyde hydrogenation.<sup>[65]</sup> Copper deposited on graphitized microfibers demonstrated lower activity and higher selectivity toward crotyl alcohol as compared to other catalysts. This was attributed to small Cu nanoparticles preferentially stabilized along the edges of the graphitic basal planes. However, no effect

of carbon support was found for hydrogenation of furfural.<sup>[66]</sup> The Cu catalysts based on graphitized CF and diamond suffered from deactivation contrary to the catalyst supported on AC.

Ma et al.<sup>[67]</sup> studied Cu nanoparticles based on different allotropic forms of carbon including graphitized carbon microfibers for N<sub>2</sub>O decomposition. The catalytic activity was found to be directly related to the copper dispersion.

Copper in combination with ZnO supported on AC, black carbon, and ACFs was used in hydrogen production during partial methanol oxidation.<sup>[68]</sup> It was concluded that a deposition of the active phase on a microporous structure leads to a lower initial activity, but a better stability with respect to Cu sintering.

A linear dependence of the activity in nitrobenzene hydrogenation on Pt dispersion was found for the catalysts based on ACFs.<sup>[43]</sup>

Activated carbon fibers were applied as a structured support for deposition of palladium nanoparticles active in hydrogenation of unsaturated hydrocarbons<sup>[41]</sup> and nitrite.<sup>[42,69]</sup> The catalysts with average Pd particle size of 3–6 nm on ACFs showed a better activity than the ones prepared on glass fibers.

### Catalytic Applications of Noble Metals on Carbon Nanofibers and Nanotubes

It was mentioned<sup>[44]</sup> that opportunities for using single-walled CNTs are rather limited, while multiwalled CNTs and CNFs seem to be more perspective.

Pd nanoparticles supported on CNFs exhibited a comparable activity in hydrogenation of nitrobenzene to aniline<sup>[53]</sup> and increased activity in hydrogenation of C=C bond of cinnamaldehyde<sup>[70]</sup> with respect to the commercial Pd catalyst based on AC. An important advantage of the CNF support is that surface area, size of fibrils, as well as mechanical strength can be controlled and mass transfer limitation can be decreased, because of the absence of micropores. A change of electronic properties of Pd particles provided by interaction with CNFs resulted in a change of their catalytic properties in 1,3-butadiene hydrogenation to butanes.<sup>[57]</sup> An increase of the Pd<sup>2+</sup> fraction in the catalysts decreased the activity and selectivity.

The following trend of specific activity was found for gas phase phenol hydrogenation over Pd catalysts: Pd/AC ~ Pd/ribbon CNFs < Pd/fishbone CNFs < Pd/SiO<sub>2</sub> ~ Pd/graphite < Pd/Ta<sub>2</sub>O<sub>5</sub>.<sup>[71]</sup> The size of the particles was in the range 6–17 nm. The authors concluded that the stronger was the Pd particles-support interaction, the higher was the reaction rate. The selectivity toward cyclohexanone and cyclohexanol was assumed to be dependent on the crystallographic orientation of Pd nanoparticles.

Pd particles (5–10 nm) supported on MWNTs showed high activity in hydrogenation of olefins in supercritical CO<sub>2</sub> and in oxygen electrocatalytic reduction.<sup>[56]</sup>

Some specific properties of Pt on the platelet type nanofibers with respect to Pt on silica in *n*-hexane isomerization were reported by Baker et al.<sup>[72]</sup> The former catalyst produced more isomers at lower temperature and higher H<sub>2</sub> partial pressure. This was assigned to the presence of a larger amount of hydrogen on the CNFs support.

Lordi, Yao, and Wei<sup>[60]</sup> applied Pt nanoparticles supported on SWNTs to hydrogenate 3-methyl-2-butenol to 3-methyl-2-butenol with high selectivity.

Ros et al.<sup>[55]</sup> used the fishbone type CNFs as a support for Rh nanoparticles (1–2 nm) applied in hydrogenation of cyclohexene. No significant effect of the size of nanoparticles on the catalytic activity was found.

Rh nanoparticles supported on graphite nanofibers were used as a catalyst in ethylene hydroformylation.<sup>[73]</sup> Their activity was compared with the activity of Rh/SiO<sub>2</sub>. They were found similar, but the selectivity toward propaldehyde was higher for Rh on nanofibers. Rh on the ribbon type nanofibers gave the highest selectivity. The morphological factor was accepted to be more important than the particle size. For the most selective catalyst, the (1 1 1) face of Rh was preferentially exposed to the gas phase.

Rh supported on MWNTs was used for hydrogenation of cinnamaldehyde and hydroformylation of hexane in liquid phase.<sup>[74]</sup> In both cases, the catalyst was found to be selective toward C=C bond hydrogenation and aldehyde production, respectively. The functionalization of nanotubes by the HNO<sub>3</sub> treatment before the Rh deposition from [Rh<sub>2</sub>Cl<sub>2</sub>(CO)<sub>4</sub>] was necessary to get an active catalyst. Otherwise, the Rh dispersion and catalyst activity were low.

Luo et al.<sup>[75]</sup> showed that Rh nanoparticles (~10 nm) supported on CNTs can decompose NO at temperatures lower than 573 K more effectively than Rh nanoparticles supported on γ-Al<sub>2</sub>O<sub>3</sub>. The Rh/CNTs catalyst was found to be more capable in keeping rhodium in metallic state indicating a strong Rh-support interaction.

The catalytic properties of Ir (30 wt.%) supported on a CNFs/carbon felt composite and alumina were compared in hydrazine decomposition.<sup>[45,76]</sup> The advantages of the former catalyst with the average metal particle size of 2 nm were the mechanical resistance, stability, low weight, and high thermal conductivity.

### Miscellaneous Applications

Antibacterial properties of Ag and Cu are well known. Activated carbon fibers demonstrate higher sorption



characteristics than granular AC. Combination of these properties in one material [Ag(Cu) nanoparticles/ACFs] is reported to be promising for water cleaning.<sup>[77]</sup>

Cu nanoparticles obtained by chemical methods were active in production of regularly coiled fishbone type CNFs by decomposition of acetylene, while nanoparticles produced from H<sub>2</sub> arc plasma revealed the ribbonlike nanofibers only.<sup>[78]</sup>

Cu filled CNTs were proposed as interconnect material for integrated circuits.<sup>[79]</sup>

Javey et al.<sup>[80]</sup> fabricated a high-performance nanotube field-effect transistor with almost zero Schottky barrier using Pd-SWNT junctions. Palladium greatly reduces the barriers for electron transport through the valence band of nanotubes.

SWNTs decorated with Pd nanoparticles were found to exhibit a significant electrical conductance modulation upon exposure to small concentrations of H<sub>2</sub> in air. The Pd nanoparticles/CNTs-based H<sub>2</sub> sensors showed high sensitivity, fast response, and reversibility at room temperature.<sup>[81]</sup>

Pd supported on the fishbone type CNFs<sup>[82]</sup> and CNTs<sup>[83,84]</sup> was studied in hydrogen storage. The hydrogen loading of 1.5 wt.% was reached at 10 MPa of H<sub>2</sub> pressure for nanofibers with specific surface area of 400 m<sup>2</sup>/g and Pd:C mole ratio close to 1. Hydrogen of 3.1 wt.% stored was reported for the 4.1 wt.% Pd/MWNT material. However, all these values are well below the 6.5 wt.% benchmark set by the U.S. Department of Energy for such kind of materials.

Development of fuel cells based on CNTs or mesoporous carbon coated by metal nanoparticles as electrodes for mobile and laptop applications was reported by some leading electronics companies.<sup>[85,86]</sup> Using CNTs with platinum nanoparticles for fuel cell purposes was discussed in a number of publications.<sup>[87-89]</sup> Higher catalytic activity and better cell performance as compared to the catalysts supported on commercial carbons were found. The current density during methanol oxidation at the Pt (~7 nm)/CNT membrane electrode was ~20 times higher than at the bulk Pt electrode. This enhancement was due to both high surface area and high electrocatalytic activity of Pt nanoparticles dispersed inside the CNTs.

The high Pt dispersion (<3 nm) on the ordered array of CNFs prepared by using mesoporous SBA-15 silica as a template also gave rise to a promising activity for O<sub>2</sub> electrocatalytic reduction.<sup>[22]</sup>

## CONCLUSIONS

Carbon micro- and nanofibers provide impressive opportunities for supporting highly dispersed noble metals. Resulting functional materials combine specific properties of metal nanoparticles and fibrous supports.

Carbon surface chemistry allows controlling metal particle size and stabilizing nanoparticles on the support. On the other hand, carbon fibrous supports represent the materials with the advantages of structured materials such as mechanical stability, improved hydrodynamic and transport properties, etc. Nanocarbons, due to their dimensions, bring new unique opportunities to control the size and morphology of supported metal nanoparticles. Today, noble metal nanoparticles supported on carbon fibrous material are already used extensively in electro- and heterogeneous catalysis. Undoubtedly, tomorrow, they will find a wide application in other fields of nanotechnology.

## REFERENCES

1. Donnet, J.B.; Bansal, C. *Carbon Fibers*; Marcel Dekker, Inc.: New York, 1990.
2. Radovic, L.R.; Rodriguez-Reinoso, F. Carbon materials in catalysis. In *Chemistry and Physics of Carbon*; Thrower, P.A., Ed.; Marcel Dekker Inc.: New York, 1997; Vol. 25, 243-358.
3. Auer, E.; Freund, A.; Pietsch, J.; Takke, T. Carbons as supports for industrial precious metal catalysts. *Appl. Catal. A* **1998**, *173* (2), 259-271.
4. Rodrigues-Reinoso, F. The role of carbon materials in heterogeneous catalysis. *Carbon* **1998**, *36* (3), 159-175.
5. Matatov-Meytal, Y.; Sheintuch, M. Catalytic fibers and cloths. *Appl. Catal. A* **2002**, *231*, 1-16.
6. Chand, S. Carbon fibers for composites. *J. Mater. Sci.* **2000**, *35* (6), 1303-1313.
7. Suzuki, M. Activated carbon fiber: fundamentals and applications. *Carbon* **1994**, *32* (4), 577-586.
8. Mochida, I.; Korai, Y.; Shirahama, M.; Kawano, S.; Hada, T.; Seo, Y.; Yoshikawa, M.; Yasutake, A. Removal of SO<sub>x</sub> and NO<sub>x</sub> over activated carbon fibers. *Carbon* **2000**, *38*, 227-239.
9. Iijima, S. Helical microtubules of graphitic carbon. *Nature* **1991**, *354* (6348), 56-58.
10. Rodriguez, N.M. A review of catalytically grown carbon nanofibers. *J. Mater. Res.* **1993**, *8* (12), 3233-3250.
11. De Jong, K.P.; Geus, J.W. Carbon nanofibers: catalytic synthesis and applications. *Catal. Rev. Sci. Eng.* **2000**, *42* (4), 481-510.
12. Dai, H. Carbon nanotubes: opportunities and challenges. *Surf. Sci.* **2002**, *500* (1-3), 218-241.
13. Serp, P.; Corrias, M.; Kalck, P. Carbon nanotubes and nanofibers in catalysis. *Appl. Catal. A* **2003**, *253* (2), 337-358.
14. Boehm, H.P. Surface oxides on carbon and their analysis: a critical assessment. *Carbon* **2002**, *40* (2), 145-149.
15. Montes-Moran, M.A.; Suarez, D.; Menendez, J.A.; Fuente, E. On the nature of basic sites on carbon surfaces: an overview. *Carbon* **2004**, *42* (7), 1219-1224.
16. Chatterjee, A.; Deopura, B.L. Carbon nanotubes and nanofibre: an overview. *Fibers Polym.* **2002**, *3* (4), 134-139.
17. Rakov, E.G. Methods for preparation of carbon nanotubes. *Russ. Chem. Rev.* **2000**, *69* (1), 35-52.

18. Huczko, A. Template-based synthesis of nanomaterials. *Appl. Phys. A: Mater. Sci. Process.* **2000**, *70* (4), 365–376.
19. Ryoo, R.; Joo, S.H.; Kruk, M.; Jaroniec, M. Ordered mesoporous carbon. *Adv. Mater.* **2001**, *13* (9), 677–681.
20. Sui, Y.C.; Cui, B.Z.; Guardian, R.; Acosta, D.R.; Martinez, L.; Perez, R. Growth of carbon nanotubes and nanofibers in porous anodic alumina films. *Carbon* **2002**, *40* (5–6), 1011–1016.
21. Kyotani, T.; Tsai, L.; Tomita, A. Preparation of ultrafine carbon tubes in nanochannels of an anodic aluminium oxide film. *Chem. Mater.* **1996**, *8* (8), 2109–2113.
22. Joo, S.H.; Choi, S.J.; Oh, I.; Kwak, J.; Liu, Z.; Terasaki, O.; Ryoo, R. Ordered nanoporous arrays of carbon supporting high dispersions of platinum nanoparticles. *Nature* **2001**, *412* (6843), 169–172.
23. Yanagishita, T.; Sasaki, M.; Nishio, K.; Masuda, H. Carbon nanotubes with a triangular cross-section, fabricated using anodic porous alumina as the template. *Adv. Mater.* **2004**, *16* (5), 429–432.
24. Satishkumar, B.C.; Vogl, E.M.; Govindaraj, A.; Rao, C.N.R. The decoration of carbon nanotubes by metal nanoparticles. *J. Phys. D* **1996**, *29* (12), 3173–3176.
25. Bulushev, D.A.; Yuranov, I.; Suvorova, E.I.; Buffat, P.A.; Kiwi-Minsker, L. Highly dispersed gold on activated carbon fibers for low-temperature CO oxidation. *J. Catal.* **2004**, *224* (1), 8–17.
26. Feldheim, D.L.; Foss, C.A., Eds. *Metal Nanoparticles: Synthesis Characterization and Applications*; Marcel Dekker, Inc.: New York, Basel, 2002.
27. Haruta, A. When gold is not noble: catalysis by nanoparticles. *Chem. Rec.* **2003**, *3* (2), 75–87.
28. Lopez, N.; Janssens, T.V.W.; Clausen, B.S.; Xu, Y.; Mavrikakis, M.; Bligaard, T.; Norskov, J.K. On the origin of the catalytic activity of gold nanoparticles for low-temperature CO oxidation. *J. Catal.* **2004**, *223* (1), 232–235.
29. Chen, S.; Zeng, H. Improvement of the reduction capacity of activated carbon fiber. *Carbon* **2003**, *41* (6), 1265–1271.
30. Fu, R.W.; Zeng, H.M.; Lu, Y. The reduction property of activated carbon-fibers. *Carbon* **1993**, *31* (7), 1089–1094.
31. Lee, Y.S.; Basova, Y.V.; Edie, D.D.; Reid, L.K.; Newcombe, S.R.; Ryu, S.K. Preparation and characterization of trilobal activated carbon fibers. *Carbon* **2003**, *41* (13), 2573–2584.
32. Fu, R.W.; Zeng, H.M.; Lu, Y. The reducing property of activated carbon-fiber and its application in the recovery of gold. *Miner. Eng.* **1993**, *6* (7), 721–729.
33. Fu, R.W.; Zeng, H.M.; Lu, Y. Studies on the mechanism of the reaction of activated carbon-fibers with oxidants. *Carbon* **1994**, *32* (4), 593–598.
34. Jia, Y.F.; Steele, C.J.; Hayward, I.P.; Thomas, K.M. Mechanism of adsorption of gold and silver species on activated carbons. *Carbon* **1998**, *36* (9), 1299–1308.
35. Bianchi, C.L.; Biella, S.; Gervasini, A.; Prati, L.; Rossi, M. Gold on carbon: influence of support properties on catalyst activity in liquid-phase oxidation. *Catal. Lett.* **2003**, *85* (1–2), 91–96.
36. Chen, J.P.; Wu, S.N. Acid/base-treated activated carbons: characterization of functional groups and metal adsorptive properties. *Langmuir* **2004**, *20* (6), 2233–2242.
37. Shim, J.W.; Park, S.J.; Ryu, S.K. Effect of modification with HNO<sub>3</sub> and NaOH on metal adsorption by pitch-based activated carbon fibers. *Carbon* **2001**, *39* (11), 1635–1642.
38. Jia, Y.F.; Xiao, B.; Thomas, K.M. Adsorption of metal ions on nitrogen surface functional groups in activated carbons. *Langmuir* **2002**, *18* (2), 470–478.
39. Ma, J.; Rodriguez, N.M.; Vannice, M.A.; Baker, R.T.K. Modifications in the morphological and chemical properties of copper supported on different allotropic forms of carbon. *J. Catal.* **1999**, *183* (1), 32–44.
40. Dandekar, A.; Baker, R.T.K.; Vannice, M.A. Carbon-supported copper catalysts I. Characterization. *J. Catal.* **1999**, *183* (1), 131–154.
41. Joannet, E.; Horny, C.; Kiwi-Minsker, L.; Renken, A. Palladium supported on filamentous active carbon as effective catalyst for liquid-phase hydrogenation of 2-butyne-1,4-diol to 2-butene-1,4-diol. *Chem. Eng. Sci.* **2002**, *57* (16), 3453–3460.
42. Matatov-Meytal, Y.; Shindler, Y.; Sheintuch, M. Cloth catalysts in water denitrification—III. pH inhibition of nitrite hydrogenation over Pd/ACC. *Appl. Catal. B* **2003**, *45* (2), 127–134.
43. Perez, M.C.M.; De Lecea, C.S.M.; Solano, A.L. Platinum supported on activated carbon cloths as catalyst for nitrobenzene hydrogenation. *Appl. Catal. A* **1997**, *151* (2), 461–475.
44. Coq, B.; Planeix, J.M.; Brotons, V. Fullerene-based materials as new support media in heterogeneous catalysis by metals. *Appl. Catal. A* **1998**, *173* (2), 175–183.
45. Ledoux, M.J.; Vieira, R.; Pham-Huu, C.; Keller, N. New catalytic phenomena on nanostructured (fibers and tubes) catalysts. *J. Catal.* **2003**, *216* (1–2), 333–342.
46. Bera, D.; Kuiry, S.C.; McCutchen, M.; Kruize, A.; Heinrich, H.; Meyyappan, M.; Seal, S. In-situ synthesis of palladium nanoparticles-filled carbon nanotubes using arc-discharge in solution. *Chem. Phys. Lett.* **2004**, *386* (4–6), 364–368.
47. Satishkumar, B.C.; Govindaraj, A.; Mofokeng, J.; Subbanna, G.N.; Rao, C.N.R. Novel experiments with carbon nanotubes: opening, filling, closing and functionalizing nanotubes. *J. Phys. B* **1996**, *29* (21), 4925–4934.
48. Matsumoto, T.; Komatsu, T.; Nakano, H.; Arai, K.; Nagashima, Y.; Yoo, E.; Yamazaki, T.; Kijima, M.; Shimizu, H.; Takasawa, Y.; Nakamura, J. Efficient usage of highly dispersed Pt on carbon nanotubes for electrode catalysts of polymer electrolyte fuel cells. *Catal. Today* **2004**, *90* (3–4), 277–281.
49. Xue, B.; Chen, P.; Hong, Q.; Lin, J.Y.; Tan, K.L. Growth of Pd, Pt, Ag and Au nanoparticles on carbon nanotubes. *J. Mater. Chem.* **2001**, *11* (9), 2378–2381.
50. Unger, E.; Duesberg, G.S.; Liebau, M.; Graham, A.P.; Seidel, R.; Kreupl, F.; Hoenlein, W. Decoration of multi-walled carbon nanotubes with noble- and transition-metal clusters and formation of CNT–CNT networks. *Appl. Phys. A* **2003**, *77* (6), 735–738.
51. Biella, S.; Porta, F.; Prati, L.; Rossi, M. Surfactant-protected gold particles: new challenge for gold-on-carbon catalysts. *Catal. Lett.* **2003**, *90* (1–2), 23–29.

52. Han, L.; Wu, W.; Kirk, F.L.; Luo, J.; Maye, M.M.; Kariuki, N.N.; Lin, Y.H.; Wang, C.M.; Zhong, C.J. A direct route toward assembly of nanoparticle-carbon nanotube composite materials. *Langmuir* **2004**, *20* (14), 6019–6025.
53. Hoogenraad, M.S.; Van Leeuwarden, R.; Vriesman, G.; Broersma, A.; Van Dillen, A.J.; Geus, J.W. Metal catalysts supported on a novel carbon. In *Preparation of Catalysts VI*; Elsevier Science Publications B V: Amsterdam, 1995; Vol. 91, 263–271.
54. Hoogenraad, M.S.; Onwezen, M.F.; Van Dillen, A.J.; Geus, J.W. Supported catalysts based on carbon fibrils. In *11th International Congress on Catalysis—40th Anniversary*; Elsevier Science Publications B V: Amsterdam, 1996; Vol. 101, 1331–1339.
55. Ros, T.G.; Keller, D.E.; van Dillen, A.J.; Geus, J.W.; Koningsberger, D.C. Preparation and activity of small rhodium metal particles on fishbone carbon nanofibres. *J. Catal.* **2002**, *211* (1), 85–102.
56. Ye, X.R.; Lin, Y.H.; Wai, C.M. Decorating catalytic palladium nanoparticles on carbon nanotubes in supercritical carbon dioxide. *Chem. Commun.* **2003**, (5), 642–643.
57. Chesnokov, V.V.; Prosvirin, I.P.; Zaitseva, N.A.; Zaikovskii, V.I.; Molchanov, V.V. Effect of the structure of carbon nanofibers on the state of an active component and on the catalytic properties of Pd/C catalysts in the selective hydrogenation of 1,3-butadiene. *Kinet. Catal.* **2002**, *43* (6), 838–846.
58. Ma, J.; Park, C.; Rodriguez, N.M.; Baker, R.T.K. Characteristics of copper particles supported on various types of graphite nanofibers. *J. Phys. Chem. B* **2001**, *105* (48), 11994–12002.
59. Chen, P.; Wu, X.; Lin, J.; Tan, K.L. Synthesis of Cu nanoparticles and microsized fibers by using carbon nanotubes as a template. *J. Phys. Chem. B* **1999**, *103* (22), 4559–4561.
60. Lordi, V.; Yao, N.; Wei, J. Method for supporting platinum on single-walled carbon nanotubes for a selective hydrogenation catalyst. *Chem. Mater.* **2001**, *13* (3), 733–737.
61. Halttunen, M.E.; Niemela, M.K.; Krause, A.O.I.; Vuori, A.I. Liquid phase methanol hydrocarbonylation with homogeneous and heterogeneous Rh and Ru catalysts. *J. Mol. Catal. A* **1996**, *109* (3), 209–217.
62. Bulushev, D.A.; Kiwi-Minsker, L.; Yuranov, I.; Suvorova, E.I.; Buffat, P.A.; Renken, A. Structured Au/FeOx/C catalysts for low-temperature CO oxidation. *J. Catal.* **2002**, *210* (1), 149–159.
63. Prati, L.; Martra, G. New gold catalysts for liquid phase oxidation. *Gold Bull.* **1999**, *32* (3), 96–101.
64. Biella, S.; Prati, L.; Rossi, M. Gold catalyzed oxidation of aldehydes in liquid phase. *J. Mol. Catal. A* **2003**, *197* (1–2), 207–212.
65. Dandekar, A.; Baker, R.T.K.; Vannice, M.A. Carbon-supported copper catalysts II. Crotonaldehyde hydrogenation. *J. Catal.* **1999**, *184* (2), 421–439.
66. Rao, R.S.; Baker, R.T.K.; Vannice, M.A. Furfural hydrogenation over carbon-supported copper. *Catal. Lett.* **1999**, *60* (1–2), 51–57.
67. Ma, J.; Rodriguez, N.M.; Vannice, M.A.; Baker, R.T.K. Nitrous oxide decomposition and reduction over copper catalysts supported on various types of carbonaceous materials. *Top. Catal.* **2000**, *10* (1–2), 27–38.
68. Navarro, R.M.; Pena, M.A.; Merino, C.; Fierro, J.L.G. Production of hydrogen by partial oxidation of methanol over carbon-supported copper catalysts. *Top. Catal.* **2004**, *30/31*, 481–486.
69. Holler, V.; Radevik, K.; Yuranov, I.; Kiwi-Minsker, L.; Renken, A. Reduction of nitrite-ions in water over Pd-supported on structured fibrous materials. *Appl. Catal. B* **2001**, *32* (3), 143–150.
70. Pham-Huu, C.; Keller, N.; Charbonniere, L.J.; Ziessle, R.; Ledoux, M.J. Carbon nanofiber supported palladium catalyst for liquid-phase reactions. An active and selective catalyst for hydrogenation of C=C bonds. *Chem. Commun.* **2000**, (19), 1871–1872.
71. Park, C.; Keane, M.A. Catalyst support effects: gas-phase hydrogenation of phenol over palladium. *J. Colloid Interface Sci.* **2003**, *266* (1), 183–194.
72. Baker, R.T.K.; Laubernds, K.; Wootsch, A.; Paal, Z. Pt/graphite nanofiber catalyst in *n*-hexane test reaction. *J. Catal.* **2000**, *193* (1), 165–167.
73. Gao, R.; Tan, C.D.; Baker, R.T.K. Ethylene hydroformylation on graphite nanofiber supported rhodium catalysts. *Catal. Today* **2001**, *65* (1), 19–29.
74. Giordano, R.; Serp, P.; Kalck, P.; Kihn, Y.; Schreiber, J.; Marhic, C.; Duvaill, J.L. Preparation of rhodium catalysts supported on carbon nanotubes by a surface mediated organometallic reaction. *Eur. J. Inorg. Chem.* **2003**, (4), 610–617.
75. Luo, J.Z.; Gao, L.Z.; Leung, Y.L.; Au, C.T. The decomposition of NO on CNTs and 1 wt% Rh/CNTs. *Catal. Lett.* **2000**, *66* (1–2), 91–97.
76. Vieira, R.; Pham-Huu, C.; Keller, N.; Ledoux, M.J. New carbon nanofiber/graphite felt composite for use as a catalyst support for hydrazine catalytic decomposition. *Chem. Commun.* **2002**, (9), 954–955.
77. Li, C.Y.; Wan, Y.Z.; Wang, J.; Wang, Y.L.; Jiang, X.Q.; Han, L.M. Antibacterial pitch-based activated carbon fiber supporting silver. *Carbon* **1998**, *36* (1–2), 61–65.
78. Qin, Y.; Zhang, Q.; Cui, Z.L. Effect of synthesis method of nanocopper catalysts on the morphologies of carbon nanofibers prepared by catalytic decomposition of acetylene. *J. Catal.* **2004**, *223* (2), 389–394.
79. Zhang, G.Y.; Wang, E.G. Cu-filled carbon nanotubes by simultaneous plasma-assisted copper incorporation. *Appl. Phys. Lett.* **2003**, *82* (12), 1926–1928.
80. Javey, A.; Guo, J.; Wang, Q.; Lundstrom, M.; Dai, H.J. Ballistic carbon nanotube field-effect transistors. *Nature* **2003**, *424* (6949), 654–657.
81. Kong, J.; Chapline, M.G.; Dai, H. Functionalized carbon nanotubes for molecular hydrogen sensors. *Adv. Mater.* **2001**, *13* (18), 1384–1386.
82. Lupu, D.; Biris, A.R.; Misan, I.; Jianu, A.; Holzhter, G.; Burkel, E. Hydrogen uptake by carbon nanofibers catalyzed by palladium. *Int. J. Hydrog. Energy* **2004**, *29* (1), 97–102.
83. Gundiah, G.; Govindaraj, A.; Rajalakshmi, N.; Dhathathreyan, K.S.; Rao, C.N.R. Hydrogen storage

- in carbon nanotubes and related materials. *J. Mater. Chem.* **2003**, *13* (2), 209–213.
84. Lueking, A.D.; Yang, R.T. Hydrogen spillover to enhance hydrogen storage—study of the effect of carbon physicochemical properties. *Appl. Catal. A* **2004**, *265* (2), 259–268.
85. <http://www.nec.co.jp/press/en/0108/3001.html> (accessed August 2001).
86. [http://www.fuelcellstoday.com/FuelCellToday/FCTFiles/FCTArticleFiles/Article\\_852\\_SAIT0804.pdf](http://www.fuelcellstoday.com/FuelCellToday/FCTFiles/FCTArticleFiles/Article_852_SAIT0804.pdf) (accessed August 2004).
87. Che, G.L.; Lakshmi, B.B.; Martin, C.R.; Fisher, E.R. Metal-nanocluster-filled carbon nanotubes: catalytic properties and possible applications in electrochemical energy storage and production. *Langmuir* **1999**, *15* (3), 750–758.
88. Li, W.Z.; Liang, C.H.; Qiu, J.S.; Zhou, W.J.; Han, H.M.; Wei, Z.B.; Sun, G.Q.; Xin, Q. Carbon nanotubes as support for cathode catalyst of a direct methanol fuel cell. *Carbon* **2002**, *40* (5), 791–794.
89. Rajesh, B.; Thampi, K.R.; Bonard, J.M.; Xanthopoulos, N.; Mathieu, H.J.; Viswanathan, B. Carbon nanotubes generated from template carbonization of polyphenyl acetylene as the support for electrooxidation of methanol. *J. Phys. Chem. B* **2003**, *107* (12), 2701–2708.

# Nonlinear Optical Materials from Self-Assembled Organic Films

**Matthew Guzy**

**Richey M. Davis**

*Department of Chemical Engineering, Virginia Technical Institute,  
Blacksburg, Virginia, U.S.A.*

**Patrick J. Neyman**

**Charles Brands**

**J. R. Heflin**

**Harry W. Gibson**

*Department of Physics Engineering, Virginia Technical Institute,  
Blacksburg, Virginia, U.S.A.*

**Kevin E. Van Cott**

*Department of Chemical Engineering, Virginia Technical Institute,  
Blacksburg, Virginia, U.S.A.*

## INTRODUCTION

Second-order non-linear optical (NLO) materials possess non-centrosymmetric structures in which there is a net orientation of an NLO-active constituent. Materials that exhibit second-order NLO properties are the active components in optoelectronic devices such as electro-optic modulators and frequency doubling devices.<sup>[1–3]</sup> Non-linear optics refers to the optical response of a material that relates the polarization vector  $P$  to an applied electric field  $E$  according to:

$$P = \chi^{(1)}E + \chi^{(2)}E^2 + \chi^{(3)}E^3 + \dots \quad (1)$$

where  $\chi^{(n)}$  is the  $n$ th-order susceptibility. The susceptibilities for the non-linear terms characterize the non-linear optical response of a material. Consider the interaction of an optical electric field at frequency  $\omega$  and amplitude  $E_\omega$

$$E_\omega(t) = E_\omega(e^{+i\omega t} + e^{-i\omega t})/2 \quad (2)$$

When a static electric field  $E_0$  is also present in a medium with a nonzero  $\chi^{(2)}$ , the second-order

polarization term becomes

$$\begin{aligned} P^{(2)}(t) &= \chi^{(2)}E^2(t) \\ &= \chi^{(2)}[E_\omega^2(e^{+2i\omega t} + e^{-2i\omega t})/4 \\ &\quad + E_\omega E_0(e^{+i\omega t} + e^{-i\omega t}) \\ &\quad + (E_\omega^2/2 + E_0^2)] \end{aligned} \quad (3)$$

The first term in Eq. (3) oscillates at frequency  $2\omega$  and depends only on the optical electric field and not the static field. This effect is referred to as second harmonic generation (SHG) and is the NLO effect directly probed in this work. The second term oscillates at frequency  $\omega$  and causes a variation in the refractive index  $n$  in the medium that is linearly proportional to  $E_0$ . This effect is known as the linear electro-optic effect and forms the basis for electro-optic modulator devices. The third term is time-independent and is referred to as optical rectification, the conversion of an oscillating electric field to a static d.c. field in the NLO material. For all three effects, the magnitude of  $\chi^{(2)}$  governs their contribution to  $P^{(2)}(t)$ . To possess nonzero even-order non-linear optical susceptibilities, a material must lack a center of inversion at the macroscopic level.<sup>[2,3]</sup> Because these second-order  $\chi^{(2)}$  nonlinear

optical effects are quadratic in the applied fields, symmetry considerations require that a material must be non-centrosymmetric to possess a non-zero  $\chi^{(2)}$ .

## OVERVIEW

The most common high  $\chi^{(2)}$  materials are ferroelectric, inorganic crystals such as lithium niobate, potassium dihydrogen phosphate, and beta-barium borate.<sup>[2,3]</sup> Growth of high-quality crystals, however, is difficult, time consuming, and expensive. However, organic NLO materials offer several performance advantages such as enhanced non-linear susceptibilities, faster modulation rates, and potentially lower device fabrication costs.<sup>[4]</sup> For organic thin films containing NLO-active chromophores,  $\chi^{(2)}$  is related to the NLO chromophore hyperpolarizability ( $\beta$ ), chromophore density ( $N$ ), orientation angle ( $\theta$ ) relative to the film normal vector, and a local field factor effect ( $F$ ) by

$$\chi^{(2)} = NF\beta\langle\cos^3\theta\rangle \quad (4)$$

For effective electro-optic modulators,  $\chi^{(2)}$  should be as large as possible. Rational design of an organic film thus involves choosing a chromophore with a suitably high  $\beta$  and incorporating it into a film with high density  $N$  and low orientation angle  $\theta$ . For effective optical waveguide performance, the film thickness should be in the range 1–10  $\mu\text{m}$ .

The objective of this work was to demonstrate that organic, low molecular weight, nonsymmetric chromophores can be integrated into films by a facile, layer-by-layer deposition process using a combination of electrostatic and covalent bonding.<sup>[5]</sup> This deposition process results in noncentrosymmetric films that exhibit significant SHG intensities where the square root of the SHG intensity scales linearly with bilayer number, indicating that deposition results in a reproducible orientation of the chromophore molecules from bilayer to bilayer up to high bilayer numbers. The effect of pH is shown to be critical in controlling both the electrostatic and covalent coupling steps.

## OVERVIEW OF ORGANIC, HIGH $\chi^{(2)}$ FILMS

In previous work, organic films exhibiting non-zero  $\chi^{(2)}$  have been made using various techniques including corona poling, Langmuir–Blodgett (LB) methods, covalent self-assembly, and, more recently, ionically self-assembled monolayers involving polyelectrolytes. Poled polymer materials are fabricated by doping a host matrix with chromophore molecules, which are then oriented by an applied electric field while the

matrix is above its glass transition ( $T_g$ ) temperature. The temperature of the matrix is then brought below the  $T_g$ , which locks in the orientation.<sup>[6]</sup> While poled polymer systems are capable of high second-order NLO activity and are easy to fabricate, the orientation of the chromophore molecules in the host is usually lost over time. The randomization of the dipole orientation in poled polymer devices occurs more quickly at elevated temperatures, and this severely limits the operating lifetime of these materials.<sup>[7]</sup> Langmuir–Blodgett films have been made with noncentrosymmetric Z- and X-type structures that exhibit relatively high values for  $\chi^{(2)}$ , but their relatively poor mechanical properties have limited their application in devices.<sup>[8]</sup>

Layer-by-layer (LBL) film deposition techniques that use intermolecular interactions such as covalent bonds, electrostatic attractions, or hydrogen bonding to drive self-assembly are particularly interesting for fabricating wholly organic and organic–inorganic hybrid films that exhibit SHG. There is a large, growing body of literature on the use of LBL methods for fabricating nanostructured films for a number of applications, including organic light emitting diodes,<sup>[9]</sup> humidity sensors,<sup>[10]</sup> biosensors,<sup>[11]</sup> photovoltaics,<sup>[12]</sup> electrochromics,<sup>[13]</sup> and non-linear optic (NLO) materials.<sup>[14]</sup> The LBL technique relying on purely electrostatic interactions, referred to hereafter in this paper as the ionically self-assembled monolayer (ISAM) process, was first developed by Iler<sup>[15]</sup> and elaborated upon by Decher, Lvov, and Schmitt<sup>[16]</sup> This process involves the sequential immersion of a charged substrate into solutions of polyelectrolytes of opposite charge.<sup>[16]</sup> A monolayer of polymer adsorbs onto the surface, resulting in charge reversal. The substrate is then removed from the solution, thoroughly rinsed to remove non-adsorbed polymer, and immersed in a solution of polyelectrolyte with a charge opposite to that of the adsorbed layer. A monolayer of polymer adsorbs, forming a bilayer with the first polymer, and the immersion process is repeated, building up a multilayer film. Reviews by Decher<sup>[17]</sup> and Hammond<sup>[18]</sup> describe many studies of films made with a variety of organic polyelectrolytes and nanoparticles.

With the ISAM method, NLO-active chromophores are oriented by the non-covalent interactions between soluble and deposited species to form multilayered films with compositions controlled at the nanometer length scale. Hefin et al.<sup>[19]</sup> and Lindsay et al.<sup>[20]</sup> demonstrated that the ISAM process can be used to create films exhibiting SHG by incorporating an NLO-active polymer as one of the constituents in a film and that these ISAM films have greater stability than poled polymer systems. Herman and Roberts<sup>[21]</sup> studied chromophore orientation in ISAM films and found that the orientation of the chromophore in the first layer can be influenced by hydrophobic interactions



between the chromophore molecule and the substrates. Furthermore, they concluded that orientation in subsequent layers is influenced by the orientation of this first layer. DeWitt and Hammond<sup>[22]</sup> showed that the average tilt angle of the charged chromophoric group in a film and the film thickness depend strongly on the solution pH values. Lee et al. showed linear growth of absorbance and thickness for films made by deposition of a polycation and a polymeric dye precursor. These films were then functionalized with the dye moiety. These films showed the expected quadratic relationship between the SHG intensity and the number of bilayers, meaning that chromophore orientation is consistent from one bilayer to the next.<sup>[23]</sup> Deposition of ordered films using reactive silane compounds has been demonstrated, but the deposition processes required organic solvents and high temperatures.<sup>[24,25]</sup>

Because of the nature of the formation of ISAM films utilizing two polymers, the NLO-active polyelectrolyte necessarily has chromophores oriented in opposite directions to provide binding to the preceding and following oppositely charged layers (Fig. 1). The opposing dipole orientations cancel one another and lead to an overall reduction in the  $\chi^{(2)}$  of the film. Thus polyelectrolyte-based ISAM films suffer from lack of orientation of chromophores within the "bulk" of a monolayer and partial cancellation of the preferentially oriented chromophores at the lower interface by chromophores at the upper interface.

A related approach that could be employed to fabricate NLO materials involves the use of low molecular weight, ionic dye molecules and polyelectrolytes as film constituents. Yamada et al.<sup>[26]</sup> fabricated films of poly(diallyldimethylammonium chloride) and Eriochrome Black T and observed linear growth of the film during the non-covalent deposition process. These films exhibited a SHG intensity that increased only for the first five bilayers and then reached a plateau. This plateau after five bilayers was attributed to the chromophore molecules in upper layers not having

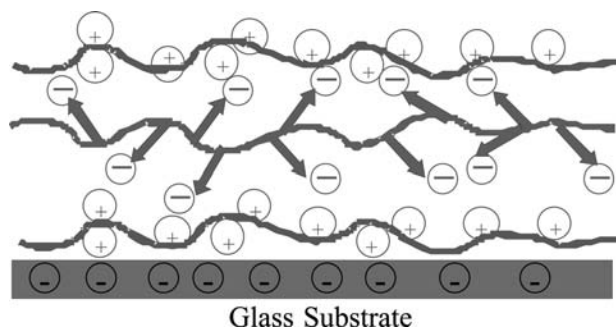


**Fig. 1** Schematic illustration of an ISAM film containing a polar non-linear optical polymer.

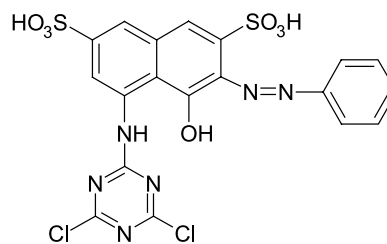


**Fig. 2** Structure of Procion Red MX-5B.

the same orientation as they did in lower layers; however, the addition of layers did not perturb the orientation of previous layers. Yet to be demonstrated is a combination of low molecular weight chromophore molecules and polyelectrolytes that can be used to construct stable NLO-active films with high bilayer numbers needed for electro-optic device fabrication.

## NON-LINEAR OPTICAL FILM FABRICATION BY COVALENT/IONIC SELF-ASSEMBLY

This present work shows that low molecular weight, non-symmetric chromophores can be stably integrated into films by a facile, layer-by-layer deposition process using both electrostatic and covalent bonding.<sup>[5]</sup> Additionally, it is shown that this deposition process results in non-centrosymmetric films that exhibit significant SHG intensities where the square root of the SHG intensity scaled linearly with bilayer number, indicating that deposition results in a reproducible orientation of the chromophore molecules from bilayer to bilayer up to high bilayer numbers. The model chromophore used is Procion Red MX-5B (Fig. 2), a reactive dye that contains a triazine ring and two sulfonic acid groups. Poly(allylamine hydrochloride) (PAH, Fig. 3) was used to provide both the nucleophilic primary amine groups for reaction with the triazine ring and the protonated amine groups for electrostatic interaction with the sulfonic acid groups of PR (Fig. 4). Koetse, Laschewsky, and Verbiest<sup>[27]</sup> earlier demonstrated that Procion Red and a reactive primary amine that was not PAH could form layer-by-layer

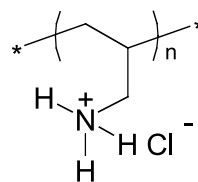


**Fig. 3** Structure of poly(allylamine hydrochloride) (PAH),  $pK_a = 8.7$ .

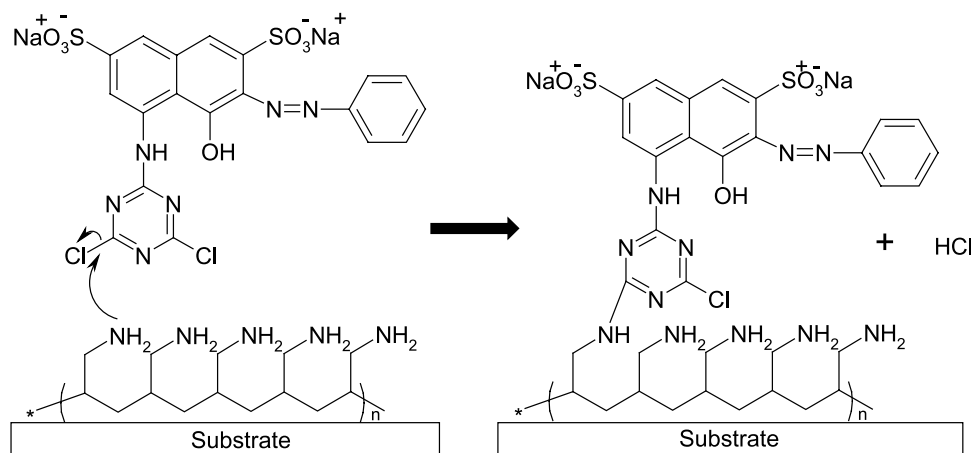


Fig. 4 Reaction between PR molecule and a previously adsorbed monolayer of PAH.

films, but no polar ordering was observed, unlike the present work.

The pH of the PR and PAH solutions was found to be a key processing variable for achieving reproducible films with a high degree of polar ordering of the PR molecules. Conditions favoring incorporation of PR by covalent bonds resulted in films with high SHG intensity. The deposition steps involve only aqueous solutions at ambient conditions, and immersion times can be as low as 2 min/monolayer.

Details of film fabrication can be found elsewhere and so only a summary is presented here.<sup>[5]</sup> The anionic/reactive Procion Red MX-5B chromophore was commercially available. The absorbance spectrum of this chromophore in deionized water solution is shown in Fig. 5. The characteristic peak for this molecule is 538 nm, which was used for all absorbance measurements.

The NLO-inactive polycation used in this study was poly(allylamine hydrochloride) (PAH; MW

~70,000 g/mol), which was also commercially available. Poly(allylamine hydrochloride) solutions at a concentration of 0.01 M on a monomer basis were used in all experiments, while the concentration of all PR solutions was 5 mg/ml. Dynamic light scattering (DLS) was used to measure the diffusion coefficient of the PAH as a function of pH to characterize the polymer solubility.<sup>[28]</sup> Deionized (DI) water with a specific resistivity above 17 M $\Omega$  cm was used in all of the experiments.

Glass microscope slides were used as the substrates on which films were deposited after the slides were rigorously cleaned.<sup>[29]</sup> The glass slide immersion time in PAH was 5 min, with the exception of the first layer which was 10 min. The immersion time in PR was 10 min. Between immersions, the substrates were vigorously agitated and rinsed with deionized water. Thorough rinsing is critical for obtaining films with good optical homogeneity. Slides were dried every 10 dips (which gives five bilayers on each side of the slide) using N<sub>2</sub> gas.

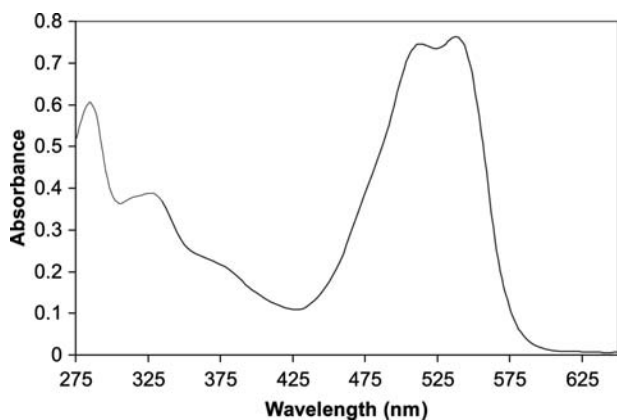
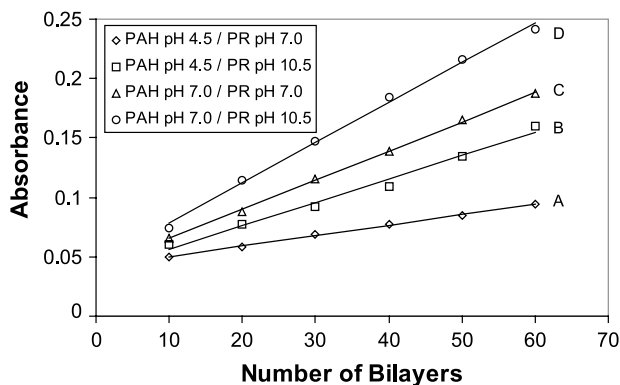


Fig. 5 Absorbance spectrum for Procion Red MX-5B, in deionized water.

## NON-LINEAR OPTICAL FILM CHARACTERIZATION

Absorbance measurements were made at a wavelength of 538 nm, and film thicknesses were measured using a variable angle spectroscopic ellipsometer.<sup>[30]</sup> Second harmonic generation measurements were performed using a 10-nsec pulse width, Q-switched Nd:YAG laser with a fundamental wavelength of 1064 nm.<sup>[31]</sup> Because the film was deposited on both sides of the substrate and the incidence angle  $\alpha$  was varied, the path length through the film on both sides varied with  $\alpha$ . This led to interference fringes of the SHG intensity. The  $\chi^{(2)}$  value was determined from the peak of the interference fringe in the vicinity of  $\alpha \sim 45^\circ$ . By comparison to



**Fig. 6** Representative plots of the absorbance at 538 nm as a function of the number of bilayers deposited.

Maker fringes in a quartz crystal wedge,  $\chi^{(2)}$  of a film was obtained from

$$\frac{\chi_{\text{film}}^{(2)}}{\chi_{\text{q}}^{(2)}} = \frac{2l_{\text{c,q}}}{\pi l_{\text{film}}} \sqrt{\frac{I_{\text{film}}^{2\omega}}{I_{\text{q}}^{2\omega}}} \quad (5)$$

where  $l_{\text{film}}$  is the total path length through the film, the coherence length of quartz,  $l_{\text{c,q}} = \lambda/[4(n^{2\omega} - n^{\omega})]$ , is 22.4  $\mu\text{m}$ , and  $\chi^{(2)}$  of quartz is  $1.92 \times 10^{-9}$  esu.

This study focused on the effect of the pH of the PR and PAH solutions on the film properties. Successful film growth was characterized by homogeneity and a linear increase in the absorbance and thickness with the number of bilayers deposited. Absorbance data for successfully deposited films are shown in Fig. 6 and Table 1. The slope characterizes the amount of dye deposited per bilayer; the standard deviation of this slope describes the reproducibility of the film deposition among replicates for a given set of experimental conditions; the correlation coefficient characterizes the reproducibility of PR deposition from bilayer to bilayer. These films displayed a linear increase in the absorbance as a function of the bilayer number.

When the pH of the PAH solutions was held constant, the amount of PR deposited per bilayer

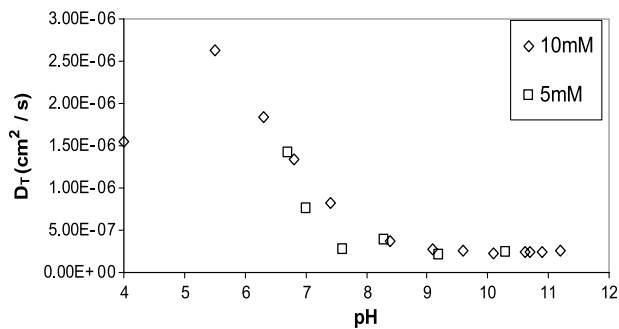


**Fig. 7** Dynamic light scattering results for the translational diffusion coefficient of PAH in solution as a function of pH at two polymer concentrations (molarity of repeat unit) with no added salt.

increased as the pH of the PR solution was increased (compare experiments A vs. B and C vs. D, Table 1). This trend was observed until the pH of the PR solution was raised to 12.0, at which point deposition of PR failed. The best PR deposition was observed when the PR solution was at a pH of 10.5. At this optimal PR deposition condition, as the pH of the PAH solution was increased from 4.5 to 7.0 (compare experiments B vs. D), a small but statistically insignificant increase in the film thickness per bilayer ( $p > 0.05$ ) and a significant increase in the amount of PR deposited per bilayer ( $p < 0.05$ ) were observed.

Poor film formation was observed for PAH solutions deposited at  $\text{pH} \geq 8.5$ . This is likely a result of incipient aggregation and insolubility of the PAH as the pH increased. The dramatic decrease in diffusion coefficient for  $\text{pH} > 7$  (Fig. 7) is consistent with the reduction in charge density of the PAH given its  $\text{p}K_{\text{a}}$  (8.7). The reduced charge density leads to reduced solubility and the formation of aggregates consisting of multiple PAH chains. Such aggregates hinder the formation of uniform, homogeneous monolayers of adsorbed PAH chains that lead to poor layer-by-layer film formation, especially when the other constituent is not a polyelectrolyte.

When the film thickness is much less than the coherence length of the material, the SHG intensity should

**Table 1** Summary of the slopes of the absorbance vs. number of bilayers and ellipsometric thicknesses for deposition of PR (0.025 m) and PR (0.025 mM)

Experiment	PAH pH	PR pH	Slope (Abs/bilayer) (correlation coefficient)	Bilayer thickness (nm)	$\chi^{(2)}$ ( $10^{-9}$ esu)
A	4.5	7.0	$8.9 \times 10^{-4} \pm 1.0 \times 10^{-5}$ (0.998)	N/A <sup>a</sup>	N/A
B	4.5	10.5	$2.0 \times 10^{-3} \pm 1.0 \times 10^{-4}$ (0.992)	$0.34 \pm 0.02$	11.2
C	7.0	7.0	$2.3 \times 10^{-3} \pm 4.0 \times 10^{-4}$ (0.999)	$0.55 \pm 0.05$	1.2
D	7.0	10.5	$3.3 \times 10^{-3} \pm 3.2 \times 10^{-4}$ (0.998)	$0.52 \pm 0.06$	11.3

For quartz,  $\chi^{(2)} = 1.92 \times 10^{-9}$  esu.

<sup>a</sup>Too thin to measure.

Source: From Ref.<sup>[25]</sup>. © permission from Angew. Chemie.

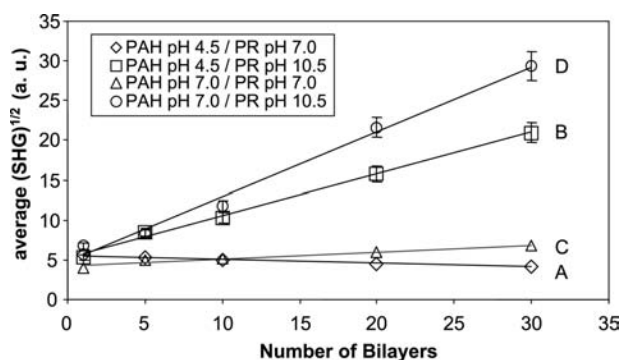


**Fig. 8** Square root of the SHG intensity as a function of the number of bilayers for various PAH/Procion Red pH conditions.

exhibit a quadratic dependence on the film thickness or, correspondingly, number of bilayers. Fig. 8 shows the square root of the peak second harmonic intensity as a function of the number of bilayers for the sets of films fabricated with different PAH and PR solution pH values. The linear dependence of the square root of the SHG intensity on the number of bilayers for the films fabricated with a PR solution at pH 10.5 (Fig. 8, experiments B and D) demonstrates that the SHG signal is due to polar ordering in each successive bilayer of the film. If the degree of ordering decreased in successive bilayers or if the SHG signal was a result of interface effects, the SHG intensity would have a subquadratic dependence on the number of bilayers. For the films fabricated with a PR pH of 7.0, there is a much weaker dependence of the SHG intensity on the number of bilayers, indicating a lesser degree of ordering.

The growth of the self-assembled films in real time was monitored using in situ second harmonic generation. In this case, a glass substrate coated with an adsorbed layer of PAH was immersed in a cuvette filled with PR dye solution. The substrate was held fixed in

the laser beam throughout the procedure. Because the glass cuvettes, the immersion solutions, and the glass substrate are all centrosymmetric, the SHG signal is due to the polar film as it grows on the substrate along with a small background signal from the air-glass and glass-liquid interfaces. The substrate was first immersed in PAH solution at pH 7.0 to produce a cationic surface. Figure 9 shows the SHG intensity as a function of time as the substrate was then immersed in a PR pH 10.5 solution. The covalent deposition of Procion Red on PAH was essentially complete in 2 min. The simplicity and potential scalability of this alternating ionic/covalent deposition process are illustrated by the in situ SHG signal that is obtained as the reactive dye is incorporated into the film. A single bilayer film is saturated with dye within about 2 min at pH 10.5. Thus multilayer films with thicknesses required for optoelectronic devices can be made just as quickly with reactive dyes as with polymeric dyes in the ISAM process. After accounting for the non-zero intercept, which is a result of the inherent non-centrosymmetry of the substrate/solvent interface effects, simple Langmuir kinetics can be used to model the dye deposition process.

## CHROMOPHORE DEPOSITION AND ORIENTATION—EFFECT OF PH

Ionic interactions alone are not sufficient for constructing LBL films with low molecular weight chromophores that exhibit polar order.<sup>[32]</sup> However, by alternating the mechanism of the deposition of each monolayer between covalent and electrostatic coupling and decoupling the chromophore orientation from the steric constraints of a polymer chain, the PR chromophore was deposited with a non-centrosymmetric orientation that is required for the film to display NLO properties such as SHG.

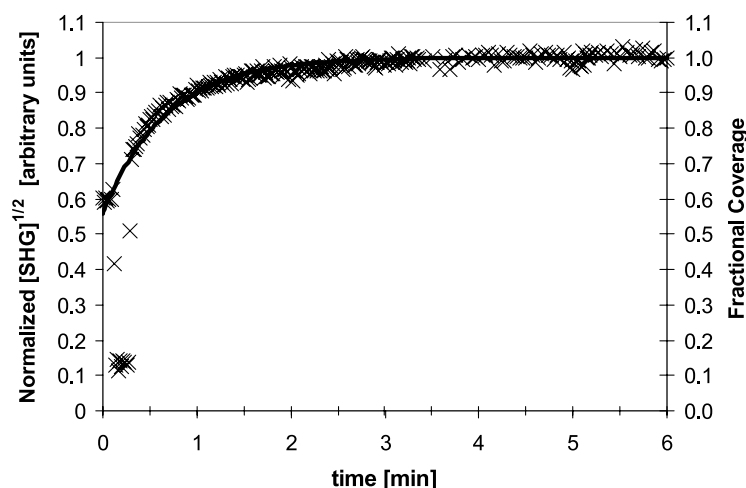


**Fig. 9** In situ measurement of the SHG intensity as Procion Red is deposited in the film.

The effects of polymer type, pH, salt concentration, and other processing variables on film deposition by physisorption of charged polymers have been studied by Decher and Schmitt,<sup>[33]</sup> Lvov et al.,<sup>[34]</sup> Rubner et al., and others.<sup>[35–42]</sup> Shiratori and Rubner<sup>[43]</sup> found that the thickness of ISAM bilayers made with weak polyelectrolytes can be varied by over an order of magnitude simply by varying the pH and ionic strength. This is particularly relevant to the present work in that it suggests a method for controlling the conformation and thickness of the adsorbed polymer layers which is critical for controlling the orientation of deposited NLO-active chromophores.

The pH determines the ionization state of the amine side groups on PAH, which affects both the conformation of the polymer upon adsorption and its subsequent reactivity with Procion Red. Efficient electrostatic deposition of PAH requires that the pH of the PAH dipping solution is maintained near or below the amino group  $pK_a$  (8.7), where the majority of the side groups will be protonated and available for interaction with the negative charges on the substrate or the sulfonate groups on the dye.<sup>[44]</sup> For cases A–D described in Table 1, the amino groups on the PAH chain were essentially fully protonated when the chains were deposited. With no additional salts in these solutions, these PAH solutions were at low ionic strengths, typically 0.003 M, so there was relatively little shielding of charged groups. Under these conditions, the fixed positive charges on the polymer chain strongly repelled each other and were strongly attracted to the negatively charged surface. These two effects led to the deposition of PAH in flat, train-like layers where the bilayer thickness was less than 1 nm/bilayer.

The PR solution pH also plays an important role in the film deposition process. The PR solution pH directly affects the degree of protonation of the previously deposited PAH layers, and thus affects the subsequent reaction kinetics for PR incorporation. At a pH above the  $pK_a$  of the side chain amines of PAH, the majority of the amines will be unprotonated and thus able to react with the triazine ring of PR. Additionally, the reactivity of the triazine ring on PR increases with increasing pH.<sup>[45]</sup> These two effects result in reactive deposition being favored as the pH is increased. The clearest example of the effect of PR

solution pH on deposition can be seen in Fig. 6 and Table 1, when the PAH pH was held constant at either pH 4.5 or 7.0, and the PR solution pH was increased from 7.0 to 10.5. The amount of dye deposited per bilayer increased as the PR solution pH was increased from 7.0 to 10.5. In fact, when the PAH pH was 4.5 and the PR pH was 7.0, very little PR was deposited at all. In addition to a fairly low reactivity of the triazine rings at pH 7.0, the PAH layers deposited at pH 4.5 did not have a sufficiently high surface concentration to allow PR deposition to occur.

Importantly, the pH of the deposition solutions affects the SHG intensities and the degree of polar ordering of the PR molecules in the film. Table 2 presents the data of Table 1 normalized to the PAH pH 4.5/PR pH 10.5 case. In addition to the absorbance/bilayer and thickness data, Table 2 also contains the normalized square root of the SHG intensity  $[(I_{2\omega})^{1/2}]$  per bilayer.

The effect of PAH solution pH on the films can be seen by comparing experiments B vs. D, where the PR solution pH is held constant at 10.5. Increasing the PAH solution pH from 4.5 to 7.0 results in increases in the absorbance per bilayer. The  $(I_{2\omega})^{1/2}$  per bilayer increases by the same relative amount (~55–60%) as the absorbance. Within this pH range, the PAH is deposited as thin, flat layers. Thus as the pH of the PAH solution is increased,  $(I_{2\omega})^{1/2}$  scales proportionally with small changes in amount of PR per bilayer, and the increase in  $(I_{2\omega})^{1/2}$  is interpreted to be a result of simply incorporating more PR into the film.

Experiments C and D keep the PAH solution pH constant at 7.0 while varying the PR solution pH from 7.0 to 10.5. In these experiments, the bilayer thickness is similar, but the absorbance per bilayer and  $(I_{2\omega})^{1/2}$  per bilayer both increase as the PR pH is increased from 7.0 to 10.5. While 42% more PR is incorporated per bilayer, the value of  $(I_{2\omega})^{1/2}$  per bilayer increases by over 800%. Thus the pH of the PR solution has a dramatic effect on the orientation of the PR molecules that are incorporated in the films. At pH 7, the reactivity of the PAH amine groups with the triazine ring of the PR is lower, and PR may be incorporated by a combination of electrostatic, hydrogen bond, and covalent interactions. Thus at conditions favoring covalent reaction between PR and PAH, a high degree of PR ordering was obtained, while at conditions not

**Table 2** Relative values of the absorbance per bilayer and  $(I_{2\omega})^{1/2}$  per bilayer, both normalized to the values for PAH at pH 4.5 and procion red at pH 10.5 as a function of deposition pH

Experiment	PAH pH	PR pH	Absorbance/bilayer	Bilayer thickness	$(I_{2\omega})^{1/2}$ /bilayer
B	4.5	10.5	1.0	1.0	1.0
C	7.0	7.0	1.15	1.61	0.17
D	7.0	10.5	1.63	1.53	1.55

favoring covalent reaction between PR and PAH, the PR deposited within the films has a more random orientation. The  $\chi^{(2)}$  values obtained for deposition of PR at pH 10.5 are  $11.2 \times 10^{-9}$  and  $11.3 \times 10^{-9}$  esu (Table 1), which are sixfold greater than quartz.

The larger SHG observed in the PR pH 10.5 case serves as confirmation of the hypothesis that alternating the mechanism of deposition in these films and decoupling of the chromophore from steric constraints of a polymer backbone can provide a route to successful deposition and orientation of a low molecular weight chromophore. In earlier studies with NLO-active polymeric dyes such as PS119<sup>[46]</sup> which consists of a poly(vinylamine) backbone with an ionic azo dye chromophore, and poly{1-4-(3-carboxy-4-hydroxyphenylazo)-benzenesulfonamido-1,2-ethanediyl, sodium salt} (PCBS), films were made under deposition conditions leading to relatively thin bilayers ( $\sim 0.2$  nm/bilayer). In both PS119 and PCBS, the NLO-active chromophores are charged side groups on the polymer chain. As observed using in situ SHG intensity measurements, polar ordering of an adsorbed chromophore layer is reduced by subsequent adsorption of the next polyelectrolyte monolayer.<sup>[47]</sup> By decoupling the NLO-active chromophore from a polymer chain, the steric constraints to achieving ordered films that are present when using a large chromophore side group were reduced. Additionally, by using a heterobifunctional chromophore in which the mechanism for chromophore deposition (i.e., covalent bonding) differs from the deposition of the polymeric component (electrostatic interactions), the competing intermolecular interactions that prevent the achievement of a high net polar ordering of the chromophore within the film can be minimized.

Finally, the structure of the polycation plays a role in chromophore orientation. Koetse, Laschewsky, and Verbiest<sup>[27]</sup> previously reported on the fabrication of films using PR and the polycation poly[*N*-(3-aminopropyl)-*N*-(4-vinylbenzyl)-*N,N*-dimethylammonium chloride] (PAVDMA). The structure of this polycation is shown in Fig. 10 and consists of a quaternary

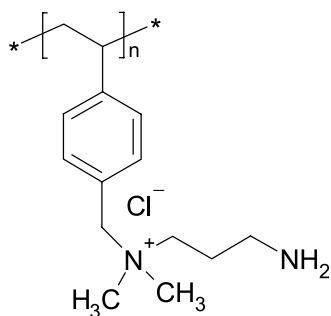


**Fig. 10** Structure of the polycation poly(*N*-(3-aminopropyl)-*N*-(4-vinylbenzyl)-*N,N*-dimethylammonium chloride) (PAVDMA).

ammonium group in addition to a primary amine. While layer-by-layer deposition of the PR chromophore was observed at pH  $\sim 9$ – $10$ , conditions that should favor covalent coupling of the PR to the primary amine, SHG results for this system showed that there was a lack of bulk polar order. The precise structural differences between PAVDMA and PAH that result in ordering of the PR when PAH is used are not known at present.

## CONCLUSION

A hybrid covalent/electrostatic deposition scheme has been demonstrated that can be used to obtain self-assembled, organic films in which there is long-range, polar ordering of a chromophore. The ordering is believed to arise from alternating the mechanism of deposition from monolayer to monolayer and decoupling the chromophore from the steric constraints of a polymer backbone. Using Procion Red MX-5B as a model reactive/anionic monomeric NLO chromophore and PAH as the cationic polyelectrolyte, films with  $\chi^{(2)}$  values  $\sim 11 \times 10^{-9}$  esu were constructed. This deposition process is highly sensitive to the pH values of both the PAH and PR solutions. In this work, we focused on the effect of pH on the film properties, and we found an operating window for optimal deposition and orientation. The PR solution pH should be high enough to favor covalent deposition. The PAH solution pH should also be as high as possible while still obtaining layer-by-layer growth of homogeneous films. While initial  $\chi^{(2)}$  values are significant, these values are far from optimized because the Procion Red chromophore is far from an ideal NLO chromophore. This methodology appears suitable for making thick films ( $1$ – $10$   $\mu\text{m}$ ) necessary for electro-optic modulator devices.

## ACKNOWLEDGMENTS

This work was supported by grant no. ECS-9907747 from the National Science Foundation.

## REFERENCES

1. Shi, Y.; Zhang, C.; Zhang, H.; Bechtel, J.; Dalton, L.; Robinson, B.; Steier, W. Low (Sub-1V) halfwave voltage polymeric electro-optic modulators achieved by controlling chromophore shape. *Science* **2000**, *288*, 119–122.
2. Boyd, R.W. *Nonlinear Optics*; Academic Press: Boston, 1992.



3. Shen, Y.R. *The Principles of Nonlinear Optics*; Wiley: New York, 1984.
4. Dalton, L.; Harper, A.; Ghosn, R.; Steier, W.; Ziari, M.; Fetterman, H.; Shi, Y.; Mustacich, R.; Jen, A.; Shea, K. Synthesis and processing of improved organic second-order nonlinear optical materials for applications in photonics. *Chem. Mater.* **1995**, *7*, 1060–1081.
5. Van Cott, K.E.; Guzy, M.; Neyman, P.; Brands, C.; Heflin, J.R.; Gibson, H.W.; Davis, R.M. Layer-by-layer deposition of low-molecular-weight molecules for second-order nonlinear optics. *Angew. Chem., Int. Ed.* **2002**, *41*, 3236–3238.
6. Singer, K.; Sohn, J.; Lalama, S. Second harmonic generation in poled polymer films. *Appl. Phys. Lett.* **1986**, *49*, 248–250.
7. Burland, D.; Miller, R.; Walsh, C. Second-order nonlinearity in poled-polymer systems. *Chem. Rev.* **1994**, *94*, 31–75.
8. Ashwell, G. Langmuir–Blodgett films: Molecular engineering of non-centrosymmetric structures for second-order nonlinear optical applications. *J. Mater. Chem.* **1999**, *9*, 1991–2003.
9. Fou, A.; Onitsuka, O.; Ferreira, M.; Rubner, M.; Swieh, B. Fabrication and properties of light-emitting diodes based on self-assembled multilayers of poly(phenylene vinylene). *J. Appl. Phys.* **1996**, *79*, 7501–7509.
10. Kleinfeld, E.; Ferguson, G. Rapid, reversible sorption of water from the vapor by a multilayered composite film: a nonstructured humidity sensor. *Chem. Mater.* **1995**, *7*, 2327–2331.
11. Caruso, F.; Furlong, D.; Ariga, K.; Ichinose, I.; Kunitake, T. Characterization of polyelectrolyte-protein multilayer films by atomic force microscopy, scanning electron microscopy, and Fourier transform infrared reflection–absorption spectroscopy. *Langmuir* **1998**, *14*, 4559–4565.
12. Piok, T.; Brands, C.; Neyman, P.; Erlacher, A.; Soman, C.; Murray, M.; Schroeder, R.; Graupner, W.; Heflin, J.R.; Marciu, D.; Drake, A.; Miller, M.; Wang, H.; Gibson, H.W.; Dorn, H.; Leising, G.; Guzy, M.; Davis, R.M. Photovoltaic cells based on ionically self-assembled nanostructures. *Synth. Met.* **2001**, *116*, 343–347.
13. Laurent, D.; Schlenoff, J. Multilayer assemblies of redox polyelectrolytes. *Langmuir* **1997**, *13*, 1552–1557.
14. Li, D.; Ratner, M.; Marks, T.; Zhang, C.; Yang, J.; Wong, G. Chromophoric self-assembled multilayers-organic superlattice approaches to thin-film nonlinear optical-materials. *J. Am. Chem. Soc.* **1990**, *112*, 7389–7390.
15. Iler, R. Multilayers of colloidal particles. *Colloid Interface Sci.* **1966**, *21*, 569.
16. Decher, G.; Lvov, Y.; Schmitt, J. Proof of multilayer structural organization in self-assembled polycation polyanion molecular films. *Thin Solid Films* **1994**, *244*, 772–777.
17. Decher, G. Fuzzy nanoassemblies: toward layered polymeric multicomposites. *Science* **1997**, *277*, 1232–1237.
18. Hammond, P. Recent explorations in electrostatic multilayer thin film assembly. *Curr. Opin. Colloid Interface Sci.* **2000**, *4*, 430–442.
19. Heflin, J.R.; Figura, C.; Marciu, D.; Liu, Y.; Claus, R.O. Thickness dependence of second-harmonic generation in thin films fabricated from ionically self-assembled monolayers. *Appl. Phys. Lett.* **1999**, *74*, 495–497.
20. Lindsay, G.; Roberts, M.; Chafin, A.; Hollins, L.; Merwin, L.; Stenger-Smith, J.; Yee, Y.; Zarras, P.; Wynne, K. Ordered films by alternating polyelectrolyte deposition of cation side chains and anionic main chain chromophoric polymers. *Chem. Mater.* **1999**, *11*, 924–929.
21. Herman, W.; Roberts, M. The sense of chromophore orientation in films made by alternate polyelectrolyte deposition. *Adv. Mater.* **2001**, *13*, 744–746.
22. DeWitt, D.; Hammond, P. Controlling orientation in optically active multilayer films. *Polym. Preprints* **2000**, *41*, 815–816.
23. Lee, S.; Balasubramanian, S.; Kim, D.; Viswanathan, N.; Bian, S.; Kumar, J.; Tripathy, S. Azo polymer multilayer films by electrostatic self-assembly and layer-by-layer post azo functionalization. *Macromolecules* **2000**, *33*, 6534–6540.
24. Lin, W.; Yitzchaik, S.; Lin, W.; Malik, A.; Durbin, K.; Richter, A.; Wong, G.; Dutta, P.; Marks, T. New nonlinear optical materials: expedient topotactic self-assembly of acentric chromophoric superlattices. *Angew. Chem., Int. Ed. Engl.* **1995**, *34*, 1497–1499.
25. Katz, H.; Scheller, G.; Putvinski, T.; Schilling, M.; Wilson, W.; Chidsey, C. Polar orientation of dyes in robust multilayers by zirconium phosphate–phosphonate interlayers. *Science* **1991**, *254*, 1485–1487.
26. Yamada, S.; Harada, A.; Matsuo, T.; Ohno, S.; Ichinose, I.; Kunitake, T. Optical second harmonic generation in alternately assembled dye–polyion multilayers. *Jpn. J. Appl. Phys.* **1997**, *36*, L1110–L1112.
27. Koetse, M.; Laschewsky, A.; Verbiest, T. Films grown from polyamines and reactive dyes by alternating polyelectrolyte adsorption/surface activation (CoMPAS). *Mater. Sci. Eng., C* **1999**, *10*, 107–113.
28. Schaefer, D.W.; Han, C.C. Quasielectric Light Scattering from Dilute and Semidilute Polymer Solution. In *Dynamic Light Scattering*; Pecora, R., Ed.; Plenum Press: New York, 1985.
29. Itano, M.; Kern, F.; Miyashita, M.; Ohmi, T. Particle removal from silicon water surface in wet cleaning process. *IEEE Trans. Semicond. Manuf.* **1993**, *6*, 258–267.
30. Azzam, R.M.; Bashara, N.M. *Ellipsometry and Polarized Light*; Elsevier: New York, 1987.
31. Neyman, P.; Guzy, M.; Shah, S.; Davis, R.M.; Van Cott, K.E.; Hang, W.; Gibson, H.W.; Brands, C.; Heflin, J.R. Novel hybrid covalent/ionic self-assembly techniques for improved second-order nonlinear optical films. *Mater. Res. Soc. Symp. Proc.* **2002**, *708*, 161–166.
32. Das, S.; Pal, A. Layer-by-layer self-assembling of a low molecular weight organic material by different electrostatic adsorption process. *Langmuir* **2002**, *18*, 458–461.
33. Decher, G.; Schmitt, J. Fine-tuning of the film thickness of ultrathin multilayer films composed of consecutively alternating layers of anionic and cationic polyelectrolytes. *Prog. Colloid & Polym. Sci.* **1992**, *89*, 160–164.
34. Lvov, Y.; Ariga, K.; Onda, M.; Ichinose, I.; Kunitake, T. A careful examination of the adsorption step in the alternate layer-by-layer assembly of linear polyanion and polycation. *Colloids Surf., A* **1999**, *146*, 337–346.

35. Caruso, F.; Lichtenfeld, H.; Donath, E.; Möhwald, H. Investigation of electrostatic interactions in polyelectrolyte multilayer films: binding of anionic fluorescent probes to layers assembled onto colloids. *Macromolecules* **1999**, *32*, 2317–2328.
36. Kleinfeld, E.; Ferguson, G. Stepwise formation of multilayered nanostructural films from macromolecular precursors. *Science* **1994**, *265*, 370–373.
37. Yoo, D.; Shiratori, S.; Rubner, M. Controlling bilayer composition and surface wettability of sequentially adsorbed multilayers of weak polyelectrolytes. *Macromolecules* **1998**, *31*, 4309–4318.
38. Clark, S.; Montague, M.; Hammond, P. Ionic effects of sodium chloride on the templated deposition of polyelectrolytes using layer-by-layer ionic assembly. *Macromolecules* **1997**, *30*, 7237–7244.
39. Lösche, M.; Schmitt, J.; Decher, G.; Bouwman, W.; Kjaer, K. Detailed structure of molecularly thin polyelectrolyte multilayer films on solid substrates as revealed by neutron reflectometry. *Macromolecules* **1998**, *31*, 8893–8906.
40. Lowack, K.; Helm, C. Molecular mechanisms controlling the self-assembly process of polyelectrolyte multilayers. *Macromolecules* **1998**, *31*, 823–833.
41. Bertrand, P.; Jonas, A.; Laschewsky, A.; Legras, R. Ultrathin polymer coatings by complexation of polyelectrolytes at interfaces: suitable materials, structures and properties. *Macromol. Rapid Commun.* **2000**, *21*, 319–348.
42. Netz, R.; Joanny, J. Adsorption of semiflexible polyelectrolytes on charged planar surfaces: charge compensation, charge reversal, and multilayer formation. *Macromolecules* **1999**, *32*, 9013–9025.
43. Shiratori, S.; Rubner, M. pH-Dependent thickness behavior of sequentially adsorbed layers of weak polyelectrolytes. *Macromolecules* **2000**, *33*, 4213–4219.
44. Fang, M.; Kim, C.; Saube, G.; Kim, H.; Waraksa, C.; Miwa, T.; Fujishima, A.; Mallouk, T. Layer-by-layer growth and condensation reactions of niobate and titanoniobate thin films. *Chem. Mater.* **1999**, *11*, 1526–1532.
45. Hermanson, G. *Bioconjugate Techniques*; Academic Press: New York, 1996.
46. Figura, C.; Neyman, P.; Marciu, D.; Brands, C.; Murray, M.; Hair, S.; Davis, R.M.; Miller, M.; Heflin, J.R. Thermal stability and immersion solution dependence of second order nonlinear optical ionically self-assembled films. *SPIE Proc.* **2000**, *3939*, 214–222.
47. Brands, C.; Neyman, P.; Guzy, M.; Shah, S.; Davis, R.; Van Cott, K.E.; Wang, H.; Gibson, H.W.; Heflin, J. In situ second harmonic generation measurements of the formation of ionically self-assembled monolayers. *SPIE Proc.* **2001**, *4461*, 311–318.

# Nucleoside- and Nucleobase-Substituted Oligopyrrolic Macrocycles

Vladimír Král

Martin Valík

Tatiana V. Shishkanova

*Department of Analytical Chemistry, Institute of Chemical Technology,  
Prague, Czech Republic*

Jonathan L. Sessler

*Department of Chemistry and Biochemistry, University of Texas at Austin,  
Austin, Texas, U.S.A.*

## INTRODUCTION

This entry summarizes the design and synthesis of conjugates resulting from the combination of nucleic acid base derivatives, particularly nucleosides and nucleotides, with oligopyrrole macrocycles. In addition to detailing the methods of preparation and fundamental chemical properties, the vision behind such projects and the various applications targeted for use by these conjugates are also described. These systems combine into one chemical entity two of the more important biological building blocks found in Nature, namely, nucleic acid bases (nucleobases) and porphyrins, and this leads to new constructs with rather unique chemical features as well as novel molecular recognition properties. Although the focus of the present chapter will be on systems containing natural nucleobase components, it is important to appreciate that the porphyrin portion of these constructs can include a range of synthetic oligopyrrole macrocycles that have no biological equivalent. This gives rise to products with unexpected supramolecular properties, including those associated with anion recognition.

## BACKGROUND

Nucleotides and nucleic acids play key roles in many biological processes ranging from information processing to energy storage and transduction. In addition, a number of nucleotide and nucleoside analogues exhibit antiviral activity. As a consequence, considerable study is devoted to simple, monomeric nucleic acid bases (“nucleobases”; NBs), both in terms of understanding their fundamental properties and in terms of developing potential new drug leads. Activity is also high in the areas of synthesis (e.g., new methods development) and sensing (i.e., finding ways to detect specific nucleic

acid derivatives selectively). The NBs also inspired supramolecular chemists as a result of their ability to undergo complementary Watson–Crick-type base pairing. This, of course, represents the most ubiquitous and fundamental kind of hydrogen bond-based molecular recognition. It thus provided an incentive to construct new, rationally designed conjugates, including covalent combinations of nucleobase with oligopyrrolic macrocycles (OPMC). These latter systems, which are the focus of this review, possess unique photophysical and molecular recognition properties that are specifically defined by the nature of the constituent NB and OPMC components, as well as the extent of “chemical communication” between two parts of what may be considered a complex, multifunctional receptor molecule. In this entry the chemistry and properties of NB–OPMC conjugates will be reviewed with a focus on the specific choice of NB, OPMC, and/or covalent linkage. However, to keep the discussion within reasonable limits, only naturally occurring purine and pyrimidine NB component(s) will be considered. By contrast, our coverage of known systems containing various linking spacer (SP) subunits and OPMCs attempts to be more comprehensive. Of the latter, which run the gamut from biomimetic to wholly synthetic, porphyrins have received the greatest attention. Thus we start our discussion with NB–SP–OPMC conjugate systems that are based on this biologically all-important chromophore.

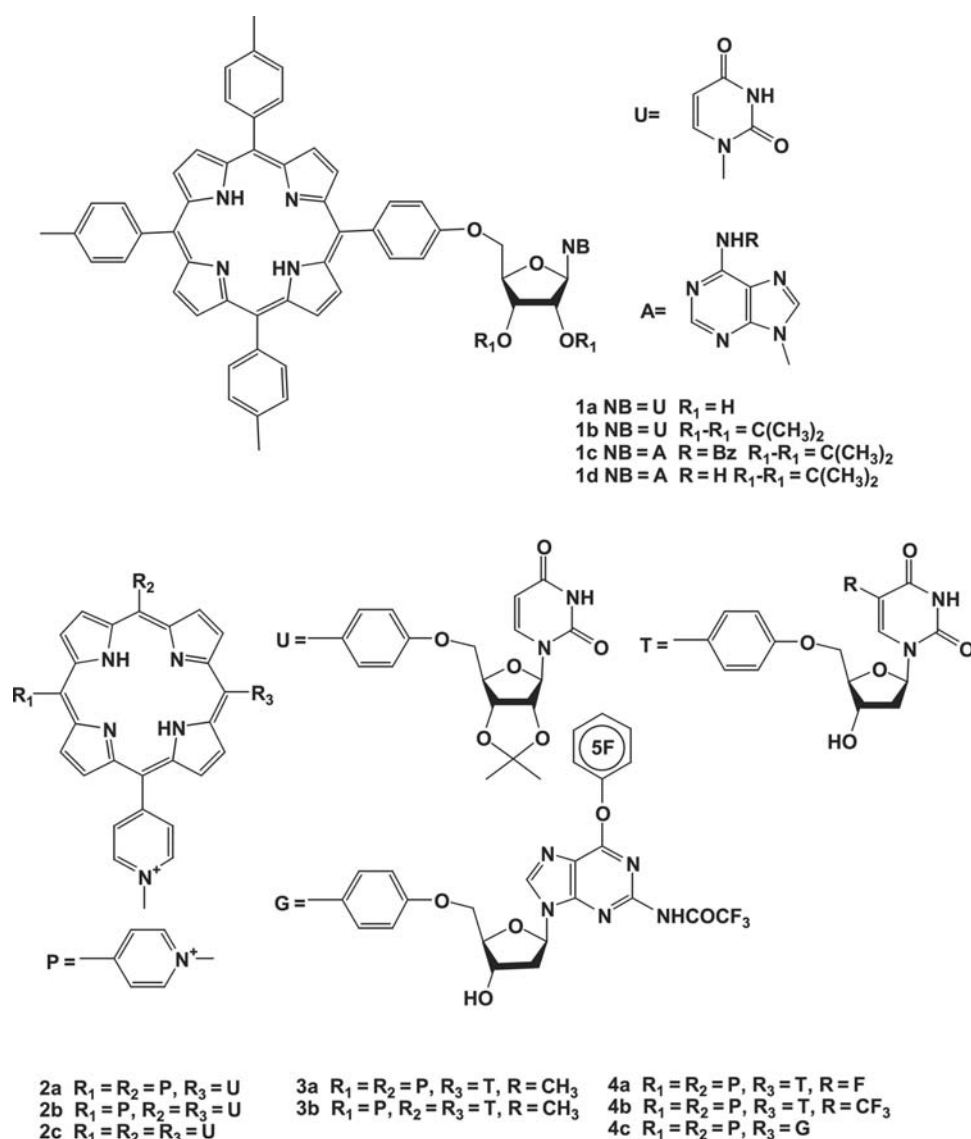
## Nucleobase–Porphyrin Derivatives

The first porphyrin nucleoside conjugates, represented by structures **1**, were synthesized by Kus and coworkers in 1990.<sup>[1]</sup> Unfortunately, these systems proved essentially insoluble in water,<sup>[2]</sup> a feature that diminished their biomedical significance and limited their

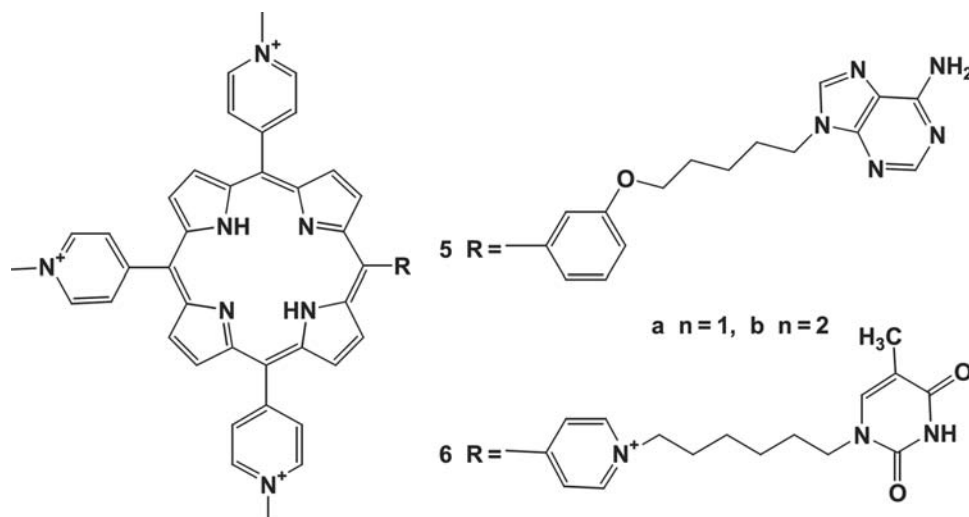
utility in terms of various targeted therapeutic applications. To overcome this problem, the *meso*-(1-methylpyridinium-4-yl)<sub>n</sub>porphyrin core was chosen as the key OPMC subunit. This choice was dictated by solubility considerations and by the recognition that *N*-methylated pyridyl porphyrins and related systems bind strongly to DNA with a preference of G–C base pair regions<sup>[3]</sup> and that certain methylated derivatives can be photoactivated to generate active species, such as single oxygen, that are known to cleave oligonucleotides.<sup>[4]</sup> The remaining *meso* positions were then used to attach the nucleoside parts. In this way, the first water soluble porphyrinyl nucleosides **2** were prepared, specifically via the condensation of *meso*-(pyridin-4-yl)<sub>n</sub>-(*p*-hydroxyphenyl)<sub>4-n</sub>porphyrins ( $n = 1-3$ ) with 5'-*O*-tosylate of 2',3'-*O*-isopropylideneuridine and subsequently subjecting the pyridine cores to

methylation.<sup>[2,5]</sup> The same synthetic strategy was used to prepare analogues containing other porphyrinyl-nucleosides, in particular the thymidine derivatives, **3**,<sup>[6]</sup> the fluorinated thymidine (**4a**, **4b**),<sup>[7]</sup> and guanosine (**4c**) porphyrinyl derivatives.<sup>[7]</sup> The biological properties of the porphyrinyl-nucleoside conjugates **2a** and **3** and their porphyrin-centered Co(II) complexes were then studied in terms of growth suppression of malignant melanoma cells.<sup>[6]</sup> Significant suppression was achieved using the Co(II) complex of porphyrinyl-dithymidine **3b**. In this instance, the extent of inhibition reached 95%. By contrast, in the case of the corresponding Co(II) complex of **3a**, containing one thymidine unit, only a low level of suppression was observed<sup>[6]</sup> (Scheme 1).

A strategy analogous to that described above was also used to prepare the two adenine-containing



Scheme 1



Scheme 2

porphyrinyl–NB derivatives<sup>[8]</sup> **5a** and **5b**. The synthesis was modified, however, such that:

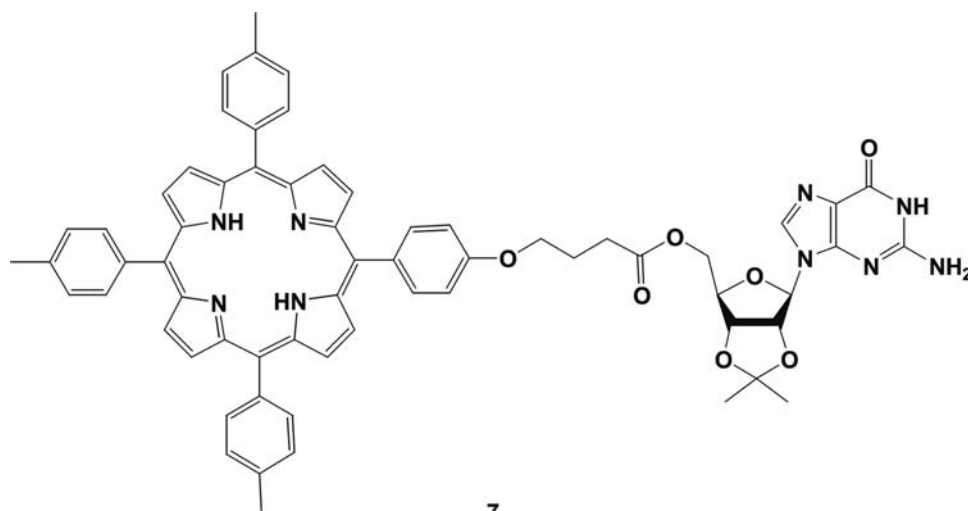
- i. The *N*-methylation step was carried out prior to forming the hybrid molecule.
- ii. The bromo derivative of the nucleobase-functionalized alkyl spacer was used instead of the tosylate employed in the case of more tightly coupled conjugates **1–4**. Unfortunately, this procedure failed to provide a more loosely linked thymidine analogue of **3a** (e.g., **6**). Thus an alternative approach was developed. It involved the treatment of 5,10,15-tris(1-methylpyridinium-4-yl)-20-(pyridin-4-yl)porphyrin with a 6-carbon bromoalkyl derivative of thymidine; this gave target **6** in almost quantitative yield.<sup>[8]</sup>

Once in hand, the interactions of **5** and **6** with nucleosides and polynucleotides were studied via UV–VIS and fluorescence-based spectroscopic titration methods. The calculated  $K_s$  values (1:1) for all combination of **5** and **6** with simple nucleosides were the same within the error of the method (ca  $1.6 \times 10^4 \text{ M}^{-1}$ ). In other words, no preference was observed between the porphyrin–nucleobase conjugates and the corresponding complementary Watson–Crick nucleotides. The absence of any significant Watson–Crick-type hydrogen bonding selectivity was interpreted as reflecting the dominance of intermolecular stacking interactions, as opposed to base-pairing ones. In the case of polynucleotide, two binding processes were inferred from the fluorimetric titration experiments. First, a set of spectroscopic changes at  $r > 0.1$  ( $r$  = ratio porphyrin/polynucleotide) were attributed to an intermolecular association of the porphyrin portion of the conjugate with the polynucleotide

polyanion. Second, a set of different emission features were observed when the intercalation binding sites were present in large excess ( $r < 0.1$ ) that were explained in terms of the porphyrin subunits intercalating into the polynucleotide backbone. Interestingly, some selectivities<sup>[8]</sup> were observed in the case of titrations carried out with polyU, with different results being seen for conjugates **5** containing complementary bases than for the corresponding noncomplementary conjugate **6**<sup>[8]</sup> (Scheme 2).

With a different focus, Masiero et al. constructed the alkyl-tethered porphyrin-guanosinyl derivative **7**. The propensity of guanosine derivatives to self-assemble into so-called G-quartets was then used to prepare a novel circular porphyrin array.<sup>[9]</sup> In terms of specifics, these researchers showed that system **7** self-assembles in chloroform solution in the presence of potassium picrate to form a supramolecular complex that consists of eight units of **7** arranged in the form of two G-quartets, as evidenced by UV–VIS, CD, and <sup>1</sup>H NMR spectroscopic studies. In the context of this work, complexation of the cation has a dramatic effect on the CD spectrum. In particular, the addition of  $\text{K}^+$  leads to the appearance of excitation couplets in both the guanine absorption and porphyrin Soret spectral regions. The couplet observed in the Soret region was deemed particularly significant inasmuch as it indicates an intermolecular electronic interaction between the porphyrin chromophores.<sup>[9]</sup> This, in turn, supports the conclusion that the porphyrins are arrayed unsymmetrically around the central  $[\text{G}]_8\text{K}^+$  “core” (Scheme 3).

Nucleobase–porphyrin constructs containing nucleosides with free ribofuranose hydroxyl groups have also been prepared. For instance, Li and Czuchajowski prepared the porphyrin nucleoside analogues (**8**) that



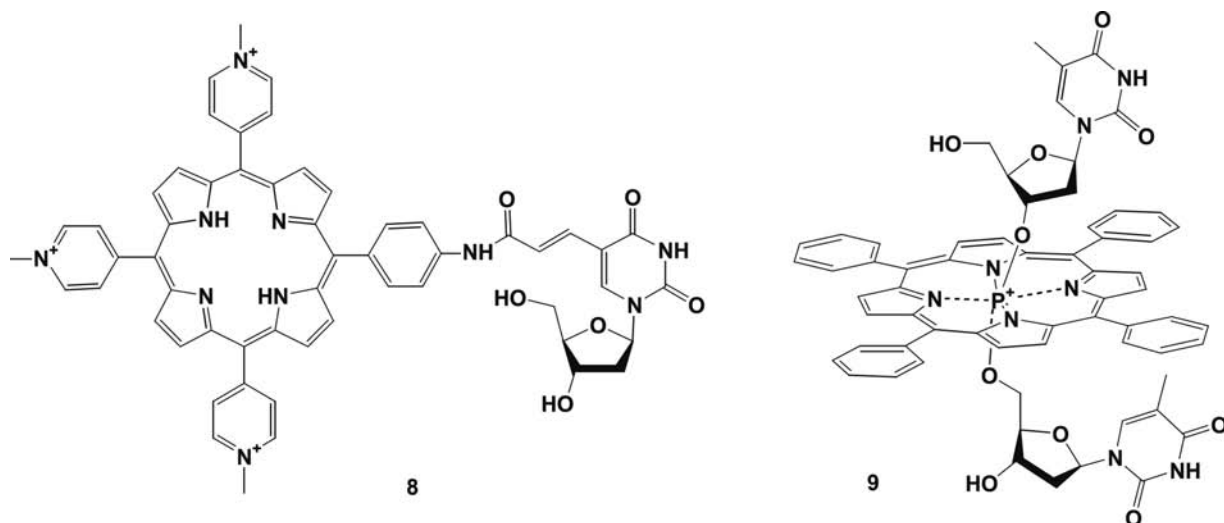
7

Scheme 3

are attractive as a potential building block for porphyrin–oligonucleotide/DNA systems wherein the number and position of the porphyrin subunits can, at least in principle, be controlled.<sup>[10]</sup> This system (**8**) was generated from (+)-6-iodo-2'-deoxyuridine and the 5,10,15-tri(4-pyridyl)-20-(*p*-acrylamidophenyl)porphyrin using a Heck reaction. Its interactions with the 20-mer oligonucleotide duplexes (dG)<sub>20</sub>–(dC)<sub>20</sub> and (dA)<sub>20</sub>–(dT)<sub>20</sub> were then studied by UV–VIS spectroscopy, as were those with the DNA plasmid-pRIT6. Comparisons with the methylated starting 5,10,15-tri(4-pyridyl)-20-(*p*-acrylamidophenyl)porphyrin revealed that, in every case, the porphyrin Soret band was red-shifted by 6–14 nm. Hypochromicity in the range of 10–54% was also observed. Interestingly, derivative **8** gave rise to a greater degree of

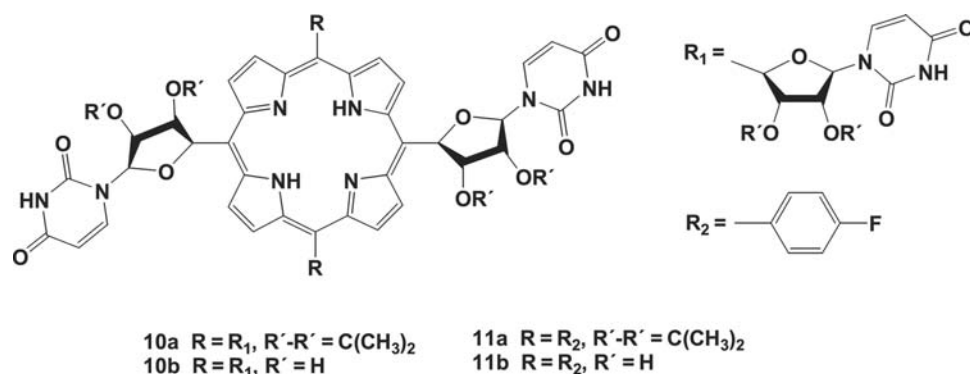
bathochromic shift and a lower level of induced hypochromicity than the corresponding 5,10,15-tri(1-methylpyridinium-4-yl)-20-(*p*-acrylamidophenyl)porphyrin “control.”<sup>[10]</sup>

In all of the above examples, the nucleosides were covalently attached to the porphyrin subunit via functionalization of a *meso* aryl substituent. This is not, however, the only way to link these two kinds of components, a point that was elegantly underscored by Goh and Czuchajowski. These researchers bound two nucleosides to the axial positions of phosphorus(V) porphyrins through the ribofuranose 3'-hydroxyl and 5'-hydroxyl substituents<sup>[11]</sup> The resulting products, potentially a mixture of three *O*-P(V) coordination isomers (vide infra), contain free 3'-hydroxyl and the 5'-hydroxyl groups (cf. structure **9**) and can thus be used,



Scheme 4





Scheme 5

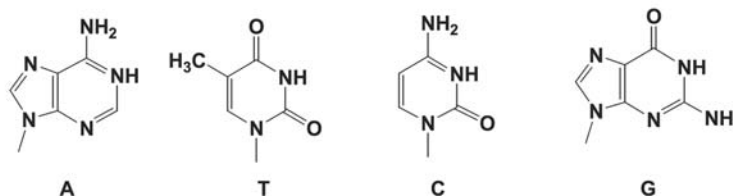
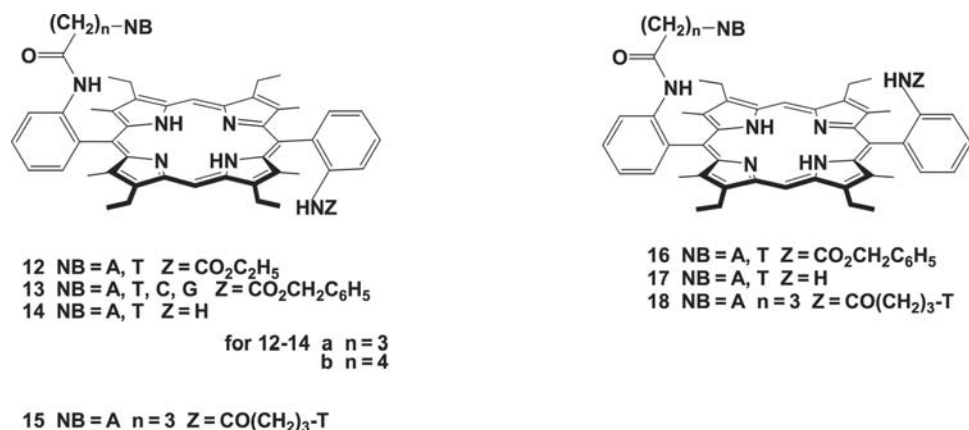
at least in principle, to prepare oligo-porphyrin DNA analogues linked through a positively charged phosphorus(V) porphyrin “backbone.” They were prepared by subjecting a dichlorophosphorus(V) tetraphenylporphyrin to nucleophilic substitution using a non-protected nucleoside as the nucleophile. The least polar and least sterically hindered 5',5'-*O*-isomer was formed with the highest yield from the three possible (and observed) products (i.e., the 3',3'-, 3',5'-, and 5',5'-*O*-isomers). However, this isomer proved less stable than the corresponding 3',3'- and 3',5'-isomers and was found to undergo rapid hydrolysis to the corresponding dihydroxyl phosphorus(V) porphyrin unless protected from light and moisture (Scheme 4).

A different kind of linked system was described by Cornia et al. These workers prepared porphyrin–uridine derivatives wherein the uridine subunits are anchored to the porphyrin macrocycle by means of robust carbon–carbon bonds (i.e., systems **10** and **11**).<sup>[12]</sup> The synthesis of these systems, which contain direct meso-ribofuranose bonds, began with the coupling of two equiv. of pyrrole to one equiv. of 2',3'-*O*-isopropylidene-5'-oxo-5'-deoxy-uridine under conditions of acid catalysis (SnCl<sub>4</sub>). The intermediate dipyrrolyl–uridyl methane was then subject to macrocyclization (BF<sub>3</sub> etherate) in the presence of 2',3'-*O*-isopropylidene-5'-oxo-5'-deoxy-uridine or 4-fluorobenzaldehyde, followed by DDQ-mediated oxidation to produce the corresponding 2',3'-*O*-isopropylidene-protected porphyrins, 5,10,15,20-tetrakisuridinylporphyrin **10a**, and 5,15-bisuridyl-10,20-(*p*-fluorophenyl)porphyrin **11a**, respectively.<sup>[12]</sup> Deprotection with aqueous trifluoroacetic acid at ambient temperature followed by neutralization with ammonia then yielded the free hydroxyl products **10b** and **11b** in nearly quantitative yield (Scheme 5).

Yet another approach to generating nucleobase–porphyrin conjugates was pursued by Hisatome et al. These workers targeted the connection of a nucleobase moiety to a porphyrin via amide linkages, relying in particular on the reaction of an aminophenylporphyrin

with an activated form of a nucleobase-bearing alkanic acid.<sup>[13,14]</sup> Unfortunately, initial efforts to affect the coupling of *anti* 5,15-bis(2-aminophenyl)porphyrin derivatives with nucleobase–alkanoic acids using standard coupling agents such as *N,N'*-dicyclohexylcarbodiimide and *N,N'*-carbonyldiimidazole under a variety of conditions gave only small amounts of the expected amide or no product at all. On the other hand, very good results were obtained in the presence of ethoxycarbonyl chloride. However, in this case, only the corresponding singly functionalized, mixed monoamide monocarbonate derivatives **12** could be separated from the reaction mixture. In light of this finding, a decision was made to protect one of the two amino groups present in the starting bis-aminophenyl porphyrin with a benzyloxycarbonyl group.<sup>[13]</sup> Subsequent coupling with a nucleobase alkanic acid afforded monofunctionalized compounds of general structure **13**.<sup>[13,14]</sup> The adenine and thymine derivatives **14** bearing free amino group were then prepared by removing the carbobenzyloxy groups from the corresponding precursors **13**. Coupling of thymine butanoic acid to **14a-A** then led to the *anti* adenine–thymine derivative **15**. The corresponding *syn* atropoisomer **18** was also prepared<sup>[13]</sup> using the same synthetic strategy, although in this instance the “intermediates” consisted of **16** and **17**, rather than **13** and **14** (Scheme 6).

As implied above, one of the prime motivations for generating porphyrinyl nucleoside, nucleotides, and oligonucleosides conjugates stemmed from a desire to produce water soluble, site-specific DNA binding and modifying systems.<sup>[15]</sup> While systems involving species containing oligonucleotides lie outside the scope of this review, it is worth noting that the covalent attachment of a photosensitizing porphyrin unit to an antisense oligonucleotide produced a system that allowed for the sequence-specific photomodification of target DNA after activation of the porphyrin subunit by photoillumination.<sup>[16]</sup>



Scheme 6

### NB-Substituted porphyrins as a model for electron transfer system

One of the more intriguing questions in the area of electron- and energy-transfer chemistry involves how covalent pathways differ from non-covalent ones in terms of mediating both short- and long-range transfer processes. Motivated by a desire to understand these issues, as well as to develop cytosine and guanine systems as new biomimetic modules for use in supramolecular ensemble construction, Sessler and coworkers prepared a series of noncovalent electron- and energy-transfer systems that contained porphyrinyl-nucleosides as key components.<sup>[17–20]</sup> These systems, which can be considered as containing a hydrogen-bonded assembled photon antenna, relied on Watson–Crick nucleobase pairing interactions between donors

and acceptors attached to functionalized guanosine and cytosine subunits.

In one early system, guanosine- and cytosine-bearing methaleted (ZnP) and nonmethaleted (H<sub>2</sub>P) porphyrins were used to construct an ensemble where photoexcitation led to energy transfer from the metalloporphyrin (characterized by a higher energy excited state) to a free-base porphyrin moiety (characterized by a lower energy excited state) in accord with Fig. 1. In this case, the requisite porphyrin–nucleobase conjugates **20** and **21** were prepared by alkylation of a nucleobase derivative bearing an amine “tail” with an electrophilic porphyrin. This provided the protected intermediates **19**. Subsequent deprotection afforded the free-base porphyrins **20** (H<sub>2</sub>P), whose metalation gave the Zn(II) porphyrin analogues **21** (ZnP)<sup>[17,21]</sup> (Scheme 7).

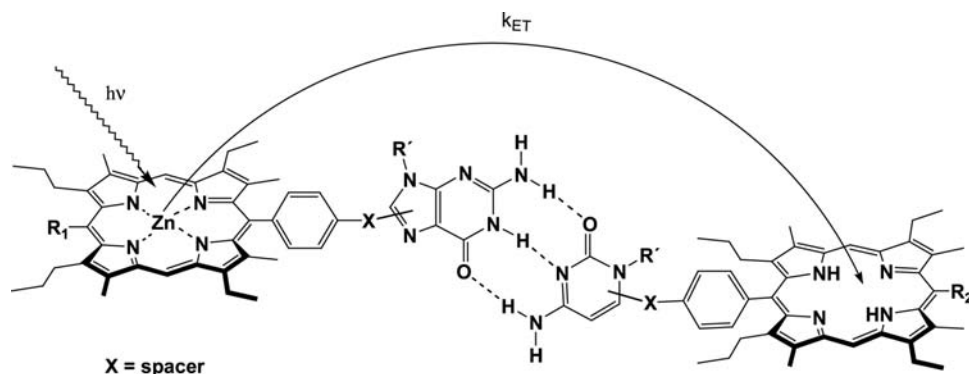
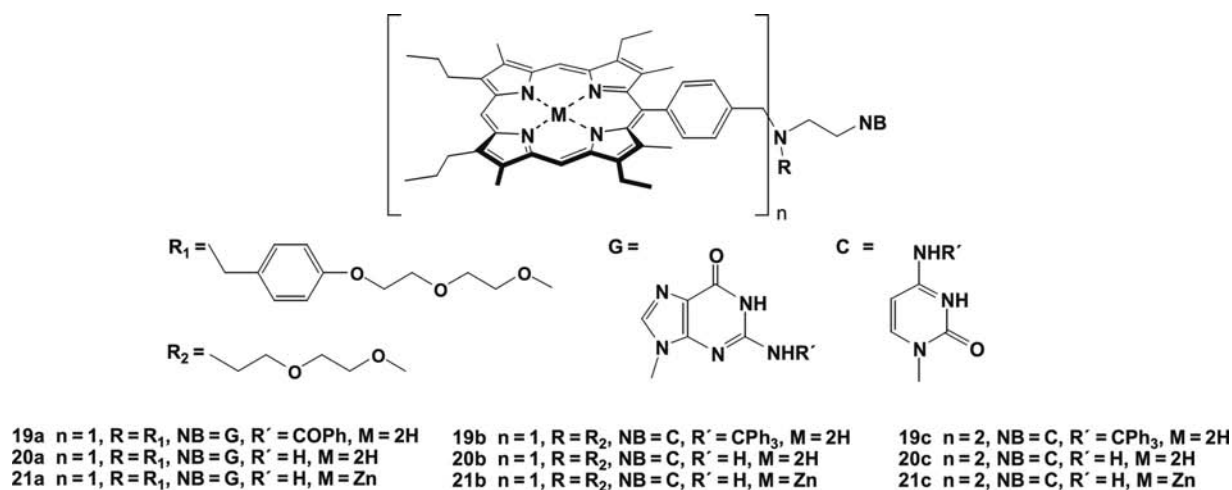


Fig. 1 Schematic representation of the hydrogen-bonded dimers **20–21** and subsequent energy transfer from ZnP **20** to H<sub>2</sub>P **21**.



Scheme 7

The photophysical characteristics of the porphyrin-nucleobase conjugates **20** and **21** and the supramolecular dimers formed as a result of their undergoing Watson-Crick-type association (Fig. 1) were then determined by studying their spectroscopic properties in ethanol-free  $CHCl_3$ . Here, both standard static fluorescence and time-resolved methods were used. The latter proved particularly revealing. For instance, when solutions containing roughly equimolar concentrations of both  $H_2P$  **20** and  $ZnP^*$  **21** were subject to laser excitation at 570 nm, the excited  $ZnP$  singlet state ( $ZnP^*$ ) was formed as the dominant product (ca. 85%). Emission from this species, essentially free of fluorescence signals arising from the corresponding free-base excited singlet,  $H_2P^*$ , could be monitored at 600 nm. Thus, varying the concentration of  $H_2P$  and studying the emission behavior of the whole system allowed the monitoring of the dimeric ensemble formation and energy transfer dynamics within it as well. At low concentrations of  $H_2P$  relative to  $ZnP$ , the fluorescence (as monitored at 600 nm) decayed with a lifetime  $\tau_1$  of  $\sim 1.5$  nsec, a value that corresponds to the singlet state lifetime of a simple, monomeric (i.e., non-complexed) photoexcited zinc(II) porphyrin (i.e.,  $ZnP^*$ ). As the

relative concentration of  $H_2P$  increased, however, the decay profiles became increasingly dual exponential in character because of the appearance of a faster decaying component that was observed in addition to the longer ca. 1.5-nsec lifetime seen in the absence of  $H_2P$ . This shorter lifetime,  $\tau_2$  (ca. 0.6–0.8 nsec), was assigned to a  $Zn$  subunit held within a base-tethered dimer that was undergoing deactivation as a result of the intra-ensemble energy transfer occurring between  $ZnP^*$  and  $H_2P$ . Energy transfer was observed also from the triplet excited state of the  $ZnP$  subunit, providing an ancillary set of data that could confirm the formation of the Watson-Crick associated ensemble. In fact, the extent of association could be calculated in quantitative terms from the observed singlet and triplet lifetimes. The resulting values, given in Table 1, confirmed the expected impression that the extent of nucleobase-nucleobase association increases in the order guanine-guanine < cytosine-cytosine < cytosine-guanine.<sup>[17]</sup>

In an effort to produce a model for electron-, as opposed to energy-, transfer, an ensemble involving the  $ZnP$ -guanosine derivative **21a** and the quinone cytosine derivative **22** was constructed via non-covalent self-assembly (Fig. 2). In  $CH_2Cl_2$ , fluorescence from the porphyrin subunit in **21a** was increasingly quenched upon the addition of concentrations of **22** (to a limit of ca. 35% total quenching at the highest concentrations used). By contrast, no fluorescence changes were observed when similar experiments were carried out in the presence of methanol or when the exocyclic amine groups of **21a** were blocked. Time-resolved fluorescence studies of an equimolar mixture of porphyrinyl-guanosine **21a** and quinone cytosine **22** displayed a biphasic profile that was almost identical to that displayed by the self-assembled dimer of **20** and **21** (Table 1).<sup>[18]</sup> Such an observation was consistent with rapid intra-ensemble electron transfer in

**Table 1** Rate constants for energy transfer ( $k_{ss}$ ) within the nucleic acid base dimers and association constants ( $K_a$ )

Porphyrins	$\tau_1$ (nsec)	$\tau_2$ (nsec)	$k_{ss}/10^8$ ( $sec^{-1}$ )	$K_a$ ( $M^{-1}$ )	Reference
<b>20c–21b</b>	1.60	0.77	6.8	48	[17]
<b>20a–21a</b>	4.41	0.82	5.1	24	[17]
<b>20b–21a</b>	1.47	0.87	4.7	225	[17]
<b>21a–22</b>	1.50	0.94	4.2	1290	[18]
<b>25–26</b>	1.80	0.74	8.0	8990	[19]
<b>24a–25</b>	1.60	0.70	8.1	22,000	[20]

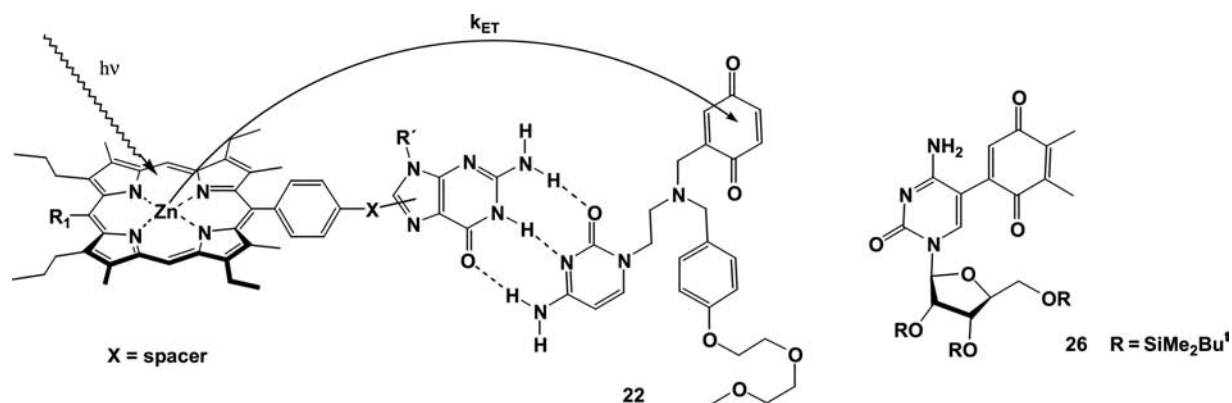


**Fig. 2** Schematic representation of the porphyrin-guanosine and quinone-cytosine ensembles and subsequent energy transfer from porphyrin to quinone parts.

the case of the porphyrin–quinone pseudodimer formed from **21a** and **22**.

While important in terms of demonstrating the utility of Watson–Crick base pairing as a means of constructing noncovalent electron transfer model systems, the above first-generation system suffered from considerable conformation flexibility. Such flexibility was thought to limit the extent to which quenching could be achieved within the self-assembled pseudodimer formed from **21a** and **22** and, as such, complicated interpretation of the observed electron transfer process. For instance, quenching arising from inter- or intracomplex diffusional encounters between the donor and acceptor, rather than through a hydrogen bond process, could be invoked to account for the observed quenching and presumed electron transfer

events. Thus more rigid, second-generation, model systems (Fig. 3) were developed.<sup>[19,20]</sup> In particular, new porphyrin–nucleobase monomers were prepared from *O*- and *N*-protected guanosine- and cytidine-substituted benzaldehyde intermediates using the MacDonald–Chang porphyrin synthesis.<sup>[22]</sup> Subsequent deprotection and selective protection of the condensation products gave rise to the guanosine (**23**) and cytidine (**24**) porphyrins. Derivative **23** was then converted into its corresponding zinc porphyrin **25** (Scheme 8).

The non-covalent donor–acceptor systems derived from porphyrin **25** and either quinone-cytidine **26** (Fig. 2) or porphyrin-cytidine **24** (Fig. 3) were then subject to analysis via time-resolved fluorescence spectroscopy. In accord with the earlier, first-generation

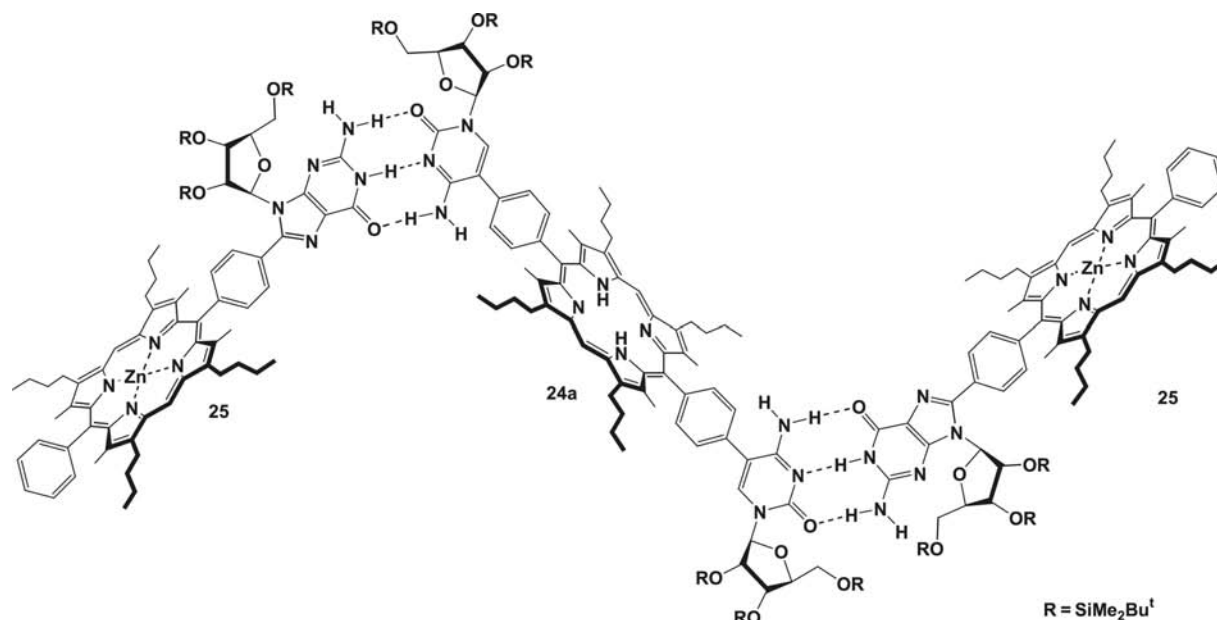
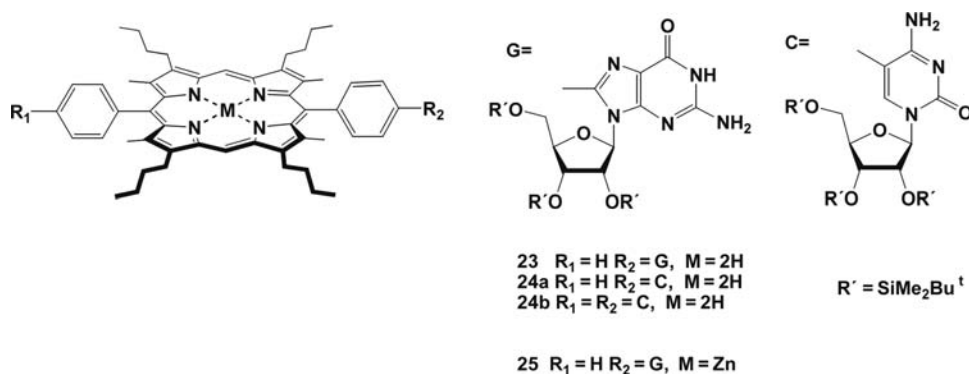


**Fig. 3** Porphyrinic array wherein two ZnP **25** and one H<sub>2</sub>P **24a** are held together in a trimeric conformation.



Scheme 8

systems described above, addition of **24** or **26** to a chloroform solution of **25** caused a primarily monoexponential fluorescence decay profile to become biphasic. The resulting decay profiles were then analyzed in terms of two exponential profiles, corresponding to two excited state components (Table 1). The fractional amplitude of the shorter-lived component, considered to reflect an intra-ensemble quenching process, increased as the concentration of the acceptor component, either **24** or **26**, was increased. The corresponding association constants,  $K_a$ , were significantly higher than those derived for the more flexible aggregate<sup>[18]</sup> formed between **21a** and **22** ( $K_a = 8990 \pm 600 M^{-1}$  for the complex formed between **25** and **26** vs.  $1290 \pm 230 M^{-1}$ ).<sup>[19]</sup>

### NB-Sapphyrin Derivative

Very different kinds of nucleobase-oligopyrrole conjugates may, in principle, be obtained when chromophores other than porphyrins are used. This is because other oligopyrrolic macrocycles are often characterized by properties that are very different than those of porphyrin. While a large number of porphyrin-like oligopyrrolic macrocycles now exist, the fact remains that, with the exception of porphyrin itself, most work in the NB-OPMC area has been largely limited to the use of sapphyrin. Sapphyrins are a class of pentapyrrolic expanded porphyrin that were first reported by Woodward (for a review, see Ref.<sup>[23]</sup>). Characterized by two relatively basic "pyridine-like" pyrrolic centers, sapphyrins are readily protonated and, in marked contradistinction to porphyrins, form complexes with a wide variety of anions, including in particular phosphates.<sup>[24,25]</sup> In fact, sapphyrin derivatives have been used to effect both nucleoside<sup>[26]</sup> and nucleotide<sup>[27]</sup> recognition. Furthermore, a silica-bound sapphyrin proved useful as a solid support for the HPLC separation of monomeric and short oligomeric nucleotides<sup>[28]</sup> at pH 7, while certain water-soluble

sapphyrins were found to bind DNA in aqueous solution at physiological pH.<sup>[29]</sup> A variety of spectroscopic studies as well as X-ray diffraction analysis established that phosphate-type species are bound to the protonated sapphyrin core via a "helicopter-like" set of hydrogen bonding interactions between the phosphate oxyanion and the pyrrolic hydrogens of the protonated macrocycle.<sup>[24]</sup>

Although unique, the phosphate binding capability of the sapphyrins is rather nonselective. For instance, the use of sapphyrin to affect the transport of nucleotide monophosphate through a model membrane (Fig. 4) consisting of an initial aqueous phase (Aq. I), an organic barrier, and a second, receiving phase (Aq. II) revealed that it is a very efficient but non-selective carrier at pH < 4 (where it exists in its diprotonated form).<sup>[30]</sup> Such findings provided an incentive for Sessler and coworkers to develop more selective systems through the construction of NB-sapphyrin conjugates. These workers considered it likely that the combination of a NB (to recognize the complementary Watson-Crick nucleobase) and a sapphyrin (to effect phosphate binding) would lead to receptors with a unique ability to bind and transport nucleotides selectively. To the extent such species could be generated and might have an important application

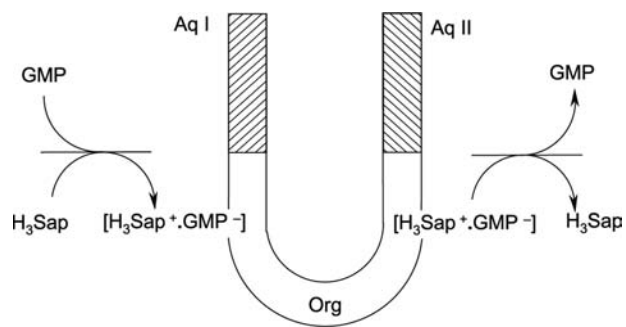
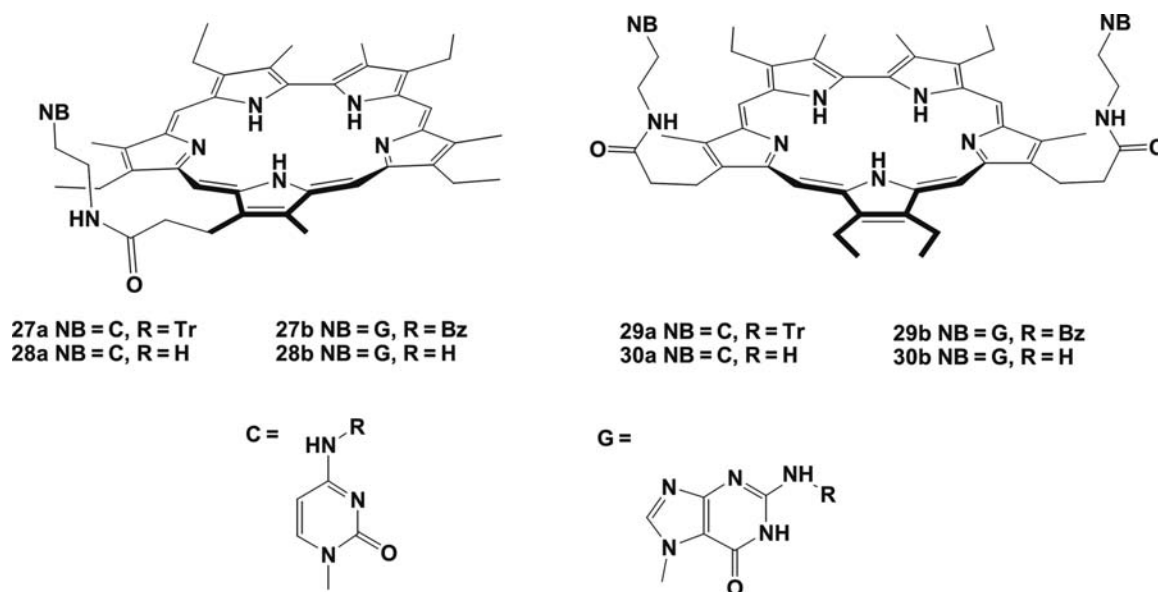


**Fig. 4** Schematic representation of GMP transport effected under synport conditions using sapphyrin as the hydrophobic phosphate-binding carrier.





Scheme 9

in the area of drug delivery; they could help affect the into-cell transport of nucleotide-based antiviral agents or, even in the limit, various antisense oligonucleotides. Important, however, as are these potential end-use applications, the initial goal was less ambitious; it was to find a saphyrin-based nucleotide carrier that would work at physiological pH. Here, it was hoped that the “extra” recognition “power” derived by linking a nucleobase recognition subunit to a saphyrin core would suffice to allow nucleotide transport at or near neutral pH.

In light of the above design considerations, systems **28** and **30** were chosen as initial targets. They were prepared by coupling protected derivatives of 2-aminoethylcytosine and 2-aminoethylcytosine with

activated forms of either a saphyrin carboxylic acid or saphyrin diacid. Following deprotection<sup>[31]</sup> of the resulting intermediates, compounds **27** and **29**, the nucleobase functionalized saphyrins **28** and **30** were obtained in good yield (Scheme 9).

As hoped, the cytosine-bearing carriers **28a** and **30a** exhibited selective transport of guanosine monophosphate through a model membrane at near-neutral pH. Interestingly, in all cases, receptor **28a** displayed a higher selectivity for GMP than its congener **30a** (Table 2). Control experiments were performed using 3, 8, 12, 13, 17, 22-hexaethyl-2, 7, 18, 23-tetramethylsaphyrin (saphyrin).<sup>[32]</sup>

The regioselectivity of carrier **28a** for the phosphate group in isomeric GMPs was also studied (Fig. 5). Here,

Table 2 Initial nucleotide-5'-monophosphate transport rates for the carriers **28a** and **30a**

Carrier	Aq. I (pH)	Aq. II	$k_T$ 5'-GMP ( $10^{-8}$ mol/cm <sup>2</sup> hr)	$k_{5'-GMP}/k_{5'-CMP}$	$k_{5'-GMP}/k_{5'-AMP}$
<b>28a</b>	6.15	H <sub>2</sub> O	1.201	101.7	7.66
<b>28a</b>	6.70	H <sub>2</sub> O	0.287	42.9	8.87
<b>28a</b>	7.05	H <sub>2</sub> O	0.001	20.1	9.49
<b>28a</b>	6.15	10 mM NaOH	1.423	26.3	2.73
<b>28a</b>	6.70	10 mM NaOH	1.228	40.8	4.36
<b>28a</b>	7.05	10 mM NaOH	0.708	43.3	9.60
<b>30a</b>	6.15	H <sub>2</sub> O	0.101	6.2	1.38
<b>30a</b>	7.05	10 mM NaOH	0.115	23.7	3.18
None	7.00	H <sub>2</sub> O	<10 <sup>-5</sup>		
Saphyrin	7.00	H <sub>2</sub> O	<10 <sup>-5</sup>		
Saphyrin	7.00	10 mM NaOH	<10 <sup>-5</sup>		



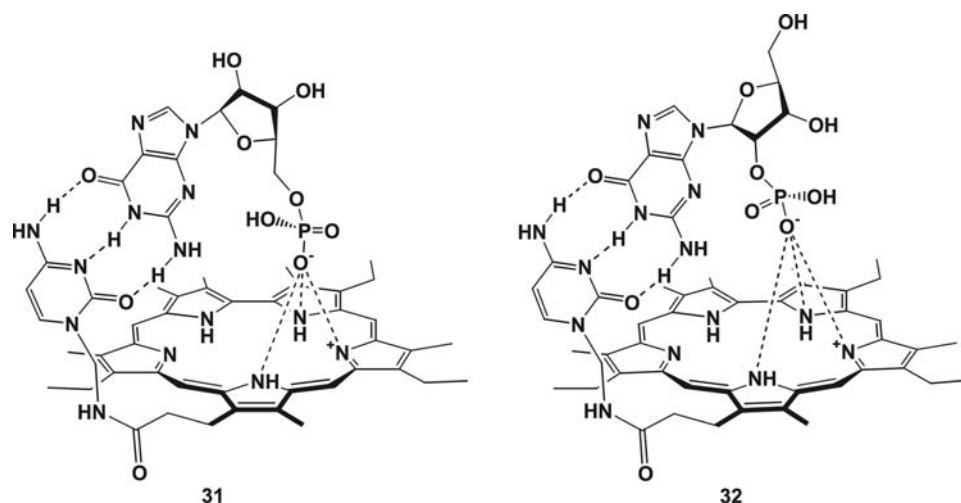


**Fig. 5** Proposed structure for the complex formed between the monoprotonated form of carrier **28a** and monobasic 5'-GMP or 2'-GMP, respectively.

the 2'-isomer of GMP was transported roughly 10 and 6 times faster than its 5'- and 3'-substituted congeners, respectively (Table 3). The association constants,  $K_a$ , of complex **31** and **32** were determined to be  $8 \times 10^3$  and  $2.2 \times 10^4 \text{ M}^{-1}$ , respectively, in methanol as judged from UV-VIS spectroscopic titrations.<sup>[31]</sup>

In the case of the guanine-bearing sapphyrins **28b** and **30b**, transport selectivity for cytosine monophosphate was observed. Compared to **28b**, the relative rates of carrier-induced, through-membrane transport were found to be smaller for the monosubstituted system, **28b**, than for doubly functionalized analogue, **30b** (Table 4).<sup>[31]</sup>

To build on the above success, a new solid phase was prepared. It was produced by attaching a cytosine-substituted sapphyrin containing a carboxylic group to aminopropyl silica gel via an amide bound (Fig. 6). An HPLC column, generated by packing this stationary phase, separated guanosine 5'-mono-, di-, and triphosphate effectively from a mixture of the mono-, di-, and triphosphates of cytidine, uridine,

adenosine, and guanosine under isocratic condition at pH 7. In addition, by using this column, it was found that all nucleotides monophosphate could be separated from one another readily under similar separation conditions.<sup>[33]</sup> Control experiments, affected using a column packed with a nucleoside-free sapphyrin-substituted silica gel,<sup>[28]</sup> allowed for the separation between mono-, di-, and triphosphates. However, no selectivity was observed. In other words, separation between the different mono-, di-, and trinucleotides present was not affected.<sup>[33]</sup>

### NB-Phthalocyanine Derivatives

Although not expanded porphyrins, phthalocyanines represent a different kind of tetrapyrrole and one of the few aromatic chromophores, other than porphyrin and sapphyrin, to be conjugated to a nucleobase. While in principle the rich chemistry of the phthalocyanines would lead one to consider that a variety of

**Table 3** Initial rates of GMP isomer transport for carriers **28a** and **30a**

Carrier	Aq. I. (pH)	Aq. II	$k_T$ 2'-GMP ( $10^{-8} \text{ mol/cm}^2 \text{ hr}$ )	$k_{2\text{'-GMP}}/k_{5\text{'-GMP}}$	$k_{2\text{'-GMP}}/k_{3\text{'-GMP}}$
<b>28a</b>	6.70	H <sub>2</sub> O	0.767	9.70	7.30
<b>28a</b>	6.70	1 mM NaOH	2.989	9.55	5.30
<b>28a</b>	7.00	H <sub>2</sub> O	0.594	11.06	7.82
<b>28a</b>	7.20	H <sub>2</sub> O	0.421	>10 <sup>2</sup>	>10 <sup>2</sup>
<b>28a</b>	7.35	H <sub>2</sub> O	0.352	>10 <sup>2</sup>	>10 <sup>2</sup>
<b>30a</b>	6.70	1 mM NaOH	0.104	3.33	2.67
None	7.00	H <sub>2</sub> O	<10 <sup>-5</sup>		
Sapphyrin	7.00	H <sub>2</sub> O	$2 \times 10^{-5}$		

**Table 4** Initial nucleotide-5'-monophosphate transport rates for the carriers **28b** and **30b**

Carrier	Aq. I (pH)	Aq. II	$k_T$ 5'-CMP ( $10^{-8}$ mol/cm <sup>2</sup> hr)	$k_{5'-CMP}/k_{5'-GMP}$	$k_{5'-GMP}/k_{5'-AMP}$
<b>28b</b>	6.70	H <sub>2</sub> O	0.129	8.96	3.15
<b>28b</b>	6.70	1 mM NaOH	0.541	9.17	3.15
<b>30b</b>	6.70	1 mM NaOH	0.147	17.5	10.5

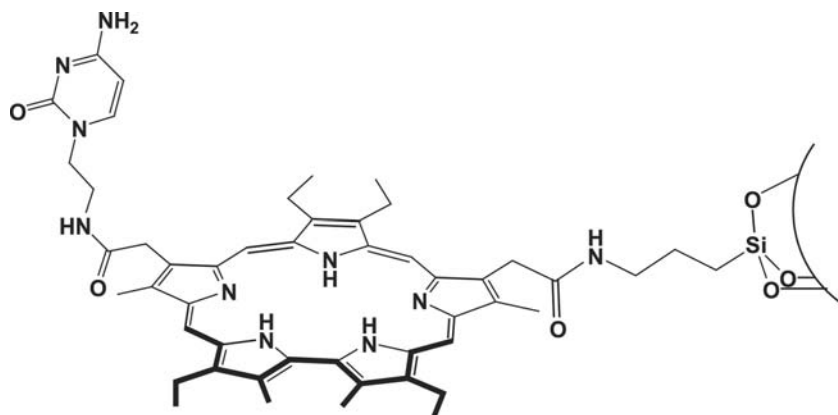
nucleobase-containing conjugates would have been prepared to date, in fact, only the adenine-containing zinc(II) phthalocyanines **33** have so far been reported in the literature. These conjugates were prepared using a procedure analogous to that used to prepare the porphyrin–nucleobase systems **5** and **7**. Specifically, treatment of tetrahydroxyphthalocyanine with an excess of 9-(2-bromoethyl) adenine and K<sub>2</sub>CO<sub>3</sub> gave the adenine–phthalocyanine conjugate **33a**. The unsymmetrical analogues **33b** and **33c** were prepared by using only one equiv. of the appropriate 9-(bromoalkyl)-adenine, followed by the addition of excess 1-bromopentane<sup>[34]</sup> (Scheme 10).

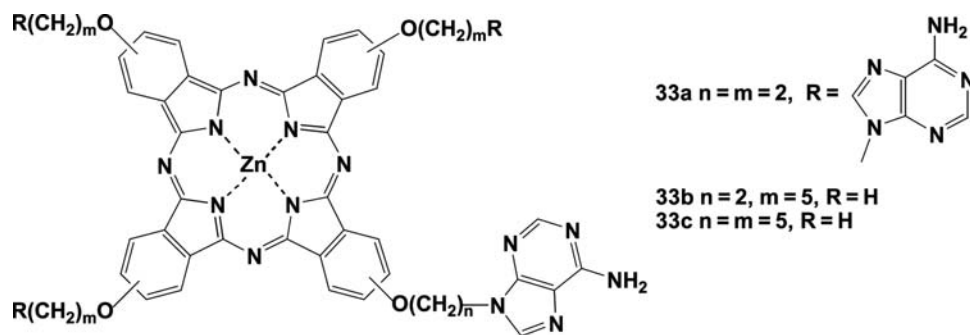
The base-pairing effects of **33a** were studied by carrying out a fluorescence-type spectroscopic titration that consisted of adding a thymine-modified 9,10-anthraquinone and monitoring the resulting decrease in emission intensity. Interestingly, in DMF/THF (9:1), the fluorescence quenching of **33b** and **33c** was modest with the extent of quenching being almost the same as was observed in experiments involving the use of 9,10-anthraquinone as a control.<sup>[34]</sup> While not constituting an absolute proof, such findings argue against the adenine-substituted conjugates **33** being able to interact strongly with species containing their Watson–Crick complement, thymine, and, as a consequence, an inability to form hydrogen bond-tethered self-assembled ensembles. If this conclusion is correct, it underscores the benefit of using cytosine–guanine interactions as supramolecular motifs as originally put forward by Sessler and coworkers.

## NB–Calix[4]pyrrole Derivatives

While traditionally the term “oligopyrrole macrocycles” refers to aromatic systems, such as porphyrin, phthalocyanine, and expanded porphyrins, in recent years increasing attention has been devoted to the development and study of non-conjugated oligopyrrolic macrocycles.<sup>[35–38]</sup> One of the best studied of such systems is calix[4]pyrrole,<sup>[35,36,39]</sup> a non-aromatic tetrapyrrolic product produced by the condensation of pyrrole with acetone. This system, whose synthetic origins can be traced back to Baeyer,<sup>[40]</sup> was “rediscovered” as a neutral anion-binding agent by Gale and coworkers in 1996.<sup>[39]</sup> This rediscovery led, inter alia, to considerations that calix[4]pyrroles could provide the basis for easier-to-make analogues of the sapphyrin-based nucleotide binding and transporting agents described above.<sup>[41]</sup> Toward this end, receptors **34** and **35** were prepared by condensing the corresponding calix[4]pyrrolecarboxylic acid with 2-aminoethylcytosine.<sup>[42]</sup> Again, the question was whether the combination of an anion binding subunit with a nucleobase binding site would allow for selective nucleotide recognition and transport, with the added wrinkle being what would be the effect of using a weaker anion binding site (Scheme 11). (As they are neutral receptors, calix[4]pyrroles show much weaker phosphate anion binding affinities than do the protonated, and correspondingly charged, sapphyrins.<sup>[41]</sup>)

In order to test the efficacy and selectivity of the calix[4]pyrrole-derived systems **34** and **35**, they

**Fig. 6** Cytosine–sapphyrin derivative immobilized on 3-aminopropyl-modified silica.



Scheme 10

were studied as nucleotide carriers, in analogy to what was done with the sapphyrin systems (vide supra), and as the key components in membrane-based ion selective electrodes (ISEs) (see Tables 5–7 and ensuing discussion).

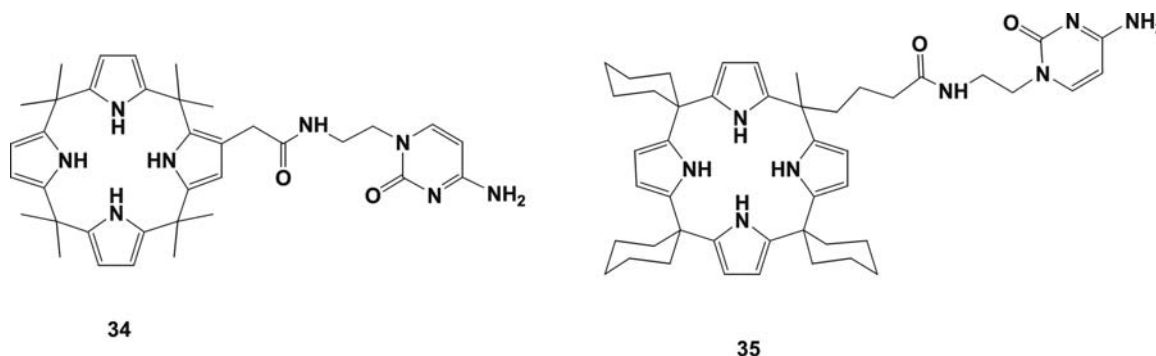
### Ion-Selective Electrode Studies

An important motivation for studying systems **34** and **35** as carrier-based ion-selective electrodes (ISE) is that analysis of such systems provides another means of testing whether a given receptor displays selectivity for a targeted analyte.<sup>[27,43–48]</sup> As true for bulk membrane transport studies (cf. Fig. 4), this method can provide insight into recognition events that take place at an aqueous–organic interface. However, it does not directly monitor binding (and/or release) per se. Rather, what is studied is the change in membrane potential observed on exposure of a liquid/polymer membrane electrode to solutions of various putative analytes. Read-out parameters thus include response (total emf change engendered by a given concentration of analyte), sensitivity (change in emf as a function of analyte concentration), and selectivity, often expressed in relative terms as a selectivity coefficient  $K_{I/J}^{Pot}$  or

selectivity factor  $k_{I/J}^{Psel}$ , where I and J represent the two competing analytes in question, and the linear range over which the response, Nernstian or otherwise, is seen.

The original benchmark for nucleotide sensors was an electrode for 5'-adenosine monophosphate (5'-AMP) that was produced by Papastathopoulos and Rechnitz.<sup>[49]</sup> This electrode consisted of a layer of suspended 5'-adenylic acid deaminase (AMP deaminase) in conjunction with an ammonia gas-sensing membrane electrode. The substrate was selectively deaminated by this enzyme to produce inosine 5'-monophosphate (5'-IMP) and  $NH_3$  in stoichiometric quantities. Monitoring the ammonia thus indirectly measured the 5'-AMP concentration present in the sample.

Because the above method represents an indirect determination, efforts have been devoted in recent years to developing more biomimetic approaches. Complementary base pairing, directed multisite hydrogen bonding interactions, specific ( $\pi$ - $\pi$ ) stacking effects, and generalized electrostatic interactions, individually or in concert, are thought to contribute to the exquisitely sensitive nucleotide recognition observed in the biological systems. Incorporating one or more of these recognition motifs into appropriately designed synthetic receptors could culminate in the



Scheme 11

**Table 5** Results of transport experiments carried out with  $\beta$ -(**34**) and *Meso*-(**35**) cytosine-functionalized calix[4]pyrroles

Carrier	$k_T$ 5'-GMP ( $10^{-11}$ mol/ cm <sup>2</sup> hr)	$k_{5'-GMP}/k_{5'-CMP}$	$k_{5'-GMP}/k_{5'-AMP}$
<b>34</b>	9.8	0.2	1.8
<b>35</b>	93	7.8	1.9

These transport studies were carried out using the set-up shown in Fig. 4 and in analogy to those discussed previously in the case of the sapphyrin-derived systems. The concentration of the carriers in the organic phase was 0.1 mM, the pH of the initial and receiving aqueous phases were 6.0 and 12.5, respectively, and the concentration of tetrabutylammonium perchlorate, added as a charge neutralizing cocarrier to the organic phase, was 0.1 mM.

production of highly specific ISEs more suited for use in various “real world” bioanalytical applications. Whether this goal will be fully realized remains to be seen. However, its pursuit has stimulated the evolutionary development of several elegant nucleotide-targeting ISEs in recent years, including (as will be discussed below) those based on calix[4]pyrrole–nucleobase conjugates.

An electrode derived from a cytosine-pendant triamine was the first ISE system to affect the potentiometric discrimination between guanine and adenine nucleotides by using complementary base-pairing and phosphate–ammonium electrostatic binding interactions within the electrode.<sup>[47]</sup> However, the multiple protonation equilibria that were a consequence of using polyamines as the electrostatic binding motif likely complicated the response mechanism and were also most probably responsible for the non-Nernstian emf slopes observed in these systems (5'-GMP:  $-10$  mV/decade;  $5 \times 10^{-4}$ – $10^{-2}$  M).

Recognizing the design limitations, it was thought that better phosphate recognition motifs would lead to improved sensors. In a previous portion of this review, it was demonstrated how this approach led to successful sapphyrin-based nucleotide carriers (e.g., systems **27a** and **28a**)<sup>[31,32,50]</sup> and, as implied above,

efforts were made to generalize this success by using calix[4]pyrroles as the anion binding cores. Thus because they were of inherent interest in their own right and because they would provide important controls for the newer calix[4]pyrrole-based systems, ISEs containing nucleobase-functionalized sapphyrins were prepared. Specifically, the guanine-bearing sapphyrins (**28b** and **30b**) were incorporated into poly(vinyl chloride) (PVC) membranes plasticized by *o*-nitrophenyl octyl ether (*o*-NPOE), and the potential response as a function of nucleotide concentration was measured using a standard Hg|Hg<sub>2</sub>Cl<sub>2</sub>|3 M KCl||0.1 M HEPES–NaOH, pH 6.6||sample|modified PVC membrane|0.1 M M KCl|AgCl|Ag cell assembly. Similar studies were carried out using the cytosine-substituted calix[4]-pyrrole conjugates **34** and **35**.

### Guanine-substituted sapphyrins

The ditopic receptor **28b** was designed to allow for specific cytosine-base recognition as well as for more general phosphate binding recognition. Its bis-(guanine)-bearing analogue, sapphyrin **30b**, a potential tritopic receptor, was thought to allow for the formation of complex-derived “triple helix” such as G–C–G motifs, wherein the bound nucleobase C-subunit would be the beneficiary of two kinds of hydrogen bonding interactions, involving both Watson–Crick and Hoogsteen recognition patterns.

At pH 6.6, sapphyrin exists as a monoprotonated, singly charged entity, whereas nucleotide monophosphates are largely dianionic. The sensitivity expected for experimental electrodes at neutral pH should thus be equal to  $-29$  mV/decade (theoretical Nernstian value for a divalent anion). The results obtained with systems **28b** and **30b** (Table 6) revealed that the doubly functionalized guanine derivative, **30b**, provided a more effective electrode system than its mono-substituted analogue. It should be noted that the sensitivity of the PVC-membranes derived from the bisguanine receptor **30b** was dependent on the time

**Table 6** Potentiometric characteristics of PVC membranes based on mono-(**28b**) and bisguanine-substituted (**30b**) sapphyrins toward nucleotides

Nucleotide	<b>28b</b>		<b>30b<sup>a</sup></b>		<b>30b<sup>b</sup></b>	
	Sensitivity (mV/decade)	Linear range (M)	Sensitivity (mV/decade)	Linear range (M)	Sensitivity (mV/decade)	Linear range (M)
5'-AMP	–32	$10^{-6}$ – $10^{-5}$	–42	$10^{-6}$ – $10^{-5}$	–30	$10^{-6}$ – $10^{-5}$
5'-CMP	–17	$10^{-5}$ – $10^{-4}$	–59	$10^{-6}$ – $10^{-4}$	–20	$10^{-6}$ – $10^{-3}$
5'-GMP	c	c	–25	$10^{-5}$ – $10^{-3}$	–58	$10^{-6}$ – $10^{-4}$

<sup>a,b</sup>The results were obtained with PVC-membranes derived from **30b** soaked in solutions of the primary analytes for 20 min (for a) and overnight (for b), respectively.

<sup>c</sup>No response.

of contact between the membrane and the nucleotide (analyte) solution, as well as the nature of the measured nucleotide (Table 6).

### Cytosine-substituted calix[4]pyrroles

In predicative work involving unfunctionalized calix[4]pyrroles,<sup>[45]</sup> it was demonstrated that simple, substituent-free calix[4]pyrroles display potentiometric selectivity to a range of anionic analytes, including phosphates, when incorporated into PVC-(*o*-NPOE) membranes and tested as ISEs. The question then became whether appending a cytosine “tail” onto the calixpyrrole skeleton would lead to the generation of nucleotide-specific ISEs and, to the extent this proved true, whether or not the choice of linkage (*meso*- vs.  $\beta$ -pyrrolic) would effect the response selectivity.<sup>[42]</sup>

Before analyzing the “tailed” systems **34** and **35**, their unfunctionalized analogues, i.e., octamethyl and cyclohexyl-substituted systems, were tested as ISE sensor elements. In neither case was evidence of pH-dependent behavior seen, at least at or near neutral pH. On the other hand, an inherent selectivity for 5'-AMP < 5'-GMP  $\approx$  5'-CMP < 5'-UMP  $\approx$  5'-TMP was observed at pH 6.6 (a value chosen to ensure a significant concentration of the dianionic forms of the nucleotides under investigation) for both systems, as judged from the extent of the anionic (negative) potentiometric response. By contrast, a slight selectivity for 5'-GMP and 5'-CMP was seen in the case of “control” electrodes made up from the hydrophobic cation, tridodecylmethylammonium chloride (TDDMACl); here, 5'-AMP (0.00) < 5'-UMP (0.07) < 5'-CMP (0.24) < 5'-GMP (0.76), where the values in parentheses refer to the selectivity coefficients ( $\log K_{5'-AMP/5-XMP}^{pot}$ ).

Taken together, these findings are consistent with the conclusion that unfunctionalized calixpyrroles mediate their observed ISE response for nucleotides by acting more as specific, nucleobase-dependent molecular recognition elements than as pure anion extractants, as is known to be true for membranes made up from TDDMACl. Support for this conclusion comes from the observation that a greater response is observed in the case of the more hydrophobic cyclohexyl-substituted system than in the octamethyl

system and that the selectivity pattern correlates with the number of accessible hydrogen bond acceptor elements (i.e., carbonyl groups) present in the nucleobase portion of the mononucleotides being studied [i.e., 5'-UMP  $\approx$  5'-TMP (two carbonyls) > 5'-GMP  $\approx$  5'-CMP (one carbonyl) > 5'-AMP (no carbonyls)]. This latter observation also rules out a response process that is dominated by direct phosphate-calixpyrrole “anion chelation”; rather, it supports the conclusion that, under the interfacial conditions of the ISE experiment, the strength and specificity of the nucleobase-calix[4]pyrrole NH interactions dominate the selectivity, even if it is the presence of the negatively charged phosphate groups that leads to the actual observation of an anionic potentiometric response.

Transport experiment demonstrated that the *meso*-substituted cytosine calix[4]pyrrole conjugate, but not its  $\beta$ -pyrrole linked congener, is capable of acting as a ditopic receptor, binding concurrently both the phosphate anion and nucleobase portions of 5'-GMP to the calixpyrrole core and cytosine “tails” of the molecule, respectively. These findings were rationalized in terms only the former is capable of binding concurrently both the phosphate and nucleobase portions and provided a backdrop against which the corresponding ISE studies could be considered. In particular, the availability of two cytosine-substituted calix[4]pyrroles, bearing the appended cytosine on either a  $\beta$ -pyrrolic (**34**) or *meso* (**35**) position, respectively, would allow the potential importance that ditopic binding interactions might play in terms of regulating a selective electrode response.

In the case of the transport studies, it proved necessary to add tetrabutylammonium perchlorate to neutralize the negative charge present in the calix[4]pyrrole-nucleotide complex that arises as a result of binding a phosphate-containing entity within a neutral receptor (cf. Table 5 and Ref.<sup>[42]</sup>). Thus a lipophilic electrically charged additive, such as TDDMACl, was also employed in the case of the PVC membranes derived from **33** and **35**. Addition of this additive served to highlight the effects of base-pairing, which proved more discernable in the case of **35** than **34**. Specifically, adding 50 mol% TDDMACl to the PVC membranes containing these two potentially

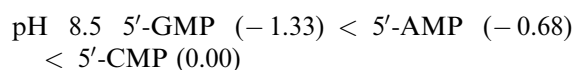
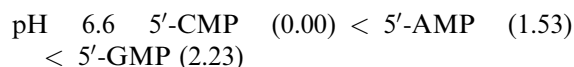
**Table 7** Effect of pH on the potentiometric selectivity of PVC membranes based on  $\beta$ - and *meso*-substituted cytosine-functionalized calix[4]pyrroles **34** ( $\log k_{5'-UMP/5-XMP}^{sel}$ ) and **35** ( $\log k_{5'-UMP/5-XMP}^{sel}$ ). These membranes additionally contained 50 mol% TDDMACl

pH	<b>34</b>			<b>35</b>		
	5'-AMP	5'-CMP	5'-GMP	5'-AMP	5'-CMP	5'-GMP
6.6	-0.07	+0.97	+0.89	+1.53	0.00	+2.23
8.5	-0.20	+0.58	+0.10	-0.68	0.00	-1.23



ditopic receptors resulted in selectivity sequences that approximated those seen in the transport experiments (Table 7; pH 6.6). Unfortunately, the inherent selectivity for 5'-GMP seen in membranes containing just TDDMACI (vide supra) complicates analysis. Thus it is not possible at present to quantify in energetic terms the specific effect of the proposed cytosine-guanosine Watson-Crick binding interactions on the experimentally determined for-analyte selectivities. Nonetheless, there is little doubt that the effect is real, and in ISEs based on suitably designed receptors, can be quite substantial.

Model membrane transport studies provide a useful potential complement to ISE studies in terms of analyzing the specificity and mode of action of a particular receptor. The fact that the transport selectivity may be influenced strongly by the rate of receptor-substrate complex formation and dissociation, and hence the pH of both aqueous phases, made it important to compare the potentiometric selectivity of the PVC-membrane electrodes based on **34** and **35** when the contacting aqueous phase was held at pH 6.6 and at 8.5. The chosen pH should approximate the conditions of potentiometric measurement to transport model when the monitored nucleotides "enter in" and "release from" bulk membrane interface. As can be seen from Table 7, the selectivity sequence for the *meso*-linked conjugate **35** is more influenced by pH than its  $\beta$ -linked congener **34**. In fact, the potentiometric selectivity of the *meso*-substituted receptor, **35**, could be reversed by changing the pH from 6.6 to 8.5, as is evident upon inspection of the following sequences:



The sensitivity to pH is as would be expected for a system where ditopic interactions are thought to be playing an important role. For instance, under conditions of high pH, where the nucleotide species would exist as a dianion, rather than a monoanion, and the nucleobase itself could bear negative charge, the ancillary benefit that would accrue from the proposed Watson-Crick base pairing interactions would be reduced if not altogether eliminated. On the other hand, the potentiometric data at high pH could help explain the relative lack of for-GMP selectivity observed in the case of the transport experiments involving receptor **34**, where the receiving phase is also held at high pH; what is observed might simply reflect the inherent preference for cytosine binding that apparently pertains at high pH. To the extent this conclusion is correct, it underscores the benefit that

can come from studying nucleobase-oligopyrrole conjugates under two rather different kinds of experimental conditions and via the use of two very different techniques. It is thus hoped that such comparisons will be carried out with other systems in the near future.

## CONCLUSION

Nucleobase-macrocylic oligopyrrole conjugates represent a new class of potential ditopic receptor. With the ability to bind the Watson-Crick complementary nucleoside or nucleotide via specific hydrogen bonding interactions and elicit some key, useful functional feature through the appended oligopyrrole, a range of chemical processes become possible that are without precedent in the case of simple, single-motif systems. These include the ability to affect selective recognition of appropriate oligonucleotide fragments, facilitate long-range energy- and electron-transfer processes, affect the specific transport and electrochemical sensing of individual nucleotides. Improvements in synthetic methodologies, coupled with an ever-increasing lexicon of available oligopyrrolic macrocycles, lead to the prediction that many new nucleobase-oligopyrrole conjugates will be constructed in the near future and that these systems will demonstrate utilities that range well beyond those that have already been described.

## ACKNOWLEDGMENTS

Financial support from the National Institutes of Health (GM 58907 to J.L.S.), financial support from the Ministry of Education of the Czech Republic Grant No. MSM 223400008, the Grant EU QLRT-2000-02360, and Grant Agency of the Czech Republic Nos. 301/98/K042, 203/03/0716, 203/02/0420, and 309/02/1193 are gratefully acknowledged.

## REFERENCES

1. Kus, P.; Knerr, G.; Czuchajowski, L. First representatives of porphyrinynucleosides. *Tetrahedron Lett.* **1990**, *31* (36), 5133-5134.
2. Czuchajowski, L.; Habdas, J.; Niedbala, H.; Wandrekar, V. Synthesis of porphyrinyl-nucleosides. *J. Heterocycl. Chem.* **1992**, *29* (2), 479-486.
3. Lipscomb, L.A.; Zhou, F.X.; Presnell, S.R.; Woo, R.J.; Peek, M.E.; Plaskon, R.R.; Williams, L.D. Structure of a DNA-porphyrin complex. *Biochemistry* **1996**, *35* (9), 2818-2823.



4. Maldoti, A.; Andreotti, L.; Molinari, A.; Borisov, S.; Vasilev, V. Photoinitiated catalysis in Nafion membranes containing palladium(II) *meso*-tetrakis-(*N*-methyl-4-pyridyl)porphyrin and iron(III) *meso*-tetrakis(2,6-dichlorophenyl)porphyrin for O<sub>2</sub>-mediated oxidations of alkenes. *Chem. Eur. J.* **2001**, *7* (16), 3564–3571.
5. Czuchajowski, L.; Habdas, J.; Niedbala, H.; Wandrekar, V. Porphyrinyl–uridines as the first water soluble porphyrinyl–nucleosides. *Tetrahedron Lett.* **1991**, *32* (51), 7511–7512.
6. Czuchajowski, L.; Niedbala, H. Synthesis and tumoricidal activity of water soluble porphyrinyl–thymidines and related porphyrins. *Bioorg. Med. Chem. Lett.* **1992**, *2* (12), 1645–1648.
7. Czuchajowski, L.; Palka, A.; Morra, M.; Wandrekar, V. Porphyrinyl–nucleosides containing fluorinated nucleobases. *Tetrahedron Lett.* **1993**, *34* (34), 5409–5412.
8. Malinowski, V.; Tumir, L.; Piantanida, I.; Zinic, M.; Schneider, H.-J. New porphyrin–nucleobase hybrid compounds and their interaction with nucleosides and nucleic acids. *Eur. J. Org. Chem.* **2002**, (22), 3785–3795.
9. Masiero, S.; Gottarelli, G.; Pieraccini, S. G-quartets as a self-assembled scaffold for circular porphyrin arrays. *Chem. Commun.* **2000**, (20), 1995–1996.
10. Li, H.; Czuchajowski, L. Compounds based on *meso*-tri(4-pyridyl)-*p*-acrylamidophenylporphyrin able to interact with DNA. *J. Heterocycl. Chem.* **1997**, *34* (3), 999–1003.
11. Goh, G.K.-M.; Czuchajowski, L. The synthesis of isomeric dithymidyl-phosphorus(V)-*meso*-tetraphenylporphyrins. *J. Porphyr. Phthalocyanines* **1997**, *1* (3), 281–285.
12. Cornia, M.; Binacchi, S.; Del Soldato, T.; Zanardi, F.; Casiraghi, G. Synthesis of novel porphyrin–uridine carbon–carbon conjugates. *J. Org. Chem.* **1995**, *60* (16), 4964–4965.
13. Hisatome, M.; Maruyama, N.; Ikeda, K.; Furutera, T.; Ishikawa, T.; Yamakawa, K. Synthesis and some spectroscopic properties of porphyrin derivatives connected with nucleobases (adenine, thymine, guanine and cytosine) by alkanamide chains. *Chem. Pharm. Bull.* **1996**, *44* (10), 1801–1811.
14. Hisatome, M.; Maruyama, N.; Furutera, T.; Ishikawa, T.; Yamakawa, K. Porphyrine coupled with nucleoside bases. Synthesis and characterization of adenine- and thymine-porphyrin derivatives. *Chem. Lett.* **1990**, (12), 2251–2254.
15. Li, H.; Czuchajowski, L. Synthesis and biomedical application of porphyrinyl nucleosides, nucleotides and oligonucleotides. *Trends Heterocycl. Chem.* **1999**, *6*, 57–77.
16. Seliger, H.; Knoller, H.; Ruck, A.; Heckelsmiller, K.; Steiner, R. Antisense oligonucleotide conjugates with photosensitizers—An update. *Nucleosides Nucleotides* **1998**, *17* (9–11), 2053–2061.
17. Harriman, A.; Magda, D.J.; Sessler, J.L. Photon antennae assembled by nucleic acid base pairing. *J. Phys. Chem.* **1991**, *95* (4), 1530–1532.
18. Harriman, A.; Kubo, Y.; Sessler, J.L. Molecular recognition via base pairing: Photoinduced electron transfer in hydrogen-bonded zinc porphyrin–benzoquinone conjugates. *J. Am. Chem. Soc.* **1992**, *114* (1), 388–390.
19. Sessler, J.L.; Wang, B.; Harriman, A. Long-range photoinduced electron transfer in an associated but noncovalently linked photosynthetic model system. *J. Am. Chem. Soc.* **1993**, *115* (22), 10418–10419.
20. Sessler, J.L.; Wang, B.; Harriman, A. Photoinduced energy transfer in associated but noncovalently linked photosynthetic model systems. *J. Am. Chem. Soc.* **1995**, *117* (2), 704–714.
21. Harriman, A.; Magda, D.J.; Sessler, J.L. Energy transfer across a hydrogen-bonded, cytosine-derived, zinc-free-base porphyrin conjugate. *J. Chem. Soc., Chem. Commun.* **1991**, (5), 345–347.
22. Chang, C.K.; Abdalmuhdi, I. Anthracene pillared cofacial diporphyrin. *J. Org. Chem.* **1983**, *48* (26), 5388–5390.
23. Sessler, J.L.; Davis, J.M. Sapphyrins: Versatile anion binding agents. *Acc. Chem. Res.* **2001**, *34* (12), 989–997.
24. Sessler, J.L.; Cyr, M.J.; Furuta, H.; Král, V.; Mody, T.; Morishima, T.; Shionoya, M.; Weghorn, S. Anion binding: A new direction in porphyrin-related research. *Pure Appl. Chem.* **1993**, *65* (3), 393–398.
25. Král, V.; Furuta, H.; Shreder, K.; Lynch, V.; Sessler, J.L. Protonated sapphyrins. Highly effective phosphate receptors. *J. Am. Chem. Soc.* **1996**, *118* (7), 1595–1607.
26. Záruba, K.; Tománková, Z.; Sýkora, D.; Charvátová, J.; Kavenová, I.; Bouř, P.; Matějka, P.; Volka, K.; Král, V. Interaction of porphyrin and sapphyrin macrocycles with nucleobases and nucleosides. Spectroscopic, quantum chemical and chromatographic investigation. *Anal. Chim. Acta* **2001**, *437*, 39–53.
27. Tohda, K.; Naganawa, R.; Lin, X.M.; Tange, M.; Umezawa, K.; Odashima, K.; Umezawa, Y.; Furuta, H.; Sessler, J.L. Liquid membrane electrodes for nucleotides based on sapphyrin, cytosine-pendant triamine and neutral cytosine derivative as sensory elements. *Sens. Actuators, B* **1993**, *14* (1-3), 669–672.
28. Iverson, B.L.; Thomas, R.E.; Král, V.; Sessler, J.L. Molecular recognition of anionic species by silica gel bound sapphyrin. *J. Am. Chem. Soc.* **1994**, *116* (6), 2663–2664.
29. Iverson, B.L.; Shreder, K.; Král, V.; Sansom, P.; Lynch, V.; Sessler, J.L. Interaction of sapphyrin with phosphorylated species of biological interest. *J. Am. Chem. Soc.* **1996**, *118* (7), 1608–1616.
30. Furuta, H.; Cyr, M.J.; Sessler, J.L. Phosphate anion binding: Enhanced transport of nucleotide monophosphates using a sapphyrin carrier. *J. Am. Chem. Soc.* **1991**, *113* (17), 6677–6678.
31. Král, V.; Sessler, J.L. Molecular recognition via base-pairing and phosphate chelation. Ditopic and tritopic sapphyrin-based receptors for the recognition and transport of nucleotide monophosphates. *Tetrahedron* **1995**, *51* (2), 539–554.
32. Král, V.; Sessler, J.L.; Furuta, H. Synthetic sapphyrin–cytosine conjugates: Carriers for selective nucleotide transport at neutral pH. *J. Am. Chem. Soc.* **1992**, *114* (22), 8704–8705.
33. Sessler, J.L.; Genge, J.W.; Král, V.; Iverson, B.L. Separation of mono-, di- and triphosphate nucleotides

- by cytosine substituted, silica-bound sapphyrin solid supports. *Supramol. Chem.* **1996**, *8*, 45–52.
34. Li, X.; Ng, D.K.P. Synthesis and spectroscopic properties of the first phthalocyanine-nucleobase conjugates. *Tetrahedron Lett.* **2001**, *42* (2), 305–309.
  35. Gale, P.A.; Sessler, J.L.; Král, V. Calixpyrroles. *Chem. Commun.* **1998**, 1–8.
  36. Gale, P.A.; Anzenbacher, P., Jr.; Sessler, J.L. Calixpyrroles II. *Coord. Chem. Rev.* **2001**, *222* (1), 57–102.
  37. Sessler, J.L.; Zimmerman, R.S.; Bucher, C.; Král, V.; Andrioletti, B. Calixphyrins. Hybrid macrocycles at the structural crossroads between porphyrins and calixpyrroles. *Pure Appl. Chem.* **2001**, *73* (7), 1041–1057.
  38. Sessler, J.L.; Maeda, H.; Mizuno, T.; Lynch, V.; Furuta, H. Quinoxaline-bridged porphyrinoids. *J. Am. Chem. Soc.* **2002**, *124* (45), 13474–13479.
  39. Gale, P.A.; Sessler, J.L.; Král, V.; Lynch, V. Calix[4]pyrroles: Old yet new anion-binding agents. *J. Am. Chem. Soc.* **1996**, *118* (21), 5140–5141.
  40. Baeyer, A. Über ein condensationsproduct von pyrrol mit aceton. *Ber. Dtsch. Chem. Ges.* **1886**, *19*, 2184–2185.
  41. Allen, W.E.; Sessler, J.L. Anion carriers: New tools for crossing membranes. *ChemTech* **1999**, *29* (9), 16–24.
  42. Sessler, J.L.; Král, V.; Shishkanova, T.V.; Gale, P.A. Cytosine substituted calix[4]pyrroles: Neutral receptors for 5'-guanosine monophosphate. *Proc. Natl. Acad. Sci. U. S. A.* **2002**, *99* (8), 4848–4853.
  43. Amemiya, S.; Buehlmann, P.; Tohda, K.; Umezawa, K. Hydrogen bond based recognition of nucleotides by neutral-carrier ion-selective electrodes. *Anal. Chim. Acta* **1997**, *341* (2–3), 129–139.
  44. Buehlmann, P.; Amemiya, S.; Nishizawa, S.; Xiao, K.P.; Umezawa, Y. Hydrogen-bonding ionophores for inorganic anions and nucleotides and their application in chemical sensors. *J. Incl. Phenom. Mol. Recognit. Chem.* **1998**, *32* (2–3), 151–163.
  45. Král, V.; Sessler, J.L.; Shishkanova, T.V.; Gale, P.A.; Volf, R. Molecular recognition at an organic-aqueous interface: Heterocalixarenes as anion binding agents in liquid polymeric membrane ion-selective electrodes. *J. Am. Chem. Soc.* **1999**, *121* (38), 8771–8775.
  46. Odashima, K.; Naganawa, R.; Radecka, H.; Kataoka, M.; Kimura, E.; Koike, T.; Tohda, K.; Tange, M.; Furuta, H.; Sessler, J.L.; Yagi, K.; Umezawa, Y. Chemical sensing based on membrane potential change induced by host-guest complexation at a membrane surface. *Supramol. Chem.* **1994**, *4*, 101–113.
  47. Tohda, K.; Tange, M.; Odashima, K.; Umezawa, K.; Furuta, H.; Sessler, J.L. Liquid membrane electrode for guanosine nucleotides using a cytosine-pendant triamine host as the sensory element. *Anal. Chem.* **1992**, *64* (8), 960–964.
  48. Umezawa, Y.; Kataoka, M.; Takami, W.; Kimura, E.; Koike, T.; Nada, H. Potentiometric adenosine triphosphate polyanion sensor using a lipophilic macrocyclic polyamine liquid membrane. *Anal. Chem.* **1988**, *60* (21), 2392–2396.
  49. Papastathopoulos, D.S.; Rechnitz, G.A. Highly selective enzyme electrode for 5-adenosine monophosphate. *Anal. Chem.* **1976**, *48* (6), 862–864.
  50. Sessler, J.L.; Furuta, H.; Král, V. Phosphate anion chelation and base-pairing. Design of receptors and carriers for nucleotides and nucleotide analogues. *Supramol. Chem.* **1993**, *1* (3–4), 209–220.

# Oil-Filled Nanocapsules

Royale S. Underhill

Emerging Materials Section, Defence Research and Development Canada–Atlantic,  
Dartmouth, Nova Scotia, Canada

## INTRODUCTION

Feynman<sup>[1]</sup> was correct when he predicted “There’s Plenty of Room at the Bottom.” Since Feynman’s talk, given at Caltech in 1959, there has been an explosion of research in the ever-shrinking areas of nanoscience. A nanometer (nano—Greek for *dwarf*) is one billionth of a meter, or ten times the size of an individual hydrogen atom. Since the mid-1980s, there has been a substantial increase in interest over the creation and use of nanocapsules,<sup>[2]</sup> a subset of nanoparticles. Nanocapsules have a number of potential applications, some of which include dye dispersants, nanoreaction vessels, and encapsulation media for fragrances, flavors, or drugs. This entry will discuss the specific case of oil-filled nanocapsules. Such structures readily encapsulate lipophilic/hydrophobic and oil-soluble compounds, allowing them to be dispersed and transported through aqueous media.

## DEFINING OIL-FILLED NANOCAPSULES

Nanoparticles have their largest dimension in the 1–200 nm range. Nanoparticles can be made of a wide range of materials: inorganic, organic, and biological. Nanoparticles are of interest in materials science for a number of reasons. Because chemical characteristics such as optical, magnetic, electrical, adsorptive, and catalytic are size-dependent, a nanoparticle may exhibit useful properties not seen in the larger bulk sample.<sup>[3]</sup> The surface area-to-volume ratio can be very high, which can increase the performance of catalysts.<sup>[3]</sup> For these reasons, material scientists are investigating a wide number of nanostructures, hoping to find new applications. One possible application is the encapsulation of guest moieties, which would be possible with hollow or filled nanoparticles. Nanocapsules are superior to nanospheres and other nanoparticles for these applications because of their high loading capacity.

The general definition of a nanocapsule is a spherical, hollow structure with a diameter less than 200 nm. The cavity can be empty or filled with a solvent, either polar or non-polar (Fig. 1). Nanocapsules can be distinguished from other nanoparticles because they have a well-defined core and shell, whereas the latter

do not. Although this definition includes coated nanoparticles, the term *nanocapsule* as referred to here is a submicrometer colloidal particle with a cavity surrounded by a shell. When made from polymers, nanocapsules have also been referred to as “hollow polymer nanostructures,” “polymer/oil composite particles”,<sup>[4]</sup> and “colloidosomes.”<sup>[5,6]</sup> Nanocapsules have been made for many years, following the example of nature, using phospholipids, which are amphiphilic. Phospholipids will self-assemble in aqueous environments to form vesicles, which have a water core and a bilayer of the phospholipid forming the shell. This is the basis of cells. In a similar manner, a single layer of phospholipid can stabilize oil droplets, resulting in liposomes (Fig. 2).

Micro-Pak, Inc. has produced lipid vesicles that can be tailored to have either aqueous or oil-filled central cavities.<sup>[7]</sup> This central cavity can be filled wholly or in part with oil such that it can be used to encapsulate hydrophobic molecules.<sup>[7]</sup> The core of these vesicles is large and unstructured, which makes it ideal as a transport vehicle. Phospholipid vesicles have two major drawbacks.<sup>[7]</sup> First, phospholipids can be degraded by a number of enzymes, thus causing problems in biomedical applications. Second, the most common phospholipids contain polyunsaturated acyl chains, which are prone to peroxidation, resulting in a fracture of the vesicle. Liposomes are generally unstable.<sup>[8]</sup> Although similar to liposomes, polymeric capsules are held together through covalent bonding in the shell, making them more robust. Thus polymeric oil-filled nanocapsules are just robust, man-made mimics of naturally occurring liposomes.

The remainder of this review is divided into three major sections. The first deals with the characterization techniques used when making nanocapsules. The second deals with research published to date, and the third briefly describes some of the possible applications for oil-filled nanocapsules.

## CHARACTERIZATION TECHNIQUES

Because of the small size and often complex formulations, a detailed characterization of nanocapsules is difficult. Some of the techniques used include quasi-elastic light scattering [QELS; also known as photon correlation

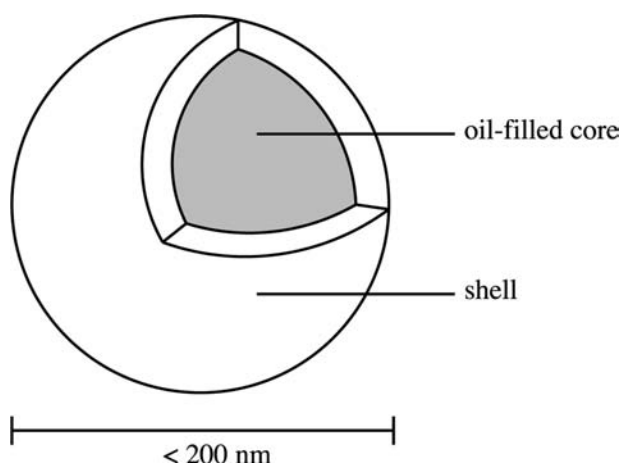


Fig. 1 Schematic of an oil-filled nanocapsule.

spectroscopy (PCS)], gel permeation chromatography (GPC), transmission electron microscopy (TEM), scanning force microscopy (SFM), and scanning electron microscopy (SEM). To date, none of these techniques has provided a clear picture of the nanocapsule shell.<sup>[9]</sup> It remains unknown as to whether the shell is a continuous or a porous network. The synthetic route used to attain the nanocapsules may also affect the nature of the shell. The characteristics of interest are morphology, size and size distribution, density, and zeta potential.

### Morphology

Morphology refers to the structural shape of the nanocapsule. This can be determined using a number of microscopy techniques. The most commonly used is TEM, with either positive staining using a heavy atom such as osmium, or negative staining where the medium surrounding the nanocapsule is stained (typically with phosphotungstate or uranyl acetate). Another technique, which has proven effective, is freeze-fracture TEM, where the polymer shell, inner core, and wall thickness are all observed. Quintanar-Guerrero et al.<sup>[10]</sup> have already used SFM for oil-filled nanocapsules. Cryoelectron microscopy and SFM have

a promising future for determining nanocapsule morphology and surface properties.<sup>[9]</sup> Scanning electron microscopy has also shown some applicability for examining the morphology of nanocapsules. It is limited by its magnification ability, but when combined with x-ray analysis, it is a powerful tool to identify nanocapsules with specific atoms. For example, it would be possible to characterize nanocapsules incorporating the iodine-containing oil, Lipiodol<sup>®</sup>.<sup>[9]</sup>

### Size and Size Distribution

For many applications, nanocapsules of specific, uniform size are desirable. Microscopy techniques are capable of giving information about size and size distribution, but have some limitations. First, the typical sample size in microscopy is very small, thus one has to make the assumption that it is representative of the whole. Second, the sample is usually dried, which may adversely affect the morphology. To obtain data on the whole population, QELS or PCS is typically used. Nanoparticles dispersed in a fluid are in constant Brownian motion. The speed of the particles is inversely proportional to their size. Photon correlation spectroscopy analyzes the frequency of shifts in the light intensity that results from the particles moving into and out of the lightpath. Time dependence provides the information needed to determine the diffusion coefficient of the nanocapsules in solutions. Once the diffusion coefficient ( $\langle D \rangle_z$ ) is determined, it can be related to the hydrodynamic radius ( $R_h$ ) of the nanocapsule using the Stokes–Einstein law:

$$R_h = \frac{kT}{6\pi\eta\langle D \rangle_z} \quad (1)$$

where  $\eta$  is viscosity and  $kT$  is the Boltzmann coefficient multiplied by temperature. The distribution of the frequency shifts in light intensity also provides the size distribution of the sample.

It is important to note that the size determined in this method is  $R_h$ , which includes a sphere of solvation

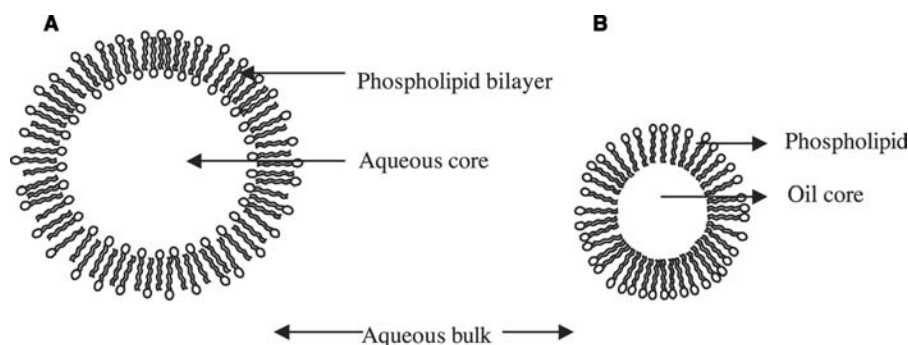


Fig. 2 Two-dimensional schematic of a 3-D phospholipid vesicle (A) and a liposome (B). The phospholipids shown actually form a shell around a 3-D sphere in each case.

around the nanocapsule. As a result, the size may appear larger than that observed in microscopy images.

Gel permeation chromatography can be performed to determine the molecular weight and polydispersity of the prepolymer.

## Density

Chouinard, Buczkowski, and Lenaerts<sup>[11]</sup> showed that nanocapsule density could be determined by isopycnic centrifugation. This technique can be performed using either a classical or analytical centrifuge. Isopycno-graphy (or equilibrium density gradient centrifugation) is a separation technique based on the differing intrinsic densities of the particles. The nanocapsules migrate through the centrifuge tube until they reach a point where they are surrounded by a solvent of equivalent density. The solvent used for nanocapsule analysis is Percoll<sup>®</sup>. The particle density can be backcalculated by comparing with a calibration curve obtained from density-calibrated particles, by collecting the zone of the gradient in which the particles accumulated, and by measuring its density.<sup>[11]</sup>

Comparing densities is a good method to determine whether the nanoparticles observed by microscopy are solid nanospheres, hollow nanocapsules, or oil-filled nanocapsules. The density of nanocapsules tends to be intermediate between that of the polymer matrix and the oil.<sup>[9]</sup> Solid nanospheres have a density equal to that of the polymer matrix. By comparing the density achieved via isopycno-graphy with the densities of the starting materials, one can determine whether nanospheres or nanocapsules are present.<sup>[11]</sup> The density can also be used to yield the nanocapsule oil/polymer composition:<sup>[9]</sup>

$$1/\rho_{\text{NC}} = X_{\text{poly}}(1/\rho_{\text{poly}}) + X_{\text{oil}}(1/\rho_{\text{oil}}) \quad (2)$$

$$X_{\text{poly}} + X_{\text{oil}} = 1 \quad (3)$$

where  $X_{\text{poly}}$  and  $X_{\text{oil}}$  are the mass fractions of the polymer and oil in the nanocapsules, respectively, and represent unknowns.  $\rho_{\text{NC}}$ ,  $\rho_{\text{poly}}$ , and  $\rho_{\text{oil}}$  are the densities of the nanocapsules, polymers, and oils, respectively.

## Zeta Potential

Zeta potential is a surface characterization technique that can be used to investigate whether a guest molecule is truly encapsulated or simply adsorbed onto the surface of a nanocapsule.<sup>[9]</sup>

Particles, when dispersed in water, have a charge because of surface-solvent interactions. For example, silica particles lose a surface proton from silanol

(Si-OH) groups to the aqueous solvent. The charged particle surface attracts a layer of counterions from the bulk solvent, leading to a double layer, whose thickness is dependent on the surface charge density. A large charge stops particles from getting close to each other because of electrostatic repulsion. Conversely, a small surface charge results in a smaller double layer, leading to flocculation.

Zeta potential is a measure (in millivolts) of the energy needed to shear the particle and its inner layer of counterions away from the bulk solvent. The higher the zeta potential is, the larger is the double layer and the more stable the nanocapsule is in the solution. Changes in zeta potential can indicate the adsorption of moieties to the surface of the nanoparticle, which have affected its double layer.

## SYNTHETIC ROUTES

Two main techniques are used to synthesize nanocapsules: the first is interfacial polymerization around a droplet, and the second is deposition of a preformed polymer at the interface of a droplet. Both techniques utilize self-assembly.

### Interfacial Polymerization

In this method, either a monomer or an amphiphilic polymer with a cross-linkable group is used and polymerization is induced at the surface of an oil droplet. This technique requires a system that can polymerize on a faster time scale than the fluctuation in the droplet geometry. The advantage of this technique is that the polymeric shell is formed *in situ*, allowing it to follow the contours of the droplet.<sup>[9]</sup> The drawback is that the cross-linking or polymerization reaction may have side reactions with other species present in the system. For example, if the nanocapsule is being used to encapsulate a drug, the monomer or cross-linkable group may have reactivity toward the drug. At the least, this would result in a reduced availability of the drug and, at its worst, this could result in toxic by-products.

Thurmond, Kowalewski, and Wooley<sup>[12]</sup> of the Washington University, St. Louis have prepared nanocapsules containing a hydrophilic shell and hydrophobic core properties. Thurmond et al. rely on self-assembly to form micelles, which are then stabilized through covalent bonding of the outer shell (Fig. 3). The result is a surface cross-linked "Knedel" (SCK).<sup>[12]</sup> The shell cross-linking provides two functions; first, it stabilizes the micelles; second, it offers the ability to control the permeability of the shell.<sup>[13]</sup> Thurmond et al.'s work was one of the first examples of chemically cross-linked nanosphere surfaces. Lowe,

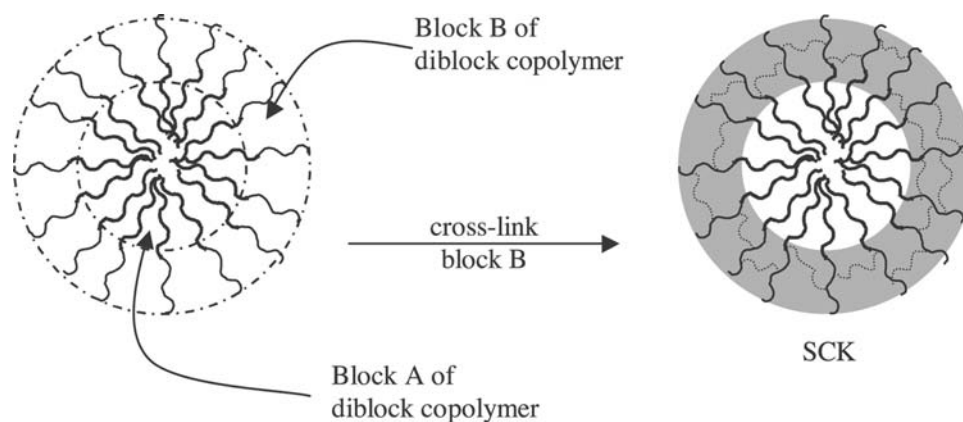


**Fig. 3** Two-dimensional schematic of a 3-D SCK. *Source:* Adapted from Ref. [12].

Billingham, and Arms<sup>[14]</sup> and Bütün et al.<sup>[15,16]</sup> have also created SCK structures. In this case, the core could be reversibly hydrated or dehydrated depending on the solution temperature resulting in a hydrophilic or hydrophobic core, respectively.

Although SCKs have core-shell structures, they are not oil-filled. They are made from unswollen micelles, thus the core is composed of the hydrophobic, alkyl chain ends of the block copolymers used to make the shell.<sup>[17]</sup> Despite this, depending on the properties of the core polymer chains (glassy, fluidlike, or crystalline), the SCKs can have a variety of core properties, including the fluidlike properties found in oil-filled nanocapsules.<sup>[18]</sup> These last properties can be achieved by using a block copolymer that has a degradable core. Huan et al.<sup>[19]</sup> and Zhang, Remsen, and Wooley<sup>[20]</sup> showed the utility of this approach by hydrolyzing the poly- $\epsilon$ -caprolactone core of SCKs. The hydrolysis products resulted in a polar core, but it is conceivable that a similar process could be used with different polymers to yield nonpolar, oil-like cores.

The synthesis of oil-filled nanocapsules using amphiphilic surfactants follows a route similar to that used to make liposomes. Oil-filled nanocapsules are created when an oil-in-water microemulsion is used as the template for the interfacial polymer layer (Fig. 4). Micrometer-sized capsules have already been proven possible<sup>[21]</sup> from regular emulsions, and the chemistry can be extended to the formation of nanocapsules from microemulsions. Such nanocapsules are water-soluble, but coating the nanocapsules with additional layers of polymers, proteins, or other materials can change solubility. Surface materials are chosen for their specific properties, such as chemical and biological resistance, adhesion, and reactivity.

Water-in-oil emulsions have been used to make nanocapsules with aqueous cores.<sup>[22]</sup> The emulsions were stirred while a shell was polymerized at the oil-water interface. Similar techniques have been used to make nanocapsules with oil cores from oil-in-water microemulsions.<sup>[4,23–26]</sup> Underhill et al.<sup>[23]</sup> utilized a microemulsion stabilized with surfactants containing

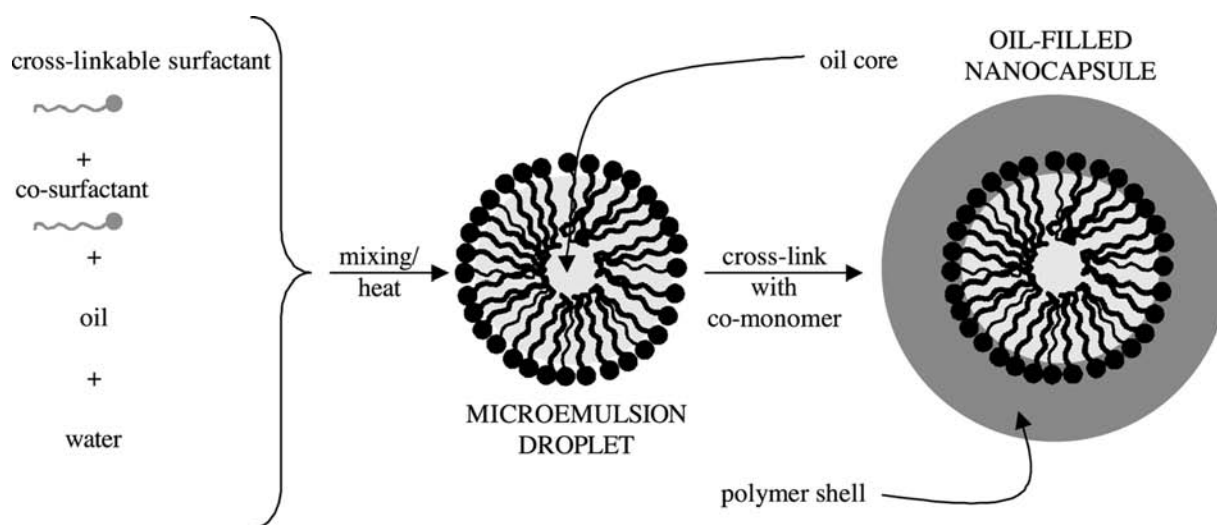


**Fig. 4** Two-dimensional of the synthesis of nanocapsules using a microemulsion as a template. *Source:* From Ref. [23].



**Table 1** Research into nanocapsules via interfacial polymerization, classified by method, system and research group

System investigated	Research group	Refs.
SCK's-Polystyrene-block-poly(4-vinyl pyridine), Poly(2-(dimethylamino) ethyl methacrylate-block-methacrylic acid), Poly( $\epsilon$ -caprolactone)-block-poly(acrylic acid)	Wooley et al., Armes et al.	[12, 14–20]
Monomer polymerization: Poly(alkylcyanoacrylate), Polystyrene, Poly(methacrylic acid), Poly(acrylonitrile)	Lenaerts et al., Couvreur et al., McDonald et al., Jang et al.	[11, 22, 24–26]
Surface cross-linkable surfactants: Polysiloxane/silicates	Duran et al.	[23]

polymerizable head groups. Once the microemulsion has been formed, subsequent steps lead to the polymerization of the surfactant with a comonomer to form a robust shell around the oil droplet. McDonald, Bouck, and Chaput<sup>[24]</sup> also used microemulsions, but utilized the change in solubility between monomers and polymers to force a polymer shell to form at the interface between the oil droplet and the aqueous continuous phase. The monomer was dissolved in the oil along with a hydrophobe and an initiator. The hydrophobe was chosen such that it was not miscible with the polymer; thus as the reaction progressed, the polymer was forced to segregate to the oil–water interface, leaving the hydrophobe forming the oil phase in the core. Typically, the hydrophobe is removed via vacuum or steam stripping. The hydrophobe diffuses through the shell to create hollow nanocapsules.<sup>[24]</sup> This is because the shell is porous enough to allow the hydrophobe to diffuse through the polymer. In the case of Jang and Ha,<sup>[26]</sup> the hydrophobe was isooctane, which is a lightweight volatile organic. If the hydrophobe is not removed, then oil-filled nanocapsules result (Table 1).

### Preformed Polymer Assembly

The alternate method to form nanocapsules is to self-assemble preformed polymers around an oil droplet (Fig. 5). Again the droplet acts as a template. This

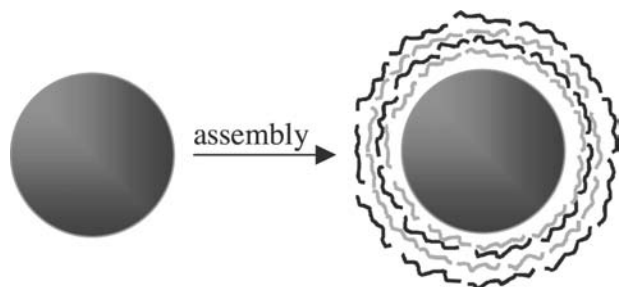


**Fig. 5.** Two-dimensional schematic of the layer-by-layer self-assembly of two different polymers (gray and black) on the surface of a template, which may be either a colloidal particle or an oil droplet. Source: Adapted from Refs.<sup>[27]</sup> and <sup>[28]</sup>

method avoids the issue of the reactivity of the cross-linkable group and the possible side reactions. The drawback is that there is less control of the size and size distribution of the resulting nanocapsules.<sup>[9]</sup>

Nanocapsules, via the self-assembly of polymers at the interface of a droplet, can be made using natural (e.g., liposomes) and/or man-made [e.g., poly(ethyleneimine)] polymers. The deposition of a pre-made polymer at the surface of a droplet can be performed following a method introduced by Lvov et al.<sup>[27,28]</sup> in the mid-1990s. The shell wall of a nanocapsule is made via layer-by-layer assembly through alternate adsorption of oppositely charged components onto a template.<sup>[29]</sup> Uncharged polymers can be used if the precipitation method is changed. In this case, the polymer is dissolved in the organic phase, which is mixed under high shear with an aqueous phase containing a hydrophilic surfactant. As the nanometer-sized droplets of oil form, the polymer precipitates at the interface with the aqueous phase and the whole nanocapsule is stabilized by the surfactant. The resulting nanocapsules can be fine-tuned to provide the desired characteristics by changing the type and amount of polymers, oils, and/or surfactants. The ratio of the organic phase to the aqueous phase also plays a role in the chemical nature of the nanocapsule.<sup>[9]</sup>

The number of layers adsorbed to the surface determines the thickness of the shell. As an alternative to adsorbing polymers to the surface, colloidosomes have

**Table 2** Research into nanocapsules via preformed polymer assembly, classified by method, system and research group

System investigated	Research group	Refs.
Emulsification-diffusion	Quintanar-Guerrero et al.	[10]
Colloidosomes	Dinsmore et al., Velev et al.	[5, 6, 30–33]
Silicate/polycation multilayers	Lvov et al.	[27, 28]
Cationic/anionic polyelectrolyte multilayers	Decher	[29]

colloidal particles adsorbed to an emulsion droplet, resulting in a selectively permeable membrane, which allows submicron particles to diffuse in but excludes larger particles.<sup>[5,6,30–33]</sup> In this case, the resulting capsules exceed the size limit imposed on the definition of nanocapsules. Despite this limitation, it is plausible that this technique could be used for smaller entities. Of concern may be that with perfectly packed spheres, the pores are approximately  $0.15d$ , where  $d$  is the diameter of the adsorbed spheres. Thus as the spheres decrease in size, so will the basic pore size, resulting in decreased permeability (Table 2).

## APPLICATIONS

Submicrometer-sized hollow particles have been explored for the encapsulation of a variety of guest molecules into their cores. They have an advantage over solid nanoparticles because their cores provide for high loading capacity. Different authors have referred to them differently; some examples include microspheres,<sup>[34,35]</sup> hollow nanoparticles,<sup>[36,37]</sup> silica particles,<sup>[38,39]</sup> nanocapsules,<sup>[11,40,41]</sup> solid lipid nanoparticles,<sup>[42]</sup> and host–guest carriers.<sup>[43,44]</sup> One of the advantages of oil-filled systems is that hydrophobic chemicals can be encapsulated and then transported at concentrations higher than their normal solubility in transport media. Supramolecular chemistry has involved numerous types of polymeric assemblies providing enhanced properties (e.g., stealth<sup>®</sup>, which is the ability of a nanoparticle to remain invisible to defense mechanisms within the body, and molecular recognition, which gives the nanoparticles the ability to target specific areas within the body). One of the limitations of such assemblies is their weak stability under changing environmental conditions. Therefore a combination of self-assembly followed by covalent bonding to create novel macromolecular architectures may be employed. The SCK nanostructured particles are being investigated for application in areas as broad as drug delivery, encapsulating agents from fragrances to food flavors, coatings, dye dispersants, pollutant removal systems, and catalysis. In the case of drug delivery, nanocapsules may be advantageous by providing protection against proteolytic degradation. In the case of the food and fragrance industries, nanocapsules are desirable because their use in encapsulating odors leads to a persistence of the odor long after application. This means a longer-lasting perfume, or a food product, which does not go “stale” as rapidly. Further variation over the three-dimensional (3-D) shape of polymer structures (e.g., the preparation of cylindrical or needle-shaped particles) is expected to generate materials of unique behavior.

As seen in the previous paragraph, oil-filled nanocapsules have a variety of applications. There are a number of articles in the literature, which outline their use in drug application technologies (see Refs. [9, 13, 34] and the references therein). Some of the biologically active compounds that nanocapsules have been proposed to encapsulate are hormonal substances, antibiotics, insulin, proteins, antigens, viruses,<sup>[45]</sup> bacteria,<sup>[38]</sup> or cells.<sup>[46]</sup> One non-biomedical application is in the cosmetic/dermatology industry. L'Oréal has been using liposomes since the early 1970s to encapsulate cosmetic ingredients.<sup>[47]</sup> Liposomes have several problems associated with their use in cosmetics.<sup>[48]</sup> First, encapsulation does not improve the bioavailability of the active ingredient. Second, liposome loading efficiency is low.<sup>[48]</sup> Last, the liposomes are not necessarily stable over all environments. Nanocapsules are superior to liposomes for this application because they address all these problems.

L'Oréal's nanocapsules have been on the market since 1995.<sup>[45,47–49]</sup> L'Oréal uses nanocapsules to encapsulate active ingredients such as vitamin A (retinol), vitamin E, vitamin C, and beta-carotene, which are most effective when they reach the deeper layers of the skin. Vitamin A is necessary for new cell generation and overall correct functioning of the epidermis.<sup>[48]</sup> Vitamin E “mops up” harmful oxygen free radicals. Both vitamins are more efficient when transported through the surface of the skin to the deep layers beneath. The nanocapsules facilitate transportation to these deep layers. The nanocapsules have a biodegradable shell, which is attacked by cutaneous enzymes, releasing the contents to the deep layers of the skin.<sup>[48]</sup>

The nanocapsules created by L'Oréal, in collaboration with the French National Research Ministry (CNRS), are made using a microemulsion technique. Two solvent phases are present, both being totally miscible with each other. The first solvent  $S_1$  is a volatile liquid (e.g., acetone), which is used to dissolve the polymer (which will constitute the shell; e.g., poly- $\epsilon$ -caprolactone), the oil phase (which will be the core), the lipophilic active compound (which will be transported within the nanocapsule), and a surfactant (which will prevent the nanocapsules from agglomerating once they are formed). The second solvent  $S_2$  is in aqueous phase and is a non-solvent for the constituents dissolved in  $S_1$ . Both  $S_1$  and  $S_2$  are mixed together via a fine stream and nanometer droplets of oil are formed, surrounded by the polymer, which is insoluble in both  $S_1$  and  $S_2$ , thus creating nanocapsules. The surface is coated with a stabilizing surfactant. As a final step, the acetone is removed under vacuum.<sup>[48]</sup>

A method of delivery alternate to the nanocapsules is the use of microemulsions. Nanocapsules are superior in terms of stability. Microemulsions can be destabilized by changes in the environment such as

temperature and pH. Nanocapsules also provide increased bioavailability because their shells protect the active ingredient(s) in the core from cutaneous enzymes, which may degrade them. Nanocapsules have been shown to penetrate the epidermis further than microemulsions (up to 30  $\mu\text{m}$ ).<sup>[45]</sup> In the case of vitamin A, the nanocapsules act as reservoirs in the uppermost layers of the epidermis, thus “stockpiling” the vitamin until the skin needs it.<sup>[48]</sup>

## CONCLUSION

Oil-filled nanocapsules consist of spherical structures typically <200 nm in diameter with a distinct core-shell structure, where the core is fluidlike and lipophilic. Oil-filled nanocapsules can be synthesized by either the polymerization of a shell, or by the self-assembly of preformed polymers around a lipophilic compound. Differing monomers, polymers, and hydrophobes have resulted in various sizes and morphologies on nanocapsules. Oil-filled nanocapsules have been examined using SEM, TEM, and SFM.

Oil-filled nanocapsules are a rapidly developing technology that shows promise in a number of areas. The areas of application are broad, and include the areas of drug delivery<sup>[9,13]</sup> and removal,<sup>[23]</sup> food science,<sup>[50]</sup> cosmetics/dermatology,<sup>[47]</sup> paints/inks and coatings, pollutant removal systems, and vessels for catalysis (e.g., nanoreactors).<sup>[8]</sup> The commonality in all these applications is the need for a reservoir or host to encapsulate a guest moiety, which otherwise may not be soluble, or may be degraded by the environment in which it is needed. When used as nanoreactors, oil-filled nanocapsules can be considered as local areas of high concentration even if the overall solution concentration is low. This may help catalysis and reactivity.

Research groups currently working on nanocapsules for drug delivery acknowledge that the nanocapsules would be more effective if the surface were altered to allow for stealth abilities (stealth refers to the nanocapsules' ability to remain invisible to the body's defense mechanisms, e.g., white blood cells). This is possible through surface functionalization with poly(ethylene oxide). Nanocapsules would also be more efficient drug delivery vessels if they could target the specific site for drug delivery (e.g., a tumor). This is known as active targeting.<sup>[13]</sup> This can be achieved if the surface of the nanocapsule is modified with ligands, which are selectively recognized by receptors on the cells of interest (e.g., tumor cells). This is of importance because it provides maximum efficiency of the drug dosage and minimizes the side effects of the drug associated with it coming into contact with non-target tissues.

In the future, nanocapsules will be better applied to topical, biomedical, cosmetic, and dermatological

applications if a biomimetic approach is adopted. The nanocapsule structure will need to be engineered such that it resembles more closely the structure of single-celled organisms. The result would be a delivery device, which would deliver its contents to a specific activity site.

Nanocapsules have already shown their utility in a number of areas and continue to show promise with the possibility of adapting them to a number of circumstances with a little bit of imagination.

## ACKNOWLEDGMENTS

The author would like to thank the members of the George and Josephine Butler Polymer Laboratory and the Engineering Research Center for Particle Science and Technology at the University of Florida as well as DRDC Atlantic for their support, both scientific and financial. Special thanks are given to Dr. R. S. Duran and Dr. G. Liu for their mentorship, and my colleagues at the DRDC Atlantic for their help and encouragement.

## REFERENCES

1. Feynman, R.P. There's Plenty of Room at the Bottom. In *Engineering and Science*; Caltech, February 1960.
2. Al Kouri Fallouh, N.; Roblot-Treupel, L.; Fessi, H.; Devissaguet, J.P.; Puisieux, F. Development of a new process for the manufacture of polyisobutylycyanoacrylate nanocapsules. *Int. J. Pharm.* **1986**, *28*, 125–132.
3. Förster, S.; Antonietti, M. Amphiphilic block copolymers in structure-controlled nanomaterial hybrids. *Adv. Mater.* **1998**, *10*, 195.
4. Tiarks, F.; Landfester, K.; Antonietti, M. Preparation of polymeric nanocapsules by miniemulsion polymerization. *Langmuir* **2001**, *17*, 908–918.
5. Dinsmore, A.D.; Hsu, M.F.; Nikolaidis, M.G.; Marquez, M.; Bausch, A.R.; Weitz, D.A. Colloidosomes: Selectively permeable capsules composed of colloidal particles. *Science* **2002**, *298*, 1006–1009.
6. <http://www.deas.harvard.edu/projects/weitzlab/research/csome.html>.
7. Wallach, D.F.H. Hybrid Paucilamellar Lipid Vesicles. US Patent 5,628,936, May 13, 1997
8. Graff, A.; Winterhalter, M.; Meier, W. Nanoreactors from polymer-stabilized liposomes. *Langmuir* **2001**, *17*, 919–923.
9. Couvreur, P.; Barratt, G.; Fattal, E.; Legrand, P.; Vauthier, C. Nanocapsule technology: A review. *Crit. Rev. Ther. Drug* **2002**, *19* (2), 99–134.
10. Quintanar-Guerrero, D.; Allemann, E.; Doelker, E.; Fessi, H. Preparation and characterization of nanocapsules from preformed polymers by a new process based on emulsification-diffusion technique. *Pharm. Res.* **1998**, *15* (7), 1056–1062.

11. Chouinard, F.; Buczkowski, S.; Lenaerts, V. Poly(alkylcyanoacrylate) nanocapsules: Physicochemical characterization and mechanism of formation. *Pharm. Res.* **1994**, *11*, 869–874.
12. Thurmond, K.B.; Kowalewski, T.; Wooley, K.L. Water-soluble Knedel-like structures: The preparation of shell-cross-linked small particles. *J. Am. Chem. Soc.* **1996**, *118*, 7239–7240.
13. Rösler, A.; Vandermeulen, G.W.M.; Klok, H.-A. Advanced drug delivery devices via self-assembly of amphiphilic block copolymers. *Adv. Drug Deliv. Rev.* **2001**, *53*, 95–108.
14. Lowe, A.B.; Billingham, N.C.; Armes, S.P. Synthesis and characterization of zwitterionic block copolymers. *Macromolecules* **1998**, *31*, 5991–5998.
15. Bütün, V.; Billingham, N.C.; Armes, S.P. Synthesis of shell cross-linked micelles with tunable hydrophilic/hydrophobic cores. *J. Am. Chem. Soc.* **1998**, *120*, 12135–12136.
16. Bütün, V.; Lowe, A.B.; Billingham, N.C.; Armes, S.P. Synthesis of zwitterionic shell cross-linked micelles. *J. Am. Chem. Soc.* **1999**, *121*, 4288–4289.
17. Thurmond, K.B.; Kowalewski, T.; Wooley, K.L. Shell cross-linked Knedels: A synthetic study of the factors affecting the dimensions and properties of amphiphilic core-shell nanospheres. *J. Am. Chem. Soc.* **1997**, *119*, 6656–6665.
18. Wooley, K.L. Shell cross-linked polymer assemblies: Nanoscale constructs inspired from biological systems. *J. Polym. Sci., A, Polym. Chem.* **2000**, *38*, 1397–1407.
19. Huan, H.; Remsen, E.E.; Kowalewski, T.; Wooley, K.L. Nanocages derived from shell cross-linked micelle templates. *J. Am. Chem. Soc.* **1999**, *121*, 3805–3806.
20. Zhang, Q.; Remsen, E.E.; Wooley, K.L. Shell cross-linked nanoparticles containing hydrolytically degradable, crystalline core domains. *J. Am. Chem. Soc.* **2000**, *122*, 3642–3651.
21. Dyatlov, V.A.; Katz, G.A. Patent WO 94/17789, August 18, 1994.
22. Lambert, G.; Fattal, E.; Pintoalphantary, H.; Gulik, A.; Couvreur, P. Polyisobutylcyanoacrylate nanocapsules containing an aqueous core as a novel colloidal carrier for the delivery of oligonucleotides. *Pharm. Res.* **2000**, *17*, 707–714.
23. Underhill, R.S.; Jovanovic, A.V.; Carino, S.R.; Varshney, M.; Shah, D.O.; Dennis, D.M.; Morey, T.E.; Duran, R.S. Oil-filled silica nanocapsules for lipophilic drug uptake: Implications for drug detoxification therapy. *Chem. Mater.* **2002**, *14*, 4919–4925.
24. McDonald, C.J.; Bouck, K.J.; Chaput, A.B.; Stevens, C.J. Emulsion polymerization of voided particles by encapsulation of a nonsolvent. *Macromolecules* **2000**, *33*, 1593–1605.
25. Jang, J.; Lee, K. Microemulsion polymerization for hollow polymer nanosphere using encapsulation of a hydrophobe. *Polym. Prepr.* **2002**, *43*, 605–606.
26. Jang, J.; Ha, H. Fabrication of hollow polystyrene nanospheres in microemulsion polymerization using triblock copolymers. *Langmuir* **2002**, *18*, 5613–5618.
27. Lvov, Y.; Ariga, K.; Onda, M.; Ichinose, I.; Kunitake, T. Alternate assembly of ordered multilayers of SiO<sub>2</sub> and other nanoparticles and polyions. *Langmuir* **1997**, *13*, 6195–6203.
28. Lvov, Y.; McShane, M.; Jones, S.; de Villiers, M. In: *Nanocapsule Technology Based on Layer-by-Layer Self-Assembly*, Abstracts of the Louisiana Conference on Commercial Applications of Microsystems, Materials and Nanotechnologies, Ruston, LA, USA, October 21–22, 2002.
29. Decher, G. Fuzzy nanoassemblies: Toward layered polymeric multicomposites. *Science* **1997**, *277*, 1232–1237.
30. Velev, O.D.; Lenhoff, A.M.; Kaler, E.W. A class of microstructured particles through colloidal crystallization. *Science* **2000**, *287*, 2240–2243.
31. Velev, O.D.; Furusawa, K.; Nagayama, K. Assembly of latex particles by using emulsion droplets as templates: 1. Microstructured hollow spheres. *Langmuir* **1996**, *12*, 2374–2384.
32. Velev, O.D.; Furusawa, K.; Nagayama, K. Assembly of latex particles by using emulsion droplets as templates: 2. Ball-like and composite aggregates. *Langmuir* **1996**, *12*, 2385–2391.
33. Velev, O.D.; Nagayama, K. Assembly of latex particles by using emulsion droplets: 3. Reverse (water in oil) system. *Langmuir* **1997**, *13*, 1856–1859.
34. Uhrich, K.E.; Cannizzaro, S.M.; Langer, R.S.; Shakesheff, K.M. Polymeric systems for controlled drug release. *Chem. Rev.* **1999**, *99*, 3181–3198.
35. Kramer, P.A. Albumin microspheres as vehicle for achieving specificity in drug delivery. *J. Pharm. Sci.* **1974**, *63*, 1646–1647.
36. Kreuter, J. Nanoparticle-based drug delivery systems. *J. Control. Release* **1991**, *16*, 169–176. and references therein.
37. Brannon-Peppas, L. Recent advances on the use of biodegradable microparticles and nanoparticles in controlled drug delivery. *Int. J. Pharm.* **1995**, *116*, 1–9.
38. Finnie, K.S.; Bartlett, J.R.; Woolfrey, J.L. Encapsulation of sulfate-reducing bacteria in a silica host. *J. Mater. Chem.* **2000**, *10*, 1099–1101.
39. Bartlett, J.; Alexandr, B.C.J. AU Patent WO0162232, August 30, 2001.
40. Speiser, A. Controlled release of drugs from microcapsules and nanocapsules. *Acta Pharm. Suec., Suppl.* **1976**, *13*, 35.
41. Watanasirichaiikul, S.; Davies, N.M.; Rades, T.; Tucker, I.G. Preparation of biodegradable insulin nanocapsules from biocompatible microemulsions. *Pharmacol. Res.* **2000**, *17*, 684.
42. Zimmerman, E.; Muller, R.H. Electrolyte- and pH-stabilities of aqueous solid lipid nanoparticle (SLN<sup>TM</sup>) dispersions in artificial gastrointestinal media. *Eur. J. Pharm. Biopharm.* **2001**, *52* (2), 203–210.
43. Orr, G.W.; Barbour, L.J.; Atwood, J.L. Controlling molecular self-organization: Formation of nanometer-scale spheres and tubules. *Science* **1999**, *285*, 1049–1052.
44. Meissner, R.S.; Rebek, J.; deMendoza, J. Autoencapsulation through intermolecular forces: A synthetic self-assembling spherical complex. *Science* **1995**, *270*, 1485–1488.

45. Handjani, R.-M.; Ribier, A. Composition for the Cosmetic and/or Pharmaceutical Treatment of the Upper Layers of the Epidermis by Topical Application to the Skin, and Corresponding Preparation Process. US Patent 6,203,802, March 20, , 2001.
46. Diaspro, A.; Silvano, D.; Krol, S.; Cavalleri, O.; Gliozzi, A. Single living cell encapsulation in nano-organized polyelectrolyte shells. *Langmuir* **2002**, *18*, 5047–5050.
47. Oger, G. The nanoscience behind beauty is serious business at L'Oréal. *Smalltimes* December 26 **2002**. ([www.smalltimes.com](http://www.smalltimes.com)).
48. Quin, F. Chemistry in Beauty, Friday Evening Discourse at the Royal Institute of Great Britain, March, 23, 2001. ([www.rigb.org/events/transcripts.html](http://www.rigb.org/events/transcripts.html)).
49. Ribier, A.; Simonnet, J.-T.; Michelet, J. Cosmetic or Dermatological Composition Comprising an Oil-in-Water Emulsion Comprising Oily Globules with a Lamellar Liquid Crystal Coating. US Patent 6,066,328, May 23, , 2000 .
50. Gibbs, B.F.; Kermasha, S.; Alli, I.; Mulligan, C.N. Encapsulation in the food industry: A review. *Int. J. Food Sci. Nutr.* **1999**, *50*, 213–224.

# One-Dimensional Electrically Conducting Polymeric Nanostructures

**Andrew D.W. Carswell**

*Department of Chemical Engineering and Materials Science, University of Oklahoma, Norman, Oklahoma, U.S.A.*

**Brian P. Grady**

*University of Oklahoma, Norman, Oklahoma, U.S.A.*

## INTRODUCTION

As the desire for smaller components heightens, techniques to fabricate materials and building blocks for materials that take advantage of the nanorealm continue to proliferate. Since the discovery of carbon nanotubes in 1991,<sup>[1]</sup> nanoscale objects fabricated from various compounds with various shapes have emerged. Although many synthetic techniques have surfaced to fabricate materials with nanoscale dimensions, there is a significant need to then arrange these materials into active and useful materials. Because of the requirement of smaller components for microelectronics, electrically conducting polymers have captured interest as materials of which nanoscale objects would be highly desirable.

Since the discovery that polyacetylene can be doped so that the electrical conductivity can be controlled over 11 orders of magnitude,<sup>[2]</sup> many studies have been carried out to better understand and improve the conductivities and properties of these polymers.<sup>[3–5]</sup> Intrinsically conducting polymers have attracted a great deal of interest as potential chemical sensors,<sup>[6]</sup> single-molecular transistors,<sup>[7]</sup> electron emitting flat panel displays,<sup>[8]</sup> and other microelectronic devices.<sup>[9]</sup> Intrinsically conducting polymers are attractive in many applications as their conductivity can be tuned by chemical manipulation of the polymer backbone, by selection of the dopant, by alteration of the doping degree, or by mixing with a matrix material producing a composite. In addition, conducting polymers offer advantages over metals and other semiconducting materials because of their good mechanical properties, stability, ease of processing, and relatively low price. Because of the desirable properties of intrinsically conducting polymers and the elevated conductivity by molecular alignment, a number of techniques have arisen to synthesize 1-D nanostructures of conducting polymers. In this entry we will review techniques that are currently available to synthesize 1-D nanoscale structures of electrically conducting polymers both in solution and on surfaces.

As conventional lithographic techniques cannot be applied to produce conducting lines in the sub-100-nm regime, the ability to render high quality 1-D wires of  $\pi$ -conjugated polymers with these dimensions is of great interest. Additionally, as the conductivity of  $\pi$ -conjugated polymers is dictated in part by molecular alignment, and the radius of gyration of polymers is generally in the tens of nanometer range, 1-D nanostructures of  $\pi$ -conjugated polymer would likely afford elevated conductivities. Although other methods do exist, techniques to fabricate 1-D nanostructures of conducting polymers evolve from the use of templates in the form of either solid materials or arranged molecules. We will begin our discussion with methods to produce 1-D nanostructures of conducting polymers in bulk solution by using “hard” or “soft” templates, and follow with techniques to fabricate 1-D nanostructures directly on surfaces.

## 1-D $\pi$ -CONJUGATED POLYMER NANOSTRUCTURES SYNTHESIZED USING “SOLID” TEMPLATES

In order to render 1-D nanostructures of  $\pi$ -conjugated polymers one must have the ability to template the shape of the polymer product. Templates are typically in the form of preformed channels in solid materials or organized molecules in bulk solution. Representative materials used as solid templates are “track-etched” polymeric membranes, porous aluminas, and aluminosilicates such as MCM-41. These materials all offer a narrow diameter confined channel in which 1-D structures can be synthesized. In 1989, Cai and Martin showed that the mesoscopic channels of “track-etched” membranes could be used to control the growth of 1-D structures of polyheterocyclics.<sup>[10]</sup> Oxidation can be carried out either chemically or electrochemically by this method. In electrochemical synthesis the support must first be coated with a thin layer of metal to act as the anode. For chemical oxidation, the membrane is first saturated with monomer



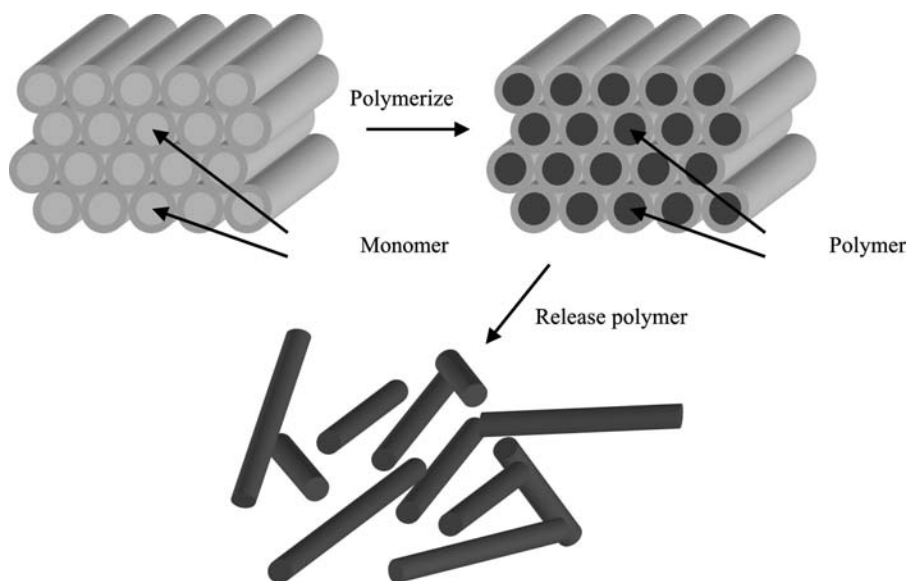


**Fig. 1** Schematic representation of the controlled 1-D synthesis of polymeric nanostructures using “hard” templates.

and then exposed to a solution containing an oxidizing agent. A general schematic for this process is shown in Fig. 1. Wires produced by the method exhibit enhanced conductivities in comparison to macroscale equivalent bulk materials. The reason for an elevation in conductivity was found to be due to a superior molecular ordering of polymer chains owing to synthesis taking place in a confined environment.<sup>[11]</sup>

Since the discovery that the pores of membranes could be used to morphologically control the growth of 1-D polymer structures, polymeric nanotubes/fibers with controllable diameters have been synthesized using nanoporous membranes<sup>[11–15]</sup> and mesoporous zeolites<sup>[16]</sup> as templates. In the case of mesoporous zeolites, polyaniline (PAni) nanofibers with diameters as small as 3 nm have been prepared within the pores of aluminosilicate MCM-41 templates.<sup>[16]</sup> Martin observed that when synthesizing PAni and polypyrrole (PPy) using the pores of track-etched polycarbonate membranes, the polymer preferentially nucleates and grows on the pore walls (Fig. 2).<sup>[12]</sup> This phenomenon can be explained in part by the polycationic forms of these polymers being solvophobically driven to the walls of the pores. This driving force is coupled with electrostatic forces between the cationic polymer and the anionic sites on the pore wall. In general, when a “molecular anchor” exists for the material being deposited, hollow tubules are favored over solid fibers.

The dimensions and pore shape of track-etched membranes have been investigated by several research groups with the conclusion that the pores are not always cylindrical and may not be of the reported diameter.<sup>[17–19]</sup> To this end, a novel method to produce reproducibly sized and shaped pores in membranes has been developed.<sup>[18]</sup> With this technique, track-etched membranes can be fabricated with perfectly cylindrical

pores with defined diameters in the range of 15–1000 nm. These membranes have been used to produce nanostructures of conjugated polymers with controllable diameters.<sup>[19,20]</sup>

Templates of aluminum oxide have also been used to electrochemically fabricate nanowires and nanotubes of PPy, PAni, and poly(3,4-ethylenedioxythiophene) with diameters of 200 nm and lengths of 10 to ~40  $\mu\text{m}$ .<sup>[21]</sup> It has been shown that the wall thickness

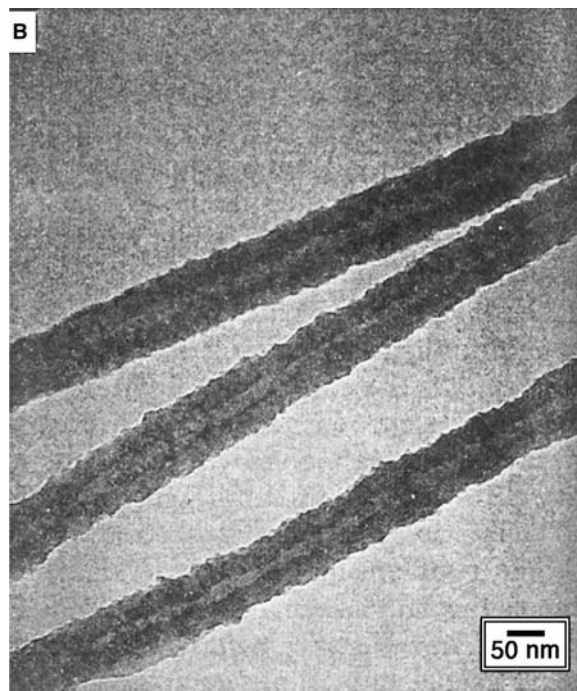


**Fig. 2** TEM image of polypyrrole nanotubules, synthesized within the pores of polycarbonate “track-etched” membranes. Source: From Ref.<sup>[12]</sup>.

of the polymer product can be controlled by the counterion and that the conductivity is influenced by the outer diameter of the tube. These nanostructures have field emission characteristics and therefore may find use as field emission displays. Anodic aluminum oxide templates have also been used to form PANi nanofibril array films that have shown interesting field emission properties.<sup>[22]</sup> Although membranes offer a route to 1-D nanostructures of conjugated polymers, a limitation inherent to the membrane synthesis technique is that post-synthesis steps are necessary to remove the polymer from the template. This process usually entails dissolving the template thereby releasing the polymer, which can unfortunately lead to damage or undesirable bundling of the product.<sup>[19]</sup>

In a similar technique, composite materials of conjugated polymer and silicas have been synthesized using a sol-gel-based method. In this approach polymerizable diacetylenic surfactants are used as template molecules for the fabrication of conjugated nanofibers in the form of a polymer/silica nanocomposite material.<sup>[23–26]</sup> In this approach silica channels are formed and packed with monomer simultaneously which in turn gives better filling of the channels as compared to post-loading approaches. More recently, this same technique has been employed using pyrrole-containing surfactants which self-organize and are then polymerized to form PPy/silica nanocomposites.<sup>[27]</sup>

### 1-D $\pi$ -CONJUGATED POLYMER NANOSTRUCTURES USING MOLECULAR INTERACTIONS AS “SOFT” TEMPLATES

In a contrasting technique in which no solid support is required, 1-D polymer nanostructures can be fabricated using a self-assembly technique. In this technique, monomer aggregates with another molecule (usually a “surfactant-like” amphiphilic molecule) to form a fiber-like assembly which is subsequently polymerized retaining the fibril morphology in the polymer product. In 1999, Huang and Wan developed a “template-free”<sup>a</sup> method to synthesize microtubes of PANi<sup>[28]</sup> and PPy<sup>[29]</sup> using  $\beta$ -naphthalene sulfonic acid ( $\beta$ -NSA) to control the polymer morphology and act as a dopant molecule. Subsequently, nanotubes of PANi with diameters in the range of 76–650 nm have been produced by this same technique and the formation mechanism has been attributed to a reaction between the basic aniline and acidic  $\beta$ -NSA to form an insoluble 1-D salt.<sup>[30]</sup> This salt then acts as a

template in the formation of the PANi nanotubes/fibers (Fig. 3). Interestingly, in this work it was found that the diameter of the PANi structures could be controlled by the ratio of  $\beta$ -NSA to aniline. When the ratio was around 2, microtubules (diameter > 100 nm) were formed but when the ratio was reduced to  $1/2$  or  $1/4$ , nanotubes (diameter < 100 nm) were favored. Since then many other organic acids have been used to fabricate 1-D nanostructures of PANi. PANi nanotubes have been synthesized in the presence of D-10-camphorsulfonic acid,<sup>[31]</sup> (4- $\{n$ -[4-(4-Nitrophenylazo)-phenoxy]alkyl}aminobenzene sulfonic acid),<sup>[32]</sup> azobenzenesulfonic acid,<sup>[33]</sup> 5-aminonaphthalene-2-sulfonic acid,<sup>[34]</sup> a sulfonated dendrimer PAMAM4.0-[naphthyl(SO<sub>3</sub>H)<sub>2</sub>]<sub>24</sub>, and hydrogensulfated fullereneol C<sub>60</sub>(OSO<sub>3</sub>H)<sub>6</sub>.<sup>[35]</sup> In all cases the chosen molecule acts as a protonic acid dopant and templating agent.

In other work, surfactants along with various inorganic acids were used to form PANi nanostructures in which the morphology, size, and electrical properties were dependent on the reaction conditions and dopant.<sup>[36]</sup> PANi nanofibers with diameters of 30–50 nm and lengths from 500 nm to several microns have been synthesized using camphorsulfonic acid at the interface between an organic and aqueous phase.<sup>[37]</sup> The dedoped nanofibers were shown to have much faster response to doping/dedoping than conventional undoped PANi films. In other work, organic acids such as  $\beta$ -NSA or *p*-toluenesulfonic acid have been used to prepare Ppy micro/nanotubes with diameters of 50–2000 nm and high conductivities.<sup>[38]</sup> Once again the properties of the polymer can be controlled by the polymerization method and conditions, or by the dopant. In a surfactant-based method, PPy nanotubes with diameters < 100 nm have been successfully

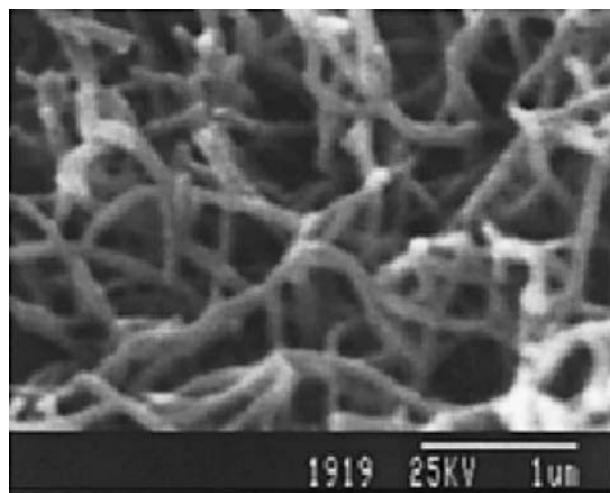


**Fig. 3** SEM image of polyaniline nanotubes (92 nm average diameter), synthesized in the presence of  $\beta$ -naphthalene sulfonic acid. Source: From Ref.<sup>[30]</sup>.

<sup>a</sup>The term “template free” is a misnomer, as described below. A more precise term would be “hard-template free.”

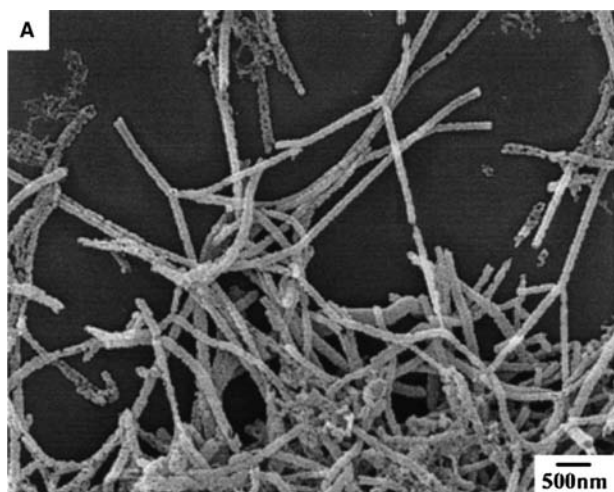


**Fig. 4** FE-SEM image of polypyrrole nanotubes (95 nm diameter), synthesized by reverse microemulsion polymerization using surfactant molecules as templates. Source: From Ref.<sup>[39]</sup>.

fabricated by a technique that uses a reverse microemulsion (Fig. 4).<sup>[39]</sup> This method employs reverse micelles that form in apolar solvents with surfactant headgroups oriented away from the solvent. Upon

addition of iron chloride, the morphology of the reverse micelles is transitioned into cylindrical micelles which can then be used as nanoreactors to carry out the controlled synthesis of a partitioned monomer (Fig. 5). All of the aforementioned studies incorporate a polymerization step in the formation of the 1-D structure.

Preformed polymers have also been shown to self-assemble into hierarchical structures, including nano-scale polymeric cylindrical structures due to molecular interactions such as hydrogen bonding and recognition.<sup>[40]</sup> Comb-shaped polymers are a class of polymers that consists of amphiphilic molecules that are either covalently or physically bonded to the polymer backbone. Interactions between the polymer backbone and appendage molecules control the self-assembled structure. Conjugated polymers, or rigid polymers, can be decorated with amphiphiles to form so-called “hairy rod” polymers, which in turn form self-organized structures. For example, high molecular weight dedoped PANi has been doped with camphorsulfonic acid (CSA) and then mixed with 4-hexylresorcinol (Hres). Hydrogen bonding between all three molecules induces self-organization into PANi cylinders with a repeat distance of 3.5 nm.<sup>[41–43]</sup> The conductivity of this material has been investigated

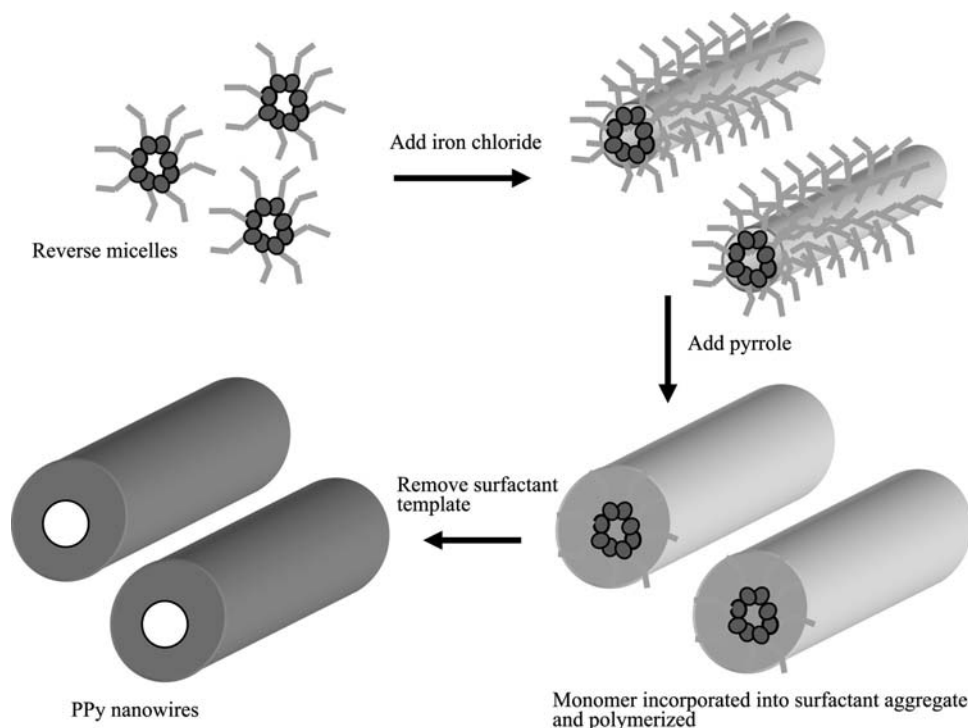


**Fig. 5** A schematic of the reverse microemulsion technique identifying four stages. In the first stage, reverse micelles form in an apolar solvent. These spherical micelles are then transitioned into cylindrical micelles by the addition of iron chloride in a second stage. Pyrrole then partitions around the cylindrical structure before being polymerized in the third step. Finally, the surfactant is removed, leaving Ppy nanotubes.

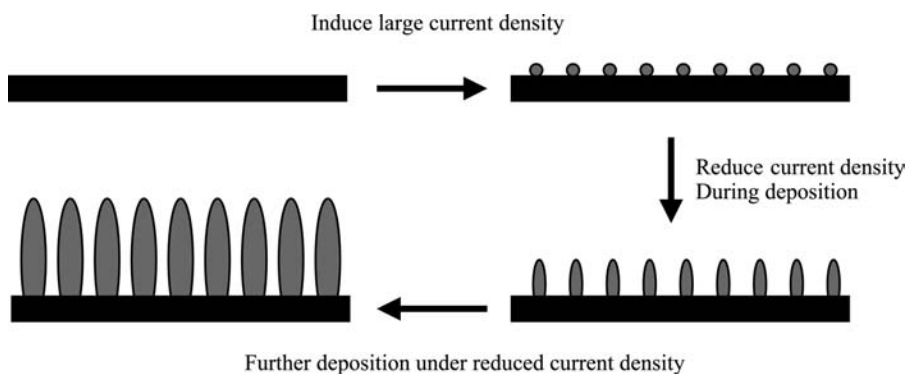


**Fig. 6** A schematic representation of a three-stage “template-free” technique in which oriented arrays of polyaniline nanotubes synthesize directly on surfaces. In stage one a large current density is applied to create nucleation sites on the substrate. In stages two and three, deposition takes place in which a reduced current density is applied forming arrays of nanowires.

and found to increase by 2 orders of magnitude when cylindrical structures were present. Once again this elevation in conductivity has been attributed to the confinement of PANi chains within the cylinders.

### 1-D $\pi$ -CONJUGATED POLYMER NANOSTRUCTURES SYNTHESIZED ON SURFACES

Because of the desire for smaller circuitry in microelectronics, new methods for depositing  $\pi$ -conjugated polymers with special resolution on surfaces are required.<sup>[44]</sup> One significant challenge to constructing microelectronic devices composed of polymeric sub-units is that the properties of the polymer remain intact after the procedure is complete. To this end a number of techniques to fabricate 1-D nanostructures of conducting polymers on surfaces have been developed.

In 2001, nanowires of a polydiacetylene compound were polymerized on the surface of graphite by using the probe tip of a scanning tunneling microscope.<sup>[45]</sup> In this work, a diacetylene compound was first adsorbed onto graphite and then a 6-nm defect site was produced on the surface. A negatively biased STM tip was then passed over the substrate, toward the defect site, leaving a line of polymer ending at the defect site. Lines of the conducting polymer were rendered with spatial resolution of around 1 nm by this method. In another similar process termed electrochemical dip-pen nanolithography (E-DPN), 3,4-ethylenedioxythiophene (EDOT) was polymerized on both semiconducting and insulating surfaces to form sub-100-nm wires.<sup>[46]</sup> In this work the tip of an atomic force microscope was coated with a thiophene derivative by immersion in a monomer/solvent solution. A negative bias was applied between the tip and substrate as it was traversed in a preprogrammed pattern above the surface of the substrate, leaving a line of poly-EDOT. Condensation facilitates the transport of material to the surface and a chemical process

immobilizes the material. Nanostructures of organic,<sup>[47,48]</sup> semiconducting,<sup>[49]</sup> and metallic materials<sup>[49,50]</sup> have also been fabricated using this process.

Recently, large arrays of oriented PANi nanowires have been grown on various substrates by a template-free method.<sup>[51]</sup> In this entry, PANi nanowires have been synthesized electrochemically on platinum, silicon, titanium, gold, carbon, and silica in a three-step procedure (Fig. 6). In the first step, a large current density is applied to create nucleation sites on the substrate followed by a second and third deposition step in which a reduced current density is applied. The PANi nanowires are mostly oriented perpendicular to the surface when flat substrates are used and grow radially in the case of colloidal particles. Such nanowires have diameters in the range of 50–70 nm and lengths of around 0.8  $\mu\text{m}$  and have been shown to be effective as sensors for peroxide detection (Fig. 7).<sup>[52]</sup>

Electrochemically synthesized conducting polymer nanowires have also been prepared by several research groups. In one such study, PPy nanowires have been synthesized on gold electrodes using self-assembled

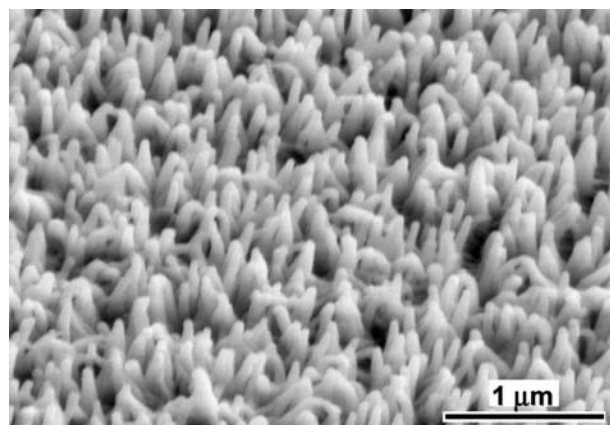


**Fig. 7** Tilted SEM image of an array of oriented polyaniline nanotubes (50–70 nm), synthesized electrochemically by a “template-free” method on a platinum surface. *Source:* From Ref.<sup>[52]</sup>.

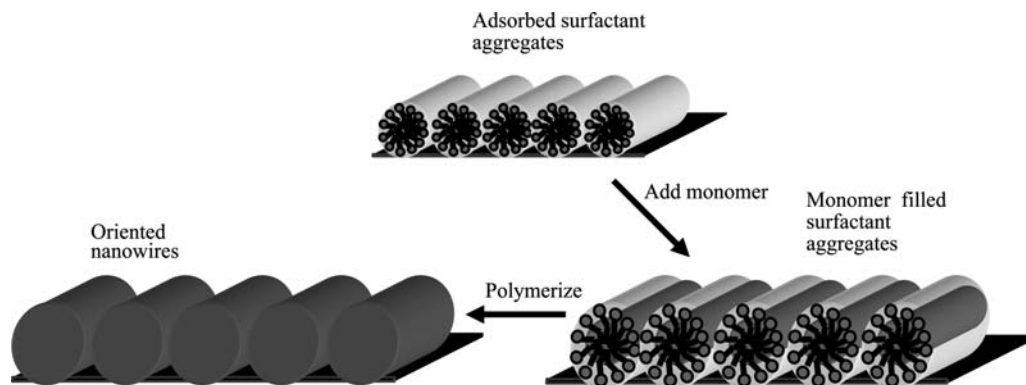


**Fig. 8** A schematic representation of a technique in which arrays of polyaniline nanowires can be synthesized parallel to the surface of graphite. The sketch may not be truly accurate as it is not clear whether surfactant aggregates form before or simultaneously with monomer-filled surfactant aggregates as both reagents are added simultaneously.

monolayers of cyclodextrins as templates.<sup>[53]</sup> These SAMs form cavities on the gold that serve as initiation points for the electrochemical polymerization of adsorbed monomers. Interestingly, when the cavities are far apart, wires are favored over dots, which form when the cavities are close together. Wires with diameters of 70 nm and lengths of 1.5  $\mu\text{m}$  have been made by this technique.

In other work, PANi nanowires have been synthesized and aligned parallel to the surface of graphite by a one-step procedure using surfactant molecules as templates.<sup>[54]</sup> Surfactants are known to adsorb onto some crystalline surfaces in aligned arrays of either hemicylindrical or cylindrical morphologies.<sup>[55]</sup> In this

technique, adsorbed arrays of surfactant are used as nanoscale reaction environments for the synthesis of aligned PANi nanowires (Fig. 8). The wires have been shown to have dimensions of around 17 and 40 nm depending on polymerization conditions and surface chemistry and will only change orientation at grain boundaries or steps on the graphite (Fig. 9). Coadsorbing molecules are known to change the morphology of adsorbed surfactant aggregates.<sup>[56–58]</sup> Similarly, manipulation of the polymer morphology between spheres and wires has been shown to occur by the incorporation of long-chain alcohols into the surfactant/monomer aggregate.

## CONCLUSION

Here we have endeavored to give an overview of techniques currently available to synthesize 1-D nanostructures of electrically conducting polymers. The drive for the fabrication of 1-D nanostructures of conjugated polymers continues to thrive with many approaches being reported recently in the literature. There is still the need for simple techniques that not only produce high-quality nanomaterials with controllable dimensions and therefore properties, but also arrange these building blocks into architectures to make viable components or products. The field of nanotechnology is still in its infancy although it has made huge strides over the last few years. The opportunities are endless for making exhilarating discoveries and inventing new devices and technologies based on materials having these dimensions.

## REFERENCES

1. Iijima, S. Helical microtubules of graphitic carbon. *Nature* **1991**, *354*, 56–58.

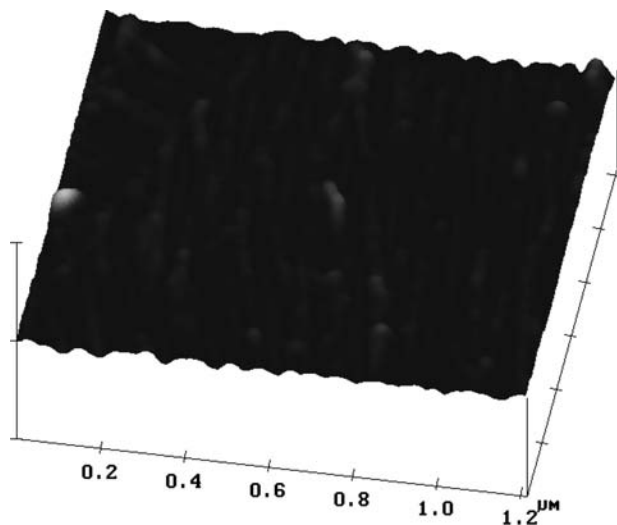


**Fig. 9** Tapping mode AFM image of 40 nm oriented polyaniline nanowires, synthesized on the surface of highly oriented pyrolytic graphite using adsorbed surfactant aggregates as templates. A change in orientation of the wires can be seen at a step or grain boundary on the graphite ( $z$ -scale 80 nm,  $x$ -scale 1.2  $\mu\text{m}$ ).

2. Chiang, C.K.; Fincher, C.R., Jr.; Park, Y.W.; Heeger, A.J.; Shirakawa, H.; Louis, E.J.; MacDiarmid, A.G. Electrical conductivity in doped polyacetylene. *Phys. Rev. Lett.* **1977**, *39*, 1098–1101.
3. MacDiarmid, A.G. “Synthetic metals”: a novel role for organic polymers (Nobel lecture). *Angew. Chem. Int. Ed.* **2001**, *40* (14), 2581–2590.
4. Shirakawa, H. The discovery of polyacetylene film: the dawning of an era of conducting polymers (Nobel lecture). *Angew. Chem. Int. Ed.* **2001**, *40* (14), 2574–2580.
5. Heeger, A.J. Semiconducting and metallic polymers: the fourth generation of polymeric materials (Nobel lecture). *Angew. Chem. Int. Ed.* **2001**, *40* (14), 2591–2611.
6. Kong, J.; Franklin, N.R.; Zhou, C.; Chapline, M.G.; Peng, S.; Cho, K.; Dai, H. Nanotube molecular wires as chemical sensors. *Science* **2000**, *287*, 622–625.
7. Yao, Z.; Postma, H.W.Ch.; Balents, L.; Dekker, C. Carbon nanotube intramolecular junctions. *Nature* **1999**, *402*, 273–276.
8. Normile, D. Nanotubes generate full-color displays. *Science* **1999**, *286*, 2056–2057.
9. Skotheim, T.A.; Elsenbaumer, R.L.; Reynolds, J.H. Conducting polymers in microelectronics. In *Handbook of Conducting Polymers*, 2nd Ed.; Dekker: New York, 1998; 921–944, Chapter 32.
10. Cai, Z.; Martin, C.R. Electronically conductive polymer fibers with mesoscopic diameters show enhanced electronic conductivities. *J. Am. Chem. Soc.* **1989**, *111*, 4138–4139.
11. Liang, W.; Martin, C.R. Template-synthesized polyacetylene fibrils show enhanced supermolecular order. *J. Am. Chem. Soc.* **1990**, *112*, 9666–9668.
12. Martin, C.R. Nanomaterials—a membrane-based synthetic approach. *Science* **1994**, *266*, 1961–1966.
13. Parthasarathy, R.V.; Martin, C.R. Template-synthesized polyaniline microtubules. *Chem. Mater.* **1994**, *6*, 1627–1632.
14. Cai, Z.; Lei, J.; Liang, W.; Menon, V.; Martin, C.R. Molecular and supermolecular origins of enhanced electronic conductivity in template-synthesized polyheterocyclic fibrils: 1. Supermolecular effects. *Chem. Mater.* **1991**, *3*, 960–967.
15. Martin, C.R.; Parthasarathy, R.; Menon, V. Template synthesis of electronically conductive polymers—a new route for achieving higher electronic conductivities. *Synth. Met.* **1993**, *55*, 1165–1170.
16. Wu, C.-G.; Bein, T. Conducting polyaniline filaments in a mesoporous channel host. *Science* **1994**, *264*, 1757–1759.
17. Ferain, E.; Legras, R. Track-etched membrane—dynamics of pore formation. *Nucl. Instrum. Methods Phys. Res., B* **1994**, *84* (3), 331–336.
18. Ferain, E.; Legras, R. Characterisation of nanoporous particle track etched membrane. *Nucl. Instrum. Methods Phys. Res., B* **1997**, *131* (1–4), 97–102.
19. Duchet, J.; Legras, R.; Demoustier-Champagne, S. Chemical synthesis of polypyrrole: structure–properties relationship. *Synth. Met.* **1998**, *98* (2), 113–122.
20. Demoustier-Champagne, S.; Ferain, E.; Legras, R.; Jérôme, C.; Jérôme, R. Electrochemically synthesized polypyrrole nanotubules: effects of different experimental conditions. *Eur. Poly. J.* **1998**, *34*, 1767–1774.
21. Joo, J.; Park, K.T.; Kim, B.H.; Kim, M.S.; Lee, S.Y.; Jeong, C.K.; Lee, J.K.; Park, D.H.; Yi, W.K.; Lee, S.H.; Ryu, K.S. Conducting polymer nanotube and nanowire synthesized by using nanoporous template: synthesis, characteristics, and applications. *Synth. Met.* **2003**, *135–136*, 7–9.
22. Wang, C.; Wang, Z.; Li, M.; Li, H. Well-aligned polyaniline nano-fibril array membrane and its field emission property. *Chem. Phys. Lett.* **2001**, *341*, 431–434.
23. Aida, T.; Tajima, K. Photoluminescent silicate microsticks containing aligned nanodomains of conjugated polymers by sol–gel-based in situ polymerization. *Angew. Chem.* **2001**, *113* (20), 3919–3922.
24. Aida, T.; Tajima, K. Photoluminescent silicate microsticks containing aligned nanodomains of conjugated polymers by sol–gel-based in situ polymerization. *Angew. Chem. Int. Ed.* **2001**, *40* (20), 3803–3806.
25. Lu, Y.; Yang, Y.; Sellinger, A.; Lu, M.; Huang, J.; Fan, H.; Haddad, R.; Lopez, G.; Burns, A.R.; Sasaki, D.Y.; Shelnett, J.; Brinker, C.J. Self-assembly of mesoscopically ordered chromatic polydiacetylene/silica nanocomposite. *Nature* **2001**, *410*, 913–917.
26. Yang, Y.; Lu, Y.; Lu, M.; Huang, J.; Haddad, R.; Xomeritakis, G.; Liu, N.; Malanoski, A.P.; Sturmayer, D.; Fan, H.; Sasaki, D.Y.; Assink, R.A.; Shelnett, J.A.; van Swol, F.; Lopez, G.P.; Burns, A.R.; Brinker, C.J. Functional nanocomposites prepared by self-assembly and polymerization of diacetylene surfactants and silicic acid. *J. Am. Chem. Soc.* **2003**, *125*, 1269–1277.
27. Ikegame, M.; Tajima, K.; Aida, T. Template synthesis of polypyrrole nanofibers insulated within one-dimensional silicate channels: hexagonal versus lamellar for recombination of polarons into bipolarons. *Angew. Chem. Int. Ed.* **2003**, *42*, 2154–2157.
28. Huang, J.; Wan, M. In situ doping polymerization of polyaniline microtubules in the presence of  $\beta$ -naphthalenesulfonic acid. *J. Polym. Sci., Part A* **1999**, *37*, 151–157.
29. Shen, Y.; Wan, M. Tubular polypyrrole synthesized by in situ doping polymerization in the presence of organic function acids as dopants. *J. Polym. Sci., Part A* **1999**, *37* (10), 1443–1449.
30. Wei, Z.; Zhang, Z.; Wan, M. Formation mechanism of self-assembled polyaniline micro/nanotubes. *Langmuir* **2002**, *18*, 917–921.
31. Zhang, L.; Wan, M. Synthesis and characterization of self-assembled polyaniline nanotubes doped with D-10-camphorsulfonic acid. *Nanotechnology* **2002**, *13*, 750–755.
32. Qiu, H.; Wan, M. Synthesis, characterization, and electrical properties of nanostructural polyaniline doped with novel sulfonic acids (4-{*n*-[4-(4-nitrophenylazo)phenoxy]alkyl}aminobenzene sulfonic acid. *J. Polym. Sci., Part A* **2001**, *39*, 3485–3497.
33. Huang, K.; Wan, M. Self-assembled nanostructural polyaniline doped with azobenzenesulfonic acid. *Synth. Met.* **2003**, *135–136*, 173–174.
34. Wei, Z.; Wan, M. Synthesis and characterization of self-doped poly(aniline-co-aminonaphthalene sulfonic



- acid) nanotubes. *J. Appl. Polym. Sci.* **2003**, *87*, 1297–1301.
35. Qiu, H.; Wan, M.; Matthews, B.; Dai, L. Conducting polyaniline nanotubes by template-free polymerization. *Macromolecules* **2001**, *34*, 675–677.
  36. Zhang, Z.; Wei, Z.; Wan, M. Nanostructures of polyaniline doped with inorganic acids. *Macromolecules* **2002**, *35*, 5937–5942.
  37. Huang, J.; Virji, S.; Weiller, B.H.; Kaner, R.B. Polyaniline nanofibers: facile synthesis and chemical sensors. *J. Am. Chem. Soc.* **2003**, *125*, 314–315.
  38. Yang, Y.; Liu, J.; Wan, M. Self-assembled conducting polypyrrole micro/nanotubes. *Nanotechnology* **2002**, *13*, 771–773.
  39. Jang, J.; Yoon, H. Facile fabrication of polypyrrole nanotubes using reverse microemulsion polymerization. *Chem. Commun.* **2003**, *6*, 720–721.
  40. Ikkala, O.; Brinke, G.T. Functional materials based on self-assembly of polymeric supramolecules. *Science* **2002**, *295*, 2407–2409.
  41. Kosonen, H.; Ruokolainen, J.; Knaapila, M.; Torkkeli, M.; Jokela, K.; Sermiaa, R.; Brinke, G.T.; Bras, W.; Monkman, A.P.; Ikkala, O. Nanoscale conducting cylinders based on self-organization of hydrogen-bonded polyaniline supramolecules. *Macromolecules* **2000**, *33*, 8671–8675.
  42. Kosonen, H.; Ruokolainen, J.; Knaapila, M.; Torkkeli, M.; Sermiaa, R.; Bras, W.; Brinke, G.T.; Ikkala, O. Self-organized supermolecules based on conducting polyaniline and hydrogen bonded amphiphiles. *Synth. Met.* **2001**, *121*, 1277–1278.
  43. Kosonen, H.; Valkama, S.; Ruokolainen, J.; Knaapila, M.; Torkkeli, M.; Sermiaa, R.; Monkman, A.P.; Brinke, G.T.; Ikkala, O. Processible conducting nanoscale cylinders due to self-organized polyaniline supramolecules. *Synth. Met.* **2003**, *137*, 881–882.
  44. Holdcroft, S. Patterning  $\pi$ -conjugated polymers. *Adv. Mater.* **2001**, *13*, 1753–1765.
  45. Okawa, Y.; Masakazu, A. Nanoscale control of chain polymerization. *Nature* **2001**, *409*, 683–684.
  46. Maynor, B.W.; Filocamo, S.F.; Grinstaff, M.W.; Liu, J. Direct-writing of polymer nanostructures: Poly(thiophene) nanowires on semiconducting and insulating surfaces. *J. Am. Chem. Soc.* **2002**, *124*, 522–523.
  47. Piner, R.D.; Zhu, J.; Xu, F.; Hong, S.H.; Mirkin, C.A. Dip pen nanolithography. *Science* **1999**, *283*, 661–663.
  48. Ivanisevic, A.; Mirkin, C.A. “Dip-pen” nanolithography on semiconductor surfaces. *J. Am. Chem. Soc.* **2001**, *123*, 7887–7889.
  49. Li, Y.; Maynor, B.W.; Liu, J. Electrochemical AFM “dip-pen” nanolithography. *J. Am. Chem. Soc.* **2001**, *123*, 2105–2106.
  50. Maynor, B.W.; Li, Y.; Liu, J. Au “Ink” for AFM “dip-pen” nanolithography. *Langmuir* **2001**, *17*, 2575–2578.
  51. Liang, L.; Liu, J.; Windisch, C.F., Jr.; Exarhos, G.J.; Lin, Y. Direct assembly of large arrays of oriented conducting polymer nanowires. *Angew. Chem. Int. Ed.* **2002**, *41* (19), 3665–3668.
  52. Liu, J.; Lin, Y.; Liang, L.; Voigt, J.A.; Huber, D.L.; Tian, Z.R.; Coker, E.; McKenzie, B.; McDermott, M.J. Templateless assembly of molecularly aligned conductive polymer nanowires: a new approach for oriented nanostructures. *Chem. Eur. J.* **2003**, *9*, 604–611.
  53. Choi, S.-J.; Park, S.-M. Electrochemical growth of nanosized conducting polymer wires on gold using molecular templates. *Adv. Mater.* **2000**, *12* (20), 1547–1549.
  54. Carswell, A.D.W.; O’Rear, E.A.; Grady, B.P. *in press*.
  55. Manne, S.; Gaub, H.E. Molecular organization of surfactants at solid-liquid interfaces. *Science* **1995**, *270*, 1480–1482.
  56. Wanless, E.J.; Davey, T.W.; Ducker, W.A. Surface aggregate phase transition. *Langmuir* **1997**, *13*, 4223–4228.
  57. Ducker, W.A.; Wanless, E.J. Surface-aggregate shape transformation. *Langmuir* **1996**, *12*, 5915–5920.
  58. Kovacs, L.; Warr, G.G. Changes in the adsorbed layer structure of cationic surfactants on mica induced by adsolubilized aromatic molecules. *Langmuir* **2002**, *18* (12), 4790–4794.

# Optical Molecular Devices

A. Prasanna de Silva

*School of Chemistry, Queen's University, Belfast, Northern Ireland*

Nathan D. McClenaghan

*School of Chemistry at Queen's University, Belfast, Northern Ireland*

## INTRODUCTION

Molecules (and supermolecules)<sup>[1,2]</sup> form the smaller size range of nano-objects, especially those that allow a degree of rational design including control of size or other properties and those that possess some useful function. This article puts the spotlight on molecules whose usefulness stems from the human comprehensibility of light signals. When a molecule is empowered with light absorption/emission, its small size can be an advantage to operate in tiny spaces but yet remain under a degree of human remote control. Most of these are sensing and switching devices,<sup>[3–5]</sup> the latter including some logic capabilities. Some of the design principles governing these will be outlined below. These are classified in terms of the formatting of chromophore/fluorophore and receptor components.<sup>[6]</sup> Chromophores and fluorophores are dyes that give light absorption signals and in the latter case, light emission signals as well. As their name suggests, receptors serve to receive species which are chemical in our cases. Thus chromo/fluorophores and receptors allow physical and chemical transactions, respectively.

## “CHROMOPHORE–RECEPTOR” SYSTEMS

The most famous optical molecular devices of this kind are the pH indicators<sup>[7]</sup> known to every student of high school chemistry. Occupation of the receptor by a proton disturbs the electron distribution of the former. Because of the direct coupling between the chromophore and the receptor, it is therefore natural that the electron distribution of the chromophore itself is disturbed (Fig. 1). The consequence is a significant change of the absorption spectrum of the chromophore. Such acid-induced color changes have brightened up many a chemistry class around the world. A common example would be **1**. In general, such  $\pi$ -electron systems have electron donor and electron acceptor terminals, which leads to charge separation in the excited state. Such fractionally charged

regions in these internal charge transfer (ICT) excited states can easily lead to observation of spectral wavelength shifts as a result of electrostatic interactions with the newly arrived target ion.

As simple as these indicators are, from a chemical standpoint, they also show a logic activity that has hitherto gone unnoticed. For instance, **2**<sup>[8]</sup> shows a simple blue shift of its absorption spectrum upon interaction with  $\text{Ca}^{2+}$ . However, this blue shift can be examined as a series of optical transmittance values obtained at different wavelengths of observation. As Fig. 2 shows, four wavelengths can be picked out to show clear  $\text{Ca}^{2+}$ -induced transmittance changes of the “low–high,” “high–low,” “low–low,” and “high–high” variety. When “high” is coded as binary 1 and “low” is coded as binary 0, these digital input–output patterns can be identified as arising from single-input logic devices of the YES, NOT, PASS 0, and PASS 1 types, respectively. Furthermore, all of these logic behaviors can be simultaneously observed because light signals are readily multiplexed. So it is clear that humble ion indicators can show superposed logic behavior, which is unknown in the semiconductor device world.

## “RECEPTOR<sub>1</sub>–CHROMOPHORE–RECEPTOR<sub>2</sub>” SYSTEMS

It is only logical to add another receptor to a “chromophore–receptor” system to develop more sophisticated formats (Fig. 3). This can be particularly productive when the two receptors are chosen to be selective, each to its own target species. For instance, **3**<sup>[8]</sup> takes in  $\text{H}^+$  and  $\text{Ca}^{2+}$  at its quinoline nitrogen and amino acid receptors, respectively. The  $\pi$ -electron system again develops a dipole in the excited state with the positive pole being near the amino acid nitrogen and the negative end being close to the quinoline nitrogen. Thus admission of  $\text{Ca}^{2+}$  causes a destabilization of the excited state and hence a blue shift of the absorption spectrum (Fig. 4). On the other hand, the

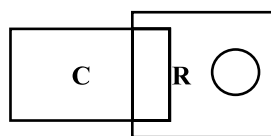


**Fig. 1** The general format of a “Chromophore (C)–Receptor (R)” system.

entry of  $H^+$  causes a stabilization of the excited state and hence a red shift of the absorption spectrum. Of course, the simultaneous treatment of **2** with  $H^+$  and  $Ca^{2+}$  gives a near cancellation of these spectral shifts. So an interesting situation arises, where the spectral effect caused by two target ions is nearly the same as what is seen in their absence. Hence we can choose a monitoring wavelength where the transmittance of light is low (coded as binary 0) when the input target species are both low ( $H^+$  and  $Ca^{2+}$  both coded as 0) or both high ( $H^+$  and  $Ca^{2+}$  both coded as 1). Furthermore, each target ion on its own causes an absorption spectral shift away from the ion-free position. So now the transmittance of light is high (coded as binary 1) when the one input target species is low and the other high ( $H^+$  coded as 1 and  $Ca^{2+}$  coded as 0 or its permutation). When these results are cast into a logic truth table (Fig. 3), we see that **3** behaves as a two-input XOR gate.

### “FLUOROPHORE–RECEPTOR” SYSTEMS

Fluorescent versions of ion indicators<sup>[9]</sup> also have a long history and their mode of action borrows extensively from their absorption-based cousins. One of

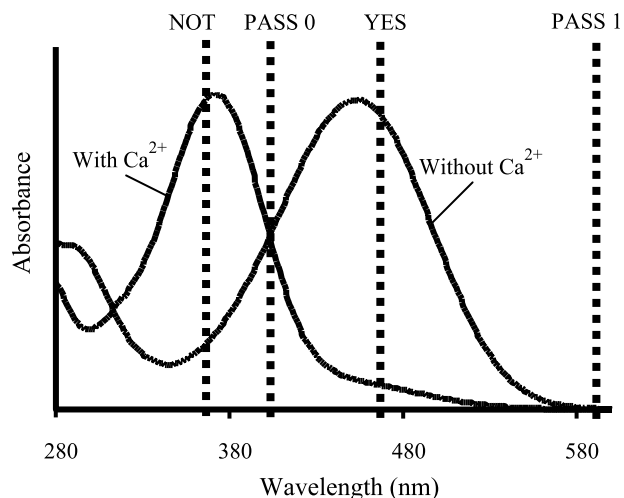
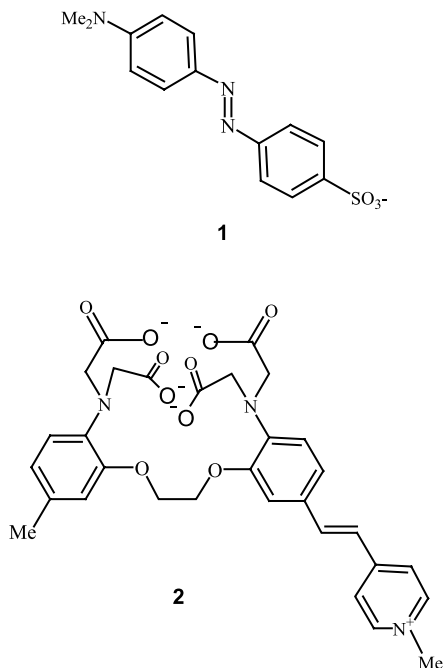
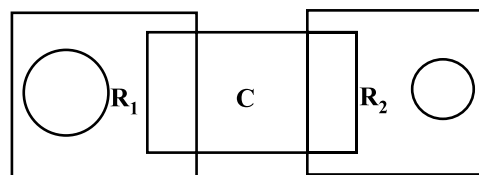


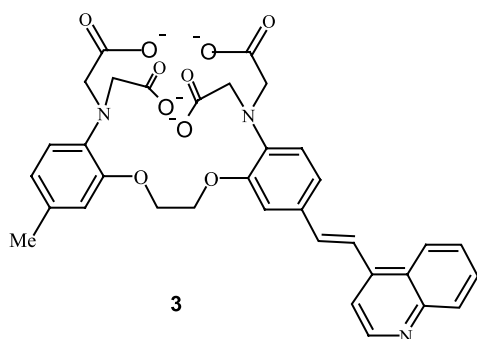
**Fig. 2** Simultaneous observation of all four single-input logic types from a single experiment with a  $Ca^{2+}$  indicator.

the significant deviations of “fluorophore–receptor” systems arises as a result of the relative temporal delay before fluorescence emerges from an excited molecule (Fig. 5). Electrostatic repulsion between the photo-produced charge separations and the receptor-incumbent target species during this time period can cause decoordination of the target. Thus the target-induced spectral change will also dissolve away. Fluorescence emission spectra are therefore weakly influenced by target binding in many “fluorophore–receptor” systems known so far, although several exceptions are available. Of course, the target-induced changes survive in the fluorescence excitation spectra, which are related to the absorption spectra anyway. Gryniewicz, Poenie, and Tsien<sup>[10]</sup> excellent  $Ca^{2+}$  sensor **4** illustrates this very well. Here is an iconic optical molecular device that has served the cellular



Input <sub>1</sub> $H^+$	Input <sub>2</sub> $Ca^{2+}$	Output Transmittance
0	0	0
0	1	1
1	0	1
1	1	0

**Fig. 3** The general format of a “Receptor<sub>1</sub> ( $R_1$ )–Chromophore (C)–Receptor<sub>2</sub> ( $R_2$ )” system and the logic truth table for the corresponding XOR gate.



physiology community for nearly two decades now by imaging  $\text{Ca}^{2+}$  populations within living cells.

### “FLUOROPHORE–SPACER–RECEPTOR” SYSTEMS

The apparently trivial addition of a spacer between a fluorophore and a receptor (Fig. 6) can completely change the device characteristics of the system. The spacer brings with it the ability to isolate components from the influence of short-range forces that normally abound in the chemical world. So the fluorophore and the receptor are forced to communicate via long-range interactions alone. These are few, and in many cases, can be reduced to one. Photoinduced electron transfer (PET), the celebrated mechanism of green plant photosynthesis, is the commonest controller of optical molecular devices of the “fluorophore–spacer–receptor” type. The fluorescence emission capability of the fluorophore is arrested by PET successfully competing for the energy of the excited state. Thus the device output is initially held in the “low” state (coded as 0). However, PET can be electrostatically stamped out,

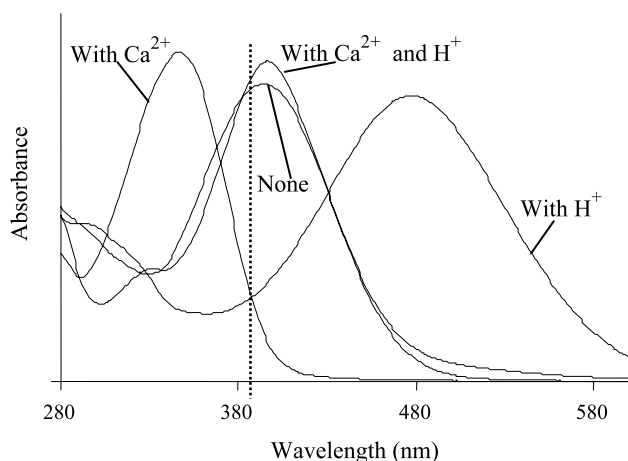


**Fig. 4** The realization of general XOR logic behavior in the transmittance output at 390 nm of the UV-Vis absorption spectra set of **3**.

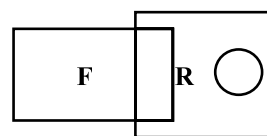
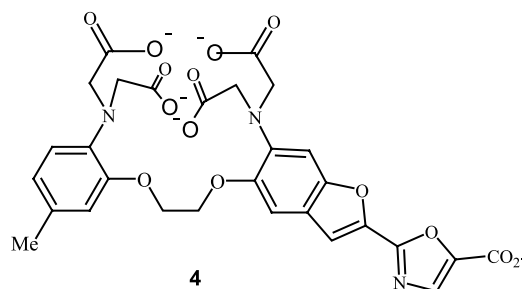


**Fig. 5.** The general format of a “Fluorophore (F)–Receptor (R)” system.

especially by charged target species when they take up residence in the receptor. Now excitation of the system will lead to no competition for the energy of the excited state. Consequently, the excited state returns to ground by emitting fluorescence as most fluorophores do. The device output is now “high” (coded as 1). Such target-induced fluorescence switching is logically a single-input YES gate. An example is the fluorescent sensor **5**<sup>[11]</sup> for  $\text{Na}^+$ , which is marketed by Roche Diagnostics for blood analysis in hospital critical care units. Cases such as **5** use more than electrostatics to enhance the fluorescence switching. The receptor within **5** is a *N*-(2-methoxyphenyl)monoaza-15-crown-5 ether, which suffers a major change in conformation upon capturing  $\text{Na}^+$ . This act reduces the electron delocalization within  $\pi$ -system of the receptor, which, in turn, makes the PET process more difficult and the fluorescence emission stronger. An extra feature within systems such as **5** is the ease with which components can be substituted for, in order to change the species being targeted or even its concentration range. So  $\text{K}^+$ -selective sensors with the same optical parameters found in **5** become available by simply replacing the receptor. Similarly, the  $\text{Na}^+$ -selective relatives of **5** such as **6**,<sup>[12]</sup> which communicate with different colors, of absorption and emission, are obtained by changing the fluorophore. Of course, the feasibility of PET must be conserved during such module replacements.

### “FLUOROPHORE–SPACER<sub>1</sub>–RECEPTOR<sub>1</sub>–SPACER<sub>2</sub>–RECEPTOR<sub>2</sub>” SYSTEMS

As observed above, a spacer ensures a high degree of modularity of systems so that individual components



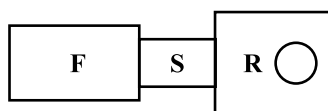
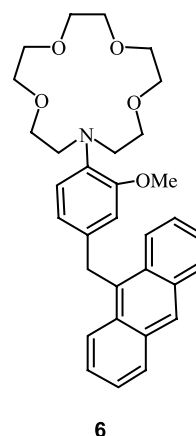
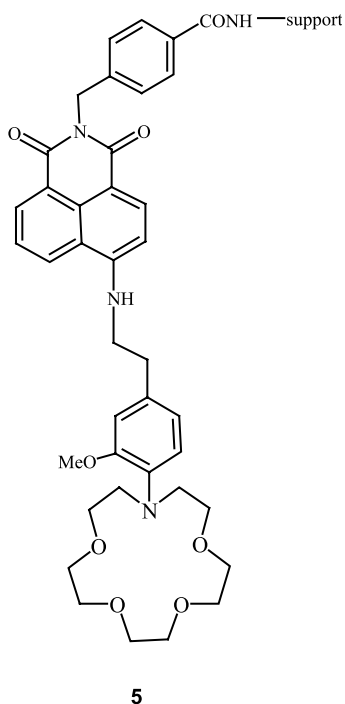


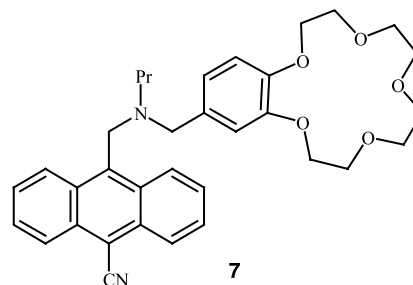
**Fig. 6** The general format of a “Fluorophore (F)–Spacer (S)–Receptor (R)” system.

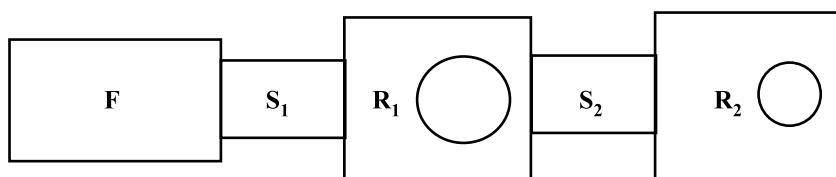
are somewhat autonomous. This not only makes PET switch system design a predictive activity but also makes PET system expansion thoroughly logical. Addition of new modules will bring with them possibilities of PET, which are each predictable (provided that electron transfer data are available). Then it becomes possible to arrange situations in which two target species arrive at suitable receptors, either alone or together. Of course, we need to have adequate selectivity within the chosen receptors so that cross-talk of target species will be minimized. Now we have two-input, one-output devices that employ the same foundations as discussed above for one-input, one-output systems. In the simplest cases, “fluorophore–spacer<sub>1</sub>–receptor<sub>1</sub>–spacer<sub>2</sub>–receptor<sub>2</sub>” systems will have two possible PET paths originating from each receptor and finishing at the fluorophore, unless each is blocked by the correct target species. So fluorescence emerges unchallenged only if both receptors are blocked by the two target species being applied as inputs. The condition of Input<sub>1</sub> = 1 and Input<sub>2</sub> = 1 is required before a “fluorophore–spacer<sub>1</sub>–receptor<sub>1</sub>–spacer<sub>2</sub>–receptor<sub>2</sub>” PET system will pass an output = 1. This



is clearly AND logic (Fig. 7). The first example of this, and the first molecular logic gate of any kind in the primary literature, was **7**.<sup>[13]</sup> This uses H<sup>+</sup> and Na<sup>+</sup> as the two inputs. There are several excellent ways of arriving at molecular AND gates now,<sup>[14–18]</sup> some of which have led to more complex logical behavior.<sup>[14,19–21]</sup>

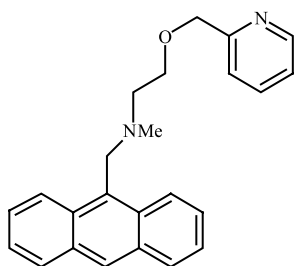
“Fluorophore–spacer<sub>1</sub>–receptor<sub>1</sub>–spacer<sub>2</sub>–receptor<sub>2</sub>” systems can also be put to uses that do not depend on binary logic. For instance, receptor<sub>1</sub> can be chosen as an electron donor amine, whereas receptor<sub>2</sub> can be chosen to be poorly electroactive. A pyridine is the choice for practical reasons, where the fluorophore is an anthracene unit within **8**.<sup>[22]</sup> Naturally, amines lose their electron donor activity upon binding to a proton. PET processes are suppressed. On the other hand, pyridines become good electron acceptors upon proton binding. PET processes are created. So the proton target species has opposite effects upon arrival at the two receptors, each with its own concentration threshold for reception. We note that a single-input species causes a single fluorescence output to be controlled in a relatively complex way. At low proton concentrations, both receptors are free and the amine launches a PET process to destroy fluorescence. At midrange proton concentrations, the more avid amine receptor picks up a proton, thereby closing its PET channel. Fluorescence flares up as a consequence. At high proton concentrations, both receptors are protonated. The





Input <sub>1</sub>	Input <sub>2</sub>	Output Fluorescence
0	0	0
0	1	0
1	0	0
1	1	1

**Fig. 7** The general format of a “Fluorophore (F)–Spacer<sub>1</sub> (S<sub>1</sub>)–Receptor<sub>1</sub> (R<sub>1</sub>)–Spacer<sub>2</sub> (S<sub>2</sub>)–Receptor<sub>2</sub> (R<sub>2</sub>)” system and the logic truth table for the corresponding AND gate.



**8**

protonated amine remains PET-disabled, but the newly formed pyridinium launches its own PET channel and extinguishes the fluorescence. Thus the fluorescence output follows a “off-on-off” pattern in response to monotonically ramping proton concentrations (Fig. 8).<sup>[22–24]</sup> Such systems are useful in being direct optical indicators of pH conditions of enzyme activity or even cellular activity. After all, the principle of “the happy medium” or “the middle way” affects everyone.

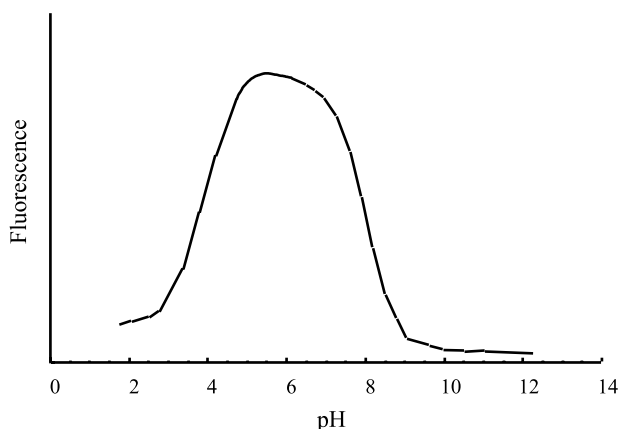


**Fig. 8** The ‘off-on-off’ fluorescence–pH profile of **8**.

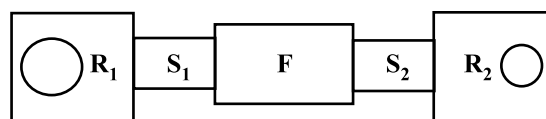
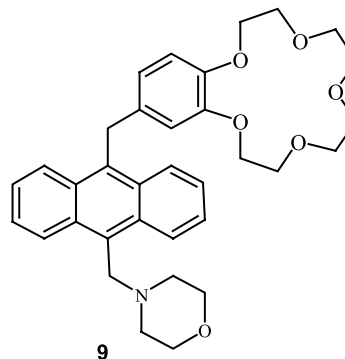


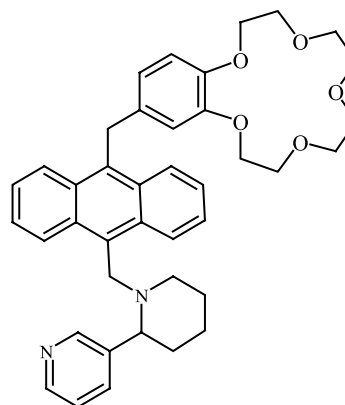
**Fig. 9** The general format of a “Receptor<sub>1</sub> (R<sub>1</sub>)–Spacer<sub>1</sub> (S<sub>1</sub>)–Fluorophore (F)–Spacer<sub>2</sub> (S<sub>2</sub>)–Receptor<sub>2</sub> (R<sub>2</sub>)” system.

### “RECEPTOR<sub>1</sub>–SPACER<sub>1</sub>–FLUOROPHORE–SPACER<sub>2</sub>–RECEPTOR<sub>2</sub>” SYSTEMS

Realizable permutations arise when a sufficiently large number of modules are contained in a system.

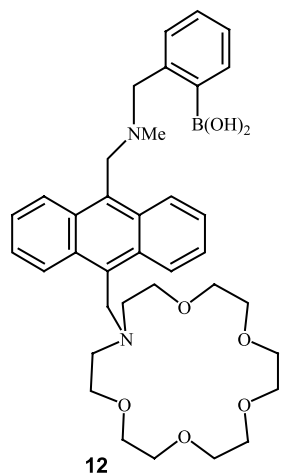
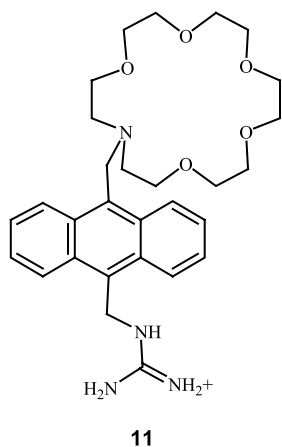


**9**



**10**





This is the case with “fluorophore–spacer<sub>1</sub>–receptor<sub>1</sub>–spacer<sub>2</sub>–receptor<sub>2</sub>” systems. A realizable permutation is to shift the fluorophore to the center of the system (Fig. 9). This act has an advantage for chemical design, because fluorescence switching efficiencies can be improved via accelerated PET processes arising from the shorter fluorophore–receptor distances involved. An example is **9**.<sup>[25]</sup> Even “receptor<sub>1</sub>–spacer<sub>1</sub>–fluorophore–spacer<sub>2</sub>–receptor<sub>2</sub>–spacer<sub>3</sub>–receptor<sub>3</sub>” systems are now in the hands of designers<sup>[26]</sup> to perform increasingly complex tasks with deceptively small molecules such as **10**.

The cases discussed above involved separate target species such as Na<sup>+</sup> and H<sup>+</sup> arriving essentially simultaneously at their respective receptors. Of course, these target species can be independently controlled to test all the input combinations for setting up truth tables to assign logic behavior. It is also feasible to build, say, two target species into separate sites of a bifunctional molecule. Now the real target becomes the bifunctional molecule itself. Naturally, such bifunctional reception can lead to enhanced selectivity of binding and detection. For example, **11**<sup>[27,28]</sup> selectively

targets amino acid zwitterions with a specified number of carbon atoms in between the ammonium and carboxylate functionalities. While the binding is enhanced, the fluorescence signaling suffers from a weakness. Indeed, the binding of the ammonium group leads to PET suppression and fluorescence enhancement. However, the capture of the carboxylate moiety reaps no such fluorescence reward owing to the lack of sufficient PET activity in the guanidinium group. Nevertheless, a nice case with two PET-active receptors is available in the form of **12** from Cooper and James.<sup>[29]</sup> Protonated glucosamine is the valuable target. The aza-18-crown-6 ether receives an ammonium group as in the case of **11**. Additionally, a diol feature is held by the aminomethylboronic acid receptor, which leads to PET suppression. So now both PET channels are blocked upon arrival of the glucosamine species in an AND logical manner. This application of AND logic systems for the enhanced binding and optical signaling is a very promising avenue of research.

## CONCLUSION

Dyes (fluorescent or not), receptors, and spacers are the building blocks that designers of optical molecular devices can play with. Combinations, or even some permutations, of these blocks can lead us to sensors, logic gates, and “off-on-off” systems already. Considering that at least some of these are demonstrably useful here and now, the number of players is bound to increase. The result will be even more interesting systems in the future.

## ACKNOWLEDGMENTS

We thank the Department of Employment and Learning, Northern Ireland and the European Union (HPRN-CT-2000-00029) for support of our efforts in this area.

## REFERENCES

1. Lehn, J.-M. *Supramolecular Chemistry*; VCH: Weinheim, 1995.
2. Balzani, V.; Scandola, F. *Supramolecular Photochemistry*; Ellis-Horwood: Chichester, 1991.
3. de Silva, A.P.; Gunaratne, H.Q.N.; Gunnlaugsson, T.; Huxley, A.J.M.; McCoy, C.P.; Rademacher, J.T.; Rice, T.E. Signaling recognition events with fluorescent sensors and switches. *Chem. Rev.* **1997**, *97*, 1515–1566.

4. Czarnik, A.W.; Desvergne, J.-P.; Eds. *Chemosensors of Ion and Molecule Recognition*; Kluwer: Dordrecht, 1997.
5. Valeur, B. *Molecular Fluorescence*; Wiley-VCH: Weinheim, 2001.
6. Bissell, R.A.; de Silva, A.P.; Gunaratne, H.Q.N.; Lynch, P.L.N.; Maguire, G.E.M.; Sandanayake, K.R.A.S. Molecular fluorescent signalling with 'fluor-spacer-receptor' systems—Approaches to sensing and switches devices via supramolecular photophysics. *Chem. Soc. Rev.* **1992**, *21*, 187–195.
7. Bishop, E.; Ed. *Indicators*; Pergamon Press: Oxford, 1972.
8. de Silva, A.P.; McClenaghan, N.D. Simultaneously multiply-configurable or superposed molecular logic systems composed of ICT (internal charge transfer) chromophores and fluorophores integrated with one- or two-ion receptors. *Chem. Eur. J.* **2002**, *8*, 4935–4945.
9. Kirkbright, G. Fluorescent Indicators. In *Indicators*; Bishop, E., Ed.; Pergamon Press: Oxford, 1972; 685–708.
10. Grynkiewicz, G.; Poenie, M.; Tsien, R.Y. A new generation of  $\text{Ca}^{2+}$  indicators with greatly improved fluorescence properties. *J. Biol. Chem.* **1985**, *260*, 3440–3450.
11. He, H.; Mortellaro, M.A.; Leiner, M.J.P.; Young, S.T.; Fraatz, R.J.; Tusa, J.K. A fluorescent chemosensor for sodium based on photoinduced electron transfer. *Anal. Chem.* **2003**, *75*, 549–555.
12. Gunnlaugsson, T.; Nieuwenhuyzen, M.; Richard, L.; Thoss, V. Novel sodium-selective fluorescent PET and optically based chemosensors: towards  $\text{Na}^+$  determination in serum. *J. Chem. Soc., Perkin Trans. 2* **2002**, 141–150.
13. de Silva, A.P.; Gunaratne, H.Q.N.; McCoy, C.P. A molecular photoionic and gate based on fluorescent signalling. *Nature* **1993**, *364*, 42–44.
14. Remacle, F.; Speiser, S.; Levine, R.D. Intermolecular and intramolecular logic gates. *J. Phys. Chem., B* **2001**, *105*, 5589–5591.
15. Lukas, A.S.; Bushard, P.J.; Wasielewski, M.R. Ultrafast molecular logic gate based on optical switching between two long-lived radical ion pair states. *J. Am. Chem. Soc.* **2001**, *123*, 2440–2441.
16. Stojanovic, M.N.; Mitchell, T.E.; Stefanovic, D. Deoxyribozyme-based logic gates. *J. Am. Chem. Soc.* **2002**, *124*, 3555–3561.
17. Pina, F.; Roque, A.; Melo, M.J.; Maestri, I.; Belladelli, L.; Balzani, V. Multistate/multifunctional molecular-level systems: light and pH switching between the various forms of a synthetic flavylum salt. *Chem. Eur. J.* **1998**, *4*, 1184–1191.
18. Inouye, M.; Akamatsu, K.; Nakazumi, H. New crown spirobenzopyrans as light- and ion-responsive dual-mode signal transducers. *J. Am. Chem. Soc.* **1997**, *119*, 9160–9165.
19. de Silva, A.P.; McClenaghan, N.D. Proof-of-principle of molecular-scale arithmetic. *J. Am. Chem. Soc.* **2000**, *122*, 3965–3966.
20. Raymo, F.M. Digital processing and communication with molecular switches. *Adv. Mater.* **2002**, *14*, 401–409.
21. Raymo, F.M.; Giordani, S. Multichannel digital transmission in an optical network of communicating molecules. *J. Am. Chem. Soc.* **2002**, *124*, 2004–2007.
22. de Silva, A.P.; Gunaratne, H.Q.N.; McCoy, C.P. Direct visual indication of pH windows: 'off-on-off' fluorescent PET (photoinduced electron transfer) sensors switches. *Chem. Commun.* **1996**, 2399–2400.
23. de Silva, S.A.; Zavaleta, A.; Baron, D.E.; Allam, O.; Isidor, E.V.; Kashimura, N.; Percarpio, J.M. A fluorescent photoinduced electron transfer sensor for cations with an off-on-off proton switch. *Tetrahedron Lett.* **1997**, *38*, 2237–2240.
24. Fabbrizzi, L.; Licchelli, M.; Poggi, A.; Taglietti, A. A versatile fluorescent system for sensing of  $\text{H}^+$ , transition metals, and aromatic carboxylates. *Eur. J. Inorg. Chem.* **1999**, 35–39.
25. de Silva, A.P.; Gunaratne, H.Q.N.; McCoy, C.P. Molecular photoionic AND logic gates with bright fluorescence and "off-on" digital action. *J. Am. Chem. Soc.* **1997**, *119*, 7891–7892.
26. de Silva, S.A.; Amorelli, B.; Isidor, D.C.; Loo, K.C.; Crooker, K.E.; Pena, Y.E. A fluorescent 'off-on-off' proton switch with an overriding 'enable-disable' sodium ion switch. *Chem. Commun.* **2002**, 1360–1361.
27. de Silva, A.P.; Gunaratne, H.Q.N.; McVeigh, C.; Maguire, G.E.M.; Maxwell, P.R.S.; O'Hanlon, E. Fluorescent signalling of the brain neurotransmitter gamma-aminobutyric acid and related amino acid zwitterions. *Chem. Commun.* **1996**, 2191–2192.
28. Sasaki, S.; Hashizume, A.; Citterio, D.; Fujii, E.; Suzuki, K. Fluororeceptor for zwitterionic form amino acids in aqueous methanol solution. *Tetrahedron Lett.* **2002**, *43*, 7243–7245.
29. Cooper, C.R.; James, T.D. Synthesis and evaluation of D-glucosamine-selective fluorescent sensors. *J. Chem. Soc., Perkin Trans. 2* **2000**, 963–969.

# Optical Nanosensors and Nanobiosensors

**Brian M. Cullum**

*Department of Chemistry and Biochemistry, University of Maryland, Baltimore County, Baltimore, Maryland, U.S.A.*

## INTRODUCTION

Advances in nanotechnology and nanofabrication have begun to have profound effects on many different scientific fields in recent years. In the field of chemical and biological sensing, one of the most significant advances in the last several decades has been the development of nanosensors, for the probing of microscopic environments. Simply stated, nanosensors are devices with dimensions on the nanometer scale that are capable of monitoring the presence of a specific chemical or class of chemicals. Although many different types of nanosensors (i.e., optical, electrochemical, etc.)<sup>[1–6]</sup> have been reported in the literature over the last two decades, this chapter will focus on nanosensors employing optical transduction methods.

As with larger optical sensors, optical nanosensors can generally be classified into one of two different classes: 1) chemical nanosensors, or 2) nanobiosensors, depending on the type of recognition element (i.e., chemical or biochemical) used to provide specificity to the sensor.<sup>[7–10]</sup> Although both of these classes of optical nanosensors are capable of obtaining quantitative measurements in many different microscopic environments, they have found an ideal application in the analysis of chemical and biochemical species present within living cells. Their small sizes allow them to be inserted and precisely positioned within individual cells to obtain spatially localized measurements of chemical species in real time.

## OVERVIEW

Prior to the development of optical nanosensors, chemical analyses inside individual living cells were limited almost entirely to the field of fluorescence microscopy, wherein a fluorescent indicator dye is introduced into a cell and allowed to diffuse throughout. When the dye comes in contact with the analyte of interest, a change in the fluorescence properties (e.g., intensity, spectral shift, etc.) of the dye occurs and fluorescence images of the entire cell are obtained. From these images, it is possible to monitor the presence of the analyte at various locations. However,

because this technique relies on imaging of the fluorescent dye, its homogenous dispersion throughout the cell is required. Unfortunately, homogeneous dispersion of dyes is often limited by intracellular conditions (i.e., pH, etc.), or prevented entirely by compartmentalization of the dye by the cell.<sup>[11]</sup> Therefore nanosensors offer significant improvements over such analyses in many cases, as they allow the user to obtain measurements at whatever location is desired without the need for homogenous dispersion of a fluorescent indicator dye.

Because of their potential for providing an enhanced understanding of cellular responses to various stimuli, several reviews have already been devoted to the subject of optical nanosensors, despite their short existence.<sup>[5,12–16]</sup> This chapter will look at the evolution of optical nanosensors from their beginning (near-field optical microscopy) to the present (biosensors capable of probing subcellular compartments of individual cells) and discuss their application to biological measurements, as well as future directions in optical nanosensing.

## EVOLUTION OF OPTICAL NANOSENSORS

Presently, the most widely reported class of optical nanosensors is fiber optic nanosensors. These sensors employ fiber optics that have been tapered on one end to diameters typically ranging between 20 and 100 nm. Although such sensors are based on the same principles as larger, conventional fiber optic sensors, their excitation process is quite different. Because the diameter of the tapered end of a fiber optic nanosensor is significantly smaller than the wavelength of light used for excitation, photons cannot escape from the tip of the fiber to be absorbed by the species of interest, as is the case in larger fiber optic sensors. Instead, excitons or evanescent fields continue to travel through the remainder of the tapered fiber's tip, providing the necessary excitation energy. Because of the weak nature of these phenomena, excitation using such a sensor is highly localized, allowing only species close to the fiber's tip to be excited. The use of tapered fiber optics to produce highly localized excitation processes (i.e., near-field excitation) arose from an area of research known as near-field optical scanning microscopy (NSOM).

## Near-Field Scanning Optical Microscopy

Near-field optical scanning microscopy is a relatively recent field of research, employing light sources and/or detectors that are smaller than the wavelength of light used for imaging.<sup>[17–20]</sup> By using such small excitation sources or detectors, images of a sample can be obtained with nanometer-scale (i.e., 10–50 nm) spatial resolution. One common method for performing such experiments is to place a pinhole in front of the detector, effectively reducing the detector's size to nanometer dimensions.<sup>[20,21]</sup> However, a variation of this technique that is growing more and more popular is to construct an excitation probe with dimensions that are smaller than the wavelength of light that is being used for sample interrogation, thereby providing a light source with sub-wavelength dimensions.<sup>[22,23]</sup> The first such excitation probe was developed by Betzig et al.<sup>[22]</sup> by tapering a single-mode optical fiber to dimensions of approximately 20 nm, thereby confining the excitation radiation to the fiber tip. Using this nanometer-scale tapered optical fiber, NSOM images of a known pattern were reconstructed with signal enhancements of greater than  $10^4$ <sup>[22,23]</sup> over previous NSOM analyses.<sup>[18,19,24,25]</sup>

### Fiber tapering methods

To construct tapered fiber optic probes for NSOM, two different processes have been developed: heated pulling and chemical etching, each capable of creating fibers with various tip diameters, taper angles, and smoothness. The first and most commonly employed of these procedures uses a heated pulling instrument, such as a laser-based micropipette puller. In this procedure, a fiber optic is placed in the micropipette puller, and a CO<sub>2</sub> laser heats the fiber while it is stretched along its major axis by a tension device (Fig. 1). As the fiber is pulled, the heated region begins to taper until, finally, the fiber is pulled into two pieces, each having one large end and one end with

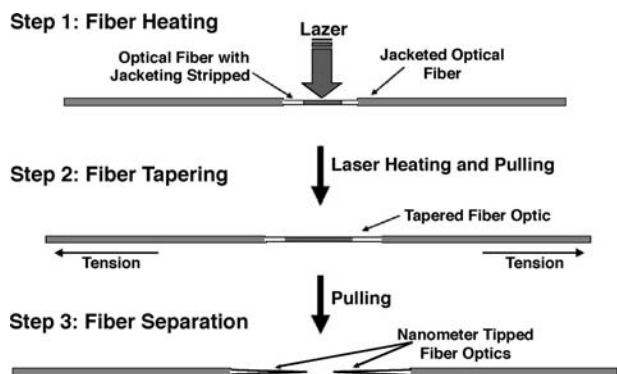


**Fig. 1** Cartoon depicting the heated pulling process used for nanofiber fabrication.

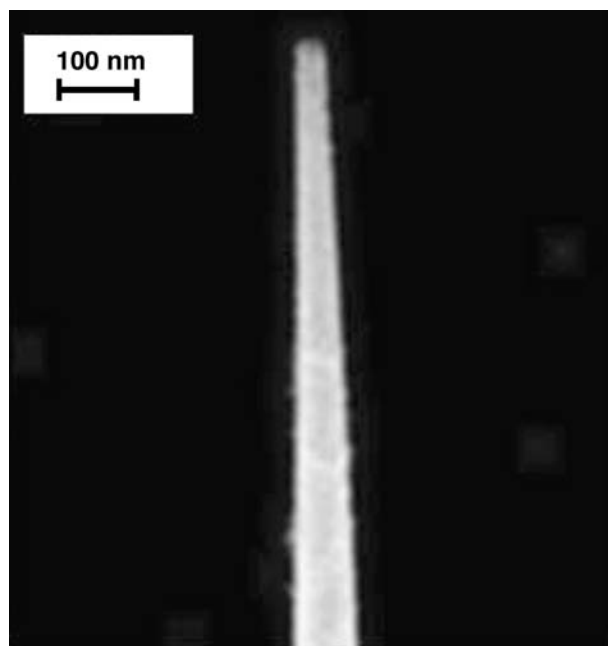


**Fig. 2** A SEM of a tapered fiber optic probe. The diameter of the tapered tip is approximately 40 nm.

nanometer-scale dimensions. By varying the heating temperature as well as the tension applied during the pulling process, tip diameters ranging in size from less than 20 nm to greater than 1000 nm have been reported.<sup>[22,26–29]</sup> A scanning electron micrograph (SEM) of an optical fiber that has been pulled with such an instrument is shown in Fig. 2. Using this technique, it is possible to produce optical fibers with highly reproducible nanometer-scale tips in just seconds.

In addition to the heated pulling process, optical fibers with nanometer-scale tips can also be produced via chemical etching. Two different variations of chemical etching have been reported in the literature: 1) Turner etching,<sup>[30,31]</sup> and 2) tube etching.<sup>[32]</sup> In both processes, hydrofluoric acid (HF) is used to etch the silica core of a fiber optic to a point. In the Turner method, the fiber is placed in the meniscus between HF and an organic overlayer, causing the HF to etch the silica and the organic overlayer to protect it. This process creates fibers with larger taper angles than those produced via the heated pulling method. These larger taper angles allow excitation light to travel closer to the tip of the fiber before being trapped, providing a more efficient excitation process. Unfortunately, because of the dual chemical nature of the etchant solution, environmental parameters such as temperature fluctuations and vibrations can cause significant batch-to-batch variations in the characteristics of the fiber tips.

Unlike Turner etching, the second chemical etching process, tube etching, employs a single-phase solution,

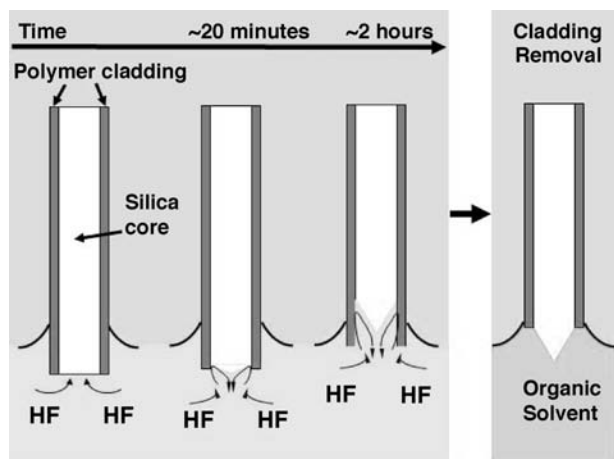


**Fig. 3** Cartoon depicting the tube etching process used for nanofiber fabrication.

thereby reducing the potential batch-to-batch variability induced by two phases. In this process, a silica core fiber having a polymer cladding is polished optically flat and one end is placed into a solution of HF. After being inserted into the HF, the silica core of the fiber begins to dissolve without affecting the cladding. Over time, the silica core continues to be etched away until it is no longer below the surface of the HF solution. When this occurs, capillary action draws HF up the walls of the polymer cladding. This HF then reaches the silica core of the fiber, where it drains back into the solution below, forming a smooth tip with a large taper angle (Fig. 3) within approximately 2 hr. To remove the surrounding polymer cladding and to expose the silica tip, the fiber is then simply placed in a suitable organic solvent. By varying the diameter of the fiber used and the depth at which it is inserted into the etching solution, accurate control over the fiber tip diameter and its taper angle can be achieved. Although this process can produce more reproducible tapered fiber optic probes than Turner etching, difficulties associated with submerging multiple fibers to the exact same depth in the HF solution make it less reproducible than the heated pulling process.

#### Application of fiber optic nanoprobes to near-field optical microscopy

One of the most significant applications of fiber optic nanoprobes to NSOM analyses of biological samples occurred when a single dye-labeled DNA molecule was detected using near-field surface-enhanced resonance Raman spectroscopy (NFSERRS).<sup>[33,34]</sup> In that work, dye-labeled DNA strands were spotted onto a surface-enhanced Raman spectroscopy (SERS) substrate that was prepared by evaporating silver on

a nanoparticle-coated surface.<sup>[33,34]</sup> Following preparation of the sample, a fiber optic nanoprobe was raster-scanned over the sample's surface, illuminating it point by point, while the resulting Raman signals were measured with a charge-coupled device (CCD). Based on the intensity of the Raman signals measured at every location, a two-dimensional image of the DNA molecules was reconstructed and normalized for surface topography based on the intensity of the Rayleigh scatter.

With the advent of fiber optic nanoprobes, NSOM promises to be an area of research that holds a great deal of promise for biological analyses. Because many biological compounds produce luminescent signals following excitation, which are typically much stronger than Raman signals, it may be possible to map out the location of individual molecules of specific chemicals in human tissues (e.g., neurotransmitters in the brain) using NSOM. Such analyses could open new horizons in the investigation of complex chemical reactions and pathways of biological systems.

#### FIBER OPTIC CHEMICAL NANOSENSORS

Shortly after the development of fiber optic nanoprobes for NSOM, they were applied to the field of chemical sensing, making it possible to obtain spatially localized measurements (i.e., less than 50 nm away from the fiber's tip) of specific chemicals in three-dimensional structures.<sup>[26]</sup> Unlike simple NSOM probes, these fiber optic chemical nanosensors have chemical recognition elements (e.g., fluorescent indicator dyes, etc.) bound to the tapered tip of the fiber to provide a degree of specificity. Because of this specificity and their ability to obtain spatially localized measurements, the monitoring of concentration gradients and spatial inhomogeneities in submicroscopic environments (e.g., cells, etc.) with chemical nanosensors is possible. However, because of the small sampling volume probed by such fiber optic chemical nanosensors, the amount of analytes present in the excitation volume at any given time is very small, making it important to use a sensitive spectroscopic analysis technique (e.g., fluorescence, etc.).

In addition to employing a sensitive spectroscopic technique, it is also important to employ a sensitive detection system, such as the one shown in Fig. 4. In such a system, the sample is excited by launching an intense light source (e.g., laser) into the proximal end of the fiber optic nanosensor. The nanosensor is then positioned in the desired location using an  $x$ - $y$ - $z$  micromanipulator or piezoelectric positioning system mounted on a microscope. Once in place, the fluorescent indicator dye immobilized on the tip of the fiber is excited, and the resulting fluorescence emission

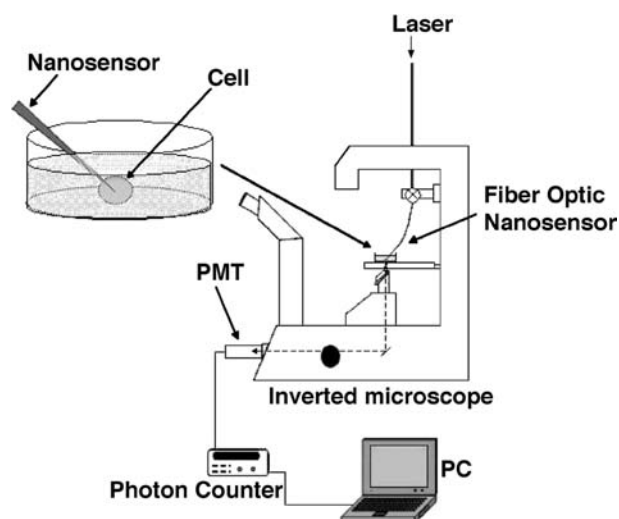


**Fig. 4** Schematic diagram depicting a typical measurement system for fiber optic nanosensor-based analyses. The nanosensor is manipulated to the location of interest using an  $x$ - $y$ - $z$  micromanipulator.

is collected and filtered by the microscope before being detected with either a photomultiplier tube (PMT) or a CCD.

### Ion-Sensitive Fiber Optic Nanosensors

The first fiber optic-based chemical nanosensors were reported in 1992 for the monitoring of pH.<sup>[26]</sup> In that original work, multimode fibers and single-mode fibers were tapered via a heated pulling process to produce tip diameters ranging from 100 to 1000 nm.<sup>[26,27]</sup> These tapered fibers were then used to fabricate pH-sensitive nanosensors via a three-step process. Immediately following the tapering process, a thick layer of aluminum was applied to the walls of the fibers using a vacuum evaporation system. This aluminum layer ensured that total internal reflection occurred over the tapered region of the fibers, where the cladding was stretched too thin. To prevent aluminum from depositing on the tips of the fibers, where the receptor molecules (i.e., fluorescent indicator dye molecules) were to be bound, the fibers were placed in an evaporator system with their tapered tips facing away from the source of the evaporating aluminum. This allowed the sides of the fibers to shadow the tips from the evaporating metal. This is illustrated in Fig. 5. Once the walls of the fibers were coated with aluminum, the silica tips were silanized to allow cross-linking to a polymer coating. The third and final step in the fabrication of these pH nanosensors consisted of attaching a pH-sensitive dye, acrylofluoresceinamine, to the silanized fiber tips through a variation of a photo-polymerization process that has been used in

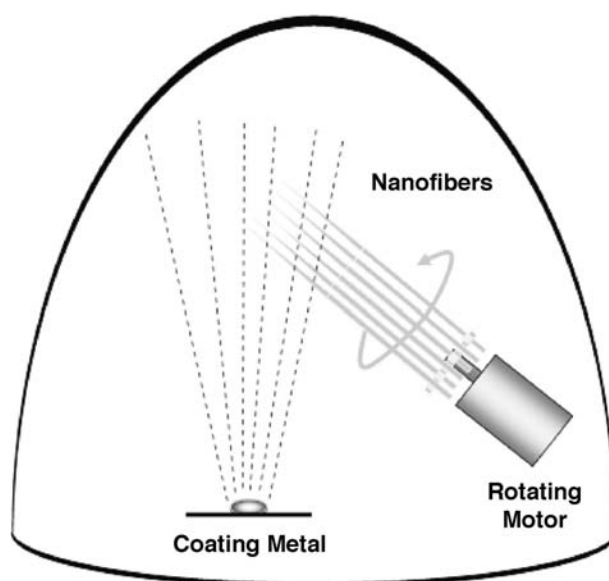


**Fig. 5** Cartoon depicting the thermal evaporation procedure used to coat the sides of the tapered fiber optic probes with metal.

the construction of larger chemical sensors.<sup>[35,36]</sup> However, unlike the larger nontapered fiber optic chemical sensors, the near-field excitation provided by these small fiber probes restricted the cross-linking of the polymer solution to the near-field of the fiber, providing a small sensing volume.

Following fabrication, the response characteristics of the pH nanosensors were evaluated. During this evaluation, the sampling volume of the nanosensors was determined to be more than six orders of magnitude smaller than conventional fiber optic chemical sensors, making them ideal for biological analyses. In addition, these nanosensors were found to be both stable and reversible to pH changes, and have response times of approximately 300 msec, which is approximately 100-fold faster than conventional fiber optic chemical sensors.

The application of fiber optic chemical nanosensors to a biologically relevant analysis was first performed by monitoring the pH of the extraembryonic space of rat conceptuses in an attempt to understand the role environmental factors play on embryonic growth.<sup>[26]</sup> In this study, pH nanosensors similar to the ones described above were inserted into the extraembryonic space of rat conceptuses, with minimal damage to the surrounding visceral yolk sac, and pH measurements were obtained. In a similar study using the same pH-sensitive nanosensors, indirect analyses of nitrite and chloride levels in the yolk sac of rat conceptuses were also performed.<sup>[37]</sup>

Since the construction of the first fiber optic nanosensors, additional fiber optic-based chemical nanosensors have been reported for the measurement



of pH,<sup>[38–41]</sup> various metal ions,<sup>[42,43]</sup> as well as nitric oxide.<sup>[44]</sup> In addition, the size of the environments in which they probe continues to become smaller. In fact, the measurement of chemical species inside individual living cells has even been reported using fiber optic chemical nanosensors. The first such intracellular measurements with fiber optic chemical nanosensors employed sodium ion (Na<sup>+</sup>)-sensitive indicator dyes immobilized onto the tips of tapered fiber optics through a process similar to that described for the pH nanosensors. These sensors were then used to measure sodium ion (Na<sup>+</sup>) concentrations in the cytoplasmic space of a single mouse oocyte, one of the largest mammalian cells (ca. 100 μm in diameter), while ion channels were opened and closed by external stimulation.<sup>[15]</sup> In addition to intracellular analyses of Na<sup>+</sup> ions, fiber optic chemical nanosensors have also been used to monitor intracellular calcium (Ca<sup>2+</sup>) ion fluctuations in vascular smooth muscle cells, following stimulation.<sup>[45]</sup> Because of the large number of cellular reactions that are signaled by fluctuations in the concentration of ionic species, and the demonstrated ability of fiber optic nanosensors to perform intracellular measurements of those ionic species, these sensors should prove to be valuable tools for future discoveries in cellular dynamics.

## FIBER OPTIC NANOBIOSENSORS

Because of the complexity of biological systems and the number of possible interference to chemical nanosensors, the need for added specificity in cellular analyses can arise. To achieve this added specificity, fiber optic nanobiosensors are often employed. Like their larger counterparts, conventional fiber optic biosensors, biological receptor molecules (i.e., antibodies, enzymes, etc.) are used to provide added specificity. The different types of bioreceptor molecules that have been used for the fabrication of fiber optic nanobiosensors include antibodies, oligonucleotides, and enzymes, thereby allowing for the detection of a wide array of analytes.

### Antibody-Based Fiber Optic Nanobiosensors

The first fiber optic nanobiosensor was reported by Alarie and VoDinh<sup>[28]</sup> in 1996. In this work, antibody-based nanobiosensors for the DNA adduct, benzo[*a*]pyrene tetrol (BPT), were developed and characterized. The fabrication of these first nanobiosensors was performed in a process very similar to that used in the development of fiber optic chemical sensors. Initially, a 600-μm-diameter multimode fiber optic was tapered down to 40 nm at the tip. After tapering, a thick layer

of silver was applied to the sides of the fiber in such a way as to prevent the coating of the fiber's tip. Next, the uncoated fiber tip was silanized, and antibodies were attached via a covalent-binding procedure.<sup>[28]</sup> Following attachment of the antibodies, the fiber optic nanobiosensors were characterized in terms of antibody binding affinity as well as sensitivity and absolute detection limits. From these measurements, it was found that the antibodies had retained greater than 95% of their native binding affinity for BPT after being bound and that the absolute detection limit for BPT using these nanobiosensors was approximately 300 zmol (i.e.,  $300 \times 10^{-21}$  mol).

Shortly after the development of this first antibody-based fiber optic nanobiosensor, several others were developed and applied to *in vitro* measurements within individual living cells.<sup>[5,29,46–48]</sup> In one such study, nanobiosensors for BPT were prepared as described above and used to obtain quantitative measurements of intracellular concentrations of BPT in the cytosol of two different cell lines: 1) rat liver epithelial cells, and 2) human mammary carcinoma cells.<sup>[29]</sup> Unlike previous intracellular analyses that employed relatively large cells (i.e., mouse oocytes and neurons), the cells analyzed in this study were spherical in shape and had diameters of approximately 10 μm, thereby demonstrating that fiber optic nanosensors and nanobiosensors could be used to analyze cells the size of typical mammalian somatic cells (i.e., 10–15 μm) without destroying them. In fact, this study also demonstrated that the insertion of a fiber optic nanosensor or fiber optic nanobiosensor into such a cell and the subsequent measurement seemed to have little effect on the cell's normal function. This was demonstrated by inserting the fiber optic nanobiosensor into the cytoplasm of a cell beginning to undergo mitosis and monitoring cell division following incubation of the nanofiber in the cell for 5 min. Fig. 6 contains an image of the fiber optic nanosensor being inserted into this cell, as well as a second image showing the two daughter cells that it divided into after approximately 2 hr.

### Molecular Beacon-Based Fiber Optic Nanobiosensors

To detect the presence of oligonucleotides (i.e., RNA, DNA, etc.) in intracellular environments, a class of fiber optic nanobiosensors that employ a relatively new type of bioreceptor molecules known as a molecular beacon has been developed.<sup>[49]</sup> Molecular beacons are hairpin-shaped oligonucleotide probes that rely on the complementarity of nucleic acids (i.e., adenine:thymine, cytosine:guanosine, etc.) to form the basis for the molecular recognition of a specific oligonucleotide sequence. As shown in Fig. 7, molecular beacons form a stem-loop structure in the absence of the target



120 minutes  
after probing  
with a fiber optic  
optic

**Fig. 6** Photograph of an individual cell that is probed with a fiber optic nanosensor as it begins to undergo mitosis, and a second photograph of that same cell approximately 2 hr later, having divided into two daughter cells.

sequence, in which a fluorophore [e.g., fluorescein isothiocyanate (FITC), etc.] on one end of the stem is in close proximity to a nonfluorescing, quenching moiety [e.g., dimethylaminophenylazobenzoic acid (DABCYL), etc.] on the other end.<sup>[50]</sup> In this state, when the fluorophore on the molecular beacon is excited, an energy transfer takes place between the excited fluorophore and the quencher, either by direct energy transfer or fluorescence resonance energy transfer (FRET), and minimal fluorescence emission occurs. However, when the loop sequence of the molecular beacon comes into contact with its complementary sequence, the stem begins to unzip, creating a spatial separation between the fluorophore and the quencher. This spatial separation in turn causes a dramatic increase in the fluorescence intensity of the molecular beacon, with some reports stating enhancements exceeding 200-fold.<sup>[51]</sup>

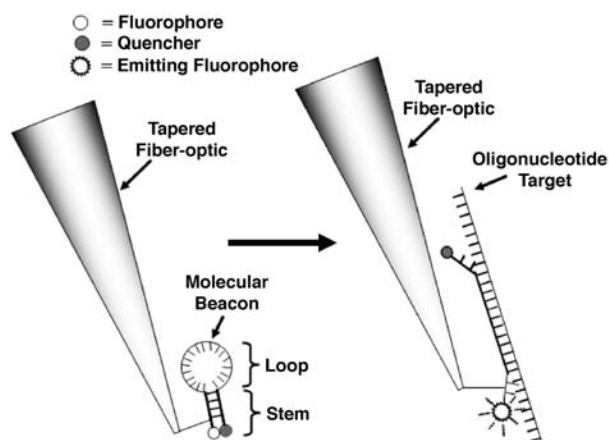


**Fig. 7** Cartoon depicting the mechanism of action of a molecular beacon.

Because of their inherent sensitivity and specificity, molecular beacons have recently been used as bioreceptor molecules in the fabrication of fiber optic nanobiosensors for single-stranded DNA and RNA.<sup>[52,53]</sup> In these works, Liu and Tan and Liu et al. attached molecular beacons to the silica core of a fiber optic nanosensor through biotin–avidin linkages. By binding the molecular beacons to the tapered tip of the fiber optic in this method, a strong attachment was achieved, while not degrading the activity of the beacon.

### Enzyme-Based Fiber Optic Nanobiosensors

In addition to the use of molecular beacons and antibodies as bioreceptor molecules, fiber optic nanobiosensors that employ enzymes for molecular recognition have also been developed.<sup>[54,55]</sup> Using enzymes as bioreceptors not only provides nanobiosensors with a high degree of specificity, but their catalytic activity can amplify the species being measured, allowing for sensitive analyses. One such enzymatic-based fiber optic nanobiosensor was developed for the indirect detection of glucose.<sup>[55]</sup> In this work, Rosenzweig and Kopelman immobilized the enzyme, glucose oxidase, and the oxygen-sensitive indicator, tris(1,10-phenanthroline) ruthenium chloride, in an acrylamide polymer on the tapered end of a nanofiber via a photopolymerization process. Therefore when the nanobiosensor is in the presence of glucose, the enzyme catalyzes the oxidation of glucose into gluconic acid, consuming oxygen. The resulting changes in oxygen levels are then measured via the oxygen-sensitive indicator dye. By using an enzymatic receptor, these nanobiosensors were capable of absolute detection limits of approximately  $10^{-15}$  mol and a sensitivity five to six orders of magnitude greater than current glucose optodes.<sup>[55]</sup>

Another example of an enzymatic nanobiosensor was developed by Tan et al. for the indirect measurement of the neurotransmitter, glutamate. In this work, glutamate dehydrogenase is bound to the tip of the fiber optic nanobiosensor to achieve molecular recognition. When the sensor is in the presence of glutamate, the nonfluorescent species, NAD, is reduced into the autofluorescent species, NADH, which can then be monitored via fluorescence spectroscopy. By relating the intensity of the NADH fluorescence to glutamate concentration, sensitive analyses were performed. Following the construction of these nanobiosensors, their usefulness was evaluated by continuously monitoring the release of glutamate from individual neurons during stimulation.

### FIBER OPTIC NANOIMAGING SENSORS

Although fiber optic nanosensors and nanobiosensors have proven to be useful tools for the spatially localized, quantitative analysis of chemical species in cells, only one sensor can be inserted into a typical mammalian somatic cell at a time, without causing significant damage.<sup>[56]</sup> This inability to monitor multiple locations simultaneously can dramatically limit the applicability of fiber optic nanosensors and nanobiosensors to many types of cellular analyses. To overcome this limitation, a couple of research groups have recently begun to develop nanoscale fiber optic imaging probes and sensors comprised of thousands of individual fibers arranged in a coherent bundle.<sup>[57,58]</sup> These nanoimaging sensors represent the latest advance in fiber optic-based nanosensors, and are capable of obtaining measurements at thousands of different locations simultaneously with nanometer-scale spatial resolution.

#### Fiber Optic Nanoimaging Probe Fabrication

Similar to single-fiber-based nanosensors and nanobiosensors, nanoimaging probes can be fabricated either through a chemical etching process, or a heated pulling process. In the chemical etching process, commercially available coherent imaging bundles with 30,000 individual fibers are etched in HF to form an array of silicon tips.<sup>[58]</sup> Following formation of the array of silicon tips, a layer of gold is sputtered over the entire surface to prevent light from escaping from the tapered sides of each fiber element. After deposition of the gold overlayer, a polymer is electrochemically deposited over the gold and heat-cured to expose the gold at the tips of the individual fiber elements. Finally, the exposed gold surface on each of the individual fiber

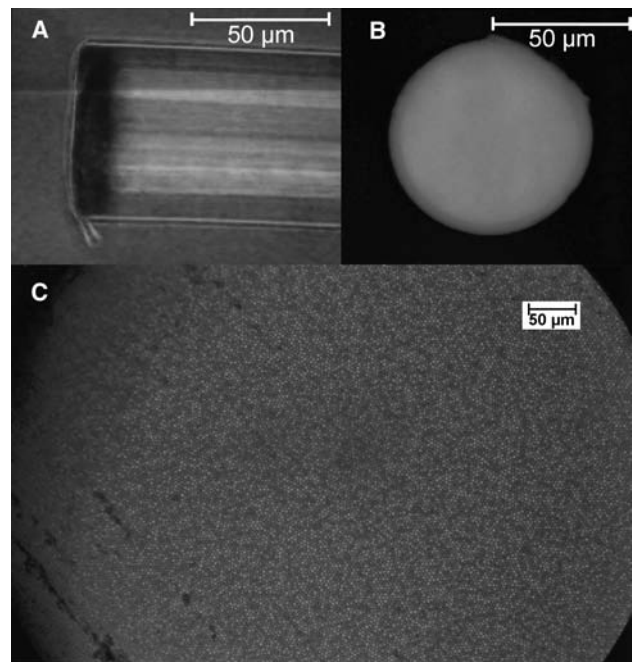


**Fig. 8** Photographs of a fiber optic nanoimaging probe that has been tapered using a heated pulling process. Panel A shows a side-on view of the fiber demonstrating the flat tip after pulling. Panels B and C are end-on views of the tapered end and the nontapered end of the fiber, respectively.

element tips is dissolved to produce free silica surfaces for spectroscopic probing.

In addition to chemical etching, nanoimaging probes have also been fabricated using a heated pulling process.<sup>[57]</sup> However, unlike the nanoimaging array created via chemical etching, the heated pulling process produces an array having a flat surface. This can be seen in Fig. 8A, which shows a side-on view of a fiber optic imaging bundle that has been tapered in a micropipette puller. To produce this flat surface, which is necessary for imaging, the delay between the final pull in the micropipette puller and the time at which the heating laser turned off is increased, thus allowing the fiber to cool off slightly and be broken, with all of the individual fiber elements being of the same length and diameter. By changing the heating temperature and the initial pull strength of the micropipette puller, fibers can be accurately and reproducibly tapered to all different diameters. Fig. 8 shows a fiber that has been tapered to have individual fiber element diameters of 800 nm on one end (Fig. 8B) and 4- $\mu$ m diameters on the untapered end (Fig. 8C).

Using these two different fabrication techniques, fiber optic nanoimaging probes and sensors that will not only allow for the quantitative measurement of individual chemical species, but also the simultaneous measurement at many different locations are being developed. Although these fiber optic imaging bundles

are too large to be inserted into individual living cells, they can be used to monitor cellular membranes without damage.

## NANOPARTICLE-BASED OPTICAL NANOSENSORS

Although fiber optic-based nanosensors have had a large impact on the fields of cellular biology and biochemistry, significant advances and variations in optical nanosensors are constantly being made, from the use of more selective bioreceptors to the development of different types of optical-based nanobiosensors. One such advance in the last several years has been the development of nanoparticle-based optochemical sensors, with nanometer-scale sizes in all three dimensions. Because of the small sizes of these sensors, a large number of them can be implanted within an individual cell at one time, allowing for the monitoring of many locations simultaneously. Although many different nanoparticle-based sensors are currently being developed, three main classes have already shown a great deal of promise for intracellular analyses. These three classes are quantum dot-based nanobiosensors, polymer-encapsulated nanosensors known as PEBBLEs, and phospholipid-based nanosensors. Each of these different classes of nanoparticle-based sensors is described in more detail below.

### Quantum Dot-Based Nanosensors

The first class of nanoparticle-based optical nanosensor that was developed involved attaching nanometer-scale semiconductor particles, known as quantum dots, to various biological receptor molecules including antibodies, oligonucleotides, and enzymes.<sup>[59–63]</sup> The quantum dots used in these nanosensors comprised ZnS particles capped with Cd–Se. By using quantum dots instead of conventional fluorescent dyes, these sensors exhibit much more intense emission as well as a much greater degree of photostability. These properties are very important when trying to monitor changes in chemical or biochemical species concentrations over time because most fluorescent dyes exhibit rapid and significant photobleaching with the small amount used in cellular analyses. Unfortunately, because quantum dot-based nanobiosensors exhibit luminescence emission whether bound to the analyte or not, there are limits to their applicability to cellular analyses. Additionally, a biocompatibility issue also exists for these sensors because the materials used to fabricate the quantum dots (e.g., Cd–Se, etc.) are toxic to cells. Because of their toxicity, there is a significant effort currently underway in many research groups to develop more biocompatible

quantum dot-based nanobiosensors to perform long-term monitoring of cellular reactions or processes.

### PEBBLEs Sensors

A second class of nanoparticle-based optical nanosensors that has already had a large impact on the fields of cellular biology and biochemistry was developed by Sasaki et al.,<sup>[64]</sup> Clark et al.,<sup>[65,66,67]</sup> Sumner et al.,<sup>[68]</sup> and Xu et al.<sup>[69,70]</sup> in the last several years. These sensors, known as PEBBLEs (probes encapsulated by biologically localized embedding), are comprised of fluorescent indicator dyes sensitive to ionic species (i.e.,  $H^+$ ,  $Ca^{2+}$ , etc.) that are embedded in 20-nm-diameter or 200-nm-diameter polymer or sol–gel spheres.<sup>[65,66]</sup> By encapsulating the fluorescent indicator dyes in a polymer matrix, they are protected from cellular degradation by proteins, while still allowing ions to pass and react with them. In addition, this polymer coating also protects the cell from the toxic effects of the dye.

Since they were first developed in 1996, PEBBLEs have been applied to the measurement of many different species (pH,  $Ca^{2+}$ , NO,  $O_2$ , and  $Zn^{2+}$ ) within individual cells.<sup>[65–70]</sup> In these analyses, large quantities of PEBBLEs are inserted in a cell, either by a gene gun or a similar device, to ensure that sensors are present at every location in which a measurement might be desired. Once the sensors have been injected into the cell, the entire cell is illuminated and the fluorescence signal from the indicator dye is measured over the autofluorescent background of the cell.

Because of the potential for intense autofluorescence from the cell, depending on the excitation wavelength used, the detection limits of such analyses can be relatively high. To overcome this problem, Anker, Behrend, and Kopelman<sup>[71]</sup> and Anker and Kopelman<sup>[72]</sup> have recently developed magnetically modulated variations of these sensors, known as MagMOONs (magnetically modulated optical nanoprobes). These MagMOONs are created around aspheric magnetic nanoparticles that can be rotated in the presence of a rotating magnetic field. As the particles begin to rotate, the optical emission from the sensor is modulated. During demodulation, the emission from the sensors can be separated from the continuous autofluorescence background signals, thereby dramatically improving the detection limit of such sensors.

### Phospholipid Sensors

The third major class of nanoparticle-based sensors that has already demonstrated a significant impact on cellular analyses is phospholipid-based sensors. Like the PEBBLEs described above, these nanosensors also

employ an encapsulation technique to ensure biocompatibility with the cell being investigated.<sup>[73–78]</sup> Within this class of nanosensors, two distinct subclasses exist: liposome sensors,<sup>[77,78]</sup> and lipobead sensors.<sup>[73,75]</sup> The first of these subclasses, liposome-based nanosensors, employs fluorescent indicator dyes encapsulated in the internal aqueous compartment of a liposome. This allows the dye, which is sensitive to a particular analyte, to retain its solution-based characteristics (i.e., spectral emission profile, Stokes shift, response time, etc.) while preventing toxic dye molecules from diffusing throughout the cell. Currently, liposome nanosensors have been developed and applied to the measurement of molecular oxygen<sup>[78]</sup> and pH<sup>[77]</sup> in various cellular environments, demonstrating a high degree of sensitivity as well as specificity.

Recently, a variation of these liposome-encapsulated nanosensors was developed by Ji et al.,<sup>[73]</sup> McNamara et al.,<sup>[75]</sup> McNamara and Rosenzweig,<sup>[79]</sup> and DeCoster et al.<sup>[80]</sup> in which the fluorescent indicator dye molecules were immobilized onto a polystyrene nanoparticle prior to being encapsulated in a phospholipid membrane. This second subclass of phospholipid-based nanosensors, known as lipobead nanosensors, is more stable and less susceptible to biological degradation than liposome-based sensors. An additional advantage of these lipobead nanosensors over liposome nanosensors or PEBBLEs is that the fluorescent indicator dyes can be partially embedded in the phospholipid membrane, allowing the measurement of a much larger number of chemical species, because the analyte does not need to diffuse through a protective coating before interacting with the dye.<sup>[73,75]</sup>

## CONCLUSION

With interest in nanotechnology and its practical use rising, the development of optical nanosensors for microscopic analyses has increased dramatically over the last decade. Since the development of the first fiber optic nanoprobe for near-field scanning optical microscopy, optical nanosensors have evolved into many different forms, each having its own distinct advantages for a particular type of analysis. Furthermore, these optical nanosensors and nanobiosensors have begun to demonstrate their ability to obtain reliable and useful measurements of chemical species within cellular and even subcellular environments. Based on the rapid impact that optical nanosensor and nanobiosensor technologies have already had on cellular biology and biomedical diagnostics, future developments (i.e., smaller, less invasive sensors; more biocompatible sensors; etc.) should revolutionize the fields of healthcare and pharmaceutical development by providing a much greater understanding of basic

cellular reaction pathways for various biological functions and diseases.

## ACKNOWLEDGMENTS

This work was supported, in part, by the University of Maryland Baltimore County. In addition, I would like to acknowledge the generous assistance of Dr. Dimitra Stratis-Cullum with the graphics.

## REFERENCES

1. Apuzzo, M.L.J.; Liu, C.Y. Things to come. *Neurosurgery* **2001**, *49* (4), 765–778.
2. Space mission for nanosensors. *Futurist* **2002**, *36* (6), 13
3. Aylott, J.W. Optical nanosensors—An enabling technology for intracellular measurements. *Analyst* **2003**, *128* (4), 309–312.
4. Cui, Y.; Wei, Q.Q.; Park, H.K.; Lieber, C.M. Nanowire nanosensors for highly sensitive and selective detection of biological and chemical species. *Science* **2001**, *293* (5533), 1289–1292.
5. Cullum, B.M.; Vo-Dinh, T. The development of optical nanosensors for biological measurements. *Trends Biotechnol.* **2000**, *18* (9), 388–393.
6. Clark, H.A.; Hoyer, M.; Parus, S.; Philbert, M.A.; Kopelman, M. Optochemical nanosensors and subcellular applications in living cells. *Mikrochim. Acta* **1999**, *131* (1–2), 121–128.
7. Nice, E.C.; Catimel, B. Instrumental biosensors: New perspectives for the analysis of biomolecular interactions. *Bioessays* **1999**, *21* (4), 339–352.
8. Weetall, H.H. Chemical sensors and biosensors, update, what, where, when and how. *Biosens. Bioelectron.* **1999**, *14* (2), 237–242.
9. Tess, M.E.; Cox, J.A. Chemical and biochemical sensors based on advances in materials chemistry. *J. Pharm. Biomed. Anal.* **1999**, *19* (1–2), 55–68.
10. Braguglia, C.M. Biosensors: An outline of general principles and application. *Chem. Biochem. Eng. Q.* **1998**, *12* (4), 183–190.
11. Haugland, R.P. Indicators for Ca<sup>2+</sup>, Mg<sup>2+</sup>, Zn<sup>2+</sup> and Other Metals. In *Handbook of Fluorescent Probes and Research Chemicals*, 6th Ed. Ed.; Spence, M.T.Z., Ed.; Molecular Probes, Inc.: Eugene, OR, 1996; 503–540.
12. Lu, J.Z.; Rosenzweig, Z. Nanoscale fluorescent sensors for intracellular analysis. *Fresenius J. Anal. Chem.* **2000**, *366* (6–7), 569–575.
13. Vo-Dinh, T.; Cullum, B.M. Biosensors and biochips: Advances in biological and medical diagnostics. *Fresenius J. Anal. Chem.* **2000**, *366* (6–7), 540–551.
14. Vo-Dinh, T.; Cullum, B.M.; Stokes, D.L. Nanosensors and biochips: Frontiers in biomolecular diagnostics. *Sens. Actuators, B, Chem.* **2001**, *74* (1–3), 2–11.
15. Tan, W.H.; Kopelman, R.; Barker, S.L.R.; Miller, M.T. Ultrasmall optical sensors for cellular measurements. *Anal. Chem.* **1999**, *71* (17), 606A–612A.

16. Cullum, B.M.; Vo-Dinh, T. Nanosensors: Development and Application of Nanosensors for Cellular Diagnostics. In *Biomedical Photonics Handbook*, 1st Ed.; Vo-Dinh, T., Ed.; CRC Press: Boca Raton, 2003.
17. Betzig, E.; Harootunian, A.; Lewis, A.; Isaacson, M. Near-field scanning optical microscopy (NSOM)—Investigation of radiation transmitted through sub-wavelength apertures. *Biophys. J.* **1985**, *47* (2), A407
18. Betzig, E.; Lewis, A.; Harootunian, A.; Isaacson, M.; Kratschmer, E. Near-field scanning optical microscopy (NSOM)—Development and biophysical applications. *Biophys. J.* **1986**, *49* (1), 269–279.
19. Durig, U.; Pohl, D.W.; Rohner, F. Near-field optical-scanning microscopy. *J. Appl. Phys.* **1986**, *59* (10), 3318–3327.
20. Pohl, D.W. Scanning Near-Field Optical Microscopy. In *Advances in Optical and Electron Microscopy*; Mulvey, T., Ed.; Academic Press: London, 1984.
21. Teague, E.C. *Scanning Microscopy Technology and Applications*; Society of Photo-Optical Instrumentation Engineering: Bellingham, 1988; Vol. 897.
22. Betzig, E.; Trautman, J.K.; Harris, T.D.; Weiner, J.S.; Kostelak, R.L. Breaking the diffraction barrier—Optical microscopy on a nanometric scale. *Science* **1991**, *251* (5000), 1468–1470.
23. Betzig, E.; Chichester, R.J. Single molecules observed by near-field scanning optical microscopy. *Science* **1993**, *262* (5138), 1422–1425.
24. Betzig, E.; Isaacson, M.; Lewis, A. Collection mode near-field scanning optical microscopy. *Appl. Phys. Lett.* **1987**, *51* (25), 2088–2090.
25. Lieberman, K.; Harush, S.; Lewis, A.; Kopelman, R. A light-source smaller than the optical wavelength. *Science* **1990**, *247* (4938), 59–61.
26. Tan, W.H.; Shi, Z.Y.; Smith, S.; Birnbaum, D.; Kopelman, R. Submicrometer intracellular chemical optical fiber sensors. *Science* **1992**, *258* (5083), 778–781.
27. Tan, W.H.; Shi, Z.Y.; Kopelman, R. Development of submicron chemical fiber optic sensors. *Anal. Chem.* **1992**, *64* (23), 2985–2990.
28. Alarie, J.P.; VoDinh, T. Antibody-based submicron biosensor for benzo a pyrene DNA adduct. *Polycycl. Aromat. Compd.* **1996**, *8* (1), 45–52.
29. Cullum, B.M.; Griffin, G.D.; Miller, G.H.; Vo-Dinh, T. Intracellular measurements in mammary carcinoma cells using fiber-optic nanosensors. *Anal. Biochem.* **2000**, *277* (1), 25–32.
30. Hoffmann, P.; Dutoit, B.; Salathe, R.P. Comparison of mechanically drawn and protection layer chemically etched optical fiber tips. *Ultramicroscopy* **1995**, *61* (1–4), 165–170.
31. Turner, D.R. US patent #4,469,5541984
32. Stockle, R.; Fokas, C.; Deckert, V.; Zenobi, R.; Sick, B.; Hecht, B.; Wild, U.P. High-quality near-field optical probes by tube etching. *Appl. Phys. Lett.* **1999**, *75* (2), 160–162.
33. Zeisel, D.; Deckert, V.; Zenobi, R.; Vo-Dinh, T. Near-field surface-enhanced Raman spectroscopy of dye molecules adsorbed on silver island films. *Chem. Phys. Lett.* **1998**, *283* (5–6), 381–385.
34. Deckert, V.; Zeisel, D.; Zenobi, R.; Vo-Dinh, T. Near-field surface enhanced Raman imaging of dye-labeled DNA with 100-nm resolution. *Anal. Chem.* **1998**, *70* (13), 2646–2650.
35. Munkholm, C.; Walt, D.R.; Milanovich, F.P. Preparation of CO<sub>2</sub> fiber optic chemical sensor. *Abstr. Pap.—Am. Chem. Soc.* **1987**, *193*, 183-ANYL.
36. Munkholm, C.; Parkinson, D.R.; Walt, D.R. Intramolecular fluorescence self-quenching of fluoresceinamine. *J. Am. Chem. Soc.* **1990**, *112* (7), 2608–2612.
37. Barker, S.L.R.; Thorsrud, B.A.; Kopelman, R. Nitrite- and chloride-selective fluorescent nano-optodes and in vitro application to rat conceptuses. *Anal. Chem.* **1998**, *70* (1), 100–104.
38. Samuel, J.; Strinkovski, A.; Lieberman, K.; Ottolenghi, M.; Avnir, D.; Lewis, A. Miniaturization of organically doped sol-gel materials—A microns-size fluorescent pH sensor. *Mater. Lett.* **1994**, *21* (5–6), 431–434.
39. McCulloch, S.A.; Uttamchandani, D. *IEE Proc., Optoelectron.* **1995**, *144* (162).
40. Tan, W.H.; Shi, Z.Y.; Kopelman, R. Miniaturized fiber optic chemical sensors with fluorescent dye-doped polymers. *Sens. Actuators, B, Chem.* **1995**, *28* (2), 157–163.
41. Song, A.; Parus, S.; Kopelman, R. High-performance fiber optic pH microsensors for practical physiological measurements using a dual-emission sensitive dye. *Anal. Chem.* **1997**, *69* (5), 863–867.
42. Koronci, I.; Reichert, J.; Heinzmann, G.; Ache, H.J. Development of a submicron optochemical potassium sensor with enhanced stability due to internal reference. *Sens. Actuators, B, Chem.* **1998**, *51* (1–3), 188–195.
43. Bui, J.D.; Zelles, T.; Lou, H.J.; Gallion, V.L.; Phillips, M.I.; Tan, W.H. Probing intracellular dynamics in living cells with near-field optics. *J. Neurosci. Methods* **1999**, *89* (1), 9–15.
44. Barker, S.L.R.; Kopelman, R. Development and cellular applications of fiber optic nitric oxide sensors based on a gold-adsorbed fluorophore. *Anal. Chem.* **1998**, *70* (23), 4902–4906.
45. Barker, S.L.R.; Kopelman, R.; Meyer, T.E.; Cusanovich, M.A. Fiber-optic nitric oxide-selective biosensors and nanosensors. *Anal. Chem.* **1998**, *70* (5), 971–976.
46. Cullum, B.M.; Vo-Dinh, T. Optical nanosensors and biological measurements. *Biofutur* **2000**, *2000* (205), A1–A6.
47. Vo-Dinh, T.; Griffin, G.D.; Alarie, J.P.; Cullum, B.M.; Sumpter, B.; Noid, D. Development of nanosensors and bioprobes. *J. Nanopart. Res.* **2000**, *2*, 17
48. Vo-Dinh, T.; Alarie, J.P.; Cullum, B.M.; Griffin, G.D. Antibody-based nanoprobe for measurement of a fluorescent analyte in a single cell. *Nat. Biotechnol.* **2000**, *18* (7), 764–767.
49. Tyagi, S. Molecular beacons: Probes that fluoresce upon hybridization. *Nat. Biotechnol.* **1995**, *14* (3), 303–309.
50. Tyagi, S.; Kramer, F.R. Molecular beacons: Probes that fluoresce upon hybridization. *Nat. Biotechnol.* **1996**, *14* (3), 303–308.
51. Fang, X.H.; Li, J.W.J.; Perlette, J.; Tan, W.H.; Wang, K.M. Molecular beacons—Novel fluorescent probes. *Anal. Chem.* **2000**, *72* (23), 747A–753A.



52. Liu, X.J.; Tan, W.H. A fiber-optic evanescent wave DNA biosensor based on novel molecular beacons. *Anal. Chem.* **1999**, *71* (22), 5054–5059.
53. Liu, X.J.; Farmerie, W.; Schuster, S.; Tan, W.H. Molecular beacons for DNA biosensors with micrometer to submicrometer dimensions. *Anal. Biochem.* **2000**, *283* (1), 56–63.
54. Cordek, J.; Wang, X.W.; Tan, W.H. Direct immobilization of glutamate dehydrogenase on optical fiber probes for ultrasensitive glutamate detection. *Anal. Chem.* **1999**, *71* (8), 1529–1533.
55. Rosenzweig, Z.; Kopelman, R. Analytical properties and sensor size effects of a micrometer-sized optical fiber glucose biosensor. *Anal. Chem.* **1996**, *68* (8), 1408–1413.
56. Cullum, B.M.; Griffin, G.D.; Vo-Dinh, T. Nanosensors for analysis of a single cell. *SPIE Proc.* **2001**, *4254*, 35–40.
57. Li, H.; Chandras, N.; Cullum, B.M. Development and optimization of SERS-based immuno-nanosensor for single cell analyses. *SPIE Proc.* **2003**, in press.
58. Walt, D. Near-field array, (accessed July 2003). <http://ase.tufts.edu/chemistry/walt/index.htm>.
59. Chan, W.C.W.; Nie, S.M. Quantum dot bioconjugates for ultrasensitive nonisotopic detection. *Science* **1998**, *281* (5385), 2016–2018.
60. Lyon, W.A.; Nie, S.M. Single molecule methodologies for DNA analysis. *Abstr. Pap.—Am. Chem. Soc.* **1997**, *213*, 49-PHYS.
61. Taylor, J.R.; Fang, M.M.; Nie, S.M. Probing specific sequences on single DNA molecules with bioconjugated fluorescent nanoparticles. *Anal. Chem.* **2000**, *72* (9), 1979–1986.
62. Zhang, C.Y.; Ma, H.; Nie, S.M.; Ding, Y.; Jin, L.; Chen, D.Y. Quantum dot-labeled trichosanthin. *Analyst* **2000**, *125* (6), 1029–1031.
63. Zhang, C.Y.; Ma, H.; Ding, Y.; Jin, L.; Chen, D.Y.; Miao, Q.; Nie, S.M. Studies on quantum dots-labeled trichosanthin. *Chem. J. Chin. Univ.—Chin.* **2001**, *22* (1), 34–37.
64. Sasaki, K.; Shi, Z.Y.; Kopelman, R.; Masuhara, H. Three-dimensional pH microprobing with an optically-manipulated fluorescent particle. *Chem. Lett.* **1996**, *25* (2), 141–142.
65. Clark, H.A.; Hoyer, M.; Philbert, M.A.; Kopelman, R. Optical nanosensors for chemical analysis inside single living cells: 1. Fabrication, characterization, and methods for intracellular delivery of PEBBLE sensors. *Anal. Chem.* **1999**, *71* (21), 4831–4836.
66. Clark, H.A.; Kopelman, R.; Tjalkens, R.; Philbert, M.A. Optical nanosensors for chemical analysis inside single living cells: 2. Sensors for pH and calcium and the intracellular application of PEBBLE sensors. *Anal. Chem.* **1999**, *71* (21), 4837–4843.
67. Clark, H.A.; Barker, S.L.R.; Brasuel, M.; Miller, M.T.; Monson, E.; Parus, S.; Shi, Z.Y.; Song, A.; Thorsrud, B.; Kopelman, R.; Ade, A.; Meixner, W.; Athey, B.; Hoyer, M.; Hill, D.; Lightle, R.; Philbert, M.A. Subcellular optochemical nanobiosensors: Probes encapsulated by biologically localised embedding (PEBBLES). *Sens. Actuators, B, Chem.* **1998**, *51* (1–3), 12–16.
68. Sumner, J.P.; Aylott, J.W.; Monson, E.; Kopelman, R. A fluorescent PEBBLE nanosensor for intracellular free zinc. *Analyst* **2002**, *127* (1), 11–16.
69. Xu, H.; Aylott, J.W.; Kopelman, R.; Miller, T.J.; Philbert, M.A. A real-time ratiometric method for the determination of molecular oxygen inside living cells using sol-gel-based spherical optical nanosensors with applications to rat C6 glioma. *Anal. Chem.* **2001**, *73* (17), 4124–4133.
70. Xu, H.; Aylott, J.; Kopelman, R. Sol-gel pebble sensors for biochemical analysis inside living cells. *Abstr. Pap.—Am. Chem. Soc.* **2000**, *219*, 97-ANYL.
71. Anker, J.N.; Behrend, C.; Kopelman, R. Aspherical magnetically modulated optical nanoprobe (MagMOONs). *J. Appl. Phys.* **2003**, *93* (10), 6698–6700.
72. Anker, J.N.; Kopelman, R. Magnetically modulated optical nanoprobe. *Appl. Phys. Lett.* **2003**, *82* (7), 1102–1104.
73. Ji, J.; Rosenzweig, N.; Jones, I.; Rosenzweig, Z. Molecular oxygen-sensitive fluorescent lipobeads for intracellular oxygen measurements in murine macrophages. *Anal. Chem.* **2001**, *73* (15), 3521–3527.
74. Ji, J.; Rosenzweig, N.; Griffin, C.; Rosenzweig, Z. Synthesis and application of submicrometer fluorescence sensing particles for lysosomal pH measurements in murine macrophages. *Anal. Chem.* **2000**, *72* (15), 3497–3503.
75. McNamara, K.P.; Nguyen, T.; Dumitrascu, G.; Ji, J.; Rosenzweig, N.; Rosenzweig, Z. Synthesis, characterization, and application of fluorescence sensing lipobeads for intracellular pH measurements. *Anal. Chem.* **2001**, *73* (14), 3240–3246.
76. Nguyen, T.; McNamara, K.P.; Rosenzweig, Z. Optochemical sensing by immobilizing fluorophore-encapsulating liposomes in sol-gel thin films. *Anal. Chim. Acta* **1999**, *400*, 45–54.
77. McNamara, K.P.; Rosenzweig, N.; Rosenzweig, Z. Liposome-based optochemical nanosensors. *Mikrochim. Acta* **1999**, *131* (1–2), 57–64.
78. McNamara, K.P.; Rosenzweig, Z. Dye-encapsulating liposomes as fluorescence-based oxygen nanosensors. *Anal. Chem.* **1998**, *70* (22), 4853–4859.
79. McNamara, K.P.; Rosenzweig, Z. Nanosized phospholipid-coated particles as biological sensors. *Abstr. Pap.—Am. Chem. Soc.* **1999**, *218*, 26-ANYL.
80. DeCoster, M.A.; Nguyen, T.; Bazan, N.G.; Rosenzweig, Z. Adherence of lectin-coated micro lipobeads to cortical neurons in cell culture. *FASEB J.* **2002**, *16* (4), A37.

# Ordered Vesicles at the Silicon–Water Interface

Duncan J. McGillivray

Physical and Theoretical Chemistry Laboratory,  
Oxford University, Oxford, U.K.

## INTRODUCTION

The purpose of this entry is to examine the stable, ordered near-surface phase of dichain cationic surfactants, which has been recently reported,<sup>[1]</sup> and to determine whether this phase can be unambiguously assigned as a vesicular phase. Such a phase would be a remarkable example of an aligned near-surface phase, extending hundreds of nanometers into solution, which exists in equilibrium with the bulk aqueous phase, and may explain the superspreading characteristics of these surfactants,<sup>[2]</sup> providing a reservoir of surfactant near the surface.

These surfactants are also widely used as fabric softeners and are the subjects of keen interest for pharmaceutical applications. They have been shown to form vesicles in dilute solutions. This is particularly significant as it extends the range of standard vesicle-forming compounds beyond phospholipids, long the gold standard of the field. Furthermore, the vesicles formed by these cationic surfactants are generally smaller than those formed from phospholipids, ranging from as small as 30 nm. These cationic vesicles are the subjects of biomedical research, where they are highly regarded as effective gene transfer agents in gene therapy.<sup>[3]</sup> Part of the success of this technique depends on the interaction between the cationic vesicle–DNA complex and the target cell membrane, which enables the DNA to cross undegraded,<sup>[4]</sup> and thus it is of interest to know how the surfactant vesicles behave near a surface.

## VESICLES

The vesicle morphology is a common motif in surfactant self-arrangement. Favored by surfactants whose packing parameter falls in the typically lamellar range ( $0.5 < pp < 1$ ), it often coexists in solution with other lamellar-type structures such as lamellar fragments or sponge phases. The precise morphology chosen for a given surfactant depends critically on the precise nature of the surfactant and its counterion and the solution conditions of the system.

The most well-studied and common vesicle-forming surfactants are phospholipids.<sup>[5]</sup> These vesicles have

been used as cell-membrane analogs<sup>[6,7]</sup> and have a great deal in common with ordinary biological cells. They do not form spontaneously, requiring significant energy input to form typically through sonication, and produce large, metastable vesicles which can grow as large as micrometers. Phospholipid vesicles are not generally monodisperse and can be both unilamellar and multilamellar. Monodispersity is often achieved by forming vesicles using a fixed-size extrusion technique.

Phospholipid vesicles are not, however, found to be stable when interacting with a solid surface. This enables them to be widely used to deposit phospholipid bilayers on surfaces for use as model membranes, where the vesicle collapses on contact to produce a lamellar bilayer at the surface.<sup>[8–10]</sup>

The range of vesicle-forming surfactant systems has recently been enlarged through the use of combinations of oppositely charged surfactants,<sup>[11–14]</sup> non-ionic surfactants,<sup>[15,16]</sup> and dichain cationic surfactants.<sup>[17–20]</sup> The vesicle-forming dichain cationic surfactants, which are the dialkyldimethylammonium bromide (DAB) family, are the focus of the work referred to as the basis of this article.

## SURFACE MEASUREMENTS

Neutron reflectometry provides the unique ability to probe the surface and near-surface region of a solid–liquid interface *non-intrusively*, an important condition for the study of such fragile systems. Neutrons of 1–10 Å wavelengths, which are typically used for surface measurements, penetrate a single crystal of silicon with greater than 70% transmittance over a path length of around 15 cm and are then reflected from the solid–liquid interface (see Fig. 1 for the standard geometry of a solid–liquid experiment). Neutron reflectometry also gives information about the near-surface structure in solution. The neutron penetration length in D<sub>2</sub>O is of the order of microns for 10-Å neutrons, although, experimentally, it is found that it is difficult to detect species which are highly disperse or rough below the surface.

The reflection experiment measures the number of neutrons reflected as a function of the wave vector

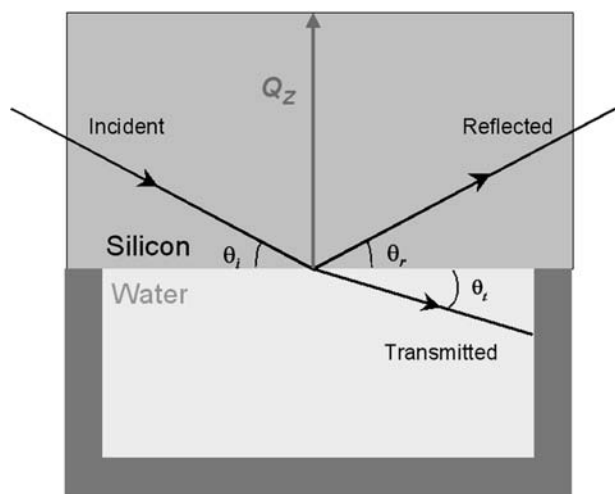


**Fig. 1** The geometry of a specular neutron reflection experiment at the solid–liquid interface, where  $\theta_i = \theta_r$  and  $Q_z$  is the vertical momentum transfer.

change on reflection (normally referred to as the momentum transfer)  $Q_z$ , which itself is a function of the wavelength of the neutrons and the angle of reflection

$$Q_z = \frac{4\pi \sin \theta}{\lambda} \quad (1.1)$$

The reflection depends on the interaction of the neutrons with the nuclei present at the surface. The extent of nuclear interaction with a neutron is described by an experimentally well-determined quantity known as the coherent scattering length  $b_{\text{coh}}$ , which varies non-systematically across the periodic table (see Table 1 for values of this parameter for a few biologically significant isotopes). In contrast to the X-ray scattering equivalent, it can be seen that hydrogen isotopes have large  $b_{\text{coh}}$ , which significantly takes a negative value for  $^1\text{H}$ . This allows simple isotopic substitution to adjust the contrast of hydrogen-containing molecules; indeed, for water, the scattering length density (SLD) can range from  $-0.58$  up to  $6.35 \text{ \AA}^{-2}$ , enabling it to be contrast-matched to many common interfaces [ $\text{SLD}(\text{Si}) = 2.07 \text{ \AA}^{-2}$ ,  $\text{SLD}(\text{Air}) = 0.0 \text{ \AA}^{-2}$ ] so that the only scattering arises from material found at the interfacial region.

**Table 1** Bound coherent scattering lengths ( $b_{\text{coh}}$ ) for biologically significant isotopes

Element	$b_{\text{coh}} (10^{-5} \text{ \AA})$	Element	$b_{\text{coh}} (10^{-5} \text{ \AA})$
$^1\text{H}$	$-3.74$	$^{12}\text{C}$	$6.65$
$^2\text{H}$ (D)	$6.67$	$^{13}\text{C}$	$6.20$
$^{16}\text{O}$	$5.81$	$^{14}\text{N}$	$9.37$

Source: Ref.<sup>[21]</sup>.

## Modeling

Data analysis is normally performed using optical matrix methods, in which the interface region is modeled as a series of homogenous layers. The layers are each characterized by a thickness [ $\tau$  ( $\text{\AA}$ )], SLD [ $\rho$  ( $\text{\AA}^{-2}$ )], and an interfacial roughness between adjacent layers [ $\sigma$  ( $\text{\AA}^{-1}$ )]. The exact reflectivity can be calculated from such a model; this can be compared with the data, and the model is then refined using least-squares minimization routines. For a more detailed discussion of the analysis of neutron reflectometry data in general, refer to Li et al.<sup>[22]</sup>

## Off-Specular Scattering

If the interface between two regions is rough on a length scale appropriate to the wavelength of the scattering neutrons, then it is possible for some reflection to occur at angles that do not equal the incident angle. In this situation, the scattering, known as off-specular scattering, contains momentum transfer in both the perpendicular ( $Q_z$ ) and horizontal ( $Q_x$ ) directions (see Fig. 2 below showing the geometry of the off-specular scattering experiment). It is therefore theoretically possible to determine, from the pattern of this scattering, information about the horizontal structure in a surface layer.

In practice, the determination of horizontal order is far from a routine procedure. Current instruments are not optimized for the detection of off-specular scattering, particularly at the small dispersive angles

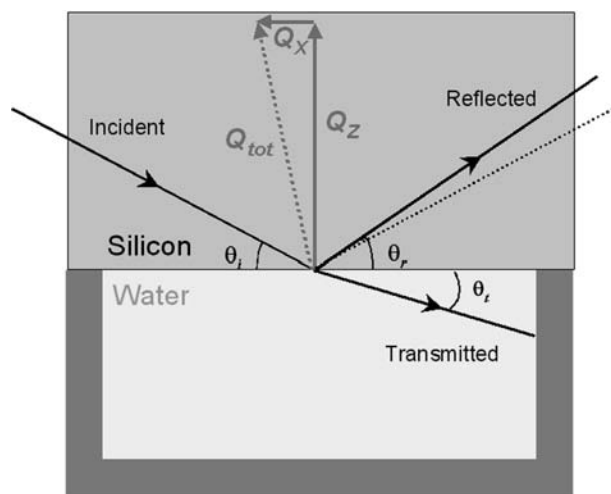


**Fig. 2** The geometry of an off-specular reflection experiment. Here the angle of the reflected beam  $\theta_r \neq \theta_i$ , and there are two components to the total momentum transfer  $Q_{\text{tot}}$ , a vertical ( $Q_z$ ) and a horizontal ( $Q_x$ ) component.

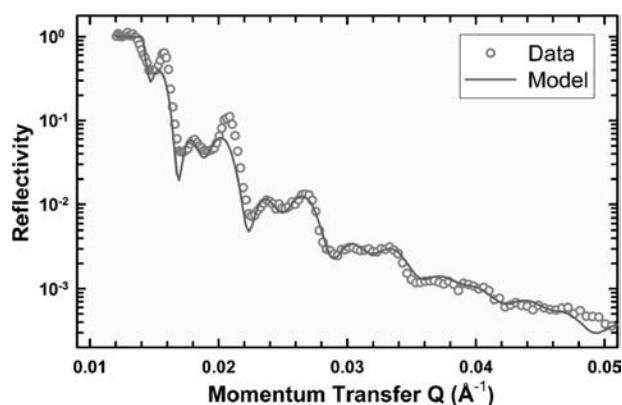


**Fig. 3** Specular reflectivity profile and simple modeled fit to data for C12C12DAB 1% w/w solution in D<sub>2</sub>O at 65°C.

necessary for these DAB measurements, and there have been few measurements making use of this ability. The most notable exceptions are in the field of magnetic thin films, where the ability of polarized neutrons to interact with magnetic fields is employed.<sup>[23]</sup>

### Bulk Solution Measurements

As an aid to modeling the surface conditions, bulk solution measurements are often used as a guide. Small-angle scattering is a well-established technique for determining bulk solution structures of surfactant solutions, which involves measuring the scattering of X-rays or neutrons from solutions in a transmission geometry. This technique is also non-perturbing, and neutron small-angle scattering shares many of the benefits of reflectometry in relation to the ability to alter contrast through the use of isotope labeling. X-ray small-angle scattering has the advantage of being able to make use of the extremely high flux available at modern synchrotron sources, enabling low-contrast (e.g., dilute) solutions to be measured, or measurements with high temporal resolution.

Cryo-transmission electron microscopy (cryo-TEM) is a much more recent technique, which involves taking a thin-film of a surfactant solution and flash-freezing it in near-freezing ethane. The freezing happens so rapidly that the water does not have time to crystallize

and is considered to be much faster than what surfactant rearrangement would be, preserving the room-temperature surfactant structure.<sup>[24]</sup> However, it has been reported that the process of thinning the surfactant solution to an appropriate thickness for flash freezing (100–200 nm) may cause changes to the surfactant structure,<sup>[25]</sup> so that the evidence from cryo-TEM images must always be considered carefully.

## RESULTS

Fig. 3 shows a typical specular reflectivity profile for a sample of C12C12DAB (didodecyldimethylammonium bromide) at 1% w/w in solution, together with a simple modeled fit to the data. The parameters of this optical matrix model can be found in Table 2. Several features are immediately clear. The primary feature is the appearance of strong quasi-Bragg peaks in the specular reflectivity profile. These peaks are indicative of a periodic structure extending into solution perpendicular to the surface. The relatively poor definition of the peaks, and the appearance of subsidiary peaks, implies that the structure consists of a limited number of repeats into the solution. In this case, it appears that the pattern is adequately fit through the use of only two layers, but more detailed modeling<sup>[1]</sup> suggests up to four may be partially complete for this sample. Samples of other DABs show very similar behavior across the same temperature range.

The modeling implies a lamellar structure aligned with the surface, consisting of broad lamellar sheets separated by large solvent-filled voids of the order of 1000 Å. Such a pattern may be observed for several morphologies at the surface, which are illustrated in Fig. 4.

It is difficult to determine from a perpendicular density profile which of these options is the one occurring at the surface. Each could give rise to a periodic density modulation, as seen in the diagram (where the characteristic repeat distance is marked), and the vertical walls in the sponge and vesicle phases would contribute negligibly to the average SLD across the voids in the structure. A significant point that arises from the fitting is that the periodic repeat layer is of low density (approximately 90% solvent content) and much thicker

**Table 2** Parameters of the optical matrix Fit to the Scattering from a C12C12DAB 1% w/w solution in D<sub>2</sub>O at 65°C

Layer	Silicon	SiO <sub>2</sub> layer	Void 1	Layer 1	Void 2	Layer 2
SLD (Å <sup>-2</sup> )	2.07	3.4	−0.2	−0.2	−0.2	−0.2
Thickness/(Å)	n/a	12.0	690	170	630	165
Roughness/(Å)	5.0	5.0	40	30	40	30
Solvent/(%)	n/a	0	100	90	100	93

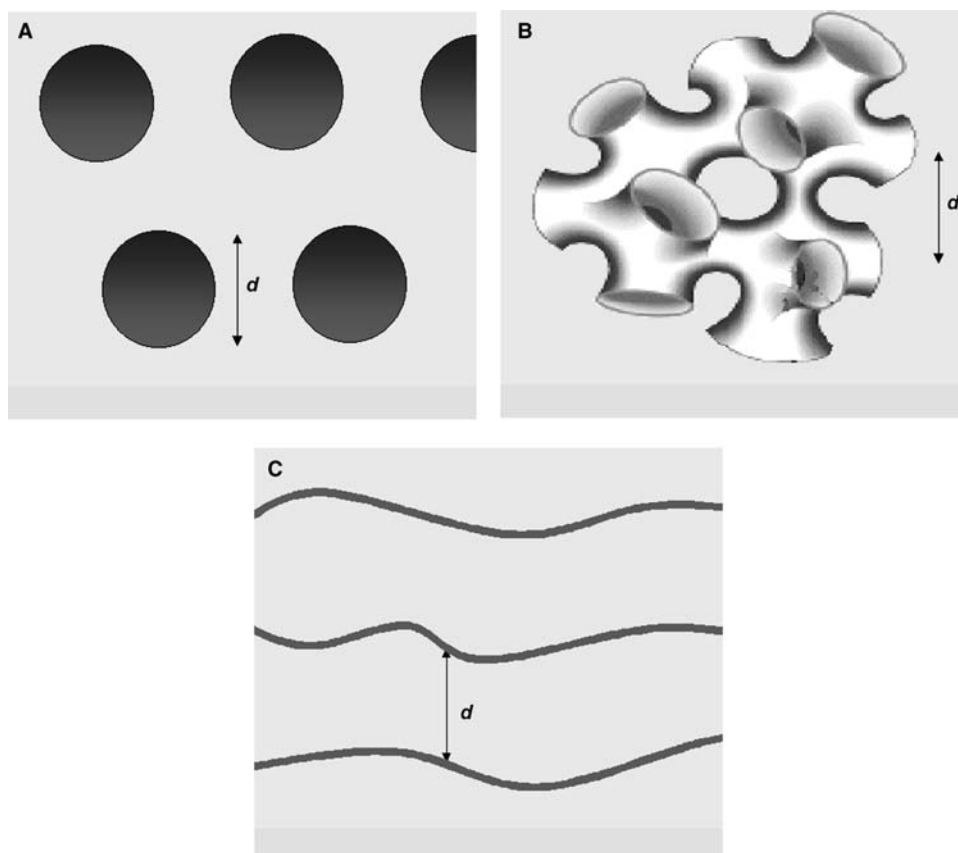


**Fig. 4** Possible morphologies giving rise to lamellar layers at the surface. (A) Vesicles aligning at the surface; (B) a sponge phase; (C) lamellar sheets, with the characteristic repeat distance  $d$  marked.

than the typical bilayer thickness for a bilayer of a C12-surfactant sheet (ca. 20 Å). The interlayer spacing is also smaller than that calculated for a simple space-filling lamellar bilayer structure at similar concentrations (ca. 2000 Å), implying that this phase does not extend throughout the solution. This coincides with surface force measurements, which do not show any evidence of this phase,<sup>[26]</sup> implying that the layering detected in reflectometry is either too diffuse, too fragile, or both to be detected by a contact method.

These facts can be rationalized differently for each of possible morphologies. For a lamellar system, this observation would be consistent with an undulating bilayer, such that the density of the layer is averaged over the undulation period. This implies undulations of a 100-Å amplitude, which is reasonable for a lamellar sheet at this temperature unconstrained by near neighbors. Conversely, for a vesicular system, the low density and thick layers could be explained by a low horizontal packing density of vesicles, as would be expected given their surface charges and the fact that the curved surface of the vesicle is being projected into a planar averaging. Similar arguments could be used for the sponge phase.

### Comparison with Bulk Structure

Some guidance can perhaps be gained from a knowledge of the bulk behavior of these surfactants. Phase diagrams have been produced for dichain cationic surfactants of these types,<sup>[17,20,27]</sup> which show some general features in common. The first is that they all form a vesicular phase at low concentrations (approximately those of the systems described here, namely, of the order of 1% w/w). The stability of these vesicles has been questioned, it being suggested that they do not form spontaneously (requiring some form of energy input to form, such as sonication or shaking)<sup>[14]</sup> and will spontaneously collapse to a lamellar phase with time.<sup>[17]</sup> The solutions reported here were indeed sonicated on dissolution, but the structuring at the surface is stable over a period of hours, with no visible changes. Another marked difference between the bulk and the surface is that the vesicles imaged in the bulk phase (e.g., through freeze-fracture electron microscopy) are polydisperse, with radii of  $1300 \pm 600$  Å for a solution of C11C12DAB imaged by freeze-fracture TEM.<sup>[20]</sup> The degree of polydispersity would need to be much lower to give rise to the quasi-Bragg peaks



seen in the specular reflectivity profiles measured for these systems.

However, it is also seen that either lamellar or sponge phases can coexist with this vesicle phase. Each of these phases is quite consistent with the simple geometric rationale of surfactant morphologies proposed by Tanford<sup>[28]</sup> and developed by Israelachvili, Mitchell, and Ninham<sup>[29]</sup> as the packing parameter for the dichain surfactants, ca. 0.6 (varying  $\pm 0.01$  depending on the chain length), lies in the middle of the range of lamellar-based structures. It appears that the bulk phase of the dichain surfactants is therefore quite complex and appears to be dependent on the precise history of the sample.

As a result, small-angle scattering and cryo-TEM experiments can be useful to determine the particular nature of these solution phases. Two representative cryo-TEM images are shown below (Fig. 5). These images clearly show that for the same sample, regions of vesicle and lamellar-like structures can be found. Indeed, other images also show that the vesicles and the lamellae were capable of coexisting in the same region. There is no evidence, however, of sponge phase structures found in any of the exposures. The lamellar structures imaged also show that the lamellae seen are not isolated lamellar sheets, but rather appear to be elongated microtubules—connected with a definite interior and exterior (as marked in Fig. 5).

Although the lack of sponge phase observed in the cryo-TEM does not of itself exclude the possibility of sponge phase being found at the surface (particularly given the nature of cryo-TEM discussed above), it seems that this phase is the least likely of the postulated options. The inherently three-dimensional continuous structure of the sponge phase does not pack well into the highly asymmetric and constrained near-surface region and, as such, would need to show some form of transition from a free bulk sponge phase to a surface phase.

In any case, the small-angle scattering experiments provide evidence that the bulk phase behaves significantly differently to the near-surface phase—direct evidence for the limited nature of the surface-induced structural alterations. Although there is some evidence of a lamellar layering in the small-angle X-ray scattering, the structure is not as pronounced as that found at the surface (see Fig. 6 for a comparison of the structuring found for C12C12DAB, 1% w/w solution, for example) nor does bulk spacing (when observed) correspond to the surface spacing.

The differences between the bulk and the near-surface are also seen in the temperature response of the two systems. The interlayer spacing of the near-surface phase is highly sensitive to the temperature, generally decreasing with increasing temperature, as seen by the shift in the quasi-Bragg peaks in the

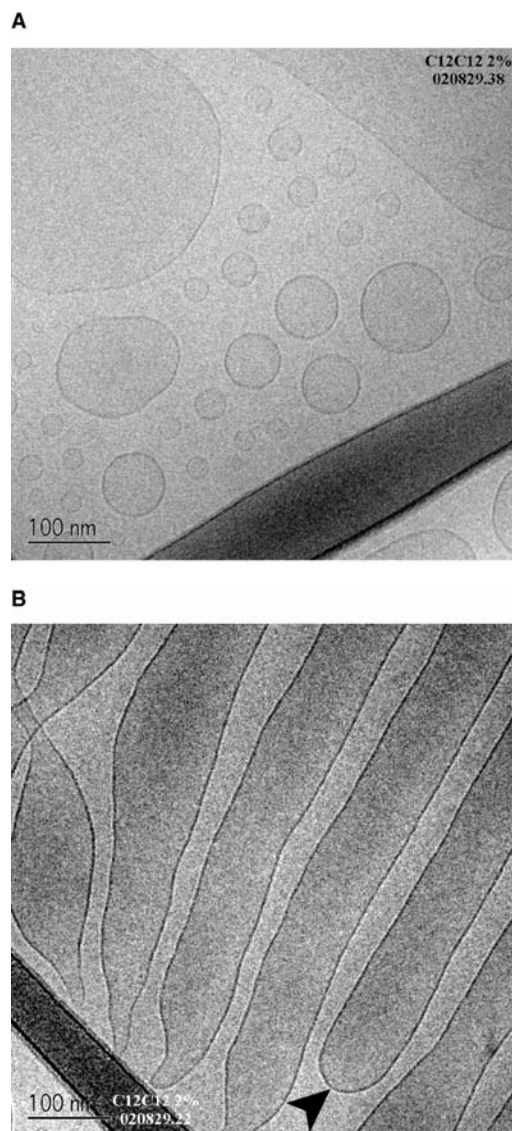


**Fig. 5** Cryo-TEM images of C12C12DAB 2% w/w solution flash-frozen from ca. 25°C; (A) showing polydisperse unilamellar vesicles in the solution; (B) showing the “extended vesicle” or microtubules. The closure is marked with an arrow. Both images are taken from different areas of the same sample, scale as marked.

scattering (Fig. 7). This type of temperature dependence at the surface has previously been reported for the lamellar phase of a 2% solution of NaAOT (sodium bis(2-ethylhexyl)sulfosuccinate) at the silicon–water interface, where the spacing changes from 270 Å at 5°C to 165 Å at 35°C.<sup>[30]</sup> In that system, the change in spacing was attributed to a change in an equilibrium between a micellar and a lamellar phase, where the surface structure was unambiguously lamellar extending thousands of layers into solution.

This change of spacing is reversible over at least a 30°C temperature range, which is also in contrast to the bulk solution, which is shown by small-angle



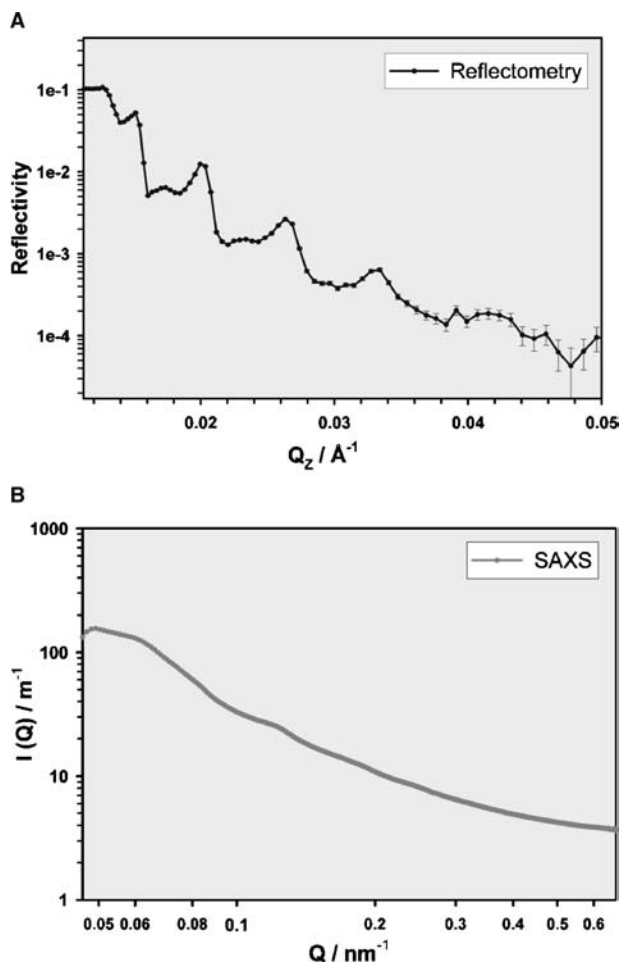


**Fig. 6** Comparison of structuring for C12C12DAB 1% w/w solution at 45°C at the surface and in the bulk solution from (A) reflectometry and (B) small-angle scattering.

scattering to be only broadly reversible (Fig. 7). This implies that the surface layer is in equilibrium at the surface and also that the time taken for the surface phase to reach this stable position is less than the equilibration time allowed after temperature changes (< 1 hr).

The temperature dependence can again be justified in terms of both the vesicular and lamellar morphologies at the surface. As the temperature increases, the solvation shell of headgroups will decrease, and the degree of ionization of the bilayer will increase—effects which will tend to increase the rigidity of the bilayer and hence decrease the degree of fluctuation–repulsion. However, this effect will be offset by the increased thermal energy of the bilayer and the increased electrostatic repulsion of the more highly charged layers, and the net effect is difficult to predict.

In the case of the vesicular morphology, in particular, attention needs to be given to the manner of how exactly the interlayer spacing might change. The direct implication is that the vesicles themselves change

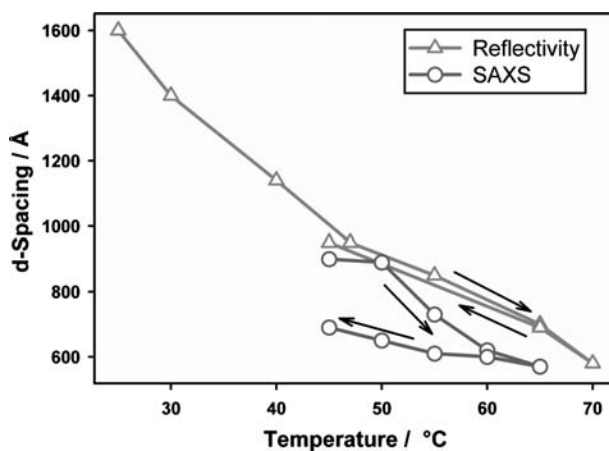


**Fig. 7** The change in the d-spacing of the surfactant solution as determined from neutron reflectivity and small-angle scattering. The arrows indicate the direction of the temperature cycles in testing the reversibility of changes.

size, achieved either through the smooth aggregation of smaller vesicles to form larger vesicles (equivalently budding material on warming) or the loss of material to free surfactant as the solubility increases with temperature. Simple calculations for C12C12DAB show, for a unilamellar spherical surfactant vesicle, that the decrease in the volume of the bilayer in going from 1100 to 600 Å (between 40°C and 70°C) is approximately 70% of the original volume, equivalent to an increase of solubility of the order of 100 times. This is much greater than the predicted change in solubility, which means the former mechanism must be dominant to explain the behavior seen here for spherical vesicles.

### Off-Specular Scattering

The samples exhibit significant off-specular scattering associated with the quasi-Bragg peaks, indicative of a degree of lateral ordering. Unfortunately, the length scale of the lateral resolution of the measurements is much larger than the equivalent vertical dimension (micrometers rather than angstroms), which means that any interference patterns on the same length scale as those found in the specular scattering, as might be envisioned from a horizontally ordered vesicular layer, would not be seen.

The scattering which is seen consists of bands of scattering across a range of  $Q_x$  at constant  $Q_z$  (Fig. 8). The question of whether this is true near-surface scattering, or instead derives from the bulk, can be answered by reference to two features of the scattering—namely, the centering of the off-specular intensity decay on the specular ridge and the appearance of curvature in the bands as a result of refraction in the  $\text{D}_2\text{O}$  sample, which is absent in the sample

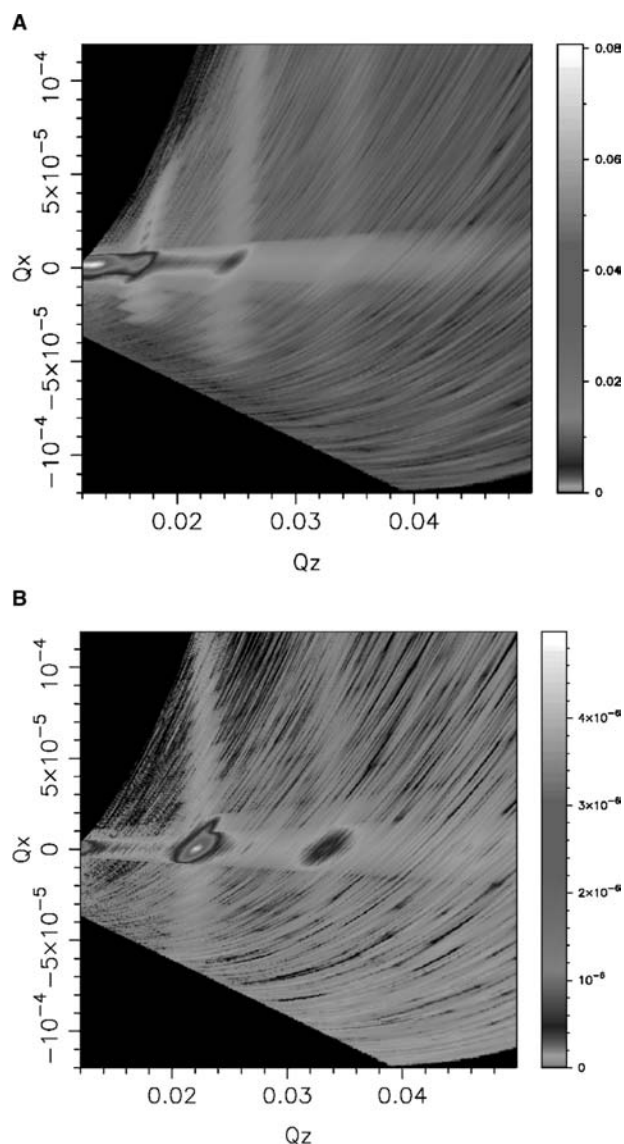


**Fig. 8** Off-specular scattering from C12C12DAB 1% w/w in (A) D<sub>2</sub>O and (B) CMSi, a mixture of H<sub>2</sub>O and D<sub>2</sub>O with a SLD equal to that of silicon crystal ( $\rho = 2.07 \times 10^{-6} \text{ \AA}^{-2}$ ).

contrast-matched to silicon (CMSi). This is also similar to the pattern seen for NaAOT and is believed to arise from correlated undulations between layers such as might be seen from the natural layer undulations.<sup>[31]</sup> These undulations might arise from either vesicular or lamellar membranes, but in the case of lamellar sheets, the large distance between the layers begs the question of the source of the correlation between the layers, failing connection between the sheets.

## CONCLUSION

While it is clear that the system in question exhibits unusual surface properties, and that there is indeed a

near-surface phase which differs from the bulk, it is extremely difficult to distinguish the possibilities that make up the structure. It is known that sponge, lamellar, and vesicular phases can exist in the solution, depending on the individual route of the preparation of the sample, but it is clear from small-angle scattering measurements that the surface is not exhibiting the same characteristics as the bulk. The exact surface density distribution, the temperature dependence of the structure, and the off-specular scattering all provide constraints on the possibilities at the surface, but none of these specifically excludes any of the candidates. A sponge phase seems the least likely because of the complexity of the phase in the dimensionally constrained near-surface region and necessity for the phase to align with the surface. Simplicity suggests that the best candidate for the surface might be a lamellar phase; this, however, represents extremely large spacing for a lamellar phase, and it is difficult then to explain the correlated nature of the undulations seen from the off-specular scattering.

The third choice, vesicles, has its own complications—in particular, that the vesicles would be more monodisperse than the bulk solution, and that the mechanism for the change in the size of the vesicles with temperature is unclear. Perhaps the most reasonable compromise is suggested by the cryo-TEM images, which show the existence of an intermediary phase between vesicular and lamellar, equivalent to extended vesicles (microtubules). However, it does not seem possible to distinguish these possibilities based on the evidence now available.

## ACKNOWLEDGMENTS

I would like to acknowledge the assistance in preparing this manuscript received from Dr. R.K. Thomas (University of Oxford, Oxford, United Kingdom) and the many useful conversations with Prof. J. Penfold (ISIS Facility, Rutherford-Appleton Lab, Didcot, United Kingdom) and Prof. A. Rennie (Studsвик, Uppsala University, Sweden). I would also like to acknowledge the assistance of Hanna Vacklin (University of Oxford) and Dr. Gunnel Karlsson at the University of Lund, Sweden, for assistance in obtaining the cryo-TEM images, and the Rhodes Trust, Oxford, for financial support through a scholarship.

## REFERENCES

1. McGillivray, D.J.; Thomas, R.K.; Rennie, A.R.; Penfold, J.; Sivia, D.S. Ordered structures of di-chain cationic surfactants at interfaces. *Langmuir* **2003**, *19* (19), 7719–7726.

2. Svitova, T.F.; Hill, R.M.; Radke, C.J. Spreading of aqueous dimethyldidodecylammonium bromide surfactant droplets over liquid hydrocarbon substrates. *Langmuir* **1999**, *15* (21), 7392–7402.
3. Miller, A.D. Cationic liposomes for gene therapy. *Angew. Chem., Int. Ed.* **1998**, *37* (13–14), 1769–1785.
4. Templeton, N.S. Liposomal delivery of nucleic acids in vivo. *DNA Cell Biol.* **2002**, *21* (12), 857–867.
5. New, R.R.C.; Ed. *Liposomes : A Practical Approach*; Oxford University Press: Oxford, 1990.
6. Fendler, J.H. *Membrane Mimetic Chemistry: Characterizations and Applications of Micelles, Microemulsions, Monolayers, Bilayers, Vesicles, Host–Guest Systems, and Polyions*; Wiley: New York, 1982.
7. Lasic, D.D.; Papahadjopoulos, D.; Eds. *Medical Applications of Liposomes*; Elsevier: Oxford, 1998.
8. Charitat, T.; Bellet-Amalric, E.; Fragneto, G.; Graner, F. Adsorbed and free lipid bilayers at the solid–liquid interface. *Eur. Phys. J., B* **1999**, *8* (4), 583–593.
9. Rapuano, R.; Carmona-Ribeiro, A.M. Supported bilayers on silica. *J. Colloid Interface Sci.* **2000**, *226* (2), 299–307.
10. Carmona-Ribeiro, A.M. Bilayer vesicles and liposomes as interface agents. *Chem. Soc. Rev.* **2001**, *30* (4), 241–247.
11. Bergstrom, M.; Pedersen, J.S. Small-angle neutron scattering (SANS) study of aggregates formed from aqueous mixtures of sodium dodecyl sulfate (SDS) and dodecyltrimethylammonium bromide (DTAB). *Langmuir* **1998**, *14* (14), 3754–3761.
12. Bergstrom, M.; Pedersen, J.S.; Schurtenberger, P.; Egelhaaf, S.U. Small-angle neutron scattering (SANS) study of vesicles and lamellar sheets formed from mixtures of an anionic and a cationic surfactant. *J. Phys. Chem., B* **1999**, *103* (45), 9888–9897.
13. Horbaschek, K.; Hoffmann, H.; Hao, J.C. Classic L-alpha phases as opposed to vesicle phases in cationic–anionic surfactant mixtures. *J. Phys. Chem., B* **2000**, *104* (13), 2781–2784.
14. Marques, E.F. Size and stability of catanionic vesicles: effects of formation path, sonication, and aging. *Langmuir* **2000**, *16* (11), 4798–4807.
15. Ma, G.; Barlow, D.J.; Lawrence, M.J.; Heenan, R.K.; Timmins, P. Small-angle neutron-scattering studies of nonionic surfactant vesicles. *J. Phys. Chem., B* **2000**, *104* (39), 9081–9085.
16. Le, T.D.; Olsson, U.; Mortensen, K. Packing states of multilamellar vesicles in a nonionic surfactant system. *Phys. Chem. Chem. Phys.* **2001**, *3* (7), 1310–1316.
17. Dubois, M.; Zemb, T. Phase-behavior and scattering of double-chain surfactants in diluted aqueous-solutions. *Langmuir* **1991**, *7* (7), 1352–1360.
18. Caboi, F.; Monduzzi, M. Didodecyldimethylammonium bromide vesicles and lamellar liquid crystal. A multinuclear NMR and optical microscopy study. *Langmuir* **1996**, *12* (15), 3548–3556.
19. Marques, E.F.; Regev, O.; Khan, A.; Miguel, M.D.; Lindman, B. Vesicle formation and general phase behavior in the catanionic mixture SDS-DDAB-water. The cationic-rich side. *J. Phys. Chem., B* **1999**, *103* (39), 8353–8363.
20. Haas, S.; Hoffmann, H.; Thunig, C.; Hoinkis, E. Phase and aggregation behaviour of double-chain cationic surfactants from the class of *N*-alkyl-*N*-alkyl'-*N*, *N*-dimethylammonium bromide surfactants. *Colloid Polym. Sci.* **1999**, *277* (9), 856–867.
21. Koester, L.; Rauch, H.; Seymann, E. Neutron scattering lengths: a survey of experimental data and methods. *Atom. Data Nucl. Data* **1991**, *49* (1), 65–120.
22. Li, Z.X.; Thirtle, P.N.; Weller, A.; Thomas, R.K.; Penfold, J.; Webster, J.R.P.; Rennie, A.R. Some improvements and extensions of the application of specular neutron reflection to the study of interfaces. *Physica, B* **1998**, *248*, 171–183.
23. Toperverg, B.P. Specular reflection and off-specular scattering of polarized neutrons. *Physica, B* **2001**, *297* (1–4), 160–168.
24. Almgren, M.; Edwards, K.; Karlsson, G. Cryo transmission electron microscopy of liposomes and related structures. *Colloids Surf., A* **2000**, *174* (1–2), 3–21.
25. Danino, D.; Talmon, Y.; Zana, R. Cryo-TEM of thread-like micelles: on-the-grid microstructural transformations induced during specimen preparation. *Colloids Surf., A* **2000**, *169* (1–3), 67–73.
26. Briscoe, W. University of Oxford, unpublished results.
27. Svitova, T.F.; Smirnova, Y.P.; Pisarev, S.A.; Berezina, N.A. Self-assembly in double-tailed surfactants in dilute aqueous-solutions. *Colloids Surf., A* **1995**, *98* (1–2), 107–115.
28. Tanford, C. Micelle shape and size. *J. Phys. Chem.* **1972**, *76* (21), 3020–3024.
29. Israelachvili, J.N.; Mitchell, D.J.; Ninham, B.W. Theory of self-assembly of hydrocarbon amphiphiles into micelles and bilayers. *J. Chem. Soc., Faraday Trans. II* **1976**, *72*, 1525–1568.
30. Li, Z.X.; Weller, A.; Thomas, R.K.; Rennie, A.R.; Webster, J.R.P.; Penfold, J.; Heenan, R.K.; Cubitt, R. Adsorption of the lamellar phase of aerosol-OT at the solid/liquid and air/liquid interfaces. *J. Phys. Chem., B* **1999**, *103* (49), 10,800–10,806.
31. Li, Z.X.; Lu, J.R.; Thomas, R.K.; Weller, A.; Penfold, J.; Webster, J.R.P.; Sivia, D.S.; Rennie, A.R. Conformal roughness in the adsorbed lamellar phase of aerosol-OT at the air–water and liquid–solid interfaces. *Langmuir* **2001**, *17* (19), 5858–5864.

# Organofullerenes in Water

Eiichi Nakamura

Hiroyuki Isobe

Department of Chemistry, University of Tokyo, Tokyo, Japan

## INTRODUCTION

Fullerenes<sup>[1–4]</sup> are entirely insoluble in water and by themselves do not show appreciable biological activity. However, suitable chemical modification allows the molecules to dissolve in aqueous solution to exhibit significant activity. In 1993, three papers reported simultaneously on the biological activities of fullerene carboxylic acids **1** and **2** (Fig. 1).<sup>[5–8]</sup> Studies ensued afterward revealed various interesting biological activities of organofullerenes owing to their photoactivity, radical quenching activity, and hydrophobicity.<sup>[9–11]</sup> The interests in biology stimulated the studies on the behavior of fullerenes in water and led to new discoveries on the formation of one- to three-dimensional supramolecular objects, including vesicle, rod, globule, membrane, and linear assemblies. Several fundamental properties of fullerenes form the background of such interest in fullerenes in water: extremely high hydrophobicity, high cohesive force between fullerene molecules,<sup>[12,13]</sup> photoactivity,<sup>[14]</sup> ability to accept and release electrons,<sup>[15]</sup> and relatively high reactivity that allows structural modifications.<sup>[16,17]</sup> This article highlights the behaviors of organofunctionalized fullerenes in water.

## BIOLOGICAL EFFECTS OF WATER-SOLUBLE FULLERENES

An obvious obstacle for the studies of fullerenes in water is the lack of solubility of fullerenes in water.<sup>[18–22]</sup> One approach to solve the issue utilizes a solubilizing agent such as polyvinylpyridone<sup>[23]</sup> or cyclodextrin,<sup>[24]</sup> and the other relies on introduction of hydrophilic function(s) by chemical modification of the molecule. Attachment of amino or hydroxyl groups<sup>[25]</sup> is straightforward but affords an inseparable mixture comprising many products of similar properties. Carbon–carbon bond forming modifications of fullerenes is more selective. The compounds **1** and **2** represent the compounds in this category (Fig. 1).

Nakamura et al.<sup>[26]</sup> synthesized the compound **1** and discovered that the compound shows significant

biological activities.<sup>[5]</sup> The compound **1** (and later its C<sub>70</sub> analog)<sup>[27]</sup> suppresses growth of mammalian cells, inhibits activity of various enzymes (including HIV protease, which they found later; Fig. 3),<sup>[28]</sup> and cuts DNA upon visible light irradiation. Later studies indicated that the cleavage is caused by active oxygen species generated by fullerene-sensitized activation of molecular oxygen in the medium (Fig. 2).<sup>[29,30]</sup> The carboxylic acid **1** does not bind to DNA.<sup>[31]</sup>

Papers from 1993<sup>[6–8]</sup> described inhibition of HIV protease by the compound **2**. The dicarboxylic acid **2** acts as a reversible inhibitor of the enzyme through binding to the cleft-like active site of the enzyme in competition with the natural peptide substrate. This shape-recognition binding is illustrated in Fig. 3 for the carboxylic acid **1**.<sup>[28]</sup> A dendritic variation of the fullerene inhibitor is studied for treatment of drug-resistant HIV.<sup>[32,33]</sup>

## Pharmacokinetics and Toxicity of Water-Soluble Fullerenes

Toxicity is the primary concern for people working on fullerenes on the bench. Although earlier studies on C<sub>60</sub> itself suggested low toxicity,<sup>[34–36]</sup> it was unclear if water-soluble fullerenes are also innocuous molecules. For the studies of the pharmacokinetic behavior of water-soluble organofullerenes, Nakamura et al.<sup>[37–40]</sup> synthesized the compounds **1** and **1-C14** starting with an alkoxy-substituted methylenecyclopropane by the use of radiolabeled trimethylenemethane chemistry as shown in Fig. 4.

The radiolabeled water-soluble fullerene **1-C14** quickly migrates through the body and accumulates mainly in the liver after a few hours. Importantly, the study also suggested that the fullerene molecule can pass through the blood–brain barrier, which was later confirmed by others.<sup>[41,42]</sup> The behavior stands in sharp contrast to the parent fullerene, which was absorbed by serum protein in blood quickly after injection.<sup>[34–36]</sup> The pharmacokinetic studies have shown that organofullerenes are excreted either slowly or rapidly depending on the substituents, which may be suitably modified under the capacity of medicinal chemists.<sup>[43]</sup>

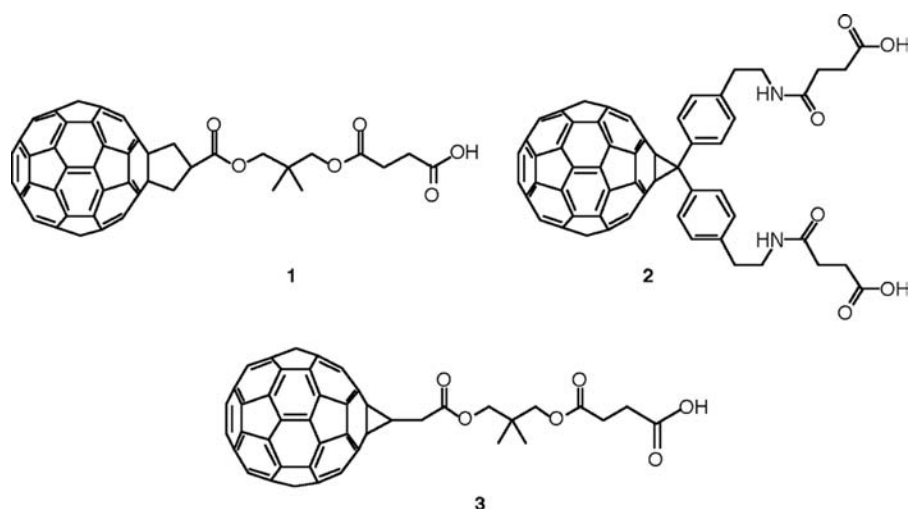


**Fig. 1** Monocarboxylic and dicarboxylic acids **1** and **2**.

The toxicity studies on the carboxylic acid **3** showed that the molecule does not show serious acute toxicity. Thus upon injection of up to 500 mg/kg quantity of the compound **3** to female mice, all mice survived for 1 week. Later studies<sup>[44-46]</sup> also indicated that the fullerene molecules do not show appreciable short-term toxicity. Long-term toxicity has so far not been reported, and little has yet been known for degradation of fullerenes in the environment.<sup>[47,48]</sup>

### Selective Binding to DNA

The initial discoveries made for the two simple molecules **1** and **2** quickly led to the studies on further application using more complex molecules. A fullerene molecule was connected to a 14-mer oligonucleotide that is complementary to single and double helix.

The fullerene/DNA conjugate **4** was found to bind to the target DNA site (Fig. 5),<sup>[49]</sup> cleaving the guanine bases in the position expected on the basis of complementary of triple helix formation. A similar result was reported for a fullerene conjugate bearing a 31-mer DNA recognition site.<sup>[50]</sup> The binding ability of such DNA/fullerene conjugates has been assessed.<sup>[51]</sup> Fullerene molecules bearing an intercalating group have been shown also to bind to double-strand DNA.<sup>[52]</sup>

One application of the above study is the photodynamic therapy of cancer. A C<sub>60</sub> derivative bearing polyether side chains was found to shrink skin cancer in mice.<sup>[53]</sup> In vivo ultrasound irradiation of fullerene-containing tissue may also suppress tumor growth.<sup>[54,55]</sup> Inactivation of virus has also been reported.<sup>[56]</sup> The actual biological targets of these approaches still remain unclear, although DNA may be a possible candidate.

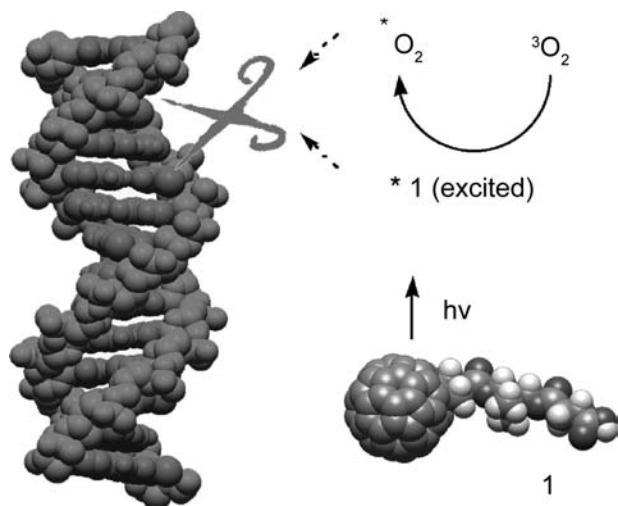


**Fig. 2** DNA cleavage by fullerene carboxylic acid **1**.

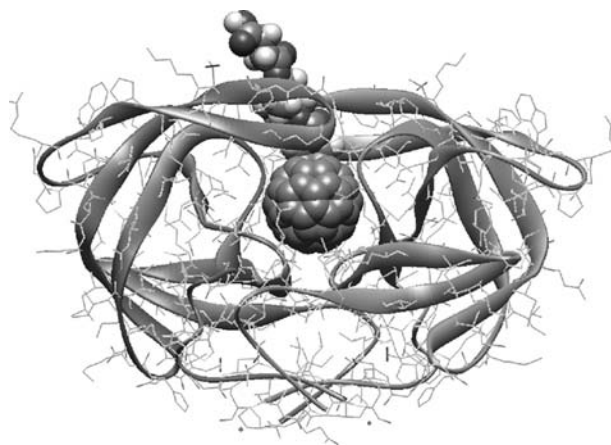


**Fig. 3** A three-dimensional model of the complex of **1** with HIV protease.

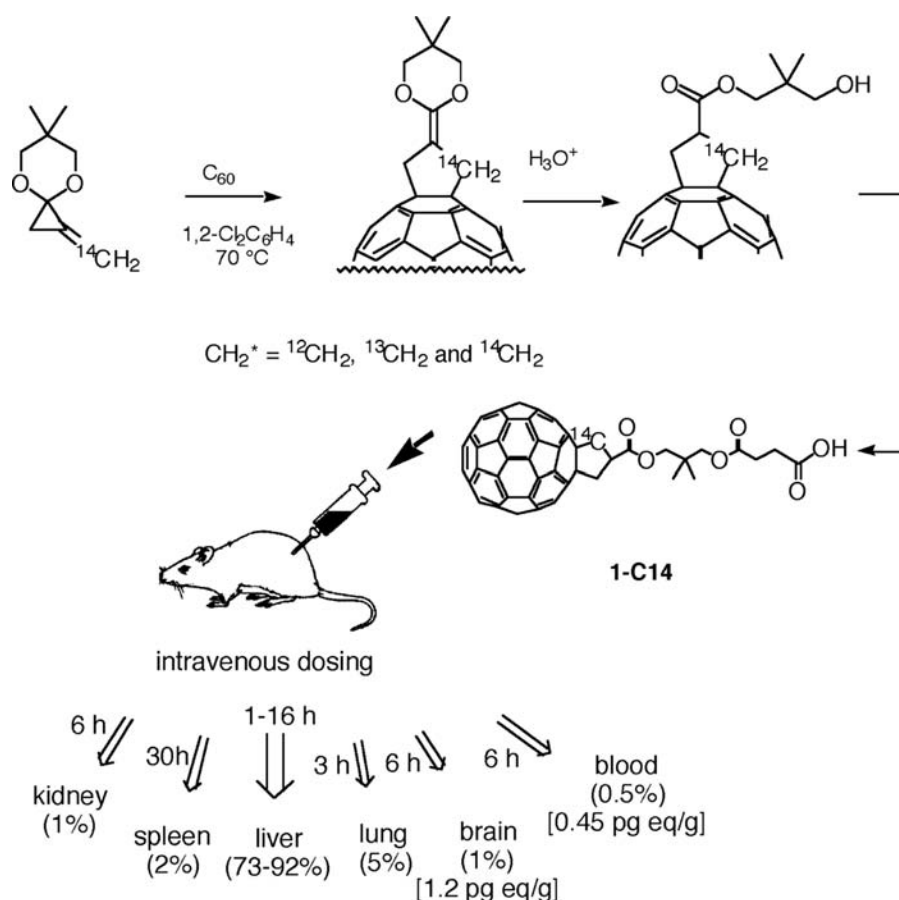


**Fig. 4** Pharmacokinetics of radiolabeled fullerene carboxylic acid **1-C14**.

## Gene Delivery

Delivery of gene into living cells through encapsulation of the gene in a “vector” is a fundamental technology in modern biology.<sup>[57]</sup> This process called “transfection” (transfer + infection) allows the production of the protein encoded in the delivered DNA within the cell. Recent studies indicated that suitably modified fullerene molecules are effective for the gene delivery.

A series of fullerenes bearing amino side chain(s) has been synthesized and was examined for their DNA binding ability as well as their transfection capability.<sup>[58]</sup> The  $C_{2}$ -chiral two-handed fullerene **5** was synthesized by double [3 + 2] cycloaddition of a bis-cyclopropenone acetal that took place with complete regioselectivity to give the desired compound.<sup>[59]</sup>

Some representative examples of the DNA-binding fullerenes (**5–8**) are shown in Chart 1.<sup>[58,60–63]</sup> As a solution of a 4.5-kbp plasmid DNA with a reporter gene

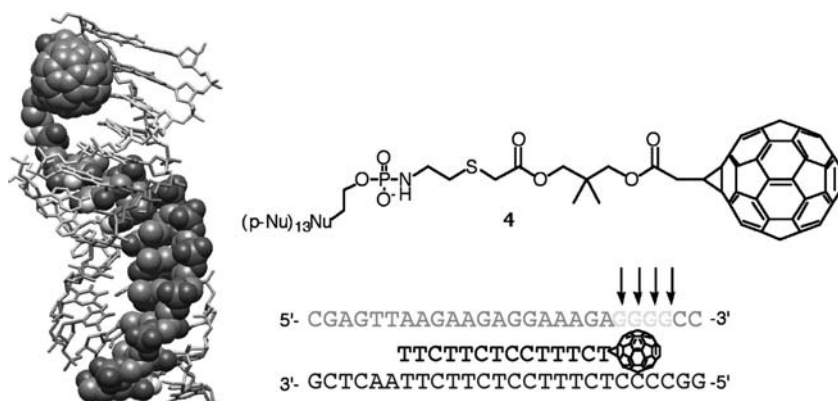


**Fig. 5** Triple helix forming fullerene/DNA conjugate **4** (CPK model), its three-dimensional binding model, and site-selective photo-cleavage of DNA (as indicated by arrows).



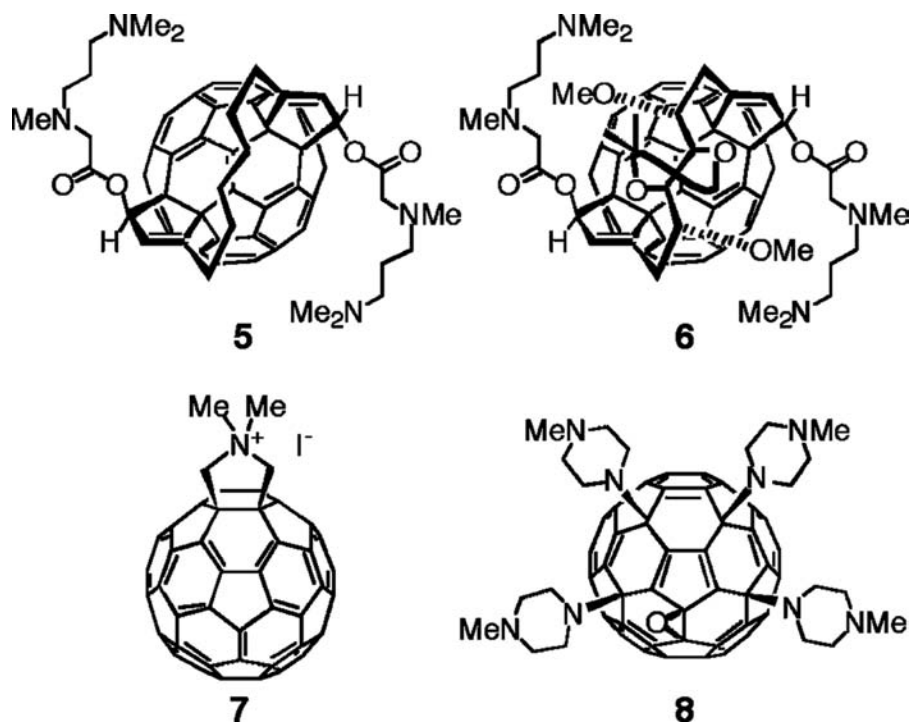


Chart 1 Representative DNA binding fullerenes examined for transfection.

was mixed together with a solution of the two-handed tetraminofullerene **5** in buffer, particles of 0.5–3  $\mu\text{m}$  diameter form as observed by optical microscope (Fig. 6). When this mixture was incubated with dividing mammalian cells, the dark-colored fullerene/DNA particles were taken into the cells, and protein production occurred. Screening of various cell lines indicated that the efficiency of this first-generation

fullerene vector is comparable to or better than the commercially available lipid-based vectors.

When a double-strand DNA is treated with an aminofullerene **7**, the fullerene molecules stick to the DNA strand without much changing the linear outline of the DNA as studied by TEM.<sup>[62,63]</sup> In spite of its binding ability, aminofullerene **7** is not effective for gene delivery.

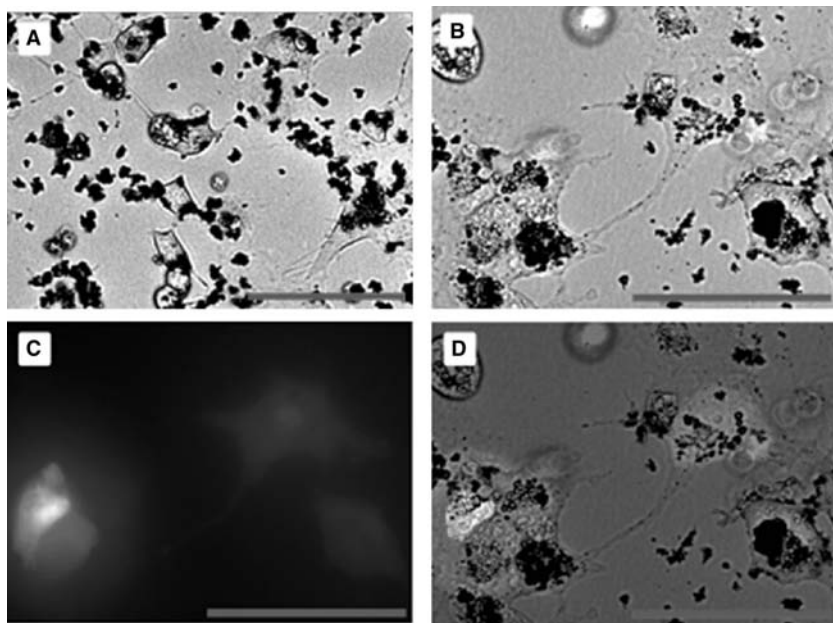
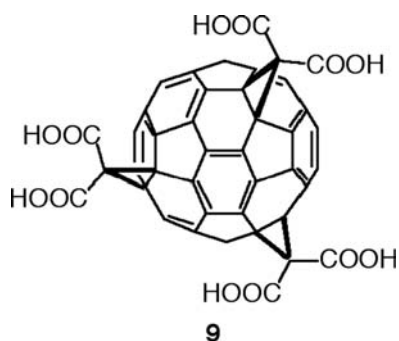


Fig. 6 Delivery of green fluorescent protein (GFP) plasmid into COS-1 cells with **5**. Bars show 100  $\mu\text{m}$ . (A) Differential interference contrast microscopy (DIC) micrograph of COS-1 cells and small black particles (1–10  $\mu\text{m}$ ) of the fullerene/DNA complex after 1-hr transfection time. (B) DIC micrograph of COS-1 cells after 2-day incubation time. (C) Fluorescence image of the area same as (B). (D) Superimposed photograph of (B) and (C). Round black clumps of 0.5–3  $\mu\text{m}$  size observed in the fluorescent cells contain fullerene materials. *Source:* Adapted from “Functionalized fullerene as a new artificial vector for transfection,” in *Angew. Chem.*<sup>[31]</sup>.

## Neuron Protection

In 1997, it was reported that the fullerene hexacarboxylic acid **9** acts as a drug for neurodegenerative diseases such as Alzheimer's, Parkinson's, or amyotrophic lateral sclerosis (ALS).<sup>[41]</sup> The activity is considered to arise from trapping of hydroxy radicals by the fullerene molecule.<sup>[64]</sup> The finding is currently developed for clinical trials.



## Endohedral Metal Complexes

Metal-containing fullerenes are attracting people's attention for their clinical applications. Biodistribution studies of <sup>166</sup>Ho<sub>x</sub>@C<sub>82</sub>(OH)<sub>y</sub> showed the uptake of the polyhydroxylated fullerene by bone without clearance and may be used as in vivo radiotracer.<sup>[42]</sup> The use of metallofullerenes as a magnetic resonance imaging (MRI) contrast agent is another area of extensive current studies. Gd@C<sub>82</sub>(OH)<sub>n</sub> was found to be a much better contrast agent than the conventional agents (i.e., a nitrogen-ligand coordinated to the metal).<sup>[65,66]</sup> The metal-containing fullerene accelerates spin relaxation (*T*<sub>1</sub>) of water protons that surrounds the fullerene molecule. The water proton relaxivity *R*<sub>1</sub> is much higher (20-folds) than that of the MRI contrast agent currently in use (e.g., Magnevist®, gadolinium-diethylenetri-aminepentaacetic acid). Polycarboxylic acid derivatives of Gd@C<sub>82</sub> also serve as an excellent contrast agent.<sup>[67]</sup>

## MOLECULAR ASSEMBLY OF WATER-SOLUBLE FULLERENES

Many of "water-soluble" fullerenes do not simply dissolve in water, but form various intriguing supramolecular structures, some of which have been unknown for conventional surfactants and lipid molecules. Various new discoveries have been made in recent years with respect to the formation of one- to three-dimensional supramolecular objects, including vesicle, rod, globule, membrane, and linear assemblies.

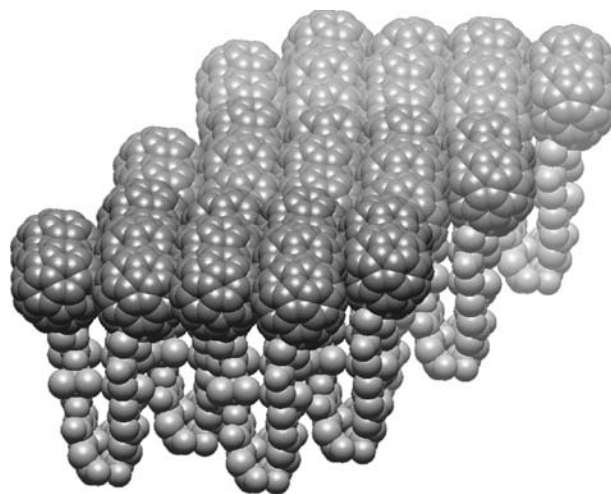


Fig. 7 Molecular model of LB film of **1**.

## Langmuir-Blodgett Film

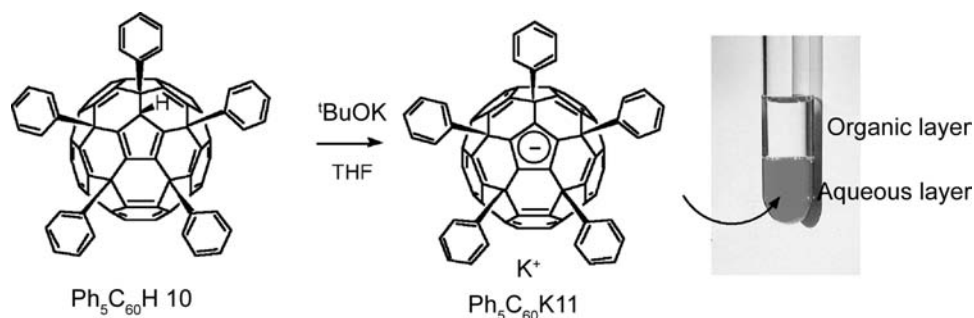
Formation of molecular layers of fullerene and their derivatives has attracted the attention of scientists for a long time, yet earlier attempts to make uniform monolayer of C<sub>60</sub> were rather unsatisfactory.<sup>[68]</sup> The amphiphilic fullerene carboxylic acid **1** was reported in 1995 to form a uniform Langmuir-Blodgett (LB) film at the water-air interface.<sup>[69]</sup> The average area per molecule determined by the  $\pi$ -A plot was 0.78 nm<sup>2</sup>, and the distance between the neighboring C<sub>60</sub> was 0.95 nm, which is close to (but slightly smaller than) the distance of 1.0 nm determined in the crystal structure of C<sub>60</sub>. Atomic force microscopic (AFM) analysis indicated that the surface contains far less defects than the LB film made from unmodified C<sub>60</sub> under similar conditions (Fig. 7).

## Nanorod and Nanoparticles

Rod-like assembly of fullerene forms when a DMSO solution of a cationic amphiphile **7** is dispersed in benzene.<sup>[62,63]</sup> The nanorods measure a diameter of 14–120 nm and a length of over 70  $\mu$ m. When the dispersion is sonicated, vesicles of various sizes and shapes form. The thickness of the vesicle wall (3–6 nm) suggests a multilamellar structure.<sup>[70]</sup> Georgakilas et al.<sup>[71]</sup> also reported that cationic amphiphiles form nanospheres and nanorods.

## Bilayer Vesicles

Ph<sub>5</sub>C<sub>60</sub>H (**10**) is an interesting hydrocarbon<sup>[72–74]</sup> in that its anion, Ph<sub>5</sub>C<sub>60</sub>K (**11**), dissolves freely in water (Scheme 1). It dissolves in water not as unimer, but as spherical aggregates.<sup>[75]</sup> Atomic force microscopy



Scheme 1

and laser light scattering (LLS) studies of the solution of **11** indicated that the solution contains bilayer vesicles and that the size distribution is quite narrow.<sup>[76]</sup> Thus upon slow addition of a THF solution to water,  $\text{Ph}_5\text{C}_{60}\text{K}$  forms spherical bilayer aggregates of 34-nm average diameter composed of about 13,000 fullerene molecules as determined by LLS (Fig. 8). This ability of  $\text{Ph}_5\text{C}_{60}\text{K}$  to form vesicles in water is the most intriguing. The  $\text{Ph}_5\text{C}_{60}$  anion amphiphile is noteworthy for its virtually all- $\text{sp}^2$  carbon framework, high structural rigidity, spherical hydrophobic moiety, and the lack of heteroatom hydrophilic sites.<sup>[77]</sup> In addition, the fullerene moiety is unique because it is highly hydrophobic but not lipophilic.

Penta-arylated  $\text{C}_{60}$  bears large aryl groups to form a cavity that can recognize another  $\text{C}_{60}$  molecule. Such a

molecule **12** looks like a badminton shuttlecock and stacks with each other to form a one-dimensional array of both in crystals and in liquid crystals (Fig. 9).<sup>[78]</sup> One may expect that, with suitable modifications, such “nanoshuttlecock” would also be useful for the formation of supramolecular structures in aqueous solutions.

### DNA/Fullerene Nanoparticles

The aforementioned experiments of gene delivery demonstrated the ability of the fullerene **5** to condense and to release DNA, and the molecular nature of the DNA condensation/release process was probed in test-tube experiments with AFM.<sup>[79]</sup> When half an equivalent/base pair of the fullerene **5** was mixed with 4-kbp plasmid DNA (Fig. 10A), the DNA molecule was condensed into a globular object seen in Fig. 10B as a flat disc of 3-nm thickness and 50-nm diameter. This condensate comprises one molecule of the plasmid DNA and about 2000 molecules of the fullerene derivative. Upon further addition of fullerene **5**, many single-molecule DNA condensates gather together to

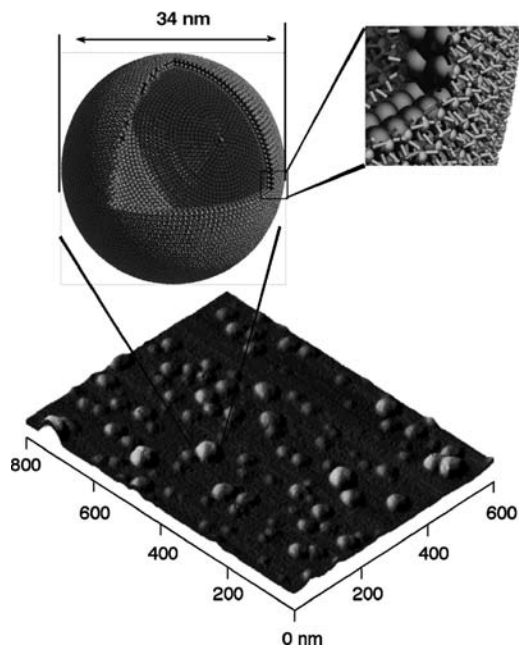


**Fig. 8** Atomic force microscopic image of bilayer vesicle of **11** and the molecular model obtained by LLS study. *Source:* Adapted from “Spherical bilayer vesicles of fullerene based surfactants in water: A laser light scattering study,” in *Science*.<sup>[76]</sup>

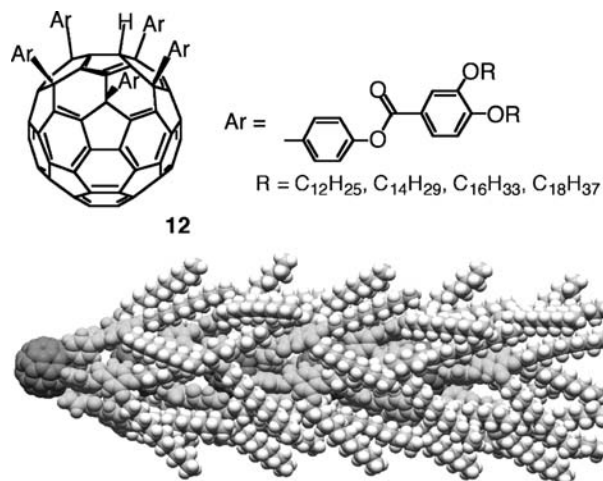


**Fig. 9** Nanoshuttlecock molecule **12** and a three-dimensional model of the stack-of-five molecules.

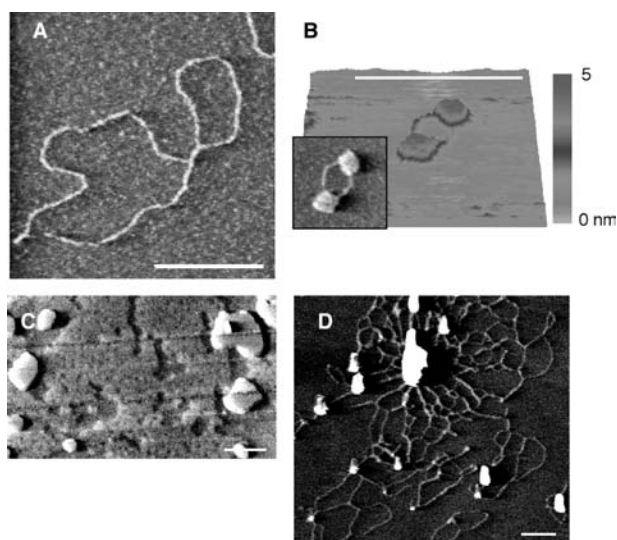


**Fig. 10** Condensation of 4-kbp plasmid DNA (A) into globules with increasing amount of **5** (B and C) and its release upon removal of fullerene (D). *Source:* Adapted from “Atomic force microscope studies on condensation of plasmid DNA with functionalized fullerene,” in *Angew. Chem.*<sup>[79]</sup>.

form the micrometer-sized object (Fig. 10c). Release of the DNA molecules from these large particles was achieved (Fig. 10d) by extractive removal of the fullerene with  $\text{CHCl}_3$ .

The formation of globular condensates composed of a single to a few DNA molecules is unique among other DNA-condensation studies based on lipid and dendrimeric molecules, which create much larger and less structurally defined DNA condensates.<sup>[80]</sup> Studies on a series of DNA-binding aminofullerenes recently showed that DNA condensation is required, but not sufficient for successful transfection.<sup>[60,61]</sup>

### Fullerene-Binding Antibody

A fullerene binding protein has been elicited purposely.<sup>[81]</sup> Immunization of mice with a  $\text{C}_{60}$ -bovine thyroglobulin (>600 kDa) conjugate elicited the desired IgG isotype antibody. Crystal structure of Fab fragment of the antifullerene antibody revealed that a shape-complementary clustering of hydrophobic amino acids forms a fullerene binding site.<sup>[82]</sup> Modeling study shows participation of the induced fit mechanism in the binding process. Interestingly, a subpopulation of the antibodies also recognizes  $\text{C}_{70}$  and even carbon nanotubes.<sup>[83–85]</sup>

### CONCLUSION

The development of the science of water-soluble fullerenes has been very rapid. The molecular design starting

from the compounds **1** and **2** has become much more elaborate and the synthesis has become more sophisticated, leading recently to the synthesis of the most complex compounds in high yield and on a large scale. Practical applications to clinical and materials uses are therefore just ahead. The science of water-soluble fullerene stimulated the studies to dissolve also carbon nanotubes in water and organic solvent.<sup>[86,87]</sup> The high cost of fullerenes has been the biggest barrier toward practical applications of any fullerene derivative, and this problem is now resolved by a large-scale production achieved by a Japanese company.<sup>[88]</sup> The cost problem is still a big issue in the use of metal-containing fullerenes, but may be resolved in the not-too-distant future.

### REFERENCES

- Osawa, E. Superaromaticity. *Kagaku* **1970**, 25 (9), 854–863.
- Kroto, H.W.; Heath, J.R.; O'Brien, S.C.; Curl, R.F.; Smalley, R.E.  $\text{C}_{60}$ -buckminsterfullerene. *Nature* **1985**, 318 (6042), 162–163.
- Krättschmer, W.; Lamb, L.D.; Fostiropoulos, K.; Huffman, D.R. Solid  $\text{C}_{60}$ —A new form of carbon. *Nature* **1990**, 347 (6291), 354–358.
- Howard, J.B.; McKinnon, J.T.; Makarovskiy, Y.; Lafleur, A.L.; Johnson, M.E. Fullerenes  $\text{C}_{60}$  and  $\text{C}_{70}$  in flames. *Nature* **1991**, 352 (6331), 139–141.
- Tokuyama, H.; Yamago, S.; Nakamura, E.; Shiraki, T.; Sugiura, Y. Photo-induced biochemical activity of fullerene carboxylic acid. *J. Am. Chem. Soc.* **1993**, 115 (17), 7918–7919.
- Friedman, S.H.; DeCamp, D.L.; Sijbesma, R.P.; Srdanov, G.; Wudl, F.; Kenyon, G.L. Inhibition of the HIV-1 protease by fullerene derivatives: Model building studies and experimental verification. *J. Am. Chem. Soc.* **1993**, 115 (15), 6506–6509.
- Sijbesma, R.; Srdanov, G.; Wudl, F.; Castoro, J.A.; Wilkins, C.; Friedman, S.H.; DeCamp, D.L.; Kenyon, G.L. Synthesis of a fullerene derivative for the inhibition of HIV enzymes. *J. Am. Chem. Soc.* **1993**, 115 (15), 6510–6512.
- Schinazi, R.F.; Sijbesma, R.; Srdanov, G.; Hill, C.L.; Wudl, F. Synthesis and virucidal activity of a water-soluble, configurationally stable, derivatized  $\text{C}_{60}$  fullerene. *Antimicrob. Agents Chemother.* **1993**, 37 (8), 1707–1710.
- Jensen, A.W.; Wilson, S.R.; Schuster, D.I. Biological applications of fullerenes: A review. *Bioorg. Med. Chem.* **1996**, 4 (6), 767–779.
- Da Ros, T.; Prato, M. Medicinal chemistry with fullerenes and fullerene derivatives. *Chem. Commun.* **1999**, (8), 663–669.
- Wilson, S.R. Nanomedicine: Fullerene and Carbon Nanotube Biology. In *Perspectives of Fullerene Nanotechnology*; Osawa, E., Ed.; Kluwer Academic: Dordrecht, 2002; 155–163.

12. Hamza, A.V.; Balooch, M. The chemisorption of C<sub>60</sub> on Si(100)-(2 × 1). *Chem. Phys. Lett.* **1993**, *201* (5–6), 404–408.
13. Deguchi, S.; Alargova, R.G.; Tsuji, K. Stable dispersions of fullerenes, C<sub>60</sub> and C<sub>70</sub>, in water. Preparation and characterization. *Langmuir* **2001**, *17* (19), 6013–6017.
14. Guldi, D.M.; Prato, M. Excited-state properties of C<sub>60</sub> fullerene derivatives. *Acc. Chem. Res.* **2000**, *33* (10), 695–703.
15. Martin, N.; Sánchez, L.; Illescas, B.; Pérez, I. C<sub>60</sub>-based electroactive organofullerenes. *Chem. Rev.* **1998**, *98* (7), 2527–2547.
16. Hirsch, A. *Chemistry of the Fullerenes*; Thieme: Stuttgart, 1994.
17. Diederich, F.; Kessinger, R. Regio- and Stereoselective Multiple Functionalization of Fullerenes. In *Templated Organic Synthesis*; Diederich, F., Stang, P.J., Eds.; Wiley-VCH: Weinheim, 2000; 189–218.
18. Ruoff, R.S.; Tse, D.S.; Malhorta, R.; Lorents, D.C. Solubility of C<sub>60</sub> in a variety of solvents. *J. Phys. Chem.* **1993**, *97*, 3379–3383.
19. Korobov, M.V.; Smith, A.L. Solubility of the Fullerenes. In *Fullerenes: Chemistry, Physics, and Technology*; Kadish, K.M., Ruoff, R.S., Eds.; Wiley: New York, 2000; 53–89.
20. Ruoff, R.S.; Malhotra, R.; Huestis, D.L.; Tse, D.S.; Lorents, D.C. Anomalous solubility behaviour of C<sub>60</sub>. *Nature* **1993**, *362* (6416), 140–141.
21. Scrivens, W.A.; Tour, J.M. Potent solvents for C<sub>60</sub> and their utility for the rapid acquisition of <sup>13</sup>C NMR data for fullerenes. *J. Chem. Soc., Chem. Commun.* **1993**, (15), 1207–1208.
22. Sivaraman, N.; Dhamodaran, R.; Kaliappan, I.; Srinivasan, T.G.; Rao, P.R.V.; Mathews, C.K. Solubility of C<sub>60</sub> in organic solvents. *J. Org. Chem.* **1992**, *57* (22), 6077–6079.
23. Yamakoshi, Y.N.; Yagami, T.; Fukuhara, K.; Sueyoshi, S.; Miyata, N. Solubilization of fullerenes into water with poly(vinylpyrrolidone) applicable to biological tests. *J. Chem. Soc., Chem. Commun.* **1994**, (4), 517–518.
24. Diederich, F.; Gómez-López, M. Supramolecular fullerene chemistry. *Chem. Soc. Rev.* **1999**, *28* (5), 263–277.
25. Chiang, L.Y.; Upasani, R.B.; Swirczewski, J.W. Versatile nitronium chemistry for C<sub>60</sub> fullerene functionalization. *J. Am. Chem. Soc.* **1992**, *114* (26), 10154–10157.
26. Prato, M.; Suzuki, T.; Foroudian, H.; Li, Q.; Khemani, K.; Wudl, F.; Leonetti, J.; Little, R.D.; White, T.; Rickborn, B.; Yamago, S.; Nakamura, E. [3 + 2] and [4 + 2] Cycloadditions of C<sub>60</sub>. *J. Am. Chem. Soc.* **1993**, *115* (4), 1594–1595.
27. Irie, K.; Nakamura, Y.; Ohigashi, H.; Tokuyama, H.; Yamago, S.; Nakamura, E. Photocytotoxicity of water-soluble fullerene derivatives. *Biosci. Biotechnol. Biochem.* **1996**, *60* (8), 1359–1361.
28. Nakamura, E.; Tokuyama, H.; Yamago, S.; Shiraki, T.; Sugiura, Y. Biological activity of water-soluble fullerenes. Structural dependence of DNA cleavage, cytotoxicity and enzyme inhibitory activities. *Bull. Soc. Chem. Jpn.* **1996**, *69* (8), 2143–2151.
29. Yamakoshi, Y.; Sueyoshi, S.; Fukuhara, K.; Miyata, N.; Masumizu, T.; Kohno, M. •OH and O<sub>2</sub><sup>•-</sup> Generation in aqueous C<sub>60</sub> and C<sub>70</sub> solutions by photoirradiation: An EPR study. *J. Am. Chem. Soc.* **1998**, *120* (47), 12363–12364.
30. Bernstein, R.; Prat, F.; Foote, C. On the mechanism of DNA cleavage by fullerenes investigated in model systems: Electron transfer from guanosine and 8-oxoguanosine derivatives to C<sub>60</sub>. *J. Am. Chem. Soc.* **1999**, *121* (2), 464–465.
31. Nakamura, E.; Isobe, H.; Tomita, N.; Sawamura, M.; Jinno, S.; Okayama, H. Functionalized fullerene as a new artificial vector for transfection. *Angew. Chem., Int. Ed.* **2000**, *39* (23), 4254–4257.
32. Brettreich, M.; Hirsch, A. A highly water-soluble dendro[60]fullerene. *Tetrahedron Lett.* **1998**, *39* (18), 2731–2734.
33. Schuster, D.I.; Wilson, S.R.; Kirschner, A.N.; Schinazi, R.F.; Schlueter-Wirtz, S.; Tharnish, P.; Barnett, T.; Ermolieff, J.; Tang, J.; Brettreich, M.; Hirsch, A. Evaluation of the anti-HIV potency of a water-soluble dendritic fullerene. *Proc. Electrochem. Soc.* **2000**, *11* (9), 267–270.
34. Nelson, M.A.; Domann, F.E.; Bowden, G.T.; Hooser, S.B.; Fernando, Q.; Carter, D.E. Effects of acute and subchronic exposure of topically applied fullerene extracts on the mouse skin. *Toxicol. Ind. Health* **1993**, *9* (4), 623–630.
35. Scrivens, W.A.; Tour, J.M.; Creek, K.E.; Pirisi, L. Synthesis of <sup>14</sup>C-labeled C<sub>60</sub>, its suspension in water, and its uptake by human keratinocytes. *J. Am. Chem. Soc.* **1994**, *116* (19), 4517–4518.
36. Moussa, F.; Roux, S.; Pressac, M.; Génin, E.; Hadchouel, M.; Trivin, F.; Rassat, A.; Céolin, R.; Szwarc, H. In vivo reaction between [60]fullerene and vitamin A in mouse liver. *New J. Chem.* **1998**, *22* (9), 989–992.
37. Nakamura, E.; Yamago, S.; Ejiri, S.; Dorigo, A.E.; Morokuma, K. Reversible generation of trimethylenemethanes by mild thermolysis of dialkoxy methylenecyclopropanes. *J. Am. Chem. Soc.* **1991**, *113* (8), 3183–3184.
38. Yamago, S.; Tokuyama, H.; Nakamura, E.; Kikuchi, K.; Kananishi, S.; Sueki, K.; Nakahara, H.; Enomoto, S.; Ambe, F. In vivo biological behavior of a water-miscible fullerene: <sup>14</sup>C labeling, absorption, distribution, excretion and acute toxicity. *Chem. Biol.* **1995**, *2* (6), 385–389.
39. Nakamura, E.; Yamago, S. Thermal reactions of dipolar trimethylenemethane species. *Acc. Chem. Res.* **2002**, *35* (10), 867–877.
40. Yamago, S.; Nakamura, E. [3 + 2] Cycloaddition of trimethylenemethane and its synthetic equivalents. *Org. React.* **2002**, *61*, 1–215.
41. Dugan, L.L.; Turetsky, D.M.; Du, C.; Lobner, D.; Wheeler, M.; Almlı, C.R.; Shen, C.K.-F.; Luh, T.-Y.; Choi, D.W.; Lin, T.-S. Carboxyfullerenes as neuroprotective agents. *Proc. Natl. Acad. Sci. U. S. A.* **1997**, *94* (17), 9434–9439.
42. Cagle, D.W.; Kennel, S.J.; Mirzadeh, S.; Alford, J.M.; Wilson, L.J. In vivo studies of fullerene-based materials

- using endohedral metallofullerene radiotracers. Proc. Natl. Acad. Sci. U. S. A. **1999**, *96* (9), 5182–5187.
43. Rajagopalan, P.; Wudl, F.; Schinazi, R.F.; Boudinot, F.D. Pharmacokinetics of a water-soluble fullerene in rats. *Antimicrob. Agents Chemother.* **1996**, *40* (10), 2262–2265.
  44. Rancan, F.; Rosan, S.; Boehm, F.; Cantrell, A.; Brellreich, M.; Schoenberger, H.; Hirsch, A.; Moussa, F. Cytotoxicity and photocytotoxicity of a dendritic C<sub>60</sub> mono-adduct and a malonic acid C<sub>60</sub> tris-adduct on Jurkat cells. *J. Photochem. Photobiol., B Biol.* **2002**, *67* (3), 157–162.
  45. Tzeng, S.-F.; Lee, J.-L.; Kuo, J.-S.; Yang, C.-S.; Murugan, P.; Tai, L.A.; Hwang, K.C. Effects of malonate C<sub>60</sub> derivatives on activated microglia. *Brain Res.* **2002**, *940* (1–2), 61–68.
  46. Chen, H.H.C.; Yu, C.; Ueng, T.H.; Chen, S.; Chen, B.J.; Huang, K.J.; Chiang, L.Y. Acute and subacute toxicity study of water-soluble polyalkylsulfonated C<sub>60</sub> in rats. *Toxicol. Pathol.* **1998**, *26* (1), 143–151.
  47. Buseck, P.R.; Tshipursky, S.J.; Hettich, R. Fullerenes from the geological environment. *Science* **1992**, *257* (5067), 215–217.
  48. Chibante, L.P.F.; Heymann, D. On the geochemistry of fullerenes: Stability of C<sub>60</sub> in ambient air and the role of ozone. *Geochim. Cosmochim. Acta* **1993**, *57* (8), 1879–1881.
  49. Boutorine, A.S.; Tokuyama, H.; Takasugi, M.; Isobe, H.; Nakamura, E.; Hélène, C. Fullerene-oligonucleotide conjugates: Photo-induced sequence-specific DNA cleavage. *Angew. Chem., Int. Ed. Engl.* **1994**, *33* (23/24), 2462–2465.
  50. An, Y.Z.; Chen, C.H.B.; Anderson, J.L.; Sigman, D.S.; Foote, C.S.; Rubin, Y. Sequence-specific modification of guanosine in DNA by a C<sub>60</sub>-linked deoxyoligonucleotide: Evidence for a non-singlet oxygen mechanism. *Tetrahedron* **1996**, *52* (14), 5179–5189.
  51. Da Ros, T.; Bergamin, M.; Vazquez, E.; Spalluto, G.; Baiti, B.; Moro, S.; Boutorine, A.; Prato, M. Synthesis and molecular modeling studies of fullerene-5,6,7-trimethoxyindole-oligonucleotide conjugates as possible probes for study of photochemical reactions in DNA triple helices. *Eur. J. Org. Chem.* **2002**, (3), 405–413.
  52. Yamakoshi, Y.N.; Yagami, T.; Sueyoshi, S.; Miyata, N. Acridine adduct of [60]fullerene with enhanced DNA-cleaving activity. *J. Org. Chem.* **1996**, *61* (21), 7236–7237.
  53. Tabata, Y.; Murakami, Y.; Ikada, Y. Photodynamic effect of polyethylene glycol-modified fullerene on tumor. *Jpn. J. Cancer Res.* **1997**, *88* (11), 1108–1116.
  54. Tabata, Y.; Ishii, T.; Aoyama, T.; Oki, R.; Hirano, Y.; Ogawa, O.; Ikada, Y. Sonodynamic Effect of Polyethylene Glycol-Conjugated Fullerene on Tumor, Perspectives of Fullerene Nanotechnology. In *Perspectives of Fullerene Nanotechnology*; Osawa, E., Ed.; Kluwer Academic: Dordrecht, 2002; 185–196.
  55. Chi, Y.; Canteenwala, T.; Chen, H.H.C.; Jeng, U.-S.; Lin, T.-L.; Chiang, L.Y. Free Radical Scavenging and Photodynamic Functions of Micelle-Like Hydrophilic Hexa(Sulfobutyl)Fullerene (FC4S). In *Perspectives of Fullerene Nanotechnology*; Osawa, E., Ed.; Kluwer Academic: Dordrecht, 2002; 165–183.
  56. Kiselev, O.I.; Kozeletskaya, K.N.; Melenevskaya, E.Y.; Vinogradova, L.V.; Keve, E.E.; Klenin, S.I.; Zgonnik, V.N.; Dumpis, M.A.; Piotrovsky, L.B. Antiviral activity of fullerene C<sub>60</sub> with the poly(*N*-vinylpyrrolidone) complex. *Mol. Cryst. Liq. Cryst. Sci. Technol., Sect. C Mol. Mater.* **1998**, *11* (1–2), 121–124.
  57. Wolff, J.A. *Gene Therapeutics: Methods and Applications of Direct Gene Transfer*; Birkhäuser: Boston, 1993.
  58. Isobe, H.; Tomita, N.; Jinno, S.; Okayama, H.; Nakamura, E. Synthesis and transfection capability of multi-functionalized fullerene polyamine. *Chem. Lett.* **2001**, (12), 1214–1215.
  59. Isobe, H.; Tokuyama, H.; Sawamura, M.; Nakamura, E. Synthetic and computational studies on symmetry-defined double cycloaddition of a new tris-annulating reagent to C<sub>60</sub>. *J. Org. Chem.* **1997**, *62* (15), 5034–5041.
  60. Isobe, H.; Tomita, N.; Nakamura, E. One-step multiple-addition of amine to [60]fullerene. Synthesis of tetra-(amino)fullerene epoxide under photochemical aerobic conditions. *Org. Lett.* **2000**, *2* (23), 3663–3665.
  61. Isobe, H.; Ohbayashi, A.; Sawamura, M.; Nakamura, E. A cage with fullerene end caps. *J. Am. Chem. Soc.* **2000**, *122* (11), 2669–2670.
  62. Cassell, A.M.; Scrivens, W.A.; Tour, J.M. Assembly of DNA/fullerene hybrid materials. *Angew. Chem., Int. Ed.* **1998**, *37* (11), 1528–1531.
  63. Cassell, A.M.; Asplund, C.L.; Tour, J.M. Self-assembling supramolecular nanostructures from a C<sub>60</sub> derivative: Nanorods and vesicles. *Angew. Chem., Int. Ed.* **1999**, *38* (16), 2403–2405.
  64. Chiang, L.Y.; Lu, F.-J.; Lin, J.-T. Free radical scavenging activity of water-soluble fullerenols. *J. Chem. Soc., Chem. Commun.* **1995**, (12), 1283–1284.
  65. Kato, H.; Kanazawa, Y.; Okumura, M.; Taninaka, A.; Yokawa, T.; Shinohara, H. Lanthanoid endohedral metallofullerenols for MRI contrast agents. *J. Am. Chem. Soc.* **2003**, *125* (14), 4391–4397.
  66. Mikawa, M.; Kato, H.; Okumura, M.; Narazaki, M.; Kanazawa, Y.; Miwa, N.; Shinohara, H. Paramagnetic water-soluble metallofullerenes having the highest relaxivity for MRI contrast agents. *Bioconjug. Chem.* **2001**, *12* (4), 510–514.
  67. Bolskar, R.D.; Benedetto, A.F.; Husebo, L.O.; Price, R.E.; Jackson, E.F.; Wallace, S.; Wilson, L.J.; Alford, J.M. First soluble M@C<sub>60</sub> derivatives provide enhanced access to metallofullerenes and permit in vivo evaluation of Gd@C<sub>60</sub>[C(COOH)<sub>2</sub>]<sub>10</sub> as a MRI contrast agent. *J. Am. Chem. Soc.* **2003**, *125* (18), 5471–5478.
  68. Mirkin, C.A.; Caldwell, W.B. Thin film, fullerene-based materials. *Tetrahedron* **1996**, *52* (14), 5113–5130.
  69. Matsumoto, M.; Tachibana, H.; Azumi, R.; Tanaka, M.; Nakamura, T.; Yunome, G.; Abe, M.; Yamago, S.; Nakamura, E. Langmuir–Blodgett film of amphiphilic C<sub>60</sub> carboxylic acid. *Langmuir* **1995**, *11* (2), 660–665.
  70. Sano, M.; Oishi, K.; Ishi-i, T.; Shinkai, S. Vesicle formation and its fractal distribution by bola-amphiphilic [60]fullerene. *Langmuir* **2000**, *16* (8), 3773–3776.



71. Georgakilas, V.; Pellarini, F.; Prato, M.; Guldi, D.M.; Mlle-Franco, M.; Zerbetto, F. Supramolecular self-assembled fullerene nanostructures. *Proc. Natl. Acad. Sci. U. S. A.* **2002**, *99* (8), 5075–5080.
72. Sawamura, M.; Iikura, H.; Nakamura, E. The first pentahapto fullerene metal complexes. *J. Am. Chem. Soc.* **1996**, *118* (50), 12850–12851.
73. Nakamura, E.; Sawamura, M. Chemistry of  $\eta^5$ -fullerene metal complexes. *Pure Appl. Chem.* **2001**, *73* (2), 355–359.
74. Sawamura, M.; Iikura, H.; Hirai, A.; Nakamura, E. Synthesis of  $\pi$ -indenyl-type fullerene ligand and its metal complexes via quantitative trisarylation of  $C_{70}$ . *J. Am. Chem. Soc.* **1998**, *120* (32), 8285–8286.
75. Sawamura, M.; Nagahama, N.; Toganoh, M.; Hackler, U.E.; Isobe, H.; Nakamura, E.; Zhou, S.-Q.; Chu, B. Pentaorgano[60]fullerene  $R_5C_{60}^-$ . A water soluble hydrocarbon anion. *Chem. Lett.* **2000**, (9), 1098–1099.
76. Zhou, S.; Burger, C.; Chu, B.; Sawamura, M.; Nagahama, N.; Toganoh, M.; Hackler, U.E.; Isobe, H.; Nakamura, E. Spherical bilayer vesicles of fullerene based surfactants in water: A laser light scattering study. *Science* **2001**, *291* (5510), 1944–1947.
77. Noguchi, H.; Takasu, M. Self-assembly of amphiphiles into vesicles: A Brownian dynamics simulation. *Phys. Rev., E* **2001**, *64* (5), 0419131–0419137.
78. Sawamura, M.; Kawai, K.; Matsuo, Y.; Kanie, K.; Kato, T.; Nakamura, E. Stacking of conical mesogens with a fullerene apex into polar columns in crystals and liquid crystals. *Nature* **2002**, *419* (6908), 702–705.
79. Isobe, H.; Sugiyama, S.; Fukui, K.-I.; Iwasawa, Y.; Nakamura, E. Atomic force microscope studies on condensation of plasmid DNA with functionalized fullerene. *Angew. Chem., Int. Ed.* **2001**, *40* (18), 3364–3367.
80. Kawaura, C.; Noguchi, A.; Furuno, T.; Nakanishi, M. Atomic force microscopy for studying gene transfection mediated by cationic liposomes with a cationic cholesterol derivative. *FEBS Lett.* **1998**, *421* (1), 69–72.
81. Chen, B.-X.; Wilson, S.R.; Das, N.; Coughlin, D.J.; Erlanger, B.F. Antigenicity of fullerenes: Antibodies specific for fullerenes and their characteristics. *Proc. Natl. Acad. Sci. U. S. A.* **1998**, *95* (18), 10809–10813.
82. Braden, B.C.; Goldbaum, F.A.; Chen, B.-X.; Kirschner, A.N.; Wilson, S.R.; Erlanger, B.F. X-ray crystal structure of an anti-buckminsterfullerene antibody Fab fragment: Biomolecular recognition of  $C_{60}$ . *Proc. Natl. Acad. Sci. U. S. A.* **2000**, *97* (22), 12193–12197.
83. Erlanger, B.F.; Brus, L.; Sheetz, M.P. Antibodies specific to fullerene nanotubes for detection and immobilization of nanotubes. *PCT Int. Appl.* **2003**, 155.
84. Erlanger, B.F.; Chen, B.-X.; Zhu, M.; Brus, L. Binding of an anti-fullerene IgG monoclonal antibody to single wall carbon nanotubes. *Nano Lett.* **2001**, *1* (9), 465–467.
85. Pantarotto, D.; Partidos, C.D.; Graff, R.; Hoebeke, J.; Briand, J.-P.; Prato, M.; Bianco, A. Synthesis, structural characterization, and immunological properties of carbon nanotubes functionalized with peptides. *J. Am. Chem. Soc.* **2003**, *125* (29), 6160–6164.
86. Bahr, J.L.; Tour, J.M. Covalent chemistry of single-wall carbon nanotube. *J. Mater. Chem.* **2002**, *12* (7), 1952–1958.
87. Hirsch, A. Functionalization of single-walled carbon nanotubes. *Angew. Chem., Int. Ed.* **2002**, *41* (11), 1853–1859.
88. Frontier Carbon Corporation <http://www.f-carbon.com>.

# Organosilanes: Molecular Assembly

Atsushi Takahara

*Institute for Fundamental Research of Organic Chemistry, Kyushu University, Fukuoka, Japan*

## INTRODUCTION

Ultrathin films of organosilane have been identified as promising nanocoating for micro- and nanoscale technologies such as electronic devices and micromachines.<sup>[1–3]</sup> As the silanol groups of organosilane monolayer prepared from organotrichlorosilane or organotrialkoxysilane strongly interact with the substrate surface, the monolayer is thermally and chemically robust compared with conventional amphiphilic monolayers. Because the chain length of organosilane is approximately 1–3 nm, the organosilane forms a uniform ultrathin film on the substrate surface.

Two methods have been proposed for the preparation of organosilane monolayers. One is chemisorption from organosilane solution,<sup>[4–7]</sup> and the other is the Langmuir–Blodgett (LB) method.<sup>[8–22]</sup> Fig. 1 shows the film-formation mechanisms of the organosilane by the LB method (A) and the chemisorption method (B). In the case of the LB method Fig. 1A, the toluene solution of organotrichlorosilane was spread on the water surface (pH = 5.8) at a controlled subphase temperature. To attain the quasi-equilibrium state of the monolayer, the monolayer was kept on the water subphase under a given constant surface pressure for 15 min. The monolayer was transferred and immobilized onto the Si-wafer substrate surface by the LB method. In the case of chemisorption Fig. 1B, organosilane molecules were deposited either from the solution or from the vapor phase. It has been clarified that the aggregation state of the organosilane monolayers prepared by the LB method shows a higher packing density than the chemisorbed monolayers.<sup>[15,22]</sup>

Organosilane monolayers, which have surfaces terminated by various functional groups, are useful for manipulation of the physicochemical properties of solid surfaces such as wettability, nanotribology, and protein adsorption behavior. A key to fabricating functional organosilane monolayers is controlling the distribution of surface functional groups. Fabricating micro- and nanodevices using a bottom-up approach requires building blocks with a precisely controlled and tunable chemical composition, morphology, and size that can be fabricated virtually at will. The

organosilane monolayer is a candidate for such a building block because of its stability and ease of fabrication. Patterned microfeatures of organosilane monolayers can be fabricated on the substrate, allowing surface physicochemical properties to be area-selectively controlled. Two methods will be discussed in this article. One of them utilizes crystallization of organosilane of the binary component monolayer at the air/water interface.<sup>[8–11]</sup> Because the diffusion of organosilane molecules at the air/water interface is slow, macroscopic phase separation is inhibited, even with the alkylsilane and fluoroalkylsilane mixed monolayers. The phase-separated monolayer is transferred to the Si-wafer substrate by the LB method. Another method utilizes photolithography by a vacuum ultraviolet (VUV) ray source.<sup>[23,24]</sup> In the case of a VUV source with  $\lambda = 172$  nm, photodecomposition of the organic moiety occurs because of the higher photon energy of the VUV ray compared with the bond energy of a typical C–C linkage. Using photolithography, one can prepare a micropatterned surface with various organosilane monolayers by repeating the photodecomposition and chemisorption processes. By changing the shape and area ratio of the patterns of the photomask, this technique enables one to control the area ratio and the wettability gap of different organosilane monolayers.

## PATTERNING OF ORGANOSILANE MONOLAYERS VIA CRYSTALLIZATION AT THE AIR/WATER INTERFACE

### Formation of Organosilane Monolayers at the Air/Water Interface

Fig. 2 shows the chemical structure of organosilanes used for monolayer preparation. Organotrichlorosilane is primarily used for monolayer preparation at the air/water interface. Lignoseric acid [LA,  $\text{CH}_3(\text{CH}_2)_{22}\text{COOH}$ ] is also used to prepare the mixed monolayers. LA is not polymerized and is also non-reactive against the silicon substrate. The chlorine groups of organosilane on the water surface were found to be substituted by hydroxyl groups. At a

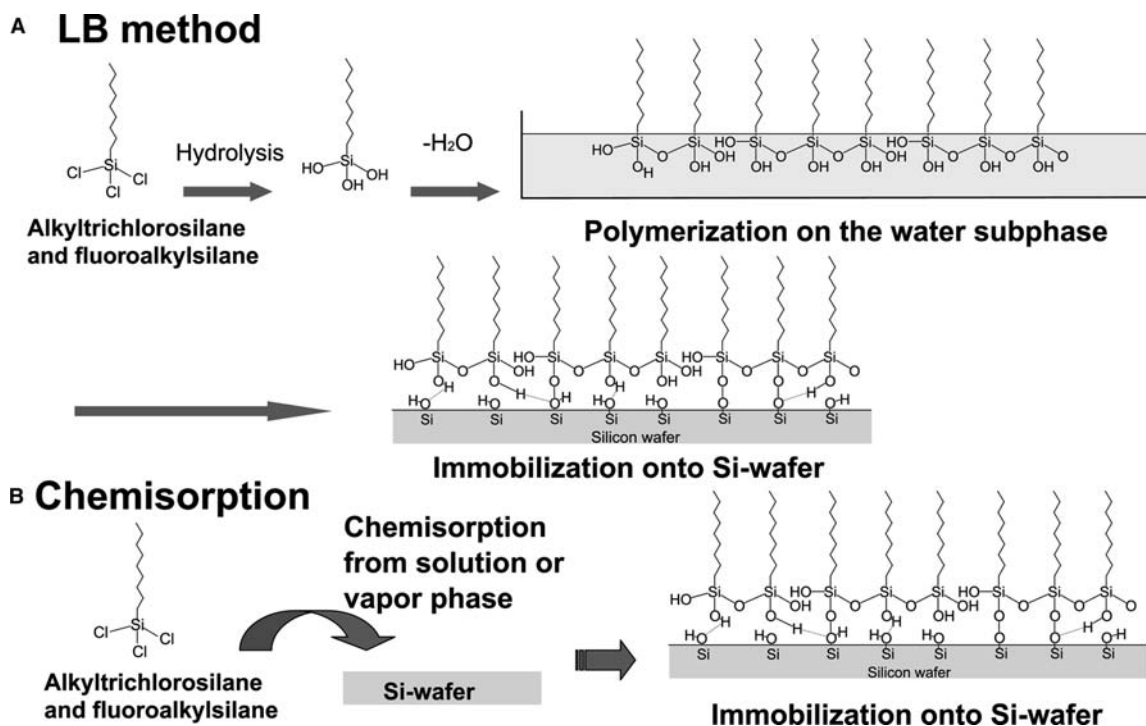


**Fig. 1** Film formation mechanism of organosilane by Langmuir–Blodgett (LB) method (A) and chemisorption method (B).

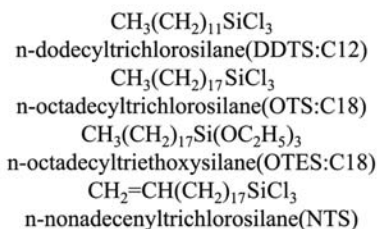
surface pressure of  $10\text{--}30\text{ mN m}^{-1}$ , the hydroxyl groups in organosilane molecules reacted with those in adjacent molecules in the case of the highly condensed monolayer, resulting in formation of a polymerized monolayer. The polymerized monolayer was easily transferred onto a Si wafer by the LB method,

and the residual hydroxyl groups could be covalently bonded with silanol groups on the Si wafer surface.

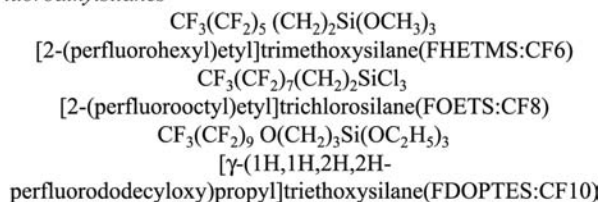
**Fig. 3** shows the surface pressure–area ( $\pi$ – $A$ ) isotherms for the *n*-octadecyltrichlorosilane (OTS), *n*-dodecyltrichlorosilane (DDTS), [1H,1H,2H,2H-perfluorododecyloxy]propyltriethoxysilane (FDOPTES), and [2-perfluorooctyl]ethyltrichlorosilane (FOETS) monolayers on the water surface at a subphase temperature of 293 K, as well as electron diffraction (ED) patterns of the monolayers transferred onto the hydrophilic SiO substrate on the EM grid at a surface pressure of approximately  $20\text{ mN m}^{-1}$ . The  $\pi$ – $A$  isotherms of the OTS and FDOPTES monolayers showed a steep increase in surface pressure with decreases in the surface area. The molecular occupied areas were determined to be  $0.24$  and  $0.29\text{ nm}^2\text{ molecule}^{-1}$  for the OTS and FDOPTES monolayers, respectively. Electron diffraction patterns of both the OTS and the FDOPTES monolayers showed hexagonal crystalline arcs at 293 K. The (10) spacings of the OTS and the FDOPTES monolayers were calculated to be ca.  $0.42$  and  $0.50\text{ nm}$  based on ED patterns, respectively.<sup>[18]</sup> These ED results make it clear that the hydrophobic alkyl and fluoroalkyl chains in the crystalline OTS and FDOPTES monolayers were closely packed in the hexagonal crystal lattice at 293 K.

High-resolution atomic force microscopy (AFM) was applied to observe the molecular arrangement of both the crystalline OTS-C18 and FDOPTES monolayers. **Fig. 3** also displays AFM images on a molecular

#### Alkylsilanes



#### Fluoroalkylsilanes



#### Aminosilane

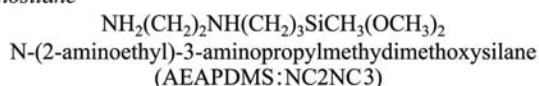


**Fig. 2** Chemical structure of organosilanes.

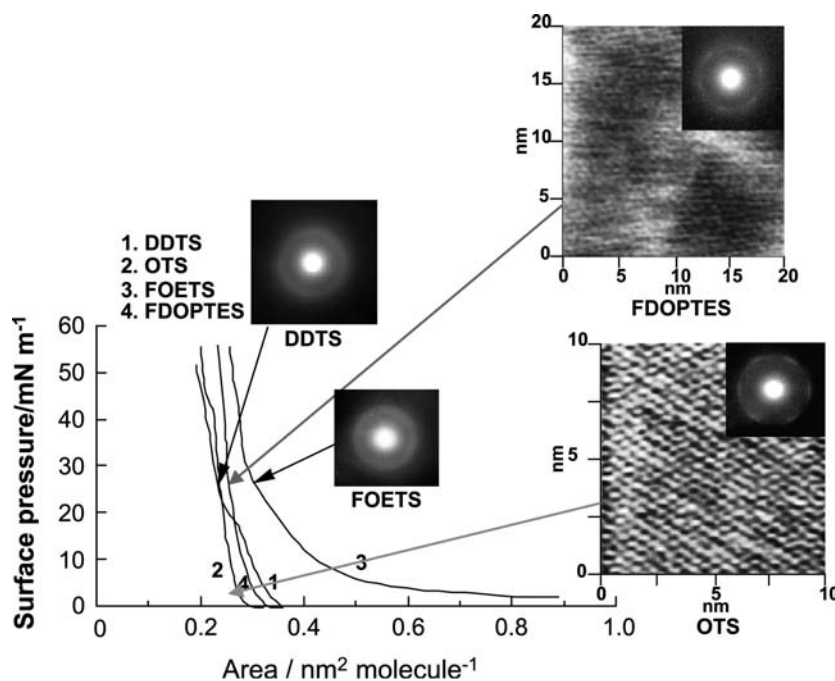


**Fig. 3**  $\pi$ - $A$  isotherms for the OTS, DDTS, FDOPTES, and FOETS monolayers on the water surface at a subphase temperature of 293 K, as well as the AFM images and ED patterns of the monolayers transferred onto the substrate at the surface pressure of around  $20 \text{ mN m}^{-1}$ .

scale for the crystalline OTS-C18 and FDOPTES monolayers transferred onto a Si wafer at a surface pressure of  $15 \text{ mN m}^{-1}$  at 293 K.<sup>[18]</sup> The (10) spacing was evaluated to be ca. 0.42 and 0.50 nm by two-dimensional fast Fourier transform (2-D-FFT). These values are in good agreement with the (10) spacings determined from the ED patterns for the crystalline OTS and FDOPTES monolayers. Thus, it is conceivable that the higher portions (the brighter dots) in the AFM images of Fig. 3 correspond to the individual methyl group of the OTS molecule and the fluoromethyl group of the FDOPTES molecule in the monolayers, respectively. In contrast, the  $\pi$ - $A$  isotherms for the DDTS monolayer and the FOETS monolayer with a shorter alkyl chain showed a gradual increase in surface pressure with decreasing surface area. In general, this can be interpreted as an indication that the monolayer is in a liquid-condensed or liquid-expanded state. In addition, the ED patterns of the DDTS and the FOETS monolayers showed an amorphous halo at 293 K. Hence, it can be envisaged that the chain lengths of hydrophobic groups of the DDTS and the FOETS molecules were not long enough to crystallize on the water subphase at 293 K.

### Phase Separation of Mixed Monolayers at the Air/Water Interface

Phase separation is expected to occur in the binary component monolayer of crystalline OTS and amorphous FOETS because of the incompatibility of OTS and FOETS. Fig. 4 shows the  $\pi$ - $A$  isotherm and the AFM

image of the scanned area  $10 \times 10 \mu\text{m}^2$  for the OTS/FOETS (50/50 mol/mol) mixed monolayer, which was transferred onto the Si wafer substrate by the LB method at a surface pressure of  $25 \text{ mN m}^{-1}$ . The height profile along the line shown in the AFM image revealed that the brighter and darker portions in the AFM image correspond to the higher and the lower

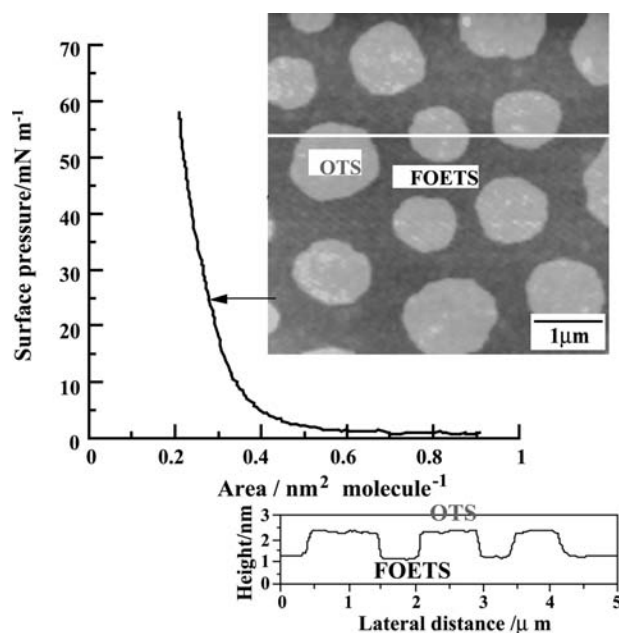


**Fig. 4**  $\pi$ - $A$  isotherm and AFM image of the scanned area  $10 \times 10 \mu\text{m}^2$  for the OTS/FOETS (50/50) mixed monolayer, which was transferred onto the Si wafer substrate by the LB method at the surface pressure of  $25 \text{ mN m}^{-1}$ .

regions of the monolayer surface, respectively. The molecular occupied area (the limiting area) of  $0.28 \text{ nm}^2 \text{ molecule}^{-1}$  for the OTS/FOETS (50/50) mixed monolayer appears to be almost equal to the average of the molecular occupied area for the OTS ( $0.24 \text{ nm}^2 \text{ molecule}^{-1}$ ) monolayer and the FOETS ( $0.31 \text{ nm}^2 \text{ molecule}^{-1}$ ) monolayer based on the molar fraction of OTS and FOETS. The OTS/FOETS mixed monolayer can be transferred onto the Si wafer substrate over a wide range of surface pressure. The transfer ratio of the OTS/FOETS mixed monolayer was ca. 1.0 at a surface pressure of  $25 \text{ mN m}^{-1}$ , indicating that the substrate surface is almost completely covered with the immobilized mixed monolayer. Also, the transfer of the OTS/FOETS mixed monolayer on the silicon substrate was confirmed by using attenuated total reflection Fourier transform infrared (ATR-FT-IR) spectroscopy and X-ray photoelectron spectroscopy (XPS). Because the area occupied by the circular flat-topped domains increases with increases in the OTS content, it is expected that the circular domains correspond to the OTS domain. The AFM line profile revealed that the circular domains were 1.1–1.3 nm higher than the surrounding area. Because the difference in molecular lengths between OTS and FOETS was ca. 1.3 nm, it can be concluded that the higher circular domains and the surrounding flat matrix regions were composed of OTS and FOETS molecules, respectively. OTS molecules formed circular domains even if the molar percent of OTS molecules was 75%. It is apparent from the ED pattern of the OTS/FOETS (75/25) mixed monolayer that the OTS domain is in a crystalline state, as the ED pattern showed a Debye ring and the magnitude of spacing corresponds to the (10) spacing of the OTS monolayer. In the case of the mixture of fluoroalkane and alkane, macroscopic phase separation was observed. However, in the case of organosilanes at the air/water interface, macroscopic phase separation such as that occurring with coalescence of the crystalline domain is inhibited because of the limited diffusion at the air/water interface.

A similar phase-separated structure was also expected for the mixed monolayer of the crystalline NTS and amorphous FOETS. Crystallization of the *n*-non-adeceyltrichlorosilane (NTS) phase was confirmed by ED.<sup>[17]</sup> Fig. 5 shows the AFM images of the mixed NTS/FOETS and carboxylated NTS (NTS<sub>COOH</sub>)/FOETS monolayers. It was clarified that the NTS/FOETS mixed monolayers were in a phase-separated state, and that circular flat-topped domains ca. 1–2 μm in diameter were surrounded by a sealike flat region. The phase separation in the mixed NTS/FOETS can also arise from crystallization of the NTS component. The NTS<sub>COOH</sub>/FOETS mixed monolayer was prepared through oxidation of the vinyl end groups of the NTS phase in the NTS/FOETS

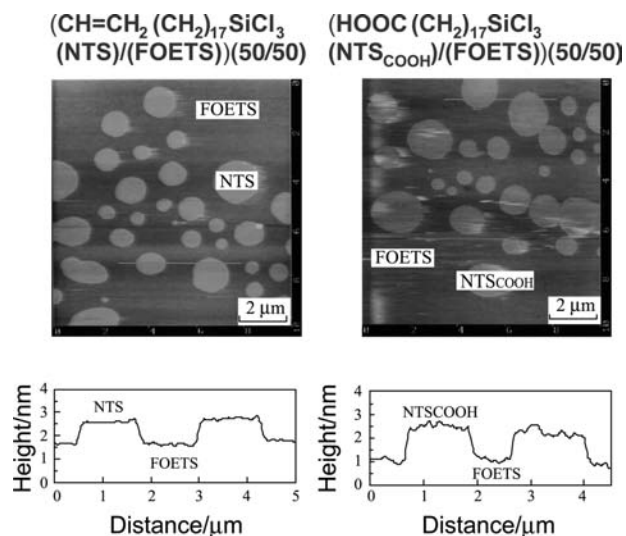


**Fig. 5** AFM images of the mixed NTS/FOETS and carboxylated NTS (NTS<sub>COOH</sub>)/FOETS monolayers.

mixed monolayer.<sup>[17]</sup> The NTS<sub>COOH</sub> monolayer showed high surface free energy, with the magnitude being comparable to that of water. The surface morphology of the NTS/FOETS mixed monolayer was not changed even after oxidation because of the presence of a strong interaction between silanol groups of NTS and the Si wafer. The height difference between the NTS<sub>COOH</sub> domain and the FOETS matrix phase in the NTS<sub>COOH</sub>/FOETS mixed monolayer was almost the same as that for the NTS/FOETS mixed monolayer. In addition, an XPS measurement was performed for the NTS/FOETS and the NTS<sub>COOH</sub>/FOETS mixed monolayers to confirm oxidation of the NTS phase. The larger ratio of oxygen/carbon atoms for the (NTS<sub>COOH</sub>/FOETS) mixed monolayer than that for the NTS/FOETS monolayer suggests that the vinyl end groups of the NTS molecules were oxidized to carboxyl groups. The magnitude of the lateral force of the NTS<sub>COOH</sub> phase was higher than that of the FOETS phase in the case of the NTS<sub>COOH</sub>/FOETS mixed monolayer in contrast to the case of the NTS/FOETS mixed monolayer. As the NTS<sub>COOH</sub> phase had hydrophilic carboxyl end groups at the surface, these end groups can presumably form intermolecular hydrogen bonds with neighboring NTS<sub>COOH</sub> molecules. Therefore, the surface of the outermost NTS<sub>COOH</sub> phase is expected to show a higher shear strength than that of the NTS phase because of a difficulty in surface deformation. Also, there is a significant contribution of adhesion force between the sample surface and the tip with regard to lateral force. Because the surface free energy of the NTS<sub>COOH</sub> phase is comparable to that of water, the water capillary force interacting between the NTS<sub>COOH</sub> monolayer surface and the hydrophilic Si<sub>3</sub>N<sub>4</sub> tip could strongly



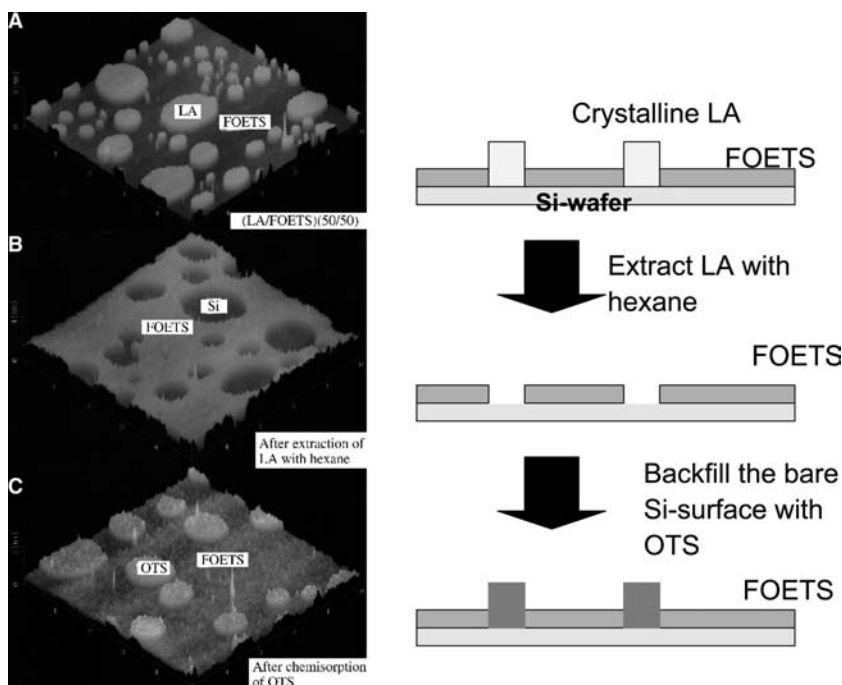


**Fig. 6** AFM images of the LA/FOETS (50/50 mol/mol) mixed monolayer (A), ghost monolayer after extraction of LA with hexane (B), and after backfill of ghost monolayer with OTS (C). *Source:* Reproduced from Ref.<sup>[13]</sup>.

contribute to the adhesion force of the  $\text{NTS}_{\text{COOH}}$  phase. It is therefore conceivable that the  $\text{NTS}_{\text{COOH}}$  phase exhibited higher lateral force than the FOETS phase because of the formation of intermolecular hydrogen bonding and a thicker adsorbed water layer as discussed above. Lateral force microscopic (LFM) and XPS measurements revealed that the phase-separated monolayer with a large surface energy gap was successfully prepared.

To investigate the various types of mixed monolayers, a novel mixed-monolayer system was designed using reactive organosilanes and a non-reactive fatty acid. A phase-separated monolayer can also be prepared from both FOETS and non-polymerizable and crystallizable amphiphiles such as stearic acid (SA) and lignoceric acid (LA). Fig. 6 shows the AFM images of the LA/FOETS (50/50 mol/mol) mixed monolayer Fig. 6A and after extraction of LA with hexane Fig. 6B. The LA/FOETS mixed monolayer was in a phase-separated state similar to the OTS/FOETS mixed monolayer as shown in Fig. 4. It is reasonable to conclude from Fig. 6A and B that the circular domains are composed of LA molecules, as the circular flat-topped domains were preferentially extracted with hexane. In addition, the FOETS matrix was not extracted with hexane because FOETS molecules were immobilized on the Si wafer surface by the Si–O–Si covalent bond and multiple hydrogen bonding. The electron diffraction of the LA/FOETS mixed monolayer showed a crystalline diffraction from LA domains. In addition, the circular domain of LA is

higher than that of FOETS by 2 nm. Because the bare Si surface with Si–OH groups was exposed to the surface, the Si phase can easily be backfilled by another organosilane through chemisorption from its solution. Thus, various types of surface modification are possible by chemisorption of various organosilanes to the FOETS monolayer with holes shown in Fig. 6B. Fig. 6C shows the AFM topographic image of the OTS/FOETS mixed monolayer prepared by the chemisorption of OTS onto the Si part of the FOETS monolayer. The surface structure of Fig. 6C was very similar to the phase-separated structure observed for the OTS/FOETS mixed monolayer directly prepared by the LB method. The OTS phase is mechanically and chemically very stable because of the polymerization and anchoring to the Si wafer. However, the domain height of the OTS phase in Fig. 6C was less than that observed for the OTS/FOETS mixed monolayer prepared by the LB method in Fig. 6C. In addition, the surface roughness of the OTS domains prepared by chemisorption was more distinct than that of the OTS domains prepared by the LB method. These results indicate that the OTS monolayer prepared by chemisorption is less ordered than that prepared by the LB method. This was also confirmed by grazing incidence X-ray diffraction (GIXD).<sup>[15,22]</sup> However, the abovementioned procedure to backfill the Si portion of the FOETS monolayer by the chemisorption of organosilane could be applicable to the preparation of two-phase monolayers in which the constituents have different surface free energies or surface chemistries.



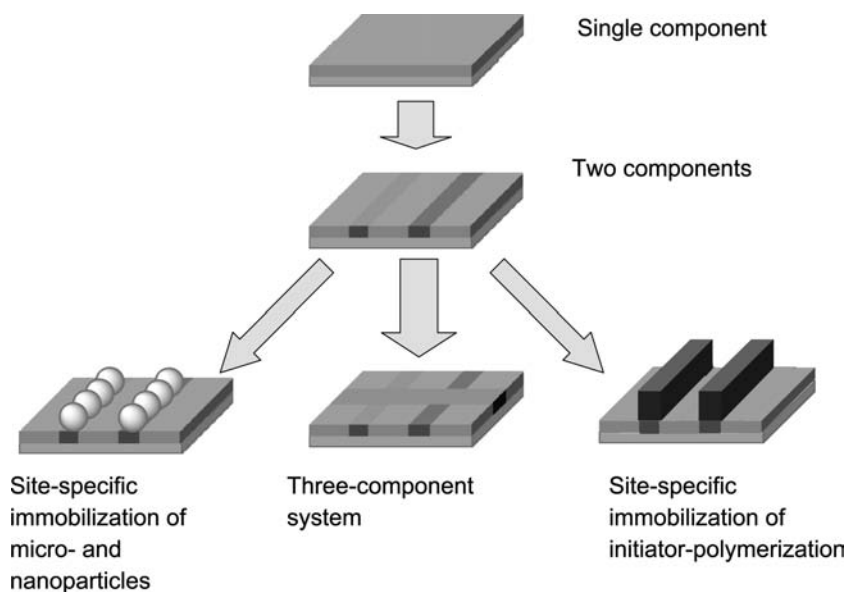


**Fig. 7** Schematic representation of surface patterning, site-specific polymerization, and site-specific immobilization of microparticles.

### FABRICATION OF MULTIPHASE ORGANOSILANE MONOLAYERS THROUGH CHEMISORPTION AND PHOTOLITHOGRAPHY

A structural surface that exhibits patterns of varying wettability can be produced by chemisorption and local photodecomposition of organosilanes. Using such patterns as templates for 3-D structures with various topographic and surface properties appears very promising. Site-specific adsorption of microparticles can be achieved by specific interactions between microparticles and a monolayer surface. Immobilization of a polymerization initiator on a functional monolayer enables site-specific polymerization, which can result in a large topography change. Fig. 7 summarizes the scheme of fabrication of micropatterned organosilane monolayers, site-specific polymerization, and immobilization of microparticles on patterned organosilane monolayers. These three processes are described in this section.

#### Preparation of a Three Component Patterned Organosilane Monolayer

Fig. 8 outlines the essential steps for fabrication of micropatterned organosilane monolayers. The first step was the preparation of organosilane-grafted Si substrates. The chemical vapor adsorption (CVA) method was used to fabricate the monolayers from organotrialkoxysilane.<sup>[25]</sup> Uniform monolayer formation was confirmed by AFM observations. Removal of the monolayer in selected areas by photodecomposition was the next step in the process. In photolithography, irradiation with VUV rays ( $\lambda = 172$  nm) leads to excitation cleavage of covalent bonds such as

C–C, C–H, and Si–C bonds, and formation of surface Si–OH residues.<sup>[25]</sup> The magnitude of water contact angle on OTES and FHETES monolayers was measured as a function of irradiation time of VUV light generated from an excimer lamp ( $\lambda = 172$  nm). VUV irradiation was done under 0.8 mm Hg of pressure. Initially, OTES and FHETES monolayers gave water contact angles larger than  $100^\circ$ . However, within 15 min, the angles approached  $0^\circ$ , which indicates that

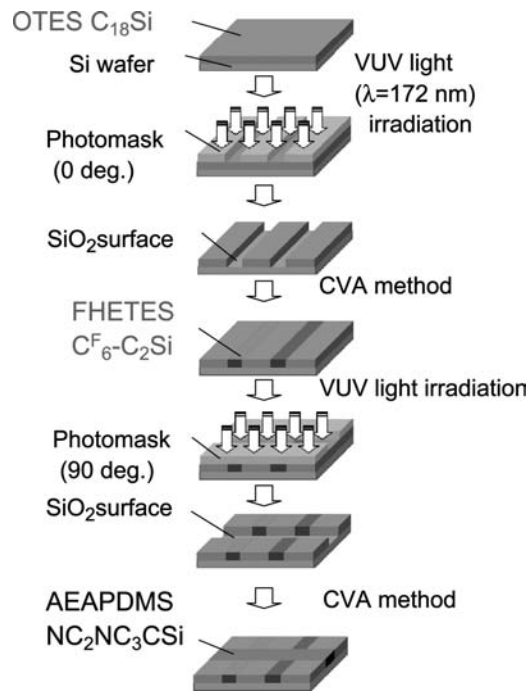


**Fig. 8** Schematic representation of site-specific photodecomposition by irradiation with VUV rays and chemisorption. *Source:* Reproduced from Ref.<sup>[24]</sup>.

almost complete removal of a monolayer can be achieved with 15-min irradiation of VUV light. The monolayer removal was also confirmed by XPS measurements. Using a photomask, one can prepare a pattern with the desired shape and a precisely controlled arrangement of surface functional groups. As an example, the preparation and characterization of an *n*-octadecyltriethoxysilane (OTES), [2-perfluorohexyl]ethyltriethoxysilane (FHETES), [2-aminoethyl]-3-aminopropylmethyldimethoxysilane (AEAPDMS) patterned surface is introduced in this section. The OTES-grafted Si wafer was irradiated for 15 min with VUV light. The second organosilane monolayer, FHETES (molecular length ca. 1.0 nm), was then introduced onto the first patterned surfaces by a similar method with alkylsilane. Formation of a ternary component monolayer requires another photodecomposition and chemisorption process, with the photomask rotated 90° from its position in the first patterning step. The OTES/FHETES sample was then irradiated with VUV, resulting in crossline micropatterns on the substrate surfaces. The third organosilane monolayer, AEAPDMS (molecular length ca. 0.9 nm), was finally introduced onto the second patterned substrate surfaces, again by the CVA method.

XPS and contact angle measurements were used to characterize the changes in the surface chemical compositions of the micropatterned organosilane monolayers. Fig. 9 shows the XPS survey scan spectra of the changes in the surface chemical compositions through the micropatterning process. The OTES monolayer showed C<sub>1s</sub>, O<sub>1s</sub>, Si<sub>2s</sub>, and Si<sub>2p</sub> peaks at 285, 533, 151, and 100 eV, respectively. The OTES/FHETES patterned Si substrate clearly showed an additional F<sub>1s</sub> peak at 690 eV, whereas the OTES/FHETES/AEAPDMS grafted Si substrates showed another N<sub>1s</sub> peak at 400 eV. Decomposition of the FHETES monolayer was revealed by the decreased intensity of the F<sub>1s</sub> peak. The grafting of organosilane monolayers was also confirmed from C<sub>1s</sub> and N<sub>1s</sub> XPS narrow-scan spectra. These results indicate that the three kinds of organosilane molecules were subsequently grafted on the substrate surfaces.

Fabrication of a micropattern with three kinds of surface functional groups was confirmed by Scanning force microscopy (SFM) observation. Fig. 10A and B shows AFM and LFM images of an OTES/FHETES/AEAPDMS three-component micropatterned organosilane monolayer, respectively. Fig. 10C and D shows the line profiles of the white lines in Fig. 10A. These figures show crossline microstructures fabricated on Si-wafer substrates. The widths of the fabricated FHETES and AEAPDMS lines were consistent with the widths of slits in the photomask. In the line profile of the AFM image as shown in Fig. 10C, the height difference between the OTES

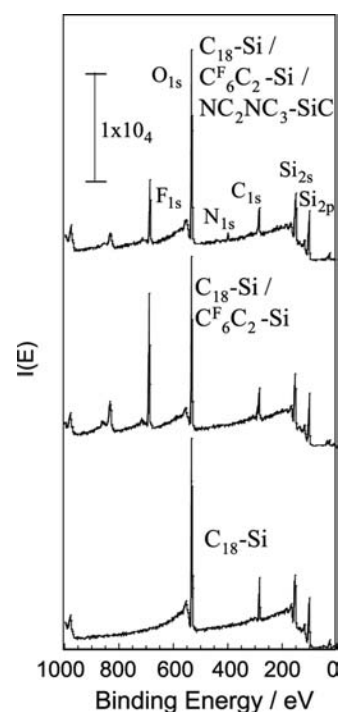


**Fig. 9** XPS survey scan spectra of the OTES, OTES/FHETES, and OTES/FHETES/AEAPDMS micropatterned Si substrates (emission angle 45°).

and FHETES surfaces was ca. 1.4 nm. The height difference corresponds to the difference in the molecular length (ca. 1.3 nm) between OTES and FHETES. In contrast, the height difference between the OTES and AEAPDMS surfaces was ca. 1.5 nm Fig. 10D, corresponding to the difference in the molecular length (ca. 1.4 nm) between OTES and AEAPDMS. The origin of the contrast in the LFM image can be explained by the difference in the surface properties of the three components, i.e., the chain rigidity, crystallinity, and chemistry of terminal functional groups of the organosilane molecules.<sup>[22]</sup> AEAPDMS-grafted areas are the brightest of the three components because the terminal amino groups exerted high lateral force due to the strong interaction between the hydrophilic amino group and the Si-OH group of the cantilever tip. The area ratio of the prepared micropatterned monolayer is in accord with that of the target value; that is, the estimated area ratio of OTES/FHETES/AEAPDMS was 4/2/3.

The introduction of a different organosilane component was also confirmed by the measurement of surface free energy. Table 1 shows the surface free energies of uniform or micropatterned organosilane monolayers. The surface free energy was calculated from the contact angles of water and methylene iodide based on Owens and Wendt's method.<sup>[26]</sup> In Table 1,  $\gamma_s^d$  and  $\gamma_s^p$  denote the dispersion and polar components of surface

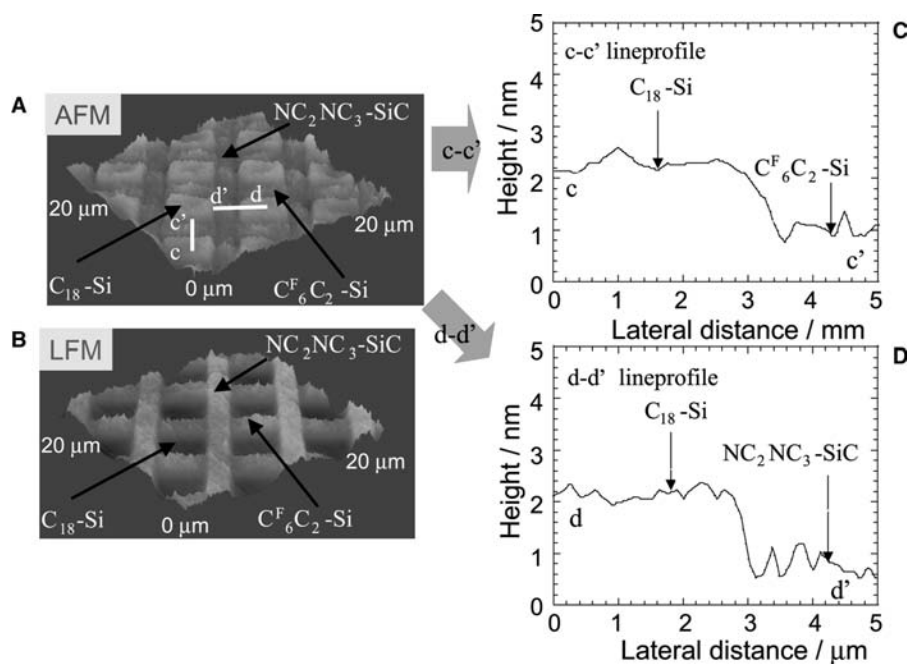


**Fig. 10** AFM and LFM images of three-component micropatterned organosilane monolayers. (A) AFM image of an OTES/FHETES/AEAPDMS micropatterned surface; (B) LFM image of an OTES/FHETES/AEAPDMS micropatterned surface; (C), (D) line profiles of white line parts in (A). Source: Reproduced from Ref.<sup>[37]</sup>.

free energy, respectively. The surface free energy of the OTES/FHETES micropatterned surface is smaller than that of the OTES monolayer surface; the decrease can be attributed to the fluoroalkyl groups of FHETES, which are known to decrease surface free energy. On the other hand, the surface free energy, especially the hydrogen-bonding component  $\gamma_s^h$ , extensively increased after the grafting of AEAPDMS; this increase can likely be attributed to the relatively high polarity of amino groups introduced in the grafted AEAPDMS monolayers.<sup>[24]</sup> Taken together with the SFM observation, this stepwise change in surface free energy confirms that the three-component organosilane surfaces had been micropatterned with highly hydrophobic and hydrophilic areas. Our patterning of three-component organosilane monolayers is expected to be a useful template for immobilizing various organic or inorganic materials on Si surfaces.

A laterally structured surface with different wetting properties may be produced by various techniques such as microcontact printing,<sup>[27]</sup> micromachining,<sup>[28]</sup> photolithography,<sup>[29]</sup> and vapor deposition.<sup>[30]</sup> If one

phase of a micropatterned surface has an affinity toward a certain liquid, the surface can be used as a template for local liquid condensation. A line-patterned high-wettability contrast surface was prepared via the local photodecomposition of an FHETMS monolayer. The advantage of this method is that the height difference of the two phases is less than 2 nm and the topographic effect on wettability can be ignored. The water-droplet formation on the micropatterned surface was directly observed with an environmental scanning electron microscope. First, the Environmental scanning electron microscope (ESEM) sample chamber was evacuated below the saturated vapor pressure (612 Pa) of water at 273 K. The sample surface was then cooled to 273 K and the vapor pressure of the ESEM sample chamber was increased to 700 Pa. Fig. 11 shows the ESEM image of the water droplet on the surface of the FHETMS/Si-OH patterned monolayer during the initial condensation process. The water began to condense on the Si-OH portion of the patterned surface. The size of the water droplet and the number of water droplets increased until the droplets coalesced in a line. Because water has a large surface free energy compared with the FHETMS phase, it is more likely to condense on the higher surface free energy region. After the vapor pressure of the ESEM sample chamber was raised to 1050 Pa, the water droplet began to bridge with droplets on the adjacent line. Because the micropatterning surface can confine liquid in distinct micropatterned regions, the surface can be used for local growth of a crystal of functional molecules<sup>[31]</sup> or as a substrate for ink-jet printing with functional molecules.<sup>[32]</sup>

**Table 1** Surface free energy of micropatterned organosilane monolayers

Organosilanes	$\gamma_{sv}$ (mJ m <sup>-2</sup> )	$\gamma_{sv}^d$ (mJ m <sup>-2</sup> )	$\gamma_{sv}^h$ (mJ m <sup>-2</sup> )
AEAPDMS	48.5	34.3	14.2
OTES	20.1	18.1	2
FHETES	14.7	13.1	1.6
OTES/FHETES	17.1	15.5	1.6
OTES/FHETES/ AEAPDMS	23.8	19.7	4.1

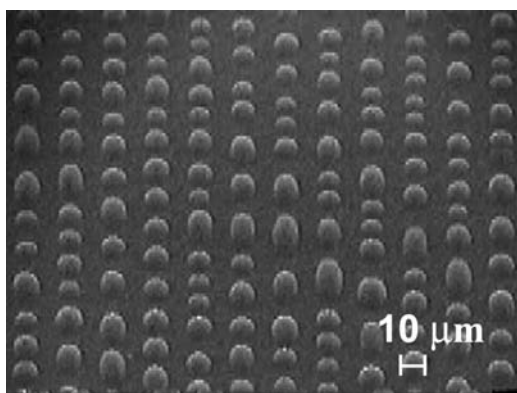


**Fig. 11** Environmental scanning electron microscopic image of a water droplet on a monolayer after exposure to water vapor at 273K. *Source:* Reproduced from Ref.<sup>[37]</sup>.

### Site-Specific Polymerization of Methacrylate Monomers

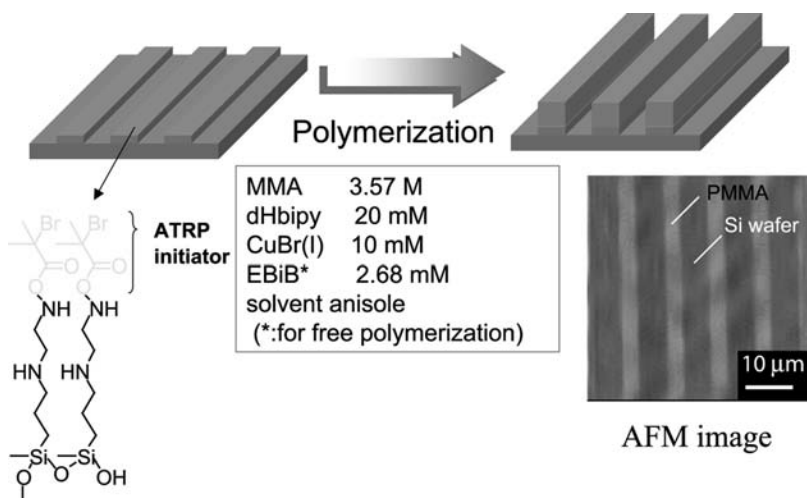
The patterned organosilane monolayers introducing an organosilane molecule with a polymerization-initiating unit are useful as template surfaces for site-specific polymerization. An atom transfer radical polymerization (ATRP) unit was immobilized as a monolayer component. Because ATRP is one of the most successful methods for polymerizing a variety of monomers in a controlled fashion,<sup>[33,34]</sup> tailor-made surface topography is possible. Several reports have described the formation of polymer thin film by radical polymerization from the immobilized ATRP initiator.<sup>[35,36]</sup>

Fig. 12 shows a schematic representation of a site-specific ATRP from a micropatterned monolayer surface.<sup>[37]</sup> Before introducing the initiator for ATRP into the organosilane monolayer system, an AEAPDMS monolayer was prepared on a Si wafer substrate surface. The prepared surface terminated by amino groups was treated with 2-bromoisobutyric acid in

the presence of a condensation agent. After the modification, the water contact angle of the obtained surface increased from 63° to 69° because of the change in the surface functional groups. Introduction of the initiating unit was further confirmed by an XPS measurement, in which the peaks attributed to Br and carbonyl carbon were observed at 68 and 287.9 eV, respectively. The resulting surface was irradiated by VUV light through a photomask. The LFM image of the patterned surface shows the presence of a pattern corresponding to the line width of the photomask used.

Surface-initiated radical polymerization of methyl methacrylate (MMA) was done in the presence of CuBr(I) and 4,4'-di-*n*-heptyl-2,2'-bipyridine in anisole. To control the polymerization process, the corresponding initiator, ethyl 2-bromoisobutyrate, was also added for bulk polymerization. The mixture was degassed, and argon was bubbled through the mixture for 20 min to ensure that oxygen was removed completely. The mixture was heated to 363 K. After several hours, the polymerization solution was cooled to room temperature to terminate the polymerization. The Si wafer was immersed in THF and rinsed with toluene to remove the adsorbed free poly(methyl methacrylate) (PMMA). The PMMA micropattern was observed by AFM.

Fig. 12 also shows the AFM image of the line-patterned PMMA ultrathin film. An AFM image revealed that the site-specific polymerization of methacrylate monomer occurred on the micropatterned surface of the ATRP initiator. The height and width of the PMMA layer is ca. 6–10 nm and ca. 5 μm, respectively. The width estimated from the AFM image is in good agreement with the line width of micropatterns of surface immobilized initiator. The formation of a PMMA layer was further confirmed by an XPS measurement, in which the characteristic



**Fig. 12** Schematic representation of the site-specific atom transfer living radical polymerization from a micropatterned monolayer surface and AFM image of line-patterned PMMA ultrathin film.

peaks attributed to the aliphatic ether and carbonyl carbons were observed at 285, 286.5, and 288.8 eV, respectively.

### Site-Specific Adsorption of Charged Microparticles

Two-dimensional alignment of micro- and nanoparticles on a substrate surface might be a promising method for fabricating functional materials, as properties of micro- and nanoparticles can be adjusted by controlling the size and surface chemistry. Various attempts have been made at the site-specific immobilization of micro- and nanoparticles.<sup>[38,39]</sup> In this study, the micropatterned organosilane monolayer with an aminosilane/fluoroalkylsilane line pattern was applied as a template surface for site-specific immobilization of negatively charged microparticles.

FHETMS and AEAPDMS were used as surface modifiers for a Si wafer substrate. The AEAPDMS/FHETMS micropattern (line width, AEAPDMS//FHETMS = 2/4  $\mu\text{m}/\mu\text{m}$ ) was fabricated by a method similar to that used to yield the multicomponent organosilane monolayer. The Si wafer substrate with a micropatterned surface was then exposed to the aqueous dispersed solution of sulfonated polystyrene (PS) microparticles at pH = ca. 6.0 for 30 min. As shown in Fig. 13, the site-specific immobilization of PS particles was successfully achieved on the micropatterned substrate surface.<sup>[40]</sup> An AFM image shows that the layers consisting of adsorbed PS microparticles are ca. 200 nm high and ca. 2  $\mu\text{m}$  wide. The height and width estimated from the AFM image is in good agreement with the diameter of PS microparticles and the line width of AEAPDMS micropatterns, respectively.

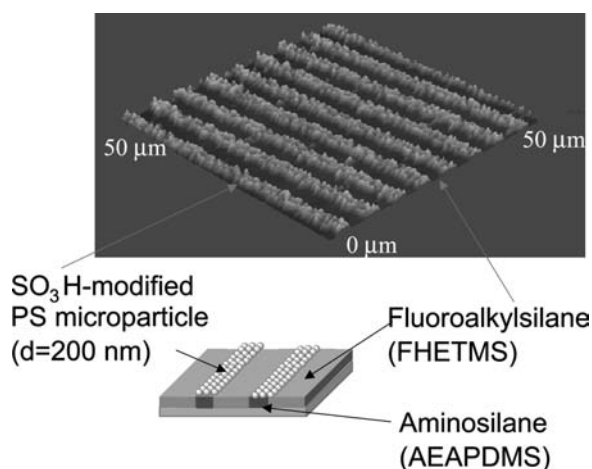


**Fig. 13** AFM image of the AEAPDMS/FHETMS monolayer after exposure to the aqueous dispersion of sulfonated PS microparticles. *Source:* Reproduced from Ref.<sup>[37]</sup>.

This result suggests that the sulfonated PS particles were adsorbed on the surface as a monolayer. The site-specific adsorption of PS particles onto the AEAPDMS grafted surfaces can be ascribed to the electrostatic interaction between negatively charged sulfonic acid groups of PS particles and positively charged amino groups of AEAPDMS-grafted surfaces.

### CONCLUSION

Patterned microfeatures of organosilane monolayers were fabricated on the substrate by two different methods. One method utilizes the crystallization of a binary component organosilane monolayer at the air/water interface. Another method utilizes the local photodecomposition by VUV light and backfilling of the decomposed area by chemisorption of organosilane monolayers. It was also revealed that micropatterned organosilane monolayers can be used as model surfaces with controlled, area-selective surface nature such as free energy, nanostructure, and chemical composition.

### ACKNOWLEDGMENTS

The author wishes to acknowledge Professor T. Kajiyama, Dr. H. Otuska, Dr. K. Tanaka, Dr. K. Kojio, M. Morita, Mr. H. Sakata, and Mr. T. Koga for their helpful discussion. This research was partially supported by Grants-in-Aid for Scientific Research Nos. 12480264 and 1200875189, the COE Research “Design and Control of Advanced Molecular Assembly Systems” (08CE2005), and the 21st-century COE Program, “Functional Innovation of Molecular Informatics” from the Ministry of Education, Culture, Sports, Science and Technology, Japan.

### REFERENCES

1. Ulmann, A. *An Introduction to Ultrathin Organic Films: From Langmuir-Blodgett to Self-Assembly*; Academic Press: San Diego, CA, 1991.
2. Tredgold, R.H. *Order in Thin Organic Films*; Cambridge University Press: Cambridge, UK, 1994.
3. Timp, G., Ed.; *Nanotechnology*; Springer: New York, 1999.
4. Sagiv, J. Organized monolayers by adsorption. I. Formation and structure of oleophobic mixed monolayers on solid surfaces. *J. Am. Chem. Soc.* **1980**, *102*, 92–98.
5. Sagiv, J. Organized monolayers by adsorption. II. Molecular orientation in mixed monolayers built on anisotropic polymeric surfaces. *Isr. J. Chem.* **1979**, *18*, 339–345.
6. Wasserman, S.R.; Tao, Y.T.; Whitesides, G.M. Structure and reactivity of alkylsiloxane monolayers formed

- by reaction of alkyltrichlorosilanes on silicon substrates. *Langmuir* **1989**, *5*, 1074–1087.
7. Parikh, A.N.; Allara, D.L.; Azouz, I.B.; Rondelez, F. An intrinsic relationship between molecular structure in self-assembled n-alkylsiloxane monolayers and deposition temperature. *J. Phys. Chem.* **1994**, *98*, 7577–7590.
  8. Ge, S.-R.; Takahara, A.; Kajiyama, T. Aggregation structure and surface properties of immobilized organosilane monolayers prepared by the upward drawing method. *J. Vac. Sci. Technol.* **1994**, *A 12*, 2530–2536.
  9. Ge, S.-R.; Takahara, A.; Kajiyama, T. Phase separated morphology of immobilized organosilane monolayer studied by scanning probe microscope. *Langmuir* **1995**, *11*, 1341–1346.
  10. Takahara, A.; Kojio, K.; Ge, S.-R.; Kajiyama, T. Scanning force microscopic studies of surface structure and protein adsorption behavior of organosilane monolayers. *J. Vac. Sci. Technol.* **1996**, *A14*, 1747–1754.
  11. Kajiyama, T.; Ge, S.-R.; Kojio, K.; Takahara, A. Scanning force microscopic study of surface structure and properties of (alkylsilane/fluoroalkylsilane) mixed monolayer. *Supramol. Sci.* **1996**, *3*, 123–130.
  12. Kojio, K.; Ge, S.-R.; Takahara, A.; Kajiyama, T. Molecular aggregation state of n-octadecyltrichlorosilane monolayer prepared at an air/water interface. *Langmuir* **1998**, *14*, 971–974.
  13. Takahara, A.; Kojio, K.; Ge, S.-R.; Kajiyama, T. Scanning force microscopy of surface structure and surface mechanical properties of organotrichlorosilane monolayers prepared by Langmuir method. In *ACS Symp. Ser.; Scanning Probe Microscopy of Polymers; Ratner, B.D., Tsukruk, V.V., Eds.; American Chemical Society: Washington, D.C., 1998; Vol. 694, 204–222.*
  14. Kojio, K.; Takahara, A.; Kajiyama, T. Formation mechanism of n-octadecyltrichlorosilane monolayer prepared at the air/water interface. *Colloids Surf., A* **2000**, *180*, 294–306.
  15. Kojio, K.; Takahara, A.; Omote, K.; Kajiyama, T. Molecular aggregation state of n-octadecyltrichlorosilane monolayers prepared by the Langmuir and chemisorption methods. *Langmuir* **2000**, *16*, 3932–3936.
  16. Kojio, K.; Takahara, A.; Kajiyama, T. Molecular aggregation state and molecular motion of organosilane monolayers prepared at the air/water interface. *Langmuir* **2000**, *16*, 9314–9320.
  17. Kojio, K.; Takahara, A.; Kajiyama, T. Aggregation structure and surface properties of 18-nonadecyltrichlorosilane monolayer and multilayer films prepared by Langmuir method. In *ACS Symp. Ser.; Silicones and Silicon-Modified Materials; American Chemical Society: Washington, D.C., 2000; Vol. 729, 332–352.*
  18. Kojio, K.; Takahara, A.; Kajiyama, T. Structure and surface properties of immobilized fluoroalkylsilane and their mixed monolayers. In *ACS Symp. Ser.; Fluorinated Surfaces, Coatings, and Films; American Chemical Society: Washington, D.C., 2001; Vol. 787, 31–47.*
  19. Takahara, A.; Ge, S.-R.; Kojio, K.; Kajiyama, T. In situ atomic force microscopic observation of albumin adsorption onto phase-separated organosilane monolayer surface. *J. Biomater. Sci., Polym. Ed.* **2000**, *11*, 111–120.
  20. Takahara, A.; Hara, Y.; Kojio, K.; Kajiyama, T. Scanning force microscopic study of protein adsorption on the surface of organosilane monolayers prepared by the Langmuir–Blodgett method. *Macromol. Symp.* **2001**, *167*, 271–284.
  21. Takahara, A.; Hara, Y.; Kojio, K.; Kajiyama, T. Plasma protein adsorption behavior onto the surface of phase-separated organosilane monolayers on the basis of scanning force microscopy. *Colloids Surf., B* **2002**, *23*, 141–152.
  22. Takahara, A.; Kojio, K.; Kajiyama, T. Effect of aggregation state on nanotribological behaviors of organosilane monolayers. *Ultramicroscopy* **2002**, *91*, 203–213.
  23. Sugimura, H.; Ushiyama, K.; Hozumi, A.; Takai, O. Micropatterning of alkyl- and fluoroalkylsilane self-assembled monolayers using vacuum ultraviolet light. *Langmuir* **2000**, *16*, 885–888.
  24. Koga, T.; Otsuka, H.; Takahara, A. Fabrication of three-component micropatterned organosilane monolayer by a stepwise photolithography process. *Chem. Lett.* **2002**, *31*, 1196–1197.
  25. Koga, T.; Morita, M.; Sakata, H.; Otsuka, H.; Takahara, A. Surface structure and properties of multi-component micropatterned organosilane monolayers prepared by stepwise photodecomposition and chemisorption process. *Int. J. Nanosci. in press.*
  26. Owens, D.K.; Wendt, R.C. Estimation of the surface free energy of polymers. *J. Appl. Polym. Sci.* **1969**, *13*, 1741–1747.
  27. Kumar, A.; Biebuyk, H.A.; Whitesides, G.M. Patterning self-assembled monolayers—applications in material science. *Langmuir* **1994**, *10*, 1498–1511.
  28. Abbott, N.L.; Folkers, J.P.; Whitesides, G.M. Manipulation of the wettability of surfaces on the 0.1-micrometer to 1-micrometer scale through micro-machining and molecular self-assembly. *Science* **1992**, *257*, 1380–1382.
  29. Calvert, J.M. Lithographic patterning of self-assembled films. *J. Vac. Sci. Technol.* **1993**, *B11*, 2155–2163.
  30. Gau, H.; Herminghaus, S.; Lenz, P.; Lipowsky, R. Liquid morphologies on structured surfaces: from microchannels to microchips. *Science* **1999**, *283*, 46–49.
  31. Kagan, C.R.; Breen, T.L.; Kosbar, L.L. Patterning organic–inorganic thin-film transistors using microcontact printed templates. *Appl. Phys. Lett.* **2001**, *79*, 3536–3538.
  32. Calvert, P. Inkjet printing for materials and devices. *Chem. Mater.* **2001**, *13*, 3299–3305.
  33. Wang, J.S.; Matyjaszewski, K. Controlled living radical polymerization—atom-transfer radical polymerization in the presence of transition metal complexes. *J. Am. Chem. Soc.* **1995**, *117*, 5614–5615.



34. Matyjaszewski, K.; Xia, J. Atom transfer radical polymerization. *Chem. Rev.* **2001**, *101*, 2921–2990.
35. Ejaz, M.; Ohno, K.; Tsujii, Y.; Fukuda, T. Controlled grafting of a well-defined glycopolymer on a solid surface by surface-initiated atom transfer radical polymerization. *Macromolecules* **2000**, *33*, 2870–2874.
36. Kong, X.; Kawai, T.; Abe, J.; Iyoda, T. Amphiphilic polymer brushes grown from the silicon surface by atom transfer radical polymerization. *Macromolecules* **2001**, *34*, 1837–1844.
37. Takahara, A.; Sakata, H.; Morita, M.; Koga, T.; Otsuka, H. Fabrication and characterization of multi-component organosilane nanofilms. *Compos. Interfaces* **2003**, *10*, 489–504.
38. Masuda, Y.; Itoh, M.; Yonezawa, T.; Koumoto, K. Low-dimensional arrangement SiO<sub>2</sub> particles. *Langmuir* **2002**, *18*, 4155–4159.
39. Fudouzi, H.; Kobayashi, M.; Shinya, N. Assembly of microsized colloidal particles on electrostatic regions patterned through ion beam irradiation. *Langmuir* **2002**, *18*, 7648–7652.
40. Koga, T.; Otsuka, H.; Takahara, A. Controlled arrangements of charged microparticles on the patterned monolayer surfaces. manuscript in preparation.

# Oxide Nanoparticles: Electrochemical Performance

**Dominique Larcher**

*Chemistry, Université de Picardie–Jules Verne, Amiens, France*

**Jean-Marie Tarascon**

*Faculté des Sciences, Université de Picardie–Jules Verne, Amiens, France*

## INTRODUCTION

Although intensively studied in a variety of fields such as catalysis, magnetism, and optics, oxide nanoparticles have just been modestly considered within the field of energy storage until these last few years that have witnessed intense developments, mainly regarding Li-ion battery technology as devoted herein.

For the last 20 years, it was a common and well-accepted belief that highly divided materials could not be suitable for extended reversible redox reaction with metallic lithium. This seems quite astonishing because most primary and secondary lithium electrochemical cell devices are based on redox reactions involving interfacial reactions between a liquid organic-based electrolyte and a solid electrode material. In fact, this idea was rooted on the belief that electrochemically driven irreversible decomposition of the organic-based electrolyte occurs at the surface of the active particles while the cell is cycled, together with possible dissolution of the solids. Thus, the higher the surface of contact between the particles and the electrolyte, the higher would be the extent of this capacity loss, hence the requirement of large particles with low surface area. Along that line, the BET surface areas of powders presently used in commercial Li-ion cells do not exceed  $2 \text{ m}^2/\text{g}$ . Recently, these prevailing ideas were seriously contradicted by several findings linked to the recent interest in nanopowders, as we will discuss in this paper. Owing to the present staggering trend toward nano objects in various research fields, too often driven by funding opportunities rather than true science, much confusion has surged about the real meaning of “nano.” Undoubtedly, the world of the so-called nanosciences is still waiting for a concrete and universal definition or at least an accurate, related size scale. Thus, we talk about nanopowders, nanostructures/nanocomposites, nanotextures, and nanoarchitected electrodes by reference to materials having a single component, two or more components intimately mixed at the nanometric scale, a porous electrode having pores and components in the nanometric scale, and finally a well-designed (either by

template deposition or by lithography) two-component system at the nanometric scale. Basically, we are prone to think that a given object, observed for a given property with a specific characterization mean, enters the “nanoworld” as soon as its size reaches a value below which the studied property starts to drastically differ from that of bulk. For instance, the significant decrease in Au particles’ melting point as their particle size becomes smaller than  $50 \text{ \AA}$  perfectly illustrates this point,<sup>[1]</sup> and for such a phenomenon  $50 \text{ \AA}$  will be the threshold value delimiting the nano/macro worlds. It is therefore unfortunate that we do not have such an equivalent to Plank’s constant that neatly separates classical mechanics from quantum mechanics.

As we march from bulk materials toward systems with small particles, new electrochemical effects are recently observed and these require the formulation of a new theoretical foundation on which to base our interpretation and understanding of the experimental data. A theoretical approach was recently undertaken and the effect of surface, particle size toward the evolution of electrochemical reactions considered. A profound effect on the chemical potential–composition curves and energy sites was demonstrated.<sup>[2]</sup> Moreover, a decrease in domain size results in a dramatic increase in grain boundaries<sup>[3]</sup> that were shown, by acting as space charge regions, to be beneficial to ionic conductivity. However, the particle size is not the only parameter that can account for the modification of properties. Indeed, the size of the crystallized reacting domains (crystallites), the specific surface area of the powder, the porosity, and the possible confinement of the matter can have a drastic influence as well.

It is surprising that the effect of the size of the reacting domains on the electrochemical properties remains almost uninvestigated, while most of the scientific fields are now, as a whole, turning toward the nanomaterials. Given the implications of the energy storage in our evolving modern society (communication, biocompatible devices), we definitively have to consider this rich domain of opportunities that lies beyond the use of nanomaterials in this field, as illustrated by the following examples.

## LITHIUM REACTIVITY THROUGH INSERTION PROCESSES

Although the principle of a Li-based secondary cell dates back to the 70s, we had to wait until the 90s for the first commercialization of reliable and safe rechargeable batteries. This impressive delay originates from numerous scientific and technological problems whose step-by-step resolution lasted decades and required sustained and crossed endeavor from physicists, chemists, and theorists. Aside from the formulation of stable electrolytes within a wide electrochemical potential window, the search for suitable electrode materials is still a major issue. The main difficulty encountered along this quest for the “ideal” insertion material is nested in the numerous criteria they have to meet all in one. They have to show high insertion capacity without undergoing drastic structural changes, low toxicity and low cost, highly separated redox potential between the cathode and anode, enhanced thermal/chemical stability toward the electrolyte, high electronic/ionic conductivities for power rate capabilities, and, finally, easy synthesis with scale-up possibilities.

Such “ideal” materials do not exist and to date only very few compounds were isolated as coming close to these requirements: ternary  $\text{LiCoO}_2$ ,  $\text{LiNiO}_2$ ,  $\text{LiMn}_2\text{O}_4$  oxides for the cathode,<sup>[4,5]</sup> and carbonaceous materials for the anode. To bypass the identified drawbacks of these materials, present studies dealing with anionic and cationic substitutions,<sup>[6]</sup> surface treatments,<sup>[7]</sup> or the making of composite materials are exploring new compromises rather than innovative and creative approaches, with the exception of a few that are exploiting lithium chemical reactivity at the nanometric scale.

Below, we give some examples showing how nanomaterials, either as electrodes or as part of the electrolyte composition, could greatly benefit the field of rechargeable Li batteries.

*LiMn<sub>2</sub>O<sub>4</sub> spinel oxide* is the first example selected to illustrate how Li-driven phase transitions associated to drastic electrode volume changes and leading to poor electrochemical performances can turn to our advantage when using small reacting domains. It has long been well known that Li insertion in this spinel framework results in a cooperative Jahn–Teller distortion together with the formation of a tetragonal phase showing a volume expansion of about 16% as compared to its cubic precursor with the overall result being very poor retention capacity upon cycling.<sup>[4,5]</sup> In contrast, when very small internal crystallites are formed by intense mechanical milling performed on crystallized powders or by precipitation techniques, this reaction appears to be very reversible.<sup>[8,9]</sup> This unexpected behavior was attributed to an isotropic

and benign expansion of the small domains as compared to the highly anisotropic and strain-inducing expansion of large ones, when the material is made by the “bake and shake” method. Because of the plasticity of the ball-milled powders, the electrode maintains its integrity upon insertion–removal of lithium ions with limited resulting loss of electrical contact.

By acting on the particle size, aside from the possibility of modifying the side effects associated to an intercalation phenomenon, one can modify the insertion mechanism by itself. This has been recently achieved for several compounds by acting on the size of the reacting domains as demonstrated through a few studies on carbonaceous materials.

*Carbonaceous materials*, owing to their both faradic and capacitive properties, are now widely implemented in Li-ion batteries and supercondensators. Their electrochemical properties are highly dependent on their texture, composition, and synthetic history. Although capacitor technology has long recognized the benefits of high-surface-area materials, it was quite recently that Li insertion in disordered and highly divided carbons turned out to be a promising approach. Such disordered/divided carbonaceous materials were, for instance, elaborated by direct preparation through pyrolysis of organic precursors or by postgrinding treatment under various conditions (atmosphere, grinding time, miller type) of crystallized carbons previously prepared at high temperatures.<sup>[10]</sup> Following the latter approach after an early appraisal of various ball-milling key parameters, carbonaceous materials having reversible specific electrochemical capacity that can reach 720 mA hr/g, which is about twice that of graphite, and low irreversible loss in the first cycle (200 mA hr/g) were fabricated. More importantly, such performance gains were not limited to one specific carbon precursor because ball milling, once the experimental parameters optimized, was shown to lead to identical texture whatever the carbonaceous precursor, stressing the universal effect of this mechanical treatment.<sup>[11]</sup> Several models have been proposed to explain this behavior, but despite this controversy, there is no doubt the origin of this increase in capacity is nested in the extremely small domains (30 Å) created by the milling.

*Hematite  $\alpha\text{-Fe}_2\text{O}_3$* <sup>[12,13]</sup> and *M<sub>3</sub>O<sub>4</sub>* (*M* = Fe, Co, Mn)<sup>[15]</sup> will be used as pedagogical examples to illustrate the effect of particle size on the electrochemical reaction path itself upon reaction with metallic lithium.

The reaction of lithium with hematite  $\alpha\text{-Fe}_2\text{O}_3$  entails a very limited solid solution domain up to a lithium critical concentration of about 0.03 lithium per formula unit, and then an irreversible transition leading to a  $\text{Li}_2\text{Fe}_2\text{O}_3$  rock-salt-type phase. It is

surprising that when using very small hematite particles, this reactivity scheme appears to be drastically different. More specifically, two batches of hematite were compared: micron-sized ( $M\text{-Fe}_2\text{O}_3$ ,  $2\text{ m}^2/\text{g}$ ,  $0.5\text{ }\mu\text{m}$  mean particle size, commercial) and nanosized ( $n\text{-Fe}_2\text{O}_3$ ,  $60\text{ m}^2/\text{g}$ ,  $200\text{ }\text{\AA}$  mean particle size, home-made) samples (Figs. 1 and 2). Quasi-equilibrium voltage evolutions along the reaction with lithium [open circuit voltage (OCV) measurements] confirm that the reduction of  $M\text{-Fe}_2\text{O}_3$  proceeds through a biphasic process ( $2.20\text{ V}$  vs.  $\text{Li}^+/\text{Li}$ ) after a very small solid solution domain. In contrast, a much longer single-phase solid solution domain (up to about one Li) is observed for  $n\text{-Fe}_2\text{O}_3$ , followed by a biphasic domain characterized by an OCV value of  $1.85\text{ V}$  vs.  $\text{Li}^+/\text{Li}^\circ$  (Fig. 3). In situ X-ray diffraction experiments (Fig. 4) further confirm these differences in reactivity when the particle size is modified. For a maximum lithium amount of one per formula unit ( $x = 1$ ),  $M\text{-Fe}_2\text{O}_3$  irreversibly transforms into a cubic rock-salt-type  $\text{Li}_2\text{Fe}_2\text{O}_3$  phase, although the  $n\text{-Fe}_2\text{O}_3$  Bragg reflections progressively and reversibly shift without any evidence for extra phase. The cell volume expansion linked to this topotactic insertion is evaluated to be 1% from  $\alpha\text{-Fe}_2\text{O}_3$  to  $\alpha\text{-Li}_1\text{Fe}_2\text{O}_3$ . As expected for such benign cationic insertion associated with small volume changes, the nanometric material exhibits higher reversible capacity and improved cycling behavior when compared to the  $M\text{-Fe}_2\text{O}_3$  batch (Fig. 5). Aside from these electrochemical aspects and the possibility of forming the  $\alpha\text{-Li}_1\text{Fe}_2\text{O}_3$  phase, recent Mössbauer and EXAFS measurements indicate that

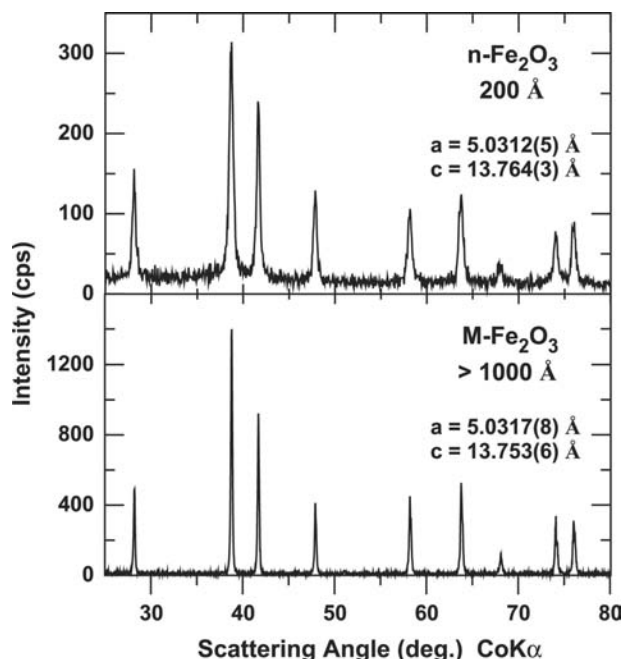


Fig. 1 X-ray diffraction patterns for  $n\text{-Fe}_2\text{O}_3$  and  $M\text{-Fe}_2\text{O}_3$ .

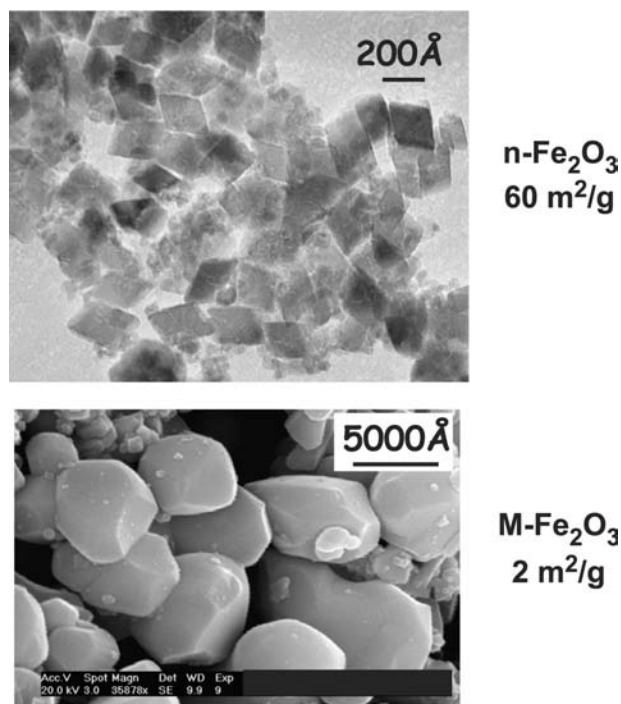


Fig. 2 TEM and SEM pictures of nanosized ( $n\text{-Fe}_2\text{O}_3$ ) and micron-sized ( $M\text{-Fe}_2\text{O}_3$ ) samples.

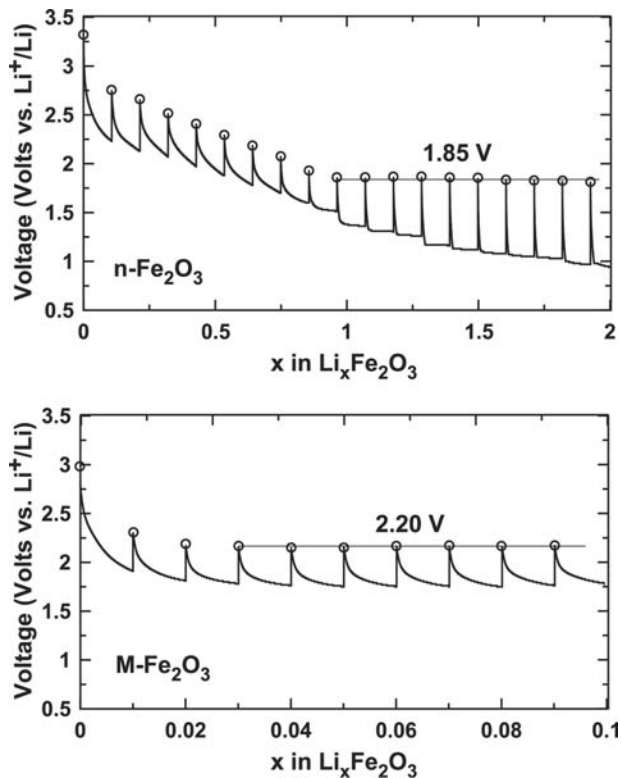
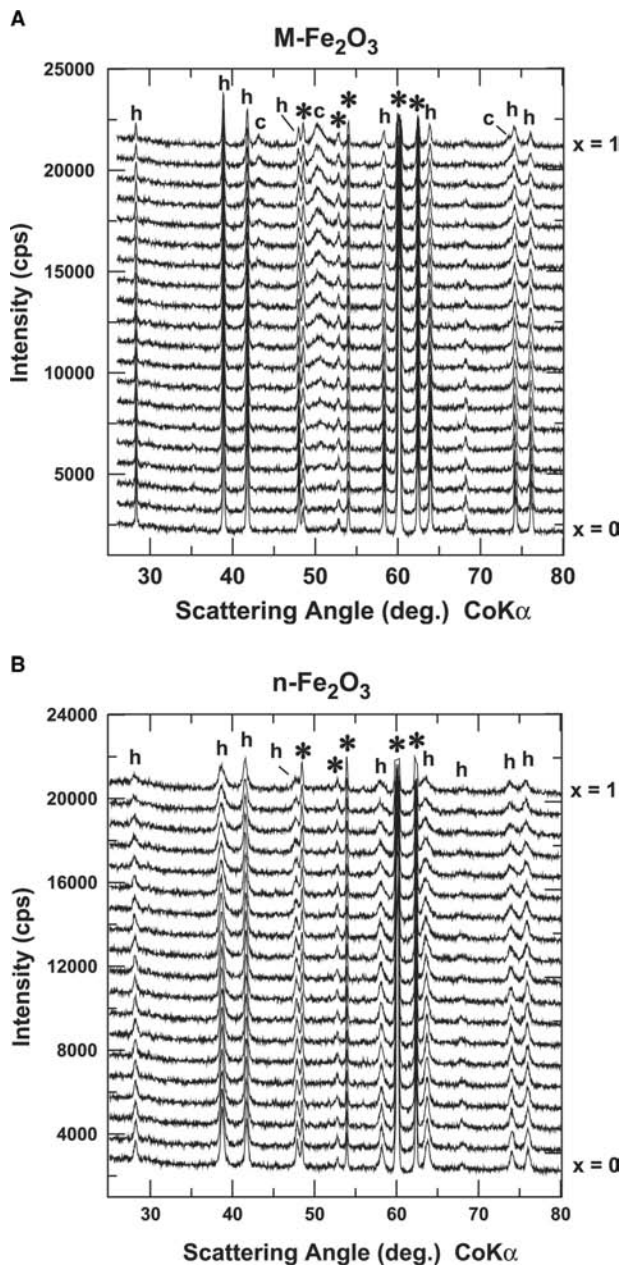
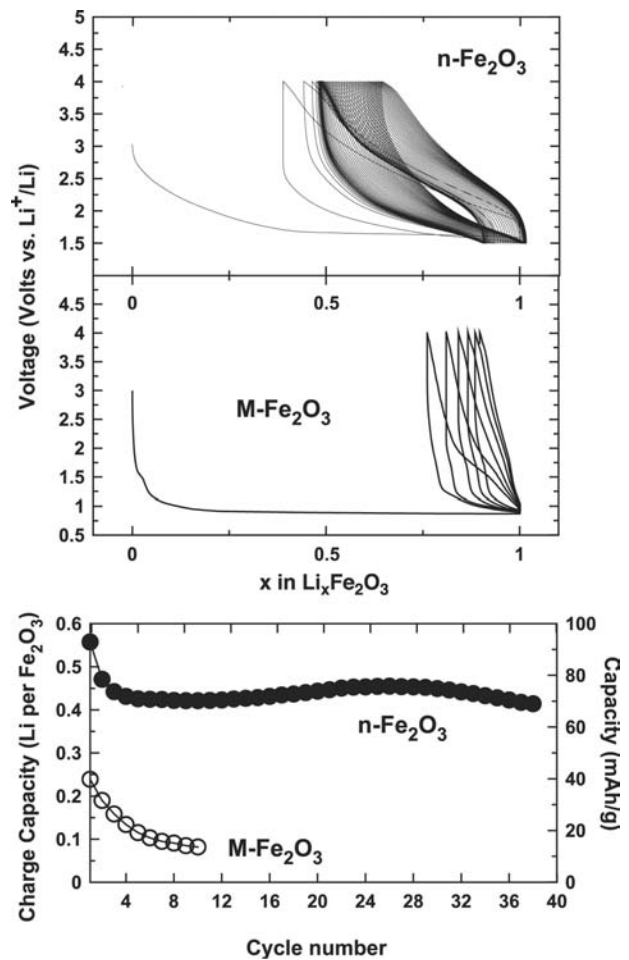


Fig. 3 Voltage–composition curves for  $n\text{-Fe}_2\text{O}_3$  and  $M\text{-Fe}_2\text{O}_3$  in Potentiostatic Intermittent Titration Technique mode. Open circles indicate the quasi-equilibrium OCVs.



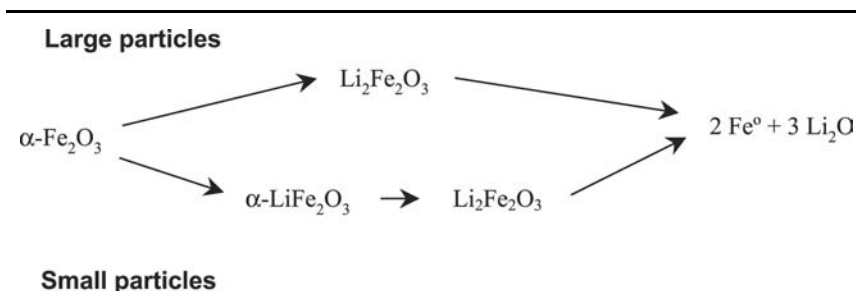
**Fig. 4** In situ X-ray diffraction patterns collected on (A) Li/M-Fe<sub>2</sub>O<sub>3</sub> and (B) Li/n-Fe<sub>2</sub>O<sub>3</sub> cells discharged at C/5 rate. The “h” and “c” labels indicate the hexagonal  $\alpha$ -Fe<sub>2</sub>O<sub>3</sub> and the cubic Li<sub>2</sub>Fe<sub>2</sub>O<sub>3</sub> phases, respectively. Asterisks indicate the peaks due to apparatus (Be, BeO).



**Fig. 5** Voltage–composition curves and capacity evolution upon cycling for Li/n-Fe<sub>2</sub>O<sub>3</sub> and Li/M-Fe<sub>2</sub>O<sub>3</sub> cells (1 Li/5 hr, 25°C).

the intimate reaction path beyond  $x = 1$  is also dependent on the particle size. For instance, we could unambiguously demonstrate a disproportionation ( $3\text{Fe}^{2+} \rightarrow 2\text{Fe}^{3+} + \text{Fe}^{\circ}$ ) mechanism along the n-Fe<sub>2</sub>O<sub>3</sub> reduction beyond  $x = 1$ , whereas it is not observed for M-Fe<sub>2</sub>O<sub>3</sub>.<sup>[13]</sup>

Finally, the overall alternative paths observed depending on the domains size could be summarized as follows:



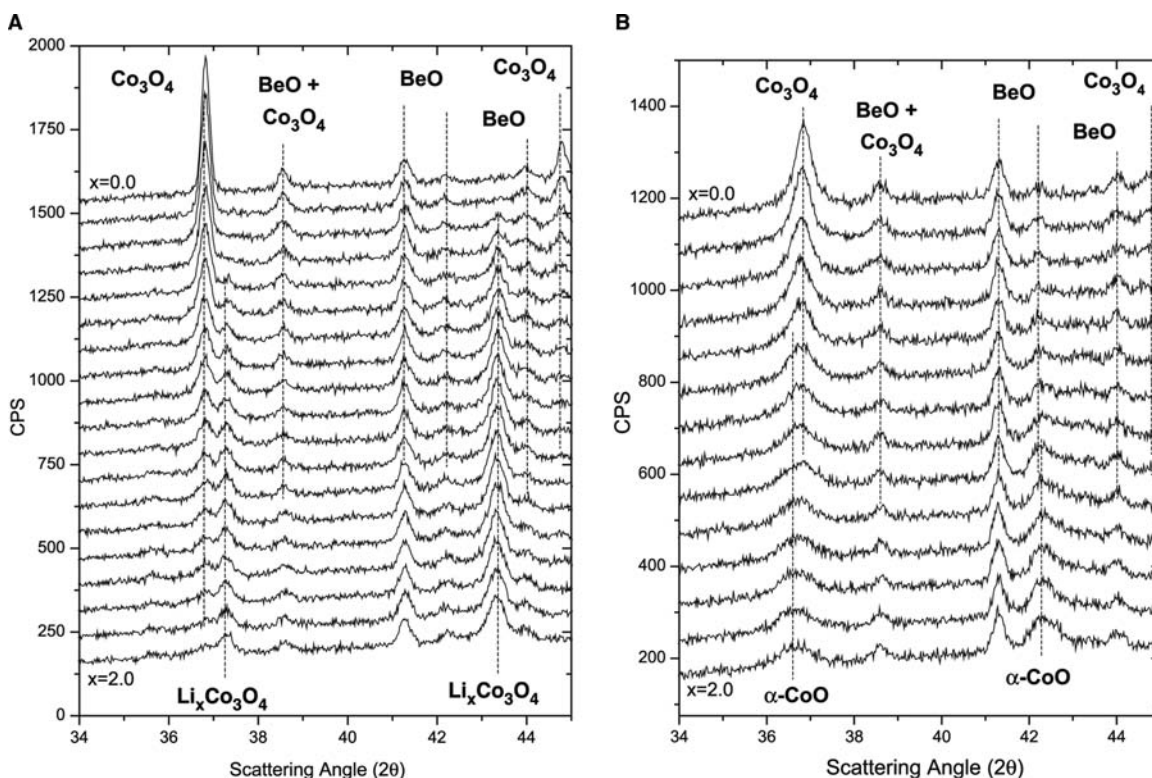
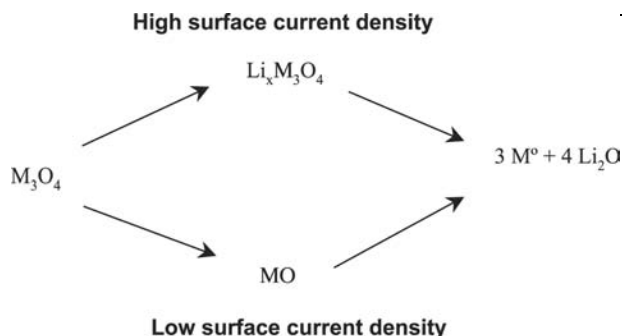


**Fig. 6** In situ X-ray diffraction patterns collected during the electrochemical reduction of Low Surface Area-Co<sub>3</sub>O<sub>4</sub> (A) and High Surface Area-Co<sub>3</sub>O<sub>4</sub> (B) at constant current (1 Li/12 hr) at 25°C. The top patterns correspond to the initial Co<sub>3</sub>O<sub>4</sub> and the bottom ones to  $x = 2.0$  Li per Co<sub>3</sub>O<sub>4</sub> (CuK<sub>α</sub>).

Similar extension of the solid solution domain by using small particles/crystallites was also recently demonstrated for compact structures such as anatase TiO<sub>2</sub>,<sup>[14]</sup> and we believe that numerous host materials disregarded for reversible lithium intercalation behave in a similar way. Thus, a completely new area is ahead of us in the search for new valuable insertion materials.

Besides hematite, numerous other materials with empty available sites are reported to irreversibly react with lithium. Among them, 3d-metal spinel materials M<sub>3</sub>O<sub>4</sub> (M = Co, Mn, Fe) are also known to transform into lithiated rock-salt type Li<sub>x</sub>M<sub>3</sub>O<sub>4</sub> structures. This is illustrated in Fig. 6. Low-surface-area Co<sub>3</sub>O<sub>4</sub> (3 m<sup>2</sup>/g) reacts with metallic lithium at constant C/12 rate (one Li in 12 hr) through a two-phase Li insertion process leading to a cubic rock-salt-type phase with the approximate composition Li<sub>~1.5</sub>Co<sub>3</sub>O<sub>4</sub> (Fig. 6A). In contrast, high-surface-area Co<sub>3</sub>O<sub>4</sub> materials (66 m<sup>2</sup>/g) behave differently because they transform into rock-salt α-CoO (Fig. 6B). The same CoO formation was observed when (3 m<sup>2</sup>/g) Co<sub>3</sub>O<sub>4</sub> powders were slowly reduced (C/100) or reacted with lithium in an intermittent mode consisting of short discharge steps followed by 2-hr relaxation periods. Note that similar current-density-driven observations were also made on

Mn<sub>3</sub>O<sub>4</sub> materials of different surface area. Such behavior fully contrasts with that of Fe<sub>3</sub>O<sub>4</sub>, as Li<sub>x</sub>Fe<sub>3</sub>O<sub>4</sub> phases are always formed whatever the reduction rate or the texture of the starting Fe<sub>3</sub>O<sub>4</sub> powders, suggesting an effect of the crystallographic nature of the spinel (normal for Co<sub>3</sub>O<sub>4</sub> as compared to inverse for Fe<sub>3</sub>O<sub>4</sub>). For Co<sub>3</sub>O<sub>4</sub> and Mn<sub>3</sub>O<sub>4</sub>, the key parameter governing the reduction reaction is therefore not the particle size but the applied current density (current/specific surface area ratio). Therefore, through these examples we demonstrate that by varying either the cycling rate or the specific surface area of the active material one can control the Li reacting path as summarized below.





## LITHIUM REACTIVITY THROUGH CONVERSION PROCESSES

Because the division state and texture of oxides used as electrode materials can drastically alter the initial intercalation process, one wonders whether the full reduction of 3d-metal oxides into metal can be affected as well. Although the size of the metallic clusters so formed are not significantly dependent on the initial oxide particle size, it was astonishing to observe, as demonstrated for various oxides such  $\text{Cu}_2\text{O}$ ,  $\text{CuO}$ ,  $\text{CoO}$ ,  $\text{NiO}$ ,  $\text{MnO}$ ,  $\text{FeO}$ ,  $\text{Fe}_2\text{O}_3$ ,  $\text{Fe}_3\text{O}_4$ , and  $\text{Co}_3\text{O}_4$ ,<sup>[16–18]</sup> a very high reversibility of these oxides toward Li according to the following reaction:



The reversibility of these conversion reactions was attributed to the in situ formation of nanometric metallic clusters embedded in a lithia matrix with, therefore, a very high metal/ $\text{Li}_2\text{O}$  surface of contact. Upon reoxidation of these nanocomposites, very small clusters of oxides are formed back. This is shown in Figs. 7–9 for  $\text{CoO}/\text{Li}$  cells. However, the formation of such nanocomposites is not the only key parameter

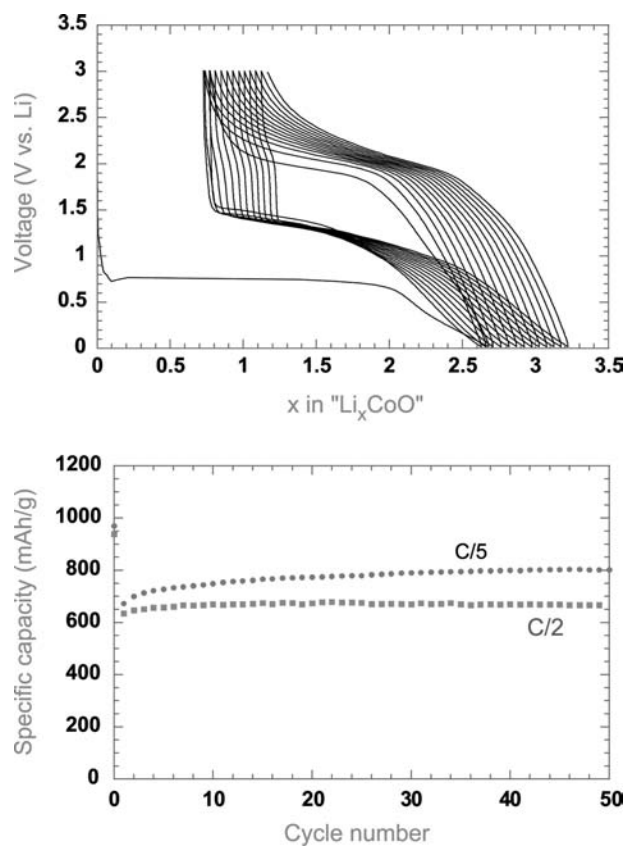


**Fig. 7** Composition–voltage curve for a  $\text{CoO}/\text{Li}$  cell (top) and evolution of the capacity as a function of the cycle number (bottom).

required for high reversibility. Indeed, when ex situ formed highly divided oxides are cycled vs. lithium, the overall cell capacity drops very quickly. This is linked to the growing of an organic gel at the surface of the particles (resulting from the decomposition/reduction of the electrolyte) that tends to electrically isolate the active particles from the current collector. The criteria for good long-term cycling behavior are twofold: 1) low surface area of the initial oxide particles and 2) in situ formed nanodomains insuring high internal contact. Note that this need of in situ nanostructure was already demonstrated in aqueous electrochemical storage using nickel hydroxide as active material.<sup>[19]</sup> These reversible conversion reactions were not only limited to oxides but were found to occur for various classes of compounds such as nitrides, fluorides, and sulfides with formation of metal/ $\text{Li}_3\text{N}$ , metal/ $\text{LiF}$ , and metal/ $\text{Li}_2\text{S}$  nanocomposites, respectively.<sup>[20–24]</sup> Thanks to the universality of these reactions, to their appealing electrochemical performances, to their intrinsic simplicity from a thermodynamic point of view, and to the large panel of materials available, it clearly appears that they represent a main opportunity for future development in the field of electrode materials. Because they involve two to three electrons per 3d metal as compared to 1, and high voltages as well (3 V for  $\text{CoF}_3$ ), such nanodriven reversible conversion reactions, owing to their staggering capacity gains over classical insertion reactions, could revolutionize the way the world stores and uses power.

## ALLOYING REACTIONS

Lithium-alloying reaction with metal such as Al, Sn, Si, Ge, Cd, Pb, and Sb is one of the most attractive alternatives to intercalation reactions.<sup>[25–29]</sup> About 25 metals or semimetals are known to form alloys with lithium and most of their combinations are active toward lithium.<sup>[30–33]</sup> These reactions offer very high capacities (Si: 4200 mA hr/g, Ge: 1600 mA hr/g, Al and Sn: 990 mA hr/g) at relatively low voltages (< 1 V vs.  $\text{Li}^+/\text{Li}^0$ ) but their cycling behavior is very poor. This detrimental characteristic is attributed to the pulverization of the material, and hence the loss of electrical contact, due to the large volume expansion of the active domains and high strain-inducing phase transitions together with the Li incorporation. Although these structural changes are intrinsic to the reactions, several attempts have been made to limit their side effects on the electrode integrity. Among them, the active/inactive nanocomposite concept represents one of the most promising exploratory routes in the field. Such composites consist of two intimately mixed materials, one reacting with lithium

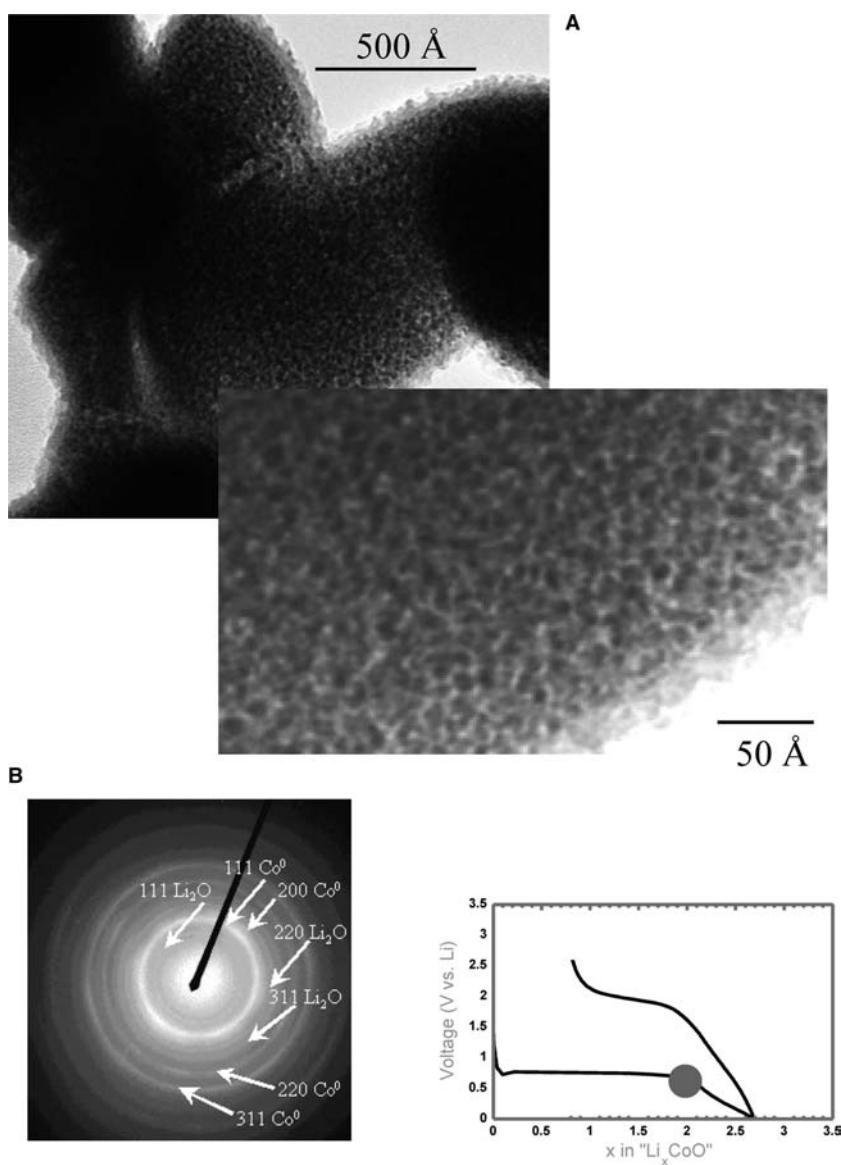


**Fig. 8** HRTEM images (A) and corresponding selected-area electron diffraction (SAED) diagram of a CoO electrode after reaction with 2 Li per CoO.

while the other acts as an inactive confining buffer. In addition, the use of small-sized metallic clusters as Li hosts considerably suppress the associated strains and therefore improve their textural response to the alloying reaction.<sup>[34,35]</sup> Several recent examples can illustrate this concept through different systems such as Sn–O based glasses,<sup>[36–39]</sup> Si–C,<sup>[40–42]</sup> Sn–Fe–C<sup>[43–45]</sup> and Sn–Mn–C.<sup>[46,47]</sup> The best experimental proof of the beneficial aspect of the buffer matrix arises from the ability to obtain several hundreds of cycles on a composite made by precipitating Sn metal at the grain boundaries of an electrochemically inactive SnFe<sub>3</sub>C matrix. However, the retention capacity was improved at the expense of a decrease in the material electrochemical capacity. Undoubtedly, alloy performance can also benefit from nanostructuring, but further developments are needed in the search for elaboration techniques to develop tailor-made nanostructure alloys.

## ELECTROLYTE

Small particles are not only involved in electrode redox mechanisms but can also be of great implications for the electrolyte conduction properties. For instance, the addition of nanometric inorganic fillers (TiO<sub>2</sub>, SiO<sub>2</sub>, Al<sub>2</sub>O<sub>3</sub>) into various types of dry or hybrid polymer systems has proved effective in improving their ionic conduction properties to a large extent without affecting their interfacial and mechanical stabilities, in the whole temperature range.<sup>[48–50]</sup> This enhancement of the conductivity was explained both in chemical terms through the introduction of a Lewis acid–base concept that considers the effect of fillers in ion–ion and ion–polymer interactions in polymeric electrolytes and in theoretical terms through a modification of diffusion and transport coefficient in space charge regions created at the nanoceramic/polymer

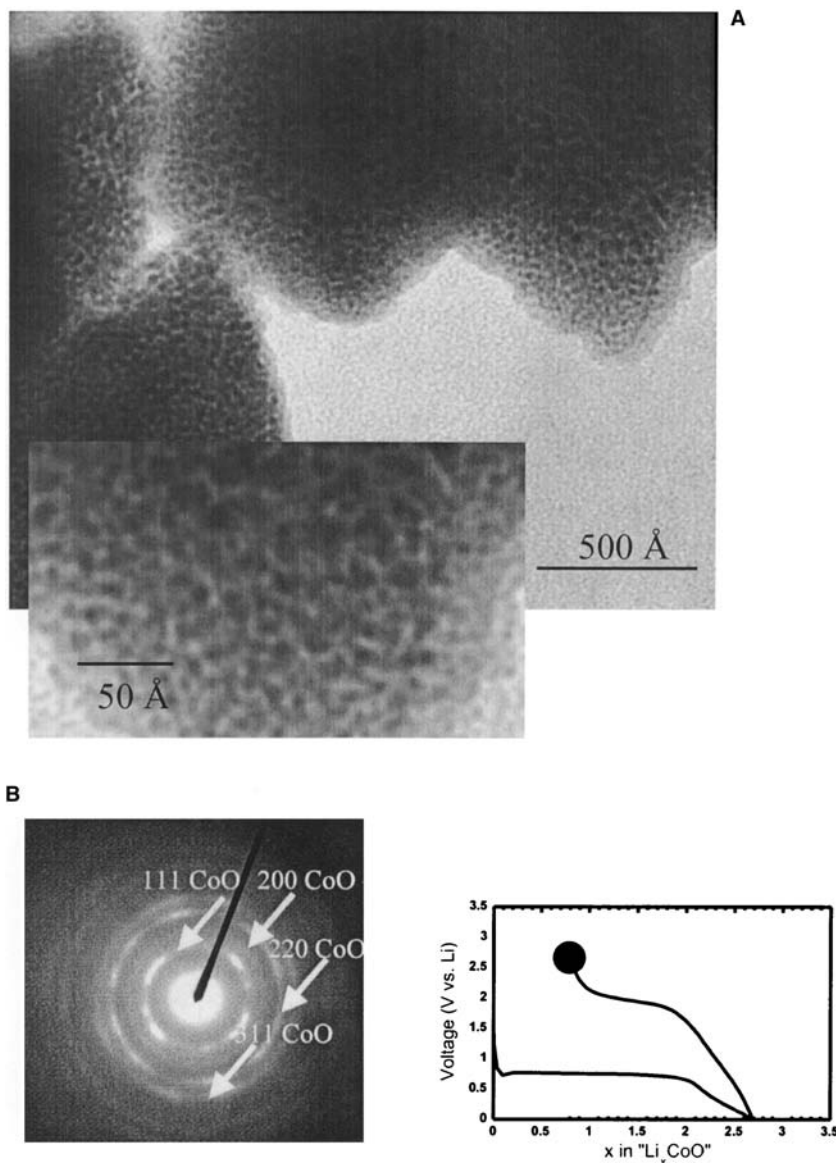


**Fig. 9** HRTEM images (A) and corresponding SAED diagram of a CoO electrode after one discharge/charge cycle.

interfaces. Present trends are devoted toward searching for new nanostructured polymers loaded with functionalized ceramic nanomaterials (e.g., nanoceramics having acid or basic surface groups). Such an approach was shown to be quite beneficial in developing highly performing protonic membranes for fuel cell applications.

## CONCLUSION

It is now evident that the entire energy storage field is moving toward nanostructures and nanoparticles. So far, only the capacitor technology was apparently concerned by this aspect and it is probably not purely coincidental that recent works have demonstrated the feasibility of hybrid capacitive/faradic

lithium cells.<sup>[51]</sup> Through this simple example, it is clear that a completely new area of opportunities is now open within the field of energy storage, both at the fundamental and applied levels. As we march from bulk materials toward systems with small particles, new electrochemical phenomena are observed and these require the formulation of a new theoretical foundation on which to base our interpretation and understanding of the experimental data. Regarding the applications, several foreseen benefits associated to nanomaterial-based Li batteries are the following: 1) an easier accommodation of structural strains for better calendar life, 2) a shorter diffusion path for enhanced electrode power capabilities, 3) an increase of the surface vs. core volume for larger double-layer capacitance contribution, and 4) an enhanced solid state reactivity to bypass

kinetics limitations so that novel reactions showing staggering electrochemical capacity gains and involving low-cost materials are becoming feasible. Such cumulated effects should translate into tremendous gain costs while preserving safety. However, although quite exciting, enthusiasm should not prevail over reality, and a few critical problems that will require cooperative endeavor and cross-sharing of knowledge accumulated for the last decades in fields such as catalysis and others remain to be solved.

## ACKNOWLEDGMENTS

The authors would like to give special thanks to L. Dupont, P. Poizot, S. Grugeon, S. Laruelle, E. Baudrin, G. Sudant (LRCS), and Y. Chabre (UJF) for their contributions to some of the data herein presented.

## REFERENCES

1. Buffat, B.; Borel, J.P. Size effect on the melting temperature of gold particles. *Phys. Rev., A* **1976**, *13*, 2287–2292.
2. Obrovac, M.N.; Dahn, J.R. Implications of finite-size and surface effects on nanosize intercalation materials. *Phys. Rev., B* **2000**, *61* (10), 6713–6719.
3. Van Hardeveld, R.; Hartog, F. The statistics of surface atoms and surface sites on metal crystals. *Surf. Sci.* **1969**, *15*, 189–230.
4. Thackeray, M.M.; de Kock, A.; Rossouw, M.H.; Liles, D.; Bittihn, R.; Hoge, D. Spinel electrodes from the Li–Mn–O system for rechargeable lithium battery applications. *J. Electrochem. Soc.* **1992**, *139*, 363–366.
5. Thackeray, M.M. Manganese oxides for lithium batteries. *Prog. Solid State Chem.* **1997**, *25*, 1–71.
6. Amatucci, G.G.; Pereira, N.; Zheng, T.; Plitz, I.; Tarascon, J.M. Enhancement of the electrochemical properties of  $\text{Li}_1\text{Mn}_2\text{O}_4$  through chemical substitution. *J. Power Sources* **1999**, *81–82*, 39–43.
7. Amatucci, G.G.; Blyr, A.; Sigala, C.; Alfonse, P.; Tarascon, J.M. Surface treatments of  $\text{Li}_{1+x}\text{Mn}_{2-x}\text{O}_4$  spinels for improved elevated temperature performance. *Solid State Ionics* **1997**, *104* (1–2), 13–25.
8. Kim, J.; Manthiram, A. Nanocomposite manganese oxides for rechargeable lithium batteries. *Electrochem. Solid-State Lett.* **1998**, *1* (5), 207–209.
9. Kang, S.-H.; Goodenough, J.B.; Rabenberg, L.K. Nanocrystalline lithium manganese oxide spinel cathode for rechargeable lithium batteries. *Electrochem. Solid-State Lett.* **2001**, *4* (5), A49–A51.
10. Disma, F.; Aymard, L.; Dupont, L.; Tarascon, J.M. Effect of mechanical grinding on the lithium intercalation process in graphites and soft carbons. *J. Electrochem. Soc.* **1996**, *143* (12), 3959.
11. Salver-Disma, F.; Tarascon, J.M.; Clinard, C.; Rouzaud, J.N. Transmission electron microscopy studies on carbon materials prepared by mechanical milling. *Carbon* **1999**, *37*, 1941–1959.
12. Larcher, D.; Masquelier, C.; Bonnin, D.; Chabre, Y.; Masson, V.; Leriche, J.-B.; Tarascon, J.-M. Effect of particle size on lithium intercalation into  $\alpha\text{-Fe}_2\text{O}_3$ . *J. Electrochem. Soc.* **2003**, *150* (1), A133–A139.
13. Larcher, D.; Bonnin, D.; Cortes, R.; Rivals, I.; Personnaz, L.; Tarascon, J.-M. Combined XRD, EXAFS and Mössbauer studies of the reduction by lithium of  $\alpha\text{-Fe}_2\text{O}_3$  with various particle size. *J. Electrochem. Soc.*, *in press*.
14. Sudant, G.; Baudrin, E.; Larcher, D.; Tarascon, J.-M. Electrochemical study of porous titanium oxide, Submitted to *Chemistry of Materials*.
15. Larcher, D.; Sudant, G.; Leriche, J.-B.; Chabre, Y.; Tarascon, J.-M. The electrochemical reduction of  $\text{Co}_3\text{O}_4$  in a lithium cell. *J. Electrochem. Soc.* **2002**, *149* (3), A234–A241.
16. Poizot, P.; Laruelle, S.; Grugeon, S.; Dupont, L.; Tarascon, J.M. Nano-sized transition-metal oxides as negative-electrode materials for lithium-ion batteries. *Nature* **2000**, *407*, 496–499.
17. Badway, F.; Plitz, I.; Grugeon, S.; Laruelle, S.; Dollé, M.; Gozdz, A.S.; Tarascon, J.-M. Metal oxides as negative electrode materials in Li-ion cells. *Electrochem. Solid-State Lett.* **2002**, *5* (6), A115–A118.
18. Obrovac, M.N.; Dunlap, R.A.; Sanderson, R.J.; Dahn, J.R. The electrochemical displacement reaction of lithium with metal oxides. *J. Electrochem. Soc.* **2001**, *148* (6), A576–A588.
19. Delahaye-Vidal, A.; Beaudoin, B.; Figlarz, M. Textural and structural studies on nickel hydroxide electrodes. I. Crystallized nickel hydroxide materials submitted to chemical and electrochemical redox cycling. *React. Solids* **1986**, *2*, 223–233.
20. Poizot, P.; Laruelle, S.; Grugeon, S.; Tarascon, J.-M. Rationalization of the low-potential reactivity of 3d-metal-based inorganic compounds toward Li. *J. Electrochem. Soc.* **2002**, *149* (9), A1212–A1217.
21. Pereira, N.; Balasubramanian, M.; Dupont, L.; McBreen, J.; Klein, L.C.; Amatucci, G.G. The electrochemistry of germanium nitride with lithium. *J. Electrochem. Soc.* **2003**, *150* (8), A1118–A1128.
22. Pereira, N.; Klein, L.C.; Amatucci, G.G. The electrochemistry of  $\text{Zn}_3\text{N}_2$  and  $\text{LiZnN}$ . A lithium reaction mechanism for metal nitride electrodes. *J. Electrochem. Soc.* **2002**, *149* (3), A262–A271.
23. Shao-Horn, Y.; Osmialowski, S.; Horn, Q.C. Reinvestment of lithium reaction mechanisms in  $\text{FeS}_2$  pyrite at ambient temperature. *J. Electrochem. Soc.* **2002**, *149* (12), A1547–A1555.
24. Poizot, P.; Laruelle, S.; Grugeon, S.; Dupont, L.; Tarascon, J.-M. Searching for new anode materials for the Li-ion technology: time to deviate from the usual path. *J. Power Sources* **2001**, *97–98*, 235–239.
25. Peled, E. The electrochemical behavior of alkali and alkaline earth metals in nonaqueous battery systems. The solid electrolyte interphase model. *J. Electrochem. Soc.* **1979**, *126*, 2047–2051.

26. Rao, B.M.L.; Francis, R.W.; Christopher, H.A. Lithium–aluminum electrode. *J. Electrochem. Soc.* **1977**, *124*, 1490–1492.
27. Nicholson, M.M. Lithium–magnesium electrodes in propylene carbonate. *J. Electrochem. Soc.* **1974**, *121*, 734–738.
28. Huggins, R.A. Lithium alloy negative electrodes formed from convertible oxides. *Solid State Ionics* **1998**, *113–115*, 57–67.
29. Huggins, R.A. Lithium alloy negative electrodes. *J. Power Sources* **1999**, *81–82*, 13–19.
30. Anani, A.; Huggins, R.A. Multinary alloy electrodes for solid state batteries. *J. Power Sources* **1992**, *38*, 351–362.
31. Benedek, R.; Thackeray, M.M. Lithium reactions with intermetallic-compound electrodes. *J. Power Sources* **2002**, *110*, 406–411.
32. Thackeray, M.M.; Vaughey, J.T.; Johnson, C.S.; Kropf, A.J.; Benedek, R.; Fransson, L.M.L.; Edstrom, K. Structural considerations of intermetallic electrodes for lithium batteries. *J. Power Sources* **2003**, *113*, 124–130.
33. Wang, J.; Raistrick, I.D.; Huggins, R.A. Behavior of some binary alloys as negative electrodes in organic solvent-based electrolytes. *J. Electrochem. Soc.* **1986**, *133*, 457.
34. Yang, J.; Winter, M.; Besenhard, J.O. Small particle size multiphase Li-alloy anodes for lithium-ion batteries. *Solid State Ionics* **1996**, *90*, 281–287.
35. Yang, J.; Takeda, Y.; Imanishi, N.; Yamamoto, O. Ultrafine Sn and SnSb<sub>0.14</sub> powders for lithium storage matrices in lithium-ion batteries. *J. Electrochem. Soc.* **1999**, *146* (11), 4009–4013.
36. Courtney, I.A.; McKinnon, W.R.; Dahn, J.R. On the aggregation of tin in SnO composite glasses caused by the reversible reaction with lithium. *J. Electrochem. Soc.* **1999**, *146* (1), 59–68.
37. Idota, Y.; Kabuto, T.; Matsufuji, A.; Maekawa, Y.; Miyasaki, T. Tin-based amorphous oxides, a high-capacity lithium-ion storage material. *Science* **1997**, *276*, 1395–1397.
38. Courtney, I.A.; Dahn, J.R. Key factors controlling the reversibility of the reaction of lithium with SnO<sub>2</sub> and Sn<sub>2</sub>BPO<sub>6</sub> glass. *J. Electrochem. Soc.* **1997**, *144* (9), 2943–2948.
39. Courtney, I.A.; Dahn, J.R. Electrochemical and in situ x-ray diffraction studies of the reaction of lithium with tin oxide composites. *J. Electrochem. Soc.* **1997**, *144* (6), 2045–2052.
40. Wilson, A.M.; Dahn, J.R. Lithium insertion in carbons containing nanodispersed silicon. *J. Electrochem. Soc.* **1995**, *142* (2), 323–326.
41. Yang, J.; Wang, B.F.; Wang, K.; Liu, Y.; Xie, J.Y.; Wen, Z.S. Si/C composites for high capacity lithium storage materials. *Electrochem. Solid-State Lett.* **2003**, *6* (8), A154–A156.
42. Wang, C.S.; Wu, G.T.; Zhang, X.B.; Qi, Z.F.; Li, W.Z. Lithium insertion in carbon–silicon composite materials produced by mechanical milling. *J. Electrochem. Soc.* **1998**, *145* (8), 2751–2758.
43. Mao, O.; Dunlap, R.A.; Dahn, J.R. Mechanically alloyed Sn–Fe(–C) powders as anode materials for Li-ion batteries. I. The Sn<sub>2</sub>Fe–C system. *J. Electrochem. Soc.* **1999**, *146* (2), 405–413.
44. Mao, O.; Dahn, J.R. Mechanically alloyed Sn–Fe(–C) powders as anode materials for Li-ion batteries. II. The Sn–Fe system. *J. Electrochem. Soc.* **1999**, *146* (2), 414–422.
45. Mao, O.; Dahn, J.R. Mechanically alloyed Sn–Fe(–C) powders as anode materials for Li-ion batteries. III. Sn<sub>2</sub>Fe:SnFe<sub>3</sub>C active/inactive composites. *J. Electrochem. Soc.* **1999**, *146* (2), 423–427.
46. Beaulieu, L.Y.; Larcher, D.; Dunlap, R.A.; Dahn, J.R. Reaction of Li with grain-boundary atoms in nanostructured compounds. *J. Electrochem. Soc.* **2000**, *147* (9), 3206–3212.
47. Beaulieu, L.Y.; Dahn, J.R. The reaction of lithium with Sn–Mn–C intermetallics prepared by mechanical alloying. *J. Electrochem. Soc.* **2000**, *147* (9), 3237–3241.
48. Scrosati, B.; Croce, F.; Persi, L. Impedance spectroscopy study of PEO-based nanocomposite polymer electrolytes. *J. Electrochem. Soc.* **2000**, *147* (5), 1718–1721.
49. Persi, L.; Croce, F.; Scrosati, B.; Plichta, E.; Hendrickson, M.A. Polyethylene oxide-based, nanocomposite electrolytes as improved separators for rechargeable lithium polymer batteries. The Li/LiMn<sub>3</sub>O<sub>6</sub> case. *J. Electrochem. Soc.* **2002**, *149* (2), A212–A216.
50. Appetecchi, G.B.; Croce, F.; Persi, L.; Ronci, F.; Scrosati, B. Transport and interfacial properties of composite polymer electrolytes. *Electrochim. Acta* **2000**, *45*, 1481–1490.
51. Du Pasquier, A.; Laforgue, A.; Simon, P.; Amatucci, G.G.; Fauvarque, J.-F. A nonaqueous asymmetric hybrid Li<sub>4</sub>Ti<sub>5</sub>O<sub>12</sub>/poly(fluorophenylthiophene) energy storage device. *J. Electrochem. Soc.* **2002**, *149* (3), A302–A306.

# Palladium Nanoclusters

Kiyotomi Kaneda  
Kwang-Min Choi  
Tomoo Mizugaki  
Kohki Ebitani

*Department of Chemical Science and Engineering, Osaka University,  
Osaka, Japan*

## INTRODUCTION

The chemistry of polynuclear metal clusters in the nanometer scale has become a central issue in materials science because of their unique functions as electronic, optical, magnetic, and catalytic devices, which bring new technologies in many industrial areas.<sup>[1–5]</sup> At present, there is some progress being made in the preparation of metal nanoclusters.<sup>[6–15]</sup> They have been synthesized by the chemical reduction of metal salts in the presence of stabilizing ligands such as surfactants,<sup>[6,7]</sup> organic polymers,<sup>[8–10]</sup> and organic bases,<sup>[11–13]</sup> which preserve the metal clusters from the agglomeration of the clusters themselves. However, the above methods hardly produce metal nanoclusters with a high degree of size dispersity.

Transition metals have been extensively used as catalysts for many organic reactions, where the oxidation state of the metal plays an important role in attaining highly selective reactions.<sup>[16–19]</sup> A multiple interaction of substrate molecules with surface metal atoms of transition metal nanoclusters would offer the possibility of unprecedented catalytic reactions. Furthermore, a creation of specific surface ensemble sites consisting of zero-valent metals and metal cations is a promising strategy for designing highly functionalized nanocluster catalysts based on cooperative action among the multiple metal species.

The purpose of this entry is to develop a new synthetic protocol of monodispersed palladium (Pd) nanoclusters at the nanometer-scale precision as high-performance catalysts. We describe here the novel synthesis of Pd nanoclusters with a high degree of size dispersity, where the standard deviation of the mean diameter ( $\sigma/d$ ) is less than 10%, by treatment of the small Pd cluster with metal nitrates such as  $\text{Cu}(\text{NO}_3)_2$  under an  $\text{O}_2$  atmosphere. This method also yielded mixed-valence states with  $\text{Pd}^0$  and cationic Pd species on the cluster surface.<sup>[20]</sup> An advantage of this synthetic method is that the particle size and the surface oxidation state of monodispersed Pd nanoclusters can be controlled by selecting the amount of the metal

nitrates and by varying the preparation time of the clusters. Furthermore, the above Pd nanoclusters are applicable to highly efficient and selective heterogeneous catalysts for liquid-phase oxidations such as acetoxylation of toluene, alcohol oxidation, and the Wacker oxidation under an atmospheric pressure of  $\text{O}_2$ .<sup>[20–22]</sup> The unique catalyses of the Pd nanoclusters are attributed to the cooperative action between zero-valent Pd and Pd cations on the surface ensemble Pd sites.

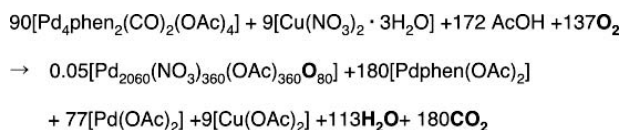
## PREPARATION OF NANOCCLUSERS

A representative example is the synthesis of the monodispersed Pd nanocluster with a mean diameter of 38 Å. A solution of  $\text{Pd}(\text{OAc})_2$  (0.20 g, 0.89 mmol) in AcOH (20 mL) was stirred at 50°C for 2 hr under continuous CO flow, yielding 0.12 g of  $\text{Pd}_4(\text{CO})_4(\text{OAc})_4 \cdot 2\text{AcOH}$  (PCA) as a yellow precipitate.<sup>[23]</sup> The obtained PCA (0.12 g, 0.155 mmol, Pd 0.62 mmol) was stirred in AcOH (2.5 mL) in the presence of 1,10-phenanthroline (phen) (0.0614 g, 0.31 mmol) at room temperature for 30 min in air to give a dark brown solution of  $\text{Pd}_4\text{phen}_2(\text{CO})_2(\text{OAc})_4$ <sup>[24]</sup> [anal. calc. for  $\text{Pd}_4\text{C}_{34}\text{H}_{28}\text{N}_4\text{O}_{10}$  (%): C, 37.9; H, 2.6; N, 5.2; found (%): C, 34.1; H, 2.7; N, 5.2].<sup>a</sup> Then, 0.0038 g of  $\text{Cu}(\text{NO}_3)_2 \cdot 3\text{H}_2\text{O}$  (0.0155 mmol) was added to the above solution and heated at 90°C under an atmospheric  $\text{O}_2$ . After 15 min, a black solid was precipitated with the consumption of 0.067 mmol  $\text{O}_2$  ( $\text{O}_2/\text{Pd} = 0.108$  mol/mol).<sup>b</sup> The precipitate was washed with AcOH for several times and dried in vacuo to yield the Pd

<sup>a</sup>An optimum mole ratio of Pd to phen in the synthesis of giant Pd clusters was found to be 2. The use of  $\text{Pd}_4\text{phen}_4(\text{CO})_2(\text{OAc})_4$  instead of  $\text{Pd}_4\text{phen}_2(\text{CO})_2(\text{OAc})_4$  did not afford giant Pd clusters.

<sup>b</sup>The amount of  $\text{O}_2$  uptake during the preparation of the Pd nanoclusters was volumetrically measured using a gas buret by trapping evolved  $\text{CO}_2$  in a cold trap at  $-120^\circ\text{C}$ .





**Scheme 1** Formation of the  $\text{Pd}_{2060}(\text{NO}_3)_{360}(\text{OAc})_{360}\text{O}_{80}$  cluster.

nanoclusters (0.032 g, ca. 30% yield based on Pd) [anal. calc. for  $\text{Pd}_{2060}(\text{NO}_3)_{360}(\text{OAc})_{360}\text{O}_{80}$  (%): C, 3.28; H, 0.41; N, 1.91; found (%): C, 3.21; H, 0.23; N, 1.34; X-ray photon spectroscopy (XPS): Pd  $3d_{5/2} = 334.5\text{--}335.2\text{ eV}$ , O  $1s = 531.5\text{ eV}$ , N  $1s = 399.4\text{ eV}$ . The XPS peak positions are referred to C  $1s$  at  $284.6\text{ eV}$  (atomic ratio by XPS: C/Pd = 0.6, N/Pd = 0.12). Copper signals were not appreciable on the clusters.]<sup>c</sup> Scheme 1 represents the formation of the Pd nanoclusters. During the preparation of the Pd nanoclusters, molecular oxygen was consumed to form  $\text{CO}_2$  and  $\text{H}_2\text{O}$ , and the oxygen species on the cluster surface.

A typical example for the immobilization of the Pd clusters on the metal oxides is described for the Pd nanocluster/ $\text{TiO}_2$ .  $\text{TiO}_2$  (JRC-TIO-2, 1.30 g) was added into the acetic acid solution of the  $\text{Pd}_4\text{phen}_2(\text{CO})_2(\text{OAc})_4$  and  $\text{Cu}(\text{NO}_3)_2 \cdot 3\text{H}_2\text{O}$ , and then stirred at  $90^\circ\text{C}$  under an atmospheric  $\text{O}_2$  (3 wt.% as Pd cluster).<sup>d</sup> The solid compound of 1.4 g was obtained after filtration, washing with acetic acid and drying under a vacuum.

In the X-ray diffraction (XRD) pattern of the Pd nanoclusters, the three peaks are observed at  $40^\circ$ ,  $46^\circ$ , and  $68^\circ$ , which correspond to the  $\{111\}$ ,  $\{200\}$ , and  $\{220\}$  planes of a face-centered cubic (fcc) lattice, respectively. The mean crystalline size of the Pd nanoclusters, calculated from the line broadening of the peak at  $40^\circ$  using the Scherrer equation, is ca.  $35\text{ \AA}$ . The particle size distribution and the ordering of Pd atoms of the Pd clusters were estimated by field emission scanning electron microscopy (FE-SEM) and high-resolution transmission electron microscopy (HR-TEM) of the Pd clusters immobilized on the  $\text{TiO}_2$  surface because the Pd nanoclusters could be immobilized on a surface of  $\text{TiO}_2$  without a change in their original cluster size and the local ordering of the Pd atoms on the cluster surface. As shown in Fig. 1A, the FE-SEM image of the Pd clusters on the  $\text{TiO}_2$  surface reveals that the Pd nanoclusters are well dispersed with a quite narrow size distribution throughout the  $\text{TiO}_2$  surface. The mean diameter ( $d$ )

of the Pd clusters is  $38\text{ \AA}$  with a standard deviation ( $\sigma$ ) of  $2.1\text{ \AA}$ , where the  $\sigma/d$  value is 6%. This particle size corresponds to that of the giant eight-shell metal cluster composed of 2060 Pd atoms as the magic number.<sup>[25]</sup> To the best of our knowledge, the Pd nanoclusters prepared by our method using metal nitrates have the narrowest size distribution of Pd nanoparticles obtained by chemical and electrochemical methods.<sup>[6–15]</sup>

Figure 2 represents the HR-TEM image of the Pd nanocluster immobilized on the  $\text{TiO}_2$  surface. A regular arrangement of Pd atoms on the Pd nanocluster surface can be clearly observed, with 17 Pd atoms along the  $\{111\}$  planes. The Pd K-edge X-ray absorption fine structure (XAFS) measurement of the Pd nanoclusters indicated that the inner part is composed of a metallic Pd atom. However, the surface analysis of the above Pd nanoclusters by XPS proved the presence of both cationic and metallic Pd species. Furthermore, the treatment of the Pd nanoclusters with a CO molecule at  $0^\circ\text{C}$  led to both  $\text{CO}_2$  evolution and CO adsorption on metallic Pd; the cationic Pd species are reduced to  $\text{Pd}^0$  during exposure to CO. The evolution of  $\text{CO}_2$  ascertains the presence of oxygen species on the surface of the Pd nanoclusters. Because the reactivity of the surface oxygen species was high enough to oxidize a CO molecule even at  $0^\circ\text{C}$ , the Pd sites responsible for the above CO oxidation would be  $\text{Pd}_2\text{O}$  species on the cluster surface.<sup>e</sup> The ratio of the  $\text{Pd}_2\text{O}$  species to the surface Pd atoms of the monodispersed Pd nanoclusters with a diameter of  $38\text{ \AA}$ , evaluated from the amounts of the formed  $\text{CO}_2$  and the CO uptake, is 23%.

A possible arrangement of the Pd atoms of the eight-shell Pd cluster with an fcc cuboctahedral shape is illustrated in Scheme 2A, where the  $\text{Pd}^0$  and  $\text{Pd}^+$  cation species are situated on the face of the nanocluster. The fraction of  $\text{Pd}^+$  ( $\text{Pd}_2\text{O}$ ) species of the surface Pd atoms was 23%, whereas those of  $\text{Pd}^{2+}$  and  $\text{Pd}^0$  species were 56% and 20%, respectively.<sup>[20]</sup> This accords with the composition of the Pd nanoclusters,  $\text{Pd}_{2060}(\text{NO}_3)_{360}(\text{OAc})_{360}\text{O}_{80}$ ; the surface-divalent Pd cations were preserved at corner/edge sites by anions of  $\text{NO}_3^-$  and  $\text{OAc}^-$ , where oxygen species were bound to the two monovalent Pd ions on the face of the nanocluster.

The use of  $\text{Fe}(\text{NO}_3)_3$  instead of  $\text{Cu}(\text{NO}_3)_2$  could also afford the Pd nanoclusters having a narrow size distribution with a mean diameter and standard deviation ( $d \pm \sigma$ ) of  $38 \pm 4.4\text{ \AA}$  ( $\sigma/d = 11\%$ ), where the fraction of the surface  $\text{Pd}_2\text{O}$  species exhibited the maximum of 22%. The composition of the eight-shell

<sup>c</sup>The  $\text{Pd}(\text{phen})(\text{OAc})_2$  complex was formed in the residual solution.

<sup>d</sup> $\text{TiO}_2$  (JRC-TIO-2) was supplied from the Catalysis Society of Japan (anatase, BET surface area:  $14\text{ m}^2\text{ g}^{-1}$ ), and is characterized by its low acidity and basicity compared with other  $\text{TiO}_2$  reference samples.

<sup>e</sup>A  $\text{Pd}^+$  species has been already reported on palladium-loaded silicoaluminophosphate molecular sieves. (See Ref.<sup>[26]</sup>)

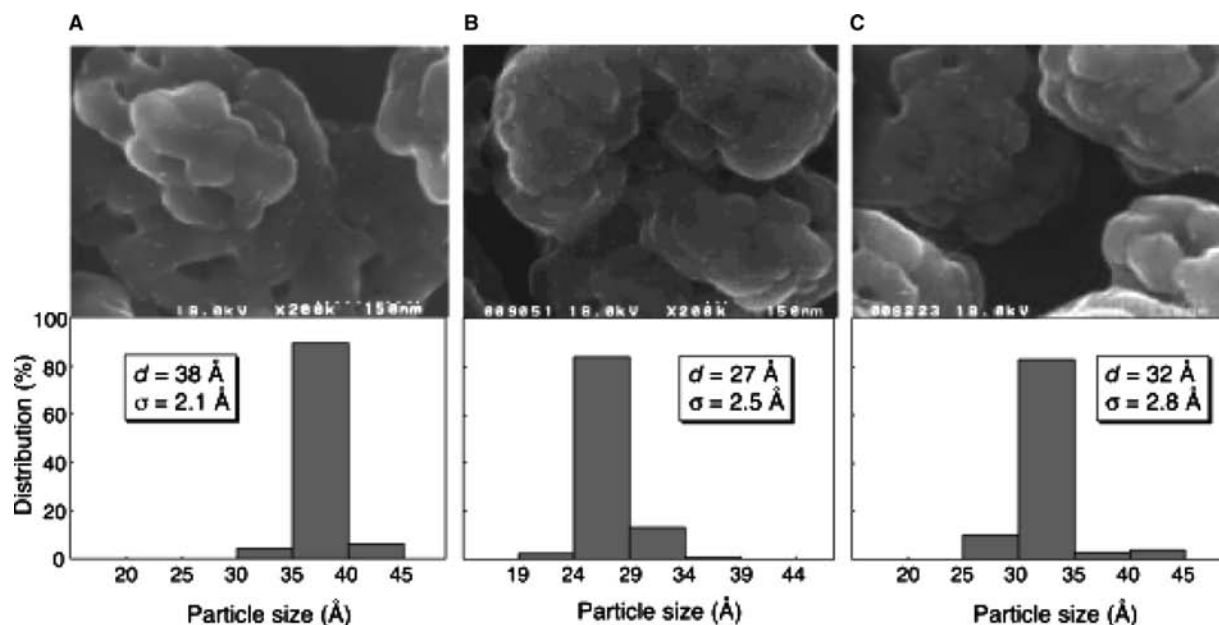


**Fig. 1** The FE-SEM photograph and the particle size distribution of the Pd nanoclusters prepared with the  $\text{Cu}(\text{NO}_3)_2/\text{PCA}$  molar ratio of (A) 0.10 (15 min), (B) 0.05 (8 min), and (C) 0.10 (10 min). The values in parentheses are the preparation times of the cluster.

Pd nanoclusters was  $\text{Pd}_{2060}(\text{NO}_3)_{250}(\text{OAc})_{470}\text{O}_{80}$ . The ratio of  $\text{OAc}^-$  to  $\text{NO}_3^-$  anions was different from that obtained for the eight-shell Pd clusters using  $\text{Cu}(\text{NO}_3)_2$ . However, the total number of anionic species situated on the cluster surface was constant, irrespective of the metal nitrates.

Furthermore, we found that the selection of the  $\text{Cu}(\text{NO}_3)_2/\text{PCA}$  molar ratio can control the particle size of the Pd nanoclusters.<sup>[20]</sup> When the  $\text{Cu}(\text{NO}_3)_2/\text{PCA}$  molar ratio was 0.05, the five-shell Pd

nanoclusters with the  $\sigma/d$  value of 9% ( $\sigma = 2.5 \text{ \AA}$ ,  $d = 27 \text{ \AA}$ ) were obtained. A typical FE-SEM image and the particle size distribution are shown in Fig. 1B. The fraction of the  $\text{Pd}^+$  species of the surface Pd atoms became 7% when the  $\text{Cu}(\text{NO}_3)_2/\text{PCA}$  molar ratio was 0.05. Scheme 2B shows a proposed structure of the five-shell Pd nanocluster composed of 560 Pd atoms whose composition is  $\text{Pd}_{560}(\text{NO}_3)_{100}(\text{OAc})_{250}\text{O}_{10}$ . It is notable that the treatment of  $\text{Pd}_4\text{phen}_2(\text{CO})_2(\text{OAc})_4$  with  $\text{Cu}(\text{NO}_3)_2 \cdot 3\text{H}_2\text{O}$  in a shorter preparation time (e.g.,  $\sim 10$  min) afforded Pd nanoclusters with a  $\sigma/d$  value of 9% ( $\sigma = 2.8 \text{ \AA}$ ,  $d = 32 \text{ \AA}$ ), as depicted in Fig. 1C. This particle size might correspond with six-shell or seven-shell clusters.<sup>[12]</sup>

The above shell-selective synthesis of monodispersed Pd clusters allows us to consider the feature

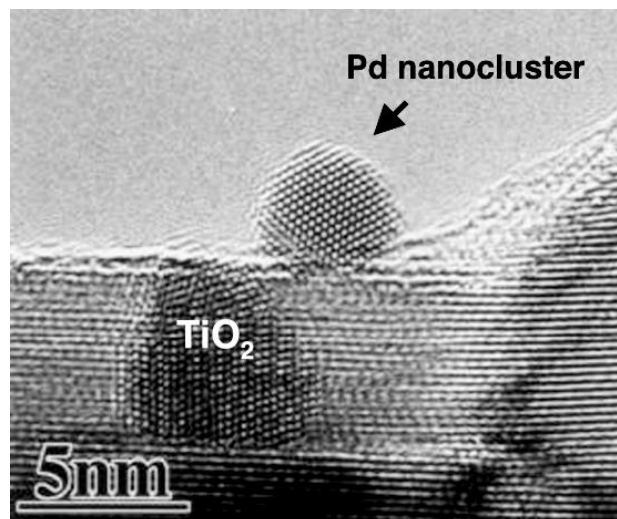
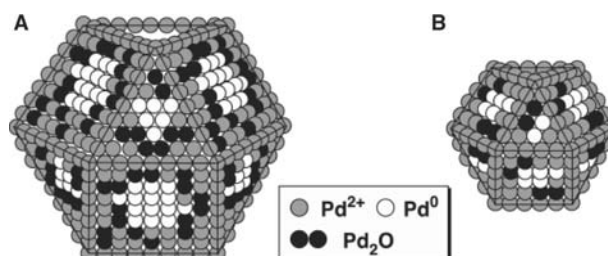


**Fig. 2** The HR-TEM image of the eight-shell Pd nanocluster immobilized on the  $\text{TiO}_2$  surface.

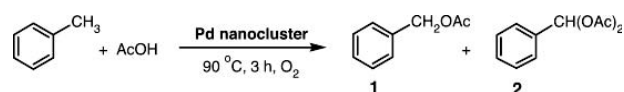


**Scheme 2** Possible structure models of (A) the eight-shell Pd nanocluster,  $\text{Pd}_{2060}(\text{NO}_3)_{360}(\text{OAc})_{360}\text{O}_{80}$ , and (B) the five-shell Pd nanocluster,  $\text{Pd}_{560}(\text{NO}_3)_{100}(\text{OAc})_{250}\text{O}_{10}$ , with an fcc cuboctahedral shape.

of nanocluster formation as follows. The metal nitrates promote the disproportionation of monovalent Pd ions of  $\text{Pd}_4\text{phen}_2(\text{CO})_2(\text{OAc})_4$  complex to yield  $\text{Pd}^0$  and  $\text{Pd}^{2+}$  cation species. The  $\text{Pd}^0$  species aggregate to form relatively small Pd assemblies. Because the amounts of  $\text{Pd}^0$  and  $\text{Pd}^{2+}$  species increase with increasing amount of the metal nitrates and duration of the treatment, the small assembly of  $\text{Pd}^0$  species is overspread with generated  $\text{Pd}^0$  species, which lead to the growth of a larger  $\text{Pd}^0$  nanocluster. Subsequently, the  $\text{Pd}^0$  atoms located at corner/edge sites of the larger cluster surface are oxidized by the metal nitrate to give  $\text{Pd}^{2+}$  cations, which are stabilized by anionic ligands such as  $\text{OAc}^-$  and  $\text{NO}_3^-$ . On the other hand, the  $\text{Pd}_2\text{O}$  surface species might be formed by the oxidation of the  $\text{Pd}^0$  ions by  $\text{O}_2$ . An additional increase in the amount of the metal nitrates resulted in a deep oxidation of the surface Pd species and also an exfoliation of  $\text{Pd}^{2+}$  ions from the cluster surface, which resulted in the formation of smaller metallic clusters together with decomposition into the monomeric  $\text{Pd}^{2+}$  complex. Indeed, both the particle size and the surface oxidation state of the Pd cluster exhibited maxima at a  $\text{Cu}(\text{NO}_3)_2/\text{PCA}$  molar ratio of 0.10.<sup>[20]</sup>

The quite narrow size distribution of the present Pd nanoclusters could be ascribed to the strong ability of the metal nitrate for the disproportionation of monovalent Pd ions of the  $\text{Pd}_4\text{phen}_2(\text{CO})_2(\text{OAc})_4$  complex that leads to a formation of a relatively small Pd assembly through a fast nucleation step of the  $\text{Pd}^0$  species. Furthermore, the partial oxidation of surface  $\text{Pd}^0$  species at the larger cluster surface with metal nitrate retards the successive growth of the nanoclusters.

Conclusively, the treatment of palladium carbonyl acetate (PCA) cluster with  $\text{Cu}(\text{NO}_3)_2$  in the presence of phen under an  $\text{O}_2$  atmosphere afforded monodispersed Pd nanoclusters containing both  $\text{Pd}^0$  and cationic Pd species on the surface. The novel preparation method described here enables a “shell-selective” synthesis of Pd nanoclusters, keeping the high monodispersity as well as a tuning of the surface fraction of  $\text{Pd}^0$ ,  $\text{Pd}^+$ , and  $\text{Pd}^{2+}$  species. Unique catalyses of



**Scheme 3** Oxidative acetoxylation of toluene in the presence of molecular oxygen catalyzed by the eight-shell Pd nanoclusters.

the Pd nanoclusters in the acetoxylation of toluene, alcohol oxidation, and the Wacker oxidation are described below.

## APPLICATION

Palladium is among the most important catalysts in organic synthesis.<sup>[17,18,27,28]</sup> Our monodispersed Pd nanoclusters will offer the possibility of unprecedented catalytic reactions based on specific surface ensemble Pd sites within a regular arrangement of multiple Pd species. We applied the monodispersed Pd nanoclusters to heterogeneous catalysts for oxidative functional transformations in liquid phase under an atmospheric  $\text{O}_2$  pressure.

### Acetoxylation of Toluene

Acetoxylation is one of the powerful methods to functionalize various kinds of C–H bonds in hydrocarbons; the acetoxy group can be facilely transformed into other functional ones. Generally, the acetoxylation of toluene occurs by using a homogeneous  $\text{Pd}(\text{OAc})_2$  complex in an acetic acid under an  $\text{O}_2$  atmosphere to give benzyl acetates, where additives of KOAc and  $\text{Sn}(\text{OAc})_2$  are indispensable.<sup>[29]</sup> In heterogeneous Pd catalysts, Pd particles on charcoal or  $\text{SiO}_2$ , as a support interacting with excess amounts of  $\text{Sn}(\text{2-ethyl-hexanoate})_2$  and KOAc, exhibit catalytic activity.<sup>[30,31]</sup> It is said that the efficient acetoxylation by Pd catalysts cannot be attained without any additives.

Our monodispersed Pd nanoclusters acted as heterogeneous catalysts for the oxidative acetoxylation of

**Table 1** Acetoxylation of toluene with various Pd catalysts in the presence of molecular oxygen<sup>a</sup>

Catalyst	Conversion (%)	Total yield of 1 + 2 (%) <sup>b</sup>	1:2
Pd nanocluster <sup>c</sup>	96	94	4.1:1
Pd nanocluster/ $\text{TiO}_2$	93	88	5.0:1
5% Pd/carbon	19	Trace	–
5% Pd/ $\text{Al}_2\text{O}_3$	21	0	–
$\text{Pd}(\text{OAc})_2$	0	0	–

<sup>a</sup>Reaction conditions: Pd 0.25 mmol, toluene 5 mmol, AcOH 4 mL, 90°C, 3 hr,  $\text{O}_2$  atmosphere.

<sup>b</sup>Yields of products were determined by gas chromatography (GC) analysis using an internal standard technique.

<sup>c</sup>Pd (0.29 mmol).

**Table 2** Aerobic oxidation of various alcohols catalyzed by Pd<sub>2060</sub>(NO<sub>3</sub>)<sub>360</sub>(OAc)<sub>360</sub>O<sub>80</sub> nanoclusters<sup>a</sup>

Entry	Substrate	Product	Catalyst	Time (hr)	Conversion (%)	Yield (%) <sup>b</sup>
1			Pd <sub>2060</sub> (NO <sub>3</sub> ) <sub>360</sub> (OAc) <sub>360</sub> O <sub>80</sub>	2	93	91
2			Pd <sub>561</sub> phen <sub>60</sub> (OAc) <sub>180</sub>	1	100	94
3			Pd(OAc) <sub>2</sub> -pyridine <sup>c</sup>	2	46	35
4			Pd <sub>2060</sub> (NO <sub>3</sub> ) <sub>360</sub> (OAc) <sub>360</sub> O <sub>80</sub>	2	100	91
5			Pd <sub>2060</sub> (NO <sub>3</sub> ) <sub>360</sub> (OAc) <sub>360</sub> O <sub>80</sub>	4	91	87
6			Pd <sub>2060</sub> (NO <sub>3</sub> ) <sub>360</sub> (OAc) <sub>360</sub> O <sub>80</sub>	5	90	83
7			Pd <sub>561</sub> phen <sub>60</sub> (OAc) <sub>180</sub>	1	100	89
8			Pd <sub>2060</sub> (NO <sub>3</sub> ) <sub>360</sub> (OAc) <sub>360</sub> O <sub>80</sub>	5	66	49 <sup>d</sup>
9			Pd <sub>561</sub> phen <sub>60</sub> (OAc) <sub>180</sub>	1	100	79
10			Pd <sub>2060</sub> (NO <sub>3</sub> ) <sub>360</sub> (OAc) <sub>360</sub> O <sub>80</sub>	14	94	80
11			Pd <sub>561</sub> phen <sub>60</sub> (OAc) <sub>180</sub>	4	47	36
12			Pd <sub>2060</sub> (NO <sub>3</sub> ) <sub>360</sub> (OAc) <sub>360</sub> O <sub>80</sub>	24	<1	Trace
13			Pd <sub>561</sub> phen <sub>60</sub> (OAc) <sub>180</sub>	24	8	1
14			Pd <sub>2060</sub> (NO <sub>3</sub> ) <sub>360</sub> (OAc) <sub>360</sub> O <sub>80</sub>	14	95	92
15			Pd <sub>561</sub> phen <sub>60</sub> (OAc) <sub>180</sub>	4	45	44
16			Pd(OAc) <sub>2</sub> -pyridine <sup>c</sup>	24	78	24
17			Pd(OAc) <sub>2</sub> -pyridine <sup>c</sup>	2	100	100
18			Pd <sub>2060</sub> (NO <sub>3</sub> ) <sub>360</sub> (OAc) <sub>360</sub> O <sub>80</sub>	14	95	91
18			Pd(OAc) <sub>2</sub> -pyridine <sup>c</sup>	4	53	50
18			Pd(OAc) <sub>2</sub> -pyridine <sup>c</sup>	2	97	95

<sup>a</sup>Reaction conditions: Pd 0.05 mmol, substrate 2 mmol, AcOH 4 mL, 60°C, O<sub>2</sub> atmosphere.

<sup>b</sup>Yields of aldehydes and ketones were determined by GC analysis using an internal standard technique.

<sup>c</sup>Substrate 2 mmol, Pd(OAc)<sub>2</sub> 0.05 mmol, pyridine 0.2 mmol, MS3A 0.5 g, toluene 4 mL, 80°C, O<sub>2</sub> atmosphere.

<sup>d</sup>Fifteen percent of 2-hexenyl acetate was formed.

toluene to benzyl acetates using molecular oxygen (Scheme 3).<sup>[20]</sup> Among the Pd nanoclusters prepared using Cu(NO<sub>3</sub>)<sub>2</sub>, the maximum catalytic activity was obtained in the case of the eight-shell Pd nanoclusters having the highest fraction of Pd<sub>2</sub>O and the divalent Pd species. It is interesting to note that the monodispersed Pd nanoclusters can efficiently catalyze the oxidative acetoxylation of toluene without any additives such as Sn(II) compounds, KOAc, and reoxidizing reagents. Furthermore, the eight-shell Pd nanoclusters showed much higher catalytic activity than conventional Pd catalysts [e.g. Pd/carbon, Pd/Al<sub>2</sub>O<sub>3</sub>, and Pd(OAc)<sub>2</sub>]. The eight-shell Pd nanoclusters immobilized on the TiO<sub>2</sub> surface

also had high catalytic activity for the acetoxylation of toluene.<sup>f</sup> These results are summarized in Table 1.

The high catalytic activity of the Pd nanoclusters is ascribed to an ensemble of the cationic Pd species and Pd<sup>0</sup> on the cluster surface. Vide supra, in the conventional oxidative acetoxylation catalyzed by Pd catalyst systems, an addition of potassium and tin compounds is indispensable. The Sn<sup>2+</sup> additives promote the

<sup>f</sup>The particle size of the Pd clusters did not change appreciably after the acetoxylation reaction. During the acetoxylation, no Pd leaching was observed by the ICP method, whose detection limit is 24 ppb.

reduction step of  $\text{Pd}^{2+}$  to  $\text{Pd}^0$ , and the resulting  $\text{Sn}^{4+}$  oxide may serve as an oxygen reservoir in oxygen-poor regimes. The potassium renders Pd particles more electropositive, which becomes susceptible to interaction with an electron-donating substrate (e.g., toluene). Because the cationic Pd atoms already exist on the surface of the Pd cluster in the present catalyst system, the addition of potassium compounds is not required to facilitate the interaction with toluene. Furthermore, tin compound is also unnecessary because the  $\text{Pd}_2\text{O}$  species acted as an oxygen reservoir through an easy interconversion between  $\text{Pd}^+$  and  $\text{Pd}^0$  species.

## Alcohol Oxidation

Recently, much attention has focused on Pd-catalyzed oxidation of alcohols into the corresponding carbonyl compounds using molecular oxygen as an environment-friendly oxidant.<sup>[32–37]</sup> In this section, we explore the catalytic potential of the monodispersed Pd nanoclusters in the aerobic oxidation of alcohols.<sup>[21]</sup>

Results of the aerobic oxidation of various alcohols catalyzed by the  $\text{Pd}_{2060}(\text{NO}_3)_{360}(\text{OAc})_{360}\text{O}_{80}$  nanoclusters are displayed in Table 2 together with those using the  $\text{Pd}_{561}\text{phen}_{60}(\text{OAc})_{180}$  cluster<sup>[38]</sup> and  $\text{Pd}(\text{OAc})_2$ -pyridine<sup>[35]</sup> catalytic systems. Our Pd nanoclusters efficiently catalyzed the oxidation of *primary* aromatic allylic alcohols to the corresponding aldehydes using molecular oxygen (entries 1, 4, and 5). It should be noted that the present Pd nanoclusters showed higher reactivity for *primary* aromatic allylic alcohols than for aliphatic ones (e.g., 3-methyl-2-buten-1-ol and 2-hexen-1-ol, entries 6 and 8). Furthermore, the oxidation of *secondary* aromatic allylic alcohols proceeded

slowly (entry 10). Interestingly, benzylic alcohols were oxidized more slowly than allylic alcohols (entries 14 and 17). This high reactivity for allylic alcohols was also exemplified in a competitive reaction of an equimolar mixture of cinnamyl alcohol and benzyl alcohol; cinnamaldehyde was selectively obtained in 92% yield, together with only 1% of benzaldehyde for 3 hr (Fig. 3).

Generally, divalent Pd catalysts are prone to oxidize benzyl alcohols, but are not suitable for the oxidation of allylic alcohols because of an irreversible coordination of allylic alcohols to the Pd species (entry 3 vs. entry 16).<sup>[35,39]</sup> The difference between the present Pd nanoclusters and conventional  $\text{Pd}^{2+}$  complexes lies in the high reactivity for allylic alcohols over benzylic alcohols. As compared with the  $\text{Pd}_{561}\text{phen}_{60}(\text{OAc})_{180}$  cluster, having  $\text{Pd}^+$  cation species throughout the surface,<sup>[38]</sup> the present Pd nanoclusters preferred aromatic allylic alcohols to aliphatic ones. Cinnamyl alcohol was completely oxidized only for 1 hr, whereas the oxidation of 3-methyl-2-buten-1-ol required 5 hr (entry 1 vs. entry 6). In contrast, using the  $\text{Pd}_{561}\text{phen}_{60}(\text{OAc})_{180}$  catalyst, the oxidation of both allylic alcohols proceeded in a similar rate (entry 2 vs. entry 7).

The highest catalytic activity was obtained for the  $\text{Pd}_{2060}(\text{NO}_3)_{360}(\text{OAc})_{360}\text{O}_{80}$  nanoclusters, which have the highest percentage of the  $\text{Pd}^+$  species among the surface Pd atoms.<sup>[21]</sup> Therefore, in a similar fashion of the above acetoxylation, we considered that the highly selective oxidation of aromatic alcohols by the Pd nanoclusters could be explained by the unique surface ensemble Pd sites; a  $\pi$ -bond interaction between aromatic allylic alcohols and the cationic  $\text{Pd}^{2+}$  species. The high selectivity for the oxidation of allylic alcohols when compared with benzyl alcohol might be related to a coordination of the C=C bond with a Pd cation (e.g.,  $\text{Pd}^{2+}$ ). Correspondingly, the distance between the Pd cation and Pd<sup>0</sup> fits with that found for the distance between a terminal  $\beta$ -carbon of a C=C bond and an oxygen atom of the OH of allylic alcohols.<sup>g</sup>

## Wacker Oxidation

The Wacker oxidation is a powerful method to synthesize methyl ketones from terminal olefins, catalyzed by an aqueous solution of  $\text{Pd}^{2+}$  salt combined with  $\text{Cu}^{2+}$  and HCl under aerobic conditions.<sup>[27]</sup> The HCl is required to achieve a favorable reoxidation of  $\text{Pd}^0$  by  $\text{Cu}^{2+}$  ions, and to prevent the aggregation of transient

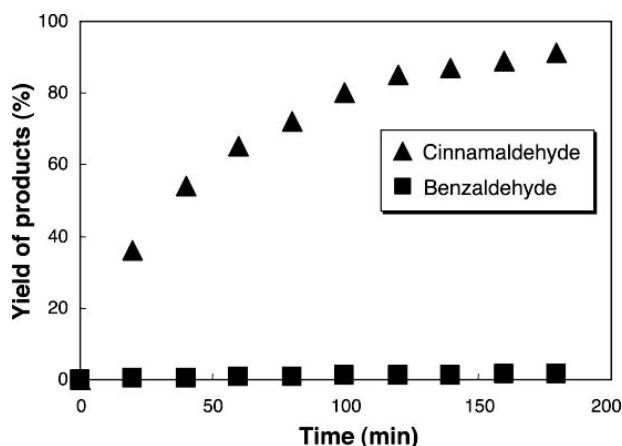
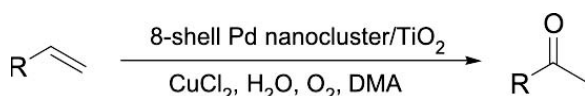


**Fig. 3** Competitive oxidation of an equimolar mixture of cinnamyl alcohol and benzyl alcohol. Reaction conditions:  $\text{Pd}_{2060}(\text{NO}_3)_{360}(\text{OAc})_{360}\text{O}_{80}$  0.0063 g (Pd; 0.05 mmol), cinnamyl alcohol 2 mmol, benzyl alcohol 2 mmol, AcOH 5 ml, 60°C,  $\text{O}_2$  atmosphere.

<sup>g</sup>The EXAFS measurement of the Pd nanoclusters showed that the average distance between the Pd species was 2.75 Å. The distance between a terminal  $\beta$ -carbon of the C=C bond and oxygen atom of the OH function of cinnamyl alcohol was ca. 3 Å, calculated by the PM3 semiempirical method as implemented in MOPAC.



**Scheme 4** The Wacker oxidation of terminal olefins catalyzed by eight-shell Pd nanoclusters immobilized on the TiO<sub>2</sub> surface.

atomic Pd<sup>0</sup> species to inactive Pd precipitates. An acidic chloride medium not only corrodes the reactor wall, but also leads to the formation of chlorinated by-products. Hence much effort has been devoted to the development of HCl-free Wacker systems.<sup>[40–42]</sup> However, there are few heterogeneous catalysts for the Wacker oxidation of unreactive higher terminal olefins in liquid phase.<sup>[43–46]</sup> We found that the Pd nanoclusters immobilized on a TiO<sub>2</sub> surface acted as a highly active and recyclable catalyst for the liquid-phase Wacker oxidation of higher terminal olefins in *N,N*-dimethylacetamide (DMA) solvent without acid additives (Scheme 4).<sup>[22]</sup>

The eight-shell Pd nanoclusters showed high catalytic activity for the oxidation of 1-decene in the presence of water and CuCl<sub>2</sub> · 2H<sub>2</sub>O under O<sub>2</sub> at atmospheric pressure to afford 2-decanone selectively. The catalytic activity of the eight-shell Pd nanoclusters was higher than that of the five-shell Pd<sub>560</sub>(NO<sub>3</sub>)<sub>100</sub>(OAc)<sub>250</sub>O<sub>10</sub> clusters. In the present oxidation, the Pd nanoclusters immobilized on the TiO<sub>2</sub> could maintain the high catalytic activity and selectivity that make the workup procedure strikingly simple. Water, O<sub>2</sub>, and CuCl<sub>2</sub> · 2H<sub>2</sub>O were necessary to obtain high yields of 2-decanone. Only three equivalents of CuCl<sub>2</sub> to Pd were sufficient for achieving high catalytic activity. It is notable that the Pd nanocluster catalysts enable the Wacker oxidation in liquid phase under acid-free conditions.

**Table 3** The wacker oxidation of various terminal olefins catalyzed by eight-shell Pd nanoclusters/TiO<sub>2</sub><sup>a</sup>

Substrate	Yield (%) <sup>b</sup>	Selectivity (%)
1-Hexane	94 <sup>c</sup>	98
1-Octene	84	98
1-Decene	88	97
1-Dodecene	83	98
<i>n</i> -Butyl vinyl ether	91	100
Vinylcyclohexane	92 <sup>d</sup>	100

<sup>a</sup>Reaction conditions: Pd 0.01 mmol, substrate 1 mmol, CuCl<sub>2</sub> · 2H<sub>2</sub>O 0.03 mmol, *N,N*-dimethylacetamide 4 mL, H<sub>2</sub>O 0.5 mL, 80°C, 2 hr, O<sub>2</sub> atmosphere.

<sup>b</sup>Yields of products were determined by GC analysis using an internal standard technique.

<sup>c</sup>50°C.

<sup>d</sup>60°C, 3 hr.

Terminal olefins such as 1-hexene, 1-octene, 1-decene, 1-dodecene, vinylcyclohexane, and *n*-butyl vinyl ether were selectively oxidized by the immobilized Pd nanocluster catalysts to give the corresponding methyl ketones and *n*-butyl acetate, respectively, in high yields within 3 hr (Table 3). Furthermore, the spent catalyst was easily separated from the reaction mixture by filtration and could be reused with retention of high activity and selectivity. However, no oxidation occurred when the filtrate was further reacted. The present Wacker oxidation proceeds via the Pd<sup>2+</sup> species on the Pd nanocluster surface. The use of even small amounts of CuCl<sub>2</sub> efficiently promoted the reoxidation of Pd<sup>0</sup> to Pd<sup>2+</sup> species, which might be ascribed to a cooperative action of Pd<sup>2+</sup>, Pd<sup>+</sup>, and Pd<sup>0</sup> species on the nanocluster surface.

## CONCLUSION

This study demonstrated the “shell-selective” synthesis and characterization of monodispersed Pd nanoclusters containing Pd<sup>0</sup>, Pd<sup>+</sup>, and Pd<sup>2+</sup> species on the surface. Each surface Pd species (e.g., Pd<sup>0</sup>, Pd<sup>+</sup>, and Pd<sup>2+</sup>) does not act individually as a catalytic site, but works cooperatively as a “trio” on the same cluster surface to attain unique catalytic performances for functional transformations under an O<sub>2</sub> atmosphere. Furthermore, the Pd nanoclusters could be immobilized on a neutral TiO<sub>2</sub> surface with retention of their original size and unique catalysis. The monodispersed Pd nanoclusters provides a new strategy to design highly *selective* Pd catalysts in many organic syntheses aiming at “green and sustainable chemistry”.<sup>[47]</sup>

## REFERENCES

- Toshima, N.; Shiraishi, Y.; Teranishi, T.; Miyake, M.; Tominaga, T.; Watanabe, H.; Brijoux, W.; Bönnemann, H.; Schmid, G. Various ligand-stabilized metal nanoclusters as homogeneous and heterogeneous catalysts in the liquid phase. *Appl. Organomet. Chem.* **2001**, *15*, 178–196.
- Rao, C.N.R.; Kulkarni, G.U.; Thomas, P.J.; Edwards, P.P. Metal nanoparticles and their assemblies. *Chem. Soc. Rev.* **2000**, *29*, 27–35.
- Aiken, J.D., III; Finke, R.G. A review of modern transition-metal nanoclusters: their synthesis, characterization, and applications in catalysis. *J. Mol. Catal., A Chem.* **1999**, *145*, 1–44.
- Moiseev, I.I.; Vargaftik, M.N. Pd cluster catalysis: a review of reactions under anaerobic conditions. *New J. Chem.* **1998**, 1217–1227.
- Schmid, G. Large clusters and colloids. Metals in the embryonic state. *Chem. Rev.* **1992**, *92*, 1709–1727.



6. Bradley, J.S.; Tesche, B.; Busser, W.; Masse, M.; Reetz, M.T. Surface spectroscopic study of the stabilization mechanism for shape-selectively synthesized nanostructured transition metal colloids. *J. Am. Chem. Soc.* **2000**, *122*, 4631–4636.
7. Bönnemann, H.; Braun, G.; Brijoux, W.; Brinkmann, R.; Tilling, A.S.; Seevogel, K.; Siepen, K. Nanoscale colloidal metals and alloys stabilized by solvents and surfactants. Preparation and use as catalyst precursors. *J. Organomet. Chem.* **1996**, *520*, 143–162.
8. Thomas, P.J.; Kulkarni, G.U.; Rao, C.N.R. Magic nuclearity giant clusters of metal nanocrystals formed by mesoscale self-assembly. *J. Phys. Chem., B* **2001**, *105*, 2417–2515.
9. Teranishi, T.; Miyake, M. Size control of palladium nanoparticles and their crystal structures. *Chem. Mater.* **1998**, *10*, 594–600.
10. Toshima, N. Nanostructured metal clusters in polymeric field as a model of artificial enzyme. *Supramol. Sci.* **1998**, *5*, 395–398.
11. Vargaftik, M.N.; Zagorodnikov, V.P.; Stolarov, I.P.; Moiseev, I.I.; Likholobov, V.A.; Kotchubey, D.I.; Chuvilin, A.L.; Zaikovskiy, V.I.; Zamaraev, K.I.; Timofeeva, G.I. A novel giant palladium cluster. *J. Chem. Soc., Chem. Commun.* **1985**, 937–939.
12. Schmid, G.; Harms, M.; Malm, J.-O.; Bovin, J.-O.; van Ruitenbeck, J.; Zandbergen, H.W.; Fu, W.T. Ligand-stabilized giant palladium clusters: Promising candidates in heterogeneous catalysis. *J. Am. Chem. Soc.* **1993**, *115*, 2046–2048.
13. Lin, Y.; Finke, R.G. Novel polyoxoanion- and  $\text{Bu}_4\text{N}^+$ -stabilized, isolatable, and redissolvable, 20–30 Å  $\text{Ir}_{300-900}$  nanoclusters: the kinetically controlled synthesis, characterization, and mechanism of formation of organic solvent-soluble, reproducible size, and reproducible catalytic activity metal nanoclusters. *J. Am. Chem. Soc.* **1994**, *116*, 8335–8353.
14. Reetz, M.T.; Helbig, W. Size-selective synthesis of nanostructured transition metal clusters. *J. Am. Chem. Soc.* **1994**, *116*, 7401–7402.
15. Reetz, M.T.; Westermann, E. Phosphine-free palladium-catalyzed coupling reactions: the decisive role of Pd nanoparticles. *Angew. Chem., Int. Ed. Engl.* **2000**, *39*, 165–168.
16. Tsuji, J. *Organic Synthesis with Palladium Compounds*; Springer-Verlag: Berlin, 1980.
17. Heck, R.F. *Palladium Reagents in Organic Syntheses*; Academic Press: London, 1985.
18. Jia, C.; Kitamura, T.; Fujiwara, Y. Catalytic functionalization of arenes and alkanes via C–H bond activation. *Acc. Chem. Res.* **2001**, *34*, 633–639.
19. Sheldon, R.A.; Kochi, J.K. *Metal Catalyzed Oxidation of Organic Compounds*; Academic Press: New York, 1981.
20. Ebitani, K.; Choi, K.-M.; Mizugaki, T.; Kaneda, K. Novel preparation of palladium nanoclusters using metal nitrates and their catalysis for oxidative acetoxylation of toluene in the presence of molecular oxygen. *Langmuir* **2002**, *18*, 1849–1855.
21. Choi, K.-M.; Akita, T.; Mizugaki, T.; Ebitani, K.; Kaneda, K. Highly selective oxidation of allylic alcohols catalysed by monodispersed 8-shell Pd nanoclusters in the presence of molecular oxygen. *New J. Chem.* **2003**, *27*, 324–328.
22. Choi, K.-M.; Mizugaki, T.; Ebitani, K.; Kaneda, K. Nanoscale palladium cluster immobilized on a  $\text{TiO}_2$  surface as an efficient catalyst for liquid-phase Wacker oxidation of higher terminal olefins. *Chem. Lett.* **2003**, *32*, 180–181.
23. Moiseev, I.I.; Stromnova, T.; Vargaftik, M.N.; Mazo, G.J.; Kuz'mina, L.G.; Struchkov, Y.T. New palladium carbonyl clusters: X-ray crystal structure of  $[\text{Pd}_4(\text{CO})_4(\text{OAc})_4] \cdot (\text{AcOH})_2$ . *J. Chem. Soc., Chem. Commun.* **1978**, 27–28.
24. Moiseev, I.I.  $\text{Pd}_4$  clusters: The sensitivity of the cluster metal core geometry to the surrounding ligands. *J. Organomet. Chem.* **1995**, *488*, 183–190.
25. Chini, P. Large metal carbonyl clusters. *J. Organomet. Chem.* **1980**, *200*, 37–61.
26. Choo, H.; Prakash, A.M.; Zhu, Z.; Kevan, L. Formation and adsorbate interactions of paramagnetic Pd(I) species in Pd(II)-exchanged NaK- and H-clinoptilolite. *J. Phys. Chem., B* **2000**, *104*, 3608–3615.
27. Tsuji, J. *Palladium Reagents and Catalysts Innovations in Organic Synthesis*; John Wiley and Sons: New York, 1998.
28. Trost, B.M. Atom economy—a challenge for organic synthesis: homogeneous catalysis leads the way. *Angew. Chem., Int. Ed. Engl.* **1995**, *34*, 259–281.
29. Bryant, D.R.; McKeon, J.E.; Ream, B.C. Palladium-catalyzed synthesis of benzyl esters from methylbenzenes. *J. Org. Chem.* **1968**, *33*, 4123–4127.
30. Benazzi, E.; Mimoun, H.; Cameron, C.J. Heterogeneous catalyzed benzylic acetoxylation of methylated aromatic hydrocarbons. *J. Catal.* **1993**, *140*, 311–327.
31. Tanielyan, S.K.; Augustine, R.L. Pd/Sn catalyst for toluene acetoxylation. *J. Mol. Catal.* **1994**, *90*, 267–289.
32. Mori, K.; Yamaguchi, K.; Hara, T.; Mizugaki, T.; Ebitani, K.; Kaneda, K. Controlled synthesis of hydroxyapatite-supported palladium complexes as highly efficient heterogeneous catalysts. *J. Am. Chem. Soc.* **2002**, *124*, 11,572–11,573.
33. Steinhoff, B.A.; Fix, S.R.; Stahl, S.S. Mechanistic study of alcohol oxidation by the  $\text{Pd}(\text{OAc})_2/\text{O}_2/\text{DMSO}$  catalyst system and implications for the development of improved aerobic oxidation catalysts. *J. Am. Chem. Soc.* **2002**, *124*, 766–767.
34. ten Brink, G.-J.; Arends, I.W.C.E.; Sheldon, R.A. Green, catalytic oxidation of alcohols in water. *Science* **2000**, *287*, 1636–1639.
35. Nishimura, T.; Onoue, T.; Ohe, K.; Uemura, S. Palladium(II)-catalyzed oxidation of alcohols to aldehydes and ketones by molecular oxygen. *J. Org. Chem.* **1999**, *64*, 6750–6755.
36. Peterson, K.P.; Larock, R.C. Palladium-catalyzed oxidation of primary and secondary allylic and benzylic alcohols. *J. Org. Chem.* **1998**, *63*, 3185–3189.
37. Kaneda, K.; Fujii, M.; Morioka, K. Highly selective oxidation of allylic alcohols to  $\alpha,\beta$ -unsaturated aldehydes using Pd cluster catalysts in the presence of molecular oxygen. *J. Org. Chem.* **1996**, *61*, 4502–4503.
38. Ebitani, K.; Fujie, Y.; Kaneda, K. Immobilization of a ligand-preserved giant palladium cluster on a

- metal oxide surface and its novel heterogeneous catalysis for oxidation of allylic alcohols in the presence of molecular oxygen. *Langmuir* **1999**, *15*, 3557–3562.
39. Blackburn, T.F.; Schwartz, J. Homogeneous catalytic oxidation of secondary alcohols to ketones by molecular oxygen under mild conditions. *J. Chem. Soc., Chem. Commun.* **1977**, 157–158.
40. ten Brink, G.-J.; Arends, I.W.C.E.; Papadogianakis, G.; Sheldon, R.A. Catalytic conversions in water: part 10. Aerobic oxidation of terminal olefins to methyl ketones catalysed by water soluble palladium complexes. *Chem. Commun.* **1998**, 2359–2360.
41. Smith, A.B., III; Cho, Y.S.; Friestad, G.K. Convenient Wacker oxidation with substoichiometric cupric acetate. *Tetrahedron Lett.* **1998**, *39*, 8765–8768.
42. Hosokawa, T.; Takano, M.; Murahashi, S.-I. The first isolation and characterization of a palladium–copper heterometallic complex bearing  $\mu_4$ -oxo atom derived from molecular oxygen. *J. Am. Chem. Soc.* **1996**, *118*, 3990–3991.
43. De Vos, D.E.; Sels, B.F.; Jacobs, P.A. Immobilization of homogeneous oxidation catalysts. *Adv. Catal.* **2001**, *46*, 1–87.
44. Yokota, T.; Sakakura, A.; Tani, M.; Sakaguchi, S.; Ishii, Y. Selective Wacker-type oxidation of terminal alkenes and dienes using the Pd(II)/molybdovanadophosphate (NPMoV)/O<sub>2</sub> system. *Tetrahedron Lett.* **2002**, *43*, 8887–8891.
45. Kishi, A.; Higashino, T.; Sakaguchi, S.; Ishii, Y. Wacker-type oxidation of cyclopentene under dioxygen atmosphere catalyzed by Pd(OAc)<sub>2</sub>/NPMoV on activated carbon. *Tetrahedron Lett.* **2000**, *41*, 99–102.
46. Tang, H.G.; Sherrington, D.C. Polymer-supported Pd(II) Wacker-type catalysts: II. Application in the oxidation of dec-1-ene. *J. Catal.* **1993**, *142*, 540–551.
47. Clark, J.; Macquarrie, D.; Eds.; *Handbook of Green Chemistry and Technology*; Blackwell Publishing: Oxford, 2002.

# Patents and Inventions

Jeffrey A. Lindeman

*Nixon Peabody LLP, Washington, District of Columbia, U.S.A.*

## INTRODUCTION

Invention is only the first step in the process of obtaining a patent. Preparing and filing a patent application is the required second step; yet, though it describes the invention, a patent application is as much a legal document as it is a technical document. In a patent application, the language of science comes under legal scrutiny. For new technology, the language of science may not easily fit into a legal document, yet it is the words used to describe and claim the invention that determine the scope of the intellectual property right deeded by the patent grant. For emerging technologies, such as nanotechnology, choosing the right words to describe and claim an invention presents a particularly unique challenge. This entry looks at the legal framework used to interpret the language of patent claims and considers how best to navigate the legal landscape to obtain robust and effective patents for nanotechnology.

This entry is written in a legal memorandum style. Citations for and references to portions of the statutes and the legal decisions discussed are included in the text rather than as endnotes.

## DEFINITIONS OF NANOTECHNOLOGY

Although still an emerging science, nanotechnology is already spanning and combining many diverse technologies, from biotechnology to circuits and machines to molecules. Despite its broad technological range, nanotechnology inventions are all characterized in terms of their small scale, their very small scale. To say size is important in nanotechnology is to understate its scientific premise. Size is everything in nanotechnology. Therefore, to patent nanotechnology, the patentable nanoscale features of the invention should be the focus of the patent specification and the patent claims.

Nanotechnology has been defined as research and technology development on the atomic, molecular, or macromolecular scale, where dimensions range from approximately 1–100 nm. Research and development efforts in nanotechnology seek to provide not only a fundamental understanding of phenomena and

materials at the nanoscale but also to create and use structures, devices, and systems that have unique properties and functions because of their very small size. These unique properties and functions include mechanisms, operation and control at the nanoscale, as well as integration of nanoscale structure and processes into larger material components, systems, and architectures. Within these larger scale assemblies, the control and construction of their structures and components remains at the nanometer scale.<sup>[1]</sup>

For patent applicants, another important definition of nanotechnology comes from the United States Patent and Trademark Office (USPTO). The USPTO arranges technology by what it terms classes and subclasses. Although this serves an administrative function, each class of technology is uniquely defined. At the USPTO, Class 977 covers nanotechnology and has the following class definition:<sup>[2]</sup>

This class provides for disclosures

- a. related to research and technology development at the atomic, molecular or macromolecular levels, in the length of scale of approximately 1–100 nm range in at least one dimension, and
- b. that provides a fundamental understanding of phenomena and materials at the nanoscale and to create and use structures, devices, and systems that have novel properties and functions because of their small and/or intermediate size.

In addition, disclosures in this class may be defined by one or more of the following statements.

- a. The novel and differentiating properties and functions of disclosures in this class are developed at a critical length scale of matter, typically under 100 nm.
- b. Nanotechnology research and development includes manipulation, processing, and fabrication under control of the nanoscale structures and their integration into larger material components, systems and architectures. Within these larger scale assemblies, the control and construction of their structures and components remains at the nanometer scale.

- c. In some particular cases, the critical length scale for novel properties and phenomena may be less than 1 nm or be slightly larger than 100 nm.
- d. The novel properties or functions, e.g., special effects, are attributed to and are intrinsic at the nanoscale.

Such nanoscale materials are infinitesimally minute arrangements of matter (i.e., nano-structural assemblages) have particularly shaped configurations formed during manufacture and are distinct from both naturally occurring and chemically produced chemical or biological arrangements composed of similar matter.

- a. Also, encompassed within this collection are disclosures related to the controlled analysis, measurement, manufacture or treatment of such nano-structural assemblages and their associated processes or apparatus specially adapted for performing at least one step in such processes.
- b. Novel and differentiating properties and functions relate to the altering of basic chemical or physical properties of the nano-structural assemblage attributed at the nanoscale.

Obviously, numerous nanotechnology inventions come within this definition.

Almost any invention can be thought of as a new and nonobvious solution to a problem. A nanoscale invention, likewise, solves problems, but in spaces of about 1–100 nm. Certainly working at the nanoscale presents unique technical problems to be solved. In the same way, preparing patent applications to adequately and appropriately protect nanotechnology inventions presents its own unique challenges.

## PATENTING NANOTECHNOLOGY

The claims of a patent define the scope of the patented invention. To claim nanotechnology, at least some word or term in the patent claim typically indicates that at least some aspect of the invention is at the nanoscale. Words, as everyone knows, are not necessarily precise. This is particularly true when words are used to describe and define technology, especially nanotechnology. Unfortunately, the nature of language makes it impossible to capture the essence of a thing in a patent application. *See Festo Corp. v. Shoketsu Kinzoku Kogyo Kabushi Co. Ltd.*, 535 U.S. 722, 731 (2002) (discussing the imprecision of language and patent infringement under the doctrine of equivalents).

The scope of a patent claim is determined by the words used to describe and claim the invention. The everyday words we often use to describe technology

or an invention do not necessarily change with a change in size, for example when one moves from the macroscale to the nanoscale. The only change is in the size of what we are describing and what the words define. If the words of a patent claim carry their everyday meaning, they may be too big for nanotechnology. The typical meaning of words in patent claims may not be sufficient to describe a nanotechnology invention, but we cannot, and we do not, simply add the prefix *nano* to every word as we discuss or write about nanotechnology. The common meaning of a word can often be acceptable for ordinary inventions—those in more established areas of technology—but patenting nanotechnology involves more careful diction. This article gives an overview of how words in patent claims are interpreted and discusses considerations for drafting patent claims to nanotechnology. As nanotechnology continues to develop, so do nanotechnology patent practice and court decisions concerning nanotechnology patents. With that in mind, we may see unique applications of patent law and practice to nanotechnology.

## The Beginning

As mentioned, inventions most often involve a new solution to a particular problem. Nanotechnology inventions involve solving problems with nanoscale technology. Simply creating a nanoscale device or performing a nanoscale process can be the new solution that is invention. Not all devices or processes can be readily manufactured or accomplished on the nanoscale. Just moving from the macroscale or from the microscale to the nanoscale can present the very problem that needs to be solved. Fig. 1A–C illustrate such a change in perspective as one moves from the macroscale to contemplating the nanoscale. There can also be new devices or processes that simply could not have existed before the advent of nanotechnology. This can provide the basis for an invention. Under U.S. law, whoever invents or discovers any new and useful process, machine, manufacture, or composition of matter, or any new and useful improvement thereof, may obtain a patent therefore. *See* 35 U.S.C. § 101.

To obtain a patent, an applicant first files a patent application with the U.S. Patent and Trademark Office. The patent application then undergoes examination by a patent examiner. The patent application must describe the invention and then conclude with one or more patent claims where the patent applicant sets out the invention to be patented. *See* 35 U.S.C. §§ 111 and 112. During examination, the patent examiner focuses on the claimed invention to ensure that it meets the statutory requirements of novelty (35 U.S.C. § 102) and unobviousness (35 U.S.C. § 103) and that

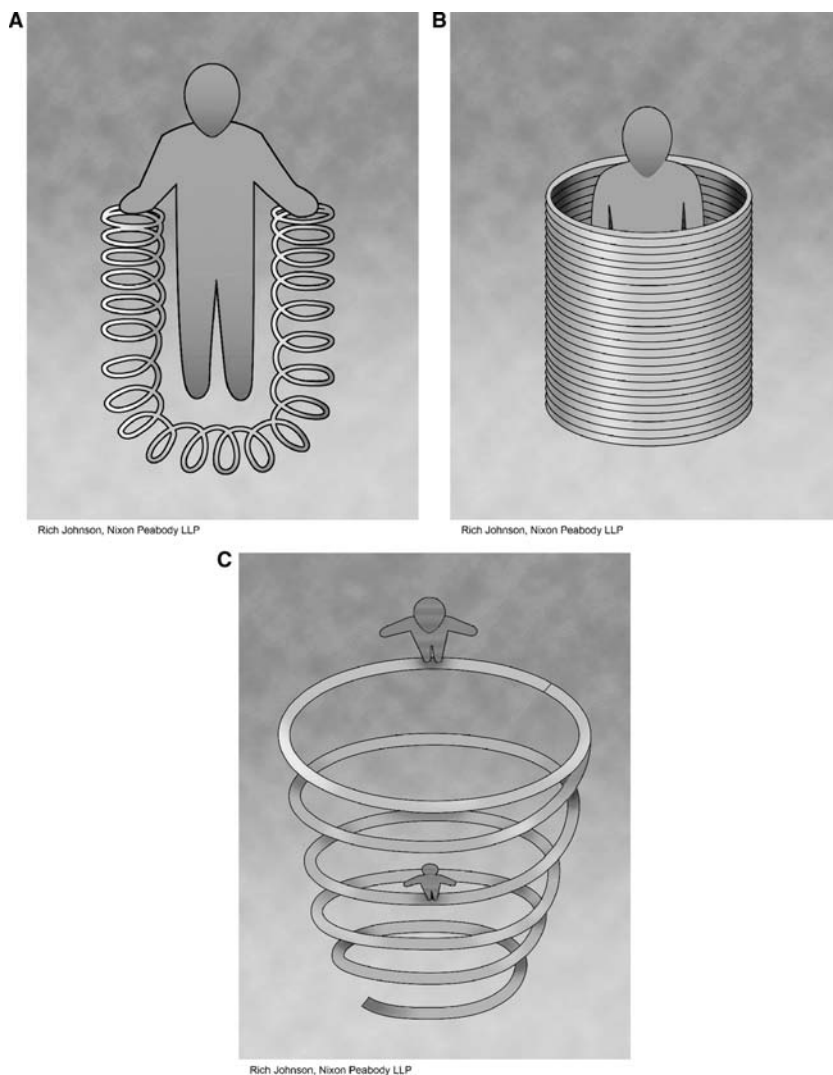


**Fig. 1** (A) The macroscale view; (B) The microscale view; (C) The nanoscale view.

the patent specification describes the claimed invention as required by statute (35 U.S.C. § 112). A patent is issued only after the patent examiner concludes that these requirements are fully met.

### Patent Claims

Patent claims define the scope of technology property rights granted in the form of a patent. A patent claim must, by statute, particularly point out and distinctly claim the subject matter that the applicant regards as his invention. 35 U.S.C. § 112, second paragraph. This is essentially a requirement for precision and definiteness of claim language. The language of the claims must make clear what they encompass. *PPG Industries, Inc. v. Guardian Industries Corp.*, 75 F.3d 1558, 1562 (Fed. Cir. 1996) (citations omitted). The standard for assessing whether a patent claim meets the statutory requirement has been stated as

follows: “If one skilled in the art would understand the bounds of the claim when read in light of the specification, then the claim satisfies section 112 paragraph 2.” *Exxon Research and Engineering Corp. v. U.S.*, 265 F.3d 1371, 1375 (Fed. Cir. 2001) citing *Miles Labs., Inc. v. Shandon, Inc.*, 997 F.2d 870, 875 (Fed. Cir. 1993). This standard has also been stated in somewhat different terms: whether “the claims at issue [are] sufficiently precise to permit a potential competitor to determine whether or not he is infringing.” *Exxon Research*, 265 F.3d at 1375 quoting *Morton Int’l, Inc. v. Cardinal Chem, Co.*, 5 F.3d 1464, 1470. (Fed. Cir. 1993).

Although patent claims are first presented by the patent applicant and then examined by the patent examiner, patent claims are often not fully tested until a patent is litigated. While being examined for patentability, patent claims are given their broadest reasonable interpretation, consistent with the specification. During examination, the patent applicant and the

patent examiner often carry on a discussion of what the terms in a patent claim mean and the scope of the invention the claims define. From the USPTO's perspective, a patent applicant always has the opportunity to amend the claims and broad interpretation by the examiner reduces the possibility that the claim, once issued in a patent, will be interpreted more broadly than is justified. Manual of Patent Examining Procedure (MPEP) § 2111.

In patent litigation, the interpretation of a patent claim, (claim construction), is a question of law for the court (the judge) to decide, not one of fact for the jury to decide. *Markman v. Westview Instruments, Inc.*, 517 U.S. 370, 384 (1996); *Gechter v. Davidson*, 116 F.3d 1454, 1457 (Fed. Cir. 1997); *Vitronics Corp. v. Conceptoronic, Inc.*, 90 F.3d 1576, 1582 (Fed. Cir. 1996). In litigation, claim language should be interpreted as one reasonably skilled in the art would have interpreted the claim at the time of invention. *Specialty Composites v. Cabot Corp.*, 845 F.2d 981, 986 (Fed. Cir. 1988) (quoting *Loctite Corp. v. Ultraseal Ltd.*, 781 F.2d 861, 867 (Fed. Cir. 1985)).

Claim construction, the determination of the meaning and scope of patent claims, begins with the language of the claims. *Vitronics Corp.*, 90 F.3d at 1582. The words of a claim are generally to be accorded their *ordinary and customary meaning*, *id.* at 1582, which is "the meaning that term would have to a person of ordinary skill in the art in question at the time of invention." *Phillips v. AWH Corp.*, 415 F.3d 1303, 1313 (Fed. Cir. 2005) (en banc). It is presumed that the person of ordinary skill in the art read the claim in the context of the entire patent, including the specification, not confining his understanding to the claim at issue. *Id.* at 1314; see also *V-Formation, Inc. v. Bennetton Group SpA*, 401 F.3d 1307, 1310 (Fed. Cir. 2005) (noting that the intrinsic record [the patent file history], "usually provides the technological and temporal context to enable the court to ascertain the meaning of the claim to one of ordinary skill in the art at the time of the invention"). Further, claim terms are presumed to be used consistently throughout the patent, such that the usage of a term in one claim can often illuminate the meaning of the same term in other claims. *Phillips*, 415 F.3d, at 1314; see also *Rexnord Corp. v. Laitram Corp.*, 274 F.3d 1336, 1342 (Fed. Cir. 2001).

For inventions in nanotechnology, *ordinary and customary meaning* may be a poor fit if an inventor intends a word to define the nanoscale aspect of the invention, particularly when its ordinary meaning does not define size or, for example, differentiate between the nanoscale or the macroscale. To effectively draft nanotechnology patent applications, especially patent claims, one should understand the legal contours of patent claim constitution, its role in defining claim

language, and, thereby, in delineating the scope of patent claims. Employing appropriate claim terminology can mean the difference between a patent claim that successfully captures the inventive nanotechnology, or one that unintentionally and unfortunately overlaps macroscale technology. Overlapping the macroscale may cause a patent claim to be invalid because it unwittingly encompasses prior art or because it fails to particularly point out and distinctly claim the subject matter of applicant's invention. See 35 U.S.C. § 112, second paragraph.

## CONSTRUING PATENT CLAIM LANGUAGE

Construing, or defining the scope of, a patent claim, a court first examines the intrinsic evidence associated with the patent, i.e., the patent claims, the patent specification, and often the patent's prosecution history. See *Gart v. Logitech, Inc.*, 115 F.3d 1334, 1339–1340 (Fed. Cir. 1997); and *O.I. Corp. v. Tekmar Co. Inc.*, 115 F.3d 1576, 1581 (Fed. Cir. 1997). The patent claims, specification, and drawings/Figs. (if present) embody the patent application an inventor files. Patent prosecution is the back and forth exchange of documents and the discussion that the patent applicant has with the patent examiner when a patent application is undergoing examination. The patent application and the patent's prosecution history provide ample opportunities (and perhaps ample pitfalls) for words to be explained or further defined. When interpreting patent claims, a court will hold a patent applicant to the definitions established in this intrinsic evidence. If the intrinsic evidence fails to clarify the meaning and scope of a claim term, extrinsic evidence (e.g., expert testimony, inventor testimony, scientific articles, treatises) may be used. *Spectrum Int'l, Inc. v. Sterillite Corp.*, 164 F.3d 1372, 1378 (Fed. Cir. 1998); *Kegel Co., Inc. v. AMF Bolwing, Inc.*, 127 F.3d 1420, 1426 (Fed. Cir. 1997). Extrinsic evidence should not be used to rebut the definition of claim meaning that is unambiguous in light of the intrinsic evidence. *Phillips*, 415 F.3d, at 1324.

In the context of those established claim construction principles, a heavy presumption nonetheless exists that a word carries its ordinary or customary meaning in the relevant art. The words used in the claims are presumed to mean what they say. The words have the full, ordinary meaning that would be attributed to those words by persons skilled in the relevant art. See *CCS Fitness, Inc. v. Brunswick Corp.*, 288 F.3d 1359, 1366, (Fed. Cir. 2002); *K-2 Corp. v. Salomon S.A.*, 191 F.3d 1356, 1362–1363 (Fed. Cir. 1999); *Johnson Worldwide Assocs., Inc. v. Zebco Corp.*, 175 F.3d 985, 989 (Fed. Cir. 1999); and *Specialty Composites v. Cabot Corp.*, 845 F.2d 981, 986 (Fed. Cir. 1988). It is the language



of the claims that frames and ultimately resolves all issues of claim interpretation. *AbTox, Inc. v. Exitron Corp.*, 122 F.3d 1019, 1023 (Fed. Cir. 1997). The resulting claim interpretation must, in the end, accord with the words chosen by the patentee to stake out the boundaries of the claimed intellectual property. See *Renishaw PLC, v. Marposs Societa' per Azioni*, 158 F.3d 1243, 1248 (Fed. Cir. 1998) citing *Thermalloy, Inc. v. Aavid Eng'g, Inc.*, 121 F.3d 691, 693 (Fed. Cir. 1997) (“Throughout the interpretation process, the focus remains on the meaning of the claim language”).

### No “Importing” Limitations into Patent Claims

While intrinsic evidence, such as the patent specification and prosecution history, must be consulted to ensure consistency of the selected meaning of a claim term, courts must take care not to import limitations into the claims. It is axiomatic that limitations must not be imported from the specification into the claims. Importing a limitation into the claims can seize the meaning of a term and push the claim construction in a different direction than the patent applicant intended. In other words, if a patent claim does not set out nanoscale limitations, a court may refuse to construe the patent claim as defining a nanoscale invention. Particular embodiments from the patent specification will not be read into patent claims when the language is broader than the particular embodiments. See *Electro Med. Sys. S.S. v. Cooper Life Sci.*, 34 F.3d 1048, 1054 (Fed. Cir. 1994). In *Specialty Composites* the court refused to limit the term plasticizer in the claims to external plasticizers when the specification and prosecution showed the term to include both external and internal plasticizers. *Specialty Composites*, 845 F.3d at 986–987. See also, *Virginia Panel Corp. v. MAC Panel Co.*, 133 F.3d 860, 865–866 (Fed. Cir. 1997) (the term “reciprocating” given its ordinary meaning and not limited to linear reciprocation); *Sojland v. Musland*, 847 F.2d 1573, 1581–1582 (Fed. Cir. 1988) (term baffle not limited to only rigid baffles and panel not limited to only panels of lattice construction).

### RELEVANT ART

A claim term takes its ordinary meaning as understood by persons skilled in the relevant art. *Rexnord Corp. v. Laitram Corp.*, 274 F.3d 1336, 1342 (Fed. Cir. 2001). It is interesting to consider what the relevant art may be for nanotechnology. Is it the particular area of technology, electrical circuits, or devices, for example? Or, is the relevant art determined only by the nanoscale aspects? Certainly, if it is not now, it will be a combination of these as distinct areas of nanotechnology continue to develop.

Patent applicants will always use common language and parlance when discussing their inventions. An entirely new language will not develop exclusively for nanotechnology. Even as areas of nanotechnology develop their own lexicons, patent applicants will use their own thoughts and words to describe their inventions. Variation in the ordinary meaning of common words as well as in accepted or customary nanotechnology terms will certainly occur and persist. Understanding that, there are four common situations when a court may constrict or restrict the ordinary meaning of a claim term:

1. the patentee acted as his or her own lexicographer;
2. the patentee distinguished the invention from the prior art;
3. the term chosen by the patentee deprives the claim of clarity; and
4. the patentee phrased the claim in means-plus-function format.

*CCS Fitness*, 288 F.3d at 1366–1367. In each of these situations the patentee actively applies a particular definition to the term in question; the term’s ordinary meaning is not necessarily any longer presumed. This is true for all areas of technology. It is likely to be particularly true for nanotechnology—now as the language of nanotechnology is developing and later once it has its own fully established lexicon and jargon.

### The Patentee as His or Her Own Lexicographer

A patentee may choose to define a term in the patent specification. If so, that defined meaning controls the meaning of that term in the patent, particularly in the patent claims. Acting as his or her own lexicographer overcomes the presumption favoring ordinary and customary meaning where the patentee has clearly set forth an explicit definition of the term different from its ordinary meaning. See *Johnson Worldwide*, 175 F.3d at 990 and *Abbott Labs. v. Novopharm*, 323 F.3d 1324 (Fed. Cir. 2003). Often a patent applicant, an inventor, will want a word in a patent claim to take its ordinary meaning. When focusing on the nanoscale aspects of a nanotechnology invention, an applicant may, however, want to avoid any uncertainty in meaning and firmly establish patentability based on the nanoscale aspects.

An illustration of where, by acting as their own lexicographer, a patent applicant controlled the meaning of a claim term is found in *Abbott Labs v. Novopharm*. The patented invention involved micronized pharmaceutical formulations of fenofibrate, which is used to treat hyperlipidemia and hypercholesterolemia.

The micronized formulation improved the bioavailability of fenofibrate. The Abbott Labs case turned on the construction of the terms *co-micronized mixture* and *co-micronization*. During prosecution, Abbott amended its claims, changing the phrase “the said composition containing fenofibrate and a solid surfactant, which have been co-micronized” to “said composition containing a co-micronized mixture of particles of fenofibrate and a solid surfactant, wherein the mean particle size of the co-micronized mixture is less than 15 μm.” *Abbott Labs*, 323 F.3d at 1327. The dispute was whether co-micronization required micronization of fenofibrate and a solid surfactant “in the absence of other excipients.” The term *co-micronization* was not known in the prior art before Abbott’s patent application, although the terms *micronization* and *co-* did have well known meanings understood by those of ordinary skill in the art. The Federal Circuit observed that the specification explicitly defined the phrase “co-micronization of fenofibrate and a solid surfactant” as “micronization of an intimate mixture of fenofibrate and a solid surfactant.” Based on this definition, the court held that Abbott had acted as its own lexicographer and concluded accordingly that the definition from the specification could be read into the claims. *Abbott Labs*, 323 F.3d at 1330. Focusing on the intimate mixture defined in the specification, the *Abbott Labs* court construed the co-micronization of fenofibrate and solid surfactant term in the claims to mean co-micronization of a mixture consisting essentially of fenofibrate and solid surfactant but not excluding minor impurities. Because the Novopharm formulation mixed fenofibrate and a solid surfactant in the presence of other significant ingredients, the Abbott patent was not infringed.

Defining your own terms as in *Abbott Labs*, acting as your own lexicographer, is not then without risk to the patent claim’s scope. For nanotechnology, however, it may be a necessity. The defined term is likely to be narrowly construed to the specific definition employed. Yet, neglecting to consider or even relying on a term’s ordinary meaning itself carries risk that the term may not be sufficiently precise to describe and distinguish the invention. Here is the true risk for nanotechnology. Simply put, care should be taken when choosing a particular word or combination of words to describe and claim the invention. Once made, that choice must be respected throughout prosecution of the patent.

### Distinguishing the Invention from the Prior Art

A term will not carry its common meaning if the patentee used a different or specific meaning of the term to distinguish the patented invention from the prior art. This can occur where the patentee distinguished the

prior art on the basis of a particular embodiment of the invention, expressly disclaimed subject matter, or described a particular embodiment as important to the invention. See *CCS Fitness*, 288 F.3d at 1366–1367. In other words, the presumption favoring ordinary meaning will be rebutted if the inventor has disavowed or disclaimed scope of coverage, by using words or expressions of manifest exclusion or restriction, representing a clear disavowal of claim scope. See *Teleflex*, 299 F.3d at 1324. *Spectrum Int’l*, 164 F.3d at 1378 (narrowing a claim term’s ordinary meaning based on statements in intrinsic evidence that distinguished the claimed invention from the prior art); *Scimed Life Sys, Inc. v. Adv. Cardiovascular Sys., Inc.*, 242 F.3d 1337, 1343–1344 (Fed. Cir. 2001) (limiting a claim term based in part on statements in the specification indicating the “all embodiments” of the claimed invention used a particular structure); *Toro Co. v. White Consol. Indus., Inc.*, 199 F.3d 1295, 1301 (Fed. Cir. 1999) (limiting claim term based in part on statements made in the specification describing a particular structure as “important to the invention”); *General Am. Transp. Corp. v. Cryo-Trans, Inc.*, 93 F.3d 766, 770 (Fed. Cir. 1996) (holding that claim language and specification made clear that openings “adjacent each of said side walls and end walls” of a rail car required the openings to be adjacent to all four walls of the railcar.); and *Modine Mfg. Co. v. United States Int’l Trade Comm’n*, 75 F.3d 1545, 1551 (Fed. Cir. 1996) (claim limited to a particular numerical range when broader range was surrendered during prosecution by amendment of the specification).

Without intending to over generalize, it is likely that much of the prior art that patent applicants will face when seeking patents for nanotechnology will be prior work done on a larger scale. Successful and patentable nanotechnology may be a patentable advance over technology previously done, for example, at the microscale. Since size may often be the touchstone for patenting nanotechnology, a patent applicant should anticipate making arguments to the patent examiner concerning the invention’s nanoscale features and the advantages those nanoscale features provide. Those arguments can constrict or restrict the meaning of claim terms to the nanoscale. This may be entirely appropriate in the context of the invention. It may or may not adversely affect claim scope, but one should consider the potential adverse impact such arguments may have on the breadth of patent protection. As has been the common theme of this article, it is best to build into patent claims the nanoscale aspect of the invention. This will often provide the opportunity to argue from the original language of the claims themselves without having to impart a particular meaning to a claim term in order to define over the prior art.

## Depriving the Patent Claim of Clarity

A claim term will not be given its ordinary meaning when doing so deprives the patent claim of clarity and requires resort to other intrinsic evidence for a definite meaning. See *Johnson Worldwide*, 175 F.3d at 990; *Gart*, 254 F.3d at 1341. *CCS Fitness*, 288 F.3d at 1367. Patents concerning nanotechnology may actually compel a court to go beyond the ordinary meaning of a term used in a patent to understand and define the nanotechnology aspects of the invention. The claim construction analysis may turn to the dictionary definition, but available dictionaries may simply not be current enough to keep pace with nanotechnology developments. A common meaning, even one expressed in a relevant dictionary, which flies in the face of the patent disclosure, is undeserving of fealty. Where there are several common meanings for a claim term, the patent disclosure often does and should serve to point away from the improper meaning and toward the proper meaning. Ultimately, the interpretation to be given a term can only be determined and confirmed with a full understanding of what the inventors actually invented and intended to claim. The construction that stays true to the claim language and most naturally aligns with the patent's discussion will be, in the end, the correct construction. See *Renishaw PLC*, 158 F.3d at 1250.

In *Renishaw PLC*, the question of infringement actually turned on the meaning of the word *when*. The patented invention involved improved touch probes used in automated manufacturing to measure the dimensions of machined parts. According to the patent claims, the touch probe generated “a trigger signal *when* said sensing tip contacts an object and said stylus holder is thereby deflected relative to said housing” (emphasis added) if *when*, applying its dictionary definitions, meant “at or after the time that”, “in the event that,” or “on the condition that” the patent was infringed. If, as the District Court construed it, *when* meant “as soon as contact was made and deflection occurred,” there was no infringement. In the patent specification, the patentee was preeminently generating a trigger signal as soon as possible. The patent specification made abundantly clear that *when* meant at the time of and not some appreciable time thereafter. *Renishaw PLC*, 158 F.3d at 1252. The *Renishaw PLC* Court applied the meaning set out in the specification, not the full range of ordinary meanings for the term *when*. The operation of the allegedly infringing probe sent a signal appreciably after contact with the workpiece and initial deflection. There was, therefore, no infringement.

In *Altiris* the Federal Circuit relied on *CCS Fitness* in affirming the District Court's claim construction of the claim term *automation code*—“means the code in the

automation partition which loads an operating system, LAN drivers for the resident NIC, and a program for reading a database on the network server to ascertain the automation commands to be executed.” See *Altiris, Inc. v. Symantec Corp.*, 318 F.3d 1363, 1374 (Fed. Cir. 2003). When interpreting the phrase, the District Court had relied in part on the specification definition because “this phrase is not commonly used in the industry and the claim language is not clear.” *Id.* The Federal Circuit tried to apply an ordinary meaning and concluded that there was not a clear definition. The Federal Circuit ultimately agreed with the District Court that the specification definition controlled, stating “the patentee chose a phrase that ‘so deprives the claim of clarity as to require resort to other intrinsic evidence for a definite meaning,’” citing *CCS Fitness*, 288 F.3d at 1366–1367 (citations and internal quotation marks omitted).

As illustrated by *Renishaw PLC* and *Altiris*, when construing the words of a patent claim one seeks to find meanings that fit with the discussion in the patent specification. Moreover, words such as *when* in *Renishaw PLC* imply time but do not by themselves define the time scale. The possible definitions of *when* discussed above demonstrate the variability inherent in language. This can lead an inventor to select a particular word and a particular meaning of that word to describe the invention. Words, however, must be used in the same way in both the claims and the specification. See *Autogiro Co. of America v. United States*, 384 F.2d 391, 397 (Ct. Cl. 1967). Consistency, then, can play a crucial role in establishing the scope of patent claims.

## Means-Plus-Function Format

An element of a patent claim may be expressed as a means or step for performing a specialized function without reciting the structure, material, or acts supporting the means or step of that function. This language is most often employed in claims to apparatus to define a portion of the apparatus in terms of its function, rather than reciting a list of possible structural elements. If means-plus-function language is used, the patent claim is construed to cover the corresponding structure, material, or acts described in the patent specification and their equivalents. For example, a volume control means for a stereo could include a knob, a sliding switch, or a remote control, if they were described in the patent specification. These claim elements are known as means-plus-function (or step-plus-function in method claims) terms. The means-plus-function language is specifically governed by statute, 35 U.S.C. § 112, ¶ 6. In fact, “a claim

limitation that employs the language ‘means...for’ invokes a rebuttable presumption that § 112, ¶ 6 applies.’ See *Gemstar-TV Guide Int’l, Inc. v. ITC*, 383 F.3d 1352, 1369 (2004) (citing *CCS Fitness, Inc. v. Brunswick Corp.*, 288 F.3d 1359, 1369 (Fed. Cir. 2002)).

To construe a means-plus-function term a court first identifies the function of the means-plus-function term. The second step is to identify the corresponding structure disclosed in the specification. See *Micro-Chem, Inc. v. Great Plains Chem. Co.*, 194 F.3d 1250, 1258 (Fed. Cir. 1999). “Structure disclosed in the specification is ‘corresponding’ structure only if the specification or prosecution history clearly links or associates that structure to the function recited in the claim.” *B. Braun Med. Inc. v. Abbot Labs*, 124 F.3d 1419, 1424 (Fed. Cir. 1997).

Means-plus-function or step-plus-function language in patent claims, while permitted by 35 U.S.C. § 112, sixth paragraph, is a convenience for the patentee. Using this language allows a patentee to define the claim term and the opportunity to identify a wide variety of structures, materials, or acts that correspond to the function. The patentee is then not necessarily limited to the *ordinary* meaning of the words in the means-plus-function or step-plus-function language. The price that must be paid for that convenience is the limiting of the claim to the means specified in the specification and their equivalents. See, *O.I. Corp.*, 115 F.3d at 1583 and *B. Braun*, 124 F.3d at 1424.

## TERMINOLOGY IN NANOTECHNOLOGY PATENT CLAIMS

The words of a claim are generally given their ordinary and customary meaning, which is the meaning that the term would have to a person of ordinary skill in the art in question at the time of the invention. *NTP, Inc. v. Research In Motion, Ltp.*, 418 F.3d 1282, 1293 (Fed. Cir. 2005). Without encountering any of the situations that narrow a claim term as discussed above, this definition can be quite broad. Certainly a patentee wants the scope of its patent claims to be construed as broadly as possible. Breadth of patent protection, however, does not always follow from broad or imprecise claim language. For nanotechnology inventions, the words used to describe the technology are quite often words that do not themselves indicate any particular size, much less the nanoscale. Yet, with nanotechnology, patentability often lies in the size of the invention. To those in traditional technologies, it may seem somewhat ironic that a patent applicant’s own actions (acting as a lexicographer, distinguishing the prior art, using means-plus-function, or defining a term such that it undermines the claim’s clarity) may constrict the

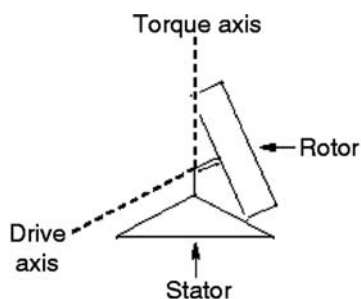
meaning of a claim term. But, for nanotechnology, a more strategic approach suggests itself—to view these traditional limitations on claim language as tools and to use them to uniquely define the patentable, nanoscale aspects of the invention. This strategic approach points to three additional considerations for patenting nanotechnology that have not been discussed above.

## Clarity of Language Does Not Mean Narrow Patent Claims

By statute, the claims of a patent must particularly point out and distinctly claim applicant’s invention. 35 U.S.C. § 112, second paragraph. Clearly defining the important aspects of the invention provides distinctness that strengthens patentability and clarity in claim scope for patent infringement. This does not mean that every aspect of an invention should be defined with the utmost detail. Using clear, appropriate technical language to describe technology does not necessarily narrow claim scope. Narrow patent claims result from overloading the claim with unnecessary details (referred to as elements or limitations of the claim)—ones that may be impossible to prove for infringement. Robust patent claims come from appropriately defining the technical features of the invention that give patentability and must be present in an infringing device. For nanotechnology, this will often mean clearly stating the nanoscale features of the invention. Other more general features, those not necessary for patentability but which describe or give context to the invention, may be included in the claim but without all their particulars.

Breadth in patent claims comes from having fewer limitations or elements in the patent claim. A patent claim having elements A, B, and C is broader than a patent claim having elements A, B, C, D, and E. The former recites only three elements necessary for infringement while the latter requires the presence of five. Well chosen claim language provides clarity as to what the claim elements are and does not necessarily sacrifice claim scope.

Related to the need for clearly defined terms, one can structure patent claims based on the inventive concept, not just the nanoscale structure. For nanotechnology, the inventive concept may be constructing a device that functions at the nanoscale. To write effective patent claims to cover that nanoscale device, focus not only on the structure and components of the device but also on its size and function. Consider how to get the key, patentable concept or function into the patent claims. For example, a *nanomotor*, such as in Fig. 2, may have turn based on the rotation of atom groups about a chemical bond. A patent claim that showed the chemical structure would be appropriate



Components of molecular motor design

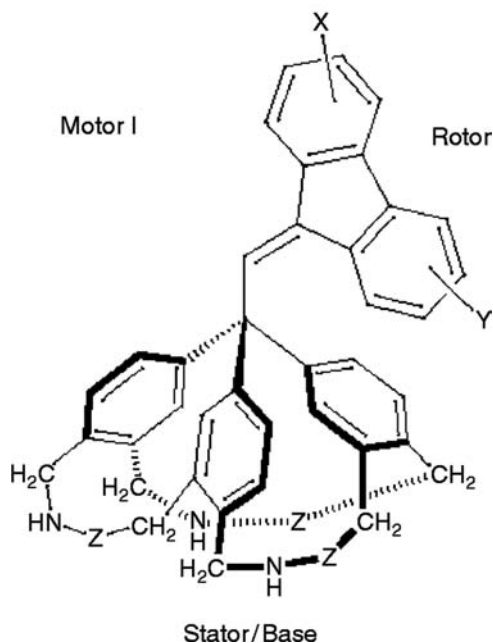


Fig. 2 Molecular motor design. Courtesy of the University of Nevada-Reno. Patent application pending.

for that nanomotor but could be limited to the specific chemical structure shown in the patent claim. Adding another patent claim where the nanomotor has rotation about a carbon-carbon single bond, for example, to provide mechanical drive provides a broader, functional scope in contrast to the claim limited to the specific chemical structure. This latter claim identifies the nanoscale in terms of the carbon-carbon bond and gives the function of the motor, “to provide mechanical drive.”

### Choosing to Define a Term

If an inventor chooses another, more limited, meaning for a claim term, then the inventor should choose deliberately and wisely. Being conscious of this choice and why it was made results in better patent application and claim drafting, as well as in potentially simplifying examination of the application and determining infringement of the eventual patent. For nanotechnology, specifically defining a term may be done not just to have clarity and certainty but also to focus on the patentable feature(s) of the invention, to exclude previously known macroscale devices. For example, Fig. 3 shows a cantilever device. Cantilevers are well known and come in all different sizes. The cantilever device in Fig. 3, however, is a nanoscale cantilever, a *nano-cantilever*. *Nano-cantilever* defines the scale of the cantilever. But, it is the uniquely defined nano-scale wires forming the cantilever that are the focus on the invention and carry the weight of patentability.

If a term is uniquely defined, a patent applicant should consider including a definition of the term in the specification. As a patent application evolves during preparation, the usage and definition of key terms should be checked to determine whether the claim terms still match their original, defined meaning or if

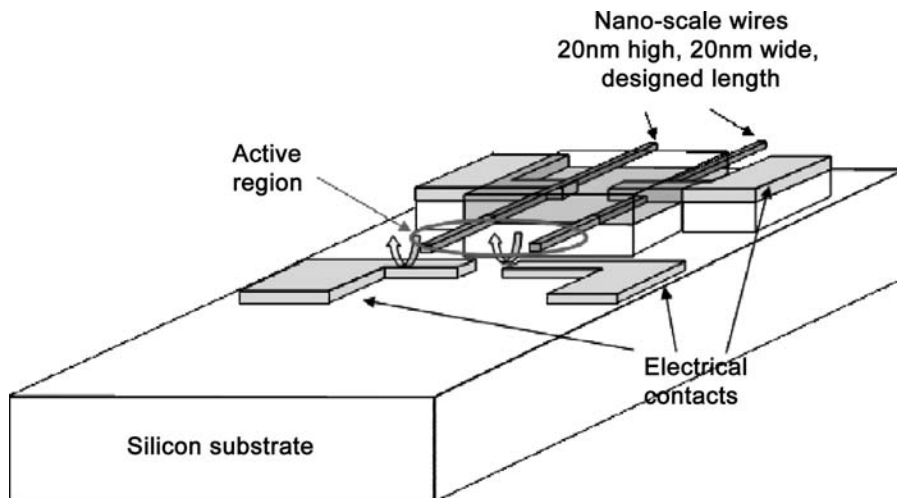


Fig. 3 Schematic of nano-cantilever using nano-scale wires and with built-in and bottom electrodes arrangement. Courtesy of Nano-Horizons, Inc., State College, PA, [www.nanohorizons.com](http://www.nanohorizons.com) Patent application pending.

editing or redefinitions is needed. It is important that the inventor(s) review both the specification and the patent claims to be satisfied with the claim language and its meaning.

### The Need for Consistency from Beginning to End

Whether a claim term is specifically defined in the patent specification or simply occurs in the patent specification and the patent claims, another key to preserving its fullest and intended meaning is consistency. This has been mentioned above, but further comment is warranted. To the extent possible, all words used in a patent claim should be used consistently, not only in the patent specification, but also in all correspondence with the USPTO. One should avoid the temptation to restate a term or limitation using different words to vary writing style (whether in drafting the application or corresponding with the USPTO). Variation in wording does not necessarily add breadth to a defined term, but it often adds ambiguity. Avoid using synonyms just for the sake of variety. Broadly, but clearly, defining a term is the appropriate way to add breadth. With the exception of identifying structures, materials, steps, etc. in the context of means-plus-function claims, listing or using alternative language for claim terms can limit the terms such that they will not reach the fullest intended meaning. It is the language of the patent claims that controls the scope of patent protection. It is that language that should be used consistently throughout the patent application and patent examination process.

### PATENTING NANOTECHNOLOGY— CONCLUSION

Nanotechnology seeks to take advantage of the unique structures, the unique properties, and the unique processes that can occur in the space of 1–100 nm. As nanotechnology advances on these nanoscale frontiers, barriers will be overcome and inventions will, undoubtedly, result, and nanotechnology patent applications will be filed. Patents are intellectual property rights in technology. In a patent, the inventive technology must

be described and then the boundaries of the intellectual property right set out in the patent claims. Thus, in a patent, the precision of science and technology takes on the imprecision of language and defines a legal property right. Using language to describe any technology then presents a challenge. Using language to describe nanotechnology, as it continues to emerge and become established, presents an even greater challenge. Yet, to obtain a patent, nanotechnology inventions must be described and claimed. Language is the only means to do this.

In patent claims, the words used are presumed to take on their full meaning. Often the common meaning of a word is just what is intended. For nanotechnology, however, the meaning of a word may not carry the needed or intended nanoscale aspects. The meaning may simply be too big for the nanotechnology invention. This requires one to consider the meaning of the words one uses to describe and claim nanotechnology inventions. An inventor should expect to be held to the words in the patent application. An inventor is not, however, left without tools to describe and claim the invention. Acting as his own lexicographer, an inventor can define the terms necessary for the invention. For nanotechnology, words can be chosen and defined to reflect the nanoscale aspects of the invention and its patentability. Choosing and defining appropriate terms for inventions in nanotechnology, and using them consistently in the patent specification, claims, and during examination, will yield strong, clear patents—ones that will provide the necessary foundation to not only patent but to also commercialize nanotechnology.

### ACKNOWLEDGMENTS

The views expressed here are the author's own views and should not be attributed to Nixon Peabody, LLP or any of its clients.

### REFERENCES

1. NSTC Definition of Nanotechnology June 12, 2000.
2. <http://www.uspto.gov/go/classification/uspc977/defs977.htm>.



# Permanent Magnets Based on Nanostructured Intermetallic Alloys

Paul McGuinness  
Andraž Kocjan  
Spomenka Kobe

*Department for Nanostructured Materials, Jožef Stefan Institute,  
Ljubljana, Slovenia*

## Abstract

Permanent magnets are vital components in many technologies, ranging from computers and domestic appliances, to many automotive, medical, and industrial applications. In simple terms, a stronger permanent-magnet material will make it possible to produce a smaller device that is capable of carrying out the same task; this is true for both static, holding applications and applications where the magnet is used in combination with electricity to produce movement. Since the development of the first steel magnets at the beginning of the 20th century, the improvements in permanent-magnet materials have been astonishing. The figure of merit used to describe the strength of a magnet, the  $BH_{\max}$ , has increased from around 4 MGOe to over 50 MGOe.

These tremendous improvements have come about as a result of discovering better materials and better methods of processing. The most recent generations of permanent magnets, which are based on a combination of one or more rare earths and transition metals like iron and cobalt, can be produced using a wide variety of methods, such as sintering, melt spinning, deposition techniques, chemical techniques, gas atomization and mechanical alloying, and result in materials with a wide range of properties. In this overview we will look at permanent magnets based on nanostructured intermetallic alloys, their properties, and their methods of production.

## HISTORICAL INTRODUCTION TO PERMANENT MAGNETS

Before the invention of the electromagnet by Sturgeon in 1925, the only permanent-magnet materials were the naturally occurring lodestone, a form of magnetite  $Fe_3O_4$ , and various forms of iron-carbon alloys. Many of these early magnets were built up from wires or strips, since these were easily magnetized by stroking them with another magnet.

The development of modern permanent magnets can be said to have begun around the end of the 19<sup>th</sup> century, with the introduction of the steel magnet.<sup>[1]</sup> The next step forward in the story of permanent magnets was made when it was realized that larger values of magnetic anisotropy were needed to produce higher coercivities. The coercivity of a permanent magnet is its ability to withstand the effects of an opposing magnetic field. These high anisotropies were found in materials that had highly anisotropic crystal structures and hexagonal or tetragonal symmetries.<sup>[2]</sup> A good example of a material with this type of structure is the common, household ferrite magnet. This is the type of magnet you will often find stuck to the door of a fridge, but is also the workhorse magnet for thousands of industrial, automotive, and domestic applications.

There were few developments in permanent magnets until the 1960s. The Second World War had seen advances in the separation and purification of rare earths, and with these metals now available, researchers began to look at combinations of rare earths and transition metals. The year 1967 saw the first reports of  $RCO_5$  (R = rare earth) materials with  $CaCu_5$ -type structures, which soon led to the commercial availability of  $SmCo_5$  magnets with properties that literally dwarfed those of ferrites,  $AlNiCos$ , and the steel magnets that had come before – albeit at a price.<sup>[3]</sup> Within a short time, it was realized that the magnetic properties of these  $SmCo_5$  magnets were being limited by the magnetization of the cobalt sub-lattice, and so a new type of magnet, based on  $R_2Co_{17}$ , quickly followed.<sup>[4]</sup> These Sm-Co magnets made possible a wide range of new applications and presented tremendous possibilities for miniaturization because of their enormous energy densities, but the high—and perhaps more importantly, the variable—price of cobalt was a problem. This situation became even worse with the cobalt crisis of 1979–1981.<sup>[5]</sup> The crisis was due to a rebellion in Zaire, source of about half of the world's cobalt, when many of the mines were flooded. The price of cobalt increased sixfold as a result, and this intensified the search for high-energy cobalt-free permanent-magnet materials. The first announcements

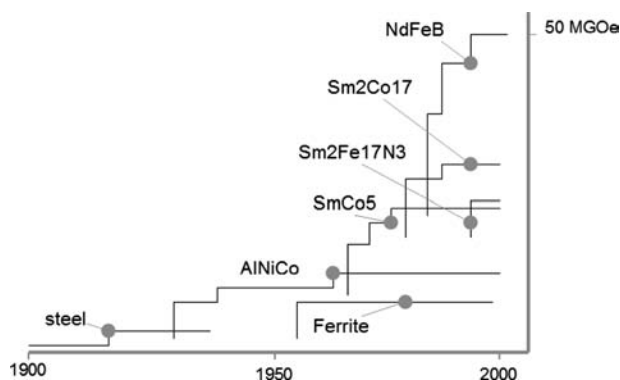


Fig. 1 Progress in permanent magnets, in terms of energy product.

of the successful production of magnets based on neodymium, iron, and boron were made at a meeting in Pittsburgh, PA, in 1983. At the same meeting, there were reports from Sumitomo Special Metals of Japan<sup>[6]</sup> and General Motors of the USA<sup>[7]</sup> of a new generation of permanent magnets based on a material with the chemical formula  $\text{Nd}_2\text{Fe}_{14}\text{B}$ . This Nd–Fe–B-type magnet was an improvement in many ways over the existing Sm–Co materials, and could be produced using a number of different techniques. The Japanese produced their Nd–Fe–B magnets via a relatively conventional powder-metallurgy sintering route, whereas the Americans had used a novel method called melt spinning. Within a few years, there were to be more reports of good magnetic properties from groups working with techniques such as mechanical alloying,<sup>[8]</sup> screen-printing,<sup>[9]</sup> sputtering,<sup>[10]</sup> ablation,<sup>[11]</sup> and techniques based on hydriding.<sup>[12]</sup>

One more major discovery has been made since the arrival of Nd–Fe–B, and that occurred in 1990, when a group in Ireland reported hard magnetic properties in nitrided Sm–Fe-based materials.<sup>[13]</sup> The  $\text{Sm}_2\text{Fe}_{17}\text{N}_3$  magnet had excellent properties, comparable in many ways to the market-leading Nd–Fe–B-based magnets, but difficulties associated with nitriding bulk samples have kept them from anything other than a niche market. A summary of the improvements made in permanent-magnet materials over the past 100 years can be seen in Fig. 1.

## PERMANENT-MAGNET PROPERTIES

To describe a permanent magnet quantitatively, we need to measure its magnetic properties. To do this, we subject the magnet to a large positive magnetic field, to saturate the magnet, and then we apply a large negative field to assess its ability to withstand a reverse magnetic field. This form of measurement

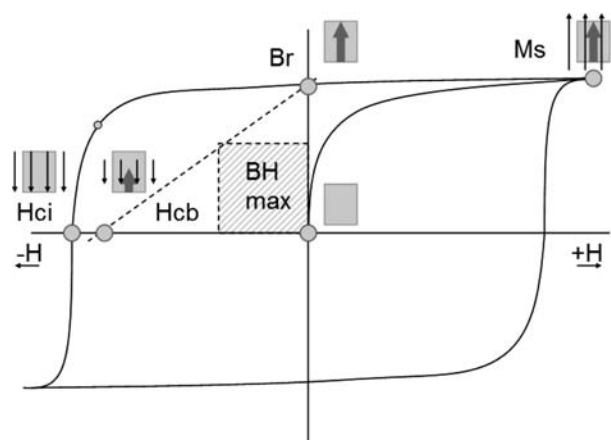


Fig. 2 Hysteresis loop of a permanent magnet.

is shown schematically in Fig. 2 and described in more detail later.

The measurement of the permanent magnet's properties begins with a completely demagnetized magnet in a zero magnetic field at the crossing point of the  $X$ -axis (the applied field) and the  $Y$ -axis (the magnetization of the sample). The state of the magnet is illustrated by the empty rectangle, i.e., the magnet is unmagnetized. The first part of the measurement involves applying a large positive magnet field ( $+H$ ). At this point, the magnet becomes fully saturated (note the arrow) while it exists in a large positive field. The next stage is to remove the applied field and look at the magnetization state of the magnet while there is no external field. With a good-quality magnet, the internal magnetization (the arrow) will remain, even in the absence of the applied field. This point on the  $Y$ -axis,  $B_r$ , is referred to as the remanence. This is followed by a demagnetization stage, where a negative field ( $-H$ ) is applied to the sample. With a sufficiently high field, the magnetization of the sample will be reduced to nothing (no arrow), and this field is referred to as the intrinsic coercivity,  $H_{ci}$ , of the magnet. For most permanent-magnet applications, we are looking for magnets with a high remanence and a high coercivity, although there are some applications when a very high coercivity would be disadvantageous. There is one other point that is important from the applications point of view, the normal coercivity,  $H_{cb}$ . This is the point where the external demagnetizing field is equal and opposite to the internal magnetization; the system, in effect, is equal to zero. This measurement is of more interest to electrical engineers than to material scientists, who are more interested in the material's performance than the performance of the system. In order that we can have a single quantity to describe the quality of a magnet, the term energy product (or  $BH_{max}$ ) has been introduced. To calculate the energy

product of a magnet, we draw a straight line from the remanence point to the normal coercivity and then measure the area of the largest rectangle that we can fit under this line. The best Nd–Fe–B magnets have energy products in excess of 50 MGOe (mega Gauss Oersted), typical Sm–Co magnets are in the range 25–30 MGOe, and ferrites are about 4 MGOe.

### COERCIVITY AND MICROSTRUCTURE IN NANOSTRUCTURED PERMANENT MAGNETS

The origin of the coercivity in all rare-earth–transition-metal permanent magnets is their high easy-axis magnetocrystalline anisotropy. However, since the coercivity remains well below the value of the anisotropy field, by a factor of about 4, the coercivity is clearly also very dependent on the nano/microstructure, with magnetization reversal being the result of the nucleation and growth of reverse magnetic domains. Sintered Nd–Fe–B magnets show two main coercivity characteristics that suggest that the coercivity mechanism is one of nucleation and growth rather than a pinning-type mechanism: unmagnetized magnets have many domains per grain, and the coercivity increases with the size of the field used to magnetize the magnet.<sup>[14]</sup> To generate high coercivities under such conditions, it is important to produce materials with a small grain size, thereby limiting the surface areas of individual grains. This is in stark contrast to permanent-magnet materials like the Sm<sub>2</sub>Co<sub>17</sub>-type magnets, where large coercivities can be generated in cast-and-annealed ingots with very large grains, and where the mechanism of the coercivity is related to the pinning of domains within the volume of the grains by precipitates.<sup>[15]</sup>

### PROCESSING INTERMETALLIC PERMANENT MAGNETS

Nd–Fe–B permanent magnets are multiphase metallic structures. Irrespective of the processing route employed to produce them, the starting point is nearly always an as-cast alloy with a composition in the region of Nd<sub>15</sub>Fe<sub>77</sub>B<sub>8</sub>. The aim when processing Nd–Fe–B magnets is twofold:

- First, reducing the grain size down to micro/nano-sizes, thereby maximizing the potential coercivity of the sample.
- Second, orienting the grains as much as possible so that the *c*-axes (which are the easy magnetic axes) of the grains are pointing in the same direction, thereby maximizing the potential remanence of the sample.

This is shown in Fig. 3, where Fig. 3A shows schematically a typical as-cast microstructure for a Nd–Fe–B alloy with a composition of Nd<sub>15</sub>Fe<sub>77</sub>B<sub>8</sub>, cast into a mold containing about 10–15 kg of material, and Fig. 3B shows schematically an idealized magnet nano/microstructure with grains in the range of 100–1000 nm.

### PROCESSING Nd–Fe–B MAGNETS VIA THE SINTERING ROUTE

From the commercial point of view, sintering is the most important method for producing Nd–Fe–B magnets; however, these magnets are better described as “micro” rather than nanostructured, and so we will not discuss them in any detail here. The reader is

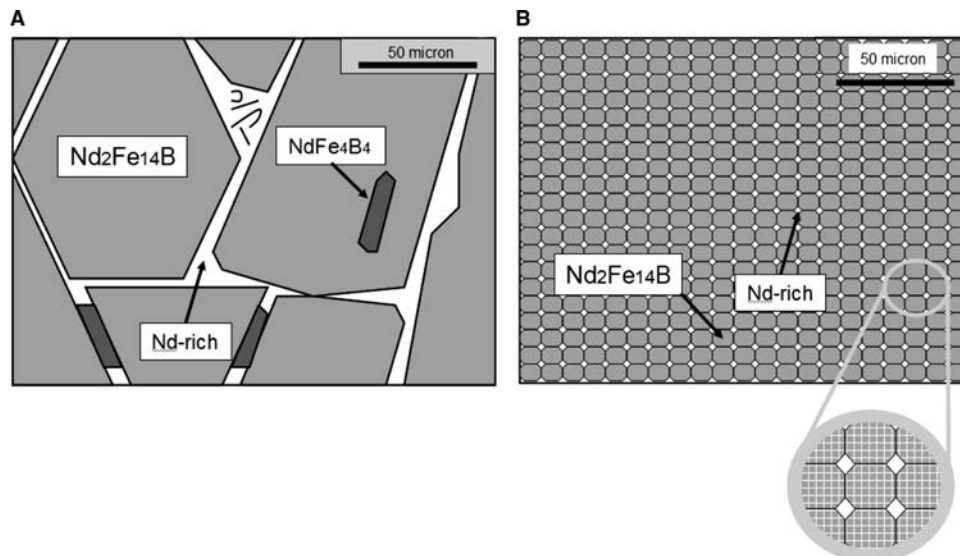


**Fig. 3** (A) Schematic microstructure of Nd<sub>15</sub>Fe<sub>77</sub>B<sub>8</sub> cast alloy. (B) Schematic micro/nanostructure of idealized permanent magnet.

referred to the extensive literature for more information on sintered Nd–Fe–B magnets.<sup>[16–18]</sup>

## PROCESSING Nd–Fe–B MAGNETS VIA THE MELT-SPINNING ROUTE

The melt-spinning production route, unlike the powder-metallurgy sintering route, was not used for previous generations of permanent magnets. The combination of melt spinning and Nd–Fe–B-type magnets was pioneered by General Motors in the USA, a development that ran in parallel with Sumitomo Special Metals' research on the sintered route for Nd–Fe–B.

In the melt-spinning process, a jet of molten alloy comes from material in an induction-melting crucible and hits a rapidly rotating water-cooled copper wheel. Under such conditions, cooling rates can be as high as  $10^6$  K/s. The Nd–Fe–B alloy tends to form in the shape of ribbons, a few centimeters long and about  $30\ \mu\text{m}$  thick, which are then thrown from the copper wheel and collected a meter or so away in a hopper. As with the sintering process, everything is carried out in a protective, inert atmosphere. A schematic diagram of the melt-spinner and some crushed Nd–Fe–B ribbons are shown in Fig. 4A and 4B.

The usual procedure involves over-quenching the ribbons to produce a largely amorphous structure, and then heat treating them at  $600\text{--}700^\circ\text{C}$  to produce  $\text{Nd}_2\text{Fe}_{14}\text{B}$  grains that are  $100\text{--}500\ \text{nm}$  in size. The grain size of melt-spun magnets tends to be smaller than with sintered magnets, but this is a consequence of many factors, not least of which is the radically different processing route. The most important feature of Nd–Fe–B melt-spun ribbons is that they are completely isotropic, i.e., there is no preferred orientation of the  $c$ -axes in the material, leading to relatively low values for the remanence. Nevertheless, the simplicity of the ribbon-production process, the intrinsic stability of the

ribbons in the atmosphere, and the ease with which these materials can be mixed with polymers and other binders and molded into intricate shapes makes them a very attractive material.<sup>[19]</sup>

## HOT PRESSING MELT-SPUN RIBBONS

These Nd–Fe–B melt-spun ribbons are also suitable for hot pressing. In such a process, the ribbon pieces are placed in a die and compacted under high loads and temperatures in the range  $700\text{--}800^\circ\text{C}$  to form 100%-dense solids. Of course, since there is no possibility of aligning the grains in a magnetic field, these materials are still isotropic, but their high density gives them an advantage over the polymer-bonded variants.<sup>[20]</sup>

## DIE-UPSET FORGING OF MELT-SPUN RIBBONS

A third possibility is to die-upset forge the compacted melt-spin ribbons.<sup>[21,22]</sup> This rather expensive process involves first of all producing a straightforward 100%-dense solid from the ribbons as described earlier, and then re-pressing the dense compact in an over-sized die, causing the material to flow in a direction perpendicular to the direction of pressing. The two hot-pressing techniques are illustrated in Fig. 5A and 5B.

This flow under pressure at high temperatures causes the material to become highly oriented along the pressing direction. This reorientation is the result of the growth of favorably oriented nanostructured grains in combination with grain-boundary sliding, boundary diffusion, and diffusion slip. The process can be enhanced by small additions of elements such as gallium,<sup>[23]</sup> although die-upsetting ratios of about 4, i.e., the compact must be reduced to a quarter of its original height, are required.

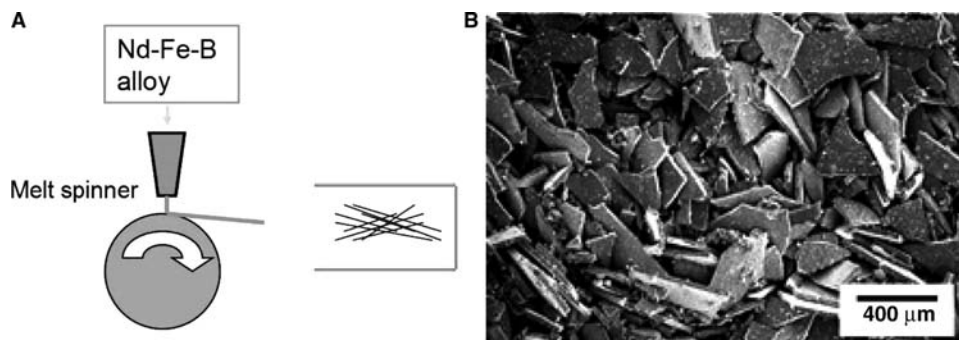


**Fig. 4** (A) Schematic diagram of melt-spinner. (B) Crushed melt-spun ribbons of Nd–Fe–B.

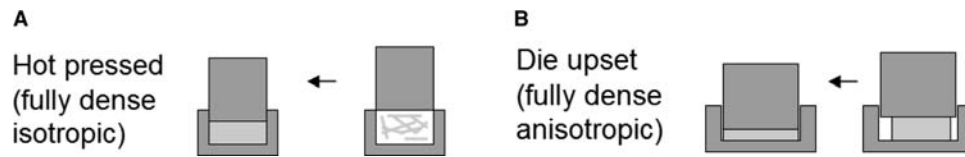
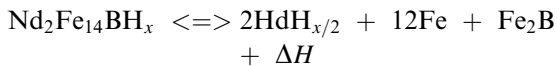


**Fig. 5** (A) Hot pressing of melt-spun powder to produce a fully dense isotropic magnet. (B) Die-upset forging of a fully dense isotropic magnet to produce an anisotropic magnet.

### PROCESSING Nd–Fe–B AND Sm–Fe–N MAGNETS VIA THE HYDROGENATION–DISPROPORTIONATION–DESORPTION–RECOMBINATION ROUTE

A third method for producing nanostructured permanent magnets from a starting material of as-cast alloy is called the hydrogenation–disproportionation–desorption–recombination process, or HDDR process.<sup>[24–31]</sup> The process involves heating the as-cast alloy in an atmosphere of hydrogen to about 700–750°C, holding for a period of minutes to hours, and then cooling the material to room temperature in vacuum. During the first stage of the process, the material reacts with hydrogen to form interstitial hydrides and a lot of cracks form in the material due to the expansion of the crystal lattice with the formation of the hydrides. However, as the temperature increases, these hydrides become unstable and the material disproportionates to form iron, ferroboron, and neodymium hydride. The disproportionation reaction can be represented as:



where  $\Delta H$  is the heat of reaction. The value of  $x$  is dependent on the hydrogen pressure used and the exact composition of the starting alloy.

The disproportionated mixture consists of a nano-dispersed mixture of iron, neodymium hydride, and ferroboron. During the second stage of the process, when the material is subjected to vacuum conditions at high temperature, the neodymium hydride desorbs to form neodymium metal, which then leads to the neodymium, iron, and ferroboron recombining to form large amounts of nanostructured  $\text{Nd}_2\text{Fe}_{14}\text{B}$  phase, together with some Nd–Fe intergranular material, only now the grain size of the  $\text{Nd}_2\text{Fe}_{14}\text{B}$  phase is in the 100–500 nm range. In simple terms, the HDDR process converts a coarse-grained as-cast material into a powdered nanostructured material via a reversible chemical reaction involving hydrogen. The process is shown schematically in Fig. 6.

As with melt-spinning, the process is intrinsically isotropic, and the resulting nanostructured HDDR powders tend to have remanences close to about half of the saturation magnetization; however, in the case of the HDDR process, it is possible to produce anisotropic material with the use of additives like zirconium,<sup>[32]</sup> hafnium,<sup>[33]</sup> and gallium,<sup>[34]</sup> and closely

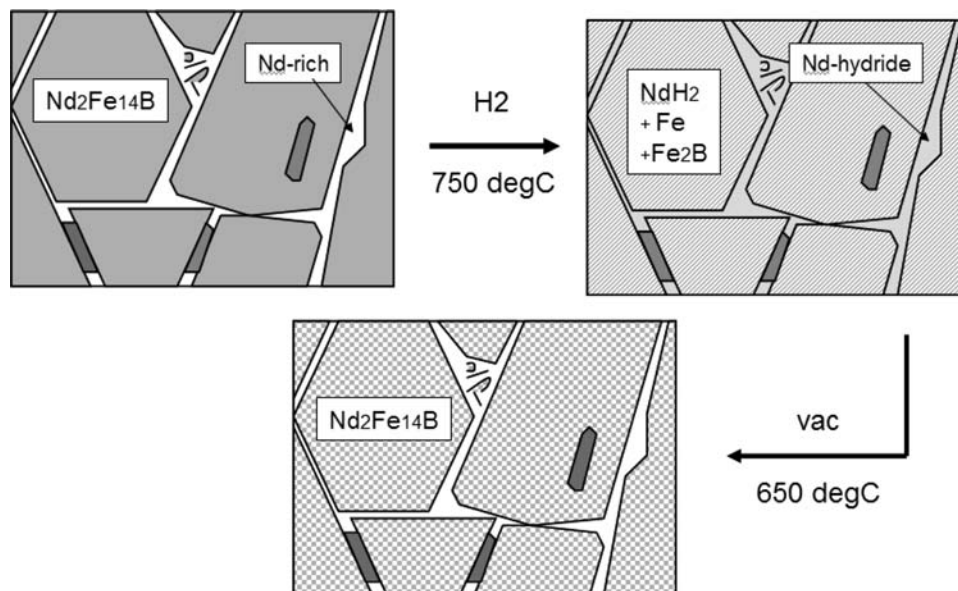


**Fig. 6** Schematic representation of the hydrogenation–disproportionation–desorption–recombination (HDDR) process.

controlled processing conditions.<sup>[35]</sup> HDDR-processed powder is also very suitable for hot pressing fully dense magnets in a procedure similar to that used for the melt-spun ribbons.<sup>[36]</sup>

## OTHER PROCESSING TECHNIQUES

Nd–Fe–B materials are remarkable in many ways, but perhaps their most remarkable characteristic is the number of different methods that can be used to produce high-coercivity permanent magnets from basically the same starting material. From the commercial point of view, the three techniques already discussed – sintering, melt-spinning, and HDDR – are the most important, but from the research perspective techniques like rapid casting,<sup>[37]</sup> hot working,<sup>[38]</sup> mechanical alloying,<sup>[39]</sup> laser ablation,<sup>[40]</sup> pulsed-laser deposition,<sup>[41]</sup> rotary forging,<sup>[42]</sup> gas atomization,<sup>[43]</sup> and explosive compaction,<sup>[44]</sup> have provided valuable insights into the capabilities and limitations of nanostructured magnets produced from the Nd–Fe–B system. From the purely scientific aspect, the most interesting nanostructured magnets produced from rare-earth–transition-metal intermetallics are exchange-coupled magnets.<sup>[45]</sup> These magnets will be described in the next section.

## EXCHANGE-COUPLED MAGNETS

Nanocomposite exchange-coupled magnets consisting of a fine mixture of magnetically hard (to provide high coercivity) and soft (to provide high magnetization) phases have attracted a lot of attention because of their remarkable magnetic properties. The exchange coupling between the two phases causes the magnetization vector of the soft phase to align with that of the hard phase, leading to a remanent magnetization of more than half of the saturation magnetization in a crystallographically isotropic structure, and this high remanence is combined with a good coercivity. Because of this, it is possible to achieve a higher  $BH_{\max}$  than with conventional isotropic uncoupled magnets.

## THE NANOSTRUCTURE–PROPERTY RELATIONSHIP IN EXCHANGE-COUPLED MAGNETS

It has been demonstrated by theory and with micro-magnetic modelling simulations<sup>[46]</sup> that the magnetic properties of nanocomposite magnets depend strongly on the intrinsic magnetic properties of the phases present and on the nano/microstructural features. Earlier studies<sup>[47]</sup> showed that in such a microstructure,

the hard and the soft phase would be exchange-coupled if the sizes of both the soft and the hard phases are of the order of twice the domain wall-width of the hard phase, which is less than 10 nm for most hard phases. Fischer et al.<sup>[48]</sup> predicted that  $M_r$  and  $H_c$  would decrease with increasing grain size and that the magnetic properties are degraded by a non-uniform nano/microstructure. Therefore, it is very important to develop a uniform nano/microstructure with very fine soft-phase grains, which are uniformly distributed in the nanocomposite magnets to obtain optimum coupling. This can be achieved by optimizing both the composition and the processing parameters.

The magnetization-reversal process in nanocomposite magnets is more complicated than with conventional magnets owing to the coexistence of the exchange-coupled hard and soft phases. The overall anisotropy constant is reduced by the soft phase, and so the coercivity is controlled by the nucleation of the reversed domains in the soft phase. This nucleation field would be very low if there was no exchange coupling between the hard and the soft phases. But, in fact, the exchange coupling significantly increases the nucleation field and thus preserves a reasonably high coercivity. This effect is generally known as exchange hardening.

## NANOPHASE MAGNETS BASED ON COBALT OR IRON AND PLATINUM

CoPt and FePt have emerged as candidates for high-performance exchange-coupled magnets with enhanced magnetic properties. Both materials have high anisotropies ( $4.9 \times 10^6 \text{ J/m}^3$  and  $6.6 \times 10^6 \text{ J/m}^3$ , respectively). However, the FePt system has the advantage of complete solid solubility at higher temperatures, and at lower temperatures the crystal structure transforms from FCC to a face-centered tetragonal structure, which has improved hard magnetic properties due to the increased anisotropy.

Zhou et al.<sup>[49]</sup> investigated improvements in the properties of FePt through exchange-coupled FePt–Fe layered films prepared by magnetron sputtering. In FePt thin films, a maximum energy product of up to  $BH_{\max} = 15 \text{ MGOe}$ , was obtained, and with CoPt thin films a maximum energy product of up to  $BH_{\max} = 50 \text{ MGOe}$  was observed.

Huang et al.<sup>[50]</sup> investigated the fabrication and magnetic properties of FePt/C films containing FePt nanoparticles to increase the coercivity when compared with normal FePt thin films. The films were produced with FePt particle sizes in the range 3–20 nm. For the films with the smallest particle sizes, the blocking temperature, which marks the boundary between hysteretic and non-hysteretic behaviour, was found to



be 200 K. For films with larger particle sizes, the blocking temperature is higher. Once the particle sizes were such that the blocking temperature was above room temperature, it was found that the coercivities were greater for the films with larger particles. A coercivity of  $1.84 \times 10^6$  A/m (23 kOe) was obtained for the 8 nm diameter particles and a coercivity of  $2.72 \times 10^6$  A/m (34 kOe) for the 15-nm diameter particles. It was also found that by depositing FePt simultaneously with carbon, the structure of the films could be controlled so that a strong perpendicular anisotropy can be produced in the films, suitable for magnetic recording-media applications.

## SUMMARY

This has been a brief overview of the processing of permanent magnets based on nanostructured alloys and the relationships between processing, nano/microstructure, and magnetic properties. We have looked mainly at the Nd-Fe-B ternary material because it is the most flexible in terms of processing – sintering, melt-spinning, and the HDDR process – and produces high-quality nanostructured magnets with useful properties for many applications.

## REFERENCES

- Petrie, R. Permanent magnet material from loadstone to rare earth cobalt, Proceedings of the Electrical/Electronics Insulation Conference, 1995, 63–64.
- Kirchmayr, H.R. Permanent magnets and hard magnetic materials. *J. Phys. D: Appl. Phys.* **1996**, *29* (11), 2763–2778.
- Strnat, K.J. Hard-magnetic properties of rare earth – transition metal alloys. *IEEE Trans. Magn.* **1972**, *MAG-8* (3), 511–516.
- Schaller, H.J.; Craig, R.S.; Wallace, W.E. Magnetic characteristics of some binary and ternary 2 – 17 compounds. *J. Appl. Phys.* **1972**, *43* (7), 3161–3164.
- Wargo, J.G. Cobalt – a supply crisis. *Min. Congr. J.* **1979**, *65* (4), 38–40.
- Sagawa, M.; Fujimura, S.; Yamamoto, S.; Matsuura, Y.; Hiraga, K. Permanent magnet materials based on the rare earth – iron – boron tetragonal compounds. *IEEE Trans. Magn.* **1984**, *MAG-20* (5 pt 2), 1584–1589.
- Croat, J.J.; Herbst, J.F.; Lee, R.W.; Pinkerton, F.E. Pr-Fe and Nd-Fe—based materials: a new class of high-performance permanent magnets. *J. Appl. Phys.* **1983**, *55* (6 pt 2A), 2078–2082.
- Schultz, L.; Wecker, J. Hard magnetic properties of Nd-Fe-B formed by mechanical alloying and solid state reaction. *Mater. Sci. Eng.* **1988**, *99*, 127–130.
- Speliotis, T.; Niarchos, D.; Falaras, P.; Tsoukleris, D.; Pepin, J. Nd-Fe-B thick films prepared by screen printing. *IEEE Trans. Magn.* **2005**, *41* (10), 3901–3903.
- Yamashita, S.; Ikeda, M.; Hara, K. Magnetic properties of Nd-Fe-B sputtered films. *IEEE Trans. J. Magn. Japan* **1988**, *3* (6), 440–441.
- Nakano, M.; Tutumi, S.; Fukunaga, H.; Jae Man Song. Preparation of Nd-Fe-B thin film magnets with high coercivity using laser ablation technique. *IEEE Trans. Magn.* **2001**, *37* (4 I), 2573–2575.
- McGuinness, P.J.; Harris, I.R.; Rozendaal, E.; Ormerod, J.; Ward, M. Production of a Nd-Fe-B permanent magnet by a hydrogen decrepitation/attritor milling route. *J. Mater. Sci.* **1986**, *21* (11), 4107–4110.
- Coey, J.M.D.; Sun, H. Improved magnetic properties by treatment of iron-based rare earth intermetallic compounds in ammonia. *J. Magn. Mater.* **1990**, *87* (3), 251–254.
- Givord, D.; Lu, Q.; Rossignol, M.F.; Tenaud, P.; Viadieu, T. Experimental approach to coercivity analysis in hard magnetic materials. *J. Magn. Mater.* **1990**, *83* (1–3), 183–188.
- Durst, K.-D.; Kronmüller, H.; Ervens, W. Investigations of the magnetic properties and demagnetization processes of an extremely high coercive Sm(Co, Cu, Fe, Zr)<sub>7.6</sub> permanent magnet: II. The coercivity mechanism. *Physica Status Solidi (A) Appl. Res.* **1988**, *108* (2), 705–719.
- Kirchmayr, H.R. Permanent magnets and hard magnetic materials. *J. Phys. D: Appl. Phys.* **1996**, *29* (11), 2763–2778.
- Higuchi, A.; Hirose, S. Sintered Nd-Fe-B permanent magnets. *IEEE Trans. Magn.* **1989**, *25* (5), 3555–3560.
- Sagawa, M. Fifteen years since the NdFeB magnet was presented. *Funtai Oyobi Fummatu Yakin/J. Japan Soc. Powder Metallurgy* **1999**, *46* (5), 457–462.
- Kramer, M.J.; Lewis, L.H.; Fabietti, L.M.; Tang, Y.; Miller, W.; Dennis, K.W.; McCallum, R.W. Solidification, microstructural refinement and magnetism in Nd<sub>2</sub>Fe<sub>14</sub>B. *J. Magn. Mater.* **2002**, *241* (1), 144–155.
- Fuerst, C.D.; Brewer, E.G. Hot-pressed Nd<sub>2</sub>Co<sub>14</sub>B magnets. *IEEE Trans. Magn.* **1989**, *25* (5), 4108–4110.
- Lee, R.W.; Brewer, E.G.; Schaffel, N.A. Processing of neodymium-iron-boron melt-spun ribbons to fully dense magnets. *IEEE Trans. Magn.* **1985**, *MAG-21* (5), 1958–1963.
- Wang, Y.R.; Guruswamy, S.; Panchanathan, V. Texture study in hot deformed magnequench NdFeB magnets. *J. Appl. Phys.* **1997**, *81* (8 PART 2A), 4450–4452.
- Steel, D.T.; Leonowicz, M.; Davies, H.A. Effect of gallium additions on the magnetic properties of die-upset forged Fe-Nd-B type melt spun alloys. *Mater. Lett.* **1995**, *23* (1–3), 43–46.
- Saje, B.; Kobe, S.; Platts, A.E.; Harris, I.R. Sm<sub>2</sub>Fe<sub>17</sub> alloy with Ta addition and the preparation procedure, EU Patent, 1996, No. 95907498.0-2211.
- Žužek, K.; McGuinness, P.J.; Kobe, S. Gaseous interactions with Sm-Fe and Sm-Fe-Ta intermetallic alloys. *J. Alloys Comp.* **1999**, *289*, 213–219.
- Žužek, K.; McGuinness, P.J.; Kobe, S. Bonded Sm-Fe-(Ta)-N materials produced via attritor milling and HDD. *J. Alloys Comp.* **1999**, *289*, 265–269.

27. Žužek, K.; McGuinness, P.J.; Dražić, G.; Kobe, S. Hydrogen absorption and desorption in Ta-doped SmFe-based alloys. *J. Alloys Comp.* **2002**, *345*, 214–220.
28. Rožman, K.Ž.; McGuinness, P.J.; Komelj, M.; Kobe, S. A kinetic evaluation of the disproportionation reaction in Sm-Fe-based materials. *J. Magn. Magn. Mater.* **2005**, *290–291* (PART 2), 1181–1183.
29. McGuinness, P.J.; Žužek, K.; Podmiljšak, B.; Kobe, S. Magnetic monitoring of the hydrogenation-decomposition-desorption-recombination process in SmFe-based alloys. *J. Appl. Phys.* **2002**, *93* (102), 6918–6920.
30. McGuinness, P.J.; Kobe, S.; Škulj, I.; Bollero, A.; Gutfleisch, O.; Devlin, E.J.; Niarchos, D. Coercivity variations with Pr- and Zr-substituted NdDyFeB-based HDDR powders. *J. Magn. Magn. Mater.* **2001**, *237* (3), 267–275.
31. Gutfleisch, O.; Harris, I.R. Fundamental and practical aspects of the hydrogenation, disproportionate, desorption and recombination process. *J. Phys. D: Appl. Phys.* **1996**, *29* (9), 2255–2265.
32. Faria, R.N.; Williams, A.J.; Harris, I.R. High anisotropy in Pr-Fe-Co-B-Zr HDDR powders. *J. Alloys Comp.* **1998**, *287* (1–2), L10–L12.
33. Takeshita, T.; Morimoto, K. Anisotropic Nd-Fe-B bonded magnets made from HDDR powders (invited). *J. Appl. Phys.* **1996**, *79* (8 PART 2A), 5040–5044.
34. Sugimoto, S.; Murai, H.; Koike, N.; Nakamura, H.; Book, D.; Tezuka, N.; Kagotani, T.; Inomata, K. Improvement of coercivity of anisotropic Nd-Fe-B HDDR powders by Ga addition. *J. Magn. Magn. Mater.* **2002**, *239* (1–3), 444–446.
35. Kwon, H.-W.; Kim, J.-H. Effect of hydrogen pressure on anisotropy of HDDR-treated Nd-Fe-B-type powder. *J. Magn. Magn. Mater.* **2006**, *304* (1), e222–e224.
36. Ragg, O.M.; Harris, I.R.; Nagel, H.; Böhm, P. Hot pressing Nd-Fe-B HDDR powders. *IEEE Trans. Magn.* **1996**, *32* (5 PART 2), 4395–4397.
37. Morimoto, K.; Kato, K.; Igarashi, K.; Nakayama, R. Magnetic properties of anisotropic Nd-Fe-B HDDR powders prepared from strip cast alloys. *J. Alloys Comp.* **2004**, *366* (1–2), 274–278.
38. Nozieres, J.P.; Perrier de la Bathie, R.; Taylor, D.W. Permanent magnets prepared by hot working cast ingots of NdFeB. *J. Magn. Magn. Mater.* **1989**, *80* (1), 88–92.
39. Zhang, Z.-D.; Liu, W.; Sun, X.K.; Zhao, X.-G.; Xiao, Q.-F.; Sui, Y.-C.; Zhao, T. Structure and magnetic properties of Nd-Fe-B-Ti prepared by mechanical alloying. *J. Magn. Magn. Mater.* **1989**, *184* (1), 101–105.
40. Nakano, M.; Tsutsumi, S.; Fukunaga, H. Magnetic properties of Nd-Fe-B thick-film magnets prepared by laser ablation technique. *IEEE Trans. Magn.* **2002**, *38* (5 I), 2913–2915.
41. Nakano, M.; Katoh, R.; Fukunaga, H.; Tutumi, S.; Yamashita, F. Fabrication of Nd-Fe-B thick-film magnets by high-speed PLD method. *IEEE Trans. Magn.* **2003**, *39* (5 II), 2863–2865.
42. Rowlinson, N.; Ashraf, M.M.; Harris, I.R. Anisotropy induced by the rotary forging of rapidly quenched Nd-Fe-B ribbons. *J. Magn. Magn. Mater.* **1990**, *87* (1–2), 1990.
43. Branagan, D.J.; Burch, J.V.; Sellers, C.H.; Hyde, T.A. Processing of Nd-Fe-B alloys by inert gas atomisation. *Powder Metallurgy* **1998**, *41* (3), 165–X.
44. Ando, S.; Mine, Y.; Takashima, K.; Itoh, S.; Tonda, H. Explosive compaction of Nd-Fe-B powder. *J. Mater. Process. Technol.* **1999**, *85* (1–3), 142–147.
45. Miao, W.F.; Ding, J.; McCormick, P.G.; Street, R. Structure and magnetic properties of mechanically milled Nd<sub>2</sub>xFe<sub>100-3xBx</sub> (x = 2–6). *J. Alloys Comp.* **1996**, *240* (1–2), 200–205.
46. Tako, K.M.; Schrefl, T.; Wongsam, M.A.; Chantrell, R.W. Finite element micromagnetic simulations with adaptive mesh refinement. *J. Appl. Phys.* **1997**, *81* (8 PART 2A), 4082–4084.
47. Kneller, E.F.; Hawig, R. The exchange-spring magnet: A new material principle for permanent magnets. *IEEE Trans. Magn.* **1991**, *27* (4), 3588–3600.
48. Fischer, R.; Schrefl, T.; Kronmüller, H.; Fidler, J. Grain-size dependence of remanence and coercive field of isotropic nanocrystalline composite permanent magnets. *J. Magn. Magn. Mater.* **1996**, *153* (1–2), 35–49.
49. Zhou, J.; Skomski, R.; Li, X.; Tang, W.; Hadjipanayis, G.C.; Sellmyer, D.J. Permanent-magnet properties of thermally processed FePt and FePt-Fe multilayer films. *IEEE Trans. Magn.* **2002**, *38* (5 I), 2802–2804.
50. Huang, Y.H.; Zhang, Y.; Hadjipanayis, G.C.; Weller, D. Fabrication and characterization of ordered FePt nanoparticles. *J. Appl. Phys.* **2003**, *93* (102), 7172–7174.

# Permanent Nanocomposite Magnets

Satoshi Hiroswawa

Research and Development Division, Sumitomo Special Metals Company, Ltd.,  
Osaka, Japan

## INTRODUCTION

Permanent magnets (PMs) are one of the key materials that support modern electronic technologies and the society that is built upon them. The basic function of a PM is to provide a static magnetic field in a limited space in which electric energy is converted into mechanical energy or vice versa. The quest for PM materials that can generate a larger magnetic flux with a given volume, or that can generate a given magnetic flux with a smaller volume, still exists even after the advent of the Nd-Fe-B anisotropic magnets.<sup>[1]</sup> The maximum magnetic energy product  $(BH)_{\max}$  exceeding  $450 \text{ kJ/m}^3$ , a magnificent record that was only a dream 20 years before, has been achieved in the Nd-Fe-B magnets prepared by controlled powder-metallurgical route.<sup>[2]</sup> An ideal permanent magnet having a rectangular hysteresis loop with the remanence value of  $B_r$  will have a  $(BH)_{\max}$  value of  $1/4\mu_0 \times B_r^2$  provided that the intrinsic coercivity is greater than one half of  $B_r/\mu_0$ .<sup>[3]</sup> As a remanence cannot exceed the saturation polarization ( $J_s$ ) of the PM material, the maximal value of  $B_r$  is  $\mu_0 J_s$ . Therefore when one reminds that  $B = J + \mu_0 H$  and that  $H < 0$  for the case under consideration, the theoretical limit of  $(BH)_{\max}$  is  $1/4 \times \mu_0 J_s^2$ , namely, a product of  $1/2 \times \mu_0 J_s$  and  $1/2 \times J_s$ . Therefore a search for a more powerful PM involves, as its principal element, a search for ferromagnetic materials that have  $J_s$  larger than that of  $\text{Nd}_2\text{Fe}_{14}\text{B}$ ,<sup>[4]</sup> the main hard magnetic component of the Nd-Fe-B magnets.

Nanocomposite PM (NPM) is a PM consisting of a combination of a hard magnetic phase (HP) and a relatively soft magnetic phase (SP) having a large  $J_s$ .<sup>[5]</sup> The concept of NPM has attracted considerable attention because of the possibility that a larger  $B_r$  than the  $J_s$  value of the currently most powerful PM (Nd-Fe-B) can be realized by combining an SP of a larger  $J_s$  than that of  $\text{Nd}_2\text{Fe}_{14}\text{B}$  (1.6 T at room temperature) as was pointed out by Skomski and Coey.<sup>[5]</sup>

The first NPM was probably  $\text{Nd}_4\text{Fe}_{81}\text{B}_{19}$  ribbons obtained by rapid solidification and a subsequent annealing treatment.<sup>[6]</sup> This material consisted of  $\text{Fe}_3\text{B}$ ,  $\text{Nd}_2\text{Fe}_{14}\text{B}$ , and a small amount of  $\alpha\text{-Fe}$ . Its  $B_r$  was approximately 1.2 T at room temperature. Because

of the isotropic nature of the material, i.e., no orientation of crystallographic axes was present, this value of  $B_r$  is smaller than the  $J_s$  of both  $\text{Fe}_3\text{B}$  and  $\text{Nd}_2\text{Fe}_{14}\text{B}$  phases. However, it is significantly larger than the expected value, which is one half of  $J_s$ ,<sup>[7]</sup> for noninteracting ensemble of hard magnetic particles of uniaxial magnetic anisotropy. This type of materials, which we classify as the  $\text{Fe}_3\text{B}/\text{Nd}_2\text{Fe}_{14}\text{B}$ -type hereafter, have been constantly improved with respect to their magnetic performance by several research groups including ourselves,<sup>[8]</sup> and form a class of commercial products that are used as a hard magnetic component of resin-bonded PM. A variety of combinations of hard magnetic and soft magnetic phases have been tried, and mechanisms of formation of nanostructures have been investigated in the past years as presented in this entry.

## PRINCIPLES

### Exchange Coupling and Critical Sizes

A composite material consisting of an HP and an SP, which are coupled via mere magnetostatic interactions or dipolar field interactions, cannot have a good hysteresis loop for practical PM applications. The reason is that the magnetization of HP, which is typically a soft magnetic phase such as  $\alpha\text{-Fe}$  or  $\text{Fe}_3\text{B}$ , easily responds to a demagnetization field. To prevent a sizable response of the SP magnetization from occurring, it is necessary to lock it by a strong coupling between SP and HP magnetic moments. Kneller and Hawig<sup>[9]</sup> discussed the role of exchange couplings in such a composite and argued that the composite can behave as if it were a single-phase PM if SP and HP are coupled via the exchange interactions between spins at the grain boundaries and if the grain sizes are smaller than the following critical values:

$$\text{for soft magnetic phase : } b_{\text{cS}} = \pi(A_{\text{S}}/2K_{\text{H}})^{1/2} \quad (1)$$

$$\text{for hard magnetic phase : } b_{\text{cH}} = b_{\text{cH}} \quad (2)$$

where  $A_S$  stands for the exchange stiffness constant of SP and  $K_H$  stands for the magnetocrystalline anisotropy constant of HP. With typical values for  $A_S$  and  $K_H$ ,  $10^{-11}$  J/m and  $2 \times 10^6$  J/m<sup>3</sup>, respectively, one obtains  $b_{cS} = b_{cH} = 5$  nm.<sup>[9]</sup>

### Remanence

Kneller and Hawig<sup>[9]</sup> further discussed about remanence and coercivity expected for a nanocomposite permanent magnet. If the saturation magnetization of HP and SP are  $J_{sH}$  and  $J_{sS}$ , respectively, and the volume ratio of HP is  $v_H$ , the saturation magnetization  $J_s$  of the composite magnet is given by

$$J_s = v_H J_{sH} + (1 - v_H) J_{sS} \quad (3)$$

The remanence  $B_r$  of the composite magnet is given by

$$B_r = v_H m_{rH} J_{sH} + (1 - v_H) m_{rS} J_{sS} \quad (4)$$

where  $m_{rH}$  and  $m_{rS}$  represent relative ratio of remanence of each component phase given by

$$m_r = B_r / J_s = \langle \cos \theta \rangle \quad (5)$$

where  $\theta$  represents the angle between the direction of the previous saturation field  $H$  and the direction of magnetization of a grain.  $\langle \cos \theta \rangle$  represents the average of  $\cos \theta$  over the entire composite. For an HP with a uniaxial magnetic anisotropy,  $\langle \cos \theta \rangle = 0.5$ , if there exists no magnetic coupling among grains. However, in the nanocomposite permanent magnet, the magnetization of SP is exchange-coupled with the magnetization of HP along their mutual grain boundaries. Therefore the resulting remanence of SP will be parallel to the magnetization of HP. If the easy direction of magnetization of the HP grains are distributed throughout the composite, the resulting magnetization state after saturation along  $H$  is inhomogeneous and numerical estimation of the values of  $m_r$  will require knowledge of space distribution of magnetization in the sample.

### Coercivity

For the optimal microstructure with  $b_{cH} = b_{cF}$ , the upper limit of the nucleation field  $H_{n0}$  is  $2K_H/J_{sS}$  for a completely aligned microstructure,<sup>[9]</sup> and it is about one half of this for isotropic polycrystallites;

$$H_{n0} = K_H / J_{sS} \quad (6)$$

which yields a coercivity value of the order of 1 MA/m for the case  $K_H = 2 \times 10^6$  J/m<sup>3</sup> and  $J_{sS} = 1.8$  T.

### The Maximum Energy Product

Skomski and Coey<sup>[5]</sup> analytically considered a case of an ideally soft magnetic inclusion of diameter  $D$  embedded in a hard magnetic matrix. The nucleation field  $H_{n0}$  reaches a plateau for  $D$  values below the Bloch wall width of HP,  $4(A_H K_H)^{1/2}$ . For larger inclusions,  $H_{n0}$  decreases as  $D^{-2}$ . The plateau value was estimated to be about 20 T for the case of  $J_{sS} = 2.15$  T,  $J_{sH} = 1.55$  T,  $A_F/A_H = 1.5$ ,  $K_F = 0$ , and  $K_H = 12$  MJ/m<sup>3</sup>, the case of  $\alpha$ -Fe inclusion in the Sm<sub>2</sub>Fe<sub>17</sub>N<sub>3</sub> matrix. For a fully aligned microstructure with rectangular hysteresis loop, they obtained an estimation for  $(BH)_{\max}$  as

$$(BH)_{\max} = 1/4 \mu_0 J_{sS}^2 \left\{ 1 - \mu_0 (J_{sS} - J_{sH}) J_{sS} / (2K_H) \right\} \quad (7)$$

and corresponding volume fraction of HP as

$$v_H = \mu_0 J_{sS}^2 / (4K_H) \quad (8)$$

For the case of  $\alpha$ -Fe inclusions in Sm<sub>2</sub>Fe<sub>17</sub>N<sub>3</sub> matrix, Eq. (7) yields  $(BH)_{\max}$  of 880 kJ/m<sup>3</sup> with only 7 vol.% of Sm<sub>2</sub>Fe<sub>17</sub>N<sub>3</sub>. However, this treatment may be oversimplified because of the assumption of the completeness in alignment and the squareness of the hysteresis loop.

### Micromagnetically Assessed Magnetic Properties

Micromagnetic calculation of inhomogeneously distributed magnetization states in exchange-coupled isotropic polycrystalline composite magnets have been performed for realistic microstructural models. Fukunaga, Kitajima, and Kanai<sup>[10]</sup> considered a model magnet composed of cubic grains of the edge length of  $L$ . Each grain is either an SP or an HP grain, the crystallographic axis of which is randomly oriented from grain to grain, namely, the magnet is an isotropic polycrystalline material. From the necessity that functional derivative of the total magnetic energy  $W$  with respect to magnetization vector of each grain to be null, a set of nonlinear equation is derived and a set of solutions is numerically obtained so that magnetic torque acting on magnetization of each grain diminishes. The solution thus obtained is not unique. When the fraction of SP is specified, the hysteresis loop depends on seven parameters; three intergranular exchange coupling constants, two intragranular exchange coupling constants, and two magnetocrystalline anisotropy constants for SP and HP. Fig. 1 shows the relationship between reduced coercivity ( $h_c$ ) and reduced remanence ( $m_r$ ) calculated with varying grain size  $L$ . Each curve corresponds to a specific value of fraction of SP (expressed as “soft” in Fig. 1). With decreasing  $L$ ,

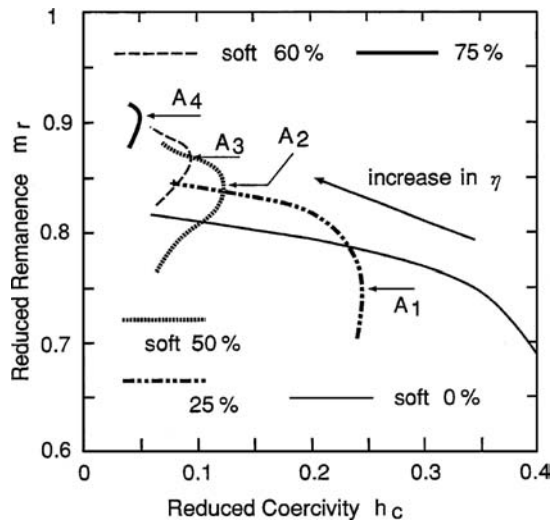


**Fig. 1** Relationship between reduced coercivity ( $h_c$ ) and reduced remanence ( $m_r$ ) calculated with varying grain size  $L$ .

the corresponding point on the curve moves from lower right to upper left, passing through a maximum of  $h_c$  when the fraction of SP is not zero. The maximum of  $h_c$  occurs because the hysteresis loop has a characteristic two-phase behavior when  $L$  is much larger than  $b_{cs}$  while the hysteresis loop becomes extremely narrow as the anisotropy energy begins to be averaged out when  $L$  is much smaller than the ferromagnetic correlation length  $(AK)^{1/2}$  as shown in Fig. 2.

The inhomogeneous distribution of directions of magnetization vectors in isotropic nanocomposite permanent magnets can be calculated by using finite-element micromagnetic calculation approach.<sup>[11]</sup> Very recently, progress in electron holography technology of transmission electron microscopy (TEM) has made observation of magnetic force lines in a nanocomposite

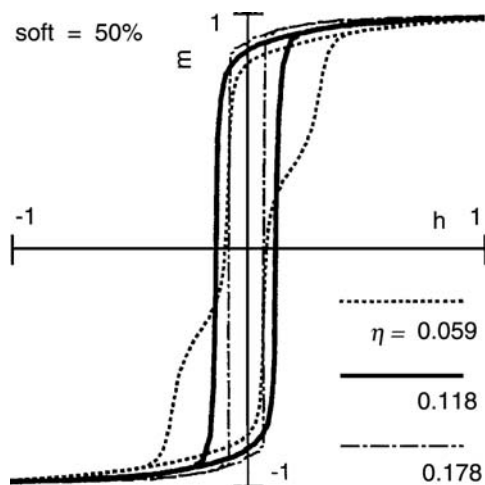


**Fig. 2** Hysteresis loops of an isotropic nanocomposite permanent magnet calculated for various fractions of soft magnetic phase (“soft” in the figure). *Source:* From Ref.<sup>[8]</sup>.

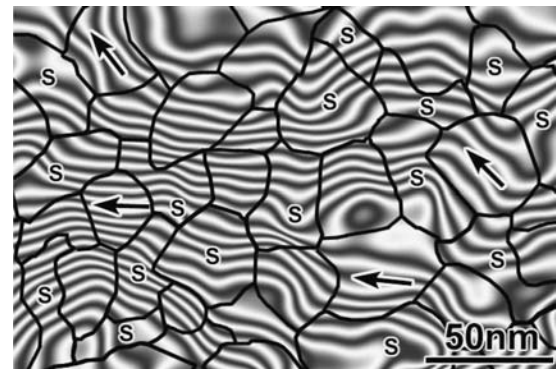


**Fig. 3** Magnetic force lines in a nanocomposite permanent magnet composed of  $\text{Fe}_3\text{B}$  and  $\text{Nd}_2\text{Fe}_{14}\text{B}$ . *Source:* Courtesy of Professor Daisuke Shindo, from Ref.<sup>[12]</sup>.

permanent magnet possible,<sup>[12]</sup> as shown in Fig. 3 for the case of SP =  $\text{Fe}_3\text{B}$  and HP =  $\text{Nd}_2\text{Fe}_{14}\text{B}$ . The white lines in Fig. 3 correspond to magnetic force lines and the net drawn by solid black lines correspond to grain boundaries. The arrows indicate the easy directions of magnetization of the  $\text{Nd}_2\text{Fe}_{14}\text{B}$  grains. Grains identified to be  $\text{Fe}_3\text{B}$  via nanobeam electron probe X-ray spectroscopy (EDX) are indicated as S.

### “Exchange-Spring” Behavior

The response of magnetization of a permanent magnet to a varying demagnetizing field is called a recoil curve. The recoil curve of an NPM has a characteristic nearly reversible response to the demagnetization field because magnetization of SP rotates in a reversible manner as long as magnetization of HP does not reverse its direction irreversibly. The reversible rotation of magnetization of SP occurs because the exchange field counteracts applied demagnetization. This characteristic recoil behavior is frequently referred to as exchange-spring, as termed by Kneller and Hawig.<sup>[9]</sup> An example of recoil curves of an  $\text{Fe}_3\text{B}/\text{Nd}_2\text{Fe}_{14}\text{B}$ -type isotropic nanocomposite magnet is shown in Fig. 4.

### POSSIBLE COMBINATIONS OF SOFT MAGNETIC AND HARD MAGNETIC PHASES

In principle, any combination of SP and HP is possible provided that they coexist in a stable or quasi stable state. Typical HP phases of interest are listed in Table 1 together with their room temperature magnetic properties. Large magnetocrystalline anisotropy in the rare-earth-based intermetallic compounds such as  $\text{SmCo}_5$  arises from the single-ion anisotropy of the rare-earth ions. On the other hand, the magnetocrystalline anisotropy in the ordered ( $L1_0$  structure) CoPt and FePt alloys is due to Pt

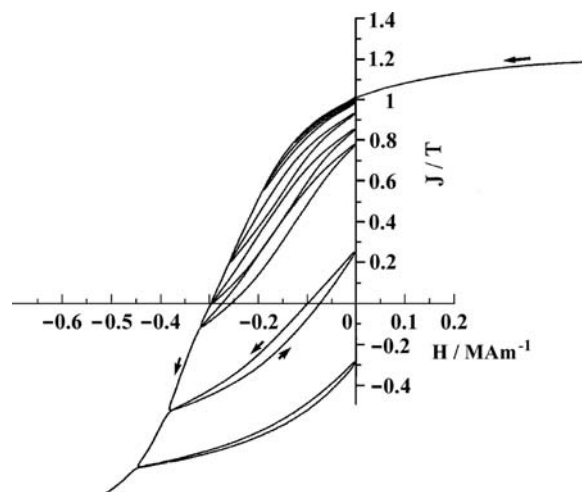


**Fig. 4** An example of recoil curves of an  $\text{Fe}_3\text{B}/\text{Nd}_2\text{Fe}_{14}\text{B}$ -type isotropic nanocomposite magnet.

atoms. For economic reasons, bulk magnets produced in industrial scales are iron-based materials, typically Nd-Fe-B. Soft magnetic phases with large  $J_s$ 's are listed in Table 2 together with their room temperature magnetic properties. For the iron-based HP,  $\alpha$ -Fe and bcc-(Fe-Co) alloys are the most promising candidates for SP. In the following, a type of a nanocomposite is designated by the SP and HP combination as SP/HP.

Because of the large  $J_s$  of  $\text{Nd}_2\text{Fe}_{14}\text{B}$ , the Fe-rich region of the Fe-Nd-B system is of a particular interest in conjunction with NPM. The volume fraction of SP can be chosen to be any value for the  $\alpha$ -Fe/ $\text{Nd}_2\text{Fe}_{14}\text{B}$  or  $\alpha$ -Fe/ $\text{Sm}_2\text{Fe}_{17}\text{N}_3$  type in terms of metallurgy. In contrast, available volume fraction of the metastable  $\text{Fe}_3\text{B}$  phase is limited in the case of the  $\text{Fe}_3\text{B}/\text{Nd}_2\text{Fe}_{14}\text{B}$  type because other metastable compounds are formed in a certain composition range.<sup>[14]</sup>

## FABRICATION TECHNIQUES FOR NANOCRYSTALLINE STRUCTURES

A nanocrystalline structure can be fabricated through rapid solidification and crystallization. The technique

**Table 1** Hard magnetic phases for nanocomposite permanent magnets and their magnetic properties at room temperature

Material	$J_s$ (T)	$K$ (MJ/m <sup>3</sup> )	Reference
$\text{SmCo}_5$	1.07	17.2	[13]
$\text{Sm}_2\text{Co}_{17}$	1.28	3.3	[13]
$\text{Nd}_2\text{Fe}_{14}\text{B}$	1.61	4.9	[13]
$\text{Sm}_2\text{Fe}_{17}\text{N}_3$	1.54	8.6	[13]
CoPt	1.00	4.9	[13]
FePt	1.43	6.6	[14]

**Table 2** Ferromagnetic phases of interest as the high-magnetization component for nanocomposite permanent magnets and their magnetic properties at room temperature

Material	$J_s$ (T)	$K$ (MJ/m <sup>3</sup> )	Reference
$\alpha$ -Fe	2.15	0.05	[13]
hcp-Co	1.81	0.53	[13]
$\text{Fe}_3\text{B}$	1.62	-0.32	[11]

most commonly used for rapid solidification of hard magnetic alloys is the melt spinning (MS) technique. In the MS technique, a melt is ejected through a small orifice onto a surface of a rotating chill wheel or roll. The surface velocity of the wheel is typically 20–50 m/sec and the cooling rate is around  $10^6$  K/sec. The crystallization process may occur either during the solidification process or during an annealing heat treatment after the alloy is quenched into an amorphous state and subsequently heated to a temperature at which atomic diffusion can take place (i.e., around 600–700°C). Empirically determined critical cooling rates for amorphous formation ( $R_c$ ) in the  $\text{Fe}_3\text{B}/\text{Nd}_2\text{Fe}_{14}\text{B}$ -type alloys are approximately  $2 \times 10^5$  K/sec. For the  $\alpha$ -Fe/ $\text{Nd}_2\text{Fe}_{14}\text{B}$ -type alloys,  $R_c$  is several times larger than this value if no additive elements that retard the crystallization process are used.

Alternative methods to fabricate a nanocrystalline structure include mechanical alloying (MA) or mechanical grinding (MG) followed by a suitable annealing treatment, vapor deposition (VD) techniques such as sputtering followed by suitable annealing treatments. Except for the VD techniques, only an isotropic nanocrystalline structure is obtained. Anisotropic or oriented films can be fabricated by sputter- or pulsed-laser-deposition (PLD) techniques.

## EXAMPLES OF NANOCOMPOSITE PERMANENT MAGNETS

Examples of nanocomposite permanent magnets are briefly discussed in this section. Their magnetic properties are summarized in Table 3.

### Isotropic Nanocomposite Permanent Magnets Based on $\alpha$ -Fe/ $\text{Nd}_2\text{Fe}_{14}\text{B}$

The fabrication of  $\text{Nd}_2\text{Fe}_{14}\text{B}$ -based permanent magnets with trace of  $\alpha$ -Fe was fabricated via MS by Yajima et al.<sup>[15]</sup> in as early as 1988.  $\text{Nd}_{10}\text{Fe}_{82}\text{B}_8$  showed a distinct indication of coarse  $\alpha$ -Fe precipitation in as-spun ribbon. Partial replacement of Fe with Zr resulted to a significant improvement of magnetic properties, but with a significant reduction of the amount of the  $\alpha$ -Fe phase resulting in a nearly single-phase  $\text{Nd}_2\text{Fe}_{14}\text{B}$ -type magnet in melt-spun  $\text{Nd}_9\text{Fe}_{72.5}$ .



**Table 3** Typical magnetic properties of isotropic nanocomposite permanent magnets

Type (SP/HP)	Composition	Preparation method	$B_r$ (T)	$H_{cJ}$ (kA/m)	$(BH)_{max}$ (kJ/m <sup>3</sup> )	Reference
$\alpha$ -Fe/Nd <sub>2</sub> Fe <sub>14</sub> B	Nd <sub>10</sub> Fe <sub>82</sub> B <sub>8</sub>	MS	0.85	541	78	[15]
	Nd <sub>9</sub> Fe <sub>72.5</sub> Co <sub>10</sub> Zr <sub>2.5</sub> B <sub>6</sub>	MS	0.89	~640	130	[15]
	Nd <sub>9</sub> Fe <sub>85</sub> B <sub>6</sub>	MS	1.10	485	158	[15]
	(70 wt.%) $\alpha$ -Fe/(30 wt.%)Nd <sub>2</sub> Fe <sub>14</sub> B	MS	1.45	207	115	[17]
	Nd <sub>8</sub> Fe <sub>87.5</sub> B <sub>4.5</sub>	MS	1.25	~500	185.2	[17]
	Nd <sub>7</sub> Fe <sub>89</sub> B <sub>4</sub>	MS	1.28	252	146	[19]
	Nd <sub>3.5</sub> Fe <sub>91</sub> Nb <sub>2</sub> B <sub>3.5</sub>	MS	1.45	215	115	[22]
	Nd <sub>6</sub> Fe <sub>87</sub> Nb <sub>1</sub> B <sub>6</sub>	MS	1.04	302	78	[22]
	Nd <sub>4</sub> Tb <sub>2</sub> Fe <sub>86</sub> Nb <sub>2</sub> B <sub>6</sub>	MS	0.72	358	41	[22]
	Nd <sub>8</sub> Fe <sub>76</sub> Co <sub>8</sub> Nb <sub>2</sub> B <sub>6</sub>	MS	1.12	512	143	[24]
(Nd <sub>0.9</sub> Dy <sub>0.1</sub> ) <sub>9</sub> (Fe <sub>0.9</sub> Co <sub>0.1</sub> ) <sub>84.5</sub> B <sub>5.5</sub> Nb <sub>1</sub>	MS-A	1.07	593	166	[25]	
$\alpha$ -Fe/Pr <sub>2</sub> Fe <sub>14</sub> B	(30.4%) $\alpha$ -Fe/(69.6%)Pr <sub>2</sub> Fe <sub>14</sub> B	MS	1.17	480	180.7	[27]
Fe <sub>3</sub> B/Nd <sub>2</sub> Fe <sub>14</sub> B	Nd <sub>4</sub> Fe <sub>80</sub> B <sub>20</sub>	MS-A	1.20	191	93.1	[6]
	Nd <sub>4.5</sub> Fe <sub>72.3</sub> B <sub>18.5</sub> Cr <sub>2</sub> Co <sub>2</sub> Cu <sub>0.2</sub> Nb <sub>0.5</sub>	MS-A	1.10	336	123	[32]
	Nd <sub>3.4</sub> Dy <sub>1</sub> Fe <sub>71.7</sub> B <sub>18.5</sub> Cr <sub>2.4</sub> Co <sub>2.4</sub> Cu <sub>0.4</sub> Zr <sub>0.2</sub>	MS-A	0.97	465	105	[32]
	Nd <sub>4.5</sub> Fe <sub>73</sub> Co <sub>3</sub> Ga <sub>1</sub> B <sub>18.5</sub>	MS-A	1.21	340	128	[36]
	Nd <sub>3.5</sub> Dy <sub>1</sub> Fe <sub>73</sub> Co <sub>3</sub> Ga <sub>1</sub> B <sub>18.5</sub>	MS-A	1.18	390	136	[36]
	Nd <sub>3.5</sub> Dy <sub>1</sub> Fe <sub>73</sub> Co <sub>3</sub> Ga <sub>1</sub> B <sub>18.5</sub>	MS	1.15	400	131.6	[41]
	Nd <sub>5.5</sub> Fe <sub>66</sub> Cr <sub>5</sub> Co <sub>5</sub> B <sub>18.5</sub>	MS-A	0.86	610	96.6	[36]
Fe-B/Nd <sub>2</sub> Fe <sub>14</sub> B	(Nd <sub>0.95</sub> La <sub>0.05</sub> ) <sub>11</sub> Fe <sub>66.5</sub> Co <sub>10</sub> Ti <sub>2</sub> B <sub>10.5</sub>	MS-A	0.94	1282	146	[39]
	Nd <sub>8</sub> Fe <sub>73</sub> Co <sub>5</sub> Hf <sub>2</sub> B <sub>12</sub>	MS	N/A	820	107	[40]
$\alpha$ -Fe/Sm <sub>2</sub> Fe <sub>17</sub> N <sub>x</sub>	Sm <sub>8</sub> Zr <sub>3</sub> Fe <sub>85</sub> Co <sub>4</sub> N <sub>x</sub>	MS-A-N	0.94	764	118	[43]
$\alpha$ -Fe/Sm <sub>2</sub> Fe <sub>17</sub> C <sub>x</sub>	Sm <sub>8</sub> Fe <sub>76</sub> Cu <sub>4</sub> Si <sub>8</sub> C <sub>4</sub>	MS		382	85	[46]
$\alpha$ -Fe/Sm <sub>2</sub> Co <sub>17</sub>	SmCo <sub>10</sub>	MA-A	0.94	318	81	[47]
(Fe, Co)/Sm-Co	Sm <sub>11.67</sub> Co <sub>58.33</sub> Fe <sub>30</sub>	MA-A	0.97	600	101	[48]
Fe <sub>3</sub> Pt/FePt	Reduced Fe <sub>3</sub> O <sub>4</sub> (4 nm)/FePt(4 nm) = 1:10	SANP	0.96	1166	160	[63]

Preparation methods: MS = melt-spinning; MA = mechanical alloying; A = annealing; N = nitrogeation; SANP = self-assembly of nanoparticles.

Co<sub>10</sub>Zr<sub>2.5</sub>B<sub>6</sub>. Manaf, Buckley, and Davies<sup>[16]</sup> prepared Nd<sub>8</sub>Fe<sub>86</sub>B<sub>6</sub> melt-spun ribbons of a high remanence, 1.12 T, which was attributed to the existence of  $\alpha$ -Fe. They investigated the microstructure of melt-spun Nd<sub>10</sub>Fe<sub>84</sub>B<sub>6</sub> by TEM and showed existence of a nanometer-sized  $\alpha$ -Fe particle at a grain junction of  $\alpha$ -Fe grains.<sup>[17]</sup> Ribbons with significant amounts of  $\alpha$ -Fe were prepared by Manaf et al.<sup>[17]</sup> One of the best energy densities achieved (185 kJ/m<sup>3</sup>) was obtained by Bauer, Seeger, and Kronmuller<sup>[18]</sup> on Nd<sub>8</sub>Fe<sub>87.5</sub>B<sub>4.5</sub> via MS under an He atmosphere. On the other hand, Inoue et al.<sup>[20]</sup> showed that an  $\alpha$ -Fe/Nd<sub>2</sub>Fe<sub>14</sub>B-type nanocomposite with a remaining amorphous phase exhibit a superior magnetic properties to fully crystalline materials. More recent micromagnetic calculation by Fukunaga, Kuma, and Kanai<sup>[21]</sup> suggested that

softening of exchange coupling in a grain boundary phase should be beneficial to increase coercivity.

Recent improvements of magnetic properties of the  $\alpha$ -Fe/Nd<sub>2</sub>Fe<sub>14</sub>B-type nanocomposite permanent magnets are based on structural refinement by use of refractory metallic elements such as Nb, Hf, Mo, and Zr.<sup>[22]</sup> These elements affect the solidification and crystallization kinetics in the  $\alpha$ -Fe/Nd<sub>2</sub>Fe<sub>14</sub>B-type nanocomposite alloys. Nb is one of the most effective elements in this sense.<sup>[22]</sup> Growth kinetics in undercooled Nd<sub>2</sub>Fe<sub>14</sub>B alloys with C and Ti or Mo addition was recently studied by Hermann and Bächer<sup>[23]</sup> using the electromagnetic levitation technique. The growth velocity of the Nd<sub>2</sub>Fe<sub>14</sub>B phase was estimated to be from 1.1 to 6.4 mm/sec, depending on the degree of supercooling, in Nd<sub>2</sub>Fe<sub>14</sub>B melt, whereas it was

reduced to 0.3–2.5 mm/sec in  $(\text{Nd}_2\text{Fe}_{14}\text{B})_{0.94}(\text{TiC})_{0.03}$  alloy. The considerable slowing down of the growth kinetics resulted in refinement of grain sizes.

One approach toward a nanocomposite permanent magnet with an improved coercivity is to increase the magnetocrystalline anisotropy of HP. Partial replacement of rare-earth ions such as Pr, Tb, and Dy for Nd in the  $\text{Nd}_2\text{Fe}_{14}\text{B}$ -type compounds results in an increase in  $K_H$  of the compound. Hadjipanayis, Withanawasam, and Krause<sup>[22]</sup> prepared melt-spun ribbons of  $\text{Nd}_6\text{Fe}_{87}\text{Nb}_1\text{B}_6$  and  $\text{Nd}_4\text{Tb}_2\text{Fe}_{86}\text{Nb}_2\text{B}_6$  and obtained  $H_{cJ}$  values of 302 and 358 kA/m, respectively. Chang et al.<sup>[24]</sup> studied effects of Co substitution for Fe and obtained good magnetic properties of  $(BH)_{\text{max}} = 143 \text{ kJ/m}^3$  for  $\text{Nd}_8\text{Fe}_{76}\text{Co}_8\text{Nb}_2\text{B}_6$ . More recently, Arai et al.<sup>[25]</sup> achieved an energy density of  $166 \text{ kJ/m}^3$  for  $(\text{Nd}_{0.9}\text{Dy}_{0.1})_9(\text{Fe}_{0.9}\text{Co}_{0.1})_{84.5}\text{B}_{5.5}\text{Nb}_1$  via the melt-spinning method, with grooved TiN-coated roll under an He atmosphere. It was rationalized that the TiN-coating layer lowered the heat transfer at the roll-ribbon interface, resulting in uniform cooling rate through the thickness of the ribbon. Better combinations of  $H_{cJ}$  and  $(BH)_{\text{max}}$  have been obtained for Pr-Fe-B nanocrystalline magnets than for the Nd-Fe-B, resulting from the higher magnetocrystalline anisotropy of  $\text{Pr}_2\text{Fe}_{14}\text{B}$  than  $\text{Nd}_2\text{Fe}_{14}\text{B}$ .<sup>[26]</sup> In a systematic study of  $\alpha$ -Fe/ $\text{Pr}_2\text{Fe}_{14}\text{B}$  melt-spun magnets, a large  $(BH)_{\text{max}}$  of  $180.7 \text{ kJ/m}^3$  was obtained for 30.4 vol.% of  $\alpha$ -Fe.<sup>[27]</sup>

### Isotropic Nanocomposite Permanent Magnets Based on Fe-B/ $\text{Nd}_2\text{Fe}_{14}\text{B}$

The first nanocomposite permanent magnet was the melt-spun  $\text{Nd}_4\text{Fe}_{80}\text{B}_{20}$ , which was of the  $\text{Fe}_3\text{B}/\text{Nd}_2\text{Fe}_{14}\text{B}$  type, composed of 73%  $\text{Fe}_3\text{B}$ , 15%  $\text{Nd}_2\text{Fe}_{14}\text{B}$ , and 12%  $\alpha$ -Fe.<sup>[4]</sup> This material had relatively large  $B_r$  of 1.2 T, but  $H_{cJ}$  was not large enough for most applications. Among various elements that have been tried to improve magnetic properties of the  $\text{Fe}_3\text{B}/\text{Nd}_2\text{Fe}_{14}\text{B}$ -based nanocomposites, Cr is one of the most effective elements to improve the intrinsic coercivity,  $H_{cJ}$ .<sup>[28]</sup> Because of the strong affinity of Cr with B, Cr is enriched in  $\text{Fe}_3\text{B}$  upon crystallization and stabilizes this phase.<sup>[29]</sup> This leads to formation of the  $\text{Fe}_3\text{B}/\text{Nd}_2\text{Fe}_{14}\text{B}$  composite even in the concentration range where formation of  $\text{Nd}_2\text{Fe}_{23}\text{B}_3$  prevails (namely for  $\text{Nd} > \sim 5 \text{ at.}\%$ ) in the ternary alloys. Accordingly, Cr addition helps to realize nanocomposites with a larger volume fraction of  $\text{Nd}_2\text{Fe}_{14}\text{B}$  and hence a large coercivity. Suzuki and Cadogan<sup>[30]</sup> pointed out that Cr has a significant effect on kinetics of phase formation and decomposition, and that it allows a reaction path in which the  $\text{Fe}_3\text{B}/\text{Nd}_2\text{Fe}_{14}\text{B}$  composite is formed as a metastable intermediate structure instead of the  $\text{Fe}_3\text{B}/\text{Nd}_2\text{Fe}_{23}\text{B}_3$  combination.

$\text{Fe}_{23}\text{B}_6$  has spontaneous magnetization of approximately 1.7 T at room temperature,<sup>[9]</sup> which is larger than that of  $\text{Fe}_3\text{B}$  (1.6 T) and  $\text{Nd}_2\text{Fe}_{14}\text{B}$  (1.6 T). Therefore the presence of this phase may be beneficial.  $\text{Fe}_{23}\text{B}_6$  crystallizes from residual amorphous phase nearly simultaneously with  $\text{Nd}_2\text{Fe}_{14}\text{B}$  at a slightly higher temperature than the crystallization temperature of  $\text{Fe}_3\text{B}$  when Nb is microalloyed in  $\text{Fe}_3\text{B}/\text{Nd}_2\text{Fe}_{14}\text{B}$ -type alloys.<sup>[31]</sup> Cu also has a prominent effect on the kinetics of  $\text{Fe}_3\text{B}$  crystallization. Three-dimensional atom probe microanalysis (3-D APM) has revealed that Cu-enriched clusters are formed upon annealing of an amorphous  $\text{Nd}_{4.5}\text{Fe}_{76.8}\text{B}_{18.5}\text{Cu}_{0.2}$  alloy well below the crystallization temperature of  $\text{Fe}_3\text{B}$ .<sup>[31]</sup> Nd is also enriched in these clusters, leaving Nd-depleted and B-enriched region around them. This region provides a chemically favored crystallization site for  $\text{Fe}_3\text{B}$ . Interestingly, simultaneous addition of very small amount of Cu and Nb resulted to significant improvement of the magnetic properties through refinement of the grain sizes.<sup>[31]</sup> The small amount of addition is sometimes referred to as “microalloying.” The impacts of microalloying of Cu and Nb on demagnetization curves and microstructure of an  $\text{Nd}_{4.5}\text{Fe}_{77}\text{B}_{18.5}$   $\text{Fe}_3\text{B}/\text{Nd}_2\text{Fe}_{14}\text{B}$ -type NPM are shown in Figs. 5 and 6.<sup>[31]</sup>

Zr is also effective in refining grain sizes in the  $\text{Fe}_3\text{B}/\text{Nd}_2\text{Fe}_{14}\text{B}$  nanocomposites. Addition of 0.1–0.5 at.% of Zr increases the crystallization temperature of particularly  $\text{Nd}_2\text{Fe}_{14}\text{B}$ . The effect of microalloying Zr is greater than that of Nb.<sup>[32]</sup> According to a recent 3-D APM analysis of Zr-Cu-doped magnets, Zr is rejected from  $\text{Fe}_3\text{B}$  and thus suppresses grain growth of this phase. Zr concentrates along grain boundaries between  $\text{Fe}_3\text{B}$  and  $\text{Nd}_2\text{Fe}_{14}\text{B}$  in the fully crystallized stage.<sup>[33]</sup>

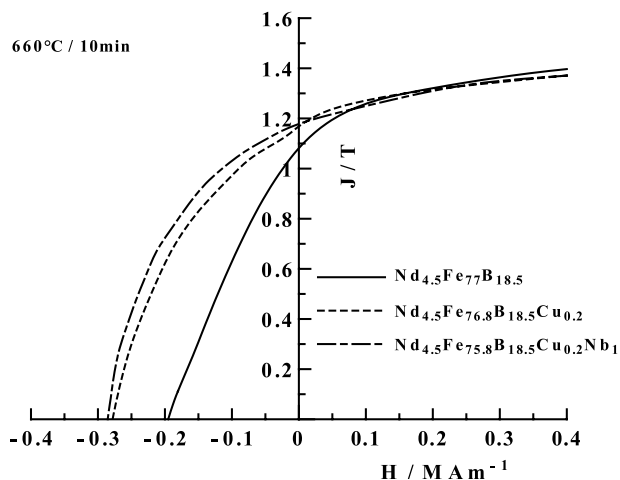


**Fig. 5** Demagnetization curves of  $\text{Nd}_{4.5}\text{Fe}_{77}\text{B}_{18.5}\text{Fe}_3\text{B}/\text{Nd}_2\text{Fe}_{14}\text{B}$ -type nanocomposites showing the impact of microalloying Cu and Nb. Source: From Ref.<sup>[31]</sup>.

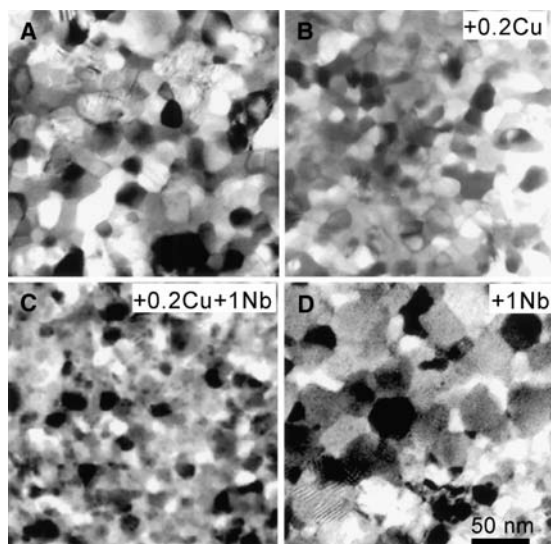


**Fig. 6** Transmission electron microscope images of (A)  $\text{Nd}_{4.5}\text{Fe}_{75.8}\text{B}_{18.5}$ , (B)  $\text{Nd}_{4.5}\text{Fe}_{76.8}\text{B}_{18.5}\text{Cu}_{0.2}$ , (C)  $\text{Nd}_{4.5}\text{Fe}_{75.8}\text{B}_{18.5}\text{Cu}_{0.2}\text{Nb}_1$ , and (D)  $\text{Nd}_{4.5}\text{Fe}_{76}\text{B}_{18.5}\text{Nb}_1$ , showing the impact of simultaneous microalloying of Cu and Nb. The average grain size is about 30, 17, 12, and 43 nm, respectively. Source: From Ref.<sup>[31]</sup>.

Compositional adjustment has yielded a relatively high coercivity material on the basis of Nd–Fe–B–Cr–Co, namely  $\text{Nd}_{4.5}\text{Fe}_{73}\text{B}_{18.5}\text{Cr}_2\text{Co}_2$ , which has  $B_r$  of 1.05 T,  $H_{cJ}$  of 378 kA/m, and  $(BH)_{\text{max}}$  of 108 kJ/m<sup>3</sup>. Simultaneous addition of small amounts of Cu and Nb to this material has been successfully carried out to improve  $(BH)_{\text{max}}$  with a slight sacrifice in  $H_{cJ}$  to yield  $\text{Nd}_{4.5}\text{Fe}_{72.3}\text{B}_{18.5}\text{Cr}_2\text{Co}_2\text{Cu}_{0.2}\text{Nb}_{0.5}$  with  $B_r$  of 1.10 T,  $H_{cJ}$  of 336 kA/m, and  $(BH)_{\text{max}}$  of 123 kJ/m<sup>3</sup>.<sup>[32]</sup> Manipulation of crystallization behavior, especially that of  $\text{Nd}_2\text{Fe}_{14}\text{B}$ , can be carried out by readjusting Cu content. An example of such compositional modifications to yield higher coercivity magnets is  $\text{Nd}_{3.5}\text{Dy}_1\text{Fe}_{71.3}\text{B}_{18.5}\text{Cr}_{2.4}\text{Co}_{2.4}\text{Cu}_{0.4}\text{Nb}_{0.5}$ , which has  $B_r$  of 0.93 T,  $H_{cJ}$  of 468 kA/m, and  $(BH)_{\text{max}}$  of 100 kJ/m<sup>3</sup>.<sup>[34]</sup> Utilizing the stronger effect of Zr to prevent grain growth, better magnetic properties have been obtained in  $\text{Nd}_{3.4}\text{Dy}_1\text{Fe}_{71.7}\text{B}_{18.5}\text{Cr}_{2.4}\text{Co}_{2.4}\text{Cu}_{0.4}\text{Zr}_{0.2}$ , which has  $B_r$  of 0.97 T,  $H_{cJ}$  of 465 kA/m, and  $(BH)_{\text{max}}$  of 105 kJ/m<sup>3</sup>.

Gallium (Ga) is another important element for improving magnetic properties of the  $\text{Fe}_3\text{B}/\text{Nd}_2\text{Fe}_{14}\text{B}$  nanocomposite.<sup>[35]</sup> One of the best  $\text{Fe}_3\text{B}/\text{Nd}_2\text{Fe}_{14}\text{B}$ -type nanocomposite is  $\text{Nd}_{3.5}\text{Dy}_1\text{Fe}_{73}\text{Co}_3\text{Ga}_1\text{B}_{18.5}$  with  $(BH)_{\text{max}}$  of 136 kJ/m<sup>3</sup>,  $B_r$  of 1.18 T, and  $H_{cJ}$  of 390 kA/m.<sup>[36]</sup> Mishra and Panchanathan<sup>[37]</sup> studied  $\text{Nd}_{3.5}\text{Dy}_1\text{Fe}_{73}\text{Co}_3\text{Ga}_1\text{B}_{18.5}$  by TEM–EDX, and observed that Ga additives were all detected in the  $\text{Nd}_2\text{Fe}_{14}\text{B}$  phase with Ga concentrations mostly near grain boundaries. More recently, a 3-D APM analysis revealed that Co and Ga atoms are partitioned to the  $\text{Nd}_2\text{Fe}_{14}\text{B}$  phase. Moreover, evidence for a slight enrichment of Ga

atoms at the  $\text{Nd}_2\text{Fe}_{14}\text{B}/\text{Fe}_3\text{B}$  interface has been found.<sup>[38]</sup>

The effects of Cr, Ti, Nb, Zr, Hf, Ta, and W on microstructure and magnetic properties of nanocomposites composed mainly of  $\text{Nd}_2\text{Fe}_{14}\text{B}$ , with minor amounts of ferromagnetic borides such as  $\text{Nd}_2\text{Fe}_{23}\text{B}_3$ , have been studied by Chang et al.<sup>[39]</sup> The formation of metastable  $\text{Nd}_2\text{Fe}_{23}\text{B}_3$  was found to be suppressed by the addition of Cr, Ti, Nb, and V in  $(\text{Nd}_{0.95}\text{La}_{0.05})_{9.5}\text{Fe}_{78}\text{M}_2\text{B}_{10.5}$ . Thermal magnetic analysis indicated existence of  $\alpha$ -Fe and an  $\text{Nd}_2\text{Fe}_{14}\text{B}$ -type phase. Considerable refinement of grain sizes was observed by TEM in  $(\text{Nd}_{0.95}\text{La}_{0.05})_{9.5}\text{Fe}_{78}\text{Cr}_2\text{B}_{10.5}$  and in  $(\text{Nd}_{0.95}\text{La}_{0.05})_{9.5}\text{Fe}_{78}\text{Ti}_2\text{B}_{10.5}$ . In a similar composition range, Chiriac et al.<sup>[40]</sup> reported that relatively good hard magnetic properties can be obtained by a chill disk melt spinning technique with a small surface velocity of only 3 m/sec in the as-cast state of  $\text{Nd}_8\text{Fe}_{73}\text{Co}_5\text{Hf}_2\text{B}_{12}$ . Thermal magnetic analysis indicated formation of  $\text{Nd}_2\text{Fe}_{14}\text{B}$ -type phase and  $\alpha$ -(Fe, Co). However, significantly better magnetic properties are obtained in as-cast alloys for the  $\text{Fe}_3\text{B}/\text{Nd}_2\text{Fe}_{14}\text{B}$ -type alloys.<sup>[41]</sup>

### Isotropic Nanocomposite Permanent Magnets Based on $\alpha$ -Fe/Sm–Fe–C, $\alpha$ -Fe/Sm–Fe–N, and Sm–Co

An  $\alpha$ -Fe/Sm<sub>2</sub>Fe<sub>17</sub>N<sub>x</sub>-type nanocomposite permanent magnet powder, the combination of the phases that was emphasized by the theoretical study of Skomski and Coey,<sup>[5]</sup> was obtained in as early as 1993 by Ding et al.<sup>[42]</sup> by mechanical alloying of Sm<sub>7</sub>Fe<sub>93</sub> followed by annealing and nitriding. The powder was isotropic and was reported to have a very large remanence of 1.75 T and a  $(BH)_{\text{max}}$  value of 204 kJ/m<sup>3</sup> after a correction for the demagnetization field. From the melt-spinning route, Yoneyama et al.<sup>[43]</sup> prepared an  $\alpha$ -Fe/SmFe<sub>7</sub>N<sub>x</sub>-type nanocomposite powder. The SmFe<sub>7</sub>N<sub>x</sub> phase has the TbCu<sub>7</sub>-type structure, which is a disordered hexagonal structure that can be derived from the Th<sub>2</sub>Zn<sub>17</sub>-type Sm<sub>2</sub>Fe<sub>17</sub> structure but with a random arrangement of dumbbell Fe pairs at the Sm sites. The addition of Co, aiming at a higher Curie temperature and remanence, resulted in a higher coercive force.

To eliminate the gas–solid reactions, namely nitriding, preparation of NPM on the basis of the Sm<sub>2</sub>Fe<sub>17</sub>C<sub>x</sub> hard magnetic compound have been attempted. Substitution of Al, Ga, Cr, and Si for Fe stabilized Sm<sub>2</sub>Fe<sub>17</sub> with high carbon concentration.<sup>[44,45]</sup> Melt-spun and annealed ribbons of  $\alpha$ -Fe/Sm<sub>2</sub>Fe<sub>15</sub>Si<sub>2</sub>C with Cu additives showed reasonable magnetic properties of  $(BH)_{\text{max}} = 85 \text{ kJ/m}^3$ .<sup>[46]</sup>

Cobalt as an SP may coexist with Sm<sub>2</sub>Co<sub>17</sub>. Isotropic nanocomposite permanent magnets were prepared by mechanical alloying processes to exhibit relatively good magnetic properties after annealing at 900°C of

$(BH)_{\max} = 81 \text{ kJ/m}^3$  for Co/Sm<sub>2</sub>Co<sub>17</sub>.<sup>[47]</sup> Somewhat better magnetic properties were obtained by mechanically alloying Sm–Co alloys and Fe powder and subsequent annealing. The finished powder of Sm<sub>11.67</sub>Co<sub>58.33</sub>Fe<sub>30</sub> had a  $(BH)_{\max}$  of  $101 \text{ kJ/m}^3$ .<sup>[48]</sup>

### Anisotropic Nanocomposite Permanent Magnet Films

Thin films prepared by vapor deposition techniques such as Ar-sputtering normally show magnetic anisotropy or texture. Therefore epitaxially grown thin films composed of soft magnetic and hard magnetic alternate layers can potentially become anisotropic nanocomposite permanent magnets of extraordinary  $(BH)_{\max}$  values. An Fe/Nd<sub>2</sub>Fe<sub>14</sub>B/Fe trilayer grown by Parhorer et al.<sup>[49]</sup> had texture with the easy direction of magnetization perpendicular to the film plane. Fe/[NdFeB/Fe]<sub>5</sub> multilayers grown by Shindo et al.<sup>[50]</sup> (Table 4) with isotropic texture in the hard magnetic layers were used to estimate the exchange-coupling constant  $J_{\text{SH}}$  between the soft and hard magnetic layers. The estimated  $J_{\text{SH}}$  value is  $2.0 \times 10^{-3} \text{ J/m}$ , which is about 1 order of magnitude smaller than the Fe/Fe and Nd<sub>2</sub>Fe<sub>14</sub>B/Nd<sub>2</sub>Fe<sub>14</sub>B couplings. Epitaxial superlattices of [Sm–Co (45 nm)/Co (30 nm)]<sub>10</sub> grown by Fullerton et al.<sup>[51]</sup> showed a relatively large  $H_{\text{cJ}}$  value of about 400 kA/m. Textured  $\alpha$ -Fe/SmFe<sub>12</sub> films in which the composite phases are randomly dispersed have been synthesized by Kato et al.<sup>[52]</sup> The film containing 25 vol.%  $\alpha$ -Fe showed  $(BH)_{\max}$  of  $152 \text{ kJ/m}^3$ . Apart from rare-earth-based systems, Liu et al.<sup>[53]</sup> succeeded to obtain a large  $(BH)_{\max}$  value of  $420 \text{ kJ/m}^3$  along the film—normal direction in an Fe<sub>3</sub>Pt/FePt multilayer film. The preparation procedure of the film included sputter deposition of Fe/Pt multilayers on a cold substrate and subsequent rapid thermal annealing of more than one step during which the Fe<sub>3</sub>Pt phase was formed.

### UTILIZATION OF NANOCOMPOSITE PERMANENT MAGNETS

The main application area of the rapidly solidified or mechanically alloyed nanocomposite permanent

magnet powders will be the resin-bonded magnet as the nanoscopic structure is metastable and cannot be maintained in the normal densification processes such as sintering. The resin-bonded magnets may be classified in compression-molded magnets and injection-molded magnets. The compression-molded magnets normally have a higher packing fraction of the magnetic composition than the injection-molded magnets. The typical packing fraction of the magnetic powder for these two types of magnets is 80 and 60 vol.%, respectively. Therefore the  $(BH)_{\max}$  of a resin-bonded magnet is only about one half of the magnetic powder used in the magnet. However, owing to the relatively simple preparation process and good dimensional accuracy originating from the molding processes, the resin-bonded magnets are widely used in electric devices such as small high-precision motors, which are used, for instance, in hard-disk drives mounted in personal computers. Rapidly solidified Nd–Fe–B powders with a small excess amount of Nd over Nd<sub>2</sub>Fe<sub>14</sub>B stoichiometry<sup>[54]</sup> have been almost exclusively used for the resin-bonded magnets. The advent of the nanocomposite permanent magnets based on the  $\alpha$ -Fe/Nd<sub>2</sub>Fe<sub>14</sub>B or Fe<sub>3</sub>B/Nd<sub>2</sub>Fe<sub>14</sub>B nanocomposite powders have added alternative choices for material engineers in this area of applications.

The R–Fe–B-based NPM powders (R is a rare-earth element) have several unique aspects when compared with the conventional Nd<sub>2</sub>Fe<sub>14</sub>B-based powders. First, NCM has compositions richer in Fe than the conventional powders, and consequently shows weaker susceptibility to oxygen or moisture. This is beneficial in massive handling of fine metallic powders in the production of bonded magnets. Second, because of the off-stoichiometric compositions, the R–Fe–B-based NPM alloys generally have greater formability of an amorphous phase, which allows application of rapid solidification techniques with relatively slow cooling rates. For instance, gas atomization may be used to produce spherical particles, which has beneficial characteristics for the injection-molding process.<sup>[55]</sup> The Fe<sub>3</sub>B/Nd<sub>2</sub>Fe<sub>14</sub>B-based NPM powders have similar morphological characteristics because of the relatively large thickness of the rapidly solidified alloys from

**Table 4** Magnetic properties of anisotropic nanocomposite permanent magnet films

Type (SP/HP)	Composition	Preparation method	$B_r$ (T)	$H_{\text{cJ}}$ (kA/m)	$(BH)_{\max}$ (kJ/m <sup>3</sup> )	Reference
$\alpha$ -Fe/Nd <sub>2</sub> Fe <sub>14</sub> B	SiO <sub>2</sub> /NdFeB/Fe/NdFeB/Cr	S	1.2	380	N/A	[49]
	Ti/Fe/[NdFeB/Fe] <sub>5</sub> /Ti	S	0.75	240	43	[50]
Co/Sm–Co	MgO/Cr/[Sm–Co(45 nm)/Co(30 nm)] <sub>10</sub> /Cr	S	N/A	500	N/A	[51]
$\alpha$ -Fe/SmFe <sub>12</sub>	(25 vol.% $\alpha$ -Fe)/(75 vol.% SmFe <sub>12</sub> )	S	1.3	240	151	[52]
Fe <sub>3</sub> Pt/FePt	Fe <sub>2</sub> Pt	S–A	1.4	1400	420	[53]

S and A denote sputtering and annealing, respectively.

which the powder particles are obtained by crushing.<sup>[8,56]</sup>

To exploit the large remanence of an NPM, the NPM powder needs to be fully consolidated. However, as mentioned above, normal densification processes such as liquid-phase sintering cannot be applied because if long-distance diffusion is to be allowed, the nanocomposite structure will be destroyed. To densify NMP, pressure-aided, moderate-temperature processes such as hot pressing must be used. Fully dense NPMs were prepared by Ono et al.<sup>[57]</sup> using spark plasma sintering method on the basis of  $\text{Nd}_{10}\text{Fe}_{75}\text{Co}_8\text{V}_1\text{B}_6$  to exhibit  $(BH)_{\text{max}} = 134 \text{ kJ/m}^3$ .

## CONCLUSION

We have witnessed an era of spectacular development of permanent magnetic materials in the last few decades. After the discovery of the  $\text{Nd}_2\text{Fe}_{14}\text{B}$  hard magnetic compound, no superior hard magnetic phase has been found. The concept of nanocomposite permanent magnet (NPM) remains the only concept that leads to designed experimentation toward a superior permanent magnet material. An NPM is a polycrystalline material composed of nanometer-sized hard magnetic phase and ferromagnetic phases that augment the total magnetization of the material. The nanosized microstructure is a prerequisite to obtain smooth J–H and B–H curves. A giant magnetic energy product reaching about  $0.7 \text{ MJ/m}^3$  may be expected in a textured NPM consisting of bcc Fe and hard magnetic phases such as  $\text{Nd}_2\text{Fe}_{14}\text{B}$  or  $\text{Sm}_2\text{Fe}_{17}\text{N}_3$ , although, in reality, only nontextured, isotropic NPM have been successfully produced in a sizable mass via rapid solidification or other techniques. Attempts to fabricate textured thin films via sputtering or laser pulse deposition<sup>[58]</sup> are among the most promising approaches. Other techniques that recently appeared may include self-organized assembly of nanoparticles prepared by means of wet chemistry,<sup>[59]</sup> spark erosion,<sup>[60]</sup> repeated cold rolling of layered stack of metallic sheets,<sup>[61]</sup> and crystallization of amorphous precursor in a magnetic field.<sup>[62]</sup> One novel and promising approach utilizes wet-chemical, self-organized assembly of nanoparticles. In the approach recently proposed by Zeng et al.,<sup>[63]</sup> both FePt and  $\text{Fe}_3\text{O}_4$  particles were incorporated as nanometer-scale building blocks into binary assemblies. Subsequent annealing under a flow of a mixture of Ar and  $\text{H}_2$  converted the assembly into FePr– $\text{Fe}_3\text{Pt}$  nanocomposites (see Table 3 for magnetic properties). Many other processes may be proposed. On the other hand, currently exploited Nd–Fe–B sintered magnets have  $(BH)_{\text{max}}$  values exceeding  $400 \text{ kJ/m}^3$  in the mass-production level. The prices of these conventional high-performance

magnets are reasonably low as a result of maturing of production techniques. Therefore the process used to produce the textured nanocomposite permanent magnets must be simple and suitable for a massive operation. Moreover, soft magnetic materials used with the hard magnetic materials as cores or yokes need to be improved to fully utilize such high-remanence hard magnets. Otherwise, the application area will be limited inside a small community.

For commercial applications, isotropic NPM has entered the stage of practical utilization as a hard magnetic ingredient for resin-bonded magnets. Indeed, NPM has some characteristics superior to those of conventional materials for this application. Some of the Fe–R-based NCM alloys have inherent characteristics that allow a high-throughput operation of the rapid solidification process and, accordingly, may be produced at a lower production cost. Therefore isotropic NPM powders will replace the conventional material in many application areas of resin-bonded magnets.

## REFERENCES

1. Sagawa, M.; Fujimura, S.; Togawa, N.; Yamamoto, H.; Matsuura, Y. New material for permanent magnets on a basis of Nd and Fe (invited). *J. Appl. Phys.* **1983**, *55* (6), 2083–2087. Part 2A.
2. Rodewald, W.; Wall, B.; Katter, M.; StÁner, K.; Steinmetz, S. Extraordinary Strong Nd–Fe–B Magnets by a Controlled Microstructure, Proceedings of the Seventeenth International Workshop on Rare Earth Magnets and Their Applications, Newark, DE, USA, August, 18–22, 2002; 2002, 25–36.
3. Buschow, K.H.J. Magnetism and Processing of Permanent Magnet Materials. In *Handbook of Magnetic Materials Vol. 10, Chap. 4*; Buschow, K.H.J., Ed.; Elsevier Science B. V., 1997; 497–593.
4. Herbst, J.F.; Corat, J.J.; Pinkerton, F.E.; Yelon, W.B. Relationships between crystal structure and magnetic properties in  $\text{Nd}_2\text{Fe}_{14}\text{B}$ . *Phys. Rev., B* **1984**, *29*, 4176–4178.
5. Skomski, R.; Coey, J.M.D. Giant energy product in nanostructured two-phase magnets. *Phys. Rev., B* **1993**, *48* (21), 15812–15816.
6. Coehoorn, R.; De Mooij, D.B.; Duchateau, J.P.W.B.; Buschow, K.H.J. Novel permanent magnet made by rapid quenching. *J. Phys.* **1988**, *C8*, 669–670.
7. Stoner, E.C.; Wohlfarth, E.P. A mechanism of magnetic hysteresis in heterogeneous alloys. *Philos. Trans. R. Soc.* **1948**, *240A*, 599–642.
8. Hiroswawa, S.; Kanekiyo, H.; Shigemoto, Y. Materials properties and utilization of  $\text{Fe}_3\text{B}/\text{Nd}_2\text{Fe}_{14}\text{B}$ -type nanocomposite permanent magnets based on Nd–Fe–Cr–Co–B. *Mater. Res. Symp. Proc.* **1999**, *577*, 141–152.
9. Kneller, E.F.; Hawig, R. The exchange-spring magnet: A new material principles for permanent magnets. *IEEE Trans. Magn.* **1991**, *27* (4), 3588–3600.

10. Fukunaga, H.; Kitajima, N.; Kanai, Y. Computer simulation of magnetic properties of nanocomposite magnets. *Mater. Trans. JIM* **1996**, *37* (4), 864–869.
11. Schrefl, T.; Fidler, J. Finite element modeling of nanocomposite magnets. *IEEE Trans. Magn.* **1999**, *35* (5), 3223–3228.
12. Shindo, D.; Park, Y.-G.; Murakami, Y.; Kanekiyo, H.; Hirosawa, S. Magnetic Domain Structure of Fe<sub>3</sub>B/Nd<sub>2</sub>Fe<sub>14</sub>B Nanocomposite Magnets Studied by Electron Holography, Proceedings of the 15th International Congress on Electron Microscopy, Durban, South Africa, September, 1–6, 2002; 2002, 299–300.
13. Skompski, R.; Coey, J.M.D. *Permanent Magnetism*; Institute of Physics Publishing Ltd.: Bristol, 1999 pp. 13, 269.
14. Buschow, K.H.J.; De Mooij, D.B.; Van Noort, H.M. Properties of metastable ternary compounds and amorphous alloys in the Nd–Fe–B system. *J. Less-Common Met.* **1986**, *125*, 135–146.
15. Yajima, K.; Nakamura, H.; Kohomoto, O.; Yoneyama, T. Microstructure of rapidly quenched Nd–Fe–Zr–B magnets. *J. Appl. Phys.* **1988**, *64*, 5528–5530.
16. Manaf, A.; Buckley, R.A.; Davies, H.A. New nanocrystalline high-performance Nd–Fe–B alloys by rapid solidification. *J. Magn. Mater.* **1993**, *128*, 302–306.
17. Manaf, A.; Al-Khafaji, M.; Zhang, P.Z.; Davies, H.A.; Buckley, R.A.; Raniforth, W.M. Microstructure analysis of nanocrystalline Fe–Nd–B ribbons with enhanced hard magnetic properties. *J. Magn. Mater.* **1993**, *128*, 307–312.
18. Bauer, J.; Seeger, M.; Kronmuller, H. Nanocrystalline FeNdB permanent magnets with enhanced remanence. *J. Appl. Phys.* **1996**, *80* (3), 1667–1672.
19. Withanawasam, L.; Hadjipanayis, G.C.; Krause, R.F. Enhanced remanence in isotropic Fe-rich melt-spun Nd–Fe–B ribbons. *J. Appl. Phys.* **1994**, *75*, 6646–6647.
20. Inoue, A.; Takeuchi, A.; Makino, A.; Masumoto, T. Hard magnetic properties of nanocrystalline Fe-rich Fe–Nd–B alloys prepared by partial crystallization of amorphous phase. *Mater. Trans., JIM* **1995**, *36* (7), 962–971.
21. Fukunaga, H.; Kuma, J.; Kanai, Y. Effects of strength of intergrain exchange interaction on magnetic properties of nanocomposite magnets. *IEEE Trans. Magn.* **1999**, *35* (5), 3235–3240.
22. Hadjipanayis, G.C.; Withanawasam, L.; Krause, R.F. Nanocomposite R<sub>2</sub>Fe<sub>14</sub>B/ $\alpha$ -Fe permanent magnets. *IEEE Trans. Magn.* **1995**, *31*, 3596–3601.
23. Hermann, R.; Bächer, I. Growth kinetics in undercooled Nd–Fe–B alloys with carbon and Ti or Mo additions. *J. Magn. Mater.* **2000**, *213*, 82–86.
24. Hamano, M.; Amsaki, M.; Mizoguchi, H.; Kobayashi, T.; Yamamoto, H.; Inoue, A. Residual amorphous phase in  $\alpha$ -Fe/NdFeB nanocomposite hard magnets. *Mat. Res. Symp. Proc.* **1999**, *577*, 187–194.
25. Arai, A.; Kato, H.; Akioka, K. Magnetic properties of (Nd,Dy)–(Fe, Co)–B–Nb and Nd–(Fe,Co)–B magnets made by the melt-spinning method with grooved and ceramic-coated roll. *IEEE Trans. Magn.* **2002**, *38* (5), 2964–2966.
26. Mendoza-Suarez, G.; Davies, H.A. The coercivities of nanophase melt-spun PrFeB alloys. *J. Alloys Compd.* **1998**, *281*, 17–22.
27. Goll, D.; Kronmüller, H. High-performance permanent magnets. *Naturwissenschaften* **2000**, *87*, 423–438.
28. Hirosawa, S.; Kanekiyo, H. Nanostructure and magnetic properties of chromium-doped Fe<sub>3</sub>B–Nd<sub>2</sub>Fe<sub>14</sub>B exchange-coupled permanent magnets. *Mater. Sci. Eng.* **1996**, *A217/218*, 367–370.
29. Sano, N.; Tomida, T.; Hirosawa, S.; Uehara, M.; Kanekiyo, H. Crystallization process of a rapidly quenched Fe–B–Nd nanocomposite magnet. *Mater. Sci. Eng.* **1998**, *A250*, 146–151.
30. Suzuki, K.; Cadogan, J.M. Formation and decomposition of Fe<sub>3</sub>B/Nd<sub>2</sub>Fe<sub>14</sub>B nanocomposite structure in Fe–Nd–B–Cr melt-spun ribbons under isothermal annealing. *J. Appl. Phys.* **1999**, *85*, 5914–5916.
31. Ping, D.H.; Hono, K.; Kanekiyo, H.; Hirosawa, S. Microstructural evolution of Fe<sub>3</sub>B/Nd<sub>2</sub>Fe<sub>14</sub>B nanocomposite magnets microalloyed with Cu and Nb. *Acta Mater.* **1999**, *47*, 4641–4651.
32. Hirosawa, S.; Miyoshi, T.; Shigemoto, Y. Effects of Cu–Nb/Zr addition on magnetic properties of Fe<sub>3</sub>B/(Nd–Dy)<sub>2</sub>Fe<sub>14</sub>B nanocomposite magnets. *IEEE Trans. Magn.* **2001**, *37*, 2558–2560.
33. Kajiwara, K.; Hono, K.; Hirosawa, S. Microstructures and the magnetic properties of Fe<sub>3</sub>B/(Nd,Dy)<sub>2</sub>Fe<sub>14</sub>B nanocomposite microalloyed with Cu and Zr. *Mater. Trans., JIM* **2001**, *42*, 1858.
34. Miyoshi, T.; Kanekiyo, H.; Hirosawa, S. Effects of Simultaneous Cu and Nb Doping on Phase Constitution and Magnetic Properties in Nd–Fe–B–Cr–Co-Based Fe<sub>3</sub>B/Nd<sub>2</sub>Fe<sub>14</sub>B-Type Nanocomposite Permanent Magnets, Proc. of the 16th International Workshop on Rare Earth Magnets and Their Applications, Sendai, Japan, September, 10–13, 2000; 2000, 495–504.
35. Kanekiyo, H.; Uehara, M.; Hirosawa, S. Microstructure and magnetic properties of high-remnance Nd<sub>5</sub>Fe<sub>71.5</sub>Co<sub>5</sub>B<sub>18.5</sub>M (M = Al, Si, Ga, Ag, Au) rapidly solidified and crystallized alloys for resin-bonded magnets. *IEEE Trans. Magn.* **1993**, *29*, 2863–2865.
36. Hirosawa, S.; Kanekiyo, H. Magnetic Properties and Microstructure of Fe<sub>3</sub>B-Based Nd–Fe–B Hard Magnetic Materials. In *Advanced Materials '93, I/B: Magnetic, Fullerene, Dielectric, Ferroelectric, Diamond and Related Materials*; Trans. Mater. Res. Soc. Jpn.; Elsevier: Amsterdam, 1994; Vol. 14B, 965–968.
37. Mishra, R.K.; Panchanathan, V.J. Microstructure of high-remnance Nd–Fe–B alloys with low-rare-earth content. *Appl. Phys.* **1994**, *75*, 6652–6654.
38. Ping, D.H.; Hono, K.; Hirosawa, S.J. Partitioning of Ga and Co atoms in a Fe<sub>3</sub>B/Nd<sub>2</sub>Fe<sub>14</sub>B nanocomposite magnet. *Appl. Phys.* **1998**, *83*, 7769–7775.
39. Chang, W.C.; Wang, S.H.; Chang, S.J.; Chen, Q. Magnetic and microstructure studied of boron-enriched (Nd<sub>0.95</sub>La<sub>0.05</sub>)<sub>11</sub>Fe<sub>76.5-x</sub>Co<sub>x</sub>Ti<sub>2</sub>B<sub>10.5</sub> (x = 0–15) melt-spun ribbons. *IEEE Trans. Magn.* **2000**, *36*, 3312–3314.
40. Czahiriac, H.; Marinescu, M.; Castano, F.J. Nd<sub>8</sub>Fe<sub>73</sub>Co<sub>5</sub>Hf<sub>2</sub>B<sub>12</sub> strip cast alloy. *J. Appl. Phys.* **2000**, *87*, 5338–5340.



41. Kanekiyo, H.; Hirosawa, S. Thick Fe<sub>3</sub>B/Nd<sub>2</sub>Fe<sub>14</sub>B nanocomposite permanent magnet flakes prepared by slow quenching. *J. Appl. Phys.* **2000**, *83*, 6265–6267.
42. Ding, J.; Street, R.; McCormick, P.G. Remanence enhancement in mechanically alloyed isotropic Sm<sub>7</sub>Fe<sub>93</sub>-nitride. *J. Magn. Magn. Mater.* **1993**, *124*, 1–4.
43. Yoneyama, T.; Yamamoto, T.; Hidaka, T. Magnetic properties of rapidly quenched high remanence Zr added Sm–Fe–N isotropic powders. *Appl. Phys. Lett.* **1995**, *67*, 3197–3199.
44. Shen, B.-G.; Wang, F.-W.; Kong, L.-S.; Gao, L.; Guo, H.-Q. Formation and magnetic properties of R<sub>2</sub>Fe<sub>17-x</sub>Ga<sub>x</sub>C<sub>2</sub> compounds prepared by arc-melting. *J. Magn. Magn. Mater.* **1993**, *127*, 267–272.
45. Chen, Z.; Hadjipanayis, G.C. Studies on the formation, structure and magnetic properties of Cr substituted Sm<sub>2</sub>(Fe,Cr)<sub>17</sub>C<sub>x</sub> compounds. *J. Magn. Magn. Mater.* **1997**, *171*, 261–266.
46. Zhang, H.-W.; Zhang, S.-Y.; Shen, B.-G. Permanent magnetic properties of nano-composite Sm<sub>2</sub>Fe<sub>15</sub>Si<sub>2</sub>C/α-Fe with Cu additive. *J. Appl. Phys.* **1999**, *85*, 4660–4662.
47. Chen, S.K.; Tsai, J.L.; Chin, T.S. Nanocomposite Sm<sub>2</sub>Co<sub>17</sub>/Co permanent magnets by mechanical alloying. *J. Appl. Phys.* **1996**, *79* (8), 5964–5966.
48. Majima, K.; Ito, M.; Umemoto, T.; Katsuyama, S.; Nagai, H. Preparation of (Sm–Co) + Fe magnetic powders by MA and their magnetic properties. *J. Jpn. Soc. Powder Metall.* **1996**, *43* (5), 629–633.
49. Parhofer, S.M.; Wecker, J.; Kurt, C.; Gieres, G.; Schultz, L. Remanence enhancement due to exchange coupling in multilayers of hard- and soft magnetic phases. *IEEE Trans. Magn.* **1996**, *32* (5), 4437–4439.
50. Snhido, M.; Ishizone, A.; Sakuma, A.; Kato, H.; Miyazaki, T.J. Magnetic properties of exchange-coupled α-Fe/Nd–Fe–B multilayer films fabricated by sputtering. *Jpn. Soc. Magn.* **1997**, *21*, 361–364.
51. Fullerton, E.E.; Jiang, J.S.; Sowers, C.H.; Pearson, J.E.; Bader, S.D. Structure and magnetic properties of exchange-spring Sm–Co/Co superlattices. *Appl. Phys. Lett.* **1998**, *72* (3), 380–382.
52. Kato, H.; Nomura, T.; Ishizone, M.; Kubota, H.; Motokawa, M. Magnetic properties of c-axis oriented SmFe<sub>12</sub>/α-Fe nanocomposite films. *J. Appl. Phys.* **2000**, *87*, 6125–6127.
53. Liu, J.P.; Luo, C.P.; Liu, Y.; Sellmyer, D.J. High energy products in rapidly annealed nanoscale Fe/Pt multilayers. *Appl. Phys. Lett.* **1998**, *72* (4), 483–485.
54. Croat, J.J.; Herbst, J.F.; Lee, R.W.; Pinkerton, F.E. Pr–Fe and Nd–Fe-based materials: A new class of high-performance permanent magnets (invited). *J. Appl. Phys.* **1984**, *55* (6), 2078–2082.
55. Ma, B.-M.; Herchenroeder, J.W.; Smith, B.; Suda, M.; Brown, D.N.; Chen, Z. Recent development in bonded Nd-FeB magnets. *J. Magn. Magn. Mater.* **2002**, *239*, 418–423.
56. Yamashita, F.; Ohara, K.; Yamagata, Y.; Fukunaga, F. High-efficiency small IPM brushless motors fabricated by directly molding Nd–Fe–B-based nano-composite magnets with a laminated steel core. *J. Jpn. Soc. Magn.* **2000**, *24*, 431–434.
57. Ono, H.; Waki, N.; Shimada, M.; Sugiyama, T.; Fujiki, A.; Yamamoto, H.; Tani, M. Isotropic bulk exchange-spring magnets with 134 kJ/m<sup>3</sup> prepared by spark plasma sintering method. *IEEE Trans. Magn.* **2001**, *37* (4), 2552–2554.
58. Cadieu, F.J. Rare Earth Transition Metal Film Permanent Magnets, Proceedings of the Seventeenth International Workshop on Rare Earth Magnets and Their Applications, Newark, DE, USA, August, 18–22, 2002; Hadjipanayis, G.C., Bonder, M.J., Eds.; Rinton Press, 2002, 416–427.
59. Chu, S.; Majetich, S.A. Applications of Amorphous Iron in SmCo<sub>5</sub>/Fe Nanocomposites, Proceedings of the Seventeenth International Workshop on Rare Earth Magnets and Their Applications, Newark, DE, USA, August, 18–22, 2002; Hadjipanayis, G.C., Bonder, M.J., Eds.; Rinton Press, 2002, 905–912.
60. Berkowitz, A.E.; Hannsen, M.F.; Vecchio, K.S.; Parker, F.T.; Harper, H.; Spada, F.E. Exchange-Spring Magnets Produced by Spark Erosion, Proceedings of the Seventeenth International Workshop on Rare Earth Magnets and Their Applications, Newark, DE, USA, August, 18–22, 2002; Hadjipanayis, G.C., Bonder, M.J., Eds.; Rinton Press, 2002, 749–759.
61. Shigu, P.H.; Yasuna, K. Nano-scale metal multilayers produced by repeated press-rolling. *Radiat. Eff. Defects Solids* **1999**, *148*, 555–562.
62. Liu, S.; Cui, S.; Bauer, R.; Leese, R.; Hilton, J.S.; Yu, R.H.; Kramp, A.; Dent, J.; Miles, D. Approach to Synthesizing Bulk, Fully Dense Anisotropic Nanocomposite Rare Earth Permanent Magnets, Proceedings of the Seventeenth International Workshop on Rare Earth Magnets and Their Applications, Newark, DE, USA, August, 18–22, 2002; Hadjipanayis, G.C., Bonder, M.J., Eds.; Rinton Press, 2002, 939–946.
63. Zeng, H.; Li, J.; Liu, J.P.; Wang, Z.L.; Sun, S.H. Exchange-coupled nanocomposite magnets by nanoparticle self-assembly. *Nature* **2002**, *420*, 395–398.

# Phase Transfer of Monosaccharides through Noncovalent Interactions

Elizabeth K. Auty  
Anthony P. Davis

*Department of Chemistry, University of Bristol, Bristol, U.K.*

## INTRODUCTION

Sugars constitute one of the major classes of biological building blocks. On one hand, they are important for physical construction (e.g., as cellulose) and energy storage (e.g., as starch). On another more subtle level, they are used by nature to label cells and biomolecules and thus to mediate a variety of biological events. Thus saccharide motifs are central to cell–cell recognition, infection of cells by pathogens, and many aspects of the immune response.<sup>[1–8]</sup>

Carbohydrates are hydrophilic molecules, which are usually freely soluble in water and show little inclination to enter organic media. Nonetheless, there are good reasons why one might wish to promote phase transfer of these species. First, there is a potential large-scale technological application in the production of “high-fructose syrup.” Hydrolysis of starch and enzymatic treatment can be used to produce a mixture of fructose and glucose, which is ca. 42% of the former. Higher levels are desirable as fructose is exceptionally sweet-tasting, and there is much interest in transport processes that might be used in enrichment procedures.<sup>[9,10]</sup> Second, there are biomedical applications for carbohydrate phase transfer. The most immediate might be in the management of diabetes, where an effective, reversible extraction system could be used as the basis for a glucose sensor.<sup>[11–14]</sup> In addition, there is fundamental interest in saccharide transport across biological membranes and the possibility of delivering carbohydrate-like drugs using phase-transfer agents. Third, the study of carbohydrate recognition has become a major area of supramolecular chemistry,<sup>[15,16]</sup> and carbohydrate phase transfer has proved useful in this context. The key challenge is to bind carbohydrates in direct competition with liquid water (their natural environment). However, it is difficult to design and handle receptors that are fully soluble in water. Extraction experiments, involving aqueous and organic phases, provide a straightforward solution to the problem. The receptor, dissolved in the organic solvent, is equilibrated with an aqueous solution of the substrate. The amount of substrate

transferred to the organic phase can be measured and used as a qualitative indication of receptor efficiency. Quantification is possible in principle,<sup>[17]</sup> although to date this has not been realized for carbohydrate substrates.

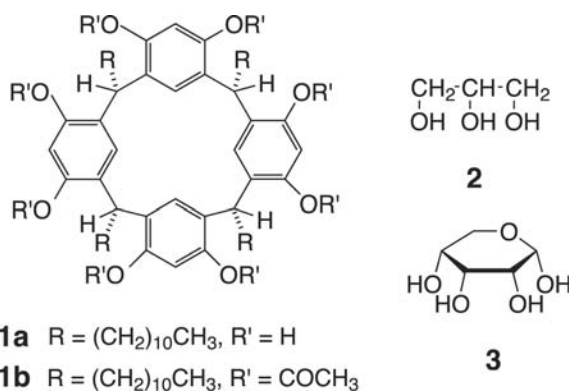
Broadly speaking, two approaches have been taken toward carbohydrate recognition in general, and toward carbohydrate phase transfer in particular. One is based on the reaction of boronic acids with diols to give cyclic boronate esters.<sup>[16,18]</sup> This strategy can be highly effective but, being based on covalent B–O bond formation, lacks biological relevance. The alternative relies on non-covalent interactions, and thus may be seen as “biomimetic.”<sup>[15]</sup> This entry discusses systems belonging to the second category only, focusing on the transfer/transport of simple monosaccharide substrates into/across non-polar phases. The account is divided into three sections covering: 1) preorganized receptor molecules; 2) less organized, micellar systems; and 3) self-assembling channels.

## PHASE TRANSFER OF MONOSACCHARIDES BY PREORGANIZED RECEPTORS

Monosaccharides are relatively large as substrates for supramolecular chemistry, possessing irregular arrays of divergent functional groups. Being mostly hydroxyls, these substituents are capable of hydrogen bonding but do not form especially strong and specific interactions (unlike, for example, carboxylate or ammonium units). Thus carbohydrate recognition is a difficult undertaking, even in the absence of water. Competition from water molecules adds to the challenge, given that the receptor must distinguish the target from competitors bearing the same functional groups. Preorganization, the correct positioning of binding groups and surfaces, is the key to solving such problems.<sup>[19]</sup> Cyclization is a useful strategy for controlling the shape of large, potentially flexible frameworks, and it is not surprising that macrocycles have featured strongly in supramolecular chemistry.<sup>[20]</sup> Macrocycles composed of rigid units possess still fewer conformational options, so that the cyclophane

architecture (a macrocycle incorporating one or more aromatic rings) is especially popular.<sup>[21,22]</sup> Most of the carbohydrate receptors with demonstrated phase transfer capability belong to this family of molecules.

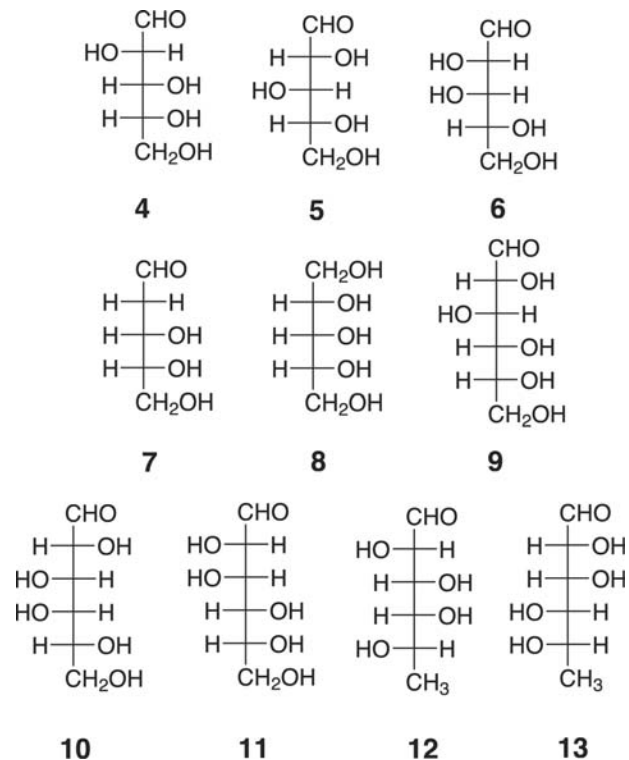
The first such system was the receptor **1a**, synthesized by Aoyama et al.<sup>[23,24]</sup> from resorcinol and dodecanal. This system is furnished with eight phenolic OH groups, capable of hydrogen bonding to the substrate hydroxyls, and four undecyl side chains, which maintain lipophilicity and organic solubility. **1a** was determined by <sup>1</sup>H nuclear magnetic resonance (NMR) to be the all-cis, bowl-shaped isomer shown, and did indeed prove soluble in apolar media such as benzene or CCl<sub>4</sub>. Dissolved in these solvents, it was capable of carrying 4 Eq of water or glycerol **2** into the organic phase. When an extraction was performed using an equimolar mixture of water and **2** ([**2**] = [water] = 11 M), only water was transferred into the organic medium with little coextraction of glycerol evident. However, when a 5.5-M solution of ribose **3** was used as the aqueous phase, the monosaccharide was extracted with water to form a complex of estimated stoichiometry: **1a**:**3**:H<sub>2</sub>O = 1:1:2. Interestingly, the ribose was found to be extracted exclusively in the  $\alpha$ -pyranose form shown, in which all the OH groups are cis. This point is discussed further below. When the *O*-acetylated macrocycle **1b** was used in the extraction experiments, neither **2** nor **3** was transferred to the organic phase, suggestive of OH...OH hydrogen bonding as the key binding interaction.



Aoyama et al. proceeded to study the extraction by **1a** of pentoses **4–8** and hexoses **9–13**. A summary of the results is given in Table 1.

Two factors seem to dominate extractability by **1a**. The first, unsurprisingly, is the hydrophilicity of the sugar [e.g., D-galactose **10** is barely detected in the organic phase, whereas L-fucose (6-deoxy-L-galactose, **12**) is readily extracted]. The second is the relative configuration of the substrates at C<sub>3</sub> and C<sub>4</sub>. Extraction seems to be favored by a cis arrangement in the Fischer projection (e.g., **3**, **4**, **7**, and **12**), which translates to cis in the pyranose form of the carbohydrates. The results

support a face-to-face binding geometry in which OH groups emerging from the same face of the saccharide are best able to form multiple interactions with the receptor.



Later work showed that methyl- $\beta$ -D-glucoside **14** could also be extracted by **1a** from water into CCl<sub>4</sub>, despite the absence of *cis*-1,2-diol units.<sup>[25]</sup> However, in this case, a 2:1 receptor/substrate ratio suggested

**Table 1** Extraction of sugars from water into CCl<sub>4</sub> by **1a**<sup>a</sup>

Sugar	Sugar/ <b>1a</b> <sup>b</sup>
D-ribose <b>3</b>	0.5
D-arabinose <b>4</b>	0.1
D-xylose <b>5</b>	vs <sup>c</sup>
D-lyxose <b>6</b>	vs <sup>c</sup>
2-deoxy-D-ribose <b>7</b>	0.8
Adonitol <b>8</b>	vs <sup>c</sup>
D-glucose <b>9</b>	vs <sup>c</sup>
D-galactose <b>10</b>	vs <sup>c</sup>
D-mannose <b>11</b>	vs <sup>c</sup>
L-fucose <b>12</b>	1.0
6-deoxy-L-mannose <b>13</b>	0.1

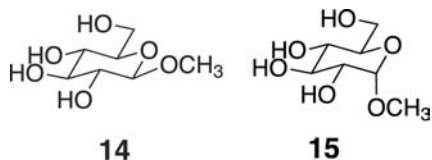
<sup>a</sup>[Sugar]<sub>aq</sub> = 2.4 M, [**1a**]<sub>org</sub> = 0.9 × 10<sup>-2</sup> M.

<sup>b</sup>Molar ratios sugar/**1a** appearing in the organic phase.

<sup>c</sup>Very small; ≤ 0.03.

Source: Ref.<sup>[24]</sup>.

a “sandwich” structure, in which receptor molecules bind to both faces of the guest. The  $\alpha$ -anomer **15**, for which the sandwich structure is probably not possible, was very poorly extracted under the same conditions.

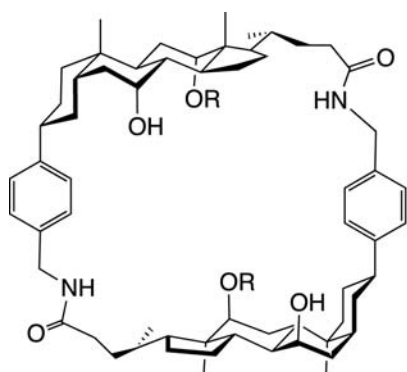
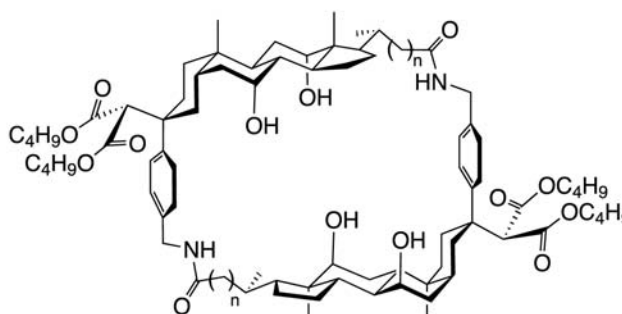
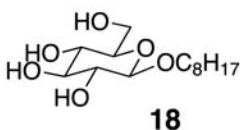


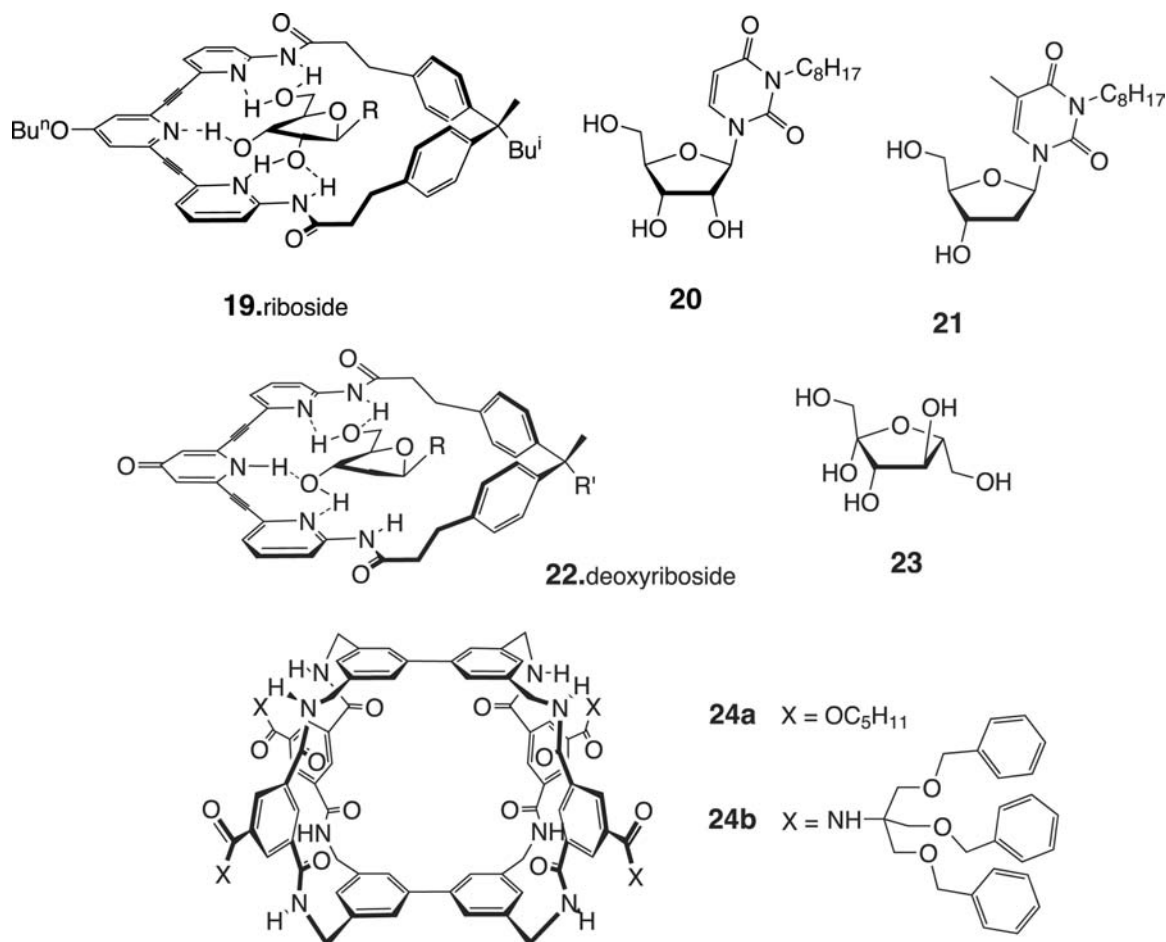
The second example of carbohydrate recognition by preorganized, macrocyclic receptors involved the steroid-derived “cholaphanes” **16**.<sup>[26,27]</sup> These molecules possess substantial cavities capable of fully surrounding a monosaccharide substrate. Up to six H-bonding groups ( $4 \times \text{OH}$  and  $2 \times \text{CONH}$ ) are available to interact with the carbohydrate, whereas the steroidal framework provides a lipophilic exterior compatible with organic media. A second generation of cholaphanes **17** featured externally directed alkyl groups to enhance lipophilicity. In this case, contraction of the side chain in steroidal precursors was used to vary cavity size and flexibility.<sup>[28]</sup>

Receptors **16** and **17** were studied mainly by NMR in homogeneous  $\text{CDCl}_3$  solution, employing organic-soluble glycosides such as **18** as substrates.<sup>[26–28]</sup> However, some extraction experiments were also performed by employing methyl- $\beta$ -D-glucoside **14**.<sup>[28]</sup> The NMR data were compatible with 1:1 complex formation, and allowed the estimation of binding constants ( $K_a$ ). For example, the following values were obtained for

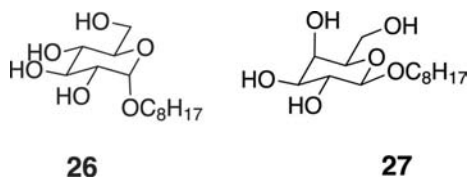
binding to **18**: **16**,  $K_a = 3100 \text{ M}^{-1}$ ; **17a**,  $K_a = 1560 \text{ M}^{-1}$ ; **17b**,  $K_a = 600 \text{ M}^{-1}$ ; and **17c**,  $K_a = 1305 \text{ M}^{-1}$ . In the extraction experiments, solutions of the receptors in chloroform were stirred with aqueous solutions of **14** (1–to 2.5 M). Perhaps surprisingly, the order of effectiveness was **17a** > **17b** > **16** > **17c**, failing to parallel the affinities to **18**. The most efficient, **17a**, was capable of extracting  $\sim 0.2$  Eq of **14** from a 1.75-M aqueous solution, and was also shown to transport this substrate through a chloroform barrier (“U-tube” experiment). Positive results were not obtained with the more hydrophilic glucose. Although not especially effective, this system performed a useful service in relating binding constants to extraction capabilities. Broadly speaking, a  $K_a$  of roughly  $10^3 \text{ M}^{-1}$  in chloroform proved sufficient to extract a moderately hydrophilic carbohydrate (**14**) from fairly concentrated ( $\sim 2 \text{ M}$ ) aqueous solutions.

A third family of macrocycles for carbohydrate phase transfer was developed by Inouye et al. Their initial system, exemplified by **19**, was especially targeted at ribofuranosides.<sup>[29]</sup> As shown, it was designed to provide a series of H-bonding interactions with the three hydroxyl groups of these substrates. In NMR titration experiments with the organosoluble  $\beta$ -D-ribofuranoside **20** and the 2-deoxy substrate **21**, binding constants of 10,000 and  $690 \text{ M}^{-1}$  were measured, respectively. The lower value for **21** is not surprising, given that it can form fewer hydrogen bonds with the receptor. The group then converted the central alkoxy pyridine unit to a pyridone, as in **22**.<sup>[30]</sup> It was hoped that the change from H-bond acceptor to donor would make the receptor more compatible with 2-deoxyfuranosides, as shown. Indeed, the binding

**16a** R = H**16b** R =  $\text{CH}_2\text{Ph}$ **17a** n = 0**17b** n = 1**17c** n = 2**18**



constant of **22** (R = Bu<sup>i</sup>) to **21** in CDCl<sub>3</sub> was found to be 19,000 M<sup>-1</sup>.



The phase-transfer capabilities of **19** and **22** were explored through solubilization experiments employing solid carbohydrate substrates and chloroform as solvent. The results are summarized in Table 2. The data show that the affinities achieved by **19** and, especially, **22** are sufficient to solubilize a full range of monosaccharides (although not necessarily extract them from water). They also reveal genuine, receptor-based selectivity. To amplify this point, a series of figures (binding constants, extraction levels) recorded for a single receptor may not be especially informative. Differences may simply reflect the fact that some substrates are more easily bound (“stickier”) than others. However, when two receptors show distinctly different preferences, receptor

structure is shown to be a major factor. In this case, **19** extracts D-ribose **3** more effectively than 2-deoxy-D-ribose **7** and fails with pyranoses **9–11**, whereas **22** prefers **7** to **3** and succeeds quite well with **9–11**.

**Table 2** Solubilization of sugars in chloroform by **19** and **22** (R' = C<sub>11</sub>H<sub>23</sub>)<sup>a</sup>

Sugar	Sugar/ <b>19</b> <sup>b,c</sup>	Sugar/ <b>22</b> (R' = C <sub>11</sub> H <sub>23</sub> ) <sup>b,d</sup>
D-ribose <b>3</b>	1.0	0.65
D-arabinose <b>4</b>	0.06	0.53
D-xylose <b>5</b>	0.5	0.52
D-lyxose <b>6</b>	0.63	0.66
2-deoxy-D-ribose <b>7</b>	0.7	1.0
D-glucose <b>9</b>	—	0.45
D-galactose <b>10</b>	—	0.32
D-mannose <b>11</b>	—	0.39
D-fructose <b>23</b>	0.2	0.52

<sup>a</sup>[Receptor]<sub>org</sub> = 10<sup>-2</sup>M.

<sup>b</sup>Molar ratios sugar/receptor appearing in solution.

<sup>c</sup>Source: Ref.<sup>[29]</sup>.

<sup>d</sup>Source: Ref.<sup>[30]</sup>.

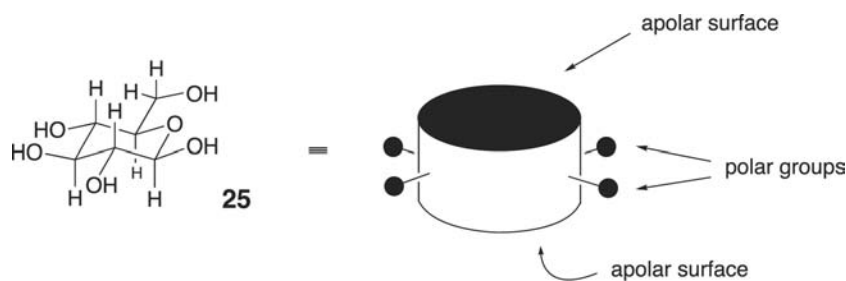


**Fig. 1** D-glucose **9** in  $\beta$ -pyranose form **25**, interpreted as polar and apolar binding regions. *Source:* From Ref.<sup>[31]</sup>.

Macrocyclic receptors **16**, **17**, **19**, and **22** are able to surround their substrates but not encapsulate them. A further advance was made by the macrotricyclic system **24**, which provides a preorganized, essentially enclosed binding site specifically designed for a monosaccharide.<sup>[31,32]</sup> In this case, the target was glucose **9**, in its native pyranose form. As shown in Fig. 1, the all-equatorial pattern of polar substituents in  $\beta$ -D-glucopyranose **25** allows the substrate to be viewed as a disk, with apolar surfaces top and bottom (corresponding to axial CH units) and a polar circumference. Accordingly, **24** consists of two parallel apolar units (biphenyls) connected by bridges containing H-bond donors/acceptors (amides). Modelling (Fig. 2) showed that **25** could fit in the cavity and make at least six intermolecular hydrogen bonds, as well as apolar CH- $\pi$  contacts.<sup>[31]</sup> The structure is reminiscent of that found in carbohydrate-binding proteins, where aromatic surfaces are often found in contact with lipophilic patches on saccharide substrates.<sup>[15]</sup>

Receptor **24** was initially prepared as tetraester **24a** and studied in homogeneous solution. Octyl glycosides **18**, **26**, and **27** were used as substrates. Binding constants were obtained by NMR in  $\text{CDCl}_3$ - $\text{CD}_3\text{OH}$  (92:8) and by fluorescence titration in  $\text{CHCl}_3$ . The results, summarized in Table 3, confirmed that the enclosed binding site yielded significant gains in affinity and selectivity. Thus the complex to  $\beta$ -glucoside **18** was formed with  $K_a \sim 10^3 \text{ M}^{-1}$  even in the presence of 8% by volume of competing methanol, and in pure  $\text{CHCl}_3$  (as used for previous systems), the value was raised to  $3 \times 10^5 \text{ M}^{-1}$ . In both media,  $\alpha$ -glucoside **26** was far less strongly bound.

The phase-transfer properties of **24** were first tested by stirring **24a** with D-glucose **9** in  $\text{CDCl}_3$ .<sup>[31]</sup> Analysis by NMR indicated that  $\sim 0.9$  Eq of **9** was solubilized, representing (as expected) an improvement on **22**. Remarkably, the glucose was detected as a 7:1 mixture of  $\beta$ -pyranose/ $\alpha$ -pyranose, presumably reflecting the preference for  $\beta$ -glucosyl revealed in Table 3.<sup>a</sup>

<sup>a</sup>The  $\beta$ : $\alpha$  ratio should normally be close to 1:1 in organic solvents.

For liquid-liquid extraction, it transpired that increased lipophilicity was required, so **24** was prepared as tetraamide **24b**.<sup>[32]</sup> Extraction experiments were performed in chloroform/water, with the results shown in Table 4. All the substrates were extracted from a 1-M aqueous solution including, for the first time, the hexoses **9**–**11**. Notable selectivity was shown for the “all-equatorial” saccharides glucose **9** and xylose **5**. Moreover, glucose, the specific target of **24**, was extracted from aqueous solutions as low as 0.1 M in concentration. Physiological glucose concentrations, at 0.005 M, are still out of reach, but with further development, this system could ultimately serve as the basis of a clinically relevant glucose sensor.

## PHASE TRANSFER OF MONOSACCHARIDES BY LESS ORGANIZED SYSTEMS

The essential characteristic required for carbohydrate phase transfer is an amphiphilic structure with a polar interior and an apolar exterior. Although preorganization of the polar interior should, in principle, be advantageous, it turns out that less organized structures can also be successful. One example is provided by thiosuccinate derivative **28**, studied by Greenspoon and Wachtel.<sup>[33]</sup> At a concentration of 50 mM, **28** was shown by x-ray scattering experiments to form “inverse micelles” (polar interior, apolar exterior) in a mixture of chloroform/cyclohexane, 1:1. Addition of D-glucose **9** (solid monohydrate) followed by centrifugation gave a clear solution, which was found by NMR to contain one molecule of glucose per nine molecules of **28**. It appears that the assembly of **28** can bind the glucose directly, without a solvation shell of water. When water was added, the glucose-derived NMR signals shifted, indicating a change in environment. Further NMR experiments with **29** as substrate, and electron spin resonance spectroscopy (ESR) studies employing **30**, confirmed that the monosaccharide unit was associated with the micelles.



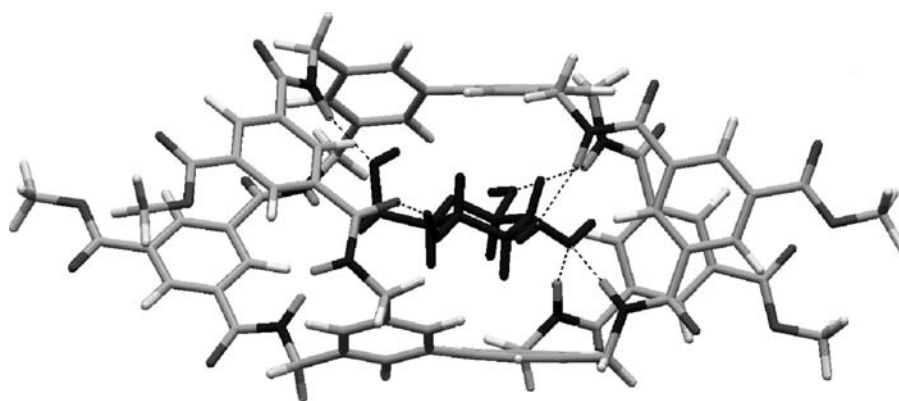


**Fig. 2** Receptor **24**, modelled as the tetramethyl ester, binding D-glucose **9** as the  $\beta$ -pyranose. The configuration shown is the baseline conformation from a 1000-step Monte Carlo molecular mechanics study. Intermolecular hydrogen bonds are shown as broken lines. *Source:* From Ref.<sup>[31]</sup>.

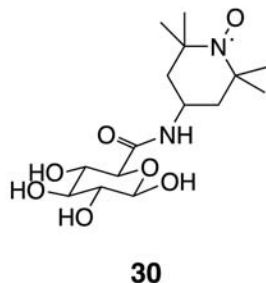
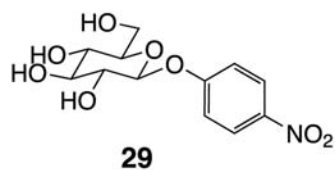
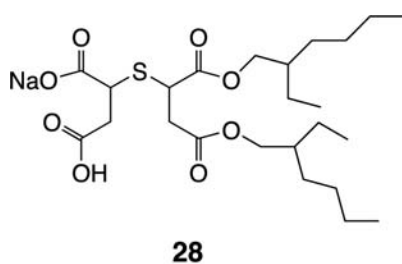


**Table 3** Binding constants ( $K_a$ ) of octyl glycosides to macrotricyclic **24a**

Substrate	$K_a$ [ $M^{-1}$ ] in	$K_a$ [ $M^{-1}$ ] in
	$CDCl_3$ - $CD_3OH$ (92:8) <sup>a</sup>	$CDCl_3$ - $CD_3OH$ (92:8) <sup>b</sup>
$\beta$ -D-glucopyranoside <b>18</b>	980 ( $\pm 2\%$ )	300,000 ( $\pm 6\%$ )
$\alpha$ -D-glucopyranoside <b>26</b>	20 ( $\pm 23\%$ )	13,000 ( $\pm 8\%$ )
$\beta$ -D-galactopyranoside <b>27</b>	220 ( $\pm 5\%$ )	110,000 ( $\pm 12\%$ )

<sup>a</sup><sup>1</sup>H NMR titrations.

<sup>b</sup>Fluorescence titrations.

*Source:* Ref.<sup>[31]</sup>.

Kobayashi et al.<sup>[34]</sup> studied **31**, a macrocyclic but flexible system best seen as a “unimolecular reversed micelle.” When **31a** dissolved in  $CCl_4$  was stirred with water, <sup>1</sup>H NMR analysis revealed the presence of ca. 40 molecules of  $H_2O$  in the organic phase. However, when 3-M solutions of D-ribose **3**, D-glucose **9**, or D-fructose **23** were substituted for water, the carbohydrate was extracted without any measurable coextraction of  $H_2O$ . In the case of D-glucose **9**, a 1 : 1 ratio of receptor/substrate was established directly by <sup>1</sup>H NMR integration, and also by reextraction of the sugar back into water. Sugar extraction, as well as water pool accommodation, were also observed with the acyclic heptakis(dihydroxyalkyl) reference host **32**, although no complexation was observed for **31b** or **33**, implying that the clustering of dihydroxyalkyl chains is essential for recognition.

Kasuga et al.<sup>[35]</sup> have shown that the lipophilic alkaline earth metal salts **34** can promote transport of monosaccharides through chloroform bulk liquid membranes. Efficiency increased with cation size, the

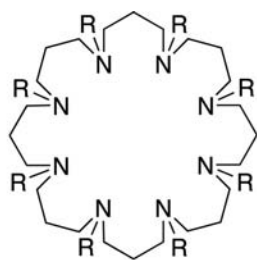
**Table 4** Extractabilities of monosaccharide substrates from water into chloroform by receptor **24b**<sup>a</sup>

Substrate	Concentration of substrate in aqueous phase (M)		
	1.0	0.5	0.1
D-ribose <b>3</b>	0.7		
D-xylose <b>5</b>	1.1		
D-glucose <b>9</b>	1.0	0.5	<0.1 <sup>b</sup>
D-galactose <b>10</b>	0.2	<0.1 <sup>b</sup>	None detectable
D-mannose <b>11</b>	<0.1 <sup>b</sup>	<0.1 <sup>b</sup>	None detectable
Methyl- $\beta$ -D-glucoside <b>14</b>	1.0		
Methyl- $\alpha$ -D-glucoside <b>15</b>	1.0		

<sup>a</sup>Molar ratios sugar/**24b** appearing in the organic phase.  $[24b]_{org} = 2.9 \times 10^{-4}$  M.

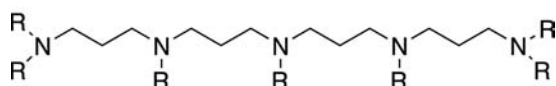
<sup>b</sup>Carbohydrate detectable, but amounts too small for quantification by NMR integration.

*Source:* Ref.<sup>[32]</sup>.

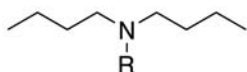


**31a** R = CH<sub>2</sub>CH(OH)CH(OH)(CH<sub>2</sub>)<sub>10</sub>CH<sub>3</sub>

**31b** R = (CH<sub>2</sub>)<sub>11</sub>CH<sub>3</sub>

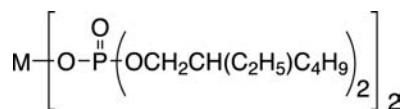


**32** R = CH<sub>2</sub>CH(OH)CH(OH)(CH<sub>2</sub>)<sub>10</sub>CH<sub>3</sub>



**33** R = CH<sub>2</sub>CH(OH)CH(OH)(CH<sub>2</sub>)<sub>10</sub>CH<sub>3</sub>

most effective carrier being **34** (M = Ba). A range of monosaccharides were tested as substrates, with the results shown in Table 5. Unsurprisingly, transport rates correlate to a fair degree with apparent substrate lipophilicity. However, the preference for D-ribose **3** over 2-deoxy-D-ribose **7** runs counter to this trend, and is especially interesting.



**34** M = Mg, Ca, Sr, Ba

## CHANNEL-MEDIATED TRANSPORT OF CARBOHYDRATES

Finally, in the special case of aqueous phases separated by a lipid bilayer, polar substrates may be transferred via channels in the membrane. Bong et al.<sup>[36]</sup> have studied a range of self-assembling channels formed from cyclic peptides composed of alternating D and L amino acids. The peptides stack through hydrogen bonding to form a toroidal version of a  $\beta$ -sheet. If a decapeptide is used, the resulting tube has an internal diameter of ca. 10 Å, enough to allow passage of a glucose molecule.<sup>[37]</sup> The cyclodecapeptide **35**, composed mainly of lipophilic D-leucine and L-tryptophan, was designed to concentrate in apolar environments. When added to liposome suspensions, it was shown by several spectroscopic techniques to incorporate into the bilayers to form H-bonded aggregates. If D-glucose **9** was entrapped in the liposomes, addition of **35** promoted efflux of the carbohydrate (measured using an enzyme-based assay). Kinetic studies were consistent with a channel, rather than carrier, transport mechanism. The analogous cyclooctapeptide, with an internal diameter of  $\sim 7.5$  Å, showed no activity.

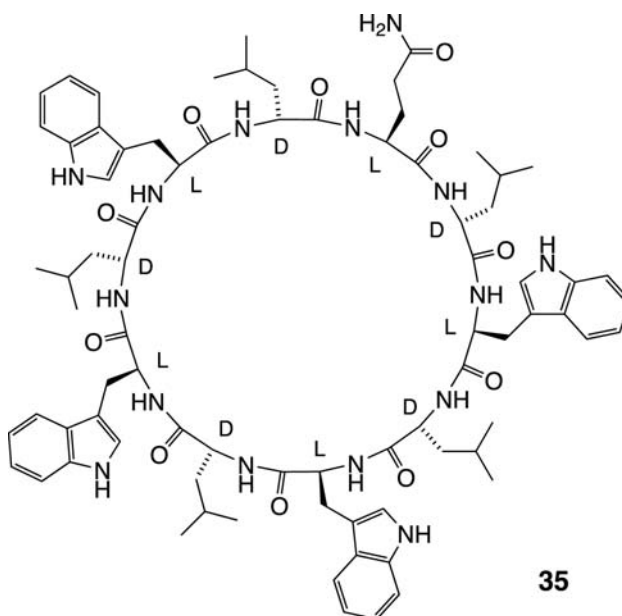
**Table 5** Transport of monosaccharides by **34** (M = Ba)<sup>a</sup>

Sugar	Amount of sugar transported after 48 hr (mmol)
D-ribose <b>3</b>	3.0 (1.7) <sup>b</sup>
D-arabinose <b>4</b>	0.4
D-xylose <b>5</b>	0.3 (0.1) <sup>b</sup>
2-deoxy-D-ribose <b>7</b>	0.5
D-glucose <b>9</b>	0.1 (0) <sup>b</sup>
D-galactose <b>10</b>	0.1
D-mannose <b>11</b>	0.4 (0.2) <sup>b</sup>
L-fucose <b>12</b>	0.7
D-fructose <b>23</b>	0.7

<sup>a</sup>[Receptor]<sub>org</sub> = 3 × 10<sup>-2</sup> M.

<sup>b</sup>Figures in parentheses refer to a competition experiment in which four monosaccharides were present simultaneously.

Source: Ref.<sup>[35]</sup>.



**35**

## CONCLUSION

In summary, the study of carbohydrate recognition through non-covalent interactions has led to a range of phase transfer systems, effective for moderate to high concentrations of substrates. It remains difficult to transport monosaccharides into apolar media from dilute aqueous solutions. However, steady progress over the past 15 years suggests that the necessary affinities will be achieved before long. Success could have important consequences, not least in diabetes treatment where improved glucose sensors are sought with some urgency.<sup>[11–14]</sup>

## ACKNOWLEDGMENTS

A.P.D. thanks all of his coworkers, whose names appear in the references, for their contributions to date and for their ongoing efforts in this area. Funding for our program on carbohydrate recognition has been provided by the EPSRC, the European Commission, the University of Bristol, and the Enterprise Ireland.

## REFERENCES

- Dwek, R.A.; Butters, T.D. Glycobiology—understanding the language and meaning of carbohydrates. *Chem. Rev.* **2002**, *102* (2), 283–284.
- Bertozi, C.R.; Kiessling, L.L. Chemical glycobiology. *Science* **2001**, *291* (5512), 2357–2364.
- Williams, S.J.; Davies, G.J. Protein–carbohydrate interactions: learning lessons from nature. *Trends Biotechnol.* **2001**, *19* (9), 356–362.
- Feizi, T.; Mulloy, B. Editorial overview: progress at the frontiers of structural glycobiology. *Curr. Opin. Struct. Biol.* **2001**, *11* (5), 585–586.
- Roseman, S. Reflections on glycobiology. *J. Biol. Chem.* **2001**, *276* (45), 41,527–41,542.
- Weis, W.I.; Drickhamer, K. Structural basis of lectin–carbohydrate recognition. *Annu. Rev. Biochem.* **1996**, *65*, 441–473.
- Sharon, N.; Lis, H. Lectins—proteins with a sweet tooth: functions in cell recognition. *Essays Biochem.* **1995**, *30*, 59–75.
- Lee, Y.C.; Lee, R.T. Carbohydrate–protein interactions: basis of glycobiology. *Acc. Chem. Res.* **1995**, *28*, 321–327.
- Altamore, T.M.; Barrett, E.S.; Duggan, P.J.; Sherburn, M.S.; Szydzik, M.L. Cavitand boronic acids mediate highly selective fructose transport. *Org. Lett.* **2002**, *4* (20), 3489–3491.
- Paugam, M.F.; Riggs, J.A.; Smith, B.D. High fructose syrup production using fructose-selective liquid membranes. *Chem. Commun.* **1996**, (22), 2539–2540.
- Tohda, K.; Gratzl, M. A microscopic, continuous, optical monitor for interstitial electrolytes and glucose. *ChemPhysChem* **2003**, *4* (2), 155–160.
- Katz, E.; Sheeney-Haj-Ichia, L.; Buckmann, A.F.; Willner, I. Dual biosensing by magneto-controlled bioelectrocatalysis. *Angew. Chem., Int. Ed. Engl.* **2002**, *41* (8), 1343–1346.
- Wei, Y.; Dong, H.; Xu, J.G.; Feng, Q.W. Simultaneous immobilization of horseradish peroxidase and glucose oxidase in mesoporous sol–gel host materials. *ChemPhysChem* **2002**, *3* (9), 802.
- Shafer-Peltier, K.E.; Haynes, C.L.; Glucksberg, M.R.; Van Duyne, R.P. Toward a glucose biosensor based on surface-enhanced Raman scattering. *J. Am. Chem. Soc.* **2003**, *125* (2), 588–593.
- Davis, A.P.; Wareham, R.S. Carbohydrate recognition through noncovalent interactions: a challenge for biomimetic and supramolecular chemistry. *Angew. Chem., Int. Ed. Engl.* **1999**, *38* (20), 2978–2996.
- James, T.D.; Sandanayake, K.R.A.S.; Shinkai, S. Saccharide sensing with molecular receptors based on boronic acid. *Angew. Chem., Int. Ed. Engl.* **1996**, *35* (17), 1911–1922.
- Ayling, A.J.; Broderick, S.; Clare, J.P.; Davis, A.P.; Pérez-Payán, M.N.; Lahtinen, M.; Nissinen, M.J.; Rissanen, K. An extraction-based assay for neutral anionophores: the measurement of high binding constants to steroidal receptors in a nonpolar solvent. *Chem. Eur. J.* **2002**, *8* (9), 2197–2203.
- Smith, B.D. Liquid membrane transport using boronic acid carriers. *Supramol. Chem.* **1996**, *7* (1), 55–60.
- Cram, D.J. Preorganization—from solvents to spherands. *Angew. Chem., Int. Ed. Engl.* **1986**, *25* (12), 1039–1057.
- Lehn, J.-M., Ed. *Comprehensive Supramolecular Chemistry*; Pergamon: Oxford, 1996.
- Diederich, F.N. *Cyclophanes*; Royal Society of Chemistry: Cambridge, 1991.
- Vögtle, F. *Cyclophane Chemistry; Synthesis, Structures, Reactions*; Wiley: Chichester, 1993.
- Aoyama, Y.; Tanaka, Y.; Toi, H.; Ogoshi, H. Polar host–guest interaction. Binding of nonionic polar compounds with a resorcinol–aldehyde cyclooligomer as a lipophilic polar host. *J. Am. Chem. Soc.* **1988**, *110*, 634–635.
- Aoyama, Y.; Tanaka, Y.; Sugahara, S. Molecular recognition of sugars via hydrogen-bonding interaction with a synthetic polyhydroxy macrocycle. *J. Am. Chem. Soc.* **1989**, *111*, 5397–5404.
- Kikuchi, Y.; Tanaka, Y.; Sutarō, S.; Kobayashi, K.; Toi, H.; Aoyama, Y. Highly cooperative binding of alkyl glucopyranosides to the resorcinol cyclic tetramer due to intracomplex guest–guest hydrogen bonding: solvophobicity/solvophilicity control by an alkyl group of the geometry, stoichiometry, stereoselectivity, and cooperativity. *J. Am. Chem. Soc.* **1992**, *114*, 10,302–10,306.
- Bonar-Law, R.P.; Davis, A.P.; Murray, B.A. Artificial receptors for carbohydrate derivatives. *Angew. Chem., Int. Ed. Engl.* **1990**, *29*, 1407.
- Bhattacharai, K.M.; Bonar-Law, R.P.; Davis, A.P.; Murray, B.A. Diastereo- and enantio-selective binding

- of octyl glucosides by a tetrahydrocholaphane. *J. Chem. Soc., Chem. Commun.* **1992**, 752.
28. Bhattarai, K.M.; Davis, A.P.; Perry, J.J.; Walter, C.J. A new generation of “cholaphanes”: steroid derived macrocyclic hosts with enhanced solubility and controlled flexibility. *J. Org. Chem.* **1997**, *62*, 8463–8473.
  29. Inouye, M.; Toshiyuki, M.; Masaru, F.; Hiroyuki, N. Molecular recognition of  $\beta$ -ribofuranosides by synthetic polypyridine–macrocyclic receptors. *J. Am. Chem. Soc.* **1995**, *117*, 12,416–12,425.
  30. Inouye, M.; Takahashi, K.; Nakazumi, H. Remarkably strong, uncharged hydrogen-bonding interactions of polypyridine–macrocyclic receptors for deoxyribofuranosides. *J. Am. Chem. Soc.* **1999**, *121* (2), 341–345.
  31. Davis, A.P.; Wareham, R.S. A tricyclic polyamide receptor for carbohydrates in organic media. *Angew. Chem., Int. Ed. Engl.* **1998**, *37* (16), 2270–2273.
  32. Ryan, T.J.; Lecollinet, G.; Velasco, T.; Davis, A.P. Phase transfer of monosaccharides through noncovalent interactions: selective extraction of glucose by a lipophilic cage receptor. *Proc. Natl. Acad. Sci.* **2002**, *99* (8), 4863–4866.
  33. Greenspoon, N.; Wachtel, E. Reverse micelles as a model system for carbohydrate binding. *J. Am. Chem. Soc.* **1991**, *113*, 7233–7236.
  34. Kobayashi, K.; Ikeuchi, F.; Inaba, S.; Aoyama, Y. Accommodation of polar guests in unimolecular polyamine–polyhydroxy cores: solubilisation of sugars in apolar organic media via intramolecular polar micro-solvation. *J. Am. Chem. Soc.* **1992**, *114*, 1105–1107.
  35. Kasuga, K.; Hirose, T.; Aiba, S.; Takahashi, T.; Hiattani, K. Transport of monosaccharides through a liquid membrane mediated by lipophilic alkaline earth metal complexes. *Tetrahedron Lett.* **1998**, *39*, 9699–9702.
  36. Bong, D.T.; Clark, T.D.; Granja, J.R.; Ghadiri, M.R. Self-assembling organic nanotubes. *Angew. Chem., Int. Ed. Engl.* **2001**, *40* (6), 988–1011.
  37. Granja, J.R.; Ghadiri, M.R. Channel mediated transport of glucose across lipid bilayers. *J. Am. Chem. Soc.* **1994**, *116*, 10,785–10,786.

# Photonic Crystal Fibers

**P. St. J. Russell**

**J. C. Knight**

**T. A. Birks**

*Department of Physics, University of Bath, Bath, U.K.*

**P. J. Roberts**

*BlazePhotonics Ltd., Bath, U.K.*

## INTRODUCTION

In 1842, the Swiss physicist Daniel Colladon<sup>[1]</sup> demonstrated that light could be guided along a curved path within a tube of transparent material. Colladon's "light pipe" was simply a narrow stream of water issuing through a hole in the side of a tank. The underlying guidance mechanism in this case was, of course, total internal reflection (TIR)—the phenomenon by which standard single-mode fiber (SMF) guides light. A typical SMF designed for communications wavelengths (Fig. 1A) has a Ge-doped silica core (synthesized by modified chemical vapor deposition),<sup>[2]</sup> a core-cladding refractive index difference of a few percent, and a core diameter of  $\sim 10\ \mu\text{m}$ , and possesses astonishing optical clarity (0.2 dB/km at 1550 nm). Although SMF has been outstandingly successful in optical telecommunications, there is still pressure to further improve its performance. For example, optical non-linearities in the solid glass core are proving complex to understand and awkward to control, and are contributing to bit error rate deterioration over long spans in wavelength division multiplexed systems. In other fields, there is a long-standing need for fibers that can carry higher power; act as versatile sensors or hosts for rare earth ions; and have multiple cores, higher non-linearities, lower non-linearities, higher birefringence, and widely engineerable dispersion.

## Annular Fibers

In the early 1970s, another kind of structure had been proposed, in theory, as an alternative to SMF (Fig. 1B). This was a cylindrical fiber that guided light by Bragg scattering at a periodic array of annular rings of high and low refractive index arranged around a central core.<sup>[3]</sup> A team in France has recently succeeded in making a solid-core version of this structure using

modified chemical vapor deposition (MCVD).<sup>[4]</sup> Work is also underway to realize a hollow-core version of a similar structure.<sup>[5]</sup>

## Photonic Crystal Fibers

In 1991, the idea emerged<sup>[6]</sup> that light might be trapped in a hollow core by means of a two-dimensional "photonic crystal" of microscopic air capillaries running along the entire length of a fiber. Appropriately designed, this array would support a photonic band gap for incidence from air, preventing the escape of light from a hollow core into the cladding and avoiding the need for TIR. It was initially far from obvious that so many new applications and developments would emerge from the photonic crystal fiber (PCF) concept.<sup>[7–9]</sup> The two basic types—with hollow and solid cores—are illustrated in Fig. 1C and D. In this entry, we review its fabrication and guidance mechanisms, numerical modelling techniques, and the numerous and growing number of applications.

## Nomenclature

The PCF idea came from the field of photonic band gap materials, not from within fiber optics. For this reason, we prefer the name PCF. It is also sometimes referred to as "holey" fiber (P. R.'s first jocular name for it, before anyone knew whether it could be made) or "microstructure" fiber.

## FABRICATION TECHNIQUES

The first working PCF emerged from the drawing tower in late 1995.<sup>[10]</sup> Since then, structures with increasing perfection and uniformity have been produced in many laboratories, using several different

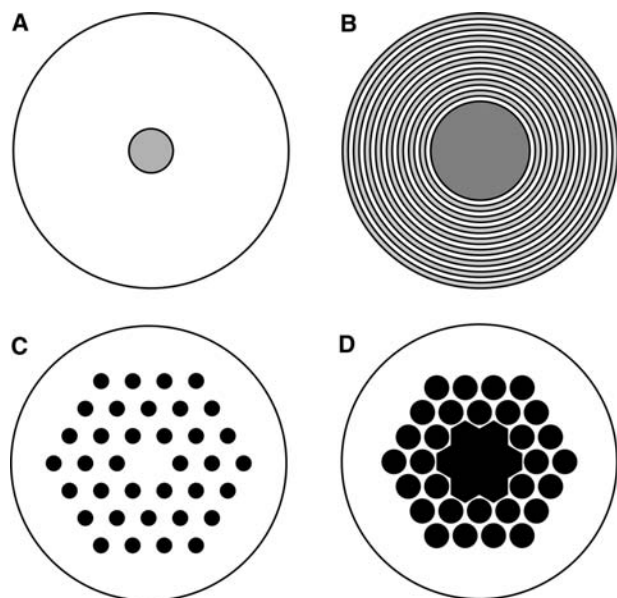


**Fig. 1** (A) Standard SMF: outer diameter, 125  $\mu\text{m}$ ; core diameter,  $\sim 9 \mu\text{m}$ ; core refractive index, a few percent higher than the silica-cladding index (1.46). (B) Annular Bragg fiber. (C) Solid-core PCF. (D) Hollow-core PCF. The black regions are hollow, and the white and grey regions denote pure and doped glass.

techniques (Fig. 2). The first stage is the production of a “preform”—a macroscopic facsimile of the nanoscopic structure in the drawn PCF. There are many ways to do this, including stacking of capillaries and rods,<sup>[11]</sup> extrusion,<sup>[12–14]</sup> sol-gel casting, injection molding, and drilling.<sup>[15]</sup>

The most widely used technique is capillary stacking (Fig. 3), a method that is especially suited to silica glass because of the ready availability of high-quality starting tubes of appropriate dimensions. Typically, meter-length capillaries with an outer diameter of around 1 mm are drawn from a starting tube of high-purity synthetic silica with a diameter of perhaps 20 mm and a length of 1 m. The inner diameter of the capillaries is largely set by the inner/outer diameter ratio of the starting tube, which might lie in the range from 0.3 up to beyond 0.9. The uniformity in diameter of the capillaries (and their circularity) should be controlled to at least 1% of the diameter, and preferably far better. When a suitable quantity of uniform capillaries is available, they are stacked horizontally by hand in a suitable jig to form a close-packed arrangement. The final stack is loosely bound with wire, before being inserted into a snug jacketing tube. It is then mounted in the preform feed assembly for drawing down to fiber.

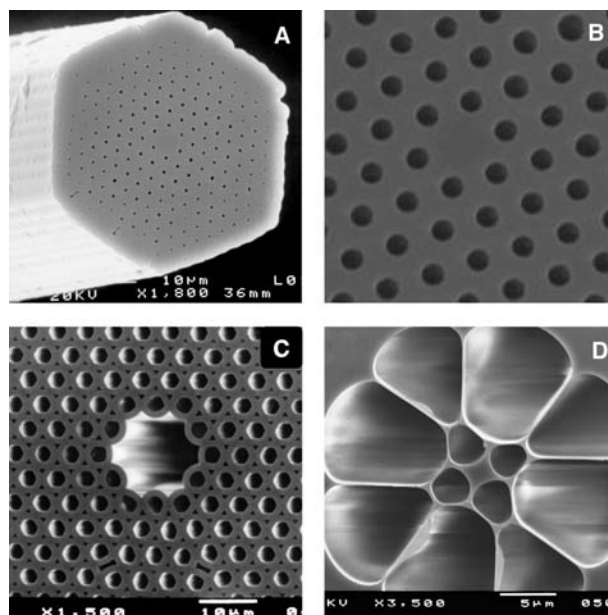


**Fig. 2** (A) The first working PCF—the solid glass core is surrounded by a triangular array of 300-nm-diameter air channels, spaced 2.3  $\mu\text{m}$  apart. From Ref.<sup>[11]</sup>. (B) Detail of a recent low-loss solid-core PCF (interhole spacing,  $\sim 2 \mu\text{m}$ ). From Refs.<sup>[26]</sup> and<sup>[35]</sup>. (C) The first hollow-core PCF. From Ref.<sup>[19]</sup>. (D) A small-core PCF extruded from Schott SF6 glass. Source: From Ref.<sup>[13]</sup>.

Extrusion is an attractive alternative route to making PCF from bulk glass. It enables the formation of structures that are not readily achievable by stacking, and requires a minimal amount of processing. Perhaps its most important application is to non-silica glass PCFs and other materials. Fig. 2D shows the cross section of a fiber extruded, through a metal die, from a commercially available glass (Schott SF6).<sup>[13]</sup>

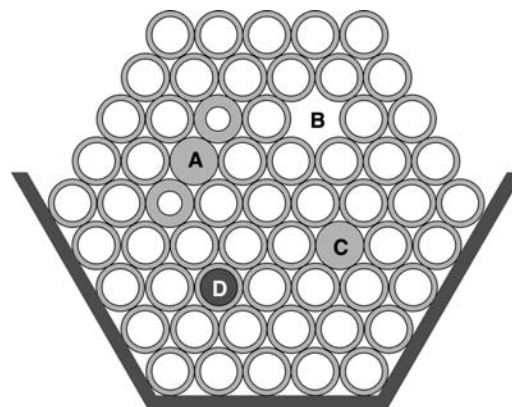


**Fig. 3** Preform stack containing (A) birefringent solid core; (B) hollow core; (C) solid isotropic core; and (D) doped core. The capillary diameters are  $\sim 1 \text{ mm}$ .



## CHARACTERISTICS OF PHOTONIC CRYSTAL CLADDING

The simplest photonic crystal cladding is a biaxially periodic, defect-free, composite material with its own well-defined dispersion and band structure. A good knowledge of its properties is essential for understanding the behavior of the guided modes that form at cores (or “structural defects” in the parlance of photonic crystals). A useful graphical tool is the propagation diagram—a map of the ranges of frequency and axial wavevector component where light is evanescent in all transverse directions regardless of its polarization state (Fig. 4).<sup>[16]</sup> The vertical axis is the normalized frequency  $k\Lambda = \omega\Lambda/c$  ( $\omega$  is the angular frequency,  $\Lambda$  is the inter-hole spacing, and  $c$  is the velocity of light in vacuum), and the horizontal axis is the normalized axial wavevector  $\beta\Lambda$ . Light is free to propagate in the white areas and is evanescent (due either to TIR or photonic band gaps) in the black regions. In any subregion of isotropic material (glass or air) at fixed optical frequency, the maximum possible value of  $\beta\Lambda$  is given by  $k\Lambda n$ , where  $n$  is the refractive index (at that frequency) of the region under consideration. For  $\beta < kn$ , light is free to propagate; for  $\beta > kn$ , it is evanescent; and at  $\beta = kn$ , the critical angle is reached—denoting the onset of TIR for light incident from a medium of index larger than  $n$ . Moving from left to right, the slanted guidelines (included in Fig. 4) denote the transitions from propagation to evanescence for glass, air, and the photonic crystal. The maximum value of  $\beta\Lambda$  in the photonic crystal cladding lies in the range  $k < \beta\Lambda < kn_s$  (where  $n_s$  is the index of silica) as expected of a glass/air composite

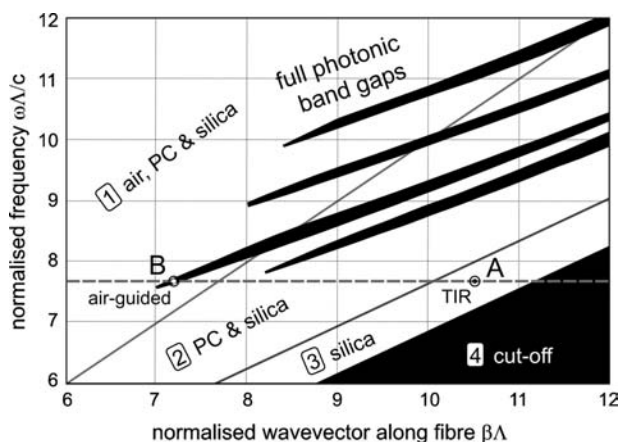


**Fig. 4** Propagation diagram for a PCF with 45% air-filling fraction. Note the different regions where light is (4) cut off completely, (3) able to propagate only in silica glass, (2) able to propagate also in the photonic crystal cladding, and (1) able to propagate in all regions. The “fingers” indicate the positions of full two-dimensional photonic band gaps. From Ref.<sup>[16]</sup>.

material. Its maximum axial refractive index depends strongly on frequency, even though neither the air nor the glass is assumed to be dispersive in the analysis. Microstructuring itself creates dispersion, through a balance between transverse energy storage and energy flow that is highly dependent on frequency. As the wavelength of the light falls, the optical fields are better able to distinguish between the glass regions and the air. The light piles up more and more in the glass or the air, causing the effective refractive index “seen” by it to change. In the limit of small wavelength  $\Lambda/\lambda \rightarrow \infty$ , the light is strongly excluded from the air holes by TIR, and the field profile freezes into a shape independent of wavelength. Treating each strand as a metallic waveguide of radius  $a = \Lambda/\sqrt{3} - d/2$  and making the approximation that the field amplitude is  $J_0(r_{z_{01}}/a)$  (where  $z_{01}$  is the first zero of the Bessel function  $J_0$ ), it may be shown that the maximum axial refractive index in the cladding is:

$$n_{\text{FSM}} \approx \sqrt{n_s^2 - \frac{z_{01}^2 \lambda^2}{4\pi^2 a^2}} \quad (1)$$

in the short wavelength limit. For a more rigorous account of this phenomenon, see Ref.<sup>[17]</sup>.

The finger-shaped regions on the diagram denote full two-dimensional photonic band gaps. Some of these extend into the region  $\beta < k$ , where light is free to propagate in vacuum, confirming the feasibility of trapping light within an empty microtube.

## CLASSES OF GUIDANCE

In SMF, guided modes form in the range of axial refractive indices  $n_{\text{cl}} < n_z < n_{\text{core}}$ , when light is evanescent in the cladding ( $n_z = \beta/k$ ). In PCF, four distinct guidance mechanisms exist: a modified form of TIR,<sup>[17,18]</sup> photonic band gap guidance,<sup>[19]</sup> a frustrated tunneling process (leading to the formation of surface states around the edge of the core),<sup>[20]</sup> and a low-leakage mechanism based on creating a low density of states in the cladding.<sup>[21]</sup>

### Modified Total Internal Reflection

This type of guidance was observed in late 1995, in the first working PCF, at a central solid core in an array of  $\sim 300$ -nm-diameter air holes, spaced  $2.3 \mu\text{m}$  apart (Fig. 2A). The striking feature of this fiber was that it was “endlessly single-mode” (i.e., the core did not ever seem to become multimode in the experiments, no matter how short the wavelength of the light).<sup>[17]</sup> Although the guidance in some respects closely resembled conventional TIR, it turned out to

have some interesting and unique features that distinguish it markedly from the standard case. These are because of the piecewise discontinuous nature of the core boundary—sections where air holes strongly block the escape of light interspersed with regions of barrier-free glass. In fact, the cladding operates in the Mie scattering regime where transverse effective wavelength (in silica) is comparable with geometrical substructures in the cladding. The zone of operation in Fig. 4 is  $n_{\text{FSM}} < n_z < n_{\text{silica}}$ .

### Photonic Band Gap: Hollow Core

Larger air-filling fractions and small interhole spacings are necessary to achieve photonic band gaps in the region  $n_z < 1$ . The relevant operating region in Fig. 4 is to the left of the vacuum line inside one of the band gap fingers. These conditions ensure that light is free to propagate—and form guided modes—within the hollow core while unable to escape into the cladding. The number  $N$  of such modes is controlled by the depth and width of the refractive index “potential well” and is given by:

$$N \approx 2\pi^2 \rho^2 (n_{\text{high}}^2 - n_{\text{low}}^2) / \lambda^2 \quad (2)$$

where  $n_{\text{high}}$  and  $n_{\text{low}}$  are the refractive indices at the edges of the photonic band gap,  $\rho$  is the core radius, and  $\lambda$  is the wavelength of light. Because the band gaps are quite narrow ( $n_{\text{high}}^2 - n_{\text{low}}^2$  is typically a few percent), the hollow core must be large if a guided mode is to exist at all. In the first working hollow-core PCF reported in 1999,<sup>[19]</sup> the core was formed by omitting

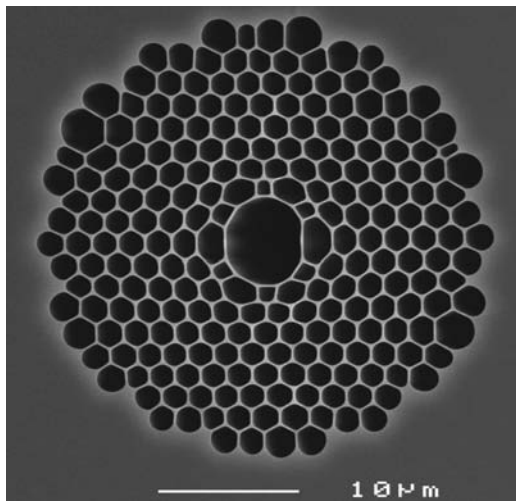


**Fig. 5** Scanning electron micrograph of a hollow-core PCF designed to guide 1064 nm light. (Transmission spectrum is plotted in Fig. 8.) Note the slightly elliptical core.

seven capillaries from the preform stack (Fig. 2C). An electron micrograph of a more recent hollow-core PCF is shown in Fig. 5.<sup>[22]</sup>

### Photonic Band Gap: Surface States

To observe unambiguous photonic band gap guidance, it is necessary to ensure that the core refractive index is lower than the cladding index. The first such PCF, demonstrated in 1998, consisted of a lattice of air holes arranged in the same way as the carbon rings in graphite. A core was formed by introducing an extra hole at the center of one of the rings, its low index precluding the possibility of TIR guidance.<sup>[20]</sup> When white light was launched into the core region, a brightly colored mode was transmitted—the colors being dependent on the absolute size to which the fiber was drawn. The modal patterns had six equally strong lobes, disposed in a flowerlike pattern around the central hole. Closer examination revealed that the light was guided not in the air holes but in the six narrow regions of glass surrounding the core. The light chose to remain in these regions, despite the close proximity of large areas of silica, full of modes. One interpretation of this behavior is that, for particular wavelengths, the phase velocity of the light in the core is not coincident with any of the phase velocities available in the transmission band created by the array of larger adjacent regions. Thus light is unable to tunnel over to them and so remains trapped in the core. This “frustrated tunneling” mechanism of photonic band gap formation can only operate in extended two-dimensional structures (similar types of behavior are seen in modes trapped within defect layers in multilayer stacks<sup>[23]</sup>). The guided modes, which can also form in hollow-core PCF, can be viewed as surface-trapped states, light being confined by TIR on the core side of a boundary and by a photonic band gap on the cladding side. The zone of operation in Fig. 4 is  $1 < n_z < n_{\text{FSM}}$ .

### Low Density-of-States Guidance

It was shown that the transmission bands can be greatly widened by fabricating a different cladding structure—a Kagomé lattice.<sup>[21]</sup> Fig. 6A shows the white-light mode emerging from such a fiber, the minimum loss being  $\sim 1$  dB/m. It turns out in this case that the density of states is greatly reduced in the cladding near the vacuum line. The consequential poor match between the core states and the greatly reduced number of cladding states slows down, but does not completely prevent, the leakage of light. The precise details of the mechanism of this case are still under study.

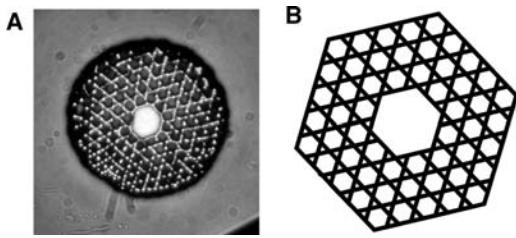


**Fig. 6** (A) PCF designed for guidance of white light. *Source:* From Ref.<sup>[21]</sup> (B) The “Kagomé” lattice in the cladding provides a low density of states (i.e., an incomplete band gap).

## CHARACTERISTICS OF GUIDANCE

### Controlling Number of Modes

In a solid-core PCF guiding by modified TIR, the number of modes guided at short wavelengths is approximately given by:

$$N \approx \frac{V^2}{2} = \frac{2\pi^2 \rho^2}{\lambda^2} (n_{\text{co}}^2 - n_{\text{cl}}^2) = \frac{z_{01}^2 \rho^2}{2a^2} \quad (3)$$

where Eq. (1) has been used to represent the cladding refractive index. This indicates that in the short wavelength limit, the number is determined solely by geometry. This behavior can be understood by viewing the array of holes as a modal filter or “sieve” (Fig. 7). The fundamental mode has a transverse effective wavelength (in the core)  $\lambda_{\text{eff}} \approx 4\Lambda$ . Thus it is unable to “squeeze between” the gaps between the holes (in the cladding), which are spaced  $\Lambda - d$  apart and are thus below the Rayleigh resolution limit  $\lambda_{\text{eff}}/2 = 2\Lambda$ . Provided the relative hole size  $d/\Lambda$  is small enough, higher-order modes are able to escape—their transverse effective wavelength is shorter so they have higher resolving power. As the holes are made larger, successive higher-order modes become trapped. Numerical modelling shows that if  $d/\Lambda < 0.43$ , the fiber is “endlessly single-mode” (i.e., it never supports any higher-order guided modes). The strong

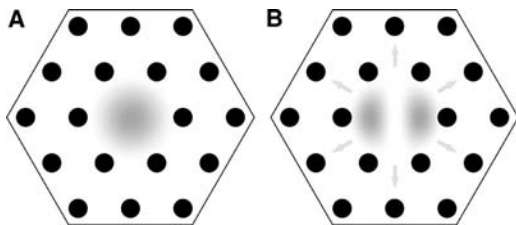


**Fig. 7** Modal filtering in a solid-core PCF. (A) The fundamental mode is trapped whereas (B) higher-order modes leak away through the gaps between the air holes.

wavelength dispersion in the photonic crystal cladding causes the core-cladding index step to fall as the wavelength gets shorter.<sup>[17,18]</sup> This counteracts the usual trend toward increasingly multimode behavior at short wavelengths. In the limit of very short wavelength, the transverse single-mode profile freezes into a constant shape that does not depend on wavelength. In this regime, the light strikes the glass–air interfaces at glancing incidence, and is strongly rejected from the air holes. As a consequence, the angular divergence (numerical aperture or NA) of the emerging light is proportional to wavelength—in SMFs, it is approximately constant owing to the appearance of more and more higher-order guided modes as the frequency increases.

### Ultralarge Mode Areas

Because this sieving process is controlled only by the size and positions of the holes and the core, it does not depend strongly on wavelength. A corollary is that the behavior is quite independent of the absolute size of the structure, making possible arbitrarily large SMF cores. A PCF with a core diameter of 22  $\mu\text{m}$  at 458 nm was reported in 1998.<sup>[24]</sup> In conventional step index fibers, where  $V < 2.405$  for single-mode operation, this would require uniformity of core refractive index to  $\sim 1$  part in  $10^5$ —this is very difficult if MCVD is used to form the doped core. Large-mode areas allow much higher power to be carried before the onset of intensity-related damage. This has obvious benefits for high-power delivery, amplifiers, and lasers.

### Restricting the Guided Wavelengths

In solid-core PCF, the refractive index of the photonic crystal cladding increases with optical frequency, tending toward the index of silica glass in the short wavelength limit. Thus if the core is made from a glass with a refractive index lower than that of silica (e.g., fluorine-doped silica), guidance is lost at wavelengths shorter than a certain threshold value.<sup>[25]</sup> Such fibers have the unique ability to prevent transmission of short wavelength light—a remarkable result when one considers that conventional fibers get better and better at guiding light as the wavelength drops.

In hollow-core PCF, guidance can only occur when a photonic band gap coincides with a core resonance. This means that only restricted bands of wavelength are guided—colored light is typically transmitted when white light is launched into the core. The attenuation spectrum of a recent hollow-core PCF, designed for low-loss transmission at 1064 nm wavelength, is given in Fig. 8.<sup>[26]</sup>

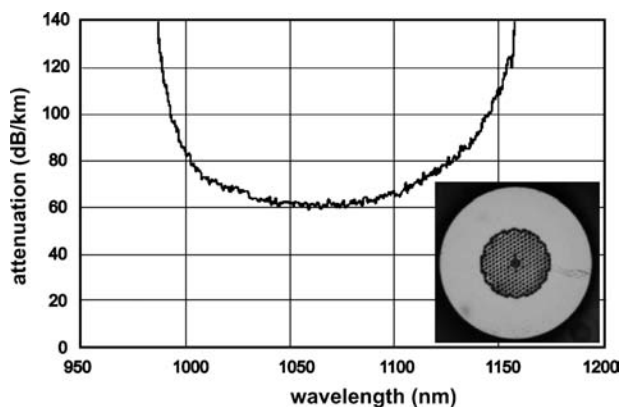


**Fig. 8** Attenuation spectrum of a hollow-core PCF designed for low-loss transmission of 1064 nm light.

## Birefringence

The modes of a perfect sixfold symmetric core are not birefringent.<sup>[27]</sup> However, in practice, even slight distortions in the structure yield a degree of birefringence, and if the core is deliberately distorted so as to become twofold symmetric (e.g., by introducing capillaries with different wall thicknesses above and below the core; Fig. 9A), extremely high values of birefringence can be achieved—some 10 times larger than in conventional fibers.<sup>[28]</sup> Experiments show that the birefringence is highly insensitive to temperature, which is important in many applications. Traditional “polarization-maintaining” fibers (bow tie, elliptical core, or Panda) contain at least two different glasses, each with a different thermal expansion coefficient. The resulting temperature-dependent stresses make birefringence a strong function of temperature.

## Dispersion

Group velocity dispersion (GVD), which causes different frequencies of light to travel at different speeds, is a crucial factor in the design of telecommunications systems. The magnitude of the GVD changes with wavelength, passing through zero at  $\sim 1.3\mu\text{m}$  in

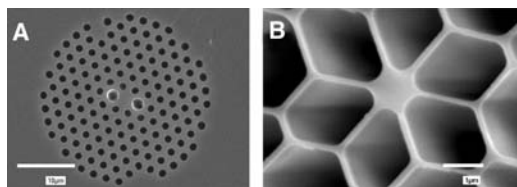


**Fig. 9** (A) Scanning electron micrograph of birefringent PCF. (B) “Cobweb” PCF with very small core and zero GVD wavelength of 560 nm. The core is only 800 nm in diameter.

conventional fiber. In PCF, the dispersion can be controlled with great freedom. For example, as the holes get larger, the core becomes more and more isolated, until it resembles an isolated strand of silica glass suspended by six thin webs of glass. If the whole structure is made very small (core diameters less than  $1\mu\text{m}$  have been made), the zero dispersion point can be shifted to wavelengths in the visible.<sup>[29,30]</sup> The “cobweb” PCF in Fig. 9B has a dispersion zero at 560 nm. By careful design, the wavelength dependence of the GVD can also be reduced. Fig. 10 shows the GVD curves of three fibers with ultraflattened low-level GVD.<sup>[31]</sup> In non-silica glasses, such as Schott SF6, the intrinsic zero dispersion wavelength is at a difference point, providing a further degree of freedom in GVD design.<sup>[13]</sup>

## Multicore

The stacking procedure makes it straightforward to produce multicore fibers. The preform stack is built up with the desired number of solid (or hollow) cores, and is drawn down to fiber in the usual manner.<sup>[33]</sup> The characteristics of coupling between the cores are unusual—the coupling strength depends on the sites chosen because the evanescent decay rate of the fields changes with azimuthal direction. Applications include curvature sensing.<sup>[34]</sup> More elaborate structures can be built up, such as fibers with inner and outer claddings designed as high-power fiber lasers.

## Attenuation Mechanisms

The optimum spacing ( $\sim 80\text{ km}$ ) between repeaters in telecommunications systems is set by the fiber attenuation, which in the best conventional fibers is limited by Rayleigh scattering to  $\sim 0.2\text{ dB/km}$  at 1550 nm wavelength. A key question is whether hollow-core or solid-core PCF can match—or perhaps improve on—this and perhaps replace rival conventional fibers in telecommunications. The answer is not yet clear, although it is easy enough to pose the questions. Are the glass–air interfaces smooth enough to avoid significant scattering out of the core or into other modes? Is Rayleigh scattering amplified by the large refractive

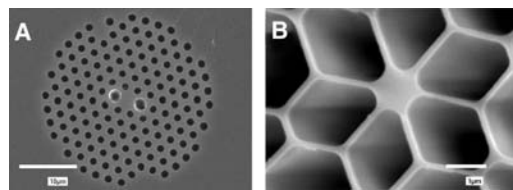


**Fig. 10** GVD profiles, against wavelength, for three different PCFs designed to have low-level ultraflattened GVD. Source: From Refs.<sup>[31]</sup> and<sup>[32]</sup>.

index step at the interfaces? Will the holes fill with water vapor and will huge water-related losses develop at 1.39  $\mu\text{m}$  wavelength, where an overtone of the OH bond absorption occurs?

### Absorption and scattering

The reported losses, from teams in Europe, Japan, and the United States, are steadily dropping, and the record now stands at 0.37 dB/km in a solid-core PCF.<sup>[35,36]</sup> Hollow-core PCF has the greatest potential for extremely low loss because the light is travelling predominantly in the hollow core. Although the best reported attenuation in hollow-core PCF is fairly high (13 dB/km),<sup>[37]</sup> values well below 0.2 dB/km seem at least feasible with further development of the technology. The prospect of improving on conventional fiber, at the same time greatly reducing the non-linearities associated with a solid glass core, is tantalizing.

### Bend loss

Conventional fibers suffer additional loss if bent beyond a certain critical radius  $R_{\text{crit}}$ , which depends on wavelength, core-cladding refractive index step, and, most notably, the third power of core radius  $a^3$ .<sup>[38]</sup> For wavelengths longer than a certain value (the “long wavelength bend edge”), all guidance is effectively lost. PCF does not escape this effect (large-mode area PCF in particular is highly sensitive to bend loss) and, in fact, in its endlessly single-mode form, PCF exhibits an unexpected *short* wavelength bend edge, caused by bend-induced coupling from fundamental to higher-order modes, which of course leak out of the core.<sup>[17]</sup> Experimentally, hollow-core PCF is remarkably insensitive to bend loss—in many cases, no appreciable drop in transmission is observed until the fiber breaks.

### Confinement loss

A fabricated PCF necessarily incorporates a finite number of holes in the cladding region. For a guided mode, the Bloch waves in the photonic crystal cladding are evanescent, just like the evanescent plane waves in the cladding of a conventional fiber. If the cladding is not thick enough, the evanescent fields at the cladding/coating boundary can be substantial, causing attenuation. In the solid-core case for small values of  $d/\Lambda$ , the resulting loss can be quite substantial unless a large number of periods is used.<sup>[31]</sup> Very similar losses are observed in the hollow-core fibers, where the “strength” of the photonic band gap (closely related to its width in  $\beta$ ) determines how many periods are needed to reduce confinement loss to acceptable levels. Numerical modelling is very useful for giving

an indication of how many periods are needed to reach a required loss level.

## NUMERICAL MODELING TECHNIQUES

The complex structure of PCF—in particular the large refractive index difference between glass and air and the resonant nature of the holes and inter-hole spaces—makes its electromagnetic analysis very challenging. Standard optical fiber analyses do not much help. Although—as we have seen in previous sections—a number of approximate models do exist, these are only useful as rough guidelines to the exact behavior. Maxwell’s equations must be solved numerically, using one of a number of specially developed techniques.<sup>[16,39–42]</sup>

The most popular technique uses a plane wave basis for the fields. This converts the wave equations into standard matrix eigenvalue problems suitable for numerical computation. The wave equation satisfied by the  $\mathbf{H}$  field is particularly amenable because, set up for  $(\omega^2/c^2)$  as an eigenvalue, it is Hermitian in form. For waveguiding structures, such as PCFs that incorporate a defect core into an otherwise periodic medium, a supercell is constructed. The supercell is made large enough so that, once tiled, the guided modes in different cores do not significantly interact. The plane wave expansion method suffers from its inability to accurately represent step changes in the dielectric function. The associated ringing or Gibb’s phenomenon introduces an inaccuracy in the solutions unless a very large number of plane wave components is retained. This problem can be alleviated by reexpressing the wave equation satisfied by the  $\mathbf{H}$  field in a variational form and by using a conjugate gradient minimization scheme.<sup>[43]</sup>

In most practical cases in photonics, a set of constant frequency modes is far more useful. Therefore it is convenient to set up Maxwell’s equation with  $\beta^2$  as an eigenvalue:

$$\left( \nabla_{\parallel}^2 + \frac{\omega^2}{c^2} \varepsilon(\mathbf{r}_{\parallel}) \right) \mathbf{H}_{\parallel} + [\nabla_{\parallel} \ln \varepsilon(\mathbf{r}_{\parallel})] \wedge (\nabla_{\parallel} \wedge \mathbf{H}_{\parallel}) = \beta^2 \mathbf{H}_{\parallel} \quad (4)$$

where the gradient operator within the square brackets only operates on the  $\ln \varepsilon(\mathbf{r}_{\parallel})$  term. This form also allows material dispersion to be naturally included. Fourier expansion of Eq. (4) can then be used to convert them to matrix eigenvalue forms.<sup>[40]</sup> Unfortunately, because of the non-Hermitian nature of Eq. (4), a variational approach cannot be invoked so straightforwardly, implying that the number of retained basis waves that can be considered in a plane wave expansion is more limited.



Other numerical techniques include expansion of the field in terms of Hermite–Gaussian functions,<sup>[29]</sup> the finite-difference time domain (FDTD) approach (a simple and versatile tool with which to explore waveguide geometries<sup>[44]</sup>), and the finite-element approach.<sup>[45]</sup> If the PCF structure comprises purely circular holes, the multipole or Rayleigh method is a particularly fast and efficient approach to use.<sup>[42]</sup> The method works by calculating the scattering of a field incident on each hole by the use of Mie scattering theory.

The most appropriate and efficient method to use for a given PCF structure depends on its geometry and which properties are required. The plane wave method is attractive for calculating mode properties because of the large number of basis waves that can be used. In common with most basis expansion methods, this method fails to accurately describe the discontinuities in the dielectric distribution and in the field at the dielectric interfaces; this necessitates the use of a large basis size. The multipole method overcomes this limitation by expanding the fields in various dielectric regions in local basis sets appropriate to the local symmetry and performs the boundary matching directly. For fibers comprising circular holes, the multipole method generally gives the quickest and most accurate results. Because no spatial mesh is required, the method naturally maintains the symmetry of the structure and the constructed eigenmodes show the correct symmetries also.

The confinement loss suffered by the guided modes is not directly accessible with the plane wave approach because of the Bloch boundary conditions that are applied. The leakage can be obtained from methods in which radiative boundary conditions outside the holey region can accurately be employed. This is automatic for the multipole method and can be achieved using boundary-element and finite-element approaches, although in the latter case, its accurate implementation (using, for example, perfectly matched layers) is not straightforward. The finite difference time domain approach can be invoked to calculate leakage loss if this is substantial, but losses at the level of a few decibels per kilometer or less, which are appropriate for most PCF fiber systems, are not resolved. This problem can be alleviated by reexpressing the wave equation satisfied by the  $\mathbf{H}$  field in a variational form and by using the conjugate gradient minimization scheme;<sup>[43]</sup> this allows many tens of thousands of plane waves to be retained in the expansions.

## INTRAFIBER DEVICES, CUTTING, AND JOINING

As PCF becomes more widely used, there is increasing demand for cleaving, low-loss splicing, multipoint

couplers, intrafiber devices, and mode area transformers. The air holes provide an opportunity not available in standard fibers—they collapse under surface tension when heated to the softening temperature of the glass. Thus not only can the fiber be stretched locally to reduce its cross-sectional area, but the microstructure can itself be altered.

PCF cleaves very cleanly using standard tools, showing slight end-face distortion only when the core crystal is extremely small (interhole spacing  $\sim 1\ \mu\text{m}$ ), and the air-filling fraction is very high ( $>50\%$ ). Solid-core PCF can be spliced successfully both to itself and to standard fiber using a fusion-splicing process. The two fiber ends are placed in intimate contact and heated to softening point. With careful control, they fuse together without distortion. Provided that the mode areas are well matched, splice losses of  $< 0.2\ \text{dB}$  can normally be achieved except when the core is extremely small (less than  $\sim 1.5\ \mu\text{m}$ ). Fusion splicing hollow-core fiber is feasible when there is a thick solid glass outer sheath (e.g., as depicted in the inset in Fig. 8), although very low splice losses can be obtained simply by placing the fibers end-to-end and clamping them—after all, the index matching fluid for hollow-core PCF is vacuum.

In many applications, it is important to be able to change the mode area without losing light. This is done traditionally using miniature bulk optics—tiny lenses precisely designed to match to a desired NA and spot size. In PCF, an equivalent effect can be obtained by scanning a heat source (flame or carbon dioxide laser) along the fiber. This causes the holes to collapse, with the degree of collapse depending on the dwell time of the heat. Drawing the two fiber ends apart at the same time provides additional control. Low loss graded transitions can fairly easily be made—mode diameter reductions as high as 5:1 have been realized with low loss. A further degree of freedom may be gained by pressurizing the holes during the taper process.<sup>[46]</sup>

The ability to cause large changes in the optical characteristics of PCF by heating is leading to a whole family of new intrafiber components. Microcouplers can be made in dual-core PCF—two optically isolated cores can be made to interact by collapsing the holes so as to allow the mode fields to expand and “talk” to each other.<sup>[47]</sup> Long period gratings, which couple the core light into the cladding within certain wavelength bands, can be made by periodic modulation of hole size.<sup>[48]</sup> Rocking a birefringent PCF to-and-fro, while scanning a carbon dioxide laser along it, results in so-called “rocking filters,” which transfer power from one polarization state to the other within a narrow band of wavelengths.<sup>[49]</sup> All these components have one great advantage over equivalent devices made in conventional fiber—being permanent changes in morphology, they are highly stable with temperature and over time.



## APPLICATIONS

The diversity of new or improved features, beyond what conventional fiber offers, means that PCFs are finding an increasing number of applications in every widening area of science and technology.

### Gas-Based Non-linear Optics

A long-standing challenge in photonics is how to maximize non-linear interactions between laser light and low-density media such as gases. Efficient non-linear processes require high intensities at low power, long interaction lengths, and good-quality transverse beam profiles. A structure conceptually capable of delivering all these requirements simultaneously is a perfectly guiding hollow-core waveguide supporting a single transverse mode with low attenuation losses. Although, theoretically, this could be realized using a perfect metal, the attenuation in real metals at optical frequencies is much too high. A number of conventional approaches have been used to alleviate this problem, including focusing a laser beam into the gas with suitable optics, using a  $\sim 200\text{-}\mu\text{m}$  bore fiber capillary to confine the gas and provide some degree of guidance for the light,<sup>[50]</sup> and employing a gas-filled high-finesse Fabry–Pérot cavity to increase the interaction length.<sup>[51]</sup> As explained in Ref.<sup>[21]</sup>, none of these approaches comes close to the performance offered by hollow-core PCF. At a bore diameter of  $10\text{ }\mu\text{m}$ , for example, a focused free space laser beam is marginally preferable to a capillary, whereas a hollow-core PCF with  $13\text{ dB/km}$  attenuation is an astonishing  $100,000\times$  more effective. Such huge enhancements are rare in physics, and point the way to dramatic improvements in all sorts of nonlinear laser–gas interactions. The first results are beginning to emerge: Recently stimulated Raman scattering was observed in a hydrogen-filled hollow-core PCF at threshold pulse energies  $\sim 100\times$  lower than previously reported.<sup>[21]</sup> Many other areas of nonlinear optics are likely to be revolutionized, such as x-ray generation in noble gases pumped by femtosecond Ti–sapphire laser pulses.<sup>[52]</sup> The conversion efficiency of this process was further enhanced recently by modulating the bore diameter so as to phase match the light and the x-rays.<sup>[53]</sup> This can be implemented in PCF by heat treatment with carbon dioxide laser light.<sup>[48]</sup>

### High-Power Transmission

Hollow-core fiber is also excellent for transmitting high continuous-wave power as well as ultrashort pulses with very high peak powers. A recent entry reports femtosecond solitons at  $1550\text{ nm}$  with peak powers of

$2\text{ MW}$  in hollow-core PCF.<sup>[54]</sup> For soliton formation, the sign and magnitude of the GVD are crucial. It has recently been reported that the GVD changes sign across the band gap, permitting choice of normal or anomalous dispersion depending on the application.<sup>[22]</sup>

### Rare Earth-Doped Lasers and Amplifiers

Rare earth-doped PCF lasers can be straightforwardly produced by incorporating doped canes in the preform stack. Many different structures can be fashioned, such as large-mode area cores and multicore lasers.

#### Ultrahigh power lasers

High-power rare earth-doped lasers and amplifiers can be fashioned in large-mode area PCF by incorporating a second, much larger, multimode core around the single-mode lasing core. Using microstructuring techniques, this “inner cladding waveguide” can be suspended by connecting it to an outer glass tube with very thin webs of glass (Fig. 11).<sup>[56]</sup> Very high inner cladding NA can be obtained ( $>0.9$ ), making it easy to launch and guide light from high-power diode bar pump lasers, which typically have very poor beam quality. The pump light is absorbed by the lasing core, and high-power single-mode operation can be achieved, as in recent reports for Yb-doped fiber lasers.<sup>[55,57]</sup>

#### Mode-locked fiber lasers

Mode-locked fiber lasers rely on control of the dispersion within the laser cavity to achieve ultrashort pulse

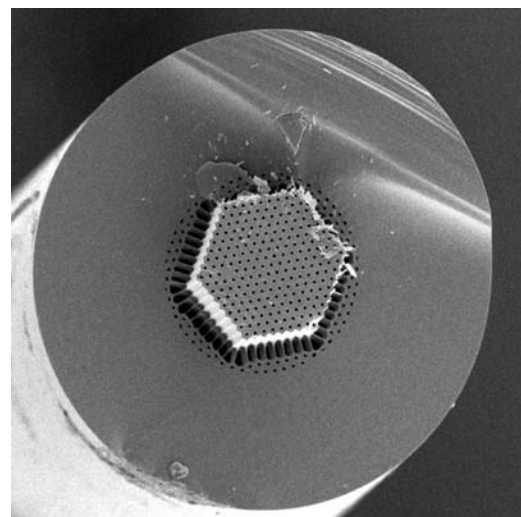


**Fig. 11** Scanning electron micrograph of a cladding-pumped PCF laser designed for high-power operation. *Source:* From Ref.<sup>[55]</sup>. The lasing core is a missing air hole close to the left-hand corner of the photonic crystal.

(subpicosecond) operation. PCF offers fine-tuning of the GVD over a wide wavelength range, making it ideal for developing a new generation of mode-locked laser systems. Laser cavities can be envisaged in which there is high local GVD but very low average dispersion over a broad wavelength range. This would allow operation in the stretched-pulse regime, or could be used simply to cancel the dispersion of other cavity components. Mode-locked fiber lasers previously were forced to operate at wavelengths beyond the 1.3- $\mu\text{m}$  zero GVD point, where the dispersion in SMF is anomalous. However, using PCF, it becomes possible to design all-fiber mode-locked systems at shorter wavelengths by shifting the zero GVD wavelength down into the visible.

### Atom and Particle Guidance

A focused light beam produces both a longitudinal (accelerating) and a transverse (trapping) force on dielectric microparticles.<sup>[58]</sup> For maximum trapping force, the intensity gradient of the light must be as high as possible. This can be achieved by focusing a high-power laser beam with a high NA lens. The Rayleigh length for such a tightly focused beam is rather short; furthermore, the high intensity will quickly accelerate the particle out of the trapping zone. Stable trapping of a particle in free space requires the longitudinal force to be balanced either by gravity or by a second (or reflected) beam. It has long been recognized that an alternative configuration offering stability would be a non-diffracting or guided beam. To guide a dielectric particle, the beam would have to be trapped in air rather than in glass, which, until very recently, was not possible. That did not stop the demonstration of guidance of both solid particles<sup>[59]</sup> and atoms<sup>[60]</sup> along a length of hollow capillary during the past decade. Of course, use of a capillary prevented the full exploitation of the possibilities of a hollow waveguide—for

the small core sizes needed for strong transverse confinement, capillary losses are very high, even on length scales of a few millimeters. The same is not true in hollow-core PCF, where core diameters of  $\sim 10\ \mu\text{m}$  can be realized with losses as low as 50 dB/km. Such a small spot size gives a strong transverse trapping force for a given longitudinal force, so that it becomes possible to envisage guiding particles even around tightly bent fibers at reasonably high speeds. The first steps toward achieving this goal were recently taken.<sup>[61]</sup>

### Sound–Light Interactions

A perennial problem in photonics is how to force sound and light to “talk” (i.e., interact more strongly). Although in theory a single photon can be deflected by annihilation or creation of a single phonon, a fair population of phonons must be used to swamp out the effects of thermal vibrations. Even so, commercial acousto-optic Bragg cells are fantastically inefficient. Driven at 500 mW power and deflecting a laser beam of 1000 nm wavelength and a power of 1 mW, a bulk 40-MHz Bragg cell uses roughly 4 billion phonons to deflect one photon. This huge overkill is largely because of the very poor overlap between sound and light. One way of improving this is to microstructure the material so as to create a frequency band where it falls silent—an acoustic or photonic band gap.<sup>[62,63]</sup> A suitable defect volume, placed within this material, will resonate at frequencies within the band gap, with the acoustic waves being unable to escape into the surrounding silence. Very high acoustic energy densities can then be reached at small drive powers, suggesting the possibility of a new class of superefficient acousto-optic component in which both sound and light are trapped at the same time in the same place. Such components would enjoy radically enhanced performance (in terms of drive power and precision). The first steps in this direction were taken recently with

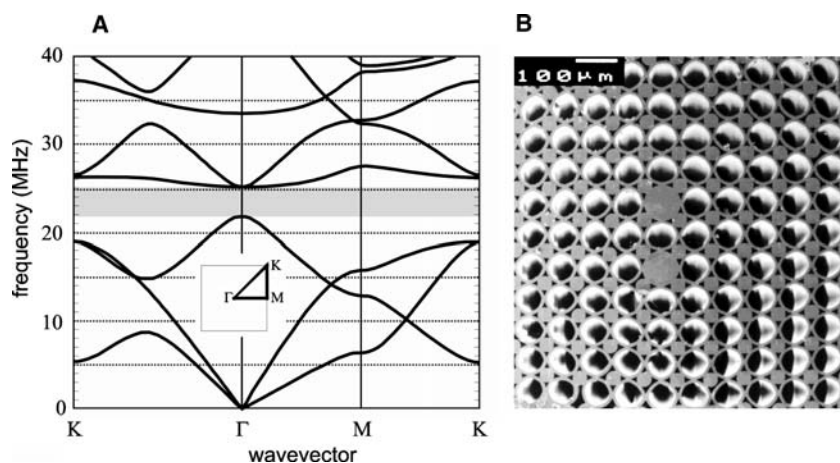


**Fig. 12** (A) Photonic band gaps of a square lattice PCF preform. (B) Full two-dimensional acoustic band gaps occur around 23 MHz, in agreement with the experiments. *Source:* From Ref.<sup>[64]</sup>.

the demonstration of intraphotonic band gap trapped resonances in the core of a square lattice PCF preform<sup>[64]</sup> (Fig. 12).

### Nonlinear Effects

The ability to enhance effective non-linearity and, at the same time, control the magnitude and wavelength dependence of the GVD makes PCF a highly versatile and complete “laboratory-in-a-fiber” for non-linear optics. Many well-known non-linear fiber optical effects (e.g., stimulated Raman scattering, four-wave mixing, self-phase modulation, modulation instability, and solitonic effects) have already been observed in short (few meters) lengths of fiber. The parameter:

$$\gamma = \omega_0 n_2 / c A_{\text{eff}} \quad (5)$$

is often used as a measure of the non-linearity of the fiber.<sup>[65]</sup> In Eq. (5),  $n_2$  is the non-linear refractive index of the fiber material ( $2.5 \times 10^{-20} \text{ m}^2 \text{ W}^{-1}$  in silica glass, and an order of magnitude or more higher for soft glasses) and  $A_{\text{eff}}$  is the effective area of the guided mode. The highest non-linearity available in conventional silica fibers is  $\gamma \sim 20 \text{ W}^{-1} \text{ km}^{-1}$  at 1550 nm wavelength<sup>[66]</sup> and  $\gamma \sim 10 \text{ W}^{-1} \text{ km}^{-1}$  at 850 nm. In comparison,  $\gamma \sim 240 \text{ W}^{-1} \text{ km}^{-1}$  at 850 nm for the PCF in Fig. 13 and non-linearities as high as  $550 \text{ W}^{-1} \text{ km}^{-1}$  at 1550 nm have been measured for PCFs based on soft glasses.<sup>[67]</sup> The fiber non-linearity is important because it sets the non-linear phase shift associated with propagation of light of a given intensity. The non-linearity can be used to calculate the nonlinear length of the fiber  $L_{\text{nl}} = (\gamma P_0)^{-1}$ , where  $P_0$

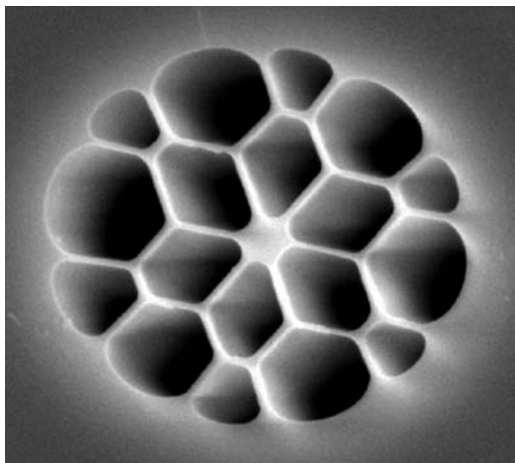


**Fig. 13** Core region of a silica/air fiber with a 1- $\mu\text{m}$  core diameter. Its unusual non-linear and dispersive properties make it a spectacular vehicle for studying non-linear fiber optics.

is the peak power. For example, for the fiber in Fig. 13, a peak power of 10 kW (easily obtained from an unamplified ultrashort pulse laser system) implies  $L_{\text{nl}} < 0.5 \text{ mm}$ . For typical values of loss (say, 100 dB/km) and dispersion (e.g., 10 psec/nm km), this non-linear length is far shorter than the fiber effective length  $L_{\text{eff}}$  and the dispersive length  $L_{\text{D}}$ .<sup>[65]</sup> Consequently, it is easy to observe extraordinary non-linear effects in such fibers. The actual non-linear processes that dominate in a particular experiment are determined by the GVD as well as the laser characteristics.

Perhaps the most dramatic application of non-linear PCF is to supercontinuum (SC) generation from picosecond and femtosecond laser pulses. When high-power pulses travel through a material their frequency spectrum can be broadened by a range of interconnected non-linear effects.<sup>[68]</sup> Until recently, the preferred pump laser was a regeneratively amplified Ti-sapphire system producing high (millijoules) energy femtosecond pulses at 800 nm wavelength and kilohertz repetition rate. Then in 2000, it was observed that highly non-linear PCF, designed with zero GVD close to 800 nm, massively broadens the spectrum of low-energy (few nanojoules) unamplified Ti-sapphire pulses launched into just a few centimeters of fiber.<sup>[69,70]</sup> Removal of the need for a power amplifier, the hugely increased 100-MHz repetition rate, and the spatial and temporal coherence of the light emerging from the core explain why this source is unique. The SC has applications in optical coherence tomography,<sup>[71]</sup> frequency metrology,<sup>[72]</sup> and all kinds of spectroscopy.

SC has been generated in different PCFs at many pump wavelengths in the range of 648 nm<sup>[73]</sup> to 1550 nm.<sup>[13]</sup> The wide range of GVD characteristics that have been demonstrated<sup>[31]</sup> in PCF in the 1550-nm wavelength band has provided a test bed<sup>[32]</sup> for non-linear fiber optics, in which the sensitivity of non-linear pulse propagation to the details of the dispersion curve can be tested. The development of conventional fiber-based optical parametric oscillators and amplifiers has been constrained by the very limited scope for engineering the GVD profile. In PCF, these constraints are lifted. The small effective mode area also offers high gain, and PCF-based oscillators based on synchronously pumped femtosecond and picosecond pump pulses have been demonstrated with relatively low powers.<sup>[74-76]</sup>

### CONCLUSION

PCFs represent a next-generation, radically improved version of a well-established and highly successful technology. In escaping from the confines of conventional fiber optics, they have created a renaissance of new

possibilities in many diverse areas of research and technology, in the process irrevocably breaking many of the tenets of received fiber optics wisdom. Over the next few years, we expect to see a gradual takeup of PCFs in many fields of application. Emerging fields of application include biotechnology, optical sensing, medical physics (imaging techniques, surgery), microparticle delivery, high-power fiber lasers, fiber-based laser delivery for manufacturing, long-haul telecommunications, and gas-based nonlinear wavelength conversion.

## REFERENCES

- Colladon, D. *Comptes Rendus* October 24 **1842**, *15*, 800–802.
- Nagel, S.R.; MacChesney, J.B.; Walker, K.L. An overview of the modified chemical vapor deposition (MCVD) process and performance. *IEEE J. Quantum Electron.* **1982**, *18*, 459–476.
- Yeh, P.; Yariv, A. Bragg reflection waveguides. *Opt. Commun.* **1976**, *19*, 427–430.
- Brechet, F.; Roy, P.; Marcou, J.; Pagnoux, D. Single mode propagation into depressed-core-index photonic-bandgap fibre designed for zero-dispersion propagation at short wavelengths. *Electron. Lett.* **2000**, *36*, 514–515.
- Johnson, S.G.; Ibanescu, M.; Skorobogatiy, M.; Weisberg, O.; Engeness, T.D.; Soljacic, M.; Jacobs, S.A.; Joannopoulos, J.D.; Fink, Y. Low-loss asymptotically single-mode propagation in large-core OmniGuide fibres. *Opt. Express* **2001**, *9*, 748–779.
- Russell, P.St.J. **1991**. private papers.
- Knight, J.C.; Birks, T.A.; Russell, P.St.J. *Holey Silica Fibres*. In *Optics of Nanostructured Materials*; Markel, V.A., George, T.F., Eds.; John Wiley and Sons: New York, 2001; 39–71.
- Birks, T.A.; Knight, J.C.; Mangan, B.J.; Russell, P.St.J. Photonic crystal fibres: An endless variety. *IEICE Trans. Electron.* **2001**, *E84-C*, 585–592.
- Russell, P.St.J. Photonic crystal fibers. *Science* **2003**, *299*, 358–362.
- Knight, J.C.; Birks, T.A.; Russell, P.St.J.; Atkin, D.M. *Pure Silica Single-Mode Fibre with Hexagonal Photonic Crystal Cladding*, Optical Fibre Communications Conference (OFC'96), San Diego, March, 1996. postdeadline paper PD3.
- Knight, J.C.; Birks, T.A.; Russell, P.St.J.; Atkin, D.M. All-silica single-mode fibre with photonic crystal cladding. *Opt. Lett.* **1996**, *21*, 1547–1549. Errata; *Opt. Lett.*, **1997**, *22*, 484–485.
- Allan, D.C.; West, J.A.; Fajardo, J.C.; Gallagher, M.T.; Koch, K.W.; Borrelli, N.F. Photonic Crystal Fibres: Effective Index and Bandgap Guidance. In *Photonic Crystals and Light Localisation in the 21st Century*; Soukoulis, C.M., Ed.; Kluwer Academic Publishers, 2001; 305–320.
- Ravi Kanth Kumar, V.V.; George, A.K.; Reeves, W.H.; Knight, J.C.; Russell, P.St.J.; Omenetto, F.G.; Taylor, A.J. Extruded soft glass photonic crystal fiber for ultrabroad supercontinuum generation. *Opt. Express* **2002**, *10*, 1520–1525.
- Kiang, K.M.; Frampton, K.; Monro, T.M.; Moore, R.; Tucknott, J.; Hewak, D.W.; Richardson, D.J.; Rutt, H.N. Extruded single-mode non-silica glass holey optical fibres. *Electron. Lett.* **2002**, *38*, 546–547.
- van Eijkelenborg, M.A.; Large, M.C.J.; Argyros, A.; Zagari, J.; Manos, S.; Issa, N.A.; Bassett, I.; Fleming, S.; McPhedran, R.C.; de Sterke, C.M.; Nicorovici, N.A.P. Microstructured polymer optical fibre. *Opt. Express* **1999**, *9*, 319–327.
- Birks, T.A.; Roberts, P.J.; Russell, P.St.J.; Atkin, D.M.; Shepherd, T.J. Full 2-D photonic band gaps in silica/air structures. *Electron. Lett.* **1995**, *31*, 1941–1942.
- Birks, T.A.; Knight, J.C.; Russell, P.St.J. Endlessly single-mode photonic crystal fibre. *Opt. Lett.* **1997**, *22*, 961–963.
- Knight, J.C.; Birks, T.A.; Russell, P.St.J.; de Sandro, J.-P. Properties of photonic crystal fibre and the effective index model. *J. Opt. Soc. Am., A* **1998**, *15*, 748–752.
- Cregan, R.F.; Mangan, B.J.; Knight, J.C.; Birks, T.A.; Russell, P.St.J.; Roberts, P.J.; Allan, D.C. Single-mode photonic band gap guidance of light in air. *Science* **1999**, *285*, 1537–1539.
- Knight, J.C.; Broeng, J.; Birks, T.A.; Russell, P.St.J. Photonic band gap guidance in optical fibres. *Science* **1998**, *282*, 1476–1478.
- Benabid, F.; Antonopoulos, G.; Knight, J.C.; Russell, P.St.J. Stimulated Raman scattering in hydrogen-filled hollow-core photonic crystal fiber. *Science* **2002**, *298*, 399–402.
- Bouwman, G.; Luan, F.; Knight, J.C.; Russell, P.St.J.; Farr, L.; Mangan, B.J.; Sabert, H. Properties of a hollow-core photonic bandgap fiber at 850 nm wavelength. *Opt. Express* **2003**, *11*, 1613–1620.
- Pechstedt, R.D.; Russell, P.St.J. Narrow-band in-line fibre filter using surface-guided Bloch modes supported by dielectric multilayer stacks. *J. Lightwave Technol.* **1996**, *14*, 1541–1545.
- Knight, J.C.; Birks, T.A.; Cregan, R.F.; Russell, P.St.J.; de Sandro, J.-P. Large mode area photonic crystal fibre. *Electron. Lett.* **1998**, *34*, 1347–1348.
- Mangan, B.J.; Arriaga, J.; Birks, T.A.; Knight, J.C.; Russell, P.St.J. Fundamental-mode cutoff in a photonic crystal fibre with a depressed-index core. *Opt. Lett.* **2001**, *26*, 1469–1471.
- [www.blazephotonics.com](http://www.blazephotonics.com).
- Steel, M.J.; White, T.P.; de Sterke, C.N.; McPhedran, R.C.; Botten, L.C. Symmetry and degeneracy in microstructured optical fibers. *Opt. Lett.* **2001**, *26*, 488–490.
- Ortigosa-Blanch, A.; Knight, J.C.; Wadsworth, W.J.; Arriaga, J.; Mangan, B.J.; Birks, T.A.; Russell, P.St.J. Highly birefringent photonic crystal fibres. *Opt. Lett.* **2000**, *25*, 1325–1327.
- Mogilevtsev, D.; Birks, T.A.; Russell, P.St.J. Group-velocity dispersion in photonic crystal fibres. *Opt. Lett.* **1998**, *23*, 1662–1664.
- Knight, J.C.; Arriaga, J.; Birks, T.A.; Ortigosa-Blanch, A.; Wadsworth, W.J.; Russell, P.St.J. Anomalous

- dispersion in photonic crystal fibres. IEEE Photonics Technol. Lett. **2000**, *12*, 807–809.
31. Reeves, W.H.; Knight, J.C.; Russell, P.St.J.; Roberts, P.J. Demonstration of ultra-flattened dispersion in photonic crystal fibres. Opt. Express **2002**, *10*, 609–613.
  32. Reeves, W.H.; Skryabin, D.V.; Biancalana, F.; Knight, J.C.; Russell, P.St.J.; Omenetto, F.G.; Efimov, A.; Taylor, A.J. Transformation and control of ultra-short pulses in dispersion-engineered photonic crystal fibres. Nature **2003**, *424*, 511–515.
  33. Mangan, B.J.; Knight, J.C.; Birks, T.A.; Russell, P.St.J.; Greenaway, A.H. Experimental study of dual-core photonic crystal fibre. Electron. Lett. **2000**, *36*, 1358–1359.
  34. MacPherson, W.N.; Gander, M.J.; McBride, R.; Jones, J.D.C.; Blanchard, P.M.; Burnett, J.G.; Greenaway, A.H.; Mangan, B.J.; Birks, T.A.; Knight, J.C.; Russell, P.St.J. Remotely addressed optical fibre curvature sensor using multicore photonic crystal fibre. Opt. Commun. **2001**, *193*, 97–104.
  35. Farr, L.; Knight, J.C.; Mangan, B.J.; Roberts, P.J. In: *Low Loss Photonic Crystal Fibre*, European Conference on Optical Communications ECOC'02, Copenhagen, 2002. postdeadline paper PD1.3.
  36. Tajima, K.; Zhou, J.; Nakajima, K.; Sato, K. In: *Ultra Low Loss and Long Length Photonic Crystal Fiber*, Optical Fiber Communication Conference (OFC 2003), Atlanta, March, 2003. postdeadline paper PD1.
  37. Smith, C.M.; Venkataraman, N.; Gallagher, M.T.; Mueller, D.; West, J.A.; Borrelli, N.F.; Allan, D.C.; Koch, K.W. Low-loss hollow-core silica/air photonic bandgap fibre. Nature **2003**, *424*, 657–659.
  38. Snyder, A.W.; Love, J.D. *Optical Waveguide Theory*; Chapman and Hall: London, 1983.
  39. Mogilevsev, D.; Birks, T.A.; Russell, P.St.J. Localised function method for modelling defect modes in 2-D photonic crystals. IEEE J. Lightwave Technol. **1999**, *17*, 2078–2081.
  40. Ferrando, A.; Miret, J.J.; Silvestre, E.; Andrés, P.; Andrés, M.V. Full-vector analysis of a realistic photonic crystal fibre. Opt. Lett. **1999**, *24*, 276–278.
  41. Roberts, P.J.; Shepherd, T.J. The guidance properties of multi-core photonic crystal fibres. J. Opt. A, Pure Appl. Opt. **2001**, *3*, S1–S8.
  42. McPhedran, R.C.; Botten, L.C.; Asatryan, A.A.; Nicorovici, N.A.; Robinson, P.A.; de Sterke, C.M. Calculation of electromagnetic properties of regular and random arrays of metallic and dielectric cylinders. Phys. Rev., E **1999**, *60*, 7614–7617.
  43. Meade, R.D.; Rappé, A.M.; Brommer, K.D.; Joannopoulos, J.D.; Alerhand, O.L. Accurate theoretical analysis of photonic band-gap materials. Phys. Rev., B **1993**, *48*, 8434–8437.
  44. Chan, C.T.; Yu, Q.L.; Ho, K.M. Order  $N$  spectral method for electromagnetic waves. Phys. Rev., B **1995**, *51*, 16635–16642.
  45. Mias, C.; Webb, J.P.; Ferrari, R.L. Finite element modelling of electromagnetic waves in doubly and triply periodic structures. IEE Proc. Optoelectron. **1999**, *146*, 111–118.
  46. Birks, T.A.; Kakarantzas, G.; Russell, P.St.J.; Murphy, D.F. Photonic crystal fibre devices. Proc. SPIE **2002**, *4943*, 142–151. (Fiber-Based Component Fabrication, Testing and Connectorization).
  47. Kakarantzas, G.; Dimmick, T.E.; Birks, T.A.; Le Roux, R.; Russell, P.St.J. Miniature all-fiber devices based on CO<sub>2</sub> laser micro-structuring of tapered fibers. Opt. Lett. **2001**, *26*, 1137–1139.
  48. Kakarantzas, G.; Mangan, B.J.; Birks, T.A.; Knight, J.C.; Russell, P.St.J. In: *Directional Coupling in a Twin Core Photonic Crystal Fiber Using Heat Treatment*, Conference on Lasers and Electro-Optics (CLEO), Baltimore, MD, May, 2001. paper JTuD2.
  49. Kakarantzas, G.; Ortigosa-Blanch, A.; Birks, T.A.; Russell, P.St.J.; Farr, L.; Couny, F.; Mangan, B.J. Structural rocking filters in highly birefringent photonic crystal fiber. Opt. Lett. **2003**, *28*, 158–160.
  50. Rabinowitz, P.; Stein, A.; Brickman, R.; Kaldor, A. Efficient tunable hydrogen Raman laser. Appl. Phys. Lett. **1979**, *35*, 739–741.
  51. Meng, L.S.; Repasky, K.S.; Roos, P.A.; Carlsten, J.L. Widely tunable continuous-wave Raman laser in diatomic hydrogen pumped by an external-cavity diode laser. Opt. Lett. **2000**, *25*, 472–474.
  52. Brabec, T.; Krausz, F. Intense few-cycle laser fields: Frontiers of nonlinear optics. Rev. Mod. Phys. **2000**, *72*, 545–591.
  53. Paul, A.; Bartels, R.A.; Tobey, R.; Green, H.; Weiman, S.; Christov, I.P.; Murnane, M.M.; Kapteyn, H.C.; Backus, S. Quasi-phase-matched generation of coherent extreme-ultraviolet light. Nature **2003**, *421*, 51–54.
  54. Ouzounov, D.G.; Ahmad, F.R.; Gaeta, A.L.; Müller, D.; Venkataraman, N.; Gallagher, M.T.; Koch, K.W. In: *Dispersion and Nonlinear Propagation in Air-Core Photonic Band-Gap Fibers*, Conference on Lasers and Electro-Optics (CLEO'03), Baltimore, June, 2003. paper CThT5.
  55. Wadsworth, W.J.; Percival, R.M.; Bouwmans, G.; Knight, J.C.; Russell, P.St.J. High power air-clad photonic crystal fibre laser. Opt. Express **2003**, *11*, 48–53.
  56. Wadsworth, W.J.; Percival, R.M.; Bouwmans, G.; Knight, J.C.; Birks, T.A.; Hedley, T.D.; Russell, P.St.J. Very high numerical aperture fibres. IEEE Phot. Tech. Lett. March **2004**, in press.
  57. Limpert, J.; Schreiber, T.; Nolte, S.; Zellmer, H.; Tünnermann, A.; Iliew, R.; Lederer, F.; Broeng, J.; Vienne, G.; Petersson, A.; Jakobsen, C. High-power air-clad large-mode-area photonic crystal fiber laser. Opt. Express **2003**, *11*, 818–823.
  58. Ashkin, A. Acceleration and trapping of particles by radiation pressure. Phys. Rev. Lett. **1970**, *24*, 156–159.
  59. Renn, M.J.; Pastel, R.; Lewandowski, H.J. Laser guidance and trapping of mesoscale particles in hollow-core optical fibres. Phys. Rev. Lett. **1999**, *82*, 1574–1577.
  60. Renn, M.J.; Montgomery, D.; Vdovin, O.; Anderson, D.Z.; Wieman, C.E.; Cornell, E.A. Laser-guided atoms in hollow-core optical fiber. Phys. Rev. Lett. **1995**, *75*, 3253–3256.
  61. Benabid, F.; Knight, J.C.; Russell, P.St.J. Particle levitation and guidance in hollow-core photonic crystal fiber. Opt. Express **2002**, *10*, 1195–1203.

62. Kushwaha, M.S.; Djafari-Rouhani, B. Sonic stop-bands for periodic arrays of metallic rods: Honeycomb structure. *J. Sound Vib.* **1998**, *218*, 697–709.
63. Economou, E.N.; Sigalas, M. Stop bands for elastic-waves in periodic composite-materials. *J. Acoust. Soc. Am.* **1994**, *95*, 1734–1740.
64. Marin, E.; Mangan, B.J.; Díez, A.; Russell, P.St.J. Acoustic Modes of a Dual-Core Square-Lattice Photonic Crystal Fibre Preform. In *Proceedings of the European Conference of Optics Communications; ECOC: Amsterdam, October, 2001*; 518–519.
65. Agrawal, G. *Nonlinear Fibre Optics*; Academic Press: Boston, 1989.
66. Onishi, M.; Okuno, T.; Kashiwada, T.; Ishikawa, S.; Akasaka, N.; Nishimura, M. Highly nonlinear dispersion-shifted fibers and their application to broadband wavelength converter. *Opt. Fiber Technol.* **1998**, *4*, 204–214.
67. Monro, T.M.; Kiang, K.M.; Lee, J.H.; Frampton, K.; Yusoff, Z.; Moore, R.; Tucknott, J.; Hewak, D.W.; Rutt, H.N.; Richardson, D.J. In: *High Nonlinearity Extruded Single-Mode Holey Optical Fibers*, Optical Fiber Communication Conference (OFC'2002), Anaheim, 2002. postdeadline paper FA1-1.
68. Alfano, R.R., Ed.; *The Supercontinuum Laser Source*; Springer-Verlag: New York, 1989.
69. Ranka, J.K.; Windeler, R.S.; Stentz, A.J. Visible continuum generation in air–silica microstructure optical fibres with anomalous dispersion at 800 nm. *Opt. Lett.* **2000**, *25*, 25–27.
70. Wadsworth, W.J.; Ortigosa-Blanch, A.; Knight, J.C.; Birks, T.A.; Man, T.-P.M.; Russell, P.St.J. Supercontinuum generation in photonic crystal fibres and optical fibre tapers—A novel light source. *J. Opt. Soc. Am., B* **2002**, *19*, 2148–2155.
71. Hartl, I.; Li, X.D.; Chudoba, C.; Ghanta, R.; Ko, T.; Fujimoto, J.G.; Ranka, J.K.; Windeler, R.S.; Stentz, A.J. Ultrahigh resolution optical coherence tomography using continuum generation in an air–silica microstructure optical fibre. *Opt. Lett.* **2001**, *26*, 608–610.
72. Holzwarth, R.; Reichert, J.; Udem, Th.; Hänsch, T.W.; Knight, J.C.; Wadsworth, W.J.; Russell, P.St.J. An optical frequency synthesiser for precision spectroscopy. *Phys. Rev. Lett.* **2000**, *85*, 2264–2267.
73. Coen, S.; Chau, A.H.L.; Leonhardt, R.; Harvey, J.D.; Knight, J.C.; Wadsworth, W.J.; Russell, P.St.J. Supercontinuum generation by stimulated Raman scattering and parametric four-wave mixing in photonic crystal fibres. *J. Opt. Soc. Am., B* **2002**, *19*, 753–764.
74. Harvey, J.D.; Leonhardt, R.; Wong, K.G.L.; Knight, J.C.; Wadsworth, W.J.; Russell, P.St.J. Scalar modulational instability in the normal dispersion regime using a PCF. *Opt. Lett.* **2003**, *28*, 2225–2227.
75. Sharping, J.E.; Fiorentino, M.; Kumar, P.; Windeler, R.S. Optical parametric oscillator based on four-wave mixing in microstructure fibre. *Opt. Lett.* **2002**, *27*, 1675–1677.
76. Tang, R.; Devgan, P.; Sharping, J.; Voss, P.; Lasri, J.; Kumar, P. *Microstructure-Fibre Based Optical Parametric Amplifier in the 1550 nm Telecom Band*, Optical Fiber Communications Conference (OFC'2003), Atlanta, March, 2003. paper ThT3.



# Photovoltaics: Organic-Based Solar Cells

Sean E. Shaheen

David S. Ginley

*National Renewable Energy Laboratory (NREL), Golden, Colorado, U.S.A.*

## INTRODUCTION

The advancement of renewable energy technology has become increasingly critical as an environmentally sustainable path to world economic and societal development. Large-scale harvesting of energy from sunlight using photovoltaic devices offers tremendous potential as a renewable energy resource. Although the field of photovoltaics has continually evolved over the last several decades, many researchers are looking beyond current device designs to what have been termed third-generation technologies. These technologies are aimed at producing significant improvements in device efficiency-to-cost ratios. This necessitates significantly improving efficiency or reducing cost or ideally both. To realize these goals, many of these technologies will need to utilize nanostructured materials and composite systems that can be tailored to have optimized electronic and optical properties.

Organic/polymeric molecule-based electronics are a promising route to meeting these needs. Organic semiconductors have emerged as a class of materials that can be specifically designed to have a wide range of chemical, optical, and electronic properties, yet they can be processed via low-cost, solution-based techniques. The field has now matured to a point where most of the fundamental photophysical and electronic phenomena of these materials are reasonably well understood. The current challenge is to fully utilize the unique properties of organic semiconductors and to specifically design and fabricate materials and devices that lead to high efficiencies. One critical aspect of these materials is the molecular morphology. It has become apparent that the particular structural arrangement of molecules in an organic semiconductor device can have a large impact on properties such as charge carrier mobility and exciton diffusion. Short-range ordering of the molecules is primarily controlled by intermolecular interactions, as well as by processing conditions such as choice of solvent. Learning how to control the morphology on longer length scales will be a necessity to produce optimized device structures.

Parallel to the development of organic semiconductors has been progress in low-cost synthetic techniques

for metal oxide semiconductors. A variety of solution-based and electrochemical routes have been developed that result in materials with well-defined, novel nanostructures that can be easily controlled by varying the fabrication conditions. This then opens up the possibility of low-cost fabrication of organic-inorganic composite structures, in which the long-range morphology of the organic molecules is determined by the three-dimensional structure of the metal oxide semiconductor. Ultimately, the development of efficient photovoltaic devices will require precise control over many parameters, including what wavelengths of light are absorbed to create excitons, the pathways available for exciton migration, the pathways and mobilities for charge carrier transport, and the alignment of energetic levels at interfaces. This entry will review existing organic photovoltaic devices and explore initial efforts at more sophisticated, yet low-cost, organic-inorganic composite structures aimed at achieving high power conversion efficiencies.

## TECHNOLOGIES FOR PHOTOVOLTAIC POWER CONVERSION

In 2001, 38.6 quads (1 quad = 1 quadrillion Btu =  $1.055 \times 10^9$  GJ) of energy, largely from fossil fuels, was consumed to produce electricity in the United States. After conversion losses, 12.7 quads of net electrical energy was output by power plants for general consumption.<sup>[1]</sup> To produce this amount of energy in 1 year would require covering a  $100 \times 100$  km square area of the Nevada desert with solar cells with a power conversion efficiency of 15%. Thus in order for photovoltaics to make a significant impact on energy production strategy, they must be produced in very large areas at low cost.

Worldwide production levels for solar cell modules have been growing rapidly over the last several years, with Japan recently taking the lead in total production volume (Table 1). Current production is dominated by single crystal and polycrystalline silicon modules, which represent a little over 82% of the market. These devices, based on silicon wafers, have been termed the “first generation” of photovoltaic technology. These

**Table 1** World photovoltaic module production, consumer and commercial (MW)

Country	1994	1995	1996	1997	1998	1999	2000	2001
Japan	16.5	16.4	21.2	35.0	49.0	80.0	128.6	171.22
United States	25.64	34.75	38.85	51.0	53.7	60.8	74.97	100.32
Europe	21.7	20.1	18.8	30.4	33.5	40.0	60.66	86.38
ROW	5.6	6.35	9.75	9.4	18.7	20.5	23.42	32.62
Total	69.44	77.6	88.6	125.8	154.9	201.3	287.65	390.54

ROW = rest of the world.

Source: PV News, Vol. 21, No.2, Feb. 2002.

are single-junction devices, which are limited by thermodynamic considerations to a maximum theoretical power conversion efficiency of 31% under direct AM1.5 sunlight.<sup>[2]</sup> Fig. 1 shows the progress over the last two decades in single crystal silicon laboratory devices, which have achieved efficiencies close to 25%.<sup>[3]</sup> Commercially produced large-area modules have efficiencies ranging from 10% to 15%.

The highest solar cell efficiencies to date have been achieved in multijunction cells based on III–V compound semiconductors (Fig. 1).<sup>[4]</sup> These devices have multiple absorbing layers, each with different band gaps. Such a device scheme allows for higher theoretically attainable efficiencies. For devices with two, three, and

“infinite” absorbing layers, the theoretical efficiency limits are 50%, 56%, and 85%, respectively.<sup>[5,6]</sup> The current record efficiency is 36.9% for a Ga<sub>0.44</sub>In<sub>0.56</sub>P/Ga<sub>0.92</sub>In<sub>0.08</sub>As/Ge triple-junction research cell, measured under concentrated light. These devices are grown epitaxially on single crystal substrates using metal-organic chemical vapor deposition or molecular beam epitaxy. Such highly sophisticated fabrication techniques are generally considered to be too expensive for large-scale commercialization and terrestrial photovoltaic energy production. However, these devices are used commercially in space-based applications, in which high efficiency is a necessity.

Over the last decade, there has been considerable effort in advancing thin-film, “second-generation”

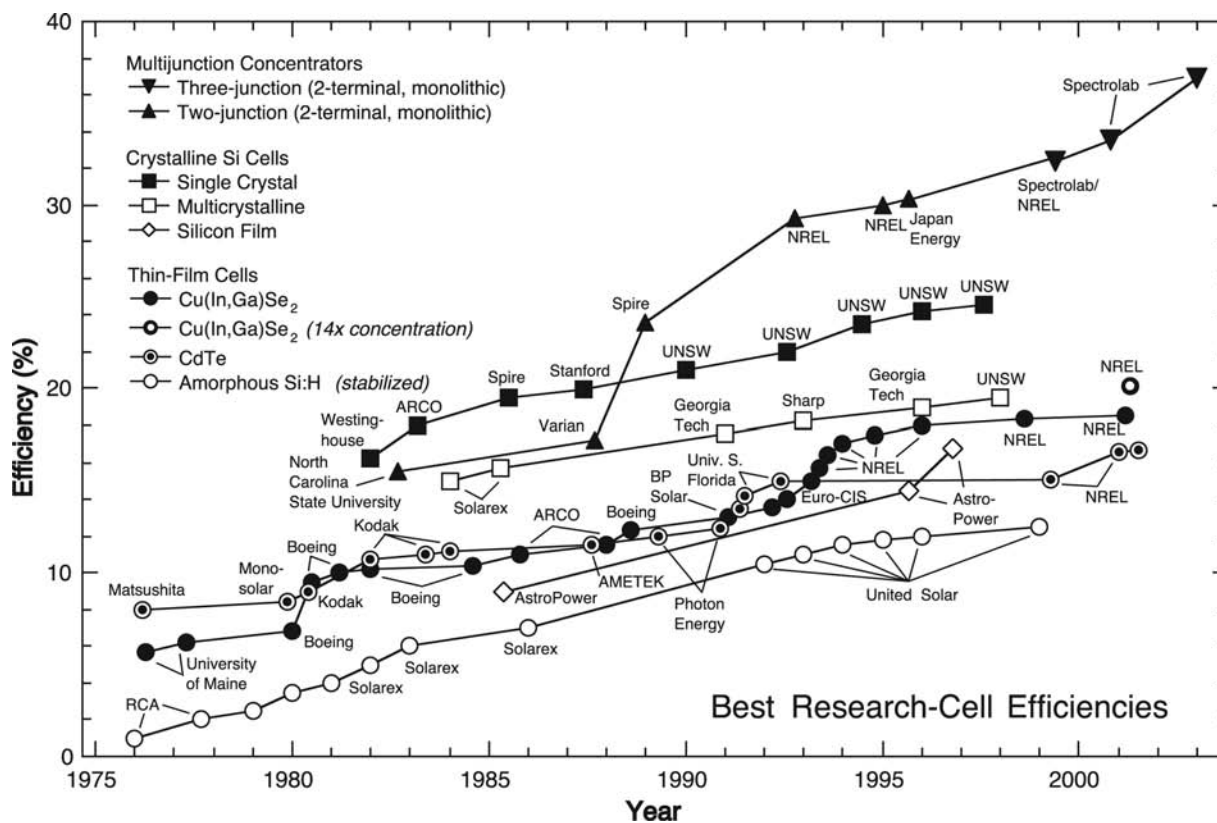


**Fig. 1** Progress of photovoltaic device efficiencies (under AM1.5 simulation solar illumination) for a variety of inorganic technologies. Source: From Ref.<sup>[4]</sup>.

Palladium - Platinum

technologies that do not require the use of silicon wafer substrates and can therefore be manufactured at significantly reduced cost. Steady progress has been made in laboratory efficiencies (Fig. 1) for devices based on CdS/CdTe, Cu(In,Ga)Se<sub>2</sub> (CIGS), and amorphous Si. These devices are fabricated using techniques such as sputtering, physical vapor deposition, and hot-wire chemical vapor deposition. Multijunction cells based on amorphous-Si and amorphous-SiGe alloys have been the most successful second-generation technology to date because of their ability to be fabricated at relatively low cost and be integrated into electronics and building roofing material. They currently constitute most of the remaining 18% of the market not covered by single crystal silicon. Currently, there are about a dozen companies supplying photovoltaic modules based on thin-film technologies, with efficiencies ranging from 7% to 13.4%. It is anticipated that these second-generation technologies will rapidly grow in commercial importance as manufacturing cost and lifetime issues are improved.

Nonetheless, these existing technologies will be hard-pressed to meet the efficiency and cost goals for the long-term outlook. This has led to the concept first coined by Prof. Martin Green of the University of New South Wales of “third-generation” technologies which would be able to show dramatic improvements in either efficiency or cost or both, as shown in Fig. 2. To meet these ambitious goals will require the development of radically new devices that operate on fundamentally different principles than current technologies. A number of novel approaches have been suggested that may be capable, at least theoretically, of more closely approaching the thermodynamic limit of 86.8% for the conversion efficiency of sunlight to electricity.<sup>[7]</sup> These embryonic concepts include hot carrier solar cells, cells with multiple electron-hole pairs per photon, multiband quantum

well and impurity solar cells, and thermophotovoltaic and thermophotonic devices. All of these concepts have been embedded in them major technical challenges with respect to developing new devices, establishing a realistic efficiency potential for the devices, and demonstrating that they are inherently manufacturable.

### Organic-Based Nanostructured Photovoltaics

The other approach to photovoltaic device development is to pursue technologies with moderate efficiency goals (<20%) but with significantly reduced fabrication costs (<\$20/m<sup>2</sup>). These are technologies that are potentially capable of the large-scale production necessary for a paradigm shift in global energy production. These would optimally be fabricated from solution-processible materials using low-temperature, non-vacuum techniques such as inkjet or screen printing. They would be compatible with low-cost, flexible substrates, thus allowing for high-throughput roll-to-roll processing as well as easy integration into existing building structures.

Organic molecular/polymeric semiconductors meet all of the above manufacturing process criteria. They are often soluble in common organic solvents and can be processed in a bench top laboratory setting. They have inherently low material costs and do not typically rely on the use of environmentally hazardous or elementally rare constituents. In addition, they have been proven to possess a wide range of optical, electronic, and mechanical properties that can be finely tuned through structural changes and molecular derivatization. In principle, they provide an enormous parameter space from which specific functionalities can be chosen to engineer novel, high-performance devices. These qualities make organic semiconductors strong candidates for a growing list of device applications. The area of flat-panel displays, in particular, is on the verge of a revolution because of advances in organic light-emitting diodes (OLEDs).<sup>[8,9]</sup> This technology is maturing rapidly, with first generation devices now on the market.

Using organic semiconductors in photovoltaic devices is now the subject of intense research. Organic molecules and  $\pi$ -conjugated polymers can have very high optical absorption coefficients (>10<sup>5</sup> cm<sup>-1</sup>), making them useful as the active layer in the device. Additionally, charge carrier mobilities, while generally several orders of magnitude lower than in conventional semiconductors, are sufficiently high to effectively transport charge out of the device. A multitude of organic solar cell device designs is currently being investigated. All of these use some form of heterojunction between electron-donating and electron-accepting molecules to create free charge carriers

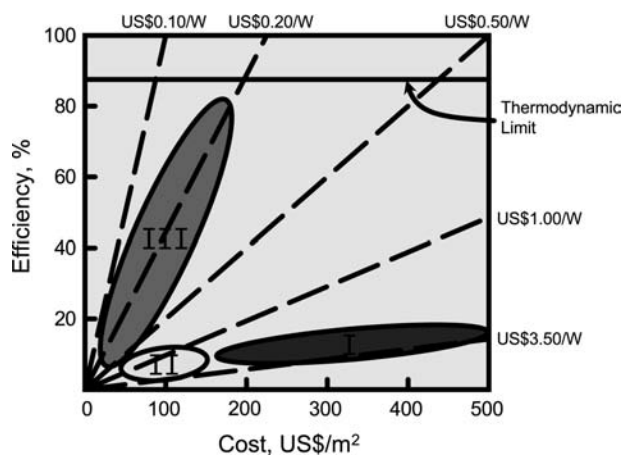


**Fig. 2** Cost-efficiency matrix for first-, second-, and third-generation photovoltaic technologies. *Source:* From Ref.<sup>[7]</sup>.

from the bound electron–hole pairs (excitons) that are characteristic of organic semiconductors. To date, the reported power conversion efficiencies of these devices under simulated solar illumination are all less than 4%.

A great deal of basic research is needed to achieve significantly higher efficiencies in organic basic devices. Some of the key issues are:

- Exciton creation—The process of light absorption to create bound electron–hole pairs.
- Exciton diffusion—Diffusion of excitons to an interface where they can be dissociated.
- Electron transfer—Transfer of electrons to acceptor molecules.
- Charge transport—Transport of electrons and holes to the electrodes.

Many of these phenomena are determined by the morphologies of the molecular structures that occur at multiple length scales within the device. Morphologies on the length scale of a few nanometers, which affect exciton diffusion rates and charge carrier mobilities for instance, are determined by intermolecular forces and the kinetics of the growth/formation process of the material. Morphologies at longer length scales (tens to hundreds of nanometers), which affect the general direction of charge transport, are also determined by these factors, at least for an all-organic material. However, organic–inorganic composite systems allow the possibility of directly controlling the arrangement of the organic molecules at longer length scales. Inorganic materials, particularly semiconducting oxides, can be fabricated using a growing number of techniques to achieve specific three-dimensional structures. These structures can be used as a scaffolding onto which an organic material can be attached to form composite materials in which all the above photovoltaic device phenomena are optimized.

In this entry, we give a brief description of the theory of charge transport in organic materials. We then provide an overview of the existing field of all-organic-based photovoltaic devices and go on to discuss current and hypothetical organic–inorganic composite devices. Finally, we examine a variety of novel semiconducting oxide structures that can be fabricated using low-temperature, solution- and electrochemical-based techniques.

## CHARGE AND EXCITON TRANSPORT IN ORGANIC SEMICONDUCTORS

Organic semiconductors can be broadly categorized as being either small molecules (molecular weight less than a few thousand atomic mass units) or polymers

(molecular weight between a few thousand and  $\sim 1$  million amu). The distinction becomes most important in determining the processing that is required in making films and devices and for the subsequent morphologies that are obtained. However, the fundamental mechanisms that underlie light absorption, exciton diffusion, and charge carrier motion are essentially the same in the two classes of molecules. These properties are governed primarily by molecular orbitals that are built-up from  $\pi$ -electrons that are delocalized across the molecule. Examples of small molecules with extended  $\pi$ -electron delocalization and  $\pi$ -conjugated polymers commonly used in organic photovoltaic devices are depicted in Fig. 3. Highest occupied molecular orbitals (HOMOs) calculated for a sexithienyl oligomer, a fullerene, and a perylene diimide are shown in Fig. 4. Charge transfer and exciton diffusion processes are largely determined by the degree to which the orbitals of adjacent molecules and molecular subunits overlap.

Charge transfer between organic molecules can be viewed within the context of the semiclassical electron transfer theory of Marcus.<sup>[10]</sup> The rate of electron transfer between two molecules is given by

$$k_{\text{ET}} = \frac{4\pi^2}{\hbar} \frac{1}{\sqrt{4\pi k_{\text{B}} T}} t^2 \exp\left(-\frac{\lambda}{4k_{\text{B}} T}\right) \quad (1)$$

where  $\hbar$  is Planck's constant,  $k_{\text{B}}$  is Boltzmann's constant,  $T$  is the temperature,  $t$  is the transfer integral describing the strength of interaction between the two molecules, and  $\lambda$  is the reorganization energy that describes the strength of the electron–phonon interaction.<sup>[11]</sup> Thus for fast charge transfer between molecules, a large interaction strength and small reorganization energy are required. Their relative orientation and the distance between them determine the degree of interaction between two molecules. For highly ordered, single- or polycrystalline molecular films of materials such as pentacenes or perylenes, this interaction strength can be sufficiently large for band transport to be observed.<sup>[11,12]</sup> However, for  $\pi$ -conjugated polymers and amorphous small-molecule materials, the large degree of disorder results in carrier bandwidths on the order of 10 meV,<sup>[13]</sup> which is far smaller than the  $\sim 0.1$  eV required for band transport to occur.<sup>[11]</sup> Instead, carrier transport in these materials occurs via polaron hopping between sites, where each site has a defined energy and geometric (positional + orientational) disorder parameter. In small-molecule materials, a “site” is considered to be an entire molecule. In conjugated polymers, however, the  $\pi$ -electrons, in reality, are not delocalized along the entire length of a polymer chain. Structural defects (kinks and bends) and chemical defects destroy the

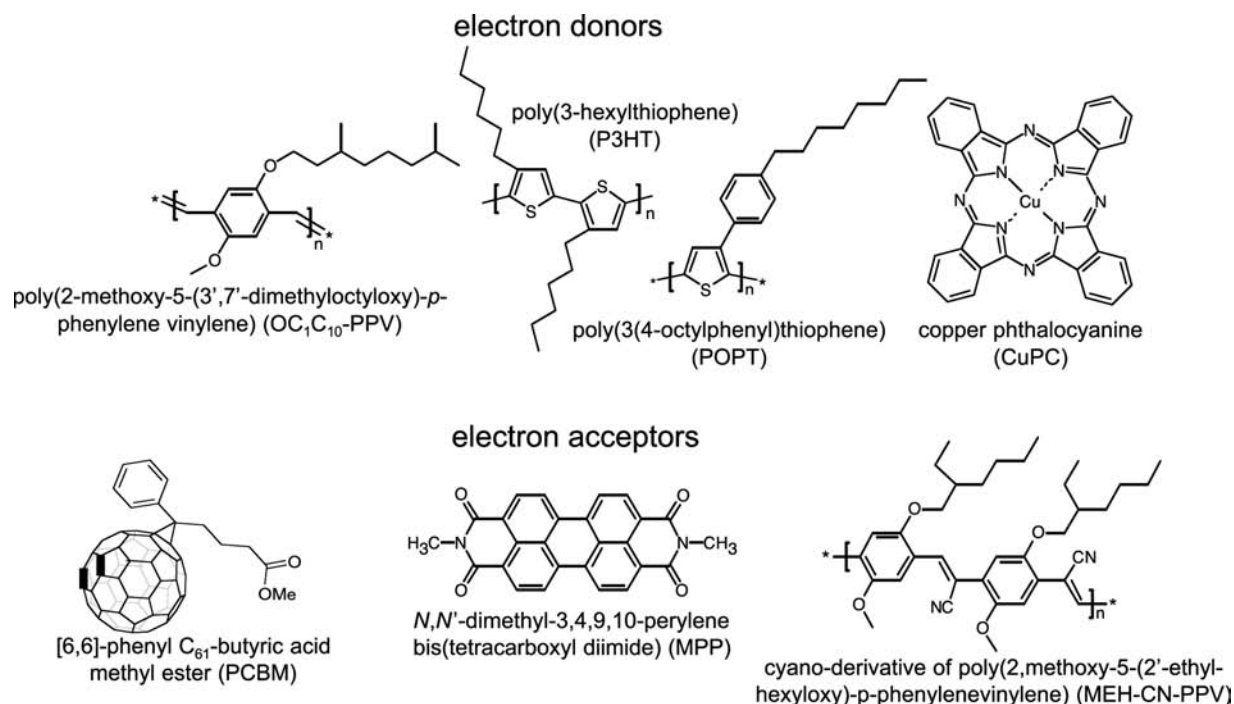


Fig. 3 Molecular structures of typical organic semiconductors that have been used in photovoltaic devices.

conjugation periodically; electronically, the polymer is a series of  $\pi$ -conjugated segments (typically 6–8 monomers long) that are bonded by non-conjugated sections. Fig. 5 illustrates carrier hopping between segments of a conjugated polymer.

The charge carrier mobility for a broad range of organic semiconductors, both small molecule and polymer, has been found experimentally to follow Poole–Frenkel behavior, in which the mobility  $\mu$  as a function of the electric field ( $E$ ) and temperature is given by

$$\mu(E, T) \propto \mu_0(T) \exp(\gamma(T)\sqrt{E}) \quad (2)$$

where  $\mu_0$  is the zero-field mobility and  $\gamma(T)$  is the coefficient of the stretched exponential that describes the temperature dependence of the field activation. This behavior has been successfully modeled with the “disorder formalism” originally developed by Bäessler.<sup>[14]</sup> The model assumes hopping between sites with Gaussian distributions of energies and geometric disorder parameters. A more recent version of the model developed by Novikov et al.,<sup>[15]</sup> which takes into account spatial correlations in the site energies, results in

$$\mu = \mu_\infty \exp \left[ - \left( \frac{3\hat{\sigma}_d}{5} \right)^2 + C_0 (\hat{\sigma}_d^{3/2} - \Gamma) \sqrt{\frac{eaE}{\hat{\sigma}_d}} \right] \quad (3)$$

where  $\mu_\infty$  is the mobility in the limit  $T \rightarrow \infty$ ,  $\hat{\sigma}_d$  is the width of the Gaussian distribution of site energies divided by  $k_B T$ ,  $C_0$  is an empirical constant,  $\Gamma$  describes the geometric disorder, and  $a$  is the intersite spacing. Using typical values of  $\sim 0.1$  eV and 2 for  $\hat{\sigma}_d$  and  $\Gamma$ , respectively, it becomes obvious that the mobility in these materials increases as the degree of disorder is decreased. Typical charge carrier mobilities in conjugated polymers that have been reported in the literature are in the range of  $10^{-6}$ – $10^{-3}$   $\text{cm}^2 \text{V}^{-1} \text{sec}^{-1}$ .<sup>[16]</sup>

Exciton motion/diffusion in organic semiconductors is determined by the same intermolecular interaction considerations as carrier transport, and thus exciton diffusion rates can also be described by hopping models involving Gaussian distributions of site energies. This has been demonstrated by thermally

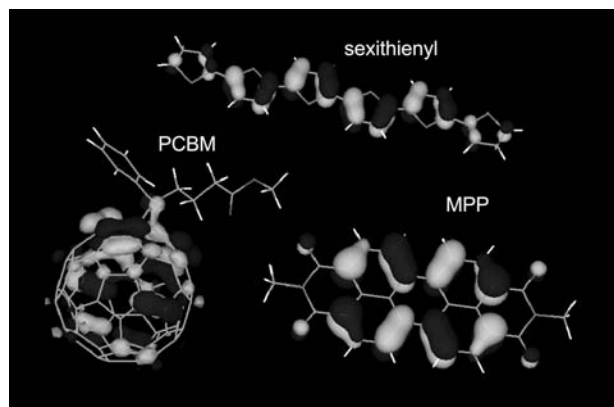
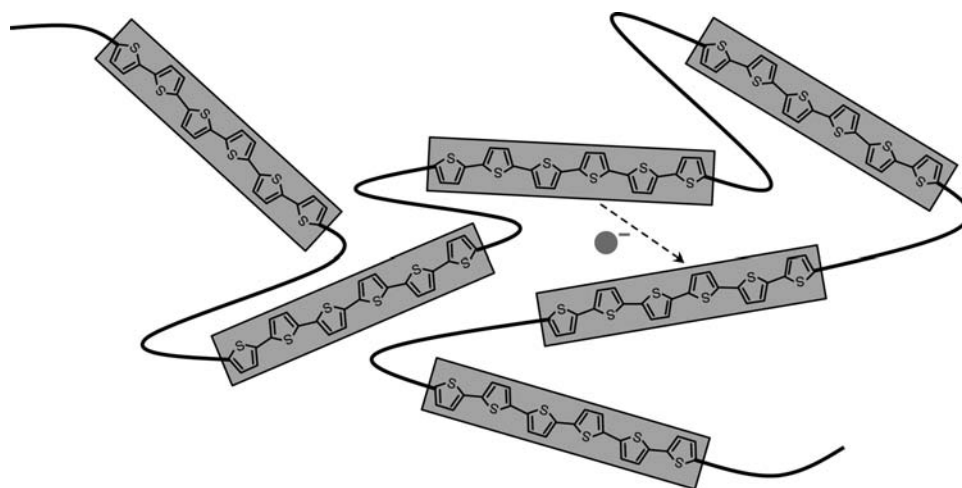


Fig. 4 Highest occupied molecular orbitals (from semiempirical calculations) of representative organic semiconductors with extended  $\pi$ -electron delocalization.





**Fig. 5** Conceptual diagram of the mechanism of charge transport by hopping in a  $\pi$ -conjugated polymer. The rectangular sections represent regions of the polymer that are fully conjugated. Between these conjugated segments are regions of polymer that are bent or twisted, or that have chemical defects that destroy the conjugation.

stimulated photoluminescence experiments on conjugated polymer films, which have been successfully modeled using double-peak Gaussian distributions to account for regions of aggregated polymer.<sup>[17]</sup> Calculations have shown that the electronic coupling between conjugated segments that are sequentially adjacent along the backbone of the polymer (that is, physically bonded but electronically isolated by a break in the conjugation) is approximately 1 order of magnitude less than the coupling between conjugated segments on different polymer chains (or on the same chain, but far away sequentially), which are close together and aligned parallel to each other.<sup>[18]</sup> This has led to the conclusion that interchain exciton hopping is a faster process than intrachain exciton hopping.<sup>[19]</sup> Analogous to the limitations on carrier transport, poor interaction strengths between adjacent segments typically lead to short exciton diffusion lengths (the average distance the exciton moves before decaying to the ground state or becoming dissociated at a defect or interface) of the order of 6–10 nm,<sup>[20]</sup> although much large exciton diffusion lengths have been reported for highly ordered materials.<sup>[21]</sup>

The main conclusion to be drawn from this section is that molecular ordering is a critical ingredient to obtain high carrier mobilities and large exciton diffusion lengths in organic semiconductors. This point is illustrated in the polymer poly(3-hexylthiophene) (P3HT). This material (when synthesized in its regioregular, head-to-tail form) has been shown to possess a large degree of molecular ordering because of efficient interdigitation of the alkyl chains of adjacent polymer chains, leading to strong  $\pi$ -stacking of the thiophene backbones (Fig. 6). As a result, this material has shown the highest hole mobility of a conjugated polymer to

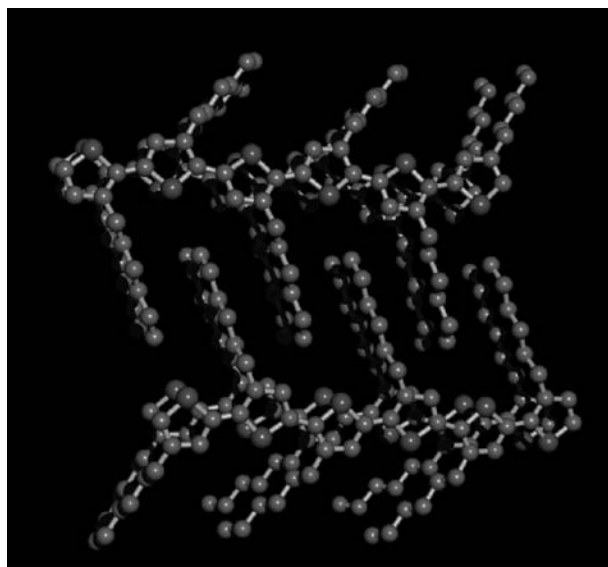


**Fig. 6** Conceptual diagram of interchain ordering in a P3HT aggregate (cyan = carbon, yellow = sulfur, hydrogen atoms are not shown).

date ( $0.1 \text{ cm}^2 \text{ V}^{-1} \text{ sec}^{-1}$ ), when measured in a field effect transistor geometry.<sup>[22]</sup> The effect of this molecular ordering on photovoltaic device performance will be discussed in the next section.

## ORGANIC PHOTOVOLTAIC DEVICES: THE PLASTIC SOLAR CELL

Photoexcitations in organic semiconductors are inherently different than in conventional inorganic semiconductors. Whereas light absorption in an inorganic



semiconductor typically leads to the immediate production of a free electron–hole pair, light absorption in an organic semiconductor results in the formation of an exciton (bound electron–hole pairs). In order for a free carrier to be generated, this exciton must be dissociated. This can happen in the presence of very high electric fields, at a defect site in the material, or at the interface between two materials that have a sufficient mismatch of their energetic levels (band offset). In the case of dissociation at the interface between two materials, an exciton created in the material with lower (higher) electron affinity diffuses to the interface, and electron (hole) transfer occurs to the material with higher (lower) electron affinity. The higher electron affinity material is referred to as the acceptor, while the lower electron affinity material is the donor. Thus one can fabricate a photovoltaic device with the structure positive electrode/donor/acceptor/negative electrode. Tang<sup>[23]</sup> using a copper phthalocyanine layer as the donor and a perylene derivative as the acceptor first did this. This device had a power conversion efficiency of about 1% under simulated solar illumination.

There are two possible driving forces in the operation of a photovoltaic device: the electrical potential gradient (the electric field) and the chemical potential gradient.<sup>[24]</sup> In a bilayer donor–acceptor device, a chemical potential gradient is established that preferentially drives electrons away from the interface toward the negative electrode and holes away from the interface toward the positive electrode. An electric field in the device, such as one established by a difference in the work functions of the positive and negative electrodes, can assist in driving charges toward the electrodes, but may not be critical to the operation of the device. The important criteria for high efficiency in such a device are large exciton diffusion lengths in both the donor and acceptor materials, fast electron transfer and slow recombination rates at the interface, and high charge carrier mobilities in both layers. Several molecular donor–acceptor pairs have been investigated for use in bilayer photovoltaic devices, including phthalocyanine–perylene,<sup>[23,25]</sup> phthalocyanine–fullerene,<sup>[26,27]</sup> polymer–polymer,<sup>[28]</sup> polymer–perylene,<sup>[29]</sup> and polymer–fullerene.<sup>[30]</sup> As a result of the short exciton diffusion lengths in these materials, only excitons that are generated within approximately 10 nm of the interface contribute to the photocurrent. This presents a serious limitation on the possible power conversion efficiency of these devices.

To overcome this problem, researchers have developed devices in which the donor and acceptor molecules are blended together in an intimate mixture to produce a “bulk heterojunction” solar cell.<sup>[31]</sup> The donor and acceptor molecules form two “interpenetrating networks” that transport holes and electrons,

respectively. In this device, an exciton generated anywhere in the bulk has only a few nanometers to diffuse before encountering an acceptor interface. After dissociation of the exciton into a free electron and a free hole, the charge carriers are transported through the bulk of the film (along their respective transport networks) to the electrodes. Directionality of the charge transport is provided by a built-in electric field in the device, which originates from a difference in effective work functions of the electrodes, as well as possibly a chemical potential gradient, which originates from “selective” electrodes that preferentially block either holes or electrons.<sup>[32]</sup>

Bulk heterojunction solar cells based on blends of a conjugated polymer with a fullerene (Fig. 7) have been among the most successful to date.<sup>[33]</sup> Photoinduced electron transfer from a conjugated polymer to a fullerene was demonstrated to occur on an ultrafast time-scale (~45 fsec) and to produce a long-lived charge-separated state, with recombination to the ground state following a power law decay ranging from 300 nsec to 1 msec.<sup>[34,35]</sup> Thus excitons generated in the conjugated polymer, which have lifetimes of several hundred picoseconds, are quickly dissociated into free carriers when they encounter a fullerene interface. These free carriers will have sufficient time to be transported to the electrodes before recombining provided that the active layer of the device is not too thick. This produces an inherent tradeoff in the device design. As the active layer is made thicker, more light is absorbed and more excitons/charge carriers are created, but the carriers spend longer time in the device and thus have a higher probability of recombining to the ground state before they can contribute to the photocurrent. This means that high carrier mobility (for both holes and electrons) is required in the elements of the blend to allow the

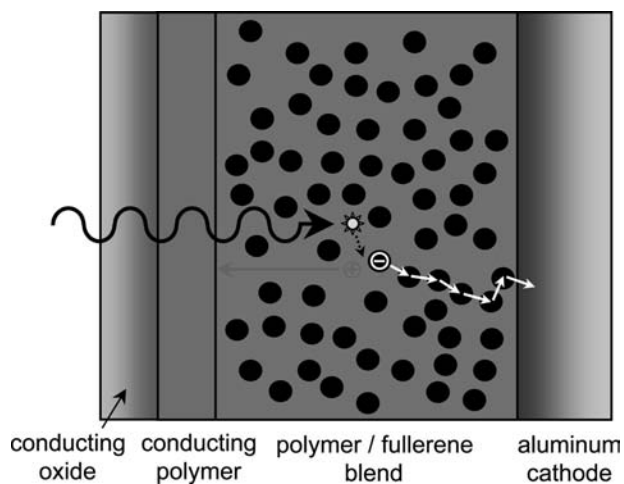


**Fig. 7** Schematic diagram of a conjugated polymer–fullerene bulk heterojunction photovoltaic device.

active layer to be thick enough to have significant optical density.

As discussed above, morphology is an important factor in determining a material's carrier mobility. Thus a critical area for development of high efficiency devices is to develop approaches that lead to improved morphologies. This has been demonstrated in conjugated polymer–fullerene bulk heterojunction solar cells in which changing the casting solvent for the active layer film can lead to a large increase in device photocurrent and efficiency.<sup>[36]</sup> Devices consisting of a blend of the polymer poly(2-methoxy-5-(3',7'-dimethyloctyloxy)-*p*-phenylene vinylene) (OC<sub>1</sub>C<sub>10</sub>-PPV) with the fullerene [6,6]-phenyl C<sub>61</sub>-butyric acid methyl ester (PCBM) (Fig. 3) showed nearly a factor of 3 enhancement in efficiency when cast from chlorobenzene as opposed to toluene. It was subsequently determined that the hole mobility in OC<sub>1</sub>C<sub>10</sub>-PPV is approximately 1 order of magnitude higher when cast from the chlorobenzene. From light-scattering measurements performed over a range of polymer concentrations, it was shown that the polymer does not truly dissolve in chlorobenzene, but instead forms a suspension.<sup>[37]</sup> A complete explanation for why this leads to higher carrier mobilities in the thin-film material has not been fully elucidated, but it has been postulated that the polymer chains collapse together into an aggregate that promotes  $\pi$ -electron sharing ( $\pi$ -stacking) between chains. Such solvent effects on carrier mobilities have also been demonstrated in the operation of OLEDs.<sup>[19]</sup> Electron mobilities in the bulk heterojunction OC<sub>1</sub>C<sub>10</sub>-PPV-PCBM blend have also been shown to be high ( $2 \times 10^{-3} \text{ cm}^2 \text{ V}^{-1} \text{ s}^{-1}$ ) when the film is cast from chlorobenzene, although, in this case, the explanation apparently is that chlorobenzene is a very good solvent for PCBM and reduces the amount of phase segregation that normally leads to large barriers to electron transport in the fullerene network.<sup>[38]</sup> Additional evidence for the effects of morphology on mobility and device performance has been reported in bulk heterojunction solar cells made from the conjugated polymer P3HT (Fig. 3). It was demonstrated that postproduction annealing of photovoltaic devices made from P3HT-PCBM blends results in a dramatic increase in device efficiency, from 0.4% to 3.5% as measured under white light illumination. This efficiency enhancement presumably arises from an increase in the ordering of the P3HT chains upon annealing.<sup>[39]</sup>

The general viability of the application of donor–acceptor systems as employed in bulk heterojunction organic solar cells has been demonstrated by a number of other recent results, including polymer–polymer<sup>[40]</sup> and polymer–quantum rod devices.<sup>[41]</sup> These all have the same criteria for high efficiency as the polymer–fullerene device, namely, small distances for exciton diffusion to an interface, exciton dissociation that is

fast, charge recombination that is slow, and large charge carrier mobilities. Reported efficiencies of organic solar cells to date have not exceeded 4% for several reasons. First, the amount of light that is absorbed by the devices is typically too small because 1) the optical band gap of the light-absorbing component is usually too large ( $>1.4 \text{ eV}$ ), resulting in poor overlap with the solar spectrum, and 2) the optical density is too small because the active layer of the device must be kept thin to limit charge carrier recombination. Second, the photovoltage that is generated is typically too low. This is limited, to first order, by the effective electronic band gap of the active layer, which is given by the difference between the HOMO level of the donor and the lowest unoccupied orbital (LUMO) level of the acceptor. Last, the fill factor, which is a measure of the quality of the diode, is too small. A necessary solution for many of these problems will be the development of new polymers and organic molecules. Concurrently, devising new ways to control the morphologies of the light-absorbing and -transporting materials to optimize the pathways for exciton/charge transport will be required. The organic–inorganic composite devices discussed in the next section provide a promising route to controlling morphologies on the nanoscale.

## ORGANIC–INORGANIC COMPOSITE PHOTOVOLTAIC DEVICE CONCEPTS

The bulk heterojunction solar cell is one approach to addressing the problem of short exciton diffusion lengths in organic semiconductors. However, the mixing of donor and acceptor species into an intimate blend introduces the problem of bulk recombination of carriers to the ground state, as previously discussed. Additionally, islands, defects, and cul-de-sacs in the transport networks that result in incomplete percolation paths may limit charge transport of one or both carriers in a bulk heterojunction cell. One promising route to high-efficiency solar cells that overcome these problems are devices that use a nanostructured, semiconducting metal oxide (such as TiO<sub>2</sub>, SnO<sub>2</sub>, or ZnO) as the electron-accepting and -transporting network. Such materials can be easily grown using low-temperature, solution-based routes to produce a variety of nanostructures, as is discussed in the next section. The topology of these nanostructures can be optimized to produce a continuous network that guarantees a percolation path for electrons to the electrode. This then opens up the possibility of organic–inorganic composite devices in which an organic semiconductor is deposited onto the surface of the oxide or used to fill the empty volume in a porous structure. In this way, the inorganic network can be used to induce a

specifically tailored morphological structure in the organic material and result in an overall device structure that has a large optical path length but short carrier-to-electrode path lengths.

The first example of a solar cell made using a porous oxide as an electron-transporting network was the solution-based, dye-sensitized solar cell.<sup>[42]</sup> In this device, a monomolecular layer of dye (typically a ruthenium complex) is chemisorbed through carboxylic acid binding groups onto the surface of a high surface area, mesoporous TiO<sub>2</sub> film. A liquid electrolyte (typically with an iodine/triiodide redox couple in an organic solvent) fills the pore spaces and makes contact to a platinum-coated counterelectrode. In the operation of the device, the dye molecules absorb light and inject electrons into the TiO<sub>2</sub>. The oxidized dye molecules are subsequently reduced by a reaction with the redox species. Transport of the charges out of the device occurs via diffusion of electrons through the TiO<sub>2</sub> and diffusion/ionic conduction of the redox species to the counterelectrode. Such devices have achieved 10% power conversion efficiency under solar illumination; however, the use of a liquid electrolyte makes them very difficult to implement for large-scale production. Recent progress has been made in replacing the liquid electrolyte with organic semiconductors, yielding devices with efficiencies reaching 3.2%.<sup>[43,44]</sup> Also, preliminary investigations into sensitizing a mesoporous oxide with quantum dots have been performed,<sup>[45]</sup> opening up the possibility of harnessing some of the “third-generation” photovoltaic mechanisms for achieving higher efficiencies such as hot carrier production or impact ionization.<sup>[46]</sup>

More recently, researchers have investigated solar cells based on conjugated polymer–semiconducting oxide composites. Such devices consist of a conjugated polymer embedded into a mesoporous metal oxide, which acts as an electron acceptor. Several studies have shown that metal oxide semiconductors can act as efficient electron acceptors for conjugated polymers.<sup>[47,48]</sup> The operation of these devices differs from that of the dye-sensitized cell in that light is absorbed in regions of the conjugated polymer potentially far from an oxide interface. Thus excitons must diffuse to an interface before electron transfer to the oxide can take place. Also, electric fields that contribute to the driving force for the current may be present in the device, which is not the case in the dye-sensitized cell because the ionic liquid shields all electric fields.<sup>[24]</sup> Several possible morphologies for such a composite device can be envisioned. As shown in Fig. 8, the polymer can be embedded in an isotropic, mesoporous oxide or in a “forest” of oxide nanorods that are vertically oriented to the substrate. To facilitate a direct path for charges to be transported to the electrode, the vertically oriented columns may be a better

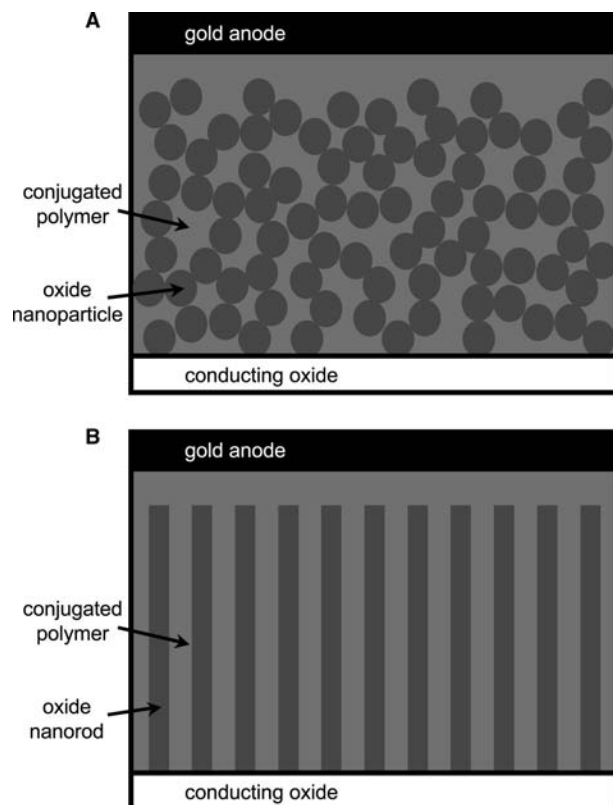


**Fig. 8** Schematic diagram of conjugated polymer–semiconducting oxide composite photovoltaic devices with (A) an isotropic, mesoporous oxide and (B) a forest of oxide nanorods.

geometry. Aside from the goal of increased power conversion efficiency, these composite devices may result in increased morphological stability and robustness compared with pure polymer films, resulting in enhanced device lifetimes.

Fabrication of organic–inorganic composite devices has been performed via several techniques. Fig. 9A shows a mesoporous SnO<sub>2</sub> structure that was fabricated by spin-coating an aqueous solution of SnO<sub>2</sub> nanoparticles (diameter ~ 9 nm) mixed with polystyrene spheres (diameter ~ 100 nm). Upon heating the film to 450°C in an oxygenated atmosphere, the SnO<sub>2</sub> nanoparticles are sintered together to form a continuous oxide network. The polystyrene spheres are burned out of the film, leaving behind voids on the size scale of 100 nm. Fig. 9B shows a composite structure fabricated by soaking the above film in a solution of the conjugated polymer OC<sub>1</sub>C<sub>10</sub>-PPV for 8 hr. The SEM image shows efficient intercalation of the polymer into the porous SnO<sub>2</sub> structure. From optical measurements, the polymer was estimated to fill 75% of the free volume of the oxide. Several thermodynamic factors contribute to the degree of intercalation of a polymer into a porous medium.<sup>[49]</sup> Osmotic pressure drives the polymer chains into the pores. However,

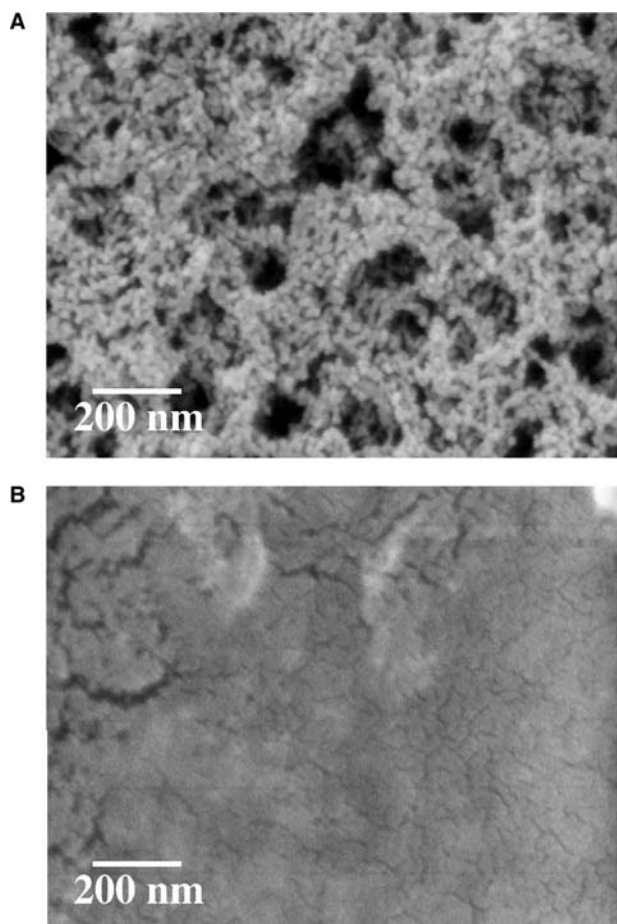


**Fig. 9** Scanning electron microscopic images of the top surfaces of (A) a porous SnO<sub>2</sub> film with a thickness of 300 nm and (B) a SnO<sub>2</sub>/conjugated polymer (OC<sub>1</sub>C<sub>10</sub>-PPV) composite film. The porous SnO<sub>2</sub> film was fabricated by sintering a solution-deposited SnO<sub>2</sub> nanoparticle/polystyrene sphere mixture. The composite structure was fabricated by solution intercalation of the polymer into the porous SnO<sub>2</sub> structure.

the entropic force is in the other direction because of the reduced number of configurational states available to the confined polymer. The force that can tip the scales in either direction is the interaction energy between the polymer and oxide surface. A strong attractive force between the polymer and the oxide can overcome the entropic drive and result in efficient intercalation into the porous volume. Whether the oxide-polymer interaction is attractive or repulsive depends on a wide range of intermolecular forces, including the hydrophobic/hydrophilic and polar character of both materials, as well as the solvent in which the polymer is dissolved.<sup>[50]</sup> The hydrophobic/hydrophilic nature of the oxide surface can be substantially altered by cleaning processes or chemical derivatization to optimize the conditions for polymer intercalation. In a system in which there is a strong oxide-polymer attraction leading to efficient

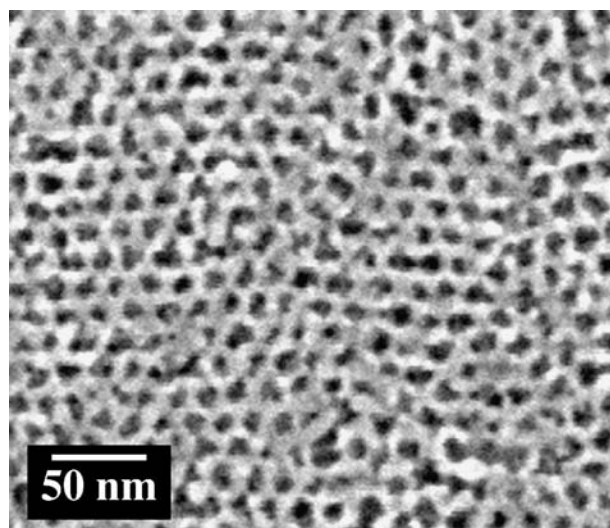


**Fig. 10** Scanning electron microscopic image of an ordered, porous TiO<sub>2</sub> film fabricated using a self-organizing block copolymer as a templating agent. *Source:* From Prof. M.D. McGehee, Dept. of Materials Science and Engineering, Stanford University.

intercalation, the intercalated polymer can become essentially insoluble in solvents that would normally dissolve it, as is the case for the composite structure shown in Fig. 9B.

Other techniques that have been demonstrated include a self-assembly approach to fabrication of mesoporous TiO<sub>2</sub> using a block copolymer as a structure-directing agent.<sup>[51]</sup> Fig. 10 shows a highly ordered, mesoporous TiO<sub>2</sub> structure fabricated via this technique. Intercalation of this structure with the conjugated polymer P3HT resulted in a solar cell with approximately 0.5% power conversion efficiency under solar illumination. Also, a technique in which a Ti(OC<sub>3</sub>H<sub>7</sub>)<sub>4</sub> precursor was blended with a conjugated polymer and subsequently annealed to form a composite film with 100% filling has been demonstrated.<sup>[48]</sup> In the next section, we examine a variety of novel, low-cost techniques for fabricating metal oxide nanostructures that could potentially be used in an organic-inorganic composite solar cell.

## NOVEL FABRICATION TECHNIQUES FOR METAL OXIDE NANOSTRUCTURES

Over the past few years, the synthesis of semiconducting nanoparticles and nanorods has advanced substantially. There is considerable work demonstrating the synthesis of nearly monodisperse particles with sizes from a few nanometers to a few hundred nanometers. This allows tremendous flexibility in controlling the material band structure. There has been a remarkable

diversity of approaches to the synthesis of nanoparticles of various structures and of nanostructured surfaces. These include solution precipitation, sol-gel approaches, self-organization, and a range of physical vapor deposition (PVD)-based approaches including pulsed laser deposition, chemical vapor deposition, and sputtering.<sup>[52–61]</sup> One of the key emerging areas for controlling particle synthesis and incorporation into composite structures is the use of appropriate chelating ligands to promote self-organization.<sup>[53,62–70]</sup> There is quite a remarkable diversity of approaches being employed to both produce and tailor nanoparticulate materials. This provides an unprecedented degree of flexibility in the development of new materials. Interestingly, however, the vast majority of the work has been on a very few materials such as CdS, CdSe, silica, and ZnO.<sup>[62,71–80]</sup> This work served well

to develop the basic tools for the synthesis and capping of the nanoparticles for self-assembly or incorporation into composites. Recent work has also developed an array of tools for the synthesis of core/shell nanoparticles where the surface of the particle is a different material than the interior.<sup>[56,73,81]</sup> Overall, the development of these synthetic techniques provides the opportunity to pick a core material based on optical, electronic, and chemical properties and then cap it with another electronic material or to derivatize it with appropriate ligands to promote incorporation into a composite, or to lead self-assembly, or to control excitation or charge transfer properties. This presents an unprecedented ability to tailor the behavior of a composite material and has significant ramifications for a wide range of applications including solar cells, catalysis, and sensors.

**Table 2** Synthetic routes for the formation of nanofibers/nanotubes from a variety of inorganic semiconductors

Material	Synthetic method	Dimensions	Reference
H-TiO <sub>2</sub> nanotubes	Hydrothermal 10 M NaOH	5 nm radius, 150 nm length	[82,83]
TiO <sub>2</sub> nanofibers	Electrospinning of ethanol solution of poly(vinyl pyrrolidone)/titanium tetraisopropoxide	10–100 nm radius, up to several centimeters length	[84]
InAs nanofibers	2InCl <sub>3</sub> + 6KBH <sub>4</sub> + 2As → 2InAs + 6KCl + 6 BH <sub>3</sub> + 3H <sub>2</sub>	15–100 nm radius, 150–1000 nm length	[85]
GaP nanorods	Benzene reflux with GaCl <sub>3</sub> , Na, and P	20–50 nm radius, 200–500 nm length	[86]
CdE (E = S, Se, Te) nanorods	Direct reaction of the elements in organic solvents	10–40 nm radius, microns length	[87]
CuInE (E = S, Se) nanorods	Elements in organic solvents	10–40 nm radius, hundreds of nanometers length	[88]
ZnO, ZnS nanocables and nanotubes	Evaporation of the oxide followed by sulfiding	5–20 nm radius, hundreds of nanometers length	[89]
ZnO nanorods	Thermal decomposition of Zn <sup>II</sup> amino complex in aqueous solution	5–10 nm, 50–100 nm, and 0.5–1.0 μm radius, up to 10 μm length	[90,91]
ZnO nanobridges and nanonails	Thermal vapor transport and condensation method	25–100 nm radius, hundreds of nanometers to 2 μm length	[92]
GaP nanorods	Catalytic decomposition of Ga <sub>2</sub> O, P, and carbon nanotubes	50 nm radius, microns length	[93]
GaO nanoribbons	Direct reaction of GaN with oxygen	10–60 nm thick, hundreds of nanometers length	[94]
MnO <sub>2</sub> nanowires	Hydrothermal reaction of MnSO <sub>4</sub> –H <sub>2</sub> O with water in presence of ammonium persulfate	5–20 nm radius, microns length	[95]
CdWO <sub>4</sub> nanorods	Hydrothermal preparation	50 nm radius, 200 nm length	[96]
BaWO <sub>4</sub> nanorods	Reverse micelle synthesis	20–50 nm radius, hundreds of nanometers length	[97,98]
Vanadium oxide nanotubes	Hydrothermal synthesis with ammonium metavanadate and amines or quaternary ammonium salts	20–100 nm radius, 100–1000 nm length	[99]
MoS <sub>2</sub> , WS <sub>2</sub> , and NbS <sub>2</sub> nanotubes	High temperature synthesis of Mo with Se	100 nm radius, microns length	[100–103]



One of the newer developments in this area has been the development of synthetic approaches to nanorods or tubes with high aspect ratios. This leads to the possibility of anisotropic three-dimensional structures. The rods can be organized very differently than spherical particles and can be selectively attached or derivatized to control incorporation into a composite. As photoactive elements, nanomaterials with high aspect ratios can be used for transport of carriers and selective transport along the fiber or tube. For tubes, it may also be possible to delineate between the interior and exterior of the tube. The formation of nanorods and or tubes has been observed for a wide variety of systems, some of which are indicated in Table 2. While this list is not exhaustive by any means, it should serve to illustrate the extensive range of possible materials available with a wide variety of surface chemistries, optical, and electronic properties. Key is that simple hydrothermal or gas phase synthesis routes, which are very flexible allowing for derivatization of the materials and are very scalable, can make many of the materials. Figs. 11 and 12 show examples of TiO<sub>2</sub> nanofibers and ZnO microcrystallites grown in aqueous solutions.

There is also a very embryonic literature on the photochemistry of nanorods/tubes indicating that very facile charge transport can occur with appropriate surface derivatization (linkers) and produce useful chemistry such as polymerization, etc.<sup>[104–108]</sup> These results support the ability to apply the tunability of the semiconducting nanostructures through quantum confinement, coupled with rapid electron/exciton

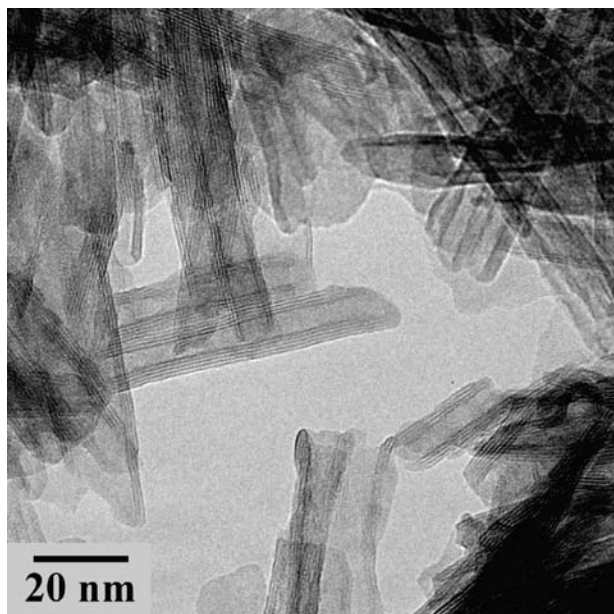


**Fig. 11** Scanning electron microscopic image of TiO<sub>2</sub> nanofibers grown from an aqueous solution at 150°C.

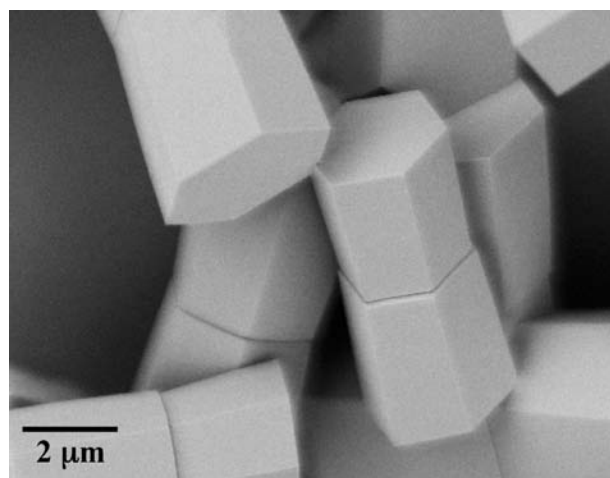


**Fig. 12** Scanning electron microscopic image of ZnO microcrystallites grown from an aqueous solution at 95°C.

transfer with appropriate incorporation of the materials into the composite structure. These initial results point to the need for extensive work to understand the nature of excitonic and charge transfer in inorganic nanorods and nanotubes as well as the specifics of how to couple the nanomaterial to the outside environment such as a polymer or catalyst entity. However, there is every reason to believe at present that the diversity of materials and ligands will allow tailoring of the energetics and kinetics to produce specific redox behavior.

## CONCLUSION

Organic semiconductors are a promising class of materials for the fabrication of low-cost, large-scale production solar cells. Current state-of-the-art organic solar cells have achieved power conversion efficiencies exceeding 3%. This is an encouraging value, but a substantial increase in performance is required for these devices to be of practical use. To achieve higher efficiencies will require controlling the morphologies of the donor and acceptor materials to simultaneously optimize the exciton and charge transport pathways while allowing for an optically thick device. Recent advances in solution-based synthesis of metal oxide and other inorganic semiconductor nanostructures bring about the possibility of low-cost organic-inorganic composite devices with optimized morphologies. Many challenges exist in this area however. Further techniques for fabricating composite structures must be identified and refined, particularly with respect to efficiently intercalating polymers into nanostructured/porous media. Also, correct alignment of the charge transport pathways to the electrodes is necessary for efficient device operation, and thus the orientation of the nanostructures with respect to



the substrate must be precisely controlled. Perhaps the most vital, yet least understood, topic in this area is the organic–inorganic interface. Optimized device structures will require good mechanical contact and strong adhesion between the two components. Electronic properties of the interface are also crucial. Exciton quenching at the interface must be fast and efficient, and the relative electronic levels of the two materials must be optimized to yield the largest possible chemical potential difference across the interface for photogenerated charges. All these require a complete understanding of the chemistry and charge transfer reactions that occur at the interface. Meeting these challenges will be necessary to realize the full potential of organic semiconductor and organic–inorganic composite devices.

## ACKNOWLEDGMENTS

The authors thank Alex Miedaner for synthesis of TiO<sub>2</sub> and ZnO nanostructures and Bobby To for production of SEM images. The authors gratefully acknowledge funding from the U.S. Department of Energy, the National Center for Photovoltaics, and from an NREL Director's Discretionary Research and Development grant under the Department of Energy contract DE-AC36-19GO10337.

## REFERENCES

1. *Annual Energy Review 2001*; Energy Information Administration; <http://www.eia.doe.gov/emeu/aer/elect.html> (accessed February 2003).
2. Shockley, W.; Queisser, H.J. Detailed balance limit of efficiency of p–n junction solar cells. *J. Appl. Phys.* **1961**, *32* (3), 510–519.
3. Green, M.A.; Emery, K.; King, D.L.; Sanekazu, I.; Wilhelm, W. Solar cell efficiency tables (version 19). *Prog. Photovolt.: Res. Appl.* **2002**, *10*, 55–61.
4. Kazmerski, L.L. 21st Century photovoltaics R&D: an expedition toward the non-conventional. In *Photovoltaics for the 21st Century*; McConnell, R.D., Kapur, V.K., Eds.; The Electrochemical Society: Washington, DC, 2001; 20–29.
5. Sze, S.M. *Physics of Semiconductor Devices*, 2nd Ed.; John Wiley & Sons: New York, 1981.
6. Marti, A.; Araujo, G.L. Limiting efficiencies for photovoltaic energy conversion in multigap systems. *Sol. Energy Mater. Sol. Cells* **1996**, *32*, 203–222.
7. Green, M.A. Third generation photovoltaics: concepts for high efficiency at low cost. In *Photovoltaics for the 21st Century*; Kapur, V.K., Ed.; The Electrochemical Society: Washington, DC, 2001; 3–19.
8. Tang, C.W.; VanSlyke, S.A. Organic electroluminescent diodes. *Appl. Phys. Lett.* **1987**, *51* (12), 913–915.
9. Friend, R.H.; Gymer, R.W.; Holmes, A.B.; Burroughes, J.H.; Marks, R.N.; Taliani, C.; Bradley, D.D.C.; Dos Santos, D.A.; Bredas, J.L.; Logdlund, M.; Salaneck, W.R. Electroluminescence in conjugated polymers. *Nature* **1999**, *397* (6715), 121–128.
10. Marcus, R.A. Electron transfer reactions in chemistry. Theory and experiment. *Rev. Mod. Phys.* **1993**, *65* (3), 599–610.
11. Bredas, J.L.; Calbert, J.P.; da Silva Filho, D.A.; Cornil, J. Organic semiconductors: a theoretical characterization of the basic parameters governing charge transport. *Proc. Natl. Acad. Sci.* **2002**, *99* (9), 5804–5809.
12. Karl, N. Charge carrier transport in organic semiconductors. *Synth. Met.* **2003**, *133–134*, 649–657.
13. Silinsh, E.A. *Organic Molecular Crystals. Their Electronic States*; Springer-Verlag: Berlin, 1980; 16pp.
14. Bässler, H. Charge transport in disordered organic photoconductors. *Phys. Status Solidi, B* **1993**, *175*, 15–56.
15. Novikov, S.V.; Dunlap, D.H.; Kenkre, V.M.; Parris, P.E.; Vannikov, A.V. Essential role of correlations in governing charge transport in disordered organic materials. *Phys. Rev. Lett.* **1998**, *81* (20), 4472–4475.
16. Martens, H.C.F.; Blom, P.W.M.; Schoo, H.F.M. Comparative study of hole transport in poly(*p*-phenylene vinylene) derivatives. *Phys. Rev., B* **2000**, *61* (11), 7489–7493.
17. Kadashchuk, A.; Skryshevski, Y.; Piryatinshki, Y.; Vakhnin, A.; Emelianova, E.V.; V.I., A.; Bässler, H.; Shinar, J. Thermally stimulated photoluminescence in poly(2,5-dioctoxy *p*-phenylene vinylene). *J. Appl. Phys.* **2002**, *91* (8).
18. Beljonne, D.; Pourtois, G.; Silva, C.; Hennebicq, E.; Herz, L.M.; Friend, R.H.; Scholes, G.D.; Setayesh, S.; Müllen, K.; Bredas, J.L. Interchain vs. intrachain energy transfer in acceptor-capped conjugated polymers. *Proc. Natl. Acad. Sci.* **2002**, *99* (17), 10,982–10,987.
19. Nguyen, T.-Q.; Martini, I.B.; Liu, J.; Schwartz, B.J. Controlling interchain interactions in conjugated polymers: the effects of chain morphology on exciton–exciton annihilation and aggregation in MEH-PPV films. *J. Phys. Chem., B* **2000**, *104*, 237–255.
20. Theander, M.; Yartsev, A.; Zigmantas, D.; Sundström, V.; Mammo, W.; Andersson, M.R.; Inganäs, O. Photoluminescence quenching at a polythiophene/C60 heterojunction. *Phys. Rev., B* **2000**, *61* (19), 12,957–12,963.
21. Gregg, B.A.; Sprague, J.; Peterson, M.W. Long-range singlet energy transfer in perylene bis(phenethylimide) films. *J. Phys. Chem., B* **1997**, *101* (27), 5362–5369.
22. Sirringhaus, H.; Brown, P.J.; Friend, R.H.; Nielsen, M.M.; Bechgaard, K.; Langeveld-Voss, B.M.W.; Spiering, A.J.H.; Janssen, R.A.J.; Meijer, W.W.; Herwig, P.; de Leeuw, D.M. Two-dimensional charge transport in self-organized, high-mobility conjugated polymers. *Nature* **1999**, *401*, 685–688.
23. Tang, C.W. Two-layer organic photovoltaic cell. *Appl. Phys. Lett.* **1986**, *48* (2), 183–185.
24. Gregg, B.A.; Hanna, M.C. Comparing organic to inorganic photovoltaic cells: theory, experiment, and simulation. *J. Appl. Phys.* **2003**, *93* (6), 3605–3614.

25. Wohrle, D.; Meissner, D. Organic solar-cells. *Adv. Mater.* **1991**, *3* (3), 129–138.
26. Pannemann, C.; Dyakonov, V.; Parisi, J.; Hild, O.; Wohrle, D. Electrical characterisation of phthalocyanine–fullerene photovoltaic devices. *Synth. Met.* **2001**, *121* (1–3), 1585–1586.
27. Yakimov, A.; Forrest, S.R. High photovoltage multiple-heterojunction organic solar cells incorporating interfacial metallic nanoclusters. *Appl. Phys. Lett.* **2002**, *80* (9), 1667–1669.
28. Granström, M.; Petritsch, K.; Arias, A.C.; Lux, A.; Andersson, M.R.; Friend, R.H. Laminated fabrication of polymeric photovoltaic diodes. *Nature* **1998**, *395*, 257–260.
29. Breeze, A.J.; Salomon, A.; Ginley, D.S.; Tillmann, H.H.; Hörhold, H.-H. Polymer–perylene diimide heterojunction solar cells. *Appl. Phys. Lett.* **2002**, *81* (16), 3085–3087.
30. Sariciftci, N.S.; Braun, D.; Zhang, C.; Srdanov, V.I.; Heeger, A.J.; Stucky, G.; Wudl, F. Semiconducting polymer–buckminsterfullerene heterojunctions—Diodes, photodiodes, and photovoltaic cell. *Appl. Phys. Lett.* **1993**, *62* (6), 585–587.
31. Yu, G.; Gao, J.; Hummelen, J.C.; Wudl, F.; Heeger, A.J. Polymer photovoltaic cells—enhanced efficiencies via a network of internal donor–acceptor heterojunctions. *Science* **1995**, *270* (5243), 1789–1791.
32. Brabec, C.J.; Shaheen, S.E.; Fromherz, T.; Padinger, F.; Hummelen, J.C.; Dhanabalan, A.; Janssen, R.A.J.; Sariciftci, N.S. Organic photovoltaic devices produced from conjugated polymer/methanofullerene bulk heterojunctions. *Synth. Met.* **2001**, *121* (1–3), 1517–1520.
33. Brabec, C.J.; Sariciftci, N.S.; Hummelen, J.C. Plastic solar cells. *Adv. Funct. Mater.* **2001**, *11* (1), 15–26.
34. Brabec, C.J.; Zerza, G.; Cerullo, G.; De Silvestri, S.; Luzzati, S.; Hummelen, J.C.; Sariciftci, N.S. Tracing photoinduced electron transfer process in conjugated polymer/fullerene bulk heterojunction in real time. *Chem. Phys. Lett.* **2001**, *340*, 232–236.
35. Nogueira, A.F.; Montanari, I.; Nelson, J.; Durrant, J.R.; Winder, C.; Sariciftci, N.S.; Brabec, C.J. Charge recombination in conjugated polymer/fullerene blended films studied by transient absorption spectroscopy. *J. Phys. Chem., B* **2003**, *107*, 1567–1573.
36. Shaheen, S.E.; Brabec, C.J.; Sariciftci, N.S.; Padinger, F.; Fromherz, T.; Hummelen, J.C. 2.5% Efficient organic plastic solar cells. *Appl. Phys. Lett.* **2001**, *78* (6), 841–843.
37. Geens, W.; Shaheen, S.E.; Wessling, B.; Brabec, C.J.; Poortmans, J.; Serdar Sariciftci, N. Dependence of field-effect hole mobility of PPV-based polymer films on the spin-casting solvent. *Org. Electron.* **2002**, *3* (3–4), 105–110.
38. Mihailitchi, V.D.; van Duren, J.K.J.; Blom, P.W.M.; Hummelen, J.C.; Janssen, R.A.J.; Kroon, J.M.; Rispen, M.T.; Verhees, W.J.H.; Wienk, M.M. Electron transport in a methanofullerene. *Adv. Funct. Mater.* **2003**, *13* (1), 43–46.
39. Padinger, F.; Rittberger, R.S.; Sariciftci, N.S. Effects of postproduction treatment on plastic solar cells. *Adv. Funct. Mater.* **2003**, *13* (1), 85–88.
40. Arias, A.C.; Corcoran, N.; Banach, M.; Friend, R.H.; MacKenzie, J.D.; Huck, W.T.S. Vertically segregated polymer-blend photovoltaic thin-film structures through surface-mediated solution processing. *Appl. Phys. Lett.* **2002**, *80* (10), 1695–1697.
41. Huynh, W.U.; Dittmer, J.J.; Alivisatos, A.P. Hybrid nanorod-polymer solar cells. *Science (Wash. D.C.)* **2002**, *295* (5564), 2425–2427.
42. O'Regan, B.; Grätzel, M. A low cost, high efficiency solar cell based on dye sensitized colloidal TiO<sub>2</sub> films. *Nature* **1991**, *353*, 737–740.
43. Krüger, J.; Plass, R.; Grätzel, M.; Matthieu, H.-J. Improvement of the photovoltaic performance of solid-state dye-sensitized device by silver complexation of the sensitizer *cis*-bis(4,4'-dicarboxy-2,2'-bipyridine)-bis(isothiocyanato) ruthenium(II). *Appl. Phys. Lett.* **2002**, *81* (2), 367–369.
44. O'Regan, B.; Lenzmann, F.; Muis, R.; Wienke, J. A solid-state dye-sensitized solar cell fabricated with pressure-treated P<sub>25</sub>-TiO<sub>2</sub> and CuSCN: analysis of pore filling and IV characteristics. *Chem. Mater.* **2002**, *14*, 5023–5029.
45. Lenzmann, F.; O'Regan, B.; Wienke, J.; Huisman, C.; Reijnen, L.; Goossens, A. Surface photovoltage measurements: a useful tool for the detection of electron injection processes in extremely thin absorber (ETA) solar cells. *Physica E* **2002**, *14*, 233–236.
46. Nozik, A.J. Quantum dot solar cells. *Physica E* **2002**, *14*, 115–120.
47. Arango, A.C.; Carter, S.A.; Brock, P.J. Charge transfer in photovoltaics consisting of interpenetrating networks of conjugated polymer and TiO<sub>2</sub> nanoparticles. *Appl. Phys. Lett.* **1999**, *74* (12), 1698–1700.
48. van Hal, P.A.; Wienk, M.M.; Kroon, J.M.; Verhees, W.J.H.; Sloof, L.H.; van Gennip, W.J.H.; Jonkheijm, P.; Janssen, R.A.J. Photoinduced electron transfer and photovoltaic response of a MDMO-PPV:TiO<sub>2</sub> bulk-heterojunction. *Adv. Mater.* **2003**, *15* (2), 118–121.
49. Lee, S.-J.E.; Chakraborty, A.K. Sequence dependence of polymer dynamics in quenched disordered media: weak attraction facilitates transport. *J. Chem. Phys.* **2002**, *117* (23), 10,869–10,876.
50. Israelachvili, J.N. *Intermolecular and Surface Forces*, 2nd Ed.; Academic Press, Inc.: San Diego, 1997.
51. Coakley, K.M.; Liu, Y.; McGehee, M.D.; Frindell, K.L.; Stucky, G.D. Infiltrating semiconducting polymers into self-assembled mesoporous titania films for photovoltaic applications. *Adv. Funct. Mater.* **2003**, *13* (4), 301–306.
52. Adams, E.W.; Bruchez, M.P., Jr. Surface modified semiconductive and metallic nanoparticles having enhanced dispersibility in aqueous media. In *PCT Int. Appl. Wo*; Quantum Dot Corporation: USA, 2002.
53. Firestone, M.A.; Csensits, R.; Seifert, S. Polymer-grafted lipid-based complex fluids as scaffolding for the formation of heterostructured nanoparticle arrays. *Polym. Prepr. (Am. Chem. Soci., Div. Polym. Chem.)* **2002**, *43* (2), 446–447.

54. Torimoto, T. Preparation of monodisperse semiconductor nanoparticles by the size selective photoetching technique and their photoelectrochemical properties. *Kagaku Kogyo* **2002**, *53* (7), 522–527.
55. Beard, M.C.; Turner, G.M.; Schmittenmaer, C.A. Size-dependent photoconductivity in CdSe nanoparticles as measured by time-resolved terahertz spectroscopy. *Nano Lett.* **2002**, *2* (9), 983–987.
56. Yan, C.; Sun, L.; Fu, X.; Liao, C. Preparation of CdS/ZnO core/shell structured nanoparticles by hydrothermal method. *Mater. Res. Soc. Symp. Proc.* **2002**, *692*, 549–553. (Progress in Semiconductor Materials for Optoelectronic Applications, 2001).
57. Kamiya, I.; Asami, H. Synthesis and functionalization of semiconductor nanoparticles by colloid chemistry. *Kagaku Sochi* **2002**, *44* (5), 41–45.
58. Baranov, I.; Hakansson, P.; Kirillov, S.; Kopniczky, J.; Novikov, A.; Obnorskii, V.; Pchelintsev, A.; Quist, A.P.; Torzo, G.; Yarmiyuchuk, S.; Zennaro, L. Desorption of nanoclusters (2–40 nm) from nanodispersed metal and semiconductor layers by swift heavy ions. *Nucl. Instrum. Methods Phys. Res., B Beam Interact. Mater. Atoms* **2002**, *193*, 798–803.
59. Kowshik, M.; Deshmukh, N.; Vogel, W.; Urban, J.; Kulkarni, S.K.; Paknikar, K.M. Microbial synthesis of semiconductor CdS nanoparticles, their characterization, and their use in the fabrication of an ideal diode. *Biotechnol. Bioeng.* **2002**, *78* (5), 583–588.
60. Monteiro, O.C.; Trindade, T. Nanochemistry of semiconductors. *Química (Lisb.)* **2002**, *84*, 49–54.
61. Kawa, M. Semiconductor Nanoparticles. In *Jpn. Kokai Tokkyo Koho, Jp.*; Mitsubishi Chemical Corp.: Japan, 2002.
62. Tan, W.; Santra, S.; Zhang, P.; Tapecc, R.; Dobson, J. Silica-Coated Nanoparticles. In *PCT Int. Appl. Wo.*; University of Florida: USA, 2001.
63. Crooks, R.M.; Chechik, V.; Lemon, B.I., III; Sun, L.; Yeung, L.K.; Zhao, M. Synthesis, characterization, and applications of dendrimer-encapsulated metal and semiconductor nanoparticles. In *Metal Nanoparticles: Synthesis, Characterization, and Applications*; Feldheim, D.L., Foss, C.A., Jr., Eds.; Dekker: New York, 2002; 261–296.
64. Hong, Y.-K.; Kim, H.; Lee, G.; Kim, W.; Park, J.-I.; Cheon, J.; Koo, J.-Y. Controlled two-dimensional distribution of nanoparticles by spin-coating method. *Appl. Phys. Lett.* **2002**, *80* (5), 844–846.
65. Mirkin, C.A.; Letsinger, R.L.; Mucic, R.C.; Storhoff, J.J.; Elghanian, R. Nanoparticles having oligonucleotides attached thereto and uses in assays. In *U.S., Us*; Nanosphere, Inc.: USA, 2002.
66. Forster, S.; Plantenberg, T. From self-organizing polymers to nanohybrid and biomaterials. *Angew. Chem. Int. Ed.* **2002**, *41* (5), 688–714.
67. Goldman, E.R.; Mattoussi, H.; Tran, P.T.; Anderson, G.P.; Mauro, J.M. Bioconjugates of luminescent CdSe–ZnS quantum dots with engineered recombinant proteins: novel self-assembled tools for biosensing. *Mater. Res. Soc. Symp. Proc.* **2001**, *642*, J2.8/1–J2.8/6 (Semiconductor Quantum Dots II).
68. van der Boom, T.; Hayes, R.T.; Zhao, Y.; Bushard, P.J.; Weiss, E.A.; Wasielewski, M.R. Charge transport in photofunctional nanoparticles self-assembled from zinc 5,10,15,20-tetrakis(perylene-diimide)porphyrin building blocks. *J. Am. Chem. Soc.* **2002**, *124* (32), 9582–9590.
69. Kovtyukhova, N.I.; Martin, B.R.; Mbindyo, J.K.N.; Mallouk, T.E.; Cabassi, M.; Smith, P.; Razavi, B.; Mayer, T.S. Layer-by-layer assembly of nanotubes and nanofilms from nanoparticles and polymer blocks for electronic applications. *NATO Sci. Ser., II: Math. Phys. Chem.* **2002**, *57*, 147–162. (Frontiers of Multifunctional Nanosystems).
70. Zhang, H.-M.; Wang, Z.-J.; Zhang, L.-G.; Yuan, J.-S. Synthesis and study of CdS nanoparticles by self-assembled monolayer. *Faguang Xuebao* **2002**, *23* (4), 369–372.
71. Pacholski, C.; Kornowski, A.; Weller, H. Self-Assembly of ZnO: From Nanodots to Nanorods, Abstracts of Papers, 224th ACS National Meeting, Boston, MA, United States, August 18–22, 2002; 2002, PHYS-374.
72. Cresce, A.V.; Ali, H.A.; Iliadis, A.A.; Lee, U.; Kofinas, P. Synthesis and characterization of self-assembled piezoelectric ZnO nanostructures and integration with Si processing. *Mater. Res. Soc. Symp. Proc.* **2002**, *728*, 115–120. (Functional Nanostructured Materials through Multiscale Assembly and Novel Patterning Techniques).
73. Sun, L.-D.; Fu, X.-F.; Qian, C.; Liao, C.-S.; Yan, C.-H. Synthesis of core/shell structural CdS/ZnO nanoparticles by hydrothermal method. *Gaodeng Xuexiao Huaxue Xuebao* **2001**, *22* (6), 879–882.
74. Manna, L.; Scher, E.C.; Alivisatos, A.P. Synthesis of soluble and processable rod-, arrow-, teardrop-, and tetrapod-shaped CdSe nanocrystals. *J. Am. Chem. Soc.* **2000**, *122* (51), 12,700–12,706.
75. Gerion, D.; Pinaud, F.; Williams, S.C.; Parak, W.J.; Zanchet, D.; Weiss, S.; Alivisatos, A.P. Synthesis and properties of biocompatible water-soluble silica-coated CdSe/ZnS semiconductor quantum dots. *J. Phys. Chem., B* **2001**, *105* (37), 8861–8871.
76. Rafeletos, G.; Norager, S.; O'Brien, P. Evidence for the chemical nature of capping in CdSe nanoparticles prepared by thermolysis in tri-*n*-octylphosphine oxide from P-edge EXAFS spectroscopy. *J. Mater. Chem.* **2001**, *11* (10), 2542–2544.
77. Chen, C.-C.; Chao, C.-Y.; Lang, Z.-H. Simple solution-phase synthesis of soluble CdS and CdSe nanorods. *Chem. Mater.* **2000**, *12* (6), 1516–1518.
78. Anikin, K.V.; Melnik, N.N.; Simakin, A.V.; Shafeev, G.A.; Voronov, V.V.; Vitukhnovsky, A.G. Formation of ZnSe and CdS quantum dots via laser ablation in liquids. *Chem. Phys. Lett.* **2002**, *366* (3,4), 357–360.
79. Sun, L.; Xu, B.; Fu, X.; Wang, M.; Qian, C.; Liao, C.; Yan, C. Carboxylic-containing copolymer as template to prepare CdS, ZnS and doped nanoparticles. *Sci. China, Ser. B: Chem.* **2001**, *44* (1), 23–30.
80. Limmer, S.J.; Hubler, T.L.; Cao, G. Nanorods of various oxides and hierarchically structured mesoporous

- silica by sol-gel electrophoresis. *J. Sol-Gel Sci. Technol.* **2003**, *26* (1/2/3), 577–581.
81. Schneider, J.J. Magnetic core/shell and quantum-confined semiconductor nanoparticles via chimie douce organometallic synthesis. *Adv. Mater. (Weinh., Ger.)* **2001**, *13* (7), 529–533.
  82. Chen, Q.; Zhou, W.; Du, G.; Peng, L.-M. Trititanate nanotubes made via a single alkali treatment. *Adv. Mater.* **2002**, *14* (17), 1208.
  83. Yao, B.D.; Chan, Y.F.; Zhang, W.F.; Yang, Z.Y.; Wang, N. Reaction mechanism of TiO<sub>2</sub> nanotubes. *Appl. Phys. Lett.* **2003**, *82* (2), 281.
  84. Li, D.; Xia, Y. Fabrication of titania nanofibers by electrospinning. *Nano Lett.* **2003**, *3* (4), 555–560.
  85. Xe, Y.; Yan, P.; Lu, J.; Wang, W.; Qian, Y. A safe low temperature route to InAs nanofibers. *Chem. Mater.* **1999**, *11*, 2619–2622.
  86. Gao, S.; Xie, Y.; Lu, J.; Du, G.; He, W.; Cui, D.; Huang, B.; Jiang, M. Mild benzene-thermal route to GaP nanorods and nanospheres. *Inorg. Chem.* **2002**, *41* (7), 1850–1854.
  87. Li, Y.; Liao, H.; Ding, Y.; Fan, Y.; Zhang, Y.; Qian, Y. Solvothermal elemental direct reaction to CdE (E = S, Se, Te). Semiconductor nanorod. *Inorg. Chem.* **1999**, *38* (7), 1382–1387.
  88. Jiang, Y.; Wu, Y.; Mo, X.; Yu, W.; Xie, Y.; Qian, Y. Elemental solvothermal reaction to produce ternary semiconductor CuInE<sub>2</sub> (E = S, Se) nanorods. *Inorg. Chem.* **2000**, *39* (14), 2964–2965.
  89. Wang, X.; Gao, P.; Li, J.; Summers, C.J.; Wang, Z.L. Rectangular porous ZnO–ZnS nanocables and ZnS nanotubes. *Adv. Mater.* **2002**, *14* (23), 1732.
  90. Vayssieres, L. Growth of arrayed nanorods and nanowires of ZnO from aqueous solutions. *Adv. Mater.* **2003**, *15* (5), 464–466.
  91. Könenkamp, R.; Boedecker, K.; Lux-Steiner, M.C.; Poschenrieder, M.; Zenia, F.; Levy-Clement, C.; Wagner, S. Thin film semiconductor deposition on free-standing ZnO columns. *Appl. Phys. Lett.* **2000**, *77* (16), 2575.
  92. Lao, J.Y.; Huang, J.Y.; Wang, D.Z.; Ren, Z.F. ZnO nanobridges and nanonails. *Nano Lett.* **2003**, *3* (2), 235–238.
  93. Tang, C.; Fan, S.; de la Chapelle, M.L.; Dang, H.; Li, P. Synthesis of gallium phosphide nanorods. *Adv. Mater. (Weinh., Ger.)* **2000**, *12* (18), 1346–1348.
  94. Dai, Z.R.; Pan, Z.W.; Wang, Z.L. Gallium oxide nanoribbons and nanosheets. *J. Phys. Chem., B* **2002**, *106*, 902–904.
  95. Wang, X.; Li, Y. Rational synthesis of α-MnO<sub>2</sub> single-crystal nanorods. *Chem. Commun. (Camb., U. K.)* **2002**, (7), 764–765.
  96. Liao, H.-W.; Wang, Y.-F.; Liu, X.-M.; Li, Y.-D.; Qian, Y.-T. Hydrothermal preparation and characterization of luminescent CdWO<sub>4</sub> nanorods. *Chem. Mater.* **2000**, *12* (10), 2819–2821.
  97. Kim, F.; Kwan, S.; Akana, J.; Yang, P. Langmuir–Blodgett nanorod assembly. *J. Am. Chem. Soc.* **2001**, *123* (18), 4360–4361.
  98. Kwan, S.; Kim, F.; Akana, J.; Yang, P. Synthesis and assembly of BaWO<sub>4</sub> nanorods. *Chem. Commun. (Camb., U. K.)* **2001**, (5), 447–448.
  99. Chen, X.; Sun, X.-M.; Li, Y. Self-assembling vanadium oxide nanotubes by organic molecular templates. *Inorg. Chem.* **2002**, *41* (17), 4524.
  100. Tenne, R. Inorganic fullerene-like materials and inorganic nanotubes from layered metal dichalcogenides and other compounds. *Abstr. Pap.-Am. Chem. Soc.* **2001**, *221st*. INOR-643.
  101. Tenne, R. Fullerene-like materials and nanotubes from inorganic compounds with a layered (2-D) structure. *Colloids Surf., A: Physicochem. Eng. Asp.* **2002**, *208* (1–3), 83–92.
  102. Zak, A.; Feldman, Y.; Lyakhovitskaya, V.; Leitus, G.; Popovitz-Biro, R.; Wachtel, E.; Cohen, H.; Reich, S.; Tenne, R. Alkali metal intercalated fullerene-like MS<sub>2</sub> (M = W, Mo) nanoparticles and their properties. *J. Am. Chem. Soc.* **2002**, *124* (17), 4747–4758.
  103. Zhu, Y.Q.; Hsu, W.K.; Firth, S.; Terrones, M.; Clark, R.J.H.; Kroto, H.W.; Walton, D.R.M. Nb-doped WS<sub>2</sub> nanotubes. *Chem. Phys. Lett.* **2001**, *342* (1,2), 15–21.
  104. Hickey, S.G.; Riley, D.J.; Tull, E.J. Photoelectrochemical studies of CdS nanoparticle modified electrodes: absorption and photocurrent investigations. *J. Phys. Chem., B* **2000**, *104* (32), 7623–7626.
  105. Hupp, J.T.; Gaal, D.A.; Leytner, S. *Kinetics, Energetics, and Dynamics of Inorganic-Dye/Semiconductor-Nanoparticle Electron Transfer Reactions*, Abstracts of Papers, 222nd ACS National Meeting, Chicago, IL, United States, August 26–30, 2001; **2001**, CHED-286.
  106. Huynh, W.U.; Dittmer, J.J.; Libby, W.C.; Whiting, G.L.; Alivisatos, A.P. Controlling the morphology of nanocrystal-polymer composites for solar cells. *Adv. Funct. Mater.* **2003**, *13* (1), 73–79.
  107. Kamat, P.V. Photophysical, photochemical and photocatalytic aspects of metal nanoparticles. *J. Phys. Chem., B* **2002**, *106* (32), 7729–7744.
  108. Torimoto, T.; Ohtani, B. Special articles: nanostructured materials for electrochemistry. Preparation and immobilization of size-quantized semiconductor nanoparticles and their photoelectrochemical properties. *Electrochemistry (Tokyo, Japan)* **2001**, *69* (11), 866–871.

# Platinum Nanoparticles: Synthesis and Catalytic Properties

Ioan Balint

*Institute of Physical Chemistry, Romanian Academy, Bucharest, Romania*

Akane Miyazaki

*Department of Environmental Chemistry and Engineering,  
Tokyo Institute of Technology, Yokohama, Japan*

## INTRODUCTION

The synthesis of metal particles with well-controlled shapes and sizes is critical for catalytic applications in structure-sensitive reactions because the rates depend significantly on the metal crystallite size as well as on the orientation of the crystalline planes.<sup>[1]</sup> The morphology–catalytic reactivity relationship is generally unclear for the catalysts prepared by classical impregnation method because the resulting metal particles are non-uniform in size and shape, and are often too small to be precisely characterized. Additionally, there is a significant support effect on the catalytic reactivity of the small metal particles.<sup>[2–4]</sup> With other preparation methods such as vapor<sup>[5]</sup> and metal cluster deposition,<sup>[6]</sup> electron beam lithography,<sup>[7]</sup> etc., it is possible to control, to some extent, the size, but not the crystallographic orientation, of the metal particles.

The colloid method is one of the most promising ways to obtain relatively monodispersed metal particles with controlled shapes.<sup>[8]</sup> Among metals, platinum is a suitable precursor because different shapes of nanoparticles can be prepared by using suitable capping polymers.<sup>[9–11]</sup> The NO/CH<sub>4</sub> reaction was chosen to investigate the structure–catalytic reactivity relationship for the well-structured Pt nanoparticles. The conventionally prepared Pt/Al<sub>2</sub>O<sub>3</sub> catalysts give relatively high selectivity to NH<sub>3</sub> and CO. Because NO/CH<sub>4</sub> reaction is structure-sensitive, significant improvements in the catalytic behavior are expected through a fine control of the morphology of Pt particles.<sup>[12,13]</sup>

The general aim of our work is to bridge the gap existing between the science of clean single crystals surfaces and the world of real catalysis. Particularly, we intend to have a better understanding of the relationship existing between the structure of the supported Pt particles and the catalytic behavior for the NO/CH<sub>4</sub> reaction. From the practical point of view, our scope is to prevent or to considerably reduce the formation of undesired reaction products, such as NH<sub>3</sub>,

CO, and N<sub>2</sub>O. The approach to fulfill the abovementioned goals was to prepare well-defined Pt nanocrystals having mainly cubic structure, to support them on alumina, and to test their specific catalytic activity for the NO/CH<sub>4</sub> reaction.

## EXPERIMENTAL

The synthesis method for the controlled shape colloidal Pt nanoparticles was reported relatively recently.<sup>[10]</sup> In principle, the procedure consisted of the reduction of K<sub>2</sub>PtCl<sub>4</sub> precursor with H<sub>2</sub> in the presence of polyacrylate capping materials.<sup>[10,11]</sup> Morphological control in the synthesis of the well-defined Pt nanoparticles was further optimized by using NIPA (polymer of *N*-isopropylacrylamide) as a capping polymer and by changing the synthesis temperature.<sup>[9]</sup> The preparation method followed in the present study consisted of the reduction of K<sub>2</sub>PtCl<sub>4</sub> (10<sup>−4</sup> M) with H<sub>2</sub> in the presence of the NIPA polymer (10<sup>−3</sup> M) in the 10–40°C temperature range.<sup>[9]</sup>

The resulting Pt nanocrystals (with mainly cubic shape) were supported by adding, under stirring, 0.1 g of  $\gamma$ -alumina (Aerosil; 100 m<sup>2</sup> g<sup>−1</sup>) to 50 ml of colloidal Pt solution to get a final loading of Pt on 1 wt.% alumina. After water was removed from the suspension by freeze-drying, the remaining solid was calcined in air at 500°C for 8 hr to remove the NIPA polymer by decomposition. The calcined catalysts was pelletized, crushed, and sieved. The 335- to 1000- $\mu$ m fraction was used for catalytic tests. The Pt colloid as well as the calcined catalyst were characterized by transmission electron microscopy (TEM; Hitachi H-8100). Additionally, the catalysts were characterized by X-ray diffraction (XRD; Rigaku Multiflex diffractometer provided with peak assignment software), by N<sub>2</sub> adsorption for measurement of physical surface (Belsorb 28 SA), and by CO chemisorption for determination of metal surface (Yuasa ChemBET-3000).

**Table 1** The morphology of the Pt particles in different stages (Pt colloid, after deposition on alumina, and after high-temperature aging) as determined by TEM, XRD, and CO chemisorption measurements

Samples	Diameter (nm)								
	Colloidal stage			Active catalyst <sup>a</sup>			Aged catalyst <sup>b</sup>		
	$d_{\text{TEM}}^c$	$d_{\text{XRD}}^d$	$d_{\text{CO}}^e$	$d_{\text{TEM}}$	$d_{\text{XRD}}$	$d_{\text{CO}}$	$d_{\text{TEM}}$	$d_{\text{XRD}}$	$d_{\text{CO}}$
Pt{polycrystalline}/Al <sub>2</sub> O <sub>3</sub>	—	—	—	2.8	—	2.4	—	—	—
Pt{100}/Al <sub>2</sub> O <sub>3</sub>	13.6	—	—	13.4	11.7	23	15.1	10.6	21

<sup>a</sup>Catalyst working in the NO/CH<sub>4</sub> reaction mixture up to 600°C.

<sup>b</sup>Catalyst aged at 950°C for 4 hr in the NO/CH<sub>4</sub> reaction mixture.

<sup>c</sup>The average size was determined from TEM micrographs by counting more than 200 Pt nanoparticles.

<sup>d</sup>Size calculated from the broadening of the XRD peak of Pt(111) ( $2\theta \approx 40^\circ$ ).

<sup>e</sup>Average size determined from CO chemisorption data.

For convenience, the alumina-supported, well-structured Pt nanocrystals will be called, hereafter, Pt{100}/Al<sub>2</sub>O<sub>3</sub>. The activity of the Pt{100}/ $\gamma$ -Al<sub>2</sub>O<sub>3</sub> catalyst (0.05 g) for the NO/CH<sub>4</sub> reaction was tested in flow system by using a quartz microreactor (i.d. = 5 mm) operating at atmospheric pressure. The total flow rate of the reactant mixture (1% NO and 0.4% CH<sub>4</sub>, balance Ar) was 50 cm<sup>3</sup> min<sup>-1</sup> standard temperature and pressure (STP). The corresponding gas hour space velocity (GHSV) was 60,000 hr<sup>-1</sup>.

The analysis of gaseous mixtures was carried out with a gas chromatograph (GL Sciences-320) equipped with a thermal conductivity detector (TCD). N<sub>2</sub>, NO, and CH<sub>4</sub> were separated by a molecular sieve 13 $\times$  column and the CO<sub>2</sub> and N<sub>2</sub>O were separated by a Porapak-Q column.

The activity of well-structured platinum catalysts (Pt{100}/Al<sub>2</sub>O<sub>3</sub>) was compared with that of a standard catalyst supplied by Engelhard Corporation Japan (lot no. H-T1150-01). The Engelhard catalyst (metal loading, 1 wt.%), hereafter called Pt{polycrystalline}/Al<sub>2</sub>O<sub>3</sub>, had metal and Brunauer–Emmet–Teller (BET) surface areas of 1.19 ( $\approx 44\%$  dispersion) and 114 m<sup>2</sup> g<sup>-1</sup>, respectively. The metal particle size, determined from chemisorption and TEM data, were 2.4 and 2.8 nm, respectively (Table 1).

The catalytic behavior in the NO/CH<sub>4</sub> reaction was expressed in terms of conversion, selectivity, and yield.<sup>[12]</sup>

## RESULTS

The configuration of NIPA thermosensitive polymer changes reversibly with temperature because a hydrophilic–hydrophobic transition takes place at  $\approx 36^\circ\text{C}$ . The influence of capping conditions on the morphology of Pt particles was investigated by carrying out the reduction of K<sub>2</sub>PtCl<sub>4</sub> both in hydrophobic and hydrophilic regions (10–40°C). The proportion of Pt cubic to other shapes passed through a maximum ( $\approx 70\%$ ) for a reduction temperature of 40°C (Fig. 1).

Fig. 2 presents the TEM images of the Pt nanoparticles in different stages. Fig. 2A shows the well-defined cubic Pt nanocrystals, of around 13 nm, in colloidal stage. Analysis by high-resolution transmission electron microscopy (HRTEM) revealed that the square particles were Pt single crystals with a surface relatively free of defects (smooth surface). The Pt nanoparticle shown in Fig. 2B is bounded by {100} facets because the distance between the adjacent lattice fringes of 0.196 nm corresponds to the interplanar distance of Pt{200}. Other crystallographic orientations (i.e., {111} and {110}) as well as steps and ledges are also possible<sup>[11]</sup> at the slightly rounded corners of the cubes. The cubic structure of the Pt nanoparticles was preserved after supporting them on alumina (Fig. 2C). The conversion of the square Pt nanoparticles to other shapes (i.e., irregular, round, and hexagonal) was observed after high-temperature aging (950°C for 4 hr) in the NO/CH<sub>4</sub> mixture (Fig. 2D). The impact of the morphological changes of the supported Pt nanoparticles on the catalytic activity and selectivity for the NO/CH<sub>4</sub> reaction will be analyzed hereafter.

Because the morphology of the Pt nanoparticles changes slightly from batch to batch and the NO/CH<sub>4</sub>

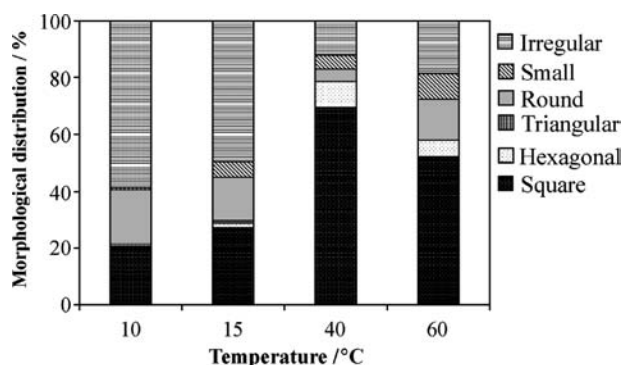


**Fig. 1** The relationship between the morphological distribution of the platinum nanoparticles in colloidal stage and the reduction temperature.



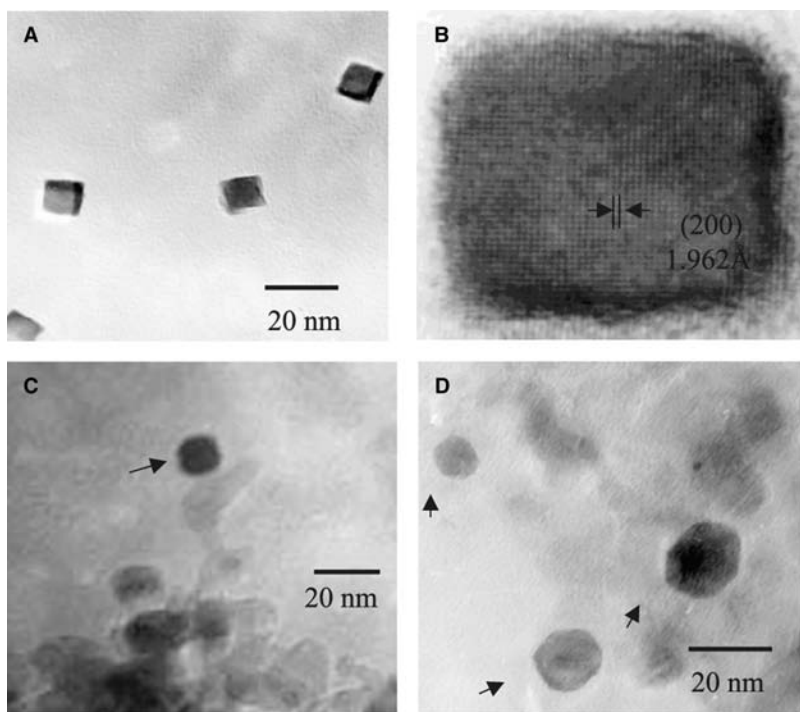


**Fig. 2** TEM images of (A) Pt colloid composed mainly of cubic nanoparticles ( $\approx 70\%$ ); (B) high magnification of an individual cubic Pt nanoparticle; (C) alumina-supported Pt nanoparticles; and (D) alumina-supported Pt nanoparticles aged at  $950^\circ\text{C}$  for 4 hr in the  $\text{NO}/\text{CH}_4$  mixture.

reaction is very sensitive to the metal structure, it is our standard procedure to characterize the Pt nanoparticles in colloidal stage as well as after deposition on alumina and catalytic tests by TEM, XRD, and CO chemisorption. Table 1 presents the average size of Pt particles in colloidal stage (TEM data), after deposition on alumina and catalytic tests up to  $600^\circ\text{C}$  (TEM, XRD, and CO chemisorption data), and after thermal aging ( $950^\circ\text{C}$ , 4 hr) in the  $\text{NO}/\text{CH}_4$  reaction mixture (TEM, XRD, and CO chemisorption data). The average size ( $d_{\text{TEM}}$ ) of the colloidal Pt nanoparticles ( $\approx 13.6\text{ nm}$ ) does not change after deposition on alumina or after catalytic reaction up to  $600^\circ\text{C}$  in the  $\text{NO}/\text{CH}_4$  reaction mixture ( $d_{\text{TEM}} \approx 13.4\text{ nm}$ ). Good thermal stability of the alumina-supported Pt nanoparticles is confirmed also by XRD data ( $d_{\text{XRD}} \approx 11.7\text{ nm}$ ).

Theoretical calculations, by considering the  $d_{\text{TEM}}$  average particle size of  $13.4\text{ nm}$ , predict a platinum dispersion of around 7%. Such a small dispersion is, in practice, difficult to measure by CO chemisorption. However, we attempted to measure it by using a sensitive chemisorption apparatus, which can generate and measure CO pulses on the order of microliters. The  $d_{\text{CO}}$  value of  $\approx 23\text{ nm}$ , determined for the catalysts working in reaction mixtures up to  $600^\circ\text{C}$ , is higher than those determined by TEM ( $d_{\text{TEM}} \approx 13.4\text{ nm}$ ) or by XRD ( $d_{\text{XRD}} \approx 11.7\text{ nm}$ ) (Table 1). Taking into account the extremely small dispersion, the low metal loading (1% Pt), and the small amount of catalyst (0.05 g) used for metal surface determination, the chemisorption data are quite satisfactory and may be

useful especially in revealing the evolution of metal surface area with temperature.

Morphological information regarding the thermally aged catalyst ( $950^\circ\text{C}$ , 4 hr in the  $\text{NO}/\text{CH}_4$  mixture) is given in Table 1 ( $d_{\text{TEM}}$ ,  $d_{\text{XRD}}$ , and  $d_{\text{CO}}$ ), Fig. 2D, as well as in Figs. 3 and 4 (morphological and size distributions, respectively). Apparently, the TEM data indicate a slight increase in particles size from  $13.4$  to  $15.1\text{ nm}$  for the thermally aged Pt nanoparticles (Table 1). In contrast, the XRD and chemisorption data ( $d_{\text{XRD}} \approx 10.6$  and  $d_{\text{CO}} \approx 21\text{ nm}$ ) suggest a slight decrease in particle size after thermal aging (Table 1). This apparent contradiction, between TEM data on one hand and chemisorption and XRD data on the other hand, will be analyzed later in the “Discussion” section.

The morphologies of the colloidal Pt nanoparticles synthesized at  $40^\circ\text{C}$  and of the thermally aged ( $950^\circ\text{C}$ , 4 hr in the  $\text{NO}/\text{CH}_4$  mixture) Pt nanoparticles supported on alumina are comparatively presented in Fig. 3. Around 53% and 17% of the colloidal Pt nanocrystals have been found to have “clear square” and “unclear square” shapes, respectively. The “clear square” particles were  $\text{Pt}\{100\}$  single crystals with surfaces relatively free of defects (Fig. 2B). The particles with “unclear square” shape were also cubic nanocrystals but with a rough surface (defected surface). Besides cubic, other shapes, such as hexagonal ( $\approx 9\%$ ), round ( $\approx 4\%$ ), small ( $\approx 5\%$ ), and irregular ( $\approx 12\%$ ), have been identified, too.

The initial morphological distribution was significantly altered after thermal aging at  $950^\circ\text{C}$  for 4 hr in

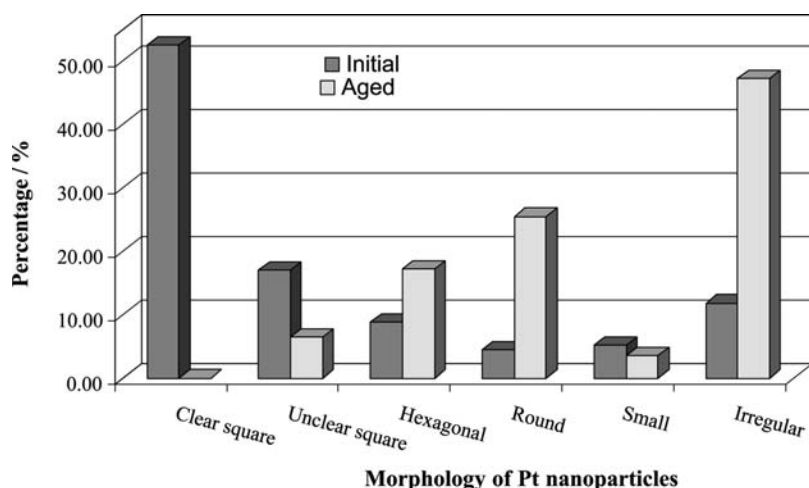


**Fig. 3** Morphological distribution of the (I) initial colloidal Pt nanocrystals deposited on  $\gamma$ - $\text{Al}_2\text{O}_3$  and (II) alumina-supported Pt nanoparticles subjected to thermal aging at  $950^\circ\text{C}$  for 4 hr in the  $\text{NO}/\text{CH}_4$  reaction mixture.

the  $\text{NO}/\text{CH}_4$  mixture. The “clear square” and the “unclear square” particles were practically completely converted to irregular ( $\approx 47\%$ ), round ( $\approx 25\%$ ), and hexagonal ( $\approx 17\%$ ).

From the Gaussian-type size distribution of the colloidal Pt nanoparticles, an average particle size of  $\approx 13.6$  nm was determined (Fig. 4, Table 1). The size distribution of the Pt nanoparticles became apparently broader after thermal aging at  $950^\circ\text{C}$  for 4 hr, but the average particle size increased only slightly, from 13.4 to 15.1 nm.

The catalytic activity of  $\text{Pt}\{100\}/\text{Al}_2\text{O}_3$  for the  $\text{NO}/\text{CH}_4$  reaction vs. temperature is presented in Fig. 5. The total conversion of NO was achieved for  $T \geq 350^\circ\text{C}$ . The concentration of  $\text{N}_2\text{O}$  goes through a maximum at  $400^\circ\text{C}$  and then decreases with increasing reaction temperature. In the lower-temperature domain ( $350$ – $500^\circ\text{C}$ ), the only product of methane oxidation was  $\text{CO}_2$ . The formation of CO was observed

for  $T \geq 500^\circ\text{C}$ . Small amounts of  $\text{NH}_3$  were detected only in the high-temperature region ( $T \geq 550^\circ\text{C}$ ). Experiments in which the catalyst was cycled up and down in the temperature range of  $300$ – $600^\circ\text{C}$  did not show any significant variations in catalytic activity.

The conversion of NO and  $\text{CH}_4$  as well as the reaction selectivity to various products are presented in Fig. 6. The reaction selectivity to  $\text{N}_2$  reaches a maximum at  $550^\circ\text{C}$  ( $\approx 99\%$ ). The selectivity to  $\text{N}_2\text{O}$  has a maximum at  $350^\circ\text{C}$  ( $\approx 40\%$ ) and then decreases with increasing reaction temperature. The selectivity to  $\text{NH}_3$  increased with increasing reaction temperature from  $\approx 1\%$  at  $550^\circ\text{C}$  to  $\approx 10\%$  at  $600^\circ\text{C}$ .

The catalytic behavior of  $\text{Pt}\{100\}/\text{Al}_2\text{O}_3$  for the  $\text{NO}/\text{CH}_4$  reaction was compared with that of a standard catalyst,  $\text{Pt}\{\text{polycrystalline}\}/\text{Al}_2\text{O}_3$ , at  $400^\circ\text{C}$  (Fig. 7) and  $500^\circ\text{C}$  (Fig. 8). In this manner, the observed differences would be ascribed to the morphological effects of the Pt particles on the  $\text{NO}/\text{CH}_4$  reaction.

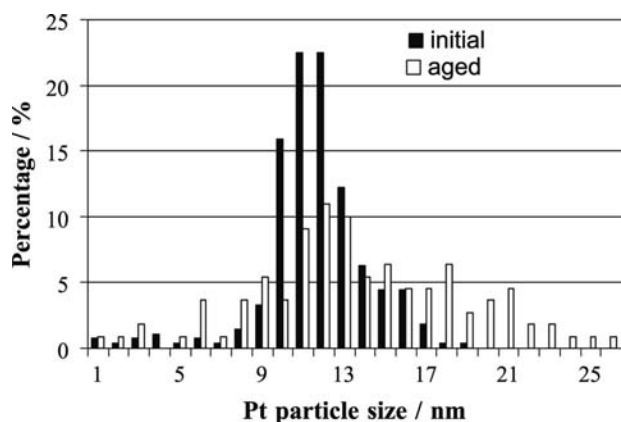


**Fig. 4** The size distribution of the (I) colloidal Pt nanoparticles supported on alumina (initial) and (II) alumina-supported Pt nanoparticles subjected to thermal aging at  $950^\circ\text{C}$  for 4 hr in the  $\text{NO}/\text{CH}_4$  reaction mixture.

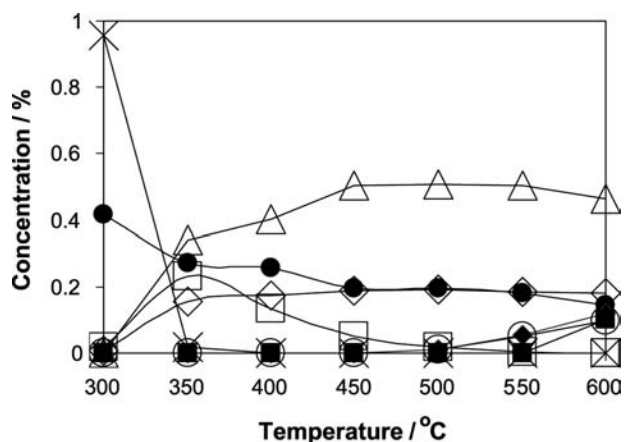


**Fig. 5** The conversion of NO to all products as a function of temperature for the  $\text{Pt}\{100\}/\text{Al}_2\text{O}_3$  catalyst. (x) NO; (●)  $\text{CH}_4$ ; (△)  $\text{N}_2$ ; (□)  $\text{N}_2\text{O}$ ; (■)  $\text{NH}_3$ ; (◇)  $\text{CO}_2$ ; (◆) CO; and (○)  $\text{H}_2$  (reactant mixture: 1% NO, 0.4%  $\text{CH}_4$ , and balance Ar).

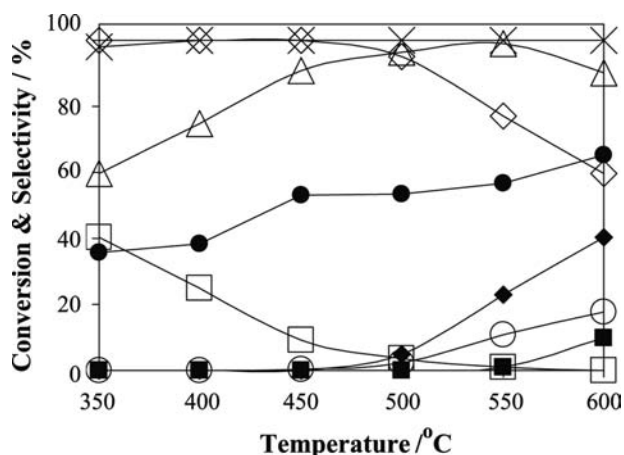


**Fig. 6** The temperature dependence of the NO/CH<sub>4</sub> reaction conversion (X) and selectivity (S) for Pt{100}/Al<sub>2</sub>O<sub>3</sub> catalysts. (×) X(NO); (●) X(CH<sub>4</sub>); (△) S(N<sub>2</sub>); (□) S(N<sub>2</sub>O); (■) S(NH<sub>3</sub>); (◇) S(CO<sub>2</sub>); (◆) S(CO); and (○) S(H<sub>2</sub>) (reactant mixture: 1% NO, 0.4% CH<sub>4</sub>, and balance Ar).

Both catalysts investigated exhibit comparable activity for NO conversion, increasing yield to N<sub>2</sub> (opposite trend for N<sub>2</sub>O) and increasing CH<sub>4</sub> conversion with temperature (Figs. 7 and 8).

Interestingly, significantly lower yields to CO and NH<sub>3</sub> were observed for the Pt{100}/Al<sub>2</sub>O<sub>3</sub> catalyst compared with the Pt{polycrystalline}/Al<sub>2</sub>O<sub>3</sub> catalyst (Figs. 7 and 8). On the other hand, the well-structured Pt nanoparticles showed higher yield to N<sub>2</sub>O.

The XRD pattern of the Pt{polycrystalline}/Al<sub>2</sub>O<sub>3</sub> presented in Fig. 9A indicates that Pt particles are too small ( $\approx 2.4$  nm) to give characteristic XRD peaks. The XRD patterns of the Pt{100}/Al<sub>2</sub>O<sub>3</sub> catalysts (Fig. 9B

and C) exhibit the characteristic XRD reflections of the large, well-crystallized Pt nanoparticles at  $2\theta \approx 40^\circ$  and  $2\theta \approx 81^\circ$ . The average sizes of Pt crystallites, calculated from the XRD peaks at  $2\theta \approx 40^\circ$  by using the Debye–Scherrer equation, were 11.7 nm for the Pt{100}/Al<sub>2</sub>O<sub>3</sub> catalyst working in the NO/CH<sub>4</sub> mixture at the 300–600°C temperature range and 10.7 nm for the same catalyst aged at 950°C for 4 hr in the reaction mixture. The XRD results suggest a remarkable size stability of the alumina-supported Pt nanocrystals.

## DISCUSSION

According to ultrahigh vacuum (UHV) investigations, the catalytic activities for numerous reactions vary from one metal crystal face to another.<sup>[14]</sup> For example, the NO/H<sub>2</sub> reaction proceeds with significantly different rates over Pt(100) and (110) monocrystals.<sup>[15]</sup> Therefore the rate of N<sub>2</sub> formation is at least five times higher on the surface of Pt(100) than on Pt(110). In fact, the studies performed on the clean surfaces predict that a strong structure–catalytic reactivity relationship should also exist in atmospheric pressure conditions.

The first step to better understand the structure–catalytic reactivity relationship is to have a good morphological control (shape and size) of the supported metal nanoparticles and to reduce or eliminate the support effect. In this way, the most important factors responsible for the significant differences observed between the catalytic behaviors of the large, well-defined Pt nanoparticles and the small, polycrystalline

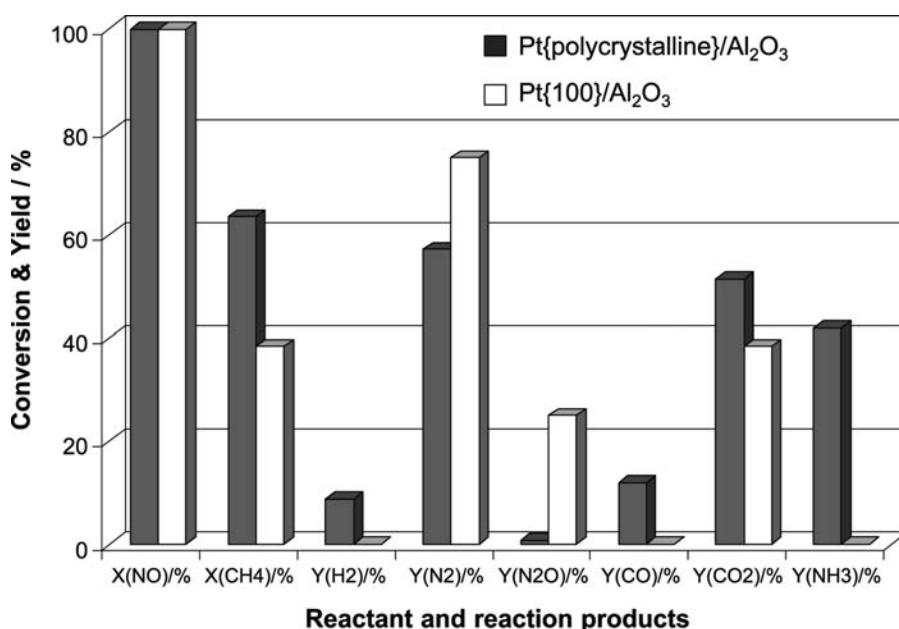


**Fig. 7** Comparison between the NO/CH<sub>4</sub> reaction conversion (X) and yield (Y), and the products for Pt{polycrystalline}/Al<sub>2</sub>O<sub>3</sub> (Engelhard) and Pt{100}/Al<sub>2</sub>O<sub>3</sub> (well-defined Pt nanoparticles) catalysts at 400°C.

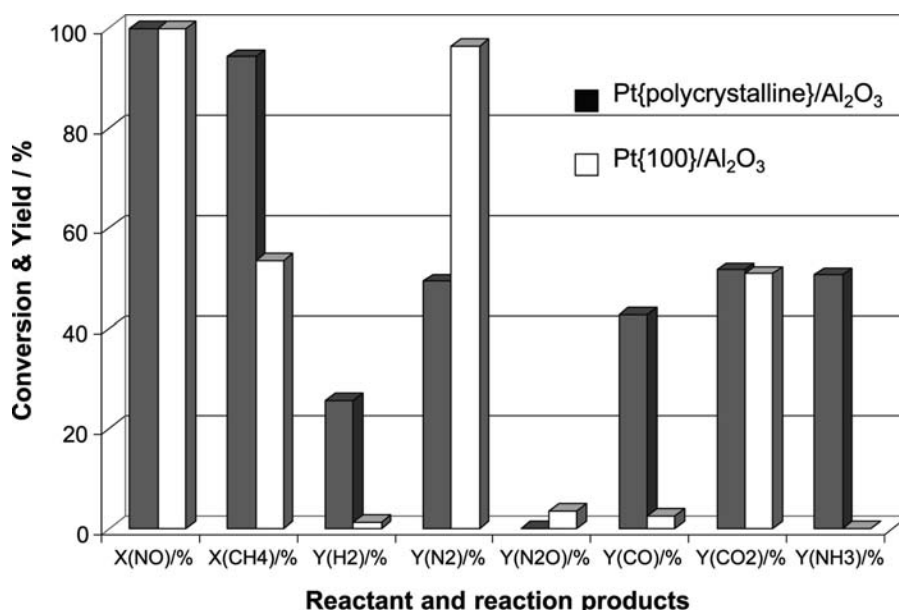


**Fig. 8** Comparison between the NO/CH<sub>4</sub> reaction conversion (X) and yield (Y), and the products for Pt{polycrystalline}/Al<sub>2</sub>O<sub>3</sub> (Engelhard) and Pt{100}/Al<sub>2</sub>O<sub>3</sub> (well-defined Pt nanoparticles) catalysts at 500°C.

Pt particles in the NO/CH<sub>4</sub> reaction can be identified and analyzed more easily. The catalytic tests show that, over the Pt{100}/Al<sub>2</sub>O<sub>3</sub> catalyst, the formation of CO and NH<sub>3</sub> is largely prevented, whereas the yield to N<sub>2</sub>O increases compared with the Pt{polycrystalline}/Al<sub>2</sub>O<sub>3</sub> catalyst.

It is clear that the interaction with the support is minimal in the case of the large (≈13 nm) Pt nanoparticles grafted after the formation on alumina. Boudart<sup>[16]</sup> observed that the catalytic behavior of particles larger than 5 nm mostly reflects the properties of bulk metals.

The main differences observed between the two catalysts compared are the dominant orientation of the crystallographic facets and the average size of Pt crystallites. The large Pt nanocrystals (≈13 nm) of the Pt{100}/Al<sub>2</sub>O<sub>3</sub> catalyst were, in majority (≈70%), cubic-shaped. In contrast, the conventional Pt{polycrystalline}/Al<sub>2</sub>O<sub>3</sub> catalyst had small, round-shaped Pt particles of ≈2.4 nm with random crystallographic orientations. The impact of the abovementioned factors, shape and size, on the catalytic behavior for the NO/CH<sub>4</sub> reaction will be discussed later in this work.

### Activation of NO

It is rational to consider that the first step of NO conversion is the dissociation from the metal surface:<sup>[17]</sup>



The absence of a reductant, which removes the strongly adsorbed O<sub>ads</sub>, prevents further NO decomposition.<sup>[18,19]</sup> We observed that in the absence of CH<sub>4</sub>, around 2–5% of NO decomposes for a short time (few minutes) over the reduced Pt{100}/Al<sub>2</sub>O<sub>3</sub> catalyst. Burch and Ramli<sup>[20]</sup> suggested that the relative activities for various catalysts reflect the ease of catalyst reduction by a reducing agent (i.e., CH<sub>4</sub>).

The dissociation of NO over the clean surfaces of metal single crystals has been intensively investigated. The most important conclusions of these studies will be briefly reviewed to explain the catalytic behavior of Pt{100}/Al<sub>2</sub>O<sub>3</sub> in the NO/CH<sub>4</sub> reaction:

- I. The NO dissociation on clean metal surfaces is a coverage-dependent process.<sup>[21]</sup> Low NO

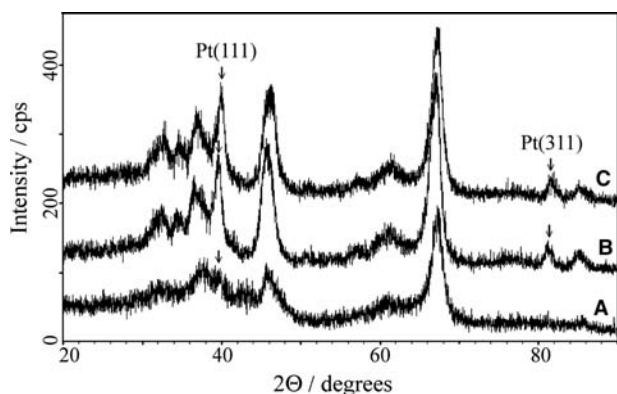


**Fig. 9** Comparative XRD patterns for polycrystalline and well-structured platinum particles supported on alumina. Spectrum (A): Pt{polycrystalline}/Al<sub>2</sub>O<sub>3</sub> (Engelhard) catalyst used in the NO/CH<sub>4</sub> reaction in the 300–600°C temperature range. Spectrum (B): Pt{100}/Al<sub>2</sub>O<sub>3</sub> (well-structured Pt nanoparticles) used in the NO/CH<sub>4</sub> reaction in the 300–600°C temperature range. Spectrum (C): Pt{100}/Al<sub>2</sub>O<sub>3</sub> after aging at 950°C for 4 hr in the NO/CH<sub>4</sub> reaction mixture.

coverage (typically  $\theta < 0.3$ ) favors the complete dissociation of NO.<sup>[22]</sup> It is likely that in real catalytic conditions, the adsorbed NO will be only partially dissociated because of the high surface coverage. Thus the molecular NO will coexist on the metal surface with  $N_{\text{ads}}$  and  $O_{\text{ads}}$  species.

- II. The dissociation of NO is very sensitive to crystallographic orientation. Desorption studies evidenced that only 5% of the adsorbed NO dissociates from Pt(111) and Pt(110), in contrast with Pt(100), which dissociates by around 50%.<sup>[22]</sup> Moreover, the Pt(111) facet is reported to be completely unreactive for NO decomposition at any coverage.<sup>[23]</sup> On the other hand, the high-index Pt planes are unusual active for NO decomposition. For example, more than 98% of the adsorbed NO is dissociated from the Pt(410) surface.<sup>[22]</sup>

Some studies pointed out that NO dissociates mainly at the steps.<sup>[17]</sup> The conventional catalyst, containing small Pt particles with random crystallographic orientation, is rich in high-index planes, edges, kinks, and steps. Therefore it is expected to show high activity for NO decomposition. In contrast, the large Pt nanocrystals have limited activity for NO decomposition because of the low concentration of high-index planes and surface defects. Our assumptions are confirmed by experimental facts. The Pt(100) single crystals are catalytically active but give a dissociation for NO  $\approx 50\%$  under conditions where the polycrystalline Pt samples give a dissociation of 75% for NO.<sup>[22]</sup> The activity for NO decomposition should have a great impact on the NO/CH<sub>4</sub> reaction selectivity to N<sub>2</sub>O and N<sub>2</sub>. We will discuss in detail these aspects in the next paragraph.

In fact, NO can be decomposed not only by metals but also by metal oxides. Winter<sup>[24]</sup> investigated the decomposition of NO to over 40 oxides (PtO<sub>x</sub> was not included in this screening) and found out that the most active oxides give a conversion of below 50% for NO. In our specific case, we could not provide evidence on the formation of PtO<sub>x</sub> species through any experimental method used [temperature-programmed reduction (TPR) and XRD]. Therefore it is safe to state that the bulk PtO<sub>x</sub> is not formed over the Pt{100}/Al<sub>2</sub>O<sub>3</sub> catalyst and, in consequence, is not involved in the decomposition of NO. On the other hand, we clearly observed that (in the absence of a reductant) the oxygen resulting from NO decomposition poisons the reaction because of the formation of a superficial layer of strongly adsorbed oxygen.<sup>[25]</sup>

In practice, NO decomposition can be even more complicated. From single crystal studies, two possible

structures have been found for the Pt(100) plane, indicated by (1 × 1) and (5 × 2).<sup>[26]</sup> The (1 × 1) surface has a square structure on a square substrate, whereas the (2 × 5) surface has a hexagonal structure on the square substrate. The (1 × 1) and (5 × 2) surfaces exhibit different adsorption and catalytic properties.<sup>[27]</sup> The dissociation of NO takes place only on the (1 × 1) phase, whereas the hexagonal one is inert.<sup>[18]</sup> However, at present, it is difficult to assess the impact of these structures, observed in UHV conditions, on catalytic behavior at atmospheric pressure.

It is likely that for a real catalyst under steady-state conditions, less active sites (e.g., terraces) will certainly come into play, so the overall reactivity will be the result of weighted contributions from various surface structure elements, dominated by active sites located at steps, edge, and kinks.<sup>[17]</sup>

### Formation of N<sub>2</sub> and N<sub>2</sub>O

There is almost a general agreement in the published literature, from catalytic investigations conducted under atmospheric pressure<sup>[2,28]</sup> and studies performed on clean metal surfaces,<sup>[22,23]</sup> that N<sub>2</sub> and N<sub>2</sub>O are formed via the following reactions:



There are also a few works assuming that N<sub>2</sub>O can be an intermediate during the reduction of NO by CH<sub>4</sub>.<sup>[29]</sup>

Our experimental results strongly support the mechanism for N<sub>2</sub>O formation described by Eq. (3). The generation of N<sub>2</sub>O is favored over the Pt{100}/Al<sub>2</sub>O<sub>3</sub> catalyst because the large, well-defined Pt nanocrystals exhibit low activity for NO decomposition. In contrast, high selectivity to N<sub>2</sub> was observed over the small ( $\approx 2.4$  nm) polycrystalline Pt particles because of the high efficiency shown for NO decomposition Eq. (2).

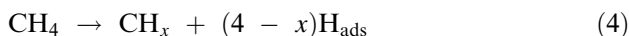
The dissociation equilibrium for NO is a temperature-dependent process. As the temperature increases, the reaction is shifted toward the dissociation of NO, thus the most favored reaction becomes the recombination of  $N_{\text{ads}}$  to give molecular N<sub>2</sub> Eq. (2) and Fig. (6).

### Conversion of CH<sub>4</sub>

Methane must overcome an activation energy barrier of around 7 kcal mol<sup>-1</sup> to chemisorb on metal surfaces, and the barrier height for breaking the C–H bond by kinetic energy is 29 kcal mol<sup>-1</sup>.<sup>[30]</sup> The dissociative adsorption of methane occurs either on the fully reduced Pt, or at mixed sites comprising Pt<sup>δ+</sup>O<sup>δ-</sup>,

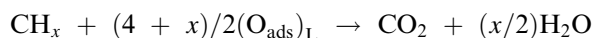


but the fully oxidized Pt surface is less active than the reduced or partially oxidized surface.<sup>[31]</sup>



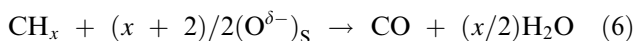
Then the  $\text{CH}_x$  and  $\text{H}_{\text{ads}}$  surface species are oxidized by the  $\text{O}_{\text{ads}}$  (resulting from NO decomposition) to  $\text{CO}_2$  and  $\text{H}_2\text{O}$  over the Pt{100}/ $\text{Al}_2\text{O}_3$  catalyst. In other words, the high oxidizing activity of the adsorbed oxygen on the surface of large Pt particles explains the high selectivity to deep oxidation products despite methane excess used in our experiments.

The structure sensitivity of methane oxidation over platinum was explained by the different reactivities of the adsorbed oxygen.<sup>[32]</sup> The higher resistance of the large Pt particles against bulk oxidation<sup>[16]</sup> explains the enhanced catalytic activity for  $\text{CH}_4$  oxidation.<sup>[32]</sup> The catalytic activity of the large Pt particles for oxidation reactions was found to be at least one order of magnitude higher than the small, well-dispersed Pt particles.<sup>[33]</sup> The chemisorbed oxygen is bound more weakly to the metal surface and therefore is more ready to react with  $\text{CH}_x$  species.<sup>[34]</sup> The oxidation of  $\text{CH}_x$  on the large Pt nanocrystals ( $\approx 13$  nm) can be described by the following equation:



The subscript “L” indicates that the oxygen is adsorbed on large Pt particles. The hydrocarbon continuously removes the pool of  $\text{O}_{\text{ads}}$  then NO dissociation continues, mainly on high index planes and surface defects.

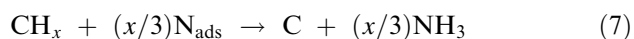
In contrast to the large Pt nanocrystals, the well-dispersed Pt particles, with an average size of 2.4 nm, give high selectivity to CO and  $\text{NH}_3$  (Figs. 7 and 8). These results can be explained as follows. The dispersed Pt particles can be successively converted, depending on the temperature, to PtO, PtO<sub>2</sub>, and, finally, PtAl<sub>2</sub>O<sub>4</sub>.<sup>[33,35]</sup> Because of the low oxidation activity of  $\text{O}^{\delta-}$  ( $\text{PtO}_x$ ) species, some of the surface  $\text{CH}_x$  species will undergo only partial oxidation:



The subscript “S” indicates that the  $\text{O}^{\delta-}$  is formed on small Pt particles.

In addition to CO, large amounts of  $\text{NH}_3$  are formed during the reduction of NO with  $\text{CH}_4$  over the conventional Pt/ $\text{Al}_2\text{O}_3$ <sup>[28]</sup> and Pt/ $\text{SiO}_2$ <sup>[36]</sup> catalysts. The selectivity to  $\text{NH}_3$  was observed to decrease with increasing oxygen concentration in reactant mixtures. It is likely that the lifetime of the  $\text{CH}_x$  and  $\text{H}_{\text{ads}}$  species on the small Pt particles is longer because of the low

oxidation ability of bulk  $\text{PtO}_x$ . Therefore the reactions responsible for ammonia formation are favored:



The formation of  $\text{NH}_3$  over Pt{100}/ $\text{Al}_2\text{O}_3$  was greatly reduced because the active oxygen chemisorbed on the large Pt particles rapidly removes, as do  $\text{CO}_2$  and  $\text{H}_2\text{O}$ , the carbonaceous and H species from the surface.

### Impact of Platinum Morphological Evolution on Catalytic Behavior

From the aforementioned results as well as from already published works,<sup>[12,13]</sup> it is clear that both the size and the facet have a determinant role in the catalytic activity of Pt particles for the NO/ $\text{CH}_4$  reaction. Morphological changes of the Pt nanoparticles are expected to take place in reaction conditions. Therefore a closer look was taken on the morphological evolution of the Pt nanoparticles with time in reaction conditions, as well as on the impact of this evolution on the catalytic behavior for the NO/ $\text{CH}_4$  reaction.

The catalyst was subjected to an accelerated thermal aging at 950°C for 4 hr in the NO/ $\text{CH}_4$  reaction mixture. Then, the catalytic behavior of the aged catalyst was checked again in the low-temperature region (300–600°C). Fig. 10 illustrates the aging effect on the catalytic behavior of alumina-supported Pt nanoparticles. For the sake of simplicity, only yields

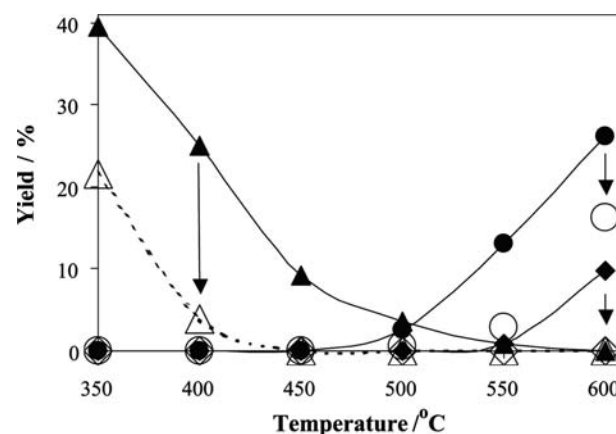


**Fig. 10** Comparison between the NO/ $\text{CH}_4$  yield to  $\text{N}_2\text{O}$  ( $\Delta$ ,  $\blacktriangle$ ), CO ( $\circ$ ,  $\bullet$ ), and  $\text{NH}_3$  ( $\diamond$ ,  $\blacklozenge$ ) for the fresh (open symbols) and high-temperature (950°C, 4 hr) aged (closed symbols) alumina-supported Pt nanoparticles in the 350–600°C temperature range (reactant mixture: 1% NO, 0.4%  $\text{CH}_4$ , and balance Ar).



to the harmful products ( $\text{N}_2\text{O}$ ,  $\text{CO}$ , and  $\text{NH}_3$ ) were compared. The main changes observed after high-temperature aging can be summarized as follows: 1) the production of  $\text{N}_2\text{O}$  and  $\text{CO}$  decreased significantly (the formation of  $\text{CO}$  was prevented below  $550^\circ\text{C}$  and the yield to  $\text{N}_2\text{O}$  became negligible at  $T \geq 400^\circ\text{C}$ ); and 2) the formation of  $\text{NH}_3$  was completely suppressed (Fig. 10).

From the data presented in Table 1 and Fig. 3, it was found that aging had little effect on particle size, but a significant effect on the shape of Pt nanocrystals. The larger  $d_{\text{TEM}}$  value observed for the aged catalyst ( $\approx 15.1$  nm) compared with the fresh catalyst ( $\approx 13.4$  nm) can be explained by the flattening of the Pt particles on the support, rather than by sintering (no sign of particle agglomeration was observed). The flattening of Pt nanoparticles (or the decrease in thickness) is supported also by the decrease in  $d_{\text{XRD}}$  value from 11.7 to 10.6 nm after aging. As we already discussed, the initially square Pt nanoparticles (relatively free of defects) were converted during thermal aging to irregular-shaped, round-shaped, and hexagonal-shaped particles (Fig. 2D). In other words, the low index facets were gradually shifted at high temperature to higher index planes. It is well known that a rearrangement of the metal surface, called “surface roughening” or “surface melting,” can take place (below the melting temperature) if it is heated above some critical temperature. It is relatively common for a surface to show one equilibrium reconstruction at low temperature and to show another equilibrium surface structure upon heating.<sup>[37]</sup> In the case of alumina-supported Pt nanoparticles, the process of surface roughening was not a reversible one.

As it was already stressed, the low index Pt planes (i.e., Pt(100))<sup>[19]</sup> are less active for NO dissociation compared with higher index planes (i.e., Pt(410))<sup>[22]</sup> or surface defects.<sup>[17]</sup> The decrease in  $\text{N}_2\text{O}$  yield for thermally aged Pt nanoparticles, rich in surface defects, can be easily explained by taking into account their high activity for NO decomposition (Fig. 10).

The reasons for the significant decrease in  $\text{CO}$  and  $\text{NH}_3$  yields after thermal aging will be given hereafter. As it was already emphasized, the small Pt particles have lower catalytic activity for oxidation reaction because they easily form  $\text{PtO}_x$  species (bulk oxide).<sup>[33]</sup> The oxygen coverage as well as the desorption temperature are significantly higher on the small ( $\approx 2$  nm) Pt particles relative to the large ( $\approx 8.3$  nm) ones.<sup>[38]</sup> For our specific case, the  $\text{CH}_x$  species, formed by the dissociative adsorption of  $\text{CH}_4$ , will be further oxidized to  $\text{CO}_x$  by oxygen resulting from the dissociation of NO. The high activity of the restructured Pt nanoparticles (thermally aged) for NO decomposition increases the supply of active oxygen, which rapidly removes surface carbonaceous species such as  $\text{CO}_2$ . As a consequence, the reaction yield to  $\text{CO}$  decreases.

The same explanation is valid in the case of ammonia formation. It is accepted that  $\text{NH}_3$  is formed in the reactions between  $\text{N}_{\text{ads}}$  and a hydrogen source, either  $\text{CH}_x$  or  $\text{H}_{\text{ads}}$ .<sup>[28]</sup> In fact, a reduction in  $\text{NH}_3$  production can be reached if the active surface oxygen rapidly removes the hydrogen sources. The high activity of the restructured (rough) Pt nanoparticles to decompose NO increases the supply of surface oxygen, which can remove, as oxidation products ( $\text{CO}_2$  and  $\text{H}_2\text{O}$ ), the hydrogen sources ( $\text{CH}_x$  and  $\text{H}_{\text{ads}}$ ) responsible for ammonia formation. Thus the recombination  $\text{N}_{\text{ads}}$  Eq. (2) becomes favored and the reaction of ammonia formation Eqs. (7) and (8) can be prevented.

## CONCLUSION

The  $\text{NO}/\text{CH}_4$  reaction is structure-sensitive, depending both on the size and the shape (facet) of the Pt nanoparticles. The “facet effect” plays an essential role in NO dissociation, and thus is responsible for the reaction selectivity to  $\text{N}_2\text{O}$  and  $\text{N}_2$ . The “size effect” is responsible for the reaction selectivity to  $\text{CO}$  and  $\text{NH}_3$  by controlling the oxygen catalytic activity.

It is clear that accurate tuning of the supported metals' morphology (size and shape) can bring in future spectacular improvements in the catalytic activity and selectivity for structure-sensitive reactions.

## REFERENCES

1. Gates, B.C. Supported metal clusters: Synthesis, structure, and catalysis. *Chem. Rev.* **1995**, *95* (3), 511–522.
2. Argo, A.M.; Odzak, J.F.; Lai, F.S.; Gates, B.C. Observation of ligands effects during alkane hydrogenation by supported metal clusters. *Nature* **2002**, *415* (6872), 623–626.
3. Balint, I.; Miyazaki, A.; Aika, K.-i. Alumina dissolution promoted by  $\text{CuSO}_4$  precipitation. *Chem. Mater.* **1999**, *11* (2), 378–383.
4. Balint, I.; Miyazaki, A.; Aika, K.-i. Alumina dissolution during impregnation with  $\text{PdCl}_4^{2-}$  in the acid pH range. *Chem. Mater.* **2001**, *13* (3), 932–938.
5. Iwasawa, Y. Supported Catalysts From Chemical Vapor Deposition and Related Techniques. In *Preparation of Solid Catalysts*; Ertl, G., Knoezinger, H., Weitkamp, J., Eds.; Wiley-VCH Verlag GmbH: Weinheim, 1999; 427–459.
6. Gates, B.C. Model of metal catalysts: Beyond single crystals. *Top. Catal.* **2001**, *14* (1–4), 173–180.
7. Somorjai, G.A. New model catalysts (platinum nanoparticles) and new techniques (SFG and STM) for studies of reaction intermediates and surface restructuring at high pressures during catalytic reactions. *Appl. Surf. Sci.* **1997**, *121/122*, 1–19.

8. Schmid, G. Cluster and Colloids, From Theory to Applications. In *The Chemistry of Transition Metal Colloids*; New York: Tokyo, 1994; 459–537.
9. Miyazaki, A.; Nakano, Y. Morphology of platinum nanoparticles protected by poly(*N*-isopropylacrylamide). *Langmuir* **2000**, *16* (18), 7109–7111.
10. Ahmadi, T.S.; Wang, Z.L.; Green, T.C.; Henglein, A.; El-Said, M.A. Shape-controlled synthesis of colloidal platinum nanoparticles. *Science* **1996**, *272* (5270), 1924–1926.
11. Wang, Z.L.; Ahmad, T.S.; El-Sayed, M.A. Steps, ledges and kinks on the surfaces of platinum nanoparticles of different shapes. *Surf. Sci.* **1997**, *380* (2–3), 302–310.
12. Balint, I.; Miyazaki, A.; Aika, K.-i. NO reduction by CH<sub>4</sub> over well-structured Pt nanocrystals supported on  $\gamma$ -Al<sub>2</sub>O<sub>3</sub>. *Appl. Catal., B* **2002**, *37* (3), 217–229.
13. Balint, I.; Miyazaki, A.; Aika, K.-i. Investigation of the morphology–catalytic reactivity relationship for Pt nanoparticles supported on alumina by using the reduction of NO with CH<sub>4</sub> as a model reaction. *Chem. Commun.* **2002**, (10), 1044–1045.
14. Somorjai, G.A. *Introduction to Surface Chemistry and Catalysis*; Wiley: New York, 1994; 319–324, Chapter 4.2.3.
15. Tanaka, K.-i.; Sasahara, A. Reconstructive activation of bimetallic surfaces. Catalytic reduction of NO with H<sub>2</sub> on Pt(100), Pt(110), Rh(100), Rh(110), and bimetallic single crystal surfaces of Rh/Pt(100), Rh/Pt(110), Pt/Rh(100), and Pt/Rh(110). *J. Mol. Catal.* **2000**, *155* (1–2), 13–22.
16. Boudart, M. Heterogeneous catalysis by metals. *J. Mol. Catal.* **1985**, *30* (1–2), 27–38.
17. Zambelli, T.; Wintterlin, J.; Trost, J.; Ertl, G. Identification of the “active sites” of a surface catalyzed reaction. *Science* **1996**, *273* (5282), 1688–1690.
18. Walker, A.V.; Gruyters, M.; King, D.A. Modeling the out-of-phase oscillatory catalytic production of N<sub>2</sub>O from NO reduction on Pt{100}. *Surf. Sci.* **1997**, *384* (1–3), L791–L797.
19. Comrie, C.M.; Weinberg, W.H.; Lambert, R.M. The adsorption of nitric oxide on platinum (111) and platinum (110) surfaces. *Surf. Sci.* **1976**, *57* (2), 619–631.
20. Burch, R.; Ramli, A. A comparative investigation of the reduction of NO by CH<sub>4</sub> on Pt, Pd, and Rh catalysts. *Appl. Catal., B* **1998**, *15* (1–2), 49–62.
21. Kao, C.T.; Blackman, G.S.; Van Hove, M.A.; Somorjai, G.A.; Chan, C.M. The surface structure and chemical reactivity of rhodium(111)-(2 × 2)-3NO by HREELS and dynamical LEED analysis. *Surf. Sci.* **1989**, *224* (1–3), 77–96.
22. Banholzer, W.F.; Masel, R.I. Nitric oxide decomposition on Pt(410). *J. Catal.* **1984**, *85* (1), 127–134.
23. Root, T.W.; Schmidt, L.D.; Fisher, G.B. Adsorption and reaction of nitric oxide and oxygen on Rh(111). *Surf. Sci.* **1983**, *134* (1), 30–45.
24. Winter, E.R.S. The catalytic decomposition of nitric oxide by metallic oxides. *J. Catal.* **1971**, *22* (2), 158–170.
25. Fritz, A.; Pitchon, V. The current state of research on automotive lean NO<sub>x</sub> catalysis. *Appl. Catal., B* **1997**, *13* (1), 1–25.
26. Vovk, E.I.; Smirnov, M.Y.; Zemlyanov, D. NO and deuterium co-adsorption on the reconstructed Pt(100)-*hex* surface: A temperature programmed reaction study. *Surf. Sci.* **2000**, *453* (1–3), 103–111.
27. Lauterbach, J.; Bonilla, G.; Pletcher, T.D. Non-linear phenomena during CO oxidation in the mbar pressure range: A comparison between Pt/SiO<sub>2</sub> and Pt(100). *Chem. Eng. Sci.* **1999**, *54* (20), 4501–4512.
28. Burch, R.; Ramli, A. A kinetic investigation of the reduction of NO by CH<sub>4</sub> on silica and alumina-supported Pt catalysts. *Appl. Catal., B* **1998**, *15* (1–2), 63–73.
29. Denton, P.; Schuurman, Y.; Giroir-Fendler, A.; Praliaud, H.; Primet, M.; Mirodatos, C. N<sub>2</sub>O as an intermediate for the formation of N<sub>2</sub> during SCR (NO): Stationary and transient conditions. *C. R. Acad. Sci., Ser. IIC Chim.* **2000**, *3* (6), 437–441.
30. Hickman, D.A.; Schmidt, L.D. Synthesis gas formation by direct oxidation of methane over Pt monoliths. *J. Catal.* **1992**, *138* (1), 267–282.
31. Burch, R.; Hayes, M.J. C–H bond activation in hydrocarbon oxidation on solid catalysts. *J. Mol. Catal., A* **1995**, *100* (1–3), 13–33.
32. Labalme, V.; Garbowski, E.; Guilhaume, N.; Primet, M. Modifications of Pt/alumina combustion catalysts by barium addition: II. Properties of aged catalysts. *Appl. Catal., A* **1996**, *138* (2), 93–108.
33. Hicks, R.F.; Qi, H.; Young, M.L.; Lee, R.G. Structure sensitivity of methane oxidation over platinum and palladium. *J. Catal.* **1990**, *122* (2), 280–294.
34. Burch, R.; Loader, P.K. Investigation of methane oxidation on Pt/Al<sub>2</sub>O<sub>3</sub> catalysts under transient reaction conditions. *Appl. Catal., A* **1995**, *122* (2), 169–190.
35. Hwang, C.-P.; Yeh, C.-T. Platinum-oxide species formed by oxidation of platinum crystallites supported on alumina. *J. Mol. Catal.* **1996**, *112* (2), 295–302.
36. Vartuli, J.C.; Gonzalez, R.D. Ammonia formation in the catalytic reduction of nitric oxide by hydrocarbons: I. Promotional effects of hydrogen. *J. Catal.* **1974**, *32* (3), 470–481.
37. Masel, R.I. *Principles of Adsorption and Reaction on Solid Surfaces*; John Wiley and Sons, Inc.: New York, 1996; 67–68.
38. Putna, E.S.; Vohs, J.M.; Gorte, R.J. Oxygen desorption from  $\alpha$ -Al<sub>2</sub>O<sub>3</sub>(0001) supported Rh, Pt and Pd particles. *Surf. Sci.* **1997**, *391* (1–3), L1178–L1182.

# Polyelectrolyte Films with Incorporated Carbon Nanotubes

Jason H. Rouse

Peter T. Lillehei

Langley Research Center, National Aeronautics and Space Administration (NASA),  
Hampton, Virginia, U.S.A.

## INTRODUCTION

Since their discovery in 1993,<sup>[1,2]</sup> the synthesis, characterization, and manipulation of single-walled carbon nanotubes (SWNT) has received considerable attention. Single-walled carbon nanotubes are composed of a graphene sheet rolled into a seamless tube to produce a material with a diameter between 1 and 2 nm and lengths of up to tens of microns. As nanotubes are comprised of an extended  $\pi$ -system, they possess a unique combination of mechanical, electronic, and optical properties.<sup>[3]</sup> Researchers have envisioned that by incorporating nanotubes within a range of materials, there is potential to produce technologically important breakthroughs such as ultrastrong but light structural materials and molecular-scale electronic devices.

This entry reviews recent reports on the incorporation of SWNTs within thin polymer films using the sequential adsorption of polyionic species.<sup>[4,5]a</sup> Using the ability to introduce acid sites on SWNTs, researchers have shown that oxidized SWNT bundles can act as polyionic species, allowing the formation of polyelectrolyte/SWNT composite thin films.<sup>[4,5]</sup> In addition to minimizing a number of problems encountered with bulk processing techniques (vide infra), such as “bottom-up” approaches to the formation of polymer/SWNT composites may permit the formation of film structures not readily achievable using bulk techniques. The preparation of polymer/SWNT composite thin films via the Langmuir–Blodgett (LB) technique<sup>[8,9]</sup> will also be reviewed.

## RESULTS AND DISCUSSION

### Difficulties with Carbon Nanotube/Polymer Composite Processing

While carbon nanotubes possess remarkable properties, their incorporation within polymer composites has been hampered by their poor solubility and the tendency to aggregate into micron-size particles.<sup>[10,11]</sup> Efforts to overcome these difficulties have primarily focused on experimenting with various bulk processing techniques, such as sonication-assisted solution mixing,<sup>[12–15]</sup> melt mixing,<sup>[16]</sup> and in situ polymerization,<sup>[17–19]</sup> and more recently, the use of SWNTs modified with groups that improve their solubility and reduce aggregation.<sup>[20–22]</sup> While these methods have allowed the formation of polymer/SWNT composites showing some mechanical improvement, the reports generally lack (sufficient) microscopy evidence detailing the extent of nanotube dispersion within the composite. Because the presence of nanotube aggregates within a composite reduces the effective number of interactions between the nanotubes and the polymer, a lower than expected mechanical reinforcement of the polymer is achieved. Additionally, large aggregates may also lower the strength of the material by providing defect sites for mechanical failure. Therefore the development of techniques that would allow the formation of composites with high loadings of well-dispersed nanotubes is of great interest.

### Functionalization of Nanotubes

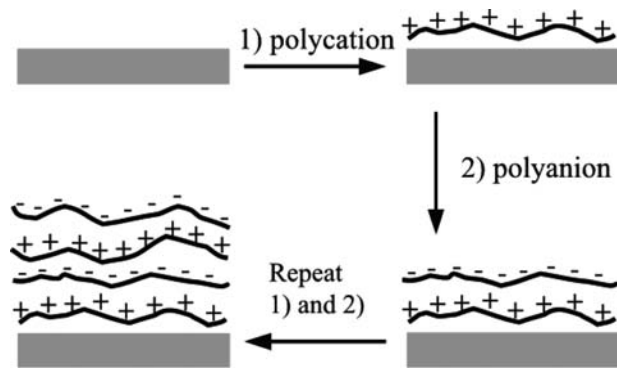
In recent years, researchers have demonstrated the ability to modify the carbon–carbon double bonds in the nanotubes and introduce functionalities that improve solubility and reduce aggregation.<sup>[23–41]</sup> A widely used modification strategy is the formation of carboxylic acids on the ends and/or sidewalls of the

<sup>a</sup>For reviews on the formation of thin films via the alternate adsorption of polyionic species, see Refs.<sup>[6,7]</sup>

nanotubes by chemical oxidation followed by further manipulation.<sup>[30–36]</sup> It has been shown that surfactant molecules and polymers can be attached to oxidized nanotubes either via zwitterionic complexation<sup>[31]</sup> or directly by converting the carboxylic acids to the corresponding esters or amides.<sup>[32–36]</sup> The presence of carboxylic acid sites on the nanotubes has also opened up the possibility of “assembling” nanotube structures.<sup>[37–41]</sup> By either attaching alkylthiol groups to the acid groups through an amide linkage<sup>[37]</sup> or by utilizing acid–metal chelation chemistry,<sup>[38–40]</sup> it has been possible to assemble shortened SWNTs vertically onto metal surfaces. The ability of these acid groups to allow oxidized SWNT bundles to act as polyanionic species and function as nanoscale building blocks within an electrostatic-based thin-film formation procedure will be discussed.<sup>[4,5]</sup>

### Electrostatic Film Formation

The formation of thin composite films via the sequential adsorption of oppositely charged species (polymeric or inorganic) has been shown to be a very versatile method of forming many types of technologically relevant structures (e.g., light-emitting diodes, humidity sensor, separation membranes, etc.)<sup>[42–50]</sup> (Scheme 1). This method of forming polymer/SWNT composites provides a number of important advantages over bulk processing techniques. First, it is possible to form films with high nanotube loading (vide infra), although the adsorption occurs from a dilute solution, helping to overcome the issue of nanotube solubility. Second, the adsorption of each component occurs from a separate solution, so the difficulty of finding a common solvent for both the nanotube and the polymer is removed. Finally, because the film is made in a stepwise manner, the morphology of the film at any point during its formation can be determined by techniques such as atomic force microscopy and



**Scheme 1** Schematic representation of the formation of a thin polymer film by the sequential adsorption of oppositely charged polyelectrolytes onto a substrate.

scanning electron microscopy (SEM), providing a clear indication of nanotube dimensions (bundle size and lengths), uniformity of surface coverage, and presence or absence of aggregates.

### Formation of Porous Polyelectrolyte/Single-Walled Carbon Nanotube Films

To assemble a polyelectrolyte/SWNT film, we first treated a silanol-bearing silicon wafer with the cationic polyelectrolyte poly(diallyldimethylammonium chloride) (PDDA).<sup>[4]</sup> The PDDA-treated wafer was then placed into a dilute *N,N*-dimethylformamide (DMF) suspension of purified HiPco nanotubes.<sup>[4]</sup> Atomic force microscopy (AFM, tapping-mode) images of the SWNTs-treated surface revealed the adsorption of a uniform and fairly dense layer of mostly SWNT bundles (5–10 nm diameter) 1–3  $\mu\text{m}$  in length (Fig. 1A). Spectroscopic characterization (X-ray photoelectron spectroscopy, Raman, UV–vis–NIR) of the nanotube bundles suggested a core–shell structure to the bundles—an inner core of pristine nanotubes surrounded by a layer of oxidized materials (nanotube or amorphous-like).<sup>[4]</sup> The reported procedure used to purify HiPco nanotubes<sup>[51]</sup> involves the oxidation of the amorphous carbon at elevated temperature, treatment with hydrochloric acid to remove the metal catalyst, and then a high-temperature annealing step

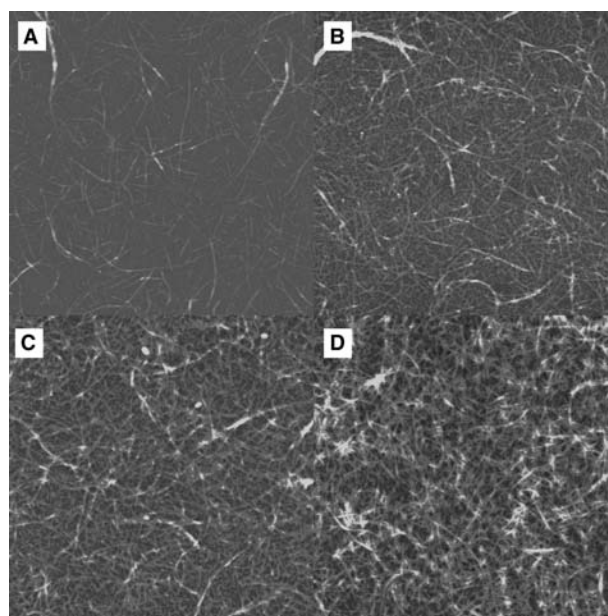


**Fig. 1** Tapping-mode AFM images of a PDDA/SWNT multilayer film prepared on a silicon wafer after various numbers of adsorption treatments: (A) PDDA/SWNT; (B) (PDDA/SWNT)<sub>3</sub>; (C) (PDDA/SWNT)<sub>6</sub>; (D) (PDDA/SWNT)<sub>9</sub>. Images are 5  $\mu\text{m}^2$  and the *z* scale in all images is 50 nm. *Source:* From Ref.<sup>[4]</sup>.

in argon to remove the oxidized groups and aromatize the nanotubes. We believe that in the case of our sample, the annealing step was insufficient to completely remove all oxidized defects present on the nanotubes. Therefore a fraction of nanotubes retained sufficient anionic character to adsorb onto a positively charged surface. While the data presented in this review concerning our research utilizes nanotubes adsorbed from this batch of purified HiPco nanotubes, for the ease of comparison, we have also been able to increase the concentration of oxidized bundles using a bulk-oxidation process. To minimize damage to the extended  $\pi$ -system, responsible for the remarkable properties of nanotubes, great care must be taken during the bulk-oxidation step to limit the number of acid sites to only that sufficient to allow for electrostatic adsorption.

Interestingly, repetitive treatment of a SWNT-terminated film with PDDA, followed again by SWNTs, produced negligible film growth. It is well known that the addition of a salt to a polyelectrolyte solution increases the amount of polyelectrolyte adsorbed per treatment by inducing the polyelectrolyte chains to adopt a globular morphology.<sup>[52–54]</sup> Hence the PDDA adsorption step was repeated with the addition of NaCl (1 M). Images of a PDDA/SWNT film after two additional PDDA–NaCl/SWNT treatments clearly indicated the buildup of a thicker layer of SWNTs on the substrate surface and that the film appeared to be porous (Fig. 1B). Compared to the sharp features of the initially adsorbed bundles (Fig. 1A), the bundles in Fig. 1B appeared to be covered with a layer of beads, indicating that PDDA was adsorbing in globular form to oxidized areas along the bundle length and not as a thin uniform layer. After six and nine adsorption cycles (Fig. 1C,D), AFM imaging revealed continued growth of a porous film. Additional confirmation of film uniformity and morphology was achieved from scanning electron microscopy performed on the nine-bilayer film. These images showed that a uniform film covered the entire silicon wafer (Fig. 2, top) and confirmed that the film was indeed porous (Fig. 2, bottom). The stepwise assembly of a 10-cycle film grown on a quartz slide was also monitored by UV–vis–NIR spectrophotometry. This experiment not only demonstrated that nanotube adsorption from cycle to cycle was reproducible but also that the adsorbed nanotube bundles had the same absorbance signature as that reported in the literature for purified HiPco nanotubes (Fig. 3).<sup>[51]</sup>

### Formation of Dense Polyelectrolyte/Single-Walled Carbon Nanotube Films

With porous films resulting from the sequential adsorption of PDDA followed by SWNTs onto a

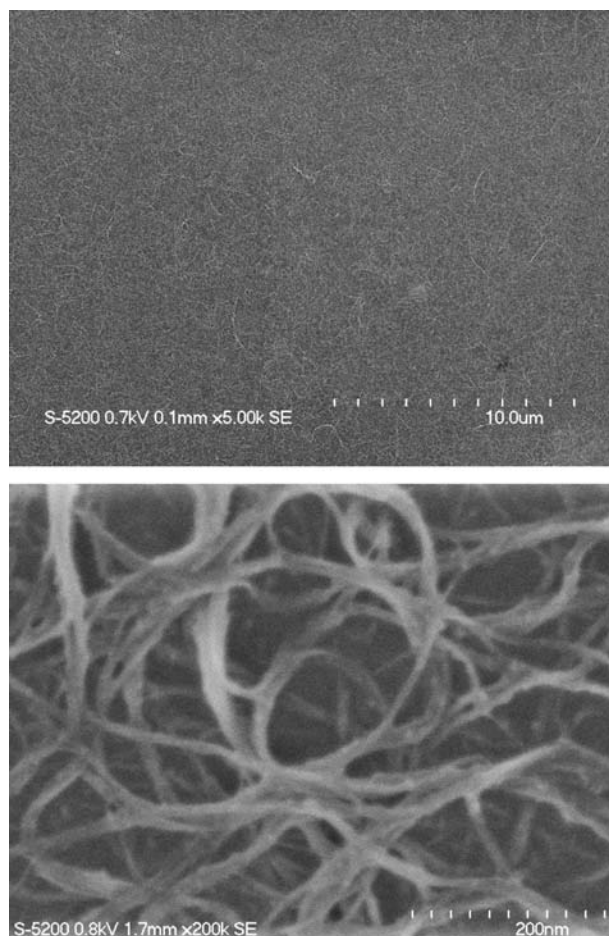


**Fig. 2** Scanning electron micrographs of a (PDDA/SWNT)<sub>9</sub> film showing film uniformity (top) and porosity (bottom).

surface, we turned our attention to modifying our adsorption protocol to permit the formation of dense films. As the nanotube adsorption onto the initial PDDA-treated surface results in approximately 15% surface coverage (Fig. 1A), we envisioned that it should be possible to adsorb the negatively charged polyelectrolyte, poly(styrene sulfonate) (PSS), onto the non-SWNT covered areas. After the PSS adsorption step, the film could then be subjected to additional PDDA/PSS treatments until the areas between the nanotube bundles are filled in, resulting in a uniform dense film. A schematic representation of this method of forming dense polyelectrolyte/SWNT films by “filling in the gaps” between the adsorbed nanotubes is shown in Scheme 2. With nanotube adsorption occurring onto a “pristine” polyelectrolyte layer at each adsorption step, this method should allow: 1) the concentration of nanotubes within each layer to be controlled from ~1% to 15% by varying the adsorption time; and 2) the vertical placement of nanotubes within the film to be controlled by increasing the number of PSS/PDDA treatments used to fill in the film.



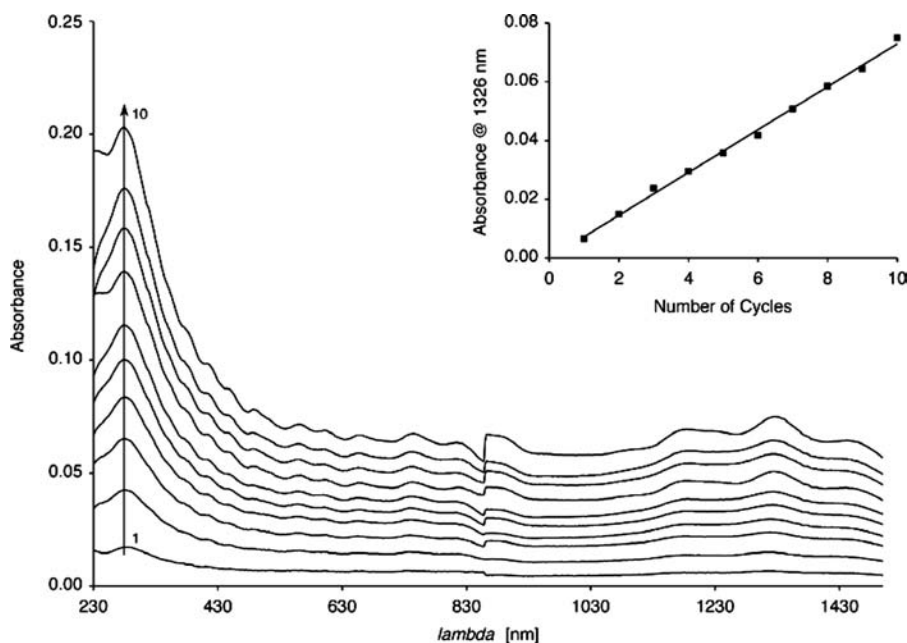
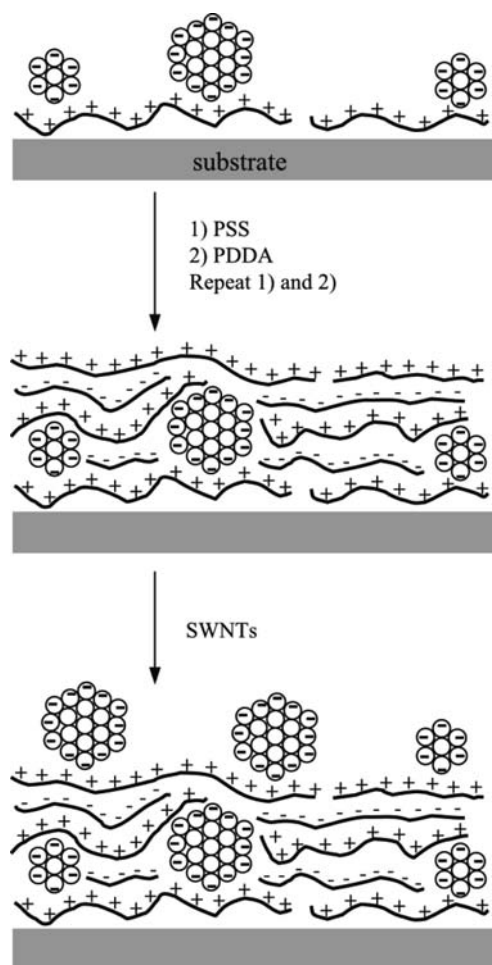


**Fig. 3** Measured UV-Vis-NIR absorbance after each PDDA/SWNT treatment for a 10-cycle film deposited on a quartz slide. The inset shows the measured absorbance at 1349 nm vs. the number of adsorption treatments; the line is a linear least-squares fit to the data. *Source:* From Ref.<sup>[4]</sup>.



**Scheme 2** Schematic representation of a method to form dense polyelectrolyte/SWNT multilayer films.

Atomic force microscopy images of a film prepared using this technique are shown in Fig. 4. A PDDA/SWNT-terminated film (Fig. 4A) was repeatedly treated with 1 wt.% aqueous solutions of PSS followed by PDDA (no NaCl was present in these solutions) until three PSS/PDDA bilayers were deposited. Images of the resultant film revealed a fairly uniform layer of polyelectrolyte with some areas indicating the presence of underlying SWNT bundles (Fig. 4B). Further treatment of the film with SWNTs, (PSS/PDDA)<sub>3</sub>, and then SWNTs demonstrated the reproducibility of both adsorbing SWNTs onto a dense film (Fig. 4C,E) and the ability to fill in the areas between the bundles with polyelectrolyte (Fig. 4D). Scanning electron microscopy imaging of the resultant PDDA/SWNT/[(PSS/PDDA)<sub>3</sub>/SWNT]<sub>2</sub> film indicated that the SWNT layer was uniformly deposited over the entire film surface (~1 × 3 cm).

In parallel to our work, Mamedov et al.<sup>[5]</sup> also reported a method of forming dense polymer/SWNT films using electrostatic interactions. In their study, SWNTs synthesized from the laser ablation of metal-doped carbon rods were refluxed in 65% HNO<sub>3</sub> under sonication to produce oxidized nanotubes that were stable in aqueous solution. Atomic force microscopy imaging revealed that the oxidized material was a mixture of individual nanotubes and 4–9 nm bundles with lengths of a few microns. As expected for water-soluble nanotubes, the UV-vis absorbance lacked the fine structure associated with pristine nanotubes. In contrast to our use of the fully quaternized PDDA, poly(ethyleneimine) (PEI), a polymer in which the degree of amine ionization can be controlled by pH, was utilized. Reminiscent of the difficulties that we incurred in

Polyelectrolyte - Polymer



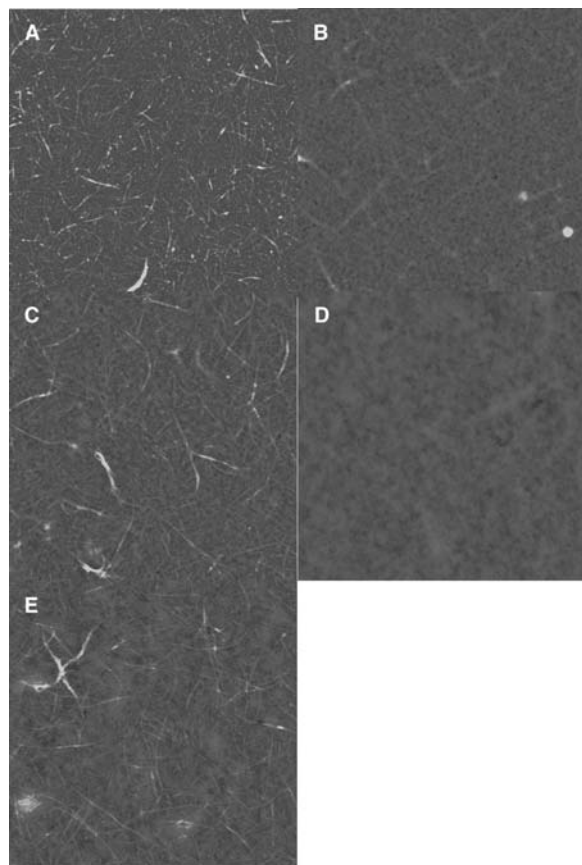


**Fig. 4** Tapping-mode AFM images of a multilayer film prepared on a silicon wafer after various adsorption treatments: (A) PDDA/SWNT; (B) (PSS/PDDA)<sub>3</sub>; (C) SWNT; (D) (PSS/PDDA)<sub>3</sub>; and (E) SWNT. The final film structure is PDDA/SWNT/[(PSS/PDDA)<sub>3</sub>/SWNT]<sub>2</sub>. Images are 5 μm<sup>2</sup> and the *z* scale in all images is 50 nm.

assembling PDDA/SWNTs without NaCl, Mamedov et al. reported the need to apply a PEI/poly(acrylic acid) (PAA) layer after every five PEI/SWNT treatments to improve linear film growth. Although it was reported that the films prepared in the study contained ~50% SWNTs from the integration of carbon and nitrogen energy dispersive X-ray (EDS) peaks, the published microscopy images (AFM, SEM, TEM) do not support such a high SWNT loading. We believe that the AFM image of the (PEI/PAA)-(PEI/SWNT)<sub>5</sub> film suggests that the loading was more likely in the 10–15% range (Fig. 1C in Ref.<sup>[51]</sup>) and consistent with our results.<sup>b</sup>

<sup>b</sup>That apparent discrepancy between the SWNT loading estimated from EDS and our interpretation of the microscopy images may reflect the assumptions made in the EDS analysis regarding the amount of PEI, PAA, SWNT, and even glutaraldehyde present within the film.

A benefit of using PEI for film formation was the ability to cross-link the assembled film. First, the amine groups on the PEI and the acid groups in the SWNTs and the PAA were allowed to react at 120°C to form amide linkages, and then the remaining amine groups were cross-linked by treating with glutaraldehyde. After removal of the PEI-PAA-SWNT cross-linked film from the silicon wafer by treatment with hydrofluoric acid, SEM imaging revealed a uniform freestanding film with no evidence of nanotube aggregation. Mechanical analysis of the resultant freestanding film demonstrated a dramatic increase in tensile strength compared to a non-cross-linked polyelectrolyte film (PEI/PAA). Unfortunately, the lack of cross-linking in the PEI/PAA film does not allow the effect of only SWNT incorporation in the polymer matrix to be quantified.

### Langmuir-Blodgett Formation of Polymer/Single-Walled Carbon Nanotube Films

An alternative method recently reported to prepare thin polymer/SWNT films involves the use of multi-layer Langmuir-Blodgett (LB) technology.<sup>[7,8]</sup> Formation of films by the LB method involves forming a dense molecular film at the water/air interface by compression, followed by transfer of the film to a hydrophobic substrate.<sup>[55]</sup> Repetition of the procedure can result in the formation of a uniform film. In both studies reported, oxidatively shortened SWNTs were functionalized with octadecyl groups and dissolved in a chloroform solution of poly(*n*-dodecylacrylamide). The polymer/SWNT solution was then spread on top of a water layer and compressed to form a film. Although UV-vis-NIR data demonstrated the repeated incorporation of SWNTs within the deposited polymer film in both studies, the reports lacked microscopy illustrating the concentration and uniformity of the incorporated SWNTs. Because the LB method requires the use of a polymer/SWNT solution, it is hampered by the same difficulties faced by solution mixing and in situ polymerization techniques (i.e., formation of a stable solution containing a high nanotube to polymer ratio without aggregation).

### CONCLUSION

This entry has reviewed recent developments of incorporating single-walled carbon nanotubes within thin polymer films via the sequential adsorption of poly-ionic species by utilizing oxidized SWNT bundles as nanoscale polyanionic building blocks. The use of a sequential adsorption protocol solves a major difficulty in forming polymer/SWNT composites, the ability to

uniformly disperse the nanotubes within the polymer matrix. Depending on the adsorption regime chosen to form the polyelectrolyte/SWNT film, it is possible to assemble either porous or dense films containing a uniform distribution of SWNT bundles with loadings of up to ~15%. Using a protocol in which the assembled polymer/SWNT film could be cross-linked and then separated from its support, it has also been shown that the mechanical properties are increased compared to non-cross-linked polyelectrolyte films. Approaches for the assembly of polymer/SWNT films using the Langmuir–Blodgett method have also been reported. As the technique requires the use of a polymer/SWNT solution in film formation, this will probably make this technique less generally useful than the sequential adsorption protocol.

## REFERENCES

- Iijima, S.; Ichihashi, T. Single-shell carbon nanotubes of 1-nm diameter. *Nature* **1993**, *363*, 603–605.
- Bethune, D.S.; Kiang, C.H.; de Vries, M.S.; Gorman, G.; Savoy, R.; Vazquez, J.; Beyers, R. Cobalt-catalyzed growth of carbon nanotubes with single-atomic-layer walls. *Nature* **1993**, *363*, 605–607.
- Ajayan, P.M. Nanotubes from carbon. *Chem. Rev.* **1999**, *99* (7), 1787–1799.
- Rouse, J.H.; Lillehei, P.T. Electrostatic assembly of polymer/single walled carbon nanotube multilayer films. *Nano Lett.* **2003**, *3* (1), 59–62.
- Mamedov, A.A.; Kotov, N.A.; Prato, M.; Guldi, D.M.; Wicksted, J.P.; Hirsch, A. Molecular design of strong single-wall carbon nanotube/polyelectrolyte multilayer composites. *Nat. Mater.* **2002**, *1*, 190–194.
- Decher, G. Fuzzy nanoassemblies: toward layered polymeric multicomposites. *Science* **1997**, *277*, 1232–1237.
- Hammond, P.T. Recent explorations in electrostatic multilayer thin films assembly. *Curr. Opin. Colloid Interface Sci.* **2000**, *4*, 430–442.
- Guo, Y.; Wu, J.; Zhang, Y. Manipulation of single-wall carbon nanotubes into aligned molecular layers. *Chem. Phys. Lett.* **2002**, *362*, 314–318.
- Guo, Y.; Minami, N.; Kazaoui, S.; Peng, J.; Yoshida, M.; Miyashita, T. Multi-layer LB films of single-walled carbon nanotubes. *Physica, B* **2002**, *323*, 235–236.
- Bahr, J.L.; Mickelson, E.T.; Bronikowski, M.J.; Smalley, R.E.; Tour, J.M. Dissolution of small diameter single-wall carbon nanotubes in organic solvents? *Chem. Commun.* **2001**, 193–194.
- Ausman, K.D.; Piner, R.; Lourie, O.; Ruoff, R.S.; Korobov, M. Organic solvent dispersions of single-walled nanotubes: toward solutions of pristine nanotubes. *J. Phys. Chem., B* **2000**, *104* (38), 8911–8915.
- Ajayan, P.M.; Schadler, L.S.; Giannaris, C.; Rubio, A. Single-walled carbon nanotube-polymer composites: strength and weakness. *Adv. Mater.* **2000**, *12* (10), 750–753.
- Kymakis, E.; Amaratunga, G.A.J. Single-walled carbon nanotube/conjugated polymer photovoltaic devices. *Appl. Phys. Lett.* **2002**, *80* (1), 112–114.
- Landi, B.J.; Raffaella, R.P.; Heben, M.J.; Alleman, J.L.; VanDerveer, W.; Gennett, T. Single wall carbon nanotube-nafion composite actuators. *Nano Lett.* **2002**, *2* (11), 1329–1332.
- Chattopadhyay, D.; Galeska, I.; Baughman, R.; Zakhidov, A.; Papadimitrakopoulos, F. Carbon nanotube/polelectrolyte composites as novel actuator materials. *Mater. Res. Soc. Symp. Proc.* **2001**, *633*, A13.39.1–A13.39.5.
- Haggenmueller, R.; Gommans, H.H.; Rinzler, A.G.; Fischer, J.E.; Winey, K.I. Aligned single-walled carbon nanotubes in composites by melt processing methods. *Chem. Phys. Lett.* **2000**, *330*, 219–225.
- Park, C.; Ounaies, Z.; Watson, K.A.; Crooks, R.E.; Smith, J.; Lowther, S.E.; Connell, J.W.; Siochi, E.J.; Harrison, J.S.; St. Clair, T.L. Dispersion of single wall carbon nanotubes by in situ polymerization under sonication. *Chem. Phys. Lett.* **2002**, *364*, 303–308.
- Barraza, H.J.; Pompeo, F.; O’Rear, E.A.; Resasco, D.E. SWNT-filled thermoplastic and elastomeric composites prepared by miniemulsion polymerization. *Nano Lett.* **2001**, *2* (8), 797–802.
- Kumar, S.; Dang, T.D.; Arnold, F.E.; Bhattacharyya, A.R.; Min, B.G.; Zhang, X.; Vaia, R.A.; Park, C.; Adams, W.W.; Hauge, R.H.; Smalley, R.E.; Ramesh, S.; Willis, P.A. Synthesis, structure, and properties of PBO/SWNT composites. *Macromolecules* **2002**, *35* (24), 9039–9043.
- Geng, H.; Rosen, R.; Zheng, B.; Shimoda, H.; Fleming, L.; Liu, J.; Zhou, O. Fabrication and properties of composites of poly(ethylene oxide) and functionalized carbon nanotubes. *Adv. Mater.* **2002**, *14* (19), 1387–1390.
- Mitchell, C.A.; Bahr, J.L.; Arepalli, S.; Tour, J.M.; Krishnamoorti, R. Dispersion of functionalized carbon nanotubes in polystyrene. *Macromolecules* **2002**, *35* (23), 8825–8830.
- Hill, D.E.; Lin, Y.; Rao, A.M.; Allard, L.F.; Sun, Y.-P. Functionalization of carbon nanotubes with polystyrene. *Macromolecules* **2002**, *35* (25), 9466–9471.
- Georgakilas, V.; Kordatos, K.; Prato, M.; Guldi, D.M.; Holzinger, M.; Hirsch, A. Organic functionalization of carbon nanotubes. *J. Am. Chem. Soc.* **2002**, *124* (5), 760–761.
- Holzinger, M.; Vostrowsky, O.; Hirsch, A.; Hennrich, F.; Kappes, M.; Weiss, R.; Jellen, F. Sidewall functionalization of carbon nanotubes. *Angew. Chem. Int. Ed.* **2001**, *40* (21), 4002–4005.
- Bahr, J.L.; Yang, J.; Kosynkin, D.V.; Bronikowski, M.J.; Smalley, R.E.; Tour, J.M. Functionalization of carbon nanotubes by electrochemical reduction of aryl diazonium salts: a bucky paper electrode. *J. Am. Chem. Soc.* **2001**, *123* (27), 6536–6542.
- Bahr, J.L.; Tour, J.M. Highly functionalized carbon nanotubes using in situ generated diazonium compounds. *Chem. Mater.* **2001**, *13* (11), 3823–3824.
- Sun, Y.; Wilson, S.R.; Schuster, D.I. High dissolution and strong light emission of carbon nanotubes in

- aromatic amine solvents. *J. Am. Chem. Soc.* **2001**, *123* (22), 5348–5349.
28. Boul, P.J.; Liu, J.; Mickelson, E.T.; Huffman, C.B.; Ericson, L.M.; Chiang, I.W.; Smith, K.A.; Colbert, D.T.; Hauge, R.H.; Margrave, J.L.; Smalley, R.E. Reversible sidewall functionalization of buckytubes. *Chem. Phys. Lett.* **1999**, *310*, 367–372.
  29. Mickelson, E.T.; Chiang, I.W.; Zimmerman, J.L.; Boul, P.J.; Lozano, J.; Liu, J.; Smalley, R.E.; Hauge, R.H.; Margrave, J.L. Solvation of fluorinated single-wall carbon nanotubes in alcohol solvents. *J. Phys. Chem., B* **1999**, *103* (21), 4318–4322.
  30. Banerjee, S.; Wong, S.S. Functionalization of carbon nanotubes with a metal-containing molecular complex. *Nano Lett.* **2002**, *2* (1), 49–53.
  31. Chen, J.; Rao, A.M.; Lyuksyutov, S.; Itkis, M.E.; Hamon, M.A.; Hu, H.; Cohn, R.W.; Eklund, P.C.; Colbert, D.T.; Smalley, R.E.; Haddon, R.C. Dissolution of full-length single-walled carbon nanotubes. *J. Phys. Chem., B* **2001**, *105* (13), 2525–2528.
  32. Sun, Y.-P.; Huang, W.; Lin, Y.; Fu, K.; Kitaygorodskiy, A.; Riddle, L.A.; Yu, Y.J.; Carroll, D.L. Soluble dendron-functionalized carbon nanotubes: preparation, characterization, and properties. *Chem. Mater.* **2001**, *13* (9), 2864–2869.
  33. Niyogi, S.; Hu, H.; Hamon, M.A.; Bhowmik, P.; Zhao, B.; Rozenzhak, S.M.; Chen, J.; Itkis, M.E.; Meier, M.S.; Haddon, R.C. Chromatographic purification of soluble single-walled carbon nanotubes (s-SWNTs). *J. Am. Chem. Soc.* **2001**, *123* (4), 733–734.
  34. Riggs, J.E.; Walker, D.B.; Carroll, D.L.; Sun, Y.-P. Optical limiting properties of suspended and solubilized carbon nanotubes. *J. Phys. Chem., B* **2000**, *104* (30), 7071–7076.
  35. Riggs, J.E.; Guo, Z.; Carroll, D.L.; Sun, Y.-P. Strong luminescence of solubilized carbon nanotubes. *J. Am. Chem. Soc.* **2000**, *122* (24), 5879–5880.
  36. Chen, J.; Hamon, M.A.; Hu, H.; Chen, Y.; Rao, A.M.; Eklund, P.C.; Haddon, R.C. Solution properties of single-walled carbon nanotubes. *Science* **1998**, *282*, 95–98.
  37. Liu, Z.; Shen, Z.; Zhu, T.; Hou, S.; Ying, L.; Shi, Z.; Gu, Z. Organizing single-walled carbon nanotubes on gold using a wet chemical self-assembling technique. *Langmuir* **2000**, *16* (8), 3569–3573.
  38. Wu, B.; Zhang, J.; Wei, W.; Cai, S.; Liu, Z. Chemical alignment of oxidatively shortened single-walled carbon nanotubes on silver surface. *J. Phys. Chem., B* **2001**, *105* (22), 5075–5078.
  39. Chattopadhyay, D.; Galeska, I.; Papadimitrakopoulos, F. Metal-assisted organization of shortened carbon nanotubes in monolayer and multilayer forest assemblies. *J. Am. Chem. Soc.* **2001**, *123* (38), 9451–9452.
  40. Cai, L.; Bahr, J.L.; Yao, Y.; Tour, J.M. Ozonation of single-walled carbon nanotubes and their assemblies on rigid self-assembled monolayers. *Chem. Mater.* **2002**, *14* (10), 4235–4241.
  41. Liu, J.; Rinzler, A.G.; Dai, H.; Hafner, J.H.; Bradley, R.K.; Boul, P.J.; Lu, A.; Iverson, T.; Shelimov, K.; Huffman, C.B.; Rodriguez-Macias, F.; Shon, Y.-S.; Lee, T.R.; Colbert, D.T.; Smalley, R.E. Fullerene pipes. *Science* **1998**, *280*, 1253–1256.
  42. Eckle, M.; Decher, G. Tuning the performance of layer-by-layer assembled organic light emitting diodes by controlling the position of isolating clay barrier sheets. *Nano Lett.* **2001**, *1* (1), 45–49.
  43. Wu, A.; Yoo, D.; Lee, J.-K.; Rubner, M.F. Solid-state light-emitting devices based on the tris-chelated ruthenium(II) complex: 3. High efficiency devices via a layer-by-layer molecular-level blending approach. *J. Am. Chem. Soc.* **1999**, *121* (20), 4883–4891.
  44. Baur, J.W.; Kim, S.; Balanda, P.B.; Reynolds, J.R.; Rubner, M.F. Thin-film light-emitting devices based on sequentially adsorbed multilayers of water-soluble poly(*p*-phenylene)s. *Adv. Mater.* **1998**, *10* (17), 1452–1455.
  45. Ho, P.K.H.; Granstrom, M.; Friend, R.H.; Greenham, N.C. Ultrathin self-assembled layers at the ITO interface to control charge injection and electroluminescence efficiency in polymer light-emitting diodes. *Adv. Mater.* **1998**, *10* (10), 769–774.
  46. Dai, J.; Jensen, A.W.; Mohanty, D.K.; Erndt, J.; Bruening, M.L. Controlling the permeability of multilayered polyelectrolyte films through derivatization, cross-linking, and hydrolysis. *Langmuir* **2001**, *17* (3), 931–937.
  47. Farhet, T.R.; Schlenoff, J.B. Ion transport and equilibria in polyelectrolyte multilayers. *Langmuir* **2001**, *17* (4), 1184–1192.
  48. Krasemann, L.; Tieke, B. Selective ion transport across self-assembled alternating multilayers of cationic and anionic polyelectrolytes. *Langmuir* **2000**, *16* (2), 287–290.
  49. Levasalmi, J.-M.; McCarthy, T.J. Poly(4-methyl-1-pentene)-supported polyelectrolyte multilayers films: preparation and gas permeability. *Macromolecules* **1997**, *30* (6), 1752–1757.
  50. Kleinfed, E.R.; Ferguson, G.S. Rapid, reversible sorption of water from the vapor by a multilayered composite film: a nanostructured humidity sensor. *Chem. Mater.* **1995**, *7* (12), 2327–2331.
  51. Chiang, I.W.; Brinson, B.E.; Huang, A.Y.; Willis, P.A.; Bronikowski, M.J.; Margrave, J.L.; Smalley, R.E.; Hauge, R.H. Purification and characterization of single-wall carbon nanotubes (SWNTs) obtained from the gas-phase decomposition of CO (HiPco process). *J. Phys. Chem., B* **2001**, *105* (35), 8297–8301.
  52. Dubas, S.T.; Schlenoff, J.B. Swelling and smoothing of polyelectrolyte multilayers by salt. *Langmuir* **2001**, *17* (25), 7725–7727.
  53. Dubas, S.T.; Schlenoff, J.B. Factors controlling the growth of polyelectrolyte multilayers. *Macromolecules* **1999**, *32* (24), 8153–8160.
  54. Losche, M.; Schmitt, J.; Decher, G.; Bouwman, W.G.; Kjaer, K. Detailed structure of molecularly thin polyelectrolyte multilayer films on solid substrates as revealed by neutron reflectometry. *Macromolecules* **1998**, *31* (25), 8893–8906.
  55. Ulman, A. *An Introduction to Ultrathin Organic Films: From Langmuir–Blodgett to Self-Assembly*; Academic Press: New York, 1991.

# Polyelectrolyte–Surfactant Complex Nanoparticles

Hans-Peter Hentze

Department of Chemical Engineering, University of Delaware,  
Newark, Delaware, U.S.A.

## INTRODUCTION

A variety of different colloidal systems can be produced by interaction between polyelectrolytes and oppositely charged surfactants. These complexes have attracted considerable interest because of their importance for both science and industrial applications.

By interaction of two oppositely charged polyelectrolytes, polyelectrolyte–polyelectrolyte complexes (PECs, or so-called symplexes) are formed. These PECs can be loose aggregates or well-defined nanoparticles.<sup>[1]</sup> In a similar way polyelectrolytes form complexes with oppositely charged surfactants and polyelectrolyte–surfactant complexes (PSCs) are obtained.<sup>[2,3]</sup> Here the mechanism of complex formation is not only based on electrostatic interactions and entropic factors, but also on the hydrophobic interaction between the surfactant tails. At surfactant concentrations below the critical micelle concentration (CMC), complex formation of polyelectrolytes with oppositely charged surfactants occurs. With increasing surfactant chain lengths, the formation of surfactant patches along the polyelectrolyte chain can be expected, because owing to hydrophobic interactions the preferred complexation binding site is the next closest position to an occupied site. This results in a zipperlike mechanism of polyelectrolyte–surfactant complex formation.<sup>[4]</sup> Typically three-dimensional networks form at concentrations above the CMC, where polyelectrolyte chains bridge discrete micelles without penetrating them.<sup>[5,6]</sup> At even higher surfactant concentrations, when all charges of the polyion are neutralized, polyelectrolyte–surfactant complexes usually precipitate from solution.<sup>[2,3,7]</sup> These bulk materials have a liquid crystalline-like mesostructure and display long-range order on the nanometer scale. The interaction between polyions and oppositely charged surfactants is a cooperative process in which the ionic head groups of the surfactant bind to the polyion, while the hydrophobic surfactant tails segregate into a hydrophobic microphase. Similar to amphiphilic block copolymers, this microphase separation occurs without macroscopic demixing.

One problem with most such polyelectrolyte–surfactant complexes is that they are usually

water-insoluble solids or semisolids and not suitable for particle applications. Within the last few years, different techniques of PSC nanoparticle synthesis have been developed to overcome this problem. These complexes are, unlike PSC bulk materials, redispersable in water or organic solvents as discrete nanoparticles without dissociation. For synthesis of PSC nanoparticles, polyelectrolytes that exhibit additional molecular entities have to be used, which provide solubility even after stoichiometric complexation and neutralization of all charges. In this way, particles are obtained that exhibit spherical core–shell structures, cylindrical or disk-shaped morphologies, or hollow spheres like vesicles. Whereas some of these morphologies appear to be equilibrium structures, others are non-equilibrium structures. The size, solubility, and morphology of PSC nanoparticles depend strongly on the molecular structure of the polyelectrolyte, the block ionomer lengths, the block length ratios, the structure and type of surfactant, and sometimes also on the way of preparation. Potential applications for this relatively new class of materials are drug and gene delivery, amphiphilic particles, and depot systems.<sup>[8,9]</sup>

## COMPLEXATION OF DOUBLE-HYDROPHILIC BLOCK COPOLYMERS—VARIOUS NANOPARTICLE MORPHOLOGIES

A very interesting family of polymers are double-hydrophilic block copolymers.<sup>[10]</sup> These consist of two covalently linked hydrophilic polymer block segments, which are chemically not equivalent, e.g., poly(ethylene oxide)-*b*-poly(sodium methacrylate). Double-hydrophilic block copolymers that contain a polymer block that is a polyelectrolyte are called block ionomers.

For the first time, redispersable nanoparticles of block ionomer–surfactant complexes have been obtained by complexation of poly(ethylene oxide)-*b*-poly(sodium methacrylate) (PEO-*b*-PMANa) with cetylpyridinium cations.<sup>[11]</sup> The segment lengths of the block ionomer were 176 and 186 repeating units for PEO and PMANa, respectively. Different aggregate morphologies could be distinguished within three

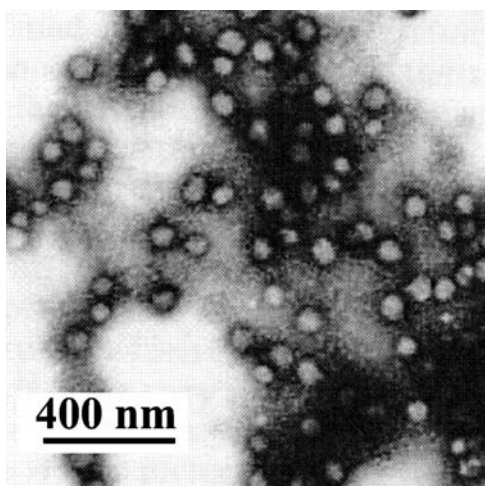


**Fig. 1** TEM micrograph of vesicles formed by the complex of PEO-*b*-PMANa with C<sub>16</sub>PyBr. *Source:* From Ref.<sup>[11]</sup>.

different surfactant concentration regions: At molar surfactant concentrations below the concentration of anionic polyion charges, the surfactant cetylpyridinium bromide (C<sub>16</sub>PyBr) binds electrostatically to the polyion and soluble complexes with negative  $\zeta$ -potentials were observed. Also, the stoichiometric and electrostatic neutral ( $\zeta = 0$ ) complexes were soluble and formed monodisperse nanoparticles with a diameter of 67 nm, as shown by dynamic light scattering (DLS) and transmission electron microscopy (TEM). A TEM micrograph is shown in Fig. 1. These discrete PSC complexes were first believed to exhibit a core-shell structure, where the core is formed by C<sub>16</sub>PyBr neutralized polyions, and the shell of PEO block segments. Later studies suggested a vesicular morphology.<sup>[12]</sup> At higher surfactant concentrations excess surfactant is incorporated into the particles, resulting in a positive  $\zeta$ -potential. The observed particles combine the properties of amphiphilic block copolymers and polyelectrolyte surfactant complexes, as they spontaneously form stable, water-soluble, and microphase separated aggregates.

Similar to mixtures of cationic and anionic single-tail surfactants,<sup>[13]</sup> spontaneous formation of vesicles is observed for the complexation of PEO-*b*-PMANa block ionomers with alkyltrimethylammonium surfactants [e.g., tetradecylammonium bromide (TTAB) or cetyltrimethylammonium bromide (CTAB)].<sup>[12]</sup> In contrast, complexation of the homopolymer PMANa with the same surfactants resulted in the formation of water-insoluble bulk materials. The wall of the PSC vesicles is composed of surfactant-neutralized polyion surrounded by the hydrophilic PEO shell, which sterically stabilizes the complexes in aqueous dispersions. The vesicular solutions are transparent or slightly opalescent. Vesicle diameters varied between 85 and

120 nm and increased with increasing chain length of the surfactant. The obtained dispersions are very stable and efficiently encapsulate and retain hydrophilic molecules in the internal aqueous volume.

The influence of the block ionomer block lengths and the surfactant structure on the solubility of PSC nanoparticles was also systematically investigated.<sup>[14]</sup> Therefore, complexation of a variety of PEO-*b*-PMANa block copolymers was performed with single-tail, double-tail, and triple-tail tetraalkylammonium surfactants. It was found that a minimum block length of PEO and a high enough block length ratio of PEO/PMANa are necessary to induce sufficient sterical stabilization in aqueous dispersions. Complex formation with stoichiometric amounts of the single-tail surfactants CTAB or C<sub>16</sub>PyBr resulted in rather small and monodisperse aggregates. These systems are believed to be in dynamic equilibrium with surfactant monomers in the dispersion. The critical aggregation concentration (CAC) was two to three orders of magnitude lower than the corresponding CMC. In contrast, the aggregate size of complexes formed with double-tailed surfactants [e.g., didodecyltrimethylammonium bromide (DDAB)] depended strongly on the way of preparation. This non-equilibrium behavior can be explained by the formation of preformed, membranelike surfactant aggregates, which is typical for double-tail surfactants. As is the case for single-tail surfactants, for triple-tail surfactants the formation of the aggregates is primarily controlled by the block ionomer structure and composition of the mixture. Different core morphologies can be expected for complexation with single- and triple-tail surfactants owing to the rather different packing parameters.

Not only linear block copolymers, but also grafted copolymers were used for PSC nanoparticle formation.<sup>[15]</sup> Unlike the vesicular morphologies formed by linear block copolymers, core-shell particles were obtained by complexation of poly(ethylene oxide)-*g*-poly(ethylene imine) (PEO-*g*-PEI) with anionic surfactants [e.g., sodium dodecyl sulfate (SDS) or sodium tetradecyl sulfate (TDS)]. In these micelle-like aggregates, apparently the hydrophobic core from the surfactant-neutralized PEI block is surrounded by the hydrophilic corona of PEO chains stabilizing the particles in aqueous media. The observed particle sizes, as determined by DLS and confirmed by TEM, are about 40–50 nm. Therefore, their size is comparable with micelle-like aggregates of amphiphilic block copolymers. The CAC was determined by fluorescence measurements using pyrene as a probe. CAC values were about two magnitudes lower than the corresponding CMC values of the pure surfactant. As the size of the obtained PSC particles is independent of the way of preparation, the complexes appear to be in equilibrium with unbound surfactants. With

increasing chain length of the anionic surfactants, excess surfactant was incorporated in the complexes, resulting in particles with negative  $\zeta$ -potentials.

Spherical core–shell morphologies can also be obtained by complexation of poly(ethylene oxide)-b-poly(ethylene imine) containing branched poly(ethylene imine) segments (PEO-b-PEI<sub>br</sub>) with the surfactant dodecanoic acid (C<sub>12</sub>).<sup>[16]</sup> In contrast, prolate particles can be obtained by complexation of the linear block copolymer PEO-b-PEI<sub>li</sub>. Even more elongated are the needlelike particles formed by C<sub>12</sub> and a PEO-b-PEI block copolymer with a cyclic architecture of the PEI segment (PEO-b-PEI<sub>cy</sub>). All these particles formed by C<sub>12</sub> and PEO-b-PEI block copolymers with a linear, branched, or cyclic PEI architecture exhibit a core–shell structure, as shown by atomic force microscopy (AFM). The core consists of poly(ethylene imine) dodecanoate surrounded by a corona of poly(ethylene oxide). All particles investigated in this study have an average size of about 200 nm (Fig. 2). Small-angle X-ray scattering (SAXS) of dried dispersions revealed that the complex formed with PEO-b-PEI<sub>cy</sub> has a lamellar morphology, while the ones of PEO-b-PEI<sub>li</sub> and PEO-b-PEI<sub>br</sub> show a lamellar-*within*-lamellar morphology.

pH-sensitive core–shell particles have been obtained in aqueous dispersions of poly(ethylene oxide)-b-poly(L-lysine) (PEO-b-PLL) complexes with retinoic acid.<sup>[17]</sup> Because of its amphiphilic properties, this vitamin A analogue can be considered as a surfactant. The complexes were characterized by SAXS as bulk material, as well as in aqueous dispersions. The diffractograms indicate that the cores of these complexes exhibit a smectic-A-like structure. By circular dichroism, an  $\alpha$ -helical conformation of L-lysine chains was found for pH values above 9. It was assumed that this conformation is stabilized by the PEO shell, as well as

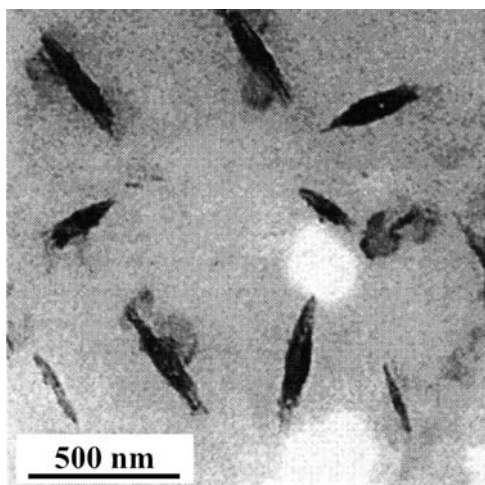


**Fig. 2** Dried dispersions of the complex of PEO–PEI<sub>br</sub> with C12 form needlelike particles. *Source:* From Ref.<sup>[16]</sup>.

by protecting retinoate molecules. Below a pH of 3.7, a random coil structure is present, while mixtures of random coils and  $\alpha$ -helices form in the intermediate pH range. The complexes can be considered as a model for pH-sensitive drug-carrier systems.

Nanoparticle dispersions of polyelectrolyte–surfactant complexes have also been made from polyelectrolyte homopolymers.<sup>[18]</sup> Non-stoichiometric complexes containing excess polyelectrolyte or surfactant are generally soluble in water, and sometimes they form well-defined, discrete aggregates. Especially, PSCs of biopolymers, such as polysaccharides or polypeptides, have been investigated for drug and gene delivery purposes. As their stoichiometric, electro-neutral complexes are not redispersible and water insoluble they are not discussed in detail in this entry.

### “REVERSE” CORE–SHELL STRUCTURES BY COMPLEXATION OF HYDROPHILIC–HYDROPHOBIC BLOCK IONOMERS

In contrast to the core–shell structure of complexes from double-hydrophilic block ionomers, complexation of hydrophilic–hydrophobic block copolymers results in “reverse” morphologies—here the non-ionic, hydrophobic block segments form the core, which is surrounded by a surfactant neutralized polyion shell. For this reason the particles can be redispersed only in solvents that are also solvents of the polyelectrolyte homopolymer complex. A major difference compared to double-hydrophilic block copolymers is the aggregation of the polyion before addition of surfactant and complexation. Micelle-like aggregates are formed in aqueous solution owing to microphase separation of the hydrophobic polymer segments. This factor might limit the possibilities of this approach to form equilibrium structures.

One example is the synthesis of nanoparticles from polystyrene-b-poly(sodium acrylate) (PS-b-PAA<sup>−</sup>) and *N*-cetylpyridinium cations (C<sub>16</sub>Py<sup>+</sup>), which precipitate from aqueous solution at stoichiometric mixing ratios of surfactant and polyion units.<sup>[19]</sup> The formed precipitate is insoluble in tetrahydrofuran and toluene, which are good solvents for PS but non-solvents for PAA<sup>−</sup>/C<sub>16</sub>Py<sup>+</sup> complexes. Instead, chloroform, a good solvent for PAA<sup>−</sup>/C<sub>16</sub>Py<sup>+</sup>, could be used for redispersion. This clearly indicates a core–shell structure with a polystyrene core surrounded by surfactant neutralized polyion segments that stabilize the particles in solution.

Similar results were obtained for complexes from poly( $\alpha$ -methylstyrene)-b-poly(*N*-ethyl-4-vinylpyridinium bromide) (PMeS-b-PE4VP) and sodium bis(2-ethylhexyl)sulfosuccinate (AOT).<sup>[20]</sup> The precipitated complexes can incorporate small excess of surfactant.



Preliminary studies showed that PSC formed by the homopolymer PE4VP and AOT were soluble in various organic solvents without dissociation of the complex, e.g., cyclohexane, chloroform, and acetone. Neither of these solvents dissolves the block ionomer PMS-b-PE4VP, but all of them are good solvents for the complexes of the block ionomer with AOT. Again, this clearly hints on the described “reverse” core–shell morphology. The particle size of the redispersed PSCs in hexane/cosolvent mixtures is about 70 nm in diameter. The spherical morphology and the size of the particles were confirmed by TEM.

## COMPLEXATION OF POLYAMPHOLYTES

Polyampholytes are polyelectrolytes that contain both anionic and cationic repeating units. Complexes of ternary polyampholytes with cationic, anionic, and neutral repeating units with perfluorododecanoic acid (FC<sub>12</sub>) have been synthesized.<sup>[21]</sup> The obtained nanoparticles are highly fluorinated and stable in aqueous dispersions. By dynamic light scattering, it was shown that discrete particles with hydrodynamic diameters of 20–35 nm were formed. The diameter and the stability of the dispersions depend strongly on the composition

of the polyampholyte. More insight into the particles' morphology was gained by small-angle X-ray scattering. The geometry of the dispersed particles was characterized by indirect Fourier transform method.<sup>[22]</sup> Disk-shaped aggregates with a diameter of 30 nm were formed by complexes from the polyampholyte with the highest content of cationic repeating units. Complexes of polyampholytes with a lower content of cationic charges formed cylindrical aggregates with a length of about 25 nm. A partially interdigitated arrangement of the surfactant tails was assumed, owing to the small thickness of the disklike aggregates (2.2 nm) and the small diameter of the formed cylinders (3 nm). An overview of the different morphologies of PSC nanoparticles formed by the different polyion precursors is given in Table 1.

## HOLLOW SPHERES FROM POLYELECTROLYTE–SURFACTANT COMPLEX NANOPARTICLES

Besides vesicle formation, hollow spheres of PSCs can be also prepared by stepwise complexation and selective dissociation of poly(ethylene imine).<sup>[23]</sup> First, non-stoichiometric complexes of PEI homopolymer

**Table 1** Overview of the different types of polyion precursors used for complexation of oppositely charged surfactants, and the resulting nanoparticle morphologies

Structure of the polyion		Surfactant (reference)	Nanoparticle morphology
Double-hydrophilic block copolymers	PEO-b-PMANa	C <sub>16</sub> PyBr <sup>[11]</sup>	Vesicles
		DOTAB <sup>[12]</sup>	
	PEO-g-PEI	TTAB <sup>[12]</sup>	
		CTAB <sup>[12]</sup>	
		SDS <sup>[15]</sup>	Core–shell
	TDS <sup>[15]</sup>		
	AOT <sup>[15]</sup>		
Hydrophilic–hydrophobic block ionomers	PEO-b-PLL	Retinoate <sup>[17]</sup>	
	PEO-b-PEI <sub>br</sub>	C <sub>12</sub> <sup>[16]</sup>	
	PEO-b-PEI <sub>li</sub>	C <sub>12</sub> <sup>[16]</sup>	Prolate particles
	PEO-b-PEI <sub>cy</sub>	C <sub>12</sub> <sup>[16]</sup>	Needlelike particles
Polyampholytes	PS-b-PAA <sup>−</sup>	C <sub>16</sub> PyBr <sup>[19]</sup>	“Reverse” core–shell structures
	PMS-b-PE4VP	AOT <sup>[20]</sup>	
Core–shell latex particles	Random copolymers from cationic, anionic and neutral monomers	FC <sub>12</sub> <sup>[21]</sup>	Disk-shaped particles and cylinders
		DOTAB <sup>[24]</sup>	Core–shell
		TTAB <sup>[24]</sup>	
		CTAB <sup>[24]</sup>	
		DDAB <sup>[24]</sup>	

with dodecanoic acid were formed. The particles display a positively charged shell of free ethylene imine units and a PEI–dodecanoic acid core. Second, poly(ethylene oxide)-*b*-poly(methacrylic acid) block copolymer with a phosphonized carboxylic acid end group was added, resulting in particles with a core of PEI–dodecanoic acid and a shell of a phosphonized block ionomer/PEI complex. By decreasing the pH value below the  $pK_a$  value of dodecanoic acid, the PEI–dodecanoic acid core was selectively dissolved. The phosphonate–PEI shell was left unchanged, forming hollow spheres with a diameter of about 400 nm. TEM micrographs reveal a porous structure of the formed PSC shells, which might have formed owing to the high osmotic pressure inside the hollow spheres induced by dissociation of the core.

### COMPLEXATION OF PREFORMED CORE–SHELL LATEX PARTICLES

Core–shell particles of PSC complexes have also been made from preformed latex particles.<sup>[24]</sup> For this purpose core–shell latex particles with a polystyrene core and a poly(ethylene oxide) shell were synthesized by cross-linking emulsion polymerization of styrene, using a PEO macroinitiator system. Subsequent sulfonation of the PS core resulted in particles with a polyelectrolyte core of poly(styrene sulfonate) surrounded by a PEO corona (PEO-*b*-PSS). Complexation with tetraalkylammonium surfactants [e.g., dodecyltrimethylammonium bromide (DOTAB)] induced microphase separation within the core. Hereby polymer latex particles with a mesostructured core and a diameter of about 400 nm were obtained (Fig. 3). By small-angle

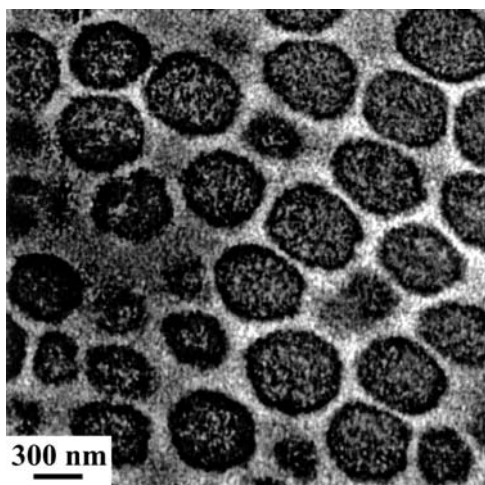


**Fig. 3** Micrograph of a microtomed sample of preformed latex particles with a PSS-TTAB core and a PEO shell. Source: Ref.<sup>[24]</sup>.

X-ray scattering, it was shown that the characteristic length of the formed core mesophase varied between 2 and 4 nm and increased with increasing chain length of the cationic surfactant.

### CONCLUSION

Complexation of block ionomers, polyampholytes, or preformed core–shell lattices enables the synthesis of well-defined, monodisperse PSC nanoparticles. Depending on the particular system, these nanoparticles form dispersions in water or organic solvents. In this way, particle applications of stoichiometric PSC have also been made possible.

Compared to bulk polyelectrolyte–surfactant complexes, the synthesis of PSC nanoparticles largely extends the opportunities of structuring nanoparticles. Morphological investigations indicate that self-assembly in these systems mainly depends on the block copolymer architecture. By using different types of polyion precursors, complexation with surfactants results in cylindrical, disk-shaped, prolate, spherical, and vesicular polymer structures. The obtained nanoparticles exhibit a long-range ordered inner mesostructure owing to microphase separation of the surfactant tails from the surfactant-neutralized polyion segments. Potential applications are especially drug and gene release systems.

### REFERENCES

1. Buchhammer, H.-M.; Petzold, G.; Lunkwitz, K. Nanoparticles based on polyelectrolyte complexes: effect of structure and net charge on the sorption capability for solvated organic molecules. *Colloid Polym. Sci.* **2000**, *278*, 841–847.
2. Zhou, S.Q.; Chu, B. Assembled materials: polyelectrolyte–surfactant complexes. *Adv. Mater.* **2000**, *12*, 545–556.
3. Thünemann, A.F. Polyelectrolyte–surfactant complexes (synthesis, structure and materials aspects). *Prog. Polym. Sci.* **2002**, *27*, 1473–1572.
4. Philipp, B.; Dawydoff, W.; Linow, K.-J. Polyelectrolyte complexes. *Z. Chem.* **1982**, *22*, 1
5. Jonsson, M.; Linse, P. Polyelectrolyte–macroion complexation. I. Effect of linear charge density, chain length, and macroion charge. *J. Chem. Phys.* **2001**, *115*, 3406–3418.
6. Macdonald, P.M.  $^2\text{H}$  NMR and polyelectrolyte–surfactant interactions: from micelles to monolayers to membranes. *Colloids Surf., A Physicochem. Eng. Asp.* **1999**, *147*, 115–131.
7. Antonietti, M.; Conrad, J.; Thünemann, A.F. Polyelectrolyte–surfactant complexes—a new type of solid, mesomorphous material. *Macromolecules* **1994**, *27*, 6007–6011.

8. Kabanov, A.V.; Vinogradov, S.V.; Suzdaltseva, Y.G.; Alakhov, V.Y. Water-soluble block polycations as carriers for oligonucleotide delivery. *Bioconjug. Chem.* **1995**, *6*, 639–643.
9. Kataoka, K.; Togawa, H.; Harada, A.; Yasugi, K.; Matsumoto, T.; Katayose, S. Spontaneous formation of polyion complex micelles with narrow distribution from antisense oligonucleotide and cationic block copolymer in physiological saline. *Macromolecules* **1996**, *29*, 8556–8557.
10. Cölfen, H. Double-hydrophilic block copolymers: synthesis and application as novel surfactants and crystal growth modifiers. *Macromol. Rapid Commun.* **2001**, *22*, 219–252.
11. Bronich, T.K.; Kabanov, A.V.; Kabanov, V.A.; Yu, K.; Eisenberg, A. Soluble complexes from poly(ethylene oxide)-block-polymethacrylate anions and *N*-alkylpyridinium cations. *Macromolecules* **1997**, *30*, 3519–3525.
12. Kabanov, A.V.; Bronich, T.K.; Kabanov, V.A.; Yu, K.; Eisenberg, A. Spontaneous formation of vesicles from complexes of block ionomers and surfactants. *J. Am. Chem. Soc.* **1998**, *120*, 9941–9942.
13. Kaler, E.W.; Murthy, A.K.; Rodriguez, B.E.; Zasadzinski, J.A. Spontaneous vesicle formation in aqueous mixtures of single-tailed surfactants. *Science* **1989**, *245*, 1371–1374.
14. Bronich, T.K.; Popov, A.M.; Eisenberg, A.; Kabanov, V.A.; Kabanov, A.V. Effects of block length and structure of surfactant on self-assembly and solution behavior of block ionomer complexes. *Langmuir* **2000**, *16*, 481–489.
15. Bronich, T.K.; Cherry, T.; Vinogradov, S.V.; Eisenberg, A.; Kabanov, V.A.; Kabanov, A.V. Self-assembly in mixtures of poly(ethylene oxide)-graft-poly(ethylene-imine) and alkyl sulfates. *Langmuir* **1998**, *14*, 6101–6106.
16. Thünemann, A.F.; General, S. Poly(ethylene oxide)-*b*-poly(ethylene imine) dodecanoate complexes: lamellar-within-lamellar morphologies and nanoparticles. *Macromolecules* **2001**, *34*, 6978–6984.
17. Thünemann, A.F.; Beyermann, J.; Kukulka, H. Poly(ethylene oxide)-*b*-poly(L-lysine) complexes with retinoic acid. *Macromolecules* **2000**, *33*, 5906–5911.
18. General, S.; Thünemann, A.F. pH-sensitive nanoparticles of poly(amino acid) dodecanoate complexes. *Int. J. Pharm.* **2001**, *230*, 11–24.
19. Lysenko, E.A.; Bronich, T.K.; Eisenberg, A.; Kabanov, V.A.; Kabanov, A.V. Block ionomer complexes from polystyrene-block-polyacrylate anions and *N*-cetylpyridinium cations. *Macromolecules* **1998**, *31*, 4511–4515.
20. Lysenko, E.A.; Bronich, T.K.; Eisenberg, A.; Kabanov, V.A.; Kabanov, A.V. Solution behavior and self-assembly of complexes from poly(*a*-methylstyrene)-block-poly(*N*-ethyl-4-vinylpyridinium) cations and aerosol OT anions. *Macromolecules* **1998**, *31*, 4516–4519.
21. Thünemann, A.F.; Wendler, U.; Jaeger, W.; Schnablegger, H. Nanoparticles of polyelectrolyte–surfactant complexes with perfluorododecanoic acid. *Langmuir* **2002**, *18*, 4500–4504.
22. Glatter, O. A new method for the evaluation of small-angle scattering data. *J. Appl. Crystallogr.* **1977**, *10*, 415–421.
23. General, S.; Rudloff, J.; Thünemann, A.F. Hollow nanoparticles via stepwise complexation and decomplexation of poly(ethylene imine). *Chem. Commun.* **2002**, *5*, 534–535.
24. Hentze, H.-P.; Khrenov, V.; Tauer, K. A new approach towards redispersable polyelectrolyte–surfactant complex nanoparticles. *Colloid Polym. Sci.* **2002**, *280*, 1021–1026.

# Polyion Complex Micelles

**Atsushi Harada**

*Department of Applied Chemistry, Graduate School of Engineering,  
Osaka Prefecture University, Osaka, Japan*

**Kazunori Kataoka**

*Department of Materials Science, Department of Materials Engineering,  
Tokyo, Japan*

## INTRODUCTION

The self-assembly of block copolymers has received considerable attention not only regarding its applications as functional materials, but also from a fundamental viewpoint. It is well known that the self-assemblies of block copolymers take various morphologies, including spherical particles, rod structures, and lamellar structures. Many studies on the block copolymer's self-assembly as spherical particles, i.e., polymeric micelles, which are characterized by a mesoscopic average diameter and a core–corona structure, have been reported. Recently, polyion complex (PIC) micelles were introduced as a new entity of polymeric micelles in aqueous medium. In this entry, we review the preparation and physicochemical properties of PIC micelles.

## PIC MICELLES

When water is used as the solvent, polymeric micelles are formed from hydrophilic–hydrophobic block copolymers driven by a hydrophobic interaction; in the formed micelles, a hydrophilic corona layer surrounds the core composed of hydrophobic segments. The formation of a corona of hydrophilic segments surrounding the core of the water-insoluble segments prevents progressive aggregation of the core and stabilizes the micelles of the block copolymers in the aqueous medium. The concept of polymeric micelle formation in an aqueous medium can be extended to include macromolecular association through a force other than hydrophobic interactions. We selected the electrostatic interaction in an aqueous medium and prepared a novel polymeric micelle system, the PIC micelle, from a pair of oppositely charged block copolymers (Fig. 1).

It is well known that an aqueous mixture of a pair of oppositely charged polyelectrolytes immediately forms visible aggregates, e.g., precipitates or coacervates, under an electrically neutral condition. In sharp contrast with this well-known phenomenon, a mixture of a pair of oppositely charged block copolymers with poly(ethylene glycol) (PEG) segments, i.e., PEG–poly( $\alpha,\beta$ -aspartic acid) block copolymer (PEG–PAA) with the PEG–poly(L-lysine) block copolymer (PEG–PLL) exhibits no precipitation even at a mixing ratio corresponding to electrical neutrality, and remains permanently transparent.<sup>[1]</sup> This is because of the formation of associates with a mesoscopic size range. The size of the formed associates is constant over a wide range of concentrations up to 1.0 wt%, and the associates also have a very small absolute zeta-potential value, suggesting that the PEG blocks effectively stabilizes the PIC core composed of PAA and PLL segments. In addition, the formed associates have an extremely narrow size distribution, which is comparable to that of natural viruses.<sup>[2]</sup> The associates have a core–corona architecture with a water-insoluble PIC formed from PAA and PLL segments, which are segregated as a core and separated from the aqueous medium by a corona composed of hydrophilic PEG segments. This type of associate was called a “polyion complex micelle” based on its structural similarity with a conventional block copolymer micelle.

The preparation procedure of PIC micelles by just mixing aqueous solutions containing oppositely charged components is simple and reproducible. It should be noted that in the case of polymeric micelles from block copolymers consisting of hydrophilic and hydrophobic segments, the exchange of solvent from the good solvent for both segments to water is usually needed to prepare the micelles with a well-defined core–corona structure; this can be done either by dialysis or by the drop-wise addition of water. The involvement

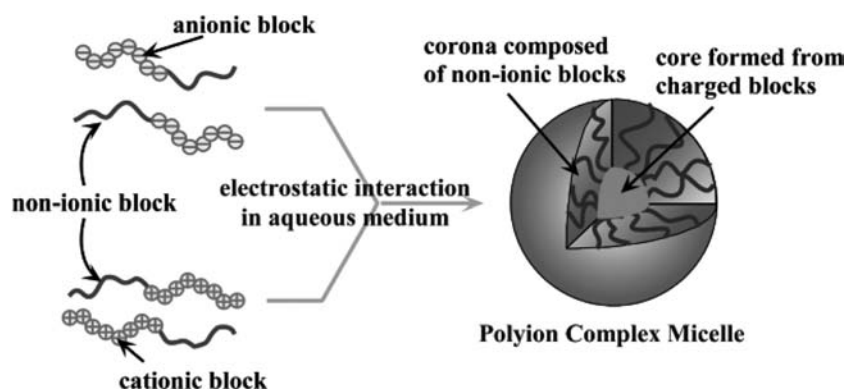


**Fig. 1** Concept of the formation of PIC micelles from a pair of oppositely charged block copolymers.

of the solvent exchange process, which is time dependent, often results in a broader distribution of the obtained micelles in terms of size and dispersion, especially for the kinetically frozen core segregation observed during the micellization of block copolymers with glassy segments. In contrast, the PIC micelle formation takes place in a buffered medium with a constant thermodynamic property. Consequently, the entire process of PIC micellization is thermodynamically regulated to give monodispersed micelles.

Polyion complex micelles were obtained from not only one pair of oppositely charged block copolymers, but also from a mixture of charged block copolymers with oppositely charged polyelectrolytes, including synthetic polymers, poly(amino acid)s, surfactants, enzymes, and DNA.<sup>[3–9]</sup> In this entry, we discuss the properties of the PIC micelles based mostly on our previous studies, in which PEG–PAA was used as an anionic block copolymer, and PEG–PLL and PLL were used as counter polymers. Because the complexation behavior and the properties of the polyion complexes generally depend on a specific combination in a pair of polyelectrolytes,<sup>[10]</sup> the properties of the PIC micelles might also depend on the combination selected for the pair of PIC core forming segments.

## PHYSICOCHEMICAL PROPERTIES OF PIC MICELLES<sup>[1,3,11]</sup>

### Hydrodynamic Radius of PIC Micelles Formed at Various Combinations

The PIC micelle solutions were prepared as follows: The PEG–PAA, PEG–PLL, and PLL block copolymers, in which the molecular weight of the PEG segment was fixed (5000 g/mol) and the polymerization degree (PD) of the charged segments was variable, were separately dissolved in sodium phosphate buffer (pH 7.4, 10 mM). The PEG–PAA solution was then added to the PEG–PLL or PLL solution to form

an electrically neutral mixture, corresponding to a (Asp):(Lys) = 1:1 ratio. The hydrodynamic radius of the PIC micelles prepared from various combinations of PEG–PAA and PEG–PLL or PLL was determined by dynamic light scattering (DLS) measurements. All combinations of PEG–PAA and PLL with varying lengths gave a sufficient scattering intensity to carry out the DLS measurements. However, for the PEG–PAA/PEG–PLL system, only a matched length pair gave an appreciable scattering intensity. It was significantly observed that there were lower scattering intensities for the combination of unmatched pairs compared with that for the matched combinations, indicating no formation of PIC micelles with a sufficiently large association number. As will be explained later, these length-unmatched pairs form associates with a minimal association number of PEG–PLL and PEG–PAA for charge compensation. All measurable combinations showed no angular dependence in the diffusion coefficient ( $D$ ), which is consistent with the assumed spherical shape. The formation of spherical micelles was also confirmed from the atomic force microscopy observations using mica as a support. Furthermore, the  $D$  values of the PIC micelles were independent of the concentration, suggesting the absence of secondary aggregates in the measured concentration region. Extrapolating the plots of the  $D$  values vs. concentration to zero concentration gave the  $D$  values at infinite dilution, from which the hydrodynamic radii ( $R_h$ ) were calculated using the Stokes–Einstein equation

$$R_h = k_b T / (6\pi\eta D)$$

where  $k_b$  is the Boltzmann constant,  $T$  is the absolute temperature, and  $\eta$  is the viscosity of the solvent. The  $R_h$  values are summarized in Table 1. The change in the  $R_h$  values with the length of the charged segments followed a different trend between PEG–PAA/PEG–PLL and PEG–PAA/PLL. In the case of PEG–PAA/PEG–PLL, the  $R_h$  values increased from 16 to 21 nm

**Table 1** Physicochemical properties of PIC micelles

PD of PAA	PD of PLL	$R_h$ (nm)	$R_g$ (m)	$R_g/R_h$	$M_{w,app}$ (g/mol)	Association number		
						PEG	PAA	PLL
<i>PEG-PAA/PEG-PLL</i>								
18	18	15.8	11.8	0.747	500,000	62	31	31
18	35				26,200	3	2	1
18	78				52,300	5	4	1
37	18				27,300	3	1	2
37	35	16.1	11.9	0.739	890,000	80	39	41
37	78				43,300	3	2	1
78	18				52,800	5	1	4
78	35				42,600	3	1	2
78	78	20.6	15.7	0.762	3,270,000	174	87	87
<i>PEG-PAA/PLL</i>								
18	20	24.3	18.2	0.749	3,430,000	235	235	212
18	45	24.8	18.7	0.754	3,390,000	237	237	95
18	82	24.6	18.5	0.752	3,410,000	236	236	52
37	20	24.4	18.4	0.754	4,570,000	258	258	477
37	45	24.7	18.7	0.757	4,490,000	253	253	208
37	82	24.5	18.6	0.759	4,510,000	255	255	117
78	20	24.2	18.0	0.744	7,470,000	307	307	1,197
78	45	24.5	18.6	0.759	7,540,000	303	303	525
78	82	24.3	18.2	0.749	7,510,000	304	304	289

with an increase in the length of the charged segments. On the other hand, the  $R_h$  values remained constant (24–25 nm) for the PEG-PAA/PLL regardless of the length of the charged segments.

### Critical Association Behavior

It is well known that polymeric micelles formed from block copolymers in selective solvents show a critical association behavior and have a characteristic critical micelle concentration. It was interesting to see whether the PIC micelles also show the critical association behavior. Also, the influence of the critical association concentration (CAC) should be taken into account for the detailed evaluation of the physicochemical properties of the PIC micelles based on static light scattering (SLS). The CAC was evaluated from the Debye plots of SLS expressed as the following equation, showing that the scattering intensity is a sensitive function of the weight-averaged molecular weight of the solute.<sup>[12]</sup>

$$KC/\Delta R(\theta) = 1/M_{w,app} + 2A_2C$$

where  $C$  is the concentration of the polymer,  $\Delta R(\theta)$  is the difference between the Rayleigh ratio of the

solution and that of the solvent,  $M_{w,app}$  is the apparent weight average molecular weight,  $A_2$  is the second virial coefficient, and  $K = [4\pi^2 n^2 (dn/dc)^2] / (N_A \lambda^4)$  ( $N_A$  is Avogadro's number). By monitoring the change in the  $KC/\Delta R(\theta)$  values with concentration, the weight-averaged molecular weight of the solute can be evaluated. In the case of the polymeric micelles having a critical association behavior, an increase in the  $KC/\Delta R(\theta)$  values with a decrease in the concentration, i.e., negative  $A_2$  values, should be observed in a concentration region below the CAC owing to a decrease in the averaged molecular weight.<sup>[12]</sup> All combinations of the PIC micelles followed a straight line with only a slight increase in the  $KC/\Delta R(\theta)$  values with an increase in the concentration, reflecting the  $A_2$  value of the PIC micelles, in the measured range from 0.01 to 4.0 mg/ml. There was no sign of a change in the  $KC/\Delta R(\theta)$  values even in the very diluted region, suggesting that the PIC micelles studied here are extremely stable upon dilution. This stability against the dilution might depend on the combination selected for the pair of core-forming polyelectrolyte segments. Indeed, a critical association behavior was observed for the micelle system prepared from PEG-PAA and the chicken egg white lysozyme.<sup>[7,13]</sup>



### Determination of $M_{w,app}$ and $R_g$

The  $M_{w,app}$  and  $R_g$  values were directly determined from the Zimm plots of SLS (Table 1). Notably, the  $M_{w,app}$  values of the PEG-PAA/PEG-PLL system were significantly different between the length-matched pairs and unmatched pairs of the charged segments. In the case of the matched pairs, the  $M_{w,app}$  values clearly depend on the length of the charged segments and increased with an increase in the length of the charged segment from 500,000 to 3,270,000 g/mol. This corresponds to association numbers for PEG-PAA and PEG-PLL from 31 to 87 as seen in Table 1. On the other hand, the length-unmatched pairs had extremely lower  $M_{w,app}$  values compared to the matched pairs. It is worthy to mention that in every unmatched combination of the block copolymers, a longer chain always had the association number of 1.0, indicating that the PEG-PAA/PEG-PLL system with an unmatched pair always forms a complex having a minimum association number to compensate their charges. These minimal charge-neutralized complexes are unable to grow further into the larger PIC micelles. The difference in the growth of the association induced an interesting feature of the PIC micelle formation, i.e., chain-length recognition, as will be introduced later.

As seen in Table 1, the  $M_{w,app}$  values of PEG-PAA/PLL were independent of the length of the PLL segment and dependent only on the length of the PAA segment in PEG-PAA. The trend of the change in the  $M_{w,app}$  values with the length of the charged segment of the block copolymer was similar between the PEG-PAA/PEG-PLL and PEG-PAA/PLL systems. The PEG-PAA/PLL system has a significantly higher  $M_{w,app}$  value than the PEG-PAA/PEG-PLL system. This significant difference in  $M_{w,app}$  reflects the difference in the association number, which is determined by the balance of several factors including the core radius, the PEG density at the core-corona interface, and the conformation of PEG in the corona.

The  $R_g$  values in Table 1 followed a similar trend in terms of the chain-length dependency on the  $R_h$  values. The  $R_g$  values increased with an increase in the length of the charged segment for the length-matched PEG-PAA/PEG-PLL system, whereas they remained at the constant value of 18.5 nm for the PEG-PAA/PLL system. The ratios of the  $R_g$  to  $R_h$  values ( $R_g/R_h$ ) are also summarized in Table 1. It is known that the  $R_g/R_h$  ratios for a hard sphere and a star molecule without a definite core are 0.775<sup>[14]</sup> and 0.707,<sup>[15]</sup> respectively. Assuming that the PIC micelles consist of a PIC core with a non-negligible size and a PEG corona layer with a density variation in the radial direction, it was reasonable to obtain  $R_g/R_h$  ratios of 0.739 to 0.762, which are between the values assumed for a star molecule and a hard sphere.

### Calculation of the Core Radius and the PEG Density at an Interface between the Core and Corona

The core radius was calculated from the density of charged segments (PAA and PLL) based on the assumption that the water volume in the PIC core may be negligible. In the former case, the core radius ( $R_{core}$ ) can be calculated from the densities of the charged segments by the following equation

$$R_{core} = [(3/4\pi)V_{core}]^{1/3} = [(3/4\pi) \cdot (M_{w,PAA}/\rho_{PAA} + M_{w,PLL}/\rho_{PLL})/N_A]^{1/3}$$

where  $V_{core}$  is the core volume of a PIC micelle, and  $M_{w,i}$  are the weight-averaged molecular weights of the PAA and PLL segments, respectively, calculated from the  $M_{w,app}$  values and the weight fractions of each segment in the PIC micelles, and the  $\rho_i$  values are the densities of PAA and PLL, respectively. The density of PAA and PLL were determined from pycnometric measurements to be 1.084 and 1.093 g/ml, respectively. The calculated  $R_{core}$  values are shown in Fig. 2. The end-to-end distances of a fully expanded model of the poly( $\alpha$ -amino acid) segments with PDs of 18, 36, and 78 were calculated to be 9.9, 19.8, and 42.1 nm, respectively.<sup>[16]</sup> The obtained  $R_{core}$  values in Fig. 2 suggest that the charged segments in the core of the PIC micelle might not have a fully elongated conformation. For both the PEG-PAA/PEG-PLL and the PEG-PAA/PLL systems, the  $R_{core}$  values clearly increased as the PD of the PAA segment in PEG-PAA increased. The PEG-PAA/PLL system has a larger  $R_{core}$  value than the PEG-PAA/PEG-PLL system when the PAA length in PEG-PAA is identical. This might be attributable to the difference between the degree of freedom of PEG-PLL and PLL during the formation of the PIC micelle with a core-corona architecture.

Furthermore, the PEG density at a core-corona interface ( $\Phi_{PEG}$ ) was determined from the association number of the PEG segment ( $N_{PEG}$ ) and the  $R_{core}$  value using the following equation

$$\Phi_{PEG} = N_{PEG}/(4\pi R_{core}^2)$$

The calculated  $\Phi_{PEG}$  values for various combinations are shown in Fig. 3. Interestingly, the  $\Phi_{PEG}$  value decreased with an increase in the length of the PAA segment in PEG-PAA, although other factors such as the  $R_h$ ,  $R_g$ ,  $M_{w,app}$ , and  $R_{core}$  values were significantly different between the PEG-PAA/PEG-PLL and PEG-PAA/PLL systems. This strongly indicates that the  $\Phi_{PEG}$  value may be a crucial factor for determining the association process of the PIC micelles. The

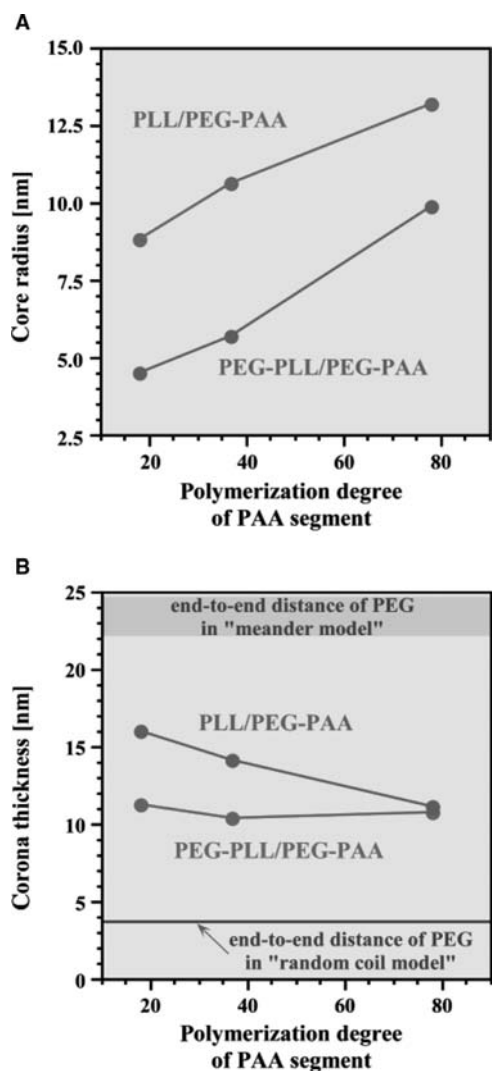


**Fig. 2** Change in core radius and corona thickness with an increase in the PD of PAA segment in PEG-PAA.

$\Phi_{\text{PEG}}$  values decreased from 0.25 to 0.14 chain/nm<sup>2</sup> with an increase in the length of the PAA segments as shown in Fig. 3.

The conformation of the PEG segments in the corona layer might also influence the properties of the PIC micelles. To evaluate the change in the PEG conformation, the corona thickness ( $R_{\text{corona}}$ ) was calculated using the following equation

$$R_{\text{corona}} = R_{\text{h}} - R_{\text{core}}$$

The calculated  $R_{\text{corona}}$  values are also shown in Fig. 2. There were different trends for the change in the  $R_{\text{corona}}$  values between the PEG-PAA/PEG-PLL and PEG-PAA/PLL systems. The  $R_{\text{corona}}$  of PEG-PAA/PLL was dependent on the length of the PAA segments and decreased with an increase in the length

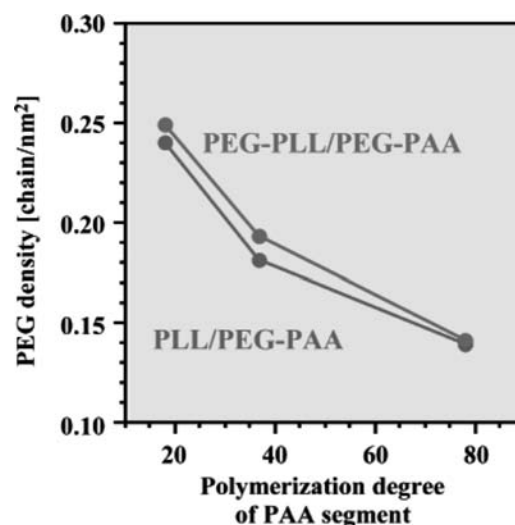


**Fig. 3** PEG density at core-corona interface.

of the PAA segments, although the  $R_{\text{corona}}$  of PEG-PAA/PEG-PLL remained constant in spite of any change in the  $\Phi_{\text{PEG}}$  values with the PD of the PAA segment. The corona thickness may be determined from the balance between the  $\Phi_{\text{PEG}}$  and the  $R_{\text{core}}$  values related to the curvature of the core. An increase in the  $\Phi_{\text{PEG}}$  and the  $R_{\text{core}}$  values oppositely influence the conformation of the PEG segments. Higher  $\Phi_{\text{PEG}}$  values induce a more elongated conformation to prevent the overlap of each PEG segment. On the other hand, a decrease in the  $R_{\text{core}}$  results in an increase in the curvature, allowing the PEG density in the corona layer to effectively decrease in the radial direction. For both the PEG-PAA/PEG-PLL and the PEG-PAA/PLL systems, a decrease in the length of the PAA segment in PEG-PAA results in the increased  $\Phi_{\text{PEG}}$  value and the decreased  $R_{\text{core}}$  value. Consequently, the opposite effects of the chain elongation and relaxation concomitantly work for the PEG segments. However, the change in the  $R_{\text{core}}$  values with the length of the charged segment of the block copolymer is more drastic for the PEG-PAA/PEG-PLL system than for the PEG-PAA/PLL system regardless of a similar trend in  $\Phi_{\text{PEG}}$  for both systems. For the PEG-PAA/PEG-PLL system, the effects of both an increased curvature because of the decreased  $R_{\text{core}}$  values and an increased  $\Phi_{\text{PEG}}$  value may compensate each other with a decrease in the length of the charged segment. On the other hand, in the case of the PEG-PAA/PLL system with a decreasing length of the PAA segment, the effect of an increased  $\Phi_{\text{PEG}}$  may be more significant than the effect of the increased curvature. Consequently, the  $R_{\text{corona}}$  value corresponding to the end-to-end distance of the PEG strands in the corona increased with a decrease in the length of the PAA segment in PEG-PAA.

## CHAIN-LENGTH RECOGNITION<sup>[17]</sup>

Molecular recognition and the resulting supramolecular assembly have received considerable attention in chemistry, biology, and applied fields. Carefully designed chemical architectures promote a precise molecular recognition, often leading to an assembly process. A common strategy to form supramolecular assemblies is the construction of spatially ordered networks of non-covalently bonded constituent molecules. Most of the studies in this area to date have focused on the design of spatially ordered structures where small differences in the steric factors of the constituent molecules significantly affect the thermodynamic stability and assembly of the system. Molecular recognition by length has been found to occur in the complexation process from the PEG-PAA and PEG-PLL systems.

The recognition of specific chain lengths upon the PIC micelle formation was directly confirmed by gel filtration chromatography (GFC) (Fig. 4). The gel filtration of the 1:1 mixture of PEG-PAA having different PAA lengths (the PDs of the PAA segments were 18 and 78, and code names were A-18 and A-78; based on content of Asp residue) provided a chromatogram with two clearly separated peaks corresponding to A-18 (elution volume: 17.4 ml) and A-78 (elution volume: 15.3 ml), respectively (Fig. 4A).

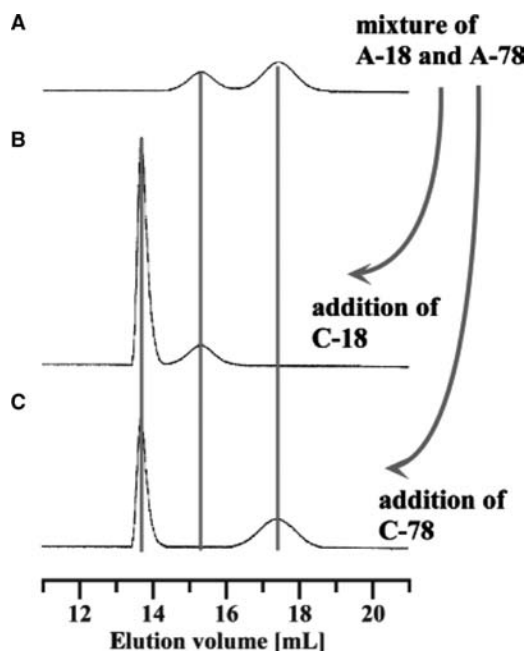


**Fig. 4** The GFC chromatograms for the mixture of PEG-PAA and PEG-PLL for varying combinations [(A) is the mixture of A-18 and A-78. (B) is PEG-PAA mixture (A) added C-18. (C) is PEG-PAA mixture (A) added C-78.] Source: From Ref.<sup>[17]</sup>.

A given amount of PEG-PLL having PLL with a PD of 18 (C-18) was then added to this mixture so as to neutralize 0.5 equivalents of Asp units in the solution. Complete disappearance of the A-18 peak from the chromatogram was observed, with the remaining A-78 peak totally intact without any change in the peak intensity (Fig. 4B). The peak corresponding to the PIC micelle was clearly observed in the exclusion volume of the chromatogram. Also, the chemical composition of the fractionated PIC micelle was determined by <sup>1</sup>H NMR in D<sub>2</sub>O containing 1.0 M NaCl, and the molar ratios for the Asp and Lys residues ([Asp]/[Lys]) in the PIC micelles were determined to be 1.0, and the observed ratio of PEG to the Asp and Lys residues was consistent with the calculated ratio assuming that the micelle exclusively includes the paired A-18 and C-18. Furthermore, the addition of PEG-PLL having PLL with a PD of 78 (C-78) to the mixture of A-18 and A-78 results in complete selection of A-78 as shown in Fig. 4C. The NMR analysis of the micelle fraction also revealed that the PIC micelle formation exclusively involves only A-78 and C-78. Thus, a pair of oppositely charged block

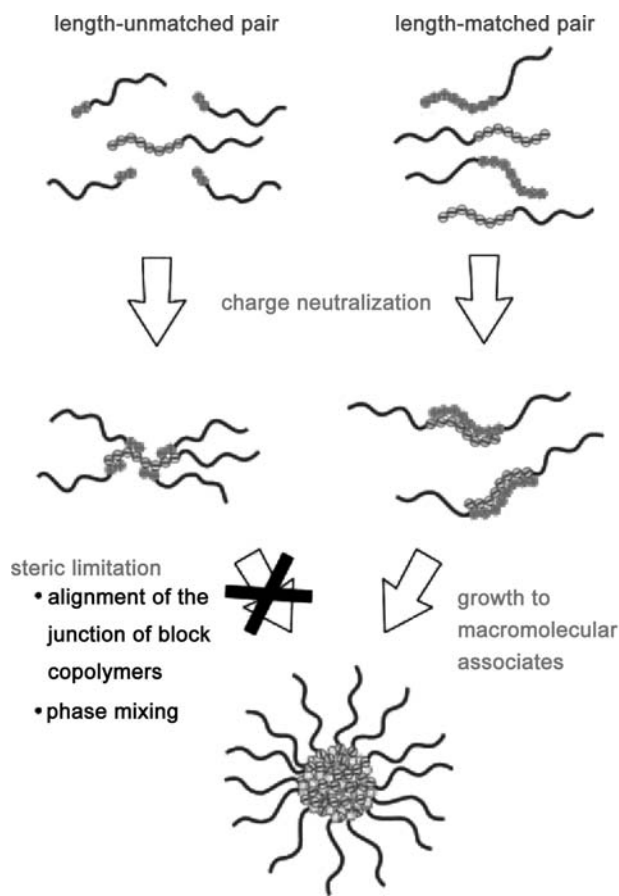


**Fig. 5** Schematic model for chain-length dependent recognition through the formation of PIC micelles. Source: From Ref.<sup>[17]</sup>.

copolymers exclusively selects matching partners with the same length of charged segments upon micellization.

As described above, the  $M_{w,app}$  values were quite different between the length-matched pairs and unmatched pairs of PEG–PAA/PEG–PLL. Although the matched pairs of PEG–PAA and PEG–PLL formed core–corona type multimolecular assemblies, i.e., PIC micelles, the unmatched pairs of PEG–PAA and PEG–PLL showed the formation of minimal charge-neutralized polyion complexes that were unable to grow further into larger PIC micelles (Fig. 5). Polymer complexes formed between unmatched pairs should be less stable than those formed with matched pairs, and consequently, in the competitive condition of coexisting matched and unmatched pairs, only the matched pairs form bimolecular complexes that grow into PIC micelles. The remaining block copolymers of unmatched length are left in the isolated form.

The key determinant in this recognition process is the strict phase separation between the PEG corona and PIC core domain, requiring regular alignment of the molecular junctions between PEG and charged segments at the interface of the two domains. Requirements for charge stoichiometry (neutralization) in the core is another essential factor in this recognition process. This eventually determines the number ratio of the participating polyanions and polycations in the core and restricts the spatial arrangement of segments in the core.

## CONCLUSIONS

We reviewed the preparation and physicochemical properties of PIC micelles in an aqueous medium. We first reported PIC micelles as a novel polymeric micelle system in 1995, using a pair of oppositely charged block copolymers. Since then, the research on the physicochemical characteristics of the PIC micelles continued in several research groups. An interesting feature of the PIC micelles, chain-length recognition, was found through fundamental studies. The length-selection property demonstrated with these flexible ionomer polymer strands provides a new approach for controlling the supramolecular assembly. Furthermore, PIC micelles have received considerable attention not only from fundamental viewpoints, but also in applied fields. In particular, the applications of PIC micelles in the biomedical field, including non-viral gene vectors have been previously reviewed.<sup>[12]</sup> Research continues on preparation and characterization of PIC micelles obtained from various combinations of polyelectrolytes.

## REFERENCES

1. Harada, A.; Kataoka, K. Formation of polyion complex micelles in an aqueous milieu from a pair of oppositely charged block copolymers with poly(ethylene glycol) segments. *Macromolecules* **1995**, *28*, 5294–5299.
2. Harada, A.; Kataoka, K. Polyion complex micelles with core-shell structure: their physicochemical properties and utilities as functional materials. *Macromolecular Symposia* **2001**, *172*, 1–9.
3. Harada, A.; Kataoka, K. Formation of stable and monodisperse polyion complex micelles in aqueous medium from poly(L-lysine) and poly(ethylene glycol)-poly(aspartic acid) block copolymer. *J. Macromol. Soc. Pure Appl. Chem.* **1997**, *A34*, 2119–2133.
4. Kabanov, A.V.; Bronich, T.K.; Kabanov, V.A.; Yu, K.; Eisenberg, A. Soluble stoichiometric complexes from poly(*N*-ethyl-4-vinylpyridinium) cations and poly(ethylene oxide)-*block*-polymethacrylate anions. *Macromolecules* **1996**, *29*, 6797–6802.
5. Bronich, T.K.; Kabanov, A.V.; Kabanov, V.A.; Yu, K.; Eisenberg, A. Soluble complexes from poly(ethylene oxide)-*block*-polymethacrylate anions and *N*-alkylpyridinium cations. *Macromolecules* **1997**, *30*, 3519–3525.
6. Gohy, J.-F.; Varshney, S.K.; Antoun, S.; Jerome, R. Water-soluble complexes formed by sodium poly(4-styrenesulfonate) and a poly(2-vinylpyridinium)-*block*-poly(ethyleneoxide) copolymer. *Macromolecules* **2000**, *33*, 9298–9305.
7. Harada, A.; Kataoka, K. Novel polyion complex micelles entrapping enzyme molecules in the core: preparation of narrowly-distributed micelles from lysozyme and poly(ethylene glycol)-poly(aspartic acid) block copolymer in aqueous medium. *Macromolecules* **1998**, *31*, 288–294.
8. Kataoka, K.; Togawa, H.; Harada, A.; Yasugi, K.; Matsumoto, T.; Katayose, S. Spontaneous formation of polyion complex micelles with narrow distribution from antisense oligonucleotide and cationic block copolymer in physiological saline. *Macromolecules* **1996**, *29*, 8556–8557.
9. Katayose, S.; Kataoka, K. Water-soluble polyion complex associates of DNA and poly(ethylene glycol)-P(L-lysine) block copolymer. *Bioconjugate Chem.* **1997**, *8*, 702–707.
10. Kabanov, V.A.; Zezin, A.B. Water-soluble nonstoichiometric polyelectrolyte complexes: a new class of synthetic polyelectrolytes. *Sov. Sci. Rev. Sect. B* **1982**, *4*, 207–282.
11. Harada, A.; Kataoka, K. Effect of charged segment length on physicochemical properties of core-shell type polyion complex micelles from block ionomers. *Macromolecules* **2003**, *36*, 4995–5001.
12. Khougaz, K.; Gao, Z.; Eisenberg, A. Determination of the critical micelle concentration of block copolymer micelles by static light scattering. *Macromolecules* **1994**, *27*, 6341–6346.
13. Harada, A.; Kataoka, K. Novel polyion complex micelles entrapping enzyme molecules in the core. 2. Characterization of the micelles prepared at

- nonstoichiometric mixing ratios. *Langmuir* **1999**, *15*, 4208–4212.
14. Douglas, J.K.; Roovers, J.; Freed, K.F. Characterization of branching architecture through “universal” ratios of polymer solution properties. *Macromolecules* **1990**, *23*, 4168–4180.
  15. Vagberg, L.J.M.; Cogan, K.A.; Gast, A.P. Light-scattering study of starlike polymeric micelles. *Macromolecules* **1991**, *24*, 1670–1677.
  16. Pauling, L.; Corey, R.B. Configurations of polypeptide chains with favored orientations around single bonds: two new pleated sheets. *Proc. Natl. Acad. Sci. USA* **1951**, *37*, 729–740.
  17. Harada, A.; Kataoka, K. Chain length recognition: Core-shell supramolecular assembly from oppositely charged block copolymers. *Science* **1999**, *283*, 65–67.
  18. Kataoka, K.; Harada, A.; Nagasaki, Y. Block copolymer micelles for drug delivery: design, characterization and biological significance. *Adv. Drug Delivery Rev.* **2001**, *47*, 113–131.
  19. Kakizawa, Y.; Kataoka, K. Block copolymer micelles for delivery of gene and related compounds. *Adv. Drug Delivery Rev.* **2002**, *54*, 203–222.
  20. Kabanov, A.V.; Kabanov, V.A. Interpolyelectrolyte and block ionomer complexes for gene delivery: physico-chemical aspects. *Adv. Drug Delivery Rev.* **1998**, *30*, 49–60.

# Polymer–Clay Nanocomposites and Polymer Brushes

**Xiaowu Fan**

**Chuanjun Xia**

*Department of Chemistry, University of Alabama at Birmingham, Birmingham, Alabama, U.S.A.*

**Rigoberto C. Advincula**

*Department of Chemistry, University of Alabama at Birmingham, Birmingham, Alabama, U.S.A., and Department of Chemistry, University of Houston, Houston, Texas, U.S.A.*

## INTRODUCTION

This entry summarizes the recent advances in the synthesis of polymer–clay nanocomposite materials and polymer brushes on clay surfaces with the focus on the in situ polymerization method. This new type of composite materials is based on a wide range of polymers as the matrix and layered silicate clays as the reinforcing filler. Its advantages, structures, and synthesis routes as well as the special properties of layered silicate are briefly introduced. Among various synthesis methods including exfoliation–adsorption, melt intercalation, and in situ polymerization, detailed discussions are focused on the in situ polymerization approach, which is then categorized by the polymerization mechanism employed. A comprehensive coverage is given to the in situ free radical polymerization method, including free radical polymerization with original clay, organoclay modified with non-reactive ammonium cations or polymerizable surfactants, and clay intercalated with cationic initiator derivatives, i.e., the surface-initiated polymerization strategy. As different strategies applied by various studies are compared, the emphasis of the discussion is placed on the synthesis scheme and the resulting structure of the nanocomposites. Short discussions on polymer brushes and in situ living polymerization methods on clay particle surfaces are offered because of the limited number of related publications. From the standpoint of the category of polymeric materials, this review is primarily based on thermoplastic polymers that can be produced by polymerizing their vinyl monomers. Other materials from other in situ polymerization mechanisms, such as ring opening polymerization, are briefly introduced at the end of this entry.

## BACKGROUND

Polymer–clay nanocomposite (PCN) materials fall into the category of organic–inorganic hybrids consisting of organic polymers as the matrix and inorganic clay minerals as the reinforcing filler. The unique characteristics of PCN materials lie in the nanometer-scale mixing of the two components and the molecular-level interactions between them. They have a wide variety of highly improved mechanical, thermal, and barrier properties as compared with those of pure polymers and their macroscale counterparts, which was demonstrated in the seminal work on nylon 6-clay hybrids (NCHs) by Toyota researchers in the early 1990s (Table 1).<sup>[1–4]</sup>

### Properties of Layered Silicates

Polymer–clay nanocomposite materials are also usually referred to as polymer-layered silicate (PLS) nanocomposites because the inorganic fillers used are mostly natural or synthetic silicate materials such as montmorillonite, hectorite, laponite, fluorohectorite, etc. They possess a unique layered morphology of ordered stacks of quasi two-dimensional silicate sheets whose dimensions are about 1 nm in thickness and a few hundred nanometers in width and length. As illustrated in Fig. 1, the crystallographic structure in one single layer consists of an edge-shared octahedral sheet of alumina or magnesia sandwiched between two tetrahedral silica sheets. Metal ions such as Na<sup>+</sup>, Li<sup>+</sup>, and Ca<sup>2+</sup> usually occupy the interlayer spacings/galleries to counterbalance the negative charges in the anionic lattice, which are generated by the isomorphous cation substitution within the layers.<sup>[5]</sup> The metal ions inside



**Table 1** Property comparison of NCH, NCC, and pure Nylon 6

Specimen (montmorillonite wt.%)	Tensile strength (MPa)	Charpy impact strength (MPa)	HDT <sup>a</sup> at 18.5 kg/cm <sup>2</sup> (°C)	Rate of water adsorption at 23°C, 1 day (%)
NCH <sup>b</sup> (4.2)	81	2.8	145	0.51
NCC <sup>c</sup> (5.0)	64	2.2	89	0.90
Nylon 6 (0)	72	2.3	65	0.87

<sup>a</sup>Heat distortion temperature (HDT).

<sup>b</sup>Nanoscale nylon 6-clay hybrid (NCH).

<sup>c</sup>Macroscale nylon 6-clay composite (NCC).

Source: Presented in Ref.<sup>[1]</sup>.

the silicate layers can be replaced by various organic cations such as alkylammonium by the cation exchange process, forming the “organically modified” layered silicate (OLS, also referred to as organoclay or organophilic clay). The exchangeable cations and layered morphology of these silicate clays lead to their two important physical properties: cation exchange capacity (CEC, often measured in the unit of meq/100 g, i.e., milliequivalents per 100 g) and specific surface area. For example, the specific area of montmorillonite clay has a range of 700–800 m<sup>2</sup>/g and its CEC varies from 80 to 150 meq/100 g.

### Structures of Polymer–Clay Nanocomposite Materials

Beyond traditional phase-separated macroscale composites, PCN materials can be structurally characterized into two categories in terms of their different

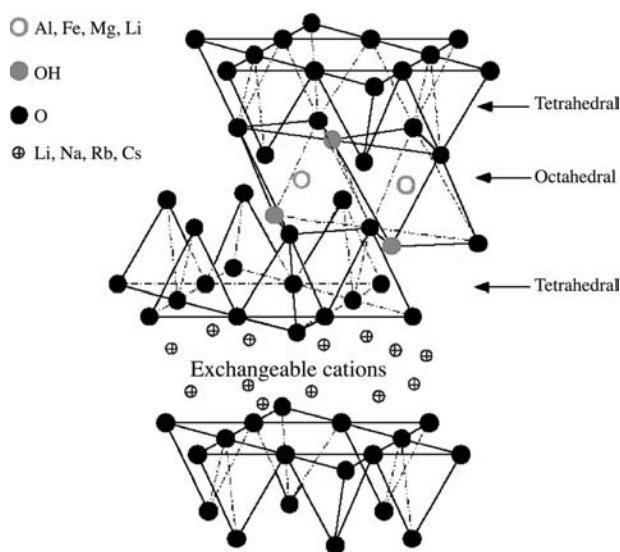


**Fig. 1.** Illustration of the structure of layered silicates. Source: From Ref.<sup>[5]</sup>. © 2003 Springer-Verlag GmbH & Co.KG.

microstructures resulting from different degrees of homogeneity between the organic and inorganic components:<sup>[6,7]</sup> 1) *Intercalated*, in which extended polymer chains are inserted between the clay layers, leading to an ordered multilayer morphology of alternating polymer/clay layers. As a result, the *d* spacing of the clay particle stacks is usually increased; 2) *exfoliated/delaminated*, in which the silicate layers are exfoliated into discrete sheets and uniformly dispersed in a continuous polymer matrix. This structure gives rise to a complete loss of the structural registry of the clay layers. Because of greater phase homogeneity with the latter, the exfoliated structure is more effective in improving the properties of the polymer, especially at very low clay loading. X-ray diffraction (XRD) *d*-spacing measurement and transmission electron microscopy (TEM) observation are two commonly used and complementary spectroscopic and microscopic tools to characterize and differentiate these microstructures. In addition to the two well-defined structures, intermediate structures comprising both intercalated and exfoliated domains are also observed. For the PCN samples of this mixed structure, the XRD peaks are often broadened and TEM analysis is imperative to characterize the overall structure.<sup>[8]</sup>

### Preparation Methods of Polymer–Clay Nanocomposite Materials

There are different numbers of synthetic routes toward PCN materials as classified by previous review articles.<sup>[9,10]</sup> The three primary methods are as follows:

- **Exfoliation–adsorption:** This generally involves the exfoliation of clay in a proper solvent and the adsorption of a soluble polymer to the clay surfaces. Polymer–clay nanocomposite materials, especially those based on polymers with high hydrophilicity, such as poly(vinyl alcohol), poly(ethylene oxide), and poly(acrylic acid), can be produced.<sup>[11,12]</sup> However, the main drawback is that a suitable solvent to promote compatibility of the inorganic clay and organic polymers is not always available.

- Melt intercalation: This is a simple mix-and-heat process, in which the layered silicate, usually organically modified, is mixed with the polymer matrix in the molten state. As compared with exfoliation–adsorption method, it is a versatile and green approach as a wide variety of polymers can be applied and no solvents are needed.<sup>[13–16]</sup> It also provides a model system in which the behavior of confined polymers can be studied.<sup>[17–22]</sup> Nonetheless, the ideal exfoliated structure is not always achieved.
- In situ polymerization: Monomers/comonomers are polymerized with the presence of original/modified clay via different polymerization mechanisms. This is also often referred to as intercalative or interlamellar polymerization, in which the chain growth is expected to be inside the galleries of the layered silicate. The advantage of this method is that as the polymerization inside the galleries progresses, the clay particles will be gradually swollen and ultimately exfoliated into discrete layers. As a result, this approach can more likely lead to PCN materials with a delaminated structure.

In this entry, we would like to focus on the strategy of in situ polymerization toward polymer brushes on clay particle surfaces and PCN materials. Details and characteristics of other methods such as template synthesis<sup>[23]</sup> and even a “general approach”<sup>[24]</sup> to PCN materials can be found in their respective reviews/reports and will not be discussed in this entry.

### Polymer Brushes on Clay Surfaces

Polymer brushes are defined as an assembly of polymer chains that are immobilized at one end to a surface by tethering, which is sufficiently dense so that the chains are forced to stretch away from the surface as a result of interchain repulsion.<sup>[25]</sup> Because of the layered morphology and negative surface charges, polymer chains that are ionically bound to clay surfaces can also be considered as polymer brushes if the surface charge density of the clay substrate is high enough so that the average distance between anionic sites is smaller than the radius of gyration of a polymer. They can exist in two different geometries. One is that the polymer brushes can be formed in bulk either by physisorption of one-end-charged polymers as described in the *exfoliation–adsorption* method (grafting-to) or by in situ polymerization using cationic monomer/initiator derivatives (grafting-from). Another is that the brushes can be grafted to/from a flat layer of clay particles on planar substrates prepared by the self-assembled monolayer (SAM) technique or the alternate polyelectrolyte deposition (APD) process.<sup>[26–28]</sup> The former

case has been extensively investigated in the form of PCN materials while there are few studies in the literature about the latter.

### METHODS OF IN SITU POLYMERIZATION

The history of in situ polymerizations with clay can be traced back to the 1960s. The type of clay involved was original clay or organoclay modified with organic cations with various functionalities. The form of polymerization ranged from bulk, solution, suspension, and emulsion. The PCN products could be thermoplastics or thermosets. Here we categorize the following in situ methods based on their individual polymerization mechanism. The emphasis of the discussion is focused on the synthetic routes and structures of the PCN materials rather than to their practical properties. It should also be noted that there is another case of in situ polymerization, in which clay minerals, especially when exchanged with transition metal cations, can also initiate/catalyze the polymerization of different monomers,<sup>[29,30]</sup> but this will not be discussed here.

#### In Situ Free Radical Polymerization

Many important thermoplastic polymers, such as polystyrene (PS) and poly(methyl methacrylate) (PMMA), can be produced by free radical polymerization mechanism using their vinyl monomers. The following discussion is focused on the PCN materials based on these two typical polymers, and in situ free radical methods are subcategorized by the initiators used.

##### Intercalative free radical polymerization using traditional initiators

Early studies on in situ free radical polymerization were focused on mixing vinyl monomers with unmodified/modified clay followed by polymerization with traditional azo, peroxide, or persulfate initiators. In the mid-1960s, in situ free radical polymerization with pristine clays was demonstrated by Blumstein<sup>[31]</sup> and Solomon and Rosser.<sup>[32]</sup> The effects of different types of clay on polymerization mechanisms and the interactions between different monomers and clay were studied. Lee and Jang<sup>[33]</sup> obtained PMMA–clay materials of intercalated structure through emulsion polymerization with original clay using potassium persulfate as the initiator. Later, they used the same method to prepare PS–clay nanocomposites. As compared with their earlier PMMA materials, the decreased *d* spacings of the intercalated PS composites were attributed to stronger hydrophobicity of the styrene monomer,

which had less compatibility to penetrate into the galleries of the hydrophilic clay.<sup>[34]</sup> Exfoliated PMMA nanocomposites was accomplished by Bandyopadhyay, Giannelis, and Hsieh<sup>[35]</sup> using different clays (montmorillonite and fluorohectorite) but similar initiator and emulsion methods. Using the same initiator, suspension polymerizations of MMA initiated with the presence of montmorillonite clay were investigated by Al-Esaimi,<sup>[36]</sup> but structural information of the composites was not reported. Structures from direct PMMA melt intercalation and in situ polymerization with alkylammonium-modified clay and 2,2'-azobisisobutyronitrile (AIBN) initiator were compared by Tabtiang, Lumlong, and Venables<sup>[37]</sup> and a finer degree of clay dispersion was observed for the latter. Exfoliated PS–clay nanocomposites were achieved by Chen, Ma, and Qi<sup>[38]</sup> using emulsion polymerization with ammonium persulfate as the initiator and cetyltrimethylammonium as the organic modifier of the clay. Similarly, Okamoto et al.<sup>[39]</sup> synthesized partially exfoliated PMMA–clay materials and intercalated PS–clay composites by bulk polymerization with lipophilized smectic clays. Later, they studied the effects of the addition of a small amount of different polar comonomers (acrylate and acrylamide derivatives) on the structure and properties of the PMMA–clay composites.<sup>[40]</sup> Likewise, Dietsche et al.<sup>[41]</sup> found that the addition of a small amount of dodecylmethacrylate (LMA) comonomer as a compatibilizer with organoclay [modified by dioctadecyldimethylammonium (DOD) cation] could promote clay exfoliation in the poly(MMA-co-LMA) matrix. By bulk polymerizations with AIBN as the initiator, Doh and Cho<sup>[42]</sup> systematically investigated the effect of different organic modifiers on the structure and properties of PS–clay nanocomposites. Although exfoliated structure was not observed, one of the three PS–clay products exhibited better clay dispersion and thermal property. The authors ascribed it to the structural affinity between the styrene monomer and the benzyl unit in one of the three alkylammonium cations employed. From the discussions above, it can be concluded that in the in situ intercalative polymerization, the compatibility between the monomer/comonomer

and organic groups in the organoclay plays an important role in the structure and properties of PCN materials. Fig. 2 illustrates the preparation method used by Chen, Ma, and Qi<sup>[38]</sup> which can also be used to schematically generalize the concept of in situ intercalative polymerization with organoclay modified by ammonium cations. Other than homopolymers, PCNs based on copolymers such as poly(styrene-co-acrylonitrile) (SAN) were also prepared by in situ polymerization with pristine or modified clay, indicating the versatility of this strategy.<sup>[43,44]</sup>

In the studies cited above, the polymer chains are freely formed and are not bound to the clay surfaces, as can be seen in Fig. 2. The following discussion will introduce recent studies on the in situ polymerization with clay modified by polymerizable cations by which a portion of the polymer chains is end-tethered to the clay surfaces. With two kinds of modified clays functionalized by charged acrylate derivatives, Biasci et al.<sup>[45]</sup> achieved intercalated PMMA–clay nanocomposites by solution polymerization initiated by AIBN. Similarly and using the same initiator, intercalated PS–clay materials were synthesized by Akelah and Moet<sup>[46,47]</sup> through ion exchanging with a vinylbenzylammonium cation and subsequent in situ free radical polymerization of styrene. As a continuation of the previous work, Dietsche et al.<sup>[41]</sup> synthesized the poly(MMA-co-LMA) materials from organoclay modified by a reactive cation containing two MMA end units [bis(2-methacryloyloxyethyl)-methyl-n-dodecyl-ammonium (DMMA)]. As compared with the old PCNs from non-reactive cation DOD, unusual combination of high stiffness and high toughness was observed in the new nanocomposites and attributed to the surface attachment of the polymers through covalent bonding with the polymerizable DMMA.<sup>[48]</sup> Exfoliated PS–clay nanocomposites were achieved from in situ bulk polymerization by Fu and Qutubuddin.<sup>[49]</sup> In their studies, organophilic clay was prepared by the insertion of a polymerizable cationic surfactant vinylbenzyltrimethylammonium chloride (VDAC), which was then directly dispersed in monomer solution followed by initiation by AIBN. They believed that exfoliation resulted from the special

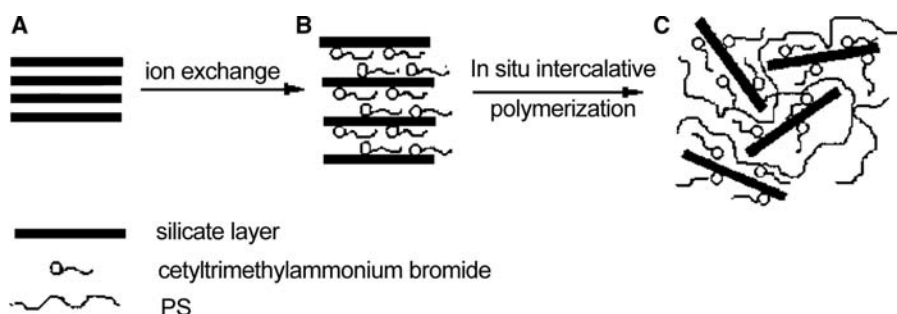


**Fig. 2** Schematic illustration of the preparation of PS–montmorillonite nanocomposite via in situ intercalative polymerization. (A) Original sodium montmorillonite. (B) Cetyltrimethylammonium bromide (CTAB) exchanged montmorillonite. (C) Exfoliated PS–montmorillonite nanocomposite. *Source:* From Ref.<sup>[38]</sup>. © 2003 Acta Materialia and Elsevier Science Inc. Ltd.

properties of the VDAC modifier: the reactivity of the vinylbenzyl group, the solubility in styrene monomer, and the better swelling ability for clay.<sup>[50]</sup> Their results were confirmed by Zhu et al.,<sup>[51]</sup> as essentially the same reactive modifier also resulted in exfoliated PS–clay nanocomposites. In their comparative studies using bulk polymerization and AIBN initiator but different cationic surfactants, better thermal stability was found in the organoclay modified by a phosphonium salt than in the other two modified by ammonium salts, which might be useful if high processing temperatures were required for the PCN materials. Similar results were recently observed by Yeh et al.<sup>[52]</sup> as they found the PMMA–clay nanocomposite from alkylphosphonium as the intercalating agent displayed higher glass transition temperature ( $T_g$ ) than that from conventional alkylammonium salt. Depending on the clay content, exfoliated, intercalated, and mixed intercalated–exfoliated structures were found in their PMMA materials via in situ solution polymerization with benzoyl peroxide (BPO) as the initiator. However, it should be noted that neither of the “onium” molecules contained polymerizable groups. Clay exfoliation in both PS<sup>[53]</sup> and PMMA–clay<sup>[54]</sup> nanocomposites was accomplished by Choi, Kim, and their coworkers through emulsion polymerizations with 2-acrylamido-2-methyl-1-propane-sulfonic acid (AMPS) as the reactive surfactant. They were able to obtain the end-tethered polymers by a reverse ion-exchange process. The copolymerization between AMPS and styrene was confirmed by NMR measurements. Likewise, Zeng and Lee<sup>[55]</sup> prepared exfoliated PS– and PMMA–clay materials by bulk polymerization with clay modified by an ammonium salt containing an MMA end unit. Furthermore, by investigating the effects of different initiators including BPO and AIBN, they also stressed that compatibility of the monomer, initiator, and organoclay could strongly influence the clay dispersion in the polymer matrix. Based on PS and PMMA, Wang et al.<sup>[56]</sup> comprehensively studied the methods for PCN materials including in situ bulk, solution, suspension, and emulsion polymerization as well as melt intercalation. The effects of different initiators and ammonium ions on the in situ polymerizations were also compared. They also found that clay exfoliation were improved by the polymerizable group in the organic modifier that could participate in the polymerization. Fig. 3 shows the synthetic route utilized by Akelah and Moet,<sup>[46]</sup> representing the scheme of tethering polymer chain to clay surfaces with cationic comonomer derivatives. Here the end-tethered chains can also be considered as polymer brushes formed in-bulk by the grafting-from approach.

From the previous discussions, it is obvious that surface-attached polymer chains through polymerizable modifiers can indeed improve clay particle

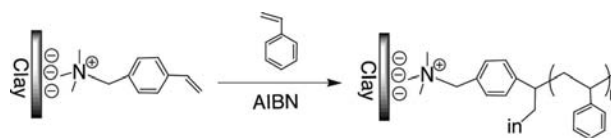


**Fig. 3** In situ polymerization scheme as employed in Ref.<sup>[46]</sup>. The free radical polymerization of styrene with clay modified by a cationic comonomer resulted in surface-bound polymer chains.

exfoliation as compared with non-reactive alkylammoniums. Besides PS and PMMA, this concept has also been demonstrated by other PCNs such as poly(acrylamide)<sup>[57]</sup> and poly(acrylonitrile)<sup>[58]</sup> via in situ polymerization using traditional free radical initiators.

It is worth mentioning that the coworkers of Dietsche further continued their previous studies<sup>[41,48]</sup> by utilizing protonated amine-terminated oligostyrene<sup>[59]</sup> and cyclic amidinium cation-terminated oligoMMA and oligostyrene<sup>[60]</sup> as organic modifiers of the clay, which was applied in the subsequent melt compounding/extrusion processes with different polymers including polystyrene, PMMA, and styrene–acrylonitrile copolymer. The cationic oligomers (number average molecular weight 3000 g/mol for amidine-terminated species and 5800 g/mol for amine-terminated species) were first synthesized by controlled free radical and anionic polymerization methods and then attached to clay surfaces by ion exchange processes. Unlike clays intercalated with various alkylammonium cations, XRD measurements were even unable to detect the significantly increased  $d$  spacings of the well-swollen organoclays inserted with the oligomeric cations. It has to be pointed out that the OLSs here are analogs to the PCNs prepared by the exfoliation–adsorption method, except that the organic components are oligomeric cations rather than water-soluble polymers. Furthermore, these end-tethered oligomers are similar to the polymer brushes on clay surfaces by the grafting-to strategy described before, except for their low molecular weight nature. Effective exfoliation was observed by scanning electron microscopy (SEM) of the PCN materials after melt intercalation. Interesting rheological and thermal properties were found to be related with the interactions among polymer matrix, oligomer brushes tethered on clay surfaces, and the clay particles themselves.<sup>[61]</sup> Citing amine-terminated oligostyrene by anionic polymerization as an example, their synthetic scheme is illustrated in Fig. 4.

#### Surface-initiated free radical polymerization using cationic initiator derivatives

As for in situ free radical polymerization with clay, polymerization initiator derivatives can also be

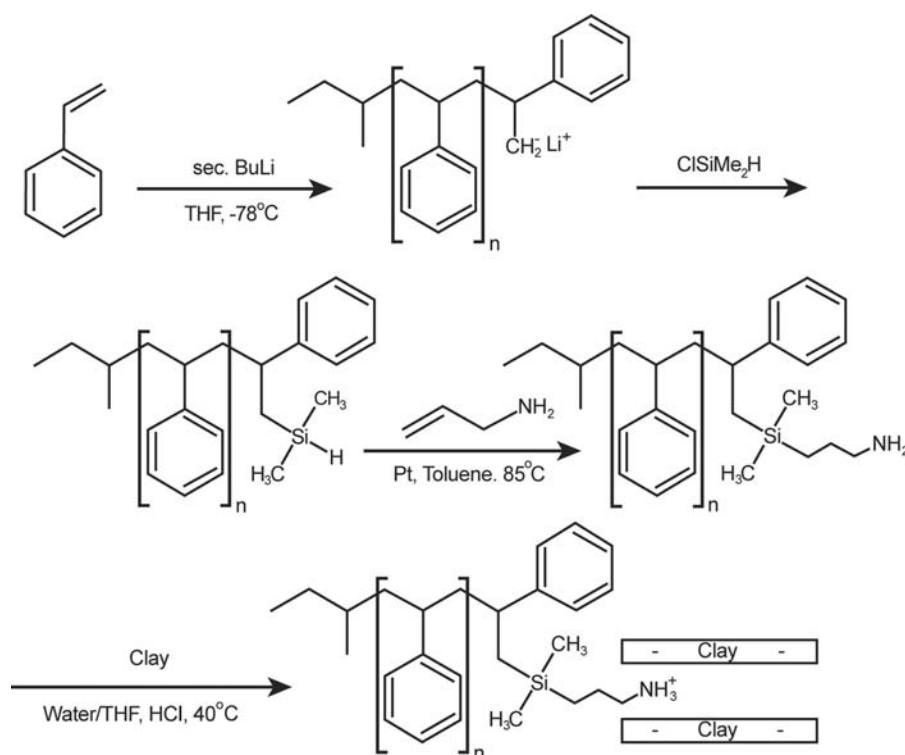


**Fig. 4** Synthesis of the oligostyrene and preparation of the organoclay. Source: From Ref.<sup>[59]</sup>. © 2003 Wiley-VCH Verlag GmbH.

inserted into clay particles' galleries instead of reactive monomer cations or non-reactive surfactants. In this case, the surface-attached initiator not only renders the clay organophilic but also provides the initiation functionality for the subsequent in situ polymerization. Because it is the surface-attached initiator that activates the polymerization process and the polymer chain actually propagates from the surface, this type of in situ polymerization is also called the surface-initiated polymerization (SIP). The advantage of in situ polymerization with the initiator-intercalated clay lies in a sound assumption that, as the bound polymer chains propagate, the ordered silicate layers can be gradually pushed apart and finally exfoliated in the polymer matrix. Furthermore, as compared with the polymerizable surfactant route discussed above, the SIP strategy can presumably generate more end-tethered polymer chains with greater length, which provide more efficiency in exfoliation. Free radical SIPs using different AIBN initiator variants were demonstrated on various surfaces including spherical silica gel particles,<sup>[62,63]</sup> planar SiO<sub>x</sub><sup>[64]</sup> and gold substrates,<sup>[65,66]</sup> etc., on which the initiators were immobilized using the SAM method through covalent bonding. As for SIPs from clay surfaces, the initiator must be rendered cationic for ionic bonding with clay surfaces. The bound polymer chains after SIP can be cleaved for analysis by a counter-ion-exchange process using an excessive amount of alkali compound with greater cationic strength such as lithium bromide.

2,2'-Azobis(isobutyramidine hydrochloride) (AIBA) is a water-soluble, commercially available, and bicationic azo compound that can be used as a surface-attached azo free radical initiator. In the mid-1960s, its feasibility was demonstrated by Dekking<sup>[67,68]</sup> through the SIPs of several vinyl monomers. By bulk and emulsion polymerization, the effects of different clays (kaolin, bentonite, and hectorite) on the kinetics of the attached initiator decomposition and the subsequent chain propagation were studied. Similarly, Meier et al.<sup>[69]</sup> also employed AIBA to polymerize styrene from high-surface-area mica powder and the SIP mechanism was investigated. Although high molecular weight grafted polymer was obtained, they argued that the surface initiation and chain propagation played a minor role in the formation of surface-attached polymers. Instead, bound chains were created by the reaction between free polymers formed in solution and the surface-bound products of AIBA decomposition. However, no structural information of the composite products was reported. Huang and Brittain,<sup>[70]</sup> employing the same AIBA initiator and suspension SIP, achieved PMMA–clay nanocomposites with exfoliated structure. For comparison, they also prepared PMMA materials based on non-reactive and polymerizable methacrylammonium-modified clays via in situ polymerization using traditional AIBN initiator. It was observed that exfoliated structure was achieved and preserved after melt processing for the nanocomposites from AIBA and methacrylammonium-modified

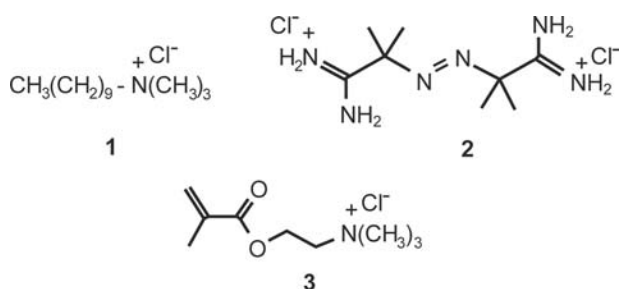


**Fig. 5** Structures of the three cations used to modify layered silicates. 1) An alkyl ammonium chloride salt; 2) the AIBA initiator; 3) a reactive surfactant containing a polymerizable MMA unit. *Source:* From Ref.<sup>[70]</sup>. © 2003 American Chemical Society.

clays. In contrast, alkylammonium organoclay yielded only the intercalated structure both before and after melt processing and an even greater degree of order after melt processing. Thus, the authors believed that the end-tethered polymer chains not only promoted clay particle exfoliation but also helped preserve the exfoliated structure at elevated temperature by hindering the aggregation of the silicate layers. Between the nanocomposites from SIP with AIBA and polymerizable cation with AIBN, better thermal stability was observed in the former. Fig. 5 shows the structures of their three cationic modifiers, which also clearly present the three foregoing concepts in OLS modifications.

We synthesized another water-soluble monocationic azo compound.<sup>[71]</sup> The advantage of this AIBN derivative is that, unlike AIBA, the positive charge at one end is pH independent, which can tolerate different polymerization conditions. In addition, the other alkyl end of the molecule can greatly enhance the homogeneity of clay-monomer/solvent mixture of the SIP system. It should also be pointed out that, other than bound polymers, free ones also form in bulk/solution resulting from the other unbound free radical after the decomposition of the azo group. Through solution SIP, this initiator was first used to graft polystyrene brushes from clay surfaces adsorbed by the SAM technique on planar substrates. Fig. 6 shows the structure of the initiator as well as the synthesis scheme of the polymer brush and the free polymer formation. By surface-sensitive characterizations including ellipsometry and surface plasmon spectroscopy (SPS), it was found that the average initiator graft density (on the order of 0.1–1 molecules/nm<sup>2</sup>) and polymer layer thickness on flat clay surfaces were much lower than those on flat SiO<sub>x</sub> substrates from which the initiator/polymer were grafted by covalent bonding (on the order of 2–3 molecules/nm<sup>2</sup> based on silane surface coupling).<sup>[72]</sup> The reason was believed to be that the charge density of clay surfaces was much lower than the density of the reactive sites of the SiO<sub>x</sub> substrates. Therefore the bound polymers grafted from clay particles existed in the morphology of “mushrooms” rather than “brushes.” It should be noted that the results

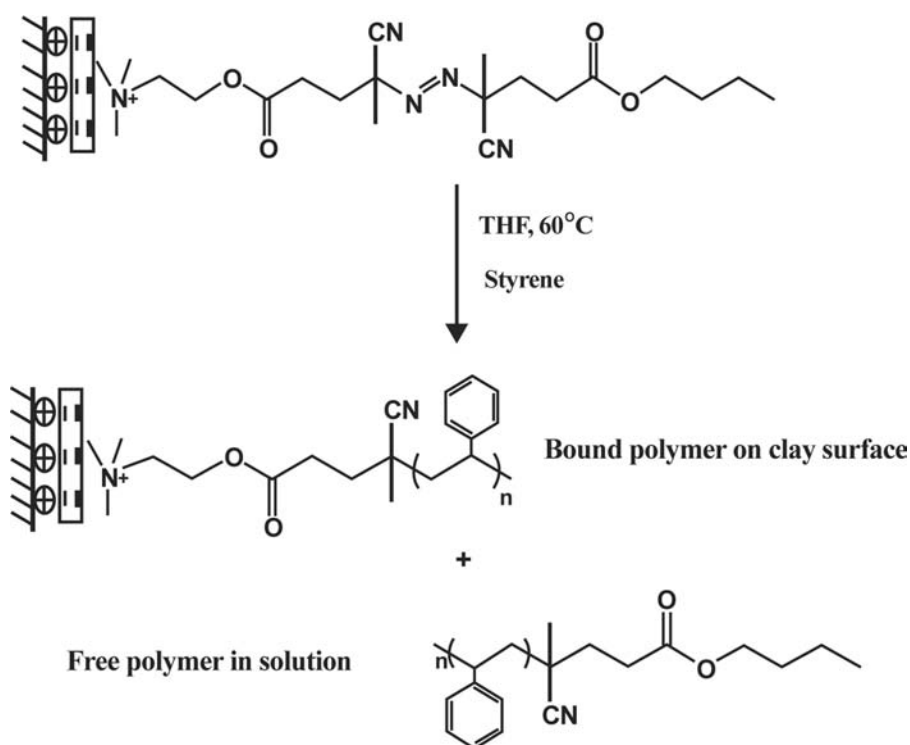


**Fig. 6** Illustration of polymer brushes grafted from clay particles adsorbed on flat substrates and free polymer formation. *Source:* From Ref.<sup>[71]</sup>. © 2003 American Chemical Society.



depend on the physical properties of a specific type of clay, i.e., its CEC and specific surface area. The graft density can be varied if another type of clay is applied.

We further synthesized another similar but bicationic initiator, which was compared with the monocationic one in terms of the structures of their modified clays and the polystyrene–clay nanocomposites from solution SIPs.<sup>[73]</sup> The structure of intercalated clays after ion exchange was first studied by XRD measurements. Despite the similar structure and chain length of the two molecules, lower  $d$  spacing and less degree of order were observed in the organoclay modified by the bicationic initiator. This result was attributed to the combination of the two attachment possibilities of the bicationic initiator: 1) The two cationic ends were attached to the same side of one clay particle and; 2) they were bound to two sides of two adjacent particles. As for the SIP products, it was found that the monocationic initiator-modified clay was more likely to produce exfoliated structure. It was also found that the molecular weights of bound polymers were lower than that of the free ones. The differences caused by the two initiators, including organophilicity of the modified clays, clay particle dispersibility during SIP, diffusion and addition kinetics of monomer, and chain transfer and termination possibilities, were discussed and compared.

Using the monocationic initiator, we also prepared PMMA–clay nanocomposites via bulk, suspension, and solution SIPs.<sup>[74]</sup> Exfoliated structure was achieved by solution and bulk methods while suspension polymerization yielded a mixed exfoliation–intercalation morphology. It was ascribed to the amphiphilic characteristic of the initiator-modified clay, which probably formed aggregation at the monomer–water interface during suspension SIP. Intriguing results such as the effect of the affinity between immobilized initiator and monomer on the product structure, molecular weights, and molecular weight distributions of free and bound polymers as shown by gel permeation chromatography (GPC) analysis, were also observed and discussed.<sup>[75]</sup> It should be noted that although the molecular weight of the bound polymer was lower

than that of the free one, it was still much higher as compared with that of the bound chains from the reactive surfactant approach, where only oligomers were obtained.<sup>[54]</sup> This proves the higher efficiency of producing long end-tethered chains in SIP methods than in the polymerizable modifier strategy. Fig. 6 can also be used to represent the synthesis scheme used here except that the monomer is MMA and the clay particle is not ionically adsorbed to a planar substrate.

## In Situ Living Polymerization

It is well known that living polymerization methods are capable of synthesizing homopolymers with narrow polydispersity and controllable molecular weight and copolymers with desired architecture. On the other hand, they generally require more demanding polymerization conditions than the ordinary free radical approach. As compared with the intensive studies on living polymerization from other surfaces with various geometry (Ref.<sup>[76]</sup> and references therein), there were just a few attempts to prepare polystyrene–clay materials through in situ surface-initiated living polymerization from clay surfaces.

### Living anionic surface initiated polymerization

We synthesized a cationic derivative of 1,1-diphenylethylene (DPE) to anionically polymerize styrene from clay surfaces.<sup>[77,78]</sup> 1,1-Diphenylethylene was first modified to be a water-soluble ammonium bromide salt and then intercalated into montmorillonite clay by ion exchange. The subsequent living anionic surface-initiated polymerization (LASIP) successfully yielded free and bound polystyrene with controllable molecular weight and narrow molecular weight distribution. However, the bound polymers had lower molecular weight than the free ones and only intercalated structure was obtained in the composite products. The authors believed that the dispersibility of intercalated clay and monomer diffusion kinetics in this heterogeneous polymerization system were critical

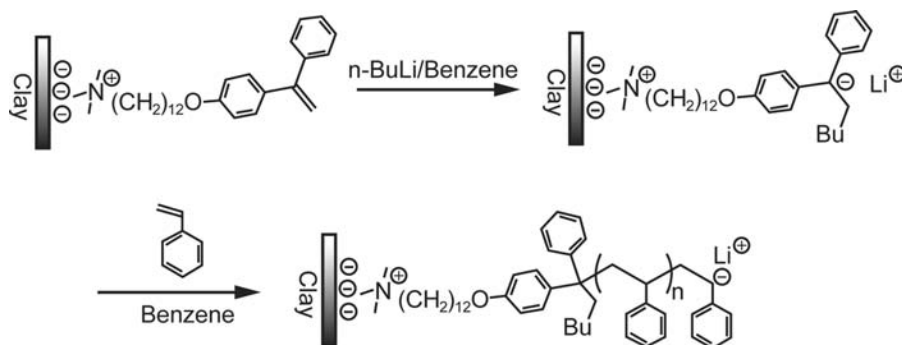


**Fig. 7** Schematic illustration of living anionic surface-initiated polymerization (LASIP) from layered clay particles. Source: From Ref.<sup>[78]</sup>. © 2003 American Chemical Society.

factors of the LASIP process. Fig. 7 shows the synthetic route.

### Living free radical polymerization

Exfoliated polystyrene–clay nanocomposites with controllable molecular weight were prepared by Weimer et al.<sup>[79]</sup> by intercalating an ammonium cation initiator containing a nitroxide moiety into the montmorillonite clay. The following living free radical polymerization (LFRP) protected by the nitroxyl group effectively produced polystyrene materials with narrow polydispersity and exfoliated structure. Moreover, while keeping the clay loading constant, they

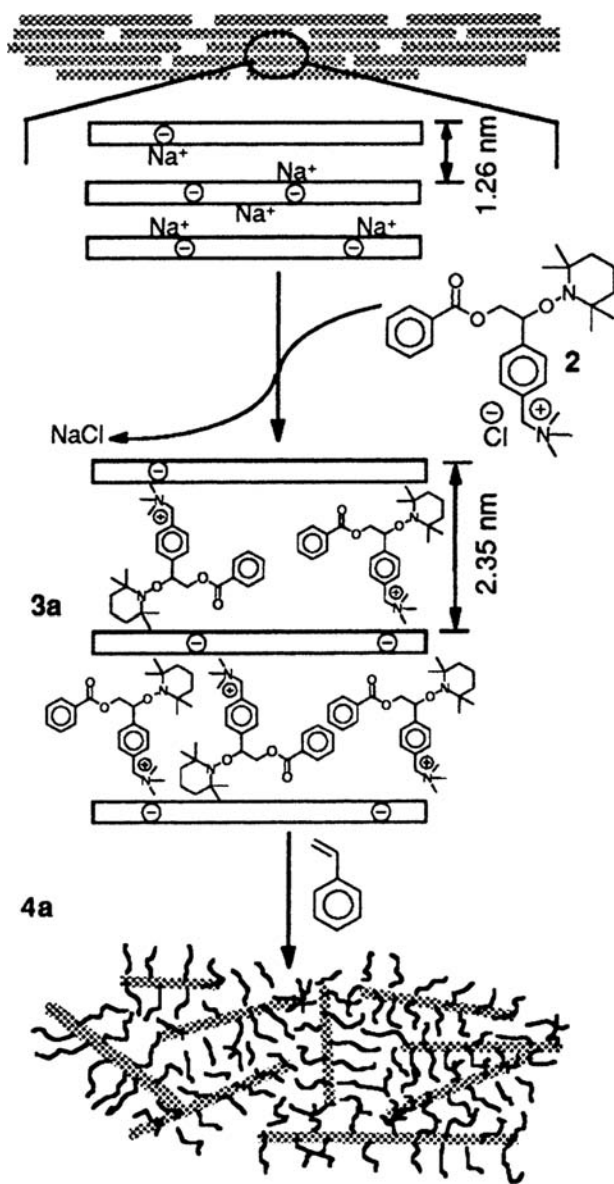


**Fig. 8** Exfoliated polystyrene–clay nanocomposites by living free radical polymerization. Source: From Ref.<sup>[79]</sup>. © 2003 American Chemical Society.

were able to control the molecular weight of the polymer matrix by varying the initiator concentration by cointercalating a non-initiating ammonium salt. The livingness of the reaction and block copolymerization viability was further confirmed by a successful effort of chain extension. It is worth mentioning that this is the first time that an exfoliated PCN material with controllable molecular weight has been achieved based on in situ polymerization with a vinyl monomer. Fig. 8 illustrates the synthesis scheme.

### Other In Situ Polymerization Methods

Other than thermoplastic polymers prepared by in situ addition polymerization of their vinyl monomers, there has been tremendous work on other polymeric materials by other polymerization mechanisms. In fact, early studies by Toyota scientists on nylon-based PCN materials demonstrated in situ ring opening polymerization of  $\epsilon$ -caprolactam with organoclays modified by protonated amino acids.<sup>[80–82]</sup> By using the similar strategy, Messersmith and Giannelis<sup>[83,84]</sup> synthesized poly( $\epsilon$ -caprolactone)–clay nanocomposites. Aside from their highly improved mechanical, thermal, and barrier properties, unique viscoelastic behaviors of those end-tethered polymers were also discovered.<sup>[85,86]</sup> The latest progress on in situ ring opening polymerization can be found in the recent reports and related reviews by Dubois et al.<sup>[87–89]</sup> Indeed, the versatility of the in situ polymerization strategy has been demonstrated by a broad spectrum of other polymers via their individual polymerization mechanism including thermosets,<sup>[90–93]</sup> elastomers,<sup>[94,95]</sup> polyolefins,<sup>[96,97]</sup> and even conducting polymers.<sup>[98–100]</sup>

### CONCLUSION

In situ polymerization synthesis methods for PCN materials and polymer brushes on clay nanoparticles are summarized and categorized. The emphasis is placed on free radical and living polymerization approaches. Earlier investigations have shown that in situ polymerization with organoclays modified by reactive modifiers, in which a portion of the polymers is attached to clay surfaces by polymerizable cations, is more likely to give exfoliated PCNs than with organoclays modified by non-reactive alkylammoniums or pristine clay. Previous studies have also demonstrated that in situ polymerization by SIP method, in which more and longer polymer chains can be end-tethered to clay surfaces by cationic initiators than by polymerizable modifiers, can also achieve effective exfoliation. The viability of achieving molecular weight-controllable PCNs has been demonstrated

as well by several attempts on in situ living polymerization approaches from clay surfaces. Although the discussions in this entry are primarily based on thermoplastic polymers from addition polymerization of their vinyl monomers, the versatility and efficiency of in situ polymerization strategy have been verified by PCNs via other in situ polymerization mechanisms, which are briefly introduced. The related report and review references are also given.

## ACKNOWLEDGMENT

The authors would like to thank the U.S. Army Research Office, Alabama Tri-Campus Materials Science Program, and the Chemistry Department of the University of Alabama at Birmingham for financial support.

## REFERENCES

- Okada, A.; Kawasumi, M.; Kurauchi, T.; Kamigaito, O. Synthesis and characterization of a nylon 6-clay hybrid. *Polym. Prepr.* **1987**, *28*, 447–448.
- Usuki, A.; Kojima, Y.; Kawasumi, M.; Okada, A.; Fukushima, Y.; Kurauchi, T.; Kamigaito, O. Synthesis of nylon 6-clay hybrid. *J. Mater. Res.* **1993**, *8* (5), 1179–1184.
- Kojima, Y.; Usuki, A.; Kawasumi, M.; Okada, A.; Fukushima, Y.; Kurauchi, T.; Kamigaito, O. Mechanical properties of nylon 6-clay hybrid. *J. Mater. Res.* **1993**, *8* (5), 1185–1189.
- Kojima, Y.; Usuki, A.; Kawasumi, M.; Okada, A.; Kurauchi, T.; Kamigaito, O. Sorption of water in nylon-6 clay hybrid. *J. Appl. Polym. Sci.* **1993**, *49* (7), 1259–1264.
- Giannelis, E.P.; Krishnamoorti, R.; Manias, E. Polymer-silicate nanocomposites: Model systems for confined polymer and polymer brushes. *Adv. Polym. Sci.* **1999**, *138*, 108–147.
- Burnside, S.D.; Giannelis, E.P. Synthesis and properties of new poly(dimethylsiloxane) nanocomposites. *Chem. Mater.* **1995**, *7* (9), 1597–1600.
- Lan, T.; Pinnavaia, T.J. Clay-reinforced epoxy nanocomposites. *Chem. Mater.* **1994**, *6* (12), 2216–2219.
- Huang, X.; Lewis, S.; Brittain, W.J.; Vaia, R.A. Synthesis of polycarbonate-layered silicate nanocomposites via cyclic oligomers. *Macromolecules* **2000**, *33* (6), 2000–2004.
- Alexandre, M.; Dubois, P. Polymer-layered silicate nanocomposites: Preparation, properties and uses of a new class of materials. *Mater. Sci. Eng., R* **2000**, *28* (1–2), 1–63.
- Lagaly, G. Introduction: From clay mineral-polymer interactions to clay mineral-polymer nanocomposites. *Appl. Clay Sci.* **1999**, *15* (1–2), 1–9.
- Ogata, N.; Kawakage, S.; Ogihara, T. Poly(vinyl alcohol)-clay and poly(ethylene oxide)-clay blend prepared using water as solvent. *J. Appl. Polym. Sci.* **1997**, *66* (3), 573–581.
- Billingham, J.; Breen, C.; Yarwood, J. Adsorption of polyamine, polyacrylic acid, and polyethylene glycol on montmorillonite: An in situ study using ATR-FTIR. *Vibr. Spectrosc.* **1997**, *14* (1), 19–34.
- Vaia, R.A.; Ishii, H.; Giannelis, E.P. Synthesis and properties of two-dimensional nanostructures by direct intercalation of polymer melts in layered silicates. *Chem. Mater.* **1993**, *5* (12), 1694–1696.
- Giannelis, E.P. Polymer layered silicate nanocomposite. *Adv. Mater.* **1996**, *8* (1), 29–35.
- Kawasumi, M.; Hasegawa, N.; Kato, M.; Usuki, A.; Okada, A. Preparation and mechanical properties of polypropylene-clay hybrids. *Macromolecules* **1997**, *30* (20), 6333–6338.
- Liu, L.; Qi, Z.; Zhu, X. Studies on nylon-6 clay nanocomposites by melt-intercalation process. *J. Appl. Polym. Sci.* **1999**, *71* (7), 1133–1138.
- Vaia, R.A.; Giannelis, E.P. Lattice of polymer melt intercalation in organically-modified layered silicates. *Macromolecules* **1997**, *30* (25), 7990–7999.
- Vaia, R.A.; Giannelis, E.P. Polymer melt intercalation in organically-modified layered silicates: Model predictions and experiment. *Macromolecules* **1997**, *30* (25), 8000–8009.
- Krishnamoorti, R.; Vaia, R.A.; Giannelis, E.P. Structure and dynamics of polymer-layered silicate nanocomposites. *Chem. Mater.* **1996**, *8* (8), 1728–1734.
- Hackett, E.; Manias, E.; Giannelis, E.P. Molecular dynamics simulations of organically modified layered silicates. *J. Chem. Phys.* **1998**, *108* (17), 7410–7415.
- Hackett, E.; Manias, E.; Giannelis, E.P. Computer simulation studies of PEO/layer silicate nanocomposites. *Chem. Mater.* **2000**, *12* (8), 2161–2167.
- Lyatskaya, Y.; Balazs, A.C. Modeling the phase behavior of polymer-clay composites. *Macromolecules* **1998**, *31* (19), 6676–6680.
- Carrado, K.A. Synthetic organo- and polymer-clays: Preparation, characterization, and materials applications. *Appl. Clay Sci.* **2000**, *17* (1–2), 1–23.
- Ishida, H.; Campbell, S.; Blackwell, J. General approach to nanocomposite preparation. *Chem. Mater.* **2000**, *12* (5), 1260–1267.
- Zhao, B.; Brittain, W.J. Polymer brushes: Surface-immobilized macromolecules. *Prog. Polym. Sci.* **2000**, *25* (5), 677–710.
- Kleinfeld, E.R.; Ferguson, G.S. Stepwise formation of multilayered nanostructural films from macromolecular precursors. *Science* **1994**, *265* (5170), 370–373.
- Kotov, N.A.; Haraszti, T.; Turi, L.; Zavala, G.; Geer, R.E.; Dekany, I.; Fendler, J.H. Mechanism of and defect formation in the self-assembly of polymeric cation-montmorillonite ultrathin films. *J. Am. Chem. Soc.* **1997**, *119* (29), 6821–6832.
- Fan, X.; Park, M.-K.; Xia, C.; Advincula, R.C. Surface structural characterization and mechanical testing by nanoindentation measurements of hybrid polymer/clay nanostructured multilayer films. *J. Mater. Res.* **2002**, *17* (7), 1622–1633.

29. Pinnavaia, T.J. Intercalated clay catalysts. *Science* **1983**, *220* (4595), 365–371.
30. Eastman, M.P.; Bain, E.; Porter, T.L.; Manyoats, K.; Whitehorse, R.; Parnell, R.A.; Hagerman, M.E. The formation of poly(methyl methacrylate) on transition metal-exchanged hectorite. *Appl. Clay Sci.* **1999**, *15* (1–2), 173–185.
31. Blumstein, A. Polymerization of adsorbed monolayers. I. Preparation of the clay-polymer complex. *J. Polym. Sci.* **1965**, *A3*, 2653–2664.
32. Solomon, D.H.; Rosser, M.J. Reactions catalyzed by minerals. Part I. Polymerization of styrene. *J. Appl. Polym. Sci.* **1965**, *9*, 1261–1271.
33. Lee, D.C.; Jang, L.W. Preparation and characterization of PMMA-clay hybrid composite by emulsion polymerization. *J. Appl. Polym. Sci.* **1996**, *61* (7), 1117–1122.
34. Noh, M.W.; Lee, D.C. Synthesis and characterization of PS-clay nanocomposite by emulsion polymerization. *Polym. Bull.* **1999**, *42* (5), 619–626.
35. Bandyopadhyay, S.; Giannelis, E.P.; Hsieh, A.J. Thermal and thermo-mechanical properties of PMMA nanocomposites. *PMSE Prepr.* **2000**, *82*, 208–209.
36. Al-Esaimi, M.M. Reaction catalyzed by montmorillonite: Polymerization of methyl methacrylate. *J. Appl. Polym. Sci.* **1997**, *64* (2), 367–372.
37. Tabtiang, A.; Lumlong, S.; Venables, R.A. The influence of preparation method upon the structure and relaxation characteristics of poly(methyl methacrylate)/clay composites. *Eur. Polym. J.* **2000**, *36* (12), 2559–2568.
38. Chen, G.; Ma, Y.; Qi, Z. Preparation and morphological study of an exfoliated polystyrene/montmorillonite nanocomposite. *Ser. Mater.* **2001**, *44* (1), 125–128.
39. Okamoto, M.; Morita, S.; Taguchi, H.; Kim, Y.H.; Kotaka, T.; Tateyama, H. Synthesis and structure of smectic clay/poly(methyl methacrylate) and clay/polystyrene nanocomposites via in situ intercalative polymerization. *Polymer* **2000**, *41* (10), 3887–3890.
40. Okamoto, M.; Morita, S.; Kim, Y.H.; Kotaka, T.; Tateyama, H. Dispersed structure change of smectic clay/poly(methyl methacrylate) nanocomposites by copolymerization with polar comonomers. *Polymer* **2001**, *42* (3), 1201–1206.
41. Dietsche, F.; Thomann, Y.; Thomann, R.; Mulhaupt, R. Translucent acrylic nanocomposites containing anisotropic laminated nanoparticles derived from intercalated layered silicates. *J. Appl. Polym. Sci.* **2000**, *75* (3), 396–405.
42. Doh, J.G.; Cho, I. Synthesis and properties of polystyrene-organoammonium montmorillonite hybrid. *Polym. Bull.* **1998**, *41* (5), 511–518.
43. Noh, M.H.; Jang, L.W.; Lee, D.C. Intercalation of styrene-acrylonitrile copolymer in layered silicate by emulsion polymerization. *J. Appl. Polym. Sci.* **1999**, *74* (1), 179–188.
44. Noh, M.H.; Lee, D.C. Comparison of characteristics of SAN-MMT nanocomposites prepared by emulsion and solution polymerization. *J. Appl. Polym. Sci.* **1999**, *74* (12), 2811–2819.
45. Biasci, L.; Agietto, M.; Ruggeri, G.; Ciardelli, R. Functionalization of montmorillonite by methyl methacrylate polymers containing side-chain ammonium cations. *Polymer* **1994**, *35* (15), 3296–3304.
46. Akelah, A.; Moet, A. Polymer-clay nanocomposites: Free-radical grafting of polystyrene on to organophilic montmorillonite interlayers. *J. Mater. Sci.* **1996**, *31* (13), 3589–3596.
47. Moet, A.; Akelah, A. Polymer-clay nanocomposites: Polystyrene grafted onto organophilic montmorillonite interlayers. *Mater. Lett.* **1993**, *18* (1–2), 97–102.
48. Dietsche, F.; Thomann, R.; Doell, W.; Mulhaupt, R. Acrylic nanocomposites containing organoclay nanofillers: Morphology development, properties and fracture behavior. *PMSE Prepr.* **2000**, *82*, 222–223.
49. Fu, X.; Qutubuddin, S. Synthesis of polystyrene-clay nanocomposites. *Mater. Lett.* **2000**, *42* (1–2), 12–15.
50. Fu, X.; Qutubuddin, S. Polymer-clay nanocomposites: Exfoliation of organophilic montmorillonite layers in polystyrene. *Polymer* **2001**, *42* (2), 807–813.
51. Zhu, J.; Morgan, A.B.; Lamelas, F.J.; Wilkie, C.A. Fire properties of polystyrene-clay nanocomposites. *Chem. Mater.* **2001**, *13* (10), 3774–3780.
52. Yeh, J.-M.; Liou, S.-J.; Lin, C.-Y.; Cheng, C.-Y.; Chang, Y.-W.; Lee, K.-R. Anticorrosively enhanced PMMA-clay nanocomposite materials with quaternary alkylphosphonium salt as an intercalating agent. *Chem. Mater.* **2002**, *14* (1), 154–161.
53. Kim, Y.K.; Choi, Y.S.; Wang, K.H.; Chung, I.J. Synthesis of exfoliated PS/Na-MMT nanocomposites via emulsion polymerization. *Chem. Mater.* **2002**, *14* (12), 4990–4995.
54. Choi, Y.S.; Choi, M.H.; Wang, K.H.; Kim, S.O.; Kim, Y.K.; Chung, I.J. Synthesis of exfoliated PMMA/Na-MMT nanocomposites via soap-free emulsion polymerization. *Macromolecules* **2001**, *34* (26), 8978–8985.
55. Zeng, C.; Lee, L.J. Poly(methyl methacrylate) and polystyrene/clay nanocomposites prepared by in-situ polymerization. *Macromolecules* **2001**, *34* (12), 4098–4103.
56. Wang, D.; Zhu, J.; Yao, Q.; Wilkie, C.A. A comparison of various methods for the preparation of polystyrene and poly(methyl methacrylate) clay nanocomposites. *Chem. Mater.* **2002**, *14* (9), 3837–3843.
57. Muzny, C.D.; Butler, B.D.; Hanley, H.J.M.; Tsvetkov, F.; Peiffer, D.G. Clay platelet dispersion in a polymer matrix. *Mater. Lett.* **1996**, *28* (4–6), 379–384.
58. Choi, Y.S.; Wang, K.H.; Xu, M.; Chung, I.J. Synthesis of exfoliated polyacrylonitrile/Na-MMT nanocomposites via emulsion polymerization. *Macromolecules* **2002**, *14* (7), 2936–2939.
59. Hoffmann, B.; Dietrich, C.; Thomann, R.; Friedrich, C.; Mulhaupt, R. Morphology and rheology of polystyrene nanocomposites based upon organoclay. *Macromol. Rapid Commun.* **2000**, *21* (1), 57–61.
60. Zilg, C.; Thomann, R.; Baumert, M.; Finter, J.; Mulhaupt, R. Organic/inorganic hybrid materials and nanocomposites based upon layered silicates modified with cyclic amides. *Macromol. Rapid Commun.* **2000**, *21* (17), 1214–1219.

61. Zilg, C.; Dietsche, F.; Hoffmann, B.; Dietrich, C.; Mulhaupt, R. Nanofillers based upon organic layered silicates. *Macromol. Symp.* **2001**, *169* (1), 65–77.
62. Prucker, O.; Ruhe, J. Synthesis of poly(styrene) monolayers attached to high surface area silica gels through self-assembled monolayers of azo initiators. *Macromolecules* **1998**, *31* (3), 592–601.
63. Prucker, O.; Ruhe, J. Mechanisms of radical chain polymerizations initiated by azo compounds covalently bound to the surface of spherical particles. *Macromolecules* **1998**, *31* (3), 602–613.
64. Prucker, O.; Ruhe, J. Polymer layers through self-assembled monolayers of initiators. *Langmuir* **1998**, *14* (24), 6893–6898.
65. Huang, W.; Skanth, G.; Baker, G.L.; Bruening, M.L. Surface-initiated thermal radical polymerization on gold. *Langmuir* **2001**, *17* (5), 1731–1736.
66. Schmidt, R.; Zhao, T.; Green, J.-B.; Dyer, D.J. Photoinitiated polymerization of styrene from self-assembled monolayers on Gold. *Langmuir* **2002**, *18* (4), 1281–1287.
67. Dekking, H.G.G. Propagation of vinyl polymers on clay surfaces. I. Preparation, structure, and decomposition of clay initiators. *J. Appl. Polym. Sci.* **1965**, *9*, 1641–1651.
68. Dekking, H.G.G. Propagation of vinyl polymers on clay surfaces. II. Polymerization of monomers initiated by free radicals attached to clay. *J. Appl. Polym. Sci.* **1967**, *11*, 23–36.
69. Meier, L.; Shelden, R.; Caseri, W.; Suter, U. Polymerization of styrene with initiator ionically bound to high surface area mica: Grafting via an unexpected mechanism. *Macromolecules* **1994**, *27* (6), 1637–1642.
70. Huang, X.; Brittain, W.J. Synthesis and characterization of PMMA nanocomposites by suspension and emulsion polymerization. *Macromolecules* **2001**, *34* (10), 3255–3260.
71. Fan, X.; Xia, C.; Fulghum, T.; Park, M.-K.; Locklin, J.; Advincula, R.C. Polymer layer grafted from clay surface on planar substrate through free radical surface initiated polymerization (SIP). *Langmuir* **2003**, *19* (3), 916–923.
72. Zhou, Q.; Wang, S.; Fan, X.; Advincula, R.C.; Mays, J. Living anionic surface-initiated polymerization (LASIP) of a polymer on silica nanoparticles. *Langmuir* **2002**, *18* (8), 3324–3331.
73. Fan, X.; Xia, C.; Advincula, R.C. Grafting of polymers from clay nanoparticles via in situ free radical surface-initiated polymerization: Monocationic versus bicationic initiators. *Langmuir* **2003**, *19* (10), 4381–4389.
74. Fan, X.; Xia, C.; Advincula, R.C. Poly(methyl methacrylate) (PMMA)-clay nanocomposites by bulk, solution, and suspension surface initiated polymerization (SIP). *Polym. Prepr.* **2003**, *44* (1), 1099–1100.
75. Fan, X.; Xia, C.; Advincula, R.C. Poly(methyl methacrylate) (PMMA)-clay nanocomposites by bulk, solution, and suspension surface initiated polymerization. (SIP). *Polymer Prepr.* **2003**, *44*, 1099–1100.
76. Zhou, Q.; Wang, S.; Fan, X.; Advincula, R.C.; Mays, J. Living anionic surface-initiated polymerization (LASIP) of a polymer on silica nanoparticles. *Langmuir* **2002**, *18* (8), 3324–3331.
77. Zhou, Q.; Fan, X.; Xia, C.; Mays, J.; Advincula, R.C. Living anionic surface initiated polymerization (SIP) of styrene from clay surfaces. *Chem. Mater.* **2001**, *13* (8), 2465–2467.
78. Fan, X.; Zhou, Q.; Xia, C.; Crsitopholi, W.; Mays, J.; Advincula, R.C. Living anionic surface-initiated polymerization (LASIP) of styrene from clay nanoparticles using surface bound 1,1-diphenylethylene (DPE) initiators. *Langmuir* **2002**, *18* (11), 4511–4518.
79. Weimer, M.W.; Chen, H.; Giannelis, E.P.; Sogah, D.Y. Direct synthesis of dispersed nanocomposites by in situ living free radical polymerization using a silicate-anchored initiator. *J. Am. Chem. Soc.* **1999**, *121* (7), 1615–1616.
80. Usuki, A.; Kojima, Y.; Kawasumi, M.; Okada, A.; Kurauchi, T.; Kamigaito, O. Characterization and properties of nylon 6-clay hybrid. *Polym. Prepr.* **1990**, *31*, 651–652.
81. Usuki, A.; Kawasumi, M.; Kojima, Y.; Okada, A.; Kurauchi, T.; Kamigaito, O. Swelling behavior of montmorillonite cation exchanged for  $\omega$ -amino acids by  $\epsilon$ -aprolactam. *J. Mater. Res.* **1993**, *8* (5), 1174–1178.
82. Okada, A.; Usuki, A. The chemistry of polymer-clay hybrids. *Mater. Sci. Eng.* **1995**, *C3* (1), 109–115.
83. Messersmith, P.B.; Giannelis, E.P. Synthesis and barrier properties of poly( $\epsilon$ -caprolactone)-layered silicate nanocomposites. *J. Polym. Sci., A, Polym. Chem.* **1995**, *33* (7), 1047–1057.
84. Messersmith, P.B.; Giannelis, E.P. Polymer-layered silicate nanocomposites: In situ intercalative polymerization of  $\epsilon$ -caprolactone in layered silicates. *Chem. Mater.* **1993**, *5* (8), 1064–1066.
85. Krishnamoorti, R.; Giannelis, E.P. Rheology of end-tethered polymer layered silicate nanocomposites. *Macromolecules* **1997**, *30* (14), 4097–4102.
86. Krishnamoorti, R.; Yurekli, K. Rheology of polymer layered silicate nanocomposites. *Curr. Opin. Colloid Interface Sci.* **2001**, *6*, 464–470.
87. Lofgren, A.; Albertsson, A.-C.; Dubois, P.; Jerome, R. Recent advances in ring-opening polymerization of lactones and related compounds. *J. Macromol. Sci., Rev. Macromol. Chem. Phys.* **1995**, *C35*, 379–418.
88. Mecerreyes, D.; Jerome, R.; Dubois, P. Novel macromolecular architectures based on aliphatic polyesters: Relevance of the coordination-insertion ring opening polymerization. *Adv. Polym. Sci.* **1999**, *147*, 1–59.
89. Lepoittevin, B.; Pantoustier, N.; Devalckenaere, M.; Alexandre, M.; Kubies, D.; Calberg, C.; Jerome, R.; Dubois, P. Poly( $\epsilon$ -caprolactone)/clay nanocomposites by in-situ intercalative polymerization catalyzed by dibutyltin dimethoxide. *Macromolecules* **2002**, *35* (22), 8385–8390.
90. Lan, T.; Kaviratna, P.D.; Pinnavaia, T.J. Mechanism of clay tactoid exfoliation in epoxy-clay nanocomposites. *Chem. Mater.* **1995**, *7* (12), 2144–2150.
91. Messersmith, P.B.; Giannelis, E.P. Synthesis and characterization of layered silicate-epoxy nanocomposites. *Chem. Mater.* **1994**, *6* (10), 1719–1725.

92. Kornmann, X.; Lindberg, H.; Berglund, L.A. Synthesis of epoxy–clay nanocomposites: Influence of the nature of the clay on structure. *Polymer* **2001**, *42* (4), 1303–1310.
93. Kornmann, X.; Berglund, L.A.; Sterte, J.; Giannelis, E.P. Nanocomposites based on montmorillonite and unsaturated polyester. *Polym. Eng. Sci.* **1998**, *38* (8), 1351–1358.
94. Wang, Z.; Pinnavaia, T.J. Nanolayer reinforcement of elastomeric polyurethane. *Chem. Mater.* **1998**, *10* (12), 3769–3771.
95. Wang, Z.; Pinnavaia, T.J. Hybrid organic–inorganic nanocomposites: Exfoliation of magadiite nanolayers in an elastomeric epoxy polymer. *Chem. Mater.* **1998**, *10* (7), 1820–1826.
96. Alexandre, M.; Dubois, P.; Sun, T.; Garces, J.M.; Jerome, R. Polyethylene-layered silicate nanocomposites prepared by the polymerization-filling technique: Synthesis and mechanical properties. *Polymer* **2002**, *43* (7), 2123–2132.
97. Sun, T.; Garces, J.M. High-performance polypropylene–clay nanocomposites by in-situ polymerization with metallocene/clay catalysts. *Adv. Mater.* **2002**, *14* (2), 128–130.
98. Hong, S.H.; Kim, B.H.; Joo, J.; Kim, J.W.; Choi, H.J. Polypyrrole–montmorillonite nanocomposites synthesized by emulsion polymerization. *Curr. Appl. Phys.* **2001**, *1* (6), 447–450.
99. Kim, B.H.; Jung, J.H.; Kim, J.W.; Choi, H.J.; Joo, J. Physical characterization of polyaniline–Na<sup>+</sup>–montmorillonite nanocomposite intercalated by emulsion polymerization. *Synth. Met.* **2001**, *117* (1–3), 115–118.
100. Lee, D.; Char, K. Thermal degradation behavior of polyaniline in polyaniline/Na<sup>+</sup>–montmorillonite nanocomposites. *Polym. Degrad. Stab.* **2002**, *75* (3), 555–560.



# Polymer Colloids and Their Metallation

Lyudmila M. Bronstein

Department of Chemistry, Indiana University, Bloomington, Indiana, U.S.A.

## INTRODUCTION

Polymer colloids with metal nanoparticles is a fast-developing field of nanoscience and nanotechnology as encapsulation of metal inside the polymer—or, vice versa, formation of polymer inside the nanocomposite colloids—show a promise for exciting applications: catalytic, optical, magnetic. Metal or semiconductor nanoparticles can be 1) formed inside the polymer colloids (block copolymer micelles, dendrimers, or other functionalized polymer colloids); 2) positioned on the outer surface of the polymer colloids; or 3) polymer layer can be formed or adsorbed on the preformed nanoparticle surface. This entry discusses the above routes to prepare polymer nanocomposite colloids considering possible advantages and disadvantages of different methods. The major methods to characterize composition and structure of these nanomaterials include those used for polymer colloid characterization and metal nanoparticle assessment. Some methods allow gathering information on both polymer and nanoparticle structure; some methods are very specific for nanoparticle characterization. Transmission electron microscopy (TEM) is widely used to characterize both polymer colloids and metal (semiconductor) nanoparticles; the latter especially provide high electron contrast. High-resolution TEM (HRTEM) is used to determine the sizes of small particles and to characterize their inner structure. X-ray diffraction (XRD) is used for crystalline nanoparticles to determine their structure and mean particle size. Scattering techniques, small angle X-ray scattering (SAXS) and small angle neutron scattering (SANS), can be used both for polymer colloid and nanoparticle assessment. The latter is possible if polymer structure does not change after particle formation so scattering from polymer particles can be subtracted. If this is not the case, anomalous SAXS is employed because it allows one to establish nanoparticle size and particle size distribution independently of changes in the nanostructured polymer. Spectroscopic techniques are often used to characterize nanoparticles because properties are dependent on nanoparticle size (Au, Ag, semiconductor nanoparticles). In the sections below, examples of polymer colloid and nanoparticle characterization are presented.

## NANOPARTICLE FORMATION INSIDE POLYMER COLLOIDS

### Nanoparticle Formation in Block Copolymer Micelles

Amphiphilic block copolymers form micelles in selective solvents (a good solvent only for one block), yet the size and shape of micelles depend on the block chemical structure, molecular weight of each block, and solvent type.<sup>[1,2]</sup> Block copolymer micelles can be treated as polymer colloids being in dynamic equilibrium with unimers (individual macromolecules in solution) and with each other, which results in exchange between micelles. Although this exchange is a slow process for block copolymer systems compared to surfactant micelles, this can ensure very useful properties (ability to assemble and disassemble in certain conditions can play very important role for some “delivery” applications) or demonstrate a disadvantage, as it can facilitate metal-species exchange between polymer colloids.

Depending on the structure of the block copolymer, nanoparticles can be formed both in the micelle core (when the core is functionalized, while corona is not) or in the corona, when the core is not functionalized.

### Nanoparticle formation in the micelle core

If the block containing the functional groups (able to react with metal compounds, giving complexes or salts) forms the micelle core, it can be loaded with a corresponding metal compound (by incorporating the metal compound in the block copolymer solution) and can further serve as a nanoreactor for nanoparticle formation. In so doing, because the core-forming block is not soluble in a selective solvent, the micelle core can be treated like a quasi solid, thus additionally stabilizing the nanoparticles. Examples of “functional” blocks are polyvinylpyridines [P2(4)VP], polymethacrylic and polyacrylic acids (PMAA and PAA), polybutadiene (PB), polyisoprene (PI), and others. A block containing no functional groups but providing solubility and micelle stability in the solution should form the micelle corona. These can be polystyrene (PS), poly(ethylene oxide) (PEO), polyisobutylene (PIB), etc.

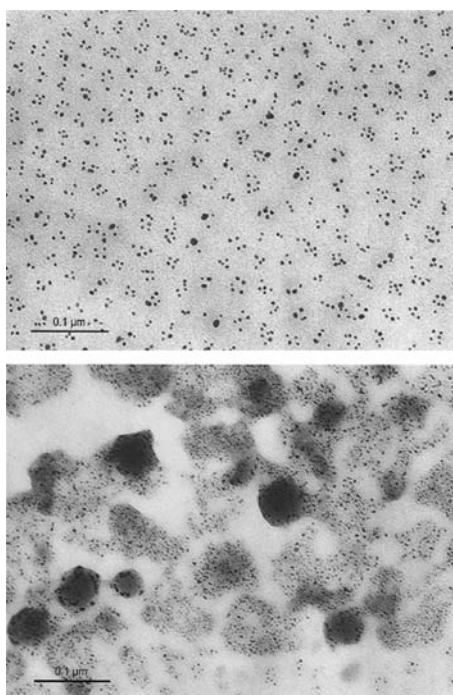


**Fig. 1** Electron micrographs of Pd colloids synthesized in PS-*b*-P4VP block copolymer micelles via reduction with hydrazine (top) and NaBH<sub>4</sub> (bottom). Source: From Ref.<sup>[9]</sup>. © 1997 by the American Chemical Society.

The synthesis of metal or semiconductor nanoparticles in the cores of amphiphilic block copolymer micelles was almost simultaneously reported by several research groups.<sup>[3–7]</sup> The metal nanoparticle formation in PS-*b*-P4VP block copolymer micelles demonstrated the strong dependence of nanoparticle morphology on the type of reducing agent. When a sluggish reducing agent is used, one nanoparticle per micelle (“cherry-like” morphology) can be formed if there is no exchange between micelles (e.g., the micelle is cross-linked).<sup>[8]</sup> Fast reduction leads to the formation of many small particles per micelle (“raspberry-like” morphology), which is considered to be preferable for catalytic applications (Fig. 1).<sup>[9]</sup> Using block copolymer micelle cores as nanoreactors allows synthesis of monometallic and bimetallic nanoparticles, yet bimetallic particle morphology depends on a metal pair,<sup>[10]</sup> i.e., on the ability of metal species to be reduced in particular conditions. For the Pd–Au pair, core–shell particles are formed with a gold core and a palladium shell. For Pd–Pt pair, cluster-in-cluster particles are obtained. These different morphologies significantly change the catalytic properties of such systems although the nanoparticle sizes are similar.<sup>[10]</sup>

Co nanoparticles of different sizes and shapes can be prepared either by incorporation of CoCl<sub>2</sub> in the PS-*b*-P2VP micelles followed by reduction or by thermal decomposition of Co<sub>2</sub>(CO)<sub>8</sub> species embedded in

the micelle cores.<sup>[11]</sup> Stable suspensions of superparamagnetic cobalt nanoparticles were also prepared in poly(dimethylsiloxane) (PDMS) carrier fluids in the presence of poly[*dimethylsiloxane-block*-(3-cyanopropyl)methylsiloxane-*block*-dimethylsiloxane] (PDMS-*b*-PCPMS-*b*-PDMS) triblock copolymers as steric stabilizers.<sup>[12]</sup> Similar to PS-*b*-P2VP, these copolymers formed micelles in toluene and served as nanoreactors for thermal decomposition of the Co<sub>2</sub>(CO)<sub>8</sub> precursor. The nitrile groups on the PCPMS central blocks are thought to adsorb onto the particle surface, while the PDMS end blocks protrude into the reaction medium to provide steric stability. Adjusting the cobalt-to-copolymer ratio can control the particle size. Transmission electron microscopy shows non-aggregated cobalt nanoparticles with a narrow size distribution and the particles are evenly surrounded with copolymer covering.

The formation of iron oxide particles in cross-linked block copolymer micelles is described in Ref.<sup>[13]</sup> A polyisoprene-*block*-poly(2-cinnamoyl ethyl methacrylate)-*block*-poly(*tert*-butyl acrylate), PI-*b*-PCEMA-*b*-PtBA, forms spherical micelles in THF/hexane mixture with 65% volume fraction of the latter. The micelles consist of a PI corona, a solvent-insoluble PCEMA shell, and a PtBA core. Their structure is locked in by photo-cross-linking the PCEMA shell to yield nanospheres (Fig. 2). Similar to core cross-linking, this approach prevents exchange between micelles. The nanospheres were made water-dispersible by hydroxylating the PI double bonds. The core was made compatible with inorganic species by removing the *tert*-butyl groups of PtBA. The possibility of using such nanospheres as nanoreactors for inorganic nanoparticle preparation was demonstrated by incorporating iron

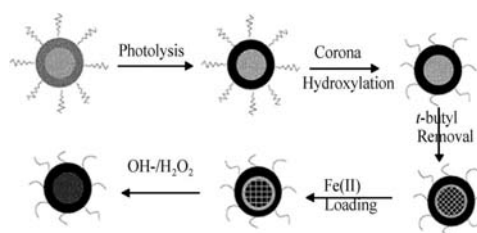


**Fig. 2** Preparation of water-dispersible magnetic nanoparticles. Photolysis cross-links the PCEMA shell (gray to dark). The PI corona chains are made water-soluble by hydroxylating the double bonds (wavy lines to free-hand lines). The core is made inorganic compatible by removing the *tert*-butyl groups (light gray to gridded pattern). Soaking the nanospheres in aqueous FeCl<sub>2</sub> enables proton exchange by Fe<sup>2+</sup> (slant to vertical grids) and the Fe<sup>2+</sup> ions are precipitated and oxidized to yield cubic  $\gamma$ -Fe<sub>2</sub>O<sub>3</sub> magnetic particles using NaOH and H<sub>2</sub>O<sub>2</sub> (last step). Source: From Ref.<sup>[13]</sup>. © 2000 by the American Chemical Society.

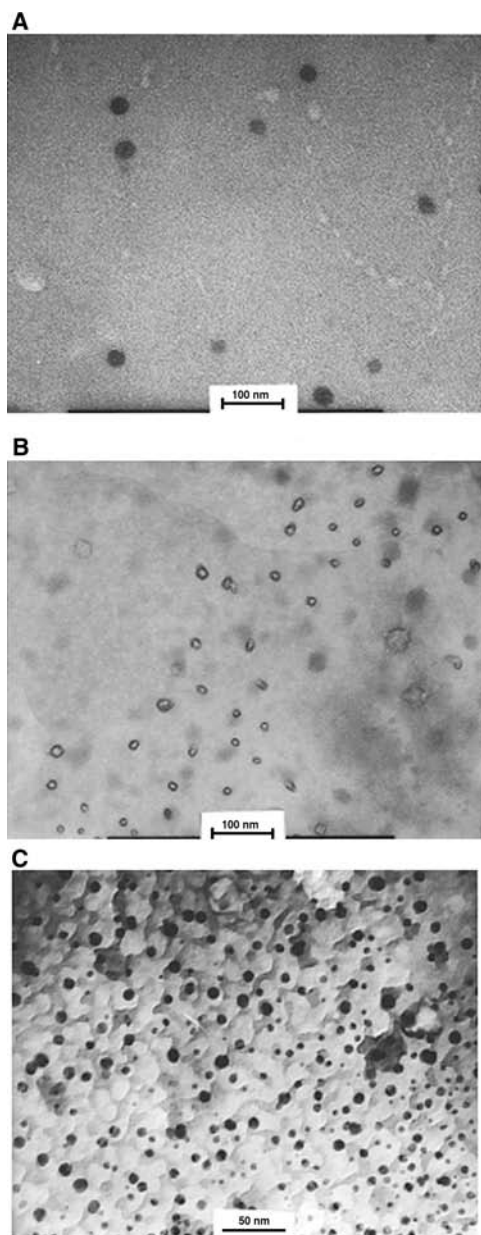


**Fig. 3** Transmission electron microscopic images of PI-*b*-PCEMA-*b*-PtBA nanospheres at each stage in the synthesis: (A) after PCEMA cross-linking and PI hydroxylation (stained with OsO<sub>4</sub> overnight); (B) after removal of *tert*-butyl groups (stained with OsO<sub>4</sub> over a weekend); and (C) after Fe<sub>2</sub>O<sub>3</sub> loading (no staining). *Source:* From Ref.<sup>[13]</sup>. © 2000 by the American Chemical Society.

salt and formation of iron oxide magnetic particles in the cores (Fig. 3).

As seen from the above examples, many amphiphilic block copolymers form micelles with a functionalized core in the organic medium. When aqueous solutions are preferred, the choice of block copolymers is very limited and metal particle formation is normally more complicated as the pH of the medium should be taken

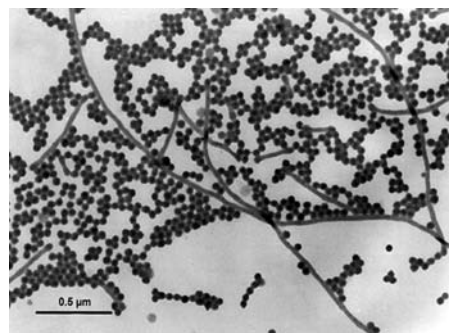


**Fig. 4** Transmission electron microscopic image of Pt nanoparticles prepared in PB-*b*-PEO micelles by NaBH<sub>4</sub> reduction. *Source:* From Ref.<sup>[15]</sup>. © 1999 by the American Chemical Society.

into consideration. A few examples of such block copolymers include P2VP-*b*-PEO and PB-*b*-PEO,<sup>[14,15]</sup> yet the former block copolymer micellization depends on the pH value:<sup>[16]</sup> At pH below 5, P2VP-*b*-PEO becomes molecularly soluble in water. At the same time, decrease of pH of the P2VP-*b*-PEO micellar solution after incorporation of metal compounds or metal nanoparticle formation results in no micelle decomposition although the micelle density decreases. In the case of PB-*b*-PEO, micelles formed in water are very dense, so they successfully fulfill two roles: They serve as nanoreactors for Pd, Pt, and Rh nanoparticle formation (Fig. 4) and as metal-particle-containing templates for mesoporous silica casting.<sup>[15]</sup>

If the P2VP block is a middle block in PS-*b*-P2VP-*b*-PEO triblock copolymer, the “layered,” well-defined micelles are formed in water with the PS core, P2VP shell, and PEO corona.<sup>[17]</sup> Here the P2VP shell serves as a nanoreactor for gold nanoparticle formation. As the shell is formed by the pH-sensitive P2VP block, the authors believe that this system can be useful for encapsulation and/or release of active species. However, one should remember that after metal particle formation, this block loses its ability to dissolve at low pH.<sup>[14]</sup> So this property can be hardly realized in this system if nanoparticles or metal complexes are formed in the P2VP shell.

The formation of spherical assemblies of CdS-containing block copolymer reverse micelles in aqueous solution was reported in Ref.<sup>[18]</sup>. These stable assemblies were formed by slow addition of water to mixtures of the reverse micelles formed by PS-*b*-PAA and single PS-*b*-PAA chains. Large compound micelles (LCMs) with quantum-confined CdS nanoparticles dispersed throughout a spherical PS stabilized in water by a layer of solubilized hydrophilic chain matrix were obtained. The size of the CdS particles (approximately 3 nm) is determined by the ionic block length of the

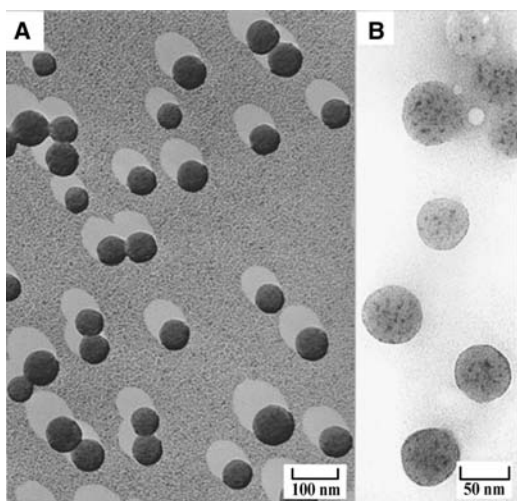


**Fig. 5** Transmission electron microscopic images of spherical aggregates in LCM, with Pd/Pt shadowing (A) and without shadowing (B). The dark particles inside the spheres are CdS nanoparticles. *Source:* From Ref.<sup>[22]</sup>. © 1998 by the American Chemical Society.

block copolymer forming the reverse micelle (Fig. 5). The formation of LCMs was found to depend on the amount of the added stabilizing copolymer. This method allows transferring the CdS nanoparticles formed in the micelle cores in organic medium to aqueous medium without loss of stability and nanoparticle aggregation.

#### Block copolymer micelle coronas

Nanoparticles can be synthesized in the corona of amphiphilic block copolymer micelles. However, if the corona is functionalized, addition of a metal salt can result in immediate formation of large aggregates because of the interaction between micelles and their precipitation; thus this method can be used only in very dilute solutions. If the corona does not contain groups able to coordinate with metal compounds, particle stabilization can be ensured because of the hydrophobic interactions with the hydrophobic core. This feature was used when synthesis of Pd, Pt, Ag, and Au nanoparticles was performed in aqueous solutions of PS-*b*-PEO and PS-*b*-PMAA by reduction of the corresponding salts in block copolymer solutions.<sup>[19,20]</sup> However, the stability of such systems, solely provided by the hydrophobic interactions with the PS core, is not satisfactory. On the other hand, accessibility of particles in the micelle coronas can be favorable from the viewpoint of catalytic applications.

Enhanced stabilization in the micelle coronas was achieved when hybrid micelles consisting of PS-*b*-PEO and surfactants were formed.<sup>[21–23]</sup> Surfactant hydrophobic tails were expected to penetrate the PS

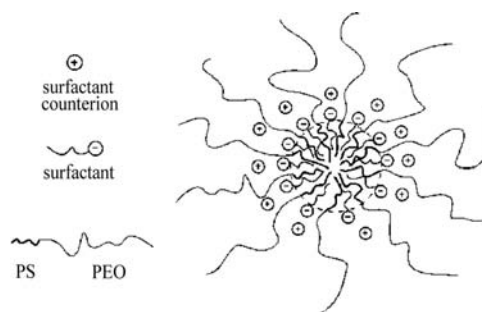


**Fig. 6** Schematic image of the PS-*b*-PEO/SDS micelle. *Source:* From Ref.<sup>[22]</sup>. © 2000 by Academic Press.

core while surfactant head groups are located on the micelle core surface or in its vicinity. As shown in Fig. 6, exchange of surfactant counterions for ions of interest would lead to saturation of the core with the given ions. Dynamic light scattering (DLS) and sedimentation in an ultracentrifuge showed that incorporation of positively or negatively charged surfactants results in increase of size and weight of micelles and micellar clusters up to a certain surfactant concentration (which is different for different surfactants). Further increase of surfactant loading (as a rule, above critical micelle concentration for surfactants) results in a moderate decrease of micelle size and weight. Incorporation of surfactant was found to increase the mobility of the PS core and to decrease the mobility of surfactant tails. Both these facts proved comicellization of block copolymer molecules and cationic or anionic surfactants. Ion exchange of surfactant counterions in the PS-*b*-PEO/CPC (cetyl pyridinium chloride) system for  $\text{PtCl}_6^{2-}$  or  $\text{PdCl}_4^{2-}$  ions results in saturation of micellar structures with Pt or Pd ions. Subsequent reduction of metal-containing hybrid micellar systems PS-*b*-PEO/CPC/ $\text{MX}_n$  with  $\text{NaBH}_4$  or  $\text{H}_2$  leads to the formation of metal nanoparticles mainly located within the micelles. The morphology and stability of Pd and Pt nanoparticles synthesized in these systems depends on the metal compound loading and the type of a reducing agent.  $\text{NaBH}_4$  reduction leads to decomposition of micellar clusters and formation of micelles with embedded nanoparticles. These systems display exceptional stability (for years) if metal salt loading does not exceed  $1.24 \times 10^{-2}$  M. Hydrogen reduction results in metal nanoparticle formation both in micelles and micellar clusters (micelle aggregates), so stability of colloidal solutions is ensured at metal salt concentration of less than  $3.36 \times 10^{-3}$  M. Rh nanoparticles with diameters of 2–3 nm have been obtained in the hybrid micelles formed by PS-*b*-PEO anionic surfactants: sodium dodecylsulfate (SDS) or sodium dodecylbenzenesulfonate (SDBS) using Rh cations  $[\text{Rh}(\text{Py})_4\text{Cl}_2]^+$  (Fig. 7). As found, nanoparticle size does not depend on the type of reducing agent

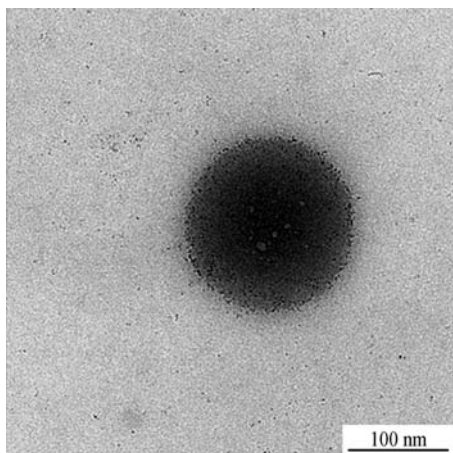


**Fig. 7** Transmission electron micrographs of Rh nanoparticles formed in the PS-*b*-PEO/SDS system. *Source:* From Ref.<sup>[22]</sup>. © 2000 by Academic Press.

(contrary to the nanoparticles formed in other block copolymer solutions),<sup>[4,14]</sup> but depends on the type of metal.<sup>[21–23]</sup> This could be governed by the strong interaction of surfactant head groups with growing nanoparticles.

Thus incorporation of surfactants in the block copolymer micelles containing no functional groups allows reliable stabilization of metal nanoparticles of 2–6 nm in size. Using both cationic and anionic surfactants allows one to explore an infinite variety of metal ions and to prepare different kinds of nanoparticles. The disadvantage of these systems is a lack of the direct methods to tune the particle size.

### Nanoparticle Formation in Dendrimers

The most commonly used and studied dendrimers (commercially available) are poly(amidoamines) (PAMAM), whose structure is presented in Ref.<sup>[24]</sup>. By varying the dendrimer size (dendrimer generation) and metal compound loading, one can vary the size of nanoparticles. Dendrimers were used for stabilization of gold and silver nanoparticles with subsequent self-assembling of metal-containing dendrimers on the surface with monolayer formation.<sup>[25]</sup> Poly(amidoamine) dendrimers with terminal hydroxyl groups were used as templates and stabilizers for controlled synthesis of monodisperse, catalytically active nanoparticles.<sup>[26]</sup> In the first step, metal ions were absorbed by the dendrimer as a result of the formation of metal complexes with amino groups. Subsequent reduction results in the formation of metal nanoparticles encapsulated in the dendrimers. For hydroxyl-terminated dendrimers, a deficiency of metal exchange between dendrimer molecules provides very narrow particle size distribution and subtle control over nanoparticle

growth: The nanoparticle size is exactly determined by the amount of metal atoms loaded in the dendrimer. These metal-containing dendrimers are water-soluble and very stable (no precipitation is observed for months). It is considered that a metal particle is formed in the cavity of the dendrimer. This location provides a certain stabilization of the particles. At the same time, the presence of functional (amino) groups allows additional stabilization of nanoparticles. Metal particle formation resembles the growth of nanoparticles in the cross-linked cores of block copolymer micelles when exchange between micelles does not occur. If PAMAM contains surface (terminal) amino groups, exchange between dendrimer molecules results in a broader particle size distribution than for PAMAM with terminal hydroxyl groups (Fig. 8).<sup>[27]</sup>

Dendrimer generation is an important factor to influence the particle characteristics.<sup>[28]</sup> Gold colloid formation upon reduction of a gold salt precursor in protonated PAMAM was studied to follow the influence of reaction conditions and dendrimer generation on the resulting polymer nanocomposite colloids.<sup>[29]</sup> Methods such as TEM, SANS, and SAXS show that the gold particles are formed inside the dendrimer and located offset from the center (probably in a dendrimer cavity). Lower generation dendrimers aggregate when nanoparticles are formed. Dendrimers of generation 6–9 can template one gold nanoparticle per dendrimer molecule; the number of gold atoms added per dendrimer determines the particle size. These data well agree with those described in Ref.<sup>[26]</sup>. For generation 10, multiple smaller gold particles per dendrimer

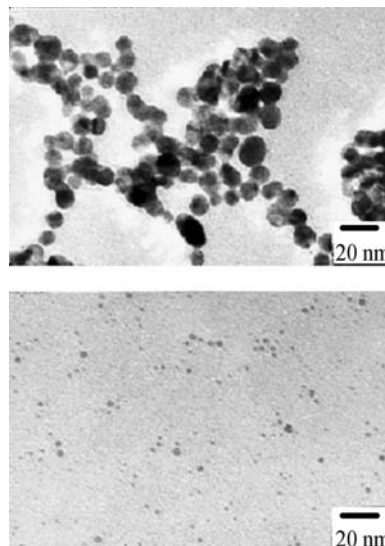


**Fig. 8** Electron micrographs of gold colloids and histograms of particle size distribution at molar ratio of surface amino group of G5 and HAuCl<sub>4</sub>: 1:1 (top) and 4:1 (bottom). *Source:* From Ref.<sup>[27]</sup>. © 1998 by the American Chemical Society.



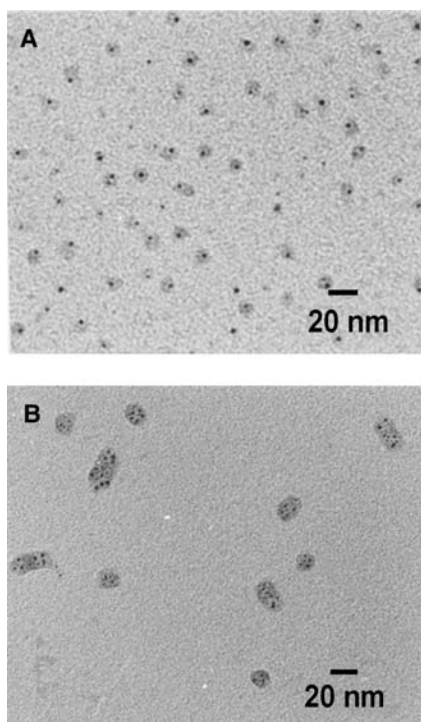


**Fig. 9** Transmission electron micrograph of gold containing G8 PAMAM (A) and G10 PAMAM (B) dendrimers obtained for 1:1 loading and slow reduction. In both cases, the dendrimers have been stained with phosphotungstic acid. Source: From Ref.<sup>[29]</sup>. © 2000 by the American Chemical Society.

were observed and dendrimers aggregated (Fig. 9). Poly(propyleneimine) dendrimers with stearyl end groups, combining both hydrophilic and hydrophobic moieties, were also used for metal particle formation.<sup>[30]</sup> These dendrimers form inverse micelles in toluene. While the initial dendrimers have a spherical structure with a collapsed core, solubilization of metal salt hydrate leads to the formation of cylindrical multidendrimer structures with swollen, metal-salt-filled dendrimer cores. When the gold salt inside the dendrimers is reduced to form colloidal particles, the cylindrical structure breaks up and spherical nanoparticles are formed. In so doing, the particle sizes are larger than would be expected if the gold-salt loading of one dendrimer formed one particle, indicating that the ions from several dendrimers are combined. Apparently, dendrimers of this kind provide no control over nanoparticle growth. In addition, these dendrimer aggregates, although resembling block copolymer micelles, are less defined and more complex. So advantages of such amphiphilic dendrimers are not evident.

Along with metal particles, a number of semiconductor particles, CdS,<sup>[31–33]</sup> CdSe,<sup>[34]</sup> and complex core-shell CdSe/ZnS,<sup>[32]</sup> were successfully prepared in dendrimers. The absorption and emission of the

CdS/PAMAM (hydroxylated) systems are a function of the generation of the dendrimer that is related to the dependence of nanoparticle size on dendrimer generation and the dependence of optical properties on a semiconductor nanoparticle size.<sup>[32]</sup>

Aqueous assemblies of adamantyl-derivatized poly(propylene imine) (PPI) dendrimers and  $\beta$ -cyclodextrin ( $\beta$ -CD) (Fig. 10) have been used as nanoreactors in the preparation of gold and platinum nanoparticles in water.<sup>[35]</sup> These particles have been formed by the reduction of aurate or platinate anions in the presence of the generation 4 ( $4_{\beta}$ -CD)<sup>32</sup> and 5 ( $5_{\beta}$ -CD)<sup>40</sup> assemblies (Fig. 11). Lower generation assemblies did not provide stable nanoparticles. The authors believe that the persistent shape of the adamantyl-derivatized dendrimers and the dense shell of adamantyl- $\beta$ -CD complexes provide a kinetic barrier for nanoparticle escape, thus prolonging their lifetime. However, particle size distribution inside  $\beta$ -CD-modified dendrimers is not particularly narrow,<sup>[35]</sup> thus demonstrating poorer control over particle size than in hydroxy-terminated PAMAM.

### Nanoparticles in Polyelectrolyte Microgels

Microgels are gel spherical particles having diameters in a nanometer range.<sup>[36,37]</sup> Internal cross-linking leads to stability of their sizes and properties, while their size (in nanometer range) ensures formation of colloidal solutions. When these microgels are formed by polyelectrolytes, they contain charged groups allowing ion exchange and solubilization in water. This allows considering microgels as nanoreactors for controlling nanoparticle growth. Gold nanoparticle formation was studied in microgels based on sulfonated PS.<sup>[38]</sup> Morphologies of nanoparticles formed are strongly determined by the degree of microgel cross-linking. The higher the cross-linking density, the higher the probability of the formation of spherical particles embedded in the microgels. The other key factor is the type of reducing agent. Fast reduction ( $\text{NaBH}_4$ ) in water leads to gold nanoparticles of 4.5 nm in diameter located in microgels. If  $\text{NaBH}_4$  is added in alkaline solution (0.1 N NaOH), it slows the reduction and results in 7-nm nanoparticles forming long “threads.” Yet only 20% of microgels contain nanoparticles. Thus slow nucleation allows Au clusters and ions to migrate out of microgel areas where aggregation easily occurs. High-resolution TEM allows determining that particles grow from one nucleus and the microgel environment governs the particle shape. In a similar fashion, Pd and Pt nanoparticles have been grown in microgels. These metal-particle-containing microgels were also used as cotemplates (along with amphiphilic PS-*b*-PEO block copolymers) for mesoporous silica



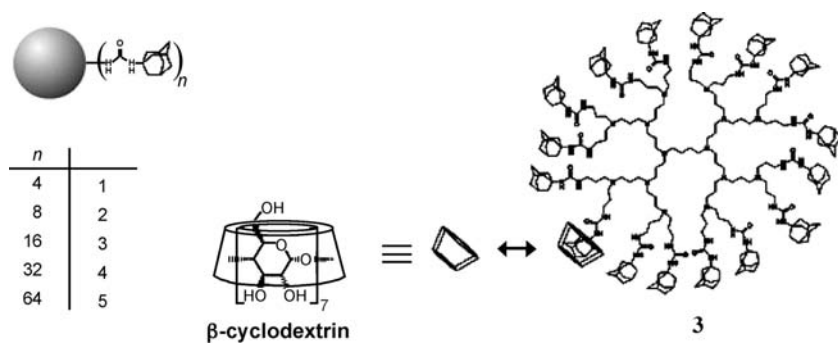


Fig. 10 Poly(propylene imine) dendrimer generations 1–5, solubilized by  $\beta$ -cyclodextrin. Source: From Ref.<sup>[35]</sup>.

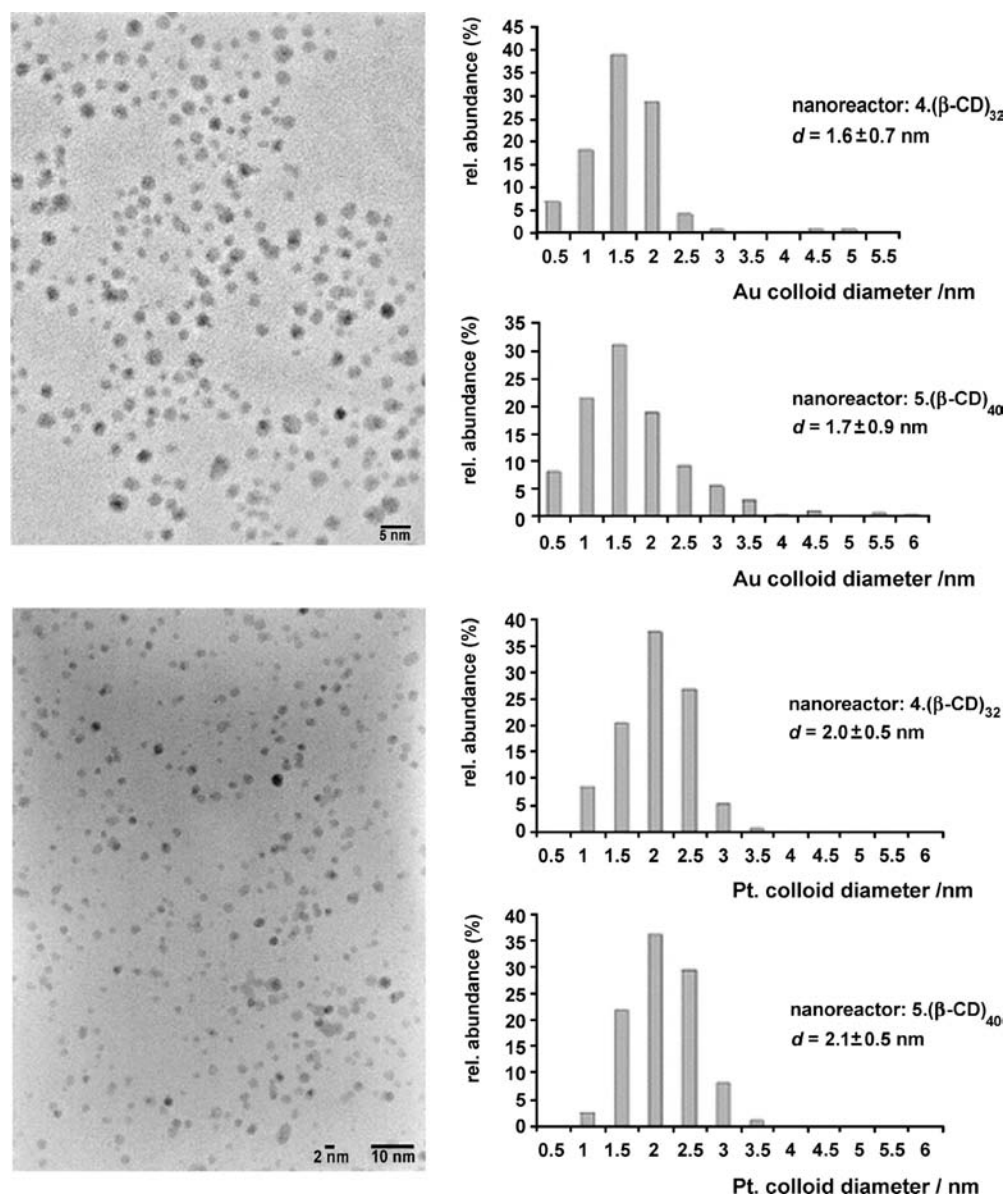
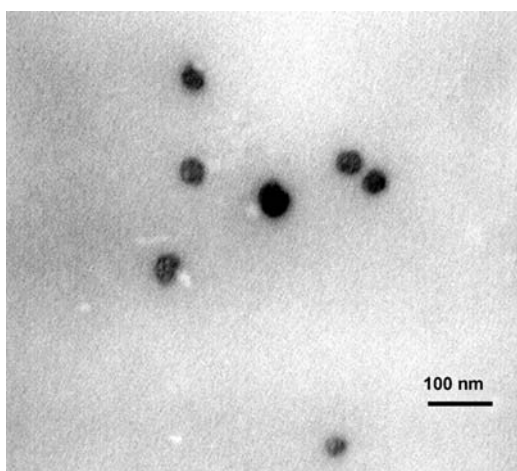


Fig. 11 Transmission electron microscopic images of gold (top) and platinum (bottom) nanoparticles stabilized by the 5 · ( $\beta$ -CD)<sub>40</sub> assembly and size distributions of colloids stabilized by 4 · ( $\beta$ -CD)<sub>32</sub> and 5 · ( $\beta$ -CD)<sub>40</sub> (amine/metal=2:1, H<sub>2</sub>O, T=25°C). Source: From Ref.<sup>[35]</sup>.

formation.<sup>[39]</sup> Here microgels play a dual role: They are nanoreactors for metal particle formation and pore-forming templates when mesoporous materials are formed.

### Nanoparticle Formation in Functionalized Polysilsesquioxane Colloids

Synthesis of functionalized polysilsesquioxane based on hydrolytic condensation of functionalized silanes was recently described in Ref.<sup>[40]</sup>. Using *N*-(6-amino-hexyl)aminopropyltrimethoxysilane (AHAPS) as a precursor, well-defined colloidal particles composed of a nearly fully condensed poly(amino-hexyl)(amino-propyl)silsesquioxane (PAHAPS) were synthesized. According to solid state <sup>29</sup>Si CP-MAS (cross-polarization magic angle spinning) nuclear magnetic resonance (NMR), PAHAPS structure contains mainly C-SiO<sub>3/2</sub> species. The sizes of PAHAPS colloids vary in the range 10–200 nm and depend on the reaction conditions: pH, solvent, and AHAPS concentration (Fig. 12). When hydrolytic condensation is carried out in water with no HCl added, self-assembling of AHAPS tails results in the formation of lamellar ordering with Bragg spacing of about 3.0 nm, which matches to two layers of fully extended AHAPS tails. When PAHAPS is fully or partially protonated (HCl is added to water), no ordering occurs. Similarly disordered structures are formed in THF, which is a good solvent for AHAPS tails. Unlike water, THF also facilitates cross-linking between colloids, so the colloids are attached to each other. Interaction of PAHAPS colloids with Pt and Pd salts followed by chemical reduction results in the formation of discrete metal nanoparticles stabilized within the colloids even at metal content of 30–45 wt.% (Fig. 13). The particle size depends on the



**Fig. 12** Transmission electron microscopic image of PAHAPS colloids obtained in water at a precursor concentration of 17 wt.%.

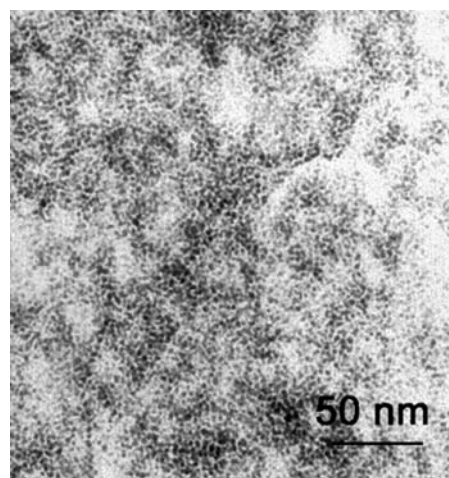


**Fig. 13** Transmission electron microscopic image of Pt nanoparticles formed in protonated PAHAPS prepared in water at a concentration of 1.5 wt.%.

type of metal compound and, in some cases, on type of the reducing agent. Particles formed after reduction of K<sub>2</sub>PtCl<sub>4</sub> within PAHAPS measure ca. 1–2 nm in diameter when the fast reducing agent (NaBH<sub>4</sub>) is reduced. With the sluggish reducing agent (hydrazine-hydrate), both small particles of 1.5 nm and larger particles with diameters of 2.5–4.0 nm are formed. When metal precursor is K<sub>2</sub>PtCl<sub>6</sub>, very narrowly distributed particles measuring about 1.5 nm are formed for both types of reducing agents. Apparently, particle nucleation does not influence the particle size when mass transfer of the PtCl<sub>6</sub><sup>2-</sup> ions is restricted. Poly(amino-hexyl)(amino-propyl)silsesquioxane colloids form very strong elastic films because of the intercolloid interactions that makes possible the formation of freestanding films and coatings of different thicknesses on various supports.

Another interesting feature of these particles is that dendrites differing in size and shape are observed to form from aqueous solutions containing PAHAPS colloids loaded with metal salts or metal nanoparticles (Fig. 14).<sup>[40]</sup> While formation of dendrites is common for a number of salts or metals,<sup>[41,42]</sup> it has not been reported so far for colloidal particles or nanoparticle-loaded colloidal systems. Because the size and shape of the dendrites produced here can be easily controlled, metal-loaded PAHAPS may be suggested as catalytically active membranes in which select surface coverage is important. Another possible application for PAHAPS loaded with metal nanoparticles is as a conductive layer between two surfaces, as described elsewhere<sup>[43]</sup> for pure Pd dendrite crystals. At the same time, unlike pure metals, metal-loaded PAHAPS possesses a number of practical advantages, including lower cost and greater structural stability.

Another precursor of interest for synthesis of polymer colloids using sol-gel reaction is octadecyldimethyl

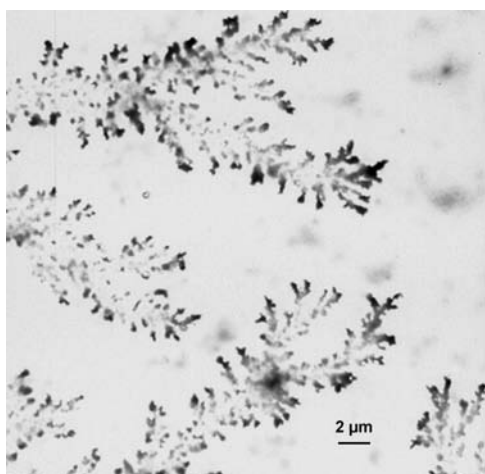


**Fig. 14** Transmission electron microscopic image of dendrites formed by PAHAPS colloids filled with Pd nanoparticles.

(3-trimethoxysilylpropyl)ammonium chloride (ODMACl). The hydrolytic condensation of this precursor both in acidic and basic solutions results in the formation of colloidal particles showing lamellar ordering with Bragg spacing  $d$  of about 3.6 nm. This Bragg spacing is significantly smaller than two layers of extended ODMACl tails, so one can assume either tilting of ODMACl chains (they are not perpendicular to the lamellar surface) or interpenetration of the tails of the two layers (or both). As the PODMACl colloids are much larger than twice the  $d$  spacing, they should have a multilamellar structure. Because PODMACl colloids contain ionic groups in their tails, they can be subjected to ion exchange that results in replacement of  $\text{Cl}^-$  ions for ions of interest:  $\text{PdCl}_4^{2-}$ ,  $\text{PtCl}_6^{2-}$ ,  $\text{AuCl}_4^-$ . The subsequent reduction leads to metal nanoparticle formation within PODMACl colloids. Moreover, independently of reducing agent type, lamellar ordering is preserved, while particle size and shape strongly depend on the nucleation rate. With  $\text{NaBH}_4$ , narrowly distributed spherical particles with a mean diameter of  $\sim 2$  nm are obtained. When nucleation is slow, particle growth is directed by the lamellar ordering, so rod-like particles of  $2 \times 13$  nm are formed and their positioning is well regulated by the ordered structure. This suggests new opportunities for growing rod-like particles derived from different metal or semiconductors within ordered polymeric colloids. Such materials can be promising for tailoring optical, magnetic, and electrical properties of nanocomposites by tuning the particle shape.

### NANOPARTICLES FORMED ON THE POLYMER COLLOID SURFACE

Micrometer and submicrometer Au-shell PS latex beads have been prepared by combining the self-assembly

and seeding methods.<sup>[44]</sup> The PS beads are first covered with positively charged poly(ethyleneimine) (PEI) via electrostatic interaction and hydrogen bonding; then, the Au shell is formed via the reaction of PEI-PS with  $\text{NH}_2\text{OH}$  and  $\text{HAuCl}_4$ . This method allows efficient control of the gold coverage and leads to relatively stable products. Using TEM, formation of Au clusters and gold nanoparticles on the surface of the PS beads was confirmed. The results suggest that the PEI polymer chains are probably stretched out on the surface of the PS beads. The UV-visible extinction spectrum for gold-covered particles is significantly affected by the plasmon resonance absorption.

For preparation of Au-shell magnetic particles, sulfonated polystyrene beads were first exchanged with  $\text{Fe}^{2+}$  ions under  $\text{N}_2$  gas flow and then treated with NaOH solution. The last stage involves heating the beads at  $100^\circ\text{C}$  for 1 h. Iron oxide layer was later covered with a gold shell as described for Au shell/PS colloids. Self-assembled structures of Au-covered particles were induced by an external magnetic field.<sup>[44]</sup> This conductive grid was suggested for use as a tunable polarizer for microwaves and milliwaves, as the conducting lines that can be switched into a non-conductive state by an external field. Waveguides for plasmon, i.e., excitation of the plasmon resonance at one end of the lines and detection at the other end, is another interesting application.

Well-dispersed Ag nanoparticles were formed in situ on the surface of poly(*N*-isopropylacrylamide, PNIPAAm)-coated polystyrene microspheres.<sup>[45]</sup> The surface-grafted PNIPAAm chains serve both as steric stabilizers to prevent the flocculation of the polystyrene particles and interact with silver salts with subsequent adsorption of the forming Ag nanoparticles onto the surfaces of the microspheres. By varying the concentrations of initiator and silver nitrate, the particle sizes and distributions for both Ag nanoparticles and polystyrene microspheres can be altered. As PNIPAAm is a well-known, temperature-sensitive polymer, the PNIPAAm-protected Pt colloids show unusual temperature dependence of activity in the aqueous hydrogenation of allyl alcohol, which can be explained by different density of PNIPAAm layer at different temperatures. In addition, Pt colloids on the microspheres show higher activity than the commercial Pt/C catalyst and retain high activity on recycling in the same reaction. Polystyrene microspheres with silver nanoparticles can be used as the active substrates for surface-enhanced Raman scattering, chemical, electronic, and optical sensors, and photocatalysts for solar energy conversion.

Another example of PS beads covered with nanoparticles is described in Ref.<sup>[46]</sup>. Surface-functionalized PS microbeads and nanobeads were prepared by grafting the *p*-acetoxystyrene monomer during the last

30 min of the fabrication of polystyrene bead core by emulsifier-free emulsion polymerization followed by hydrolysis of the acetoxy group by a base. The size of the resulting beads is mostly dictated by the size of the core. Hydroxyl-derivatized polystyrene microspheres have been used for anchoring catalytically active silver and ruthenium nanoparticles. This was performed by adsorption of preformed nanoparticles on the functionalized bead surface. The bead formation, surface functionalization, and coating with metal nanoparticles were studied using scanning electron microscopy (SEM), TEM, energy dispersive X-ray spectrometry (EDS), Fourier-transform IR spectrometry, and Auger analysis.

### NANOPARTICLES WITH ADSORBED POLYMER LAYER

Any nanoparticle synthesis in polymer solution normally results in the adsorption of polymer molecules on the nanoparticle surface. Usually, these materials are not considered as metallated polymer colloids. Nevertheless, in some cases including ones cited below, adsorption or chemical interaction of polymers with nanoparticles is accompanied with formation of a polymer layer of different nature than that used for nanoparticle synthesis.

Reduction of Pd, Pt, or Au ions in dimethyl sulfoxide (DMSO) solution by a  $\pi$ -conjugated poly(dithiafulvene) (PDF) having strong electron-donating properties resulted in the adsorption of oxidized polymer on the forming nanoparticle surface, which protected the metal nanoparticles (Fig. 15).<sup>[47]</sup> As found, all the DF units of PDF were uniformly oxidized by electron transfer, which means that they participated in the reduction, and resided on the particle surface.

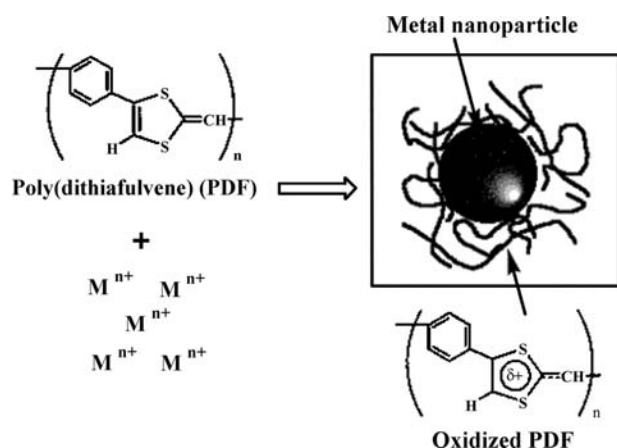


**Fig. 15** Schematic illustration of the formation of the PDF-protected metal nanoparticles via reduction of metal ions by the  $\pi$ -conjugated, electron-donating PDF. *Source:* From Ref.<sup>[47]</sup>. © 2002 by the American Chemical Society.

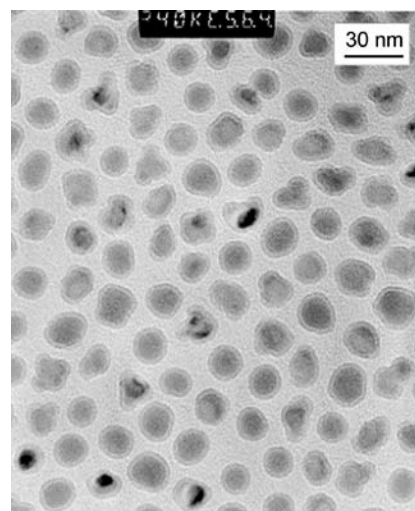


**Fig. 16** Transmission electron microscopic image of PIB-coated nanoparticles made with 80 g of  $Fe(CO)_5$  and 11 g of PIB-TEPA (tetraethylenepentamine). *Source:* From Ref.<sup>[48]</sup>. © 2002 by the American Chemical Society.

The average size of the formed Pt nanoparticles increased with the increases of the PDF concentration and reaction temperature. All of the Pt nanoparticles formed at different temperatures showed narrow size distribution, high dispersibility, and great thermal stability.

Magnetic materials comprised of polymer-iron nanoparticle composites have been prepared by thermal decomposition of iron pentacarbonyl in the presence of ammonia and several types of polymeric dispersants.<sup>[48]</sup> The nanoparticles consist of metallic cores, each of which is coated with a strongly bound polymer layer (Fig. 16). The polyisobutylene- and polyethylene-based dispersants lead to more uniform particle sizes and the materials are composed principally of individual core-shell particles. Large, complex particles, formed by the aggregation of smaller particles, as well as simple core-shell particles, were obtained with polystyrene-based dispersants in 1-methylnaphthalene. Aggregation leading to complex particles was found to be a result of a mismatch between the solubility parameters of the dispersant and the reaction solvent. When the solvent was better matched with the solubility parameter of polystyrene, simple core-shell nanoparticles of fairly uniform size were obtained. Electron diffraction revealed that the core material is iron. High-resolution TEM showed highly ordered or crystalline regions within the polymer shell, possibly because of the dense packing of the strongly bound dispersant chains (Fig. 17). Magnetic interactions between particles cause formation of secondary structures such as clusters, coils, loops, and strings of particles. The nanocomposites can be dispersed in organic solvents or cast as films. The

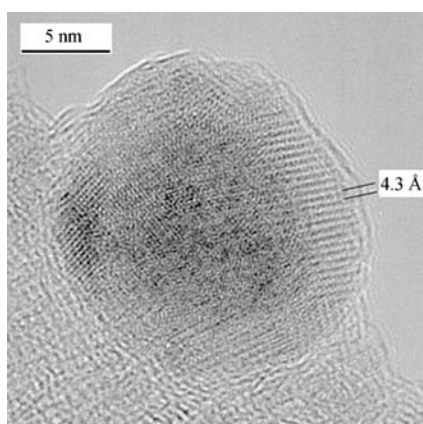


**Fig. 17** High-resolution TEM image of PIB-coated nanoparticles made with 60 g of  $\text{Fe}(\text{CO})_5$  and 11 g of PIB-TEPA. Lattice planes are visible in the shell region of the particles. Source: From Ref.<sup>[48]</sup>. © 2002 by the American Chemical Society.

polystyrene-iron composites are rigid solids at room temperature but can be melted at temperatures of 65–100°C. The nanoparticle composites showed different magnetic behavior depending on the particle size. Samples with the smallest particles proved to be superparamagnetic but their saturation magnetizations were low. Hysteresis was observed for materials with larger particles, and the materials possessed larger magnetizations. The magnetization was correlated with the particle size where samples with larger particles showed higher magnetizations. The samples with higher iron contents, achieved using higher iron pentacarbonyl loadings or by removing unbound polymer dispersant, showed the highest magnetization.

## CONCLUSION

This entry clearly shows several approaches to constructing nanocomposite polymer colloids containing nanoparticles. In all cases, polymer colloids are soluble in organic or aqueous media (depending on the exterior of the colloids) and retain solubility after nanoparticle formation. This key feature allows the formation of thin deposited or freestanding films (the latter were obtained with block copolymer micelles and functionalized polysilsesquioxane colloids) that makes possible a number of important applications for nanolithography in optical and magnetic materials. For catalytic applications, both homogeneous (solutions) and heterogeneous systems (after deposition on the support) proved to be promising with the polymer colloids filled with nanoparticles. It is worth mentioning that the polymer nanoenvironment significantly changes the nanoparticle properties via modification

of the nanoparticle surface with polymer groups; therefore the choice of polymer type and structural organization of polymer colloids play a crucial role in material properties and should be taken into consideration for specific material application.

## REFERENCES

1. Hamley, I.U. *The Physics of Block Copolymers*; Oxford University Press: Oxford, UK, 1998.
2. Förster, S.; Antonietti, M. Amphiphilic block copolymers in structure-controlled nanomaterial hybrids. *Adv. Mater.* **1998**, *10* (3), 195–217.
3. Antonietti, M.; Henz, S. Supermolecular structures at polymers. A way towards intelligent materials? *Nachr. Chem. Tech. Lab.* **1992**, *40* (3), 308–314.
4. Antonietti, M.; Wenz, E.; Bronstein, L.; Seregina, M. Synthesis and characterization of noble metal colloids in block copolymer micelles. *Adv. Mater.* **1995**, *7* (12), 1000–1005.
5. Spatz, J.P.; Roescher, A.; Möller, M. Gold nanoparticles in micellar poly(styrene)-*b*-poly(ethylene oxide) films. Size and interparticle distance control in monodisperse films. *Adv. Mater.* **1996**, *8* (4), 337–340.
6. Moffitt, M.; McMahon, L.; Pessel, V.; Eisenberg, A. Size control of nanoparticles in semiconductor-polymer composites. 2. Control via sizes of spherical ionic microdomains in styrene-based diblock ionomers. *Chem. Mater.* **1995**, *7* (6), 1185–1192.
7. Saito, R.; Okamura, S.; Ishizu, K. Introduction of colloidal silver into poly(2-vinylpyridine) microdomains of microphage-separated poly(styrene-*b*-2-vinylpyridine) film. 3. Poly(2-vinylpyridine) spherical microdomain. *Polymer* **1993**, *34* (6), 1189–1195.
8. Bronstein, L.; Antonietti, M.; Valetsky, P. Metal colloids in block copolymer micelles: formation and material properties. In *Nanoparticles and Nanostructured Films*; Fendler, J.H., Ed.; Wiley-VCH Verlag: Weinheim, 1998; 145–171.
9. Seregina, M.V.; Bronstein, L.M.; Platonova, O.A.; Chernyshov, D.M.; Valetsky, P.M.; Hartmann, J.; Wenz, E.; Antonietti, M. Preparation of noble-metal colloids in block copolymer micelles and their catalytic properties in hydrogenation. *Chem. Mater.* **1997**, *9* (4), 923–931.
10. Bronstein, L.M.; Chernyshov, D.M.; Volkov, I.O.; Ezernitskaya, M.G.; Valetsky, P.M.; Matveeva, V.G.; Sulman, E.M. Structure and properties of bimetallic colloids formed in polystyrene-*block*-poly-4-vinylpyridine micelles: Catalytic behavior in selective hydrogenation of dehydrolinalool. *J. Catal.* **2000**, *196* (2), 302–314.
11. Platonova, O.A.; Bronstein, L.M.; Solodovnikov, S.P.; Yanovskaya, I.M.; Obolonkova, E.S.; Valetsky, P.M.; Wenz, E.; Antonietti, M. Cobalt nanoparticles in block copolymer micelles. Preparation and properties. *Colloid Polym. Sci.* **1997**, *275* (5), 426–431.
12. Rutnakornpituk, M.; Thompson, M.S.; Harris, L.A.; Farmer, K.E.; Esker, A.R.; Riffle, J.S.; Connolly, J.; St. Pierre, T.G. Formation of cobalt nanoparticle

- dispersions in the presence of polysiloxane block copolymers. *Polymer* **2002**, *43* (8), 2337–2348.
13. Underhill, R.S.; Liu, G. Triblock nanospheres and their use as templates for inorganic nanoparticle preparation. *Chem. Mater.* **2000**, *12* (8), 2082–2091.
  14. Bronstein, L.M.; Sidorov, S.N.; Valetsky, P.M.; Hartmann, J.; Coelfen, H.; Antonietti, M. Induced micellization by interaction of poly(2-vinylpyridine)-*block*-poly(ethylene oxide) with metal compounds. Micelle characteristics and metal nanoparticle formation. *Langmuir* **1999**, *15* (19), 6256–6262.
  15. Bronstein, L.; Kraemer, E.; Berton, B.; Burger, C.; Foerster, S.; Antonietti, M. Successive use of amphiphilic block copolymers as nanoreactors and templates: preparation of porous silica with metal nanoparticles. *Chem. Mater.* **1999**, *11* (6), 1402–1405.
  16. Martin, T.J.; Prochazka, K.; Munk, P.; Webber, S.E. pH-dependent micellization of poly(2-vinylpyridine)-*block*-poly(ethylene oxide). *Macromolecules* **1996**, *29* (18), 6071–6073.
  17. Gohy, J.-F.; Willet, N.; Varshney, S.; Zhang, J.-X.; Jerome, R. Core-shell-corona micelles with a responsive shell. *Angew. Chem., Int. Ed.* **2001**, *40* (17), 3214–3216.
  18. Moffitt, M.; Vali, H.; Eisenberg, A. Spherical assemblies of semiconductor nanoparticles in water-soluble block copolymer aggregates. *Chem. Mater.* **1998**, *10* (4), 1021–1028.
  19. Mayer, A.B.R.; Mark, J.E.; Morris, R.E. Palladium and platinum nanocatalysts protected by amphiphilic block copolymers. *Polym. J.* **1998**, *30* (3), 197–205.
  20. Mayer, A.B.R.; Mark, J.E. Transition metal nanoparticles protected by amphiphilic block copolymers as tailored catalyst systems. *Colloid Polym. Sci.* **1997**, *275* (4), 333–340.
  21. Bronstein, L.M.; Chernyshov, D.M.; Timofeeva, G.I.; Dubrovina, L.V.; Valetsky, P.M.; Obolonkova, E.S.; Khokhlov, A.R. Interaction of polystyrene-*block*-poly(ethylene oxide) micelles with cationic surfactant in aqueous solutions. Metal colloid formation in hybrid systems. *Langmuir* **2000**, *16* (8), 3626–3632.
  22. Bronstein, L.M.; Chernyshov, D.M.; Timofeeva, G.I.; Dubrovina, L.V.; Valetsky, P.M.; Khokhlov, A.R. The hybrids of polystyrene-*block*-poly(ethylene oxide) micelles and sodium dodecyl sulfate in aqueous solutions: interaction with Rh ions and Rh nanoparticle formation. *J. Colloid Interface Sci.* **2000**, *230* (1), 140–149.
  23. Bronstein, L.M.; Chernyshov, D.M.; Vorontsov, E.; Timofeeva, G.I.; Dubrovina, L.V.; Valetsky, P.M.; Kazakov, S.; Khokhlov, A.R. Comicecellization of polystyrene-*block*-poly(ethylene oxide) with cationic and anionic surfactants in aqueous solutions: Indications and limits. *J. Phys. Chem., B* **2001**, *105* (38), 9077–9082.
  24. Zeng, F.; Zimmerman, S.C. Dendrimers in supramolecular chemistry: from molecular recognition to self-assembly. *Chem. Rev.* **1997**, *97* (5), 1681–1712.
  25. Bar, G.; Rubin, S.; Cutts, R.W.; Taylor, T.N.; Zawodzinski, T.A., Jr. Dendrimer-modified silicon oxide surfaces as platforms for the deposition of gold and silver colloid monolayers: preparation method, characterization, and correlation between microstructure and optical properties. *Langmuir* **1996**, *12* (5), 1172.
  26. Zhao, M.; Crooks, R.M. Dendrimer-encapsulated Pt nanoparticles: synthesis, characterization, and applications to catalysis. *Adv. Mater.* **1999**, *11* (3), 217–220.
  27. Esumi, K.; Suzuki, A.; Aihara, N.; Usui, K.; Torigoe, K. Preparation of gold colloids with UV irradiation using dendrimers as stabilizer. *Langmuir* **1998**, *14* (12), 3157–3159.
  28. Crooks, R.M.; Lemon, B.I.; Sun, L.; Yeung, L.K.; Zhao, M. Dendrimer-encapsulated metals and semiconductors: synthesis, characterization, and applications. *Topics Curr. Chem.* **2001**, *212* (Dendrimers III), 81–135.
  29. Gröhn, F.; Bauer, B.J.; Akpalu, Y.A.; Jackson, C.L.; Amis, E.J. Dendrimer templates for the formation of gold nanoclusters. *Macromolecules* **2000**, *33* (16), 6042–6050.
  30. Gröhn, F.; Bauer, B.J.; Amis, E.J. Hydrophobically modified dendrimers as inverse micelles: formation of cylindrical multidendrimer nanostructures. *Macromolecules* **2001**, *34* (19), 6701–6707.
  31. Sooklal, K.; Huang, J.; Murphy, C.J.; Hanus, L.; Ploehn, H.J. Inorganic quantum dot-organic dendrimer nanocomposite materials. *Mater. Res. Soc. Symp. Proc.* **1999**, *576*, 439–444.
  32. Lemon, B.I.; Crooks, R.M. Preparation and characterization of dendrimer-encapsulated CdS semiconductor quantum dots. *J. Am. Chem. Soc.* **2000**, *122* (51), 12,886–12,887.
  33. Donners, J.J.J.M.; Hoogenboom, R.; Schenning, A.P.H.J.; van Hal, P.A.; Nolte, R.J.M.; Meijer, E.W.; Sommerdijk, N.A.J.M. Fabrication of organic-inorganic semiconductor composites utilizing the different aggregation states of a single amphiphilic dendrimer. *Langmuir* **2002**, *18* (7), 2571–2576.
  34. Seker, F.; Ellis, A.B. Probing polymer adsorption using an emissive semiconductor substrate: Adsorption of poly(acrylic acid) onto cadmium selenide. *Macromolecules* **2000**, *33* (2), 582–589.
  35. Michels, J.J.; Huskens, J.; Reinhoudt, D.N. Dendrimer-cyclodextrin assemblies as stabilizers for gold and platinum nanoparticles. *J. Chem. Soc., Perkin Trans.* **2002**, *2* (1), 102–105.
  36. Antonietti, M. Microgels—polymers with a special molecular architecture. *Angew. Chem.* **1988**, *100* (12), 1813–1817.
  37. Antonietti, M.; Bremser, W.; Schmidt, M. Microgels: model polymers for the crosslinked state. *Macromolecules* **1990**, *23* (16), 3796–3805.
  38. Antonietti, M.; Gröhn, F.; Hartmann, J.; Bronstein, L. Nonclassical shapes of noble-metal colloids by synthesis in microgel nanoreactors. *Angew. Chem., Int. Ed.* **1997**, *36* (19), 2080–2083.
  39. Whilton, N.T.; Berton, B.; Bronstein, L.; Hentze, H.-P.; Antonietti, M. Organized functionalization of mesoporous silica supports using prefabricated metal-polymer modules. *Adv. Mater.* **1999**, *11* (12), 1014–1018.
  40. Bronstein, L.M.; Linton, C.; Karlinsey, R.; Stein, B.; Svergun, D.I.; Zwanziger, J.W.; Spontak, R.J. Synthesis of metal-loaded poly(aminohexyl)(aminopropyl)silsesquioxane colloids and their self-organization into dendrites. *Nano Lett.* **2002**, *2* (8), 873–876.



41. Honjo, H.; Ohta, S. Dense-branching morphology of an ammonium chloride crystal. *Phys. Rev., A* **1992**, *45* (12), R8332–R8335.
42. Zeng, H.C.; Lim, L.C. Secondary ionic forces in lead molybdate melt solidification. *J. Mater. Res.* **1998**, *13* (6), 1426–1429.
43. Bernier, W.E.; Bundga, E.G. Conductive adhesive having a palladium matrix interface between two metal surfaces. **2001**, US 6331119.
44. Ji, T.; Lirtsman, V.G.; Avny, Y.; Davidov, D. Preparation, characterization, and application of Au-shell/polystyrene beads and Au-shell/magnetic beads. *Adv. Mater.* **2001**, *13* (16), 1253–1256.
45. Chen, B.C.-W.; Chen, M.-Q.; Serizawa, T.; Akashi, M. In-situ formation of silver nanoparticles on poly (*N*-isopropylacrylamide)-coated polystyrene microspheres. *Adv. Mater.* **1998**, *10* (14), 1122–1126.
46. Greci, M.T.; Pathak, S.; Mercado, K.; Prakash, G.K.S.; Thompson, M.E.; Olah, G.A. Poly(*p*-hydroxystyrene) grafted polystyrene nanospheres: excellent hosts for silver and ruthenium nanoparticles. *J. Nanosci. Nanotech.* **2001**, *1* (1), 3–6.
47. Zhou, Y.; Itoh, H.; Uemura, T.; Naka, K.; Chujo, Y. Synthesis of novel stable nanometer-sized metal (M=Pd, Au, Pt) colloids protected by a pi-conjugated polymer. *Langmuir* **2002**, *18* (1), 277–283.
48. Burke, N.A.D.; Stoeber, H.D.H.; Dawson, F.P. Magnetic nanocomposites: preparation and characterization of polymer-coated iron nanoparticles. *Chem. Mater.* **2002**, *14* (11), 4752–4761.

# Polymer-Mediated Self-Assembly of Nanoparticles

Tyler B. Norsten  
Amitav Sanyal  
Roy Shenhar  
Vincent M. Rotello

*Department of Chemistry, University of Massachusetts, Amherst, Massachusetts, U.S.A.*

## INTRODUCTION

Polymer self-assembly of nanoparticles yields stabilized metal and semiconductor nanocomposites as well as provides access to structured nanoscale materials. The properties of these materials can be tuned by varying the size and shape of the metal cluster as well as by altering the composition of the monolayer that covers the particles. Furthermore, the functionality and structure of the polymer can be modified, which lends an additional element of control to the entire assembly process. This “bottom-up” approach provides a methodology that is complementary to “top-down” lithographic methods, providing access to structures smaller and with greater 3-dimensional (3-D) control than is possible through sophisticated lithographic techniques such as electron-beam lithography.<sup>[1–4]</sup> Presently, one of the major obstacles facing nanotechnology is the successful integration of these two general approaches. Multiscale engineering of this sort would allow for the fabrication of intricate functional devices with atomic level structural control that manifests and spans itself into the macroscopic world.

One of the key initial goals in polymer-mediated nanoparticle assembly is the design of catalytic nanocomposites. We have therefore designated a section within this entry solely to polymer–nanoparticle assemblies as applied to catalytic systems. The remaining sections describe the use of polymers to assemble nanoparticles into interesting and potentially useful architectures. Because of lack of space, this entry is not an exhaustive review of the literature but instead contains selected examples, which we feel highlight many of the different methodologies that have been employed for the assembly of polymer-based nanoparticle composites. When necessary the reader will be directed to more in-depth articles and reviews that contain information pertinent to the area.

## GENERAL APPROACHES TO POLYMER-MEDIATED ASSEMBLY OF NANOPARTICLES

Metal and semiconductor nanoparticles embedded within polymer matrices are attractive materials as

they share the processing and handling advantages of bulk materials as well as unique possessing properties arising from the nanoscopic size of the components. Traditional preparation of polymer–nanoparticle composites has been accomplished by in situ generation of metal nanoclusters, typically by chemical reduction of a metal salt contained within a polymer matrix (Fig. 1, route A). The primary function of the polymer matrix is to provide a protective barrier against aggregation of the metal particles during this reduction process. As shown in Fig. 1, a variety of different polymers (homopolymers, block copolymers, and dendrimers) have been employed in this regard in an effort to create well-ordered nanocomposite materials for various applications.

A similar but separate approach involves the assembly of polymer scaffolds with preformed monolayer-protected clusters (MPCs). Monolayer-protected clusters already contain a surface monolayer that prevents the metal from agglomerating and allows for ease of handling and processing (Fig. 1, route B). As such, MPCs can be readily dispersed into polymer matrices taking advantage of designed interfacial interactions between the monolayer functional groups and the polymer backbone. Multiple groups have demonstrated over the past several years that the latter approach provides a versatile alternative method for the fabrication of novel nanoparticle-polymeric materials.

## POLYMER SCAFFOLDS AND NANOPARTICLE BUILDING BLOCKS

### Polymer Scaffolds

Polymers are large molecular structures in which many small repeat units are linked together. These repeat units can be linked together in a linear array, as is the case with the homopolymers and block copolymers described in Fig. 1, or in branched fashion as is the case with dendrimers. Many different routes were followed to synthetically prepare the various types of polymers described in this entry; however, because of space limitations this is beyond the scope of the present chapter.

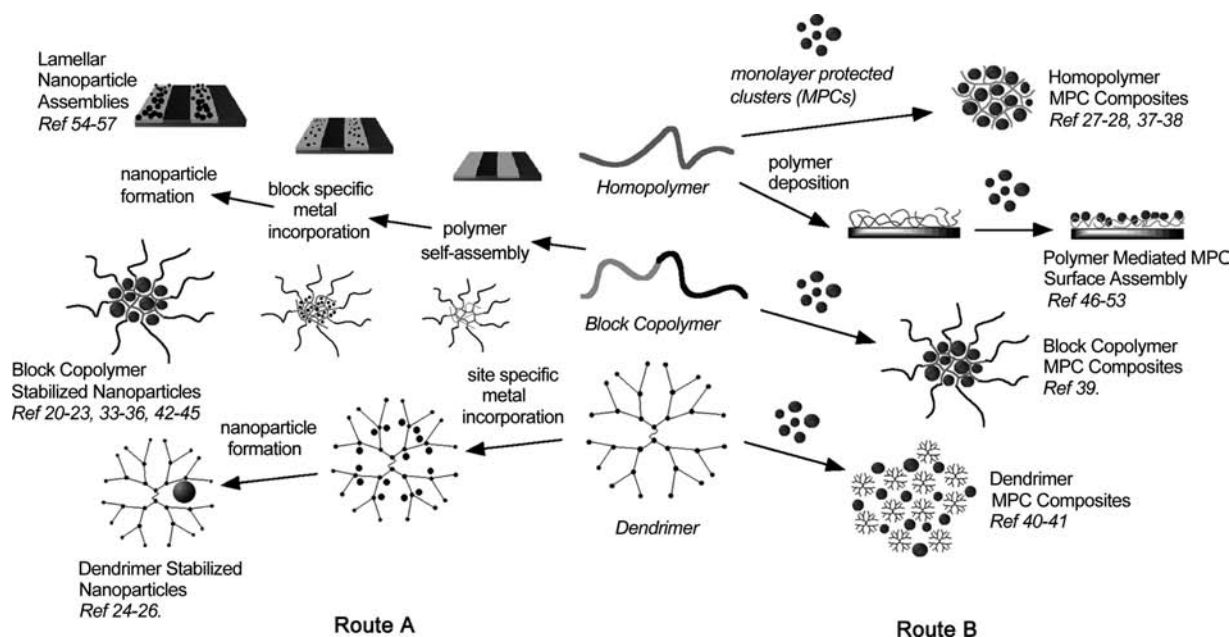


**Fig. 1** Polymer-mediated approaches to fabrication of ordered nanocomposites. Route A: In situ formation of particles within polymer matrices. Route B: Polymer-mediated assembly of preformed monolayer protected clusters (MPCs).

Suffice it to say there has been significant recent progress in the area of polymer synthesis specifically with respect to the formation of block copolymers via living polymerization techniques.<sup>[5-7]</sup>

Block copolymers represent a new and significant class of materials because of their remarkable ability to form unique micro- and nanophase morphologies. These properties are unattainable with homopolymers or their corresponding polymer blends. Diblock copolymers differ from traditional homopolymers in that two chemically distinct polymer chains are covalently connected end-to-end. The immiscibility of the different blocks with each other or with a solvent causes these polymers to phase separate, as such diblock copolymers are able to self-assemble into solvent-stabilized micelles, vesicles, and regular surface stabilized lamellar, cylindrical, or spherical arrays. Several examples will illustrate how appropriately functionalized diblock copolymers are able to incorporate nanoparticles or their precursor metal salts into specific polymer blocks.

Dendrimers are hyperbranched polymers that differ from their traditional linear counterparts in that the repeating units cascade outwardly from a central core rather than elongating in a linear fashion.<sup>[8]</sup> Dendrimers with sufficient layers (generations) take on 3-D/globular morphologies containing interior voids and cavities capable of accommodating guest species. Functionality can be accurately placed throughout the core and at the periphery of dendrimers providing control over such features as site-specific molecular recognition events, interior cavity

size, and overall polymer solubility. The internal attributes described above have been used to incorporate nanoparticles inside of dendrimers, while their distinct generational size-dependent morphologies have been used to define interparticle spacing between metal nanoparticles.

The use of biological polymers such as DNA to assemble and organize nanoparticles is an attractive strategy as the degree of non-covalent complementarity between these polymers can be effectively tuned. As the scope of nanoparticle-biopolymer interactions is exceedingly large in essence commanding its own chapter, we will not cover the topic here, there are, however, several recent examples worth noting that exemplify this type of assembly strategy.<sup>[9-11]</sup>

## Nanoparticle Building Blocks

Fig. 1 describes two of the most typically followed routes to the formation of polymer-nanoparticle composites. Route A generally involves using the polymer as both a template for the formation of nanoparticles into nano- or microdomains defined by the polymer as well as an organic stabilizer to prevent agglomeration after nanoparticle formation. Fairly monodisperse nanoparticles can be assembled using this methodology; however, in many instances the supporting polymer matrix does not offer long-term stability against agglomeration of the metal cores.

Route B typically involves the assembly of polymers with preformed nanoparticles already possessing a

stabilizing monolayer. One of the most frequently encountered MPCs is that of the alkanethiolate-stabilized gold cluster synthesized by the solution-phase method developed by Brust et al.<sup>[12]</sup> (Fig. 2). In this procedure chemical reduction of a gold salt by a hydride-reducing agent in the presence of thiol capping ligands furnishes the desired monolayer-protected nanoparticles. By carefully controlling the reaction conditions and by varying the stoichiometry of the metal salt to capping ligand a variety of different core sizes (1.5–8 nm) can be obtained.

Surface modifications of these nanoparticles can be achieved through a place exchange reaction, where new incoming thiol ligands displace monolayer thiols on the parent MPC to afford mixed monolayer-protected clusters (MMPCs).<sup>[13]</sup> This monolayer modification technique is extremely versatile as it allows for the incorporation of virtually any functionalized thiol into the preexisting monolayer. This permits the interfacial interactions on the surface of the nanoparticle to be precisely tuned to that of the assembling polymer strands.

Gold MPCs are attractive building blocks for the fabrication of nanoscale architectures as their synthesis permits good control over their size and polydispersity. Furthermore, the alkanethiolate monolayer provides excellent stability to intercore agglomeration both in air and in solution. This permits the particles to be handled (i.e., dissolved in solvents, isolated, dispersed in matrices) multiple times without significant degradation occurring and allows for easy characterization using standard solution-phase techniques such as nuclear magnetic resonance (NMR), infrared (IR), and UV–VIS spectroscopy.<sup>[14]</sup>

There are many other types of metallic, bimetallic, and semiconductor nanoparticles available;<sup>[15,16]</sup> however, in most instances, the chemistries of their formation are quite harsh, which substantially reduces the variety of functionalities that can be placed in their protecting monolayers. This makes assembling these types of nanoparticles into extended ordered structures substantially more difficult. Nanoparticle chemistry is still very much in its infancy and it is only a matter

of time before new procedures are created or existing procedures are modified to permit a wider variety of functionalities onto these other types of nanoparticles.

Monolayer-protected clusters clearly provide excellent “building blocks” of regular shape and size for the fabrication of larger ordered structures. These attributes provide part of the solution to the problem of multiscale fabrication as discussed earlier. What remains is their successful incorporation into desired functional ensembles.

## ASSEMBLIES OF NANOPARTICLES FOR CATALYTIC APPLICATIONS

Creation of nanoparticle assemblies possessing an open, porous framework is an attractive strategy for catalyst design. Various noble metals such as palladium, platinum, etc., are used for catalysis in numerous important chemical transformations, including hydrogenation, oxidation, and Heck coupling.<sup>[17–19]</sup> A high surface area-to-volume ratio is desirable for the creation of efficient heterogeneous catalysts as the cost of these precious metals is significant. Small nanoparticles (1–4 nm) are excellent candidates for catalysts in this respect as they exhibit extremely high surface area-to-volume ratios by virtue. Catalytically active materials obtained by metal nanoparticles dispersed in polymeric matrices display increased stability, improved processability, recyclability, and solubility in a variety of organic solvents.

A major thrust in the area of nanoparticle-based catalysts has been the preparation of palladium colloids within the micelles of amphiphilic block copolymers.<sup>[20]</sup> Forster and Antonietti have utilized poly-4-vinylpyridine-*b*-polystyrene (P4VP-*b*-PS) as the block copolymer and Pd(OAc)<sub>2</sub> as the palladium source in the preparation of metal colloids (Fig. 3). Distinct colloidal morphologies can be obtained by carefully controlling the method of reduction: A “raspberry morphology” is created with rapid reduction vs. a “cherry morphology” with a slower reduction rate.<sup>[21]</sup> Colloidal aggregates with the “raspberry morphology,” where

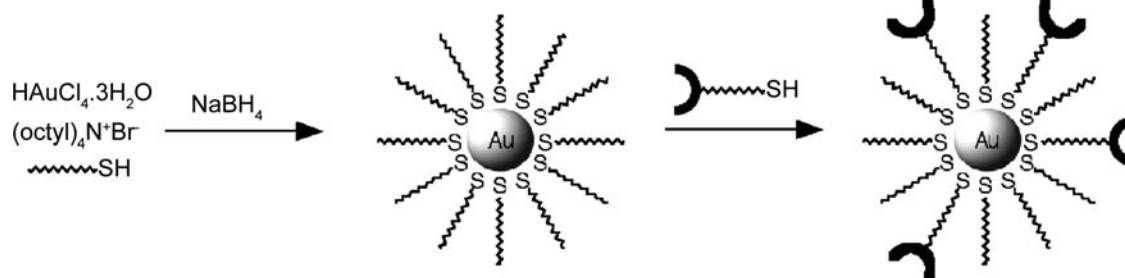


**Fig. 2** Brust et al.’s solution phase MPC synthesis,<sup>[12]</sup> followed by MMPC synthesis using the place exchange process developed by Murray.<sup>[13]</sup>

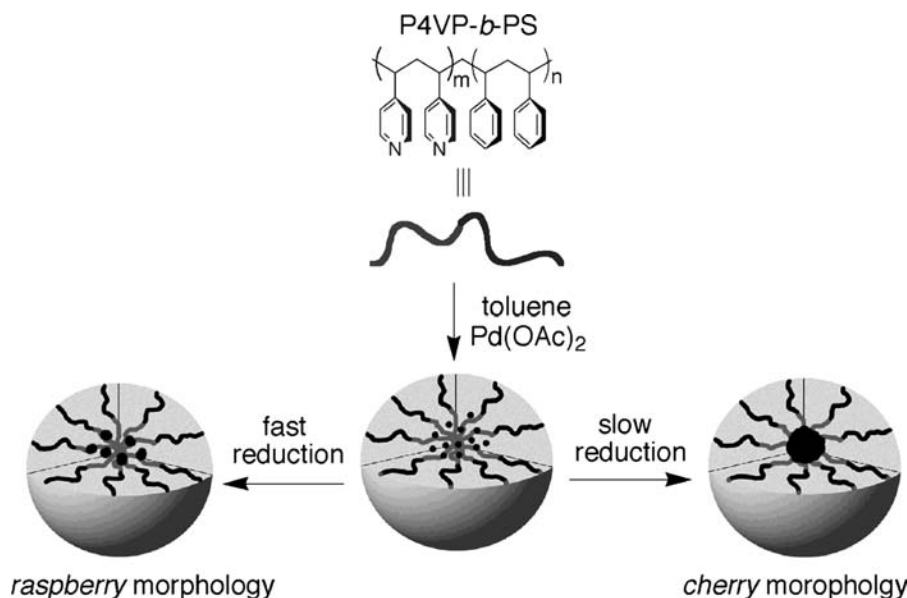


**Fig. 3** Preparation of palladium colloids in P4VP-*b*-PS block copolymer micelles.

the particle size is smaller, demonstrated excellent catalytic activity in the carbon-carbon bond forming Heck reaction. Although the catalyst reactivities were similar to other widely used phosphine ligand/Pd complexes, the polymer-bound Pd nanoparticle catalyst showed much higher stability.

Li and coworkers have shown that palladium nanoparticles stabilized by poly(*N*-vinyl-2-pyrrolidone) (PVP) can be used as efficient catalysts for Suzuki coupling reactions in 40% ethanolic aqueous media.<sup>[22]</sup> Good conversions were obtained upon refluxing for 12–48 hr; however, the PVP homopolymer does not provide adequate stability under such harsh reaction conditions as precipitation of the palladium metal occurs at the end of the reaction.

Underhill and Liu have employed triblock copolymer cross-linked nanospheres as templates for Pd nanoparticles.<sup>[23]</sup> Micelles of a polyisoprene-*b*-poly(2-cinnamoyloxyethyl methacrylate)-*b*-poly(*tert*-butyl acrylate) (PI-*b*-PCEMA-*b*-PtBA) were formed in 65% hexane/THF mixture. The micelles consisted of PI coronas, PCEMA shells, and PtBA cores. Photocross-linking the PCEMA shell produced stable nanospheres, hydroxylation of the terminal isoprene units provided water-dispersibility, and subsequent

hydrolysis of the PtBA groups provided poly(acrylic acid) (PAA) cores capable of complexing PdCl<sub>2</sub>. Loading of PdCl<sub>2</sub> into the acrylic acid core followed by reduction using hydrazine yielded polymer-stabilized palladium nanoparticles (Fig. 4). These palladium-loaded nanospheres were used to study hydrogenation reactions of tetraethylammonium bromide, vinylacetic acid, methylmethacrylate, and ethylene glycol dimethylacrylate. Although the diffusion barriers created by the encapsulating nanospheres led to slightly lower reaction rates compared to palladium black, the hydrogenation kinetics can be controlled by changing the pH as the core structure of the nanospheres is pH sensitive, which ultimately affects the transport of charged substrates into the nanospheres.

Dendrimers have also been used to sequester nanoparticles within their hyperbranched polymer architectures. Crooks et al. have employed poly(amidoamine) (PAMAM) and poly(propylene imine) (PPI) dendrimers as templates for the in situ generation of nanoparticles within the polymer shell of the dendrimer in an effort to create catalytically active nanocomposites.<sup>[24]</sup> Monodisperse nanoparticles can be created inside the dendrimer shell by first introducing a metal salt that strongly complexes to the interior tertiary

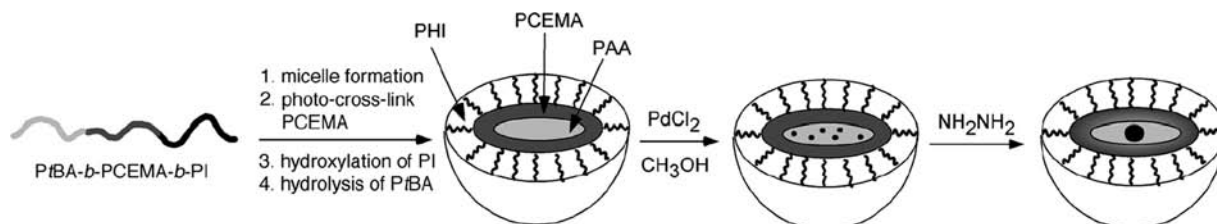


**Fig. 4** Cross-linked triblock copolymer nanospheres encapsulating Pd nanoparticles.

amine groups followed by subsequent reduction of the metal ions producing a trapped-stabilized zero-valent metal nanoparticle. They were able to demonstrate size selective hydrogenation catalysis of  $\alpha$ -substituted allyl alcohols by employing Pd stabilized by hydroxy-terminated PAMAM dendrimers (Fig. 5).<sup>[25]</sup> As generations were added to the dendrimers (G4OH  $\rightarrow$  G6OH  $\rightarrow$  G8OH) turnover frequencies of all the substrates decreased. Furthermore, within a given generation of dendrimer the turnover frequencies were always smaller for the larger substrates. The observed selectivity is a result of the steric crowding at the periphery of the dendrimer, which increases with the dendrimers generation. In essence, the periphery of the dendrimer behaves like a molecular filter which can be tuned in a generational fashion, ultimately hampering access of larger substrates to the catalytically active site.

Recently, Mecking et al. have utilized amphiphilic hyperbranched poly(glycerols) to prepare catalytically active and stable palladium colloids.<sup>[26]</sup> This amphiphilic *dendrimer-like* molecule is capable of solubilizing precursor palladium salts (e.g., PdCl<sub>2</sub>, Pd(OAc)<sub>2</sub>) in non-polar solvents such as toluene and chloroform. Slow reduction using hydrogen results in stable colloidal palladium. The authors suggest that the *soft* binding polyglycerols tend to avoid any ligand poisoning that may result in the amine-functionalized systems because of stronger coordination between the metal and the polymer–ligand. Subsequent catalytic hydrogenation reactions on cyclohexene using this amphiphile-stabilized palladium colloid proceeded at an impressive rate of 700 turnovers hr<sup>-1</sup>, with no significant decrease in rate during recyclable use.

In the example shown above, Crooks et al. employed the hindering effect of a dendrimer sheath in an advantageous way to obtain size selective catalytic discrimination. The polymer casing effectively controls substrate access to the catalytically active site. In general, however, this tends to be a drawback of polymer-supported catalysts as the substrates must find their way through the stabilizing polymer shell in order to reach the buried metal catalyst. This

ultimately results in inefficient mass transport mechanisms for these types of catalysts.

In an alternative approach to the polymer-stabilized nanoparticle catalysts described above, we employ directed self-assembly strategies to develop porous catalyst systems. Mixed monolayer-protected clusters of catalytically active metals can be utilized as building blocks in the presence of a suitable polymeric mediator to obtain macromolecular assemblies. Subsequent removal of the stabilizing polymers and ligands through calcination provides materials with tailored catalytic properties and with improved access to the catalytically active sites.

Preliminary studies to investigate this strategy involved a polymer-mediated three-component system employing both carboxylic acid-terminated gold and SiO<sub>2</sub> nanoparticles, and an amine-functionalized polystyrene random copolymer.<sup>[27]</sup> This type of assembly strategy is based on acid–base chemistry resulting in the electrostatic attraction between the basic polymer and the acidic nanoparticles when combined. Well-integrated nanocomposites were obtained upon the addition of the polymer to a mixture of the two nanoparticles, whereas segregated clusters were formed upon premixing of one of the MPCs with the polymer followed by the addition of the other nanoparticle.

This strategy was then applied to fabricate high-efficiency palladium catalysts.<sup>[28]</sup> Preformed SiO<sub>2</sub>–COOH/poly-NH<sub>2</sub> was used as a scaffold to assemble catalytically active Pd–COOH nanoparticles. The two-phase assembly strategy was necessary to obtain a high exposure of the catalytic metal on the surface of the final aggregate. Calcination removed all of the organic matter creating a highly porous Pd–SiO<sub>2</sub> composite material free of any polymer and monolayer stabilizers (Fig. 6).

The catalytic activity of the calcinated aggregates was investigated for the hydrogenation of 9-decen-1-ol. High turnover frequencies (TOF) (10,100 hr<sup>-1</sup> for the 1:1:1 w/w/w composition of Pd/Si/polymer, respectively) were observed, compared to the 7200 hr<sup>-1</sup> found under the same conditions for the commercial 1% Pd/C catalyst (Fig. 7). In addition, these systems

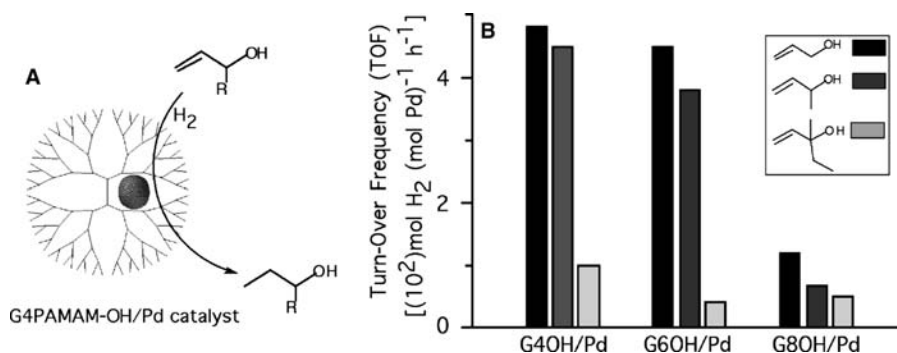


**Fig. 5** (A) Representation of a PAMAM-stabilized Pd nanoparticle catalyzing the hydrogenation of  $\alpha$ -substituted allyl alcohols. (B) Turn-over frequencies of the hydrogenation reactions of various allyl alcohols with generation 4-, 6-, and 8-hydroxy-terminated dendrimers.



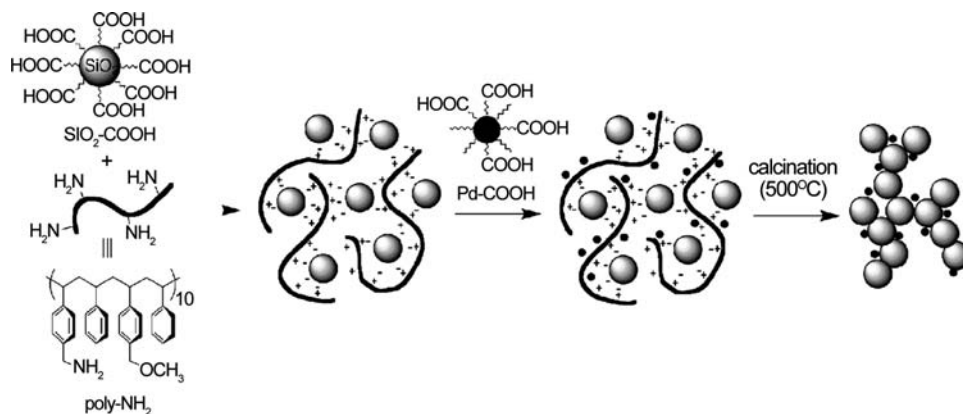


Fig. 6 Formation of the SiO<sub>2</sub>-stabilized Pd nanoparticle catalyst via the three component self-assembly strategy.

proved to be excellent catalysts for Heck coupling reactions between electronically activated bromoarenes and styrene or methyl acrylate at very low catalyst loadings (0.045 mol% of Pd).

Unlike commonly used homogeneous Pd-catalysts, all of the nanoparticle-based catalysts described above required no activation by additional ligands such as phosphines and most could be recycled with only small decreases in their activity. Furthermore, nanoparticle catalysts are much simpler both to separate from their reaction mixtures and to recycle than typical homogeneous catalysts. The combination of these attributes makes them particularly attractive and useful catalysts for a variety of chemical transformations.

## ORGANIZED NANOPARTICLE ASSEMBLIES

The creation of discrete organized nanoparticle assemblies provides a structural motif for nanotechnology.<sup>[29–31]</sup> Highly structured, 3-D nanocomposites display unique magnetic, electronic, and optical behaviors that are both size and distance dependent. An effective way to control both the size and assembly of metallic nanoparticles is through the use of diblock

copolymers. As discussed earlier, diblock copolymers consist of two chemically distinct segments capable of organizing into various structural morphologies because of microphase separation. The size and morphology of the domains are easily controlled by varying the lengths of the individual blocks.<sup>[32]</sup> These self-assembled structures can act as scaffolds for patterning with metallic nanoparticles, employing selective wetting or complexation of the polymeric domains with metal clusters.

Rutnakornpituk and coworkers were able to prepare superparamagnetic cobalt nanoparticles within poly[di-methylsiloxane]-*b*-poly[(3-cyanopropyl)methylsiloxane]-*b*-poly[di-methylsiloxane] (PDMS-PCPMS-PDMS) triblock copolymer templates.<sup>[33]</sup> The copolymer forms micelles in toluene with the PCPMS block being oriented toward the interior of the micelle. Introduction of the cobalt precursor (Co<sub>2</sub>(CO)<sub>8</sub>) into the PCPMS block followed by subsequent thermal decomposition of the metal carbonyl complex yields stable nanoparticles. It is thought that the nitrile groups adhere to the particle surface while the bulky PDMS endblocks provide the steric stability against the core-to-core agglomeration.

Moore and coworkers synthesized several metal nanoparticle clusters using ionomers as templates.<sup>[34]</sup> The size of such ionic microdomains in these

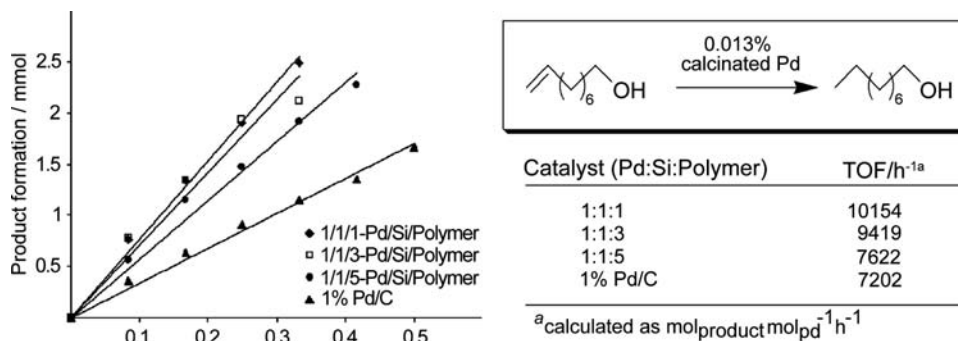
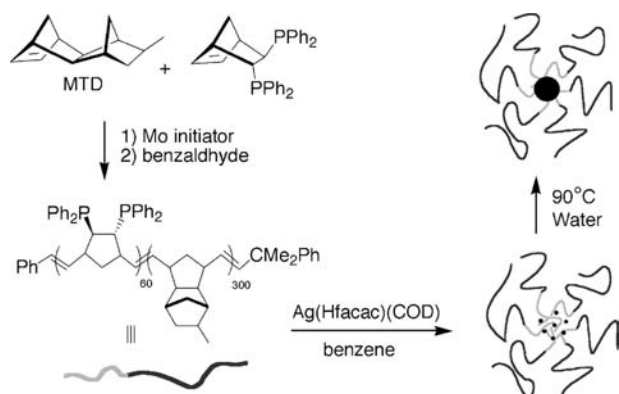


Fig. 7 Rates of product formation in hydrogenation reactions of 9-decen-1-ol with different polymer ratios.

ion-containing copolymers can be controlled by choice of structure of the ionic monomer, whereas in diblock ionomers with spherical microdomains, the radii of the ionic core can be varied between 15 and 100 nm by varying the ionic block length. Utilizing these as microcompartments for nanocluster synthesis allows control over their size. In this approach the control of aggregate size is achieved primarily through ionomer aggregate size and not through varying ion concentration and subsequent annealing conditions.

Ng Cheong Chan et al. have demonstrated that block copolymers created from living ring opening metathesis polymerization reactions of methyltricyclododecene (MTD) and metal-functionalized norbornene monomers can yield stable nanoparticles. They have shown that both a precursor metal complex ( $\text{Ag}(\text{Hfacac})(\text{COD})$ )<sup>[35]</sup> as well as preformed monolayer-stabilized  $\text{CdSe}$ <sup>[36]</sup> nanoparticles can be incorporated into MTD and phosphine-functionalized norbornene block copolymers. In the case of the silver nanoparticles, the silver salts coordinate to the phosphine ligands within the core of solvent-stabilized micelles. Heating the silver-loaded micelles in water produces single nanoclusters (Fig. 8). Both fabrication methods yield stable spherical nanocomposites, but the latter method (akin to route B in Fig. 1) allows for the introduction of preformed nanoparticles that display a much narrower particle size distribution.

We have developed a different approach for using polymer scaffolds to direct the assembly of preformed nanoparticles. Our approach, which we have coined “bricks-and-mortar” self-assembly, involves functionalized nanoparticles as the building blocks or “bricks,” and polymer scaffolds bearing complementary recognition units that serve as the “mortar.” The complementary recognition motif is based on the three-point hydrogen bond between thymine-functionalized gold



**Fig. 8** Phosphine-containing diblock copolymer (bottom left) forming silver-loaded micelles (bottom right). Subsequent thermal treatment leads to stabilized individual silver nanoclusters (top right).

nanoparticles (Au-thy) and diaminotriazine-functionalized polystyrene (poly-triaz) (Fig. 9).

Addition of a triazine-substituted random copolymer (poly-triaz) to concentrated solutions of thymine-functionalized gold nanoparticles (Au-thy) in non-polar solvents results in the formation of insoluble aggregates.<sup>[37]</sup> The TEM images of the THF-soluble fraction of the poly-triaz/Au-thy precipitate revealed the formation of large spherical clusters approximately 100 nm in diameter composed of 3000–7000 individual gold particles (Fig. 10). Small-angle X-ray scattering (SAXS) analysis of the aggregates suggests that the nanoparticles are regularly dispersed within the polymer matrix providing evidence that individual polymer strands weave the nanoparticles together. When hydrogen bonding is disrupted, as is the case with the methylated Au-thy nanoparticles, no such aggregates are formed. This provides direct evidence that the specific hydrogen bonding interactions between the polymer and the nanoparticle drive the assembly process.

Thermal control of the assembly process leads to aggregates of well-defined size and morphology. For instance, highly size-dispersed networks of spherical aggregates were obtained by performing the assembly at 10°C, while performing the aggregation at –20°C yields even larger, individual aggregates. These aggregates are 5–10 times larger than the aggregates formed at 23°C, ranging from 0.5 to 1 μm in diameter and composed of 0.6–5.0 million (!) individual Au-thy nanoparticles, and are among the most complex synthetic self-assembled structures ever constructed.

A follow-up study was undertaken aimed at understanding how secondary molecular interactions such  $\pi$ - $\pi$  stacking in combination with the primary three-point hydrogen bonding interaction would influence the overall aggregation process.<sup>[38]</sup> Here various combinations of nanoparticle and polymer were synthesized containing different recognition elements consisting of either an electron-rich anthracene moiety or an electron-poor naphthalimide moiety in conjunction with a primary hydrogen bonding element. This study showed that weaker secondary interactions are indeed important to aggregate formation and that overall aggregate morphology is directly related to supramolecular events that occur at the colloid-polymer interface.

While we were able to demonstrate a limited level of control over the size and the morphology using monoblock copolymers by carrying out the assembly at different temperatures, we were never able to fully rationalize the observed trends. A solution to this problem is to employ a diblock copolymer where one of the blocks is functionalized as before and the second block remains unfunctionalized.<sup>[39]</sup> In this approach the functionalized block will provide the required hydrogen bonding interactions for the assembly, while

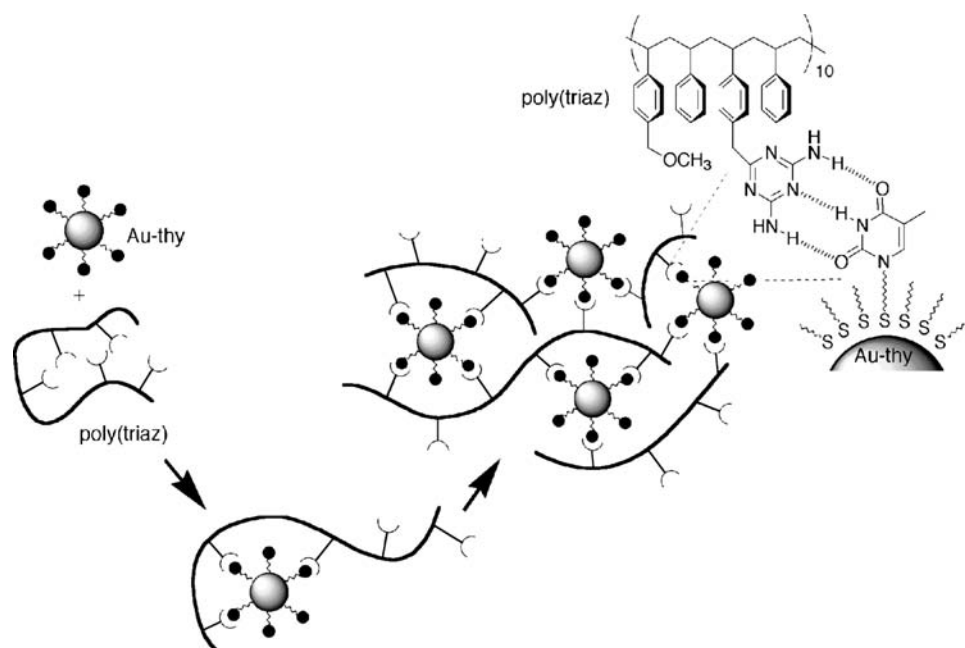


**Fig. 9** Three-point hydrogen bonding recognition between thymine-capped gold nanoparticles and diaminotriazine-functionalized polymers leads to extended network formation.

the inert second block will prevent extensive network formation. As only the functionalized block is capable of incorporating nanoparticle, the overall core size should depend primarily on the length of the functionalized block (Fig. 11A).

The feasibility of diblock-based control of aggregate size was demonstrated by employing three symmetric diblock copolymers (Fig. 11B) with varying total lengths. Combining Au-thy with the various polymers (A–C) results in aggregates with core sizes of  $13.2 \pm 1.3$ ,  $13.9 \pm 1.2$ , and  $19.4 \pm 1.8$  nm, respectively, as revealed by TEM analysis. Dynamic light scattering (DLS) experiments of the polymer micelles reveal the effective hydrodynamic radii  $R_h$  (core and polystyrene corona) to be 18.7, 27.1, and 31.1 nm for

the polymers (A–C), respectively. Comparison of core size by TEM to the overall aggregate size observed by DLS suggests that the polymer segments within the core are extended as compared to the polystyrene segments lying in the exterior, as the corona contributes less than half of the overall radius (Fig. 11C).

The ability to control the spacing between nanoparticles is an important issue as the electronic, and in certain cases the magnetic, properties of the nanoclusters are affected by neighboring particles. We were able to employ the size-dependent properties displayed by different generations of PAMAM dendrimers to both assemble and control the distance between gold nanoparticles.<sup>[40]</sup> Electrostatic self-assembly between the dendrimer and nanoparticle components was provided

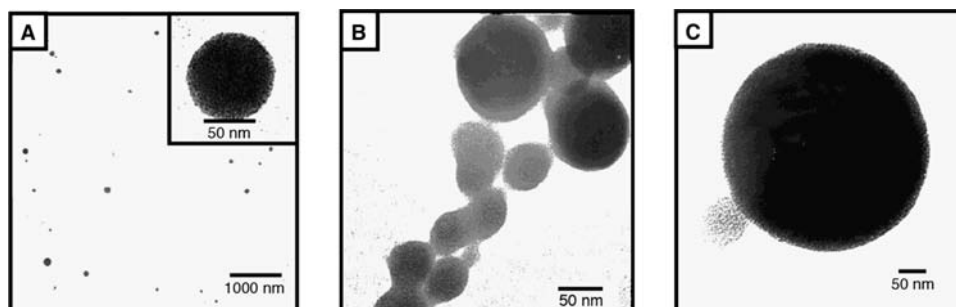


**Fig. 10** (A) TEM of Au-thy/poly-triaz aggregates formed at 23°C. Inset: Representative self-assembled nanoparticle-polymer microspheres. (B) TEM of Au-thy/poly-triaz aggregate network formed at 10°C. (C) TEM of Au-thy/poly-triaz spherical aggregate formed at -20°C.

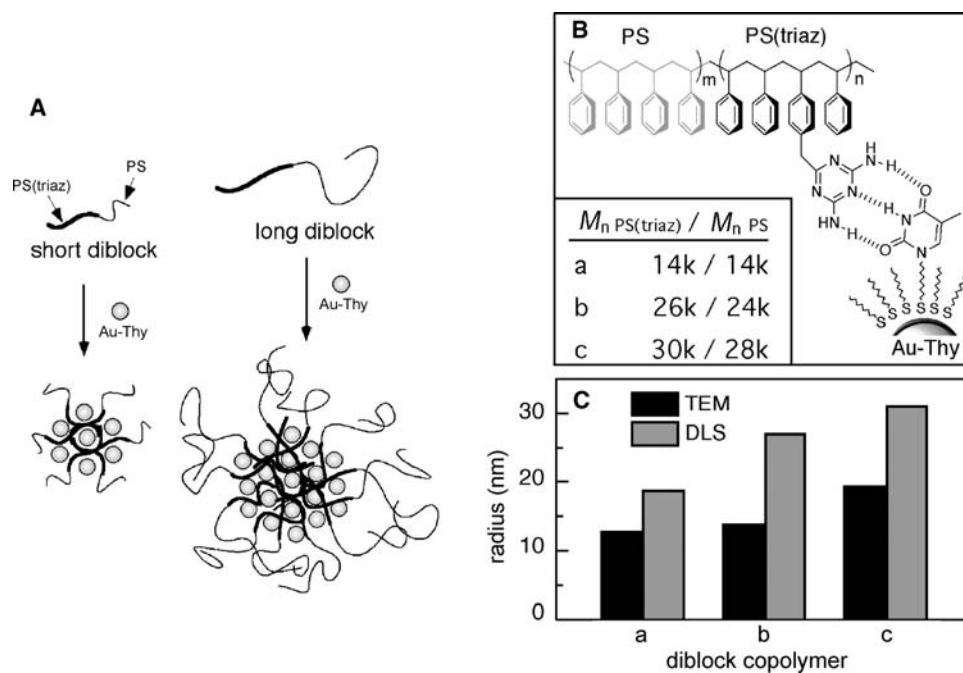


**Fig. 11** (A) Schematic representation of diblock length controlling nanoparticle core and corona size. (B) Different length PS(triaz)-*b*-PS polymers assembled with Au-Thy. (C) Observed nanoparticle core size by TEM compared to hydrodynamic radii of the micelles determined by DLS.

by salt-bridge formation between a carboxylic acid-functionalized nanoparticle and the terminal amine groups on PAMAM dendrimers (Fig. 12).

Examination of the resulting assemblies by TEM revealed that varying the ratios of MMPC to dendrimer resulted in two distinct morphologies. Low dendrimer to MMPC ratios led to network-like structures, which showed little evidence of spatial control. In contrast, high ratios of dendrimer to MMPC (10:1 based

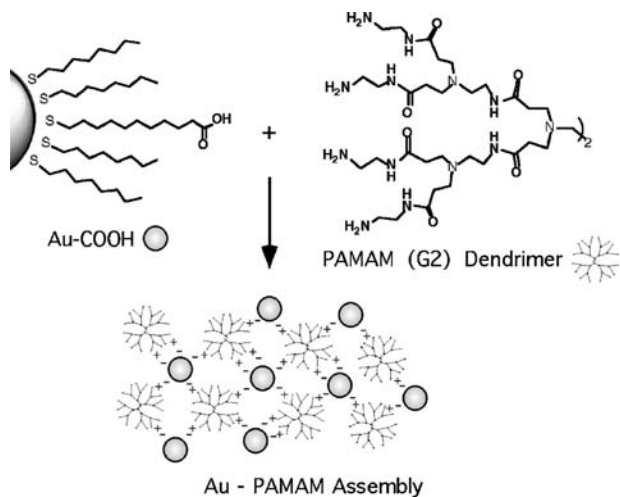


**Fig. 12** Schematic representation of electrostatic self-assembly of carboxylic acid gold nanoparticles and PAMAM dendrimers.

on functional group equivalence) resulted in spherical aggregates ranging from 0.5 to 1.5  $\mu\text{m}$  in diameter (Fig. 13A). In these assemblies, qualitative differences in inter-MMPC spacing could be readily discerned.

Quantification of interparticle distance in the dendrimer MMPC nanocomposites was obtained using SAXS. When the carboxylic acid-functionalized nanoparticle was assembled with PAMAM dendrimers, the primary peak shifted to lower  $q$  values (translating into greater interparticle distances) as the particle is assembled with larger dendrimers ( $G_0 \rightarrow G_1 \rightarrow G_2 \rightarrow G_4 \rightarrow G_6$ ), (Fig. 13). This example clearly demonstrates how different generations of dendrimers can be effectively used to control the spacing between nanoparticles.

Dendrimer-nanoparticle composites have also been used to form functional sensors.<sup>[41]</sup> Vossmeier et al.

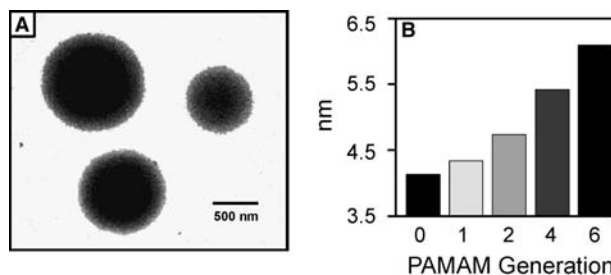


**Fig. 13** (A) Self-assembled nanoparticle-dendrimer microspheres. (B) Graph of correlation between PAMAM generation and interparticle spacing derived from SAXS data.

Polyelectrolyte - Polymer

created thin films of chemically cross-linked gold nanoparticles and polyphenylene dendrimers and deposited them onto glass substrates containing interdigitated gold electrodes. The rigid polyphenylene dendrimer provides a highly porous film for the incorporation of analyte while the nanoparticles provide a high surface-to-volume ratio leading to excellent signal transduction through the film. They were able to show ppm sensitivity to various volatile organic compounds (VOCs) such as toluene and tetrachloroethylene by measuring the change in electrical resistance through the films after exposure to the VOCs. This example demonstrates how the directed assembly of polymers and nanoparticles can lead to working composite devices.

### HIGHLY ORGANIZED POLYMER-NANOPARTICLE ASSEMBLIES ON SURFACES

The previous examples show how polymers have been used to both create finite ordered nanoparticle arrays and assemble nanoparticles into discrete ordered entities extending into the microscale realm. The formation of these large complex structures from small polymeric building blocks is a testament to the power of self-assembly. For many purposes, the controlled ordering at this level may be adequate; nevertheless, functional device applications such as nanoelectronics or memory media (optical or magnetic) require higher degrees of ordering. To create such sophisticated devices it is essential to fabricate not only highly *ordered* arrays but also arrays that are highly *extended* over vast distances (nm→cm).

To this end, Spatz and coworkers have used micelles obtained from diblock copolymers of polystyrene-polyvinylpyridine (PS-*b*-PVP)<sup>[42,43]</sup> and polystyrene-polyethylene oxide (PS-*b*-PEO)<sup>[44]</sup> for synthesis of

metallic and semiconductor nanoparticles. In the case of the PS-*b*-PVP, the pyridine units within the micellar cores can uptake transition metal salts because of hard acid/soft base interactions (Fig. 14). This strategy allows one to obtain size-controlled synthesis of gold nanoparticles by controlling the amount of the precursor salt. Micelles containing the gold salt arranged into quasi-hexagonal packing when transferred onto a flat surface. Subsequent treatment with oxygen plasma completely removed all of the polymeric material yielding highly ordered bare gold nanoclusters.<sup>[45]</sup> Reducing the gold salts in the micellar core before plasma treatment gave clusters of similar size. Varying the concentration of metal salt allows one to obtain cluster sizes from 1 to 15 nm, whereas changing the length of the blocks allows one to get interparticle distances from 30 to 140 nm.

Using a different approach, similar to that of the layer-by-layer (LBL) assembly of oppositely charged polyanions developed by Decher,<sup>[46]</sup> Schmid, Bäuml, and Beyer were able to assemble [Au<sub>55</sub>(Ph<sub>2</sub>PC<sub>6</sub>H<sub>4</sub>SO<sub>3</sub>H)<sub>12</sub>Cl<sub>6</sub>] clusters onto poly(ethyleneimine) (PEI)-covered surfaces (Fig. 15).<sup>[47]</sup> They found that the clusters ordered on the surface into the typical hexagonally close-packed arrangement, but they also found large domains of nanoparticles with an unusual cubic lattice structure. They attribute this high level of surface ordering to the use of PEI with a moderate molecular weight (60,000), which they believe allows the polymer to uncoil on the surface creating a more ordered polymer template. In this case the nanoparticles are packed immediately next to one another as there is no thick polymer sheath surrounding the nanoparticle. There are several examples of LBL assemblies containing multiple layers of polymers with gold,<sup>[48-51]</sup> semiconductor,<sup>[52]</sup> or magnetic nanoparticles,<sup>[53]</sup> and the interested reader is directed to those references.

Using the MTD and phosphine-functionalized norbornene block copolymers as described earlier (Fig. 8),

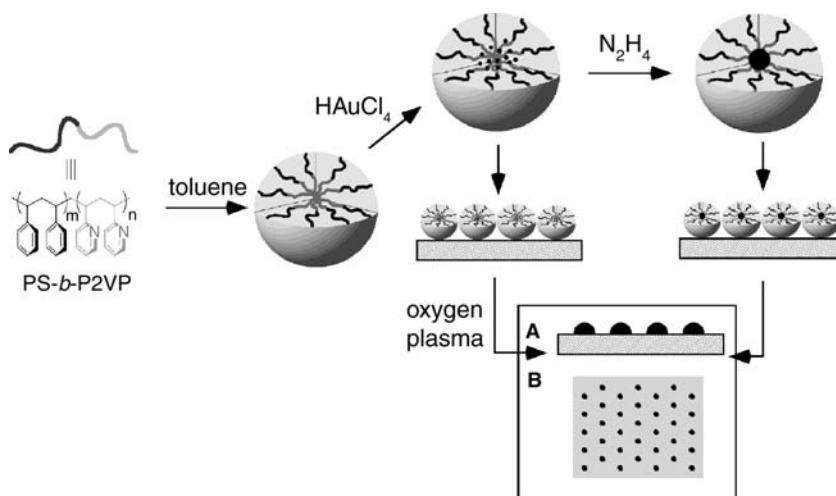


**Fig. 14** Deposition of nanoparticles in a block copolymer micelle onto a surface. (A) Subsequent removal with oxygen plasma yields bare nanoparticles. (B) Schematic representation showing hexagonal packing arrangement of nanoparticles.

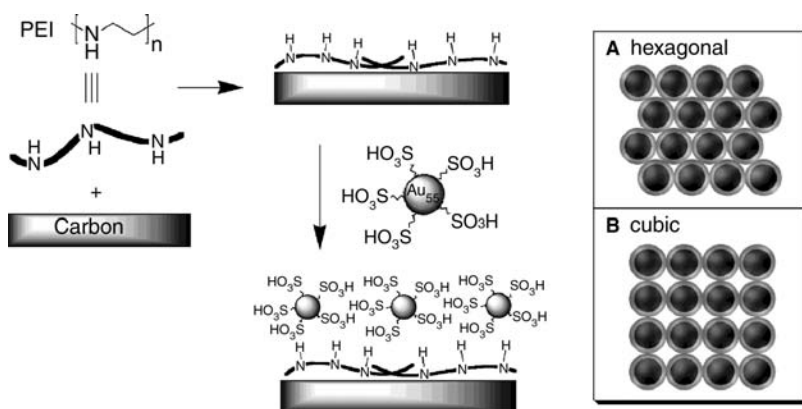


**Fig. 15** Poly(ethyleneimine)-mediated assembly of sulfonated gold nanoparticles arranging into (A) hexagonal and (B) cubic-packed formations.

Ng Cheong Chan et al. were able to form ordered surface assemblies of silver and gold nanoparticles.<sup>[54]</sup> In these studies the phosphine-containing block of the copolymer can selectively coordinate, in a “dative” fashion, to gold and silver, forming coordination complexes in benzene solutions. Films cast from the block copolymer silver solutions yielded lamellar structures while those cast from the gold solutions gave cylinders. Thermally annealing the films yielded striped domains of silver nanoparticles (2–10 nm in diameter) and spherical domains of gold nanoparticles (1.5–4 nm). In both cases long-range ordering occurred and the interdomain spacing was consistent with the length of the unfunctionalized block. This type of methodology

was extended to the incorporation of zinc and cadmium into similar norbornene block copolymers to form the sulfides of these metals within specific lamellar block copolymer microdomains.<sup>[55]</sup>

More recently, Lopes and Jaeger have demonstrated that ultrathin films of phase-separated diblock copolymers can be utilized as templates allowing for the incorporation of metal nanoclusters with selectivity approaching 100% into the desired domain.<sup>[56,57]</sup> In these studies metal vapors were allowed to permeate an ultrathin film consisting of laterally alternating domains of PS and PMMA, obtained using a PS-*b*-PMMA diblock copolymer (Fig. 16). The PS domains preferentially absorb Au and Ag, while the PMMA domains show preference for In, Pb, Sn, and Bi. Near-perfect selective absorption is observed for the deposition of Ag. In the cases where the deposition is only partially selective to one block, selectivity is obtained by annealing the system above the glass transition temperature of the diblock copolymer. Depending on the annealing protocol, distinct separate nanoparticles could be formed within the decorated polymer block. Alternatively, metal nanowires can be obtained by a repeated deposition and annealing sequence. It was shown that the *nanowire* diblock templates display linear current–voltage (*I*-*V*) characteristics over a wide range of conditions, while the *nanoparticle* diblocks exhibit highly nonlinear *I*-*V* curves.

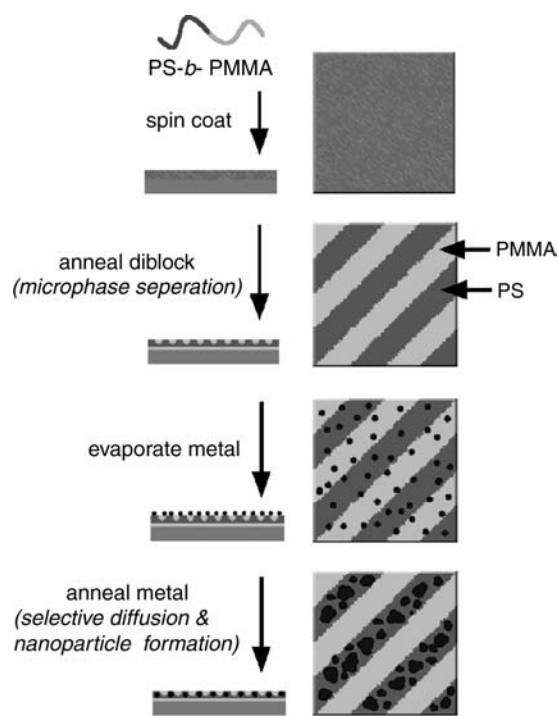


**Fig. 16** Steps for creating ordered arrays of nanoclusters and nanowires in phase-separated PMMA-*b*-PS diblock copolymer films.

## CONCLUSION

Polymer-mediated assembly of nanoparticles is a versatile and effective method for the creation of nanocomposite materials. The ability to chemically control both the polymer structure and the nanoparticle core and shell at the molecular level provides access to a wide variety of resulting materials with tunable properties. This combinatorial approach, coupled with the wealth of structures that can be obtained through self-assembly, makes polymer–nanoparticle composites



potentially useful for a variety of applications. Nanoparticle chemistry and polymer self-assembly are still emerging disciplines and as such we are just beginning to learn the rules that govern their assembly. As we learn these rules and begin to put them to the test, both the complexity and the resulting utility of nanoparticle-polymer composites will increase dramatically.

## REFERENCES

- Jager, E.W.H.; Smela, E.; Inganas, O. Microfabricating conjugated polymer actuators. *Science* **2000**, *290*, 1540–1545.
- Chen, Y.; Pepin, A. Nanofabrication: conventional and nonconventional methods. *Electrophoresis* **2001**, *22*, 187–207.
- Craighead, H.G. Nanoelectromechanical systems. *Science* **2000**, *290*, 1532–1535.
- Wallraff, G.M.; Hinsberg, W.D. Lithographic imaging techniques for the formation of nanoscopic features. *Chem. Rev.* **1999**, *99*, 1801–1821.
- Matyjaszewski, K.; Xia, J. Atom transfer radical polymerization. *Chem. Rev.* **2001**, *101*, 2921–2990.
- Hawker, C.J.; Bosman, A.W.; Harth, E. New polymer synthesis by nitroxide mediated living radical polymerizations. *Chem. Rev.* **2001**, *101*, 3661–3688.
- Hadjichristidis, N.; Pitsikalis, M.; Pispas, S.; Iatrou, H. Polymers with complex architecture by living anionic polymerization. *Chem. Rev.* **2001**, *101*, 3747–3792.
- Newkome, G.R.; Moorefield, C.N.; Vögtle, F. *Dendritic Molecules—Concepts, Syntheses, Perspectives*; VCH: Weinheim, 1996.
- Cao, Y.C.; Jin, R.; Mirkin, C.A. Nanoparticles with Raman spectroscopic fingerprints for DNA and RNA detection. *Science* **2002**, *297*, 1536–1540.
- Mucic, R.C.; Storhoff, J.J.; Mirkin, C.A.; Letsinger, R.L. DNA-directed synthesis of binary nanoparticle network materials. *J. Am. Chem. Soc.* **1998**, *120*, 12,674–12,675.
- Mann, S.; Shenton, W.; Li, M.; Connolly, S.; Fitzmaurice, D. Biologically programmed nanoparticle assembly. *Adv. Mater.* **2000**, *12*, 147–150.
- Brust, M.; Walker, M.; Bethell, D.; Schiffrin, D.J.; Whyman, R. Synthesis of thiol-derivatized gold nanoparticles in a 2-phase liquid-liquid system. *J. Chem. Soc., Chem. Commun.* **1994**, 801–802.
- Templeton, A.C.; Hostetler, M.J.; Warmoth, E.K.; Chen, S.W.; Hartshorn, C.M.; Krishnamurthy, V.M.; Forbes, M.D.E.; Murray, R.W. Gateway reactions to diverse, polyfunctional monolayer-protected gold clusters. *J. Am. Chem. Soc.* **1998**, *120*, 4845–4849.
- Templeton, A.C.; Wuelfing, M.P.; Murray, R.W. Monolayer-protected cluster molecules. *Acc. Chem. Res.* **2000**, *33*, 27–36.
- Toshima, N.; Yonezawa, T. Bimetallic nanoparticles—novel materials for chemical and physical applications. *New J. Chem.* **1998**, *22*, 1179–1201 and references cited therein.
- Schmidt, G.; Bäuml, M.; Geerkens, M.; Heim, I.; Osemann, C.; Sawitowski, T. Current and future applications of nanoclusters. *Chem. Soc. Rev.* **1998**, *28*, 179–185.
- Clapham, B.; Reger, T.S.; Janda, K.D. Polymer-supported catalysis in synthetic organic chemistry. *Tetrahedron* **2001**, *57*, 4637–4662.
- Aiken, J.D.; Finke, R.G. A review of modern transition-metal nanoclusters: their synthesis, characterization, and applications in catalysis. *J. Mol. Catal., A Chem.* **1999**, *145*, 1–44.
- Centi, G.; Perathoner, S. Oxidation catalysts: new trends. *Curr. Opin. Solid State Mater. Sci.* **1999**, *4*, 74–79.
- Forster, S.; Antonietti, M. Amphiphilic block copolymers in structure-controlled nanomaterial hybrids. *Adv. Mater.* **1998**, *10*, 195–217.
- Klingelhofer, S.; Heitz, W.; Greiner, A.; Oestreich, S.; Forster, A.M. Preparation of palladium colloids in block copolymer micelles and their use for the catalysis of the heck reaction. *J. Am. Chem. Soc.* **1997**, *119*, 10,116–10,120.
- Li, Y.; Hong, X.M.; Collard, D.M.; El-Sayed, M.A. Suzuki cross-coupling reactions catalyzed by palladium nanoparticles in aqueous solution. *Org. Lett.* **2000**, *2*, 2385–2388.
- Underhill, R.S.; Liu, G. Preparation and performance of Pd particles encapsulated in block copolymer nanospheres as a hydrogenation catalyst. *Chem. Mater.* **2000**, *12*, 3633–3641.
- Crooks, R.M.; Zhao, M.; Sun, L.; Chechik, V.; Yeung, L.K. Dendrimer-encapsulated metal nanoparticles: synthesis, characterization, and applications to catalysis. *Acc. Chem. Res.* **2001**, *34*, 181–190.
- Niu, Y.; Yeung, L.K.; Crooks, R.M. Size-selective hydrogenation of olefins by dendrimer-encapsulated palladium nanoparticles. *J. Am. Chem. Soc.* **2001**, *123*, 6840–6846.
- Mecking, S.; Thomann, R.; Holger, F.; Sunder, A. Preparation of catalytically active palladium nanoclusters in compartments of amphiphilic hyperbranched polyglycerols. *Macromolecules* **2000**, *33*, 3958–3960.
- Boal, A.K.; Galow, T.H.; Ilhan, F.; Rotello, V.M. Binary and ternary polymer-mediated “bricks and mortar” self-assembly of gold and silica nanoparticles. *Adv. Funct. Mater.* **2001**, *11*, 461–465.
- Galow, T.H.; Drechsler, U.; Hanson, J.A.; Rotello, V.M. Highly reactive heterogeneous heck and hydrogenation catalysts constructed through “bottom-up” nanoparticle self-assembly. *Chem. Commun.* **2002**, 1076–1077.
- Shipway, A.N.; Katz, E.; Willner, I. Nanoparticle arrays on surfaces for electronic, optical, and sensor applications. *ChemPhysChem* **2000**, *1*, 18–52.
- Murray, C.B.; Kagan, C.R.; Bawendi, M.G. Synthesis and characterization of monodisperse nanocrystals and close-packed nanocrystal assemblies. *Annu. Rev. Mater. Sci.* **2000**, *30*, 545–610.
- Forster, S.; Plantenberg, T. From self-organizing polymers to nanohybrid biomaterials. *Angew. Chem., Int. Ed. Engl.* **2002**, *41*, 688–714.

32. Russell, T.P. Copolymers at surfaces and interfaces. *Curr. Opin. Colloid Interface Sci.* **1996**, *1*, 107–115.
33. Rutnakornpituk, M.; Thompson, M.S.; Harris, L.A.; Farmer, K.E.; Esker, A.R.; Riffle, J.S.; Connolly, J.; St. Pierre, T.G. Formation of cobalt nanoparticle dispersions in the presence of polysiloxane block copolymers. *Polymer* **2002**, *43*, 2337–2348.
34. Moore, R.B.; Bittencourt, D.; Gauthier, M.; Williams, C.E.; Eisenberg, A. Small-angle X-ray scattering investigations of ionomers with variable-length side-chains. *Macromolecules* **1991**, *24*, 1376–1382.
35. Ng Cheong Chan, Y.; Schrock, R.R.; Cohen, R.E. Synthesis of single silver nanoclusters within spherical microdomains in block copolymer films. *J. Am. Chem. Soc.* **1992**, *114*, 7295–7296.
36. Fogg, D.E.; Radzilowski, L.H.; Blanski, R.; Schrock, R.R.; Thomas, E.L. Fabrication of quantum dot/polymer composites: phosphine-functionalized block copolymers as passivating hosts for cadmium selenide nanoclusters. *Macromolecules* **1997**, *30*, 417–426.
37. Boal, A.K.; Ilhan, F.; DeRouchey, J.E.; Thurn-Albrecht, T.; Russell, T.P.; Rotello, V.M. Self-assembly of nanoparticles into structured spherical and network aggregates. *Nature* **2000**, *404*, 746–748.
38. Boal, A.K.; Gray, M.; Ilhan, F.; Clavier, G.M.; Kapitzky, L.; Rotello, V.M. Bricks and mortar self-assembly of nanoparticles. *Tetrahedron* **2002**, *58*, 765–770.
39. Frankamp, B.L.; Uzun, O.; Ilhan, F.; Boal, A.K.; Rotello, V.M. Recognition-mediated assembly of nanoparticles into micellar structures with diblock copolymers. *J. Am. Chem. Soc.* **2002**, *124*, 892–893.
40. Frankamp, B.L.; Boal, A.K.; Rotello, V.M. Controlled interparticle spacing through self-assembly of Au nanoparticles and poly(amidoamine) dendrimers. *J. Am. Chem. Soc.* **2002**, *124*, 15146–15147.
41. Vossmeier, T.; Guse, B.; Besnard, I.; Bauer, R.E.; Müllen, K.; Yasuda, A. Gold nanoparticle/polyphenylene dendrimer composite films: preparation and vapor-sensing properties. *Adv. Mater.* **2002**, *14*, 238–242.
42. Möller, M.; Kunstle, H.; Kunz, M. Inorganic nanoclusters in organic glasses—novel materials for electro-optical applications. *Synth. Met.* **1991**, *41*, 1159–1162.
43. Spatz, J.P.; Sheiko, A.; Möller, M. Ion-stabilized block copolymer micelles: film formation and intermicellar interaction. *Macromolecules* **1996**, *29*, 3220–3226.
44. Spatz, J.P.; Roescher, A.; Möller, M. Gold nanoparticles in micellar poly(styrene)-*b*-poly(ethylene oxide) films—size and interparticle distance control in monodisperse films. *Adv. Mater.* **1996**, *8*, 337–340.
45. Spatz, J.P.; Mössmer, S.; Hartmann, C.; Möller, M.; Herzog, T.; Krieger, M.; Boyen, H.-G.; Ziemann, P.; Kabius, B. Ordered deposition of inorganic clusters from micellar block copolymer films. *Langmuir* **2000**, *16*, 407–415.
46. Decher, G. Fuzzy nanoassemblies: towards layered polymeric multicomposites. *Science* **1997**, *277*, 1232–1237.
47. Schmidt, G.; Bäuml, M.; Beyer, N. Ordered two-dimensional monolayers of Au<sub>55</sub> clusters. *Angew. Chem. Int. Ed.* **2000**, *39*, 181–183.
48. Hao, E.; Lian, T. Buildup of polymer/Au nanoparticle multilayer thin films based on hydrogen bonding. *Chem. Mater.* **2000**, *12*, 3392–3396.
49. Schmitt, J.; Decher, G.; Dressick, W.J.; Brandow, S.L.; Geer, R.E.; Shashidhar, R.; Calvert, J.M. Metal nanoparticle/polymer superlattice films: Fabrication and control of layer structure. *Adv. Mater.* **1997**, *9*, 61–65.
50. Feldheim, D.L.; Grabar, K.C.; Natan, M.J.; Mallouk, T.E. Electron transfer in self-assembled inorganic polyelectrolyte/metal nanoparticle heterostructures. *J. Am. Chem. Soc.* **1996**, *118*, 7640–7641.
51. Freeman, R.G.; Grabar, K.C.; Allison, K.J.; Bright, R.M.; Davis, J.A.; Guthrie, A.P.; Hommer, M.B.; Jackson, M.A.; Smith, P.C.; Walter, D.G.; Natan, M.J. Self-assembled metal colloid monolayers: an approach to SERS substrates. *Science* **1995**, *267*, 1629–1632.
52. Gao, M.; Zhang, X.; Yang, B.; Li, F.; Shen, J. Assembly of modified CdS particles/cationic polymer based on electrostatic interactions. *Thin Solid Films* **1996**, *284–285*, 242–245.
53. Sun, S.; Anders, S.; Haumann, H.F.; Thiele, J.-U.; Baglin, J.E.E.; Thomson, T.; Fullerton, E.E.; Murray, C.B.; Terris, B.D. Polymer mediated self-assembly of magnetic nanoparticles. *J. Am. Chem. Soc.* **2002**, *124*, 2884–2885.
54. Ng Cheong Chan, Y.; Schrock, R.R.; Cohen, R.E. Synthesis of silver and gold nanoclusters within microphase-separated diblock copolymers. *Chem. Mater.* **1992**, *4*, 24–27.
55. Cummins, C.C.; Schrock, R.R.; Cohen, R.E. Synthesis of ZnS and CdS within ROMP block copolymer microdomains. *Chem. Mater.* **1992**, *4*, 27–30.
56. Lopes, W.A.; Jaeger, H.M. Hierarchical self-assembly of metal nanostructures on diblock copolymer scaffolds. *Nature* **2001**, *414*, 735–738.
57. Lopes, W.A. Nonequilibrium self-assembly of metals on diblock copolymer templates. *Phys. Rev., E* **2002**, *65*, 031606 (1–14).

# Polymer Molding: Nanostructure Replication

Daniel B. Wolfe

J. Christopher Love

George M. Whitesides

*Department of Chemistry and Chemical Biology, Harvard University,  
Cambridge, Massachusetts, U.S.A.*

## INTRODUCTION

This entry discusses materials and techniques used to generate polymer replicas of nanostructures by molding, embossing, and printing. Nanostructures are defined as those that have lateral dimensions of less than 100 nm. The effect of spatially confining materials to these dimensions gives rise to physical, electronic, mechanical, magnetic, and optical properties, e.g., quantum behavior,<sup>[1,2]</sup> superparamagnetism,<sup>[3]</sup> depressed melting point,<sup>[4,5]</sup> and increased hardness,<sup>[6,7]</sup> that differ, at times significantly, from those of microstructures and macrostructures.

The fabrication and characterization of nanostructures are important for applications in optics,<sup>[8]</sup> computation,<sup>[9]</sup> data storage,<sup>[10,11]</sup> specialty materials,<sup>[7]</sup> and biology.<sup>[12]</sup> Most processes for producing electrically, magnetically, and optically functional devices containing nanostructures include four basic steps: 1) fabrication of a “master” (i.e., a substrate from which replicas are formed); 2) replication of the master; 3) transfer of the replica into a functional material (e.g., semiconductor or metal); and 4) registration of the pattern of a master (the same as or different than the one used originally) with that of the replica for multilayer structures. This article focuses on the polymers and the molding techniques useful for the second step of this process.

## OVERVIEW

### Why Replication of Nanostructures into Polymers?

Replication of nanostructures into photosensitive polymers by photolithography is routine in fundamental and applied research and in commercial manufacturing.<sup>[13]</sup> The process replicates features from a photomask that is prepared by a serial lithographic technique such as electron-beam lithography,<sup>[14,15]</sup> focused-ion milling,<sup>[16–18]</sup> or scanning probe lithography.<sup>[19–21]</sup> The fabrication of masters by these

techniques is slow ( $\sim 10 \text{ hr/cm}^2$ ) because each feature in the mask is drawn individually. The lateral dimensions of the structures that can be patterned by photolithography are limited by the wavelength of the illumination source; state-of-the-art, 157-nm sources can fabricate features as small as 50 nm.<sup>[22]</sup> The techniques for making masters and for sub-100-nm photolithography require specialized, expensive equipment; such equipment is readily accessible in industry, but is not commonly available in academic research laboratories.

### Advantages and Disadvantages of Replication of Nanostructures into Polymers

Replication of nanostructures by the molding of polymers shares the attractive feature of photolithography (that is, it can replicate all the features on a master in one step), but with a much lower limit, in principle, for the lateral dimensions of features ( $\sim 1 \text{ nm}$ ) than that for photolithography. This limit is set by the size of the molecules in the replica. The molding of polymers has four advantages over photolithography: 1) the techniques can replicate nanostructures over large areas ( $> 1 \text{ m}^2$ ); 2) the dimensions of the features replicated into polymers are not distorted by problems common to photolithographic techniques (e.g., variations in focus, intensity, and exposure dose); 3) the materials and the facilities necessary are inexpensive and readily accessible; and 4) the process may be compatible with low-cost manufacturing processes (e.g., roll-to-roll processing).

The replication of nanostructures by molding in polymers has seen only limited commercial applications to date. Replication of sub-10-nm features is still difficult to obtain reproducibly over large areas because of lateral collapse of the features in the polymeric replica. Defect densities are currently too high for use in most high-performance electronic devices; no defects must be observed over an area of several square centimeters for commercial applications. The process of replication does not reduce the dimensions of features; that is, the dimensions of the features

defined in the master must be the same as those desired in the replica. This characteristic differs from photolithography where dimensions in a mask can be reduced optically.

## POLYMER MATERIALS AND PROPERTIES FOR USE IN REPLICAS

Table 1 summarizes some of the types of polymers used to replicate masters by molding and the properties relevant to molding. Two properties that influence the quality of a polymer replica are the coefficient of thermal expansion of the master and the polymer and the dimensional change in the polymer during curing. The dimensions of features defined in masters or replicas made of polymers with large coefficients of thermal expansion can be distorted by changes in the temperature. The polymer replica also can shrink during curing because of evaporation of solvents, cross-linking of the polymer, and/or thermal expansion of the polymer (for heat-based curing)<sup>[23]</sup> These processes can also yield replicas with distorted features.

Some processes of replication reshape thin films of polymers by softening them at elevated temperatures; the temperature at which the polymer softens is the glass transition temperature ( $T_g$ ). Low glass transition temperatures (i.e.,  $45^\circ\text{C} < T_g < 150^\circ\text{C}$ ) can minimize distortions of the critical dimensions of the features because of thermal expansion of the master during

heating and thermal contraction of the replica during cooling. Temperatures within this range also make the process compatible with a wide range of substrate materials (e.g., polymers and low-melt glasses).

Mechanical instabilities in the polymers can lead to vertical and lateral collapse of the features in the replica. The elasticity or the tensile modulus of the material used to make the replica determines the importance of these distortions. They are significant for nanostructures defined in polymers that have a low tensile modulus ( $< 2\text{ MPa}$ ), and they limit the minimum dimension ( $> 300\text{ nm}$ ) and the minimum aspect ratio (0.4; height/width) of the features these polymers (e.g., derivatives of polydimethylsiloxane (PDMS) such as 184-PDMS and s-PDMS) can replicate.<sup>[24–26]</sup> A number of groups have developed formulations of PDMS (e.g., *h*-PDMS and *hν*-PDMS) that have a medium to high elastic modulus (4–10 MPa).<sup>[23,27,28]</sup> These formulations of PDMS are particularly useful for the replication of nanostructures, as they can replicate features with lateral dimensions as small as 30 nm and with vertical dimensions as small as 2 nm.<sup>[27,29]</sup>

The process removing a rigid replica from a rigid master can damage the fragile nanostructures defined on each surface. The physical toughness of the polymer is an indication of how much stress it can tolerate before cracking. The potential for damage to the features in the master and in the replica decreases when using a polymer with a tensile strength of  $> 0.1\text{ MPa}$

**Table 1** Properties of polymers used commonly in replication

	Tensile modulus (MPa)	Toughness (MPa)	Surface free energy (dyn/cm <sup>2</sup> )	Coefficient of linear thermal expansion (ppm/°C)	Glass transition temperature (°C)	Method of curing	Commercially available
Poly(dimethyl siloxane) (PDMS)							
184-PDMS <sup>a</sup>	1.8, <sup>[23]</sup>	4.77 <sup>[23]</sup>	21.6	260–310 <sup>b</sup>	N/A	Heat	Yes
<i>h</i> -PDMS <sup>[27]</sup>	8.2 <sup>[23]</sup>	0.02 <sup>[23]</sup>	~ 20	450 <sup>[27]</sup>	N/A	Heat	No
<i>hν</i> -PDMS <sup>[23]</sup>	3.4 <sup>[23]</sup>	0.13 <sup>[23]</sup>	~ 20	300 <sup>[23]</sup>	N/A	UV-light	No
s-PDMS <sup>c</sup>	0.6 <sup>[23]</sup>	0.41 <sup>[23]</sup>	~ 20	–	N/A	UV-light	Yes
Poly(methyl methacrylate)	2200–3100 <sup>d</sup>	195 <sup>d</sup>	36.5	50–90 <sup>d</sup>	85–105°C <sup>c</sup>	N/A	Yes
Poly (vinylchloride)	2400–4100 <sup>d</sup>	65	39	50–100 <sup>d</sup>	75–105°C <sup>c</sup>	N/A	Yes
Poly(styrene)	2300–3300 <sup>d</sup>	36.52 <sup>d</sup>	33	50–83 <sup>d</sup>	74–100°C <sup>c</sup>	N/A	Yes
Poly(urethane)	20–70 <sup>e</sup>	75–80 <sup>e</sup>	28–30	30–60	N/A	UV-light	Yes
Novalac Photoresist	~ 6000–9000	~ 100–110	43.6	30–50	~ 120°C <sup>c</sup>	N/A	Yes

<sup>a</sup>Sylgard 184 available from Dow Corning.

<sup>b</sup>Dow Corning technical data sheet for Sylgard 184.

<sup>c</sup>RMS-033 available from Gelest.

<sup>d</sup>Modern Plastics Encyclopedia 1999, p B158 to B216.

<sup>e</sup>Norland Optical Adhesives technical data sheets.

(e.g., PDMS) as the material for the replica. Polymers with a high toughness tend to have a low tensile modulus.

The surface free energy of the polymer is a parameter that determines the ease of release of the polymer replica from the master and thus the damage to the replicated nanostructures during this process. PDMS is a useful material for use in replicas because it has a low surface free energy ( $\sim 21.6$  dyn/cm).<sup>[30]</sup> After molding, the surface energy of PDMS replica can be lowered further to  $\sim 12$  dyn/cm by coating the surface with a fluorosilane;<sup>[31,32]</sup> this process makes the surface properties of the stamp similar to poly(tetrafluoroethylene) (Teflon<sup>®</sup>).

## TECHNIQUES FOR THE REPLICATION OF NANOSTRUCTURES BY THE MOLDING OF POLYMERS

### Replica Molding

Replica molding is a technique used routinely to fabricate macroscale and microscale objects, e.g., compact disks, digital versatile disks (DVD), holograms, and plastic parts, by molding a polymer against ceramic, metallic, or rigid plastic masters (Fig. 1). Typically, the surface of the master is modified chemically to lower its surface free energy by coating it with a fluorinated molecule or polymer; this layer facilitates the separation of the master from the replica after molding. Damage to the nanostructures defined in the master and/or the replica occurs most commonly during this separation. The use of elastomeric polymers in replica molding helps to minimize damage to the nanostructures, especially in the replica, during separation because of the toughness and elasticity of the polymers. An example of replica molding into PDMS is the replication of rings of photoresist into a composite polymer made of a thin layer ( $40\ \mu\text{m}$ ) of *h*-PDMS and a thick layer ( $>1$  mm) of 184 PDMS (Fig. 2). The composite PDMS structure can replicate

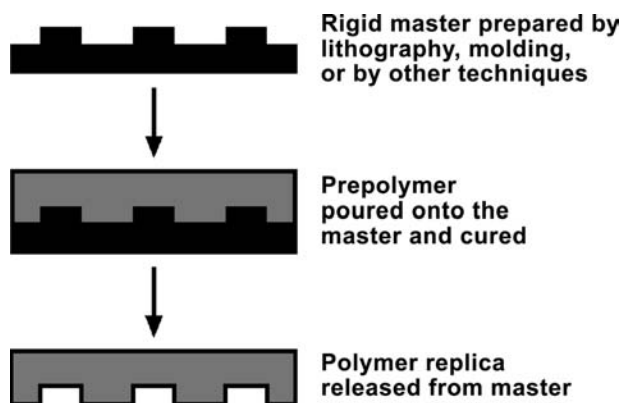


Fig. 1 Scheme for replica molding.

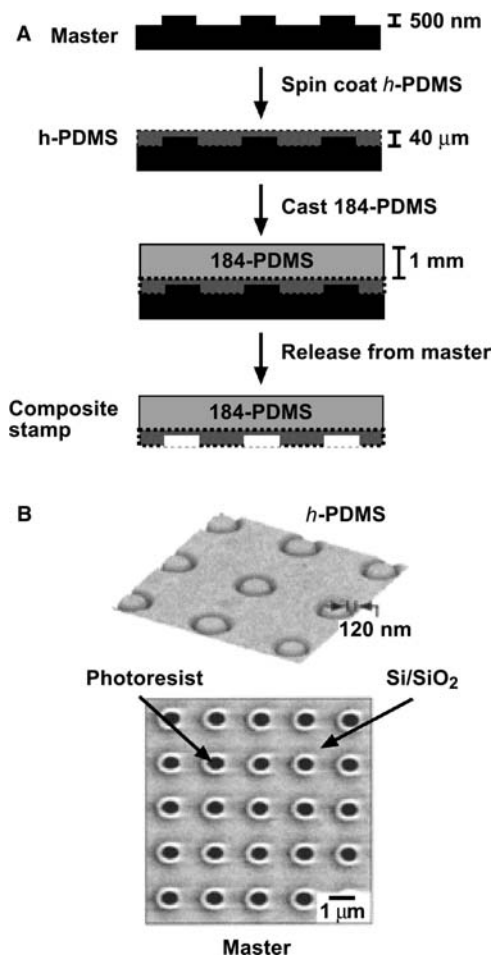
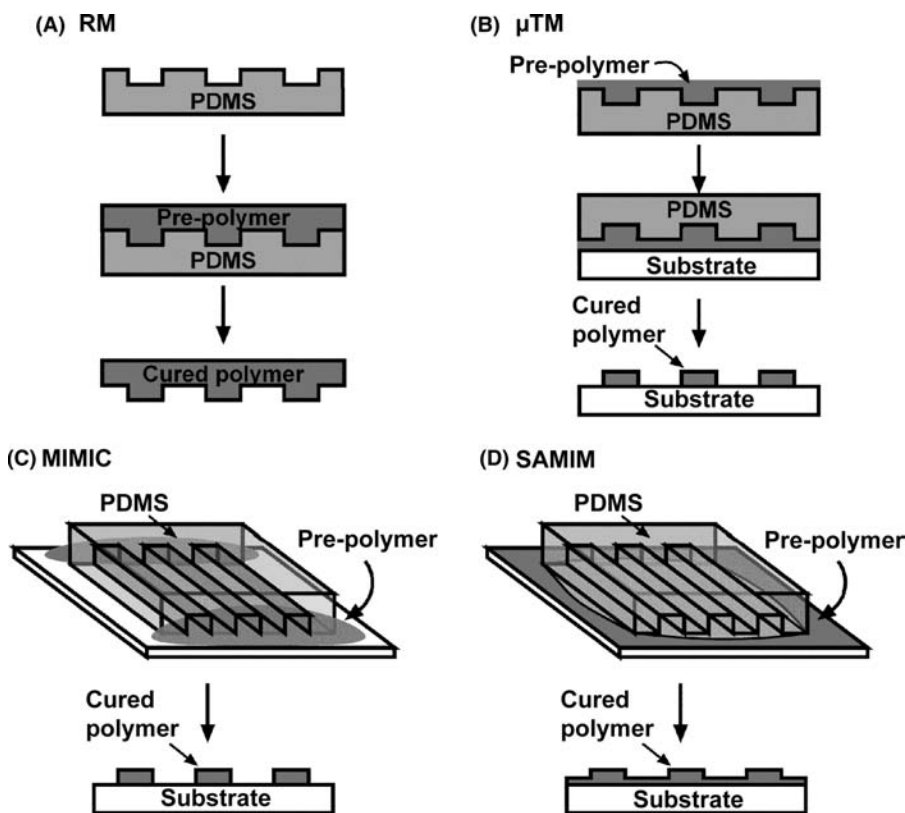


Fig. 2 (A) Scheme for replica molding a master into a *h*-PDMS/184 PDMS composite polymer. (B) An atomic force micrograph of the replica (top) and a scanning electron micrograph of the master (bottom). *Source:* The scheme and images in (B) are reproduced with permission from the *American Chemical Society*. From Ref.<sup>[28]</sup>.

sub-100-nm features by molding and can be removed easily from a master without damaging the nanostructures on either surface.<sup>[27,28]</sup>

### Soft Lithography

Soft lithography is a suite of techniques that use a PDMS-based stamp—prepared by replica molding—as the master (Fig. 3).<sup>[13,31,32]</sup> Replica molding (RM),<sup>[33]</sup> microtransfer molding ( $\mu\text{TM}$ ),<sup>[34]</sup> micromolding in capillaries (MIMIC),<sup>[35]</sup> and solvent-assisted micromolding (SAMIM)<sup>[36]</sup> are four soft-lithographic techniques that replicate features by the molding of polymers. For many of these techniques, the inherent low surface free energy of PDMS is enough to permit the stamp to be separated from the replica without the need of a release layer.



**Fig. 3** Schematic illustrations of the procedures used in the corresponding soft lithographic techniques. (A) Replica molding (RM); (B) microtransfer molding ( $\mu$ TM); (C) micromolding in capillaries (MIMIC); (D) solvent-assisted micromolding (SAMIM).

### Replica molding

The soft lithographic version of replica molding uses a PDMS stamp as the master instead of a rigid material (Fig. 3A). Fig. 4 shows the replica molding of nanostructures into an UV-curable polyurethane. The PDMS stamp can be used repeatedly; no measurable

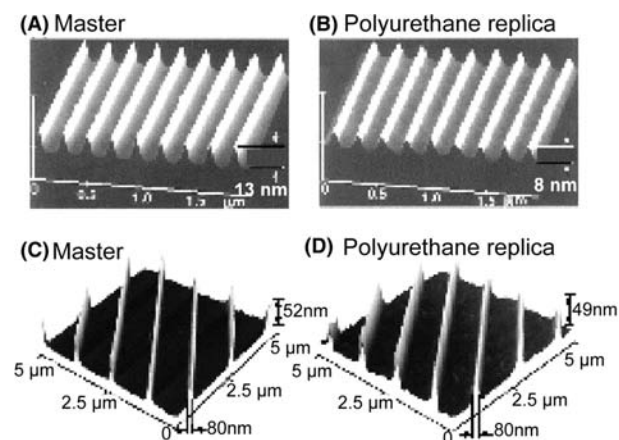


**Fig. 4** Atomic force micrographs of (A) a chrome master; (B) a polyurethane replica of the master produced by replica molding; (C) atomic force micrographs of chrome master; (D) atomic force micrographs of polyurethane replica. *Source:* The images in this figure are reproduced with permission from *Advanced Materials*. From Ref.<sup>[33]</sup>.

difference in feature quality is observed after successive replication into polyurethane more than 20 times from the same stamp.

### Microtransfer molding

Microtransfer molding prepares a replica by first filling the recessed regions of the stamp with a curable prepolymer (Fig. 3B). The excess prepolymer is scraped from the surface of the stamp using a thin slab of PDMS; this scraping process does not remove the excess polymer completely, and, often, a thin film of excess polymer remains on the replica. The filled stamp is placed onto a rigid substrate under slight pressure. The prepolymer is cured by the appropriate technique, and the mold is removed manually. This technique is well suited for UV-curable materials because the PDMS stamp is optically transparent above  $\sim 290$  nm.

### Micromolding in capillaries

Micromolding in capillaries uses capillarity to fill channels in a PDMS stamp with a photocurable or thermally curable polymer (Fig. 3C). A PDMS-based stamp is placed in conformal contact with a surface. The stamp is topographically patterned with a series of channels that extend from one end of the stamp to the other. A drop of liquid prepolymer placed at one

Polyelectrolyte - Polymer



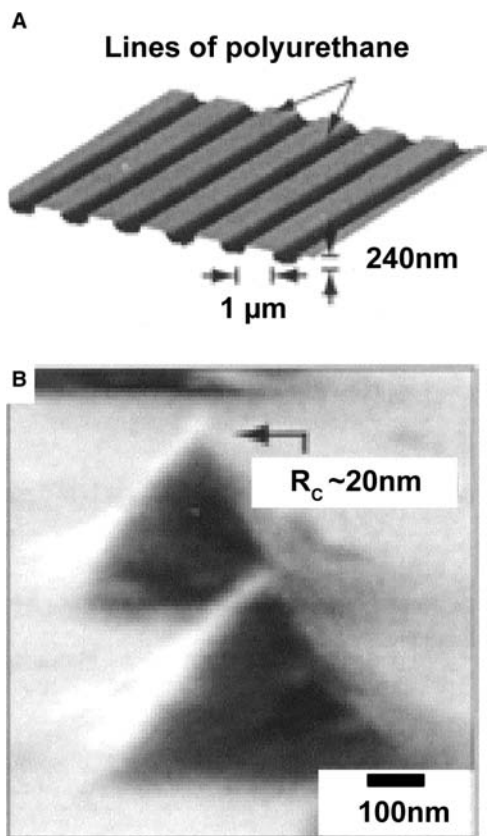


**Fig. 5** (A) Atomic force micrograph of lines of photoresist patterned by MIMIC. (B) Scanning electron micrograph of Novalac photoresist patterned by SAMIM. *Source:* The images are reproduced with permission from *The American Chemical Society*. From Ref.<sup>[28]</sup>.

end of the stamp fills the channels by capillarity. The polymer is cured once the entire channel network is filled. The replication of nanochannels in a 184-PDMS stamp is difficult because the channels tend to collapse when the stamp is placed in contact with a surface.<sup>[28]</sup> Composite stamps of *h*-PDMS and 184-PDMS overcome this limitation and can be used to replicate features with critical dimensions below 300 nm (Fig. 5A). Unlike  $\mu$ TM, this technique does not produce an excess polymer film on the replica.

#### Solvent-assisted micromolding

Solvent-assisted micromolding is similar operationally to traditional embossing techniques, but it uses solvent to reshape a polymer rather than elevated temperatures, and it uses an elastomeric stamp instead of a rigid master (Fig. 3D). Elastomeric stamps are especially useful in embossing because the stamp conforms to the surface of the polymer and contacts uniformly over large areas. The stamp is wet with a solvent for the polymer that is to be molded and placed in contact with a thin film of this polymer. The solvent is

allowed to evaporate, and the stamp is removed to reveal the replica in the polymer. Air bubbles and voids in the replica as a result of poor evaporation of the solvent before removal of the stamp are not observed because the stamp is gas-permeable. This process has been demonstrated for a number of polymers including: Novalac photoresists, poly(styrene), poly(methylmethacrylate), cellulose acetate, poly(vinyl chloride), and precursors to conjugated organic polymers.<sup>[36]</sup> An example of nanostructures prepared by this technique is in Fig. 5B. The molded structure can also act as its own optical element for further size reduction of the features.<sup>[37]</sup>

#### Advantages and disadvantages of soft lithography

The advantages of soft lithography are that: 1) it uses inexpensive materials and equipment; 2) it can replicate over large areas and on nonplanar surfaces; 3) it uses stamps that are compatible with a large number of polymers; and 4) it uses stamps that are gas-permeable. The disadvantages are that: 1) the PDMS molds are not compatible with many organic solvents or high temperatures; 2) the softness of PDMS can cause distortions in molded structures; 3) the use of PDMS-based stamps requires careful temperature control because of the high coefficient of thermal expansion; that is, small changes in temperature can change the dimensions of the nanostructures; and 4) the registration of multilayer patterns is difficult.

#### Imprint Lithographies

Step-and-flash imprint lithography (developed by Willson et al.<sup>[38–41]</sup>) and nanoimprint lithography (developed by Chou et al.<sup>[42–44]</sup>) are two forms of imprint lithography that are used for the replication of nanostructures into polymers. Both techniques work by placing a topographically patterned, rigid master in contact with a formable material coated on a rigid surface. The rigid master is prepared by photolithographic replication of the features into a polymer that is coated on a rigid substrate (e.g., quartz and silicon). The structures are transferred into the substrate by etching.

#### Step-and-flash imprint lithography

Step-and-flash imprint lithography uses a low-viscosity, photocurable polymer as the material for the replica (Fig. 6)<sup>[41]</sup> The low viscosity of the polymer eliminates the need for high temperatures and pressures. A quartz master is placed in contact with the photocurable polymer under slight pressure. Flood illumination through the backside of the master cures the polymer replica. The master is transparent to the

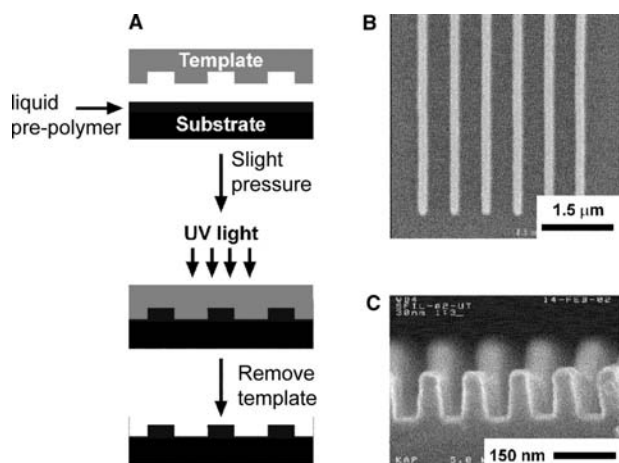


**Fig. 6** (A) Schematic illustration of step-and-flash imprint lithography. (B) Scanning electron micrograph of lines of polymer on a silicon substrate patterned by the technique. (C) Scanning electron micrograph of the cross-section of the lines in (B). *Source:* The images in (B) and (C) are reproduced with permission from *Proceedings of the SPIE*. From Ref.<sup>[45]</sup>.

wavelengths necessary to cure the polymer. Treatment of the surface of the master with a fluorosilane lowers its surface free energy and facilitates the removal of the master from the replica. The technique can replicate features with lateral dimensions greater than 30 nm and with aspect ratios as high as 8:1 (for 50-nm lines).<sup>[41,45]</sup> Step-and-flash lithography is “self-cleaning” because particulates on the surface of the master are trapped in the replica during the curing process. Repeated use of a master actually lowers the density of defects in the replica.<sup>[46]</sup>

The advantages of step-and-flash imprint lithography are that: 1) it is a room-temperature technique and is therefore not subject to thermal- or pressure-induced deformations of the nanostructures; 2) it is a rapid process (< 5 min/cycle);<sup>[40,47]</sup> and 3) it uses optically transparent masters that permit alignment of the replica with underlying features. The disadvantages are that: 1) the masters are more difficult to prepare than those used in soft lithography; 2) the replication of non-planar masters is difficult;<sup>[48]</sup> and 3) the technique is not good for the replication of isolated, recessed features in the master.<sup>[41]</sup>

### Nanoimprint lithography

Nanoimprint lithography differs from step-and-flash imprint lithography in that it reshapes a polymer at temperatures above its glass transition point, e.g., 90–100°C, and requires high pressures, e.g., 50–100 bar (Fig. 7).<sup>[43,44]</sup> The high temperatures lower the viscosity of the polymer enough to fill the master uniformly. The replica and mold are allowed to cool before separation.

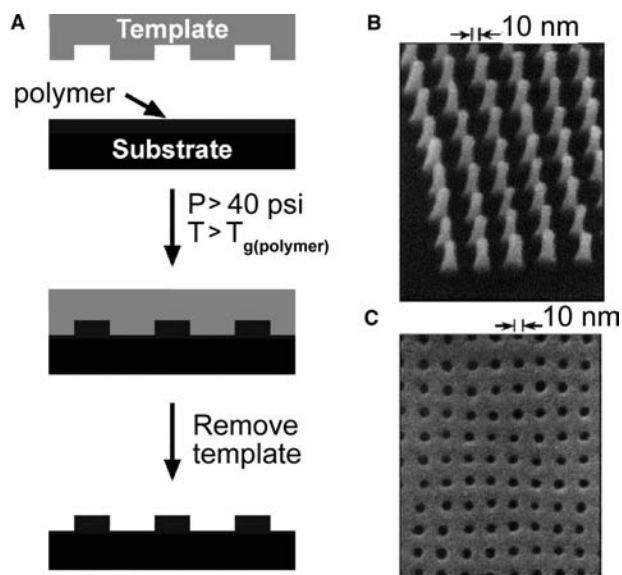


**Fig. 7** (A) Schematic illustration of the process used in nanoimprint lithography. (B) Scanning electron micrograph of the SiO<sub>2</sub> master. (C) Scanning electron micrograph of the polymer replica of the master in (B) made by nanoimprinting. *Source:* The images in (B) and (C) are reproduced by permission of *MRS Bulletin*. From Ref.<sup>[43]</sup>.

The technique can replicate nanostructures as small as 10 nm and aspect ratios as large as 10:1.<sup>[43]</sup> Transparent masters can be used to permit multilevel registration of replicas. Nanoimprint lithography can be carried out in a sequential, step-by-step process similar to that of step-and-flash. The fidelity of replication of nanostructures with critical dimensions of less than 50 nm is poor over large areas because the polymer chains in the materials used in the replicas tend to relax and spread over distances of tens of nanometers.<sup>[47]</sup> These factors can only be corrected by designing the original master to account for polymer shrinkage in the processing steps. Another disadvantage of nanoimprinting is that it requires 10–15 min per replication for the heating and cooling cycles; this interval is 3–5 times longer than that necessary for the entire replication process for step-and-flash imprint lithography and some soft lithographic techniques.<sup>[47]</sup>

### Uses for Polymeric Replicas with Nanostructures

Replication of nanostructures into polymers is used to make electronic,<sup>[49–59]</sup> optical,<sup>[60–64]</sup> and mechanical<sup>[65–69]</sup> devices. Single-layer, subwavelength, optical elements, e.g., frequency-selective surfaces (Fig. 8A), are one example of such a device fabricated by soft lithography.<sup>[57,62,70,71]</sup> A master was replicated into Novalac photoresist by solvent-assisted micromolding. The replica acted as a photomask, and the edges of the raised features

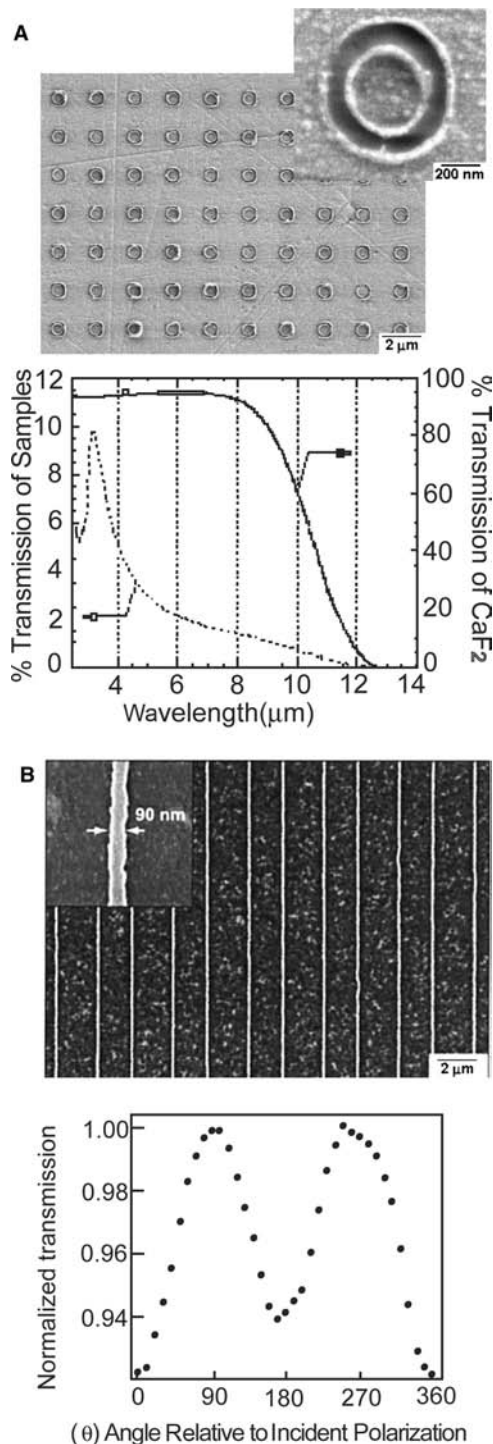


**Fig. 8** (A) Scanning electron micrograph of rings of nickel formed by lift-off of a photoresist patterned by phase-shifting photolithography and the corresponding transmission spectrum as a function of wavelength for the sample and the CaF<sub>2</sub> substrate. (B) Lines of palladium formed by lift-off of photoresist patterned by phase-shifting photolithography and the corresponding plot of the intensity of the transmitted light as a function of angle of polarization. *Source:* Figure (A) is reproduced with permission from *The Optical Society of America*. Figure (B) is reproduced with permission from *The American Chemical Society*. From Refs.<sup>[28,62]</sup>.

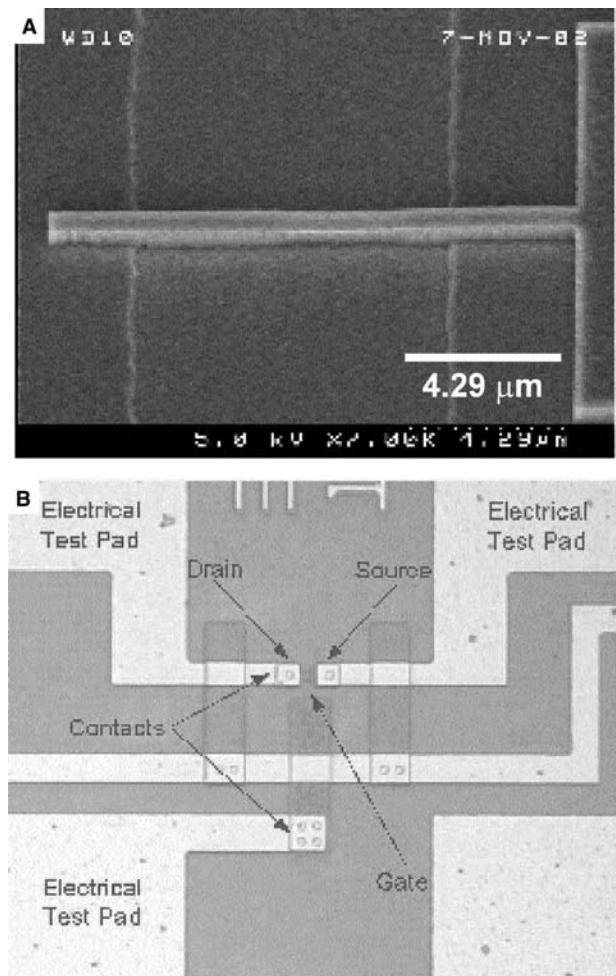


**Fig. 9** (A) Scanning electron micrograph of a polymer gate made by step-and-flash imprint lithography. (B) Optical micrograph of the complete MOSFET device that incorporates the polymer gate in (A). *Source:* The images are reproduced with permission from *Proceedings of the SPIE*. From Ref.<sup>[77]</sup>.

were transferred into the underlying photoresist upon exposure to UV-light. The PDMS replica prepared by standard replica molding was used to fabricate polarizers by a similar, phase-shifting lithography technique (Fig. 8B).<sup>[70]</sup> The PDMS replicas can also be used to replicate nanostructures into metals by microcontact printing. This process uses the PDMS replica as a stamp to print an organic molecule selectively onto a metal surface. This molecule acts as an etch resist and permits the selective etching of unprotected regions. This technique was used to fabricate polarizers,<sup>[28]</sup> hydrogen-gas sensors,<sup>[72]</sup> transistors,<sup>[50,52]</sup> and microelectromechanical systems (MEMS) devices.<sup>[69,73]</sup> The imprint lithographies use the polymer replica as an etch resist to transfer the pattern of the replica into a functional material. These techniques have been used to make photonic crystals,<sup>[74]</sup> polarizers,<sup>[75,76]</sup> photodetectors,<sup>[56]</sup> and transistors (Fig. 9).<sup>[58,59,77]</sup>

## CONCLUSION

Although replication will not replace the techniques used currently for the preparation of masters, it is extremely useful as a research tool for the rapid prototyping of devices using nanostructures. The combination of the two techniques could enable the fabrication of nanostructures to become routine and cost-effective. Polymeric replicas containing nanostructures may be most useful in the process of fabricating low-cost, low-to-medium performance optical and electronic devices (e.g., RF-ID tags, large area displays, optical filters, and polarizers). Efforts to improve the capabilities of replication will lead to the fabrication of new devices based on the unique properties of nanostructures.

## REFERENCES

- Bukowski, T.J.; Simmons, J.H. Quantum dot research: current state and future prospects. *Crit. Rev. Solid State Mater. Sci.* **2002**, *27* (3 and 4), 119–142.
- Alivisatos, P. Colloidal quantum dots. From scaling laws to biological applications. *Pure Appl. Chem.* **2000**, *72* (1–2), 3–9.
- Sun, X.-C. Microstructure characterization and magnetic properties of nanomaterials. *Mol. Phys.* **2002**, *100* (19), 3059–3063.
- Jiang, Q.; Yang, C.C.; Li, J.C. Melting enthalpy depression of nanocrystals. *Mater. Lett.* **2002**, *56* (6), 1019–1021.
- Wu, Y.; Yang, P. Melting and welding semiconductor nanowires in nanotubes. *Adv. Mater.* **2001**, *13* (7), 520–523.
- Ohji, T. Strengthening mechanisms of nanocomposites. *Mater. Integr.* **2000**, *13* (11), 3–8.
- Koch, C. Bulk behavior of nanostructured materials. *Nanostruct. Sci. Technol.* **1999**, 93–111.
- Chung, S.-J.; Kim, K.-S.; Lin, T.-C.; Shen, Y.; Markowicz, P.; He, G.S.; Prasad, P.N. Nanophotonics: nanoscale optical interactions. *Mol. Cryst. Liq. Cryst. Sci. Technol., Sect. A* **2002**, *374*, 59–66.
- Tsu, R. Challenges in nanoelectronics. *Nanotechnology* **2001**, *12* (4), 625–628.
- Menon, A.K.; Gupta, B.K. Nanotechnology: a data storage perspective. *Nanostruct. Mater.* **2000**, *11* (8), 965–986.
- Kirk, K.J. Nano-magnets for sensors and data storage. *Contemp. Phys.* **2000**, *41* (2), 61–78.
- Taton, T.A. Nanostructures as tailored biological probes. *Trends Biotechnol.* **2002**, *20* (7), 277–279.
- Whitesides, G.M.; Love, J.C. The art of building small. *Sci. Am.* **2001**, *285* (3), 32–41.
- Gibson, J.M. Reading and writing with electron beams. *Phys. Today* **1997**, 56–61.
- Pease, R.F.W. Nanolithography and its prospects as a manufacturing technology. *J. Vac. Sci. Technol., B* **1992**, *10* (1), 278–285.
- Li, H.-W.; Kang, D.-J.; Blamire, M.G.; Huck, W.T.S. Focused ion beam fabrication of silicon print masters. *Nanotechnology* **2003**, *14* (2), 220–223.
- Lehrer, C.; Frey, L.; Petersen, S.; Ryssel, H. Limitations of focused ion beam nanomachining. *J. Vac. Sci. Technol., B* **2001**, *19* (6), 2533–2538.
- Longo, D.M.; Benson, W.E.; Chraska, T.; Hull, R. Deep submicron microcontact printing on planar and curved substrates utilizing focused ion-beam fabricated printheads. *Appl. Phys. Lett.* **2001**, *78* (7), 981–983.
- Crommie, M.F.; Lutz, C.P.; Eigler, D.M. Confinement of electrons to quantum corrals on a metal surface. *Science* **1993**, *262* (5131), 218–220.
- Mirkin, C.A. Dip-pen nanolithography: Automated fabrication of custom multicomponent, sub-100-nanometer surface architectures. *MRS Bull.* **2001**, *26* (7), 535–538.
- Sulchek, T.; Grow, R.J.; Yaralioglu, G.G.; Minne, S.C.; Quate, C.F.; Manalis, S.R.; Kiraz, A.; Aydine, A.; Atalar, A. Parallel atomic force microscopy with optical interferometric detection. *Appl. Phys. Lett.* **2001**, *78* (12), 1787–1789.
- Itani, T.; Wakamiya, W.; Cashmore, J.; Gower, M. 157-nm lithography with high numerical aperture lens for sub-70 nm node. *Microelectron. Eng.* **2003**, *67–68*, 39–46(Complete).
- Choi, K.M.; Rogers, J.A. A photocurable poly(dimethylsiloxane) chemistry designed for soft lithographic molding and printing in the nanometer regime. *J. Am. Chem. Soc.* **2003**, *125* (14), 4060–4061.
- Delamarche, E.; Schmid, H.; Michel, B.; Biebuyck, H. Stability of molded polydimethylsiloxane microstructures. *Adv. Mater.* **1997**, *9* (9), 741–746.
- Hui, C.Y.; Jagota, A.; Lin, Y.Y.; Kramer, E.J. Constraints on microcontact printing imposed by stamp deformation. *Langmuir* **2002**, *18* (4), 1394–1407.
- Rogers, J.A.; Paul, K.E.; Whitesides, G.M. Quantifying distortions in soft lithography. *J. Vac. Sci. Technol., B* **1998**, *16* (1), 88–97.
- Schmid, H.; Michel, B. Siloxane polymers for high-resolution, high-accuracy soft lithography. *Macromolecules* **2000**, *33* (8), 3042–3049.
- Odom, T.W.; Love, J.C.; Wolfe, D.B.; Paul, K.E.; Whitesides, G.M. Improved pattern transfer in soft lithography using composite stamps. *Langmuir* **2002**, *18* (13), 5314–5320.
- Gates, B.G.; Whitesides, G.M. Unpublished work.
- Clarson, S.J.; Semlyen, J.A.; Eds. *Siloxane Polymers*; Prentice Hall: Englewood Cliffs, NJ, 1993.
- Xia, Y.; Whitesides, G.M. Soft lithography. *Angew. Chem., Int. Ed. Engl.* **1998**, *37* (5), 550–575.
- Xia, Y.; Whitesides, G.M. Soft lithography. *Annu. Rev. Mater. Sci.* **1998**, *28*, 153–184.
- Xia, Y.; McClelland, J.J.; Gupta, R.; Qin, D.; Zhao, X.-M.; Sohn, L.L.; Celotta, R.J.; Whitesides, G.M. Replica molding using polymeric materials: a practical step toward nanomanufacturing. *Adv. Mater.* **1997**, *9* (2), 147–149.
- Zhao, X.-M.; Xia, Y.; Whitesides, G.M. Fabrication of three-dimensional micro-structures: microtransfer molding. *Adv. Mater.* **1996**, *8* (10), 837–840.

35. Xia, Y.; Kim, E.; Whitesides, G.M. Micromolding of polymers in capillaries: applications in microfabrication. *Chem. Mater.* **1996**, *8*, 1558–1567.
36. Kim, E.; Xia, Y.; Zhao, X.-M.; Whitesides, G.M. Solvent-assisted microcontact molding: a convenient method for fabricating three-dimensional structures on surfaces of polymers. *Adv. Mater.* **1997**, *9* (8), 651–654.
37. Odom, T.W.; Thalladi, V.R.; Love, J.C.; Whitesides, G.M. Generation of 30–50 nm structures using easily fabricated, composite PDMS masks. *J. Am. Chem. Soc.* **2002**, *124* (41), 12,112–12,113.
38. Bailey, T.C.; Johnson, S.C.; Sreenivasan, S.V.; Ekerdt, J.G.; Willson, C.G.; Resnick, D.J. Step and flash imprint lithography: an efficient nanoscale printing technology. *J. Photopolym. Sci. Tech.* **2002**, *15* (3), 481–486.
39. Colburn, M.; Grot, A.; Amistoso, M.N.; Choi, B.J.; Bailey, T.C.; Ekerdt, J.G.; Sreenivasan, S.V.; Hollenhorst, J.; Willson, C.G. Step and flash imprint lithography for sub-100-nm patterning. *Proc. SPIE Int. Soc. Opt. Eng.* **2000**, *3997*, 453–457. (Emerging Lithographic Technologies IV).
40. Colburn, M.; Johnson, S.; Stewart, M.; Damle, S.; Bailey, T.C.; Choi, B.; Wedlake, M.; Michaelson, T.; Sreenivasan, S.V.; Ekerdt, J.; Willson, C.G. Step and flash imprint lithography: a new approach to high-resolution patterning. *Proc. SPIE Int. Soc. Opt. Eng.* **1999**, *3676*, 379–389. (Pt. 1, Emerging Lithographic Technologies III).
41. Colburn, M.; Bailey, T.; Choi, B.I.; Ekerdt, J.G.; Sreenivasan, S.V.; Willson, C.C. Development and advantages of step-and-flash lithography. *Solid State Technol.* **2001**, *44* (7), 67, 68, 71, 73–76, 78.
42. Chou, S.Y.; Krauss, P.R.; Renstrom, P.J. Nanoimprint lithography. *J. Vac. Sci. Technol., B* **1996**, *14* (6), 4129–4133.
43. Chou, S.Y. Nanoimprint lithography and lithographically induced self-assembly. *MRS Bull.* **2001**, *26* (7), 512–517.
44. Chou, S.Y.; Krauss, P.R.; Renstrom, P.J. Imprint lithography with 25-nanometer resolution. *Science* **1996**, *272* (5258), 85–87.
45. Resnick, D.J.; Bailey, T.; Dauksher, W.J.; Mancini, D.; Nordquist, K.J.; Ainley, E.; Gehoski, K.; Baker, J.H.; Johnson, S.; Meissl, M.; Sreenivasan, S.V.; Ekerdt, J.; Willson, C.G. High resolution templates for step and flash imprint lithography. *Proc. SPIE Int. Soc. Opt. Eng.* **2002**, *4688*, 205.
46. Bailey, T.; Smith, B.; Choi, B.J.; Colburn, M.; Meissl, M.; Sreenivasan, S.V.; Ekerdt, J.G.; Willson, C.G. Step and flash imprint lithography: defect analysis. *J. Vac. Sci. Technol., B* **2001**, *19* (6), 2806–2810.
47. Sotomayor Torres, C.M.; Zankovych, S.; Seekamp, J.; Kam, A.P.; Clavijo Cedeno, C.; Hoffmann, T.; Ahopelto, J.; Reuther, F.; Pfeiffer, K.; Bleidiessel, G.; Gruetzner, G.; Maximov, M.V.; Heidari, B. Nanoimprint lithography: an alternative nanofabrication approach. *Mater. Sci. Eng., C* **2003**, *C23* (1–2), 23–31.
48. Ruchhoeft, P.; Colburn, M.; Choi, B.; Nounu, H.; Johnson, S.; Bailey, T.; Darmle, S.; Stewart, M.; Ekerdt, J.; Sreenivasan, S.V.; Wolfe, J.C.; Willson, C.G. Patterning curved surfaces: template generation by ion beam proximity lithography and relief transfer by step and flash imprint lithography. *J. Vac. Sci. Technol., B* **1999**, *17* (6), 2965–2969.
49. Deng, T.; Goetting, L.B.; Hu, J.; Whitesides, G.M. Microfabrication of half-wave rectifier circuits using soft lithography. *Sens. Actuators, A* **1999**, *75*, 60–64.
50. Hu, J.; Beck, R.G.; Deng, T.; Westervelt, R.M.; Maranowski, K.D.; Gossard, A.C.; Whitesides, G.M. Using soft lithography to fabricate GaAs/AlGaAs heterostructure field effect transistors. *Appl. Phys. Lett.* **1997**, *71* (14), 2020–2022.
51. Hu, J.; Beck, R.G.; Westervelt, R.M.; Whitesides, G.M. The use of soft lithography to fabricate arrays of Schottky diodes. *Adv. Mater.* **1998**, *10*, 574–577.
52. Jeon, N.L.; Hu, J.; Whitesides, G.M.; Erhardt, M.K.; Nuzzo, R.G. Fabrication of silicon MOSFETs using soft lithography. *Adv. Mater.* **1998**, *10* (17), 1466–1469.
53. Rogers, J.A. Rubber stamping for plastic electronics and fiber optics. *MRS Bull.* **2001**, *26* (7), 530–534.
54. Koide, Y.; Such, M.W.; Basu, R.; Evmenenko, G.; Cui, J.; Dutta, P.; Hersam, M.C.; Marks, T.J. Hot microcontact printing for patterning ITO surfaces. Methodology, morphology, microstructure, and OLED charge injection barrier imaging. *Langmuir* **2003**, *19* (1), 86–93.
55. Zhang, F.; Nyberg, T.; Inganaes, O. Conducting polymer nanowires and nanodots made with soft lithography. *Nano Lett.* **2002**, *2* (12), 1373–1377.
56. Yu, Z.; Schablitsky, S.J.; Chou, S.Y. Nanoscale GaAs metal-semiconductor-metal photodetectors fabricated using nanoimprint lithography. *Appl. Phys. Lett.* **1999**, *74* (16), 2381–2383.
57. Guo, L.; Krauss, P.R.; Chou, S.Y. Nanoscale silicon field-effect transistors fabricated using imprint lithography. *Appl. Phys. Lett.* **1997**, *71* (13), 1881–1883.
58. Austin, M.; Chou, S.Y. Fabrication of nanocontacts for molecular devices using nanoimprint lithography. *J. Vac. Sci. Technol., B* **2002**, *20* (2), 665–667.
59. Austin, M.D.; Chou, S.Y. Fabrication of 70 nm channel length polymer organic thin-film transistors using nanoimprint lithography. *Appl. Phys. Lett.* **2002**, *81* (23), 4431–4433.
60. Yang, P.; Wirnsberger, G.; Huang, H.; Cordero, S.R.; McGehee, M.D.; Scott, B.; Deng, T.; Whitesides, G.M.; Chmelka, B.F.; Buratto, S.K.; Stucky, G.D. Mirrorless lasing from mesostructured waveguides patterned by soft lithography. *Science* **2000**, *287* (5452), 465–467.
61. Schueller, O.J.A.; Zhao, X.-M.; Whitesides, G.M.; Smith, S.P.; Prentiss, M. Fabrication of liquid-core waveguides by soft lithography. *Adv. Mater.* **1999**, *11* (1), 37–41.
62. Paul, K.E.; Zhu, C.; Love, J.C.; Whitesides, G.M. Fabrication of mid-infrared frequency-selective surfaces (FSS) using soft lithography. *Appl. Opt.* **2001**, *40* (25), 4557–4561.
63. Love, J.C.; Wolfe, D.B.; Jacobs, H.O.; Whitesides, G.M. Microscope projection photolithography for rapid prototyping of masters with micron-scale features for use in soft lithography. *Langmuir* **2001**, *17* (19), 6005–6012.
64. Xia, Y.; Kim, E.; Zhao, X.-M.; Rogers, J.A.; Prentiss, M.; Whitesides, G.M. Complex optical surfaces by replica

- molding against elastomeric masters. *Science* **1996**, *273*, 347–349.
65. Brittain, S.; Paul, K.; Zhao, X.-M.; Whitesides, G. Soft lithography and microfabrication. *Phys. World* **1998**, *11* (5), 31–36.
  66. Schueller, O.J.A.; Brittain, S.T.; Whitesides, G.M. Fabrication of glassy carbon microstructures by soft lithography. *Sens. Actuators, A* **1999**, *72*, 125–139.
  67. Xu, B.; Arias, F.; Whitesides, G.M. Making honeycomb microcomposites by soft lithography. *Adv. Mater.* **1999**, *11* (6), 492–495.
  68. Xu, B.; Arias, F.; Brittain, S.T.; Zhao, X.-M.; Grzybowski, B.; Torquato, S.; Whitesides, G.M. Making negative Poisson's ratio microstructures by soft lithography. *Adv. Mater.* **1999**, *11* (14), 1186–1189.
  69. Yang, H.; Deschatelets, P.; Brittain, S.T.; Whitesides, G.M. Fabrication of high performance ceramic microstructures from a polymeric precursor using soft lithography. *Adv. Mater.* **2001**, *13* (1), 54–58.
  70. Rogers, J.A.; Paul, K.E.; Jackman, R.J.; Whitesides, G.M. Generating  $\sim 90$  nanometer features using near-field contact-mode photolithography with an elastomeric phase mask. *J. Vac. Sci. Technol., B* **1998**, *26* (1), 59–68.
  71. Paul, K.E.; Prentiss, M.G.; Whitesides, G.M. Patterning spherical surfaces at the two-hundred-nanometer scale using soft lithography. *Adv. Funct. Mater.* **2003**, *13* (4), 259–263.
  72. Wolfe, D.B.; Love, J.C.; Paul, K.E.; Chabynyc, M.L.; Whitesides, G.M. Fabrication of palladium-based microelectronic devices by microcontact printing. *Appl. Phys. Lett.* **2002**, *80* (12), 2222–2224.
  73. Jackman, R.J.; Brittain, S.T.; Adams, A.; Wu, H.; Prentiss, M.G.; Whitesides, S.; Whitesides, G.M. Three-dimensional metallic microstructures fabricated by soft lithography and microelectrodeposition. *Langmuir* **1999**, *15* (3), 826–836.
  74. Guo, L.J.; Cheng, X.; Chao, C.Y. Fabrication of photonic nanostructures in nonlinear optical polymers. *J. Mod. Opt.* **2002**, *49* (3/4), 663–673.
  75. Yu, Z.; Deshpande, P.; Wu, W.; Wang, J.; Chou, S.Y. Reflective polarizer based on a stacked double-layer subwavelength metal grating structure fabricated using nanoimprint lithography. *Appl. Phys. Lett.* **2000**, *77* (7), 927–929.
  76. Wang, J.; Schablitsky, S.; Yu, Z.; Wu, W.; Chou, S.Y. Fabrication of a new broadband waveguide polarizer with a double-layer 190 nm period metal-gratings using nanoimprint lithography. *J. Vac. Sci. Technol., B* **1999**, *17* (6), 2957–2960.
  77. Smith, B.; Stacey, N.A.; Donnelly, J.P.; Onsongo, D.M.; Bailey, T.C.; Mackay, C.J.; Sreenivasan, S.V.; Banerjee, S.K.; Ekerdt, J.; Willson, C.G. Employing step and flash imprint lithography for gate level patterning of a MOSFET device. *Proc. SPIE Int. Soc. Opt. Eng.* **2003**, *5037*, 1029–1034.



# Polymer Nanocomposites with Nanoparticle and Carbon Nanotube Fillers

**B. J. Ash**

*Sandia National Laboratories, Albuquerque, New Mexico, U.S.A.*

**A. Eitan**

**L. S. Schadler**

*Department of Materials Science and Engineering, Rensselaer Polytechnic Institute, Troy, New York, U.S.A.*

## INTRODUCTION

Polymer nanocomposites are composites with a polymer matrix and a filler with at least one dimension less than 100 nm. The fillers can be plate-like (clays), high aspect ratio nanotubes, and lower aspect ratio or equiaxed nanoparticles. While some nanofilled composites (carbon black<sup>[1]</sup> and fumed silica<sup>[2,3]</sup>-filled polymers) have been used for over a century, in recent years the dedicated research and development of nanofilled polymers has greatly increased. This is due to our increased ability to synthesize and manipulate a broad range of nanofillers and significant investment by government and industry in this field.

Current interest in nanocomposites has been generated and maintained because nanoparticle and carbon nanotube-filled polymers exhibit unique combinations of properties not achievable with traditional composites. For example, the inclusion of equiaxed nanoparticles in thermoplastics, and particularly semicrystalline thermoplastics, increases the yield stress, the tensile strength, and Young's modulus<sup>[4]</sup> compared to pure polymer. Other examples include scratch-resistant transparent amorphous thermoplastic coatings.<sup>[5]</sup> These combinations of properties can be achieved because of the small size of the fillers, the large surface area the fillers provide, and in many cases the unique properties of the fillers themselves. As will be shown, in many cases these large changes in the material properties require small to modest nanofiller loadings. Unlike traditional micron-filled composites, these novel fillers often alter the properties of the entire polymer matrix while, at the same time, imparting new functionality because of their chemical composition and nanoscale size.

This entry will give a general introduction to polymer nanocomposites and address what is unique to nanofillers compared to traditional micron-scale fillers. The second section will briefly address nanofiller surface modification and the third will provide specific

examples of mechanical, electrical, and optical properties in nanoparticle-filled polymers. The last section provides a detailed description of the mechanical properties of nanotube-filled polymers and a brief description of some electrical and optical properties that have been reported.

## WHAT MAKES NANOCOMPOSITES UNIQUE

The small size of nanofillers leads to several factors that distinguish nanocomposites from traditional composites. First of all, nanofillers are small mechanical, optical, and electrical defects compared to micron-scale fillers. This means that the addition of nanofillers to a polymer does not necessarily lead to a decrease in the ductility of the polymer and in some cases can increase it.<sup>[6,7]</sup> It also means that below about 50 nm,<sup>[8]</sup> many fillers do not scatter light significantly. Thus it is possible to make composites with altered electrical or mechanical properties that maintain their optical clarity. Finally, as small electrical defects, nanofillers do not concentrate electromagnetic fields as sharply as micron-scale fillers and indeed may act to trap charge and increase the electrical breakdown strength of polymers.

Secondly, although many properties of a material are said to be intrinsic, they often depend upon matter being assembled above a critical length scale. When the nanoparticles decrease below this size, the properties of the particles can differ significantly from the bulk material; thus variations in melting temperature, color, magnetization, and charge capacity are often observed.<sup>[9]</sup>

Third, the small size of the fillers leads to an exceptionally large interfacial area in the composites. Fig. 1A shows the surface area per unit volume as a function of particle size for spherical particles that are ideally dispersed. If one compares the surface area of a 10- $\mu\text{m}$  carbon fiber to that of a 1-nm single-walled nanotube

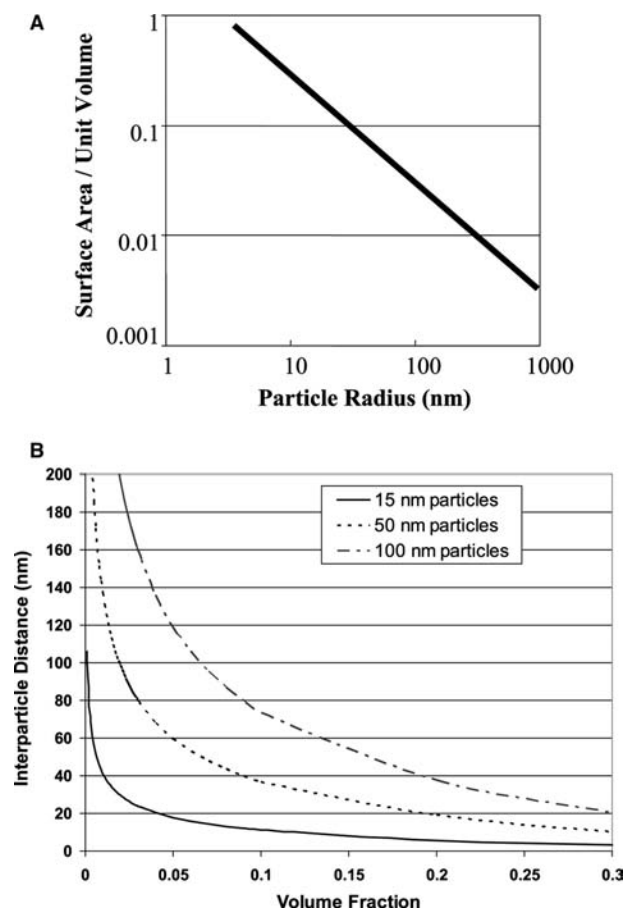


**Fig. 1** (A) The surface area per unit volume as a function of particle size for spherical particles showing the large surface area in nanoparticles. (B) The interparticle spacing of nanoparticles arranged on a simple cubic lattice showing the variation with particle size (15, 50, and 100 nm diameter) and volume fraction.

(SWNT) for the same total volume of the two, the surface area increases by a factor of 10,000. In addition (Fig. 1B), the interparticle spacing decreases such that at small volume fractions of filler, the interparticle spacing is similar to the radius of gyration of the polymer ( $\sim 100$  Å). The high surface area becomes even more significant when one considers that there is an interaction zone (IZ) surrounding the filler. This is a region in which the structure and properties have been altered because of the presence of the filler. It could be a region of altered chemistry, polymer conformation, chain mobility, degree of cure, or crystallinity. This zone of affected polymer has been approximated to be between 2 and 9 nm thick,<sup>[10]</sup> but may be much larger. If we assume that this IZ is about 10 nm in thickness, then at 2.5 vol.% of a 20-nm equiaxed nanoparticle well dispersed, 37% of the polymer has different properties from the bulk polymer. Therefore the IZ can be a significant portion, if not the entire bulk, of the matrix.

Thus the nanofillers can alter the expected properties of the composite considerably.

An example of the influence of the IZ on behavior can be seen by monitoring the glass transition temperature,  $T_g$ . The  $T_g$  of a bulk part can be raised and lowered with the addition of nanoparticles due to the immobilization of polymer chains by the particles or, conversely, an increase in polymer mobility due to non-interacting particles. Both increasing<sup>[11–13]</sup> and decreasing<sup>[14,15]</sup>  $T_g$  cases have been shown. The physical nature and extent of this IZ has recently been probed through some recent work on multiwalled carbon nanotubes (MWNTs).<sup>[16]</sup> In this study, a solvent processing method was used to make MWNT polymer nanocomposites. Upon observation of the composite fracture surface, a polymer layer was observed on the nanotubes (Fig. 2) that had pulled out of the opposing side of the fracture. This “sheath” was confirmed to be polymer from the matrix, but with obviously altered thermal and mechanical properties from the bulk. The thickness of this interfacial layer increased with chemical modification of the nanotubes.

Nanoparticles can also influence the polymerization, curing, or crystallization aspects of polymer synthesis. For example, nanoparticles can serve as nucleation sites in semicrystalline polymers and result in changes in crystalline content and spherulite structure.<sup>[17]</sup> Fig. 3 shows an AFM micrograph of unfilled polyethylene and nanoparticle-filled polyethylene. Note that in the case of the nanofilled polyethylene, the crystalline structure is much less organized.<sup>[18]</sup> Similar results have been seen in polyethylene terephthalate (PET).<sup>[19]</sup>

## SURFACE MODIFICATION OF NANOFILLERS

The nanoscale sizes and subsequently higher surface energies of nanofillers lead to some unique challenges in the processing of these materials. The most critical of these challenges is dispersion of the nanofiller. Any agglomeration of the filler reduces the interfacial area in the composites and thus reduces the opportunity to take advantage of the unique nanofiller properties mentioned in the previous section. Thus aggregated nanoparticles are simply micron fillers.

Controlling the size and degree of agglomeration of nanoparticles is difficult due to their large radius of curvature and subsequent increase in surface energy. As these high surface area fillers tend to aggregate, silanes and organotitanates are used extensively both to tailor the particle surface properties to mimic the surrounding matrix and to lower their surface energy and reduce their tendency to agglomerate.<sup>[20–22]</sup> Other methods to alter the surface properties of the nanoparticles include radiation grafting,<sup>[23]</sup> chemical vapor

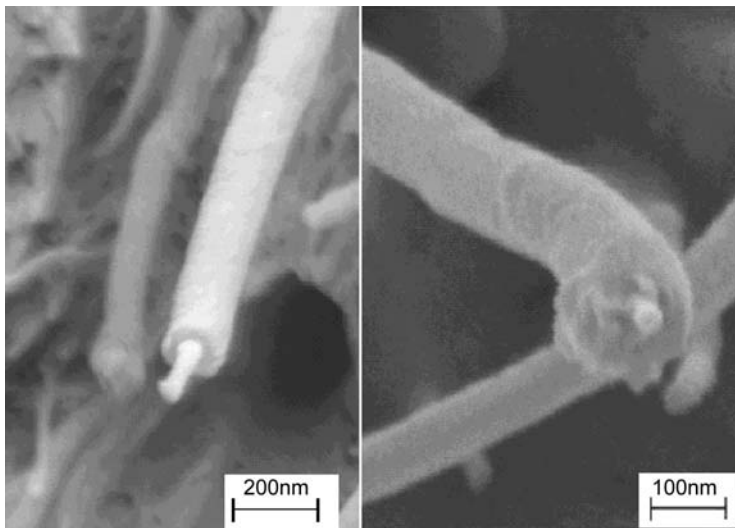


**Fig. 2** Polymer-coated nanotubes observed in the fracture surface of MWNT reinforced polycarbonate composite. *Source:* From Ref.<sup>[16]</sup>.

deposition, and a host of complicated synthesis procedures that attempt to polymerize polymer chains off of initiating agents coupled to the surface.<sup>[24–26]</sup> An excellent review by Caruso<sup>[27]</sup> provides an extensive background on the modification of nanoparticle surfaces. In addition to achieving better dispersion, these techniques control the nature of the interaction between the nanofillers and the polymer and thus the properties and size of the IZ.

Carbon nanotubes not only tend to agglomerate but are often prepared in a bundle-like structure, as illustrated in Fig. 4. In order to take advantage of their high surface area for interacting with the polymer, the bundles have to be separated into individual nanotubes. For MWNT this can usually be accomplished with sonication.<sup>[28,29]</sup> For SWNT, exfoliation is a more difficult process but progress is being made.<sup>[30–34]</sup> The challenge is in exfoliating the bundles without shortening the SWNT and introducing significant numbers of defects. Once the nanotubes have been separated, it is important to disperse them uniformly in the polymer matrix, preventing agglomeration of nanotubes. This

is accomplished with functional groups which also mediates the interaction of the nanotubes with the polymer.

Non-covalent surface modification of carbon nanotubes includes all treatments that cause a change in the functional groups that face the solvent (or the polymer), without modifying the chemical nature of the nanotube. The advantage of the non-covalent surface modification is that the basic structure and hence the mechanical and electrical properties of the tubes are not affected due to the modification.<sup>[35]</sup> Non-covalent attachment is possible if there is a secondary bonding between these groups and the surface of the nanotube.<sup>[36,37]</sup> For example, wrapping of the nanotubes by polymer chains, in particular conjugated polymers, has been observed.<sup>[36,38–40]</sup>

Covalent attachment of chemical groups to the outer wall of the nanotubes can occur particularly at defect sites. One example is the attack of the defect sites by concentrated nitric acid, in order to form carboxylic acid groups.<sup>[41]</sup> The reaction with nitric acid also eliminates the catalysts that are left from the

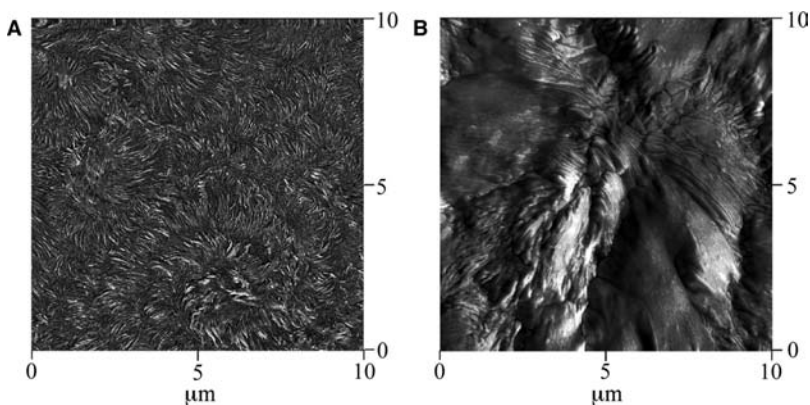


**Fig. 3** Atomic force micrographs showing the change in crystalline morphology for unfilled and nanofilled low-density polyethylene, (A) neat low density polyethylene, (B) low-density polyethylene with 5 wt.% titania nanoparticles. *Source:* From Ref.<sup>[18]</sup>.

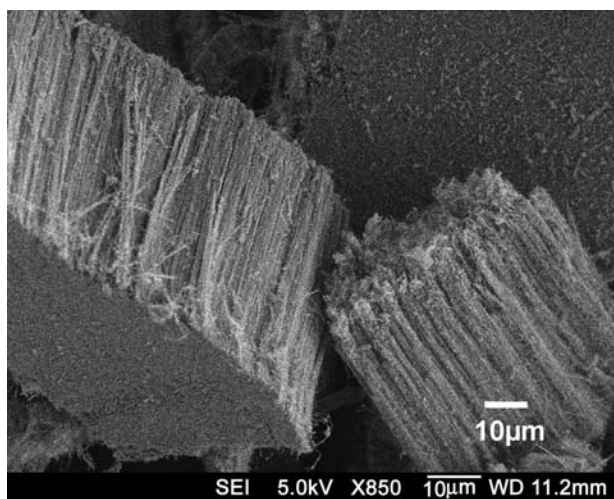


**Fig. 4** An SEM micrograph showing the bundled nature of multiwalled carbon nanotubes grown using a chemical vapor deposition process.

nanotubes preparation process. This reaction has been applied on SWNT and MWNT. The resultant carboxylated nanotubes can then be further covalently modified by means of reactions based on the carboxylic acid groups.<sup>[42,43]</sup> There are also other variations of the chemical oxidation of carbon nanotubes (for example, applying a mixture of sulfuric acid and  $H_2O_2$ <sup>[44]</sup>). The presence of carboxylic acid groups on the nanotube walls enables various reactions for the further attachment of functional groups.<sup>[43,45–50]</sup>

Other types of covalent surface modification of carbon nanotubes are based on chemical reactions between the carbon–carbon bond structures and specific reagents such as fluorination<sup>[51]</sup> or on radical attachments.<sup>[52,53]</sup> These reactions and many others<sup>[54–58]</sup> enable tailoring of the nanofillers to the specific application and environment. The potential for using surface modification to improve the properties of nanotube-reinforced polymer composites has just begun to be explored.

## NANOPARTICLE-FILLED POLYMER PROPERTIES

Nanoparticle fillers are relatively equiaxed with diameters less than 100 nm (Fig. 5). Nanoparticles (carbon black) have been used as fillers in polymers for the past century, but the advent of new particle synthesis techniques has made available industrial quantities of ceramic, piezoelectric, metal, and even polymer nanoparticles for use in polymer nanocomposite research. Synthesis of these nanoparticles is accomplished using a variety of methods, each with its own advantages and disadvantages.<sup>[59]</sup> This section focuses mainly on the

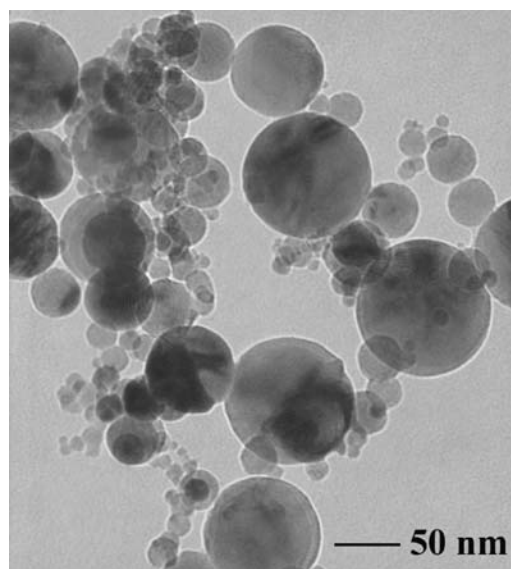


**Fig. 5** Typical poly-disperse oxide nanoparticles synthesized in a forced gas condensation process.

unique mechanical, thermal, optical, and electrical properties obtained when nanoparticles are used as fillers in polymer systems.

## Mechanical Properties

One of the primary reasons for adding fillers to polymers is to improve mechanical performance. Traditional polymer composites filled with micron-size fillers often show improvements in stiffness and heat resistance in the form of increases in modulus, yield strength, and glass transition temperature.<sup>[4,60]</sup> In micron-filled composites, unfortunately, this often comes at the cost of a substantial reduction in ductility, and sometimes in impact strength, because of stress concentrations caused by the fillers. Well-dispersed nanofillers, on the other hand, are able to improve modulus and strength, and to maintain or even improve ductility because they are much smaller than the critical crack size for polymers and need not initiate failure. In addition, large amounts of traditional fillers are often required to achieve the desired properties, often diminishing the weight-savings gained in using low-density polymers.

Polymer nanocomposites have been shown to provide unique combinations of mechanical and thermal properties often at very low filler weight fractions. For example, dramatic improvements in the yield stress (30%) and Young's modulus (170%) have been shown in nanofilled polypropylene compared to micron-filled polypropylene.<sup>[61]</sup> These composites also showed no decrease in the strain-to-failure when filled with silica ranging from 7 to 40 nm in diameter (Fig. 6).



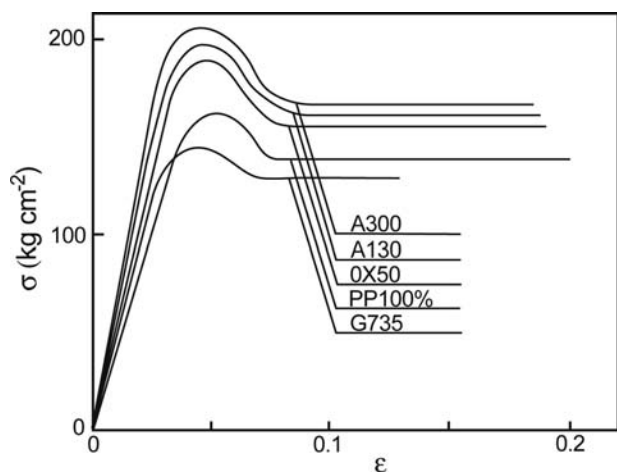


**Fig. 6** Stress–strain curves of a silica/polypropylene (PP) nanocomposite with fillers of four different diameters (A300 and A130 = nanosilica-filled PP, PP100% = neat polymer, and G735 = micron-filled PP). *Source:* From Ref.<sup>[4]</sup>.

In addition, nylon 6 filled with 50-nm silica particles displayed increases in tensile strength (15%), strain-to-failure (150%), Young's modulus (23%), and impact strength (78%) with only 5 wt.% nanoparticles.<sup>[62]</sup> In a rubbery polyurethane elastomer, Petrovic and Zhang<sup>[63,64]</sup> found that a sixfold increase in the elongation-at-break and a threefold increase in the modulus were achievable with 40 wt.% 12-nm silica compared to micron-size filler that embrittled the polymer. Furthermore, the nanocomposites showed no reduction in transparency even at these relatively high loadings unlike the micron-size filled systems. In attempting to modify an already two-phase system, Zhang et al.<sup>[65]</sup> filled high impact polystyrene (HIPS) with nanoparticles and showed increases in notched impact, tensile strength, and elastic modulus of the blend. In a study by Ash et al., the mode of yielding in polymethylmethacrylate, a brittle thermoplastic polymer, was changed from dilatational (craze) to shear

by the incorporation of nanoparticles that showed no affinity for the matrix polymer.<sup>[66]</sup> Extensions as high as 80% but averaging 30% were routinely seen and were accompanied by a necking phenomenon (Fig. 7). The transition from crazing to shear yielding was hypothesized to be due to poorly bonded nanoparticles that are well dispersed in the polymer matrix. In this way, the polymer was hypothesized to detach from the nanoparticles and deform in response to the tensile stress, thus delocalizing the yield damage and preventing the typical craze-to-fracture brittle failure.

The most dramatic increases in the modulus of nanocomposites occur in the region above the  $T_g$ . Often, these increases are much greater (4000%) than those that occur below  $T_g$ .<sup>[14,67]</sup> This is hypothesized to be due to the creation of crosslinks, either temporary or permanent, between nanoparticles and polymer which serve to increase the plateau modulus. Indeed, the ability to strictly control the size and surface activity of nanoparticles in recent dynamic mechanical studies on silica/polyvinylacetate nanocomposites above the  $T_g$  has shed new light on the non-linear reinforcement behavior of rubbery melts.<sup>[68]</sup> In this study, the modulus of the polymer nanocomposite melt is shown to vary depending on the imposition of a large or small amplitude strain. The corresponding hypothesis concludes that the nanoparticles act as centers for trapped, non-labile polymer chains that serve as temporary entanglements. In this work, the destruction and eventual recovery of the network offer an alternative to the particle filler networks widely believed to be responsible for the behavior known as the Payne effect.<sup>[69]</sup>

Studies of the wear behavior of nanofilled polymer composites have also demonstrated encouraging results. In composites using micron-size fillers, the wear resistance increases, but often the coefficient of friction does as well. In silica/epoxy nanocomposites at low volume fractions ( $\sim 2$  vol.%), however, sliding wear tests showed that both the frictional coefficient

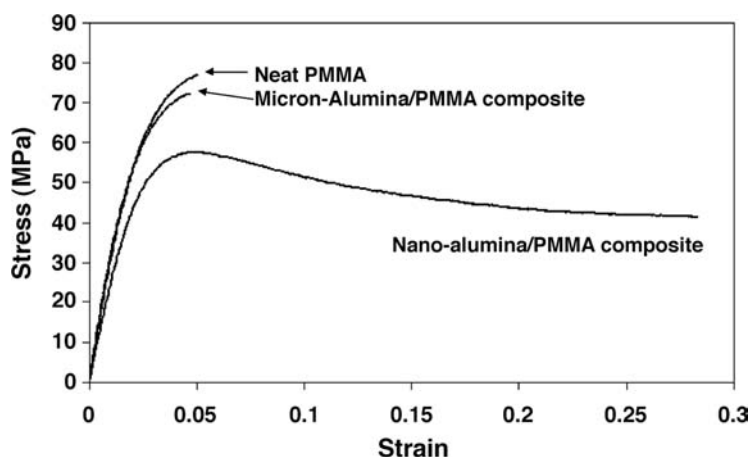


**Fig. 7** Stress–strain curves for alumina/polymethyl methacrylate (PMMA) nanocomposites showing transformation from brittle to ductile behavior at 5 wt.% 39-nm-diameter alumina nanoparticles. *Source:* From Ref.<sup>[66]</sup>.

and the specific wear rate were lower than either the unfilled epoxy or epoxy filled with micron-size fillers.<sup>[70]</sup> This is significant because most filled systems display the decreased wear rate, but also show an increase in the friction coefficient. Nanoparticles are theorized to be able to significantly reduce wear rates because the wear mechanism changes from severe abrasion wear to mild sliding wear. This is due to the reduction in the angularity of the filler particles and the fact that the transfer film, where abrasion is taking place, can be strengthened because the nanoparticles would have the capability of blending well with wear particles. In addition, the material removal of nanoparticulate composites is thought to be much milder than that of conventional composites because the fillers have the same size as the segments of the surrounding polymer chains.<sup>[70]</sup>

The scratch resistance of nanocomposites is also improved over their micron counterparts.<sup>[71]</sup> Ng et al. reported that nano-TiO<sub>2</sub>-filled epoxy showed greater scratch resistance with the scratch track being much smoother than either the neat polymer or a micron-filled system.<sup>[72]</sup> In addition, the depth and width of the scratch track decreased in the nanofilled system. This behavior has also been seen in alumina/gelatin nanocomposites.<sup>[73]</sup>

Nanoparticles have also been recently used to reinforce shape memory polymers for microelectromechanical systems (MEMS) applications. Gall et al.<sup>[74]</sup> demonstrated that the microhardness and elastic modulus could be increased through the use of SiC nanoparticles. In this case, the small size of the MEMS devices necessitates the use of nanoparticles for incorporation into the device, but the nanoparticles actually increased the force of recovery from 300 mN for the unfilled resin to 450 mN for a 20 wt.% nano-filled composite.

As with most mechanical systems, the property enhancements shown above experience an initial increase followed by a decrease usually in the 2–5 vol.% range. The observation of a particular weight fraction at which mechanical behavior is optimized has been observed in other nanocomposite studies.<sup>[14,62,65]</sup> It is obvious that at lower particle loadings, there is generally not enough material altered by the presence of the particles to permit large-scale changes in material properties. Higher loadings induce agglomeration, which degrades the polymer performance through, for example, inclusion of voids that can act as preferential sites for crack initiation and failure.

## Thermal Properties

The thermal properties of polymers and their composites are important from a mechanical stability

perspective as well as a processing perspective. Thus the ability to alter this behavior, either by increasing or decreasing the processing or service temperature, is highly important in finding new markets for polymer products.

One of the most widely measured values to quantify thermal properties in polymers is the glass transition temperature. Changes in the glass transition temperature,  $T_g$ , as a function of the filler content have been reported for a variety of polymer composites containing a wide variety of nanoscale fillers. Most researchers report an increase in the  $T_g$  as a function of filler content;<sup>[10,14,75]</sup> in fact, Avella and coworkers have shown a 35°C increase in the  $T_g$  of PMMA filled with just 6 wt.% CaCO<sub>3</sub> nanoparticles.<sup>[76]</sup> On the other hand, decreases in the nanocomposite  $T_g$  have also been reported.<sup>[11,15]</sup>

The increases in  $T_g$  have been linked to the immobilization of the matrix within an IZ which hinders cooperative motion by raising the energy barrier for intermolecular chain movement.<sup>[11,75]</sup> However, attempts to relate the  $T_g$  reductions to existing theories of the glass transition have been limited. Becker, Mueller, and Schmidt<sup>[11]</sup> reported that, over the range of filler volume fractions considered (0–10 vol.%), the  $T_g$  of their acetoxypolypropyltrimethoxysilane (APTS)-treated silica-filled PMMA–HEMA copolymer system decreased by 16°C, while the  $T_g$  of their composites prepared with as-received filler decreased by 9°C. This was contrasted with the increases in  $T_g$  observed for 10-nm silica coated with methacryloxypropyltrimethoxysilane (MPTS). In these latter specimens, the  $T_g$  increased by 10°C at 10 vol.% filler. However, the 100-nm silica used in the study produced no changes in the  $T_g$  with either coating at any filler concentration. Thus the increased surface area of the 10-nm silica and the interface between the APTS- and MPTS-coated particles and the polymer dramatically changed the polymer mobility in the bulk at fairly low volume fractions resulting in both increasing and decreasing  $T_g$  values.

In some instances, the particle, IZ, and matrix have been modeled as a core-shell scheme to incorporate the interaction zone/low mobility region. If the volume fraction of the interaction zone is high enough, this model shows two  $T_g$ s, while most researchers do not see this, there have been reports that show the additional relaxation mode corresponding to the restricted polymer network in contact with the nanofiller.<sup>[77,78]</sup>

Recent work by Sternstein and Zhu<sup>[68]</sup> on silica/polyvinylacetate nanocomposites indicates that a greater far-field effect is at work in altering chain dynamics than simply a local immobilization of the polymer chain as has been previously suggested.<sup>[78]</sup> This far-field effect may have a very large effect on



the glass transition as shown recently by Ash, Schadler, and Siegel<sup>[15]</sup> In this work, the  $T_g$  of alumina/PMMA nanocomposites at 1.0 wt.% filler drops by 25°C when compared to the neat polymer (Fig. 8). Further additions of filler do not lead to additional  $T_g$  reductions. This novel thermal behavior is shown to vary with particle size, but this dependence can be normalized with respect to specific surface area. The nanocomposite  $T_g$  phenomenon is hypothesized to be due to non-adhering nanoparticles that act as well-dispersed internal void/polymer interfaces that break up the percolating structure of dynamically heterogeneous domains recently suggested by Long and Lequeux<sup>[79]</sup> to be responsible for the  $T_g$  reductions in polymer ultrathin films.<sup>[80]</sup> The results also point to a dramatically increased scope of the so-called IZ and its “far-field” effect on the entire matrix.

A closely related topic in polymers and nanocomposites is the diffusivity of these materials. Studying gas transport of nanosilica-filled polymer by <sup>129</sup>Xe NMR permeativity increased with increasing filler content while retaining gas molecule size selectivity.<sup>[81]</sup> Similar results were shown using pulsed field gradient (PFG) NMR techniques with an order of magnitude increase in translational diffusion seen at 30 wt.% silica in a random copolymer.<sup>[82]</sup>

## Optical Properties

As stated in the Introduction, the scattering of light by nanoscale particles is markedly reduced when the particle size is decreased less than 50 nm.<sup>[8]</sup> Thus nanoparticles may be added to polymers to increase wear, toughness, etc., while maintaining the optical transparency that many organic materials possess. An excellent review, both historical and current, of

the phenomena of light absorption and scattering by nanoparticles in solution and in nanocomposites was recently given by Caseri.<sup>[8]</sup> Apart from maintaining clarity in the visible wavelengths, adding nanoparticles can add interesting functionality in the form of UV absorption<sup>[83]</sup> and the alteration of the refractive index of the matrix polymer. The addition of TiO<sub>2</sub> nanoparticles to many polymers results in such a material where the particles act to absorb the UV radiation and increase the refractive index.<sup>[71,84]</sup> Indeed, nanocomposites of lead sulfide and polyethylene oxide now boast a refractive index of 3.9,<sup>[3,85]</sup> while gold nanoparticles contained in gelatin have reduced the refractive index to about 1.<sup>[86]</sup> Dichoric behavior has also been observed in nanoparticle-filled polymers that have been highly stretched, resulting in “string of pearls”-type structures of fillers with very high aspect ratios. In these composites, the interaction with polarized light varies with the direction of both the incoming radiation and the orientation of the filler strands and results in both color<sup>[87]</sup> and intensity changes.<sup>[88]</sup> This type of composite response can be used in the liquid crystal displays<sup>[8]</sup> or in strain-based schemes for light-filtering devices.

## Electrical Properties

The opportunities to tune the electrical properties of polymers with nanocomposites extend beyond enhancing conductive polymers; superparamagnetism in magnetic materials<sup>[89,90]</sup> or tunable band gaps in quantum dot semiconductor arrays show promise when incorporated into polymers for additional functionality. In addition, the percolation threshold has been shown to be lower in nanocomposites than in traditional filled composites with values as low as

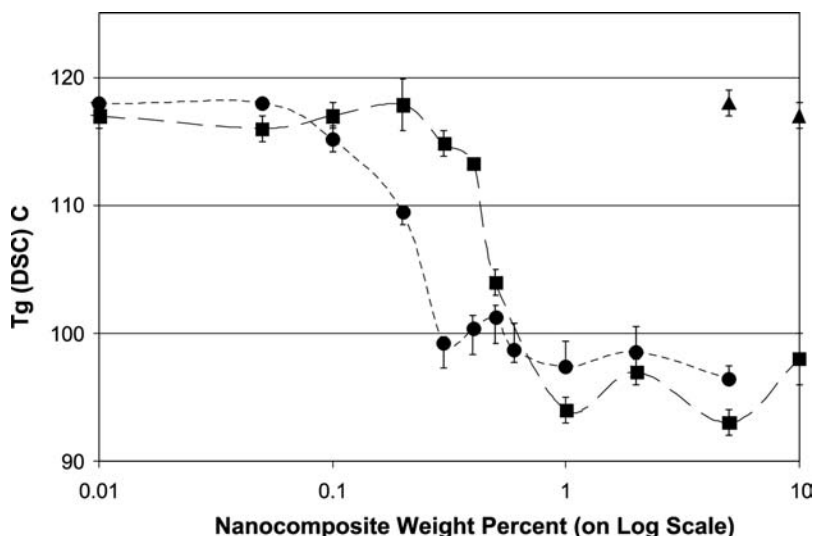


**Fig. 8** Glass transition behavior of alumina/PMMA nanocomposites (■—38/39-nm alumina, ●—17-nm alumina). Note that the filler weight fraction is plotted on a log scale to show the behavior of the lower values more clearly. The neat PMMA is plotted as 0.01 wt.% on the above graph. Following coating with GPS, the  $T_g$  returns to the neat value (▲—GPS-coated). *Source:* From Ref.<sup>[15]</sup>.

0.03 vol.% reported.<sup>[91]</sup> Hong et al. using a ZnO/LDPE nanocomposite showed a lower percolation limit and a slower decrease in the resistivity with nanofiller concentration compared to conventional composite.<sup>[92]</sup> The dielectric breakdown strength of nanocomposites can also be enhanced over compositions with micron-scale fillers.<sup>[18]</sup>

In addition to traditional filler roles, organic-inorganic nanocomposites have found their way into etch resists used in semiconductor nanolithography. With line sizes in CMOS technology approaching 100 nm, adding silica nanoparticles to traditional organic resists, such as PMMA, have been shown to increase rigidity and display a higher glass transition temperature which enhances resist performance for nanometer pattern fabrication.<sup>[93]</sup>

### CARBON NANOTUBE/POLYMER NANOCOMPOSITES

Carbon nanotubes are in some ways the ideal fiber. The almost defect-free structure of the nanotubes results in mechanical properties that are comparable to those of a graphene sheet. Recent studies have focused on the assessment of the mechanical properties of carbon nanotubes through both experiment and modeling. The Young's modulus of these almost-perfect fibers has been predicted to be between 0.64 and 5.0 TPa for a SWNT.<sup>[94–100]</sup> The tensile strength of SWNTs was calculated to range from 50 to 100 GPa depending on the type and number of defects present.<sup>[101]</sup> The nanometer-scale size of the nanotubes introduces technical difficulties in the experimental measurement of their mechanical properties. However, Yu and coworkers conducted tensile testing experiments on individual MWNTs that were attached to opposing AFM tips on both ends.<sup>[102]</sup> They obtained values of 11–63 GPa for the tensile strength and 270–950 GPa for the elastic modulus of the MWNT. Yu and coworkers also conducted tensile tests on SWNT bundles and obtained 320–1470 GPa for the elastic modulus.<sup>[103]</sup> Thus the strengths obtained by experimental measurements are lower than the calculated values, possibly due to intrinsic nanotube defects that cause premature mechanical failure or to other errors in the experimental methodology. Indirect measurements have yielded similar values for modulus and strength.<sup>[104,105]</sup>

In addition to their unique mechanical properties, carbon nanotubes have a high aspect ratio, high thermal conductivity, high electrical conductivity, and low coefficient of thermal expansion.<sup>[106]</sup> In short, carbon nanotubes theoretically have the properties of an ideal graphite fiber. This alone makes them attractive for incorporation into polymers. In addition,

their small size introduces the possibility of synthesizing transparent materials with low volume fractions of filler.

### Mechanical Properties

Studies have been conducted in order to explore the mechanical properties of nanotube-reinforced polymer composites, keeping in mind the challenges to be addressed. MWNT-polystyrene films were prepared from solution in toluene and tested in tension.<sup>[28]</sup> 1 wt.% of MWNT caused an increase of 36% in the elastic modulus, and 25% increase in strength. In another study, 5 wt.% MWNT-epoxy samples were prepared and tested under tension and compression.<sup>[107]</sup> An increase of 20% in the tensile elastic modulus and the compression elastic modulus was observed. Insights into the mechanisms of load transfer were discussed for this system, because of the interesting behavior of the composites under tension and compression, as measured by Raman spectroscopy (see next section for details). In another study, carbon nanofiber reinforced poly(etherether)ketone (PEEK) nanocomposites were prepared by twin-screw extrusion and tested by dynamic mechanical analysis and tensile tests.<sup>[108]</sup> A gradual increase in the elastic modulus as a function of nanofiber concentration was observed such that a loading of 15 wt.% nanofibers resulted in a 40% increase in the modulus. The effect of non-covalent modification of carbon nanotubes on the mechanical and thermal properties of nanotube-epoxy composite was investigated<sup>[37]</sup> using polyoxyethylene 8 lauryl as a surfactant. In this work by Gong et al. an increase of 25°C in the glass transition temperature and a 30% increase in the elastic modulus, as measured by dynamic mechanical analysis, were observed with the incorporation of only 1 wt.% nanotubes. Using polyvinylidene fluoride, again as a non-covalent modifier, in MWNT-polymethyl methacrylate (PMMA) nanocomposites<sup>[109]</sup> the dispersion of the nanotubes in the polymer was better, and the storage modulus, as measured by dynamic mechanical analysis, increased. In situ polymerization has been attempted also in the presence of carbon nanotubes, in order to achieve the participation of the nanotubes in the polymerization process and hence get a covalent attachment of the growing polymer chains to the nanotube surface. Such a study was conducted with methyl methacrylate polymerization and MWNT.<sup>[110]</sup> Evidence for nanotube-polymer interactions was observed from the examination of the fracture surface of the composites. An increase in the heat deflection temperature was also observed with the incorporation of nanotubes. This in situ polymerization procedure was also used in a SWNT-polyimide system.<sup>[111]</sup> In this

research the electrical conductivity of the nanocomposite increased by 10 orders of magnitude at 0.2 wt.% SWNT loading while the mechanical properties also improved. Fluorinated MWNT-reinforced polyvinyl alcohol composites were prepared and mechanically tested.<sup>[112]</sup> A 400% increase in the storage modulus (as measured by dynamic mechanical analysis) was obtained for 4 wt.% functionalized MWNT composite as compared to pure polyvinyl alcohol.

From a mechanical properties viewpoint, the characteristic bending and looping of SWNTs is problematic if the maximum reinforcement is to be obtained. Therefore research has been conducted to align the nanotubes by magnetic fields<sup>[113]</sup> and by melt spinning.<sup>[114]</sup> In both cases nanocomposites with anisotropic properties were obtained with increases in the elastic modulus realized in the alignment orientation.

Few if any of the nanotube-filled polymer composites reported in the literature have achieved the properties expected by their high modulus and strength. This is because of three closely related factors: dispersion, load transfer, and volume fraction. For example, SWNTs are synthesized in bundles. In the bundle form, the load-bearing portion of the bundle is only the outermost tubes. The tubes inside the bundle slide are relative to the others and do not carry significant load. To solve this problem, the SWNT must be separated from the bundles and as mentioned earlier progress is being made in this area. MWNTs on the other hand, can be separated from their bundles. MWNTs however, are concentric tubes with poor bonding between the carbon layers. Therefore even if the outermost tube of a MWNT is carrying load, the inner layers may not be. This also reduces their efficiency. Finally, the high surface area of the nanotubes makes it difficult to process composites with high volume fractions of fillers because the viscosity of the nanotube/matrix mixture is prohibitively high.

### Electrical and Optical Properties

One likely application of nanotube-filled polymers is for applications requiring high electrical conductivity. Their high aspect ratio leads to percolation at extremely low loadings. A recent paper claimed percolation at 0.0025 wt.%<sup>[115]</sup> and several others report levels near 0.3 wt.%.<sup>[116]</sup> This low percolation loading and relatively high conductivity leads to the promise of transparent conducting coatings or other multifunctional applications where the conductivity is improved, but other properties are not compromised. Changes in conductivity as high as 8 orders of magnitude have been observed in nanotube/PPV composites with little loss in photoluminescence/electroluminescence yield. In addition, the mechanical strength simultaneously

improved.<sup>[117]</sup> In situ polymerization under sonication has also been used to assist the dispersion of SWNT in a polyimide matrix. Enhancement of the conductivity by 10 orders of magnitude was measured in this system for 0.2 wt.% of SWNT, while maintaining transparency of the nanocomposite.<sup>[111]</sup> Alignment has also been found to improve conductivity.<sup>[114]</sup> The conductivity that can be achieved is somewhat limited by the mixture of semiconducting and metallic nanotubes produced. Improvements in the ability to separate metallic from semiconducting nanotubes will likely lead to further improvements in conductivity. Other electrical properties such as permittivity have also been investigated.<sup>[118]</sup>

The conduction properties of nanotubes can also be used to alter the optical response of polymers. For example, functionalization of nanotubes and doping of chemically modified nanotubes in low concentration to photoactive polymers such as PPV have been shown as a means to alter the hole transport mechanism and hence the optical emission of the polymer.<sup>[119]</sup> Such hole-collecting properties seem to be a quite general property of some conjugated polymers. Specifically, SWNTs in a polymer matrix trap holes injected from the anode in organic light emitting diodes (OLEDs).<sup>[120]</sup>

The optical limiting behavior of polymer nanotube-filled composites has been investigated with success. It has been reported that polymerization of phenylacetylene in the presence of short nanotubes results in a solvated product of tubules wrapped with poly(phenylacetylene). The optical limiting properties of this composite are excellent and far better than the pristine polymer and polymer filled with other carbon structures. They also fare well in photovoltaic applications suggesting that such nanocomposites could find an array of potential applications in optics-related and laser-based technologies.<sup>[121]</sup>

### NANOTUBE AND NANOPARTICLE COMPOSITE MODELS

The dramatic changes in mechanical properties observed in nanofillers challenge existing theories of mechanical reinforcement. In traditional composites, the modulus can be predicted, usually between upper and lower bounds,<sup>[122]</sup> by modeling the effectiveness of load transfer from the matrix to the polymer. As the particles are, in large part, stiffer than the surrounding matrix, this load transfer results in a stiffer composite than the neat polymer. With the nanoparticles, however, the “span” required for effective load transfer is extremely small and thus can contribute only a small portion of the dramatic gains in modulus seen in nanocomposites. In addition, because of their

unique geometry, the theoretical modeling of the mechanical behavior of nanotube polymer composites is even more complex. The hollow shape of the nanotubes, the wall-wall interactions in MWNT, and the molecular level interactions between the nanotubes and the polymer matrix have to be considered in these models. Odegard and coworkers<sup>[123]</sup> transformed the SWNT and the neighboring polymer chains into an effective fiber. By using molecular dynamic considerations, the effects of nanotube alignment and length on the elastic modulus were calculated. These theoretical calculations were compared to the experimental results of SWNT-polyimide composite mechanical properties.

Addressing the presence of a large volume fraction of the IZ that has properties different from the bulk polymer is also paramount to successful modeling. The alteration of the matrix that takes place at the IZ, as previously mentioned, is a likely candidate for property enhancement. Modeling the IZ is difficult; however, as imperfect bonding, mechanical stresses, and chemical interactions can all play a decisive role in determining its behavior. Ji et al.<sup>[124]</sup> recently modified a composite model to incorporate the interphase zone and were able to successfully model the increases in the modulus of a clay/nylon-6 nanocomposite system. Their treatment modeled the interphase zone as a linear gradient change in the modulus between the surface of the filler and the matrix and introduced the critical effect of particle size (through the increase in volume fraction of the interphase) into the theory. The curves predicted by the model were shown to be in good agreement with the experimental nanocomposite mechanical behavior.

## CONCLUSION

Polymer nanocomposites incorporating carbon nanotubes or nanoparticles are a novel class of composite materials that are often multifunctional, adding the unique optical, electrical, or mechanical properties of the nanofillers while maintaining, if not enhancing, the neat polymer properties. These composites are often characterized by low volume fractions of filler, which may then affect the entire matrix, due to their large surface-area-to-volume ratio, through an interaction zone. The unique nature of these particles presents both challenges and unique opportunities to create a wide range of multifunctional polymer composites.

## REFERENCES

1. Bueche, A.M. Filler reinforcement of silicone rubber. *J. Polym. Sci.* **1957**, *25*, 139–149.

2. Kuriakose, B.; De, S.K.; Bhagawan, S.S.; Sivaramkrishnan, R.; Athithan, S.K. Dynamic mechanical properties of thermoplastic elastomers from polypropylene-natural rubber blend. *J. Appl. Polym. Sci.* **1986**, *32*, 5509–5521.
3. Sumita, M.; Shizuma, T.; Miyasaka, K.; Shikawa, K.J. Effect of reducible properties of temperature, rate of strain, and filler content on the tensile yield stress of nylon 6 composites filled with ultrafine particles. *Macromol. Sci.-Phys.* **1983**, *B22*, 599–616.
4. Sumita, M.; Tsukumo, Y.; Miyasaka, K.; Ishikawa, K. Tensile yield stress of polypropylene composites filled with ultrafine particles. *J. Mater. Sci.* **1983**, *18*, 1758–1764.
5. Li, T.; Chen, Q.; Schadler, L.S.; Siegel, R.W.; Mendel, J.; Irvin, G.C., Jr. Scratch behavior of nanophase Al<sub>2</sub>O<sub>3</sub>-filled gelatin films. *Polym. Compos.* **2002**, *23* (6), 1076–1086.
6. Ruan, S.L.; Gao, P.; Yang, X.G.; Yu, T.X. Toughening high performance ultrahigh molecular weight polyethylene using multiwalled carbon nanotubes. *Polymer* **2003**, *44*, 5643–5654.
7. Ash, B.J.; Stone, J.; Rogers, D.F.; Schadler, L.S.; Siegel, R.W.; Benicewicz, B.C.; Apple, T. Investigations into the thermal and mechanical behavior of PMMA/alumina nanocomposites. *Mater. Res. Soc. Symp. Proc.* **2001**, *661*, KK2.10.1–KK2.10.6.
8. Caseri, W. Nanocomposites of polymers and metals or semiconductors: Historical background and optical properties. *Macromol. Rapid Commun.* **2000**, *21*, 705–722.
9. Siegel, R.W. Nanophase Materials. In *Encyclopedia of Applied Physics*; Trigg, G.L., Ed.; VCH Publishing: Weinheim, 1994; Vol. 11.
10. Hergeth, W.; Steinau, U.; Bittrich, H.; Simon, G.; Schmutzler, K. Polymerization in the presence of seeds: Part IV. Emulsion polymers containing inorganic filler particles. *Polymer* **1989**, *30*, 254–258.
11. Becker, C.; Mueller, P.; Schmidt, H. Optical and thermomechanical investigations on thermoplastic nanocomposites with surface modified silica nanoparticles. *SPIE* **1998**, *3469*, 88–98.
12. Carotenuto, G.; Nicolais, L.; Kuang, X.; Zhu, Z. A method for the preparation of PMMA-SiO<sub>2</sub> nanocomposites with high homogeneity. *Appl. Compos. Mater.* **1995**, *2*, 385–393.
13. Wang, Z.; Pinnavaia, T.J. Hybrid organic-inorganic nanocomposites: Exfoliation of magadiite nanolayers in an elastomeric epoxy polymer. *Chem. Mater.* **1998**, *10*, 1820–1826.
14. Becker, C.; Krug, H.; Schmidt, H. Tailoring of thermomechanical properties of thermoplastic nanocomposites by surface modification of nanoscale silica particles. *Mater. Res. Soc. Symp. Proc.* **1996**, *435*, 237–242.
15. Ash, B.J.; Schadler, L.S.; Siegel, R.W. Glass transition behavior of alumina/polymethylmethacrylate nanocomposites. *Mater. Lett.* **2002**, *55*, 83–87.
16. Ding, W.; Eitan, A.; Fisher, F.T.; Chen, X.; Dikin, D.A.; Andrews, R.; Brinson, L.C.; Ruoff, R.S. Direct observation of polymer sheathing in carbon

- nanotube—Polycarbonate composites. *Nano Lett.* **2003**, *3* (11), 1593–1587.
17. Chan, C.M.; Wu, J.; Li, J.X.; Cheung, Y.K. Polypropylene/calcium carbonate nanocomposites. *Polymer* **2002**, *43*, 2981–2992.
  18. Ma, D.L.; Onnesby, C.; Martensson, E.; Siegel, R.W.; Schadler, L.S. Influence of nanoparticle surface water on the breakdown strength of nanoparticle filled low density polyethylene. **2003**.
  19. Bhimaraj, P.; Freudenberg, K.; Action, J.; Sawyer, G.; Schadler, L. Enhancement in wear resistance and self-lubrication of PET through addition of nanofillers. **2003**.
  20. Abboud, M.; Turner, M.; Duguet, E.; Fontanille, M. PMMA-based composite materials with reactive ceramic fillers: Part I. Chemical modification and characterization of ceramic particles. *J. Mater. Chem.* **1997**, *7*, 1527.
  21. Wang, S.; Wang, M.; Lei, Y.; Zhang, L. Anchor effect of poly(styrene maleic anhydride)/TiO<sub>2</sub> nanocomposites. *J. Mater. Sci. Lett.* **1999**, *18*, 2009–2012.
  22. Caris, C.; van Elven, L.; van Herk, A.; German, A. Polymerization of MMA (methyl methacrylate) at the surface of inorganic submicron particles. *Br. Polym. J.* **1989**, *21*, 133–140.
  23. Rong, M.Z.; Zhang, M.Q.; Zheng, Y.X.; Zeng, H.M.; Friedrich, K. Improvement of tensile properties of nano-SiO<sub>2</sub>/PP composites in relation to percolation mechanism. *Polymer* **2001**, *42*, 3301–3304.
  24. von Werne, T.; Patten, T. Atom transfer radical polymerization from nanoparticles: A tool for the preparation of well-defined hybrid nanostructures and for understanding the chemistry of controlled/‘living’ radical polymerizations from surfaces. *J. Am. Chem. Soc.* **2001**, *123*, 7497–7505.
  25. Weimer, M.W.; Chen, H.; Giannelis, E.P.; Sogah, D.Y. Direct synthesis of dispersed nanocomposites by in situ living free radical polymerization using a silicate-anchored initiator. *J. Am. Chem. Soc.* **1999**, *121*, 1615–1616.
  26. Tsubokawa, N.; Kogure, A.; Maruyama, K.; Sone, Y.; Shimomura, M. Graft polymerization of vinyl monomers from inorganic ultrafine particles initiated by azo groups introduced onto the surface. *Polym. J.* **1990**, *22*, 827–833.
  27. Caruso, F. Nanoengineering of particle surfaces. *Adv. Mater.* **2001**, *13*, 11–22.
  28. Qian, D.; Dickey, E.C.; Andrews, R.; Rantell, T. Load transfer and deformation mechanisms in carbon nanotube–polystyrene composites. *Appl. Phys. Lett.* **2000**, *76* (20), 2868–2870.
  29. Dalton, A.B.; Bayrne, H.J.; Coleman, J.N.; Curran, S.; Davey, A.P.; McCarthy, B.; Blau, W. Optical absorption and fluorescence of multi-walled nanotube–polymer composites. *Synth. Met.* **1999**, *102*, 1176–1177.
  30. Kahn, M.G.C.; Banerjee, S.; Wong, S.S. Solubilization of oxidized single-walled carbon nanotubes in organic and aqueous solvents through organic derivatization. *Nano Lett.* **2002**, *2* (11), 1215–1218.
  31. Bower, C.; Kleinhammes, A.; Wu, Y.; Zhou, O. Intercalation and partial exfoliation of single-walled carbon nanotubes by nitric acid. *Chem. Phys. Lett.* **1998**, *288*, 481–486.
  32. Nagasawa, S.; Yudasaka, M.; Hirahara, K.; Ichihashi, T.; Ijima, S. Effect of oxidation on single-wall carbon nanotubes. *Chem. Phys. Lett.* **2000**, *328*, 374–380.
  33. Chen, J.; Hamon, M.A.; Hu, H.; Chen, Y.; Rao, A.M.; Eklund, P.C.; Haddon, R.C. Solution properties of single-walled carbon nanotubes. *Science* **1998**, *282*, 95–98.
  34. Niyogi, S.; Hamon, M.A.; Hu, H.; Zhao, B.; Bhowmik, B.; Sen, R.; Itkis, M.E.; Haddon, R.C. Chemistry of single-walled carbon nanotubes. *Acc. Chem. Res.* **2002**, *35*, 1105–1113.
  35. Carrillo, A.; Swartz, J.A.; Gamba, J.M.; Kane, R.S.; Chakrapani, N.; Wei, B.; Ajayan, P. Noncovalent functionalization of graphite and carbon nanotubes with polymer multilayers and gold nanoparticles. *Nano Lett.* **2003**, *3* (11), 1437–1440.
  36. Chen, J.; Liu, H.; Weimer, W.A.; Halls, M.D.; Waldeck, D.H.; Walker, G.C. Noncovalent engineering of carbon nanotube surfaces by rigid, functional conjugated polymers. *J. Am. Chem. Soc.* **2002**, *124* (31), 9034–9035.
  37. Gong, X.; Liu, J.; Baskaran, S.; Voise, R.D.; Young, J.S. Surfactant-assisted processing of carbon nanotube/polymer composites. *Chem. Mater.* **2000**, *12*, 1049–1052.
  38. O’Connell, M.J.; Boul, P.; Ericson, L.M.; Huffman, C.; Wang, Y.; Haroz, E.; Kuper, C.; Tour, J.; Ausman, K.D.; Smalley, R.E. Reversible water-solubilization of single-walled carbon nanotubes by polymer wrapping. *Chem. Phys. Lett.* **2001**, *342*, 265–271.
  39. Czerw, R.; Guo, Z.; Ajayan, P.M.; Sun, T.-P.; Carroll, D.L. Organization of polymers onto carbon nanotubes: A route to nanoscale assembly. *Nano Lett.* **2001**, *1* (8), 423–427.
  40. McCarthy, B.; Coleman, J.N.; Crezw, R.; Dalton, A.B.; in het Panhuis, M.; Drury, A.; Brenier, P.; Nagy, J.B.; Lahr, B.; Byrne, H.J.; Carroll, D.L.; Blau, W.J. A microscopic and spectroscopic study of interactions between carbon nanotubes and a conjugated polymer. *J. Phys. Chem., B* **2002**, *106* (9), 2210–2216.
  41. Hamon, M.A.; Hu, H.; Bhowmik, P.; Niyogi, S.; Zhao, B.; Itkis, M.E.; Haddon, R.C. End-group and defect analysis of soluble single-walled carbon nanotubes. *Chem. Phys. Lett.* **2001**, *347*, 8–12.
  42. Lin, Y.; Rao, A.M.; Sadanadan, B.; Kenik, E.A.; Sun, Y.-P. Functionalization of multiple-walled carbon nanotubes with aminopolymers. *J. Phys. Chem., B* **2002**, *106* (6), 1294–1298.
  43. Hill, D.E.; Rao, A.M.; Allard, L.F.; Sun, Y.-P. Functionalization of carbon nanotubes with polystyrene. *Macromolecules* **2002**, *35* (25), 9466–9471.
  44. Zhao, W.; Song, C.; Pehrsson, P.E. Water-soluble and optically PH-sensitive single-walled carbon nanotubes from surface modification. *J. Am. Chem. Soc.* **2002**, *124* (42), 12418–12419.
  45. Liu, J.; Rinzler, A.G.; Dai, J.H.; Hafner, J.H.; Bradley, R.K.; Boul, P.J.; Lu, A.; Iverson, T.; Shelimov, K.; Huffman, C.B.; Rodriguez-Macias, F.; Shon, Y.S.;

- Lee, T.R.; Colbert, D.T.; Smalley, R.E. Fullerene pipes. *Science* **1998**, *280*, 1253–1256.
46. Hamon, M.A.; Chen, J.; Hu, H.; Chen, Y.; Itkis, M.E.; Rao, A.M.; Eklund, P.C.; Haddon, R.C. Dissolution of single-walled carbon nanotubes. *Adv. Mater.* **1999**, *11* (10), 834–840.
47. Baker, S.E.; Cai, W.; Lasseter, T.L.; Weidkamp, K.P.; Hamers, R.J. Covalently bonded adducts of deoxyribonucleic acid (DNA) oligonucleotides with single-wall carbon nanotubes: Synthesis and hybridization. *Nano Lett.* **2002**, *2* (12), 1413–1417.
48. Huang, W.; Fernando, S.; Allard, L.F.; Sun, Y.-P. Solubilization of single-walled carbon nanotubes with diamine-terminated oligomeric poly(ethylene glycol) in different functionalization reactions. *Nano Lett.* **2003**, *3* (4), 565–568.
49. Huang, W.; Taylor, S.; Fu, K.; Lin, Y.; Zhang, D.; Hanks, T.W.; Rao, A.M.; Sun, Y.-P. Attaching proteins to carbon nanotubes via diimide-activated amidation. *Nano Lett.* **2002**, *2* (4), 311–314.
50. Banerjee, S.; Wong, S.S. Synthesis and characterization of carbon nanotube–nanocrystal heterostructures. *Nano Lett.* **2002**, *2* (3), 195–200.
51. Mickelson, E.T.; Huffman, C.B.; Rinzler, A.G.; Smalley, R.E.; Hauge, R.H.; Margrave, J.L. Fluorination of single-wall carbon nanotubes. *Chem. Phys. Lett.* **1998**, *296*, 188–194.
52. Ying, Y.; Saini, R.K.; Liang, F.; Sadana, A.K.; Billups, W.E. Functionalization of carbon nanotubes by free radicals. *Org. Lett.* **2003**, *5* (9), 1471–1473.
53. Holzinger, M.; Votrowsky, O.; Hirsch, A.; Henrich, F.; Kappes, M.; Weiss, R.; Jellen, F. Sidewall functionalization of carbon nanotubes. *Angew. Chem., Int. Ed.* **2001**, *40* (21), 4002–4005.
54. Banerjee, S.; Wong, S.S. Structural characterization, optical properties, and improved solubility of carbon nanotubes functionalized with Wilkinson's catalyst. *J. Am. Chem. Soc.* **2002**, *124*, 8940–8948.
55. Georgakilas, V.; Kordatos, K.; Prato, M.; Guldi, D.M.; Holzinger, M.; Hirsch, A. Organic functionalization of carbon nanotubes. *J. Am. Chem. Soc.* **2002**, *124* (5), 760–761.
56. Dyke, C.A.; Tour, J.M. Solvent-free functionalization of carbon nanotubes. *J. Am. Chem. Soc.* **2003**, *125*, 1156–1157.
57. Velasco-Santos, C.; Martínez-Hernández, A.L.; Lozada-Cassou, M.; Alvarez-Castillo, A.; Castaño, V.M. Chemical functionalization of carbon nanotubes through an organosilane. *Nanotechnology* **2002**, *13*, 495–498.
58. Bahr, L.J.; Tour, J.M. Highly functionalized carbon nanotubes using in situ generalized diazonium compounds. *Chem. Mater.* **2001**, *13* (11), 3823–3824.
59. Ajayan, P.M.; Braun, P.; Schadler, L.S. *Nanocomposite Science and Technology*; Wiley-VCH Verlag GmbH & Co. KGaA: Weinheim, Germany, 2003.
60. Hussain, M.; Nakahara, A.; Nishijima, S.; Niihara, K. Fracture behavior and fracture toughness of particulate filled epoxy composites. *Mater. Lett.* **1996**, *27*, 21–25.
61. Sumita, M.; Tsukihi, H.; Miyasaka, K.; Ishikawa, K. Dynamic mechanical properties of polypropylene composites filled with ultrafine particles. *J. Appl. Polym. Sci.* **1984**, *29*, 1523–1530.
62. Ou, Y.; Yang, F.; Yu, Z. A new conception on the toughness of nylon 6/silica nanocomposite prepared via in situ polymerization. *J. Polym. Sci., B, Polym. Phys.* **1998**, *36*, 789–795.
63. Petrovic, Z.S.; Zhang, W. Glassy and elastomeric polyurethanes filled with nano-silica particles. *Mat. Sci. Forum* **2000**, *352*, 171–176.
64. Petrovic, Z.S.; Javni, I.; Waddon, A.; Banhegyi, G. Structure and properties of polyurethane–silica nanocomposites. *J. Appl. Polym. Sci.* **2000**, *76*, 133–151.
65. Zhang, J.; Wang, X.; Lu, L.; Li, D.; Yang, X. Preparation and performance of high-impact polystyrene (HIPS)/nano-TiO<sub>2</sub> nanocomposites. *J. Appl. Polym. Sci.* **2003**, *87*, 381–385.
66. Ash, B.J.; Rogers, D.F.; Wiegand, C.J.; Schadler, L.S.; Siegel, R.W.; Benicewicz, B.C.; Apple, T. Mechanical properties of Al<sub>2</sub>O<sub>3</sub>/polymethylmethacrylate nanocomposites. *Polym. Compos.* **2002**, *23*, 1014–1025.
67. Zhang, Q.; Archer, L.A. Poly(ethylene oxide)/silica nanocomposites: Structure and rheology. *Langmuir* **2002**, *18*, 10435–10442.
68. Sternstein, S.S.; Zhu, A.-J. Reinforcement mechanism of nanofilled polymer melts as elucidated by nonlinear viscoelastic behavior. *Macromolecules* **2002**, *35*, 7262–7273.
69. Payne, A.R. The dynamic properties of carbon black-loaded natural rubber vulcanizates. *J. Appl. Polym. Sci.* **1962**, *6*, 368–372.
70. Zhang, M.Q.; Rong, M.Z.; Yu, S.L.; Wetzel, B.; Friedrich, K. Effect of particle surface treatment on the tribological performance of epoxy based nanocomposites. *Wear* **2002**, *253*, 1086–1093.
71. Hwang, D.K.; Moon, J.H.; Shul, Y.G.; Jung, K.T.; Kim, D.H.; Lee, D.W. Scratch resistant and transparent UV-protective coating on polycarbonate. *J. Sol-Gel Sci. Technol.* **2003**, *26*, 783–787.
72. Ng, C.B.; Schadler, L.S.; Siegel, R.W. Synthesis and mechanical properties of TiO<sub>2</sub>–epoxy nanocomposites. *J. Nanostruct. Mater.* **1999**, *12* (1–4), 507–510.
73. Li, T.; Chen, Q.; Schadler, L.S.; Siegel, R.W. Scratch behavior of nanoparticle Al<sub>2</sub>O<sub>3</sub>-filled gelatin films. *Polym. Compos.* **2002**, *23*, 1076–1086.
74. Gall, K.; Dunn, M.L.; Liu, Y.; Finch, D.; Lake, M.; Munshi, N.A. Shape memory polymer nanocomposites. *Acta Mater.* **2002**, *50*, 5115–5126.
75. Iisaka, K.; Shibayama, K. Mechanical alpha-dispersion and interaction in filled polystyrene and polymethylmethacrylate. *J. Appl. Polym. Sci.* **1978**, *22*, 3135–3143.
76. Avella, M.; Errico, M.E.; Martuscelli, E. Novel PMMA/CaCO<sub>3</sub> nanocomposites abrasion resistant prepared by an in situ polymerization process. *Nano Lett.* **2001**, *1*, 213–217.
77. Arrighi, V.; McEwen, I.J.; Qian, H.; Serrano Prieto, M.B. The glass transition and interfacial layer in styrene–butadiene rubber containing silica nanofiller. *Polymer* **2003**, *44*, 6259–6266.



78. Tsagaropoulos, G.; Eisenberg, A. Direct observation of two glass transitions in silica-filled polymers. Implications for the morphology of random ionomers. *Macromolecules* **1995**, *28*, 396–398.
79. Long, D.; Lequeux, F. Heterogeneous dynamics at the glass transition in van der Waals liquids, in the bulk and in thin films. *Eur. Phys. J., E* **2001**, *4*, 371.
80. Mattsson, J.; Forrest, J.A.; Borgesson, L. Quantifying glass transition behavior in ultrathin free-standing polymer films. *Phys. Rev., E* **2000**, *62*, 5187–5200.
81. Merkel, T.C.; Toy, L.G.; Andrady, A.L.; Gracz, H.; Stejskal, E.O. Investigation of enhanced free volume in nanosilica-filled poly(1-trimethylsilyl-1-propyne) by  $^{129}\text{Xe}$  NMR spectroscopy. *Macromolecules* **2003**, *36*, 353–358.
82. Zhong, J.; Wen, W.Y.; Jones, A.A. Enhancement of diffusion in a high-permeability polymer by the addition of nanoparticles. *Macromolecules* **2003**, *36*, 6430–6432.
83. Kyprianidou-Leodidou, T.; Margraf, P.; Caseri, W.; Suter, U.W.; Walther, P. Polymer sheets with a thin nanocomposite layer acting as a UV filter. *Polym. Adv. Technol.* **1997**, *8*, 505–512.
84. Nussbaumer, R.J.; Caseri, W.R.; Smith, P.; Tervoort, T. Polymer-TiO<sub>2</sub> nanocomposites: A route towards visually transparent broadband UV filters and high refractive index materials. *Macromol. Mater. Eng.* **2003**, *288*, 44–49.
85. Weibel, M.; Caseri, W.; Suter, U.W.; Kiess, H.; Wehrli, E. Polymer nanocomposites with ‘ultrahigh’ refractive index. *Polym. Adv. Technol.* **1991**, *2*, 75–80.
86. Zimmermann, L.; Weibel, M.; Caseri, W.; Suter, U.W.; Walther, P. Polymer nanocomposites with ‘ultralow’ refractive index. *Polym. Adv. Technol.* **1993**, *4*, 1–7.
87. Dirix, Y.; Darribere, C.; Heffels, W.; Bastiaansen, C.; Caseri, W.; Smith, P. Optically anisotropic polyethylene-gold nanocomposites. *Appl. Opt.* **1999**, *38*, 6581–6586.
88. Ash, B.J. Investigation into the Thermal and Mechanical Behavior of Alumina/Polymethylmethacrylate Nanocomposites. In *Ph.D. Thesis*; Rensselaer Polytechnic Institute, 2003; 108–113.
89. Roy, S.; Das, D.; Chakravorty, D.; Agrawal, D.C. Magnetic properties of glass-metal nanocomposites prepared by the sol-gel route and hot pressing. *J. Appl. Phys.* **1993**, *74*, 4746–4749.
90. Morup, S.; Tronc, E. Superparamagnetic relaxation of weakly interacting particles. *Phys. Rev. Lett.* **1994**, *72*, 3278–3281.
91. Banerjee, P.; Mandel, B.M. Conducting polyaniline nanoparticle blends with extremely low percolation thresholds. *Macromolecules* **1995**, *28*, 3940–3943.
92. Hong, J.I.; Schadler, L.S.; Siegel, R.W.; Martensson, E. Rescaled electrical properties of ZnO/LDPE nanocomposites. *Appl. Phys. Lett.* **2003**, *82*, 1956–1958.
93. Gonsalves, K.E.; Merhari, L.; Wu, H.; Hu, Y. Organic-inorganic nanocomposites: Unique resists for nanolithography. *Adv. Mater.* **2001**, *13*, 703–714.
94. Treacy, M.M.J.; Ebbesen, T.W.; Gibson, J.M. Exceptionally high young’s modulus for individual carbon nanotubes. *Nature* **1996**, *381* (6584), 678–680.
95. Gao, G.H.; Cagin, T.; Goddard, W.A. Energetics, structure, mechanical and vibrational properties of single-walled carbon nanotubes. *Nanotechnology* **1998**, *9* (3), 184–191.
96. Lu, J.P. Elastic properties of carbon nanotubes and nanoropes. *Phys. Rev. Lett.* **1997**, *79* (7), 1297–1300.
97. Sanchez-Portal, D.; Artacho, E.; Soler, J.M.; Rubio, A.; Ordejon, P. Ab initio structural, elastic, and vibrational properties of carbon nanotubes. *Phys. Rev., B* **1999**, *59*, 12677–12688.
98. Yakobson, B.I.; Barber, C.J.; Bembhole, J. Nanomechanics of carbon tubes: Instabilities beyond linear response. *Phys. Rev. Lett.* **1996**, *76* (14), 2511–2514.
99. Zhou, X.; Zhou, J.J.; Ou-Yang, Z.C. Strain energy and Young’s modulus of single-wall carbon nanotubes calculated from electronic energy-band theory. *Phys. Rev., B* **2000**, *62* (20), 13692–13696.
100. Popov, V.N.; Van Doren, V.E.; Balkanski, M. Elastic properties of single-walled carbon nanotubes. *Phys. Rev., B* **2000**, *61* (4), 3078–3084.
101. Belytschko, T.; Xiao, S.P.; Schatz, G.C.; Ruoff, R.S. Atomistic simulations of nanotube fracture. *Phys. Rev., B* **2002**, *65* (23), 235430/1–8.
102. Yu, M.F.; Lourie, O.; Dyer, M.J.; Moloni, K.; Kelly, T.F.; Ruoff, R.S. Strength and breaking mechanism of multiwalled carbon nanotubes under tensile load. *Science* **2000**, *287*, 637–640.
103. Yu, M.F.; Files, B.S.; Arepalli, S.; Ruoff, R.S. Tensile loading of ropes of single wall carbon nanotubes and their mechanical properties. *Phys. Rev. Lett.* **2000**, *84* (24), 5552–5555.
104. Krishnan, A.; Dujardin, E.; Ebbesen, T.W.; Yanilos, P.N.; Treacy, M.M.J. Young’s modulus of single-walled nanotubes. *Phys. Rev., B* **1998**, *58*, 14013.
105. Lourie, O.; Wagner, H.D. Evaluation of Young’s modulus of carbon nanotubes by micro-Raman spectroscopy. *J. Mater. Res.* **1998**, *13* (9), 2418–2422.
106. Thostenson, E.T.; Ren, Z.F.; Chou, T.W. Advances in the science and technology of carbon nanotubes and their composites: A review. *Compos. Sci. Technol.* **2001**, *61* (13), 1899–1912.
107. Schadler, L.S.; Giannaris, S.C.; Ajayan, P.M. Load transfer in carbon nanotube epoxy composites. *Appl. Phys. Lett.* **1998**, *73* (26), 3842–3844.
108. Sandler, J.; Werner, P.; Shaffer, M.S.P.; Demchuk, V.; Altstädt, V.; Windle, A.H. Carbon-nanofibre-reinforced poly(ether ether ketone) composites. *Compos., Part A* **2002**, *33*, 1033–1039.
109. Jin, Z.; Pramoda, K.P.; Goh, S.H.; Xu, G. Poly(vinylidene fluoride)-assisted melt-blending of multiwalled carbon nanotube/poly(methyl methacrylate) composites. *Mater. Res. Bull.* **2002**, *37*, 271–278.
110. Jia, Z.; Wang, Z.; Xu, C.; Liang, J.; Wei, B.; Wu, D.; Zhu, S. Study on poly(methyl methacrylate) carbon nanotube composites. *Mater. Sci. Eng., A* **1999**, *271*, 395–400.
111. Park, C.; Ounaies, Z.; Watson, K.A.; Crooks, R.E.; Smith, J., Jr.; Lowther, S.E.; Connell, J.W.; Siochi,

- E.J.; Harrison, J.S.; St. Clair, T.L. Dispersion of single wall carbon nanotubes by in situ polymerization under sonication. *Chem. Phys. Lett.* **2002**, *364*, 303–308.
112. Geng, H.Z.; Rosen, R.; Zheng, B.; Shimoda, H.; Fleming, L.; Liu, J.; Zhou, O. Fabrication and properties of poly(ethylene oxide) and functionalized carbon nanotubes. *Adv. Mater.* **2002**, *14* (19), 1387–1390.
113. Kimura, T.; Ago, H.; Tobita, M.; Ohshima, S.; Kyotani, M.; Yumura, M. Polymer composites of carbon nanotubes aligned by a magnetic field. *Adv. Mater.* **2002**, *14* (19), 1380–1383.
114. Hagenmueller, R.; Gommans, H.H.; Rinzler, A.G.; Fischer, J.E.; Winey, K.I. Aligned single-wall carbon nanotubes in composites by melt processing methods. *Chem. Phys. Lett.* **2000**, *330*, 219–225.
115. Sandler, J.K.W.; Kirk, J.E.; Kinloch, I.A.; Shaffer, M.S.P.; Windle, A.H. Ultra-low electrical percolation threshold in carbon-nanotube-epoxy composites. *Polymer* **2003**, *19* (44), 5893–5899.
116. Benoit, J.-M.; Corraze, B.; Lefrant, S.; Bernier, P.; Chauvet, O. Electric Transport Properties and Percolation in Carbon Nanotubes/PMMA Composites. In *Making Functional Materials with Nanotubes*; Mater. Res. Soc. Symp. Proc. Materials Research Society, 2002; Vol. 706, 85–90.
117. Coleman, J.; Dalton, A.; Curran, S.; Rubio, A.; Davey, A.; Drury, A.; McCarthy, B.; Lahr, B.; Ajayan, P.; Roth, S.; Barklie, R.; Blau, W. Phase separation of carbon nanotubes and turbostratic graphite using a functional organic polymer. *Adv. Mater.* **2000**, *12*, 213–216.
118. Grimes, C.A.; Mungle, C.; Kouzoudis, D.; Fang, S.; Eklund, P.C. The 500 MHz to 5.50 GHz complex permittivity spectra of single-wall carbon nanotube-loaded polymer composites. *Chem. Phys. Lett.* **2000**, *319* (5,6), 460–464.
119. Ago, H.; Shaffer, M.S.P.; Ginger, D.S.; Windle, A.H.; Friend, R.H. Electronic interaction between photoexcited poly(p-phenylene-vinylene) and carbon nanotubes. *Phys. Rev., B* **2000**, *61*, 2286.
120. Woo, H.S.; Czerw, R.; Webster, S.; Carroll, D.L.; Ballato, J.; Strevens, A.E.; O'Brien, D.; Blau, W.J. Hole blocking in carbon nanotube-polymer composite organic light emitting diodes based on poly(m-phenylene-vinylene-co-2,5 dioctoxy-p-phenylene). *Appl. Phys. Lett.* **2000**, *77*, 1393–1395.
121. Tang, B.Z.; Xu, H. Preparation, alignment, and optical properties of soluble poly(phenylacetylene)-wrapped carbon nanotubes. *Macromolecules* **1999**, *32*, 2569.
122. Nielsen, L.; Landel, R. *Mechanical Properties of Polymers and Composites*; Marcel Dekker Inc.: New York, 1994. Chapter 7.
123. Odegard, G.M.; Gates, T.S.; Wise, K.E.; Park, C.; Siochi, E.J. Constitutive modeling of nanotube-reinforced polymer composites. *Compos. Sci. Technol.* **2003**, *63*, 1671–1687.
124. Ji, X.L.; Jing, J.K.; Jiang, W.; Jiang, B.Z. Tensile modulus of polymer nanocomposites. *Polym. Eng. Sci.* **2002**, *42*, 983–993.

# Polymer Nanofibers Prepared by Electrospinning

Roland Dersch

Andreas Greiner

Joachim H. Wendorff

*Philipps-Universität Marburg, Marburg, Germany*

## INTRODUCTION

The use of fibers has a long history, the traditional application being in clothing. Natural fibers such as silk, wool, or cotton provide attractive properties for such applications. Fiber diameters characteristic of such natural fibers are 15–40  $\mu\text{m}$  for sheep wool, approximately 20  $\mu\text{m}$  for cotton, and approximately 20  $\mu\text{m}$  for cultivated silk. Natural fibers compete in this area of applications with synthetic fibers. Man-made fibers are predominantly produced by melt spinning, which leads to fiber diameters typically in the range from about 5 to more than 70  $\mu\text{m}$ , thus covering the diameter range characteristic of natural fibers. To produce such fibers, the polymer melt is pumped through a spinneret. Fiber stretching is applied not only to obtain a certain reduction of the diameter but also to simultaneously enhance the chain orientation and mechanical properties.

## OVERVIEW

The range of fiber end-uses is obviously not restricted to clothing. Among others, fibers are used as sorbants, for thermal insulation, filtration, protective clothing, in composites to reinforce a polymer matrices, etc. Such applications frequently require the reduction of the fiber diameter to obtain microfibers, ultramicrofibers down to nanofibers, for example for increase of efficiency by increase of the specific surface area. Polymer fibers with diameters down to 10 nm and below are in demand for a broad range of applications to be discussed below in more detail. These include nanoscaled reinforcement, tissue engineering, specialty fibers, and templates for the formation of hollow fibers with inner diameters in the nanometer range.<sup>[1–9]</sup>

Melt blowing invented close to 50 years ago has become a process of choice for the production of microfibers. It is basically a process in which a high-velocity stream of gases or fluids—steam, air, or other fluids—blows molten thermoplastic resins from an extruder die tip onto a substrate, a conveyor, or a

take-up screen. The characteristic feature is that this process provides a fine fiber web; that is, non-wovens rather than textile fibers.

Another approach toward microfibers involves the spinning of two polymers together to form fine-diameter fibers within the matrix of the second polymer. The matrix is dissolved to yield the microfiber. A related approach consists in splitting the composite fiber by mechanical forces, a high-velocity stream of water. None of these techniques is able to produce polymer fibers down to the nanometer range. The only technique currently available to yield such extremely thin fibers is electrospinning, which is also called electrostatic spinning.

The intention of this review on electrospinning of polymers is not to be comprehensive nor to demonstrate the historical evolution but rather to show concepts and disclose further challenges in electrospinning.

## ELECTROSPINNING PROCESS: THEORETICAL BACKGROUND

The experimental observation is that electrospinning is able to yield well-defined nanofibers with diameters down to a few nanometers for many polymers. Yet a broad range of parameters seems to influence fiber formation and it is a frequent observation that electrospinning does not give rise to homogeneous fibers but rather to beaded fibers; that is, fibers in combination with droplets (Fig. 1). Theory is helpful for understanding the main mechanism causing fiber formation and how particular parameters affect fiber formation.

In electrospinning, a strong electrical field is applied to a droplet formed by a polymer solution or polymer melt at the tip of a die acting as one of the electrodes (Fig. 2). The charging of the fluid leads, as shown by Taylor<sup>[10]</sup> in a set of papers, to a conical deformation of the droplet—the well-known Taylor cone and eventually to the ejection of a jet from the tip of the cone. Taylor found that the critical field required for such deformation is strongly controlled by the surface tension. The electric dispersion of liquids based on this

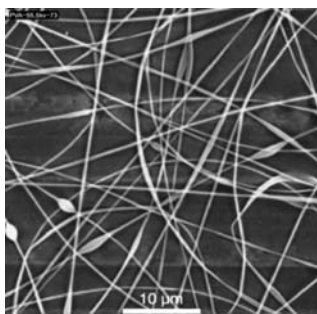


**Fig. 1** Beaded poly(vinylalcohol) fibers by electrospinning from aqueous solution.

phenomenon is widely used today, for instance in ink jet printing, for crop spraying, to prepare aerosols from liquids, and to produce propellants for rockets.

In electrospinning of fibers, the conventional view is that the charged viscoelastic jet is accelerated toward the counter electrodes, and rapidly thins during this period because of elongation and evaporation of the solvent. In some cases, splitting of the jet into multiple jets has been observed leading to a further thinning.<sup>[11]</sup> Solidification takes place and solid fibers are randomly deposited onto the substrate with a deposition rate in the order of several meters per second.<sup>[12]</sup>

However, a more detailed experimental and theoretical analysis has shown that the electrospinning process is much more complex.<sup>[13–19]</sup> It is controlled by various types of instabilities such as the Rayleigh instability, an axisymmetric instability, and finally by a so-called whipping or bending instability. In particular, the whipping instability has been identified as the one controlling elongation and thinning of the electrospun fibers. The other

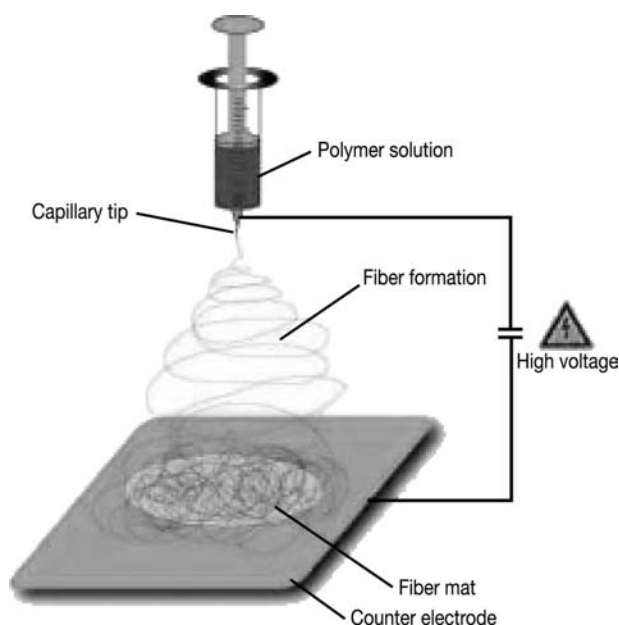


**Fig. 2** Schematical graph of the electrospinning setup.

types of instability causes fluctuations of the radius of the jet and may eventually result in droplet formation.

The Rayleigh instability in the presence of electrical fields is the electrical counterpart of the well-known surface energy driven Rayleigh instability observed for liquid threads in the absence of external forces. This type of instability is characterized by statistical fluctuation of the radius of the jet and the growth of such fluctuations with specific wavelength. The effect of an applied field is that the wavelength for fluctuations with positive growth rate is shifted to larger and larger wavelength with increasing field strength until these fluctuations are finally suppressed at a still larger field strength.

However, the jet is still unstable because a new type of instability—the so-called axisymmetric mode. A statistical modulation of the radius of the jet induces a modulation of the density of the surface charges. These modulations result in tangential stresses, which in turn accelerate the liquid and thus enhance the modulation of the radius. Again, the formation of droplets can be the final state. It is the absolute value of the charge density at the surface, which controls other factors when this instability becomes dominant.

Finally, the whipping or bending type of instability occurs at higher field strengths and this is apparently the most important type for electrospinning of fibers. The strong thinning of the jet as well as the strong elongational deformation, which takes place during electrospinning, has been attributed to this mode of instability. For large static charge densities, the whipping mode tends to dominate because high-charge densities at the surface simultaneously tend to suppress both the Rayleigh and the axisymmetric mode of instability. It has even been claimed that the onset threshold for electrospinning corresponds to the excitation of the whipping mode.

The whipping mode corresponds to long-wavelength oscillations of the centerline of the jet; that is, the jet is subjected to bending modes. Dipolar components arise if a charged jet is subjected to bending because the charge density is no longer uniform across the cross section of the jet. An elastic force resulting from the viscous flow of the liquid counteracts the bending mode. This force is related to the rate of strain and thus to the time derivative of the curvature of the jet. For larger static charge densities, the whipping mode tends to dominate because high surface charges simultaneously suppress the axisymmetric mode.

These theoretical considerations point out the important role of surface charge and thus of the conductivity of the material used for spinning as well as of the surface energy. The role of viscoelastic properties of solutions or melts are less well known and require further experimental investigations. Furthermore, the expectations are that structure formation processes have to rapidly occur during electrospinning because of the large

deposition rates, which in turn should lead to non-equilibrium structures within the nanofibers. A second feature should be high orientations as a result of the strong deformation, which occur in the whipping mode.

## PARAMETERS AFFECTING FIBER FORMATION

Fiber diameters and the absence or presence of beads are features that have to be reproducibly controlled. A set of parameters including surface free energy, viscosity, electrical conductivity, molecular weight, and its distribution control fiber formation can have an effect on the formation of beaded fibers. In the following, experimental results will be discussed exploring the importance of these parameters.

### Surface Free Energy

The critical field for the onset of fiber formation is predicted to be proportional to the square root of the surface tension. This finding is roughly in agreement with experimental findings. The more important question is whether this parameter affects fiber diameters. The observation is that a variation of surface free energy keeping the other controlling parameters constant did not significantly modify the fiber diameter.

### Electrical Conductivity

A second key parameter is the conductivity of the melt or solution.<sup>[20,21]</sup> An increase of the conductivity is expected to increase the surface charge density, which in turn should lead to a stabilization of the whipping modes giving rise to fiber extension. Furthermore, bead formation arising from other modes of instability should be suppressed. Experiments performed on solutions of polylactide (PLA) in dichloromethane doped with various amount of pyridinium formate showed that in fact an increasing concentration of the dopant lead to a reduction of bead formation and to smaller diameters of the fibers (Fig. 3).

These results agree in principle with those from Baumgarten.<sup>[22]</sup> The prediction was that the final fiber diameter depends on the conductivity and that it varies as the cube root of the resistivity. Baumgartner also stated that only droplets are generated if the conductivity is too high and he also reported that no continuous spinning could be achieved if the conductivity is too low. The reason is that the flow rate is too small in this case.

### Concentration of the Polymer in Solution

There is a direct correlation between concentration and fiber diameter. For instance, a decrease of the PLA

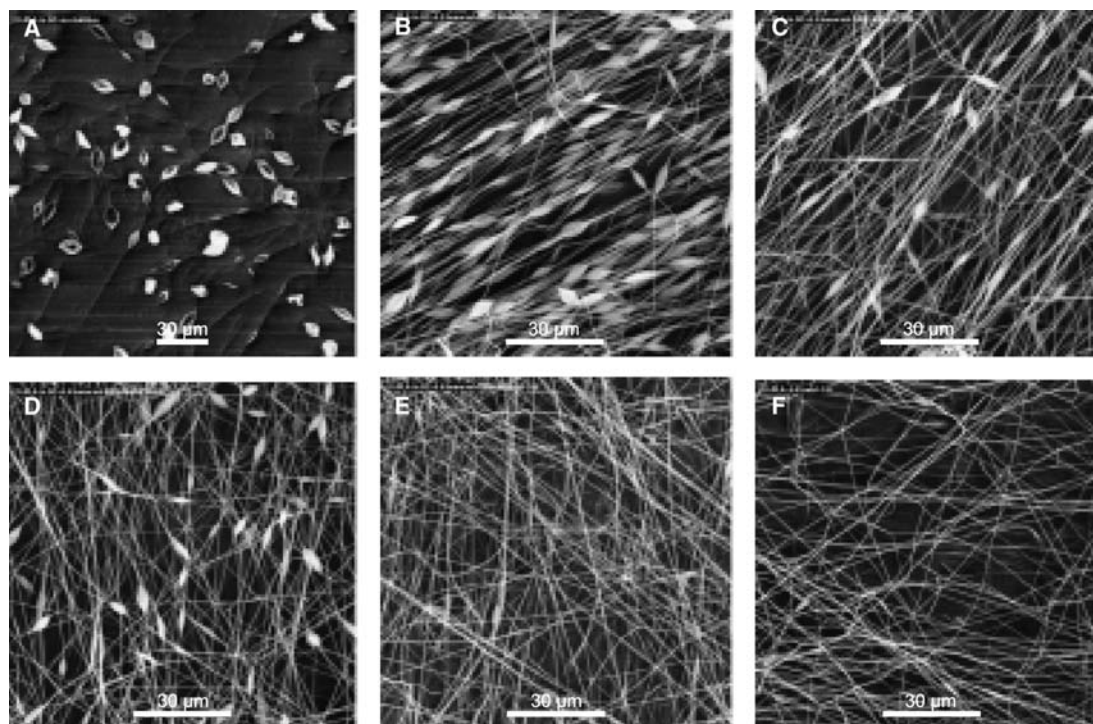


**Fig. 3** Scanning electron microscopy images of electrospun PLA fibers from 2% PLA solution in dichloromethane with different concentrations (w/w in solution) of pyridinium formate: (A) 0%; (B) 0.2%; (C) 0.3%; (D) 0.4%; (E) 0.6%; (F) 0.8%.

concentration in dichloromethane from 5 to 0.8 wt.% causes a reduction of the fibers from approximately 500–1000 to approximately 10–70 nm.<sup>[20]</sup> Provisions have to be made to reduce bead formation. Electrospinning from more diluted solutions requires a certain degree of electrical conductivity.

Subsequent investigations revealed that the control of the fiber diameter, the presence or absence of drop formation, the control of the surface morphology, and also the control of the texture of the web that is produced by electrospinning depend on a much broader range of parameters. These are among other thermodynamic properties of the solvent and the polymer—vapor pressure, crystallization and glass transition temperature, solubility of the polymer in the solvent or mixture of solvent. A reduction in molecular weight or an increase of the concentration of the lower molecular weight component in blends have been found to cause a reduction of the fiber diameter.

The concept of electrospinning is simple; yet, it is a demanding task to adjust the electrospinning parameters for a given system to be able to spin nanofibers in a controlled manner.

## A BRIEF SURVEY ON ELECTROSPUN POLYMER SYSTEMS

A broad range of polymer systems has been subjected to electrospinning. Most of the papers published on electrospinning of polymer fibers consider spinning from solution. One advantage of electrospinning is that water can be used as a solvent. Water-soluble polymers such as poly(ethylenoxide) (PEO) or poly(vinylalcohol) (PVA) can thus be electrospun.<sup>[21,23,24]</sup> Electrospinning without any solvent from the melt was reported by Larrando and Manley<sup>[25–27]</sup> for poly(propylene) and poly(ethylene terephthalate), although true nanofibers as major products have not been obtained so far by melt electrospinning. Besides PEO and PVA, electrospinning of numerous polymers to nanofibers has been reported including poly(acrylonitrile),<sup>[28]</sup> PLA,<sup>[9,20,29]</sup> poly(styrene),<sup>[11]</sup> poly(methylmethacrylate),<sup>[30]</sup> poly(amides),<sup>[12]</sup> poly(imides),<sup>[31]</sup> poly(caprolactone),<sup>[32,33]</sup> and poly(vinylidene fluoride),<sup>[11]</sup> just to name a few.

Electrospinning of blends<sup>[34–37]</sup> or composites<sup>[9,37–41]</sup> considerably broadens the range of fiber properties and applications and might lead to novel functionalities. Polymer nanofibers can be loaded with drugs or other biologically active molecules by spinning of polymers from ternary solutions containing the reagent. For example, Kenawy et al.<sup>[42]</sup> studied the release of tetracycline hydrochloride from poly(ethylene-co-vinylacetate), PLA, and a blend thereof. Similarly, but with a different purpose, He<sup>[43]</sup> investigated electrospinning of PVA–Pt/TiO<sub>2</sub> and subsequent photocatalytic

degradation of the PVA nanofibers. Core–shell fibers with concentric variation of concentrations were obtained by concentric coelectrospinning of a solution of palladium(II)acetate (core) and PEO (shell),<sup>[44]</sup> which can be extended to other systems as well.

## STRUCTURE FORMATION DURING ELECTROSPINNING

A characteristic feature of the electrospinning process is the rapid evaporation of the solvent in the case of solution spinning and the rapid temperature decrease in the case of electrospinning from the melt. Thus structure formation has to happen on a millisecond scale. The nucleation of crystals should therefore be strongly quenched. A second feature is the strong deformation taking place during the whipping mode, which should give rise to orientational process within the fibers.

Experiments performed on nanofibers made from polymers able to crystallize such as polyamides, polyethylene oxide, or PLA have revealed that crystals are able to grow. In fact, the degree of crystallinity and the perfection of the crystal are not much different from those observed for thicker fibers obtained from melt extrusion or for thicker films.<sup>[45]</sup>

High degrees of crystal orientation have been found for various electrospun polymers including polyethylene oxide and polyamides (Fig. 4). Performing selected area electron diffraction studies, it was shown for polyamide fibers that the degree of orientation directly obtained by electrospinning corresponds to the one obtained for melt-extruded fibers only after considerable stretching. On the other hand, no crystal orientation has been reported for electrospun fibers made from PLAs.<sup>[46]</sup> It is currently not obvious why crystal orientation is absent in this case. Crystal formation, degree of crystallinity, and the crystal orientation are parameters that considerably affect properties and functions of the fibers.

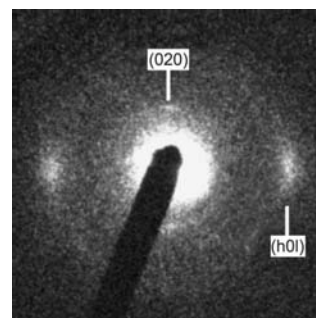


**Fig. 4** Crystal orientation in PA6 fibers as obtained from selective area electron diffraction on an individual fiber with a diameter of 50 nm.



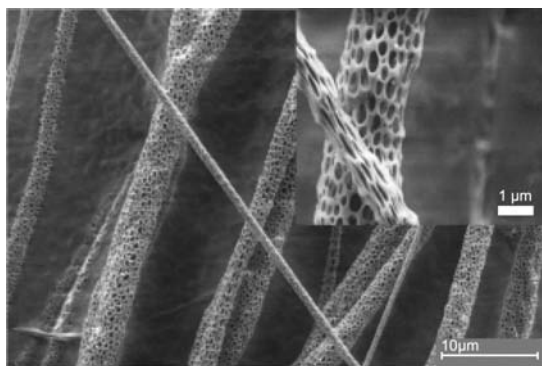


**Fig. 5** Nanoporous electrospun PLA nanofibers from a dichloromethane solution.

The properties and functionality of electrospun nanofibers can be also modified by their surface morphology. The concept is to use phase-separation processes during electrospinning. One approach considers electrospinning of ternary systems composed of two incompatible polymers and a solvent.<sup>[34]</sup> The resulting nanofibers are characterized in this case by phase morphologies corresponding either to cocontinuous spinodal type morphologies or dispersed binodal-like morphologies. Such internally structured fibers are of interest for many applications. Yet one might also selectively remove one of the components to generate fibers characterized by porous structures or other types of topologies. Such surface topologies are known to affect surface free energy, wetting, as well as adhesion. The experimental finding is that such types of phase separation processes may also occur during electrospinning in binary systems composed of one polymer and a solvent.<sup>[29,30]</sup> PLA nanofibers electrospun from dichloromethane solution typically show a nanoporous surface (Fig. 5).

Nanoporous electrospun fibers were also obtained for a variety of other polymer systems such as polycarbonates or polystyrene.<sup>[30]</sup> Interestingly, electrospinning at different humidities had a significant effect on the porosity of the electrospun fibers. It has been concluded that pore formation arising from rapid solvent evaporation most likely occurred because of the formation of water droplets from atmospheric water as a result of the evaporative cooling of the polymer solution on its way to the counter electrode in the electrospinning process.

## APPLICATIONS OF ELECTROSPUN NANOFIBERS

Electrospun nanofibers offer wide applications such as in the fields of specialty filters,<sup>[47]</sup> tissue engineering,<sup>[4]</sup> wound healing,<sup>[48]</sup> reinforcement,<sup>[1,49]</sup> protective

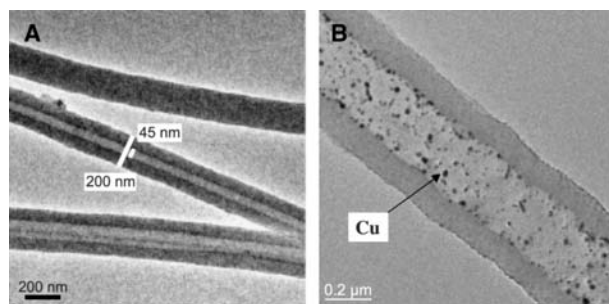


**Fig. 6** Transmission electron micrograph of poly(*p*-xylylene) (PPX) nanotubes (A) and of PPX nanotubes loaded by copper nanoparticles.

clothing,<sup>[2,50]</sup> drug release,<sup>[42]</sup> sensors,<sup>[51]</sup> catalysis,<sup>[52,53]</sup> and templating,<sup>[8,9,54,55]</sup> to name a few. Presently, most patents on electrospinning are focused on applications rather than on new materials or on new processes. Commercialized applications were accomplished by several companies worldwide in specialty filters (air filtration, coalescence filters) with an increasing market in the coming years. Tissue engineering is going to be another successful field of applications for electrospun biodegradable nanofibers (e.g., PLA) because cells including stem cells grow well on these nanofibers. An additional plus is the large potential for loading of electrospun nanofibers by biologically active agents ranging from salts to drugs and proteins.<sup>[42,56]</sup> Protective clothing, in particular in combination with special reagents, is expected to enhance the performance of military protective clothing.<sup>[6]</sup> The main focus here is on trapping of aerosols of chemical and biological warfare agents.

A unique application of electrospun nanofibers is their use as templates for the preparation of other nano-objects such as nanotubes.<sup>[8,9,55,56]</sup> Coating of electrospun nanofibers by different materials and coating techniques and subsequent removal of the core template fibers generates a whole set of nanotubes of different sizes and materials combinations, which has by far not been exploited (Fig. 6). The versatility of this approach is enhanced again by the option of loading of electrospun nanofibers directly during electrospinning or coelectrospinning.<sup>[44]</sup>

## CONCLUSION

As electrospinning of polymers is a rather old technique that has just recently been rediscovered, a new community has been established dealing with electrospinning. The number of papers is exponentially increasing as obvious from the papers published per year. The technique will be certainly optimized within the next few years but a precise understanding of the impact of different processing parameters based on

empirical observations together with theoretical considerations will be a key issue for optimum results. Many new open questions remain concerning materials choice but major new developments are expected in the area of structuring of electrospun nanofibers, loading of nanofibers by new additives for special applications, and the development of smart nanofibers. Clearly, a major driving force of new developments in the field of electrospun nanofibers will be new applications, which nicely unites researchers from different areas such as polymers, physics, engineering, inorganic and organic chemistry, medicine, pharmacy, or rheology, to name a few.

## REFERENCES

- Bergshoef, M.M.; Vancso, G.J. Transparent nanocomposites with ultrathin, electrospun nylon-4,6 fiber reinforcement. *Adv. Mater.* **1999**, *11*, 1362.
- Gibson, P.W.; Schreuder-Gibson, H.L.; Rivin, D. Electrospun fiber mats: Transport properties. *AIChE J.* **1999**, *45*, 190.
- Boland, E.; Wnek, G.; Simpson, D.; Pawlowski, K.; Bowlin, G.L. Tailoring tissue engineering scaffolds using electrostatic processing techniques: A study of poly(glycolic acid) electrospinning. *J. Macromol. Sci., Pure Appl. Chem.* **2001**, *38*, 1231.
- Li, W.J.; Laurencin, C.T.; Catterson, E.J.; Tuan, R.S.; Ko, F.K. Electrospun nanofibrous structure: A novel scaffold for tissue engineering. *J. Biomed. Mater. Res.* **2002**, *60*, 613.
- Shortkroff, S.; Li, Y.; Thornhill, T.S.; Rutledge, G.C. Cell growth on electrospun PCL scaffolds. *Polym. Mater. Sci. Eng.* **2002**, *87*, 457.
- Schreuder-Gibson, H.; Gibson, P.; Senecal, K.; Sennett, M.; Walker, J.; Yeomans, W.; Ziegler, D.; Tsai, P.P. Protective textile materials based on electrospun nanofibers. *J. Adv. Mater.* **2002**, *34*, 44.
- Tsai, P.P.; Schreuder-Gibson, H.; Gibson, P. Different electrostatic methods for making electret filters. *J. Electrostat.* **2002**, *54*, 333.
- Bognitzki, M.; Hou, H.Q.; Ishaque, M.; Frese, T.; Hellwig, M.; Schwarte, C.; Schaper, A.; Wendorff, J.H.; Greiner, A. Polymer, metal, and hybrid nano- and mesotubes by coating degradable polymer templates fibers (TUFT process). *Adv. Mater.* **2000**, *12*, 637.
- Hou, H.; Jun, Z.; Reuning, A.; Schaper, A.; Wendorff, J.H.; Greiner, A. Poly(*p*-xylylene) nanotubes by coating and removal of ultrathin polymer template fibers. *Macromolecules* **2002**, *35*, 2429.
- Taylor, G.I. Electrically driven jets. *Proc. R. Soc. A* **1969**, *313*, 453.
- Koombhongse, S.; Liu, W.X.; Reneker, D.H. Flat polymer ribbons and other shapes by electrospinning. *J. Polym. Sci., Part B, Polym. Phys.* **2001**, *39*, 2598.
- Reneker, D.H.; Chun, I. Nanometre diameter fibres of polymer, produced by electrospinning. *Nanotechnology* **1996**, *7*, 216.
- Hohman, M.M.; Shin, M.; Rutledge, G.; Brenner, M.P. Electrospinning and electrically forced jets. I. Stability theory. *Phys. Fluids* **2001**, *13*, 2201.
- Hohman, M.M.; Shin, M.; Rutledge, G.; Brenner, M.P. Electrospinning and electrically forced jets. II. Applications. *Phys. Fluids* **2001**, *13*, 2221.
- Yarin, A.L.; Koombhongse, S.; Reneker, D.H. Bending instability in electrospinning of nanofibers. *J. Appl. Phys.* **2001**, *89*, 3018.
- Shin, Y.M.; Hohman, M.M.; Brenner, M.P.; Rutledge, G.C. Electrospinning: A whipping fluid jet generates submicron polymer fibers. *Appl. Phys. Lett.* **2001**, *78*, 1149.
- Reneker, D.H.; Yarin, A.L.; Fong, H.; Koombhongse, S. Bending instability of electrically charged liquid jets of polymer solutions in electrospinning. *J. Appl. Phys.* **2000**, *87*, 4531.
- Yarin, A.L.; Koombhongse, S.; Reneker, D.H. Taylor cone and jetting from liquid droplets in electrospinning of nanofibers. *J. Appl. Phys.* **2001**, *90*, 4836.
- Fridrikh, S.; Yu, J.; Brenner, M.; Rutledge, G.C. Controlling the fiber diameter during electrospinning. *Phys. Rev. Lett.* **2003**, *90*, art. no. 144502.
- Jun, Z.; Hou, H.; Schaper, A.; Wendorff, J.; Greiner, A. Poly-L-lactide nanofibers by electrospinning—Influence of solution viscosity and electrical conductivity on fiber diameter and fiber morphology. *E-Polymers* **2003**, art. no. 009.
- Doshi, J.; Reneker, D.H. Electrospinning process and applications of electrospun fibers. *J. Electrostat.* **1995**, *35*, 151.
- Baumgarten, P. Electrostatic spinning of acrylic microfibers. *J. Colloid Interface Sci.* **1971**, *36*, 71.
- Ding, B.; Kim, H.Y.; Lee, S.C.; Shao, C.L.; Lee, D.R.; Park, S.J.; Kwag, G.B.; Choi, K.J. Preparation and characterization of a nanoscale poly(vinyl alcohol) fiber aggregate produced by an electrospinning method. *J. Polym. Sci., Part B, Polym. Phys.* **2002**, *40*, 1261.
- Jaeger, R.; Bergshoef, M.M.; Battle, C.M.I.; Schönherr, H.; Vancso, G.J. Electrospinning of ultra-thin polymer fibers. *Macromol. Symp.* **1998**, *127*, 141.
- Larrondo, L.; Manley, R.S.J. Electrostatic fiber spinning from polymer melts 2. Examination of the flow field in an electrically driven jet. *J. Polym. Sci., Part B, Polym. Phys.* **1981**, *19*, 921.
- Larrondo, L.; Manley, R.S.J. Electrostatic fiber spinning from polymer melts 3. Electrostatic deformation of a pendant drop of polymer melt. *J. Polym. Sci., Part B, Polym. Phys.* **1981**, *19*, 933.
- Larrondo, L.; Manley, R.S.J. Electrostatic fiber spinning from polymer melts 1. Experimental—Observations on fiber formation and properties. *J. Polym. Sci., Part B, Polym. Phys.* **1981**, *19*, 909.
- Chun, I.; Reneker, D.; Fong, H.; Fang, X.; Dietzel, J.; Tan, N.; Kearns, K. Carbon nanofibers from polyacrylonitrile and mesophase pitch. *J. Adv. Mater.* **1999**, *31*, 36.
- Bognitzki, M.; Czado, W.; Frese, T.; Schaper, A.; Hellwig, M.; Steinhart, M.; Greiner, A.; Wendorff, J.H. Nanostructured fibers via electrospinning. *Adv. Mater.* **2001**, *13*, 70.

30. Megelski, S.; Stephens, J.; Chase, D.; Rabolt, J.F. Micro- and nanostructured surface morphology on electrospun polymer fibers. *Macromolecules* **2002**, *35*, 8456.
31. Nah, C.; Han, S.; Lee, M.; Kim, J.; Lee, D.S. Characteristics of polyimide ultrafine fibers prepared through electrospinning. *Polym. Int.* **2003**, *52*, 429.
32. Reneker, D.H.; Kataphinan, W.; Theron, A.; Zussman, E.; Yarin, A.L. Nanofiber garlands of polycaprolactone by electrospinning. *Polymer* **2002**, *43*, 6785.
33. Lee, K.; Kim, H.; Khil, M.; Ra, Y.; Lee, D.R. Characterization of nano-structured poly(epsilon-caprolactone) non-woven mats via electrospinning. *Polymer* **2003**, *44*, 1287.
34. Bognitzki, M.; Frese, T.; Steinhart, M.; Greiner, A.; Wendorff, J.H.; Schaper, A.; Hellwig, M. Preparation of fibers with nanoscaled morphologies: Electrospinning of polymer blends. *Polym. Eng. Sci.* **2001**, *41*, 982.
35. Huang, L.; Nagapudi, K.; Apkarian, R.; Chaikof, E.L. Engineered collagen-PEO nanofibers and fabrics. *J. Biomater. Sci., Polym. Ed.* **2001**, *12*, 979.
36. Lee, S.H.; Yoon, J.W.; Suh, M.H. Continuous nanofibers manufactured by electrospinning technique. *Macromol. Res.* **2002**, *10*, 282.
37. Wu, G.; Miura, T.; Asai, S.; Sumita, M. Carbon black-loading induced phase fluctuations in PVDF/PMMA miscible blends: Dynamic percolation measurements. *Polymer* **2001**, *42*, 3271.
38. Kenawy, E.R.; Bowlin, G.L.; Mansfield, K.; Layman, J.; Simpson, D.G.; Sanders, E.H.; Wnek, G.E. Release of tetracycline hydrochloride from electrospun poly(ethylene-co-vinylacetate), poly(lactic acid) and a blend. *J. Control. Release* **2002**, *81*, 57.
39. Wang, C.; Hong, Y.; Qingbiao, Y.; Yunus, T.; Li, Z.; Guo, N.; Zhao, Y.; Liu, W.; Hao, X.; Fei, Q. Array of nanoparticles in PAN nanofiber. *Polym. Prep.* **2002**, *43*, 1387.
40. Yang, Q.; Li, D.; Hong, Y.; Li, Z.; Wang, C.; Qiu, S.; Wei, Y. Preparation and characterization of a pan nanofibre containing Ag nanoparticles via electrospinning. *Synth. Met.* **2003**, *137*, 973.
41. Fong, H.; Liu, W.D.; Wang, C.S.; Vaia, R.A. Generation of electrospun fibers of nylon 6 and nylon 6-montmorillonite nanocomposite. *Polymer* **2002**, *43*, 775.
42. Kenawy, E.; Bowlin, G.; Mansfield, K.; Layman, J.; Simpson, D.; Sanders, E.; Wnek, G.E. *J. Control. Release* **2002**, *81*, 57.
43. He, C.G.J. The preparation of PVA-Pt/TiO<sub>2</sub> composite nanofiber aggregate and the photocatalytic degradation of solid-phase polyvinyl alcohol. *Polym. Degrad. Stab.* **2003**, *81*, 117.
44. Zussman, E.; Yarin, A.; Sun, Z.; Wendorff, J.; Greiner, A. Compound core/shell polymer nanofibers by co-electrospinning. *Adv. Mater.* **2003**, *15*, 1929.
45. Dersch, R.; Liu, T.; Schaper, A.; Greiner, A.; Wendorff, J.H. Electrospun nanofibers: Internal structure and intrinsic orientation. *J. Polym. Sci., Polym. Chem.* **2003**, *41*, 545.
46. Zong, X.; Kim, K.; Fang, D.; Ran, S.; Hsiao, B.; Chu, B. Structure and process relationship of electrospun bioabsorbable nanofiber membranes. *Polymer* **2002**, *43*, 4403.
47. Jacobsen, M. The nonwovens industry meets the filtration business. *Non-wovens Ind.* May **1991**, 36.
48. Jin, H.; Fridrikh, S.; Rutledge, G.; Kaplan, D.L. Electrospinning *Bombyx mori* silk with poly(ethylene oxide). *Biomacromolecules* **2002**, *3*, 1233.
49. Kim, J.S.; Reneker, D.H. Mechanical properties of composites using ultrafine electrospun fibers. *Polym. Compos.* **1999**, *20*, 124.
50. Schreuder-Gibson, H.; Gibson, P.; Senecal, K.; Sennett, M.; Walker, J.; Yeomans, W.; Ziegler, D.; Tsai, P.P. Protective textile materials based on electrospun nanofibers. *J. Adv. Mater.* **2002**, *34*, 44.
51. Wang, X.; Drew, C.; Lee, S.; Senecal, K.; Kumar, J.; Samuelson, L.A. Electrospinning technology: A novel approach to sensor application. *J. Macromol. Sci., Pure Appl. Chem.* **2002**, *A39*, 1251.
52. Jun, Z.; Sun, Z.; Greiner, A., submitted.
53. Jia, H.; Zhu, G.; Vugrinovich, B.; Kataphinan, W.; Reneker, D.; Wang, P. Enzyme-carrying polymeric nanofibers prepared via electrospinning for use as unique biocatalysts. *Biotechnol. Prog.* **2002**, *18*, 1027.
54. Caruso, R.A.; Schattka, J.H.; Greiner, A. Titanium dioxide tubes from sol-gel coating of electrospun polymer fibers. *Adv. Mater.* **2001**, *13*, 1577.
55. Dong, H.; Jones, W. A fiber templating approach to conducting polymer nanotubes. *Polym. Mater. Sci. Eng.* **2002**, *87*, 273.
56. Luu, Y.; Kim, K.; Hsiao, B.; Chu, B.; Hadjiargyrou, M. Development of a nanostructured DNA delivery scaffold via electrospinning of PLGA and PLA-PEG block copolymers. *J. Control. Release* **2003**, *89*, 341.

# Polymer–Nanoparticle Composites

Kevin Sill  
Seunghoo Yoo  
Todd Emrick

*Department of Polymer Science and Engineering, University of Massachusetts,  
Amherst, Massachusetts, U.S.A.*

## INTRODUCTION

The rapid development in the chemistry of nanoparticles over the past 20 years has driven tremendous advances in the field. While there remains significant interest in the use of nanoparticles as fillers in polymer materials to enhance physical and mechanical properties, many are now engaging in research efforts that focus on precise structures of nanoparticles in polymers, including their assembly in arrays and along interfacial boundaries. The combination of precise organic chemistry on nanoparticle materials has led to developments in the growth of polymers from nanoparticle surfaces, allowing one to tailor the properties of the particles by the choice of polymer and its inherent functionality. Such nanoparticle–polymer composite materials are generating interest in several applications, including electronic and optical materials, based on the properties of metallic and semiconductor particles used. In addition, efforts in catalysis are under way using nanoparticles in polymer scaffolds. These and other topics form the basis of this review article, which will start in the next section with a brief account of early studies in the field, and progress from clay-based composites to metallic- and semiconductor-based nanoparticle–polymer composites.

## NANOPARTICLES IN POLYMERS: FROM CLAY TO SEMICONDUCTORS

The integration of nanoparticles into polymers is of significant theoretical and experimental interest, with a rich history in the polymer and engineering communities. Inorganic fillers have been used for some time in conjunction with organic polymer materials, largely in an effort to enhance the physical and mechanical properties over those of the polymers alone. In the mid-19th century, research efforts by Charles and Nelson Goodyear, pioneers in the chemistry of rubber, showed that vulcanized rubber can be toughened significantly by the addition of zinc oxide and magnesium sulfate.<sup>[1–3]</sup> In the early 1900s, Leo Baekeland

investigated the use of silicate clay in phenolic resins that helped Bakelite®, the first mass-produced synthetic polymer composite, become a commercial success.<sup>[1–4]</sup> Many additional commodity materials have been developed based on the enhanced properties that result from filling rubber with clay.<sup>[5]</sup> More recently, it was found that rubber particles embedded in nylon and other polymer matrices afford composites with outstanding impact resistance.<sup>[6]</sup> These are among the many examples of composite materials on which new research efforts have been constructed. These efforts have focused on the integration of a variety of nanoscopic materials into polymers and the impact of these composites over a broad spectrum of applications, from engineering plastics to electronic materials to biotechnology.

There is no question that nanotechnology is revolutionizing the scientific approach across many disciplines, including chemistry, biology, materials science, engineering, and theory.<sup>[7–10]</sup> For example, research centered on nanoscopic materials extends from the semiconductor industry, where the ability to produce nanometer-scale features leads to faster and less expensive transistors,<sup>[11–13]</sup> to biotechnology, where, e.g., luminescent nanoparticles are extremely interesting as bioprobes.<sup>[14–16]</sup> Tremendous advances in characterization technology is a common thread through all disciplines in nanotechnology, where nanoscopic objects and materials can be visualized with greatly improved resolution relative to only 10–15 years ago. Fig. 1 illustrates a few examples of “nanomaterials” with dimensions of 1 micron and less. In the nanoparticle–polymer area, current efforts now reach far beyond (or below) the use of micron-sized particle fillers (e.g., layered silicates) and into very small metallic and semiconductor nanoparticles as small as 1–2 nm in diameter.

This entry will highlight recent research in the area of polymer–nanoparticle composites, focusing especially on preparative techniques that afford well-dispersed nanocomposites, because such dispersion is a major target in the field. A leading discussion of clay-based nanocomposites will be followed by a focus

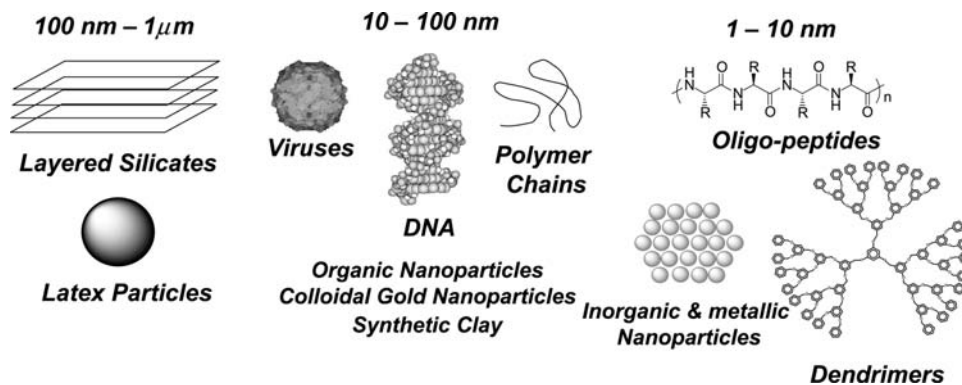


Fig. 1 Building blocks for nanotechnology.

on metallic and semiconductor-based hybrid materials. The use of polymers as a means to provide exquisite order to nanoparticles will be described, based on the ability of polymer materials to assemble into nanostructures. Finally, potential applications of polymer–nanoparticle composites will be discussed, with a special focus on the use of dendritic polymers and nanoparticles for catalysis.

### Clay–Nanoparticle Polymer Composites

The use of clay (i.e., hydrated silicates of aluminum) in combination with polymer materials can provide significant advantages in physical properties relative to the polymers alone.<sup>[17]</sup> Early discoveries in this area described blends of layered silicate nanoparticles with nylon-6 to afford composites with greatly enhanced thermal and mechanical properties.<sup>[18–20]</sup> Further advances in such composites in terms of melt processing allow these materials to be prepared in the absence of organic solvents.<sup>[21]</sup> Manias and coworkers have developed polypropylene–montmorillonite composites by varying the volume fraction of montmorillonite nanoparticles and varying block lengths of polypropylene–styrene or polypropylene–poly(methyl-methacrylate) copolymers to probe mechanical and thermal properties.<sup>[22]</sup> For example, a 3% inorganic loading into polypropylene gave a 30% increase in Young's modulus and a 30°C increase in heat deflection temperature when compared to native

polypropylene. In addition, there is significant interest in the fire-retardant properties of polymer–clay nanocomposites, as integration of clay into the structure inhibits the inherent flammability of most organic-based polymers.<sup>[23]</sup>

Significant challenges are associated with blending polymers and nanoparticles to afford homogeneous, well-dispersed inorganic material within the polymer. In order for dispersion to be achieved, the entropic penalty associated with addition of the nanoparticles must be balanced by favorable enthalpic interactions. Typical polymer–clay hybrids composed of layered nanoparticles (silicates, talc, and mica) are aggregated to some degree, as the immiscibility of clay in the polymer leads to a very close proximity of sheets to one another.<sup>[24]</sup> The degrees of dispersion in these composites are generally referred to as unmixed (highly aggregated), intercalated (minimally aggregated), and exfoliated (well dispersed). In the intercalated case, polymer chains interpenetrate stacked silicate layers with small separation distances (few nanometers) between the layers. In the exfoliated or delaminated morphology, the silicate layers are well dispersed within the polymer matrix (Fig. 2). When polar polymers are used, exfoliation can be achieved by the addition of a surfactant to the material, typically a long-chain alkylammonium salt. However, for non-polar polymers such as poly(ethylene) and poly(propylene), the addition of a surfactant is not sufficient to overcome the entropic penalty; thus a functional comonomer such as methyl methacrylate

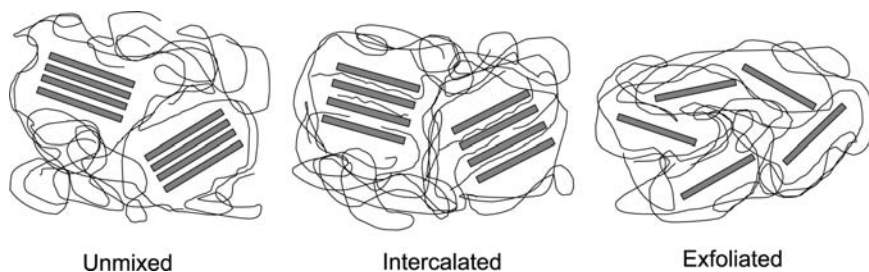


Fig. 2 Depiction of three types of clay–polymer hybrid materials showing different levels of particle dispersion.

must be incorporated into the nonpolar polymer to allow nanoparticle dispersion within the matrix.<sup>[22]</sup> Advances in processing have also led to decreased aggregation in clay–polyethylene materials, such as the use of supercritical CO<sub>2</sub> during polyethylene extrusion.<sup>[25,26]</sup> Because the physical properties of these composites depend on the ability to produce controlled intercalation or exfoliation, the interest in small molecule and polymeric additives tuned to this target is growing significantly.

Recent studies by Balazs and coworkers describe models based on self-consistent field theory to determine the interactions needed to allow polymer chains to penetrate nanoparticle layers or sheets, leading to a further increase in the composite's physical properties.<sup>[27]</sup> Their findings indicate that the introduction of small amounts of functionalized polymers to the homopolymer system will greatly increase the thermodynamic stability of the clay–polymer composite and increase the degree of intercalation or exfoliation in the system. Based on these and other findings, a much research has been dedicated to optimizing the properties of these clay–polymer systems based on blend ratio, degree of cross-linking, curing behavior, and size and dispersity of the nanoparticles.<sup>[28]</sup>

### Composites of Polymers with Metallic and Semiconductor Nanoparticles

Related to research efforts in clay–nanoparticle composite materials are efforts to integrate metallic and semiconductor nanoparticles into polymer materials. While targets such as controlled dispersion and self-assembly parallel those of the clay-based materials, the metal and semiconductor-based composites offer clearly distinct materials in that electronic, magnetic, and optical properties offered by the particles are now present. For example, nanoparticles composed of gold, cobalt, palladium, copper, and cadmium selenide are of great interest for their potential role in nanotechnology applications.<sup>[29–34]</sup> Nanoparticles such as these are generally synthesized by “bottom-up” chemistry that affords nanoparticles with narrow size distributions. Very small nanoparticles (i.e., <10 nm) are especially interesting for the quantum confinement effects inherent in particles of that size.<sup>[29,30,35]</sup> Semiconductor nanoparticles such as cadmium selenide and cadmium telluride are of special interest because of their narrow (ca. 20–25 nm FWHM) and tunable (based on size) fluorescence emission wavelengths.<sup>[30,36]</sup> Key to the behavior of these nanoparticles is their organic ligand shell that provides a protective encapsulating layer to prevent aggregation and oxidative or chemical degradation, all of which serve to diminish or destroy the nanoscopic integrity and properties of the nanoparticles (Fig. 3).

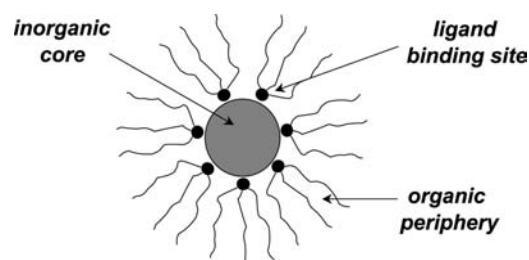


**Fig. 3** Representation of nanoparticles passivated by organic ligands.

To provide dispersion of these organic-capped nanoparticles in a polymer matrix, there must be favorable interactions between the nanoparticle ligands and the polymer environment. Several approaches have been investigated, such as 1) mimicking the nanoparticle ligand coverage with side chains on the polymer structure; 2) preparing polymers that contain ligands to bind to the nanoparticles; 3) the attachment of polymers to the nanoparticles by functionalized chain-ends, also known as “grafting-to”; and 4) the attachment of polymerization initiators to nanoparticle surfaces, followed by polymer growth from outward from the surface, also known as “grafting-from.” Method 4 is proving to be an excellent approach whereby a high density of initiators can be attached to nanoparticles, and a diverse range of monomers can then be grown off the particles; this will serve as the focus of the next section.

### POLYMER GROWTH FROM NANOPARTICLE SURFACES

Functionalization of nanoparticles with polymer chains opens new avenues in nanostructured materials and composites by tailoring the interactions of the nanoparticle with its environment based on the properties of the polymer encapsulant. This concept may be used to introduce an enormous diversity of chemical functionality into composite systems that can be used directly, or modified further. This chemical functionality can be tailored to provide specific solubility or miscibility, or used for further coupling chemistry, e.g., to reactive surfaces.

There are two general methods used for attachment of polymers to nanoparticle surfaces. The first is coupling of end-functionalized polymers onto the surface of nanoparticles in a “grafting-to” approach. Although this procedure is commonly used because of the simplicity of the approach, less than optimum grafting density may result, because of the steric shielding that arises on placement of each successive polymer chain onto the nanoparticle. Some recent examples using this



“grafting-to” method include thiol-functionalized polystyrene (PS) grafted to gold nanoparticles,<sup>[37]</sup> pyridine-functionalized poly(ethylene glycol) grafted to CdSe nanoparticles,<sup>[38]</sup> thiol-functionalized poly-(caprolactone) grafted to CdS nanoparticles,<sup>[39]</sup> and a variety of copolymers with end-thiol functionality, including water-soluble particles, for stabilization of gold nanoparticles.<sup>[40]</sup>

The second method used to connect polymers and nanoparticles involves polymerization from the nanoparticle surface, using nanoparticles functionalized appropriately with polymerization-active ligands. The appeal of this “grafting-from” method is derived from the facile attachment of small molecules to the nanoparticle surface relative to chain-end functionalized polymers, and the ability to subsequently grow a compact shell of polymers outward from the surface. Critical to this “grafting-from” process is the compatibility of the nanoparticle with the polymerization conditions chosen, such that neither the attachment of functional ligands nor the polymerization process appreciably alters the fundamental features of the nanoparticles. Although these requirements pose a considerable challenge, much progress has been made in recent years. It should be noted that nanoparticle surfaces differ from flat surfaces as substrates in the “grafting-from” process, as higher surface curvature of the spherical nanoparticle can reduce steric crowding during chain growth, which may lead to more effective polymerization from the nanoparticles.

Polymerization techniques utilized in the “grafting-from” method include controlled radical polymerization, “living” anionic polymerization, and ring-opening metathesis polymerization (ROMP).<sup>[41]</sup> Optimum control over the properties of these composites can be achieved by varying the type of nanoparticle and by adjusting the composition, molecular weight, and functionality of the attached polymer shell. ROMP is proving to be especially useful in grafting from nanoparticles, due in part to the excellent chemical tolerance of the ruthenium-based catalysts used in ROMP, and the mild conditions under which they perform. Watson and coworkers recently reported the surface functionalization of gold nanoparticles with polymerizable moieties that were used to prepare nanocomposites by ROMP.<sup>[41]</sup> This was accomplished by functionalization of gold nanoparticles with 1-mercapto-10-(*exo*-5-norbornen-2-oxy)decane, where the thiol group binds to the gold surface, and a ROMP-active functionality is left available for polymerization. *bis*(Tricyclohexylphosphine)benzylidene ruthenium dichloride (i.e., first-generation Grubbs catalyst) was used as a surface-immobilized ROMP catalyst, and a ferrocene-substituted norbornene was then polymerized from the nanoparticle surface (Fig. 4). The “living” nature of this ROMP method was demonstrated by the preparation of block copolymers from the gold surface, using two different ferrocene esters. Cyclic voltammetry of the composite exhibited two distinguishable waves characteristic of oxidation/reduction of the different ferrocenyl moieties. From the integrated current

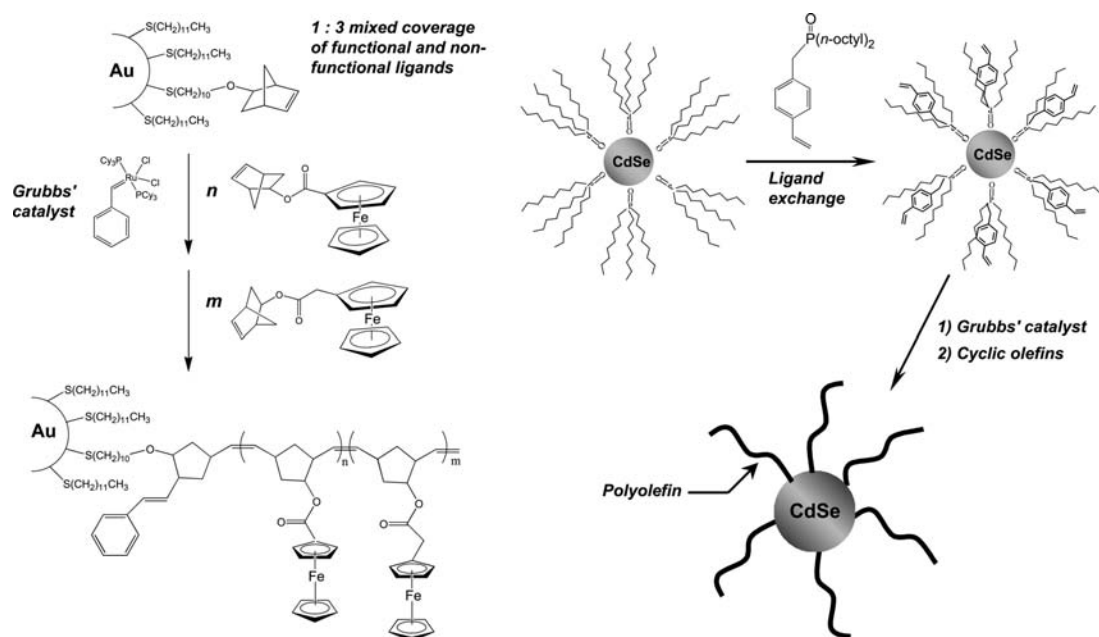


**Fig. 4** Schematic representation of the preparation of polyolefin-functionalized gold (left) and CdSe (right) nanoparticles by ring-opening metathesis techniques.

1 : 9 mixed ratio of functional and non-functional ligands

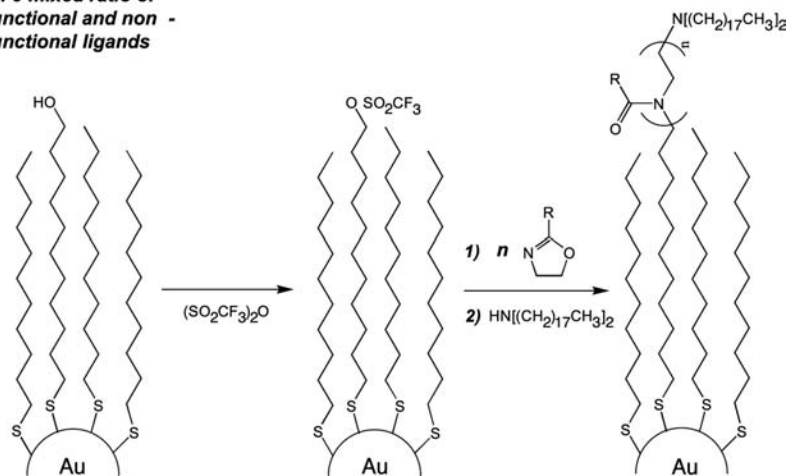


**Fig. 5** Reaction scheme of gold-nanoparticle-initiated cationic polymerization of 2-substituted oxazolines.

associated with these waves, a copolymer composition of 1.4:1 [poly(*exo*-5-norbornen-2-yl-ferrocenecarboxylate):poly(*exo*-5-norbornen-2-yl-ferroceneacetate)] was calculated.

Recently, Skaff and coworkers applied the “grafting-from” concept to semiconductor nanoparticles, using ca. 3-nm CdSe nanoparticles and cyclooctene-based monomers.<sup>[42]</sup> This involved the synthesis and use of a new ligand for CdSe, *p*-vinylbenzyl-di-*n*-octylphosphine oxide, prepared from di-*n*-octylphosphine oxide and 4-vinylbenzyl chloride. This ligand is first used to functionalize the nanoparticles, followed by metathesis chemistry of the vinyl moiety with Grubbs’ catalyst (generation 1) to afford a macroinitiator that is suitable for polymerization of cyclic olefins (Fig. 4). For example, cyclooctene was polymerized outward from the surface of the macroinitiator nanoparticle, and excellent particle dispersion was observed in the resulting poly(cyclooctene)–CdSe hybrid material. In addition, other cyclic olefins such as *exo*-7-oxanorbornene-2,3-dicarboxylic anhydride and *exo*-*N*-ethyl-7-oxanorbornene-2,3-dicarboxylimide proved applicable to this approach, and it is expected that many other cyclic olefins could be polymerized from this versatile nanoparticle-based macroinitiator.

Jordan and coworkers used  $\omega$ -functionalized self-assembled monolayers of thiolates on gold nanoparticles to initiate living cationic ring-opening polymerizations of 2-oxazoline monomers.<sup>[43]</sup> *N,N*-di-*n*-Octadecylamine was introduced as a terminating agent to provide a hydrophobic region and thus afford an amphiphilic polymer shell around the gold core. A schematic illustration of the preparation of such nanoparticles is given in Fig. 5. Tethered polymers were liberated from the nanoparticles by using NaCN solution and analyzed by matrix-assisted laser desorption ionization time-of-flight (MALDI TOF) mass spectrometry. These polymerizations were observed to proceed in a living fashion, as judged from the linear

relationship between molecular weight of the grafted polymer after cleavage from the nanoparticle surface and reaction time.

Surface-initiated anionic polymerization from nanoparticle surfaces has also been reported, e.g., using 1,1-diphenylethylene with a chlorosilane end group to functionalize silica nanoparticles, followed by anionic polymerization of styrene (Fig. 6).<sup>[44]</sup> Although the molecular weight distributions ( $M_w/M_n = 1.2$ – $1.8$ ) of the surface-bound polymers were broader than typical solution anionic polymerization, this is a rare example where living anionic polymerization is performed on nanoparticle surfaces; it will be interesting to see the progress in this area in terms of which nanoparticle compositions can be used in conjunction with the living anionic chemistry.

Atom transfer radical polymerization (ATRP) is among the most extensively exploited methods for polymer growth from nanoparticle surfaces. Recent studies on ATRP from silica<sup>[45–47]</sup> and core-shell CdS/SiO<sub>2</sub> nanoparticles<sup>[48]</sup> have demonstrated the ability to grow well-defined PS or poly(methylmethacrylate) (PMMA) layers from these modified inorganic surfaces. In these studies, some interesting effects of nanoparticle size were reported. In the case of 75-nm-diameter silica nanoparticles, good molecular weight control of PS was observed. However, the growth-from method on larger silica nanoparticles (300-nm diameter) did not show characteristics of a living polymerization. This was attributed to the high ratio of monomer to initiator per unit mass of silica used in the latter case. However, in each case the CdS/SiO<sub>2</sub> nanoparticles were dispersed throughout the polymer, with no signs of aggregation.

Other examples of the preparation of polymer-attached particles by “grafting-from” ATRP methods were reported by Hallensleben and coworkers.<sup>[49,50]</sup> In this case, *tris*(2-dimethylaminoethyl)amine was used as the ATRP ligand, which enabled the polymerization to

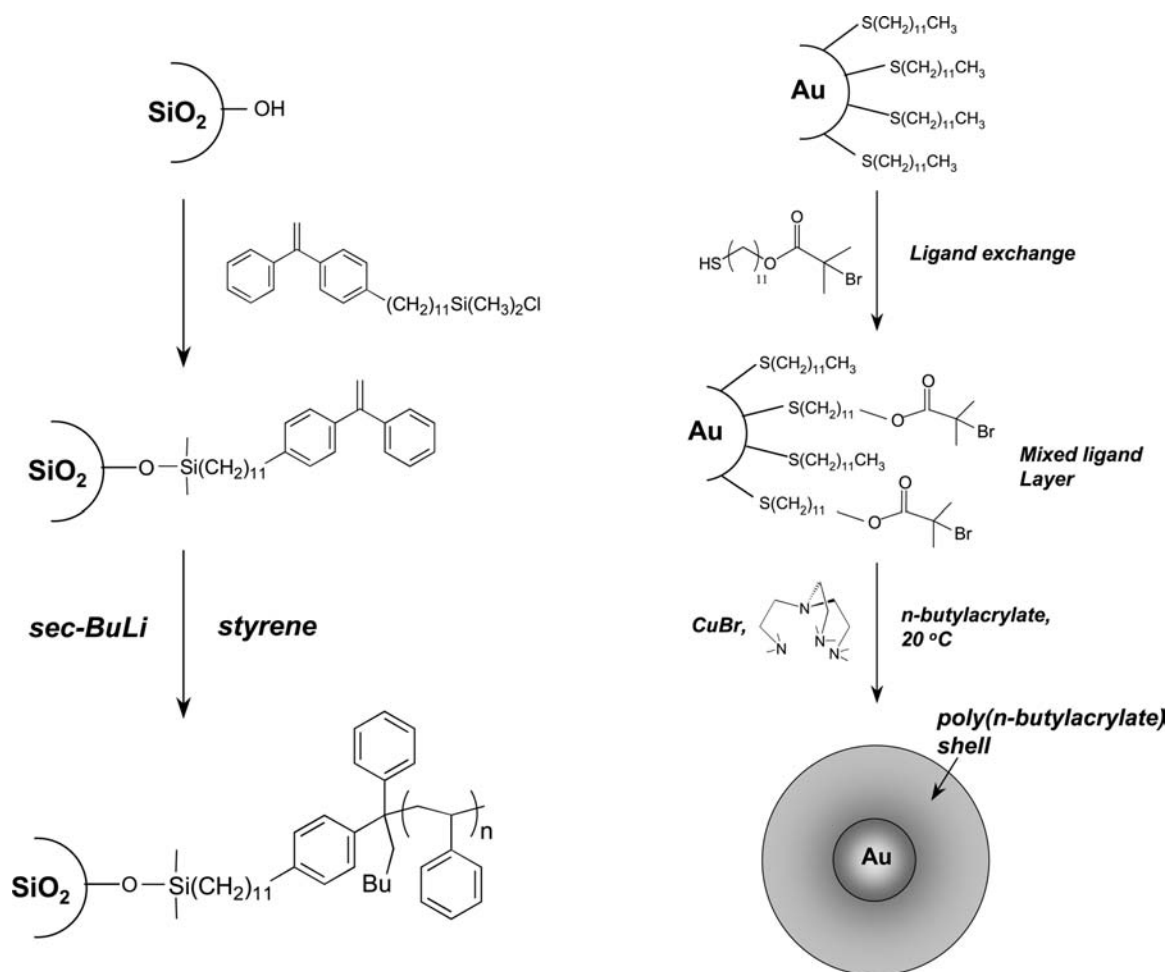


**Fig. 6** Schematic representation of polymer growth from nanoparticle surfaces by anionic polymerization (left) and atom transfer radical polymerization (right).

proceed at room temperature (Fig. 6). This low reaction temperature has the advantage of suppressing side reactions, such as desorption of thiol-functionalized ATRP initiators from the gold surface, and thermal initiation of *n*-butylacrylate monomer.<sup>[50]</sup> Gold nanoparticles had varying numbers of the polymer chains, which resulted in a relatively broad molecular weight distribution, as judged by the gel permeation chromatography (GPC) trace of poly(*n*-butylacrylate)-grafted gold nanoparticles.

An interesting approach to prepare silica nanoparticle–polymer hybrid materials has been demonstrated by Mori et al., where a hyperbranched polymer (HBP) was grown from the particle surface.<sup>[51]</sup> Typical hyperbranched polymerizations that proceed by polycondensation chemistry would result in cross-linked networks when performed in the presence of functionalized nanoparticles that participate in the chemistry. However, in this case self-condensing vinyl polymerization<sup>[52]</sup> of an acrylic “inimer” was used, where the inimer functions as both a monomer and an initiator. This inimer is designated as “AB\*,” where A is a vinyl

group and B\* is a functional group that can be transformed to an active center capable of initiating polymerization. Bulk polymerization of the inimer, 2-(2-bromopropionyloxy)ethyl acrylate, with the silica nanoparticles functionalized with 2-bromoisobutyryl fragment (B\*) was performed via ATRP, resulting in the formation of HBP shell on the silica surface (Fig. 7). These efforts are promising for providing diverse polymer architecture to nanoparticle-based composites, because HBPs have distinctive chemical and physical properties due to their globular shape and many end groups. This may also provide a rapid alternative to the synthesis of dendrimer–nanoparticle hybrid materials, which require the tedious dendritic synthesis.<sup>[53,54]</sup>

## ORDERED ASSEMBLIES OF NANOPARTICLE–POLYMER COMPOSITES

Well-ordered nanoparticles within polymers are expected to provide access to new materials that

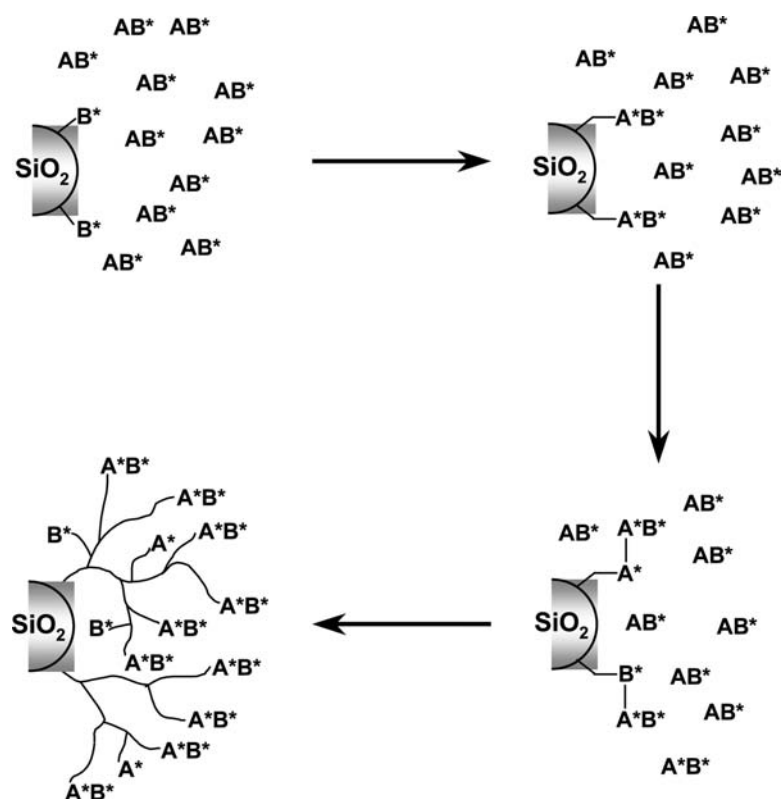


Fig. 7 Schematic representation of self-condensing vinyl polymerization of  $AB^*$  inimer from functionalized silica nanoparticles.

combine the unique physical properties of the particles with the superior processibility of the polymers. The ability to control the assembly of nanoparticles in materials promises advances in information storage, nanoelectronics, and quantum computing. A variety of nanoparticle assembly methods are under investigation, e.g., into superlattice structures reported by Murray and Bawendi for CdSe nanoparticles with aliphatic ligands of various size.<sup>[33,55]</sup> These highly ordered structures are prepared by slow crystallization to give ordered nanoparticle assemblies with remarkably few defects.

Theoretical models of Balasz and coworkers are addressing the impact of nanoparticles on phase separation in A–B diblock copolymers.<sup>[32,56–58]</sup> These calculations are driven by a combination of self-consistent field theory, which is preferred for diblock copolymers, and density functional theory, which is optimal for studying ordered colloidal particles. The theory accounts for key parameters such as nanoparticle size, chain length of the polymer blocks, and the relevant interaction parameters, including those between nanoparticles and polymer A, nanoparticles and polymer B, and polymer A with polymer B. These models show that nanoparticles can be directed to the center or the edges of phase-separated lamella or spherical domains by choosing systems with the appropriate parameters. The increased complexity of the system that results from placing ligands on the nanoparticles

would certainly have an impact on the outcome of these calculations.

A report by Fogg et al. in 1997 on nanoparticle–polymer assemblies was one of the early papers to address specific polymer–nanoparticle interactions to promote assembly in phase-separated systems.<sup>[59]</sup> In this study, a diblock copolymer was prepared by ROMP, where one of the blocks contained phosphine or phosphine oxide moieties as nanoparticle ligands. This diblock copolymer was annealed in the presence of CdSe nanoparticles, resulting in polymeric phase separation and the nearly exclusive presence of the nanoparticles within the functionalized block, as shown by transmission electron microscopy (TEM) analysis, and illustrated schematically in Fig. 8.

Several research groups have recently been active in the field of polymer–nanoparticle composites and assemblies. Rotello and coworkers have been active in self-assembly of gold nanoparticles that are functionalized with ligands that contain recognition sites.<sup>[60,61]</sup> Specifically, gold nanoparticles were synthesized with aliphatic thiols containing a specific hydrogen bonding sequence, specifically triazine and diaminopyridine derivatives. When these nanoparticles are blended with a polymer or block copolymer containing the complementary hydrogen bond sequence recognition of the two components drives the self-assembly process. Several other methods have been reported for producing ordered assemblies of polymers and nanoparticles.

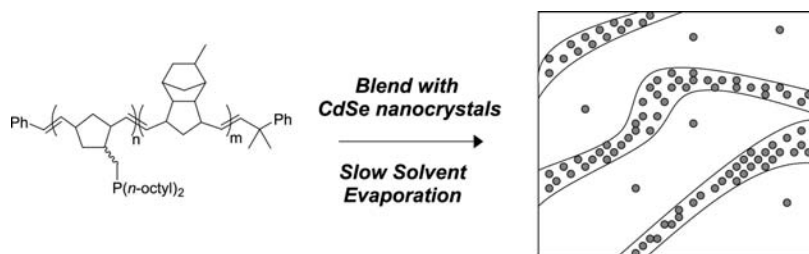


**Fig. 8** Schematic representation of nanoparticle segregation to the ligand-rich phase of an AB diblock copolymer.

For example, Kotov and coworkers have prepared “nanorainbows” using a multilayer approach,<sup>[60–62]</sup> where a thin polymer film of poly(diallyldimethylammonium chloride) containing cadmium telluride nanoparticles is deposited onto a quartz slide. Subsequent deposition of larger cadmium telluride nanoparticles with progressively longer wavelengths (e.g., yellow, orange, and red) were then deposited in layer-by-layer fashion. This resulted in a multilayer film that has a color gradient oriented normal to the surface, a material of interest in photonic and electronic devices.

Recent work by Lopes showed self-assembly of various nanoparticles (e.g., gold, silver, indium, and lead) within a PS–PMMA diblock copolymer matrix under nonequilibrium conditions.<sup>[63]</sup> Under appropriate annealing conditions, the polymer matrix will phase separate into an ordered lamella structure with the nanoparticles residing exclusively in the polystyrene phase because of the more favorable gold–polystyrene interactions. At loadings of 30% gold particles, the polystyrene blocks are capable of conducting an electric charge, essentially converting the polystyrene segments into nanowires. Yuan and coworkers have studied amphiphilic triblock copolymers, such as poly(ethylene oxide-*b*-propylene oxide-*b*-ethylene oxide) as scaffolds for nanostructured silica.<sup>[64]</sup> When cast from an acidic ethanol solution containing tetraethoxysilane (TEOS), a silica precursor, the copolymer undergoes phase separation to afford an assembly of polymer cylinders. The hydrophilic poly(ethylene oxide) and TEOS form the periphery, and the hydrophobic poly(propylene oxide) is found at the center of the cylinders. The nanostructured silica

is formed by calcination of the TEOS, yielding a hollow silica cylinder with a wall thickness of ca. 4 nm.

A different approach to nanoparticle assemblies was reported by Misner and coworkers using templates prepared from diblock copolymers.<sup>[65]</sup> These templates consist of a cylindrical PMMA phase within a PS matrix, where the cylinder diameter is of the order of 15–20 nm.<sup>[66,67]</sup> CdSe nanoparticles were driven into these cylinders by capillary forces present on withdrawal of the templates from dilute solutions of CdSe nanocrystals (Fig. 9). This method is quite promising in that nanoparticle coverage in the template was shown to be approximately 70% by TEM (i.e., 70% of the cylinders are filled with nanoparticles), and conditions were developed to the point where >95% of the nanoparticles reside in the cylinders rather than on the PS matrix. Solid-state fluorescence measurements of these templates showed that the nanoparticles retained their fluorescence throughout the assembly and substrate removal (acid etching) process, and that fluorescence intensity could be controlled by changing the concentration of solution into which the templates were dipped. New deposition methods currently under investigation are expected to produce templates with complete coverage.<sup>[68]</sup>

A novel technique for controlling the location of nanoparticles has been demonstrated by Firestone and coworkers.<sup>[69]</sup> This report shows that by controlling the surface characteristics of silver nanoparticles, one can control their location within a multitier phospholipid bilayer system. Particles that are passivated by lithium dodecyl sulfate reside entirely in the aqueous layer, while alkyl derivatized particles are in the hydrocarbon portion of a lipid bilayer. The use of

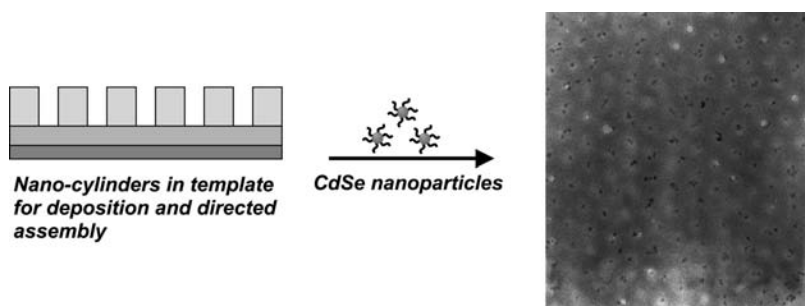


**Fig. 9** Nanoparticle-filled templates prepared from self-assembled diblock copolymers are used to direct the assembly of nanoparticles.

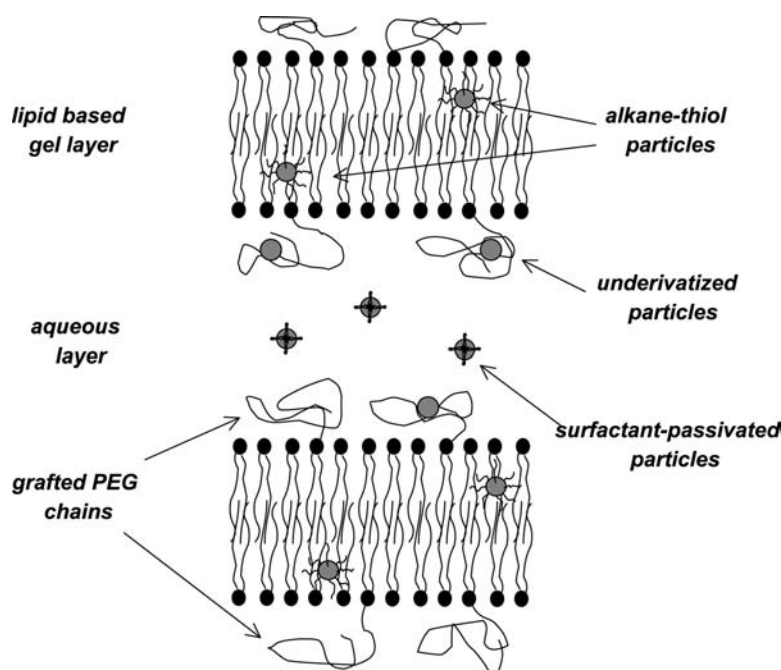


**Fig. 10** Schematic representation of a lipid-based gel with selective nanoparticle placement that depends on the nanoparticle ligand environment.

underivatized silver particles results in assembly at the lipid–water interface (Fig. 10). The authors suggest that the particle interacts with the poly(ethylene oxide) (PEO) chains that have been grafted to some of the surfactant molecules. These hydrophilic polymer chains extend from the bilayer into the aqueous phase, and passivate the bare silver particles. Interestingly, it has been shown by small-angle X-ray scattering that these particles do not aggregate within the fluid, leaving their unique optical and electronic properties intact.

## NANOPARTICLE–POLYMER COMPOSITES FOR CATALYSIS

Catalytic methods are of vital importance in the chemical and petroleum industries. Catalysts represent the oldest commercial application of nanoparticles, typically consisting of small metal particles, often in the nanometer size regime, that are dispersed on a microporous oxide. Many studies on the catalytic properties of metal surfaces, such as platinum,<sup>[70,71]</sup> nickel,<sup>[72]</sup> iron,<sup>[73,74]</sup> and molybdenum<sup>[75,76]</sup> have been explored since the 1920s.<sup>[77]</sup>

Catalytic processes are greatly affected by the complexity of catalyst surface composition and structure. The catalytic efficiencies of metals increase dramatically with increasing surface-to-volume ratio; thus nanoparticles have inherent advantages. As the high surface energy associated with nanoparticles leads to aggregation, the use of surface-confined stabilizers has been induced. Ideally, these stabilizers should

possess rather weak surface activity, as strong adsorption would diminish significantly the catalytic activity. Protective stabilizers can influence not only the stability of the catalyst but also the catalytic properties by creating specific environments around the active sites.

Aside from the conventional commercialized catalytic processes, there have been some very interesting recent studies on nanoparticles in catalysis of organic reactions. For example, El-Sayed reported that Pd nanoparticles stabilized by poly(*N*-vinyl-2-pyrrolidone) (PVP) efficiently catalyze Suzuki cross-coupling reactions in aqueous medium.<sup>[78]</sup> Successful coupling of arylboronic acids to aryl iodides gave reasonably high yields even though the Pd particles precipitated during the reaction. The reaction rate was observed to depend on the Pd concentration in a linear fashion, indicating that catalysis occurs on the Pd surface. Hydroxyl-terminated poly(amido amine) (PAMAM) dendrimers and polystyrene-*b*-poly(sodium acrylate) were also reported to be efficient stabilizers for the Pd nanoparticles in the Suzuki reactions between phenylboronic acid and iodobenzene.<sup>[79]</sup> Overall, the careful choice of the type of stabilizer, metal precursors, as well as reaction conditions can lead to the preparation of the desired catalyst system.

Dendrimers have been recognized as suitable hosts for metal nanoparticles for a variety of reasons. Their uniform composition and three-dimensional structure provides a homogeneous environment for the particles, whereas their periphery of terminal end groups can be controlled in terms of functionality to control solubility and allow for catalyst recovery. Substrate



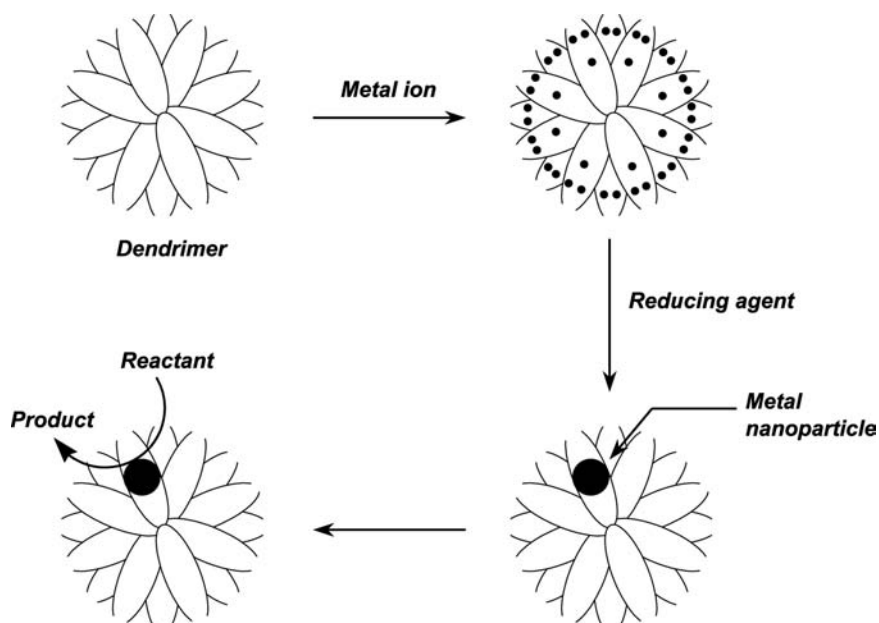


**Fig. 11** Schematic illustration of the synthesis of metal nanoparticles within a dendrimer template.

selectivity can be affected by the size and polarity of the terminal groups, and the size of the host dendrimer can be varied systematically through well-defined growth chemistry that affords dendritic macromolecules with precise structures and molecular weights.

Dendrimers have been used as both templates and stabilizers for nanoparticles, and have been found to effectively impede their aggregation. In some cases, nanoparticles are confined within the host dendrimer by steric effects, without significant surface passivation. Metal nanoparticles can be sequestered within dendrimers by adsorbing suitable precursor metal ions into the template dendrimer and subsequently reducing the composite (Fig. 11). Several systems have been explored with dendrimers, e.g., in the group of Crooks dendrimer-encapsulated metal nanoparticles were prepared in fluorosol media, leading to easy separation and recycling of the catalyst. Chechik and Crooks describe a case where Pd nanoparticles in PAMAM dendrimers were complexed with carboxylic end groups of perfluoropolyethers in fluorosolvents.<sup>[80]</sup> Hydrogenation of various alkenes, including 1-hexene and methylacrylate, was performed to assess the catalytic activity of the system. Pd–dendrimer nanocomposites were observed to be catalytically active without appreciable loss of activity after 12 cycles. The wide range of turnover frequency numbers was observed exhibiting the possibility of selective hydrogenation; more polar substrates were hydrogenated faster because of the hydrophilic interior of the dendrimer that promotes contact between the metal nanoparticles and the polar substrates.

Yeung and Crooks also presented examples of carbon–carbon bond formation in biphasic fluorosol/

organic solvent systems catalyzed by dendrimer-encapsulated nanoparticles.<sup>[81]</sup> The perfluorinated polyether-derivatized poly(propylene imine) (PPI) dendrimers containing Pd(0) nanoparticles effectively catalyzed Heck couplings of aryl halides with *n*-butylacrylate. Because PPI dendrimers are more stable at elevated temperatures than PAMAM dendrimers, they are better suited for the Heck reaction, which requires high temperatures and long reaction times. Whereas the selectivity for the production of *n*-butyl-*trans*-formylcinamate was previously reported to be in the 74–98% range in the absence of the dendritic stabilizer,<sup>[82]</sup> the PPI–Pd(0) catalyst provides 100% selectivity for the *trans* isomer. This result suggested that the sterically confined environment of the dendritic interior may impart regioselectivity.<sup>[83,84]</sup> It should be noted that the activity of catalysts can also be influenced by the dendrimer size. Equal amounts of metal nanoparticles of nearly the same particle size could be prepared within dendrimers of varying generations. A fifth-generation dendrimer/Pd(0) catalyst gave substantially greater product yield than the fourth-generation catalyst, which Crooks attributes to the larger dendrimer host that provides a less confining space for the Pd nanoparticles, resulting in easier access of substrate to the particle.<sup>[81]</sup>

Dendrimer–nanoparticle composites have been used in conjunction with supercritical CO<sub>2</sub>, an alternative to hydrocarbon solvents, and a “greener” approach to catalysis with nanoparticles. Crooks has previously shown that Pd nanoparticles, encapsulated by PPI dendrimers having covalently grafted perfluorinated-polyether chains, were easily solubilized in this supercritical medium without requiring perfluorinated ligands or

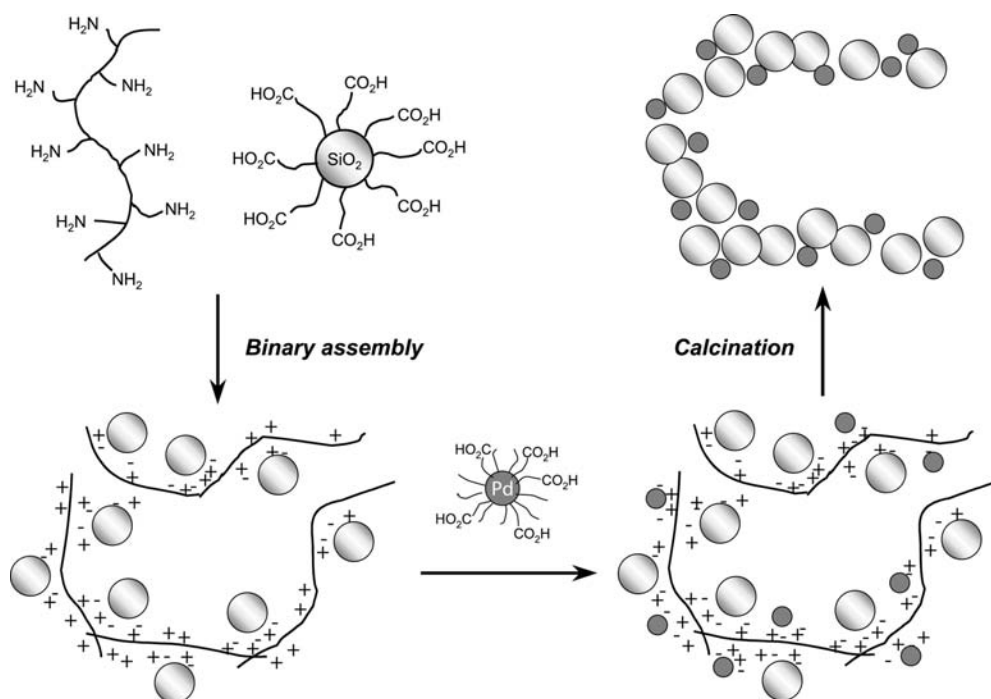


**Fig. 12** Formation of palladium and silica nanoparticle catalysts directed by the interactions of functionalized polymers and nanoparticles.

toxic solvents.<sup>[84]</sup> Whereas the standard Pd-catalyzed Heck coupling between iodobenzene and methylacrylate resulted in the *cis*- and/or *trans*-cinnamate product, the CO<sub>2</sub>-soluble Pd-based nanocomposite exclusively produced methyl 2-phenylacrylate. The high selectivity is presumably related to both the steric environment of the dendrimer template and the properties of supercritical CO<sub>2</sub> because the same dendrimer-encapsulated Pd(0) yielded only the *trans*-cinnamate product using organic/fluorocarbon solvent system instead of supercritical CO<sub>2</sub>.<sup>[81]</sup>

Amphiphilic block copolymers have been used for the stabilization of metal nanoparticles.<sup>[85–88]</sup> They are versatile components for polymer–metal systems because they can offer several options for tuning the system in catalytic applications. PS-*b*-PMMA and PS-*b*-PEO block copolymers were observed to be suitable for controlling both metal size and size distribution. The catalytic activities of the palladium and platinum nanoparticles stabilized by block copolymers were tested by hydrogenation of cyclohexene, which provided 100% conversion. The nanoparticle morphologies and catalytic activities were strongly dependent on many factors, including the type and ratio of polymer blocks, choice of metal precursor type, and the reduction method and conditions. These findings suggested that amphiphilic block copolymers could offer a tremendous versatility to the design of tailored catalysts.

Galow and coworkers have reported electrostatic-mediated assembly of highly reactive heterogeneous

catalysts in which mixed monolayer protected clusters (MMPCs) were used as both building blocks and active catalysts.<sup>[89]</sup> Catalysts were formed through calcinations of the mixture of palladium colloid and silica–polymer aggregates (Fig. 12). A series of hydrogenation reactions and Heck reaction were performed and substantially high catalytic ability was observed. In the case of the Heck reaction between nitroarene and styrene, only 0.045 mol% of Pd was required to show a dramatic improvement over commercial counterparts.

The fabrication of nanoparticle-based templates that exhibit site-isolated nanoparticles in long-range ordered arrays may be ideal for some catalytic applications; thus future efforts in catalysis will be directed toward constructs as described in Fig. 9 above. Such studies, performed previously with CdSe nanoparticles, should translate well to other nanoparticle systems studied in catalysis. Because selectivity is not understood as well as activity, future research should focus on achieving exceedingly high selectivity for the desired product. Through systematic variation of particle size and interparticle distance by using block copolymer templates with different molecular weight, structural ingredients responsible for selectivity of catalyst may be investigated in the near future.

## CONCLUSION

In summary, it is clear that nanoparticle–polymer composite materials are playing an increasingly important

role in nanotechnology. This article has summarized only a few of the many outstanding achievements in the field. As our ability to prepare and assemble these composites continues to improve, the specificity of the applications that can be addressed will increase accordingly. Nevertheless, progress to date has been most impressive, and all indications point toward further growth in the future.

## ACKNOWLEDGMENTS

T.E. gratefully acknowledges the contributions of his group in nanoparticle-polymer composite materials, including Kevin Sill, Dr. Seunghoo Yoo, Habib Skaff, Rui Hong, Qingling Zhang, and Korisha Ramdhanie. Financial support for T.E.'s research group in nanoparticle-polymer composites was provided by the National Science Foundation (CAREER grant #0239486), the Eastman Kodak Company, and the U.S. Army Center of Excellence at U.Mass. Amherst.

## REFERENCES

- Goodyear, C. Improvement in India-Rubber Fabrics. US Patent 3633, June 15, 1844.
- Goodyear, C. Procedure for the fabrication of objects which are more or less hard, bendable, or elastic from natural or synthetic rubber in conjunction with other materials. *Dinglers Polytech. J.* **1856**, CXXXIX, 376-390.
- Goodyear, N. Improvement in the Manufacture of India-Rubber. US Patent 8075, May 6, 1851.
- Baekeland, L.H. Bakelite, a new composition of matter: Its synthesis, constitution, and uses. *Sci. Am., Suppl.* **1909**, 68, 322.
- Baekeland, L.H. Method of Molding Articles. US Patent 939,966, January 29, 1909.
- Sheldon, R.P. *Composite Polymeric Materials*; Applied Science Publishers Ltd.: Essex, England, 1982.
- Shipway, A.N.; Katz, E.; Willner, I. Nanoparticle arrays on surfaces for electronic, optical, and sensor applications. *Chem. Phys. Chem.* **2000**, 1, 18-52.
- Gudiksen, M.S.; Lauthon, L.J.; Wang, J.; Smith, D.C.; Lieber, C.M. Growth of nanowire superlattice structures for nanoscale photonics and electronics. *Nature* **2002**, 415, 617-620.
- Service, R.F. Nanotechnology—Biology offers nanotech a helping hand. *Science* **2002**, 298, 2322-2323.
- Williams, K.A.; Veenhuizen, P.T.M.; de la Torre, B.G.; Eritja, R.; Dekker, C. Nanotechnology—Carbon nanotubes with DNA recognition. *Nature* **2002**, 420, 761.
- Wang, F.C.; Zhang, W.E.; Yang, C.H.; Yang, M.J.; Bennett, B.R.; Wilson, R.A.; Stone, D.R. A tunneling field-effect transistor with 25 nm metallurgical channel length. *Appl. Phys. Lett.* **1997**, 70, 3005-3007.
- Conley, W.; Dean, K.; Miller, D.; Rich, G.; Graffenberg, V.; Patel, S.; Lin, S.H.; Jamieson, A.; Hung, R.; Yamada, S.; Pinnow, M.; MacDonald, S.; Chambers, C.; Osborne, B.; Patterson, K.; Somervell, M.; Trinquet, B.; Tran, H.V.; Cho, S.; Chiba, T.; Byers, J.; Tomas, B.; Shafer, G.; DesMarteau, D.; Klopp, J.; Frechet, J.; Sanders, D.; Grubbs, R.; Ober, C.; Korner, H.; Willson, C.G. Developments in materials for 157 nm photore-sists. *Solid State Technol.* **2001**, 44, 63-68.
- Black, C.T.; Guarini, K.W.; Milkove, K.R.; Baker, S.M.; Russell, T.P.; Tuominen, M.T. Integration of self-assembled diblock copolymers for semiconductor capacitor fabrication. *Appl. Phys. Lett.* **2001**, 79, 409-411.
- Mattoussi, H.; Mauro, J.M.; Goldman, E.R.; Green, T.M.; Anderson, G.P.; Sundar, V.C.; Bawendi, M.G. Bioconjugation of highly luminescent colloidal CdSe-ZnS quantum dots with an engineered two-domain recombinant protein. *Phys. Status Solidi, B Basic Res.* **2001**, 224, 277-283.
- Gerion, D.; Parak, W.J.; Williams, S.C.; Zanchet, D.; Micheel, C.M.; Alivisatos, A.P. Sorting fluorescent nanocrystals with DNA. *J. Am. Chem. Soc.* **2002**, 124, 7070-7074.
- Jaiswal, J.K.; Mattoussi, H.; Mauro, J.M.; Simon, S.M. Long-term multiple color imaging of live cells using quantum dot bioconjugates. *Nat. Biotechnol.* **2003**, 21, 47-51.
- Zerda, A.S.; Caskey, T.C.; Lesser, A.J. Highly concentrated, intercalated silicate nanocomposites: Synthesis and characterization. *Macromolecules* **2003**, 36, 1603-1608.
- Kojima, Y.; Usuki, A.; Kawasumi, M.; Okada, A.; Fukushima, Y.; Kurauchi, T.; Kamigaito, O. Mechanical-properties of nylon 6-clay hybrid. *J. Mater. Res.* **1993**, 8, 1185-1189.
- Kojima, Y.; Usuki, A.; Kawasumi, M.; Okada, A.; Kurauchi, T.; Kamigaito, O. Synthesis of nylon-6-clay hybrid by montmorillonite intercalated with epsilon-caprolactam. *J. Polym. Sci., Part A, Polym. Chem.* **1993**, 31, 983-986.
- Usuki, A.; Kojima, Y.; Kawasumi, M.; Okada, A.; Fukushima, Y.; Kurauchi, T.; Kamigaito, O. Synthesis of nylon 6-clay hybrid. *J. Mater. Res.* **1993**, 8, 1179-1184.
- Vaia, R.A.; Ishii, H.; Giannelis, E.P. Synthesis and properties of 2-dimensional nanostructures by direct intercalation of polymer melts in layered silicates. *Chem. Mater.* **1993**, 5, 1694-1696.
- Manias, E.; Touny, A.; Wu, L.; Strawhecker, K.; Lu, B.; Chung, T.C. Polypropylene/montmorillonite nanocomposites. Review of the synthetic routes and materials properties. *Chem. Mater.* **2001**, 13, 3516-3523.
- Porter, D.; Metcalfe, E.; Thomas, M.J.K. Nanocomposite fire retardants—A review. *Fire Mater.* **2000**, 24, 45-52.
- Carrudo, K.A. Synthetic organo- and polymer-clays: Preparation, characterization, and materials applications. *Appl. Clay Sci.* **2000**, 17, 1-23.
- Caskey, T.; Lesser, A.J.; McCarthy, T.J. Supercritical CO<sub>2</sub> welding of laminated linear low density polyethylene films. *Polym. Eng. Sci.* **2001**, 41, 2259-2265.

26. Kung, E.; Lesser, A.J.; McCarthy, T.J. Morphology and mechanical performance of polystyrene/polyethylene composites prepared in supercritical carbon dioxide. *Macromolecules* **1998**, *31*, 4160–4169.
27. Balazs, A.C.; Singh, C.; Zhulina, E.; Lyatskaya, Y. Modeling the phase behavior of polymer/clay nanocomposites. *Acc. Chem. Res.* **1999**, *32*, 651–657.
28. Varghese, H.; Bhagawan, S.S.; Thomas, S. Effects of blend ratio, crosslinking systems and fillers on the morphology, curing behavior, mechanical properties, and failure mode of acrylonitrile butadiene rubber and poly(ethylene-*co*-vinyl acetate) blends. *J. Appl. Polym. Sci.* **1999**, *71*, 2335–2364.
29. Alivisatos, A.P. Perspectives on the physical chemistry of semiconductor nanocrystals. *J. Phys. Chem.* **1996**, *100*, 13226–13239.
30. Peng, Z.A.; Peng, X. Formation of high-quality CdTe, CdSe, and CdS nanocrystals using CdO as precursor. *J. Am. Chem. Soc.* **2001**, *123*, 183–184.
31. Skaff, H.; Ilker, M.F.; Coughlin, E.B.; Emrick, T.S. Preparation of cadmium selenide–polyolefin composites from functional phosphine oxides and ruthenium-based metathesis. *J. Am. Chem. Soc.* **2002**, *124*, 5729–5733.
32. Thompson, R.B.; Ginzburg, V.V.; Matsen, M.W.; Balazs, A.C. Block copolymer-directed assembly of nanoparticles: Forming mesoscopically ordered hybrid materials. *Macromolecules* **2002**, *35*, 1060–1071.
33. Murray, C.B.; Kagan, C.R.; Bawendi, M.G. Self-organization of CdSe nanocrystallites into three-dimensional quantum dot superlattices. *Science* **1995**, *270*, 1335–1338.
34. Sooklal, K.; Hanus, L.H.; Ploehn, H.J.; Murphy, C.J. A blue-emitting CdS/dendrimer nanocomposite. *Adv. Mater.* **1998**, *10*, 1083–1087.
35. Brus, L. Chemical approaches to semiconductor nanocrystals. *J. Phys. Chem. Solids* **1998**, *59*, 459–465.
36. Lee, J.; Sundar, V.C.; Heine, J.R.; Bawendi, M.G.; Jensen, K.F. Full color emission from II–VI semiconductor quantum dot–polymer composites. *Adv. Mater.* **2000**, *12*, 1102–1105.
37. Corbierre, M.K.; Cameron, N.S.; Sutton, M.; Mochrie, S.G.J.; Lurio, L.B.; Ruhm, A.; Lennox, R.B. Polymer-stabilized gold nanoparticles and their incorporation into polymer matrices. *J. Am. Chem. Soc.* **2001**, *123*, 10411–10412.
38. Skaff, H.; Emrick, T. The use of 4-substituted pyridines to afford amphiphilic, pegylated cadmium selenide nanoparticles. *Chem. Commun.* **2003**, 52–53.
39. Carrot, G.; Scholz, S.M.; Plummer, C.J.G.; Hilborn, J.G.; Hedrick, J.L. Synthesis and characterization of nanoscopic entities based on poly(caprolactone)-grafted cadmium sulfide nanoparticles. *Chem. Mater.* **1999**, *11*, 3571–3577.
40. Lowe, A.B.; Sumerlin, B.S.; Donovan, M.S.; McCormick, C.L. Facile preparation of transition metal nanoparticles stabilized by well-defined (Co)polymers synthesized via aqueous reversible addition–fragmentation chain transfer polymerization. *J. Am. Chem. Soc.* **2002**, *124*, 11562–11563.
41. Watson, K.J.; Zhu, J.; Nguyen, S.T.; Mirkin, C.A. Hybrid nanoparticles with block copolymer shell structures. *J. Am. Chem. Soc.* **1999**, *121*, 462–463.
42. Skaff, H.; Ilker, M.F.; Coughlin, E.B.; Emrick, T. Preparation of cadmium selenide–polyolefin composites from functional phosphine oxides and ruthenium-based metathesis. *J. Am. Chem. Soc.* **2002**, *124*, 5729–5733.
43. Jordan, R.; West, N.; Ulman, A.; Chou, Y.M.; Nuyken, O. Nanocomposites by surface-initiated living cationic polymerization of 2-oxazolines on functionalized gold nanoparticles. *Macromolecules* **2001**, *34*, 1606–1611.
44. Zhou, Q.Y.; Wang, S.X.; Fan, X.W.; Advincula, R.; Mays, J. Living anionic surface-initiated polymerization (LASIP) of a polymer on silica nanoparticles. *Langmuir* **2002**, *18*, 3324–3331.
45. von Werne, T.; Patten, T.E. Preparation of structurally well-defined polymer–nanoparticle hybrids with controlled/living radical polymerizations. *J. Am. Chem. Soc.* **1999**, *121*, 7409–7410.
46. von Werne, T.; Patten, T.E. Atom transfer radical polymerization from nanoparticles: A tool for the preparation of well-defined hybrid nanostructures and for understanding the chemistry of controlled/“living” radical polymerizations from surfaces. *J. Am. Chem. Soc.* **2001**, *123*, 7497–7505.
47. Perruchot, C.; Khan, M.A.; Kamitsi, A.; Armes, S.P.; von Werne, T.; Patten, T.E. Synthesis of well-defined, polymer-grafted silica particles by aqueous ATRP. *Langmuir* **2001**, *17*, 4479–4481.
48. Farmer, S.C.; Patten, T.E. Photoluminescent polymer/quantum dot composite nanoparticles. *Chem. Mater.* **2001**, *13*, 3920–3926.
49. Nuss, S.; Bottcher, H.; Wurm, H.; Hallensleben, M.L. Gold nanoparticles with covalently attached polymer chains. *Angew. Chem., Int. Ed.* **2001**, *40*, 4016–4018.
50. Bottcher, H.; Hallensleben, M.L.; Nuss, S.; Wurm, H. ATRP grafting from silica surface to create first and second generation of grafts. *Polym. Bull.* **2000**, *44*, 223–229.
51. Mori, H.; Seng, D.C.; Zhang, M.F.; Muller, A.H.E. Hybrid nanoparticles with hyperbranched polymer shells via self-condensing atom transfer radical polymerization from silica surfaces. *Langmuir* **2002**, *18*, 3682–3693.
52. Frechet, J.M.J.; Henmi, M.; Gitsov, I.; Aoshima, S.; Leduc, M.R.; Grubbs, R.B. Self-condensing vinyl polymerization—An approach to dendritic materials. *Science* **1995**, *269*, 1080–1083.
53. Wang, Y.A.; Li, J.J.; Chen, H.Y.; Peng, X.G. Stabilization of inorganic nanocrystals by organic dendrons. *J. Am. Chem. Soc.* **2002**, *124*, 2293–2298.
54. Wang, R.Y.; Yang, J.; Zheng, Z.P.; Carducci, M.D.; Jiao, J.; Seraphin, S. Dendron-controlled nucleation and growth of gold nanoparticles. *Angew. Chem., Int. Ed.* **2001**, *40*, 549–552.
55. Sun, S.H.; Murray, C.B. Synthesis of monodisperse cobalt nanocrystals and their assembly into magnetic superlattices (invited). *J. Appl. Phys.* **1999**, *85*, 4325–4330.
56. Thompson, R.B.; Ginzburg, V.V.; Matsen, M.W.; Balazs, A.C. Predicting the mesophases of copolymer–nanoparticle composites. *Science* **2001**, *292*, 2469–2472.
57. Lee, J.Y.; Thompson, R.B.; Jasnow, D.; Balazs, A.C. Effect of nanoscopic particles on the mesophase

- structure of diblock copolymers. *Macromolecules* **2002**, *35*, 4855–4858.
58. Lee, J.Y.; Thompson, R.B.; Jasnow, D.; Balazs, A.C. Entropically driven formation of hierarchically ordered nanocomposites. *Phys. Rev. Lett.* **2002**, *89*.
  59. Fogg, D.E.; Radzilowski, L.H.; Dabbousi, B.O.; Schrock, R.R.; Thomas, E.L.; Bawendi, M.G. Fabrication of quantum dot-polymer composites: Semiconductor nanoclusters in dual-function polymer matrices with electron-transporting and cluster-passivating properties. *Macromolecules* **1997**, *30*, 8433–8439.
  60. Boal, A.K.; Galow, T.H.; Ilhan, F.; Rotello, V.M. Binary and ternary polymer-mediated “bricks and mortar” self-assembly of gold and silica nanoparticles. *Adv. Funct. Mater.* **2001**, *11*, 461–465.
  61. Boal, A.K.; Gray, M.; Ilhan, F.; Clavier, G.M.; Kapitzky, L.; Rotello, V.M. Bricks and mortar self-assembly of nanoparticles. *Tetrahedron* **2002**, *58*, 765–770.
  62. Mamedov, A.A.; Belov, A.; Giersig, M.; Mamedova, N.N.; Kotov, N.A. Nanorainbows: Graded semiconductor films from quantum dots. *J. Am. Chem. Soc.* **2001**, *123*, 7738–7739.
  63. Lopes, W.A. Nonequilibrium self-assembly of metals on diblock copolymer templates. *Phys. Rev., E* **2002**, *65*, 031606.
  64. Yuan, Y.J.; Hentze, H.P.; Arnold, W.M.; Marlow, B.K.; Antonietti, M. Fabrication of nanostructured silica using a triblock copolymer template. *Nano Lett.* **2002**, *2*, 1359–1361.
  65. Misner, M.J.; Skaff, H.; Emrick, T.; Russell, T.P. Directed deposition of nanoparticles using diblock copolymer templates. *Adv. Mater.* **2003**, *15*, 221–224.
  66. Mansky, P.; Russell, T.P.; Hawker, C.J.; Pitsikalis, M.; Mays, J. Ordered diblock copolymer films on random copolymer brushes. *Macromolecules* **1997**, *30*, 6810–6813.
  67. Huang, E.; Pruzinsky, S.; Russell, T.P.; Mays, J.; Hawker, C.J. Neutrality conditions for block copolymer systems on random copolymer brush surfaces. *Macromolecules* **1999**, *32*, 5299–5303.
  68. Sill, K.; Yoo, S.H. Unpublished results.
  69. Firestone, M.A.; Williams, D.E.; Seifert, S.; Csencsits, R. Nanoparticle arrays formed by spatial compartmentalization in a complex fluids. *Nano Lett.* **2001**, *1*, 129–135.
  70. Zaera, F.; Somorjai, G.A. Hydrogenation of ethylene over platinum (111) single-crystal surfaces. *J. Am. Chem. Soc.* **1984**, *106*, 2288–2293.
  71. Yeates, R.C.; Turner, J.E.; Gellman, A.J.; Somorjai, G.A. The oscillatory behavior of the CO oxidation reaction at atmospheric pressure over platinum single crystals: Surface analysis and pressure dependent mechanisms. *Surf. Sci.* **1985**, *149*, 175–190.
  72. Goodman, D.W.; Kelly, R.D.; Madey, T.E.; Yates, J.T. Kinetics of the hydrogenation of CO over a single crystal nickel catalyst. *J. Catal.* **1980**, *63*, 226–234.
  73. Spencer, N.D.; Somorjai, G.A. Iron single crystals as ammonia synthesis catalysts: Effect of surface structure on catalyst activity. *J. Catal.* **1982**, *74*, 129–135.
  74. Dwyer, D.J.; Hardenbergh, J.H. The catalytic reduction of carbon monoxide over iron surfaces: A surface science investigation. *J. Catal.* **1984**, *87*, 66–76.
  75. Youchang, X.; Naasz, B.M.; Somorjai, G.A. Alcohol synthesis from CO and H<sub>2</sub> over molybdenum sulfide. The effect of pressure and promotion by potassium carbon. *Appl. Catal.* **1986**, *27*, 233–241.
  76. Gellman, A.J.; Farias, M.H.; Somorjai, G.A. The catalytic hydrodesulfurization of thiophene on the Mo (100) crystal surface. *J. Catal.* **1984**, *88*, 546–548.
  77. Somorjai, G.A. The evolution of surface chemistry. A personal view of building the future on past and present accomplishments. *J. Phys. Chem., B* **2002**, *106*, 9201–9213.
  78. Li, Y.; Hong, X.M.; Collard, D.M.; El-Sayed, M.A. Suzuki cross-coupling reactions catalyzed by palladium nanoparticles in aqueous solution. *Org. Lett.* **2000**, *2*, 2385–2388.
  79. Li, Y.; El-Sayed, M.A. The effect of stabilizers on the catalytic activity and stability of Pd colloidal nanoparticles in the Suzuki reactions in aqueous solution. *J. Phys. Chem. B* **2001**, *105*, 8938–8943.
  80. Chechik, V.; Crooks, R.M. Dendrimer-encapsulated Pd nanoparticles as fluorous phase-soluble catalysts. *J. Am. Chem. Soc.* **2000**, *122*, 1243–1244.
  81. Yeung, L.K.; Crooks, R.M. Heck heterocoupling within a dendritic nanoreactor. *Nano Lett.* **2001**, *1*, 14–17.
  82. Moineau, J.; Pozzi, G.; Quici, S.; Sinou, D. Palladium-catalyzed Heck reaction in perfluorinated solvents. *Tetrahedron Lett.* **1999**, *40*, 7683–7686.
  83. Chow, H.F.; Mak, C.C. Dendritic bis(oxazoline)copper(II) catalysts. 2. Synthesis, reactivity, and substrate selectivity. *J. Org. Chem.* **1997**, *62*, 5116–5127.
  84. Yeung, L.K.; Lee, C.T.; Johnston, K.P.; Crooks, R.M. Catalysis in supercritical CO<sub>2</sub> using dendrimer-encapsulated palladium nanoparticles. *Chem. Commun.* **2001**, 2290–2291.
  85. Mayer, A.B.R.; Mark, J.E. Transition metal nanoparticles protected by amphiphilic block copolymers as tailored catalyst systems. *Colloid Polym. Sci.* **1997**, *275*, 333–340.
  86. Mayer, A.B.R.; Mark, J.E.; Morris, R.E. Palladium and platinum nanocatalysts protected by amphiphilic block copolymers. *Polym. J.* **1998**, *30*, 197–205.
  87. Mayer, A.B.R.; Mark, J.E. Immobilization of palladium nanoparticles on latex supports and their potential for catalytic applications. *Angew. Makromol. Chem.* **1999**, *268*, 52–58.
  88. Mayer, A.B.R.; Mark, J.E. Poly(2-hydroxyalkyl methacrylates) as stabilizers for colloidal metal nanoparticles. *Polymer* **2000**, *41*, 1627–1631.
  89. Galow, T.H.; Drechsler, U.; Hanson, J.A.; Rotello, V.M. Highly reactive heterogeneous heck and hydrogenation catalysts constructed through ‘bottom-up’ nanoparticle self-assembly. *Chem. Commun.* **2002**, 1076–1077.

# Polymer Nanowires Conjugated by Controlled Chain Polymerization

Yuji Okawa

Masakazu Aono

Nanomaterials Laboratory, National Institute for Materials Science,  
Ibaraki, Japan

## INTRODUCTION

The present-day silicon-based electronic devices have grown more powerful as their basic subunit, the transistor, has shrunk in size. However, the laws of quantum mechanics and the limitations of fabrication techniques may soon prevent further reduction. Thus we must develop a novel device concept, which can be applied at the nanometer scale. This exploration of a novel device concept beyond silicon-based transistors is analogous to the search for a replacement for the vacuum tube half a century ago, and its discovery will make a profound impact on society in this century. Many ideas have been proposed for the novel device concept, and one promising possibility is the construction of novel electronic devices using organic molecules.<sup>[1–14]</sup> However, even if we could make individual molecules that function as single-molecule transistors or diodes, the next problem would be the absence of good methods by which to arrange them in the desired pattern and to interconnect them with one another. Regarding this problem, it is necessary to develop a method of fabricating conductive wires of nanometer width (nanowires) at designated positions.

We usually use metals for wires whose width is larger than the order of micrometers. However, in the case of nanowires, the use of metals becomes much more difficult because of their poor stability and difficulties in their fabrication. If we want to use metals for nanowires, we must devise some method of stabilizing them.<sup>[15]</sup> Hence many materials other than metals have been considered as candidates for nanowires, including inorganic compounds,<sup>[16]</sup> carbon nanotubes,<sup>[4,8,9,12,14,17–19]</sup> DNA,<sup>[20–24]</sup> and other conductive organic molecules or polymers,<sup>[25–30]</sup> although we must conduct further basic studies before we can put them to practical use.

In this entry, we will present a method of fabricating a conjugated polymer nanowire at designated positions by controlling linear chain polymerization using the probe tip of a scanning tunneling microscope (STM).<sup>[29,30]</sup> A demonstration is presented for a self-ordered monomolecular layer of 10,12-pentacosadiynoic acid and 10,12-nonacosadiynoic acid, which are

amphiphilic diacetylene compounds, adsorbed on a graphite substrate. We have succeeded in controlling the initiation and termination of chain polymerization with a spatial precision on the order of 1 nm. The obtained polydiacetylene is a conjugated polymer, so that we can expect that it will become conductive when excess electrons or holes are supplied to it from the surroundings.

## SELF-ORDERED MOLECULAR LAYER

The monomer molecules we use are diacetylene compounds with the general formula  $R-C\equiv C-C\equiv C-R'$ , where  $C\equiv C-C\equiv C$  is the diacetylene moiety, and R and R' are substituent groups. It is well known that this molecular species in the form of solid crystals<sup>[31]</sup> or Langmuir–Brodgett films<sup>[32]</sup> polymerizes into polydiacetylene compounds on appropriate stimulation such as heating or ultraviolet irradiation (Fig. 1). Several studies have dealt with STM observations of physisorbed layers of various diacetylene compounds on graphite surfaces.<sup>[33–35]</sup> According to those studies, a variety of molecular arrangements are formed depending on the species of substituent groups, the method of film preparation, and the incorporation of foreign molecules.

In our work, we chose 10,12-pentacosadiynoic acid [ $CH_3(CH_2)_{11}-C\equiv C-C\equiv C-(CH_2)_8COOH$ ] and 10,12-nonacosadiynoic acid [ $CH_3(CH_2)_{15}-C\equiv C-C\equiv C-(CH_2)_8COOH$ ] as monomer molecules. These two species gave essentially the same results. To prepare their thin films, the monomer molecules were dissolved in chloroform and the solution was applied onto the surface of purified water. After the evaporation of chloroform, the thin films of monomer molecules on the water surface were transferred to a freshly cleaved surface of highly oriented pyrolytic graphite (HOPG) by nearly horizontal dipping.

The STM images were recorded using the Digital Instruments NanoScope STM system under ambient conditions in the constant current mode. A typical STM image of the 10,12-pentacosadiynoic acid layer is shown in Fig. 2A. The image consists of parallel bright lines separated by two different alternating



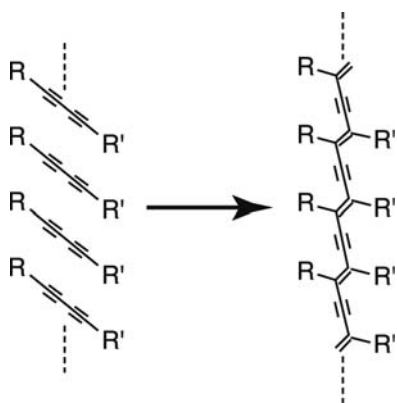


**Fig. 1** Polymerization of diacetylene compounds into polydiacetylene compounds.

spacings of about 3.0 and 3.8 nm, indicating that the 10,12-pentacosadiynoic acid molecules on the graphite surface are self-ordered after the transfer from the water surface. A magnified STM image of the layer is shown in Fig. 2B, in which individual molecules are

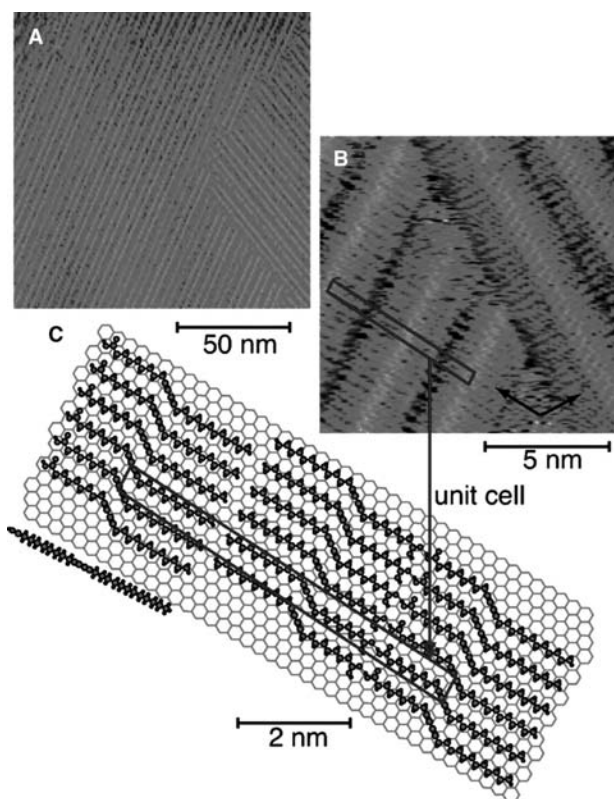


**Fig. 2** (A) Typical STM image of 10,12-pentacosadiynoic acid layer on a graphite surface (sample bias voltage  $V_S = -1.0$  V; tunneling current  $I_t = 0.07$  nA). (B) Magnified STM image of the layer ( $V_S = +0.5$  V;  $I_t = 1.0$  nA). The arrows in the image indicate the main crystal axes of graphite. (C) Top and side views of the proposed model for molecular arrangement. *Source:* From Ref.<sup>[30]</sup>; © American Institute of Physics, 2001.

resolved. Based on such STM images, we proposed the molecular arrangement shown in Fig. 2C. The molecules are aligned in phase to form straight chains and the chains are arranged such that the COOH end groups of a chain are opposite to those of a neighboring chain. Each bright line in Fig. 2A corresponds to the linear array of diacetylene moieties in Fig. 2C because the multiple bonds are, in general, observed to be higher than single bonds in STM images.<sup>[36]</sup>

At appropriately small sample biases and high tunneling currents, the STM image of the graphite substrate can be observed. On comparing such an image with the images of the molecular layer taken previously, it was found that the alkyl side chains of each molecule are oriented parallel to the main crystal axis of graphite. For many other molecules on graphite surfaces, it has been reported that their alkyl chains are also oriented parallel to the main crystal axis of graphite.<sup>[34,36–40]</sup> In Fig. 2B, a modulation of the image contrast is observed as a moiré pattern because of the lattice mismatch between the molecular layer and the graphite substrate. The periodicity of the moiré modulation indicates that the spacing between neighboring molecules in the molecular layer is 0.47 nm.

## PHOTOPOLYMERIZATION

First, we examined whether such chain polymerization could be induced by ultraviolet irradiation in the monomer film described above, and how the created polymers are observed in STM images. For this purpose, the molecular layer was irradiated with ultraviolet light from a low-pressure mercury lamp (254 nm wavelength and 1.3 mW/cm<sup>2</sup> power density at the sample position) for a period of 20 min.

Fig. 3A shows a typical STM image of the 10,12-pentacosadiynoic acid layer after ultraviolet irradiation. As we can see, very bright lines appeared. One of these very bright lines is imaged on a magnified scale at various sample biases, as shown in Fig. 3B–E. The number density of the very bright lines increased almost linearly with increasing duration of ultraviolet irradiation, as shown in Fig. 3F. Hence these very bright lines are considered to be polydiacetylenes, created by the photopolymerization of the linear array of diacetylene moieties.

The moiré modulation described above was also observed for the polymer, as seen in Fig. 3C. An important point is that the moiré pattern in the created polymer is the same as that in the monomer array. This means that the spacing between the alkyl side chains in the polymer is the same as that in the monomer—0.47 nm. This also indicates that the orientation of the alkyl chains is maintained parallel to the main crystal axis of graphite even after polymerization.

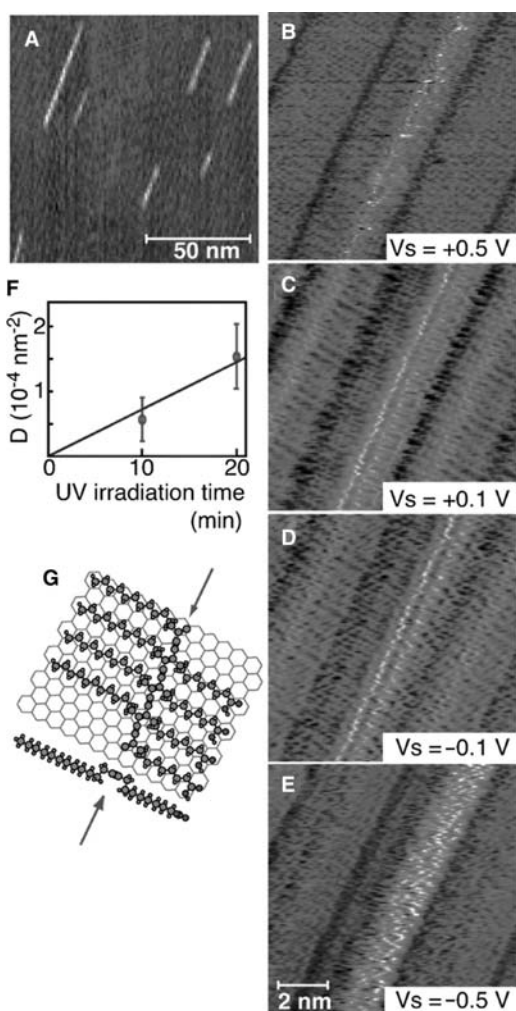


**Fig. 3** (A) An STM image obtained after ultraviolet irradiation ( $V_S = -1.0$  V;  $I_t = 0.07$  nA). (B–E) Magnified STM images of a polymer obtained at the same tunneling current ( $I_t = 0.1$  nA) and various sample biases  $V_S$ . (F) Plots of the number density of the polymer  $D$  against the duration of ultraviolet irradiation. (G) The proposed structural model of a polymer. The arrows indicate the backbone of polydiacetylene. Source: From Ref.<sup>[30]</sup>; © American Institute of Physics, 2001.

Based on these results, we proposed the structural model for the polymer, as shown in Fig. 3G. In this model, the polydiacetylene backbone is raised so that the alkyl side chains are parallel to the main crystal axis of the graphite substrate.

The most plausible mechanism of photopolymerization is illustrated in Fig. 4, by analogy with the case of bulk crystals of diacetylene compounds.<sup>[41]</sup> In the array of monomer molecules (Fig. 4A), the diacetylene moiety of one of the molecules is excited by photoabsorption into an excited state. As shown in Fig. 4B, a diradical state in the *trans* form with an unpaired electron at either end is a reasonable representation of the lowest excited  $\pi\pi^*$  singlet or triplet state located at 3.7 and 3.1 eV above the  $\pi\pi$  ground state,-

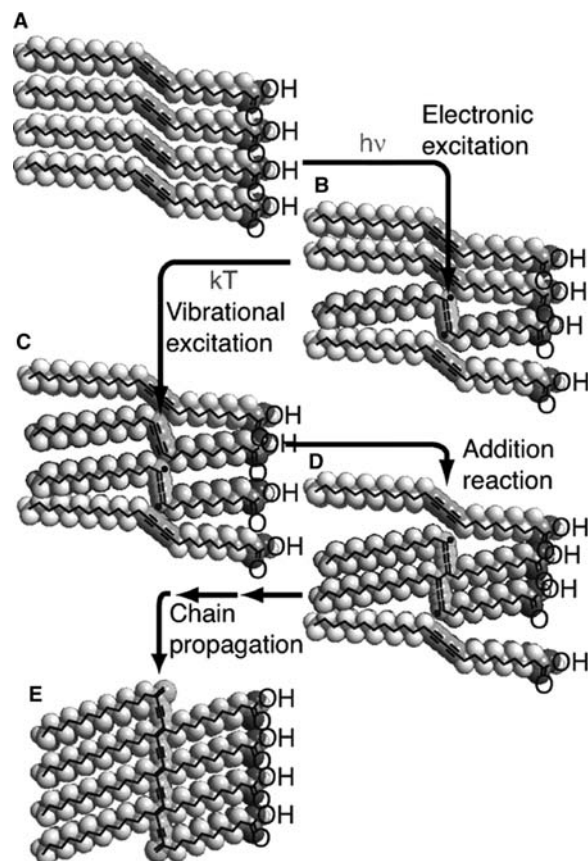


**Fig. 4** Illustration of the mechanism of photopolymerization. (A) Array of the monomer molecules. (B) Diradical formation by photoabsorption. (C) Approach of a neighboring diacetylene moiety by vibrational excitation. (D) Dimer formation by an addition reaction. (E) Extended chain propagation. Source: From Ref.<sup>[30]</sup>; © American Institute of Physics, 2001.

respectively.<sup>[42,43]</sup> Within the lifetime of the diradical state, if a neighboring diacetylene moiety on either side approaches the diradical because of thermal vibration (Fig. 4C), an addition reaction occurs, forming a dimer of diacetylene (Fig. 4D). Because the created dimer of diacetylene still has radicals at both ends, a similar addition reaction occurs on both ends. Hence the repetition of such addition reaction occurs and results in extended chain polymerization, as shown in Fig. 4E. Therefore we can expect that if the excited diradical state in the first step (Fig. 4B) can be created by stimulation with the STM tip instead of photoabsorption, the extended chain polymerization will follow.

#### CHAIN POLYMERIZATION INITIATED BY A SCANNING TUNNELING MICROSCOPE TIP

Fig. 5A shows an STM image of the 10,12-pentacosadiynoic acid layer. The same area was imaged again in Fig. 5B, in which the STM tip is scanned rapidly in the

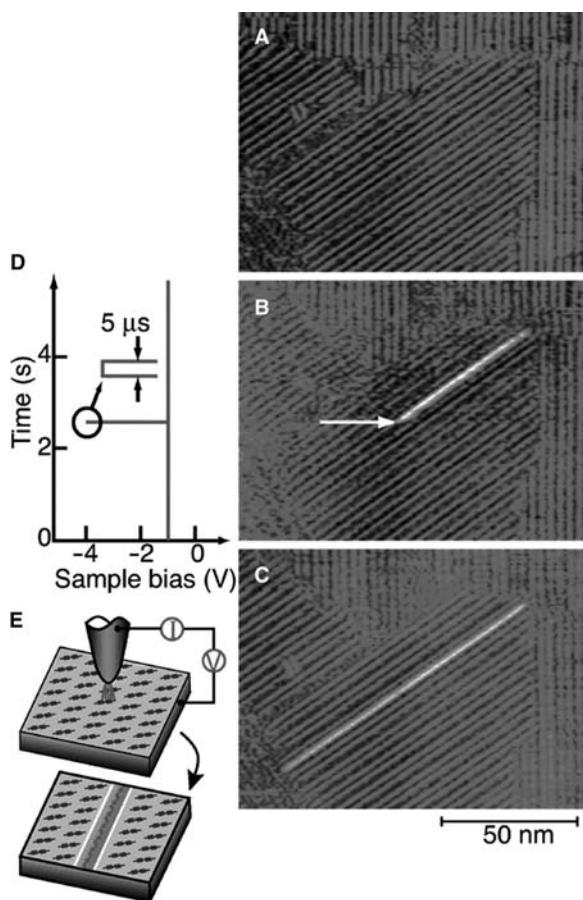


**Fig. 5** (A) An STM image of the original monomolecular layer of 10,12-pentacosadiynoic acid ( $V_S = -1.0$  V;  $I_t = 0.07$  nA). (B) Image of the same area observed from the bottom to the top, but with pulsed sample bias voltage applied at the point indicated by the arrow. (C) The same area imaged once again. (D, E) Diagrams illustrating the initiation of chain polymerization using an STM tip. Source: From Ref.<sup>[30]</sup>; © American Institute of Physics, 2001.

horizontal direction and slowly from the bottom to the top at a sample bias of  $-1$  V. When the tip passed the point indicated by an arrow, a pulsed sample bias ( $-4$  V in height and  $5 \mu\text{s}$  in width) was applied, as shown on the left-hand side of the figure. As can be seen, a very bright line appeared starting from the point where the pulsed sample bias was applied. This very bright line is identical in structure to those observed in Fig. 3. Namely, stimulation with the STM tip induced chain polymerization and created a polymer. The same area was imaged once again and the result is shown in Fig. 5C. We can see that chain polymerization occurred on both sides of the point of stimulation.

In the case of Fig. 5B, a negative pulsed sample bias ( $-4.0$  V) was applied, and we found that chain polymerization occurred at both polarities of the pulsed sample bias. This is seen in Fig. 6, where the frequency of the occurrence of chain polymerization  $P_{\text{STM}}$  is

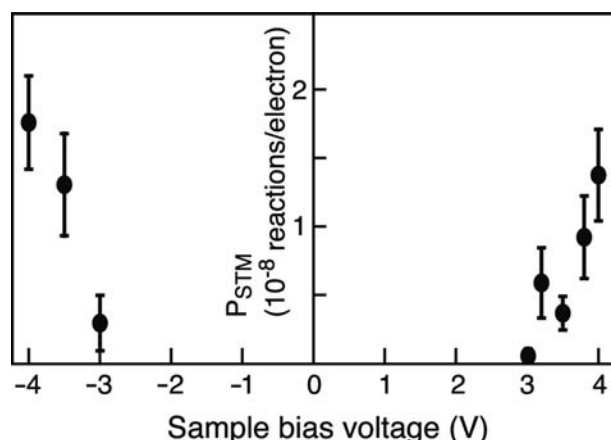


**Fig. 6** Plots of the frequency of occurrence of chain polymerization  $P_{\text{STM}}$  in units of reactions per electron against the height of the pulsed sample bias voltage  $V_S$ . Source: From Ref.<sup>[30]</sup>; © American Institute of Physics, 2001.

plotted against the height of the pulsed bias voltage  $V_S$  at both polarities; these measurements were carried out using a 10,12-pentacosadiynoic acid layer at a fixed pulse width of  $10 \mu\text{s}$  while monitoring the tunneling current. As we can see, the reaction probability was symmetric with respect to the polarity of the pulsed sample bias, and the threshold voltage for polymerization was  $2.9 \pm 0.2$  V. This value is close to the energy separation between the  $\pi\pi$  ground state and the lowest excited  $\pi\pi^*$  triplet state of the diacetylene moiety— $3.1$  eV.<sup>[43]</sup> This suggests that the diacetylene moiety was excited by electrons tunneling between the tip and the substrate, which passed inelastically through the intermediate molecular layer.

As seen in Fig. 5C, the polymers created were usually terminated at domain boundaries. In other words, the chain polymerization initiated by the STM tip propagated in the domain without any additional energy other than thermal energy, and terminated when it encountered the domain boundary that acted as a kind of structural defect. Exploiting the fact that the chain reaction is terminated by a structural defect, we can also control the termination of chain polymerization by forming an artificial structural defect in advance. An example of a 10,12-nonacosadiynoic acid layer is presented in Fig. 7. First, the original monomolecular layer was imaged (Fig. 7A). Then we created an artificial defect at the center of the image, as shown in Fig. 7B, using a previously reported method.<sup>[44]</sup> Namely, an STM tip was placed at that position and a high pulsed sample bias ( $+5$  V in height and  $10 \mu\text{s}$  in width) was applied (Fig. 7F and G). The created defect was a hole with a diameter of  $6$  nm in the graphite substrate. The same area was imaged again from the top to the bottom, as shown in Fig. 7C, but a pulsed sample bias ( $-4$  V in height and  $5 \mu\text{s}$  in width) was



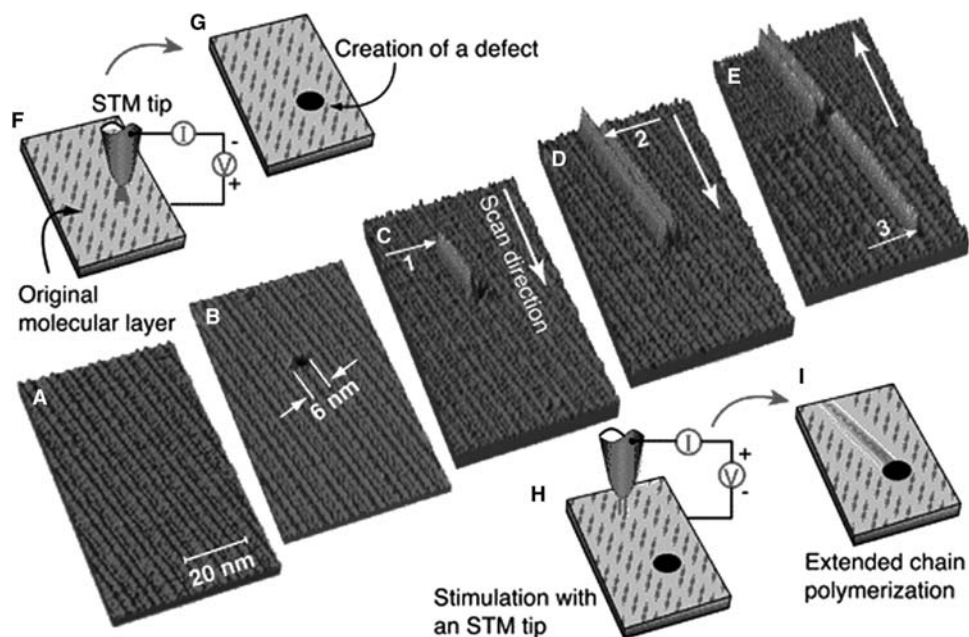


**Fig. 7** (A) An STM image of the original monomolecular layer of 10,12-nonacosadiynoic acid ( $V_s = -1.0$  V;  $I_t = 0.07$  nA). (B) Creation of an artificial defect in advance with an STM tip. (C) First chain polymerization, initiated at the point indicated by arrow 1 and terminated at the artificial defect. (D, E) Second and third chain polymerizations initiated at the points indicated by arrows 2 and 3, respectively. (F, G) Diagrams illustrating the creation of an artificial defect in advance. (H, I) Diagrams illustrating the initiation and termination of chain polymerization. *Source:* From Ref.<sup>[29]</sup>; © Macmillan Magazines Ltd., 2001.

applied when the scanning tip passed the point marked by arrow 1. A very bright line appeared between the point of stimulation and the artificial defect, indicating that chain polymerization was initiated at the stimulation point and terminated at the artificial defect (Fig. 7H and I). We imaged the same area once more from the top to the bottom, as shown in Fig. 7D, applying another pulsed sample bias when the tip passed the point marked by arrow 2. In this case as well, chain polymerization was initiated at the indicated point and terminated at the artificial defect. Note the chain polymerization initiated at the point marked by arrow 1 propagated on both sides of the point, as described above. In a similar manner, we created a third polymer nanowire by initiating chain polymerization at the point marked by arrow 3 in Fig. 7E.

This result shows that we can control the initiation and termination of chain polymerization with spatial precision on the order of 1 nm. Furthermore, this result also indicates that at least three polymer nanowires can be connected to an object as small as 6 nm. This means that the source, drain, and gate electrode of a nano-scale single-molecule transistor, for instance, will be connectable.

### ADVANTAGES OF THE METHOD

It is well known that we can manipulate individual atoms or molecules with an STM tip,<sup>[45–48]</sup> so we

should be able to create nanowires using such atom-by-atom crafting. It is also known that if a thin molecular film is stimulated by a biased STM tip, a local chemical reaction or reorientation is sometimes induced,<sup>[49–53]</sup> so that continuous modification will be possible by scanning of a biased STM tip. Although such work is essential to fundamental advances, the chain polymerization technique used in our work has several advantages.

First, the nanowires obtained are guaranteed to have perfect structures without any defects. If defects exist, the chain reaction itself will be terminated, as has been discussed above. Hence if the chain reaction proceeds, the nanowire reaction product is guaranteed to have perfect structures. For a chain reaction proceeding in a large domain without any defects, polymers longer than 500 nm have been observed. Furthermore, a single conducting polymer chain in a free state, such as a solution, generally has a coiled conformation, which prevents the occurrence of  $\pi$ -electron conjugation along the whole chain. In contrast, the polydiacetylene nanowires on a graphite surface obtained in our method are straight, so they can be considered ideal  $\pi$ -conjugated systems. Second, the nanowires are stable at room temperature. Third, we can create a long nanowire by applying only one pulsed bias voltage at one point; the propagation speed of the chain reaction is high (we roughly estimated the propagation speed of the chain polymerization to be

0.1–1 m/sec), so that the entire process is accomplished in a short time. Fourth, the process required no additional energy for the chain propagation reaction, other than the first stimulation.

The controlled chain reaction methods have many advantages for the fabrication of nanosized structures. However, despite these advantages, reports on controlled chain reaction are few (Lopinski et al.<sup>[54]</sup> have reported another type of chain reaction—a spontaneous growth of a molecular styrene line from a silicon dangling bond).

Finally, we would like to discuss whether or not the nanowires are conductive. According to electronic energy band calculations for various polydiacetylene compounds,<sup>[55–57]</sup> their polydiacetylene backbones have almost the same band structure and are nearly independent of substituent groups. Namely, the conjugated  $\pi$ -electrons of the polydiacetylene backbone form valence and conduction bands, which are separated by an energy gap of about 1.6 eV.<sup>[57]</sup> Because of the existence of this band gap, the polydiacetylene backbone is expected to be a nonconductor. However, because the highest valence band and the lowest conduction band have fairly strong dispersions,<sup>[57]</sup> the polydiacetylene backbone should act as an electronically conductive nanowire on the transfer of charge from the surroundings. For example, excess electrons, created by light illumination on a polydiacetylene chain, move in response to an electronic field with an ultrahigh drift mobility,<sup>[58]</sup> and the conductivity of polydiacetylene films increases on doping with iodine.<sup>[59]</sup> The polymer nanowire on the graphite surface created by our method is also expected to be conductive if a charge transfer between the polymer and the graphite surface exists. We are now planning to measure the conductivity of the polymer nanowire.

## CONCLUSION

We have demonstrated that we can initiate the linear propagation of the chain polymerization of unsaturated organic molecules at any predetermined point and terminate it at another predetermined point with a spatial precision on the order of 1 nm, using the probe tip of an STM. In our demonstration, we used a self-ordered monomolecular layer of the amphiphilic diacetylene compounds, 10,12-pentacosadiynoic acid and 10,12-nonacosadiynoic acid. Because the polydiacetylene backbone has a conjugated  $\pi$ -electron system, we can expect that it will function as an electrically conductive nanowire when charge is transferred from the surroundings.

In the future, this method will be useful for fabricating novel molecular devices comprising conjugated polymer nanowires, and for interconnecting novel

nanoelectronic devices. Furthermore, because the obtained polymer is considered to be a long, linear, conductive nanowire with high structural perfection, it will be an ideal system for the basic study of the physics of one-dimensional conductors. We also hope that this work will provide a new experimental method for chemists investigating the kinetics and mechanisms of chain reactions.

## REFERENCES

1. Aviram, A.; Ratner, M.A. Molecular rectifiers. *Chem. Phys. Lett.* **1974**, *29* (2), 277–283.
2. Aviram, A. Molecules for memory, logic, and amplification. *J. Am. Chem. Soc.* **1988**, *110* (17), 5687–5692.
3. Joachim, C.; Gimzewski, J.K. An electromechanical amplifier using a single molecule. *Chem. Phys. Lett.* **1997**, *265*, 353–357.
4. Tans, S.J.; Verschueren, A.R.M.; Dekker, C. Room-temperature transistor based on a single carbon nanotube. *Nature* **1998**, *393*, 49–52.
5. Collier, C.P.; Wong, E.W.; Belohradsky, M.; Raymo, F.M.; Stoddart, J.F.; Kuekes, P.J.; Williams, R.S.; Heath, J.R. Electronically configurable molecular-based logic gates. *Science* **1999**, *285*, 391–394.
6. Chen, J.; Reed, M.A.; Rawlett, A.M.; Tour, J.M. Large on–off ratios and negative differential resistance in a molecular electronic device. *Science* **1999**, *286*, 1550–1552.
7. Joachim, C.; Gimzewski, J.K.; Aviram, A. Electronics using hybrid-molecular and mono-molecular devices. *Nature* **2000**, *408*, 541–548.
8. Batchold, A.; Hadley, P.; Nakanishi, T.; Dekker, C. Logic circuits with carbon nanotube transistors. *Science* **2001**, *294*, 1317–1320.
9. Liu, X.; Lee, C.; Zhou, C.; Han, J. Carbon nanotube field-effect inverters. *Appl. Phys. Lett.* **2001**, *79* (20), 3329–3331.
10. Xue, J.; Forrest, S.R. Organic thin-film transistors based on bis(1,2,5-thiadiazolo)-*p*-quinobis(1,3-dithiole). *Appl. Phys. Lett.* **2001**, *79* (22), 3714–3716.
11. Collier, C.P.; Jeppesen, J.O.; Luo, Y.; Perkins, J.; Wong, E.W.; Heath, J.R.; Stoddart, J.F. Molecular-based electronically switchable tunnel junction devices. *J. Am. Chem. Soc.* **2001**, *123* (50), 12,632–12,641.
12. Derycke, V.; Martel, R.; Appenzeller, J.; Avouris, Ph. Carbon nanotube inter- and intramolecular logic gates. *Nano Lett.* **2001**, *1* (9), 453–456.
13. Kwok, K.S.; Ellenbogen, J.C. Moletronics: future electronics. *Mater. Today* **2002**, *5* (2), 28–37.
14. Cui, J.B.; Burghard, M.; Kern, K. Room temperature single electron transistor by local chemical modification of carbon nanotubes. *Nano Lett.* **2002**, *2* (2), 117–120.
15. Hong, B.H.; Bae, S.C.; Lee, C.-W.; Jeong, S.; Kim, K.S. Ultrathin single-crystalline silver nanowire arrays formed in an ambient solution phase. *Science* **2001**, *294*, 348–351.
16. Chen, Y.; Ohlberg, D.A.A.; Medeiros-Ribeiro, G.; Chang, Y.A.; Williams, R.S. Self-assembled growth of

- epitaxial erbium disilicide nanowires on silicon(001). *Appl. Phys. Lett.* **2000**, *76* (26), 4004–4006.
17. Iijima, S. Helical microtubules of graphitic carbon. *Nature* **1991**, *354*, 56–58.
  18. Tans, S.J.; Devoret, M.H.; Dai, H.J.; Thess, A.; Smalley, R.E.; Geerligs, L.J.; Dekker, C. Individual single-wall carbon nanotubes as quantum wires. *Nature* **1997**, *386*, 474–477.
  19. Wildöer, J.W.G.; Venema, L.C.; Rinzler, A.G.; Smalley, R.E.; Dekker, C. Electronic structure of atomically resolved carbon nanotubes. *Nature* **1998**, *391*, 59–62.
  20. Braun, E.; Eichen, Y.; Sivan, U.; Ben-Yoseph, G. DNA-templated assembly and electrode attachment of a conducting silver wire. *Nature* **1998**, *391*, 775–778.
  21. Fink, H.W.; Schönenberger, C. Electrical conduction through DNA molecules. *Nature* **1999**, *398*, 407–410.
  22. Porath, D.; Bezryadin, A.; de Vries, S.; Dekker, C. Direct measurement of electrical transport through DNA molecules. *Nature* **2000**, *403*, 635–638.
  23. Kasujov, A.Y.; Kociak, M.; Gueron, S.; Reulet, B.; Volkov, V.T.; Klinov, D.V.; Bouchiat, H. Proximity-induced superconductivity in DNA. *Science* **2001**, *291*, 280–282.
  24. Yoo, K.-H.; Ha, D.H.; Lee, J.-O.; Park, J.W.; Kim, J.; Kim, J.J.; Lee, H.-Y.; Kawai, T.; Choi, H.Y. Electrical conduction through poly(dA)–poly(dT) and poly(dG)–poly(dC) DNA molecules. *Phys. Rev. Lett.* **2001**, *87* (19), 198102.
  25. Bumm, L.A.; Arnold, J.J.; Cygan, M.T.; Dunbar, T.D.; Burgin, T.P.; Jones, L.; Allara, D.L.; Tour, J.M.; Weiss, P.S. Are single molecular wires conducting? *Science* **1996**, *271*, 1705–1707.
  26. Reed, M.A.; Zhou, C.; Muller, C.J.; Burgin, T.P.; Tour, J.M. Conductance of a molecular junction. *Science* **1997**, *278*, 252–254.
  27. Langlais, V.J.; Schlittler, R.R.; Tang, H.; Gourdon, A.; Joachim, C.; Gimzewski, J.K. Spatially resolved tunneling along a molecular wire. *Phys. Rev. Lett.* **1999**, *83* (14), 2809–2812.
  28. Shimoura, T.; Akai, T.; Abe, T.; Ito, K. Atomic force microscopy observation of insulated molecular wire formed by conducting polymer and molecular nanotube. *J. Chem. Phys.* **2002**, *116* (5), 1753–1756.
  29. Okawa, Y.; Aono, M. Nanoscale control of chain polymerization. *Nature* **2001**, *409*, 683–684.
  30. Okawa, Y.; Aono, M. Linear chain polymerization initiated by a scanning tunneling microscope tip at designated positions. *J. Chem. Phys.* **2001**, *115* (5), 2317–2322.
  31. Wegner, G. Topochemical polymerization of monomers with conjugated triple bonds. *Makromol. Chem.* **1972**, *154*, 35–48.
  32. Tieke, B.; Lieser, G.; Wegner, G. Polymerization of diacetylenes in multilayers. *J. Polym. Sci., Polym. Chem. Ed.* **1979**, *17*, 1631–1644.
  33. Rabe, J.P.; Buchholz, S.; Askadskaya, L. Scanning tunneling microscopy of several alkylated molecular moieties in monolayers on graphite. *Synth. Met.* **1993**, *54*, 339–349.
  34. Grim, P.C.M.; Feyter, S.D.; Gesquière, A.; Vanoppen, P.; Rücker, M.; Valiyaveetil, S.; Moessner, G.; Müllen, K.; De Schryver, F.C. Submolecularly resolved polymerization of diacetylene molecules on the graphite surface observed with scanning tunneling microscopy. *Angew. Chem., Int. Ed. Engl.* **1997**, *36* (23), 2601–2603.
  35. Takami, T.; Ozaki, H.; Kasuga, M.; Tsuchiya, T.; Mazaki, Y.; Fukushi, D.; Ogawa, A.; Uda, M.; Aono, M. Periodic structure of a single sheet of a clothlike macromolecule (atomic cloth) studied by scanning tunneling microscopy. *Angew. Chem., Int. Ed. Engl.* **1997**, *36* (24), 2755–2757.
  36. Hibino, M.; Sumi, A.; Hatta, I. Atomic images of saturated and unsaturated fatty acids at liquid/graphite interface and difference of tunneling currents between them observed by scanning tunneling microscopy. *Jpn. J. Appl. Phys.* **1995**, *34* (2A), 610–614. Part 1.
  37. Groszek, A.J. Selective adsorption at graphite/hydrocarbon interfaces. *Proc. R. Soc. Lond., A* **1970**, *314*, 473–498.
  38. McGonigal, G.C.; Bernhardt, R.H.; Thomson, D.J. Imaging alkane layers at the liquid / graphite interface with the scanning tunneling microscope. *Appl. Phys. Lett.* **1990**, *57* (1), 28–30.
  39. Rabe, J.P.; Buchholz, S. Commensurability and mobility in two-dimensional molecular patterns on graphite. *Science* **1991**, *253*, 424–427.
  40. Venkataraman, B.; Breen, J.J.; Flynn, G.W. Scanning tunneling microscopy studies of solvent effects on the adsorption and mobility of triacontane/triacontanol molecules adsorbed on graphite. *J. Phys. Chem.* **1995**, *99* (17), 6608–6619.
  41. Neumann, W.; Sixl, H. The mechanism of the low temperature polymerization reaction in diacetylene crystals. *Chem. Phys.* **1981**, *58*, 303–312.
  42. Takabe, T.; Tanaka, M.; Tanaka, J. The electronic spectra of diphenylacetylene and 1,3-butadiyne. *Bull. Chem. Soc. Jpn.* **1974**, *47* (8), 1912–1916.
  43. Bertault, M.; Fave, J.L.; Schott, M. The lowest triplet state of a diacetylene. *Chem. Phys. Lett.* **1979**, *62* (1), 161–165.
  44. Albrecht, T.R.; Dovek, M.M.; Kirk, M.D.; Lang, C.A.; Quate, C.F.; Smith, D.P.E. Nanometer-scale hole formation on graphite using a scanning tunneling microscope. *Appl. Phys. Lett.* **1989**, *55* (17), 1727–1729.
  45. Eigler, D.M.; Schweizer, E.K. Positioning single atoms with a scanning tunneling microscope. *Nature* **1990**, *344*, 524–526.
  46. Kobayashi, A.; Grey, F.; Williams, R.S.; Aono, M. Formation of nanometer-scale grooves in silicon with a scanning tunneling microscope. *Science* **1993**, *259*, 1724–1726.
  47. Avouris, Ph.; Walkup, R.E.; Rossi, A.R.; Akpati, H.C.; Nordlander, P.; Shen, T.-C.; Lyding, J.W.; Abeln, G.C. Breaking individual chemical bonds via STM-induced excitations. *Surf. Sci.* **1996**, *363* (1–3), 368–377.
  48. Shen, T.C.; Wang, C.; Tucker, J.R. Al nucleation on monohydride and bare Si(001) surfaces: Atomic scale patterning. *Phys. Rev. Lett.* **1997**, *78* (7), 1271–1274.
  49. Dujardin, G.; Walkup, R.E.; Avouris, Ph. Dissociation of individual molecules with electrons from the tip of a scanning tunneling microscope. *Science* **1992**, *255*, 1232–1235.



50. Stipe, B.C.; Rezaei, M.A.; Ho, W.; Gao, S.; Persson, M.; Lundqvist, B.I. Single-molecule dissociation by tunneling electrons. *Phys. Rev. Lett.* **1997**, *78* (23), 4410–4413.
51. Ma, L.P.; Yang, W.J.; Xie, S.S.; Pang, S.J. Ultrahigh density data storage from local polymerization by a scanning tunneling microscope. *Appl. Phys. Lett.* **1998**, *73* (22), 3303–3305.
52. Patitsas, S.N.; Lopinski, G.P.; Hul'ko, O.; Moffatt, D.J.; Wolkow, R.A. Current-induced organic molecule–silicon bond breaking: Consequences for molecular devices. *Surf. Sci. Lett.* **2000**, *457*, L425–L431.
53. Gao, H.J.; Sohlberg, K.; Xue, Z.Q.; Chen, H.Y.; Hou, S.M.; Ma, L.P.; Fang, X.W.; Pang, S.J.; Pennycook, S.J. Reversible, nanometer-scale conductance transitions in an organic complex. *Phys. Rev. Lett.* **2000**, *84* (8), 1780–1783.
54. Lopinski, G.P.; Wayner, D.D.M.; Wolkow, R.A. Self-directed growth of molecular nanostructures on silicon. *Nature* **2000**, *406*, 48–51.
55. Karpfen, A. Ab initio studies on polymers: IV. Polydiacetylenes. *J. Phys., C. Solid State Phys.* **1980**, *13*, 5673–5689.
56. Brédas, J.L.; Chance, R.R.; Silbey, R.; Nicolas, G.; Durand, Ph. A nonempirical effective Hamiltonian technique for polymers: application to polyacetylene and polydiacetylene. *J. Chem. Phys.* **1981**, *75* (1), 255–267.
57. Salaneck, W.R.; Fahlman, M.; Lapersonne-Meyer, C.; Fave, J.-L.; Schott, M.; Lögdlund, M.; Brédas, J.L. Electronic structure of 4-BCMU polydiacetylene studied by angle-dependent photoelectron spectroscopy. *Synth. Met.* **1994**, *67*, 309–314.
58. Donovan, K.J.; Sudiwala, R.V.; Wilson, E.G. Fast photoconduction in Langmuir–Blodgett multilayers of polydiacetylenes. *Thin Solid Films* **1992**, *210/211*, 271–273.
59. Day, D.R.; Lando, J.B. Conduction in polydiacetylene bilayers. *J. Appl. Polym. Sci.* **1981**, *26*, 1605–1612.

# Polypropylene and Thermoplastic Olefins Nanocomposites

Francis M. Mirabella, Jr.

Analytical Department, Equistar Chemicals, LP, Cincinnati, Ohio, U.S.A.

## INTRODUCTION

The purpose of this chapter is to review the progress toward the preparation of polypropylene/clay and thermoplastic olefin/clay nanocomposites. Further, the structure and properties of these type of nanocomposites are discussed and, where possible, structure/property relationships are described. Lastly, the progress toward the achievement of commercially viable nanocomposites of this type is assessed.

Polyolefins account for about 185 billion pounds per year or about 50% of the total worldwide plastic's industry production. Polypropylene (PP) accounts for about 20% of this total or 74 billion pounds per year production. Therefore polypropylene is one of the most widely used thermoplastics not only because of its balance of physical and mechanical properties, but also because of its environmental friendliness (e.g., recyclability) and low cost. The most common type is isotactic PP, while syndiotactic PP is a minor contributor to the PP market. Polypropylene has an attractive combination of low density, high stiffness and toughness, and heat distortion temperature above 100°C, which endows it with extraordinary versatility of properties and applications ranging from molded parts to films and fibers. Innovative catalyst and process technologies have significantly simplified its production, resulting in the minimization of catalyst residues, waxy byproducts, and low stereoregularity components, by the use of high activity and highly stereoselective catalysts, such as Ziegler–Natta and metallocene catalysts. Highly energy-efficient processes, such as gas phase and liquid-pool processes, have minimized the need for solvents. Polypropylene offers ready means for recycling by remolding or feedstock recovery or by recovery of its energy content in power plants and steel mills. It has also continued to make inroads into the engineering plastics markets by replacing more expensive and less environmentally friendly resins. The addition of mineral fillers to polypropylenes has widened its sphere of applications by enhancing its stiffness properties. However, the concomitant effect is typically a decrease in toughness properties because the inorganic filler particles act as stress concentrators.

Montmorillonite (mmt) is the most common clay mineral used in polymer/clay hybrids and is composed

of an octahedral alumina sheet sandwiched between two tetrahedral silica sheets. The anionically charged sheets, or clay platelets, are strongly held together by cations, such as  $\text{Na}^+$ ,  $\text{Li}^+$ ,  $\text{Ca}^{2+}$ ,  $\text{Fe}^{2+}$ , and  $\text{Mg}^{2+}$ . The tightly bound stacks of clay platelets may be readily separated by simple dissolution in a polar solvent, such as water. In addition, the natural clay is miscible with polar polymers in which the platelets readily disperse. However, separation of the clay platelets in a nonpolar polymer is difficult. The thickness of the individual clay platelets is about 1 nm and the gallery spacing (spacing is defined in terms of d-spacing from X-ray diffraction and small-angle X-ray scattering, which is the distance from one clay platelet center to the next) of the platelets in natural clay is about 1 nm. Organic modification of the clay with alkyl ammonium chlorides, in which the alkyl chain is typically composed of 6 to 15 carbons, expands the gallery spacing to about 2.2 to 2.4 nm in typical commercial organoclays. Addition of maleic anhydride-modified PP often results in intercalated clay with gallery spacing of greater than 3 nm. The typically desired state is, upon addition of PP, the complete dispersion, i.e., exfoliation and dispersal, of the clay platelets so that there is no correlation between platelets and therefore no maxima in the X-ray scattering pattern. Considering that clay is composed of platelets that are about 1 nm in thickness and around 1000 nm in lateral dimensions and assuming a density of 2.65 g/cm<sup>3</sup> yields an upper limit of about 750 m<sup>2</sup>/g surface area per gram for fully exfoliated clay. This is 5 to 10 times the surface area per gram achievable with ordinary fillers. Exfoliated clay in polymers was shown to endow unique properties to the system, such as increased T<sub>g</sub>, increased stiffness, maintenance of impact strength, increased barrier to gases and liquids, increased flame retardancy, etc.

## POLYPROPYLENE

### Structure

The extraordinary property enhancements accessible through the formation of polymer/clay mineral hybrid systems were pioneered by Toyota workers about a decade ago. In a series of papers, the synthesis of

nylon-6/clay hybrids was described by the swelling of natural montmorillonite (fractionated from bentonite) with  $\epsilon$ -caprolactam to form an intercalated compound, followed by the thermolytic polymerization of the  $\epsilon$ -caprolactam to nylon-6.<sup>[1,2]</sup> The remarkable enhancements of the thermal and mechanical properties of the nylon-6 were further reported by the Toyota workers.<sup>[3]</sup> The dispersion of the silicate layers in such nylon-6/montmorillonite hybrids is generally excellent. The clay platelets are essentially completely exfoliated, resulting in a morphology as shown in the transmission electron microscopy (TEM) photomicrograph in Fig. 1. The clay platelets are seen to be completely dispersed and uncorrelated with each other. Therefore no X-ray signal from a periodic stacking of clay platelets would be expected from x-ray diffraction (XRD) or small angle x-ray scattering (SAXS) measurements.

In a technological advancement of this development, Vaia, Ishii, and Giannelis<sup>[4]</sup> reported the formation of polymer/clay hybrids by the direct intercalation of polystyrene in organically modified montmorillonite. The montmorillonite was modified with alkyl ammonium cations to maximize the enthalpic interactions of the

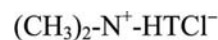
modified clay with the polystyrene and thus overcome the unfavorable loss of conformational entropy associated with the confinement of the polymer inside the clay galleries. The intercalated polymer was claimed to exist in a collapsed, two-dimensional conformation, and, as evidence of this, it was demonstrated that the normal glass transition temperature of the polystyrene was essentially absent for the intercalated polymer.<sup>[4]</sup> In further work, this group studied the chain dynamics of polystyrene in organically modified clay hybrids. They defined an effective diffusion coefficient and found that it increased with increasing alkyl chain length of the alkyl ammonium cation functional groups on the clay.<sup>[5]</sup>

The organic modification of natural clay minerals typically involves exchange of cations on the natural clay with alkyl ammonium cations. Commercial mmt typically is modified with hydrogenated tallow, which is ~65% C<sub>18</sub>, 30% C<sub>16</sub>, and 5% C<sub>14</sub> alkyl chain lengths. The typical commercial organoclay is modified with an alkyl ammonium compound as shown in Fig. 2.

Two alternative synthetic routes were proposed by Manias et al.<sup>[6]</sup> to prepare organically modified mmt that would be readily dispersed in polypropylene. These small-scale studies were intended to explore the thermodynamics required to intercalate and exfoliate mmt with polypropylene. The first route relied on improving the favorability of the polypropylene–mmt enthalpic interactions to disperse the mmt. This was performed by functionalizing the polypropylene with 0.5–1.0 mol% of methyl styrene monomer. This random copolymer was then further functionalized with maleic anhydride and ethanol resulting in three random copolymers of polypropylene. The functionalized PP/dimethyl dioctadecylammonium–mmt hybrid systems were formed by static melt intercalation in a vacuum oven at 180°C. The organo-mmt was observed by XRD to be intercalated with the functionalized PP and by TEM measurements to be dispersed in these random polypropylene copolymers to the extent of about 25–40% exfoliated clay platelets. The second route relied on decreasing the enthalpic interactions between the surfactant and the mmt. This is expected to effectively render the polymer–mmt interactions more favorable. This was performed by the partial fluorination of the alkyl chains in an mmt. The mmt was organically modified with dimethyldioctadecyl ammonium and with partially fluorinated alkyltrichlorosilane. The



**Fig. 1.** Transmission electron microscopy photomicrograph of nylon/clay nanocomposite.



HT = hydrogenated tallow

HT = 65% C<sub>18</sub>, 30% C<sub>16</sub> and 5% C<sub>14</sub>

**Fig. 2.** Structure of typical organic modifier for clay.

organically modified mmt was statically melt intercalated with neat polypropylene. Measurements by XRD showed that the mmt was intercalated by the PP, indicating that the thermodynamics were favorable for nanocomposite formation. Further shear mixing of these two types of systems was expected to lead to further dispersion of the mmt in the polymer.

The promise of extraordinary improvement in end-use properties of polyolefin/clay hybrid systems has spurred great interest and intensive activity on the part of the players in the polyolefin and allied industries. Academic participation in these developments has also been vigorous. Optimistic predictions were made early in the drive to apply nanotechnology to the polyolefins industry. Probably, partly because of the promise of the technological benefits of nanotechnology and to the large size of the polyolefins industry, it was predicted that the largest impact of nanocomposites on the plastics industry would be in polyolefins. Wilson<sup>[7]</sup> of Inspired Innovations, LLC, predicted that nanocomposite versions of polyolefins will displace engineering thermoplastics and thermosets in many traditional applications and will open new opportunities to displace metal and glass in many traditional applications. Well over one-half of all the current applications for polymers could be improved by this new technology, according to Wilson. This author predicted millions of tons of nanocomposite polyolefin production and replacement of an equal amount of annual glass and metal production for the foreseeable future. Sinclair,<sup>[8]</sup> STA Research, predicted that polypropylene would be the largest growth polymer in nanocomposites and that PP nanocomposites would reach a volume of millions of tons per year by 2010. Both of these prognosticators emphasized that complete exfoliation of the clay was required to imbue the polyolefins with the improved end-use properties that could drive such massive commercial volumes of polyolefin nanocomposites. However, these goals could only be achieved by overcoming the very problematic dispersion of naturally polar clay in nonpolar polymers.

The attraction of clay mineral additives is their low cost to recover from the earth in their natural state. The incorporation of the clay in polypropylene, on the other hand, requires much more than natural clay. The technological challenges to formulating stable polypropylene/clay nanocomposites have proven to be formidable. Furthermore, the achievement of enhanced end-use properties has barely been explored because of this inability to form the systems with suitable clay dispersions.

Although studies continue aiming at novel modification of clay and functionalized polymer for improving the intercalation and exfoliation of the clay in polypropylene, the vast majority of experimental

studies and commercial developments employ polypropylene with maleated polypropylene (PP-MA), or more rarely another functionalized PP, as a compatibilizer to form PP/clay nanocomposite hybrid systems. The approximate individual costs of organically modified mmt and PP-MA are about five times that of the polymer on a per pound basis. This means that the production of polypropylene nanocomposites with properties sufficiently enhanced to justify the additional costs is a doubly formidable problem.

In the earliest studies, the morphology of several systems was determined to compare various strategies to form intercalated and exfoliated polypropylene/clay hybrids systems. Low molecular weight polypropylene (12,000–30,000) functionalized with maleic anhydride or hydroxyl groups was found to intercalate into C<sub>18</sub>-mmt.<sup>[9]</sup> Higher concentrations of functionalization were correlated with successful intercalation of the PP into the clay, while lower concentrations failed to exhibit intercalation of the PP. The same group then showed that PP homopolymer was not intercalated into Na-mmt, but a polyolefin diol was used to intercalate diasteryldimethylammonium-mmt followed by exfoliation of the clay by PP homopolymer.<sup>[10]</sup> In a further study, these workers employed PP-MA with two concentrations of maleic anhydride functionalization to intercalate C<sub>18</sub>-mmt, followed by exfoliation of the clay with PP homopolymer.<sup>[11]</sup> It was found that too high a concentration of maleic anhydride functionalization resulted in immiscibility of the PP-MA compatibilizer with the PP homopolymer. The reinforcement of the system was judged best for the lower concentration of maleic anhydride in the PP-MA, which had a higher storage modulus and good miscibility with the PP homopolymer.

Many groups, to investigate strategies for improved clay dispersion in polypropylene and to probe the resulting morphologies, extended the foregoing early work by Okada et al. It was confirmed in some of these studies that PP homopolymer could not intercalate into organoclays.<sup>[12,13]</sup> The use of considerable amounts of PP-MA compatibilizer was necessary to intercalate the clay and to facilitate subsequent exfoliation of the clay platelets by PP homopolymer.<sup>[12,13]</sup> Xu et al.<sup>[12]</sup> found that C<sub>16</sub>-mmt was intercalated in composites containing 2 wt.% clay only when the concentration of PP-MA (containing 0.9 wt.% maleic anhydride) exceeded 10 wt.% in the composite. Similarly, Walter et al.<sup>[13]</sup> found that C<sub>18</sub>-synthetic clay was intercalated in polypropylene composites containing 7 wt.% clay and 20 wt.% PP-MA (containing 4.2 wt.% maleic anhydride), but that no intercalation of the PP occurred in the absence of the PP-MA. Fig. 3 shows TEM photomicrographs of a 7 wt.% clay composite with no PP-MA exhibiting no intercalation of the clay (Fig. 3A) and a 7 wt.% clay composite with

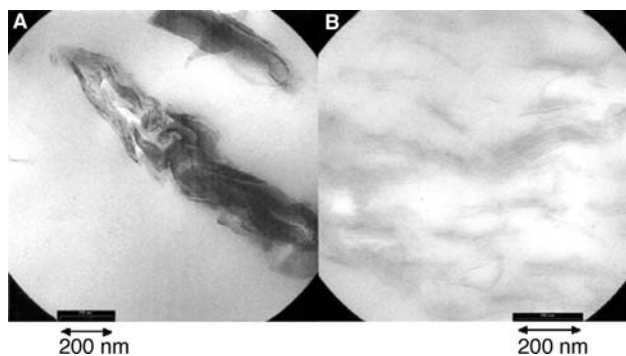


**Fig. 3.** Transmission electron microscopic image of polypropylene compound containing 10 vol.% organophilic fluoromica (M100/ODA) without addition of PP-g-MA compatibilizer (A, left) and the corresponding ME100/DA nanocomposite obtained in the presence of 20 wt.% PP-g-MA compatibilizer. *Source:* From Ref.<sup>[13]</sup> with permission from Marcel Dekker, Inc.

20 wt.% PP-MA exhibiting intercalation of the clay and some evidence of exfoliation of the clay “tactoids” by the PP homopolymer (Fig. 3B). Tactoids are defined as stacks of clay platelets that are intercalated with polymer chains, thereby expanding the galleries between succeeding clay platelets, as in Fig. 3B. Tactoids are distinguished from clay particles, which are composed of closely spaced clay platelets, which do not exhibit expanded galleries, as in Fig. 3A.

Reichert et al.<sup>[14]</sup> showed that the alkyl chain in clays organically modified with alkylammonium cations must exceed 8 carbon atoms in length to promote intercalation and that increasing the concentration of the maleic anhydride functionality in the PP-MA promoted exfoliated nanocomposite systems with PP homopolymer matrices. Alkyl chain lengths of C<sub>4</sub> to C<sub>8</sub> gave a similar clay interlayer distance of 1.3 nm, while C<sub>16</sub> and C<sub>18</sub> chain lengths afforded spacing of 1.7 and 2 nm, respectively (the nonmodified synthetic clay spacing was 0.95 nm). This indicated that sufficient molar mass of the alkyl chain in the organically modified clay was necessary to promote favorable interactions of the silicate organic modifier with the polymer chains intercalating the clay platelets. This type of observation was made in original work on organic modification of clay to promote intercalation of clay by nonpolar species.<sup>[15,16]</sup> Reichert et al.<sup>[17]</sup> further investigated the stability of polypropylene composites prepared with PP with Mw = 350,000, 20 wt.% of PP-MA with Mw = 32,000, and 4.2 wt.% MA and 5 wt.% of C<sub>18</sub>-synthetic clay melt blended in a twin screw at 200°C. The as-prepared system exhibited typical nanocomposite morphology with well-intercalated tactoids and partial exfoliation of clay platelets in TEM photomicrographs, as well as a broad “hump” in the wide angle x-ray scattering (WAXS) pattern

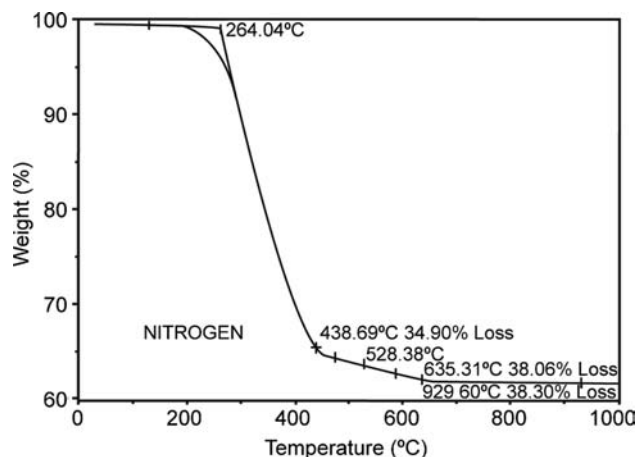


**Fig. 4.** Thermogravimetric analysis curve of Cloisite 20 A™ (Southern Clay Products) organo-mmt. The onset of thermal decomposition is at 190°C.

indicative of a broad distribution of interlayer distances. Upon annealing of the material at 220°C for 200 min, the morphology observed in the TEM appeared to show a collapse of the structure to much more tightly spaced stacks and no evidence of partial exfoliation of clay platelets. However, it was argued on the basis of WAXS data on this system that because no peak was observed and the broad “hump” observed for the as-prepared and the broad “hump” observed for the annealed system, the clay exfoliation was further improved by the annealing process. The upper temperature limit of stability of the organic functionality, i.e., alkylammonium cations (C<sub>18</sub>-ammonium cation in this case), on typical clays is about 190°C, as shown in Fig. 4.<sup>[18]</sup> Above this temperature, the organic functionality degrades and the intercalated clay tactoids characteristically collapse to a stacked platelet structure. This appears to be the case in this study and the TEM photomicrograph showing clay platelet stacks was strong evidence for collapse of the intercalated clay tactoids at the annealing temperature of 220°C.<sup>[17]</sup>

Many other studies of clay dispersion in polypropylene are available. Analytical methods to probe the morphology in such systems were discussed by Morgan and Gilman.<sup>[19]</sup> They recommended TEM as the best means to qualitatively assess the degree of dispersion of clay in polymer matrices. Their TEM photomicrographs demonstrated that unintercalated clay platelet stacks, intercalated tactoids, and exfoliated platelets could be recognized. They recommended XRD to measure d-spacing in ordered, unintercalated stacks and ordered, intercalated tactoids, but cautioned that XRD is insufficient for determining disordered and exfoliated clay because these exhibit no reflection peak. These analytical methods were used to probe the morphology in studies of melt intercalated

PP/clay hybrid systems.<sup>[20–27]</sup> These studies all relied on significant concentrations of a functionalized polypropylene (predominantly PP-MA) to intercalate organically modified clay (predominantly alkylammonium-mmt) in a PP homopolymer matrix, followed by shearing of the melt to exfoliate the clay to the extent possible. In all cases, the best dispersion of the clay observed was partially as ordered, intercalated tactoids and partially as disordered, exfoliated clay platelets; however, nonuniform dispersion of the clay was commonly observed in all of these studies. The factors investigated were the MA concentration of the functionalized PP-MA and the concentration of PP-MA in the blend,<sup>[12,20,24,26,27]</sup> various melt compounding techniques,<sup>[12,20–22,25]</sup> and organic modification of clay.<sup>[23,24]</sup>

More uniform dispersion of alkylammonium-mmt in polypropylene was achieved by the intercalative polymerization of propylene in the galleries of the clay.<sup>[28]</sup> The TEM photomicrographs showed that the clay platelets were uniformly dispersed in the polypropylene. This strategy is attractive because no functionalized polypropylene compatibilizer is required; however, in situ polymerization of monomers in the clay galleries has not been demonstrated for commercial practice. Therefore melt intercalation remains the desired strategy for commercial production of polypropylene/clay hybrid nanocomposites. This goal has not been achieved for widespread commercial practice.

### Mechanism of exfoliation

A mean-field, lattice-based model of polymer intercalation in organically modified silicates was presented by Vaia and Giannelis.<sup>[29,30]</sup> The thermodynamic factors which control polymer intercalation into the clay galleries were outlined in terms of an interplay between entropic and energetic factors. The entropic penalty for confining the polymer inside the clay gallery may be partially compensated for by an increase in entropy of the surfactant chains (alkyl chains on organic modifier) as the clay layers separate. Although the tethered alkyl chains cannot increase their entropy by an increase in translational freedom, the expanded gallery spacing permits increased conformational entropy. Intercalation will be thermodynamically possible when favorable polymer–organically modified silicate energetic interactions overcome any unfavorable entropic factors. Further separation, i.e., driving exfoliation, depends on maximization of favorable polymer–surface interactions with the organically modified silicate, as well as minimization of unfavorable interactions with the tethered alkyl chains of the organic modifier. This explains the use of polymer functionalization with polar moieties. The polar functionalities on polypropylene participate in polar–polar interactions with the silicate surface, decreasing the free energy of

the system. If the total free energy of the system is decreased by the combined entropic and energetic factors, then intercalation and exfoliation may occur.

The further effects of shear forces on intercalated clay stacks (tactoids) have been elucidated by subsequent studies.<sup>[31,32]</sup> Fornes et al.<sup>[31]</sup> proposed a model explaining exfoliation of intercalated silicate stacks by the stepwise skewing of the silicate sheets in the tactoids, followed by peeling, one-by-one, of the silicate layers off the silicate stacks by combined diffusion/shearing, as shown in Fig. 5. The tactoids were shown to first skew apart forming shorter stacks of fewer and fewer numbers of silicate layers, followed by peeling of the individual layers off the tactoids forming exfoliated and dispersed layers, without short-range order with other silicate layers. The matrix polymer needs to have sufficient affinity for the silicate surface to cause spontaneous wetting of the surface to drive exfoliation. This is the required thermodynamic driving force. However, shear forces play a kinetic role by driving the peeling of silicate layers off the tactoids during the residence time of the system in the shear process. It was found that the higher the melt viscosity of the matrix polymer, the greater the stress exerted on the tactoids, driving this skewing and peeling process. Therefore higher

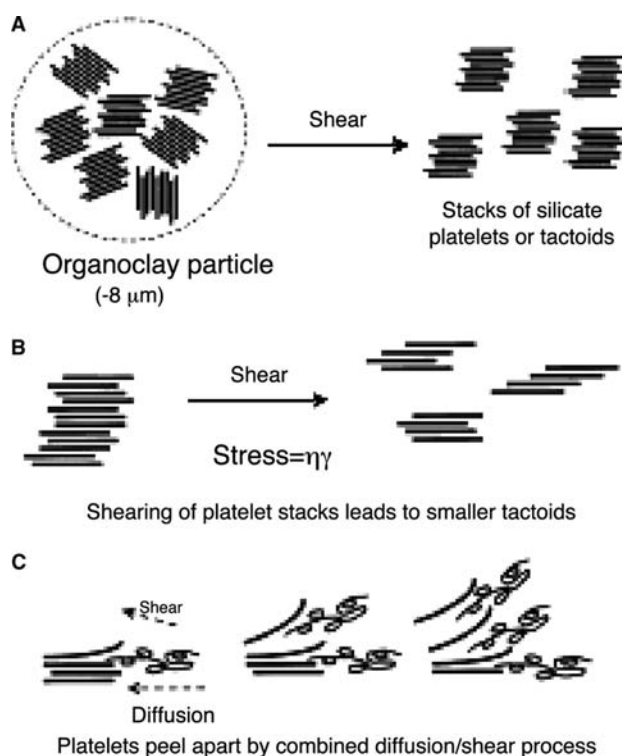


**Fig. 5.** Stepwise mechanism of clay platelet exfoliation in the melt compounding of nanocomposites: (A) organoclay particle breakup, (B) clay tactoid breakup, and (C) platelet exfoliation. *Source:* From Ref.<sup>[31]</sup> with permission from Elsevier Science Ltd.



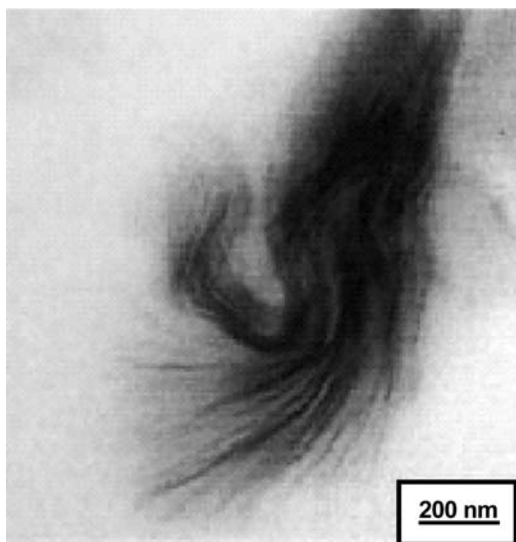


**Fig. 6.** Transmission electron micrograph of silicate layers peeling apart via a fan-shaped intermediate. Source: From Ref.<sup>[32]</sup> with permission from John Wiley and Sons, Inc.

molecular weight matrix polymer was associated with higher stresses and a higher degree of exfoliation. This model was supported by a further experimental study in which the clay tactoid was observed to be in the process of peeling apart in TEM images, as shown in Fig. 6.<sup>[32]</sup> The silicate layers in the tactoid can be seen to be sliding and peeling apart from one another, like a deck of cards, in Fig. 6.

## CRYSTALLIZATION

The effects of crystallization on polypropylene/clay hybrids have been investigated from two vantage points. The effects of the clay on the crystallization of the polypropylene matrix and the effects of the crystallization of the polypropylene on the clay morphology have been reported. The rate of crystallization was found to be increased for polypropylene-mmt nanocomposites as compared with neat polypropylene, as measured by crystallization half-times determined from differential scanning calorimetric data.<sup>[33,34]</sup> The nucleating effect of mmt has also been discussed in detail.<sup>[35,36]</sup> The nucleating effect was found to strongly depend on the origin and treatment of the mmt.<sup>[35]</sup> The spherulite diameter was decreased in PP-MA/mmt nanocomposites, as compared with neat polypropylene, in quiescent isothermal crystallization.<sup>[36]</sup>

The quiescent, isothermal crystallization kinetics of PP/PP-MA/mmt nanocomposites were found to be slightly retarded in comparison to the neat polypropylene, but were not significantly different from the PP/PP-MA blend.<sup>[26]</sup> However, marked

flow-induced acceleration of crystallization for PP/PP-MA/mmt nanocomposites was observed at strain rates for which flow had only a modest effect on the neat PP.<sup>[26]</sup> This behavior of the PP/PP-MA/mmt nanocomposites was further inferred to be largely due to the PP-MA compatibilizer, by comparing a blend of the PP/PP-MA, under these conditions.

The detailed crystalline morphology of the polypropylene matrix in PP/PP-MA/mmt nanocomposites has been reported.<sup>[36–38]</sup> Modifications observed were a fibrous crystalline morphology, instead of the usual spherulitic morphology after quiescent, isothermal crystallization.<sup>[38]</sup> Okamoto et al.<sup>[36,37]</sup> reported an interfibrillar structure composed of a disordered arrangement of crosshatched lamellae among the dispersed clay platelets, which arose after quiescent, isothermal crystallization of a PP-MA/mmt nanocomposite because of crystallization occurring between clay particles, thereby disordering the usual spherulitic structure. Polarized optical microscopy, XRD, SAXS, and TEM measurements were correlated to propose a morphology in which fibrils of about 3–5 polypropylene lamellae reside between dispersed clay platelets, forming a disordered spherulitic superstructure.

Okamoto et al.<sup>[36,39]</sup> proposed an intercalation mechanism of PP-MA into mmt in PP-MA/mmt nanocomposites involving the interplay of crystallization and residence time in the melt state. Their results indicated that slower rate of crystallization permits more time for the polymer to intercalate the mmt by diffusing into the clay galleries, while faster crystallization rate inhibits this diffusion. They found that clay gallery spacing, measured by XRD, became larger as crystallization temperature was increased near the melting temperature. Interestingly, because crystallization is also slow just above glass transition temperature ( $T_g$ ), it was similarly claimed, based on XRD measurements, that clay gallery spacing became larger for crystallization just above the glass transition temperature. In addition, gallery spacing was increased as clay concentration in the nanocomposite was decreased.

## MECHANICAL PROPERTIES

A primary goal for nanocomposites is to achieve enhanced mechanical properties. The addition of inorganic fillers to polymers is widely practiced in the plastics industry. The common enhancement to polymer mechanical properties, by the addition of talc, calcium carbonate, glass fibers, wollastonite, glass beads, mica, wood flour, etc., is the increase in stiffness (Young's modulus, tensile modulus, and flexural modulus), while strength properties (tensile strength, elongation at break, and flexural strength) and toughness (Izod and

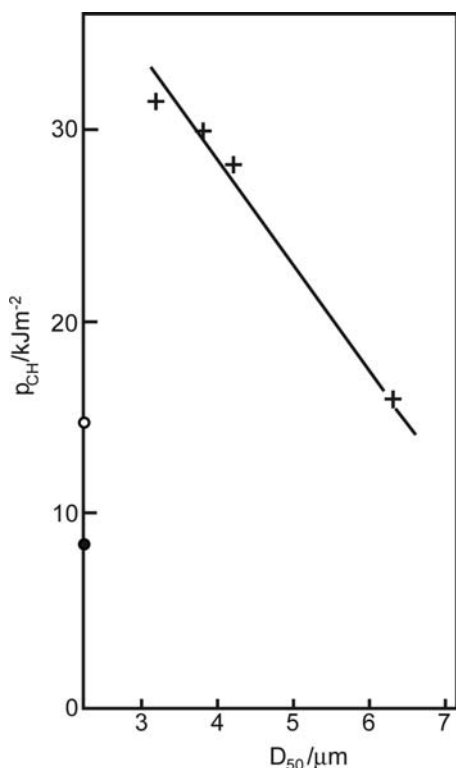


**Fig. 7.** Composite Charpy notch toughness vs. talc mean particle size of ternary composite (26 wt.% talc). *Source:* From Ref.<sup>[40]</sup> with permission from John Wiley and Sons, Inc.

Charpy impact strength) may decrease or be maintained.<sup>[40,41]</sup> The degradation in strength and toughness properties is a result of the concentration, degree of dispersion, and particle size of the inorganic filler.<sup>[40,41]</sup> Typically, the degradation in properties is correlated with the size of the particulate because the particle acts as a stress concentrator, thereby initiating cracks and degrading strength and toughness properties.<sup>[40,41]</sup> For example, the decrease in notched Charpy impact strength vs. talc particle diameter is shown in Fig. 7.

The early promise of nanocomposites was to provide a type of inorganic filler that would enhance stiffness and strength properties, while simultaneously maintaining or even improving toughness properties.<sup>[1]</sup> This development was expected to be related to three unique structural characteristics of nanofiller particles: 1) their approximately 1-nm size in one dimension; 2) their large aspect ratio; and 3) their ability to be preferentially oriented because of the large aspect ratio.

Another advantage, demonstrated by Walter et al.,<sup>[13]</sup> was the increase in matrix reinforcement achievable with nanocomposites with much lower inorganic filler concentration. The effectiveness of nanodispersed silicate relative to microdispersed talcs is shown in Fig. 8.

In the case of polypropylene, the further significant challenge is to achieve property enhancements that

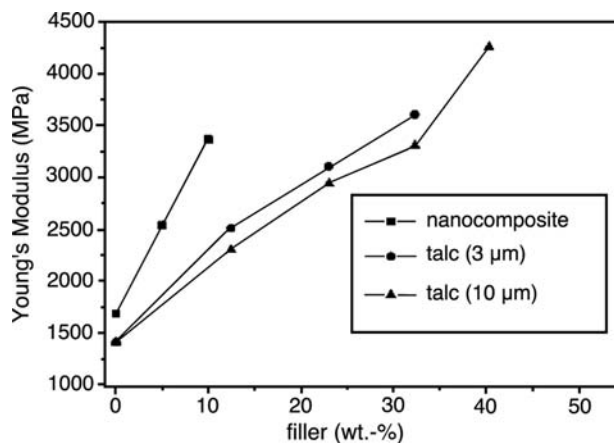


**Fig. 8.** Young's modulus of polypropylene compounds, prepared by melt compounding, as a function of filler content using organophilic fluoromica and talc with 3 and 10  $\mu\text{m}$  average particle diameter. *Source:* From Ref.<sup>[13]</sup> with permission from Marcel Dekker, Inc.

justify the incremental cost increase associated with the production of nanocomposites. This challenge is formidable because of the very low cost of polypropylene resins.

There have been relatively few studies on polypropylene nanocomposite properties and structure/property relationships in nanocomposites. This is partly because of the fact that the formation of anything approaching ideal PP nanocomposites has been unsuccessful. Therefore, as stated previously, most work has focused on the preparation and characterization of PP nanocomposites.

Early studies by Toyota workers, led by Hasegawa et al.,<sup>[42]</sup> focused on the increase of the dynamic storage modulus. PP/PP-MA/C18-mmt nanocomposites were formed, e.g., by blending 5 wt.% mmt and 22 wt.% PP-MA (MA acid number 52 mg KOH/g) with isotactic PP. It was found that only large concentrations of PP-MA afforded reasonable clay dispersion; however, even in these type blends partial exfoliation and partial intercalation (as intercalated tactoids of mmt) were observed in TEM measurements. In the nanocomposite blend cited above, the storage modulus was 1.8 times higher than that of the corresponding PP at 80°C. Hasegawa et al.<sup>[43]</sup> prepared PP-MA (0.2 wt.% MA)/C18-mmt (5.3 wt.% mmt) nanocomposites, which exhibited apparently complete exfoliation of the mmt, and had 1.9 times higher tensile modulus than the PP-MA matrix polymer. However, a simple PP/C<sub>18</sub>-mmt composite had a slightly higher tensile modulus than this PP-MA/C18-mmt nanocomposite.

Reichert et al.<sup>[14]</sup> made an extensive study of PP/PP-MA/synthetic clay compounds prepared with fluoromica-modified synthetic clays, organically modified with alkyl chains ranging in length from C<sub>4</sub> to C<sub>18</sub>.

These workers found that 10 wt.% synthetic clay modified with C<sub>16</sub> organic modifier in conjunction with 20 wt.% PP-MA with 4.2 wt.% MA was sufficient to achieve effective PP matrix reinforcement. This nanocomposite exhibited exfoliated and well-dispersed silicate layers in the TEM and an increase in Young's modulus from 1490 to 3460 MPa and yield stress from 33 to 44 MPa with respect to bulk PP. However, notched Izod impact strength decreased from 1.7 to 1.4 kJ/m<sup>2</sup> with respect to bulk PP.

In other studies, polypropylene/clay nanocomposites exhibited enhancements in tensile strength and modulus<sup>[44]</sup> and also flexural strength and modulus.<sup>[45]</sup> Improvements in tensile properties were shown to be accompanied by maintenance or modest increases in fracture toughness.<sup>[46,47]</sup>

Monotonic increase in tensile modulus and decrease in elongation at break were observed for PP-MA/tallow-mmt nanocomposites up to 20 wt.% clay.<sup>[48]</sup> Tensile modulus increased rapidly up to about 5 wt.% clay, but then remained constant up to about 15 wt.% clay and then decreased at up to 20 wt.% clay. Notched impact strength remained approximately constant up to 20 wt.% clay, exhibiting modest increases between about 3 and 10 wt.% clay. The best mechanical properties were observed for the highest molecular weight PP-MA.

In a study of PP/PP-MA/C<sub>16</sub>-mmt nanocomposites, it was found that the best intercalation efficiency was achieved by the highest concentration of PP-MA (20–30 wt.%) and by a higher concentration of MA (0.9 wt.% better than 0.6 wt.%) in the PP-MA.<sup>[12]</sup> Tensile strength and notched Izod impact strength were found to increase and then decrease according to similar patterns, as shown in Figs. 9 and 10, as

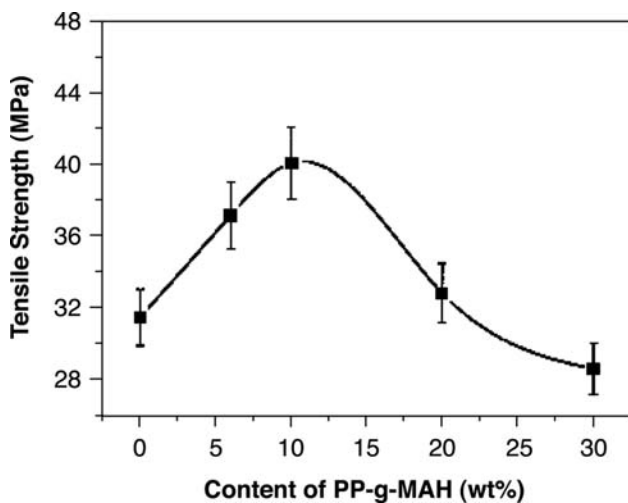


**Fig. 9.** Plot of tensile strength vs. concentration of PP-g-MAH. The mass percent of Org-MMT was 2 wt.%. *Source:* From Ref.<sup>[12]</sup> with permission from John Wiley and Sons, Inc.

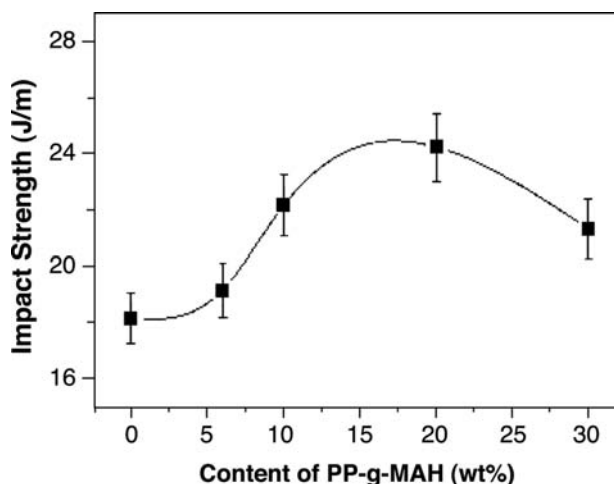


**Fig. 10.** Plot of impact strength vs. concentration of PP-g-MAH. The mass percent of Org-MMT was 2 wt.%. *Source:* From Ref.<sup>[12]</sup> with permission from John Wiley and Sons, Inc.

PP-MA concentration in the nanocomposite increased at 2 wt.% mmt concentration. Attempts to intercalate the same clay with the bulk polypropylene indicated little or no entry of the PP into the clay galleries.

The incorporation of radiation-grafted SiO<sub>2</sub> nanoparticles into polypropylene was shown to lead to well-dispersed SiO<sub>2</sub> nanoparticles grafted to the PP homopolymer matrix.<sup>[49]</sup> Reinforcement and toughening of the PP matrix were observed at concentrations between 0.5 and 5 wt.% SiO<sub>2</sub>.

The micromechanics of nanocomposites reinforced with platelet-shaped fillers was addressed by the development of a theoretical model.<sup>[50]</sup> The model was aimed at predicting the buckling of platelets in reinforced materials under compressive loading. The model predicted a critical strain above which platelet buckling would lead to reduction in the compressive modulus relative to the tensile modulus. The model predicted a significant reduction in reinforcement efficiency as a result of incomplete exfoliation of platelets into “pseudoparticle” stacks containing polymer layers sandwiched between successive clay platelets (tactoids), rather than into individual perfectly exfoliated and well-dispersed platelets. The model also predicted the reduction of reinforcement efficiency as a result of the deviation of the platelet from perfect biaxial in-plane orientation.

The common finding in these studies of the mechanical properties of polypropylene nanocomposites is that a large concentration of PP-MA is necessary to produce intercalated and exfoliated compounds with polypropylene. The nanocomposites exhibit imperfect dispersion of the clay with morphologies containing partial intercalated tactoids and partial exfoliated clay platelets. The improvements of polypropylene properties (tensile and toughness) are

typically not sufficient to justify the additional costs to modify the polypropylene.

## RHEOLOGY

The effects of clay and the orientation of the clay platelets on the rheology of polypropylene nanocomposites have been an area of particular interest, secondary to mechanical properties.<sup>[25,51–59]</sup> The rheological response of PP/PP-MA/mmt nanocomposites was studied.<sup>[58,59]</sup>

Lele et al. found that the zero-shear viscosity of the compatibilized nanocomposites (PP/PP-MA/tallow-mmt) was at least 3 orders of magnitude higher than that of the matrix PP and the uncompatibilized hybrids, as shown in Fig. 11. The strong dependence of melt viscosity on clay concentration was claimed to arise from frictional interactions between the silicate layers and not because of immobilization of confined chains between silicate layers. At low shear rates, a 3-D percolated structure of dispersed clay tactoids

having a high zero-shear viscosity was postulated. At higher shear rates, this network was speculated to break, imparting a solid-like behavior to the melt, which exhibited yielding and decreasing viscosity as shear rate increased. Rheo-XRD experiments gave direct evidence of flow-induced orientation of the clay tactoids. Yielding was linked to the cooperative orientation of the clay. The rheological data for the uncompatibilized hybrid exhibited a much lower zero-shear viscosity and much less pronounced yield behavior, and the corresponding rheo-XRD data showed a smaller orientation of the clay tactoids.

This dramatic increase in low shear rate viscosity has been utilized to prepare polypropylene homopolymers and copolymers/clay compounds with improved melt strength in extrusion for the production of films, fibers, and a variety of molded articles.<sup>[60]</sup> The rheology of such clay compounds was shown to be controllable by the variation of the ratio of PP-MA compatibilizer/clay.

## BARRIER

The enhancement of barrier properties of polypropylene is obviously an important application for nanocomposites. The platelet morphology of dispersed clay would be expected to impart enhanced barrier properties to fabricated articles, and extraordinary barrier properties might be imparted by the preferential orientation of the platelets in such fabricated articles. Blow-molded containers, based on high-density polyethylene (HDPE)/mmt nanocomposites, were shown to have a much higher barrier to organic liquids compared with the neat HDPE.<sup>[61]</sup> The HDPE was melt-compounded with mmt, and the blow-molding process was optimized to obtain a high degree of orientation of the exfoliated clay platelets to maximize barrier performance. However, there have been only a few reports concerning the enhancement of barrier properties in polypropylene.<sup>[6,62]</sup> These workers reported that the permeability of PP/PP-MA/mmt or PP-MA/mmt nanocomposites, containing 4 wt.% mmt, was one-half of that of the matrix material, while solvent uptake was also decreased accordingly.

## FLAMMABILITY AND THERMAL STABILITY

Montmorillonite-based fillers have been shown to promote flame retardancy in polypropylene composites. The mechanism of this flame-retardant behavior has been shown to be based on the formation of a carbonaceous-char layer on the outer surface of the composite article by Gilman et al.<sup>[63]</sup> The surface char layer was found to have a high concentration of mmt

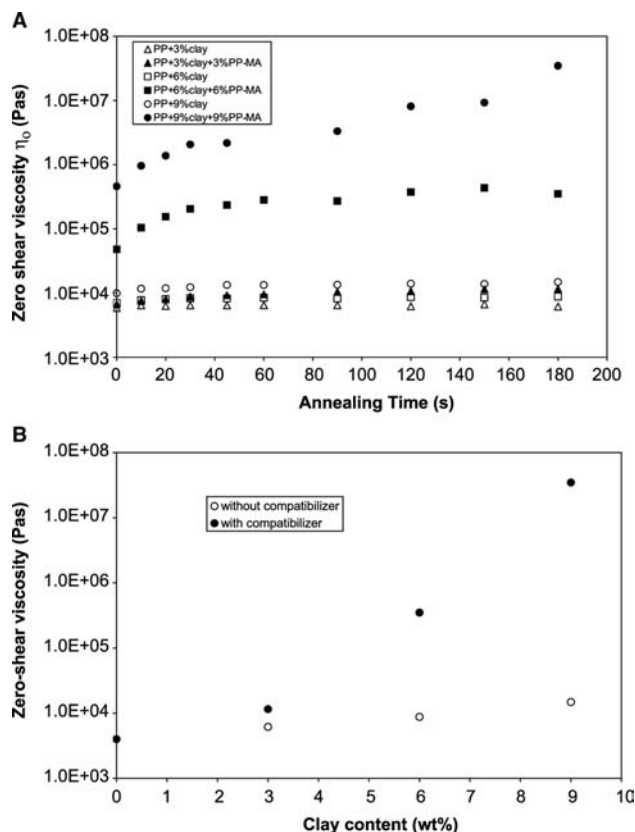


**Fig. 11.** (A) Zero shear viscosity as a function of annealing time for several PPCH samples in the presence (denoted by filled symbols) and absence (denoted by open symbols) of PP-MA. (B) Zero-shear viscosity as a function of clay content for samples with and without compatibilizer. *Source:* From Ref.<sup>[58]</sup> with permission from the American Chemical Society.

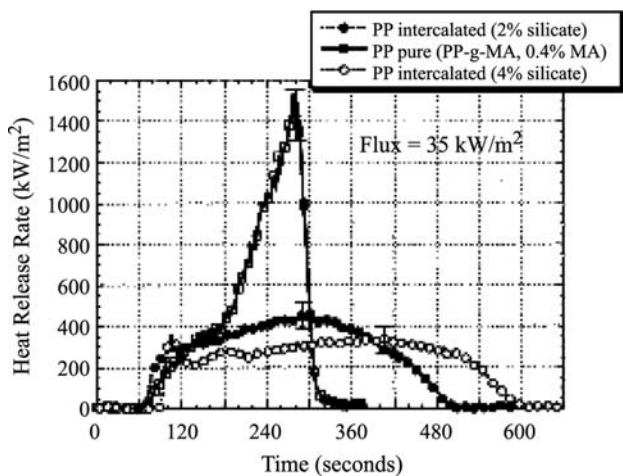


**Fig. 12.** Comparison of the heat release rate (HRR) for pure PPgMA and two PPgMA-layered silicate nanocomposites, at  $35 \text{ kW/m}^2$  heat flux, showing a 70–80% reduction in peak HRR for the nanocomposites with a mass fraction of only 2 or 4 wt.% layered silicate, respectively. *Source:* From Ref.<sup>[63]</sup> with permission from the American Chemical Society.

layers and was claimed to become an excellent insulator and mass transport barrier, slowing oxygen diffusion into the surface and the escape of combustion products out of the surface. These workers showed that the heat release rate (HRR) was 75% lower for PP-MA/mmt (4 wt.%) nanocomposite compared with the neat PP-MA matrix (Fig. 12). In addition, the mass loss rate (MLR) of the same PP-MA/mmt (4 wt.%) nanocomposite was about one-quarter of that of the PP-MA matrix polymer (Fig. 13). These workers further found that the type of layered silicate, degree of dispersion, and the processing conditions affected the magnitude of the flammability reduction in the nanocomposites.

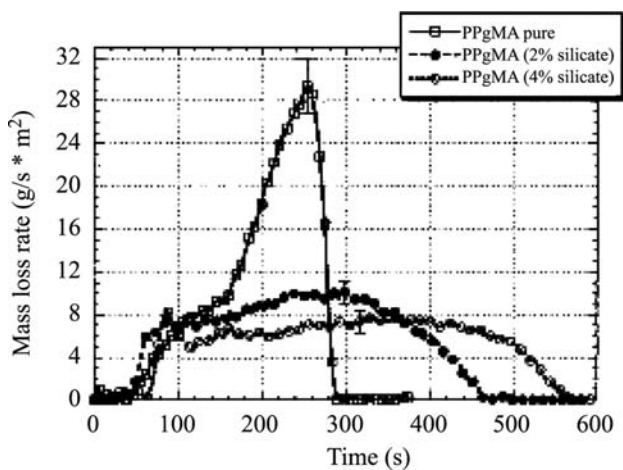


**Fig. 13.** Mass loss rate plots for PPgMA and two PPgMA-layered silicate nanocomposites. *Source:* From Ref.<sup>[63]</sup> with permission from the American Chemical Society.

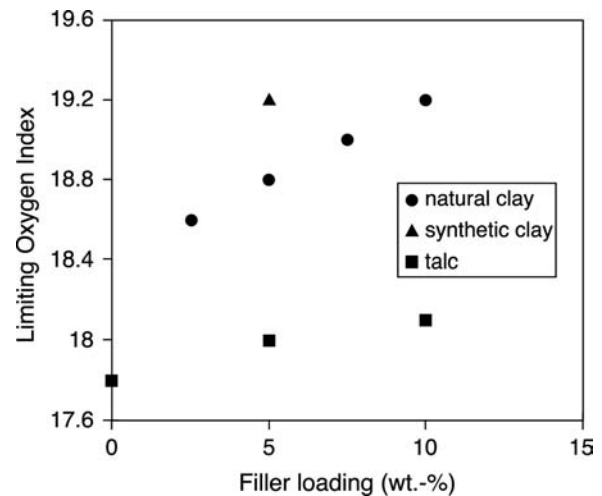


**Fig. 14.** Limiting oxygen index of composites with different inert fillers. *Source:* From Ref.<sup>[64]</sup> with permission from John Wiley and Sons, Inc.

In another study, similar results were obtained and explained by a similar mechanism, based on the formation of a char layer.<sup>[64]</sup> A comparison was made between nanocomposites, based on a PP-MA matrix, containing 2.5 to 10 wt.% clay, with talc composites having the same PP-MA matrix. It was found that the limiting oxygen index (LOI, ASTM 2863-87) was increased for the PP-MA/clay nanocomposites over the talc composites (Fig. 14). Furthermore, the time from ignition to the first occurrence of dripping was shown to increase with clay loading (Fig. 15). Burning was reported to be much less intensive in the nanocomposites in comparison to the neat matrix polymer. In addition, ash layers of about 1 mm in thickness were formed on the nanocomposites, which were correlated with the minimization of burning intensity and

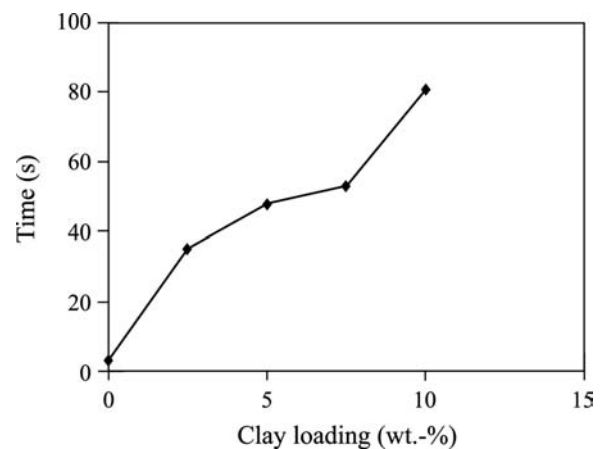


**Fig. 15.** Time from taking off the gas flame from the sample to the dripping of first burning parts. *Source:* From Ref.<sup>[64]</sup> with permission from John Wiley and Sons, Inc.

dripping. In other studies, it was similarly reported that HRR and time-to-ignition were reduced in PP/clay nanocomposites.<sup>[6,65,66]</sup>

The detailed thermal behavior and the formation of char layers on PP/PP-MA/clay nanocomposites were reported.<sup>[67]</sup> The thermal oxidation process of the polymer was significantly slowed in the nanocomposites exhibiting high char yield. The inhibition of oxidation was explained on the basis of a physical barrier effect of the surface char layer, by ablative reassembling of the silicate and by a chemical catalytic action, because of the silicate and of the amine modifier on the silicate.

## HEAT DEFLECTION TEMPERATURE

The heat deflection temperature (HDT) of a PP/fluoro-organo-mmt nanocomposite was found to increase from 109°C to 152°C compared to the neat PP.<sup>[6]</sup> The increase in HDT was attributed to better mechanical stability of the nanocomposite and not to an increase in melting temperature, which remained invariant in the nanocomposite relative to the neat PP.

## ELECTRICAL PROPERTIES

A process to prepare electrically conducting PP-MA/graphite nanocomposites was reported.<sup>[68]</sup> It was found that the percolation threshold for conductivity was much lower than that of conventional conducting composites.

## THERMOPLASTIC OLEFINS

Although the vast majority of work that has been published, relative to propylene-based polymers, concerns the development of polypropylene nanocomposites, there has been little incentive to commercially produce these compositions. Polypropylene is a very low cost commodity thermoplastic and the improvements in the properties so far demonstrated for polypropylene nanocomposites have not justified the increased cost to produce nanocomposites commercially.

On the other hand, far more interest has been generated in developing thermoplastic olefin (TPO) nanocomposites. The applications of TPOs, especially targeted for nanocomposite development, are those in the automotive sector. Thermoplastic olefins are usually reinforced with large quantities (up to 50 vol.%) of mineral fillers, such as talc and calcium carbonate. The outlook of replacing these conventional composites with lighter weight and better-performing nanocomposites has driven intensive efforts to achieve this objective. Because of the much

higher cost basis of TPOs, relative to polypropylene homopolymer, this objective appears to be much easier to achieve.

Some relative disadvantages of PP are that it is brittle and has poor low-temperature properties. However, the addition of a rubber, such as ethylene-propylene rubber (EPR), or ethylene-propylene-diene-monomer (EPDM) results in dramatic improvements in the impact strength and low-temperature properties. These rubber-modified PPs have a greatly expanded sphere of applications, relative to PP, and are often called impact copolymer-polypropylene (ICP) and thermoplastic olefins (TPOs). Rubber toughening of polypropylene continues to be an active area of investigation.<sup>[69]</sup> It is well known from previous studies that, among other factors, the rubber particle diameter is of critical importance.<sup>[69–71]</sup> These studies indicate that the modification in the rubber domain size to an optimum diameter improves the impact strength of PP. It is also well known that the addition of the rubber to polypropylene results in a decrease in stiffness.<sup>[72]</sup> Thus although successes in improving the impact properties of PP have been attained by rubber toughening, its application, e.g., in the automotive industry, is still limited because of the opposing trends of stiffness and toughness.

An attractive strategy to improve the stiffness, while maintaining the impact strength of PP and rubber-modified PP, is the formation of nanocomposites. Addition of mineral fillers, such as talc, CaCO<sub>3</sub>, and glass to PP, provides an increase in stiffness, but these particulates are stress concentrators and result in concomitant decrease in impact strength.<sup>[73,74]</sup> The fact that the filler is at the nanometer-size scale in these systems gives promise of achieving improved stiffness without significant loss of impact strength.<sup>[75]</sup> This is under the assumption that the clay platelets do not act as stress concentrators because of their nanometer size scale. Thus this desirable combination of improved stiffness and maintenance of impact strength by the addition of clay in TPOs, if attained, could boost the application of TPOs in the automotive and other industries.

For example, Oldenbo<sup>[76]</sup> from Volvo Car Corp., Sweden, recently presented data regarding the effect of addition of clay on the impact and flexural properties of TPO/clay nanocomposites. The desirable combination of improvement in stiffness and maintenance of impact strength was not observed in that study. Monotonic increase in stiffness was observed, but a precipitous decrease in impact was observed, as clay loading increased. The decrease in impact strength was ascribed to the lack of good dispersion of the clay. The existence of clay tactoids and “chunks” was supposed to be the cause of poor impact strength because these acted as stress concentrators.



Very little work has been published on the development of TPO nanocomposites. Much of what has been published resulted from the joint development of TPO nanocomposites for injection-molded automotive components by General Motors Research and Basell Polyolefins. This joint development was described in a publication, which highlighted the process ability advantages of a TPO/clay nanocomposite over a conventional TPO/talc composite.<sup>[77]</sup> This TPO nanocomposite is covered in patents assigned to Basell Poliolefine Italia S.p.A.<sup>[78]</sup> and Basell Technology Company BV.<sup>[79]</sup> No reports on the morphology and the specific degree of intercalation and exfoliation of the clay in the material developed by General Motors Research and Basell Polyolefins have been published.

This development and other similar developments of TPO/clay nanocomposites for automotive and other applications were heavily reported in the trade literature.<sup>[80–87]</sup> In one of these trade journal articles, it was claimed that, “much of the development work done before 1998 with natural montmorillonites having amorphous silica impurities is of little practical value.”<sup>[83]</sup> This claim was based on the proposition that large proportions of amorphous silica in the clay substantially degrade impact strength and elongation, increase opacity or haze levels, and increase gas permeability.

A study of the requirements for preparing exfoliated TPO/C<sub>18</sub>-mmt nanocomposites was reported.<sup>[88]</sup> It was noted that nanocomposite properties were dependent not only on exfoliation of the clay, but also on the structure and properties of the silicate / polymer matrix interface. The optimization of the organoclay structure for the maximum enhancement of TPO/clay nanocomposite mechanical properties was discussed.

The effect of varying clay loading on the morphology of TPO/clay nanocomposites was studied using atomic force microscopy, transmission electron microscopy, and X-ray diffraction.<sup>[89]</sup> Thermoplastic olefin/clay nanocomposites were made at clay loadings varying from 0.6 to 6.7 wt.%. The morphology of these TPO/clay nanocomposites was investigated with atomic force microscopy (AFM), transmission electron microscopy (TEM), and X-ray diffraction (XRD). The ethylene-propylene rubber (EPR) particle morphology in the TPO was found to undergo progressive particle breakup and decrease in particle size, as clay loading increased in the range from 0.6 to 5.6 wt.% clay. Transmission electron micrographs showed that the clay platelets preferentially segregate to the rubber–particle interface. The breakup of the EPR particles was suspected to be a result of the increasing melt viscosity observed as clay loading increased and/or the accompanying chemical modifiers on the clay, acting as interfacial agents, reducing the interfacial tension with concomitant reduction in particle size. The clay

morphology was mainly as intercalated tactoids with a minor amount of exfoliated and dispersed clay platelets evident in the TEM photomicrographs. Flexural modulus increased monotonically as clay loading increased. Impact strength was maintained or decreased modestly as clay loading increased.

## CONCLUSION

Polypropylene is one of the most widely used thermoplastics not only because of its balance of physical and mechanical properties, but also because of its environmental friendliness (e.g., recyclability) and low cost. Although the addition of mineral fillers to polypropylenes enhances the stiffness properties, the concomitant effect is typically a decrease in toughness properties because the inorganic filler particles act as stress concentrators. Therefore the formation of propylene-based polymer/clay nanocomposites is an area of intensive investigation.

Considering that clay is composed of platelets that are about 1 nm in thickness and around 1000 nm in lateral dimensions and assuming a density of 2.65 g/cm<sup>3</sup> yields an upper limit of about 750 m<sup>2</sup>/g surface area per gram for fully exfoliated clay. This is 5 to 10 times the surface area per gram achievable with ordinary mineral fillers. Exfoliated clay in polymers has been shown to endow unique properties to the system, such as increased T<sub>g</sub>, increased stiffness, maintenance of impact strength, increased barrier to gases and liquids, increased flame retardancy, etc.

The tightly bound stacks of clay platelets in natural clay may be readily separated by simple dissolution in a polar solvent; however, separation of the clay platelets in a nonpolar polymer is difficult. Therefore organic modification of natural clay minerals is required to disperse the clay in polypropylenes. This typically involves exchange of cations on the natural clay with alkyl ammonium cations with alkyl chains of varying lengths. However, the vast majority of experimental studies and commercial developments employ polypropylene with maleated polypropylene (PP-MA), or more rarely another functionalized PP, as a compatibilizer to form PP/clay nanocomposites with reasonable dispersion of the clay.

These polypropylene nanocomposites have exhibited enhancements in mechanical properties, rheological properties, barrier to gases and liquids, flammability, thermal stability, heat deflection temperature, and electrical properties. Although the majority of work that has been published, relative to propylene-based polymers, concerns the development of polypropylene nanocomposites, there has been little incentive to commercially produce these compositions because polypropylene is a very low cost commodity

thermoplastic and the improvements in the properties so far demonstrated have not justified the increased cost to produce nanocomposites commercially.

On the other hand, far more interest has been generated in developing thermoplastic olefin (TPO) nanocomposites. The applications of TPOs, especially targeted for nanocomposite development, are those in the automotive sector. The major initiative in the development of TPO nanocomposites was that of General Motors Research and Basell Polyolefins to develop TPO nanocomposites for injection-molded automotive components. Automotive TPOs are usually reinforced with large quantities (up to 50 vol.%) of mineral fillers, such as talc and calcium carbonate. Replacing these conventional composites with lighter weight and better-performing TPO nanocomposites has driven these efforts. Because of the much higher cost basis of TPOs, relative to polypropylene homopolymer, this objective appears to be much easier to achieve. The processability advantages of a TPO/clay nanocomposite over a conventional TPO/talc composite have been reported, but no reports on the morphology and the specific degree of intercalation and exfoliation of the clay in the material developed by General Motors Research and Basell Polyolefins have been published.

Therefore the state of development of polypropylene homopolymer or TPO nanocomposites is currently in an early stage. From the technical standpoint, the formation of nanocomposites with uniformly dispersed clay remains a daunting challenge. From the commercial standpoint, the production of economically viable nanocomposites, i.e., with properties enhanced to the extent that the increased cost of production is justified, also remains a daunting challenge. Certainly, the research that is progressively reported, which better defines and innovates upon the structure and properties of polypropylene and TPO nanocomposites, continues to spur interest in commercial development. The outlook remains bright, but formidable challenges, both technical and commercial, abound.

## REFERENCES

- Kojima, Y.; Usuki, A.; Kawasumi, M.; Okada, A.; Fukushima, Y.; Kurauchi, T.; Kamigaito, O. Mechanical properties of nylon 6–clay hybrid. *J. Mater. Res.* **1993**, *8* (5), 1185–1189.
- Kojima, Y.; Usuki, A.; Kawasumi, M.; Okada, A.; Kurauchi, T.; Kamigaito, O. Synthesis of nylon-6–clay hybrid by montmorillonite intercalated with epsilon-caprolactam. *J. Polym. Sci., Part A, Polym. Chem.* **1993**, *31* (4), 983–986.
- Usuki, A.; Kojima, Y.; Kawasumi, M.; Okada, A.; Fukushima, Y.; Kurauchi, T.; Kamigaito, O. Synthesis of nylon 6–clay hybrid. *J. Mater. Res.* **1993**, *8* (5), 1179–1184.
- Vaia, R.A.; Ishii, H.; Giannelis, E.P. Polymer-layered silicate nanocomposites: In situ intercalative polymerization of epsilon-caprolactone in layered silicates. *Chem. Mater.* **1993**, *5* (8), 1064–1066.
- Manias, E.; Chen, H.; Krishnamoorti, R.; Genzer, J.; Kramer, E.J.; Giannelis, E.P. Intercalation kinetics of long polymers in 2 nm confinements. *Macromolecules* **2000**, *33* (21), 7955–7966.
- Manias, E.; Touny, A.; Wu, L.; Strawhecker, K.; Lu, B.; Chung, T.C. Polypropylene/montmorillonite nanocomposites. Review of the synthetic routes and materials properties. *Chem. Mater.* **2001**, *13* (10), 3516–3523.
- Wilson, P.S. Nanocomposite Market Opportunities. In *Nanocomposites 2001: Delivering New Value to Plastics*, Executive Conference Management, Chicago, June 25–27, 2001; Plymouth, MI, 2001.
- Sinclair, K. The Market Potential for Nanocomposites: Quantifying the Opportunities. In *Nanocomposites 2001: Delivering New Value to Plastics*, Executive Conference Management, Chicago, June 25–27, 2001; Plymouth, MI, 2001.
- Kato, M.; Usuki, A.; Okada, A. Synthesis of polypropylene oligomer–clay intercalation compounds. *J. Appl. Polym. Sci.* **1997**, *66* (9), 1781–1785.
- Usuki, A.; Kato, M.; Okada, A.; Kurauchi, T. Synthesis of polypropylene–clay hybrid. *J. Appl. Polym. Sci.* **1997**, *63* (1), 137–139.
- Kawasumi, M.; Hasegawa, N.; Kato, M.; Usuki, A.; Okada, A. Preparation and mechanical properties of polypropylene–clay hybrids. *Macromolecules* **1997**, *30* (20), 6333–6338.
- Xu, W.; Liang, G.; Wang, W.; Tang, S.; He, P.; Pan, W.-P. PP-PP-g-MA-Org-MMT nanocomposites. I. Intercalation behavior and microstructure. *J. Appl. Polym. Sci.* **2003**, *88* (14), 3225–3231.
- Walter, P.; Mader, D.; Reichert, P.; Mulhaupt, R.J. Novel polypropylene materials. *J. Macromol. Sci., Pure Appl. Chem.* **1999**, *A36*, 1613–1639.
- Reichert, P.; Nitz, H.; Klinke, S.; Brandsch, R.; Thomann, R.; Mulhaupt, R. Poly(propylene)/organoclay nanocomposite formation: Influence of compatibilizer functionality and organoclay modification. *Macromol. Mater. Eng.* **2000**, *275* (2), 8–17.
- Hofmann, U. The chemistry of clays possessing a high swelling capacity (bentonites). *Angew. Chem.* **1956**, *68*, 53–61.
- Weiss, A. Organic derivatives of micaceous layered silicates. *Angew. Chem.* **1963**, *75*, 113–122.
- Reichert, P.; Hoffmann, B.; Bock, T.; Thomann, R.; Mulhaupt, R.; Friedrich, C. Morphological stability of poly(propylene) nanocomposites. *Macromol. Rapid Commun.* **2001**, *22* (7), 519–523.
- Southern Clay Products Inc. *Material Safety Data Sheet, Cloisite 15A and 20A*.
- Morgan, A.B.; Gilman, J.W. Characterization of polymer-layered silicate (clay) nanocomposites by transmission electron microscopy and X-ray diffraction: A comparative study. *J. Appl. Polym. Sci.* **2003**, *87* (8), 1329–1338.

20. Kim, K.-N.; Kim, H.; Lee, J.-W. Effect of interlayer structure, matrix viscosity and composition of a functionalized polymer on the phase structure of polypropylene–montmorillonite nanocomposites. *Polym. Eng. Sci.* **2001**, *41* (11), 1963–1969.
21. Zhang, Q.; Wang, Y.; Fu, Q. Shear-induced change of exfoliation and orientation in polypropylene/montmorillonite nanocomposites. *J. Polym. Sci., Part B, Polym. Phys.* **2003**, *41* (1), 1–10.
22. Chen, L.; Wong, S.-C.; Pisharath, S. Fracture properties of nanoclay-filled polypropylene. *J. Appl. Polym. Sci.* **2003**, *88* (14), 3298–3305.
23. Liu, X.; Wu, Q. PP/clay nanocomposites prepared by grafting–melt intercalation. *Polymer* **2001**, *42* (25), 10013–10019.
24. Kaempfer, D.; Thomann, R.; Mulhaupt, R. Melt compounding of syndiotactic polypropylene nanocomposites containing organophilic layered silicates and in situ formed core/shell nanoparticles. *Polymer* **2002**, *43* (10), 2909–2916.
25. Koo, C.M.; Kim, S.O.; Chung, I.J. Study on morphology evolution, orientational behavior, and anisotropic phase formation of highly filled polymer-layered silicate nanocomposites. *Macromolecules* **2003**, *36* (8), 2748–2757.
26. Somwangthanoj, A.; Lee, E.C.; Solomon, M.J. Early stage quiescent and flow-induced crystallization of intercalated polypropylene nanocomposites by time-resolved light scattering. *Macromolecules* **2003**, *36* (7), 2333–2342.
27. Marchant, D.; Jayaraman, K. Strategies for optimizing polypropylene–clay nanocomposite structure. *Ind. Eng. Chem. Res.* **2002**, *41* (25), 6402–6408.
28. Ma, J.; Qi, Z.; Hu, Y. Synthesis and characterization of polypropylene/clay nanocomposites. *J. Appl. Polym. Sci.* **2001**, *82* (14), 3611–3617.
29. Vaia, R.A.; Giannelis, E.P. Lattice model of polymer melt intercalation in organically-modified layered silicates. *Macromolecules* **1997**, *30* (25), 7990–7999.
30. Vaia, R.A.; Giannelis, E.P. Polymer melt intercalation in organically-modified layered silicates: Model predictions and experiment. *Macromolecules* **1997**, *30* (25), 8000–8009.
31. Fornes, T.D.; Yoon, P.J.; Keskkula, H.; Paul, D.R. Nylon 6 nanocomposites: The effect of matrix molecular weight. *Polymer* **2001**, *42* (25), 9929–9940.
32. Schon, F.; Thomann, R.; Gronski, W. Shear controlled morphology of rubber/organoclay nanocomposites and dynamic mechanical analysis. *Macromol. Symp.* **2002**, *189* (1), 105–110.
33. Xu, W.; Ge, M.; He, P. Nonisothermal crystallization kinetics of polypropylene/montmorillonite nanocomposites. *J. Polym. Sci., Part B, Polym. Phys.* **2002**, *40* (5), 408–414.
34. Hambir, S.; Bulakh, N.; Jog, J.P. Polypropylene/clay nanocomposites: Effect of compatibilizer on the thermal, crystallization and dynamic mechanical behavior. *Polym. Eng. Sci.* **2002**, *42* (9), 1800–1807.
35. Pozsgay, A.; Frater, T.; Papp, L.; Sajo, I.; Pukanszky, B. Nucleating effect of montmorillonite nanoparticles in polypropylene. *J. Macromol. Sci., Phys.* **2002**, *B41* (4–6), 1249–1265.
36. Maiti, P.; Nam, P.H.; Okamoto, M.; Hasegawa, N.; Usuki, A. Influence of crystallization on intercalation, morphology, and mechanical properties of polypropylene/clay nanocomposites. *Macromolecules* **2002**, *35* (6), 2042–2049.
37. Nam, P.H.; Maiti, P.; Okamoto, M.; Kotaka, T.; Hasegawa, N.; Usuki, A. A hierarchical structure and properties of intercalated polypropylene/clay nanocomposites. *Polymer* **2001**, *42* (23), 9633–9640.
38. Hambir, S.; Bulakh, N.; Kodgire, P.; Kalgaonkar, R.; Jog, J.P. PP/clay nanocomposites: A study of crystallization and dynamic mechanical behavior. *J. Polym. Sci., Part B, Polym. Phys.* **2001**, *39* (4), 446–450.
39. Maiti, P.; Nam, P.H.; Okamoto, M.; Kotaka, T.; Hasegawa, N.; Usuki, A. The effect of crystallization on the structure and morphology of polypropylene/clay nanocomposites. *Polym. Eng. Sci.* **2002**, *42* (9), 1864–1871.
40. Svehlova, V.; Poloucek, E. Mechanical-properties of talc-filled polypropylene—influence of filler content, filler particle-size and quality of dispersion. *Angew. Makromol. Chem.* **1994**, *214*, 91–99.
41. Maiti, S.N.; Mahapatro, P.K. Mechanical-properties of I-PP/CaCO<sub>3</sub> composites. *J. Appl. Polym. Sci.* **1991**, *42* (12), 3101–3110.
42. Hasegawa, N.; Kawasumi, M.; Kato, M.; Usuki, A.; Okada, A. Preparation and mechanical properties of polypropylene–clay hybrids using a maleic anhydride-modified polypropylene oligomer. *J. Appl. Polym. Sci.* **1998**, *67* (1), 87–92.
43. Hasegawa, N.; Okamoto, H.; Kato, M.; Usuki, A. Preparation and mechanical properties of polypropylene–clay hybrids based on modified polypropylene and organophilic clay. *J. Appl. Polym. Sci.* **2000**, *78* (11), 1918–1922.
44. Zhang, Q.; Wang, K.; Men, Y.; Fu, Q. Dispersion and tensile behavior of polypropylene/montmorillonite nanocomposites produced via melt intercalation. *Chin. J. Polym. Sci.* **2003**, *21* (3), 359–367.
45. Kodgire, P.; Kalgaonkar, R.; Hambir, S.; Bulakh, N.; Jog, J.P. PP/clay nanocomposites: Effect of clay treatment on morphology and dynamic mechanical properties. *J. Appl. Polym. Sci.* **2001**, *81* (7), 1786–1792.
46. Hernandez-Luna, A.; D’Souza, N.A.; Renade, A.; Drewniak, M. Skin-core Effects in Polypropylene Nanocomposites. In *Affordable Materials Technology: Platform to Global Value and Performance*, 47th International SAMPE Symposium, Long Beach, CA, May 12–16, 2002; Society for the Advancement of Material and Process Engineering: Covina, CA, 2002, 1100–1106.
47. Wong, S.-C.; Chen, L. Mechanical and Fracture Properties of Nanoclay-Filled Polypropylene. In *ANTEC 2002, San Francisco*; CA, May 5–9, 2002; Society of Plastics Engineers: Brookfield, CT, 2002; Vol. 2, 1466–1469.
48. Svoboda, P.; Zeng, C.; Wang, H.; Lee, L.J.; Tomasko, D.L. Morphology and mechanical properties of polypropylene/organoclay nanocomposites. *J. Appl. Polym. Sci.* **2002**, *85* (7), 1562–1570.
49. Rong, M.Z.; Zhang, M.Q.; Zheng, Y.X.; Zeng, H.M.; Walter, R.; Friedrich, K. Structure–property relationships of irradiation grafted nano-inorganic particle filled

- polypropylene composites. *Polymer* **2001**, *42* (1), 167–183.
50. Brune, D.A.; Bicerano, J. Micromechanics of nanocomposites: Comparison of tensile and compressive elastic moduli, and prediction of effects of incomplete exfoliation and imperfect alignment on modulus. *Polymer* **2002**, *43* (2), 369–387.
  51. Solomon, M.J.; Abdulwahab, A.S.; Seefeldt, K.F.; Somwangthanaroj, A.; Varadan, P. Rheology of polypropylene/clay hybrid materials. *Macromolecules* **2001**, *34* (6), 1864–1872.
  52. Reichert, P.; Bock, T.; Thomann, R.; Mulhaupt, R.; Friedrich, C. Morphological stability of poly(propylene) nanocomposites. *Macromol. Rapid Commun.* **2001**, *22* (7), 519–523.
  53. Marchant, D.; Jayaraman, K. Rheological Probing of Structure in Polypropylene/Clay Nanocomposites. In *ANTEC 2001*; Dallas, TX, May 6–10, 2001; Society of Plastics Engineers: Brookfield, CT, 2001; Vol. 2, 2130–2134.
  54. Krishnamoorti, R.; Ren, J.; Siva, A.S. Shear response of layered silicate nanocomposites. *J. Chem. Phys.* **2001**, *114* (11), 4968–4973.
  55. Nam, P.H.; Maiti, P.; Okamoto, M.; Kotaka, T.; Nakayama, T.; Takada, M.; Oshima, M. Foam processing and cellular structure of polypropylene/clay nanocomposites. *Polym. Eng. Sci.* **2002**, *42* (9), 1907–1918.
  56. Koo, C.M.; Kim, M.J.; Choi, M.H.; Kim, S.O.; Chung, I.J. Mechanical and rheological properties of the maleated polypropylene-layered silicate nanocomposites with different morphology. *J. Appl. Polym. Sci.* **2003**, *88* (6), 1526–1535.
  57. Boucard, S.; Duchet, J.; Gerard, J.F.; Prele, P.; Gonzalez, S. Processing of polypropylene–clay hybrids. *Macromol. Symp.* **2003**, *194* (1), 241–246.
  58. Galgali, G.; Ramesh, C.; Lele, A. A rheological study on the kinetics of hybrid formation in polypropylene nanocomposites. *Macromolecules* **2001**, *34* (4), 852–858.
  59. Lele, A.; Mackley, M.; Galgali, G.; Ramesh, C. In situ rheo-X-ray investigation of flow-induced orientation in layered silicate-syndiotactic polypropylene nanocomposite melt. *J. Rheol.* **2002**, *46* (5), 1091–1110.
  60. Mehta, S.D.; Shankernarayanan, M.J.; Mavridis, H. *PCT Application 03/022917 A1*; March 20, 2003.
  61. Kenig, S.; Ophir, A.; Shepelev, O.; Weiner, F. High Barrier Blow Molded Containers Based on Nano Clay Composites. In *ANTEC 2002, San Francisco, CA, May 5–9, 2002*; Society of Plastics Engineers: Brookfield, CT, 2002; Vol. 2, 794–798.
  62. Manias, E.; Touny, A.; Wu, L.; Lu, B.; Chung, T.C. Polypropylene/silicate nanocomposites, synthetic routes and materials properties. *Polym. Mater. Sci. Eng.* **2000**, *82*, 282–283.
  63. Gilman, J.W.; Jackson, C.L.; Morgan, A.B.; Harris, R., Jr.; Manias, E.; Giannelis, E.P.; Wuthenow, M.; Hilton, D.; Phillips, S.H. Flammability properties of polymer-layered-silicate nanocomposites. Polypropylene and polystyrene nanocomposites. *Chem. Mater.* **2000**, *12* (7), 1866–1873.
  64. Wagenknecht, U.; Kretzschmar, B.; Reinhardt, G. Investigations of fire retardant properties of polypropylene–clay-nanocomposites. *Macromol. Symp.* **2003**, *194* (1), 207–212.
  65. Wang, D.; Wilkie, C.A. In-situ reactive blending to prepare polystyrene–clay and polypropylene–clay nanocomposites. *Polym. Degrad. Stab.* **2003**, *80* (1), 171–182.
  66. Morgan, A.B.; Harris, J.D. Effects of organoclay Soxhlet extraction on mechanical properties, flammability properties and organoclay dispersion of polypropylene nanocomposites. *Polymer* **2003**, *44* (8), 2313–2320.
  67. Zanetti, M.; Camino, G.; Reichert, P.; Mulhaupt, R. Thermal behaviour of poly(propylene) layered silicate nanocomposites. *Macromol. Rapid Commun.* **2001**, *22* (3), 176–180.
  68. Shen, J.-W.; Chen, X.M.; Huang, W.-Y. Structure and electrical properties of grafted polypropylene/graphite nanocomposites prepared by solution intercalation. *J. Appl. Polym. Sci.* **2003**, *88* (7), 1864–1869.
  69. Jang, B.Z.; Uhlmann, D.R.; Vander Sande, J.B. Rubber-toughening in polypropylene. *J. Appl. Polym. Sci.* **1985**, *30* (6), 2485–2504.
  70. Jang, B.Z.; Uhlmann, D.R.; Vander Sande, J.B. The Rubber Particle Size Dependence of Crazing in Polypropylene. In *ANTEC 84*; Society of Plastics Engineers: Brookfield, CT, 1984; 549–551, New Orleans, LA, April 30–May 3, 1984.
  71. Mehrabzadeh, M.; Hossein Nia, K. Impact modification of polypropylene by ethylene propylene copolymer-grafted maleic anhydride. *J. Appl. Polym. Sci.* **1999**, *72* (10), 1257–1265.
  72. Lu, J.; Wei, G.-X.; Sue, H.-J.; Chu, J. Toughening mechanisms in commercial thermoplastic polyolefin blends. *J. Appl. Polym. Sci.* **2000**, *76* (3), 311–319.
  73. Radosta, J.A. Improving the Impact-Stiffness Balance of Mineral Filled Polyolefins with Surface Modified Talc. In *ANTEC 84*; New Orleans, LA, April 30–May 3, 1984; Society of Plastics Engineers: Brookfield, CT, 1984; 145–149.
  74. Marshall, C.J.; Rozett, R.; Kunkle, A.C. Effects of mica as a filler in polyolefins and PVC. *Plast. Compd.* **1985**, *8* (7), 69–74.
  75. Svoboda, P.; Zeng, C.; Wang, H.; Lee, L. Structure and Mechanical Properties of Polypropylene/Organoclay Nanocomposites. In *Nanocomposites 2001: Delivering New Value to Plastics*; Executive Conference Management, Plymouth, MI, 2001.
  76. Oldenbo, M. TPO-Nanocomposites for Automotive Exterior Bodypanels: Potentials and Experiences from Evaluations of Commercial Materials. In *Nanocomposites 2001: Delivering New Value to Plastics*; Executive Conference Management: Chicago, June 25–27, Plymouth, MI, 2001.
  77. Okonski, D.A. Injection molding a polyolefin-based nanocomposite versus a talc-filled TPO. *Mater. Res. Symp. Proc.* **2002**, *702*, 265–276.
  78. Bishop, C.E.; Niyogi, S.G. Intercalated Clay Useful for Making an Alpha-Olefin Polymer Material Nanocomposite. US Patent 6,500,892, December 31, 2002.
  79. Niyogi, S.G. Nanocomposites Made from Polypropylene Graft Copolymers. US Patent 6,451,897, September 17, 2002.
  80. US polymer manufactures are working on nanocomposites. *Addit. Polym.* **1999**, *1999* (2), 9–10.

81. Grande, J.A. Olefin-based nanocomposites hold potential for automotive. *Mod. Plast. Int.* **1999**, *29* (1), 35–36.
82. Garces, J.M.; Moll, D.J.; Bicerano, J.; Fibiger, R.; McLeod, D. Polymeric nanocomposites for automotive applications. *Adv. Mater.* **2000**, *12* (23), 1835–1839.
83. Mapleston, P. Tiny mineral fillers bring big benefits in compounding. *Mod. Plast. Int.* **2000**, *30* (11), 72–74.
84. Murphy, J. Nanocomposites—It's a question of picking the winners. *Plast. Addit. Compound.* **2000**, *2* (5), 30–32.
85. Leaversuch, R. Nanocomposites: Broaden roles in automotive, barrier packaging. *Plast. Technol.* **2001**, *47* (10), 64–69.
86. Nanocomposite body panels. *High Perform. Plast.* **2001**, 8–9.
87. Sall, K. Smaller is better. *Eur. Plast. News* **2002**, *29* (3), 14.
88. Merinska, D.; Malac, Z.; Hrnčirik, J.; Simonik, J.; Trlica, J.; Pospisil, M.; Capkova, P.; Weiss, Z. Modification of Clay Intercalate Structure and Properties of TPO Based Nanocomposites. In *ANTEC 2001*; Dallas, TX, May 6–10, 2001; Society of Plastics Engineers: Brookfield, CT, 2001; 2, 2166–2170.
89. Mehta, S.; Mirabella, F.M.; Rufener, K.; Bafna, A. TPO/clay nanocomposites: Morphology and mechanical properties. *J. Appl. Polym. Sci.* *in press*.

# Porous Alumina Templates for Nanofabrication

**Latika Menon**

*Department of Physics and the Center for Nanotechnology,  
Texas Tech University, Lubbock, Texas, U.S.A.*

## INTRODUCTION

Currently, nanotechnology is concerned with fabrication of useful materials at the nanoscale level for applications in nanodevices. Several methods are being used for nanofabrication,<sup>[1–10]</sup> e-beam lithography, interference lithography, cluster method, etc. One commonly used method is the use of membranes with nanosized holes. When the holes are filled up with appropriate materials, it leads to formation of a self-assembled nanoarray. Some commonly used membranes are polycarbonate membranes and nanoporous alumina membranes. Use of porous alumina membranes is particularly noteworthy.<sup>[11]</sup> These are aluminum oxide membranes with nanosized cylindrical holes perpendicular to the surface of the film. The membranes are available commercially in some fixed sizes with specific pore diameters. They can also be prepared very easily in the laboratory using electrochemical means. Fabrication conditions can be controlled to achieve desired pore length and diameter, and they can be used in many different ways to prepare a variety of nanostructured materials, magnetic metals and alloys, semiconductor alloys and heterostructures, superconductors, carbon nanotubes, etc. This entry briefly reviews some of the ongoing research in the area of nanofabrication using porous alumina templates.

## FABRICATION OF NANOPOROUS ALUMINA TEMPLATE

It is well known that a thin (2–5 nm) film of aluminum oxide always forms on the surface of aluminum exposed to air. This is because of oxidation of aluminum in the presence of oxygen and water vapor. The reactions occurring during the process are



and



The oxidation process can be hastened by anodizing or oxidizing aluminum in the presence of an acid. Anodization in a weak acid leads to formation of a non-porous barrier layer of aluminum oxide. In contrast, a strong acid can partially dissolve aluminum oxide. Anodization in a strong acid (pH < 4) therefore results in a porous aluminum oxide film (commonly known as porous alumina) because of a competing mechanism of oxide growth and partial dissolution of aluminum oxide by hydrogen ions.<sup>[12,13]</sup>

In the laboratory, a commercially available aluminum foil is first electropolished to create a clean, shiny, flat surface (roughness ~5–10 nm). Electropolishing is carried out under d.c. conditions in an electrolyte commonly called the L1 electrolyte. It consists of 1050 mL ethyl alcohol, 150 mL butyl cellosolve, 93 mL perchloric acid, and 205 mL distilled water. The optimum voltage is of the order of 30–60 V, and the optimum electropolishing time is of the order of 10–30 sec.<sup>[14–16]</sup> The electropolished Al surface is then anodized in the presence of an acid. In this process, the Al foil is placed at the anode, while a Pt mesh is used as cathode (Fig. 1). A d.c. voltage is applied across the two electrodes. A moderately strong acid (for example, 15% sulfuric acid, 3% oxalic acid, or 5% phosphoric acid) is used as electrolyte. During the process of anodization, a thin film of nanoporous aluminum oxide forms at the surface of aluminum as shown in the schematic cross-section diagram in Fig. 2.

The pores are cylindrical, straight, and are open at the top. The pores do not grow all the way into the aluminum surface. There is a thin barrier layer of aluminum oxide separating the porous alumina layer from the bottom aluminum layer. The thickness of the barrier layer and the diameter of the pores are controlled by fabrication conditions, namely, the acid used and the voltage applied. Some commonly used acids are 3% oxalic, 15% sulfuric, and 5% phosphoric acid. The smallest pore diameters are obtained by anodization in 15% sulfuric acid at low voltages, and the largest pore diameters are obtained for anodization in 5% phosphoric acid at higher voltages. Pore densities are typically of the order of  $10^{10}$ – $10^{11}$  pores/cm<sup>2</sup>. Barrier layer thickness is in the range of tens of



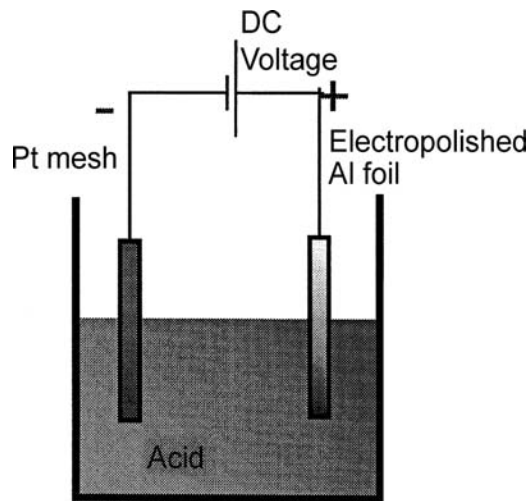


**Fig. 1** Schematic diagram showing a typical anodization process.

nanometers. Pore diameters are in the range of 8–200 nm. Theoretical modeling of pore growth and dependence of pore parameters on fabrication conditions are discussed in detail in Refs.<sup>[17–19]</sup> The length of the pores is controlled by time of anodization. Increased time of anodization leads to longer pore lengths. Some typical AFM images of templates prepared by anodization under different conditions are shown in Figs. 3 and 4. The pores are highly ordered over length scales of the order of 5–10  $\mu\text{m}$ . The extent of ordering can be increased slightly by annealing the Al foil prior to anodization and also by carrying out a multistep anodization process.<sup>[20]</sup> In a multistep process, Al foil is first anodized for a very long time (typically 12–18 hr). Long time anodization causes the pores to rearrange and reduces the number of

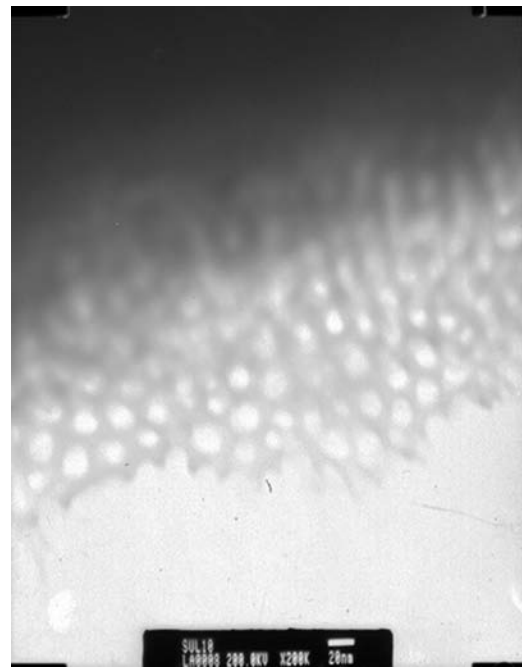


**Fig. 3** Transmission Electron Microscope image of a template anodized in 15% sulfuric acid at 10 V showing an array of pores with diameter  $\sim 10$  nm.

defects and dislocations. It also leads to formation of a very thick alumina template. The thick template is dissolved away in a 0.2 M chromic–0.4 M phosphoric acid mixture at 60°C which leaves behind a textured Al surface consisting of an array of ordered bumps.

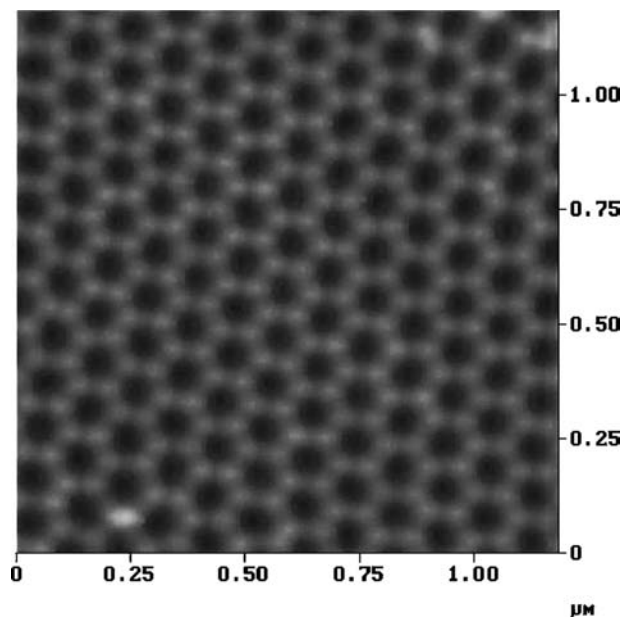


**Fig. 4** Atomic force microscopic image of a template anodized in 3% oxalic acid at 40 V showing an array of pores with diameter 50 nm.

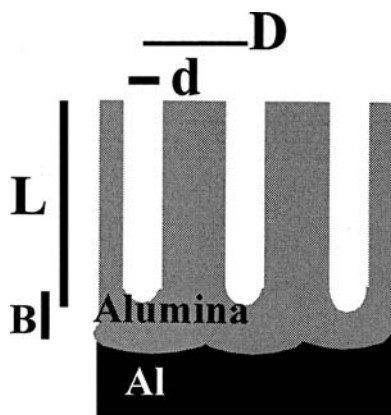


**Fig. 2** Schematic cross-sectional diagram of a typical porous alumina template showing the nanoporous layer, the barrier layer and the aluminum layer ( $L$  is the pore length,  $d$  is the pore diameter,  $D$  is the interpore spacing, and  $B$  is the thickness of the barrier layer).

Reanodization of the textured Al surface for the desired length of time leads to a well-ordered nanoporous template (Fig. 4). Instead of a multistep anodization process, an initial ordered nanoindentation of the Al surface can also be used to improve the ordering of the subsequent pore array.<sup>[21]</sup>

## NANOFABRICATION METHODS USING POROUS ALUMINA

Once the templates are fabricated with the desired pore size, they can be used in many different ways to fabricate nanoarrays. Some of these methods are discussed in this section.

### Electrodeposition

Alternating current electrodeposition is the simplest way to fill the pores with the appropriate material. For example, to prepare an array of Fe nanowires inside the pores, a 0.1 M aqueous solution of  $\text{FeSO}_4$  can be used. Porous alumina and the Pt mesh are the electrodes. An a.c. voltage is applied across the two electrodes. The frequency and voltage are optimized. In the solution,  $\text{FeSO}_4$  dissociates into  $\text{Fe}^{2+}$  ions and  $(\text{SO}_4)^{2-}$  ions. During every negative half-cycle, Fe ions are reduced to Fe atoms and deposit inside the pores.

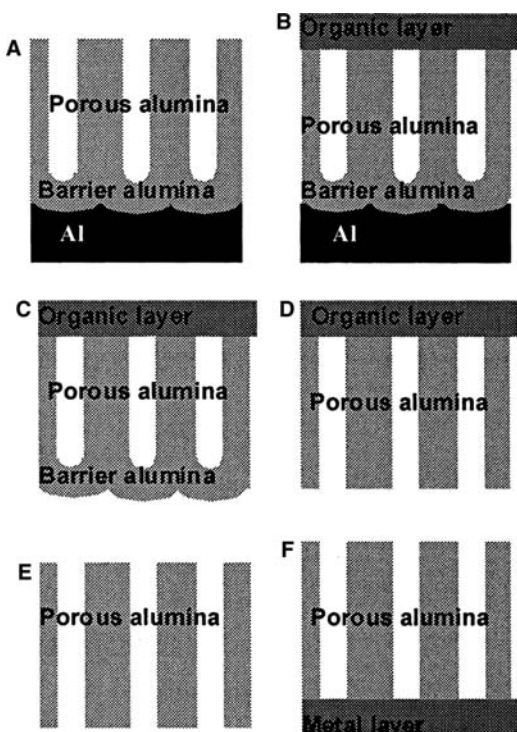


**Fig. 5** Sequence of steps to prepare a template in contact with a conducting substrate to achieve d.c. electrodeposition.

Fig. 5 shows a cross-section SEM image of a nanoporous alumina membrane containing Fe nanowires. Using a similar electrodeposition method, nanoarrays of other magnetic metals, for example, Co and Ni, can also be prepared. Alloys, for example, FeCo and CoNi, can be prepared by using an electrolyte containing the appropriate ratio of the constituent materials. The two materials are then subsequently electrodeposited into the pores under optimized a.c. conditions to create alloy nanoarrays. The magnetic properties of Fe, Co, Ni, and FeCo nanoarrays are discussed in “Magnetic Nanoarrays.” Other materials, for example, thermoelectric materials such as Bi,<sup>[22]</sup> superconducting Pb,<sup>[23]</sup> conducting materials Cu and Au,<sup>[24]</sup> and conducting polymers,<sup>[25]</sup> may also be synthesized inside the pores by using the appropriate electrolyte.

To carry out d.c. electrodeposition, the barrier layer below the pores must be removed. This can be achieved by following the sequence of steps shown in Fig. 6. The top nanoporous layer is first coated with a protective organic layer. The sample is then soaked in 3%  $\text{HgCl}_2$  solution to remove the bottom Al layer. This is followed by soaking in 5% phosphoric acid solution for a predetermined length of time to remove the alumina layer at the bottom. The top organic layer is finally removed by soaking in ethyl alcohol solution. This leaves behind a through-hole template. One side is coated with a thin conducting layer, e.g., Au. Using an appropriate electrolyte, nanowires can be deposited inside the pores under d.c. conditions, using a three-terminal setup and a potentiostat. The Pt mesh is used as the counterelectrode, porous alumina is used as the working electrode, and a third electrode, for example, calomel electrode, is used as reference electrode. The voltage between the reference electrode and the

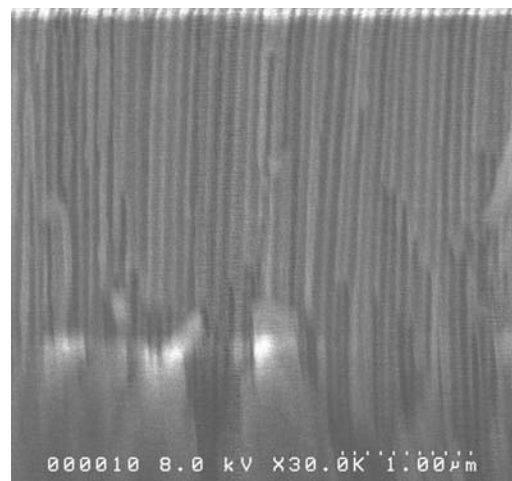


**Fig. 6** Scanning electron microscope cross-section image showing an array of pores containing Fe nanowires. Pore diameter  $\sim 50$  nm. *Source:* From J. Yun, Texas Tech University.

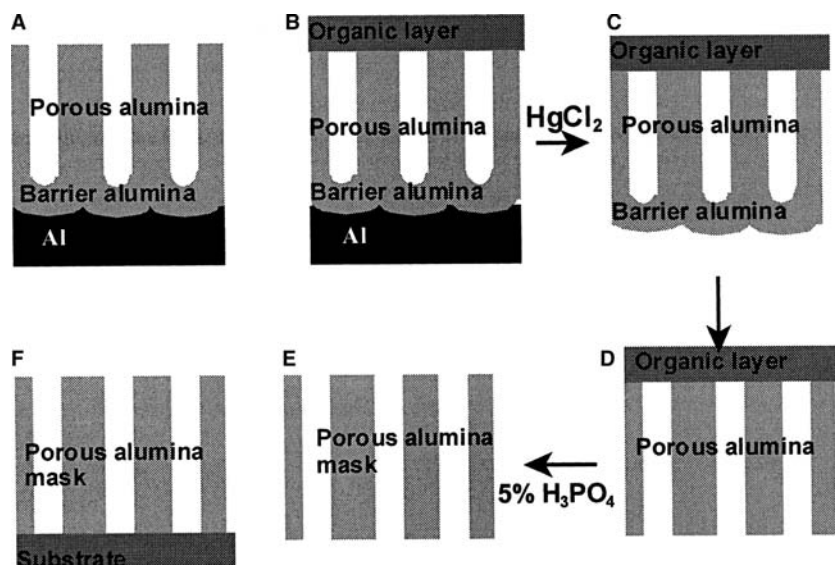


Fig. 7 Sequence of steps to process a nanoporous alumina template for transfer onto a substrate.

alumina is adjusted so that it is higher than the standard reduction potential of the element to be deposited. The standard reduction potentials are obtained from literature. Direct current electrodeposition is particularly useful in the deposition of multilayered nanowires for applications in Giant Magnetoresistance (GMR) devices and other semiconductor-based spintronic structures. Multilayer nanowires with layers as thin as a few angstroms may be fabricated in porous alumina using electrodeposition.<sup>[26]</sup> This is achieved using separate electrolytes for the two components or by using a single electrolyte. The electrolyte is prepared such that it consists of only a trace amount of the nobler element, A, in comparison with the second element, B. The deposition voltage is continually switched between two values, one at which only A is deposited and the other at which both A and B are deposited. By keeping only a trace amount of the nobler metal, A, in the electrolyte, it is ensured that the amount of metal in the AB layer is small, so that its deposition is diffusion-limited. The process may be carried out by adjustment of either the current density (galvanostatic) or the potential (potentiostatic).

#### Transfer of Porous Alumina onto Substrate

In this method, alumina template is transferred to an appropriate substrate, so that it is in direct contact with the substrate. Several processing steps are necessary to separate the template from the parent aluminum film. The sequence of steps is shown in Fig. 7. The sample is initially anodized for a very short time, sufficient to produce a thin nanoporous layer  $\sim 0.1$ – $0.5 \mu\text{m}$ . A protective organic coating is then applied to the top porous layer. The bottom Al and the barrier

alumina layer are etched away in  $\text{HgCl}_2$  solution and 5% phosphoric acid solution, respectively. Dry etching methods, for example, plasma etching or focused ion beam milling, may also be used to remove the barrier layer.<sup>[27,28]</sup> In the final stage, the organic coating is dissolved away in ethyl alcohol. This leaves behind a thin through-hole nanoporous alumina layer. The layer is carefully transferred onto a substrate, dried, and subsequently used as a mask for deposition of nanoarrays of various materials. Fig. 8 shows an AFM of an array of Co nanodots prepared in this manner on a Si substrate. One difficulty with this method is the very small area of the prepared masks.

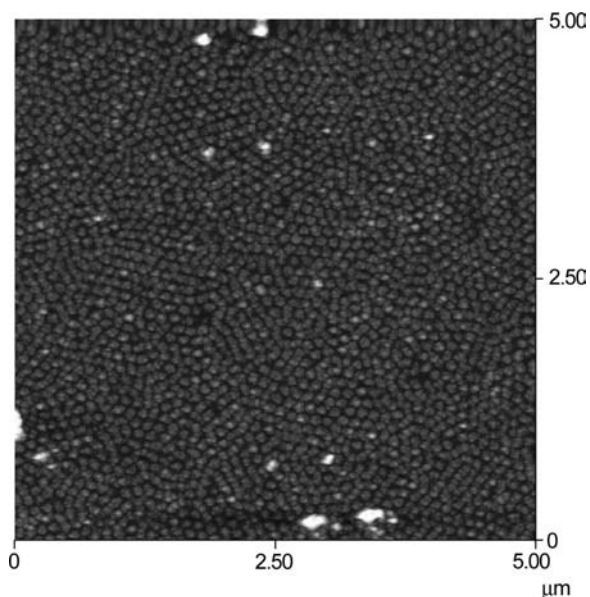


Fig. 8 Atomic force microscopic image showing an array of Co nanodots on a Si substrate.

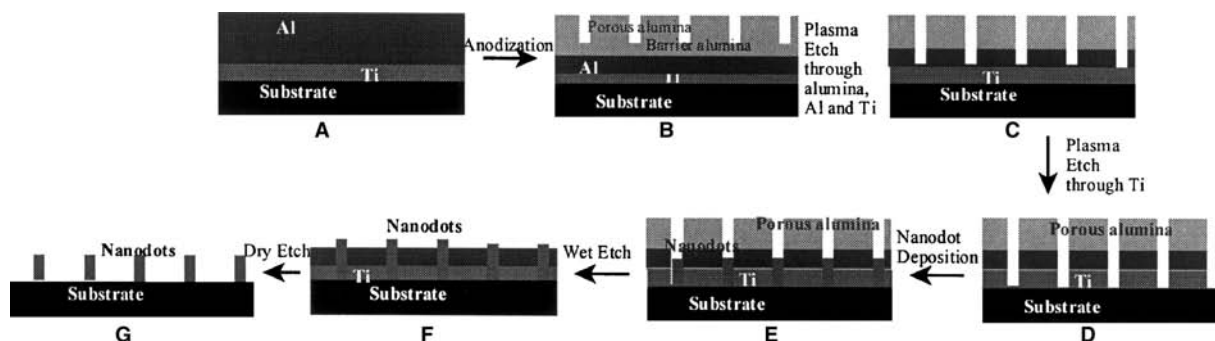


Fig. 9 Sequence of steps to deposit nanoporous alumina template on a substrate.

This is because of the very small thickness of the masks ( $\sim 0.1\text{--}0.5\ \mu\text{m}$ ) and the very brittle nature of aluminum oxide. This problem can be overcome if porous alumina is directly deposited (instead of being transferred) on a substrate.

### Direct Deposition of Porous Alumina on a Substrate

In our laboratory, we have recently demonstrated a novel method to deposit nanoporous alumina template on a substrate.<sup>[29]</sup> The method also allows transfer of the nanoporous template pattern onto the bottom substrate. The technique combines anodization process to produce template arrays and plasma etching through the pores. The sequence of steps is shown schematically in Fig. 9. We used silicon wafers as the starting substrate material, although in principle, the method can be extended to any other substrate, for example, epitaxial GaN.<sup>[30]</sup> A 5-nm-thick adhesion layer of Ti is deposited onto Si substrate by e-beam evaporation followed by a 1- $\mu\text{m}$ -thick layer of Al. Without the Ti layer, the subsequently deposited nanoporous alumina membrane is found to peel from the Si substrate. The aluminum film is anodized in an acid under d.c. conditions for 2–3 min. A cross-section SEM image of the as-deposited template is shown in Fig. 10. The remaining Al layer following anodization and the alumina layer produced by the anodization process are clearly seen. The presence of a thin barrier layer of alumina (U-shaped barrier) is also seen at the pore bottoms. The thickness of the barrier layer in this case is only of the order of 10–20 nm. One major problem for applications based on this method is posed by etching of this barrier layer to pattern layers directly below. Wet chemical etching methods, such as dilute phosphoric acid, although attempted in the past by other research groups,<sup>[31,32]</sup> are not particularly useful. In addition to removing the barrier layer, it also causes pore widening, thus increasing pore diameter and, in some cases, completely removing the alumina film.

We have used plasma etching to anisotropically remove the barrier layer without changing pore diameter. Plasma etching was carried out using a commercial inductively coupled plasma system with reactive ion etching (RIE).  $\text{Cl}_2$  diluted with Ar was used as etchant. The etch process required critical control over various parameters, in particular, etch power and etch time. Details of the process are described in Ref.<sup>[29]</sup> Cross-section image of the final product after a 60-sec etch at 200-W RIE power is shown in Fig. 11. The pores in the top nanoporous alumina layer can be clearly seen. In addition, the etch has penetrated through the barrier region and continued down through the Al to the Ti adhesion layer. Some of the Al nanotubes produced by the process have snapped in cleaving, showing the hexagonal shape of the parent hole template. Following breakthrough of the barrier layer, etch time can be varied to control the depth of the aluminum pores. In fact, with the appropriate

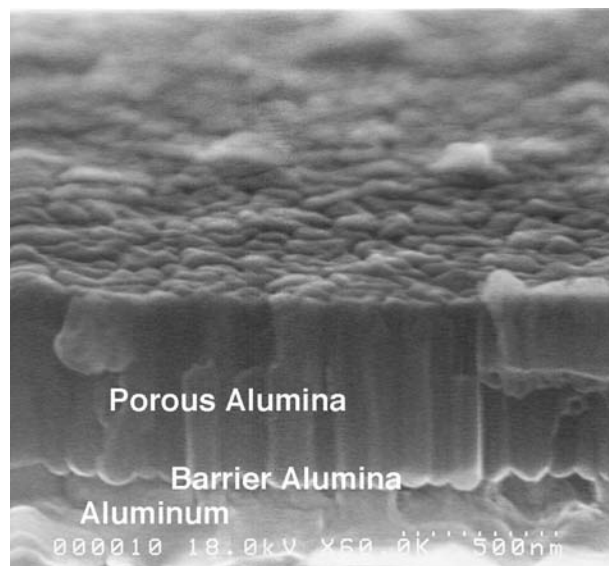
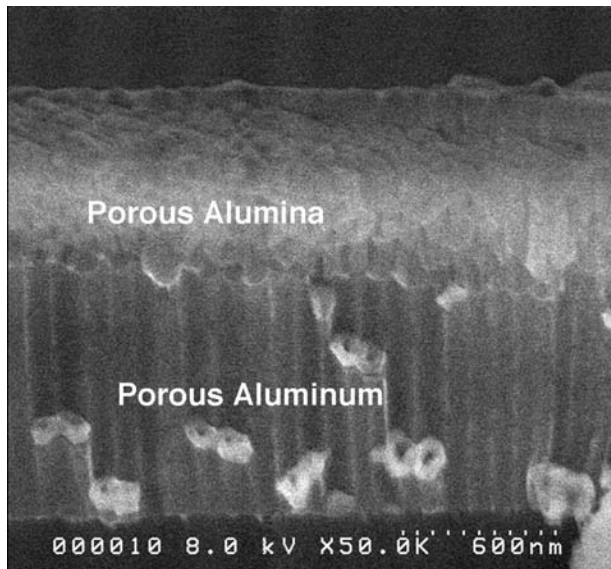


Fig. 10 Left: SEM cross-section image before plasma etch showing nanoporous alumina layer at the top, barrier layer followed by aluminum layer below.





**Fig. 11** Right: Cross-section image postplasma etch showing porous alumina layer and the porous aluminum layer below. *Source:* From J. Yun, M. Holtz, Texas Tech Univ.

etchant, the etch can even be continued through the Ti layer into the bottom substrate. In this manner, a nanoporous pattern, which mirrors the pattern on the initial nanoporous alumina template, can be created on any substrate. The top nanoporous alumina layer can easily be removed by soaking in a mixed solution of 0.2 M chromic/0.4 M phosphoric acid. Fig. 12 shows an AFM image of the top view of the aluminum template postremoval of the porous alumina layer. The pore diameter is of the order of 50–60 nm similar

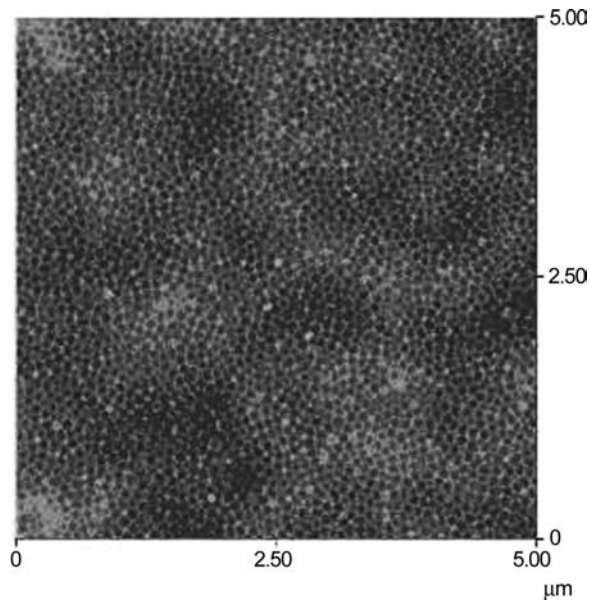


**Fig. 12** Top view AFM image showing pores on aluminum layer.

to that of the initial alumina film. In the final stage, nanoarrays of various materials can be synthesized by depositing/growing them inside the pores.

## SELF-ASSEMBLED NANOARRAYS

Using the various methods discussed, nanoarrays of different materials have been successfully deposited. These include magnetic materials, semiconductor compounds, superconductors, and carbon nanotubes. A brief description of the properties of these nanoarrays is given below.

### Magnetic Nanoarrays

Current magnetic recording media are based on magnetic thin films where the information is stored on grains. To increase data storage density in such media, one must either reduce the size of the grains or reduce the number of grains that constitute each bit. Reducing the number of grains leads to increased noise and decreased size of grains leads to superparamagnetism where thermal energies alone are enough to flip the magnetization direction. These limits depend mainly on the anisotropy constant of the material and the aspect ratio of the grains. For present-day magnetic media, the superparamagnetic limit will be reached at densities of about 100 Gb/in<sup>2</sup>. Patterned media consisting of isolated single-domain islands where each island stores one bit of information are expected to overcome the above problem. It is thought that for such patterned media (with anisotropy constant equal to that of present-day magnetic media), storage densities as high as 1 Tb/in<sup>2</sup> will be achievable. For such large densities, the size of the islands will have to be around 10 nm. Using porous alumina, one can easily fabricate nanomagnetic islands with feature size down to 10 nm. Materials such as Fe, Co, and Ni electrodeposited into the nanopores serve as a model system for the study of magnetic properties, interactions, and thermal stability of nanometer-sized particles. Several research groups have carried out investigations on the magnetic properties of Fe, Co, and Ni nanowires electrodeposited in porous alumina.<sup>[33–37]</sup> The standard synthesis procedure has been to use a.c. electrodeposition. The wires are in the form of cylinders positioned perpendicular to the film plane in a regular array. The wires have been characterized using electron diffraction measurements. Fig. 13 shows a TEM image of Fe nanowires released from alumina template and dispersed onto a substrate. The wire diameter is of the order of 10 nm. High-resolution TEM images of the wires reveal that the wires are polycrystalline in nature with grain sizes ranging from ~5 to 50 nm.

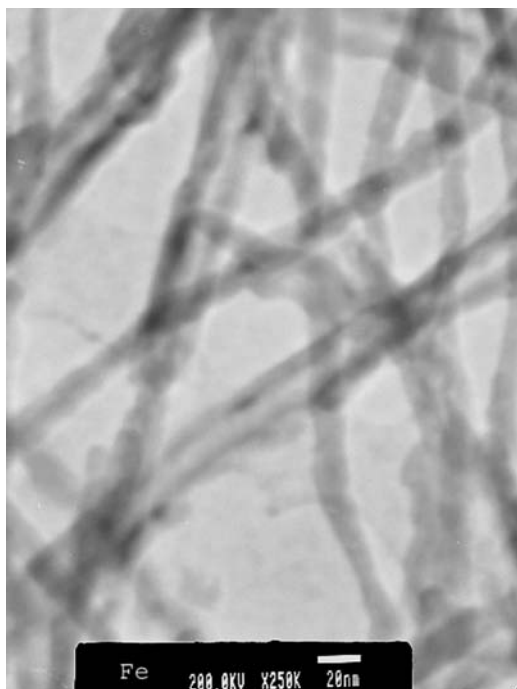


**Fig. 13** Transmission electron microscopic image of Fe nanowires released from porous alumina.

Electron diffraction image for Fe nanowires is also shown in Fig. 14. Analysis of the image confirms a bcc crystal structure for these nanowires. Similar studies for Co and Ni nanowires reveal an hcp structure for Co and fcc structure for Ni nanowires.<sup>[38,39]</sup>

Magnetic properties of these nanowires exhibit strong perpendicular anisotropy. Fig. 15 shows a typical magnetization vs. field image for an array of

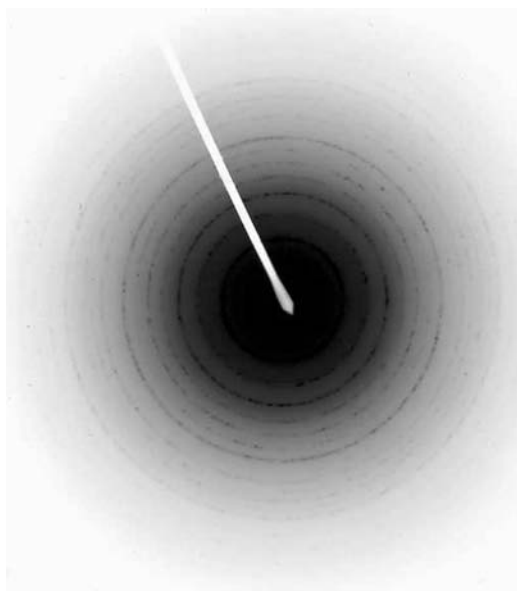


**Fig. 14** Electron diffraction image of Fe nanowires.

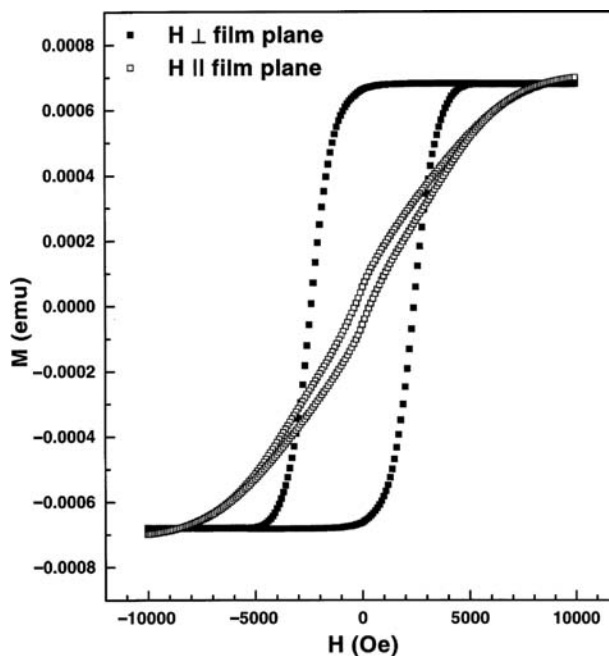


**Fig. 15** Magnetization vs. field for an array of Fe nanowires in the perpendicular and parallel direction.

Fe nanowires electrodeposited inside porous alumina. The diameter of the wires is around 10 nm, and the length is of the order of 1 μm. In the direction perpendicular to the film plane, the coercivity is very high, about 2341 Oe (remanence ratio 0.96), and in the parallel orientation, the coercivity is only about 300 Oe (remanence ratio 0.055). The nanowires thus possess uniaxial anisotropy with easy axis perpendicular to the film plane. The large anisotropy arises mostly from shape anisotropy because of the cylindrical shape of the nanowires. For a cylinder-shaped entity, the demagnetizing factor for field parallel and perpendicular to the cylinder axis are 0 and  $2\pi$ , respectively. The shape anisotropy therefore forces the magnetization to be in the axial direction and is given by  $2\pi M_s$ , where  $M_s$  is the saturation magnetization. The anisotropy field can be estimated by extrapolating the magnetization curves using the  $M_s$  values for bulk Fe ( $1710 \text{ emu/cm}^3$ ) and is estimated to be of the order of 8 kOe for Fe nanowires. These may be compared with theoretically predicted shape anisotropy field of  $2\pi M_s$  ( $\sim 10.7 \text{ kOe}$  for Fe nanowires) for an infinite cylinder. The large perpendicular coercivity suggests resistance to magnetization reversal. The large perpendicular squareness in comparison to the parallel squareness indicates large remanent magnetization. All of these factors, large perpendicular squareness, high remanence, and the large coercivities, may make these materials useful for magnetic recording media.<sup>[40,41]</sup> For such applications, it is necessary to investigate the dependence of magnetic properties on size of the nanostructure.



We have carried out a systematic investigation of the magnetic properties of Fe nanowires as a function of length and diameter of nanowires.<sup>[42]</sup> For large length of the nanowires, of the order of microns, the coercivity  $H_c$  was found to be somewhat independent of length for fixed wire diameter. The coercivity, however, depends critically on the diameter of the wires. In general, the coercivity is found to decrease with increasing wire diameter. For example, Fe nanowires of diameter 32 nm exhibit a coercivity of  $\sim 2158$  Oe which is about 200 Oe smaller than that for wires of diameter 9 nm. The decrease in coercivity is a result of development of multidomain structure in larger nanowires.

An interesting feature is observed for wires with very small diameter,  $<13$  nm. As seen in Fig. 16, for diameter  $<13$  nm, the coercivity is found to decrease. The maximum in coercivity therefore occurs at a wire diameter of about 13 nm and has a value of about 2640 Oe. In contrast to the behavior at 300 K, at 5 K, the coercivity exhibits a maximum for the smallest wire diameter investigated, namely, 9 nm (Fig. 16). The coercivity is around 3700 Oe at 5 K. Unlike the behavior at 300 K, for increasing wire diameter, the coercivity continually decreases. The non-monotonic behavior at 300 K, in contrast to that at 5 K, can be explained as follows. At such small sizes, the wire diameter is much smaller than a single domain. Ferromagnetic domains cannot form and superparamagnetism dominates. Accordingly, the coercivity is low. Indeed, Li and Metzger<sup>[43]</sup> reported very small activation volumes,  $\sim 1.0 \times 10^{-18} \text{ cm}^3$ , for small diameter Fe nanowires at room temperature. This value is very close to the theoretical superparamagnetic limit.<sup>[44]</sup> The superparamagnetic effect will contribute to

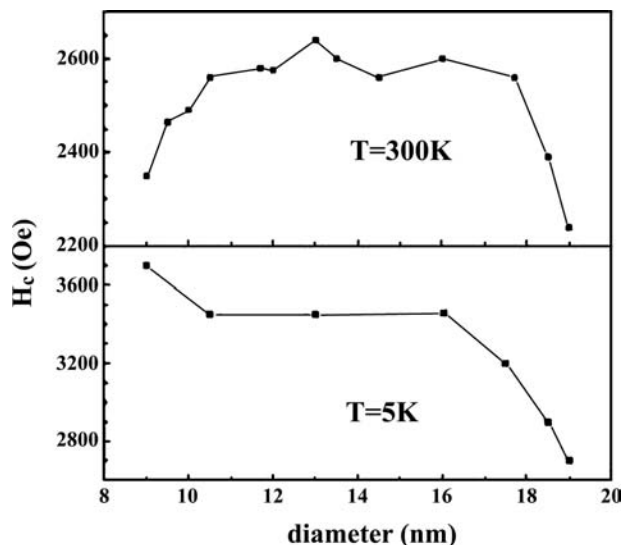


Fig. 16 Coercivity as a function of wire diameter for Fe nanoarrays, at room temperature and at 5 K.

magnetization at low temperature below blocking temperature leading to the increase of coercivity at 5 K. Magnetic interaction between the wires is an important factor in recording media and can be estimated by measuring the quantity defined as  $\Delta M$ .

$$\Delta M = I_d(H) - (1 - 2I_r(H)) \quad (3)$$

where  $I_r(H)$  is d.c. demagnetization remanence and  $I_r(H)$  is isothermal remanence. For isothermal remanent magnetization measurements, the sample was first demagnetized. A magnetic field was then applied and reset to zero and the remanent magnetization was measured. This was carried out for different field values, and the isothermal remanent magnetization curve was obtained as a function of the field. In the case of the d.c. demagnetization curve, the sample was first saturated in a high field of 13 kOe and the remanent magnetization was obtained at various values of the reversal field. Fig. 17 shows the  $\Delta M$  plots for Fe wires with different diameters. All of them show negative peaks, suggesting presence of magneto-static interaction.

Magnetic properties of Co and Ni nanoarrays electrodeposited in porous alumina have also been studied in great detail by various authors. The largest coercivities for Ni nanowires have been reported by Nielsch et al.<sup>[36]</sup> They obtained coercivity of  $\sim 1200$  Oe for highly ordered Ni wires of diameter 30 nm with remanence of the order of 100%. The diameter of the wires was varied in the range 30 to 55 nm while keeping the nanowire distance constant (100 nm) and found that the coercivity drops to 600 Oe (remanence  $\sim 30\%$ )

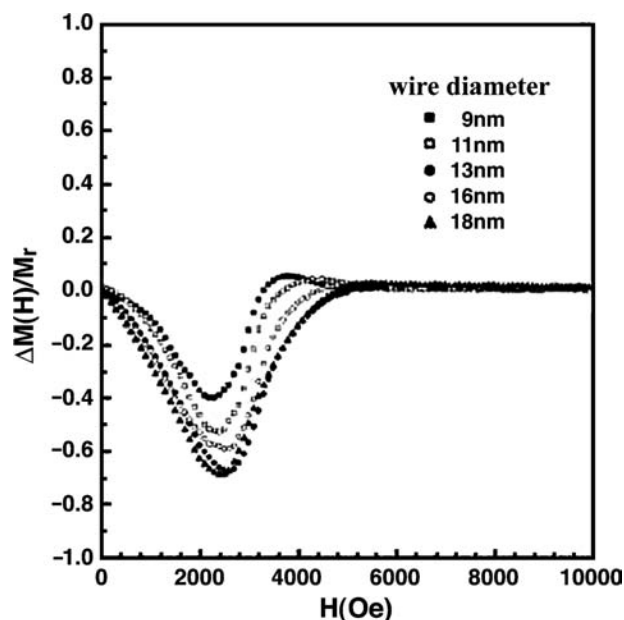


Fig. 17  $\Delta M$  plots for Fe nanowires of varying diameter.

for wires of diameter 55 nm. Magnetic measurements for Co nanowires in anodic alumina templates have been studied extensively by Zeng et al.<sup>[45]</sup> For a fixed wire diameter of about 10 nm, as the nanowire length is increased,  $H_c$  is found to increase steeply until a constant value of about 2300 Oe is approached at wire lengths of about 200 nm. For larger wire lengths, the coercivity is more or less independent of length. For wire lengths of the order of 500–1000 nm, the coercivity is found to decrease gradually with increasing nanowire diameter. This is accompanied by shearing of the hysteresis loop. Both the decrease of  $H_c$  and the shearing of the loop are attributed to magnetostatic interactions.

Time dependence of magnetic properties of Fe, Co, and Ni nanoarrays has been studied.<sup>[46–48]</sup> Quantities such as magnetic viscosity and activation volume have been calculated, and models for reversal mechanism in these nanowires have been extensively investigated. Typically, the activation volume for wires with diameter of the order of 10 nm is calculated to be of the order of  $\sim 4 \times 10^{-18} \text{ cm}^3$ . This value is much smaller than the physical wire volumes, which indicates that magnetization reversal starts in a small region of wires. Magnetic reversal mechanisms such as coherent rotation and curling treat the wires as perfect homogeneous cylinders. However, the coherent rotation and curling modes are delocalized and could lead to activation volumes much larger than those observed. A more reasonable explanation of the reduced coercivities and thermal activation volumes encountered in electrodeposited nanowires is morphological inhomogeneities. Transmission electron microscopic results indicate a considerable degree of polycrystallinity with crystallite diameter of about 5 nm. Polycrystalline wires can be interpreted as random-anisotropy ferromagnets where interatomic exchange tries to align the local spins, but the exchange stiffness has to compete against random-anisotropy forces associated with the local uniaxial anisotropy. As a consequence, the magnetization processes become localized.<sup>[49]</sup> The localization length or physical activation volume strongly depends on crystallite size.

As discussed earlier, in nanowires, magnetic anisotropy originates mainly from shape anisotropy. Large-shaped anisotropies can result from large saturation magnetization, which, in turn, can lead to large coercivity. This suggests that large coercivities are expected in FeCo nanowires because in bulk form, these alloys exhibit large saturation magnetization ( $1950 \text{ emu/cm}^3$  for 35 at.% Co) which is larger than both Fe and Co. We have successfully electrodeposited FeCo alloys into the pores.<sup>[50]</sup> For these arrays, we did observe coercivity for some FeCo nanowires to be larger than that of Fe and Co. The coercivity is found to be 2600 Oe for  $\text{Fe}_{0.93}\text{Co}_{0.07}$ , 2900 Oe for  $\text{Fe}_{0.67}\text{Co}_{0.33}$ ,

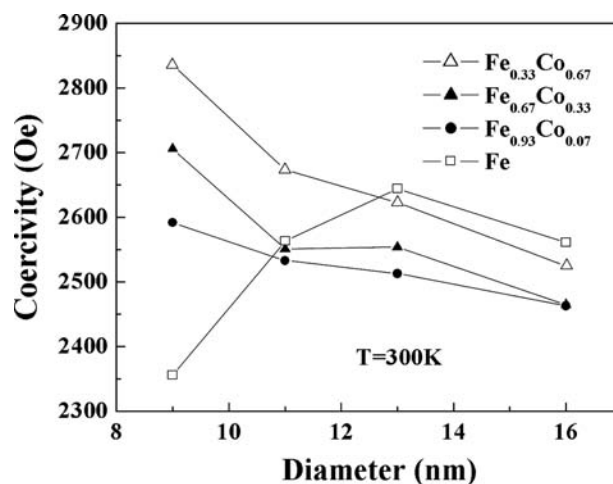


Fig. 18 Variation of coercivity as a function of wire diameter for FeCo alloys.

2850 Oe for  $\text{Fe}_{0.33}\text{Co}_{0.67}$ , and 2400 Oe for  $\text{Fe}_{0.07}\text{Co}_{0.93}$ . The coercivity is largest for  $\text{Fe}_{0.33}\text{Co}_{0.67}$  and  $\text{Fe}_{0.67}\text{Co}_{0.33}$  samples and is much higher than those obtained for Fe (2400 Oe) and Co (1900 Oe) prepared under similar conditions. As in the case of elemental Fe, Co, and Ni nanoarrays, we obtained very high squareness ratio ( $\sim 1$ ) for most of the samples, suggesting excellent perpendicular magnetization characteristics. Fig. 18 shows the variation of coercivity as a function of diameter of the nanowires for all the  $\text{Fe}_{1-x}\text{Co}_x$  alloys. Length of the nanowires is kept constant in all the samples ( $\sim 3 \mu\text{m}$ ). It is noted that contrary to the behavior of pure Fe, Fe–Co alloys show no maximum in coercivity as a function of wire diameter, suggesting that the superparamagnetic behavior is eliminated even for the smallest diameter wires (9 nm) used in this study. With increasing Co addition, the saturation magnetization and hence shape anisotropy constant of Fe–Co alloys are increased, which should result in higher energy barrier  $E$  (given by  $KV$ , where  $K$  is the anisotropy constant and  $V$  is the volume).

## Semiconductor Nanoarrays

Alternating current or direct current electrodeposition can be used to fabricate arrays of semiconducting nanowires/nanodots in porous alumina. Electrochemically, the most easily fabricated semiconductors are the II–VI semiconductors of the type CdS, CdSe, etc. This can be achieved using three different methods. In the first method used by Moskovits,<sup>[51]</sup> a metal capable of forming a semiconductor is first electrodeposited into the pores of alumina. The top surface of the porous aluminum oxide is then etched away in an acid to expose the ends of the metallic array of wires. The deposited metal is then allowed to react with a liquid

or gaseous reagent to convert them chemically to a semiconductor. For example, cadmium particles can be converted to CdS by reaction with sulfur vapor or hydrogen sulfide. Gallium particles may be converted to GaAs by reaction with arsine.

In the second method, sulfuric acid is a.c.-electrolyzed causing the sulfide atoms to be deposited in the pores. This is followed by a.c. electrodeposition of Cd into the pores, allowing the S atoms to react chemically with the Cd atoms, causing formation of CdS. Instead of a.c. electrodeposition of Cd, one may simply soak the porous template containing S atoms into a boiling solution of cadmium sulfate.

In the third method, the electrolyte used for the electrodeposition is non-aqueous unlike that used for magnetic materials.<sup>[52,53]</sup> For the preparation of semiconductor nanowires of MX (M = Cd, Pb, Zn and X = S, Se, Te), a solution of dimethylsulfoxide containing a salt of M (50 mM) and elemental X (S or Se) is used. For example, CdS is electrodeposited using a 50-mM solution of cadmium perchlorate and 50 mM S in a dimethylsulfate solution. A small amount of lithium perchlorate is also added to improve the conductivity.

We have successfully prepared nanowires of CdS, CdSe, PbSe, ZnSe, etc. using the deposition methods described above. Details of our studies on these nanoarrays and their possible device applications are discussed in detail in Ref. <sup>[54]</sup>. Such nanowire arrays can be used to study their electrical properties and thus investigate their potential applications in devices such as diodes, transistors, photodetectors, and light-emitting devices. Semiconductor nanodots and nanowire devices could be the building blocks for digital nanoelectronics, an integrated circuit technology which will permit downscaling to be carried beyond what is currently achievable.

## Energetic Nanocomposite Nanoarrays

Energetic materials are a class of substances consisting of an appropriate mixture of a fuel and oxidizer material. When ignited, they release a large amount of energy because of an exothermic reaction. Such materials have several applications, in explosives, propellants, etc. Recently, it has been found that when fabricated in the form of nanocomposites, the energetic properties are highly enhanced.<sup>[55]</sup>

Using porous alumina templates, we have developed two novel methods to fabricate these materials. In both methods, a thin film of Al is the fuel material and Fe oxide nanowires are the oxidizer material. Al film is prepared by means of thermal evaporation, while the nanowires are prepared by means of electrodeposition inside nanoporous alumina templates. We have found that presence of aluminum oxide around the wires inhibits direct interaction between Al and iron oxide. The aluminum oxide barrier layer and the aluminum oxide around the wires therefore need to be completely removed. Fig. 19 shows the sequence of steps that we followed to achieve this.<sup>[56]</sup> The electrodeposited sample is first coated with a thin organic layer. The sample is then soaked in 3% mercuric chloride solution, which removes the bottom Al layer. The top organic layer protects Fe wires inside the pores from being etched away by mercuric chloride solution. In the next step, the organic layer is removed in ethyl alcohol solution and the sample is dried. The sample is now soaked in a mixture of chromic-phosphoric acid at 60°C to partially etch the pores from the top revealing Fe wires. The sample is rinsed and dried, and a thin film of Al (50 nm) is coated on top by means of thermal evaporation. Al film is therefore in contact with the Fe nanowires. The sample is annealed at 100°C for a few minutes to improve the interface contact between Al

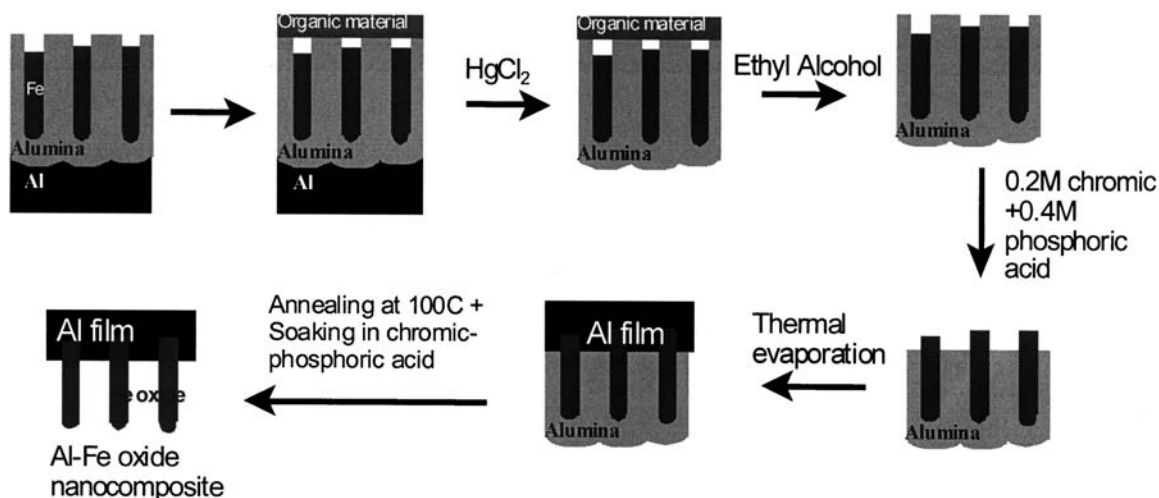


Fig. 19 Sequence of steps to prepare Al-Fe oxide nanocomposites (method 1).

and the Fe nanowires. It is then soaked in chromic-phosphoric acid mixture to etch away the remaining aluminum oxide film. This leaves behind an Al film attached to an array of Fe nanowires. The sample is cleaned, dried, and annealed to completely remove trace amounts of water vapor and also to convert Fe nanowires into Fe oxide. In method 2 (see Fig. 20 for sequence of steps), a thin film of photoresist material is deposited on a glass wafer followed by thermal evaporation of a thin layer of aluminum (50-nm thickness). A commercial Al foil is anodized separately under d.c. conditions at 40 V in 3% oxalic acid for 30 min, creating a nanoporous template with pore diameter of the order of 50 nm. Fe nanowires are electrodeposited inside the pores under a.c. conditions. The sample is then soaked in a mixed solution of 0.2 M chromic/0.4 M phosphoric acid at 60°C. The acid mixture dissolves aluminum oxide completely leaving behind the Fe wires in solution. This solution is poured onto the thermally evaporated Al film. The Al film is annealed at 100°C to improve adhesion of Fe nanowires, followed by rinsing and drying to remove traces of the acid. The sample is then soaked in a solution of acetone to dissolve the photoresist material. This leaves behind the final product, Al-Fe oxide nanocomposite film, which is rinsed in methanol followed by annealing at 100°C for a few minutes to remove all traces of water vapor. Al-Fe oxide nanocomposite prepared using these two methods is found to ignite readily under flame ignition, indicating several possible applications of these materials in explosives, propellants, and other military applications.

### Carbon Nanotube Arrays

Carbon nanotubes<sup>[57]</sup> can be viewed as rolled-up sheets of graphite with diameters approximately a few nanometers. They can be either metallic or semiconducting,

with band gaps that can be controlled by controlling the tube diameter. Several applications are envisioned for these materials. Carbon nanotube electronics are expected to provide a viable alternative to silicon when chip feature sizes cannot be made any smaller using silicon.<sup>[58]</sup> Nanotube electronics are also expected to provide great progress in computer miniaturization and computing power. They have potential applications in cold-cathode flat panel displays because of their excellent field emission properties.<sup>[59]</sup> Carbon nanotubes can be used to encapsulate other materials such as Fe, Co, etc.<sup>[60]</sup> They can be used in infrared imaging, inert membranes for biomedicine, etc. They can be placed on an Scanning Probe Microscopy (SPM) tip to manipulate molecules with sub-angstrom accuracy.<sup>[61]</sup> The tips are atomically precise with chemistry similar to C<sub>60</sub>, and thus serve as functional elements with a wide variety of molecular fragments. Functionalizing carbon nanotube tips will allow mechanical manipulation of many molecular systems on various surfaces with sub-angstrom accuracy.

For several of the applications described above, particularly in nanotube electronics, it is necessary to be able to control the growth of carbon nanotubes both with respect to size and orientation. Carbon nanotube arrays have been successfully synthesized in ordered porous alumina templates.<sup>[62-66]</sup> The diameter and spacing of the carbon nanotubes are controlled by controlling the diameter and interpore spacing in porous alumina. Most of the methods involve initial deposition of Co inside the pores which act as catalyst for the growth of carbon nanotubes. Earliest demonstration of carbon nanotube synthesis in porous alumina was provided by Li et al.<sup>[65,66]</sup> A small amount of Co is electrodeposited in the pores, and the templates are heated in a tube furnace at 600°C for 4-5 hr under CO flow (100 cm<sup>3</sup>/min). The CO flow is then replaced by a mixture of 10% acetylene in nitrogen at a flow rate of 100 cm<sup>3</sup>/min for about 2 hr at

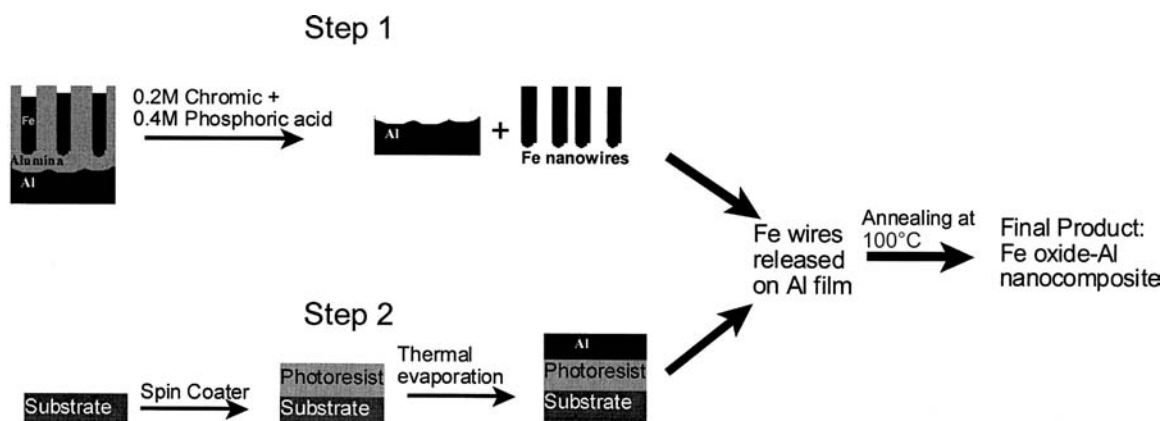


Fig. 20 Sequence of steps to prepare Al-Fe oxide nanocomposite (method 2).

650°C. The samples are then annealed for 15 hr in nitrogen leading to formation of an array of carbon nanotubes. The carbon nanotubes produced in porous alumina templates have the following common characteristic features: they always grow perpendicular to film plane, are multiwalled, have uniform sizes, and are open-ended. The growth of carbon nanotubes inside pores by catalytic decomposition of organic vapors has been postulated as either base or tip growth.<sup>[67]</sup> Scanning electron microscopic studies indicate residual Co/Fe catalyst in the base of the tubes, indicating that a tip growth mechanism could be responsible for the tube growth. It is also thought that the surrounding alumina may also be acting as a catalyst in nanotube growth.<sup>[68]</sup>

Field emission characteristics of ordered carbon nanotubes have been investigated.<sup>[63–69]</sup> Yuan et al.<sup>[63]</sup> demonstrated excellent field emission characteristics for these nanotube arrays. In their measurements, they removed the barrier layer between the aluminum and the porous layer. Field emission was seen to begin at a relatively low electric field ( $\sim 2.8$  V/ $\mu$ ). They measured a very large emission current 0.08 mA/cm<sup>2</sup> at 3.6 V/mm, much greater than that reported by Davydov et al.<sup>[69]</sup> for as-prepared nanotube arrays (in presence of barrier layer). Over a period of 150 hr, no significant reduction in emission current was observed. In contrast, in the presence of the barrier layer, the current density was found to decrease rapidly with time over a period of a few minutes. Another reason for the enhanced field emission may be related to the open-ended nature of the carbon nanotubes, which results in smaller radius of curvature than the closed ends, thus causing electrons to be emitted more easily. In a similar study, Jeong et al.<sup>[70]</sup> measured a turn-on field of 1.9–2.1 V/ $\mu$ m and a field enhancement factor of 3360–5200. In their samples, the barrier layer is absent and the density of carbon nanotubes was very small,  $\sim 10^7$  tips/cm<sup>2</sup>. The intertube distance is therefore higher, minimizing field screening effect and, in turn, enhancing field emission effect.<sup>[71]</sup> Field emitter arrays with such high emitting efficiency are expected to have applications in flat panel displays in the near future. For application in nanoelectronics, it is sometimes necessary to be able to make connections between carbon nanotubes. One solution is to directly prepare T- or Y-junction carbon nanotubes. In general, pores inside nanoporous alumina are straight when the anodization voltage is kept fixed during anodization. However, one can create branched pores inside alumina by changing the anodization voltage during anodization. In particular, Y-shaped pore forms in porous alumina when the anodization voltage is reduced by a factor of 1/2 during the anodization. Li et al.<sup>[66]</sup> synthesized Y-junction carbon nanotubes in such templates by using Co as a catalyst and

by pyrolysis of acetylene at 650°C. Papadopoulos et al.<sup>[72]</sup> obtained electronic transport measurements on both individual and parallel arrays of Y-junction nanotubes synthesized in porous alumina. Non-linear transport and rectifying behavior was observed. This behavior can be explained in terms of a change in band gap across the junction caused by the change in diameter across the junction. Y-junction carbon nanotubes are thus a realization of semiconductor heterostructures in the nanometer scale. Y-shaped nanotubes and nanowires are expected to have possible applications in room-temperature single electron transistor and spintronic devices.

## CONCLUSION

In conclusion, porous alumina is indeed a versatile template. It allows fabrications of a variety of nanostructures in the form of nanoarrays with feature sizes as small as 10 nm. As described in this entry, characterization and measurement of appropriate properties of the nanoarrays can be easily carried out. It allows investigation of several fundamental phenomena at the nanoscale level and also allows for investigation of potential applications of nanostructures in future high-performance nanoscale devices.

## ACKNOWLEDGMENTS

Most of the work described in this entry (unless specified) has been carried out by the author and her colleagues at the University of Nebraska-Lincoln and at Texas Tech University, Lubbock. The author would like to thank S. Bandyopadhyay, N. Kouklin, X.Z. Li, P.F. Williams, M. Holtz, K. Zhu, and J. Yun for useful discussions, collaborations, and help with experiments. Several aspects of the work are supported by grants from National Science Foundation, Office of Naval Research, and the Department of Army.

## REFERENCES

1. Edelstein, A.S. *Nanomaterials: Synthesis, Properties and Applications*; Edelstein, A.S., Camarata, R.C., Eds.; Institute of Physics Publishers: Bristol, Philadelphia, 1996.
2. Shalaev, V.M.; Moskovits, M. *Nanostructured Materials: Clusters, Composites and their Films*; ACS Symposium Series; American Chemical Society Editions: Washington, DC, 1997; Vol. 679.
3. Fendler, J.H. *Nanoparticles and Nanostructured Films: Preparation, Characterization and Applications*; Wiley-VCH: Weinheim, Germany, 1998.

4. Murray, C.B.; Kagan, C.R.; Bawendi, M.G. Self-organization of CdSe nanocrystallites into three-dimensional quantum dot superlattices. *Science* **1995**, *270*, 1335.
5. Andres, R.P.; Bielefeld, J.D.; Henderson, J.I.; Janes, D.B.; Kolagunta, V.R.; Kubiak, C.P.; Mahoney, W.J.; Osifchin, R.G. Self-assembly of a two-dimensional superlattice of molecularly linked metal clusters. *Science* **1996**, *273*, 1690.
6. Shi, J.; Gider, S.; Babcock, K.; Awschalom, D.D. Magnetic clusters in molecular beams, metals, and semiconductors. *alumina*. *Science* **1996**, *271*, 937.
7. Billas, I.M.L.; Becker, J.A.; Chatelain, A.; de Heer, W.A. Magnetic moments of iron clusters with 25 to 700 atoms and their dependence on temperature. *Phys. Rev. Lett.* **1993**, *71*, 4067.
8. White, R.L.; New, R.M.H.; Pease, R.F.W. Patterned media: A viable route to 50 Gbit/in.<sup>2</sup> and up for magnetic recording? *IEEE Trans. Magn.* **1997**, *33*, 990.
9. Chou, S.Y.; Wei, M.S.; Krausse, P.R.; Fischer, P.B. Single-domain magnetic pillar array of 35 nm diameter and 65 Gbits/in<sup>2</sup> density for ultrahigh density quantum magnetic storage. *J. Appl. Phys.* **1994**, *76*, 6673.
10. Ross, C.A.; Smith, H.I.; Savas, T.; Schattenburgh, M.; Farhoud, M.; Hwang, M.; Walsh, M.; Abraham, M.C.; Ram, R.J. Fabrication of patterned media for high density magnetic storage. *J. Vac. Sci. Technol. B* **1999**, *17*, 3168.
11. Menon, L. Synthesis of Nanowires Using Porous Alumina. In *Advances in Nanophase Materials and Nanotechnology (Vol. Quantum Dots and Nanowires)*; Bandyopadhyay, S., Nalwa, H.S., Eds.; American Scientific Publishers, 2003. (the "Series Editors").
12. Lohrengel, M.M. Thin anodic oxide layers on aluminum and other valve metals: High field regime. *Mater. Sci. Eng.* **1993**, *R11*, 243.
13. Keller, F.; Hunter, M.S.; Robinson, D.L. Structural features of oxide coatings on aluminum. *J. Electrochem. Soc.* **1953**, *100*, 411.
14. Bandyopadhyay, S.; Miller, A.E.; Chang, H.-C.; Banerjee, G.; Yuzhakov, V.; Yue, D.-F.; Ricker, R.E.; Jones, S.; Eastman, J.A.; Baugher, E.; Chandrasekhar, M. Electrochemically assembled quasi-periodic quantum dot arrays. *Nanotechnology* **1996**, *7*, 360.
15. Ricker, R.E.; Miller, A.E.; Yue, D.-F.; Banerjee, G.; Bandyopadhyay, S. Nanofabrication of a quantum dot array: Atomic force microscopy of electropolished aluminum. *J. Electron. Mater.* **1996**, *25*, 1585.
16. Bandyopadhyay, S.; Menon, L.; Kouklin, N.; Zeng, H.; Sellmyer, D.J. Electrochemically self-assembled quantum dot arrays. *J. Electron. Mater.* **1999**, *28*, 515.
17. Li, A.P.; Miller, F.; Gösele, U. Polycrystalline and monocrystalline pore arrays with large interpore distance in anodic alumina. *Electrochem. Solid-State Lett.* **2000**, *3*, 131.
18. O'Sullivan, J.P.; Wood, G.C. *Proc. R. Soc. Lond., Ser. A* **1970**, *317*, 511.
19. Jessensky, O.; Müller, F.; Gösele, U. Self-organized formation of hexagonal pore arrays in anodic alumina. *Appl. Phys. Lett.* **1998**, *72*, 1173.
20. Masuda, H.; Fukuda, K. Ordered metal nanohole arrays made by a two-step replication of Honeycomb structures of nanoporous alumina. *Science* **1995**, *268*, 1466.
21. Masuda, H.; Yamada, H.; Satoh, M.; Asoh, H.; Nakao, M.; Tamamura, T. Highly ordered nanochannel-array architecture in anodic alumina. *Appl. Phys. Lett.* **1997**, *71*, 2770.
22. Zhang, Z.; Ying, J.Y.; Dresselhaus, M.S. Bismuth quantum-wire arrays fabricated by a vacuum melting and pressure injection process. *J. Mater. Res.* **1998**, *13*, 1745.
23. Yi, G.; Schwarzacher, W. Single crystal superconductor nanowires by electrodeposition. *Appl. Phys. Lett.* **1999**, *74*, 1746.
24. Hornyak, G.L.; Patrissi, C.J.; Martin, C.R. Fabrication, characterization and optical properties of gold-nanoparticle/porous-alumina composites: The non-scattering Maxwell-Garnett limit. *J. Phys. Chem., B* **1997**, *101*, 1548.
25. Martin, C.R. Nanomaterials—A membrane-based synthetic approach. *Science* **1994**, *266*, 1961.
26. Schwarzacher, W. Metal nanostructures a new class of electronic devices. *Electrochem. Soc. Interface* **1999**, *8*, 20–24.
27. Liang, J.; Chik, H.; Yin, A.; Xu, J. Two-dimensional superlattices of nanostructures: Nonlithographic formation by anodic alumina membrane template. *J. Appl. Phys.* **2002**, *91* (4), 2544–2546.
28. Kanamori, Y.; Hane, K.; Sai, H.; Yugami, H. 100 nm period silicon antireflection structures fabricated using a porous alumina membrane mask. *Appl. Phys. Lett.* **2001**, *78*, 142.
29. Menon, L.; Kanchibotla, B.R.; Patibandla, S.; Aurongzeb, D.; Holtz, M.; Yun, J.; Zhu, K. Anodization and plasma etching of nanopore patterns on a generic substrate. Submitted to *Appl. Phys. Lett.*
30. Menon, L.; Holtz, M. et al., unpublished.
31. Rabin, O.; Herz, P.R.; Cronin, S.B.; Lin, Y.-M.; Akinwande, A.I.; Dresselhaus, M.S. Nanofabrication using self-assembled alumina templates. *Mater. Res. Soc. Symp.* **2001**, *636*, D4.7.1.
32. Huang, Q.; Lye, W.-K.; Longo, D.M.; Reed, M.L. Sub-micron patterned anodic oxidation of aluminum thin films. *Mater. Res. Symp. Proc.* **2001**, *636*, D9.49.1.
33. AlMawlawi, D.; Coombs, N.; Moskovits, M. Magnetic properties of Fe deposited into anodic aluminum oxide pores as a function of particle size. *J. Appl. Phys.* **1991**, *70*, 4421.
34. Metzger, R.M.; Kononov, V.V.; Sun, M.; Xu, T.; Zangari, G.; Xu, B.; Benakli, M.; Doyle, W.D. Magnetic nanowires in hexagonally ordered pores of alumina. *IEEE Trans. Magn.* **2000**, *36*, 30.
35. Skomski, R.; Zeng, H.; Zheng, M.; Sellmyer, D.J. Magnetic localization in transition-metal nanowires. *Phys. Rev., B* **2000**, *62*, 3900.
36. Nielsch, K.; Wehrspohn, R.B.; Barthel, J.; Kirschner, J.; Gsele, U.; Fischer, S.F.; Kronmüller, H. Hexagonally ordered 100 nm period nickel nanowire arrays. *Appl. Phys. Lett.* **2001**, *79*, 1360.



37. Li, F.; Zhang, L.; Metzger, R.M. On the growth of highly ordered pores in anodized aluminum oxide. *Chem. Mater.* **1998**, *10*, 2470.
38. Strijkers, G.J.; Dalderop, J.H.J.; Broaksteeg, M.A.A.; Swagten, H.J.M.; de Jonge, W.J.M. Structure and magnetization of arrays of electrodeposited Co wires in anodic alumina. *J. Appl. Phys.* **1999**, *86*, 5141.
39. Zheng, M.; Menon, L.; Zeng, H.; Liu, Y.; Bandyopadhyay, S.; Kirby, R.D.; Sellmyer, D.J. Magnetic properties of Ni nanowires in self-assembled arrays. *Phys. Rev., B* **2000**, *62*, 12282.
40. Whitney, T.M.; Jiang, J.S.; Searson, P.C.; Chien, C.L. Fabrication and magnetic properties of arrays of metallic nanowires. *Science* **1993**, *261*, 1316.
41. Iwasaki, S.; Nakamura, Y. An analysis for the magnetization mode for high density magnetic recording. *IEEE Trans. Magn.* **1977**, *MAG-13*, 1272.
42. Menon, L.; Zheng, M.; Zeng, H.; Bandyopadhyay, S.; Sellmyer, D.J. Size dependence of the magnetic properties of electrochemically self-assembled Fe quantum dots. *J. Electron. Mater.* **2000**, *29*, 510.
43. Li, F.; Metzger, R.M. Activation volume of a-Fe particles in alumite films. *J. Appl. Phys.* **1997**, *81*, 3806.
44. Koster, E.; Arnoldssen, T.C. *Magnetic Recording*; Mee, C.D., Daniel, E.D., Eds.; McGraw-Hill: New York, 1987; Vol. 1.
45. Zeng, H.; Zheng, M.; Skomski, R.; Sellmyer, D.J.; Liu, Y.; Menon, L.; Sellmyer, D.J. Magnetic properties of self-assembled Co nanowires of varying length and diameter. *J. Appl. Phys.* **2000**, *87*, 4718.
46. Li, F.; Metzger, R.M. Activation volume of a-Fe particles in alumite films. *J. Appl. Phys.* **1997**, *81*, 3806.
47. Bao, X.; Li, F.; Metzger, R.M. Synthesis and magnetic properties of electrodeposited metal particles on anodic alumite film. *J. Appl. Phys.* **1996**, *79*, 4866.
48. Liberatos, A.; Chantrell, R.W.; Sterring, E.R.; Lodder, J.C. Magnetic viscosity in perpendicular media. *J. Appl. Phys.* **1991**, *70*, 4431.
49. Skomski, R.; Zeng, H.; Zheng, M.; Sellmyer, D.J. Magnetic localization in transition-metal nanowires. *Phys. Rev., B* **2000**, *62*, 3900.
50. Menon, L.; Bandyopadhyay, S.; Liu, Y.; Zeng, H.; Sellmyer, D.J. Magnetic and structural properties of electrochemically self-assembled Fe<sub>1-x</sub>Cox nanowires. *J. Nanosci. Nanotechnol.* **2001**, *1*, 149.
51. Moskovits, M. Semiconductors and Method for Their Manufacture International Patent Publication #5202290, 1993.
52. Baranski, A.S.; Fawcett, W.R. The electrodeposition of metal chalcogenides. *J. Electrochem. Soc.* **1980**, *127*, 766.
53. Xu, D.; Shi, X.; Guo, G.; Gui, L.; Tang, Y. Electrochemical preparation of CdSe nanowire arrays. *J. Phys. Chem., B* **2000**, *104*, 5061.
54. Bandyopadhyay, S. Nanoarrays: Electrochemically self-assembled. In *Dekker Encyclopedia of Nanoscience and Nanotechnology*, 2E; Schwarz, J.A., Contescu, C.I., Putyera, K., Eds.; Taylor & Francis: New York, NY, 2009; Vol. 4, 2502–2513.
55. Pantoya, M.; Granier, J. Modeling Laser Ignition and Heat Propagation in Nanocomposite Thermites, Proceedings of the 8th AIAA/ASME Joint Thermophysics and Heat Transfer Conference, 2002. Paper No. AIAA-2002-3030.
56. Menon, L. et al., unpublished.
57. Hellemans, A. IBM researchers devise nanotube ICs. *IEEE Spectrum* **2001**, *38*, 26.
58. Iijima, S. Helical microtubules of graphitic carbon. *Nature* **1991**, *354*, 56.
59. Rinzler, A.G.; Hafner, J.H.; Nikolaev, P.; Luo, L.; Kim, S.G.; Tomanek, D.; Nordlander, P.; Colbert, D.T.; Smalley, R.E. Unraveling nanotubes: Field emission from an atomic wire. *Science* **1995**, *269*, 1550.
60. Liu, S.; Zhu, J. Carbon nanotubes filled with long continuous cobalt nanowires. *Appl. Phys., A* **2000**, *70*, 673.
61. Dai, H.; Hafner, J.H.; Rinzler, A.G.; Colbert, D.T.; Smalley, R.E. Nanotubes as nanoprobe in scanned probe microscope. *Nature* **1996**, *384*, 147.
62. Suh, J.S.; Lee, J.S. Highly ordered two-dimensional carbon nanotube arrays. *Appl. Phys. Lett.* **1999**, *75*, 2047.
63. Yuan, Z.H.; Huang, H.; Dang, H.Y.; Cao, J.E.; Hu, B.H.; Fan, S.S. Field emission property of highly ordered monodispersed carbon nanotube arrays. *Appl. Phys. Lett.* **2001**, *78*, 3127.
64. Iwasaki, T.; Motoi, T.; Den, T. Multiwalled carbon nanotubes growth in anodic alumina nanoholes. *Appl. Phys. Lett.* **1999**, *75*, 2044.
65. Li, J.; Moskovits, M.; Haslett, T.L. Nanoscale electrodeless metal deposition in aligned carbon nanotubes. *Chem. Mater.* **1998**, *10*, 1963.
66. Li, J.; Papadopoulos, C.; Xu, J.M.; Moskovits, M. Highly-ordered carbon nanotube arrays for electronics applications. *Appl. Phys. Lett.* **1999**, *75*, 367.
67. Baker, R.T.K. Catalytic growth of carbon filaments. *Carbon* **1989**, *27*, 315.
68. Thess, A.; Lee, R.; Nikolaev, P.; Dai, H.; Petit, P.; Robert, J.; Xu, C.; Hee Lee, Y.; Kim, S.G.; Rinzler, A.G.; Colbert, D.T.; Scuseria, G.E.; Tomanek, D.; Fischer, J.E.; Smalley, R.E. Crystalline ropes of metallic carbon nanotubes. *Science* **1996**, *273*, 483.
69. Davydov, D.N.; Sattari, P.A.; AlMawlawi, D.; Osika, A.; Haslett, T.L.; Moskovits, M. Field emitters based on porous aluminum oxide templates. *J. Appl. Phys.* **1999**, *86*, 3983.
70. Jeong, S.-H.; Hwang, H.-Y.; Lee, K.-H.; Jeong, Y. Template-based carbon nanotubes and their application to a field emitter. *Appl. Phys. Lett.* **2001**, *78*, 2052.
71. Nilsson, L.; Groening, O.; Emmenegger, C.; Kuettel, O.; Schaller, E.; Schalpbach, L.; Kind, H.; Bonard, J.-M.; Kern, K. Scanning field emission from patterned carbon nanotube films. *Appl. Phys. Lett.* **2000**, *76*, 2071.
72. Papadopoulos, C.; Rakitin, A.; Li, J.; Vedenev, A.S.; Xu, J.M. Electronic transport in Y-junction carbon nanotubes. *Phys. Rev. Lett.* **2000**, *85*, 3476.

# Porphyrinic Materials: Self-Assembly on Surfaces

**Charles Michael Drain**

*Department of Chemistry and Biochemistry, Hunter College, City University of New York, and Rockefeller University, New York, New York, U.S.A.*

**James D. Batteas**

*Surface and Microanalysis Science Division, National Institute of Standards and Technology (NIST), Gaithersburg, Maryland, U.S.A.*

**Gabriela Smeureanu**

**Sandeep Patel**

*Department of Chemistry and Biochemistry, Hunter College, City University of New York, New York, New York, U.S.A.*

## INTRODUCTION

For the foreseeable future, the vast majority of commercial electronics, photonics, and other devices will be in the solid state and incorporated onto or into a substrate—although there are substantial efforts to change this paradigm.<sup>[1]</sup> To date, most of these surface structures are manufactured by a “top-down” approach wherein various layers of a material are selectively added or removed. The formation of organic light-emitting diodes (OLEDs), for example, generally requires the careful deposition of several to several tens of layers of various organic and inorganic materials, and the thickness of each must be precisely controlled. An alternative “bottom-up” approach exploits knowledge of intermolecular interactions to self-assemble molecules into supramolecular structures, self-organize molecules into monolayers, or electrostatically deposit films layer by layer.<sup>[1–5]</sup> The degree of predictable and long-range molecular order decreases from self-assembly to self-organization to layer by layer. Notable applications of the second mode of bottom-up assembly are the deposition of thin films of liquid crystals and mesogens for various display applications.<sup>[6–9]</sup> Because exact alignment of molecules is not usually possible with the layer-by-layer approach, applications of this method to date have focused on modifications of large surface areas. This entry focuses on the methods and applications of self-assembled and self-organized porphyrinic materials on surfaces; however, many of the themes and methods discussed are applicable to a variety of other chromophores and other organic molecules. Porphyrinoids are tetrapyrrolic macrocycles that are excellent molecules for various commercial applications because of their remarkable stability, considering their rich photonic properties.

A crucial step toward the application of nanoscaled photonic devices is the ability to design and create increasingly larger architectures of interactive molecules and to incorporate these entities into device components.<sup>[2–5]</sup> For example, the tessellation of molecules into specific designs on surfaces<sup>[10,11]</sup> remains a significant challenge (Fig. 1). The efficiency of electronic and energy transfer in organic-based materials depends on both the molecule and the architecture of these molecules in the device. Other major considerations include the interconnections between the organic material and inorganic components as well as environmental factors. In addition to increasing the performance and efficiency of devices, the components of devices that are molecule-based will be more environmentally benign than much of the inorganic materials they replace.

## DEFINITIONS AND SCOPE

### Porphyrinoids

Porphyrins are tetrapyrrole macrocycles (Fig. 2) found in nature in systems such as hemoglobin, myoglobin, various cytochromes (*C*, *P*<sub>450</sub>, etc.), chlorophylls, methyl-Co-M reductase in methanogenic bacteria, and a plethora of other biological systems.<sup>[12]</sup> They function as transporters of small molecules such as dioxygen, mediators of electron transport, oxidation catalysts, light-harvesting and energy transport conduits, and catalysts for the reduction of a methyl thioether, respectively. Although porphyrins can bind virtually every metal in the periodic table (and a few nonmetals), in biological systems these metals are usually Mg, Fe, Co, and Ni—where the redox chemistry of the latter three provides the function. The limited flexibility and restricted aperture of the square planar

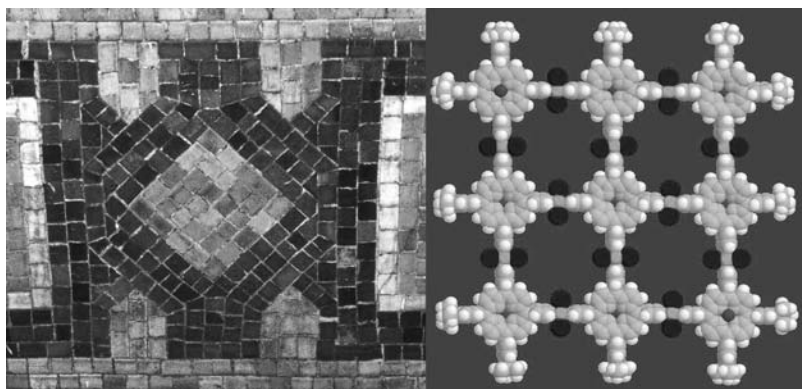


**Fig. 1** Although there has been substantial progress in the assembly of molecules on surfaces, the tessellation of even simple patterns such as the one on the left (from the New York City subway) is currently not feasible because of the large numbers of specific intermolecular interactions needed to distinguish and place the molecules in the pattern. The 21-particle nonamer of porphyrins on the right represents one of the best examples of molecular tessellation on a surface.

ligand modulate both the redox potential and the coordination geometry of bound metals, which in turn modulate the redox and photophysical properties of the macrocycle. The remarkable stability of the macrocycle (it is found in shale oils as a vanadium complex) and the wide distribution in nature have indicated to some researchers that porphyrins may be prebiotic.<sup>[12]</sup>

Because of their biological relevance and diverse functions, a large number of porphyrin derivatives

have been synthesized in the laboratory in the last decades using the methods of Adler, Longo, and Shergalis<sup>[13]</sup> and Lindsey<sup>[14]</sup> and, more recently, a solventless “green” synthesis.<sup>[15]</sup> These methods have allowed commercial applications of porphyrin derivatives that include oxidation catalysts, blood substitutes, therapeutics, sensors/actuators, photonic materials, dyes, and various forms of “toners” in photolithography. In the past decade, there has been substantial effort to create and characterize the properties of multiporphyrinic systems for materials applications.<sup>[16–18]</sup> Two related macrocycles—phthalocyanines and porphyrazines—have also been the subject of much research for similar applications, but multichromophoric systems of these dyes are less well developed at present.<sup>[19–22]</sup> Although all three types of macrocycles have related photophysical properties, the porphyrins have been the primary focus of research because of synthetic accessibility and greater solubility in organic solvents.

In the context of nanotechnology and materials chemistry, the aforementioned properties of porphyrinoids can be exploited for a variety of applications that include: [1] molecular electronics,<sup>[4,23–26]</sup> [2] components of nanoscaled sensors, actuators,<sup>[27–34]</sup> and photonics,<sup>[35–38]</sup> [3] both structural and chemically active elements in molecule-constructed molecular sieves,<sup>[39–45]</sup> [4] catalysts,<sup>[46]</sup> and [5] part of biomolecular encapsulating systems.<sup>[47,48]</sup> For many of these applications, the precise geometric alignment of the chromophores in the materials is essential for function. The problem, then, is how to make nanomaterials of organic compounds wherein a few to a few hundred molecules are brought together in a predefined or predictable geometry—as opposed to aggregates, colloids, and gels (all of which have important applications in nanotechnology as well). The remarkable progress in organic chemistry has provided many elegant molecular systems with more than one porphyrin linked by covalent bonds.<sup>[14,25,49–65]</sup> These include acetylene, phenylacetylene, bridged, fused, and other linkages. For many of these molecular systems, the interspatial

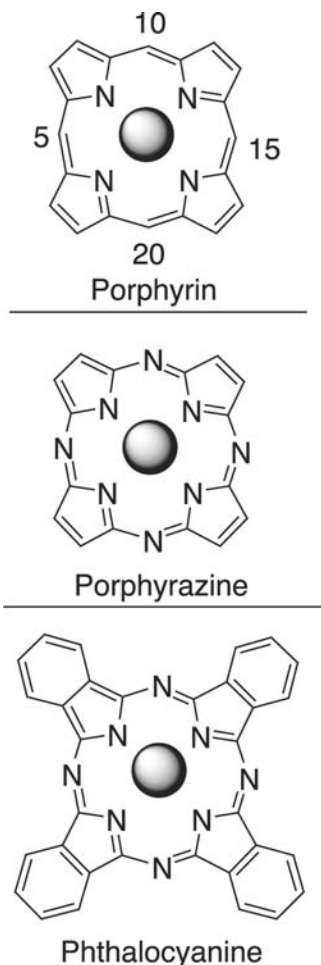


**Fig. 2** The three basic porphyrinoid pigments.

relationships of the macrocycle are well defined. However, the significant limitation of these molecular systems is that the product yield drops precipitously as the number of chromophores increases. There are a variety of polymeric systems bearing porphyrins, or with porphyrins as part of the polymeric chain where the dispersity varies from system to system, but the yields are generally better than for the above molecular system.<sup>[31,66–77]</sup> Both the molecular and polymeric systems have provided a wealth of information of the nature of energy and electron transport mediated by the porphyrins and the various linkers, as well as the means to gate these processes. Several functional materials have also been reported, *vide supra*. The focus of this review is on self-assembled and self-organized porphyrinic systems on surfaces.

## Supramolecular Chemistry

Self-assembly and self-organization are spontaneous processes that allow simple components to form more complex and more ordered systems.<sup>[78–85]</sup> In terms of molecules, the spontaneous *self-assembly* of a given set of molecules results in a discrete supramolecular entity or three-dimensional lattice, whereas the spontaneous *self-organization* of a set of molecules results in systems that are usually not discrete and ordered in only one or two dimensions. The former is usually less tolerant of defects or errors in structure than the latter. Much of the initial inspiration and concept for both self-processes comes from the study and observation of biological systems. For example, the self-assembly of a set of helical proteins into a discrete ion channel relies on the complex intermolecular interactions between the component molecules. One may observe the opening and closing of a single ion channel that gates ionic currents across a lipid membrane (which is an example of a self-organizing system). The intermolecular interactions are governed by the electron distributions in molecular orbitals and by complementary shapes or structures. For purposes of discussion, the intermolecular interactions are heuristically classified and include hydrogen bonding, electrostatic interactions, coordination chemistry, and van der Waals forces acting in concert. The “lock-and-key” concept for shape complementarity has a long history.<sup>[78,79]</sup> Thus nature provides a plethora of examples, which demonstrate that self-assembly and self-organization are effective means to build complex, functional structures in good yields. The self-assembly of discrete supramolecular systems generally relies on the use of component molecules designed with specific intermolecular interactions such as H-bonds, metal ion coordination, and sometimes electrostatics because these noncovalent bonds are directional and stronger than

other intermolecular forces.<sup>[1]</sup> However, the self-organization of materials generally relies on a greater number of weaker, nonspecific interactions such as dipolar, van der Waals, and hydrophobic/hydrophilic forces. Crystals of supramolecular systems are an example of structures that arise from both directional and nondirectional intermolecular interactions.<sup>[39,40,82,84,86,87]</sup> In most cases, the architectures of molecules arising from both self-processes are the thermodynamic products.

## Supramolecular Systems on Surfaces

The advantages of using supramolecular chemistry to construct materials that can serve as components of nanoscaled devices include the ability to construct complex structures efficiently, but there are several significant technical challenges. The reversibility of the intermolecular interactions that allow self-assembly and self-organization to result in thermodynamic products in high yields also means that the structure of the system is sensitive to environmental factors such as concentration, temperature, ionic strength, etc.<sup>[10,11,17,88]</sup> Because the formation of the desired nanoarchitectures of organic molecules generally proceeds in solutions and these are to be incorporated onto surfaces as components of devices, the first challenge is to deposit the self-assembled or self-organized system onto an appropriate substrate. The inherent concentration changes during deposition and solvent evaporation may significantly alter the supramolecular structure, or result in undesirable aggregates. Other factors such as surface chemistry and surface energetics may also affect the structure of self-assembled or self-organized systems. The second challenge is to design supramolecular systems on surfaces that are stable to the operating conditions of the device. Device stability to thermal fluctuations, redox chemistry, environmental changes such as humidity, and dioxygen is crucial. But all of these factors can affect the equilibrium of self-assembled systems, thus also the structure and function. There are numerous examples of porphyrin-containing self-organized monolayers,<sup>[89–92]</sup> thin films,<sup>[20,93,94]</sup> and polymeric materials<sup>[95]</sup> on surfaces; however, there are only a few examples of self-assembled (discrete, monodispersed) systems that can be deposited onto surfaces with high structural fidelity that are stable at room temperature. These last constructs are the primary subject of this entry.

An important aspect of all types of nanoscaled materials on surfaces is the role of surface chemistry and surface energetics in determining the final structure/orientation of the molecules. This is especially true of self-assembled and self-organized systems because the surface properties may induce unanticipated

structural changes, or may be exploited as a further means of dictating the final structure.<sup>[10,11]</sup> A host of surface chemical preparations can be utilized to modify the surface chemistry, and hence the surface energetics of the substrate, which impacts the structure of adsorbing supramolecular materials. For example, Au surfaces can be modified by self-assembly of alkanethiol-based compounds. The chemistry of glass or mica surfaces can be readily changed by organosilanes, allowing for the generation of hydrophobic or hydrophilic surfaces. Chemical modification of the surface can even allow the direct assembly of species on surfaces by providing the appropriate anchor groups on which to build. Weakly bound aggregates, such as those organized by  $\pi$ -stacking, can be made to either retain or lose their initial solution structure depending on the competition between the interaggregate interactions, the interactions of the component molecules, and the interactions of the aggregates with the surface. This has been readily demonstrated by the adsorption of porphyrinic nanoparticles on surfaces.<sup>[10,11,96,97]</sup>

## Applications

Some of the applications of these porphyrinic materials are envisioned to be in the areas of molecular electronics<sup>[5,98]</sup> and photonic materials.<sup>[2,3,23,26]</sup> The latter applications exploit both the functionality and the rigid structure of porphyrins to make materials such as molecular sieves,<sup>[39,42]</sup> catalysts,<sup>[99]</sup> sensors,<sup>[100]</sup> actuators,<sup>[24]</sup> and non-linear optics.<sup>[101]</sup> Elegant synthetic organic work has yielded discrete multiporphyrinic systems held together by covalent bonds using a variety of linkers,<sup>[25,49–57,61,102–111]</sup> or by direct fusion of the porphyrin macrocycles.<sup>[58–62,112,113]</sup> In addition to the development of new synthetic methods, these types of molecules have provided insights into the complexities of photo-induced electron/energy transfer processes<sup>[51,104,105]</sup> in terms of chromophore geometry, role of the linker, and dynamics of the molecule. However, the overall yield of discrete molecular systems containing more than a few porphyrins is too low to be commercially viable for all but the most specialized applications. Similarly, numerous polymers of/with porphyrins have also yielded interesting materials that have a distribution of polymeric and photonic properties because of polydispersity and the subtly different environments of the chromophores.<sup>[70–73,114]</sup> For many of the aforementioned applications, control of both the relative positions of the macrocycles and the nano-scaled size of the system is necessary for the function.<sup>[1]</sup> Since the first publications on self-organizing<sup>[115,116]</sup> and self-assembling porphyrins via H-bonds<sup>[117]</sup> and coordination chemistry,<sup>[118]</sup> there has been an exponential annual increase in the number or reports of

multiporphyrinic systems made by these methods.<sup>[10,11,17,23,52,81,88,96,97,115–127]</sup> The primary focus of this entry will be on the developments of the last few years because there are several reviews and entries that cover a large body of work on the chemistry, properties, and applications of porphyrins up to early 2000.<sup>[52,81,85,126]</sup> There are also a variety of reviews on both self-assembly and multiporphyrin systems.<sup>[16,43,65,125,126,128–132]</sup>

## SELF-ORGANIZED PORPHYRINIC FILMS ON SURFACES

Because self-organized systems are generally less ordered and more tolerant of defects both in solution and on surfaces than self-assembled systems, these types of systems are generally easier to make. Thus the majority of work on porphyrinic materials on surfaces use self-organizing systems, which can be divided into two categories: [1] thin films<sup>[93,94]</sup> deposited as polymers or by layer-by-layer methods,<sup>[133–135]</sup> and [2] monolayers chemically attached via covalent<sup>[89,136–138]</sup> or coordination bonds to the surface,<sup>[139]</sup> or as (mono)-layers adsorbed onto the surface. To date, most of the demonstrated applications for nanoscaled porphyrinic materials on surfaces have been in the area of electrodes, wherein these types of layered films are used to modify electrodes to make them selective for various analytes, and/or to modify surface/electrode chemistry. Other applications in molecular electronics are in the early stages of development.

## Polymers and Layer-by-Layer Adsorption

The deposition of polymers and molecules onto surfaces via the layer-by-layer technique can be summarized as follows. Dipping a charged substrate into a solution containing an organic molecule or polymer of the opposite charge results in a thin film or layer of the material on the surface. After annealing and rinsing, the coated substrate is dipped into a second solution that has molecules or polymer(s) with the charge opposite to the first layer. This alternate layering can be repeated, but the structural fidelity generally decreases with increasing number of layers. The density of defects in each layer and the interpenetration of the layers are major issues for most layer-by-layer systems, but these are difficult to quantify on the molecular scale and may not be important for some applications. An early example of this technique used the tetraanionic tetra-4-sulfonatophenylporphyrin (TSPP) and a tetra-4-pyridylporphyrin (TPyP), where each of the four pyridyl groups coordinates with cationic RuBiPy<sub>2</sub> units (BiPy = 2,2'-bipyridine).<sup>[133]</sup> Other methods to make layers of porphyrins include the use

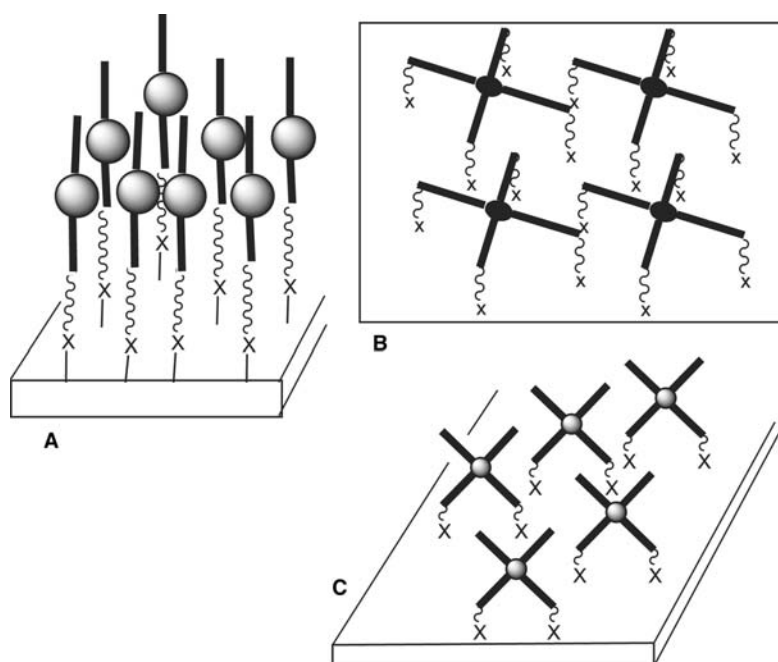


**Fig. 3** Chemical attachment of a hydrocarbon bearing a porphyrin at one end to a surface can be accomplished in a variety of ways by matching the reactivity of the substrate to the functional group on the opposite end. Some examples:  $x = \text{S}$  on gold,  $x = \text{PO}_3^{2-}$  on zirconium, and  $x = \text{O}$  on glass. The orientation of the porphyrin depends on the number and location of the reactive groups, as well as the nature of the hydrocarbon linker. The planes of the macrocycles are at an angle to the substrate surface in (A) and (C), and nearly parallel in (B). Some two-dimensional order can be found in small domains, but not globally.

of TPyP and Pd(II) in a layer-by-layer method wherein the first porphyrin is attached to a glass surface via an alkane linker (Fig. 3A). The substrate is then dipped in a solution of Pd(II), rinsed, and dipped in a solution of TPyP.<sup>[140]</sup> Again the defect density is not well established.

The stepwise self-organization of a bis-bipyridinium–porphyrin dyad and gold nanoparticles on a conductive indium tin oxide (ITO) surface results in a system where the redox properties are significantly different than the component molecules.<sup>[141]</sup> A cationic polyamine adsorbed onto glass promotes adsorption of anionic TSPP.<sup>[142]</sup> The electrostatic association of cobalt TPyP coordinated to four cationic Ru(BiPy)<sub>2</sub> moieties with anionic Zn(II)TSPP in layer-by-layer films on electrodes has been used to examine nitrite oxidation as an analytical application.<sup>[143]</sup> Indium tin oxide electrodes modified with porphyrin–fullerene dyads as the active layer give rise to improved light-harvesting properties in the visible region.<sup>[134,144]</sup> The synthesis and characterization of electropolymerized thin films of tetra(4-aminophenyl)porphyrin from an aqueous solution onto electrodes to form an emeraldine-type polymer was reported,<sup>[31]</sup> although the morphology of the film was not well defined. A five-component light-harvesting and electron transfer system using this alternating cationic/anionic porphyrin system was also reported.<sup>[145]</sup>

## Monolayers

The formation of uniform molecular films of porphyrins on solid surfaces can be accomplished by a variety of means, ranging from covalent attachment, to

coordination chemistry, to adsorption. The formation and properties of Langmuir–Blodgett films of porphyrin derivatives at the air–water interface have been well studied but are beyond the scope of the present discussion unless these films are then transferred to a solid support. Historically, the chemical, electrostatic, or adsorptive attachment of hydrocarbons to an appropriate surface to yield a uniform molecular layer is referred to as self-assembled monolayers (SAMs); however, these materials are more accurately described as self-organizing systems because they result in dynamic two-dimensional systems and generally do not exhibit specific intermolecular interactions. There has been considerable research on SAMs; some of the concepts found in numerous reports on porphyrin-containing monolayers are discussed below.

## Chemically Bound

One of the most common routes to monolayered materials on surfaces is to chemically bind (Fig. 3) a hydrocarbon bearing a reactive functional group to an appropriate surface. Most often, this method uses a thiol group (or its precursors) to react with gold surface, and there are numerous examples with porphyrins.<sup>[89,91,137,146–148]</sup> The gold–sulfur bond is reasonably strong, but there is some mobility along the surface. Other substrates such as ITO<sup>[147]</sup> and polypyrrole<sup>[149]</sup> have also been used. Using standard reactions for the derivitization of glass yields porphyrins on transparent supports, but the order of these systems is generally less than similar gold constructs. The nature of the hydrocarbon linker modulates the



physical properties, and therefore the photonic activity, of the monolayer. Carboxylate moieties have been used to organize monolayers of porphyrinic materials on surfaces such as gold<sup>[92,150–152]</sup> and mica,<sup>[93]</sup> and at the air–water interface<sup>[153]</sup> for later transfer to a solid support. The weaker substrate–molecule interactions of these systems allow more facile modification of the surface after formation of the monolayer, but it also results in less well-defined structures. A hybrid system with octacarboxylate porphyrins adsorbed facedown onto a gold surface surrounded by a bolaamphiphile monolayer has been reported.<sup>[154,155]</sup> The motivation behind this work is to make nanoscaled test tubes on the surface for catalytic or sensing applications. Phosphates are well known to bind to zirconium, and this system has been used to form porphyrin monolayers.<sup>[17,83,156–158]</sup>

Monothiolated porphyrins covalently bound to gold surfaces (shown schematically in Fig. 3A) have been formed with a variety of orientations relative to the surface plane. Control of such orientation has been the subject of many investigations. For instance, it has been shown that the length of alkane linkers between the porphyrin and gold surfaces affects their relative orientations. For smaller chains, odd numbers of methylene groups exhibit a more perpendicular orientation, whereas an even number results in a more parallel arrangement.<sup>[159]</sup> In addition, post-assembly metal insertion has been shown to avoid unexpected disorder in the monolayer.<sup>[137]</sup> Structural control of the monolayer is needed for various applications that require defined chromophore architectures. Surface catalysis requires such a condition, and porphyrinic monolayers attached to gold surfaces have been shown to better control the rate and selectivity of the electrocatalytic oxidation of ascorbic acid.<sup>[46]</sup> Other applications include biorecognition surfaces for attaching cells, proteins, and other biomolecules, which also require rigid, enzyme-like clefts on the surface for biomolecule attachment.<sup>[160]</sup> Artificial photosynthesis, photocatalysis,<sup>[136,138,147,161]</sup> and molecular photonics<sup>[147,159]</sup> using porphyrinoids are also under development. Well-defined aggregates are better able to harvest light<sup>[91,159]</sup> than the lone metal/composite surface, and these dyes are used to increase the absorption of near-infrared (IR) light for photocatalysis.<sup>[91]</sup> Furthermore, three-dimensional architectures of nanosize particles provide even more light-harvesting efficiency than the two-dimensional layers. This has been demonstrated by the synthesis of an air-stable alkanethiolate monolayer-protected gold cluster.<sup>[136]</sup> Porphyrin monolayers have also been the subject of surface plasmon excitation studies.<sup>[89,163]</sup> Gold surfaces have proven to be an effective excitation source for porphyrin monolayers. Although gold is the most commonly studied solid substrate, other possible

surfaces continue to be explored. Porphyrins have been attached through a silane bond to glass<sup>[163,164]</sup> and ITO.<sup>[147]</sup> In the former case,<sup>[164]</sup> instead of directly linking the porphyrin to the surface, the glass was silylated beforehand and the porphyrin was connected via amide coupling. For example, a freebase porphyrin monolayer on glass was designed for heavy metal detection in environmental applications. In the latter case,<sup>[147]</sup> ITO was chosen to increase the quantum yield because of its semiconducting properties. The ITO exhibited remarkably better photocurrent generation than a similar system on gold because gold introduces an undesirable electron transfer quenching not observed with semiconductors. More complex (structural, redox, and optical) photonic triple-decker molecules containing porphyrins, phthalocyanines, and both porphyrins and phthalocyanines have been used to form monolayers with more complex redox and optical properties.<sup>[148,165–169]</sup> The increased physical chemical complexity affords an opportunity to design and characterize devices that act as multistate counters for molecular electronics applications.

Hipps et al. have carried out extensive scanning tunneling microscopy (STM) studies of porphyrin and phthalocyanine monolayers on metal surfaces. Scanning tunneling microscopy studies revealed that well-ordered two-dimensional arrays form from vapor-deposited films on Au(111) and that the atomic structure of the rings could be observed. Contrast differences were readily obtained for metalation of the macrocycle, and the differing chemical properties of the pendent groups could be used to vary the surface structure.<sup>[170–172]</sup> Other surfaces such as Cu(100) have been used for STM studies as well.<sup>[157]</sup> The electrochemical potential of an electrode surface can also modulate the self-assembly of porphyrinic systems.<sup>[173]</sup>

Another means to organize two different chromophores—one per layer—is to use porphyrins bearing two different functional groups. By these means, one functional group is used to attach the porphyrin to the surface, which poises the second functional group on the opposite side of the macrocycle to form supramolecular or covalent bonds with a second chromophore in a second step. The subsequent layers are added with varying degrees of structural fidelity to the initial layer. Because of the increasing propensity for defects with increasing number of layers, characterization of multilayer systems is often more difficult.

## Coordination Chemistry

There have been numerous reports on systems where exocyclic ligands such as pyridine on the porphyrins coordinate to metal ions bound to the surface by

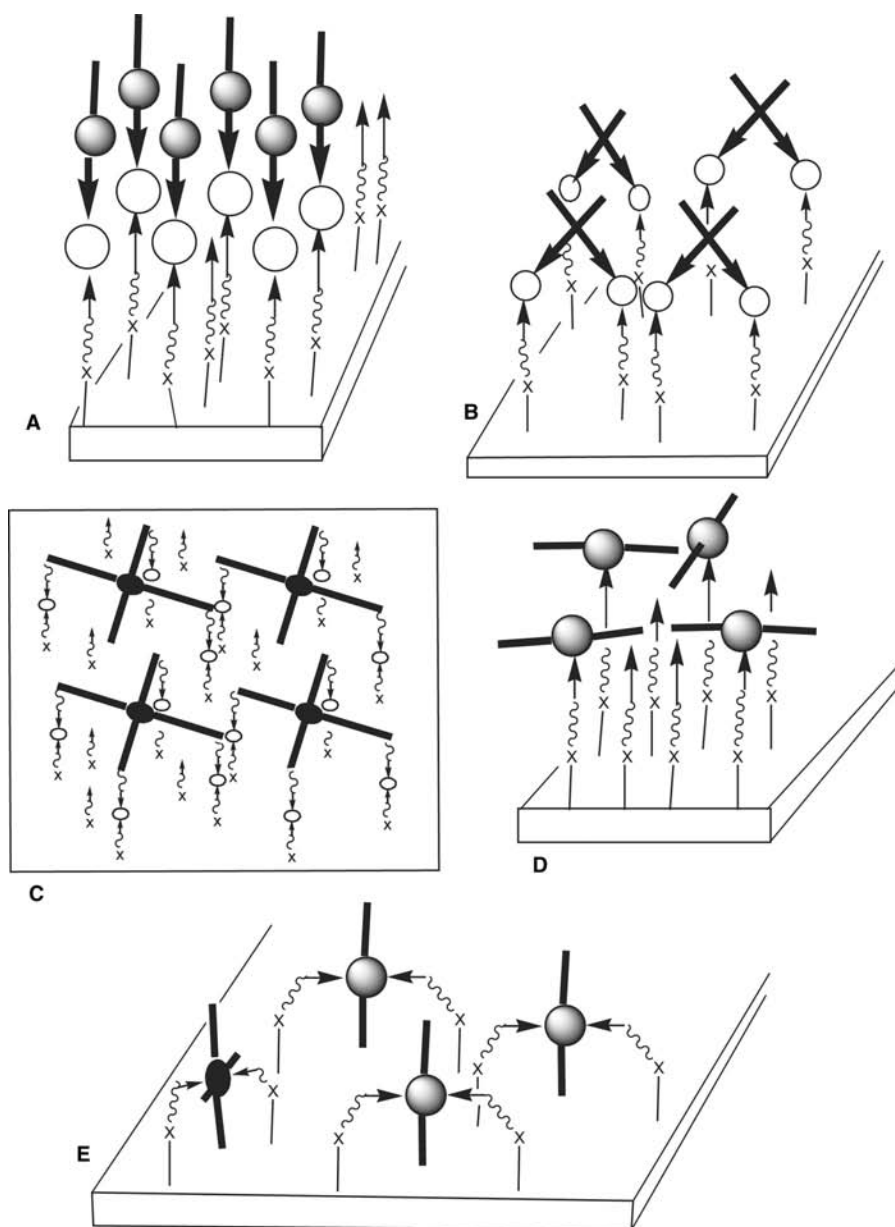


**Fig. 4** Organization of monolayers on surfaces using coordination chemistry. As in Fig. 3, the relative orientation of the porphyrin plane to the surface depends on the mode and topology (number of bonds between the macrocycle and the surface). (A)–(C) use ligands on the porphyrin to coordinate to metal ions attached to the surface by ligands chemically bound to the surface. (D) and (E) use chemically attached ligands that coordinate to metalloporphyrins either at one or two axial positions. X can be a variety of organic or inorganic functional groups and depends on the surface chemistry. The arrowheads indicate the connectivity mediated by ligand coordination. Not all surface-bound ligands are used.

ligands, which are chemically attached to the surface (Fig. 4A–C). Conceptually, this approach (e.g., Refs.<sup>[95,150,174]</sup>) is similar to the chemically attached self-organized monolayers. Surfaces modified with covalently bound ligands can also directly bind metalloporphyrins in the axial position(s) (e.g., Ref.<sup>[175]</sup>) (Fig. 4D and E). The chemistry used to attach these various ligands is essentially the same as that used for the self-organized monolayers where the nature of the surface dictates the range of suitable functional groups. This method affords a great deal of design flexibility in terms of porphyrin orientation and placement of functional groups. The linkers most commonly used contain pyridine, which ligates to the metal center,<sup>[174,176,177]</sup> or carboxylic acid-terminated hydrocarbon chain, which hydrogen-bonds

to complementary groups on the macrocycle.<sup>[150]</sup> An advantage of using hydrogen bonding is that the center of the porphyrin remains functionally available for applications such as catalysis or molecular recognition,<sup>[178]</sup> and allows the use of freebase porphyrins. For coordination bonds, a variety of metals can be used, although zinc<sup>[174,176]</sup> and cobalt<sup>[176,177,179]</sup> are the most common. Systems using metalloporphyrins allow for the utilization of the metal center for catalysis<sup>[176,177]</sup> and nanoscaled optical devices.<sup>[174,177]</sup> In special cases, a single type of linker can symmetrically ligate the metal on both axial positions of a metalloporphyrin,<sup>[33,180]</sup> such as pyridine ligands coordinating an iron or cobalt center. These types of assemblies (Fig. 4E) can be used to study electronic changes involved in the reversible binding of dioxygen,<sup>[33]</sup> or

to study the optical spectroscopy of metalloporphyrins on surfaces.<sup>[180]</sup>

There are several examples of two-dimensional monolayers where a ligand is covalently attached to the substrate and this binds to an axial position of a metalloporphyrin.<sup>[160,175–177,179,181,182]</sup> This method to make monolayers on surfaces generally orients the plane of the porphyrin parallel to the plane of the surface, but there is sufficient room for the macrocycle to tilt such that a range of orientations is possible. These may be investigated by surface plasmon resonance, surface-enhanced Raman scattering, and surface-enhanced IR absorption.<sup>[37,89,146,162]</sup> Interactions of analytes with these porphyrin-modified surfaces may be exploited as a means of chemical identification and sensing. As mentioned above, the relative orientation of the porphyrin rings with respect to each other and with respect to the surface is of paramount importance to the photonic properties of the system. An elegant way to use coordination chemistry to orient metalloporphyrins perpendicular to the surface is to make monolayers with flexible linkers and ligands that generally are poised to bind 6-coordinate metalloporphyrins in both axial positions (Fig. 4E), resulting in layers with the plane of the macrocycle generally perpendicular to the surface.<sup>[139,180]</sup>

### Adsorption of Liquid Crystalline and Mesogenic Materials

One of the early successes in the self-organization of a porphyrin-based device utilized liquid crystal-type

interactions to form thin films of a photoconducting zinc porphyrin with eight dodecyloxy groups on the pyrroles.<sup>[4,183,184]</sup> Electron–hole pairs are generated on irradiation of a section of a device that has this porphyrin derivative placed between two optically transparent electrodes with an applied electric field. The device then performs as a high-density nanosecond charge trap that can be used as an optical memory device. Similar porphyrins were used to make liquid crystal thin films between ITO-coated glass slides, which displayed electric field-modulated near-field photoluminescence.<sup>[185]</sup> These studies show that there is a correlation between the device's physical properties and the morphology of the self-organized, photoactive, organic layer. Other liquid crystal-forming porphyrins with properties dependent on the nature and position of the hydrocarbon have also been reported.<sup>[186–188]</sup> The attachment of long-chain hydrocarbons allows for the two-dimensional organization of porphyrins (Fig. 5)<sup>[92]</sup> and phthalocyanines<sup>[189–191]</sup> on surfaces, which can be characterized by scanning probe microscopy.<sup>[192,193]</sup>

There are several examples of discrete multiporphyrin arrays with long-chain hydrocarbons appended on the periphery that induce the formation of monolayers by the Langmuir–Blodgett method. Then, these can be transferred to surfaces such as glass with reasonable structural integrity.<sup>[64,194,195]</sup> These films are early examples of using a secondary procedure to self-organize self-assembled supermolecules. A good example of an alternating current light-emitting device based on Langmuir–Blodgett films of porphyrins was

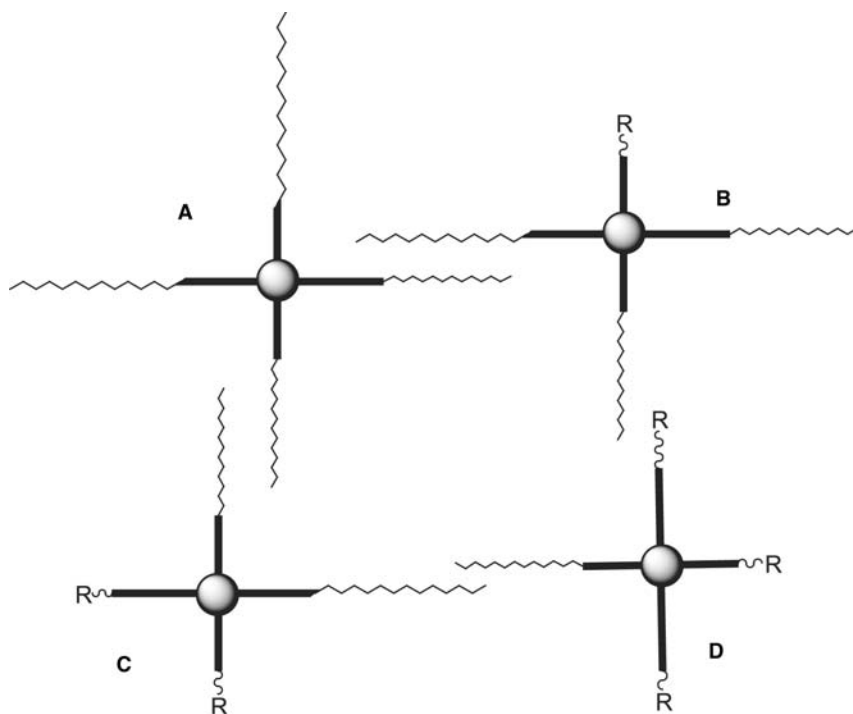


**Fig. 5** Porphyrins bearing long-chain hydrocarbons that serve as liquid crystal-forming motifs can be adsorbed on surfaces. The R-group can be a variety of polar and non-polar functional groups. The number and topology of the hydrocarbon chains and the nature of R-groups govern the molecule–surface and molecule–molecule interactions thus the resulting organization on the surface.

reported,<sup>[196]</sup> where the transient character of electroluminescence is explained in terms of a space charge-assisted electron injection.

Solid vesicle membranes made of bixin–porphyrin derivatives have been reported to form stable colloidal solutions, which can be photopolymerized to yield 30- to 120-nm spheres<sup>[197]</sup> and cast onto surfaces. Self-assembled fibrillar networks are formed from porphyrins bearing two lipid groups on the same side of the macrocycle.<sup>[198]</sup>

## Outlook

The self-organization of porphyrins on a variety of surfaces can be accomplished via covalent attachment, coordination chemistry, and electrostatic interactions. The choice of substrate and mode of attachment is dictated by the desired function of the surface-bound photonic material. In general, the relative orientation of the macrocycle to the plane of the substrate can be reasonably designed, but the horizontal two-dimensional structure of the porphyrins is usually much less ordered or organized than simple SAMs. The two-dimensional order that is observed results from weak porphyrin–porphyrin interactions and is generally found only in small domains, rather than globally. The extent of these organized domains varies with the mode of surface assembly found in Figs. 3–5. This does not imply that these systems are not well suited for some purposes, but rather that long-range surface organization is not easily achieved by these

approaches. The applications of these systems can be as diverse as the mode of assembly, the nature of the porphyrin, the choice of substrate, and the properties of the linkage. All of these parameters can be systematically changed to modulate the material/device properties and to optimize catalytic, sensor, and photonic functions.

## SELF-ASSEMBLED PORPHYRINIC MATERIALS ON SURFACES

As discussed in the “Introduction,” there are several challenges to using self-assembled and self-organized structures in commercial devices, which can be generally ascribed to issues of structural and chemical stability. One of the first examples of self-assembled porphyrin arrays that address the above issues is a self-assembled nonamer (Fig. 6A). The  $3 \times 3$  tessellation of nine porphyrins of three topologies (+, T, and L-shaped) is mediated by the *trans* coordination geometry of Pd(II) in a variety of organic solvents. These non-amers (which are the third generation of self-assembled porphyrin arrays mediated by metal ion coordination) can then self-organize into columnar stacks of 1 to ~20 layers to form  $6.5 \times 0.5$ –10 nm nanoscaled aggregates.<sup>[122]</sup> The length of the columnar stack can be fine-tuned by the choice of appended alkane, solvent, metalloporphyrin, and by kinetics.<sup>[11,88]</sup> These stacks can be deposited onto glass surfaces without any observable change in structure or function because of the weak interactions between the

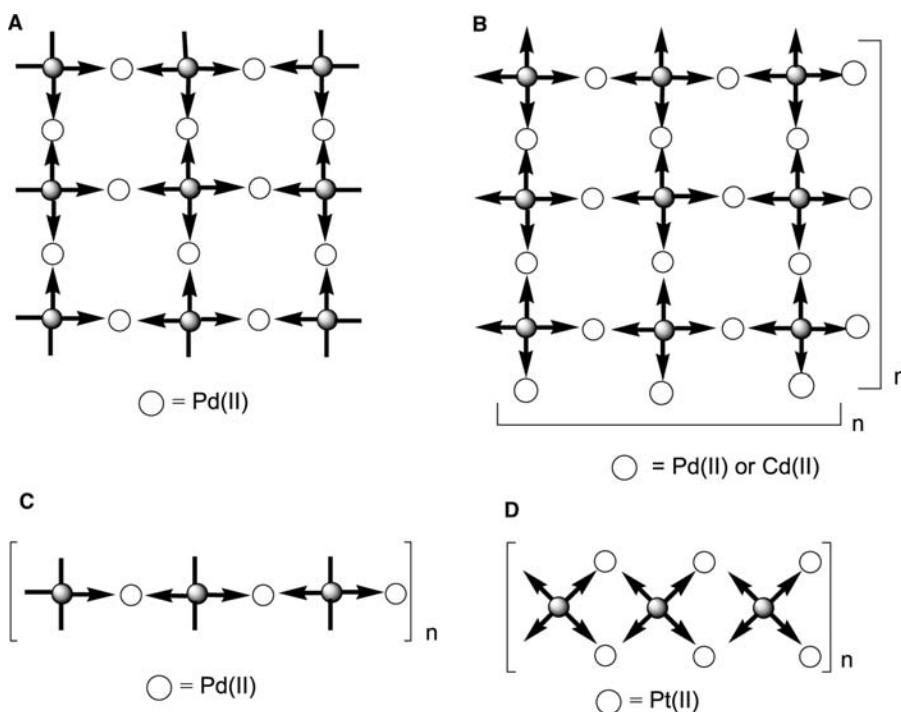


**Fig. 6** Self-assembled porphyrinic arrays and polymers. (A) A 21-particle porphyrin non-amer can be placed on Au(111) surfaces with high structural fidelity, or nanoscaled aggregates can be placed on a variety of surfaces. (B) Two-dimensional polymers with an as yet unspecified defect density are formed using a similar chemistry. (C, D) Short one-dimensional polymers can also be made with a distribution of lengths depending on the thermodynamics of the coordination bonds and topology. The arrowheads indicate the connectivity mediated by ligand coordination.



aggregate and the substrate and the strength of the intermolecular forces holding the nonamer and the stack together. Conversely, the individual (non-aggregated) non-amer can be deposited on an Au(111) surface—an example of a purely self-assembled structure deposited on a surface. Most importantly for applications, all of these constructs and their photonic functions are stable in air at room temperature for years.<sup>[10]</sup> The next challenge will be to self-organize the self-assembled non-amers into two-dimensional arrays on surfaces.

The ability to control the size of the nanoscale aggregates of porphyrin nonamers is an important consideration for many applications, *vide supra*. This can be accomplished by a variety of means. The nature of the peripheral R-group affects the solubility of the non-amer and thus the heights of the nanoaggregates can be varied from  $\sim 10$  nm, where R = H, to  $\sim 7$  nm, where R = methyl, to  $\sim 5$  nm, where R = *tert*-butyl as observed by atomic force microscopy (AFM) on glass.<sup>[10,11]</sup> The metalation state of the porphyrin and the choice of metal affect the internonamer interactions both by electrostatics and by altering the  $\pi$ -stacking energetics. The average height for the R = *tert*-butyl freebase is  $\sim 5$  nm, for the Zn(II) derivative is  $\sim 7$  nm, and the Co(II) is about 11 nm, as observed by AFM on glass.<sup>[10,11]</sup> The surface–non-amer interactions also play a role in the size of the nanoparticle found on a substrate; thus single non-amers are observed by AFM and STM on Au(111). The average columnar height is  $\sim 3$  nm on mica, and the average height is  $\sim 5$  nm for the freebase R = *tert*-butyl on glass. During the equilibration process, 20- to 150-nm aggregates are observed, which ultimately result in the above  $< 15$  nm columnar stacks, although the structural arrangement of the non-amers within these is not known at this time. These large aggregates can be deposited on surfaces, and after solvent evaporation, they are trapped in this aggregation state. These samples are as stable as the smaller  $\sim 5$ -nm particles. In addition to influencing the height of the columnar nanoaggregates, the R-groups that constitute the side surfaces also play a role in determining interaggregate associations. Thus non-amers bearing dodecyloxyphenyl groups were constructed in the expectation that these long hydrocarbon chains would assist in the organization of the non-amers, and the columnar aggregates on surfaces. UV–visible spectroscopy, dynamic light scattering (DLS), and  $^1\text{H}$  nuclear magnetic resonance (NMR) spectroscopy indicate that this non-amer is indeed formed in solution. However, neither the non-amers nor the columnar aggregates are observed by AFM on gold or glass, respectively. These results indicate that the additional surface–non-amer interactions arising from the 12 hydrocarbon chains is sufficient to break apart the non-amer on

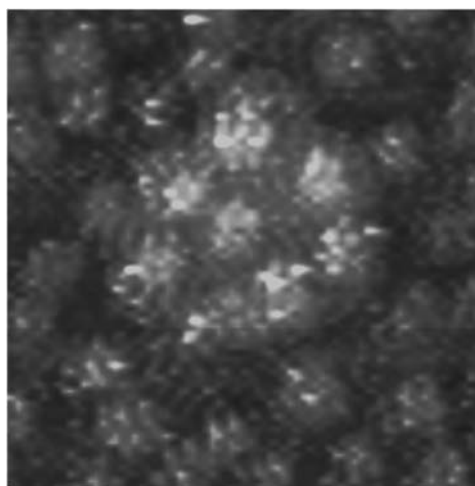


**Fig. 7** Scanning tunneling microscopy indicates that the 12 dodecyloxyphenyl groups interact strongly with an Au surface and break apart the nonamer to yield individual nonassembled porphyrins. Area,  $20 \times 20$  nm;  $\delta z$ ,  $\sim 0.5$  nm.

gold (Fig. 7), and to form amorphous films on glass. This is clear evidence that there is a careful balance between the intermolecular interactions in self-assembled supramolecular systems and the energetics of binding these systems to surfaces.

Using similar design strategies, several two-dimensional arrays/polymers (Fig. 6B) are formed from TPyP and Cd(II) using Langmuir–Blodgett methods, which then can be deposited on surfaces,<sup>[199]</sup> or the equivalent Pd(II) linked array can be made with the layer-by-layer method.<sup>[135]</sup> These are two examples of methods to make self-organized two-dimensional monolayers using specific intermolecular interactions, but the long-range order (or defect density) is not well established in either case.

When deposited on a variety of surfaces, small one-dimensional porphyrinic tapes (Fig. 6C and D) result in a variety of aggregates and little organization. To obtain better surface organization of these types of systems, long-chain hydrocarbons have been placed on the peripheral phenyl groups of a Pd(II)-linked dimer.<sup>[200]</sup> However, this system tends to form non-uniform films and rings of varying heights, radii, and thickness largely because of solvent evaporation during the deposition process. One likely explanation for this variation in surface topology of this particular dimer is that there is substantial flexibility in the relative orientations of the two macrocycles. As a result, both the dimer–dimer and dimer–surface interactions are not well defined.

To construct self-assembled arrays that then self-organize into reasonably uniform films on surfaces, two porphyrinic squares bearing dodecyloxyphenyl groups on the periphery were constructed, as shown

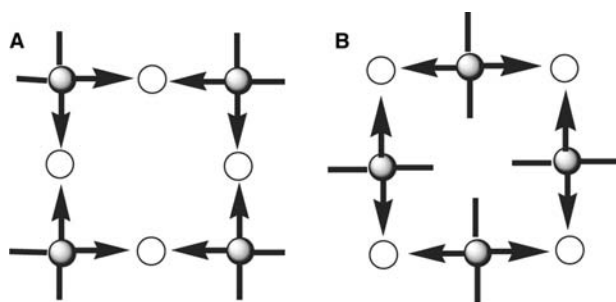


**Fig. 8** Two porphyrinic supramolecular tetramers: (A) square results from the  $90^\circ$  topology of the pyridyl groups on these porphyrins and the architecturally complementary  $180^\circ$  coordination geometry of  $\text{Pd(II)Cl}_2$ ; and (B) cube results from the  $180^\circ$  topology of the pyridyl groups on the isomeric porphyrins and the architecturally complementary  $90^\circ$  coordination geometry of  $\text{Pt(II)Cl}_2$ . The eight remaining substituents are dodecyloxyphenyl groups. The arrowheads indicate the connectivity mediated by ligand coordination.

schematically in Fig. 8. The intent was that there would be much less conformational flexibility, compared to the above dimer; therefore the intersupramolecular forces would be more defined, and a more ordered film would result. These squares are constructed using the same design strategy as the first discrete porphyrin assemblies reported—pyridyl porphyrins with  $\text{Pd(II)}$  and  $\text{Pt(II)}$ .<sup>[118]</sup> Because the  $\text{Pt-Py}$  bond is stronger than the  $\text{Pd-Py}$  bond, assemblies using  $\text{Pt}$  as a linker are more robust. Consistent with previous findings, these supramolecular squares with dodecyloxy groups are all well characterized in solution by NMR, UV-visible, and mass spectral analyses. The conformation of **8A** is largely planar as illustrated because the  $90^\circ$  topology of the rigid corner macrocycles prevents much twisting about the pyridyl- $\text{Pd(II)}$  bond, but the conformation of **8B** is boxlike or parallelogram-like because there can be substantial rotation about the pyridyl- $\text{Pt(II)}$  bonds. The calculated structure showing the bond rotations is shown in Fig. 9. This means that the dodecyloxyphenyl groups of **8A** are essentially coplanar with the plane of the supramolecular square, but in **8B**, these groups are directed along two faces of the box. The orientation of these liquid crystal-forming groups has a significant influence on the resultant structure of the films on glass surfaces, such that films from **8B**-type squares are reasonably uniform, whereas those from **8A**-type squares are much less so. The relative number/strength of the van der Waals forces per supermolecule may be largely responsible for these observations. Although both **8A** and **8B** have eight alkane groups, only two per side of Fig. 8A can interact with a coplanar neighbor, but four alkanes interact with the neighbors of **8B**. This hypothesis is born out by AFM studies of these two supramolecular squares



**Fig. 9** MM2-calculated structure of a porphyrinic cube using  $\text{Pt(II)Cl}_2$  corners. The H and dodecyloxyphenyl groups are left out for clarity.

deposited on glass. **8B** tends to form thin films that are 2–5 nm thick, whereas Fig. 8A forms small islands of variable thickness. An **8B**-type square with *tert*-butylphenyl groups was made for comparison with the supermolecule with dodecyloxyphenyl groups. As expected, the *tert*-butylphenyl-substituted square does not form films but rather small aggregates similar to those observed for the non-amer discussed above. This is a clear indication that the number, position, and nature of the R-groups are of paramount importance to the self-organization of self-assembled arrays of porphyrins. Comparisons between the non-amer and the tetrameric species reveal that the size and conformational flexibility of the supermolecule also dictate the organization of these entities on surfaces. Further studies on the interactions of all of these systems on different surfaces will reveal the role of surface chemistry/energetics in the organization of supramolecular porphyrinic systems.

Adsorption of the dodecyloxyphenyl-functionalized porphyrin square on glass shows that a thin ( $\sim 2$  nm) film is formed. The thickness of this film is in general agreement with the dimensions of a single central square unit, as shown schematically in Fig. 10. The film is composed of both nanoparticles of these subunits and larger domains/islands (Fig. 11), which are found to be much more uniform in height than those of the porphyrin rings using a  $\text{Pd}$ -linked dimer.<sup>[200,201]</sup> Annealing of the samples may yield more organized structures, and temperature-dependent studies are currently underway.



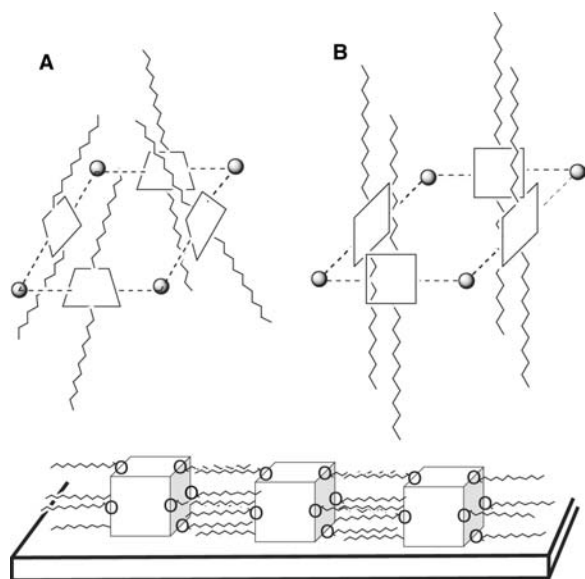


**Fig. 10** Two possible conformations of the tetramer in Fig. 8B (top) and possible interactions between the supramolecular tetramers in Fig. 8B (bottom).

## Outlook

The ability to deposit specifically designed self-assembled (discrete) supramolecular structures onto surfaces without change in structure or function remains a significant challenge for the exploitation of this methodology in real-world applications and devices. However, self-organized monolayer systems are more accessible because of the tolerance for local defects, but the horizontal dimensions of these are generally quite large. The layer-by-layer method has both advantages (ease of preparation) and disadvantages (greater defect density than SAMs), but may find

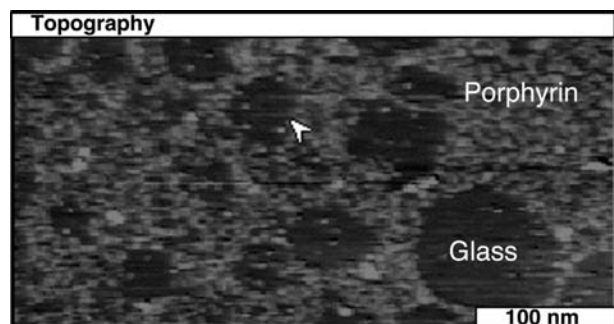


**Fig. 11** Topographic AFM image of the dodecyloxyphenyl-functionalized porphyrin square **8B** on glass formed by drop casting and evaporation of solvent. The film is composed of nanoscale particles  $\sim 2$  nm in height. The uncovered regions are glass (dark open circles). A bright (indicating higher topography) spot appears where multiple particles have stacked together and were not removed by rinsing.

numerous applications as sensors, and other systems requiring surface modification. The adsorption of a  $\text{La(III)(TPyP)}_2$  sandwich compound onto a liquid Hg surface can provide access to two-dimensional arrays on this and other surfaces when they are chemically cross-linked with a dibromohydrocarbon.<sup>[202,203]</sup> The overall structure of these systems is likely a grid, but because the cross-linking step results in kinetic rather than thermodynamic products, the degree or order is likely not comparable to self-assembled/organized systems. This work is notable because it is an attempt to organize porphyrin sandwich compounds on surfaces with greater structural stability and a degree of order different from monolayers of similar compounds.

## CONCLUSION

The use of porphyrins and porphyrinoids for self-assembly and self-organization of molecules and ions to create functional, photonic materials has been the cornerstone of much research because of their structural rigidity, chemical stability, and rich photochemical and electrochemical properties. The facile modulation of the photonic properties of porphyrins<sup>[27,36,51,204,205]</sup> is accomplished both by the choice of metal ion and by the choice of substituents on the macrocycle. Steric crowding and distortions of the macrocycle can alter the excited state lifetimes of some nickel porphyrins by six orders of magnitude.<sup>[206,207]</sup> The placement of self-assembled/organized porphyrinoids on surfaces<sup>[89–92,95,146,150,152,173,174,182,208,209]</sup> remains a key issue toward the use of these systems in materials and devices,<sup>[10,11]</sup> and scanning probe methods for both discerning functional properties and organization have been used.<sup>[208–210]</sup> Although the focus of much of the research discussed herein is on nanoscaled materials<sup>[3,5,10,11,23,68,93,97,125,134,141,146,152,154,158,183,193,201,210–220]</sup> in which at least one dimension is less than a few nanometers, some applications of porphyrinoids require larger, less defined structures such as nanoscaled colloids between about 100 and 600 nm for catalysis, or less well-defined or controllable surface structures.<sup>[210–220]</sup> To date, the methods to self-assemble discrete multiporphyrinic systems of this size are limited, but aggregates of this size have been made and deposited on surfaces.<sup>[97]</sup> These particles exhibit enhanced catalytic activity and have novel photonic properties. The rapid advances in supramolecular chemistry, surface chemistry, and physical chemistry indicate that molecule-based materials have a bright future.

## ACKNOWLEDGMENTS

Funding from the National Science Foundation (CHE-0135509 and IGERT DGE-9972892), the

Israel–U.S. Binational Science Foundation (1999082), and the National Institutes of Health (SCORE) is gratefully acknowledged.

## REFERENCES

- Alivisatos, A.P.; Barbara, P.F.; Castleman, A.W.; Chang, J.; Dixon, D.A.; Klein, M.L.; McLendon, G.L.; Miller, J.S.; Ratner, M.A.; Rossky, P.J.; Stupp, S.I.; Thompson, M.E. From molecules to materials: current trends and future directions. *Adv. Mater.* **1998**, *10* (16), 1297–1336.
- Tour, J.M. Molecular electronics. Synthesis and testing of components. *Acc. Chem. Res.* **2000**, *33* (11), 791–804.
- Lent, C.S. Bypassing the transistor paradigm. *Science* **2000**, *88*, 1597–1599. June 2.
- Fox, M.A. Fundamentals in the design of molecular electronic devices: long-range charge carrier transport and electronic coupling. *Acc. Chem. Res.* **1999**, *32* (3), 201–207.
- Ellenbogen, J.C.; Love, J.C. Architectures for molecular electronic computers: 1. Logic structures and an adder designed from molecular electronic diodes. *Proc. IEEE* **2000**, *88* (3), 386–426.
- Collinson, S.R.; Bruce, D.W. Chapter 7: Metallomesogens—supramolecular organization of metal complexes in fluid phases. In *Transition Metals in Supramolecular Chemistry*; Sauvage, J.-P., Ed.; John Wiley and Sons Ltd.: New York, 1999; 285–369.
- Donnio, B.; Bruce, D.W. Metallomesogens. In *Structure and Bonding*; Springer-Verlag: Berlin, 1999; Vol. 95, 193–247.
- Monobe, H.; Miyagawa, Y.; Mima, S.; Sugino, T.; Uchida, K.; Shimizu, Y. Photoconductive properties of a mesogenic long-chain tetraphenylporphyrin oxovanadium(IV) complex. *Thin Solid Films* **2001**, *393* (1–2), 217–224.
- Shimizu, Y.; Matsuno, J.; Miya, M.; Nagata, A. The first aluminum discotic metallomesogen: hydroxo-[5,10,15,20-tetrakis(4-*n*-dodecaphenyl)-porphyrinato]-aluminum(III). *Chem. Commun.* **1994**, 2411–2412.
- Drain, C.M.; Batteas, J.D.; Flynn, G.W.; Milic, T.; Chi, N.; Yablon, D.G.; Sommers, H. Designing supramolecular porphyrin arrays that self-organize into nanoscale optical and magnetic materials. *Proc. Natl. Acad. Sci. U. S. A.* **2002**, *99*, 6498–6502.
- Milic, T.N.; Chi, N.; Yablon, D.G.; Flynn, G.W.; Batteas, J.D.; Drain, C.M. Controlled hierarchical self-assembly and deposition of nanoscale photonic materials. *Angew. Chem., Int. Ed. Engl.* **2002**, *41*, 2117–2119.
- Mauzerall, D.C. Evolution of porphyrins. *Clin. Dermatol.* **1998**, *16*, 195–201.
- Adler, A.D.; Longo, F.R.; Shergalis, W. Mechanistic investigations of porphyrin syntheses: I. Preliminary studies on *meso*-tetraphenylporphyrin. *J. Am. Chem. Soc.* **1964**, *86* (15), 3145–3149.
- Lindsey, J.S. Porphyrin synthesis. In *The Porphyrin Handbook*; Kadish, K.M., Smith, K.M., Guillard, R., Eds.; Academic Press: New York, 2000; Vol. 1, 45–118.
- Drain, C.M.; Gong, X. Synthesis of *meso*-substituted porphyrins in air without solvents or catalysts. *Chem. Commun.* **1997**, 2117–2118.
- Chou, J.-H.; Kosal, M.E.; Nalwa, H.S.; Rakow, N.A.; Suslick, K.S. Applications of porphyrins and metalloporphyrins to materials chemistry. In *The Porphyrin Handbook*; Kadish, K.M., Smith, K.M., Guillard, R., Eds.; Academic Press: New York, 2000; Vol. 6, 43–131.
- Drain, C.M.; Hupp, J.T.; Suslick, K.S.; Wasielewski, M.R.; Chen, X. A perspective on four new porphyrin-based functional materials and devices. *J. Porphy. Phthalocyanines* **2002**, *6* (4), 241–256.
- Chambron, J.-C.; Heitz, V.; Sauvage, J.-P. Noncovalent multiporphyrin assemblies. In *The Porphyrin Handbook*; Kadish, K.M., Smith, K.M., Guillard, R., Eds.; Academic Press: New York, 2000; Vol. 6, 1–42.
- Valkova, L.; Borovkov, N.; Kopranenkov, V.; Pisani, M.; Bossi, M.; Rustichelli, F. Some features of the molecular assembly of copper porphyrazines. *Mater. Sci. Eng., C* **2002**, *22* (2), 167–170.
- Valkova, L.; Borovkov, N.; Maccioni, E.; Pisani, M.; Rustichelli, F.; Erokhin, V.; Patternoilli, C.; Nicolini, C. Influence of molecular and supramolecular factors on sensor properties of Langmuir–Blodgett films of *tert*-butyl-substituted copper azaporphyrins towards hydrocarbons. *Colloids Surf., A Physicochem. Eng. Asp.* **2002**, *198–200*, 891–896.
- Lange, S.J.; Nie, H.; Stern, C.L.; Barrett, A.G.M.; Hoffman, B.M. Peripheral palladium(II) and platinum(II) complexes of bis(dimethylamino)porphyrazine. *Inorg. Chem.* **1998**, *37* (25), 6435–6443.
- Engelkamp, H.; Middelbeek, S.; Nolte, R.J.M. Self-assembly of disk-shaped molecules to coiled-coil aggregates with tunable helicity. *Science* **1999**, *284* (5415), 785–788.
- Burrell, A.K.; Wasielewski, M.R. Porphyrin-based nanostructures: routes to molecular electronics. *J. Porphy. Phthalocyanines* **2000**, *4* (5), 401–406.
- Fabbrizzi, L.; Licchelli, M.; Pallavicini, P. Transition metals as switches. *Acc. Chem. Res.* **1999**, *32* (10), 846–853.
- Wagner, R.W.; Lindsey, J.S.; Seth, J.; Palaniappan, V.; Bocian, D.F. Molecular optoelectronic gates. *J. Am. Chem. Soc.* **1996**, *118* (16), 3996–3997.
- Hong, F.T. Relevance of light-induced charge displacements in molecular electronics: design principles at the supramolecular level. *J. Mol. Electron.* **1989**, *5*, 163–185.
- Mines, G.A.; Tzeng, B.C.; Stevenson, K.J.; Li, J.; Hupp, J.T. Microporous supramolecular coordination compounds as chemosensory photonic lattices. *Angew. Chem., Int. Ed. Engl.* **2002**, *41* (1), 154–157.
- Rakow, N.A.; Suslick, K.S. A colorimetric sensor array for odour visualization. *Nature* **2000**, *406*, 710–713.
- Andrew, R.; Seiji, S. Cooperative binding in selective sensors, catalysts and actuators. *Coord. Chem. Rev.* **2000**, *205* (1), 157–199.

30. Keefe, M.H.; Benkstein, K.D.; Hupp, J.T. Luminescent sensor molecules based on coordinated metals: a review of recent developments. *Coord. Chem. Rev.* **2000**, *205* (1), 201–228.
31. Bruti, E.M.; Giannetto, M.; Mori, G.; Seeber, R. Electropolymerization of tetrakis(*o*-aminophenyl)porphyrin and relevant transition metal complexes from aqueous solution. The resulting modified electrodes as potentiometric sensors. *Electroanalysis* **1999**, *11* (8), 565–572.
32. Purrello, R.; Gurrieri, S.; Lauceri, R. Porphyrin assemblies as chemical sensors. *Coord. Chem. Rev.* **1999**, *190–192*, 683–706.
33. Ashkenasy, G.; Ivanisevic, A.; Cohen, R.; Felder, C.E.; Cahen, D.; Ellis, A.B.; Shanzer, A. Assemblies of “hinged” iron–porphyrins as potential oxygen sensors. *J. Am. Chem. Soc.* **2000**, *122* (6), 1116–1122.
34. Wu, D.G.; Ashkenasy, G.; Shvarts, D.; Ussyshkin, R.V.; Naaman, R.; Shanzer, A.; Cahen, D. Novel NO biosensor based on the surface derivatization of GaAs by “hinged” iron porphyrins. *Angew. Chem., Int. Ed. Engl.* **2000**, *39* (24), 4496–4500.
35. Sun, S.-S.; Lees, A.J. Transition metal based supramolecular systems: synthesis, photophysics, photochemistry and their potential applications as luminescent anion chemosensors. *Coord. Chem. Rev.* **2002**, *230* (1–2), 170–191.
36. Wosnick, J.H.; Swager, T.M. Molecular photonic and electronic circuitry for ultra-sensitive chemical sensors. *Curr. Opin. Chem. Biol.* **2000**, *4* (6), 715–720.
37. O’Brien, M.J.; Pérez-Luna, V.H.; Brueck, S.R.; López, G.P. A surface plasmon resonance array biosensor based on spectroscopic imaging. *Biosens. Bioelectron.* **2001**, *16* (1–2), 97–108.
38. Ozoemena, K.; Nyokong, T. Voltametric characterization of the self-assembled monolayer(SAM) of octabutylthiophthalocyaninatoiron(II): a potential electrochemical sensor. *Electrochim. Acta* **2002**, *47* (25), 4035–4043.
39. Diskin-Posner, Y.; Dahal, S.; Goldberg, I. Crystal engineering of metalloporphyrin zeolite analogues. *Angew. Chem., Int. Ed. Engl.* **2000**, *39* (7), 1288–1292.
40. Diskin-Posner, Y.; Patra, G.K.; Goldberg, I. Crystal engineering of 2-D and 3-D multiporphyrin architectures: the versatile topologies of tetracarboxyphenylporphyrin-based materials. *Eur. J. Inorg. Chem.* **2001**, (10), 2515–2523.
41. Goldberg, I. Design strategies for supramolecular porphyrin-based materials. *Cryst. Eng. Commun.* **2002**, *4*, 109–116.
42. Kumar, R.K.; Diskin-Posner, Y.; Goldberg, I. Solid-state supramolecular chemistry of porphyrins. Ligand-bridged tetraphenylmetalloporphyrin dimers. *J. Incl. Phenom. Macrocycl. Chem.* **2000**, *37*, 219–230.
43. Kosal, M.E.; Suslick, K.S. Microporous porphyrin and metalloporphyrin materials. *J. Solid State Chem.* **2000**, *152* (1), 87–98.
44. Kosal, M.E.; Chou, J.-H.; Suslick, K.S. A calcium-bridged porphyrin coordination network. *J. Porphy. Phthalocyanines* **2002**, *6* (6), 377–381.
45. Zimmerman, S.C.; Wendland, M.S.; Rakow, N.A.; Zharov, I.; Suslick, K.S. Synthetic hosts by monomolecular imprinting inside dendrimers. *Nature* **2002**, *418*, 399–403.
46. Lu, X.; Jin, J.; Kang, J.; Lv, B.; Liu, H.; Geng, Z. The characterization of 5-[[4-(4-mercapto)phenylmethoxy]phenyl-10,15,20-tris(phenyl)porphyrin cobalt(II) self-assembled monolayers (SAMs) and its electrocatalytic oxidation for ascorbic acid. *Mater. Chem. Phys.* **2003**, *77* (3), 952–957.
47. Ikeda, A.; Ayabe, M.; Shinkai, S.; Sakamoto, S.; Yamaguchi, K. A self-assembled porphyrin-based dimeric capsule constructed by a Pd(II)–pyridine interaction which shows efficient guest inclusion. *Org. Lett.* **2000**, *2* (23), 3707–3710.
48. Johnston, M.R.; Latter, M.J.; Warrenner, R.N. Porphyrin-containing molecular capsules: metal mediated dimerization of a bis-porphyrin cavity. *Org. Lett.* **2002**, *4* (13), 2165–2168.
49. Ambroise, A.; Li, J.; Yu, L.; Lindsey, J.S. A self-assembled light-harvesting array of seven porphyrins in a wheel and spoke architecture. *Org. Lett.* **2000**, *2* (17), 2563–2566.
50. Bothner-By, A.A.; Dadok, J.; Johnson, T.E.; Lindsey, J.S. Molecular dynamics of covalently linked multiporphyrin arrays. *J. Phys. Chem.* **1996**, *100* (44), 17551–17557.
51. Holten, D.; Bocian, D.F.; Lindsey, J.S. Probing electronic communication in covalently linked multiporphyrin arrays. A guide to the rational design of molecular photonic devices. *Acc. Chem. Res.* **2002**, *35* (1), 57–69.
52. Lindsey, J.S. Self-assembly in synthetic routes to molecular devices. Biological principles and chemical perspectives: a review. *New J. Chem.* **1991**, *15* (2–3), 153–180.
53. Fletcher, J.T.; Therien, M.J. Strongly coupled porphyrin arrays featuring both pie-cofacial and linear-pie-conjugative interactions. *Inorg. Chem.* **2002**, *41* (2), 331–341.
54. Fletcher, J.T.; Therien, M.J. Extreme electronic modulation of the cofacial porphyrin structural motif. *J. Am. Chem. Soc.* **2002**, *124* (16), 4298–4311.
55. Kumble, R.; Palese, S.; Lin, V.S.-Y.; Therien, M.J.; Hochstrasser, R.M. Ultrafast dynamics of highly conjugated porphyrin arrays. *J. Am. Chem. Soc.* **1998**, *120* (44), 11489–11498.
56. Lin, V.S.Y.; DiMaggio, S.G.; Therien, M.J. Highly conjugated, acetylenyl bridged porphyrins: new model for light-harvesting antenna systems. *Science* **1994**, *264*, 1105–1111.
57. Moore, K.T.; Fletcher, J.T.; Therien, M.J. Syntheses, NMR and EPR spectroscopy, electrochemical properties, and structural studies of [5,10,15,20-Tetrakis(perfluoroalkyl) porphinato] iron (II) and iron (III) complexes. *J. Am. Chem. Soc.* **1999**, *121* (22), 5196–5209.
58. Aratani, N.; Osuka, A.; Kim, Y.H.; Jeong, D.H.; Kim, D. Extremely long, discrete *meso-meso*-coupled porphyrin arrays. *Angew. Chem., Int. Ed. Engl.* **2000**, *39* (8), 1458–1462.

59. Aratani, N.; Osuka, A. Synthesis of *meso-meso* linked hybrid porphyrin arrays by Pd-catalyzed cross-coupling reaction. *Org. Lett.* **2001**, *3* (26), 4214–4216.
60. Aratani, N.; Osuka, A. Monodisperse giant porphyrin arrays. *Macromol. Rapid Commun.* **2001**, *22*, 725–740.
61. Osuka, A.; Tanabe, N.; Zhang, R.; Maruyama, K. An efficient synthesis of linear porphyrin arrays. *Chem. Lett.* **1993**, 1505–1508.
62. Nakano, A.; Osuka, A.; Yamazaki, T.; Nishimura, Y.; Akimoto, S.; Yamazaki, I.; Itaya, A.; Murakami, M.; Miyasaka, H. Modified windmill porphyrin arrays: Coupled light-harvesting and charge separation, conformational relaxation in the S1 state, and S2–S2 energy transfer. *Chem. Eur. J.* **2001**, *7* (14), 3134–3150.
63. Biemans, H.A.M.; Rowan, A.E.; Verhoeven, A.; Vanoppen, P.; Latterini, L.; Foekema, J.; Schenning, A.P.H.J.; Meijer, E.W.; de Schryver, F.C.; Nolte, R.J.M. Hexakis porphyrinato benzenes. A new class of porphyrin arrays. *J. Am. Chem. Soc.* **1998**, *120* (43), 11,054–11,060.
64. Foekema, J.; Schenning, A.; Vriezema, D.M.; Benneker, F.B.G.; Norgaard, K.; Kroon, J.K.M.; Bjornholm, T.; Feiters, M.; Rowan, A.E.; Nolte, R.H.M. Synthesis of multi-porphyrin arrays and study of their self-assembly behavior at the air–water interface. *J. Phys. Org. Chem.* **2001**, *14*, 501–512.
65. Burrell, A.K.; Officer, D.L.; Plioger, P.G.; Reid, D.C.W. Synthetic routes to multiporphyrin arrays. *Chem. Rev.* **2001**, *101* (9), 2751–2796.
66. Hecht, S.; Ihre, H.; Frechet, J.M.J. Porphyrin core star polymers: synthesis, modification, and implication for site isolation. *J. Am. Chem. Soc.* **1999**, *121* (39), 9239–9240.
67. Friend, R.H.; Gymer, R.W.; Holmes, A.B.; Burroughes, J.H.; Marks, R.N.; Tallani, C.; Bradley, D.D.C.; Dos Santos, D.A.; Bredas, J.L.; Logdlund, M.; Salaneck, W.R. Electroluminescence in conjugated polymers. *Nature* **1999**, *397*, 121–128.
68. Hernandez-Lopez, J.L.; Bauer, R.E.; Chang, W.-S.; Glasser, G.; Grebel-Koehler, D.; Klapper, M.; Kreiter, M.; Leclaire, J.; Majoral, J.-P.; Mittler, S. Functional polymers as nanoscopic building blocks. *Mater. Sci. Eng., C* **2003**, *23* (1–2), 267–274.
69. Inoue, K. Functional dendrimers, hyperbranched and star polymers. *Prog. Polym. Sci.* **2000**, *25* (4), 453–571.
70. Jiang, B.; Yang, S.-W.; Jones, W.E., Jr. Conjugated porphyrin polymers: control of chromophore separation by oligophenylenevinylene bridges. *Chem. Mater.* **1997**, *9* (10), 2031–2034.
71. Jiang, B.; Yang, S.W.; Bailey, S.L.; Hermans, L.G.; Niver, R.A.; Bolcar, M.A.; Jones, W.E., Jr. Toward transparent molecular wires: electron and energy transfer in transition metal derivatized conducting polymers. *Coord. Chem. Rev.* **1998**, *171* (1), 365–386.
72. Jiang, B.; Yang, S.-W.; Lam, P.T.; Jones, W.E., Jr. Design and synthesis of new conjugated porphyrin copolymers for optical–electronic applications. *Mater. Res. Soc. Symp. Proc.* **1998**, *488*, 323–328.
73. Jiang, B.; Yang, S.-W.; Jones, W.E., Jr. Metalloporphyrin polymers bridged with conjugated cyano-substituted stilbene units. *Synag. Met.* **1998**, *94* (2), 205–210.
74. Miura, A.; Yanagawa, Y.; Tamai, N. Excitation energy transfer of porphyrin in polymer thin films by time-resolved scanning near-field optical microspectroscopy. *J. Microsc.* **2001**, *202* (2), 401–407.
75. Wen, L.; Li, M.; Schlenoff, J.B. Polyporphyrin thin films from the interfacial polymerization of mercaptoporphyrins. *J. Am. Chem. Soc.* **1997**, *119* (33), 7726–7733.
76. Screen, T.E.O.; Thorne, J.R.G.; Denning, R.G.; Bucknall, D.G.; Anderson, H.L. Amplified optical nonlinearity in a self-assembled double-strand conjugated porphyrin polymer ladder. *J. Am. Chem. Soc.* **2002**, *124* (33), 9712–9713.
77. Twyman, L.J.; King, A.S.H. Formation of A<sub>2</sub>B<sub>2</sub> supramolecular porphyrin co-polymers. *Chem. Commun.* **2002**, 910–911.
78. Lehn, J.-M. Toward complex matter: supramolecular chemistry and self-organization. *Proc. Natl. Acad. Sci. U. S. A.* **2002**, *99* (8), 4763–4768.
79. Lehn, J.-M. Perspectives in supramolecular chemistry—from molecular recognition towards molecular information processing and self-organization. *Angew. Chem., Int. Ed. Engl.* **1990**, *29*, 1304–1319.
80. Lehn, J.-M. Perspectives in supramolecular chemistry—from molecular recognition towards self-organisation. *Pure Appl. Chem.* **1994**, *66* (10/11), 1961–1966.
81. Lawrence, D.S.; Jiang, T.; Levett, M. Self-assembling supramolecular complexes. *Chem. Rev.* **1995**, *95* (6), 2229–2260.
82. Moulton, B.; Zaworotko, M.J. From molecules to crystal engineering: supramolecular isomerism and polymorphism in network solids. *Chem. Rev.* **2001**, *101* (6), 1629–1658.
83. Nguyen, S.T.; Gin, D.L.; Hupp, J.T.; Zhang, X. Supramolecular chemistry: functional structures on the mesoscale. *Proc. Natl. Acad. Sci. U. S. A.* **2001**, *98* (21), 11849–11850.
84. Tabellion, F.M.; Seidel, S.R.; Arif, A.M.; Stang, P.J. Discrete supramolecular architecture vs. crystal engineering: The rational design of a platinum-based bimetallic assembly with a chairlike structure and its infinite, copper analogue. *J. Am. Chem. Soc.* **2001**, *123* (31), 7740–7741.
85. Whitesides, G.M.; Simanek, E.E.; Mathias, J.P.; Seto, C.T.; Chin, D.N.; Mammen, M.; Gordon, D.M. Non-covalent synthesis: using physical organic chemistry to make aggregates. *Acc. Chem. Res.* **1995**, *28* (1), 37–44.
86. Aakeroy, C.B.; Seddon, K.R. The hydrogen bond and crystal engineering. *Chem. Soc. Rev.* **1993**, 397–407.
87. Desiraju, G.R. Hydrogen bridges in crystal engineering: interactions without borders. *Acc. Chem. Res.* **2002**, *35* (7), 565–573.
88. Drain, C.M. Self-organization of self-assembled photonic materials into functional devices: Photo-switched conductors. *Proc. Natl. Acad. Sci. U. S. A.* **2002**, *99*, 5178–5182.
89. Ishida, A.; Majima, T. Exchange reaction of a decanethiol self-assembled monolayer with porphyrin disulfides observed by surface plasmon enhanced fluorescence spectroscopy. *Chem. Commun.* **1999**, 1299–1300.

90. Kong, D.-S.; Wan, L.-J.; Han, M.-J.; Pan, G.-B.; Lei, S.-B.; Bai, C.-L.; Chen, S.-H. Self-assembled monolayer of a Schiff base on Au(111) surface: electrochemistry and electrochemical STM study. *Electrochim. Acta* **2002**, *48* (4), 303–309.
91. Ishida, A.; Majima, T. Photocurrent generation of a porphyrin self-assembly monolayer on a gold film electrode by surface plasmon excitation using near-infrared light. *Chem. Phys. Lett.* **2000**, *322* (3–4), 242–246.
92. Zhang, Z.; Yoshida, N.; Imae, T.; Xue, Q.; Bai, M.; Jiang, J.; Liu, Z. A self-assembled monolayer of an alkanolic acid-derivatized porphyrin on gold surface: A structural investigation by surface plasmon resonance, ultraviolet–visible, and infrared spectroscopies. *J. Colloid Interface Sci.* **2001**, *243* (2), 382–387.
93. Imae, T.; Niwa, T.; Zhang, Z. Atomic force microscopic observation of the molecular orientation in ultrathin films of alkanolic acid-derivatized porphyrins on a mica surface. *J. Nanosci. Nanotechnol.* **2002**, *2* (1), 37–40.
94. Oberg, K.; Eliasson, B. A method for screening of coverage and film thickness of monolayers by projection of molecular electron density surface onto a substrate plane. *Mater. Lett.* **2001**, *49* (3–4), 147–153.
95. Sarno, D.M.; Grosfeld, D.; Jiang, B.; Afriyie, J.O.; Matienzo, L.J.; Jones, W.E., Jr. Self-assembled molecular architectures on surfaces: new strategies involving metal–organic copolymers. *Langmuir* **2000**, *16* (15), 6191–6199.
96. Drain, C.M.; Shi, X.; Milic, T.; Nifiatis, F. Self-assembled multiporphyrin arrays mediated by self-complementary quadruple hydrogen bond motifs. *Chem. Commun.* **2001**, 287–288.
97. Gong, X.; Milic, T.; Xu, C.; Batteas, J.D.; Drain, C.M. Preparation and characterization of porphyrin nanoparticles. *J. Am. Chem. Soc.* **2002**, *124* (48), 14,290–14,291.
98. Kwok, K.S.; Ellenbogen, J.C. Moletronics: future electronics. *Mater. Today* **2002**, *5* (2), 28–37.
99. Merlau, M.L.; Mejia, M.D.P.; Nguyen, S.T.; Hupp, J.T. Artificial enzymes formed through directed assembly of molecular square encapsulated epoxidation catalysts. *Angew. Chem., Int. Ed. Engl.* **2001**, *40* (22), 4239–4242.
100. Borovkov, V.V.; Lintuluoto, J.M.; Sugeta, H.; Fujiki, M.; Arakawa, R.; Inoue, Y. Supramolecular chirogenesis in zinc porphyrins: equilibria, binding properties, and thermodynamics. *J. Am. Chem. Soc.* **2002**, *124* (12), 2993–3006.
101. Ogawa, K.; Zhang, T.; Yoshihara, K.; Kobuke, Y. Large third-order optical nonlinearity of self-assembled porphyrin oligomers. *J. Am. Chem. Soc.* **2002**, *124* (1), 22–23.
102. Anderson, S.; Anderson, H.L.; Bashall, A.; McPartlin, M.; Sanders, J.K.M. Assembly and crystal structure of a photoactive array of five porphyrins. *Angew. Chem., Int. Ed. Engl.* **1995**, *34* (10), 1096–1099.
103. Wilson, G.S.; Anderson, H.L. A conjugated triple strand porphyrin array. *Chem. Commun.* **1999**, 1539–1540.
104. Ambroise, A.; Wagner, R.W.; Rao, P.D.; Riggs, J.A.; Hascoat, P.; Diers, J.R.; Seth, J.; Lammi, R.K.; Bocian, D.F.; Holtén, D.; Lindsey, J.S. Design and synthesis of porphyrin-based optoelectronic gates. *Chem. Mater.* **2001**, *13* (3), 1023–1034.
105. Benites, M.D.R.; Johnson, T.E.; Weghorn, S.; Yu, L.; Rao, P.D.; Diers, J.R.; Yang, S.I.; Kirmaier, C.; Bocian, D.F.; Holtén, D.; Lindsey, J.S. Synthesis and properties of weakly coupled dendrimeric multiporphyrin light-harvesting arrays and hole-storage reservoirs. *J. Mater. Chem.* **2002**, *12* (1), 65–80.
106. Li, J.; Lindsey, J.S. Efficient synthesis of light-harvesting arrays composed of eight porphyrins and one phthalocyanine. *J. Org. Chem.* **1999**, *64* (25), 9101–9108.
107. Roth, K.M.; Gryko, D.T.; Clausen, C.; Li, J.; Lindsey, J.S.; Kuhr, W.G.; Bocian, D.F. Comparison of electron-transfer and charge-retention characteristics of porphyrin-containing self-assembled monolayers designed for molecular information storage. *J. Phys. Chem., B* **2002**, *106* (34), 8639–8648.
108. Yu, L.; Lindsey, J.S. Rational syntheses of cyclic hexameric porphyrin arrays for studies of self-assembling light-harvesting systems. *J. Org. Chem.* **2001**, *66* (22), 7402–7419.
109. Hyslop, A.G.; Kellett, M.A.; Iovine, P.M.; Therien, M.J. Suzuki porphyrins: new synthons for the fabrication of porphyrin-containing supramolecular assemblies. *J. Am. Chem. Soc.* **1998**, *120* (48), 12,676–12,677.
110. LeCours, S.M.; Guan, H.W.; DiMaggio, S.G.; Wang, C.H.; Therien, M.J. Push–pull arylethynyl porphyrins: new chromophores that exhibit large molecular first-order hyperpolarizabilities. *J. Am. Chem. Soc.* **1996**, *118* (6), 1497–1503.
111. de Rege, P.J.F.; Williams, S.A.; Therien, M.J. Direct evaluation of electronic coupling mediated by hydrogen-bonds: implications for biological electron transfer. *Science* **1995**, *269*, 1409–1413.
112. Smith, K.M.; Jaquinod, L.; Vicente, M.G.H. Oligomeric porphyrin arrays. *Chem. Commun.* **1999**, 1771–1782.
113. Tsuda, A.; Furuta, H.; Osuka, A. Syntheses, structural characterizations, and optical and electrochemical properties of directly fused diporphyrins. *J. Am. Chem. Soc.* **2001**, *123* (42), 10,304–10,321.
114. Jiang, H.; Su, W.; Hazel, J.; Grant, J.T.; Tsukruk, V.V.; Cooper, T.M.; Bunning, T.J. Electrostatic self-assembly of sulfonated C60–porphyrin complexes on chitosan thin films. *Thin Solid Films* **2000**, *372* (1–2), 85–93.
115. Drain, C.M.; Christensen, B.; Mauzerall, D. Photogating of ionic currents across a lipid bilayer. *Proc. Natl. Acad. Sci. U. S. A.* **1989**, *86*, 6959–6962. September.
116. Drain, C.M.; Mauzerall, D. An example of a working charge sensitive ion conductor (CSIC). *Bioelectrochem. Bioenerg.* **1990**, *24*, 263–266.
117. Drain, C.M.; Fischer, R.; Nolen, E.; Lehn, J.M. Self-assembly of a bis-porphyrin cage induced by molecular recognition between complementary hydrogen bonding sites. *Chem. Commun.* **1993**, 243–245.

118. Drain, C.M.; Lehn, J.M. Self-assembly of square multiporphyrin arrays by metal ion coordination. *Chem. Commun.* **1994**, 2313–2315.
119. Drain, C.M.; Mauzerall, D.C. Photogating of ionic currents across lipid bilayers: hydrophobic ion conductance by an ion chain mechanism. *Biophys. J.* **1992**, *63*, 1556–1563.
120. Drain, C.M.; Mauzerall, D.C. Photogating of ionic currents across the lipid bilayer: electrostatics of ions and dipoles inside the membrane. *Biophys. J.* **1992**, *63*, 1544–1555.
121. Drain, C.M.; Russel, K.C.; Lehn, J.M. Self-assembly of a multi-porphyrin supramolecular macrocycle by hydrogen bond molecular recognition. *Chem. Commun.* **1996**, *42*, 337–338.
122. Drain, C.M.; Nifiatis, F.; Vasenko, A.; Batteas, J.D. Porphyrin tessellation by design: metal-mediated self-assembly of large arrays and tapes. *Angew. Chem., Int. Ed. Engl.* **1998**, *37* (17), 2344–2347.
123. Drain, C.M.; Cheng, K.F.; Grohmann, K. Porphyrins linked directly to the 5,5' positions of 2,2'-bipyridine: a new supramolecular building block and switch. *Inorg. Chem.* **2003**, *42* (6), 2075.
124. Shi, X.; Barkigia, K.M.; Fajer, J.; Drain, C.M. Design and synthesis of porphyrins bearing rigid hydrogen bonding motifs: highly versatile building block is for self-assembly of polymers and discrete arrays. *J. Org. Chem.* **2001**, *66* (20), 6513–6522.
125. Philp, D.; Stoddart, J.F. Self-assembly in natural and unnatural systems. *Angew. Chem., Int. Ed. Engl.* **1996**, *35*, 1154–1196.
126. Imamura, T.; Fukushima, K. Self-assembly of metallo-pyridylporphyrin oligomers. *Coord. Chem. Rev.* **2000**, *198* (1), 133–156.
127. Swiegers, G.F.; Malefetse, T.J. Classification of coordination polygons and polyhedra according to their mode of self-assembly: 2. Review of the literature. *Coord. Chem. Rev.* **2002**, *225* (1–2), 91–121.
128. Sliwa, W.; Mianowska, B. Metalloporphyrin arrays. *Transit. Met. Chem. (Dordrecht, Neth.)* **2000**, *25* (5), 491–504.
129. Swiegers, G.F.; Malefetse, T.J. New self-assembled structural motifs in coordination chemistry. *Chem. Rev.* **2000**, *100* (9), 3483–3537.
130. Toma, H.E.; Araki, K. Supramolecular assemblies of ruthenium complexes and porphyrins. *Coord. Chem. Rev.* **2000**, *196* (1), 307–329.
131. Wojaczynski, J.; Latos-Grazynski, L. Poly- and oligo-metalloporphyrins associated through coordination. *Coord. Chem. Rev.* **2000**, *204* (1), 113–171.
132. Chen, C.-T.; Suslick, K.S. One-dimensional coordination polymers: application to materials science. *Coord. Chem. Rev.* **1993**, *128* (1–2), 293–322.
133. Araki, K.; Wagner, M.J.; Wrighton, M.S. Layer-by-layer growth of electrostatically assembled multilayer porphyrin films. *Langmuir* **1996**, *12* (22), 5393–5398.
134. Guldi, D.M.; Pellarini, F.; Prato, M.; Granito, C.; Troisi, L. Layer-by-layer construction of nanostructured porphyrin–fullerene electrodes. *Nano Lett.* **2002**, *2* (9), 965–968.
135. Qian, D.-J.; Nakamura, C.; Miyake, J. Layer-by-layer assembly of metal-mediated multiporphyrin arrays. *Chem. Commun.* **2001**, 2312–2313.
136. Imahori, H.; Arimura, M.; Hanada, T.; Nishimura, Y.; Yamazaki, I.; Sakata, Y.; Fukuzumi, S. Photoactive three-dimensional monolayers: Porphyrin–alkanethiolate-stabilized gold clusters. *J. Am. Chem. Soc.* **2001**, *123* (2), 335–336.
137. Nishimura, N.; Ooi, M.; Shimazu, K.; Fujii, H.; Uosaki, K. Post-assembly insertion of metal ions into thiol-derivatized porphyrin monolayers on gold. *J. Electroanal. Chem.* **1999**, *473* (1–2), 75–84.
138. Imahori, H.; Hasobe, T.; Yamada, H.; Nishimura, Y.; Yamazaki, I.; Fukuzumi, S. Concentration effects of porphyrin monolayers on the structure and photoelectrochemical properties of mixed self-assembled monolayers of porphyrin and alkanethiol on gold electrodes. *Langmuir* **2001**, *17* (16), 4925–4931.
139. Ashkenasy, G.; Kalyuzhny, G.; Libman, J.; Rubinstein, I.; Shanzer, A. Functional monolayers with coordinatively embedded metalloporphyrins. *Angew. Chem., Int. Ed. Engl.* **1999**, *38* (9), 1257–1261.
140. Qian, D.J.; Nakamura, C.; Ishida, T.; Wenk, S.O.; Wakayama, T.; Takeda, S.; Miyake, J. Palladium-mediated stepwise assembly of three-dimensional organized multiporphyrin arrays directly on solid substrates. *Langmuir* **2002**, *18* (26), 10,237–10,242.
141. Lahav, M.; Gabriel, T.; Shipway, A.N.; Willner, I. Assembly of a Zn(II)–porphyrin–bipyridinium dyad and Au-nanoparticle superstructures on conductive surfaces. *J. Am. Chem. Soc.* **1999**, *121* (1), 258–259.
142. Castriciano, M.A.; Romeo, A.; Scolaro, L.M. Aggregation of *meso*-tetrakis(4-sulfonatophenyl)porphyrin on polyethyleneimine in aqueous solutions and on glass surface. *J. Porphy. Phthalocyanines* **2002**, *6* (6), 431–438.
143. da Rocha, J.R.C.; Demets, G.J.-F.; Bertotti, M.; Araki, K.; E. Toma, H. Charge transfer at electrostatically assembled tetraethenated porphyrin modified electrodes. *J. Electroanal. Chem.* **2002**, *526* (1–2), 69–76.
144. Ikeda, A.; Hatano, T.; Shinkai, S.J.; Akiyama, T.; Yamada, S. Efficient photocurrent generation in novel self-assembled multilayers comprised of [60] fullerene–cationic homooxocalix [3] arene inclusion complex and anionic porphyrin polymer. *J. Am. Chem. Soc.* **2001**, *123* (20), 4855–4856.
145. Kaschak, D.M.; Lean, J.T.; Waraksa, C.C.; Saube, G.B.; Usami, H.; Mallouk, T.E. Photoinduced energy and electron transfer reactions in lamellar polyanion/polycation thin films: toward an inorganic “leaf”. *J. Am. Chem. Soc.* **1999**, *121* (14), 3435–3445.
146. Ishida, A.; Majima, T. Surface plasmon excitation of porphyrin self-assembly monolayers on an Au surface. *Nanotechnology* **1999**, *10*, 308–314.
147. Yamada, H.; Imahori, H.; Nishimura, Y.; Yamazaki, I.; Fukuzumi, S. Remarkable enhancement of photocurrent generation by ITO electrodes modified with a self-assembled monolayer of porphyrin. *Chem. Commun.* **2000**, *19*, 1921–1922.
148. Roth, K.M.; Dontha, N.; Dabke, R.B.; Gryko, D.T.; Clausen, C.; Lindsey, J.S.; Bocian, D.F.; Kuhr, W.G.



- Molecular approach toward information storage based on the redox properties of porphyrins in self-assembled monolayers. *J. Vac. Sci. Technol., B* **2000**, *18* (5), 2359–2364.
149. Hanks, T.W.; Bergman, B.; Dillon, P. Design and synthesis of porphyrin-containing arrays on polypyrrole surfaces. *Synag. Met.* **2001**, *121* (1–3), 1431–1432.
  150. Sharma, C.V.K.; Broker, G.A.; Szulczewski, G.J.; Rogers, R.D. Self-assembly of freebase-and metallated-tetrapyrrolylporphyrins to modified gold surfaces. *Chem. Commun.* **2000**, 1023–1024.
  151. Zhang, Z.; Imae, T. Surface enhanced infrared absorption and UV-Vis spectroscopic study of a monolayer film of protoporphyrin IX Zinc (II) on gold. *Stud. Surf. Sci. Catal.* **2001**, *132*, 585–588.
  152. Zhang, Z.; Imae, T. Hydrogen-bonding stabilized self-assembled monolayer film of a functionalized diacid, protoporphyrin IX Zinc(II), onto a gold surface. *Nano Lett.* **2000**, *1* (5), 241–243.
  153. Choudhury, B.; Weedon, A.C.; Bolton, J.R. Effects of molecular organization on photophysical behaviour: 1. Steady-state fluorescence and fluorescence quantum yield studies of Langmuir–Blodgett monolayers of some surfactant porphyrins. *Langmuir* **1998**, *14* (21), 6192–6198.
  154. Skupin, M.; Li, G.; Fudickar, W.; Zimmermann, J.; Roeder, B.; Fuhrhop, J.-H. Methylammonium groups at the solid walls of nanometer-sized, water-filled monolayer gaps as binding sites for a tetraanionic porphyrin. *J. Am. Chem. Soc.* **2001**, *123* (15), 3454–3461.
  155. Fudickar, W.; Zimmermann, J.; Ruhlmann, L.; Schneider, J.; Roder, B.; Siggel, U.; Fuhrhop, J.-H. Fluorescence quenching and size selective heterodimerization of a porphyrin adsorbed to gold and embedded in rigid membrane gaps. *J. Am. Chem. Soc.* **1999**, *121* (41), 9539–9545.
  156. Benítez, I.O.; Bujoli, B.; Camus, L.J.; Lee, C.M.; Odobel, F.; Talham, D.R. Monolayers as models for supported catalysts: zirconium phosphonate films containing manganese(III) porphyrins. *J. Am. Chem. Soc.* **2002**, *124* (16), 4363–4370.
  157. Loppacher, C.; Bammerlin, M.; Guggisberg, M.; Meyer, E.; Guntherodt, H.J.; Luthi, R.; Schlittler, R.; Ginzewski, J.K. Forces with submolecular resolution between the probing tip and Cu-TBPP molecules on Cu(100) observed with a combined AFM/STM. *Appl. Phys., A* **2001**, *72* (7), S105–S108.
  158. Hupp, J.T.; Nguyen, S.T. Functional nanostructured molecular material. *Electrochem. Soc. Interface* **2001**, 28–32.
  159. Imahori, H.; Norieda, H.; Nishimura, Y.; Yamazaki, I.; Higuchi, K.; Kato, N.; Motohiro, T.; Yamada, H.; Tamaki, K.; Arimura, M.; Sakata, Y. Chain length effect on the structure and photoelectrochemical properties of self-assembled monolayers of porphyrins on gold electrodes. *J. Phys. Chem., B* **2000**, *104* (6), 1253–1260.
  160. Boeckl, M.S.; Bramblett, A.L.; Hauch, K.D.; Sasaki, T.; Ratner, B.D.; J.W. Rogers, J. Self-assembly of tetraphenylporphyrin monolayers on gold substrates. *Langmuir* **2000**, *16* (13), 5644–5653.
  161. Imahori, H.; Nishimura, Y.; Norieda, H.; Karita, H.; Yamazaki, I.; Sakata, Y.; Fukuzumi, S. Photoinduced energy transfer in mixed self-assembled monolayers of pyrene and porphyrin. *Chem. Commun.* **2000**, 8, 661–662.
  162. Ishida, A.; Sakata, Y.; Majima, T. Surface plasmon excitation of a porphyrin covalently linked to a gold surface. *Chem. Commun.* **1998**, 57–58.
  163. Delmarre, D.; Meallet, R.; Bied-Charreton, C.; Pansu, R.B. Heavy metal ions detection in solution, in sol–gel and with grafted porphyrin monolayers. *J. Photochem. Photobiol., A Chem.* **1999**, *124*, 23–28.
  164. McCallien, D.W.J.; Burn, P.L.; Anderson, H.L. Chelation of diamine ligand to zinc porphyrin monolayers amide-linked to glass. *J. Chem. Soc., Perkin Trans.* **1997**, *1* (17), 2581–2586.
  165. Clausen, C.; Gryko, D.T.; Dabke, R.B.; Dontha, N.; Bocian, D.F.; Kuhr, W.G.; Lindsey, J.S. Synthesis of thiol-derivatized porphyrin dimers and trimers for studies for architectural effects on multibit information storage. *J. Org. Chem.* **2000**, *65* (22), 7363–7370.
  166. Gryko, D.T.; Clausen, C.; Lindsey, J.S. Thiol-derivatized porphyrins for attachment to electroactive surfaces. *J. Org. Chem.* **1999**, *64* (23), 8635–8647.
  167. Gryko, D.T.; Zhao, F.; Yasserli, A.A.; Roth, K.M.; Bocian, D.F.; Kuhr, W.G.; Lindsey, J.S. Synthesis of thiol-derivatized ferrocene-porphyrins for studies of multibit information storage. *J. Org. Chem.* **2000**, *65* (22), 7356–7362.
  168. Li, J.; Gryko, D.; Dabke, R.B.; Diers, J.R.; Bocian, D.F.; Kuhr, W.G.; Lindsey, J.S. Synthesis of thiol-derivatized europium porphyrinic triple-decker sandwich complexes for multibit molecular information storage. *J. Org. Chem.* **2000**, *65* (22), 7379–7390.
  169. Schweikart, K.-H.; Malinovskii, V.L.; Diers, J.R.; Yasserli, A.A.; Bocian, D.F.; Kuhr, W.G.; Lindsey, J.S. Design, synthesis, and characterization of prototypical multistate counters in three distinct architectures. *J. Mater. Chem.* **2002**, *12* (4), 808–828.
  170. Hips, K.W.; Mazur, U. An experimental study of the line shape of orbital mediated tunneling bands seen in inelastic tunneling spectroscopy. *J. Phys. Chem., B* **2000**, *104* (19), 4707–4710.
  171. Hips, K.W.; Scudiero, L.; Barlow, D.E.; Cooke, M.P. A self-organized 2-dimensional bifunctional structure formed by supramolecular design. *J. Am. Chem. Soc.* **2002**, *124* (10), 2126–2127.
  172. Scudiero, L.; Hips, K.W.; Barlow, D.E. Scanning tunneling microscopy, orbital-mediated tunneling spectroscopy, and ultraviolet photoelectron spectroscopy of Nickel (II) octaethylporphyrin deposited from vapor. *J. Phys. Chem., B* **2002**, *106* (5), 996–1003.
  173. He, Y.; Ye, T.; Borguet, E. Porphyrin self-assembly at electrochemical interfaces: Role of potential modulated surface mobility. *J. Am. Chem. Soc.* **2002**, *124* (40), 11,964–11,970.
  174. Kanayama, N.; Kanbara, T.; Kitano, H. Complexation of porphyrin with a pyridine moiety in self-assembled monolayers on metal surfaces. *J. Phys. Chem., B* **2000**, *104* (2), 271–278.

175. Zhang, Z.; Hu, R.; Liu, Z. Formation of a porphyrin monolayer film by axial ligation of protoporphyrin IX Zinc to an amino-terminated silanized glass surface. *Langmuir* **2000**, *16* (3), 1158–1162.
176. Cruz, F.D.; Driaf, K.; Berthier, C.; Lameille, J.-M.; Armand, F. Study of a self-assembled porphyrin monomolecular layer obtained by metal complexation. *Thin Solid Films* **1999**, *349* (1–2), 155–161.
177. Liu, Z.; Zhu, Z.; Hou, S.; Zhang, Z. Preparation and characterization of a porphyrin self-assembled monolayer with a controlled orientation on gold. *Langmuir* **2000**, *16* (2), 537–540.
178. Linton, B.; Hamilton, A.D. Formation of artificial receptors by metal-templated self-assembly. *Chem. Rev.* **1997**, *97*, 1669–1680.
179. Armand, F.; Albouy, P.-A.; Cruz, F.D.; Normand, M.; Huc, V.; Goron, E. Interconnection of porphyrins in Langmuir–Blodgett and self-assembled monolayers by means of silver acetylide bridges. *Langmuir* **2001**, *17* (11), 3431–3437.
180. Kalyuzhny, G.; Vaskevich, A.; Ashkenasy, G.; Shanzer, A.; Rubinstein, I. UV/Vis spectroscopy of metalloporphyrin and metallophthalocyanine monolayers self-assembled on ultrathin gold films. *J. Phys. Chem., B* **2000**, *104* (34), 8238–8244.
181. Offord, D.A.; Sachs, S.B.; Ennis, M.S.; Eberspacher, T.A.; Griffin, J.H.; Chidsey, C.E.D.; Collman, J.P. Synthesis and properties of metalloporphyrin monolayers and stacked multilayers bound to an electrode in site specific axial ligation to a self-assembled monolayer. *J. Am. Chem. Soc.* **1998**, *120* (18), 4478–4487.
182. Zhang, Z.; Imae, T.; Sato, H.; Watanabe, A.; Ozaki, Y. Surface-enhanced Raman scattering and surface-enhanced infrared absorption spectroscopic studies of a metalloporphyrin monolayer film formed on pyridine self-assembled monolayer-modified gold. *Langmuir* **2001**, *17* (15), 4564–4568.
183. Liu, C.-Y.; Pan, H.-L.; Fox, M.A.; Bard, A.J. High-density nanosecond charge trapping in thin films of the photoconductor ZnODEP. *Science* **1993**, *261*, 897–899.
184. Liu, C.-Y.; Pan, H.-L.; Fox, M.A.; Bard, A.J. Reversible charge trapping/detrapping in a photoconductive insulator of liquid crystal zinc porphyrin. *Chem. Mater.* **1997**, *9* (6), 1422–1429.
185. Adams, D.M.; Kerimo, J.; Liu, C.Y.; Bard, A.J.; Barbara, P.F. Electric field modulated near-field photo-luminescence of organic thin films. *J. Phys. Chem., B* **2000**, *104* (29), 6728–6736.
186. Patel, B.R.; Suslick, K.S. Discotic liquid crystals from a bis-pocketed porphyrin. *J. Am. Chem. Soc.* **1998**, *120* (45), 11,802–11,803.
187. Kimura, M.; Saito, Y.; Ohta, K.; Hanabusa, K.; Shirai, H.; Kobayashi, N. Self-organization of supramolecular complex composed of rigid dendritic porphyrin and fullerene. *J. Am. Chem. Soc.* **2002**, *124* (19), 5274–5275.
188. Burrows, H.D.; Gonsalves, A.M.R.; Leitao, M.L.P.; Miguel, M.D.G.; Pereira, M.M. Phase transitions and self-assembly in *meso*-tetrakis(undecyl)porphyrin. *Supramol. Sci.* **1997**, *4* (3–4), 241–246.
189. Lei, S.B.; Wang, C.; Yin, S.X.; Wang, H.N.; Xi, F.; Liu, H.W.; Xu, B.; Wan, L.J.; Bai, C.L. Surface stabilized porphyrin and phthalocyanine two-dimensional network connected by hydrogen bonds. *J. Phys. Chem., B* **2001**, *105* (44), 10,838–10,841.
190. Ohshiro, T.; Ito, T.; Buhlmann, P.; Umezawa, Y. Scanning tunneling microscopy with chemically modified tips: discrimination of porphyrin centers based on metal coordination and hydrogen bond interactions. *Anal. Chem.* **2001**, *73* (5), 878–883.
191. Qiu, X.; Wang, C.; Zeng, Q.; Xu, B.; Yin, S.; Wang, H.; Xu, S.; Bai, C. Alkane-assisted adsorption and assembly of phthalocyanines and porphyrins. *J. Am. Chem. Soc.* **2000**, *122* (23), 5550–5556.
192. Giancarlo, L.C.; Flynn, G.W. Scanning tunneling and atomic force microscopy probes of self-assembled, physisorbed monolayers: peeking at the peaks. *Annu. Rev. Phys. Chem.* **1998**, *49* (1), 297–336.
193. Liu, G.; Xu, S.; Qian, Y. Nanofabrication of self-assembled monolayers using scanning probe lithography. *Acc. Chem. Res.* **2000**, *33* (7), 457–466.
194. Ogi, T.; Ohkita, H.; Ito, S.; Yamamoto, M. Preparation of porphyrin mono- and multi-layer films based on the polymer Langmuir–Blodgett method. *Thin Solid Films* **2002**, *415* (1–2), 228–235.
195. Richardson, T.H.; Dooling, C.M.; Worsfold, O.; Jones, L.T.; Kato, K.; Shinbo, K.; Kaneko, F.; Tregonning, R.; Vysotsky, M.O.; Hunter, C.A. Gas sensing properties of porphyrin assemblies prepared using ultra-fast LB deposition. *Colloids Surf., A Physicochem. Eng. Asp.* **2002**, *198–200*, 843–857.
196. Chowdhury, A.; Pal, A.J. Alternating current light-emitting devices based on Langmuir–Blodgett films of a porphyrin derivative: space charges in device operation. *Thin Solid Films* **2001**, *385* (1–2), 266–270.
197. Komatsu, T.; Tsuchida, E.; Böttcher, C.; Donner, D.; Messerschmidt, C.; Siggel, U.; Stocker, W.; Rabe, J.P.; Fuhrhop, J.-H. Solid vesicle membrane made of *meso*-tetrakis[(bixinylamino)-*o*-phenyl]porphyrins. *J. Am. Chem. Soc.* **1997**, *119* (48), 11,660–11,665.
198. Sagawa, T.; Fukugawa, S.; Yamada, T.; Ihara, H. Self-assembled fibrillar networks through highly oriented aggregates of porphyrin and pyrene substituted by dialkyl L-glutamine in organic media. *Langmuir* **2002**, *18* (19), 7223–7228.
199. Qian, D.-J.; Nakamura, C.; Miyake, J. Multiporphyrin array from interfacial metal-mediated assembly and its Langmuir–Blodgett films. *Langmuir* **2000**, *16* (24), 9615–9619.
200. Latterini, L.; Blossey, R.; Hofkens, J.; Vanoppen, P.; De Schryver, F.C.; Rowan, A.E.; Nolte, R.J.M. Ring formation in evaporating porphyrin derivative solutions. *Langmuir* **1999**, *15* (10), 3582–3588.
201. Foubert, P.; Vanoppen, P.; Martin, M.; Gensch, T.; Hofkens, J.; Helser, A.; Seeger, A.; Taylor, R.M.; Rowan, A.E.; Nolte, R.J.M.; Schryver, F.C.D. Mechanical and optical manipulation of porphyrin rings at the submicrometre scale. *Nanotechnology* **2000**, *11* (1), 16–23.
202. Magnera, T.F.; Peslherbe, L.M.; Körblóvá, E.; Michl, J. The organometallic ‘Molecular Tinkertoy’ approach

- to planar grid polymers. *J. Organomet. Chem.* **1997**, *548* (1), 83–89.
203. Michl, J.; Magnera, T.F. Two-dimensional supramolecular chemistry with molecular tinkertoys. *Proc. Natl. Acad. Sci. U. S. A.* **2002**, *99* (8), 4788–4792.
  204. Kalyanasundaram, K.; Grätzel, M. Applications of functionalized transition metal complexes in photonic and optoelectronic devices. *Coord. Chem. Rev.* **1998**, *177* (1), 347–414.
  205. Liddell, P.A.; Kodis, G.; Moore, A.L.; Moore, T.A.; Gust, D. Photonic switching of photoinduced electron transfer in a dithienylethene–porphyrin–fullerene triad molecule. *J. Am. Chem. Soc.* **2002**, *124* (26), 7668–7669.
  206. Drain, C.M.; Gentemann, S.; Roberts, J.A.; Nelson, N.Y.; Medforth, C.J.; Jia, S.; Simpson, M.C.; Smith, K.M.; Fajer, J.; Shelnut, J.A.; Holten, D. Picosecond to microsecond photodynamics of a nonplanar nickel porphyrin: Solvent dielectric and temperature effects. *J. Am. Chem. Soc.* **1998**, *120* (15), 3781–3791.
  207. Drain, C.M.; Kirmaier, C.; Medforth, C.; Nurco, D.; Smith, K.M.; Holten, D. Dynamic photophysical properties of conformationally distorted nickel porphyrins: 1. Nickel(II) dodecaphenylporphyrin. *J. Phys. Chem.* **1996**, *100* (29), 11984–11993.
  208. Deng, W.; Fujita, D.; Ohgi, T.; Yokoyama, S.; Kamikado, K.; Mashiko, S. STM-induced photon emission from self-assembled porphyrin molecules on a Cu(100) surface. *J. Chem. Phys.* **2002**, *117* (10), 4995–5000.
  209. Furukawa, M.; Tanaka, H.; Sugiura, K.; Sakata, Y.; Kawai, T. Fabrication of molecular alignment at the specific sites on Cu(111) surfaces using self-assembly phenomena. *Surf. Sci.* **2000**, *445* (1), L58–L63.
  210. Thomas, P.J.; Berovic, N.; Laitenberger, P.; Palmer, R.E.; Bampos, N.; Sanders, J.K.M. Room temperature manipulation of self-organised supramolecular nanostructures with a scanning tunnelling microscope. *Chem. Phys. Lett.* **1998**, *294* (1–3), 229–232.
  211. Belanger, S.; Hupp, J.T. Porphyrin-based thin-film molecular materials with highly adjustable nanoscale porosity and permeability characteristics. *Angew. Chem., Int. Ed. Engl.* **1999**, *38* (15), 2222–2224.
  212. Cherian, S.; Wamser, C.C. Adsorption and photoactivity of tetra(4-carboxyphenyl)porphyrin (TCPP) on nanoparticulate TiO<sub>2</sub>. *J. Phys. Chem., B* **2000**, *104* (15), 3624–3629.
  213. Leininger, S.; Olenyuk, B.; Stang, P.J. Self-assembly of discrete cyclic nanostructures mediated by transition metals. *Chem. Rev.* **2000**, *100* (3), 853–908.
  214. Stupp, S.I.; Pralle, M.U.; Tew, G.N.; Li, L.; Sayar, M.; Zubarev, E.R. Self-assembly of organic nano-objects into functional materials. *MRS Bull.* **2000**, 42–48.
  215. Vlckova, B.; Smejkal, P.; Michl, M.; Prochazka, M.; Mojzes, P.; Lednický, F.; Pflieger, J. Surface-enhanced resonance Raman spectroscopy of porphyrin and metalloporphyrin species in systems with Ag nanoparticles and their assemblies. *J. Inorg. Biochem.* **2000**, *79* (1–4), 295–300.
  216. Georgakilas, V.; Pellarini, F.; Prato, M.; Guldi, D.M.; Melle-Franco, M.; Zerbetto, F. Supramolecular self-assembled fullerene nanostructures. *Proc. Natl. Acad. Sci. U. S. A.* **2002**, *99* (8), 5075–5080.
  217. Sloufova-Srnova, I.; Vlckova, B. Two-dimensional assembling of Au nanoparticles mediated by tetrapyrrolylporphyrin molecules. *Nano Lett.* **2002**, *2* (2), 121–125.
  218. van der Boom, T.; Hayes, R.T.; Zhao, Y.; Bushard, P.J.; Weiss, E.A.; Wasielewski, M.R. Charge transport in photofunctional nanoparticles self-assembled from zinc 5,10,15,20-tetrakis(peryleneimide)porphyrin building blocks. *J. Am. Chem. Soc.* **2002**, *124* (32), 9582–9590.
  219. Zenkevich, E.I.; Shulga, A.M.; von Borczyskowski, C. Multistep photoinduced electron transfer in self-organised nanoscale porphyrin triads. *Physica, E, Low-Dimens. Syst. Nanostruct.* **2002**, *14* (1–2), 277–281.
  220. Zenkevich, E.I.; Borczyskowski, C.V.; Shulga, A.M.; Bachilo, S.; Rempel, U.; Willert, A. Self-assembled nanoscale photomimetic models: structure and related dynamics. *Chem. Phys.* **2002**, *275* (1–3), 185–209.

# Printed and Molded Nanostructures: Photonic Applications

**John A. Rogers**

*Department of Materials Science and Engineering and Beckman Institute,  
University of Illinois at Urbana–Champaign, Urbana, Illinois, U.S.A.*

## INTRODUCTION

Many classes of components for integrated optics and optoelectronics rely on structures with nanometer features sizes (typically a fraction of the optical wavelength at which they operate) for couplers, filters, laser resonators, etc.<sup>[1]</sup> Similar but more advanced devices that use photonic crystals<sup>[2]</sup> as well as a variety of subwavelength elements<sup>[3,4]</sup> for bulk optics also make use of arrays of nanostructures to achieve desired optical effects. Traditionally, techniques borrowed from the microelectronics industry, such as photolithography and electron beam lithography, have been employed for these applications. The operational complexity of these methods, their high capital costs, and certain inherent limitations associated with them create research interest in alternative fabrication techniques.<sup>[5,6]</sup> Two relatively recent approaches to patterning photonic nanostructures use advanced forms of printing and molding, two of the conceptually oldest forms of lithography. These methods offer sub-micron resolution along with patterning capabilities that are well suited to this class of application. This entry summarizes these methods and demonstrates their use in fabricating a range of components for integrated optics.

## HIGH-RESOLUTION STAMPS AND MOLDS

High-resolution stamps and molds can be formed with electron beam lithography or photolithography according to the procedures illustrated in Fig. 1. Casting and curing a polymer against a pattern of resist formed with these techniques (known as the “master”) yields polymeric elements that can serve as stamps and molds. Many elements can be produced from a single master and each element can be used many times. Similar molds and stamps can be made out of the material that serves as the substrate for the master by using the resist to generate surface relief, through selective etching. There are currently two classes of printing techniques that use these stamps for patterning with

submicron resolution—microcontact printing ( $\mu$ CP)<sup>[7,8]</sup> and nanotransfer printing (nTP).<sup>[9,10]</sup> In  $\mu$ CP, an elastomeric stamp [usually poly(dimethylsiloxane), PDMS; Dow Corning, Inc.] is used to print patterns of chemical inks. In nTP, a hard or an elastomeric stamp delivers a solid ink material to a substrate.  $\mu$ CP offers typical edge resolution of 50–200 nm depending on the inks and substrates. Demonstrated resolution in nTP is in the range of 5–20 nm. The stamps for these techniques can also be used as high resolution molds for embossing relief structures into polymers and other soft materials.<sup>[5]</sup>

## Microcontact Printing

It was mainly developed for use with inks that form self-assembled monolayers (SAMs) of alkanethiolates on gold and silver. The procedures for carrying out  $\mu$ CP in these systems are simple: A stamp, inked with a solution of alkanethiol, is brought into contact with the surface of a substrate to transfer ink molecules to regions where the stamp and substrate contact. The resolution and effectiveness of this method relies on conformal contact between the stamp and the surface of the substrate, rapid formation of highly ordered monolayers,<sup>[11]</sup> and autophobicity of the SAM,<sup>[12]</sup> which effectively blocks the reactive spreading of the ink across the surface. It can pattern SAMs over relatively large areas (up to  $\sim 0.25$  ft<sup>2</sup> have been demonstrated in prototype electronic devices)<sup>[13]</sup> in a single impression.

Fig. 2 schematically illustrates the use of  $\mu$ CP and wet etching to pattern a thin film of Au. Fig. 3 shows scanning electron microscope (SEM) images of representative nanopatterns of gold (20-nm thick, thermally evaporated with a 2.5-nm layer of Ti as an adhesion promoter) that were fabricated on silicon wafers using this approach. In both of these examples, the masters for the stamps consist of photoresist patterned on silicon wafers with projection-mode photolithography. Placing a few drops of a  $\sim 1$  mM solution of hexadecanethiol (HDT) in ethanol on the surface of the stamps, and then blowing them dry with a stream of nitrogen

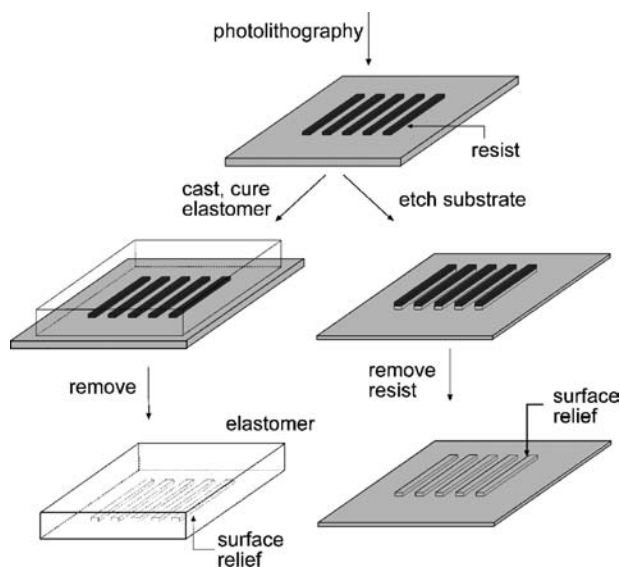


**Fig. 1** Schematic illustration of two representative methods for producing high-resolution stamps and molds. Both begin with photolithography to pattern a thin layer of resist on a flat substrate, such as a silicon wafer. This structure, known as the master, is converted to a stamp or mold either by etching or by molding. In the first case, the resist acts as a mask for etching the underlying substrate. Removing the resist yields a stamp or a mold. In the molding approach, a pre-polymer is cast against the relief structure formed by the patterned resist on the substrate. Curing (thermally or optically) and then peeling the resulting solid polymer away from the substrate completes the process.

prepares them for printing. Contacting the metal film for a few seconds with the stamp produces a patterned self-assembled monolayer (SAM) of HDT. An aqueous etchant removes the unprinted regions of the gold.<sup>[14]</sup> The patterns in Fig. 3 have edge roughness of  $\sim 50$ – $100$  nm. This resolution, which is typical for  $\mu$ CP, is determined by the grain size of the metal films, the isotropic etching process, slight reactive spreading of the inks and edge disorder in the patterned SAMs. Patterns with these feature sizes are useful for many applications in integrated optics, and especially those at the infrared wavelengths ( $1.5 \mu\text{m}$ ) that are predominant in communication systems.

### Nanotransfer Printing

Nanotransfer printing (nTP) is a more recent high-resolution printing technique that uses surface chemistries as interfacial “glues” and “release” layers to control the transfer of solid material layers from relief features on a stamp to a substrate.<sup>[9,10]</sup> This approach, which is illustrated in Fig. 4, is purely additive (i.e., material is only deposited in locations where it is needed) and it can generate complex patterns of single

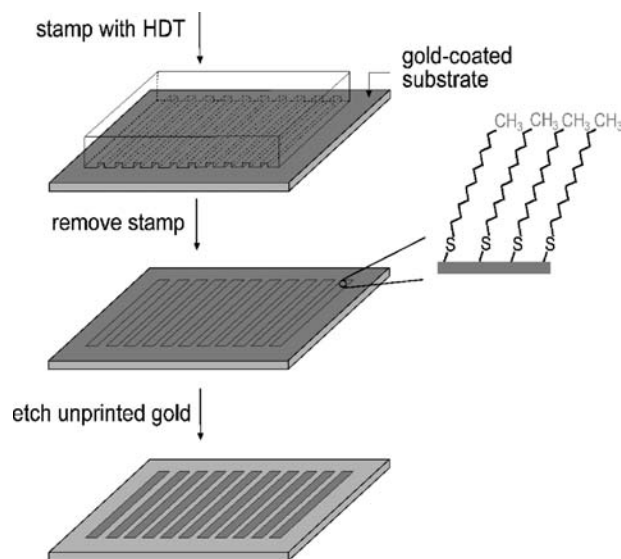


**Fig. 2** Schematic illustration of an example of microcontact printing. The first step involves “inking” a “stamp” with a solution of hexadecanethiol (HDT) in ethanol. Contacting the stamp to a thin film of gold on a substrate produces a patterned SAM of HDT. The printed SAM can act as a resist for the aqueous-based wet etching of the exposed regions of the Au. The resulting pattern of conducting gold can be used to build devices of various types.

or multiple layers of materials with nanometer resolution over large areas in a single process step. It does not suffer from surface diffusion or edge disorder in the patterned “inks” of  $\mu$ CP nor does it require post-printing etching or deposition steps to produce structures of functional materials. The method involves four components: 1) a stamp (rigid, flexible, or elastomeric) with relief features in the geometry of the desired pattern; 2) a method for depositing a thin layer of solid material onto the raised features of this stamp; 3) a means for bringing the stamp into intimate

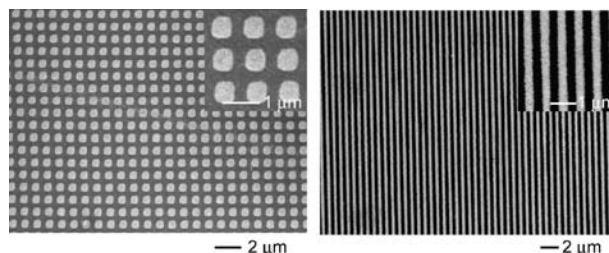


**Fig. 3** Scanning electron micrographs of typical structures formed by microcontact printing a self-assembled monolayer ink of hexadecanethiol onto thin gold films followed by etching of the unprinted areas. The left frame shows an array of Au (20-nm thick) dots with  $\sim 500$ -nm diameters. The right frame shows printed lines of Au (20-nm thick). The edge resolution of features in both of these patterns is  $\sim 50$ – $100$  nm.



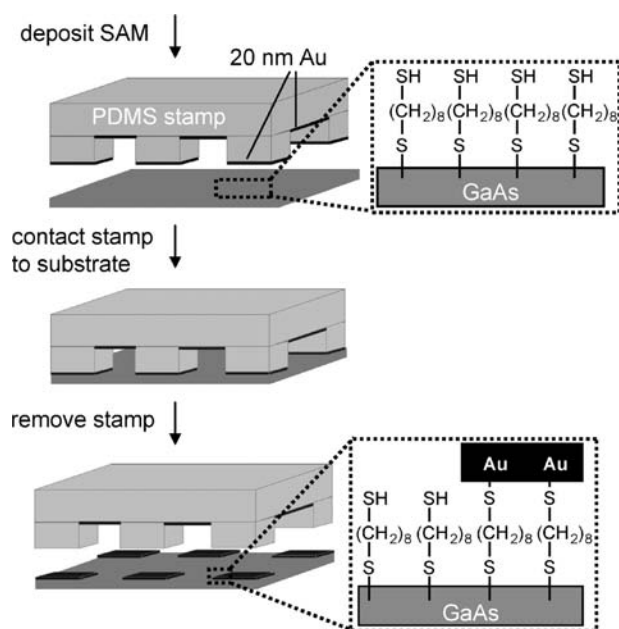


**Fig. 4** Schematic illustration of procedures for nanotransfer printing a pattern of Au on a GaAs substrate. A uniform monolayer of 1,8-octanedithiol molecules is formed on the GaAs using vapor or solution phase deposition. Evaporating a collimated flux of Au (20 nm) onto an elastomeric stamp forms layers on the recessed and raised regions but not on the sidewalls. Contacting this stamp with the substrate leads to Au–S bonds. Removing the stamp leaves a pattern of gold on the substrate in the geometry of relief on the stamp. The transferred gold patterns are effectively “glued” to the surface by strong Ga–S, As–S, and S–Au bonds at the interface. The insets highlight the idealized orientation of the dithiol molecule on GaAs surface; control experiments indicate that the unreacted thiol endgroups are generally oriented away from the wafer surface.

physical contact with a substrate; and 4) surface chemistries that prevent adhesion of the deposited material to the stamp and promote its strong adhesion to the substrate. nTP has been demonstrated with SAMs and other surface chemistries for printing onto flexible and rigid substrates with hard inorganic and soft polymer stamps.<sup>[9,10,15]</sup> Fig. 4 presents a set of procedures for using nTP to pattern a thin layer of Au with a surface transfer chemistry that relies on Au–S bonding and self-assembled monolayers.<sup>[15]</sup> The process begins with fabrication of rigid or elastomeric stamps using the procedures of Fig. 1. Careful control of the processing steps yields features of relief with nearly vertical or slightly reentrant sidewalls. Directional deposition of Au (or other materials) onto the surfaces of such stamps yields coatings only on the raised and recessed regions and not on the sidewalls. The depth of relief on the stamps is typically  $>200$  nm for patterning metal films with thicknesses  $<50$  nm.

In the case of Fig. 4, contacting a gold-coated PDMS stamp to a GaAs substrate that has a self-assembled dithiol monolayer on its surface leads to thiol-gold linkages at the interface. Removing the stamp (to which the gold does not adhere) leaves behind a pattern of gold in the geometry of the raised regions of the stamp.<sup>[15]</sup> Similar procedures can be used with a wide range of stamps, patterned materials, substrates, and surface chemistries. Fig. 5 shows some representative examples. The resolution of nTP is limited mainly by the roughness at the edges of the films that are deposited on the stamps and by the stamps themselves. This edge roughness is less than 5–20 nm for evaporated gold and stamps fabricated by electron beam lithography. There is no observable degradation in feature sharpness or resolution because of the transfer process. Care must be taken to use optimized deposition and printing conditions in order to avoid nanocracking in the transferred layer, especially when patterns of rigid materials are printed from deformable stamps onto deformable surfaces. In the applications that we have explored, even when they might exist, the nanocracks (which are not visible with conventional optical or scanning electron microscopes) do not significantly affect the functional properties of the devices (e.g., resistivity test structures, organic transistors and simple circuits, photonic structures, thin film capacitors, etc.).

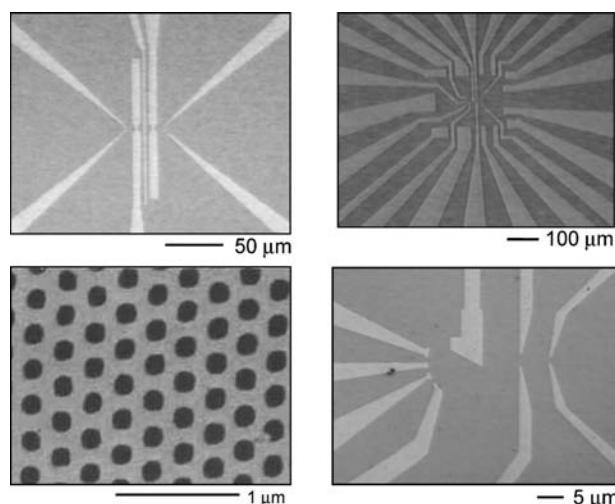


**Fig. 5** Optical micrographs of patterns of Au (15-nm thick) formed on plastic (top left and bottom left frames), silicon (top right frame), and GaAs (bottom right frame) substrates with nanotransfer printing. The transfer chemistry in the top left case relies on silane self-assembled monolayers with exposed thiol groups. The chemistry for the patterns in the top and bottom right cases relies on surface dehydration reactions. The bottom right pattern used a dithiol chemistry. The minimum feature sizes and the edge resolution are limited, in all cases, by the stamps.



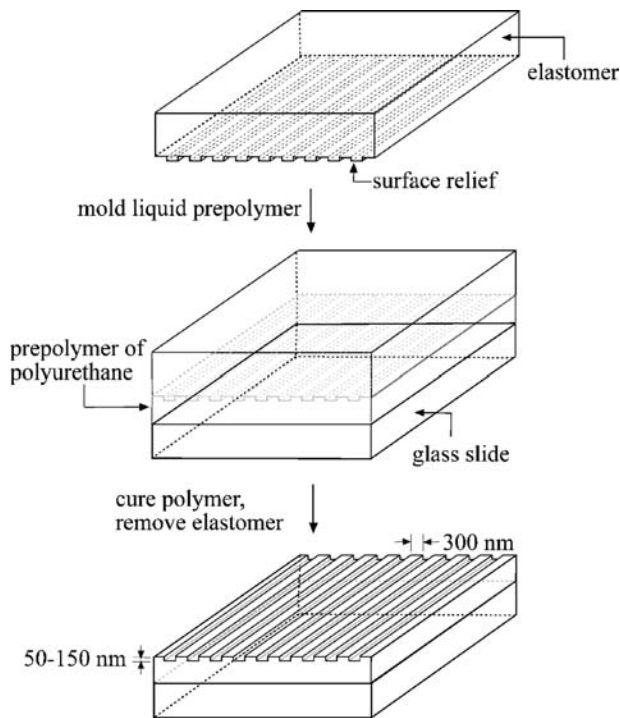


**Fig. 6** Schematic illustration of molding procedures for defining distributed feedback gratings for lasers. The gratings are formed by exposing a thin film of a photocurable polymer to ultraviolet light through an elastomeric mold.

### Nanomolding

The stamps used for  $\mu$ CP and nTP can also serve as molds for generating relief surface relief features in other materials. Nanoimprint lithography and related embossing methods represent one class of such techniques that use hard stamps and thermally softened polymers or photocurable liquids.<sup>[5]</sup> The use of elastomeric materials for “soft” molds yields a related type of

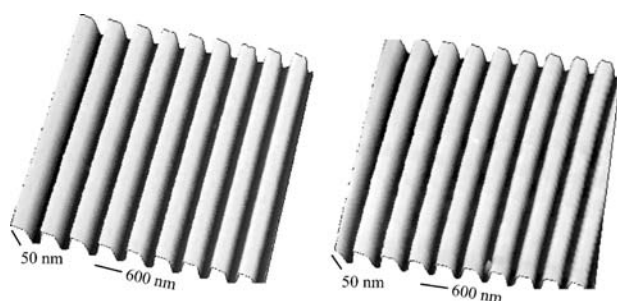


**Fig. 7** Atomic force micrographs of distributed feedback grating structures. The right frame was collected from a photolithographically defined pattern in a thin layer of SiO<sub>2</sub> on a silicon wafer. The left frame was collected from a polymer replica generated with an elastomeric mold produced from the structure illustrated on the right.

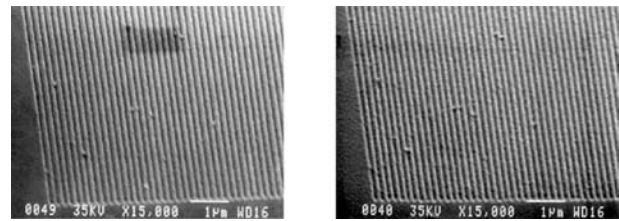


**Fig. 8** Scanning electron micrographs of 200 nm period distributed feedback gratings in a thin layer of SiO<sub>2</sub> on a silicon wafer (left frame) and in a thin layer of a photocurable polymer on a glass slide (right frame). The structure in silica was formed by direct write electron beam lithography and etching. The structure in the photopolymer was defined by molding using an elastomeric mold formed by casting and curing against the silica structure.

technique which, because of the flexibility of the molding elements, can be used for large-area patterning of nanostructures even in fragile materials.<sup>[6]</sup> Fig. 6 shows procedures for using this approach to generate features of relief in a thin photocurable polymer. The transparent PDMS mold allows the photopolymer to be cured by exposure to ultraviolet light passing through the mold. In the case illustrated here, the pattern consists of a distributed feedback grating for a laser that emits in the visible spectrum. Fig. 7 presents atomic force microscope images of a relief pattern generated by photolithography and etching of a thin layer of SiO<sub>2</sub> on a silicon substrate (left frame) and a fifth generation replica grating (right frame) in a photocurable polyurethane (NOA 72, Norland) formed by using the procedures of Fig. 6 with a PDMS mold generated from the SiO<sub>2</sub> structure.<sup>[16]</sup> These procedures are effective for pattern replication down to the 50–100-nm scale. Fig. 8 shows scanning electron micrographs of 100 nm lines and spaces fabricated by

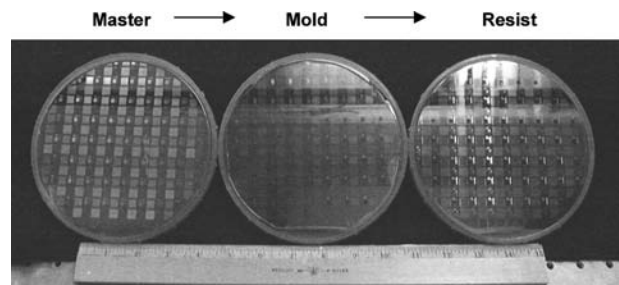


**Fig. 9** Images of a large-area master (6-in. silicon wafer with patterned photoresist; left frame), a large-area mold formed from this master (middle frame), and a molded thin film (2  $\mu$ m thick) of photopolymer formed using this mold (right frame). The mechanical flexibility and elastomeric nature of the mold are key features that allow this type of large-area replication. The lateral feature sizes in this pattern range from 200 nm to 1 cm. The relief depth ranges from 1 to 0.25  $\mu$ m.

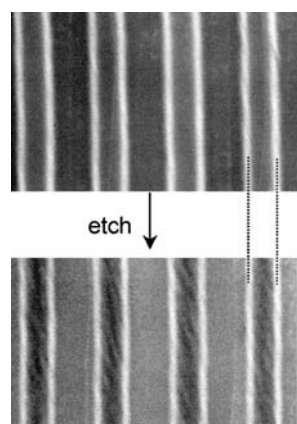


**Fig. 10** Scanning electron micrographs showing molded features of relief in a thin polymer film before (top frame) and after (bottom frame) reactive ion etching to remove the thin regions.

electron beam lithography and etching in  $\text{SiO}_2$  (left frame) and a replica grating structure in a molded polymer (right frame).<sup>[17]</sup> Below these sizes, the mechanical properties of the mold can be limiting;<sup>[18–21]</sup> newer elastomers with comparatively high modulus and physical toughness can extend the resolution of these procedures deep into the sub-100-nm regime.<sup>[18,20]</sup>

The resolution and replication fidelity illustrated in Figs. 7 and 8 can be achieved over large areas. Fig. 9 shows a master, a mold, and a replicated pattern in a thin polymer film carried out with and on 6-in. silicon wafers. The ability to flex and bend the mold allows contact with the thin spin cast photopolymer to be initiated at the center of the wafer. As the contact line is gradually allowed to move toward the edges of the substrate, air is pushed out, thereby eliminating trapped air pockets of the type that are difficult to avoid in more conventional embossing and

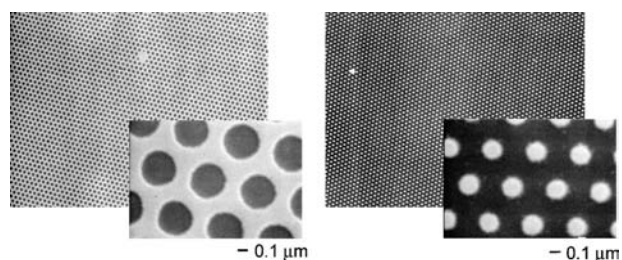


**Fig. 11** Scanning electron micrographs of nanopatterns of tungsten (left frame) and gold (right frame) formed by etching through a sacrificial polymer resist defined by molding and etching.

imprinting techniques that use rigid molds. The mechanical flexibility of the mold is also important for release because it allows the mold to be removed from the substrate by bending and peeling, in way that avoids damage to the substrate or the mold.

The wafer-scale results illustrated in Fig. 9 incorporate features with lateral dimensions down to 200 nm. This relief can be converted into isolated polymer nanostructures by etching to remove the thin regions of the molded films. Fig. 10 shows SEMs of a molded thin polymer film before and after exposure to an oxygen reactive ion etch. Careful control of the etching conditions can enable removal of the thin regions of the molded films without significant changes in the lateral dimensions of the features. The isolated polymer lines that are generated by these procedures can be used in the same way that patterned photoresist is used in conventional semiconductor processing. In the examples illustrated in Fig. 11, similar polymer structures were used for dry etching a pattern into underlying films of tungsten and gold. This molding and etching approach provides an alternative route to building the types of structures that can be formed by  $\mu\text{CP}$  and  $\text{nTP}$ .

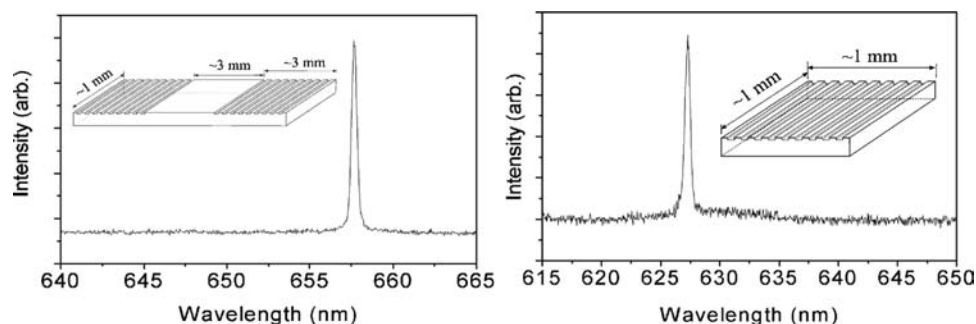


**Fig. 12** Schematic illustrations and emission spectra of plastic lasers that use molded resonators based on surface relief distributed Bragg reflectors (DBRs) and distributed feedback gratings (DFBs) on glass substrates. The grating periods are  $\sim 600$  nm in both cases. The lasers use thin-film plastic gain media deposited onto the printed gratings. The emission profiles, the lasing thresholds, and other characteristics of these devices are comparable to similar lasers that use resonators formed by high-resolution projection-mode photolithography.

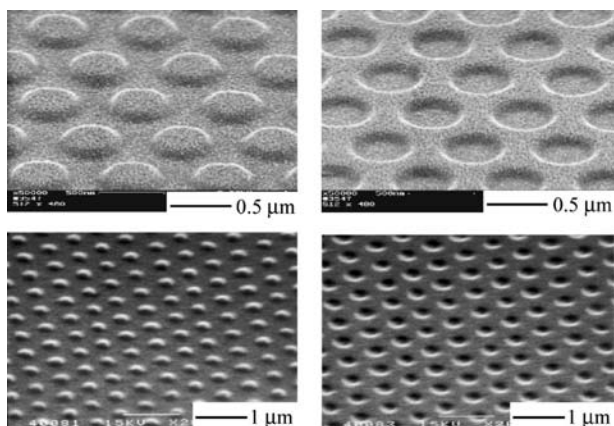


**Fig. 13** Scanning electron micrographs of four photonic crystal structures ( $\sim 50$ -nm deep) molded onto the surfaces of sol-gel-derived glass films. [The slight “graininess” in these images is due to a thin coating of gold ( $\sim 5$  nm) deposited to eliminate charging.]

## APPLICATIONS

Nanopatterns such as those described in the preceding discussion can be used for a variety of photonic devices. To build lasers out of molded or printed surface relief structures (which not only yields functional devices but also demonstrates the quality of these structures—defect density, spatial coherence, uniformity, etc.—for other applications), a thin layer of organic gain media is deposited on top of the structure to define a planar waveguide that confines light to the surface. The thickness of this layer is chosen to support a single transverse mode. Photopumping the structure generates lasing as a result of feedback associated with reflections from the grating. A lower-order interaction couples light out of the waveguide. For the examples described in this article, a third-order interaction with the grating provides the feedback and a first-order interaction leads to output coupling.

**Fig. 12** shows the typical performance of plastic lasers that use printed and molded distributed feedback (DFB) and distributed Bragg (DBR) resonators with spin-coated thin film (150–200-nm thick) gain media of 2-(4-biphenyl)-5-(4-*tert*-butylphenyl)-1,3,4-oxadiazole doped with 1 wt.% Coumarin 490 and DCMII (Exciton, Inc.).<sup>[16]</sup> Photopumping these structures with 2-nsec pulses from a nitrogen laser with intensities  $>5$  kW/cm<sup>2</sup> leads to multimode lasing at resolution-limited linewidths and wavelengths corresponding to the third harmonic of the gratings. The spectra and the threshold intensities for lasing are similar to those observed in lasers that use SiO<sub>2</sub> gratings generated with photolithography. They are better than those that we observed from gratings formed by pressing heated thin polymer films against rigid templates.<sup>[22]</sup>

The same printing and molding techniques can be used with more unusual materials and laser structures. **Fig. 13** shows images of some two-dimensional photonic crystal structures molded into a type of sol-gel derived glass<sup>[23]</sup> as examples. This class of material, known as an organically modified silicate, consists of interpenetrating organic and inorganic networks prepared by using a metal alkoxide with a reactive organic moiety. This hybrid matrix forms, at relatively low temperatures, thick, mechanically hard coatings with good optical properties. To generate fine patterns of surface relief in these films, the curing is carried out while the film is in contact with a PDMS mold.<sup>[23]</sup> The structures in **Fig. 13** are molded in organically modified silicate films several microns thick and consist of periodic arrays of cylindrical posts or holes with submicron diameters, arrayed in triangular, square, and honeycomb lattices. The images suggest that the structures are replicated with a spatial resolution that comfortably exceeds both the smallest dimensions of the features ( $\sim 150$  nm) in these sol-gel-derived photonic crystals and in structures ( $\sim 250$  nm) that are useful for applications in telecommunications.

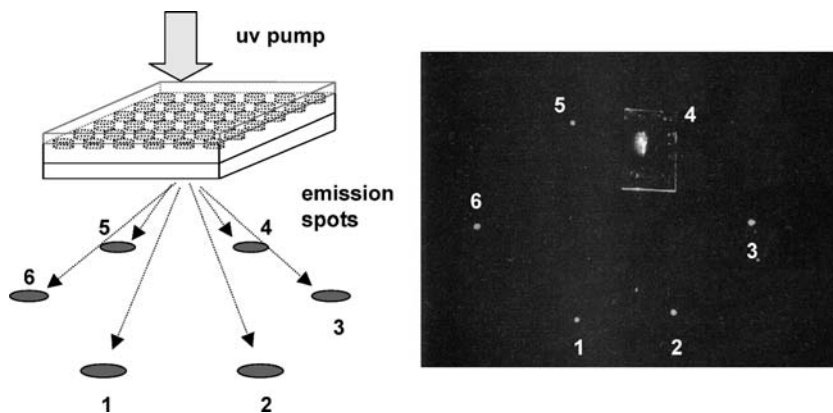


**Fig. 14** Schematic illustration (left frame) and optical image (right frame) of emission from a photopumped photonic crystal laser that uses a molded resonator of cylindrical depressions  $\sim 50$ -nm deep, with 400-nm diameters and center-to-center separations of 600 nm in a layer of an organically modified silicate glass film on glass slide. In this device, the crystal acts both as the resonator to provide feedback for the laser and the output coupler.

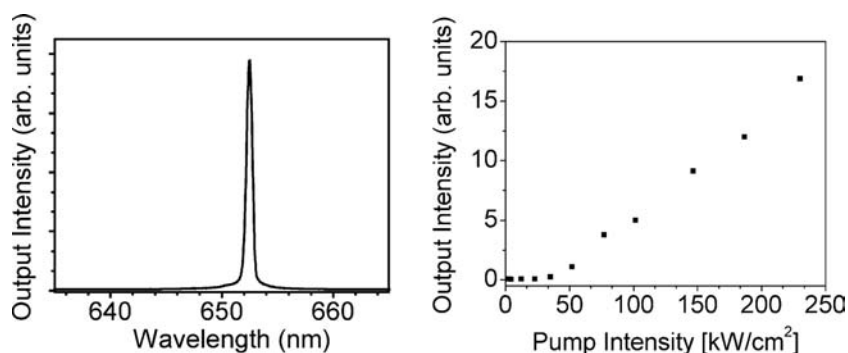


**Fig. 15** Emission spectrum (left frame) and output intensity as a function of pump intensity (right frame) for a photopumped laser that uses a molded two-dimensional photonic crystal as a resonator. The narrow emission linewidth (instrument limited), the well-defined emission spots and the relatively low lasing threshold provide evidence that the quality of the molded resonator is high (i.e., spatially uniform and free of defects).

Depositing thin films (150–200-nm thick) of organic gain materials [8-hydroxyquinolino aluminum (Alq) and the laser dye, DCMII] onto these molded patterns produces lasers that operate due to Bragg reflections induced by the photonic lattice.<sup>[23]</sup> Fig. 14 illustrates the photopumping geometry (left frame) and an image of the spatial pattern of laser emission (right frame). A typical spectrum (left frame) and the measured dependence of the output intensity on the intensity of the pump light (right frame) are shown in Fig. 15. The lasing threshold ( $\sim 50 \text{ kW}/\text{cm}^2$ ) and the emission spectra are, to within device-to-device variations, identical to those of similar lasers that use photolithographically defined resonators in  $\text{SiO}_2$ .<sup>[24]</sup>

Printing and molding procedures not only provide a simple, low-cost route to structures that can be fabricated with other approaches, but they also enable some unique patterning capabilities. For example,  $\mu\text{CP}$  can be used to form DFB resonators directly on the top surfaces ridge waveguides.<sup>[25]</sup> In certain cases, there are

manufacturing advantages to forming the gratings after defining the waveguides. Achieving this process sequence with photolithography is challenging because spin cast layers of photoresist develop large and undesired thickness variations due to dewetting at the sharp edges of relief associated with the waveguides. Fig. 16 illustrates the procedures for using  $\mu\text{CP}$  for this patterning task.<sup>[25]</sup> The bottom left frame shows an optical micrograph of the printed gold lines. Sublimation of a  $\sim 200$ -nm film of Alq doped with 0.5–5.0 wt.% DCMII onto the resonators produces waveguide DFB lasers. The bottom right frame of Fig. 16 shows the emission profile. Once the ridge waveguide DFB structure has been fabricated, it can be used as a master for producing a mold with two levels of relief.<sup>[17]</sup> The structure can then be rapidly replicated by molding in a single step. Fig. 17 shows the procedures and micrographs of the master and a typical replica in a photopolymer.

This basic type of laser can also be produced by molding the relief structure directly into the organic

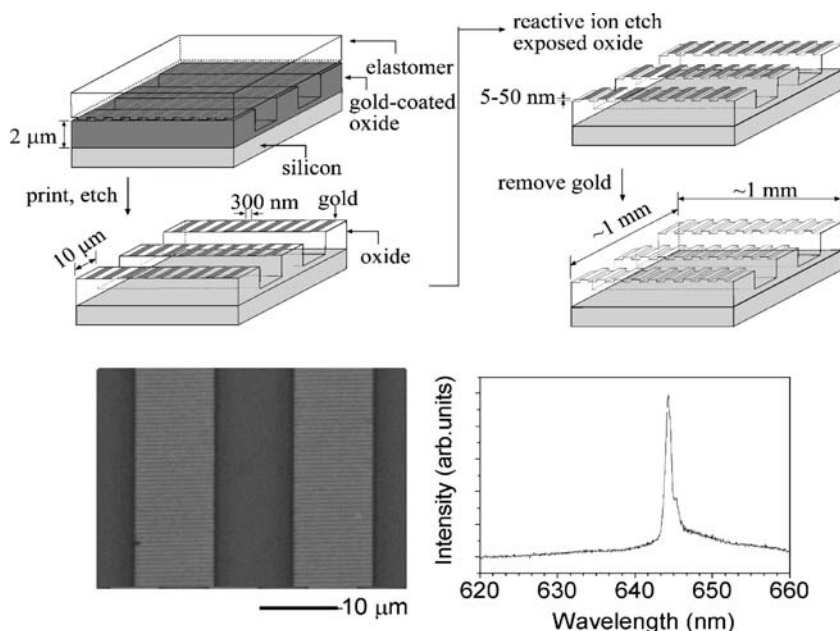


**Fig. 16** Schematic illustration (top frames) of steps for microcontact printing high-resolution gratings directly onto the top surfaces of ridge waveguides. The printing defines a sacrificial etch mask of gold, which is subsequently removed. The bottom left frame shows a top-view optical micrograph of printed gold lines on the ridge waveguides. The bottom right frame shows the emission output of a plastic photopumped laser that uses the printed structure and a thin evaporated layer of gain media.



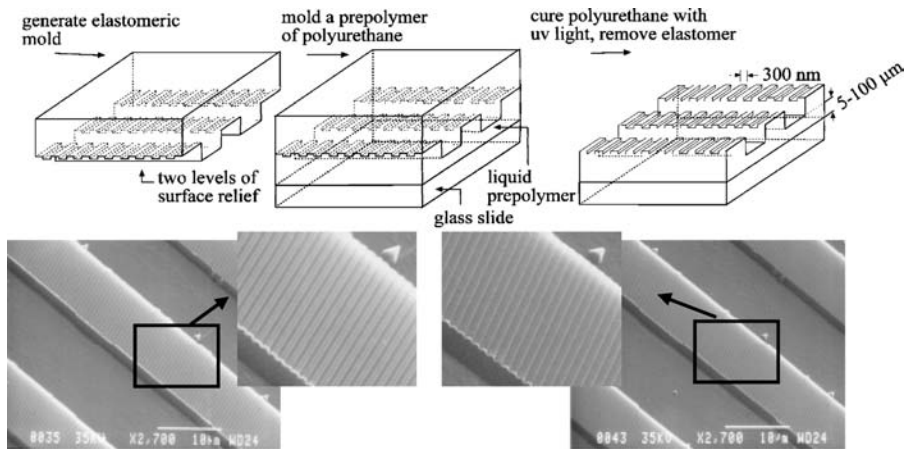


**Fig. 17** Schematic illustration (top frames) of the use of a two-level mold to produce, in a single step, distributed feedback ridge waveguide laser resonators. The scanning electron micrographs on the right show the silica master that was used for the mold (top frame) and a molded replica in a photocurable polymer (bottom frame).

gain material.<sup>[25]</sup> Fig. 18 shows the procedures. In this case, a PDMS mold is placed in contact with a thin layer of gain material that is evaporated onto the waveguides. Exposing this film to ultraviolet laser light while in contact with the mold softens the material and causes it to conform to the relief of the mold. Removing the PDMS mold after this procedure leaves a surface relief DFB grating embossed onto the gain material itself. Photopumping this structure leads to lasing; a typical spectrum is shown in Fig. 18. We have also used this same basic soft molding approach to pattern relief features into thin films of the polymer poly(*p*-phenylene vinylene) (PPV) to structure light emission in polymer light-emitting diodes (Figure 19).

A PPV film cast on top of a piece of glass coated with indium tin oxide was molded during solvent evaporation using a PDMS mold. A uniform top electrode consisted of a uniform bilayer of Al/Ca. Here thickness relief produced by the molding leads to light output from only the thin regions of the film at certain voltages.<sup>[26]</sup> This sort of direct patterning of thin layers of electroactive organics could have important applications in the emerging field of active organic optoelectronics. These classes of mechanically and chemically fragile materials are difficult or impossible to pattern with conventional approaches because of their chemical incompatibility with the required photoresists, developers, and solvents.

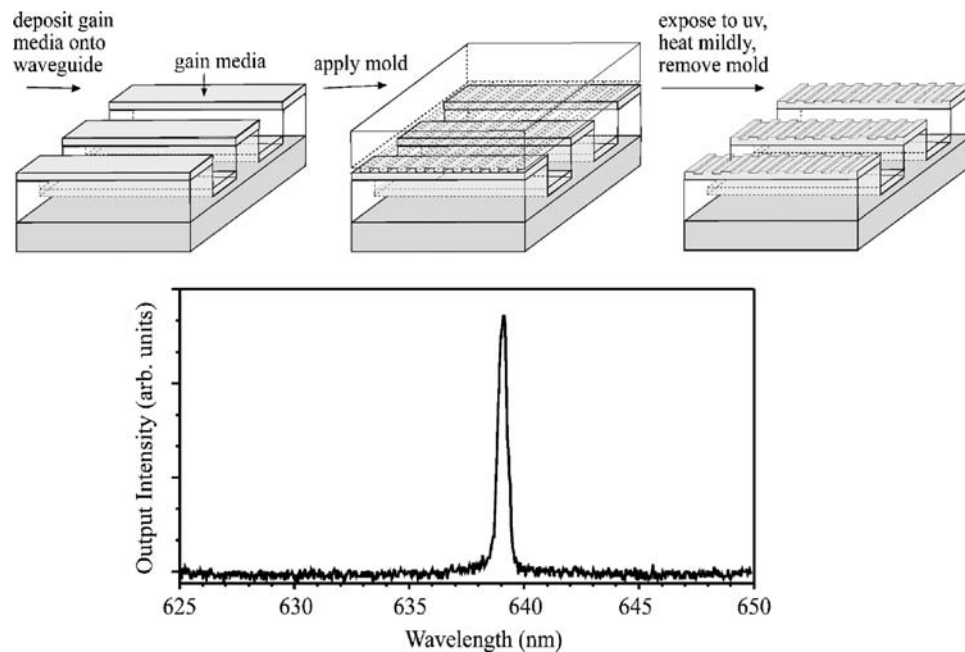


**Fig. 18** Schematic illustration (top frames) of procedures for molding high-resolution gratings directly onto the surface of a thin layer or organic gain material. Photopumping this structure leads to lasing. The bottom frame shows a typical emission spectra.

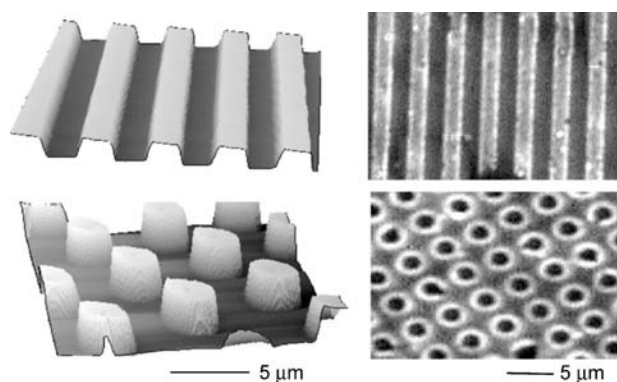


**Fig. 19** Atomic force micrographs (left frames) of surface relief structure molded into a thin film of poly(*p*-phenylene vinylene) on a thin film of indium tin oxide on a glass slide. The right frames show optical micrographs of the patterns of emission that results from diodes that are formed by depositing Al/Ca on top of the molded films.

## CONCLUSION

This entry summarizes some of our recent work in the development and application of unconventional methods for fabricating photonic nanostructures, with examples of their use in organic optoelectronics. Integrated optics represents a field where new or emerging techniques for nanofabrication could find important niche applications. The dimensional requirements for registration and alignment (2–500 μm typically) in these systems is much less demanding than the requirements on the minimum feature sizes (~100–300 nm for the devices described here). As a result, the complex and highly engineered systems that are required for nanoscale registration are not needed, and the challenges associated with achieving nanoscale overlay accuracy with deformable molds and stamps can be avoided.<sup>[27]</sup> These features greatly simplify the potential introduction of these new lithographic methods into realistic manufacturing settings. Compared to other types of unconventional approaches that have nanometer resolution (e.g., imprint lithography, embossing, etc.) the printing and molding methods described here are attractive, in part because they are directly compatible with classes of organic active materials. The technologies that emerge from the combined use of soft materials and soft patterning methods for photonics have a strong potential to yield important classes of devices for future optical communication networks, information displays, and other systems.

## ACKNOWLEDGMENTS

The author would like to thank all of the collaborators that contributed to the work described here.

## REFERENCES

1. Tamir, T.; Ed. *Integrated Optics*, 2nd; Springer-Verlag, 1985.
2. Yablonovich, E. Photonic crystals: semiconductors of light. *Sci. Am.* December **2001**, 47–55 and references therein.
3. Clapham, P.B.; Hutley, M.C. Reduction of lens reflexion by the ‘moth eye’ principle. *Nature (Lond.)* **1973**, *244*, 281–282.
4. Enger, R.C.; Case, S.K. Optical elements with ultrahigh spatial-frequency surface corrugations. *Appl. Opt.* **1983**, *22*, 3220–3228.
5. Mirkin, C.A.; Rogers, J.A. Emerging methods for micro- and nanofabrication. *MRS Bull.* **2001**, *26*, 506–507 and references therein.
6. Xia, Y.; Rogers, J.A.; Paul, K.E.; Whitesides, G.M. Unconventional methods for fabricating and patterning nanostructures. *Chem. Rev.* **1999**, *99* (7), 1823–1848.
7. Kumar, A.; Whitesides, G.M. Features of gold having micrometer to centimeter dimensions can be formed through a combination of stamping with an elastomeric stamp and an alkanethiol ink followed by chemical etching. *Appl. Phys. Lett.* **1993**, *63*, 2002–2004.
8. Michel, B.; Bernard, A.; Bietsch, A.; Delamarche, E.; Geissler, M.; Juncker, D.; Kind, H.; Renault, J.P.; Rothuizen, H.; Schmid, H.; Schmidt-Winkel, P.; Stutz, R.; Wolf, H. Printing meets lithography: soft approaches to high-resolution printing. *IBM J. Res. Develop.* **2001**, *45*, 697–719.
9. Loo, Y.-L.; Willett, R.W.; Baldwin, K.; Rogers, J.A. Interfacial chemistries for nanoscale transfer printing. *J. Am. Chem. Soc.* **2002**, *124* (26), 7654–7655.
10. Loo, Y.-L.; Willett, R.W.; Baldwin, K.; Rogers, J.A. Additive, nanoscale patterning of metal films with a stamp and a surface chemistry mediated transfer process: Applications in plastic electronics. *Appl. Phys. Lett.* **2002**, *81* (3), 562–564.
11. Larsen, N.B.; Biebuyck, H.; Delamarche, E.; Michel, B. Order in microcontact printed self-assembled monolayers. *J. Am. Chem. Soc.* **1997**, *119*, 3017–3026.
12. Biebuyck, H.A.; Whitesides, G.M. Self-organization of organic liquids on patterned self-assembled monolayers of alkanethiolates on gold. *Langmuir* **1994**, *10*, 2790–2793.
13. Rogers, J.A.; Bao, Z.; Baldwin, K.; Dodabalapur, A.; Crone, B.; Raju, V.R.; Kuck, V.; Katz, H.; Amundson, K.; Ewing, J.; Drzaic, P. Paper-like electronic displays: large area, rubber stamped plastic sheets of electronics and electrophoretic inks. *Proc. Natl. Acad. Sci.* **2001**, *98* (9), 4835–4840.
14. Xia, Y.N.; Zhao, X.M.; Kim, E.; Whitesides, G.M. A selective etching solution for use with patterned self-assembled monolayers of alkanethiolates on gold. *Chem. Mater.* **1995**, *7*, 2332–2337.
15. Loo, Y.-L.; Hsu, J.W.P.; Willett, R.L.; Baldwin, K.W.; West, K.W.; Rogers, J.A. High-resolution transfer printing on GaAs surfaces using alkane dithiol self-assembled monolayers. *J. Vac. Sci. Technol. B* **2002**, *20*, 2853–2856.



16. Rogers, J.A.; Meier, M.; Dodabalapur, A. Using stamping and molding techniques to produce distributed feedback and Bragg reflector resonators for plastic lasers. *Appl. Phys. Lett.* **1998**, *73* (13), 1766–1768.
17. Rogers, J.A.; Bao, Z.; Dodabalapur, A.; Schueller, O.J.A.; Whitesides, G.M. Printing, molding and near-field photolithographic methods for patterning organic lasers, smart pixels and simple circuits. *Synth. Met.* **2000**, *115* (1–3), 5–11.
18. Schmid, H.; Michel, B. Siloxane polymers for high-resolution, high-accuracy soft lithography. *Macromolecules* **2000**, *33*, 3042–3049.
19. Odom, T.W.; Love, J.C.; Wolfe, D.B.; Paul, K.E.; Whitesides, G.M. Improved pattern transfer in soft lithography using composite stamps. *Langmuir* **2002**, *18*, 5314–5320.
20. Choi, K.M.; Rogers, J.A. A photocurable poly(dimethylsiloxane) for soft lithography in the nanometer regime. *J. Am. Chem. Soc.* **2003**, *125*, 4060–4061.
21. Hui, C.Y.; Jagota, A.; Lin, Y.Y.; Kramer, E.J. Constraints on microcontact printing imposed by mechanical deformation. *Langmuir* **2002**, *18* (4), 1394–1407.
22. Berggren, M.; Dodabalapur, A.; Slusher, R.E.; Timko, A.; Nalamasu, O. Organic solid-state lasers with imprinted gratings on plastic substrates. *Appl. Phys. Lett.* **1998**, *72*, 410–411.
23. Schueller, O.J.A.; Whitesides, G.M.; Rogers, J.A.; Meier, M.; Dodabalapur, A. Fabrication of photonic crystal lasers by nanomolding of sol-gel glasses. *Appl. Opt.* **1999**, *38* (27), 5799–5802.
24. Berggren, M.; Dodabalapur, A.; Slusher, R.E.; Bao, Z.; Timko, A.; Nalamasu, O. *Electron. Lett.* **1998**, *34*, 90–91.
25. Rogers, J.A.; Meier, M.; Dodabalapur, A. Distributed feedback ridge waveguide lasers fabricated by nanoscale printing and molding on non-planar substrates. *Appl. Phys. Lett.* **1999**, *74* (22), 3257–3259.
26. Rogers, J.A.; Bao, Z.; Dhar, L. Fabrication of patterned electroluminescent polymers that emit in geometries with features into the sub-micron range. *Appl. Phys. Lett.* **1998**, *73* (3), 294–296.
27. Rogers, J.A.; Paul, K.E.; Whitesides, G.M. Quantifying distortions in soft lithography. *J. Vac. Sci. Technol., B* **1998**, *16*, 88–97.

# Protein Adsorption Kinetics under an Applied Electric Field

Paul R. Van Tassel

Department of Chemical Engineering, Yale University,  
New Haven, Connecticut, U.S.A.

## INTRODUCTION

The dimensions of the largest naturally occurring molecular species and those of the smallest manmade features converge at the nanoscale. Proteins, the basic building blocks of living organisms, are among the larger molecules in nature with dimensions ranging from 1 to 100 nm. Materials incorporating proteins are therefore true nanomaterials. Of particular importance are thin films of proteins immobilized at a solid substrate. Biosensing, tissue engineering, enzymatic catalysis, and bioelectronics are just a few of the areas in which immobilized layers of proteins play a key role.

The tendency of proteins to attach to interfacial regions is well documented.<sup>[1–4]</sup> Ionic, van der Waals, solvation, and donor–acceptor interactions all play important roles in rendering the interfacially adsorbed state to be thermodynamically favored over the solution state.<sup>[1]</sup> Proteins are colloidal objects, possessing a distribution of surface charge and, in an electrolytic solution, a distribution of weakly associated counterions. Their interaction with a solid substrate is thus expected to be sensitive to the substrate's charge distribution. By controlling the polarization of an adsorbing surface (i.e., applying an electric field), one alters this charge distribution and therefore the surface–protein interaction. This possibility is understandably appealing to those wishing to control the adsorption process, perhaps desiring adsorbed layers of preferred orientation or spatial distribution. However, the interaction between proteins and surfaces is complex and predicting adsorbed layer properties by considering the contributions from the interaction modes listed above remains a significant challenge. Adding an electric field makes the problem even more complex. Thus while influencing an adsorbed protein layer with an electric field is both possible and desirable, the outcome is as yet poorly understood.

In this contribution, we review the field of protein adsorption kinetics under an applied electric field. By focusing on kinetics, we limit ourselves to studies where adsorbed layer properties are measured in situ during the electroformation process. We begin with a brief presentation of certain basic theoretical

considerations. We then introduce the methods employed to measure protein adsorption kinetics under an applied electric field. Next, we introduce some of the key results, grouping our presentation by investigator. A perspective on future directions is then given and this is followed by a conclusion. By summarizing some of the key accomplishments and open questions, we hope to guide future efforts to produce nanoscale devices employing adsorbed protein layers formed under an electric field.

## THEORY

An applied electric field may affect protein adsorption in two ways. The first of these deals with transport. Proteins are composed of amino acids, some of which contain acidic/basic sites. Thus at all but the isoelectric pH, the protein will possess a net charge and thus migrate in response to an electric field. Because the charge distribution is generally not spherically symmetric, the electric field also imposes a torque on the molecule, causing it to rotate. Of course, electric-field-induced migration and rotation must compete against the molecule's thermal diffusive motion, so these influences are only observed in excess of some threshold field strength. The second principal effect of an applied electric field involves the direct interaction between the electrode and the protein upon close approach. The alteration of electrode potential brings about various physicochemical changes in the surface itself and alters the counterion distribution away from the surface; these two effects influence the protein–surface interaction and affect such properties as the rate of attachment, protein orientation, and the rate and extent of subsequent post-adsorption changes in orientation and conformation.

The transport of protein in a (assumedly laminar) flowing solution to the surface may be described by the general transport relation

$$\frac{\partial c}{\partial t} + \vec{v} \cdot \vec{\nabla} c = \vec{\nabla} \cdot \left( D \vec{\nabla} c + \frac{cq\vec{E}}{\zeta} \right) \quad (1)$$

where  $c$  is the protein concentration,  $t$  is the time,  $\vec{v}$  is the fluid flow velocity vector,  $D$  is the diffusivity,  $q$  is the effective protein charge,  $\vec{E}$  is the electric field vector, and  $\zeta$  is the friction coefficient (a measure of the viscous drag on the protein). The flow field must be known in advance to solve Eq. (1). So long as the concentration is quite low, one may neglect the influence of the migrating proteins on the fluid and solve for the flow field using the standard Navier–Stokes equation.

The two terms on the right side of Eq. (1) represent the contributions from thermal diffusion and electric-field-induced migration, respectively. It is interesting to consider the limiting cases where one is much larger than the other. Neglecting the second term gives pure convective diffusion. One may approximate the flux to the surface by assuming steady shear flow and a perfect sink boundary condition at the adsorbing surface. In this case, the flux may be approximated by  $J(x, t) = Dc_b/\delta(x, t)$ , where  $c_b$  is the bulk protein concentration and

$$\delta(x, t) = \frac{(45Dx/2a)^{1/3}}{f\left(\frac{4Dt}{(45Dx/2a)^{2/3}}\right)} \quad (2)$$

is the convective diffusion boundary layer, a function of the diffusivity ( $D$ ), the distance along the surface in the direction of the flow ( $x$ ), the shear rate ( $a$ ), and the time ( $t$ ).<sup>[5,6]</sup> The function  $f(\tau)$  is the inverse of  $\tau(f) = [1 - (1 - f^3)^{2/3}]/2f^2$  for  $\tau < 1/2$  and  $f(\tau) = 1$  for  $\tau > 1/2$ . Pure convective diffusion is therefore characterized by an initially zero flux that increases steadily to a steady flux at dimensionless time,  $\tau$ , equals 1/2.

Neglecting the first term in Eq. (1) is equivalent to ignoring diffusive motion. In this case, assuming an electric field normal to the surface of magnitude  $E$ , fully developed shear flow, and a no-slip, perfect sink boundary condition, the concentration profile is given by

$$c(x, z, t) = c_b H\left(azt + \frac{aqEt^2}{2\zeta} - x\right) \quad (3)$$

where  $z$  is the height above the surface and  $H$  is the Heaviside function [i.e.,  $H(\xi) = 1$  for  $\xi > 0$  and  $H(\xi) = 0$  for  $\xi < 0$ ].<sup>[6]</sup> The flux to the surface is thus

$$J(x, t) = \frac{c_b q E}{\zeta} H\left(\frac{aqEt^2}{2\zeta x} - 1\right) \quad (4)$$

Pure electrophoretic migration is therefore characterized by an initial period of zero flux, during a time of  $\sqrt{2\zeta x/aqE}$ , followed by a steady flux.

In the absence of transport limitations, the rate of adsorption may be expressed as

$$\frac{d\Gamma}{dt} = k_a c_b \Phi - \sum_i k_{d,i} \Gamma_i \quad (5)$$

where  $\Gamma$  is the density of adsorbed protein (mass per area),  $k_a$  is the adsorption rate constant,  $\Phi$  is the one-body cavity function, and  $k_{d,i}$  and  $\Gamma_i$  are the desorption rate constant and the density of protein in the  $i$ th structural state, respectively (these states may denote various conformations, orientations, or states of aggregation).<sup>[7]</sup> The cavity function is defined as  $\Phi = \langle e^{-u/kT} \rangle_{\Gamma, T}$ , where  $u$  is the potential energy of a single molecule interacting with the surface and with all of the previously adsorbed molecules ( $u$  depends on position and orientation),  $k$  is the Boltzmann constant,  $T$  is the absolute temperature, and the brackets represent an averaged quantity, over all representations of the adsorbed layer at density  $\Gamma$  and temperature  $T$ , according to their appropriate weights, and over all orientations and positions of the single “reference” molecule. All of the quantities on the right of Eq. (5) (except  $c_b$ ) may be altered by application of an electric field.

To make quantitative predictions, the potential energy of interaction between protein molecules and the charged surface must be calculated. The electrostatic contribution to this energy may be determined using Poisson–Boltzmann<sup>[8–12]</sup> or density functional<sup>[13,14]</sup> approaches.

## EXPERIMENTAL METHODS

In this section, we review the experimental methods used to measure protein adsorption kinetics, in situ, under an applied electric field.

### Impedance Measurements

Impedance measurements involve the application of an alternating voltage across an electrode/solution interface.<sup>[15–17]</sup> The solution is modeled as a resistor and the interface as an impedor and a capacitor in series. The capacitance is simply the imaginary part of the measured impedance. Adsorbed molecules (e.g., organics and proteins) displace ions and solvent from the interface; this changes the charge distribution and thereby the interfacial capacitance. The capacitance is thus an indirect measure of the extent of adsorption and structure of the adsorbed layer.

## Reflectometry

Reflectometry involves measuring the reflection of polarized light at the interface between two optical media. In fact, two reflections are measured: one for the electric field component perpendicular to the plane of incidence (transverse electric or s-wave) and one for the electric field component parallel to the plane of incidence (transverse magnetic or p-wave). At a certain angle of incidence (the Brewster angle), the p-wave reflection vanishes and around this angle, the reflectivity, or square of the amplitude of the p-wave reflection, and ellipticity, or ratio of p- and s-wave reflections, become very sensitive to interfacial heterogeneity, as brought about, for example, by adsorption of biomolecules. By assuming the adsorbed layer to be uniform in refractive index, both its thickness and refractive index may be determined. By further assuming a linear dependence of refractive index on concentration, the adsorbed density is calculable. Silica is typically used as the adsorbing substrate; thus to apply an electric field, a conducting coating is needed. Bos et al.<sup>[18]</sup> have developed a reflectometry method using silica coated with a ca. 100-nm layer of indium tin oxide (ITO). An important caveat is that the intensity ratio changes in the presence of an applied voltage and this must be considered when calculating the amount of adsorbed protein.

## Quartz Crystal Microbalance

A quartz crystal microbalance (QCM) consists of a thin disk of (piezoelectric) crystalline quartz sandwiched between thin film metal electrodes. Upon application of an alternating voltage, the crystal undergoes thickness shear mode vibration. The mass adsorbed to the electrode surface, including the trapped solvent, is simply proportional to the frequency shift. In addition, the dissipation of energy following voltage removal, as measured by the decay of the oscillation amplitude, is a sensitive measure of the viscoelastic properties of an adsorbed layer. Khan and Wernet<sup>[19]</sup> have developed a QCM method in which a voltage is applied between an electroconductive polymer film-coated adsorbing surface and a counterelectrode.

## Optical Waveguide Lightmode Spectroscopy

Optical waveguide lightmode spectroscopy (OWLS) is based on the phase shift associated with multiple interfacial reflections: when either the s- or p-wave undergoes a total phase shift equal to an integral multiple of  $2\pi$  upon one complete traversal of a planar, dielectric waveguide sandwiched between media of lower refractive index, a standing wave is excited in

the waveguiding film. Because of their dependence on reflection, the phase shifts are sensitive to interfacial heterogeneity—and the thickness, refractive index, and density of an adsorbed biomolecular layer can be readily determined. Optical waveguide lightmode spectroscopy is normally applied to non-conductive substrates. To allow for detection in the presence of an electric field, Brusatori et al.<sup>[6,20]</sup> and Bearinger et al.<sup>[21]</sup> have developed OWLS methods employing an indium tin oxide coating.

## Total Internal Reflection Fluorescence

When light traversing an optically dense medium approaches an interface with a more optically rare medium at an angle exceeding a critical value of  $\theta_{\text{crit}} = \sin^{-1}(n_{\text{rare}}/n_{\text{dens}})$ , a total internal reflection occurs and an evanescent wave of exponentially decaying intensity penetrates the rarer medium. In total internal reflection fluorescence (TIRF) spectroscopy, the evanescent wave excites fluorescent probes attached to the biomolecules and detection of the emission associated with their decay provides information on the density, composition, and conformation of adsorbed molecules. Fraaije et al.<sup>[22]</sup> and Asanov et al.<sup>[23,24]</sup> have extended TIRF methods to measure protein adsorption under an applied electric field.

## RESULTS

Bernabeu and Caprani<sup>[15]</sup> have measured the adsorption of fibrinogen and albumin to a carbon electrode using an impedance method. They observed the initial rate and the overall extent of adsorption of these two negatively charged proteins to decrease with increasing voltage, in apparent violation of electrostatic rules [Fig. 1](#). The authors explained this in terms of adsorbed counterions. On a platinum (i.e., more hydrophilic) surface, the rate and overall extent yielded minima at an intermediate electrode potential.

Feng and Andrade<sup>[16]</sup> have investigated the adsorption of several proteins on low-temperature isotropic carbon electrodes, also using an impedance method. They generally find the extent and initial rate of adsorption to decrease with increasing electrode potential, irrespective of protein charge and solution ionic strength [Fig. 2](#). In contrast, on a gold electrode, the extent and initial rate varied according to electrostatics. At higher pH, they did note a maximum in adsorbed amount at an intermediate potential—consistent with behavior of organics at metal surfaces—and surmised that similar behavior may hold at other pH values, provided a sufficiently large potential range. This non-monotonic behavior is explained by

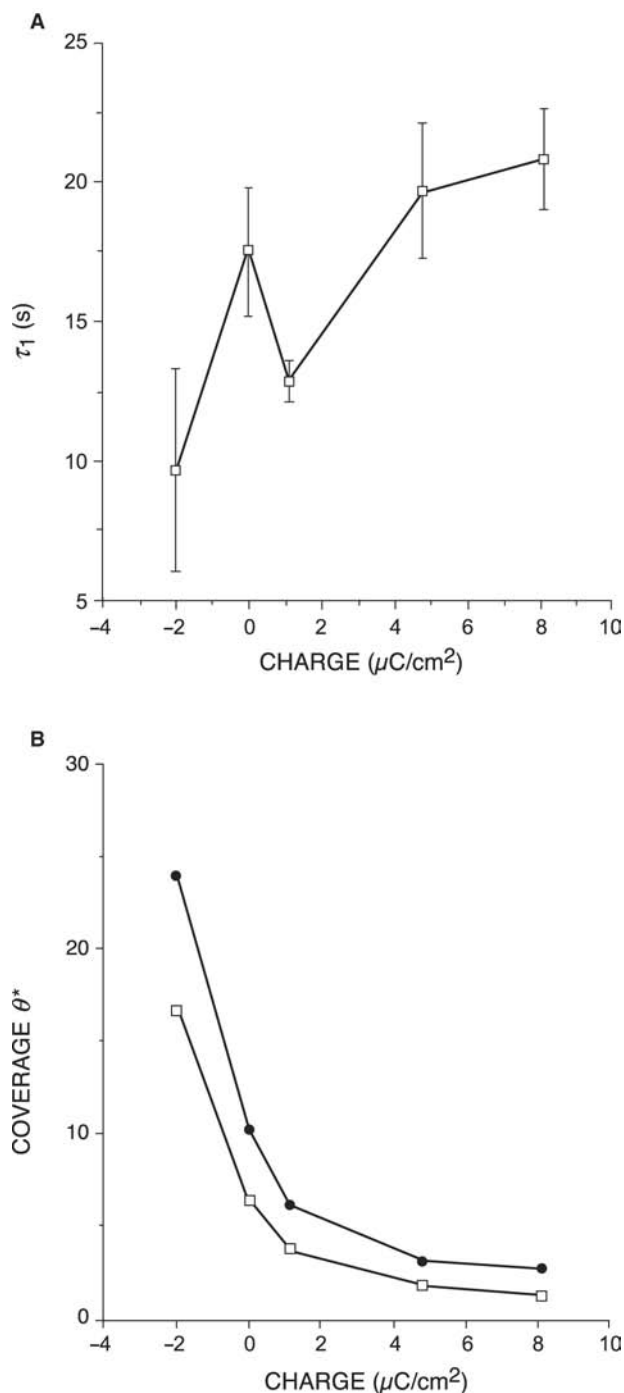


**Fig. 1** (A) The characteristic time of adsorption and (B) the amount adsorbed at saturation in the initially adsorbed state (bottom line) and the conformationally altered state (upper line) vs. electrode potential for fibrinogen adsorbing to a carbon electrode as measured using an impedance method. *Source:* From Ref.<sup>[15]</sup>.

the hydrophobic effect: at a hydrophobic surface of near-zero charge, the contacting water is highly ordered and thus its displacement is highly favored entropically, whereas at a more charged hydrophobic

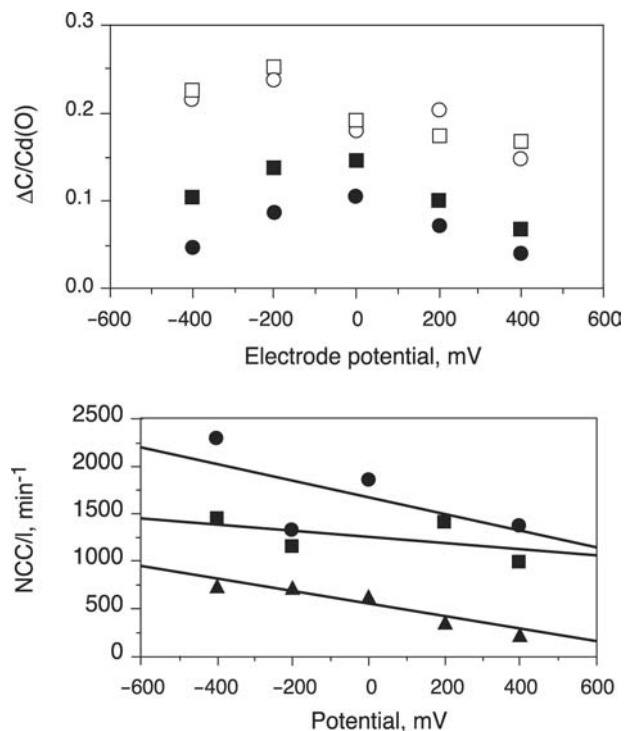


**Fig. 2** (A) Normalized capacitance change because of adsorption of 0.5 g/L human serum albumin (circles) and 0.1 g/L lysozyme (squares) from acidic (pH = 4.0, open) and basic (pH = 10.6, solid) solutions as functions of carbon electrode potential as measured by an impedance method. (B) Initial rates of normalized capacitance change for 0.50 g/L human serum albumin (circles), 0.05 g/L human plasma fibrinogen, 0.50 g/L superoxide dismutase, and 0.10 g/L lysozyme onto a carbon electrode as a function of electrode potential. The change in interfacial capacitance is a measure of the extent of surface coverage. *Source:* From Ref.<sup>[16]</sup>.

surface, the contacting water is less ordered and thus more difficult to displace by adsorbing molecules.

Fievet et al.<sup>[17]</sup> have also used impedance methods to measure protein adsorption onto a carbon electrode. They observed both the adsorbed amount and the initial adsorption rate to exhibit a maximum at an intermediate electrode potential and attributed this as well to a hydrophobic effect.

Bos et al.,<sup>[18]</sup> using reflectometry, observed a modest influence of an applied electric field on the adsorption of several proteins onto indium tin oxide under most conditions. Most observations followed electrostatic arguments, but an exception was lysozyme at pH = 9.9 Fig. 3, where a significant increase in adsorbed amount of this positively charged protein was observed at ITO potentials exceeding 300 mV (vs. Ag/AgCl). This was explained by a local pH effect: the  $\text{H}^+$  concentration decreased with increasing electrode potential, thereby causing the protein to become less positive (or even slightly negative).

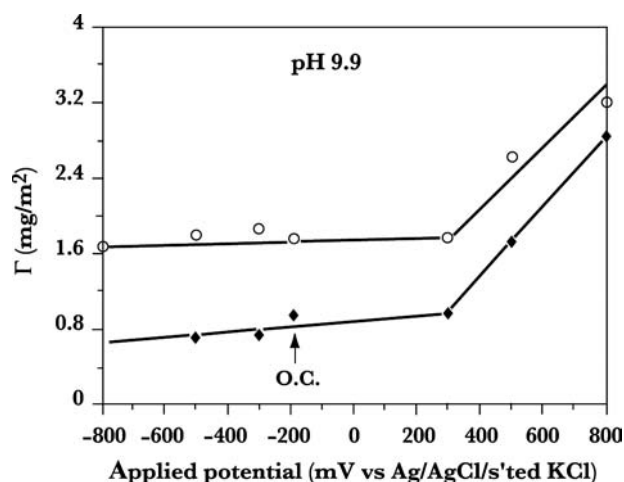


**Fig. 3** The amount of lysozyme (open symbols) and ribonuclease (closed symbols) from a solution at  $\text{pH} = 9.9$ , following 15 min of exposure to an indium tin oxide surface, as a function of applied voltage as measured using reflectometry. *Source:* From Ref.<sup>[18]</sup>.

Khan and Wernet<sup>[19]</sup> used a quartz crystal microbalance to investigate the adsorption of glucose oxidase onto an electroconducting polyanion-doped polypyrrole film. Although the study focused on enzymatic activity following adsorption, of particular significance was the demonstration of a kinetic isotherm under an applied potential Fig. 4.

Fraaije et al.<sup>[22]</sup> have used total internal reflection fluorescence to investigate the voltage dependence of the amount and mean orientation of cytochrome *c* adsorbed onto tin oxide. The fluorescent intensity as a result of absorption of both the p-wave and the s-wave of the incident light was measured, and it was

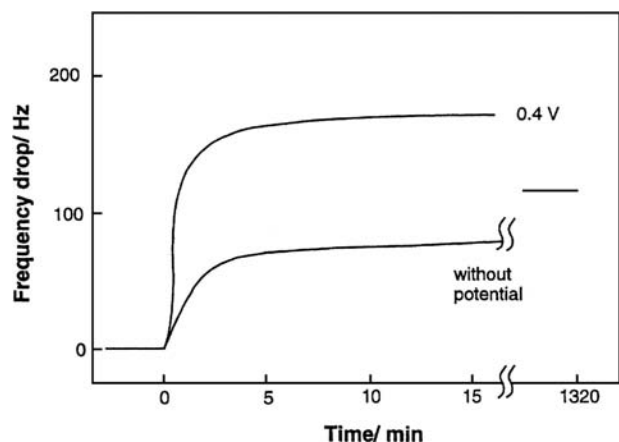


**Fig. 4** The amount of glucose oxidase adsorbed to a sulfated poly  $\beta$  hydroxyether-doped polypyrrole film vs. time at an open circuit potential and under an applied potential difference of 0.4 V as measured using a quartz crystal microbalance. *Source:* From Ref.<sup>[19]</sup>.

determined that over a fairly significant voltage range (from 0 to 1 V vs. Ag/AgCl), little change in adsorbed amount or mean orientation occurs. In contrast, changing the pH or the surface coverage of the adsorbed protein resulted in changes in mean orientation angle  $7^\circ$  and  $4^\circ$ , respectively.

Asanov et al.<sup>[23]</sup> have used TIRF to measure the adsorption of bovine serum albumin onto tin oxide under an applied electric field. They find little effect on adsorption at anodic potentials (negative surface charge) but a significant increase in adsorption at increasingly cathodic potentials. This behavior again contradicts one's expectations based on electrostatics. However, it was noted that the adsorption behavior correlates strongly with the adsorbing substrate's water contact angle; thus it appears that hydrophobic forces are at play. These authors have also investigated the voltage-induced desorption of biospecifically bound species, with a goal of developing a regenerable biosensing platform.<sup>[24]</sup> Their findings are impressive: the rate and extent of desorption could be greatly enhanced by the application of an oscillating voltage Fig. 5. In particular, the desorption time constant was decreased from  $10^5$  sec in the absence of an applied potential to 300 sec in the presence of a square wave potential alternating from  $-0.7$  to  $+1.1$  V.

Brusatori et al.<sup>[6,20]</sup> have investigated the adsorption of albumin and cytochrome *c* onto ITO using OWLS. The raw data of a typical experiment appear in Fig. 6. Following a baseline measured under flowing solvent

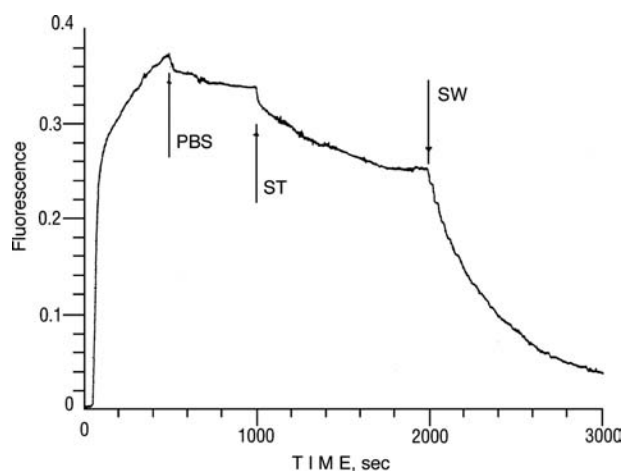


**Fig. 5** The fluorescence detected (a measure of the adsorbed amount) from labeled antibiotin adsorbing onto a biotinylated indium tin oxide electrode. At the first arrow, the protein solution is replaced by a pure PBS buffer solution. At the second arrow, the open circuit potential is replaced by a saw tooth polarization from  $-0.7$  to  $+1.1$  V at  $0.1$  V/sec. At the third arrow, the potential is changed to a square wave polarization from  $-0.7$  to  $+1.1$  V at a time period of 5 sec. *Source:* From Ref.<sup>[24]</sup>.



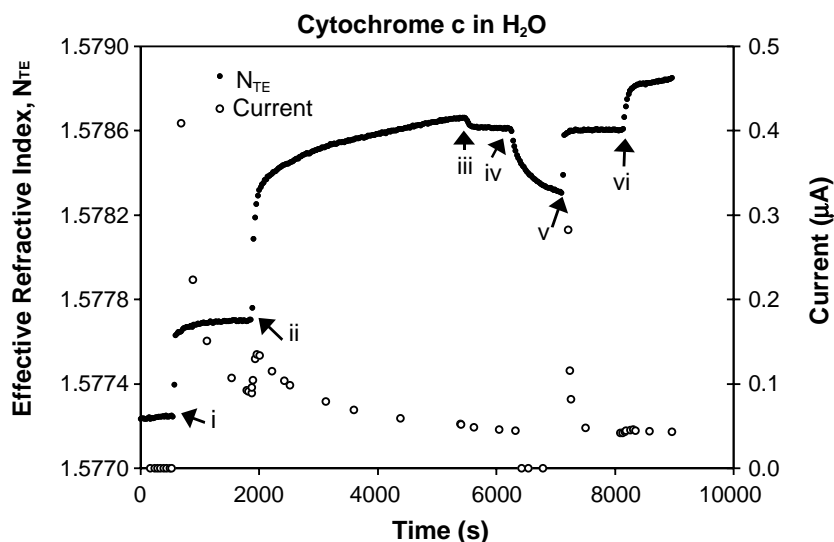


**Fig. 6** The effective refractive index (a measure of the adsorbed amount from optical waveguide lightmode spectroscopy) and the current during cytochrome *c* adsorption from water onto indium tin oxide as a function of time. At point i, a voltage difference of 1.0 V is applied. At point ii, the protein solution is introduced. At point iii, the protein solution is replaced by a buffer solution. At point iv, the system is returned to an open circuit potential, and at point v, the 1.0-V voltage difference is reapplied. At point vi, the protein solution is reintroduced. *Source:* Taken from Ref.<sup>[6]</sup>.

(deionized water in this case), application of an electric field (1.0 V over a 1.0-mm distance) between the adsorbing substrate and a platinum counterelectrode (i) yields an increase in the measured effective refractive index, the fundamental output signal of OWLS. This increase is not fully understood, but is likely a result of interfacial double-layer charging, to penetration of small ions into the ITO and/or the underlying silicon titanium oxide films (even in deionized water, carbonate and other ionic impurities are present), or to mild oxidation of the ITO. The current increases initially but then decreases, as would occur for a resistor and capacitor in series. Upon addition of cytochrome *c* in water (ii), the signal greatly increases because of optical changes at the interface brought about by adsorption. A return to the deionized water (iii) causes only a small signal reduction, indicating that only a small quantity of protein desorbs. When the electric field is removed (iv), a decreased signal results. However, this is not a result of further desorption as a reapplication of the field (v) returns the signal to its previous level. Finally, a reintroduction of the protein (vi) yields an additional signal increase. This additional adsorption is likely a result of an increased amount of area on the surface open for adsorption. The cause of this increased available area is likely aggregation among the adsorbed molecules.

The surface density vs. time for albumin and cytochrome *c*, in a water solvent, adsorbing to ITO under a range of applied voltage appears in Fig. 7. Clearly, adsorption is significantly enhanced under an applied electric field. In fact, at voltages exceeding 1.0 V, no true adsorption plateau is reached. If a rectangular array of adsorbed proteins is assumed, the saturated monolayer density would be  $0.46 \mu\text{g}/\text{cm}^2$ . Thus

multilayer adsorption is occurring, at least to some extent, in all but the open circuit potential curve of Fig. 7. In Fig. 8, the adsorption rate vs. adsorbed amount is shown. In all curves, an initial increase in adsorption rate is noted, reflecting transport limitations. The subsequent decrease in adsorption rate is a result of surface filling. Thus the initial surface limited kinetics of albumin increase significantly with applied voltage, while those of cytochrome *c* are not affected. At longer times, however, the rate of adsorption for cytochrome *c* also is increased by the presence of the electric field. The transport-limited adsorption rate vs. time (insets) shows that only albumin transport is directly influenced by the field, likely because of its greater overall (negative) charge. While solvent and local pH effects could be influencing these results, the major contributing factor is the preferential adsorption, under an applied field, at patches on the protein surface of complementary charge.

## PERSPECTIVES

An applied electric field offers an opportunity to influence the structure and formation kinetics of an adsorbed protein layer. The literature now contains several examples of this.<sup>[6,15–20,22–24]</sup> However, it is striking the extent to which observed behavior deviates from that expected by basic electrostatics. There is little agreement on the cause of such behavior and therefore on the very nature of the electric field's influence on protein adsorption. Explanations put forth invoke surface-bound counterions, local pH effects, interfacial solvent structure, and protein charge heterogeneity. Below, we comment upon each of these effects.

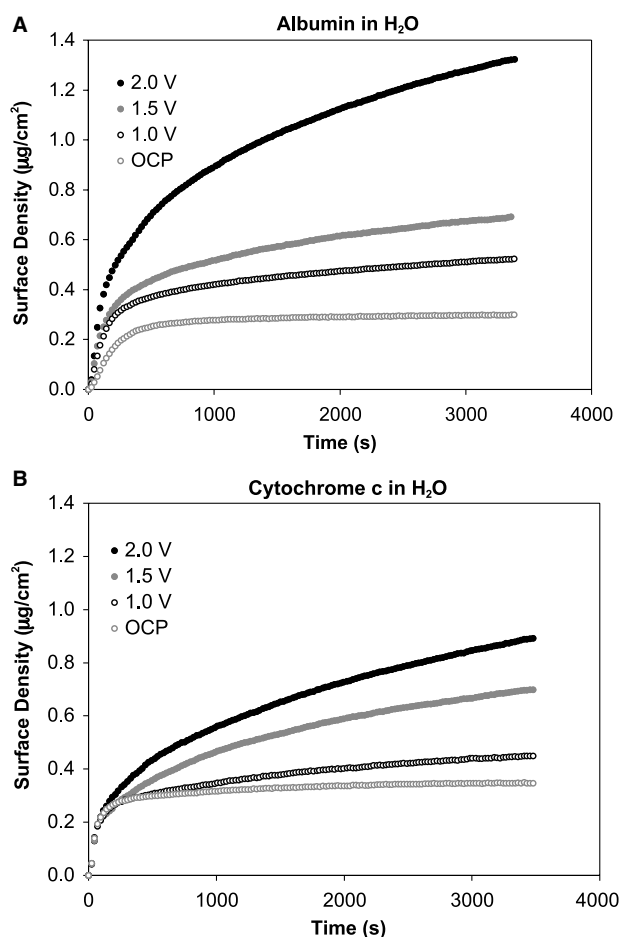


**Fig. 7** The amount of (A) albumin and (B) cytochrome *c* from a water solution adsorbed to an indium tin oxide surface as a function of time for various applied voltages as measured by optical waveguide lightmode spectroscopy. *Source:* Taken from Ref.<sup>[6]</sup>.

### Surface-Bound Counterions

Could similarly charged surfaces be attracted to one another given the presence of a third, oppositely charged species? At first glance, this would seem unlikely because counterions would at most completely compensate the charge, leaving two neutral surfaces. The classic Poisson–Boltzmann approach, in which solvated electrolytic species are assumed uncorrelated, predicts only repulsion between like charged objects in an electrolytic solution. However, there are examples where charge overcompensation may occur. A spectacular recent example of this is the layer-by-layer method of growing thin films by exposing a substrate alternatively to solutions of polyanions and polycations.<sup>[25]</sup> Although not fully understood theoretically, the idea is that charged sites on the polyions exchange nearly completely with smaller ions at the surface for entropic reasons. However, in addition to sites contacting

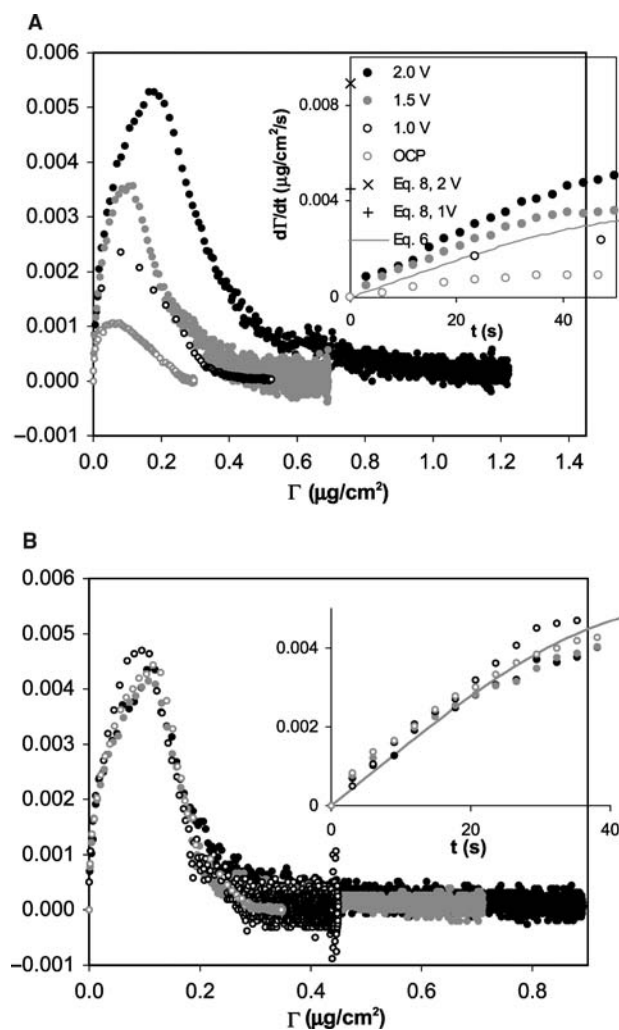


**Fig. 8** The rate of adsorption vs. amount adsorbed for (A) albumin and (B) cytochrome *c* from water onto indium tin oxide as a function of adsorbed amount (and, in the insets, as a function of time) for various applied voltages as measured by optical waveguide lightmode spectroscopy. *Source:* Taken from Ref.<sup>[6]</sup>.

the surface, the polyions generally contain additional charged sites that extend away from the surface, thus resulting in a charge overcompensation. However, this type of charge overcompensation would not be expected from the relatively small ionic species present in most protein adsorption systems.

### Local pH Effects

Proteins are amphoteric, i.e., possess a number of acid/base sites whose charge is pH-dependent. Because a positively (negatively) charged surface will repel solvated protons (hydroxide ions) and thus raise (lower) the pH near to the surface, the sign of a protein's

overall change could change upon approach to the surface. In this case, attraction that is indeed electrostatic in origin may follow. Could this effect explain the antielectrostatic behavior reported in the literature? Evidence to suggest otherwise lies in the following observation: the degree of buffering has been shown to have little effect on these antielectrostatic adsorption trends.<sup>[20]</sup>

### Solvent Interfacial Structure

Solvent molecules (typically water) at or near a solid substrate often experience a hindered rotation relative to those far from the interfacial region. If liberated from the surface via, for example, displacement by an adsorbed protein, a net entropy gain results. An estimation of the rotational contribution to the entropy is given by the statistical mechanical result for an ideal gas rigid rotor,  $S_{\text{rot}} = Nk \ln q_{\text{rot}}$ , where  $N$  is the number of molecules,  $k$  is the Boltzmann constant, and  $q_{\text{rot}}$  is the rotational partition function. For water at 300 K,  $q_{\text{rot}} \approx 30$ , so the contribution per mole of water liberated from the surface is about 28 J/K mol. An average-sized protein might result in the liberation of 50 water molecules, so the contribution to the overall free energy of adsorption at 300 K from the solvent rotation would be about  $-420$  kJ/mol. Of course, this is an upper bound because the molecules at the surface do possess some rotational freedom. This estimate would most accurately apply to water at a neutral, hydrophobic surface, where the molecules are expected to be very ordered. As the magnitude of surface charge is increased, the water becomes more disordered, i.e., may experience enhanced rotation, and the free energy gain from its liberation is thus diminished. As several of the above-mentioned studies show trends consistent with these thoughts, the role of solvent structure in the overall influence of an applied electric field cannot be discounted.

### Protein Charge Heterogeneity

Based on electrostatics, can a positively (negatively) charged protein be attracted to a positively (negatively) charged surface? Within the Poisson–Boltzmann approach, the answer is yes, according to Asthagiri and Lenhoff,<sup>[10]</sup> so long as both protein and surface contain charge heterogeneity. The idea is that regions of complementary charge may come into close contact, while overall repulsion is sufficiently screened by counterions so that a net attraction occurs. Brusatori, Tie, and Van Tassel invoke this reasoning to explain the increase in adsorption observed for positively charged cytochrome *c* with increasing adsorbent potential.<sup>[6]</sup>

### CONCLUSION

An applied electric field offers the possibility of controlling the structure of an adsorbed protein layer. This represents a powerful method of producing nanostructured coatings for biosensing and biomaterials applications. Only in the past few years have techniques become available to measure the adsorbed layer properties in situ during formation. While it remains to fully resolve a number of puzzling observations—and while quantitative prediction of the effects of the electric field, such as counterion binding, local pH enhancement, solvent structure, and charge heterogeneity, remains sparse—the prospects are strong for a general understanding, in the not-to-distant future, of the influence of an electric field on protein adsorption, and the engineering of protein coatings to near-exact specifications using voltage-based methods is certainly a realistic and laudable goal.

### ACKNOWLEDGMENTS

The author thanks the National Institutes of Health, under Grant # R01-EB00258, for financial support.

### REFERENCES

- Haynes, C.A.; Norde, W. Globular proteins at solid/liquid interfaces. *Colloids Surf., B Biointerfaces* **1994**, *2*, 517–566.
- Malmsten, M. Formation of adsorbed protein layers. *J. Colloid Interface Sci.* **1998**, *207* (2), 186–199.
- Malmsten, M.; Ed. *Biopolymers at Interfaces*; Surfactant Science Series; Marcel Dekker: New York, 1998; Vol. 75.
- Van Tassel, P.R. Biomolecules at interfaces. In *Encyclopedia of Polymer Science and Technology*, 3rd Ed.; Wiley Interscience: New York, 2003; 285–305.
- Calonder, C.; Van Tassel, P.R. Kinetic regimes of protein adsorption. *Langmuir* **2001**, *17* (14), 4392–4395.
- Brusatori, M.A.; Tie, Y.; Van Tassel, P.R. Protein adsorption kinetics under an applied electric field: an optical waveguide lightmode spectroscopy study. *Langmuir* **2003**, *19* (12), 5089–5097.
- Tie, Y.; Calonder, C.; Van Tassel, P.R. Protein adsorption: kinetics and history dependence. *J. Colloid Interface Sci.* **2003**, *268* (1), 1–11.
- Roth, C.M.; Lenhoff, A.M. Electrostatic and Van-Der-Waals contributions to protein adsorption—comparison of theory and experiment. *Langmuir* **1995**, *11* (9), 3500–3509.
- Roth, C.M.; Lenhoff, A.M. Electrostatic and Vanderwaals contributions to protein adsorption—computation of equilibrium-constants. *Langmuir* **1993**, *9* (4), 962–972.

10. Asthagiri, D.; Lenhoff, A.M. Influence of structural details in modeling electrostatically driven protein adsorption. *Langmuir* **1997**, *13* (25), 6761–6768.
11. Oberholzer, M.R.; Lenhoff, A.M. Protein adsorption isotherms through colloidal energetics. *Langmuir* **1999**, *15* (11), 3905–3914.
12. Ravichandran, S.; Talbot, J. Mobility of adsorbed proteins: a Brownian dynamics study. *Biophys. J.* **2000**, *78* (1), 110–120.
13. Carignano, M.A.; Szeleifer, I. Adsorption of model charged proteins on charged surfaces with grafted polymers. *Mol. Phys.* **2002**, *100* (18), 2993–3003.
14. Fang, F.; Szeleifer, I. Competitive adsorption in model charged protein mixtures: equilibrium isotherms and kinetics behavior. *J. Chem. Phys.* **2003**, *119* (2), 1053–1065.
15. Bernabeu, P.; Caprani, A. Influence of surface-charge on adsorption of fibrinogen and or albumin on a rotating-disk electrode of platinum and carbon. *Biomaterials* **1990**, *11* (4), 258–264.
16. Feng, L.; Andrade, J.D. Protein adsorption on low-temperature isotropic carbon. 2. Effects of surface-charge of solids. *J. Colloid Interface Sci.* **1994**, *166* (2), 419–426.
17. Fievet, P.; Mullet, M.; Reggiani, J.C.; Pagetti, J. Influence of surface charge on adsorption of a hydrophobic peptide onto a carbon surface by capacitance measurements. *Colloids Surf., A Physicochem. Eng. Asp.* **1998**, *144* (1–3), 35–42.
18. Bos, M.A.; Shervani, Z.; Anusiem, A.C.I.; Giesbers, M.; Norde, W.; Kleijn, J.M. Influence of the electric potential of the interface on the adsorption of proteins. *Colloids Surf., B Biointerfaces* **1994**, *3* (1–2), 91–100.
19. Khan, G.F.; Wernet, W. Adsorption of proteins on electro-conductive polymer films. *Thin Solid Films* **1997**, *300* (1–2), 265–271.
20. Brusatori, M.A.; Van Tassel, P.R. Biosensing under an applied voltage using optical waveguide lightmode spectroscopy. *Biosens. Bioelectron.* **2003**, *18* (10), 1269–1277.
21. Bearinger, J.P.; Voros, J.; Hubbell, J.A.; Textor, M. Electrochemical optical waveguide lightmode spectroscopy (EC-OWLS): a pilot study using evanescent-field optical sensing under voltage control to monitor polycationic polymer adsorption onto indium tin oxide (ITO)-coated waveguide chips. *Biotechnol. Bioeng.* **2003**, *82* (4), 465–473.
22. Fraaije, J.; Kleijn, J.M.; Vandergraaf, M.; Dijt, J.C. Orientation of adsorbed cytochrome-C as a function of the electrical potential of the interface studied by total internal-reflection fluorescence. *Biophys. J.* **1990**, *57* (5), 965–975.
23. Asanov, A.N.; DeLucas, L.J.; Oldham, P.B.; Wilson, W.W. Heteroenergetics of bovine serum albumin adsorption from good solvents related to crystallization conditions. *J. Colloid Interface Sci.* **1997**, *191* (1), 222–235.
24. Asanov, A.N.; Wilson, W.W.; Odham, P.B. Regenerable biosensor platform: a total internal reflection fluorescence cell with electrochemical control. *Anal. Chem.* **1998**, *70* (6), 1156–1163.
25. Decher, G.; Schlenoff, J.B.; Eds. *Multilayer Thin Films*; Wiley-VCH: Weinheim, 2003.

# Protein Nanotubes as Building Blocks

Hiroshi Matsui

Department of Chemistry, Hunter College, City University of New York,  
New York, New York, U.S.A.

## INTRODUCTION

Nanometer scale self-assemblies of biological molecules, such as protein nanotubes, play important roles in nature to regulate biological activities. It is a natural progress to synthesize protein nanotubes in order to mimic those biological functions and apply for medical applications such as drug delivery and medical imaging. Although it appears to be unlikely, peptide nanotubes are also applied to non-biological fields such as electronics, sensors, catalysis, and optics because those smart, selective peptide functions can be applied in various device fabrication processes. Those new types of building blocks with smart biological functions may offer more economical, reproducible, accurate, and simpler methods in device fabrications. In this entry, various examples of natural and synthetic protein nanotubes and their functionalizations for particular applications are discussed.<sup>[1–32]</sup>

## OVERVIEW

Protein nanotubes are tubular assemblies of proteins. The production of protein nanotubes can be synthetic or natural. They are generally produced via their direct self-assemblies into tubular structures<sup>[33]</sup> or their self-assemblies on template nanotubes.<sup>[34–37]</sup> While the direct nanotube assemblies from protein monomers without templates are normally achieved in vitro,<sup>[38,39]</sup> there are some examples that protein nanotubes are self-assembled in solutions in the presence of divalent metal ions.<sup>[40]</sup> With the aid of surfactants, some proteins were also demonstrated to be assembled as a tubular form.<sup>[41]</sup> Molecular self-assembly is robust and reproducible under the controlled experimental conditions.<sup>[42,43]</sup> For example, protein nanotubes are grown in solution via self-assembly with high reproducibility and monodispersity.<sup>[40]</sup> Thermodynamics controls chemical structures and dimensions of self-assembled nanotubes<sup>[44]</sup> and it can be determined by external experimental conditions such as pH, temperature, solvents, and pressure.<sup>[45]</sup> Protein nanotubes such as virus, phages, and microtubules are also produced via natural self-assembly with high reproducibility and monodispersity inside cells. The chemical structures of natural protein nanotubes can be modified

via mutations, which gives flexibility to design protein nanotubes.<sup>[46]</sup> Therefore the use of self-assemblies either synthetically or naturally has an advantage to mass-produce monodisperse and chemically identical nanotubes. Because protein nanotubes are water-soluble, it makes their size separation easier if necessary.

While the self-assembly nature offers some interesting features in protein nanotubes, they may not display useful physical properties as shown in metal and semiconductor nanowires for particular devices such as electronics and sensors. Then what makes protein nanotubes special compared with other inorganic nanotubes/nanowires? I believe that features of protein nanotubes distinguished from other nanotubes are their flexibility in the functionality and their molecular recognition. All proteins have some functions and those functions can be used to introduce new properties into protein nanotubes, desired for particular building blocks in specific nanodevices. For example, proteins can mineralize various metals and semiconductors selectively via their molecular recognition and biomineralization, which are routinely operated in living systems.<sup>[47,48]</sup> Positioning of protein nanotubes can be achieved through biological recognitions of proteins toward their complementary ligands.

In this entry, I would like to categorize the features of protein nanotubes into four characteristic functions: 1) coating, 2) arrangement, 3) sensing, and 4) mechanical motion. In the coating section, biomineralization of protein nanotubes is discussed. In the placement section, organization and location-specific immobilization of protein nanotubes are explained via biological recognitions such as inorganic-protein and protein-protein interactions. Physical property changes of protein nanotubes via biological recognition-induced adsorption of target molecules can be used for their detections and quantitative analysis, as explained in the “Sensing” section. In the “Mechanical motion” section, motor functions of protein nanotubes by converting chemical energy into mechanical force are summarized.

## COATING

To apply protein nanotubes as building blocks for various nanodevices, functionalizations of protein nanotubes via coatings are very effective. Choices of

proteins are dependent upon what types of materials to be coated. Tobacco mosaic virus (TMV) was used to mineralize CdS, PbS, silica, and iron oxides on the outer surfaces of TMV.<sup>[49,50]</sup> Tobacco mosaic virus, a hollow protein nanotube, is a stable virion with 18 nm in diameter and 300 nm in length, self-assembled from the protein monomers. The repeated protein subunits on the nanotubes offer the nucleation sites to produce highly crystalline semiconductor coatings. Figure 1A shows CdS nanotubes fabricated by exposing a buffered suspension of TMV in 10 mM CdCl<sub>2</sub> to H<sub>2</sub>S gas for up to 6 hr. High-resolution transmission electron micrograph (HRTEM) of the CdS nanotubes in Fig. 1B indicates that the CdS coating consists of aggregates of crystalline CdS nanoparticles with 5 nm in diameter, whose fringe space matches a (111) lattice plane of the zinc-blende structure. Modified TMV nanotubes at the C-terminus via a single site mutation were also synthesized as template nanotubes to

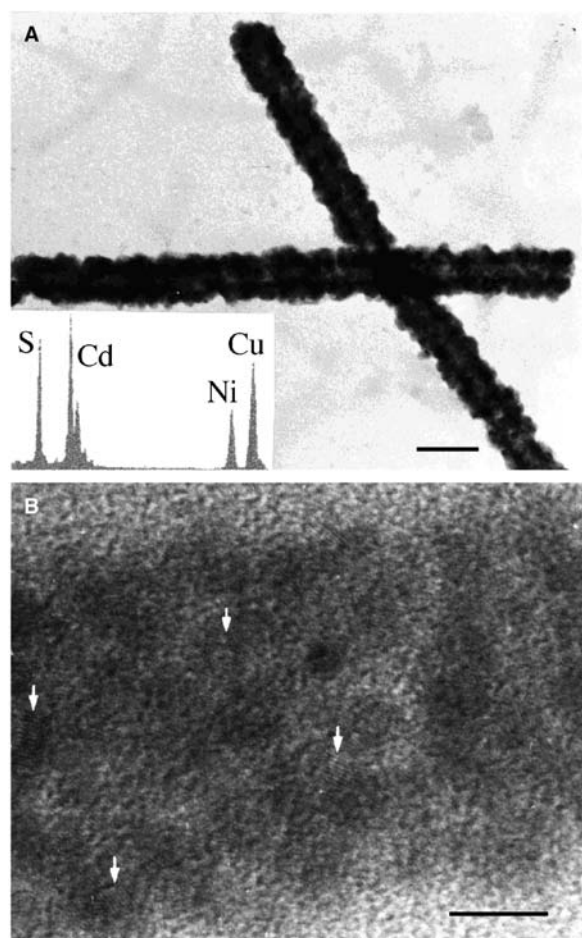


**Fig. 1** TEM images of (A) CdS-coated TMV nanotubes, scale bar=50 nm, inset: corresponding EDX spectrum (Ni and Cu peaks arise from TEM grid and sample holder). (B) CdS nanocrystals (white arrows) on the TMV nanotube in high magnification, scale bar = 10 nm. Source: From Ref.<sup>[49]</sup>. © (1999) Wiley-VCH Verlag GmbH.

improve their selectable chemospecificity.<sup>[46]</sup> The modified TMV nanotubes have lysine units on the outer surfaces of the nanotubes and these sites can be used to immobilize functional molecules via *N*-hydroxy succinamide chemistry (Fig. 2). This mutant TMV nanotube functionalized with fluorophor selectively mineralized Cu via photoreduction of Cu ions. Another example of biomineralization of protein nanotubes is to produce magnetic nanofibers by using rod-shaped bacterium as templates.<sup>[51]</sup> A single *bacillus subtilis* bacterium is an organism with cells of approximately 0.7 μm in diameter and up to 4 μm in length. Two types of iron oxide nanoparticles, magnetite (Fe<sub>3</sub>O<sub>4</sub>) and maghaemite (γ-Fe<sub>2</sub>O<sub>3</sub>), were mineralized on the bacterial threads. The magnetization data showed that the magnetic field-dependent switching behavior was markedly sharp when single domains of iron oxide nanoparticles were aligned to the easy axes of the nanotubes. This alignment was achieved when the magnetic nanotube synthesis was conducted within an external magnetic field.

Microtubules, self-assembled from cytoskeletal proteins in vitro, were used as template nanotubes to coat Pd.<sup>[38]</sup> The subunits of purified porcine brain tubulin were cross-linked by glutaric dialdehyde and this process yielded stabilized microtubules, whose diameter is 4–5 nm and length is about 8 μm. This resulting microtubule remained intact up to 90°C for approximately 1 hr in the pH range from 4 to 9. The improved microtubule mineralized Pd with trisodium citrate or dimethylamine borane at 90°C. The trisodium citrate produced smaller Pd nanocrystals with a mean diameter of 1.9 nm and the dimethylamine borane produced larger Pd nanocrystals with a mean diameter of 3.1 nm (Fig. 3A). HRTEM micrograph of the highly monodisperse Pd nanocrystals on the nanotubes imaged the (111) plane of a pure metallic Pd phase (Fig. 3B). Pd nanocrystals were found to grow on both α- and β-tubulin subunits of the protein nanotubes and the histidine residues likely serve as nucleation sites for the Pd biomineralization on the nanotubes.

Improved metal nanocrystal coatings were demonstrated on the biological nanotubes incorporating sequenced peptides that can mineralize specific metals via biological recognitions.<sup>[52]</sup> This sequence consisting of histidine and alanine residues not only produced monodisperse Au nanocrystals on the nanotube surfaces but also controlled the density and the size of nanocrystals by tuning the sequenced peptide conformations (Fig. 4).<sup>[53]</sup> The histidine residue captured Au ions (ClAuPMe<sub>3</sub>) and the reduction of those trapped Au ions led to monodisperse nanocrystal formation with an average diameter of 5 nm on the nanotubes. The change in experimental conditions such as pHs and ion concentrations in the nanocrystal growth solution induced the ion-peptide conformation change



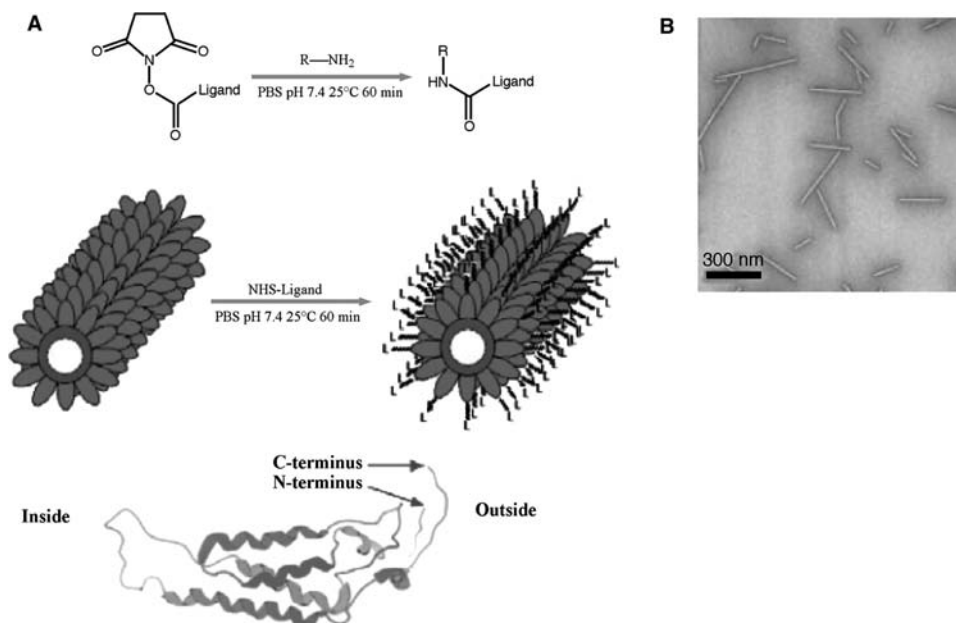


**Fig. 2** (A) The upper panel: the facile NHS chemical reaction; the middle panel: the structure of TMV nanotube and a schematic to introduce ligands on the TMV nanotube surface via the NHS chemistry; the lower panel: the structure of the protein monomer for the TMV nanotube and the relative positions of the monomer in the TMV nanotube. (B) Electron micrograph of m-TMV nanotubes. *Source:* From Ref.<sup>[46]</sup>. © (2002) Institute of Physics Publishing.

and this structural transformation controlled the size and the distribution of Au nanocrystals on the nanotubes. It should be noted that metallic nanocrystals with a diameter below 6 nm are in the size domain to observe significant conductivity change by changing the packing density.<sup>[54]</sup> Therefore this system may be useful as a conductivity-tunable building block by controlling the nanocrystal size and the distribution.

## ARRANGEMENT

There are several techniques to align nanotubes by using electronic fields, magnetic fields, microfluidics,

and hydrophobic interactions.<sup>[26–30]</sup> But when multiple types of nanotubes are necessary to be aligned respectively in more complex device configurations, the above methods may not be sufficient. For example, consider fabricating a nanodevice whose configuration has two nanotubes crossing perpendicular to each other (Fig. 5). In this configuration, when one nanotube is coated by a metal and the other nanotube is coated by a semiconductor, this nanodevice will function as a switch in memory circuits for reading and writing information.<sup>[6,55]</sup> Whereas these device elements can be switched between well-defined on-and-off states by transiently charging the coated nanotubes to produce

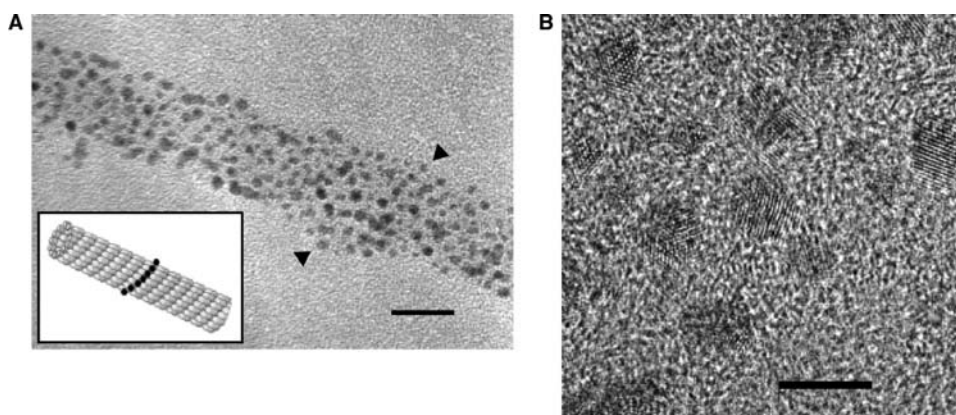


**Fig. 3** (A) TEM image of palladium nanoparticles immobilized on a microtubule, scale bar = 20 nm. (B) HRTEM image of palladium nanoparticles on the microtubule, scale bar = 5 nm. *Source:* From Ref.<sup>[38]</sup>. © (2002) Wiley-VCH Verlag GmbH.

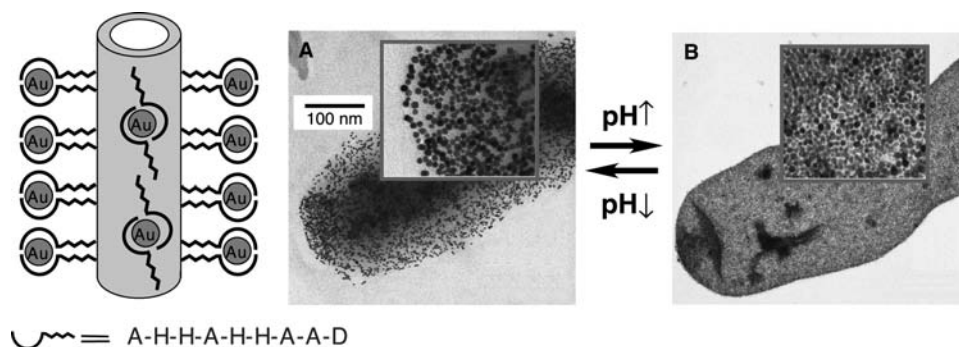


**Fig. 4** TEM images of Au nanocrystals regulated by the sequenced histidine-rich peptides on the nanotubes. Au nanocrystals were grown by reducing the Au ion-nanotube solution after incubating Au ions for 10 days at (A) pH = 8.5, and (B) pH = 11.5. Insets show the TEM images in higher magnification. *Source:* From Refs.<sup>[52]</sup> and<sup>[53]</sup>.

attractive and repulsive electrostatic forces,<sup>[55]</sup> aligning two or more types of nanotubes in desired directions precisely is not an easy task by the techniques described above.

By functionalizing circuit elements and connecting wires with biomolecular recognition of complementary connecting units while in solution, we can mimic biological systems, in which organic/inorganic nanoscale building blocks are routinely and precisely turned into complex structures for biological function with almost perfect reproducibility. In theory, protein nanotubes, which can recognize and selectively bind a well-defined region on complementary protein-patterned substrates, can be used as building blocks to assemble three-dimensional nanoscale architectures by placing them at the uniquely defined positions. As shown in Fig. 5, an antigen 1 nanotube can be aligned on antibody 1 areas while an antigen 2 nanotube recognizes and immobilizes on antibody 2 surfaces. Therefore the immobilization of protein nanotubes onto the antibody self-assembled monolayers (SAMs) will be “programmed” (i.e., protein nanotubes recognize binding sites and attach automatically) in aqueous solution without any complicated multistep fabrication procedures. To demonstrate the feasibility of this scheme, the streptavidin-coated nanotubes were dispersed on

biotin-incorporated SAMs in solution, and their selective immobilization onto the biotin-incorporated SAMs was observed after 1 day (Fig. 6).<sup>[56]</sup> Protein-functionalized nanotubes were positioned to interconnect patterned complementary protein-SAM/Au surfaces via protein-protein interactions; however, uniform coverage of proteins on template nanotubes also caused the nanotube aggregations on the complementary protein-SAM surfaces.<sup>[56]</sup> One solution to produce the nanotube-bridge configurations with minimum nanotube aggregations could be selective protein immobilization at the ends of nanotubes. We recently demonstrate that this location-specific protein immobilization on nanotubes was established by using Au nanocrystal masks.<sup>[57]</sup> As a proof-of-principle, avidin was used to be immobilized only at the ends of peptide nanotubes with the nanotube end-fabrication method, as outlined in Fig. 7. The approach involves thiolation of the nanotube sidewalls [step (i)] and Au nanocrystal coating to mask the sidewalls of nanotubes [step (ii)], followed by incubating nanotubes with sulforhodamine-labeled avidin [step (iii)]. After avidin molecules were immobilized at the ends (with no Au nanocrystals) and the sidewalls (with Au nanocrystals) of the nanotubes, the Au nanocrystals on the sidewalls were chemically etched and the proteins at the ends remained attached

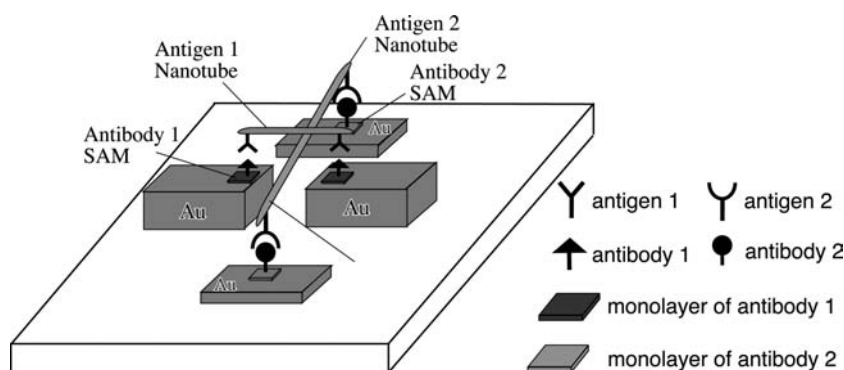


**Fig. 5** Illustration of proposed scheme to assemble multiple protein nanotubes into device configurations via biological recognitions between the protein nanotubes and the complementary protein-patterned surfaces.

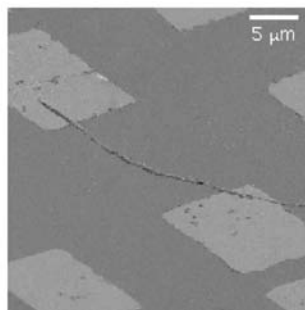
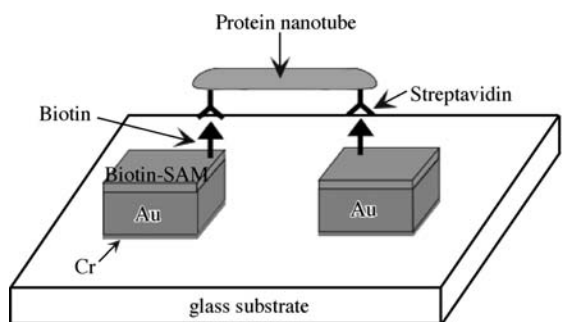


**Fig. 6** Illustration and SEM image of a streptavidin-functionalized nanotube immobilized onto the complimentary biotin SAMs/Au substrates. *Source:* From Ref.<sup>[56]</sup>.

without denaturing [step (iv)]. The chemical etching of the Au nanocrystal masks on the sidewalls of nanotubes removed avidin molecules from the sidewalls; however, avidin molecules at the nanotube ends remained bound.<sup>[57]</sup> After sulforhodamine-labeled avidin was incubated into the Au nanocrystal-masked nanotube solution for 36 hr [step (iii) in Fig. 7], the protein was immobilized on the entire nanotube surface shown by fluorescence micrograph of the resulting nanotube (Fig. 8A). This fluorescence image was dramatically changed after the Au nanocrystals on the nanotube sidewall were etched by iodine in step (iv). After etching the Au nanocrystals from the nanotube surface, fluorescing areas of the sulforhodamine-labeled avidin were limited to the ends of the

nanotube and fluorescence at the nanotube sidewall was diminished, as shown in Fig. 8B. These fluorescence micrographs confirm that the protein remained bound to the peptide nanotube ends after the chemical Au nanocrystal etching. This chemical etching process did not denature the avidin on the nanotubes and the nanotube ends could still recognize the complementary biotin after the etching process.<sup>[57]</sup> This result is particularly important to this proposed research because denaturing proteins at the nanotube ends via the chemical etching process could prevent the use of this protein nanotube as building blocks for nanodevices due to the loss of the biological recognition function. Our preliminary result indicates that these end-functionalized nanotubes reduced the nanotube aggregation about five times on

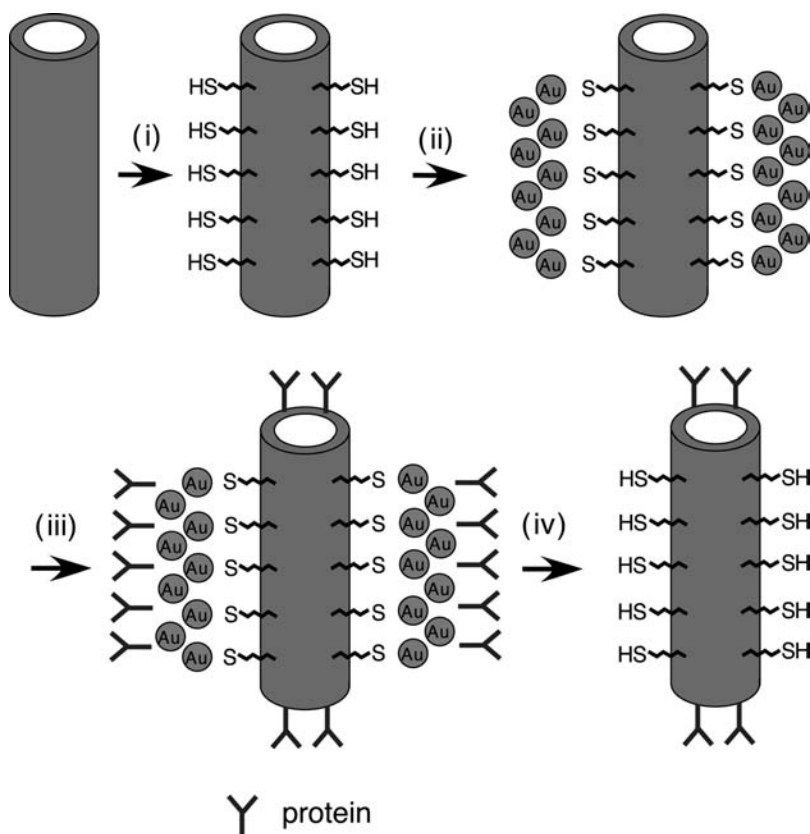


**Fig. 7** Procedure to immobilize proteins at the ends of nanotubes using Au nanocrystals as protective masks. *Source:* From Ref.<sup>[57]</sup>.

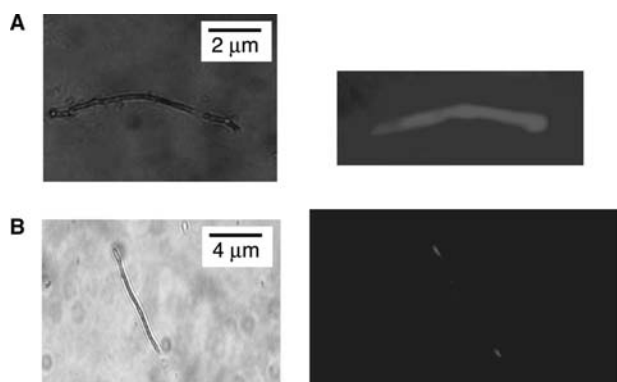


**Fig. 8** Fluorescence micrographs of (A) the Au nanocrystal-masked nanotube incubated with sulforhodamine-labeled avidin [step (iii) in Fig. 7], (B) the nanotube with sulforhodamine-labeled avidin after etching the Au nanocrystals [step (iv) in Fig. 7]. *Source:* From Ref.<sup>[57]</sup>.

the biotin-SAMs compared to the nanotubes whose entire surfaces were coated by avidin.<sup>[57]</sup>

The location-specific assembly of protein nanotubes was also achieved via biological recognitions between inorganic surfaces and phages.<sup>[58]</sup> Phages and natural protein nanotubes with 6.6 nm in diameter and approximately 880 nm in length (Fig. 9A) can be modified to have specific peptide sequences on the surfaces to recognize and bind specific inorganic surface after multiple cycles of the peptide selection processes. To identify appropriate peptide sequences of phages to recognize specific inorganic surfaces, Whaley and coworkers used a combinatorial library of genetically engineered bacteriophage.<sup>[58]</sup> For example, this peptide combinatory approach identified proteins that specifically bind GaAs (100) and they were self-assembled on the patterned GaAs surfaces (Fig. 10).<sup>[59]</sup> The specificity of binding exerted the level over the recognition of crystal orientations.

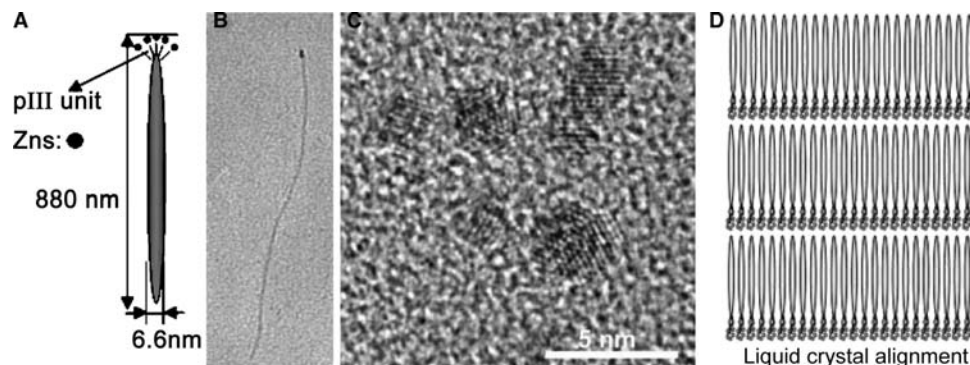


**Fig. 9** (A) Illustration of phage and ZnS nanocrystals (the PIII peptide unit and the ZnS nanocrystal bound to the phage are not drawn in scale). (B) TEM image of an individual phage and ZnS nanocrystals. (C) HRTEM image of 0.01% phage-ZnS suspension, showing lattice fringe images of ZnS nanocrystals. (D) Illustration of liquid crystal alignment of the phage-ZnS nanocrystal complexes. *Source:* From Ref.<sup>[60]</sup>. © (2002) American Association for the Advancement of Science.

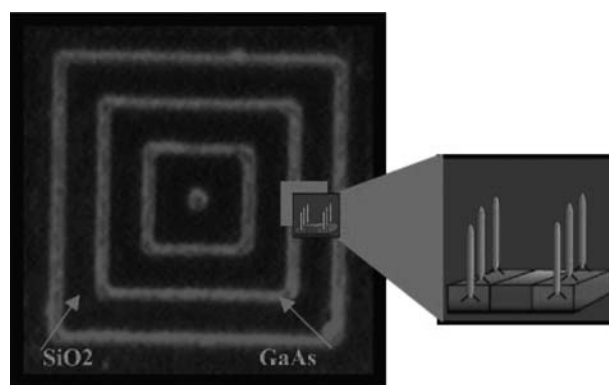


**Fig. 10** Fluorescence image of tetramethyl rhodamine-labeled phages selectively assembled on the patterned (100) GaAs surfaces. The red lines (1 μm across) correspond to GaAs and the black spaces (4 μm across) are SiO<sub>2</sub>. *Source:* From Ref.<sup>[59]</sup>. © (2002) National Academy of Science, U.S.A.

Those genetically engineered bacteriophage-nanocrystal complexes can also be arranged into ordered films.<sup>[60]</sup> For example, when phages were engineered to recognize ZnS, they mineralized highly crystalline ZnS nanocrystals at the end of the tubules in ZnCl<sub>2</sub>/Na<sub>2</sub>S solutions (Fig. 9B,C). Under the optimized experimental conditions, those phages with ZnS nanocrystals were spontaneously assembled into self-supporting hybrid films whose order structures were maintained over a centimeter-length scale (Fig. 9D). These films showed the liquid crystalline phase behaviors and they could be modulated by solvent concentrations and an external magnetic field.<sup>[60]</sup> The monodispersity of the genetically engineered phages and the ease in incorporating and aligning various types of inorganic nanocrystals by molecular cloning techniques and genetic selections are advantageous to apply the protein nanotube-based materials in the field of liquid crystals.



## SENSING

As pointed out above, one of the key functions of proteins is to recognize specific molecules and ions. The molecular recognitions of proteins are dependent on the shapes of target molecules because multiple hydrogen bonds, electrostatic interactions, and hydrophobic interactions between target molecules and proteins in a well-defined spatial pattern provide the excellent selectivity of protein bindings.<sup>[61]</sup> Therefore it is natural to apply the molecular recognition of protein nanotubes to sense and diagnose target molecules.

A planar field effect transistor (FET) has been used mostly as a nanotube-based sensor configuration. Modification of the gate oxide in the carbon nanotube-based FET allowed monitoring a conductance change due to the adsorption of analytes.<sup>[62]</sup> The practical aspect of the FET is that the FET can serve as a highly sensitive real-time electrically based sensor. The sensitivity of carbon nanotube-based FET sensors was in the regime of single-molecule detection.<sup>[62]</sup>

Cui and coworkers assembled antigen nanowires, antigen-coated silicon nanowires, as building blocks into the FET sensors.<sup>[63]</sup> The single-crystal boron-doped (p-type) silicon nanowires, prepared by a nanocluster-mediated vapor-liquid-solid growth method,<sup>[64]</sup> were aligned by a microfluidic technique between two electrodes, a source and a drain (Fig. 11).<sup>[29]</sup> The reversible, real-time antigen-nanowire sensor was fabricated by functionalizing the silicon nanowire template with biotin via the drop deposition, and this sensor system could detect conductivity changes under m-antibiotin adsorption on the functionalized nanowires.<sup>[63]</sup> A linear change in the nanowire conductance as a function of m-antibiotin concentration was observed as shown in

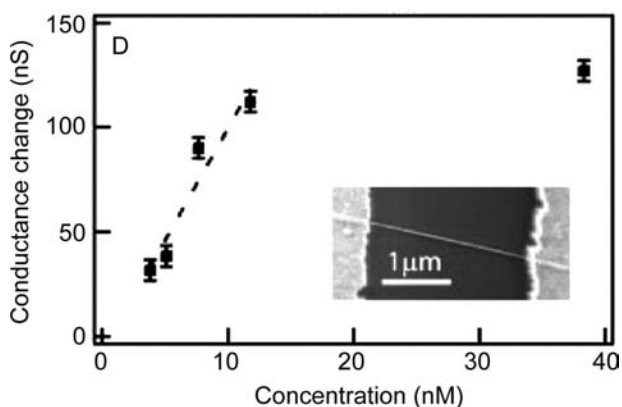


**Fig. 11** Plot of the conductance change of a biotin-modified Si nanowire vs. m-antibiotin concentration. (Inset) SEM image of a typical FET configuration: a Si nanowire connecting two electrodes, a source and a drain. *Source:* From Ref.<sup>[63]</sup>. © (2001) American Association for the Advancement of Science.

Fig. 11. The correlation between linear current ( $I$ ) vs. voltage ( $V$ ) was transformed to the conductance ( $dI/dV$ ). The detection of m-antibiotin in this sensor system was achieved below 10 nM, while the detection limit for streptavidin could reach in the order of pM.<sup>[63]</sup>

## MECHANICAL MOTION

There have been major attempts to synthesize chemically powered nanoscale engines driven by light or chemical energy.<sup>[65,66]</sup> The weaknesses of the synthetic nanoscale motors are as follows: 1) they often stall when operated under load; and 2) they have a low cycle time.<sup>[61]</sup> In contrast, motor proteins are better engines at this point as the man-made motors are fueled by electrical or thermal energy with an efficiency of around 30% while protein motors are driven by direct conversion from chemical energy with an efficiency as high as 90%.<sup>[67]</sup> Therefore motor proteins have been studied extensively not only to understand the mechanism for their mechanical motions regulating cell activities but also to fabricate high-performance nanoscale engines. There are two types of well-studied protein motors, translational motors and rotary motors. Translation protein motors transport on the complimentary protein nanotubes. While development of rotary protein-based nanodevices has also been very active,<sup>[68]</sup> rotary protein motors are not discussed in this entry.

Conformational changes of motor proteins produce mechanical forces and motions fueled by the interconversion of chemical energy.<sup>[69]</sup> Translational motor proteins move along their complementary nanotubes via the energy conversion. Microtubules, protein nanotubes in diameter of 25 nm, are tracks to guide a translational motor protein, kinesin. Kinesins transport vesicles, chromosomes, and protein complexes using these tracks throughout the intracellular environment.<sup>[70]</sup> For example, kinesins transfer encapsulated neurotransmitters from cores of nerve cells to synaptic clefts in order to excite next nerve cells.<sup>[61]</sup>

Kinesins are elongated heterotetrameric proteins and contain adenosine triphosphate (ATP) and microtubule binding sites.<sup>[30]</sup> The side-by-side motor domains alternately bind and release the tubulin subunits of a microtubule,  $\alpha$ - and  $\beta$ -tubulins, in a walking type of motion.<sup>[71]</sup> The walking motion is fueled by the hydrolysis of ATP from adenosine diphosphate (ADP), initiated by a proton gradient across a cell membrane. The kinetically more dynamic end of the microtubule is terminated with the  $\beta$ -tubulin (black circles in Fig. 12A) whose relative polarity is positive, whereas the opposite end is terminated with  $\alpha$ -tubulin (white circles in Fig. 12A) whose relative polarity is negative. The overall structural polarity of microtubules is recognized by motor proteins, which determine the

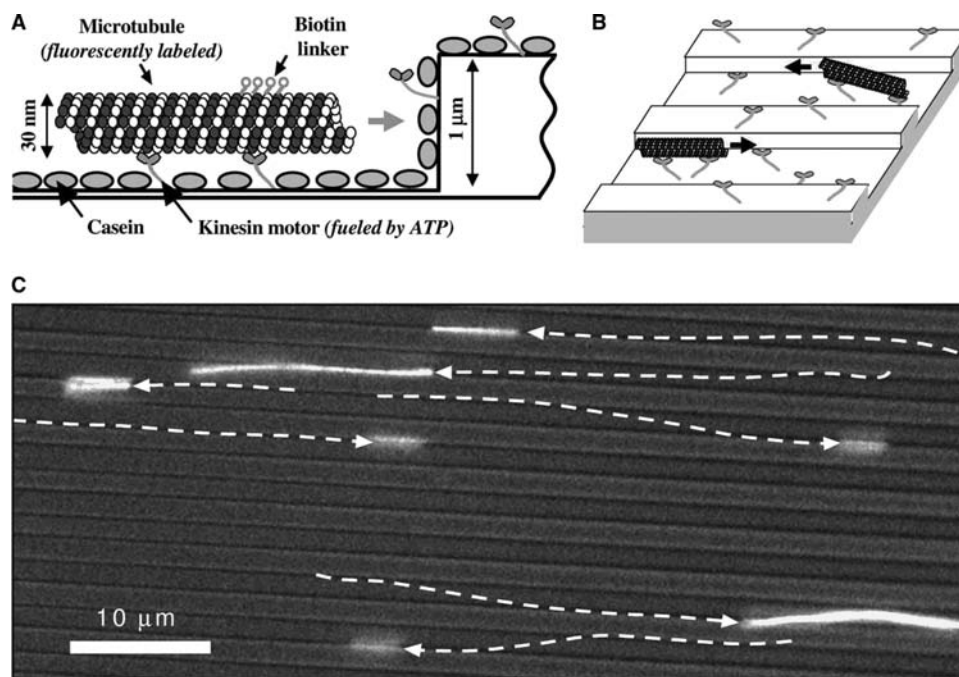


**Fig. 12** (A) Illustration of the microtubule transport on kinesin motor surfaces. (B) Illustration of a typical geometry of the kinesin motor track. (C) Micrograph of photolabeled microtubules moving in channels ( $2\ \mu\text{m}$  wide) on a patterned polyurethane substrate. The dotted lines are the paths of individual microtubules. *Source:* From Ref.<sup>[61]</sup>. © (2002) the Materials Research Society.

direction of their motion along the microtubule surface as kinesin steps only toward the plus end.<sup>[72]</sup> Myosins are another family of translational protein motors that move along actin nanotubes for cell motility and muscle contraction.<sup>[61]</sup>

While there have been extensive effort to manipulate this molecular transport machinery outside cells and fabricate as moving building blocks of nanodevices driven by kinesin/myosin motor proteins,<sup>[71]</sup> their applications require to overcome technical problems such as the orientation of force generation toward the desired direction, the optimization of surface conditions and geometries, and the stability of the motor protein–protein nanotube systems.<sup>[73]</sup>

Motor protein–protein nanotube integrated systems have been fabricated in two configurations: 1) moving motor proteins on protein nanotube tracks; and 2) moving protein nanotubes on motor protein-patterned surfaces. The first configuration is analogous to the geometry found in cells.<sup>[70]</sup> When kinesins and microtubules were integrated to develop nanodevices, the majority of effort has been focused on positioning and alignment of microtubules.<sup>[30,70,71,73]</sup> The microtubules must be aligned precisely in order to transport cargoes attached to motor proteins toward the proper destinations. For example, Limberis and Stewart transported silicon microchips with genetically engineered kinesin motors to particular locations guided by patterned microtubules on substrates.<sup>[71]</sup>

The second configuration is the inversed geometry used in nature. Various surface topologies with lithographically fabricated ridges and valleys were examined as motor protein tracks to guide protein nanotubes inside the ridges or valleys (Fig. 12B). The difficulty in this scheme is that microtubules tend to escape from the valleys by binding the sidewalls of valleys, slowly climb up, and then move toward different directions.<sup>[74]</sup> This escaping motion of microtubules on a kinesin-coated polyurethane surface patterned with  $2\text{-}\mu\text{m}$ -wide and  $1\text{-}\mu\text{m}$ -deep channels is shown in Fig. 12C. In this figure, the bottom of the channels is in focus and the plateaus in between are out of focus. Some microtubules were staying in the channels but most of them moved up and down in the grooves.<sup>[74]</sup> The patterned myosin surfaces were shown to direct the actin nanotube movement in one direction more effectively.<sup>[75]</sup> Recently, the myosin gel substrate also appeared to regulate the movement of the cross-linked actin nanofibers in one direction (Fig. 13).<sup>[67]</sup> The optimal solution to engineer motor protein/protein nanotube tracks seems to be an optimized combination of chemical and topological track patterns,<sup>[74]</sup> and the myosin/actin system may be chemically favorable to reduce the nanotube sliding motions.

Those motor protein/protein nanotube systems have potential to be applied in the fields of mechanical engineering, biomedical engineering, and electronics. Coupling motors/nanotubes with gears or rotors



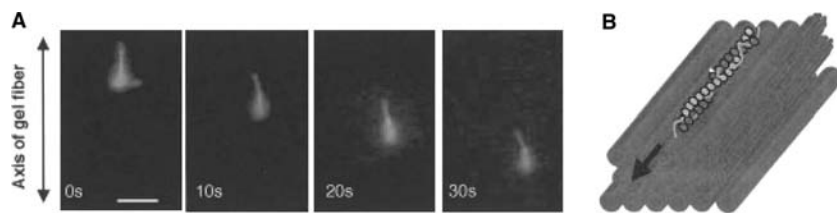


**Fig. 13** (A) Sequential fluorescence images of the cross-linked actin gel movement on the oriented myosin gels. (B) Illustration of the actin gel movement on the myosin gels. *Source:* From Ref.<sup>[67]</sup>. © (2002) Wiley-VCH Verlag GmbH.

may be used as switches or valves in microfluidic channels.<sup>[70]</sup> It is encouraging that recently motion of microtubules can be turned on and off sequentially on patterned motor protein substrates triggered by UV-induced release of caged ATP via the enzymatic ATP degradation, which is a crucial feature to develop the switches and the valves.<sup>[74]</sup> Motor protein-based microgenerators, pumps, and biosensors can be applied in medical implants.<sup>[71]</sup> For example, the motor protein-based microgenerators can power implanted microdevices for monitoring physiological processes because the mechanochemical energy of motor proteins is transduced to an electrical current. In any applications described above, alignments and chemical controls of protein nanotubes will be crucial to develop nanodevices from these smart components.

## CONCLUSION

Protein nanotubes have distinguished characters compared with other nanotubes. Obviously, protein-assembled nanotubes are biocompatible and broad biological applications can be expected. Molecular recognition is another unique function in protein nanotubes. The molecular recognition, such as an antibody–antigen recognition, images the complementarity of a lock and a key—the lock being antibody and the key being antigen that is recognized via the spatial fit and non-covalent interactions to form the specific antibody–antigen complex. This specificity will make protein nanotubes smart building blocks for high-performance chemical sensors. When multiple antibodies are patterned wisely on surfaces, resulting device configurations, after antigen–nanotubes recognize and position onto their complementary regions, will be achieved via their robust self-assembling processes. This approach may build certain device configurations in an economical and simple manner. Coupling between protein nanotubes and motor proteins certainly offers intriguing potential to build nanodevices powered by converting chemical energy into mechanical force. When physical properties of protein nanotubes are not suitable to certain applications, protein nanotubes can be functionalized to add the desired physical properties. For example, if conductive nanotubes need to be placed at a certain position, protein nanotubes can be coated with

conductive metals via biomineralization after protein nanotubes are positioned at the desired position via molecular recognitions. To date, fabrication of protein nanotubes and organization of protein nanotubes have been investigated, respectively. Applications of protein nanotubes as building blocks in real-world nanodevices will be accelerated once those two outcomes are integrated.

Of course, this field is still extremely young and there are many concerns and hurdles to overcome. For example, proteins typically lose their functions within days or weeks unless they are frozen.<sup>[61]</sup> They degrade by various and often competing mechanisms, including thermal and enzymatic degradation as well as precipitation. For the applications in the coating and the arrangement of nanotubes, proteins need to be active during the nanotube assembly, which is normally achieved in a short time because of robust self-assembly. Therefore the protein degradation may not be a crucial issue for these applications. But when protein nanotubes are applied to the devices necessary to transform one structure to the other repeatedly or to detect target molecules over and over again, proteins must be evolved to survive under harsh environmental conditions.<sup>[76,77]</sup>

Various difficulties in applying protein nanotubes as building blocks of nanodevices will be overcome if we keep learning from nature. There are many natural protein nanotubes/nanofibers whose excellent properties are known, but their chemical structures remain unsolved. For example, a tensile strength of spider dragline silk is comparable with steel and its elasticity is comparable with rubber.<sup>[78]</sup> This unique combination makes the spider dragline silk mechanically superior to any other man-made materials. But it was just recently that the protein sequences and structures of the spider dragline silk were understood.<sup>[78]</sup> Progress in understanding unsolved natural protein nanotubes and mimicking those nanotubes will make protein nanotubes more attractive to apply them as building blocks for various nanometer-scaled devices.

## ACKNOWLEDGMENT

I would like to thank my co-workers for the past four years for their hard work in the development of protein nanotubes and their applications: S. Pan,

G.E. Douberly, P. Porrata, Yung-fou Chen, Lingtao Yu, Ramin Djalali, and Ipsita Banerjee. I also would like to acknowledge the financial supports from the National Science Foundation CAREER Award (EIA-0133493), the National Science Foundation NER program (ECS-0103430), and the U.S. Department of Energy (DE-FG-02-01ER45935).

## REFERENCES

- Tans, S.J.; Devoret, M.H.; Dai, H.; Thess, A.; Smalley, R.E.; Geerligs, L.J.; Dekker, C. Individual single-wall carbon nanotubes as quantum wires. *Nature* **1997**, *386* (6624), 474–477.
- Bockrath, M.; Cobden, D.H.; McEuen, P.L.; Chopra, N.G.; Zettl, A.; Thess, A.; Smalley, R.E. Single-electron transport in ropes of carbon nanotubes. *Science* **1997**, *275* (5308), 1922–1925.
- Dai, H.; Kong, J.; Zhou, C.; Franklin, N.; Tomblor, T.; Cassel, A.; Fan, S.; Chapline, M. Controlled chemical routes to nanotube architectures, physics, and devices. *J. Phys. Chem., B* **1999**, *103* (51), 11,246–11,255.
- Dai, H.; Wong, E.W.; Lieber, C.M. Probing electrical transport in nanomaterials: conductivity of individual carbon nanotubes. *Science* **1996**, *272* (5261), 523–526.
- Shim, M.; Kam, N.W.S.; Chen, R.J.; Li, Y.M.; Dai, H.J. Functionalization of carbon nanotubes for biocompatibility and biomolecular recognition. *Nano Lett.* **2002**, *2* (4), 285–288.
- Rueckes, T.; Kim, K.; Joselevich, E.; Tseng, G.Y.; Cheung, C.-L.; Lieber, C.M. Carbon nanotube-based non-volatile random access memory for molecular computing. *Science* **2000**, *289* (5476), 94–97.
- Diehl, M.R.; Yaliraki, S.N.; Beckman, R.A.; Barahona, M.; Heath, J.R. Self-assembled, deterministic carbon nanotube wiring networks. *Angew. Chem., Int. Ed. Engl.* **2001**, *41* (2), 353–356.
- Bachtold, A.; Hadley, P.; Nakanishi, T.; Dekker, C. Logic circuits with carbon nanotube transistors. *Science* **2001**, *294* (5545), 1317–1320.
- Collins, P.G.; Arnold, M.S.; Avouris, P. Engineering carbon nanotubes and nanotube circuits using electrical breakdown. *Science* **2001**, *292* (5517), 706–709.
- Cheung, C.L.; Kurtz, A.; Park, H.; Lieber, C.M. Diameter-controlled synthesis of carbon nanotubes. *J. Phys. Chem., B* **2002**, *106* (10), 2429–2433.
- Chattopadhyay, D.; Lastella, S.; Kim, S.; Papadimitrakopoulos, F. Length separation of Zwitterion-functionalized single wall carbon nanotubes by GPC. *J. Am. Chem. Soc.* **2002**, *124* (5), 728–729.
- Doorn, S.K.; Fields, R.E.; Hu, H.; Hamon, M.A.; Haddon, R.C.; Selegue, J.P.; Majidi, V. High resolution capillary electrophoresis of carbon nanotubes. *J. Am. Chem. Soc.* **2002**, *124* (12), 3169–3174.
- Zhao, B.; Hu, H.; Niyogi, S.; Itkis, M.E.; Hamon, M.A.; Bhowmik, P.; Meier, M.S.; Haddon, R.C. Chromatographic purification and properties of soluble single-walled carbon nanotubes. *J. Am. Chem. Soc.* **2001**, *123* (47), 11,673–11,677.
- Joselevich, E.; Lieber, C.M. Vectorial growth of metallic and semiconducting single-wall carbon nanotubes. *Nano Lett.* **2002**, *2* (10), 1137–1141.
- Bahr, J.L.; Tour, J.M. Covalent chemistry of single-wall carbon nanotubes. *J. Mater. Chem.* **2002**, *12* (7), 1952–1958.
- Duan, X.; Huang, Y.; Cui, Y.; Wang, J.; Lieber, C.M. Indium phosphide nanowires as building blocks for nanoscale electronic and optoelectronic devices. *Nature* **2001**, *409* (6816), 66–69.
- Yu, J.-Y.; Chung, S.-W.; Heath, J.R. Silicon nanowires: preparation, device fabrication, and transport properties. *J. Phys. Chem., B* **2000**, *104* (50), 11,864–11,870.
- Mbindyo, J.K.N.; Mallouk, T.E.; Mattzela, J.B.; Kratochvilova, I.; Razavi, B.; Jackson, T.N.; Mayer, T.S. Template synthesis of metal nanowires containing monolayer molecular junctions. *J. Am. Chem. Soc.* **2002**, *124* (15), 4020–4026.
- Shelimov, K.B.; Davydov, D.N.; Moskovits, M. Template-grown high-density nanocapacitor arrays. *Appl. Phys. Lett.* **2000**, *77* (11), 1722–1724.
- Gudixsen, M.S.; Wang, J.F.; Lieber, C.M. Synthetic control of the diameter and length of single crystal semiconductor nanowires. *J. Phys. Chem., B* **2001**, *105* (19), 4062–4064.
- Li, Y.M.; Kim, W.; Zhang, Y.G.; Rolandi, M.; Wang, D.W.; Dai, H.J. Growth of single-walled carbon nanotubes from discrete catalytic nanoparticles of various sizes. *J. Phys. Chem., B* **2001**, *105* (46), 11,424–11,431.
- Huynh, W.U.; Dittmer, J.J.; Alivisatos, A.P. Hybrid nanorod-polymer solar cells. *Science* **2002**, *295* (5564), 2425–2427.
- Murphy, C.J.; Jana, N.R. Controlling the aspect ratio of inorganic nanorods and nanowires. *Adv. Mater.* **2002**, *14* (1), 80–82.
- Mayers, B.; Gates, B.; Yin, Y.D.; Xia, Y.N. Large-scale synthesis of monodisperse nanorods of Se/Te alloys through a homogeneous nucleation and solution growth process. *Adv. Mater.* **2001**, *13* (8), 1380–1384.
- Landes, C.F.; Link, S.; Mohamed, M.B.; Nikoobakht, B.; El-Sayed, M.A. Some properties of spherical and rod-shaped semiconductor and metal nanocrystals. *Pure Appl. Chem.* **2002**, *74* (9), 1675–1692.
- Smith, P.A.; Nordquist, C.D.; Jackson, T.N.; Mayer, T.S.; Martin, B.R.; Mbindyo, J.; Mallouk, T.E. Electric field assisted assembly and alignment of metallic nanowires. *Appl. Phys. Lett.* **2000**, *77* (9), 1399–1401.
- Ural, A.; Li, Y.M.; Dai, H.J. Electric field-aligned growth of single-walled carbon nanotubes on surfaces. *Appl. Phys. Lett.* **2002**, *81* (18), 3464–3466.
- Hone, J.; Llaguno, M.C.; Nemes, N.M.; Johnson, A.T.; Fischer, J.E.; Walters, D.A.; Casavant, M.J.; Schmidt, J.; Smalley, R.E. Electrical and thermal transport properties of magnetically aligned single wall carbon nanotube films. *Appl. Phys. Lett.* **2000**, *77* (5), 666–668.
- Huang, Y.; Duan, X.F.; Wei, Q.Q.; Lieber, C.M. Directed assembly of one-dimensional nanostructures into functional networks. *Science* **2001**, *291* (5504), 630–633.
- Limberis, L.; Magda, J.J.; Stewart, R.J. Polarized alignment and surface immobilization of microtubules of

- kinesin-powered nanodevices. *Nano Lett.* **2001**, *1* (5), 277–280.
31. Liu, J.; Casavant, M.J.; Cox, M.; Walters, D.A.; Boul, P.; Lu, W.; Rimberg, A.J.; Smith, K.A.; Colbert, D.T.; Smalley, R.E. Controlled deposition of individual single-walled carbon nanotubes on chemically functionalized templates. *Chem. Phys. Lett.* **1999**, *303* (1–2), 125–129.
  32. Krupke, R.; Malik, S.; Weber, H.B.; Hampe, O.; Kappes, M.M.; v. Lohneysen, H. Patterning and visualizing self-assembled monolayers with low-energy electrons. *Nano Lett.* **2002**, *2* (10), 1161–1164.
  33. Almasy, R.J.; Janson, C.A.; Hamlin, R.; Xuong, N.H.; Eisenberg, D. Novel subunit–subunit interactions in the structure of glutamine-synthetase. *Nature* **1986**, *323* (6086), 304–309.
  34. Douberly, G.E.J.; Pan, S.; Walters, D.; Matsui, H. Fabrication of protein tubules: immobilization of proteins on peptide tubules. *J. Phys. Chem., B* **2001**, *105* (9), 7612–7618.
  35. Huang, W.; Taylor, S.; Fu, K.; Lin, Y.; Zhang, D.; Hanks, T.W.; Rao, A.M.; Sun, Y.-P. Attaching proteins to carbon nanotubes via diimide-activated amidation. *Nano Lett.* **2002**, *2* (4), 311–314.
  36. Zhang, S.; Marini, D.M.; Hwang, W.; Santoso, S. Design of nanostructured biological materials through self-assembly of peptides and proteins. *Curr. Opin. Chem. Biol.* **2002**, *6* (6), 865–871.
  37. Azamian, B.R.; Davis, J.J.; Coleman, K.S.; Bagshaw, C.B.; Green, M.L.H. Bioelectrochemical single-walled carbon nanotubes. *J. Am. Chem. Soc.* **2002**, *124* (43), 12,664–12,665.
  38. Behrens, S.; Rahn, K.; Habicht, W.; Bohm, K.-J.; Rosner, H.; Dinjus, E.; Unger, E. Nanoscale particle arrays induced by highly ordered protein assemblies. *Adv. Mater.* **2002**, *14* (22), 1621–1625.
  39. Dabrowski, M.D.; Chen, J.P.; Shi, H.Q.; Chen, W.C.; Atkins, W.M. Strategies for protein-based nanofabrication: Ni<sup>2+</sup>-NTA as a chemical mask to control biologically imposed symmetry. *Chem. Biol.* **1998**, *5* (12), 689–697.
  40. Schurke, P.; Freeman, J.C.; Dabrowski, M.J.; Atkins, W.M. Metal-dependent self-assembly of protein tubes from *Escherichia coli* glutamine synthetase. *J. Biol. Chem.* **1999**, *274* (39), 27963–27968.
  41. Mishra, B.; Thomas, B.N. Phospholipid/protein cones. *J. Am. Chem. Soc.* **2002**, *124* (24), 6866–6871.
  42. Whitesides, G.M. Self-assembling materials. *Sci. Am.* **1995**, *273* (3), 146–149.
  43. Shimizu, T.; Kogiso, M.; Masuda, M. Vesicle assembly in microtubules. *Nature* **1996**, *383* (6600), 487–488.
  44. Fenniri, H.; Deng, B.-L.; Ribbe, A.E.; Hallenga, K.; Jacob, J.; Thiyagarajan, P. Entropically driven self-assembly of multichannel rosette nanotubes. *Proc. Natl. Acad. Sci. U. S. A.* **2002**, *99*, 6487.
  45. Shimizu, T. Bottom-up synthesis and structural properties of self-assembled high-axial-ratio nanostructures. *Macromol. Rapid Commun.* **2002**, *23* (5–6), 311–331.
  46. Demir, M.; Stowell, M.H.B. A chemoselective biomolecular template for assembling diverse nanotubular materials. *Nanotechnology* **2002**, *13* (4), 541–544.
  47. Whitling, J.M.; Spreitzer, G.; Wright, D.W. A combinatorial and informatics approach to CdS nanoclusters. *Adv. Mater.* **2000**, *12* (18), 1377–1380.
  48. Slocik, J.M.; Moore, J.T.; Wright, D.W. Monoclonal antibody recognition of histidine-rich peptide encapsulated nanoclusters. *Nano Lett.* **2002**, *2* (3), 169–173.
  49. Shenton, W.; Douglas, T.; Young, M.; Stubbs, G.; Mann, S. Inorganic–organic nanotube composites from template mineralization of tobacco mosaic virus. *Adv. Mater.* **1999**, *11* (3), 253–256.
  50. Douglas, T.; Young, M. Virus particles as templates for materials synthesis. *Adv. Mater.* **1999**, *11* (8), 679–681.
  51. Field, M.; Smith, C.J.; Awshalom, D.D.; Mayes, E.L.; Davis, S.A.; Mann, S. Ordering nano-meter scale magnets using bacterial thread templates. *Appl. Phys. Lett.* **1998**, *73* (12), 1739–1741.
  52. Djalali, R.; Chen, Y.-F.; Matsui, H. Au nanowire fabrication from sequenced histidine-rich peptide. *J. Am. Chem. Soc.* **2002**, *124* (46), 13,660–13,661.
  53. Djalali, R.; Chen, Y.-F.; Matsui, H. Au nanocrystal growth on nanotubes controlled by conformations and charges of sequenced peptide templates. *J. Am. Chem. Soc.* **2003**, *125* (19), 5873–5879.
  54. Beverly, K.C.; Sample, J.L.; Sampaio, J.F.; Remacle, F.; Heath, J.R.; Levine, R.D. Quantum dot artificial solids: understanding the static and dynamic role of size and packing disorder. *Proc. Natl. Acad. Sci. U. S. A.* **2002**, *99*, 6456.
  55. Matsui, H.; Dagani, R. Building from the bottom up. *C&EN* **October 16, 2000**, 27.
  56. Matsui, H.; Porrata, P.; Douberly, G.E.J. Protein tubule immobilization on self-assembled monolayers on Au. *Nano Lett.* **2001**, *1* (9), 461–464.
  57. Banerjee, I.A.; Yu, L.; Matsui, H. Location-specific biological functionalization on nanotubes: attachment of proteins at the ends of nanotubes using Au nanocrystal masks. *Nano Lett.* **2003**, *3* (3), 283–287.
  58. Whaley, S.R.; English, D.S.; Hu, E.L.; Barbara, P.F.; Belcher, A.M. Selection of peptides with semiconductor binding specificity for directed nanocrystal assembly. *Nature* **2000**, *405*, 665.
  59. Seeman, N.C.; Belcher, A.M. Emulating biology: building nanostructures from the bottom up. *Proc. Natl. Acad. Sci. U. S. A.* **2002**, *99* (2), 6451–6455.
  60. Lee, S.W.; Mao, C.B.; Flynn, C.E.; Belcher, A.M. Ordering of quantum dots using genetically engineered viruses. *Science* **2002**, *296* (5569), 892–895.
  61. Vogel, V. Learning from proteins how to enhance the performance of synthetic nanosystems. *MRS Bull.* **2002**, *27* (12), 972–978.
  62. Kong, J.; Franklin, N.R.; Zhou, C.W.; Chapline, M.G.; Peng, S.; Cho, K.J.; Dai, H.J. Nanotube molecular wires as chemical sensors. *Science* **2000**, *287* (5453), 622–625.
  63. Cui, Y.; Wei, Q.Q.; Park, H.K.; Lieber, C.M. Nanowire nanosensors for highly sensitive and selective detection of biological and chemical species. *Science* **2001**, *293* (5533), 1289–1292.
  64. Cui, Y.; Duan, X.; Hu, J.; Lieber, C.M. Doping and electrical transport in silicon nanowires. *J. Phys. Chem., B* **2000**, *104* (22), 5213–5216.

65. Feringa, B.L. In control of motion: from molecular switches to molecular motors. *Acc. Chem. Res.* **2001**, *34* (6), 504–513.
66. Stoddart, J.F. Molecular machines. *Acc. Chem. Res.* **2001**, *34* (6), 410–411.
67. Kakugo, A.; Sugimoto, S.; Gong, J.P.; Osada, Y. Gel machines constructed from chemically cross-linked actins and myosins. *Adv. Mater.* **2002**, *14* (16), 1124–1126.
68. Soong, R.K.; Bachand, G.D.; Neves, H.P.; Olkhovets, A.G.; Craighead, H.G.; Montemagno, C.D. Powering an inorganic nanodevice with a biomolecular motor. *Science* **2000**, *290* (5496), 1555–1558.
69. Howard, J. *Mechanics of Motor Proteins and the Cytoskeleton*; Sinauer Associates, Publishers: Sunderland, MA, 2001.
70. Brown, T.B.; Hancock, W.O. A polarized microtubule array for kinesin-powered nanoscale assembly and force generation. *Nano Lett.* **2002**, *2* (10), 1131–1135.
71. Limberis, L.; Stewart, R.J. Toward kinesin-powered microdevices. *Nanotechnology* **2000**, *11* (2), 47–51.
72. Schnapp, B.J.; Reese, T.S.; Nechtold, R. Kinesin is bound with high affinity to squid axon organelles that move to the plus-end of microtubules. *J. Cell. Biol.* **1992**, *119*, 389–399.
73. Stracke, R.; Bohm, K.J.; Burgold, J.; Schacht, H.-J.; Unger, E. Physical and technical parameters determining the functioning of a kinesin-based cell-free motor system. *Nanotechnology* **2000**, *11* (2), 52–56.
74. Hess, H.; Clemmens, J.; Qin, D.; Howard, J.; Vogel, V. Light-controlled molecular shuttles made from motor proteins carrying cargo on engineered surfaces. *Nano Lett.* **2001**, *1* (5), 235–239.
75. Nicolau, D.V.; Taguchi, T.; Taniguchi, H.; Yoshikawa, S. Negative and positive tone protein patterning on e-beam/deep-UV resists. *Langmuir* **1999**, *15* (11), 3845–3851.
76. Arnold, F.H. Combinatorial and computational challenges for biocatalyst design. *Nature* **2001**, *409* (6817), 253–257.
77. Schultz, P.G.; Lerner, R.A. Antibody catalysis: completing the circle. *Nature* **2002**, *418*, 485.
78. Oroudjev, E.; Soares, J.; Arcidiacono, S.; Thompson, J.B.; Fossey, S.A.; Hansma, H.G. Segmented nanofibers of spider dragline silk: atomic force microscopy and single-molecule force spectroscopy. *Proc. Natl. Acad. Sci. U. S. A.* **2002**, *99* (2), 6460–6465.

# Proteins: Structure and Interaction Patterns to Solid Surfaces

Thomas J. Webster

Department of Biomedical Engineering, Purdue University, West Lafayette, Indiana, U.S.A.

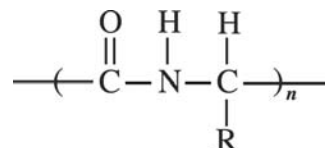
## INTRODUCTION

Advances in several critical research fields (processing, catalytic, optical, actuation, electrical, mechanical fields, etc.) have started to benefit from new technological advancements in the area of nanotechnology.<sup>[1–22]</sup> Nanotechnology can be broadly defined as the use of materials and systems whose structures and components exhibit novel and significantly changed properties when control is gained at the atomic, molecular, and supramolecular levels. Specifically, such advances have been found for materials when particulate size is decreased to below 100 nm. However, to date, relatively few advantages have been described for biological applications (specifically, those involving protein interactions). This entry elucidates several promising examples of the control nanophase materials have in manipulating interactions with proteins to improve traditional biological applications (such as for improving implantable devices, filtration systems, bioMEMS, etc.). Such advances were previously unimaginable with conventional materials possessing large micron size particulates. To describe the promise nanophase materials have in revolutionizing interactions with biology, this entry will start with a review of protein structure and interaction with solid surfaces. The entry will then continue with reports from the literature providing evidence of unique interactions proteins can have with nanophase materials.

## PROTEIN STRUCTURE

Proteins are essential to health and, in fact, mean “of first importance” in Greek. This is for a very good reason because initial protein interactions with material surfaces control subsequent cell functions essential for tissue engineering/implant applications, antibody interactions for immunoassays and/or biodegradation devices, and bacteria interactions involved in problems such as marine fouling and infection. Clearly, understanding protein size and structure will aid investigators in either maximizing or minimizing protein interactions with surfaces to improve these technologies.

Proteins are polyamides formed by a step reaction polymerization between the amino and carboxyl groups of amino acids:



where R is a characteristic side group and  $n$  is the number of repeating units. Depending on the side group, the molecular structure of the protein will drastically change. The simplest side group in protein structure is hydrogen, which will form the amino acid glycine (abbreviated Gly). The geometry of Gly is shown in Fig. 1 as a hypothetical flat sheet with a repeating distance of 0.72 nm.<sup>[23]</sup> Although the R side group in proteins can be diverse (as will soon be discussed), there are many commonalities between proteins, namely, size and structure in the nanometer regime. To date, the fundamental nanometer size of proteins has been largely ignored and not appreciated when considering approaches to control initial protein interactions with surfaces. Thus it is first important to describe protein structure to discuss how nanotechnology can be utilized to influence protein interactions. There are four important levels of protein structure to consider: primary, secondary, tertiary, and quaternary; these will be discussed in the sections that follow.

## Primary Protein Structure

The primary structure of a protein is its linear sequence of amino acids. Each amino acid is linked to another through peptide bonds (Fig. 2).<sup>[23]</sup> Because there are 20 amino acids found in man (11 of which are synthesized in the human body: Ala, Arg, Asn, Asp, Cys, Glu, Gln, Gly, Pro, Ser, and Tyr; and 9 of which are synthesized elsewhere but are essential to human diet: His, Ile, Leu, Lys, Met, Phe, Thr, Trp, and Val) (Fig. 3),<sup>[24]</sup> many sequences are possible to create numerous proteins with diverse properties. Moreover, these 20 amino acids are themselves diverse (Table 1)<sup>[25–27]</sup>

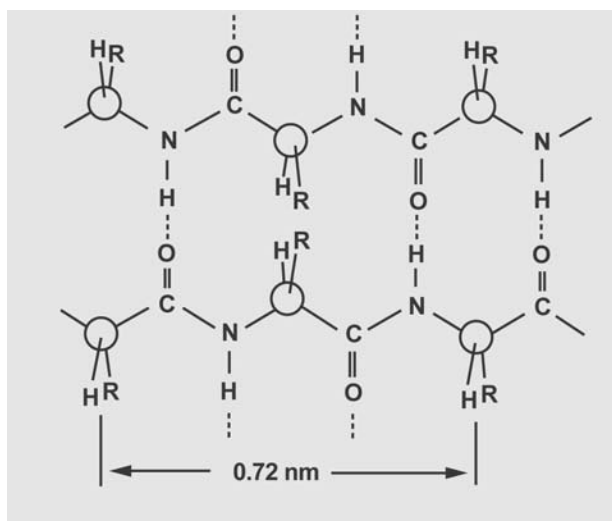


**Fig. 1** The geometry of proteins as a hypothetical flat sheet with a repeating distance of 0.72 nm. *Source:* From Ref.<sup>[23]</sup>.

and may be classified according to a number of categories: such as either aliphatic amino acids, amino acids with hydroxyl-containing or sulfur-containing side chains, aromatic amino acids, basic amino acids, cyclic amino acids, or acidic amino acids and their amides, as presented in Fig. 3. Other amino acid classifications that are often utilized when considering initial protein interactions with material surfaces are either non-polar, polar, or ionized, labeled as either N, P, or I in Fig. 3, respectively.

Some amino acids have side chains (or residues) that carry no charge at any pH yet exhibit strong polar character (e.g., Ser and Thr).<sup>[23]</sup> Ionizable side chains vary from fairly acidic ones (such as Asp and Glu, which are fully negative at the physiological pH of 7.4) to more basic amino acids (such as the imidazole group in His, which has a positive charge at a pH of 7.4) and the still more basic amino acids that carry full charges at a pH of 7.4 (specifically, Lys and Arg).<sup>[23]</sup> Yet another group of amino acids has no acid, base, or polar character in their residues as shown by their generally much lower solubility in water (such as Ala, Val, Leu, Ile, Met, Trp, and Pro). For these reasons, it should not be surprising why proteins exist with a wide range of properties, as

shown in Table 2, and this is just from considering protein primary structure.<sup>[25,26,28–32]</sup>

## Secondary Structure

The secondary structure of proteins consists of regions of ordered structures in the protein chain (Fig. 4A and B).<sup>[23]</sup> Two main secondary structures of proteins are very common: the  $\alpha$ -helix (Fig. 4A) and the  $\beta$ -pleated sheet (Fig. 4B). The degree of secondary structures in proteins varies to a large amount. For example, in structural proteins such as silk and wool, secondary structures are extensive and thus determine the overall shape of such proteins.<sup>[23]</sup> In addition, myoglobin and hemoglobin (proteins involved in oxygen transport and storage) have extensive  $\alpha$ -helical secondary structure. In contrast, some proteins possess very little secondary structure such as the digestive enzyme chymotrypsin.

Both the  $\alpha$ -helix and  $\beta$ -pleated sheet secondary protein structures are controlled by hydrogen bonding mechanisms, as illustrated in Fig. 4. Hydrogen bonding mechanisms are electrostatic attractions between oxygen of one chemical group and hydrogen of another chemical group. The  $\alpha$ -helix results from the coiling of the protein chain such that the peptide bonds making up the backbone are able to form hydrogen bonds with each other (presented as curved lines in Fig. 4A). These hydrogen bonds are directed along the axis of the helix, and thus amino acid residues (portions of the amino acid not participating in the peptide bond) extend at right angles from the helix with minimal steric hindrance that further stabilizes the  $\alpha$ -helix. The  $\beta$ -pleated sheet is a layering of protein chains in which each layer is held together by hydrogen bonds between the peptide links (presented as curved lines in Fig. 4B). The amino acid residues are situated at right angles to the sheets with, again, minimal steric hindrance that further stabilizes the  $\beta$ -pleated sheet.

## Tertiary Structure

The tertiary structure of proteins is the overall three-dimensional shape of the protein (Fig. 5).<sup>[23]</sup> Protein

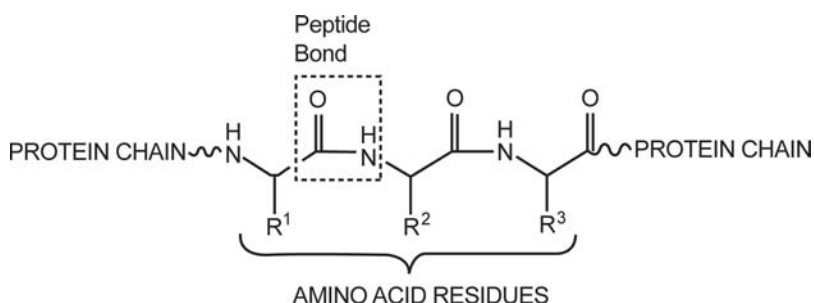


**Fig. 2** Each amino acid is linked to another in proteins through peptide bonds. Note that the R group characteristic of each amino acid is often referred to as an amino acid residue. *Source:* From Ref.<sup>[23]</sup>.



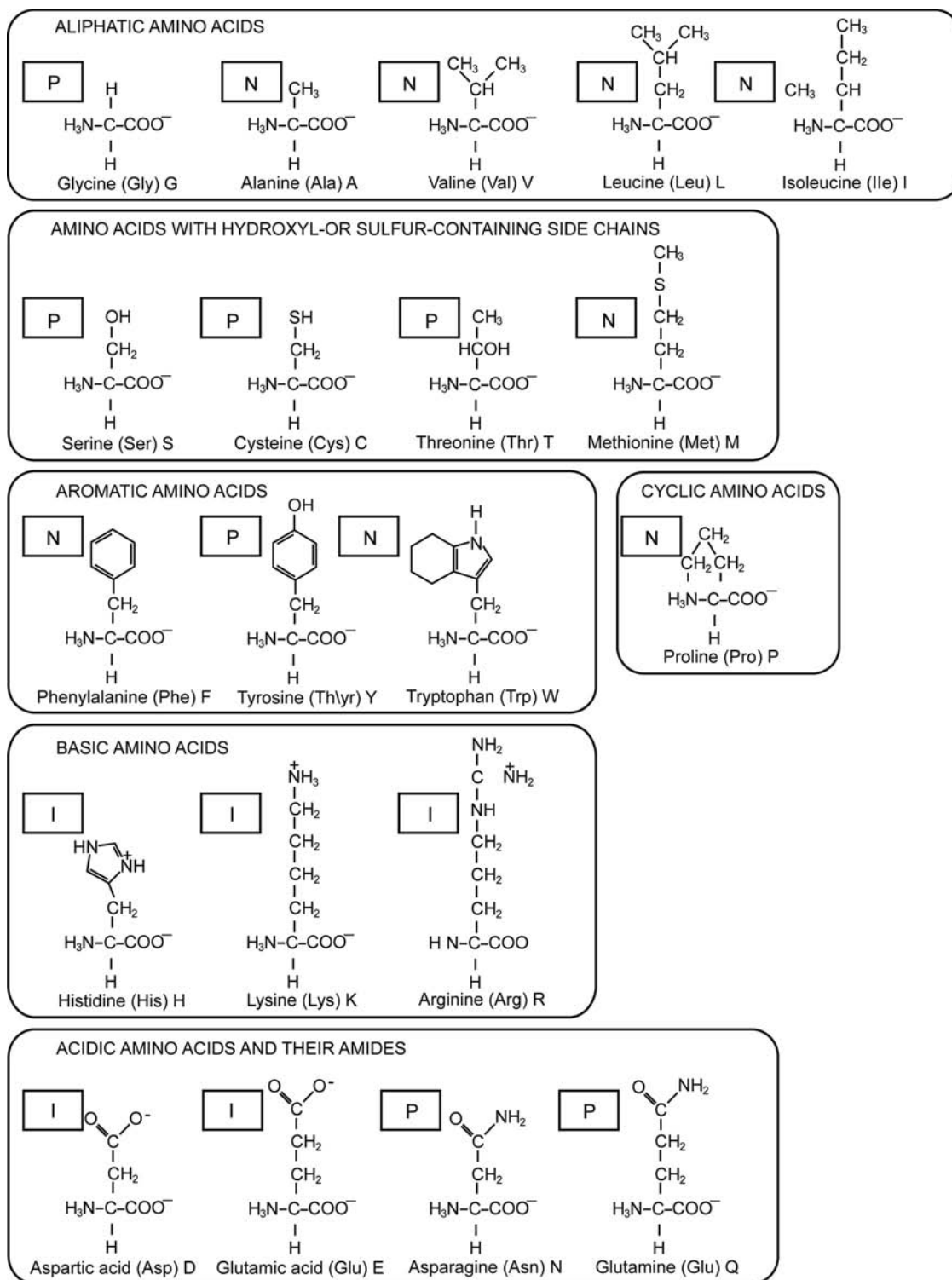


**Fig. 3** Twenty common amino acids. N, P, and I are non-polar, polar, and ionized residue categories, respectively, that appear to the left of each amino acid. *Source:* From Refs.<sup>[23]</sup> and <sup>[24]</sup>.

tertiary structure can either possess little order for many structural proteins, or be extremely complicated for other proteins such as enzymes that fold up on themselves to form more complex structures. Clearly,

the tertiary structure of proteins is a consequence of primary structure as it depends on spontaneous interactions between different amino acids and, under aqueous conditions, spontaneous interactions between

**Table 1** Diverse properties of amino acid residues

Amino acid (three-letter and one-letter abbreviations)	Charge	Hydrophobicity (kcal/mol) <sup>a</sup>	Surface tension (erg/cm <sup>2</sup> /mol/l lowering of the surface tension of water)
Isoleucine (Ile or I)	Neutral	0.73	-15.2
Phenylalanine (Phe or F)	Neutral	0.61	-17.3
Valine (Val or V)	Neutral	0.54	-3.74
Leucine (Leu or L)	Neutral	0.53	-21.9
Tryptophan (Trp or W)	Neutral	0.37	-9.6
Methionine (Met or M)	Neutral	0.26	-3.01
Alanine (Ala or A)	Neutral	0.25	0.96
Glycine (Gly or G)	Neutral	0.16	1.12
Cysteine (Cys or C)	0 to -1	0.04	0.69
Tyrosine (Tyr or Y)	0 to -1	0.02	-15.1
Proline (Pro or P)	Neutral	-0.07	-0.49
Threonine (Thr or T)	Neutral	-0.18	0.59
Serine (Ser or S)	Neutral	-0.26	0.76
Histidine (His or H)	0 to 1	-0.40	1.03
Glutamic acid (Glu or E)	0 to -1	-0.62	0.86
Asparagine (Asn or N)	Neutral	-0.64	1.17
Glutamine (Gln or Q)	Neutral	-0.69	1.21
Aspartic acid (Asp or D)	0 to -1	-0.72	0.96
Lysine (Lys or K)	0 to 1	-1.1	0.92
Arginine (Arg or R)	0 to 1	-1.8	1.03

<sup>a</sup>Transfer from hydrophobic to more hydrophilic phase; increased positive value means more hydrophobic.  
Source: Refs.<sup>[25-27]</sup>.

amino acids and water as will be discussed. Because of the properties of the amino acids and the order in which amino acids are bonded (i.e., protein primary structure), select electrostatic interactions will be created for predictable tertiary structures. This automatic folding of proteins occurs even as proteins are synthesized within ribosomes of cells. As individual proteins are synthesized, residues of each amino acid will either attract, repel, or remain indifferent to residues of another amino acid. Thus regions of the protein will twist and turn to minimize unfavorable and to maximize favorable interactions to form a consistent shape or three-dimensional tertiary structure, as illustrated in Fig. 5 (please note repulsive and attracting forces resulting in a favorable protein shape).

There are four main interactions among residues of amino acids that contribute to the tertiary structure of proteins, each with different strengths: covalent, ionic, hydrogen, and van der Waals bonds. Of these interactions, covalent bonds are the strongest, as indicated in Table 3.<sup>[23]</sup> For example, when two Cys amino acids come in close proximity, a covalent bond between sulfur in each residue can be formed as a result of oxidation (Fig. 6A).<sup>[23]</sup> This covalent bond can have

a strength approaching 250 kJ/mol.<sup>[23]</sup> Ionic bonds are also a strong interaction force (approximately 20 kJ/mol),<sup>[23]</sup> which occurs between chemical groups having opposite charges. For example, ionic bonds are often formed between the carboxylate ion of an acidic residue (such as Asp) and the ammonium ion of a basic residue (such as Lys), as presented in Fig. 6B.<sup>[23]</sup> As previously mentioned, hydrogen bonds are formed between electronegative atoms, such as oxygen, and protons attached to electronegative atoms. Hydrogen bonding between two Ser amino acids is illustrated in Fig. 6C.<sup>[23]</sup> The forces can be quite strong in the range of 7–40 kJ/mol.<sup>[23]</sup> Lastly, van der Waals forces result from interactions between hydrophobic molecules (e.g., between two aromatic residues such as Phe, as presented in Fig. 6D). They result from unequal distributions of electrons between residues such that an area of high electron density on one residue has an attraction for an area of low electron density on another residue. These forces are the weakest of those discussed (1.9 kJ/mol).

Based on Table 3, one might expect that the most important or influential binding forces are those with the highest strength. On the contrary, generally

**Table 2** Diverse properties of proteins

Protein	Function	Location	Size (kDa)	Shape (Å)	Stability	Surface activity
Albumin	Carrier	Blood	65	42 × 141	Denatures at 60°C	Low on polyethylene
Fibrinogen	Clotting	Blood	340	460 × 60 (trinodular string)	Denatures at 56°C	High on polyethylene
IgG	Antibody	Blood	165	T-shaped		Low on polyethylene
Lysozyme	Bacterial lysis	Tear; hen egg	14.6	45 × 30 (globular)	$\Delta G_n = -14$ kcal/mol	High on negatively charged surfaces
Hemoglobin	Oxygen carrier	Red blood cells	65	55 (spherical)	Normal form	Very high on polyethylene
Hemoglobin S	Oxygen carrier	Sickle red blood cells	65	55 (spherical)	Less than hemoglobin	Much higher air-water activity than hemoglobin
Myoglobin	Oxygen carrier	Muscle	16.7	45 × 35 × 25 (spherical)	$\Delta G_n = -12$ kcal/mol	
Collagen	Matrix factor	Tissue	285	3000 × 15 (triple helical rod)	Melts at 39°C	
Bacteriorhodopsin	Membrane protein		26	30–40 long		High at cell membrane
Tryptophan synthase $\alpha$ subunit (wild type)	Enzyme		27		$\Delta G_n = -8.8$ kcal/mol; denatures at 55°C	High air-water activity compared to ovalbumin
Tryptophan synthase variant $\alpha$ subunit	Enzyme		27		$\Delta G_n = -16.8$ kcal/mol	Much less active at air-water interface than wild type

Source: Refs.<sup>[25,26,28–32]</sup>

speaking, the most important binding forces for the tertiary structure of proteins are those with the weakest strength (i.e., van der Waals and hydrogen bonding forces), whereas the least important forces are those with the highest strength (specifically, covalent and ionic bonding forces). One reason for this is because, compared with ionic and covalent bonding, there are many more opportunities for van der Waals and hydrogen bonding interactions in protein tertiary structure. A simple reexamination of amino acid chemical structures, as given in Fig. 3, can provide the answer as to why this is true. For example, the only covalent bond that is readily seen in protein tertiary structure is the disulfide bond.<sup>[23]</sup> The only amino acid capable of creating such a bond, when in juxtaposition to itself, is Cys.<sup>[23]</sup> In contrast, there are eight amino acids capable of promoting van der Waals interactions (specifically, Gly, Ala, Val, Leu, Ile, Phe, Pro, and Met).<sup>[23]</sup> However, it is important to note that for some proteins (small polypeptides such as the hormones vasopressin and oxytocin), covalent bonding mechanisms are more important, but for the majority of proteins, these bonds play a minor role in mediating

tertiary structure compared with the other bonding mechanisms listed in Table 3. The same is true for ionic and hydrogen bonding mechanisms. Specifically, significantly more amino acids are capable of forming hydrogen bonds (eight: Ser, Thr, Cys, Asn, Gln, His, Tyr, and Trp) than ionic bonds (four: Asp, Glu, Lys, and Arg).<sup>[23]</sup>

Another reason for the increased importance of the weaker-strength interactions in controlling tertiary structure is the fact that proteins exist in aqueous media. Thus residues of amino acids must interact with water, which is a highly polar compound that forms strong hydrogen bonds (as presented in Fig. 5). In addition, water can also accept a proton to become positively charged and can form ionic bonds to several amino acids including Asp and Glu. This makes water an important medium for influencing the tertiary structure of proteins because it can form either hydrogen or ionic bonds with the following groups of amino acids: Ser, Thr, Cys, Asn, Gln, His, Tyr, Asp, Glu, Lys, and Arg.<sup>[23]</sup> These hydrophilic amino acids are either polar or ionizable, as given in Fig. 3. The remaining non-polar amino acids (Ala, Val, Leu, Ile, Phe, Pro, and Met)

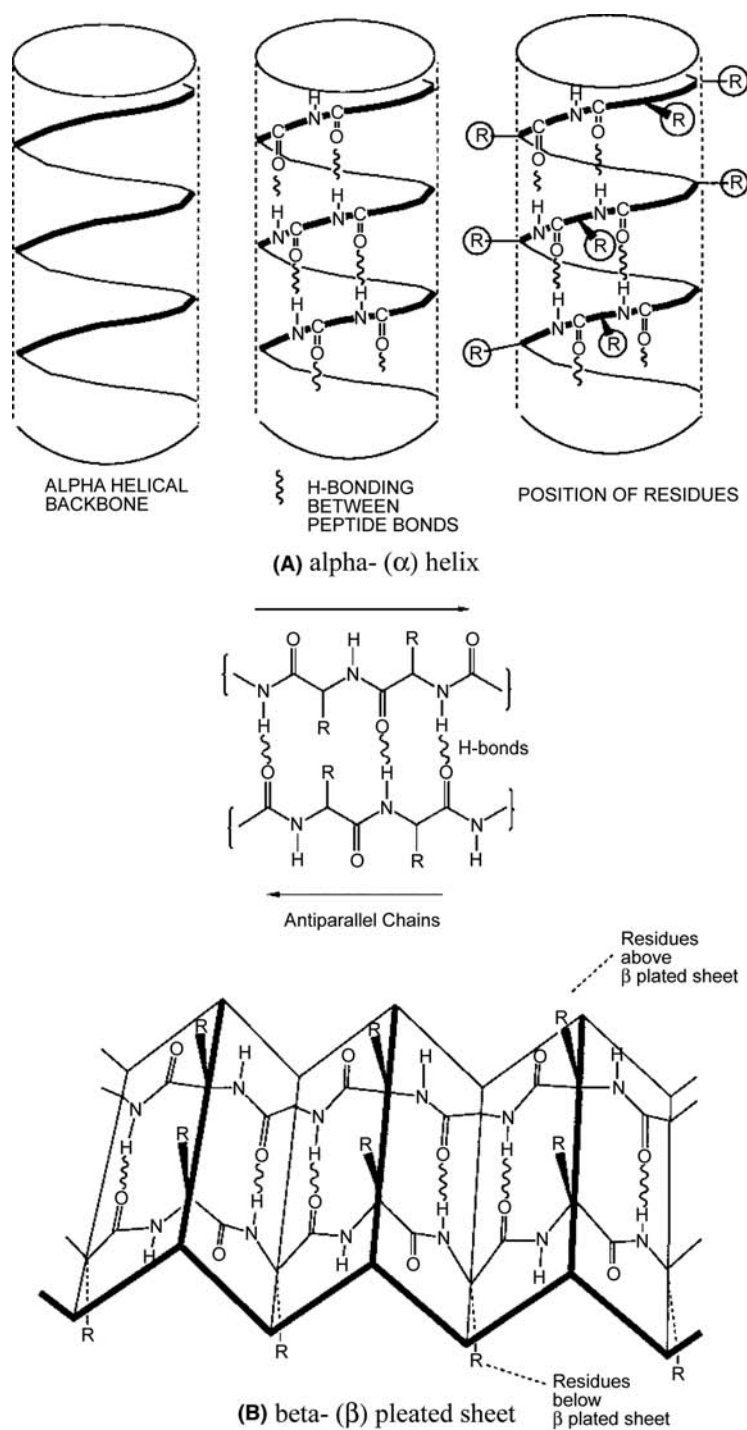


**Fig. 4** Secondary protein structures: (A)  $\alpha$ -helix and (B)  $\beta$ -pleated sheet. *Source:* From Ref.<sup>[23]</sup>.

are hydrophobic and thus are repelled by water. In this manner, it can be expected that the most stable tertiary structures of proteins in aqueous media are those where most of the hydrophobic and hydrophilic amino acids are on the inside and outside of the protein, respectively (Fig. 5). This is why most soluble proteins exhibit spherical or globular tertiary shapes, although fibrinogen (an important protein for blood clotting) does not follow this trend as it is more elongated than spherical.

Globular tertiary protein structures have several consequences in terms of amino acid interactions. The hydrophobic amino acids on the inside of the protein tertiary structure (avoiding interaction with water) are forced to interact with each other because of this tertiary structure. However, the number of ionic and hydrogen bonds contributing to the tertiary structure is reduced because the hydrophilic amino acids on the exterior of the protein form ionic and/or hydrogen bonds with water. For these reasons, hydrophobic—not

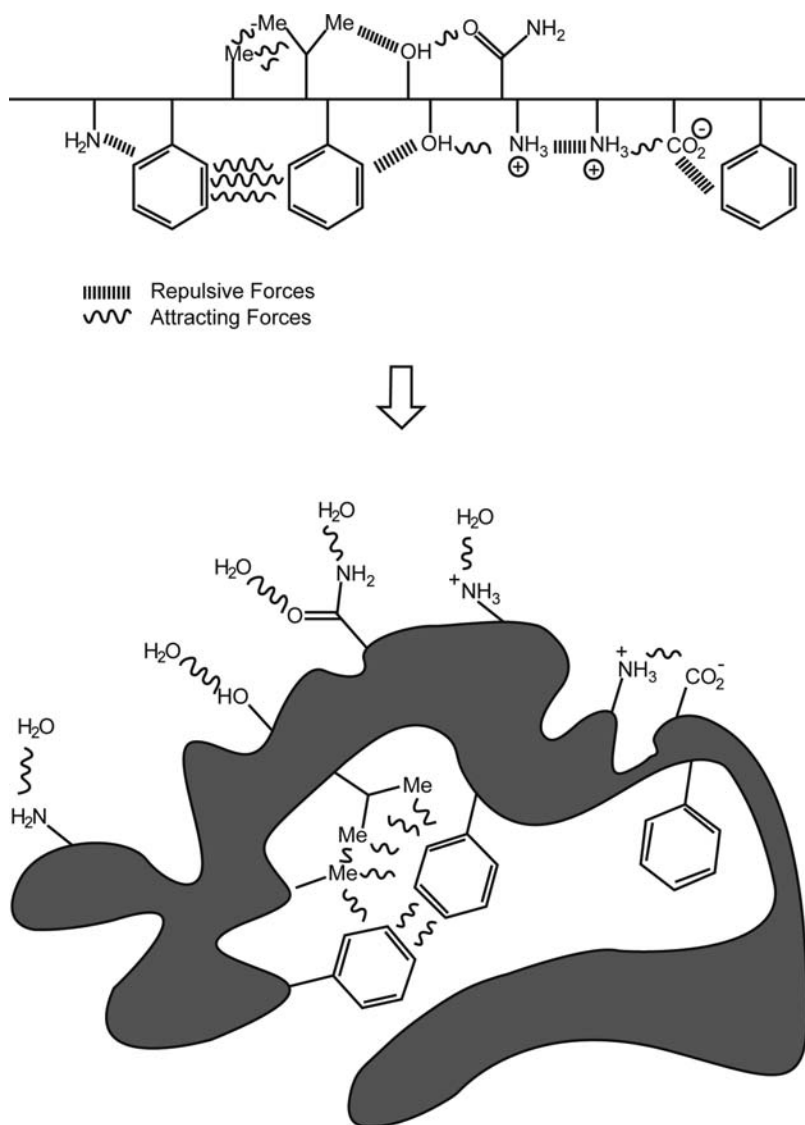


**Fig. 5** Tertiary protein structure. *Source:* From Ref.<sup>[23]</sup>.

hydrophilic—interactions control the tertiary structure of proteins. However, as will be discussed, hydrophilic and hydrophobic amino acid locations on the outer and inner cores of the protein, respectively, will drastically change as proteins initially come in contact with solid surfaces.

Of course, repulsion forces between amino acid residues in close proximity can also aid in protein tertiary

structure. For example, residues that are hydrophilic (such as amino functional groups in Gln) would repel amino acid residues that are hydrophobic (such as an aromatic ring in Phe) when in close position. Similarly, two residues that are identical in charge will repel each other until a more favorable interaction between residues is created.

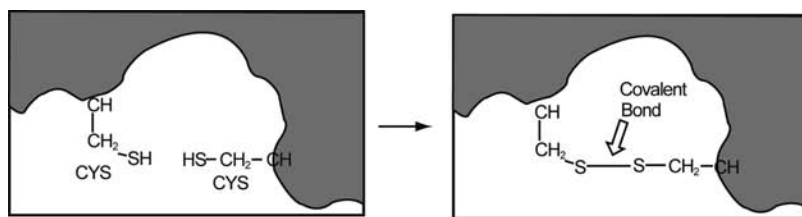
### Quaternary Structure

Only proteins that possess numerous subunits have quaternary structure. How these subunits interact will determine the quaternary structure of that protein. An example of a well-studied quaternary protein structure is hemoglobin, which is composed of four protein subunits as described by secondary structure: two identical  $\alpha$  subunits and two identical  $\beta$  subunits (Fig. 7).<sup>[24]</sup> Of course, interactions between amino acid

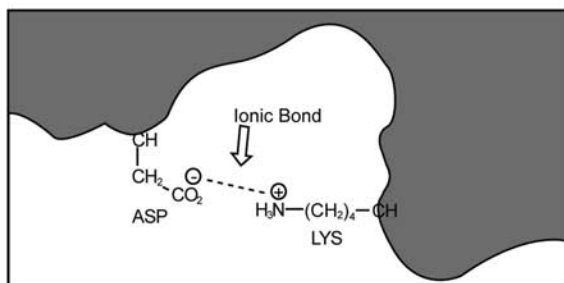
**Table 3** Strengths of bonds controlling tertiary protein structure

Type of bond	Strength (kJ/mol)
Covalent (S–S)	250
Ionic	20
Hydrogen	7–40
Van der Waals	1.9

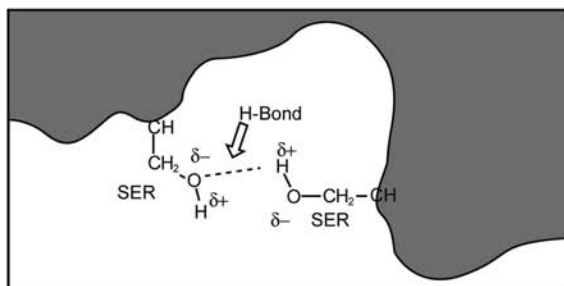
*Source:* Ref.<sup>[23]</sup>.



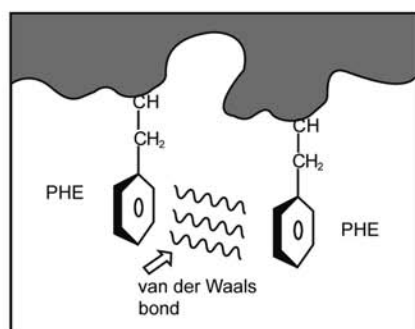
(A) covalent bonds



(B) ionic bonds



(C) hydrogen bonds



(D) van der Waals bonds

**Fig. 6** Four main interactions among residues of amino acids: (A) covalent, (B) ionic, (C) hydrogen, and (D) van der Waals bonds. *Source:* From Ref.<sup>[23]</sup>.

residues on the exterior of the protein's tertiary structure will control quaternary structure. Thus ionic bonding mechanisms, which control the placement of hydrophilic amino acids on the exterior of protein tertiary structure in an aqueous environment, now play another important role in determining quaternary structure. Similarly, hydrophobic interactions have an essential role in determining quaternary structure.

For example, it is clearly not possible for all hydrophobic amino acids to be placed on the interior of proteins; some may be present on the exterior. Thus a small hydrophobic area between adjacent subunits in the quaternary structure of proteins may be formed through hydrophobic interactions because these groups would have a preferred interaction of facing each other, rather than being exposed to the aqueous



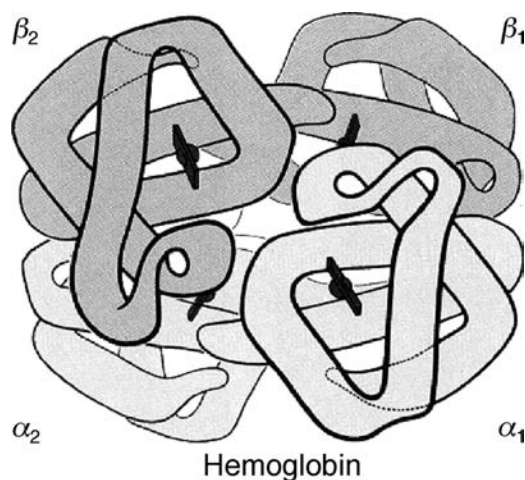


**Fig. 7** Quaternary structure of hemoglobin. *Source:* From Ref.<sup>[24]</sup>.

environment. This is another example of how important hydrophobic interactions are in controlling protein structure.

Although the structure of proteins has been well studied for a number of years, only in the past several decades have investigators begun to elucidate mechanisms of protein interactions with solid substrates. Knowledge of protein structure has certainly aided these researchers in understanding properties of surfaces that mediate protein interactions. “Protein Interactions with Surfaces” will describe some of these findings.

## PROTEIN INTERACTIONS WITH SURFACES

Although proteins may interact in a wide range of media, such as at the air–water interface in the case of interfacial coagulation/foaming, this section will primarily discuss interactions at the solid–liquid interface because the most promising applications of nanophase materials in a biological context have been observed at this intersection.<sup>[33–42]</sup> Because proteins can interact with surfaces in two main ways—adsorption and orientation (or conformation)—the next sections will focus on these aspects beginning with adsorption.

### Principles of Protein Adsorption

A great deal of attention has been focused on protein structure in aqueous media in this entry. This is because soluble proteins present in biological fluids (e.g., blood plasma) are the type of proteins that are involved in immediate adsorption to surfaces.<sup>[43]</sup> In contrast, insoluble proteins that comprise tissues (such as collagen and elastin) are not normally free to diffuse

to a solid surface; however, these proteins may appear on solid surfaces of implantable devices because of synthesis and deposition by cells.<sup>[25]</sup>

In as short a time that can be measured (i.e., less than 1 sec), soluble proteins become adsorbed to surfaces.<sup>[25]</sup> This is true for applications incorporating implants (such as orthopedic, vascular, etc.), bioseparation devices, immunoassays, catheters, and biosensors, or for any device involved in protein contact from a liquid surface to a solid surface. In seconds to minutes, a monolayer of adsorbed protein will form on solid surfaces.<sup>[25]</sup> Typical values for protein adsorption on solid surfaces are in the range of  $1 \mu\text{g}/\text{cm}^2$  and exhibit a plateau with respect to initial protein concentration.<sup>[25]</sup> That is, protein adsorption will reach a maximum and will not be influenced by higher initial bulk protein concentrations. Moreover, the surface concentration of proteins adsorbed on a material surface is often 1000 times more concentrated than in the bulk phase.<sup>[25]</sup> It is apparent that because there is a limited amount of space on a material surface, extreme competition exists for protein adsorption to solid surfaces. Depending on the two major driving forces for protein adsorption from liquid to solid surfaces (specifically, the relative bulk concentration of each protein in solution and the properties of the surface that control protein reactivity), the outcome of this competitive adsorption process is that the surface will be rich in some proteins while poor in others. Because proteins have vastly different properties and thus reaction to surfaces, as shown in Table 2,<sup>[25,26,28–32]</sup> protein adsorption will clearly be different depending on material chemistry, wettability, roughness, charge, etc.

It is also imperative to note that with some exceptions, protein adsorption to material surfaces is irreversible and thus leads to “immobilization” of specific proteins because they are, for the most part, not free to diffuse away.<sup>[44]</sup> Harsh treatments, such as using detergents (such as sodium dodecyl sulfate [SDS]), are usually required to remove adsorbed proteins from a material surface.<sup>[40]</sup> Clearly, because of this efficiency, proteins have an inherent tendency to adsorb on surfaces as a tightly bound adsorbate, and removing unwanted protein adsorption (or fouling) from surfaces has consequently become an active area of research.<sup>[45–47]</sup>

### Kinetics of Protein Adsorption

The kinetics of protein adsorption to solid surfaces can be described as a very fast initial phase that is diffusion-limited followed by a slower phase until steady state is realized.<sup>[25]</sup> A plot of the initial amount of protein adsorbed vs. the square root of time results

**Table 4** Positive enthalpy change of protein adsorption to surfaces

Protein	Surface	Enthalpy change of adsorption (mJ/m <sup>2</sup> )
Horse serum albumin	$\alpha$ -Fe <sub>2</sub> O <sub>3</sub>	+1.9 at pH = 5
		+7.0 at pH = 7
RNase	Negatively charged polystyrene with high surface charge density	+4 at pH = 5
		-2 at pH = 11

Source: Refs.<sup>[25,31,41]</sup>

in a linear characteristic typical of diffusion-controlled processes.<sup>[25]</sup> It can be speculated that during the later phase, protein adsorption is slowed because of the competition to locate a position sterically unhindered on the surface.<sup>[25]</sup>

### Thermodynamics of Protein Adsorption

Because protein adsorption appears to be irreversible,<sup>[25,40,44]</sup> the thermodynamics of protein adsorption is difficult to characterize. However, there have been several studies providing insights into the thermodynamics of protein adsorption.<sup>[25,31,41]</sup> For example, some studies have determined direct measurements of the heat of adsorption for several proteins on a variety of surfaces, as indicated in Table 4.<sup>[25,31,41]</sup> Positive enthalpies have been documented on spontaneous adsorption, thus providing evidence that protein adsorption is entropically driven under certain circumstances. [Remembering that  $\Delta G = \Delta H - T\Delta S$ , with a positive  $\Delta H$  (enthalpy),  $\Delta S$  (entropy) must be positive to keep  $\Delta G$  (free energy) negative to provide for a spontaneous reaction.] It is now generally agreed on that all protein adsorption processes are strongly driven by entropic changes.<sup>[25]</sup> The presence of entropic factors in protein adsorption to solid surfaces could arise because of the thermodynamics of water binding to the surface and the limited protein unfolding that occurs once adsorbed.<sup>[25]</sup>

### Principles of Protein Orientation

As previously mentioned, protein adsorption is only one manner in which proteins interact with solid surfaces. The orientation of proteins in the adsorbed monolayer must also be considered because this interaction leads to extreme consequences in the ultimate function of a device.<sup>[36,44]</sup> For example, for implant, biosensor, or immunoassay applications, particular amino acids in proteins are well known to bind to a

variety of cells, antibodies, or other agents that drastically influence device function. An example of the importance of protein orientation for the capture of cells is illustrated in Fig. 8.<sup>[48]</sup> Protein orientation will alter from surface to surface because proteins are not uniform in properties (Table 2) or structure. The existence of regions that are largely acidic/basic and hydrophobic/hydrophilic, and with select amino acids exposed to the aqueous media will greatly influence how that protein will adsorb to a surface, and thus its orientation, once adsorbed. As previously mentioned, proteins are not free to rotate once adsorbed because of multiple bonding mechanisms and thus immediately on adsorption, proteins are fixed in a preferred orientation or bioactivity.<sup>[25]</sup>

Under certain extreme conditions (e.g., conditions that are outside of the physiological range, or outside the range of 0–45°C and pH 5–8, and in aqueous solutions of about 0.15 M ionic strength), proteins may lose their normal structure.<sup>[25]</sup> In other words, under such conditions, the spherical or globular tertiary structure most soluble proteins assume in aqueous media will unfold or denature. The structure of denatured proteins has been described as a random coil structure similar to those found in synthetic polymers.<sup>[25]</sup> Because the structure of the protein has changed from that of a hydrophilic/hydrophobic exterior/interior to a more random arrangement, often times denatured proteins lose their solubility, become less dense (folded protein structures have densities of approximately 1.4 g/cm<sup>3</sup>), and ultimately lose their bioactivity.<sup>[25]</sup> Although there have been many examples of protein denaturation in solution, in general, there have been few reports of full protein denaturation on material surfaces.<sup>[25]</sup> That is, generally, proteins adsorbed at the solid-liquid interface are not fully denatured and retain some degree of structure.

### Properties that Influence Protein Interactions

Not only do properties of proteins determine the degree of protein interaction with surfaces, but properties of the media and the surface (specifically, wettability, surface energy, chemistry, roughness, etc.) also influence the degree of protein interactions.<sup>[48]</sup> This is true because proteins are relatively large in size and have correspondingly great numbers of charged amino acid residues of varying acidity/basicity well distributed on the exterior of the protein. Therefore the inherent polyelectrolytic behavior of proteins becomes increasingly important depending on conditions of the aqueous media (such as alterations in pH and ionic strength). The polyelectrolytic property of proteins provides for exciting design criteria to engineer surfaces to either maximize or minimize protein

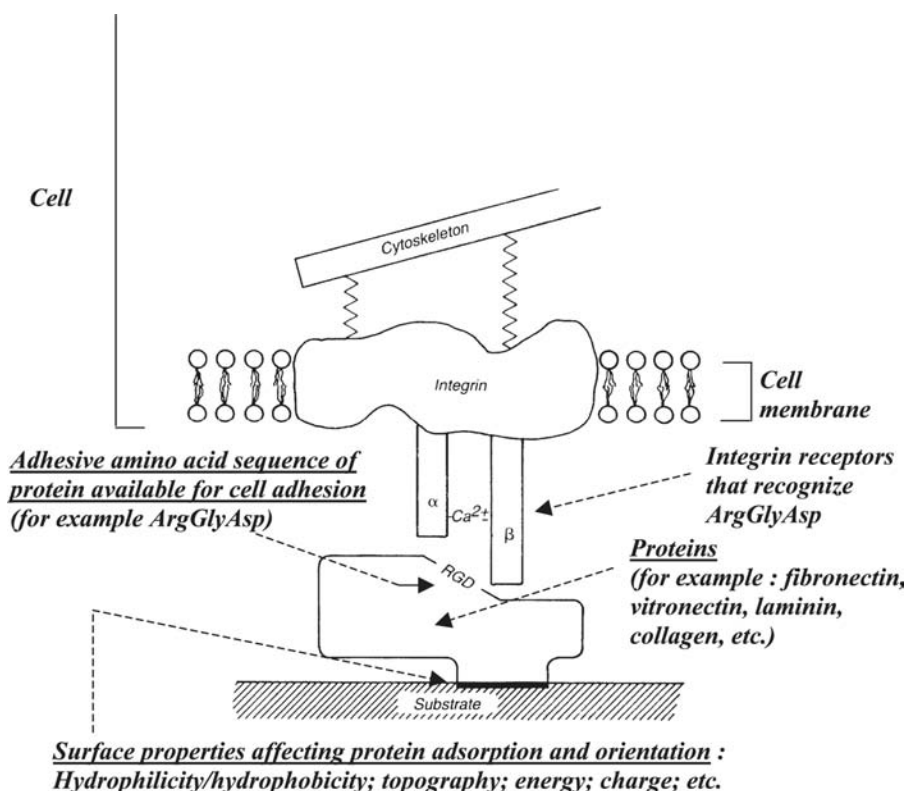


**Fig. 8** Control of surface-protein interactions for capture of cells. Source: From Ref.<sup>[48]</sup>.

interactions. Not surprisingly, at a neutral or slightly charged surface and at a pH in which the net charge on the protein is minimal (i.e., near the isoelectric pH), most proteins will exhibit maximum adsorption.<sup>[25]</sup> For surfaces with a large net charge, initial protein interactions will be dominated by the degree of the opposite charge on the surface.<sup>[25,48]</sup> Thus to develop a surface to maximize interactions with a protein displaying a large positive charge, one needs to design a surface with a large negative charge (such as one with numerous hydroxyl groups).

Simple consideration of the spatial organization of amino acids can also be used in the design of surfaces to enhance protein interactions.<sup>[39]</sup> As previously discussed, hydrophilic and hydrophobic amino acids are present primarily on the exterior and the interior of soluble proteins, respectively. This spatial arrangement has a direct consequence on the initial interaction of proteins with surfaces. For example, for the most part, a surface that initiates interactions with the exterior hydrophilic amino acid residues can promote adsorption. In contrast, for the interior hydrophobic amino acid residues to interact with a material surface, the soluble protein would have to unfold or lose tertiary structure, which is unlikely under normal conditions. For this reason, it can be reasoned that the types of amino acid residues that will initially react with a material surface are only those that exhibit largely polar properties (Fig. 3). Thus to minimize interactions with hydrophobic regions of proteins, one could design a surface

with a large degree of hydrophobicity (such as polymers with numerous nonfunctionalized benzene rings).

Several studies have confirmed speculations that properties (such as chemistry, charge, topography, etc.) of surfaces dictate select interactions (specifically, the type, concentration, and conformation/bioactivity) of proteins.<sup>[43,49-53]</sup> It has been reported in the literature that changes in the type and concentration (up to 2100%, 74%, and 53% for albumin,<sup>[52]</sup> fibronectin,<sup>[54]</sup> and vitronectin,<sup>[55,56]</sup> respectively) of protein adsorption on materials depend on surface properties such as chemistry (i.e., either polymer, metal, or ceramic), hydrophilicity/hydrophobicity, roughness, and surface energy. Specifically, maximum vitronectin,<sup>[56]</sup> fibronectin,<sup>[54]</sup> and albumin<sup>[43,52]</sup> adsorption was noted on hydrophilic ceramic surfaces with high surface roughness and/or energies. Despite these promising studies providing some level of understanding between material properties and protein adsorption, few (if any) studies have accurately correlated material properties to protein orientation. This lack of correlation may be because of a previous failure to create surfaces with features similar in size to those of proteins (i.e., at the nanometer level).

## THE PROMISE OF NANOPHASE MATERIALS FOR ENHANCING PROTEIN INTERACTIONS

Nanophase materials are new formulations of materials that are composed of particulates of the same

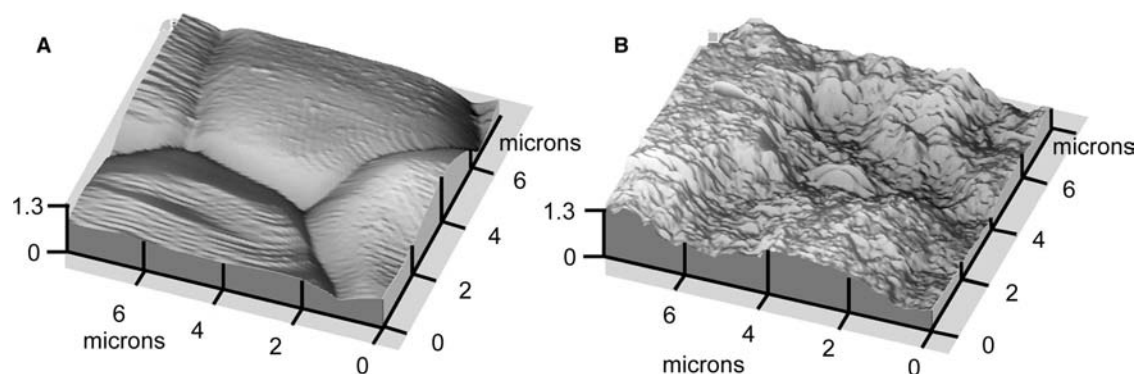


**Fig. 9** Representative atomic force images of (A) conventional materials compared to (B) nanophase materials (specifically, titania is depicted here). *Source:* From Ref.<sup>[35]</sup>.

atoms but are fewer (less than tens of thousands) and smaller (less than 100 nm in diameter) than conventional forms (which contain several billions of atoms and have particulate sizes in microns to millimeters in diameter).<sup>[15]</sup> Representative images of nanophase compared with conventional materials are presented in Fig. 9.<sup>[35]</sup> The rationale, followed by experimental evidence that surface properties of nanophase materials enhance initial protein interactions, is expounded in the sections that follow.

### Rationale

Surface properties (such as area, charge, and topography) depend on the particulate (such as grain) size of a material.<sup>[1,4,7,15,21,22]</sup> In this respect, nanophase materials that, by their very nature, possess higher surface areas with increased portions of surface defects (such as edge/corner sites) and/or grain boundaries<sup>[1,7]</sup> have special advantageous properties that remain largely unexplored for applications involving biology. To date, the increased surface reactivity of nanomaterials has been utilized for catalytic applications exclusively;<sup>[1,7]</sup> for example, compared with conventional (greater than 100 nm in average grain size) magnesium oxide (MgO),

nanophase (i.e., 4 nm average grain size) MgO possessed an increased number of atoms at the surface, higher surface area (100–160 m<sup>2</sup>/g compared with 200–500 m<sup>2</sup>/g, respectively), less acidic OH<sup>-</sup> groups (because of a much higher proportion of edge sites for the nanophase MgO to cause delocalization of electrons) (Fig. 10), increased adsorption of acidic species, and increased destructive adsorption of organophosphorous and chlorocarbons.<sup>[1,7]</sup> Because such promising results have been found when utilizing nanophase materials in catalytic applications, it is intriguing to ponder what promise these materials may have in applications involving protein interactions.

### Experimental Evidence

Some of the best examples of how nanophase—compared with conventional—materials alter interactions with proteins are outlined in investigations of the potential use of nanostructured materials as the next generation of bone implants.<sup>[33–42]</sup> Reports in the literature have determined that new bone synthesis is enhanced on materials with grain sizes less than 100 nm.<sup>[33–42]</sup> Investigations of the underlying mechanisms revealed that the initial adsorbed

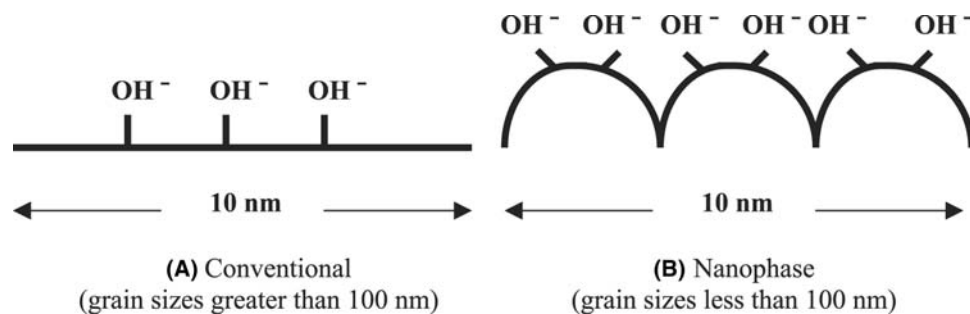


**Fig. 10** Special surface properties of nanophase materials pertinent for protein interactions. Compared to (A) conventional materials, (B) nanophase materials possess a greater number of atoms at the surface, higher surface areas, and less acidic OH<sup>-</sup> groups (because of an increase in electron delocalization) in the hydroxide layer. *Source:* From Refs.<sup>[1]</sup> and <sup>[7]</sup>.

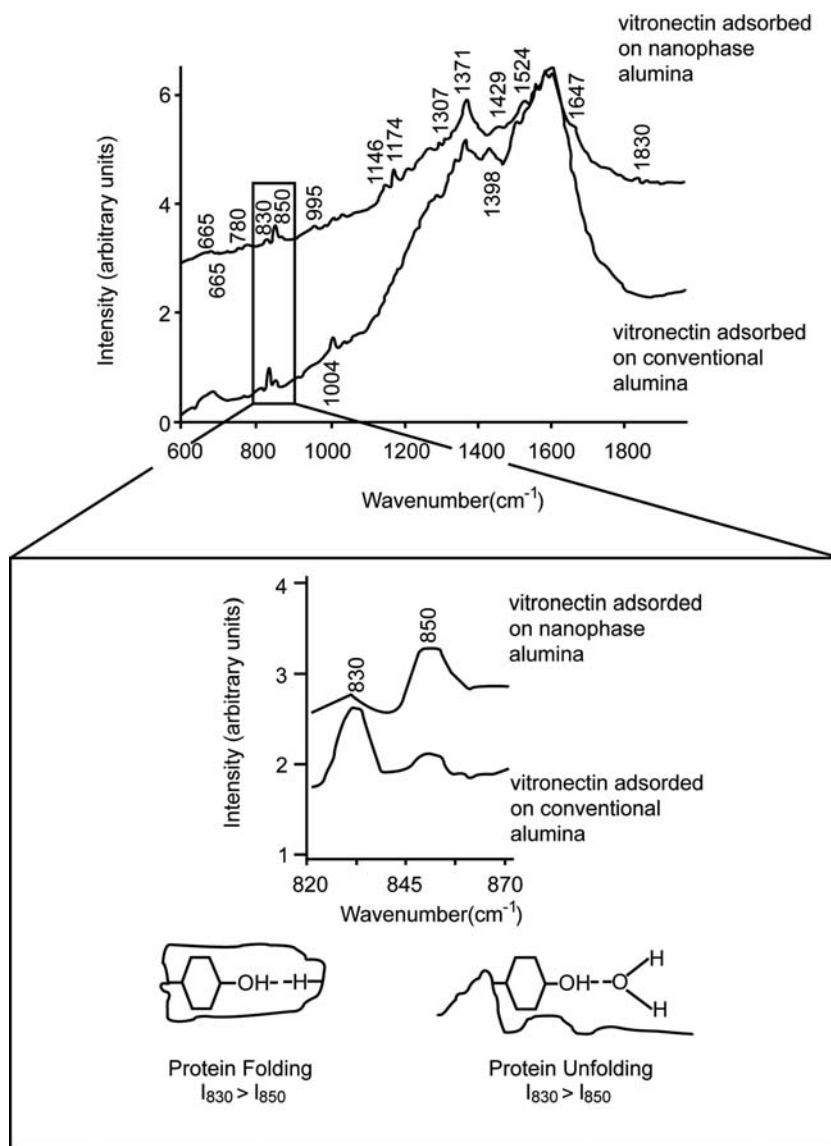


**Fig. 11** Surface-enhanced Raman scattering technique provided evidence of increased unfolding of the proteins (specifically, vitronectin in this example) adsorbed on nanophase compared to conventional grain-sized ceramics. *Source:* From Ref.<sup>[40]</sup>.

concentration,<sup>[36]</sup> conformation,<sup>[40]</sup> and bioactivity<sup>[40]</sup> of proteins contained in blood serum were responsible for the select enhanced functions of osteoblasts (or bone-forming cells) on nanophase materials. Of first importance, the cumulative adsorption of proteins contained in serum was significantly higher on smaller, nanometer grain-sized ceramics.<sup>[36]</sup> In particular, the interaction of four proteins (fibronectin, vitronectin, laminin, and collagen—proteins all known to enhance osteoblast function)<sup>[36]</sup> increased greatly on nanophase compared with conventional ceramics.<sup>[36]</sup> For example, by just decreasing grain size to below 100 nm, select competitive vitronectin adsorption increased by 10% on alumina formulations. These studies demonstrated that initial enhanced calcium adsorption on nanophase ceramics was a key mechanism for increased protein interactions.<sup>[36]</sup>

Calcium-mediated protein adsorption affected the orientation of proteins adsorbed on nanophase ceramics as well.<sup>[40]</sup> Specifically, a novel adaptation of the standard surface-enhanced Raman scattering (SERS) technique provided evidence of increased unfolding of the aforementioned proteins adsorbed on nanophase compared with conventionally grain-sized ceramics (Fig. 11).<sup>[40]</sup> Unfolding of these proteins promoted the availability of specific cell-adhesive epitopes (such as the amino acid sequence Arg-Gly-Asp) that undoubtedly increased bone cell adhesion and function (this interaction is depicted in Fig. 8); evidence supporting this claim was further provided by these investigators through competitive cell adhesion inhibition studies.<sup>[40]</sup> These studies were the first to demonstrate that by decreasing grain size (or, in effect, decreasing the size of surface features) to below 100 nm (thus becoming closer to the fundamental size of

proteins), interactions of proteins were altered in ways previously unobserved on conventional formulations.

It is interesting to consider what properties of nanophase ceramics manipulated protein adsorption and orientation to benefit new bone formation needed for orthopedic implant applications. Select adsorption of proteins important for bone cell function was enhanced by simply decreasing the grain size of the ceramics into the nanometer regime. Equally as important, the tertiary structure of the proteins (namely, the positioning of the Arg–Gly–Asp amino acid sequence in the interior of some of these proteins)<sup>[57]</sup> was manipulated and partially unfolded to expose cell-adhesive epitopes. Because of these novel observations, the investigators characterized several key material properties of nanophase ceramics to find some insights into these interactions.

One may speculate that increased surface area (up to 30% for alumina)<sup>[35]</sup> of nanophase materials is the only property leading to increased adsorption of proteins. However, although this property certainly holds promise for biofiltration, bioseparation applications, etc., literature reports have normalized increased protein adsorption to the increased surface area observed on nanophase ceramics, and have still found enhanced protein adsorption.<sup>[36]</sup> Thus it is clear that the greater surface area that results from nanostructured surface features compared with conventionally structured surface features is not the only property promoting interactions with proteins.

Increased protein adsorption may be directly related to the reported increased surface wettability of nanophase over conventional ceramics.<sup>[35]</sup> It was previously suspected that nanophase ceramics have much greater surface reactivity because of an increased number of atoms at the surface, greater amounts of grain boundaries at the surface, and higher proportions of edge sites (Fig. 10).<sup>[7]</sup> This was confirmed by studies that provided evidence of aqueous contact angles three times smaller than when alumina grain size was reduced from 167 to 24 nm.<sup>[35]</sup> As previously discussed, because proteins assume a tertiary structure with mostly hydrophilic amino acid residues on the exterior of globular shapes, a material surface with increased wettability (or hydrophilic) properties should increase interactions with hydrophilic regions of proteins to, subsequently, enhance unfolding of that protein to expose interior amino acids important for cell adhesion.

In addition, large topographical differences resulting from grain size as well as pore size differences were found between nanophase and conventional ceramics as expected (Fig. 9).<sup>[35]</sup> Specifically, surface roughness increased by 35–50% on nanophase compared with conventional grain size ceramics.<sup>[35]</sup> These investigators hypothesized that, for the first time, because of

the ability to create surface topographies with features that approximate the size of proteins, extreme control over protein orientation can result. For example, because of protein stereochemical structure and ceramic pore size dimensions (in angstrom regime compared with micron regime for nanophase and conventional ceramics, respectively), many of these nanostructured proteins important for bone cell function adsorbed in preferential orientations to smaller pores sizes in nanophase ceramics.<sup>[36,42]</sup> Some of the larger proteins contained in blood plasma (such as albumin not important for bone cell function) were preferentially sterically excluded from angstrom-sized pores of nanostructured ceramics.<sup>[36,42]</sup> In addition, variations in ceramic surface topography on the same order of magnitude as the size of proteins influenced adsorbed protein orientation, and thus the availability of select amino acid sequences, to promote bone-forming cell function. Because of protein dimension in the nanometer regime, through the use of nanostructured topographies, scientists can now modify a surface to control and manipulate adsorbed protein conformation; this is, most likely, the largest unexplored and promising potential at the intersection of protein interactions and nanophase materials. These studies demonstrate that the reported high surface reactivity nanophase materials have in enhancing catalytic applications can be transferred to benefit applications involving protein interactions.

## CONCLUSION

Nanostructured materials provide alternatives not yet fully explored for controlling interactions with proteins. Because technologies now exist to manipulate materials at the atomic, molecular, and supramolecular levels, surfaces can be designed at a dimension similar to that of proteins—the nanometer level. Moreover, in conjunction with this promise, nanophase materials have special surface properties because of an inherent increased number of atoms at the surface, large surface areas, higher proportions of edge sites, and a greater number of material defects (such as grain boundaries for ceramics) at the surface. When these concepts are fully appreciated and realized, it will be possible to design highly engineered surfaces for improving implantable devices, filtration systems, bioseparations, bioMEMS, etc. Such advances were previously unimaginable with conventional materials. Fundamental knowledge of protein dimension, structure, and organization is essential toward this goal. As the disciplines of protein biology and nanophase material science develop and mature, the design criteria mentioned in this chapter for controlling protein interactions will be expanded and refined. Undoubtedly, nanophase



materials have the potential to become the next generation-of-choice proactive materials for innovative biotechnology and biomedical applications that could have profound impact in many diverse fields that involve interactions with proteins.

## REFERENCES

- Baraton, M.I.; Chen, X.; Gonsalves, K.E. FTIR study of nanostructured alumina nitride powder surface: determination of the acidic/basic sites by CO, CO<sub>2</sub>, and acetic acid adsorptions. *Nanostruct. Mater.* **1997**, *8*, 435.
- Bohn, R.; Haubold, R.; Birringer, R.; Gleiter, H. Nanocrystalline intermetallic compounds—An approach to ductility. *Scr. Metall. Mater.* **1991**, *25*, 811.
- Carry, C.; Mocellin, A. Structural superplasticity in single phase crystalline ceramics. *Ceram. Int.* **1987**, *13* (2), 89–98.
- Catledge, S.; Vohra, Y. Effect of nitrogen addition on the microstructure and mechanical properties of diamond films grown using high-methane concentrations. *J. Appl. Phys.* **1999**, *86* (1), 698–700.
- Ciftcioglu, M.; Mayo, M.J. Processing of Nanocrystalline Ceramics. In *Superplasticity in Metals, Ceramics, and Intermetallics Symposium Proceedings*; Mayo, M.J., Kobayashi, M., Wadsworth, J., Eds.; Materials Research Society: Pittsburgh, 1990; 77–86.
- Cui, Z.; Hahn, H. Tensile deformation of nanostructured TiO<sub>2</sub> at low temperatures. *Nanostruct. Mater.* **1992**, *1*, 419.
- Klabunde, K.J.; Strak, J.; Koper, O.; Mohs, C.; Park, D.; Decker, S.; Jiang, Y.; Lagadic, I.; Zhang, D. Nanocrystals as stoichiometric reagents with unique surface chemistry. *J. Phys. Chem.* **1996**, *100*, 12,141.
- Mayo, M.; Siegel, R.W.; Liao, Y.X.; Nix, W.D. Nanoindentation of nanocrystalline ZnO. *J. Mater. Res.* **1992**, *7*, 973.
- Mayo, M.; Siegel, R.W.; Narayanasamy, A.; Nix, W.D. Mechanical properties of TiO<sub>2</sub> as determined by nanoindentation. *J. Mater. Res.* **1990**, *5*, 1073.
- Nieman, G.W. Processing and Mechanical Behavior of Nanocrystalline Cu, Pd, and Ag. In *Ph.D. Thesis*; Northwestern University, 1991.
- Nieman, G.W.; Weertman, J.R.; Siegel, R.W. Microhardness of nanocrystalline palladium and copper produced by inert gas condensation. *Scr. Metall.* **1989**, *23*, 2013.
- Nieman, G.W.; Weertman, J.R.; Siegel, R.W. Mechanical behavior of nanocrystalline metals. *J. Mater. Res.* **1991**, *6*, 1012.
- Nieman, G.W.; Weertman, J.R.; Siegel, R.W. Mechanical behavior of nanocrystalline Cu and Pd. In *Microcomposites and Nanophase Materials*; Van Aken, D.C., Ed.; TMS: Warrendale, PA, 1991; 15 pp.
- Siegel, R.W. Nanophase materials. In *Encyclopaedia of Applied Physics*; VCH Publishers, Inc.: New York, NY, 1994; 11, 173–199.
- Siegel, R.W. Creating nanophase materials. *Sci. Am.* **1996**, *275*, 42.
- Siegel, R.W.; Fougere, G.E. Mechanical properties of nanophase materials. In *Nanophase Materials: Synthesis–Properties–Applications*; Hadjipanayis, G.C., Siegel, R.W., Eds.; Kluwer: Dordrecht, 1994.
- Siegel, R.W.; Fougere, G.E. Mechanical properties of nanophase metals. *Nanostruct. Mater.* **1995**, *6*, 205.
- Siegel, R.W.; Fougere, G.E. Grain size dependent mechanical properties on nanophase materials. *Mater. Res. Soc. Symp. Proc.* **1995**, *362*, 219.
- Toprani, N.; Catledge, S.; Vohra, Y. Interfacial adhesion and toughness of nanostructured diamond coatings. *J. Mater. Sci.* **2000**, *15* (5), 1052–1055.
- Weertman, J.R.; Farkas, D.; Hemker, K.; Kung, H.; Mayo, M.; Mitra, R.; van Swygenhoven, H. Structure and mechanical behavior of bulk nanocrystalline materials. *MRS Bull.* **1999**, *24* (2), 44–50.
- Wu, S.J.; DeJong, L.C.; Rahaman, M.N. Sintering of nanophase  $\gamma$ -Al<sub>2</sub>O<sub>3</sub> powder. *J. Am. Ceram. Soc.* **1996**, *79*, 2207.
- Barringer, E.A.; Bowen, H.K. Formation, packing, and sintering of monodispersed TiO<sub>2</sub> powders. *Commun. Am. Ceram. Soc.* **1982**, *12*, C199.
- Patrick, G.L. *An Introduction to Medicinal Chemistry*; Oxford University Press: New York, 1995; 15–26.
- Suckling, K.E.; Suckling, C.J. *Biological Chemistry*; Cambridge University Press: New York, 1980.
- Horbett, T.A. Proteins: structure, properties and adsorption to surfaces. In *Biomaterials Science: An Introduction to Materials in Medicine*; Ratner, B.D., Hoffman, A.S., Schoen, A.S., Lemmons, J.E., Eds.; Academic Press: New York, 1996; 133–140.
- Eisenberg, D. Three-dimensional structure of membrane and surface proteins. *Annu. Rev. Biochem.* **1984**, *53*, 595–623.
- Bull, H.B.; Breese, K. Surface tension of amino acid solutions: a hydrophobicity scale of the amino acid residues. *Arch. Biochem. Biophys.* **1974**, *161*, 665–670.
- Peters, T. Serum Albumin. In *Advances in Protein Chemistry*; Anfinsen, C.B., Edsall, J.T., Richards, F.M., Eds.; Academic Press: New York, 1985; Vol. 37, 161–245.
- Stryer, L. *Biochemistry*, 2nd Ed.; W. H. Freeman: San Francisco, 1981.
- Loeb, W.F.; Mackey, W.F. A “cuvette method” for the determination of plasma fibrinogen. *Bull. Am. Soc. Vet. Clin. Pathol.* **1972**, *1*, 5–8.
- Norde, W.; Lyklema, J. Why proteins prefer interfaces. *J. Biomater. Sci., Polym. Ed.* **1991**, *2*, 183–202.
- Yutani, K.; Ogasahara, K.; Tsujita, T.; Sugino, Y. Dependence of conformational stability on hydrophobicity of the amino acid residue in a series of variant proteins substituted at a unique position of tryptophan synthase alpha subunit. *Proc. Natl. Acad. Sci. U.S.A.* **1987**, *84*, 4441–4444.
- Webster, T.J.; Siegel, R.W.; Bizios, R. An in vitro evaluation of nanophase alumina for orthopaedic/dental applications. In *Bioceramics 11: 11th International Symposium on Ceramics in Medicine*; LeGeros, R.Z., LeGeros, J.P., Eds.; 1998; 273 pp.
- Webster, T.J.; Siegel, R.W.; Bizios, R. Design and evaluation of nanophase alumina for orthopaedic/dental applications. *Nanostruct. Mater.* **1999**, *12*, 983.

35. Webster, T.J.; Siegel, R.W.; Bizios, R. Osteoblast adhesion on nanophase ceramics. *Biomaterials* **1999**, *20*, 1221.
36. Webster, T.J.; Ergun, C.; Doremus, R.H.; Siegel, R.W.; Bizios, R. Specific proteins mediate enhanced osteoblast adhesion on nanophase ceramics. *J. Biomed. Mater. Res.* **2000**, *51* (3), 475.
37. Webster, T.J.; Siegel, R.W.; Bizios, R. Enhanced functions of osteoblasts on nanophase ceramics. *Biomaterials* **2000**, *21*, 1803.
38. Webster, T.J.; Siegel, R.W.; Bizios, R. Enhanced Surface and Mechanical Properties of Nanophase Ceramics for Increased Orthopaedic/Dental Implant Efficacy. In *Bioceramics 13: 13th International Symposium on Ceramics in Medicine Conference Proceedings*; Giannini, S., Moroni, A., Eds.; 2000; 321 pp.
39. Webster, T.J. Nanophase ceramics: the future orthopedic and dental implant material. In *Advances in Chemical Engineering*; Ying, J.Y., Ed.; Academic Press: New York, 2001; *27*, 125–166.
40. Webster, T.J.; Schadler, L.S.; Siegel, R.W.; Bizios, R. Mechanisms of enhanced osteoblast adhesion on nanophase alumina involve vitronectin. *Tissue Eng.* **2001**, *7* (3), 291–301.
41. Webster, T.J.; Ergun, C.; Doremus, R.H.; Siegel, R.W.; Bizios, R. Enhanced functions of osteoclast-like cells on nanophase ceramics. *Biomaterials* **2001**, *22* (11), 1327–1333.
42. Webster, T.J.; Siegel, R.W.; Bizios, R. Nanoceramic surface roughness enhances osteoblast and osteoclast functions for improved orthopaedic/dental implant efficacy. *Scr. Mater.* **2001**, *44*, 1639–1642.
43. Horbett, T.A. Principles underlying the role of adsorbed plasma proteins in blood interactions with foreign materials. *Cardiovasc. Pathol.* **1993**, *2*, 137S–148S.
44. Horbett, T.A. Techniques for protein adsorption studies. In *Techniques of Biocompatibility Testing*; Williams, D.F., Ed.; CRC Press: Boca Raton, FL, 1986; 183–214.
45. Horbett, T.A.; Brash, J.L. Proteins at interfaces: current issues and future prospects. In *Proteins at Interfaces: Physicochemical and Biochemical Studies*; Horbett, T.A., Brash, J.L., Eds.; American Chemical Society: Washington, DC, 1987; 343, 1–33.
46. Horbett, T.A. Protein adsorption on biomaterials. In *Biomaterials: Interfacial Phenomena and Applications*; Cooper, S.L., Peppas, N.A., Eds.; American Chemical Society: Washington, DC, 1982; 199, 233–244.
47. Andrade, J.D. Principles of protein adsorption. In *Surface and Interfacial Aspects of Biomedical Polymers*; Andrade, J., Ed.; Plenum Publ.: New York, 1985; 1–80.
48. Schakenraad, J.M. Cell: their surfaces and interactions with materials. In *Biomaterials Science: An Introduction to Materials in Medicine*; Ratner, B.D., Hoffman, A.S., Schoen, A.S., Lemmons, J.E., Eds.; Academic Press: New York, 1996; 141–147.
49. Sinha, R.K.; Tuan, R.S. Regulation of human osteoblast integrin expression by orthopedic implant materials. *Bone* **1996**, *18*, 451–457.
50. Brunette, P.M. The effect of surface topography of cell migration and adhesion. In *Surface Characterization of Biomaterials: Progress in Biomedical Engineering*; Ratner, B.D., Ed.; Elsevier: New York, 1988; Vol. 6, 203–217.
51. Davies, J.E. The importance and measurement of surface charge species in cell behavior at the biomaterial interface. In *Surface Characterization of Biomaterials: Progress in Biomedical Engineering*; Ratner, B.D., Ed.; Elsevier: New York, 1988; 6, 219–234.
52. Luck, M.; Paulke, B.R.; Schroder, W.; Blunk, T.; Muller, R.H. Analysis of plasma protein adsorption on polymeric nanoparticles with different surface characteristics. *J. Biomed. Mater. Res.* **1998**, *39*, 478–485.
53. Curtis, A.; Wilkinson, C. Review: topographical control of cells. *Biomaterials* **1997**, *18* (24), 1573–1583.
54. Degasne, I.; Basle, M.F.; Demais, V.; Hure, G.; Lesourd, M.; Grolleau, B.; Mercier, L.; Chappards, D. Effects of roughness fibronectin and vitronectin on attachment, spreading, and proliferation of human osteoblast-like cells (Saos-2) on titanium surfaces. *Calcif. Tissue Int.* **1999**, *64* (6), 499–507.
55. Dalton, B.A.; McFarland, C.D.; Gengenbach, T.R.; Griesser, H.J.; Steele, J.G. Polymer surface chemistry and bone cell migration. *J. Biomater. Sci., Polym. Ed.* **1995**, *9* (8), 781–799.
56. Lopes, M.A.; Monteiro, F.J.; Santos, J.D.; Serro, A.P.; Saramago, B. Hydrophobicity, surface tension, and zeta potential measurements of glass-reinforced hydroxyapatite composites. *J. Biomed. Mater. Res.* **1999**, *45* (4), 370–375.
57. Ayad, S.; Boot-Handford, R.; Humphries, M.J.; Kadler, K.E.; Shuttleworth, A. *The Extracellular Matrix Factsbook*; Academic Press: San Diego, CA, 1994.

# Quantum Dot Arrays: Electromagnetic Properties

Sergey A. Maksimenko

Gregory Ya. Slepyan

*Institute of Nuclear Problems, Belarus State University, Minsk, Belarus*

## INTRODUCTION

A fundamental breakthrough in semiconductor device physics is connected with the recent progress in the synthesis of sheets of nanoscale narrow-gap insertions in a host semiconductor—quantum dots (QDs). The key peculiarity of QDs is related to the spatial confinement of charge carriers and their discrete energy levels determined by QD size and shape. The shape is dictated by the growth kinetics and the parameters of the materials governing the thermodynamics of growth. The large body of recent results on the physical properties of QDs and their utilization for the QD laser design has been discussed in Ref.<sup>[1]</sup>.

Apart from charge carrier confinement, there exists a class of effects governed by the intrinsic spatial inhomogeneity of the QD heterostructures. Transparent and dissipative heterogeneous media with small inclusions of one material into another material, conventionally referred to as composite materials, exhibit, in general, new mechanical, electronic, as well as optical properties, which are not inherent to each individual component.<sup>[2]</sup> In the case of QD heterostructures, a conventional picture is modified because of specific properties of excitons, coupled electron–hole states, which define the QD response. First, excitonic composite is constituted by resonant particles and, consequently, is characterized by resonant response; moreover, inverse population is possible owing to the discrete energy spectrum of excitons. Thus a QD-based composite is a resonant active system. Another specific property of QD composites appears owing to the quantum nature of excitons: the exciton Bohr radius  $a_B$  can either exceed the QD linear extension (strong confinement regime), or be much less (weak confinement regime). In the latter case, often realized in experiments, the QD electromagnetic response becomes nonlocal<sup>[3]</sup> (i.e., constitutive relations for polarization of the QD medium take the form of integral operators). Electromagnetic properties of QD-based composites are the focus of the present paper. Consideration is based on earlier published articles of various authors.<sup>[4–10]</sup>

## BASIC RELATIONS

### Effective Permittivity Tensor for Three-Dimensional Structures

Electromagnetic properties of composites are usually modelled in the framework of the effective medium approach,<sup>[2]</sup> which implies electromagnetic field averaging over material inhomogeneities. Thus a homogeneous medium with effective constitutive parameters (ECPs), such as conductivity, susceptibility, and permittivity, instead of a composite, is being considered. The effective parameters are expressed in terms of the generic and the geometrical parameters of the inclusions and the host medium. The general approach for estimating the effective parameters of a composite material is as follows: First, the field scattered by a single inclusion in the host medium is found; then, the scattering contributions from all inclusions are summed and averaged over a vanishingly small region. For this approach to hold, all inclusions must be electrically small (i.e., their linear size must be small compared with the wavelength). Quantum dot-based structures completely satisfy that condition in the visible range.

There are a large number of different modifications of the effective medium theory. Among them, we choose the Maxwell Garnett approach as it is based on rigorous solutions of the integral equations of macroscopic electrodynamics<sup>[11]</sup> for composites with small volume fractions of inclusions ( $f_V < 0.4$ – $0.5$ ) (i.e., a weak modification of the electronic spectrum and the gain of QD ensemble are assumed as compared with that of individual QDs). In the framework of the Maxwell Garnett approach, rigorous derivation of the effective permittivity tensor has been first presented in Refs.<sup>[12]</sup> and<sup>[13]</sup> (also Ref.<sup>[2]</sup>) where it has been shown that a composite medium comprising a regular ensemble of uniform-sized, electrically small, dielectric inclusions dispersed in a host dielectric material is characterized by the effective permittivity tensor as follows:

$$\hat{\epsilon}(\omega) = \epsilon_h + f_V \epsilon_h \hat{\alpha}(\omega) [1 + f_V \hat{\delta} \hat{\alpha}(\omega)]^{-1} \quad (1)$$

where  $\hat{\alpha}(\omega)$  is the polarizability tensor of a single QD and  $\hat{\delta}$  is the lattice tensor completely determined by the array

geometry. Furthermore, the dielectric constant of the host material  $\epsilon_h$  is assumed to be real, frequency-independent, and equal to the permittivity of the QD material far away from the exciton resonance.

Eq. (1) states that the QD ensemble comprises an optically anisotropic medium even if both the QD and host materials are isotropic. Thus we predict electromagnetic anisotropy of the gain in QD arrays because of the diffraction of the electromagnetic field by inclusions. The diffraction manifests itself in two ways. First, the effective permittivity tensor depends on the array geometry involving the electromagnetic interaction between inclusions. Second, the polarizability of a single QD depends on its shape because of the depolarizing field. Assuming the linear size of the lattice elementary cell to be much less than the wavelength, it has been shown that components of the lattice tensor are given by integrals as follows:

$$\begin{aligned}\delta_{ij} &= \frac{1}{4\pi} \int_{\Omega} \frac{r_i r_j}{r^5} d^3 r \text{ if } i \neq j \text{ and} \\ \delta_{ii} &= \frac{1}{4\pi} \int_{\Omega} \frac{3r_i^2 - r^2}{r^5} d^3 r\end{aligned}\quad (2)$$

where  $\Omega$  is the elementary cell volume,  $r$  is the radius vector of a point inside the elementary cell,  $r = |r|$ ; indices stand for Cartesian components. Note that lattice tensor (2) is found without any reference to specific properties of QDs as quantum-mechanical objects.

### Effective Boundary Conditions for Planar Structures

In many cases, a planar array of QDs with intrinsic two-dimensional (2-D) periodicity of characteristic period much less than the optical wavelength can be treated as a more adequate and realistic model.<sup>[1]</sup> Below we present a general method for the evaluation of the electromagnetic response of planar arrays of QDs. This method, conventionally referred to as the effective boundary condition (EBC) method, has been originally developed for microwaves and antenna theory,<sup>[14–16]</sup> and has found a wide application in these fields. Similar approaches have also been developed in acoustics, hydrodynamics, and elasticity theory. Recently, the EBC method has been extended to low-dimensional nanostructures, such as quantum wells,<sup>[17,18]</sup> carbon nanotubes,<sup>[19,20]</sup> and semicontinuous metal films.<sup>[21]</sup> The basic idea of the EBC method is that a smooth homogeneous surface is considered instead of the initial structure, and appropriate EBCs for the electromagnetic field are stated for this surface. These conditions are chosen in such a way that the spatial structures of the electromagnetic field, because of an effective current induced on the homogeneous

surface, and the electromagnetic field of the real current in the initial structure turn out to be identical at some distance away from the surface. Material characteristics of the structure as well as its geometrical parameters are included in coefficients of EBCs. In essence, the EBC method is a modification of the effective medium theory as applied to 2-D confined structures. A detail description of the EBC method as applied to planar QD structures has been presented in Ref.<sup>[7]</sup>

Effective boundary conditions, in the form of two-sided impedance boundary conditions, were first formulated for the linear electrodynamics of single-shell and multishell carbon nanotubes.<sup>[19]</sup> Using this analysis, the EBC method has been extended to planar QD structures and corresponding EBCs have been derived.<sup>[7]</sup>

$$\begin{aligned}\mathbf{n} \times \mathbf{n} \times (\mathbf{H}^I - \mathbf{H}^{II}) &= -\frac{2\pi}{c} \mathbf{n} \times \hat{\sigma}(\mathbf{E}^I + \mathbf{E}^{II}) \\ \mathbf{n} \times (\mathbf{E}^I - \mathbf{E}^{II}) &= -\xi \mathbf{n} \times \nabla[\mathbf{n} \cdot (\mathbf{E}^I + \mathbf{E}^{II})]\end{aligned}\quad (3)$$

where  $\mathbf{n} \parallel \mathbf{e}_z$  is the normal to the QD layer, and  $\hat{\sigma}$  and  $\xi$  are coefficients completely determined by the shape and size of QDs. Nonzero components of the tensor  $\hat{\sigma}$ ,  $\sigma_{ij}$  ( $i, j = x, y$ ), constitute  $2 \times 2$  surface conductivity tensor  $\hat{\sigma}_{\parallel}$ . For quadratic lattice with period  $d$ , it can easily be found that:

$$\hat{\sigma}_{\parallel} = i \frac{\epsilon_h \omega}{d^2} \left[ \hat{\mathbf{I}}_{\parallel} + \frac{\delta_x}{d^2} \hat{\alpha}_{\parallel} \right]^{-1}, \quad \xi = \frac{2\pi \alpha_{zz}}{d^2 + \delta_z \alpha_{zz}} \quad (4)$$

Here  $\hat{\mathbf{I}}_{\parallel}$  is the  $2 \times 2$  unit tensor, and  $\hat{\alpha}_{\parallel}$  is given by the in-plane components  $\alpha_{ij}$  ( $i, j = x, y$ ) of the QD polarizability tensor. Coefficients  $\delta_{x,z}$  are derived from Eq. (2) for planar quadratic elementary cell.<sup>[7]</sup>

Eq. (3) constitutes the complete system of EBCs for electromagnetic field in low-dimensional nanostructures. They have been obtained in an ordinary way, by the averaging of a microscopic field over a physically infinitesimal volume. The technique of macroscopic averaging is similar to that which introduces the constitutive parameters for bulk media, but differs in that the averaging occurs in boundary conditions rather than in field equations. Correspondingly, the averaging was carried out over the 2-D surface but not over the three-dimensional (3-D) spatial element. Thus in electrodynamics of low-dimensional structures, EBCs play the same role as constitutive relations in the electrodynamics of bulk media. A theory is applicable in both strong and weak confinement regimes. Although EBCs have been derived for 2-D periodical structures with quadratic lattices, they keep validity for the arbitrary configuration of elementary cell and for planar layers with random distributions

of QDs. The derived EBCs turn out to be analogous to well-known boundary conditions for quantum wells (QWs)<sup>[17]</sup> if spatial dispersion in the latter can be neglected (i.e., in the limit of infinitely large exciton mass). Thus a planar layer comprising a 2-D array of QDs can be treated as an effective QW.

## POLARIZABILITY OF A SINGLE QUANTUM DOT

For practical utilization of the derived ECPs (Eq. (1)) or EBCs (Eq. (3)), the polarizability tensor of an isolated QD requires to be known. For the simplest configuration of QDs (spheres, disks), this tensor can be found analytically whereas direct numerical simulation is required for more complicated configurations. A conventional phenomenological model of gain in a QD is based on a semiclassical theory of two-level systems, which gives the equation of motion for the mean polarization  $\mathbf{P}$  caused by transitions between levels:<sup>[22]</sup>

$$\left[ \frac{\partial^2}{\partial t^2} + \frac{2}{\tau} \frac{\partial}{\partial t} + \omega_0^2 \right] \mathbf{P} = -\frac{\omega_0}{2\pi\epsilon_h} \hat{\mathbf{g}}_0 \mathbf{E}_L \quad (5)$$

Here  $\omega_0$  is the resonant frequency of the transition,  $\tau$  is the exciton dephasing time, and  $\mathbf{E}_L$  is the macroscopic local field inside the QD. The tensor  $\hat{\mathbf{g}}_0$  is a phenomenological parameter expressed in terms of the QD dipole moment  $\boldsymbol{\mu}$  diadic:

$$\hat{\mathbf{g}}_0 = \mp \frac{4\pi}{\hbar V} \boldsymbol{\mu} \boldsymbol{\mu}$$

Here,  $V$  is the QD volume, and upper and bottom signs correspond to ground and excited states, respectively, so that  $\|\hat{\mathbf{g}}_0\| > 0$  in an inverted medium. If QD comprises an isotropic material, orientational averaging leads to the change  $\boldsymbol{\mu} \boldsymbol{\mu} \rightarrow |\boldsymbol{\mu}_0|^2 \hat{\mathbf{I}}/3$ , where  $\boldsymbol{\mu}_0$  is the matrix element of the dipole moment of the corresponding bulk sample.

For time-harmonic fields, the solution of Eq. (5) in the vicinity of the resonance gives the well-known Lorentz contribution to medium polarizability:

$$\hat{\alpha}(\omega) = \frac{1}{\epsilon_h} \frac{\hat{\mathbf{g}}_0}{\omega - \omega_0 + i/\tau} \quad (6)$$

This dependence on the isotropic  $\hat{\mathbf{g}}_0$  is commonly used as a phenomenological model of the dispersion and the gain of a single QD. However, relation (6) assumes an infinite, isotropic, homogeneous medium and can serve only as a rough approximation to the case under consideration: the polarizability of a single QD turns out to be distinct from that given by Eq. (6). Indeed, the

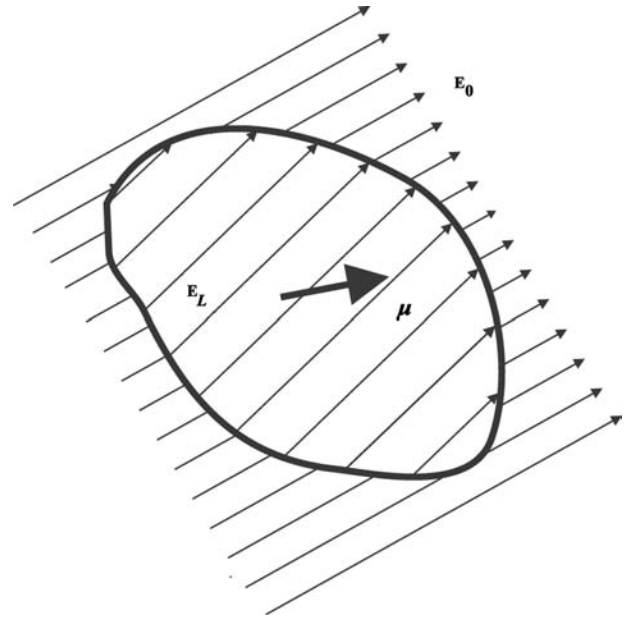


**Fig. 1** Schematic picture of correlation between acting and local fields in electrically small scatterer. The local field is assumed to be homogeneous.

local field  $\mathbf{E}_L$  inside the QD is different from the external acting field  $\mathbf{E}_0$  (Fig. 1). The depolarization field determines this difference by:<sup>[23]</sup>

$$\mathbf{E}_L = \mathbf{E}_0 - 4\pi \hat{\mathbf{N}} \mathbf{P} \quad (7)$$

where  $\hat{\mathbf{N}}$  is the depolarization tensor. This tensor is symmetrical<sup>[24]</sup> (also Ref.<sup>[10]</sup>) and depends only on the shape of the scattering object:

$$N_{\alpha\beta} = -\frac{1}{4\pi V} \int_V \int_V \frac{\partial^2}{\partial r_\alpha \partial r_\beta} \frac{1}{|\mathbf{r} - \mathbf{r}'|} d^3\mathbf{r} d^3\mathbf{r}'$$

Here  $r_{\alpha,\beta} = x, y, z$ . For a sphere,  $\hat{\mathbf{N}} = \hat{\mathbf{I}}/3$ ; for an ellipsoid, this tensor is diagonal on a basis related to the ellipsoid's axes.<sup>[23]</sup> For more complex objects, its elements can be found only numerically.

Substitution of Eq. (7) into Eq. (5) results in a set of equations for three coupled oscillators, which describe the tensorial polarizability of QD in the vicinity of resonance:

$$\hat{\alpha}(\omega) = \frac{1}{\epsilon_h} \frac{1}{(\omega - \omega_0 + i/\tau) \hat{\mathbf{I}} + \hat{\mathbf{g}}_0 \hat{\mathbf{N}}/\epsilon_h} \hat{\mathbf{g}}_0 \quad (8)$$

In this equation, we neglect the linewidth change provided by depolarization.<sup>[5]</sup> Thus one can conclude that the QD's shape reflects itself as a fine structure of the resonance, which itself is a superposition of three bands with frequencies  $\omega_0 - \Delta\omega_j$ , where  $\Delta\omega_j$  are the eigenvalues of the inner tensor product  $\hat{\mathbf{g}}_0 \hat{\mathbf{N}}/\epsilon_h$ . Note

that this diffraction-induced shift is analogous to that which occurs in ferromagnetic resonance, where the resonance frequencies of small-sized grains and infinite continuous media are different because of the effects of demagnetization.<sup>[23]</sup> Depolarization shift has been ignored in Ref.<sup>[25]</sup> under the construction of the electromagnetic response theory of QD arrays. For spherical isotropic QDs, the tensors  $\hat{\mathbf{N}}$  and  $\hat{\mathbf{g}}_0$  are isotropic and the fine structure manifests itself as a polarization-independent shift of the resonance line.<sup>[26,27]</sup> Let us estimate the shift using well-known data for QD characteristics and relations for the exciton radiative lifetime in a medium  $\hbar/\tau_{\text{rad}} = 4k_1^3|\mu_0|^2/3$ , where  $k_1 = \sqrt{\epsilon_h}\omega_0/c$ . Then, the depolarization shift can be written by:

$$\Delta\omega = \pm \frac{4\pi}{9\hbar V} |\mu_0|^2 = \pm \frac{1}{\tau_{\text{rad}}} \frac{\pi}{Vk_1^3} \quad (9)$$

For GaAs spherical QDs with radius in the range  $R = 2\text{--}4$  nm, dielectric constant  $\epsilon_h = 12.25$ , and radiative lifetime  $\tau_{\text{rad}} \cong 1$  nsec,<sup>[1]</sup> at the wavelength  $\lambda = 1.3$   $\mu\text{m}$ , formula (9) gives  $\hbar\Delta\omega \sim 10\text{--}1$  meV, respectively. This estimate correlates well with the theoretical predictions given in Refs.<sup>[4,5,28]</sup> Note that the Bohr radius for such QDs is about 10 nm,<sup>[1]</sup> so that the strong confinement approximation used above is valid. For experimental detection of the predicted fine structure, the value  $\Delta\omega$  must exceed the linewidth provided by radiative decay and homogeneous broadening because of dephasing. From Eq. (9), it follows that the inequality  $\Delta\omega \gg 1/\tau_{\text{rad}}$  holds true for any realistic arbitrary-shaped QDs. Analysis shows that the dominant contribution to the homogeneous broadening gives exciton–phonon interactions. Recent low-temperature ( $T = 20\text{--}40$  K) measurements<sup>[29–31]</sup> give the homogeneous linewidth  $\sim 1\text{--}20$   $\mu\text{eV}$ . Analogous estimates follow from calculations presented in Ref.<sup>[32]</sup> at  $T = 77$  K. Thus at low temperatures, the predicted value of the shift turns out to be sufficiently large to be measured. At room temperature, the homogeneous linewidth grows up to  $\sim 0.2\text{--}1$  meV.<sup>[1,31,32]</sup> This magnitude is comparable to the depolarization shift. However, even in that case, local field effects are of importance for adequate prediction of spectral line shape. Note that the optical absorption and gain of an isolated QD could be distinguished owing to the depolarization shift—blue in the former case and red in the latter one.<sup>[27]</sup>

### Physical Interpretation

Physical interpretation of the depolarization field effect can be given by an analogy with the  $\mathbf{k} \cdot \mathbf{p}$  theory of bulk crystals<sup>[33]</sup> utilizing the concept of electron–hole

effective mass. For spherical QD, using the standard expression for  $\omega_0$  and the given expression for  $\Delta\omega$ , we obtain:

$$\hbar(\omega_0 + \Delta\omega) = \epsilon_g + \frac{\hbar^2\kappa_{nl}^2}{2R^2M} \pm \frac{|\mu|^2}{R^3} \quad (10)$$

where  $M$  is the mass of electron–hole pair in QD,  $\epsilon_g$  is the width of the forbidden bandgap,  $\kappa_{nl}$  is the  $n$ th root of the Bessel function  $J_{l+1/2}(\cdot)$ , and indices  $n$  and  $l$  define the working mode in the oscillator spectrum. The third term in the right-hand part of this equation describes the depolarization field contribution. The right-hand part of the equation can be rewritten as:

$$\epsilon_g + \hbar^2\kappa_{nl}^2/2R^2M_{\text{eff}}$$

with  $M_{\text{eff}}$  given by:

$$M_{\text{eff}} = M \left[ 1 \pm \frac{|\mu|^2 M}{\hbar^2\kappa_{nl}^2 R} \right]^{-1}$$

The quantity  $M_{\text{eff}}$  can be interpreted as effective mass of the electron–hole pair in the QD. Thus electromagnetic effects at the QD boundary (QD depolarization) change the exciton effective mass. Analogous consideration for the case of asymmetrically shaped QDs leads to the tensorial effective mass, which gives rise to the polarization-dependent splitting of the gain band.<sup>[4,5]</sup>

### The Role of Nonlocality

In the weak confinement regime, when the exciton Bohr radius is much less than the QD linear extension, the QD electromagnetic response becomes nonlocal: The constitutive relation for medium polarization takes the form of the integral operator as follows:<sup>[34]</sup>

$$\mathbf{P}(\mathbf{r}) = \frac{DF(\mathbf{r})}{\omega - \omega_0 + i/\tau} \Lambda \quad (11)$$

where

$$\Lambda = \int_V F(\mathbf{r}') \mathbf{E}_L(\mathbf{r}') d^3\mathbf{r}', \quad D = -2|\mu|^2\Phi^2(0)/\hbar \quad (12)$$

The function  $F(\mathbf{r})$  is the envelope function of the exciton ground state whereas the function  $\Phi(r) = \exp(-r/a_B)/\sqrt{\pi a_B^3}$ <sup>[35]</sup> describes the electron–hole relative motion. Inside, QD retardation can be neglected and thus local and acting fields are coupled by:

$$\mathbf{E}_L(\mathbf{r}) = \mathbf{E}_0(\mathbf{r}) + \nabla \nabla \cdot \int_V \frac{\mathbf{P}(\mathbf{r}')}{|\mathbf{r} - \mathbf{r}'|} d^3\mathbf{r}' \quad (13)$$



Assuming polarization to be constant over the QD volume, Eq. (13) is reduced to relation (7). Eq. (13) allows us to find vector  $\Lambda$  by omitting the procedure of evaluation of the local electromagnetic field  $\mathbf{E}_L(\mathbf{r})$ ; to do this, let us multiply this equation by the function  $F(\mathbf{r})$  and integrate it over the QD volume. As a result, we obtain:

$$\Lambda \approx F_0 \mathbf{E}_0 + \frac{\tilde{\mathbf{g}}_0}{\omega - \omega_0 + i/\tau} \hat{\mathbf{N}}' \Lambda$$

where

$$F_0 = \int_V F(\mathbf{r}') d^3 \mathbf{r}', \quad \tilde{\mathbf{g}}_0 = \frac{4\pi\epsilon_h}{V} F_0^2 D \quad (14)$$

and the 3-D tensor  $\hat{\mathbf{N}}'$  is given by its components:

$$N'_{\alpha\beta} = -\frac{V}{4\pi F_0^2} \int_V \int_V F(\mathbf{r}) F(\mathbf{r}') \frac{\partial^2}{\partial r_\alpha \partial r_\beta} \times \frac{1}{|\mathbf{r} - \mathbf{r}'|} d^3 \mathbf{r} d^3 \mathbf{r}' \quad (15)$$

In the far zone, the electromagnetic field scattered by QD is characterized by the Hertz potential:

$$\Pi^e = \frac{e^{ik_1 r}}{r} \int_V \mathbf{P}(\mathbf{r}') d^3 \mathbf{r}' = \frac{e^{ik_1 r}}{r} D F_0 \Lambda$$

Substituting the above relation for  $\Lambda$  into this formula and taking into account the relation:<sup>[23]</sup>

$$\Pi^e = \frac{V}{4\pi r} e^{ik_1 r} \hat{\alpha} \mathbf{E}_0$$

we come to Eq. (8) for the polarizability tensor of an isolated QD with the change  $\hat{\mathbf{g}}_0 \rightarrow \tilde{\mathbf{g}}_0 \hat{\mathbf{I}}$  and  $\hat{\mathbf{N}} \rightarrow \hat{\mathbf{N}}'$ . Thus the special law of nonlocality (Eq. (11)) inherent to an isolated QD admits the description of the electromagnetic field scattering by the QD using the polarizability tensor independent of the incident field structure. In other words, the nonlocality changes the values of the polarizability tensor components but does not change the general representation of the scattering operators compared with the strong confinement regime. The above result admits extension of the Maxwell Garnett approach to 3-D composites constituted by QDs in weak confinement regimes.

Let us estimate depolarization shift in the weak confinement regime for a spherical QD of the radius  $R$ . Exciton wavefunction for an isolated spherical QD is as follows (e.g., Ref.<sup>[26]</sup>):

$$F(r) \equiv F_{nlm} = C_{nl} Y_{lm}(\vartheta, \varphi) J_{l+1/2}(\kappa_{nl} \rho / R) / \sqrt{\rho}$$

where  $Y_{lm}(\theta, \varphi)$  is the spherical harmonics;  $J_{l+1/2}(x)$  is the Bessel function;  $\kappa_{nl}$  is its  $n$ th root;  $\rho$ ,  $\theta$ , and  $\varphi$  are

the spherical coordinates; and indices  $n$  and  $l$  define the working mode in the oscillator spectrum. Coefficient  $C_{nl} = \sqrt{2} [R J_{l+3/2}(\kappa_{nl})]^{-1}$  provides orthonormalization of functions  $F_{nlm}$ . Furthermore, we restrict ourselves to the case  $l = m = 0$ . By integrating Eqs. (14) and (15), we obtain  $F_0^2 = 32\pi R^3 / \kappa_{n0}^2$ ,  $N_{xx} = N_{yy} = N_{zz} = \kappa_{n0}^2 / 72$ . This allows us to evaluate the depolarization shift of the exciton resonance in the weak confinement regime:

$$\Delta\omega = \pm \frac{4}{3\tau_{\text{rad}}} \frac{\pi}{V k_1^3} \left( \frac{R}{a_B} \right)^3 \quad (16)$$

This shift is different from that given by Eq. (9) for spherical QDs in the strong confinement regime. Because  $V \sim R^3$ , formula (16) states the independence of the depolarization shift on the QD radius in the weak confinement regime. Choosing excitonic modes with another set of numbers  $n, l, m$ , we obviously obtain another magnitude of components  $\hat{\mathbf{N}}'$  and, consequently, another magnitude of the polarizability tensor  $\hat{\alpha}$  (Eq. 8). Thus we come to a peculiar property of the weak confinement regime: Depolarization depends on the excitonic mode number. This property follows from the nonlocality of the exciton polarization. Unlike that, in the strong confinement regime, the depolarization tensor  $\hat{\mathbf{N}}$  is completely determined by the QD geometry.

## BIREFRINGENCE IN QUANTUM DOT ARRAYS

In this section, the general consideration developed above applies to the tetragonal lattice composed of certainly shaped identical QDs. The tetragonal lattice serves as a geometrical model for an ensemble of separated QDs vertically stacked with finite period.<sup>[1]</sup> Let QD be a spheroid with the axis of symmetry directed along the lattice vector  $\mathbf{e}_z$  (Fig. 2). This model admits analytical treatment in the framework of the effective medium theory presented above. Indeed, for the chosen QD shape and the lattice geometry, the depolarization tensor  $\hat{\mathbf{N}}$  and the lattice tensor  $\hat{\delta}$  turn out to be diagonal in the Cartesian basis depicted in Fig. 2,<sup>[13]</sup> and eigenvalues of these tensors corresponding to the basis vectors  $\mathbf{e}_x$  and  $\mathbf{e}_y$  are degenerated. Furthermore, the tensor  $\hat{\mathbf{g}}_0$  must also show the same properties in these coordinates by reasoning of symmetry. In such a situation, the effective permittivity tensor  $\hat{\epsilon}(\omega)$  (Eq. 1) of a composite can be expressed in terms of Cartesian basis diadics by:

$$\hat{\epsilon}(\omega) = \epsilon_H (\mathbf{e}_x \mathbf{e}_x + \mathbf{e}_y \mathbf{e}_y) + \epsilon_E \mathbf{e}_z \mathbf{e}_z \quad (17)$$

where

$$\epsilon_\sigma(\omega) = \epsilon_h + \frac{f_V \alpha_\sigma(\omega)}{1 + f_V \delta_\sigma \alpha_\sigma(\omega)} \quad (18)$$

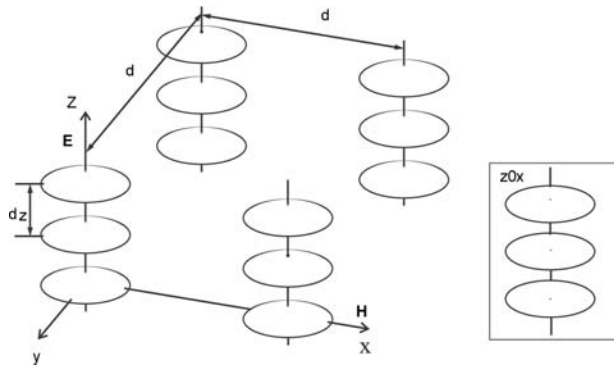


**Fig. 2** Array of vertically stacked disklike QDs arranged on a tetragonal lattice.

and  $\sigma = E, H$  refers to light polarized along ( $E$ -polarization) or normal ( $H$ -polarization) to the  $z$ -axis. The polarizability components  $\alpha_\sigma$  follow from Eq. (8) and have the form:

$$\alpha_\sigma(\omega) = \frac{1/\varepsilon_h}{\omega - (\omega_0 - g_0^\sigma N_\sigma / \varepsilon_h) + i/\tau} \quad (19)$$

In accordance with Ref.<sup>[23]</sup>, for spheroid, the depolarization factors  $N_\sigma$  are as follows:

$$\begin{aligned} N_E &= \frac{e^2 + 1}{e^3} (e - \arctan e), \\ N_H &= \frac{1}{2} (1 - N_E) \end{aligned} \quad (20)$$

where  $e = [a^2/b^2 - 1]^{1/2}$  is the spheroid eccentricity, and  $a$  and  $b$  are the spheroid semi-axes in the  $xy$ -plane and the  $z$ -direction, respectively. These formulae hold true for both disklike ( $a > b$ ) and cigarlike ( $a < b$ ) spheroids. Infinite stretching of the spheroids ( $a/b \rightarrow 0$ ) results in  $N_E \rightarrow 0$  and  $N_H \rightarrow 1/2$ , and Eq. (19) reproduces the polarizabilities of cylinders (e.g., Ref.<sup>[4]</sup>). The geometrical coefficients  $\delta_\sigma$  for a tetragonal lattice have been derived in Ref.<sup>[13]</sup> (also Refs.<sup>[4]</sup> and<sup>[5]</sup>):

$$\begin{aligned} \delta_E &= \frac{1}{4\pi} \left[ \left( 18 - \frac{10}{\beta^2} \right) \arctan \frac{Q}{\beta^2} + 30 \frac{1 - \beta^2}{\beta^4} \right. \\ &\quad \left. \times \left( 2 \arctan Q - \ln \frac{1 + Q}{1 - Q} \right) \right] \\ \delta_H &= \frac{1}{4\pi} \left[ \left( 18 + \frac{20}{\beta^2} - \frac{30}{\beta^4} \right) \arctan Q \right. \\ &\quad \left. + 15 \frac{1 - \beta^2}{\beta^4} \ln \frac{1 + Q}{1 - Q} \right] \end{aligned} \quad (21)$$

where  $\beta = d_z/d$  is the ratio of lattice periods in the  $z$ -direction and in the  $x$ -direction or  $y$ -direction,  $Q = \beta/\sqrt{2 + \beta^2}$ . The above expressions are not valid for  $\beta \ll 1$  or  $\beta \gg 1$ . For a cubic lattice,  $\beta = 1$  and the electromagnetic interaction of QDs

becomes isotropic:  $\delta_E = \delta_H = 1/3$ . Thus for the chosen QD shape and array configuration, we have found the geometrical coefficients  $N_\sigma, \delta_\sigma$  needed for the evaluation of the array effective dielectric function. These two coefficients correspond to two different mechanisms responsible for the modification of the gain in the array. The first mechanism is related to diffraction at individual QDs. Although QDs are assumed to be electrically small and, by this reason, the diffraction can be described within the dipole approximation, its role turns out to be essential owing to the resonant nature of the exciton. It is obvious that the diffraction-induced shift does not depend on the exciton dephasing time  $\tau$  and the volume fraction  $f_V$  of QDs. The second mechanism inducing a frequency shift is a collective effect and is defined by electromagnetic interaction between QDs in the ensemble. This contribution depends on lattice type. The combined effect of both mechanisms can easily be obtained from Eq. (19):

$$\Delta\omega_\sigma = \frac{g_0^\sigma}{\varepsilon_h} (N_\sigma + f_V \delta_\sigma) \quad (22)$$

Different from the geometrical coefficients  $N_\sigma, \delta_\sigma$ , the quantities  $g_0^\sigma$  are phenomenological parameters, which must be invoked with consideration of the outside.

Eq. (17) shows that, in the language of crystal optics,<sup>[11]</sup> the QD composite being considered is effectively a uniaxial dielectric continuum with the  $z$ -axis as its preferred axis. The phenomenon of birefringence is characteristic for this medium: Both ordinary and extraordinary planewave propagations can occur in it.<sup>[36]</sup> The refractive indices of these waves ( $n_H$  and  $n_E$ , respectively) are given by:<sup>[36]</sup>

$$n_H = \sqrt{\varepsilon_H}, \quad n_E = \sqrt{\frac{\varepsilon_E \varepsilon_H}{\varepsilon_H + (\varepsilon_E - \varepsilon_H) \cos^2 \theta}} \quad (23)$$

where  $\theta$  is the angle between the  $z$ -axis and the propagation direction. The polarization vector of the ordinary wave is normally directed to the plane constituted by the  $z$ -axis and the propagation direction. Eq. (23) shows that  $n_H = n_E$  when the propagation direction coincides with the  $z$ -axis ( $\theta = 0$ ), and  $n_E = \sqrt{\varepsilon_E}$  when the propagation occurs in the  $xy$ -plane ( $\theta = \pi/2$ ). Substitution of Eqs. 19–21 into Eq. (18) and then into Eq. (23) allows us to evaluate the anisotropic macroscopic gain for QD arrays for both polarizations:

$$g_{H,E} = \text{Im}(n_{H,E}) \quad (24)$$

Below we discuss the computation of  $g_{H,E}$  by Eqs. (18), (23), and (24).

## Numerical Estimates and Discussion

The analytics presented above implies composite medium constituted by uniform two-level insertions in the host. Actually, QDs in ensemble are characterized by essential size dispersion and multilevel structure of the exciton spectrum. These factors provide inhomogeneous line broadening, which is beyond the above consideration. As a first step to take the effect into account, we introduce into analytics phenomenological parameters  $g_0 = |\hat{g}_0|$  and  $\tau$  as collective characteristics of the ensemble. A simple estimate of  $g_0$  using experimental data can be given in the following way. The parameter  $g_0$  is related to the material gain per dot  $g_{\text{mat}}$  by  $g_{\text{mat}} \approx kg_0/2\Gamma_{\text{inh}}\sqrt{\epsilon_h}$ , where  $\Gamma_{\text{inh}}$  is the inhomogeneous broadening width in the measured QD sample. The value of  $g_{\text{mat}}$  is extracted from experimental measurements of the QD ensemble gain. Letting  $g_{\text{mat}} \cong 10^5 \text{ cm}^{-1}$  and  $\Gamma_{\text{inh}} \cong 10^{13} \text{ sec}^{-1}$ ,<sup>[1]</sup> for  $\lambda = 1300 \text{ nm}$ , one can obtain  $|g_0| \cong 10^{14} \text{ sec}^{-1}$ . The value of the experimentally estimated maximum material gain correlates with theoretical predictions.<sup>[37,38]</sup> The above estimate is used further for calculations.

Fig. 3 demonstrates the polarization-dependent shift of the resonance energy of macroscopic gain for the case  $g_0^E = g_0^H$  at different magnitudes of the effective dephasing time and  $\theta = \pi/2$ . In the case of disklike QDs, the gain band for  $H$ -polarized field directed

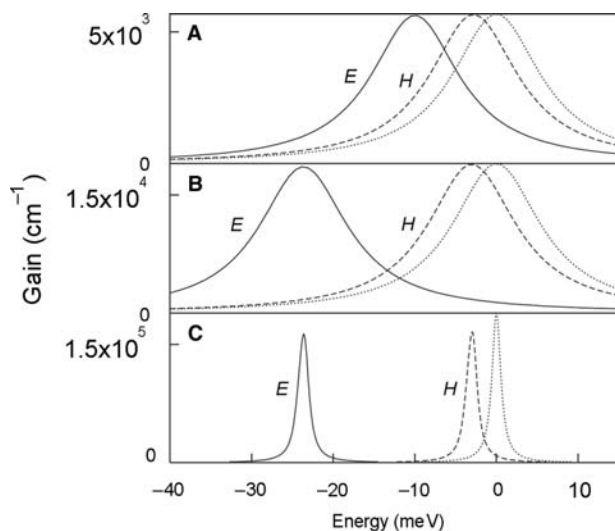


**Fig. 3** Macroscopic gain bands for  $E$ -polarized and  $H$ -polarized fields (solid and dashed lines, respectively) for an array of disk QDs arranged on a cubic (A) and tetragonal (B, C) lattice and different dephasing times  $\tau = 0.1$  psec (A, B) and  $\tau = 1$  psec (C). Vertical stacking period  $\beta = 1$  (A), 0.3 (B, C); QD's volume fraction  $f_V = 0.02$  (A), 0.07 (B, C);  $B/A = 0.33$ ;  $A/D = 0.25$ ; host dielectric constant  $\epsilon_h = 12.25$ ; and wavelength  $\lambda = 1 \mu\text{m}$ . Also shown by dotted lines are the gain bands of QD ensembles defined by Eq. (6) with isotropic  $\hat{g}_0$ . Source: From Ref.<sup>[5]</sup>.

toward the long axis of the disc possesses the smaller shift. The polarization dependence of the shift results in an appreciable polarization splitting of the gain bands for  $E$ -polarization and  $H$ -polarization, which become completely resolved for sufficiently large dephasing times (Fig. 3C). Thus radiation from an active composite must be linearly polarized at a given frequency.

As it has been pointed out above, the analytical treatment illustrated by Fig. 3 is invalid at  $\beta \ll 1$  and  $\beta \gg 1$ . Fig. 4 demonstrates polarization splitting of the gain band for cubic (Fig. 4A) and tetragonal lattices (Fig. 4B and C) of disklike QDs, obtained via direct numerical simulation by the minimal autonomic block (MAB) method.<sup>[5]</sup> Comparison with Fig. 3 shows that for cubic lattices (Figs. 3A and 4A), the polarization splitting effect manifests itself in the same manner, distinguished only in that the peak gains for  $E$ -polarized and  $H$ -polarized waves are slightly different in the last case. The situation is changed as  $\beta$  decreases (i.e., disks approach each other along the  $z$ -axis as far as they are in contact). Instead of the splitting increase demonstrated by Fig. 3B, we see a reverse tendency (Fig. 4B) up to the interchange of the  $E$ -polarized and  $H$ -polarized peaks for closely stacked pyramids (Fig. 4C). Note that the relative location of the  $E$ -polarized and  $H$ -polarized peaks in last case correlates with analytical results for quantum wires presented in Ref.<sup>[4]</sup>. Thus from an electrodynamic point

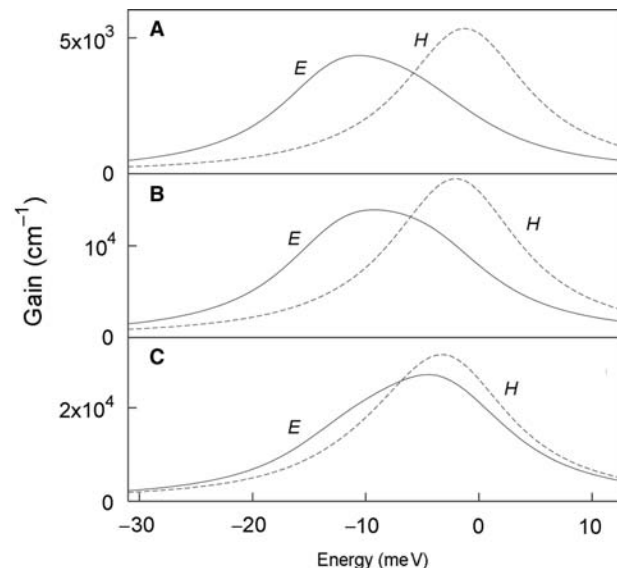


**Fig. 4** Macroscopic gain bands for  $E$ -polarized and  $H$ -polarized fields (solid and dashed lines, respectively) for an array of disklike QDs arranged on a cubic (A) and tetragonal (B, C) lattice. The input parameters  $\epsilon_h$ ,  $\lambda$ ,  $B/A$ , and  $A/D$  are the same as in Fig. 3. Dephasing time is  $\tau = 0.1$  psec. Vertical stacking period  $\beta = 1$  (A), 0.3 (B), and 0.2 (C). QD's volume fraction  $f_V = 0.02$  (A), 0.07 (B), and 0.1 (C). Source: From Ref.<sup>[5]</sup>.

of view, closely stacked QDs form a corrugated quantum wire. The corrugation is responsible for the quantitative difference in the polarization splitting for closely stacked QDs (Fig. 4B) and cylindrical quantum wires.<sup>[4]</sup> Numerical results for slablike QDs at  $\beta \rightarrow 0$  correlate well with the analytics. The fact that the tendency inherent in the polarization splitting for closely stacked QDs cannot be derived from analytical treatment reflects both the restrictiveness of the Maxwell Garnet formalism of the effective medium approach utilized in our paper and the use of approximate expressions (Eq. (21)) for the geometrical coefficients  $\delta_\sigma$ .

Fig. 5 demonstrates the formation of the gain band fine structure in tetragonal lattices of disklike QDs for the  $E$ -polarized field (extraordinary wave; Eq. (23)) at oblique propagation with respect to the  $z$ -axis. As is predicted by Eq. (23), the  $H$ -polarized field exhibits single resonance coinciding with that for  $E$ -polarization at  $\theta = 0$ . Owing to the high symmetry of pyramids, the MAB method simulation for arrays of disklike and pyramidal QDs shows that both models of the QD shape manifest qualitatively similar behavior differing in the shift values and peak amplitudes. It should be noted that the band fine structure illustrated in the particular case given by Fig. 5 must be involved in considering the interpretation of any polarization effects in QD arrays.

In general, also the anisotropic shape of QD causes different oscillator strengths for transitions involving  $E$ -polarized and  $H$ -polarized fields.<sup>[37]</sup> To estimate the influence of different gains for different polarizations, we considered the case when the gain for  $E$ -polariza-

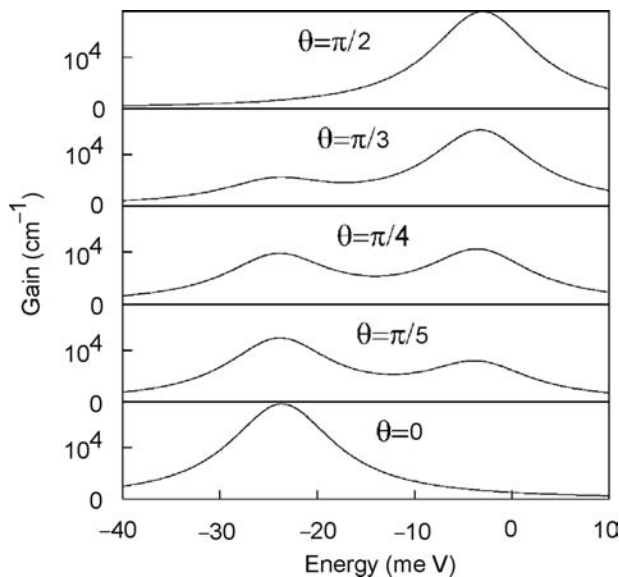


**Fig. 5** Macroscopic gain of  $E$ -polarized field by disk DQs arranged on a tetragonal lattice for different  $\theta$  from  $\pi/2$  to 0 as indicated. Lattice and individual QD parameters are as in Fig. 3. (B). *Source:* From Ref.<sup>[5]</sup>.

tion is lower and the case when the gain for  $H$ -polarization is higher (Fig. 6) compared with the case of equal gains in Fig. 3A and B (parameter  $g_0$  in Eq. (8) is the diagonal tensor). To make the effect clearer, we select also a longer exciton dephasing time. The remarkable result is that the gain peak of  $E$ -polarization locates closer to the QD resonance energy because the decrease of the gain peak dominates over the corresponding depolarization coefficient and results in smaller shifts than follow from Eq. (9).

To verify the predicted effects experimentally, a structure with a dense array of QDs was fabricated at the Abram Ioffe Physical Technical Institute (St. Petersburg). The structure represented 12 stacks of arrays of ZnCdSe disklike QDs formed in a self-organized way. The growth, structural, and basic optical properties of the structure are given in Ref.<sup>[39]</sup>. The areal density of QDs in a single sheet was about  $10^{12} \text{ cm}^{-2}$ ; the ZnCdSe dots had a lateral size of  $\sim 4 \text{ nm}$  and a height of  $\sim 1.2 \text{ nm}$ . The dots were incorporated in a ZnSe matrix and separated with 5-nm ZnSe spaces.<sup>[39,40]</sup> At low excitation density in edge geometry, QD photoluminescence (PL) is linearly polarized<sup>[5,40]</sup> throughout the PL band with a degree of polarization of 50% of the  $H$ -component (alignment as in Fig. 1). This effect is related to the anisotropy in optical transition matrix elements for  $H$ -polarizations and  $E$ -polarizations originating from the disklike shape of the QDs and the heavy-hole-like nature of

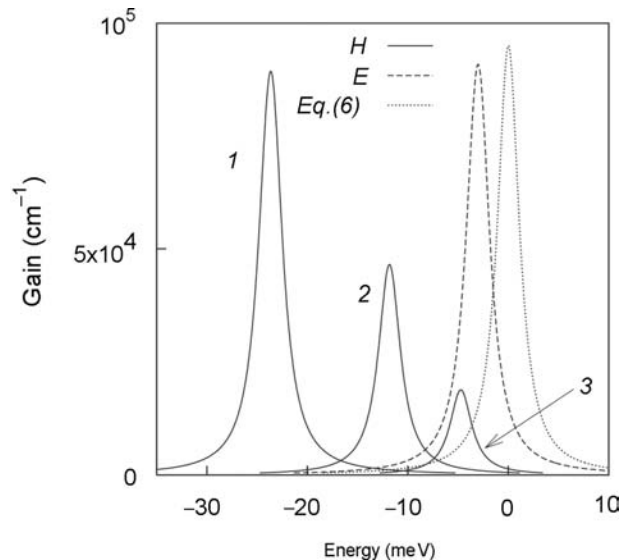


**Fig. 6** Macroscopic gain of  $H$ -polarized field (solid curves) by disklike QDs arranged on a tetragonal lattice for different anisotropic gains with  $g^E/g^H = 1.0(1), 4.0(2), 12.0(3)$ , normal incidence  $\theta = \pi/2$ ,  $\tau = 0.5 \text{ psec}$ , and other parameters as in Fig. 5. Dashed curve = a gain band for  $E$ -polarization; dotted curve = a gain band of a QD ensemble defined by Eq. (6) with isotropic  $\hat{g}_0$ . (From Ref.<sup>[5]</sup>.)

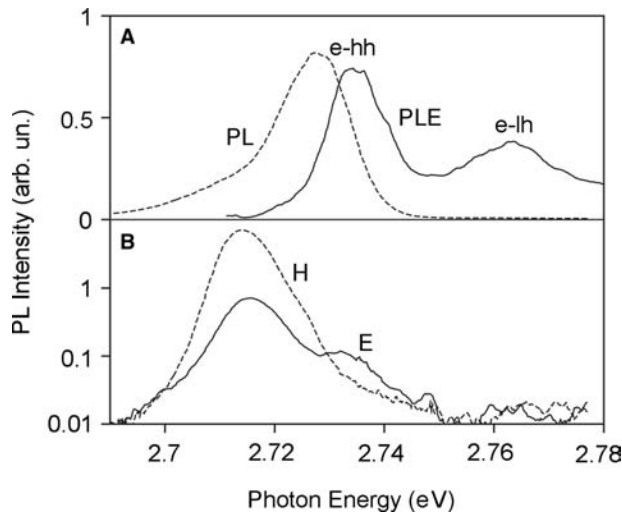


**Fig. 7** Photoluminescence (PL) and photoluminescence excitation (PLE) spectra (A) and *E*-polarized and *H*-polarized spectra of stimulated emission in edge geometry (B) for the observation temperature = 7 K, excitation density = 1 MW/cm<sup>2</sup>, and energy of exciting photon  $E_{ex} = 2.88$  eV. Source: From Ref.<sup>[4]</sup>.

the QD exciton. The light-hole-like exciton QD state is also seen in the PL excitation spectrum and is shifted significantly away from the spectral range of interest. With increase in excitation density, gain develops<sup>[39]</sup> and causes a strong superlinear growth of the PL intensity. Spectra of the *H*-components and *E*-components of stimulated emission are shown in Fig. 7B. The predominantly *H*-polarized component is shifted from the QD resonance revealed in the PL excitation and optical reflectance spectra (Fig. 7A). The degree of polarization of this component strongly increases with excitation density. At the same time, we distinctly observe an appearance of a second separate peak in the *E*-component at energies closer to the QD resonance. The intensity of the *E*-polarized peak is much smaller, pointing to a smaller gain coefficient as compared with that for the *H*-polarized peak at lower photon energy. Therefore the peak location of the *E*-component corresponds to the predictions of the calculations for the case of different gain coefficients for *E*-polarizations and *H*-polarizations (Fig. 6).

### Reflectance of Planar Array of Quantum Dots

As was pointed out above, a planar layer comprising a 2-D ensemble of QDs can be treated as an effective QW. As a result, the formalism of investigation of QWs can be extended to QD arrays by introducing effective integral parameters of the array defined by Eq. (4). In particular, it can easily be shown that EBCs (Eq. (3)) describe a QW of the thickness  $L_{QW}$  with the

tensorial dielectric function given by Eq. (17):

$$\begin{aligned}\varepsilon_H(\omega) &= \varepsilon_h - \frac{4\pi i}{\omega} \sigma_{xx} L_{QW}, \\ \varepsilon_E(\omega) &= \frac{\varepsilon_h}{1 + 2\xi/L_{QW}}\end{aligned}$$

Reflection coefficients for such a QW are given by:<sup>[17]</sup>

$$\begin{aligned}r_H(\omega) &= \frac{ik\eta_H}{2\sqrt{\varepsilon_h} \cos \theta - ik\eta_H}, \\ r_E(\omega) &= \frac{ik[\eta_H \cos^2 \theta + \varepsilon_h^2 \eta_E \sin^2 \theta]}{2\sqrt{\varepsilon_h} \cos \theta - ik[\eta_H \cos^2 \theta - \varepsilon_h^2 \eta_E \sin^2 \theta]}\end{aligned}\quad (25)$$

where  $\theta$  is the angle of incidence and:

$$\begin{aligned}\eta_H &= L_{QW}[\varepsilon_H(\omega) - \varepsilon_h], \\ \eta_E &= L_{QW} \left[ \frac{1}{\varepsilon_E(\omega)} - \frac{1}{\varepsilon_h} \right]\end{aligned}$$

For spherical particles, after substituting  $L_{QW} \rightarrow 2R$ ,<sup>[7]</sup> Eq. (25) describes the reflection from the planar array of QDs. Thus we state the mathematical equivalence of optical properties of a 2-D periodical layer of QDs and an isolated quantum well. It should be stressed that the mechanisms of electron transport processes and oscillator strengths in each case are essentially different. Nevertheless, the equivalence makes it possible to extend to QD-based planar structures with more complicated configurations (finite-sized QD layer, QD layer in microcavity, several QD layers, etc.) the well-developed mathematical formalism of investigation of quantum wells.<sup>[41]</sup> Namely this equivalence provides promising potentiality of the derived EBCs for particular electrodynamic problems in QD-based structures. In particular, the threshold current for QD-based lasers can be evaluated by analogy with solutions of corresponding problems for the QW lasers; the EBC method allows us to analyze electromagnetic responses of a QD layer (or a multilayer structure) placed in microcavity—this is very important for the design of QD-based semiconductor lasers.<sup>[1]</sup>

### CONCLUSION

In our paper, we have discussed the electromagnetic response properties of 2-D and 3-D inhomogeneous semiconductor heterostructures—excitonic composites—constituted by QDs imbedded in a transparent host medium. The Maxwell Garnett approach of the effective medium theory and its modification—impedance

boundary conditions—have been applied to study 3-D and 2-D structures, respectively. The depolarization shift of the QD gain band and, in anisotropically shaped QDs, the polarization-dependent splitting of this band have been predicted to exist as manifestation of the local field effects. Both types of the exciton localization—strong and weak confinement regimes—with a pronounced non-locality in the latter regime have been addressed. The basic result is that in both cases, spatially local constitutive relations describe QD composites although the electromagnetic response of an isolated QD in the weak confinement regime is spatially nonlocal. The nonlocality manifests itself in specific dependence of the effective constitutive parameters on the geometry and electronic properties of a single QD.

In our consideration, we have restricted ourselves to the simplest model of excitonic composites—the perfect lattice of identical QDs—whereas experimentally, available structures show intrinsic size dispersion and periodicity violation. These effects may be characterized by a distribution function and taken into account by a theory of irregular excitonic composites. Elaboration of such a theory is the topical question. Another essential restriction of the analysis presented is that nonclassical light–matter interactions have been left beyond the analysis. The quantum nature of light interacting with an excitonic composite is expected to be of importance for many problems where collections of excitons are involved: quantum computing, electromagnetic fluctuations, etc. Both topical questions will be addressed elsewhere in the future.

## ACKNOWLEDGMENT

The research is partially supported through the NATO Science for Peace Program under project SfP-972614.

## REFERENCES

1. Bimberg, D.; Grundmann, M.; Ledentsov, N.N. *Quantum Dot Heterostructures*; John Wiley and Sons: Chichester, 1999.
2. Lakhtakia, A., Ed. *Selected Papers on Linear Optical Composite Materials*; SPIE Optical Engineering Press: Bellingham, WA, 1996.
3. Cho, K. Mechanisms for LT splitting of polarization waves: A link between electron–hole exchange interaction and depolarization shift. *J. Phys. Soc. Jpn.* **1999**, *68* (2), 683–691.
4. Slepyan, G.Ya.; Maksimenko, S.A.; Kalosha, V.P.; Ledentsov, N.N.; Bimberg, D.; Alferov, Zh.I. Polarization splitting of the gain band in quantum wire and quantum dot arrays. *Phys. Rev., B* **1999**, *59* (19), 12275–12278.
5. Maksimenko, S.A.; Slepyan, G.Ya.; Kalosha, V.P.; Maly, S.V.; Ledentsov, N.N.; Herrmann, J.; Hoffmann, A.; Bimberg, D.; Alferov, Zh.I. Electromagnetic response of 3D arrays of quantum dots. *J. Electron. Mater.* **2000**, *29* (5), 494–503.
6. Maksimenko, S.A.; Slepyan, G.Ya.; Ledentsov, N.N.; Kalosha, V.P.; Hoffmann, A.; Bimberg, D. Light confinement in a quantum dot. *Semicond. Sci. Technol.* **2000**, *15* (5), 491–496.
7. Slepyan, G.Ya.; Maksimenko, S.A.; Kalosha, V.P.; Hoffmann, A.; Bimberg, D. Effective boundary conditions for planar quantum-dot structures. *Phys. Rev., B* **2001**, *64* (12), no. 125326.
8. Maksimenko, S.A.; Slepyan, G.Ya.; Kalosha, V.P.; Ledentsov, N.N.; Hoffmann, A.; Bimberg, D. Size and shape effects in electromagnetic response of quantum dots and quantum dot arrays. *Mater. Sci. Eng., B* **2001**, *82* (1–3), 215–217.
9. Slepyan, G.Ya.; Maksimenko, S.A.; Hoffmann, A.; Bimberg, D. Local field effects in an isolated quantum dot: Self-consistent microscopic approach. *Phys. Status Solidi, A* **2002**, *190* (2), 555–559.
10. Slepyan, G.Ya.; Maksimenko, S.A.; Hoffmann, A.; Bimberg, D. Quantum optics of a quantum dot: Local-field effects. *Phys. Rev., A* **2002**, *66* (6), no. 063804.
11. Born, M.; Wolf, E. *Principles of Optics*, 6th Ed.; Pergamon Press: Oxford, 1985. Sec. 14.5.
12. Von Faxen, H. Der Zusammenhang zwischen den Maxwell'schen Gleichungen für Dielektrika und den atomistischen Ansätzen. *Z. Phys.* **1920**, *2* (3), 218–229.
13. Khiznjak, N.A. *Integral Equations of Macroscopic Electrodynamics*; Naukova Dumka: Kiev, 1986 (in Russian).
14. Weinstein, L.A. *The Theory of Diffraction and the Factorization Method*; Golem: New York, 1969.
15. Ilyinsky, A.S.; Slepyan, G.Ya.; Slepyan, A.Ya. *Propagation, Scattering and Dissipation of Electromagnetic Waves*; Peter Peregrinus: London, 1993.
16. Hoppe, D.J.; Rahmat-Samii, Y. *Impedance Boundary Conditions in Electromagnetics*; Taylor and Francis: Washington, 1995.
17. Atanasov, R.; Bassani, F.; Agranovich, V.M. Mean-field polariton theory for asymmetric quantum wells. *Phys. Rev., B* **1994**, *49* (4), 2658–2666.
18. Zaluzny, M.; Nalewajko, C. Coupling of infrared radiation to intersubband transitions in multiple quantum wells: The effective-medium approach. *Phys. Rev., B* **1999**, *59* (20), 13043–13053.
19. Maksimenko, S.A.; Slepyan, G.Ya. Electrodynamic Properties of Carbon Nanotubes. In *Electromagnetic Fields in Unconventional Structures and Materials*; Singh, O.N., Lakhtakia, A., Eds.; John Wiley and Sons: New York, 2000; 217–255.
20. Maksimenko, S.A.; Slepyan, G.Ya. Electrostatics of carbon nanotubes. *J. Commun. Technol. Electron.* **2002**, *47* (3), 235–252.
21. Shubin, V.A.; Sarychev, A.K.; Clerc, J.P.; Shalaev, V.M. Local electric and magnetic fields in semicontinuous metal films: Beyond the quasistatic approximation. *Phys. Rev., B* **2000**, *62* (16), 11230–11244.



22. Pantell, R.H.; Puthoff, H.E. *Fundamentals of Quantum Electronics*; John Wiley and Sons: New York, 1969.
23. Landau, L.D.; Lifshitz, E.M. *Electrodynamics of Continuous Media*; Pergamon Press: Oxford, 1960.
24. Kleinman, R.E. Low Frequency Electromagnetic Scattering. In *Electromagnetic Scattering*; Uslenghi, P.L.E., Ed.; Academic Press: New York, 1978; 1–28.
25. Kayanuma, Y. Resonant interaction of photons with a random array of quantum dots. *J. Phys. Soc. Jpn.* **1993**, *62* (1), 346–356.
26. Schmitt-Rink, S.; Miller, D.A.B.; Chemla, D.S. Theory of the linear and nonlinear optical properties of semiconductor microcrystallites. *Phys. Rev., B* **1987**, *35* (15), 8113–8125.
27. Hanewinkel, B.; Knorr, A.; Thomas, P.; Koch, S.W. Optical near-field response of semiconductor quantum dots. *Phys. Rev., B* **1997**, *55* (20), 13715–13725.
28. Keller, O. Local fields in the electrodynamics of mesoscopic media. *Phys. Rep.* **1996**, *268* (2–3), 85–262.
29. Regelman, D.V.; Mizrahi, U.; Gershoni, D.; Ehrenfreund, E.; Schoenfeld, W.V.; Petroff, P.M. Semiconductor quantum dot: A quantum light source of multicolor photons with tunable statistics. *Phys. Rev. Lett.* **2001**, *87* (25), no. 257401.
30. Birkedal, D.; Leosson, K.; Hvam, J.M. Long lived coherence in self-assembled quantum dots. *Phys. Rev. Lett.* **2001**, *87* (22), no. 227401.
31. Borri, P.; Langbein, W.; Schneider, S.; Woggon, U.; Sellin, R.L.; Ouyang, D.; Bimberg, D. Exciton relaxation and dephasing in quantum-dot amplifiers from room to cryogenic temperature. *IEEE J. Sel. Top. Quantum Electron.* **2002**, *8* (5), 984–991.
32. Verzelen, O.; Ferreira, R.; Bastard, G. Excitonic polarons in semiconductor quantum dots. *Phys. Rev. Lett.* **2002**, *88* (14), no. 146803.
33. Yu, P.Y.; Cardona, M. *Fundamentals of Semiconductors. Physics and Material Properties*; Springer-Verlag: Berlin, 2001.
34. Fu, Y.; Willander, M.; Ivchenko, E.L. Photonic dispersions of semiconductor-quantum-dot-array-based photonic crystals in primitive and face-centered cubic lattices. *Superlattices Microstruct.* **2000**, *27* (4), 255–264.
35. Hanamura, E. Very large optical nonlinearity of semiconductor microcrystallites. *Phys. Rev., B* **1988**, *37* (3), 1273–1279.
36. Yariv, A.; Yeh, P. *Optical Waves in Crystals*; John Wiley and Sons: New York, 1983, Sec. 4.6.
37. Asada, M.; Miyamoto, Y.; Suematsu, Y. Gain and the threshold of three dimensional quantum dot lasers. *IEEE J. Quantum Electron.* **1986**, *32*, 1915–1933.
38. Asryan, L.V.; Suris, R.A. Inhomogeneous line broadening and the threshold current density of a semiconductor quantum dot laser. *Semicond. Sci. Technol.* **1996**, *11* (4), 554–567.
39. Strassburg, M.; Kutzer, V.; Pohl, U.W.; Hoffmann, A.; Broser, I.; Ledentsov, N.N.; Bimberg, D.; Rosenauer, A.; Fischer, U.; Gerthsen, D.; Krestnikov, I.L.; Maximov, M.V.; Kop'ev, P.S.; Alferov, Zh.I. Gain studies of (Cd, Zn)Se quantum islands in a ZnSe matrix. *Appl. Phys. Lett.* **1998**, *72* (8), 942–944.
40. Krestnikov, I.L.; Strassburg, M.; Caesar, M.; Hoffmann, A.; Pohl, U.W.; Bimberg, D.; Ledentsov, N.N.; Kop'ev, P.S.; Alferov, Zh.I.; Litvinov, D.; Rosenauer, A.; Gerthsen, D. Control of the electronic properties of CdSe submonolayer superlattices via vertical correlation of quantum dots. *Phys. Rev., B* **1999**, *60* (12), 8695–8703.
41. Bastard, G. *Wave Mechanics Applied to Semiconductor Heterostructures*; Les editions de Physique: Les Ulis, 1988.

# Quantum Dot Lasers

**Mikhail V. Maximov**

*Ioffe Physico-Technical Institute, St. Petersburg, Russia*

**Nikolai N. Ledentsov**

*Institut für Festkörperphysik, Technische Universität Berlin, Berlin, Germany*

## INTRODUCTION

Quantum dot (QD) lasers emerged about decade ago and now they are one of the most rapidly developing and exciting areas in the field of semiconductor optoelectronics. Properly optimized QD lasers show better performance than conventional quantum well (QW) lasers: low threshold current, enhanced temperature stability, high differential efficiency, increased differential gain, and small linewidth enhancement factor resulting in reduced filamentation and chirp. Self-organized QDs offer the possibility to reach emission wavelengths that are larger than those obtainable with quantum wells of the same material system.

In this entry we discuss the fundamentals of QD lasers. The criteria for the optimization of QD lasers for different applications are considered. Experimental demonstrations of the advantages of QD lasers are presented. The latest experimental results on edge-emitting and vertical cavity surface emitting QD lasers are reviewed. Possible short-term commercial applications of QD lasers are also discussed.

## ADVANTAGES OF QUANTUM DOT LASERS

The concept of carrier confinement has been of primary importance in the development of semiconductor laser. The invention of the double heterostructure,<sup>[1,2]</sup> in which carriers in a narrow-gap material are confined by wide bandgap barriers, made possible the first continuous wave (CW) operation of semiconductor lasers at room temperature and their practical implementation. The next breakthrough occurred when Dingle and Henry proposed the idea to “exploit quantum effects in heterostructure semiconductor lasers to produce wavelength tunability” and to achieve “lower lasing thresholds” via “the change in the density of states which results from reducing the number of translational degrees of freedom of the carriers”.<sup>[3]</sup> It was also shown that if the number of translational degrees of freedom of charge carriers is decreased below two, a

singularity occurs in the density of states (Fig. 1). This singularity increases light absorption or light amplification (gain). An ultimate case of size quantization is realized in QDs. A QD is a coherent inclusion of a narrow-gap material in a wide-gap matrix in which electrons are quantized in all three spatial directions. Thus a single semiconductor QD exhibits a discrete  $\delta$ -function-like energy spectrum similar to that in a real atom, keeping the advantage of direct current injection, impossible in other types of lasers based on atomic transitions.

The physical advantages of QD lasers resulting from  $\delta$ -function-like density of states are:

- Low threshold current
- High material gain
- High temperature stability of the threshold current (characterized by characteristic temperature  $T_0$ )
- High differential efficiency
- High differential gain
- Small  $\alpha$ -factor and correspondingly reduced filamentation and chirp (shift of the lasing wavelength with current)

In addition, QD medium has some advantages, which are not directly related to size quantization effects:

- The possibility to reach emission wavelengths that are larger than those obtainable with quantum wells of the same material system. For instance, lasing at wavelengths up to 1.32  $\mu\text{m}$  is demonstrated for InAs QDs on GaAs substrate, in contrast to QW devices, in which lasing is limited to approximately 1.15  $\mu\text{m}$ .
- Dramatically reduced carrier lateral transport. Carrier capture in QDs is very fast and carrier localization in QDs is very efficient. This leads to a number of advantages of using QD medium in laser applications: larger catastrophic optical damage threshold due to decreased facet overheating, increased lifetime, enhanced radiation hardness, and the possibility to fabricate narrow stripes via

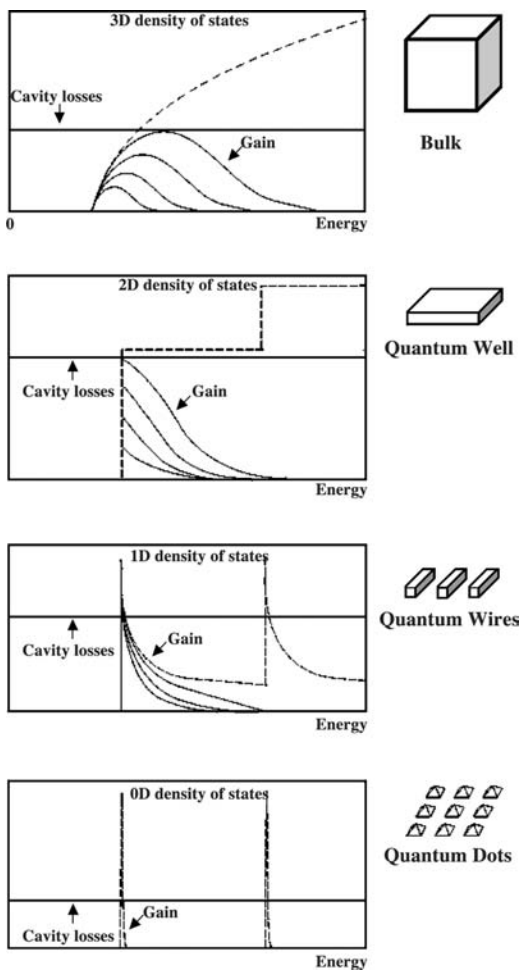


**Fig. 1** A schematic sketch of the density of states (dashed curves) and gain spectra (solid curves) in bulk material, quantum well, quantum wires, and quantum dots. Schematic morphology is shown on the right.

etching through active area without increase in surface recombination.

Some of the basic advantages of QD lasers such as improvement in the temperature stability of the threshold current,<sup>[4]</sup> high material gain,<sup>[5]</sup> and the possibility of remarkable reduction in the laser threshold were already described in the first theoretical works on QD lasers. These works, however, were generally based on simplified assumptions such as infinite barriers, no QD size fluctuations, one confined electron and hole level, and ultrafast energy relaxation of injected carriers. More recent theoretical models had to take into account such complications as finite barriers, many electron and hole levels (effect of excited states), QD size fluctuations, many body effects, radiative and non-radiative recombination in the optical confinement layer (OCL; wide-gap matrix), charge neutrality violation in QDs, etc. It was shown that the characteristics

of QD lasers depend dramatically on the parameters characterizing QD array (QD lateral size, height and corresponding position of energy levels, QD density, and size dispersion) as well as on the structure design: thickness of the OCL, doping profiles in the cladding layers and in the OCL, the band offsets at the interface between the OCL and the cladding layers. Depending on the abovementioned parameters the performance of QD lasers can be very good or poor. To get the best performance, an optimization of QD array parameters should be done consistently with the optimization of the structure design. Optimization for certain applications (low threshold current, high output power, etc.) should be done according to different criteria, and in many applications a combination of these criteria needs to be taken into account.

High temperature stability of the threshold current as the main fingerprint of QD lasers was demonstrated already in the first injection laser based on self-organized QDs.<sup>[6]</sup> Further realization of the advantages of QD lasers was associated with the improvement in QD growth and the development of more sophisticated QD growth techniques. At present, all the advantages of QD lasers are basically experimentally proved. At the same time we believe that there is still room for improvement in the characteristics of QD lasers. Experimental and theoretical studies of QD lasers are exploding in scientific areas and further progress in the field of QD lasers can be foreseen. Recently, the first commercial QD lasers have been announced.<sup>[7]</sup>

## QUANTUM DOTS GROWTH

Realization of QD lasers became possible owing to the progress in self-organized growth. The deposition of a material with a lattice constant different from that of the substrate was shown to result in a spontaneous formation of three-dimensional (3-D) islands (for a review, see Ref.<sup>[8]</sup>). In most practical cases, for instance for the deposition of InGaAs on GaAs, first a 2-D layer grows on the substrate and island formation occurs only after a certain critical thickness is exceeded. Thus QD array is situated on top of a thin initial planar layer (so-called wetting layer). This growth mode is referred to as Stranski–Krastanow growth mode. Under certain growth parameters, arrays of highly uniform coherent islands can be formed. Each island generates long-range strain fields in the substrate and interaction of the island via these fields favors island lateral ordering in a 2-D lattice.

The characteristics of QD lasers depend dramatically on the parameters characterizing QD array.<sup>[9]</sup> Already in the first injection QD laser based on QDs formed in simple Stranski–Krastanow growth mode, insufficient carrier localization in QDs and their

thermal escape to the wetting layer and the OCL were shown to be a disadvantage, deteriorating the device performance at high temperatures.<sup>[6]</sup> As simple Stranski–Krastanow growth provides only limited control of the interrelated size and density of the islands, extensive investigations have been conducted to overcome these limitations and to optimize the properties of QD arrays. Novel advanced approaches such as vertically coupled QDs<sup>[10]</sup> lead to a considerable improvement in the performance of QD lasers.

Present best performance QD lasers are based on QDs formed by the technological approach that we refer to as activated alloy phase separation (AAPS).<sup>[11,12]</sup> In this approach the original Stranski–Krastanow InAs islands are formed by depositing a certain amount ( $D_{IS}$ ) of InAs ( $D_{IS} = 1.7\text{--}3$  ML). The original islands are then overgrown with an average thickness  $H$  of  $\text{In}_x\text{Ga}_{1-x}$  As alloy layer ( $H = 0\text{--}6$  nm,  $x = 0\text{--}0.20$ ). The strain field induced by each island leads to a migration of In atoms toward it and, correspondingly, to an increase in its effective volume. The increase in the original island volume as well as partial strain relaxation in such QDs embedded in an  $\text{In}_x\text{Ga}_{1-x}$  As layer and a narrowing of the matrix bandgap results in a higher confinement of electron and hole levels with a corresponding red-shift of the photoluminescence (PL) emission.<sup>[12,13]</sup> Lasers based on QDs formed by the AAPS enable it to reach lasing wavelengths above  $1.3\ \mu\text{m}$  for the structures grown on GaAs substrates, which is not possible with the use of InGaAs QWs. The AASP process sensitively depends on the size and density of the InAs nanostressors, i.e., the InAs deposition amount ( $D_{IS}$ ), as well as on the thickness ( $H$ ), and on the composition ( $x$ ) of the  $\text{In}_x\text{Ga}_{1-x}$  As alloy layer. To achieve high QD confinement energy (long emission wavelength), narrow QD size distribution, and simultaneously prevent formation of dislocations and large dislocated clusters, a careful optimization of growth parameters is required and described in detail in Ref.<sup>[12]</sup>

A growth sequence very similar to AAPS is referred to by the authors as a “dots in a well” (DWELL) design.<sup>[14]</sup> In the DWELL design the original Stranski–Krastanow islands are formed on a several-nanometer-thick  $\text{In}_x\text{Ga}_{1-x}$  As buffer layer. To the best of our knowledge QDs formed by AAPS and DWELL have very similar properties. More details on the growth and optical properties of InAs–GaAs QDs emitting in long-wavelength optical region can be found in review.<sup>[15]</sup>

### EQUILIBRIUM VS. NONEQUILIBRIUM CARRIER DISTRIBUTION IN QUANTUM DOT ARRAY

Depending on the sample temperature and the confinement of electron and hole energy levels with respect to

the continuum, the carrier distribution within the QD array can be either equilibrium or non-equilibrium.<sup>[9]</sup> At high temperatures or (and) low confinement energies the characteristic times of thermally excited escapes of electrons and holes from a QD are small compared to the radiative lifetime in QDs. Thermal carrier emission, lateral transport via the wetting layer and matrix, and then recapture result in the quasi-equilibrium distribution of carriers in the array with the corresponding quasi-Fermi levels determined by the pumping level. As a consequence of such carrier redistribution, the level occupancies (and numbers of carriers) in various QDs will differ.

At low temperatures or (and) efficient confinement of electron and hole energy levels, the radiative lifetime in QDs is small compared with the characteristic times of thermally excited escapes of the carriers from a QD. A carrier captured by a QD having no time to leave a QD recombines in the same QD. The redistribution of carriers from one QD to another and establishment of quasi-Fermi levels for the conduction and valence bands do not occur. As the initial numbers of carriers injected into various QDs are the same, the level occupancies are also the same there.

Carrier distribution dramatically affects the dependence of gain spectra on the injection current.<sup>[9]</sup> In case of non-equilibrium distribution, the gain spectrum copies the shape of the curve corresponding to the dispersion of QD ground-state transition energies (Gaussian). The spectra are scaled along the vertical axis by a factor equal to the mean population inversion in QDs (Fig. 2A). In case of quasi-equilibrium the “gradual” filling of the curve occurs with the increase in pumping level (Fig. 2B).

### SPONTANEOUS EMISSION AND GAIN

The first theoretical simulations of QD lasers were based on the assumption of one electron and one hole level in a QD. In actual QDs the energy level structure is much more complex.<sup>[13,16]</sup> In a pyramidal QD with base length larger than 14 nm there are several electron and hole levels.<sup>[16]</sup> Because of piezoelectric effect and Coulomb interaction there is no degeneracy, even accidental, of the excited states. However, several excited-state transitions may act as one “effective” transition if their energies are close. The absorption (gain) spectrum of the “effective” transition will be a superposition of absorption (gain) spectra corresponding to individual excited-state transitions with close energies. The maximal absorption (gain) of this superposition can be higher than that of the ground-state transition.<sup>[17]</sup>

Typical electroluminescence (EL) spectra of a laser based on QDs with narrow size distribution are

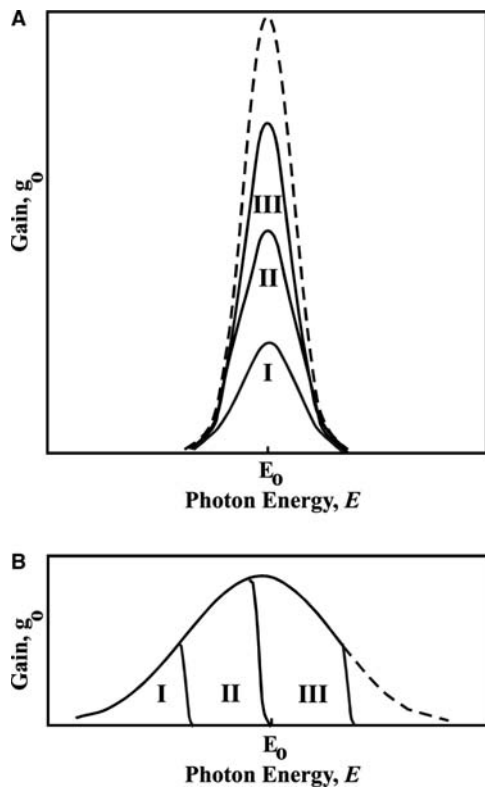


**Fig. 2** Gain spectra for the cases corresponding to non-equilibrium (A) and equilibrium (B) filling of QDs. The curves are numbered in ascending order of population inversion in a QD. The dashed curve corresponds to the population inversion equal to unity.  $E_0$  is the energy of the ground state transition in an average sized QD. *Source:* From Ref.<sup>[9]</sup>.

shown in Fig. 3. A 200- $\mu\text{m}$ -long stripe was used. Short stripes are essential to measuring the EL spectrum shape correctly. The longer the stripe the higher the probability of high energy photons corresponding to the emission from excited states to be reabsorbed and contribute to the final emission from lower energy levels. By contrast, lower energy photons corresponding to the emission from the ground state easily leave the structure. The reabsorption effect can modify the EL spectra. Moreover, in short stripes, the spontaneous emission can be studied even at high current densities. At the lowest excitation density, the emission mainly originates from the ground-state transition. At higher excitation densities, the first and the second short wavelength peaks become apparent. Strong level filling occurs at high injection currents because of the limited number of QD energy states. At all temperatures, EL lines from the ground- and excited-state transitions are relatively narrow (40–60 nm) and well resolved. Emission due to the wetting layer/InGaAs layer is also seen in the spectra at 0.97  $\mu\text{m}$  at room temperature (the QDs are embedded in a QW formed by

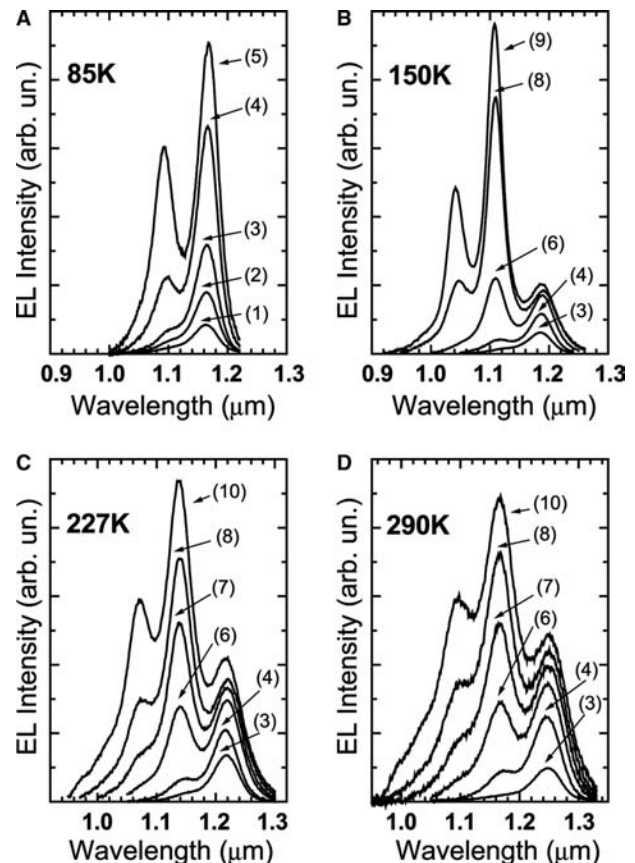


**Fig. 3** Electroluminescence spectra from a 200- $\mu\text{m}$ -long stripe at different injection currents and temperatures: (1) 12.5, (2) 25, (3) 50, (4) 125, (5) 250, (6) 500, (7) 1250, (8) 2500, (9) 3750, and (10) 5000  $\text{A}/\text{cm}^2$ .

the wetting layer and InGaAs layer with nominal thickness  $H$ ). Each of the two short wavelength QD peaks is likely to be a superposition of two or more closely located peaks from transitions involving different electron and hole sublevels. At 80 K, the lasing starts at a current density of 500  $\text{A}/\text{cm}^2$ , whereas at 290 K the device is in the spontaneous emission mode up to 5  $\text{kA}/\text{cm}^2$ .

Modal gain spectra of a laser structure based on three sheets of QDs formed by the AAPS are shown in Fig. 4. The surface density of QDs estimated from TEM images was  $4\text{--}5 \times 10^{10} \text{cm}^{-2}$ . The spectra are measured by the variable-stripe length method with varying current injection. The maxima at 1.254 and 1.18  $\mu\text{m}$  correspond to the ground- and first excited-state transitions. At current densities of about 900  $\text{A}/\text{cm}^2$  the gain of the ground-state transition saturates. The gain saturation effect is a consequence of the limited surface density of QDs, inhomogeneous broadening of the QD array, and the limited QD radiative emission rate. The maximum modal gain for the transition from the  $i$ th electron level to the  $j$ th hole



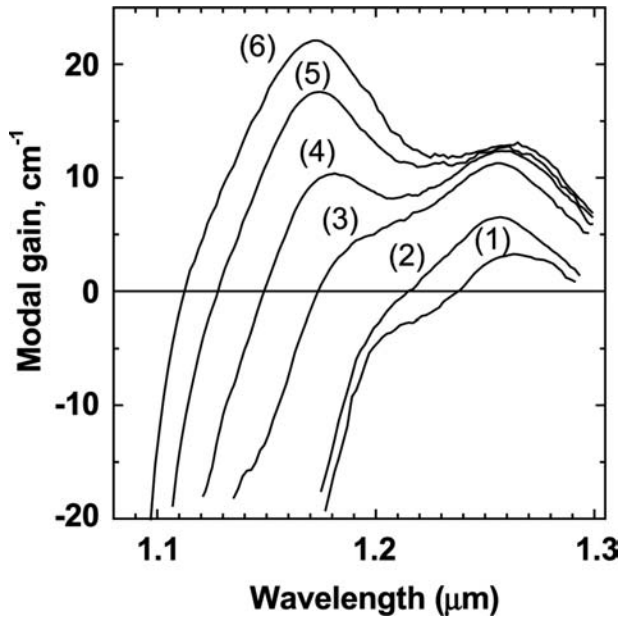


**Fig. 4** Modal gain spectra at different injection currents: (1) 98, (2) 195, (3) 487, (4) 975, (5) 1950, and (6) 2925 A/cm<sup>2</sup>.

level is:<sup>[17]</sup>

$$g_{ij}^{\max} = \frac{\xi}{4} \left[ \frac{\bar{\lambda}_{ij}}{\sqrt{\bar{\epsilon}_{ij}}} \right]^2 d_{ij} \frac{1}{\tau_{ij}^{\text{QD}}} \frac{\hbar}{(\Delta\epsilon)_{\text{inhom},ij}} \frac{\bar{\Gamma}_{ij}}{\bar{a}} N_S Z_L \quad (1)$$

where

$\xi$  is a numerical constant ( $\xi = 1/\pi$  and  $\xi = 1/\sqrt{2\pi}$  for Lorentzian and Gaussian QD-size distribution functions, respectively);

$\bar{\lambda}_{ij} = 2\pi\hbar c/\bar{E}_{ij}$  (a wavelength at transition  $\bar{E}_{ij}$ );

$d_{ij}$  is the degeneracy of the transition;

$\bar{a}$  is the mean size of QDs;

$Z_L$  is the number of QD layers;

$N_S$  is the surface density of QDs in a layer;

$\bar{\epsilon}_{ij}$  is a dielectric constant;

$\tau_{ij}^{\text{QD}}$  is the spontaneous radiative lifetime for the  $i \rightarrow j$  transition;

$(\Delta\epsilon)_{\text{inhom},ij}$  is the inhomogeneous line broadening for the  $i \rightarrow j$  transition;

$\bar{\Gamma}_{ij}$  is the modal optical confinement factor in a QD layer (along the transverse direction in the waveguide) for the  $i \rightarrow j$  transition.

The measured maximum (saturated) modal gain of the ground-state transition is 12 cm<sup>-3</sup> (4 cm<sup>-1</sup> per

QD sheet). For a laser structure based on 10 stacks of similar QDs the measured maximum modal gain was above 25 cm<sup>-1</sup>.<sup>[11]</sup>

In equilibrium filling of QDs, the general relationship between the gain and spontaneous emission spectra has been shown to hold for an arbitrary number of radiative transitions and an arbitrary QD-size distribution.<sup>[17]</sup> Thus gain spectrum can be derived from the measured spontaneous emission spectrum (and vice versa).

### EFFECT OF EXCITED-STATE TRANSITIONS ON THE THRESHOLD CHARACTERISTICS OF A QUANTUM DOT LASER

Depending on the relationship between the separation of the ground- and excited-state transition energies and the inhomogeneous broadening, either a smooth or a step-like change in the lasing wavelength with losses occurs.<sup>[18,19]</sup> The multiple transition effect on threshold characteristics, in particular on the lasing wavelength, was theoretically studied in Ref.<sup>[17]</sup>. We consider two optical transitions and assume that maximal gain for the “effective” excited-state transition is higher than that for the ground-state transition. The following situations can arise:<sup>[17]</sup>

1. Large separation of the mean transition energies and small inhomogeneous broadening. The gain and the spontaneous emission spectra for different injection current levels are shown in Fig. 5A and B, respectively. As the injection current density at the lasing threshold is a monotonically increasing function of the losses  $\beta$ , the dependence of the laser characteristics on the injection current density will also represent the dependence on the losses, and vice versa. At  $\beta < g_1^{\max}$ , the gain peak is near the energy of the ground-state transition ( $\bar{E}_1$ ) and, hence, lasing occurs via this transition ( $\lambda \approx \bar{\lambda}_1$ , where  $\lambda$  is the lasing wavelength and  $\bar{\lambda}_1$  is the wavelength of the ground-state transition). For  $\beta$ , somewhat less than  $g_1^{\max}$ , there is a shift in the peak position, and for  $g_1^{\max} < \beta < g_2^{\max}$ , the peak is seen near the energy of the excited-state transition ( $\bar{E}_2$ ). Lasing then occurs via the excited-state transition ( $\lambda \approx \bar{\lambda}_2$ , where  $\lambda$  is the lasing wavelength and  $\bar{\lambda}_2$  is the wavelength of the excited-state transition). The lasing wavelength and threshold current density  $j_{\text{th}}$  are shown in Fig. 6 as a function of losses. The break in  $\partial j_{\text{th}}/\partial\beta$  at  $\beta \approx g_1^{\max}$  reflects the shift of the lasing wavelength. As the modal gain peak is equal to the losses at lasing threshold, it is obvious that the curve for the threshold



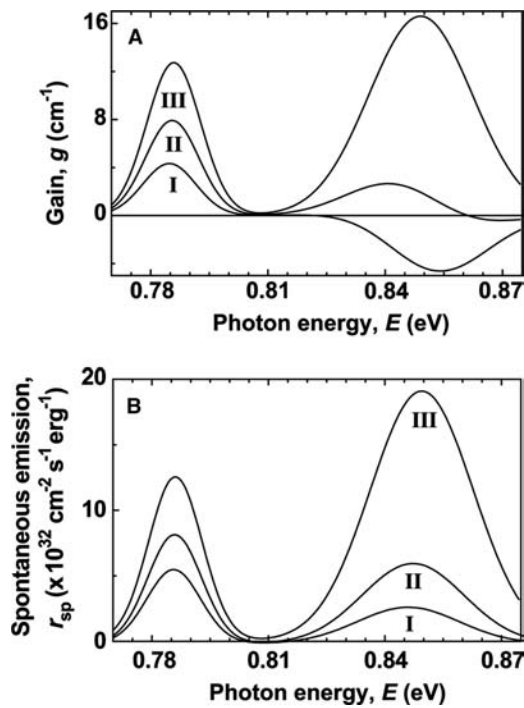


**Fig. 5** Gain (A) and spontaneous emission spectra (B) at different injection currents for a model structure in case of large separation of the mean transition energies and small inhomogeneous broadening. I:  $j = 6.8 \text{ A cm}^{-2}$ , II:  $j = 18 \text{ A cm}^{-2}$ ,  $j_3 = \infty$  (saturated  $g$  and  $r_{sp}$ ). Source: From Ref.<sup>[17]</sup>.

current density against losses also represents the gain peak vs. the injection current density (the gain-current curve) if the abscissa and the ordinate are interchanged.

2. Small separation of the mean transition energies and large inhomogeneous broadening. The character of the change in the gain and the

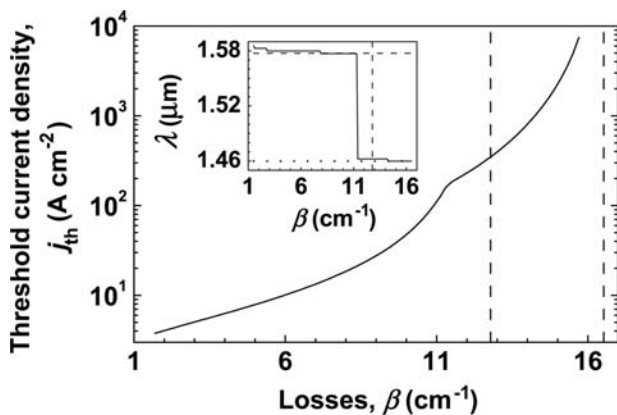


**Fig. 6** Threshold current density and lasing wavelength (the inset) against losses. The parameters are the same as in Fig. 5. The vertical dashed lines are for  $g_1^{\text{max}}$  and  $g_2^{\text{max}}$ . The horizontal dashed and dotted lines in the inset are for  $\bar{\lambda}_1$  and  $\bar{\lambda}_2$ . Source: From Ref.<sup>[17]</sup>.

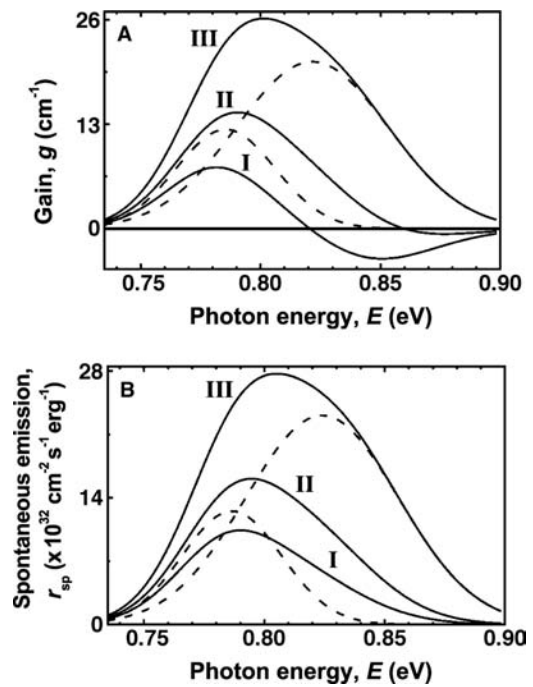


**Fig. 7** Gain (A) and spontaneous emission (B) spectra at different injection currents for a model structure in case of small separation of the mean transition energies and large inhomogeneous broadening, I:  $j = 20.7 \text{ A cm}^{-2}$ , II:  $j = 39.7 \text{ A cm}^{-2}$ ,  $j_3 = \infty$  (saturated  $g$  and  $r_{sp}$ ). Source: From Ref.<sup>[17]</sup>.

spontaneous emission spectra with injection current as well as the lasing wavelength dependence on losses are shown in Figs. 7 and 8, respectively. There is a smooth change in  $\lambda$  with  $\beta$ . The lasing wavelength  $\lambda$  can be significantly below  $\bar{\lambda}_1$  for high losses. Nevertheless, it is hard to construct a situation where  $\lambda$  approaches

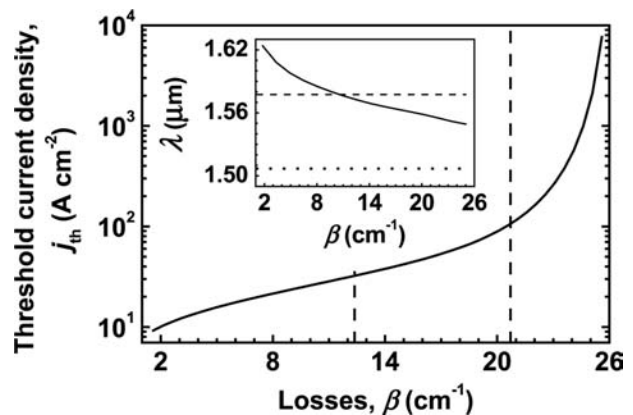


**Fig. 8** Threshold current density and lasing wavelength (the inset) against losses. The parameters are the same as in Fig. 7. The vertical dashed lines are for  $g_1^{\text{max}}$  and  $g_2^{\text{max}}$ . The horizontal dashed and dotted lines in the inset are for  $\bar{\lambda}_1$  and  $\bar{\lambda}_2$ . Source: From Ref.<sup>[17]</sup>.

$\bar{\lambda}_2$ . This is because the position of the gain spectrum peak is determined by the overlap of the transition lines, and the inhomogeneous broadening of the excited-state transition is always larger than that of the ground-state transition. Thus the position of the gain spectrum peak is closer to that of the ground-state transition. Therefore when the lasing wavelength changes smoothly with losses, it is impossible to derive information on the energy of the excited-state transition directly from this dependence.

Near-threshold lasing and EL spectra of a laser structure based on three sheets of QDs formed by the AAPS (the same as was used to measure spontaneous emission and gain spectra; Figs. 3 and 4) are shown in Fig. 9. The inhomogeneous broadening is less than the separation of the mean transition energies (situation 1 takes place). For a long stripe, where the external loss is small, the gain of the ground-state transition is sufficient to overcome the total loss, and lasing occurs via the ground-state transition (Fig. 9A). In shorter stripes, with larger external loss, the gain of the ground-state transition is not sufficient to

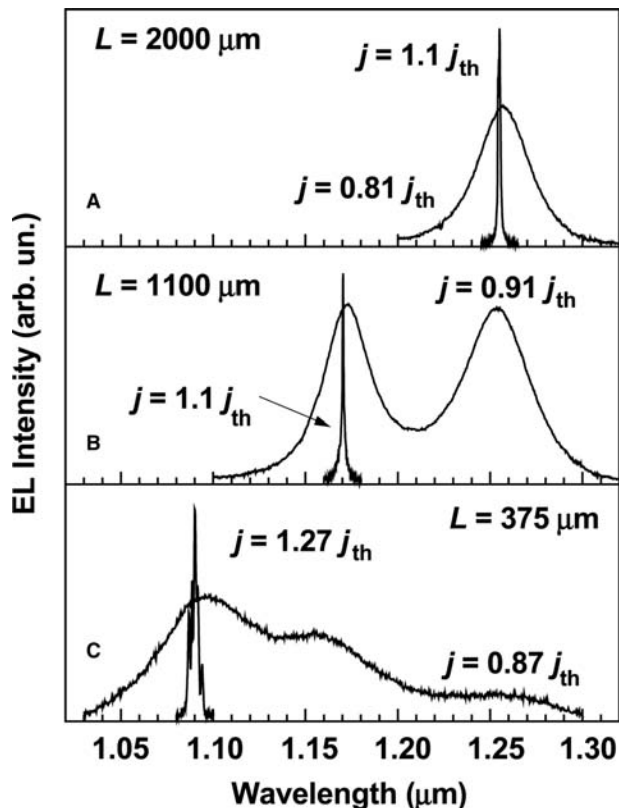


Fig. 9 Electroluminescence spectra showing spontaneous emission and lasing. Different stripe lengths are used.

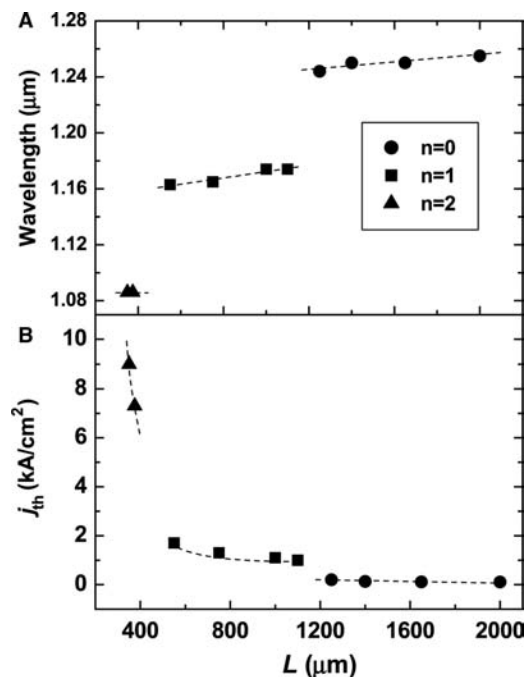


Fig. 10 Dependence of the lasing wavelength (A) and the threshold current density (B) on the cavity length.  $n = 0$ , 1, and 2 denote the ground, first, and second excited states, respectively.

overcome the total loss, and the lasing proceeds via the first excited-state transition (Fig. 9B); the threshold current density increases dramatically. The shortest devices lase via the second excited-state transition (Fig. 9C) at a very high threshold current density. The dependence of the lasing wavelength and the threshold current density on the cavity length is summarized in Fig. 10. When the lasing occurs via the ground-state transition (for cavities longer than 1.2 mm) the threshold current density increases only slightly as the cavity length decreases.

## THRESHOLD CURRENT DENSITY

Lower threshold current density in QD lasers as compared to those based on quantum wires and QWs was predicted in early theoretical works and greatly motivated experimental and theoretical research in the field of QD lasers. More detailed theoretical studies revealed dramatic dependence of threshold current on the parameters of QD array among which the most important are the QD density and the inhomogeneous broadening.<sup>[9]</sup> Thus, for instance, it was shown that lasing could never be achieved if QD density is less than certain critical density or inhomogeneous broadening exceeds the critical value. In Ref.<sup>[20]</sup>, the following inequality for interrelated tolerable values of structure

parameters was obtained:

$$\frac{4}{\xi} \left[ \frac{\sqrt{\varepsilon}}{\lambda_0} \right]^2 \tau_{\text{QD}} \frac{a}{\Gamma} \frac{(\Delta\varepsilon)_{\text{inhom}}}{\hbar} \frac{1}{N_S} \frac{1}{L} \ln \frac{1}{R} \leq 1 \quad (2)$$

where most values are defined in Eq. (1), and where  $R$  is the facet reflectivity and  $L$  is the cavity length.

Hence Eq. (2) relates the tolerable values of the three parameters,  $N_S$ ,  $(\Delta\varepsilon)_{\text{inhom}}$ , and  $L$ , to each other. The critical tolerable value of each of the three parameters is related to the given values of the other two. The more perfect the QD array [the less the  $(\Delta\varepsilon)_{\text{inhom}}$ ] or the longer the cavity the less is the minimum surface density of QDs  $N_S^{\text{min}}$ . The denser the QD ensemble (the greater the  $N_S$ ) or the longer the cavity the greater is  $(\Delta\varepsilon)_{\text{inhom}}^{\text{max}}$ . The more perfect the QD array or the denser the QD ensemble the less is the minimum cavity length  $L^{\text{min}}$ .

When one of the structure parameters is close to its critical tolerable value, the mean (averaged over the lateral direction) electron and hole level occupancies in QDs tend to unity—the electron and hole levels are fully occupied. This demands infinitely high free-carrier densities in the OCL and, correspondingly, infinitely high injection current. For the advantages of a QD laser to be attained in practice, structure parameters should be well away from the critical values. Fig. 11 shows the dependence of the normalized threshold current on the normalized surface QD density for a model structure.<sup>[9,20]</sup> There is an optimal surface QD density minimizing threshold current. For  $N_S < N_S^{\text{min}}$ , the lasing is impossible to attain (the gain cannot overcome losses).

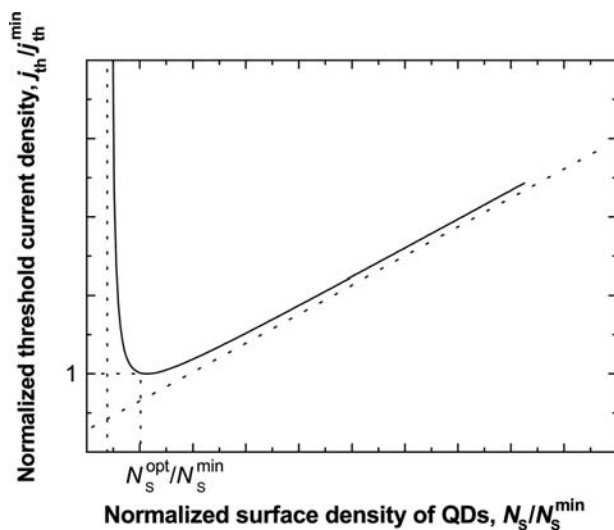


**Fig. 11** Normalized threshold current density vs. the normalized surface QD density for a model structure. *Source:* From Ref.<sup>[9]</sup>.

Recent progress in crystal growth has resulted in arrays of In(Ga,As)–GaAs QD with a relatively small ( $< 10\%$ ) inhomogeneous broadening. Low threshold current densities of  $26 \text{ A/cm}^2$ <sup>[14]</sup> and  $19 \text{ A/cm}^2$ <sup>[21]</sup> at  $300 \text{ K}$ , and  $6 \text{ A/cm}^2$  at  $4 \text{ K}$ <sup>[22]</sup> for long devices with HR facet coatings based on a single sheet of QDs have been achieved. However, differential efficiency of such lasers was low. In commercial lasers, high differential efficiency is required and, thus, HR coatings cannot be applied to the front facet. Here the measure of quality is the value of threshold current density per single QW or QD layer. The best values of  $7\text{--}10 \text{ A/cm}^2$  per QD layer were realized in devices with a large number of QD stacks<sup>[11]</sup> and high differential efficiency. A record low transparency current of  $6 \text{ A/cm}^2$  per dot layer, an internal quantum efficiency of  $98\%$ , and an internal loss below  $1.5 \text{ cm}^{-1}$  have been demonstrated in a QD laser grown by MOCVD.<sup>[23]</sup>

## DEFECT REDUCTION TECHNIQUES

Growth of QDs especially large-sized ones with high confinement energy for electrons and holes may be accompanied by the formation of defects and large dislocated clusters. This problem can be eliminated by applying specially developed in situ defect-reduction techniques, which permits selective elimination of dislocated objects without affecting coherent QDs.<sup>[24]</sup> A schematic diagram illustrating the reduction of dislocation density is shown in Fig. 12. The QDs are overgrown with a thin (1 nm) GaAs layer (Fig. 12B) at a temperature corresponding to that of QD formation ( $480^\circ\text{C}$ ). Then the substrate temperature is raised to  $600^\circ\text{C}$ . The thin cap layer only partly covers the large dislocated InAs clusters allowing the InAs to evaporate in the annealing step (Fig. 12C). The smaller coherent QDs, being completely covered, are only weakly affected. Fig. 13 shows transmission electron microscopy (TEM) images for the samples grown with and without the annealing step. The density of dislocated islands in the sample grown without the annealing step is  $\sim 10^9 \text{ cm}^{-2}$ . No dislocated islands are revealed in the structure grown with the annealing step.

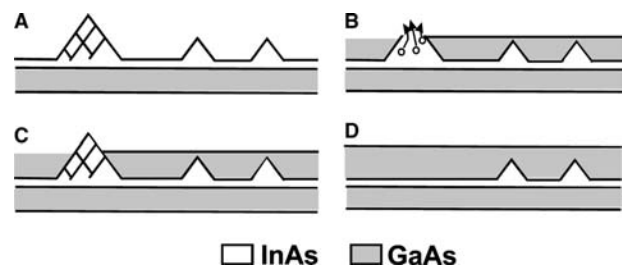


**Fig. 12** A schematic illustrating reduction of dislocation density.

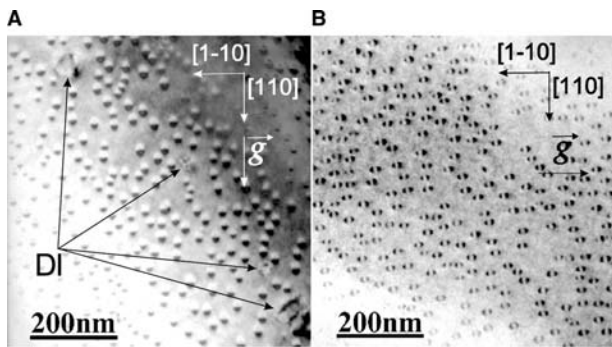


**Fig. 13** Plan view bright field (220) TEM images of the structures grown without (A) and with (B) the annealing step. DI denotes dislocated islands.

The application of defect reduction techniques is especially important in case of lasers based on multiple QD stacks. Even small density of dislocations and large dislocated clusters in the first QD sheet result in a drastic deterioration of the properties of upper QD sheets. The use of defect reduction techniques results in a dramatic improvement in the characteristics of QD lasers (Fig. 14). More than sevenfold decrease in the threshold current is observed for a structure based on 10 QD stacks.

## TEMPERATURE CHARACTERISTICS

Ultrahigh temperature stability of threshold current was predicted for ideal QD lasers (infinite barriers,

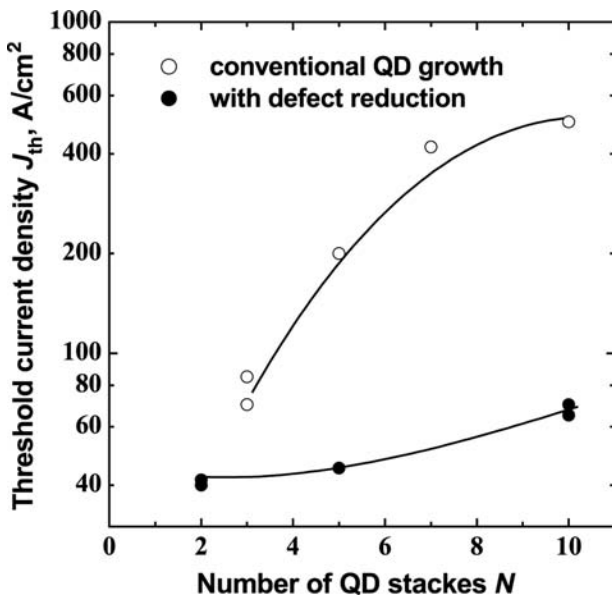


**Fig. 14** Threshold current densities for the structures with various numbers of QD stacks grown without and with defect reduction. A design with negligible external losses is used.

no fluctuation of QD sizes, etc.) to be one of the main advantages over conventional (QW lasers.<sup>[4]</sup> Usually, the temperature dependence of the threshold current density ( $j_{th}$ ) is described by the characteristic temperature defined as

$$\frac{1}{T_0} = \frac{1}{j_{th}} \frac{\partial j_{th}}{\partial T}$$

In actual laser structures there are several reasons for  $j_{th}$  to be temperature dependent:

- The presence of carriers in the OCL and their radiative and nonradiative recombination processes give rise to an additional component of the threshold current, which is governed by the thermal escape of carriers from QDs and depends exponentially on temperature.<sup>[9]</sup>
- Inhomogeneous broadening of QD array. This effect is similar to that due to recombination in the OCL in the sense that the inhomogeneous line broadening is associated with undesired pumping of non-lasing QDs. So long as the electron and hole populations in the nonlasing QDs are in equilibrium with those in the active QDs, the fraction of threshold current arising from the recombination in non-lasing QDs depends on temperature, and the characteristic temperature is no longer infinite.<sup>[25]</sup>
- The charge neutrality violation in QDs makes the threshold current component, associated with the recombination in QDs, to be also temperature dependent.<sup>[26]</sup>
- Small energy separation between the discrete hole levels.<sup>[27]</sup>
- Temperature dependence of free carrier absorption.

Because of these effects the threshold current and its temperature stability depend dramatically on the parameters characterizing the QD array (surface density of QDs, QD size dispersion, and carrier localization energies in QDs) as well as on the structure design (p-type modulation doping in the active region, thickness of the OCL, doping profiles in the cladding layers and in the OCL, the band offsets at the interface between the OCL and the cladding layers, and the cavity length).

Most of the theoretical works simulate temperature dependence of the threshold current under the assumption of either equilibrium or nonequilibrium carrier distribution in the QD array. Recently, it has been shown that transition from non-equilibrium to equilibrium distribution can result in a very unusual behavior of temperature dependence of the threshold current unique for QD lasers. Fig. 15 shows the temperature dependence of the threshold current density for a

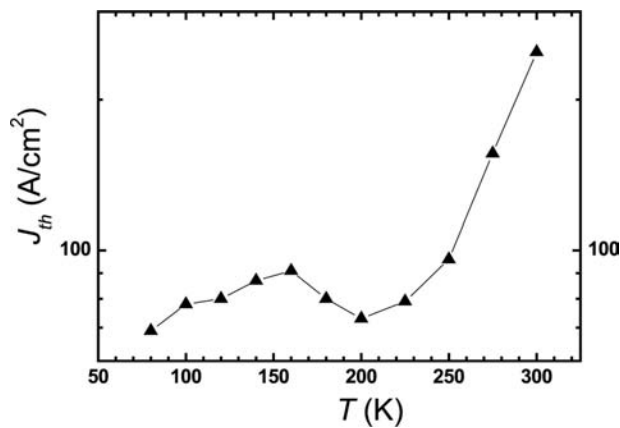


**Fig. 15** N-shape temperature dependence of the threshold current density for a laser with narrow QD size dispersion and low threshold current density. Cavity length is 2 mm.

high-performance QD laser.<sup>[28]</sup> At  $T < T_1$  ( $T_1 = 150$  K in our case), threshold current density  $j_{th}$  only weakly increases with the temperature. This increase can be attributed to the presence of carriers in the OCL and their radiative and non-radiative recombination. Then at  $T > T_1$ , threshold current density decreases with the temperature. Thus at  $T_1 < T < T_2$  ( $T_2 = 200$  K in our case), the temperature dependence of the threshold current is described by a negative  $T_0$ .<sup>[29]</sup> Finally, at  $T > T_2$ , threshold current density starts to increase, with the temperature steeper as compared to low temperature range. Temperatures  $T_1$  and  $T_2$  depend on the confinement of electron and hole energy levels with respect to the continuum and inhomogeneous broadening of QD arrays. For QD arrays with weak confinement and larger inhomogeneous broadening,  $T_1$  can be very low and was not observed in the early experiments.<sup>[29]</sup>

For commercial applications it is essential to have a high value of  $T_0$  at temperatures above 300 K. Several approaches have been proposed to improve the  $T_0$  values such as placing of QDs in a QW,<sup>[30]</sup> increasing the bandgap of the matrix,<sup>[29]</sup> etc. However, even in some cases the  $T_0$  values were increased (up to 350 K in Ref.<sup>[30]</sup>) threshold current density was also high. First high characteristic temperature operation (160 K) at ambient temperature (below 40°C (313 K)) together with low threshold current density (70 A/cm<sup>2</sup> for 3-fold stacked QDs) was realized in Ref.<sup>[31]</sup> for a design with negligible external losses in pulsed mode.

Very high characteristic temperature in QD lasers ( $T_0 = 230$  K up to 80°C (353 K)) was recently demonstrated by applying a QD p-modulation doping technique;<sup>[32]</sup> the approach, which was earlier proposed to improve the performance of QW lasers.<sup>[33]</sup> The penalty of p-doping was reduced differential efficiency

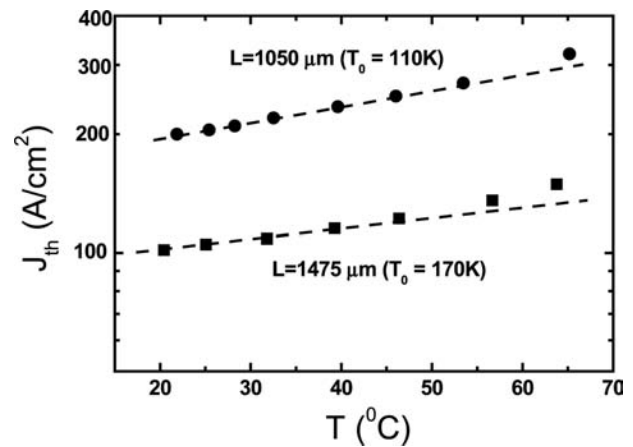


**Fig. 16** High-temperature stability of the threshold current for a high-performance QD laser emitting at 1.3 μm. The active area is based on five QD stacks.

(<20% in Ref.<sup>[32]</sup>). Recently, using undoped 5 fold-stacked QDs, it became possible to increase the  $T_0$  value to 170 K (Fig. 16) between 10°C (283 K) and 65°C (338 K) without paying a penalty of increased internal losses.<sup>[34]</sup> Remarkably, this device simultaneously showed low threshold current density (100 A/cm<sup>2</sup>, 1.5 mm cavity length, uncoated) and high differential efficiency (85%).

## TIME-RESPONSE

The modulation bandwidth of QD lasers was measured by different groups and is typically 5–10 GHz.<sup>[35–39]</sup> The high-speed performance of QD lasers was shown to be limited by the long “quantum capture” time of injected carriers.<sup>[40]</sup> The value of this parameter, which includes transport through the heterostructure, continuum to bound capture time, and intersubband carrier relaxation, varies with injection current and the number of dot levels in the active region. The carrier capture time measured in Refs.<sup>[40]</sup> and<sup>[41]</sup> quantitatively agrees with the modulation bandwidth value of 5 GHz. More direct femtosecond differential transmission measurements have been made by using the pump-probe technique.<sup>[35]</sup> These measurements have been done as a function of temperature (4–300 K) and excitation level (number of carriers per dot). It was shown that, in addition to intersubband electron relaxation in the dots, carrier reemission to the barrier and wetting layers and the density of available states in these regions also play significant roles in determining the carrier dynamics, particularly at elevated temperatures. It is therefore worthwhile to use QD with high confinement energy to suppress carrier reemission from QDs to the WL and OCL. Indeed, in QD amplifiers the use of QDs with high confinement energy (large-sized



QDs) resulted in a significant improvement in gain dynamic.<sup>[42]</sup>

The “hot-carrier” problem (or gain compression) can be overcome by injecting electrons directly to the lasing states<sup>[43,44]</sup> and thus bypassing the usual injection process over the heterojunction barriers. By tunnel injection, “cold” electrons are introduced into the lasing subband of the active (gain) region (resonantly or phonon assisted) at or near the Fermi level at a rate higher than the stimulated emission rate, and the electron distribution remains quasi-Fermi even at large drive currents. The hole thermalization rates are usually very large because of the high density of states and band mixing. Hot-carrier effects, mentioned earlier, can therefore be minimized. By utilizing tunnel injection of electrons, enhanced small-signal modulation bandwidth,  $f_{-3\text{ dB}}$ , and reduced temperature sensitivity of the threshold current, characterized by  $T_0$ , were measured in  $\text{In}_{0.4}\text{Ga}_{0.6}\text{As}/\text{GaAs}$  self-organized quantum dot ridge waveguide lasers. Values of  $f_{-3\text{ dB}} = 15\text{ GHz}$  at  $283\text{ K}$  and  $T_0 = 237\text{ K}$  for  $278\text{ K} < T < 318\text{ K}$  are measured in these devices.<sup>[45]</sup> However, threshold current density of the laser was high.

Passive mode locking was achieved at  $1.3\text{ }\mu\text{m}$  in oxide-confined, two-section, bistable QD lasers with an integrated intracavity QD saturable absorber.<sup>[46]</sup> Fully mode-locked pulses at a repetition rate of  $7.4\text{ GHz}$  with a duration of  $17\text{ psec}$  were observed under appropriate bias conditions. No self-pulsation accompanied the mode locking. These results suggest that a carefully designed QD laser is a candidate for ultrashort pulse generation.

## LINewidth ENHANCEMENT FACTOR

The linewidth enhancement factor  $\alpha$  is a key parameter to characterize the dynamic behavior of semiconductor lasers. It is usually defined as  $\alpha = 4\pi/\lambda(dn/dN)(dg/dN)^{-1}$ , where  $N$  is the carrier density,  $n$  is the refractive index, and  $g$  is the optical gain. In narrow stripe lasers, large values of  $\alpha$  can result in antiguiding, whereas in broad area devices this leads to self-focusing, filamentation, and chirp under modulation. Typically,  $\alpha$  is about 2 for InGaAs single QW lasers at carrier densities corresponding to threshold.<sup>[47]</sup> A record low value of  $\alpha = 0.5$  has been reported.<sup>[48]</sup>

The linewidth enhancement factor can be calculated from the gain spectrum using the Kramers–Kronig relations. In the case of a QD laser with a dot ensemble showing a perfect Gaussian energy distribution and only one energy level for electrons and holes, the gain spectrum is perfectly symmetric around the peak gain energy. In this case, the differential gain is also symmetric about the peak gain energy at which lasing occurs. Thus the differential refractive index change

calculated using the Kramers–Kronig relations is exactly zero at the lasing energy, and the QD laser with a quasi ideally distributed (symmetric) ensemble of QDs exhibits a chirp-free operation.<sup>[49]</sup> Participation of excited states might cause a nonsymmetric gain curve, which increases the linewidth enhancement factor. A narrow QD distribution and well-resolved energy levels of  $1.3\text{-}\mu\text{m}$  QD lasers favor substantial reduction in  $\alpha$ . The linewidth enhancement factor below the onset of gain saturation has been measured to be as small as 0.1 in QD lasers,<sup>[50]</sup> which is significantly lower than values reported for QW lasers.

For nearly all applications large spatial coherence of the laser light is needed to focus the beam. Narrow stripe devices with index guiding that gives rise to fundamental transverse mode operation are limited in the output power by the onset of catastrophic optical mirror damage (COMD).<sup>[51]</sup> The solution of gain-guided broader area devices has been fraught with the problem of filamentation and higher order modes, which destroy the spatial coherence.<sup>[52]</sup> As beam filamentation strongly depends on the linewidth enhancement factor ( $\alpha$ -factor),<sup>[53]</sup> QD-lasers, which are conjectured to show a reduced  $\alpha$ -factor, are expected to show suppressed filamentation compared to QW lasers.

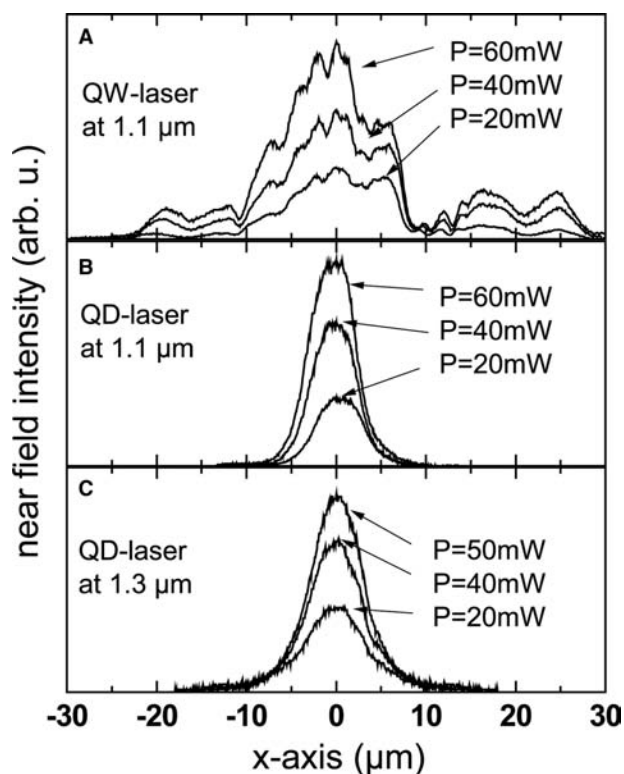


**Fig. 17** Near field cross sections in horizontal direction (slow axis) for  $6\text{-}\mu\text{m}$  stripe QW laser emitting at  $1.1\text{ }\mu\text{m}$  (A), QD laser emitting at  $1.1\text{ }\mu\text{m}$  (B), and QD laser emitting at  $1.3\text{ }\mu\text{m}$  (C). Cavity length is  $1.3\text{ mm}$  in all cases.



Recently, near-fields and beam-qualities ( $M^2$ ) were compared for a narrow stripe 1.1- $\mu\text{m}$  emitting QW laser, a 1.1- $\mu\text{m}$  emitting QD laser, and a 1.3- $\mu\text{m}$  emitting QD laser.<sup>[54]</sup> The cross section in the lateral direction (slow axis) of the near fields for output powers of 20, 40, and 60 mW is shown in Fig. 17A for the QW laser and in Fig. 17B and C for the QD lasers emitting at 1.1 and 1.3  $\mu\text{m}$ , respectively. The near fields of the QD lasers are Gaussian for all output powers up to 60 mW. In the QW laser, filamentation is present already at an output power of 20 mW. With increasing output power, filamentation increases with more sharp peaks appearing in the beam profile. Additionally, for higher drive currents side lobes next to the laser ridge emerge, too. The beam qualities ( $M^2$ ) were studied as a function of stripe width for QW and QD lasers.<sup>[54]</sup> At an output power of 20 mW,  $M^2$  increases for the QW laser from a value of 2.6 for a 3- $\mu\text{m}$  stripe laser to 4.7 for a 10- $\mu\text{m}$  stripe laser. Thus even for a narrow stripe width of 3  $\mu\text{m}$  no lateral fundamental mode emission could be achieved for this gain-guided QW laser. In the case of the QD lasers the situation is quite different. Lateral fundamental mode emission ( $M^2 \leq 2$ ) is demonstrated up to a stripe width of 8  $\mu\text{m}$  for the 1.1- $\mu\text{m}$  QD laser and up to 9  $\mu\text{m}$  for the 1.3- $\mu\text{m}$  QD laser at an output power of 20 and 45 mW, respectively.

## REDUCED CARRIER LATERAL TRANSPORT

Three-dimensional carrier localization in QDs leads to a dramatically reduced lateral carrier spreading in the active area of QD lasers. Carrier capture time from the GaAs matrix to the wetting layer was measured to be less than 1 psec for QDs emitting at long wavelengths.<sup>[55]</sup> The capture from the wetting layer into the QDs is also very efficient.<sup>[56]</sup> The fabrication of single-mode lasers may require etching through an active region. For QW devices this would lead to non-radiative recombination of carriers within a diffusion length at the processed surfaces. In contrast, in a QD structure, carrier transport in the lateral direction is suppressed, which makes the surface recombination insignificant. Thus leakage currents in narrow stripe QD lasers are expected to be lower than those in QW devices. In Ref.<sup>[56]</sup>, bright photoluminescence at 300 K was demonstrated from very small 0.2- $\mu\text{m}$  mesas at room temperature, indicating that using QDs as an active medium indeed permits a dramatic reduction of the surface recombination in deeply etched devices.

In QD lasers, lateral transport toward defects in the active area and, correspondingly, non-radiative recombination are also suppressed. This results in reduced sensitivity of the performance of QD lasers to defects in the active area. The influence of high-energy proton

irradiation on the device properties of QD lasers was investigated in Ref.<sup>[57]</sup>. Quantum dot lasers demonstrated enhanced radiation hardness in contrast to QW devices, which indicates that using QDs is promising for lasers in hard radiation environment. First degradation experiments on QD lasers demonstrated the potential of QD lasers for increased operation lifetime.<sup>[58,59]</sup>

## HIGH-POWER OPERATION

High differential efficiency, low threshold current, and suppression of filamentation make QD lasers very promising for high-power applications. Recently, light-current characteristics in QW, quantum wire, and QD lasers have been theoretically treated.<sup>[60]</sup> Quantum dot lasers were shown to have a major advantage over conventional QW laser from the viewpoint of high-power operation. According to Ref.<sup>[60]</sup>, in properly optimized QD lasers the light-current characteristic is linear with both the internal and external quantum efficiency being close to unity up to very high injection current densities (15 kA/cm<sup>2</sup>). Output power in excess of 10 W at an internal quantum efficiency higher than 95% was shown to be attainable in broad area devices.

Present broad-area QD lasers emitting in a spectral range of 0.94–1.3  $\mu\text{m}$  show CW output powers of 3–6 W.<sup>[61–64]</sup> Fig. 18 shows the pulsed performance of QD lasers based on 10-fold stacked QDs. The cavity length is 1.45 mm and uncoated facets are used. Differential efficiency as high as 85% and a threshold current density as low as 90 A/cm<sup>2</sup> are realized. The characteristic temperature is 150 K in a temperature range of 0–70°C. All the key numbers are better than those for commercial InP-based 1.3- $\mu\text{m}$  devices. Narrow

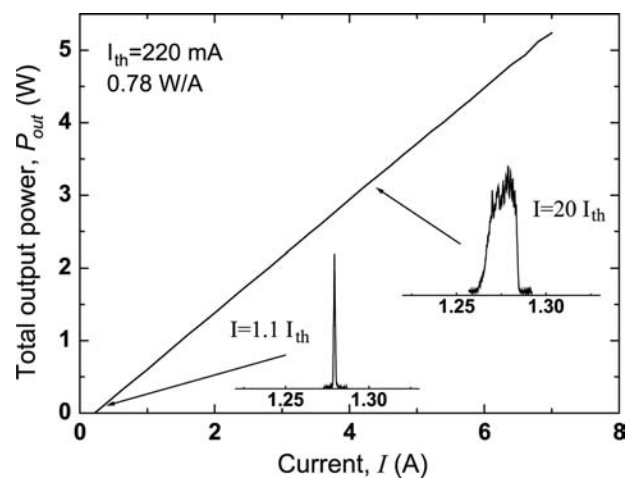


**Fig. 18** Pulsed light-current characteristic at room temperature of a broad area QD laser emitting at 1.3  $\mu\text{m}$ . Stripe width is 100  $\mu\text{m}$ , stripe length is 1.5 mm.

7- $\mu\text{m}$ -wide stripes demonstrated single-transverse-mode kink-free CW operation up to 330 mW for uncoated facets.<sup>[65]</sup>

### VERTICAL CAVITY SURFACE EMITTING LASERS BASED ON QUANTUM DOTS

Vertical cavity surface emitting lasers (VCSELs) emitting at 1.3  $\mu\text{m}$  are very promising for use in high-bit-rate transmission lines for telecommunications. Until recently only the InP/InGaAsP material system has been utilized to fabricate long-wavelength semiconductor lasers because the crystal composition of InGaAsP can be adjusted to produce emitters in the required wavelength region. However, the performance of current long-wavelength lasers still lags behind that of their shorter-wavelength counterparts. The problem limiting the performance of InP-based QW devices is a strong temperature dependence of their characteristics caused by insufficient electron confinement in the active region.<sup>[66]</sup> This leads to poor temperature stability of the threshold current and emission wavelength, as well as to high values of threshold current densities. Besides, the cost of InP-based devices is substantially higher than that for GaAs-based ones.

An additional disadvantage as far as fabrication of commercial long-wavelength vertical cavity lasers based on traditional InGaAsP–InP heterostructures is concerned is the lack of adequate Bragg mirrors. Mirrors of InGaAsP–InP layers have a small refractive index difference. Thus a Bragg mirror with 50 or more periods is required to achieve the reflectivity value ( $>0.99$ ) needed for lasing. The introduction of wafer-bonded GaAs/AlGaAs Bragg mirrors to InP-based active regions has led to an improvement in device performance.<sup>[67]</sup> However, the wafer-fusion technique represents a complex technological process and therefore expensive for large-scale production. In addition,

bonded interfaces have low quality, resulting in, for example, increased resistance. Other recent approaches (using top metamorphic AlAs–GaAs DBR, or using AlGaAsSb-based DBRs on InP substrates) do not solve the problem of reliability and cost efficiency, and may be competitive only until the production-oriented GaAs-based technology is developed. Thus for the fabrication of commercial 1.3- $\mu\text{m}$  VCSELs it is essential that the whole structure, including the active area, is grown on the same GaAs substrate, which would enable it to use monolithic high-contrast lattice-matched GaAs–Al(Ga)As or oxidized GaAs–AlO Bragg mirrors.

Two approaches are successfully applied for long-wavelength GaAs-based VCSELs: using InGaAs–GaAs QDs and nitrogen doping of InGaAs layers.<sup>[68]</sup> Self-organized QDs are particularly advantageous for VCSELs as they offer the possibility to realize very low threshold current density and high temperature stability in properly optimized devices. Owing to suppressed carrier lateral transport very small VCSELs can be fabricated without a deterioration of operating characteristics.

The first 1.3- $\mu\text{m}$  VCSELs grown on GaAs substrate was realized in Ref.<sup>[69]</sup>. The VCSEL design is schematically shown in Fig. 19. The microcavity is surrounded by (p) and (n)  $\text{Al}_{0.98}\text{Ga}_{0.02}\text{As}$  layers (less than  $\lambda/4$ -thick) followed by  $1\lambda$ -thick (p) and (n)GaAs current spreading/intracavity contact spacer layers doped to  $10^{18}\text{ cm}^{-3}$ . Intracavity contacts are used. The spacer layers are followed by DBRs composed of alternating  $\text{Al}_{0.98}\text{Ga}_{0.02}\text{As}$  and  $\lambda/4$ -thick GaAs layers. The  $\text{Al}_{0.98}\text{Ga}_{0.02}\text{As}$  layers in the DBR, as well as those surrounding the optical cavity, are selectively oxidized to form Al(Ga)O. The QDs are centered in a  $1\lambda$ -thick GaAs optical microcavity, whose edges are doped to  $10^{17}\text{ cm}^{-3}$ . The ends of the microcavity are composed of  $\text{Al}_x\text{Ga}_{1-x}\text{As}$  linearly graded from  $x = 0.02$  up to 0.98. The CW light power–current–voltage ( $L$ – $I$ – $V$ )

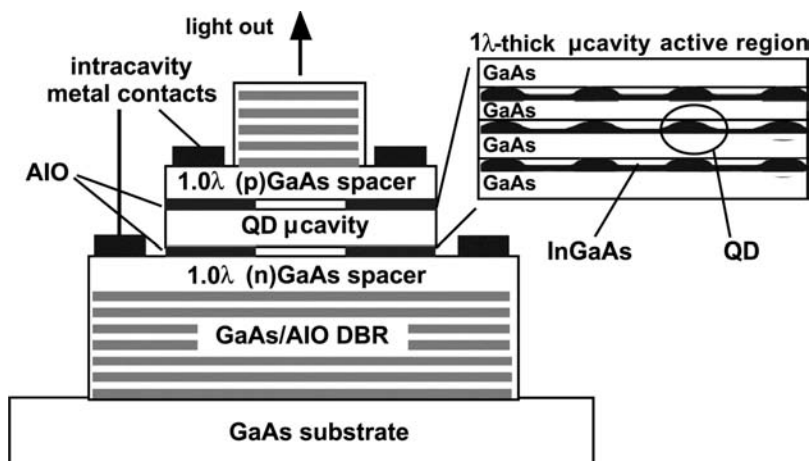


**Fig. 19** A schematic cross section of vertical cavity surface emitting laser with QD active region, oxide current aperture, and oxide DBRs.

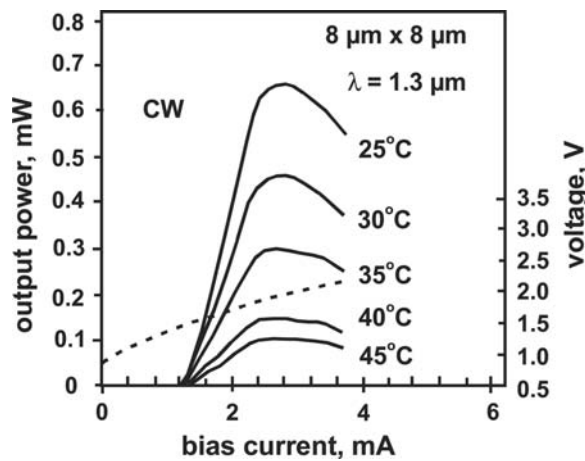


Fig. 20  $L$ - $I$ - $V$  curves of a 1.3- $\mu\text{m}$  emitting GaAs-based QD VCSEL at various temperatures.

characteristics of a QD VCSEL are shown in Fig. 20. The threshold current of the QD VCSEL remains practically unchanged with temperature increase. The electroluminescence measurements from a test structure indicate that the lasing proceeds via the QD ground-state transition. The maximum differential efficiency is 64%. The emission wavelength is near 1.3  $\mu\text{m}$  (1.28–1.306  $\mu\text{m}$  depending on the particular position on the wafer). Variation in the threshold current across the wafer is  $\sim 10\%$ . The lasing threshold (1.2 mA) is constant down to 0.5- $\mu\text{m}$  oxide apertures, due to reduced carrier lateral diffusion. During the lifetime test in excess of 700 hr CW at 35°C no change in the performance of the device is found.

## CONCLUSION

Since the first realization of injection lasing<sup>[6]</sup> via self-organized QDs, tremendous progress has been achieved in the field of QD lasers. Development of sophisticated growth techniques resulted in arrays of In(Ga,As)-GaAs QD with a relatively small (<10%) inhomogeneous broadening, large confinement energies of electrons and holes, and emission wavelength of about 1.3  $\mu\text{m}$ . Lasers based on such QD arrays demonstrated unique characteristics such as low threshold current density, high temperature stability of threshold current, high differential efficiency, and small linewidth enhancement factor ( $\alpha$ -factor). The QDs are also very promising as an active medium for high-performance, cost-efficient, 1.3- $\mu\text{m}$  VCSELs. We believe that further progress in QD growth as well as deeper understanding of the physics of QD lasers will result in the perfection of their characters, reveal new exciting properties, and finally lead to a new generation of high-performance commercial devices for different applications.

## ACKNOWLEDGMENTS

This work was done in collaboration with Zh.I. Alferov, D.Bimberg, N.A. Cherkashin, A.Yu. Egorov, I.N. Kajander, P.S. Kop'ev, A.R. Kovsh, J.A. Lott, N.A. Maleev, I.I. Novikov, C. Ribbat, R. Sellin, Yu.M. Shernyakov, and A.F. Tsatsul'nikov. We are very grateful to L.V. Asryan for helpful discussions and kind permission to reproduce parts of his works. We acknowledge the support of the INTAS, the Russian Foundation of Basic Research, the Volkswagen Foundation, and the Alexander von Humboldt Foundation. MVM thanks the Alexander von Humboldt Foundation for the fellowship.

## REFERENCES

1. Alferov, Zh.I.; Kazarinov, R.F. *Double Heterostructure Laser, Authors Certificate No 27448, Application No 950840 with a priority from March 30, 1963.*
2. Kroemer, H. A proposed class of heterojunction injection lasers. Proc. IEEE **1963**, *51*, 1782–1784. Submitted October 14, 1963.
3. Dingle, R.; Henry, C.H. Quantum Effects in Heterostructure Lasers. U.S. Patent No. 3982207, 21 September 1976
4. Arakawa, Y.; Sakaki, H. Multidimensional quantum well laser and temperature dependence of its threshold current. Appl. Phys. Lett. **1982**, *40* (11), 939–941.
5. Asada, M.; Miyamoto, Y.; Suematsu, Y. Gain and the threshold of three-dimensional quantum-box lasers. IEEE J. Quantum Electron. **1986**, *22* (9), 1915–1921.
6. Kirstaedter, N.; Ustinov, V.M.; Ruvimov, S.S.; Maximov, M.V.; Kop'ev, P.S.; Alferov, Zh.I.; Richter, U.; Werner, P.; Gosele, U.; Heydenreich, J. Low threshold, large to injection laser emission from InGaAs quantum dots. Electron. Lett. **1994**, *30* (9), 416–417.
7. <http://www.compoundsemiconductor.net/articles/news/6/3/21/1> (accessed March 2003).
8. Bimberg, D.; Grundmann, M.; Ledentsov, N.N. *Quantum Dot Heterostructures*; John Wiley & Sons: Chichester, 1999.
9. Asryan, L.V.; Suris, R.A. Inhomogeneous line broadening and the threshold current density of a semiconductor quantum dot laser. Semicond. Sci. Technol. **1996**, *11* (4), 554–567.
10. Ledentsov, N.N.; Shchukin, V.A.; Grundmann, M.; Kirstaedter, N.; Böhrer, J.; Schmidt, O.; Bimberg, D.; Ustinov, V.M.; Egorov, A.Yu.; Zhukov, A.E.; Kop'ev, P.S.; Zaitsev, S.V.; Gordeev, N.Yu.; Alferov, Zh.I.; Borovkov, A.I.; Kosogov, A.O.; Ruvimov, S.S.; Werner, P.; Gösele, U.; Heydenreich, J. Direct formation of vertically coupled quantum dots in Stranski-Krastanow growth. Phys. Rev., B **1996**, *54* (12), 8743–8750.
11. Kovsh, A.R.; Maleev, N.A.; Zhukov, A.E.; Mikhrin, S.S.; Vasil'ev, A.R.; Shernyakov, Yu.M.; Maximov, M.V.; Livshits, D.A.; Ustinov, V.M.; Alferov, Zh.I.

- Ledentsov, N.N.; Bimberg, D. InAs/InGaAs//GaAs quantum dot lasers of 1.3  $\mu\text{m}$  range with high (88%) differential efficiency. *Electron. Lett.* **2002**, *38* (19), 1104–1106.
12. Maximov, M.V.; Tsatsul'nikov, A.F.; Volovik, B.V.; Sizov, D.S.; Shernyakov, Yu.M.; Kaiander, I.N.; Zhukov, A.E.; Kovsh, A.R.; Mikhlin, S.S.; Ustinov, V.M.; Alferov, Zh.I.; Heitz, R.; Shchukin, V.A.; Ledentsov, N.N.; Bimberg, D.; Musikhin, Yu.G.; Neumann, W. Tuning quantum dot properties by activated phase separation of an InGa(Al)As alloy grown on InAs stressors. *Phys. Rev., B* **2000**, *62* (24), 16,671–16,680.
  13. Guffarth, F.; Heitz, R.; Schliwa, A.; Stier, O.; Ledentsov, N.N.; Kovsh, A.R.; Ustinov, V.M.; Bimberg, D. Strain engineering of self-organized InAs quantum dots. *Phys. Rev., B* **2001**, *64* (15), 085305–085312.
  14. Liu, G.T.; Stintz, A.; Li, H.; Malloy, K.J.; Lester, L.F. Extremely low room-temperature threshold current density diode lasers using InAs dots in  $\text{In}_{0.15}\text{Ga}_{0.85}$  As quantum well. *Electron. Lett.* **1999**, *35*, 1163–1165.
  15. Maximov, M.V.; Ledentsov, N.N.; Ustinov, V.M.; Alferov, Zh.I.; Bimberg, D. GaAs-based 1.3  $\mu\text{m}$  InGaAs quantum dot lasers: A status report. *J. Electron. Mater.* **2000**, *29* (5), 476–486.
  16. Stier, O.; Grundmann, M.; Bimberg, D. Electronic and optical properties of strained quantum dots modeled by 8-band  $k$   $p$  theory. *Phys. Rev., B* **1999**, *59* (8), 5688–5701.
  17. Asryan, L.V.; Grundmann, M.; Ledentsov, N.N.; Stier, O.; Suris, R.A.; Bimberg, D. Effect of excited-state transitions on the threshold characteristics of a quantum dot laser. *IEEE J. Quantum Electron.* **2001**, *37* (3), 418–425.
  18. Shoji, H.; Nakata, Y.; Mukai, K.; Sugiyama, Y.; Sugawara, M.; Yokoyama, N.; Ishikawa, H. Lasing characteristics of self-formed quantum-dot lasers with multistacked dot layer. *IEEE J. Sel. Top. Quantum Electron.* **1997**, *3* (2), 188–195.
  19. Maximov, M.V.; Asryan, L.V.; Yu, M.; Tsatsul'nikov, A.F.; Kaiander, I.N.; Nikolaev, V.V.; Kovsh, A.R.; Mikhlin, S.S.; Ustinov, V.M.; Zhukov, A.E.; Alferov, Z.I.; Ledentsov, N.N.; Bimberg, D. Gain and threshold characteristics of long wavelength lasers based on InAs/GaAs quantum dots formed by activated alloy phase separation. *IEEE J. Quantum Electron.* **2001**, *37* (5), 676–683.
  20. Asryan, L.V.; Suris, R.A. Longitudinal spatial hole burning in a quantum-dot laser. *IEEE J. Quantum Electron.* **2000**, *36* (10), 1151–1160.
  21. Park, G.; Shchekin, O.B.; Huffaker, D.L.; Deppe, D.G. Low-threshold oxide-confined 1.3- $\mu\text{m}$  quantum-dot laser. *IEEE Photonics Technol. Lett.* **2000**, *12* (3), 230–232.
  22. Park, G.; Shchekin, O.B.; Csutak, S.; Deppe, D.G. Room-temperature continuous-wave operation of a single-layered 1.3  $\mu\text{m}$  quantum dot laser. *Appl. Phys. Lett.* **1999**, *75* (11), 3267–3269.
  23. Sellin, R.; Ribbat, Ch.; Grundmann, M.; Ledentsov, N.N.; Bimberg, D. Close-to-ideal device characteristics of high-power InGaAs/GaAs quantum dot lasers. *Appl. Phys. Lett.* **2000**, *78* (9), 1207–1209.
  24. Ledentsov, N.N.; Maximov, M.V.; Bimberg, D.; Maka, T.; Sotomayor Torres, C.M.; Kochnev, I.V.; Krestnikov, I.L.; Lantratov, V.M.; Cherkashin, N.A.; Musikhin, Yu.M.; Alferov, Zh.I. 1.3  $\mu\text{m}$  luminescence and gain from defect-free InGaAs–GaAs quantum dots grown by metal-organic chemical vapour deposition. *Semicond. Sci. Technol.* **2000**, *15* (6), 604–607.
  25. Asryan, L.V.; Luryi, S. Tunneling-injection quantum-dot laser: ultrahigh temperature stability. *IEEE J. Quantum Electron.* **2001**, *37* (7), 905–910.
  26. Asryan, L.V.; Suris, R.A. Charge neutrality violation in quantum dot lasers. *IEEE J. Sel. Top. Quantum Electron.* **1997**, *3* (1), 148–157.
  27. Shchekin, O.B.; Deppe, D.G. The role of p-type doping and the density of states on the modulation response of quantum dot lasers. *Appl. Phys. Lett.* **2002**, *80* (15), 2758–2760.
  28. Novikov, I.I.; Maximov, M.V.; Shernyakov, Yu.M.; Gordeev, N.Yu.; Kovsh, A.R.; Zhukov, A.E.; Mikhlin, S.S.; Maleev, N.A.; Vasil'ev, A.P.; Ustinov, V.M.; Alferov, Zh.I.; Ledentsov, N.N.; Bimberg, D. Temperature characteristics of low threshold and high efficient quantum-dot lasers emitting in the wavelength range 1.25–1.29  $\mu\text{m}$ . *Semiconductor* **2003**, *37* (10), 1239–1242.
  29. Zhukov, A.E.; Ustinov, V.M.; Egorov, A.Yu.; Kovsh, A.R.; Tsatsul'nikov, A.F.; Ledentsov, N.N.; Zaitsev, S.V.; Gordeev, N.Yu.; Kop'ev, P.S.; Alferov, Zh.I. Negative characteristic temperature of InGaAs quantum dot injection laser. *Jpn. J. Appl. Phys.* **1997**, *36* (6B), 4216–4218.
  30. Maximov, M.V.; Kochnev, I.V.; Shernyakov, Y.M.; Zaitsev, S.V.; Gordeev, N.Yu.; Tsatsul'nikov, A.F.; Sakharov, A.V.; Krestnikov, I.L.; Kop'ev, P.S.; Alferov, Zh.I.; Ledentsov, N.N.; Bimberg, D.; Kosogov, A.O.; Werner, P.; Gösele, U. InGaAs/GaAs quantum dot lasers with ultrahigh characteristic temperature ( $T_0 = 385$  K) grown by metal organic chemical vapour deposition. *Jpn. J. Appl. Phys.* **1997**, *36* (6B), 4221–4223.
  31. Shernyakov, Yu.M.; Bedarev, D.A.; Kondrat'eva, E.Yu.; Kop'ev, P.S.; Kovsh, A.R.; Maleev, N.A.; Maximov, M.V.; Mikhlin, S.S.; Tsatsul'nikov, A.F.; Ustinov, V.M.; Volovik, B.V.; Zhukov, A.E.; Alferov, Zh.I.; Ledentsov, N.N.; Bimberg, D. 1.3  $\mu\text{m}$  GaAs-based laser using quantum dots obtained by activated spinodal decomposition. *Electron. Lett.* **1999**, *35* (11), 898–900.
  32. Shchekin, O.B.; Ahn, J.; Deppe, D.G. High temperature performance of self-organised quantum dot laser with stacked p-doped active region. *Electron. Lett.* **2002**, *38* (14), 712–713.
  33. Vahala, K.J.; Zah, C.E. Effect of doping on the optical gain and the spontaneous noise enhancement factor in quantum well amplifiers and lasers studied by simple analytical expressions. *Appl. Phys. Lett.* **1988**, *52* (23), 1945–1947.
  34. Ledentsov, N.N. Long-wavelength quantum-dot lasers on GaAs substrates: From media to device concepts. *IEEE J. Sel. Top. Quantum Electron.* **2002**, *8* (5), 1015–1024.

35. Bhattacharya, P.; Kamath, K.K.; Singh, J.; Klotzkin, D.; Phillips, J.; Jiang, H.T.; Chervela, N.; Norris, T.B.; Sosnowski, T.; Laskar, J.; Murty, M.R. In(Ga)As/GaAs self-organized quantum dot lasers: DC and small-signal modulation properties. *IEEE Trans. Electron Devices* **1999**, *46* (5), 871–883.
36. Klotzkin, D.; Kamath, K.; Vineberg, K.; Bhattacharya, P.; Murty, R.; Laskar, J. Enhanced modulation bandwidth (20 GHz) of  $\text{In}_{0.4}\text{Ga}_{0.6}$  As–GaAs self-organized quantum-dot lasers at cryogenic temperatures: role of carrier relaxation and differential gain. *IEEE Photonics Technol. Lett.* **1998**, *10* (7), 932–934.
37. Krebs, R.; Klopff, F.; Rennon, S.; Reithmaier, J.P.; Forchel, A. High frequency characteristics of InAs/GaInAs quantum dot distributed feedback lasers emitting at 1.3  $\mu\text{m}$ . *Electron. Lett.* **2001**, *37* (20), 1223–1225.
38. Mao, M.-H.; Heinrichsdorff, F.; Krost, A.; Bimberg, D. Study of high frequency response of self-organized stacked quantum dot lasers at room temperature. *Electron. Lett.* **1997**, *33* (19), 1641–1642.
39. Kuntz, M.; Ledentsov, N.N.; Bimberg, D.; Kovsh, A.R.; Ustinov, V.M.; Zhukov, A.E.; Shernyakov, Yu.M. Spectrotemporal response of 1.3  $\mu\text{m}$  quantum-dot lasers. *Appl. Phys. Lett.* **2002**, *81* (20), 3846–3848.
40. Klotzkin, D.; Kamath, K.; Bhattacharya, P. Quantum capture times at room temperature in high-speed  $\text{In}_{0.4}\text{Ga}_{0.6}$  As–GaAs self-organized quantum-dot lasers. *IEEE Photonics Technol. Lett.* **1997**, *9* (10), 1301–1303.
41. Heitz, R.; Veit, M.; Ledentsov, N.N.; Hoffmann, A.; Bimberg, D.; Ustinov, V.M.; Kop'ev, P.S.; Alferov, Zh.I. Energy relaxation by multiphonon processes in InAs/GaAs quantum dots. *Phys. Rev., B* **1997**, *56* (16), 10,435–10,445.
42. Borri, P.; Schneider, S.; Langbein, W.; Woggon, U.; Zhukov, A.E.; Ustinov, V.M.; Ledentsov, N.N.; Alferov, Zh.I.; Ouyang, D.; Bimberg, D. Ultrafast carrier dynamics and dephasing in InAs quantum-dot amplifiers emitting near 1.3- $\mu\text{m}$ -wavelength at room temperature. *Appl. Phys. Lett.* **2001**, *79* (16), 2633–2635.
43. Yoon, H.; Sun, H.C.; Bhattacharya, P.K. Dynamic linewidth of tunneling injection laser. *Electron. Lett.* **1994**, *30* (20), 1675–1677.
44. Asryan, L.V.; Luryi, S. Tunneling-injection quantum-dot laser: ultrahigh temperature stability. *IEEE J. Quantum Electron.* **2001**, *37* (7), 905–910.
45. Bhattacharya, P.; Ghosh, S. Tunnel injection  $\text{In}_{0.4}\text{Ga}_{0.6}$  As/GaAs quantum dot lasers with 15 GHz modulation bandwidth at room temperature. *Appl. Phys. Lett.* **2002**, *80* (19), 3482–3484.
46. Huang, X.; Stintz, A.; Li, H.; Lester, L.F.; Cheng, J.; Malloy, K.J. Passive mode-locking in 1.3  $\mu\text{m}$  two-section InAs quantum dot lasers. *Appl. Phys. Lett.* **2001**, *78* (19), 2825–2827.
47. Bossert, D.J.; Gallant, D. Improved method for gain/index measurements of semiconductor lasers. *Electron. Lett.* **1996**, *32* (4), 338–339.
48. Dutta, N.K.; Hobson, W.S.; Vakhshoori, D.; Han, H.; Freeman, P.N.; de Jong, J.F.; Lopata, J. Strain compensated InGaAs–GaAsP–InGaP laser. *IEEE Photonics Technol. Lett.* **1996**, *8* (7), 852–854.
49. Bimberg, D.; Kirstaedter, N.; Ledentsov, N.N.; Alferov, Zh.I.; Kop'ev, P.S.; Ustinov, V.M. InGaAs–GaAs quantum-dot lasers. *IEEE J. Sel. Top. Quantum Electron.* **1997**, *3* (2), 196–205.
50. Newell, T.C.; Bossert, D.J.; Stintz, A.; Fuchs, B.; Malloy, K.J.; Lester, L.F. Gain and linewidth enhancement factor in InAs quantum-dot laser diodes. *IEEE Photonics Technol. Lett.* **1999**, *11* (12), 1527–1529.
51. Moser, A.; Latta, E.-E.; Webb, D.J. Thermodynamics approach to catastrophic optical mirror damage of AlGaAs single quantum well lasers. *Appl. Phys. Lett.* **1989**, *52* (12), 1152–1154.
52. Chang-Hasnain, C.J.; Kapon, E.; Bhat, R. Spatial mode structure of broad-area semiconductor quantum well lasers. *Appl. Phys. Lett.* **1989**, *54* (30), 205–207.
53. Marcianite, J.R.; Agrawal, G.P. Nonlinear mechanisms of filamentation in broad-area semiconductor lasers. *IEEE J. Quantum Electron.* **1996**, *32* (4), 590–596.
54. Ribbat, Ch.; Sellin, R.L.; Kaiander, I.; Hopfer, F.; Ledentsov, N.N.; Bimberg, D.; Kovsh, A.R.; Ustinov, V.M.; Zhukov, A.E.; Maximov, M.V. Complete suppression of filamentation and superior beam quality in quantum-dot lasers. *Appl. Phys. Lett.* **2003**, *82* (6), 952–954.
55. Graham, L.A.; Huffaker, D.L.; Deppe, D.G. Spontaneous lifetime control in a native-oxide-apertured microcavity. *Appl. Phys. Lett.* **1999**, *74* (17), 2408–2410.
56. Maximov, M.V.; Sotomayor Torres, C.M.; Volovik, B.V.; Ramushina, E.M.; Skopina, V.I.; Ustinov, V.M.; Gurevich, S.A.; Alferov, Zh.I.; Ledentsov, N.N.; Bimberg, D. Impact of carrier lateral transport and surface recombination on the PL efficiency of mesas with self-organized quantum dots. *Phys. Status Solidi, A* **2001**, *188* (3), 955–959.
57. Ribbat, C.; Sellin, R.; Grundmann, M.; Bimberg, D.; Sobolev, N.A.; Carmo, M.C. Enhanced radiation hardness of quantum dot lasers to high energy proton irradiation. *Electron. Lett.* **2001**, *37* (3), 174–175.
58. Lundina, E.Yu.; Shernyakov, Yu.M.; Maximov, M.V.; Kayander, I.N.; Tsatsul'nikov, A.F.; Ledentsov, N.N.; Zhukov, A.E.; Maleev, N.A.; Mikhlin, S.S.; Ustinov, V.M.; Alferov, Zh.I.; Bimberg, D. Long-term stability of long-wavelength ( $> 1.25 \mu\text{m}$ ) quantum-dot lasers fabricated on GaAs substrates. *Tech. Phys.* **2003**, *48* (1), 131–132.
59. Sellin, R.L.; Ribbat, C.; Bimberg, D.; Rinner, F.; Konstanzer, H.; Kelemen, M.T.; Mikulla, M. High-reliability MOCVD-grown quantum dot laser. *Electron. Lett.* **2002**, *38* (16), 883–884.
60. Asryan, L.V.; Luryi, S.; Suris, R.A. Internal efficiency of semiconductor lasers with a quantum-confined active region. *IEEE J. Quantum Electron.* **2003**, *39* (3), 404–418.
61. Zhukov, A.E.; Kovsh, A.R.; Mikhlin, S.S.; Maleev, N.A.; Ustinov, V.M.; Livshits, D.A.; Tarasov, I.S.; Bedarev, D.A.; Maximov, M.V.; Tsatsul'nikov, A.F.; Soshnikov, I.P.; Kop'ev, P.S.; Alferov, Zh.I.; Ledentsov, N.N.; Bimberg, D. 3.9 W CW power from sub-monolayer quantum dot diode laser. *Electron. Lett.* **1999**, *35* (21), 1845–1847.

62. Kovsh, A.R.; Zhukov, A.E.; Livshits, D.A.; Egorov, A.Y.; Ustinov, V.M.; Maximov, M.V.; Musikhin, Yu.G.; Ledentsov, N.N.; Kop'ev, P.S.; Alferov, Zh.I.; Bimberg, D. 3.5 W CW operation of quantum dot laser. *Electron. Lett.* **1999**, *35* (14), 1161–1163.
63. Sellin, R.L.; Ribbat, Ch.; Grundmann, M.; Ledentsov, N.N.; Bimberg, D. Close-to-ideal device characteristics of high-power InGaAs–GaAs quantum dot lasers. *Appl. Phys. Lett.* **2001**, *78* (9), 1207–1209.
64. Klopff, F.; Reithmaier, J.P.; Forchel, A.; Collot, P.; Krakowski, M.; Calligaro, M. High-performance 980 nm quantum dot lasers for high-power applications. *Electron. Lett.* **2001**, *37* (6), 353–354.
65. Maximov, M.V.; Shernyakov, Yu.M.; Kaiander, I.N.; Bedarev, D.A.; Kondrat'eva, E.Yu.; Kop'ev, P.S.; Kovsh, A.R.; Maleev, N.A.; Mikhrin, S.S.; Tsatsul'nikov, A.F.; Ustinov, V.M.; Volovik, B.V.; Zhukov, A.E.; Alferov, Zh.J.; Ledentsov, N.N.; Bimberg, D. Single transverse mode operation of long wavelength ( $\sim 1.3 \mu\text{m}$ ) InAsGaAs quantum dot laser. *Electron. Lett.* **1999**, *35* (23), 2038–2039.
66. Seki, S.; Oohasi, H.; Sugiura, H.; Hirono, T.; Yokoyama, K. Dominant mechanism for limiting the maximum operating temperature of InP-based multiple-quantum-well lasers. *J. Appl. Phys.* **1996**, *79* (5), 2192–2197.
67. Margalit, N.M.; Babic, D.I.; Streubel, K.; Mirin, R.P.; Mars, D.E.; Bowers, J.E.; Hu, E.L. Laterally oxidized long wavelength cw vertical-cavity lasers. *Appl. Phys. Lett.* **1996**, *69* (4), 471–472.
68. Choquette, K.D.; Klem, J.F.; Fischer, A.J.; Blum, O.; Allerman, A.A.; Fritz, I.J.; Kurtz, S.R.; Breiland, W.G.; Sieg, R.; Geib, K.M.; Scott, J.W.; Naone, R.L. Room temperature continuous wave InGaAsN quantum well vertical-cavity lasers emitting at  $1.3 \mu\text{m}$ . *Electron. Lett.* **2000**, *36* (16), 1388–1390.
69. Lott, J.A.; Ledentsov, N.N.; Ustinov, V.M.; Maleev, N.A.; Zhukov, A.E.; Kovsh, A.R.; Maximov, M.V.; Volovik, B.V.; Alferov, Zh.I.; Bimberg, D. InAs–InGaAs quantum dot VCSELs on GaAs substrates emitting at  $1.3 \mu\text{m}$ . *Electronics Lett.* **2000**, *36* (16), 1384–1385.



# Quantum Dots: Electronic Coupling and Structural Ordering

Glenn S. Solomon

*Department of Electrical Engineering, Stanford University,  
Stanford, California, U.S.A.*

## INTRODUCTION

Current epitaxial crystal growth techniques, with their precise monolayer (ML) control, have led to abrupt heterointerfaces in III–V and group IV semiconductors. This remarkable heterointerface control is responsible for 1-D carrier confinement in the growth direction: When a thin layer is formed from a more narrow bandgap material in the larger bandgap host, a quantum well (QW) is formed. In the III–V material system, this QW has had a dramatic impact in both semiconductor research and mainstream semiconductor technology. Although significant effort has been concentrated toward extending this control to 2-D and 3-D confinement with quantum wires and quantum dots, the results have been encouraging but not resounding. This is generally because lithography techniques typically used to provide increased lateral confinement do not have the monolayer resolution that is available through epitaxial growth techniques. Furthermore, because of interfacial damage, it is difficult to directly pattern active regions using processing. Although useful structures can be fabricated using surface patterning,<sup>[1–4]</sup> these techniques are not suitable for all structures. In the 1990s, a purely epitaxial technique was developed to produce quantum dots in the InAs/GaAs and Ge/Si semiconductor systems. This technique utilizes the strain-induced islanding of the Stranski–Krastanow (SK) growth mode, in which the growth surface islands compensate for the increase in energy caused by extra interface surface with a decrease in accumulated strain energy.

The formation of quantum dots by strain-induced islanding has provided a simple, lithography-free method to produce dense ensembles of quantum dots. Unlike the classical self-assembly processes in non-epitaxial systems, in this system, the energies associated with the epitaxial growth process still dominate those that drive the nanostructure formation process. The result is nanostructure features that are not identical but still similar. Strain-induced island formation is perhaps more akin to other surface and interface phenomena such as surface spinodal decomposition,<sup>[5]</sup> surface reconstruction, and ledge-and-step formation.<sup>[6]</sup> In fact, our general observation is that the

ensemble uniformity and spatial periodicity of InAs islands follow more closely these processes than the self-organized formation of more classical structures such as carbon nanotubes<sup>[7]</sup> or self-assembled protein structures.<sup>[8]</sup> Unfortunately, the dominance of the epitaxial process and the large surface migration processes common in this growth lead to large inhomogeneous island size distributions: The spectral features are broadened with respect to QWs, and the narrow, atomic-like transitions are lost in the ensemble broadening. Nevertheless, the association of self-organization with strain-induced islanding, specifically with respect to direct bandgap semiconductors, has done much to focus attention on the possible utility of this system. Although the phenomenological process of strain-induced islanding was observed 60 years ago, the association of spectral features with these islands was made by Tabuchi et al.,<sup>[9]</sup> whereas the general possibilities of this system have been noted, developed, and championed by Leonard, Noda, and Sasaki<sup>[10]</sup> This research is encouraging and lively, and with further fine-tuning of the growth processes, as was needed in the development of the successful QW technology, inhomogeneous broadening can be reduced.

## OVERVIEW

The strain-induced quantum dot formation approach has been used effectively to investigate the 0-D structure in nanoscale systems leading to a rich array of results.<sup>[11–13]</sup> New devices, where the active regions are composed of these quantum dot ensembles, have demonstrated improved characteristics. However, except for the improved thermal stability of lasers demonstrated by Heinrichsdorff et al.,<sup>[14]</sup> most of these improvements result not from the 0-D confined system but from material compliance. For example, the useful wavelength range of light-emitting diodes (LEDs) and lasers based on GaAs substrates has been extended, but this is not a result of increased carrier confinement. In addition, nearly all of these results rely on the random arrays of islands with slightly varying sizes, and the quest for atomic-like ensembles, either ordered or random, has not been demonstrated to date. This is

clearly because of the less dominant, secondary role of the energies that drive this ordering process in epitaxial systems.

However, there are benefits to the integration of self-ordering processes with epitaxial deposition. Creating active regions away from processing interfaces and placing these regions within doping and barrier structures while utilizing semiconductor processing and fabrication techniques are attractive approaches to nanostructure fabrication. To this end, we have investigated ways in which vertical growth precision can be incorporated to develop new structures and improve the size and spatial distribution of the strain-induced quantum dot ensemble. In this chapter, we discuss the effect of epitaxially layering InAs islands with small spacer layers of the GaAs host crystal<sup>[15,16]</sup> as a technique to create either small, well-controlled, vertically coupled structures, or as a mechanism to create an ordered surface array of quantum dots. Because of the strain distribution present around the InAs islands, GaAs deposited on top of an InAs island layer preferentially migrates away from individual InAs dots, resulting in a planarized growth front. If the deposited GaAs is thin enough so that the strain field is still present on the GaAs surface, when subsequent InAs is deposited, there is preferential migration to regions above InAs islands. In this way, InAs island layers, separated by thin GaAs spacer layers, can be vertically aligned in columns.<sup>[17]</sup>

Two properties can be optimized using these columns. First, the confined energy states within the InAs quantum dots are no longer isolated when two InAs dots are vertically aligned and separated by only a thin GaAs spacer layer. The energy states couple or extend into the adjacent dots.<sup>[15]</sup> Second, in a subsurface dot layer, the strain distribution from adjacent InAs dots can interact so that a surface strain distribution results, which is a superposition of strain distribution of the subsurface InAs dots.<sup>[18]</sup> In regions where island density is larger than some equilibrium value, the strain from individual subsurface islands will interfere so that the surface strain will be a superposition of the subsurface distribution. In regions where the island density is smaller than some critical value, the adjacent strain fields from subsurface islands will not interfere as significantly and the resulting surface strain distribution will have regions unaffected by subsurface islands. By depositing multiple island layers, the surface strain distribution can, in theory, be made uniformly periodic. Because the surface strain distribution resulting from the superposition of subsurface island strain affects the surface diffusion, increased spatial ordering of InAs islands on the surface can result. Furthermore, because the size distribution of dots in a layer is affected by variations in the nutrient field surrounding a stable island by creating a more

uniform spatial distribution of nucleation sites, the island size distribution can be made more uniform. Thus subsurface layers of InAs dots can be used to create a more structurally and spatially uniform top layer of quantum dots. When optimized to enhance coupling between vertical dots, we call the structures “vertically coupled quantum dot columns.” When optimized to enhance surface quantum dot uniformity, we call the structures “subsurface island superlattices.”

Before discussing the details of the vertical quantum dot layers, we discuss two salient features of single-layer InAs quantum dot ensembles: the control of ensemble density and the state of in-plane localization. Both of these effects depend on molecular beam epitaxy (MBE) growth conditions. The “Introduction” provides a general introduction to the formation of single quantum dot layers by this technique, in addition to particular discussions of ensemble density and localization. The rest of the chapter is broken into two sections on multiply quantum dot layer growth. The vertical electronic coupling in quantum dot columns is first discussed, whereas ordering by subsurface island superlattices follows.

## SINGLE-LAYER InAs QUANTUM DOT ENSEMBLES

### Theory of Island Formation

In homoepitaxial crystal growth of cubic materials, the (100) growth surface is the lowest energy facet plane.<sup>[19]</sup> If the growth temperature and flux rates are appropriate, adatom attachment on the growth surface is to kink and ledge sites, or at island nucleation regions. Thus crystal growth proceeds by the lateral growth of kinks and ledges, or by the expansion of/at monolayer-scale high islands. Ideally, as one monolayer is filled, new monolayer-high nucleation sites are created, and the 2-D (100) growth surface propagates. In contrast, during heterogeneous crystal growth, as more adatoms are deposited onto the growing surface, this growth surface can go through structural changes that can be as dramatic as the complete loss of epitaxial coherency, or as small as changes in surface reconstruction, surface roughness, or abruptness of a heterointerface.<sup>[20–23]</sup> In the case of InAs on GaAs, the lattice mismatch is 7.2%. The critical thickness for relaxation by dislocation generation is 45 Å, or approximately 15 unstrained InAs monolayers according to the Matthews–Blakeslee model.<sup>[24]</sup> This critical thickness is based on the mechanical equilibrium of an existing interfacial dislocation. A more accurate theory, based only on the energy density required to generate (not propagate) an interfacial dislocation, indicates the complete absence of a critical

thickness.<sup>[25]</sup> Although this approach cannot be assumed accurate at such large misfit, it does suggest a significantly smaller critical thickness. Because of the similar InAs and GaAs crystal structures, at least one chemisorbed monolayer of InAs can be assumed to be stable on the GaAs substrate. Below the critical thickness or after a chemisorbed layer, a metastable phase can exist. This is phenomenologically known as the SK growth regime.<sup>[26]</sup> In the SK growth of InAs on GaAs, there is a thickness region where excess strain is partially accommodated by surface islanding. This growth regime is a transitional growth mode between a compliant planar growth regime that characterizes ideal MBE growth and a plastically relaxed growth, because as islands grow and merge, the surface area can no longer expand to accommodate the increasing strain energy.

Without kinetic effects, island size and shape are predominantly determined by the Gibbs free energy balance:

$$\mu = \mu_0 + \frac{1}{2} \mathbf{S}_{ijkl} \sigma_{ij}(x) \sigma_{kl}(x) V_0 + \gamma K V_0 \quad (1)$$

where  $V_0$  is the molecular volume,  $\gamma$  is the surface tension, and  $K$  is the surface curvature (the inverse of the radius of curvature).  $\mathbf{S}_{ijkl}$  is the compliance matrix and  $\sigma_{kl}(x)$  is the stress field at  $x$ .  $S_{ijkl} \sigma_{kl}(x) = \epsilon_{ij}$  is the strain, so that  $1/2 \epsilon_{ij}(x) \sigma_{kl}(x) V_0$  is the accumulated strain energy.  $\gamma K V_0$  is the extra surface energy and  $\mu_0$  is the total unstrained planar crystal energy. If the epitaxial lattice mismatch were not present, the strain would be absent and the curvature ( $K$ ) that minimizes the system energy would be zero—corresponding to a flat surface. Thus the lattice mismatch strain leads to a non-flat growth surface with an island size determined by the minimization of Eq. (1). Entropy-of-mixing terms and reduction in the strain energy because of alloy mixing in the near-surface region are not included in Eq. (1). Because of surface diffusion limitations, the surface curvature will take the form of a periodic roughness  $a \cos kx$ , where  $a$  is the roughness amplitude and  $k$  is the roughness wavenumber. If  $\tau$  and  $n$  are the local in-plane and surface normals, whereas  $x$  and  $y$  denote the global crystal in-plane and normal directions, then by geometry, the stresses on the traction free surface are:

$$\begin{aligned} \sigma_{\tau\tau} &= \sigma_{xx} \cos^2 \theta + \sigma_{yy} \sin^2 \theta + 2\sigma_{xy} \cos \theta \sin \theta, \\ \sigma_{\tau n} &= \sigma_{nn} = 0, \quad \text{along the surface} \end{aligned} \quad (2)$$

To solve for  $\sigma_{\tau\tau}$ , an Airy solution of the form:

$$\Phi = \frac{\sigma_y^2}{2} + (A + By)e^{-ky} \sin(kx) \quad (3)$$

is used. The stress on the islanding surface is:<sup>[27–29]</sup>

$$\sigma_{xx} = \sigma(1 - ka(ky - 2))e^{-ky} \sin(kx) \quad (4)$$

where the  $y$  origin is taken as the mean surface. As more materials are deposited, the amplitude  $a$  increases. When  $a$  approaches the thickness of the heteroepitaxial layer, the troughs of the roughened surface begin to impinge on the heterointerface and stop because the mismatch is no longer present. The trough regions become extended as more materials are transferred away from the interface region to the peaks of the roughened surface, resulting in distinct islands.<sup>[20]</sup> The island shape is determined by the details of the facet-dependent surface energy  $\gamma$ . In the InAs/GaAs system, the islands are formed from (136) facets.<sup>[30]</sup>

Based on Eq. (1), as heteroepitaxial material is deposited, the growth surface remains initially flat until the accumulated strain energy exceeds the energy associated with creating extra surface area. The flat region is called the wetting layer in SK growth, and is inherent in this growth mode. Although the concept of critical thickness mentioned previously is based on a continuum model, there has been theoretical<sup>[31–33]</sup> and experimental evidence<sup>[34]</sup> showing dislocation and crack nucleation at island edges, suggesting that the islands formed during growth play a more central role in the transition to relaxed heterogeneous crystal growth.

## Experimental Control of Quantum Dot Properties

### Growth of dislocation-free islands

Except where noted, the InAs dot structures described in this chapter were constructed from epitaxial layers deposited in a Varian Gen II MBE system. The system uses an As<sub>2</sub> flux that is produced by thermally decomposing the As<sub>4</sub> flux commonly used as the arsenic source in MBE. In addition, the As source has an adjustable valve, so that the V/III flux ratio can be precisely controlled. In this way, we can control the surface diffusivity of In. The V/III beam equivalent pressure ratio is kept at 9 for all layers, except where noted. Except where noted, the InAs island region and all subsequent depositions were conducted at 500°C, as measured by the substrate thermocouple, which corresponds to 457°C using a more accurate optical technique.<sup>[35]</sup> Where growth temperature is varied, it is reported as thermocouple temperature and is approximately 50°C higher than the actual temperature. Each InAs island layer is composed of the equivalent of 3 ML of planar InAs deposited at a rate varied between 0.1 and 0.2 μm/hr. The GaAs growth rate was 0.2 μm/hr. Photoluminescence (PL) spectra

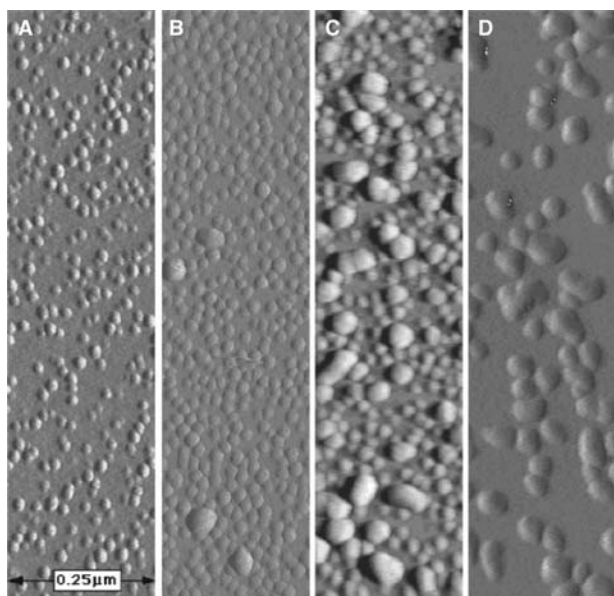


**Fig. 1** AFM images of InAs islands formed from various amounts of InAs deposition at 500°C. (A) After 2 ML on InAs, (B) 3 ML of InAs, (C) 4 ML of InAs, and (D) after 6 ML of InAs. The InAs islands are not covered with GaAs, but left bare for AFM imaging. The AFM is conducted *ex situ*, under ambient conditions.

were obtained using an Ar<sup>+</sup> ion laser with samples mounted in a circulation He cryostat, except for the LEDs, which are measured at room temperature.

Atomic force microscopy (AFM) images of the islanding surface for different InAs coverages are shown in Fig. 1.<sup>[36]</sup> This figure shows the transition in the SK growth regime between isolated 3-D island growth and coalesced island growth at 500°C. Fig. 1A shows isolated islanding at 2 ML of surface coverage. Just below this coverage (2 ML) of InAs, the epitaxial surface is planar. This abrupt transition to island growth just below 2 ML has been observed by several groups.<sup>[9,36,37]</sup> With 2 ML of deposited InAs, the average island diameter is 150 Å. Transmission electron microscopy (TEM) investigations<sup>[9]</sup> indicate that these islands are defect-free. When the equivalent of three planar monolayers of InAs (Fig. 1B) has been deposited, the additional material is accommodated by an increase in island size and density. The island size increases because more materials have been deposited and migrate to the islands. The increase in island density is more complicated and is related to the local wetting layer structure. Because of the lattice mismatch, the wetting layer thickness is only 1.8 ML. Thus very small differences in thickness and strain energy at different sample positions, corresponding to the equivalent thickness on the order of 0.2 ML (0.6 Å), will result in regions that are still growing planarly because this critical wetting layer thickness has not

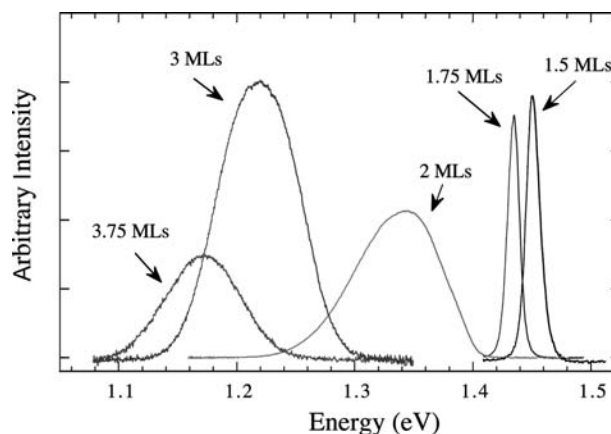


**Fig. 2** The 8-K PL of several samples, which contain InAs thicknesses that vary between 1.5 and 3.75 ML. There is a transition from planar growth to dot growth between 1.75 and 2 ML. The intensity decrease at 3 and 3.75 ML is because of non-radiative recombination.

been exceeded, and regions that contain islands because the critical wetting layer thickness has been exceeded. As more materials are deposited, the planar thickness is exceeded over more regions of the sample and the island density increases.

When an additional 1 ML of InAs is deposited, so that the total InAs deposited is 4 ML (Fig. 1C), a significant change in surface topology is evident. The distribution in island size increases significantly and it appears that there are two distinct types of islands. The larger islands are formed by the coalescing of initially isolated islands, which have plastically relaxed through dislocation generation.<sup>[34,38]</sup> By 6 ML of InAs deposition (Fig. 1D), the transition to a surface topology of plastically relaxed islands is complete.

Fig. 2 shows PL spectra corresponding to the structural transformations observed in Fig. 1. The PL measurements of InAs QWs and quantum dots formed with varying thicknesses of InAs were taken at 8 K using a lock-in technique with a cooled Ge detector for the quantum dot spectra and a Si detector for the QW spectra. The InAs layers have GaAs barriers and are located 500 Å below the sample surface. When 1.5 and 1.75 ML of InAs are deposited, the observed luminescence energy and linewidth are consistent with a uniform InAs (or InGaAs) QW. When the total deposited thickness increases from 1.5 to 1.75 ML, there is a red shift in the spectral peak position because the width of the QW increases. When an additional 0.25 ML is added so that the total deposited InAs is 2 ML, the spectral peak position and shape change dramatically. This is the transition to the quantum dot ensemble structure shown in Fig. 1. This shift occurs when only 0.25 ML (0.75 Å) is added to the surface. The correlation of luminescence structure with the

change in physical structure clearly shows that the luminescence originates from the InAs dot regions. In the QD ensembles, the average height is 40 Å and the dots are unalloyed, whereas in the QW, the thickness is less than 40 Å and the well is alloyed with GaAs because of vertical diffusion. It will be shown later in the entry that significant alloying is present in the QW region but absent in the quantum dot region, leading to a higher energy bandgap in the QW region than in the QD region. Both the bandgap shift and the change in confinement contribute to the red shift in QD luminescence with respect to the QW luminescence. The QD linewidth increases because of the size distribution in the dot ensemble. The luminescence is attributed to an ensemble of InAs dots of different sizes and shapes that each have very narrow, atomic-like spectral linewidths.<sup>[39,40]</sup> The integrated intensity also increases when the deposited thickness changes from 2 to 3 ML. This is because of an increase in InAs dot density, as seen in Fig. 1. When the amount of deposited InAs is increased from 3 to 3.75 ML, the spectral peak position again shifts to lower energy because of the increasing size of the InAs islands. However, the integrated intensity now begins to decrease because of defect generation, which acts as non-radiative recombination site.

One of the major issues in the fabrication of quantum dots by strain-induced islanding is that the narrow, atomic-like emission from single quantum dots is hidden in the inhomogeneously broadened ensemble luminescence. Although it is not the purpose of this chapter to investigate the characteristics of single quantum dots, it is instructive to briefly investigate the emission from the isolated quantum dots forming the ensemble. By reducing the number of quantum dots sampled, single quantum dot features can be observed. This can be accomplished by etching posts into the quantum dot sample and observing the luminescence from individual posts. In Fig. 3A, PL from a single InAs quantum dot layer sample is shown. The wetting layer position is 850 nm and the peak of the quantum dot ensemble emission is 885 nm (1.40 eV). Posts isolating the quantum dot layer were fabricated by electron beam lithography and dry etching, after which microphotoluminescence measurements were made on isolated posts. These measurements were made by G. S., M. Pelton, and Y. Yamamoto. In Fig. 3B, microphotoluminescence from a single 2000-nm post is shown. The spectrum shows luminescence from a large number of closely spaced quantum dot features. By reducing the post size, the number of quantum dots within a post is reduced. In Fig. 3C, the post size is reduced to 100 nm and emission from a single quantum dot can be observed. The typical linewidth is 0.9 Å (140 μeV) and is limited by the spectrometer resolution. The linewidth of the

wetting layer peak at 850 nm is not significantly reduced because it is a continuous 2-D feature, where the major contribution to luminescence broadening is the thickness variation in the growth direction that fluctuates on spatial scale much smaller than the post diameter.

### Substrate temperature

The substrate temperature also affects the InAs QD size and luminescence properties. Fig. 4 shows PL spectra from InAs QD samples where each sample consists of the equivalent of 3 ML of InAs, and only the growth temperature has been varied. The growth temperature was changed from 515°C to 455°C. As the growth temperature is decreased, the spectral peak representing the QD ensemble undergoes a blue shift and the linewidth is reduced. The blue shift in the spectral peak position is because of the reduction in the average dot size. In Fig. 5, an AFM image of the bare dot surface of two samples is shown. The two growth temperatures are 455°C and 500°C. The dot size is reduced from 200 Å to less than 150 Å because of the reduction in In surface diffusion. The dots formed at the lower temperature are less distinct than the dots formed at 500°C. Although the quantum dots are less uniform when grown at 455°C, the spectral linewidth is smaller than in the well-formed QDs grown at 500°C.

To explain this result, we first show that the small-scale roughness in the lower-temperature samples does not have a significant effect on luminescence broadening. Assume that a quantum dot exciton has a Hamiltonian of the form  $H = H_e + H_h + V_{eh} = H_{ex}$ , where  $H_e$  and  $H_h$  are the Hamiltonians for individual electrons and holes, and  $V_{eh}$  is the Coulomb attractive potential. Now assume that in a quantum dot, the individual electrons and holes have a Hamiltonian that is perturbed by roughness potentials  $V_{e,d}$  and  $V_{h,d}$ , respectively. If  $H_{e,0}$  and  $H_{h,0}$  are the unperturbed QD electron and hole Hamiltonians, the new Hamiltonian is  $H = H_{ex,0} + V_{e,d} + V_{h,d}$ . Assuming that the exciton is in the ground state, so that  $H_0|R_{cm},1s\rangle = E_{R_{cm}}|R_{cm},1s\rangle$ , the variation in the confining potential of the exciton is:

$$\Delta V_{exc,d} = \langle R, 1s | V_{e,d}(z) + V_{h,d}(z) | R, 1s \rangle \quad (5)$$

which we approximate by a combined potential energy component and a geometrical component, so that:

$$\Delta V_{exc} = \Delta V_{rough} \left( \frac{\lambda_c}{a_B} \right)^n \quad (6)$$

where  $\Delta V_{rough}$  is the change in Coulombic attraction because of local variations in confinement,  $\lambda_c$  is the wavelength of roughness perturbation,  $a_B$  is the exciton Bohr radius, and  $n$  is a geometrical factor that increases as

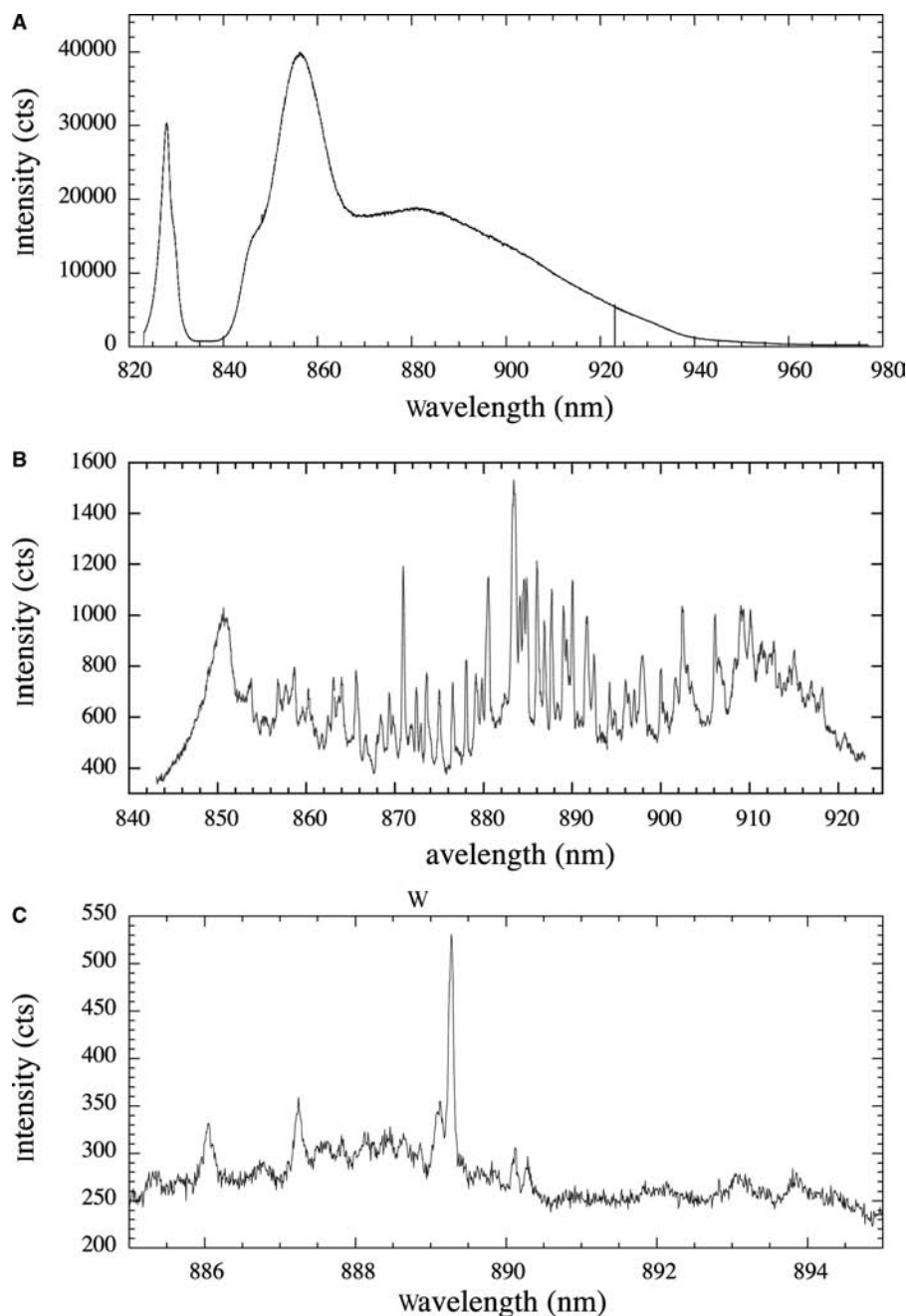


**Fig. 3** The 4-K microphotoluminescence of etched posts containing quantum dots. In (A), the unprocessed sample shows the inhomogeneously broadened luminescence from the QD ensemble. The wetting layer is at 850 nm. In (B), luminescence from many individual quantum dots in a 2- $\mu\text{m}$  post is shown. In (C), luminescence in a single quantum dot in a 100-nm post is shown.

the confinement goes from 1-D to 3-D.  $\Delta V_{\text{rough}}$  cannot be larger than the Coulomb binding energy, or new confinement regions are formed. In addition,  $\lambda_c$  values larger than  $a_B$  lead to inhomogeneous broadening. Thus the maximum broadening occurs when  $\lambda_c$  and  $\Delta V_{\text{rough}}$  are of the order of  $a_B$  and the Coulomb binding energy, respectively. This occurs for our case of InAs dots in GaAs when the dot radius equals the exciton radius, which is approximately 100 Å. Because the small-scale roughness that is dominant in the lower-temperature sample is much smaller than 100 Å, it does not significantly contribute to the ensemble luminescence broadening.

In fact, the structure of the lower-temperature dot sample reduces the broadening for a different reason. Because the barriers between the quantum dots are not well defined, the excitons (or electrons and holes) can become partially extended into adjacent quantum dots. This leads to reduced spectral broadening because these carriers interact with an average potential. If  $\bar{H}$  is the average Hamiltonian and  $\Delta H_i$  is the variation from this average seen by carrier  $i$ , then the energy variation in ground-state excitons is:

$$\Delta V = \sum_i \langle R_i, 1s | \Delta H_i | R_i, 1s \rangle \quad (7)$$



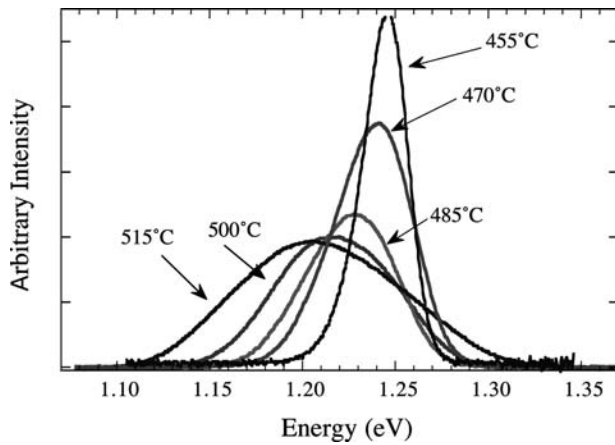


**Fig. 4** Spectra of dot structures grown at different growth temperatures. Each sample contains a dot layer composed of the planar equivalent of 3 ML of planar InAs with an undoped GaAs cap.

But this is reduced as the exciton samples more dots (and is eliminated completely in the trivial case when the exciton samples all of the dots). Therefore the broadening decreases as the dots become less defined and the carriers become less localized. The reduction in spectral broadening can be further enhanced if acoustic phonon scattering is present between the partially extended states of adjacent quantum dots. This scattering will allow carriers to move to the lowest energy state of the overlapping states. In such a case, the luminescence spectrum will no longer be Gaussian: The higher energy component of the Gaussian distribution will be reduced as carriers relax into the lower energies of the partially overlapping states. Evidence of this can be observed in Fig. 4, where the luminescence spectrum of the sample grown at 455°C is no longer symmetrical.

Although the PL linewidth is reduced and excitons become less localized in any particular dot, this is not coupling from overlapping identical states, nor is this complete delocalization and band formation. The observed narrowing is a result of the weakened in-plane localization, not a result of any increased

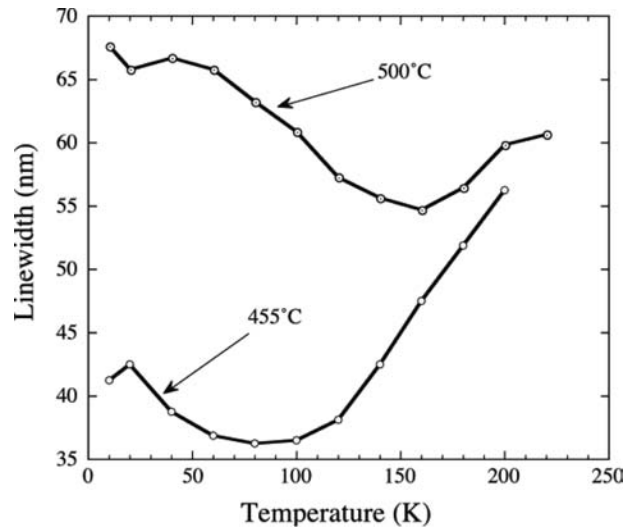


**Fig. 6** The spectral linewidth as a function of temperature for two samples fabricated at different growth temperatures. The narrowing in linewidth as the temperature initially increases is because of reduced localization.

uniformity in the dot ensemble. Additional confirmation of our model can be seen by investigating the variation in the spectral linewidth with sample (cryostat) temperature during measurement. At low temperatures, the spectral broadening is dominated by inhomogeneous broadening from the QD ensemble, whereas at high cryostat temperatures, the spectral broadening is dominated by thermal broadening. Fig. 6 shows the results of variable-temperature PL for the two cases described above. An unusual feature in the figure is the initial decrease in spectral linewidth observed in both samples with increasing sample temperature. The linewidth reduction is caused by a decrease in the inhomogeneous broadening as the sample temperature increases. The presence of further spectral linewidth narrowing confirms that complete delocalization is not present. We believe that the increased spectral linewidth reduction is because of variable range hopping between quantum dot regions. This is a thermally activated process involving states of varying energy. We note that thermionic

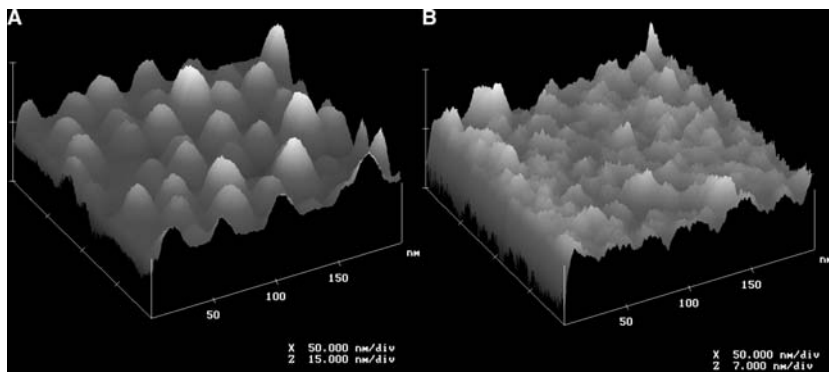


**Fig. 5** AFM images of the bare dot surface of two samples identically prepared, except for the growth temperature. In (A), the growth temperature is 500°C, whereas in (B), the growth temperature is 455°C, as measured by the substrate thermocouple. The vertical height scales are indicated and are different in these two images.

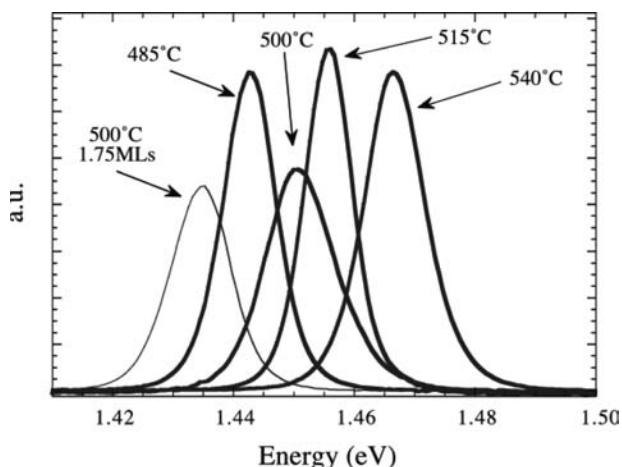


**Fig. 7** PL spectra of QWs grown at different growth temperatures with thickness of either 1.5 or 1.75 ML.

emission above the quantum dot barriers is an unlikely explanation because the barrier between the confined states and the QW wetting region is too large to be of issue at this temperature.

We have confirmed that the QDs formed at low growth temperatures are distinct from the wetting layer QW regions by fabricating QWs with 1.5 and 1.75 ML of InAs. Results of low-temperature PL measurements on these samples are shown in Fig. 7. The data in Figs. 4 and 7 have been combined into Fig. 8. A linear

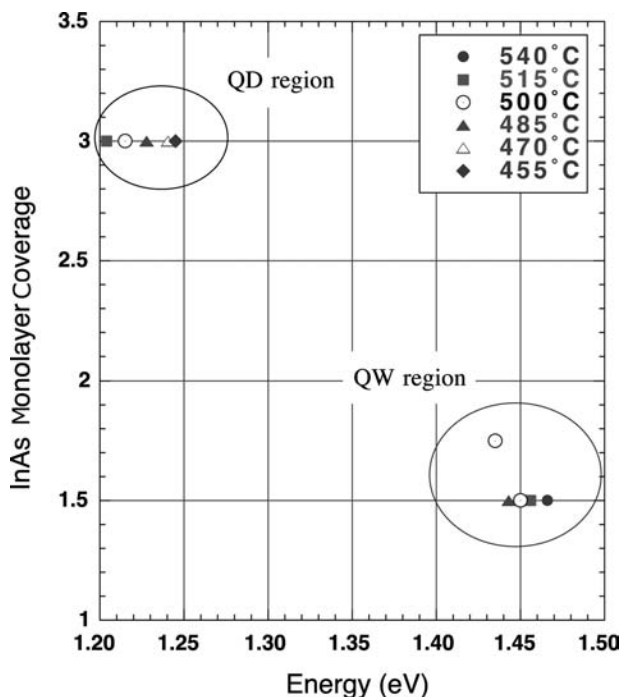


**Fig. 8** PL spectra of QWs and quantum dots grown at different growth temperatures indicating that even at low temperature, the quantum dots luminescence is distinctly shifted from the QW luminescence.

fit is shown between the 1.5- and 1.75-ML QWs grown at 500°C and is extended to the 3-ML region of the figure. Although the 3-ML QD spectral peak position converges to approximately 1.25 eV, the linear fit from the QW region is at a much higher energy; it is clear that the PL peak of the QD ensemble is not converging to the QW (wetting layer) peak position. Although the QD luminescence blue shifts with decreasing growth temperature, the QW luminescence red shifts because of a combination of reduced In desorption and reduced alloying.

V/III flux ratio and quantum dot density

One of the largest determinants of the density of QDs formed using MBE is the V/III flux ratio.<sup>[41]</sup> Fig. 9 shows AFM images of surfaces where the V/III flux ratio has been varied while the InAs growth rate is maintained constant at 0.19 μm/hr. The V/III ratio is decreased from 36 in Fig. 9A to 18 in Fig. 9B, and finally to 9 in Fig. 9C. As the V/III ratio decreases, the 3-D island density increases, whereas the island diameter remains unchanged. The island density changes from 42% for a V/III ratio of 36, to 49% for a V/III ratio of 18, to 81% for a V/III ratio of 9. In MBE growth, decreasing the V/III ratio increases the In surface migration length. If the island density can be modulated by adjusting the In adatom surface diffusion on the islanding surface, then the island

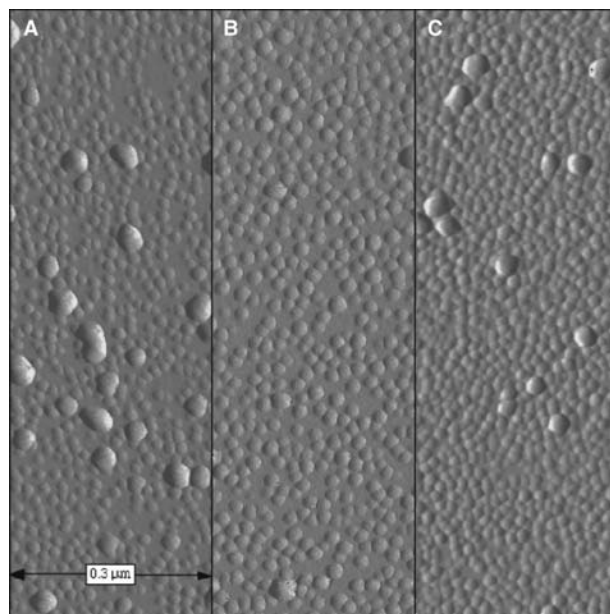


**Fig. 9** AFM images of the difference in island density when the V/III flux ratio is changed from 36 in (A), to 18 in (B), and, finally, to 9 in (C). In all cases, the growth temperature was 500°C, the growth rate was 0.19 μm/hr, and 3 ML of InAs were deposited.

diameter should also change, but this is not observed. However, decreasing the V/III ratio also increases the In adatom surface diffusivity in the wetting layer, allowing it to approach a more equilibrium state with respect to uniform strain and uniform roughening. This situation allows for a more uniform and simultaneous transformation to an islanding surface, and hence a more dense island distribution on top of the wetting layer.

Decreasing the V/III flux ratio increases the concentration-dependent surface diffusion in the wetting layer and hence increases the 2-D island size (pill boxes) in the wetting layer. It is important to make clear the distinction between 3-D islands nucleating on top of the wetting layer and 2-D islands contributing to the layer-by-layer growth of the wetting layer. The 2-D islands nucleate between surface steps and coalesce into a layer. In typical MBE growth, their density and hence average size at which they coalesce are affected by surface diffusion: Increasing surface diffusion can lead to larger 2-D islands in the wetting layer. A layer composed of larger 2-D islands will have a more uniform strain distribution than one composed of smaller 2-D islands because of relaxation at island edges; thus this leads to a more uniform transition to an islanded surface and an increased 3-D island density. In addition, the increased surface diffusion will also allow the growth front to roughen more uniformly, and hence more uniformly develop into 3-D islands of increased density. Although two effects within the wetting layer that will increase the 3-D island density on top of this region have been described, it is not known whether one or both of these effects dominate.

## ELECTRONIC COUPLING IN VERTICALLY ALIGNED QUANTUM DOTS

### Quantum Dot Columns

In addition to the limitations of lithographically defined quantum dots described in the “Introduction,” currently, lithography can only be used to define in-plane features and cannot be used to form arbitrary 3-D quantum dot arrays. In this section, we show how arrays of InAs islands in a matrix of GaAs can be vertically stacked and vertically aligned, and we show that such a structure produces electronically coupled quantum dots in the growth direction. Vertical alignment of islands was demonstrated several years ago.<sup>[42]</sup> These results showed the vertical alignment of two layers in the context of a degenerative roughness process in InGaAs QWs in GaAs, and was believed to be associated with dislocation generation. Here we show the vertical alignment of up to 75 islanding layers

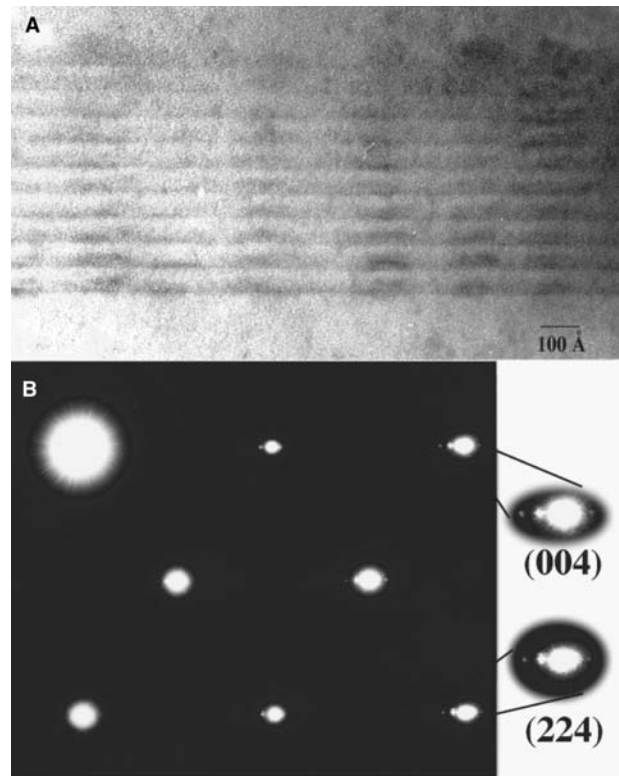


**Fig. 10** (A) TEM (110) cross-sectional image of several columns of vertically aligned InAs islands (dark regions). (B) Selected area diffraction pattern of TEM sample in (A) showing superlattice diffraction spots in the (001) growth direction.

with no associated dislocation generation. These vertically aligned islands have been designed to be electronically coupled by using a thin GaAs spacer layer so that the vertical barrier between dots is small. Although these vertical columns do not provide the freedom to make arbitrary 3-D arrays, this technique produces in situ vertical 1-D QD arrays.

In these structures, the thickness of the GaAs spacer layer between InAs islanding layers is defined as the thickness between adjacent wetting layers, and not the thickness between islands. For a 56-Å GaAs spacer layer, the separation between islands in adjacent islanding layers is approximately 15 Å. In Fig. 10A, a high-resolution TEM image of 10 layers of InAs dots shows several vertically aligned InAs dot columns. The sample is tilted slightly off the zone axis to reduce strain contrast, so that the dark regions in the layered structure are predominantly from the increased scattering of the heavier In atoms. The top InAs layer produces much larger, more rounded, and diffuse islands, which we believe are more heavily alloyed with GaAs than the InAs islands in the lower layers. The presence of a new InAs wetting layer close to the peak of the lower islands inhibits mixing of GaAs with the InAs islands. AFM measurements indicate that the

islands are approximately 180 Å in diameter, which is confirmed in Fig. 10A. AFM measurements also indicate that the in-plane island size does not change significantly when islanding layers of 10 or fewer are added.<sup>[16]</sup> Although the small spacer thickness impedes vertical alloying with GaAs, the island shape remains consistent with (113) sides, as observed by other workers.<sup>[43]</sup> Several TEM images made perpendicular to the zone axis to enhance the lattice contrast were investigated for dislocations in the layer island regions; none was observed. A search for dislocations at the upper interface between the InAs islands and the GaAs cap was done by tilting the sample up to 30° off the zone axis; again, no dislocations were observed.

A selected area diffraction (SAD) pattern is shown in Fig. 10B. Superlattice and InAs diffraction spots are present at all non-in-plane reciprocal lattice points. Of particular interest are the bright and faint reflections to the left of the GaAs reflections for non-in-plane reflections, such as the (004) reflection. Calculations indicate that the brighter secondary spots are because of the superlattice unit cell and are determined from the average composition and lattice constant of the superlattice. The faint reflections further to the left of the GaAs spot are because of InAs and a higher-order superlattice reflection. In reciprocal space directions that are not the growth direction or the in-plane direction, such as the [224] direction, the InAs reflections correspond to an in-plane InAs lattice constant that is pseudomorphically strained. Because the InAs islands form aligned columns, there are two separate diffracting regions that are structurally connected: the wetting layer regions without columns and the column regions. High-resolution X-ray diffraction (HRXRD) in the [001] direction will be discussed later and confirms that the superlattice diffraction results from the pseudomorphically strained wetting layer region. Because of the high island density, if the islands were relaxed through a dislocation mechanism, this relaxation should extend to the wetting layer region; however, this is not observed.

In Fig. 11, a high-resolution TEM cross section highlighting a single column of InAs islands is shown. It clearly indicates the individual InAs islands and their vertical alignment. The 1.8-ML InAs wetting layer<sup>[44]</sup> is not observed. X-ray diffraction (XRD) and cross-sectional STM results discussed in “Theory of Quantum Dot Vertical Alignment” show that the wetting layer diffuses vertically; therefore it is very difficult to image with the microscope. The island height is approximately 40 Å, but is difficult to accurately determine because, at the island peaks, only a small number of InAs atoms remain in cross section to contribute to the contrast, and the observed cross section may not intersect the island centers. The lower island interface

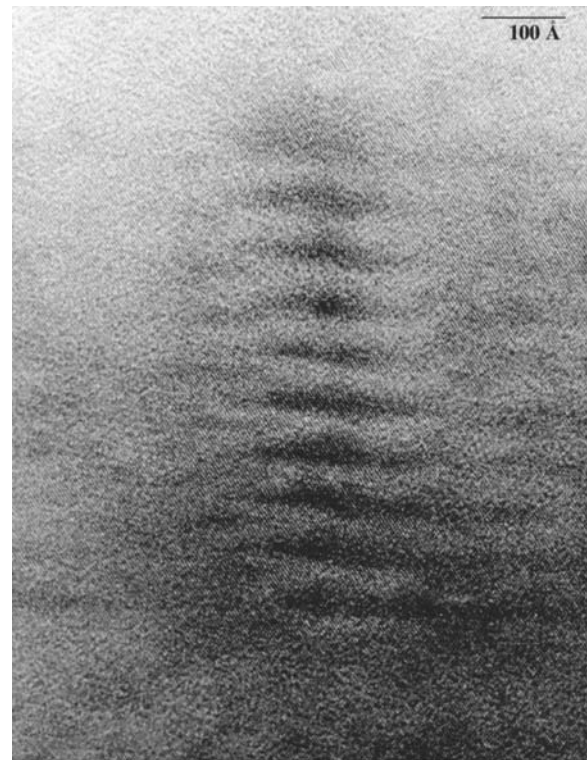


**Fig. 11** TEM image showing one column of vertically aligned InAs islands. The island height is approximately 40 Å, and the in-plane dimension is approximately 180 Å.

is flat and abrupt, indicating that the GaAs fills in and smoothes the islanding interface. As in Fig. 10, the island dimensions in the uppermost islanding layer are much larger and, from the contrast change, appear to be alloyed with GaAs. To the right of the island column in Fig. 11 is a four- or five-layer column that does not continue through the upper layers. This decrease in island density after five layers is also observed in our AFM results<sup>[16]</sup> and is consistent with predictions by Tersoff, Teichert, and Lagally<sup>[18]</sup>

### Theory of Quantum Dot Vertical Alignment

The vertical alignment of InAs islands is easily understood within the context of an energy balance between interface free energy terms and the lattice mismatch-induced strain energy. The islands form to reduce the large heteroepitaxial free energy component and allow the strain in InAs to partially relax. Because the InAs is partially relaxed, subsequent GaAs deposition is favored in the non-islanding regions, and the valleys between islands will be initially filled. When the islands are covered, the GaAs on top of the islands is locally more stressed than the GaAs in adjacent regions between the islands. When a new InAs islanding layer is initiated, the locally stressed GaAs regions above the



old InAs regions become favorable low-energy attachment sites.

The stress field on the islanding surface was described in Eq. (4) as:<sup>[27–29]</sup>

$$\sigma_{xx} = \sigma(1 - ka(ky - 2)e^{-ky} \sin(kx))$$

The strain is  $\epsilon_i = S_{ij}\sigma_{ij}$ , where  $S_{ij}$  is the compliance matrix. The surface strain is largest on the crest of the islands. Therefore Ga adatoms attaching to the crystal surface at island peaks are more strained than in non-island regions: There is a strain gradient toward the area between the islands. Thus In adatoms see a potential gradient in the opposite direction. The gradient is expressed as:

$$V = M\sigma_{\tau,\tau} \quad (8)$$

The mobility  $M$  is given by:

$$M = \frac{D}{kT} \quad (9)$$

where  $D$  is the diffusivity and  $kT$  is the thermal energy. The flux  $J$  along the surface is proportional to this gradient through the surface adatom concentration  $c$ . But if a concentration gradient develops, it also affects the surface flux, so that:

$$J = V\nabla c - D\nabla c = -D\left(\frac{c}{kT}\nabla V + \nabla c\right) \quad (10)$$

If the stress gradient exceeds the concentration gradient, Ga adatoms diffuse to the planar regions, whereas In adatoms diffuse to the island regions.

The local strain relaxation that occurs by islanding in one layer facilitates preferential island formation directly on top of islands in subsequent layers. The islanding process reduces the interface energy by limiting the contact of InAs with the GaAs underlayer, and allows the InAs free surface to partially relax. This partial relaxation is expected to be removed as the InAs island is covered by GaAs. However, if only a thin layer of GaAs is added to the islanding layer, the removal of the partial relaxation will not be complete and the strain field from the buried InAs island will extend to the surface, leaving the GaAs locally strained and possibly distorted. In such a case, the region above a buried InAs island will act as a preferential nucleation site for further islands. Note that the InAs wetting layer and islands form a coupled system, yet SAD and XRD indicate that the wetting layer is unchanged by this preferential islanding and stacking process. The TEM and AFM observations that there is only a marginally small change in the island size with the addition of 10 island layers implies that the

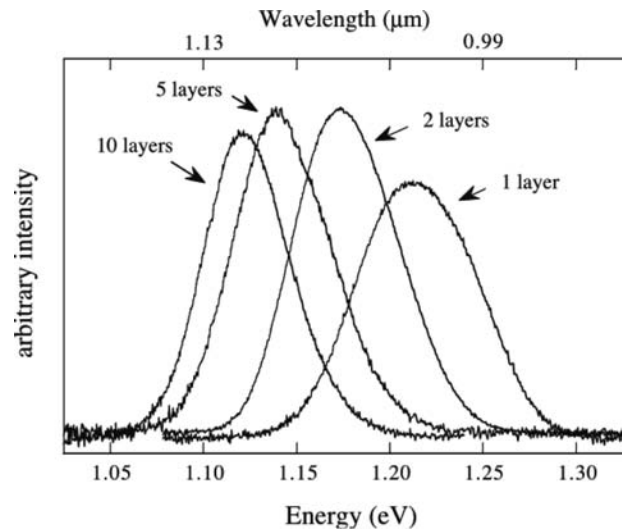


**Fig. 12** The 8-K PL of vertically stacked dot layers. The variation in spectral peak position and linewidth is shown when the number of stacked dot layers changes from 1 to 10.

modification of the local surface strain state by the buried InAs island is not yet pronounced enough to measurably change the lattice mismatch.

### Electronic Coupling in Quantum Dot Columns

Results from 8 K PL measurements are shown in Fig. 12. The single-layer sample is the 3-ML spectrum shown in Fig. 2. Again, the broad luminescence of the single-layer sample is a result of variations in the size of the InAs islands. It is observed that for increasing layers of InAs islands, the spectral peak position shifts to lower energies and the spectral linewidth decreases. In comparison to the single island layer centered at 1.22 eV, the PL peak shifts 73 meV for five layers of islands and an additional 19 meV for 10 layers of islands. Because TEM and AFM measurements show that the change in the island size is small, we attribute the shift in spectral peak position to vertical coupling between InAs islands within a column. There is a 25% reduction in the spectral linewidth between the single islanding layer and the 10 islanding layers. In all cases, the spectral lineshape is Gaussian.

The spectral peak shift and linewidth reduction result from vertical coupling of islands in a column. The tunneling between vertical islands allows carriers to migrate to the lowest energy dot in the column, resulting in a spectral peak shift to lower energy. However, because the number of dots contributing to the spectra is many orders of magnitude larger than the 10 dots in each column, this effect is not responsible for the spectra changes observed here. Vertical coupling also results in spectral peak shifts and linewidth

changes by reducing the ground-state confinement energy of each dot column. A miniband is formed; it is the sum of the bonding and antibonding states from the overlap of the individual wavefunctions in a column. The individual dot is approximated as either a sphere or a box with infinite potential barriers so that the linewidth of the ensemble is proportional to:

$$E \sum_i \left( \frac{\Delta\chi_i}{\chi_i} \right) \quad (11)$$

where  $E$  is the coupled energy level.  $\Delta\chi_i$  and  $\chi_i$  are the variation of the size and the average size of an island in the  $i$ th direction, respectively. The tight-binding formalism is used to model the coupling and resulting energy. In the tight-binding model for a superlattice:

$$E = E_i + S_i + 2T_i \cos(qd) \quad (12)$$

where  $E_i$  is the uncoupled energy in each dot,  $S_i$  is the energy change in each dot when an adjacent dot perturbs the barrier potential, and  $T_i \cos(qd)$  is the wave function overlap term, with dot spacing  $d$  and wavevector  $q$ . Here the bandwidth  $4T_i$  is approximated to increase as  $e^{-c(d-1)}$ , where  $c$  is a fitting parameter weighting the overlap and  $d$  is the number of coupled dots. In this analysis, the spectral peak position and spectral linewidth are fitted using the same coupling parameter, and it is assumed that conduction band coupling is dominant. The fit to the peak position and spectral linewidth is shown in Fig. 13. It is found that the peak shift and the reduction in linewidth can be fully attributed to the change in ground-state energy because of coupling.

The strongest coupling state results if all of the dots within a column have the same energy. This coupling will produce the largest spectral peak shift. However, such a state will not result in the largest reduction in

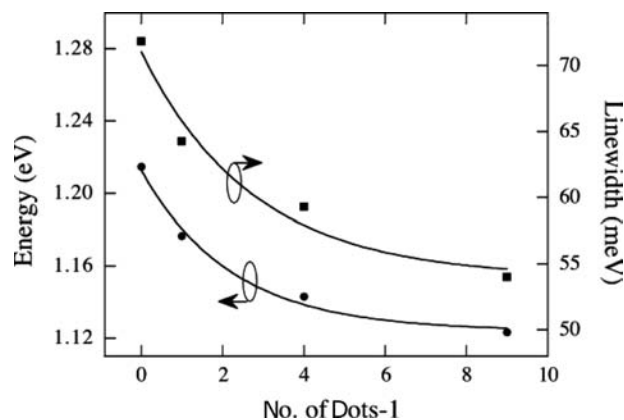


**Fig. 13** Changes in (A) spectral linewidth and (B) energy are shown as a function of the number of vertical islanding layers. Both exponential fits use the same fitting parameter.

the energy linewidth because if all of the dots within a column have the same energy, the in-plane size variations will insure a variation in the lowest miniband state in the ensemble of columns. The weak coupling state, where carriers tunnel through the vertical barriers in a dot column, produces small changes in spectral peak position and linewidth. These changes arise from the increased spatial extent of the dot wavefunctions and not from the strong overlap of coupled states. An interesting case is the intermediate coupling state, in which the vertical variation in the island size in a single column has the same distribution as the in-plane island size variation in an island layer. This coupling state produces the largest reduction in spectral linewidth because all of the dot columns now have the same size distribution. Because it has been shown that a significant element of the in-plane island size variation is caused by small spatial flux non-uniformities across the growth surface,<sup>[45]</sup> it is unlikely that the vertical distribution in island size can be made equal to the in-plane island distribution. Thus some significant inhomogeneous spectral broadening will always remain, as is the case here.

An additional source of spectral red shift and linewidth reduction is that as the number of island layers increases, the islands may be increasing in size or relaxing. This has not been observed in these 10-layer samples in our TEM or AFM characterization; however, changes in island size are observed in larger columns, as will be seen later in this chapter. If such changes were present here (yet too small to observe) and were responsible for the energy shift, we still do not observe spectral features from individual dot layers in the column, which would result in increased linewidths. Thus even in this scenario, weak coupling (tunneling) from islands in a column to the lowest energy state in the column would still be present.

The coupling in columns can be further investigated by varying the spacer layer thickness between the InAs island layers. The spacer layer thickness in a 10-islanding layer structure was changed between 40 and 50 Å, and 75 and 85 Å. Because these thicknesses are the approximate thicknesses between the wetting layer regions of adjacent islanding layers, the actual vertical spacing between islands varies between 0 and 45 Å. The 8-K PL results for these structures are shown in Fig. 14. The results indicate an increased spectral peak shift in the 40 Å spacer sample as compared with the 50-Å sample. This is consistent with the increased coupling that would be associated with a thinner spacer region. In addition, the spectral linewidth increases when the spacer layer thickness is reduced to 40 Å. The increased spectral linewidth is caused by a disruption in the island structure because the spacer layer is now approximately equal to the island height. However, the spectral peak shift is smaller in the sample with



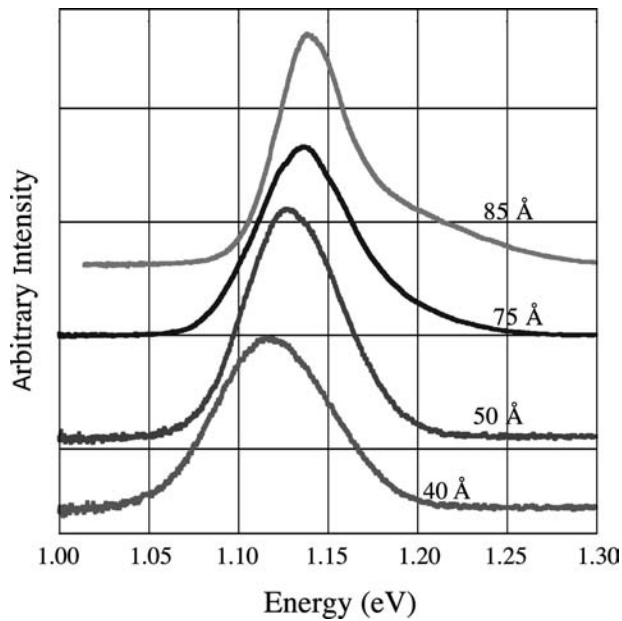


**Fig. 14** The effect of varying the spacer layer thickness from 40 to 85 Å is shown. The energy shift is because of the change in electronic coupling. The narrowest linewidth is found in the sample with a 50-Å spacer layer.

the 85-Å GaAs spacer than the sample with the 50-Å GaAs spacer. Here the increased spacer thickness reduces the electronic coupling between islands. In addition, a broad, high-energy shoulder is also apparent in the spectrum with the 85-Å spacer. This shoulder is caused by isolated or only partially aligned islands, where coupling is either not present or is diminished. In Fig. 15, the sample composed of 10 QD layers with

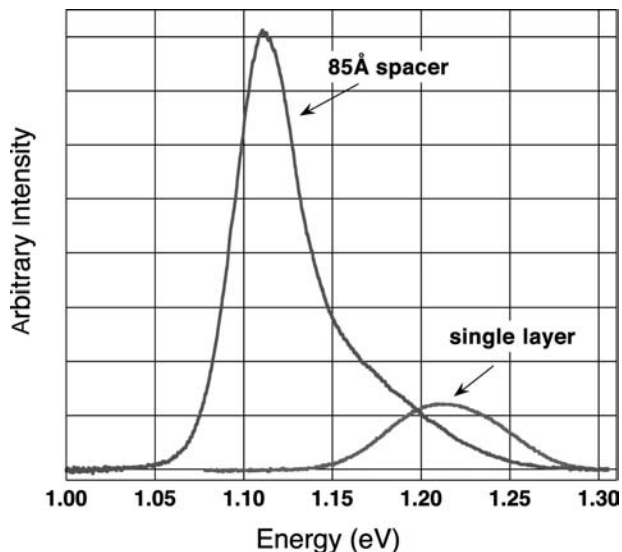


**Fig. 15** The 8-K PL of a 10-layer QD sample with an 85-Å spacer is compared to a single-layer sample to show how the larger spacer layer produces a broad high-energy spectral shoulder that indicates incomplete columns.

85-Å GaAs spacer regions is shown with the single-layer sample to further illustrate the how the high-energy shoulder corresponds with isolated or partially aligned columns.

We have shown that the wavefunctions of the isolated dots become vertically extended in the vertically aligned dot columns. When the states become vertically extended, the carriers occupying these states become delocalized and sample an average dot potential. This situation is similar to the in-plane delocalization that results when dots formed at low growth temperatures have rough, poorly defined structures (see “Single-Layer InAs Quantum Dot Ensembles” and Fig. 6) and there is in-plane delocalization when the PL temperature is raised, except that the vertical columns are a controlled 1-D chain of dots. We would not expect an increase in the PL measurement temperature to reduce the luminescence linewidth as with the single-layer samples. In Fig. 16, the variation in spectral linewidth with varying sample temperatures is shown for a single InAs QD ensemble sample and one with 10 InAs QD layers. Although the single-layer sample shows the effects of inhomogeneous broadening discussed in “Theory of Quantum Dot Vertical Alignment,” the 10-layer sample does not and is predominately thermally broadened.

## LEDs Using Coupled Quantum Dots

It is naturally desirable to extend device performance successes gained using QWs in electronic and optoelectronic devices to structures with more reduced density of states (DOS), such as quantum wires and quantum dots. For optoelectronics, the implementation of such structures should result in increasingly efficient LEDs, lower threshold lasers, and novel non-linear optical devices if: 1) the QD size is reduced to allow for room temperature applications; 2) the QD size uniformity is improved to take advantage of the sharp resonances in the QD DOS; and 3) reliable and simple fabrication techniques are developed. The QD structures described earlier have large-enough confinement energies for room temperature applications; however, the variation in the dot size leads to large inhomogeneous broadening and a loss of the sharp luminescence from the 0-D energy states. We believe that a major advantage of the self-assembled QDs is the high dot densities that can be produced in these self-organized random arrays. As shown in “Electronic Coupling in Quantum Dot Columns,” these densities can approach 80% of the ideal close-packed array density, and will be important for optoelectronic device applications.<sup>[41]</sup> In addition, we believe that the multilayer dot column structure will have an additional impact on optoelectronics. Other groups have made impressive contributions in QD lasers<sup>[46]</sup> (see the entry in this book by D. Bimberg),

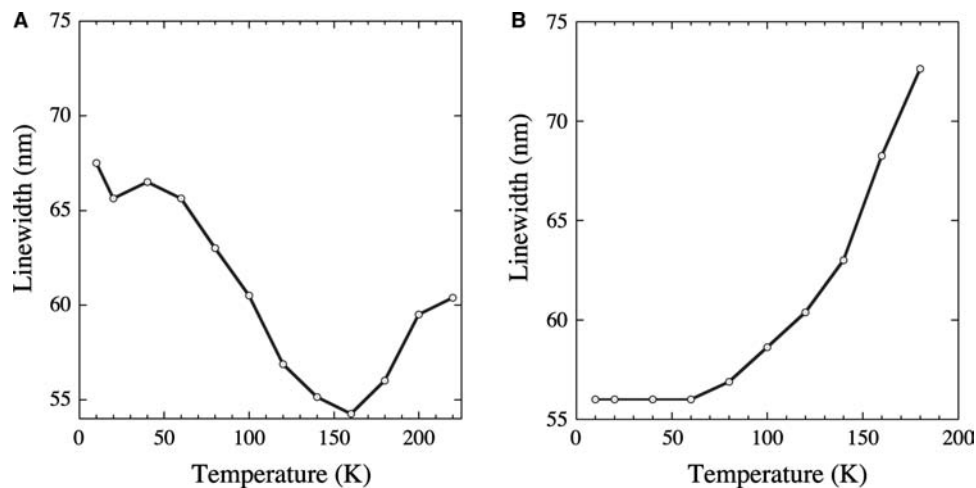


**Fig. 16** Variable temperature PL of (A) a single-layer InAs dot sample and (B) 10-layer InAs quantum dots layers.

and it is not our desire to describe such results. However, we would like to show in this section how some of the properties of these dot columns can be used in optoelectronic device structures.

The vertical columns of quantum dots described in “Electronic Coupling in Quantum Dot Columns” can be used to increase the optically active volume of LEDs. LEDs are demonstrated in which the active regions are composed of columns of InAs QDs containing either 1, 5, or 10 QDs. Measurements indicate that the single dot layer diode is more efficient than the coupled multidot column diodes. However, at high injection levels, spectra show that much of the luminescence intensity in the single-layer sample is because of the QW formed by the preislanding (wetting) layer and recombination in the doped cladding regions. Luminescence from these regions is nearly eliminated in the multidot column samples. Thus these columnar QD structures may be important to understand high injection conditions, such as lasing. Because of variations in the island size, these diodes are spectrally broad and the sharp spectral features associated with 0-D DOS of these structures are lost. However, of considerable practical importance for optical communications is that spectral peak emission at  $1.3\ \mu\text{m}$  has been achieved.<sup>[47]</sup>

The LED structures consist of an n-type GaAs bottom cladding layer of  $0.75\ \mu\text{m}$  and a p-type GaAs top cladding layer of  $0.29\ \mu\text{m}$ . The diode intrinsic region is  $0.11\ \mu\text{m}$  thick and contains an active region of either 1, 5, or 10 InAs island layers in a GaAs matrix. The devices were wet etched to form  $20 \times 20\ \mu\text{m}$  mesas. The devices are bottom-emitting and only a portion of the light that is generated in the intrinsic region reaches the bottom interface. The numerical aperture (NA) of the collecting objective is 0.25. Therefore neglecting scattered light from different interfaces

passing into the objective, only about 1% of the light generated in the intrinsic region is collected by the objective and measured.

Light output collected through the substrate for the three LEDs is shown in the power output vs. current ( $L-I$ ) curves of Fig. 17. Two features are apparent. First, in the linear region of each curve, the slope of the diode with only a single quantum dot layer is higher than the slope of the diodes containing multidot columns. As the number of dots in a column increases, the steady-state carrier concentration throughout the active regions becomes more non-uniform, diminishing the radiative recombination rate. Carrier transport, particularly hole transport, is slowed because the carriers must tunnel through several dots in a column to recombine. Additional evidence of decreased radiative recombination rate is the small flattened onset region in the diodes containing multi-QD columns. If the non-radiative recombination rate is increased, then more current is required to overcome the non-radiative recombination and the slope of the  $I-V$  curve is initially decreased. The second feature seen is an increase in saturation current and peak intensity. Because there are more dots available, there is now an increased number of states for which recombination can occur. Thus as the number of dots in a column increases, the optically active QD volume increases; this shows the effectiveness of the vertically aligned, columnar QD system. The luminescence in these diodes comes from two distinct regions: the QW wetting layer, and the QDs nucleated on top of the QW. As will be seen, at high currents, a significant portion of the luminescence from the single QD layer diode observed in the  $L-I$  curve originates outside the QD region, whereas the luminescence is well confined to the QD regions in the diodes containing columns of multiple QDs.

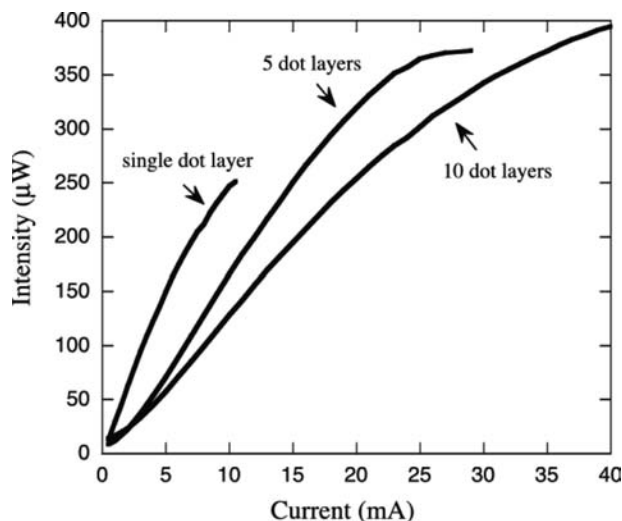


**Fig. 17** The light output vs. bias current for three LEDs that use either single, 5, or 10 dot layers at the device active region.

The spectra of diodes containing columns of 1, 5, or 10 InAs QDs are shown in Fig. 18. As the number of QD layers increases, the spectral peak position of the diode shifts to longer wavelengths and the spectral line-width decreases (Fig. 12). As the current increases in each of the diodes, luminescence from the doped GaAs cladding region increases at 900 nm. This luminescence feature is the luminescence shoulder from recombination in the doped region of the diodes where band-gap narrowing is present. From top-emitting LED samples, it is estimated that one-half of the feature (the region below 900 nm) is absorbed by the GaAs substrate. Carriers travel through the active region and recombine with majority carriers in the doped region. The prominence of this feature is significantly reduced as the number of QDs in the dot columns is increased because carriers are more effectively captured in the InAs dot region. The spectra of the diodes with a single QD layer (Fig. 18A) exhibit an additional feature between the main QD peak and the luminescence from recombination in the barriers, which is absent in the diodes containing columns of multiple QDs. This extra peak is because of radiative recombination in the QW wetting layer region. The peak position is well modeled, assuming a strained, coherent InAs wetting layer (QW) with a wetting layer thickness of 1.8 ML, a thickness observed in Fig. 1 and by other researchers.<sup>[43,44]</sup> The coupling of dots in the QD columns is larger than the coupling between QWs, so that the dominant carrier transport is through the QD columns.

As the current increases in the diodes, the spectral peaks in all samples shift to shorter wavelengths. The LEDs are biased under d.c. conditions. Sample heating is not responsible for this effect because it will reduce

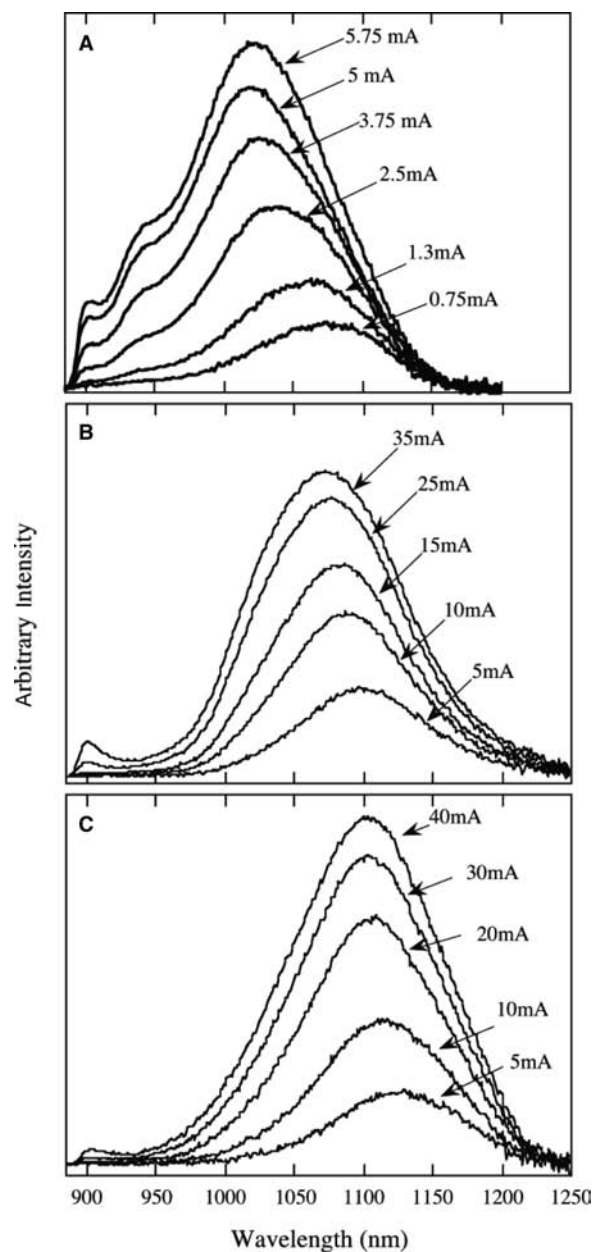


**Fig. 18** Luminescence spectra for three diodes with different numbers of quantum dot layers in the active region with various current bias. (A) Single quantum dot layer, (B) columns of five quantum dots, and (C) columns of 10 quantum dots.

both the InAs and GaAs bandgaps similarly and produce a red shift in each. The spectral shifts with bias are larger in the single-layer QD diode, whereas they are equal in the two multi-QD column samples. In all cases, the spectral peak shift stabilizes at higher currents. The spectral peak shifts result when the lower-energy states from larger QDs become saturated. The extra shift in the single QD layer sample results from the proportionally larger luminescence from the QW wetting layer.

A comparison of the three different diodes at the same current of 15 mA is shown in Fig. 19. In the

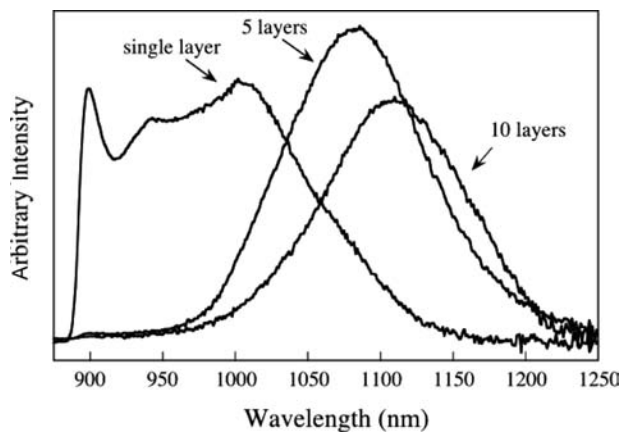


**Fig. 19** Comparison of the three diodes with columns of 1, 5, and 10 quantum dots using the same current of 15 mA.

single-layer QD diode, the intensity increase between 6 mA (Fig. 18A) and 15 mA results almost entirely from recombination in the QW InAs wetting layer and the GaAs barrier region; the energy states contributing to the main 0-D spectral peak luminescence are saturating. Thus this luminescence is a mixture of light from the 2-D QWs and light from the 0-D QDs. The luminescence intensity of the diodes containing the multi-QD columns results entirely from the 0-D energy states. At 15 mA, the peak intensity of the diode with five dot columns is larger than the peak intensity with 10 dot columns. Even without scaling, it is apparent that the internal quantum efficiency of the device is reduced between the 5- and 10-dot column samples.

An approximate comparison of internal quantum efficiency can be made by comparing the diodes when the current per QD layer is equal, and the luminescence intensity is scaled by the number of QDs in a column. This is shown in Fig. 20, where the current per dot

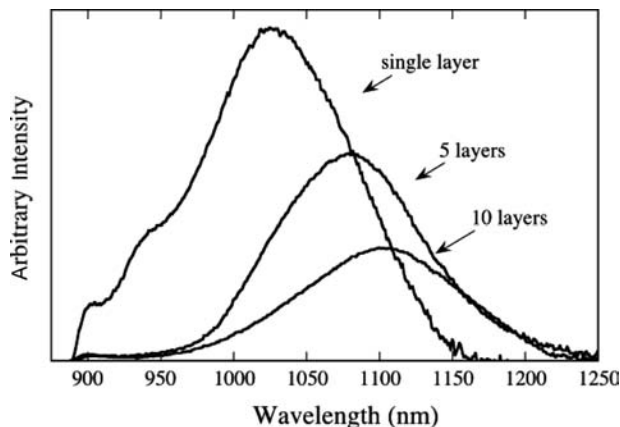


**Fig. 20** Comparison of the three diodes with columns of 1, 5, and 10 quantum dots where the current per quantum dot layer is constant at 3 mA for each of the three diodes. The luminescence from each diode is divided by the number of QD layers in each diode.

layer is 3 mA. The normalized peak intensity of the diode with the single dot layer is the highest of all the diodes, so that even with respect to only the 0-D luminescence, the single-layer diode has the highest efficiency. As observed in multiple quantum well (MQW) LEDs, holes are not being evenly distributed throughout the multi-QD column active region because their large effective mass reduces their tunneling probability between QDs in a column. However, the effects of non-radiative recombination processes, such as recombination at crystalline imperfections, must also be considered. This does not appear to be the case because the slope of the  $I$ - $V$  curves of diodes with either 5 or 10 dot columns is similar, implying that there is no significant increase in nonradiative recombination between the two diodes.

In summary, the increased active volume of the columnar structure containing multiple QDs leads to increased peak luminescence intensity and reduced carrier recombination in the doped GaAs region. However, this comes with a penalty, which is a decrease in luminescence efficiency as the QD column size increases. It is believed that the reduced luminescence is because of a partitioning of holes in the QD columns, but other effects such as non-radiative recombination at structural defects cannot be ignored. Finally, in the diodes containing QD columns, the luminescence from the QW wetting layers regions is eliminated because the coupling within the dot columns facilitates carrier transport through the QD columns. This is a significant advantage to using the quantum dot columns because early laser structures appear to lase through the wetting layer states or excited states of the dots. Because of the hole partitioning in columns with many dot layers, an optimum quantum dot active region should contain columns with a limited number quantum dots. The number will vary depending on the structure, but the results shown here indicate that columns containing about five QDs adequately balance the reduction in QW luminescence without significant hole transport penalties.

## IN-PLANE InAs ISLAND ORDERING USING A SUBSURFACE ISLAND SUPERLATTICE

### Columns Composed of Many Quantum Dot Layers

The focus of “LEDs Using Coupled Quantum Dots” was the electrical coupling that can occur in vertical columns of a small number of quantum dot layers. A different effect can be observed when a large number of layers are stacked. In this regime, the column structure can increase the structural and spatial uniformity of the uppermost in-plane QD ensemble. Although we



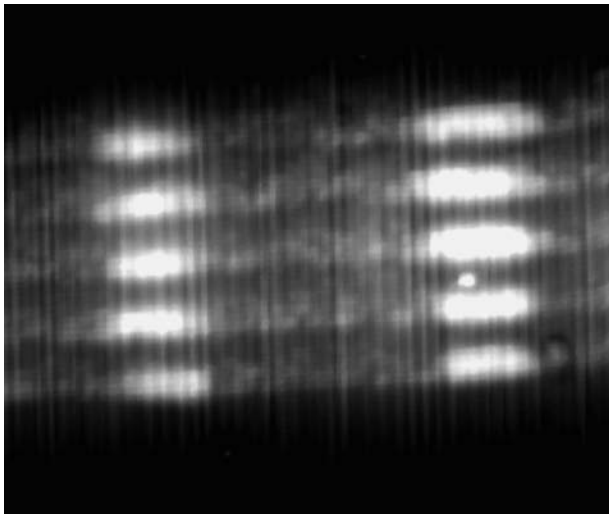


**Fig. 21** Cross-sectional STM empty states image of two columns of InAs quantum dots (bright) in a GaAs matrix (dark). The field of view is  $600 \text{ \AA}$  in (110) (horizontal) and in (001) (vertical). *Source:* W. Wu and J. R. Tucker.

have explored some of the structural properties of these columns in “LEDs Using Coupled Quantum Dots” using TEM, we will more closely examine these properties using AFM, XRD, and cross-sectional scanning tunneling microscopy (STM).

A cross-sectional STM image of columns of five InAs QDs is shown in Fig. 21. Here the image size is  $600 \times 600 \text{ \AA}$ . This and other STM images were made by W. Wu and J. R. Tucker at the University of Illinois, Urbana-Champaign. These samples are prepared by in situ cleaving in a  $5.5 \times 10^{-11}$  Torr chamber to expose the (110) surface. The measurements are made at room temperature. The STM image is an empty states image derived from current variations across the surface when electrons tunnel from the STM tip to available states in the valence band. Because of the charge transfer on the (110) III–V unreconstructed surface, empty valence band states are localized on the group III sublattice. Thus this imaging highlights Ga or In atoms. Because of the narrower bandgap of InAs and the larger size of the In atom (which pushes the exposed In further out into the vacuum), the tunneling current is higher in the In-rich regions than in the Ga-rich regions. Hence, the contrast is directly related to the mole fraction of In. In these images, discrete bright areas are the result of In surface atoms. Fainter bright spots are assumed to be from In atoms in the next group III layer below the surface.<sup>[48,49]</sup>

This image, as well as other STM images, are consistent with the TEM micrographs. The in-plane dot diameters in Fig. 21 are approximately  $130 \text{ \AA}$  and the heights are  $30 \text{ \AA}$ . The spacing between the two columns is  $200 \text{ \AA}$ . As in cross-sectional TEM, the exact diameter cannot be measured directly from these images because

the cleave does not necessarily bisect the center of the QDs. TEM and STM are complimentary measurements. The advantage of this STM technique will be seen later in this section: Although TEM images are formed by columns of atoms in the plane of the image, the STM images are formed from states close to the surface. Thus individual In atoms that have diffused into GaAs regions can be imaged with STM. In addition, the DOS can also be examined using STM by sweeping the tip voltage.

We now focus on uniformity improvements that can be made using large columns containing up to 75 layers of dots. In these structures, there is an interaction between neighboring columns, which imposes a strain field on the growing surface and can lead to dot ensembles of both increased size uniformity and increased spatial uniformity. We begin by showing that, despite the layering of dots to form columns, the InAs diffusion from these dots is limited, especially with respect to the large InAs diffusion observed in the wetting layer regions.

In Fig. 22, a cross-sectional STM image of two adjacent 20-layer columns of InAs islands is shown. As in Fig. 21, the STM image is an empty states image highlighting tunneling current differences associated with Ga or In. In Fig. 22A, a speckled band, which is the planar wetting layer region, is present between the dot columns. This region has been shown by various groups to consist of between 1.6 and 1.8 ML of InAs, determined through reflection high-energy electron diffraction (RHEED). Although it has been shown in earlier InAs planar epitaxy studies that the surface segregation in this layer results in a broadly alloyed region,<sup>[48–50]</sup> in strain-induced quantum dot research, it is often assumed that this region remains relatively intact. In Fig. 22A, the In diffusion can be easily seen to extend to the height of the InAs dots, which is approximately six unit cells.

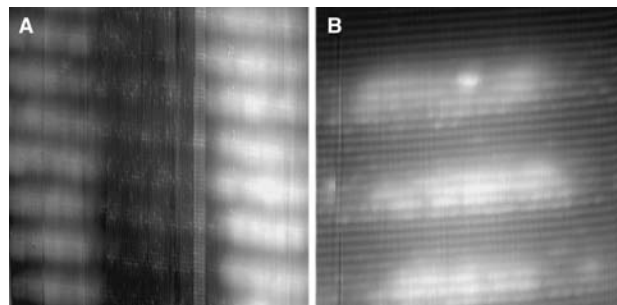


**Fig. 22** Cross-sectional STM image of (A) the region between two 20-layer quantum dot columns showing In diffusion between dot columns, and (B) the region around a column indicates no significant In diffusion from the dot regions. *Source:* W. Wu and J. R. Tucker.

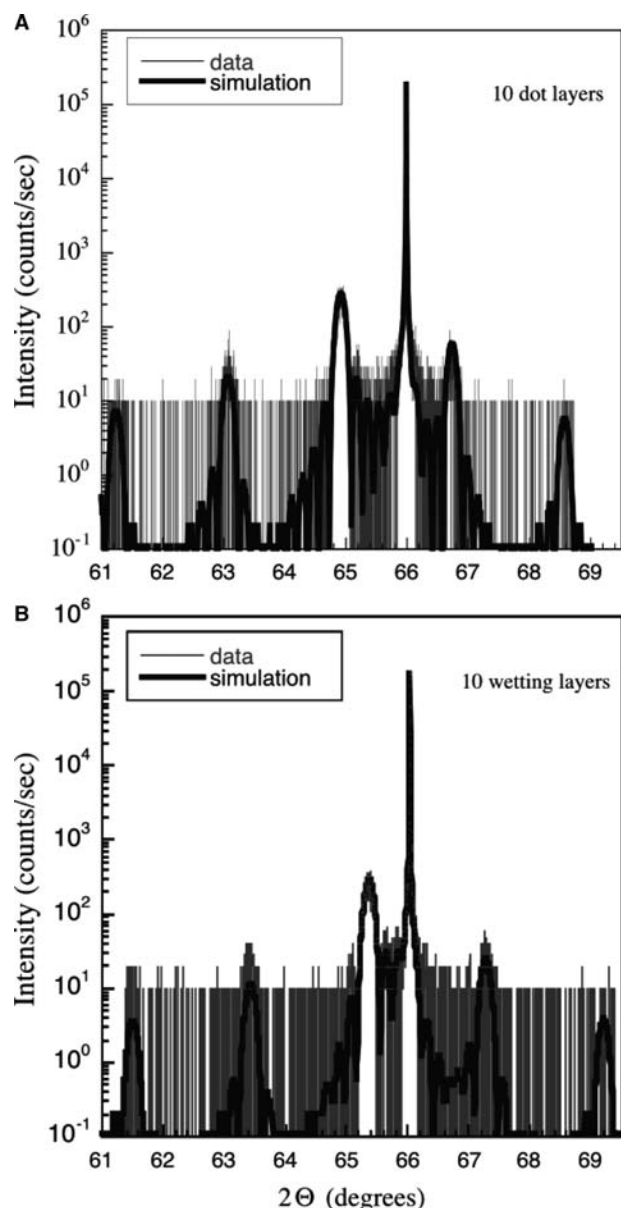


**Fig. 23** X-ray diffraction from (A) a 10-dot layer sample formed in the columnar structure, and (B) a QW 10-wetting-layer sample (nominally planar InAs layers). Simulations are shown in black. In both cases, the superlattice diffraction is caused by the wetting layer regions.

We have observed the global structure of this wetting layer region using XRD. In Fig. 23A, XRD results are shown for a sample consisting of 10 InAs dot layers. The XRD was conducted using a Philips 4 crystal X-ray diffractometer. In the figure, we observe superlattice diffraction from a supercell consisting of the GaAs spacer and the InAs. Peaks for the  $n = 0$ ,  $\pm 1$ , and  $\pm 2$  reflections are present, with the (004) GaAs substrate peak residing between the  $n = 0$  and  $n = 1$  reflections. A fit using a dynamic diffraction model gives (Fig. 23A) a strained InAs thickness of 1.9 ML

( $\pm 0.2$  ML) and a GaAs thickness of 52 Å. Our interpretation of these results is that the wetting layers (in the dots wetting layer system) are the only contribution to the superlattice diffraction. Because Fig. 23A represents symmetrical diffraction about the (004) GaAs reflection, the dot regions, with their varying InAs and GaAs vertical sections, should not contribute to superlattice diffraction. The only extensive regions with periodic structure in the growth direction are the regions of the sample without InAs dots where only the wetting layers are present. To verify this result, XRD was conducted on a similar sample with only InAs wetting layers. This sample is composed of 10 periods of 1.5 ML of InAs; the GaAs spacer layer is 50 Å. The results are shown in Fig. 23B. When fitted using the same diffraction model, the best fit occurs for 1.5 ML (approximately 9 Å) of strained InAs.

This measured value of 1.9 ML for the 10-layer dot sample is close to the 1.8-ML wetting layer thickness observed by other researchers using RHEED. The RHEED measurements determined the equivalent amount of materials deposited leading to the dot transition, whereas this XRD measurement determines the wetting layer thickness after the dot transition. Because the transition to island growth results in an overall change in the surface topology, it is interesting to note that the wetting layer thickness is unchanged by the transition to islanding.

The width and decay of the superlattice diffraction in Fig. 23 indicate the uniformity of the wetting layers over the superlattice and the intermixing of the InAs wetting layers and GaAs spacer layers. The model indicates that the wetting has an alloyed profile, which decreases exponentially from  $\text{In}_{.99}\text{Ga}_{.01}\text{As}$  to  $\text{In}_{.10}\text{Ga}_{.90}\text{As}$  in 18 Å, or nearly two-thirds of the dot height. In addition, a small amount of In is present throughout the GaAs region. This diffusion of InAs in GaAs has been observed by other researchers in thin InAs QWs in GaAs.<sup>[48–50]</sup> The diffusion is the result of surface segregation of In. Like the InAs island formation, the surface segregation is a mechanism by which the lattice-mismatched strain can be reduced. After InAs has been deposited on the GaAs surface and GaAs deposition again begins, the In atoms switch sites with surface Ga adatoms. This strain-driven diffusion of In to the surface reduces the total system energy because the surface In is not completely constrained by the GaAs lattice. The complete sequence of In diffusion occurs as follows. Through the initial deposition of less than 2 ML of equivalently planar InAs, the InAs surface remains generally planar, except for some surface roughness that may be present to reduce strain. With the addition of a small amount of In to the surface, the surface transforms from planar to 3-D islands. However, through XRD, we have shown that the wetting layer region remains. If the



InAs deposition is terminated before plastic relaxation and the surface is covered with GaAs, In from the planar region surface segregates, leading to an alloyed region between the dots. A consequence of this segregation is that the InAs quantum dots are now less laterally confined because the vertically diffused In decreases the lateral confining potential.

In contrast to the In diffusion present in spaces between the dots, the In in the dot regions is remarkably stable. This can be seen in Fig. 22B, where an STM empty state tunneling image of three vertically aligned dots is shown. The shape of these dots is pancake-like and is the typical shape we observe in all samples. Although the bottom interface of each dot is abrupt, the top interface of the dot is also quite sharp; no isolated In atoms are observed in the vertical regions between the dots, as are seen in the spacer regions away from the dots. In addition, no In concentration gradient is observed to go away from the dots into the wetting layer regions (in the in-plane direction), further indicating the stability of the In in the dots.

We believe that the InAs in the dot regions is resistant to lateral and vertical diffusion because this InAs exists in regions where the lattice constant remains slightly dilated toward the InAs lattice constant. In the wetting layer regions, the InAs is strained to the GaAs lattice constant, and the full effect of strain-enhanced diffusion is present. In fact, if the GaAs regions surrounding the InAs dots have the GaAs lattice constant, then the small difference in lattice constant between the two regions inhibits InAs diffusion away from the dots [Eq. (10)].

### Increased Structural Uniformity

It has been theoretically and experimentally shown<sup>[18,41]</sup> that the vertical column structure increases the upper layer dot size uniformity and nearest-neighbor spatial

uniformity. The increased uniformity is the result of stress fields from the subsurface dot layers affecting the adatom diffusion on the new surface layer. Suppose that the initial dot density is large compared with the adatom surface diffusion length, and the strain fields from adjacent columns overlap. Because the nucleation of an InAs island occurs at a strain maximum, overlapping columns produce maxima that are closer together. With increased layering of islands, the strain maxima become closer together and columns will eventually be eliminated. If the initial dot density is sparse compared with the adatom surface diffusion length and the island strain distribution, new dots will nucleate between existing columns. Overall, some equilibrium density of islands will result. In this state, the strain field should be periodic over the growth surface; the spacing between strain maxima will be determined by strain, overlayer thickness, and surface diffusion. The nearest-neighbor distance between nucleating dots will become constant, resulting in uniform nutrient fields around each dot and thus a more uniform dot size distribution. In our work, we assume that the ideal equilibrium surface of a single dot layer is a dense array of dots in which the dots form from strain-induced surface roughness. Therefore the formation of columns should decrease the dot density in the uppermost dot layer.

A decrease in island density and an increased island uniformity are immediately apparent when comparing the bare InAs dot surfaces after a single layer of dots and after 20 layers of dots have been deposited. This is shown in the AFM images of Fig. 24. A statistical evaluation of the AFM images in Fig. 24 is found in Figs. 25 and 26. In Fig. 25, a comparison of the variation in height in the single-layer and 20-layer samples is shown. The average height increases from 43 Å in the single sample to 65 Å in the 20-layer sample. The full width at half maximum (FWHM) of the dot height is reduced from 17 to 10 Å between the single-layer and

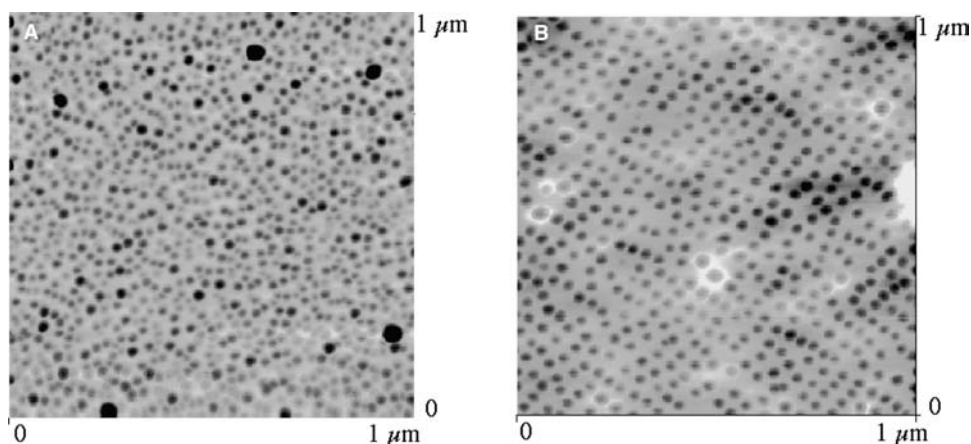
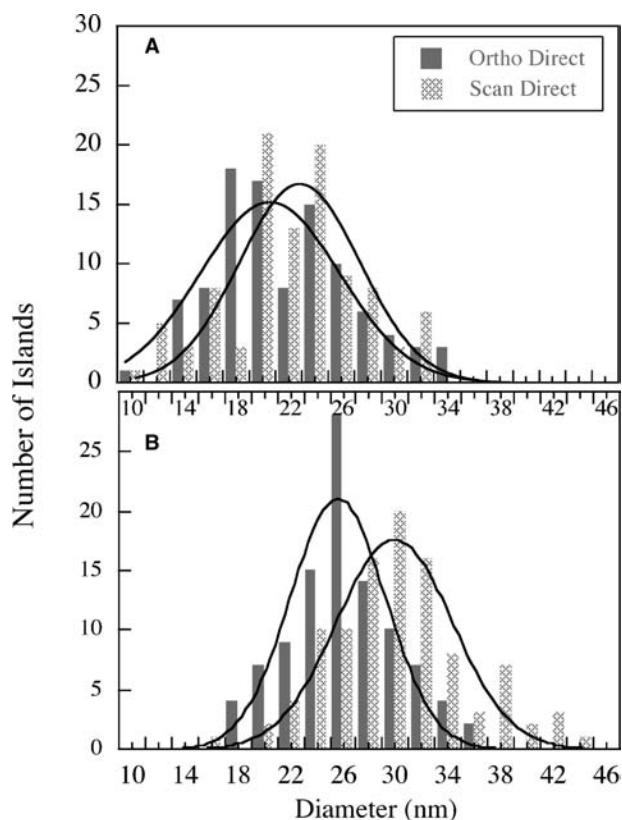
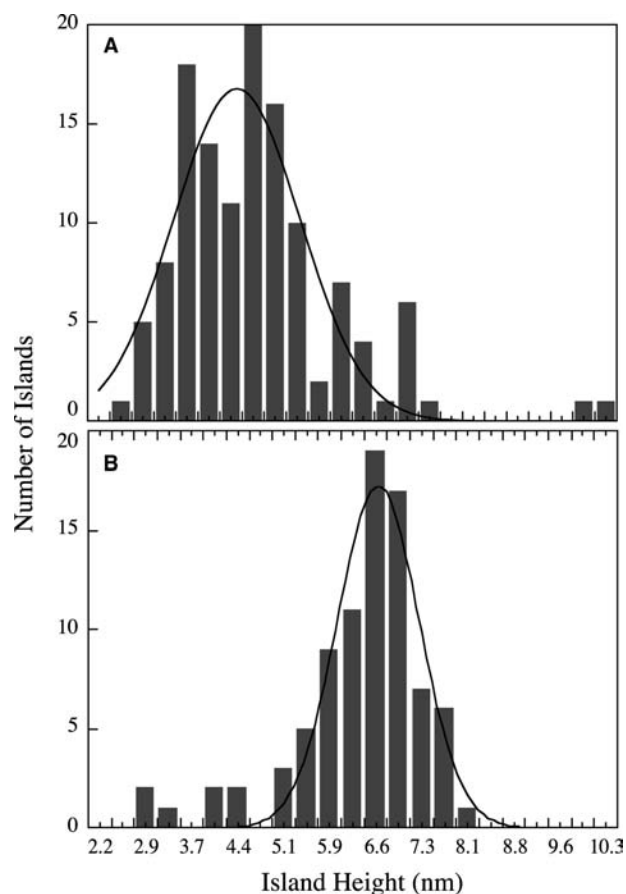


Fig. 24 AFM image of (A) the top surface of a single layer of InAs dots, and (B) of the top surface after 20 layers of dots.



**Fig. 25** In-plane dot diameter variations determined from AFM, where (A) is for a single layer of InAs dots and (B) is after 20 layers of InAs dots.

20-layer samples, even though the average dot height has increased in the 20-layer sample. In Fig. 26, a comparison of the variation in the in-plane dot diameter between the two samples is shown. The in-plane area is not circular but elliptical, and the two differently shaded regions in Fig. 26 represent the orthogonal directions with maximum and minimum values. (We cannot observe the facet planes in our AFM imaging, and it is assumed that the island base is rectangular or parallelogram.) As for the average dot height, the in-plane diameter has increased after 20 dot layers. The average in-plane diameter of the single dot layer is 218 Å, whereas the average in-plane diameter after 20 dot layers is 273 Å. The distribution of the in-plane diameter has also narrowed: The FWHM of the diameter distribution is reduced from 50 Å (single layer) to 41 Å (20 dot layers). There is a small but observable difference between the height increase and the diameter increase in the 20-layer dot distribution. The average height increases more than the average diameter, so that the ratio of height to in-plane radius changes from 0.4 to 0.48 after 20 layers (i.e., these dots are more hemispherical). The increase in dot height and diameter is in agreement with the reduced island density observed in Fig. 24. Because the dot density is reduced and the



**Fig. 26** Height variations determined from AFM (A) for a single layer of dots and (B) after 20 layers of dots.

wetting layer thickness is unchanged (Fig. 23A), the dot size must increase. The reduction in the size variation in height and diameter is because of the more uniform local dot environment resulting from stacking the dot layers. Because the strain field in the dot layers becomes more periodic with each dot layer, dots are nucleated with more uniform nearest-neighbor distances, and hence more uniform nutrient fields. These more uniform surroundings lead to more uniform dot sizes.

Cross-sectional STM reveals the way in which the dot columns are eliminated. Empty states images of 20 dot layers are shown in Fig. 27. In Fig. 27A, three columns that are not terminated are shown, and indicate the well-aligned dot column structure. In Fig. 27B, several columns are eliminated through the dot layering process. Two types of column elimination are present, yet it is not clear whether these two types of elimination are indeed distinct. The first process is by simple extinction: The column abruptly ends. Such a column is observed in Fig. 27B on the left. The second type of column elimination is observed on the right: Two columns merge after only two dot layers, whereas still another column dramatically bends

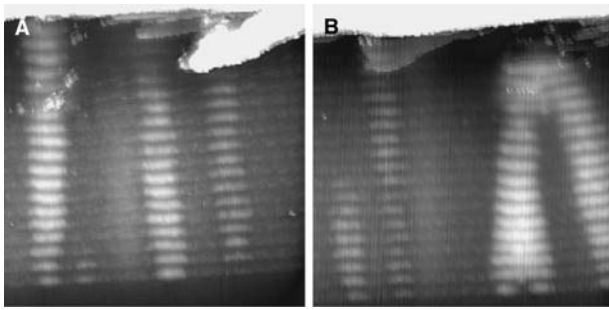


**Fig. 27** Cross-sectional STM images in two regions of a 20-layer dot column structure. On the left (A), column uniformity is maintained except for a small truncated column. On the right (B), two columns merge, and then the resulting column merges with a third column. *Source:* W. Wu and J. R. Tucker.

toward this stable column until it eventually merges and is eliminated. Because we only probe in one cross-sectional plane, we cannot be sure that the column that abruptly ends does not bend inward away from the surface; however, the abruptness in which the column ends suggests that this is not the case.

If one column exerts more of an effect on the resulting strain field, then the position of the new dot will be closer to this column. Such a description will account for the abrupt type of column elimination we observe. However, the slow bending of columns is a more dynamic process. In this case, we believe that overlapping strain fields from columns produce a situation in which distinct minima in misfit exist near each column, but that an overall lattice change between the columns shifts one or more of these minima toward the region between columns. It is unlikely that the observed bending is caused by competing nutrient fields because this situation would drive columns away from each other, and this is not observed.

### Increased Spatial Uniformity

When a large number of island layers are deposited, the strain created by adjacent columns interacts to

create a surface strain distribution. We have just shown how this imposed strain distribution leads to structural ordering of the quantum dot ensemble on the surface. Similarly, the strain distribution becomes a template that can lead to spatial ordering of the new island layer. In investigating the limits of this ordering, we have determined that, under various crystal growth conditions, a surface unit cell of islands is formed on the upper layer of the superlattice. Although some translational properties of the unit cell are observed, providing initial evidence of a 2-D surface lattice of quantum dots, a well-ordered lattice is not found. We demonstrate that this occurs because in this material system, with a (100) growth surface, surface diffusion effects and bulk strain effects compete in a manner that breaks complete translational symmetry. Adjusting growth parameters can diminish this effect.

An example of the variation in quantum dot ensembles with variations in spacer layer thickness and number of layers can be seen in Fig. 28. The first two images in Fig. 28 have different subsurface InAs dot layer parameters. In Fig. 28A, the subsurface multidot structure has 30 InAs dot layers, each containing the equivalent of 2.5 ML of planar InAs. The thickness between each wetting layer region is 55 Å, and the growth temperature was 500°C. In Fig. 28B, the subsurface multilayer contains 50 dot layers, the wetting layer spacer is 75 Å, and the growth temperature is 525°C. In “Single-Layer InAs Quantum Dot Ensembles” and our previous work,<sup>[36]</sup> we showed that the higher the growth temperature is, the larger is the average InAs dot size. Thus the GaAs spacer layer must be increased in the sample grown at a higher temperature so that the growth surface can planarize between dot layers. In Fig. 28A and B, a qualitative alignment along  $\langle 100 \rangle$  can be seen. Ordering in single-layer samples, if present at all, is along [110] and is because of step bunching.<sup>[6]</sup> An example of this is shown in Fig. 28C, where the growth parameters were adjusted to maximize step bunching. In contrast to the  $\langle 100 \rangle$  alignment seen in Fig. 28A and B, the alignment in Fig. 28C is in the vertical [110] direction. The alignment is caused by anisotropic surface diffusion because of

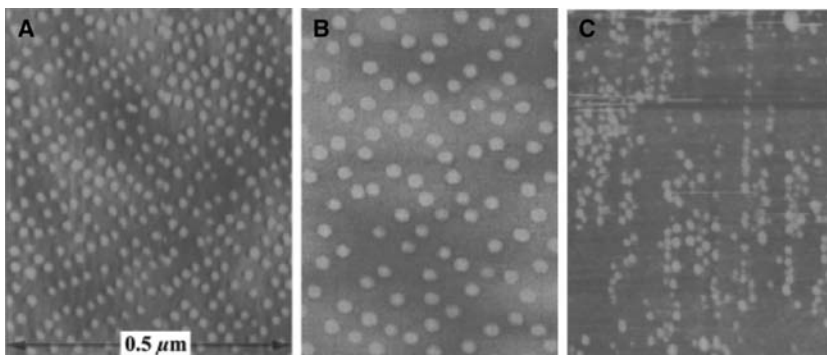


**Fig. 28** AFM images of after (A) 30 layers of InAs dots ( $T_g = 500^\circ\text{C}$ ), (B) 75 layers of InAs dots ( $T_g = 525^\circ\text{C}$ ), and (C) a single layer of dots grown to enhance surface step bunching.

ledge and surface reconstruction.<sup>[51]</sup> In contrast, the surface alignment of InAs dots in  $\langle 100 \rangle$  in samples containing subsurface dot multilayers is because of the interaction of the strain fields from the buried dots.

We can begin to see the extent of the spatial ordering present in these structures by making reciprocal space surface maps of AFM images. The Fourier transforms of the AFM images for the single-layer and the 30-layer samples shown in Fig. 28 are shown in Fig. 29. In the Fourier space image of the single island layer sample, only a centered peak is present, indicating there is no regular nearest-neighbor distance between islands. In the 30-layer sample, there is both regular nearest-neighbor distance and orientation. The nearest-neighbor directions are only approximately the  $\langle 100 \rangle$  directions, as shown by the thin lines added in the vertical and diagonal directions. Our explanation for this is that, although the strain distribution on the surface drives the unit cell of dots to have a nearest-neighbor direction in  $\langle 100 \rangle$ , the surface diffusion has a different preferential orientation. The anisotropic surface diffusivity in a sense competes with subsurface strain and pushes the nearest-neighbor direction slightly away from  $\langle 100 \rangle$ . We will show later in this entry that the situation is even more interesting because the second nearest-neighbor directions from the strain distribution will be shown to be  $\langle 110 \rangle$ , but because of the anisotropic surface diffusion, these unit cell directions are no longer degenerate.

In the case of an isotropic material, the region above a subsurface island is strained and becomes an advantageous site for island formation because the dilated lattice constant is closer to the InAs lattice than the surrounding surface. The strain interaction of two subsurface islands has been calculated for the isotropic case.<sup>[52]</sup> We use one island as an infinitesimal “test island” in analogy to the test charge in electrostatics, with the convention that it induces a negative strain in the crystal. The strain distribution on the surface from an island submerged a distance  $L$  from the

surface is:<sup>[18]</sup>

$$\epsilon(x) = C \frac{1}{(x^2 + L^2)^{\frac{3}{2}}} \left( 1 - \frac{3L^2}{(x^2 + L^2)} \right) \quad (13)$$

where  $C$  is constant. If two islands are in close proximity, the resulting surface strain distribution is the superposition of the strain distributions of the individual islands. On the 2-D surface, the possible first nearest-neighbor island positions fall on a circle. If the surface diffusion rate is adequate, the highest density of islands (a hexagonal cell) will result. If enough layers are deposited, different surface regions will coalesce into a close-packed 2-D hexagonal arrangement.

What is interesting to us is the effect of the crystal symmetry on this result. Thus for the moment, we ignore the surface diffusion effect and determine the nearest-neighbor arrangement from crystal symmetry. The nearest-neighbor ordering observed in Fig. 29 can be explained by the anisotropic properties of the GaAs zinc-blend crystal structure. The  $\langle 100 \rangle$  directions are elastically soft<sup>[53]</sup> (i.e., they have relatively small elastic moduli). Thus it is expected that nearest-neighbors should be in these directions. We investigate the effect of the anisotropic elasticity tensor on the orientation of the surface ordering by calculating the surface strain from a single buried island as a function of crystallographical orientation, and then assuming that the total strain from a buried layer of many islands is the linear superposition of the strain from individual islands. We do this by using a known isotropic solution<sup>[54]</sup> for an isolated subsurface island and adopting it to the anisotropic case. A more accurate but still approximate solution can be developed using the elastic stress tensor of a cubic crystal. However, approximations must still be made and, for our purposes, this simple solution is adequate. We use a Green’s function approach for a buried elliptical island where the island dimensions have been determined from the cross-sectional STM discussed in “Increased Structural Uniformity.” Following Hooke’s law, the stress  $\sigma$  and strain  $\epsilon$  are related by the elastic tensor  $c_{ijkl}$  by  $\sigma = c_{ijkl}\epsilon$ . For rotation about the surface normal, we assume that the inverse of the elastic tensor (denoted by  $s_{ijkl}$ ) is a slowly varying function of the orientation in GaAs, so that the already known isotropic Green’s functions can be applied. The displacement is related to stress  $\sigma^*$  induced by the buried InAs island by  $c_{ijkl}\mathbf{u}_{i,j,k,l} = \sigma_{ij}^*$ , where  $ij,kl$  indicates partial differentiation by the cyclical indices  $k$  and  $l$ . Then:

$$u_i(x) = -c_{jlmn}\epsilon * \int_{\Omega} G_{ij,l}(\mathbf{x} - \mathbf{x}')d\mathbf{x}' \quad (14)$$

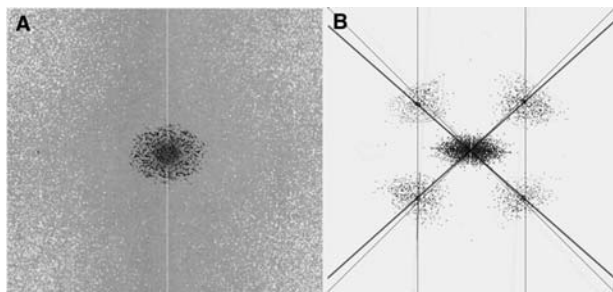


**Fig. 29** Fourier transform of the AFM images of the surface of two InAs QD samples: (A) single-QD layer and (B) 30-QD layer.



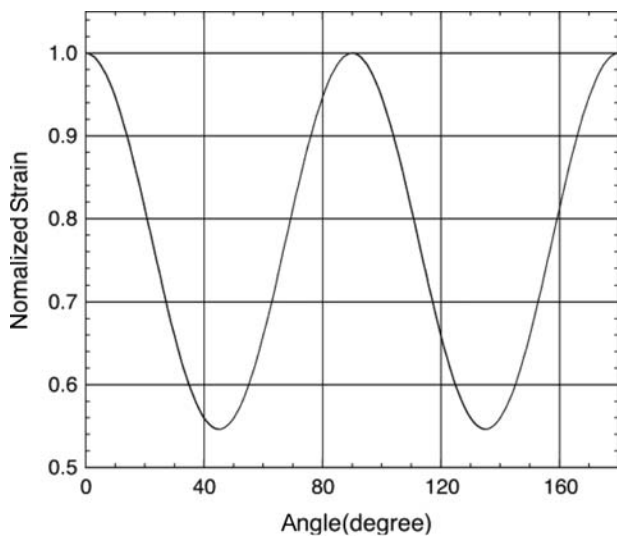
is a solution for the displacement. An image island above the surface is used to force the surface tractions to zero. The strain is related to the displacement by  $\epsilon_{ij} = 1/2(u_{i,j} + u_{j,i})$  and leads to surface strain as a function of position  $x$  and crystallographical orientation  $\theta$ :

$$\epsilon_{ij}(x, \theta) = -\frac{\epsilon^* s_{11}(\theta) + s_{12}(\theta)}{4\pi s_{11}(\theta) - s_{12}(\theta)} \left( \int_{\Omega_1} \left( \frac{1}{R_1} \right)_{ij} dx' \right) + \left( 3 + \frac{4s_{12}(\theta)}{s_{11}(\theta)} \right) \int_{\Omega_2} \left( \frac{1}{R_2} \right)_{ij} dx' \quad (15)$$

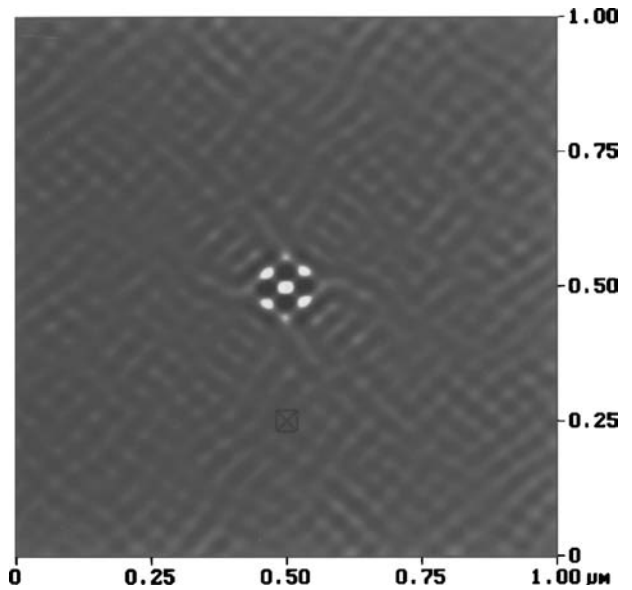
The subsurface island is region  $\Omega_1$ , whereas the image island is region  $\Omega_2$ .  $R_1$  is  $|x - x'|$ , where  $x'$  is on  $\Omega_1$ , and  $R_2$  is the distance between a point in  $\Omega_2$  and  $x$ . The  $\theta$  dependence of the above equation can be evaluated by transformation of the stiffness constants  $s_{ijkl}(\theta)$  into a rotating coordinate system on the surface and centered above an island. This transformation is  $s_{ij} = \sum_{m,n} s_{mn} q_{mi} q_{nj}$  where  $q_{ij}$  is the transformation coefficient and is of second order in the directional cosines.

Fig. 30 shows the variation of the surface strain as a function of crystallographical orientation. The maximum strain is in the  $\langle 100 \rangle$  directions. Because InAs island nucleation will occur preferentially where the GaAs crystal is biaxially expanded, this direction becomes the nearest-neighbor direction.

In the Fourier-transformed AFM images, we would like to investigate higher-order modes related to the second nearest-neighbors. Therefore we have examined the autocovariance of the images. In Fig. 31, the autocovariance of the AFM image from Fig. 28A is shown.



**Fig. 30** The normalized angular variation in strain on the GaAs surface caused by an island below the surface. Zero degrees is taken in the  $[100]$  direction.



**Fig. 31** 2-D autocovariance of the AFM image in Fig. 28A.

This sample contains 30 InAs dot layers. The autocovariance of a function  $f$  is defined as:

$$\mathbf{R}_{ff}(\mu, \nu) = \lim_{T \rightarrow \infty} \frac{1}{2T} \int_{-T}^T f(x, y) f(x + \mu, y + \nu) dx dy \quad (16)$$

Here  $f$  is a functional representation of the real space image in the  $x$ - $y$  plane,  $\mu$  and  $\nu$  are the  $x$  and  $y$  translations, and  $T$  is a spatial limit. We now investigate primary unit cell directions by taking slices through this transformation. Figure 32 shows autocovariance data from two samples in the  $\langle 110 \rangle$  and  $\langle 100 \rangle$  directions. Peaks in the figure indicate a translational correlation. In the single-layer case, shown in Fig. 32A, there is only a central peak, indicating no correlation between islands. In Fig. 32B, we show autocovariance sections of a sample grown at 500°C with 30 InAs dot layers, separated by 55 Å GaAs spacer layers. Here the single satellite peaks in the  $\langle 110 \rangle$  and  $\langle 100 \rangle$  directions near the central peak indicate the InAs quantum dot unit cell; once again,  $\langle 100 \rangle$  is only approximate. From the figure, the first nearest-neighbor directions are in the predominantly  $\langle 100 \rangle$  directions, whereas the second nearest-neighbor direction is  $[\bar{1}10]$  and the third nearest-neighbor direction is  $[110]$ . Because the subsurface strain should create four nearest-neighbors in  $\langle 100 \rangle$ , we believe that both the deviation from this direction and the nondegeneracy of the orthogonal second and third nearest-neighbors result from the anisotropic surface diffusion. The longer-wavelength, lower-intensity oscillations in Fig. 32B are the result of large-scale surface roughness, possibly because of steps on the

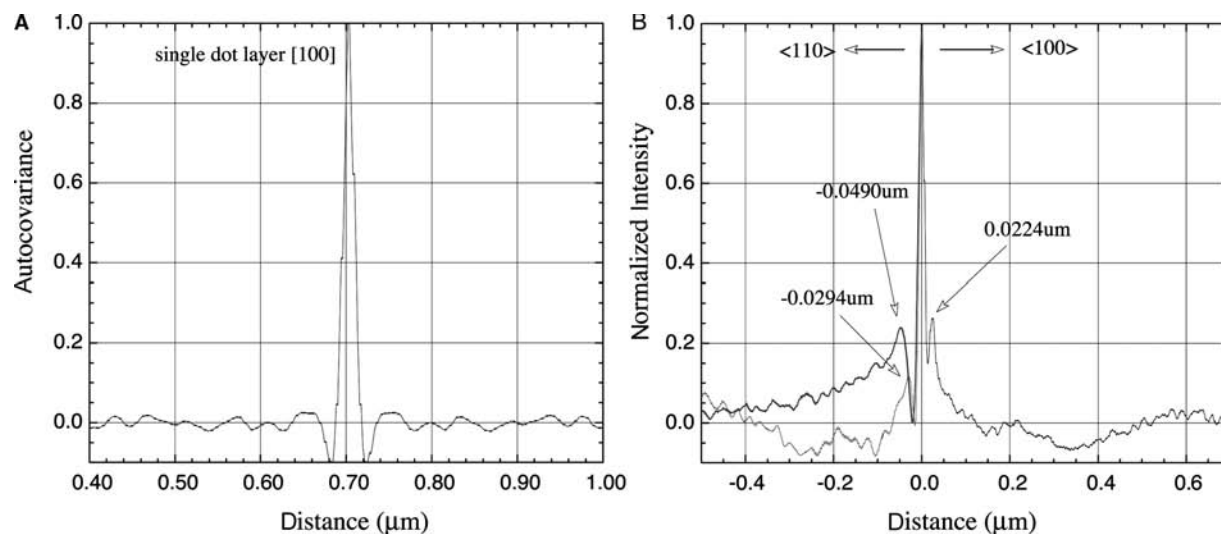


**Fig. 32** Autocovariance of AFM images in the  $\langle 110 \rangle$  and  $[100]$  directions: (A) a single dot layer sample, and (B) a 30-layer dot sample. The 30-layer sample has 55 Å spacer layers and was fabricated at 500°C.

surface. On top of this low-frequency roughness, some periodic intensity fluctuations can be seen, especially in one of the  $\langle 110 \rangle$  directions. This periodicity matches the fundamental unit cell distance and shows the translational symmetry in these directions.

To optimize the unit cell periodicity, we can adjust the crystal growth parameters. Figure 33 shows the autocovariance of images from two samples grown at 525°C. In Fig. 33A, 50 layers of InAs dots have been used, whereas in Fig. 33B, the number of InAs dot layers has been increased to 75. In both cases, the spacer layer thickness is 100 Å. Compared with the earlier samples grown at 500°C, this spacer layer thickness has been increased because of the increased dot size at

increased growth temperatures. In Fig. 33A, nearest-neighbor periodicity can be seen in both the  $\langle 110 \rangle$  and  $[100]$  directions. The nearest-neighbor distance has grown from 225 to 525 Å because of the increasing dot size with increasing growth temperature.<sup>[36]</sup> In Fig. 33B, the autocovariance shows a much more pronounced periodicity in the first, second, and third nearest-neighbor directions. We now see clear evidence of the emergence of a surface lattice of QDs. The condition that improves the surface lattice structure is primarily increased growth temperature.

We can combine the information from Figs. 32 and 33 to begin to understand why the quantum dots form only a weakly organized lattice. The lattice is weak

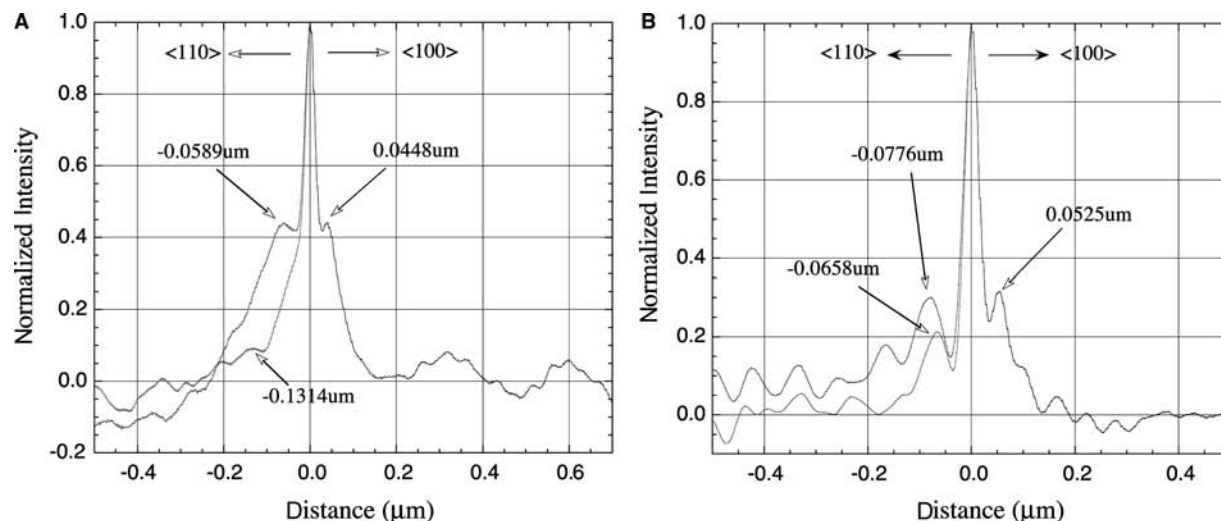


**Fig. 33** Autocovariance of AFM images in the  $\langle 110 \rangle$  and  $[100]$  directions for two structures fabricated at 525°C: (A) 50 layers of InAs dots were used in the subsurface structure, whereas in (B), 75 layers were used.



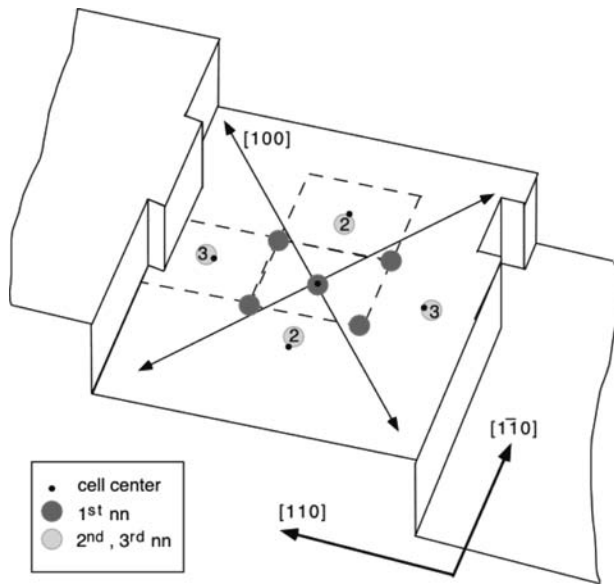


**Fig. 34** The unit cell is shown on a ledged surface. The unit cell is shown as a broken line whose center is translated to the small black dots. Experimentally determined first, second, and third nearest-neighbor sites are indicated by larger dots. The translated unit cell does not align with the second and third nearest-neighbors.

because the ratio of the first, second, and third nearest-neighbor distances does not allow for the complete filling of the surface. The anisotropic surface strain distribution creates a template for a cubic lattice of InAs dots. This process would create first nearest-neighbor sites in the  $\langle 100 \rangle$  directions. However, the surface diffusion of In or Ga adatoms is also anisotropic because of surface reconstruction and ledge dynamics. Because the surface diffusion is larger in  $[110]$ ,<sup>[51]</sup> the linear dot density in this direction should be largest. When these

two processes are combined, the degeneracy in the  $\langle 110 \rangle$  directions is lifted and the second nearest-neighbor sites in  $[1\bar{1}0]$  become closer than in  $[110]$ . In addition, the first nearest-neighbor site is rotated toward  $[110]$  because of the anisotropic surface diffusion.

The angular difference from the ideal first nearest-neighbor position ( $\langle 100 \rangle$ ) and the experimentally determined position is approximately  $3.5^\circ$ . This small difference from the ideal subsurface strain-driven case, where the first nearest-neighbor orientation should be  $\langle 100 \rangle$ , shows that the surface diffusion does not dominate the island ordering. However, it is enough to inhibit the formation of a well-ordered surface lattice. A cartoon of the quantum dot unit cell is shown in Fig. 34. The large dark circles represent the first nearest-neighbors, and the slight misalignment from  $\langle 100 \rangle$  can be seen. The second and third nearest-neighbors are represented by the large, lighter-colored circles. The anisotropy in the surface diffusion length,<sup>[51]</sup> attachment kinetics, and nucleation in orthogonal  $\langle 110 \rangle$  directions makes the nearest-neighbor distance in  $[1\bar{1}0]$  shorter than the nearest-neighbor distance in  $[110]$ . Finally, because of the anisotropy on the surface, the surface QD unit cell cannot be translated to fill the surface—no lattice is formed. This is seen in Fig. 34, where the small black dots represent the center of the translated unit cell. These smaller black dots do not fall on the second and third nearest-neighbor sites.

As the growth temperature increases, the anisotropy is reduced; this is shown in Fig. 35. As the growth temperature is increased, the difference in length between the second and third neighbors is reduced and the deviation from the ideal ratios between the first, second, and third nearest-neighbors is reduced. From Fig. 32 (510°C) and Fig. 33B (525°C), the ratio between the second and third nearest-neighbors is reduced from

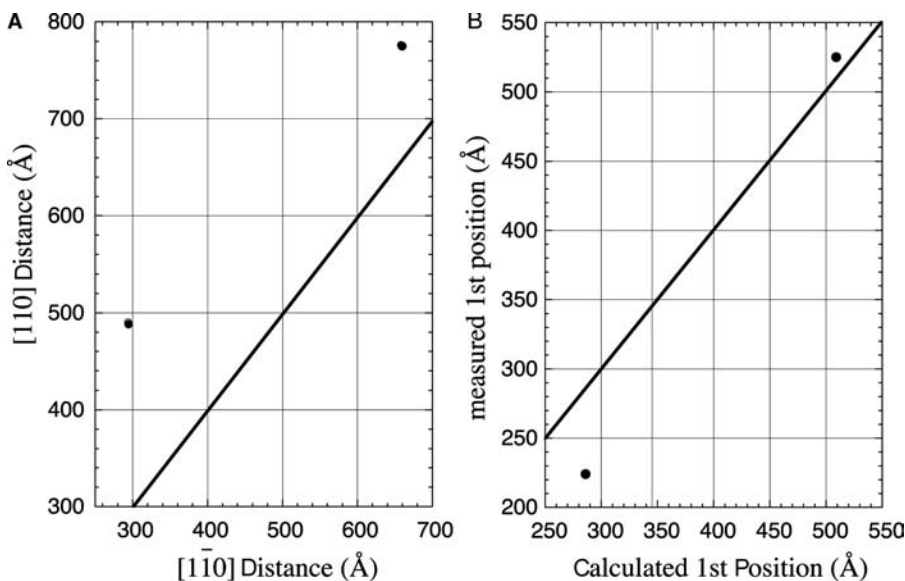


**Fig. 35** The variation from an ideal rectangular unit cell is shown for samples grown at 510°C and 525°C. In (A), the  $[110]$  to  $[1\bar{1}0]$  nearest-neighbor distances are compared. The solid line indicates an ideal rectangular cell. In (B), the first nearest-neighbor distance is calculated based on the second and third nearest-neighbor distances, and compared to the measured values.

1.70 to 1.15. The reduction in anisotropy shows that the effect of surface diffusion is reduced. If the second and third nearest-neighbors are used to calculate the first nearest-neighbor position based on a simple rectangular lattice, the deviation from the ideal position drops from 0.22 to only 0.035 as the temperature is increased from 510°C to 525°C. Thus as the growth temperature increases, a more ideal simple rectangular unit cell can be formed. This more ideal unit cell is more easily translated on the surface to form a lattice. We believe that the increased growth temperature reduces the anisotropy in the surface diffusion. Although an increased growth temperature would create larger terrace lengths in an unstrained GaAs surface, this may not be the case in the strained surface. Further work is necessary to confirm these results and develop a better understanding of the interplay between the subsurface strain and the surface diffusion. However, from this work, the spatial ordering from a subsurface superlattice structure of dot layers is improved with increased growth temperature.

Finally, it is important to note that the competition between surface diffusion and subsurface strain shown here is a manifestation of our particular crystal system and substrate orientation. Other systems with different surface reconstructions and ledge dynamics, or other vicinal or crystallographical surfaces will certainly act differently.

## CONCLUSION

We began this chapter by highlighting certain aspects of strain-induced quantum dot formation. These dots are formed in dense arrays. Although the density and uniformity of these ensembles can be controlled by adjusting the growth parameters, inhomogeneous broadening continues to mask the atomlike nature of the quantum dot states. Two features of this system were discussed. First, the luminescence linewidth was compared with the dot structure. It was shown that, although the linewidth is reduced in samples made at lower growth temperatures, the dots are less distinct. The decreasing linewidth is the result of reduced localization as the wavefunctions of individual dots in the ensemble begin to extend into adjacent dots. Second, the density of the dot ensemble was shown to be a function of the V/III flux ratio. In some applications, a high density is important, and we show how to maximize the density and implications of the process on dot formation.

The main purpose of this chapter is to develop the idea of using stacks of InAs quantum dot layers. These structures can be used in two ways. First, when only a small number of dot layers are stacked, columns of dots form electronically coupled structures. In analogy

to coupled QWs, changing the number of dot layers and the spacer layer thickness between them can tune the coupling. As a simple test of the structures, LEDs were fabricated, and it was shown that luminescence from the wetting layer and higher dot states could be suppressed using these column structures. Second, when a large number of dot layers are used, the surface size and spatial distributions can be improved. However, the experimental improvements are limited in our system because of competition between subsurface strain and surface diffusion. The way in which these two processes interact is clearly evident in the AFM images. Higher growth temperatures reduce the anisotropic surface diffusion effect, leading to an extended lattice. This lattice is present, but is not perfect, and perhaps other substrate orientations or material systems may offer improvements.

This work is just the beginning of efforts to create ensembles of atomlike quantum dots using epitaxial crystal growth. Although GaAs and InAs are used in these experiments, this work is not limited to III-V materials or even semiconductors. If well-ordered arrays of quantum dots can be created, promising device and fundamental physics opportunities await. In the device world, regular arrays of quantum dots allow for lithographical alignment and possibilities of logic and memory devices. As well, many of the experiments in atomic physics can be repeated using quantum dots. An interesting extension of this work would be the combination of the two aspects of the vertical column structures: the fabrication of structures in which a subsurface island superlattice of one material is used to make a surface strain distribution that increases the ordering in the surface layers, whereas a small number of quantum dots of a different material are grouped together in short columns as a coupled active region.

## ACKNOWLEDGMENTS

This work was only made possible through collaborations with and support from many people. The STM images were performed by W. Wu in J. R. Tucker's laboratory at the University of Illinois at Urbana-Champaign. TEM images were made with A. F. Marshall (Center for Materials Research at Stanford University). AFM and autocovariance data were obtained and analyzed with the help of S. Komarov (Photonics and Electronics Laboratory at Stanford University). G. S. would like to thank Y. Yamamoto for continued support. We would like to thank M. Pelton for critical discussions and helpful comments. This work was supported by the DARPA and ONR through contract nos. N00014-93-1 and N00014-97-1, and by the JST through the ERATO Quantum Fluctuation Project.

## REFERENCES

1. Matsumoto, K.; Ishii, M.; Segawa, K.; Oka, Y.; Vartanian, B.J.; Harris, J.S., Jr. *Appl. Phys. Lett.* **1996**, *68*, 34.
2. Tarucha, S.; Austing, D.G.; Honda, T.; Hage, R.; Kouwenhoven, L.P. *Jpn. J. Appl. Phys.* **1997**, *36*, 3917.
3. Yano, K.; Ishii, T.; Hashimoto, T.; Kobayashi, T.; Murai, F.; Seki, K. *Appl. Phys. Lett.* **1995**, *67*, 828.
4. Bockelmann, U.; Heller, W.; Filoramo, A.; Roussignol, Ph. *Phys. Rev., B* **1997**, *55*, 4456.
5. Ipatova, I.P.; Malyshkin, V.G.; Shchukin, V.A. *J. Appl. Phys.* **1993**, *74*, 7198.
6. Tersoff, J.; Phang, Y.H.; Zhang, Z.; Lagally, M.G. *Phys. Rev. Lett.* **1995**, *75*, 2730.
7. Lijima, S. *Nature* **1991**, *354*, 56.
8. Tanford, C. *Science* **1978**, *200*, 1012.
9. Tabuchi, M.; Noda, S.; Sasaki, A. *Science and Technology of Mesoscopic Structures*; Springer-Verlag: Tokyo, Japan, 1992; 375.
10. Leonard, D.; Krishnamurthy, M.; Reaves, C.M.; Denbaars, S.P.; Petroff, P.M. *Appl. Phys. Lett.* **1993**, *63*, 3203.
11. Medeiros-Ribeiro, G.; Lenard, D.; Petroff, P.M. *Appl. Phys. Lett.* **1995**, *66*, 1767.
12. Heitz, R.; Grundmann, M.; Ledentsov, N.N.; Eckey, L.; Veit, M.; Bimberg, D.; Ustinov, V.M.; Egorov, A.Yu.; Zhukov, A.E.; Kop'ev, P.S.; Alferov, Sh.I. *Appl. Phys. Lett.* **1996**, *68*, 361.
13. Hessman, D.; Castrillo, P.; Pistol, M.E.; Samuelson, L. *Appl. Phys. Lett.* **1996**, *69*, 749.
14. Heinrichsdorff, F.; Mao, M.H.; Kirstaedter, N.; Krost, A.; Bimberg, D.; Kosogov, A.O.; Werner, P. *Appl. Phys. Lett.* **1997**, *71*, 22.
15. Solomon, G.S.; Trezza, J.A.; Marshall, A.F.; Harris, J.S., Jr. *Phys. Rev. Lett.* **1996**, *76*, 952.
16. Solomon, G.S.; Trezza, J.A.; Harris, J.S., Jr. *J. Vac. Sci. Technol., B* **1996**, *14*, 2208.
17. Xie, Q.; Madhukar, A.; Chen, P.; Kobayashi, N.P. *Phys. Rev. Lett.* **1995**, *75*, 2542.
18. Tersoff, J.; Teichert, C.; Lagally, M.G. *Phys. Rev. Lett.* **1996**, *76*, 1675.
19. Tiller, W.A. *The Science of Crystallization: Microscopic Interfacial Phenomena*; Cambridge University Press: Cambridge, England, 1991; 172 pp.
20. Gao, H. *Int. J. Solids Struct.* **1990**, *28*, 703.
21. Freund, L.B.; Jonsdottir, F. *J. Mech. Phys. Solids* **1993**, *41*, 1245.
22. Orr, B.G.; Kessler, D.; Synder, C.W.; Sander, L. *Europhys. Lett.* **1992**, *19*, 33.
23. Vanderbilt, D.; Wickham, L.K. *Mater. Res. Soc. Symp. Proc.* **1991**, *202*, 555.
24. Matthews, J.W.; Blakeslee, A.E. *J. Cryst. Growth* **1974**, *27*, 118.
25. People, R.; Bean, J.C. *Appl. Phys. Lett.* **1985**, *47*, 322.
26. Stranski, I.N.; Krastanow, L. *Akad. Wiss. Wien Math. Naturwiss. Kl. Abt. 2B Chemie* **1937**, *146*, 797. We add this reference for historical context.
27. Mullins, W.W. *J. Appl. Phys.* **1957**, *28*, 333.
28. Asaro, R.J.; Tiller, W.A. *Metall. Trans.* **1972**, *3*, 1789.
29. Srolovitz, D.J. *Acta Metall.* **1989**, *37*, 621.
30. Lee, H.; Lowe-Webb, R.; Yang, W.; Sercel, P.C. *Appl. Phys. Lett.* **1998**, *72*, 812.
31. Gao, H. *J. Mech. Phys. Solids* **1991**, *39*, 443.
32. Gao, H. *J. Mech. Phys. Solids* **1994**, *42*, 741.
33. Freund, L.B.; Johnson, H.T.; Kukta, R.V. *Mater. Res. Soc. Symp. Proc.* **1995**, 359.
34. Guha, S.; Madhukar, A.; Rajkumar, K.C. *Appl. Phys. Lett.* **1990**, *57*, 210.
35. Hellman, E.S.; Harris, J.S., Jr. *J. Cryst. Growth* **1987**, *81*, 38.
36. Solomon, G.S.; Trezza, J.A.; Harris, J.S., Jr. *Appl. Phys. Lett.* **1995**, *66*, 991.
37. Leonard, D.; Pond, K.; Petroff, P.M. *Phys. Rev., B* **1994**, *50*, 11,687.
38. Lin, X.W.; Liliental-Weber, Z.; Washburn, J.; Weber, E.R. *J. Vac. Sci. Technol., B* **1994**, *12*, 2562.
39. Marzin, J.Y.; Gerard, J.M.; Izrael, A.; Barrier, D.; Bastard, G. *Phys. Rev. Lett.* **1994**, *73*, 716.
40. Fafard, S.; Leonard, D.; Merz, J.L.; Petroff, P.M. *Appl. Phys. Lett.* **1994**, *65*, 1388.
41. Solomon, G.S.; Trezza, J.A.; Harris, J.S., Jr. *Appl. Phys. Lett.* **1995**, *66*, 3161.
42. Goldstein, L.; Glas, F.; Marzin, J.Y.; Charasse, M.N.; Le Roux, G. *Appl. Phys. Lett.* **1985**, *47*, 1099.
43. Nabetani, Y.; Ishikawa, T.; Noda, S.; Sasaki, A. *J. Appl. Phys.* **1994**, *76*, 347.
44. Leonard, D.; Fafard, S.; Pond, K.; Zhang, Y.H.; Merz, J.L.; Petroff, P.M. *J. Vac. Sci. Technol., B* **1994**, *12*, 2516.
45. Gerard, J.M.; Genin, J.B.; Lefebvre, J.; Moison, J.M.; Lelouch, N.; Barthe, F. *J. Cryst. Growth* **1995**, *150*, 351.
46. Lott, J.A.; Ledentsov, N.N.; Ustinov, V.M.; Egorov, A.Yu.; Zhukov, A.E.; Kop'ev, P.S.; Alferov, Zh.I.; Bimberg, D. *Electron. Lett.* **1997**, *33*, 1150.
47. Mirin, R.P.; Ibbetson, J.P.; Nishiad, K.; Gossard, A.C.; Bowers, J.E. *Appl. Phys. Lett.* **1996**, *67*, 3795.
48. Zheng, J.F.; Walker, J.D.; Salmeron, M.B.; Weber, E.R. *Phys. Rev. Lett.* **1994**, *72*, 2414.
49. Pfister, M.; Johnson, M.B.; Alvarado, S.F.; Salemink, H.W.M.; Marti, U.; Martin, D.; Morier-Genoud, F.; Reinhart, F.K. *Appl. Phys. Lett.* **1995**, *67*, 1459.
50. Sauvage-Simkin, M.; Garreau, Y.; Pinchaux, R.; Veron, M.B.; Landesman, J.P.; Nagle, J. *Phys. Rev. Lett.* **1995**, *75*, 3485.
51. Ohta, K.; Kojima, T.; Nakagawa, T. *J. Cryst. Growth* **1989**, *95*, 71.
52. Maradudin, A.A.; Wallis, R.F. *Surf. Sci.* **1980**, *91*, 423.
53. Okada, T.; Weatherly, G.C.; McComb, D.W. *J. Appl. Phys.* **1997**, *81*, 2185.
54. Mura, T. *Micromechanics of Defects in Solids*; Martinus Nijhoff: Netherlands, 1982; 93.

# Quantum Dots: Inelastic Light Scattering from Electronic Excitations

Christian Schüller

*Institut für Angewandte Physik und Zentrum für Mikrostrukturforschung,  
Universität Hamburg, Hamburg, Germany*

## INTRODUCTION

Electrons confined in semiconductor quantum systems are a field of enormous and still growing research interest because they allow, in specially tailored systems, the investigation of fundamental properties, such as many-particle interactions of electrons in reduced dimensions. In this entry, we give an overview of experimental and theoretical investigations of electronic excitations in semiconductor quantum dots. Optical spectroscopy techniques, such as far-infrared (FIR) transmission<sup>[1–7]</sup> and resonant Raman scattering, i.e., inelastic light scattering (ILS),<sup>[8–12]</sup> are ideal tools to study the spectrum of elementary excitations of these systems. Since the work of Pinczuk et al.<sup>[13]</sup> on 2-D intersubband excitations in GaAs–AlGaAs quantum wells, it has been known that besides collective spin-density (SDEs) and charge-density excitations (CDEs), one can observe nearly unrenormalized excitations—the so-called single-particle excitations (SPEs)—in ILS experiments. Both SDEs and CDEs are collective excitations; SDEs are affected by exchange interaction while CDEs are affected by the full Coulomb interaction of the electrons. However, the origin of the SPEs, which seem to be unaffected by the particle–particle interaction, has posed a puzzle. Electronic excitations, and also SPEs in particular, could subsequently be observed in lower-dimensional systems, based on modulation-doped GaAs–AlGaAs quantum wells, and also particularly in quantum dots.<sup>[8–10]</sup> In an experimental work, it was shown that SPEs can be observed in low-dimensional electron systems under conditions of extreme resonance, when the laser energy is close to the fundamental band gap of the structures.<sup>[10]</sup> Thus SPEs are created in a resonant density-fluctuation scattering process,<sup>[14,15]</sup> whereas collective SDEs and CDEs ensue from an excitonic third-order scattering process.<sup>[10,16,17]</sup> Many theories of non-resonant Raman scattering accurately describe the energetic positions of the collective excitations, as well as the wave-vector and magnetic-field dependence of the CDE and SDE.<sup>[18–21]</sup> However, they fail in predicting the experimentally observed relative strengths of the different modes. Furthermore, the occurrence

of SPE cannot be explained within the confines of these theories. It has been known for a long time that valence-band states play a crucial role<sup>[22,23]</sup> in carrying out a correct treatment of the resonant scattering cross section. Recent theoretical papers on quantum wires<sup>[15,24,25]</sup> and quantum dots<sup>[26]</sup> showed that inclusion of the valence-band states indeed significantly changes the intensities of the excitations. During the past decade, self-assembled InAs quantum dots (SAQDs) have also proven to be highly interesting quantum structures, both from a technological as well as from a fundamental physics point of view. They exhibit relatively large quantization energies in the range of about 50 meV. In most experiments reported so far, SAQDs have been investigated by optical spectroscopy, in particular photoluminescence (PL). Nowadays, PL experiments on single dots are well established, which overcome the inhomogeneously broadened linewidths in typical ensemble measurements.<sup>a</sup> It has also been demonstrated that it is possible to charge SAQD with single electrons<sup>[28]</sup> via the application of external gate structures. So far, there are only two reports in literature about ILS experiments on electronic excitations in InGaAs SAQD.<sup>[29,30]</sup> In this contribution, ILS experiments on collective CDEs in InAs SAQD with tunable electron numbers  $N$  are described. In these experiments,  $N$  can be controlled at  $N = 1–6$ .

The entry is organized as follows. In the section “Characteristics of Quantum Dots and Experimental Details,” we describe the quantum-dot structures under investigation: modulation-doped GaAs–AlGaAs quantum dots and InAs SAQD, and give a brief discussion of the electronic structure and the excitations of these systems. Furthermore, the experimental realization of ILS is outlined in this section. In the section “Scattering Mechanisms,” a summarized description of the scattering mechanisms, which lead to the creation of electronic excitations in quantum dots, is provided. In the section “Experiments on GaAs–AlGaAs Deep-Etched Quantum Dots,” we start to

<sup>a</sup>For a recent review, see Ref.<sup>[27]</sup>.

discuss experiments on modulation-doped GaAs–AlGaAs quantum dots. There, basics such as parity selection rules are elaborated. The section “Experiments on InAs Self-Assembled Quantum Dots” summarizes recent experiments on InAs SAQD, which contain only a small number of electrons and which can be regarded as artificial atoms.

## CHARACTERISTICS OF QUANTUM DOTS AND EXPERIMENTAL DETAILS

### Preparation of Quantum Dots

The vast majority of ILS experiments on electronic excitations in quantum dots have been performed on modulation-doped GaAs–AlGaAs structures. Fig. 1A shows a scanning electron micrograph of deep-etched quantum dots. Typical sizes of these structures are on the order of several hundred nanometers. In many cases, 2-D electron systems, realized in modulation-doped single quantum wells, are used as a starting material. In Fig. 1A, the location of such a 25-nm-wide quantum well is indicated by thick dashed lines. By a reactive-ion etching process, the pillar-shaped quantum dots were defined. Typically, such deep-etched structures contain electron numbers on the order of several hundreds. An alternative and very effective way to produce quasi zero-dimensional semiconductor structures is the so-called self-assembled growth of InAs quantum dots. Here the lattice mismatch between GaAs, which is used as the starting material, and InAs is exploited. The minimization of strain energy leads to the formation of small InAs islands, if InAs is grown on a GaAs surface. In contrast to the etched structures,

the typical lateral sizes of these islands are on the order of only a few tens of nanometers. Therefore they exhibit much larger quantization energies. Fig. 1B displays a transmission electron micrograph of an InAs quantum dot, embedded in GaAs. The boundaries of the InAs dot are indicated by a white dashed line. It has been shown that electrons can be filled into these quantum boxes either by modulation doping<sup>[29]</sup> or by application of external gates.<sup>[28]</sup> With the application of gates, it is even possible to fill in single electrons in a very controlled way. Fig. 1C shows a schematic picture of the band structure of an InAs SAQD sample, as used in Ref.<sup>[30]</sup> There, an inverted modulation-doped AlGaAs–GaAs structure serves as a back contact. By application of a voltage between the back contact and a metallic front gate, the dots can be charged with single electrons, which then tunnel from the two-dimensional electron system (2DES) to the dots.

### Electronic Ground State and Excitations

As will be explained below, in the etched GaAs dots, as well as in the InAs SAQD,<sup>[31]</sup> the lateral external confining potential is to a good approximation parabolic. In the deep-etched samples, the potential is determined by the homogeneously distributed ionized remote donors in the AlGaAs barrier and negatively charged surface states. By analytical calculations, one can show that this lateral potential, which acts on a test electron within the structure (*external* potential), is in  $x$  and  $y$  directions (lateral directions) in good approximation parabolic.<sup>[32]</sup> Therefore we will start our investigations by assuming that the corresponding single-particle energies are given by the eigenvalues of a

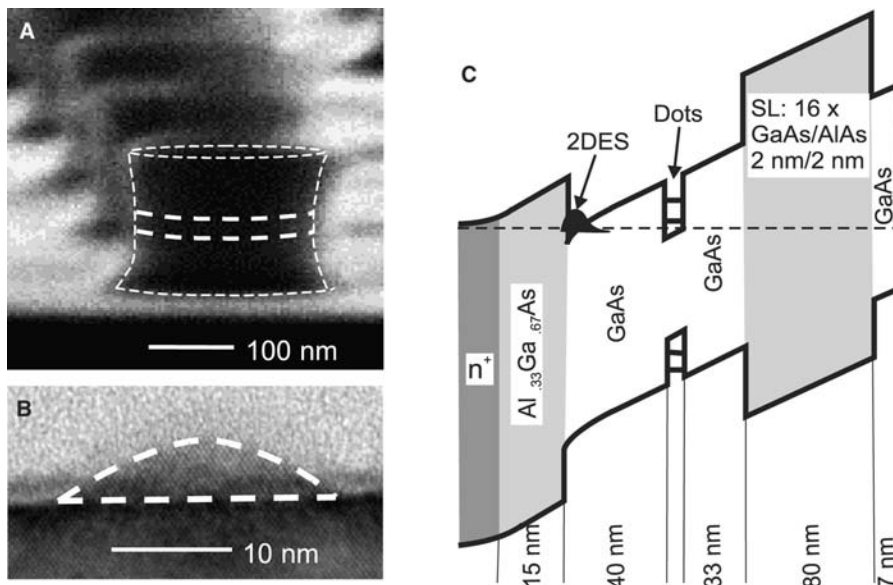


**Fig. 1** (A) Scanning electron micrograph of deep-etched GaAs–AlGaAs quantum dots. The white dashed lines mark one of the dots. The long dashes indicate the active electron layer. (B) Transmission electron micrograph of an InAs quantum dot. The white dashed lines mark the borders of the InAs island. (With permission of S. Mendach.) (C) Schematic band structure of an InAs SAQD sample with a two-dimensional electron system (2DES) as a back contact.

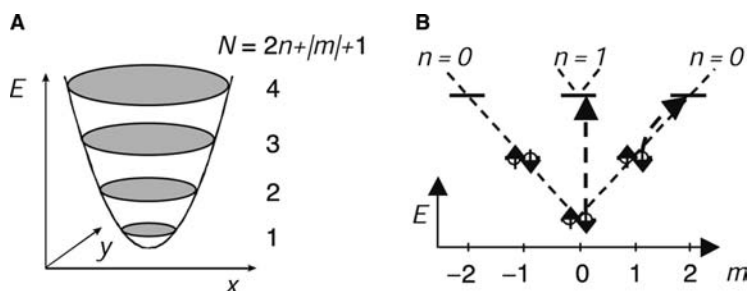


Fig. 2 (A) Schematic picture of the lateral potential of a quantum dot. (B) Energy levels of a quantum dot with parabolic potential. The curved dashed arrows indicate possible excitations of single electrons.

two-dimensional harmonic oscillator

$$E_{nm} = \hbar\Omega_0(2n + |m| + 1) = N\hbar\Omega_0 \quad (1)$$

Here the two relevant quantum numbers are the radial quantum number  $n = 0, 1, 2, \dots$  and the azimuthal or angular-momentum quantum number  $m = 0, \pm 1, \pm 2, \dots$ . We define a lateral quantum number  $N = (2n + |m| + 1)$ , which characterizes the  $2N$ -fold degenerate discrete levels, as sketched in Fig. 2A. Naturally, the presence of many other electrons in the sample leads to a screening of the potential, which acts on the test electron. Theoretically, this is described, e.g., in a self-consistent Hartree calculation of the ground state. Thus the effective lateral potential is flattened in the center of the dot, i.e., it becomes more and more square-well-like. This results, in a mean field approach, in a decrease of the single-particle level spacings and to a lifting of degeneracies. For simplicity, we stay for the moment in the simple picture, where we assume that also the effective, or Hartree, potential is parabolic which is a good approximation for the ground state of dots with small electron numbers.

In such a single-particle picture, the electronic excitations, which can be created in the inelastic light scattering process, are transitions of electrons from occupied to unoccupied levels, as, e.g., sketched in Fig. 2B. In Fig. 2B, the energy levels for a parabolic quantum dot, which contains six electrons, is shown in more detail. The corresponding radial- and angular-momentum quantum numbers are indicated. Of course, in a real interacting system, the electronic excitations will be collective excitations, CDEs and SDEs, which are affected by Coulomb interaction.

For large electron numbers, on the order of 100 or more, it is instructive to leave the quasiparticle picture described above for a while, and discuss the electronic excitations in terms of plasma oscillations of the electrons. For CDEs, in that case, some of the excitations are also called confined plasmons. For all following considerations, we assume that the external potential is parabolic. Consequently, the simplest CDE is a plasma oscillation where all electrons oscillate in phase in the quantum dot back and forth. This situation is, for a fixed time, schematically shown in Fig. 3A, where a dark color should indicate a large

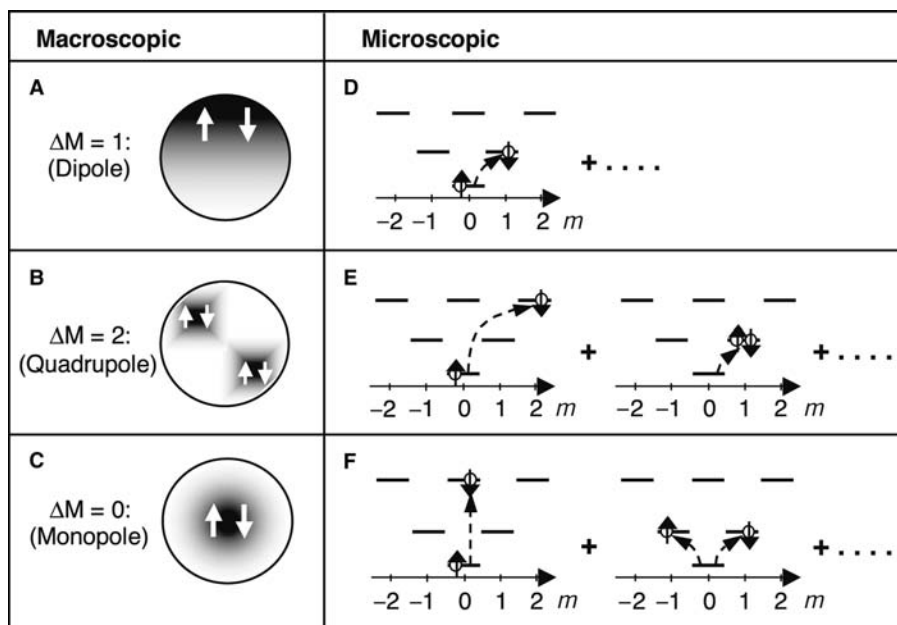


Fig. 3 Schematic drawings of the electron-density distributions for different confined plasmon modes [(A)–(C)]. Microscopic picture for the excitations of a parabolic quantum dot with two electrons [(D)–(F)].



induced electron density. White indicates an induced positive charge distribution. Hence the induced electron density has, in this case, one node. Obviously, this excitation has a large dipole moment. It is also called the first confined plasmon or Kohn's mode, because, for the case of a parabolic external potential, its energy exactly equals the quantization energy of the external potential, and the energy of the lowest energy dipole excitation is independent of the number of electrons  $N$  in the dot. This fact is known as the so-called generalized Kohn's theorem.<sup>[33]</sup> The dipole excitation is characterized by a change of  $\Delta M = 1$  of the total angular-momentum quantum number  $M$ , i.e., the angular momentum of the  $N$ -electron system. This will become clearer when we discuss the microscopic picture below. The CDEs with the next higher energies are the quadrupole excitation corresponding to  $\Delta M = 2$  [Fig. 3B], and the monopole excitation with a change in total angular momentum of  $\Delta M = 0$  [Fig. 3C]. The next higher excitation would again be a dipole excitation (not shown here), which is additionally accompanied by a change in the radial quantum number  $n$ . In all CDEs, the electrons with spin up and spin down oscillate in phase against the positively charged background. This is schematically indicated by the white arrows in Fig. 3. This means that the CDEs are strongly affected by the direct part of the Coulomb interaction, which in most cases results in a blueshift of the excitations. In contrast, in the corresponding SDEs, the electrons with spin up and spin down oscillate with a phase shift of  $\pi$ . For the *spin dipole* excitation (not shown here), corresponding to the CDE in Fig. 3A, e.g., this means that the center of mass of the charge does not oscillate. Thus the energies of the SDEs are only renormalized by exchange-correlation interaction and are therefore redshifted. We note here already that, in experiments on zinc-blende semiconductors, SDEs and CDEs can be distinguished by polarization selection rules.<sup>[34]</sup> CDEs are observed if the polarizations of the incoming and scattered light are parallel to each other (*polarized* geometry), and, for SDEs, the polarizations have to be perpendicular (*depolarized* geometry).

In the following, we will discuss how this macroscopic picture translates into the quasiparticle picture, which we introduced at the beginning. This makes sense for small electron numbers only, otherwise it would be too complicated. The simplest interacting system that comes to mind is a quantum dot with two electrons. In Fig. 3D–F, the dipole, quadrupole, and monopole CDEs are schematically shown for a two-electron quantum dot, respectively. More precisely, Fig. 3D–F pictorially displays the occupation of the Slater determinants, which predominantly contribute to the two-particle wavefunctions of the respective excited states. The exact many-particle

wavefunction can always be written as an infinite series of single-particle Slater determinants. Fig. 3D–F exhibits the occupation of the most important Slater determinants of the respective excited states. The ground state of a two-electron dot has a total angular momentum of  $M = 0$ , because both electrons occupy the  $s$  level with  $m = 0$ . In Fig. 3, one can see that for the dipole excitation, the angular momentum of the excited state is  $M = 1$ , for the quadrupole excitation,  $M = 2$ , and, for the monopole excitation,  $M = 0$ . For CDEs, as displayed in Fig. 3, the spin is preserved during the excitation ( $\Delta S = \Delta S_z = 0$ ). For the excitation of SDEs, which are triplet excitations,  $\Delta S = 1$ , and  $\Delta S_z$  can take on values of 1,  $-1$ , and 0. This means that spinflip transitions of electrons are involved in SDEs. For zero magnetic field,  $B = 0$ , the three triplet excitations with  $\Delta S_z = 0, \pm 1$ , corresponding to the same excitation type (e.g., spin dipole, spin monopole, etc.), are degenerate. As already noted, we expect the SDEs to have lower energies than the corresponding CDEs because they experience no direct Coulomb interaction.

## Experimental Details

For resonant ILS experiments, tunable lasers such as dye lasers or Ti:sapphire lasers are used. Usually, the samples are kept in a cryostat at low temperatures, typically below 10 K. A special feature of ILS spectroscopy is that a finite wave vector  $\mathbf{q}$  can be transferred to the excitations. This is achieved by tilting the sample with respect to the incident and scattered beams. Fig. 4 schematically displays the most often used backscattering geometry, which allows the largest wave-vector transfer  $\mathbf{q}$  into the system. Here  $\mathbf{k}_i$  and  $\mathbf{k}_s$  represent the wave vector of the incident and inelastically scattered photons, respectively. Under the assumption that the wavelengths of the incident,  $\lambda_i$ , and scattered light,  $\lambda_s$ , are almost equal ( $\lambda_i \sim \lambda_s$ , which is a good approximation because light in the visible or near-infrared range is used to excite excitations with energies in the FIR), the equation  $\mathbf{q} \sim 4\pi\lambda_i \sin\Theta$  holds for the relation of  $\mathbf{q}$  vs. the tilt angle  $\Theta$ . The experiments discussed in this entry were performed using backscattering geometry. A Ti:sapphire laser

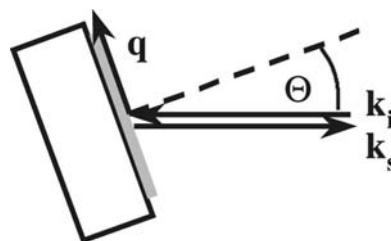


Fig. 4 Sketch of the backscattering configuration.

was applied for excitation, and the ILS signals were detected with a triple Raman spectrometer, equipped with a cooled, charge-coupled device detector. The samples were mounted in cryostats at temperatures between  $T = 2\text{ K}$  and  $T = 12\text{ K}$ .

### SCATTERING MECHANISMS

In this section, the dominant scattering mechanisms, which lead to the light scattering in low-dimensional electron systems, are qualitatively discussed. In general, the inelastic light scattering by electronic excitations in semiconductor microstructures with relatively small numbers of electrons can be observed only under specific interband resonance conditions. That means that in the scattering process, valence-band states are involved as intermediate states. Nevertheless, most of the theoretical work concerning the dynamic Raman response in microstructures is performed for non-resonant conditions, neglecting the valence-band structure. We summarize here the dominant *resonant* scattering processes, which are fragmentarily present in the literature, and which we found in our experiments on quantum wells, wires, and dots to be the dominant ones.<sup>[14]</sup>

The coupling of the radiation with the electron system is taken into account by replacing the momentum  $\mathbf{p}$  of the electron by  $\mathbf{p} + e\mathbf{A}$  in the Hamiltonian  $H_0$  of the unperturbed system.  $\mathbf{A}$  is the vector potential of the electromagnetic field.

$$H = \frac{1}{2m} \sum_i [(\mathbf{p}_i + e\mathbf{A}(\mathbf{r}_i))^2 + U(\mathbf{r}_i)] + V_{e-e} + V_{e-ph}$$

$$= H_0 + \frac{1}{2m} \sum_i [(A(\mathbf{r}_i))^2 + \mathbf{p}_i A(\mathbf{r}_i) + A(\mathbf{r}_i) \mathbf{p}_i] \quad (2)$$

$V_{e-e}$  is the Coulomb interaction,  $V_{e-ph}$  the electron-phonon interaction, and  $U$  includes the lattice-periodic potential as well as all types of external potentials. For simplicity, the spin-orbit coupling is neglected in Eq. (2). In a perturbation theory approach, the last three terms of Eq. (2) can be treated as the perturbation. Here the  $A^2$  terms give contributions to the light scattering cross section in *first* order, the  $\mathbf{pA}$  terms in *second*-order perturbation theory. The  $\mathbf{pA}$  terms, together with either the Coulomb interaction  $U_{e-e}$  of a photoexcited exciton with the electron system, or the electron-phonon interaction  $V_{e-ph}$  of a photoexcited exciton with the phonon bath, give contributions in *third*-order perturbation theory.  $V_{e-ph}$  leads to the scattering by phonons, which shall not be discussed here. The second-order (SOP) and third-order light scattering processes (TOP) appear to be the dominant ones in electronic Raman scattering on microstructures because they exhibit a resonant behavior.<sup>[35]</sup> In Fig. 5, transitions which contribute to the second- [Fig. 5A,B] and third-order [Fig. 5C] processes in quantum dots are sketched. Valence band levels are marked by  $|v\rangle$ , and conduction band levels by  $|c\rangle$ . In the first step of the two-step SOP, an electron is excited from a valence band level to a conduction band state. In the second step, an electron, either with the same or with opposite spin as the photoexcited electron, recombines with the hole in the valence band. Thus as a net effect, either a non-spinflip or spinflip single-particle excitation has been created in the conduction band. In the third step of the three-step SOP, another SPE is created by Coulomb interaction. This represents the screening of the SPE by other SPEs in the system. This screening also leads to the formation of collective CDEs and SDEs by direct and exchange Coulomb coupling. For non-resonant conditions, the SPEs are screened by the interaction. This is formally implemented by the

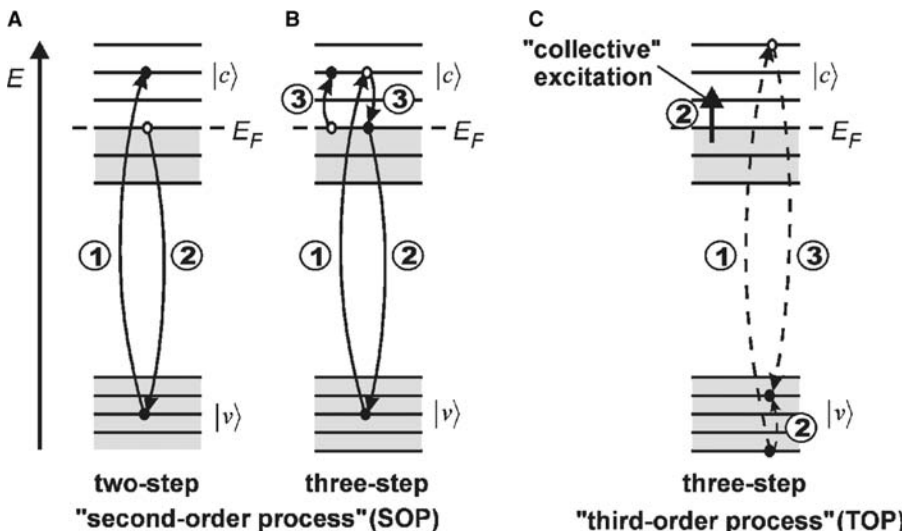


**Fig. 5** Schematic pictures of the (A) two-step, (B) three-step second-order scattering processes, and (C) a three-step third-order process, which contribute to the resonant ILS in quantum dots. *Source:* From Ref.<sup>[14]</sup>.

cancellation of the two-step SOP contribution by the three-step SOP in the scattering cross section for off-resonance conditions. In experiments on deep-etched GaAs samples with relatively large electron numbers, it was observed that under conditions of extreme resonance, which means that the laser frequency is in the vicinity of the fundamental bandgap of the underlying 2-D structure, quasi unscreened SPEs occur. They show stronger resonance enhancements than the collective excitations.<sup>[10]</sup> This means that the above-mentioned cancellation of terms does not hold in the case of extreme resonance and thus single-particle-like excitations can be observed. A quite similar behavior was reported for intraband excitations in n-type GaAs bulk samples.<sup>[36]</sup>

It was found that for laser energies well above the bandgap, an excitonic third-order scattering process, as for the case of quantum dots displayed in Fig. 5C, is the dominant one (for 2-D excitations, see Refs.<sup>[16,17]</sup>). For this scattering mechanism, which is assisted by the Coulomb interaction, in the first step the incident photon creates an exciton with a hole in the valence band and an electron in a higher conduction band level. This exciton is scattered by direct and exchange Coulomb interaction with the electron system into another state, where, e.g., as drawn in Fig. 5C, the hole is scattered into another state. By this scattering process, a collective excitation (SDE or CDE) is created in the conduction band system. In the third step, the scattered exciton recombines. This scattering process exhibits very sharp and intense resonance profiles in a plot of the scattered intensity vs. laser energy.<sup>[16]</sup> It was found that this TOP is the dominant scattering mechanism for excitation of collective SDEs and CDEs in low-dimensional GaAs samples.<sup>[10]</sup>

In the following, we elucidate these scattering processes in more detail. The scattering cross section is given by<sup>[34]</sup>

$$\frac{d^2\sigma}{d\Omega d\omega} = \frac{\omega_S}{\omega_I} \frac{e^4}{c^4 m^4} S(\omega) \quad (3)$$

where the structure factor  $S(\omega)$  is defined as

$$S(\omega) = \sum_F |\langle F | V_{\text{eff}} | I \rangle|^2 \delta(E_F - E_I - \hbar\omega) \quad (4)$$

$\omega_I$  ( $\omega_S$ ) is the frequency of the incident (scattered) photon, and  $\hbar\omega = \hbar\omega_I - \hbar\omega_S$  is the energy transfer.  $V_{\text{eff}}$  is the effective operator, which describes the transition of the system from the many-particle initial state  $|I\rangle$  with energy  $E_I$  to the final state  $|F\rangle$  with energy  $E_F$ . Using the second-quantization technique, this effective operator of the light scattering  $V_{\text{eff}}$  can, in a many-particle system, be expanded in terms of creation ( $\hat{c}^+$ ) and

annihilation ( $\hat{c}$ ) operators of single-electron states<sup>[17]</sup>

$$V_{\text{eff}} = \sum_{\alpha,\beta} \gamma_{\alpha\beta} \hat{c}_\beta^+ \hat{c}_\alpha \quad (5)$$

Here each  $\alpha$  and  $\beta$  represents a set of quantum numbers  $(n,m,\sigma)$ , for the radial, azimuthal, and spin quantum numbers of the corresponding state, respectively. If we treat, for a moment, the excitons as simple electron-hole pairs without interaction, which for a quantitative analysis is certainly not correct, the scattering amplitudes  $\gamma_{\alpha\beta}$  can approximately be written as

$$\gamma_{\alpha\beta} \propto \langle \alpha | e^{iqr} | \beta \rangle e_I e_S + \frac{1}{m} \sum_{\beta'} \frac{\langle \alpha | \mathbf{p} \mathbf{A}_S | \beta' \rangle \langle \beta' | \mathbf{p} \mathbf{A}_I | \beta \rangle}{E_\beta - E_{\beta'} + \hbar\omega_I} + \sum_{\nu,\nu'} \frac{\langle \beta | \mathbf{p} \mathbf{A}_S | \nu' \rangle \langle \nu' | U_{e-e} | \nu \rangle \langle \nu | \mathbf{p} \mathbf{A}_I | \alpha \rangle}{(E_\beta - E_{\nu'} + \hbar\omega_S)(E_\alpha - E_\nu - \hbar\omega_I)} \quad (6)$$

where, in the last two terms, we have written only the strongest resonant term. The first term in Eq. (6) represents the non-resonant contributions from the  $A^2$  terms in first-order perturbation theory. Here the scalar product of the polarization vectors of the incident ( $e_I$ ) and scattered ( $e_S$ ) photon shows that this non-resonant term yields only scattering by plasmons (CDEs). Spin-flip processes, which are necessary for the excitation of SDEs, are only possible in the resonant second and third terms. The second term describes second-order processes, as schematically shown in Fig. 5A, and the third term represents third-order resonant scattering, as displayed in Fig. 5C.

To illustrate this, Fig. 6 shows experimental ILS spectra of electronic excitations in deep-etched GaAs quantum dots with 240 nm geometrical diameter and about 200 electrons per quantum dot. The spectra in the lower part were recorded at laser energies well above the effective bandgap. In the lowest spectrum at a laser energy of  $E_L = 1587$  meV, three peaks can be observed, which can be identified as SDEs because of polarization selection rules. (We will come to the detailed interpretation of the excitations in the section ‘‘Experiments on GaAs–AlGaAs Deep-Etched Quantum Dots.’’) Correspondingly, the peaks in the polarized spectrum can be identified as CDEs. We have found that CDEs, in particular, exhibit a very sharp [full width at half-maximum (FWHM)  $\sim 3.5$  meV] resonance profile in this range of laser energies—which leads us to the interpretation that this scattering by *collective* excitations is caused by the third-order TOP, as discussed before. If the laser frequency is slightly lowered (spectra at  $E_L = 1585$  meV in Fig. 6), additional broad features appear, especially in the polarized spectrum, which then slowly evolve into intense peaks, by further lowering  $E_L$  toward the bandgap. These features are marked in Fig. 6 by dotted arrows. Under conditions of extreme resonance

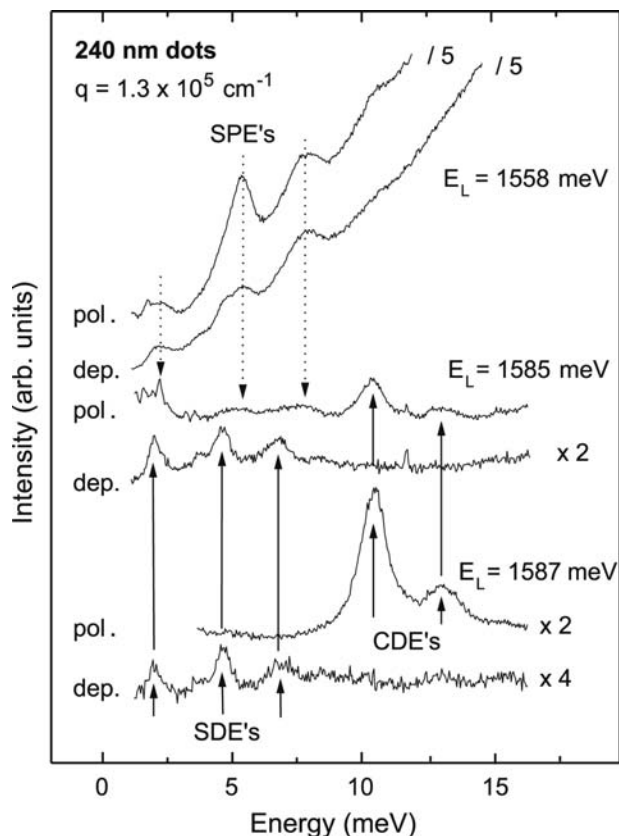


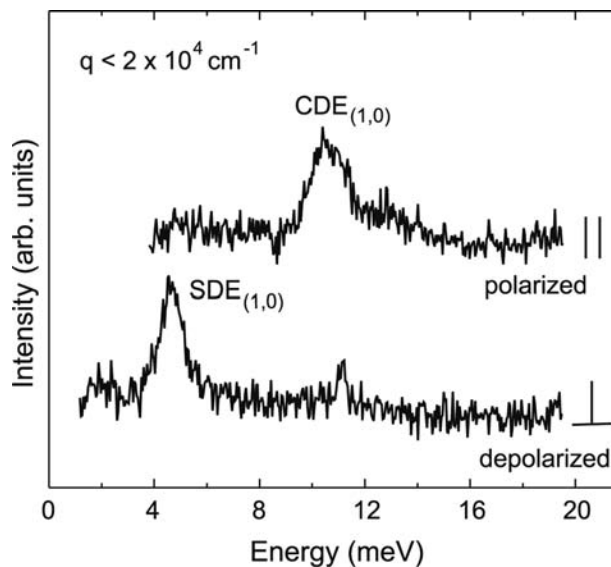
**Fig. 6** Polarized and depolarized ILS spectra of deep-etched GaAs–AlGaAs quantum dots for different laser energies  $E_L$ . Source: From Ref.<sup>[37]</sup>.

(e.g.,  $E_L = 1558$  meV in Fig. 6), these peaks dominate the spectra and are present in both polarization configurations. Therefore we interpret them, within the framework described above, as SPEs, which are caused by an SOP under conditions of extreme resonance. We note that the observation of similar SPEs in multi-layered quantum dots were reported by Lockwood et al.<sup>[9]</sup> From the experimental spectra in Fig. 6, we can directly deduce for the corresponding collective SDEs and CDEs the energy renormalizations due to many-particle interactions.<sup>[10]</sup>

### EXPERIMENTS ON GaAs–AlGaAs DEEP-ETCHED QUANTUM DOTS

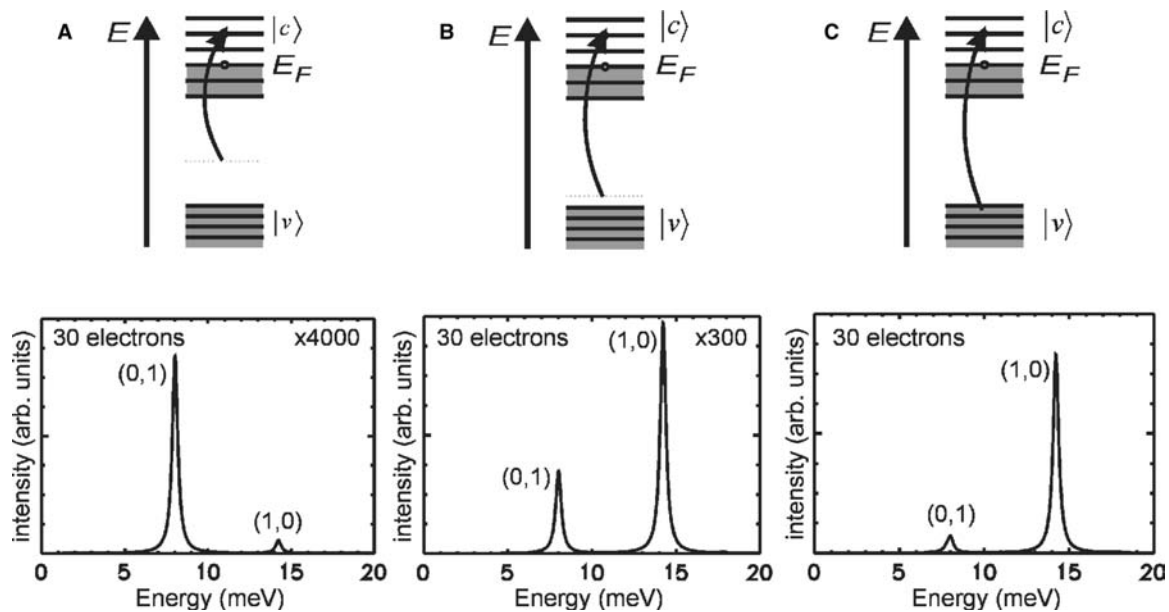
In this section, we focus on ILS experiments on modulation-doped GaAs dots in more detail. In particular, we will discuss parity selection rules for the collective excitations and the importance of resonant excitation.

Fig. 7 shows experimental ILS spectra of quantum dots with approximately 200 electrons per dot.<sup>[37]</sup>



**Fig. 7** Polarized and depolarized ILS spectra of 240 nm GaAs–AlGaAs quantum dots with approximately 200 electrons per dot. Source: From Ref.<sup>[37]</sup>.

In these experiments in backscattering geometry, the wave-vector transfer  $q$  parallel to the plane of the dot was close to zero. In each scattering configuration, depolarized and polarized, there is one mode visible. On general grounds, one can say that in a symmetric system, the allowed modes have even parity because the ILS process is a two-photon process. This is in contrast to direct absorption, which is a one-photon process. Consequently, the observed SDE and CDE are even-parity modes. Referring to the section “Characteristics of Quantum Dots and Experimental Details,” we find that the lowest energy modes with even parity are the monopole modes with  $\Delta M = 0$ . The modes are labeled  $(\Delta n, \Delta m)$  corresponding to the changes in radial ( $\Delta n$ ) and angular-momentum ( $\Delta m$ ) quantum numbers, respectively, of the involved transitions. The assignment of the SDE was deduced from its magnetic field behavior<sup>[11]</sup> (not shown here) and the CDE is considered in more detail below. We want to note here that the polarized spectrum demonstrates the exclusion principle between FIR and Raman spectroscopy: the FIR-allowed mode  $CDE_{(0,1)}$ , the Kohn’s mode, has odd parity and hence a large dipole moment (in the section “Characteristics of Quantum Dots and Experimental Details”). It has, for the sample displayed in Fig. 7, an energy of about 6 meV and is not visible at all in the Raman spectrum (Fig. 7). On the other hand, the Raman-allowed monopole mode [ $CDE_{(1,0)}$ ] has no dipole moment at all. Considering that the induced density of this mode has only nodes in radial direction [see Fig. 3C], it can also be regarded as a so-called breathing mode. Thus the experiments demonstrate that, for resonant ILS on circularly



**Fig. 8** Calculated ILS spectra for a quantum dot with 30 electrons for (A) off-resonance, (B) close-to-resonance, and (C) resonant conditions. The schematic pictures show the different resonance conditions. The curved arrows indicate the laser energies. *Source:* From Ref.<sup>[37]</sup>.

symmetric dots at approximately zero wave-vector transfer, the general parity selection rules hold.

In the following, we will elucidate these parity selection rules from the theoretical point of view in more detail. Most of the calculations of ILS spectra for low-dimensional electron systems have been carried out for non-resonant conditions, because in such cases, one does not have to deal with the complex valence-band states. Fig. 8 shows a series of calculated resonant ILS spectra for off-resonance and for different resonance conditions.<sup>[37]</sup> The calculations have been performed for a 30-electron quantum dot with  $\hbar\Omega_0 = 8$  meV for the external potential. In Fig. 8A, the laser energy was chosen to be far away from resonance, i.e., off-resonance conditions. Under experimental conditions, in this regime the scattered intensities are much too low to be observable. Note that the calculated spectrum in Fig. 8A is multiplied by a factor of 4000 to be of comparable strength with the resonant spectrum in Fig. 8C. One can observe in Fig. 8A that, in the off-resonance case, the parity selection rules have completely changed: for the sake of curiosity, the FIR-allowed Kohn's mode [CDE<sub>(0,1)</sub>] is the dominant mode. As the laser energy approaches resonance, the situation changes, and, under resonance conditions [Fig. 8C], the experimentally observed parity selection rules are confirmed, i.e., the monopole mode CDE<sub>(1,0)</sub> is the dominant mode in the polarized spectrum. This clearly demonstrates that, for a correct description of the relative intensities of the excitations, the resonant scattering process is crucial.

An at least partial breakdown of the parity selection rules can be achieved by the transfer of a finite wave vector  $\mathbf{q}$  parallel to the plane of the dot. Fig. 9 shows a series of depolarized and polarized spectra for the same dots in Fig. 7 for different wave-vector transfer  $\mathbf{q}$ . As  $\mathbf{q}$  increases, symmetry-forbidden modes (the spin dipole mode SDE<sub>(0,1)</sub>, and a higher dipole mode CDE<sub>(1,1)</sub>) gain relative intensity. Furthermore, the spin quadrupole mode SDE<sub>(0,2)</sub>—which, for a parabolic effective potential, would be energetically degenerate with the spin monopole mode SDE<sub>(1,0)</sub> if interaction effects are neglected—becomes visible.<sup>[11]</sup> A so-far unsolved puzzle focuses on why the violation of parity selection rules with wave-vector transfer  $\mathbf{q}$  is much stronger for SDEs than for CDEs.

## EXPERIMENTS ON InAs SELF-ASSEMBLED QUANTUM DOTS

### Few-Electron Quantum-Dot Atoms

It has been demonstrated that, by application of metallic gates, InAs SAQD can be charged with single electrons. For experiments that will be described below, a special sample design, where a 2-D electron system was used as a back contact, was applied (for details, see Ref.<sup>[30]</sup>). The charging of dots can be monitored in situ by capacitance measurements (Fig. 10, inset). For the ILS experiments, resonant excitation was achieved by tuning the laser to the  $E_0 + \Delta$  gap of the InAs SAQD



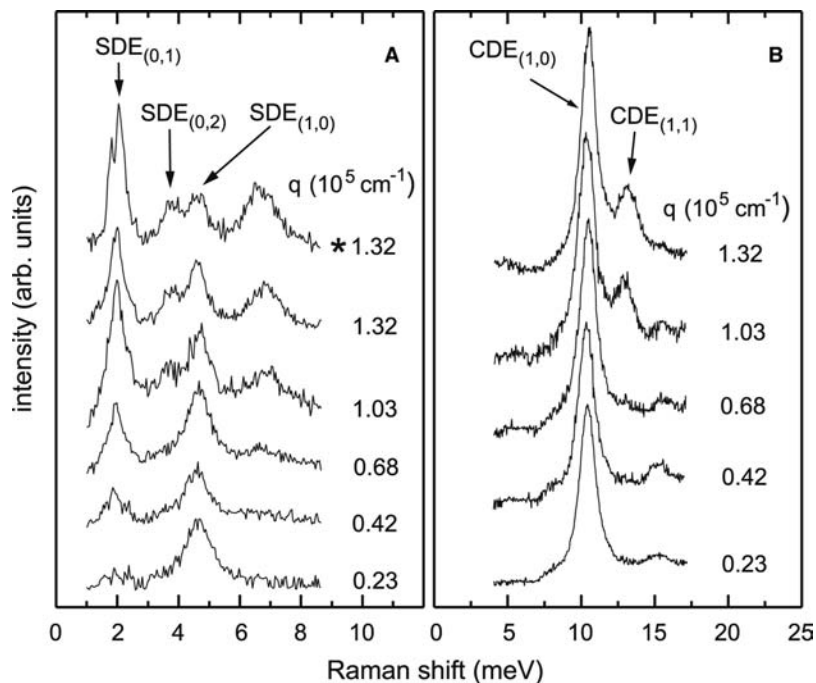


Fig. 9 (A) Depolarized and (B) polarized ILS spectra of GaAs quantum dots for different wave-vector transfer  $q$ . Source: From Ref.<sup>[11]</sup>.

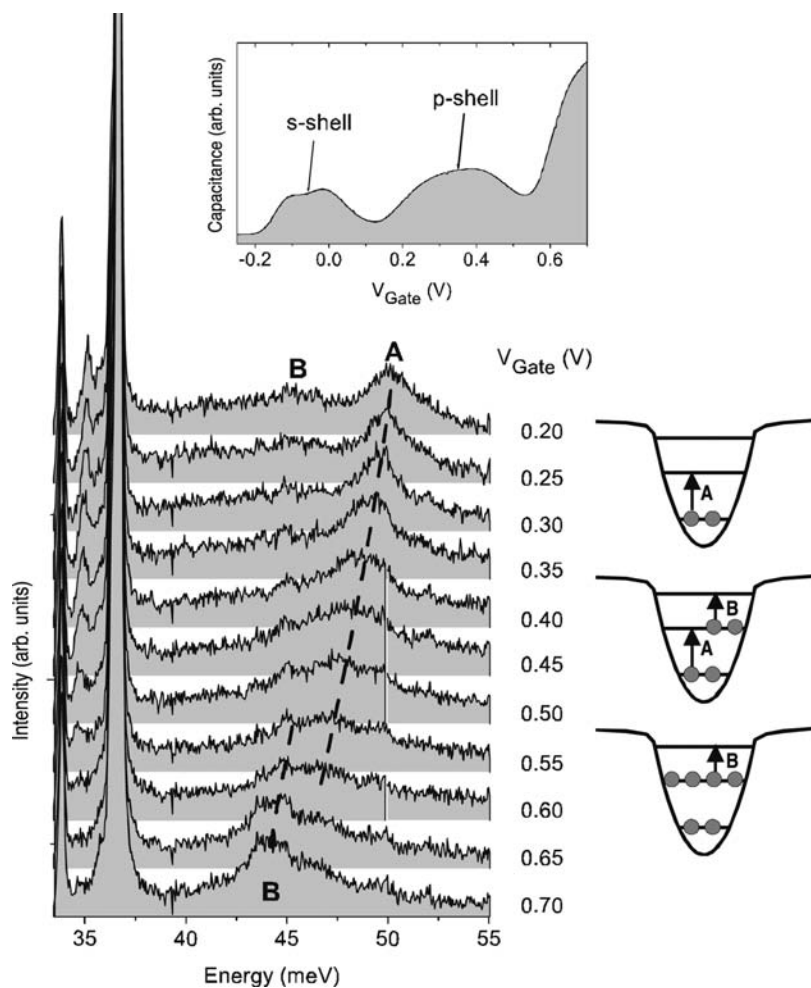


Fig. 10 Series of polarized ILS spectra of InAs SAQD for different gate voltages  $V_{Gate}$ . The upper inset shows a capacitance measurement of the sample. On the right-hand side, different electron configurations in the dots are schematically shown. Source: From Ref.<sup>[30]</sup>.



( $\sim 1.65$  eV), which is far above the fundamental PL transition energies of the structure ( $\sim 1.1$ – $1.2$  eV). Fig. 10 displays a series of polarized ILS spectra. At  $E = 33.4$  meV and  $E = 36.6$  meV, two sharp lines can be observed that result from the TO- and LO-phonon excitations of the GaAs bulk material in the structure. At higher energies, broader bands are visible in the range 45–55 meV (labeled as A and B), which we attribute to CDEs of the electrons in the quantum dots. Both the positions and the linewidths of these bands change with applied gate voltage  $V_{\text{Gate}}$ . The capacitance trace, displayed in the inset of Fig. 10, shows that, by varying  $V_{\text{Gate}}$ , the s- and the p-shell of the quantum dots can be charged with electrons. The doublet structure around  $V_{\text{Gate}} = -0.05$  V stems from the charging of the s shell with two electrons, and, at the broad plateau at positive  $V_{\text{Gate}}$ , the p-shell is loaded with four electrons. The bands A in Fig. 10 were interpreted to be a result of transition of electrons from the s to the p shell (s–p transitions) of the quasiatoms, and the B bands from p–d transitions:<sup>[30]</sup> it was assumed that 2–3 confined single-particle energy levels exist in the quantum dots, which is schematically shown in the drawings on the right-hand side of Fig. 10. Here three selected situations with  $N = 2$ ,  $N = 4$ , and  $N = 6$  electrons per quantum dot are sketched in a single-particle picture. The vertical arrows indicate possible transitions of single electrons. The SAQD stick out of the InAs wetting layer. Therefore the dot potentials are flattened at the edges because of the wetting-layer continuum. This leads to the situation that the single-particle transition, sketched as B in the inset of Fig. 10, has a smaller energy than the transition A. So far, in the interpretation, only transitions between single-particle states have been considered. Within this simplified picture, one is not able to explain the observed shift of excitation A (s–p transitions) with increasing electron number  $N$  in the quantum dots, as observed in Fig. 10. In the voltage range where the p-shell is filled with electrons ( $V_{\text{Gate}} \sim 0.2$ – $0.6$  V), we find, in Fig. 10, a shift of A to lower energies and a broadening of the transition.

More accurately, the experimentally observed excitations are of course collective CDEs of the few-electron quantum dots, and are therefore affected by Coulomb interaction. To take account of this, model calculations where the excitation energies were calculated by using exact numerical diagonalization of the Hamilton operator

$$H = \sum_{i=1}^N \left[ \frac{\mathbf{p}_i^2}{2m^*} + \frac{m^*}{2} \Omega_0^2 \mathbf{r}_i^2 \right] + \frac{e^2}{4\pi\epsilon\epsilon_0} \times \sum_{i \neq j}^N \frac{1}{|\mathbf{r}_i - \mathbf{r}_j|} \quad (7)$$

of the  $N$ -electron quantum dot were performed.<sup>[30]</sup> There, a two-dimensional quantum dot with a parabolic confining potential in lateral direction [ $\mathbf{r} = (r_x, r_y)$ ] with quantization energy  $\hbar\Omega_0 = 50$  meV was assumed. By exact numerical diagonalization, the low-energy excitations of the  $N$ -electron quantum dot were determined, where, during the excitation, the total spin is preserved. This selects the excitations, which one expects in polarized ILS spectra (CDEs). Fig. 11 exhibits the calculated excitation energies for electron numbers  $N = 2$ – $6$  in the quantum dot. The vertical bars mark the energetic positions of the few-particle excitations. First, one can see that, independent of  $N$ , there is always an excitation at the energy  $\hbar\Omega_0 = 50$  meV of the external confining potential. This represents the Kohn's mode. However, for  $N > 2$ , in the calculations additional mode energies appear below the energy of the Kohn's mode. These are a consequence of the different possible final states of the electrons after excitation. For very small electron numbers, these different final states make a significant difference in the energy of the state. For  $N = 3$ , e.g., the configuration where two electrons in the  $p$  shell have antiparallel spin has the lowest energy. With increasing electron numbers, more complex electron configurations occur that can have different energies. The most important result of Fig. 11, concerning the experiments, is that with

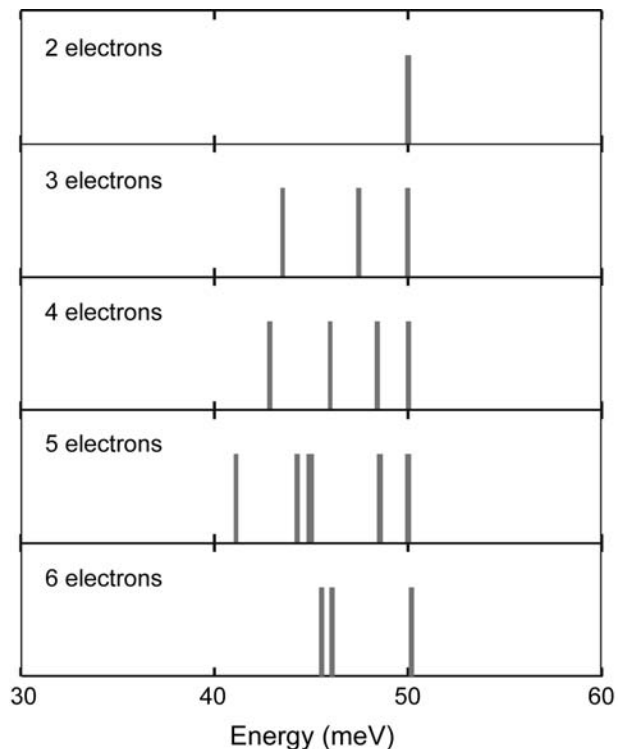


Fig. 11 Calculated few-electron excitation energies for a parabolic InAs quantum dot. Source: From Ref.<sup>[30]</sup>.

increasing  $N$ , the spectral weight of the low-energy excitations shifts to lower energies. This might ascribe the shift and broadening of the s-p transitions, as observed in the experiments (band A in Fig. 10), to be due to additional excitations at lower energies, which cannot be individually resolved in the ensemble experiment. Clearly, the model can only qualitatively explain the experiments. The most important limitation is the assumption of a parabolic potential, which deviates from the more realistic form (sketched in Fig. 10) and which cannot account for the lower energy of band B. However, one should note that the important qualitative result, i.e., the appearance of additional collective modes at lower energies for increasing electron number, is independent of the choice of parameters and the form of the confining potential. This leads to the conclusion that these results might generally apply for quantum-dot atoms.

## CONCLUSION

There is a variety of theoretical and experimental literature on ILS spectroscopy of electronic excitations in quantum dots. Most of the experiments have been performed on modulation-doped GaAs-AlGaAs quantum dots. In these mesoscopic systems with electron numbers on the order of 100 per quantum dot, CDEs, SDEs, and SPEs could be observed. More sophisticated theoretical models demonstrated, in comparison with experiments, the importance of the resonant scattering process, including valence-band states as intermediate states, for a correct description of, e.g., parity selection rules. Recently, resonant ILS experiments on InAs SAQD with tunable electron numbers have been reported. This opens the road for the investigation of excitations in few-electron quantum dot atoms. With the prospect of single-dot Raman spectroscopy, in the future one might be able to observe and resolve electronic excitations as individual sharp lines, caused by interaction effects of few electrons in artificial atoms.

## ACKNOWLEDGMENTS

I would like to thank many colleagues who contributed to our work, as listed in the references, and B. Wunsch for providing the theoretical results, which were used to prepare Fig. 3D–F. In particular, I am grateful to D. Heitmann for his support and critical reading of the manuscript. This work was supported by the Deutsche Forschungsgemeinschaft via SFB 508 and a Heisenberg Grant (SCHU 1171/2).

## REFERENCES

1. Reed, M.A.; Randall, J.N.; Aggarwal, R.J.; Matyi, R.J.; Moore, T.M.; Wetsel, A.E. Observation of discrete electronic states in a zero-dimensional semiconductor nanostructure. *Phys. Rev. Lett.* **1988**, *60* (6), 535–537.
2. Hansen, W.; Smith, T.P., III; Lee, K.Y.; Brum, J.A.; Knoedler, C.M.; Hong, J.M.; Kern, D.P. Zeeman bifurcation of quantum-dot spectra. *Phys. Rev. Lett.* **1989**, *62* (18), 2168–2171.
3. Sikorski, C.; Merkt, U. Spectroscopy of electronic states in InSb quantum dots. *Phys. Rev. Lett.* **1989**, *62* (18), 2164–2167.
4. Demel, T.; Heitmann, D.; Grambow, P.; Ploog, K. Nonlocal dynamic response and level crossings in quantum-dot structures. *Phys. Rev. Lett.* **1990**, *64* (7), 788–791.
5. Lorke, A.; Kotthaus, J.P. Coupling of quantum dots on GaAs. *Phys. Rev. Lett.* **1990**, *64* (21), 2559–2562.
6. Meurer, B.; Heitmann, D.; Ploog, K. Single-electron charging of quantum-dot atoms. *Phys. Rev. Lett.* **1992**, *68* (9), 1371–1374.
7. Bollweg, K.; Kurth, T.; Heitmann, D.; Gudmundsson, V.; Vasiliadou, E.; Grambow, P.; Eberl, K. Detection of compressible and incompressible states in quantum dots and antidots by far-infrared spectroscopy. *Phys. Rev. Lett.* **1996**, *76* (15), 2774–2777.
8. Strenz, R.; Bockelmann, U.; Hirler, F.; Abstreiter, G.; Böhm, G.; Weimann, G. Single-particle excitations in quasi-zero- and quasi-one-dimensional electron systems. *Phys. Rev. Lett.* **1994**, *73* (22), 3022–3025.
9. Lockwood, D.J.; Hawrylak, P.; Wang, P.D.; Sotomayor Torres, C.M.; Pinczuk, A.; Dennis, B.S. Shell structure and electronic excitations of quantum dots in a magnetic field probed by inelastic light scattering. *Phys. Rev. Lett.* **1996**, *77* (2), 354–357.
10. Schüller, C.; Biese, G.; Keller, K.; Steinebach, C.; Heitmann, D.; Grambow, P.; Eberl, K. Single-particle excitations and many-particle interactions in quantum wires and dots. *Phys. Rev., B* **1996**, *54* (24), R17304–R17307.
11. Schüller, C.; Keller, K.; Biese, G.; Ulrichs, E.; Rolf, L.; Steinebach, C.; Heitmann, D.; Eberl, K. Quasiatomic fine structure and selection rules in quantum dots. *Phys. Rev. Lett.* **1998**, *80* (12), 2673–2676.
12. Biese, G.; Schüller, C.; Keller, K.; Steinebach, C.; Heitmann, D.; Grambow, P.; Eberl, K. Coupling of lateral and vertical electron motion in GaAs-AlGaAs quantum wires and dots. *Phys. Rev., B* **1996**, *53* (15), 9565–9567.
13. Pinczuk, A.; Schmitt-Rink, S.; Danan, G.; Valladares, J.P.; Pfeiffer, L.N.; West, K.W. Large exchange interactions in the electron gas of GaAs quantum wells. *Phys. Rev.* **1989**, *63* (15), 1633–1636.
14. Schüller, C. Raman Spectroscopy of Quantum Dots. In *Festkörperprobleme/Advances in Solid State Physics*; Kramer, B., Ed.; Vieweg: Braunschweig/Wiesbaden, 1999; Vol. 38, 167–181.
15. Das Sarma, S.; Wang, D.-W. Resonant Raman scattering by elementary electronic excitations in semiconductor structures. *Phys. Rev. Lett.* **1999**, *83* (4), 816–819.

16. Danan, G.; Pinczuk, A.; Valladares, J.P.; Pfeiffer, L.N.; West, K.W.; Tu, C.W. Coupling of excitons with free electrons in light scattering from GaAs quantum wells. *Phys. Rev., B* **1989**, *39* (8), 5512–5515.
17. Govorov, A.O. Resonant light scattering induced by Coulomb interaction in semiconductor microstructures. *J. Phys. Condens. Matter* **1997**, *9*, 4681–4690.
18. Steffens, O.; Suhrke, M. Novel spin features in Raman spectra of few-electron quantum dots. *Phys. Rev. Lett.* **1999**, *82* (19), 3891–3894.
19. Pi, M.; Barranco, M.; Emperador, A.; Lipparini, E.; Serra, Ll. Current-density-functional approach to large quantum dots in intense magnetic fields. *Phys. Rev., B* **1998**, *57* (23), 14783–14792.
20. Serra, Ll.; Barranco, M.; Emperador, A.; Pi, M.; Lipparini, E. Spin and density longitudinal response of quantum dots in the time-dependent local-spin-density approximation. *Phys. Rev., B* **1999**, *59* (23), 15290–15300.
21. Lipparini, E.; Barranco, M.; Emperador, A.; Pi, M.; Serra, Ll. Transverse dipole spin modes in quantum dots. *Phys. Rev., B* **1999**, *60* (12), 8734–8742.
22. Mooradian, A. Light scattering from single-particle electron excitations in semiconductors. *Phys. Rev. Lett.* **1968**, *20* (20), 1102–1104.
23. Blum, F.A. Inelastic light scattering from semiconductor plasmas in a magnetic field. *Phys. Rev., B* **1970**, *1* (3), 1125–1135.
24. Sasseti, M.; Kramer, B. Resonant Raman scattering by collective modes of the one-dimensional electron gas. *Phys. Rev. Lett.* **1998**, *80* (7), 1485–1488.
25. Wang, D.W.; Millis, A.J.; Das Sarma, S. Where is the Luttinger liquid in one-dimensional semiconductor quantum wire structures? *Phys. Rev. Lett.* **2000**, *85* (21), 4570–4573.
26. Steinebach, C.; Schüller, C.; Heitmann, D. Single-particle-like states in few-electron quantum dots. *Phys. Rev., B* **2000**, *61* (23), 15600–15602.
27. Gammon, D.; Steel, D.G. Optical studies of single quantum dots. *Phys. Today* October **2002**, *55* (10), 36–41.
28. Drexler, H.; Leonard, D.; Hansen, W.; Kotthaus, J.P.; Petroff, P.M. Spectroscopy of quantum levels in charge-tunable InGaAs quantum dots. *Phys. Rev. Lett.* **1994**, *73* (16), 2252–2255.
29. Chu, L.; Zrenner, A.; Bichler, M.; Böhm, G.; Abstreiter, G. Raman spectroscopy of In(Ga)As/GaAs quantum dots. *Appl. Phys. Lett.* **2000**, *77* (24), 3944–3946.
30. Brocke, T.; Bootsman, M.-T.; Wunsch, B.; Tews, M.; Pfannkuche, D.; Heyn, Ch.; Hansen, W.; Heitmann, D.; Schüller, C. Inelastic light scattering on few-electron quantum-dot atoms. *Physica E*. **2004**, *22* (1–3), 478–481.
31. Wojs, A.; Hawrylak, P.; Fafard, S.; Jacak, L. Electronic structure and magneto-optics of self-assembled quantum dots. *Phys. Rev., B* **1996**, *54* (8), 5604–5608.
32. Merkt, U. Far-infrared spectroscopy of quantum dots. *Physica B* **1993**, *189*, 165–175.
33. Maksym, P.A.; Chakraborty, T. Quantum dots in a magnetic field: Role of electron–electron interactions. *Phys. Rev. Lett.* **1990**, *65* (1), 108–111.
34. Hamilton, D.; McWhorter, A.L. Raman Scattering from Spin-Density Fluctuations in n-GaAs. In *Light Scattering Spectra of Solids*; Wright, G.B., Ed.; Springer: New York, 1969; 309 pp.
35. Burstein, E.; Pinczuk, A.; Mills, D.L. Inelastic light scattering by charge carrier excitations in two-dimensional plasmas: Theoretical considerations. *Surf. Sci.* **1980**, *98*, 451–468.
36. Pinczuk, A.; Brillson, L.; Burstein, E. Resonant light scattering by single-particle electronic excitations in n-GaAs. *Phys. Rev. Lett.* **1971**, *27* (6), 317–320.
37. Schüller, C.; Steinebach, C.; Heitmann, D. Spin- and charge-density excitations in quantum dots: A Raman study. *Solid State Commun.* **2001**, *119*, 323–331.

# Quantum Dots: Phonons in Self-Assembled Multiple Germanium Structures

Jianlin Liu

Department of Electrical Engineering, University of California–Riverside,  
Riverside, California, U.S.A.

Aleksandr Khiton

Kang L. Wang

Electrical Engineering Department, University of California–Los Angeles,  
Los Angeles, California, U.S.A.

## INTRODUCTION

Self-assembled Ge quantum dots by the Stranski–Krastanov growth mode have attracted much attention for many years. Similar to the purpose of the research on short-period Si/Ge superlattices and Er-doped Si, self-assembled Ge/Si quantum dots may be exploited to fabricate Si-based on-chip light emitting sources for 1.55- $\mu\text{m}$  fiberoptic communication applications. Takagahara and Takeda<sup>[1]</sup> and Ren<sup>[2]</sup> have theoretically predicted that an indirect-to-direct conversion of the optical transition of SiGe quantum dots would occur whenever the sizes of the quantum dots were small enough. In order to increase the component of quasi-direct transition of the Ge/Si quantum dot system and thus to enhance light emission intensity of the quantum dots for practical applications, the understanding of non-radiative recombination mechanisms (such as phonon-assisted process) is essential.

To probe phonons from self-assembled semiconductor quantum dots, Raman spectroscopy is an efficient and indispensable experimental tool. Up to date, several groups have already reported Raman scattering studies of self-assembled quantum dots of group III–V systems, such as (In, Ga, Al)Sb/GaAs,<sup>[3]</sup> InSb/InP,<sup>[4]</sup> In(Ga)As/GaAs,<sup>[5–9]</sup> InAs/InP,<sup>[10–13]</sup> (Al, Ga)As/InAs,<sup>[14]</sup> InAs/AlAs,<sup>[15,16]</sup> and GaN/(Si)AlGaIn,<sup>[17,18]</sup> group II–VI system, such as CdSe/ZnSe,<sup>[19]</sup> and group IV system, i.e., Ge/Si.<sup>[20–38]</sup> Optical phonon spectra of any of these systems were basically used to extract the chemical composition of the quantum dots as a result of interdiffusion between the dots and the surrounding media or the substrates. It should be pointed out that a few other techniques for the determination of composition of self-assembled quantum dots have been reported. These include scanning tunneling microscopy,<sup>[39]</sup> transmission electron microscopy (TEM) with high-resolution imaging,<sup>[40]</sup> electron energy loss spectrometry,<sup>[41]</sup> X-ray energy disperse spectrometry,<sup>[42]</sup> high-resolution X-ray

diffraction,<sup>[43,44]</sup> and scanning TEM.<sup>[45]</sup> Most of these techniques are capable to show non-uniform dot material distribution in the dots. Optical phonon Raman scattering method is simple and direct to give an average concentration of the dots. In contrast to the tremendous research on optical phonons, the effort on the research of phonon process in the low-frequency acoustic spectral region, however, is much smaller. In self-assembled Ge quantum dot system, for example, one early work reported the observation of equal-distance acoustic peaks in 25-period Ge quantum dot superlattices.<sup>[21]</sup> Afterwards, Milekhin et al. investigated folded longitudinal acoustic phonons in their Ge dot superlattices and explained the acoustic vibrations by the elastic continuum model.<sup>[26–29]</sup> Recently, resonant Raman scattering by acoustic phonons in double- and multilayered Ge dot structures was reported and the observed equal-distance oscillation peaks were explained by interference and ordering effects.<sup>[32,33]</sup> The origins of these observed low-frequency acoustic phonon spectra in Ge dot superlattices therefore remain unclear and debatable because there is a lack of systematic studies, such as the dependence of acoustic phonons on island sizes and other island-related parameters.<sup>[23]</sup>

In this entry, we systematically study Raman scattering by optical and acoustic phonons in multiple Ge quantum dots. The analysis of GeGe and SiGe optical phonon features takes the phonon confinement effect, strain effect, and atomic intermixing into account. Acoustic phonons are found to originate from folded acoustic phonons associated with a superlattice and can be explained by elastic continuum model.

## RESULTS ON SELF-ASSEMBLED MULTIPLE GE QUANTUM DOTS

All samples were grown on Si (100) wafers using a solid source molecular beam epitaxy (MBE) system.

Samples A, B, and C were grown at 540°C with 10 periods of Ge and Si bilayers and contained a Ge coverage of 12, 15, and 18 Å, respectively. Samples D and E were grown with the same Ge layer thickness of 15 Å but at different growth temperatures of 500°C and 600°C, respectively. In addition, sample D has 10-period Ge and Si bilayers while sample E contains 22 periods. The Si spacer layer thickness of 20 nm was used for all superlattices. No cap Si layers were grown intentionally on these samples for convenience of atomic force microscopy (AFM) characterizations. Transmission electron microscopy measurements were exploited as well to obtain the size, density, and uniformity of the self-assembled dots. Raman scattering measurements were performed on a Renishaw Raman Imaging 2000 system with a 514 Ar<sup>+</sup> laser as the excitation light source in the backscattering configuration.

Fig. 1A shows a typical cross-sectional TEM image of sample A. Ten-period vertically correlated layers of Ge dots are evident. The dots in the different layers (beyond the third Ge layer) are identical in size and shape. This observation is also seen for other dot samples. Fig. 1B and C shows an AFM image, and height and base statistic analysis of sample A, respectively. Gaussian distributions were used to fit the data. Most of the dots appear as pyramid and the average dot base and height are 11.9 and 110.4 nm, respectively. Similar measurements have been performed on other samples as well. The growth parameters and structural data were summarized in Table 1. It should be noted that the structural data were from AFM measurements only and not calibrated by TEM characterizations.

## Optical Phonons

Fig. 2 shows the Raman spectra of the dot samples in the spectral region of SiGe and GeGe optical phonons. Similar SiGe (from 400 to 420 cm<sup>-1</sup>) and GeGe lines (near 300 cm<sup>-1</sup>) are observed for dot samples. The frequency position of SiGe optical phonons more or less represents the degree of the interdiffusion between Si spacers and Ge dots. Samples A, B, and C have almost the same Si-Ge optical phonon line shape. The peak frequency changes slightly from 418 cm<sup>-1</sup> for sample A with a nominal Ge thickness of 1.2 nm to 416 cm<sup>-1</sup> for sample C with a nominal Ge thickness of 1.8 nm. To understand this, we shall notice that the interdiffusion arises from both thermal diffusion and strain-induced diffusion. As the same growth temperature of 540°C was used for the three samples, the degree of interdiffusion due to thermal management is the same. The slight difference in frequency therefore comes from the difference in strain-induced diffusion. The thicker Ge was deposited the more relaxation was presented in the dots (as will be discussed in detail

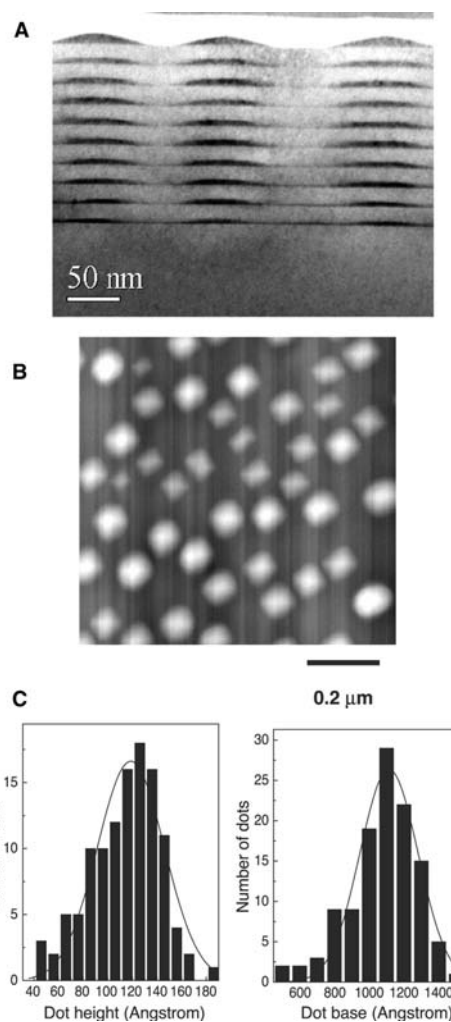


**Fig. 1** (A) TEM image of sample A. Vertically correlated islands are evident. (B) AFM image of sample A. Most of the islands appear as square-based pyramids and the island density is determined to be  $3.6 \times 10^9 \text{ cm}^{-2}$ . (C) Statistical base diameter and height distributions of the Ge islands of sample A. A typical Gaussian peak is used to fit the distribution data. The most probable height and base diameter are 11.9 and 110.4 nm, respectively.

in the following). Strain-induced interdiffusion in the samples with thicker nominal Ge thickness is smaller. The resulting lower frequency can be understood with the following picture: The eigen-frequency of these optical phonons is determined by the effective stretching force constant for each bond and the mass of atoms at the end of each bond. For example, SiSi optical phonon band is centered at 520 cm<sup>-1</sup> for all of the samples and the substrate (not shown in the figure), considering the force constant of SiSi to be 39.5 N/m, and atomic weight of 28.1 for Si.<sup>[46]</sup> Likewise, optical phonons of crystal Ge can be found at 300 cm<sup>-1</sup> with the GeGe bond force constant of 35 N/m and atomic weight of 72.6. Any mixture of Si and Ge leads to SiGe optical



**Table 1** Growth parameters and structural data of the samples

Sample	Ge layer thickness (Å)	Si layer thickness (nm)	Growth $T$ (°C)	Dot base (nm)	Dot height (nm)	Density (cm <sup>-2</sup> )
A	12	20	540	110.4	11.9	$3.6 \times 10^9$
B	15	20	540	122.0	14.0	$4.1 \times 10^9$
C	18	20	540	122.2	16.0	$3.5 \times 10^9$
D	15	20	500	114.7	15.1	$5.9 \times 10^8$
E	15	20	600	175.5	10.2	$2.6 \times 10^8$

phonons with the frequency in between 300 and 520 cm<sup>-1</sup>. For simplicity, we assume that Ge quantum dots are fixed and only Si atoms move. At a situation of stronger interdiffusion, more Si atoms are introduced into Ge dots. Thus SiGe optical phonon band has a frequency closer to SiSi optical phonon band, which is exactly the case for samples A through C. Likewise, much lower frequency position of 406 cm<sup>-1</sup> for sample D and slightly larger frequency of about 420 cm<sup>-1</sup> for sample E compared with that of sample B (due to the same nominal Ge) can also be explained by the above picture.

Now let us analyze the GeGe optical phonons in the samples. It is important to note that the GeGe modes from the dot samples are different from the second-order transverse acoustic (2TA) phonon mode<sup>[47]</sup> for Si at 303 cm<sup>-1</sup>. For comparison, the vertical dotted line is plotted at 300 cm<sup>-1</sup> to represent the optical phonon position for bulk crystalline Ge. The frequency positions of the GeGe optical phonons in dot samples are shifted slightly to higher frequencies with respect to their bulk value. There are several mechanisms to

cause a Raman shift of GeGe optical phonons. The first one is phonon confinement. It is known that the optical phonon branches of bulk Ge are quadratic and, moreover, nearly flat at the Brillouin zone center ( $k \cong 0$ ). Confined optical phonons in a nanocrystal are equivalent to those vibrations in an infinite crystal whose wave vector is given by  $m\pi/d$ , where  $m$  is an integer and  $d$  is the size of the nanocrystal, in our case, the height of the dots. In the dots with a very small height of 1.5–2 nm,<sup>[21]</sup> the phonon confinement effect was observed to result in a shift less than 2 cm<sup>-1</sup>. As the dot size for the present samples is much larger than the lattice constant of Ge, the wave vector is extremely small, leading to insignificant phonon confinement effect.

The size confinement effect of optical phonons in quantum dots with small size should give rise to a shift of phonon band to lower frequency side due to the negative dispersion of the optical phonon branch. A compressive strain on the dots in the lateral directions as a result of the lattice mismatch of Si and Ge, however, leads to a GeGe mode shift to the higher frequency side. This concept can be written as:<sup>[48]</sup>

$$\omega = \omega_0 + \frac{1}{2\omega_0} [p\varepsilon_{zz} + q(\varepsilon_{xx} + \varepsilon_{yy})] \quad (1)$$

where  $\omega$  is the Ge-Ge mode frequency induced by a biaxial strain,  $\omega_0$  is the frequency of the Ge zone-center LO phonon;  $p$  and  $q$  are the Ge deformation potentials;  $\varepsilon_{xx}$  and  $\varepsilon_{yy}$  are the biaxial strain  $(a - a_0)/a$  with  $a$  and  $a_0$  being unstrained and strained lattice constants, respectively. The physical parameters used in Eq. (1) can be obtained from Ref.<sup>[34]</sup>. For fully strained pure Ge on Si, we obtain  $\omega = 317.4$  cm<sup>-1</sup>. The large difference between this calculated number and the experimental GeGe mode values (close to 300 cm<sup>-1</sup> as shown in Fig. 2) suggests that the dots are not fully strained as assumed in the calculation. By using Eq. (1) and the experimental GeGe optical phonon frequencies  $\omega$ , the residual biaxial strain ( $\varepsilon_{xx}$ ) on the quantum dots can be estimated and listed in Table 2. Very small residual strain values obtained suggest the dots are almost fully relaxed.

An obvious reason of the strain relaxation is the atomic intermixing at the Si–Ge interface. The degree

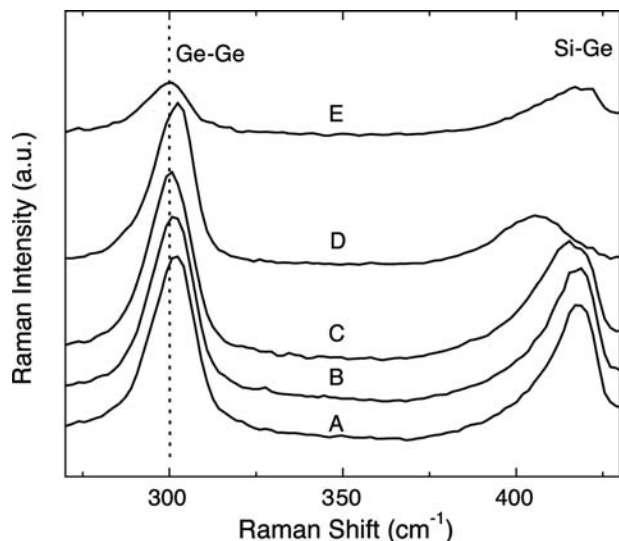


**Fig. 2** Raman spectra of the dot samples. Similar SiGe and GeGe lines are observed for these samples. The frequency positions of the GeGe optical phonons in dot samples are shifted slightly to higher frequencies with respect to their bulk value (300 cm<sup>-1</sup>).



**Table 2** The experimental GeGe mode frequencies, integrated peak intensity ratios, and calculated Ge composition in dots and residual in-plane strain in the dot samples

Sample	$\omega(\text{GeGe}) (\text{cm}^{-1})$	$\omega(\text{SiGe}) (\text{cm}^{-1})$	$I_{\text{GeGe}}/I_{\text{SiGe}}$	Ge composition in dots	$\varepsilon_{XX} (10^{-3})$
A	302	418	1.45	0.48	-4.8
B	301.1	417.5	1.45	0.48	-2.65
C	300.5	416	1.45	0.48	-1.2
D	302.4	406	2.14	0.58	-5.8
E	300.4	419.5	1.29	0.45	-0.96

of the interface intermixing can be determined by the integrated peak intensity ratio  $I_{\text{GeGe}}/I_{\text{SiGe}}$  as the intensity depends on the relative number of corresponding bonds. This concept was used for SiGe alloy<sup>[49]</sup> and Ge quantum dots<sup>[37]</sup> and can be expressed as:

$$\frac{I_{\text{GeGe}}}{I_{\text{SiGe}}} \cong B \frac{x}{2(1-x)} \quad (2)$$

where  $x$  is the average Ge concentration and the coefficient  $B$  is related to the Bose factor and the frequencies of GeGe and SiGe optical modes of the alloy. It is found that the coefficient  $B$  varies weakly with alloy composition and is determined to be 3.2.<sup>[50]</sup>  $I_{\text{GeGe}}/I_{\text{SiGe}}$  can be obtained from the spectra in Fig. 2. The Ge concentrations in quantum dots estimated by this method are listed in Table 2. It should be noted that the estimation by such interpolation is rough because the Si 2TA phonons and optical phonons from wetting layers have not been subtracted in the calculation. Moreover, the composition obtained is an average value, which does not show any information about composition distribution in the dots.

Fig. 3 plots the GeGe peak position as a function of the Ge concentration in the dots. Symbols are experimental data. Solid straight lines 1 and 2 are used to guide the eyes and indicate that the different GeGe mode frequency is obtained for dots not only with different Ge concentrations but also with a similar Ge concentration. Solid line 3 is a calculation result using Eq. (1). In this calculation, we assume the same  $\omega_0$  and other deformation potentials for pure Ge. This approximation is reasonable because the interdiffusion occurs in the interface and the “core” of the dots remains pure Ge. For example, the non-uniform Ge content in the dots has been proved by elemental distribution analysis using an electron filtering imaging method in TEM<sup>[51]</sup> and scanning TEM.<sup>[45]</sup> The in-plane strain  $\varepsilon_{xx}$  used can be written as  $(a_{\text{Si}_{1-x}\text{Ge}_x} - a_0)/a_{\text{Si}_{1-x}\text{Ge}_x}$  with the lattice parameter of an alloy with Ge concentration of  $x$  determined by Vegard's law  $a_{\text{Si}_{1-x}\text{Ge}_x} = xa_{\text{Ge}} + (1-x)a_{\text{Si}}$ , where  $a_{\text{Ge}}$  and  $a_{\text{Si}}$  are lattice parameters of pure Ge and Si, respectively. Simple calculations show, for example, in-plane strain to be  $-0.02$  for an alloy with Ge

concentration of 0.48 (samples A, B, and C), leading to a GeGe mode frequency of  $308.3 \text{ cm}^{-1}$ . The calculated values show a considerable shift from the value obtained for fully strained Ge on Si ( $317.4 \text{ cm}^{-1}$ ); however, these are still larger than the peak frequencies of the GeGe modes of the samples A through E. As a matter of fact, the absolute value of the residual strain on the dots shown in Table 2 is much smaller than the absolute value estimated here by interdiffusion only. Moreover, the picture of interdiffusion does not completely account for the peak position difference for the different samples with the same Ge composition as of line 3 in Fig. 3. The above analysis suggests that additional strain relaxation mechanisms exist apart from Ge/Si interdiffusion. We believe that this additional strain relaxation comes from the process of the formation of Ge dots.

The relaxation of the dots in addition to atomic interdiffusion consists of the relaxation of the surface-layered dots and the relaxation of the embedded dots.

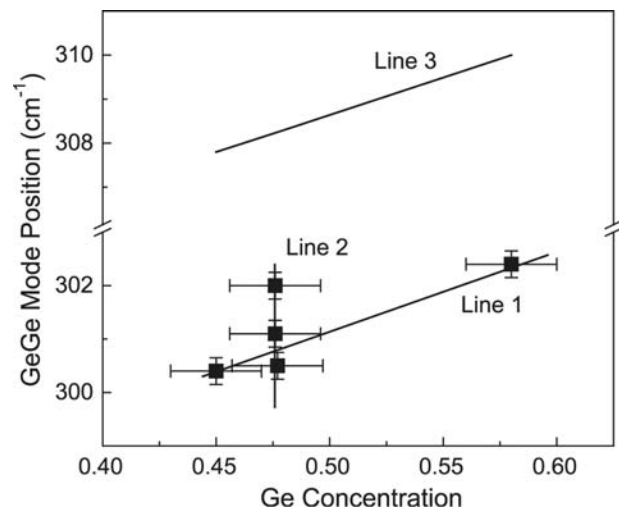


**Fig. 3** GeGe mode position as a function of Ge concentration in dots. Ge concentration is obtained by means of the integrated intensity ratio of optical phonons of GeGe and SiGe. Solid lines 1 and 2 are used to guide the eyes. The results show that the different GeGe mode frequency is obtained for dots not only with different Ge concentrations but also with a similar Ge concentration. Line 3 is the calculated data by assuming Si/Ge interdiffusion only.

The relaxation of the surface-layered dots is related to the nature of Stranski–Krastanov growth mode. When Ge is deposited on Si, it first takes a layer-by-layer growth format. As the Ge film exceeds its critical thickness, it becomes rough by forming pyramidal islands to relieve strain energy. As more Ge is deposited, the islands transform from the pyramid shape to the dome shape, leading to more strain relaxation. Atomic force microscopy measurements on our samples indeed showed, for example, the pyramid-over-dome ratio decreases as the increase of the Ge deposition for these samples grown at the same temperature of 540°C.<sup>[25]</sup> The relaxation is also induced by the dot embedding effect. Sutter and Lagally have used a strain-driven atom diffusion model to show that the dot shape transforms to truncated shape after the growth of Si layer on top.<sup>[52]</sup> Indeed, we have observed this transition from the cross-section TEM measurements. Because of the capping process, the in-plane strain is relaxed.<sup>[39]</sup>

After recognizing all the above relaxation mechanisms, we can fully explain the observed GeGe optical phonon frequencies. First, let us take a look at line 1 of Fig. 3. This line represents the GeGe mode trend of a set of samples (C, D, and E) grown at different temperatures. GeGe mode frequency changes from 302.4 to 300.4 cm<sup>-1</sup> when the Ge concentration decreases from 0.58 to 0.45 as a result of growth temperature from 500°C to 600°C, indicating that the sample grown at higher temperature induces stronger interface intermixing, or more strain relaxation. Quantitative calculations using Eq. (1) show that a shift of 2.2 cm<sup>-1</sup> is obtained for the present interdiffusion difference in the three samples (as can be seen from line 3 in Fig. 3). This number is almost the same as the experimental observed shift, suggesting that the strain relaxation from the different degrees of interdiffusion is the main factor responsible for the different frequencies of the GeGe mode in this set of samples. In other words, the overall effect of the dot shape transition on the GeGe mode frequency is about the same for the three samples. Line 2 in Fig. 3 represents another set of samples (A, B, and C). As shown previously, this set of samples has the same Ge concentration in the dots. Nevertheless, the GeGe optical phonon frequency is different and the largest difference is 1.5 cm<sup>-1</sup>. This suggests different strains are present on the dots in different samples, which arises from the different dot morphologies in the different samples, such as pyramid-over-dome ratios, dot height-over-base ratios, and embedding effect.

The above-analyzed, negligible phonon confinement effect but dominant atomic intermixing and/or strain effect in determining frequencies of optical phonons for quantum dot samples can also be proved by performing annealing experiments. Fig. 4A shows the Raman spectra of sample A under rapid thermal

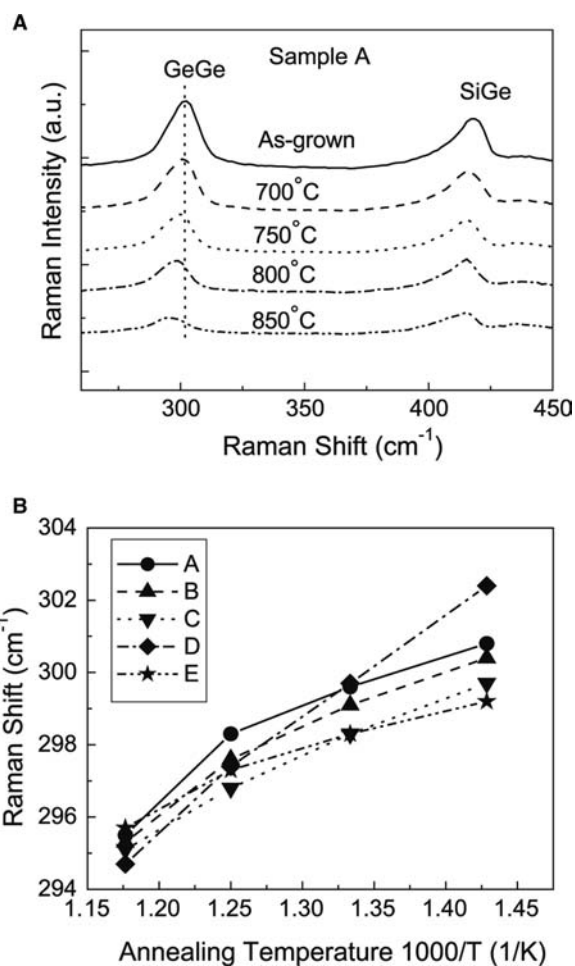


**Fig. 4** (A) Raman spectra of sample A under RTA for 5 min at different temperatures, and (B) Raman shift as a function of annealing temperature for different samples.

annealing (RTA) for 5 min at different temperatures. The vertical dotted line is plotted at the center of GeGe mode from as-grown sample for comparison. The GeGe Raman line broadens and shifts to lower frequencies as the annealing temperature increases. This phenomenon was also observed when annealing other samples. Fig. 4B shows the annealing temperature dependence of the Raman shift for the dot samples grown at different temperature. After 850°C annealing for 5 min, the GeGe optical mode shifts downward by as much as 8, 6–7, and 5 cm<sup>-1</sup> for the samples grown at 500°C, 540°C, and 600°C, respectively. The intermixing after annealing leads to fully relaxed SiGe alloy-like dots, causing the observed peak shift.

## Acoustic Phonons

Fig. 5A shows the Raman spectra of the samples A, B, and C, which were grown with the same temperature and different Ge layer thickness. The vertical dot lines

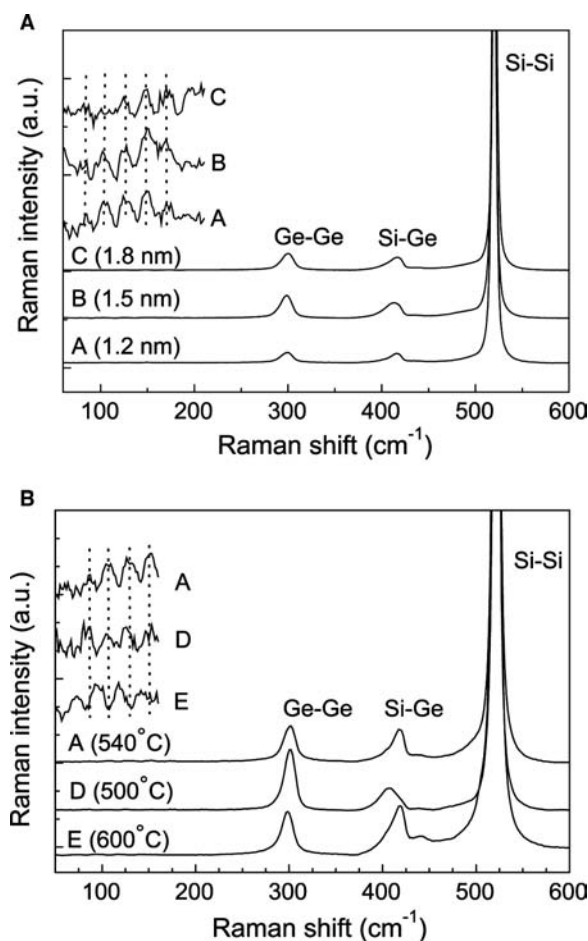


**Fig. 5** Raman spectra of the samples with (A) different nominal Ge thicknesses of 1.2, 1.5, and 1.8 nm for samples A, B, and C, respectively, and (B) with different growth temperatures of 540°C, 500°C, and 600°C for samples A, D, and E, respectively. Acoustic phonon modes with the same frequencies are observed for different Ge-thickness samples, while different frequencies and periods are observed for different samples with different growth temperatures.

are used to facilitate the comparison among the samples. Similar SiSi, SiGe, and GeGe optical vibration peaks are seen at around 520, 415, and 300  $\text{cm}^{-1}$ , respectively. Besides these peaks, low-frequency oscillation peaks are observed for all of the three samples around 84.3, 104.7, 126.6, 150, and 171.8  $\text{cm}^{-1}$ , respectively. These nearly equal-distance peaks with a period of about 20  $\text{cm}^{-1}$  are higher-order acoustic phonons. The lower orders were attenuated by the Rayleigh line rejection filter and thus were not observed. An interesting phenomenon is that the acoustic peak frequencies do not scale with the dot size. Lamb's theory predicts that confined phonon frequency should be inversely proportional to the nano-crystal size<sup>[53]</sup> and was shown to be true for a number of nano-crystal systems such as  $\text{CdS}_x\text{Se}_{1-x}$  in glasses<sup>[54]</sup> and Si in  $\text{SiO}_2$  matrix.<sup>[55]</sup> The present result suggests that the observed

low-frequency peaks are not confined phonon modes in quantum dots.

Fig. 5B shows the Raman spectra of the samples A, D, and E, which were grown at different temperatures. The vertical dot lines are again used here to facilitate the comparison among the samples. Acoustic phonons for different samples have different frequencies. Specifically, acoustic phonon peak frequencies for sample A have been assigned in Fig. 5A. Sample D has acoustic phonons around 71.4, 95.7, 118.8, and 141  $\text{cm}^{-1}$ , and sample E has acoustic phonons around 83.8, 105.8, 126.8, and 149.8  $\text{cm}^{-1}$ . The period of these nearly equal-distance peaks is about 24, 22, and 20 for samples D, E, and A, respectively.

There are two possibilities, which may be used to explain the observed periodic acoustic phonons.<sup>[56]</sup> The first one is that these are probably phonon modes confined in quantum wells where zone-edge phonon modes have been made, "allowed" by breakdown of wave vector conservation. The second one is that they are associated with a superlattice where low-frequency zone-edge phonon modes have been folded into zone center. The first concept has been used to explain the periodic acoustic phonon oscillations in the InAs/InP self-assembled quantum dots.<sup>[12]</sup> The period of the periodic acoustic phonons can be expressed by:

$$\Delta\omega = \frac{1}{2L} \cdot \frac{v}{c} \quad (3)$$

where  $L$  is the thickness of the quantum layer,  $v$  is the sound velocity of the phonons, and  $c$  is the speed of the light. If the observed phonons were the confined phonons in the Si spacer layers, then with the velocity  $v_{\text{Si}} = 8.44 \times 10^5 \text{ cm/sec}$ <sup>[57]</sup> and the peak periods of 20–24  $\text{cm}^{-1}$  for the present samples, we would obtain the Si layer thicknesses for our samples to be around 5.9–7 nm. The designed thickness of Si spacer thickness for all the samples was 19–20 nm. The actual effective thickness of Si spacer layers has shrunk to around 14 nm characterized by cross-sectional TEM. The reason is that Si spacers were deposited on curvature surfaces containing three-dimensional dots. A similar situation was often observed when growing short-period superlattices on relaxed substrate, which consisted of cross-hatch undulation patterns. The layer deposited on top was stretched as a result of undulation and the effective thickness along the growth direction was shrunk. The effective thickness of about 14 nm for the present samples, however, is still more than two times of the calculated 5.9–7 nm, suggesting that these phonons have nothing to do with the confinement in the Si spacers. Likewise, the phonons are not confined phonons in the wetting layers either. Samples grown at different temperatures lead to different wetting layer thickness because of Si/Ge

interdiffusion. Different from the dots grown at much lower temperature (300°C)<sup>[26]</sup> or by the use of anti-mony as surfactant,<sup>[34]</sup> where the wetting layers were more or less around 3–4 MLs, the wetting layers in this set of samples had the thickness in the region of 15–20 Å with cross-sectional TEM characterizations (not shown here). Therefore the wetting layers are not pure Ge but SiGe alloy. Phonon velocity for SiGe can be obtained by the linear interpolation of LA phonon velocity of Si and Ge. Simple calculations showed that one could never obtain an agreeable solution compared with the experimental results.

The above analysis leaves the only possible origin for these phonons, i.e., they are folded acoustic modes related to the periodicity of the superlattice. Rytov's elastic continuum model<sup>[58]</sup> has been well applied for folded acoustic phonons in quantum well superlattices and was also seen to explain the acoustic phonon features in Ge dot multilayers<sup>[26–29]</sup> and InAs/GaAs dot multilayers.<sup>[14]</sup> In this model, the acoustic phonon dispersion can be written as:

$$\cos(qd) = \cos\left(\frac{\omega d_1}{V_1}\right) \cos\left(\frac{\omega d_2}{V_2}\right) - \frac{1}{2} \left(R + \frac{1}{R}\right) \times \sin\left(\frac{\omega d_1}{V_1}\right) \sin\left(\frac{\omega d_2}{V_2}\right) \quad (4)$$

where  $q$  is the superlattice wave vector perpendicular to the layers and is roughly determined to be  $q \cong 4\pi n' / \lambda_L$ , where  $\lambda_L$  is the incident laser light wavelength and  $n'$  is the refractive index of the material at that wavelength. In addition,  $R = (V_1\rho_1)/V_2\rho_2$ ,  $d = d_1 + d_2$ ,  $d_1$  and  $d_2$ ,  $\rho_1$  and  $\rho_2$ , and  $V_1$  and  $V_2$  are the thickness, density, and sound velocity in Ge and Si layers, respectively. The physical parameters can be obtained from Ref.<sup>[57]</sup>. The model designed for quantum well superlattice can be considered as a zero-order approximation to the real quantum dot superlattice as it does not take into account quantum dot shape, size, and density. It was suggested in Ref.<sup>[27]</sup> to use nominal thickness of Ge layer as an effective thickness  $d_2$ . Nevertheless, with this rough approximation, good agreement with experimental data was achieved.<sup>[26–29]</sup> Following this approach, with the effective Si spacer layer thicknesses of about 14 nm and wetting layer thicknesses of about 1.5 nm in our samples, we calculated the phonon dispersion and showed acoustic phonon peak period of 19–21 cm<sup>-1</sup>, which was close to the experimentally observed 20–24 cm<sup>-1</sup>. Therefore we conclude that the observed low-frequency modes are folded acoustic phonons. More accurate description of the acoustic spectra of semiconductor quantum dot superlattices will require rigorous calculations of acoustic phonon scattering on quantum dot as well as multiple scattering effect produced by quantum dot ensemble in each layer.

## CONCLUSION

We have studied Raman scattering from optical phonons and acoustic phonons in the Ge quantum dot superlattices. The GeGe optical phonon frequencies of the dot samples were larger than 300 cm<sup>-1</sup> but within 3 cm<sup>-1</sup>, indicating that the dots were relaxed in the superlattices. Strain relaxation was found not only from the atomic interdiffusion but also from the dot morphology transition both for the surface dots and the embedded dots. The annealing experiments also proved that the strain relaxation and intermixing were the key parameters for the observed optical phonons. Optical phonon studies show that Raman spectroscopy is an efficient tool for the determination of the average compositions and strains for zero-dimensional quantum dots. Periodic oscillations in the lower frequency region were observed for quantum dot superlattice samples. These acoustic phonons were found to be related to superlattice period and could be well explained by the elastic continuum model.

Furthermore, the method for analysis of phonons in the above Ge quantum dot superlattice system can be generally used for other quantum dot systems, such as, InGaSb/GaAs, InSb/InP, InGaAs/GaAs, InAs/InP, AlGaAs/InAs, InAs/AlAs, and GaN/(Si)AlGaN, CdSe/ZnSe, and so on. Phonon spectra in these material systems depend on the physical parameters of superlattice, such as concentration in dots, dot size, and period thickness. In the case of very small dots with high density (e.g., greater than 10<sup>11</sup> cm<sup>-2</sup>), multiple scattering effects may play an important role in the modification of phonon spectra. The phonon densities of states in quantum dot superlattices change as seen from the strong modification of phonon spectra with the appearance of quantum dots and can be used to calculate the thermal conductivities of superlattices. Research has shown a great reduction of thermal conductivities in quantum dot superlattices, which have great applications in the fabrication of new-generation solid-state thermoelectric devices. Phonon spectra modification by quantum dots also suggests the potential applications of quantum dot superlattices as phonon lenses, filters, and reflectors for phonon-assisted lasers in indirect-band gap material systems.

## ACKNOWLEDGMENTS

The authors wished to thank Dr. S. G. Thomas of Motorola Semiconductor Products Sector for performing some of the TEM characterizations and Prof. Peter Y. Yu of UC Berkeley for valuable discussions. This work was funded by the DoD MURI-ONR program on Thermoelectrics (N00014-97-1-0516) and the AFOSR MURI program on phonon engineering (F49620-00-1-0328).

## REFERENCES

1. Takagahara, T.; Takeda, K. Theory of the quantum confinement effect on excitons in quantum dots of indirect-gap materials. *Phys. Rev., B* **1992**, *46*, 15,578.
2. Ren, S.Y. Quantum confinement of edge states in Si crystallites. *Phys. Rev., B* **1997**, *55*, 4665.
3. Bennett, B.R.; Shanabrook, B.V.; Magno, R. Phonons in self-assembled (In,Ga,Al)Sb quantum dots. *Appl. Phys. Lett.* **1996**, *68*, 958.
4. Armelles, G.; Utzmeier, T.; Postigo, P.A.; Briones, F.; Ferrer, J.C.; Peiro, P.; Cornet, A. Raman scattering of InSb quantum dots grown on InP substrates. *J. Appl. Phys.* **1997**, *81*, 6339.
5. Zanelatto, G.; Pusep, Yu.A.; Moshegov, N.T.; Toropov, A.I.; Basmaji, P.; Galzerani, J.C. Raman study of the topology of InAs/GaAs self-assembled quantum dots. *J. Appl. Phys.* **1999**, *86*, 4387.
6. Artus, L.; Cusco, R.; Hernandez, S.; Patane, A.; Polimeni, A.; Henini, M.; Eaves, L. Quantum-dot phonons in self-assembled InAs/GaAs quantum dots: dependence on the coverage thickness. *Appl. Phys. Lett.* **2000**, *77*, 3556.
7. Chu, L.; Zrenner, A.; Bichler, M.; Bohm, G.; Abstreiter, G. Raman spectroscopy of In(Ga)As/GaAs quantum dots. *Appl. Phys. Lett.* **2000**, *77*, 3944.
8. Toda, Y.; Moriwaki, O.; Nishioka, M.; Arakawa, Y. Resonant Raman scattering of optical phonons in self-assembled quantum dots. *Physica, E* **2000**, *8*, 328.
9. Galzerani, J.C.; Puseb, J.A. Raman spectroscopy characterization of InAs self-assembled quantum dots. *Physica, B* **2002**, *316*, 455.
10. Groenen, J.; Priester, C.; Carles, R. Strain distribution and optical phonons in InAs/InP self-assembled quantum dots. *Phys. Rev., B* **1999**, *60*, 16013.
11. Prieto, J.A.; Armelles, G.; Groenen, J.; Carles, R. Size and strain effects in the E1-like optical transitions of InAs/InP self-assembled quantum dot structures. *Appl. Phys. Lett.* **1999**, *74*, 99.
12. Huntzinger, J.R.; Groenen, J.; Cazayous, M.; Mlayah, A.; Bertrn, N.; Paranthoen, C.; Dehaese, O.; Carrere, H.; Bedel, E.; Armelles, G. Acoustic-phonon Raman scattering in InAs/InP self-assembled quantum dots. *Phys. Rev., B* **2000**, *61*, R10547.
13. Yin, J.; Wang, X.; Yin, Z.; Du, G.; Yang, S. InAs self-assembled quantum dots on GaAs/InP by low-pressure metal-organic chemical vapour deposition. *Semicond. Sci. Technol.* **2001**, *16*, 715.
14. Tenne, D.A.; Haisler, V.A.; Toropov, A.I.; Bakarov, A.K.; Gutakovsky, A.K.; Zahn, D.R.T.; Shebanin, A.P. Raman study of self-assembled GaAs and AlAs islands embedded in InAs. *Phys. Rev., B* **2000**, *61*, 13785.
15. Tenne, D.A.; Haisler, V.A.; Bakarov, A.K.; Toropov, A.I.; Gutakovsky, A.K.; Shebanin, A.P.; Zahn, D.R.T. Self-assembled islands in the (Ga,Al)As/InAs heteroepitaxial system studied by Raman spectroscopy. *Phys. Status Solidi, B* **2001**, *224*, 25.
16. Tenne, D.A.; Bakarov, A.K.; Toropov, A.I.; Zahn, D.R.T. Raman study of self-assembled InAs quantum dots embedded in AlAs: Influence of growth temperature. *Physica, E* **2002**, *13*, 199.
17. Kuball, M.; Gleize, J.; Tanaka, S.; Aoyagi, Y. Resonant Raman scattering on self-assembled GaN quantum dots. *Appl. Phys. Lett.* **2001**, *78*, 987.
18. Kuball, M.; Gleize, J.; Tanaka, S.; Aoyagi, Y. On phonon confinement effects and free carrier concentration in GaN quantum dots. *Phys. Status Solidi, B* **2001**, *228*, 195.
19. Rho, H.; Smith, L.M.; Jackson, H.E.; Lee, S.; Dobrowolska, M.; Furdyna, J.K. Interface phonons in CdSe/ZnSe self-assembled quantum dot structures. *Phys. Status Solidi, B* **2001**, *224*, 165.
20. Liu, J.L.; Tang, Y.S.; Wang, K.L.; Radetic, T.; Gronsky, R. Raman scattering from a self-organized Ge dot superlattice. *Appl. Phys. Lett.* **1999**, *74*, 1863.
21. Liu, J.L.; Jin, G.; Tang, Y.S.; Luo, Y.H.; Wang, K.L.; Yu, D.P. Optical and acoustic phonon modes in self-organized Ge quantum dot superlattices. *Appl. Phys. Lett.* **2000**, *76*, 586.
22. Liu, J.L.; Tang, Y.S.; Wang, K.L. Response to "comment on 'Raman scattering from a self-organized Ge dot superlattices'". *Appl. Phys. Lett.* **1999**, *75*, 3574.
23. Liu, J.L.; Jin, G.; Tang, Y.S.; Luo, Y.H.; Wang, K.L.; Yu, D.P. Response to "Comment on 'Optical and acoustic phonon modes in self-assembled Ge quantum dot superlattices'". *Appl. Phys. Lett.* **2001**, *78*, 1162.
24. Liu, J.L.; Jin, G.; Tang, Y.S.; Luo, Y.H.; Lu, Y.; Wang, K.L.; Yu, D.P. Study of phonons in self-organized multiple Ge quantum dots. *J. Electron. Mater.* **2000**, *29*, 554.
25. Liu, J.L.; Wan, J.; Jiang, Z.M.; Khitun, A.; Wang, K.L.; Yu, D.P. Optical phonons in self-assembled Ge quantum dot superlattices: Strain relaxation effects. *J. Appl. Phys.* **2002**, *92*, 6804.
26. Milekhin, A.; Stepina, N.P.; Yakimov, A.I.; Nikiforov, A.I.; Schulze, S.; Zahn, D.R.T. Raman scattering of Ge dot superlattices. *Eur. Phys. J., B* **2000**, *16*, 355.
27. Milekhin, A.; Stepina, N.P.; Yakimov, A.I.; Nikiforov, A.I.; Schulze, S.; Zahn, D.R.T. Raman scattering studies of Ge dot superlattices. *Appl. Surf. Sci.* **2001**, *175*, 629.
28. Milekhin, A.; Nikiforov, A.I.; Pchelyakov, O.P.; Schulze, S.; Zahn, D.R.T. Phonons in self-assembled Ge/Si structures. *Physica, E* **2002**, *13*, 982.
29. Milekhin, A.; Nikiforov, A.I.; Pchelyakov, O.P.; Schulze, S.; Zahn, D.R.T. Self-selective Raman scattering in self-assembled Ge/Si quantum dot superlattices. *Nanotechnology* **2002**, *13*, 55.
30. Teo, K.L.; Qin, L.; Noordin, I.M.; Karunasiri, G.; Shen, Z.X.; Schmidt, O.G.; Eberl, K.; Queisser, H.J. Effects of hydrostatic pressure on Raman scattering in Ge quantum dots. *Phys. Rev., B* **2001**, *63*, 121306.
31. Qin, L.; Teo, K.L.; Shen, Z.X.; Peng, C.S.; Zhou, J.M. Raman scattering of Ge/Si dot superlattices under hydrostatic pressure. *Phys. Rev., B* **2001**, *64*, 075312.
32. Cazayous, M.; Huntzinger, J.R.; Groenen, J.; Mlayah, A.; Christiansen, S.; Strunk, H.P.; Schmidt, O.G.; Eberl, K. Resonant Raman scattering by acoustic phonons in Ge/Si self-assembled quantum dots: interferences and ordering effects. *Phys. Rev., B* **2000**, *62*, 7243.

33. Cazayous, M.; Groenen, J.; Huntzinger, J.R.; Mlayah, A.; Schmidt, O.G. Spatial correlations and Raman scattering interferences in self-assembled quantum dot multilayers. *Phys. Rev., B* **2001**, *64*, 033306.
34. Kwok, S.H.; Yu, P.Y.; Tung, C.H.; Zhang, Y.H.; Li, M.F.; Peng, C.S.; Zhou, J.M. Confinement and electron-phonon interactions of the  $E_1$  exciton in self-organized Ge quantum dots. *Phys. Rev., B* **1999**, *59*, 4980.
35. Persans, P.D.; Deelman, P.W.; Stokes, K.L.; Schowalter, L.J.; Byrne, A.; Thundat, T. Optical studies of Ge islanding on Si(111). *Appl. Phys. Lett.* **1997**, *70*, 472.
36. Guedj, C.; Beyer, A.; Muller, E.; Grutzmacher, D. Raman spectroscopy of carbon-induced germanium dots. *Appl. Phys. Lett.* **2001**, *78*, 1742.
37. Groenen, J.; Carles, R.; Christiansen, S.; Albrecht, M.; Dorsch, W.; Strunk, H.P.; Wawra, H.; Wagner, G. Phonons as probes in self-organized SiGe islands. *Appl. Phys. Lett.* **1997**, *71*, 3856.
38. Gaiduk, P.I.; Larsen, A.N.; Hansen, J.L.; Mudryj, A.V.; Samtsov, M.P.; Demenshenok, A.N. Self-assembly of epitaxially grown Ge/Si quantum dots enhanced by As ion implantation. *Appl. Phys. Lett.* **2001**, *79*, 4025.
39. Liu, N.; Tersoff, J.; Baklenov, O.; Holmes, A.L., Jr.; Shih, C.K. Nonuniform composition profile in  $\text{In}_{0.5}\text{Ga}_{0.5}\text{As}$  alloy quantum dots. *Phys. Rev. Lett.* **2000**, *84*, 334.
40. Rosenauer, A.; Fischer, U.; Gerthsen, D.; Forster, A. Composition evaluation of  $\text{In}_x\text{Ga}_{1-x}\text{As}$  Stranski-Krastanow-island structures by strain state analysis. *Appl. Phys. Lett.* **1997**, *71*, 3868.
41. Walther, T.; Humphreys, C.J.; Cullis, A.G. Observation of vertical and lateral Ge segregation in thin undulating SiGe layers on Si by electron energy-loss spectroscopy. *Appl. Phys. Lett.* **1997**, *71*, 809.
42. Chaparro, S.A.; Drucker, J.; Zhang, Y.; Chandrasekhar, D.; McCartney, M.R.; Smith, D.J. Strain-driven alloying in Ge/Si(100) coherent islands. *Rev. Lett.* **1999**, *83*, 1199.
43. Wiebach, T.; Schmidbauer, M.; Hanke, M.; Raidt, H.; Kohler, R. Strain and composition in SiGe nanoscale islands studied by x-ray scattering. *Phys. Rev., B* **2000**, *61*, 5571.
44. Jiang, Z.M.; Jiang, X.M.; Jiang, W.R.; Jia, Q.J.; Zheng, W.L.; Qian, D.C. Lattice strains and composition of self-organized Ge dots grown on Si(001). *Appl. Phys. Lett.* **2000**, *76*, 3397.
45. Harvey, A.; Davock, H.; Dunbar, A.; Bangert, U.; Goodhew, P.J. Three-dimensional compositional analysis of quantum dots. *J. Phys., D, Appl. Phys.* **2001**, *34*, 636.
46. Alonso, M.I.; Winer, K. Raman spectra of c-Si $_{1-x}$ Ge $_x$  alloys. *Phys. Rev., B* **1989**, *39*, 10,056.
47. Uchinokura, K.; Sekine, T.; Matsuura, E. Critical-point analysis of the two-phonon Raman spectrum of silicon. *J. Phys. Chem. Solids* **1974**, *35*, 171.
48. Cerdeira, F.; Buchenauer, C.J.; Pollak, F.H.; Cardona, M. Stress-induced shifts of first-order Raman frequencies of diamond- and zinc-blende-type semiconductors. *Phys. Rev., B* **1972**, *5*, 580.
49. Renucci, M.A.; Renucci, J.B.; Cardona, M., III. *Disordered Systems: Raman Scattering in Ge-Si Alloys*; Proceedings of the 2nd International Conference on Light Scattering in Solids; Flammarion: Paris, 1971; 326pp.
50. Mooney, P.M.; Dacol, F.H.; Tsang, J.C.; Chu, J.O. Raman scattering analysis of relaxed Ge $_x$ Si $_{1-x}$  alloy layers. *Appl. Phys. Lett.* **1993**, *62*, 2069.
51. Liao, X.Z.; Zou, J.; Cockayne, D.J.H.; Qin, J.; Jiang, Z.M.; Wang, X.; Leon, R. Strain relaxation by alloying effects in Ge islands grown on Si (100). *Phys. Rev., B* **1999**, *60*, 15,605.
52. Sutter, P.; Lagally, M.G. Embedding of nanoscale 3D SiGe islands in a Si matrix. *Phys. Rev. Lett.* **1998**, *81*, 3471.
53. Lamb, H. *Proc. Lond. Math. Soc.* **1882**, *13*, 189.
54. Champagnon, B.; Andrianasolo, B.; Ramos, A.; Gandais, M.; Allais, M.; Benoit, J. Size of Cd(S,Se) quantum dots in glasses: correlation between measurements by high-resolution transmission electron microscopy, small-angle x-ray scattering, and low-frequency inelastic Raman scattering. *J. Appl. Phys.* **1993**, *73*, 2775.
55. Fujii, M.; Kanzawa, Y.; Hayashi, S.; Yamamoto, K. Raman scattering from acoustic phonons confined in Si nanocrystals. *Phys. Rev., B* **1996**, *54*, 8373.
56. Yu, P.Y. Comment on "optical and acoustic phonon modes in self-organized Ge quantum dot superlattices". *Appl. Phys. Lett.* **2001**, *78*, 1160.
57. Lockwood, D.J.; Dharma-Wardana, M.W.C.; Baribeau, J.-M.; Houghton, D.C. Folded acoustic phonons in Si/Ge $_x$ Si $_{1-x}$  strained-layer superlattices. *Phys. Rev., B* **1987**, *35*, 2243.
58. Rytov, S.M. *Akust. Z.* **1956**, *2*, 71.



# Raman Spectroscopy of Carbon Nanotube–Polymer Composites

**Bin Chen**

*National Aeronautics and Space Administration (NASA),  
Moffett Field, California, U.S.A.*

## INTRODUCTION

Natural carbon exhibits its distinct properties in two forms: diamond, an insulator, gives the strongest mechanical strength; graphite, a brittle material, conducts electricity at room temperature. A recently synthesized carbon form, the carbon nanotube (CNT), combines the mechanical strength of diamonds with the electric conductivity of graphite. However, the as-grown form of this almost perfect new material is actually a mixture of semiconducting and metallic tubes, in the approximate 2:1 ratio estimated by the tight binding model.<sup>[1]</sup> Furthermore, as-grown single-wall nanotubes (SWNTs) generally possess a very high aspect ratio of length to diameter (on the order of 1000:1). They tend to bundle together as ropelike hydrophobic aggregates—not an individual tube of either semiconductor or metallic tube. However, controlling growth and follow-up processing and treatment conditions can change the metallic and semiconducting ratio in the mixture (see “Carbon Nanotubes”).

To take advantage of their unique electronic properties, mixed SWNT bundles can be dispersed and separated to tailor to various device applications. One ideal matrix for separation and self-assembly is a scheme using polymers consisting of a carbon backbone because of their structural compatibility. The electric conductivity of the filler-based polymer composite is substantially increased with CNT loading. Raman frequency shifts have demonstrated their non-covalent interfacial interactions, through tensile and strain as well as compression transferred by the outer and inner layers of the multiwalled nanotube (MWNT), respectively.<sup>[2,3]</sup> These interfacial interactions, along with the high aspect ratio (D/L in the order of 1:1000), are believed to enhance conduction path through hopping and tunneling in the composite.

The study and design of the CNT/polymer composite emerged with increased knowledge of the interactions in the composites. Most recently, CNT-based composites appear promising for applications in telecommunication,<sup>[4]</sup> actuators,<sup>[5,6]</sup> photovoltaic cells,<sup>[7]</sup> light-emitting diodes (LEDs),<sup>[8]</sup> field emission<sup>[9]</sup>

and radiation shielding.<sup>[10]</sup> The performance and lifetime of devices are enhanced through CNT composites. This also opens a venue for many non-conducting polymer applications with good structural stability and flexible processability. Because mobility can be increased to avoid electrostatic effect, the composites can be used for passive electronic components as well as electromagnetic shielding.<sup>[11]</sup> By forming the CNT composites, we overcome the disadvantages pertinent to nonconducting polymers to improve their performance as a result of the superior electric, thermal, and mechanical properties of CNT.

## RAMAN SPECTROSCOPY BACKGROUND

The interfacial molecular structure studied by the high-throughput micro-Raman probes is correlated with macroscopic physical properties. In particular, resonant Raman spectroscopy probes the electronic density of states (DOS) singularity band gap by tuning the Raman excitation energies. The optical approach has the advantage of eliminating the contact between the electrode and the nanometer-scale material. It has become a very powerful technique to study the electronic properties of nanostructured materials.

Figure 1 shows the energy level diagram of the Raman effect. When the monochromatic light excites matter (solid, liquid, or gas), it scatters light as a result of relaxation from virtual states, which are short-lived and distorted by the oscillating electric field of the incident light. A photon is immediately emitted or absorbed during the scattering. Depending on higher or lower vibration states, it relaxes back, resulting in stoke and antistoke scatterings, respectively. A small percentage of light scatters the same frequency as the incident light when it relaxes back to the same vibration state as the initial state (called Rayleigh scattering). When the incident light matches the electronic transition states, resonance scattering occurs with an intensity of up to  $10^8$  over the nonresonance intensity. Thus the electronic band gap can be measured.

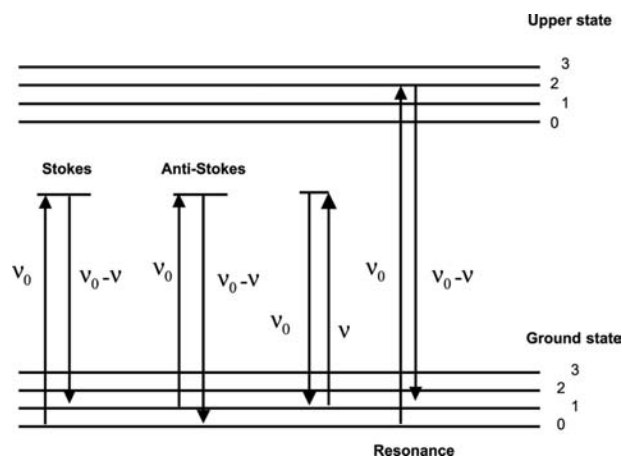


Fig. 1 Energy level diagram of Raman scattering effect.

Raman spectroscopy emerged as a powerful tool to study carbonaceous materials in recent years with the breakthrough in charge-coupled detectors and laser radiation sources. Both polymer and CNT have very high percentages of the chemical composition of carbon. The high polarizability intensity of the carbon bond (C–C or C=C) results in especially strong Raman scattering in these classes of materials. Although infrared (IR) spectroscopy is frequently used for probing the polymer side-chain vibration symmetry, Raman spectroscopy is an ideal technique to study the properties of polymer backbones, the CNT lattice structure, and their interactions in composites.

Raman spectroscopy has been used to study the polymer vibration structure of backbone composition, conformation, and crystallinity. Targeting the conjugation length, chain conformation, interchain interaction, and polaron–bipolaron ratio, the correlation of

the electronic and chemical structural changes of polymers can be established.<sup>[12]</sup> In the CNT composite, the polymer structure changes caused by the CNT loading can be monitored by the Raman frequency shift and lines shape analysis.

Fig. 2 shows the Raman spectra of crystalline diamonds, graphites, and SWNTs. Like its parent forms of diamond and graphite, SWNT also processes distinct spectroscopic signatures. The characteristic D-band and G-band correspond to  $sp^3$  and  $sp^2$  vibration modes displayed in diamonds and graphites, respectively. The quasi one-dimensional (1-D) CNT also displays nanometer-scale signatures in tangential modes (TMs) and radial breathing modes (RBMs) regions. The rich information about structure provided by Raman spectroscopy has been also demonstrated in probes of CNT chirality, size, and defects.

A detailed analysis of SWNT structures and SWNT Raman modes can be found in an excellent review<sup>[1]</sup> and the entry on “Single-Walled Carbon Nanotubes: Geometries, Electronic Properties, and Actuation.” Briefly, SWNT is a graphene sheet rolled into a cylindrical shape with very high aspect ratio. The axial symmetry exhibits the spiral conformation called chirality. The CNT belongs to  $D_{nh}$  ( $n$  is even number),  $D_{nd}$  ( $n$  is odd number), and  $C_n$  (achiral) groups. The G-band is formed through graphite Brillouin zone folding. According to group theory, the TM exhibits  $A_1$ ,  $E_1$ , and  $E_2$  symmetries that are Raman-active; the characteristic Raman signature consists of TMs including G-bands around  $1590\text{ cm}^{-1}$  and D-bands around  $1350\text{ cm}^{-1}$ ; another signature band is the second-order Raman mode at  $1730\text{ cm}^{-1}$  in the single-walled CNT. In the TM region, the line shape displays a symmetric profile around  $1590\text{ cm}^{-1}$  for semiconductor SWNTs; a

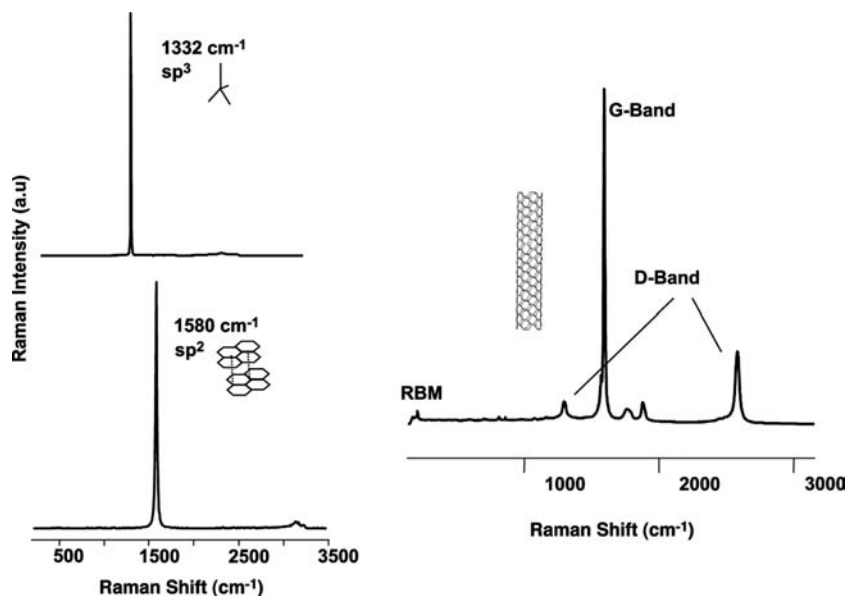


Fig. 2 Raman spectra of crystalline diamond, graphite, and SWNT in visible excitations.

broad asymmetric G-band around  $1560\text{ cm}^{-1}$ , as well as a sharp band around  $1580\text{ cm}^{-1}$  are characteristic features associated with metallic SWNT in the bundle.<sup>[13]</sup> Usually, Breit–Wigner–Fano (BWF) line shape is used to fit the lower-frequency component of the G-band. This phonon and electron continuum Raman line shapes can be obtained from:

$$I(\omega) = I_0 \left\{ 1 + \frac{(\omega - \omega_0)/q\Gamma}{2 \left\{ 1 + \left( \frac{\omega - \omega_0}{\Gamma} \right)^2 \right\}} \right\} \quad (1)$$

where  $I_0$ ,  $\omega_0$ ,  $1/q$ , and  $\Gamma$  are intensity, renormalized frequency, the interaction of the phonon with continuum states, and the broadening parameter, respectively.<sup>[14]</sup>

The energies of allowed optical transitions (ATOs) are determined by both the diameter and the chirality of the SWNT,<sup>[15]</sup> as schematically illustrated in Fig. 3.

Below  $500\text{ cm}^{-1}$ , the frequencies are contributed from the RBM  $\Omega$ . The SWNT diameter  $d$  is computed<sup>[16,17]</sup> from the low-frequency Raman spectra region using a phenomenological Eq. (2)

$$\Omega_{\text{RBM}}(\text{cm}^{-1}) = \alpha/d \text{ (nm)}, \quad \text{where } \alpha = 248\text{ cm}^{-1}\text{nm} \quad (2)$$

The MWNT consists of tens of SWNTs. The stacking and assembly of each tube rarely align perfectly.

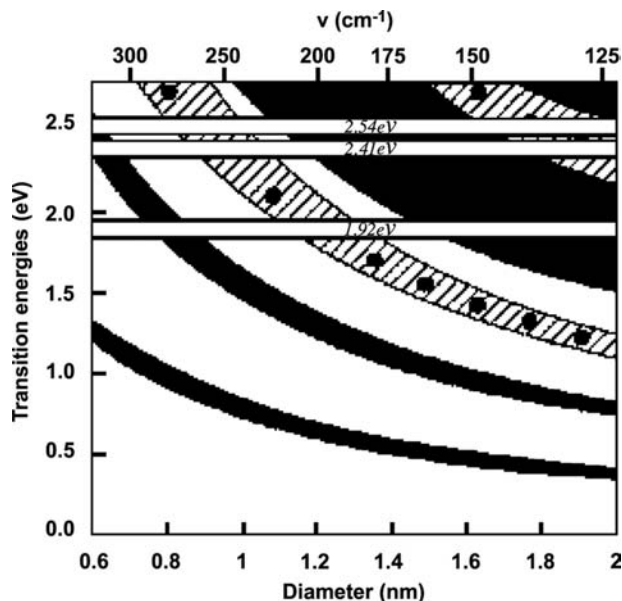


**Fig. 3** Allowed optical transitions for SWNT with various diameters and chiralities calculated in the zone folding scheme. Black areas correspond to semiconducting tubes; dashed areas correspond to metallic tubes. The laser energies are labeled in write frames. The maximum of Raman intensity is expected for RBMs and TMs at the high and low limit of the frames, respectively. *Source:* ©APS, 2001.

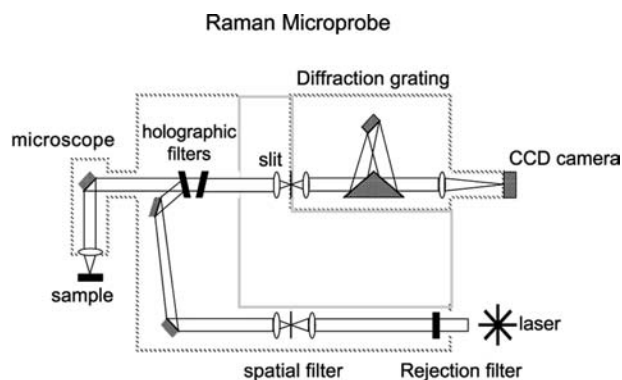


**Fig. 4** The schematic illustration of a typical micro-Raman instrument setup. *Source:* Renishaw, Inc.

illumination of a small region at the center of the field of view

Two forms are commonly observed in experiments: bamboo structure and cone shape stacking. Tube stacking generally lowers the symmetry of the CNT. The Raman mode resulting from these two stacking assemblies gives the secondary defect-induced mode at about  $1612\text{ cm}^{-1}$  as a shoulder peak in the D-band. The cap at the end of the tube is usually open with the larger-diameter CNTs and chemical treatments. This feature can be monitored for MWNTs undergoing purification and dispersion because of their interactions with chemical agents and the chemical environment. The G-band to D-band ratio is substantially lower than that of SWNTs.

The confocal microscopic Raman probe enables the study of unique properties exhibited in nanometer-scale composite materials in the volume order of  $1\text{ }\mu\text{m}$ . Various techniques such as polarized Raman and Raman imaging<sup>[18]</sup> became possible for the study of SWNT interactions in non-conjugated polymer matrices in high spatial resolution. The interfacial van der Waals interaction of SWNTs in the polymer composite demonstrates important contributions to many physical properties.

The Raman instrument is generally composed of three parts: the excitation light source, the spectrometer, and the detection apparatus. Fig. 4 is the schematic setup of a typical micro-Raman from Renishaw, Inc. The setup enables relative low laser power (2–3 mW) focused on the  $1\text{-}\mu\text{m}^2$  sample spot, providing the necessary high spatial resolution for nanomaterial studies.

## SYNTHESIS OF CNT/POLYMER COMPOSITES

### In Situ Growth

It is a challenge to control the growth process, but managing it effectively is nevertheless an effective

way to obtain homogeneous composite films and to achieve a uniform CNT dispersion.

UV and chemical-polymerized composites were processed by polymerization of monomers in the presence of SWNTs (an initiator sometimes is added as needed) in the sonication bath. The same polymerization can incorporate SWNTs into a polymer matrix through ionic surfactant solution, with a concentration slightly higher than the critical micelle concentration. This second polymerization approach is so-called “emulsion-processed.” Either oil or water-soluble initiators maybe added to accelerate the polymerization. The third method is electropolymerization. The CNTs will be used either as the electrode onto which the polymer is deposited, or as part of the electrolyte to be codeposited. When the CNT array is used as the electrode, the composite formed through the polymerization occurs on the surface of the CNT electrode. As the nanotube is dispersed with a monomer in the organic solution as a mixed electrolyte, the composite forms homogeneously onto a conventional electrode such as platinum. The redox potential, oxidation–reduction cycle time, and choice of dopant ions<sup>[19,20]</sup> in the electrolyte and the functional group in the CNT all act as control parameters to adjust composite film thickness and conductivity. Conducting polymers, such as polypyrrole (PPy), are commonly synthesized with either scheme.<sup>[21,22]</sup>

### Shear Field Processing

SWNTs are added to a solution of polymer in toluene or *N,N*-dimethylformamide solution. High sonic power is briefly (a few minutes) used to break up the CNT aggregates, and then low power is applied to the sonic bath for a few hours. Generally, a few percent of CNTs remain in the solution other than those precipitated as aggregates. After a few days of settlement, the polymer/CNT composite from the supernatant can either be piped out and cast as thin film, or further thermally blended. In the latter, the composite can be dried in the oven and then melt-pressed above its glass transition temperatures a few times to ensure uniform mixing. The anisotropic effect introduced in the melt-blended process may seem predominant than in situ-polymerized composites. Some researchers<sup>[23]</sup> believe that the different thermal expansions between SWNTs and PMMAs can significantly contribute to their interfacial adhesion. This causes stress and improves alignment between the two components in the melt-blended composite in anisotropic directions. For example, molecular dynamic simulations of polyethylenes and SWNT composites show that the polyethylene diffusion coefficient is 30% higher in the direction in which its backbone is parallel to the SWNT axial direction than perpendicular to it.

### INTERFACIAL INTERACTIONS IN THE COMPOSITE OF INCREASED ELECTRIC CONDUCTIVITY

Some of the processing conditions have subtle, yet profound, impacts on composite properties. Raman studies show that applied sonication shear field strength during CNT composite formation can introduce defects to the CNT sidewall, change its diameter,<sup>[24,25]</sup> or even open the end caps on the tubes. The defect sites are usually the most active sites where the charge transfer most likely occur. The chemical interaction usually occurs on the CNT tip because the fullerene-like cap is more reactive. The less invasive noncovalent interaction generally happens along the CNT sidewall in the form of van der Waals, hydrogen bond, or electrostatic interactions, all of which are more commonly observed in the polymer composites. Raman analysis is a very sensitive technique for investigating these interactions. The G-band and D-band ratio in the Raman shift can illustrate processing and growth-related mechanisms. However, the backbone conformation changes of the polymer in conjunction with the diameter changes of the CNT routinely probed by Raman spectroscopy are likely the causes of the constituent components electronic conductivity increases in the polymer composites.

In many cases, the measured conductivity change depends on interactions on the molecular level for nanometer-scale composites. Raman spectroscopy has demonstrated that the electronic DOS band gap of CNTs in the composite can be influenced by interactions formed during the composite formation.

### PMMA/SWNT Composites

The polymethyl methacrylate (PMMA/CNT) composites are among the most studied composites. The electronic conductivity of the MWNT composite is increased by several orders of magnitude.<sup>[26]</sup> Because there is no conjugated bond in PMMA to interact with the CNT, the interfacial interactions are likely to play important roles in composite formation. Therefore this is an ideal system to investigate the structure and conductivity changes simultaneously. These changes can be interplayed with direct conductivity measurements, as well as optical probes to electronic DOS through resonant Raman spectroscopy.

The PMMA/SWNT composite is fabricated into a spun fiber by the melt-processed film and analyzed by Raman spectroscopy.<sup>[27]</sup> The SWNT could either position itself to the fiber axis, or isotropically disperse in the composite. Fig. 5 shows the polarized Raman spectra of the composite. The intensity dependence of the RBMs with respect to the laser incident angles

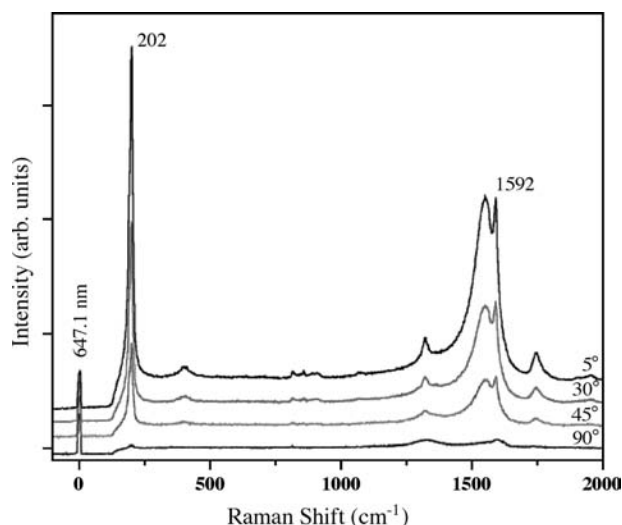


**Fig. 5** Raman spectra of SWNT/PMMA nanocomposite fiber at the indicated fiber angles with respect to the incident laser polarization axis. Spectra were recorded using the 647.1-nm excitation, with the analyzed polarization parallel to the incident polarization. The angle-dependent intensity of the breathing mode of the SWNTs ( $202\text{ cm}^{-1}$ ) was used to determine the extent of nanotube alignment relative to the fiber axis. *Source:* ©Elsevier Science B.V., 2000.

demonstrates that the SWNT is highly anisotropically aligned with the fiber axis. This corresponds to the much higher conductivity directly measured in the fiber axial direction, as opposed to the lower conductivity perpendicular to the processing flow direction.

Apparently, further investigations are needed of the PMMA and SWNT structural details that affect the change of conductivity. The changes of SWNT sizes

with loading have been studied with Raman spectroscopy by using multiple wavelength excitations.<sup>[28]</sup> At both 514- and 1064-nm excitations, Fig. 6A shows that SWNT RBM frequency upshifts toward larger-diameter distributions as calculated from Eq. (2). The PMMA composites with SWNT loadings of 2.5%, 5%, 10%, and 20% are also studied with resonant conditions at 1064 and 647 nm for semiconducting and metallic SWNTs, respectively. These two excitations correspond to the first semiconducting and metallic DOS singularity bandgaps, respectively. In the 1064-nm excitation that corresponds to the semiconducting SWNT, Fig. 6B shows that among the five components in the TM region ( $1553, 1568, 1573, 1592,$  and  $1597\text{ cm}^{-1}$ ), the intensities of the three peaks located at  $1553, 1568,$  and  $1573\text{ cm}^{-1}$  decrease in the composites. More drastically, in the 633-nm laser excitation that corresponds to the metallic SWNT, the relative ratio of  $1543/1558\text{ cm}^{-1}$  in the G-band is reversed from the pristine SWNT. This is an indication of the increased percentage of metallic SWNT because the G-band line shape featured by the BWF fit in Eq. (1) in the metallic SWNT resonant condition. The other possibility is that PMMA/SWNT interaction replaces the interface in the SWNT bundles. Furthermore, the interaction between SWNT and PMMA is investigated in full width at half maximum (FWHM). The FWHM increases with SWNT loadings, and decreases with excitation wavelengths go from 458, 514, 676, to 1064 nm. The observed G-band blue shifts and the SWNT diameter increases, clearly demonstrating the van der Waals interaction between SWNT/PMMA in the composites, in place of intertube interactions in the pristine SWNT.

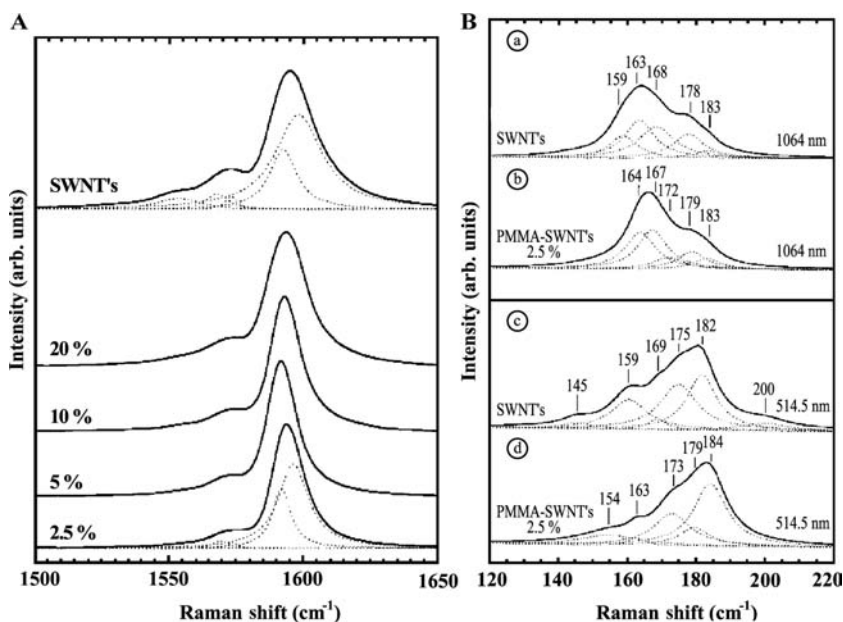


**Fig. 6** (A) Raman spectra of PMMA/SWNT composites and SWNT films in the frequency range  $1500\text{--}1650\text{ cm}^{-1}$  with 1064 nm excitation. The spectra are resolved for PMMA/SWNT composites of 2.5% concentration and SWNTs. (B) Decomposition of low-frequency bands: (A) SWNT film with 1064 nm excitation; (B) PMMA/SWNT film for 2.5% concentration with 1064 nm excitation; (C) SWNT film with 514.5 nm excitation; and (D) PMMA/SWNT film for 2.5% concentration with 514.5 nm excitation. *Source:* ©Elsevier Science S.A., 2000.

The interfacial interaction in SWNT/PMMA composites can be further illustrated by Raman studies on two differently processed composites.<sup>[29]</sup> Figure 7A gives the Raman results of melt-processed and UV-polymerized composites in the metallic resonant excitation energy at 633 nm (1.96 eV). SWNT Raman spectra are used for reference. Comparing to both UV-polymerized composites and pristine SWNTs, the melt-blended composite exhibits a significant difference in the SWNT G-band line shape profiles around  $1590\text{ cm}^{-1}$ . The G-band in UV-polymerized composites retains the same Lorentzian line shape as that of the pristine SWNT. The broader G-band feature in the thermally treated composite can be fit with the BWF line shape for the SWNT diameter between 1.2 and 1.6 nm in the AOT,<sup>[30]</sup> as discussed in Fig. 3. The BWF line shape is the signature of metallic SWNTs resulting from the coupling between the phonon and the electronic continuum.<sup>[31]</sup> The predominant metallic feature shown in Fig. 7A demonstrates a significant increase of the metallic SWNT percentage in the melt-blended composites. The SWNT in the UV-polymerized composite, in which PMMA exhibits no anisotropic effect, retains the same chirality as in the pristine SWNT sample.

The anisotropic interfacial interaction between PMMA and SWNT in the melt-blended composite can be monitored by the PMMA backbone conformation change, especially when the C–H stretching in the backbone is amplified by Fermi resonance.<sup>[32,33]</sup> The stretching symmetry contributions from the backbone relative to the side chain are significantly different

in the two composites examined. The relative ratio of the C–H<sub>2</sub> stretch bands to the side-chain C–C and C–O stretching mode is 30% higher in the melt-blended composite than that in the UV-polymerized composite. Schematically, the C–H<sub>2</sub> stretching is little affected by the anisotropic SWNT/PMMA interactions in Fig. 7B; however, it is hindered by isotropic SWNT/PMMA interactions in Fig. 7C. Because the side-chain vibrations are not sensitive to the orientation of PMMA/SWNT interaction, the higher intensity of the C–H<sub>2</sub> stretching band suggests the likely stronger anisotropic interaction between PMMAs and SWNTs. This interaction is believed to cause metallic SWNT enrichment in the melt-blended composite.

The electric conductivity increase investigated by Raman spectroscopy was also confirmed by composite dielectric measurements.<sup>[34]</sup> The higher dielectric constant is obtained for the melt-blended composite than for the UV-polymerized composite. This is consistent with the possible dipole interaction enhanced by the anisotropic interaction between the PMMA and SWNT in the melt-blended composite. The strain-induced band gap change<sup>[35]</sup> possibly could also contribute to the increase of the metallic percentage of SWNTs in the melt-blended composites.

## Other Polymer Composites

The similar interfacial interaction effect on the conductivity in PMMA/SWNT composites has been observed in several other polymer composites.

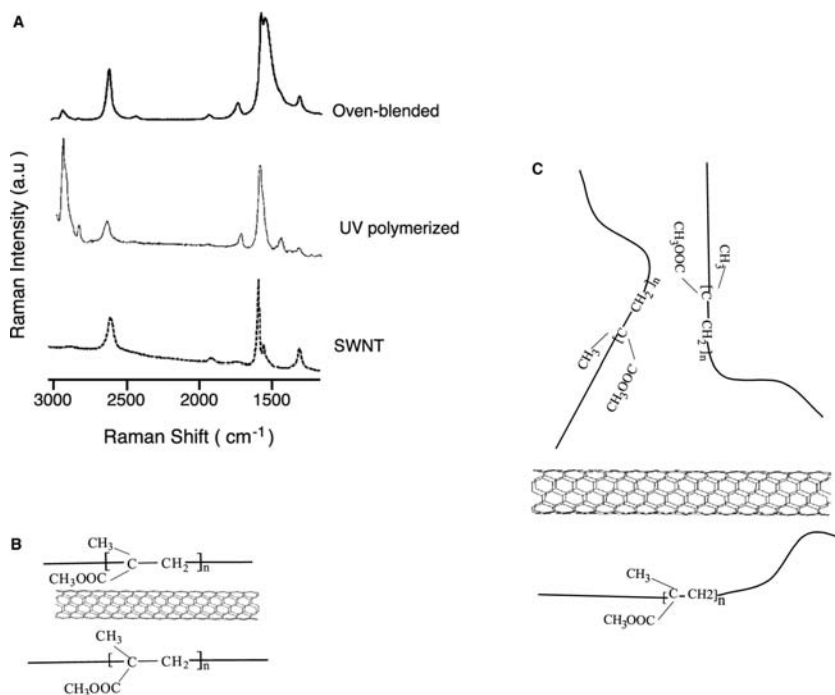


**Fig. 7** (A) Raman spectra of the two PMMA/SWNT composites and pristine SWNT excited at 633 nm. The G-band of SWNTs in the melt-blended composite around  $1590\text{ cm}^{-1}$  is distinctly different. This line shape fits with the BWF line shape and is recognized as the signature for a metallic SWNT. The G-band in UV-polymerized composites retains the same Lorentzian line shape as in pristine SWNT. (b, c) Schematic illustrations of the PMMA and SWNT anisotropic and isotropic interactions in the melted-blended and UV-polymerized composites, respectively. The anisotropic interaction between SWNT side wall and PMMA backbone has little effect on side-chain vibrations, but will affect the backbone C–H<sub>2</sub> stretch because axial stretching can be blocked by SWNT/PMMA if not aligned.



The in situ-polymerized rigid polymer poly(*p*-phenylene)benzobisoxazole (PBO)/SWNT composite is similarly prepared as UV-polymerized PMMA/SWNT composites.<sup>[36]</sup> Its measured conductivity remained the same as that of the neat polymer, possibly because of a lack of strong interfacial interactions in the composite, which is not detectable from Raman studies.

The conductivity of polystyrene and SWNT composites formed from a miniemulsion process increases by ten order of magnitude at 8.5% SWNT loading.<sup>[37]</sup> The interactions between polystyrene and SWNT in the composites are both exhibited in the Raman spectra. The SWNT G-line at  $1580\text{ cm}^{-1}$  shifted to higher frequencies whereas the RBM upshifted. The loss of intensity of polymer C=C stretch modes at  $1670\text{ cm}^{-1}$  is also observed among the polystyrene Raman modes.

Polyimide (PI)-based composites appeared to increase electric conductivity with SWNT loading. Conductivity percolation is reached with SWNT loading between 0.02% and 0.1%.<sup>[38]</sup> The interactions in CNT/PI nanocomposites can be controlled to increase polaron mobility and quantum efficiency. The Raman results of this photovoltaic electrolyte material suggest the charge transfer mechanism correspondingly.<sup>[39]</sup>

### CHARGE TRANSFER AND STRONG $\pi$ INTERACTION IN COMPOSITE WITH INCREASED ELECTRIC CONDUCTIVITY

The SWNT G-band is very sensitive to the doping and charge process. The Raman frequency shifts depending on the types of donor or acceptor. The charge transfer between halogen or alkali metal and SWNT was first demonstrated by Raman studies<sup>[40]</sup> shown in Fig. 8. The TM frequency shifts in the SWNT sidewall around  $1550\text{ cm}^{-1}$  show the changes in accordance with the corresponding diameter changes in RBM. The charge transfer soften mode is identified as BWF interference in the alkali metal-doped SWNT bundle. The  $\pi$  electron transfer from the carbon to the acceptor ( $\text{Br}_2$ ,  $\text{I}_2$ ) or donor (K, Rb) is believed to introduce both TM and RBM changes.

The  $\pi$ -stacking of the planar pyrenylene  $\pi$ -moiety in the 1-pyrenebutanoic acid succinimidyl ester with the CNT graphite basal plane forms a very stable self-assembled composite,<sup>[41]</sup> which changes the SWNT from hydrophobic to hydrophilic nature. This structure interaction was schematically illustrated in Fig. 9. Although Raman studies are not reported for this composite, the strong interaction was investigated by another similar polymer composite in terms of charge transfer. The Raman studies of composites of the aromatic perylene-doped SWNTs are believed to have a charge transfer in the G-band modes.<sup>[42]</sup> Fig. 10 shows the similar Raman shifts as observed

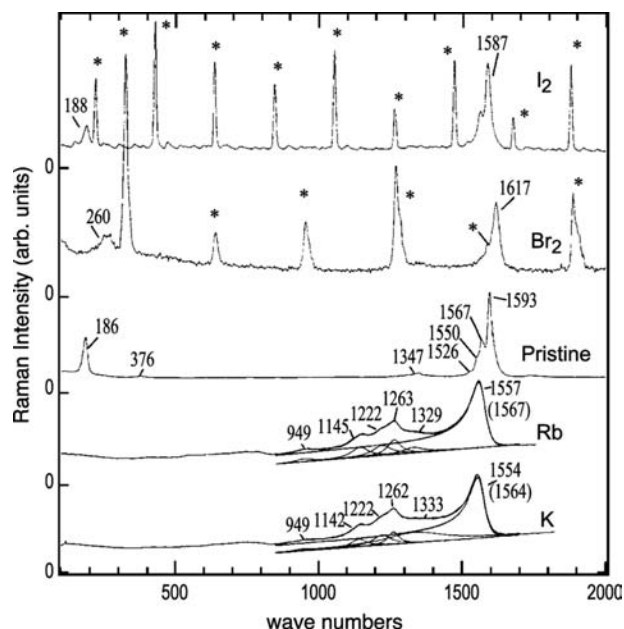


**Fig. 8** Raman scattering spectra for pristine SWNT bundles reacted with various donor and acceptor reagents. From top to bottom:  $\text{I}_2$ ,  $\text{Br}_2$ , pristine SWNT, Rb, and K. The backscattering spectra were taken at  $T = 300\text{ K}$  using  $514.5\text{ nm}$  radiation. In the spectra for both halogen-doped SWNT bundles, a harmonic series of peaks (indicated with asterisk) is observed, which are identified with the fundamental stretching frequency  $\omega_s$ :  $\sim 220\text{ cm}^{-1}$  ( $\text{I}_2$ ) and  $\sim 324\text{ cm}^{-1}$  ( $\text{Br}_2$ ). The spectra have been scaled so that the strongest SWNT feature appears to have the same intensity. In the vicinity of the strongest high-frequency mode around  $1550\text{ cm}^{-1}$ , the Raman spectra for SWNTs doped with K or Rb are fitted with superposition of Lorentzian functions and an asymmetric BWF line shape on a linear continuum. Source: ©Macmillan Publishers, 1997.

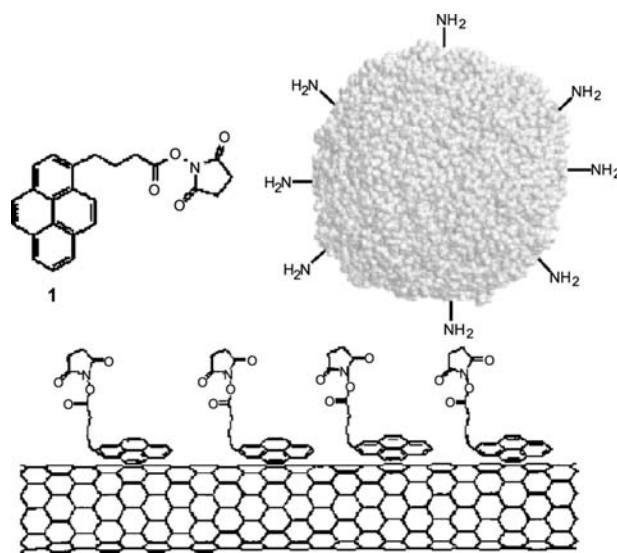


**Fig. 9** 1-Pyrenebutanoic acid succinimidyl ester 1 irreversibly adsorbing onto the sidewall of a SWNT via  $\pi$ -stacking. Source: ©ACS, 2001.

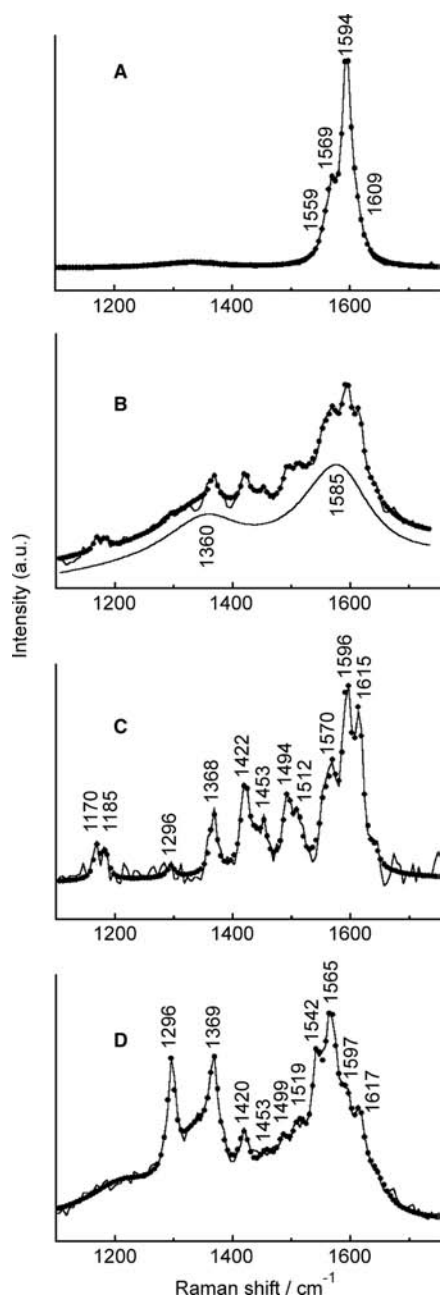


**Fig. 10** Typical Raman spectra in different areas. (A) Spectrum of pristine nanotube G-band is fitted by Lorentzian curves peaking at  $1559\text{ cm}^{-1}$  ( $E_{2g}$  mode),  $1569\text{ cm}^{-1}$  ( $A_{1g}$ ),  $1594\text{ cm}^{-1}$  ( $A_{1g}+E_{1g}$  modes), and  $1609\text{ cm}^{-1}$  ( $E_{2g}$  mode). (B) Spectrum of perylene-doped tubes in zone B. (C) Signatures of perylene–tube interaction after subtraction of the asymmetric background and of the growing fluorescence background in zone B. (D) Spectrum of perylene-doped tubes in another area. *Source:* ©Elsevier Science B.V., 2002.

in alkali and halogen doping in the SWNT. Although the strong perylene modes, such as  $1296\text{ cm}^{-1}$ , are not observed in the areas investigated by Raman spectra, the inactive SWNT vibrational modes around  $1542$ ,  $1549$ , and  $1610\text{ cm}^{-1}$  in the G-band emerge in

the composite and exhibit different degrees of enhancement because of perylene doping interaction.

The PmPV composite is well studied by various spectroscopy techniques. PmPV is an important photovoltaic and LED material in optoelectronic applications. The CNT composite is expected to improve device performance by optimizing the SWNT loading, tube length, and its chirality. The scanning tunneling microscopy (STM) results indicate that PmPV, as a coiling polymer, is interacting with SWNT with periodical surface wrapping,<sup>[43]</sup> as shown in Fig. 11. The wrappings are refractive and conform to the sidewall lattice structure of the SWNT. The electric conductivity increased up to eight orders of magnitude at 8.5% MWNT loading. At less than 7% SWNT loading, an increase of one order of magnitude to  $1.5 \times 10^{-9}$  S/m was observed; between 7% and 11% loading, an increase in conductivity of eight orders of magnitude has been observed; whereas the conductivity plateaus to 3 S/m after 36% loading.<sup>[44]</sup> The interactions in the composite possibly enhance polaron mobility through the change of the polymer backbone conformation and through a better hopping and tunneling path. It is believed that PmPV significantly reduces electron delocalization and vibrational freedom after the interaction with SWNT in the composite.

The dependence of increased conductivity on CNT loading in the composites is established by Raman studies under resonant conditions of the semiconducting

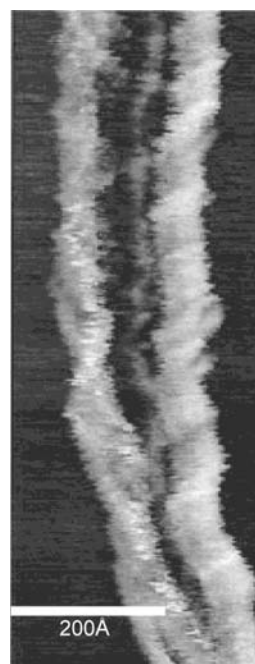


**Fig. 11** STM image of two PmPV-coated SWNTs lying on HOPG substrate. The ordered coating can be seen in the tube on the right. There are two individual tubes on the left, separating at the bottom. *Source:* ©ACS, 2002.

and metallic SWNTs, respectively.<sup>[45]</sup> At 676 nm wavelength excitation resonant with the metallic SWNT, the polymer vinylene stretch mode at  $1627\text{ cm}^{-1}$  evolves into two well-defined modes at  $1630$  and  $1625\text{ cm}^{-1}$ . The SWNT TM of  $1598\text{ cm}^{-1}$  is simultaneously downshifted to  $1593\text{ cm}^{-1}$ , whereas the  $1568\text{ cm}^{-1}$  mode disappears. The RBMs measured with laser excitation energies resonant at the semiconducting condition display the upshifts by about  $7\text{ cm}^{-1}$ ; the relative intensity ratio of the individual frequencies is also changed. The SWNT diameter distributions derived from Eq. (1) indicate that the diameters shift toward smaller size distribution in the composites. However, the D-band to G-band ratio is significantly changed, which suggests that  $\text{sp}^3$  carbon may act as the active site that interacts with PmPV. The spectroscopy evidence of these vibration symmetry changes from both PmPV and SWNT, combined with STM studies, show the helix wrapping of PmPV backbone around the MWNT sidewall with strong interactions. The luminescence study shows no quenching, which is usually associated with the charge transfer mechanism. Therefore it can be concluded that the composite conductivity increases are because of the PmPV backbone's strong  $\pi$ - $\pi$  interactions with the SWNT sidewall, rather than charge transfer mechanism.

The majority of the pristine LED polymer materials needed to be doped to achieve high-enough carrier mobility for device application. The polaron and bipolaron ratio not only reflects the conductivity of the composite, but also is the direct result of the symmetry change of the polymer because of the interaction of the CNT with the polymer.

The electropolymerized polypyrrole (PPy)/CNT thin film composite has attracted considerable attention. Being a conjugated polymer, PPy has strong electron and phonon interactions (called polaron) in the lattice. It resembles an ionic lattice, so bipolaron can form through interactions between neighboring polarons. Two significant changes in the MWNT symmetry mode are shown in the curve-fitting results of Raman spectra at 633 nm excitation.<sup>[46]</sup> First, the defect-induced MWNT shoulder peak D' at  $1612\text{ cm}^{-1}$  substantially decreased after the composite film formation. The normalized intensity ratio of D-band to G-band significantly decreases from 2.5 in the MWNT arrays to 0.4 in the composite film. This indicates that the MWNT sidewall  $\text{sp}^3$  graphitic carbon interacts with PPy. The observed decrease of the D-band intensity is similarly demonstrated in the PmPV/SWNT composite as well.<sup>[8]</sup> Therefore the symmetry of both MWNT and PPy is expected to change. Examine the bipolaron (labeled with\*) and polaron (labeled with †) pair<sup>[47]</sup> in Fig. 12. MWNT composites have much higher bipolaron contributions than in the CPE composite. Furthermore, bipolaron-only<sup>[48]</sup> mode

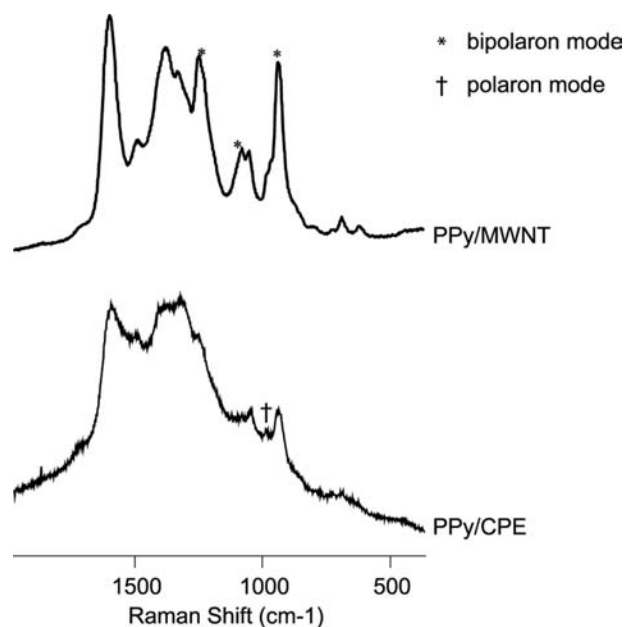


**Fig. 12** Raman spectra of PPy electropolymerized at (A) MWNT array electrode, and (B) at carbon paste electrode. In the MWNT/PPy composite, the dipolaron modes at  $986$  and  $1051\text{ cm}^{-1}$  (labeled with\*) corresponding to polaron modes (labeled with †)  $986$  and  $1051\text{ cm}^{-1}$  are much higher than that in the CPE/PPy composite. The bipolaron mode at  $1247\text{ cm}^{-1}$  is only observed in the MWNT/PPy composite. However, the polaron mode at  $1044\text{ cm}^{-1}$  is more predominant in the CPE/MWNT film. The skeletal band C–N stretching mode at  $1487\text{ cm}^{-1}$  shoulder is higher in the MWNT/PPy composite, indicating stronger backbone vibrations.

at  $1247\text{ cm}^{-1}$  is only observed in the MWNT/PPy composite film. However, the polaron mode at  $1044\text{ cm}^{-1}$  is more predominant in the CPE/MWNT film. In addition, the skeletal band<sup>[49]</sup> C–N stretching mode at  $1487\text{ cm}^{-1}$  shoulder is higher in the MWNT/PPy composite, indicating stronger backbone vibrations. All the Raman results suggest better PPy backbone conjugation in the MWNT composite than that in the CPE composite. When PPy electropolymerized onto the highly orientated electrode array, its backbone conforms to the MWNT sidewall. Therefore the polymer chain deformations, kinks, twists, and angle distortions between aromatic ring planes can be reduced. The high bipolaron density enhances conjugation in the MWNT/PPy composite film. Thus the resultant film is structurally very stable and highly conductive. This preferred configuration is confirmed by the SEM image of the MWNT after composite formation. The remarkable uniformity of this widely studied<sup>[50,51]</sup> composite film can be understood because of its unique nanostructural interactions.

Recently, Raman analyses have become a powerful technique to identify the separation of metallic and

semiconductor SWNTs in both the bulk quantity and the nanoscale approach.

Resonant Raman analysis is used to probe the conductivity of SWNTs treated in the polar organic solvent, with octadecylamine (ODA) possibly self-assembled onto SWNTs.<sup>[52]</sup> The Raman line shape analysis around frequency of TMs is used for gauging semiconducting and metallic features under the respective resonant conditions. The resonant Raman spectroscopy concludes the predominant semiconducting and metallic compositions in the supernatant and precipitant, respectively.

Raman study of CNT conductivity has also been successful in nanodevices.<sup>[53]</sup> Both RBM and TM frequencies are used to analyze compositions in the electrode and in the suspension after the a.c. electric field on a pair of microelectrodes laid out on the oxidized Si substrate. The induced dipole moment migrates the metallic SWNTs to the electrodes, leaving the semiconducting SWNT in the suspension. The polarized Raman also shows the highly aligned nanotube along the electric field. In this application, the in situ microscopic Raman probe demonstrates the ideal technique to study CNT conductivity beyond macroscopic chemical environments.

## CONCLUSION

Recent research progress in Raman spectroscopy demonstrates that it is an ideal technique to study the electronic conductivity of the CNT and polymer composites in two approaches. In the first approach, the vibration symmetry studies of the CNT and polymer are directly correlated with conductivity measurements, providing possible mechanisms of the composite electronic conductivity change caused by nanostructural interactions. In the second approach, Raman spectroscopy directly probes the composite electronic DOS band gap through resonant scattering. The implications of interfacial interaction, as well as charge transfer between the constituent components in the composite are studied by Raman spectroscopy. The Raman spectroscopy study will guide processing conditions, including thermal treatment and shear field strength, as well as polymerization specifications for better control in electronic and optical applications.

## REFERENCES

- Saito, R.; Dresselhaus, G.; Dresselhaus, M.S. *Physical Properties of Carbon Nanotubes*; Imperial College Press: London, 1998.
- Wagner, H.D.; Lourie, O.; Feldman, Y.; Tenne, R. Stress-induced fragmentation of multiwall carbon nanotubes in a polymer matrix. *Appl. Phys. Lett.* **1998**, *72*, 188.
- Schadler, L.S.; Giannaris, S.C.; Ajayan, P.M. Load transfer in carbon nanotube epoxy composites. *Appl. Phys. Lett.* **1998**, *73*, 3842.
- Chen, Y.-C.; Raravikar, N.R.; Schadler, L.S.; Ajayan, P.M.; Zhao, Y.P.; Lu, T.-M.; Wang, G.-C.; Zhang, X.-C. Ultrafast optical switching properties of single-wall carbon nanotube polymer composites at 1.55  $\mu\text{m}$ . *Appl. Phys. Lett.* **2002**, *81* (6), 975.
- Landi, B.J.; Raffaele, R.P.; Heben, M.J.; Alleman, J.L.; Van Derveer, W.; Gennett, T. Single wall carbon nanotube–nafion composite actuators. *Nano Lett.* **2002**, *2* (2), 1329.
- Baughman, R.; Cui, C.; Zakhidov, A.A.; Iqbal, Z.B.J.N.; Spinks, G.M.; Wallace, G.G.; Mazzoldi, A.; De Rossi, D.; Rinzler, A.G.; Jaszinski, O.; Roth, S.; Keresz, M. Carbon nanotube actuators. *Science* **1999**, *284*, 1340.
- Kymakis, E.; Amaratunga, G.A.J. Single-wall carbon nanotube/conjugated polymer photovoltaic devices. *Appl. Phys. Lett.* **2002**, *80* (1), 112.
- Curran, S.A.; Ajayan, P.M.; Blau, W.J.; Carroll, D.L.; Coleman, J.N.; Dalton, A.B.; Davey, A.P.; Drury, A.; McCarthy, B.; Maier, S.; Strevens, A. A composite from poly(*m*-phenylenevinylene-*co*-2,5-dioctoxy-*p*-phenylenevinylene) and carbon nanotubes: A novel material for molecular optoelectronics. *Adv. Mater.* **1998**, *10*, 1091.
- Alexandrou, I.; Kymakis, E.; Amaratunga, G.A.J. Polymer–nanotube composites: burying nanotubes improves their field emission properties. *Appl. Phys. Lett.* **2002**, *80*, 1435.
- Muisener, P.A. O'Rourke; Clayton, L.; D'Angelo, J.; Harmon, J.P.; Sikder, A.K.; Kumar, A.; Cassell, A.M.; Meyyappan, M. Effects of gamma radiation on poly(methyl methacrylate)/single-wall nanotube composites. *J. Mater. Res.* **2002**, *17*, 2507.
- Chung, D.D.L. Electromagnetic interference shielding effectiveness of carbon materials. *Carbon* **2001**, *39*, 279.
- Yacoby, Y.; Enrenfreund, E. Light scattering in solids VI. In *Topics in Applied Physics*; Cardona, M., Güntherodt, G., Eds.; Springer: Heidelberg, 1991; Vol. 68.
- Rao, R.; Richter, E.; Bandow, S.; Chase, B.; Eklund, P.C.; Williams, K.A.; Fang, S.; Subbaswamy, K.R.; Menon, M.; Thess, A.; Smalley, R.E.; Dresselhaus, G.; Dresselhaus, M.S. Diameter-selective Raman scattering from vibrational modes in carbon nanotubes. *Science* **1997**, *275*, 187.
- Klein, M.V. *Light Scattering in Solids I*; Cardona, M., Ed.; Springer-Verlag: Berlin, 1983; 169 pp.
- Brown, S.D.; Corrio, P.; Marucci, A.; Dresselhaus, M.S.; Pimenta, M.A.; Kneipp, K. Anti-stokes Raman spectra of single-walled carbon nanotubes. *Phys. Rev., B.* **2000**, *61*, R5137.
- Jorio, A.; Saito, R.; Hafner, J.H.; Lieber, C.M.; Hunter, M.; McClure, T.; Dresselhaus, G.; Dresselhaus, M.S. Structural (*n*, *m*) determination of isolated single-wall carbon nanotubes by resonant Raman scattering. *Phys. Rev. Lett.* **2001**, *86* (6), 1118.
- Alvares, L.; Righi, A.; Guillard, T.; Rols, S.; Anglaret, E.; Laplaze, D.; Sauvajol, J.L. Resonant Raman study

- of the structure and electronic properties of single-wall carbon nanotubes. *Chem. Phys. Lett.* **2000**, *316*, 186.
18. Debarre, A.; Jaffiol, R.; Richard, A.; Tchénio, P. Raman hyperspectral imaging applied to chemical co-localization in diluted samples of perylene-doped nanotubes. *Chem. Phys. Lett.* **2002**, *366*, 274.
  19. Liu, Y.; Hwang, B.-J. Identification of oxidized polypyrrole on Raman spectrum. *Synth. Met.* **2000**, *113*, 203.
  20. Iriyama, Y.; Hanawa, M. Plasma polymerization of pyrrole and structures and properties of the polymerized films. *Polym. J.* **2001**, *33*, 419.
  21. Chen, G.Z.; Shaffer, M.S.P.; Coleby, D.; Dixon, G.; Zhou, W.; Fray, D.J.; Windle, A.H. Carbon nanotube and polypyrrole composites: coating and doping. *Adv. Mater.* **2000**, *12* (7), 522.
  22. Chen, J.H.; Huang, Z.P.; Wang, D.Z.; Yang, S.X.; Wen, J.G.; Ren, Z.F. Electrochemical synthesis of polypyrrole/carbon nanotube nanoscale composites using well-aligned carbon nanotube arrays. *Appl. Phys., A* **2001**, *73*, 129.
  23. Wei, C.; Srivastava, D.; Cho, K. Thermal expansion and diffusion coefficients of carbon nanotube–polymer composites. *Nano Lett.* **2002**, *2* (6), 647.
  24. Cinke, M.; Li, J.; Chen, B.; Cassell, A.; Delzeit, L.; Han, J.; Meyyappan, M. Pore structure of raw and purified HiPco single-walled carbon nanotubes. *Chem. Phys. Lett.* **2002**, *365*, 69.
  25. Liao, K.; Li, S. Interfacial characteristics of a carbon nanotube–polystyrene composite system. *Appl. Phys. Lett.* **2001**, *79*, 4225.
  26. Sandler, J.; Shaffer, M.S.P.; Prasse, T.; Bauhofer, W.; Schulte, K.; Windle, A.H. Development of a dispersion process for carbon nanotubes in an epoxy matrix and the resulting electrical properties. *Polymer* **1999**, *40*, 5967.
  27. Haggemuller, R.; Gommans, H.H.; Rinzler, A.G.; Fischer, J.E.; Winey, K.I. Aligned single-wall carbon nanotubes in composites by melt processing methods. *Chem. Phys. Lett.* **2000**, *330*, 219.
  28. Stephan, C.; Nguyen, T.P.; Lamy de la Chapelle, M.; Lefrant, S.; Journet, C.; Bernier, P. Characterization of single-walled carbon nanotubes–PMMA composites. *Synth. Met.* **2000**, *108*, 139.
  29. Chen, B.; Cinke, M.; Li, J.; Meyyappan, M.; Chi, Z.; Harmon, J.P.; Muisener, P.A.O.; Clayton, L.; D'Angelo, J. Modifying electronic property of the single-walled carbon nanotube through anisotropic polymer interaction: a Raman study. *Adv. Funct. Mater.*, submitted for publication.
  30. Kataura, H.; Kumazawa, Y.; Maniwa, Y.; Umez, U.; Suzuki, S.; Ohtsuka, Y.; Achiba, Y. Optical properties of single-wall carbon nanotubes. *Synth. Met.* **1999**, *103*, 2555.
  31. Brown, S.D.M.; Jorio, A.; Corio, P.; Dresselhaus, M.S.; Dresselhaus, G.; Saito, R.; Kneipp, K. Origin of the Breit–Wigner–Fano lineshape of the tangential G-band feature of metallic carbon nanotubes. *Phys. Rev., B* **2001**, *63*, 155414.
  32. Bulkin, B.J.; Krishnamachan, A. Vibrational spectra of liquid crystals: IV. Infrared and Raman spectra of phospholipid–water mixtures. *J. Am. Chem. Soc.* **1972**, *94*, 1109.
  33. Gabor, B.P.; Peticolas, W.L. On the quantitative interpretation of bromemembranal structure. *Raman spectroscopy. Biochim. Biophys. Acta* **1977**, *465*, 260.
  34. Chen, B.; Li, J.; Lu, Y.; Cinke, M.; Au, D.; Partridge, H.; Meyyappan, M.; Harmon, J.P.; Muisener, P.A.O.; Clayton, L.; D'Angelo, J. Characterizations of enriched metallic single-walled carbon nanotubes in polymer composite. *Macromol. Symp.*, submitted for publication.
  35. Yang, L.; Han, J. Electronic structure of deformed carbon nanotubes. *Phys. Rev. Lett.* **2000**, *85* (1), 154.
  36. Kumar, S.; Dang, T.D.; Arnold, F.E.; Bhattacharyya, A.R.; Min, B.G.; Zhang, X.; Varia, R.A.; Park, C.; Adams, W.W.; Hauge, R.H.; Smalley, R.E.; Ramesh, S.; Willis, P.A. Synthesis, structure, and properties of PBO/SWNT composites. *Macromolecules* **2002**, *35*, 9039.
  37. Barraza, H.J.; Pompeo, F.; O'Rear, E.A.; Resasco, D.E. SWNT-filled thermoplastic and elastomeric composites prepared by miniemulsion polymerization. *Nano Lett.* **2002**, *2* (8), 797.
  38. Park, C.; Ounaies, Z.; Watson, K.A.; Crooks, R.E.; Smith, J., Jr.; Lowether, S.E.; Connell, J.W.; Siochi, E.J.; Harrison, J.S.; St. Clair, T.L. Dispersion of single wall carbon nanotubes by in situ polymerization under sonication. *Chem. Phys. Lett.* **2002**, *364*, 303.
  39. Wise, K.E.; Park, C.; Siochi, E.J.; Harrison, J.S. Stable dispersion of single wall carbon nanotubes in polyimide: the role of noncovalent interactions. *Chem. Phys. Lett.*, submitted for publication.
  40. Rao, A.M.; Eklund, P.C.; Bandow, S.; Thess, A.; Smalley, R.E. Evidence for charge transfer in doped carbon nanotube bundles from Raman scattering. *Nature* **1997**, *388*, 257.
  41. Chen, R.J.; Zhang, Y.; Wang, D.; Dai, H. Noncovalent sidewall functionalization of single-wall carbon nanotubes for protein immobilization. *J. Am. Chem. Soc.* **2001**, *123*, 3838.
  42. Débarre, A.; Jaffiol, R.; Richard, A.; Tchénio, P. Raman hyperspectral imaging applied to chemical co-localization in diluted samples of perylene-doped nanotubes. *Chem. Phys. Lett.* **2002**, *366*, 274.
  43. McCarthy, B.; Coleman, J.N.; Czerw, R.; Dalton, A.B.; in het Panhauis, M.; Maitis, A.; Drury, A.; Bernier, P.; Nagy, J.B.; Lahr, B.; Byrne, H.J.; Carroll, D.L.; Blau, W.J. A microscopic study of interactions between carbon nanotubes and a conjugated polymer. *J. Phys. Chem., B* **2002**, *106*, 2210.
  44. Coleman, J.N.; Curran, S.; Dalton, A.B.; Davey, A.P.; McCarthy, B.; Blau, W.; Barklie, R.C. Percolation-dominated conductivity in a conjugated-polymer–carbon–nanotube composite. *Phys. Rev., B* **1998**, *58* (12), R7492.
  45. Dalton, A.B.; Stephan, C.; Coleman, J.N.; McCarthy, B.; Ajayan, P.M.; Lefrant, S.; Bernier, P.; Blau, W.J.; Byrne, H.J. Selective interaction of a semiconjugated organic polymer with single-wall nanotubes. *J. Phys. Chem., B* **2000**, *104*, 10,012.

46. Chen, B.; Li, J.; Delzeit, L.; Partridge, H.; Meyyapan, M. Raman analysis of in-situ electropolymerized carbon nanotube and polypyrrole composite. *Nano Lett.*, submitted for publication.
47. Mikat, J.; Orgzall, I.; Hochheimer, H.D. Raman spectroscopy of conducting polypyrrole under high pressure. *Phys. Rev., B* **2002**, *65*, 174202.
48. Furukawa, Y.; Tazawa, S.; Fujii, Y.; Harada, I. Raman spectra of polypyrrole and its 2,5-<sup>13</sup>C-substituted and C-deuterated analogues in doped and undoped states. *Synth. Met.* **1988**, *24*, 329.
49. Jenden, C.M.; Davidson, R.G.; Turner, T.G. A Fourier transform-Raman spectroscopic study of electrically conducting polypyrrole films. *Polymer* **1993**, *34*, 1649.
50. Chen, J.H.; Huang, Z.P.; Wang, D.Z.; Yang, S.X.; Li, W.Z.; Wen, J.G.; Ren, Z.F. Electrochemical synthesis of polypyrrole films over each of well-aligned carbon nanotubes. *Synth. Met.* **2002**, *125*, 289.
51. Gao, M.; Huang, S.; Dai, L.; Wallace, G.; Gao, R.; Wang, Z. Aligned coaxial nanowires of carbon nanotubes sheathed with conducting polymers. *Angew. Chem., Int. Ed. Engl.* **2000**, *39*, 3664.
52. Chattopadhyay, D.; Galeska, I.; Papadimitrakopoulos, F. A route for bulk separation of semiconducting from metallic single-wall carbon nanotubes. *J. Am. Chem. Soc.* **2003**, *125*, 3370.
53. Krupke, R.; Hennrich, F.; v. Lohneysen, H.; Kappes, M. Separation of metallic from semiconducting single-walled carbon nanotubes. *Science* **2003**, *301*, 344.



# Ring Structures from Nanoparticles and Other Nanoscale Building Blocks

Zhen Liu

Rastislav Levicky

*Department of Chemical Engineering, Columbia University,  
New York, New York, U.S.A.*

## INTRODUCTION

Over the last two decades nanomaterials have attracted growing interest because of their unique, potentially useful electronic, magnetic, and optical properties. For example, carbon nanotubes possess tunable electronic structure from metals to insulators. Nanoparticles can act as “artificial atoms” which, when assembled into meso- or macroscopic structures may lead to novel functional materials. Thus self-assembled particle arrays not only preserve the properties of individual particles but can also exhibit new behaviors due to interparticle correlations and coupling. The ability to organize nanoscale components into specific geometrical arrangements, with defined interconnections, underpins much of their promise for future applications as well as current fundamental studies. Here we focus on the organization of nanoparticles and, to a lesser extent, other nanoscopic building blocks into ringlike arrangements ranging over five decades of length scale, from macroscopic ( $\sim 1$  mm) to nanoscopic ( $\sim 10$  nm). In addition to the simple geometry of a ring, a variety of other arrangements have been realized. For example, following earlier reports of close-packed crystalline nanoparticle superstructures,<sup>[1–5]</sup> Korgel et al. analyzed nanoparticle self-assembly into superlattices in detail highlighting the effects of size-selection, ligand coverage, and interparticle attraction.<sup>[6]</sup> Detailed reviews on the fabrication and properties of nanoparticle superlattices are now available.<sup>[7,8]</sup> Other efforts have focused on organizing nanoparticles according to highly specific biological interactions<sup>[9–19]</sup> or using self-organized polymeric media such as block copolymers to spatially template nanoparticle synthesis and distribution.<sup>[20–28]</sup> Albeit the focus of this review restricts it from broadly considering the general theme of nanomaterial self-assembly, the above and related efforts continue to make critical advances toward functional materials and devices incorporating nanoscale components.

The formation of ringlike assemblies, whether over macroscopic or nanoscale dimensions, is intriguing for reasons other than simple curiosity about their physical or chemical origin. Thus continuous rings, for example, will develop circulating currents when magnetic flux is applied across the ring.<sup>[29]</sup> This “persistent” current has a periodicity as a function of the enclosed magnetic flux. Moreover, the electronic states of the ring are likewise functions of the applied field, leading to magnetically tunable optical and other properties that, in addition to being fundamentally interesting, may provide unique capabilities in applications. While a variety of routes to microscopic rings have been reported, including lithography,<sup>[30]</sup> direct chemical synthesis,<sup>[31]</sup> and diffusive coalescence on free liquid surfaces,<sup>[32]</sup> self-assembly of ring structures using wetting and capillary phenomena has perhaps been the most common. By its nature, self-assembly often provides a facile fabrication route, and generally similar methods can be effectively used to organize different particle types, making these methods fairly general. In what follows, various mechanisms that have led to the formation of ring structures will be described.

## SELF-ASSEMBLY OF MACROSCOPIC RINGS

Ringlike patterns formed by precipitated solute particles that are visible to the naked eye, such as coffee rings, are familiar phenomena. The formation of macroscopic ( $\sim 1$  mm to  $\sim 1$  cm) ring patterns from non-wetting droplets placed on a solid support was investigated by Deegan et al.<sup>[33]</sup> The mechanism presented by these authors invoked pinning of the contact line of the drying droplet as the carrier solvent evaporates. In order to maintain the contact line pinned at its initial position in the face of continued evaporation, a capillary flow of solvent is engendered from the interior of the droplet to its perimeter. Dispersed solute particles are carried by this resulting outflow to the edge where they accumulate (Fig. 1A). When the

droplet fully dries, a ringlike residue consisting of the accumulated particles remains. Notably, in this mechanism the ring formation is largely independent of the nature of the underlying surface, the deposited solute particles, and the carrier solvent. Maenosono and collaborators formed millimeter scale annular rings by precipitating 4–6-nm CdS and CdSe nanoparticles from a suspension droplet (Fig. 1B).<sup>[34]</sup> These authors postulated that, in addition to the pinning of the droplet's contact line as discussed by Deegan et al., convection from the suspension droplet to its perimeter where ring assembly occurs could be driven by the capillary pressure from the meniscus curvature within the porous, drying ring of nanoparticles. In this model, the capillary pressure produces an effective pressure-driven suction of solvent into the ring. Both mechanisms are potentially operative in the formation of macroscopic rings of nanoparticles and provide useful insights into how such arrays may be assembled.

## SELF-ASSEMBLY OF MICRON-SIZED RINGS

A number of investigators reported micron-scale annular ring assemblies of various nanometer subunits such as nanocrystals, nanotubes, and even small organic molecules. The origins of these microscopic structures are likely very different from those of macroscopic rings. Ohara and Gelbart observed micron-sized rings of nanoparticles,<sup>[35]</sup> possibly originating from the accumulation of particles along the rims of dewetting holes formed during the evaporation of nanoparticle suspensions on solid supports.<sup>[36]</sup> In these studies, the particle suspensions wetted the underlying support. Maillard and coworkers presented that thermocapillary flows engendered within an evaporating particle suspension could also lead to microrings and even hexagonal meshes of nanocrystals.<sup>[37,38]</sup> Stowell and Korgel observed the self-assembly of nanoparticles into rings and honeycomb networks.<sup>[39]</sup> The selection

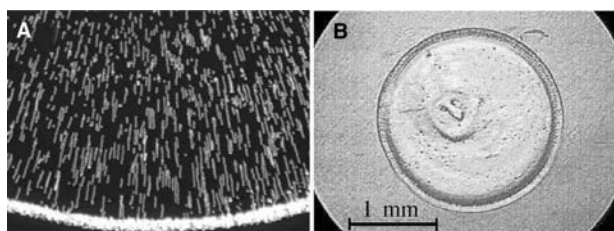


**Fig. 1** (A) Motion of microspheres driven by the capillary flow of solvent from the interior to the periphery in an evaporating water droplet.<sup>[33]</sup> (B) Optical microscope photograph of a CdS ring with an outer diameter of 0.23 cm. *Source:* From Ref.<sup>[34]</sup>.

of a particular geometry was attributed to the variation of the thermal susceptibility of the suspension's surface tension because of the presence of nanoparticles, triggering a transition from hole nucleation in the evaporating film to Marangoni instability-induced convective flow. Microrings formed from other materials include a report by Schenning et al. of such structures generated from disk-like porphyrin molecules. These authors suspected that the rings formed as a result of hole nucleation possibly induced by foreign particles.<sup>[40]</sup> In the following discussion some of these mechanisms are examined in greater detail.

## Thermocapillary Mechanisms

As discussed by Maillard et al. and others,<sup>[37–39]</sup> convective flow driven by variations in surface tension at the free interface of a thin evaporating liquid film can engender film rupture and hence the formation of holes or dry patches around which nanoparticles deposit. The physical origins of thermocapillary flows in liquid films have been well documented (e.g., see Ref.<sup>[41]</sup> for a review). For sufficiently thin (less than about 1 mm) volatile liquid films, evaporation generates a temperature gradient between the film's lower and upper boundaries due to the removal of latent heat, leaving the free upper surface cooler. Local fluctuations in the extent of cooling cause variations in the interfacial tension of this interface, with surface tension  $\gamma$  typically decreasing with temperature  $T$  according to a thermal coefficient  $B = -d\gamma/dT$ . As a result, the liquid from warmer surface regions where the interfacial tension is lower is pulled along the surface to spread over the cooler regions, where it is forced to move downward into the film as it cannot accumulate without limit. Simultaneously, warm liquid is fed upward to the warmer surface regions. Viscous coupling propagates this convective flow throughout the film to establish three-dimensional convective cells as illustrated in Fig. 2.

As evaporation proceeds, the thinning film may eventually rupture at the accompanying depressions, exposing the nearly bare substrate to form holes.<sup>[42–44]</sup> Evaporation and/or interfacial dewetting then drive the growth of the holes. When film rupture and subsequent hole growth occur in a suspension layer of nanoparticles, the particles can collect at the expanding hole rims eventually leaving behind drying patterns in the shape of rings (Fig. 3A). Possibly, the hole rims become pinned before complete drying of the film due to a build-up of frictional interaction between particles accumulated at the hole rim and the underlying surface.

A dimensionless Marangoni number,  $M_a = (B\Delta T h)/(\rho\nu\kappa)$ , is customarily used to compare the time

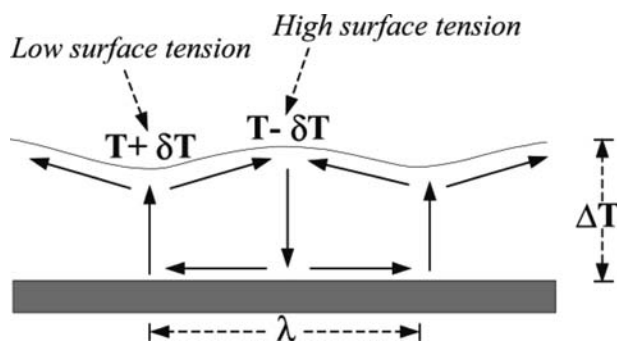


**Fig. 2** Illustration of thermocapillary convective flows in volatile liquid films. The mean temperature drop across the film is  $\Delta T$ .  $\lambda$  is a characteristic wavelength of the induced convective cells.

scale for the propagation of temperature disturbances across the thickness of the film with that needed to establish convective flow.<sup>[45,46]</sup> Temperature perturbations leading to the establishment of convective flow must be sufficiently long lived, corresponding to a critical  $M_a$  value above which convective flow becomes possible, and below which Marangoni instabilities will not appear. The critical  $M_a$  depends on the boundary conditions at the film's interfaces.<sup>[45,46]</sup> At the most basic level, convective flow is favored by greater temperature variation across the film ( $\Delta T$ ), film thickness ( $h$ ), and susceptibility of interfacial tension to variation in temperature ( $B$ ), but is suppressed by increases in the liquid's kinematic viscosity ( $\nu$ ), density ( $\rho$ ), or thermal diffusivity ( $\kappa$ ).

## Wetting Mechanisms

For apolar liquids and surfaces interacting purely via long-range dispersive forces, a drop of solvent placed on a solid support is typically characterized as either "wetting," meaning it thins so as to fully cover the support, or "non-wetting," meaning it beads up and forms a finite contact angle with the solid support. More completely, a set of classification rules can be devised that incorporate not only long-range apolar interactions but also short-range "contact" forces due to polar interactions.<sup>[47]</sup> By appropriate balancing of short polar and long-range apolar interactions, additional wetting states become possible including coexistence of thin wetting films with macroscopic, non-wetting droplets, and of dewetting thin films even when thicker layers of the same liquid wet. In considering the formation of microring assemblies from evaporating films, the approximation of either strictly (i.e., irrespective of film thickness) wetting or non-wetting liquids is usually sufficient as the surfaces and organic solvents used have been largely apolar in nature.

Ohara and Gelbart theoretically analyzed microring formation from evaporating particle suspensions when the suspension wets the surface.<sup>[35]</sup> Their analysis was motivated by accompanying experiments in which dilute nanoparticle solutions in wetting organic solvents such as hexane or toluene were spread on carbon-coated TEM grids and allowed to dry.<sup>[36]</sup> Drying patterns consisting of  $\sim 1\text{-}\mu\text{m}$ -diameter rings were found (Fig. 3B). As a wetting liquid film evaporates,

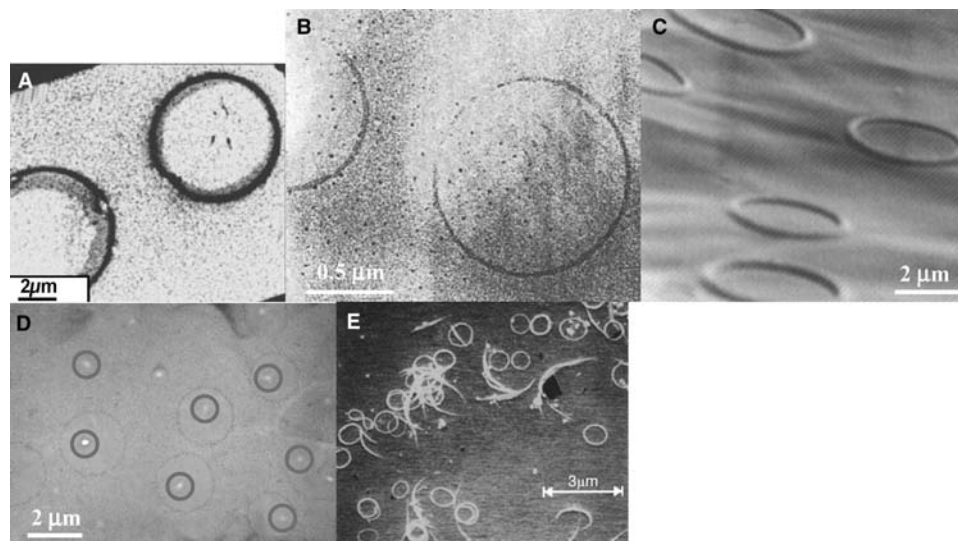


**Fig. 3** (A) Microrings formed from ferrite nanocrystals precipitated out of hexane after deposition on a TEM grid under air.<sup>[37,38]</sup> (B) A microring of organically functionalized Ag nanocrystals precipitated out of hexane solution.<sup>[35]</sup> (C) Porphyrin rings generated from evaporating chloroform solutions.<sup>[40]</sup> (D) Microrings of gold nanocrystals prepared by spin coating from octane solutions on a polymer film (surface defects were indicated by red circles). (E) Nanotube rings formed after irradiation of bulk suspensions with ultrasound. *Source:* From Ref.<sup>[50]</sup>.

it will continue to thin until the film thickness decreases to nearly molecular dimensions, on the order of a few nanometers. At this stage, further thinning leads to increasing loss of attractive liquid–liquid dispersive interactions, which prefer to thicken the film. Ohara and Gelbart argue that, rather than dry uniformly to zero thickness, the film may seek to maintain a minimal thickness  $t_e$  to counteract the loss of favorable liquid–liquid interactions, following a previous theoretical analysis for non-volatile liquid films by de Gennes.<sup>[48]</sup> In their model, as evaporation proceeds, the drying film will develop holes which will expand so as to maintain remnant wetted regions at the thickness  $t_e$ . The holes would open once the film thickness decreases sufficiently for free energy barrier to hole nucleation to become comparable to the thermal background  $kT$ , where  $k$  is the Boltzmann constant. For typical solvents this occurs at thicknesses of  $\sim 1$  nm. Once holes open and grow, nanoparticles can collect at the receding rims in a manner analogous to that described above for thermocapillary flows, leaving behind drying patterns in the shape of rings. Alternately, for sufficiently thin wetting films, holes can nucleate simply by spontaneous local evaporation of liquid molecules to form a dry patch or because of the presence of surface heterogeneities (e.g., a small non-wettable region).

Schenning et al. observed micron-sized ring assemblies composed of porphyrin molecules.<sup>[40]</sup> Their experimental procedure was similar to those used to form rings of nanoparticles. A droplet of porphyrin molecules in a solvent such as chloroform was placed on a substrate and allowed to evaporate for 10 sec, followed by draining of the remaining solution with filter paper. These authors suggested that the ringlike patterns originate from the nucleation of holes engendered by possibly combined influences of 1) non-wetability of the surface by the liquid; 2) progressive thinning of the liquid due to evaporation; and 3) deposition of foreign particles (e.g., from the laboratory ambient) that lowers the free energy barrier for hole nucleation. As the holes nucleate and grow, porphyrin molecules would accumulate at the rim increasing their concentration. Eventually, the concentration will exceed solubility and a condensed porphyrin phase will precipitate out to form the ring structures (Fig. 3C).

Liu and Levicky observed that spin coating of nanoparticles from organic solvents on polymer films produced micron-sized rings very similar to those reported by Ohara et al. and others.<sup>[35–40]</sup> Spin coating instead of droplet drying was used to better control deposition conditions. Samples for transmission electron microscopy (TEM) were prepared as reported previously.<sup>[28]</sup> From TEM micrographs, these authors identified that microrings formed around defects in the polymer film (Fig. 3D). Based on this evidence, ring

formation was attributed to defect-induced nucleation of holes in the spin-coated particle solution followed by particle accumulation at the hole rims, leaving microring drying patterns as discussed above. The defects appear white in the images (Fig. 3D), suggesting that the polymer film is thinner (possibly punctured) at those locations. Others have similarly connected surface topography with nucleation of holes and subsequent formation of drying patterns. For example, step edge defects on highly oriented pyrolytic graphite surfaces led to the formation of ringlike patterns from drying collagen solutions.<sup>[49]</sup>

Microring assembly will, in general, also depend on other factors such as solute concentration and evaporation speed. Clearly, rings cannot form if the solute (e.g., nanoparticle) concentration is too low because of the insufficiency of available material. Moreover, microring formation, at least in wetting systems, appears favored by faster rates of evaporation. For instance, in experiments by the present authors in which nanoparticle suspensions were spin coated from relatively low volatility, wetting solvents such as octane, microrings did not form if the deposition speed was below 100 rpm or if static evaporation was used. Presumably, under such wetting conditions, a nucleated hole can quickly seal unless solvent evaporation from the hole rim is sufficient to ensure hole growth.

### Other Types of Microrings

Microrings of carbon nanotubes have also been reported.<sup>[50,51]</sup> Martel and coworkers observed microrings of single-walled carbon nanotubes (SWNTs) following ultrasound irradiation of nanotubes in a warm solution of sulfuric acid and hydrogen peroxide (Fig. 3E). This process shortens the SWNTs and evidently can cause them to coil into rings. The physical origin of coiling was suggested to stem from tube bending due to the nucleation of bubbles on the hydrophobic surfaces of the SWNTs during ultrasound irradiation, followed by subsequent bubble collapse. Once a tube becomes coiled into a ring, the strain energy of bending can be balanced by physical van der Waals attraction along the nanotubes. This renders the rings highly permanent, sufficiently so that they can be recovered by filtering. High yields of rings, up to 50%, were reported.

### SELF-ASSEMBLY OF NANOSCALE RINGS

Rings with diameters ranging from 10 to 100 nm have been made out of magnetic nanoparticles or metal nanocrystals by several groups. In contrast to

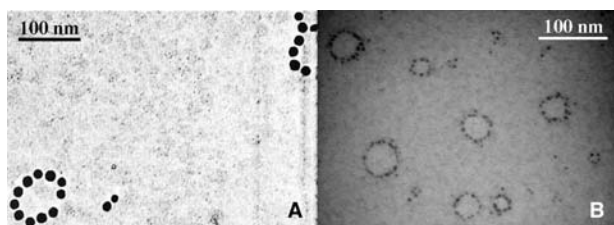


**Fig. 4** (A) Nanorings formed by 16-nm cobalt nanoparticles.<sup>[13]</sup> (B) Nanorings composed of 2.5-nm gold nanocrystals, formed by spin coating from octane solutions.

micron-sized rings, these structures are approximately one particle wide along their perimeter (Fig. 4). The self-assembly mechanisms, as may be expected, are distinct from those effective for forming macro- or microrings and involve magnetostatic particle interactions in the case of magnetic nanoparticles.<sup>[52,53]</sup> The present authors have also assembled nanoscopic rings from metal nanoparticles by spin coating nanoparticle solutions on thin polymer films.

### Magnetostatic Mechanisms

Tripp et al. synthesized weakly ferromagnetic cobalt nanoparticles (~30 nm in diameter), possessing a 3- to 0.4-nm oxide layer.<sup>[52]</sup> The nanoparticles were dispersed in toluene or  $\text{CH}_2\text{Cl}_2$  in the presence of a resorcinarene as a stabilizing surfactant. Droplets of nanoparticle solution containing surfactant were deposited on carbon-coated TEM grids and allowed to dry. If the concentration of surfactant was sufficiently high, this procedure produced a large population of nanorings with diameter in the range of 50 to 100 nm. A possible mechanism for ring formation is minimization of magnetostatic energy realized when a string of magnetic dipoles (i.e., a string of “head-to-tail” aligned ferromagnetic Co nanoparticles) closes, thus eliminating unpaired magnetic poles at its ends. Notably, without sufficient surfactant the Co nanoparticles aggregated into dense, continuous layers or “rafts.” The need for the non-volatile resorcinarene surfactant in the assembly of rings was believed to stem from kinetic stabilization attributed to the enhancement of the viscosity of the deposited particle layer. Otherwise, at low surfactant concentrations, the nanoparticles were sufficiently mobile to rearrange into more thermodynamically stable, dense aggregates. Other aggregate structures, such as oriented strings of particles, were also identified with preference for a particular geometry somewhat adjustable by application of external magnetic fields.

A previous report by Puntès et al. similarly described, among many other structures, the self-assembly of nanorings from ferromagnetic Co

nanoparticles (Fig. 4A).<sup>[53]</sup> Closed motifs, such as nanorings, did not form with smaller Co nanoparticles that were superparamagnetic rather than ferromagnetic. These results indicate that the permanency of the particles’ magnetic dipole plays a crucial role in facilitating the formation of closed loops or rings. In the work of Puntès et al., the Co nanoparticles had a thin organic coating and were deposited onto carbon-coated TEM grids from evaporating suspensions.

### Assembly of Nanorings on Polymer Films

Polymer media have been used to template spatial distributions of nanometer-sized particles in a variety of ways, including in situ synthesis of nanoparticles in ordered block copolymer matrices,<sup>[54–56]</sup> introduction of premade nanoparticles into the bulk or on the surface of such media,<sup>[25,57–61]</sup> or via additional routes exploiting polymeric micelles<sup>[62,63]</sup> or multilayered structures.<sup>[64–69]</sup> Liu and coworkers have been investigating the organization of nanoparticles in polymer “brushes,”<sup>[28]</sup> which are monolayers of polymer chains tethered by one end to a planar support. The polymer brushes consist of poly(ethylenepropylene) (PEP) chains and are typically between 5 and 20 nm in thickness. The PEP chains incorporated a shorter polystyrene (PS) endblock to provide anchoring to an underlying film of PS homopolymer. Dodecanethiol-stabilized gold nanoparticles about 2.5 nm in diameter were spin coated on top of the polymer brush from octane and their drying patterns imaged by TEM. On some specimens, rings of nanoparticles 10 to 50 nm in diameter were observed in high yields (Fig. 4B). The underlying physical cause of ring assembly has not yet been identified.

### CONCLUSION

Fabrication of structures at submicron length scales is a difficult yet crucial capability in advancing devices and technologies that may one day incorporate nanomaterials. Prospective examples of applications include novel analytical tools, ultrasmall chemical sensors, optoelectronics, and new reagents and catalysts for use in chemistry and biology. The last few years have seen rapid developments in the self-assembly of a variety of structures from nanoparticles and other components such as nanotubes or nanorods. This brief review has specifically emphasized the methods for organizing tiny building blocks into ring-shaped assemblies, with the predominance of the responsible physical phenomena traced to wetting and hydrodynamics of thin liquid films. Even as the theme of self-assembly in nanomaterial science continues to expand,



as illustrated by this report, at least for specific geometries general methods can begin to be formulated.

## ACKNOWLEDGMENTS

During the writing of this work, Zhen Liu was supported by the MRSEC program of the National Science Foundation (DMR-0213574) and by the Donors of The Petroleum Research Fund, administered by the American Chemical Society.

## REFERENCES

- Murray, C.B.; Kagan, C.R.; Bawendi, M.G. Self-organization of CdSe nanocrystallites into three-dimensional quantum dot superlattices. *Science* **1995**, *270*, 1335.
- Kagan, C.R.; Murray, C.B.; Nirmal, M.; Bawendi, M.G. Electronic energy transfer in CdSe quantum dot solids. *Phys. Rev. Lett.* **1996**, *76*, 1517.
- Harfenist, S.A.; Wang, Z.L.; Alvarez, M.M.; Vezmar, I.; Whetten, R.L. Highly oriented molecular Ag nanocrystal arrays. *J. Phys. Chem.* **1996**, *100*, 13904.
- Taleb, A.; Petit, C.; Pileni, M.P. Synthesis of highly monodisperse silver nanoparticles from AOT reverse micelles: A way to 2D and 3D self-organization. *Chem. Mater.* **1997**, *9*, 950.
- Andres, R.P.; Bielefeld, J.D.; Henderson, J.I.; Janes, D.B.; Kolagunta, V.R.; Kubiak, C.P.; Mahoney, W.J.; Osifchin, R.G. Self-assembly of a two-dimensional superlattice of molecularly linked metal clusters. *Science* **1996**, *273*, 1690.
- Korgel, B.A.; Fullman, S.; Connolly, S.; Fitzmaurice, D. Assembly and self-organization of silver nanocrystal superlattices: Ordered "soft spheres". *J. Phys. Chem., B* **1998**, *102*, 8379.
- Murray, C.B.; Kagan, C.R.; Bawendi, M.G. Synthesis and characterization of monodisperse nanocrystals and close-packed nanocrystal assemblies. *Annu. Rev. Mater. Sci.* **2000**, *30*, 545.
- Collier, C.P.; Vossmeier, T.; Heath, J.R. Nanocrystal superlattices. *Annu. Rev. Phys. Chem.* **1998**, *49*, 371.
- Storhoff, J.J.; Mirkin, C.A. Programmed materials synthesis with DNA. *Chem. Rev.* **1999**, *99*, 1849.
- Niemeyer, C.M. Self-assembled nanostructures based on DNA: Towards the development of nanobiotechnology. *Curr. Opin. Chem. Biol.* **2000**, *4*, 609.
- Braun, E.; Eichen, Y.; Sivan, U.; Ben-Yoseph, G. DNA-templated assembly and electrode attachment of a conducting silver wire. *Nature* **1998**, *391*, 775.
- Coffer, J.L.; Bigham, S.R.; Li, X.; Pinizzotto, R.F.; Rho, Y.G.; Pirtle, R.M.; Pirtle, I.L. Dictation of the shape of mesoscale semiconductor nanoparticle assemblies by plasmid DNA. *Appl. Phys. Lett.* **1996**, *69*, 3851.
- Alivisatos, A.P.; Johnsson, K.P.; Peng, X.; Wilson, T.E.; Loweth, C.J.; Bruchez, M.P.; Schultz, P.G. Organization of "nanocrystal molecules" using DNA. *Nature* **1996**, *382*, 609.
- Mirkin, C.A.; Letsinger, R.L.; Mucic, R.C.; Storhoff, J.J. A DNA-based method for rationally assembling nanoparticles into macroscopic materials. *Nature* **1996**, *382*, 607.
- Taton, T.A.; Mucic, R.C.; Mirkin, C.A.; Letsinger, R.L. The DNA-mediated formation of supramolecular mono- and multilayered nanoparticle structures. *J. Am. Chem. Soc.* **2000**, *122*, 6305.
- Torimoto, T.; Yamashita, M.; Kuwabata, S.; Sakata, T.; Mori, H.; Yoneyama, H. Fabrication of CdS nanoparticle chains along DNA double strands. *J. Phys. Chem., B* **1999**, *103*, 8799.
- Niemeyer, C.M.; Burger, W.; Peplies, J. Covalent DNA-streptavidin conjugates as building blocks for novel biometallic nanostructures. *Angew. Chem., Int. Ed.* **1998**, *37*, 2265.
- Willner, I.; Patolsky, F.; Wasserman, J. Photoelectrochemistry with controlled DNA-cross-linked CdS nanoparticle arrays. *Angew. Chem., Int. Ed.* **2001**, *40*, 1861.
- Cassell, A.M.; Scrivens, W.A.; Tour, J.M. Assembly of DNA/fullerene hybrid materials. *Angew. Chem., Int. Ed.* **1998**, *37*, 1528.
- Chan, Y.N.C.; Schrock, R.R.; Cohen, R.E. Synthesis of silver and gold nanoclusters within microphase-separated diblock copolymers. *Chem. Mater.* **1992**, *4*, 24.
- Ciebien, J.F.; Clay, R.T.; Sohn, B.H.; Cohen, R.E. Brief review of metal nanoclusters in block copolymer films. *New J. Chem.* **1998**, *22*, 685.
- Fogg, D.E.; Radzilowski, L.H.; Dabbousi, B.O.; Schrock, R.R.; Thomas, E.L.; Bawendi, M.G. Fabrication of quantum dot-polymer composites: Semiconductor nanoclusters in dual-function polymer matrices with electron-transporting and cluster-passivating properties. *Macromolecules* **1997**, *30*, 8433.
- Zehner, R.W.; Lopes, W.A.; Morkved, T.L.; Jaeger, H.; Sita, L.R. Selective decoration of a phase-separated diblock copolymer with thiol-passivated gold nanocrystals. *Langmuir* **1998**, *14*, 241.
- Spatz, J.P.; Mossmer, S.; Hartmann, C.; Moller, M.; Herzog, T.; Krieger, M.; Boyen, H.G.; Ziemann, P.; Kabius, B. Ordered deposition of inorganic clusters from micellar block copolymer films. *Langmuir* **2000**, *16*, 407.
- Lopes, W.A.; Jaeger, H.M. Hierarchical self-assembly of metal nanostructures on diblock copolymer scaffolds. *Nature* **2001**, *414*, 735.
- Thompson, R.B.; Ginzburg, V.V.; Matsen, M.W.; Balazs, A.C. Predicting the mesophases of copolymer-nanoparticle composites. *Science* **2001**, *292*, 2469.
- Lee, J.Y.; Thompson, R.B.; Jasnow, D.; Balazs, A.C. Entropically driven formation of hierarchically ordered nanocomposites. *Phys. Rev. Lett.* **2002**, *89*, art. no.-155503.
- Liu, Z.; Pappacena, K.; Cerise, J.; Kim, J.; Durning, C.J.; O'Shaughnessy, B.; Levicky, R. Organization of nanoparticles on soft polymer surfaces. *Nano Lett.* **2002**, *2*, 219.



29. Lorke, A.; Luyken, R.J.; Govorov, A.O.; Kotthaus, J.P.; Garcia, J.M.; Petroff, P.M. Spectroscopy of nanoscopic semiconductor rings. *Phys. Rev. Lett.* **2000**, *84*, 2223.
30. Rabiei, P.; Steier, W.H.; Zhang, C.; Dalton, L.R. Polymer micro-ring filters and modulators. *J. Lightwave Technol.* **2002**, *20*, 1968.
31. Li, Z.J.; Chen, X.L.; Li, H.J.; Tu, Q.Y.; Yang, Z.; Xu, Y.P.; Hu, B.Q. Synthesis and Raman scattering of GaN nanorings, nanoribbons and nanowires. *Appl. Phys., A* **2001**, *72*, 629.
32. Yang, B.; Scheidtmann, J.; Mayer, J.; Wuttig, M.; Michely, T. Fragmentation, rings and coarsening: Structure and transformations of nanocrystal aggregate networks on a liquid surface. *Surf. Sci.* **2002**, *497*, 100.
33. Deegan, R.D.; Bakajin, O.; Dupont, T.F.; Huber, G.; Nagel, S.R.; Witten, T.A. Capillary flow as the cause of ring stains from dried liquid drops. *Nature* **1997**, *389*, 827.
34. Maenosono, S.; Dushkin, C.D.; Saita, S.; Yamaguchi, Y. Growth of a semiconductor nanoparticle ring during the drying of a suspension droplet. *Langmuir* **1999**, *15*, 957.
35. Ohara, P.C.; Gelbart, W.M. Interplay between hole instability and nanoparticle array formation in ultrathin liquid films. *Langmuir* **1998**, *14*, 3418.
36. Ohara, P.C.; Heath, J.R.; Gelbart, W.M. Self-assembly of submicrometer rings of particles from solutions of nanoparticles. *Angew. Chem., Int. Ed. Engl.* **1997**, *36*, 1078.
37. Maillard, M.; Motte, L.; Ngo, A.T.; Pileni, M.P. Rings and hexagons made of nanocrystals: A Marangoni effect. *J. Phys. Chem., B* **2000**, *104*, 11871.
38. Maillard, M.; Motte, L.; Pileni, M.P. Rings and hexagons made of nanocrystals. *Adv. Mater.* **2001**, *13*, 200.
39. Stowell, C.; Korgel, B.A. Self-assembled honeycomb networks of gold nanocrystals. *Nano Lett.* **2001**, *1*, 595.
40. Schenning, A.P.H.J.; Benneker, F.B.G.; Geurts, H.P.M.; Liu, X.Y.; Nolte, R.J.M. Porphyrin wheels. *J. Am. Chem. Soc.* **1996**, *118*, 8549.
41. Oron, A.; Davis, S.H.; Bankoff, S.G. Long-scale evolution of thin liquid films. *Rev. Mod. Phys.* **1997**, *69*, 931.
42. Burelbach, J.P.; Bankoff, S.G.; Davis, S.H. Nonlinear stability of evaporating condensing liquid-films. *J. Fluid Mech.* **1988**, *195*, 463.
43. Tan, M.J.; Bankoff, S.G.; Davis, S.H. Steady thermocapillary flows of thin liquid layers: I. Theory. *Phys. Fluids, A* **1990**, *2*, 313.
44. Burelbach, J.P.; Bankoff, S.G.; Davis, S.H. Steady thermocapillary flows of thin liquid layers: II. Experiment. *Phys. Fluids, A* **1990**, *2*, 322.
45. Pearson, J.R.A. On convection cells induced by surface tension. *J. Fluid Mech.* **1958**, *4*, 489.
46. Nguyen, V.X.; Stebe, K.J. Patterning of small particles by a surfactant-enhanced Marangoni-Bénard instability. *Phys. Rev. Lett.* **2002**, *88*, 164501.
47. Sharma, A. Relationship of thin film stability and morphology to macroscopic parameters of wetting in the apolar and polar systems. *Langmuir* **1993**, *9*, 861.
48. de Gennes, P.-G. Wetting: Statics and dynamics. *Rev. Mod. Phys.* **1985**, *57*, 827.
49. Thiele, U.; Mertig, M.; Pompe, W. Dewetting of an evaporating thin liquid film: Heterogeneous nucleation and surface instability. *Phys. Rev. Lett.* **1998**, *80*, 2869.
50. Martel, R.; Shea, H.R.; Avouris, P. Rings of single-walled carbon nanotubes. *Nature* **1999**, *398*, 299.
51. Liu, J.; Dai, H.; Hafner, J.H.; Colbert, D.T.; Smalley, R.E.; Tans, S.J.; Dekker, C. Fullerene "crop circles". *Nature* **1997**, *385*, 780.
52. Tripp, S.L.; Pusztay, S.V.; Ribbe, A.E.; Wei, A. Self-assembly of cobalt nanoparticle rings. *J. Am. Chem. Soc.* **2002**, *124*, 7914.
53. Puentes, V.F.; Krishnan, K.M.; Alivisatos, A.P. Colloidal nanocrystal shape and size control: The case of cobalt. *Science* **2001**, *291*, 2115.
54. Chan, Y.N.C.; Craig, G.S.W.; Schrock, R.R.; Cohen, R.E. Synthesis of palladium and platinum nanoclusters within microphase-separated diblock copolymers. *Chem. Mater.* **1992**, *4*, 885.
55. Ciebien, J.F.; Clay, R.T.; Sohn, B.H.; Cohen, R.E. Brief review of metal nanoclusters in block copolymer films. *New J. Chem.* **1998**, *22*, 685.
56. Bronstein, L.; Seregina, M.; Valetsky, P.; Breiner, U.; Abetz, V.; Stadler, R. Transition metal complex induced morphology change in an ABC-triblock copolymer. *Polym. Bull.* **1997**, *39*, 361.
57. Fogg, D.E.; Radzilowski, L.H.; Dabbousi, B.O.; Schrock, R.R.; Thomas, E.L.; Bawendi, M.G. Fabrication of quantum dot-polymer composites: Semiconductor nanoclusters in dual-function polymer matrices with electron-transporting and cluster-passivating properties. *Macromolecules* **1997**, *30*, 8433.
58. Lin, B.H.; Morkved, T.L.; Meron, M.; Huang, Z.Q.; Viccaro, P.J.; Jaeger, H.M.; Williams, S.M.; Schlossman, M.L. X-ray studies of polymer/gold nanocomposites. *J. Appl. Phys.* **1999**, *85*, 3180.
59. Zehner, R.W.; Lopes, W.A.; Morkved, T.L.; Jaeger, H.; Sita, L.R. Selective decoration of a phase-separated diblock copolymer with thiol-passivated gold nanocrystals. *Langmuir* **1998**, *14*, 241.
60. Hamdoun, B.; Ausserre, D.; Joly, S.; Gallot, Y.; Cabuil, V.; Clinard, C. New nanocomposite materials. *J. Phys. II* **1996**, *6*, 493.
61. Lopes, W.A. Nonequilibrium self-assembly of metals on diblock copolymer templates. *Phys. Rev., E* **2002**, *65*, 1063.
62. Spatz, J.P.; Roescher, A.; Moller, M. Gold nanoparticles in micellar poly(styrene)-*b*-poly(ethylene oxide) films-size and interparticle distance control in monodisperse films. *Adv. Mater.* **1996**, *8*, 337.
63. Bronstein, L.; Kramer, E.; Berton, B.; Burger, C.; Forster, S.; Antonietti, M. Successive use of amphiphilic block copolymers as nanoreactors and templates: Preparation of porous silica with metal nanoparticles. *Chem. Mater.* **1999**, *11*, 1402.

64. Kotov, N.A.; Dekany, I.; Fendler, J.H. Layer-by-layer self-assembly of polyelectrolyte–semiconductor nanoparticle composite films. *J. Phys. Chem.* **1995**, *99*, 13065.
65. Schmitt, J.; Decher, G.; Dressick, W.J.; Brandow, S.L.; Geer, R.E.; Shashidhar, R.; Calvert, J.M. Metal nanoparticle/polymer superlattice films: Fabrication and control of layer structure. *Adv. Mater.* **1997**, *9*, 61.
66. Caruso, F.; Caruso, R.A.; Mohwald, H. Nanoengineering of inorganic and hybrid hollow spheres by colloidal templating. *Science* **1998**, *282*, 1111.
67. Joly, S.; Kane, R.; Radzilowski, L.; Wang, T.; Wu, A.; Cohen, R.E.; Thomas, E.L.; Rubner, M.F. Multilayer nanoreactors for metallic and semiconducting particles. *Langmuir* **2000**, *16*, 1354.
68. Gao, M.Y.; Richter, B.; Kirstein, S. White-light electroluminescence from a self-assembled Q-CdSe/PPV multilayer structures. *Adv. Mater.* **1997**, *9*, 802.
69. He, J.A.; Valluzzi, R.; Yang, K.; Dolukhanyan, T.; Sung, C.M.; Kumar, J.; Tripathy, S.K.; Samuelson, L.; Balogh, L.; Tomalia, D.A. Electrostatic multilayer deposition of a gold-dendrimer nanocomposite. *Chem. Mater.* **1999**, *11*, 3268.

# Risk Assessment and Benefits

Douglas Mulhall

Marsh Harbour, Bahamas

## INTRODUCTION

Risk assessment is the foundation of our capacity to evaluate economic, health, and ecological impacts. Yet, a wave of scientific discovery is transforming our understanding of not only risk but also the environments that sustain us. This will force basic changes to how we evaluate risk and make decisions to restrict new technology.

Until we acknowledge such changes and incorporate them into our assessment of risk, it will not be possible for detractors or supporters of nanotechnologies to accurately evaluate their risks and benefits.

## OVERVIEW

Some critics perceive the risk of nanomaterials as too great to go ahead with until we study them further.<sup>[1]</sup> The most often-cited example is the risk that out-of-control nanomachines, which use carbon-based life forms for an energy source, will turn everything alive into “gray goo” as they multiply. Technology luminaries such as Eric Drexler and Robert Freitas,<sup>a</sup> Ray Kurzweil and Bill Joy,<sup>b</sup> along with science fiction writers such as Michael Crichton<sup>c</sup> have explored such potential threats. Related debates have often spilled over into the legislative arena as governments have limited development of biotechnologies such as stem cell research,<sup>[6]</sup> while initiating investigations into ways of restricting nanotechnology.<sup>[7]</sup>

These debates are similar to those presented in the early 1950s when it was postulated that nuclear proliferation would get out of control and lead to

contamination of the whole world. As with the nuclear argument, critics say that this new generation of technologies may be too volatile to control. Similar arguments were made about the machine gun at the turn of the century. As every new major technology comes along, fears are expressed that it may annihilate humanity.

Many scientists disagree with these arguments and say that the potential benefits outweigh the potential risks.<sup>d</sup> They point to near-term benefits such as nano-scale methods that can detect and target diseases far more precisely and less invasively than we do today. Vast improvements in energy efficiency created by a new generation of solar cells may also solve our energy supply problems, they argue. They say further that while the destructive power of technologies has been growing enormously, this has not hindered the expansion of civilization on Earth so far.

So we are faced with a familiar quandary: risk the benefits or eliminate the risks?

Principles for controlling powerful technologies, so that we can manage risks and get benefits, have been around for some time. For example, as early as 1950 the well-known science fiction writer Isaac Asimov put forward his “Laws of Robotics.”<sup>[9,10]</sup> Organizations that specialize in nanotechnology, such as the Foresight Institute have developed principles for managing nanotechnology risks.<sup>[11]</sup> Still other organizations such as the Center for Responsible Nanotechnology have drafted ethical guidelines to help cope with disruptive economic and social impacts.<sup>[12]</sup>

These works are each helpful. Together they may constitute the beginnings of a regulatory framework for administering technology risks. Yet by themselves and together they are still incomplete.

This article briefly describes three considerations that could transform the debate: *Technologies that merge with ecology, enhanced intelligence, and punctuated equilibrium*. Finally, the article shows how these discoveries may completely change the regulatory

<sup>a</sup>The term “gray goo” was put forward by Eric Drexler in 1986 in Ref.<sup>[2]</sup> and has been extensively quoted and misquoted. For a summary of the gray goo discussion, see Ref.<sup>[3]</sup>.

<sup>b</sup>Sun Microsystems co-founder Bill Joy<sup>[4a]</sup> revitalized the concept of voluntary relinquishment of dangerous technologies that was put forward by other scientists in relation to earlier technologies such as nuclear weapons. Inventor Ray Kurzweil disagrees with this approach. A summary of the discussion is found in Ref.<sup>[4b]</sup>.

<sup>c</sup>Eric Drexler’s 1980’s description of uncontrollable nanobots was given great popularity by the science fiction novel: Ref.<sup>[5]</sup>.

<sup>d</sup>Updates on the nanoethics debates, are found in the December and February newsletter of Ref.<sup>[8]</sup>.

paradigm. This entry is necessarily limited on space and I encourage the interested reader to look at my book-length work *Our Molecular Future*<sup>[13]</sup> and the reference list for more details and information.

## BACKGROUND

Some scientists have begun to describe a point known as the “Singularity,” where the rate of technology convergence makes it impossible for human beings to accurately forecast the near future. If this point is approaching, then it seems that all the present discussions by environmentalists, scientists, and government regulators over how to regulate nanotechnologies may soon become moot, because the process will be out of our hands regardless of what we do, unless we impose a draconian ban on all new technology development. Given our history, such a ban seems improbable; therefore we must consider the implications of exponentially accelerating technologies.

The ideas that *Homo sapiens*—as we are presently constituted—won’t be able to control our own destiny, and that some other form of development that we can’t comprehend right now may take over from present paradigms, seem so fatalistic that many people don’t dare to consider such thoughts. These confound the basic human tenet of belief in the future. Yet with technology rapidly progressing, and with the particularly accelerating advances in nanotechnologies—that are described throughout this encyclopedia—we must consider such a possibility as a starting point in the discussion over how to regulate the risks posed by new technologies. Nor do we need to be fatalistic about it, because there are avenues whereby we can participate in the accelerated evolution that has begun to occur.

Just in the same way that the atomic bomb transformed the concepts of security and war, so advanced technologies are already upending conventional notions of evolution. For example, it has now become clear that computers have started to solve problems in ways that their human designers do not comprehend. Chess Grand Master Gary Kasparov acknowledged this reality many years ago when, after having been defeated by a computer at his own game, he stated that he had lost to “an alien.”<sup>[14]</sup> This was rapidly followed by the development of genetic computing where software using genetic algorithms was used to design circuits in ways that human designers couldn’t fully comprehend.<sup>[15]</sup>

Why is this so relevant right now to the discussion over regulation of nanotechnology?

The extrapolation to be drawn from this is that because some computers already exceed human intelligence in limited areas, that nanotechnology-enabled artificial intelligence will increasingly supercede our

own. Given that it would be extremely difficult to regulate something that is smarter than a human, again we are confronted with this possibility that the regulatory discussion is moot.

However, such a viewpoint—and the fears expressed about “runaway” technology—overlook one central development. Human intelligence and machine intelligence are beginning to merge. As they do, the possibilities for anticipating and regulating development of further technologies take on a new light.

The perceptual problem that we face today is that most discussions over regulation of nanotechnologies are based on the assumption that while technology continues to evolve rapidly, *Homo sapiens* will somehow continue to evolve as we have for millennia: slowly and biologically. If this is true, then we can stop the discussion over regulation, because the rate of technological evolution is already exceeding the rate of biological evolution, and will render *Homo sapiens* intelligence obsolete or at least inferior.

However, this article looks at another possibility: that evolution of human intelligence is about to accelerate past our biological limitations into another realm. If so, this will transform the regulatory landscape.

Furthermore, our growing understanding of the natural environment is showing us that we may have no choice but to proceed, because history demonstrates that sooner or later nature will create conditions that make our existence on Earth difficult or untenable unless we take measures to protect ourselves.

## NEW FACTORS THAT MAY TRANSFORM RISK ASSESSMENT

Using Life Cycle Assessment methodologies,<sup>[16–18]</sup> combined with an examination of new technological developments and new discoveries about the natural environment, these emerging theories and technologies can be identified as having the potential to profoundly transform the present paradigm of technology regulation.

### Technologies That Merge with the Natural Environment

Ray Kurzweil, who pioneered technologies such as the flatbed scanner, argues that technology is a continuation of evolution by other means.<sup>[19]</sup> This implies that our technologies are becoming an integral part of the ecology. What are the physical manifestations of this?

Smart Dust<sup>[20]</sup> comprises a massive array of micro-machines made of nanoscale components that ride on air or water currents, undetectable to the human eye. Each expendable machine can have a camera,

communications device, and varying sensors for chemicals, temperature, and sound. It has its own rechargeable energy source. It can serve as the eyes, ears, nose, and guidance mechanism for everyone from soldiers to hurricane watchers. It may soon cost a fraction of a penny to manufacture, and its prototype exists today. It forms part of a massive array that delivers information to one or hundreds of computers in one or many locations. It may soon be in our environment in the trillions, delivering information about everything from troop to sewage movements.

This nanoscale level of incursion into—and integration with—the ecology suggests emergence of an *intelligent environment*. Just as the natural environment exercises its own type of intelligence by passing on information from generation to generation via DNA, so we are creating an intelligent human-built environment not just alongside that, but also as part of it. An intelligent environment has elements that are able to sense virtually every part of the ecology, from the epicenter of earthquakes to the heart of a hurricane and the heartbeat of every species, then interpret what this means and how to react. Right now, we are only at the very first primitive stages of this, but our sensing capacities are accelerating.

Such intelligent particles are also gaining the capacity to *self-assemble*. Several universities have pioneered self-assembling photovoltaic materials that generate and conduct an electric current (see entry on “Photovoltaics for the Next Generation: Organic-Based Solar Cells”).<sup>[21]</sup> These materials can be painted onto surfaces, thus eliminating the need for solar panels. Such chemical self-assembly is only a primitive precursor to molecular assembly that is described in other entries to this encyclopedia.

When we combine self-assembly with intelligent sensing at the nanometer scale, then multiply it a trillion-fold, we see that our technology is becoming an integral part of the ecology instead of just impacting it, and that human technologies may soon be indistinguishable from the natural environment. This is a profound transition.

Furthermore, such pervasive intelligence is developing outside the human brain, but also in deep contact with it.

### Enhanced Intelligence Changes the Groundrules

Hans Moravec, of Carnegie Mellon’s Robotics Institute, has shown convincingly—as have others—that the rate of acceleration in information processing is logarithmic.<sup>[22]</sup> Not only is the capacity to process ones and zeros multiplying, but the *rate* at which it is multiplying is also increasing.

For millennia, this exponential rate was barely perceptible, because it took thousands, then hundreds,

then tens of years for such capacity to multiply, from the abacus to the microprocessor, and now the nano-processor.

Today, this exponential acceleration enables superfast manufacturing by machines and software. An example of this is desktop manufacturing that is transforming desktop printing into three-dimensional desktop manufacturing of products.<sup>[23]</sup>

Such hyperchange is upending the ground rules for intelligence, and by extension for environmental risk management.

Most risk assessment today implicitly assumes that evolution of human intelligence will proceed in the same way that it has over the past few thousands of years—that is, gradually.

Here are examples of why this assumption may be wrong.

In 2001, a computer used “genetic computing”<sup>[24]</sup> to build a thermostat and actuator that were superior to the counterparts designed by a human. The computer’s programmers were unable to trace how the computer reached its conclusion. This is because genetic algorithms allow computers to solve problems in their own way without human intervention.

Machines with enhanced intelligence do certain things far faster and better than we do. Not everything, but many things. Stockbrokers now use algorithms that forecast commodity markets more accurately than humans do.<sup>[25]</sup> Satellites that repair themselves and make unilateral data transmission decisions are already in orbit.<sup>[26]</sup>

Moreover, massive networks are enhancing our own intelligence. It is now possible for the layperson to perform Internet searches in real time to get answers to complex questions. This acceleration in data retrieval *by the general population* constitutes a mass enhancement to our own memories.

At the more specialized level, remote robotic surgery is creating a networked medical “mind” that can perform operations in and from many locations at once.<sup>[27]</sup>

The extraordinary development is that human intelligence and primitive forms of machine “intelligence” are merging already. This is apparent from the use of artificial retinas for the blind, where computer microchips are implanted in the eye then connected to the optical nerve. They interpret and relay visual information to the brain. The merging of human intelligence with genetic algorithms and massive networks is being applied to modeling of, for example, climate change, but it has only just begun to be applied to evaluation of phenomena such as those described below.

### Understanding Punctuated Equilibrium

The theory of *punctuated equilibrium*<sup>[28]</sup> was first proposed in 1972 by Niles Eldredge and Harvard

evolutionary biologist Stephen Jay Gould.<sup>[41]</sup> This holds that evolutionary change occurs relatively rapidly in comparatively brief periods of environmental stress, separated by longer periods of evolutionary stability. After many years of skepticism, their theory is now gaining acceptance. This is because proof is emerging.

Intelligent tools, such as those described earlier, are helping us to discover that the natural ecology experiences periodic instability that threatens our society; not just in the extended time frames that we used to think.

In 1994, Comet Shoemaker–Levy 9 (SL9) hit Jupiter,<sup>[29]</sup> blasting holes the size of Earth in its atmosphere. Had this hit the Earth, human life would have been virtually extinguished. Only recently have we developed the tools to see such distant impacts, and until such technologies were invented we could only theorize about how often catastrophic collisions occur.

Before that, it was thought that such upheavals happened only every few million years and that we'd have lots of time to see them coming. SL9 demolished this idea. It demonstrated that we live in a galaxy where life can be snuffed out on a planetary scale without warning—in this era, not just the distant past.

Furthermore, scientists have found that smaller events have upset the ecology here on Earth. Ice core and tree ring records show that around the year A.D. 536 an unknown event triggered a catastrophic cooling of the Northern Hemisphere, resulting in years without summers that led to wholesale crop failures and starvation.<sup>[30]</sup>

Thousands of samples taken from ice cores and tree rings around the world show that naturally induced climate flips occur more frequently than we once thought they do, and that they don't only unfold over centuries but also erupt in a few years.<sup>[31,32]</sup>

At the regional scale, in 1700, a fracture at the Cascadia subduction zone produced a gigantic tsunami that scoured much of the Pacific coast for miles inland, where many of our cities now stand.<sup>[33]</sup> In 1958, a 1,500-foot wave swept away a forest after a mountain collapsed into Lituya Bay, Alaska.<sup>[34]</sup>

At the nanometer scale we are also getting a surprise. Researchers have discovered vast numbers of nanoscale organisms that are a hundred times smaller than most bacteria. In geology, they are named nanobacteria,<sup>[35]</sup> nanobes, and nanoarchaea.<sup>[36]</sup> In human ecology, a similar-sized entity has been labeled *Nanobacterium sanguineum* or blood nanobacteria.<sup>[37]</sup> Despite the name, it may not be a bacterium at all, but instead seems to be a newly discovered infection with the unusual ability to form a tough shell consisting of the same type of calcium found in many diseases. For decades, researchers have seen evidence that epidemic illnesses such as heart disease are triggered by infection.<sup>[38]</sup> This was proven for stomach ulcers

decades ago, but for other illnesses no one could find a culprit. Now it seems that one has been discovered,<sup>[39]</sup> as chronicled in the book *Has Heart Disease Been Cured?*<sup>[40]</sup>

If the existence of such organisms turns out to be valid after the hot discussion over them is resolved, then it may fundamentally alter our understanding of how ecology works, what constitutes an ecosystem, and how epidemics decimate populations.

The reality that has been overlooked by environmental agencies and theorists is that many of these nano- and macro-scale phenomena pose deep threats to our society. Agencies such as the United States Federal Emergency Management Agency (FEMA) and United States Environmental Protection Agency (EPA) have few defenses against them. Such agencies usually do not consider how to adapt to climate altering super-volcanoes or epidemics from strange nano-organisms, because these are perceived as indefensible, or they haven't entered the awareness of the organizations yet.

Thus, punctuated equilibrium is not part of the risk assessment framework. As such, a chunk of the equation is missing. This is especially true when considering the relative risks and benefits posed by nanotechnologies. Such technologies may be driving the next “punctuation” in evolution by upending longstanding paradigms. At the same time they may give us the tools to protect ourselves from newly discovered big natural threats. Such is the contradictory reality of the two-edged sword.

## MATCH NATURE'S COMPLEXITY

The convergence of these discoveries may let us achieve something that we have only dreamed of until now: how to match nature's complexity.

Right now, most of our technologies are unable to match the complexity of natural environments. For example, we use antibiotics to cure bacterial infections, but they lose their potency when the environment that they work in adapts to them. We build power lines to survive ice storms, but our miscalculation of the worst scenarios leads to collapses that paralyze our high-technology infrastructures.

Most of our agricultural, medical, energy, transportation, and housing systems are in a constant struggle to respond to the complexity of the natural environment.

Yet this imbalance may shift. Molecular technologies are empowering us to find solutions that replicate natural processes at the molecular level (for some examples, see entries on “Biomedical Applications: Tissue Engineering, Therapeutic Devices, and Diagnostic Systems” and “Nanomaterials: New Trends.”).



We may see energy grids based on solar “paint” that slash the political and economic risks associated with fossil fuel infrastructures. Our drugs may be so precise that they backfire only occasionally instead of generating widespread immune responses as they do now.

This nascent capacity to match nature’s complexity constitutes the next environmental revolution. Over the centuries, such efforts to replicate natural processes have been criticized as arrogant and unachievable approaches to nature, and today are sparking a political and religious furor. Nonetheless, they may soon force us to redefine the boundaries of risk assessment.

## WHAT TO DO

These new realities—enhanced intelligence, technologies that merge with the environment, and newly understood evolutionary paradigms—are the elephants in the room of risk assessment. To cope with them, we must initiate a new regulatory discussion. We must first acknowledge that the yardsticks for measuring risk are being moved dramatically by our own rapidly expanding knowledge.

Just a few small examples: Although nanoscale organisms have been identified in geological formations and the human body since the early 1990s, few projects have examined the implications for human or natural ecology or for environmental chemistry. NASA is studying it, as are the universities of Texas, McGill (Canada), Regensburg (Germany), Kuopio (Finland), Melbourne (Australia), and others. However, no major government initiative is considering the implications. At the opposite end of the scale, few if any governmental, environmental, or disaster preparedness agencies are examining newly discovered mega-scale anomalies such as the naturally induced climate flip of circa A.D. 536, or the giant west coast tsunami of 1700. These would certainly disrupt natural ecosystems and civilized society if they recurred today, and evidence suggests that they may.

No disaster preparedness or environmental agency yet examines how nanotechnologies might be used for adapting to such phenomena. Future initiatives may develop, but at this time they are not apparent. To rectify this, the author has suggested that a forum be held under the auspices of one or several of the nanotechnology Non-Governmental Organizations such as The Foresight Institute or Center for Responsible Nanotechnology, to examine such an issue.

Examples of technologies that might help us to adapt to “nature’s time bombs,” and to explosive risks that may be posed by nanotechnologies themselves, include:

- Artificially intelligent software that is transforming the way that we make products and carry out

business. The role that artificial and enhanced intelligence will play in risk assessment is so far understudied and overlooked. This takes us to the heart of the issue of evolution of human intelligence relative to thousands of years of biological evolution. Likewise, technologies that are merging with the human body and mind, such as artificial retinas and other implants, merit far greater attention, as these are the stepping stones to development of *Homo sapiens* who have enhanced evaluative capacities.

- Superstrong nanostructured materials such as aerogels that exist now and that may let human settlements withstand mega-hurricanes, earthquakes, and tornadoes without causing more environmental damage than they prevent. Furthermore, the self-assembling and disassembling properties of other newer materials may protect us from more serious near-earth object threats that are now considered impossible to defend against, and that have been badly misjudged as too infrequent to worry about.
- “Desktop manufacturing” that may replace thousands of polluting factories while producing materials such as self-assembling solar materials that may stabilize our energy supplies.
- Nanomedicine that is opening the doors to new solutions for many prevalent diseases, and that may stop epidemics that have retarded human progress for millennia.
- Many other technologies that are cited throughout this encyclopedia and constitute an excellent basis to start with.

Of equal importance is the process used to evaluate them. By expanding the interdisciplinary approach to technology, it is possible and necessary to bring together experts in fields that are infrequently combined. These include:

- Computer scientists who have applied artificially intelligent software to technologies that might be used for environmental adaptation and risk assessment.
- Biochemists, geologists, and physicians who discovered nanobacteria in the environment and human body, and also developed treatments that seem to reverse nanobacterial infections.
- Climatologists, geologists, and astronomers who uncovered evidence of recurring climate disruptions, giant tsunamis, and near-earth object collisions.
- Scientists who have developed adaptive technologies such as desktop manufacturing and self-assembling photovoltaic materials that may let us adapt rapidly to big ecological changes.
- Critics who have proposed moratoria on nanomanufacturing.

## CONCLUSION

By focusing such wide-ranging expertise on the challenges depicted in this article, risk assessment could be made into a more effective tool for proponents, detractors, and users of advanced technologies.

## CREDIT LINE

This essay is an adaptation of a paper “Reassessing Risk Management” by Douglas Mulhall, presented in the 2003 Proceedings of the World Future Society, WorldFuture 2003: 21st Century Opportunities and Challenges: An Age of Destruction or An Age of Transformation, edited by Howard F. Didsbury Jr. (World Future Society, 2003). <http://www.wfs.org/2003confvol.htm>.

## REFERENCES

1. *The Big Down, Atomtech Technologies Converging at the Nano Scale*; ETC Group, January, 2003. [online] [www.etcgroup.org/documents/TheBigDown.pdf](http://www.etcgroup.org/documents/TheBigDown.pdf) [May 15, 2003].
2. Drexler, E. *Engines of Creation: The Coming Era of Nanotechnology*; Doubleday: New York, 1986. [online] [http://www.foresight.org/EOC/EOC\\_Chapter\\_11.html](http://www.foresight.org/EOC/EOC_Chapter_11.html) [October 22, 2003].
3. *Ecophagy and Gray Goo*; 2002; Compiled by Robert A Freitas Jr. [online] <http://www.foresight.org/Nano-medicine/Ecophagy.html> [October 23, 2003].
- 4a. Joy, B. Why the future doesn't need us. *Wired Mag.* April 2000, (8.04). [online] <http://www.wired.com/wired/archive/8.04/joy.html>.
- 4b. Kurzweil, R. Promise and peril of the 21st century. *CIO Magazine* Fall/Winter 2003 issue. [online] <http://www.cio.com/archive/092203/kurzweil.html> [October 23, 2003].
5. Crichton, M. *Prey*; Harper Collins: New York, 2003.
6. *European Parliament Bans Stem Cell Research*; Reuters, April 10, 2003[online] [October 23, 2003]
7. Oger, G. Nanotech riddle: How green is Europe's 'goo'? *Small Times* August 14 2003. [online] [http://www.smalltimes.com/document\\_display.cfm?document\\_id=6495](http://www.smalltimes.com/document_display.cfm?document_id=6495) [October 22, 2003].
8. CMP-Cientifica. [www.cmpcientifica.com/cientifica/frameworks/generic/public\\_users/tnt\\_weekly/subscribe.htm](http://www.cmpcientifica.com/cientifica/frameworks/generic/public_users/tnt_weekly/subscribe.htm).
9. Asimov, I. *I, Robot*; Genome Press: New York, 1950.
10. Asimov, I. *Robots and Empire*; Doubleday: New York, 1985. Updated.
11. *Foresight Guidelines on Molecular Nanotechnology*-Foresight Institute June 2000 [online] [www.Foresight.org/guidelines/current.html](http://www.Foresight.org/guidelines/current.html) [October 23, 2003].
12. Phoenix, C.; Treder, M. *Three Systems of Action: A Proposed Application for Effective Administration of Molecular Nanotechnology*; Center for Responsible Nanotechnology, Revised November 2003. [online] [www.crnano.org/systems.htm](http://www.crnano.org/systems.htm) [December 25, 2003].
13. Mulhall, D. *Our Molecular Future: How Nanotechnology, Robotics, Genetics, and Artificial Intelligence Will Transform Our World*; Prometheus Books: Amherst, NY, 2002.
14. Chang, G. *World Chess Champion Loses Game 2 Against Computer 'Deep Blue' Amidst Media Frenzy*; Discovery: Canada, May 6, 1997. [online] <http://www.exn.ca/Stories/1997/05/05/01.asp> [October 22, 2003].
15. Yasunaga, M.; Kim, J.H.; Yoshihara, I. The Application of Genetic Algorithms to the Design of Reconfigurable Reasoning VLSI Chips, International Symposium on Field Programmable Gate Arrays Archive Proceedings of the 2000 ACM/SIGDA Eighth International Symposium on Field Programmable Gate Arrays, Monterey, CA, United States, 2000, 116–125.
16. Braungart, M.; Engelfried, J.; Mulhall, D. *Criteria for Sustainable Development of Products and Production*; Fresenius Environmental Bulletin; Birkhauser Verlag: Basel, Switzerland, 1993; 2, 70–77.
17. Mulhall, D. Tools for adapting to big ecosystem changes. *Futures Res. Q.* Fall 2000, 16 (3), 49–61.
18. Mulhall, D. Redefining Earth: A conceptual framework for nanoecology. *Nanotechnol. Mag.* December 2001.
19. Kurzweil, R. Are We Spiritual Machines?. In *The Material World: "Is That All There Is?"*; Future Positive; June 18, 2002. [online] [futurepositive.synearth.net/2002/06/20](http://futurepositive.synearth.net/2002/06/20).
20. *Smart Dust* DARPA research Web site describing project on micro air vehicles, [online] [roboticseecs.berkeley.edu/~pister/SmartDust/](http://roboticseecs.berkeley.edu/~pister/SmartDust/) [March 15, 2003].
21. Solar Cells Go Organic. In *The Economist, Technology Quarterly*; July 20, 2002. [online] [www.economist.com/science/tq/displayStory.cfm?story\\_id=1176099](http://www.economist.com/science/tq/displayStory.cfm?story_id=1176099) [March 14, 2003].
22. Moravec, H. Robot. In *Power and Presence*; Oxford, 1998; 60“The number of MIPS in \$1,000 of computer from 1900 to the present,” [online] [www.frc.ri.cmu.edu/~hpm/book98/fig.ch3/p060.html](http://www.frc.ri.cmu.edu/~hpm/book98/fig.ch3/p060.html) [March 15, 2003].
23. Personal fabrication on demand. *Wired Mag.* April 9 2001, 9 (4).
24. Koza, J.R., (Stanford University); Bennett, F.H., III (Genetic Programming Inc.); Andre, D., (University of California, Berkeley); Keane, M.A., (Econometrics Inc.) Chapter V. Genetic Programming III: Darwinian Invention and Problem Solving. In *Automated Synthesis of Analog Electrical Circuits*; Morgan Kaufmann, 1999.
25. Cliff, D. *Artificial Trading Agents for Online Auction Marketplaces*; HP Labs: Bristol. [online] [www.uk.hpl.hp.com/people/dave\\_cliff/traders.htm](http://www.uk.hpl.hp.com/people/dave_cliff/traders.htm) [March 15, 2003].
26. Satellite trio to test artificial intelligence software. *Aviat. Week* May 30 2001 *AviationNow.com*, [online] [www.aviationnow.com/avnw/news/channel\\_space.jsp?view=story&id=news/ssat0530.xml](http://www.aviationnow.com/avnw/news/channel_space.jsp?view=story&id=news/ssat0530.xml) [ March 15, 2003].
27. *FDA Approves New Robotic Surgery Device*; July 11, 2000 *Food & Drug Administration news release* [online] [www.fda.gov/bbs/topics/NEWS/NEW00732.html](http://www.fda.gov/bbs/topics/NEWS/NEW00732.html).

28. Gould, S.J. Darwinian Fundamentalism. In *New York Review of Books*; June 12, 1997. [online] [www.nybooks.com/articles/1151](http://www.nybooks.com/articles/1151) [March 17, 2003].
29. Bruton, D. *Frequently Asked Questions About the Impact of Comet Shoemaker-Levy 9 with Jupiter*; Institute for Scientific Computation, February 2, 1996. [online] [www.isc.tamu.edu/~astro/sl9/cometfaq2.html#Q3.1](http://www.isc.tamu.edu/~astro/sl9/cometfaq2.html#Q3.1) [August 29, 2001].
30. Stothers, R.B. Mystery cloud of 536 A.D.. *Sci. Front.* May-June **1984**, (33). Reprinted from R.B. Stothers, "Mystery Cloud of A.D. 536," *Nature*, 307 (1984), 344, [online] [August 12, 2001].
31. Alley, R.B. *The Two Mile Time Machine: Ice Core, Abrupt Climate Change, and Our Future*; Princeton University Press: Princeton, NJ, 2000.
32. Baillie, M.G.L. *A Slice Through Time: Dendrochronology and Precision Dating*; Routledge: London, 1995.
33. Nelson, A.R.; Atwater, B.F.; Bobrowsky, P.T.; Bradley, L.-A.; Claque, J.J.; Carver, G.A.; Darienzo, M.E.; Grant, W.C.; Krueger, H.W.; Sparks, R.; Stafford, T.W.; Stuiver, M. Radiocarbon evidence for extensive plate boundary rupture about 300 years ago at the Cascadia subduction zone. *Nature* November 23 **1995**, 378.
34. *The 1958 Lituya Bay Tsunami*; University of Southern California Tsunami Research Group [online] [www.usc.edu/dept/tsunamis/alaska/1958/webpages/index.html](http://www.usc.edu/dept/tsunamis/alaska/1958/webpages/index.html) [March 17, 2003].
35. Folk, R.L. Nanobacteria: Surely not figments, but what under heaven are they?. *Nat. Sci.* March 4 **1997**. [online] [naturalscience.com/ns/articles/01\\_03/ns\\_folk.html](http://naturalscience.com/ns/articles/01_03/ns_folk.html) [January 25, 2003].
36. Huber, H.; Hohn, M.J.; Rachel, R.; Fuchs, T.; Wimmer, V.C.; Stetter, K.O. A new phylum of archaea represented by a nanosized hyperthermophilic symbiont. *Nature* May 2 **2002**, 417, 63–67.
37. Kajander, E.O.; Ciftcioglu, N.; Miller-Hjelle, M.A.; Hjelle, J.T. Nanobacteria: Controversial pathogens in nephrolithiasis and polycystic kidney disease. *Curr. Opin. Nephrol. Hypertens.* **2001**, 10, 445–452.
38. Mawhorter, S.D.; Lauer, M.A. Is atherosclerosis an infectious disease?. *Clevel. Clin. J. Med.* May **2001**, 68 (5).
39. Rasmussen, T.E.; Kirkland, B.L.; Charlesworth, J.; Rodgers, G.P.; Severson, S.R.; Rodgers, J.; Folk, R.L.; Miller, V.M. *Electron Microscope and Immunological Evidence of Nanobacterial-Like Structures in Calcified Carotid Arteries, Aortic Aneurysms and Cardiac Valves*; March 6, 2002 Mayo Clinic and Foundation: Rochester, Minnesota; University of Texas, Austin.
40. Mulhall, D.; Hansen, K. *Has Heart Disease Been Cured?*; The Writers' Collective: Rhode Island, 2003. [www.calcify.com](http://www.calcify.com).
41. Eldredge, N.; Gould, S.J. *Punctuated Equilibria: An Alternative to Phyletic Gradualism*; Paleobiology; Schopf, T.J.M., Ed.; Freeman and Company: San Francisco, 1972.

*Encyclopedia of*

# Nanoscience and Nanotechnology

*Second Edition*

## Volume VI

*Pages 3709 through 4429*

*Scanning – Zeolite*

Scanning –  
Self-Assembled

Self-Assembly –  
Self-Organized

Semiconductor –  
Sensors

Silane – Silicon

Single – Smart

Soft –  
Supramolecular

Surface – Three

Titania – Zeolite

# Scanning Near-Field Photolithography

Graham J. Leggett

Department of Chemistry, University of Sheffield,  
Sheffield, S. Yorkshire, U.K.

## INTRODUCTION

Optical methods continue to surprise us. The Abbé limit, of approximately  $\lambda/2$ , was once thought to be an insurmountable barrier to their exploitation, but the ingenuity of physicists continues to confound this unduly pessimistic outlook. There are currently a number of tools, including near-field,<sup>[1]</sup> two-photon,<sup>[2]</sup> fluorescence-based,<sup>[3]</sup> and plasmonic techniques<sup>[4]</sup> that all offer subdiffraction limit spatial resolution. Moreover, while the end of photolithography has been forecast for about two decades, the semiconductor device industry remains firmly wedded to it as its primary manufacturing tool, and electronic engineers have been very creative in adapting it to facilitate the onward progress of their industry along the path charted by Moore's Law. However, at the very smallest length scale, electron beam lithography has continued to be seen as the gold standard fabrication tool. While electron beam methods are serial ones and do not readily translate into a manufacturing environment, they have been thought to offer a degree of resolution beyond the reach of photolithography.

Here we review new work that suggests this view is incorrect. By using scanning near-field photolithography (SNP), it is possible to generate structures in organic monolayers that are comparably small to anything fabricated by electron beam lithography. Importantly, however, these approaches, based on the excitation of photochemical reactions, are capable of being implemented under ambient conditions or even under fluid. Although such near-field lithographic tools are in their infancy, they offer exciting prospects for use in lithography at extremely small length scales, along with a capability to manipulate biomolecular and organic molecular systems that are inaccessible to electron beam methods. Combined with multiplexing, they may, given their lower cost, offer much greater potential for commercial exploitation than has ever been the case for electron beam lithography, and they may prove a valuable tool in the drive toward highly miniaturized molecular devices and materials.

## NEAR-FIELD SCANNING OPTICAL MICROSCOPY

In surface microscopy, near-field scanning optical microscopy (NSOM, also known as scanning near-field optical microscopy, or SNOM) has provided access to nanometer-scale optical characterization. The original concept for NSOM was developed by Synge, early in the 20th century. His ideas revolved around the use of small optical apertures to characterize materials. Ordinarily, when light is passed through an optical aperture smaller than the Abbé limit, it undergoes diffraction, imposing a lower limit on resolution (also called the diffraction limit). Synge proposed that an optical aperture could be used for subdiffraction limit imaging provided it was brought adequately close to a solid surface.<sup>[5–7]</sup> Under such conditions, illumination occurs in the near field, effectively meaning that light from the aperture interacts with the sample before diffraction can occur (Fig. 1). Although the underlying concept was very simple, its realization in practice was much more challenging, because for it to be effective, the separation between the aperture and the sample must be very small indeed (nm distances) and must be maintained within a very small range of tolerance during the course of the whole experiment. The empirical corroboration for Synge's ideas was eventually provided in 1972 by Ash and Nichols,<sup>[8]</sup> who achieved a resolution of  $\lambda/60$  with 3 cm microwaves. Although this result was impressive, it represented, at that wavelength, a resolution that was still a macroscopic distance.

A significant leap forward was made by Betzig and Trautman in 1992. They used an optical fiber, drawn to a narrow apex and coated with a metal film to constrain the electric field, to image samples.<sup>[9]</sup> They claimed that a resolution of 12 nm was feasible, but only after deconvolution of the probe geometry. This spatial resolution has unfortunately not been widely reproduced. While subdiffraction-limit imaging is feasible, and a variety of types of characterization are possible,<sup>[10]</sup> fiber-based approaches have generally proved difficult to implement. Generally speaking, the best resolution achieved has been approximately equal to the probe aperture, typically ca 50 nm, and usually, the

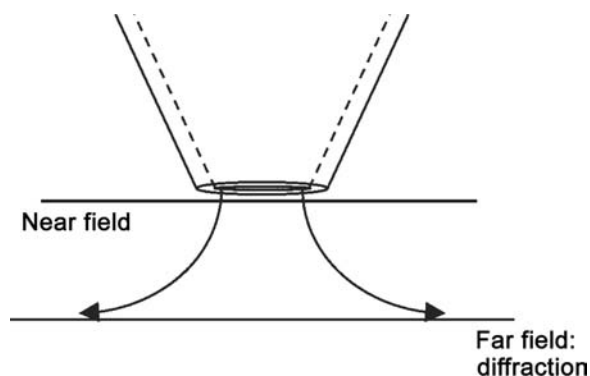


**Fig. 1** By bringing a surface close to a small aperture, it is possible for light to emerge from the aperture without undergoing diffraction.

resolution has been poorer than this—often significantly so. One of the problems of fiber-based methods is that the reproducible preparation of small apertures with high transmissions is difficult.

Recently, there has been a growing interest in the use of what are termed “apertureless” NSOM methods. These exploit the fact that irradiation of a metallic tip held in close proximity to a solid surface using a suitably polarized light may lead to a very pronounced enhancement of the electric field in a small region beneath the tip.<sup>[11]</sup> A variety of optical phenomena may be excited in this way. The tip may, for example, act as an antenna, a phenomenon referred to rather evocatively as the lightning-rod effect, yielding a strongly focused field. A surface plasmon mode may be excited at the tip. Again, the electric field associated with the plasmon excitation exhibits a pronounced confinement. Fluorescence resonance energy transfer between donor and acceptor systems attached to the tip and the sample surface may occur,<sup>[12]</sup> offering exciting prospects for the characterization of biological systems. Two-photon absorption<sup>[13]</sup> and other nonlinear phenomena, such as second harmonic generation,<sup>[14]</sup> have also been reported. While many of these techniques are currently difficult to implement, they offer extraordinary capability. For example, Hartschuh et al. carried out an apertureless Raman investigation of single-walled carbon nanotubes.<sup>[15,16]</sup> They reported Raman spectra from single nanotubes, with a spatial resolution of ca 25 nm. These results constitute an exciting advance for near-field microscopy and spectroscopy. Such progress suggests that after a long gestation period, NSOM may be on the verge of delivering the kind of fruit that it has long promised.

## LITHOGRAPHY USING NSOM

In photolithography, light is typically directed through a mask at a layer of photoresist. The light exposes the

resist, leading to either the cross-linking of oligomeric material or the removal of a photosensitive material, and the formation of a photopattern that may subsequently be used to transfer structures into the underlying substrate. Clearly, it is possible to fabricate smaller features by simply reducing the dimensions of the gaps in the mask through which the light passes, and for many years the semiconductor device manufacturers have been able to do this. However, eventually the diffraction limit is reached. At this point, light is diffracted as it passes through the mask. There are several solutions to this, including reducing the wavelength of the light used. In principle, a photolithography mask may be placed in contact with the sample (rather than being placed away from it, as in projection photolithography), to try to exploit near-field effects. However, the great problem with this is ensuring that the mask remains genuinely within the near-field regime across the whole of its area. The tiniest specs of dust or small variations in substrate topography would mean that significant portions of the mask were not in contact and diffraction would occur.

The adaptation of a scanning near-field optical microscope represents another solution. While mask-based processes offer the advantage of parallel fabrication of large numbers of structures, there are other applications for photolithography, outside of electronic device fabrication, where the ability to excite different processes at different locations on the sample is a distinct advantage (for example, the immobilization of biological molecules using light-directed processes).<sup>[17,18]</sup> Moreover, the development of high-speed scanning systems<sup>[19]</sup> and multiplexing technologies<sup>[20]</sup> both provide potentially important new routes to high-throughput fabrication.

In a fiber-based NSOM system, the aperture at the end of the optical fiber constitutes a nanoscopic light source. Provided the probe is maintained in close proximity to the sample at all times, the dimensions of the illuminated region will be determined, to a first approximation, by the dimensions of the probe. Given that the fabrication of probes with 50 nm apertures is technically feasible with reasonable repeatability, and that the transmission will in any case decrease sharply at smaller aperture dimensions, it would seem, a priori, feasible to aim for a resolution of ca 50 nm in well-optimized circumstances. The first report of the use of NSOM to conduct lithography, by Betzig et al.,<sup>[21]</sup> suggested that this was realistic. Using an optical fiber probe, controlled by shear-force modulation, they wrote structures into a Co/Pt multilayer film using visible light (488 and 514 nm). In regions heated near to the Curie temperature of the medium (ca 300°C), domains were formed with opposite magnetization that could subsequently be imaged using NSOM. When adequate powers (ca 5 mW input power from



an argon ion laser) were utilized, it was possible to write features with diameters of 60 nm. Optimization of the conditions relied upon ensuring that adequate power was passed through the probe to ensure sample heating and, at the same time, that the input power was not great enough to damage the aluminum coating on the probe.

Building on this promising start, Krausch and coworkers utilized an NSOM to expose films of conventional photoresist.<sup>[22–24]</sup> Using an argon ion laser ( $\lambda = 454$  nm), they were able to write structures as small as  $\lambda/5$  (ca 80 nm) into Hoechst Novalack AZ 6612, a resist based on a phenol–formaldehyde resin, which becomes base-soluble on exposure to light. The features formed in the photoresist represented a mechanical replica of the intensity distribution in the optical near field of the tip. It was found that the features could be fitted with a Gaussian intensity distribution with a width of approximately 100 nm, and a height of ca 15 nm. A grating was fabricated with a period of 164 nm and a line width of 82 nm. These results confirmed that by using NSOM, it was possible to break the diffraction limit in lithographic mode by a significant margin.

Smolyaninov Mazzoni, and Davis utilized a standard negative-tone resin-based photoresist (Shipley KTI 747) in studies using UV light from an excimer laser (248 nm).<sup>[25]</sup> Exposure of the resist using an NSOM led to the photochemical generation of a cross-linked network that was insoluble in the developer. The resulting specimens were characterized before development, by using shear-force imaging with the same probe employed to modify the sample, and after development, by AFM. A nonlinear dependence of the feature size on the light power was reported. Under optimal conditions, features of size ca 100 nm could be written with an uncoated optical fiber.

Although these results represented excellent progress, they nevertheless leave much to be desired. In particular, these early studies failed to realize the optimal resolution expected a priori—matching the diameter of the optical fiber aperture. One of the problems was that these photoresist films had a finite thickness—tens of nanometers at best. However, the electric field associated with an optical aperture in the near field is known to diverge comparatively rapidly within dielectric layers.<sup>[11]</sup> This may mean significant spreading of the excitation in the resist layer. Moreover, the approach of Betzig et al. relied upon localized heating; thermal migration away from the region exposed beneath the fiber aperture may lead to an additional broadening effect. These problems were realized by Fujihara and coworkers,<sup>[26,27]</sup> who sought to restrict the thickness of the resist by utilizing monolayer systems. They prepared Langmuir–Blodgett films of a photochromic material containing

4-octyl-4'-[5-carboxypentamethyleneoxy)azobenzene. On exposure to UV light ( $\lambda = 350$  nm), this molecule undergoes a *cis–trans* conformational change. The change may be reversed by the action of heat or light. They reported a resolution of 130 nm. Although this does not represent an improvement on the work described above, it nevertheless suggests that such systems have a useful role to play.

Conjugated polymers have a broad range of potential applications arising from their electrical and optical properties. There has been significant interest in exploiting the susceptibility of conjugated polymers to photooxidation as a means for patterning them at the nanometer scale, using an NSOM to deliver excitation to localized regions in polymer films. Wei et al. studied thin films of (3,4-diphenyl-2,5-thienylene vinylene). They reported comparatively diffuse structures with line widths of ca 200 nm.<sup>[28]</sup> Buratto and coworkers patterned films of poly[2-methoxy, 5-(2'-ethyl hexyloxy)-*p*-phenylene vinylene] using light from an argon ion laser coupled to an NSOM.<sup>[29,30]</sup> They also reported a line width of 200 nm. In part, no doubt, the poor resolution in these studies was a consequence of the finite thickness of the resist. Credo et al.<sup>[30]</sup> also studied the exposure of *tris*-8-hydroxyquinoline aluminum ( $\text{Alq}_3$ ) films. Here there was an additional problem in that active species created by the initial exposure of the sample diffused away from the region of initial exposure. On small length scales, even small amounts of diffusion may cause a significant degradation of the resolution. In studies of self-assembled dye layers, they also reported degradation of resolution; but, in this case, it was because of the migration of energy through the resist material rather than the diffusion of active species. Once again, the finite film thickness (50 nm) may well account for much of the migration of heat energy. Studies of the near-field exposure of conjugated polymer films have generally failed to yield dimensions that are authentically nanometer scaled (i.e., less than 200 nm), and much of this can be attributed to the problems associated with the finite thicknesses of even the highest quality materials prepared by techniques such as spin-coating. More recently, for example, Riehn et al. patterned PPV layers with a resolution of, at best, 160 nm.<sup>[31]</sup> They modeled the behavior using the Bethe–Bouwkamp model, and determined that a surface of constant intensity was formed, which just touched the substrate under a 40 nm precursor film and had an extent of approximately half the diameter of the feature prepared experimentally. They proposed the formation of a central core surrounded by a gel phase. The steep profile of the electric field predicted by their model indicated that the polymer at the top of the sample absorbed 20 times the dose of the polymer at the substrate.

These studies have focused on organic systems. However, some authors have sought to pattern inorganic materials using methods based on near-field microscopy. Madsen et al. used an NSOM coupled to an argon ion laser to write oxide structures into hydrogen-passivated silicon surfaces, which were then used as resists during etching of the Si substrate with KOH.<sup>[32]</sup> The structures observed were complex, but consisted of a central line with a full width at half maximum height of, in one case, 111 nm, and in another, 126 nm. These narrow structures were bordered by slightly wider features attributed to an interference pattern dominated by far-field excitation through the sidewalls of the uncoated fiber used. Narrower structures (50 nm) were observed in the absence of the optical excitation, attributed to the presence of the electrostatic potential between the probe and the amorphous Si layer. Significant improvements were produced when aluminum-coated fibers were used. The Al coating prevented far-field emission through the fiber walls, and resulted in the formation of much better defined structures with widths not much in excess of 50 nm.<sup>[33]</sup> These structures represent some of those most clearly resolved in these early studies.

Herndon et al. also used NSOM-based methods to fabricate structures in hydrogen-passivated silicon.<sup>[34]</sup> They explored wavelengths down to 248 nm, using argon ion and excimer lasers. The threshold dose required to fully expose the resist was found to decline with the wavelength of the light used. However, the lines written had widths that were comparatively large—in the range of 140–320 nm. Like Madsen et al., they also found that modification could occur in the absence of optical excitation.

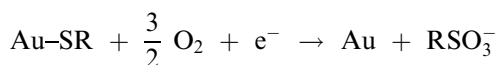
Hosaka and coworkers examined a different inorganic system, amorphous Ge–Sb–Te films, whose structure could be modified by localized heating by light from a pulsed diode laser, emitting at 785 nm and delivered through an NSOM probe.<sup>[35,36]</sup> They achieved somewhat superior resolution, demonstrating the fabrication of 60 nm structures. A variety of other approaches have been explored, some of which are more complex and use less conventional resist materials. For example, Yamamoto et al. studied the deposition of zinc using the photo-dissociation of gas-phase dimethyl zinc.<sup>[37]</sup> While they reported the formation of sub-100 nm structures, these were comparatively ill defined. Better images were reported of 200 nm zinc structures. Hong et al. combined near-field microscopy with a micropipette filled with photore-sist.<sup>[38]</sup> While their paper demonstrates an innovative modification of the method, they were only able to fabricate structures that were some hundreds of nanometers in size. Finally, Philipona et al. examined the direct attachment of biological molecules to photosensitive monolayers of a diazine molecule.<sup>[39]</sup> This

represented a significant step into a new area of application, but it proved only possible to create comparatively large (hundreds of nanometers) structures.

## PHOTOCHEMISTRY OF SELF-ASSEMBLED MONOLAYERS

Summarizing the progress described above, it may reasonably be said that NSOM-based approaches had yielded new and, in some cases, unique capabilities, without yielding the kind of routinely very high resolution that might have been hoped in the earliest studies. The thickness of the resist layer has been demonstrated to be critical, with the potential for the spread of the excitation, through the divergence of the electric field, the diffusion of reactive species formed by photoexcitation, and thermal migration, increasing with film thickness. Many of these phenomena may be controlled through the selection of an appropriate resist material. In this section, we describe how the use of self-assembled monolayers (SAMs) of alkanethiols adsorbed on gold surfaces has provided unambiguous evidence not only that structures significantly smaller than 100 nm may be fabricated routinely, but also that near-field techniques can rival the power of electron beam lithography for such materials.

Alkanethiols,  $\text{HS}(\text{CH}_2)_n\text{X}$ , adsorb spontaneously onto gold surfaces, forming dense, well-ordered monolayers, SAMs, that provide versatile templates for the construction of complex molecular architectures.<sup>[40]</sup> Li et al.<sup>[41]</sup> and Tarlov and Newman<sup>[42]</sup> reported that on extended exposure to the air, the alkylthiolate adsorbate species was oxidized to yield an alkylsulfonate:



Huang and Hemminger<sup>[43]</sup> and Tarlov, Burgess, and Gillen<sup>[44]</sup> demonstrated that the same process could be initiated by exposure of SAMs to light from a mercury arc lamp. They found that unlike the adsorbates in the pristine monolayer, the sulfonate oxidation products were only weakly bound, and could be displaced, either by rinsing or by immersion in a solution of a second thiol, to generate a chemical pattern. The process is illustrated in Fig. 2, where a carboxylic acid-terminated thiol is photopatterned. After immersion of the sample in a solution of a methyl-terminated thiol, a chemical pattern is formed that may be imaged using a variety of methods including friction force microscopy (FFM). (Fig. 3), scanning electron microscopy (SEM)<sup>[45]</sup> and imaging secondary ion mass spectrometry (SIMS).<sup>[46]</sup> The advantage of depositing both chemistries in a solution-phase self-assembly process is

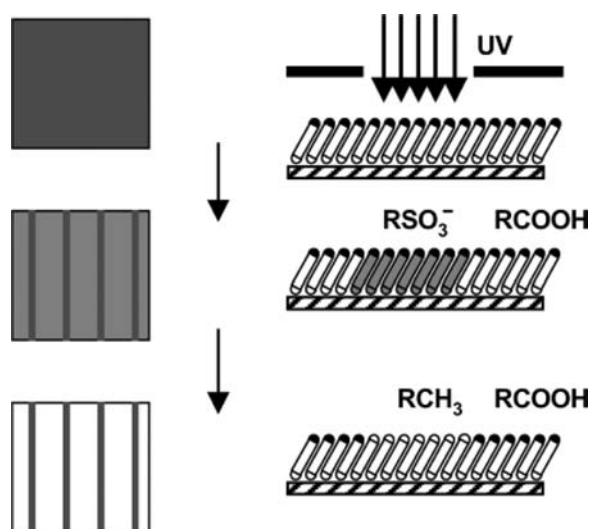


**Fig. 2** Schematic diagram illustrating the photopatterning of a SAM. A carboxylic acid-terminated SAM is formed and then exposed to UV light through a mask. In exposed areas, the adsorbates are oxidized to weakly bound alkylsulfonates, which are displaced by a contrasting solution-phase thiol in the final step.

that the entire specimen exhibits well-ordered adsorbates with relatively low defect densities.

The mechanism of photooxidation has been the subject of some debate. Early on, it was proposed by Hemminger and coworkers that the process was initiated by the formation of hot electrons at the gold surface. However, this idea did not have direct support.

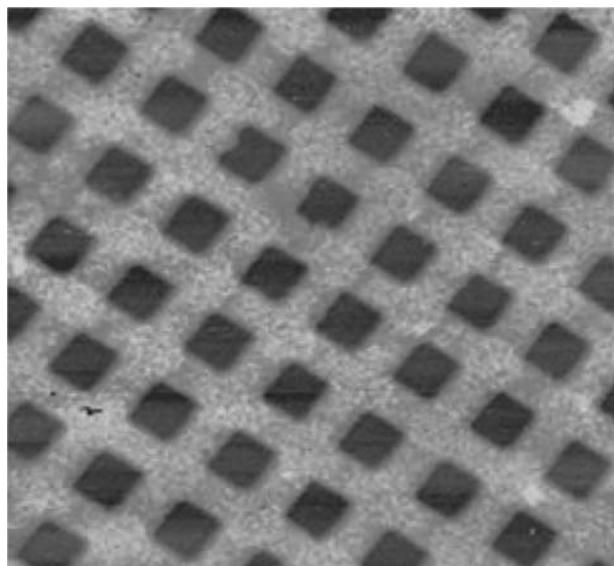


**Fig. 3** An  $80\ \mu\text{m} \times 80\ \mu\text{m}$  FFM image of a patterned SAM. The pattern consists of regions functionalized by  $\text{HS}(\text{CH}_2)_{11}\text{CH}_3$  (dark contrast) and  $\text{HS}(\text{CH}_2)_{10}\text{COOH}$  (bright). Source: From Ref.<sup>[55]</sup>.

Studies in the authors' laboratory demonstrated that for SAMs adsorbed on both gold<sup>[47]</sup> and silver surfaces,<sup>[48]</sup> the rate of oxidation decreased with increasing adsorbate chain length, correlating with the decrease in alkyl chain mobility associated with the increased dispersion interaction between long alkyl chains, and suggesting that penetration of oxygen species to the air–sulfur interface was the rate-limiting step. For adsorbates capable of forming hydrogen bonds between their terminal groups, the rate of oxidation was found to be even slower,<sup>[49]</sup> suggesting that the resulting network of hydrogen bonding interactions impeded the diffusion of oxygen. A radical proposal was made by Bohn and coworkers<sup>[50,51]</sup> and by Norrod and Rowlen,<sup>[52]</sup> who suggested that the process was not in fact a photochemical one, but involved the ozonolysis of adsorbate molecules. Critically, all of the studies published till date had utilized mercury arc lamps, which typically exhibited broad emission spectra. They suggested that short wavelength light generated by a mercury arc lamp could initiate ozone formation, and that ozone species could oxidize the adsorbate molecules in the SAM. In studies of the oxidation of hexadecanethiol SAMs, they claimed that the interposition of a filter that blocked short wavelength radiation between the lamp and the source extinguished the photooxidation process.<sup>[50]</sup>

This finding, if correct, would have meant that it will be difficult to utilize such approaches for near-field excitation, because a methodology based upon the creation of gaseous reagents would be unlikely to yield significant spatial control of reactivity. However, using a lamp equipped with a filter designed to eliminate ozone formation, Brewer et al. provided clear evidence that oxidation of SAMs could occur in the absence of ozone.<sup>[53]</sup> It was found that monolayers of carboxylic acid-terminated SAMs on both gold and silver surfaces oxidized rapidly to yield alkylsulfonates when exposed to light with a wavelength of 254 nm. Recently, a more detailed kinetic study has been carried out using static SIMS, to determine rates of photooxidation.<sup>[54]</sup> Significant differences were observed between the rates of oxidation under these well-defined conditions and those measured using mercury arc lamp sources. Unexpectedly, when exposed to 254 nm light, acid terminated thiols oxidize much faster than methyl-terminated adsorbates—the direct opposite of the observation made earlier for an arc lamp source. This is explained by differences in the mechanisms of oxidation. The dominance of intermolecular interactions in determining the rate of oxidation during exposure to the arc lamp source suggests that gaseous reagents are important under those conditions, in agreement with the predictions of Bohn and coworkers.<sup>[50]</sup> However, when a well-defined light source emitting at 254 nm is used, these species are absent, and it is

believed that hot electron formation provides the main impetus for SAM oxidation. Measurements of the contact potential differences of SAMs on Au and Ag have yielded data that reveal differences in SAM work functions that are consistent with such an explanation.<sup>[54]</sup> In particular, it was found that the work functions of carboxylic acid-terminated SAMs are larger than the energy of a 254 nm photon. As a result, absorption of a UV photon may lead to the promotion of an electron from the Fermi level to an excited state, but not to photoemission. These excited electrons may tunnel into an antibonding state in the adsorbate sulfur atom, leading to oxidation. In contrast, the work functions of methyl terminated SAMs are smaller than the photon energy, meaning that photoemission may occur. Photoemitted electrons will have small kinetic energies, and most likely be scattered by the alkyl chains above the surface, but nevertheless the number of electrons available for the initiation of oxidation will be significantly reduced. The transfer of hot electrons from the Fermi level to the adsorbate sulfur thus becomes the rate-limiting step, although adsorbate order still plays a role. For example, carboxylic acid-terminated thiols pack less closely on silver than on gold, and a concomitant increase was reported in the rate constants for photooxidation.

## NANOPHOTOPATTERNING OF SAMS

These findings indicate that SAMs are a suitable system for developing into a resist for ultra-high resolution photolithography. Not only are the monolayers very well defined, but also, through the use of hot-electron stimulated oxidation of the adsorbate sulfur atom, produce a resist that may effectively be regarded as the monatomic layer of sulfur atoms that forms at the gold–adsorbate interface. This clearly represents the thinnest conceivable resist layer. A priori, therefore, one would expect to be able to exploit the full potential for spatial resolution offered by near-field lithographic techniques, with the resolution being determined, as a first approximation, by the diameter of the aperture in the NSOM probe. Fig. 4 illustrates the process schematically. An NSOM fiber, coupled to a suitable light source (a frequency-doubled argon ion laser, emitting at 244 nm is well suited to the purpose) is traced across the sample surface. Wherever the probe travels, the adsorbate molecules are exposed to UV light, leading to their oxidation to alkylsulfonates. On immersion of the sample in a solution of a contrasting thiol, the oxidation products are displaced by solution-phase thiols, which adsorb at the surface and form a chemical pattern: The new adsorbate occupies the exposed areas, while the original adsorbate continues to occupy the rest of the surface.

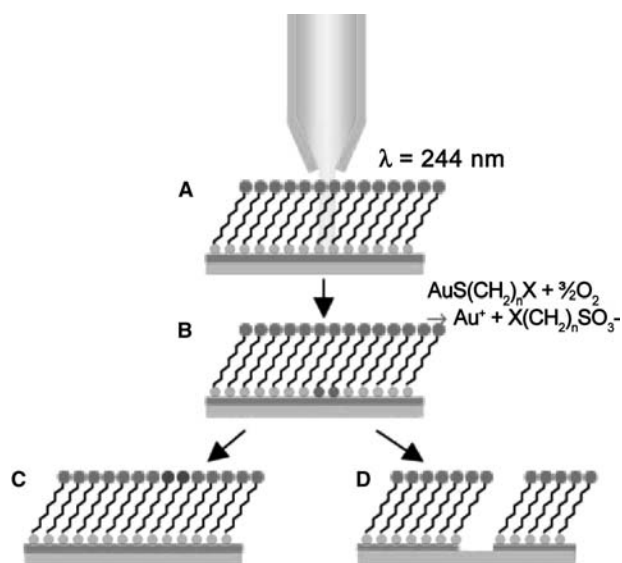


**Fig. 4** A schematic diagram illustrating the application of SNP. A sample is exposed to UV light from an NSOM (A), leading to local oxidation (B) and either replacement of the oxidation products by a contrasting thiol (C), or etching of the gold underlying the oxidized regions (D). *Source:* From Ref.<sup>[56]</sup>.

Initial studies were very promising.<sup>[57]</sup> Monolayers of carboxylic acid-terminated thiols were formed and selectively exposed to UV light from an NSOM probe. On immersion in a solution of methyl-terminated thiol, the oxidation products were displaced leading to a chemical pattern. Fig. 5 shows scanning probe microscopy data on such samples. In this illustration, the adsorbate molecules had identical chain lengths. As a result, the AFM topographical image shows no contrast. The only difference between the two regions of the surface is in the identity of the terminal group. Friction force microscopy (FFM) is a powerful tool for probing the compositions and molecular organization of molecular monolayers. FFM provides a convenient mean for quantifying the extent of SAM photooxidation. In Fig. 5, the FFM image reveals clear contrast between regions of the surface with different chemistries: the lines of methyl-terminated thiols exhibit dark contrast compared to the surrounding carboxylic acid-terminated regions of the surface, because they have smaller coefficients of friction than the high surface energy, polar adsorbates.

The lines in Fig. 5 have widths of ca 40 nm. In our experience, this level of performance can be reproduced routinely provided probes of adequately good quality are used. However, this does not represent the limit of performance achievable by SNP. Indeed, even the achievement of a line width of 40 nm deserves comment, because this is smaller than the diameter of the aperture in the probe. A priori, one would have

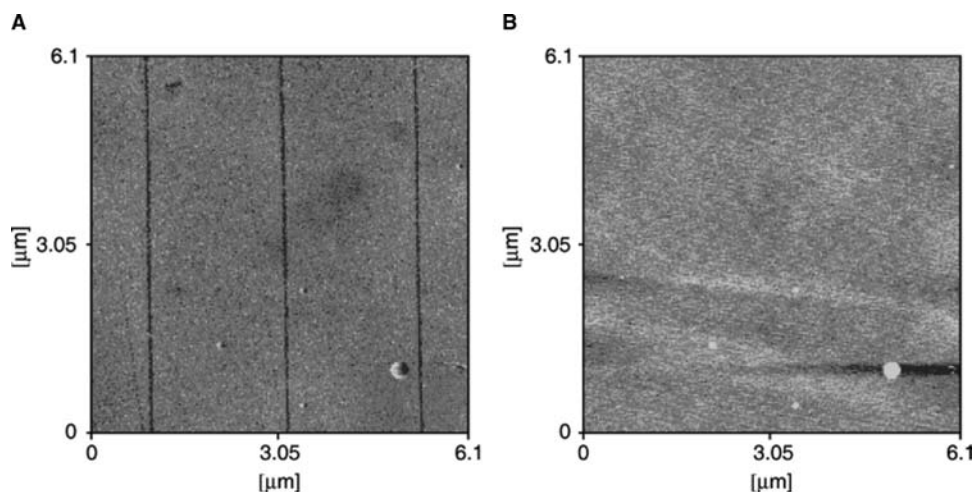


**Fig. 5** Friction force (A) and topographical (B) AFM images of lines of methyl-terminated thiols written into a carboxylic acid-terminated SAM using SNP. *Source:* From Ref.<sup>[57]</sup>.

expected the best performance to yield a feature size comparable to the aperture diameter, because of the extent to which the electric field associated with the optical near field diverges under the aperture. Resolutions better than the aperture diameter have proved to be readily reproducible. Recently, line widths of ca 20 nm were reported in SAMs of alkanethiols (Fig. 6), corresponding to a resolution of  $\lambda/12$ .<sup>[58]</sup> This significantly exceeds the performance of previous photolithographic techniques. However, this does not represent the limit of performance: recently a line width of 9 nm (i.e.,  $\lambda/27$ ) was achieved. For these materials, this kind of performance matches the resolution of electron

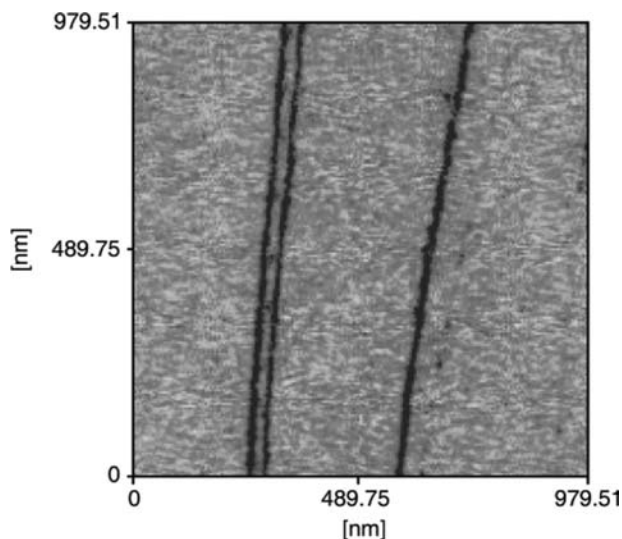


**Fig. 6** Matching the performance of electron beam lithography by photochemical means. Lines of methyl-terminated thiol only 20 nm wide written into an acid-terminated SAM by SNP. *Source:* From Ref.<sup>[58]</sup>.

beam lithography, which is an impressive achievement for an ambient technique that utilizes significantly less complex and less expensive apparatus. However, the question arises, how is it feasible to achieve such a resolution, when the aperture in the NSOM probe is, at best, 50 nm in diameter?

It has been observed that the resolution achievable in SNP is dependent upon the morphology of the underlying substrate. The substrates upon which our SAMs are prepared are typically polycrystalline, consisting of grains that have diameters in the range of 10–100 nm. The grain size may be readily varied by altering the rate of deposition of the metal. As the grain size of the gold substrate decreases, so does the line width. This is illustrated graphically in Fig. 7. As the grains become larger, the line width increases, reaching a limiting value that is approximately equal to the diameter of the aperture in the probe. The limit

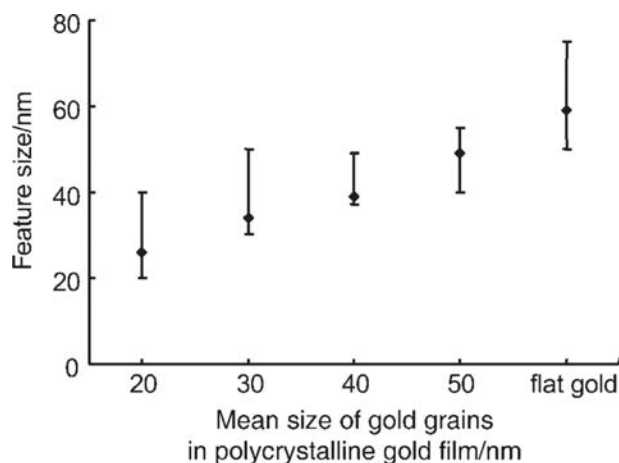


**Fig. 7** The variation in line width as a function of the grain size of the underlying gold film in SNP. *Source:* From Ref.<sup>[58]</sup>.



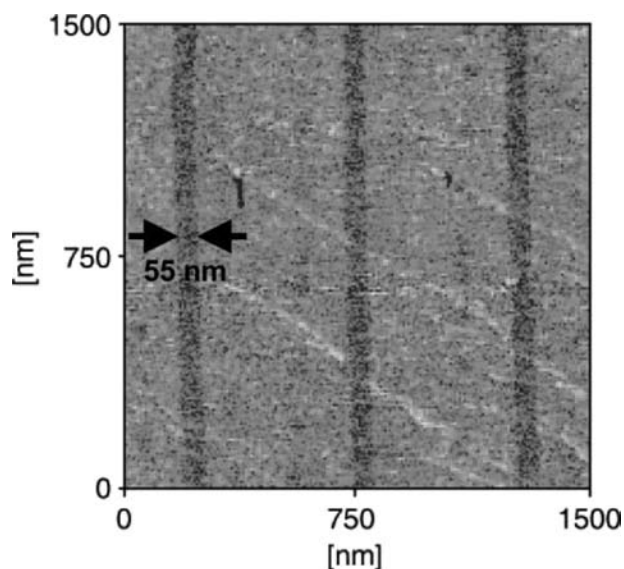


**Fig. 8** Lines of methyl-terminated adsorbates fabricated in a carboxylic acid-terminated SAM formed on an atomically flat gold substrate. *Source:* From Ref.<sup>[58]</sup>.

of large grain size is represented by an atomically flat, epitaxially deposited gold film. For such a substrate, we were only able to achieve a grain size comparable to the diameter of the aperture (Fig. 8). These data may be rationalized in the following way. When a metallic asperity is exposed to optical excitation in the near field, it may function like an antenna, causing a very pronounced enhancement in the intensity of the electric field in a small region around the apex of the asperity. This phenomenon is referred to as the “lightning-rod effect” and it forms the basis of apertureless NSOM (see below). We have speculated that the grains in the gold film function like an array of antennae, leading to a confinement of the excitation as the probe traverses the sample and resulting in the photochemical reaction being confined to a very small region of the surface. Although this sounds like a rather specific phenomenon, it may in fact be applicable to a wide range of systems. For example, a variety of metals and some semiconductors are known to yield a similar effect (it is thus not confined to gold). Moreover, there are potentially exciting possibilities if one could utilize an apertureless excitation, by combining this substrate-mediated localization with further confinement by the tip itself. Such phenomena may also be helpful in imaging applications of NSOM. An “inverted lightning rod effect” may thus prove a valuable tool for the manipulation and characterization of surface structure on even smaller length scales than those indicated in Fig. 6.

Samples patterned using SNP may be utilized in a variety of ways. For example, aldehyde-functionalized polymer nanoparticles have been attached to

amine-terminated regions in carboxylic acid-terminated SAMs. Proteins may also be patterned using SNP. In protein patterning on any length scale, the most difficult problem is the prevention of nonspecific adsorption, because proteins tend to adhere strongly to most surfaces. On the nanometer scale, any such problems are accentuated. In a region of several  $\mu\text{m}^2$ , a few nonspecifically adsorbed protein molecules may be missed; compared to a feature of size comparable to a protein molecule, they will be much more problematic. One particularly significant contribution to the field of protein adsorption has been the use of oligo(ethylene glycol) (OEG)-terminated thiols to resist protein adsorption.<sup>[59]</sup> These are so effective in reducing non-specific adsorption that it becomes insignificant even on molecular length scales. Using SNP, regions in an OEG-terminated SAM may be selectively oxidized and replaced, either with an adsorbate that does not resist protein adsorption, leading to localized adsorption on transfer to the biological medium, or with an adsorbate to which proteins may be covalently attached. One approach adopted in the author’s laboratory is to introduce carboxylic acid-terminated adsorbates into regions of an OEG-terminated SAM and then attach proteins using well-established carbodiimide-coupling chemistry, originally established for use on larger length scales. In conjunction with SNP, this approach yields protein features with line widths smaller than 100 nm.<sup>[60]</sup>

Structures formed by SNP have also been used to fabricate 3-D structures in metal films.<sup>[56,61]</sup> After exposure of a SAM to UV light from the NSOM probe, the sample may be immersed in a solution of an etchant for the underlying substrate, such as the ferri/ferrocyanide etchant reported by Xia et al.<sup>[62]</sup> Fig. 9 shows an AFM image of a structure fabricated in a monolayer of hexadecanethiol using this approach, together with a cross-section through the structure. The AFM data indicate that the width of the nanotrench is only 50 nm. Recent work using electron microscopy to characterize similar structures suggests that in such circumstances the AFM image probably gives a significant overestimate of the trench width because of the convolution of the topographical profile of the surface with the tip geometry. However, even at a width of 50 nm, such data provide clear evidence that this is a convenient and powerful approach to the patterning of metal films. Subsequently, the gold nanostructures may be used as masks for anisotropic etching of the underlying substrate.

These data provide clear evidence that SNP is a powerful tool for patterning SAMs of alkanethiols. However, there are strong reasons to believe that similar performance levels should be feasible for other materials. The basis for the extremely high resolution achieved for alkanethiol systems is the exploitation of



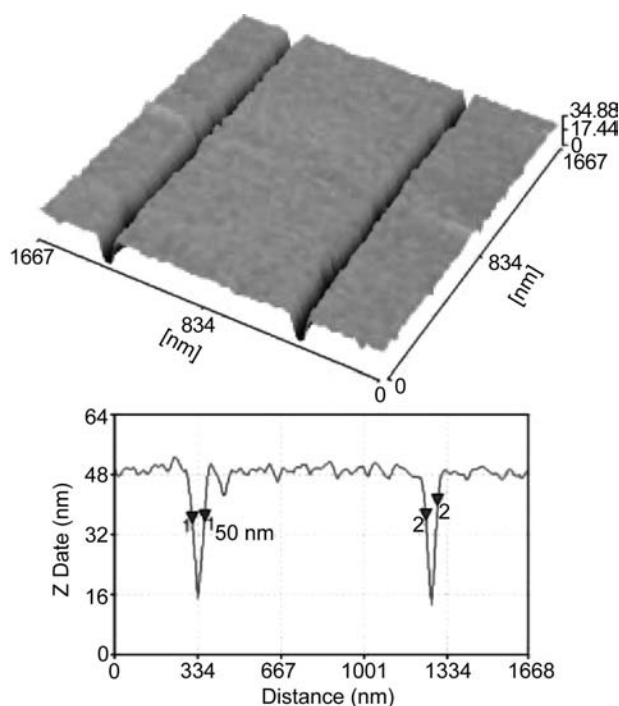


**Fig. 9** AFM image of nanotrenches etched into gold using an SNP-patterned SAM of hexadecanethiol as the resist.

a specific photochemical reaction that is confined to a functional group (the thiol head group) distributed with monolayer coverage on a solid surface. There is a large group of systems that fit this classification. Current work in the author's laboratory is focused on monolayers on silicon and other surfaces and initial results are very promising.<sup>[61]</sup> In principle, it seems that SNP should be extendable to a broad class of organic monolayer systems.

## APERTURELESS METHODS

Apertureless methods have recently made an enormous impact on surface characterization by NSOM, enabling significant improvements in spatial resolution to be achieved. Till date, they have been little used for lithography. However, Royer and coworkers have provided evidence that apertureless techniques offer significant potential in lithographic applications. Their motivation was to use photosensitive films as a means of observing the field enhancement beneath an apertureless NSOM probe.<sup>[63,64]</sup> Azobenzene films were spin-coated onto glass with a thickness estimated to be 200 nm. Despite the thickness of the resist layer, it proved possible to fabricate lines with a width of ca 50 nm and dots as small as 30 nm.<sup>[65]</sup> These samples were subject to the limitations of the resist films employed in previous studies using aperture-based

methods, but the resolution was significantly improved and approached the performance achieved for SAMs. Given the advances in resolution from those systems to the thiol-on-gold system, it is possible that SAMs may yield even greater enhancements in resolution in conjunction with apertureless lithography.

The principal problem with apertureless methods is the far-field exposure of the region around the tip, which may lead to complications in lithographic operation because it may cause exposure of the resist. Although the electric field may be enhanced directly under the tip, the finite period of time required to write structures means that the far-field exposure may nevertheless be substantial. However, one route of potential value in this respect is the use of non-linear optical processes, such as two-photon absorption. Because the cross-section for two-photon absorption is related to the square of the electric field strength, significantly greater absorption will occur under the tip than in the surrounding regions, potentially enabling near-field modification in the absence of significant far-field exposure. The feasibility of such approaches has been demonstrated by Yin et al.,<sup>[66]</sup> who fabricated features with widths of ca 70 nm in a photoresist film.

## CONCLUSIONS

Scanning near-field photolithography is a technique that offers great promise in the fabrication of molecular nanostructures. While early attempts to utilize near-field scanning optical microscopes to pattern materials yielded mixed results, alkanethiol SAMs provide simple, convenient and highly effective resists, enabling the initial hopes for the methodology not only to be realized, but also to be surpassed. Operating under ambient conditions, and requiring no special sample preparation procedures, it facilitates the fabrication of structures comparably small to those made by electron beam lithography. The resulting structures may readily be utilized for the immobilization of biological molecules and for the etching of 3-D structures into the underlying substrate. It is thus clear that the careful selection of resist materials enables SNP to compete very favorably with other nanofabrication techniques. Moreover, it offers the benefits of ambient operation. Because there is a large number of photochemical reactions that may be used to modify surfaces, techniques based on near-field optical excitation are extremely attractive and potentially offer enormous flexibility for the fabrication of complex molecular nanostructures. In conjunction with apertureless excitation, it is not inconceivable that a resolution significantly better than 10 nm may be achieved, reflecting advances in near-field microscopy. Combined with the ability to selectively excite

photochemical transformations, this would represent a powerful capability. There are good grounds, therefore, for continuing to explore the possibilities offered for nanofabrication by near-field optical processes.

## ACKNOWLEDGMENT

The author is grateful to the EPSRC and the RSC Analytical Chemistry Trust Fund for their support.

## REFERENCES

1. Alkaiji, M.M.; Blaikie, R.J.; McNab, S.J. Nanolithography in the evanescent near field. *Adv. Mater.* **2001**, *13*, 877–887.
2. Hanninen, P.E.; Hell, S.W.; Saol, J.; Soini, E. Two-photon excitation 4Pi confocal microscope: enhanced axial resolution microscope for biological research. *Appl. Phys. Lett.* **1995**, *66*, 1698–1700.
3. Klar, T.A.; Jakobs, S.; Dyba, M.; Egner, A.; Hell, S.W. Fluorescence microscopy with diffraction resolution barrier broken by stimulated emission. *Proc. Natl. Acad. Sci. U.S.A.* **2000**, *97*, 8206–8210.
4. Srituravanich, W.; Fang, N.; Sun, C.; Luo, Q.; Zhang, X. Plasmonic Lithography. *Nano Lett.* **2004**, *4*, 1085–1088.
5. Syngé, E.H. A suggested method for extending microscopic resolution into the ultra-microscopic region. *Phil. Mag.* **1928**, *6*, 356–362.
6. Syngé, E.H. A microscopic method. *Phil. Mag.* **1931**, *11*, 65–80.
7. Syngé, E.H. An application of piezo-electricity to microscopy. *Phil. Mag.* **1932**, *13*, 297–300.
8. Ash, E.A.; Nicholls, G. Super-resolution aperture scanning microscope. *Nature* **1972**, *237*, 510–512.
9. Betzig, E.; Trautman, J.K. Near-field optics: microscopy, spectroscopy and surface modification beyond the diffraction limit. *Science* **1992**, *257*, 189–195.
10. De Serio, M.; Zenobi, R.; Deckert, V. Looking at the nanoscale: scanning near-field optical microscopy. *Trends Anal. Chem.* **2003**, *22*, 70–77.
11. Novotny, L.; Pohl, D.W.; Hecht, B. Light confinement in scanning near-field optical microscopy. *Ultramicroscopy* **1995**, *61*, 1–9.
12. Shubeita, G.T.; Sekatskii, S.K.; Dietler, G.; Potapova, I.; Mews, A.; Basche, T. Scanning near-field optical microscopy using semiconductor nanocrystals as a local fluorescence and fluorescence resonance energy transfer source. *J. Microsc.* **2003**, *210*, 274–278.
13. Sánchez, E.J.; Novotny, L.; Xie, X.S. Near-field fluorescence microscopy based on two-photon excitation with metal tips. *Phys. Rev. Lett.* **1999**, *82*, 4014–4017.
14. Bouhelier, A.; Beversluis, M.; Hartschuh, A.; Novotny, L. Near-field second-harmonic generation induced by local field enhancement. *Phys. Rev. Lett.* **2003**, *90*, 013903.
15. Hartschuh, A.; Sanchez, E.J.; Xie, X.S.; Novotny, L. High-resolution near-field Raman microscopy of single-walled carbon nanotubes. *Phys. Rev. Lett.* **2003**, *90*, 095503.
16. Hartschuh, A.; Pedrosa, H.N.; Novotny, L.; Krauss, T.D. Simultaneous fluorescence and Raman scattering from single carbon nanotubes. *Science* **2003**, *301*, 1354–1356.
17. Fodor, S.P.A.; Read, J.L.; Pirrung, M.C.; Stryer, L.; Liu, A.T.; Solas, D. Light-directed, spatially addressable parallel chemical synthesis. *Science* **1991**, *251*, 767–773.
18. Yang, Z.; Frey, W.; Oliver, T.; Chilkoti, A. Light-activated affinity micropatterning of proteins on self-assembled monolayers on gold. *Langmuir* **2000**, *16*, 1751–1758.
19. Humphris, A.D.L.; Hobbs, J.K.; Miles, M.J. Ultrahigh-speed scanning near-field optical microscopy capable of over 100 frames per second. *Appl. Phys. Lett.* **2003**, *83*, 6–8.
20. Vettiger, P.; Despont, M.; Drechsler, U.; Durig, U.; Haberle, W.; Lutwyche, M.I.; Rothuizen, H.E.; Stutz, R.; Widmer, R.; Binnig, G.K. The “Millipede”—more than one thousand tips for future AFM data storage. *IBM J. Res. Devel.* **2000**, *44*, 323–340.
21. Betzig, E.; Trautman, J.K.; Wolfe, R.; Gyorgy, E.M.; Finn, P.L.; Kryder, M.H.; Chang, C.-H. Near-field magneto-optics and high density data storage. *Appl. Phys. Lett.* **1992**, *61*, 142–144.
22. Wegscheider, S.; Kirsch, A.; Mlynek, J.; Krausch, G. Scanning near-field optical lithography. *Thin Sol. Films* **1995**, *264*, 264–267.
23. Krausch, G.; Wegscheider, S.; Kirsch, A.; Bielefeldt, H.; Meiners, J.C.; Mlynek, J. Near field microscopy and lithography with uncoated fiber tips: a comparison. *Optics Comm.* **1995**, *119*, 283–288.
24. Krausch, G.; Mlynek, J. Surface modification in the optical near field. *Microelectron. Eng.* **1996**, *32*, 219–228.
25. Smolyaninov, I.I.; Mazzoni, D.L.; Davis, C.C. Near-field direct-write ultraviolet lithography and shear force microscopic studies of the lithographic process. *Appl. Phys. Lett.* **1995**, *67*, 3859–3861.
26. Jiang, S.; Ichihashi, J.; Monobe, H.; Fujihara, M.; Ohtsu, M. Highly localized photochemical processes in LB films of photochromic material by using a photon scanning tunnelling microscope. *Optics Comm.* **1994**, *106*, 173.
27. Fujihara, M.; Monobe, H.; Muramatsu, H.; Ataka, T. Near-field optical microscopic recording on Langmuir-Blodgett (LB) films and chemically modified surfaces. *Ultramicroscopy* **1995**, *57*, 176.
28. Wei, P.K.; Hsu, J.H.; Fann, W.S.; Hsieh, B.R. Surface modification of conjugated polymers: an application of near-field optical microscopy in sub-micron photochemistry. *Synth. Met.* **1997**, *85*, 1421–1422.
29. DeAro, J.A.; Gupta, R.; Heeger, A.J.; Buratto, S.K. Nanoscale oxidative patterning and manipulation of conjugated polymer thin films. *Synth. Met.* **1999**, *102*, 865–868.
30. Credo, G.M.; Lowman, G.M.; DeAro, J.A.; Carson, P.J.; Winn, D.L.; Buratto, S.K. Probing nanoscale

- photo-oxidation in organic films using spatial hole-burning near-field scanning optical microscopy. *J. Chem. Phys.* **2000**, *112*, 7864–7872.
31. Riehn, R.; Charas, A.; Morgado, J.; Cacialli, F. Near-field optical lithography of a conjugated polymer. *Appl. Phys. Lett.* **2003**, *82*, 526–528.
  32. Madsen, S.; Mullenborn, M.; Birkelund, K.; Grey, F. Optical near-field lithography on hydrogen-passivated silicon surfaces. *Appl. Phys. Lett.* **1996**, *69*, 544–546.
  33. Madsen, S.; Bozhevolnyi, S.I.; Birkelund, K.; Mullenborn, M.; Hvam, J.M.; Grey, F.J. Oxidation of hydrogen-passivated silicon surfaces by scanning near-field optical lithography using uncoated and aluminium-coated fiber probes. *J. Appl. Phys.* **1997**, *82*, 49–53.
  34. Herndon, M.K.; Collins, R.T.; Hollingsworth, R.E.; Larson, P.R.; Johnson, M.B. Near-field scanning optical lithography using amorphous silicon photoresists. *Appl. Phys. Lett.* **1999**, *74*, 141–143.
  35. Imura, R.; Shintani, T.; Nakamura, K.; Hosaka, S. Nanoscale modification of phase change materials with near-field light. *Microelectron. Eng.* **1996**, *30*, 387–390.
  36. Hosaka, S.; Kikukawa, A.; Koyanagi, H.; Shintani, T.; Miyamoto, M.; Nakamura, K.; Etoh, K. SPM-based data storage for ultrahigh density recording. *Nanotechnology* **1997**, *8*, A58–A62.
  37. Yamamoto, Y.; Kurogi, M.; Ohtsu, M.; Polonski, V.; Lee, G.H. Fabrication of nanometric zinc pattern with photodissociated gas-phase diethylzinc by optical near field. *Appl. Phys. Lett.* **2000**, *76*, 2173–2175.
  38. Hong, M.-H.; Kim, K.H.; Bae, J.; Jhe, W. Scanning nanolithography using a material-filled nanopipette. *Appl. Phys. Lett.* **2000**, *77*, 2604–2606.
  39. Philipona, C.; Chevelot, Y.; Leonard, D.; Mathieu, H.J.; Sigrist, H.; Marquis-Weible, F. A scanning near-field optical microscope approach to biomolecule patterning. *Bioconjugate Chem.* **2001**, *12*, 332–336.
  40. Xia, Y.; Whitesides, G.M. Soft lithography. *Angew. Chem. Int. Ed.* **1998**, *37*, 550–575.
  41. Li, Y.; Huang, J.; McIver, R.T.; Hemminger, J.C. Characterization of thiol self-assembled films by laser desorption Fourier transform mass spectrometry. *J. Am. Chem. Soc.* **1992**, *114*, 2428–2432.
  42. Tarlov, M.J.; Newman, J.G. Static secondary ion mass spectrometry of self-assembled alkanethiol monolayers on gold. *Langmuir* **1992**, *8*, 1398–1405.
  43. Huang, J.; Hemminger, J.C. Photooxidation of thiols in self-assembled monolayers on gold. *J. Am. Chem. Soc.* **1993**, *115*, 2243–2343.
  44. Tarlov, M.J.; Burgess, D.R.F.; Gillen, G. UV photopatterning of alkanethiolate monolayers self-assembled on gold and silver. *J. Am. Chem. Soc.* **1993**, *115*, 5305–5306.
  45. Cooper, E.; Wiggs, R.; Hutt, D.A.; Parker, L.; Leggett, G.J.; Parker, T.L. Rates of attachment of fibroblasts to self-assembled monolayers formed by the adsorption of alkylthiols onto gold surfaces. *Mater. Chem.* **1997**, *7*, 435–441.
  46. Cooper, E.; Leggett, G.J. Influence of tail-group hydrogen bonding on the stabilities of self-assembled monolayers of alkylthiols on gold. *Langmuir* **1999**, *15*, 1024–1032.
  47. Hutt, D.A.; Leggett, G.J. Dependence of rates of photo-oxidation of self-assembled monolayers on adsorbate alkyl chain length. *J. Phys. Chem.* **1996**, *100*, 6657–6662.
  48. Hutt, D.A.; Cooper, E.; Leggett, G.J. Structure and mechanism of photo-oxidation of self-assembled monolayers of alkylthiols on silver studied by XPS and static SIMS. *J. Phys. Chem. B* **1998**, *102*, 174–184.
  49. Cooper, E.; Leggett, G.J. Static SIMS studies of self-assembled monolayers: the influence of adsorbate chain length and terminal functional group on rates of photo-oxidation of alkylthiols on gold. *Langmuir* **1998**, *14*, 4795–4801.
  50. Zhang, Y.; Terrill, R.H.; Tanzer, T.A.; Bohn, P.W. Ozonolysis is the primary cause of UV photooxidation of alkanethiolate monolayers at low irradiance. *J. Am. Chem. Soc.* **1998**, *120*, 2654.
  51. Zhang, Y.; Terrill, R.H.; Bohn, P.W. Ultraviolet photochemistry and ex situ ozonolysis of alkanethiol self-assembled monolayers on gold. *Chem. Mater.* **1999**, *11*, 2191.
  52. Norrod, K.L.; Rowlen, K.L. Ozone-induced oxidation of self-assembled decanethiol: contributing mechanism for “photooxidation”? *J. Am. Chem. Soc.* **1998**, *120*, 2656.
  53. Brewer, N.J.; Rawsterne, R.E.; Kothari, S.; Leggett, G.J. Oxidation of self-assembled monolayers by UV light with a wavelength of 254 nm. *J. Am. Chem. Soc.* **2001**, *123*, 4089–4090.
  54. Brewer, N.J.; Janusz, S.J.; Critchley, K.; Evans, S.D.; Leggett, G.J. Photo-oxidation of self-assembled monolayers by exposure to light of wavelength 254 nm: a static SIMS study. *J. Phys. Chem.* **2005**, *109*, 11,247–11,256.
  55. Chong, K.S.L.; Sun, S.; Leggett, G.J. Measurement of the kinetics of photo-oxidation of self-assembled Monolayers by friction force microscopy. *Langmuir* **2005**, *21*, 3903–3909.
  56. Sun, S.; Leggett, G.J. Generation of nanostructures by scanning near-field photolithography of self-assembled monolayers and wet chemical etching. *Nano Lett.* **2002**, *2*, 1223–1227.
  57. Sun, S.; Chong, K.S.L.; Leggett, G.J. Nanoscale molecular patterns fabricated using scanning near-field optical lithography. *J. Am. Chem. Soc.* **2002**, *124*, 2414–2415.
  58. Sun, S.; Leggett, G.J. Matching the resolution of electron beam lithography using scanning near-field photolithography. *Nano Lett.* **2004**, *4*, 1381–1384.
  59. Sigal, G.B.; Mrksich, M.; Whitesides, G.M. Effect of surface wettability on the adsorption of proteins and detergents. *J. Am. Chem. Soc.* **1998**, *120*, 3464–3473.
  60. Chong, K.S.L. Fabrication of Molecular Nanostructures by Scanning Near-Field Optical Lithography. Ph.D.thesis, The University of Sheffield, 2004.
  61. Sun, S.; Chong, K.S.L.; Leggett, G.J. Photopatterning of self-assembled monolayers at 244 nm and applications to the fabrication of functional microstructures and nanostructures. *Nanotechnol.* **2005**, *16*, 1798–1808.

62. Xia, Y.; Zhao, X.-M.; Kim, E.; Whitesides, G.M. A selective etching solution for use with patterned self-assembled monolayers of alkanethiolates on gold. *Chem. Mater.* **1995**, *7*, 2332–2337.
63. Wurtz, G.; Bachelot, R.; H'dhili, F.; Royer, P.; Triger, C.; Ecoffet, C.; Lougnot, D.-J. Photopolymerisation induced by optical field enhancement in the vicinity of a conducting tip under laser illumination. *Jpn. J. Appl. Phys.* **2000**, *39*, L98–L100.
64. H'dhili, F.; Bachelot, R.; Lerondel, G.; Barchiesi, D.; Royer, P. Near-field optics: direct observation of the field enhancement below an apertureless probe using a photosensitive polymer. *Appl. Phys. Lett.* **2001**, *79*, 4019–4021.
65. Bachelot, R.; H'dhili, F.; Barchiesi, D.; Lerondel, G.; Fikri, R.; Royer, P. Apertureless near-field optical microscopy: a study of the local tip field enhancement using photosensitive azobenzene-containing films. *J. Appl. Phys.* **2003**, *94*, 2060–2072.
66. Yin, X.; Fang, N.; Zhang, X.; Martini, I.B.; Schwartz, B.J. Near-field two-photon nanolithography using an apertureless optical probe. *Appl. Phys. Lett.* **2002**, *81*, 3663–3665.

# Scanning Probe Lithography: Polymeric and Biomolecular Nanostructures

Stefan Zauscher

*Department of Mechanical Engineering and Materials Science, Duke University,  
Durham, North Carolina, U.S.A.*

## INTRODUCTION

One central goal of materials engineering is to produce hierarchical materials that are ordered over a range of length scales and in which larger-scale structural and physicochemical properties are controlled by molecular characteristics.<sup>[1]</sup> Fabricating molecular, polymeric, and biomolecular structures on surfaces and controlling their architecture on the nanometer length scale is important for a wide range of applications. For example, the ability to pattern surfaces with polymers and biomacromolecules has important applications in biosensors,<sup>[2]</sup> proteomic chips,<sup>[3]</sup> and nanofluidic devices.<sup>[4]</sup> To date, fabrication of micropatterns and microstructures for these applications has relied on either photolithography<sup>[2,5,6]</sup> or an ensemble of related techniques termed “soft lithography”,<sup>[7]</sup> that use elastomeric stamps or molds. These techniques have been extremely successful at the micrometer length scale or larger, but have a number of inherent limitations that preclude their extension to the nanometer length scale. X-ray lithography<sup>[8–10]</sup> requires expensive mask alignment equipment, and the photoresists and developers commonly used are incompatible with many organic and biomolecules. Furthermore, like electron beam lithography,<sup>[8,11,12]</sup> it requires expensive ultrahigh vacuum equipment.

This review will focus on methods that allow for molecular-level control in the fabrication of polymeric and biomolecular nanostructures using scanning probe lithography (SPL),<sup>[13–15]</sup>. Among all the available nanofabrication techniques, SPL has unique advantages because of its simplicity and capability to both manipulate and image nanostructures on surfaces. In contrast to other nanofabrication methods, SPL, which is capable of resolution less than 50 nm<sup>[16]</sup> is technologically simpler, significantly cheaper, and therefore a much more widely accessible method to most researchers, requiring only a scanning probe microscope (SPM) such as a scanning tunneling microscope (STM),<sup>[17]</sup> an atomic force microscope (AFM)<sup>[18]</sup>, or a near-field scanning optical microscope (NSOM)<sup>[19,20]</sup> (Fig. 1).

SPL can behave like an interactive plotter, registering with nanostructures on a surface, while offering resolution comparable to electron beam lithography.<sup>[21]</sup> The slow-speed serial nature of the lithography process can be circumvented by employing cantilever arrays.<sup>[22]</sup>

## METHODOLOGY

Direct manipulation of both self-assembly and supramolecular chemistry are critical to materials engineering on the nanoscale. Generally, two fabrication approaches are used: a “bottom-up” or “grafting from” approach, which constructs supramolecular ensembles by synthesis of functionalized, small molecular units, using, for example, surface initiated polymerization; and a “grafting to” approach that seeks to directly manipulate and position macromolecules, proteins, or ligands on a surface with nanometer precision.

### Self-Assembled Affinity Templates

Highly ordered and spatially confined self-assembled monolayers (SAMs) serve as initiator platforms for polymerization of polymer brushes and as growth templates for directed self-assembly of synthetic and biomolecules. The molecules forming these “affinity templates” are typically bifunctional, where the surface binding group (silane<sup>[23]</sup> or thiol<sup>[24,25]</sup>) is chosen to match the substrate chemistry. The linker, usually an inert hydrocarbon chain, connects the surface binding group with the ligating, functional head group, often a hydroxyl (–OH) or carboxyl (–COOH) group.

### Surface-Initiated Polymerization

Attaching polymer brushes<sup>[26]</sup> with thicknesses on the molecular scale to solid surfaces allows one to tailor the surface properties of materials by imparting desirable energetic, mechanical, and electrical functionalities. The in situ formation of polymer brushes in a “grafting-from” approach, using patterned SAMs of

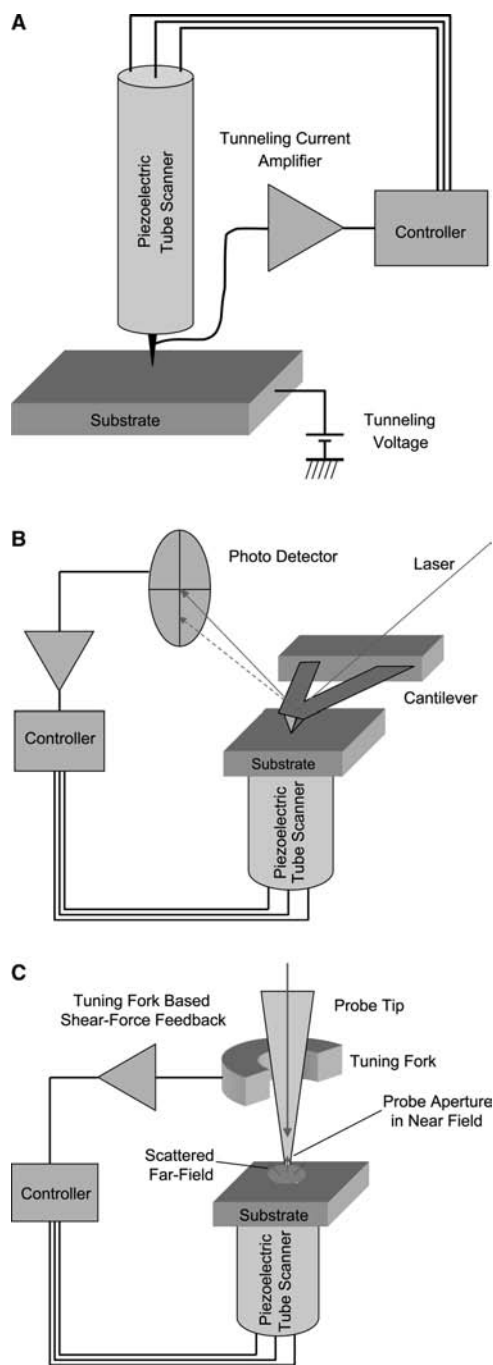


**Fig. 1** Schematic view of scanning probe microscopes. (A) Scanning tunneling microscope (STM), (B) atomic force microscope (AFM), and (C) near-field scanning optical microscope (NSOM).

an initiator, provides spatial flexibility and achieves higher packing densities than possible in a “grafting-to” approach.<sup>[27,28]</sup>

Seminal work by Prucker and Rühle<sup>[27,28]</sup> led the way for generating polymer brushes in a “grafting from” approach using free radical polymerization. Although the templated fabrication of polymeric

nanostructures from the “bottom-up” has been prototypically demonstrated, and many methods to initiate polymerization reactions have been used (e.g., anion,<sup>[29]</sup> cation,<sup>[30]</sup> radical,<sup>[27]</sup> plasma,<sup>[31]</sup> condensation,<sup>[32]</sup> photochemical,<sup>[33]</sup> electrochemical,<sup>[34]</sup> and ring-opening metathesis polymerization.<sup>[35–37]</sup>), preparation of precisely patterned, surface-attached polymeric structures with controlled lengths, conformational geometries, functionality, and properties is still in its infancy. So far, atom-transfer radical polymerization (ATRP) has been the workhorse polymerization methodology used by researchers attempting to prepare surface-attached polymer brushes of controlled structure<sup>[38,39]</sup> This transition metal-based, controlled radical polymerization chemistry produces functional polymers with defined molecular weight and polydispersity, and as a result of the “living” nature of the catalyst, allows the ready synthesis of block copolymers.

### Protein Grafting

The precision with which one can organize large molecular structures, such as proteins, depends on the quality and chemical functionality of the affinity template nanostructure.<sup>[40]</sup> Ideally, the template surface and background polymers are chosen so that the protein to be grafted selectively links either with the template or the background only. Some approaches for protein grafting or “immobilization” rely on physisorption, while others make use of chemical bonds between protein and substrate, particularly if the patterned protein is subjected to hydrodynamic or other physical forces. Covalent immobilization methods include formation of amide, imine, and disulfide bonds. While these approaches are relatively simple, they often preclude direct control over protein orientation on the surface, which is problematic if protein binding to its recognition partners is desired. Recently, Hyun et al.<sup>[41]</sup> developed a new nanofabrication method allowing control over molecular orientation by using molecular recognition mediated protein immobilization.

### SCANNING PROBE LITHOGRAPHY

Shortly after the invention of the scanning probe microscope, it was realized that the tips used for imaging could also be used to modify the surfaces. Since then, many SPL techniques have been developed based on various chemical, physical, and electrical modifications of surfaces, including mechanical scratching,<sup>[42–44]</sup> electrochemical anodization of silicon surfaces,<sup>[45,46]</sup> decomposition of self-assembled



monolayers,<sup>[45,47–49]</sup> electric field induced chemical reactions,<sup>[50,51]</sup> and electrochemical reactions in solution using electrochemical STM tips.<sup>[52–57]</sup> Several comprehensive reviews of SPM related lithography can be found in the literature.<sup>[16,58]</sup>

Depending on the instrument design, either the probe tip scans relative to a stationary sample surface, or the surface is scanned relative to a stationary tip. Scanning is typically achieved through piezoelectric actuators. The requirement for accurate tip positioning has driven SPM design to use closed-loop scanning to compensate for the non-linear and often hysteretic behavior of piezoelectric actuators. Increasing interest in scanning probe lithography has also spurred the development of user interfaces that allow the user to program arbitrary motions of the tip relative to the sample,<sup>[59]</sup> and several SPM manufacturers now offer lithography packages. Current methods for fabricating polymer nanostructures include nanoshaving and nanografting, dip-pen nanolithography (DPN), direct-write DPN, and near-field scanning optical lithography.

### Nanoshaving and Nanografting

Perhaps the simplest method for fabricating patterned substrates is nanoshaving, in which SAM adsorbates are mechanically displaced while the cantilever tip is dragged over the surface, leaving behind a patterned surface.<sup>[42,44,60]</sup> Large contact pressure during patterning<sup>[44]</sup> creates large shear forces that exceed the displacement threshold of the usually chemisorbed molecules (Fig. 2A). In nanografting, the AFM tips

are again used to displace thiol molecules from adsorption sites; however, cantilever and SAM are now immersed in a solution of a different thiol<sup>[43]</sup> (Fig. 2B).

These thiols in solution immediately self-assemble on the newly exposed gold surface left behind as the tip shaves the matrix SAM. The resulting SAM patterns can now be used as affinity templates for protein immobilization<sup>[40]</sup> or for surface initiated nanopolymerization.

### Dip-Pen Nanolithography

More recently, a new SPL technique, “dip-pen” nanolithography (DPN),<sup>[61,62]</sup> has permitted patterning of monolayer films of thiolated organic molecules with sub-100-nm resolution onto gold substrates. The technology uses the spontaneous condensation of water vapor between the AFM tip and substrate to transport organic molecules from the AFM tip to the surface in the area specifically defined by the tip–surface interaction<sup>[63]</sup> (Fig. 3).

To draw on a familiar analogy, the AFM tip acts as a “pen,” the organic molecules act as “ink,” and the surface acts as “paper” to “draw” the nanostructures. DPN allows direct patterning of nanoscale structures in both serial and parallel fashions.<sup>[64]</sup> Attractive features of DPN over most other SPL techniques are its simplicity—it requires no liquid cells—and its ability to create various nanostructures in a “direct-write” fashion. Furthermore, as long as the tip can be inked with a solution containing the reactant of interest and a capillary meniscus maintained between the tip and surface, there appears to be little limitation on the types of molecules that can be transferred onto a

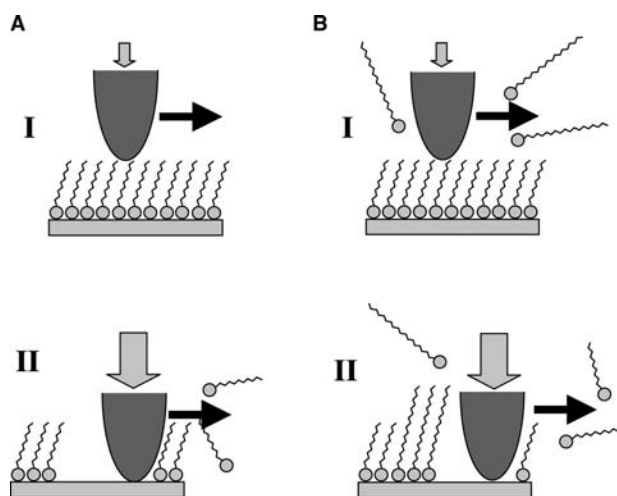


**Fig. 2** Schematic diagrams of two basic manipulation mechanisms using AFM: (A) nanoshaving and (B) nanografting. The corresponding imaging (I) and fabrication (II) modes are depicted in the top and bottom rows, respectively. *Source:* From Ref.<sup>[44]</sup>. © 2000, American Chemical Society.

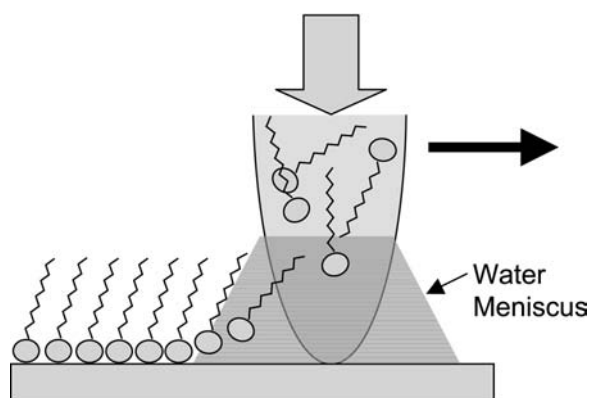


**Fig. 3** Schematic representation of dip-pen nanolithography (DPN). A water meniscus forms between the AFM tip, typically coated with a  $\omega$ -functionalized alkane thiol (e.g., mercapto-hexadecanoic acid) and a gold substrate. The size of the meniscus, which is controlled by relative humidity, affects the thiol transport rate, the effective tip–substrate contact area, and DPN resolution.

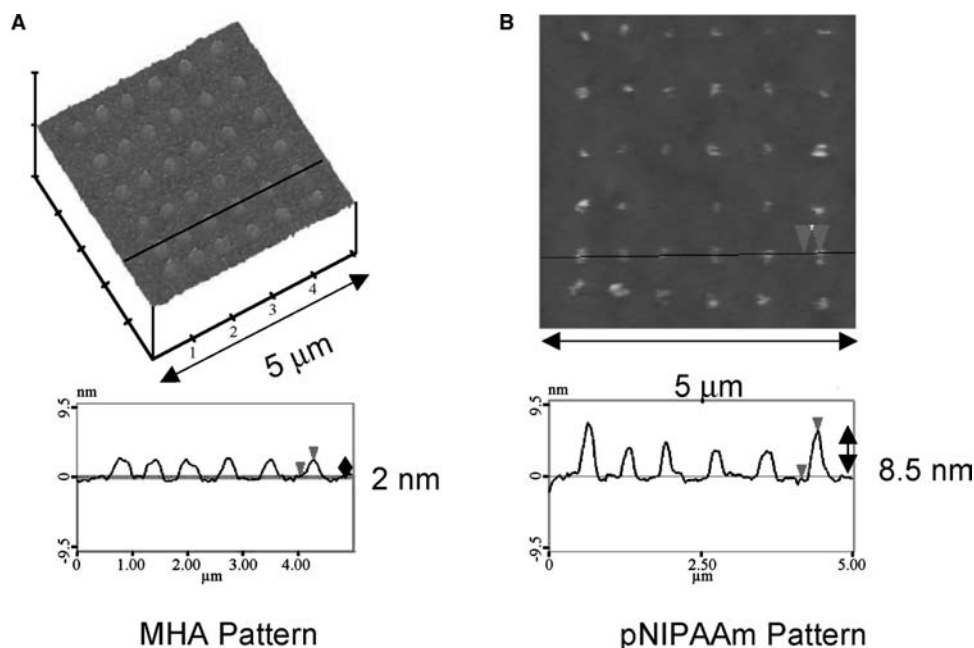


**Fig. 4** Surface initiated nanopolymerization (SINP) of *N*-isopropylacrylamide (NIPAAm) on a mercaptohexadecanoic acid (MHA) pattern, conjugated with free radical initiator. (A) AFM lateral force height image of MHA patterned with DPN and typical cross section (contact mode in air). (B) AFM height image of the corresponding pNIPAAm pattern and typical cross section (TappingMode® in air). The feature height after 30 hr reaction time ranges between 7 and 9 nm, and is amplified at the pattern boundary. *Source:* From Ref.<sup>[65]</sup>. © 2003, Materials Research Society.

surface. Thus DPN enables a large number of additive chemical reactions to be performed on diverse substrates with nanometer resolution comparable to that achieved with electron-beam lithography. However, to achieve this nanometer resolution, DPN requires molecularly smooth gold substrates.

Recently, Ahn, Lee, and Zauscher<sup>[65]</sup> combined surface initiated polymerization with DPN in a fabrication process termed “surface initiated nanopolymerization” (SINP) to fabricate patterned, surface-confined, stimulus-responsive polymer brushes (Fig. 4). In this approach, mercaptohexadecanoic acid (MHA) was patterned on gold thin films by DPN (Fig. 4A) and subsequently conjugated with a free radical initiator. The cross-sectional profile of a pattern with 300-nm dots reveals that the polymer brush height at the periphery of the pattern is larger than that in the center (Fig. 4B).

These and other results suggest that the rate of polymerization, and thus the brush height in uncontrolled free radical polymerizations of *N*-isopropylacrylamide (NIPAAm), are affected by pattern size. This may likely be attributable to the density of initiator immobilized on the surface and limited monomer diffusion to the surface of the growing brush (1-D).<sup>[28]</sup> Diffusional freedom is larger at pattern boundaries (2-D) and polymer growth is usually larger there.

Controlled/living radical polymerization methods, such as atom transfer radical polymerization (ATRP),

decrease the probability of bimolecular termination reactions, yielding polymer brushes of uniform molecular weight and controlled composition. Kaholek et al.<sup>[66]</sup> succeeded in fabricating stimulus-responsive polymer patterns with linewidths of 200 nm, by directly patterning the initiator thiol using DPN, and subsequent amplification of the pattern using ATRP of NIPAAm in an organometallic catalyst solution (Fig. 5).

The preparation of patterned protein surfaces using DPN was first demonstrated by Demers et al.<sup>[67]</sup> and Lee et al.<sup>[68]</sup> who physisorbed lysozyme and immunoglobulin G (IgG) onto DPN nanopatterned mercaptohexadecanoic acid (MHA) templates, achieving feature sizes on the order of 100 nm. By backfilling with a protein-resistant oligoethylene glycol-terminated alkanethiol SAM,<sup>[69]</sup> they avoided non-specific protein adsorption that could have led to large background signals and complicated differentiation between active and inactive areas of the substrate.

A method for molecular-recognition mediated, stepwise fabrication of patterned protein nanostructures with feature sizes on the order of 200 nm was recently developed in the author’s laboratory (Fig. 6).<sup>[41]</sup>

In this method, an amine-terminated biotin derivative was covalently conjugated with a chemically activated MHA SAM nanopattern, patterned with DPN on gold. The patterned surface was then incubated

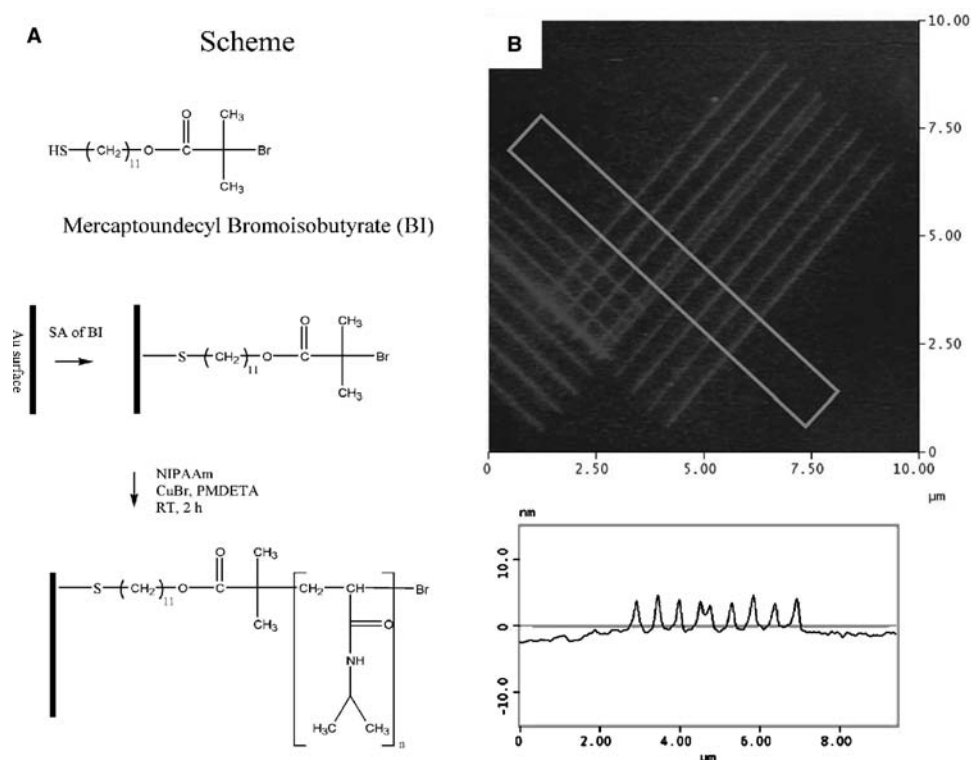


**Fig. 5** Surface initiated nanopolymerization of NIPAAm using atom transfer radical polymerization (ATRP) on directly patterned initiator thiol. (A) Reaction scheme. (B) AFM height image of the resulting pNIPAAm line pattern showing a line width of 220 nm line and a brush height of 5.7 nm (TappingMode<sup>TM</sup> in Milli-Q<sup>TM</sup> water).

with streptavidin whose binding to the pattern was mediated by molecular recognition between biotin and streptavidin. The patterned streptavidin surface functioned as a universal platform for molecular-recognition mediated protein immobilization through use of biotinylated molecules. “Smart,” reversible protein nanopatterns were fabricated by using iminobiotin as the molecular recognition partner. These structures are pH-sensitive and allow for the reversible immobilization of iminobiotin tagged proteins. This latter

characteristic makes possible the regeneration of the nanopattern.

The concept of “smart,” regenerable protein patterns was carried one step further by Hyun et al.,<sup>[70]</sup> who developed a new method for the fabrication of stimulus-responsive polypeptide nanostructures using DPN. They created an array comprising elastin-like polypeptide (ELP) nanodots with a diameter of approximately 200 nm on gold against a non-fouling oligoethylene glycol-terminated alkanethiol SAM (Fig. 7).

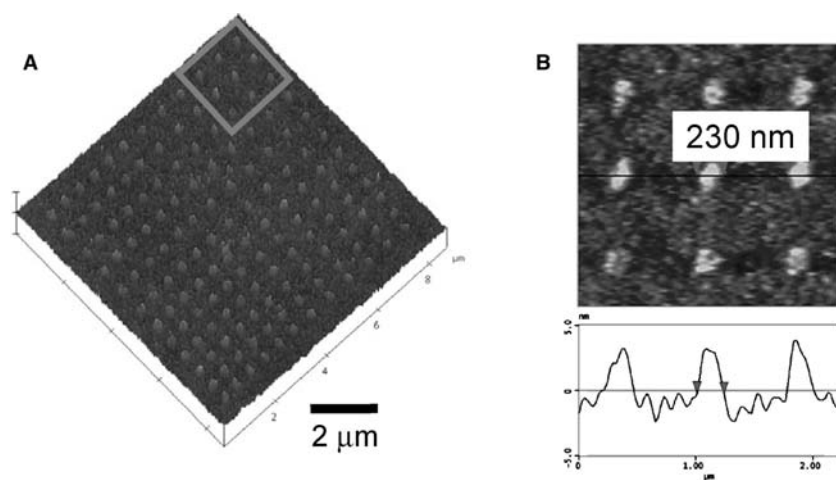


**Fig. 6** AFM height images of Biotin-BSA nanopatterns (TappingMode<sup>TM</sup> in Milli-Q<sup>TM</sup> water). (A) 144 dot pattern with average feature size of 230 nm. (B) Zoom of the area indicated by the square in panel (A) and representative cross section showing the typical feature size. *Source:* From Ref.<sup>[41]</sup>. © 2002, American Chemical Society.

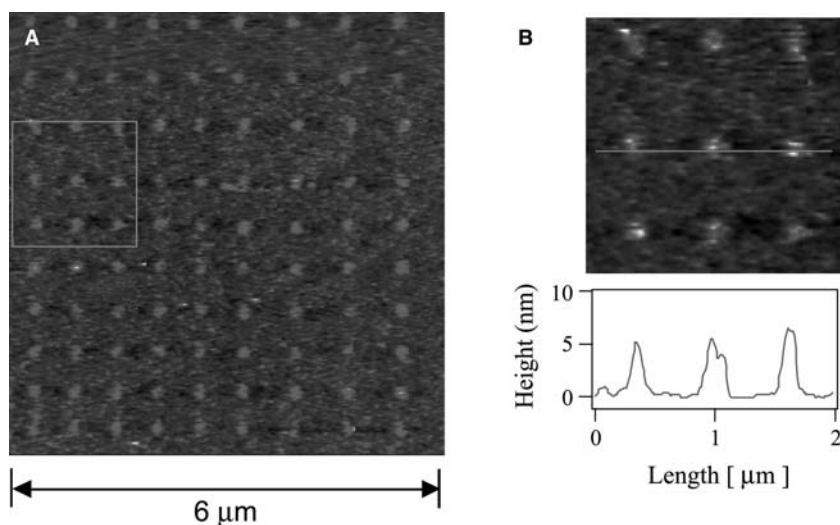


**Fig. 7** (A) AFM TappingMode<sup>®</sup> height image of a  $10 \times 9$  elastin-like polypeptide (ELP) dot array in PBS buffer. (B) Enlarged view of area indicated in panel (A) and representative cross section, showing a feature size of about 200 nm.

ELPs, chemically grafted onto self-assembled monolayers on gold, exhibit an interfacial hydrophilic–hydrophobic phase transition in response to increased temperature or ionic strength. This stimulus-response behavior of ELP nanopatterns can be harnessed for the reversible immobilization of small amounts of ELP-tagged proteins from solution, which is important for protein detection and purification on the nanoscale.

### Direct-Write DPN

Direct-write DPN of polymeric and biomolecular structures has great appeal as an efficient nanofabrication method. For example, tip-directed in-situ polymerization potentially eliminates multiple-step processing that currently requires amplification of a pattern in a bulk polymerization step. Even greater advantages present themselves for direct-write DPN of proteins in areas of drug discovery, diagnostics, and proteomics, as it offers the possibility of generating arrays made from more than one protein.

Until recently, DPN has been used to fabricate affinity arrays from small organic molecules that aid in the directed deposition of proteins and biomacromolecules from solution.<sup>[41,68,70]</sup> Demers et al.<sup>[67]</sup> developed a variation of DPN that directly writes oligonucleotides on metals and insulators. A key strategy for the success of this approach was the use of matched ink–substrate combinations, directing the transfer of oligonucleotides onto the substrate. Lee, Kim, and Mikin<sup>[71]</sup> recently developed an innovative approach for directly writing proteins using DPN. This method hinges on the realization that protein transfer from the tip onto the substrate requires a biocompatible and hydrophilic (non-fouling) tip surface layer (Fig. 8).

The latter was achieved by tip-surface treatment with a poly(ethylene-glycol)silane. Directed, and orientationally controlled protein deposition on the

substrate surface is possible by judicious matching of surface and protein functionality.<sup>[71,72]</sup>

Current photolithography, microcontact printing, template synthesis, and scanning electrochemical microlithography techniques can yield conducting polymer microstructures, but these techniques possess significant limitations for patterning structures of  $< 100$ -nm dimensions. The availability of a wide range of monomers enables direct-writing of polymeric materials with a wide range of interesting electronic and electrooptical properties at the nanoscale level. Li, Maynov, and Liu<sup>[73]</sup> have recently introduced a variation of DPN, in which the water meniscus on the AFM tip is not only used as the transfer medium but

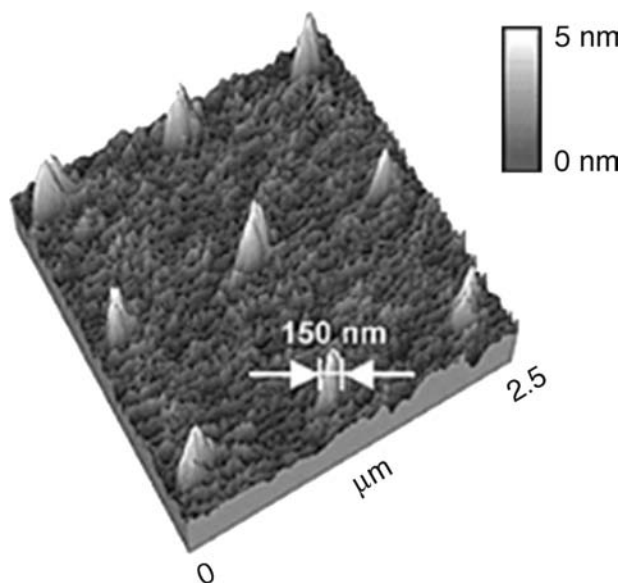


**Fig. 8** Protein nanoarray prepared via direct-write DPN. Contact mode height image of a Lysozyme nanodot array with a feature size of about 150 nm. *Source:* From Ref.<sup>[71]</sup>. © 2003 American Chemical Society.

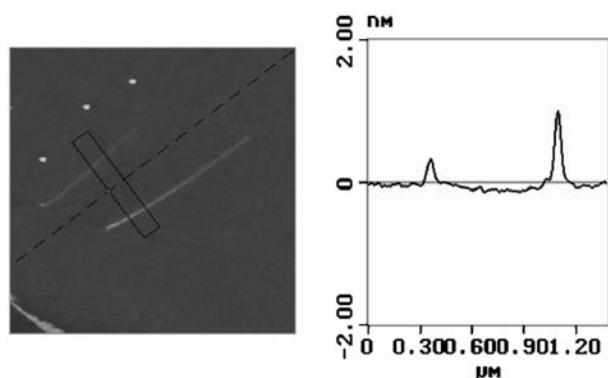


**Fig. 9** Tip-directed electrochemical polymerization of 3,4-ethylenedioxythiophene. AFM height image (contact mode in air) showing two polymer lines each about 50 nm wide. *Source:* From Ref.<sup>[74]</sup>. © 2001, American Chemical Society.

also serves as a nanometer-sized electrochemical cell in which metal salts can be dissolved, electrochemically reduced, and ultimately deposited on a surface.<sup>[73]</sup> They showed that electrochemical DPN can be used to directly fabricate conducting polythiophene nanostructures on semiconducting and insulating surfaces in the sub-100-nm size scale.<sup>[74]</sup> To pattern these nanostructures, a negative bias voltage was applied between the AFM tip and a silicon surface, and the tip was translated across the surface in a preprogrammed pattern. The applied voltage electrochemically polymerized the monomer, resulting in tip-defined deposition of poly-3,4-ethylenedioxythiophene on the substrate (Fig. 9).

### Near-Field Scanning Optical Lithography

To date, photolithography is perhaps the most successful microfabrication technology, as most microelectronic circuits are produced via photolithographic methods. In conventional photolithography, the lateral resolution is determined by the Abbe diffraction limit (a far-field effect), which limits the feature size to about half the wavelength of the radiation used. The diffraction limit can be circumvented if the photosensitive sample is placed in the optical near-field of the focusing elements.<sup>[19,75]</sup> Optical lithography in the evanescent near field is mainly developed as a static patterning process by using a shadow mask in close proximity to a photoresist layer during exposure.<sup>[76]</sup>

In near-field scanning optical lithography (NSOL), this approach is taken one step further by inducing photopolymerization only in the vicinity of the probe tip (Fig. 10A).<sup>[19,75]</sup> In most NSOL techniques, laser radiation is coupled directly into a tapered single-mode optical fiber where the small fiber aperture limits the intensity of the deliverable radiation. Another NSOL

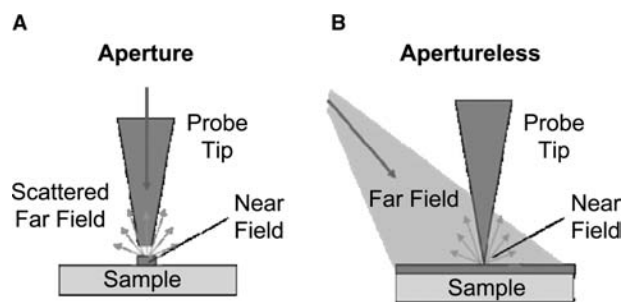


**Fig. 10** Two possible configurations for scanning near-field optical lithography. (A) NSOM aperture probe where radiation enters the region of interest in the near field through the probe. (B) Aperture-less NSOM using far field illumination. Intensity amplification occurs beneath the probe tip in the optical near field.

technique capitalizes on the field enhancement of optical radiation in the near field of a conducting SPM tip due to photon absorption (Fig. 10B).<sup>[77–79]</sup>

This approach is of considerable interest for surface nanopatterning and nanofabrication as it circumvents the use of delicate optical fibers and instead makes use of readily available laser sources and focusing optics.

Wurtz et al.<sup>[79]</sup> report on photopolymerization of a photoresist formulation induced by optical field enhancement in the near field of a conducting tip.<sup>[78,80]</sup> The free radical polymerization reaction was triggered by an actinic light activated sensitizer dye that, in the triplet state, reacts with amine to form free radicals. The threshold energy necessary to trigger a reaction is high and requires relatively large field intensities. Sufficiently large fields were only achieved in close proximity to the tip apex of a conducting AFM cantilever. Polymeric features with 70-nm lateral feature size were fabricated (Fig. 11).

These results are significant because they demonstrate that direct nanopolymerization in the evanescent

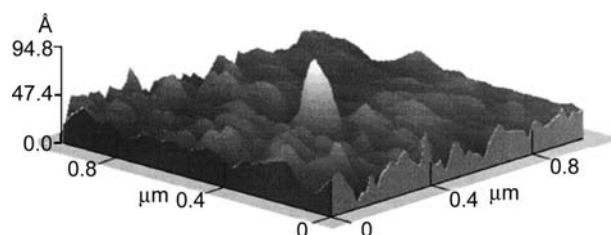


**Fig. 11** Aperture-less near-field scanning optical lithography where the optical field enhancement at the tip initiates locally the photopolymerization process. AFM height image (TappingMode<sup>TM</sup> in air) showing a nanometer scale polymer feature polymerized from a photo-polymerizable formulation (resist). *Source:* From Ref.<sup>[39]</sup>. © 2000, Japanese Institute of Pure and Applied Physics.

near-field of a conducting AFM tip is possible, and affords an elegant way for patterning surfaces with polymers.

## CONCLUSION

Advances in the area of scanning probe lithography have made available techniques, such as dip-pen nanolithography and nanografting, that allow fabrication of polymeric structures on surfaces on the nanoscale. While significant progress has been made in nanopatterning of biomacromolecules using affinity templates and direct writing, nanofabrication of polymeric structures from the “bottom up” using scanning probe lithography has only been prototypically demonstrated. Thus there is now a need to build more complex polymeric structures with precisely controlled lengths, conformational geometries, and chemical functionalities. In pursuit of these goals, techniques must be further developed which allow for the controlled synthesis of surface-attached polymers.

Several factors need to be addressed for the viability of SPL as a fabrication technology for polymeric nanostructures beyond the laboratory scale: 1) lateral resolution; 2) alignment; 3) reliability; and 4) throughput. While items 1)–3) are intrinsic capabilities associated with SPMs, a considerable restriction is presented by the slow, serial nature of the patterning process—one tip creates a single feature at a time. Recent developments of massively parallel proximal probe systems have been demonstrated,<sup>[22]</sup> and offer prospects toward achieving cost-effective, high-throughput “direct write” fabrication. The development of complex patterns is only possible through sufficient automation of the instrumentation and through pattern generation making use of computer-aided design (CAD). Progress in this area is of primary importance for the evolution of existing SPL nanofabrication strategies.

## ACKNOWLEDGMENTS

The author would like to thank the National Science Foundation for support through grants NSF EEC-021059 and NSF DMR-0239769 CAREER AWARD. The author is grateful to Ken C. Caster for helpful discussions. The help of Chris Markley in preparing this manuscript is acknowledged.

## REFERENCES

- Dan, N. Synthesis of hierarchical materials. *Trends Biotechnol.* **2000**, *18* (9), 370–374.
- Blawas, A.S.; Reichert, W.M. Protein patterning. *Biomaterials* **1998**, *19* (7–9), 595–609.
- Mrksich, M.; Whitesides, G.M. Patterning self-assembled monolayers using microcontact printing—A new technology for biosensors. *Trends Biotechnol.* **1995**, *13* (6), 228–235.
- Beebe, D.J.; Moore, J.S.; Yu, Q.; Liu, R.H.; Kraft, M.L.; Jo, B.H.; Devadoss, C. Microfluidic tectonics: A comprehensive construction platform for microfluidic systems. *Proc. Natl. Acad. Sci. U. S. A.* **2000**, *97* (25), 13488–13493.
- Hengsakul, M.; Cass, A.E.G. Protein patterning with a photoactivatable derivative of biotin. *Bioconjug. Chem.* **1996**, *7* (2), 249–254.
- Mooney, J.F.; Hunt, A.J.; McIntosh, J.R.; Liberko, C.A.; Walba, D.M.; Rogers, C.T. Patterning of functional antibodies and other proteins by photolithography of silane monolayers. *Proc. Natl. Acad. Sci. U. S. A.* **1996**, *93* (22), 12287–12291.
- Xia, Y.N.; Whitesides, G.M. Soft lithography. *Angew. Chem. Int. Ed.* **1998**, *37* (5), 551–575.
- Chen, Z.W. Nanometric-scale electron-beam lithography. *Adv. Electron. El. Phys.* **1992**, *83*, 107–201.
- Tandon, U.S.; Pant, B.D.; Kumar, A. An overview of x-ray-lithography for use in semiconductor-device preparation. *Vacuum* **1991**, *42* (18), 1219–1228.
- Tolfree, D.W.L. Microfabrication using synchrotron radiation. *Rep. Prog. Phys.* **1998**, *61* (4), 313–351.
- Craighead, H.G.; Mankiewich, P.M. Ultra-small metal-particle arrays produced by high-resolution electron-beam lithography. *J. Appl. Phys.* **1982**, *53* (11), 7186–7188.
- Pease, R.F.W. Nanolithography and its prospects as a manufacturing technology. *J. Vac. Sci. Technol., B* **1992**, *10* (1), 278–285.
- Kim, Y.; Lieber, C.M. Machining oxide thin-films with an atomic force microscope—Pattern and object formation on the nanometer scale. *Science* **1992**, *257* (5068), 375–377.
- Wada, Y. Possible application of micromachine technology for nanometer lithography. *Microelectron. J.* **1998**, *29* (9), 601–611.
- Quate, C.F. Scanning probes as a lithography tool for nanostructures. *Surf. Sci.* **1997**, *386* (1–3), 259–264.
- Nyffenegger, R.M.; Penner, R.M. Nanometer-scale surface modification using the scanning probe microscope: Progress since 1991. *Chem. Rev.* **1997**, *97* (4), 1195–1230.
- Binnig, G.; Rohrer, H. Scanning tunneling microscopy. *Helv. Phys. Acta* **1982**, *55* (6), 726–735.
- Binnig, G.; Quate, C.F.; Gerber, C. Atomic force microscope. *Phys. Rev. Lett.* **1986**, *56* (9), 930–933.
- Betzig, E.; Trautman, J.K. Near-field optics—Microscopy, spectroscopy, and surface modification beyond the diffraction limit. *Science* **1992**, *257* (5067), 189–195.
- Dunn, R.C. Near-field scanning optical microscopy. *Chem. Rev.* **1999**, *99* (10), 2891–2927.
- Mirkin, C.A.; Rogers, J.A. Emerging methods for micro- and nanofabrication. *MRS Bull.* **2001**, *26* (7), 506–508.
- Vettiger, P.; Despont, M.; Drechsler, U.; Durig, U.; Haberle, W.; Lutwyche, M.I.; Rothuizen, H.E.; Stutz,



- R.; Widmer, R.; Binnig, G.K. The “millipede”—More than one thousand tips for future AFM data storage. *IBM J. Res. Develop.* **2000**, *44* (3), 323–340.
23. Ulman, A. Self-assembled monolayers of alkyltrichlorosilanes—Building-blocks for future organic materials. *Adv. Mater.* **1990**, *2* (12), 573–582.
24. Bain, C.D.; Whitesides, G.M. Molecular-level control over surface order in self-assembled monolayer films of thiols on gold. *Science* **1988**, *240* (4848), 62–63.
25. Strong, L.; Whitesides, G.M. Structures of self-assembled monolayer films of organosulfur compounds adsorbed on gold single-crystals—Electron-diffraction studies. *Langmuir* **1988**, *4* (3), 546–558.
26. Zhao, B.; Brittain, W.J. Polymer brushes: Surface-immobilized macromolecules. *Prog. Polym. Sci.* **2000**, *25* (5), 677–710.
27. Prucker, O.; Rühle, J. Synthesis of poly(styrene) monolayers attached to high surface area silica gels through self-assembled monolayers of azo initiators. *Macromolecules* **1998**, *31* (3), 592–601.
28. Prucker, O.; Rühle, J. Mechanism of radical chain polymerizations initiated by azo compounds covalently bound to the surface of spherical particles. *Macromolecules* **1998**, *31* (3), 602–613.
29. Jordan, R.; Ulman, A.; Kang, J.F.; Rafailovich, M.H.; Sokolov, J. Surface-initiated anionic polymerization of styrene by means of self-assembled monolayers. *J. Am. Chem. Soc.* **1999**, *121* (5), 1016–1022.
30. Ingall, M.D.K.; Honeyman, C.H.; Mercure, J.V.; Bianconi, P.A.; Kunz, R.R. Surface functionalization and imaging using monolayers and surface-grafted polymer layers. *J. Am. Chem. Soc.* **1999**, *121* (15), 3607–3613.
31. Chen, W.; Fadeev, A.Y.; Hsieh, M.C.; Oner, D.; Youngblood, J.; McCarthy, T.J. Ultrahydrophobic and ultralyophobic surfaces: Some comments and examples. *Langmuir* **1999**, *15* (10), 3395–3399.
32. Husemann, M.; Mecerreyes, D.; Hawker, C.J.; Hedrick, J.L.; Shah, R.; Abbott, N.L. Surface-initiated polymerization for amplification of self-assembled monolayers patterned by microcontact printing. *Angew. Chem. Int. Ed.* **1999**, *38* (5), 647–649.
33. Prucker, O.; Naumann, C.A.; Rühle, J.; Knoll, W.; Frank, C.W. Photochemical attachment of polymer films to solid surfaces via monolayers of benzophenone derivatives. *J. Am. Chem. Soc.* **1999**, *121* (38), 8766–8770.
34. Gurtner, C.; Wun, A.W.; Sailor, M. Surface modification of porous silicon by electrochemical reduction of organo halides. *Angew. Chem. Int. Ed.* **1999**, *38* (13–14), 1966–1968.
35. Fürstner, A. Olefin metathesis and beyond. *Angew. Chem. Int. Ed.* **2000**, *39* (17), 3013–3043.
36. Grubbs, R.H.; Chang, S. Recent advances in olefin metathesis and its application in organic synthesis. *Tetrahedron* **1998**, *54* (18), 4413–4450.
37. Ivin, K.J.; Mol, J.C. *Olefin Metathesis and Metathesis Polymerization*; Academic Press: San Diego, 1997.
38. Matyjaszewski, K.; Xia, J.H. Atom transfer radical polymerization. *Chem. Rev.* **2001**, *101* (9), 2921–2990.
39. Patten, T.E.; Matyjaszewski, K. Copper(I)-catalyzed atom transfer radical polymerization. *Acc. Chem. Res.* **1999**, *32* (10), 895–903.
40. Liu, G.Y.; Amro, N.A. Positioning protein molecules on surfaces: A nanoengineering approach to supramolecular chemistry. *Proc. Natl. Acad. Sci. U. S. A.* **2002**, *99* (8), 5165–5170.
41. Hyun, J.; Ahn, S.J.; Lee, W.K.; Chilkoti, A.; Zauscher, S. Molecular recognition-mediated fabrication of protein nanostructures by dip-pen lithography. *Nano Lett.* **2002**, *2* (11), 1203–1207.
42. Xu, S.; Liu, G.Y. Nanometer-scale fabrication by simultaneous nanoshaving and molecular self-assembly. *Langmuir* **1997**, *13* (2), 127–129.
43. Xu, S.; Miller, S.; Laibinis, P.E.; Liu, G.Y. Fabrication of nanometer scale patterns within self-assembled monolayers by nanografting. *Langmuir* **1999**, *15* (21), 7244–7251.
44. Liu, G.Y.; Xu, S.; Qian, Y.L. Nanofabrication of self-assembled monolayers using scanning probe lithography. *Acc. Chem. Res.* **2000**, *33* (7), 457–466.
45. Sugimura, H.; Nakagiri, N. Scanning probe anodization: Nanolithography using thin films of anodically oxidizable materials as resists. *J. Vac. Sci. Technol., A, Vac. Surf. Films* **1996**, *14* (3), 1223–1227.
46. Legrand, B.; Stievenard, D. Nanooxidation of silicon with an atomic force microscope: A pulsed voltage technique. *Appl. Phys. Lett.* **1999**, *74* (26), 4049–4051.
47. Sugimura, H.; Takai, O.; Nakagiri, N. Multilayer resist films applicable to nanopatterning of insulating substrates based on current-injecting scanning probe lithography. *J. Vac. Sci. Technol., B* **1999**, *17* (4), 1605–1608.
48. Zamborini, F.P.; Crooks, R.M. Nanometer-scale patterning of metals by electrodeposition from an STM tip in air. *J. Am. Chem. Soc.* **1998**, *120* (37), 9700–9701.
49. Gorman, C.B.; Carroll, R.L.; He, Y.F.; Tian, F.; Fuierer, R. Chemically well-defined lithography using self-assembled monolayers and scanning tunneling microscopy in nonpolar organothiol solutions. *Langmuir* **2000**, *16* (15), 6312–6316.
50. Maoz, R.; Frydman, E.; Cohen, S.R.; Sagiv, J. “Constructive nanolithography”: Inert monolayers as patternable templates for in-situ nanofabrication of metal–semiconductor–organic surface structures—A generic approach. *Adv. Mater.* **2000**, *12* (10), 725–731.
51. Maoz, R.; Frydman, E.; Cohen, S.R.; Sagiv, J. Constructive nanolithography: Site-defined silver self-assembly on nanoelectrochemically patterned monolayer templates. *Adv. Mater.* **2000**, *12* (6), 424–429.
52. Kolb, D.M.; Ullmann, R.; Will, T. Nanofabrication of small copper clusters on gold(111) electrodes by a scanning tunneling microscope. *Science* **1997**, *275* (5303), 1097–1099.
53. Hofmann, D.; Schindler, W.; Kirschner, J. Electrodeposition of nanoscale magnetic structures. *Appl. Phys. Lett.* **1998**, *73* (22), 3279–3281.
54. Randler, R.J.; Kolb, D.M.; Ocko, B.M.; Robinson, I.K. Electrochemical copper deposition on Au(100): A

- combined in situ STM and in situ surface x-ray diffraction study. *Surf. Sci.* **2000**, *447* (1–3), 187–200.
55. Schindler, W.; Hofmann, D.; Kirschner, J. Nanoscale electrodeposition: A new route to magnetic nanostructures?. *J. Appl. Phys.* **2000**, *87* (9), 7007–7009.
  56. Yang, R.; Evans, D.F.; Hendrickson, W.A. Writing and reading at nanoscale with a scanning tunneling microscope. *Langmuir* **1995**, *11* (1), 211–213.
  57. Forouzan, F.; Bard, A.J. Evidence for faradaic processes in scanning probe microscopy on mica in humid air. *J. Phys. Chem., B* **1997**, *101* (50), 10876–10879.
  58. Bard, A.J.; Denuault, G.; Lee, C.; Mandler, D.; Wipf, D.O. Scanning electrochemical microscopy—A new technique for the characterization and modification of surfaces. *Acc. Chem. Res.* **1990**, *23* (11), 357–363.
  59. Cruchon-Dupeyrat, S.; Porthun, S.; Liu, G.Y. Nanofabrication using computer-assisted design and automated vector-scanning probe lithography. *Appl. Surf. Sci.* **2001**, *175*, 636–642.
  60. Kenseth, J.R.; Harnisch, J.A.; Jones, V.W.; Porter, M.D. Investigation of approaches for the fabrication of protein patterns by scanning probe lithography. *Langmuir* **2001**, *17* (13), 4105–4112.
  61. Piner, R.D.; Zhu, J.; Xu, F.; Hong, S.H.; Mirkin, C.A. “Dip-pen” nanolithography. *Science* **1999**, *283* (5402), 661–663.
  62. Hong, S.H.; Zhu, J.; Mirkin, C.A. A new tool for studying the in situ growth processes for self-assembled monolayers under ambient conditions. *Langmuir* **1999**, *15* (23), 7897–7900.
  63. Piner, R.D.; Mirkin, C.A. Effect of water on lateral force microscopy in air. *Langmuir* **1997**, *13* (26), 6864–6868.
  64. Mirkin, C.A.; Hong, S.H.; Demers, L.M.; Zhu, J.; Eidelman, A.A. Multiple-ink-dip pen nanolithography. *Abstr. Pap. Am. Chem. Soc.* **2000**, *219*, U285
  65. Ahn, S.-J.; Lee, W.-K.; Zauscher, S. Fabrication of Stimulus—Responsive Polymeric Nanostructures by Proximal Probes. In *Bioinspired Nanoscale Hybrid Systems*; Schmid, G., Simon, U., Stranick, S.J., Arrivo, S.M., Hong, S., Eds.; Materials Research Society: Warrendale, PA, 2003; Vol. 735, C11.54.11–C11.54.16.
  66. Kaholek, M.; Lee, W.-K.; LaMattina, B.; Caster, K.C.; Zauscher, S. Polymerization, Nanopatterning, and Characterization of Surface Confined, Stimulus-Responsive Polymer Brushes. In *Polymer Brushes: From Synthesis to Functional Microstructures*; Brittain, W.J., Advincula, R.C., R  he, J., Caster, K.C., Eds.; John Wiley & Sons: New York, 2003. Submitted.
  67. Demers, L.M.; Ginger, D.S.; Park, S.J.; Li, Z.; Chung, S.W.; Mirkin, C.A. Direct patterning of modified oligonucleotides on metals and insulators by dip-pen nanolithography. *Science* **2002**, *296* (5574), 1836–1838.
  68. Lee, K.B.; Park, S.J.; Mirkin, C.A.; Smith, J.C.; Mrksich, M. Protein nanoarrays generated by dip-pen nanolithography. *Science* **2002**, *295* (5560), 1702–1705.
  69. Prime, K.L.; Whitesides, G.M. Self-assembled organic monolayers—Model systems for studying adsorption of proteins at surfaces. *Science* **1991**, *252* (5009), 1164–1167.
  70. Hyun, J.; Lee, W.-K.; Nath, N.; Chilkoti, A.; Zauscher, S. Stimulus-responsive elastin-like polypeptide nanostructures. *Nano Lett.* **2003**. Submitted.
  71. Lee, K.B.; Lim, J.H.; Mirkin, C.A. Protein nanostructures formed via direct-write dip-pen nanolithography. *J. Am. Chem. Soc.* **2003**, *125* (19), 5588–5589.
  72. MacBeath, G.; Schreiber, S.L. Printing proteins as microarrays for high-throughput function determination. *Science* **2000**, *289* (5485), 1760–1763.
  73. Li, Y.; Maynor, B.W.; Liu, J. Electrochemical AFM “dip-pen” nanolithography. *J. Am. Chem. Soc.* **2001**, *123* (9), 2105–2106.
  74. Maynor, B.W.; Filocamo, S.F.; Grinstaff, M.W.; Liu, J. Direct-writing of polymer nanostructures: Poly (thiophene) nanowires on semiconducting and insulating surfaces. *J. Am. Chem. Soc.* **2002**, *124* (4), 522–523.
  75. Wegscheider, S.; Kirsch, A.; Mlynek, J.; Krausch, G. Scanning near-field optical lithography. *Thin Solid Films* **1995**, *264* (2), 264–267.
  76. Alkaisi, M.M.; Blaikie, R.J.; McNab, S.J. Nanolithography in the evanescent near field. *Adv. Mater.* **2001**, *13* (12–13), 877–887.
  77. Inouye, Y.; Kawata, S. Near-field scanning optical microscope with a metallic probe tip. *Opt. Lett.* **1994**, *19* (3), 159–161.
  78. Jersch, J.; Demming, F.; Hildenhagen, L.J.; Dickmann, K. Field enhancement of optical radiation in the nearfield of scanning probe microscope tips. *Appl. Phys., A: Mater. Sci. Process.* **1998**, *66* (1), 29–34.
  79. Wurtz, G.; Bachelot, R.; H’Dhili, F.; Royer, P.; Triger, C.; Ecoffet, C.; Lougnot, D.J. Photopolymerization induced by optical field enhancement in the vicinity of a conducting tip under laser illumination. *Jpn. J. Appl. Phys., Part 2-Lett.* **2000**, *39* (2A), L98–L100.
  80. Ecoffet, C.; Espanet, A.; Lougnot, D.J. Photopolymerization by evanescent waves: A new method to obtain nanoparts. *Adv. Mater.* **1998**, *10* (5), 411–414.

# Scanning Single-Electron Transistor Microscopy

N. B. Zhitenev

T. A. Fulton

*Bell Laboratories, Lucent Technologies, Murray Hill, New Jersey, U.S.A.*

## INTRODUCTION

The devices of nanotechnology will require fabrication and characterization tools capable of near-atomic resolution, such as scanning probe devices. These employ a small, ultrasharp tip placed upon the surface of a solid. The tip measures an electrical, mechanical, or thermal property of the surface on a scale that ranges from 100 nm down to the size of a single atom. The most familiar and widely used devices of this class are the scanning tunneling microscope and the atomic-force microscope. The scanning device being discussed here detects the electric fields arising from charge on a surface. It is capable of seeing individual electrons and even much smaller amounts of charge. The device is a marriage of the sharp-tip scanning probe geometry with the single-electron transistor (SET).<sup>[1,2]</sup> The SET is based on the quantum-mechanical phenomenon of electron tunneling and the principle of Coulomb blockade. It has a conductance that is unusually sensitive to an external electric field, such as provided by the charge  $e$  of a nearby electron. A probe with this capability having atomic-scale spatial resolution would potentially be a powerful tool for surface characterization in both technology and surface science. The present-date SET probes have not reached this status. So far the demonstrated resolution for charge on the surface of a solid is of order  $0.001e$  with a spatial resolution of  $\sim 30$  nm. The operation has been restricted to liquid He temperature ( $<4$  K). The performance of SET probes can be expected to improve in the future as new nanoscale fabrication techniques become available.

## NATURE OF THE SINGLE-ELECTRON TRANSISTOR

The SETs used here are based on the metal–metal tunnel junction.<sup>[3]</sup> It consists of two metal electrodes separated by a thin insulating layer a few nanometers thick. Electrons can pass through the thin insulator by quantum-mechanical tunneling. In this process, an electron will spontaneously disappear from one electrode at random times and immediately reappear in the other.

A voltage bias  $V$  applied between the electrodes produces a net tunneling current  $I$ . A tunnel junction between two normal metals shows an ohmic conductance like a resistor. Unlike a resistor, however, the current has a granular nature, as it is made up of the random passage of individual charges of size  $e$ . This granularity is a significant factor in the operation of the SET.

The SET is a two-tunnel-junction device as shown schematically in Fig. 1. It has two conducting leads (X and Y in Fig. 1) that make contact with a much smaller, intermediate metal island (Z in Fig. 1). There may also be a gate (G in Fig. 1) that is capacitively coupled to the island. The island is connected to the leads by tunnel junctions (J1 and J2 in Fig. 1). A fundamental goal of the design is to make the total capacitance of the island,  $C$ , as small as practical. For a fixed geometry this capacitance scales with the size. In most cases, the bulk of  $C$  arises from the two tunnel junctions, where the separation of the conductors is  $\sim 1$ – $2$  nm.

At first sight, this configuration is two ordinary tunnel junctions in series and one might expect ohmic conductance. But the small capacitance  $C$  of the island imposes a strong restriction on the current flow that leads to a more complicated and interesting behavior known as Coulomb blockade. Except for fine details, the behavior can be understood by a simple circuit analysis. Three factors play a major role: the granular nature of the tunneling current, the electrostatic energy involved in changing the charge of the island by a single electron (!), and the use of a gate to modify this energy.

Suppose that electrode Y is at ground potential and a (negative) bias  $V$  is applied to electrode X, causing electrons to flow through the two junctions from X to Y. In the nature of tunnel junctions, this flow is not continuous. It occurs, rather, as an intermittent series of abrupt transfers of individual lumps of charge  $e$  through J1 from X to Z, and concurrently through J2 from Z to Y. For typical SET operation the current magnitude is  $\sim 1$  nA and the time interval between the arrivals and departures of electrons from the island is  $\sim 150$  psec. This is much longer than the tunneling time. Hence for most of the time, no current flows and the charge state of the island stays

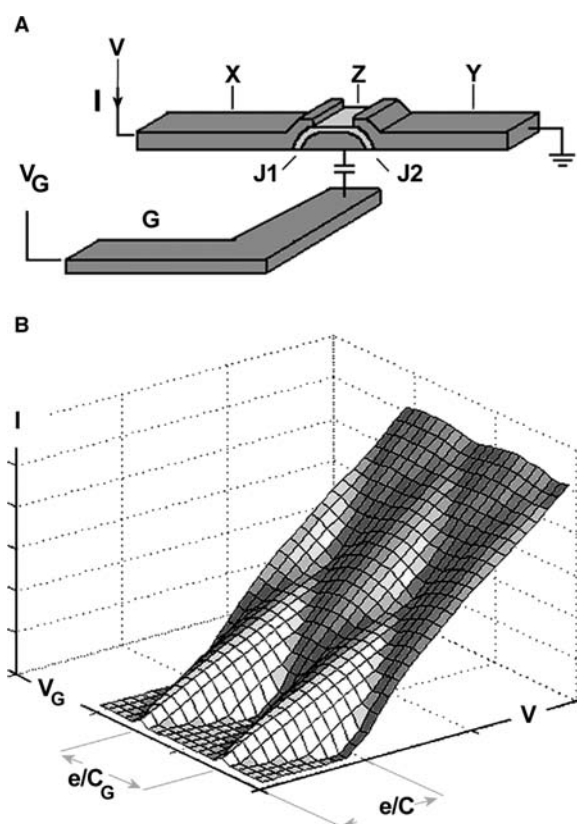


**Fig. 1** Schematic of an SET: (A) Input electrode X at bias  $V$ . Output electrode Y at ground potential. Central region Z is insulated from X and Y by a thin insulator (shown in gray). Tunnel junctions J1 and J2 provide electrical contact from X and Y to Z. Current  $I$  flows from X to Y. A nearby gate G with bias  $V_G$  has a capacitance  $C_G$  to Z. (B) Calculated dependence of  $I$  on bias  $V$  and gate bias  $V_G$  for two identical junctions of resistance  $R$  and capacitance  $C'$ . The dependence is nonlinear on a voltage scale of  $e/C$  where  $C = 2C' + C_G$ . For fixed  $V$ ,  $I$  is periodic in  $V_G$  with period  $e/C_G$ . At low  $V$ , the Coulomb blockade suppresses  $I$  over a range of  $V$  and  $V_G$ . At higher  $V$  the dependence is approximately given by  $I = 2R(V - |e/2C|)$ .

fixed. The voltage  $V_Z$  of the island is also fixed and can be calculated by simple electrostatics, using only the mutual capacitances between Z and the other electrodes X, Y, and G, the biases  $V$  and  $V_G$  of X and G, and the number of excess electrons in residence on Z. As the tunneling electrons arrive and depart, they charge or discharge the capacitance  $C$  of the island, causing its voltage  $V_Z$  to increase and decrease by an amount  $e/C$ . The associated charging energy is  $e^2/2C$ . Whenever an arriving electron tunnels through J1, the voltage bias across J1,  $V - V_Z$ , is decreased by  $e/C$ , and that across J2,  $V_Z$ , is increased by this amount, and vice versa for an electron departing through J2. The rates of tunneling of the two junctions are similarly affected.

This influence of the charging energy is so strong it can stop the tunneling completely. At  $T = 0$  K, if the voltage bias across one of the junctions is smaller than  $e/2C$ , electrons cannot tunnel through that junction. To do so would impart a negative kinetic energy, in classical terms, to that electron. Moreover, if both junctions have a bias  $< e/2C$  at once, as may happen at total bias  $V < e/C$ , the tunneling events halt altogether. The SET displays a complete Coulomb blockade of the current flow. At finite temperature, the current is still greatly suppressed up to  $T \sim (e^2/2C)/k_B$ . The current is also partially suppressed by this effect at higher  $V$ , up to a few  $e/C$ , while the tunneling events in the two junctions tend to be anticorrelated.

Importantly for device purposes, the Coulomb blockade can be lifted by the voltage  $V_G$  of the gate G. Because the gate is capacitively coupled to the island with mutual capacitance  $C_G$  a fractional portion  $C_G/C$  of  $V_G$  is added to  $V_Z$ . Thus the biases of the two junctions can be adjusted by the gate voltage, one being increased and the other decreased. In this way, the bias of one of the junctions can be increased above  $e/2C$ , causing tunneling to begin again. This modulation of the SET conduction is actually an oscillating function of  $V_G$  with a period  $e/C_G$ . As  $V_G$  is increased electrons are added periodically to the island through one of the junctions resetting  $V_Z$  and the junction biases. Fig. 1B shows the calculated dependence of  $I$  on  $V$  and  $V_G$  for an SET formed by two identical junctions.

Finally, if a charged object is brought near the SET, the island voltage  $V_Z$  is shifted by electrostatic induction, changing the SET conductance. A single electron put very close to the island has the same effect as an increase of the gate voltage by one period. Thus the SET can be used as a sensitive scanning probe capable of detecting tiny amounts of charge.

## THE SINGLE-ELECTRON TRANSISTOR AS A SCANNING DEVICE

To use the SET as a scanning device, it is necessary to achieve a close proximity between the SET island and the surface to be studied. The traditional type of SET fabricated by electron beam lithography on a flat substrate is hard to exploit for scanning. To fabricate an SET in a sharp-point geometry suitable for scanning, an alternative lower-tech approach has been used.<sup>[4]</sup> The substrate is a glass or quartz cylinder of approximately  $\sim 1$  mm in diameter that is sharpened at one end into a micropipette shape. The sharpened end forms a cone with an angle  $\sim 10$ – $20^\circ$ . The very tip is truncated by a small flat area with a  $\sim 50$ -nm diameter. This plateau on the end is where the SET island is to be located. This truncated-cone geometry allows an SET to be formed by a simple angled-evaporation technique, without any lithography.

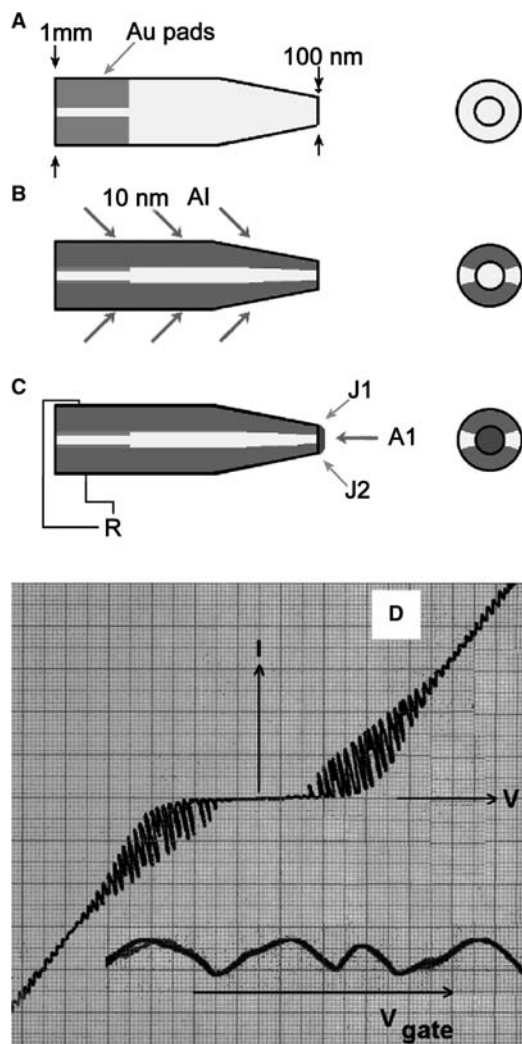


**Fig. 2** (A–C) Sketch of three stages in the formation of an SET on a sharp tip. Front views are at the left and side views, looking along the tip from the sharp end, are at the right. The size of the plateau at the tip is exaggerated for clarity. (A) Gold contact pads are prepared on the stem of the tip. (B) X and Y electrodes are made by evaporation of aluminum from top and bottom. The aluminum is then lightly oxidized. (C) Al evaporation from the sharp end forms the Z electrode on the plateau and junctions J1 and J2 at the edges of the plateau. The resistance  $R$  is monitored. (D) The upper curve shows the dependence of  $I$  on  $V$  and  $V_G$  for an experimental scanning SET. The oscillations in  $I$  are induced by rapid large oscillations in  $V_G$  as  $V$  is varied slowly. At low  $V$ , the  $I$ – $V$  curve differs from that in Fig. 1B because the electrodes are superconducting here. The lower curve shows the semi-periodic variation of  $I$  at fixed  $V$  for this SET. The irregular period and regions of hysteresis are commonly seen in the scanning SETs. They are due to the very thin, partly granular films used in the fabrication in this geometry.

The process (Fig. 2) has the following steps. First, gold contact pads are prepared along opposite sides of the rod excluding the lower, sharper part of the tip. The rod is then clamped in a detachable part of

the scanning apparatus and electrical connections are attached to the contact pads. Next, aluminum is evaporated from opposing sides producing two separate coatings that are aligned with and overlap the gold pads and extend down the conical part of the tip to the end. The films form the X and Y leads of the SET. During these evaporations the plateau is shadowed and stays uncoated. At this point, a low pressure of oxygen is briefly created in the vacuum system producing a thin oxide coating on the two aluminum films. A final aluminum evaporation is then performed with the sharp end pointing into the evaporant stream. At this orientation the small plateau and the adjacent edges of the X and Y films are coated with a single patch of conducting film. This forms the island Z of the SET. The two junctions are formed by the overlap of the Z film with the oxidized edges of the X and Y films. The sides of the cone and the rest of the rod receive much less evaporant flux owing to the shallow angle of incidence and acquire a much thinner, electrically discontinuous coating. Here it is helpful to monitor the resistance of the device to determine when the region Z first becomes electrically continuous. This completes the formation of the SET scanning tip. Typically, the thickness of the films is  $\sim 10$ – $20$  nm, the size of the SET island is  $< 100$  nm, the total area of the tunnel junctions is  $< 1000$  nm<sup>2</sup>, the junction resistance is  $\sim 1$  M $\Omega$ , and the charging energy  $e^2/2C$  is a few millielectron volts.

The tip, the sample to be studied, and the rest of the scanning apparatus are then cooled to liquid He temperatures. At low temperature the device is tested for characteristic SET behavior. Samples with conducting regions on the surface may be used as a gate to test the response of the SET. The upper curve in Fig. 2D shows the relationship between current  $I$  and voltage  $V$  for a typical SET used for scanning. The bottom curve shows dependence of  $I$  on gate voltage  $V_G$ . The capacitance  $C_G$  between the sample and the island can be determined from the period of oscillations. The value of  $C_G$  serves also to monitor and control the distance between the tip and the sample surface as the tip is lowered to the working height. This capacitance increases approximately logarithmically with decreasing distance at larger separations, and more steeply at smaller separations. Another indicator of the height, particularly at close separation, is provided by the resolution of the features seen in scanning the SET along a line. The final separation between the tip and the sample is  $\sim 5$  nm. At this height, a typical period  $e/C_G$  is  $\sim 30$ – $200$  mV. Any unintentional light mechanical contact made during the approach does not destroy the SET tip. On average, this whole procedure starting from a bare tip has about a 50% success rate in producing a usable scanning device. Typical runs last for periods ranging from days to months.

## IMAGING WITH THE SINGLE-ELECTRON TRANSISTOR

To proceed with the scanning, the SET is biased at fixed voltage and the SET current is recorded. Generally, the operating point is set so that the current varies linearly with the magnitude of electric flux picked up by the island. In cases when the signal is larger than one electron, feedback to the gate is used to extend the linear dynamic range. In this mode, the feedback voltage is recorded in addition to the SET current. The SET tip is scanned in a raster pattern across an area of interest at fixed height.

The signals seen by the SET tip may have several contributions. These include free charges, polarization of dielectrics, and image charges on conductors, as well as signals stemming from external biases on conducting regions, variations in contact potentials, and from current flow. For brevity, these are lumped together as d.c. electric-field signals. In addition, one can measure at the same time an a.c. signal, the response to a low-frequency stimulation of the system. This helps in extracting the small signal of interest from the larger d.c. signal background, e.g., the a.c. voltage pattern caused by an a.c. current flow. Data acquisition rates are about 1 pixel per second for the signal levels of about 0.1% of an electron flux terminating on the island of the SET.

So far, the samples studied with the scanning SET have been heterostructures of GaAs/AlGaAs grown on GaAs chips. The heterostructures contain a high-mobility two-dimensional electron gas, or 2DEG, buried  $\sim 100$  nm below the surface. These devices provide a reasonably well-characterized, clean semiconductor system whose flat surfaces have charge patterns suitable for testing the scanning SET. The main motivation for choosing this system, however, is that the 2DEG displays the quantum Hall effect (QHE),<sup>[5,6]</sup> which has been a long-time major topic of interest in condensed-matter physics. The electric-field images have provided a new tool for investigations of this topic.

### Images of Surface Charge Patterns

Fig. 3A shows d.c. electric-field images seen at the surface of these heterostructures. The pattern appears random with no apparent theme. The typical amplitude corresponds to a few tenths of an electron flux and the spatial size of features is limited by the SET resolution. This type of pattern can be expected. The heterostructure samples contain a fairly high concentration of charged donors,  $>10^{12}$  cm<sup>-2</sup>, at a depth of  $\sim 50$  nm, and a compensating charge density forms on the semiconductor surface. Both of these charge layers contribute to the surface electric fields seen by the SET.

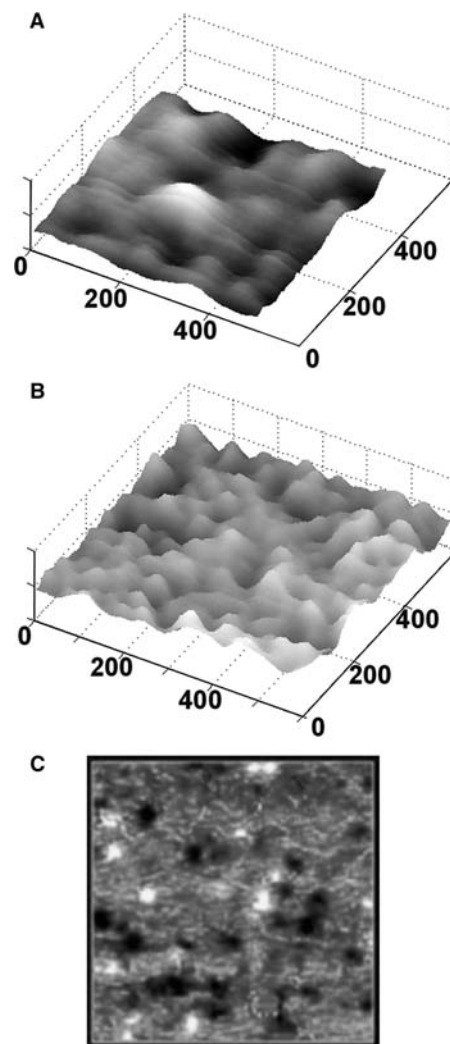


**Fig. 3** (A) A typical electric field image (d.c. signal) seen by a scanning SET in a  $500 \times 500$ -nm area over the surface of a GaAs/AlGaAs heterojunction with an underlying 2DEG. The random pattern is due to the unresolved surface charge density of  $\sim 10^{12}$  charges/cm<sup>2</sup>. (B) The highest resolution electric-field image seen to date, taken in a  $600 \times 600$ -nm region of undoped GaAs. The small peaks have a density of about  $3 \times 10^{10}$  cm<sup>-2</sup> which may be the total number of charges trapped at the surface. (C) Effect of optical illumination on surface charges. The panel shows the difference of electric field images in a  $2 \times 2$ - $\mu$ m area taken before and after brief illumination by a light emitting diode. The white and black spots arise from sites (donor atoms) that acquired or lost a single electron charge.

But the individual charges are too closely spaced,  $\sim 10$  nm, to be resolved. Statistical fluctuations in the charge density would produce a random pattern of the sort seen in Fig. 3A.

The highest surface resolution obtained to date is shown in the image in Fig. 3B. This shows a  $600 \times 600$ -nm region of the GaAs surface where the heterostructure doped regions have been etched away.



The apparent resolution of the structure is  $\sim 30$  nm, and up to  $\sim 0.2$  electrons are induced on the SET island in the regions of maximum signal. The pattern appears to be partly correlated as opposed to the example above. In this undoped region, the surface charge density is much less than that in the doped heterostructure regions, and it is conceivable that the features shown are the individual charges.

The distribution of charges is fixed at low temperature and such patterns persist for weeks. However, an exposure to light excites carriers in the semiconductor and induces changes in these patterns at randomly positioned spots. These changes result from the ionization or neutralization of individual donors or surface sites (Fig. 3C).

### Studies of the Quantum Hall Effect

The QHE is an exotic form of the ordinary Hall effect. This effect, commonly observed in metals and semiconductors, occurs in a conductor subjected to a magnetic field and having a current flowing perpendicular to the field. In this situation a potential, or Hall voltage, is found to be present in the direction transverse to both current and field. This potential arises from the Lorentz force acting upon the electrons. The Hall resistance, the ratio of the Hall voltage to the current, is proportional to the field strength and inversely proportional to the carrier density.

The integer QHE occurs in situations where the Hall resistance of a high-mobility two-dimensional electron (or hole) gas is measured at temperatures  $< 10$  K, and much lower, and in a magnetic field  $B$  of several Tesla.<sup>[5,6]</sup> It is found that whenever the filling factor, the normalized ratio  $\nu = n(h/e)/B$  between the 2DEG density  $n$  and magnetic field  $B$ , is approximately an integer  $N = 1, 2, 3, \dots$ , the Hall resistance does not increase linearly with  $B$  but instead becomes constant exactly equal to  $(h/e^2)/N$ . Here  $h$  is Planck's constant and  $e$  is the electronic charge. This quantization of the Hall resistance is the signal feature of the QHE. The quantization is intimately related with the notion of electron localization. The localization is caused by disorder in the potential seen by the 2DEG electrons. The fascinating physics of the QHE has led to two separate Nobel prizes over the last 20 years.

The scanning SET images taken at the surface of the heterostructures at high  $B$  and low  $T$  show a rich hierarchy of phenomena associated with the QHE.<sup>[7]</sup> On a larger scale there are contact potential features in the 2DEG in the form of linear structures that move about as a function of magnetic field as illustrated in Fig. 4. The four panels show overlapping  $15 \times 15$ - $\mu\text{m}$  areas of a heterostructure having a 2DEG conducting layer 100 nm below the surface. The average 2DEG density

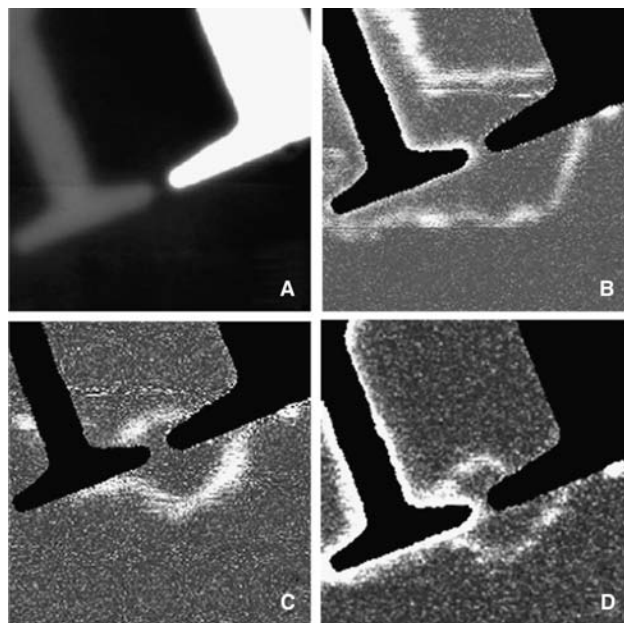


**Fig. 4** Electric-field images related to the quantum Hall effect. These  $15 \times 15$ - $\mu\text{m}$  images are taken in the same general area over the surface of a GaAs/AlGaAs heterojunction with an underlying 2DEG. The density of the electrons in the 2DEG is  $\sim 10^{11} \text{ cm}^{-2}$  but has about  $\pm 30\%$  variation with location. Part of the surface is covered by two t-shaped metal gates. A) d.c. signal (1-V scale) showing a biased gate (white) and an unbiased gate (gray). The remaining surface of the semiconductor is featureless on this scale. B–D) The a.c. signals ( $\sim 1$ -mV scale) seen in this region induced by a small uniform variation of  $n$ . B) Magnetic field  $B \sim 2.3$  T. The white lines are contact potential features occurring at points where the local density  $n$  corresponds to a filling factor of 2 at this field. C)  $B = 2.0$  T. The contact potential features of B) have moved to a region of  $\sim 15\%$  lower density. D)  $B = 4.0$  T. The filling factor is now 1 at the same locations as in C). The unusually large variations in the 2DEG density  $n$  seen here are associated with leakage of surface charge from a biased gate. This charge partially depletes the underlying 2DEG.

is  $\sim 10^{11} \text{ cm}^{-2}$ , varying substantially with location. Magnetic field  $B$  ranges from 2 to 4 T. This corresponds to the regime of the QHE for filling factors  $\nu = 1$  and 2. All images in Fig. 4 are taken in the feedback mode mentioned above. Fig. 4A shows the feedback voltage ( $\sim 1$ -V scale) corresponding to the overall d.c. signal. The primary features are the metal gates patterned on the sample surface. The right gate is biased at  $\sim -0.6$  V producing the largest signal shown as white. The left gate is unbiased but shows up relative to the surrounding semiconductor owing to  $\sim 0.2$  V of contact potential between the two. This large-scale picture has a relatively low resolution because the scanning SET is positioned  $\sim 50$  nm above the surface. While the semiconductor region appears featureless in this image, there is structure on the 50-mV scale near the biased gate.

The signature of the QHE appears at a smaller  $\sim 1$ -mV scale and is superimposed on the much larger signals discussed above. This signal is extracted by an a.c. modulation technique. Applying an a.c. voltage to a gate underneath the 2DEG produces a small variation in the 2DEG density,  $\sim 0.1\%$ . The corresponding a.c. component in the SET signal is displayed in Fig. 4B. The contact potential features are the bright lines located between the gates and in the lower part of the picture. These mark the contours along which the spatially varying carrier density  $n$  is equal exactly to  $n = 2 \times B/(h/e)$  for  $B = 2.3$  T. At lower magnetic field (e.g., Fig. 4C) the contours move to positions of lower local density always appearing at the local filling factor  $\nu = 2$ . By adjusting the magnetic field, one can map out the inhomogeneous density of the 2DEG. Fig. 4D shows the contours at  $\nu = 1$  that appear at exactly the same location as in Fig. 4C for magnetic field two times higher.

The contact potential features result from the energy level structure of the quantum states of a high-mobility 2DEG. At high  $B$ , the energy levels are grouped into a set of narrow energy bands, known as Landau levels, separated by gaps. The lower energy levels are occupied by the 2DEG electrons. The filling factor  $\nu$  is an integer whenever the electrons just fill up a Landau-level band. Additional electrons must be located in the higher Landau band of states, a few millielectron volts up in energy. In an inhomogeneous 2DEG there might be spatial regions with filling factor less than some integer  $N$  where a Landau band is almost filled up and adjacent regions with filling factor greater than  $N$  where the next Landau band is partly filled. An analogous situation is that of p–n junctions in a semiconductor. In a semiconductor with spatial gradients in donor and acceptor density some areas may be p-type and adjacent areas n-type. A contact potential equal to the energy gap develops across the p–n boundaries. A similar effect occurs in the inhomogeneous 2DEG. Here again a contact potential equal to the energy gap occurs between areas having filling factors less than  $N$  and greater than  $N$ . When the charge density is increased uniformly, the boundaries between these two areas shift sideways. The features seen in the a.c. signal in Fig. 4B–D are caused by the movement of such boundaries. With changes in magnetic field  $B$  these boundaries have been observed to move across the sample surface, tracing out the density contours. Such boundaries are seen over a wide range of  $B$  in a variety of twisting shapes, sometimes forming loops indicating local density extrema. The shapes of these boundaries are reflected, to a degree, in the larger-scale variations in the surface potential, indicating that the density is perturbed by the surface charge in these images.

The accepted picture of the QHE assigns a central role to the peculiar behavior of the 2DEG electrons

at these boundaries where the local filling factor is an integer, known also as incompressible strips.<sup>[8]</sup> Current flows without dissipation along these boundaries, perpendicular to the local voltage gradients, and experiences a very high resistance in flowing across the boundaries. The location of the boundaries with respect to the position of the voltage contacts determines whether a quantized Hall resistance will be measured. Single-electron-transistor images of the voltage induced by a flowing current have confirmed that it is much distorted by the presence of such a boundary in the current path.<sup>[7]</sup>

Higher resolution SET images of the boundary regions just described have revealed that they contain an intriguing variety of complicated structure. The structure arises from the localization of some of the 2DEG electrons.<sup>[9]</sup> A typical example is shown in Fig. 5. These panels show the a.c. response of the SET in a  $1 \times 1\text{-}\mu\text{m}^2$  area induced by a small change in the density of the 2DEG, the same way as for

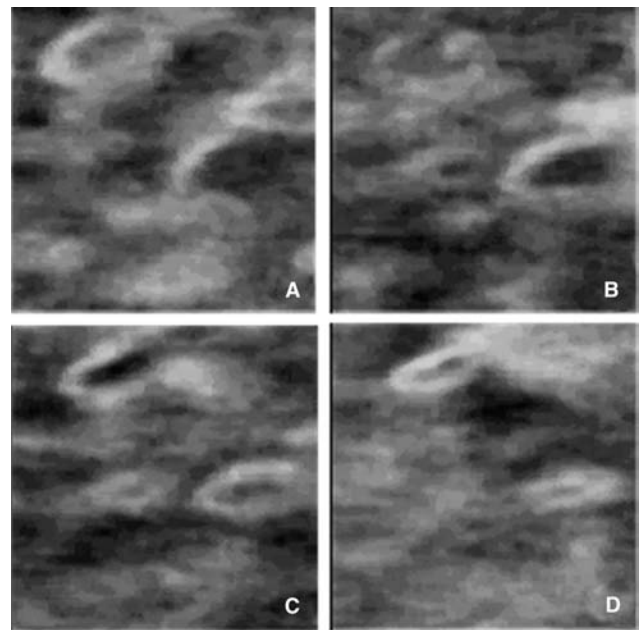


**Fig. 5** Grayscale maps ( $\sim 0.1$ -mV scale) of the a.c. signal seen by the scanning SET. The area is  $1 \times 1\ \mu\text{m}^2$ . The conditions are set similar to Fig. 4D and the fine structure within the strip with local filling factor  $\sim 1$  is studied. The average density is increased by  $\sim 1.8$  electrons/ $\mu\text{m}^2$  between successive panels. Dark color represents positive a.c. signal while bright contours are regions with the phase of a.c. signal opposite to the a.c. excitation at the gate electrode (negative signal). The ring-shaped contours on different panels are seen collapsing to common centers as the density is increased. These sequences of collapsing rings are the visualization of the Coulomb blockade occurring at localized electron sites within the 2DEG. The specific appearances of these charging events are determined by the interaction of the localized electrons with each other and with the scanning SET tip.

Fig. 4B–D. The total number of electrons in the area shown is  $\sim 1300$ . In successive panels an additional  $\sim 1.8$  electrons are added to the area substantially changing the a.c. signal pattern. The strength of the signals ( $\sim 0.1$  mV) occurring in these patterns indicates that the bright features are due to the addition or subtraction of individual electrons from the immediate vicinity of the tip. Theoretical considerations of the QHE lead to the conclusion that the electrons occupying a fully filled Landau band form an insulator-like incompressible fluid. Any small excess or deficit in the complete filling gives rise to a low density of singly charged quasi particles. These are trapped in small variations in the local disorder potential and interact with each other to form, in some theories, a sort of electron glass or crystal. Although the picture is complicated by a fairly strong interaction between the tip and the electrons, it may be that the images shown in Fig. 5 are of such a two-dimensional solid.

## CONCLUSION

The present-day SET scanning devices have been able to make a significant contribution to studies of electronic properties of materials at a nanoscale level complementing other characterization techniques. Smaller devices of the same geometry will have improved spatial resolution and higher operating temperature. Even with the current fabrication procedures some SET scanning devices have been made that have shown operation at around 50 K. It is believed that ultimately an SET of atomic size can be developed, and that its operation and performance will be similar to that of the present-day SETs. This will require new techniques of fabrication, similar perhaps to those considered for molecular electronics.

## ACKNOWLEDGMENTS

We would like to acknowledge Harold Hess, Michael Yoo, Amir Yacoby, Larue Dunkelberger, Robert Chichester, Loren Pfeiffer, and Ken West who contributed equally with the present authors to the development of the technique and the associated research.

## REFERENCES

1. Fulton, T.A.; Dolan, G.J. Observation of single-electron charging effects in small tunnel junctions. *Phys. Rev. Lett.* **1987**, *59* (1), 109–112.
2. Grabert, H., Devoret, M.H., Eds.; Introduction to Single Charge Tunneling; Plenum Press: New York, 1991.
3. Giaever, I. Energy gap in superconductors measured by electron tunneling. *Phys. Rev. Lett.* **1960**, *5* (4), 147–148.
4. Yoo, M.J.; Fulton, T.A.; Hess, H.F.; Willett, R.L.; Dunkelberger, L.N.; Chichester, R.J.; Pfeiffer, L.N.; West, K.W. Scanning single-electron transistor microscopy: imaging individual charges. *Science* **1997**, *276* (5312), 579–582.
5. von Klitzing, K.; Dorda, G.; Pepper, M. New method for high-accuracy determination of the fine-structure constant based on quantized Hall resistance. *Phys. Rev. Lett.* **1980**, *45* (6), 494–497.
6. Prange, R.E.; Girvin, S.M.; Eds. *The Quantum Hall Effect*; Springer: New York, 1990.
7. Yacoby, A.; Hess, H.F.; Fulton, T.A.; Pfeiffer, L.N.; West, K.W. Electrical imaging of the quantum Hall state. *Solid State Commun.* **1999**, *111* (1), 1–13.
8. Chklovskii, D.B.; Lee, P.A. Transport properties between quantum Hall plateaus. *Phys. Rev., B* **1993**, *48* (24), 18,060–18,078.
9. Zhitenev, N.B.; Fulton, T.A.; Yacoby, A.; Hess, H.F.; Pfeiffer, L.N.; West, K.W. Imaging of localized electronic states in the quantum Hall regime. *Nature* **2000**, *404* (6777), 473–476.

# Self-Assembled Monolayers: Adsorption and Desorption from Alkanethiols on Gold

Pieter Stroeve

Department of Chemical Engineering and Materials Science, University of California–Davis, Davis, California, U.S.A.

## INTRODUCTION

There is considerable interest in thin molecular nanofilms made from the self-assembly of species. A current area of research is the assembly of multilayers of alternating surfactants, proteins, and polymers to form macromolecular assemblies with unique functions and properties. Such properties can be directional in conducting electricity and propagating light or transferring mass. An example is the use of different types of surfactants and polymers, in a multilayer stack, to design selective membranes. Another interest is in using biopolymers with surfactants at the solid–water interface for selective barrier coatings for biosensors that may also be compatible with biological species. Yet another possibility is to use the self-assembly of surfactants on the solid–water interface to pattern the deposition of biopolymers on surfactants (Fig. 1). Self-assembled thiol monolayers (SAMs) on gold are often used as model solid–water interfaces, because these surfaces have unique properties. This is yet another area that has become a subject of active research. This entry will review the formation of SAMs and the adsorption and desorption of molecules on the SAMs to create nanofilms.

## SELF-ASSEMBLED MONOLAYERS OF ALKANETHIOLS ON GOLD

Self-assembled monolayers can be formed from alkanethiols on the surface of gold.<sup>[1–4]</sup> Alkanethiol SAMs have become a widely used tool for the design of surfaces and for the study of phenomena on surfaces.<sup>[5–8]</sup> Many studies have focused on SAMs formed on evaporated films of gold and Au(111) single crystals. The SAMs of alkanethiols on gold films are formed by rinsing the gold films with absolute ethanol (100%) followed by immersion in ethanolic solutions of alkanethiols (about 1 mM) for at least 24 hr. Upon removal from solution, samples must be thoroughly rinsed with absolute ethanol and dried under a stream

of nitrogen. X-ray diffraction has been used to show that the predominant crystallographic orientation of evaporated gold deposited on mica<sup>[9]</sup> and silicon single crystals<sup>[10]</sup> is Au(111). The structure of SAMs formed on Au(111) from solutions of long-chain alkanethiols [i.e.,  $\text{CH}_3(\text{CH}_2)_n\text{SH}$ ,  $n \geq 9$ ] has been extensively studied. Scanning tunneling microscopy (STM)<sup>[11]</sup> and electron diffraction<sup>[12]</sup> show that the sulfur atoms form a commensurate  $(\sqrt{3} \times \sqrt{3})R30^\circ$  structure with a nearest sulfur–sulfur spacing of 4.97 Å. Helium atom diffraction,<sup>[13–15]</sup> low energy electron diffraction (LEED),<sup>[16]</sup> grazing-angle X-ray diffraction,<sup>[17]</sup> and atomic force microscopy (AFM)<sup>[18]</sup> show that the alkyl chains form hexagonal lattices with a unit mesh constant of  $\sim 5$  Å that is consistent with the  $(\sqrt{3} \times \sqrt{3})R30^\circ$  structure of sulfur atoms (Fig. 2A). The specific area of each alkyl chain within this structure is  $21.7 \text{ \AA}^2/\text{molecule}$ .<sup>[6,15]</sup> Other studies, however, also indicate the presence of unit cells containing more than one chain. Band splitting in infrared spectra at low temperatures ( $< 300 \text{ K}$ ) suggests a packing structure of two chains per unit cell.<sup>[19]</sup> Helium atom diffraction (temperature  $< 100 \text{ K}$ ) suggests a rectangular  $(3 \times 2\sqrt{3})$  unit mesh of alkyl chains that is commensurate with the  $(\sqrt{3} \times \sqrt{3})R30^\circ$  structure<sup>[20]</sup> (Fig. 2A). The packing arrangement can also be described as a  $c(4 \times 2)$  superlattice of alkyl chains with respect to the fundamental  $(\sqrt{3} \times \sqrt{3})R30^\circ$  structure of sulfur atoms. The existence of a superlattice is supported by results of grazing-angle X-ray diffraction<sup>[20–22]</sup> and ultrahigh vacuum STM.<sup>[23]</sup> Because the nearest sulfur–sulfur spacing (4.97 Å) for the structure shown in Fig. 2A is larger than the closest spacing of the alkyl chains ( $\sim 4.24 \text{ \AA}$ ),<sup>[24]</sup> the alkyl chains tilt from the surface normal to maximize their van der Waals interactions.<sup>[25]</sup> A simple geometric calculation indicates a tilt angle of about  $30^\circ$  from the surface normal. Ellipsometric measurements<sup>[2,3]</sup> in conjunction with grazing-angle infrared spectroscopy<sup>[3,6,10,16,26–28]</sup> have confirmed that the alkyl chains are tilted by about  $30^\circ$  from the surface normal and rotated around the chain axis by an angle (twist angle) of about  $52^\circ$  on surfaces of evaporated gold and Au(111) single



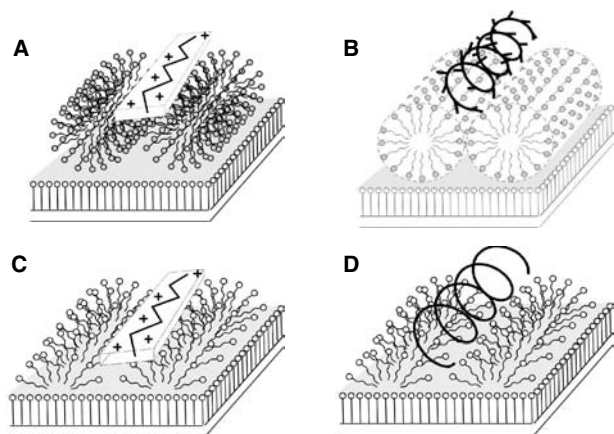


**Fig. 1** Schematic presentation of polymer macromolecules (linear and helical) with different conformations aligned by surface self-assembled, full- (A, B), and hemimicelles (C, D) of surfactants on a self-assembled thiol monolayer on gold.

crystals. Both the position ( $2918\text{ cm}^{-1}$ ) and the width of the absorbance peak corresponding to the asymmetric stretch of the methylene groups suggest the formation of close-packed, crystalline-like monolayers with a nearly all *trans* configuration. The intensities of the symmetric and the asymmetric methyl modes in the IR spectra of odd and even chain lengths are substantially different,<sup>[27,28]</sup> leading to the conclusion that the transition dipole of the symmetric methyl mode in a chain with an odd number of carbons is tilted from the surface normal more than that for a canted chain with an even number of carbons. The reverse situation exists for the asymmetric methyl mode.

Fenter et al.<sup>[22]</sup> have proposed a different structure for SAMs formed from long-chain alkanethiols on Au(111). They interpreted grazing-angle X-ray diffraction patterns to infer the presence of a S–S distance similar to that of a disulfide. This packing arrangement of the sulfur atoms along with a *gauche* defect at the S–C bond leads to the  $c(4 \times 2)$  superlattice.<sup>[20–23]</sup> Results from a simulation based on quantum mechanics are consistent with this structure and suggest that the alkyl chains are canted by  $28.3^\circ$  from the surface normal.<sup>[29]</sup> This tilt angle is close to that estimated from the thiolate structure as stated above.

The packing and orientation of chains within SAMs have been studied on surfaces of gold other than (111), including (110)<sup>[15]</sup> and (100)<sup>[12,15,16]</sup> surfaces. From those studies, it has been shown that the crystal structure of the surface of the gold substrate does influence the structure of a SAM. On a Au(110) surface with a rectangular unit lattice ( $2.88 \times 4.07\text{ \AA}$ ), helium atom diffraction suggests that the terminal methyl groups of docosyl mercaptan [ $\text{CH}_3(\text{CH}_2)_{21}\text{SH}$ ] form a commensurate  $c(2 \times 2)$  structure with  $a = b = 4.99\text{ \AA}$  and  $\alpha = 109.5^\circ$  (Fig. 2B) at low temperatures ( $<100\text{ K}$ ).<sup>[15]</sup>

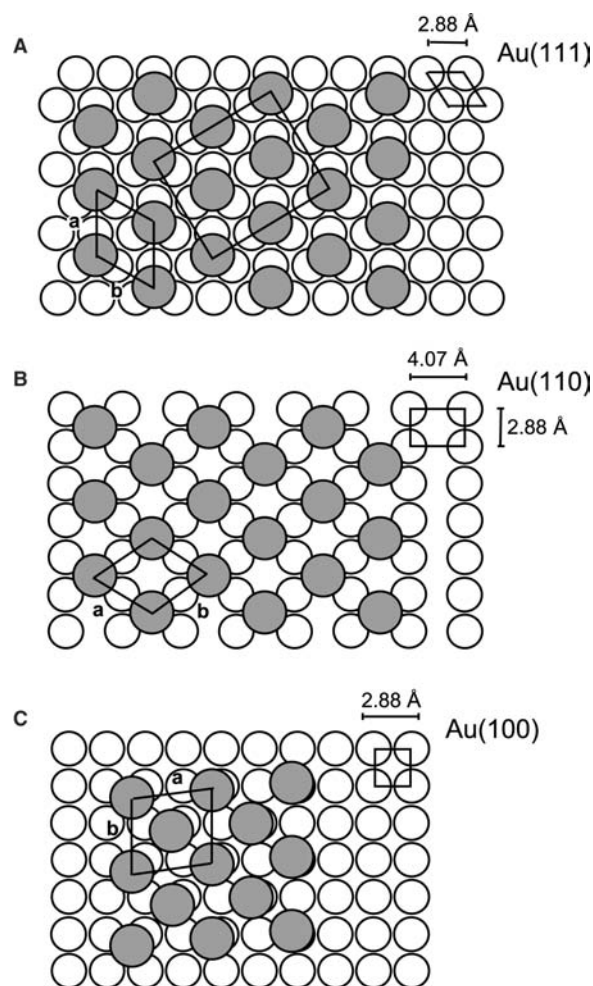


**Fig. 2** Schematic illustrations of the structure of SAMs formed from alkanethiols on single crystals of gold. Open circles represent gold atoms and shaded circles represent alkyl chains. The chain tilt and twist are not shown for clarity. (A) Au(111). The smaller rhombus shows the Au(111) lattice. The larger rhombus shows a commensurate  $(\sqrt{3} \times \sqrt{3})R30^\circ$  unit mesh with  $a = b = 4.97\text{ \AA}$  and  $\alpha = 120^\circ$  (angle between  $a$  and  $b$ ). The rectangle denotes a  $c(4 \times 2)$  superlattice with respect to the  $(\sqrt{3} \times \sqrt{3})R30^\circ$  structure. (B) Au(110). Also shown is a commensurate  $c(2 \times 2)$  unit mesh with  $a = b = 4.99\text{ \AA}$  and  $\alpha = 109.5^\circ$ . (C) Au(100). Also shown is an oblique incommensurate structure with  $a = b = 5.97\text{ \AA}$  and  $\alpha = 95^\circ$ . Source: Reprinted from Ref.<sup>[30]</sup> with permission.

The resulting area per chain ( $23.6\text{ \AA}^2/\text{molecule}$ ) is larger than that on a (111) surface (as noted above,  $21.7\text{ \AA}^2/\text{molecule}$ ). Thus the chains on the (110) surface tilt more from the surface normal (the tilt angle is estimated to be about  $37^\circ$  based on geometric considerations) than on the (111) surface.<sup>[15]</sup> The structure of SAMs formed on Au(100) [square unit lattice ( $2.88 \times 2.88\text{ \AA}$ )] has also been reported. In a study using electron diffraction, the alkyl chains of

$\text{CH}_3(\text{CH}_2)_{21}\text{SH}$  were found to be packed more densely on Au(100) than on Au(111).<sup>[12]</sup> A study using LEED has shown that  $\text{CH}_3\text{SH}$  forms a commensurate  $c(2 \times 2)$  overlayer on Au(100) when vapor-deposited at 300 K.<sup>[16]</sup> The interchain spacing of this structure is too small, however, to accommodate longer chains with extended all-*trans* conformation. An expanded structure for long chains was suggested. An oblique unit mesh of terminal methyl groups of  $\text{CH}_3(\text{CH}_2)_{21}\text{SH}$  with  $a = b = 5.97 \text{ \AA}$  and  $\alpha = 95^\circ$  on the Au(100) surface (Fig. 2C, two molecules per mesh) at low temperatures ( $<100 \text{ K}$ ) was observed by helium atom diffraction.<sup>[15]</sup> This structure suggests that the alkyl chains are incommensurate with the (100) lattice. The area per chain is  $17.8 \text{ \AA}^2$ , which is smaller than those on Au(111) and (110) surfaces. The above results support the idea that the alkyl chains are packed more densely on Au(100) than on Au(111) and (110) surfaces. A study of IR spectroscopy at low temperatures (160 K) shows that the tilt angle of chains on the Au(100) surface is only  $\sim 14^\circ$  from the surface normal.<sup>[16]</sup> Consequently, the intensities of the methyl stretching modes in the IR spectra between odd and even chain lengths are almost indistinguishable.<sup>[16]</sup>

Hou, Abbott, and Stroeve<sup>[30]</sup> reported an investigation of SAMs formed from alkanethiols on the surface of both electroless gold and evaporated gold supported by a variety of substrates. They adapted the procedure for electroless plating reported by Menon and Martin<sup>[31]</sup> so as to deposit thin films of electroless gold on glass microscope slides, high index glass, and polycarbonate membranes. The capability to form SAMs on electroless gold is important for two principal reasons. First, electroless gold can be easily prepared in any wet chemical laboratory. Second, electroless gold can be deposited onto complex and internal surfaces where procedures of evaporation cannot be used. On both evaporated gold and electroless gold, densely packed SAMs were formed. Because electroless gold has a crystallographic texture that is more dispersed than evaporated films of gold, the structures of SAMs formed on these two surfaces were not identical.

## PROTEIN ADSORPTION AND DESORPTION

Self-assembled monolayers formed from  $\omega$ -substituted alkanethiols on the surface of gold have been used as model surfaces in a number of past studies of the interactions of proteins with surfaces.<sup>[32–35]</sup> Multilayer systems based on biotinylated alkanethiols and streptavidin have been used in schemes for the immobilization of Fab fragments of antibodies on surfaces,<sup>[32]</sup> and SAMs formed from NHS-activated disulfides have been used to form enzyme-based electrodes by covalent

immobilization of glutathione reductase.<sup>[33]</sup> Cytochrome *c*, when adsorbed to SAMs formed from mercaptoundecanoic acid, has also been shown to be active and to possess a formal potential nearly identical to that of cytochrome *c* bound to physiological membranes.<sup>[34]</sup>

Past studies of the interactions of proteins and SAMs formed from alkanethiols on gold have used either planar surfaces prepared by electron beam or thermal deposition of gold<sup>[36,37]</sup> or highly curved surfaces formed by using colloidal gold.<sup>[38–41]</sup> Whereas planar interfaces prepared by the evaporation of gold have surface areas that are too small to be generally useful for biological assays based on measurements of bulk concentrations of analytes, colloidal particles ( $\sim 1\text{--}10 \text{ nm}$  in size) are not large enough to pack (unsupported) in columns through which reagents can be readily passed.

Dubrovsky et al.<sup>[42]</sup> reported modification of the surface properties of microparticles of silica (silica gel) by electroless deposition of gold on the surface of silica gel and self-assembly of monolayers formed from  $\text{X}(\text{CH}_2)_{11}\text{SH}$  [ $\text{X} = \text{CH}_3, \text{OH}, \text{COOH}$ , and  $(\text{OCH}_2\text{CH}_2)_2\text{OH}$ ] on the surface of the deposited gold. Whereas the proteolytic enzyme subtilisin BPN' adsorbed irreversibly from aqueous solution (100 mM Tris buffer, 10 mM  $\text{CaCl}_2$ , pH 8.6) on the surface of untreated silica gel, reversible adsorption of subtilisin BPN' was achieved on silica gel coated with gold and derivatized with SAMs formed from  $\text{HO}(\text{CH}_2\text{CH}_2\text{O})_2(\text{CH}_2)_{11}\text{SH}$ . The results demonstrated the usefulness of gold-coated silica gel for preparation of supports for chromatography and biological assays with controlled surface properties.

The extent of irreversible adsorption of subtilisin BPN' onto bare silica gel and modified silica gel was determined by measuring the absorbance of a solution of enzyme before and after passage through a column containing gel. The measurements were performed in Tris buffer at pH 8.6, which corresponds to the isoelectric point of subtilisin BPN' and a maximum in the hydrolytic activity of the enzyme. First, the column was contacted with 3 mL of Tris buffer containing 32 nmol of subtilisin BPN' for 40 min. Following this contact period, a 14-mL buffer was passed through the column and eluent samples of 1 mL each were collected. The concentration of enzyme in the eluent was measured and the amount of enzyme adsorbed to the gel was determined. The amount of enzyme irreversibly adsorbed to the gel after the completion of elution is shown in Table 1. Whereas 14 nmol of subtilisin BPN' was irreversibly adsorbed to untreated silica gel, Dubrovsky et al.<sup>[42]</sup> observed no irreversible adsorption of the enzyme onto gel presenting di(ethylene glycol) groups. The gold-coated gel (not treated with a SAM) irreversibly adsorbed 8 nmol of subtilisin



**Table 1** Moles of subtilisin BPN' irreversibly adsorbed (in 100 mM Tris buffer at pH 8.6) on the following surfaces: Bare silica gel; silica gel covered with a layer of electroless gold; and silica gel covered with a layer of electroless gold and derivatized with SAMs formed from  $\text{CH}_3(\text{CH}_2)_{11}\text{SH}$ ,  $\text{HO}(\text{CH}_2)_{11}\text{SH}$ , and  $\text{HO}(\text{CH}_2\text{CH}_2\text{O})_2(\text{CH}_2)_{11}\text{SH}$

Stationary phase (500 mg)	Irreversibly adsorbed subtilisin BPN' (nmol)
Silica gel (untreated)	14
Electroless gold on silica gel	8
$\text{CH}_3(\text{CH}_2)_{11}\text{SH}$ on electroless gold on silica gel	2
$\text{HO}(\text{CH}_2)_{11}\text{SH}$ on electroless gold on silica gel	1
$\text{HO}(\text{CH}_2\text{CH}_2\text{O})_2(\text{CH}_2)_{11}\text{SH}$ on electroless gold on silica gel	0

Source: From Ref.<sup>[42]</sup> with permission.

BPN', and thus the SAM is needed to prevent irreversible adsorption. Because the bare silica gel irreversibly adsorbs subtilisin BPN' whereas the gold-coated silica gel supporting the SAMs formed from  $\text{HO}(\text{CH}_2\text{CH}_2\text{O})_2(\text{CH}_2)_{11}\text{SH}$  does not, one can conclude that electroless gold in combination with the SAMs can be used to block sites on the silica gel responsible for irreversible adsorption of subtilisin BPN'. It can also be seen that the extent of irreversible adsorption of subtilisin BPN' to the SAMs presenting hydroxyl (OH) and methyl groups ( $\text{CH}_3$ ) is also small. In these cases, however, the volume of buffer required to elute a specified fraction of the adsorbed protein was greater than for SAMs presenting di(ethylene glycol) groups.

## SURFACTANT ADSORPTION AND DESORPTION

An improved understanding of surfactant adsorption and desorption on solid–aqueous interfaces is of crucial importance in many practical applications including detergency, wetting, pharmaceuticals, biomaterials, cosmetics, decontamination, and oil recovery.<sup>[43]</sup> Atomic force microscopy has been used to image surface-adsorbed surfactant structures directly in surfactant solutions.<sup>[44]</sup> In addition to monolayers and bilayers, a wide variety of surface micelles on solid surfaces have been found, such as hemicylinders, cylinders, hemispheres, and spheres. It is now generally accepted that hemimicelles may be formed by the adsorption of charged surfactants on hydrophobic surfaces. The formation of full micellar structures is often found in the adsorption of charged surfactants on hydrophilic surfaces.

Knowledge of the aggregate structure of the adsorbed surfactant layer, as well as the surface excess concentration and the rates of adsorption and desorption, is necessary to fully characterize the adsorption behavior, which is dependent on the interaction of the surfactant with surfaces of different nature and charge. Soluble surfactants can associate with surfaces due to van der Waals forces or coulombic interactions with hydrophobic or charged portions of the surface to form different surface structures.<sup>[44–48]</sup> The literature on surfactant adsorption on solid–liquid interfaces often contains kinetic adsorption data where mass transfer in the fluid played a role. Although such studies have merit in comparing different conditions, the presence of mass transfer complicates analysis, and, consequently, the intrinsic kinetics is usually not reported.

Sodium dodecyl sulfate is a well-studied material because of its practical importance. Sodium dodecyl sulfate is known to hydrolyze over time to form dodecanol, which enhances the adsorption of sodium dodecyl sulfate (SDS) below the critical micelle concentration (cmc) (8.1 mM) and decreases the adsorbed amount above the cmc.<sup>[49]</sup> The dodecanol impurity can exist in commercially available SDS if used as received. Thus SDS must be purified before use in adsorption studies. There exists a large amount of information on the structure and equilibrium of SDS adsorption on a variety of surfaces using AFM, Fourier transformed infrared spectroscopy (FTIR), and other surface-sensitive techniques. However, less attention has been given to SDS adsorption and desorption kinetics because of the difficulty of exploring fast kinetic processes. Sigal, Mkrbich, and Whitesides<sup>[45,46]</sup> employed a BIACore surface plasmon resonance (SPR) in a flow configuration to elucidate information on equilibrium adsorption and adsorption kinetics of SDS on hydrophobic and hydrophilic surfaces made by SAMs on gold. Assuming first-order kinetics, the maximum adsorption constant their SPR equipment could measure was  $k_a < 0.1 \text{ sec}^{-1}$ . Because of these limitations they did not report specific values for the adsorption and desorption kinetics. Levchenko et al.<sup>[50]</sup> constructed a SPR system with a laminar flow cell and high SPR measurement rate that allowed monitoring the adsorption kinetics at various flow rates with  $k_a$  of up to  $10 \text{ sec}^{-1}$ . By increasing the flow rate in the flow cell (expressed in terms of the Reynolds number), the limit at which kinetics controls the process of adsorption or desorption could be achieved so that the intrinsic kinetics could be measured. Consistent with previous results in the literature, they found that recrystallization of SDS was necessary to eliminate trace amounts of dodecanol. The SDS adsorption and desorption rates increased with bulk SDS concentration in the monomer regime reaching a maximum at

the cmc. At and above the cmc of SDS, the adsorption and desorption rates became nearly constant as shown in Fig. 3. The experimental results show that the SDS monomers play a dominant role in the adsorption and desorption on SAMs, and that micelles in the solution do not increase the adsorption rate when mass transfer limitations are negligible. The data suggested that the kinetics of adsorption and surface micelle formation for hemicylinders is a slower process than the adsorption and formation of hemispheres.

## ADSORPTION AND DESORPTION OF POLYMERS

Copolymers that have constituent blocks with different affinities for their surroundings exhibit amphiphilic properties; that is, they, like more conventional surfactants, self-organize or self-assemble at interfaces and in solution to minimize contact between less compatible parts. This behavior can be exploited to change the properties of surfaces and to enhance solubilities in solution. Lately, the emphasis has shifted toward the

design and creation of functional, adsorption-driven, self-assembled nanostructures.<sup>[51–53]</sup> Understanding the modality of interactions between polymers and surfaces is fundamental in the pursuit of this task. Brandani and Stroeve<sup>[54]</sup> reported on the equilibrium behavior of adsorption (and desorption) from solution of a series of copoly(ethyleneoxide–propyleneoxide–ethyleneoxide), PEO–PPO–PEO triblock copolymers (Pluronic) on a gold surface modified by a methyl-terminated self-assembled monolayer of a long-chain alkanethiol ( $\text{CH}_3(\text{CH}_2)_{10}\text{SH}$ ). The simplified notation  $E_nP_mE_n$  for Pluronic PEO–PPO–PEO will be used here, where  $n$  and  $m$  are the repeat units. Brandani and Stroeve<sup>[54]</sup> monitored the adsorbed amounts of Pluronic on the hydrophobic SAM with SPR. The study showed that the adsorbed amounts go through a maximum near the cmc, as shown in Fig. 4, and thus the process was not consistent with a Langmuir isotherm. The occurrence of non-Langmuir-type behavior for Pluronic or similar systems has already been seen in the past.<sup>[55,56–59]</sup> The maximum is generally attributed to polydispersity, and in fact it has been reported that these polymers have a bimodal distribution with an additional lower molecular weight, more hydrophobic fraction.<sup>[60]</sup> Brandani and Stroeve<sup>[54]</sup> found that the adsorption–desorption process was partially irreversible as shown in Fig. 5. They employed AFM in the liquid environment on a selected number of cases to discern the morphology of the copolymer-coated surfaces. Atomic force microscopy observations showed that globular micelle-like aggregates were present at the surface for the more hydrophobic species P103 ( $E_{17}P_{60}E_{17}$ ). In contrast, a uniform

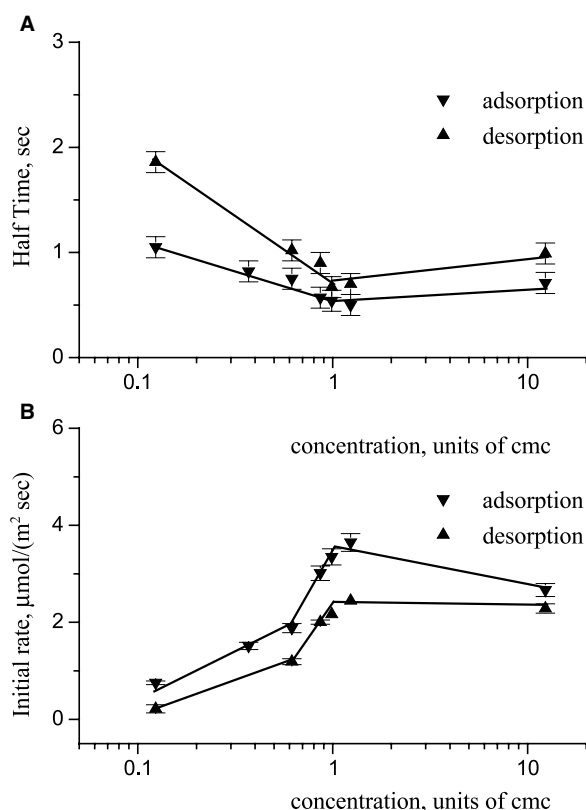


**Fig. 3** Half times (A) and initial rates (B) of SDS adsorption on and desorption from SAMs of undecanethiol as a function of surfactant concentration. The cmc is 8.1 mM. Source: Reprinted from Ref.<sup>[50]</sup> with permission.

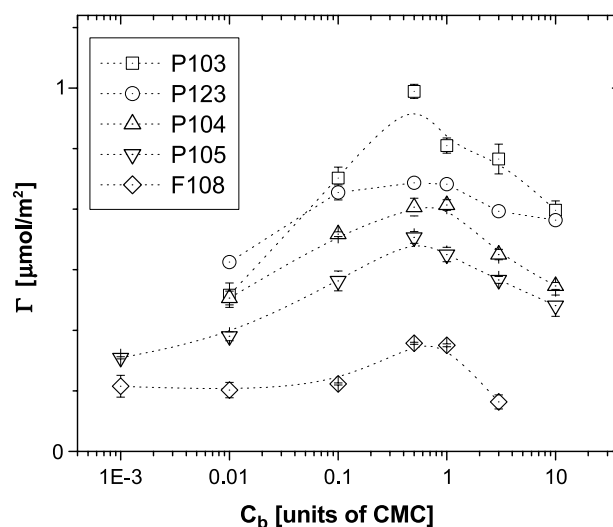


**Fig. 4** Adsorption isotherms for Pluronic P103 ( $E_{17}P_{60}E_{17}$ ), P123 ( $E_{19}P_{69}E_{19}$ ), P104 ( $E_{27}P_{61}E_{27}$ ), P105 ( $E_{37}P_{56}E_{37}$ ), and F108 ( $E_{132}P_{50}E_{132}$ ). Source: Reprinted from Ref.<sup>[54]</sup> with permission.

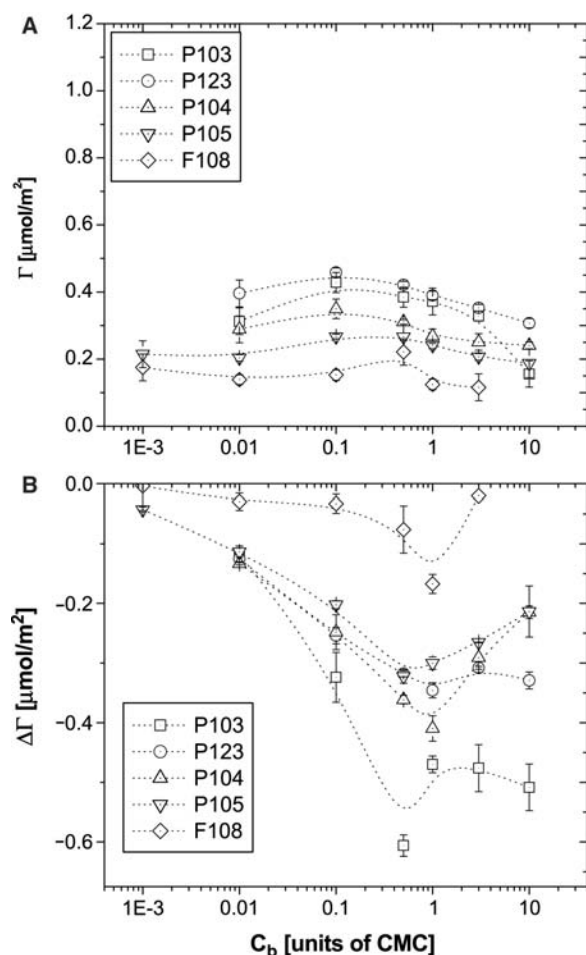


**Fig. 5** Desorption isotherms for Pluronic P103 ( $E_{17}P_{60}E_{17}$ ), P123 ( $E_{19}P_{69}E_{19}$ ), P104 ( $E_{27}P_{61}E_{27}$ ), P105 ( $E_{37}P_{56}E_{37}$ ), and F108 ( $E_{132}P_{50}E_{132}$ ): (A) residual amount left on the surface at the end of the desorption experiment; (B) absolute change in surface excess concentration (residual minus adsorbed amount at the start of the desorption experiment). *Source:* Reprinted from Ref.<sup>[54]</sup> with permission.

monolayer-like morphology was observed for the more hydrophilic Pluronic P105 ( $E_{37}P_{56}E_{37}$ ).

In another study, Brandani and Stroeve<sup>[61]</sup> reported on the kinetic rates of adsorption from solution of the same family of Pluronic on a gold surface modified by a methyl-terminated self-assembled monolayer of a long-chain alkanethiol ( $\text{CH}_3(\text{CH}_2)_{10}\text{SH}$ ). They monitored the kinetics with the SPR technique, whose high time resolution (0.1 sec) allowed them to follow the evolution of these systems even for characteristic times of a few seconds. The adsorption and desorption data were analyzed in the context of a mass transfer corrected Langmuir kinetics model. While the model was only able to reproduce the observations for very dilute solutions, or for the initial stages of the processes, it nevertheless allowed the authors to discriminate the onset of different mechanisms of adsorption.

The study showed that, for a series of compounds with the same length of the PPO block, the character of the adsorption process was affected by the relative balance of the hydrophilic and hydrophobic content within the copolymer: higher hydrophobic content leads to enhanced adsorption rates past the cmc. This was consistent with observations from their earlier study of the morphology of polymer-coated surfaces by AFM.

Brandani and Stroeve<sup>[62]</sup> also reported on Pluronic adsorption and desorption from SAMs of a hydrophilic thiol. The thiols adsorbed at much lower surface concentrations compared to the studies on hydrophobic SAM.<sup>[61]</sup> Brandani and Stroeve<sup>[62]</sup> reported that the adsorbed amounts, at equilibrium, go through a maximum near the critical micelle concentration and that the adsorption–desorption process is reversible for the Pluronic that adsorb in relatively significant amounts. They observed enhanced adsorption rates past the CMC regardless of the relative balance of the hydrophilic and hydrophobic content within the triblock copolymer. The triblock species with a higher hydrophobic content exhibited higher equilibrium adsorption values but lower kinetic rates.

## MACROMOLECULAR ASSEMBLIES

Using SDS as a surfactant and poly(diallyldimethylammonium chloride) (PDDA) as a polyelectrolyte, Artyukhin et al.<sup>[63]</sup> formed a surfactant–polymer macromolecular complex on a model surface of a positively charged 2-aminoethanethiol (cysteamine) SAM on gold. First, SDS adsorption on cysteamine and subsequent adsorption of PDDA on the preformed SDS layer achieved the complex formation. Successful deposition of the PDDA layer on SDS without noticeable surfactant desorption showed that the complex formation was a fast process. The presence of SDS–PDDA complex on a cysteamine-modified gold substrate was observed by SPR and FTIR. Surface

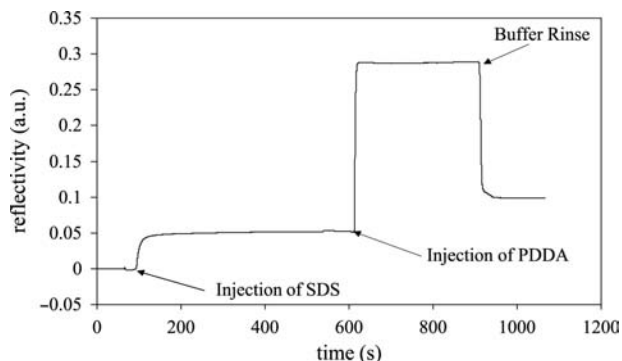


**Fig. 6** Adsorption kinetics of 1 cmc SDS and 0.2 M PDDA on SAM. *Source:* Reprinted from Ref.<sup>[63]</sup> with permission.

**Table 2** Calculated thicknesses and surface concentrations of SDS on cysteamine/gold and PDDA on SDS/cysteamine/gold obtained at different SDS concentrations and a PDDA concentration of 0.2 M, All in 5 mM Phosphate 7.0 Buffer<sup>a</sup>

Concentrations		Thickness (Å)		Surface concentration (μmol/m <sup>2</sup> )	
SDS (cmc)	PDDA (M)	SDS	PDDA	SDS	PDDA
0.1	0.2	3	5	1.03	1.14
0.2	0.2	5	7	1.71	1.6
1	0.2	17	11	5.82	2.51

<sup>a</sup>Data obtained from reflectance vs. angle scan curves.

Source: From Ref.<sup>[63]</sup> with permission.

plasmon resonance experiments on the kinetics of SDS adsorption followed by the adsorption of a flexible chain cationic polyelectrolyte are shown in Fig. 6. The PDDA can be adsorbed on SDS adsorbed on a positively charged SAM.<sup>[63]</sup> The decrease after the water rinse is due to the change in the refractive index, and not due to loss of PDDA or SDS. At equilibrium, the final thickness of SDS is 1.7 nm and for PDDA it is 1.1 nm, as calculated from the reflectance vs. angle scan curves (not shown). These thickness values are similar to those found for singular component adsorption,<sup>[63]</sup> indicating similar thicknesses (Table 2). Artyukhin et al. found that sequential adsorption of surfactants and polyelectrolytes to form stable surfactant–polymer complexes at the solid–water interface is possible if the adsorption rate of the polyelectrolytes is faster than the desorption rate of the surfactant.<sup>[63]</sup> Thus, it is critical to know the intrinsic rates of adsorption and desorption of surfactants on SAMs, and of polymers on surfactants. Kinetic rates can also give insight on the physics of adsorption. It should be of interest to study the use of externally applied voltages to a surface to influence the kinetics of adsorption and desorption of surfactants and polymers.

## CONCLUSION

Unique macromolecular structures can be assembled on SAMs of alkanethiols. The advantage of the use of SAMs on gold is that these model surfaces are well characterized and reproducible in any laboratory. Further, by using functional groups, the surfaces can be tailor-made to be hydrophobic, hydrophilic, charged, or to have reactive chemical groups at the surface. The competition of adsorption and desorption on the surfaces needs to be taken into account when macromolecular assemblies are created by depositing several layers of molecules on top of each other.

Generally, for physisorption of molecules on molecular layers, the desorption rate for molecules in the last deposited layer must be much lower than the adsorption rate of the next deposited species to form the next layer of molecules. The competitions between desorption and adsorption rates can be understood from measurement of the intrinsic kinetics of the kinetic processes. In the case of chemisorption of different molecules on a previously deposited molecular layer, the rate of chemisorption of the new molecules must be much faster than the rate of desorption of the previously deposited molecules.

## REFERENCES

1. Nuzzo, R.G.; Allara, D.L. Small-molecule chemisorption in nickel disilicide: implications for heterogeneous catalysts. *J. Am. Chem. Soc.* **1983**, *105*, 4481–4483.
2. Bain, C.D.; Troughton, E.B.; Tao, Y.-T.; Evall, J.; Whitesides, G.M.; Nuzzo, R.G. Formation of monolayer films by the spontaneous assembly of organic thiols from solution onto gold. *J. Am. Chem. Soc.* **1989**, *111*, 321–335.
3. Porter, M.D.; Bright, T.B.; Allara, D.L.; Chidsey, C.E.D. Spontaneously organized molecular assemblies: 4. Structural characterization of *n*-alkyl thiol monolayers on gold by optical ellipsometry, infrared spectroscopy, and electrochemistry. *J. Am. Chem. Soc.* **1987**, *109*, 3559–3568.
4. Whitesides, G.M.; Laibinis, P.E. Wet chemical approaches to the characterization of organic surfaces: self-assembled monolayers, wetting, and the physical-organic chemistry of the solid–liquid interface. *Langmuir* **1990**, *6*, 87–96.
5. Ulman, A. Formation and structure of self-assembled monolayers. *Chem. Rev. (Washington, D.C.)* **1996**, *96* (4), 1533–1554.
6. Dubois, L.H.; Nuzzo, R.G. Synthesis, structure, and properties of model organic surfaces. *Annu. Rev. Phys. Chem.* **1992**, *43*, 437–463.
7. Ulman, A. *An Introduction to Ultrathin Organic Films: From Langmuir–Blodgett to Self-Assembly*; Academic Press: San Diego, CA, 1991; 279–298.
8. Rubinstein, I.; Steinberg, S.; Tor, Y.; Shanzer, A.; Sagiv, J. Ionic recognition and selective response in self-assembling monolayer membranes on electrodes. *Nature* **1988**, *332*, 426–429.
9. Chidsey, C.E.D.; Loiacono, D.N.; Sleator, T.; Nakahara, S. STM study of the surface morphology of gold on mica. *Surf. Sci.* **1988**, *200*, 44–66.
10. Nuzzo, R.G.; Fusco, F.A.; Allara, D.L. Spontaneously organized molecular assemblies: 3. Preparation and properties of solution adsorbed monolayers of organic disulfides on gold surfaces. *J. Am. Chem. Soc.* **1987**, *109*, 2358–2368.
11. Widrig, C.A.; Alves, C.A.; Porter, M.D. Scanning tunneling microscopy of ethanethiolate and *n*-octadecanethiolate monolayers spontaneously adsorbed

- at gold surfaces. *J. Am. Chem. Soc.* **1991**, *113*, 2805–2810.
12. Strong, L.; Whitesides, G.M. Structures of self-assembled monolayer films of organosulfur compounds adsorbed on gold single crystals: electron diffraction studies. *Langmuir* **1988**, *4*, 546–558.
  13. Chidsey, C.E.D.; Liu, G.-Y.; Rowntree, P.; Scoles, G. Molecular order at the surface of an organic monolayer studied by low energy helium diffraction. *J. Chem. Phys.* **1989**, *91*, 4421–4423.
  14. Camillone, N., III; Chidsey, C.E.D.; Liu, G.-Y.; Putvinski, T.M.; Scoles, G. Surface structure and thermal motion of *n*-alkane thiols self-assembled on gold(111) studied by low-energy helium diffraction. *J. Chem. Phys.* **1991**, *94*, 8493–8502.
  15. Camillone, N., III; Chidsey, C.E.D.; Liu, G.-Y.; Scoles, G.J. Substrate dependence on the surface structure and chain packing of docosyl mercaptan self-assembled on the (111), (110), and (100) faces of single-crystal gold. *Chem. Phys.* **1993**, *98*, 4234–4245.
  16. Dubois, L.H.; Zegarski, B.R.; Nuzzo, R.G. Molecular ordering of organosulfur compounds on gold(111) and gold(100): adsorption from solution and in ultrahigh vacuum. *J. Chem. Phys.* **1993**, *98*, 678–688.
  17. Samant, M.G.; Brown, C.A.; Gordon, J.G., II. Structure of an ordered self-assembled monolayer of docosyl mercaptan on gold(111) by surface X-ray diffraction. *Langmuir* **1991**, *7*, 437–439.
  18. Alves, C.A.; Smith, E.L.; Porter, M.D. Atomic scale imaging of alkanethiolate monolayers at gold surfaces with atomic force microscopy. *J. Am. Chem. Soc.* **1992**, *114*, 1222–1227.
  19. Nuzzo, R.G.; Korenic, E.M.; Dubois, L.H. Studies of the temperature-dependent phase behavior of long chain *n*-alkyl thiol monolayers on gold. *J. Chem. Phys.* **1990**, *93*, 767–773.
  20. Camillone, N., III; Chidsey, C.E.D.; Liu, G.-Y.; Scoles, G.J. Superlattice structure at the surface of a monolayer of octadecanethiol self-assembled on gold(111). *Chem. Phys.* **1993**, *98*, 3503–3511.
  21. Fenter, P.; Eisenberger, P.; Liang, K.S. Chain-length dependence of the structures and phases of alkanethiols (CH<sub>3</sub>(CH<sub>2</sub>)*n*-1SH) self-assembled on gold(111). *Phys. Rev. Lett.* **1993**, *70*, 2447–2450.
  22. Fenter, P.; Eberhardt, A.; Eisenberger, P. Self-assembly of *n*-alkyl thiols as disulfides on Au(111). *Science* **1994**, *266*, 1216–1218.
  23. Poirier, G.E.; Tarlov, M.J. The *c*(4 × 2) superlattice of *n*-alkanethiol monolayers self-assembled on Au(111). *Langmuir* **1994**, *10*, 2853–2856.
  24. Ulman, A.; Eilers, J.E.; Tillman, N. Packing and molecular orientation of alkanethiol monolayers on gold surfaces. *Langmuir* **1989**, *5*, 1147–1152.
  25. Wunderlich, B. *Macromolecular Physics*; Academic Press: New York, 1973, Chapter II.
  26. Allara, D.L.; Nuzzo, R.G. Spontaneously organized molecular assemblies: 2. Quantitative infrared spectroscopic determination of equilibrium structures of solution-adsorbed *n*-alkanoic acids on an oxidized aluminum surface. *Langmuir* **1985**, *1*, 52–66.
  27. Nuzzo, R.G.; Dubois, L.H.; Allara, D.L. Fundamental studies of microscopic wetting on organic surfaces: 1. Formation and structural characterization of a self-consistent series of polyfunctional organic monolayers. *J. Am. Chem. Soc.* **1990**, *112*, 558–569.
  28. Laibinis, P.E.; Whitesides, G.M.; Allara, D.L.; Tao, Y.-T.; Parikh, A.N.; Nuzzo, R.G.J. Comparison of the structures and wetting properties of self-assembled monolayers of *n*-alkanethiols on the coinage metal surfaces, copper, silver, and gold. *Am. Chem. Soc.* **1991**, *113*, 7152–7167.
  29. Gerdy, J.J.; Goodard, W.A., III. Atomistic structure for self-assembled monolayers of alkanethiols on Au(111) surfaces. *J. Am. Chem. Soc.* **1996**, *118*, 3233–3236.
  30. Hou, Z.; Abbott, N.L.; Stroeve, P. Electroless gold as a substrate for self-assembled monolayers. *Langmuir* **1998**, *14*, 3287–3297.
  31. Menon, V.P.; Martin, C.R. Fabrication and evaluation of nanoelectrode ensembles. *Anal. Chem.* **1995**, *67*, 1920–1928.
  32. Willner, I.; Katz, E.; Riklin, A.; Kashner, R. Mediated electron transfer in glutathione reductase organized in self-assembled monolayers on gold electrodes. *R. J. Am. Chem. Soc.* **1992**, *114*, 10,965–10,966.
  33. Spinke, J.; Liley, M.; Guder, H.J.; Angermaler, L.; Knoll, W. Molecular recognition at self-assembled monolayers: the construction of multicomponent multilayers. *Langmuir* **1993**, *9*, 1821–1825.
  34. Song, S.; Clark, R.A.; Bowden, E.F.; Tarlov, M.J. Characterization of cytochrome *c*/alkanethiolate structures prepared by self-assembly on gold. *J. Phys. Chem.* **1993**, *97*, 6564–6572.
  35. Mrkish, M.; Grunwell, J.R.; Whitesides, G.M. Biospecific adsorption of carbonic anhydrase to self-assembled monolayers of alkanethiolates that present benzenesulfonamide groups on gold. *J. Am. Chem. Soc.* **1995**, *117*, 12,009–12,010.
  36. Prime, K.L.; Whitesides, G.M. Self-assembled organic monolayers: model systems for studying adsorption of proteins at surfaces. *Science* **1991**, *252*, 1164–1167.
  37. Prime, K.L.; Whitesides, G.M. Adsorption of proteins onto surfaces containing end-attached oligo(ethylene oxide): a model system using self-assembled monolayers. *J. Am. Chem. Soc.* **1993**, *115*, 10,714–10,721.
  38. Brust, M.; Walker, M.; Bethell, D.; Schiffrin, D.J.; Whyman, R. Synthesis of thiol-derivatized gold nanoparticles in a two-phase liquid-liquid system. *J. Chem. Soc.* **1994**, *1994*, 801–802.
  39. Grabar, K.C.; Allison, K.J.; Baker, B.E.; Bright, R.M.; Brown, K.R.; Freeman, R.G.; Fox, A.P.; Keating, C.D.; Musick, M.D.; Natan, M.J. Two-dimensional arrays of colloidal gold particles: a flexible approach to macroscopic metal surfaces. *Langmuir* **1996**, *12*, 2353–2361.
  40. Grabar, K.C.; Brown, K.R.; Keating, C.D.; Stranick, S.J.; Tang, S.-L.; Natan, M.J. Nanoscale characterization of gold colloid monolayers: a comparison of four techniques. *Anal. Chem.* **1997**, *69*, 471–477.
  41. Keating, C.D.; Kovaleski, K.M.; Natan, M.J. Protein: colloid conjugates for surface enhanced raman

- scattering: stability and control of protein orientation. *J. Phys. Chem. B* **1998**, *102*, 9404–9413.
42. Dubrovsky, T.B.; Hou, Z.; Stroeve, P.; Abbott, N.L. Self-assembled monolayers formed on electroless gold deposited on silica gel: a potential stationary phase for biological assays. *Anal. Chem.* **1999**, *17*, 327–332.
  43. Goddard, E.D. *Interactions of Surfactants with Polymers and Proteins*; Goddard, E.D., Ananthapadmanabhan, K.P., Eds.; CRC Press, Inc.: N.W. Boca Raton, FL, 1993.
  44. Tiberg, F.; Brinck, J. Adsorption and surface-induced self-assembly of surfactants at the solid–aqueous interface. *Curr. Opin. Colloid Interface Sci.* **2000**, *4*, 411–419.
  45. Sigal, G.B.; Mkrsich, M.; Whitesides, G.M. Using surface plasmon resonance spectroscopy to measure the association of detergents with self-assembled monolayers of hexadecanethiolate on gold. *Langmuir* **1997**, *13*, 2749–2755.
  46. Sigal, G.B.; Mkrsich, M.; Whitesides, G.M. Effect of surface wettability on the adsorption of proteins and detergents. *J. Am. Chem. Soc.* **1998**, *120*, 3464–3473.
  47. Bain, C.D.; Whitesides, G.M. Formation of monolayers by the coadsorption of thiols on gold: variation in the length of the alkyl chain. *J. Am. Chem. Soc.* **1989**, *111*, 7164–7175.
  48. Chaudhury, M.K.; Whitesides, G.M. Correlation between surface free energy and surface constitution. *Science* **1992**, *255*, 1230–1232.
  49. Turner, S.F.; Clarke, S.M.; Rennie, A.R.; Thirtle, P.N.; Cooke, D.J.; Li, Z.X.; Thomas, R.K. Adsorption of sodium dodecyl sulfate to a polystyrene/water interface studied by neutron reflection and attenuated total reflection infrared spectroscopy. *Langmuir* **1999**, *15*, 1017–1023.
  50. Levchenko, A.A.; Argo, B.P.; Vidu, R.; Talroze, R.V.; Stroeve, P. Kinetics of sodium dodecyl sulfate adsorption on and desorption from self-assembled monolayers. *Langmuir* **2002**, *18*, 8464–8471.
  51. Chakraborty, A.K.; Golumbfskie, A.J. Polymer adsorption-driven self-assembly of nanostructures. *Annu. Rev. Phys. Chem.* **2001**, *52*, 537–573.
  52. Muthukumar, M.; Ober, C.K.; Thomas, E.L. Competing interactions and levels of ordering in self-organizing polymeric materials. *Science* **1997**, *277*, 1225–1232.
  53. Peppas, N.A.; Langer, R. New challenges in biomaterials. *Science* **1994**, *263*, 1715–1720.
  54. Brandani, P.; Stroeve, P. Adsorption and desorption of PEO–PPO–PEO triblock copolymers on a self-assembled hydrophobic surface. *Macromolecules* **2003**, *36*, 9492–9501.
  55. Eskilsson, K.; Tiberg, F. Equilibrium and kinetic properties of triblock copolymers at hydrophobic surfaces. *Macromolecules* **1997**, *30*, 6323–6332.
  56. Munch, M.R.; Gast, A.P. A study of block copolymer adsorption kinetics via internal reflection interferometry. *J. Chem. Soc. Faraday Trans.* **1990**, *86*, 1341–1348.
  57. Amiji, M.M.; Park, K. Analysis on the surface adsorption of PEO/PPO/PEO triblock copolymers by radiolabeling and fluorescence techniques. *J. Appl. Polym. Sci.* **1994**, *52*, 539–544.
  58. Eskilsson, K.; Tiberg, F. Interfacial properties of triblock copolymers at hydrophilic surfaces. *Macromolecules* **1998**, *31*, 5075–5083.
  59. Eskilsson, K.; Grant, L.M.; Hansson, P.; Tiberg, F. Self-aggregation of triblock copolymers at the solid silica–water interface. *Langmuir* **1999**, *15*, 5150–5157.
  60. Nolan, S.L.; Phillips, R.J.; Cotts, P.M.; Dungan, S.R. Light scattering study on the effect of polymer composition on the structural properties of PEO–PPO–PEO micelles. *J. Colloid Interface Sci.* **1997**, *191*, 291–302.
  61. Brandani, P.; Stroeve, P. Kinetics of adsorption and desorption of PEO–PPO–PEO triblock copolymers on a self-assembled hydrophobic surface. *Macromolecules* **2003**, *36*, 9502–9509.
  62. Brandani, P.; Stroeve, P. Kinetics and equilibria of adsorption of PEO–PPO–PEO triblock copolymers on a hydrophilic self-assembled monolayer on gold. *Macromolecules* **2004**, *37*, 6640–6643.
  63. Artyukhin, A.; Burnham, K.J.; Levchenko, A.A.; Talroze, R.V.; Stroeve, P. Polyelectrolyte adsorption onto a surface confined surfactant. *Langmuir* **2003**, *19*, 2243–2248.



# Self-Assembled Monolayers: Chemical and Physical Modification under Vacuum

Jessica Torres  
Anthony J. Wagner  
Christopher C. Perry  
Glenn M. Wolfe  
D. Howard Fairbrother

*Johns Hopkins University, Baltimore, Maryland, U.S.A.*

## INTRODUCTION

Self-assembled monolayers (SAMs) are highly organized nanoscale films formed by the chemisorption of organic molecules (e.g., alkanethiols and alkanesiloxanes) onto solid substrates (e.g., Au and Si). The organized structure, chemical design flexibility, and facile preparation of SAMs have made them popular models for the study of interfacial phenomena and important systems in the development of new technologies. For example, there is current interest in using SAMs as the template for molecular resists, nanopatterned surfaces, and highly selective sensors. However, some of these applications require specific properties that demand the selective chemical and physical modification of existing SAMs. In addition to their potential technological applications, a study of the chemical transformations that accompany the modification of SAMs can also provide a detailed molecular-level understanding of the interfacial processes that accompany reactions at polymeric surfaces.

Modification of SAMs can be accomplished using either wet chemical or vacuum-based treatments. A number of advantages are inherent in the use of vacuum conditions during the modification of SAMs, including better control over the extent of reaction and the greater ease of in situ reaction monitoring. In this entry, we focus on the chemical processes that accompany the vacuum-based modification of several chemically distinct types of SAMs adsorbed on Au substrates, specifically alkanethiolate SAMs, semi-fluorinated SAMs, and alkanethiolate SAMs functionalized at the vacuum/film interface. The chemical modification of these SAMs has been investigated during exposure to three distinctly different types of reactive species, specifically ionizing radiation, atomic radicals, and vapor-deposited metal atoms.

One of the frequent motivations for the chemical and physical modification of SAMs is the desire to selectively modify or control the interfacial properties

of the organic interface. Results from our investigations indicate that the surface selectivity of a given modification treatment is strongly dependent on both the nature of the reactive species and the chemical composition of the SAM. For example, because of the greater penetration depth of electrons and X-rays relative to the thickness of typical SAMs, the modification of SAMs by ionizing radiation results in a nonsurface-selective process initiated by electron-stimulated bond cleavage events throughout the film. These events produce an initial period of modification characterized by desorption and structural disordering, leading to the formation of a cross-linked carbonaceous overlayer.

## OVERVIEW

The surface-selective modification of SAMs is favored by the presence of labile chemical bonds at the vacuum/film interface and reactive gas-phase species. For example, the initial reactivity of vapor-phase Ti atoms with nitrile-terminated SAMs leads to the selective formation of TiN at the vacuum/film interface. Similarly, reactions of atomic oxygen (AO) and chlorine with alkanethiolate SAMs are initially dominated by reactions at the vacuum/film interface, leading to the incorporation of new oxygen and chlorine-containing carbon functional groups, respectively. In contrast, reactions of AO with semifluorinated SAMs are initiated at the film/substrate interface, leading to desorption of intact adsorbate chains.

SAMs are organized molecular assemblies typically attached to solid substrates through the formation of a covalent bond between the head group of the adsorbate and the surface of the solid substrate (Fig. 1). The ordered structure that subsequently develops during adsorption is derived, in part, from intermolecular forces that exist between the hydrophobic chains of adsorbate molecules. Through the appropriate choice

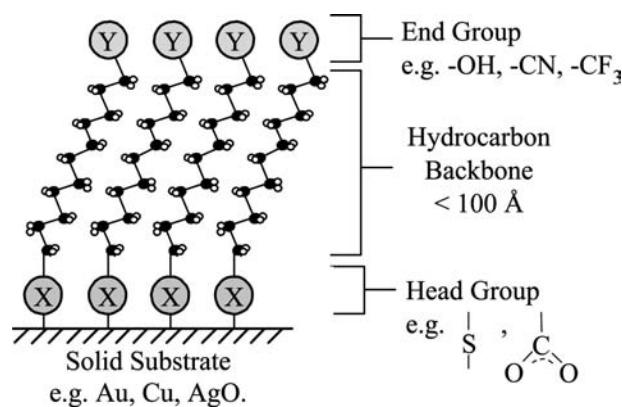


**Fig. 1** Schematic of a SAM, where X represents the head groups that chemisorb the adsorbate to the solid substrate and Y represents the chemical functionality expressed at the SAM surface.

of adsorbate, controlled chemical functionalities can be expressed at the surface of the SAM (Fig. 1). These organic layers can be bound to a number of substrates including noble metals (Au, Ag, and Cu),<sup>[1]</sup> semiconductors (Si),<sup>[2]</sup> and oxide surfaces<sup>[3]</sup> by using an appropriate head group. Compared with thin films prepared by chemical vapor deposition (CVD) or molecular beam epitaxy, SAMs exhibit a number of advantages, which include: 1) ease of preparation; 2) the ability to tailor the chemical identity of end groups and thus the chemical characteristics of the organic interface (Fig. 1); and 3) local and long-range order.

The study of SAM systems has resulted in an improved molecular-level understanding of the factors that control adhesion,<sup>[4]</sup> wetting,<sup>[1]</sup> and friction.<sup>[5]</sup> Related studies have focused on examining the potential technological applications of SAMs. For example, octadecyltrichlorosilane SAMs coated on  $\text{Si}_3\text{N}_4$  tips have been found to improve the quality of images<sup>[6]</sup> obtained during atomic force microscopy (AFM) measurements by avoiding the unwanted effects of water adsorption on the tip. The chemical and physical design flexibilities of SAMs also make them attractive candidates for the creation of highly selective electrodes and sensors,<sup>[7]</sup> modeling and immobilization of artificial biomolecular surfaces,<sup>[8]</sup> miniaturization of electronic components,<sup>[9–11]</sup> and creation of molecular switches.<sup>[12]</sup> SAMs have also been considered as candidates for the creation of patterned surfaces that could be useful in the construction of microelectronic components,<sup>[13–16]</sup> whereas nanoparticles functionalized by SAMs have been proposed for the creation of selective DNA sensors.<sup>[17]</sup>

These applications of SAMs for new technologies have also led to the development of surface modification methodologies that can modify their physical and chemical properties. For example, in the design

of chemical sensors, the surface of SAMs must be modified/controlled so that they exhibit exclusive adhesion properties toward the target analyte.<sup>[7]</sup> Similarly, in creating miniaturized electronic components, the non-conducting surface of SAMs needs to be modified through the selective incorporation of metals at the film's interface.<sup>[10]</sup>

The two main approaches to the modification of SAMs employ either wet chemical or vacuum-based treatments. Wet chemical treatments are easily accessible experimentally and can be used to incorporate new surface functionalities into SAMs. For example, the bromination of hexadecylsiloxane SAMs on Si substrates<sup>[18]</sup> can be accomplished through UV irradiation of the SAM while immersed in a  $\text{CCl}_4$  solution containing dissolved  $\text{Br}_2$ . Although wet chemical methods are generally experimentally facile, modification can result in the loss of structural integrity of the SAM<sup>[19]</sup> and contamination of the surface. Vacuum-based modification protocols offer the advantage of being solvent-free, fast, and environmentally benign. In addition, in situ surface-sensitive analytical techniques such as X-ray photoelectron spectroscopy (XPS) and reflection absorption infrared spectroscopy (RAIRS) can be employed to measure and control the extent of the modification.

Under vacuum conditions, SAMs can also serve as effective models for polymeric interfaces and thereby provide detailed mechanistic information regarding molecular-level events that accompany modification processes.<sup>[20]</sup> In this respect, SAMs offer a number of important advantages over bulk polymeric substrates. SAMs can readily be created free from impurities whose presence would otherwise compromise the interpretation of changes in the film's chemical and physical characteristics. In contrast, polymeric interfaces often contain additives or surface impurities.<sup>[11]</sup> The ultrathin nature of SAMs ( $< 100 \text{ \AA}$ ) also facilitates the quantitative analysis of changes in the film's chemical composition using electron-based surface spectroscopic techniques, whereas analogous studies on polymers are often overwhelmed by the signal contribution from bulk species. In addition, the ultrathin nature of the film facilitates the determination of erosion by monitoring the intensity of the substrate signal.<sup>[21,22]</sup> In contrast to bulk polymeric films, the temperature of SAMs can also be controlled by heating or cooling the solid substrate,<sup>[21]</sup> enabling temperature effects to be investigated.

In this entry, we focus on the vacuum-based physical and chemical modification of semifluorinated and alkanethiolate-based SAMs adsorbed on Au substrates during exposure to a range of reactive species, including electrons, vapor-phase metal atoms, AO, and atomic chlorine. Emphasis is placed on the modification process and its dependence on the interplay between the reactive species and the chemical nature of the SAM.

## EXPERIMENTAL

### Surface Analysis

XPS and SAM modifications were performed in the same ultrahigh vacuum (UHV) chamber, with typical base pressures on the order of  $5 \times 10^{-9}$  Torr. Details of the UHV system and associated capabilities can be found in previous publications.<sup>[23–25]</sup> All XPS spectra were collected using a non-monochromatic Mg K $\alpha$  anode operating at 15 kV and 300 W with 45° take-off angle, relative to the sample normal. Binding energy scales were referenced to the CC/CH<sub>2</sub> peak in the C(1s) region centered at 284.6 eV. XPS data fitting was performed using 100% Gaussian peaks and Shirley background subtractions.

### Sample Preparation

Polycrystalline gold substrates were cleaned by Ar<sup>+</sup> sputtering and then placed into 5-mM solutions of relevant thiols for 10–24 hr. Semifluorinated SAMs were prepared using 1*H*,1*H*,2*H*,2*H*-perfluorodecanethiols (HS(CH<sub>2</sub>)<sub>2</sub>(CF<sub>2</sub>)<sub>7</sub>CF<sub>3</sub>), alkanethiolate SAMs from hexadecane thiols (HS(CH<sub>2</sub>)<sub>15</sub>CH<sub>3</sub>), and nitrile-terminated SAMs from 12-mercaptododecanenitrile (HS(CH<sub>2</sub>)<sub>11</sub>CN). Following immersion, samples were washed in ethanol, water, and hexane, placed into the spectrometer's fast-entry load-lock cell, and pumped to high vacuum ( $2 \times 10^{-5}$  Torr), before being introduced into the UHV chamber.

### X-ray-Induced Modification of SAMs

X-ray-induced modification of SAMs was accomplished with a nonmonochromatic X-ray source operating at 15 kV and 300 W.

### Radical Modification of SAMs

Atomic oxygen and chlorine used during the chemical modification of SAMs were generated using a thermal gas cracker (TC-50; Oxford Applied Research). This gas cracker thermally dissociates molecular gases such as oxygen or chlorine into a stream of atomic, low-energy reactive species to produce a mixture of O(<sup>3</sup>P) and O<sub>2</sub>, or Cl(<sup>2</sup>P) and Cl<sub>2</sub>, hereafter referred to as atomic O (AO) or atomic Cl, respectively. A description of the radical source can be found in previous publications.<sup>[21,22,26]</sup>

### Vapor-Phase Metallization of SAMs

The metal evaporation source used to deposit Ti, Fe, Ni, Cu, and Au on the nitrile-terminated SAM was

prepared by tightly winding wires of each of the aforementioned metals around a 0.5-mm-diameter Ta or W filament. The metal source was resistively heated using a d.c. power source. To avoid the effects of secondary heating, a Ta shield with a 0.5-mm-diameter hole was placed in front of the evaporation source.

### X-RAY AND ELECTRON-INDUCED MODIFICATION OF SEMIFLUORINATED SAMs

The interaction of X-rays and electrons with SAMs is important in a number of scientific and technological applications. For example, X-ray and electron-induced changes in SAMs can be utilized for surface patterning at the nanometer scale, finding use in a variety of fields that include microelectronics and sensor design.<sup>[27]</sup> X-ray modification can also be used to induce chemical changes in SAMs. This is well illustrated in a study by Dressick et al.,<sup>[13]</sup> where X-ray treatment of SAMs containing benzyl chloride groups led to selective C–Cl bond cleavage and the subsequent formation of surface aldehyde and/or ketone groups. Electrons have also been shown to be effective in releasing important bioregulatory drugs such as nitric oxide from surface-functionalized SAMs.<sup>[28]</sup>

The study of the interaction of X-rays and electrons with SAMs can also be used to model the X-ray-induced modification of polymers by providing detailed information about the chemical nature of the species evolving at the surface, rates of reactions, and irradiation-induced structural changes.<sup>[20,23]</sup> Understanding of these events can also help in predicting the lifetimes of polymers used as coatings on spacecraft as they enter low Earth orbit.<sup>[23,29]</sup> Furthermore, it is important to understand the interaction of ionizing radiation with SAMs to elucidate the unintentional modification that can occur during the spectroscopic characterization of organic films with electron-based spectroscopic techniques such as XPS and low-energy electron diffraction (LEED).<sup>[30]</sup>

Studies have shown that X-ray-induced changes in organic films are initiated by secondary electrons ejected from the film and the substrate during X-ray excitation. The idea that electrons, and not X-rays, are responsible for the changes in the SAM on X-ray exposure has been demonstrated by Laibinis, Graham, and Biebuyck<sup>[31]</sup> and Graham et al.<sup>[32]</sup> where the rate of defluorination for –CO<sub>2</sub>CF<sub>3</sub> and –NHCOF<sub>3</sub> terminated SAMs was found to scale with the substrate's secondary electron yield. In another study, Moon et al.<sup>[27]</sup> followed the modification of nitrobenzaldimine monolayers as a function of the incident photon energy (300–800 eV). Results showed that the modification rates were similar regardless of the incident photon energy, supporting the idea that the secondary

substrate electrons, rather than the primary photons, are responsible for the chemical and physical modification of the organic film.

In the following discussion, we present results from the X-ray-induced modification of semifluorinated SAMs [derived from  $\text{CF}_3(\text{CF}_2)_7(\text{CH}_2)_2\text{SH}$ , hereafter referred to as CF-SAMs] adsorbed on Au,<sup>[20,23,30,33]</sup> focusing on the chemical changes that SAMs undergo and the consequential physical modification to the film. The use of semifluorinated SAMs enables the employment of XPS to quantitatively measure the chemical changes taking place under X-ray exposure, including the loss of fluorine, carbon, and sulfur.

### X-ray-Induced Modification of Semifluorinated SAMs

For short exposures (<120 min), the X-ray-induced modification of CF-SAMs leads to competing electron-stimulated C–F, C–C, and S–Au bond-breaking processes. This fact is illustrated in Fig. 2 by the decrease in the F(1s):Au(4f), C(1s):Au(4f), and S(2p):Au(4f) ratios. Stochastic simulations indicate that the relative magnitude of rate constants associated with these bond-breaking processes decreases in the order of C–F > S–Au > C–C during this initial period of X-ray exposure.<sup>[33]</sup> The simultaneous occurrence of these events is indicative of the lack of selectivity inherent in the X-ray-induced SAM modification process. This results from the fact that the X-ray penetration depth is much greater than the thickness of the film, leading to the release of secondary electrons that react throughout the entire SAM. Fig. 3 pictorially illustrates the desorption of F species, intact adsorbate chains, and alkyl fluoride ( $\text{C}_x\text{F}_y$ ) fragments that result from C–F, S–Au, and C–C bond-breaking events, respectively. In a separate near-edge X-ray absorption fine structure spectroscopy (NEXAFS) study, analogous results have been found to accompany the electron-induced modification of alkanethiolate SAMs adsorbed on gold, leading to simultaneous C–H, C–C, C–S, and S–Au bond cleavage.<sup>[34,35]</sup>

During the initial period of X-ray-induced modification, carbon-containing radicals produced from C–F and C–C bond-breaking events remain tethered to the Au substrate. Bimolecular reactions between proximate carbon-containing radicals lead to the formation of a disordered cross-linked structure.<sup>[36]</sup> Similarly, Au–S bond cleavage leads to the ejection of some intact adsorbate chains and also to the production of radiation-induced C–S–C bonds, localized at the film/vacuum interface.<sup>[34,35,37]</sup> These transformations characterizing the initial period of X-ray-induced modification to CF-SAMs are depicted

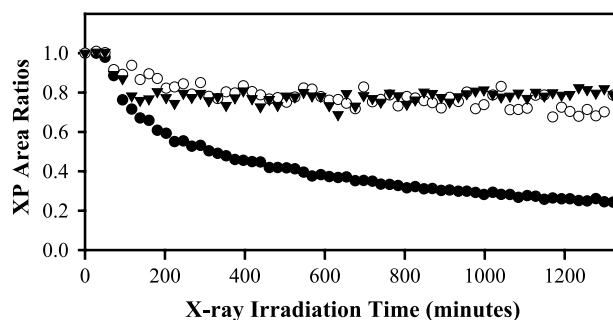


**Fig. 2** Variation in the chemical composition of a semifluorinated SAM [ $\text{CF}_3(\text{CF}_2)_7(\text{CH}_2)_2\text{S-Au}$ ] as a function of X-ray exposure, followed by the F(1s):Au(4f) (●), S(2p):Au(4f) (○), and C(1s):Au(4f) (▼) XPS area ratios. Ratios were normalized to the values obtained for the untreated film to show changes relative to the native semifluorinated SAM.

pictorially in Fig. 3. This carbonaceous, partially fluorinated, cross-linked structure stabilizes the film against additional carbon and sulfur desorption, as shown in Fig. 2 by the invariant C(1s):Au(4f) and S(2p):Au(4f) ratios for prolonged X-ray exposures. The absence of sustained C and S desorption can be explained by fact that once a cross-linked structure has been produced, additional C desorption requires the simultaneous cleavage of two C–C bonds along the same chain, which is an extremely low-probability event.<sup>[30,36]</sup> In contrast, the loss of fluorine is observed continuously because any fluorine is attached to the film through a single C–F bond that can be cleaved by an electron-stimulated process to yield volatile fluorine species. This is shown pictorially in Fig. 3.

As a result of the structural changes that accompany X-ray-induced changes to the CF-SAM, the electron-stimulated loss of fluorine is the only bond-breaking process that contributes to desorption for prolonged X-ray exposures. Indeed, a detailed mechanistic understanding of the processes that lead to fluorine desorption for prolonged X-ray exposures can be derived from the spectral changes in the C(1s) region, as shown in Fig. 4. Initially, the C(1s) XP spectra have three component peaks corresponding to the  $\text{CF}_3$  (292.8 eV),  $\text{CF}_2$  (290.5 eV), and  $\text{CC/CH}_2$  (284.5 eV) functional groups characteristic of CF-SAMs. Upon X-ray exposure, defluorination is evidenced by the decrease in intensity of the  $\text{CF}_3$  and  $\text{CF}_2$  component peaks with the concomitant appearance of  $\text{CFCF}_n$  and  $\text{CFC}$  peaks and the growth of the  $\text{CC/CH}_2$  peak. Fluorine loss for prolonged X-ray exposures is proportional to the concentration of C–F bonds in the film, consistent with a first-order process.<sup>[33]</sup> Indeed, the evolution of the film's chemical composition [based on changes to the C(1s) region] after the film has stabilized toward carbon and sulfur

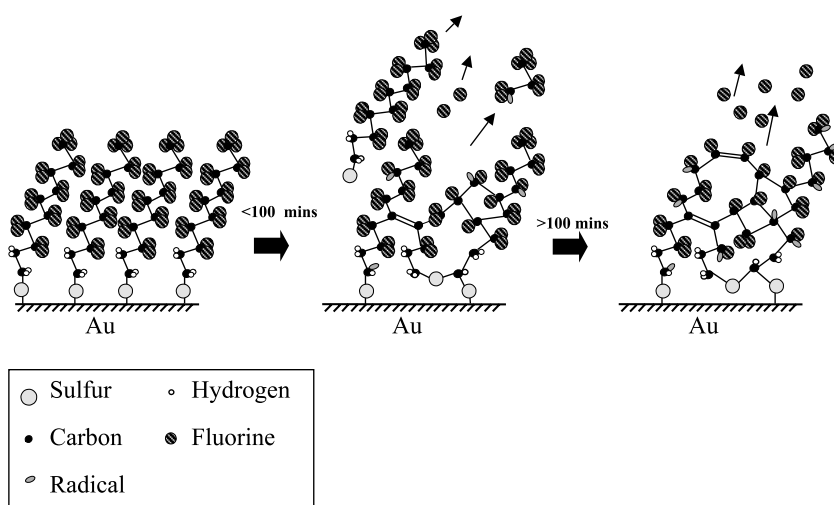


**Fig. 3** Schematic representation of the X-ray-induced modification of a semi-fluorinated SAM as a function of X-ray exposure time.

desorption can be well fitted by a kinetic model where defluorination is postulated to occur via a series of consecutive C–F bond-breaking processes (i.e.,  $\text{CF}_3 \rightarrow \text{CF}_2 \rightarrow \text{CF} \rightarrow \text{C}$ ).<sup>[33]</sup>

Our results indicate that the chemical modification of CF-SAMs by means of X-ray exposures proceeds with a lack of chemical selectivity, rendering this a relatively poor means for achieving controlled modification of SAMs. However, in the context of surface patterning, it appears that X-rays or low-energy electron beams can be used to create surface features that exhibit hydrophobicity distinct from the<sup>[37]</sup> and highly

hydrophobic CF-SAMs. However, the inability of X-rays and low-energy electrons to completely remove the carbon overlayer is undesirable for most lithographic applications, where there is interest in creating distinct regions that contain native SAM structures and regions where the SAM has been completely removed and the substrate has been exposed.

### CHEMICAL MODIFICATION OF SAMs WITH ATOMIC RADICALS

There is interest in modifying SAMs through the introduction of new chemical functionalities to attain a film with specific chemical and physical properties. Chemically modified SAMs have applications that include the development of functionalized electrodes to achieve selective sensing capabilities<sup>[7]</sup> and the understanding of the specific surface interactions of protein and biological materials.<sup>[8]</sup> Surface selectivity is often a desirable aspect of a chemical modification process because many chemical and physical properties are determined by interfacial characteristics.

Ion beam and plasma treatments represent two popular vacuum-based means of modifying polymeric interfaces. Ion implantation surface modification strategies are derived from the collision of energetic ions (typically >1 keV) with a material, resulting in bond-breaking events and the incorporation of new functional groups.<sup>[38]</sup> Although ion implantation is a well-developed methodology for modifying polymeric substrates, its application to SAMs is limited by the fact that sputtering effects dominate over the incorporation of new chemical functionality for typical ion beam energies. Recently, ion beam-induced modification of SAMs has been accomplished by collisions involving polyatomic ions with low-energy ions (<100 eV).<sup>[39]</sup> However, such ion beam modification

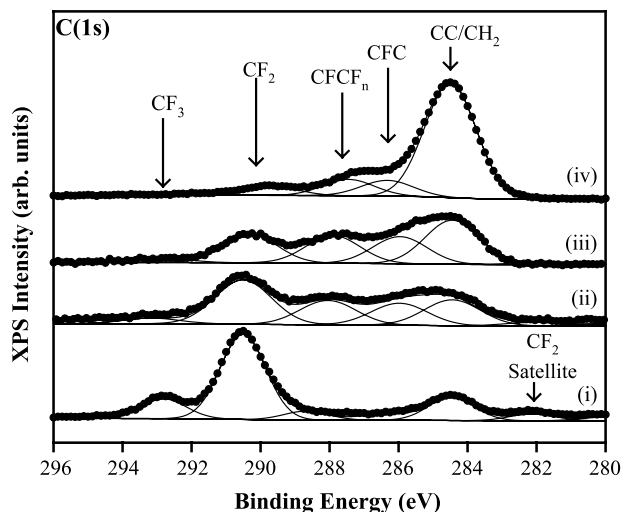


**Fig. 4** Variation in the C(1s) XP spectral region of a semi-fluorinated SAM as a function of X-ray exposure. (A) Shows the native semifluorinated SAM fitted to a combination of  $\text{CC}/\text{CH}_2$ ,  $\text{CF}_2$ , and  $\text{CF}_3$  species. The following spectra show the semifluorinated SAM after X-ray exposure, fitted with additional  $\text{CFCF}_n$  and  $\text{CFC}$  species. Data are shown in filled circles ( $\bullet$ ), whereas fits, backgrounds, and envelopes are shown as solid lines.

of SAMs is limited by the need for dedicated and expensive equipment capable of generating such low-energy ions.<sup>[40]</sup> Plasma treatments are another potential method to achieve the chemical modification of SAMs. Plasmas are highly reactive media that contain ions, neutrals, radicals, electrons, and ionizing radiation.<sup>[41]</sup> Plasma-based surface interactions represent one of the most widely employed means for polymer surface modification.<sup>[41]</sup> However, the competition between film removal with the incorporation of new chemical functionality limits the general applicability of this approach for the chemical modification of SAMs.<sup>[42,43]</sup>

These difficulties, inherent in the use of ion beams and plasmas to modify SAMs can in principle be overcome by the use of free radical species. A wide range of radicals can be formed under vacuum conditions, either by photodissociation or thermal dissociation of a parent molecule, resulting in the formation of species with relatively low kinetic energies (<10 eV). The low kinetic energy of radicals ensures that the modification of a SAM will be dominated by the inherent chemical reactivity of the radical, rather than sputtering. Furthermore, in contrast to ions, the extremely low kinetic energies of radical species limits their effective penetration depth, often facilitating selective reactivity at the vacuum/film interface.<sup>[21,22,26]</sup>

In this section, we detail the modification of semifluorinated and alkanethiolate SAMs with AO and atomic chlorine. AO and chlorine incorporation into organic films often produce opposite effects on interfacial properties (e.g., hydrophobicity). Because of its

relative abundance in low Earth orbit, there is also particular interest in following the reactions of AO ( $O^3P$ ) with well-defined organic films (SAMs) to elucidate the elementary reaction steps responsible for the well-documented weight loss of polymeric coatings used on spacecraft.<sup>[44]</sup>

### Modification of Semifluorinated SAMs with AO

The modification of semifluorinated SAMs by AO was monitored by following the evolution of the C(1s) XP spectral region (Fig. 5A), the integrated area of the C(1s) and F(1s) XPS regions (Fig. 5B), and the oxygen uptake measured from the O(1s) region (Fig. 5C). The native semifluorinated SAM (CF-SAM), derived from  $CF_3(CF_2)_7(CH_2)_2SH$  adsorbed on Au, exhibits the characteristic  $CF_3$ ,  $CF_2$ , and  $CC/CH_2$  peaks in the C(1s) region, as shown in Fig. 5A. During the initial stages of oxygen exposure (<90 min), the C(1s) spectral envelope and the C(1s) and F(1s) XPS areas in Fig. 5B remain unchanged. Taken in conjunction with a lack of oxygen uptake in the CF-SAM during this initial period of AO exposure, these results indicate an initial period of inertness toward AO. This inability of AO to chemically modify the vacuum/film interface can be attributed to the combined effect of the chemical inertness of C–F and C–C bonds toward AO and the limited penetration depth of AO within the well-ordered semifluorinated SAM.

AO-induced modification of the CF-SAM is initiated by the permeation of oxygen to the film/

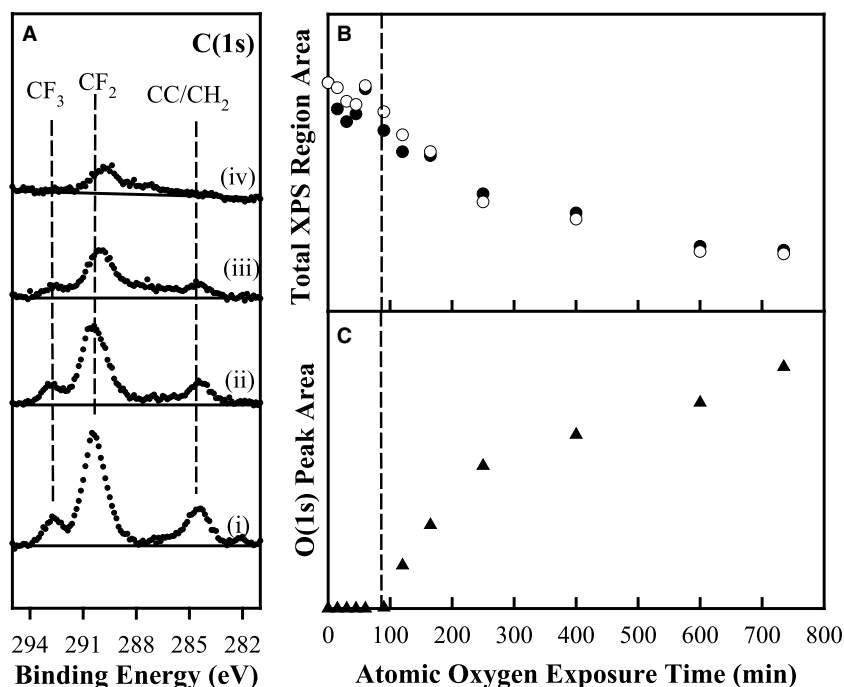


**Fig. 5** Modification of semifluorinated SAMs [ $CF_3(CF_2)_7(CH_2)_2S-Au$ ] by AO. (A) Shows the variation in the C(1s) XP spectral region of semifluorinated SAMs after (i) 0, (ii) 120, (iii) 250, and (iv) 600 min of AO exposure. (B) Shows the total C(1s) (●) and F(1s) (○) XPS areas as a function of AO exposure. Areas were normalized to the values obtained for the untreated film to reflect changes relative to the native semifluorinated SAM. (C) Shows the production of  $Au_2O_3$  (▲) calculated from the area of the fitted peak in the O(1s) region. The vertical dashed line in (B) and (C) indicates the AO exposure for which  $Au_2O_3$  is produced. (A)–(C) were compiled from the same data set. Each data point represents individual AO exposures to separate semifluorinated SAMs, rather than consecutive exposures to the same semifluorinated SAM.



substrate interface as shown in Fig. 7A. Although the detailed mechanism responsible for the oxygen migration through the semifluorinated SAMs cannot be determined unambiguously from XPS studies, it is reasonable to assume that AO permeation and subsequent reactivity are initiated in proximity to defect sites within the SAM, rather than uniformly throughout the film. AO-induced reactivity at the film/substrate interface is evidenced experimentally by the oxidation of sulfur groups producing  $\text{RSO}_3$ <sup>[22]</sup> and the formation of  $\text{Au}_2\text{O}_3$  (Fig. 5C). AO reactions at the film/substrate interface also lead to the desorption of intact adsorbate chains, as shown in Fig. 7A. This is responsible for the fact that fluorine and carbon are lost from the film at equal rates, evidenced by the nearly constant C(1s) spectral profile observed despite the decrease in the integrated C(1s) XPS area (shown in Fig. 5B) and the fact that the C(1s):F(1s) ratio remains essentially constant during the entire AO exposure. In conclusion, the presence of a fully fluorinated surface does indeed appear to provide limited protection toward the effects of chemical modification by AO, although the long-term stability of the CF-SAM toward the effects of AO is compromised by the instability of the C–H, C–S, and S–Au bonds at the film/substrate interface toward AO.

### Modification of Alkanethiolate SAMs with AO

In contrast to semifluorinated SAMs, the modification of alkanethiolate SAMs is initiated exclusively at the

vacuum/film interface because of the facility of AO-mediated H-atom abstraction from C–H bonds. The selective reactivity of alkanethiolate SAM surfaces toward AO is evidenced experimentally by the appearance of spectral intensity in both the C(1s) (Fig. 6A) and O(1s) regions characteristic of oxygen-containing carbon functionality ( $\text{CO}_x$  species) in the absence of  $\text{RSO}_3$  or  $\text{Au}_2\text{O}_3$  production (Fig. 6C).<sup>[22]</sup> Simultaneous changes in the C(1s):Au(4f) area ratio in Fig. 6B indicate that during the early stages of AO-induced modification, the production of new chemical functionality proceeds in the absence of any significant erosion of the native SAM; this is shown schematically in Fig. 7B. Thus it appears that under controlled conditions (corresponding to short AO exposures), the vacuum/film interface of alkanethiolate SAMs can be modified by AO as a means to tailor the physical and chemical properties of the interface (e.g., adhesion and hydrophobicity) while the hydrocarbon backbone of the SAM is retained.

However, prolonged exposures of AO result in etching of the alkanethiolate SAM, as evidenced by the decrease in area of the C(1s) region in Fig. 6A and B. The removal of the hydrocarbon overlayer for prolonged AO exposures can be attributed to the production of volatile species, namely CO and  $\text{CO}_2$ , as presented in Fig. 7B. On AO exposures in excess of 300 min, the hydrocarbon overlayer thickness becomes smaller than the oxygen penetration depth, enabling AO to penetrate to the film/substrate interface, producing  $\text{RSO}_3$  and  $\text{Au}_2\text{O}_3$  (Fig. 6C). Continued AO

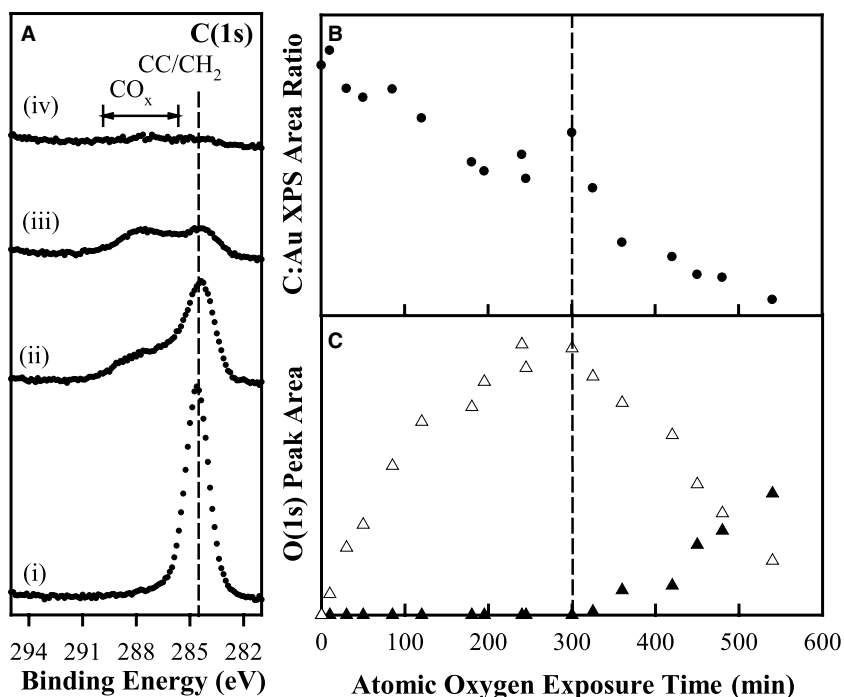


**Fig. 6** Modification of alkanethiolate SAMs  $[\text{CH}_3(\text{CH}_2)_{15}\text{S-Au}]$  by AO. (A) Shows the variation in the C(1s) XP spectral region of alkanethiolate SAM after (i) 0, (ii) 120, (iii) 360, and (iv) 540 min of AO exposure. (B) Shows the C(1s):Au(4f) (●) XPS area ratio normalized to the value obtained for the untreated film. (C) Shows the production of  $\text{CO}_x$  ( $\Delta$ ) and  $\text{Au}_2\text{O}_3$  ( $\blacktriangle$ ) species, calculated from the area of the fitted peaks in the O(1s) XPS region. The vertical dashed line in (B) and (C) indicates when  $\text{Au}_2\text{O}_3$  is produced. (A)–(C) were compiled from the same data set. Each data point represents individual AO exposures to separate alkanethiolate SAMs, rather than consecutive exposures to the same alkanethiolate SAM.

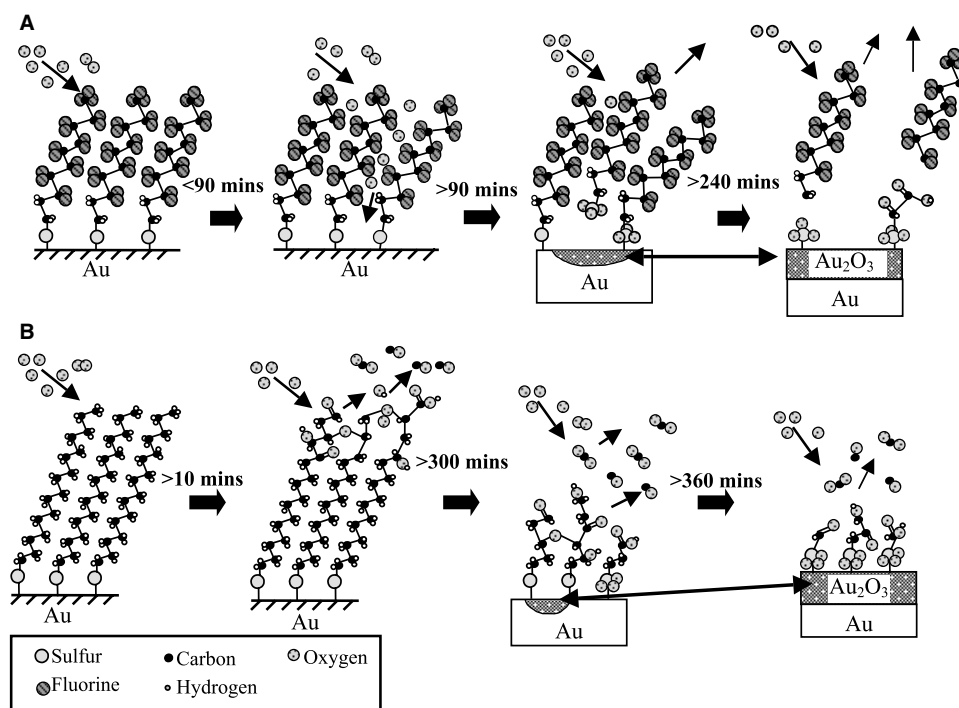


**Fig. 7** Schematic representation of the AO modification of (A) semifluorinated and (B) alkanethiolate SAMs as a function of AO exposure time.

exposure results in the complete etching of the film, as illustrated in (Figs. 5A and B and 7B).

A comparison of the reactivity of semifluorinated and hydrocarbon alkanethiolate SAMs reveals that for a patterned surface containing both species, selective modification of the alkanethiolate portion can be accomplished during controlled exposures to AO. Furthermore, the AO modification of hydrocarbon surfaces could also represent a viable alternative to oxygen-based plasma treatments for thin films and coatings where substrate erosion must be minimized. For prolonged AO exposures, etching of both alkanethiolate and semifluorinated SAMs will occur, although film erosion is initiated at the substrate/film interface in the case of semifluorinated SAMs and at the vacuum/film interface for alkanethiolate SAMs.

### Modification of Alkanethiolate SAMs with Atomic Chlorine

The reactions of alkanethiolate SAMs with atomic chlorine lead to the production of mono- (CCl) and dichlorinated (CCl<sub>2</sub>) species (Fig. 8A). Chlorine incorporation is initiated by Cl-mediated hydrogen abstraction from C–H bonds, generating volatile HCl species.<sup>[45]</sup> This process creates alkyl radicals in the film whose subsequent reactions with either atomic or molecular chlorine lead to the production of CCl and

CCl<sub>2</sub> species. In contrast to AO reactions with alkanethiolate SAMs, atomic chlorine-based modification of alkanethiolate SAM occurs in the absence of film erosion. This is evidenced by the invariant C(1s):Au(4f) ratio presented in Fig. 8B and is a reflection of the fact that atomic chlorine species are unable to induce C–C bond cleavage.

Related experiments on polymeric substrates<sup>[26]</sup> revealed that chlorination under these vacuum conditions created a strong depth-dependent concentration of chlorine-containing functional groups in the surface, with a predominance of chlorinated groups near the vacuum interfacial region. The observed concentration gradient is attributed to a combination of cross-linking reactions between alkyl radicals and steric effects because of the presence of bulky CCl and CCl<sub>2</sub> groups, with both effects limiting chlorine incorporation into the film.<sup>[26]</sup> The same reasons are also ascribed to the limited chlorination of alkanethiolate SAMs, indicated by the continued presence of CC/CH<sub>2</sub> species (Fig. 8A) even after chlorine uptake in the film has reached a maximum value (Fig. 8C); this is illustrated in Fig. 9. Evidence for the surface-selective chlorination of SAMs has also been reported during the photochlorination of 1-octadecene SAMs on Si substrates,<sup>[46]</sup> where IR studies reveal the disappearance of methyl groups after photochlorination while methylene groups still remain.

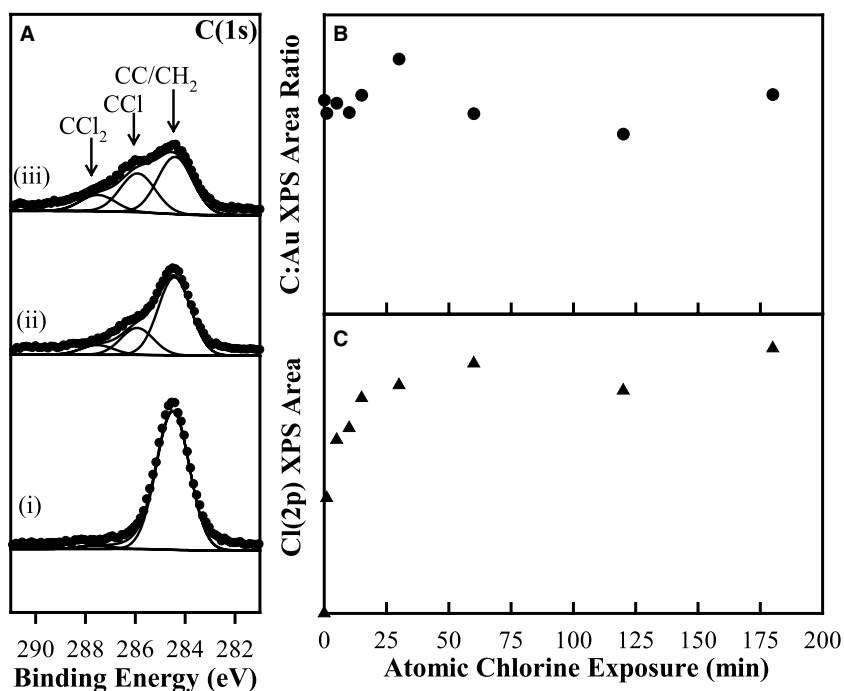


**Fig. 8** Modification of alkanethiolate SAMs [ $\text{CH}_3(\text{CH}_2)_{15}\text{S-Au}$ ] by atomic chlorine. (A) Shows the variation in the C(1s) XP spectral region of alkanethiolate SAMs after (i) 0, (ii) 10 and (iii) 30 min of atomic chlorine exposure. (B) Shows the C(1s):Au(4f) ( $\bullet$ ) XPS area ratio normalized to the value obtained for the untreated alkanethiolate SAM. (C) Shows the incorporation of atomic chlorine into the alkanethiolate SAM measured by the increase in area of the  $\text{CCl}_x$  ( $x = 1, 2$ ) ( $\blacktriangle$ ) fitted doublet peaks in the Cl(2p) XPS region. (A)–(C) were compiled from the same data set. Each data point represents individual atomic chlorine exposures to separate alkanethiolate SAMs, rather than consecutive exposures to the same alkanethiolate SAM.

## VAPOR-PHASE METALLIZATION OF SAMS

The chemical modification of SAMs by means of metal vapor deposition has been proposed as a possible route for the formation of nanometer-scaled micro-electronic components. Employing this approach, molecular-scale capacitors and dielectrics consisting of a molecular-sized organic insulating unit (the SAM)<sup>[47]</sup> located between two conductive metallic surfaces<sup>[48,49]</sup> could be prepared. However, to determine if the fabrication of such devices can be reliably achieved

using vapor-phase metal deposition, a molecular-level understanding of the chemical processes taking place at the metal/organic interfaces during metallization must be developed.<sup>[10]</sup> It is also essential to understand these elementary processes because of the requirement for reliable performance in any discrete metal–organic–metal device, which dictates that the growth of the deposited metal should be restricted to the film/vacuum interface.<sup>[50]</sup>

Previous research has shown that chemical reactivity between end groups of the SAM and incident

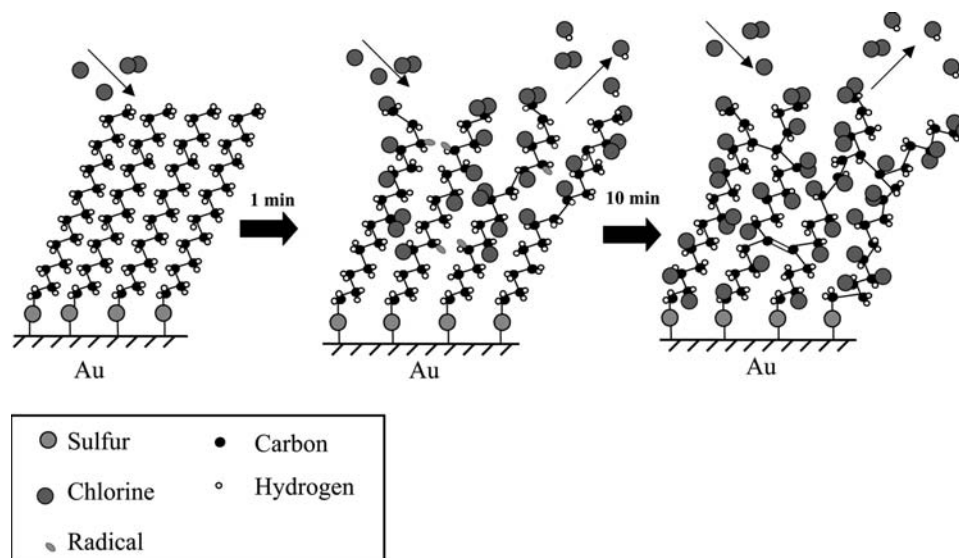


**Fig. 9** Schematic representation of the atomic chlorine-induced modification of alkanethiolate SAMs as a function of exposure time.

vapor-phase metal atoms promotes nucleation and metallic growth at the SAM vacuum/film interface.<sup>[9,48,49]</sup> The relationship between the chemical composition of SAMs and metal reactivity is exemplified by recent studies on the vapor-phase aluminum metallization of hydrocarbon-based SAMs on Au substrates, functionalized at the vacuum/film interface with different head groups [methyl ( $-\text{CH}_3$ ), alcohol ( $-\text{OH}$ ), ether ( $-\text{OCH}_3$ ), ester ( $-\text{CO}_2\text{CH}_3$ ), and carboxylic acid ( $-\text{CO}_2\text{H}$ )].<sup>[9,49,51]</sup> Aluminum metal was selected because of its importance in the microelectronics industry.<sup>[9]</sup> Results from these studies revealed that methyl-terminated SAMs were unreactive during Al deposition, allowing Al to penetrate to the film/substrate interface.<sup>[9]</sup> In contrast, for alcohol-, ester-, and carboxylic acid-terminated SAMs, the deposited aluminum reacted at the vacuum/film interface to form Al-O-C complexes, preventing Al penetration to the Au substrate.<sup>[9,49,51]</sup> When ether-terminated SAMs were used, Al also initially reacted with O at the vacuum/film interface. Upon continued deposition, however Al penetrated through the film to the Au substrate, an effect ascribed to the weak interaction of Al with ether functional groups.<sup>[49]</sup> These results illustrate that the chemical reactivity of functional groups at the vacuum/film interface of the SAM with vapor-phase metal atoms plays a crucial role in determining the stability and integrity of a metal/organic interface in any molecular device.

Vapor-phase metallization of model organic interfaces, such as SAMs, has also become an important experimental tool for modeling the chemical interactions occurring at metal/polymer interfaces.<sup>[11,48,52]</sup> Physical vapor deposition (PVD) is widely used to

metallize polymers encountered in microelectronics,<sup>[11]</sup> data, and food storage devices,<sup>[53]</sup> and in the development of biomaterials for implants.<sup>[54]</sup> Because the depth of metal interactions within polymeric substrates is typically limited to the top few nanometers, surface reactions are particularly important in determining overall adhesion properties.<sup>[11]</sup> However, the nature of chemical reactions taking place at the metal/polymer interface is often difficult to assess because of the multifunctional and heterogeneous nature of most polymer surfaces, particularly those that have been pretreated (e.g., with plasmas) prior to PVD of metal overlayers.<sup>[55,56]</sup> These disadvantages can be largely overcome by the application of SAMs as models for polymeric interfaces, allowing us to study reactions on ultrathin, well-ordered organic interfaces that can be prepared with discrete chemical functionality.

We have recently examined the reactivity of a common chemical functional group expressed at the vacuum/film interface of an alkanethiolate SAM with different vapor-deposited metal atoms. In particular, we have explored the reactions of a nitrile-terminated SAM (CN-SAM) with a variety of different metals (Au, Cu, Ni, Fe, and Ti).<sup>[57]</sup> Interest in these systems was motivated, in part, by the reported presence of nitrile groups following  $\text{N}_2$ -based plasma treatments of hydrocarbon-based polymers prior to metallization.<sup>[58,59]</sup> In addition, the 12-mercaptododecanenitrile ( $\text{HS}(\text{CH}_2)_{11}\text{CN}$ ) precursor for the CN-SAM can be readily synthesized and contains the chemically robust nitrile functional group, making it an ideal candidate for more generalized applications.<sup>[60]</sup>

Fig. 10 shows representative N(1s) and C(1s) XP spectral regions of the native CN-SAM following

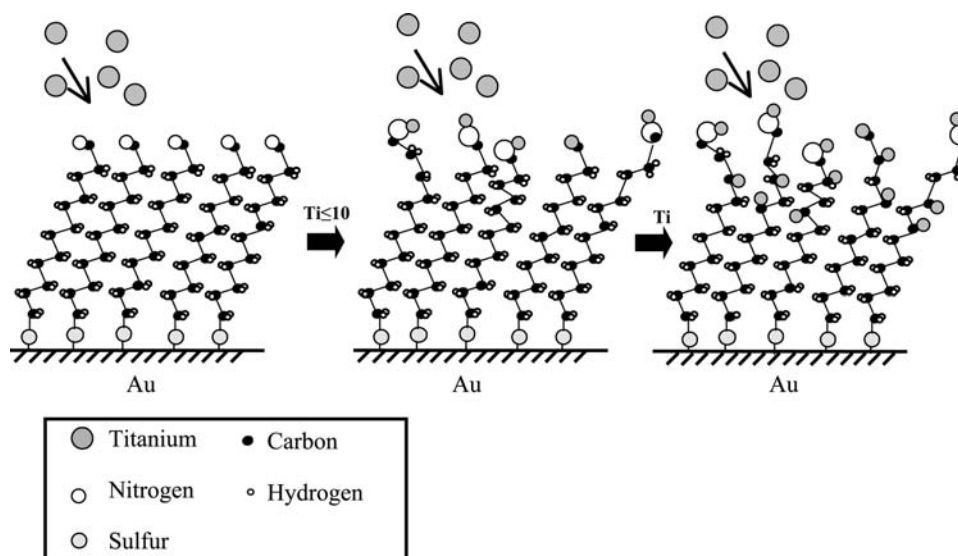


**Fig. 10** Variation in the N(1s) and C(1s) XP spectral regions of nitrile-terminated SAMs exposed to  $\approx 20\%$  of Au, Cu, Ni, Fe, and Ti measured from the elemental composition of the XPS spectrum.

exposure to vapor-phase Au, Cu, Ni, Fe, and Ti atoms. In addition to the peak at 284.6 eV in the C(1s) region corresponding to the CC/CH<sub>2</sub> groups present in the hydrocarbon backbone of the SAM, Fig. 10 shows spectral characteristics of C≡N functionality, notably a peak in the N(1s) region at 399.6 eV and a corresponding C≡N peak at 286.8 eV in the C(1s) region. Upon Au and Cu metallization, the N(1s) peak broadened, probably as a result of increased physical heterogeneity in the system. However, no evidence of metal–nitrogen bond formation was observed<sup>[57,61]</sup> and based on previous studies,<sup>[11,48,62,63]</sup> it is anticipated that Au and Cu will penetrate through the SAM to the Au substrate.

During the vapor-phase deposition of Ni, Fe, and Ti, Fig. 10 reveals that a lower binding energy peak is observed in the N(1s) spectral region. This new species is indicative of the formation of a metal–nitrogen linkage, possibly a metal nitride.<sup>[57]</sup> It should be noted that the Ni reactivity observed in our study is in contrast to previous investigations by Herdt, Jung, and Czanduha,<sup>[48]</sup> where Ni vapor deposition on CN-SAMs exhibited no reactivity. In the case of Ti metallization, the C(1s) spectral profile also shows the appearance of an additional peak at lower binding energies indicative of titanium carbide formation, which is not observed during Au, Cu, Ni, or Fe deposition.

The relative reactivity of different metals with organic functional groups during vapor-phase metallization has been explained based on differences in heat released during metal condensation ( $\Delta H_{\text{vap}}$ ).<sup>[64]</sup> However, in several studies of polymer metallization, we have found a poor correlation between the reactivity of metal atoms deposited on both functionalized SAMs and polymers and  $\Delta H_{\text{vap}}$ .<sup>[20,24,25,57,65]</sup> For

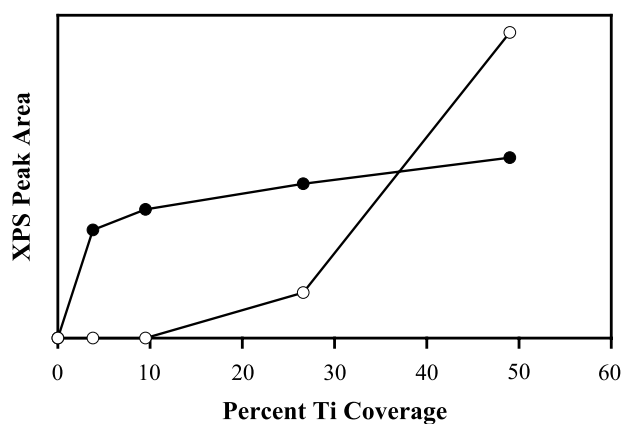


**Fig. 11** Variation in the concentration of TiN (●) and TiC (○) species as a function of Ti coverage. TiC and TiN peak areas were derived from the fitted peaks in the C(1s) and N(1s) regions, respectively.

example, during the metallization of nylon 6 ( $-\text{NH}(\text{CH}_2)_5\text{CO}-_n$ ), vapor-deposited Fe atoms were found to activate the carbonyl group (forming a Fe–O linkage), whereas Ni was unreactive with this same functional group, despite the fact that Ni has a larger  $\Delta H_{\text{vap}}$  than Fe [ $\Delta H_{\text{vap}}(\text{Fe}) = 415 \text{ kJ mol}^{-1}$ ;  $\Delta H_{\text{vap}}(\text{Ni}) = 425 \text{ kJ mol}^{-1}$ ].<sup>[57]</sup> Similarly, in the context of Fig. 10, Fe exhibits a greater degree of reactivity with the nitrile group compared with Ni for comparable metal exposures. A more reliable guide to metal reactivity has been found based on the strength of new metal-containing bonds (e.g., metal–nitrogen) that can form during metallization. The strength of these bonds decreases from left to right along a transition metal series and also decreases as a given series is descended. From spectral trends shown in Fig. 10,

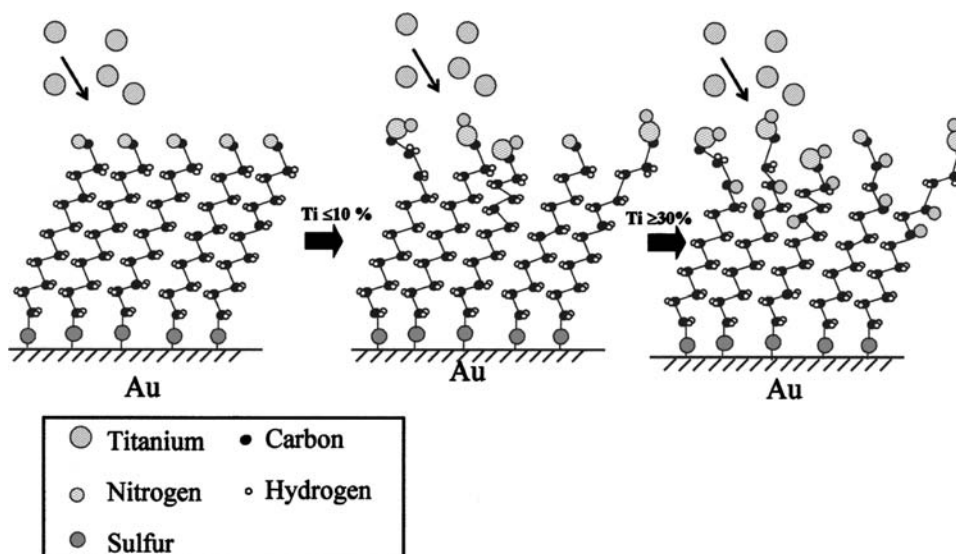


**Fig. 12** Schematic representation of the Ti deposition on nitrile-terminated SAMs as a function of Ti coverage.



the predicted reactivity from this argument yields  $\text{Ti} > \text{Fe} > \text{Ni} > \text{Cu} > \text{Au}$ , which is in agreement with the results shown here for the nitrile group as well as for other organic functional groups studied in our laboratory.<sup>[25,52,57,65]</sup>

In the case of Ti, reactivity is observed at the vacuum/film interface (titanium nitride formation) as well as within the hydrocarbon backbone of the SAM (titanium carbide formation). Fig. 11 shows the area of the fitted Ti–N peak in the N(1s) region and the Ti–C peak in the C(1s) region as a function of Ti coverage. The fact that TiN is an exclusive product observed for short Ti exposures is indicative of a surface-selective reaction. However, on longer exposures, Ti penetration to the hydrocarbon backbone of the SAM is evidenced by the formation of TiC. These results, summarized schematically in Fig. 12, suggest that surface-selective modification of the CN-SAM can be attained during low Ti coverage. Similarly, we anticipate that Ni and Fe deposition on the CN-SAM will also produce an initially surface-selective process. However, despite the reactivity of initial vapor-deposited Ti atoms with nitrile functionality located at the film/vacuum interface, the resultant structure is permeable, enabling Ti migration through this interfacial region and initiating subsequent reactivity within the hydrocarbon backbone of the film. Thus although Ti exhibits initial surface selectivity in its reaction with the CN-SAM, exposures must be carefully controlled to create a discrete metal/organic interface.

## CONCLUSION

Results have been presented on the vacuum-based physical and chemical modification of SAMs studied with in situ XPS. These studies illustrate that the nature of the physical and chemical modification within the SAM is controlled by the relationship between the reactive gas-phase species (vapor-phase metal atoms, radicals, and electrons) and the chemical composition of the SAM.

The importance of the chemical identity of the reactive species in the modification process is demonstrated in metallization studies on nitrile-terminated alkanethiolate SAMs, where the initial site of reactivity can initially be localized at the film/vacuum interface through an appropriate choice of metal atom. Similarly, in the case of radical reactions with alkanethiolate SAMs, the significance of the radical's chemical identity is evidenced by the observation of film erosion during exposure to AO, whereas reactions with atomic chlorine proceed in the absence of substrate erosion.

The importance of the SAM's chemical composition is illustrated in the reactions of alkanethiolate and semifluorinated SAMs with AO. Thus during the initial stages of AO exposure to alkanethiolate SAMs, the incorporation of O-containing chemical functionalities is restricted to the vacuum/film interface because of the lability of C–H bonds toward H-atom abstraction. In contrast, for semifluorinated SAMs, AO-induced reactivity is initiated exclusively at the film/substrate interface, leading to desorption of intact adsorbate chains because of the inertness of C–F and C–C bonds present at the vacuum/film interface. In contrast to SAM modification by vapor-phase metal atoms or atomic radicals, the X-ray-induced modification of semifluorinated SAMs exemplifies a non-selective modification process because it proceeds through a combination of C–C, C–F, C–S, and S–Au bond-breaking events throughout the SAM, leading to the formation of a largely stabilized, cross-linked carbonaceous overlayer.

## ACKNOWLEDGMENTS

Support for this research was provided by a National Science Foundation CAREER award (No. 9985372), a grant from the Petroleum Research Fund (PRF No. 35281-G5, G6) administered through the American Chemical Society and the Howard Hughes Summer Research Fellowship.

## REFERENCES

1. Laibinis, P.E.; Whitesides, G.M.; Allara, D.L.; Tao, Y.T.; Parikh, A.N.; Nuzzo, R.G. Comparison of the structures and wetting properties of self-assembled monolayers of *n*-alkanethiols on the coinage metal surfaces, copper, silver, and gold. *J. Am. Chem. Soc.* **1991**, *113* (19), 7152–7167.
2. Linford, M.R.; Chidsey, C.E.D. Alkyl monolayers covalently bonded to silicon surfaces. *J. Am. Chem. Soc.* **1993**, *115* (26), 12,631–12,632.
3. Tao, Y.T. Structural comparison of self-assembled monolayers of *n*-alkanoic acids on the surfaces of silver, copper, and aluminum. *J. Am. Chem. Soc.* **1993**, *115* (10), 4350–4358.
4. Quon, R.A.; Ulman, A.; Vanderlick, T.K. Impact of humidity on adhesion between rough surfaces. *Langmuir* **2000**, *16* (23), 8912–8916.
5. Choi, J.; Ishida, T.; Kato, T.; Fujisawa, S. Self-assembled monolayer on diamond-like carbon surface: formation and friction measurements. *Tribol. Int.* **2003**, *36* (4–6), 285–290.
6. Wei, Z.Q.; Wang, C.; Bai, C.L. Surface imaging of fragile materials with hydrophobic atomic force microscope tips. *Surf. Sci.* **2000**, *467* (1–3), 185–190.



- Gooding, J.J.; Hibbert, D.B. The application of alkanethiol self-assembled monolayers to enzyme electrodes. *Trends Anal. Chem.* **1999**, *18* (8), 525–533.
- Ferreti, S.; Paynter, S.; Russell, D.A.; Sapsford, K.E.; Richardson, D.J. Self-assembled monolayers: a versatile tool for the formulation of bio-surfaces. *Trends Anal. Chem.* **2000**, *19* (9), 530–540.
- Hooper, A.; Fisher, G.L.; Konstadinidis, K.; Jung, D.; Nguyen, H.; Opila, R.; Collins, R.W.; Winograd, N.; Allara, D.L. Chemical effects of methyl and methyl ester groups on the nucleation and growth of vapor-deposited aluminum films. *J. Am. Chem. Soc.* **1999**, *121* (35), 8052–8064.
- Haynie, B.C.; Walker, A.V.; Tighe, T.B.; Allara, D.L.; Winograd, N. Adventures in molecular electronics: how to attach wires to molecules. *Appl. Surf. Sci.* **2003**, *203–204*, 436–443.
- Opila, R.L.; Eng, J.J. Thin film and interfaces in microelectronics: composition and chemistry as function of depth. *Prog. Surf. Sci.* **2002**, *69* (4–6), 125–163.
- Donhauser, Z.J.; Mantooh, B.A.; Kelly, K.F.; Bumm, L.A.; Monnell, J.D.; Stapleton, J.J.; Price, D.W., Jr.; Rawlett, A.M.; Allara, D.L.; Tour, J.M.; Weiss, P.S. Conductance switching in single molecules through conformational changes. *Science* **2001**, *292*, 2303–2307.
- Dressick, W.J.; Dulcey, C.S.; Brandow, S.L.; Witschi, H.F.; F., N.P. Proximity X-ray lithography of siloxane and polymer films containing benzyl chloride functional groups. *J. Vac. Sci. Technol., A* **1999**, *17* (4), 1432–1440.
- Eck, W.; Stadler, V.; Geyer, W.; Zharnikov, M.; Götzhäuser, A.; Grunze, M. Generation of surface amino groups on aromatic self-assembled monolayers by low energy electron beams—a first step towards chemical lithography. *Adv. Mater.* **2000**, *12* (11), 805–808.
- Tarlov, M.J.; Burgess, D.R.F.; Gillen, G. UV photopatterning of alkanethiolate monolayers self-assembled on gold and silver. *J. Am. Chem. Soc.* **1993**, *115* (12), 5305–5306.
- Yang, X.M.; Peters, R.D.; Kim, T.K.; Nealey, P.F.; Brandow, S.L.; Chen, M.S.; Shirey, L.M.; Dressick, W.J. Proximity X-ray lithography using self-assembled alkylsiloxane films: resolution and pattern transfer. *Langmuir* **2001**, *17* (1), 228–233.
- McIntosh, C.M.; Esposito, E.A., III; Boal, A.K.; Simard, J.M.; Martin, C.T.; Rotello, V.M. Inhibition of DNA transcription using cationic mixed monolayer protected gold clusters. *J. Am. Chem. Soc.* **2001**, *123* (31), 7626–7629.
- Baker, M.V.; Watling, J.D. Functionalization of alkylsiloxane monolayers via free-radical bromination. *Langmuir* **1997**, *13* (7), 2027–2032.
- Swalen, J.D.; Allara, D.L.; Andrade, J.D.; Chandross, E.A.; Garoff, S.; Israelachvili, J.; McCarthy, T.J.; Murray, R.; Pease, R.F.; Rabolt, J.F.; Wynne, K.J.; Yu, H. Molecular monolayers and films. *Langmuir* **1987**, *3* (6), 932–950.
- Perry, C.C.; Carlo, S.R.; Wagner, A.J.; Vecitis, C.; Torres, J.; Kolegraf, K.; Fairbrother, D.H. Self-assembled monolayers as models for polymeric interfaces. In *Thin Films: Preparation, Characterization and Applications*; Soriaga, M.P., Stickney, J., Bottomley, L.A., Kim, Y., Eds.; Kluwer Academic/Plenum Publishers: New York, 2002; 215–230.
- Torres, J.; Perry, C.C.; Bransfield, S.J.; Fairbrother, D.H. Radical reactions with organic thin films: chemical interaction of atomic oxygen with an X-ray modified self-assembled monolayer. *J. Phys. Chem., B* **2002**, *106* (24), 6265–6272.
- Wagner, A.J.; Wolfe, G.M.; Fairbrother, D.H. Dynamics of atomic oxygen reactions with semi-fluorinated and *n*-alkanethiolate self-assembled monolayers. *J. Chem. Phys.* submitted for publication.
- Wagner, A.J.; Han, K.; Vaught, A.L.; Fairbrother, D.H. X-ray induced modification of semifluorinated organic thin films. *J. Phys. Chem., B* **2000**, *104* (14), 3291–3297.
- Carlo, S.R.; Perry, C.C.; Torres, J.; Wagner, A.J.; Vecitis, C.; Fairbrother, D.H. Surface reaction of vapor phase Ti atoms with halogen and nitrogen containing polymers studied using in situ XPS and AFM. *Appl. Surf. Sci.* **2002**, *195* (1–4), 93–106.
- Perry, C.C.; Torres, J.; Carlo, S.; Fairbrother, D.H. Reactivity of Cu with poly-tetrafluoroethylene and polyvinyl chloride: effect of pre- and post-metallization modification on the metal–polymer interface. *J. Vac. Sci. Technol., A* **2002**, *20* (5), 1690–1698.
- Torres, J.; Perry, C.C.; Wagner, A.J.; Fairbrother, D.H. Interaction of chlorine radicals with polyethylene and hydrocarbon thin films under vacuum conditions—a comparison with atomic oxygen reactivity. *Surf. Sci.* **2003**, *543*, 75–76.
- Moon, J.H.; Kim, K.J.; Kang, T.H.; Kim, B.; Kang, H.; Park, J.M. Selective cleavage of the nitro group from a nitrophenyl monolayer by synchrotron soft X-ray. *Langmuir* **1998**, *14* (20), 5673–5675.
- Kim, C.O.; Jung, J.W.; Kim, M.; Kang, T.H.; Ihm, K.; Kim, K.J.; Kim, B.; Park, J.W.; Nam, H.W.; Hwang, K.J. Low energy electron beam irradiation promoted selective cleavage of surface furoxan. *Langmuir* **2003**, *19* (10), 4504–4508.
- Rasoul, F.A.; Hill, D.J.T.; George, G.A.; O'Donnell, J.H. A study of a simulated low Earth environment on the degradation of FEP polymer. *Polym. Adv. Technol.* **1998**, *9* (1), 24–30.
- Wagner, A.J.; Carlo, S.; Vecitis, C.; Fairbrother, D.H. Effect of X-ray irradiation on the chemical and physical properties of a semifluorinated self-assembled monolayer. *Langmuir* **2002**, *18* (5), 1542–1549.
- Laibinis, P.E.; Graham, R.L.; Biebuyck, H.A.; Whitesides, G.M. X-ray damage to CF<sub>3</sub>CO<sub>2</sub>-terminated organic monolayers on Si/Au: Principal effect of electrons. *Science* **1991**, *254* (5034), 981–983.
- Graham, L.R.; Bain, C.D.; Biebuyck, H.A.; Laibinis, P.E.; Whitesides, G.M. Damage to CF<sub>3</sub>CONH-terminated organic self-assembled monolayers (SAMs) on Al, Ti, Cu and Au by Al K $\alpha$  X-rays is due principally to electrons. *J. Phys. Chem.* **1993**, *97*, 9456–9464.

33. Perry, C.C.; Wagner, A.J.; Fairbrother, D.H. Electron stimulated C–F bond breaking kinetics in fluorine-containing organic thin films. *Chem. Phys.* **2002**, *280*, 111–118.
34. Müller, H.U.; Zharnikov, M.; Völkel, B.; Schertel, A.; Harder, P.; Grunze, M. Low-energy electron-induced damage in hexadecanethiolate monolayers. *J. Phys. Chem., B* **1998**, *102* (41), 7949–7959.
35. Zharnikov, M.; Geyer, W.; Götzhäuser, A.; Frey, S.; Grunze, M. Modification of alkanethiolate monolayers on Au-substrate by low energy electron irradiation: alkyl chains and the S/Au interface. *Phys. Chem., Chem. Phys.* **1999**, *1*, 3163–3171.
36. Wirde, M.; Gelius, U.; Dunbar, T.; Allara, D.L. Modification of self-assembled monolayers of alkanethiols on gold by ionizing radiation. *Nucl. Instrum. Methods, B* **1997**, *131*, 245–251.
37. Frey, S.; Heister, K.; Zharnikov, M.; Grunze, M. Modification of semifluorinated alkanethiolate monolayers by low energy electron irradiation. *Phys. Chem., Chem. Phys.* **2000**, *2* (9), 1979–1987.
38. Garbassi, F.; Morra, M.; Occhiello, E. Physical modifications. In *Polymer Surfaces from Physics to Technology*, revised and updated edition Ed.; Wiley: New York, 1997; 238–246.
39. Hanley, L.; Lim, H.; Schultz, D.G.; Garbis, S.; Yu, C.; Ada, E.T.; Wijesundara, M.B.J. Energetics, timescales, and chemistry of low energy molecular ion–organic surface collisions. *Nucl. Instrum. Methods, B* **1999**, *157* (1–4), 174–182.
40. Winger, B.E.; Laue, H.J.; Horning, S.R.; Julian, R.K., Jr.; Lammert, S.A.; Riederer, D.E., Jr.; Cooks, R.G. Hybrid BEEQ tandem mass spectrometer for the study of ion/surface collision processes. *Rev. Sci. Instrum.* **1992**, *63* (12), 5613–5625.
41. Cahn, M.C.; Ko, T.M.; Hiraoka, H. Polymer surface modification by plasmas and photons. *Surf. Sci. Rep.* **1996**, *24* (1–2), 3–54.
42. Elms, F.M.; George, G.A. Plasma reactions of self-assembled monolayers to model oxygen atom effects on polymers. *Polym. Adv. Technol.* **1998**, *9* (1), 31–37.
43. Clouet, F.; Shi, M.K. Interactions of polymer model surfaces with cold plasmas: hexatriacontane as a model molecule of high-density polyethylene and octadecyl octadecanoate as a model of polyester: I. Degradation rate versus Time and Power. *J. Appl. Polym. Sci.* **1992**, *46* (11), 1955–1966.
44. Schuler, P.; Mojazza, H.B.; Haghihat, R. Atomic oxygen resistant films for multi-layer insulation. *High Perform. Polym.* **2000**, *12*, 113–123.
45. Garton, D.J.; Minton, T.K.; Alagia, M.; Balucani, N.; Casavecchia, P.; Volpi, G.G. Comparative dynamics of Cl(<sup>2</sup>P) and O(<sup>3</sup>P) interactions with hydrocarbon surface. *J. Chem. Phys.* **2000**, *112* (13), 5975–5984.
46. Linford, M.R.; Chidsey, C.E.D. Surface functionalization of alkyl monolayers by free-radical activation: gas phase photochlorination with Cl<sub>2</sub>. *Langmuir* **2002**, *18* (16), 6217–6221.
47. Boulas, C.; Davidovits, J.V.; Rondelez, F.; Vuillaume, D. Ultra-low conductivity through insulating self-assembled organic monolayers. *Microelectron. Eng.* **1995**, *28* (1–4), 217–220.
48. Herdt, G.C.; Jung, D.R.; Czanderna, A.W. Weak interactions between deposited metal overlayers and organic functional groups of self-assembled monolayers. *Prog. Surf. Sci.* **1995**, *50* (1–4), 103–129.
49. Fisher, G.L.; Walker, A.V.; Hooper, A.E.; Tighe, T.B.; Bahnck, K.B.; Skriba, H.T.; Reinard, M.D.; Haynie, B.C.; Opila, R.L.; Winograd, N.; Allara, D.L. Bond insertion, complexation, and penetration pathways of vapor-deposited aluminum atoms with HO- and CH<sub>3</sub>O-terminated organic monolayers. *J. Am. Chem. Soc.* **2002**, *124* (19), 5528–5541.
50. Zhou, C.; Deshpande, M.R.; Reed, M.A.; Jones, L.; Tour, J.M. Nanoscale metal self-assembled monolayer metal heterostructures. *Appl. Phys. Lett.* **1997**, *71* (5), 611–613.
51. Fisher, G.L.; Hooper, A.E.; Opila, R.L.; Allara, D.L.; Winograd, N. The interaction of vapor-deposited Al atoms with CO<sub>2</sub>H groups at the surface of a self-assembled alkanethiolate monolayer on gold. *J. Phys. Chem., B* **2000**, *104* (14), 3267–3273.
52. Carlo, S.R.; Wagner, A.J.; Fairbrother, D.H. Iron metallization of fluorinated organic films: a combined XPS and AFM study. *J. Phys. Chem., B* **2000**, *104* (28), 6633–6641.
53. Ziegler, P.; Vallat, M.F.; Haidara, H.; Schultz, J. Polyester/aluminum adhesion: improvement by heat treatments. *J. Mater. Sci.* **1997**, *32* (7), 1809–1813.
54. Bödo, P.; Sundgren, J.E. Adhesion of evaporated titanium to polyethylene: effects of ion bombardment pretreatment. *J. Vac. Sci. Technol., A* **1984**, *2* (4), 1498–1502.
55. Friedrich, J.F.; Unger, W.E.S.; Lippitz, A.; Koprinarov, I.; Kuhn, G.; Weidner, S.; Vogel, L. Plasma pretreatment of polymer surfaces—relevance to adhesion of metals. In *Metallized Plastics: 5 and 6. Fundamental and Applied Aspects*; Mittal, K.L., Ed.; VSP International Science: Utrecht, The Netherlands, 1998; 271–293.
56. Ringenbach, A.; Jugnet, Y.; Duc, T.M. Interfacial chemistry in Al and Cu metallization of untreated and plasma treated polyethylene and poly(ethylene terephthalate). *J. Adhes. Sci. Technol.* **1995**, *9* (9), 1209–1228.
57. Wagner, A.J.; Wolfe, G.M.; Fairbrother, D.H. Reactivity of vapor-deposited metal atoms with nitrogen-containing polymers and organic surfaces studied by in situ XPS. *Appl. Surf. Sci.* **2003**, *219*, 317–328.
58. Petrat, F.M.; Wolany, D.; Schwede, B.C.; Wiedmann, L.; Benninghoven, A. In situ ToF-SIMS/XPS investigation of nitrogen plasma-modified polystyrene surfaces. *Surf. Interface Anal.* **1994**, *21* (5), 274–282.
59. Wagner, A.J.; Fairbrother, D.H.; Reniers, F. A comparison of polyethylene surfaces modified by plasma generated neutral nitrogen species and nitrogen ions. *Plasma Polym.* **2003**, *8* (2), 119–134.

60. Frey, S.; Shaporenko, A.; Zharnikov, M.; Harder, P.; Allara, D.L. Self-assembled monolayers of nitrile-functionalized alkanethiols on gold and silver substrates. *J. Phys. Chem., B* **2003**, *107* (31), 7716–7725.
61. Jung, D.R.; King, D.E.; Czanterna, A.W. Metal overlayers on organic functional groups of self-organized molecular assemblies: II. X-ray photoelectron spectroscopy of interactions of Cu/CN on 12-mercaptododecanenitrile. *J. Vac. Sci. Technol., A* **1993**, *11* (4), 2382–2386.
62. Herdt, G.C.; King, D.E.; Czanterna, A.W. Penetration of deposited Au, Cu, and Ag overlayers through alkanethiol self-assembled monolayers on gold or silver. In *Metallized Plastics: 5 and 6. Fundamental and Applied Aspects*; Mittal, K.L., Ed.; VSP International Science: Utrecht, The Netherlands, 1998; 169–201.
63. Herdt, G.C.; Jung, D.R.; Czanterna, A.W. Penetration of deposited Ag and Cu overlayers through alkanethiol self-assembled monolayers on gold. *J. Adhes.* **1997**, *60* (1–4), 197–222.
64. Sacher, E. Fluoropolymer metallization for microelectronic applications. *Prog. Surf. Sci.* **1994**, *47* (3), 273–300.
65. Carlo, S.R.; Perry, C.C.; Torres, J.; Fairbrother, D.H. Metallization of poly(vinylchloride) by Fe, Ni, Cu, Ag and Au. *J. Vac. Sci. Technol., A* **2002**, *20* (2), 350–355.

# Self-Assembled Monolayers: Surface Nanostructure Effect on Wetting

Jun Yang  
Jingmin Han  
Kelvin Isaacson  
Daniel Y. Kwok

*Department of Mechanical Engineering, University of Alberta,  
Edmonton, Alberta, Canada*

## INTRODUCTION

The determination of solid–vapor ( $\gamma_{sv}$ ) and solid–liquid ( $\gamma_{sl}$ ) interfacial tensions is of importance in a wide range of problems in pure and applied sciences. For example, the process of particle adhesion can be modeled by the net free energy change  $\Delta F^{\text{adh}}$  of the system during the adhesion process, which depends explicitly on the solid (particle) surface tensions: The net free energy change per unit surface area for the adhesion process of a square particle is given by:

$$\Delta F^{\text{adh}} = \gamma_{pv} - \gamma_{pl} - \gamma_{sl} \quad (1)$$

where  $\gamma_{pv}$  and  $\gamma_{pl}$  are the particle–vapor and particle–liquid interfacial tensions, respectively. If  $\Delta F^{\text{adh}} < 0$ , the adhesion process is thermodynamically favorable. The work of adhesion  $W^{\text{adh}}$  is simply:

$$W^{\text{adh}} = -\Delta F^{\text{adh}} \quad (2)$$

Because of the difficulties involved in measuring directly the surface tension involving a solid phase, indirect approaches are called for. Several independent approaches have been used to estimate solid surface tensions, including direct force measurements,<sup>[1–9]</sup> contact angles,<sup>[10–17]</sup> capillary penetration into columns of particle powder,<sup>[18–21]</sup> sedimentation of particles,<sup>[22–25]</sup> solidification front interaction with particles,<sup>[25–32]</sup> film flotation,<sup>[33–37]</sup> gradient theory,<sup>[38–41]</sup> the Lifshitz theory of van der Waals forces,<sup>[41–44]</sup> and the theory of molecular interactions.<sup>[45–50]</sup> Among these methods, contact angle measurements are believed to be the simplest.

We report low-rate dynamic contact angle data of various liquids on self-assembled monolayers (SAMs) of octadecanethiol on annealed and non-annealed gold. It was found that the interpretation of solid surface tensions using contact angle data on less well-prepared polycrystalline non-annealed gold surfaces can be misleading. Our findings were supported by

reflectance infrared (IR) spectra and atomic force microscopy (AFM) data indicating that surface nanostructure, defects, and polycrystallinity can be important factors for a systematic study of wettability on SAMs in terms of surface energetics. We found that the contact angle and adhesion patterns of various liquids on SAMs of octadecanethiol adsorbed onto annealed gold substrates are consistent with recent experimental data for the relatively thick polymer-coated surfaces. The variation of surface structure in terms of surface energetics can be estimated only when a fundamental understanding of contact angles and surface tensions is known.

## CONTACT ANGLE MEASUREMENTS

Contact angle measurement is easily performed by establishing the tangent (angle) of a liquid drop with a solid surface at the base. The attractiveness of using contact angles  $\theta$  to estimate the solid–vapor and solid–liquid interfacial tensions is because of the relative ease with which contact angles can be measured on suitably prepared solid surfaces. It is apparent in the literature that this seeming simplicity can be misleading.

The possibility of estimating solid surface tensions from contact angles relies on a relation that was recognized by Young<sup>[51]</sup> in 1805. The contact angle of a liquid drop on an ideal solid surface is defined by the mechanical equilibrium of the drop under the action of three interfacial tensions: solid–vapor  $\gamma_{sv}$ , solid–liquid  $\gamma_{sl}$ , and liquid–vapor  $\gamma_{lv}$ . This equilibrium relation is known as Young's equation:

$$\gamma_{lv} \cos \theta_Y = \gamma_{sv} - \gamma_{sl} \quad (3)$$

where  $\theta_Y$  is the Young contact angle (i.e., a contact angle that can be inserted into Young's equation). The experimentally accessible contact angles may or may not be equal to  $\theta_Y$ , as there exist many metastable contact angles that are not equal to  $\theta_Y$ .

Several contact angle approaches,<sup>[10–17]</sup> of current interest, were largely inspired by the idea of using Young's equation for the determination of surface energetics. Although these approaches are, logically and conceptually, mutually exclusive, nevertheless, they share the following basic assumptions:

1. All approaches rely on the validity and applicability of Young's equation for surface energetics from experimental contact angles.
2. Pure liquids are always used; surfactant solutions or mixtures of liquids should not be used because they would introduce complications because of preferential adsorption.
3. The values of  $\gamma_{lv}$ ,  $\gamma_{sv}$ , and  $\gamma_{sl}$  are assumed to be constant during the experiment (i.e., there should be no physical/chemical reaction between the solid and the liquid).
4. The liquid surface tensions of the test liquids should be higher than the anticipated solid surface tension.
5. The values of  $\gamma_{sv}$  going from liquid to liquid are also assumed to be constant (i.e., independent of the liquids used).

Recent contact angle studies<sup>[52–54]</sup> have shown the complexities of contact angle phenomena, which prevent the use of measurements for surface energetic calculations, by means of low-rate dynamic contact angle measurements using an automated drop shape analysis. It was found that there were three apparent contact angle complexities that violated the basic assumptions made in the interpretation of contact angles for solid surface tensions:

1. Slip/stick of the three-phase contact line.
2. The contact angle increases/decreases as the drop front advances.
3. The liquid surface tension changes as the drop front advances.

These contact angles should not be used for the determination of solid surface tensions. With respect to the first point, slip/stick of the three-phase contact line indicates that Young's equation is not applicable. An increase/decrease in the contact angle and a change in the liquid surface tension as the drop front advances violate the expectation of no physical/chemical reaction. Therefore when the experimental contact angles and liquid surface tensions are not constant, they should be disregarded. After eliminating the meaningless (non-constant) data, experimental contact angles on a large number of polymer surfaces yield smooth curves of  $\gamma_{lv} \cos \theta$  vs.  $\gamma_{lv}$ ,  $\cos \theta$  vs.  $\gamma_{lv}$ , and  $W_{sl}$  vs.  $\gamma_{lv}$  for one and the same solid surface.<sup>[52–63]</sup> Changing the solid surface shifts the curve in a very regular

manner, suggesting the following relations:

$$\gamma_{lv} \cos \theta = f_1(\gamma_{lv}, \gamma_{sv}) \quad (4)$$

$$\cos \theta = f_2(\gamma_{lv}, \gamma_{sv}) \quad (5)$$

$$W_{sl} = f_3(\gamma_{lv}, \gamma_{sv}) \quad (6)$$

We reproduce in Fig. 1 the adhesion and contact angle patterns for six surfaces: fluorocarbon FC722,<sup>[52]</sup> hexatriacontane,<sup>[64–67]</sup> cholesteryl acetate,<sup>[64–66]</sup> poly(*n*-butyl methacrylate),<sup>[56]</sup> poly(methyl methacrylate/*n*-butyl methacrylate),<sup>[68]</sup> and poly(methyl methacrylate).<sup>[57]</sup> This and other results suggest the existence

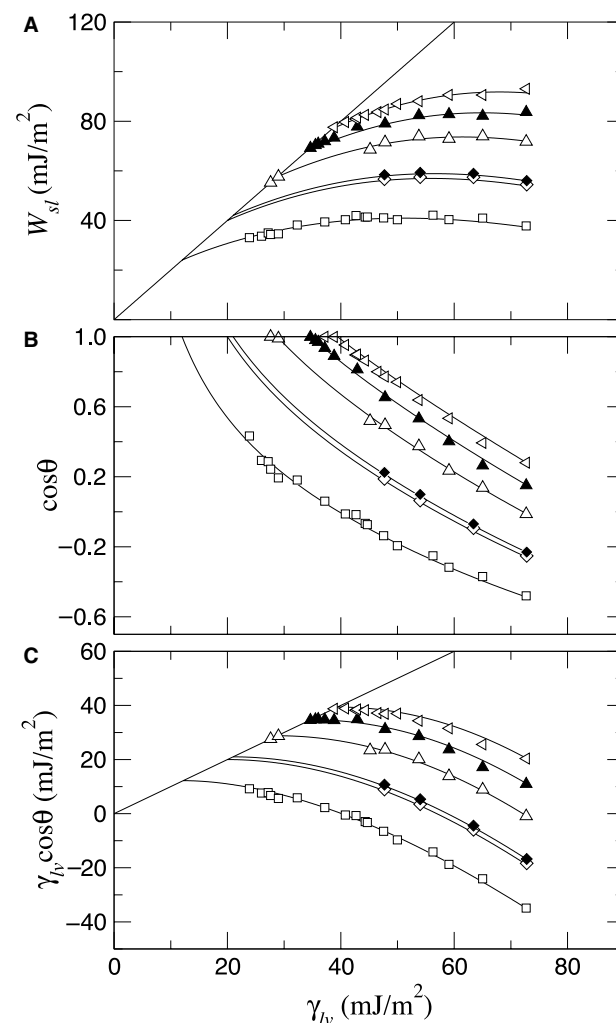


**Fig. 1** (A) The solid–liquid work of adhesion  $W_{sl}$ ; (B) the cosine of the contact angle  $\cos \theta$ ; and (C) the liquid vapor surface tension times the cosine of the contact angle  $\gamma_{lv} \cos \theta$  vs. the liquid–vapor surface tension  $\gamma_{lv}$  for fluorocarbon FC722 ( $\square$ ), hexatriacontane ( $\diamond$ ), cholesteryl acetate ( $\triangle$ ), poly(*n*-butyl methacrylate) ( $\triangle$ ), poly(methyl methacrylate/*n*-butyl methacrylate) ( $\blacktriangle$ ), and poly(methyl methacrylate) ( $\triangleleft$ ) surfaces.

of universal adhesion and contact angle patterns for low-energy solid surfaces. However, a question arises as to whether the low-rate dynamic measurements giving constancy of  $\theta$  and  $\gamma_{lv}$  will always guarantee that the above contact angle assumptions are fulfilled and the patterns in Fig. 1 are unique.

Because these measurements were performed on relatively thick polymer-coated surfaces, it is legitimate to question if the selection of surfaces was biased. In this entry, we purposely selected a thin monomolecular film as our substrate, prepared by SAMs of octadecanethiol adsorbed onto gold. The choice of octadecanethiol SAM is because of its popularity and ease of generating different wettabilities.<sup>[69–74]</sup> To our knowledge, a systematic study of the low-rate dynamic contact angle measurements on SAMs in terms of solid surface tensions has not been performed. A review of literature on contact angle data for octadecanethiol  $\text{CH}_3(\text{CH}_2)_{17}\text{SH}$  SAM on Au suggests that the dependence of  $W_{sl}$ ,  $\gamma_{lv} \cos \theta$ , and  $\cos \theta$  on  $\gamma_{lv}$  is not unique and is different from those shown in Fig. 1. A question arises as to whether the patterns in Fig. 1 do not exist for these monomolecular films, or are there other reasons that complicate our interpretation. The aim of this work is to investigate if the relationships and patterns shown in Fig. 1 exist only for the thick polymer surfaces and not for the relatively thin monolayers by means of low-rate dynamic contact angle measurements. As a second objective, we also study how surface nanostructure and defects of octadecanethiol SAM adsorbed onto gold affect wetting in terms of solid surface tension interpretation.

## EXPERIMENTAL

### Materials

Silicon wafers of test grade were obtained from Wafer World (West Palm Beach, FL) in circular discs of about 10 cm diameter and were cut into rectangular shapes of about  $2.5 \times 5$  cm. Gold shot (99.999%) and titanium shot (99.995%) were obtained from Kurt

J. Lesker (Clairton, PA). Ethanol (100%) was obtained from the Chemistry Department at the University of Alberta (Edmonton, Alberta, Canada). Octadecanethiol [ $\text{CH}_3(\text{CH}_2)_{17}\text{SH}$ ] was obtained from Aldrich and used as received. Six liquids were chosen for contact angle measurements. Selection was based on the following criteria: 1) they should include a wide range of intermolecular forces; 2) they should be non-toxic; and 3) the liquid surface tension should be higher than the anticipated solid surface tension.<sup>[10,14,21,75]</sup> They are listed in Table 1.

### Preparation of Self-Assembled Monolayers

Supported gold films were prepared by sequentially evaporating titanium ( $\sim 10$  nm) and gold ( $\sim 100$  nm) onto small rectangular silicon wafers in a diffusion-pumped vacuum chamber at  $\sim 10^{-6}$  Torr. The chamber was backfilled with air and the substrates were used within 48 hr of preparation. The evaporated surfaces were rinsed with ethanol before SAM formation. Self-assembled monolayers were prepared by immersing into 1 mM  $\text{CH}_3(\text{CH}_2)_{17}\text{SH}$  in ethanol overnight. The resulting surfaces were rinsed with ethanol and blown dry by nitrogen before use. Evaporated gold substrates were also flame-annealed for  $\sim 30$  sec using a Bunsen burner under ambient laboratory condition. After  $\sim 1$  min, the annealed substrate was then immersed into 1 mM  $\text{CH}_3(\text{CH}_2)_{17}\text{SH}$  in ethanol overnight.

### Characterization of Self-Assembled Monolayers

Self-assembled monolayers were first characterized by a Sopra GES5 Variable Angle Spectroscopic Ellipsometer. Ellipsometry measurements were performed using a rotating polarizer in the tracking analyzer mode. A broad band of light (300–850 nm) from a 75-W Xe arc lamp is linearly polarized and directed onto the film surface at an incident angle of  $75^\circ$  from the surface normal. The  $\tan \Psi$  and  $\cos \Delta$  for each bare gold substrate were measured as references immediately after evaporation. After immersion into 1 mM

**Table 1** Experimental advancing and receding contact angles on SAMs of octadecanethiol  $\text{CH}_3(\text{CH}_2)_{17}\text{SH}$  adsorbed onto Au

Liquid	$\gamma_{lv}$ (mJ/m <sup>2</sup> )	$\theta_a$ (°)	$\theta_r$ (°)
Water	72.70 ± 0.09	119.1 ± 0.8	100.2 ± 0.7
Formamide	59.08 ± 0.01	88.7 ± 0.8	63.0 ± 1.4
Ethylene glycol	47.55 ± 0.02	81.5 ± 0.6	66.4 ± 1.1
Bromonaphthalene	44.31 ± 0.05	67.2 ± 0.8	44.1 ± 0.8
Decanol	28.99 ± 0.01	50.7 ± 0.5	38.2 ± 1.1
Hexadecane	27.62 ± 0.01	45.4 ± 0.4	<20.0

Error bars are 95% confidence limits.



octadecanethiol/ethanol solution overnight, a new set of  $\tan \Psi$  and  $\cos \Delta$  for each substrate was measured again using an ambient film substrate model for regression with known refractive index ( $n$  and  $k$ ) for octadecanethiol adsorbed onto gold. The refractive index for octadecanethiol adsorbed onto gold as a function of wavelength was independently obtained from a Sopra GXR Grazing X-ray Reflectometer, rather than assuming an index of refraction (e.g.,  $n = 1.46$ ) at a given wavelength (e.g.,  $\lambda = 6328 \text{ \AA}$ ) as typically performed in the literature. Such spectroscopic measurements are expected to provide more accurate results in ellipsometer thickness because the optical constants for a range of wavelengths were used simultaneously. The thickness was calculated according to the following equation:

$$(\tan \Psi)e^{(i\Delta)} = f(n_i k_i T_i)$$

where  $n$  and  $k$  are the optical constants of the film, and  $T$  is its thickness; subscript  $i$  represents different wavelengths. The averages of three measurements made at each location on the sample were used to calculate the thickness of each sample.

Reflectance IR spectra of SAMs of octadecanethiol onto Au were obtained by using a Thermo Nicolet Nexus 670 Spectrometer equipped with a VeeMax glazing angle accessory. A p-polarized light was incident at  $70^\circ$  from the surface normal and the reflected light was detected by means of an MCT-A detector cooled with liquid nitrogen. The spectra resolution was  $2 \text{ cm}^{-1}$ . Spectra were referenced to the corresponding bare (anneal and non-annealed) Au substrates and 1024 scans were obtained for good signal-to-noise ratios. An IR gain of two was selected for all reflectance IR measurements to ensure that the input IR signals are constant. Samples were rinsed with ethanol and blown dry by  $\text{N}_2$  prior to characterization.

Atomic force microscopy measurements were performed using a Digital Instruments Nanoscope IIIa atomic force microscope (Digital Instruments, Santa Barbara, CA). Standard silicon nitride cantilevered probes were used with a force/spring constant in the range between 0.06 and 0.58 N/m. The AFM images of annealed and non-annealed Au surfaces were captured by using contact mode under ambient laboratory conditions. The surfaces were cut into  $1 \times 1$ -cm samples to fit onto a  $1.5 \times 1.5$ -cm sample stage.

## Contact Angle Measurements

Contact angle measurements were chosen as the last step for the characterization of SAMs. A Linux version of the axisymmetrical drop shape analysis profile (ADSA-P) was used for sessile drop contact angle measurements. Axisymmetrical drop shape analysis

profile is a technique used to determine liquid–fluid interfacial tensions and contact angles from the shape of axisymmetrical menisci (i.e., from sessile as well as pendant drops).<sup>[76,77]</sup> Assuming that the experimental drop is Laplacian and axisymmetrical, ADSA-P finds a theoretical profile that best matches the drop profile extracted from an image of a real drop, from which the surface tension, contact angle, drop volume, surface area, and three-phase contact radius can be computed. The strategy employed is to fit the shape of an experimental drop to a theoretical drop profile according to the Laplace equation of capillarity, using surface/interfacial tension as an adjustable parameter. The best fit identifies the correct surface/interfacial tension from which the contact angle can be determined by a numerical integration of the Laplace equation. Details of the methodology and experimental setup can be found elsewhere.<sup>[52,53,76–78]</sup>

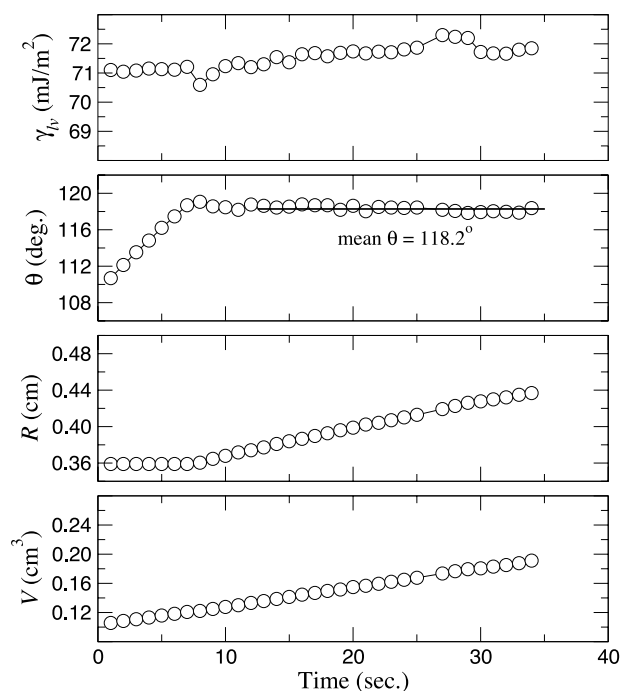
Sessile drop experiments were performed by ADSA-P to determine the advancing and receding contact angles. Temperature and relative humidity were maintained at  $23.0 \pm 0.5^\circ\text{C}$  and at about 40%, respectively, by means of an independent central air conditioning unit in the laboratory. It was found that because ADSA-P assumes an axisymmetrical drop shape, the values of liquid surface tensions measured from sessile drops are very sensitive to even a very small amount of surface imperfection, such as roughness and heterogeneity, whereas contact angles are less sensitive. Therefore the liquid surface tensions used in this study were independently measured by applying ADSA-P to a pendant drop because the axisymmetry of the drop is enforced by using a circular capillary. Results of the liquid surface tension from previous studies<sup>[52,56,57]</sup> are reproduced in Table 1.

In this study, at least five and up to 15 dynamic contact angle measurements at velocities of the three-phase contact line in the range from 0.1 to 1.0 mm/min were performed for each liquid. The choice of this velocity range was based on previous studies,<sup>[52,53,79,80]</sup> which showed that low-rate dynamic contact angles at these velocities were essentially identical to the static contact angles for these relatively smooth surfaces. Liquids were supplied from below the surface through a hole of  $\sim 1$  mm in diameter on the substrate by means of a motorized syringe system. Details of this setup can be found elsewhere.<sup>[52,53]</sup>

## RESULTS AND DISCUSSION

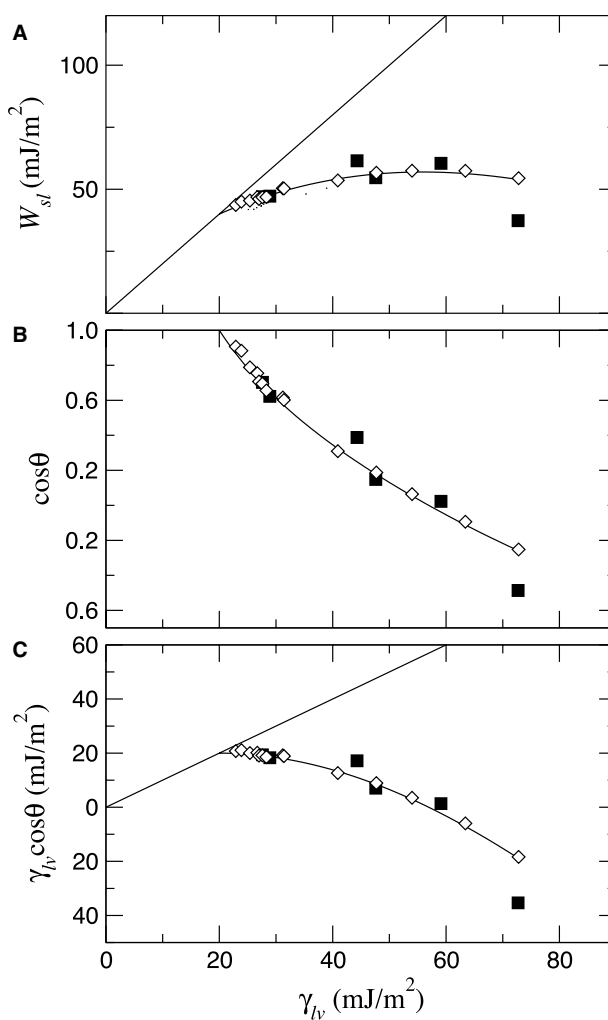
### Formation of Self-Assembled Monolayers on Polycrystalline Gold

Fig. 2 displays a typical low-rate dynamic contact angle of water on SAMs of octadecanethiol



**Fig. 2** Low-rate dynamic contact angles of water on SAMs of octadecanethiol  $\text{CH}_3(\text{CH}_{17})_2\text{SH}$  adsorbed onto Au.

$\text{CH}_3(\text{CH}_2)_{17}\text{SH}$  adsorbed onto Au. As can be seen, increasing the drop volume  $V$  linearly from 0.11 to  $0.12\text{ cm}^3$  increases the apparent contact angle  $\theta$  from ca.  $110^\circ$  to  $118^\circ$  at essentially constant three-phase contact radius  $R$ . This is because of the fact that even carefully putting an initial water drop from above on a solid surface can result in a contact angle somewhere between advancing and receding angles. A further increase in the drop volume causes the three-phase contact line to advance, with  $\theta$  essentially constant as  $R$  increases. Increasing the drop volume in this manner ensures the measured  $\theta$  to be an advancing contact angle. Because the contact angles are essentially constant after  $R = 0.37\text{ cm}$  and according to Ref.<sup>[53]</sup>, these contact angles can be used for the determination of solid surface tensions. The averaged contact angle of  $118^\circ$  in Fig. 2 is consistent with the literature values.<sup>[81,82]</sup> The experimental results for the other five liquids also yield essentially constant contact angles; these results, together with the receding angles, are summarized in Table 1. The solid-liquid work of adhesion  $W_{sl}$ ,  $\cos \theta$ , and  $\gamma_{lv} \cos \theta$  vs.  $\gamma_{lv}$  for these liquids is plotted in Fig. 3. However, there are significant scatters in these data even though the procedures of low-rate dynamic contact angles were used to distinguish meaningful angles from meaningless ones. Comparison of this figure with Fig. 1 suggests that the two patterns are different. A question arises as to whether or not the patterns shown in Fig. 1 are unique only for thick polymer surfaces and not for other surfaces such as monolayers.



**Fig. 3** (A) The solid-liquid work of adhesion  $W_{sl}$ ; (B) the cosine of the contact angle  $\cos \theta$ ; (C) the liquid vapor surface tension times the cosine of the contact angle  $\gamma_{lv} \cos \theta$  vs. the liquid-vapor surface tension  $\gamma_{lv}$  for hexatriacontane ( $\diamond$ ) and SAMs of octadecanethiol  $\text{CH}_3(\text{CH}_2)_{17}\text{SH}$  adsorbed onto Au ( $\blacksquare$ ).

From the point of view of surface energetics, we note that a water contact angle of  $119.1^\circ$  (Table 1) for a surface exposing purely methyl groups [ $\text{CH}_3(\text{CH}_2)_{17}\text{S}/\text{Au}$ ] appears to be too high. For example, the experimental advancing contact angles of water on polystyrene, hexatriacontane, Teflon PTFE, and fluorocarbon are expected to be  $90\text{--}92^\circ$ ,  $105\text{--}107^\circ$ ,  $108\text{--}110^\circ$ , and  $118\text{--}120^\circ$ , respectively, as summarized in Table 2. This comparison suggests that SAMs of octadecanethiol adsorbed onto Au, which are supposed to expose mainly methyl groups, should have a solid surface tension similar to that of fluorocarbon ( $118\text{--}120^\circ$ ) and lower than that of Teflon PTFE ( $108\text{--}110^\circ$ ). These interpretations are questionable. From a surface energetic viewpoint, if SAMs of octadecanethiol adsorbed onto Au expose only methyl

**Table 2** Comparison of expected water contact angles on fluorocarbons, PTFE, polystyrene (PS), and poly (methyl methacrylate) (PMMA) with that measured on SAMs of octadecanethiol  $\text{CH}_3(\text{CH}_2)_{17}\text{SH}$  adsorbed onto Au

Surface	Water contact angle (°)
Fluorocarbon	118–120
PTFE	108–110
Hexatriacontane	105–107
PS	90–92
PMMA	73–75
$\text{CH}_3(\text{CH}_2)_{17}\text{S}/\text{Au}$	118–120

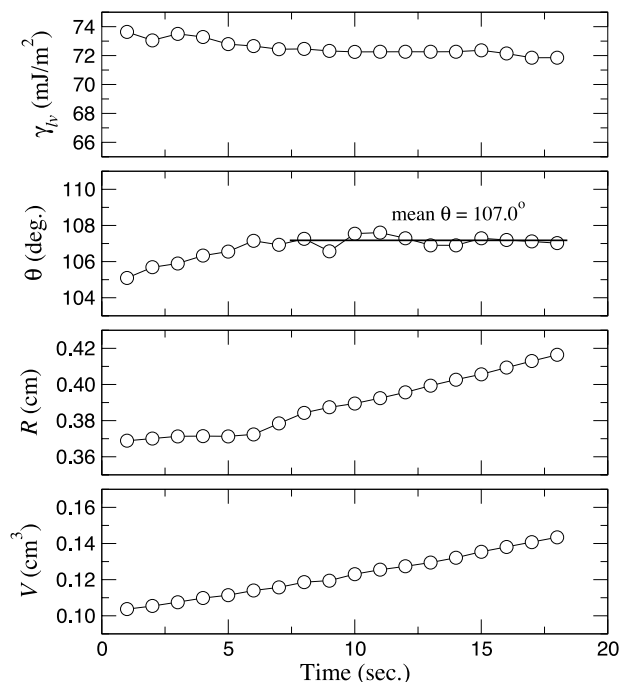
groups, we would expect them to behave very much like a hexatriacontane surface (with water advancing angles between  $105^\circ$  and  $107^\circ$ ) because both surfaces have predominately methyl groups exposed to the surface. The only apparent difference is that the former is a monolayer and the latter is a thick crystalline and well-ordered surface. The hexatriacontane surface was prepared by vapor deposition, of which the surface quality was so good that there was no contact angle hysteresis for water.<sup>[66]</sup> Self-assembled monolayers with methyl groups cannot possibly have a solid surface tension as low as that of fluorocarbon. We also superimposed the contact angle data of octadecanethiol SAM/Au onto those of the hexatriacontane in Fig. 3 and found that the monolayer data appear to fluctuate around those of the hexatriacontane. We wish to point out that the conventional thinking regarding contact angles is that they are indicators for surface hydrophobicity in terms of solid surface tensions (e.g., higher contact angle implies lower surface energy and, similarly, lower contact angle suggests higher surface energy). Such an interpretation is not necessarily conclusive for the systems considered here as will be illustrated and discussed later. We speculate that the discrepancy may come from additional and unexpected effects of changing solid–liquid interfacial tensions on the contact angles through the variation of surface structures, even though the solid–vapor surface tension might have been constant. If  $\gamma_{sv}$  and  $\gamma_{lv}$  are constant, changes in  $\theta$  suggest that  $\gamma_{sl}$  is changing. In “Formation of Self-Assembled Monolayers on Annealed Gold,” we will quantify such effects by looking into the surface structures of octadecanethiol SAMs adsorbed onto Au.

It is commonly known in the literature<sup>[83,84]</sup> that thermally evaporated gold yields smoother and better polycrystalline structures than that by sputtering. It has also been found that SAMs on thermally annealed gold have larger terraces with less surface defects.<sup>[85,86]</sup> Thus SAMs on annealed gold are typically used in AFM studies to obtain atomic resolution pictures.

As a matter of fact, most contact angle studies of SAMs on gold were prepared either by sputtering or thermal evaporation because of the relatively simple procedures.<sup>[81,87–89]</sup> To our knowledge, no systematic contact angle study on SAMs has yet been performed and has looked into the details of how surface structures affect wetting in terms of surface energetic interpretation using thermally annealed gold. Thus we will investigate in “Formation of Self-Assembled Monolayers on Annealed Gold” low-rate dynamic contact angles on octadecanethiol monolayers formed on thermally annealed gold, in an attempt to isolate any (possible) effect of surface structures and defects on solid surface tension interpretation.

### Formation of Self-Assembled Monolayers on Annealed Gold

Fig. 4 shows the low-rate dynamic contact angle results of water on SAMs of octadecanethiol adsorbed onto a thermally annealed gold substrate. Similar to the experimental results in Fig. 2, as  $V$  increases at the beginning,  $\theta$  increases at constant  $R$ . This is because of the fact that such contact angles are not truly advancing angles and that it takes time for the drop front to advance. As  $V$  increases further, the three-phase contact radius  $R$  moves and the contact angle remains rather constant. Averaging the contact

**Fig. 4** Low-rate dynamic contact angles of water on SAMs of octadecanethiol  $\text{CH}_3(\text{CH}_2)_{17}\text{SH}$  adsorbed onto annealed gold.

**Table 3** Experimental advancing and receding contact angles on SAMs of octadecanethiol  $\text{CH}_3(\text{CH}_2)_{17}\text{SH}$  adsorbed onto evaporated (non-annealed) and annealed gold

Liquid	$\gamma_{lv}$	Non-annealed		Annealed	
		$\theta_a$ (°)	$\theta_r$ (°)	$\theta_a$ (°)	$\theta_r$ (°)
Water	72.7	$119.1 \pm 0.8$	$100.2 \pm 0.7$	$106.9 \pm 0.5$	$92.3 \pm 0.9$
Formamide	59.1	$88.7 \pm 0.8$	$63.0 \pm 1.4$	$92.4 \pm 1.5$	$69.2 \pm 1.9$
Ethylene glycol	47.6	$81.5 \pm 0.6$	$66.4 \pm 1.1$	$81.6 \pm 2.4$	$68.2 \pm 1.6$
Bromonaphthalene	44.3	$67.2 \pm 0.8$	$44.1 \pm 0.8$	$76.1 \pm 0.9$	$64.3 \pm 1.3$
Decanol	28.9	$50.7 \pm 0.5$	$38.2 \pm 1.1$	$53.2 \pm 0.9$	$45.1 \pm 1.3$
Hexadecane	27.6	$45.4 \pm 0.4$	<20.0	$45.7 \pm 0.8$	$35.4 \pm 2.2$

Error bars are 95% confidence limits.

angle yields a mean value of  $107.0^\circ$ . We see that this water contact angle value ( $107.0^\circ$ ) is significantly lower than that shown in Fig. 2 ( $118.2^\circ$ ) on the evaporated (non-annealed) gold. We also note that the contact

angle obtained here ( $107.0^\circ$ ) for the  $\text{CH}_3(\text{CH}_2)_{17}\text{S}$  or thermally annealed gold is similar to those obtained on the hexatriacontane (cf. Table 2) and paraffin. This result agrees with the expectation that a monolayer surface exposing predominately methyl groups should have a similar solid surface tension, and hence contact angle, as those of hexatriacontane and paraffin surfaces. Low-rate dynamic contact angle measurements for the remaining five liquids were performed and found to be also constant. These angles, together with the receding angles, are summarized in Table 3.

It is of interest to plot these contact angles in Fig. 5 together with those on the hexatriacontane surface. We see that the apparent scatter in Fig. 3 has disappeared in Fig. 5 using the contact angles on the annealed samples. The resulting  $W_{sl}$ ,  $\cos \theta$ , and  $\gamma_{lv} \cos \theta$  vs.  $\gamma_{lv}$  curves are quite smooth and similar to those shown in Fig. 1. We conclude that the experimental results in Fig. 5 are compatible with the functional relationships in Eqs. (4–6). The origin of the difference in experimental patterns between the nonannealed and annealed gold will be discussed below.

### Characterizations by Ellipsometry, Fourier Transform Infrared Spectroscopy, and Atomic Force Microscopy

The ellipsometer thickness for octadecanethiol  $\text{CH}_3(\text{CH}_2)_{17}\text{SH}$  adsorbed onto annealed gold was consistently 21 Å, whereas that formed on the non-annealed Au varied between 20 and 21 Å. Although this difference is not statistically significant, we noticed that the experimental  $\tan \Psi$  and  $\cos \Delta$  for the non-annealed Au samples did not always match those of the theoretical curves. Nevertheless, our thicknesses are consistent with those reported in the literature.<sup>[82]</sup>

The reflectance spectra for SAMs derived from octadecanethiol on Au and annealed Au are shown

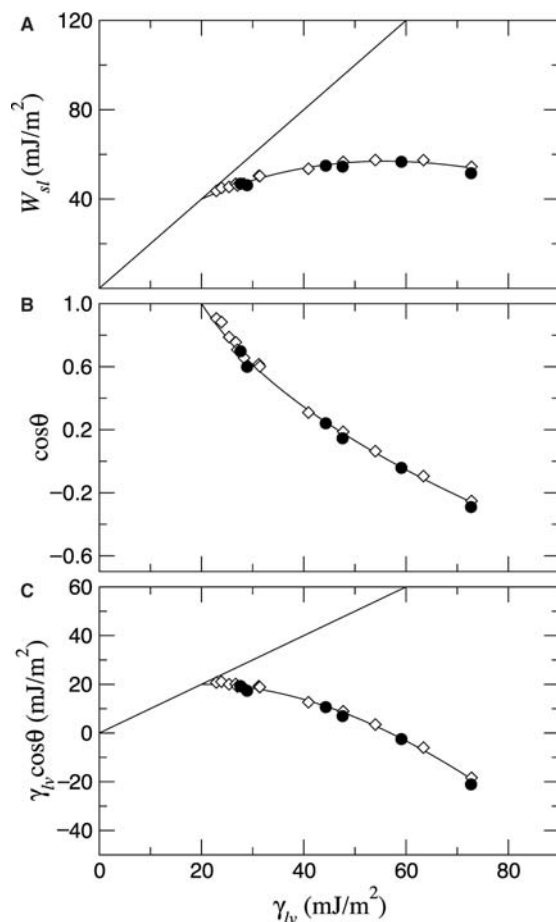


**Fig. 5** (A) The solid–liquid work of adhesion  $W_{sl}$ ; (B) the cosine of the contact angle  $\cos \theta$ ; and (C) the liquid vapor surface tension times the cosine of the contact angle  $\gamma_{lv} \cos \theta$  vs. the liquid–vapor surface tension  $\gamma_{lv}$  for hexatriacontane ( $\diamond$ ) and SAMs of octadecanethiol  $\text{CH}_3(\text{CH}_2)_{17}\text{SH}$  adsorbed onto thermally annealed Au ( $\bullet$ ).

in Fig. 6. In both spectra of Fig. 6, the asymmetrical methylene peaks appeared at  $\sim 2918\text{ cm}^{-1}$ . This indicates a primarily trans-zigzag extended hydrocarbon chain with few gauche conformers. Both spectra demonstrate that SAMs of octadecanethiol adsorbed onto Au and annealed Au are highly crystalline. However, the intensities of the methylene peaks are larger on Au and smaller on the annealed Au. The difference in the peak intensity could reflect different canted orientations for the polymethylene chains on these surfaces, or different amounts of the polymethylene chains that the IR detected. Because the tilt of the chain on the Au substrate for alkanethiolate SAMs is known to be  $\sim 30^\circ$  and this structural orientation is unlikely to be changed by annealing, we speculate that the difference in the intensity of the asymmetrical methylene peaks appears at  $\sim 2918$  and  $2850\text{ cm}^{-1}$ , indicating different amounts of polymethylene chains that were detected by the IR. The spectrum for the adsorbed layer of octadecanethiol on non-annealed Au exhibits a higher dichroic ratio ( $\sim 2$ ) for the methylene adsorption modes [ $\nu_a(\text{CH}_2)/\nu_s(\text{CH}_2)$ ], and that on the annealed Au exhibits a much lower dichroic ratio ( $\sim 1.3$ ). We also note the lower asymmetrical methyl intensity  $\nu_a(\text{CH}_3)$  at  $2964$  (asym)  $\text{cm}^{-1}$  and the higher symmetrical methyl intensity  $\nu_s(\text{CH}_3)$  at  $2879$  (sym)  $\text{cm}^{-1}$  for SAMs on annealed Au in Fig. 6, suggesting that the methyl groups are oriented more toward the surface normal. These features in the spectra provide evidence that SAMs of octadecanethiol on non-annealed Au have a structure that is not the same as that on the annealed Au. Independent AFM images shown in Fig. 7 suggest that the annealed Au has larger terraces (as much as 200 nm), whereas that of the non-annealed Au has much smaller gold steps.

From the interpretation of the above IR and AFM results, we constructed a model in Fig. 8 that illustrates a possible arrangement of octadecanethiol adsorbed onto non-annealed and annealed Au. From the schematic, it is expected that the reflectance IR would detect more methylenes per unit projected area on the non-annealed Au than that for the annealed Au. This is because of the polycrystallinity nature of non-annealed Au that causes variations of the methyl and methylene groups exposed to water. The schematic also supports the IR results for lower asymmetrical methyl intensity and higher symmetrical methyl intensity for SAMs on the annealed Au, as the methyl groups are oriented more toward the surface normal than those on the non-annealed Au.

### Wetting Interpretation in Terms of Solid Surface Tensions

Contact angle interpretation requires extreme experimental care to ensure that all of the commonly accepted assumptions are not violated. It is apparent in Table 3 that, in general, the contact angle hysteresis  $H = \theta_a - \theta_r$  decreases for the annealed gold substrate, suggesting better surface quality. The slightly larger errors for the contact angle data of octadecanethiol adsorbed onto annealed Au were because of the variation of our annealing procedures. From the AFM results above, we conclude that the non-annealed surface consists of smaller gold steps, whereas that of the annealed Au has larger terraces and less defects, as illustrated schematically in Fig. 8. In the case of the non-annealed samples, water could “see” deeper of the surface layer (the methylenes) under the methyl

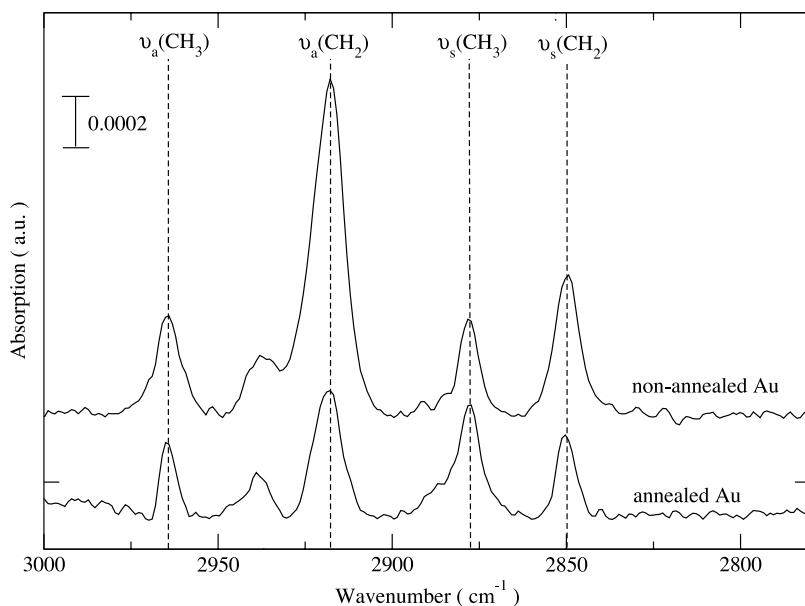


**Fig. 6** Grazing incidence polarized infrared spectra for SAMs of octadecanethiol  $\text{CH}_3(\text{CH}_2)_{17}\text{SH}$  adsorbed onto evaporated (non-annealed) and annealed gold. The approximate positions of the methylene modes are  $2918$  (asym) and  $2850$  (sym)  $\text{cm}^{-1}$ , and those for the methyl modes are  $2964$  (asym),  $2935$  (sym, Fermi resonance), and  $2879$  (sym)  $\text{cm}^{-1}$ . The spectra have been offset vertically for clarity.



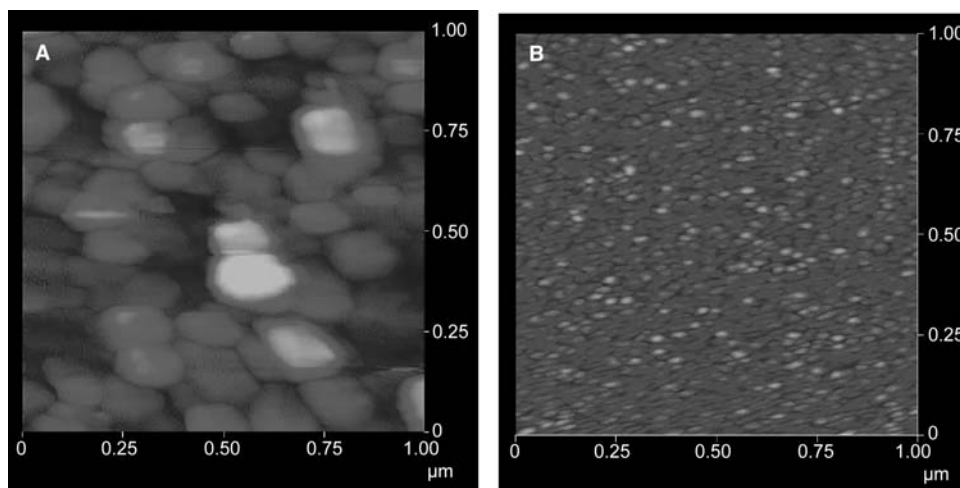


**Fig. 7** Atomic force microscopy images of (A) annealed Au and (B) non-annealed Au for a scan size of 1  $\mu\text{m}$ .

groups because of the relatively less packed monolayers as a result of smaller gold steps or defects. This allows the formation of additional intermolecular interactions between water and the methylenes in the solid–liquid interface. In this case, the surface no longer consists of predominantly methyl groups, but a mixture of methyl and methylene groups in the solid–liquid interfacial region. These molecular interactions with methylenes would result in a higher, additional, interfacial tension between the solid–liquid interface  $\Delta\gamma_{sl}$ , and is illustrated schematically in Fig. 9. This additional effect is believed to have less influence on the solid–vapor interface because of the presence of the relatively less dense water vapor on the solid–vapor interface. Assuming that  $\gamma_{sv}$  is roughly constant for both annealed and non-annealed surfaces, an increase

in  $\gamma_{sl}$  for the latter would cause the contact angle to increase from that of a surface where water can only “see” most of the outer methyl groups and less methylene groups. Thus it appears that the change in the contact angle is a result of additional and unexpected formation of intermolecular interactions in the solid–liquid interface for less packed monolayers. The magnitude would depend, of course, on the intermolecular strength, polarity of the liquid, and structures of the monolayers. In this case, even though we apparently fix our substrate, the intermolecular interactions would not be the same for a given pair of liquid and solid, depending on the surface defect, structure, polycrystallinity, and arrangement of monolayers. In Table 3, we also note that the advancing contact angles for the annealed and non-annealed surfaces are nearly identical

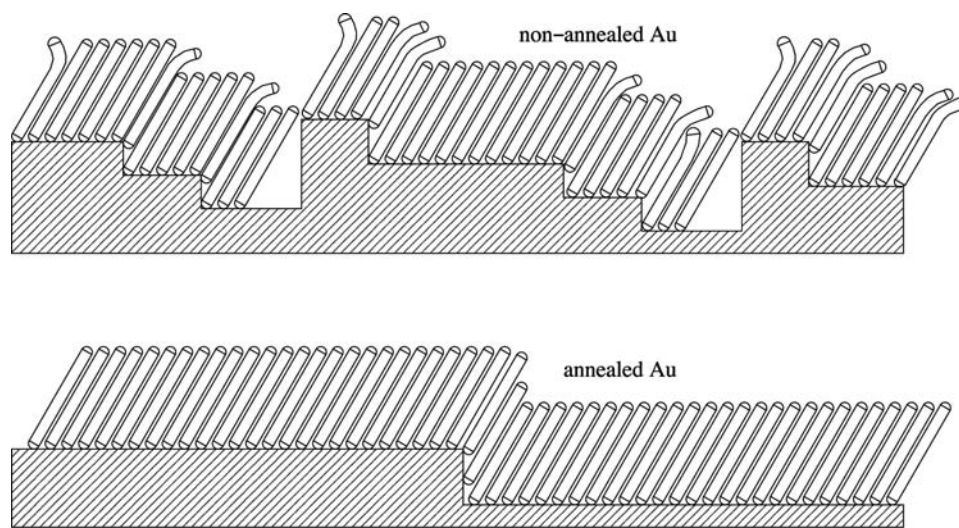


**Fig. 8** Schematic illustration of SAM assembly on two different Au substrates. The upper figure demonstrates the SAM assembly of octadecanethiol adsorbed onto non-annealed Au with smaller gold steps. The lower figure illustrates the SAM assembly of octadecanethiol adsorbed onto annealed Au with larger terraces.



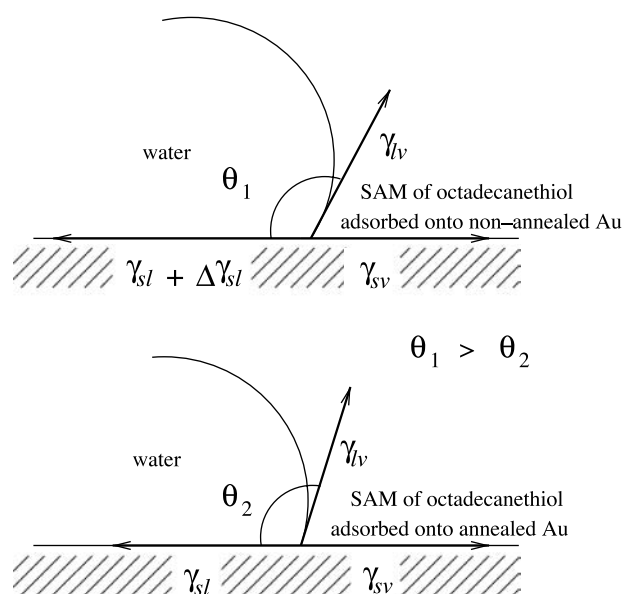


**Fig. 9** Schematic illustration of how the variation of surface structures affects the solid–liquid interfacial tension  $\gamma_{sl}$  for SAMs of octadecanethiol on non-annealed and annealed Au.  $\Delta\gamma_{sl}$  in the upper figure represents the increase in the solid–liquid interfacial tension from that of an annealed Au. Given that the liquid vapor interfacial tension  $\gamma_{lv}$  and the solid–vapor interfacial tension  $\gamma_{sv}$  remain unchanged, an increase in  $\Delta\gamma_s$  results in a higher contact angle  $\theta_1$  than that of the annealed Au,  $\theta_2$ .

and did not change very much for both ethylene glycol and hexadecane. However, the molecular interactions between hexadecane/ $\text{CH}_3(\text{CH}_2)_{17}\text{SH}$  and ethylene glycol/ $\text{CH}_3(\text{CH}_2)_{17}\text{SH}$  on two different Au surfaces are not clearly known. We conclude that, whatever these interactions are, they appear to be insensitive to the structural changes and surface defects of the monolayers. If the intermolecular interactions change drastically as we change the substrate's surface preparation for a given liquid, this violates our expectation of constant solid properties along the curves shown in Figs. 1, 3, and 5. Interpretation of such angles on the non-annealed ones would be difficult.<sup>[90–92]</sup> Because the annealed surfaces contain less defects, additional variation of the solid–liquid interfacial interactions  $\Delta\gamma_{sl}$  would be minimal. We conclude that the surface structures of the underlying gold on which the monolayers of octadecanethiol are formed can affect directly the interpretation of contact angles. Only when a fundamental framework (such as that shown in Fig. 1 or Fig. 5) has been established can the variation of the interfacial interactions from liquid to liquid as an additional effect be studied more systematically. With the above stipulation, the variation of  $\gamma_{sl}$  as a result of surface structural change can be estimated if we assume  $\gamma_{sv}$  for the non-annealed and annealed Au to

be the same. Therefore a  $\Delta\gamma_{sl}$  of  $12.9 \text{ mJ/m}^2$  can be estimated by taking the difference in the water advancing angles,  $\Delta\gamma_{sl} = [72.7(\cos 107 - \cos 118)]$ , using Young's equation. This value represents an increase in  $\gamma_{sl}$  because of the variation of surface structures of octadecanethiol SAMs adsorbed onto Au when interacting with water. However, conventional thinking would have interpreted the water contact angle of  $118^\circ$  for octadecanethiol SAMs on Au to have a much lower solid surface tension similar to that of fluorocarbon ( $\gamma_{sv} = \sim 12 \text{ mJ/m}^2$ ), rather than a  $\gamma_{sv}$  of  $19\text{--}20 \text{ mJ/m}^2$  for methyl-terminated surfaces.

## CONCLUSION

We conclude that the surface defect, structure, and crystallinity of SAMs of octadecanethiol adsorbed onto gold can affect the interpretation of contact angles in terms of solid surface tensions. The contact angle and adhesion patterns of various liquids for SAMs of octadecanethiol adsorbed onto annealed gold are consistent with recent experimental findings on the relatively thick polymer-coated surfaces. We also found that interpretation of solid surface tensions using contact angle data on less well-prepared polycrystalline gold surfaces can be misleading. The variation of surface structures in terms of surface energetics can be estimated only when a fundamental understanding of contact angles and surface tensions is achieved.

## ACKNOWLEDGMENTS

This research was supported financially, in part, by the Natural Sciences and Engineering Research Council (NSERC) of Canada, the Canada Research Chair Program (CRCP), and the Canada Foundation for Innovation (CFI). J. Y. acknowledges support from the Province of Alberta through an Alberta Ingenuity studentship. D. Y. K. thanks Prof. P. E. Laibinis, Dr. R. Michalitsch, and Dr. N. Kim for helpful discussion, and Prof. J. Malisya for the atomic force microscope.

## REFERENCES

1. Derjaguin, B.V.; Muller, V.M.; Toporov, Y.P. On different approaches to the contact mechanics. *J. Colloid Interface Sci.* **1980**, *73*, 293–294.
2. Johnson, K.L.; Kendall, K.; Roberts, A.D. Surface energy and the contact of elastic solids. *Proc. R. Soc. Lond., A* **1971**, *324*, 301–320.
3. Muller, V.M.; Yushchenko, V.S.; Derjaguin, B.V. General theoretical consideration of the influence of surface

- forces on contact deformations and the reciprocal adhesion of elastic spherical particles. *J. Colloid Interface Sci.* **1983**, *92*, 92–101.
- Fogden, A.; White, L.R. Contact elasticity in the presence of capillary condensation: I. The nonadhesive Hertz problem. *J. Colloid Interface Sci.* **1990**, *138*, 414–430.
  - Pashley, R.M.; McGuiggan, P.M.; Horn, R.G.; Ninham, B.W. Forces between bilayers of cetyltrimethylammonium bromide in micellar solutions. *J. Colloid Interface Sci.* **1988**, *126*, 569–578.
  - Christenson, H.K. Interactions between hydrocarbon surfaces in a non-polar liquid: Effect of surface properties on solvation forces. *J. Phys. Chem.* **1986**, *90*, 4–6.
  - Claesson, P.M.; Blom, C.E.; Horn, P.C.; Ninham, B.W. Interactions between water-stable hydrophobic Langmuir–Blodgett monolayers on mica. *J. Colloid Interface Sci.* **1986**, *114*, 234–242.
  - Pashley, P.M.; McGuiggan, P.M.; Pashley, R.M. A study of surfactant solution wetting on mica. *Colloids Surf.* **1987**, *27*, 277–287.
  - Pashley, R.M.; McGuiggan, P.M.; Ninham, B.W.; Evans, D.F. Attractive forces between uncharged hydrophobic surfaces—Direct measurements in aqueous-solution. *Science* **1985**, *229*, 1088–1089.
  - Zisman, W.A. *Contact Angle, Wettability and Adhesion, Advances in Chemistry Series, No. 43*; American Chemical Society: Washington, DC, 1964.
  - Fowkes, F.M. Attractive forces at interfaces. *Ind. Eng. Chem.* **1964**, *56* (12), 40–52.
  - Driedger, O.; Neumann, A.W.; Sell, P.J. An equation of state approach for surface free energies. *Kolloid-Z. Z. Polym.* **1965**, *201*, 52–57.
  - Neumann, A.W.; Good, R.J.; Hope, C.J.; Sejpal, M. An equation-of-state approach to determine surface tension of low-energy solids from contact angles. *J. Colloid Interface Sci.* **1974**, *49*, 291–304.
  - Spelt, J.K.; Li, D. *Applied Surface Thermodynamics*; Spelt, J.K., Neumann, A.W., Eds.; Marcel Dekker Inc.: New York, 1996; 239–292.
  - Owens, D.K.; Wendt, R.C. Estimation of the surface free energy of polymer. *J. Appl. Polym. Sci.* **1969**, *13*, 1741–1747.
  - van Oss, C.J.; Chaudhury, M.K.; Good, R.J. Interfacial Lifshitz–van der Waals and polar interactions in macroscopic systems. *Chem. Rev.* **1988**, *88*, 927–941.
  - Good, R.J.; van Oss, C.J. *Modern Approaches to Wettability: Theory and Applications*; Schrader, M., Loeb, G., Eds.; Plenum Press: New York, 1992; 1–27.
  - Bruil, H.G. The determination of contact angles of aqueous surfactant solutions on powders. *Colloid Polym. Sci.* **1974**, *252*, 32–38.
  - Cheever, G.D. Interrelationships between pigment surface energies and pigment dispersions in polymer solutions. *J. Coat. Technol.* **1983**, *55*, 53–63.
  - Kilau, H.W. Coal wetting ability of surfactant solutions and the effect of multivalent anion additions. *Colloids Surf.* **1987**, *26*, 217–242.
  - Grundke, K.; Bogumil, T.; Gietzelt, T.; Jacobasch, H.J.; Kwok, D.Y.; Neumann, A.W. Wetting measurements on smooth, rough and porous solid surfaces. *Prog. Colloid Polym. Sci.* **1996**, *101*, 58–68.
  - Vargha-Butler, E.I.; Zubovits, T.K.; Absolom, D.R.; Neumann, A.W. Surface-tension effects in the sedimentation of polymer particles in various liquid-mixtures. *J. Dispers. Sci. Technol.* **1985**, *6* (3), 357–379.
  - Vargha-Butler, E.I.; Moy, E.; Neumann, A.W. Sedimentation behavior of low surface-energy powders in different non-polar liquid-systems. *Colloids Surf.* **1987**, *24*, 315–324.
  - Vargha-Butler, E.I.; Zubovits, T.K.; Absolom, D.R.; Neumann, A.W. Surface-tension effects in the sedimentation of coal particles in various liquid-mixtures. *Chem. Eng. Commun.* **1985**, *33*, 255–276.
  - Li, D.; Neumann, A.W. *Applied Surface Thermodynamics*; Spelt, J.K., Neumann, A.W., Eds.; Marcel Dekker Inc.: New York, 1996; 509–556, 557, 628.
  - Omenyi, S.N.; Neumann, A.W. Thermodynamic aspects of particle engulfment by solidifying melts. *J. Appl. Phys.* **1976**, *47*, 3956–3962.
  - Corte, A.E. Vertical migration of particles in front of a moving freezing plane. *J. Geophys. Res.* **1962**, *67*, 1085.
  - Hoekstra, P.; Miller, R.D. On the mobility of water molecules in the transition layer between ice and a solid surface. *J. Colloid Interface Sci.* **1967**, *25*, 166–173.
  - Cissé, J.; Bolling, G.F. A study of the trapping and rejection of insoluble particles during freezing of water. *J. Cryst. Growth* **1971**, *10*, 67.
  - Cissé, J.; Bolling, G.F. The steady-state rejection of insoluble particles by salol grown from the melt. *J. Cryst. Growth* **1971**, *11*, 25–28.
  - Zubko, A.M.; Lobonov, V.G.; Nikonova, V.V. Reaction of foreign particles with a crystallization front. *Sov. Phys. Crystallogr.* **1973**, *18*, 239–241.
  - Chen, K.H.; Wilcox, W.R. Anomalous influence of body force on trapping of foreign particles during solidification. *J. Cryst. Growth* **1977**, *40*, 214–220.
  - Fuerstenau, D.W.; Williams, M.C. Characterization of the lyophobicity of particles by film flotation. *Colloids Surf.* **1987**, *22*, 87–91.
  - Fuerstenau, D.W.; Williams, M.C. A new method for characterization of the surface energy of hydrophobic particles. *Part. Charact.* **1987**, *4*, 7–13.
  - Fuerstenau, D.W.; Williams, M.C. A simple floatation method for rapidly assessing the hydrophobicity of coal particles. *Int. J. Miner. Process.* **1987**, *20*, 153.
  - Fuerstenau, D.W.; Williams, M.C.; Narayanan, K.S.; Diao, J.; Urbina, R. Assessing the wettability and degree of oxidation of coal by film flotation. *Energy Fuels* **1988**, *2*, 237–241.
  - Fuerstenau, D.W.; Diao, J.; Hanson, J. Estimation of the distribution of surface sites and contact angles on coal particles from film flotation data. *Energy Fuels* **1990**, *4*, 34–37.
  - Hemingway, S.J.; Henderson, J.R.; Rowlinson, J.R. The density profile and surface tension of a drop. *Faraday Symp. Chem. Soc.* **1981**, *16*, 33–43.
  - Guermeur, R.; Biquard, F.; Jacolin, C. Density profiles and surface-tension of spherical interfaces—Numerical results for nitrogen drops and bubbles. *J. Chem. Phys.* **1985**, *82*, 2040–2051.

40. Carey, B.S.; Scriven, L.E.; Davis, H.T. Semi-empirical theory of surface-tension of binary-systems. *AIChE J.* **1980**, *26*, 705–711.
41. Moy, E.; Neumann, A.W. *Applied Surface Thermodynamics*; Spelt, J.K., Neumann, A.W., Eds.; Marcel Dekker Inc.: New York, 1996; 333–378.
42. Hamaker, H.C. The London–van der Waals attraction between spherical particles. *Physica* **1937**, *4*, 1058–1072.
43. Israelachvili, J.N.; Tabor, D. The measurement of van der Waals dispersion forces in the range 1.5 to 130 nm. *Proc. R. Soc. Lond., A* **1972**, *331*, 19–38.
44. van Giessen, A.E.; Bukman, D.J.; Widom, B. Contact angles of liquid drops on low-energy solid surfaces. *J. Colloid Interface Sci.* **1997**, *192*, 257–265.
45. Reed, T.M. The theoretical energies of mixing for fluorocarbon–hydrocarbon mixtures. *J. Phys. Chem.* **1955**, *55*, 425–428.
46. Fender, B.E.F.; Halsey, G.D., Jr. *J. Chem. Phys.* **1962**, *36*, 1881.
47. Sullivan, D.E. Surface-tension and contact-angle of a liquid–solid interface. *J. Chem. Phys.* **1981**, *74*, 2604–2615.
48. Matyushov, D.V.; Schmid, R. Calculation of Lennard–Jones energies of molecular fluids. *J. Chem. Phys.* **1996**, *104*, 8627–8638.
49. Kwok, D.Y.; Neumann, A.W. Contact angle interpretation: Combining rule for solid–liquid intermolecular potential. *J. Phys. Chem., B* **2000**, *104*, 741–746.
50. Zhang, J.; Kwok, D.Y. Calculation of solid–liquid work of adhesion patterns from combining rules for intermolecular potentials. *J. Phys. Chem., B* **2002**, *106*, 12594–12599.
51. Young, T. An essay on the cohesion of fluids. *Philos. Trans. R. Soc. Lond.* **1805**, *95*, 65.
52. Kwok, D.Y.; Lin, R.; Mui, M.; Neumann, A.W. Low-rate dynamic and static contact angles and the determination of solid surface tensions. *Colloids Surf., A Physicochem. Eng. Asp.* **1996**, *116*, 63–77.
53. Kwok, D.Y.; Gietzelt, T.; Grundke, K.; Jacobasch, H.J.; Neumann, A.W. Contact angle measurements and contact angle interpretation: I. Contact angle measurements by axisymmetric drop shape analysis and a goniometer sessile drop technique. *Langmuir* **1997**, *13*, 2880–2894.
54. Kwok, D.Y.; Lam, C.N.C.; Li, A.; Leung, A.; Wu, R.; Mok, E.; Neumann, A.W. Measuring and interpreting contact angles: A complex issue. *Colloids Surf., A Physicochem. Eng. Asp.* **1998**, *142*, 219–235.
55. Kwok, D.Y.; Lam, C.N.C.; Li, A.; Leung, A.; Neumann, A.W. Low-rate dynamic contact angles on noninert poly(propene-*alt*-*N*-(*n*-alkyl)maleimide) copolymers by an automated axisymmetric drop shape analysis (ADSA-P). *Langmuir* **1998**, *14*, 2221–2224.
56. Kwok, D.Y.; Leung, A.; Li, A.; Lam, C.N.C.; Wu, R.; Neumann, A.W. Low-rate dynamic contact angles on poly(*n*-butyl methacrylate) and the determination of solid surface tensions. *Colloid Polym. Sci.* **1998**, *276*, 459–469.
57. Kwok, D.Y.; Leung, A.; Lam, C.N.C.; Li, A.; Wu, R.; Neumann, A.W. Low-rate dynamic contact angles on poly(methyl methacrylate) and the determination of solid surface tensions. *J. Colloid Interface Sci.* **1998**, *206*, 44–51.
58. Kwok, D.Y.; Lam, C.N.C.; Li, A.; Zhu, K.; Wu, R.; Neumann, A.W. Low-rate dynamic contact angles on polystyrene and the determination of solid surface tensions. *Polym. Eng. Sci.* **1998**, *38*, 1675–1684.
59. Kwok, D.Y.; Li, A.; Lam, C.N.C.; Wu, R.; Zschoche, S.; Pöschel, K.; Gietzelt, T.; Grundke, K.; Jacobasch, H.J.; Neumann, A.W. Low-rate dynamic contact angles on poly[styrene-*alt*-(hexyl/10-carboxydecyl(90/10)maleimide)] and the determination of solid surface tensions. *Macromol. Chem. Phys.* **1999**, *200* (5), 1121–1133.
60. Kwok, D.Y.; Lam, C.N.C.; Neumann, A.W. Wetting behavior and solid surface tensions for a 70:30 copolymer of polystyrene and poly(methyl methacrylate). *Colloid J.* **2000**, *62* (3), 324–335.
61. Kwok, D.Y.; Wu, R.; Li, A.; Neumann, A.W. Contact angle measurements and interpretation: Wetting behavior and solid surface tensions for poly(alkyl methacrylate) polymers. *J. Adhes. Sci. Technol.* **2000**, *14* (5), 719–743.
62. Kwok, D.Y.; Li, A.; Neumann, A.W. Low-rate dynamic contact angles on poly(methyl methacrylate/ethyl methacrylate, 30/70) and the determination of solid surface tensions. *J. Polym. Sci., B, Polym. Phys.* **1999**, *16*, 2039–2051.
63. del Río, O.I.; Kwok, D.Y.; Wu, R.; Alvarez, J.M.; Neumann, A.W. Contact angle measurements by axisymmetric drop shape analysis and an automated polynomial fit program. *Colloids Surf., A Physicochem. Eng. Asp.* **1998**, *143*, 197–210.
64. Hellwig, G.H.E.; Neumann, A.W. *5th International Congress on Surface Activity, Section B*; Barcelona, 1968; 687.
65. Hellwig, G.H.E.; Neumann, A.W. Temperature dependence of contact angles of the system water/cholesteryl acetate. *Kolloid-Z. Z. Polym.* **1969**, *229*, 40–46.
66. Neumann, A.W. Contact angles and their temperature dependence: Thermodynamic status, measurement, interpretation. *Adv. Colloid Interface Sci.* **1974**, *4*, 105–191.
67. Kwok, D.Y.; Neumann, A.W. Contact angle measurements and contact angle interpretation. *Adv. Colloid Interface Sci.* **1999**, *81*, 167–249.
68. Kwok, D.Y.; Lam, C.N.C.; Li, A.; Neumann, A.W. Low-rate dynamic contact angles on poly(methyl methacrylate/*n*-butyl methacrylate) and the determination of solid surface tensions. *J. Adhes.* **1998**, *68*, 229–255.
69. Ulman, A. *An Introduction to Ultrathin Organic Films from Langmuir–Blodgett to Self-Assembly*; Academic Press: Boston, 1991.
70. Bhatia, R.; Garrison, B.J. Phase transitions in a methyl-terminated monolayer self-assembled on Au(111). *Langmuir* **1997**, *13*, 765–769.
71. Zamborini, F.P.; Crooks, R.M. Corrosion passivation of gold by *N*-alkanethiol self-assembled monolayers: Effect of chain length and end group. *Langmuir* **1998**, *14*, 3279–3286.
72. Schoenfish, M.H.; Pemberton, J.E. Air stability of alkanethiol self-assembled monolayers on silver and gold surfaces. *J. Am. Chem. Soc.* **1998**, *120*, 4502–4513.

73. Lusk, A.T.; Jennings, G.K. Characterization of self-assembled monolayers formed from sodium *S*-alkyl thiosulfates on copper. *Langmuir* **2001**, *17*, 7830–7836.
74. Parikh, A.N.; Allara, D.L. Quantitative-determination of molecular-structure in multilayer thin-films of biaxial and lower symmetry from photon spectroscopies: 1. Reflection infrared vibrational spectroscopy. *J. Chem. Phys.* **1992**, *96*, 927–945.
75. Kwok, D.Y.; Ng, H.; Neumann, A.W. Experimental study on contact angle patterns: Liquid surface tensions less than solid surface tensions. *J. Colloid Interface Sci.* **2000**, *225* (2), 323–328.
76. Rotenberg, Y.; Boruvka, L.; Neumann, A.W. Determination of surface tension and contact angle from the shape of axisymmetric fluid interfaces. *J. Colloid Interface Sci.* **1983**, *93*, 169–183.
77. Cheng, P.; Li, D.; Boruvka, L.; Rotenberg, Y.; Neumann, A.W. Automation of axisymmetric drop shape-analysis for measurement of interfacial-tensions and contact angles. *Colloids Surf.* **1990**, *43*, 151–167.
78. Lahooti, S.; del Río, O.I.; Cheng, P.; Neumann, A.W. *Applied Surface Thermodynamics*; Spelt, J.K., Neumann, A.W., Eds.; Marcel Dekker Inc.: New York, 1996; 441–507.
79. Kwok, D.Y.; Li, D.; Neumann, A.W. *Applied Surface Thermodynamics*; Spelt, J.K., Neumann, A.W., Eds.; Marcel Dekker Inc.: New York, 1996; 413–440.
80. Kwok, D.Y.; Budziak, C.J.; Neumann, A.W. Measurements of static and low-rate dynamic contact angles by means of an automated capillary rise technique. *J. Colloid Interface Sci.* **1995**, *173*, 143–150.
81. Laibinis, P.E.; Nuzzo, R.G.; Whitesides, G.M. Structure of monolayers formed by coadsorption of 2 normal-alkanethiols of different chain lengths on gold and its relation to wetting. *J. Phys. Chem.* **1992**, *96*, 5097–5105.
82. Laibinis, P.E.; Whitesides, G.M.; Allara, D.L.; Tao, Y.T.; Parikh, A.N.; Nuzzo, R.G. Comparison of the structures and wetting properties of self-assembled monolayers of normal-alkanethiols on the coinage metal-surfaces, Cu, Ag, Au. *J. Am. Chem. Soc.* **1991**, *113*, 7152–7167.
83. Nuzzo, R.G.; Fusco, F.A.; Allara, D.L. Spontaneously organized molecular assemblies: 3. Preparation and properties of solution adsorbed monolayers of organic disulfides on gold surfaces. *J. Am. Chem. Soc.* **1987**, *109*, 2358–2368.
84. Guo, W.; Jennings, G.K. Use of underpotentially deposited metals on gold to affect the surface-catalyzed formation of polymethylene films. *Langmuir* **2002**, *18*, 3123–3126.
85. Haiss, W.; Lackey, D.; Sass, J.K.; Bescoke, K.H. Atomic resolution scanning tunneling microscopy images of Au(111) surfaces in air and polar organic solvents. *J. Chem. Phys.* **1991**, *95*, 2193–2196.
86. Delamarche, E.; Michel, B.; Kang, H.; Gerber, C. Thermal-stability of self-assembled monolayers. *Langmuir* **1994**, *10*, 4103–4108.
87. Shon, Y.S.; Lee, T.R. Chelating self-assembled monolayers on gold generated from spiroalkanedithiols. *Langmuir* **1999**, *15*, 1136–1140.
88. Vanderah, D.J.; Meuse, C.W.; Silin, V.; Plant, A.L. Synthesis and characterization of self-assembled monolayers of alkylated 1-thiahexa(ethylene oxide) compounds on gold. *Langmuir* **1998**, *14*, 6916–6923.
89. Weinstein, R.D.; Yan, D.; Jennings, G.K. Self-assembled monolayer films from liquid and supercritical carbon dioxide. *Ind. Eng. Chem. Res.* **2001**, *40*, 2046–2053.
90. Drelich, J.; Miller, J.D. Examination of Neumann equation-of-state for interfacial tensions. *J. Colloid Interface Sci.* **1994**, *167*, 217–220.
91. Amirfazli, A.; Kwok, D.Y.; Gaydos, J.; Neumann, A.W. Line tension measurements through drop size dependence of contact angle. *J. Colloid Interface Sci.* **1998**, *205*, 1–11.
92. Drelich, J.; Wilbur, J.L.; Miller, J.D.; Whitesides, G.M. Contact angles for liquid drops at a model heterogeneous surface consisting of alternating and parallel hydrophobic hydrophilic strips. *Langmuir* **1996**, *12*, 1913–1922.

# Self-Assembled Quantum Dots: Atomic Scale Engineering

S. Oktyabrsky

Alain E. Kaloyeros

*College of Nanoscale Science and Engineering, State University of New York at Albany,  
Albany, New York, U.S.A.*

## Abstract

This entry describes critical challenges, opportunities, approaches, and recent results in the science and technology of heteroepitaxial semiconductor zero-dimensional structures known as quantum dots (QDs). Focus is placed on the controlled fabrication and tight management of the properties of self-assembled QD through design, epitaxial growth, and modification of QD heterostructures using nanoscale engineering techniques, for example, surface kinetics control, shape engineering, and band-structure engineering. Examples of applications are described where the advantageous properties of the engineered QD ensembles have been demonstrated.

## INTRODUCTION

Heteroepitaxial semiconductor zero-dimensional structures known as quantum dots (QDs) are arguably the most developed quantum-type entities. Control of such entities can be achieved in a relatively straightforward manner using current technologies, thus leading to many potentially exciting applications.

In this context, this entry presents a review of the fabrication and properties of self-assembled QDs. Given that self-assembly is controlled by the thermodynamics and kinetics of the specific system under study, the entry begins with a brief overview of the mechanism of self-assembly and the main processes that drive the nucleation and evolution of a QD structure. Typically, the phenomenon of self-assembly is exploited to control the structure laterally, while in the growth direction it is managed directly by growth control (usually through composition control) with atomic-scale precision. The overview is followed by a description of key techniques to improve carrier localization and carrier dynamics in the QD ensemble. Modification of QD heterostructures using nanoscale engineering protocols is then discussed, including pertinent methods for QD shape, strain, and heterostructure band engineering. Examples are provided of applications where the distinctive properties of engineered QD ensembles have been demonstrated.

## HETEROEPITAXIAL QUANTUM DOTS

Manipulation of materials at the atomic scale opens enormous opportunities for the development of novel applications, devices, and processes. Among the many nano-engineered systems proposed over the years, one of the most exciting and probably the most mature is

heteroepitaxial quantum confined semiconductor structures. These structures can be classified as quantum wells (QWs) and QDs. Over two decades of research in both areas have resulted in significant advances, including the demonstration of various electronic devices such as microwave transistors, laser diodes, and photodetectors, just to name a few. These advances are attributed primarily to the development of two semiconductor growth approaches, namely, molecular beam epitaxy (MBE) and metal-organic vapor phase epitaxy (MOVPE). These approaches are capable of producing quantum-confined heterostructures with highly controlled purity, epitaxial quality, and interfacial sharpness.

A QW consists typically of an ultra-thin film with a thickness of a few nanometer (nm) grown usually on gallium arsenide (GaAs) or indium phosphide (InP) substrates. Its main advantages include single-dimension quantization of the electronic spectrum and reasonably strong carrier localization. As a result, single QW and multiple stacked quantum well structures are responsible for a reduction of more than an order of magnitude in the threshold current in semiconductor laser diodes and an increase in mobility in two-dimensional electron gas in field-effect transistors. Quantum wells have also enabled the fabrication of far-infrared quantum cascade lasers.

A QD consists typically of a few nm-size particles of one semiconductor material embedded into a matrix consisting of a wider bandgap semiconductor. Its main advantage is achievement of ultimate zero-dimensional localization. Remarkably, the electronic spectrum of individual QDs is quantized in all three directions, as is the case for atoms and molecules. In this respect, the electronic spectrum of QDs is determined by the type of semiconductor materials used for the QD and matrix, as well as quantum confinement and strain in the QD.

Quantum dot ensembles are more attractive than QWs for electronic and, especially, photonic devices, such as lasers,<sup>[1]</sup> infrared photodetectors,<sup>[2,3]</sup> broad spectrum superluminescent light emitting diodes (LEDs)<sup>[4,5]</sup> due to their enhanced performance. A case in point is the projected performance of QD-based laser diodes. According to theoretical predictions, heterojunction lasers with QD active media will exhibit superior characteristics in comparison with conventional QW lasers,<sup>[1,6]</sup> including higher efficiency at elevated temperatures, higher thermal stability, improved reliability, and faster dynamics. The primary reason for this superiority is the discrete atom-like electronic spectrum of QDs without any thermal spreading of carriers.

The ability to fully exploit the exciting benefits of QD ensembles still presents some challenges, mainly due to (i) inhomogeneous broadening of the QD electronic spectrum resulting from the size dispersion of QDs, (ii) existence of excited states in the dots, (iii) relatively slow relaxation of carriers to the ground level in the QDs, and (iv) poor localization of carriers at room temperature because of escape of carriers from the QDs to the wetting layer and barrier. These problems can be potentially solved through various atomic-scale engineering approaches, as discussed in what follows.

### TEMPLATING VS. SELF-ASSEMBLY

The most common approach for growing heteroepitaxial QDs relies on the phenomenon of self-organization in epitaxial heterostructures with high lattice mismatch between the structures. The most widely explored heterosystem is In(Ga)As/(Al)GaAs structures with up to 7% lattice mismatch (Fig. 1). The growth of InAs QDs on GaAs surface is usually described rather simplistically in terms of a classic Stranski–Krastanov growth mechanism, where the structure attains the lowest total free energy through a trade-off between strain energy in the growing film and the surface free energy of the islands. According to this mechanism, after formation of a thin coherent wetting layer, growth spontaneously becomes three-dimensional through the assembling of islands. In reality, the mechanism of self-assembly is further complicated by the involvement of kinetics in addition to thermodynamics.

To obtain more uniform QD density and enable the formation of periodic arrays of QDs, various types of nanolithographic patterning or templating methods using either e-beam or scanning probe techniques were proposed and evaluated.<sup>[7]</sup> Electron beam lithography accompanied with wet or dry etching<sup>[8,9]</sup> was employed to pattern the QD structures with the lateral dimensions down to 20 nm. Nanolithographic methods

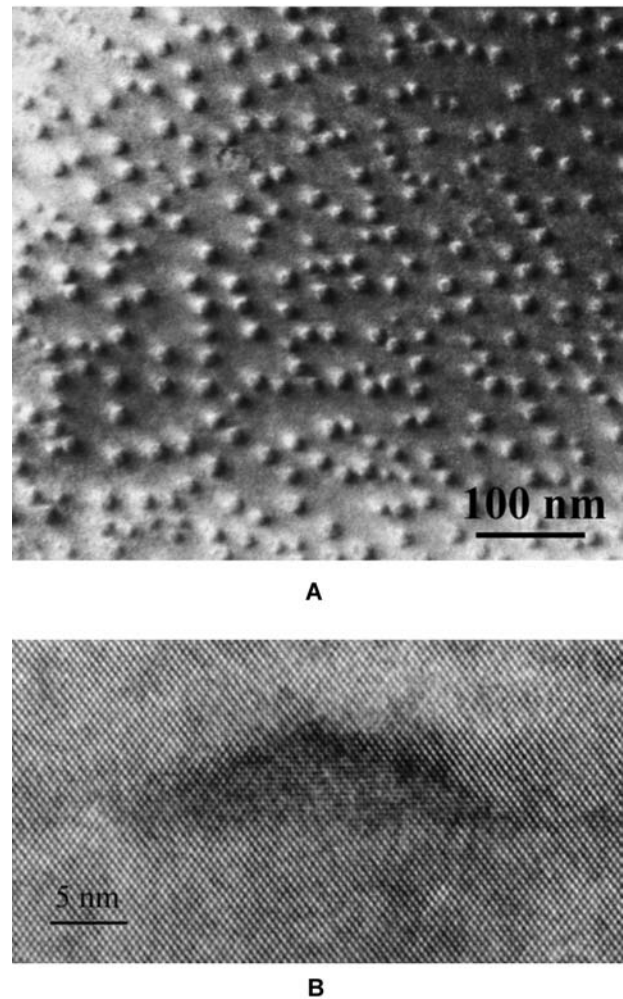


**Fig. 1** (A) Plane-view transmission electron microscopy (TEM) image of InAs quantum dots grown on AlAs surface. The lateral size is about 14 nm and lateral density is about  $10^{11} \text{ cm}^{-2}$ ; (B) high-resolution TEM micrograph of an InAs QD grown on (100) GaAs surface. (111) lattice fringes of GaAs/InAs are visible in the image. InAs QD appears as darker pyramid with 20 nm base and 8 nm height.

involve direct atomic force microscopy (AFM) oxidation of the GaAs surface<sup>[10]</sup> or formation of scanning tunneling microscopy (STM) current-induced deposits<sup>[11]</sup> followed by the MBE growth of self-assembled InGaAs QDs. In situ ultra-high vacuum nanolithography techniques include direct electron-beam writing with subsequent chlorine etching of the GaAs surface to provide arrays of holes serving as nucleation sites for the InAs islands.<sup>[12]</sup> Though QD formation has been successfully demonstrated, these nanoscale methods so far generate a high defect density, which introduces traps and recombination centers in the active medium of the device. These features result in low quality material in comparison with the self-assembly method. In addition, nanolithographic



**Table 1** Properties of self-assembled InAs QD ensemble prepared for laser gain medium and associated optimization trade-offs

QD property	Demonstrated optimum	Trade-offs
Narrow size distribution (small inhomogeneous broadening)	25–35 meV at $h\nu = 1.1$ eV	High density High efficiency
Strong localization	400–500 meV at RT	High density
Large ground-excited states separation	~100 meV	Fast relaxation to GS
High density	$\sim(8-12) \times 10^{10} \text{ cm}^{-2}$ per layer	Strong localization, high efficiency
High efficiency (defects)	Close to 100%	High density
High efficiency (e–h overlap)	Symmetrical shape	High density
Fast carrier transport to GS	~5–10 ps at RT	Thermal stability

patterning or templating methods exhibit very low throughput, making scalability a serious issue.

### BASIC PROPERTIES OF SELF-ASSEMBLED QD ENSEMBLES

Self-assembly is driven by the thermodynamics and kinetics of 2D-to-3D phase transformation, which limit the ability to vary QD properties to a narrow window. Any improvement to one QD parameter results in degradation of other properties. Table 1 lists key parameters and associated trade-offs for a self-assembled InAs QD ensemble used in a laser medium. A narrow QD size distribution, high QD density, and high radiation recombination efficiency are essential for the formation of a QD medium with high optical gain, whereas strong carrier localization and large energy separation between ground and excited states are needed for laser thermal stability. Fast carrier transport to the lasing state (preferably ground state)

results in higher saturation gain and faster modulation properties.

In this respect, the narrowest size distribution is achieved in QD sheets with low areal density, where growth of one island is less affected by other islands in proximity. Self-assembly results in a large QD size distribution, thus giving rise to wide inhomogeneously broadened emission spectra (Fig. 2). A single QD energy level is extremely narrow  $\sim 10 \mu\text{eV}$  (Fig. 3), but the narrowest spectrum for an ensemble of QDs is  $\sim 25-35$  meV. Creating a QD medium with more uniform size distribution is a significant challenge because island size distribution, or more accurately, island volume distribution, is determined by the kinetics of fluctuations in phase transformation. If the island size fluctuations were purely statistical (varying around some equilibrium size), the variation in number of atoms would be on the order of  $N^{-1/2}$  ( $N$  is the number of atoms in the island). A typical InAs QD with  $\langle N \rangle = 3000$  atoms would have fluctuations of  $\sim 50$  atoms, corresponding to an inhomogeneous broadening

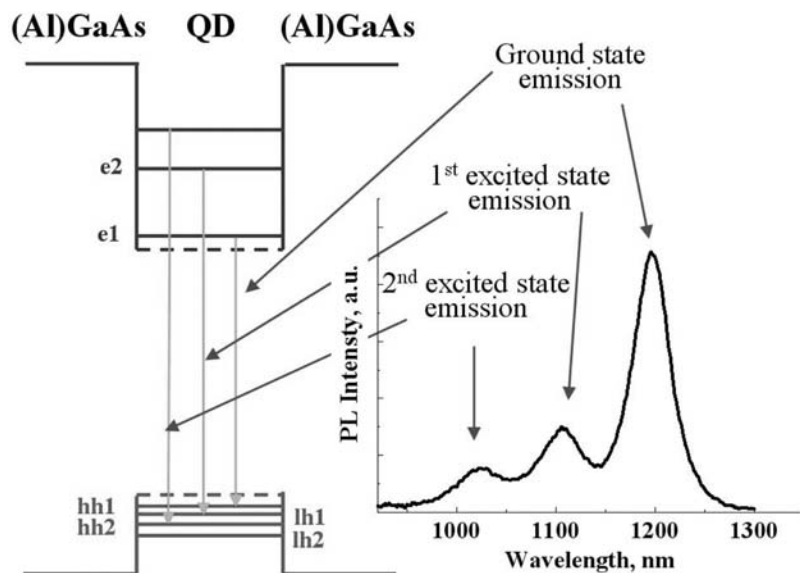


**Fig. 2** Schematic diagram of the electron–hole pair energy levels in a QD heterostructure and room-temperature photoluminescence spectrum of QD ensemble. QD luminescence results from transitions between quantum-confined levels of electrons and holes in the QD potential. Width of the spectrum is determined by inhomogeneous broadening due to QD size distribution.

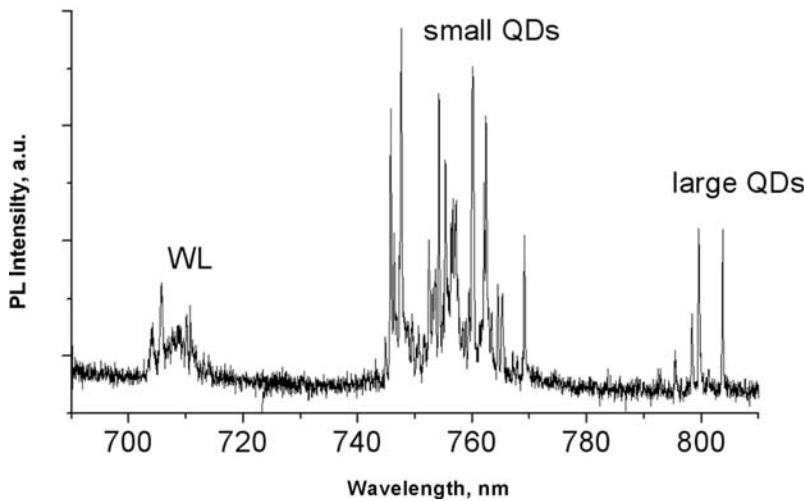


**Fig. 3** Near-field photoluminescence of small QD cluster taken at liquid helium temperature. Each narrow peak corresponds to PL of individual dot. *Source:* J. Merz and A. Mintairov, University of Notre Dame.

of the emission line of  $\sim 3$  meV as can be estimated from Fig. 4.<sup>[13]</sup> Practically, the full-width at half-maximum (FWHM) of QD luminescence band is usually 30–50 meV, and is quite higher than the simple statistics of the number of condensed atoms. Island size distribution is determined by the dynamics of island formation and could be controlled by nanoengineering methods, as described here.

As mentioned earlier, the benefits of QDs are attributed mainly to strong carrier localization. To maintain localization at higher temperatures, the separation between ground and excited levels ( $\Delta_{exc}$ ) and the barrier height in QDs should be made much larger than the thermal energy. This separation is determined by QD barrier height and shape. Barrier height decreases when QD size decreases due to increased quantum confinement energy. Therefore, smaller dots with high density provide lower localization energy than larger dots

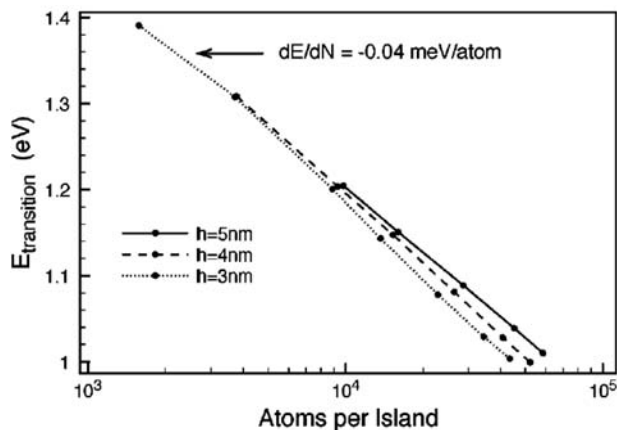


**Fig. 4** Emission energies as a function of QD volume, expressed as the total number of atoms in the dot for three different QD heights. *Source:* Reprinted with permission from Pryor.<sup>[13]</sup>

with low density. Additionally, high QD density is essential to achieving higher gain in the laser medium, a feature that is critical to the performance of miniature lasers such as vertical cavity surface-emitting lasers (VCSELs) and short edge-emitting laser diodes. High QD density mediums ( $>10^{11}$  cm<sup>-2</sup>) suffer from poorer localization and lower radiative efficiency, the latter most likely due to higher defect density in the heterostructures with increased InAs/GaAs interface area.

Management of electronic and optical properties of QDs, such as homogeneous and inhomogeneous electronic spectrum and defects that define non-radiative recombination and carrier dynamics, relies on understanding the basic technology–structure–property relationships that control their performance. A set of physical phenomena essential for understanding these relationships is given in Table 2. These phenomena serve as basis for the development of effective management methods (somewhat interrelated), as discussed in the following sections.

**Table 2** Processes involved in QD formation and associated phenomena

Process	Associated phenomena
Nucleation of QDs	Thermodynamics and kinetics of 2D–3D phase transition Adatom diffusion
Evolution of QDs	Tendency towards larger dots with time Evaporation and intermixing of In
Overgrowth of QDs	Segregation of In Lateral redistribution of In
Post-growth control	Diffusion of species Stress-induced redistribution

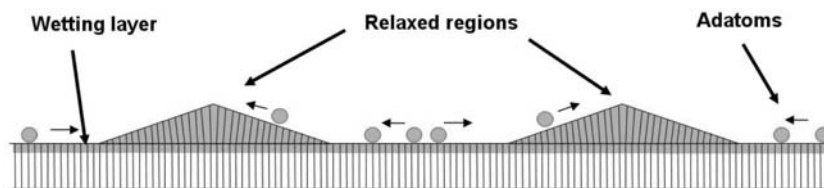


**Fig. 5** Schematic drawing illustrating QD self-assembly. Two main driving forces for self-assembled growth: (i) strain energy is lower in 3D structure than in the uniform 2D strained layer, and (ii) stress term in surface chemical potential drives adatoms towards the top of the islands.

## QD SELF-ASSEMBLY

### Control of QD Nucleation

The nucleation of InAs QDs utilizes the large ( $\sim 7\%$ ) lattice mismatch between InAs and GaAs to promote the formation of strained 3D InAs islands through the Stranski–Krastanow growth mode. At first, InAs grows pseudomorphically on top of GaAs, forming a strained film (wetting layer) with a thickness on the order of  $\sim 1.5$  ML.<sup>[14]</sup> At this critical thickness, it becomes energetically favorable for InAs to form islands, or QDs, which allows the effective release of strain as shown in Fig. 5.

The main driving force for QD self-assembly is the stress term in surface chemical potential, which drives adatoms towards the top of the islands. Therefore, it is obvious that the characteristics of the developing QDs are strongly affected by the process temperature and underlying surface chemistry. Figure 6 exhibits the dependence of InAs QD density on the growth temperature for GaAs and AlAs underlayers. Though the growth conditions are somewhat different in experiments reported by various investigators, resulting in different absolute values of QD densities, the trend is quite clear. The Arrhenius behavior with

$\sim 2.0$  eV activation energy is evident up to QD densities as high as  $10^{12}$  cm<sup>-2</sup>.<sup>[15,16]</sup> The density of dots is consistently higher by approximately a factor of 2, if formed on AlAs surface. This behavior is attributed to the lower surface diffusion rates of In adatoms on AlAs.

Atomic force microscopy imaging of the QDs allows assessment of QD size and heights (Fig. 7). As expected from transmission electron microscopy (TEM) studies, AFM results indicate that the dots grown on AlAs surface are smaller and have higher densities. When the QDs are grown at 475°C, the aspect ratio is about 6 for the dots on GaAs surface, and slightly higher on AlAs. In both cases, total thickness of deposited InAs was kept identical, 2.4 ML. Hence, there is no noticeable difference in the total volume of the QDs grown on AlAs or GaAs. In this context, further overgrowth, along with cooling down of surface dots, may change the QD resulting size and shape. Accordingly, the ultimate QD heterostructures may contain QDs of varying features and characteristics. In fact, it will be shown in the next section that (volume  $\times$  density) can be controlled through a QD overgrowth process.

Manipulation of the chemistry of the underlying surface at the monolayer (ML) scale can be effective

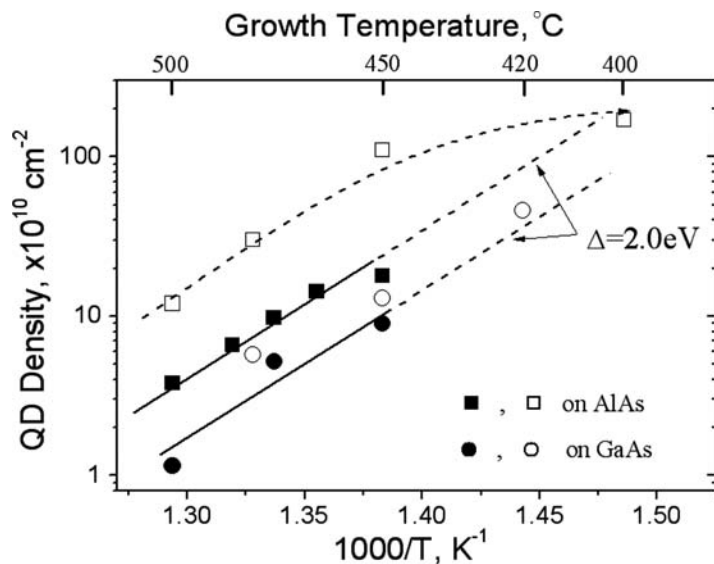


**Fig. 6** Arrhenius plot of InAs QDs areal density. The solid (black) symbols correspond to GaAs and 2 ML AlAs, as measured by TEM.<sup>[14]</sup> The open (white)-symbols are from Ref.<sup>[53]</sup> (circles) and Ref.<sup>[54]</sup> (squares), with the circles and squares corresponding to growth on, respectively, GaAs and thick AlAs, as measured by AFM. Straight lines correspond to activation energy of 2.0 eV. Source: Reprinted with permission from Ref.<sup>[14]</sup>

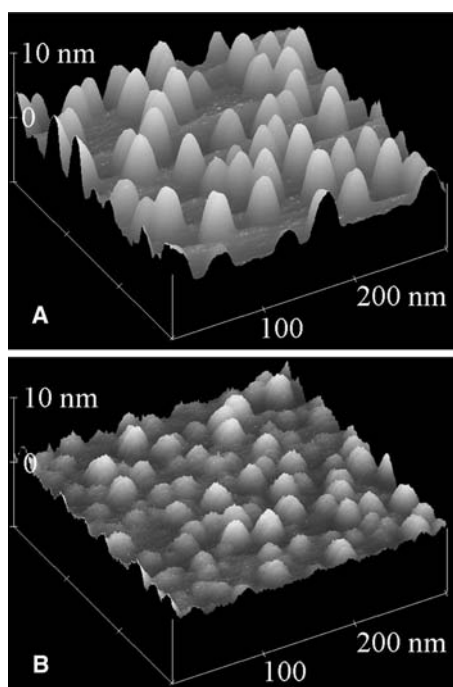


**Fig. 7** AFM images of QDs grown on AlAs and GaAs surfaces at 475°C. The QD ensembles have almost identical average lateral size: 31 nm on GaAs, and 27 nm on AlAs), different aspect ratio ( $d/h$ ):  $\sim 6$  on GaAs and  $\sim 11$  on AlAs; lower QD density on GaAs  $\sim 5.2 \times 10^{10} \text{ cm}^{-2}$ , and  $\sim 9.8 \times 10^{10} \text{ cm}^{-2}$  on AlAs.

at fine-tuning QD size, leading to direct changes in the optical properties of QD structures. Figure 8 plots photoluminescence (PL) intensity and linewidth dependence on ground state transition energy of QDs,  $E_g$ . Noticeable degradation in PL intensity and broader size distribution were measured for QDs grown on AlAs surface. The intermediate properties were obtained for QDs grown on 1 ML of GaAs on short period superlattice (SPSL) terminated by AlAs.

### SURFACE EVOLUTION OF QDs AND QDs OVERGROWTH

As mentioned earlier, overgrowth of QDs can lead to significant changes in their overall characteristics. The overgrowth process reveals the following major trends: (i) evolution of QDs on the surface towards larger QDs with lower density; (ii) QD evolution may be preserved by a capping layer deposition; and (iii) redistribution of In from QDs may occur when capping is slow. These trends are discussed in more detail here.

Trend (i) is quite obvious and results from the fact that uncapped dots that exist on a bare surface for the longest time exhibit the largest volume. It is well

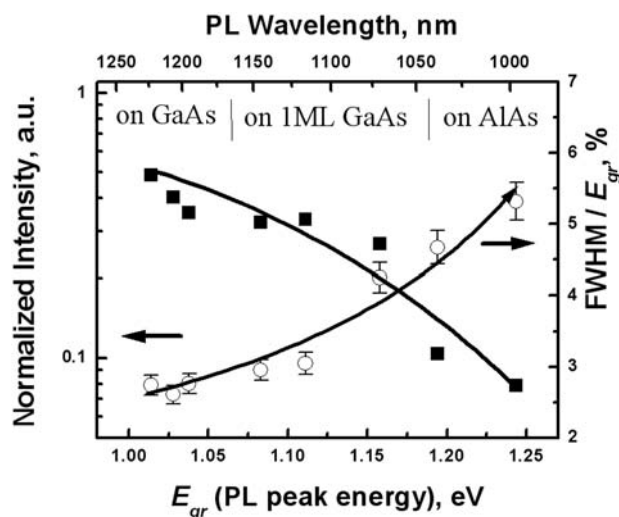


**Fig. 8** Normalized room temperature PL intensity and linewidth,  $\text{FWHM}/E_{gr}$ , corresponding to size distribution versus ground state PL energy  $E_{gr}$  for QD ensembles grown on various underlayers *Source*: Reprinted from Ref.<sup>[16]</sup> with permission of Springer Science and Business Media.

understood that if the QD growth process is allowed to progress, surface redistribution of In adatoms will continue and the islands will become larger and larger. This has been shown both experimentally<sup>[17]</sup> and through theoretical modeling.<sup>[18]</sup> This conclusion is very important for understanding QD growth mechanisms because it indicates that there is no thermodynamic equilibrium size for the QDs on the surface, and the QDs will be growing on the surface as long as they are not overgrown.

Of course, some other requirements should be met for this process to continue, such as maintaining the As equilibrium overpressure, confinement (evaporation or solution) of In atoms to the surface, and the absence of plastic strain relaxation. The initial size and density of QDs is determined by the characteristics of critical nuclei at the 2D–3D phase transformation, and after this transformation takes place within a few seconds, the QDs start growing slowly by dissolution of the smaller dots. To prevent QD evolution on the surface, fast capping is essential since it can “freeze” the growing surface.

Processes (ii) and (iii) compete with each other. A few ML thick AlAs layer deposited at a fast rate is a good candidate for the capping layer.<sup>[19]</sup> In fact, a comparison of fast and slow capping with thin GaAs or AlAs layers using AFM, TEM, and PL studies<sup>[16]</sup> has shown that fast AlAs capping results in the ensemble of the highest density. On the other hand, the observed reduction in QD size with other capping procedures is due to a segregation and lateral redistribution of In from the dots to the surrounding matrix.

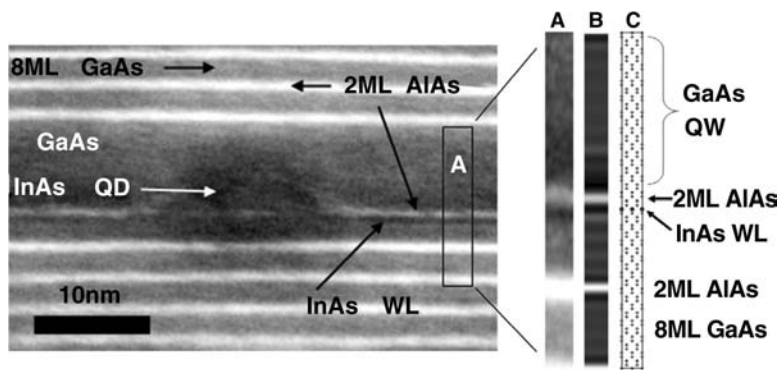


**Fig. 9** Left: (002) dark field TEM image of InAs QD embedded in a SPSL. Right: (A) Magnified (002) DF image of the frame “A” including two periods of (2 ML-AlAs)/(8 ML-GaAs) SPSL,  $\sim 1$  ML InAs wetting layer (WL), 2 ML AlAs capping layer, 20 ML GaAs QW; (B) multislice image simulation of the image in (A) using a supercell as depicted in (C), with  $\text{In}_{0.5}\text{Al}_{0.5}\text{As}$  alloyed wetting layer and Indium segregation into GaAs; and (C) Supercell used in the image simulation viewed along [110] direction. *Source:* Reprinted from Ref.<sup>[16]</sup> with permission of Springer Science and Business Media.

Indium is known to segregate at the growing surface even at relatively low growth temperatures (450–500°C). The reported values for the In segregation efficiency parameter are high and almost identical for AlAs and GaAs overgrowth:  $R = 0.86$  for both GaAs and AlAs overgrowth at 480°C;<sup>[14]</sup>  $R = 0.82$ <sup>[20]</sup> for GaAs; and  $R = 0.77$  for AlAs<sup>[20,21]</sup> at 530°C. As a result, the InAs redistribution thickness is about 6 ML. An indication of In segregation can be found from analysis of TEM images. Figure 9 shows a (002) dark field image of a QD assembled on GaAs surface and capped with 2 ML AlAs, with arrows pointing to heterostructure features.

The image contrast variations simulated using multislice package (MacTempas<sup>®</sup>) indicated vertical In distribution in the region above the wetting/capping layers within  $\sim 6$  ML and incorporation of Al atoms (alloy formation) into the wetting layer. In segregation alone cannot account for the difference in QD capping by GaAs or AlAs layers. Since the In surface segregations are found to be almost identical for GaAs and AlAs, the difference in QD capping with GaAs or AlAs layers is most likely to be due to lateral redistribution of In resulting from different adatom mobility on the two surfaces.

### SHAPE ENGINEERING OF QDs

All-epitaxial InAs QDs assembled on GaAs or AlAs surfaces typically exhibit pyramidal or close to pyramidal shapes, which is determined by the surface energy of the growing InAs islands. A high-resolution UHV STM image reveals the corresponding QD shape with dominant  $\{137\}$  (or  $\{136\}$ ) and  $\{111\}$  facets, as shown in Fig. 10.<sup>[22–24]</sup> This pyramidal shape is responsible for the quite poor interaction between the electron and hole. More specifically, the electron and hole ground state wave functions have a small overlap integral due to a stress-induced piezoelectric field that separates electrons and holes,<sup>[25]</sup> thus resulting in reduced optical gain in the QD systems.<sup>[26]</sup> QDs with more

symmetric shapes, such as spheres or disks would be preferable to strengthen the electron–hole interaction.

The shape of QDs also determines the energy splitting between the ground state and excited states. In III–V semiconductor QDs, quantum confinement splitting of holes is usually much smaller than that of electrons due to significantly large effective mass of heavy holes. Though the binding energies of the ground states are mainly controlled by QD volume, the splitting between the ground s-like and first excited p-like conduction states ( $\Delta_{\text{exc}}$ ) increases with the increase in height-to-base ratio of the pyramid<sup>[26]</sup> and also with the increase in the barrier height. Quantum dot ensemble with high  $\Delta_{\text{exc}}$  is required for thermally stable lasers. Control of shape and  $\Delta_{\text{exc}}$  allows fabrication of quantum dot infrared photodetectors (QDIPs) in the 3–14  $\mu\text{m}$  range. Large height-to-base QD ratio results in a reduced dependence of IR sensitivity on polarization, and the volume and shape determine the spectral range of the resulting photodetector.<sup>[28,29]</sup>

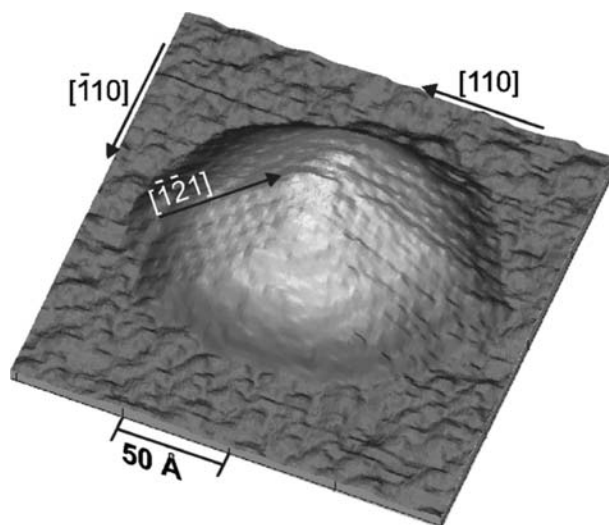


**Fig. 10** Atomically resolved STM image of uncapped InAs QD grown on GaAs(100) at 450°C. *Source:* Reprinted with permission from Ref.<sup>[22]</sup>.

The height-to-base aspect ratio can be controlled using the “punctuated island growth” method developed by Mukhametzhanov et al.<sup>[30]</sup> It was found that the lateral size remains remarkably unchanged with further InAs deposition, if growth is interrupted after deposition of  $\sim 1.7$  ML. The added material (up to 3 ML) after “punctuation” increased the height and density of the dots, while keeping the lateral size almost unchanged at about 24 nm. This approach resulted in impressive low inhomogeneous linewidth broadening value of 26 meV.

An effective shape-managing method was also proposed by Wasilewski et al.<sup>[31]</sup> It employs heating (flushing) of partially overgrown dots to reduce pyramidal shapes to disk-like shapes. Figure 11 demonstrates a further developed method of shape management of QD ensemble.<sup>[32]</sup> The InAs QDs were embedded into 2 ML-AlAs/8 ML-GaAs SPSL barriers with a GaAs overlayer (up to 25 ML in thickness) on top of the QDs. After capping of the freshly formed QDs with 2 ML-thick AlAs layer to prevent coarsening of the islands and In redistribution, the QDs were overgrown with a GaAs layer with a thickness corresponding approximately to the QD heights

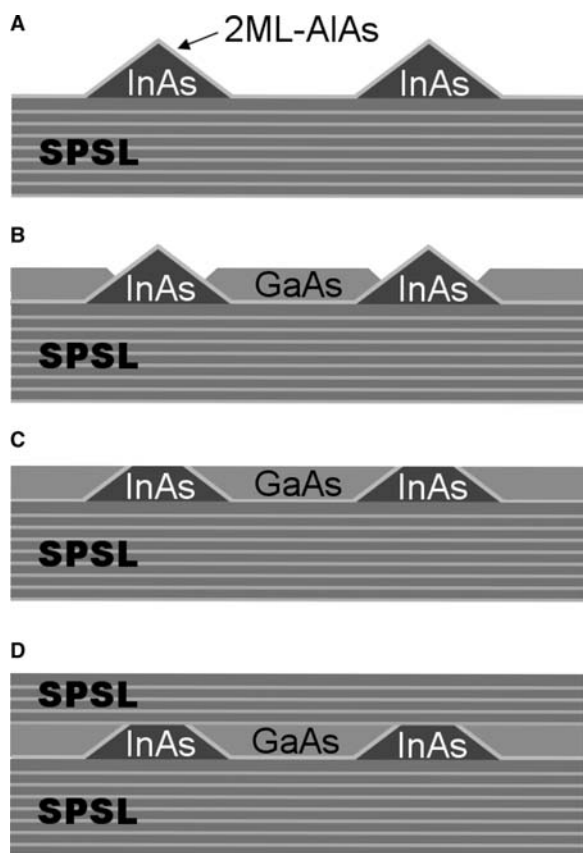


**Fig. 11** (A)–(D) Shape management step-by-step procedure.

( $\sim 6$  nm). Owing to high mobility of Ga adatoms, GaAs layer does not cover the QDs entirely but tends to cover the low stress area between the QDs (Fig. 11B). Then, the sample is rapidly heated by an additional  $100^\circ\text{C}$ , resulting in indium redistribution mainly at the top of QDs. This treatment leads to changes in the shape and volume of QD. Finally, the structure is overgrown by a thin layer of GaAs to form a QW for efficient collection of carriers, and further, by SPSL (Fig. 11D).

The shape management procedure described results in the QDs with a shape of truncated pyramids with flat tops entirely covered by an AlAs layer, even after subjecting the partially overgrown dots to a heating (truncation) step (Fig. 11D). The shape-engineered QD ensemble has demonstrated better volume uniformity because larger QDs lose more In during the truncation procedure. This reduces the inhomogeneous broadening of the emission spectrum below 30 meV.<sup>[33]</sup> The beneficial (more symmetrical) shape of the QDs was shown to increase the electron–hole coupling, which allowed higher emission efficiency and saturated ground state gain of  $16\text{ cm}^{-1}$  in a triple-layer structure, which is almost doubled when compared with similar non-truncated QD structures.

AlAs capping affected mostly the energy separation between ground and first excited states. In this context, the optimized structures demonstrated a 90–100 meV separation that is considerably higher than the thermal energy. Apart from the increase in electron–hole coupling through shape engineering, a more typical approach to maximum gain increase is through increase in total density of QDs through the addition of further layers. Noticeable advantages of shape-engineered QD ensembles for multilayer QDs are due to reduced roughness for the entire structure with very smooth top SPSL interfaces [as contrasted with wave-shape top SPSL interfaces in non-truncated QDs in Fig. 12(A) and (B)]. It is worth noting that a medium with seven truncated QD layers separated by thin 20 nm interlayer barrier distances (total thickness of  $\sim 125$  nm) with maximum in-plane gain of  $31\text{ cm}^{-1}$  was recently demonstrated.<sup>[34]</sup>

## STRAIN ENGINEERING OF QDs

Given the role of strain as the driving force for QD formation in heteroepitaxial systems, control of strain is a valuable tool for manipulation of QD properties. As reported earlier, tighter 7.2% misfit in InAs/GaAs system typically produces QDs with lateral dimensions of about 20 nm with density in the range of  $10^{10}$ – $10^{11}\text{ cm}^{-2}$ . Lower 3.2% misfit in InAs/InP results in larger dots (30–50 nm lateral size) with low density ( $10^8$ – $10^9\text{ cm}^{-2}$ ).<sup>[34]</sup> The latter can provide significantly



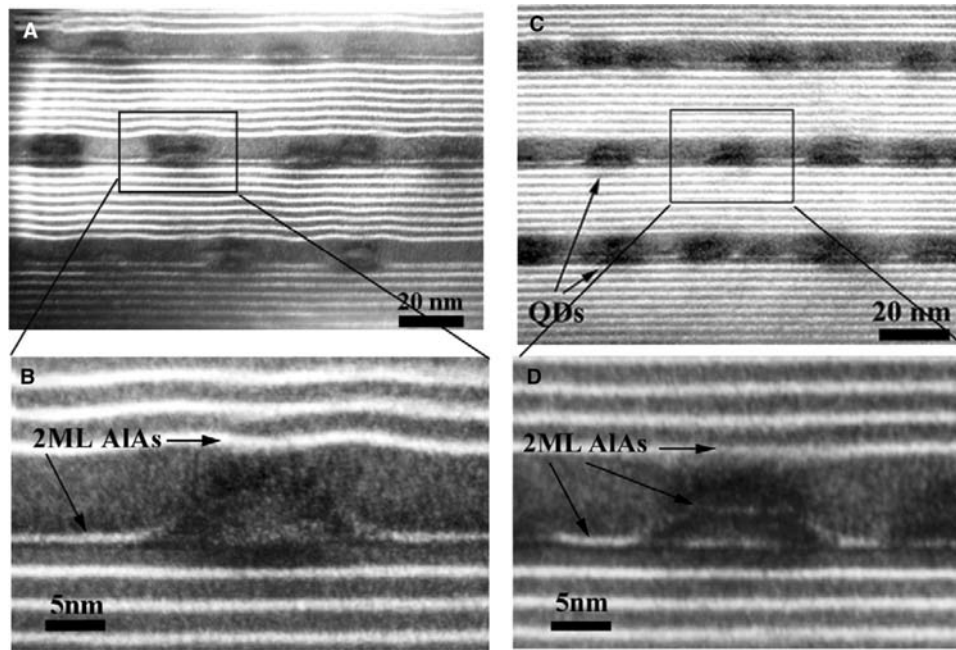


**Fig. 12** TEM images [(200) dark field] of triple-layer InAs QDs embedded in a (2 ML-AIAs)/(8 ML-GaAs) SPSL: (A) non-truncated QDs in SPSL with top AIAs; and (B) magnified image; (C) shape-engineered QDs in SPSL with top AIAs; and (D) magnified image. *Source:* Reprinted from Ref.<sup>[16]</sup> with permission of Springer Science and Business Media.

red-shifted emission in the 1.4–2  $\mu\text{m}$  range, and therefore, is important for telecommunication applications.<sup>[35]</sup>

Epitaxial heterostructures do not provide many options to control strain on any given substrate. In fact, creation of a virtual substrate with a lateral lattice constant different from that of GaAs or InP (i.e., the commercially available high quality III–V substrates) results in the formation of misfit dislocations with inevitable reduction in layer quality. Nevertheless, it is proven possible to control nucleation and growth of QDs via manipulation of the lateral strain field. Quantum dot produce non-uniform lateral strain in the subsequent layers of the structure, which facilitates preferential nucleation of islands directly on top of the existing QDs (Fig. 13). This phenomenon was used by several groups to develop vertically coupled QDs to modify the electronic spectrum, increase the effective density of states in the medium, and enhance the uniformity of dot size and column spacing distributions.<sup>[36–38]</sup>

In addition, the composition and thickness of strained InGaAs underlayers and overlayers were used to control both emission energy and carriers escape energy by means of strain and band structure manipulation.<sup>[39]</sup> This approach is generally believed to be the most promising to red-shift the emission spectrum of GaAs-based structures toward fiber wavelengths of 1.3 and possibly 1.55  $\mu\text{m}$ .

## BAND ENGINEERING OF QD HETEROSTRUCTURES

An important and very useful feature of heteroepitaxial semiconductor structures is the ability to engineer their band structure and to control their electronic spectrum and transport properties. This feature makes group III–V heteroepitaxial QDs unique. For example,

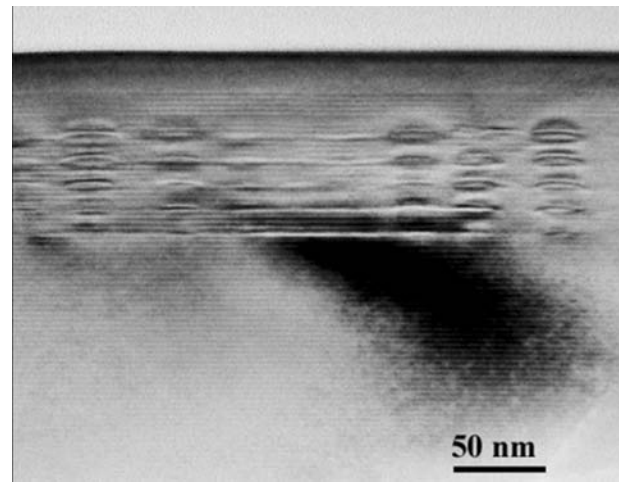


**Fig. 13** Cross-sectional TEM image of 5-layer QD stack in SPSL with the spacing of 12 nm demonstrating vertical alignment of QDs.

free-standing QDs (nanoparticles) or QDs in an insulating matrix, although usually easier to produce and having better uniformity, retain high and uncontrollable energy barriers, and therefore, are of limited use in electronic and optoelectronic applications.

Barrier height around heteroepitaxial InAs QDs is relatively easy to control by varying the composition of the surrounding layers. To increase the bandgap of the QD matrix, it might be beneficial to utilize AlAs/GaAs SPSL as a barrier material instead of an AlGaAs alloy (Figs. 9 and 12). The SPSL or “digital alloy” is a high-quality wide-bandgap material, which can be grown at low temperature (<500°C) required for QD growth. In addition, SPSL provides another variable to control QD growth since both GaAs and AlAs surfaces can be readily used as a starting surface for QD deposition.

Band engineering provides the means to control transport and dynamics of carriers in the structure. A good example is a dots-in-a-well (DWELL) structure where InAs QDs are imbedded into an InGaAs QW. In this structure, if used as a laser gain medium, QW works as an efficient reservoir for capturing carriers, which significantly improve their collection into QDs, and therefore improve modal gain and internal quantum efficiency. As a result, laser diodes with record low threshold current density of 16 A/cm<sup>2</sup> were demonstrated.<sup>[40]</sup> In addition, this DWELL approach was used to red-shift the emission spectrum of QDs down to 1.3 μm by varying the composition of the InGaAs quantum well matrix.<sup>[41]</sup>

The DWELL approach has proved to be very promising for broadening the gain spectrum needed for superluminescent LEDs used, for example, in optical coherence tomography. The shape of the broad emission band can be tailored by varying the composition of InGaAs QWs of a multi-dot-in-well stack.<sup>[5]</sup>

## LOCALIZATION ENERGY

As noted above, strong carrier localization in QDs is responsible for the major advantages in a QD laser medium. Thermal escape of carriers from the QDs negatively impacts the device parameters, such as gain in the laser medium. The same process is responsible for thermal quenching of QD luminescence due to recombination of the carriers outside the dots. Obviously, strong localization requires large barrier for carrier escape, large energy separation between the ground and excited state levels, and lack of intermediate levels with high density of states, such as those in a wetting layer. In general, this set of requirements is good enough to ensure localization.<sup>[42]</sup> It should be emphasized that a wide bandgap barrier, such as AlGaAs, by itself is not enough to guarantee strong localization of the carriers in the dots.

Thermal quenching of photoluminescence of QDs in QW structure fabricated using nanoengineering approaches described in the previous section (Fig. 12) is shown in Fig. 14 with a corresponding band diagram in the inset 2). Within the capture/escape events, carriers are usually considered to behave as excitons or correlated electron–hole pairs, rather than independent electrons and holes. The validity of this approach is justified by the fact that the activation energy for the escape process is typically equal to the sum of the barrier heights for electrons and holes. Le Ru et al.<sup>[43]</sup> have recently argued that more realistic independent capture/escape of electrons and holes will also give a barrier height for thermal escape equal to the sum of the barrier heights for electrons and holes under realistic experimental conditions, such as strong thermal quenching. Therefore, the observed large barrier for escape from QDs (450 meV) simply corresponds to the transitions between ground QDs and the GaAs QW states as in Fig. 14.

The nanoengineered QDs described exhibit over two orders of magnitude higher tolerance to non-radiative defects than QWs at room temperature, as measured by introduction of radiative defects with ion implantation and monitoring the luminescence efficiency.<sup>[42]</sup> There are two reasons for QD defect tolerance. First, a large barrier energy for carrier escape from the QDs results in a high temperature offset (~250 K) for carrier escape from the dots. Second, low non-radiative rate in the barrier material (which is a 7.5 nm-thick GaAs QW in these samples) extends

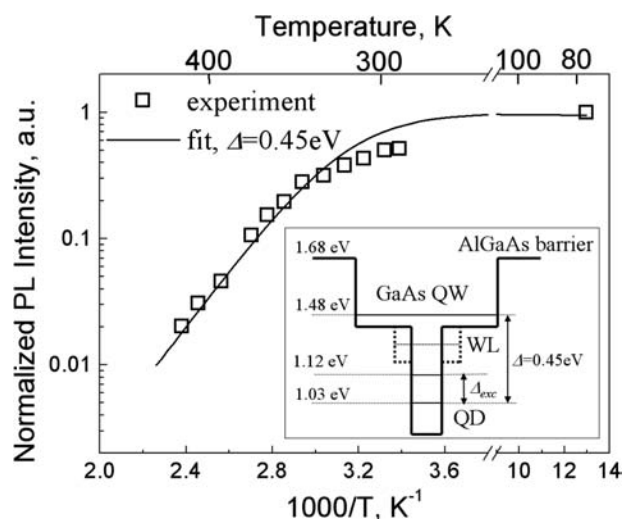


**Fig. 14** Arrhenius plot of integrated PL intensity in nanoengineered QD structures. Symbols correspond to the experimental data and the line is a fit with the dynamic model,<sup>[42]</sup> which neglects the carrier escape through intermediate levels. Inset: Band structure of electron–hole pairs in nanoengineered QDs in QW.

the high probability of carrier recombination in the QDs to temperatures as high as 320 K and, consequently, shifts the PL thermal quenching offset to higher temperatures. These properties provide a way for significant improvement in reliability and radiation hardness of optoelectronic devices.

## CARRIER DYNAMICS

Many optoelectronic applications, such as lasers (in particular VCSELs) and superluminescent LEDs, require high optical gain, which is difficult to achieve using QD medium due to its low density of states (proportional to the QD density) when compared with QWs. However, this gain can be increased by the nanoengineering approaches described above through reduction of inhomogeneous broadening in the QD ensemble, enhancement of overlap between electrons and holes, and reduction of escape of carriers from the lasing (ground state) QD levels.

Carrier capture and further relaxation to the ground level of a QD is relatively slow ranging from 5 to 50 ps depending on doping, and carrier and QD densities. Shorter relaxation times are usually attributed to electron–hole scattering,<sup>[44]</sup> while longer times are due to slower phonon scattering,<sup>[45]</sup> also known as “phonon bottleneck”.<sup>[46]</sup> An effective way to improve the gain is to increase the capture rate of carriers into QDs using tunnel injection from QWs.<sup>[47–49]</sup> In this case, QW is working as a reservoir for electrons and holes with high density of states and, therefore, with large capture cross-section. Hence, carrier capture in QWs is more efficient than in QDs, and may provide a path for fast carriers transfer into the dots by resonant tunneling. As a result, tunnel-coupled QW-QDs medium exhibited extremely high maximum saturated gain,<sup>[47]</sup> and impressive 23 GHz modulation bandwidth as a result of fast tunneling time into QDs of about 1.7 ps as shown in Fig. 15.<sup>[48]</sup> This fast tunneling rate is comparable with the stimulated emission rate at high injection currents, thus reducing gain suppression and improving saturation gain of the medium.

Fig. 16 shows a (200) dark-field TEM image of tunnel-coupled well-on-dots structure. This multilayer structure has smooth interfaces as a result of the QD shape-engineering (truncation) procedure described above. Immediately after QD truncation, a tunnel barrier consisting of 5 ML(GaAs) + 2 ML-(AlAs) + 4 ML(GaAs) is grown, followed by a 3 nm-thick  $\text{In}_{0.33}\text{Ga}_{0.67}\text{As}$  QW on top of the tunnel structure. Fast carrier transport from QW into QDs is believed to be due to LO phonon-assisted tunneling. It is proved, for example, by photoluminescence measurements of the described tunnel structure where the broad QD band consists of multiple narrow peaks, separated by

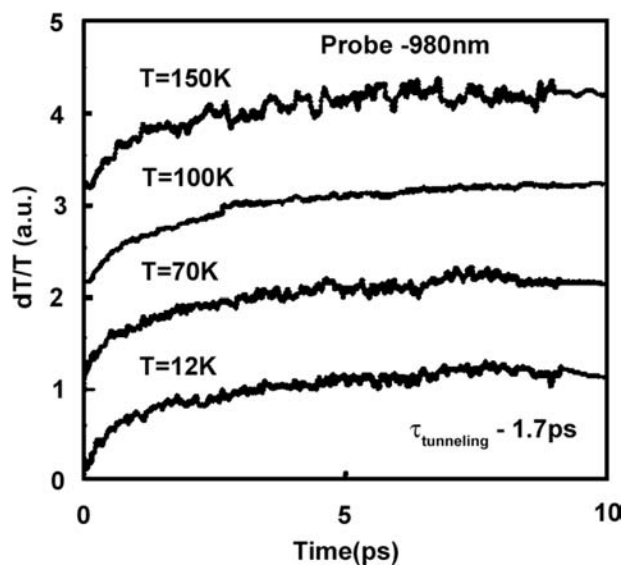


**Fig. 15** Pump-probe differential transmission signal from a QW–QD tunnel injection heterostructure taken at different temperatures. The gain (pump) pulse at 800 nm generates carriers in the heterostructure, and the probe pulse at 980 nm monitors population of the QD levels. *Source:* Reprinted with permission from Ref.<sup>[48]</sup>.

energies equal to LO phonon energy of  $\sim 37$  meV.<sup>[49]</sup> In this case, the resonant tunneling process occurs only in those QDs with energy levels shifted by multiple LO phonon energies from the QW level.

**Table 3** summarizes relevant parameters for different QD laser media fabricated using the nanoengineering methods described here. Shape-engineering improves the gain almost by a factor of 2. Another twofold enhancement may be obtained through a

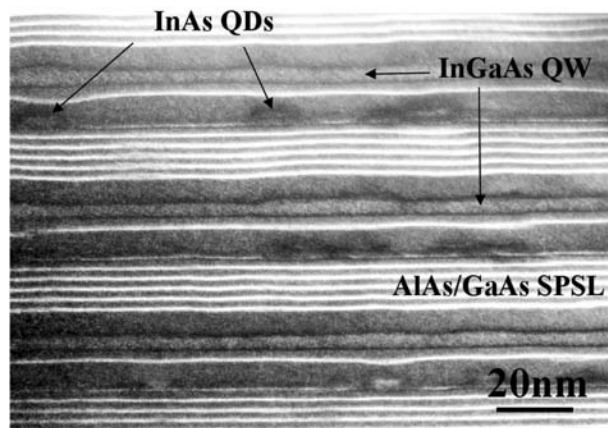


**Fig. 16** TEM (200) dark-field micrographs of QW-on-QDs tunnel structure. The InGaAs QW is separated from the top of the InAs QDs by a GaAs/AlAs barrier. The AlAs layers appear bright, while GaAs appears dark under these conditions.

**Table 3** Comparison of resonant tunnel injection lasers with multilayer QD lasers.  $\lambda_{\text{las}}$  is a lasing wavelength,  $J_{\text{th}}$  is threshold current density,  $L_{\text{min}}$  is minimum cavity length for lasing with cleaved mirrors. All the lasers tested were fabricated using the same waveguide design

MQD lasers	3xQD non-truncated	3xQD	7xQD	3x (QW on QDs)
$\lambda_{\text{las}}$ ( $\mu\text{m}$ )	1.23	1.22	1.12	1.13–1.11
Minimum $J_{\text{th}}$ ( $\text{A}/\text{cm}^2$ )	78	56	155	255
$L_{\text{min}}$ (mm)	1.73	0.87	0.41	0.13
Max. modal gain (per layer) ( $\text{cm}^{-1}$ )	9 (3)	16 (5.3)	31 (4.4)	90 (30)

simple increase in the number of QD layers from 3 to 7. The slight reduction of gain per layer is most likely due to lower injection efficiency in a thicker double heterostructure. A significant fivefold improvement of the modal gain is achieved in the tunnel QW–QD structures shown in Fig. 14. These structures were recently used in an all-epitaxial VCSEL.<sup>[51]</sup>

It is important that the tunnel QW–QD structures have the beneficial properties of QDs even though some lateral transport exists during the operation. For example, frequency chirping and linewidth enhancement factor remain significantly less ( $\sim 5$  times) than that in QW laser.<sup>[50]</sup>

## CONCLUSIONS

Semiconductor quantum dot structures with a discrete atomic-like electronic spectrum have significant physical advantages over those commonly used in optoelectronic devices quantum wells. While growth of semiconductor heterostructures with QDs is relatively easy, it is essential to employ various nanotechnology technologies to maximize projected benefits. A number of methods have been employed recently to improve carrier localization and carrier dynamics in QD ensembles. These methods employ self-assembly to control the structure laterally, and atomically precise component deposition from MBE or MOVPE to achieve the same control in the growth direction. It is reasonable, therefore, to expect major breakthroughs in both the physics and applications of QDs through the development of methods for 3D control of heterostructures via patterning or templating technologies paving a road toward single QD devices.<sup>[52]</sup>

## ACKNOWLEDGMENTS

The authors acknowledge the support by SRC, DARPA, NYSTAR, and NSF through the IFC and INDEX Centers.

## REFERENCES

1. Bimberg, D.; Grundmann, M.; Heinrichsdorff, F.; Ledentsov, N.N.; Ustinov, V.M.; Zhukov, A.E.; Kovsh, A.R.; Maximov, M.V.; Shernyakov, Y.M.; Volovik, B.V.; Tsatsul'nikov, A.F.; Kop'ev, P.S.; Alferov, Z.I. Quantum dot lasers: Breakthrough in optoelectronics. *Thin Solid Films* **2000**, *367* (1–2), 235–249.
2. Ye, Z.; Campbell, J.C.; Chen, Z.; Kim, E.T.; Madhukar, A. Quantum dot infrared photodetectors. *Proc. SPIE* **2002**, *4656*, 16–24.
3. Chakrabarti, S.; Stiff-Roberts, A.D.; Bhattacharya, P.; Gunapala, S.; Bandara, S.; Rafol, S.B.; Kennerly, S.W. High-temperature operation of InAs-GaAs quantum-dot infrared photodetectors with large responsivity and detectivity. *IEEE Photon. Tech. Lett.* **2004**, *16* (5), 1361–1363.
4. Li, L.H.; Rossetti, M.; Fiore, A.; Occhi, L.; Velez, C. Wide emission spectrum from superluminescent diodes with chirped quantum dot multilayers. *Electron. Lett.* **2005**, *41* (1), 41–43.
5. Ray, S.K.; Groom, K.M.; Alexander, R.; Kennedy, K.; Liu, H.Y.; Hopkinson, M.; Hogg, R.A. Design, growth, fabrication, and characterization of InAs/GaAs 1.3  $\mu\text{m}$  quantum dot broadband superluminescent light emitting diode. *J. Appl. Phys.* **2006**, *100* (10), 103105–103103.
6. Arakawa, Y.; Sakaki, H. Multidimensional quantum well laser and temperature dependence of its threshold current. *Appl. Phys. Lett.* **1982**, *40*, 939–941.
7. Bimberg, D.; Grundmann, M.; Ledentsov, N.N. *Quantum Dot Heterostructures*; John Wiley and Sons: New York, NY, 1999.
8. Forchel, A.; Schilling, O.; Wang, K.H.; Ils, P.; Oshinowo, J.; Kieseling, F.; Braun, W. InP/InGaAs nanofabrication and optical characterization. Conference Proceedings, Seventh International Conference on Indium Phosphide and Related Materials, Hokkaido, Japan, 1995; IEEE: Piscataway, NJ, USA, 1995, 660–663.
9. Tang, Y.S.; Sotomayor Torres, C.M. Damage, strain and quantum confinement issues in dry etched semiconductor nanostructures. *MRS Proc.* **1996**, *405*, 99–108.
10. Okada, Y.; Amano, S.; Kawabe, M.; Shimbo, B.N.; Harris, J.S., Jr. Nanoscale oxidation of GaAs-based semiconductors using atomic force microscope. *J. Appl. Phys.* **1998**, *83* (4), 1844–1847.



11. Nakamura, H.; Kohmoto, S.; Ishikawa, T.; Asakawa, K. Novel nano-scale site-controlled InAs quantum dot assisted by scanning tunneling microscope probe. *Physica E* **2000**, *7* (3–4), 331–336.
12. Ishikawa, T.; Kohmoto, S.; Asakawa, K. Site control of self-organized InAs dots on GaAs substrates by in situ electron-beam lithography and molecular-beam epitaxy. *Appl. Phys. Lett.* **1998**, *73* (12), 1712–1714.
13. Pryor, C. Geometry and material parameter dependence of InAs/GaAs quantum dot electronic structure. *Phys. Rev. B* **1999**, *60* (4), 2869–2874.
14. Yakimov, M.; Tokranov, V.; Agnello, G.; Van Eisdien, J.; Oktyabrsky, S. In situ monitoring of formation of InAs quantum dots and overgrowth by GaAs or AlAs. *J. Vac. Sci. Technol. B* **2005**, *23* (3), 1221–1225.
15. Shiramine, K.; Itoh, T.; Muto, S. Critical cluster size of InAs quantum dots formed by Stranski-Krastanow mode. *J. Vac. Sci. Technol. B* **2004**, *22* (2), 642–646.
16. Oktyabrsky, S.; Tokranov, V.; Agnello, G.; Van Eisdien, J.; Yakimov, M. Nano-engineering approaches to self-assembled InAs quantum dot laser medium. *J. Electron. Mater.* **2006**, *35* (5), 822–833.
17. Moison, J.M.; Houzay, F.; Barthe, F.; Leprince, L.; Andre, E.; Vatel, O. Self-organized growth of regular nanometer-scale InAs dots on GaAs. *Appl. Phys. Lett.* **1994**, *64* (2), 196–198.
18. Heyn, C.; Dumat, C. Formation and size evolution of self-assembled quantum dots. *J. Crystal Growth* **2001**, *227–228*, 990–994.
19. Ferdos, F.; Wang, S.; Wei, Y.; Sadeghi, M.; Zhao, Q.; Larsson, A. Influence of initial GaAs and AlAs cap layers on InAs quantum dots grown by molecular beam epitaxy. *J. Crystal Growth* **2003**, *251* (1–4), 145–149.
20. Rosenauer, A.; Gerthsen, D.; Van Dyck, D.; Arzberger, M.; Bohm, G.; Abstreiter, G. Quantification of segregation and mass transport in In/sub x/Ga/sub 1-x/As/GaAs Stranski-Krastanow layers. *Phys. Rev. B* **2001**, *64* (24), 245334/245331–245315.
21. Schowalter, M.; Rosenauer, A.; Gerthsen, D.; Arzberger, M.; Bichler, M.; Abstreiter, G. Investigation of In segregation in InAs/AlAs quantum-well structures. *Appl. Phys. Lett.* **2001**, *79* (26), 4426–4428.
22. Marquez, J.; Geelhaar, L.; Jacobi, K. Atomically resolved structure of InAs quantum dots. *Appl. Phys. Lett.* **2001**, *78* (16), 2309–2311.
23. Eisele, H.; Jacobi, K. Erratum: atomically resolved structure of InAs quantum dots [Appl. Phys. Lett. **2001**, *78*, 2309]. *Appl. Phys. Lett.* **2007**, *90* (12), 129902.
24. Lee, H.; Lowe-Webb, R.; Yang, W.; Sercel, P.C. Determination of the shape of self-organized InAs/GaAs quantum dots by reflection high energy electron diffraction. *Appl. Phys. Lett.* **1998**, *72* (7), 812–814.
25. Grundmann, M.; Stier, O.; Bimberg, D. InAs/GaAs pyramidal quantum dots: Strain distribution, optical phonons, and electronic structure. *Phys. Rev. B* **1995**, *52* (16), 11,969–11,981.
26. Asryan, L.V.; Grundmann, M.; Ledentsov, N.N.; Stier, O.; Suris, R.A.; Bimberg, D. Maximum modal gain of a self-assembled InAs/GaAs quantum-dot laser. *J. Appl. Phys.* **2001**, *90* (3), 1666–1668.
27. Kim, J.; Wang, L.W.; Zunger, A. Comparison of the electronic structure of InAs/GaAs pyramidal quantum dots with different facet orientations. *Phys. Rev. B* **1998**, *57* (16), R9408–R9411.
28. Ryzhii, V.; Khmyrova, I.; Pipa, V.; Mitin, V.; Willander, M. Device model for quantum dot infrared photodetectors and their dark-current characteristics. *Semicon. Sci. Technol.* **2001**, *16* (5), 331–338.
29. Chen, Z.; Baklenov, O.; Kim, E.T.; Mukhametzhanov, I.; Tie, J.; Madhukar, A.; Ye, Z.; Campbell, J.C. Normal incidence InAs/Al/sub x/Ga/sub 1-x/As quantum dot infrared photodetectors with undoped active region. *J. Appl. Phys.* **2001**, *89* (8), 4558–4563.
30. Mukhametzhanov, I.; Wei, Z.; Heitz, R.; Madhukar, A. Punctuated island growth: An approach to examination and control of quantum dot density, size, and shape evolution. *Appl. Phys. Lett.* **1999**, *75* (1), 85–87.
31. Wasilewski, Z.R.; Fafard, S.; Mccaffrey, J.P. Size and shape engineering of vertically stacked self-assembled quantum dots. *J. Crystal Growth* **1999**, *201–202*, 1131–1135.
32. Tokranov, V.; Yakimov, M.; Katsnelson, A.; Lamberti, M.; Oktyabrsky, S. Shape engineered InAs quantum dots with stabilized electronic properties. *Proc. SPIE* **2003**, *4999*, 79–88.
33. Tokranov, V.E.; Yakimov, M.; Katsnelson, A.; Lamberti, M.; Agnello, G.; Oktyabrsky, S. Nano-engineered InAs quantum dot active medium for laser diodes. *Proc. SPIE* **2004**, *5365* (1), 72–79.
34. Mccaffrey, J.P.; Robertson, M.D.; Poole, P.J.; Riel, B.J.; Fafard, S. Interpretation and modeling of buried InAs quantum dots on GaAs and InP substrates. *J. Appl. Phys.* **2001**, *90* (4), 1784–1787.
35. Notzel, R.; Anantathanasarn, S.; Van Veldhoven, R.P.J.; Van Otten, F.W.M.; Eukemans, T.J.; Trampert, A.; Satpati, B.; Barbarin, Y.; Bente, E.A.J.M.; Oei, Y.S.; Vries, T.D.; Geluk, E.J.; Smalbrugge, B.; Smit, M.K.; Wolter, J.H. Self assembled InAs/InP quantum dots for telecom applications in the 1.55 μm wavelength range: Wavelength tuning, stacking, polarization control, and lasing. *Jap. J. Appl. Phys. Part 1* **2006**, *45* (8B), 6544–6549.
36. Solomon, G.S.; Trezza, J.A.; Marshall, A.F.; Harris, J.S., Jr. Vertically aligned and electronically coupled growth induced InAs islands in GaAs. *Phys. Rev. Lett.* **1996**, *76* (6), 952–955.
37. Mukhametzhanov, I.; Heitz, R.; Zeng, J.; Chen, P.; Madhukar, A. Independent manipulation of density and size of stress-driven self-assembled quantum dots. *Appl. Phys. Lett.* **1998**, *73* (13), 1841–1843.
38. Lita, B.; Goldman, R.S.; Phillips, J.D.; Bhattacharya, P.K. Nanometer-scale studies of vertical organization and evolution of stacked self-assembled InAs/GaAs quantum dots. *Appl. Phys. Lett.* **1999**, *74* (19), 2824–2826.
39. Seravalli, L.; Minelli, M.; Frigeri, P.; Franchi, S.; Guizzetti, G.; Patrini, M.; Ciabattini, T.; Geddo, M. Quantum dot strain engineering of InAs/InGaAs nanostructures. *J. Appl. Phys.* **2007**, *101* (2), 24,313–24,341.

40. Liu, G.; Stintz, A.; Li, H.; Malloy, K.J.; Lester, L.F. Extremely low room-temperature threshold current density diode lasers using InAs dots in In/sub 0.15/Ga/sub 0.85/As quantum well. *Electron. Lett.* **1999**, *35* (14), 1163–1165.
41. Ustinov, V.M.; Maleev, N.A.; Zhukov, A.E.; Kovsh, A.R.; Egorov, A.; Lunev, A.V.; Volovik, B.V.; Krestnikov, I.L.; Musikhin Yu, G.; Bert, N.A.; Kop'ev, P.S.; Alferov Zh, I.; Ledentsov, N.N.; Bimberg, D. InAs/InGaAs quantum dot structures on GaAs substrates emitting at 1.3  $\mu\text{m}$ . *Appl. Phys. Lett.* **1999**, *74* (19), 2815–2817.
42. Oktyabrsky, S.; Lamberti, M.; Tokranov, V.; Agnello, G.; Yakimov, M. Room-temperature defect tolerance of band-engineered InAs quantum dot heterostructures. *J. Appl. Phys.* **2005**, *98* (5), 53,512–53,531.
43. Le Ru, E.C.; Fack, J.; Murray, R. Temperature and excitation density dependence of the photoluminescence from annealed InAs/GaAs quantum dots. *Phys. Rev. B* **2003**, *67* (24), 245318–245341.
44. Siegert, J.; Marcinkevicius, S.; Zhao, Q.X. Carrier dynamics in modulation-doped InAs/GaAs quantum dots. *Phys. Rev. B* **2005**, *72* (8), 85,316–85,851.
45. Heitz, R.; Grundmann, M.; Ledentsov, N.N.; Eckey, B.L.; Veit, M.; Bimberg, D.; Ustinov, V.M.; Egorov, A.Y.; Zhukov, A.E.; Kop'ev, P.S.; Alferov, Z.I. Multiphonon-relaxation processes in self-organized InAs/GaAs quantum dots. *Appl. Phys. Lett.* **1996**, *68* (3), 361–363.
46. Benisty, H.; Sotomayor-Torres, C.M.; Weisbuch, C. Intrinsic mechanism for the poor luminescence properties of quantum-box systems. *Phys. Rev. B* **1991**, *44* (19), 10,945–10,948.
47. Walter, G.; Chung, T.; Holonyak, N. High-gain coupled InGaAs quantum well InAs quantum dot AlGaAs-GaAs-InGaAs-InAs heterostructure diode laser operation. *Appl. Phys. Lett.* **2002**, *80*, 1126–1128.
48. Bhattacharya, P.; Ghosh, S.; Pradhan, S.; Singh, J.; Wu, Z.K.; Urayama, J.; Kim, K.; Norris, T.B. Carrier dynamics and high-speed modulation properties of tunnel injection InGaAs-GaAs quantum-dot lasers. *IEEE J. Quantum Electron.* **2003**, *39*, 952–962.
49. Chang, S.W.; Chuang, S.L.; Holonyak, N. Phonon- and auger-assisted tunneling from a quantum well to a quantum dot. *Phys. Rev. B* **2004**, *70* (12), 125312–125321.
50. Fathpour, S.; Bhattacharya, P.K.; Ghosh, S. Low line-width enhancement factor and chirp and suppressed filamentation in tunnel injection In/sub 0.4/Ga/sub 0.6/As self-assembled quantum dot lasers. *Proc. SPIE* **2004**, *5361* (1), 29–34.
51. Tokranov, V.; Yakimov, M.; Van Eisdien, J.; Oktyabrsky, S. All-epitaxial VCSELs with tunnel InGaAs-InAs gain medium QW-QD. *Proc. SPIE* **2007**, *6481*, 79–86.
52. Michler, P. *Single Quantum Dots. Fundamentals, Applications and New Concepts*; Michler, P., Ed.; Springer-Verlag: Berlin, Germany, 2003.
53. Suekane, O.; Okui, T.; Takata, M.; Hasegawa, S.; Nakashima, H. Growth temperature dependence of InAs islands grown on GaAs (001) substrates, Conference Proceedings, 13<sup>th</sup> International Conference on Indium Phosphide and Related Materials, Nara, Japan, 2001; IEEE: Piscataway, NJ, USA, 2001, 288–291.
54. Ballet, P.; Smathers, J.B.; Yang, H.; Workman, C.L.; Salamo, G.J. Control of size and density of InAs/(Al, Ga)As self-organized islands. *J. Appl. Phys.* **2001**, *90* (1), 481–487.



# Self-Assembled Quantum Dots: Electronic Structures and Optical Properties

Andrew Williamson

Lawrence Livermore National Laboratory, Livermore, California, U.S.A.

## INTRODUCTION

As evidenced by many of the entries in this encyclopedia, the past decade has witnessed a series of significant advances in the growth of semiconductor nanostructures. These nanostructures range in size from a few atoms up to several million atoms and have been produced by myriad synthesis techniques.<sup>[1]</sup> In this entry, we describe calculations of the electronic and optical properties of self-assembled (so-called Stranski–Krastanow) quantum dots produced by molecular beam epitaxy.<sup>[2,3]</sup> Even more dramatic than the advances in the growth of these structures has been the development of extremely sophisticated techniques for measuring the optical, electronic, magnetic, and transport properties of these quantum dot systems. The availability of such high-quality measurements for a wide range of properties presents theorists with the formidable challenge of constructing models that can explain the origins of these experimental observations in terms of the underlying energy states of the quantum dots.

Calculating such energy states in self-assembled semiconductor quantum dots is rendered particularly challenging by a number of factors:

1. The quantum dots contain a large number of atoms. A typical self-assembled quantum dot has a base of  $\sim 300 \text{ \AA}$  and a height of  $\sim 50 \text{ \AA}$ . Therefore the dot itself may contain  $\sim 10^5$  atoms. This dot then needs to be surrounded by a barrier material to isolate it from other dots. Therefore a representative system containing both the dot and barrier typically contains  $\sim 10^6$  atoms.
2. By the nature of the growth process, self-assembled quantum dots are highly strained. For example, in the most common InAs/GaAs material combination, the lattice mismatch is 7%. Therefore an accurate solution of the strain profile in the system is required before the electronic structure can be calculated.
3. The valence band maximum (VBM) in III–V semiconductor materials is threefold degenerate (in the absence of strain and spin–orbit splitting),

therefore any realistic approach must describe at least the band mixing between the three valence band edge states.

4. In InAs, the bulk band gap is 0.42 eV and the spin–orbit splitting is 0.38 eV, therefore the mixing between valence and conduction band states and split off states also have to be taken into account.
5. In a zero-dimensional InAs/GaAs quantum dot system, the charge carriers are artificially confined inside the dot, which is typically smaller than the bulk excitonic radius—the “Strong Confinement” regime. This dramatically enhances the Coulomb interaction between charges in the dot and strongly modifies the dielectric screening.

## OVERVIEW

The standard theoretical approach to this problem has been to adapt effective mass-based techniques and their more sophisticated extension, the  $\mathbf{k}\cdot\mathbf{p}$  method, which has been extremely successful in explaining a range of properties of bulk semiconductors. In essence, these methods expand the single-particle wavefunctions of the system in a basis of bulk Bloch orbitals derived from the Brillouin zone center ( $\Gamma$  point). If a sufficient number of basis states are included, this expansion provides an excellent description of the band structure of the bulk material close to the  $\Gamma$  point. However, errors in the predicted energy rapidly increase as one moves away from the zone center. To improve the description of the band structure away from the zone center, one typically includes more and more basis functions in the expansion of the wavefunctions. The successes of this effective mass model in describing spectroscopic and transport properties in both three-dimensional bulk systems and two-dimensional quantum well structures are well documented. This model was also demonstrated to be able to provide at least a qualitative picture of the energy states in zero-dimensional systems. However, some of this success is mitigated by the fact that often, the

parameters in the model have to be refit to the nanostructure system itself. Recently, a direct comparison<sup>[4]</sup> between an eight-band  $\mathbf{k}\cdot\mathbf{p}$  calculation and a full pseudopotential calculation for a pyramidal InAs quantum dot embedded within bulk GaAs showed a generally good agreement between the two techniques. However, the higher symmetry imposed by the  $\mathbf{k}\cdot\mathbf{p}$  approach acts to omit certain energy level splittings and polarization anisotropies. The  $\mathbf{k}\cdot\mathbf{p}$  approach also overconfined both electrons and holes level by  $\sim 50$  meV.

Instead, in this entry, we describe our method of choice, the empirical pseudopotential method (EPM) approach to calculating the energy states in semiconductor quantum dots. This approach has several advantages over the conventional effective mass approach to the problem:

1. Once a pseudopotential has been developed to describe the bulk system, there are no adjustable parameters for describing a heterostructure system.
2. The EPM method has the same accuracy, whether it is describing a three-dimensional bulk system, a two-dimensional quantum well, a one-dimensional quantum wire, or a zero-dimensional quantum dot.
3. The EPM method provides an *atomistic* description of the system. Therefore the correct symmetry of the underlying crystal lattice is reproduced. In addition, an atomistic description of interfaces between materials is also maintained.

We begin with a detailed description of each of the stages required in a typical EPM calculation of the energy states in a semiconductor quantum dot. Then we describe a series of applications of the EPM technique to studying a range of optical and electronic properties of self-assembled quantum dots.

## DESCRIPTION OF PSEUDOPOTENTIAL TECHNIQUES

To calculate the energy states associated with various electronic excitations in self-assembled quantum dots requires three stages of calculation:

1. Assume the shape and composition and compute the strain:  
We first construct a supercell containing both the quantum dot and surrounding barrier material. Sufficient barrier material is used, so that when periodic boundary conditions are applied to the system, the electronic and strain

interactions between dots in neighboring cells is negligible. The atomic positions within the supercell are relaxed by minimizing the strain energy described by an atomistic force field<sup>[5,6]</sup> including bond bending, bond stretching, and bond bending–bond stretching interactions. More details of the atomistic relaxation are given in the section “Calculation of the Strain Profile.”

2. Set up the pseudopotential single-particle equation:

A single-particle Schrödinger equation is set up at the relaxed atomic positions,  $\{\mathbf{R}_{nz}\}$

$$\begin{aligned}\hat{H}\psi_i(\mathbf{r}) &= \left\{ -\frac{\beta}{2}\nabla^2 + \sum_{nz} \hat{v}_z(\mathbf{r} - \mathbf{R}_{nz}) \right\} \psi_i(\mathbf{r}) \\ &= \epsilon_i \psi_i(\mathbf{r})\end{aligned}\quad (1)$$

The potential for the system is written as a sum of strain-dependent, screened atomic pseudopotentials,  $v_z$ , that are fit to bulk properties extracted from experiment and first-principles calculations. For more details of the constructing of the Hamiltonian see the section “[Constructing the Single-Particle Hamiltonian.](#)”

3. Calculate the screened, interparticle many-body interactions:

The calculated single-particle wavefunctions are used to compute the electron–electron, electron–hole, and hole–hole direct,  $J_{ee}$ ,  $J_{eh}$ ,  $J_{hh}$ , and exchange  $K_{ee}$ ,  $K_{eh}$ ,  $K_{hh}$  Coulomb energies. For more details, see the section “[Calculation of ‘Two-Body’ Interactions.](#)”

The main approximations involved in our method are as follows: 1) the fit of the pseudopotential to the experimental data of bulk materials is never perfect; and 2) we neglect self-consistent iterations in that we assume that the screened pseudopotential drawn from a bulk calculation is appropriate for the dot. Our numerical convergence parameters are: 1) the size of the GaAs barrier separating periodic images of the dots; and 2) the number of basis functions used in the expansion of the wavefunctions (see the sections “[Expansion in a Plane Wave Basis](#)” and “[Expansion in a Linear Combination of Bloch Bands](#)” for more details).

## Calculation of the Strain Profile

To obtain an *atomistic* description of the strain profile in a heterostructure system, we construct an expression for the strain energy in terms of few-body potentials

between actual atoms

$$E_{\text{strain}} = \sum_{ij} V_2(\mathbf{R}_i - \mathbf{R}_j) + \sum_{ijk} V_3(\hat{\Theta}_{ijk}) + \dots \quad (2)$$

where  $V_2$  is a two-body term,  $V_3$  is a three-body function of the bond angle,  $\hat{\Theta}_{ijk}$ . The functional form of these terms is taken to be strain-independent. The strain is determined by minimizing  $E_{\text{strain}}$  with respect to atomic positions  $\{\mathbf{R}\}$ .

Our chosen expression for the elastic strain energy, is a generalization (G-VFF) of the original valence force field (VFF)<sup>[5,7]</sup> model. Our implementation of the VFF includes bond stretching, bond angle bending, and bond length/bond angle interaction terms. This enables us to accurately reproduce the  $C_{11}$ ,  $C_{12}$ , and  $C_{44}$  elastic constants in a zincblende bulk material. We have also included higher-order bond stretching terms, which yield the correct dependence of the Young's modulus with pressure. The expression for the G-VFF total energy is:

$$\begin{aligned} E_{\text{G-VFF}} = & \sum_i \sum_j^{n_i} \frac{3}{8} [\alpha_{ij}^{(1)} \Delta d_{ij}^2 + \alpha_{ij}^{(2)} \Delta d_{ij}^3] \\ & + \sum_i \sum_{k>j}^{n_i} \frac{3\beta_{jik}}{8d_{ij}^0 d_{ik}^0} [(\mathbf{R}_j - \mathbf{R}_i) \cdot (\mathbf{R}_k - \mathbf{R}_i)] \\ & - \cos \theta_{jik}^0 [d_{ij}^0 d_{ik}^0]^2 + \sum_i \sum_{k>j}^{n_i} \frac{3\sigma_{ijk}}{d_{ik}^0} \Delta d_{ij} \\ & \times [(\mathbf{R}_j - \mathbf{R}_i) \cdot (\mathbf{R}_k - \mathbf{R}_i) - \cos \theta_{jik}^0 d_{ij}^0 d_{ik}^0] \end{aligned} \quad (3)$$

where  $\Delta d_{ij} = [(\mathbf{R}_i - \mathbf{R}_j)^2 - d_{ij}^{02}]/d_{ij}^0$ . Here,  $\mathbf{R}_i$  is the coordinate of atom  $i$  and  $d_{ij}^0$  is the ideal (unrelaxed) bond distance between atom types of  $i$  and  $j$ . Also,  $\theta_{jik}^0$  is the ideal (unrelaxed) angle of the bond angle  $j$ - $i$ - $k$ .  $\sum^{n_i}$  denotes the summation over the nearest neighbors of atom  $i$ . Example values of  $\alpha$ ,  $\beta$ , and  $\sigma$  can be found in Ref.<sup>[8]</sup>.

For an InGaAs alloy system, the bond angle and bond length/bond angle interaction parameters  $\beta$ ,  $\sigma$  for the mixed cation Ga-As-In bond angle are taken as the algebraic average of the In-As-In and Ga-As-Ga values. In Fig. 1, we show the result of a G-VFF calculation for the strain profile in a lens-shaped InAs quantum dot embedded within GaAs. The trace of the strain is plotted in a (010) plane through the center of the dot. It shows that, to a first approximation, the InAs dot is subjected to a uniform compressive strain and the GaAs barrier is slightly expanded around the interface with the dot.

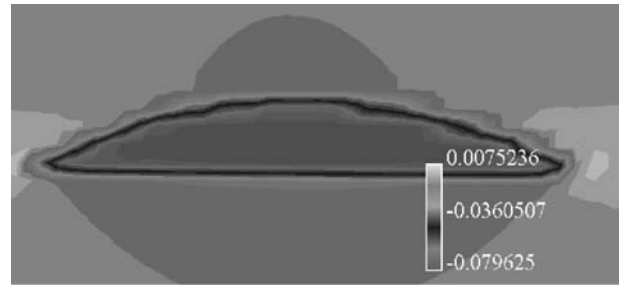


**Fig. 1** Contour plot of the hydrostatic strain profile in a lens-shaped, self-assembled InAs/GaAs quantum dot with a base of 252 Å and a height of 35 Å.

## Constructing the Single-Particle Hamiltonian

We construct the single-particle Hamiltonian as

$$\hat{H} = -\frac{\beta}{2} \nabla^2 + \sum_{nz} \hat{v}_z(\mathbf{r} - \mathbf{R}_{nz}) \quad (4)$$

where  $\mathbf{R}_{nz}$  is the G-VFF relaxed position of the  $n$ th atom of type  $\alpha$ . Here  $\hat{v}_z(\mathbf{r})$  is a screened empirical pseudopotential for atomic type  $\alpha$ . It contains a local part and a non-local, spin-orbit interaction part.

The local potential part is designed to include dependence on the local hydrostatic strain  $\text{Tr}(\epsilon)$ :

$$v_\alpha^{\text{loc}}(r; \epsilon) = v_\alpha^{\text{eq}}(r; 0) [1 + \gamma_\alpha \text{Tr}(\epsilon)] \quad (5)$$

where the  $\gamma_\alpha$  is a fitting parameter. The zero strain potential  $v_\alpha^{\text{eq}}(r; 0)$  is expressed in reciprocal space  $q$  as

$$v(q) = a_0(q^2 - a_1)/[a_2 e^{a_3 q^2} - 1] \quad (6)$$

where  $a_{0,1,2,3}$  are fitting parameters. The local hydrostatic strain  $\text{Tr}(\epsilon)$  for a given atom at  $\mathbf{R}$  is defined as  $\Omega_R/\Omega_0 - 1$ , where  $\Omega_R$  is the volume of the tetrahedron formed by the four atoms bonded to the atom at  $\mathbf{R}$ .  $\Omega_0$  is the volume of that tetrahedron in the unstrained condition. The need for explicit dependence of the atomic pseudopotential on strain in Eq. (5) results from the following: While the description in Eq. (4) of the total pseudopotential as a superposition of atomic potentials situated at specific sites,  $\{\mathbf{R}_{nz}\}$ , does capture the correct local symmetries in the system, the absence of a self-consistent treatment of the Schrödinger equation deprives the potential from changing in response to strain. In the absence of a strain-dependent term, the volume dependence of the energy of the bulk valence band maximum is incorrect. While self-consistent descriptions show that the volume deformation potential  $a_v = dE_v/d \ln \Omega$  of the valence band maximum is *negative* for GaAs, GaSb, InAs, InSb, and for all II-VI, this qualitative behavior cannot be

obtained by a non-self-consistent calculation that lacks a strain-dependent pseudopotential.

In Eq. (4), the kinetic energy of the electrons has been scaled by a factor of  $\beta$ . The origin of this term is as follows: In an accurate description of the crystal band structure, such as the GW method, a general, spatially non-local potential,  $V(r,r')$ , is needed to describe the self-energy term. In the absence of such a term, the occupied band width of an inhomogeneous electron gas is too large compared to the exact many-body result. However, to a first approximation, the leading effects of this non-local potential,  $V(r,r')$ , can be represented by scaling the kinetic energy. This can be obtained by Fourier transforming  $V(r,r')$  in reciprocal space,  $q$ , then making a Taylor expansion of  $q$  about zero. We find that the introduction of such a kinetic energy scaling,  $\beta$ , permits a simultaneous fit of both the effective masses and energy gaps. In this study, we fit  $\beta = 1.23$  for both GaAs and InAs.

The pseudopotential parameters in Eqs. (5) and (6) were fitted to the bulk band structures, experimental deformation potentials and effective masses, and first-principles calculations of the valence band offsets of GaAs and InAs. The alloy bowing parameter for the GaInAs band gap (0.6 eV) is also fitted. An example of the quality of the pseudopotential fit for GaAs and InAs can be found in Ref.<sup>[9]</sup>.

## Solving the Single-Particle Hamiltonian

We have developed two techniques for solving for the eigenstates of Eq. (4). The choice of technique depends on the size of the heterostructure system being studied, i.e., the number of electrons in the system, and the desired level of accuracy. The two techniques are distinguished by: 1) the choice of the basis set for expanding the single-particle eigenstates of Eq. (4); and 2) the algorithm used to solve for the eigenstates within that particular basis. In our first approach, we expand the eigenstates in a *plane wave* basis and use the folded spectrum method to obtain eigenstates in a given energy window. In the second approach, we expand the eigenstates in a basis of *bulk Bloch orbitals* and use a Lanczos algorithm to obtain eigenstates.

### Expansion in a plane wave basis

The conventional basis set for performing calculations of the electronic band structure of periodic materials, such as bulk semiconductors, is the plane wave basis.

$$\psi_i(\mathbf{r}) = \sum_{\mathbf{G}}^{E_{\text{cut}}} c_{\mathbf{G}}^i e^{i\mathbf{G}\cdot\mathbf{r}} \quad (7)$$

Within this basis, one can easily utilize fast Fourier transforms to convert the wavefunctions from a real-space to reciprocal-space representation. The matrix elements of the Hamiltonian in Eq. (4) in the basis of Eq. (7) can be written as

$$\hat{H}_{\mathbf{G},\mathbf{G}'} = \frac{1}{2} \mathbf{G}^2 \delta_{\mathbf{G},\mathbf{G}'} + V_{\text{local}}(\mathbf{G} - \mathbf{G}') + V_{\text{nonlocal}}(\mathbf{G}, \mathbf{G}') \quad (8)$$

The conventional variation al approach to solving for the eigenstates of Eq. (8) is to minimize the energy  $\langle \psi_0 | \hat{H} | \psi_0 \rangle$ , of the groundstate wavefunction,  $\psi_0$ , by varying its expansion coefficients,  $c_{\mathbf{G},0}$ . To find higher states, one needs to orthogonalize each  $\psi_i$  to all previously converged energy eigenstates below it. This orthogonalization process scales as the third power of the number of states and so only small systems with up to a few hundred electrons can be solved in this manner.

To enable us to study heterostructure systems containing  $10^6$  electrons, we instead “fold” the spectrum of eigenstates about a specified reference energy and hence solve<sup>[10,11]</sup> for the eigenstates of the equation

$$(\hat{H} - \epsilon_{\text{ref}})^2 \psi_i = (\epsilon - \epsilon_{\text{ref}})^2 \psi_i \quad (9)$$

where  $\epsilon_{\text{ref}}$  is a chosen reference energy. By placing  $\epsilon_{\text{ref}}$  within the band gap of the quantum dot system, and close to the valence band maximum (VBM) or conduction band minimum (CBM), one is then able to calculate the top few valence states or the bottom few conduction states, respectively. As quantum confinement effects act to lower (raise) electron (hole) levels in the quantum dot compared to the bulk, one can ensure that  $\epsilon_{\text{ref}}$  falls within the band gap of the dot simply by placing it within the bulk band gap of the dot material. By applying the  $\hat{H}$  operator twice, it is easy to see that the eigenstates of Eq. (9) are also eigenstates of the Hamiltonian in Eq. (4). Therefore, the process of folding the spectrum does not introduce any additional approximations compared to the conventional  $N^3$  scaling algorithms. It simply removes the need to calculate all the low-energy eigensolutions and then orthogonalize to each of these states. By removing the need for this costly orthogonalization, the folded spectrum algorithm is able to scale linearly with the number of electrons in the system. A version of this folded spectrum code was developed<sup>[12]</sup> for parallel supercomputers, which linearly scales up to hundreds of processors and is able to handle systems containing up to  $10^7$  electrons. Typically, a calculation requires 20–50 plane waves per atom in the system and so these parallel calculations are effectively finding selective eigenstates of a matrix of order  $10^8$ .

## Expansion in a linear combination of bloch bands

For larger quantum dot heterostructure systems containing several million atoms, using a plane wave basis set to expand the single-particle eigenstates becomes too computationally demanding, even when the folded spectrum method is employed. Instead, we choose to use a more physically intuitive basis set, namely a linear combination of bulk bands (LCBB).<sup>[13]</sup>

$$\psi_i(\mathbf{r}) = \sum_s \sum_{n,k} c_{s,n,k}^{(i)} u_{s,n,k}(\mathbf{r}) e^{i\mathbf{k}\cdot\mathbf{r}} \quad (10)$$

where  $u_{s,n,k}(\mathbf{r})$  is the cell periodic part of the bulk Bloch wavefunction for structure,  $s$ , at the  $n$ th band and the  $k$ th  $k$ -point. As these states form a physically more intuitive basis than traditional plane waves, the number of bands and  $k$ -points can be significantly reduced to keep only the physically important bands and  $k$ -points. This method was recently generalized to strained semiconductor heterostructure systems<sup>[14]</sup> and to include the spin-orbit interaction. To study an  $\text{In}_x\text{Ga}_{1-x}\text{As}$  quantum dot embedded within a GaAs barrier, we typically use an LCBB basis derived from a set of structures,  $s$ . This allows us to directly include the effects of strain on the basis functions. The structures used are as follows: 1) unstrained, bulk InAs at zero pressure; 2) unstrained, bulk GaAs at zero pressure; 3) bulk InAs subjected to the strain value in the center of the InAs dot; and 4) bulk InAs subjected to the strain value at the tip of the InAs dot. For an  $\text{In}_x\text{Ga}_{1-x}\text{As}$  quantum dot system, where we expect the electron and hole states to be derived from around the bulk  $\Gamma$  point, the wavevectors,  $\{k\}$ , include all allowed values within a given cutoff of the zone center. For calculations of electron states, we find we only need to include the band index,  $n$ , around the  $\Gamma_{1c}$  point. For the hole states, we also include the three bands around the  $\Gamma_{15v}$  point. As the number of  $k$ -points and bands in the LCBB basis is increased, the eigenstates converge to those calculated using a converged basis, such as the above plane wave basis with a large cutoff,  $E_{\text{cut}}$ . Therefore we can use a plane wave, folded spectrum calculation as a reference to judge when our LCBB basis set is sufficient. We find that to study a typical quantum dot system, a basis set containing 10,000 bulk bands produces single-particle energies that are converged with respect to basis size, to within 1 meV.

## Calculation of “Two-Body” Interactions

Using screened Hartree Fock theory, the energy associated with loading  $N$  electrons and  $M$  holes into a

quantum dot can be expressed<sup>[15]</sup> as

$$\begin{aligned} E_{MN} = & \sum_i -\epsilon_{h_i} m_i + \sum_{i<j} (J_{ij}^{\text{hh}} - K_{ij}^{\text{hh}}) m_i m_j \\ & + \sum_i \epsilon_{e_i} n_i + \sum_{i<j} (J_{ij}^{\text{ee}} - K_{ij}^{\text{ee}}) n_i n_j \\ & - \sum_{ij} (J_{ij}^{\text{eh}} - K_{ij}^{\text{eh}}) n_i m_j \end{aligned} \quad (11)$$

where the electron and hole levels are denoted by  $e_0, e_1, e_2, \dots$ , and  $h_0, h_1, h_2, \dots$ , respectively. The  $n_i$  and  $m_i$  are the electron and hole occupation numbers, respectively, such that  $\sum_i n_i = N$  and  $\sum_i m_i = M$ . The  $\epsilon_i$  are the single-particle energies of the  $i$ th state,  $J_{ij}$  and  $K_{ij}$  are the direct and exchange Coulomb integrals between the  $i$ th and  $j$ th electronic states. For example, by using Eq. (11), in the strong confinement regime where kinetic energy effects dominate over the effects of exchange and correlation, an exciton involving an electron excited from hole state  $i$  to electron state  $j$  can be expressed as

$$E_{ij}^{\text{exciton}} = (\epsilon_{e_j} - \epsilon_{h_i}) - J_{ji}^{\text{eh}} + K_{ji}^{\text{eh}} \delta_{S,0} \quad (12)$$

The direct and exchange Coulomb energies are defined<sup>[16]</sup> as

$$\begin{aligned} J_{ijkl} &= \iint \frac{\psi_i^*(\mathbf{r}_1) \psi_j(\mathbf{r}_2) \psi_k^*(\mathbf{r}_1) \psi_l(\mathbf{r}_2)}{\bar{\epsilon}(\mathbf{r}_1 - \mathbf{r}_2) |\mathbf{r}_1 - \mathbf{r}_2|} d\mathbf{r}_1 d\mathbf{r}_2 \\ K_{ijkl} &= \iint \frac{\psi_i^*(\mathbf{r}_1) \psi_j(\mathbf{r}_2) \psi_k^*(\mathbf{r}_2) \psi_l(\mathbf{r}_1)}{\bar{\epsilon}(\mathbf{r}_1 - \mathbf{r}_2) |\mathbf{r}_1 - \mathbf{r}_2|} d\mathbf{r}_1 d\mathbf{r}_2 \end{aligned} \quad (13)$$

where  $\bar{\epsilon}$  is connected to a phenomenological, screened dielectric function,<sup>[17]</sup>  $\epsilon(\mathbf{r}, \mathbf{r}', R)$ , by,

$$\frac{1}{\bar{\epsilon}(\mathbf{r}, \mathbf{r}'') |\mathbf{r} - \mathbf{r}''|} = \int d\mathbf{r}' \epsilon^{-1}(\mathbf{r}, \mathbf{r}'; R) \frac{1}{|\mathbf{r}'' - \mathbf{r}'|} \quad (14)$$

where  $R$  is the diameter of the quantum dot being studied.

## RECENT APPLICATIONS

One of the long-standing problems that has held back the development of accurate models for the energy states in semiconductor quantum dot heterostructures is the need to accurately determine the size, shape, and composition of quantum dot samples. This problem is further compounded by the fact that, while it is possible to determine the shape of dots by using atomic force microscopy (AFM) *before* they have been capped with a GaAs “barrier,” it is believed that the capping process itself induces the diffusion of gallium into the dots and diffusion of indium from the dots into the surrounding matrix. Hence AFM data for

the size and shape of *uncapped* dots is only of limited use in evaluating the quality of theoretical models for *capped* dots. Therefore a major determining factor in our choice of which systems to apply the above EPM techniques to has been the continuing experimental progress in the characterization of self-assembled quantum dots. The earliest quantum dot samples were believed to contain pure InAs, pyramidal structures, with {101} facets (Fig. 2) forming 45° angles between the facets and the base. Following this interpretation of the structure, early calculations were also performed assuming a pyramidal geometry. In the section “Pyramidal Quantum Dots: Single-Particle Electron and Hole States,” we compare the results of our initial calculations for pyramidal InAs quantum dots embedded within GaAs with those from other theoretical techniques. More recent characterization using cross-sectional transmission electron microscopy (TEM) and scanning tunneling microscopy (STM) measurements of *capped* dots has predicted that a more realistic dot geometry and composition is a lens-shaped  $\text{In}_x\text{Ga}_{1-x}$  As quantum dot. In the section “Lens-Shaped Dots: The Effect of Changing the Shape and Composition Profile,” we present results of calculations for the energy states, excitonic band gaps, and Coulomb matrix elements in lens-shaped  $\text{In}_x\text{Ga}_{1-x}$  As quantum dots. These calculations were used in combination with a range of measured properties to help to determine both the geometry and composition of these quantum dots.

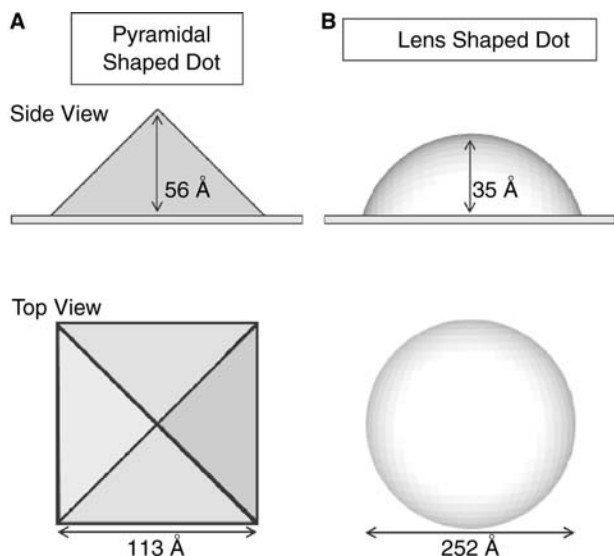


**Fig. 2** The assumed geometry of the (A) pyramidal and (B) lens-shaped dots described in the sections “Pyramidal Quantum Dots: Single-Particle Electron and Hole States” and “Lens-Shaped Dots: The Effect of Changing the Shape and Composition Profile.”

### Pyramidal Quantum Dots: Single-Particle Electron and Hole States

The EPM techniques described in the section “Description of Pseudopotential Techniques” have been applied to the study of pyramidal self-assembled quantum dots in several publications.<sup>[17–19]</sup> The assumed pyramidal geometry is illustrated in Fig. 2A. in Fig. 3 we schematically show the single-particle energy levels that are typically calculated. The five lowest energy electron states are labeled in increasing energy from  $e_0$  to  $e_4$  and the three highest energy hole states are labeled in order of decreasing energy from  $h_0$  to  $h_2$ . The single-particle wavefunctions corresponding to each of these electron and hole states are illustrated in Fig. 4. Fig. 4 shows only the square of the envelope function,  $f(\mathbf{r})$ , for each of the single-particle states,  $i$ , defined as

$$f^i(\mathbf{r}) = \sum_{\mathbf{k}} c_{n,\mathbf{k}}^i e^{i\mathbf{k}\cdot\mathbf{r}} \quad (15)$$

where the  $c_{n,\mathbf{k}}^i$  are the coefficients of the  $i$ th single-particle wavefunction,  $\psi_i(\mathbf{r})$ , when expanded in a basis of bulk Bloch orbitals representing a large number of bands,  $N$ , at the Brillouin zone center ( $\Gamma$  point),

$$\psi_i(\mathbf{r}) = \sum_{n=1}^N \sum_{\mathbf{k}} c_{n,\mathbf{k}}^i u_{n,\Gamma}(\mathbf{r}) e^{i\mathbf{k}\cdot\mathbf{r}} \quad (16)$$

The expansion coefficients,  $c_{n,\mathbf{k}}^i$ , are obtained by projecting each of the calculated single-particle states onto this zone center basis,

$$c_{n,\mathbf{k}}^i = \langle \psi_i(\mathbf{r}) | u_{n,\Gamma}(\mathbf{r}) e^{i\mathbf{k}\cdot\mathbf{r}} \rangle \quad (17)$$

Plotting the envelope function squared,  $f(\mathbf{r})^2$ , instead of the wavefunction squared,  $\psi_i(\mathbf{r})^2$ , has the effect of averaging out the atomic-scale oscillations in the wavefunction, purely for graphical purposes. In all our calculations, the atomistic structure of the EPM technique automatically includes both the envelope,  $f(\mathbf{r})$ , and atomistic,  $u_{n,\Gamma}(\mathbf{r})$ , contributions to the wavefunctions. A useful intuitive guide to interpreting the single-particle electron states is to consider the eigenstates of the  $\hat{L}_z$  operator.<sup>[3]</sup> The first six bound electron states corresponding to  $l_z = 0, \pm 1$ , and  $\pm 2$ . The first state  $e_0$ , has  $l_z = 0$  and is commonly described as *s*-like as it has no nodes. The  $e_1$  and  $e_2$  states have  $l_z = \pm 1$ , and are *p*-like with nodal planes (110) and ( $\bar{1}10$ ). The  $e_3, e_4$ , and  $e_5$  states have  $l_z = \pm 2$  and 0, respectively, and are commonly described as  $d_{x^2 - y^2}$ ,  $d_{xy}$ , and  $2s$ , respectively. Obviously, the square base of the pyramid reduces the symmetry of the dot from  $C_\infty$  to  $C_{4v}$ . In addition, the underlying zincblende atomistic structure further reduces the



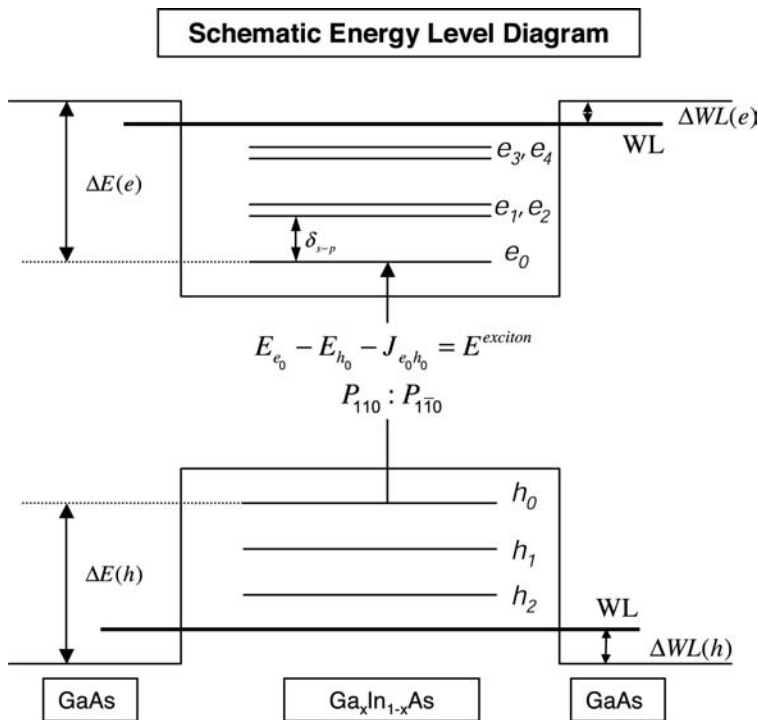


**Fig. 3** A schematic representation of the single-particle energy levels in a self-assembled quantum dot. The five lowest energy electron states are labeled in increasing energy from  $e_0$  to  $e_4$ , and the three highest energy hole states are labeled in order of decreasing energy from  $h_0$  to  $h_2$ . The electron and hole binding energies are labeled  $\Delta E(e, h)$ , and the wetting layer energies with respect to the GaAs VBM and CBM are labeled  $\Delta WL(h, e)$ .

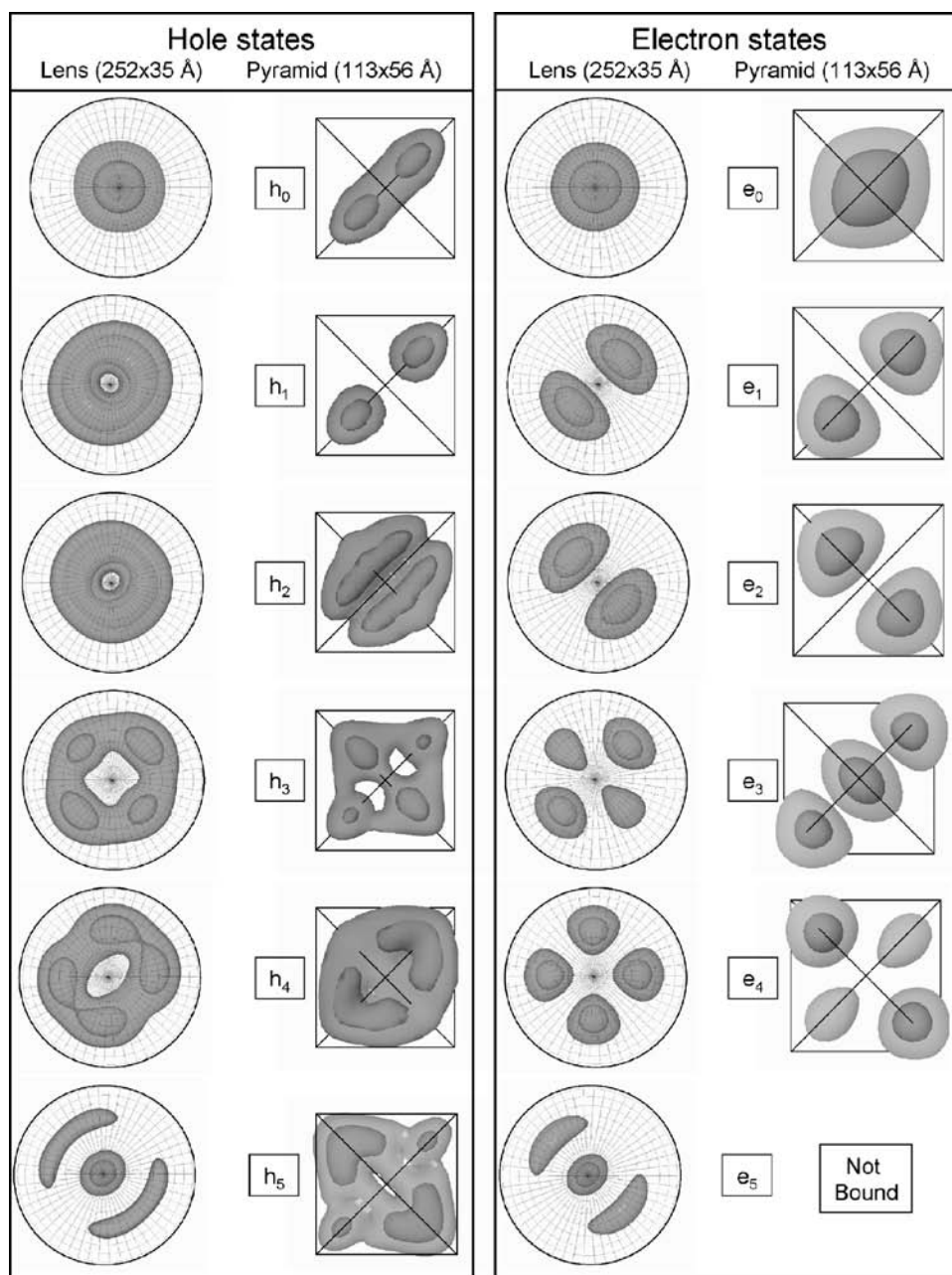
symmetry to  $C_{2v}$ . Hence, the  $e_0$  to  $e_5$  states correspond to the  $a_1, b_1, b_2, a_1, a_2,$  and  $a_1$  irreducible representations of the  $C_{2v}$  group, rather than eigenstates of  $\hat{L}_z$ . The alignment of the  $e_1$  and  $e_2p$ -states along the  $[110]$  and  $[1\bar{1}0]$  directions results from the underlying zincblende lattice structure. Note that this simple analysis neglects the effects of the spin-orbit interaction, which further reduces the symmetry from the  $C_{2v}$  group to a double group with the same single representation for all the states. In our calculations, the spin-orbit interaction is included, but it produces no significant effects for the electron states. For the pyramidal dot studied in Fig. 4, the small size of the dot ( $113 \text{ \AA}$  base) and the relatively light effective mass of electrons in InAs ( $0.023 m_0$ ) results in a large quantum confinement of the electron states which, in turn, pushes these states up in energy so that only the five states  $e_0$  to  $e_4$  are bound in the pyramidal dot. Here our definition of a bound electron (hole) state is that its energy is lower (higher) than the bulk GaAs CBM (VBM).

Fig. 4 also shows calculated envelope functions squared for the hole states in the pyramidal InAs/GaAs quantum dot. As there is a strong mixing between the original bulk Bloch states with  $\Gamma_{8v}$  and  $\Gamma_{7v}$  symmetry, the hole states cannot be interpreted as the solutions of a single-band Hamiltonian. The larger effective mass for holes results in a reduced quantum confinement of the hole states and consequently, many more bound hole states. Only the six bound hole states with the highest energy are shown in Fig. 4.

In Fig. 5, we show how the energy of the lowest 4 electron states and highest 4 hole states in a pyramidal InAs quantum dot depends on the size of the dot. It shows that, as the size of the dot increases, the quantum confinement of the electrons and holes in the dot is reduced and therefore the electron levels decrease in energy and the hole levels increase in energy. Reducing the quantum confinement by increasing the size of the dots also acts to increase the number of bound states in the dot. For example, the  $e_3$  state is bound for dots with a base size greater than  $90 \text{ \AA}$ , but is higher than the wetting layer energy for dots with a base less than  $90 \text{ \AA}$ , and is therefore effectively unbound. It is interesting to compare these results with earlier calculations by: 1) Grundman, Stier, and Bimberg<sup>[20]</sup> and Cusak, Briddon, and Jaros<sup>[21]</sup> who applied single band effective techniques to pyramidal InAs dots with base sizes ranging from  $60$  to  $160 \text{ \AA}$  and found only a single bound state; and 2) eight-band  $\mathbf{k}\cdot\mathbf{p}$  calculations by Jiang and Singh<sup>[22]</sup> and Pryor,<sup>[23]</sup> who found three bound electron states over a similar range of sizes. Therefore we conclude that obtaining even qualitative estimates for the quantum confinement energies in these systems requires a multiband technique of at least eight bands.

### Lens-Shaped Dots: The Effect of Changing the Shape and Composition Profile

In the section “Pyramidal Quantum Dots: Single-Particle Electron and Hole States,” we discussed the



**Fig. 4** Top view of the calculated electron and hole wavefunctions squared for pyramidal and lens-shaped InAs quantum dots embedded in GaAs, with bases of 252 and 113 Å and heights of 25 and 56 Å. The grey and dark gray isosurfaces represent 20% and 60% of the maximum charge density, respectively.

single-particle electron and hole states in an idealized, pure InAs, pyramidal quantum dot. Recently, considerable evidence has emerged that, in fact, a more realistic geometry for self-assembled InAs/GaAs quantum dots is that of a lens-shaped dot<sup>[24–31]</sup> (see Fig. 2B). In addition to modifying the predicted shape of self-assembled quantum dots, recent measurements<sup>[32–35]</sup> also indicate that the composition of these dots differs from the pure InAs that was originally assumed. In Table 1, we show the results

of calculations for a pure InAs, lens-shaped quantum dot, with a base of 252 Å and a height of 35 Å, embedded within GaAs [column (a)]. Table 1 also shows the experimentally measured of the electron levels, the electron–electron splittings and electron–hole Coulomb energies, the magnetic field dependence, and the excitonic band gap measured in Refs.<sup>[26]</sup> and<sup>[30]</sup>. The agreement between the measured energy level spacings, Coulomb energies and magnetic field response with our theoretical lens-shaped model is

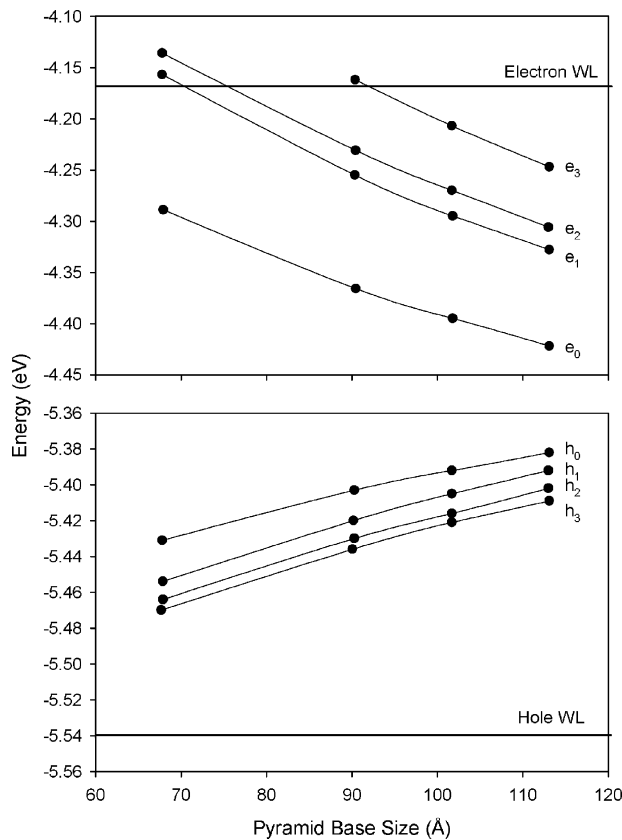


**Fig. 5** The dependence of the energy of the four lowest electron states and four highest hole states on the base size of a pyramidal InAs quantum dot. The horizontal lines show the energy of the groundstate electron and hole energies in a 1-ML-thick InAs WL.

generally good. Both the model and experiment find: 1) a large spacing,  $\delta_{sp}$  ( $\sim 50$ – $60$  meV), between the  $s$ -like  $e_0$  state and the  $p$ -like  $e_1$  state; 2) a small spacing,  $\delta_{pp}$  ( $\sim 3$  meV), between the two  $p$ -like  $e_1$  and  $e_2$  states; and 3) a large spacing ( $\sim 55$  meV) between the  $p$ -like  $e_2$  state and the  $d$ -like  $e_3$  state.

These electron level spacings are similar to those found for pyramidal quantum dots<sup>[18]</sup> [see Table 1, column (g)]. However, because of the lower pyramidal symmetry, the spacings of the two  $p$ -like and  $d$ -like states,  $\delta_{pp}$  and  $\delta_{dd}$ , are larger (26 and 23 meV, respectively). Both the model and experiment also find similar values for the Coulomb energies,  $J(e_0e_0)$  and  $J(e_0h_0)$  ( $\sim 25$  meV).

The calculated hole binding energy of  $\Delta E(h) = 193$  meV is in good agreement with those of Berryman, Lyon, and Segev<sup>[36]</sup> ( $\sim 240$  meV) and Itskevich et al.<sup>[37]</sup> ( $\sim 250$  meV). The calculated electron–electron and electron–hole Coulomb energies are in reasonable agreement with those extracted from Refs.<sup>[26]</sup> and<sup>[30]</sup>. For the integrals  $J_{e_0e_0}^{ee}$ ,  $J_{e_0e_1}^{ee}$ ,  $J_{e_1e_1}^{ee}$ , and  $J_{e_0h_0}^{eh}$ , we calculate values of 31, 25, 25, and 37,

respectively, compared to measured values of 23, 24, 18, and 33.3 meV. The calculated ratios of absorption intensities for light polarized along  $[110]$  and  $[\bar{1}\bar{1}0]$  directions, defined as

$$\lambda = \frac{P_{[110]}}{P_{[\bar{1}\bar{1}0]}} = \frac{\langle \psi_{e_0} | r_{[110]} | \psi_{h_0} \rangle^2}{\langle \psi_{e_0} | r_{[\bar{1}\bar{1}0]} | \psi_{h_0} \rangle^2} \quad (18)$$

are  $\lambda = 1.03$  and 1.2, respectively, for the  $e_0 - h_0$  recombination in lens and pyramidal shaped, pure InAs dots.

In the lens-shaped dot, we find a difference in the average positions of the  $h_0$  and  $e_0$  states,  $d_{h_i, e_j}$ , of around 1 Å. This is smaller than the value that we calculated for a pyramidal quantum dot, where we find the hole approximately 3.1 Å higher than the electron.

In summary, the assumed lens-shaped geometry with a pure InAs composition produces a good agreement with measured level splitting, Coulomb energies, and magnetic field dependence. Detailed inspection of the remaining differences reveals that the calculations systematically *overestimate* the splittings between the single-particle electron levels ( $\delta_{sp}$ : 65 vs. 50 meV,  $\delta_{pd}$ : 68 vs. 48 meV) and *underestimate* the excitonic band gap (1032 vs. 1098 meV).

### Pure InAs dots: The effects of lens shape and size

Focusing only on the lens shape, we examine the effect of changing the height and base of the assumed geometry. Calculations were performed on similar lens-shaped, pure InAs dots where 1) the base of the dot was increased from 252 to 275 Å, while keeping the height fixed at 35 Å, [column (b)] and 2) the height of the dot was decreased from 35 to 25 Å, while keeping the base fixed at 252 Å, [column (c)]. These show that decreasing the height of the dot increases the quantum confinement and hence increases the splittings of the electron and hole levels ( $\delta_{sp}$ : from 65 to 69 meV and  $\delta_{h_0, h_1}$ : from 8 to 16 meV). Decreasing the height of the dot also acts to increase the excitonic band gap from 1032 to 1131 meV by pushing up the energy of the electron levels and pushing down the hole levels. Conversely, increasing the base of the dot decreases both the splittings of the single-particle levels ( $\delta_{sp}$ : from 66 to 61 meV) and the band gap (1032–1016 eV). These small changes in the geometry of the lens-shaped dot have only a small effect on electronic properties that depend on the shape of the wavefunctions. The electron–electron and electron–hole Coulomb energies remain relatively unchanged, the magnetic field induced splitting remain at 20 meV, the polarization anisotropy ( $\lambda$ ) remains close to 1.0, and the excitonic dipole,  $d_{h_i, e_j}$ , remains negligible. In summary, reducing either the height or the base of the

**Table 1** Calculated single particle electron and hole energy level spacings, electron and hole binding energies,  $\Delta E(e,h)$ , electron–electron and electron–hole Coulomb energies, excitonic band gap (all in meV), exciton dipole moment and polarization anisotropy for lens-shaped and pyramidal  $\text{Ga}_x\text{In}_{1-x}\text{As}$  quantum dots embedded within GaAs

Geometry (Å)	Lens calculations						Pyramid calculation	Lens experiment <sup>[26,30]</sup>
	(a)	(b)	(c)	(d)	(e)	(f)	(g)	
	$252 \times 35$	$275 \times 35$	$252 \times 25$	$252 \times 35$	$252 \times 35$	$275 \times 35$	$200 \times 100$	
% Ga at base, tip	0, 0	0, 0	0, 0	15, 15	30, 0	15, 15	0, 0	
$e_1 - e_0$	65	57	69	58	64	52	108	50
$e_3 - e_2$	68	61	67	60	63	57	64	48
$e_2 - e_1$	2	2	2	2	3	2	26	2
$e_2 - e_1$ (15 T)	20	20	18	21	20	17		19
$e_4 - e_3$	4	3	4	4	3	1	23	
$h_0 - h_1$	8	12	16	13	14	11	15	
$h_1 - h_2$	7	6	5	5	6	5	20	
$h_2 - h_3$	6	10	14	13	14	9	1	
$\Delta E(e)$	271	258	251	209	192	204	171	
$\Delta E(h)$	193	186	174	199	203	201	198	
$J_{e_0e_0}$	31	29	32	29	31	28	40	23
$J_{e_0e_1}$	25	24	26	24	24	24	35	24
$J_{e_1e_1}$	25	24	26	25	24	26	36	~18
$J_{h_0h_0}$	30	27	39	32	28	30	31	
$J_{e_0h_0}$	30	28	35	31	29	29	31	33.3
$E_{\text{gap}}$	1032	1016	1131	1080	1125	1083	1127	1098
$d_{e_0,h_0}$ (Å)	0.16	-0.37	0.5	0.5	1.2	0.5	3.1	
$\lambda = P_{110} : P_{\bar{1}\bar{1}0}$	1.03	1.01	1.04	1.05	1.08	1.08	1.20	

dot increases quantum confinement effects and hence increases energy spacings and band gaps, while not significantly effecting the shape of the wavefunctions.

### Interdiffused In(Ga)As/GaAs lens-shaped dots

We next investigate the effect of changing the composition of the quantum dots, while keeping the geometry fixed. Recently, there have been several experiments<sup>[33,34,38]</sup> suggesting that a significant amount of Ga diffuses into the nominally pure InAs quantum dots during the growth process. We investigate two possible mechanisms for this Ga in-diffusion: 1) Ga diffuses into the dots during the growth process from all directions producing a dot with a uniform Ga composition  $\text{Ga}_x\text{In}_{1-x}\text{As}$ ; and 2) Ga diffuses up from the substrate, as suggested in Ref.<sup>[38]</sup>. To investigate the effects of these two methods of Ga in-diffusion on the electronic structure of the dots, we compare pure InAs dots embedded in GaAs with  $\text{Ga}_x\text{In}_{1-x}\text{As}$ , random alloy dots embedded in GaAs, where the Ga composition,  $x$ , 1) is fixed at 0.15, [column (d)] and

2) varies linearly from 0.3 at the base to 0 at the top of the dot, [column (e)].

Table 1 shows that increasing the amount of Ga in the dots acts to decrease the electron level spacings ( $\delta_{\text{sp}}$ : from 65 to 58 for  $x = 0.15$ ). It also acts to increase the excitonic band gap from 1032 to 1080 and 1125 meV, respectively. The electron binding energy,  $\Delta E(e)$ , is decreased by the in diffusion of Ga (from 271 to 209 and 192 meV), while the hole binding energy,  $\Delta E(h)$ , is relatively unaffected. This significant decrease in the electron binding energy considerably improves the agreement with experiments on other dot geometries.<sup>[36,39]</sup>

As with changing the size of the dots, we find that Ga in-diffusion has only a small effect on properties that depend on the shape of the wavefunctions. The calculated electron–electron and electron–hole Coulomb energies are almost unchanged, while the average separation of the electron and hole,  $d_{h,e}$ , increases from 0.16 to 0.5 and 1.2 Å and the polarization ratio,  $\lambda$ , and magnetic field response are also unchanged.

Table 1 shows that the dominant contribution to the increase in the excitonic band gap and reduction in

electron binding energy, results mostly from an increase in the energy of the *electron* levels as the Ga composition is increased. This can be understood by considering the electronic properties of the bulk  $\text{Ga}_x\text{In}_{1-x}\text{As}$  random alloy. The unstrained valence band offset between GaAs and InAs is  $\sim 50$  meV,<sup>[40]</sup> while the conduction band offset is  $\sim 1100$  meV and hence changing the Ga composition,  $x$ , has a large effect on the energy of the electron states and only a small effect on the hole states.

In summary, the effect of Ga in-diffusion is to reduce the spacing of the electron levels while significantly increasing their energy and hence increasing the band gap. We find that only the average Ga composition in the dots is important to their electronic properties. Whether this Ga is uniformly or linearly distributed throughout the dots has a negligible effect.

The effects of changing the *geometry* of the lens-shaped, pure InAs dots on the single-particle energy levels can be qualitatively understood from single-band, effective mass arguments. These predict that decreasing any dimension of the dot increases the quantum confinement and hence, the energy level spacings and the single-particle band gap will increase. Note that as the dominant quantum confinement in these systems arises from the vertical confinement of the electron and hole wavefunctions, changing the height has a stronger effect on the energy levels than changing the base. In this case, decreasing the height by 10 Å has a much stronger effect on the energy spacings and on the band gap than increasing the base by 23 Å.

As increasing (decreasing) the dimensions of the dot acts to decrease (increase) both the level spacings and the gap, it is clear that changing the dot geometry alone will not significantly improve the agreement with experiment as this requires a simultaneous *decrease* in the energy level splittings and *increase* in the band gap. However, Ga in-diffusion into the dots acts to *increase* the band gap of the dot while decreasing the energy level spacings. Table 1 shows that adopting a geometry with a base of 275 Å and a height of 35 Å and a uniform Ga composition of  $\text{Ga}_{0.15}\text{In}_{0.85}\text{As}$  produces the best fit to the measurements in Refs.<sup>[26]</sup> and<sup>[30]</sup>.

## CONCLUSION

In conclusion, we believe we have successfully demonstrated that modern empirical pseudopotential techniques, coupled with atomistic strain calculations, provide a powerful technique for calculating the electronic structure of semiconductor nanostructures containing several million atoms.

Our results strongly suggest that to obtain accurate agreement between theoretical models and

experimental measurements for standard lens-shaped quantum dots, one needs to adopt a model of the quantum dot that includes some Ga in-diffusion within the quantum dot. When 15% Ga in-diffusion is included, we obtain an excellent agreement between state-of-the-art multiband pseudopotential calculations and experiments for a wide range of electronic properties. We are able to fit/predict most observable properties to an accuracy of  $\pm 5$  meV, which is sufficient to make predictions of both the geometry and composition of the dot samples.

The techniques described above have recently been extended to describing the decay of multiple excitons in semiconductor quantum dots. For more details, see Refs.<sup>[9]</sup> and<sup>[41]</sup>.

## ACKNOWLEDGMENTS

The author would like to thank Alex Zunger, Lin-Wang Wang, Andrew Canning, Alberto Franceschetti, and John Shumway for collaborations on the above projects. The work performed by the author at the National Renewable Energy Laboratory was supported by the Department of Energy Basic Energy Sciences, Division of Materials Science under contract No. DE-AC36-98-GO10337. The work performed by the author at Lawrence Livermore National Laboratory was performed under the auspices of the DOE by the University of California, Lawrence Livermore National Laboratory under contract No. W-7405-Eng-48.

## REFERENCES

1. Yoffe, A. Low-dimensional systems: quantum size effects and electronic properties of semiconductor microcrystallites (zero-dimensional systems) and some quasi-two-dimensional systems. *Adv. Phys.* **2002**, *51*, 799.
2. Bimberg, D.; Grundmann, M.; Ledentsov, N. *Quantum Dot Heterostructures*; Wiley: Chichester, 1998.
3. Jacak, L.; Hawrylak, P.; Wojs, A. *Quantum Dots*; Springer: Berlin, 1998.
4. Wang, L.; Williamson, A.; Zunger, A.; Jiang, H.; Singh, J. Comparison of the kp and direct diagonalization approaches to the electronic structure of InAs/GaAs quantum dots. *Appl. Phys. Lett.* **2000**, *76*, 339.
5. Keating, P. Effect of invariance requirements on the elastic strain energy of crystals with application to the diamond structure. *Phys. Rev.* **1966**, *145*, 637.
6. Pryor, C.; Kim, J.; Wang, L.; Williamson, A.; Zunger, A. Comparison of two methods for describing the strain profiles in quantum dots. *J. Appl. Phys.* **1998**, *83*, 2548.
7. Martin, R. Elastic properties of zns structure semiconductors. *Phys. Rev.*, **B 1970**, *1*, 4005.
8. Williamson, A. *Energy States in Quantum Dots*; World Scientific: Singapore, 2002, Chapter 1.



9. Williamson, A.; Grossman, J.; Hood, R.; Puzder, A.; Galli, G. Quantum Monte Carlo calculations of nanostructure optical properties: application to silicon quantum dots. *Rev. Rev. Lett.* **2002**, *89*, 196803.
10. Wang, L.; Zunger, A. *Semiconductor Nanoclusters*; Elsevier Science: Amsterdam, 1996.
11. Wang, L.W.; Zunger, A. Solving Schrodingers equation around a desired energy-application to silicon quantum dots. *J. Phys. Chem.* **1994**, *100*, 2394.
12. Canning, A.; Wang, L.W.; Williamson, A.; Zunger, A. Parallel empirical pseudopotential electronic structure calculations for million atom systems. *J. Comp. Physiol.* **2000**, *160*, 29.
13. Wang, L.; Franceschetti, A.; Zunger, A. Million-atom pseudopotential calculation of gamma-x mixing in GaAs/AlAs superlattices and quantum dots. *Phys. Rev. Lett.* **1997**, *78*, 2819.
14. Wang, L.-W.; Zunger, A. Linear combination of bulk bands method for large-scale electronic structure calculations on strained nanostructures. *Phys. Rev., B* **1999**, *59*, 15,806.
15. Franceschetti, A.; Williamson, A.; Zunger, A. Addition spectra of quantum dots: the role of dielectric mismatch. *J. Phys. Chem.* **2000**, *104*, 3398.
16. Franceschetti, A.; Zunger, A. Direct pseudopotential calculation of exciton coulomb and exchange energies in semiconductor quantum dots. *Phys. Rev. Lett.* **1997**, *78*, 915.
17. Williamson, A.; Zunger, A. Effect of interfacial states on the binding energies of electrons and holes in InAs/GaAs quantum dots. *Phys. Rev., B* **1998**, *58*, 6724.
18. Kim, J.; Wang, L.; Zunger, A. Comparison of the electronic structure of InAs/GaAs pyramidal quantum dots with different facet orientations. *Phys. Rev., B* **1998**, *57*, R9408.
19. Wang, L.; Kim, J.; Zunger, A. Electronic structures of [110]-faceted self-assembled pyramidal InAs/GaAs quantum dots. *Phys. Rev., B* **1999**, *59*, 5678.
20. Grundmann, M.; Stier, O.; Bimberg, D. InAs/GaAs pyramidal quantum dots: strain distribution, optical phonons, electronic structure. *Phys. Rev., B* **1995**, *52*, 11,969.
21. Cusak, M.; Briddon, P.; Jaros, M. Electronic structure of InAs/GaAs self-assembled quantum dots. *Phys. Rev., B* **1996**, *54*, 2300.
22. Jiang, H.; Singh, J. Conduction band spectra in self-assembled InAs/GaAs dots: a comparison of effective mass and an eight-band approach. *Appl. Phys. Lett.* **1997**, *71*, 3239.
23. Pryor, C. Eight-band calculations of strained InAs/GaAs quantum dots compared with one-, four-, six-band approximations. *Phys. Rev., B* **1998**, *57*, 7190.
24. Drexler, H.; Leonard, D.; Hansen, W.; Kotthaus, J.; Petroff, P. Spectroscopy of quantum levels in charge-tunable InGaAs quantum dots. *Phys. Rev. Lett.* **1994**, *73*, 2252.
25. Medeiros-Ribeiro, G.; Leonard, D.; Petroff, P. Electron and hole energy levels in InAs self-assembled quantum dots. *Appl. Phys. Lett.* **1995**, *66*, 1767.
26. Fricke, M.; Lorke, A.; Kotthaus, J.; Medeiros-Ribeiro, G.; Petroff, P. Shell structure and electron-electron interaction in self-assembled InAs quantum dots. *Europhys. Lett.* **1996**, *36*, 197.
27. Miller, B. Few-electron ground states of charge-tunable self-assembled quantum dots. *Phys. Rev., B* **1997**, *56*, 6764.
28. Warburton, R.; Durr, C.; Karraill, K.; Kotthaus, J.; Medeiros-Ribeiro, G.; Petroff, P. Charged excitons in self-assembled semiconductor quantum dots. *Phys. Rev. Lett.* **1997**, *79*, 5282.
29. Schmidt, K.; Medeiros-Ribeiro, G.; Garcia, J.; Petroff, P. Size quantization effects in InAs self-assembled quantum dots. *Appl. Phys. Lett.* **1997**, *70*, 1727.
30. Warburton, R.; Miller, B.; Durr, C.; Bodefeld, C.; Karrai, K.; Kotthaus, J.; Medeiros-Ribeiro, G.; Petroff, P.; Huant, S. Coulomb interactions in small charge-tunable quantum dots: a simple model. *Phys. Rev., B* **1998**, *58*, 16,221.
31. Schmidt, K.; Medeiros-Ribeiro, G.; Petroff, P. Photoluminescence of charged InAs self-assembled quantum dots. *Phys. Rev., B* **1998**, *58*, 3597.
32. Yang, W.; Lee, H.; Johnson, J.; Sercel, P.; Norman, A. Electronic structure of self-organized InAs/GaAs quantum dots bounded by (136) facets. *Phys. Rev., B* **2000**, *64*, 2784.
33. Metzger, T.; Kegel, I.; Paniago, R.; Peisl, J. Grazing incidence x-ray scattering: an ideal tool to study the structure of quantum dots. *J. Phys., D, Appl. Phys.* **1999**, *32*, A202.
34. Garcia, J.; Medeiros-Ribeiro, G.; Schmidt, K.; Ngo, T.; Feng, J.; Lorke, A.; Kotthaus, J.; Petroff, P. Intermixing and shape changes during the formation of InAs self-assembled quantum dots. *Appl. Phys. Lett.* **1997**, *71*, 2014.
35. Rubin, M.; Medeiros-Ribeiro, G.; O'Shea, J.; Chin, M.; Lee, E.; Petroff, P.; Narayanamurti, V. Imaging and spectroscopy of single InAs self-assembled quantum dots using ballistic electron emission microscopy. *Phys. Rev. Lett.* **1996**, *77*, 5268.
36. Berryman, K.; Lyon, S.; Segev, M. Electronic structure and optical behavior of self-assembled InAs quantum dots. *J. Vac. Sci. Technol., B* **1997**, *15* (4), 1045.
37. Itskevich, I.; Skolnick, M.; Mowbray, D.; Trojan, I.; Lyapin, S.; Wilson, L.; Steer, M.; Hopkinson, M.; Eaves, L.; Main, P. Excited states and selection rules in self-assembled InAs/GaAs quantum dots. *Phys. Rev., B* **1999**, *60*, R2185.
38. Fry, P.; Itskevich, I.; Mowbray, D.; Skolnick, M.; Finley, J.; Barker, J.; O'Reilly, E.; Wilson, L.; Larkin, I.; Maksym, P.; Hopkinson, M.; Al-Khafaji, M.; David, J.; Cullis, A.; Hill, G.; Clark, J. Inverted electron-hole alignment in InAs-GaAs self-assembled quantum dots. *Phys. Rev. Lett.* **2000**, *84*, 733.
39. Tang, Y.; Rich, D.; Mukhametzhonov, I.; Chen, P.; Hadhukar, A. Self-assembled InAs/GaAs quantum dots studied with excitation dependent cathodoluminescence. *J. Appl. Phys.* **1998**, *84*, 3342.
40. Wei, S.; Zunger, A. Calculated natural band offsets of all II-VI and III-V semiconductors: Chemical trends and the role of cation d orbitals. *Appl. Phys. Lett.* **1998**, *72*, 2011.
41. Williamson, A.; Franceschetti, A.; Zunger, A. Multi-excitons in self-assembled InAs/GaAs quantum dots: a pseudopotential, many-body approach. *Europhys. Lett.* **2001**, *53*, 59.



# Self-Assembled Silane Monolayers: Cyano-to-Carboxylic Termination Conversion

**Chandra Sekhar Palla**

*Department of Chemical Engineering, University of Delaware, Newark, Delaware, U.S.A.*

**Alexander Couzis**

*Department of Chemical Engineering, City College of City University of New York, New York, New York, U.S.A.*

## INTRODUCTION

In recent years, there has been an increasing interest in the study and development of molecularly thin films such as self-assembled monolayers (SAMs) and Langmuir–Blodgett (LB) films. SAMs provide a unique way of altering just the surface properties of a material, by modifying the terminal functional groups displayed on the surface without altering or affecting the bulk properties of the material. The ability to modify just the surface properties gives rise to several technological applications such as protective coatings,<sup>[1]</sup> lubrication layers,<sup>[2]</sup> membranes for chemical and biochemical sensors,<sup>[3–7]</sup> templates for crystal growth,<sup>[8]</sup> fabrication of nanoparticles,<sup>[9–12]</sup> micropatterning,<sup>[13,14]</sup> and molecularly thin transistors,<sup>[15]</sup> to name a few.

SAMs are molecular assemblies that are formed by spontaneous adsorption of surfactant molecules (amphiphiles), present either in solution or vapor phase, onto the surface of an appropriate substrate. The three classical types of SAMs are: 1) silanes on hydroxylated surfaces;<sup>[16–23]</sup> 2) alkanethiols on gold, copper, or silver surfaces;<sup>[1,18,24–27]</sup> and 3) long-chain carboxylic acids on aluminum oxide surfaces.<sup>[28–30]</sup> The quality of the SAM depends on the head group, the hydrocarbon chain length,<sup>[1,20,31,32]</sup> the terminal functional group, the solvent used,<sup>[33]</sup> the amount of water present in the solvent<sup>[17]</sup> (specifically for silane SAMs), and the preparation temperature.<sup>[21,32,34,35]</sup>

In this entry, we present the results of the modification of the CN terminal functional group of 11-cyanoundecyltrimetjoxysilane (CUTMS) monolayer to the COOH terminal group by a simple hydrolysis reaction. SAMs with a COOH terminal group are technologically interesting, as the ionization state of these groups is sensitive to the pH of the surrounding environment.<sup>[25,26]</sup> By varying the pH of the surface, the terminal groups are transformed from all COOH (at low pH) to all COO<sup>−</sup> (at high pH), or a mixture of COOH and COO<sup>−</sup> (at intermediate pH values).

By controlling the pH, the ratio of the number densities of the COOH group to the COO<sup>−</sup> groups is controlled, which in turn determines the local structure and arrangement of the surface groups. Thus in an indirect way, the structure and arrangement of the COOH and COO<sup>−</sup> groups on the surface are fine-tuned by just controlling the pH of the system. We also demonstrate this interconvertibility of COOH ↔ COO<sup>−</sup> by controlling the pH using both modified CUTMS monolayer and LB film of stearic acid. From quantitative analyses of the infrared spectra of COOH and COO<sup>−</sup> groups, the number densities of these groups present on the surface have been independently determined. This also provides a tool to determine the extent of reaction or conversion of the cyano groups to carboxyl groups.

## FORMATION AND REACTIVITY OF SAMs

The structure and properties of organized thin films have been widely studied. These efforts have focused on understanding the formation mechanism and structural features of these films. Various techniques have been employed such as contact angle measurements,<sup>[24,25]</sup> Fourier transform infrared spectroscopy (FTIR),<sup>[1,26,31,36]</sup> ellipsometry,<sup>[37–40]</sup> X-ray reflectivity,<sup>[41]</sup> X-ray photoelectron spectroscopy (XPS),<sup>[41–45]</sup> and scanning probe microscopy.<sup>[17,34,35,46]</sup>

Researchers now agree that SAMs with long hydrocarbon chains form ordered and densely packed structures, with the methylene groups of the hydrocarbon chain aligned, for the most part, in an all-trans conformation.<sup>[1,31]</sup> It has been also observed that the crystallinity in the structure of the monolayer formed increases with increasing hydrocarbon chain length. It is believed that this increased crystallinity (or packing density) in the structure of the monolayer is a result of the energetically favorable, weak, intermolecular chain–chain interactions. Whereas, it has been observed

that short-chain molecules form disorder structures because of the increase of gauche conformations resulting from decreasing van der Waals interactions between the shorter chains.<sup>[1,31]</sup> Chain length also affects the mechanism of formation of these monolayers.

Iimura, Nakajima, and Kato<sup>[31]</sup> have studied SAMs of trichlorosilanes of varying hydrocarbon chain lengths using FTIR as a function of temperature. In their studies, they found that the silanes with a chain length of 16 methylene groups or less always existed in liquid state (disordered state) for all the temperatures above 0°C. They have attributed that the temperature at which the monolayers were prepared was above the critical phase transition temperature. In analogy with three-dimensional matter, the monolayer existed as crystalline (solid state) for temperatures below the critical transition temperature and existed as disordered liquid state for temperatures above the transition temperature. Independently, Jennings et al.<sup>[1]</sup> in their studies with SAMs of alkanethiols on gold, have noticed that the disorder in the structure increased with a decrease in hydrocarbon chain length, when prepared at the same temperature. As a result, SAMs of long-chain alkyl silanes are formed via a solid–gas phase transition process on the surface, whereas short-chain alkyl silanes form uniform, liquidlike films.<sup>[20]</sup>

When compared with siloxane-based SAMs, alkanethiol SAMs on gold surfaces are widely studied because of the ease by which they can be prepared.<sup>[24–27]</sup> Thiol monolayers are formed via the covalent linkage between the surface gold atom and the sulfur atom of the alkanethiol molecule.<sup>[24–27]</sup> Because of the lack of reactivity between the various terminal functional groups and the sulfur surface binding group, alkanethiol surfactants with different terminal functionalized groups can be prepared a priori to the adsorption process and monolayer formation, thus making it convenient to prepare thiol-based monolayers with varying functionalized groups. Thiol-based monolayers can also be modified by simple synthetic approaches. Several researchers have successfully converted thiols of one functional group to another.<sup>[47,48]</sup> However, these thiol-based SAMs are relatively fragile both thermally and chemically, which restricts the conditions that can be employed for subsequent surface modification.<sup>[49–51]</sup>

Contrary to thiol-based SAMs, silane-based SAMs are thermally and chemically robust. Silane-based SAMs are thermally stable even at temperatures approaching 600 K in an inert nitrogen environment.<sup>[52,53]</sup> However, because of the high reactivity of the electrophilic trifunctional silane group, the functional groups that can be incorporated on silane SAMs are restricted. Because of this limitation, several useful functional groups such as alcohols, carboxylic acids, amines, amides, thiols, phosphines, enamines, enol

ethers, etc. must either be protected in non-nucleophilic form, or introduced subsequent to the monolayer assembly. In addition to this, any functional group present on the alkyl tether must be sterically small enough to allow a close-packed, well-ordered SAM to form on a hydroxylated surface.

Because of the reasons mentioned above, several researchers have been investigating ways of modifying silane-based SAMs to form monolayers of various terminal functional groups. Lee et al.<sup>[54]</sup> Balachander and Sukenik,<sup>[55]</sup> Barness et al.<sup>[56]</sup> Collins and Sukenik,<sup>[57]</sup> and Grisar et al.<sup>[58]</sup> have successfully demonstrated the transformation of Br, CN, SCN, and SCOC<sub>2</sub>H<sub>5</sub> functionalities to N<sub>3</sub>, NH<sub>2</sub>, SH, SO<sub>3</sub>H, SCH<sub>2</sub>CH<sub>2</sub>, and SO<sub>2</sub>CH<sub>2</sub>CH<sub>2</sub> by nucleophilic substitution using various reagents and reacting conditions. Fryxell et al.<sup>[59]</sup> have shown *N,N*-dimethylethylenediamine (DMED) amidation, hydroxylamine amidation, and hydrazine amidation by nucleophilic displacement. Koloski et al.<sup>[60]</sup> have demonstrated nucleophilic displacement reactions on benzyl halide SAMs. Kakkar et al.<sup>[61]</sup> and Yam, Tong, and Kakkar<sup>[62]</sup> have used a simple acid–base hydrolytic chemistry approach to form SAMs of long-chain alcohols terminated with alkyl, phenyl, and acetylene groups. Kim et al.<sup>[63]</sup> have chemically modified SAMs of inert or hydrophobic nature to reactive or hydrophilic state by exposing the monolayers to soft X-rays in air. Wade et al.<sup>[64]</sup> have converted hydroxyl-terminated SAMs to ester, or ether-terminated, by using low-energy collisions of polyatomic cations. Table 1 presents examples of various transformations reported in the literature and of reagents used.

## EXPERIMENTAL

### Materials

11-Cyanoundecyltrimethoxysilane (CUTMS) was purchased from United Chemical Technologies and octadecyltrichlorosilane (OTS; 95% purity) was obtained from Sigma Aldrich Co. Chloroform, toluene, and concentrated sulfuric acid were purchased from Fisher Scientific. Anhydrous grade hexadecane was purchased from Sigma Aldrich Co. Stearic acid was purchased from Fluka. Nochromix crystals used for cleaning purposes were obtained from Godax Laboratories. Silicon wafers used were obtained from Montco Silicon Technologies (Spring City, PA). The silicon wafers used in our experiments have a thickness of 450–500 μm, are double-sided polished, and of orientation (111). Silicon and germanium internal reflection elements [dimensions: 50 × 10 × 3 mm; orientation: (111)] used for infrared spectroscopy were obtained from Harrick Scientific Corp. All chemicals were used as purchased

**Table 1** In situ transformation of monolayers into different functional groups

Monolayer (silanes)	Reagent	In situ transformation
(CH <sub>2</sub> ) <sub>16</sub> Br	NaSCN	(CH <sub>2</sub> ) <sub>16</sub> SCN
(CH <sub>2</sub> ) <sub>16</sub> Br	NaN <sub>3</sub>	(CH <sub>2</sub> ) <sub>16</sub> N <sub>3</sub>
(CH <sub>2</sub> ) <sub>16</sub> SCN	LiAlH <sub>4</sub>	(CH <sub>2</sub> ) <sub>16</sub> SH
(CH <sub>2</sub> ) <sub>16</sub> SCOCH <sub>3</sub>		(CH <sub>2</sub> ) <sub>16</sub> SH
((CH <sub>2</sub> ) <sub>16</sub> S) <sub>2</sub>		(CH <sub>2</sub> ) <sub>16</sub> SH
(CH <sub>2</sub> ) <sub>16</sub> CN	LiAlH <sub>4</sub> or BH <sub>3</sub>	(CH <sub>2</sub> ) <sub>16</sub> NH <sub>2</sub>
(CH <sub>2</sub> ) <sub>16</sub> N <sub>3</sub>	LiAlH <sub>4</sub> or SnCl <sub>2</sub>	(CH <sub>2</sub> ) <sub>16</sub> NH <sub>2</sub>
(CH <sub>2</sub> ) <sub>16</sub> Br	Na <sub>2</sub> S	((CH <sub>2</sub> ) <sub>16</sub> ) <sub>2</sub> S
(CH <sub>2</sub> ) <sub>16</sub> Br	Na <sub>2</sub> S <sub>2</sub>	((CH <sub>2</sub> ) <sub>16</sub> S) <sub>2</sub>
((CH <sub>2</sub> ) <sub>16</sub> ) <sub>2</sub> S	H <sub>2</sub> O <sub>2</sub>	((CH <sub>2</sub> ) <sub>16</sub> ) <sub>2</sub> SO <sub>2</sub>
(CH <sub>2</sub> ) <sub>16</sub> SH		(CH <sub>2</sub> ) <sub>16</sub> SO <sub>3</sub> H
(CH <sub>2</sub> ) <sub>16</sub> SH	Br <sub>2</sub>	((CH <sub>2</sub> ) <sub>16</sub> S) <sub>2</sub>
(CH <sub>2</sub> ) <sub>16</sub> X	CH <sub>3</sub> COONa	(CH <sub>2</sub> ) <sub>16</sub> OH
(CH <sub>2</sub> ) <sub>16</sub> OH	CXH <sub>2</sub> COX	(CH <sub>2</sub> ) <sub>17</sub> COOX
(CH <sub>2</sub> ) <sub>16</sub> X	C <sub>6</sub> H <sub>4</sub> CH <sub>2</sub> XCH <sub>2</sub> X ( <i>α,α'</i> -dibromo- <i>p</i> -xylene)	(CH <sub>2</sub> ) <sub>16</sub> C <sub>6</sub> H <sub>4</sub> CH <sub>2</sub> X
(CH <sub>2</sub> ) <sub>16</sub> COOH	LiAlH <sub>4</sub> or BH <sub>3</sub>	(CH <sub>2</sub> ) <sub>16</sub> CH <sub>2</sub> OH
(CH <sub>2</sub> ) <sub>16</sub> CH <sub>2</sub> OH	RCOCl	(CH <sub>2</sub> ) <sub>16</sub> CH <sub>2</sub> OCOR
(CH <sub>2</sub> ) <sub>16</sub> COOH	PCl <sub>5</sub>	(CH <sub>2</sub> ) <sub>16</sub> COCl
(CH <sub>2</sub> ) <sub>16</sub> COCl	ROH	(CH <sub>2</sub> ) <sub>16</sub> COOR
(CH <sub>2</sub> ) <sub>16</sub> COCl	RNH <sub>2</sub>	(CH <sub>2</sub> ) <sub>16</sub> CONHR
-C <sub>6</sub> H <sub>4</sub> CH <sub>2</sub> X	Li-EDA	-C <sub>6</sub> H <sub>4</sub> CH <sub>2</sub> NHCH <sub>2</sub> CH <sub>2</sub> NH <sub>2</sub>
-C <sub>6</sub> H <sub>4</sub> CH <sub>2</sub> X	Li-PYR	-C <sub>6</sub> H <sub>4</sub> CH <sub>2</sub> C <sub>5</sub> H <sub>4</sub> N
(CH <sub>2</sub> ) <sub>16</sub> CH=CH <sub>2</sub>	HX (peroxide)	(CH <sub>2</sub> ) <sub>16</sub> CH <sub>2</sub> CH <sub>2</sub> X
(CH <sub>2</sub> ) <sub>16</sub> CH=CH <sub>2</sub>	KmnO <sub>4</sub> or HCO <sub>2</sub> OH	(CH <sub>2</sub> ) <sub>16</sub> CHOHCH <sub>2</sub> OH
(CH <sub>2</sub> ) <sub>16</sub> Br	<sup>-</sup> SCH <sub>2</sub> CHNH <sub>2</sub> COO <sup>-</sup>	(CH <sub>2</sub> ) <sub>16</sub> SCH <sub>2</sub> CHNH <sub>2</sub> COO <sup>-</sup>
((CH <sub>2</sub> ) <sub>16</sub> CO <sub>2</sub> CH <sub>2</sub> CF <sub>3</sub> ) <sub>2</sub>	NH <sub>2</sub> (CH <sub>2</sub> ) <sub>2</sub> N(CH <sub>3</sub> ) <sub>2</sub>	((CH <sub>2</sub> ) <sub>16</sub> CO) <sub>2</sub> N(CH <sub>2</sub> ) <sub>2</sub> N(CH <sub>3</sub> ) <sub>2</sub>
((CH <sub>2</sub> ) <sub>16</sub> CO <sub>2</sub> CH <sub>2</sub> CF <sub>3</sub> ) <sub>2</sub>	NH <sub>2</sub> OH	(CH <sub>2</sub> ) <sub>16</sub> CONHOOC(CH <sub>2</sub> ) <sub>16</sub>
((CH <sub>2</sub> ) <sub>16</sub> CO <sub>2</sub> CH <sub>2</sub> CF <sub>3</sub> ) <sub>2</sub>	NH <sub>2</sub> NH <sub>2</sub>	(CH <sub>2</sub> ) <sub>16</sub> CONHNHOC(CH <sub>2</sub> ) <sub>16</sub>

without any further purification. Deionized water with a resistivity of 18 MΩcm from a Millipore system was used in all our experiments.

### Cleaning Protocols

Silicon crystals were thoroughly cleaned before use. The crystals were first sonicated in a freshly prepared Nochromix solution for 30 min. The Nochromix solution was prepared by dissolving the Nochromix crystals in sulfuric acid and stirring the solution until it became clear. The Nochromix treatment was followed by rinsing with water and subsequent sonication in water for 30 min. Then the crystals were further cleaned using a plasma cleaner (model PDC-32G; Harrick Scientific Corp.). Plasma treatment was performed under an argon environment at low pressure. After the plasma treatment, the crystals were again

cleaned with Nochromix and deionized water. The same procedure was followed for silicon wafers, with the exception of plasma treatment.

### Monolayer Preparation

The cleaned substrates (crystals or wafer) were immersed in a solvent mixture of a known surfactant concentration for a fixed amount of time. After the end of the time period, the substrates were thoroughly rinsed with chloroform to remove physisorbed molecules from the substrate surface.

### CUTMS Monolayer Deposition

For CUTMS monolayers, the concentration of the CUTMS silane solution was maintained between

4 and 5 mM. Chloroform, toluene, and hexadecane were used as solvents. The deposition time was varied from minutes to days. A stable uniform monolayer formed after 24 hr.

### Modification of CUTMS Monolayer

The –CN terminal groups of the CUTMS monolayer prepared as mentioned above were transformed into –COOH groups by a simple hydrolysis reaction. The CUTMS monolayer was kept in a 50:50 (vol/vol) solution mixture of 15% hydrochloric acid and deionized water maintained at 75°C. Before modifying the CUTMS monolayer, the substrates were annealed at 150°C for about 2 hr. The monolayer was not stable for the abovementioned reaction conditions, unless it was annealed. The monolayer molecules desorbed if the substrate was kept for durations of more than 1.5 hr.

### OTS Monolayer Deposition

For the OTS monolayer, a mixture of hexadecane, carbon tetrachloride, and chloroform in the ratio of 30:5:3 by volume, respectively, was used in the OTS solution preparation. The substrate was immersed for 30 min in the above-prepared solution.

### LB Film of Stearic Acid

One hundred microliters of 1.34 mg/mL of a solution of stearic acid in chloroform was spread on a subphase (deionized Millipore water, 18 M $\Omega$ ) maintained at 20°C and at a pH of 2.0 (by adding HCl) in a KSV 2000 dual-compartment LB trough. The solution was allowed to stabilize for about 15 min for the chloroform to evaporate. The trough barriers compressed the surface until the surface pressure reached the desired value of 30 mN/m, at which time the transfer of the LB monolayer onto an OTS-coated (hydrophobic) silicon crystal was performed. At that surface pressure, before transferring, the stearic acid layer was allowed to stabilize for another 30 min to minimize any fluctuations. The transfer speed was maintained at 2.5 mm/min. The structure and orientation information of the transferred film was then obtained from IR measurements.

### Contact Angle Measurements

Contact angle goniometry was used to characterize the prepared monolayers. A 2- $\mu$ L drop of deionized water was placed on the sample surface and the contact angle

was measured within 2 min after the drop was placed to reduce errors caused by evaporation of water drop. The measurements were taken at different locations of the sample. All the values reported are an average of five to six measurements.

### Ellipsometry

The thickness information of the monolayer was obtained using a variable-angle null ellipsometer (Rudolph Instruments). A He–Ne laser beam, corresponding with a wavelength of 632.8 nm, is incident on the substrate. The thickness and refractive index of the monolayer are evaluated from the changes in polarization and the reflectivity of incident parallel and perpendicular polarized light beams. Principally, the ellipsometer is supposed to evaluate both the refractive index and the thickness of the thin film simultaneously, but because of instrument limitations in obtaining data for thin films, the refractive index of the film is assumed and the thickness is calculated. Organic films have a refractive index of approximately 1.46, and we have assumed this value as the refractive index for all our monolayers.

### IR Measurements

IR spectra were measured using a Bio-Rad FTS 175 spectrometer. Spectra were collected as interferograms with a resolution of 4 cm<sup>-1</sup> and Fourier-transformed with triangular apodization. Monolayer spectra were obtained by averaging attenuated total internal reflection (ATR) modes to 100–200 scans. Spectra of liquid samples were obtained in transmission mode using NaCl windows. For quantitative analysis, peaks were fitted with a Lorentzian function. The integrated absorbance value was the area under the appropriate peak. However, the readers have to be cautioned that the absorbance value (or peak area) is very sensitive to the type of fit used and baseline selection. For consistency in results, one has to maintain the same procedures throughout the quantitative analysis.

## RESULTS AND DISCUSSION

### Spectral Features

A typical spectrum of a CUTMS monolayer formed on a silicon substrate after a deposition time of 24 hr is shown in Fig. 1. Some of the important vibrational modes pertaining to methyl and methylene symmetric and asymmetric stretching modes are shown in Table 2. The asymmetric stretching mode of the

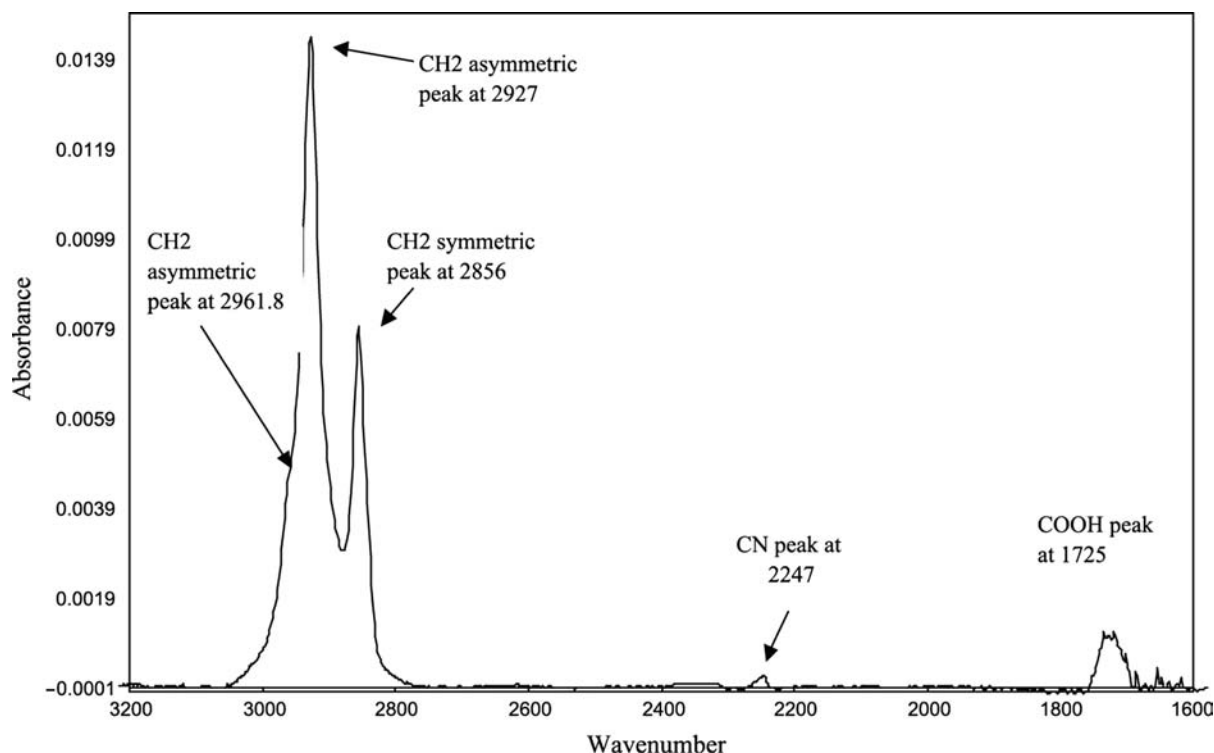


Fig. 1 Typical spectrum of CUTMS monolayer formed on a silicon crystal.

methylene group reveals a great deal of information on local molecular order and packing.<sup>[21,65]</sup> How this information is used to get the packing density and coverage is discussed later. The methylene asymmetric stretching modes for the CUTMS monolayer appear at  $\sim 2927\text{ cm}^{-1}$  and those of symmetric stretching modes appear at  $2856\text{ cm}^{-1}$ . These values correspond to a liquidlike structure. The spectrum was compared with the solution spectrum of CUTMS in anhydrous chloroform, obtained independently using NaCl windows in transmission mode. The details of the spectral features are shown in Table 2. The asymmetric and symmetric peaks of  $\text{CH}_2$  of the liquid spectrum match closely those of the CUTMS monolayer. Slight differences in the spectra of molecules at the surface and in the solution are attributed to the small degree of ordering as the molecules are being anchored to the substrate by one end.

**Table 2** Peak positions of important vibrations between CUTMS liquid and monolayer spectra

	$\text{CH}_2$ asymmetric	$\text{CH}_2$ symmetric	CN	COOH
Liquid CUTMS	2930	2857	2250	–
CUTMS monolayer	2927	2856	2248	1725

The difference in spectral values is not considerably different, indicating that the monolayer formed resembles a liquidlike structure.

### Formation and Structure of Silane SAMs

The formation of SAMs of silanes on silicon substrates is a three-step process. First, the trichloro or trimethoxy groups of silanes are hydrolyzed either in the solution, because of the presence of trace amounts of water in the solvent, or near the surface of the substrate, where a thin water film of two to three monolayers is present. The importance of the thin water film on the final structure and formation of the OTS monolayers was largely studied and reported.<sup>[19,22]</sup> Silberzan et al. have reported that for a good, uniform monolayer, a thin water film is necessary. Second, these hydrolyzed silanes react with surface hydroxyl groups and get chemically adsorbed on the surface. Finally, as the monomers adsorb on the surface because of weak van der Waals chain–chain interactions, the molecules order and arrange themselves. In the case of OTS molecules, where the packing density is considerably high, silanols of neighboring molecules form cross-links and a two-dimensional siloxane network. The ability of the molecules to pack depends on several factors such as the chain length of the hydrocarbon chain, the end terminal group, and the head group. Some of these aspects are discussed later.

There is a possibility of these hydrolyzed monomers reacting in the solvent and forming oligomers in the bulk itself, before actually adsorbing onto the surface.<sup>[66,67]</sup> The process of polymerization (oligomerization)

depends on several factors such as the amount of water present in the bulk solution, the incubation time of the silane solution before the deposition process, and the susceptibility of the trichloro or trimethoxy silanes to be converted to hydroxyl groups.<sup>[68–70]</sup> Fig. 1 shows a peak at  $2961.8\text{ cm}^{-1}$  corresponding to the  $\text{CH}_3$  asymmetric stretch of the methoxy group attached to the silicon head group. This clearly indicates that the hydrolysis of CUTMS monomers was not complete. Trichloro silanes are more susceptible to hydrolysis. However, the reaction rate for a methoxy ( $\text{OCH}_3$ ) or ethoxy ( $\text{OC}_2\text{H}_5$ ) is relatively slow when compared with chlorosilanes.<sup>[71]</sup> The  $\text{CH}_3$  peak could be seen even after long deposition times, thus emphasizing the low hydrolysis rates of the methoxy groups. After a uniform layer of CUTMS was formed, the total amount of molecules adsorbed on the surface did not increase even with an increase in deposition time. The total amount adsorbed is qualitatively discerned from the total integrated absorbance value. Details of the actual qualitative analysis are given later. One reason for incomplete methoxy group hydrolysis is the low water content in solvents used in our experiments. Vallant et al.<sup>[67]</sup> in their studies with alkoxy silanes, had to perform the hydrolysis reaction of alkoxy groups in a water-rich tetrahydrofolate (THF) solvent before using the silanes for monolayer formation.

Fig. 1 also shows peaks at  $2248$  and  $1725\text{ cm}^{-1}$  corresponding to the cyano ( $\text{C}\equiv\text{N}$ ) and carbonyl ( $\text{C}=\text{O}$ ) stretching bands, respectively. The peak at  $2248\text{ cm}^{-1}$  is because of the presence of cyano groups in the monomer. However, we believe that the presence of the  $\text{C}=\text{O}$  peak is because of the transformation of some of the CN groups to carboxylic acid ( $\text{COOH}$ ) groups caused by hydrolysis. A similar behavior of acetylchlorides transforming to carboxylic acid groups during monolayer formation was observed by Cheng, Scherson, and Sukenik<sup>[26]</sup> They reported that the rapid hydrolysis of acid chloride to carboxylic acid is likely because of the presence of a thin water film of adsorbed water on the surface of the ATR element and the relatively high local concentration of HCl formed during the growth of the siloxane network. The effect of solvent on monolayer formation was studied. Table 3 shows details of all the important

**Table 3** Peak positions of methylene symmetric and asymmetric vibrations of CUTMS monolayer prepared in different solvents

Solvent used	$\text{CH}_2$ asymmetric	$\text{CH}_2$ symmetric
Chloroform	2927	2856
Hexadecane	2928	2857
Toluene	2927	2856

Data show that there is no considerable effect of solvent on the monolayer structure of CUTMS.

spectral features observed under different solvent conditions. The solvents used were chloroform, toluene, and carbon tetrachloride. As can be seen, there are no considerable differences in spectral features under different solvent environments.

The kinetics of CUTMS monolayer formation was studied from contact angle measurements. Fig. 2 shows the variation of contact angle with deposition time. The solvent used was chloroform. Measurements were taken within 10 min after the removal of the sample from the solution. As can be seen from this figure, the contact angle reaches a constant value of  $55^\circ$  after about 12 hr. However, to guarantee that the monolayer formation process is complete, we have used for all our experiments a deposition time of at least 24 hr. The equilibrium contact angle of  $55^\circ$  is less than the value of  $65^\circ$  reported by Balachander and Sukenik<sup>[55]</sup> for surfaces formed by 1-cyano-16-trichlorosilyl hexadecane. One reason for this contact angle difference is the formation of  $\text{COOH}$  groups as monolayer formation proceeds, as we have described earlier. The other plausible reason for this difference is the difference in packing densities of monolayers formed by two surfactants. We have used an 11-carbon-chain-length surfactant, whereas Balachander and Sukenik have used a 16-carbon-chain-length surfactant. The packing density of molecules depends on hydrocarbon chain length. As the hydrocarbon chain length increases, lateral chain–chain dispersive interactions increase, leading to higher surface coverage and ordering. These chain–chain dispersive interactions are also present in short-chain molecules. However, the energy gain because of these interactions is comparatively less than the equivalent gain for long chains. Thus to minimize the free energy of the system, the molecules decrease entropic penalty by packing less densely. On heating to  $150^\circ\text{C}$  for a few hours, the contact angle reached a steady state value of  $70^\circ$ . The value was very stable and was independent of heating time.

The thickness of the film was found to vary from  $10 \pm 2$  to  $14 \pm 2\text{ \AA}$ . The length of the fully extended CUTMS monomer was calculated to be  $\sim 14\text{ \AA}$  using the CACHE<sup>®</sup> software. The thickness obtained is reasonable because in a disordered structure, the molecules will be inclined at an angle to the surface normal instead of being fully extended. A simple geometrical calculation gives an angle of inclination to the surface normal as large as  $55^\circ$ . The molecules are oriented in all possible angles from  $0^\circ$  to  $55^\circ$  to the surface normal. Even the densely packed monolayers of OTS on hydroxylated surfaces and alkanethiols on gold surfaces are found to be inclined to the surfaces from dichroic measurements. However, the difference in both of them lies in the order and the packing. The schematic in Fig. 3 depicts the idea of molecular order and direction. In densely packed monolayers, all the



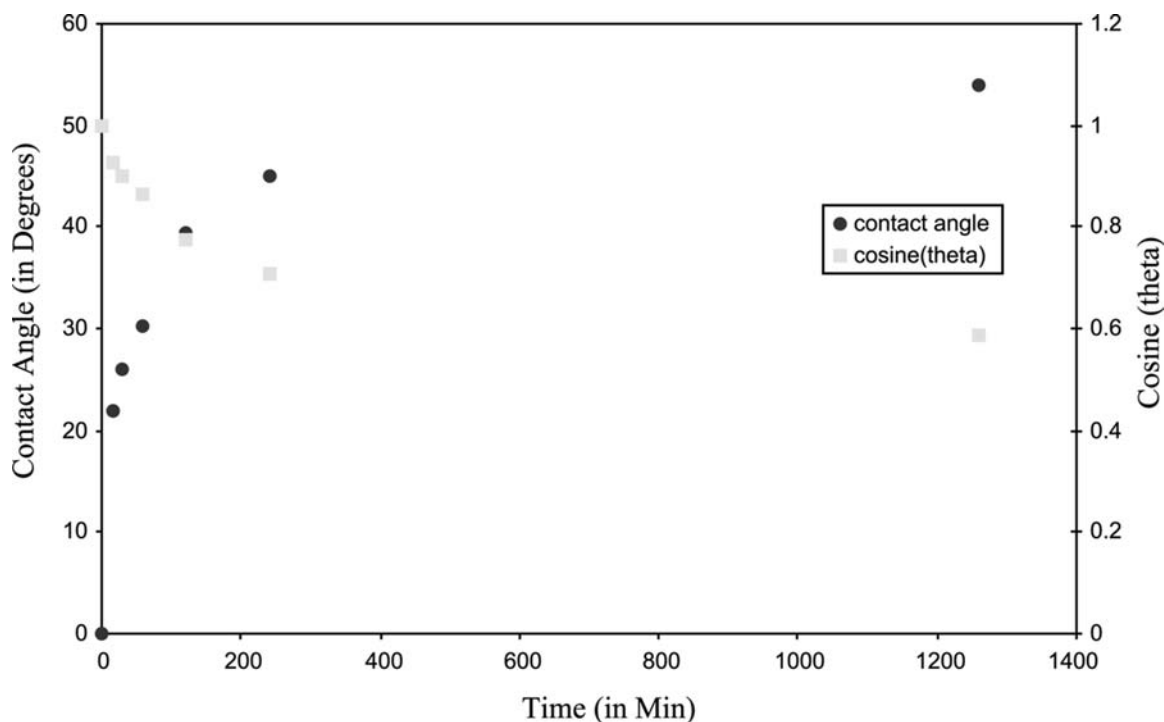


Fig. 2 Variation in contact angle of the CUTMS monolayer with increase in deposition time.

molecules are aligned in the same direction, or, in other words, the molecules have a net order parameter value, which is non-zero. However, the molecules in the CUTMS monolayer, although inclined, are not aligned in a particular direction. The order parameter, if one can be defined, will be lesser than that for the densely packed monolayers. Dense packing, caused by weak

van der Waals interactions between chains, brings in a local order of molecules arranged on the surface.

### Modification of Carboxyl-Terminated SAMs

The terminal groups of CUTMS monolayers were modified to COOH groups by a simple hydrolysis reaction, as described in “Experimental.” The kinetics of the reaction was followed by contact angle and IR measurements. The changes in contact angle with reaction time are shown in Fig. 4. The contact angle reached an equilibrium value of  $\sim 32^\circ$  after approximately 45 min. A contact angle of  $30\text{--}40^\circ$  on monolayers with COOH terminal groups is reported by Wasserman, Tao, and Whitesides.<sup>[23]</sup> This clearly indicates that the terminal groups have been converted to COOH groups. The mole fractions of CN and COOH groups present on the surface, as the reaction proceeds, were calculated using the Cassie equation:

$$\cos(\theta_{\text{avg}}) = f_{\text{COOH}} \cos(\theta_{\text{COOH}}) + f_{\text{CN}} \cos(\theta_{\text{CN}})$$

where  $f_{\text{COOH}}$  and  $f_{\text{CN}}$  correspond to the mole fraction of COOH and CN terminal groups, respectively;  $\theta_{\text{COOH}}$  and  $\theta_{\text{CN}}$  correspond to the equilibrium contact angle when the whole monolayer is filled with either COOH or CN groups, respectively; and  $\theta_{\text{avg}}$  is the contact angle on the surface containing a mixture of COOH and CN groups. The variation of  $f_{\text{COOH}}$  and

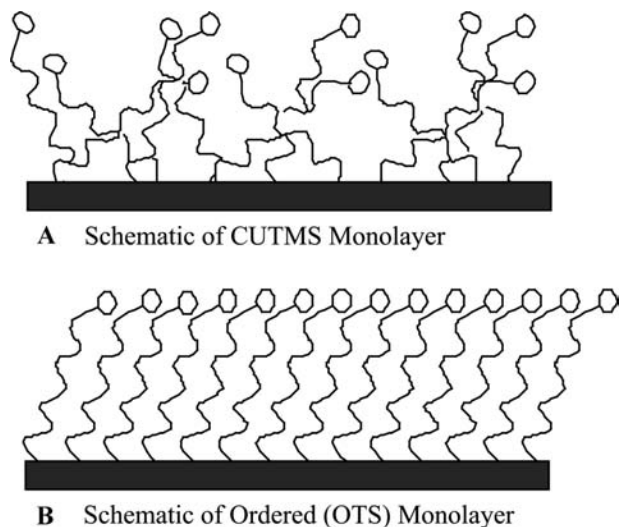


Fig. 3 Schematic of (A) CUTMS and (B) OTS monolayers. Molecules of the CUTMS monolayer are randomly oriented in all possible directions and are loosely packed. Whereas, molecules of the OTS monolayer are densely packed and are oriented in a particular direction.

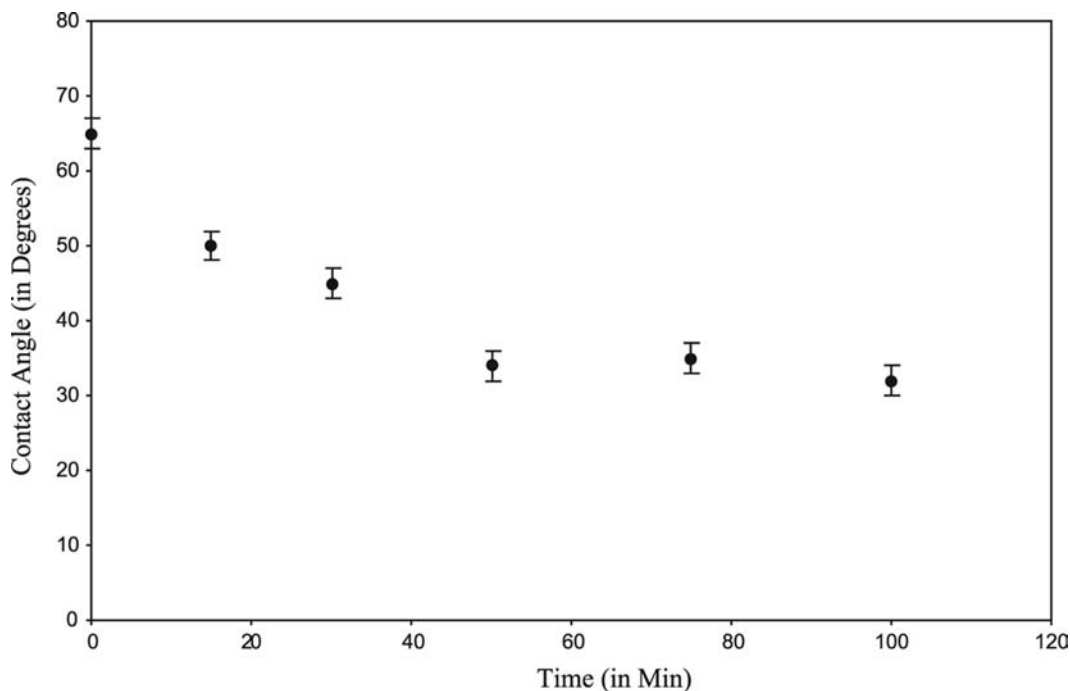


Fig. 4 Variation in contact angle as the reaction proceeds.

$f_{CN}$  is shown in Fig. 5. ( $\theta_{COOH}$  was taken as  $32^\circ$  and  $\theta_{CN}$  was taken as  $70^\circ$ .)

The changes in COOH and CN peak intensities were also followed by IR. A typical spectrum is shown

in Fig. 6. The spectrum clearly indicates a decrease in CN peak ( $2253\text{ cm}^{-1}$ ) and an increase in COOH peak ( $1702\text{ cm}^{-1}$ ). The decrease in CN peak intensity is plotted in Fig. 7. As expected, COOH groups are

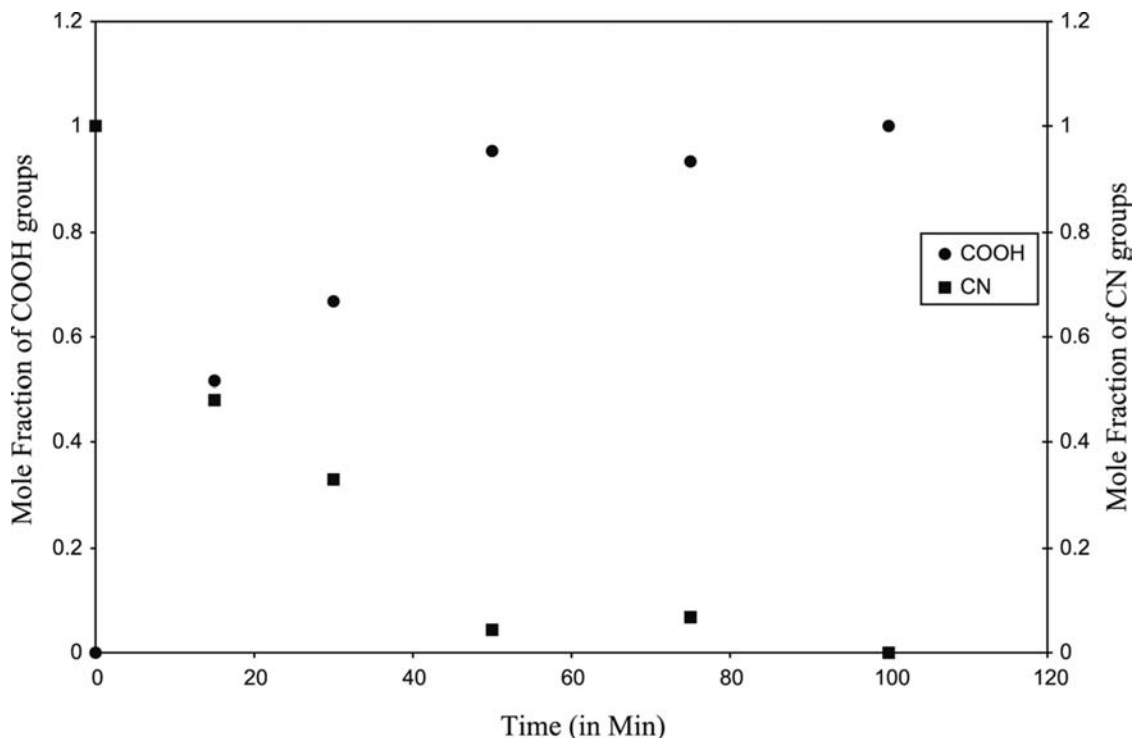
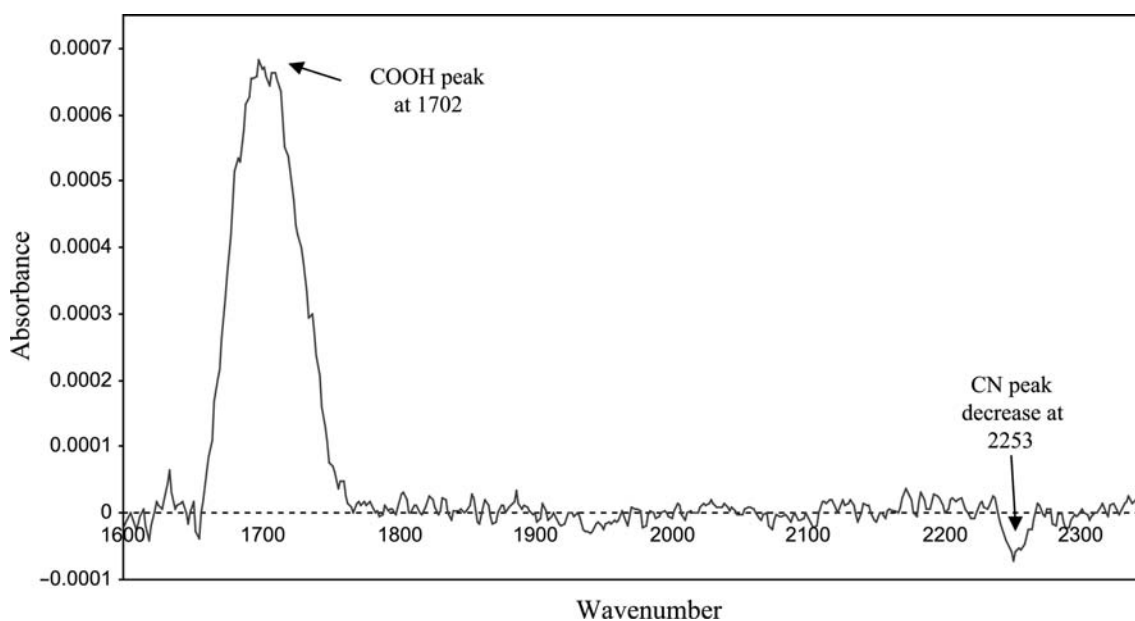


Fig. 5 Fraction of COOH and CN groups present on surfaces as the reaction proceeds (calculated using the Cassie equation).



**Fig. 6** Spectrum shows an increase in COOH peak at 1702 and a decrease in CN peak at 2253 as the reaction proceeds.

highly sensitive to pH changes, and  $\text{COOH} \leftrightarrow \text{COO}^-$  can be interchangeably converted back and forth by changing the pH. Fig. 8 shows the spectra of the modified COOH surface at different pH values. At a pH value of 2, which is below the  $\text{p}K_a$  value of the surface, the monolayer is terminated with COOH groups.

The peak at  $1718\text{ cm}^{-1}$  confirms that. When the same sample was immersed in a solution with a pH value of 7.5, which was above the  $\text{p}K_a$  value of the surface, the terminal groups were converted to  $\text{COO}^-$ . Spectrum B in Fig. 8 shows a peak split. The peak at  $1590\text{ cm}^{-1}$  corresponds to  $\text{COO}^-$  stretching. The broad

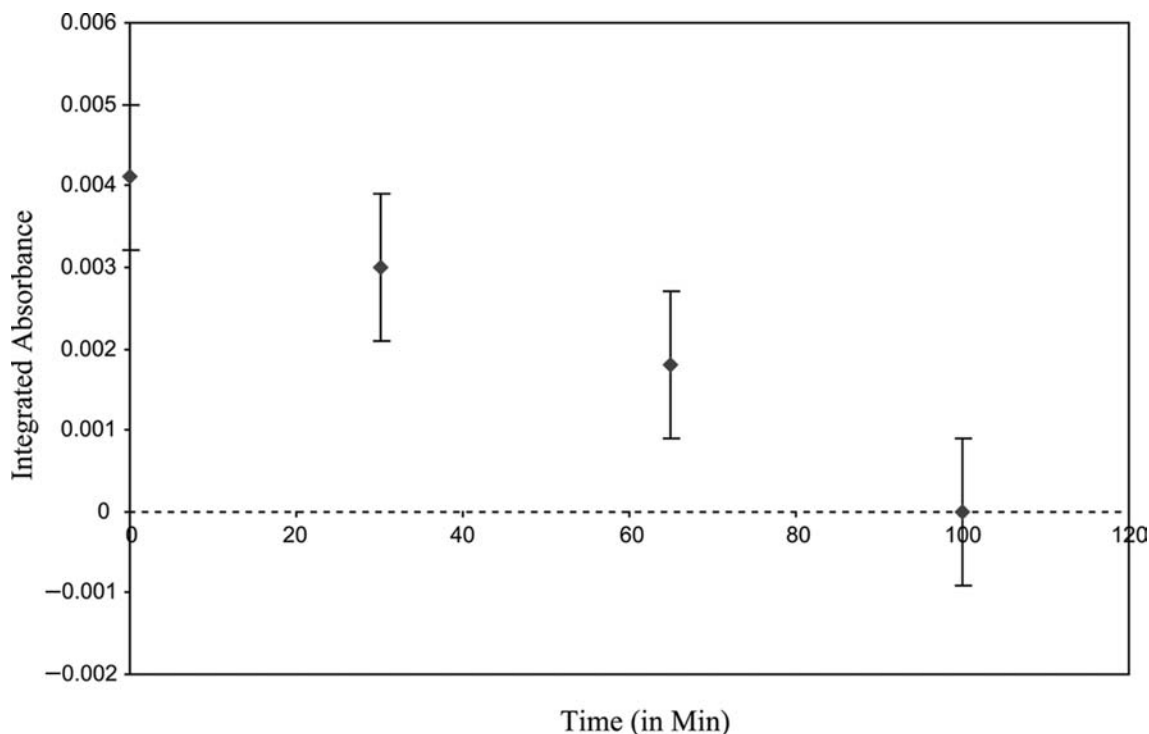


**Fig. 7** Decrease in CN peak intensity as the reaction proceeds.

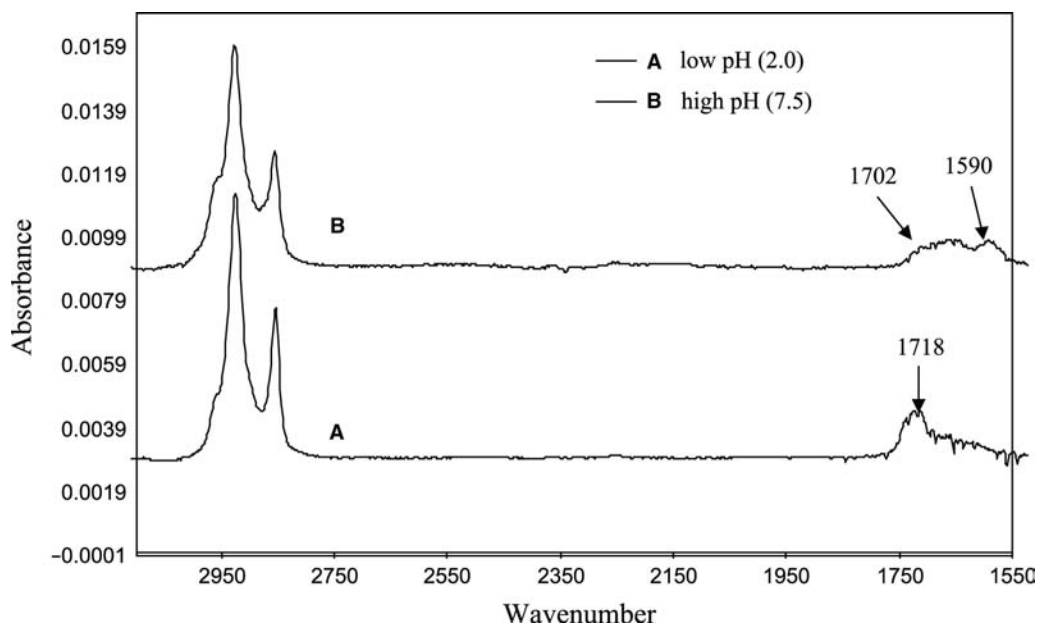


**Fig. 8** (A) Spectrum of monolayer after reaction at low pH (2.0); only COOH groups are present. (B) Spectrum of monolayer at pH 7.5 after reaction; both COOH and COO<sup>-</sup> exist.

peak between 1650 and 1725 cm<sup>-1</sup> corresponds to the unconverted COOH and the surface-bound water. Cheng, Scherson, and Sukenik<sup>[26]</sup> have calculated the pK<sub>a</sub> value of the monolayer from changes of COOH and COO<sup>-</sup> peaks and found that value to be 5.4.

### Surface Coverage

In this section, we report the results regarding our measurements of the surface coverage by CUTMS surfactants. We have measured the surface coverage of

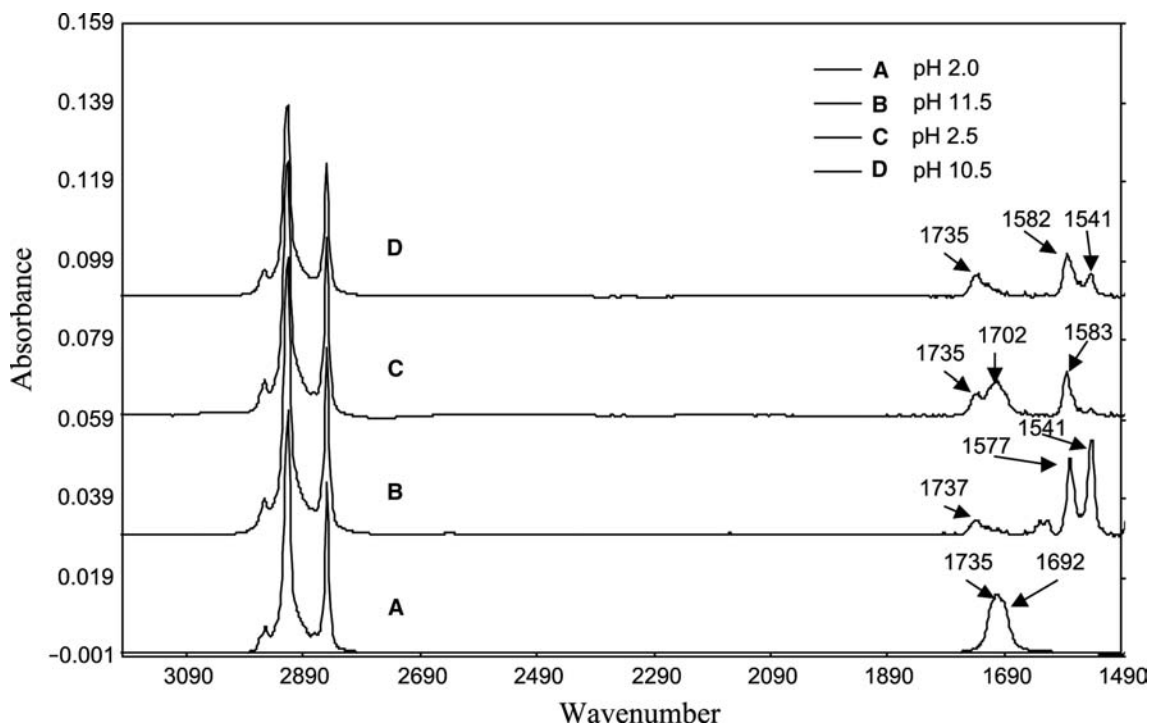


**Fig. 9** (A) LB film of stearic acid at pH 2.0; (B) LB film immersed in calcium chloride solution of pH 11.5; (C) LB film again immersed in a solution of pH 2.5; and (D) LB film again immersed in a sodium hydroxide solution of pH 10.

**Table 4** Peak positions of methylene symmetric and asymmetric vibrations for OTS SAM and stearic acid LB film

	CH <sub>2</sub> asymmetric	CH <sub>2</sub> symmetric
OTS SAM	2919	2850
Stearic acid LB film	2917	2949.6

Both of them form a densely packed, crystalline structure.

molecules by the protocol first developed by Kumar et al.<sup>[36]</sup> where the surface coverage  $\Gamma$  is given by  $\Gamma = A/\epsilon$ , where  $A$  is the integrated absorbance and  $\epsilon$  is the molar emissivity. Furthermore, Kumar et al. have also found that the molar emissivity measured for the CH<sub>2</sub> asymmetric peak in monolayers is  $\sim 1.5$  times that obtained from liquid solutions. The difference in  $\epsilon$  values is attributed to the packing and ordering of surfactants onto the solid surface.

In this study, we have used the LB film of stearic acid to estimate  $\epsilon_{\text{CH}_2}$ ,  $\epsilon_{\text{COOH}}$ , and  $\epsilon_{\text{COO}^-}$ . Calculation of these values provides a tool to quantitatively measure the molecular coverage, extent of conversion, and relative coverage of COOH and COO<sup>-</sup>. The LB film of stearic acid was transferred onto a silicon substrate coated with the OTS monolayer using the method described in “Experimental.” The IR spectrum of the transferred stearic acid LB film is shown in Fig. 9. Details of the prominent peaks for the OTS monolayer and the LB film of stearic acid are given in Table 4. The peaks at 2917 and 2850 cm<sup>-1</sup> corresponding to CH<sub>2</sub> asymmetric and symmetric stretch-

ing bands, respectively, indicate that the LB film is crystalline and uniform. The peak at 1702 cm<sup>-1</sup> corresponds to the C=O stretching band of COOH groups. When COOH groups are apart, COOH groups exist as monomers and the peak is seen between 1720 and 1740 cm<sup>-1</sup>. However, when molecules are closely packed, then neighboring COOH molecules interact with one another (hydrogen bonding) and exist as dimers. Crooks, Sun, and Kepley<sup>[72]</sup> have seen a similar phenomenon in carboxylic acid-terminated thiol SAMs. A shoulder at 1692 cm<sup>-1</sup> confirms the strong intermolecular interaction between neighboring molecules.

The sensitivity of COOH groups to pH of the surrounding environment was proven by immersing the substrate coated with the stearic acid LB film in a CaCl<sub>2</sub> solution of pH 11.5 for approximately 30 min. Fig. 9B shows the spectrum of the resulting substrate. As can be seen, the peak at 1702 cm<sup>-1</sup> vanished and a very small peak, corresponding to COOH groups existing as monomers, appeared at 1737 cm<sup>-1</sup>. Two peaks appeared at 1577 and 1541 cm<sup>-1</sup> corresponding to free COO<sup>-</sup> groups and bonded COO<sup>-</sup> groups, respectively. The interchangeability of COOH and COO<sup>-</sup> groups was proven by immersing the above sample in deionized water of pH 2.4 for about 30 min. Fig. 9C shows the spectrum of the same. As can be seen, two distinct peaks appear at 1703 and 1583 cm<sup>-1</sup>. These two peaks correspond to COOH existing as dimers and COO<sup>-</sup> existing as free monomers, respectively. There is also a shoulder at 1735 cm<sup>-1</sup> corresponding to free monomers of COOH groups. If the immersion time is increased, the spec-

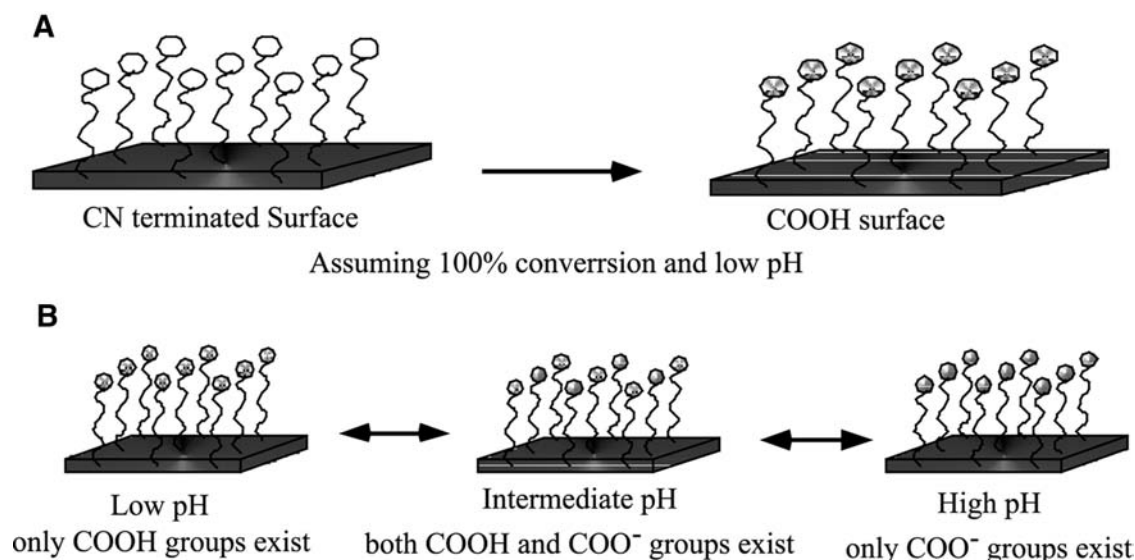


**Fig. 10** (A) Schematic of a CN-terminated monolayer modified to COOH terminal groups. Conditions: 1:1 (vol/vol) of 15% HCl and water at a temperature of 75°C. (B) Schematic showing the dependence of COOH terminal groups on the pH of the environment. At low pH, the surface is only covered with COOH groups; at high pH, the surface is covered with COO<sup>-</sup> groups; at intermediate pH values, the surface is covered with both COOH and COO<sup>-</sup> groups.

**Table 5** Peaks of COOH and COO<sup>-</sup> (bounded and unbounded) of stearic acid LB film at various pH values

pH	COOH		$A_{\text{COOH}}$	COO <sup>-</sup>		$A_{\text{COO}^-}$
	Unbound monomers	Bounded dimers		Unbound monomers	Bounded dimers	
2.0	–	1702 and shoulder at 1692	0.5260	–	–	–
11.5	1737	–	0.0695	1577	1541	0.678
2.4	1735	1702	0.4229	1583	–	0.159
10.5	1735	–	–	1582	1541	–

Integrated absorbance values are also given in the table. No differentiation was drawn between bounded and unbounded COOH and COO<sup>-</sup> in the calculation of integrated absorbance values.

trum looks identical to the spectrum of Fig. 9A. Thus COOH dimers, monomers, and COO<sup>-</sup> monomers coexist on the surface. Fig. 9D shows the spectrum when the sample was immersed again in a solution of high pH (10.5) for about 20 min. The spectral features of Fig. 9B and D are qualitatively very similar. The difference in quantities arises from the difference in deposition times and pH. The schematic in Fig. 10A and B depicts the whole process in short.

For quantitative analysis, the maximum packing density of the stearic acid LB film was set at 18 Å<sup>2</sup> per molecule. This assumption is drawn from the  $\pi$ -A isotherm of the stearic acid LB film obtained on a sub-phase of pH 2. Absorbance values for the CH<sub>2</sub> asymmetric and symmetric stretching bands were obtained by fitting the data with a Lorentzian peak. All the spectra were baseline-corrected before peak fitting analysis was done. For COOH and COO<sup>-</sup> peaks, the peaks were not fitted and the absorbance values were evaluated by calculating the area between two wavenumbers. Details of absorbance values for CH<sub>2</sub>, COOH, and COO<sup>-</sup> and calculated molar absorptivities for the respective groups are given in Table 5. Using  $A_{\text{CH}_2} = N\varepsilon_{\text{CH}_2}(\Gamma)^*\Gamma_{\text{CH}_2}$ , where  $N$  is the number of reflections in the ATR element ( $N$  was geometrically determined to be 18) and  $\Gamma$  is the molecular coverage of the stearic acid monolayer [mol/cm<sup>2</sup>],  $\varepsilon_{\text{CH}_2}$  was found to be  $4.12 \times 10^6$  cm/mol per CH<sub>2</sub> group.

Because the vibrational frequencies for COOH and COO<sup>-</sup> differ by a considerable amount, we have assumed the values of  $\varepsilon_{\text{COOH}}$  and  $\varepsilon_{\text{COO}^-}$  to be different. However, we did not differentiate between the freely existing and bounded COOH and COO<sup>-</sup> groups.

From Fig. 9B, because the total number of COOH and COO<sup>-</sup> should be constant and equal to the molecular coverage of the monolayer, one can write:

$$\begin{aligned} A_{\text{COOH}}/\varepsilon_{\text{COOH}} + A_{\text{COO}^-}/\varepsilon_{\text{COO}^-} &= \Gamma \\ &= A_{\text{COOH}}/\varepsilon_{\text{COOH}} \end{aligned}$$

This allows us to determine the ratio of the molar emissivities of the charged and the uncharged carboxylates  $\varepsilon_{\text{COO}^-}/\varepsilon_{\text{COOH}}$  to be 1.48. The data from Fig. 9C were used for a consistency check and the values agreed.

Similarly,  $\varepsilon_{\text{CH}_2}$ , obtained from stearic acid calculations, was used to evaluate the molecular coverage of the CUTMS monolayer. The molecular coverage of CUTMS monolayers was evaluated to be in the range of 45–60 Å<sup>2</sup> per molecule. The value of 45–60 Å<sup>2</sup> per molecule indicates that the surface monolayer exists in a rather disordered, liquidlike structure, which is further verified by the position of methylene asymmetric and symmetric stretching bands, as discussed earlier.

## CONCLUSION

We have used contact angle measurements, ellipsometry, and IR reflection measurements to characterize the structure of a cyano-terminated monolayer formed by the adsorption of CUTMS on a silicon substrate. We have characterized the structure of the monolayer before and after hydrolysis of the terminal cyano group. CUTMS forms a monolayer film that has a liquidlike, disordered structure. The coverage of CUTMS molecules was found to be approximately between 45 and 60 Å<sup>2</sup> per molecule. The –CN terminal groups of CUTMS monolayer were converted to COOH terminal groups by a simple hydrolysis reaction. The kinetics of the reaction was followed using IR and contact angle measurements. COOH groups are very sensitive to the pH of the surrounding environment and can be reversibly ionized by changing the pH of the wetting solution.

## ACKNOWLEDGMENTS

We acknowledge the support from the National Science Foundation (CTS 9872082, CTS 9871798, and CTS 0079677).

## REFERENCES

- Jennings, G.K.; Munro, J.C.; Yong, T.-H.; Laibinis, P.E. Effect of chain length on the protection of copper by *n*-alkanethiols. *Langmuir* **1998**, *14*, 6130–6139.



- de Gennes, P.G. Wetting: Statics and dynamics. *Rev. Mod. Phys.* **1985**, *57*, 827–863.
- Lahiri, J.; Isaacs, L.; Grzybowski, B.; Carbeck, D.J.; Whitesides, G.M. Biospecific binding of carbonic anhydrase to mixed SAMs presenting benzenesulfonamide ligands: A model system for studying lateral steric effects. *Langmuir* **1999**, *15*, 7186–7198.
- Ottova, A.; Tvarozek, V.; Racek, J.; Sabo, J.; Ziegler, W.; Hianik, T.; Tein, H.T. Self-assembled BLMs: Biomembrane models and biosensor applications. *Supramol. Sci.* **1997**, *4*, 101–112.
- Piletsky, S.A.; Wulff, G.; Piletskaya, E.V.; Panasyuk, T.L.; Elskaya, A.V.; Levi, R.; Karube, I. Imprinted membranes for sensor technology: Opposite behavior of covalently and noncovalently imprinted membranes. *Macromolecules* **1998**, *31*, 2137–2140.
- Rubinstein, I.; Steinberg, S.; Tor, Y.; Shanzer, A.; Sagiv, J. Ionic recognition and selective response in self-assembling monolayer membranes on electrodes. *Nature* **1988**, *332*, 426–429.
- Schierbaum, K.D.; Weiss, T.; Velzen, E.U.T.V.; Engbersen, J.F.J.; Reinhoudt, D.N.; Gopel, W. Molecular recognition by self-assembled monolayers of cavitand receptors. *Science* **1994**, *265*, 1413–1415.
- Lochhead, M.J.; Letellier, S.R.; Vogel, V. Assessing the role of interfacial electrostatics in oriented mineral nucleation at charged organic monolayers. *J. Phys. Chem., B* **1997**, *101*, 10821–10827.
- Jiang, P.; Liu, Z.-F.; Cai, S.-M. Electron transport on a single CdS nanocrystal formed on self-assembled monolayer at room temperature. *Surf. Sci.* **2001**, *486*, L507–L512.
- Li, L.S.; Lianhua Qu, R.L.; Xiaogang, P.; Zhao, Y.; Li, T. Preparation and structure of quantum-sized cadmium sulfide grown in amphiphilic oligomer Langmuir–Blodgett films. *Thin Solid Films* **1998**, *327–329*, 408–411.
- Li, L.S.; Jin, J.; Tian, Y.Q.; Zhao, Y.Y.; Li, T.J.; Du, Z.L.; Ma, G.H.; Zheng, N. Studies of nanoparticulate cadmium sulfide in amphiphilic polymaleic acid octadecanol ester Langmuir–Blodgett films. *Supramol. Sci.* **1998**, *5*, 475–478.
- Zhang, L.; Shen, G.; Pan, Z.; Lu, Z. Transmission electron microscope investigation of cadmium sulfide nanoparticles grown under Langmuir monolayer. *Mater. Chem. Phys.* **1998**, *55*, 160–163.
- Sugimura, H.; Ushiyama, K.; Hozumi, A.; Takai, O. Micropatterning of alkyl- and fluoroalkylsilane self-assembled monolayers using vacuum ultraviolet light. *Langmuir* **2000**, *16*, 885–888.
- Whitesides, G.M.; Aizenberg, J.; Black, A.J. Controlling local disorder in self-assembled monolayers by patterning the topography of their metallic supports. *Nature* **1999**, *398*, 495–498.
- Schon, J.H.; Bao, Z. Nanoscale organic transistors based on self-assembled monolayers. *Appl. Phys. Lett.* **2002**, *80*, 847–849.
- Sagiv, J. Organized monolayers by adsorption: I. Formation and structure of oleophobic mixed monolayers on solid surfaces. *J. Am. Chem. Soc.* **1980**, *102* (1), 92–98.
- Kumar, N.; Malderelli, C.; Steiner, C.; Couzis, A. Formation of nanometer domains of one chemical functionality in a continuous matrix of a second chemical functionality by sequential adsorption of silane self-assembled monolayers. *Langmuir* **2001**, *17*, 7789–7797.
- Sabatani, E.; Rubinstein, I.; Maoz, R.; Sagiv, J. Organized self-assembling monolayers on electrodes: Part I. Octadecyl derivatives on gold. *J. Electroanal. Chem.* **1987**, *219*, 365–371.
- Angst, D.L.; Simmons, G.W. Moisture absorption characteristics of organosiloxane self-assembled monolayers. *Langmuir* **1991**, *7*, 2236–2242.
- Bierbaum, K.; Grunze, M.; Basaki, A.A.; Chi, L.F.; Schrepp, W.; Fuchs, H. Growth of self-assembled *n*-alkyltrichlorosilane films on Si(100) investigated by atomic force microscopy. *Langmuir* **1995**, *11*, 2143–2150.
- Parikh, A.N.; Allara, D.L.; Azouz, I.B.; Rondelez, F. An intrinsic relationship between molecular structure in self-assembled *n*-alkylsiloxane monolayers and deposition temperature. *J. Phys. Chem.* **1994**, *98*, 7577–7590.
- Silberzan, P.; Leger, L.; Ausserre, D.; Benattar, J.J. Silanation of silica surfaces. A new method of constructing pure or mixed monolayers. *Langmuir* **1991**, *7*, 1647–1651.
- Wasserman, S.R.; Tao, Y.-T.; Whitesides, G.M. Structure and reactivity of alkylsiloxane monolayers formed by reaction of alkyltrichlorosilanes on silicon substrates. *Langmuir* **1989**, *5*, 1074–1087.
- Creager, S.E.; Clarke, J. Contact-angle titrations of mixed omega-mercaptoalkanoic acid/alkanethiol monolayers on gold. Reactive vs nonreactive spreading, and chain length effects on surface  $pK_a$  values. *Langmuir* **1994**, *10*, 3675–3683.
- Bain, C.D.; Whitesides, G.M. A study by contact angle of the acid–base behavior of monolayers containing omega-mercaptocarboxylic acids adsorbed on gold: An example of reactive spreading. *Langmuir* **1989**, *5*, 1370–1378.
- Cheng, S.S.; Scherson, D.A.; Sukenik, C.N. In situ attenuated total reflectance Fourier transform infrared spectroscopy study of carboxylate-bearing, siloxane-anchored, self-assembled monolayers: A study of carboxylate reactivity and acid–base properties. *Langmuir* **1995**, *11*, 1190–1195.
- Wang, J.; Frostman, L.M.; Ward, M.D. Self-assembled thiol monolayers with carboxylic acid functionality: Measuring pH-dependent phase transitions with the quartz crystal microbalance. *J. Phys. Chem.* **1992**, *96*, 5224–5228.
- Maoz, R.; Sagiv, J. On the formation and structure of self-assembling monolayers: I. A comparative ATR-wettability study of Langmuir–Blodgett and adsorbed films on flat substrates and glass microbeads. *J. Colloid Interface Sci.* **1984**, *100*, 465–496.
- Sagiv, J.; Iscovici, R.; Gun, J. On the formation and structure of self-assembling monolayers: II. A comparative study of Langmuir–Blodgett and adsorbed films using ellipsometry and IR reflection–absorption spectroscopy. *J. Colloid Interface Sci.* **1984**, *101*, 201–213.

30. Couzis, A.; Gulari, E. Adsorption of sodium laureate from its aqueous solution onto an alumina surface. A dynamic study of the surface-surfactant interaction using attenuated total reflection Fourier transform infrared spectroscopy. *Langmuir* **1993**, *9*, 3414–3421.
31. Iimura, K.-I.; Nakajima, Y.; Kato, T. A study on structures and formation mechanisms of self-assembled monolayers of *n*-alkyltrichlorosilanes using infrared spectroscopy and atomic force microscopy. *Thin Solid Films* **2000**, *379*, 230–239.
32. Brzoska, J.B.; Azouz, I.B.; Rondelez, F. Silanization of solid substrates: A step toward reproducibility. *Langmuir* **1994**, *10*, 4367–4373.
33. Kallury, K.M.R.; Macdonald, P.M.; Thompson, M. Effect of surface water and base catalysis on the silanization of silica by (aminopropyl)alkoxysilanes studied by X-ray photoelectron spectroscopy and <sup>13</sup>C cross-polarization/magic angle spinning nuclear magnetic resonance. *Langmuir* **1994**, *10*, 492–499.
34. Carraro, C.; Yauw, O.W.; Sung, M.M.; Maboudian, R. Observation of three growth mechanisms in self-assembled monolayers. *J. Phys. Chem., B* **1998**, *102*, 4441–4445.
35. Carraro, C.; Yauw, O.W.; Sung, M.M.; Maboudian, R.; Kim, Y. Reversible liquid-liquid transitions in the early stages of monolayer self-assembly. *J. Phys. Chem., B* **2000**, *104*, 1556–1559.
36. Kumar, V.; Krishnan, S.; Steiner, C.; Maldarelli, C.; Couzis, A. Measurement of infrared molar absorptivity of a surfactant adsorbed onto a solid substrate over a wide range of surface concentrations using octadecyltrichlorosilane Langmuir-Blodgett transferred films. *J. Phys. Chem., B* **1998**, *102*, 5152–5159.
37. Porter, M.D.; Bright, T.B.; Allara, D.L.; Chidsey, C.E.D. Spontaneously organized molecular assemblies: 4. Structural characterization of *n*-alkyl thiol monolayers on gold by optical ellipsometry, infrared spectroscopy, and electrochemistry. *J. Am. Chem. Soc.* **1987**, *109* (12).
38. Paudler, M.; Ruths, J.; Riegler, H. Analysis of multiple-angle ellipsometry of uniaxial ultrathin organic films at the air-water interface and determination of the refractive indices of behenic acid monolayers. *Langmuir* **1992**, *8* (1), 184–189.
39. Meuse, C.W. Infrared spectroscopic ellipsometry of self-assembled monolayers. *Langmuir* **2000**, *16* (24), 9483–9487.
40. Wasserman, S.R.; Whitesides, G.M.; Tidswell, I.M.; Ocko, B.M.; Pershan, P.S.; Axe, J.D. The structure of self-assembled monolayers of alkylsiloxanes on silicon: A comparison of results from ellipsometry and low-angle X-ray reflectivity. *J. Am. Chem. Soc.* **1989**, *111* (15), 5852–5861.
41. Brandow, S.L.; Chen, M.S.; Aggarwal, R.; Dulcey, C.S.; Calvert, J.M.; Dressick, W.J. Fabrication of patterned amine reactivity templates using 4-chloromethylphenylsiloxane self-assembled monolayer films. *Langmuir* **1999**, *15*, 5429–5432.
42. Dulcey, W.J.D.C.S.; Chen, M.-S.; Calvert, J.M. Photochemical studies of (aminoethylaminomethyl)phenethyltrimethoxysilane self-assembled monolayer films. *Thin Solid Films* **1996**, *284–285*, 568–572.
43. Heiney, P.A.; Gruneberg, K.; Fang, J.; Dulcey, C.; Sashidhar, R. Structure and growth of chromophore-functionalized (3-aminopropyl)triethoxysilane self-assembled on silicon. *Langmuir* **2000**, *16*, 2651–2657.
44. Hooper, A.E.; Werho, D.; Hopson, T.; Palmer, O. Evaluation of amine- and amide-terminated self-assembled monolayers as molecular glues for Au and SiO<sub>2</sub> substrates. *Surf. Interface Anal.* **2001**, *31*, 809–814.
45. Sieval, A.B.; Linke, R.; Heij, G.; Meijer, G.; Zuilhof, H.; Sudholter, E.J.R. Amino-terminated organic monolayers on hydrogen-terminated silicon surfaces. *Langmuir* **2001**, *17*, 7554–7559.
46. Doudevski, I.; Hayes, W.A.; Woodward, J.T.; Schwartz, D.K. Atomic force microscope imaging of molecular aggregation during self-assembled monolayer growth. *Colloids Surf., A Physicochem. Eng. Asp.* **2000**, *174*, 233–243.
47. Lukkari, J.; Kleemola, K.; Meretoja, M.; Ollonqvist, T.; Kankare, J. Electrochemical post-self-assembly transformation of 4-aminothiophenol monolayers on gold electrodes. *Langmuir* **1998**, *14*, 1705–1715.
48. Tillman, N.; Ulman, A. Formation of multilayers by self-assembly. *Langmuir* **1989**, *5*, 101–111.
49. Delamarche, E.; Michel, B.; Kang, H.; Gerber, C. Thermal stability of self-assembled monolayers. *Langmuir* **1994**, *10*, 4103–4108.
50. Bensebaa, F.; Ellis, T.H.; Badia, A.; Lennox, R.B. Thermal treatment of *n*-alkanethiolate monolayers on gold, as observed by infrared spectroscopy. *Langmuir* **1998**, *14*, 2361–2367.
51. Tam-Chang, S.-W.; Biebuyck, H.A.; Whitesides, G.M.; Jeon, N.; Nuzzo, R.G. Self-assembled monolayers on gold generated from alkanethiols with the structure RNHCO CH<sub>2</sub>SH. *Langmuir* **1995**, *11*, 4371–4382.
52. Sung, M.M.; Kluth, G.J.; Yauw, O.W.; Maboudian, R. Thermal behavior of alkyl monolayers on silicon surfaces. *Langmuir* **1997**, *13*, 6164–6168.
53. Sung, M.M.; Kluth, G.J.; Maboudian, R. Thermal behavior of alkylsiloxane self-assembled monolayers on the oxidized Si(100) surface. *Langmuir* **1997**, *13*, 3775–3780.
54. Lee, Y.W.; Reed-Mundell, J.; Sukenik, C.N.; Zull, J.E. Electrophilic siloxane-based self-assembled monolayers for thiol-mediated anchoring of peptides and proteins. *Langmuir* **1993**, *9*, 3009–3014.
55. Balachander, N.; Sukenik, C.N. Monolayer transformation by nucleophilic substitution: Applications to the creation of new monolayer assemblies. *Langmuir* **1990**, *6*, 1621–1627.
56. Barnes, Y.; Gershevit, O.; Sekar, M.; Sukenik, C.N. Functionalized silanes for the preparation of siloxane-anchored monolayers. *Langmuir* **2000**, *16*, 247–251.
57. Collins, R.J.; Sukenik, C.N. Sulfonate-functionalized, siloxane-anchored, self-assembled monolayers. *Langmuir* **1995**, *11*, 2322–2324.
58. Grisar, H.; Cohen, Y.; Aurbach, D.; Sukenik, C.N. Highly doped silicon electrodes for the electrochemical modification of self-assembled siloxane-anchored

- monolayers: A feasibility study. *Langmuir* **2001**, *17*, 1608–1619.
59. Fryxell, G.E.; Rieke, P.C.; Wood, L.L.; Engelhard, M.H.; Williford, R.E.; Graff, G.L.; Campbell, A.A.; Wiacek, R.J.; Lee, L.; Halverson, A. Nucleophilic displacements in mixed self-assembled monolayers. *Langmuir* **1996**, *12*, 5064–5075.
  60. Koloski, T.S.; Dulcey, C.S.; Haralson, Q.J.; Calvert, J.M. Nucleophilic displacement reactions at benzyl halide self-assembled monolayer film surfaces. *Langmuir* **1994**, *10*, 3122–3133.
  61. Kakkar, A.K.; Yitzchaik, S.; Roscoe, S.B.; Kubota, F.; Allan, D.S.; Marks, T.J. Chromophoric self-assembled nonlinear optical multilayer materials. Synthesis, properties, and structural interconversions of assemblies with rodlike alkynyl chromophores. *Langmuir* **1993**, *9*, 388–390.
  62. Yam, C.M.; Tong, S.S.Y.; Kakkar, A.K. Simple acid–base hydrolytic chemistry approach to molecular self-assembly: Thin films of long chain alcohols terminated with alkyl, phenyl, and acetylene groups on inorganic oxides surfaces. *Langmuir* **1998**, *14*, 6941–6947.
  63. Kim, T.K.; Yang, X.M.; Peters, R.D.; Sohn, B.H.; Nealey, P.F. Chemical modification of self-assembled monolayers by exposure to soft X-rays in air. *J. Phys. Chem., B* **2000**, *104*, 7403–7410.
  64. Wade, N.; Gologan, B.; Vincze, A.; Cooks, R.G.; Sullivan, D.M.; Bruening, M.L. Esterification and ether formation at a hydroxyl-terminated self-assembled monolayer surface using low-energy collisions of polyatomic cations. *Langmuir* **2002**, *18*, 4799–4808.
  65. Parikh, A.N.; Liedberg, B.; Atre, S.V.; Ho, M.; Allara, L.D. Correlation of molecular organization and substrate wettability in the self-assembly of *n*-alkylsiloxane monolayers. *J. Phys. Chem.* **1995**, *99*, 9996–10008.
  66. Peters, R.D.; Nealey, P.F.; Crain, J.N.; Himpel, F.J. A near edge X-ray absorption fine structure spectroscopy investigation of the structure of self-assembled films of octadecyltrichlorosilane. *Langmuir* **2002**, *18*, 1250–1256.
  67. Vallant, T.; Brunner, H.; Mayer, U.; Hoffmann, H.; Resch, R.; Grasserbauer, M.; Friedbacher, G. Formation of self-assembled octadecylsiloxane monolayers on mica and silicon surfaces studied by atomic force microscopy and infrared spectroscopy. *J. Phys. Chem., B* **1998**, *102*, 7190–7197.
  68. Kessel, C.R.; Granick, S. Formation and characterization of a highly ordered and well-anchored alkylsilane monolayer on mica by self-assembly. *Langmuir* **1991**, *7*, 532–538.
  69. Oostendorp, D.J.; Bertrand, G.L.; Stoffer, O.J. Kinetics and mechanism of the hydrolysis and alcoholysis of alkoxy silanes. In *Silanes Coupling Agents*; VSP: Utrecht, 1992; 159–179.
  70. Osterholtz, F.D.; Pohl, E.R. Kinetics of the hydrolysis and condensation of organofunctional alkoxy silanes: A Review. In *Silanes Coupling Agents*; VSP: Utrecht, 1992; 119–141.
  71. Brinker, C.J.; Scherer, G.W. *Sol–Gel Science: The Physics and Chemistry of Sol–Gel Processing*; Academic Press, 1990.
  72. Crooks, R.M.; Sun, L.; Kepley, L.J. Molecular interactions between organized, surface-confined monolayers and vapor-phase probe molecules: Hydrogen-bonding interactions. *Langmuir* **1992**, *8*, 2101–2103.

# Self-Assembled Structures

**Anna Cristina Samia**

*Chemistry Division, Argonne National Laboratory, Argonne, Illinois, U.S.A.*

**Xiao-Min Lin**

*Material Science Division, Chemistry Division and Center for Nanoscale Materials, Argonne National Laboratory, Argonne, Illinois, U.S.A.*

## INTRODUCTION

Spontaneous organization of matter into hierarchical ordered structures is ubiquitous in nature.<sup>[1]</sup> From a single strand of DNA in a biological cell to a colony of king penguins on an Antarctic island, self-assembled structures exist not only on molecular level, but also on a macroscopic length scale. Under a strict definition, self-assembly is a process whereby a large quantity of pre-existing components undergo spontaneous organization to form larger structures driven by internal interactions or external constraints. The assembled structures may retain the properties of their constituent building blocks, but more importantly, can demonstrate new collective phenomena due to the interactions between their components.

Under this definition, crystallization of atoms driven by the formation of covalent or ionic bonds is a self-assembling process. However, it is the self-assembly process driven by noncovalent interaction that has attracted much more attention lately. This is largely because the energy associated with noncovalent bonds is comparable to thermal energy. Thus, a slight variation of interaction or temperature can drive the same system into vastly different structures. This is partly responsible for the existing complexity of nature. Understanding the mechanism for self-assembly is not only of fundamental interest, but may also lead to many technological applications. While the vast majority of self-assembled structures exist in biological systems, this review is from the material's point of view with only a few exceptions. This is largely due to our own research interests as well as the practical consideration that it is impossible to cover every aspect of these research activities in a short review. Nevertheless, we hope to capture the essence of self-assembly, and refer interested readers to several other excellent review articles and monographs published in this encyclopedia and elsewhere.<sup>[2–15]</sup>

## SELF-ASSEMBLY IN MOLECULAR SYSTEMS

The development of synthetic chemistry has led to the construction of many large molecules with well-defined

sizes, functional groups, and chiralities. Most of these molecules such as vitamin B<sub>12</sub> are based on the sequential formation of covalent bonds.<sup>[16]</sup> However, it is becoming increasingly clear that constructing even larger structures would require more efficient synthetic pathways.<sup>[6]</sup> One approach is to mimic nature where covalent bonds are used to construct functional building blocks, and these building blocks are subsequently assembled into well-defined super-structures through non-covalent interactions. Self-assembly of these molecular units has provided a powerful means for designing molecular systems with novel structures and properties.

## Surfactants and Lipids

Amphiphiles, such as surfactants and lipids, are molecules containing both hydrophobic and hydrophilic components. They self-assemble into a variety of structures, such as micelles, bilayers, and vesicles, in both aqueous and organic solvents. The competing interactions that drive this self-assembly arise from the attractive interfacial tension at the hydrocarbon–water interface, the repulsive steric interactions and the electrostatic force between the molecular head groups.

From the thermodynamics point of view, the formation of molecular aggregates is determined by the relative change in chemical potential ( $\mu_N - \mu_1$ ) when the molecules form a finite size aggregate consisting of  $N$  monomers. For simple alkane molecules in water, the change of chemical potential is monotonic with size,  $(\mu_N - \mu_1) \sim (\mu_\infty - \mu_1) + \alpha kT/N^P$ , where  $\mu_\infty$  and  $\mu_1$  are chemical potentials of the infinite solid and single molecule, respectively,  $\alpha kT$  is the binding energy in the aggregate, and the index  $P$  is determined by the dimensionality of the aggregate. Although finite size aggregates do form for simple alkane molecules above the critical micelle concentration (CMC), the population number of these aggregates decreases rapidly with their size. On the other hand, amphiphilic molecules have a minimum in chemical potential at a finite aggregation number. This is because the attractive

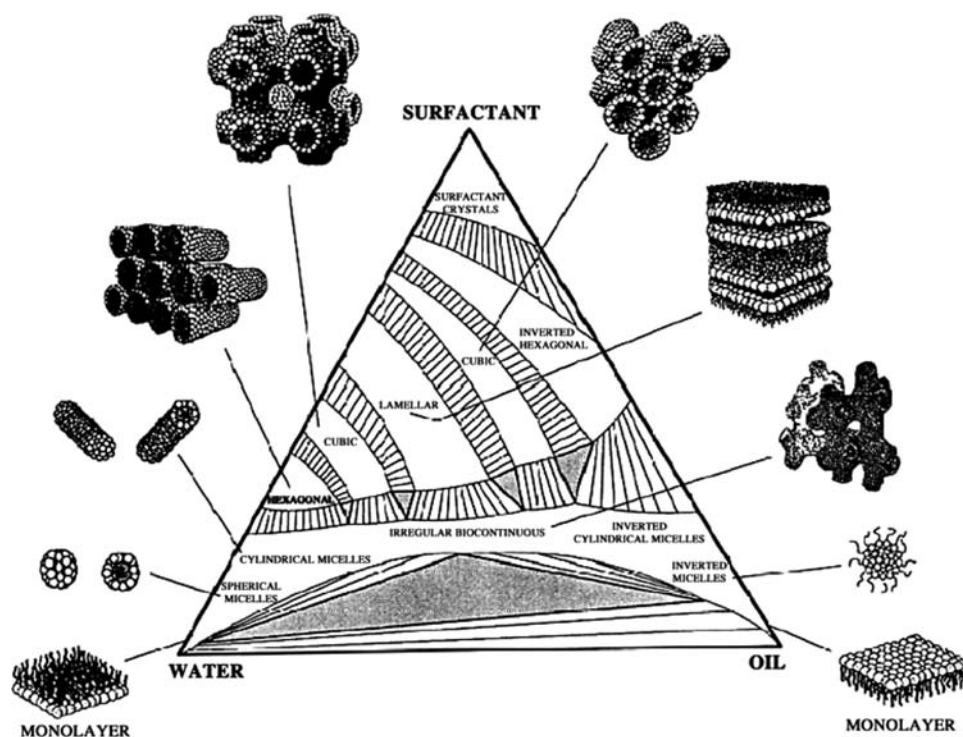


**Fig. 1** Amphiphiles can adopt a variety of structures as shown in this figure by simply changing the conditions, such as concentration, pH and temperature. *Source:* From Ref.<sup>[17]</sup>. © 1991, J. Coll. Inter. Sci.

interaction is proportional to the surface area of the molecule's head group whereas the repulsive interaction has an inverse proportionality. So, there is an optimum surface area  $a_0$  for the amphiphilic molecule, and finite size aggregates can form with a large population number.

Self-assembled structures obtained by this competing interaction can be determined by a simple geometrical packing parameter  $v/(a_0l_c)$ , where  $v$  is the volume of the molecule and  $l_c$  is the critical chain length. At low monomer concentrations, spherical micelles form when  $(v/(a_0l_c)) < (1/3)$ , cylindrical micelles form when  $(1/3) < (v/(a_0l_c)) < (1/2)$ , flexible bilayers and vesicles form when  $(1/2) < v/(a_0l_c) < 1$ , planar bilayers form when  $(v/a_0l_c) \sim 1$  and inverted micelles form when  $(v/a_0l_c) > 1$ . Fig. 1 shows some of the most widely studied structures. One interesting phenomenon is that even with the same amphiphile, the packing parameter can change with the environmental conditions, such as the pH of the solvent, the salt concentration and the temperature. As a result, self-organized structures will change correspondingly. This has a significant implication in biological membranes, because biological lipids with different packing parameters can form complex structures with different curvatures while maintaining the flexibility to respond to the changing environment. When the monomer concentration increases, the interaction between the

aggregates becomes more important, which leads to the change of aggregate shape and further organization of aggregates into several liquid crystalline phases (Fig. 1). For instance, the phase diagram of the binary system of water–dodecyltrimethyl ammonium chloride contains a micellar phase at low concentrations, two cubic phases, one hexagonal phase and one lamellar phase at high surfactant concentrations.<sup>[5]</sup> The lamellar phases consist of alternating bilayers that can easily slip relative to each other. Among various liquid crystalline phases, it is more difficult to detect the cubic phase since its isotropic structure cannot be revealed by standard polarized light microscopy. The cubic phase between the micellar and hexagonal phase is made of short rod-like aggregates. The cubic phase in the high amphiphile concentration region has a bicontinuous structure in which a single bilayer of molecules folds its way in space separating the two aqueous compartments.

While the thermodynamic phases created by amphiphile self-assembly have been well characterized, little is known about the kinetics of the phase transition between different structures.<sup>[18]</sup> This is largely because the transitions between different phases exhibit a very broad range of time scales, varying from submicroseconds to many days. Recently, light scattering, small-angle x-ray scattering (SAXS) and small-angle neutron scattering (SANS) have been adopted to investigate the kinetics of phase transitions.<sup>[19]</sup> Time resolved SAXS

experiments on a mixture of a cationic surfactant (tetradecyltrimethyl ammonium hydroxide) and an anionic surfactant (Texapon N<sub>70</sub>-H) show that the transition from micelles to vesicles is a multistep process.<sup>[20]</sup> Globular mixture micelles form very quickly upon mixing. Subsequent bilayer formation has a time scale of 500–1000 msec. The bilayer then closes up in a much slower process (5–100 sec) to form vesicles. Experiments on pentaethylene glycol mono-*n*-dodecyl ether (C<sub>12</sub>E<sub>5</sub>) in D<sub>2</sub>O under increasing pressure show a transformation from cylindrical micelles to ordered hexagonal micellar bundles, possibly due to the pressure induced freezing of the hydrophobic core.<sup>[21]</sup>

### Block Copolymers

This principle of self-assembly, based on combining motifs with different interfacial energies in a single molecule, also applies to polymers.<sup>[22,23]</sup> Copolymers are macromolecules that contain chemically distinct polymer blocks that are linked covalently. Synthetic developments based on living anionic, cationic, and radical polymerization have generated diblock, triblock, and multiblock copolymers that are arranged as linear chains, grafts, or star shapes.<sup>[24]</sup> Diblock copolymers are the most widely studied systems.

At low concentrations in solutions, block copolymers readily form micelles, with a CMC much lower than the typical surfactants or lipids. For diblock copolymers, micelles have a well-defined structure with a core consisting of the insoluble A block and a shell of the soluble B block. The size of the resulting micelles, which is characterized by the aggregation number  $Z$  (i.e., the number of molecules in a micelle), depends on the degree of polymerization of the soluble block  $N_A$  and insoluble block  $N_B$  through a simple relation,  $Z = Z_0 N_A^2 N_B^{-0.8}$ .<sup>[25]</sup> Thus, the diameter of the micelles can be directly tuned by the degree of polymerization of each block. Because of the possibility to tune the aggregate properties by varying either the type, the size, or the relative proportion of the constituting blocks, diblock micellar aggregates are able to provide a much wider range of applications than normal surfactants, including being used as tunable nanoreactors for colloidal synthesis,<sup>[26]</sup> and drug and gene delivery.<sup>[27]</sup>

In bulk materials, block copolymers phase-separate into a variety of mesoscopic structures upon cooling below the glass transition temperature. The sizes of the domains created by microphase separation are typically in the range of 10–100 nm. Electron microscopy<sup>[28]</sup> and SANS<sup>[29]</sup> have been used extensively to investigate the phase separated structures. These studies have shown that the morphologies of segregated diblock copolymer microphases depend upon the degree of polymerization  $N = N_A + N_B$ , the relative composition of the two constituent blocks

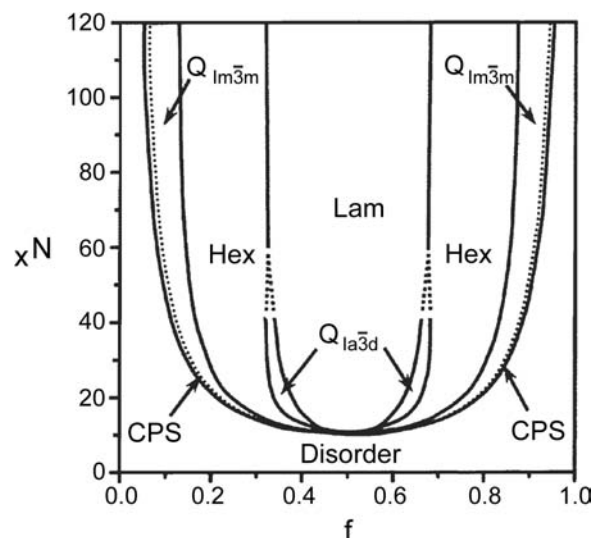


**Fig. 2** Phase diagram for a structurally symmetric coil-coil diblock copolymer. Lam = lamellae, Hex = hexagonally packed cylinders,  $Q_{Ia3d}$  = bicontinuous cubic with  $Ia3d$  symmetry,  $Q_{Im3m}$  = body-centered cubic, CPS = close-packed sphere. Source: From Ref.<sup>[32]</sup>. © 2001, Chem. Rev.

$f_A = N_A/N$ , the Flory–Huggins interaction parameter  $\chi$  between the two blocks and the temperature. A predicted stable microstructure, shown in Fig. 2, includes lamellae, hexagonally packed cylinders, body-centered cubic spheres, close-packed spheres, and bicontinuous cubic network phases with  $Ia3d$  symmetry. These structures have been verified experimentally.<sup>[30,31]</sup>

For a thin film of block copolymer, the interfacial energy of polymer/substrate and polymer/air become additional driving forces to affect the morphology of phase separation.<sup>[23,33]</sup> Fig. 3(A) shows the schematic cross-section diagram of polystyrene-*b*-poly(ethylene-*alt*-propylene). Polystyrene (PS) prefers to wet the silicon nitride/polymer interface, whereas the poly(ethylene-*alt*-propylene) (PEP) prefer the polymer/air interface.<sup>[34]</sup> The thickness of these PS-*b*-PEP film are quantized in odd multiples of  $L/2$ , with  $L/2$  being the size of the molecule. Recently, there has been growing effort to control the microdomain orientation and induce long-range lateral ordering in these thin films. So far, this has been achieved through applying an electric field, directional crystallization or confining the polymer on a patterned surface.<sup>[34–37]</sup> Fig. 3(C) and Fig. 3(D) show that cylindrical PS-*b*-PEP domains and spherical Polystyrene(PS)-*b*-polyferrocenyldimethylsilane (PFS) domains can be aligned in the trough lithographically patterned on a substrate.

### Supramolecular Systems

The highly selective and directional nature of the hydrogen bond makes it an ideal candidate for



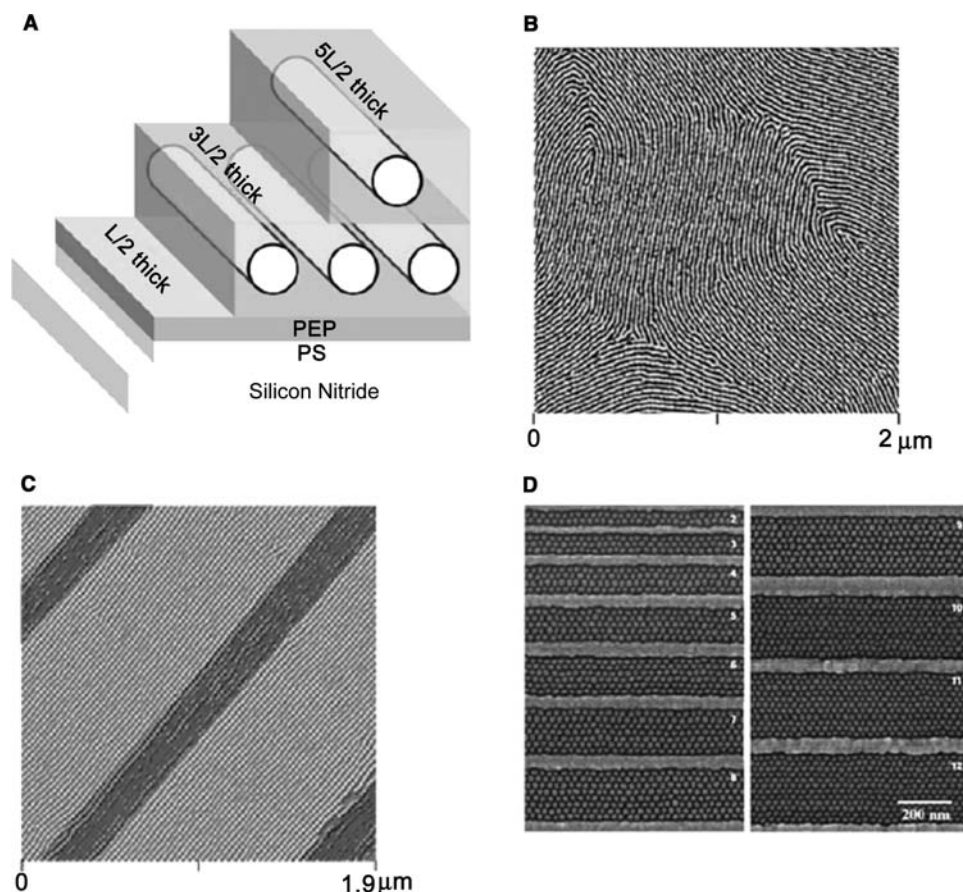


**Fig. 3** (A) Schematic diagram for a PS-*b*-PEP thin film organized on a silicon nitride substrate. (B) Tapping mode of cylindrical fingerprint structure of PS-*b*-PEP film. (C) Alignment of PS-*b*-PEP cylinders in the trough of a grating. *Source:* From Ref.<sup>[34]</sup>, © 2004, Langmuir. (D) Well-aligned PS-*b*-PFS spherical domains in the trough of a patterned surface. *Source:* From Ref.<sup>[37]</sup>, © 2001, Nature Mater.

constructing large assemblies of molecular building blocks. The strength of hydrogen bonds is relatively weak (3–5 kcal/mol). Furthermore, the enthalpic gain to form such bonds must overcome the entropy loss due to the reduction of molecular translation and conformation. Therefore, multi-hydrogen bond motifs are typically used to construct a stable assembly. Derivatives of 2-ureido-4-pyrimidone have a strong tendency to polymerize with self-complementary DDAA (donor–donor–acceptor–acceptor) hydrogen bonds. Depending on the geometry of this bonding motif in the molecule, linear polymers and reversible networks can be formed (Fig. 4). The network created by hydrogen bonding has a strong temperature dependent rheology. Multicomponent self-assembled structures based on the cyanuric acid–melamine motif were studied by Whitesides.<sup>[38]</sup> It was shown that these molecules form stacked rosettes, which can be further used for the self-assembly of multiporphyrin arrays.

By designing molecules with well-defined chirality, self-enclosed cyclic structures can form instead of straight polymeric chains. Bis-lactam molecules,

designed by Brienne and coworkers, form a ring structure due to the stereochemical arrangement of their hydrogen bonding sites [Fig. 5(A)].<sup>[40]</sup> Two sets of complementary triple hydrogen motifs in molecules such as Fig. 5(B) spontaneously form hexameric aggregates.<sup>[41]</sup> Self-assembled capsules, which contain molecules or ions inside their cavities, are formed using concave building blocks like glycoluril, calixarenes, or resorcinarenes [Fig. 5(C)].<sup>[42]</sup> One example based on complementary hydrogen bonding of glycoluril has created a “molecular tennis ball” [Fig. 5(D)].<sup>[43]</sup> The study of the dynamics of guest exchange in this tennis ball structures leads to the conclusion that optimal binding between the guest molecules and the capsule occurs when approximately 55% of the capsule volume is occupied.

Dendrimers are globular macromolecules in which all bonds emerge radially from a central focal point and with the repeating units converging to a branch point.<sup>[45]</sup> The distinctive features of dendrimers are their layered architecture, globular shape, multifunctional periphery, and radially controlled chemical composition. These features provide a unique oppor-

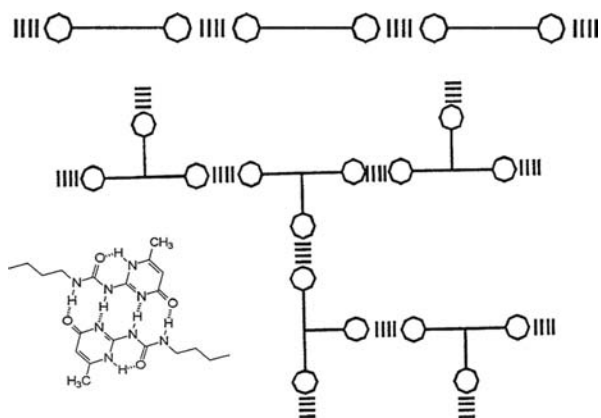


**Fig. 4** Schematic representation of reversible polymer architectures obtained from bifunctional and trifunctional pyrimidone derivatives. *Source:* From Ref.<sup>[39]</sup>. © 1997, Science.

tunity to transform dendritic structures into a variety of supramolecular architectures. Hydrogen-bonding interactions offer an effective route for creating such supramolecular structures. Using this approach, Zimmerman and co-workers prepared a remarkable family of dendrimers, which consisted of six Fréchet-type polyether dendrons, which fitted with two isophthalic acid units at their focal point.<sup>[46]</sup> In this case, six subunits were brought together by hydrogen bonds to construct supramolecular dendritic structures up to four generations. The resulting self-assembled macromolecule was disk-shaped with 9 nm in diameter and 2 nm in thickness. The shape of the first generation monodendron building blocks affects the superstructures they eventually form. Monodendrons with a flat, tapered shape organize into cylindrical dendrimers, which further organize into thermotropic hexagonal columnar phase ( $\Phi_h$ ) (Fig. 6A), whereas the spherical

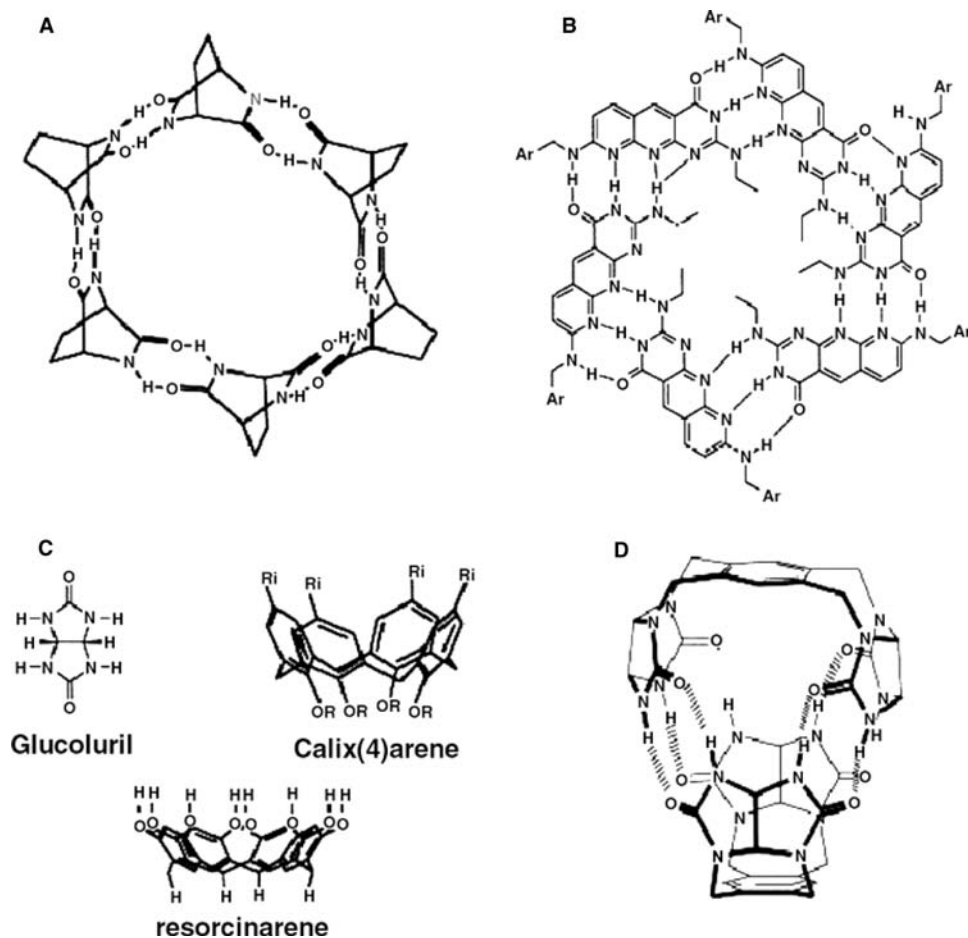


**Fig. 5** (A) Chiral dilactam form ring structure. *Source:* From Ref.<sup>[40]</sup>. © 1997, Helv. Chim. Acta. (B) Cyclic hexamer formed by triple hydrogen bonds in a DDA:AAD motif. *Source:* From Ref.<sup>[41]</sup>. © 1997, J. Am. Chem. Soc. (C) Molecular building blocks Glucoloril, calix(4)arene, and resorcinarene. *Source:* From Ref.<sup>[44]</sup>. © 1999, Curr. Opi. Coll. Inter. Sci. (D) “Tennis ball” structure formed by glycoluril-based building blocks. *Source:* From Ref.<sup>[43]</sup>. © 1993, Angew. Chem. Int. Ed. Engl.

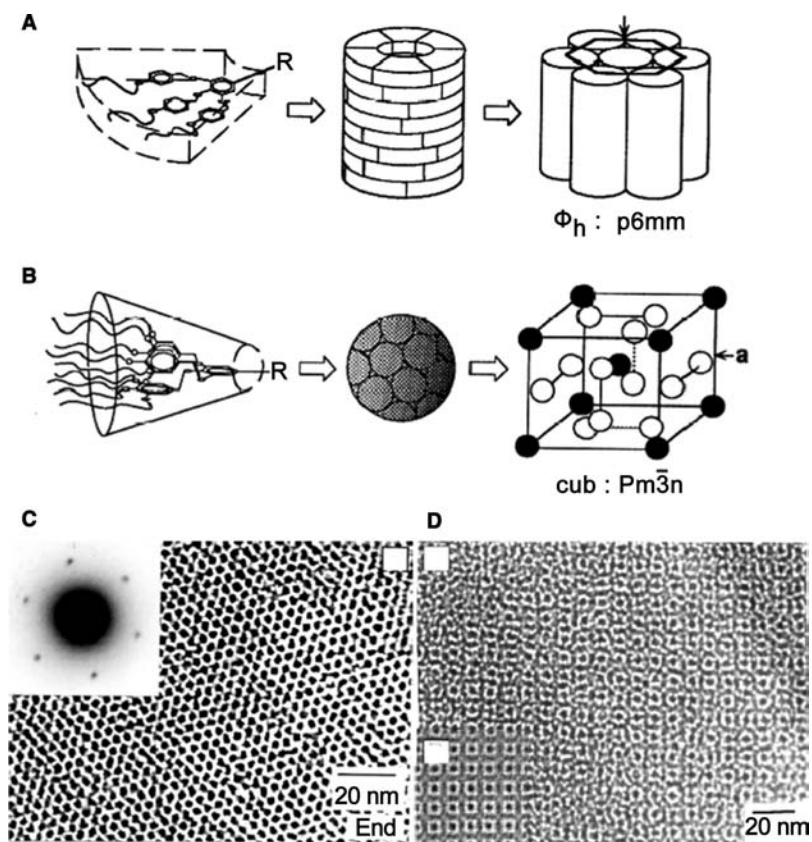


**Fig. 6** (A) Self-assembly of first generation, flat, tapered monodendrons into a cylindrical dendrimer and the subsequent formation of  $p6mm \Phi_h$  LC phase. (B) Self-assembly of second generation conical monodendron into spherical dendrimer and the subsequent formation of  $Pm\bar{3}n$  cubic LC phase. (C) Phase contrast TEM image of homeotropically aligned  $\Phi_h$  LC phase. (D) TEM image of  $Pm\bar{3}n$  cubic LC phase. *Source:* From Ref.<sup>[47]</sup>. © 1997, Science.

monodendrons form a homeotropic cubic liquid crystalline (LC) phase of  $Pm\bar{3}n$  symmetry [Fig. 6(B)].<sup>[47,48]</sup> Using a similar approach, Aida and coworkers<sup>[49]</sup> have prepared luminescent superhelical fibers, by exploiting weak metal–metal interactions to create hierarchical self-organization of small dendrimers. Owing to their sizes and unique optical and electronic properties, these supramolecular structures could have great potential applications in display, storage, and electronic devices.

### SELF-ASSEMBLY OF NANOSCALE BUILDING BLOCKS

Building blocks with a nanoscale dimension (typically <100 nm) have different properties compared with their bulk counterparts. For instance, the absorption and photoluminescence of semiconductor quantum dots show a strong size dependence.<sup>[50,51]</sup> Charge injection onto a single quantum dot has to overcome a strong Coulomb charging energy. The magnetic moments of the surface atoms are strongly enhanced due to unquenched orbital moments in transition metal clusters.<sup>[52]</sup> Fundamentally, all these new phenomena can be attributed to two major effects on the nanometer scale, namely, the quantum confinement of charge and spin,<sup>[53]</sup> and the low coordination of surface atoms.<sup>[54]</sup>

Developments in colloidal chemistry during the past two decades have produced a variety of high-quality nanoscale building blocks with many unique properties.<sup>[7,55–58]</sup> Although it is possible to study and utilize the physical properties of nanoparticles on a single particle level, it remains a technically challenging task. On the other hand, experiments on macroscopic 2D and 3D nanocrystal superlattices are more accessible. Self-assembly of nanocrystal building blocks not only provides a way to connect the nanoscale dimension to the macroscopic length scale, but it also creates a revolutionary new class of materials. New collective behavior is expected to emerge if there is a strong coupling between building blocks.<sup>[8,59]</sup>

Self-assembly of nanocrystals upon evaporation of solvents leads to spontaneous organization of particles. Based on this approach, many nanocrystal self-assemblies have been formed, including CdSe, CdS, Au, Ag, Co, FePt, CoO, Fe<sub>2</sub>O<sub>3</sub>.<sup>[60–67]</sup> Such assemblies are driven by interparticle van der Waals interactions. For a polydisperse colloid, this leads to size segregation because the interparticle interaction is size dependent. The balancing force to create a stable structure is provided by either steric repulsion from surface ligands or the electrostatic interactions from the surface charges. X-ray diffraction (XRD) and electron diffraction are typically used to characterize the structure. The

packing structures thus formed are slightly different from the crystal structure formed by atoms, because nanocrystals are typically polyhedral and thus create non-isotropic interactions between the different building blocks. Therefore, the size and shape of nanocrystals can affect the packing structure dramatically. For instance, it was found that truncated octahedral Ag nanocrystals form fcc superlattices, and there is a strong orientational order among particles in the superlattices.<sup>[68]</sup> For quasi-spherical gold nanoparticles, it was found that the crystallographic structure of the self-assembly depends on the ratio between the ligand chain length ( $L$ ) and the size of the metal core  $D_{\text{core}}$ :  $\xi = 2L/D_{\text{core}}$ .<sup>[50]</sup> This relates to a simple property like the “softness” of the particles (relative interaction strength) with the resultant self-assembled structure, with fcc as the hard-sphere limit and bcc in the soft limit. Assembly of building blocks with more anisotropy, such as nanorods, can create nematic and smectic liquid crystal phases.<sup>[69]</sup>

Mixing different nanoparticles with selected size ratio forms binary colloidal crystals with AB, AB<sub>2</sub>, AB<sub>5</sub>, and AB<sub>13</sub> structures, depending on the concentration ratio of the components. Two-dimensional binary lattices were demonstrated using two different sizes of gold nanoparticles.<sup>[71]</sup> Recently, three-dimensional binary lattices consisting of 11 nm  $\gamma$ -Fe<sub>2</sub>O<sub>3</sub> nanoparticles and 6 nm PbSe nanocrystals were also demonstrated.<sup>[70]</sup> Fig. 7 shows a TEM image of such a binary lattice. In these multicomponent nanocrystal assemblies, the properties of each component may be engineered individually. By tuning the coupling between different functionalities, it may be possible to obtain new properties that are otherwise difficult to obtain.

Kinetics also plays an important role in nanoscale self-assemblies. For evaporation-induced self-assemblies, percolating networks of nanocrystals are typically obtained because of the highly non-equilibrium process of solvent evaporation.<sup>[72,73]</sup> Despite this, for dodecanethiol ligated gold nanocrystals, it was shown that a highly ordered nanocrystal monolayer with domain sizes up to tens of micrometers can be formed by adding an excess amount of ligand molecules in the solution.<sup>[74]</sup> Recent in situ SAXS experiments (Fig. 8) demonstrated that the presence of excess thiol induces superlattice domain formation at the liquid–air interface rather than at the liquid–substrate interface.<sup>[75]</sup> Evaporation kinetics plays an important role in this process. With a fast evaporation rate, 2D superlattices nucleate and grow into a highly ordered structure. On the other hand, if the evaporation rate is slow enough, the 2D superlattices formed at the liquid–air interface are not stable, and the formation of 3D superlattices occurs in the interior of the droplet.

Nanoparticles functionalized with complementary linker molecules can spontaneously self-assemble into

macroscopic structures due to the chemical recognition ability of the surface ligands. Many such lock-and-key type of linker molecules have been investigated. Triple hydrogen bond motifs were used to assemble nanocrystals.<sup>[76]</sup> Gold nanocrystals ligated with DNA molecules form nanocrystal dimers and trimers when a complementary strand of DNA is added.<sup>[50,77]</sup> Streptavidin ligated gold nanoparticles were shown to form a two-dimensional array on a biotin-labeled glass substrate or form linear chains on biotin-labeled DNA chains.<sup>[78,79]</sup> The antigen–antibody recognition scheme was also used to create bimetallic aggregates.<sup>[80]</sup> Because of their intrinsic diversity, these biological scaffolds have the potential to create a rich family of self-organized structures. Such prospects have been shown recently using DNA scaffolds, where linear chains, ribbons, and branches of nanocrystal arrays were created.<sup>[79–81]</sup>

The self-assembly of nanoscale building blocks can also be induced by a pre-fabricated template. This template can be created by the molecular-scale self-assembly. An example was demonstrated in the evaporation of gold and silver onto a phase-separated polystyrene-*b*-poly(methyl methacrylate) film (Fig. 9).<sup>[82]</sup> Gold and silver particles spontaneously form in the polystyrene domain rather than the poly(methyl methacrylate) domain. This hierarchical self-assembly is driven by the different diffusion rates of metal atoms on the different polymer surfaces. When thiolated gold colloid is mixed with a solution of polystyrene-*b*-poly(4-vinylpyridine), which forms hexagonally ordered micelles upon evaporation, gold nanocrystals preferentially distribute themselves in the polystyrene coronas. If at the same time, the FeCl<sub>3</sub> precursor embedded in the PVP domains is oxidized, Fe<sub>2</sub>O<sub>3</sub> particles form in the PVP cores, thus creating a binary nanocrystal superlattice.<sup>[83]</sup>

## SELF-ASSEMBLY OF SUBMICROMETER TO MILLIMETER PARTICLES

A variety of different systems contain submicrometer particles with sizes ranging from 100 nm to 1  $\mu\text{m}$ . These include common substances such as milk, ink, and smoke. Studies on the self-organization of these particles have not only revealed a myriad of interesting phenomena associated with crystal structures and phase transitions, but have also led to many applications in pharmaceutical and cosmetic industries.<sup>[9]</sup> Most recently, the prospect of using these assemblies for photonic applications became a focus area.<sup>[84]</sup> Particles in an aqueous environment experience a strong, long-range, Hamaker-type van der Waals attraction that is balanced by a repulsive electrostatic double layer. These interactions together create a secondary minimum, well-described by DLVO theory, which



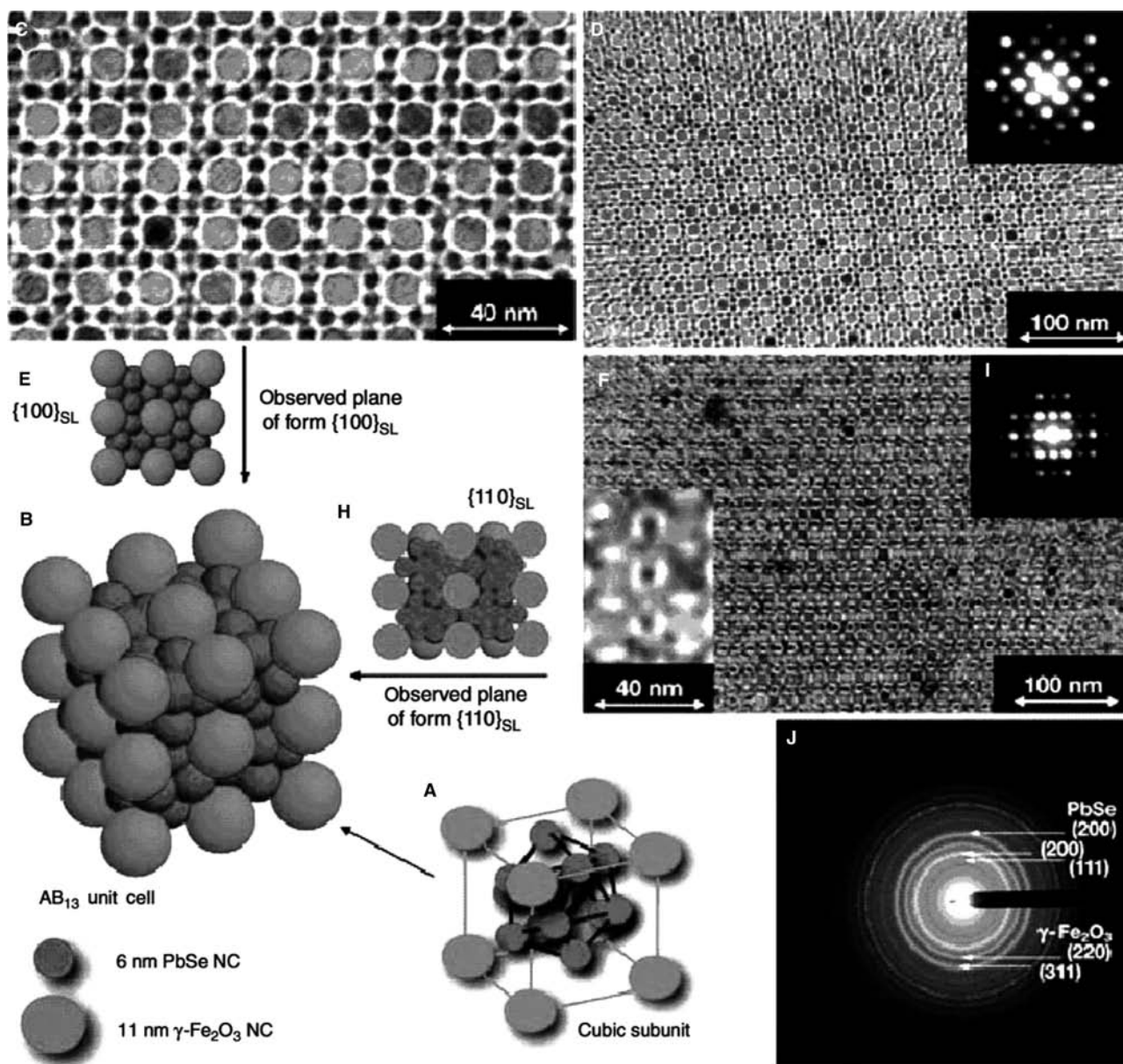


**Fig. 7** Transmission electron micrographs and sketches of AB<sub>13</sub> superlattices (SL) of 11 nm Fe<sub>2</sub>O<sub>3</sub> and 6 nm PbSe NCs. (A) Cubic subunit of the AB<sub>13</sub> unit cell. (B) AB<sub>13</sub> unit cell. (C) Projection of a 100 SL plane at high magnification. (D) As in (C) but at low magnification; inset: small-angle electron diffraction pattern from a corresponding 6 μm<sup>2</sup> area. (E) Depiction of a 100 plane. (F) Projection of a 110 SL plane. (G) As (F) but at high magnification. (H) Depiction of the projection of the 110 plane. (I) Small-angle electron diffraction pattern from a 6 μm<sup>2</sup> 110 SL area. (J) Wide-angle electron diffraction pattern of an AB<sub>13</sub>-superlattice (SAED of a 6 μm<sup>2</sup> area) with indexing of the main diffraction rings for PbSe and Fe<sub>2</sub>O<sub>3</sub> (maghemite). Source: From Ref.<sup>[70]</sup>. © 2003, Nature.

can lead to the assembly of stable supercrystals.<sup>[4]</sup> The range of the interaction is characterized by the Debye length, which can be tuned by changing the ionic strength of the colloidal solution. If the repulsive force is too weak, irreversible fractal aggregation or gel formation occur. The majority of the research has so far concentrated on systems with either hard sphere repulsive interaction or relatively weak attractive interactions.

For hard spheres confined in a finite volume, entropic effects can drive the system to crystallize when the volume fraction ( $\phi$ ) is above the freezing concentration.<sup>[85]</sup> Both the simulations and experiments<sup>[86–88]</sup> have shown that the colloid remains a liquid when  $\phi < 0.494$ , becomes a coexisting mixture of liquid and crystals when  $0.494 < \phi < 0.545$  and finally crystallizes when  $0.545 < \phi < 0.74$ . While the lowest energy crystal structure is still under debate, experiments both on earth

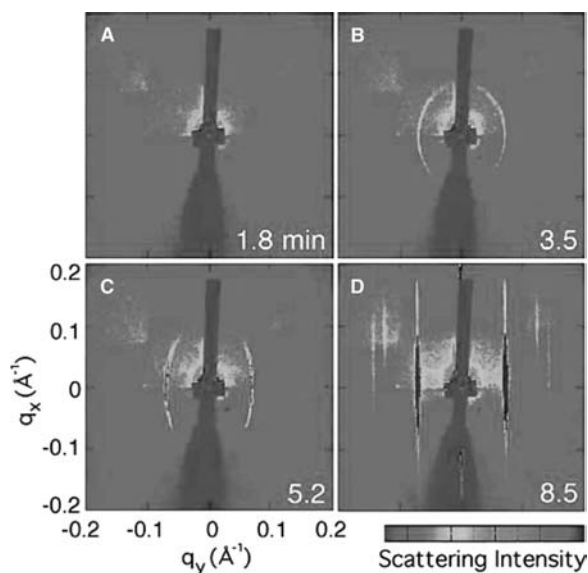


**Fig. 8** In situ SAXS patterns of 2D NCSs formation during droplet evaporation. Time in units of minutes is in reference to the deposition of the colloid droplet. The average diameter of the nanocrystals is 7.5 nm, as determined by TEM. Cross bar feature in each frame is the shadow image of the beam stop. *Source:* From Ref.<sup>[75]</sup>. © 2004, Phys. Rev. Lett.

and under microgravity both yield random stacking of hexagonal close pack structure (r.h.c.p.).<sup>[89,89]</sup> Face-centered cubic structures only form when the volume fraction is deep into the crystallization region and the sample is maintained undisturbed for a long time. If the volume fraction of the colloid is increased very rapidly into the crystal phase  $\phi > 0.58$ , a glassy state

is obtained. This was first confirmed experimentally by Pusey and van Megen.<sup>[88,91]</sup>

When the range of the interaction or the nature of the interaction between submicrometer particles changes, the formation of the crystal phase occurs at a very different volume fraction, and it can also lead to different crystal structures of the crystal phase. Polystyrene spheres trapped at the liquid–air interface interact through a long-range dipole–dipole interaction, which can also lead to the formation of two-dimensional triangular lattices.<sup>[92]</sup> Large floating particles can also deform the liquid surface enough to create long-range capillary forces due to the curvature of the surface. Smaller particles, however, can only deform the surface enough when they are nearly in contact with the solid substrate.<sup>[93]</sup> These techniques can be used to create extraordinary ordering, and have been recently used to self-assemble photonic band gap crystals of exceptional quality.<sup>[94]</sup> A weak long-range attractive interaction can also be induced by adding nonabsorbing polymers into the colloid.<sup>[95]</sup> Because of the finite radius of gyration ( $r_g$ ) of the added polymer, it will be excluded in the depletion layer surrounding the particles. The osmotic pressure exerted on the particles because of the depletion region will lead to the formation of particle assemblies. Attraction of a sufficiently long range will also introduce a gas phase transition, which depends keenly on the range of the attraction. At a high volume fraction that typically forms a glassy state in hard spheres, tuning the depletion attraction by adding a nonabsorbing polymer can induce transition from a repulsive glass state to a fluid state, followed by a re-entrant transition to

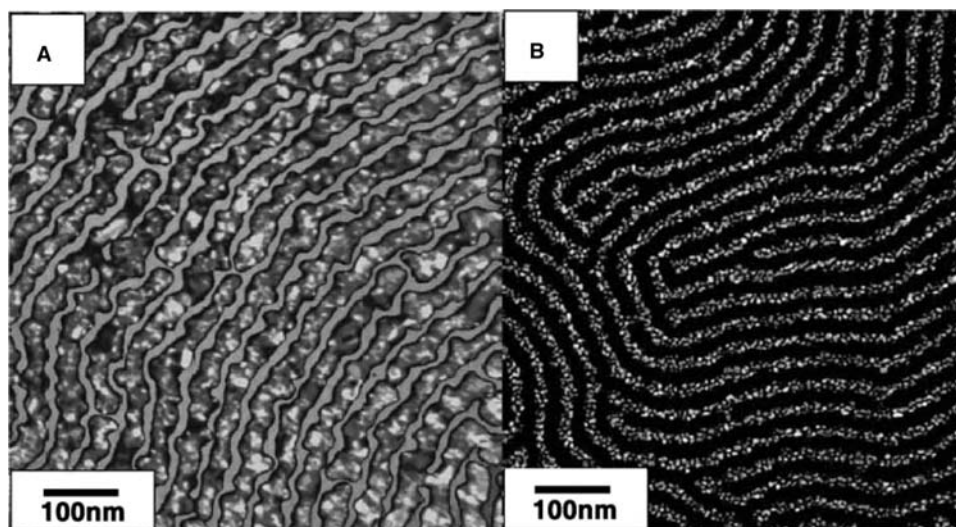


**Fig. 9** (A) Silver and (B) gold atoms selectively decorate polystyrene domains to form nanoscale chains after thermal evaporation of the metals onto the phase separated polystyrene-*b*-poly(methylmethacrylate) film.<sup>[82]</sup> *Source:* Courtesy of Prof. Heinrich Jaeger from University of Chicago.



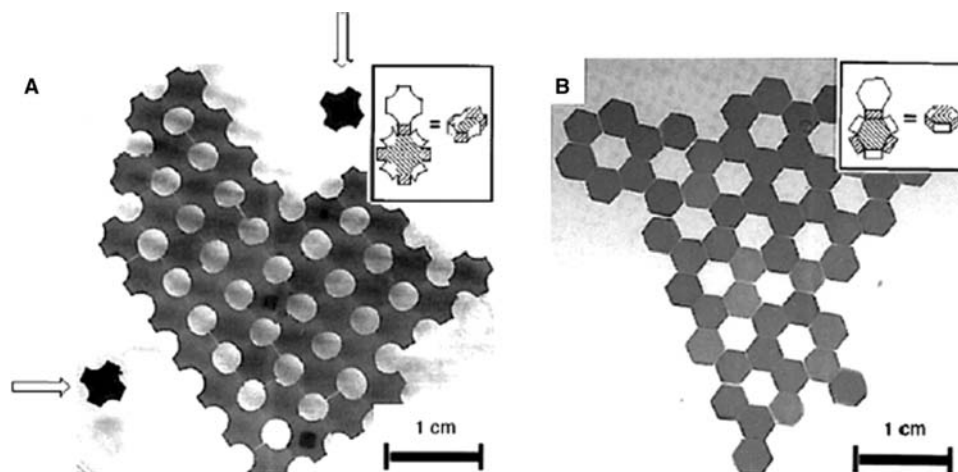


**Fig. 10** Crystalline aggregates generated by the self-assembly of millimeter-size (A) crosses that have hydrophobic ends and (B) hexagons that have three hydrophobic side faces. *Source:* From Ref.<sup>[100]</sup>. © 1997, Science.

an attractive glass state. This was first predicted by theory and has been recently confirmed by experiment.<sup>[96–98]</sup> Depletion interaction can also drive crystallization at the interface. A patterned surface can induce crystal growth into macroscopic structures that are determined by the symmetry of the surface patterns.<sup>[99]</sup>

Several interesting experiments also exist which examined the self-assembly of tens of micron to millimeter size particles with different shapes and hydrophobicities.<sup>[100]</sup> Hexagons made of polydimethylsiloxane with different hydrophobic surfaces interact selectively to form different 2D structures at the water-perfluorodecalin interface (Fig. 10). Different strengths of attractive interaction caused by capillary forces can also drive phase segregation of different particles. Such an assembly scheme has later been developed for 3D stacking of hexagonal polyurethane rods and 10  $\mu\text{m}$  metal blocks that are functionalized with self-assembled monolayers.<sup>[101]</sup>

## CONCLUSIONS

Compared with the complexity and diversity of biological self-assembled systems, man-made self-assembled systems, some of them outlined in the previous sections, are essentially still very primitive. The size range and the shape of the building blocks are quite limited, and the structures created from these building blocks are rather simple. Nevertheless, studies on many simple model systems have led to a better understanding of the basic energetic driving forces for the self-assembly process.

There are several promising directions in the near future. One area is to develop hierarchical schemes to control self-assembly at all length scales, therefore

creating materials entirely from self-assembly. Such efforts have already yielded some interesting results, with one example being the surfactant mediated crystallization of colloidal crystals.<sup>[102]</sup> In another aspect, much of the understanding of self-assembly has been limited to static systems, with the main focus on equilibrium structures. Dynamic self-assembly, where systems undergo constant energy exchange with their environment and have different phase transitions, will draw more research attention in the future, largely because nature itself is essentially a dynamic and evolving system.<sup>[2]</sup> Therefore, it is crucial to develop new in situ experimental techniques with high spatial and temporal resolutions. Ultimately, creating materials that have the same complexity as biological systems through self-assembly is the holy grail in this research field. It is therefore, not a surprise that there is tremendous interest in developing biomimetic self-assembled systems.

## ACKNOWLEDGMENTS

This work was supported by the University of Chicago–Argonne National Laboratory Consortium for Nanoscience Research, U.S. Department of Energy, Basic Energy Sciences–Materials Sciences, under Contract #W-31-109-ENG-38.

## REFERENCES

1. Ball, P. *Self-Made Tapestry: Pattern Formation in Nature*; Oxford Press: Oxford, 1998.
2. Whitesides, G.M.; Grzybowski, B. Self-assembly at all scales. *Science* **2002**, *295*, 2418–2421.

- Fendler, J.H. Chemical self-assembly for electronic applications. *Chem. Mater.* **2001**, *13*, 3196–3210.
- Israelachvili, J.N. *Intermolecular and Surface Forces*; Academic Press Ltd.: San Diego, 2003.
- Evans, D.F.; Wennerström, H. *The Colloidal Domain Where Physics, Chemistry, Biology, and Technology Meet*; Wiley-VCH: New York, 1999.
- Philp, D.; Stoddart, J.F. Self-assembly in natural and unnatural systems. *Angew. Chem. Int. Ed. Engl.* **1996**, *35*, 1155–1196.
- Murray, C.B.; Kagan, C.R.; Bawendi, M.G. Synthesis and characterization of monodisperse nanocrystals and close-packed nanocrystal assemblies. *Annu. Rev. Mater. Sci.* **2000**, *30*, 545–610.
- Zhang, J.; Wang, Z.L.; Liu, J.; Chen, S.; Liu, G. *Self-assembled Nanostructures*; Kluwer Academic: New York, 2003.
- Weitz, D.A.; Russel, R.B. New developments in colloidal science. *MRS Bull.* **2004**, *29* (2), 82–84.
- Evans, L.S.; Gale, P.A. Anion-templated self-assembly: inorganic compounds. In *Dekker Encyclopedia of Nanoscience and Nanotechnology*, 2E; Schwarz, J.A., Contescu, C.I., Putyera, K., Eds.; Taylor & Francis: New York, NY, 2009; Vol. 1, 178–190.
- Sevin, K. Metallomacrocyclic selective ion receptors. In *Dekker Encyclopedia of Nanoscience and Nanotechnology*, 2E; Schwarz, J.A., Contescu, C.I., Putyera, K., Eds.; Taylor & Francis: New York, NY, 2009; Vol. 3, 2202–2210.
- Kretzschmar, I.; Reed, M.A. Nanoparticle arrays: optical and electronic applications. In *Dekker Encyclopedia of Nanoscience and Nanotechnology*, 2E; Schwarz, J.A., Contescu, C.I., Putyera, K., Eds.; Taylor & Francis: New York, NY, 2009; Vol. 4, 2856–2867.
- Pileni, M.P. Nanocrystals synthesized in colloidal self-assemblies. In *Dekker Encyclopedia of Nanoscience and Nanotechnology*, 2E; Schwarz, J.A., Contescu, C.I., Putyera, K., Eds.; Taylor & Francis: New York, NY, 2009; Vol. 4, 2581–2591.
- Lin, X.M.; Parthasarathy, R.; Jaeger, H.M. Nanocrystal arrays: self-assembly and physical properties. In *Dekker Encyclopedia of Nanoscience and Nanotechnology*, 2E; Schwarz, J.A., Contescu, C.I., Putyera, K., Eds.; Taylor & Francis: New York, NY, 2009; Vol. 4, 2568–2580.
- Santhanam, V.; Andres, R.P. Metal nanoparticles: self-assembly into electronic nanostructures. In *Dekker Encyclopedia of Nanoscience and Nanotechnology*, 2E; Schwarz, J.A., Contescu, C.I., Putyera, K., Eds.; Taylor & Francis: New York, NY, 2009; Vol. 3, 2079–2090.
- Woodward, R.B. The total synthesis of vitamin B<sub>12</sub>. *Pure. Appl. Chem.* **1973**, *33*, 145–177.
- Vinson, P.K.; Bellare, J.R.; Davis, H.T.; Miller, W.G.; Scriven, L.E. Direct imaging of surfactant micelles, vesicles, discs, and ripple phase structures by cryo-transmission electron microscopy. *J. Coll. Interface Sci.* **1991**, *142* (1), 74–91.
- Gradzielski, M. Kinetics of morphological changes in surfactant systems. *Curr. Opin. Colloid Interface Sci.* **2003**, *8*, 337–345.
- Egelhaaf, S.U.; Schurtenberger, P. Micelle-to-vesicle transition: a time-resolved structural study. *Phys. Rev. Lett.* **1999**, *82* (13), 2804–2807.
- Schmölzer, S.; Grabner, D.; Gradzielski, M.; Narayanan, T. Millisecond-range time-resolved small-angle x-ray scattering studies of micellar transformation. *Phys. Rev. Lett.* **2002**, *88* (25), 258, 301–258, 304.
- Bossev, B.P.; Kline, S.R.; Israelachvili, J.N.; Paulaitis, M.E. Pressure-induced freezing of the hydrophobic core leads to a  $L_1 \rightarrow H_1$  phase transition for C<sub>12</sub>E<sub>5</sub> micelles in D<sub>2</sub>O. *Langmuir* **2001**, *17* (25), 7728–7731.
- Bates, F.S.; Fredrickson, G.H. Block copolymer thermodynamics: theory and experiment. *Annu. Rev. Phys. Chem.* **1990**, *41*, 525–557.
- Fasolka, M.J.; Mayes, A.M. Block copolymer thin films: physics and applications. *Annu. Rev. Mater. Res.* **2001**, *31*, 323–355.
- Föster, S.; Antonietti, M. Amphiphilic block copolymers in structure-controlled nanomaterial hybrids. *Adv. Mater.* **1998**, *10* (3), 195–217.
- Föster, S.; Zisenis, M.; Wenz, E.; Antonietti, M.J. Micellization of strongly segregated block copolymers. *J. Chem. Phys.* **1996**, *104* (24), 9956–9970.
- Moffitt, M.; McMahan, L.; Pessel, V.; Eisenberg, A. Size control of nanoparticles in semiconductor-polymer composites. 2. control via sizes of spherical ionic micro-domains in styrene-based diblock ionomers. *Chem. Mater.* **1995**, *7* (6), 1185–1192.
- Yokoyama, M.; Okano, T.; Sakurai, Y.; Ekimoto, H.; Shibasaki, C.; Kataoka, K. Toxicity and antitumor activity against solid tumors of micelle-forming polymeric anticancer drug and its extremely long circulation in blood. *Cancer Res.* **1991**, *51*, 3229–3236.
- Mortensen, K.; Talmon, Y. Cryo-TEM and SANS microstructural study of pluronic polymer solutions. *Macromolecules* **1995**, *28* (26), 8829–8834.
- Mortensen, K. Structural studies of aqueous solutions of PEO-PPO-PEO triblock copolymers, their micellar aggregates and mesophases: a small-angle neutron scattering study. *J. Phys. Condens. Matter* **1996**, *8*, A103–A124.
- Hamley, I.W.; Koppi, K.A.; Rosedale, J.H.; Bates, F.S.; Almdal, K.; Mortensen, K. Hexagonal mesophases between lamellae and cylinders in a diblock copolymer melt. *Macromolecules* **1993**, *26*, 5959–5970.
- Bahadur, P. Block copolymers—their microdomain formation (in solid state) and surfactant behavior (in solution). *Curr. Sci.* **2001**, *80* (8), 1002–1007.
- Lee, M.; Cho, B.K.; Zin, W.C. Supramolecular structures from rod-coil block copolymers. *Chem. Rev.* **2001**, *101* (12), 3869–3892.
- Krausch, G.; Magerle, R. Nanostructured thin films via self-assembly of block copolymers. *Adv. Mater.* **2002**, *14* (21), 1579–1583.
- Sundrani, D.; Darling, S.B.; Sibener, S.J. Hierarchical assembly and compliance of aligned nanoscale polymer cylinders in confinement. *Langmuir* **2004**, *20* (12), 5091–5099.
- Morkeved, T.L.; Lu, M.; Urbas, A.M.; Ehrichs, E.E.; Jaeger, H.M.; Mansky, P.; Russell, T.P. Local control

- of microdomain orientation in diblock copolymer thin films with electric fields. *Science* **1996**, *273*, 931–933.
36. Park, C.; De Rosa, C.; Thomas, E.L. Large area orientation of block copolymer microdomains in thin films via directional crystallization of a solvent. *Macromolecules* **2001**, *34* (8), 2602–2606.
37. Cheng, J.Y.; Mayes, A.M.; Ross, C.A. Nanostructure engineering by templated self-assembly of block copolymers. *Nat. Mater.* **2004**, *3*, 823–828.
38. Mammen, M.; Shakhnovich, E.I.; Deutch, J.M.; Whitesides, G.M. Estimating the entropic cost of self-assembly of multiparticle hydrogen-bonded aggregates based on the cyanuric acid–melamine lattice. *J. Org. Chem.* **1997**, *62*, 2619–2621.
39. Sijbesma, R.P.; Beijer, F.H.; Brunsveld, L.; Folmer, B.J.B.; Hirschberg, J.H.K.K.; Lange, R.F.M.; Lowe, J.K.L.; Meijer, E.W. Reversible polymers formed from self-complementary monomers using quadruple hydrogen bonding. *Science* **1997**, *278* (5343), 1601–1604.
40. Brienne, M.J.; Gabard, J.; Leclercq, M.; Lehn, J.M.; Cheve, M. Synthesis of chiral bicyclic bis-lactam components for the controlled self-assembly of hydrogen-bonded arrays. *Helv. Chim. Acta.* **1997**, *80*, 856–875.
41. Kolutchin, S.V.; Zimmerman, S.C. Self-assembly mediated by the donor–donor–acceptors: acceptor–acceptor–donor (DDA:AAD) hydrogen-bonding motif: formation of a robust hexameric aggregates. *J. Am. Chem. Soc.* **1998**, *120*, 9092–9093.
42. Conn, M.M.; Rebek, J.J. Self-assembled capsules. *Chem. Rev.* **1997**, *97*, 1647–1668.
43. Wyler, M.; de Mendoza, J.; Rebek, J.J. Dynamics of assembly and guest exchange of new molecular hosts—solvation and the energetics of encapsulation. *Angew. Chem. Int. Ed. Engl.* **1993**, *32*, 1699.
44. Sijbesma, R.P.; Meijer, E.W. Self-assembly of well-defined structures by hydrogen bonding. *Curr. Opin. Coll. Interface Sci.* **1999**, *4*, 24–32.
45. Frchet, J.M.J. Dendrimers and supramolecular chemistry. *Proc. Natl. Acad. Sci.* **2002**, *99* (8), 4782–4787.
46. Zimmerman, S.C.; Zeng, F.W.; Reichert, D.E.C. Self-assembling dendrimers. *Science* **1996**, *271* (5252), 1095–1098.
47. Hudson, S.D.; Jung, H.T.; Percec, V.; Cho, W.D.; Johansson, G.; Ungar, G.; Balagurusamy, V.S.K. Direct visualization of individual cylindrical and spherical supramolecular dendrimers. *Science* **1997**, *278*, 449–452.
48. Percec, V.; Cho, W.D.; Mosier, P.E.; Ungar, G.; Yeardeley, D.J.P. Structural analysis of cylindrical and spherical supramolecular dendrimers quantifies the concept of monodendron shape control by generation number. *J. Am. Chem. Soc.* **1998**, *120* (43), 11,061–11,070.
49. Enomoto, M.; Kishimura, A.; Aida, T. Coordination metallacycles of an achiral dendron self-assemble via metal–metal interaction to form luminescent superhelical fibers. *J. Am. Chem. Soc.* **2001**, *123* (23), 5608–5609.
50. Alivisatos, A.P. Semiconductor clusters, nanocrystals, and quantum dots. *Science* **1996**, *271*, 933–937.
51. Murray, C.B.; Norris, D.J.; Bawendi, M.G.; Synthesis and characterization of nearly monodisperse CdE (E = S, Se, Te) semiconductor nanocrystallines. *J. Am. Chem. Soc.* **1993**, *115*, 8706–8715.
52. Bucher, J.; Douglass, D.C.; Bloomfield, L.A. Magnetic properties of free cobalt clusters. *Phys. Rev. Lett.* **1991**, *66* (23), 3052–3055.
53. Halperin, W.P. Quantum size effects in metal particles. *Rev. Mod. Phys.* **1986**, *58* (3), 533–606.
54. Klabunde, K. *Nanoscale Materials in Chemistry*; Wiley: New York, 2001.
55. Lee, S.M.; Jun, Y.W.; Cho, S.N.; Cheon, J. Single-crystalline star-shaped nanocrystals and their evolution: programming the geometry of nanobuilding blocks. *J. Am. Chem. Soc.* **2002**, *124* (38), 11,244–11,245.
56. Song, Q.; Zhang, Z.J. Shape control and associated magnetic properties of spinel cobalt ferrite nanocrystals. *J. Am. Chem. Soc.* **2004**, *126* (19), 6164–6168.
57. Jana, N.; Gearheart, L.; Murphy, C.J. Wet chemical synthesis of high aspect ratio cylindrical gold nanorods. *J. Phys. Chem. B* **2001**, *105* (19), 4065–4067.
58. Peng, Z.A.; Peng, X. Mechanisms of the shape evolution of cdse nanocrystals. *J. Am. Chem. Soc.* **2001**, *123* (7), 1389–1395.
59. Pileni, M.P. Nanocrystal self-assemblies: fabrication and collective properties. *J. Phys. Chem. B* **2001**, *105*, 3358–3371.
60. Murray, C.B.; Kagan, C.R.; Bawendi, M.G. Self-organization of CdSe nanocrystallites into three-dimensional quantum dot superlattices. *Science* **1995**, *270*, 1335–1338.
61. Hu, H.; Brust, M.; Bard, A.J. Characterization and surface charge measurement of self-assembled CdS nanoparticle films. *Chem. Mater.* **1998**, *10*, 1160–1165.
62. Stoeva, S.; Klabunde, K.J.; Sorensen, C.M.; Dragieva, I. Gram-scale synthesis of monodisperse gold colloids by the solvated metal atom dispersion method and digestive ripening and their organization into two- and three-dimensional structures. *J. Am. Chem. Soc.* **2002**, *124* (10), 2305–2311.
63. Wang, Z.L.; Harfenist, S.A.; Vezmar, I.; Whetten, R.L.; Bentley, J.; Evans, N.D.; Alexander, K.B. Superlattices of self-assembled tetrahedral Ag nanocrystals. *Adv. Mater.* **1998**, *10*, 808–812.
64. Sun, S.H.; Murray, C.B. Synthesis of monodisperse cobalt nanocrystals and their assembly into magnetic superlattices. *J. Appl. Phys.* **1999**, *85*, 4325–4330.
65. Sun, S.H.; Murray, C.B.; Weller, D.; Folks, L.; Moser, A. Monodisperse FePt nanoparticles and ferromagnetic FePt nanocrystal superlattices. *Science* **2000**, *287*, 1989–1992.
66. Yin, J.S.; Wang, Z.L. Ordered self-assembly of tetrahedral oxide nanocrystals. *Phys. Rev. Lett.* **1997**, *79*, 2570–2573.
67. Bentzon, M.D.; Wouterghem, J.V.; Mørup, S.; Thölen, A.; Koch, C.J.W. Ordered aggregates of ultrafine iron-oxide particle-super crystals. *Philos. Mag. B* **1989**, *60*, 169–178.
68. Harfenist, S.A.; Wang, Z.L.; Alvarez, M.M.; Vezmar, I.; Whetten, R.L. Hexagonal close packed thin films

- of molecular Ag-nanocrystal arrays. *J. Phys. Chem. B* **1996**, *100*, 13,904–13,910.
69. Kim, F.; Kwan, S.; Akana, J.; Yang, P. Langmuir–Blodgett nanorod assembly. *J. Am. Chem. Soc.* **2001**, *123* (18), 4360–4361.
  70. Redl, F.X.; Cho, K.-S.; Murray, C.B.; O'Brian, O. Three-dimensional binary superlattices of magnetic nanocrystals and semiconductor quantum dots. *Nature* **2003**, *423* (6943), 968–971.
  71. Kiely, C.J.; Fink, J.; Brust, M.; Bethell, D.; Schiffrin, D.J. Spontaneous ordering of bimodal assemblies of nanoscopic gold clusters. *Nature* **1998**, *396*, 444–446.
  72. Tang, J.; Ge, G.; Brus, L.E. Gas–liquid–solid phase transition model for two-dimensional nanocrystal self-assembly on graphite. *J. Phys. Chem. B* **2002**, *106* (22), 5653–5658.
  73. Moriarty, P.; Taylor, M.D.R.; Brust, M. Nanostructured cellular networks. *Phys. Rev. Lett.* **2002**, *89* (24), 248,303–248,307.
  74. Lin, X.M.; Jaeger, H.M.; Sorensen, C.M.; Klabunde, K.J. Formation of long-range-ordered nanocrystal superlattices on silicon nitride substrates. *J. Phys. Chem. B* **2001**, *105* (17), 3353–3357.
  75. Narayanan, S.; Wang, J.; Lin, X.M. Dynamical self-assembly of nanocrystal superlattices during colloidal droplet evaporation by in situ small-angle x-ray scattering. *Phys. Rev. Lett.* **2004**, *93* (13), 135,503–135,506.
  76. Boal, A.K.; Ilhan, F.; DeRouchey, J.E.; Thurn-Albrecht, T.; Russell, T.P.; Rotello, V.M. Self-assembly of nanoparticles into structured spherical and network aggregates. *Nature* **2000**, *404*, 746–748.
  77. Mirkin, C.A.; Letsinger, R.L.; Mucic, R.C.; Storhoff, J.J. A DNA-based method for rationally assembling nanocrystals into macroscopic materials. *Nature* **1996**, *382*, 607–609.
  78. Grabar, K.C.; Freeman, R.G.; Hommer, M.B.; Natan, M.J. Preparation and characterization of Au colloid mono-layer. *Anal. Chem.* **1995**, *67* (4), 735–743.
  79. Li, H.; Park, S.H.; Reif, J.H.; LaBean, T.H.; Yan, H. DNA-templated self-assembly of protein and nanoparticle linear arrays. *J. Am. Chem. Soc.* **2004**, *126* (2), 418–419.
  80. Shenton, W.; Davis, S.A.; Mann, S. Directed self-assembly of nanoparticles into macroscopic materials using antibody–antigen recognition. *Adv. Mater.* **1999**, *11* (6), 2135–2138.
  81. Warner, M.G.; Hutchison, J.E. Linear assemblies of nanoparticles electrostatically organize on DNA scaffolds. *Nat. Mater.* **2003**, *2*, 272–276.
  82. Lopes, W.A.; Jaeger, H.M. Hierarchical self-assembly of metal nanostructures on diblock copolymer scaffolds. *Nature* **2001**, *414*, 735–738.
  83. Sohn, B.; Choi, J.; Yoo, S.; Yun, S.; Zin, W.; Jung, J.C.; Kane-hara, M.; Hirata, T.; Teranishi, T. Directed self-assembly of two kinds of nanoparticles utilizing monolayer films of diblock copolymer micelles. *J. Am. Chem. Soc.* **2003**, *125* (21), 6368–6369.
  84. Joannopoulos, J.D.; Meade, R.D.; Winn, J.N. *Photonic Crystals: Molding the Flow of Light*; Princeton University Press: Princeton, 1995.
  85. Gast, A.P.; Russel, W.B. Simple ordering in complex fluids. *Phys. Today*. **1998**, *12*, 24–30.
  86. Wood, W.W.; Jacobsen, J.D. Preliminary results from recalculation of the Monte Carlo equation of state of hard spheres. *J. Chem. Phys.* **1957**, *27*, 1207–1208.
  87. Adler, B.J.; Wainwright, T.E. Phase transition for a hard sphere system. *J. Chem. Phys.* **1957**, *27*, 1208–1209.
  88. Pusey, P.N.; van Meegen, W. Phase behavior of concentrated suspensions of nearly hard colloidal spheres. *Nature* **1986**, *320*, 340–342.
  89. Pusey, P.N.; van Meegen, W.; Bartlett, P.; Ackerson, B.J.; Rarity, J.G.; Underwood, S.M. Structure of crystals of hard colloidal spheres. *Phys. Rev. Lett.* **1989**, *63* (25), 2753–2756.
  90. Zhu, J.; Li, M.; Rogers, R.; Meyer, W.; Ottewill, R.H.; Crew, S.S.S.; Russel, W.B.; Chaikin, P.W. Crystallization of hard-sphere colloids in microgravity. *Nature* **1997**, *387*, 883.
  91. Pusey, P.N.; van Meegen, W. Observation of a glass transition in suspensions of spherical colloidal particles. *Phys. Rev. Lett.* **1987**, *59* (18), 2083–2086.
  92. Pieranski, P. Two-dimensional interfacial colloidal crystals. *Phys. Rev. Lett.* **1980**, *45* (7), 569–572.
  93. Denkov, N.; Velev, O.; Kralchevski, P.; Ivanov, I.; Yoshimura, H.; Nagayama, K. Mechanism of formation of two-dimensional crystals from latex particles on substrates. *Langmuir* **1992**, *8* (12), 3183–3190.
  94. Vlasov, Y.A.; Bo, X.; Sturm, J.C.; Norris, D.J. On-chip natural assembly of silicon photonic bandgap crystals. *Nature* **2001**, *414* (6861), 289–293.
  95. Poon, W.C.K. The physics of a model colloid–polymer mixture. *J. Phys.: Condens. Matter.* **2002**, *14* (33), R859–R880.
  96. Bergenholtz, J.; Fuchs, M. Nonergodicity transitions in colloidal suspensions with attractive interactions. *Phys. Rev.* **1999**, *E59* (5), 5706–5715.
  97. Fabbian, L.; Götze, W.; Sciortino, F.; Tartaglia, P.; Thiery, F. Ideal glass–glass transitions and logarithmic decay of correlations in a simple system. *Phys. Rev. E.* **1999**, *59* (2), R1347–R1350.
  98. Pham, K.N.; Puertas, A.M.; Bergenholtz, J.; Egelhaaf, S.U.; Moussaid, A.; Pusey, P.N.; Schofield, A.B.; Cates, M.E.; Fuchs, M.; Poon, W.C.K. Multiple glassy states in a simple model system. *Science* **2002**, *296* (5565), 104–106.
  99. Lin, K.; Crocker, J.C.; Prasad, V.; Schofield, A.; Weitz, D.A.; Lubensky, T.C.; Yodh, A.G. Entropically driven colloidal crystallization on patterned surfaces. *Phys. Rev. Lett.* **2000**, *85* (8), 1770–1773.
  100. Bowden, N.; Terfort, A.; Carbeck, J.; Whitesides, G.M. Self-assembly of mesoscale objects into ordered two-dimensional arrays. *Science* **1997**, *276*, 233
  101. Oliver, S.R.J.; Bowden, N.; Whitesides, G.M. Self-assembly of hexagonal rod arrays based on capillary forces. *J. Coll. Interface Sci.* **2000**, *224* (2), 425–428.
  102. Ramos, L.; Lubensky, T.C.; Dan, N.; Nelson, P.; Weitz, D.A. Surfactant-mediated two-dimensional crystallization of colloidal crystals. *Science* **1999**, *286*, 2325–2328.

# Self-Assembled Thin Films: Optical Characterization

**Herbert Wormeester**

*Faculty of Science and Technology, University of Twente, Enschede, The Netherlands*

**E. Stefan Kooij**

*Faculty of Science and Technology, Department of Solid State Physics,  
University of Twente, Enschede, The Netherlands*

**Bene Poelsema**

*Faculty of Applied Physics, University of Twente, Enschede, The Netherlands*

## INTRODUCTION

Many different materials with truly new physical and chemical properties, consisting of controllably deposited colloid particles, are being developed. Particles with a variety of intrinsic properties are used, their sizes varying over at least three orders of magnitude. For photonic band gap materials, particle sizes are in the (sub)micron range, whereas for magnetic applications, such as ultra-high-density storage devices, they are in the low-nanometer range.<sup>[1,2]</sup> A prerequisite for studying colloidal systems is the ability to characterize them unambiguously under relevant conditions. Among the large number of methods available for characterizing colloids and their superstructures, scanning electron microscopy (SEM) and transmission electron microscopy (TEM) are by far the most popular.<sup>[1–7]</sup> For both very small as well as relatively large particles these are the most employed *ex situ* techniques. The use of various scanning probe microscopies—atomic force microscopy (AFM), scanning tunneling microscopy (STM), and magnetic force microscopy (MFM)—among colloid scientists is increasing; with these techniques experiments are also typically performed *ex situ*.<sup>[8,9]</sup> In fact, only optical methods have been employed *in situ*. For larger colloids, imaging techniques such as conventional<sup>[5,10]</sup> or confocal<sup>[11]</sup> microscopy are used. For sizes much smaller than the wavelength of light, such as with gold nanoparticles, only non-imaging (lateral averaging) *in situ* techniques are available. These include primarily ultraviolet/visible (UV/vis) absorption spectroscopy<sup>[1,6,8,9]</sup> and also optical reflection techniques such as reflectometry and ellipsometry.<sup>[12–15]</sup> The major advantage of ellipsometry as compared to reflectometry is its sensitivity to very small perturbations at an interface. Not only the deposition process but also the drying processes of (nano)colloidal particles at a solid–liquid interface can be studied.<sup>[12–14]</sup> However, both the *in situ* and *ex situ* capabilities of the

aforementioned reflection techniques depend on an unambiguous interpretation of recorded optical spectra.

Much work is devoted to the optical characterization of adsorbed proteins.<sup>[15]</sup> The optical contrast between these protein films and other layers is usually small because of the absence of light absorption in the visible and a refractive index of 1.35–1.4, i.e., close to water and glass. The approach developed by de Feijter, Benhamine, and Veer<sup>[16]</sup> gives satisfactory results in such cases. However, for larger colloids and light absorbing particles, such as metal nanocrystals, this approach no longer suffices.

This entry is devoted to the optical characterization of Au nanocolloids (radius  $a = 6.6$  nm) adsorbed from solution onto a naturally oxidized silicon substrate. An unambiguous optical characterization of such a colloidal system is not straightforward. We present an analysis of ellipsometry spectra in the coverage range up to 40%. A comparison of the optically determined coverage with the coverage determined with SEM serves as a benchmark for the quality of the description of the optical response.

The standard approach in the analysis of the optical spectra is to describe the optical properties of a heterogeneous layer, such as an adsorbed layer of colloids, with an effective medium approximation (EMA). In this entry, we will show that commonly used approaches as the Bruggeman and Maxwell-Garnett EMA do not give adequate results. However, the so-called thin film theory developed by Bedeaux and Vlioger<sup>[17]</sup> gives an excellent description of the optical response. In this theory, the incorporation of image dipoles and laterally interacting entities is essential. We will show that an extension which modifies the strength of the image dipole is required. This is necessary for two reasons: 1) there is a large optical contrast between the ambient and the silicon substrate, and 2) the presence of the natural oxide layer also influences the image dipole contribution. This oxide layer has a limited thickness that is three times smaller than

the radius of the colloids, and thus the silicon–silicon oxide interface affects the image dipole contribution. A prerequisite for the description of the optical properties of the colloid layer is the knowledge of the optical characteristics of a single entity. The limited size of the Au colloids results in a different polarizability than that of bulk gold.<sup>[18]</sup> An experimental determination of the absorbance of the Au colloid suspension provides the required modification of the dielectric function of bulk gold in order to incorporate size effects.

## GOLD COLLOID PREPARATION AND DEPOSITION

### Preparation

Colloidal gold suspensions are prepared by standard citrate reduction.<sup>[7,19]</sup> Typically, 100 mL of 1 mM HAuCl<sub>4</sub> (Aldrich) aqueous solution is heated to 100°C under refluxing conditions. While the solution is stirred vigorously, 10 mL of 38.8 mM sodium citrate (Merck) is quickly added, resulting in color changes of the originally yellow solution to transparent, to dark blue/gray, and finally, after approximately 2 min, to burgundy red, which marks the end of the reaction. The mixture is kept at 100°C for 15 min and subsequently cooled to room temperature with continuous stirring.

The particle size was determined by three different methods. (HR)TEM measurements show that the gold particles are spherical multidomain crystallites with a radius of 6.4 nm; the size dispersion amounts to  $\sigma = 8\text{--}10\%$ . Second, the average height of particles in AFM images amounts to a radius of 6.6 nm; laterally, the size of the particles is overestimated because of tip convolution. These AFM images are obtained using a Molecular Imaging PicoSPM system, operated in AAC Mode or MAC Mode, using silicon cantilevers with a typical resonance frequency of 65 kHz (Nanosensors); for MAC Mode, magnetically coated (Molecular Imaging) cantilevers are used. Finally, X-ray fluorescence measurements (XRF 2400 Cr spectrometer with a spot diameter of 10 mm) are performed to determine the number of gold atoms on the surface. This is compared to the number density of gold particles obtained from AFM images on the same samples. The average number of gold atoms per nanocrystal amounts to  $7.62 \times 10^4$ ; using the bulk density of gold (19.32 g/cm<sup>3</sup>), one obtains a particle radius of 6.7 nm.

Assuming that all gold ions in solution are consumed in the formation of the colloids, and with an average particle radius  $a = 6.6$  nm, the number density of particles in suspension amounts to  $N = 7.70 \times 10^{18} \text{ m}^{-3}$ . The tip-colloid convolution is quite large in AFM images, and the lateral dimensions of the colloid double in AFM images. This leads to a rather

cumbersome determination of the surface particle density. Therefore, images obtained from low-voltage SEM are used to determine this. Fractional surface coverages are determined by counting the number of colloids in a particular area and multiplying by  $\pi a^2$ , with  $a = 6.6$  nm the average particle radius.

### Substrates

Polished silicon wafers with a 1.5-nm native oxide are cleaved into  $12 \times 12\text{-mm}^2$  pieces. Before handling, these substrates are cleaned ultrasonically in methanol for at least 15 min. A high surface affinity for the colloidal gold particles is achieved by derivatization of the silicon substrates in a 10% 3-aminopropyltriethoxysilane (APTES) in methanol solution for 60 min, followed by thorough rinsing in methanol. After drying in a nitrogen flow, the samples are immersed in water for 15 min. Deposition of the gold particles is done by immersion of the derivatized substrates in the colloidal suspension, typically for a few hours; underivatized samples do not show any deposition of gold on the surface. After rinsing with water, the samples are dried in a nitrogen gas flow.

### Single-Particle Optical Characterization

An accurate, quantitative optical characterization of thin colloidal gold films is possible only if the dielectric function of the individual particles is known. Owing to their small size the optical properties of nanocrystals is markedly different from those of bulk material. Therefore, we first study the optical properties of single colloidal particles in suspension by means of optical absorbance spectroscopy. Optical extinction spectra are obtained with an HP8452-A UV/vis spectrophotometer. The optical path of the cuvette is  $\ell = 10^{-2}$  m. The extinction coefficient  $\sigma_{\text{ext}}$  of our as-prepared colloidal gold suspension, calculated from absorbance measurements,<sup>a</sup> is shown in Fig. 1 as a function of wavelength. The maximum at 519 nm, often referred to as the surface plasmon resonance, results in a pink color of the suspension, in good agreement with previous work. Upon dilution of the suspension, the entire extinction spectrum scales linearly with the particle concentration. Apparently, the extinction is dominated by absorption (which is proportional to the particle number density), and scattering can be neglected as expected for particles much smaller than the wavelength of the light.<sup>[18]</sup> In this Rayleigh regime ( $a \ll \lambda$ ) the extinction

<sup>a</sup>The extinction coefficient  $\sigma_{\text{ext}}$  defined by  $I/I_0 = \exp(-\sigma_{\text{ext}}z)$ , with  $I/I_0$  the attenuation of the light intensity at depth  $z$  in the suspension, is determined from the optical absorbance  $A$  given by  $A = -\log I/I_0$ , using the known optical path length  $\ell = 10^{-2}$  m.



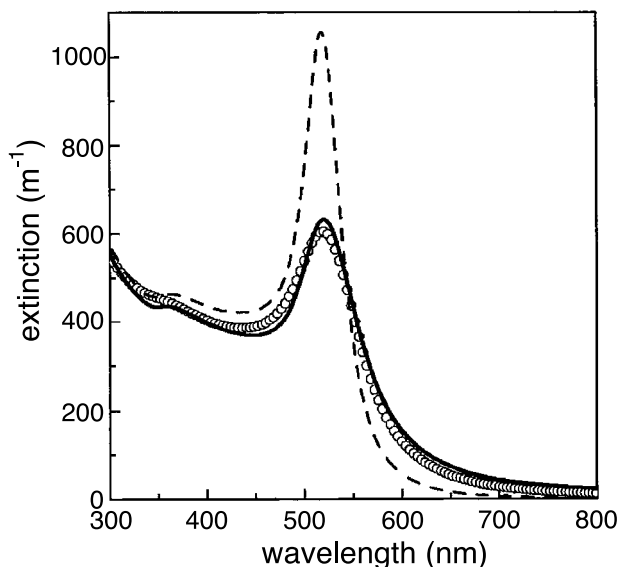


**Fig. 1** Wavelength-dependent extinction coefficient of an as-prepared colloidal solution, obtained from a measured absorbance spectrum.<sup>1a</sup> Calculated extinction coefficients using bulk (dashed line) and modified (solid line) dielectric functions are also shown.

cross section is due to dipolar absorption only; the scattering cross section and higher multipolar contributions (such as quadrupole extinction and scattering) are strongly suppressed in this size regime.<sup>[20]</sup> The extinction coefficient is thus given by

$$\sigma_{\text{ext}} = \frac{2\pi N \sqrt{\epsilon_1}}{\epsilon_0 \lambda} \text{Im}(\alpha) \quad (1)$$

with  $N$  the particle number density,  $\lambda$  the wavelength of the light, and  $\epsilon_1$  the dielectric function of the medium in which the colloids are suspended. The single-particle polarizability  $\alpha$  is related to the dielectric function through the Clausius–Mosotti relation:

$$\alpha = 3\epsilon_1 \epsilon_0 V \frac{\epsilon - \epsilon_1}{\epsilon + 2\epsilon_1} \quad (2)$$

where  $V = (4/3)\pi a^3$  is the particle volume,  $\epsilon_0 = 8.85 \times 10^{-12}$  F/m is the permittivity of vacuum, and  $\epsilon$  is the complex dielectric function of the particle. The bulk dielectric function for gold<sup>b[21]</sup> is shown in Fig. 2 by the dashed lines. In Fig. 1, the dashed line shows the calculated extinction using the aforementioned bulk optical properties of gold. Qualitatively, the features of the measured spectrum are reproduced. The extinction maxima are at the same wavelength, but the calculated peak is considerably higher and markedly narrower. Nevertheless, the difference between

<sup>b</sup>The bulk dielectric function of gold was determined using spectroscopic ellipsometry on a 1.5- $\mu\text{m}$ -thick gold film on mica.

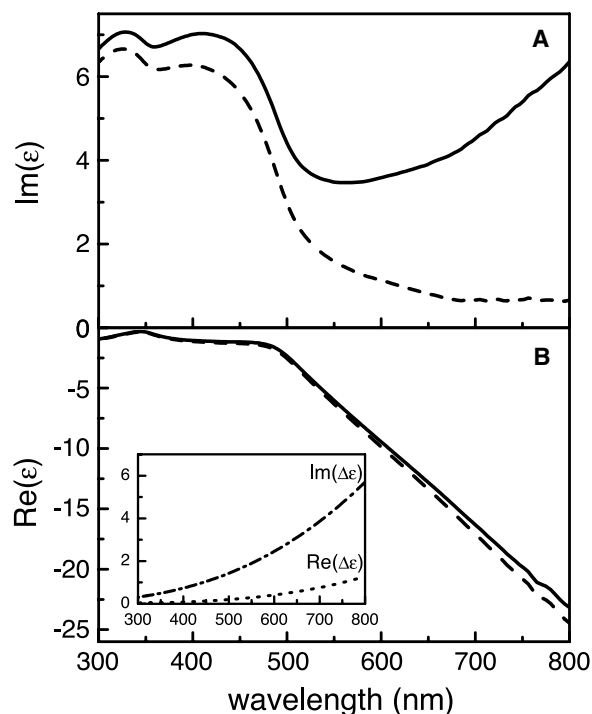


**Fig. 2** (A) Imaginary and (B) real parts of the complex dielectric function of gold. The dashed lines refer to bulk values<sup>1b[21]</sup> and the solid lines depict the modified dielectric function, as described in the text. The inset shows the wavelength-dependent corrections  $\Delta\epsilon_1$  and  $\Delta\epsilon_2$  of the real and imaginary parts, respectively.

measured and calculated extinction is negligible on the small-wavelength side of the spectrum. A similar decrease of the height and broadening of the peak for gold nanocrystals with a size below approximately 30 nm has been observed.<sup>[22]</sup> However, it is surprising that these spectra are often only compared qualitatively and merely the position of the surface plasmon resonance is considered.

The differences between calculated and measured extinction can be accounted for by considering the limited electron mean free path because of the small particle size.<sup>[20,23]</sup> Within the classical electrical conductivity theory, the overall relaxation frequency for bulk material  $\Gamma_\infty = \sum \Gamma_i$  is composed of contributions  $\Gamma_i$  because of interactions with phonons, electrons, impurities, and lattice defects. Assuming that only electrons near the Fermi surface (with Fermi velocity  $v_F$ ) contribute to the conductivity, the mean free path  $\ell_\infty$  is related to  $\Gamma_\infty$  through  $\Gamma_\infty = v_F/\ell_\infty$ . For gold,  $\ell_\infty$  amounts to 42 nm. As our colloidal particles are markedly smaller than this, the effective mean free path is considerably reduced. Following Matthiessen's rule, the additional scattering of conduction electrons gives rise to an extra term in the relaxation frequency

$$\Gamma(r) = \Gamma_\infty + A \frac{v_F}{a} \quad (3)$$

in which  $A = 4/3$  is a theory-related constant. This size-dependent relaxation frequency leads to an alteration of the dielectric function  $\varepsilon(\lambda, r) = \varepsilon_{\text{bulk}}(\lambda) + \Delta\varepsilon(\lambda, r)$  that now also becomes size dependent. The correction  $\Delta\varepsilon(\lambda, r)$  of the dielectric function because of intrinsic size effects can be expressed in terms of a difference of two Drude expressions:<sup>[23]</sup>

$$\Delta\varepsilon = \frac{\omega_p^2}{\omega} \left( \frac{1}{\omega + i\Gamma_\infty} - \frac{1}{\omega + i\Gamma(a)} \right) \quad (4)$$

where  $\omega = 2\pi c/\lambda$ , with  $c$  the speed of light. As this simple model takes into account only free electron effects, the correction is largest at longer wavelengths.

With the size-dependent dielectric function  $\varepsilon(\lambda, r)$ , we are able to calculate the modified extinction employing Eqs. (1) and (2). The plasma frequency  $\omega_p$  and the Fermi velocity  $v_F$  are not known for these small particles. With the bulk values  $\omega_p = 8.8 \text{ eV}$  and  $v_F = 1.39 \times 10^6 \text{ m/sec}$ , the best fit upon varying  $a$  (shown by the solid line in Fig. 1) yields a particle radius  $a = 4.2 \text{ nm}$ . This value is much lower than the physical nanocrystal radius of  $6.6 \text{ nm}$ . Several reasons for this discrepancy can be envisaged. First, the TEM images reveal that the gold nanoparticles generally consist of multiple crystalline domains. This enhances scattering of electrons and decreases the electron mean free path even further, compared with the bulk value. Furthermore, the radius obtained by fitting is very sensitive to  $\omega_p$  and  $v_F$ , the exact values of which are not known for these small particles. The shift of the surface plasmon resonance of nanocolloidal gold suspensions with varying dielectric constant of the solvent<sup>[24]</sup> yields a plasma frequency  $\omega_p = 9.9 \text{ eV}$ . The best fit with this value inserted into Eq. (4) yields  $a = 5.3 \text{ nm}$ . The sensitivity to the precise value of  $v_F$  is comparable.

The modified dielectric functions are shown in Fig. 2 by the solid lines; the inset depicts the corrections  $\text{Re}(\Delta\varepsilon)$  and  $\text{Im}(\Delta\varepsilon)$  of the real and imaginary parts, respectively. As mentioned above, the correction is largest at longer wavelengths and much more pronounced for  $\text{Im}(\varepsilon)$ . The calculated extinction coefficient using this modified dielectric function yields a broader but also lower peak. At longer wavelengths, between 550 and 800 nm, the tail of the extinction is much higher compared to that calculated using the bulk dielectric function, in agreement with experimental observations.

## OPTICAL CHARACTERIZATION OF COLLOIDAL ASSEMBLIES

### Spectroscopic Ellipsometry on Thin Island Films

Ellipsometry measures the ratio of the reflection coefficient of light polarized parallel,  $r_p$ , and perpendicular,

$r_s$ , to the plane of incidence.<sup>[25]</sup> The complex ratio  $\rho$  is defined as

$$\rho \equiv \frac{r_p}{r_s} \equiv \tan(\Psi) \cos(\Delta) \quad (5)$$

For a single interface,  $r_p$  and  $r_s$  represent the Fresnel reflection coefficients. Historically, the complex quantity  $\rho$  is expressed in the two angles  $\Psi$  and  $\Delta$ .

In our experiments, we used a homebuilt rotating polarizer spectroscopic ellipsometer equipped with a Xe lamp and a scanning monochromator.<sup>[26]</sup> Measurements are performed, both in situ during deposition and ex situ after deposition, in the visible region of the spectrum at wavelengths between 300 and 800 nm at a fixed incident angle of  $70^\circ$ .

Fig. 3 shows a 3-D representation of the evolution of ellipsometric spectra with increasing gold colloid coverages in the range from 0% to 35%. Absolute

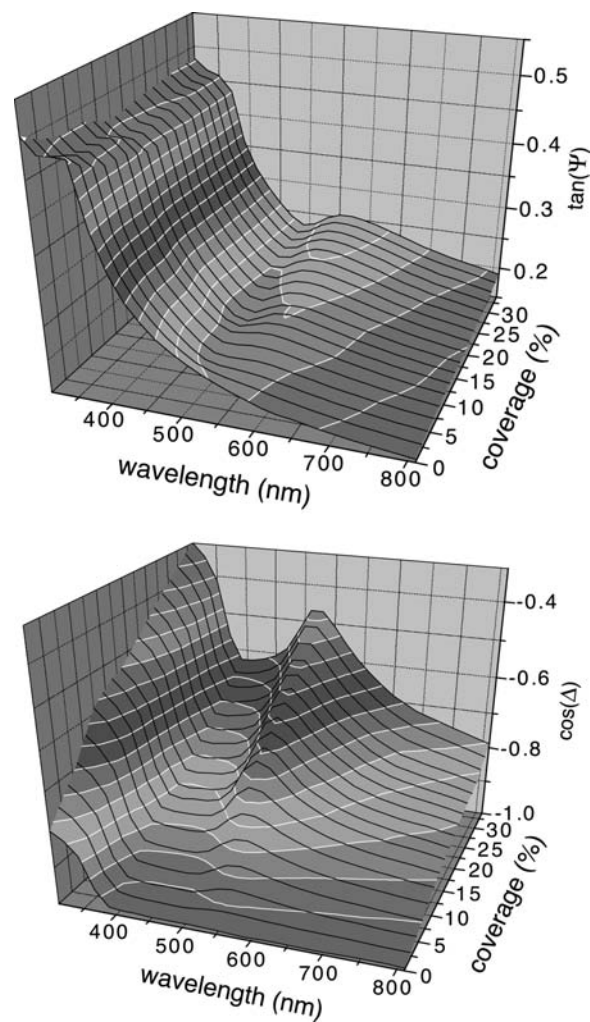


**Fig. 3** Ellipsometry spectra measured for various coverages up to 40%. The 3-D representation of  $\tan \Psi$  and  $\cos \Delta$  gives a good view of the change in spectra with increasing coverage.

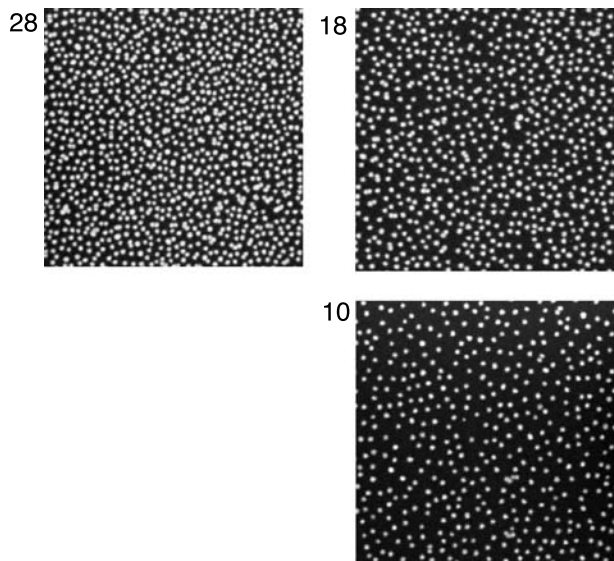


**Fig. 4** SEM images for three coverages as indicated in percent.

surface coverages are determined from SEM images such as those shown in Fig. 4 for three specific coverage values. The deposition of colloidal gold particles has a marked effect on the ellipsometry measurements. As expected for a thin layer of deposited material, the change in  $\cos \Delta$  is much more pronounced than the change in  $\tan \Psi$ . Apart from an increase in  $\cos \Delta$  over the entire wavelength range, a characteristic peak develops with increasing numbers of gold particles on the surface. The position of the peak maximum near 520 nm corresponds to the surface plasmon resonance of the gold colloids (Fig. 1).

### Analysis of Ellipsometric Spectra

Although the actual ellipsometry measurement is relatively simple, the analysis of the results is often complicated.<sup>[25,27]</sup> A model is required for the system under consideration, which can then be used to simulate or fit the results. The optical response of a multilayered structure with known dielectric functions can be simulated using the Abeles matrix algorithm. Details of the original method are described by Azzam and Bashara.<sup>[27]</sup> Two types of matrices are employed. One describes the transition from medium  $m$  to medium  $m + 1$  and is defined as

$$\mathbf{I}_{m,m+1} = \frac{1}{t_{m,m+1}} \begin{pmatrix} 1 & r_{m,m+1} \\ r_{m,m+1} & 1 \end{pmatrix} \quad (6)$$

with  $r_{m,m+1}$  and  $t_{m,m+1}$  the Fresnel reflection and transmission coefficients. Another matrix describes the light passage through the medium and involves the phase

factors

$$\mathbf{L}_m = \begin{pmatrix} e^{-i\Delta_m} & 1 \\ 1 & e^{-i\Delta_m} \end{pmatrix} \quad (7)$$

where  $\Delta_m = (2\pi/\lambda)d_m n_m \cos(\theta_m)$ , with  $\lambda$  the wavelength of the light in vacuum (nm),  $d_m$  the thickness of layer  $m$  (nm),  $\theta_m$  the angle of the light, and  $n_m$  the refractive index of medium  $m$ . The angles in the various media are related through Snell's law:  $n_m \sin(\theta_m) = n_{m+1} \sin(\theta_{m+1})$ .

For our system consisting of a colloidal gold layer ( $m = 2$ ) and a silicon dioxide film ( $m = 3$ ) on a silicon substrate ( $m = 4$ ) in contact with the ambient (air or aqueous solution;  $m = 1$ ), a matrix product is defined

$$\mathbf{A} = \mathbf{I}_{1,2} \mathbf{L}_2 \mathbf{I}_{2,3} \mathbf{L}_3 \mathbf{I}_{3,4} \quad (8)$$

and the overall reflection coefficient is calculated from  $r = A_{21}/A_{11}$ . For both the parallel and perpendicular polarizations the reflection coefficients  $r_p$  and  $r_s$  can be obtained by inserting the appropriate Fresnel coefficients in Eq. (6), and the ellipsometric ratio in Eq. (5) can be calculated.

### Effective Medium Theories

For homogeneous media the wavelength-dependent dielectric function is generally obtained from the literature or by performing an ellipsometric measurement on bulk material. However, determining the dielectric properties of inhomogeneous media consisting of different materials is not straightforward. Effective medium theories have been developed, which provide a relation between the effective dielectric function of the medium and the dielectric functions of its constituents.<sup>[20]</sup> For two types of spherical inclusions with sizes much smaller than the wavelength of light, one can write for the effective dielectric function  $\epsilon_{\text{eff}}$

$$\frac{\epsilon_{\text{eff}} - \epsilon_h}{\epsilon_{\text{eff}} + 2\epsilon_h} = f_a \frac{\epsilon_a - \epsilon_h}{\epsilon_a + 2\epsilon_h} + f_b \frac{\epsilon_b - \epsilon_h}{\epsilon_b + 2\epsilon_h} \quad (9)$$

with  $\epsilon_a$  and  $\epsilon_b$  the dielectric functions of the inclusions in a host matrix with  $\epsilon_h$ . The volume fractions of the materials are given by  $f_a$  and  $f_b$ . Replacing  $f_b$  by  $1 - f_a$  and substituting  $\epsilon_h = \epsilon_{\text{eff}}$  gives the EMA established by Bruggeman,<sup>[28]</sup> whereas inserting  $\epsilon_h = \epsilon_b$  corresponds to the Maxwell-Garnett<sup>[29]</sup> approximation. Both these approximations are commonly used in the description of an ensemble of adsorbed colloidal particles.<sup>[14]</sup>

The dielectric function of the colloidal layer can be mimicked using an EMA in combination with the surface coverage determined from SEM images. The volume fraction  $f$  in Eq. (9) for spherical particles is related to the surface coverage through  $\phi = 1.5f$ .

With the Abeles matrices in Eqs. (6) and (7) the optical response of our multilayered sample can be calculated and compared to the experimental spectra. In Fig. 5, the experimental ellipsometry result of a colloidal gold film with coverage  $\phi = 12\%$  is compared to calculations using the Bruggeman (dashed line) and Maxwell-Garnett (dotted line) EMAs. A thickness of 13.2 nm was used for the colloidal film with a volume fraction  $f = 8.0\%$ . In both simulations, considerable differences are observed in comparison with the experimental data. This is most clearly visible in  $\cos \Delta$ . Apart from being lower, the calculation using the Bruggeman EMA exhibits a shift of the peak maximum in  $\cos \Delta$ . The Maxwell-Garnett approximation yields a peak in  $\cos \Delta$ , which is in qualitative agreement with the experimental result, but is much too low. Increasing the volume fraction  $f$  (corresponding to a higher coverage) results in increasing discrepancy between the

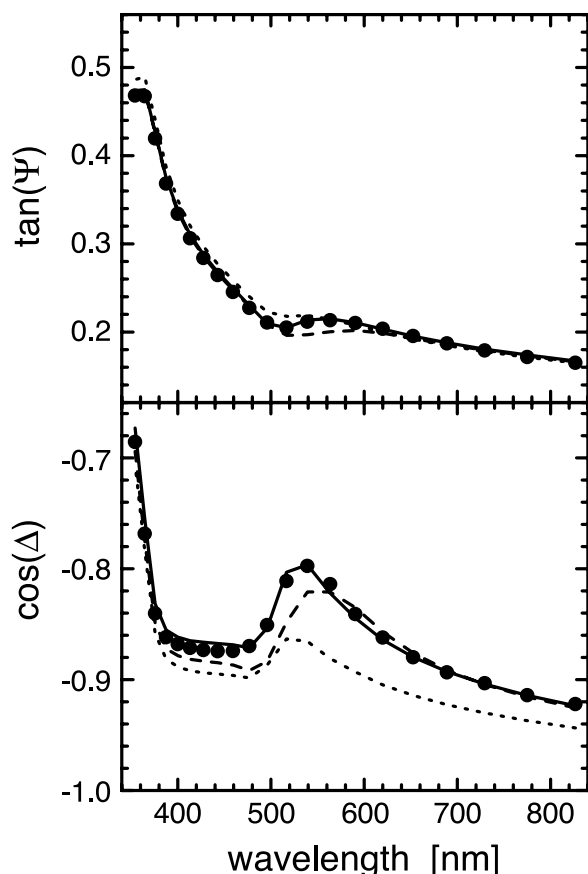


**Fig. 5** Calculated ellipsometry spectra for a silicon/silicon oxide sample with 12% gold coverage. The Bruggeman (dashed lines) and Maxwell-Garnett (dotted lines) EMAs were used to model the dielectric function of the colloidal film with the fill fraction  $f = 8\%$ . The solid lines represent a calculation using the thin island film theory, including image dipoles and lateral interaction with a surface coverage equal to that obtained with SEM. The filled circles represent the ellipsometry data for a film with  $\phi = 12\%$ .

measured spectra and simulations with both the Bruggeman and the Maxwell-Garnett EMA.

### Thin Island Film Theory

The main problem associated with the aforementioned effective medium theories is that in their derivation it was assumed that the effective medium is isotropic in three dimensions. Obviously, this is no longer valid for the monolayer of nanocolloids considered here. A description of the optical properties of particulate films is provided by the thin island film theory as originally described by Bedeaux and Vlieger.<sup>[30,31]</sup> The various extensions of this theory describe the influence of image dipoles and the lateral distribution of the particulates and were also derived for non-spherical particulates. This theory describes the optical response of the constituent entities, which are small compared to the wavelength of the light, in terms of excess optical susceptibilities. Recently, Koper<sup>[14]</sup> and Bedeaux and Vlieger<sup>[17]</sup> published elaborate reviews on this theory. Böhmer, van der Zeeuw, and Kopel described an application of the theory to a reflectometry experiment.<sup>[12]</sup>

The optical response to an electromagnetic field of a particulate is, in a good approximation, described in terms of polarizabilities parallel and perpendicular to the interface, respectively,

$$\begin{aligned}\gamma &= \phi 4a\epsilon_a \frac{\epsilon - \epsilon_a}{\epsilon + 2\epsilon_a} \\ \beta &= \phi \frac{4a}{\epsilon_a} \frac{\epsilon - \epsilon_a}{\epsilon + 2\epsilon_a}\end{aligned}\quad (10)$$

where  $\epsilon$  and  $\epsilon_a$  represent the dielectric functions of the spheres (gold in this case) and the suspending medium (air/water) and  $\phi = n\pi a^2$  is the surface coverage with  $a$  the particle radius and  $n$  the particle density. The reflection and transmission coefficients depend on the polarization of the light and are given by

$$\begin{aligned}r_1^s &= \frac{X^s}{1 - X^s} \\ t_1^s &= \frac{1}{1 - X^s}\end{aligned}\quad (11)$$

for s-polarized light, with

$$X^s = \frac{\pi i \gamma}{\lambda n_1 \cos(\theta_1)}\quad (12)$$

and by

$$\begin{aligned}r_1^p &= \frac{X^p}{1 - X^p} - \frac{Y^p}{1 - Y^p} \\ t_1^s &= 1 + \frac{X^p + Y^p - 2X^p Y^p}{(1 - X^p)(1 - Y^p)}\end{aligned}\quad (13)$$

for p-polarized light with

$$X^p = \frac{\pi i \beta (n_1)^3 \sin^2(\theta_1)}{\lambda \cos(\theta_1)} \quad (14)$$

$$Y^p = \frac{\pi i \gamma \cos(\theta_1)}{\lambda n_1}$$

The Abeles film matrix for such a particulate film in terms of these reflection and transmission coefficients is given by

$$\mathbf{F} = \frac{1}{t_1} \begin{pmatrix} 1 & -r_1 \\ r_1 & t_1^2 - r_1^2 \end{pmatrix} \quad (15)$$

For our system the modified overall matrix becomes

$$\mathbf{A} = \mathbf{F} \mathbf{L}_F \mathbf{I}_{1,3} \mathbf{L}_3 \mathbf{I}_{3,4} \quad (16)$$

The layer matrix  $\mathbf{L}_F$  is identical to  $\mathbf{L}_m$  in Eq. (7), but with a phase factor  $\Delta = (2\pi/\lambda) h n_1 \cos \theta_1$ , where  $h$  is the height of the excess susceptibilities above the Fresnel interface. Often, the distance  $h = a$  between the bare substrate and the particle centers is used. Note that the film matrix  $\mathbf{F}$  is different from the interface matrix  $\mathbf{I}_{m,m+1}$  as for an interface  $r_{m,m+1} = -r_{m+1,m}$ , which is obviously not true for the reflection coefficients  $r_1^s$  and  $r_1^p$  of a thin particulate film.

The solid lines in Fig. 5 show  $\cos \Delta$  and  $\tan \Psi$ , calculated with the thin island film theory for a particulate film using a coverage  $\phi = 12\%$  in Eq. (10). Clearly, the measured features both in  $\cos \Delta$  and  $\tan \Psi$  are reproduced much better than with the Bruggeman or Maxwell-Garnett EMAs (dashed and dotted lines, respectively). Note that as mentioned in a previous section, we used a modified dielectric function for the gold. With the bulk values, a much higher peak in  $\cos \Delta$  is calculated, and the agreement between experiment and simulation is considerably worse.

Not only should the spectra be reproduced, but the coverage determined optically must also correspond to that measured by counting the particle density in SEM images such as those in Fig. 4. This comparison is shown in Fig. 6. The difference between the two ways of determining the coverage is enhanced in the bottom panel, which depicts the ratio of the optically determined coverage and the coverage determined with SEM. From these images, it is clear that for coverages below approximately 15%, the coverage is overestimated in ellipsometry, whereas above 15% it is underestimated. The latter arises because we neglected lateral interaction of neighboring particles, whereas the overestimation at low coverage arises because we neglected image dipole effects, i.e., the perpendicular interaction. The polarizabilities defined by Eq. (10) are thus regarded as due to noninteracting particles, i.e., the bare dipole.

Fig. 7 shows the measured ellipsometry spectrum of two comparable coverages. One of these spectra (filled

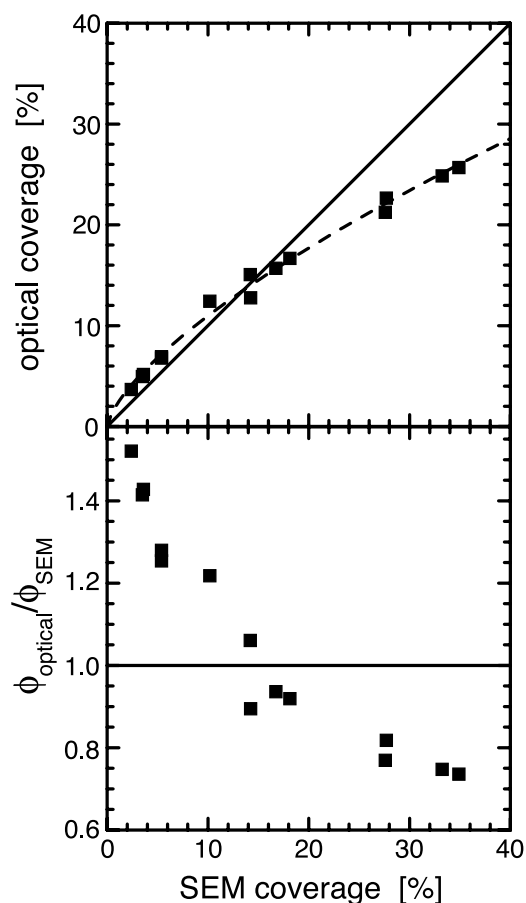


**Fig. 6** Comparison of the coverage determined with SEM and the one obtained from the thin island film theory, considering the colloids as noninteracting bare dipoles (top). The solid line indicates a one-to-one correspondence, whereas the dotted line serves as a guide to the eye. Also shown is the ratio of the optically determined coverage and the SEM coverage (bottom).

circles) shows a marked broadening of the plasmon feature in both  $\cos \Delta$  and  $\tan \Psi$ . This broadening is due to coagulation of the particles on the surface as is also observed with AFM and SEM. Coagulation of two or more particles leads to a shift in the plasmon energy<sup>[20]</sup> and is thus directly observed in the ellipsometry spectra. In the analysis presented in this entry, only spectra that do not show this broadening are considered. Coagulation can occur for various reasons such as an unstable solution because of a high salt concentration or an excess amount of APTES on the sample surface. The latter occurs if the substrate is not properly rinsed in methanol after immersion in APTES.

#### Image dipoles and lateral interaction

Yamaguchi, Yoshida, and Kinbara<sup>[32]</sup> and Bedeaux and Vlieger<sup>[30]</sup> considered the influence of image dipoles on the optical response of small particulates



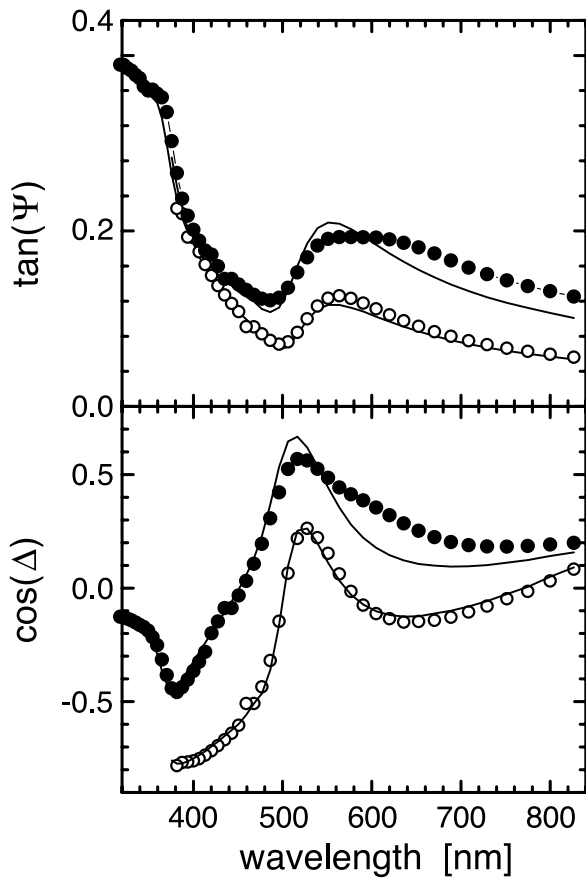


**Fig. 7** Ellipsometric spectra measured with (filled circles) and without (open circles) coagulation. The best fit obtained with the thin island film theory for both cases is shown.

on a surface. Haarmans and Bedeaux considered the influence of the lateral distribution on the optical response.<sup>[33]</sup> The incorporation of image dipole effects and lateral interaction with neighboring particles leads to a modification of the one particle polarizabilities. Haarmans and Bedeaux<sup>[17,34]</sup> have shown that these changes are adequately described by an expansion of the potential distribution up to quadrupole order. The optical response is thus described as the response of an ensemble of non-interacting particles with effective polarizabilities  $\gamma$  and  $\beta$  given by:

$$\begin{aligned} \gamma_{qu} &= \phi \frac{4a\epsilon_a}{3} \\ &\times \frac{(\epsilon - \epsilon_a)(\epsilon_a + L1_p(\epsilon - \epsilon_a))}{(\epsilon_a + L_p(\epsilon - \epsilon_a))(\epsilon_a + L1_p(\epsilon - \epsilon_a)) + \Lambda_p(\epsilon - \epsilon_a)^2} \\ \beta_{qu} &= \phi \frac{4a}{3\epsilon_a} \\ &\times \frac{(\epsilon - \epsilon_a)(\epsilon_a + L1_z(\epsilon - \epsilon_a))}{(\epsilon_a + L_z(\epsilon - \epsilon_a))(\epsilon_a + L1_z(\epsilon - \epsilon_a)) + \Lambda_z(\epsilon - \epsilon_a)^2} \end{aligned} \quad (17)$$

Here,  $L_p$  and  $L_z$  represent the dipolar correction terms and  $L1_p$  and  $L1_z$ ,  $\Lambda_p$  and  $\Lambda_z$  are the quadrupole depolarization factors. Using

$$B_{sa} = \frac{\epsilon_a - \epsilon_s}{\epsilon_a + \epsilon_s} \quad (18)$$

with  $\epsilon_a$  the dielectric function of the substrate, these correction terms are given by:

$$\begin{aligned} L_p &= \frac{1}{3} \left( 1 + 2\sqrt{\frac{\pi}{5}} I_2(\phi) + 2\sqrt{\frac{\pi}{5}} B_{sa} I_{2r}(\phi) \right) \\ L_z &= \frac{1}{3} \left( 1 - 4\sqrt{\frac{\pi}{5}} I_2(\phi) + 4\sqrt{\frac{\pi}{5}} B_{sa} I_{2r}(\phi) \right) \\ L1_p &= \frac{2}{5} \left( 1 - \frac{8}{3}\sqrt{\pi} I_4(\phi) + \frac{8}{3}\sqrt{\pi} B_{sa} I_{4r}(\phi) \right) \\ L1_z &= \frac{2}{5} \left( 1 + 4\sqrt{\pi} I_4(\phi) + 4\sqrt{\pi} B_{sa} I_{4r}(\phi) \right) \\ \Lambda_p &= \frac{8}{35}\pi \left( I_3(\phi)^2 - B_{sa}^2 I_{3r}(\phi)^2 \right) \\ \Lambda_z &= \frac{24}{35}\pi \left( I_3(\phi)^2 - B_{sa}^2 I_{3r}(\phi)^2 \right) \end{aligned} \quad (19)$$

The integral quantities  $I_l$  and  $I_{lr}$ , with  $l = 2,3,4$ , take into account the spatial distribution of the nanoparticles on the surface in terms of the correlation function  $g(r)$ . Haarmans and Bedeaux<sup>[34]</sup> showed that up to 40% surface coverage, the specific lateral distribution has no influence on the optical response. This implies that the isotropic distribution can be used for the integral quantities providing analytical expressions for the quantities in Eq. (19):

$$\begin{aligned} I_2(\phi) &= -\sqrt{\frac{5}{4\pi}} \frac{\phi}{2} \\ I_{2r}(\phi) &= \sqrt{\frac{5}{4\pi}} \left( \frac{1}{8} - \frac{\phi}{4\sqrt{2}} \right) \\ I_3(\phi) &= 0 \\ I_{3r}(\phi) &= \sqrt{\frac{7}{4\pi}} \frac{1}{16} \left( -1 + \frac{\phi}{\sqrt{2}} \right) \\ I_4(\phi) &= \frac{3}{64\sqrt{\pi}} \phi \\ I_{4r}(\phi) &= \sqrt{\frac{9}{4\pi}} \frac{1}{32} \left( 1 - \phi \frac{3}{8\sqrt{2}} \right) \end{aligned} \quad (20)$$

In Fig. 8,  $\gamma$  and  $\beta$  are shown for both the bare dipoles and the modified values with up to quadrupole interactions taken into account. The strength of the image dipoles was evaluated by inserting the silicon dielectric function in Eq. 16. In the limit of zero coverage, because of the incorporation of the image dipole effect the slopes of the curves are different from those obtained using the bare dipole approximation. Above



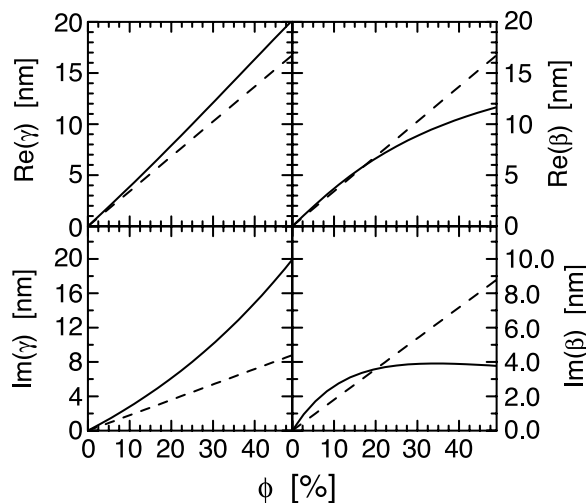


**Fig. 8** Real and imaginary part of  $\gamma$  and  $\beta$  at 517 nm for the bare dipole approximation (dashed line) and after taking into account the influence of an isotropic distribution of colloids and their image dipole up to quadrupole order (solid line).

20%,  $\beta$  shows an overestimation in the bare dipole model, whereas for  $\gamma$  an underestimation is noted for all coverages. These two effects cancel each other for a coverage of about 20% and results in good correspondence between the optical and AFM-determined coverage. The image dipole effect is especially noteworthy because Si has a relative high dielectric function compared to many oxide materials commonly used as substrates. In this case,  $B_{sa}$  is  $-0.89$  at a wavelength of 517 nm, whereas for instance the value of  $B_{sa}$  for quartz is almost three times smaller. Fig. 9 shows the relation between the optical and SEM-determined coverages with and without the influence of the image dipoles and lateral interaction. The incorporation of these two effects leads to a significant improvement of the one-to-one relation that should exist between the coverage determinations.

#### Modified image dipole contribution

The Au colloids with radius  $a = 6.6$  nm are deposited on the 1.5-nm natural oxide layer of the silicon substrates. The silicon oxide interface is covered with an approximately 0.3-nm-thick layer of APTES, which gives a total layer thickness  $d = 1.8$  nm. This layer is only a fraction of the particle radius  $a$ , and gives rise to the question of where the image dipole is located, i.e., in the silicon oxide layer, in the silicon substrate, or in a combination of the two. The influence of the substrate choice for the image dipole contribution is also shown in Fig. 9. Assuming a pure silicon substrate gives rise to an underestimation of the optical coverage, whereas a pure  $\text{SiO}_2$  layer leads to an overestimation, a modification of the image dipole strength is thus required.

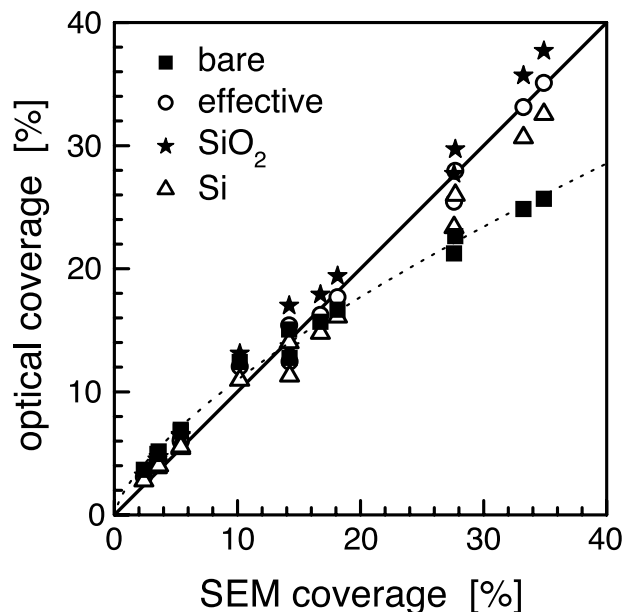


**Fig. 9** The coverage as determined with spectroscopic ellipsometry, analyzed by taking into account the lateral distribution and image dipole effects as a function of the coverage determined with SEM. The lateral distribution was evaluated for an isotropic distribution with silicon as the substrate for the image dipole (triangles), silicon oxide as the substrate for the image dipole (full star), a modified image dipole strength (open circle), and for the bare dipole approximation (full squares). The dotted line is a guide to the eye, whereas the full line reflects a one-to-one relation between the two coverages.

The strength of the image dipole contribution  $B(d)$  for a dipole placed at distance  $a + d$  above a homogeneous substrate falls off with  $[a/(a + d)]^3$ ,

$$\begin{aligned} B(d) &= -\frac{\varepsilon_s - \varepsilon_a}{\varepsilon_s + \varepsilon_a} \left( \frac{a}{a + d} \right)^3 \\ &= B_{sa} \left( \frac{a}{a + d} \right)^3 \end{aligned} \quad (21)$$

with  $\varepsilon_s$  and  $\varepsilon_a$  the dielectric functions of the substrate and ambient, respectively.<sup>[17]</sup> The strength of the image dipole contribution for our system is thus expected to be bound between values for the image dipole contribution given by a silicon substrate and that of a silicon oxide substrate, i.e., between  $B = -0.89$  and  $B = -0.365$ , respectively. For image dipoles, the value  $B$  is treated as a reflection coefficient.<sup>[35]</sup> An expansion with reflection and transmission coefficients of both interfaces combined with the attenuation factor given by the thickness  $d$  of the layer yields an effective image dipole strength

$$B^{\text{eff}}(d) = \frac{B_{la} + B_{sl} \left( \frac{a}{a + d} \right)^3}{1 + B_{la} B_{sl} \left( \frac{a}{a + d} \right)^3} \quad (22)$$

where  $B_{la}$  and  $B_{sl}$  represent the image dipole strengths for the thin layer–ambient and substrate thin layer, respectively. The value of  $B^{eff}$  is plotted as a function of the thickness of the  $\text{SiO}_2$  layer in Fig. 10. Only the real part of  $B^{eff}$  is considered because the imaginary part is negligible at a wavelength of 517 nm. The rapid change of  $B^{eff}$  with thickness leads to a considerably reduced value of the image dipole contribution already for thin oxide layers.

The influence of a thin silicon oxide layer on the polarizabilities  $\gamma$  and  $\beta$  is shown in Fig. 11. Especially for  $\beta$ , a marked difference is observed in both the real and imaginary parts. The most substantial difference is observed in the imaginary part of  $\beta$  in the 10–30% coverage range.

Fig. 9 shows the influence of the modified image dipole on the comparison of optical coverage and SEM coverage. The correction made by incorporating  $B^{eff}$ , yields a one-to-one correspondence between the optically and SEM-determined coverages.

## CONCLUSIONS

We have presented a detailed study of the optical properties of colloidal gold films assembled on naturally oxidized silicon derivatized with APTES. Knowledge of both the single-particle diameter and its polarizability is a prerequisite for a quantitative analysis of the surface coverage for in situ and ex situ

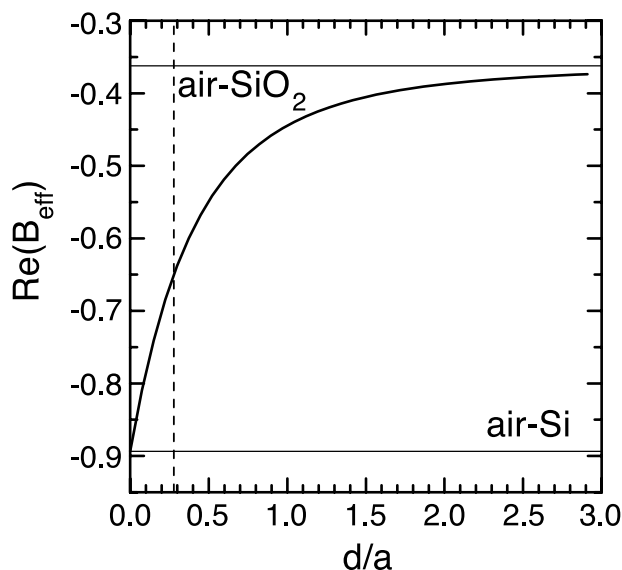


**Fig. 10** The value of the real part of  $B^{eff}$  at 517 nm as a function of thickness  $d$  of the  $\text{SiO}_2$  layer, normalized to the colloid radius  $a$ . The limit for  $d = 0$  is equal to the value for an air–Si interface and the limiting value for a large oxide thickness is equivalent to an air– $\text{SiO}_2$  interface. The dashed line indicates the value of  $d/a$  for a system considered here with  $d = 1.8$  nm and  $a = 6.6$  nm.

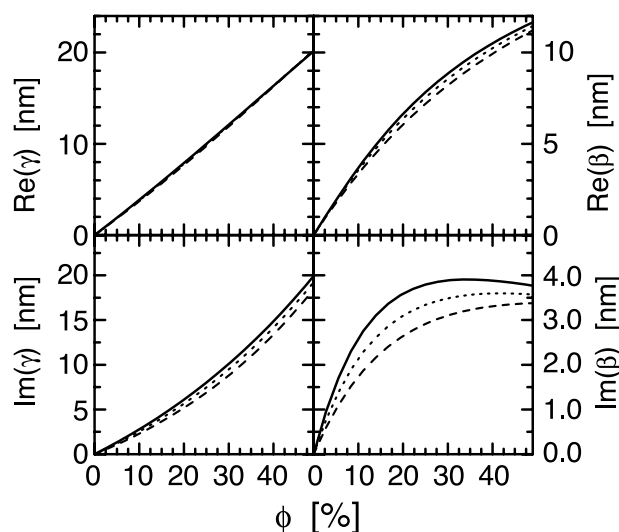


**Fig. 11** The influence of different substrates on the image dipole contribution for  $\gamma$  and  $\beta$ . Depicted are the results obtained assuming a Si substrate (solid line),  $\text{SiO}_2$  (dashed line), and the effective substrate for a  $d = 1.8$ -nm oxide layer (dotted line) as described in the text.

characterization with ellipsometry. The diameter of the particle is usually determined from TEM, although AFM or a combination of AFM and XRF provides useful alternatives. An absorbance measurement of the colloid solution gives an excellent basis for the determination of the one-particle polarizability. The polarizability of the Au nanocolloids used in this entry is influenced by the finite size of the colloid. This reduces the effective mean free path of the electrons. Using Mathiessen's rule, a relation between the bulk dielectric function and optical properties of a single Au nanocolloid can be established.

The standard analysis procedure of ellipsometric spectra of samples, such as our gold nanocrystal-on-silicon assemblies, involves an EMA for the dielectric function of the adsorbed colloid layer. However, both the commonly used Maxwell-Garnet and Bruggeman approaches lead to highly inaccurate results.

The thin island film theory developed by Bedeaux and Vlieger, which treats the deposited colloids as excess polarizabilities, allows an accurate calculation of the optical properties. The image dipole and the lateral interaction between the dipoles have to be taken into account. However, up to 40% coverage the details of the lateral distribution of the particles are of little importance. This allows the use of an isotropic distribution. The Au colloids were deposited on naturally oxidized silicon substrates. This implies that the radius of the colloid is three times larger than the thickness of the silicon oxide layer. A modification of the strength of the image dipole contribution is required to take into account the limited thickness of the oxide layer. Such a modification gives a one-to-one relation between

the optically determined and the SEM-determined coverage. This results in an excellent capability of optical techniques for both in situ and ex situ unambiguous characterization of colloid nanocrystal assemblies.

## ACKNOWLEDGMENT

This work is part of the research program of the Stichting voor Fundamenteel Onderzoek der Materie (FOM), and was financially supported by the Nederlandse Organisatie voor Wetenschappelijk Onderzoek (NWO).

## REFERENCES

- Murray, C.B.; Kagan, C.R.; Bawendi, M.G. Synthesis and characterization of monodisperse nanocrystals and close-packed nanocrystal assemblies. *Annu. Rev. Mater. Sci.* **2000**, *30*, 545–610.
- Puntes, V.F.; Krishnan, K.M.; Alivisatos, P. Synthesis, self-assembly, and magnetic behavior of a two-dimensional superlattice of single-crystal epsilon-Co nanoparticles. *Appl. Phys. Lett.* **2001**, *78*, 2187–2189.
- van Blaaderen, A. Materials science—opals in a new light. *Science* **1998**, *282*, 887–888.
- Giersig, M.; Mulvaney, P. Preparation of ordered colloid monolayers by electrophoretic deposition. *Langmuir* **1993**, *9*, 3408–3413.
- Trau, M.; Saville, D.A.; Aksay, I.A. Field-induced layering of colloidal crystals. *Science* **1996**, *272*, 706–709.
- Jana, N.R.; Gearheart, L.; Murphy, C.J. Seeding growth for size control of 5–40 nm diameter gold nanoparticles. *Langmuir* **2001**, *17*, 6782–6786.
- Grabar, K.C.; Freeman, R.G.; Hommer, M.B.; Natan, M.J. Preparation and characterization of Au colloid monolayers. *Anal. Chem.* **1995**, *67*, 735–743.
- Grabar, K.C.; Brown, K.R.; Keating, C.D.; Stranick, S.J.; Tang, S.-L.; Natan, M.J. Nanoscale characterization of gold colloid monolayers: a comparison of four techniques. *Anal. Chem.* **1997**, *69*, 471–477.
- Schmitt, J.; Mächtle, P.; Eck, D.; Möhwald, H.; Helm, C.A. Preparation and optical properties of colloidal gold monolayers. *Langmuir* **1999**, *15*, 3256–3266.
- Böhmer, M. In situ observation of 2-dimensional clustering during electrophoretic deposition. *Langmuir* **1996**, *12*, 5747–5750.
- Dinsmore, A.D.; Weeks, E.R.; Prasad, V.; Levitt, A.C.; Weitz, D.A. Three-dimensional confocal microscopy of colloids. *Appl. Opt.* **2001**, *40*, 4152–4159.
- Böhmer, M.R.; van der Zeeuw, E.A.; Koper, G.J.M. Kinetics of particle adsorption in stagnation point flow studied by optical reflectometry. *J. Colloid Interface Sci.* **1995**, *197*, 242–250.
- Baum, T.; Benthell, D.; Brust, M.; Schiffrin, D.J. Electrochemical charge injection into immobilized nanosized gold particle ensembles: potential modulated transmission and reflectance spectroscopy. *Langmuir* **1999**, *15*, 866–871.
- Koper, G.J.M. Optical properties of colloidal films. *Colloids Surf., A* **2000**, *165*, 39–57.
- Arwin, H. Spectroscopic ellipsometry and biology: recent developments and challenges. *Thin Solid Films* **1998**, *313–314*, 764–774.
- de Feijter, J.A.; Benhamins, J.; Veer, F.A. Ellipsometry as a tool to study the adsorption behaviour of synthetic and biopolymers at the air–water interface. *Biopolymers* **1978**, *17*, 1759–1772.
- Bedeaux, D.; Vlieger, J. *Optical Properties of Surfaces*; Imperial College Press, 2002.
- van Hulst, H.C. *Light Scattering by Small Particles*; Dover Publications: New York, 1981.
- Frens, G. Controlled nucleation for the regulation of the particle size in monodisperse gold solutions. *Nat., Phys. Sci.* **1973**, *241*, 20–22.
- Kreibig, U.; Vollmer, M. *Optical Properties of Metal Clusters*; Springer-Verlag: Berlin, 1995.
- Johnson, P.B.; Christy, R.W. Optical constants of the noble metals. *Phys. Rev., B* **1972**, *6*, 4370–4379.
- Dinsmore, A.D.; Weeks, E.R.; Prasad, V.; Levitt, A.C.; Weitz, D.A. Three-dimensional confocal microscopy of colloids. *Appl. Opt.* **2001**, *40*, 4152–4159.
- Klebtsov, N.G.; Bogatyrev, V.A.; Dykman, L.A.; Mel'nikov, A.G. Spectral properties of colloidal gold. *Opt. Spectrosc.* **1996**, *80*, 113–121.
- Mulvany, P. Surface plasmon spectroscopy of nanosized metal. *Langmuir* **1996**, *12*, 788–800.
- Tompkins, H.G.; McGahan, W.A. *Spectroscopic Ellipsometry and Reflectometry: A User's Guide*; John Wiley & Sons, Inc.: New York, 1999.
- de Nijs, J. *Ellipsometry and the Ti/c-Si Solid State Reaction*; Ph.D. thesis; Univ. Twente: Enschede, 1989.
- Azzam, R.M.A.; Bashara, N.H. *Ellipsometry and Polarized Light*; North Holland: Amsterdam, 1987.
- Bruggeman, D.A.G. Berechnung verschiedener physikalischen konstanten von heterogenen substanzen. *Ann. Phys.* **1935**, *24*, 636–664.
- Maxwell-Garnett, J.C. Colours in metal glasses and in metallic films. *Philos. Trans. R. Soc. Lond., A* **1904**, *203*, 385–420.
- Bedeaux, D.; Vlieger, J. A phenomenological theory of the dielectric properties of thin films. *Physica* **1973**, *67*, 55–77.
- Bedeaux, D.; Koper, G.J.M.; van der Zeeuw, E.A.; Vlieger, J.; Wind, M.M. The definition and use of optical invariants for thin island films. *Physica, A* **1994**, *207*, 285–292.
- Yamaguchi, T.; Yoshida, S.; Kinbara, A. Optical effect of the substrate on the anomalous absorption of aggregated silver films. *Thin Solid Films* **1974**, *21*, 173–187.
- Haarmans, M.T.; Bedeaux, D. The polarizability and the optical properties of lattices and random distributions of small metal spheres on a substrate. *Thin Solid Films* **1993**, *224*, 117–131.
- Haarmans, M.T.; Bedeaux, D. Optical properties of thin films up to second order in the thickness. *Thin Solid Films* **1995**, *258*, 213–223.
- Jackson, J.D. *Classical Electrodynamics*; Wiley, 1999.

# Self-Assembly and Chirality of Molecules at Interfaces

Dalia G. Yablon

Corporate Research Strategies, ExxonMobil Research and Engineering,  
Annandale, New Jersey, U.S.A.

Self-Assembly –  
Self-Organized

## INTRODUCTION

Chirality is a subtle molecular property that has a profound impact in nature. A chiral object or enantiomer is defined as one that has a nonsuperimposable mirror image, in the same way that a left hand is related to a right hand. Although this geometric distinction may seem trivial, it plays a very significant role in a molecule's functionality and has especially important consequences for many biological molecules and pharmaceutical drugs. One of the more infamous and tragic examples of the role chirality plays in a molecule's functionality is the drug thalidomide, administered in the 1950s to pregnant women to alleviate nausea: It was discovered that only one enantiomer of thalidomide was safe whereas the other enantiomer caused severe birth defects. Pharmaceutical companies invest tremendous resources into synthesizing enantiomerically pure compounds or separating racemic compounds (where equal amounts of left- and right-handed molecules are present) into enantiomerically pure forms. Not only are enantiomers extremely difficult to separate, but they are also difficult to identify because all of their chemical properties—except for the direction in which they rotate plane-polarized light—are identical. Therefore classical chemical techniques such as nuclear magnetic resonance (NMR), circular dichroism (CD), and other forms of spectroscopy cannot identify the absolute chirality of a given molecule, and many techniques require some sort of chemical modification of the enantiomer (e.g., forming a diastereomer) to achieve even a relative differentiation between enantiomers.

Scanning tunneling microscopy (STM) has become an obvious and highly relevant technique with which to study chiral systems. The ability of the scanning tunneling microscope to observe molecules on an atom-by-atom basis with angstrom-level resolution makes it a natural choice for detailed, high-resolution studies of chiral molecules and chiral surface structures. The scope of STM studies on chiral systems is too large to be covered in a single article, and so here we focus on surface studies of physisorbed self-assembled monolayers at the liquid–solid interface (i.e., ambient conditions).

## OVERVIEW

This entry aims to explore the many different ways in which chirality affects surface structures. This discussion includes examples of chiral molecules forming interfacial domains that can be chiral or achiral, achiral molecules forming surface structures that possess 2-D chirality, and finally mixtures of chiral and achiral molecules that lead to interesting and often unexpected surface formations. The organization of this article is described below. In “Direct Determination of Chirality of Individual Molecules: 2-Br-Hexadecanoic Acid on Graphite,” we discuss the recent achievement of direct determination of chirality of individual molecules initially achieved by both Fang, Giancarlo, and Flynn<sup>[1]</sup> and Lopinski et al.,<sup>[2]</sup> and we focus on Fang et al.'s study of self-assembly of racemic 2-Br-hexadecanoic acid at the liquid–solid interface. This achievement was critical to the progress of using STM to study chiral systems and serves as a basis for much of the ensuing work described here. In “Self-Assembly of Chiral Molecules at the Interface,” we examine the wide variety of surface structures formed by chiral molecules (both enantiomers and racemates). We continue in “Self-Assembly of Achiral Molecules into Enantiomorphous Domains at the Interface” by discussing the fascinating topic of chiral surface structures formed by *achiral* molecules, and we focus on the specific example of self-assembly of hexadecanoic acid. Although this topic may seem peculiar at first, the imposition of two-dimensional order by the surface onto three-dimensional molecules has many symmetry-breaking properties that lead to a wealth of such systems. In “Achiral Molecules Mixed with Chiral Molecules and Their Effect on Self-Assembly,” we combine achiral molecules with chiral molecules to examine the effect of the former on self-assembly of chiral molecules. The case study explored mixtures of different-length unsubstituted fatty acids with racemic 2-Br-hexadecanoic acid at the liquid–solid interface.

Many of the studies described take advantage of molecules with chemical marker groups. Marker groups are chemical functional groups contained within

a molecular adsorbate that exhibit unusually high or low contrast in the STM topograph relative to the rest of the molecule. This unusual contrast can be used to locate particular functionalities within a given molecule. A number of physisorbed molecular systems that contain such markers have been successfully explored on graphite, and the unusual image contrast arises from both the functional group's topographic positioning and its electronic coupling to the surface. Finally, several of the investigations discussed here involve long-chain functionalized hydrocarbons, popular molecules for STM investigations of self-assembled monolayers physisorbed on graphite and MoS<sub>2</sub> surfaces. In general, these molecules lie flat on the substrate, and the hydrocarbon chains are in a *trans* orientation.

### DIRECT DETERMINATION OF CHIRALITY OF INDIVIDUAL MOLECULES: 2-BR-HEXADECANOIC ACID ON GRAPHITE

Individual molecules in a physisorbed self-assembled monolayer of racemic 2-Br-hexadecanoic acid [CH<sub>3</sub>(CH<sub>2</sub>)<sub>13</sub>CHBrCOOH] dissolved in phenyloctane solution were imaged at the graphite-liquid interface with an STM.<sup>[1]</sup> Previous studies on long-chain *n*-carboxylic acids have shown that these molecules physisorb on graphite with the hydrocarbons flat on the substrate and the carboxyl end groups oriented toward each other to facilitate hydrogen bonding. These studies also reveal that the carboxyl end group always appears with “darker” contrast compared to the rest of hydrocarbon chain, thus making the carboxylic acid functionality a *dark* chemical marker group.<sup>[1,3]</sup> Similarly, bromine atoms at a nonterminal position along the hydrocarbon chain or at a terminal position in the *gauche* conformation appear with bright contrast and are positioned “up” pointing away from the graphite surface,<sup>[4-6]</sup> making the bromine a *bright* chemical marker group.

An STM topograph of a pair of 2-Br-hexadecanoic acid molecules is shown in Fig. 1 accompanied by a schematic of the arrangement of the molecules.<sup>[1]</sup> The dark circles (found between the bright white spots) are unambiguously ascribed to the carboxylic acid groups marked as -COOH. The large “bright” spot (marked as Br in the figure) is attributed to the location of the bromine atom. Given the relative position of the bromine atom and the carboxyl group, the orientation of the rest of the alkyl chain is determined, as the bromine atom lies between the carboxyl group and the rest of the alkyl chain. Thus the alkyl chain associated with the lower of the two labeled bromine atoms (marked as Br in the figure) is represented by the lower set of numbers 1 to 14, where the numbers correspond to small topographic protrusions along the alkyl tail. These

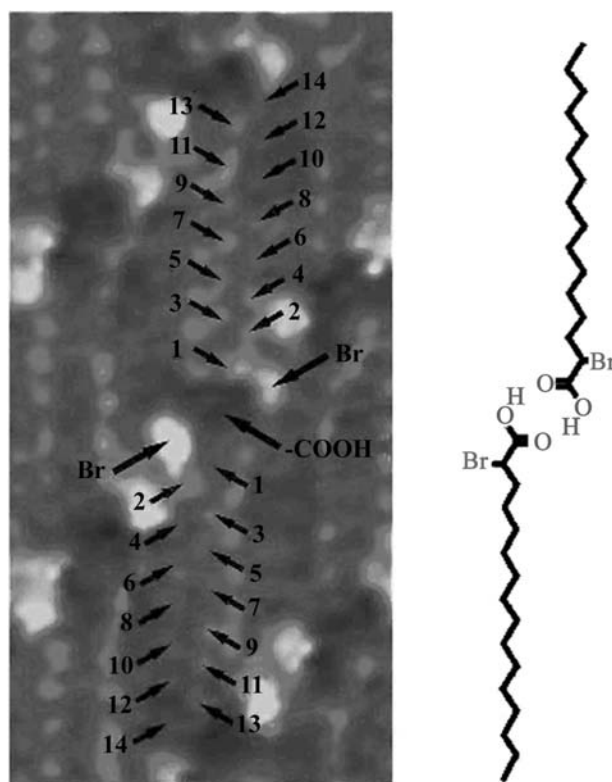


**Fig. 1** Enlarged portion of a constant current image of *R*-2-bromohexadecanoic acid at the interface of a phenyloctane solution and the graphite basal plane. *Source:* From Ref. <sup>[1]</sup>. © 1998 by the American Chemical Society.

small spots are ascribed to the positions of those hydrogen atoms of the adsorbed hydrocarbon molecules protruding farthest out of the molecular plane.<sup>[7]</sup>

Based on the above assignment with bright bromine atoms sticking up,<sup>[4]</sup> the molecule can be easily identified as the *R*-2-Br-hexadecanoic acid because the relative positions of three of the four groups attached to the chiral carbon have been directly determined (Br, COOH, alkyl tail) and the fourth (hydrogen atom) is right beneath the bromine atom, as shown in Fig. 1. The atomic resolution obtained in this STM image has enabled us to determine the absolute configuration of a single organic molecule directly, i.e., without the help of any compound of known chirality. Similarly, Lopinski et al.<sup>[2]</sup> conducted a study of short-chain alkenes on silicon in ultrahigh vacuum and were also able to directly determine the chirality of the *SS* and *RR* enantiomers of adsorbed *trans*-2-butene on an Si(100) surface.

### SELF-ASSEMBLY OF CHIRAL MOLECULES AT THE INTERFACE

The resolution of a racemic mixture of chiral molecules into enantiomers was first observed by Louis Pasteur

in his famous experiment in 1848 on a solution of racemic sodium ammonium tartrate, which he resolved into enantiomorphic crystals.<sup>[8]</sup> This phenomenon translates to the 2-D interface where numerous examples exist of spontaneous resolution of racemic molecules into enantiomorphous domains possessing 2-D chirality, where an enantiomorphous domain is described as one possessing nonsuperimposable mirror-image morphology. Racemic 2-Br-hexadecanoic acid spontaneously resolves into domains that are mirror images of each other.<sup>[1]</sup> A racemic mixture of a binaphthalene dithiol compound on gold was also found to form domains of enantiomeric purity,<sup>[9]</sup> where the study of a self-assembled monolayer of a racemic mixture of 1,2-dihydroxyoctadecane revealed a lamellar-like alternation of enantiomeric purity.<sup>[10]</sup> Clusters of nitronaphthalene were enantiomorphic on the Au(111) image and the STM tip was used to manipulate and separate the enantiomorphic clusters in a molecular analog to Pasteur's experiment.<sup>[11]</sup> An extension of this study explored a coverage-driven, chiral-phase transition of nitronaphthalene clusters on gold.<sup>[12]</sup> An experiment that investigated the effects of the impact of different substrate structures on the packing of chiral molecules revealed that a racemic mixture of thiaheterohelicene on Au(111) resolved into chiral structures only on the steps and not on the terraces. However, many racemic mixtures do not resolve into enantiomorphous domains on a surface as shown for a racemic mixture of physisorbed secondary alcohol molecules<sup>[13]</sup> and formamide molecules at the interface.<sup>[14]</sup>

With the increasing synthetic ability to separate racemic molecules into pure enantiomers, a formidable challenge for chemists as so many properties of chiral isomers are identical, STM studies of chiral systems are not limited to racemic mixtures but also include investigations of enantiomerically pure substances. Enantiomerically pure formamide molecules are found to form enantiomorphous domains.<sup>[14]</sup> Similarly, chiral terephthalic acid derivatives<sup>[15]</sup> and their polymorphs<sup>[16]</sup> have been found to form enantiomorphous self-assembled monolayers. Many chiral liquid crystals also form enantiomorphous domains.<sup>[17]</sup> Conformations of chiral dendrimers have also been explored with STM.<sup>[18]</sup>

A discussion of self-assembly of chiral molecules should also include, at least briefly, the study of chiral surfaces. An elegant approach to formation of a chiral surface is described by Lopinski et al.<sup>[19]</sup> where the sterically hindered 1*S*(+)-3-carene molecule is demonstrated to enantiospecifically chemisorb onto Si(100) surface in a bonding arrangement that is predicted to be very stable. Although many other chiral surface structures formed by adsorbed molecules are described in this article, for the most part they are *physisorbed*, which makes them stable only in the specified liquid–solid

environment in which the experiments were conducted. A different approach to chiral surfaces is to form high Miller index surfaces of single metal crystals; such surfaces have been demonstrated to be chiral.<sup>[20]</sup> Enantiospecific chemical reactions of chiral molecules have also been explored on such chiral surfaces.<sup>[20–22]</sup>

## SELF-ASSEMBLY OF ACHIRAL MOLECULES INTO ENANTIOMORPHOUS DOMAINS AT THE INTERFACE

Surfaces possess symmetry-breaking properties that affect the resultant surface structures formed by *achiral* molecules. Molecules that are achiral in three dimensions can form arrays on the surface that result in a 2-D chiral surface structure. A 2-D chiral surface structure is one in which the adsorbed molecule has a non-superimposable mirror image when the adsorbed molecule is *confined* to motion (i.e., rotation/translation) within the surface plane. This concept is illustrated further below as we examine the specific case of self-assembly of hexadecanoic acid at the graphite–liquid interface.<sup>[23,24]</sup>

Free hexadecanoic acid [ $\text{CH}_3(\text{CH}_2)_{14}\text{COOH}$ ] is an achiral molecule that is always superimposable with its mirror image in three dimensions. This property dramatically changes when hexadecanoic acid is adsorbed onto a graphite surface, for now the molecule is fixed in a plane instead of being able to freely rotate in three dimensions. Two hexadecanoic acid molecules will adsorb onto a graphite surface in a manner that allows the carboxylic acid functional groups to hydrogen-bond together; Fig. 2a depicts a model with two such molecules whose conformations have been labeled “A”. When this pair is reflected through a mirror plane demarcated by the black line, the resultant molecules on graphite adopt the configuration labeled “B”, which (in the restricted two-dimensional world of the interface) is a nonsuperimposable mirror image of the “A” molecules on the surface. The surface ultimately drives hexadecanoic acid to self-assemble in two distinct enantiomorphous domains that possess 2-D chirality. Such 2-D chiral films are generally formed on a graphite surface for fatty acids with an even number of carbon atoms, but not for fatty acids with an odd number of carbon atoms. Two-dimensional arrays arising from the assembly of molecules configured in the “A” or “B” arrangements are presented in Fig. 2b.

Achiral molecules forming enantiomorphous domains on the surface is not an uncommon phenomenon and has been documented via high-resolution SPM studies. Other examples have been observed for discotic liquid crystals,<sup>[25]</sup> for a liquid crystal phase of achiral molecules investigated via optical microscopy,<sup>[26]</sup>



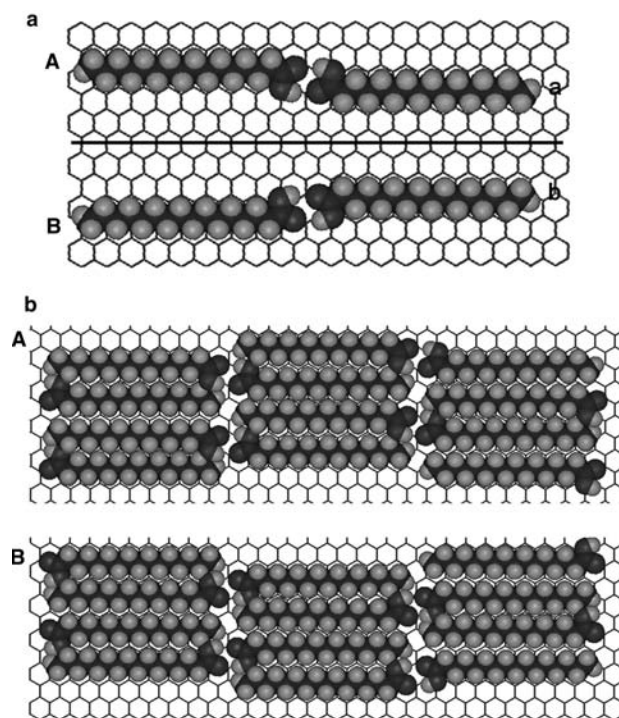


**Fig. 2** The two-dimensional chiral nature of achiral hexadecanoic acid physisorbed onto a graphite surface is shown in (a). The “B” molecules on graphite are the mirror image of the “A” molecules on the surface, reflected through the mirror plane indicated by a black bar. Hexadecanoic acid self-assembles into the two distinct enantiomorphous (possessing mirror-image morphology) domains depicted in (b). Source: From Ref. [24]. © 2000 by the American Chemical Society.

for calcium arachidate assembled on mica probed by atomic force microscopy (AFM),<sup>[27]</sup> for achiral formamide,<sup>[14]</sup> and for adenine molecules adsorbed onto molybdenum disulfide observed via STM.<sup>[28]</sup> Like fatty acids, 1-nitronaphthalene adopts a pseudochirality when adsorbed onto gold, which influences the formation of supramolecular clusters and chains.<sup>[29]</sup> Achiral diamide molecules form supramolecular lamellae that express chirality as observed by STM.<sup>[30]</sup>

### ACHIRAL MOLECULES MIXED WITH CHIRAL MOLECULES AND THEIR EFFECT ON SELF-ASSEMBLY

As discussed in the last three sections, chiral and achiral molecules can form a wide variety of surface structures that range from the formation of achiral surface domains by chiral molecules to enantiomorphous domains created by achiral molecules. This leads us to address the question of what happens when achiral molecules are mixed with chiral molecules? Such

studies have a vastly increased complexity because interadsorbate interactions play a role in determining the surface structure in addition to other adsorbate–adsorbate and adsorbate–surface interactions. Nevertheless, to date, several interesting studies have been undertaken to explore the effects of achiral molecules on self-assembly of chiral molecules. In some instances, the achiral molecules are simply represented as solvent that coadsorbs with the solute as in the work on isophthalic acid derivatives dissolved in 1-heptanol,<sup>[31]</sup> where the achiral molecules were found to express the chirality of the overall monolayer formed by the chiral solute. A similar phenomenon occurred in the study of substituted acids dissolved in alcoholic solvents.<sup>[32]</sup>

A particularly interesting study described below examines an odd/even effect of achiral unsubstituted fatty acids on the self-assembly of chiral 2-Br-hexadecanoic acid at the liquid–solid interface. The achiral molecules form a template that directs the chiral molecules to form interfacial domains either with enantiomeric purity<sup>[24]</sup> or domains with both enantiomers simultaneously present.<sup>[33]</sup> In the latter case, different templates can be chosen to create alternating lamellae of *R*- and *S*-2-Br-hexadecanoic acid or patterns with *R*- and *S*-2-Br-hexadecanoic acid stripes on the surface, thus allowing for the simultaneous detection of both enantiomers within one interfacial domain.

### Hexadecanoic Acid with Racemic 2-Br-Hexadecanoic Acid

Mixtures of the chiral molecule, 2-Br-hexadecanoic, with the achiral molecule, hexadecanoic acid, exhibit long-range order when physisorbed onto a graphite substrate. Multiple domains are formed extending in width from 30 nm to over 100 nm. Fig. 3A,C shows representative STM topograph for two different domains of a mixture of hexadecanoic acid with racemic 2-Br-hexadecanoic acid imaged at the phenyloctane–graphite interface. This image depicts well-ordered lamella separated by dark troughs. The troughs in Fig. 3A,C primarily contain dark circular regions that are sporadically accompanied by bright spots. The individual dark regions (topographical depressions) are assigned to the positions of pairs of hydrogen-bonding carboxylic acid groups<sup>[1,3]</sup> whereas the bright spots (topographical protrusions) correspond to bromine atoms, which appear bright when they are located at a nonterminal position along the hydrocarbon chain.<sup>[4,6]</sup> The presence or absence of the chemical marker bromine (bright) near the COOH (dark) group provides a straightforward and facile differentiation of the two chemical species in this mixture despite their similar lengths.

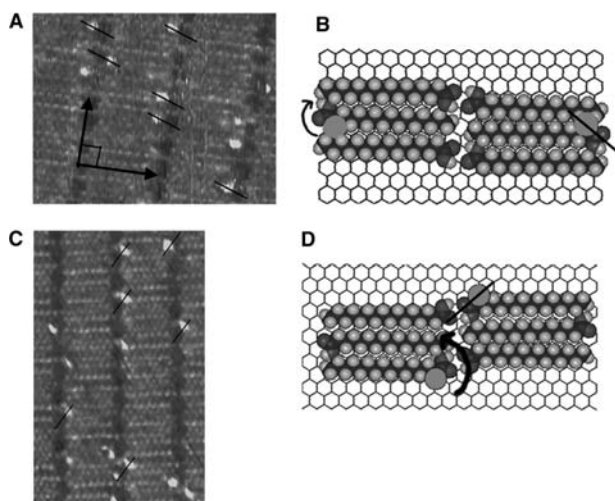


**Fig. 3** (A) An enlarged portion of a domain of racemic 2-Br-hexadecanoic acid with hexadecanoic acid imaged at the liquid–solid interface where all the brominated molecules are *R*-2-Br-hexadecanoic acid, accompanied by a corresponding model in (B). (C) A second domain of racemic 2-Br-hexadecanoic acid with hexadecanoic acid is shown where all the 2-Br-hexadecanoic acid molecules are identified as the *S* chiral conformers of the molecule with a corresponding model shown in (D). *Source:* From Ref. [24]. © 2000 by the American Chemical Society.

Note that unlike the 45° angle between the lamella direction and molecular axis present in pure 2-Br-hexadecanoic acid from Fang et al.'s work,<sup>[1]</sup> images of the 2-Br-hexadecanoic acid/hexadecanoic acid mixture display a 90° angle (marked by the arrows) between these two axes. Pure hexadecanoic acid self-assembles with a 90° lamellar–molecular axis angle. The 45° molecular–lamellar structure in racemic 2-Br-hexadecanoic acid is driven by favorable Br–Br attractive interactions, which here are effectively shut down in mixtures where the probability that two Br-containing molecules will be found adjacent to each other is low.

Two different domains are found on the surface, represented by STM images in Fig. 3A,C. The relative orientation of the bromine atoms to the carboxylic acid groups remains consistent throughout a single domain. All of the bromine atoms in Fig. 3a lie either above and to the left of the carboxyl group or below and to the right of the carboxyl group. Black lines have been superimposed on some of the individual carboxyl/bromine combinations to denote this arrangement. Fig. 3B presents a molecular model representation of this surface organization.

A different marker group positioning is found in the STM image of a second domain shown in Fig. 3C, where the bromine/carboxyl group orientation is the mirror image of that presented in Fig. 3A,B. Fig. 3D provides a molecular model representation of Fig. 3C where the orientation of the bromine/COOH orientation is marked by a black line.

Determination of the absolute chirality of individual 2-Br-hexadecanoic acid molecules has been described in detail elsewhere<sup>[1,4]</sup> and can be assigned from the relative orientations of the three dissimilar groups on the chiral carbon center that are all clearly present in the STM image—the bromine atom, carboxylic acid group, and the remainder of the alkyl chain. Thus the brominated molecules in Fig. 3A,B

are assigned as *R*-2-Br-hexadecanoic acid, and the brominated molecules in Fig. 3C,D are *S*-2-Br-hexadecanoic acid.

In summary, two phenomena clearly stand out in the self-assembled monolayer of a mixture of two coadsorbates, achiral hexadecanoic acid and chiral 2-Br-hexadecanoic acid. First, the ability to effect a specific self-assembly of 2-Br-hexadecanoic by introducing hexadecanoic acid into the solution has been demonstrated. The element of control for this feature is the “forced” opening of the angle between the molecular axis and the lamellar direction from 45° to 90° in the mixed self-assembly. Second, racemic 2-Br-hexadecanoic acid coadsorbed with hexadecanoic acid segregates into separate chiral domains when the solution is applied to a graphite surface. This phenomenon is attributed to a curious effect of the two-dimensional graphite surface on one element in the mixture, the achiral hexadecanoic acid molecules. In fact, physisorption of hexadecanoic acid on a graphite surface causes it to separate into two distinct domains that exhibit nonsuperimposable mirror-image morphology (enantiomorphous domains) as discussed in “Self-Assembly of Achiral Molecules into Enantiomorphous Domains at the Interface.” These enantiomorphous domains necessarily lead to a resolution of *R*- or *S*-2-bromohexadecanoic acid in the self-assembled monolayer when the mixture is physisorbed onto a graphite surface.

### Heptadecanoic Acid with 2-Br-Hexadecanoic Acid

Another example of the templating effect of achiral molecules on chiral molecules is observed in the mixture of heptadecanoic acid [ $\text{CH}_3(\text{CH}_2)_{15}\text{COOH}$ ] with racemic 2-Br-hexadecanoic acid. A mixture of heptadecanoic

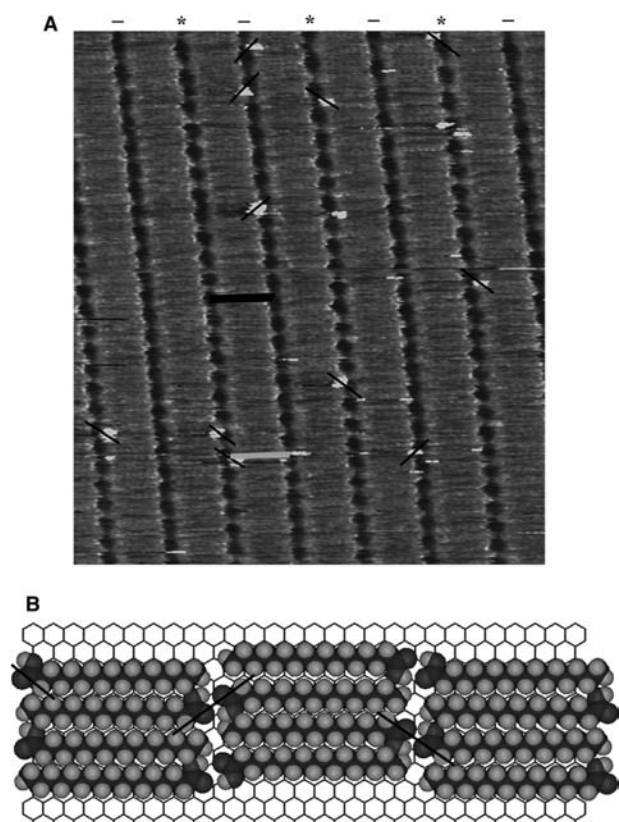


**Fig. 4** (A) An  $18 \times 18 \text{ nm}^2$  STM constant-current topograph of a mixture of heptadecanoic acid with racemic 2-Br-hexadecanoic acid [ $\text{CH}_3(\text{CH}_2)_{13}\text{CHBrCOOH}$ ]. The brominated molecules in the (\*) troughs are identified as *R*-2-Br-hexadecanoic acid while those in the (-) troughs are *S*-2-Br-hexadecanoic acid. (B) A molecular model depicts a typical domain of a heptadecanoic acid/racemic 2-Br-hexadecanoic acid mixture. *Source:* From Ref. [33]. © 2002 by the American Chemical Society.

acid with racemic 2-Br-hexadecanoic acid forms well-ordered domains when physisorbed onto a graphite surface at the liquid–solid interface. A representative STM topograph is shown in Fig. 4A, where a single molecular length of heptadecanoic acid is depicted by a black bar and a single molecular length of 2-BrHA is marked by a gray bar. The chemical marker fatty acid groups (dark) and bromine atoms (bright) are again used to differentiate the two molecules on the surface.

The relative orientation of the bromine atoms to the carboxylic acid groups is identical in *alternating* troughs of this self-assembly pattern; black bars have been superimposed over the COOH/bromine orientation to highlight this configuration. For example, the bromine atoms (bright spots) in the troughs arbitrarily marked by (\*) are either below and to the right or above and to the left of the carboxylic acid group (dark round region). In contrast, the bromine atoms in the troughs arbitrarily marked by (-) are all either below and to the left or above and to the right of the

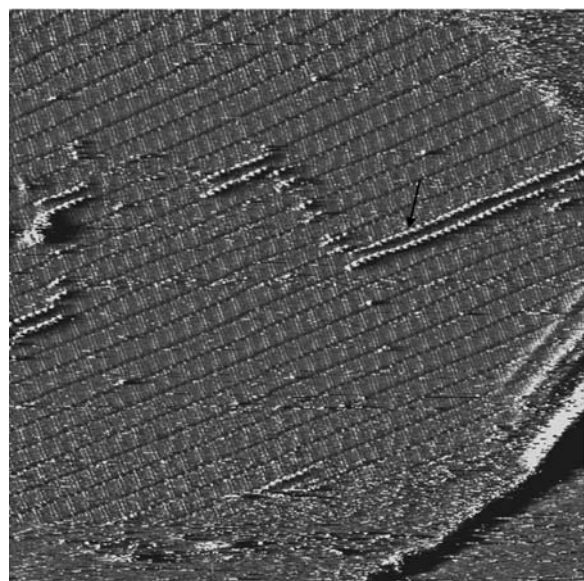
carboxylic acid groups. The relative positioning of the bromine atoms to the carboxylic acid groups in the (\*) troughs in Fig. 4A is the mirror image of the positioning of the bromine atoms to the carboxylic acid groups in the (-) troughs. Fig. 4B provides a molecular model based on a typical region of the self-assembled monolayer where the orientation of the carboxylic acid group with respect to the accompanying bromine in the alternating troughs is accordingly reflected. Thus, in these mixtures, each lamella is composed of alternating *R*- and *S*-2-Br-hexadecanoic acid molecules giving rise to the enantiomeric alternation along the starred (\*) and minus (-) troughs.

Determination of the absolute chirality of individual 2-Br-hexadecanoic acid molecules has been described in detail elsewhere.<sup>[1,4]</sup> Thus the brominated molecules that appear in those troughs arbitrarily marked by a (\*) are identified as *R*-2-Br-hexadecanoic acid, while the brominated molecules in the troughs arbitrarily marked by a (-) are readily recognizable as *S*-2-Br-hexadecanoic acid. In addition, a mixture of heptadecanoic acid with enantiomerically pure *R*-2-Br-hexadecanoic acid revealed a self-assembled structure where the bright spots (corresponding to brominated molecules) appear in every other trough.

### Longer-Chain Fatty Acid Templates with 2-Br-Hexadecanoic Acid

Self-assembled monolayers of mixtures of 2-Br-hexadecanoic acid with longer-chain fatty acids such as nonadecanoic acid and eicosanoic acid have also been studied with high-resolution scanning tunneling microscopy.<sup>[34]</sup> These mixtures reveal quasi phase segregation, as the length of the unsubstituted achiral fatty acid chain becomes significantly different from that of 2-bromohexadecanoic acid, resulting in a surface structure containing microdomains of brominated molecules and fatty acids. This is in contrast to mixtures of 2-Br-hexadecanoic acid with either hexadecanoic acid or heptadecanoic acid where these mixtures formed fully miscible surface structures.

An STM topograph of a mixture of 2-Br-hexadecanoic acid with nonadecanoic acid on graphite is shown in Fig. 5. Mixtures of 2-Br-hexadecanoic acid with both eicosanoic acid and nonadecanoic acid induce the formation of brominated “stripes” or bands within the greater domain of pure fatty acid; these bands are marked by a black arrow in Fig. 5. These bands are homochiral (meaning each band contains only one enantiomer), but which enantiomers are present depends on the length of the fatty acid template. So mixtures of 2-Br-hexadecanoic acid with eicosanoic acid form surface domains that will contain both *R*- and *S*-2-Br-hexadecanoic acid, while



80 nm

**Fig. 5** An  $80 \times 80$  nm constant-height topograph of a mixture of racemic 2-Br-hexadecanoic acid with nonadecanoic acid. The surface structure is dominated by dark troughs, which are composed of carboxylic acid groups of nonadecanoic acid. Bright spots appear in illuminated bands (highlighted by a black arrow), which are composed of single enantiomers of 2-Br-hexadecanoic acid (i.e., bands are homochiral).

mixtures with nonadecanoic acid form surface structures that contain either *R*- or *S*-2-Br-hexadecanoic acid. This quasi phase segregation is similar to the study of various coadsorbed fluorinated isophthalic acid derivatives where a difference in chain length of three carbon atoms induced formation of microdomains but coadsorbates with a difference in chain length of one carbon atom formed a miscible surface structure.<sup>[35]</sup>

## CONCLUSION

Scanning tunneling microscopy (STM) is a powerful and uniquely suited technique to study chiral surface structures with atomic resolution. In this article, we focus on 2-D chiral self-assembled monolayers formed at the liquid–solid interface. Systems composed of chiral molecules, achiral molecules, mixtures of chiral and achiral molecules, and inherently chiral surfaces have been discussed to reveal a part of the rich and diverse role chirality plays in influencing surface formations and self-assembled monolayers at the liquid–solid interface. Ongoing work in the area of STM investigations of chiral systems include expanding the pool of candidates that can be studied, useful applications of symmetry-breaking properties of surfaces, and a more complete understanding of the subtle effects

that chiral molecules and surfaces have on the self-assembly process.

## REFERENCES

1. Fang, H.; Giancarlo, L.C.; Flynn, G.W. Direct determination of the chirality of organic molecules by scanning tunneling microscopy. *J. Phys. Chem., B* **1998**, *102*, 7311–7315.
2. Lopinski, G.P.; Moffatt, D.J.; Wayner, D.D.M.; Wolkow, R.A. Determination of the absolute chirality of individual adsorbed molecules using the scanning tunneling microscope. *Nature* **1998**, *392*, 909–911.
3. Hibino, M.; Sumi, A.; Hatta, I. Atomic images of saturated and unsaturated fatty acids at liquid/graphite interface and difference of tunneling currents between them observed by scanning tunneling microscopy. *Jpn. J. Appl. Phys.* **1995**, *34*, 610–614; 3354–3359.
4. Yablon, D.G.; Guo, J.; Knapp, D.; Fang, H.; Flynn, G.W. Scanning tunneling microscopy investigation of a chirally pure molecule at the liquid–solid interface: Unambiguous topographic markers. *J. Phys. Chem., B* **2001**, *105*, 4313–4316.
5. Cyr, D.M.; Venkataraman, B.; Flynn, G.W.; Black, A.; Whitesides, G.M. Functional group identification in scanning tunneling microscopy of molecular adsorbates. *J. Phys. Chem.* **1996**, *100*, 13747–13759.
6. Claypool, C.L.; Faglioni, F.; Matzger, A.J.; Goddard, W.A.; Lewis, N.S. Effects of molecular geometry on the STM image contrast of methyl- and bromo-substituted alkanes and alkanols on graphite. *J. Phys. Chem., B* **1999**, *103*, 9690–9699.
7. Liang, W.; Whangbo, M.-H.; Wawkuszewski, A.; Cantow, H.J.; Magonov, S.N. Electronic origin of scanning tunneling microscopy images and carbon skeleton orientation of normal alkanes adsorbed on graphite. *Adv. Mater.* **1993**, *5*, 817–821.
8. Pasteur, L. C.R. *Hebd. Seances Acad. Sci.* **1848**, *26*, 535–539.
9. Ohtani, B.; Shintani, A.; Uosaki, K. Two-dimensional chirality: Self-assembled monolayer of an atropisomeric compound covalently bound to a gold surface. *J. Am. Chem. Soc.* **1999**, *121*, 6515–6516.
10. Qian, P.; Nanjo, H.; Yokoyama, T.; Suzuki, T.M. STM observation of chiral 1,2-Dihydroxyoctadecane monolayer self-assembled on the graphite surface. *Chem. Lett.* **1998**, *11*, 1133.
11. Bohringer, M.; Morgenstern, K.; Schneider, W.; Berndt, R. Separation of a racemic mixture of two-dimensional molecular clusters by scanning tunneling microscopy. *Angew. Chem., Int. Ed.* **1999**, *38*, 821–823.
12. Bohringer, M.; Schneider, W.-D.; Berndt, R. Real space observation of a chiral phase transition in a 2-D organic layer. *Angew. Chem., Int. Ed.* **2000**, *39*, 792.
13. LePoullennec, C.; Cousty, J.; Xie, Z.X.; Mioskowski, C. Self-organization of physisorbed secondary alcohol molecules on a graphite surface. *Surf. Sci.* **2000**, *448*, 93–100.

14. DeFeyter, S.; Gesquiere, A.; Wurst, K.; Amabilino, D.B.; Veciana, J.; DeSchryver, F.C. Homo- and hetero-chiral supramolecular tapes from achiral, enantiopure, and racemic promesogenic formamides: Expression of molecular chirality in two and three dimensions. *Angew. Chem., Int. Ed.* **2001**, *40*, 3217.
15. DeFeyter, S.; Gesquiere, A.; Grim, P.C.M.; DeSchryver, F.C. Expression of chirality and visualization of stereogenic centers by scanning tunneling microscopy. *Langmuir* **1999**, *15*, 2817.
16. DeFeyter, S.; Gesquiere, A.; DeSchryver, F. Chiral polymorphism: A scanning tunneling microscopy study. *Langmuir* **2000**, *16*, 9887–9894.
17. Walba, D.M.; Stevens, F.; Clark, N.A.; Parks, D.C. Detecting molecular chirality by scanning tunneling microscopy. *Acc. Chem. Res.* **1996**, *29*, 591–597.
18. Hermann, B.A.; Hubler, U.; Jess, P.; Lang, H.P.; Guntherodt, H.-J.; Greiveldinger, G.; Rheiner, P.B.; Murer, P.; Sifferlen, T.; Seebach, D. Chiral dendrimers on a Pt(100) surface investigated by STM. *Surf. Interface Anal.* **1999**, *27*, 507.
19. Lopinski, G.P.; Moffatt, D.J.; Wayner, D.M.; Zgierski, M.Z.; Wolkow, R.A. Asymmetric induction at a silicon surface. *J. Am. Chem. Soc.* **1999**, *121*, 4532–4533.
20. McFadden, C.F.; Cremer, P.S.; Gellman, A.J. Adsorption of chiral alcohols on “Chiral” metal surfaces. *Langmuir* **1996**, *12* (10), 2483.
21. Gellman, A.J.; Horvath, J.D.; Buelow, M.T. Chiral single crystal surface chemistry. *J. Mol. Catal., A: Chem.* **2001**, *167*, 3–11.
22. Ahmadi, A.; Attard, G.; Feliu, J.; Rodes, A. Surface reactivity at “chiral” platinum surfaces. *Langmuir* **1999**, *15*, 2420–2424.
23. Hibino, M.S.A.; Tsuchiya, H.; Hatta, I. Microscopic origin of the odd-even effect in monolayer of fatty acids formed on a graphite surface by scanning tunneling microscopy. *J. Phys. Chem., B* **1998**, *102*, 4544–4547.
24. Yablon, D.G.; Giancarlo, L.C.; Flynn, G.W. Manipulating self-assembly with archiral molecules: An STM study of chiral segregation by achiral adsorbates. *J. Phys. Chem., B* **2000**, *104*, 7627–7635.
25. Charra, F.; Cousty, J. Surface-induced chirality in self-assembled monolayer of discotic liquid crystals. *Phys. Rev. Lett.* **1998**, *80*, 1682–1685.
26. Link, D.R.; Natale, G.; Shao, R.; MacLennan, J.E.; Clark, N.A.; Korblova, E.; Walba, D.M. Spontaneous formation of macroscopic chiral domains in a fluid smectic phase of achiral molecules. *Science* **1997**, *278*, 1924–1927.
27. Viswanathan, R.; Zasadzinski, J.A.; Schwartz, D.K. Spontaneous chiral symmetry breaking by achiral molecules in a Langmuir-Blodgett film. *Nature* **1994**, *368*, 440–443.
28. Sowerby, S.J.; Heckl, W.M.; Petersen, G.B. Chiral symmetry breaking during the self-assembly of monolayers from achiral purine molecules. *J. Mol. Evol.* **1996**, *43*, 419–424.
29. Bohringer, M.; Morgenstern, K.; Schneider, W.-D.; Berndt, R.; Mauri, F.; Vita, A.D.; Car, R. Two-dimensional self-assembly of supramolecular clusters and chains. *Phys. Rev. Lett.* **1999**, *83*, 324–327.
30. Lim, R.; Li, J.; Li, S.F.Y.; Feng, Z.; Valiyaveetil, S. The formation of two-dimensional supramolecular chiral lamellae by diamide molecules at the solution/graphite interface: A scanning tunneling microscopy study. *Langmuir* **2000**, *16*, 7023–7030.
31. DeFeyter, S.; Grim, P.C.M.; Rucker, M.; Vanoppen, P.; Meiners, C.; Sieffert, M.; Valiyaveetil, S.; Mullen, K.; DeSchryver, F.C. Expression of chirality by achiral coadsorbed molecules in chiral monolayers observed by STM. *Angew. Chem., Int. Ed.* **1998**, *37*, 1223–1226.
32. Wintgens, D.; Yablon, D.G.; Flynn, G.W. Packing of HO(CH<sub>2</sub>)<sub>14</sub>COOH and HO(CH<sub>2</sub>)<sub>15</sub>COOH on graphite at the liquid-solid interface observed by scanning tunneling microscopy: Methylene unit direction of self-assembly structures. *J. Phys. Chem., B* **2002**, *106* (21), 5470–5475.
33. Yablon, D.G.; Wintgens, D.; Flynn, G.W. Odd/even effect in self-assembly of chiral molecules at the liquid-solid interface: An STM investigation of coadsorbate control of self-assembly. *J. Phys. Chem., B* **2002**, *106*, 5470.
34. Yablon, D.G.; Flynn, G.W. **2002**, in preparation.
35. Gesquiere, A.; Abdel-Mottaleb, M.A.; DeSchryver, F. Imaging of a Fluorine-substituted isophthalic acid derivative on graphite with scanning tunneling microscopy. *Langmuir* **1999**, *15*, 6821–6824.



# Self-Assembly of Coordination Cages

Laura Pirondini  
Enrico Dalcanale

Dipartimento di Chimica Organica e Industriale, Università di Parma, Parma, Italy

## INTRODUCTION

Why is self-assembly so appealing to nanoscience in general and nanotechnology in particular? One answer is, in Whitesides's words: "Self-assembly is one of the few practical strategies for making ensembles of nanostructures."<sup>[1]</sup>

The key issue in self-assembly is that the desired structures are quantitatively formed by simply mixing the programmed components under thermodynamic control. Unlike covalent synthesis, self-assembly is a reversible process. This is a very attractive feature because it allows the system to self-repair possible structural deficiencies.

## OVERVIEW

Of the self-assembly protocols developed so far, metal-directed self-assembly is particularly appealing as a result of the large number of structural motifs and bond energies that are available through coordination chemistry. The most important feature is the great directionality offered by metal–ligand coordinative bonds compared to weak electrostatic and  $\pi$ – $\pi$  stacking interactions or even hydrogen bonding. Moreover, coordinative metal bond offers great versatility due to different transition-metal complexes and multidentate ligands available as building blocks and to bond energies that are between the range of the strong covalent bond in carbon-based molecules and the weak interactions in biological systems. The final shape of the self-assembled entity is not only defined through the metal-complex coordination geometry, but also through the orientation of the ligand interaction sites.

Molecules with a wide variety of topologies and shapes have been constructed in this way, including boxes, cages, catenanes, dendrimers, grids, helicates, rotaxanes, and others. (For recent reviews on this topic, see Refs.<sup>[2–7]</sup>.)

Container molecules are unique among synthetic molecular receptors because of their peculiar encapsulation properties.<sup>[8,9]</sup> Guests of different sizes, shapes, and charges have been trapped within their interior in a timescale that can span from microseconds to

infinity. Desired features of container molecules comprise selectivity in guest encapsulation, control of guest orientation and dynamics within the cage, and reversibility, which allows guest uptake and release under controlled conditions. The ability of such container molecules to confine<sup>[10]</sup> and stabilize<sup>[11]</sup> their guests makes them particularly attractive for many potential applications, ranging from specific drug release to catalysis<sup>[12–14]</sup> and memory-storage devices.<sup>[15]</sup>

Metal-directed self-assembly has been employed to construct container molecules presenting internal cavities of molecular dimensions, capable of trapping ions and neutral molecules.<sup>[16]</sup> The need of highly preorganized, multidentate ligands presenting concave surfaces has led some researchers to resort to calixarenes (for the first report on calixarene-based coordination cages, see Refs.<sup>[17]</sup>; see also Ref.<sup>[18]</sup>) and cavitands (for the first report on cavitand-based coordination cages, see Ref.<sup>[19]</sup>) as source of rigid molecular scaffolds. The present account will focus on the design and self-assembly of cavitand-based coordination cages.

After a comprehensive survey of the literature in the field, the evolution of coordination cages in our group in terms of size, structure, and adaptability to different self-assembly conditions will be presented. Besides our own efforts, three other groups have engaged in the preparation, characterization, and complexation studies of cavitand-based coordination cages. They have in common the synthetic strategy adopted for the introduction of the ligands, which relies on functionalizing the apical positions of methylene-bridged cavitands.

Harrison and coworkers introduced four iminodiacetate moieties as chelating ligands (cavitand **I**, Fig. 1). Treatment with  $\text{CoCl}_2$  under basic conditions led to the formation of cage **IIa**, with the four octahedrally coordinated  $\text{Co(II)}$  connecting two cavitand **I** scaffolds.<sup>[20]</sup> Cage **IIa**, which has been structurally characterized, presents two very interesting features: 1) it is water-soluble; 2) the self-assembly process is pH dependent: At pH values below 2, the carboxyl groups and amine nitrogen atoms are protonated and do not coordinate  $\text{Co(II)}$  ions; upon addition of base at pH 5, cage **IIa** is formed. Taking advantage of the hydrophobic effect, they have been able to include several small lipophilic guests within the cage such



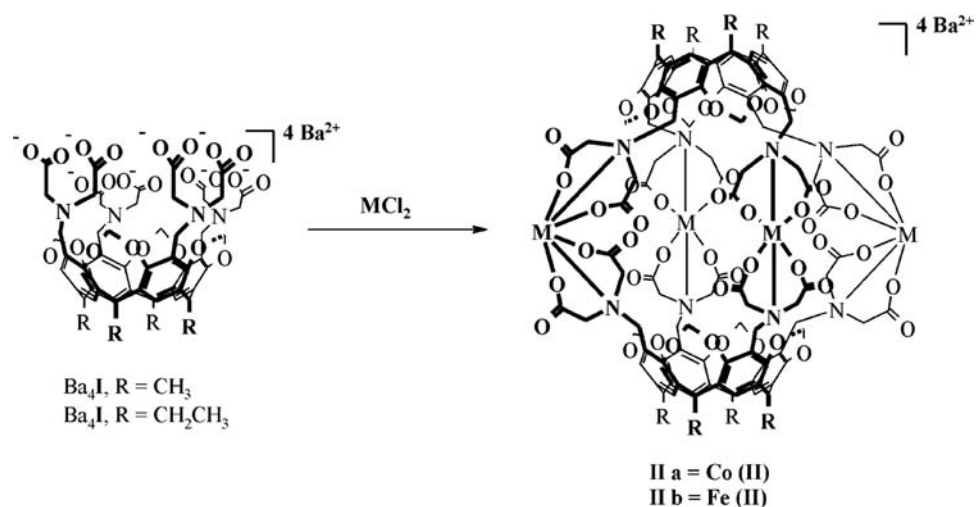


Fig. 1 Harrison's approach to cavitand-based coordination cages.

as aromatic molecules, alkanes, haloalkanes, and alcohols.<sup>[21]</sup> Large upfield shifts in the proton resonances (30–40 ppm) of the encapsulated guest are observed: Thus the cage behaves as a NMR (nuclear magnetic resonance) shift reagent for the included guest. Using the same cavitand ligand, the corresponding Fe<sub>4</sub> cage **IIb** has been prepared and structurally characterized.<sup>[22]</sup> These cages also form grids in the solid state.<sup>[23]</sup> The carboxylate groups bind cations such as Ca<sup>2+</sup>, Sr<sup>2+</sup>, and Ba<sup>2+</sup>, connecting the cages among them in the solid state. The resulting three-dimensional network formed presents channels and pores, whose size can be controlled by varying the cation size.<sup>[24]</sup>

Beer and coworkers have reported the metal-assembled synthesis of trimeric and tetrameric host

architectures **III** and **IV** assembled from dithiocarbamate (dtc) cavitand ligands and zinc or copper ions (Fig. 2).<sup>[25]</sup> In the case of **III**, the three cavitand cups provide the corners for an equilateral molecular triangle with two zinc ions positioned at the midpoints of each side. The Zn(II) ions coordinate two bidentate dtc moieties and a pyridine molecule. Treatment of the same cavitand ligand with Cu(II) acetate provided an intermediate Cu(II) complex that was oxidized to the octanuclear Cu(III) cages **IV**[I<sub>3</sub>]<sub>7</sub>[I]·6H<sub>2</sub>O by treatment with iodine. In this case, four cavitands lie at the apices of a distorted tetrahedron, and are connected to each other by eight Cu(III) ions. The novelty of this approach is in the formation of higher stoichiometric species with respect to the other cases, leading to wider

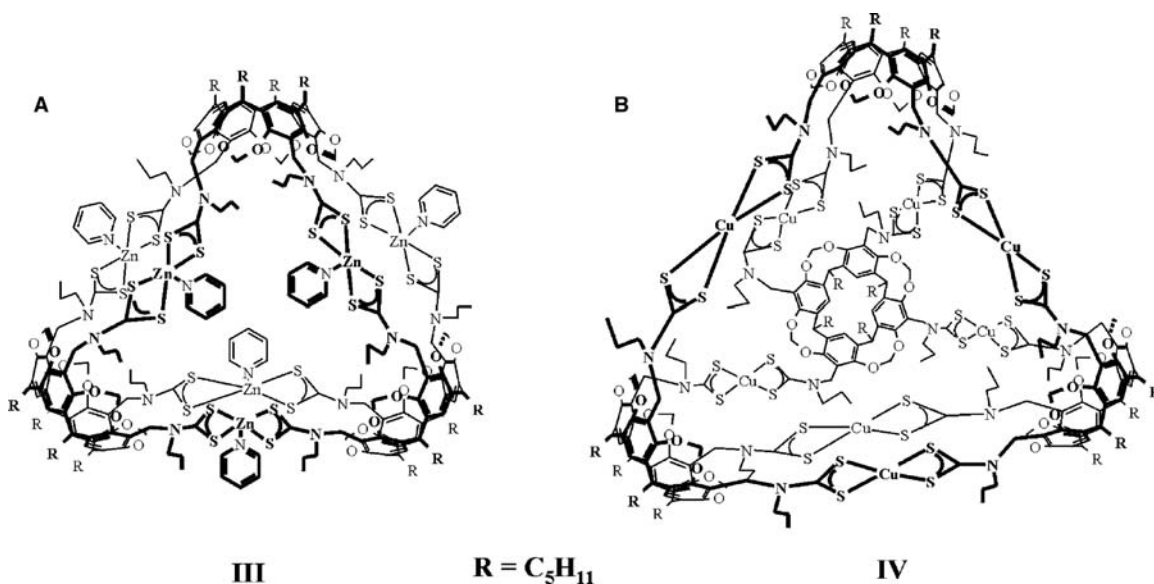


Fig. 2 (A) Hexanuclear Zn(II) complex **III**; (B) octanuclear Cu(III) complex **IV**.

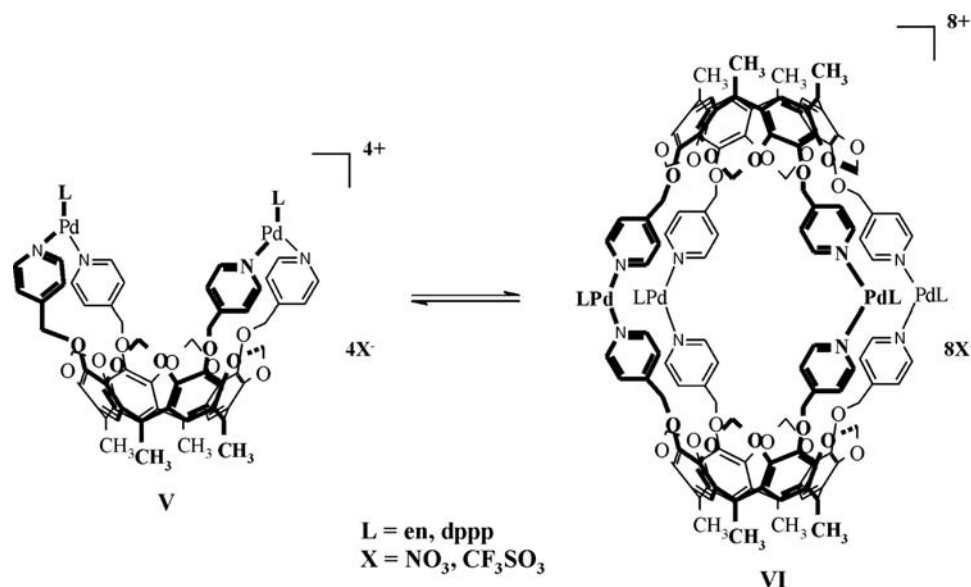


Fig. 3 Solvent-driven equilibrium between cage VI and metalated cavitand V.

cavities and larger portals. The complexation properties in organic solvents of the trimeric cage III have been explored, using fullerene as guest.<sup>[26]</sup> The selectivity in binding C<sub>60</sub> has been attributed to the presence of 16 sulfur atoms that interact with the electron-deficient guest.

A third approach has been carried out by Hong and collaborators, connecting four pyridine ligands to the apical positions of a cavitand through methyleneoxy spacers. When the pyridyl nitrogen is *para* with respect to the spacer, coordination cages VI are formed upon exposure to square-planar metal precursors such as Pd(en)(NO<sub>3</sub>)<sub>2</sub>.<sup>[27]</sup> Evidences of cage formation come from vapor pressure osmometry <sup>1</sup>H NMR, and electrospray ionization mass spectrometry (ESI-MS) experiments, but these cages have not been structurally characterized yet. Cage VI binds positively charged *N*-alkylpyridinium derivatives in acetone solution as a result of strong cation- $\pi$  interactions. In this particular case, the self-assembly is solvent-dependent (Fig. 3): Cage VI formation is favored by apolar solvents, while cavitand complex V is formed as unique product in water solution.<sup>[28]</sup> This result seems to imply that the solvation of the inner space of cavitand-based coordination cages is pivotal for cage self-assembly.

## SELF-ASSEMBLY OF COORDINATION CAGES IN SOLUTION

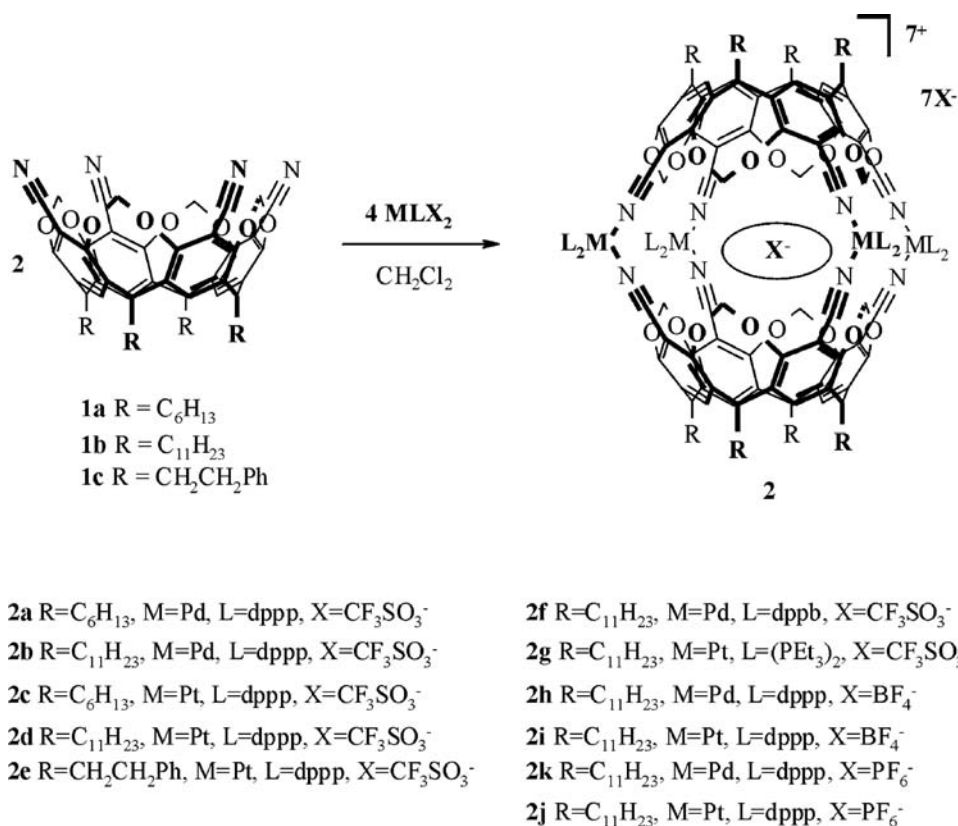
### Nitrile-Based Coordination Cages

Among the coordination cages studied in our group, the archetype is cage of general structure 2, which is

composed of two tetracyanocavitand derivatives connected through four Pd(II) or Pt(II) square-planar complexes (Scheme 1).<sup>[19,29]</sup> Such cages were assembled by simply mixing cavitand 1 with different metal precursors MLX<sub>2</sub> [M = Pd, Pt; L = dppp, dppb, (PEt<sub>3</sub>)<sub>2</sub>;<sup>a</sup> X = CF<sub>3</sub>SO<sub>3</sub> (= OTf), BF<sub>4</sub>, PF<sub>6</sub>] in a 1:2 molar ratio. Multinuclear NMR spectroscopy (<sup>13</sup>C, <sup>31</sup>P, and <sup>19</sup>F), ESI-MS, matrix-assisted laser desorption/ionization-time of flight (MALDI-TOF) mass spectrometry, and vapor phase osmometry (VPO) confirmed the dimeric structure of the cage with respect to the cavitand ligands. Their <sup>1</sup>H NMR spectra showed the complete absence of absorptions belonging to both precursors and the formation of a new set of signals, indicative of the presence of a single highly symmetric compound (*D*<sub>4h</sub> symmetry). The triflate counterions of all cages experience two different environments: Their <sup>19</sup>F NMR spectra exhibited two singlets in a 7:1 integral ratio, the bigger one at about -78 ppm, typical of non-coordinated ionic triflates, and a smaller one shifted upfield at about -82 ppm, indicative of the encapsulation of one triflate anion inside the cage.

Additional evidences for the self-assembly of the cages were obtained by using electrospray mass spectrometry (ESI-MS). (For studies of non-covalent aggregation by ESI-MS, see Refs.<sup>[30]</sup>.) Electrospray ionization mass spectrometry proved to be a powerful technique for the investigation of coordination cages in terms of 1) characterization; 2) individuation of

<sup>a</sup>Ligand abbreviations: dppp = 1,3-bis(diphenylphosphino)-propane; dppb = 1,3-bis(diphenylphosphino)-butane; dppe = 1,3-bis(diphenylphosphino)-ethane, dppm = 1,3-bis(diphenylphosphino)-methane; en = ethylenediamine.



**Scheme 1** Self-assembly of Pd and Pt cage molecules. *Source:* From Ref.<sup>[29]</sup>. © 2001 by the American Chemical Society.

competitive oligomeric species; and 3) presence of solvent molecules trapped within the cages. For **2a–e**, ESI-MS showed prominent [M-2CF<sub>3</sub>SO<sub>3</sub>]<sup>2+</sup> and [M-3CF<sub>3</sub>SO<sub>3</sub>]<sup>3+</sup> peaks.

Suitable crystals of **2d** for X-ray analysis were obtained from a dichloromethane–benzene solvent mixture (Fig. 4). The cage is filled with a single triflate anion, without any ancillary solvent molecule present.

The internal cavity resembles an oblate sphere: The long axis, defined as the distance between opposite Pt atoms, is 13.5(1) Å, the short axis is 12.1(1) Å and is defined as the distance between the centroids of the four resorcinarene methine carbons. These distances are in agreement with the dimensions of the cavity calculated using the Graphical Representation and Analysis of Structural Properties (GRASP)

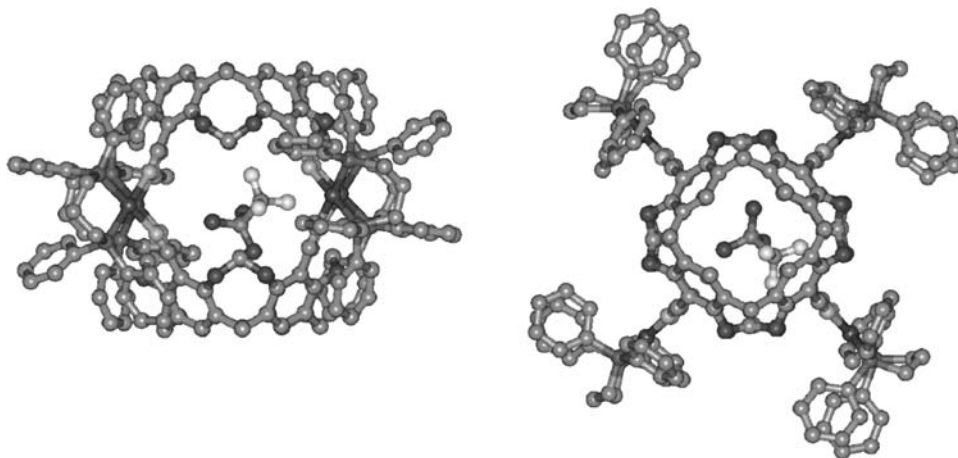


**Fig. 4** X-ray crystal structure of cage **2d**. *Source:* From Ref.<sup>[29]</sup>. © 2001 by the American Chemical Society.

program.<sup>[31]</sup> The included triflate cannot escape from the lateral portals without breaking a coordinative bond.

### Control of the self-assembly process

The self-assembly process leads to coordination cages via formation of four square-planar transition metal complexes. The *cis* coordination geometry, a necessary condition for cage self-assembly (CSA), is imposed using dppp as chelating ligand. Therefore the following structural parameters have been examined as the key factors controlling the self-assembly process: (1) choice of chelating ligand, transition metal, and counterions of the metal precursor; (2) preorganization and stiffness of the tetradentate cavita nd ligand.

(1) The influences of the chelating ligand and of the type of metal have been analyzed by mixing cavita nd **1b** with organometallic triflate precursors **3a–h** and **4a**, under standard self-assembly conditions. The results are reported in Table 1. All the chosen complexes assume square-planar coordination geometry in solution, except for Ni(dppp)(OTf)<sub>2</sub>**3e**, which in solution is in equilibrium between the tetrahedral and square-planar forms.

The effect of varying the chelate ring size has been examined in the Pd series (entries 1,3,6,8). The results clearly indicate that the CSA is highly sensitive to distortion from the optimal square-planar arrangement of the four ligands provided by dppp, particularly when the P–M–P angle is smaller than 90°. In fact, in the case of dppb (**3h**, entry 8) partial cage formation was observed at 300 K, which became complete at 373 K. In the other two cases (entries 1 and 3), the CSA was completely suppressed at any temperature. The X-ray crystal structure of **2d** supports these results, showing almost no strain in the coordination sphere of the four Pt complexes. Likewise, exchange of dppp with dppe in the Pt complexes (compare entries 4 and 7) destabilizes

the cage with respect to open oligomers. The partial CSA observed in the case of **4a** to give cage **2g** (entry 9) at room temperature demonstrates that the absence of a chelating ligand destabilizes the cage with respect to alternative open species. The influence of the transition metal has been highlighted in the M(dppe)(OTf)<sub>2</sub> and M(dppp)(OTf)<sub>2</sub> series (entries 2–7). The observed trend in cavita nd nitriles coordination is Pt > Pd > Ni in accordance with the relative strength of the CN–M dative bonds.

Another basic factor to be considered for CSA is the selection of the counterions, which must be weakly coordinated to the metal precursor to allow the exchange with the nitriles of the cavita nd ligands. Cage self-assembly proceeded with noncoordinating counterions such as triflate, BF<sub>4</sub><sup>–</sup>, and PF<sub>6</sub><sup>–</sup>, but failed with the acetate, trifluoroacetate, and tosylate anions, which are too strongly coordinated to the metal to undergo ligand exchange with the nitriles.

(2) The preorganization of the cavita nd ligand is another essential ingredient of the self-assembly recipe. The influence of the rigidity of the tetradentate cavita nd ligand and the relative orientation of the four cyano substituents on the cage self-assembly have been evaluated introducing conformationally mobile ethylene-bridged cavita nds. In this case, CSA is possible only with Pt complexes, which provide sufficient coordinative strength toward nitriles to freeze the cavita nd in the required cone conformation. Their Pd analogs failed to give CSA under the same conditions (Table 2).

Also, in this case, inclusion of a single anion has been detected by <sup>19</sup>F NMR. A second interesting feature connected to the use of ethylene-bridged cavita nds is the temperature effect on CSA: In all cases, the process is partial at 300 K and complete only above 350 K. This different behavior points out that, in terms of preorganization of the cavita nd ligands, conformational rigidity is more important than optimal coordination

**Table 1** Cage self-assembly (CSA) using cavita nd **1b** as tetradentate ligand and organometallic precursors **3a–h**, **4a**

Entry	Organometallic precursor	Outcome
1	Pd(dppm)(OTf) <sub>2</sub> ( <b>3a</b> ) (72.7°) <sup>a</sup>	No CSA
2	Ni(dppe)(OTf) <sub>2</sub> ( <b>3b</b> ) (86.9°) <sup>a</sup>	No CSA
3	Pd(dppe)(OTf) <sub>2</sub> ( <b>3c</b> ) (85.8°) <sup>a</sup>	No CSA
4	Pt(dppe)(OTf) <sub>2</sub> ( <b>3d</b> ) (85.1°) <sup>a</sup>	Oligomers formation at 300 K; partial CSA at 373 K
5	Ni(dppp)(OTf) <sub>2</sub> ( <b>3e</b> )	No CSA
6	Pd(dppp)(OTf) <sub>2</sub> ( <b>3f</b> ) (90.6°) <sup>a</sup>	CSA ( <b>2b</b> )
7	Pt(dppp)(OTf) <sub>2</sub> ( <b>3g</b> ) (89.3°) <sup>a</sup>	CSA ( <b>2d</b> )
8	Pd(dppb)(OTf) <sub>2</sub> ( <b>3h</b> ) (97.6°) <sup>a</sup>	Partial CSA at 300 K; CSA at 373 K ( <b>2f</b> )
9	<i>Cis</i> -Pt(PEt <sub>3</sub> ) <sub>2</sub> (OTf) <sub>2</sub> ( <b>4a</b> )	Partial CSA at 300 K; CSA at 328 K ( <b>2g</b> )

<sup>a</sup>P–M–P angle of M(dppx)Cl<sub>2</sub> complexes taken from the crystal structures.

Source: Ref.<sup>[29]</sup>. © 2001 by the American Chemical Society.

**Table 2** Influence of cavitand preorganization on cage self-assembly (CSA)

Entry	Organometallic precursor	<b>1b</b> R=C <sub>11</sub> H <sub>23</sub>	<b>5</b> R=C <sub>11</sub> H <sub>23</sub>
1	Pd(dppm)(OTf) <sub>2</sub>	No CSA	No CSA
2	Pd(dppe)(OTf) <sub>2</sub>	No CSA	No CSA
3	Pd(dppp)(OTf) <sub>2</sub>	CSA	No CSA
4	Pd(dppp)(BF <sub>4</sub> ) <sub>2</sub>	CSA	No CSA
5	Pd(dppp)(PF <sub>6</sub> ) <sub>2</sub>	CSA	No CSA
6	Pd(dppb)(OTf) <sub>2</sub>	CSA <sup>a</sup>	No CSA
7	Pt(dppp)(OTf) <sub>2</sub>	CSA	CSA <sup>b</sup>
8	Pt(dppp)(BF <sub>4</sub> ) <sub>2</sub>	CSA	CSA <sup>b</sup>
9	Pt(dppp)(PF <sub>6</sub> ) <sub>2</sub>	CSA	CSA <sup>b</sup>

<sup>a</sup>The CSA is partial at 300 K and complete at 373 K.

<sup>b</sup>The CSA is partial at 300 K and complete at 353 K.

Source: Ref.<sup>[29]</sup>. © 2001 by the American Chemical Society.

geometry; in fact, ethylene-bridged cavitand ligands, despite having the perfect biting angle for CSA, require an entropic price to be frozen in the cone conformation necessary for CSA.

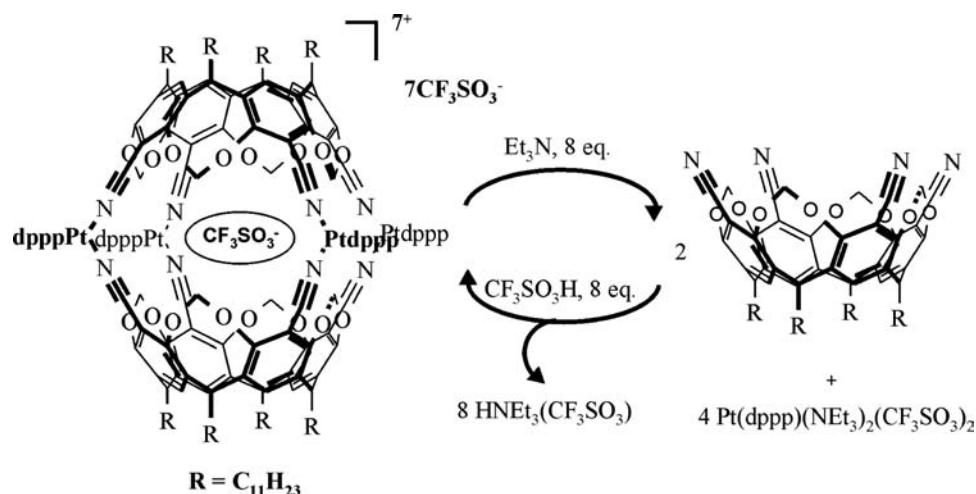
#### Thermodynamics and kinetics of the cage self-assembly

Calorimetric experiments were conducted in tetrachloroethane as solvent at different temperatures to quantify the enthalpic contribution to the self-assembly. In the case of cage **2d** at 298 K, the CSA process is strongly endothermic ( $\Delta H^0 = +57.7 \pm 0.7 \text{ kJ mol}^{-1}$ ); therefore cage formation is *entropy driven*. (For the thermodynamics of self-assembly, see Refs.<sup>[32,33]</sup>). The endothermic nature of CSA can be rationalized in terms of desolvation of the cage components and particularly of the included anion in the self-assembly process, which leads to the entropic overriding of the unfavorable positive  $\Delta H^0$  of formation. The enthalpic opposition has been explained by taking in account the large enthalpic costs associated with ion desolvation.

As the anion exchange experiments require dissociation/recombination of the coordination cages, the kinetic stability of Pd and Pt cages deserves special attention. A rough estimate of the dissociation/recombination timescale can be obtained by monitoring the ligand exchange between a preformed cage and a competitive ligand. This estimate, although not

accurate, is sufficient for the purpose of choosing the optimal anion exchange conditions. (For a detailed NMR study of the exchange process in hydrogen-bonded cal[4]arenes capsules, see Ref.<sup>[34]</sup>). Two set of experiments were directly performed in the NMR tube. Addition of cavitand **1c** to a CDCl<sub>3</sub> solution of cage **2b** at 300 K led to the immediate formation of three new species in solution, identified as cavitand **1b**, Pd heterocage [**1b**(Pdcomplex)<sub>4</sub>**1c**], and Pd homocage [**1c**(Pdcomplex)<sub>4</sub>**1c**], respectively, and to the decrease of **2b**. In the same experiment performed on Pt cage **2d**, the ligand exchange is negligible immediately after the addition, with an equilibration time of over 4 hr at 300 K. The same experiment, repeated at 330 K, led to immediate ligand exchange. Therefore the dynamics of dissociation/recombination, slow on the NMR timescale in both cages, is fast on the human timescale at ambient temperature only for **2b**, a further evidence of the greater strength of the Pt–NC dative bond compared to that of Pd–NC.

Control of the self-assembly process was achieved through metal–ligand exchange (Scheme 2). Addition of eight equivalents of a competing ligand such as triethylamine to preformed **2d** led to complete and clean disassembly of the cage into its cavitand components and [Pt(dppp)(NEt<sub>3</sub>)<sub>2</sub>(OTf)<sub>2</sub>]. Subsequent addition of eight equivalents of triflic acid restored the original Pt complex, which immediately quantitatively reassembled the cage.



**Scheme 2** Control of the self-assembly of the Pt cage. *Source:* From Ref.<sup>[19]</sup>. © 1997 by Wiley-VCH.

### Selectivity in anion encapsulation

The Born equation<sup>[35]</sup> allows to estimate the free energy of solvation of an ion of radius  $r$  (Å)<sup>b</sup> and charge  $z$  in a given solvent. For monovalent anions such as  $BF_4^-$ ,  $PF_6^-$ , and  $CF_3SO_3^-$  in chloroform, we have  $\Delta G_{m,solv}^\circ = -550 r^{-1} \text{ kJ mol}^{-1}$ . Because encapsulation requires desolvation of the anion, our expectation was that inclusion selectivity in a given cage would have been dictated by the relative enthalpy of solvation of the anions, thus favoring the larger, less-solvated ones. Accordingly, in our case, the predicted selectivity should have been  $CF_3SO_3^- > PF_6^- > BF_4^-$ . Two trends are observed: 1) at 300 K in the presence of stoichiometric amounts of the competing ion, the encapsulation preference is in the order  $BF_4^- > CF_3SO_3^- \gg PF_6^-$ , which becomes complete for  $BF_4^-$  in the presence of an excess of  $(NBu_4^+)$  ( $BF_4^-$ ); 2) at 333 K under stoichiometric conditions, the slight prevalence of  $BF_4^-$  vs.  $CF_3SO_3^-$  is reversed in favor of the latter. The discrepancy between observed and expected selectivity in anion encapsulation led us to further investigate the matter both experimentally and via computer modeling. Once again, ESI-MS turned out to be a very valuable investigation tool, enabling to detect the presence of solvent molecules trapped within the cages.<sup>[36]</sup> For all cages having  $CF_3SO_3^-$  and  $PF_6^-$  as counterions, ESI-MS gave  $[M-2X]^{2+}$  and  $[M-3X]^{3+}$  as prominent ions, both in chloroform and acetone as solvents, while in the case of  $BF_4^-$  the base peaks correspond to the  $m/z$  values expected for  $[CHCl_3@M-2BF_4]^{2+}$ ,  $[CHCl_3@M-3BF_4]^{3+}$ ,  $[acetone@M-2BF_4]^{2+}$ , and  $[acetone@M-3BF_4]^{3+}$ , respectively.

<sup>b</sup>Even if the Born equation is strictly valid only for spherical ions, it also gives a good approximation of  $\Delta G_{m,solv}^\circ$  for non-spherical ones.

These results imply that there is enough room in the cavity for one molecule of solvent only in the case of encapsulated  $BF_4^-$ , while in the other two cases the anion is included alone, as proven in the case of  $CF_3SO_3^-$  by the crystal structure. These findings were confirmed by molecular modeling carried out using the GRASP program. Only for  $BF_4^-$  is the cavity sufficiently wide to accommodate an ancillary solvent molecule, thus reducing the enthalpic cost required for the desolvation of  $BF_4^-$ . This renders  $BF_4^-$  the preferred encapsulated anion at 300 K. The change in selectivity observed upon increasing the temperature to 333 K is the result of the higher-cage occupancy factor of  $BF_4^- \cdot CHCl_3$  with respect to  $CF_3SO_3^-$ . At higher temperatures, the entropic term favors  $CF_3SO_3^-$ , as its movements are less restricted in the confined space of the cavity with respect to the couple  $BF_4^- \cdot CHCl_3$ . This additional entropic cost for  $BF_4^- \cdot CHCl_3$  is sufficient to reverse the selectivity pattern observed at 300 K.

This first class of coordination cages gave us the possibility of exploring and understanding the main factors driving CSA. The following structural parameters have been found to be the key elements controlling CSA: 1) a P–M–P angle close to 90° between the chelating ligand and the metal precursor; 2) square planar Pd and Pt as metal centers; 3) a weakly coordinated counterion; 4) preorganization of the tetradentate cavitated ligand.

On the other side, this CSA protocol has some limitations. The major ones are:

1. The internal volume of this first type of cages is only  $250 \text{ \AA}^3$ , which is not sufficient to include guests of nanosize dimensions.
2. Cage self-assembly is highly sensitive to distortion from the optimal square-planar arrangement: Chelating ligands in the metal precursors with



L–M–L angle close to 90° are required. For this reason, dppp ligands are favored with respect to dppb; no self-assembly has been observed in the case of dppe, dppm, and ethylenediamine.

- The nitrile ligands require weakly coordinating counterions to enter the coordination sphere of the metal; for example,  $\text{CF}_3\text{SO}_3^-$ ,  $\text{PF}_6^-$ ,  $\text{BF}_4^-$  worked, whereas  $\text{CH}_3\text{CO}_2^-$ ,  $\text{PhCOO}^-$ , and  $\text{CF}_3\text{CO}_2^-$  did not.
- Only a limited pool of solvents is compatible with CSA: Many solvents such as  $\text{CH}_3\text{CN}$  and dimethyl sulfoxide (DMSO) compete with nitriles for coordination to the metal centers, reducing the applicability of this methodology.

### Enlarged Nitrile-Based Coordination Cages

The demand for cages with internal cavities of nanoscopic dimensions, able to encapsulate large guests or be used as reaction chambers, can be fulfilled either by increasing the number of self-assembled components<sup>[37,38]</sup> or by enlarging the size of the reacting ligands. Following this second approach, self-assembly of nanosize coordination cages **7a–b** using tetradentate cavitand ligands **6a–b** is reported. Phenyl groups were chosen as spacers introduced at the upper rim of **6** to extend the cavity size<sup>[39]</sup> while retaining the relative orientation of the cyano groups and the rigidity of the cavitand framework, both essential for cage formation. Tetracyanophenyl cavitands **6a,b** were synthesized by a known procedure from the corresponding

tetrabromophenyl cavitands<sup>[40]</sup> through reaction with  $\text{CuCN}$  in 1-methyl-2-pyrrolidinone (NMP).

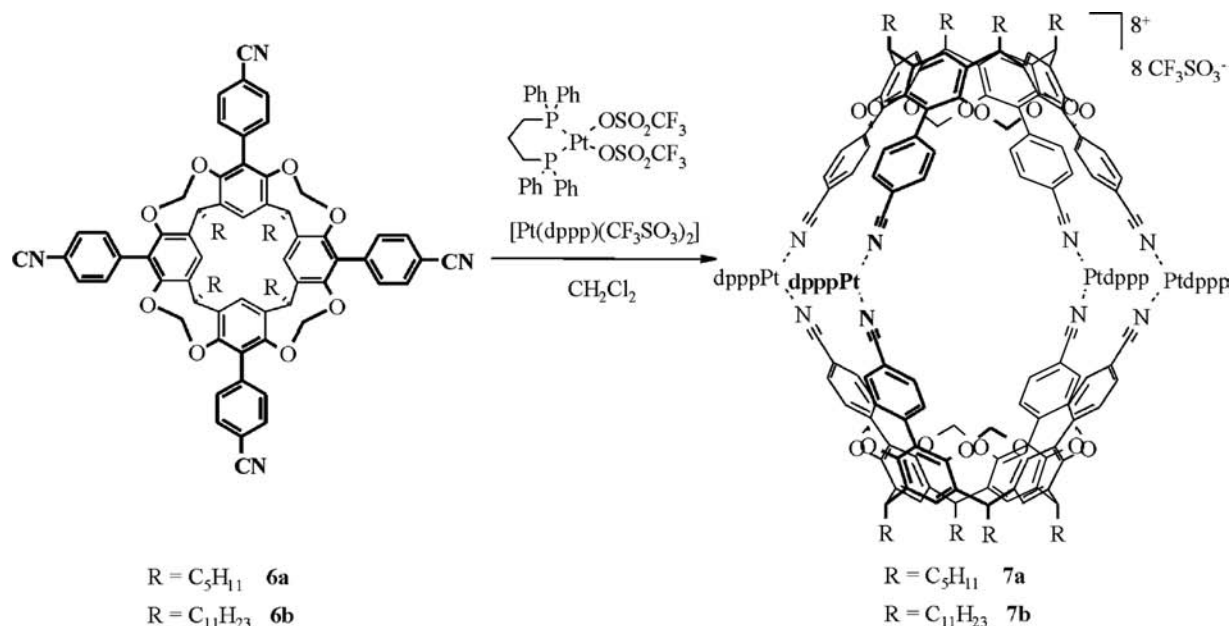
As in the previous case, cages **7a–b** were obtained in quantitative yield mixing **6a–b** with  $\text{Pt}(\text{dppp})$  ( $\text{CF}_3\text{SO}_3^-$ )<sub>2</sub> in a 1:2 molar ratio in dichloromethane at room temperature (Scheme 3). The less-soluble cage **7a** precipitated out of the solution and was collected in pure form by filtration.

No permanent inclusion of the  $\text{CF}_3\text{SO}_3^-$  counterions was observed by <sup>19</sup>F-NMR even at low temperature. Rapid exchange with solvent molecules occurs as a result of the large dimensions of the lateral portals. Their dimensions as well as the internal cavity volume were evaluated by modeling the cage structure. The internal volume is ca. 1100 Å<sup>3</sup>, over four times that of its short analog.

Deepening the cavitand precursor while retaining the relative orientation of the cyano groups and the rigidity of the cavitand framework has proved to be a viable strategy for the preparation of large coordination cages. The drawback of such approach lies in the reduced stability of these larger cages as a result of the lability of the CN–M coordinative bond.

### Pyridine-Based Coordination Cages

To overcome this limit, a strong metal–ligand interaction is necessary to operate cage self-assembly in a wide range of solvents. To this purpose, we designed and synthesized new cavitands bearing pyridines (for references on cages derived from multidentate pyridine



**Scheme 3** Self-assembly of cages **7a,b**. Source: From Ref.<sup>[39]</sup>. © 2001 by Elsevier Science Ltd.

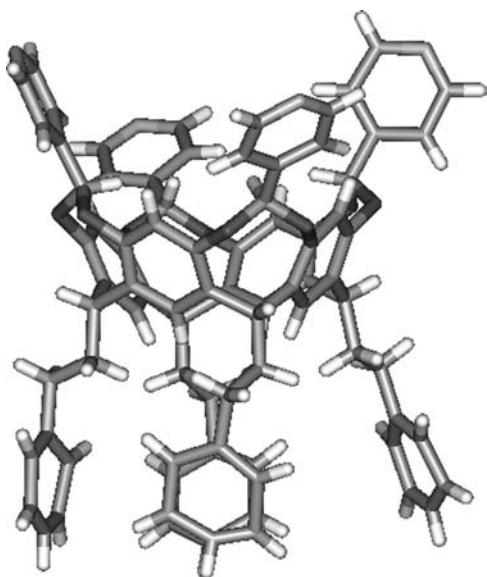


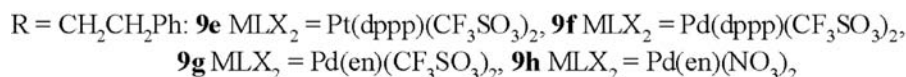
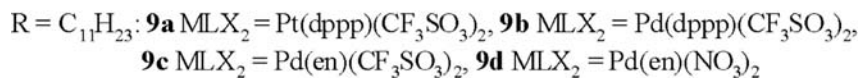
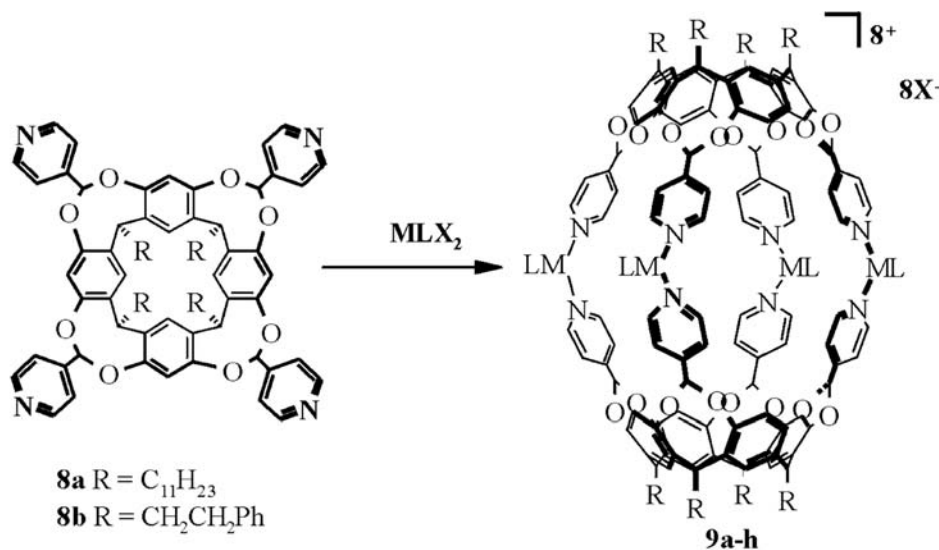
**Fig. 5** X-ray crystal structure of the phenethyl cavitand **8b**. Source: From Ref.<sup>[44]</sup>. © 2002 by the National Academy of Sciences.

ligands, see Refs.<sup>[41–43]</sup>) instead of nitriles as ligands for the coordination to the metal centers.<sup>[44]</sup> The pyridyl groups are positioned on the bridging units and not on the apical positions of the resorcinarene.

The synthesis of these deep-cavity cavitands,<sup>[45]</sup> of general structure **8a–b**, was performed by bridging the corresponding resorcinarenes with 4-( $\alpha,\alpha'$ -dibromo-methyl)pyridine.

In all cases, the low yields (10–12%) of the desired (oooo) isomer with the four pyridyl groups pointing outward (o) the cavity are due to the competitive formation of useless isomers having one (iooo) or two (iioo, ioio) pyridyl groups pointing inward (i). The correct stereochemical assignment of the oooo isomer has been confirmed by the X-ray crystal structure of cavitand **8b** (Fig. 5). From the crystal structure of the tetradentate cavitand, it is possible to evaluate the  $\alpha$  angle of the pyridyl ligands relative to the  $C_{4v}$  symmetry axis: The estimated value is  $42^\circ$ , close to the ideal value of  $45^\circ$  required for the formation of strainless square-planar complexes. Therefore the cavitand ligand is correctly preorganized for CSA.

The typical procedure for cage formation is shown in the case of cavitands **8a** and **8b** and various metal precursors  $MLX_2$  ( $M = Pd, Pt; L = dppp, en; X = CF_3SO_3, NO_3$ ) (Scheme 4): By mixing the two components in a 1:2 molar ratio at room temperature in solvents such as  $CH_2Cl_2, CHCl_3, acetone, or DMSO$ , cages **9a–h** were obtained in quantitative yields. In all cases,  $^1H$  NMR spectra showed the formation of a



**Scheme 4** Self-assembly of cages **9a–h**. Source: From Ref.<sup>[44]</sup>. © 2002 by the National Academy of Sciences.

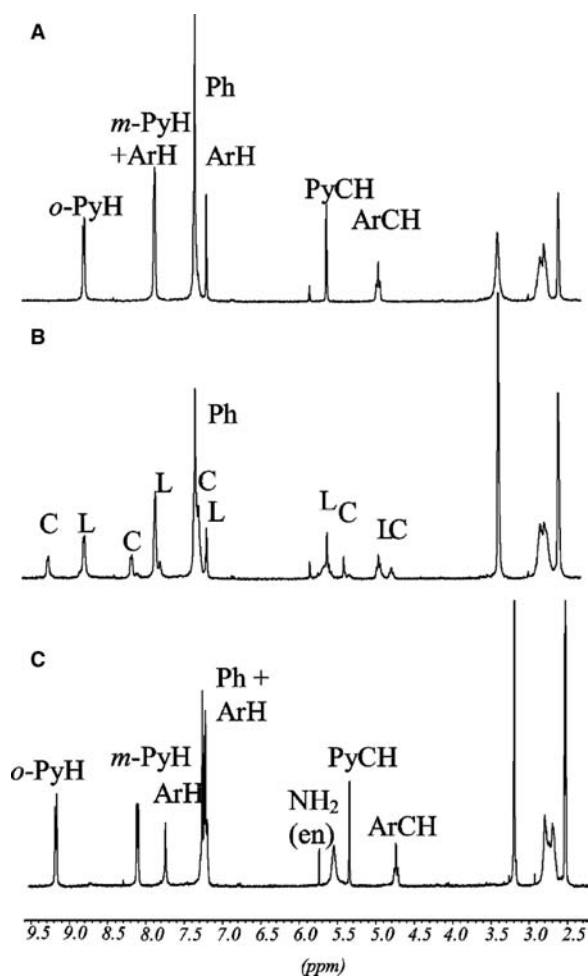


**Fig. 6** Self-assembly of cage **9h** monitored via  $^1\text{H}$  NMR: (A) spectrum of cavitant **8b** in  $\text{DMSO-}d_6$ ; (B) mixture of free cavitant ligand (L) and cage (C) after addition of slightly less than 1 eq. of  $\text{Pd}(\text{en})(\text{NO}_3)_2$ ; (C) cage **9h** as single product after addition of 2 eq. of  $\text{Pd}(\text{en})(\text{NO}_3)_2$ . *Source:* From Ref.<sup>[44]</sup>. © 2002 by the National Academy of Sciences.

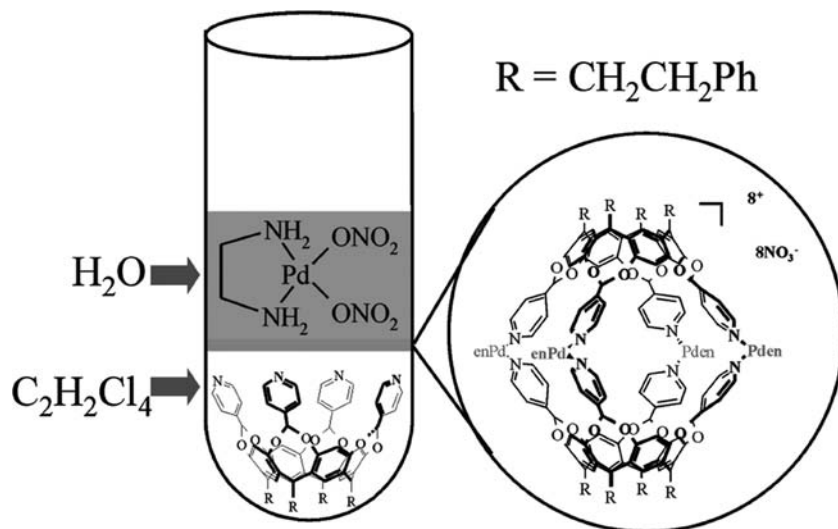


**Fig. 7** Cage formation at the water / organic solvent interface. *Source:* From Ref.<sup>[44]</sup>. © 2002 by the National Academy of Sciences.

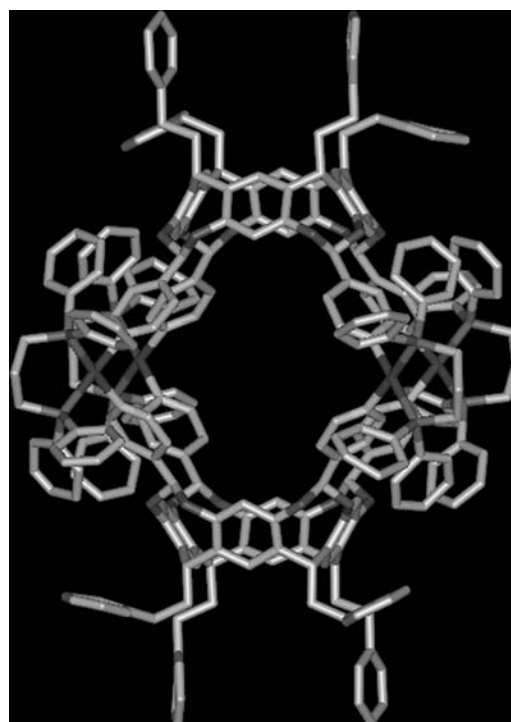


**Fig. 8** Preliminary X-ray crystal structure of  $\text{Pddppp}(\text{OTf})_2$ -cage **9f**.

new set of signals, indicative of the presence of a single highly symmetric compound ( $D_{4h}$  symmetry).

The intramolecular CSA process is the only one detected via  $^1\text{H}$  NMR (Fig. 6): Adding slightly less than 1 eq. of  $\text{Pd}(\text{en})(\text{NO}_3)_2$  to a solution of cavitant **8b** led to the formation of a mixture of Pd-cage and free cavitant. After the addition of the second equivalent of metal precursor, the  $^1\text{H}$  NMR spectrum showed the signals of cage **9h** as the only product.

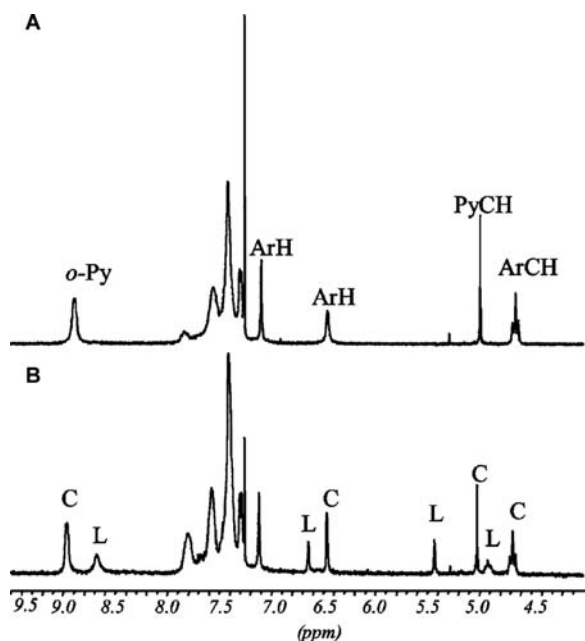


**Fig. 9** (A) Cage **9b** in the presence of an excess of  $\text{NEt}_3$  at 300 K; (B) partial disassembly of the cage (C) into its cavitand component (L) after heating at 323 K for few minutes. Source: From Ref.<sup>[44]</sup>. © 2002 by the National Academy of Sciences.

The robustness of the M–Py coordination allowed to perform CSA in polar and competitive solvents such as DMSO or acetonitrile, where the nitrile-based coordination cages immediately decompose. The solubility properties of cages **9a–h** can be tuned by appropriately choosing the counterion, chelating ligand, and R substituents at the lower rim of the cavitand ligand. In particular, the solubility of the cages in DMSO or even in DMSO/ $\text{H}_2\text{O}$  mixtures (up to 3:1 ratio) has been achieved by introducing the highly hydrophilic  $\text{NO}_3^-$  counterion as in the case of **9d** and **9h**. The different solubility properties of the cage components have been exploited to perform CSA in a liquid–liquid two-phase system. In a typical experiment, cavitand **8b** (1 eq.) dissolved in 1,1,2,2-tetrachloroethane was exposed to an aqueous solution of  $\text{Pd}(\text{en})(\text{NO}_3)_2$  (2.5 eq.) in a test tube (Fig. 7). A solid immediately formed at the interface, which became more abundant over time.  $^1\text{H}$  NMR analysis of the recovered solid indicated the formation of cage **9h** in pure form. A MALDI-TOF experiment directly performed on the solid sample confirmed the attribution, ruling out the possibility of the formation of a sheet-like network at the interface.<sup>c</sup> This last result is particularly interesting because

<sup>c</sup>In principle, a sheet-like network that contains both components in a 2:1 ratio could also form at the interface and subsequently rearrange into cage **9h** upon dissolution in DMSO.

liquid–liquid interfaces represent another potentially useful field of action for self-assembly protocols, which has barely been explored so far.<sup>[46]</sup>

We were able to obtain good crystals of the  $\text{Pd}(\text{dppp})(\text{OTf})_2$ -cage **9f** from an acetone solution of the cage (Fig. 8). A preliminary X-ray crystal structure of the cage shows the formation of four square-planar complexes. The cavity can be accessed through the four large lateral portals, of 12.3 Å (close Pd–Pd distance)  $\times$  10.8 Å (apical Ar–Ar distance), large enough to allow the entrance/egress of solvent molecules as well as triflate anions, in accordance with  $^{19}\text{F}$  NMR experiments. The dimensions of the internal cavity turned out to be 17.2  $\times$  15.7 Å. Calculations by GRASP highlight the larger dimensions of these pyridine-based cages with an internal volume of 840 Å<sup>3</sup>, which are over three times bigger with respect to the corresponding nitrile-based ones (250 Å<sup>3</sup>).

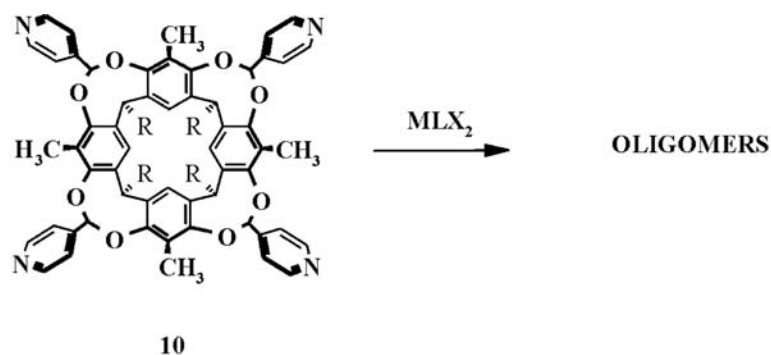
Several attempts to disassemble Pt and Pd cages were performed. Pd cage **9b** was disassembled into its cavitand component and  $[\text{Pd}(\text{dppp})(\text{NEt}_3)_2(\text{CF}_3\text{SO}_3)_2]$  in the presence of an excess of  $\text{NEt}_3$  as competitive ligand (32 eq.) at 323 K (Fig. 9), whereas, under the same conditions, the  $^1\text{H}$  NMR spectrum of the corresponding Pt cage **9a** remained unchanged. This is consistent with the greater Pt–N bond strength with respect to that of Pd–N.

The kinetic stability of the Pt cages<sup>d</sup> has been assessed via ESI-MS. A ligand-exchange experiment was performed starting from two Pt cages, **9a** and **9e**, different for the chains at the lower rim (R =  $\text{C}_{11}\text{H}_{23}$  and  $\text{CH}_2\text{CH}_2\text{Ph}$ ): Both cages were separately analyzed via ESI-MS, showing  $[\text{M}-2\text{CF}_3\text{SO}_3]^{2+}$ ,  $[\text{M}-3\text{CF}_3\text{SO}_3]^{3+}$ , and  $[\text{M}-4\text{CF}_3\text{SO}_3]^{4+}$  ions. Then they were mixed in a 1:1 molar ratio at room temperature, giving a spectrum resulting from the simple addition of the signals owing to the two homocages. Upon heating the mixture, the ESI-MS spectrum exhibited a third set of peaks belonging to the heterocage in a statistic 1:2:1 ratio with the signals of the homocages.

### Suppressing cage self-assembly

Introduction of methyl groups at the apical position of the resorcinarene completely switched off the CSA process. Addition of three different precursor complexes, such as  $\text{Pt}(\text{dppp})(\text{CF}_3\text{SO}_3)_2$ ,  $\text{Pd}(\text{dppp})(\text{CF}_3\text{SO}_3)_2$ , and  $\text{Pt}(\text{PET}_3)_2(\text{CF}_3\text{SO}_3)_2$ , to a solution of **10** resulted in the precipitation of stone-like oligomeric species only slightly soluble in most organic solvents (Scheme 5). The

<sup>d</sup>Dynamic interconversion of similar square-planar Pd(II) complexes with pyridyl cycloveratrylenes has been shown by Shinkai et al. to occur at room temperature.<sup>[47]</sup>



$R=C_3H_{11}$ ;  $MLX_2=Pt(dppp)(CF_3SO_3)_2$ ,  $Pd(dppp)(CF_3SO_3)_2$ ,  $Pt(PEt_3)_2(CF_3SO_3)_2$ .

**Scheme 5** Oligomeric self-assembly with cavitand **10**.

experiment has been followed by  $^1H$  NMR: The solution became heterogeneous as soon as the first equivalent of metal precursor was added and the spectrum showed a broadening of all the peaks, indicative of oligomer formation. No significant changes were observed by adding the second equivalent of precursor complexes or after heating. This is an evidence of how sensitive CSA is to the preorganization of the molecular components: In fact, a further requirement for efficient CSA is the conformational freedom of the four diverging pyridine ligands, to allow the formation of strainless square-planar connecting units. The presence of the methyl groups at the apical position forces the pyridine ligands to

preferentially assume a tilted orientation with respect to the cavity, hampering cage self-assembly, and instead favoring oligomerization via the formation of square-planar complexes among several cavitand ligands.

### SURFACE-DIRECTED SELF-ASSEMBLY OF COORDINATION CAGES

The idea behind this approach is to exploit the thermodynamic control and reversibility of CSA for the generation of three-dimensional architectures directly on surfaces, which is one of the key requirements for the

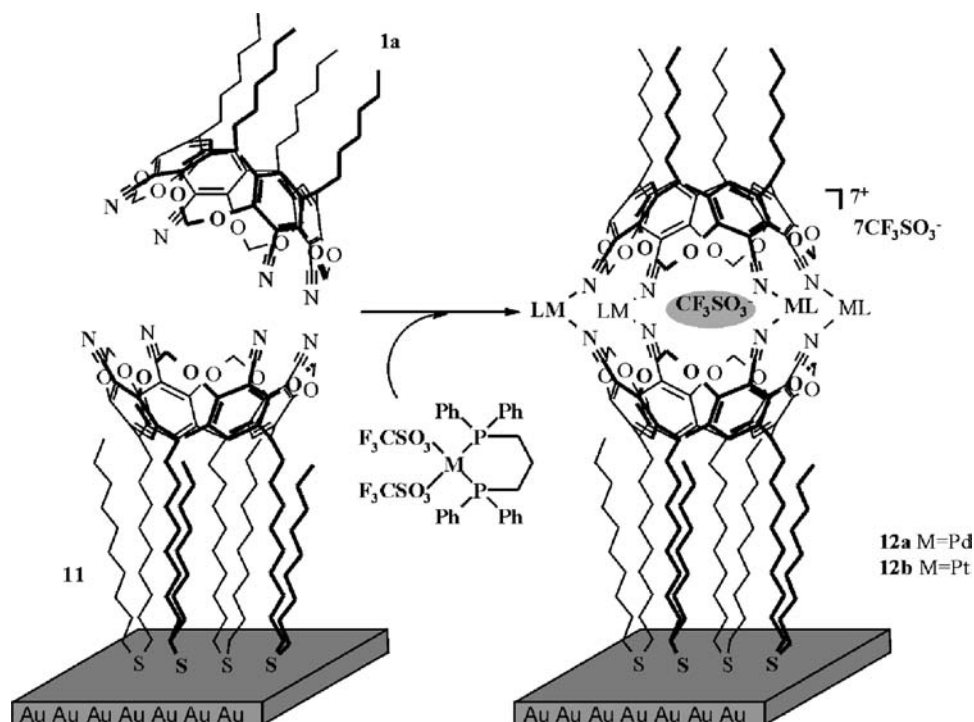


**Fig. 10** Representation of the self-assembly reaction that leads to the formation of cages on a SAM.

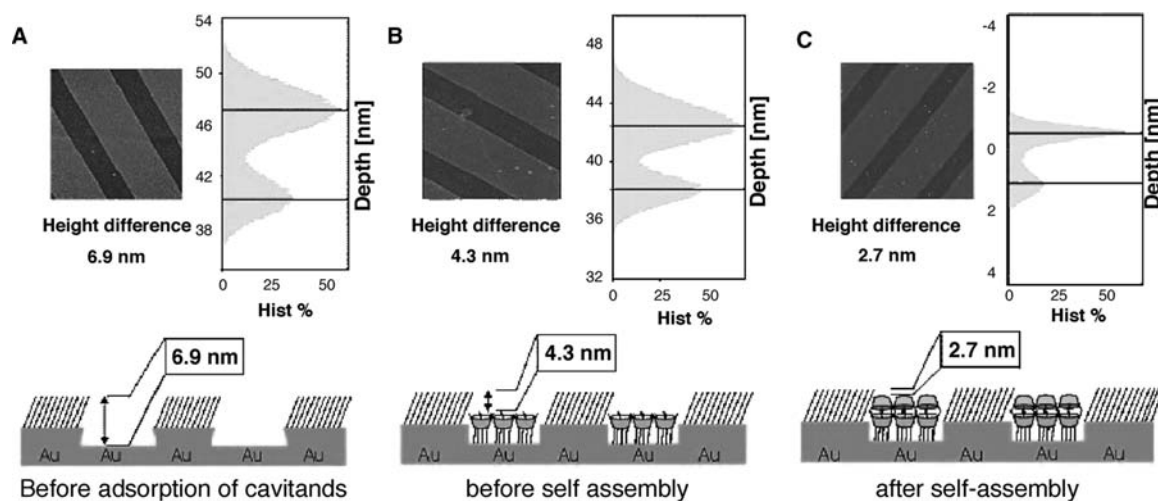


**Fig. 11** Self-assembly of coordination cages on  $\mu$ -CP substrates. The AFM picture, the corresponding histogram, and a schematic representation of the surface is shown for each. *Source:* From Ref.<sup>[49]</sup>. © 2001 by Wiley-VCH.

development of nanotechnology and molecular electronics.<sup>[48]</sup> The clean, precise, and reversible modification of surfaces represents an important opportunity to expand the application range of self-assembly.

Our group, in collaboration with Reinhoudt et al.,<sup>[49]</sup> have recently reported an intriguing example of generation of coordination cages directly on surfaces by using self-assembled monolayers (SAMs) as molecular platforms. At first, monolayers of **11** were prepared by adsorption of the thioether chains on gold surface; then, self-assembly of the cages occurred directly on the SAMs through the addition of a solution of **1a**, and of Pd(dppp)(OTf)<sub>2</sub> (cage **12a**) in one case and Pt(dppp)(OTf)<sub>2</sub> (cage **12b**) in the other (Fig. 10). The formation of these cages on SAMs of **11** was proven by contact angle measurements, electrochemistry, X-ray photoelectron spectroscopy (XPS), and atomic force microscopy (AFM).

A series of control experiments were performed to prove that self-assembly of the cages occurs on the surface of the SAMs via metal coordination. Treatment of the SAM of **12a** with triethylamine shifts the equilibrium toward the formation of M(dppp)(NEt<sub>3</sub>)<sub>2</sub>(OTf)<sub>2</sub> plus uncomplexed cavitand **11**. Complete disassembly of the cages on the SAM was monitored by electrochemistry, in full agreement with the expectations.

The formation of the molecular cages was directly monitored by atomic force microscopy (AFM). For this purpose, microcontact-printed templates were created using standard soft lithography methods.<sup>[50]</sup> These templates showed the presence of very regular features over large areas (Fig. 11). Stripes with a lower height correspond to areas exposing bare gold, while stripes with a higher topographic profile are covered by the SAM of 11-mercaptoundecanol. After deposition of a monolayer of cavitand **11** on the bare gold

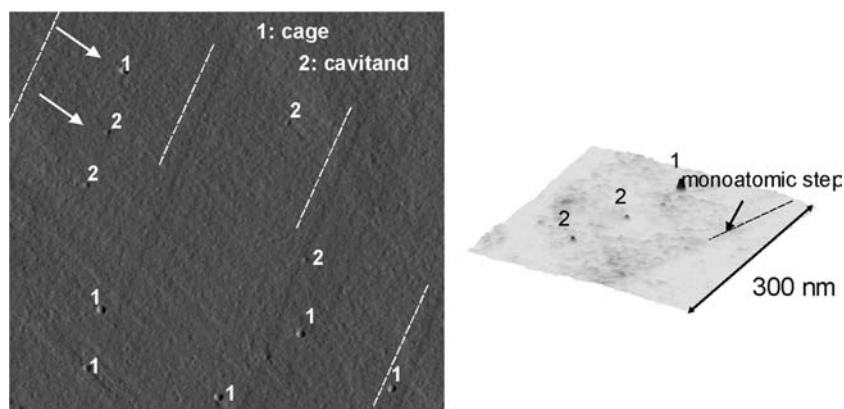


**Fig. 12** Atomic force microscopy image and height profiles of individual cages.



grooves, AFM was used to directly measure the differences in the height profile.

The height difference of 2.6 nm (Fig. 11A,B) is consistent with the formation of a monolayer of **11**. The formation of the molecular cages on the printed layers was performed using the same procedure as for the full monolayers. A difference of 4.2 nm was measured after assembly of the cages (Fig. 11C), a value that is consistent with the calculated dimensions of the assembly. The self-assembly of the cages was monitored by comparing the relative height differences.

Moreover, the insertion of sulfides into SAMs of thiols has been recently investigated by Reinhoudt's group.<sup>[51]</sup> A SAM was prepared where single cavitands could be detected far apart from each other by AFM to individually study the formation of the coordination cages. Insertion of cavitand **11** into a monolayer of mercaptoundecanol was achieved by soaking SAMs of thiol into a 0.1 mM solution of **11** in ethanol. Under this experimental conditions, an average of 20–25 molecules per square micron were inserted into the SAM.<sup>c</sup> Extensive washing with large amounts of solvents ensured the removal of all physisorbed material. Atomic force microscopy experiments and profile analysis showed the presence of individual round entities that were protruding from the flat monolayer. A height-profile analysis revealed that these entities all had the expected size of approximately 2 nm. As for the full SAMs, formation of the cages **12a** and **12b** was performed on these samples as described above for the full monolayers. Atomic force microscopy analysis on the new samples proved the presence of two different types of features: 1) individual dots with heights of about 4 nm; and 2) individual dots with heights of about 2 nm (Fig. 12). The two different entities were attributed to the two different species, the cavitand and the coordination cages adsorbed on Au, respectively.

## CONCLUSION

Cage self-assembly represents a successful strategy for the construction of three-dimensional objects having inner cavities of molecular dimensions. The driving force behind this research effort can be attributed to the following factors: 1) precise control of the CSA process via rational design of the molecular components; 2) the reversibility of the process that conveys

self-repairing properties and responsiveness to external stimuli; and 3) extension of the CSA process to interfaces and surfaces.

This last feature in particular opens new avenues to the metal-directed self-assembly of supramolecular species. In the specific case of cavitand-based coordination cages, single-molecule addressing on surfaces of confined molecules having peculiar electric, magnetic, or optical properties can be envisioned.

## REFERENCES

- Whitesides, G.M.; Grzybowski, B. Self-assembly at all scales. *Science* **2002**, *295* (5564), 2418–2421.
- Lehn, J.-M. Self-processes-programmed supramolecular systems. In *Supramolecular Chemistry: Concepts and Perspectives*; Lehn, J.-M., Ed.; VCH: Weinheim, Germany, 1995; 139–197.
- Baxter, P.N.W. Metal ion directed assembly of complex molecular architectures and nanostructures. In *Comprehensive Supramolecular Chemistry*; Lehn, J.-M., Atwood, J.L., Davis, J.E.D., MacNicol, D.D., Vogtle, F., Eds.; Pergamon Press: Oxford, U.K., 1996; Vol. 9, 165–211. Chapter 5.
- Fujita, M. Self-assembled macrocycles, cages, and catenanes containing transition metals in their backbones. In *Comprehensive Supramolecular Chemistry*; Lehn, J.-M., Atwood, J.L., Davis, J.E.D., MacNicol, D.D., Vogtle, F., Eds.; Pergamon Press: Oxford, U.K., 1996; Vol. 9, 253–282. Chapter 7.
- Fujita, M. Metal-directed self-assembly of two- and three-dimensional synthetic receptors. *Chem. Soc. Rev.* **1998**, *27* (6), 417–425.
- Saalfrank, R.W.; Demleitner, B. Ligand and metal control of self-assembly in supramolecular chemistry. In *Perspectives in Supramolecular Chemistry*; Sauvage, J.P., Ed.; Wiley-VCH: Weinheim, 1999; Vol. 5, 1–51.
- Leininger, S.; Olenyuk, B.; Stang, P.J. Self-assembly of discrete cyclic nanostructures mediated by transition metals. *Chem. Rev.* **2000**, *100* (3), 853–908.
- Cram, D.J.; Cram, J.M. *Container Molecules and Their Guests, Monographs in Supramolecular Chemistry*; Stoddart, J.F., Ed.; Royal Society of Chemistry: Cambridge, U.K., 1994; Vol. 4.
- Rebek, J., Jr. Assembly and encapsulation with self-complementary molecules. *Chem. Soc. Rev.* **1996**, *25* (4), 255–264.
- Jasat, A.; Sherman, J.C. Carceplexes and hemicarceplexes. *Chem. Rev.* **1999**, *99* (4), 931–967.
- Warmuth, R. Inner-phase stabilization of reactive intermediates. *Eur. J. Org. Chem.* **2001**, *3*, 423–437.
- Kang, J.; Kang, J., Jr. Acceleration of a Diels–Alder reaction by a self-assembled molecular capsule. *Nature* **1997**, *385*, 50–52.
- Kang, J.; Hilmersson, G.; Santamaría, J.; Rebek, J., Jr. Diels–Alder reactions through reversible encapsulation. *J. Am. Chem. Soc.* **1998**, *120*, 3650–3656.

<sup>c</sup>By increasing the soaking time, the number of adsorbed molecules increases.

14. Yoshizawa, M.; Kusukawa, T.; Fujita, M.; Yamaguchi, K. Ship-in-a-bottle synthesis of otherwise labile cyclic trimers of siloxanes in a self-assembled coordination cage. *J. Am. Chem. Soc.* **2000**, *122*, 6311–6312.
15. van Wageningen, A.M.A.; Timmerman, P.; van Duynhoven, J.P.M.; Verboom, W.; van Veggel, F.C.J.; Reinhoudt, D.N. Calix[4]arene-based (hemi)carcerands and carceplexes: Synthesis, functionalization, and molecular modeling study. *Chem. Eur. J.* **1997**, *3* (4), 639–654.
16. Caulder, D.L.; Raymond, K.N. Supermolecules by design. *Acc. Chem. Res.* **1999**, *32* (11), 975–982.
17. Fujimoto, K.; Shinkai, S. Synthesis of and amine recognition with a Cu(II)-bridged biscalix[4]arene. *Tetrahedron Lett.* **1994**, *35*, 2915.
18. Ikeda, A.; Yoshimura, M.; Udzu, H.; Fukuhara, C.; Shinkai, S. Inclusion of [60]fullerene in a homooxacalix[3]arene-based dimeric capsule cross-linked by a Pd(II)–pyridine interaction. *J. Am. Chem. Soc.* **1999**, *121* (17), 4296–4297.
19. Jacopozzi, P.; Dalcanale, E. Metal-induced self-assembly of cavitand-based cage molecules. *Angew. Chem., Int. Ed. Engl.* **1997**, *36* (6), 613–615.
20. Fox, O.D.; Dalley, N.K.; Harrison, R.G. A metal-assembled, pH-dependent, resorcinarene-based cage molecule. *J. Am. Chem. Soc.* **1998**, *120* (28), 7111–7112.
21. Fox, O.D.; Leung, J.F.-Y.; Hunter, J.M.; Dalley, N.K.; Harrison, R.G. Metal-assembled cobalt(II) resorc[4]arene-based cage molecules that reversibly capture organic molecules from water and act as NMR shift reagents. *Inorg. Chem.* **2000**, *39* (4), 783–790.
22. Fox, O.D.; Dalley, N.K.; Harrison, R.G. Structure and small molecule binding of a tetranuclear iron(II) resorc[4]arene-based cage complex. *Inorg. Chem.* **1999**, *38* (25), 5860–5863.
23. Harrison, R.G.; Dalley, N.K.; Nazarenko, A.Y. Metal-promoted assembly of organic-based cages into a porous material. *Chem. Commun.* **2000**, *15*, 1387–1388.
24. Harrison, R.G.; Fox, O.D.; Meng, M.O.; Dalley, N.K.; Barbour, L.J. Cation control of pore and channel size in cage-based metal-organic porous materials. *Inorg. Chem.* **2002**, *41* (4), 838–843.
25. Fox, O.D.; Drew, M.G.B.; Beer, P.D. Resorcinarene-based nanoarchitectures: metal-directed assembly of a molecular loop and tetrahedron. *Angew. Chem., Int. Ed.* **2000**, *39* (1), 136–140.
26. Fox, O.D.; Drew, M.G.B.; Wilkinson, E.J.S.; Beer, P.D. Cadmium- and zinc-directed assembly of nano-sized, resorcinarene-based host architectures which strongly bind C<sub>60</sub>. *Chem. Commun.* **2000**, *5*, 391–392.
27. Park, S.J.; Hong, J.-I. Self-assembled nanoscale capsules between resorcin[4]arene derivatives and Pd(II) or Pt(II) complexes. *Chem. Commun.* **2001**, *17*, 1554–1555.
28. Park, S.J.; Shin, D.M.; Sakamoto, S.; Yamaguchi, K.; Chung, Y.K.; Lah, M.S.; Hong, J.-I. Water-soluble supramolecular bowls formed by intra-clipping of resorcin[4]arene-based ligands with Pd(II) ions. *Chem. Commun.* **2003**, *8*, 998–999.
29. Fochi, F.; Jacopozzi, P.; Wegelius, E.; Rissanen, K.; Cozzini, P.; Marastoni, E.; Fiscaro, E.; Manini, P.; Fokkens, R.; Dalcanale, E. Self-assembly and anion encapsulation properties of cavitand-based coordination cages. *J. Am. Chem. Soc.* **2001**, *123* (31), 7539–7552.
30. Schalley, C.A.; Martín, T.; Obst, U.; Rebek, J., Jr. Characterization of self-assembling encapsulation complexes in the gas phase and solution. *J. Am. Chem. Soc.* **1999**, *121* (10), 2133–2138.
31. Mecozzi, S.; Rebek, J., Jr. The 55% solution: a formula for molecular recognition in the liquid state. *Chem. Eur. J.* **1998**, *4* (6), 1016–1022.
32. Chi, X.; Guerin, A.J.; Haycock, R.A.; Hunter, C.A.; Sarson, L.D. The thermodynamics of self-assembly. *J. Chem. Soc. Chem. Commun.* **1995**, *24*, 2563–2565.
33. Ercolani, G. Physical basis of self-assembly macrocyclizations. *J. Phys. Chem., B* **1998**, *102* (29), 5699–5703.
34. Mogck, O.; Pons, M.; Böhmer, V.; Vogt, W. NMR studies of the reversible dimerization and guest exchange processes of tetra urea calix[4]arenes using a derivative with lower symmetry. *J. Am. Chem. Soc.* **1997**, *119* (24), 5706–5712.
35. Marcus, Y. *Ion Solvation*; Wiley & Sons: Chichester, 1985.
36. Schalley, C.A.; Castellano, R.K.; Brody, M.S.; Rudkevich, D.M.; Siuzdak, G.; Rebek, J., Jr. Investigating molecular recognition by mass spectrometry: characterization of calixarene-based self-assembling capsule hosts with charged guests. *J. Am. Chem. Soc.* **1999**, *121* (19), 4568–4579.
37. Takeda, N.; Umemoto, K.; Yamaguchi, K.; Fujita, M. A nanometre-sized hexahedral coordination capsule assembled from 24 components. *Nature* **1999**, *398*, 794–796.
38. Olenyuk, B.; Whiteford, J.A.; Fechtenkötter, A.; Stang, P.J. Self-assembly of nanoscale cuboctahedra by coordination chemistry. *Nature* **1999**, *398*, 796–799.
39. Cuminetti, N.; Ebbing, M.H.K.; Prados, P.; De Mendoza, J.; Dalcanale, E. Enlarged cavitand-based coordination cages. *Tetrahedron Lett.* **2001**, *42* (3), 527–530.
40. von dem Bussche-Hünnefeld, C.; Helgeson, R.C.; Bühring, D.; Knobler, C.B.; Cram, D.J. Bowl shaped cavitands dimerize and complex certain organic guests in organic solvents which themselves are poor guests. *Croat. Chem. Acta* **1996**, *69* (2), 447–458.
41. Fujita, M.; Nagao, S.; Ogura, K. Guest-induced organization of a three-dimensional palladium(II) cagelike complex. A prototype for “induced-fit” molecular recognition. *J. Am. Chem. Soc.* **1995**, *117*, 1649–1650.
42. Ikeda, A.; Yoshimura, M.; Tani, F.; Naruta, Y.; Shinkai, S. Construction of a homooxacalix[3]arene-based dimeric capsule crosslinked by a Pd(II)–pyridine interaction. *Chem. Lett.* **1998**, *7*, 587–588.
43. Zhong, Z.; Ikeda, A.; Ayabe, M.; Shinkai, S.; Sakamoto, S.; Yamaguchi, K. Metal-mediated self-assembly of pyridylcalixarenes: prevention of intramolecular metal chelation is essential in constructing molecular capsules. *J. Org. Chem.* **2001**, *66* (3), 1002–1008.
44. Pirondini, L.; Bertolini, F.; Cantadori, B.; Ugozzoli, F.; Massera, C.; Dalcanale, E. Design and self-assembly of wide and robust coordination cages. *Proc. Natl. Acad. Sci. U. S. A.* **2002**, *99* (8), 4911–4915.
45. Green, J.O.; Baird, J.-H.; Gibb, B.C. Reduced-symmetry deep-cavity cavitands. *Org. Lett.* **2000**, *2* (24), 3845–3848.

46. Bowden, N.; Terfort, A.; Carbeck, J.; Whitesides, G.M. Self-assembly of mesoscale objects into ordered two-dimensional arrays. *Science* **1997**, *276* (5310), 233–235.
47. Zhong, Z.; Ikeda, A.; Shinkai, S.; Sakamoto, S.; Yamaguchi, K. Creation of novel chiral cryptophanes by a self-assembling method utilizing a pyridyl–Pd(II) interaction. *Org. Lett.* **2001**, *3* (7), 1085–1087.
48. Service, R.F. Can chemists assemble a future for molecular electronics? *Science* **2002**, *295* (5564), 2398–2399.
49. Levi, S.A.; Guatteri, P.; van Veggel, F.C.J.M.; Vancso, G.J.; Dalcanale, E.; Reinhoudt, D.N. Direct observation of surface-controlled self-assembly of coordination cages by using AFM as a molecular ruler. *Angew. Chem., Int. Ed.* **2001**, *40*, 1892–1896.
50. Xia, Y.; Whitesides, G.M. Soft lithography. *Angew. Chem., Int. Ed.* **1998**, *37*, 550–575 and references within.
51. Friggeri, A.; Schönherr, H.; van Manen, H.-J.; Huisman, B.-H.; Vancso, G.J.; Huskens, J.; van Veggel, F.C.J.M.; Reinhoudt, D.N. Insertion of individual dendrimer molecules into self-assembled monolayers on gold: a mechanistic study. *Langmuir* **2000**, *16* (20), 7757–7763.

# Self-Assembly Directed by NH-O Hydrogen Bonding

Katrina A. Jolliffe  
Leonard F. Lindoy

*Department of Chemistry, University of Sydney, Sydney, New South Wales, Australia*

## INTRODUCTION

Following comments on the nature of hydrogen bonding as well as on self-assembly as it applies to supramolecular systems, the role of N–H...O hydrogen bonding in the formation and properties of a variety of supramolecular structures obtained by self-assembly from their molecular components is reviewed. The structures, which range from simple host–guest systems to complex entities such as nanotubes and hydrogen-bonded polymers, serve to exemplify the manner by which hydrogen bonds of the above type may be utilized in achieving particular molecular architectures.

Emphasis in the treatment is given to structure–function relationships underlying the various architectures described.

## MOLECULAR SELF-ASSEMBLY

The self-assembly of molecular or ionic components to form nanometer-scale structures held together by (generally) weak intermolecular interactions is a phenomenon of fundamental importance to the expanding field of supramolecular chemistry.<sup>[1,2]</sup> The latter is driven, in part, by a generally increased appreciation of the latent steric and electronic information inherent in the wide diversity of molecular building blocks that are either already available or that are capable of being synthesized. The self-assembly process requires that molecular recognition between the assembling components initially occurs and this in turn implies that such components be designed such that steric and electronic complementarity occurs between their respective binding sites.

Supramolecular assemblies have been constructed that exhibit novel properties that include unusual redox and/or electron transfer properties, photoactivity, conductivity, as well as non-linear optical behavior. Interest in such behavior for application in new supramolecular “devices” has remained a further motivation for the continuing interest in the synthesis of new assemblies of the above type.

An important outcome of employing weak non-covalent interactions for the construction of

supramolecular assemblies is that their formation is normally readily reversible because the final assembly remains in thermodynamic equilibrium with its components. As a consequence, supramolecular systems of this type have an inherent capacity for assembly “error correction” that is not normally available to systems that are fully covalently bound. In the present context, the “preorganization effect,” first proposed by Cram,<sup>[3]</sup> is also worth mentioning. This concept can provide a useful aid for rationalizing the strength of binding between the components in particular supramolecular systems. In essence, Cram proposed that the more closely the binding sites of a host molecule are structurally preorganized for binding to a guest, the greater will be the binding strength between host and guest in the resulting assembled species.

## HYDROGEN BONDING

Hydrogen bonding is the most directional of all the intermolecular interactions and is also the most widely used interaction in forming supramolecular structures.<sup>[4]</sup> Hydrogen bond formation has been studied for around a century and is now recognized to cover a wide variety of interaction types involving a bound hydrogen atom (X–H, the donor) and one or more acceptors, which may be an atom or an unsaturated molecule. In view of the diversity, it is not easy to offer a precise definition covering all aspects of hydrogen bonding.<sup>[1]</sup> In a recent review of hydrogen bonds, Steiner<sup>[5]</sup> offered the following description: An X–H...A interaction is called a “hydrogen bond,” if 1) it constitutes a local bond, and 2) X–H acts as proton donor to A. Some common hydrogen bond donor groups are C–H, N–H, O–H, S–H, P–H, F–H, Cl–H, Br–H, and I–H, while acceptor groups include N, O, P, S, F, Cl, Br, and I as well as a range of unsaturated aliphatic and aromatic compounds; the degree of directionality in the resulting hydrogen bond is quite dependent on the polarity of the donor. The strength of such bonds can range from very weak to substantial, typically falling in the approximate range of 3–40 kcal mol<sup>−1</sup>. In this entry, we are concerned with the use of hydrogen bonds of the type N–H...O for

the construction of supramolecular assemblies exhibiting a range of architectures. Hydrogen bonds of this latter type typically fall into the “moderate” strength category, with X...A distances in the range 2.5–3.3 Å and bond angles greater than 130°. [6] Although individual hydrogen bonds may be quite weak, in supramolecular systems (as is often also the case in most hydrogen-bonded biological systems), a number of hydrogen bonds may act in unison resulting in, overall, strong forces operating between the individual molecular components. [7] Similarly, hydrogen bonds tend to cooperatively act with other intermolecular interactions, such as van der Waals forces, such that the overall free energy of the assembled system is minimized.

Self-assembly processes involving NH–O hydrogen bonds have now been reported to generate an impressive range of different supramolecular architectures. Examples include simple (1:1) host–guest systems, molecular tweezers, zippers, boxes, large cyclic assemblies, grids, capsules, rotaxanes, catenanes, helices, knots, tubes, dendrimers, and other polymeric systems. Representative examples of selected systems chosen from this list are now discussed.

## SIMPLE SYSTEMS

The simplest type of “self-assembly” is the 1:1 complexation of two molecules, often described as host–guest complexation. Numerous simple host–guest complexes have been investigated and an understanding of the factors affecting their formation has provided a solid platform for the preparation of larger self-assembled aggregates.

Some of the earliest examples of host–guest complexes involving NH–O hydrogen bonding are the complexes formed between 18-C-6 crown ethers and ammonium ions. In these complexes, three of the ether oxygens form hydrogen bonds with the ammonium NH groups. [8,9] This recognition motif has been utilized to prepare more complicated structures (see below).

Hamilton et al. [10,11] have designed a series of receptors containing six inwardly facing hydrogen bonding sites in a cleft, such that they perfectly complement the six available hydrogen bonding groups in 5,5-disubstituted barbiturates. The formation of 1:1 complexes with high association constants [e.g.,  $1.37 \times 10^6 \text{ M}^{-1}$  for the complex **1:2** (Fig. 1)] was established by <sup>1</sup>H NMR experiments, including titrations and by UV–visible and fluorescence spectroscopy titration experiments.

Molecular receptors for nucleic acids have also been designed. For example, Rebek et al. [12–14] have prepared a number of receptors that form complexes with adenine using a combination of hydrogen bonding and  $\pi$ – $\pi$  stacking interactions. A receptor utilizing a similar

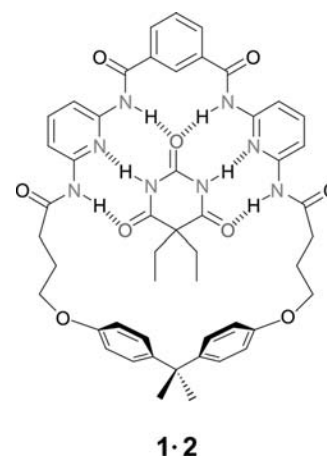


Fig. 1 Structure of the complex **1:2**.

combination of hydrogen bonding and  $\pi$ – $\pi$  stacking interactions has also been designed to complex thymine. [15]

Molecules containing self-complementary hydrogen bonding sites can self-assemble to form dimers or polymers. For example, the rigid dipyrindone **3** forms discrete dimers **4** (Fig. 2) in both dilute CHCl<sub>3</sub> solution (as determined by vapor pressure osmometry, VPO) and in the solid state. In contrast, the dipyrindone **5**, which can not dimerize, forms linear polymeric aggregates **6** (Fig. 2). [16] A less rigid analog of **3** was found to dimerize in solution, but X-ray crystallographic analysis showed that linear polymeric aggregates formed in the solid state. [17]

Recently, the dimerization of a guanidiniocarbonyl pyrrole carboxylate zwitterion **7** (Fig. 3) was described. The dimer is held together by two bifurcated hydrogen bonds and two NH–O hydrogen bonds, which are strengthened by ionic attraction. Dimerization constants of the order of  $10^{10} \text{ M}^{-1}$  in DMSO and  $170 \text{ M}^{-1}$  in water were estimated by <sup>1</sup>H NMR dilution studies. A neutral analog with an essentially identical hydrogen bonding pattern but lacking the ionic interactions was found to dimerize in CDCl<sub>3</sub>; however, addition of small amounts of DMSO resulted in virtually complete dissociation of the complex. [18]

## MORE COMPLEX SYSTEMS

Numerous “polytopic” receptors have been designed for molecules with more than one functional group capable of forming NH–O hydrogen bonds. An early example of a ditopic receptor, comprising a crown ether linked to a macrocyclic polyamine, was studied by Kimura, Fujioka, and Kodama [19] This molecule complexes dopamine in aqueous solution through the formation of ion-pair-reinforced NH–O hydrogen

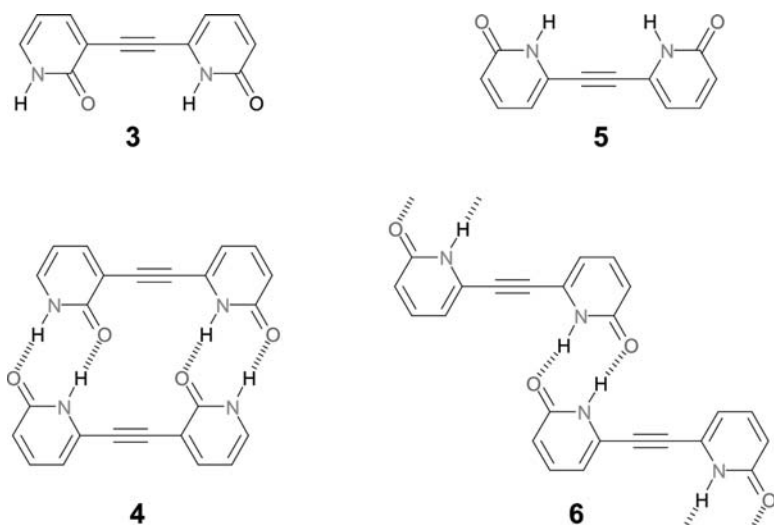


Fig. 2 Dipyridones **3** and **5** and the hydrogen-bonded dimer **4** and polymer **6**.

bonds between the crown ether and the ammonium ion and between the partially protonated azacrown and the electron-donating phenolic oxygens of dopamine.

Schrader et al.<sup>[20,21]</sup> have developed a number of receptors for biologically relevant molecules. The adrenaline host **8** was designed such that the phosphonates bind the ammonium functional group of adrenaline **9** through an ion-pair-reinforced NH-O hydrogen bond and the amide NH's provide hydrogen bonding sites for the catechol oxygen substituents (Fig. 4). Additional interactions are provided by  $\pi$ - $\pi$  stacking of the catechol between the two nitroarene units. <sup>1</sup>H NMR studies indicated that a 1:1 complex is formed between **8** and adrenaline **9** with a binding constant of  $153 \text{ M}^{-1}$  in  $\text{D}_2\text{O}$ -MeOD (1:1).

A series of oligoamides prepared from isophthalic acid and a bisaniline derivative undergo self-assembly via a combination of NH-O hydrogen bonds and edge-to-face aromatic interactions to form double-stranded "zipper" complexes in solution (Fig. 5).<sup>[22]</sup> Evidence for the association comes from <sup>1</sup>H NMR dilution and titration experiments in  $\text{CDCl}_3$  and  $\text{CDCl}_3$ - $\text{CD}_3\text{OD}$  (95:5) together with X-ray crystal structure analysis. The stability of the dimers was found to increase as the length of the oligomer

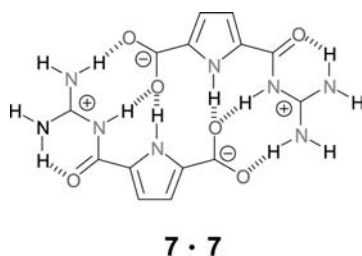


Fig. 3 Hydrogen-bonded dimer formed upon dissolution of **7** in DMSO or  $\text{H}_2\text{O}$ .

increased, indicating significant cooperativity in the intermolecular interactions along the chain.

## CYCLIC ASSEMBLIES

Whilst it is relatively simple to control the self-assembly of two components, the self-assembly of multiple components into a single aggregate is more difficult to engineer. One technique that has been successfully employed in the self-assembly of multiple components is hydrogen-bond-mediated cyclic aggregation, using either self-complementary molecules or mixtures of molecules with complementary hydrogen bonding sites.

An example of the above strategy is the self-assembly of the pyrido[4,3-g]quinoline **10** to form the cyclic trimer **11** held together by six NH-O hydrogen

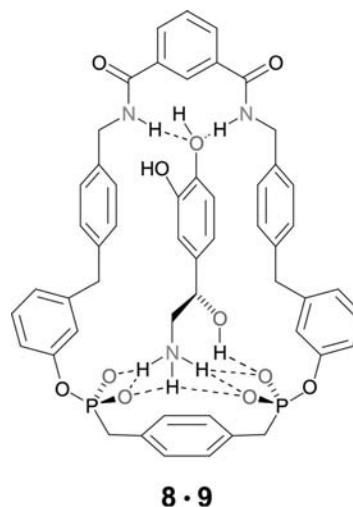


Fig. 4 Structure of the complex **8:9**.



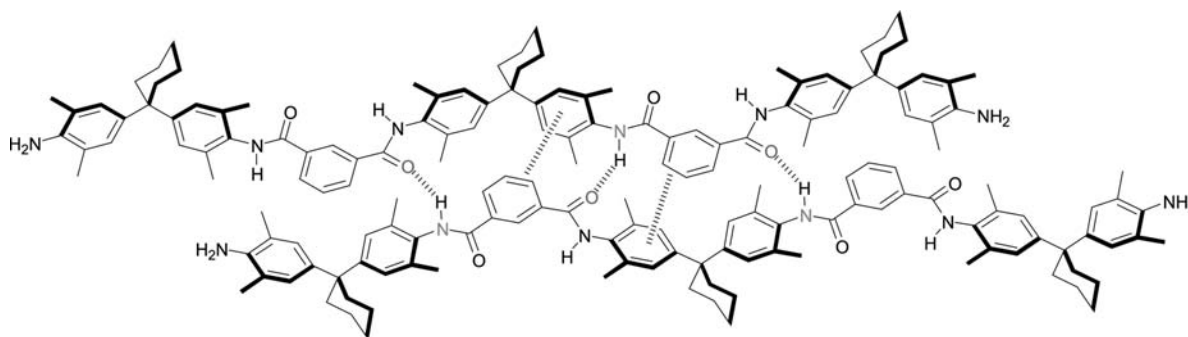


Fig. 5 Double stranded “zipper.”

bonds (Fig. 6). The formation of a cyclic trimer was confirmed by a combination of VPO and  $^1\text{H}$  NMR studies and the cyclic assembly was found to be very stable in  $\text{CDCl}_3$  solution ( $K_{\text{ass}} = 20,000 \text{ M}^{-2}$ ).<sup>[23]</sup>

The self-assembly of two-faced, “Janus-type” molecules, which incorporate the AAD hydrogen bonding sequence of cytosine and the DDA sequence of guanine, has been observed by both Lehn, Silvestri, and Lehn<sup>[24]</sup> and Mascal et al.<sup>[25]</sup> The  $60^\circ$  angle between the hydrogen bonding faces of these molecules dictates the formation of cyclic hexamers, both in solution and the solid state.

Using a similar array of hydrogen bonding donor and acceptor sites, Zimmerman and coworkers have found that cyclic hexamers assemble upon dissolution of **12** in  $\text{CDCl}_3$ ,  $d_8$ -toluene and  $d_8$ -THF (Fig. 7).<sup>[26]</sup> In this case, six secondary hydrogen bonds may serve to further stabilize the aggregate, which remains the predominant species in solution in both DMSO–chloroform (1:9) and 8% aqueous THF mixtures. This and similar recognition motifs have been employed in the formation of self-assembled dendrimers.<sup>[27,28]</sup>

Upon crystallization of a 1:1 mixture of cyanuric acid (CA) and melamine (M), a hydrogen-bonded lattice with several recognizable motifs, including a cyclic rosette **13** (Fig. 8), is observed.<sup>[29]</sup> Using appropriately substituted M and CA derivatives, the self-assembly of cyclic aggregates based on this rosette motif has been explored by the groups of Whitesides and Reinhoudt.

A series of hydrogen-bonded cyclic aggregates have been prepared by Whitesides et al., who employed both peripheral crowding and preorganization strategies to favor the formation of cyclic over linear aggregates. The first of these systems contains three M units attached to a central “hub” by semirigid spokes to produce a “tritopic” receptor ( $\text{HubM}_3$ ).<sup>[30,31]</sup>  $\text{HubM}_3$  forms a complex with three molecules of neohexylisocyanurate **14** to form the cyclic rosette **15** (Fig. 9). Double and triple rosette aggregates have been prepared using a similar strategy and aggregates incorporating both linked melamine and linked isocyanurate components have also been prepared. These aggregates have been

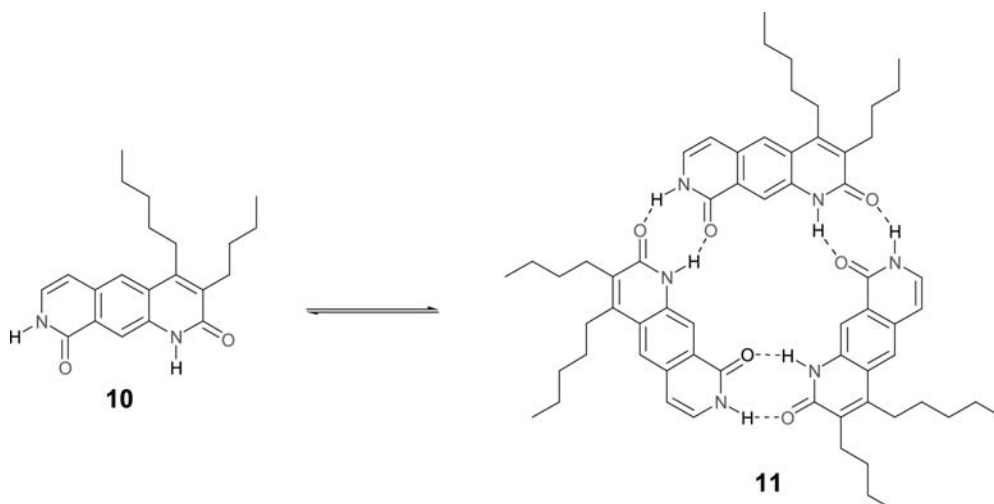
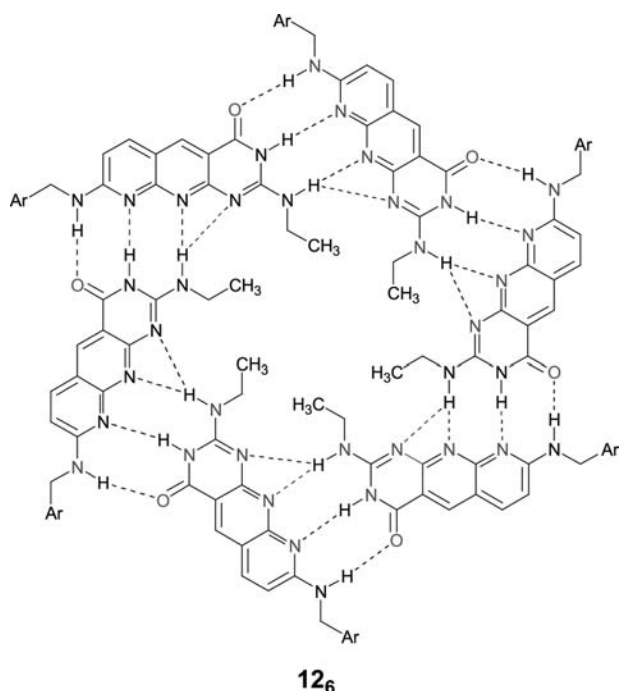


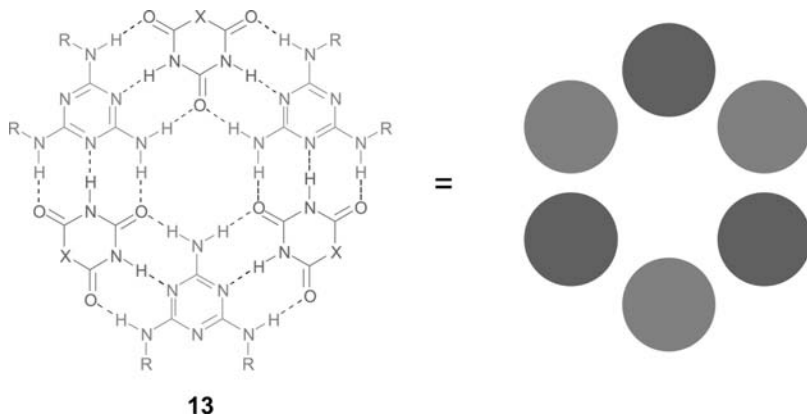
Fig. 6 Self-assembly of a cyclic trimer.



**Fig. 7** Cyclic hexamer formed upon self-assembly of six molecules of **12**.

characterized using a combination of  $^1\text{H}$  NMR spectroscopy (including titrations), VPO, and gel phase chromatography (GPC).

Reinhoudt and coworkers have used a similar pre-organization strategy to prepare aggregates comprising multiple-stacked rosettes. In these systems, a number of calix[4]arene derivatives, diametrically substituted with two melamine substituents on the upper rim, are connected with various linker units. Three of these melamine “strings” then complex the appropriate number of isocyanurate or barbiturate derivatives to give aggregates comprising multiple rosettes. Recently, this strategy has been employed in the self-assembly of 27 molecules, via 144 hydrogen bonds, to form an aggregate with eight stacked rosette motifs, which



was characterized using a combination of MALDI-TOF mass spectrometry,  $^1\text{H}$  NMR, and GPC.<sup>[32,33]</sup> The use of either chiral melamine or chiral cyanurate components in the formation of these aggregates has been found to result in the formation of homochiral self-assembled structures.<sup>[34–38]</sup>

## MOLECULAR CAPSULES AND BOXES

A considerable number of self-assembling capsules have now been reported, many of which incorporate arrays of  $\text{N-H}\cdots\text{O}$  hydrogen bonds.<sup>[39]</sup> The resulting three-dimensional structures incorporate enclosed cavities that are frequently occupied by included solvent or other molecules. Shimizu and Rebek<sup>[40]</sup> have prepared a number of systems of this type. For example, the group has reported the synthesis and assembly of self-complementary calix[4]arenes derivatives, which, on dimerization, yield discrete capsules. One system of this type was based on the cone-conformer of tetrabenzylcalixarene **16** that had been further functionalized by the appending of four urea groups to the periphery of the large aperture of the cone (Fig. 10). Individual urea groups from two such half capsules intermesh in an alternate fashion such that they interlink in a head to tail manner to provide the “glue” for connecting the two half capsules; a total of sixteen  $\text{NH}\cdots\text{O}$  contacts are involved in this arrangement (Fig. 10). The resulting cavity in this case is sufficiently large to encapsulate guests such as ethyl benzene and *p*-xylene.

Schall and Gokel<sup>[41]</sup> have described the formation of the molecular “box” given by **17** (Fig. 11).  $^1\text{H}$  NMR chemical shift data were used to assign the nature of the hydrogen bond patterns for this species in  $\text{CDCl}_3$ . Signal broadening was observed in the spectrum and this was interpreted as suggesting the likely presence of more than one aggregate type under the conditions used for the experiment.

**Fig. 8** Cyclic rosette motif observed in the crystal lattice of a 1:1 mixture of melamine and cyanuric acid.

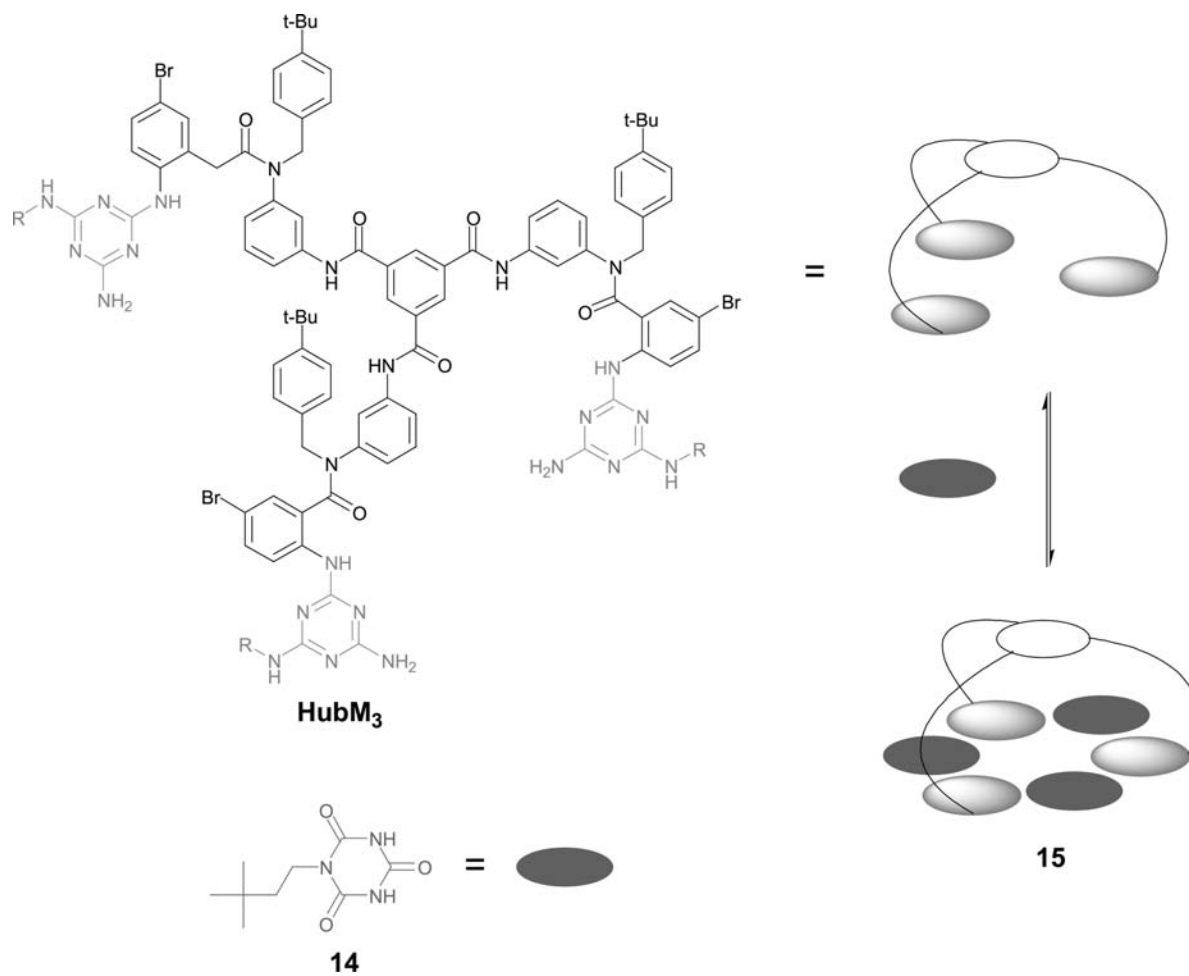


**Fig. 9** Formation of a cyclic rosette by self-assembly of four components.

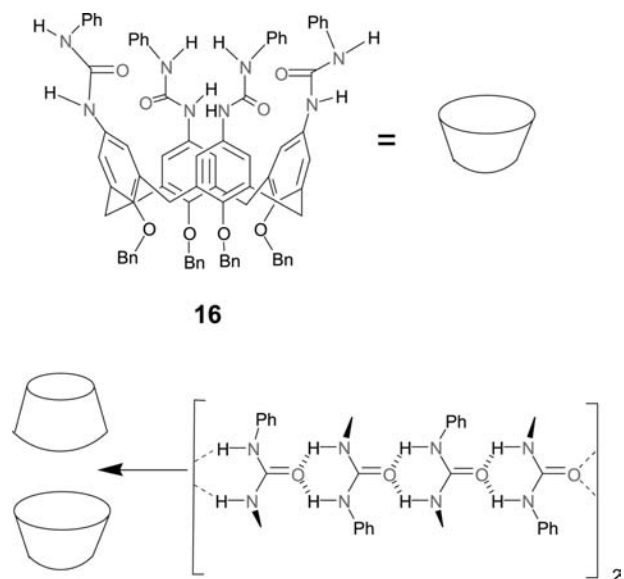


**Fig. 10** Self-assembly of a molecular capsule.

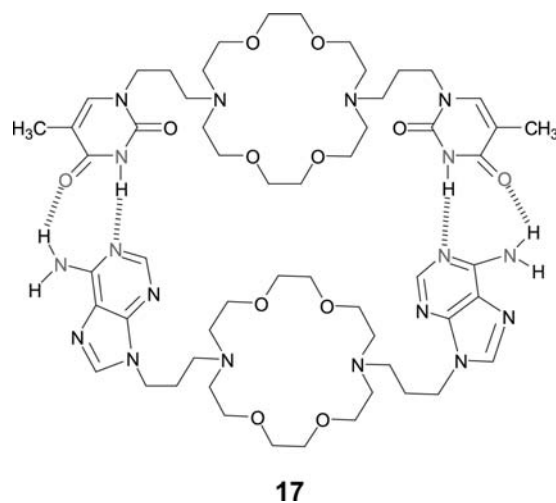


**Fig. 11** A self-assembled molecular box.

## ROTAXANES AND CATENANES

The use of NH-O hydrogen bonding to promote the threading process in the formation of a range of catenanes, pseudorotaxanes, and rotaxanes has been reported.<sup>[42,43]</sup>

In a typical reaction of this type, a cationic dialkylammonium-containing moiety interacts with a suitable crown ether, e.g., dibenzo-24-crown-8, in a solvent such as chloroform or dichloromethane.<sup>[44]</sup> The success of this procedure relies on the strong tendency for the  $\text{-NH}^{2+}$ -group to be encircled by the macrocycle such that hydrogen bonds form between the NH groups of the cation and the ring polyether oxygens, with the alkyl substituents protruding on either side of the ring. The resulting pseudorotaxane may then be converted into a rotaxane by appending bulky stopper groups to the termini of each alkyl portion of the threaded component to sterically block dissociation of the assembled product.

Ashton et al.<sup>[45]</sup> have been successful in producing a range of  $[n]$ -rotaxanes using the “threading followed by stoppering” strategy discussed above. For example, using the bis-azidomethyl-substituted *p*-xylene- $\alpha,\alpha'$ -dibenzylammonium dicationic salt **18**·**2PF<sub>6</sub><sup>-</sup>** and dibenzo-24-crown-8, both the corresponding [2]-catenane and [3]-catenane were prepared. The structure of the latter dication is illustrated by **19** (Fig. 12). In each case, the bulky “stoppers” were attached by means of two dipolar cycloadditions involving reaction of the azido groups with acetylene-dicarboxylate. The X-ray structure of **19**·**2PF<sub>6</sub><sup>-</sup>** shows that this [3]-rotaxane is stabilized by a combination of  $[\text{N-H}\cdots\text{O}]$ ,  $[\text{C-H}\cdots\text{O}]$ , and  $\pi$ - $\pi$  stacking interactions. Not surprisingly, the X-ray structure of the corresponding intermediate

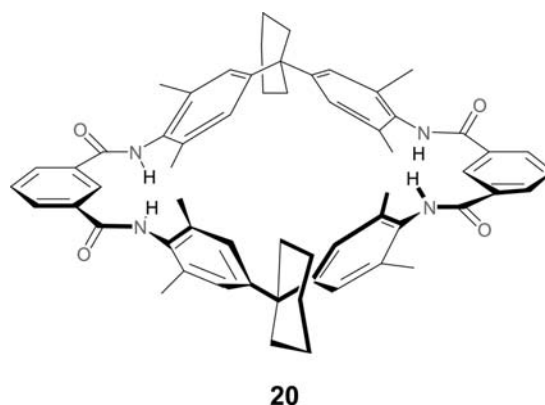


**Fig. 13** Amide macrocycle **20**. Two molecules of **20** intertwine to form a catenane during the macrocyclization reaction.

[3]-pseudorotaxane shows a very similar (supramolecular) structure to that found for the above rotaxane product.

Different groups<sup>[46–48]</sup> have reported the formation of a series of uncharged [2]-catenanes incorporating amide linkages that are intimately associated with the “interlinking” self-assembly of these species. For example, the [2]-catenane consisting of two interlinked rings of type **20** (Fig. 13) was isolated from a one-pot, double macrocyclization reaction from the required precursors in 34% yield.<sup>[42]</sup> The X-ray structure of the product was subsequently determined<sup>[49]</sup> and shows that the two macrocycles are locked together by a total of six hydrogen bonds that include bifurcated hydrogen bonds from the amide groups of an isophthaloyl subunit in each ring to a carbonyl oxygen belonging to the other ring. For this system, as well as for the related derivatives referred to above, the intermolecular

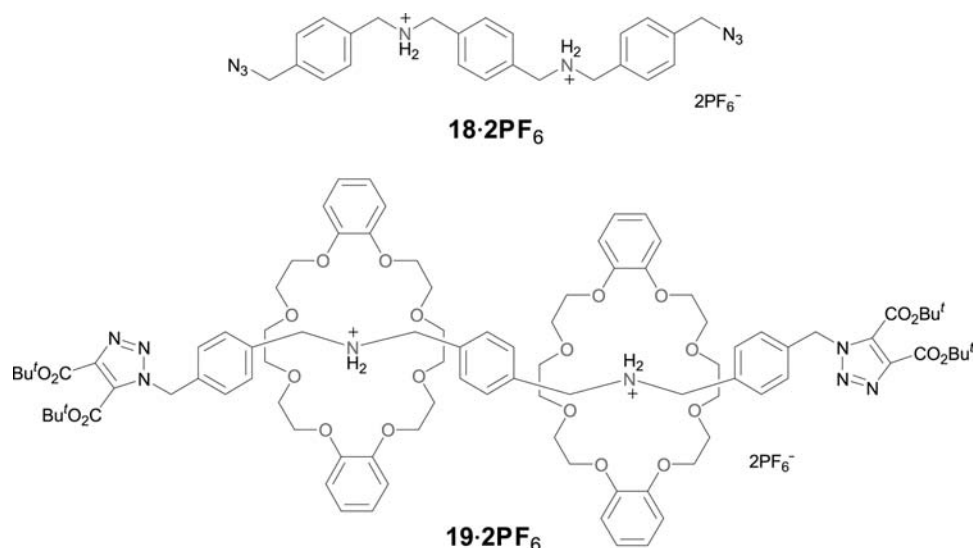


**Fig. 12** Diammonium “thread” **18** and a [3]-rotaxane.

interactions (which may also involve  $\pi$  interactions in particular cases) clearly play an additional role in acting as templates during the crucial interlinking step.

## HELICAL STRUCTURES

The helical structures found throughout nature (e.g.,  $\alpha$ -helical polypeptides) have inspired the design of synthetic oligomers that fold into helices. Numerous interactions are available to hold such “foldamers” in a well-defined conformation and NH–O hydrogen bonding has been employed in many cases.

Oligoamides that incorporate aromatic rings in their backbones are more rigid than their aliphatic counterparts and can be directed to adopt helical structures using hydrogen bonding between backbone substituents. Oligoanthranilides form intramolecular hydrogen bonds between adjacent amide NH and CO groups. Linking these units with either pyridine-2,6-carboxamide or 4,6-dimethoxy-1,3-diamino benzene derivatives introduces turns into the H-bonded oligomers **21** (Fig. 14), resulting in the formation of extended helical structures.<sup>[50,51]</sup> Similarly, helices have been formed from oligomers of 5-amino-2,4-dimethoxybenzoic acids **22** (Fig. 14) (or analogs in which longer alkyl ethers are present at the 2- and 4-positions).<sup>[52,53]</sup> In this case, hydrogen bonds between the amide NH and the ether substituents together with the *meta*-substitution pattern of the aromatic rings results in the backbone adopting a helical conformation which has a 10 Å cavity. Substitution of some of the *m*-substituted aromatic rings with *p*-substituted analogs permits the formation of helices with larger internal cavities (>30 Å).<sup>[54]</sup> Evidence for the helical nature of these molecules comes from 2-D <sup>1</sup>H NMR experiments, which show end-to-end NOE contacts in CDCl<sub>3</sub> or mixtures of CDCl<sub>3</sub> and DMSO, together with X-ray crystal structure data for a number of compounds that clearly show that these molecules adopt a helical conformation in the solid state.

Berl et al.<sup>[55]</sup> have found that a “heptamer” formed from alternating 2,6-diaminopyridine and 1,3-benzenedicarboxylate units forms helices around a central cyanurate template that has complementary hydrogen bonding sites. In the absence of the template, multiple conformers are present in solution as a result of free rotation about the aryl–CO bonds. Introduction of the cyanurate template results in a single conformer that exhibited end-to-end NOE contacts in the <sup>1</sup>H NMR spectrum, indicating the stabilization of a helical structure.

## SELF-ASSEMBLY OF NANOTUBES

The self-assembly of tubular structures is of great interest because of the large number of potential applications for these nanotubes. Two major classes of nanotubes have been assembled using NH–O hydrogen bonding: those formed by the stacking of macrocycles to form continuous tubes and those formed by interdigitating peptidic side chains attached to rigid rod scaffolds to form  $\beta$ -barrels.

Ghadiri et al.<sup>[56,57]</sup> observed that the controlled acidification of a solution of the cyclic octapeptide cyclo-[-(L-Gln-D-Ala-L-Glu-D-Ala)<sub>2</sub>-] **23** resulted in the self-assembly of hollow tubular structures with an internal diameter of approximately 7 Å **24** (Fig. 15). A number of other cyclic D,L  $\alpha$ -peptides have been found to form self-assembled nanotubes under the appropriate conditions.<sup>[58,59]</sup> Both the exterior surface properties and the internal diameters of the nanotubes may easily be altered upon changing the amino acid side chains and the number of amino acids in the cycle, respectively; thereby providing self-assembled structures that can be tailored for specific applications. It has also been found that cyclic  $\beta^3$ -peptides can form similar tubular structures with an internal pore.<sup>[60,61]</sup> The formation of cylindrical assemblies using macrocycles composed of cystine-bridged bisamides or bisureas has also been reported.<sup>[62]</sup>

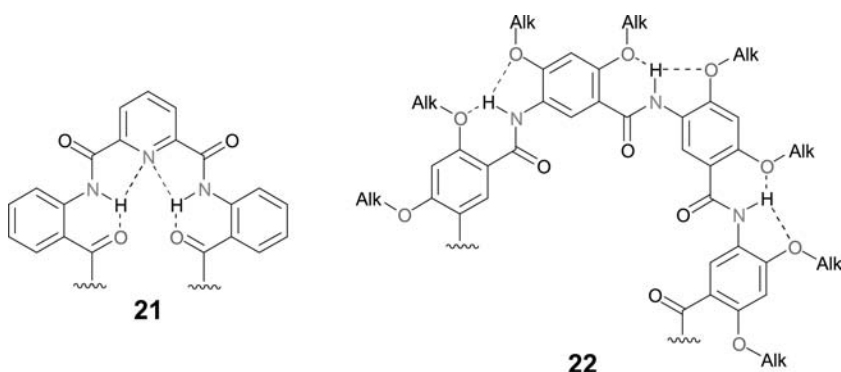


Fig. 14 Oligomers that adopt helical structures.

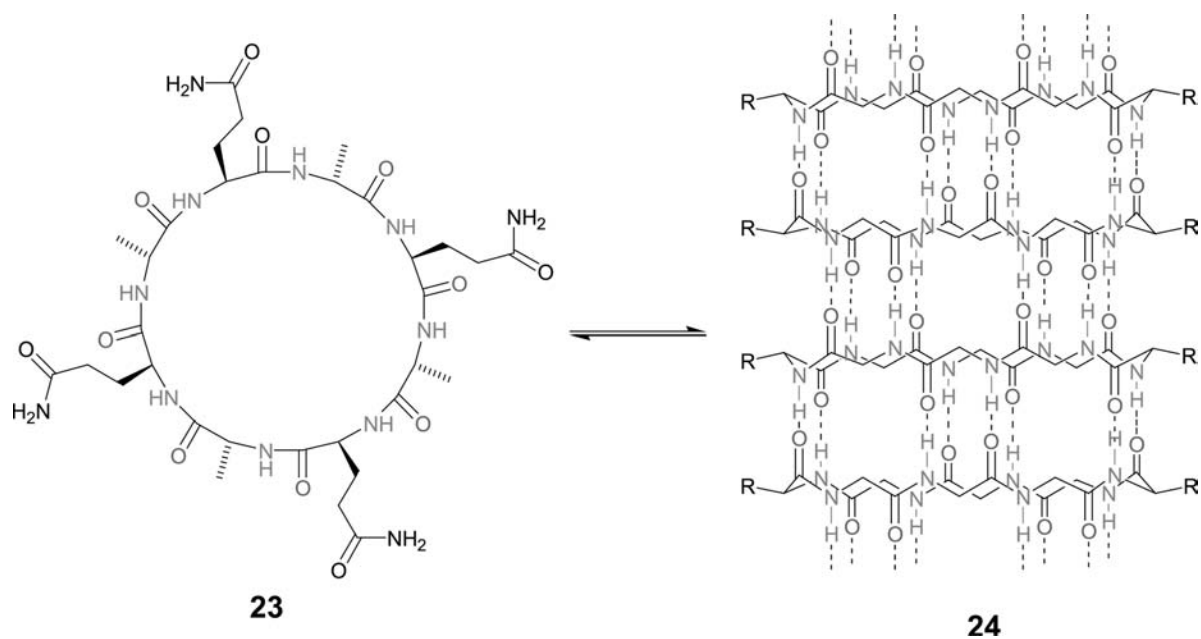


Fig. 15 Self-assembly of nanotubes from stacked cyclic peptides.

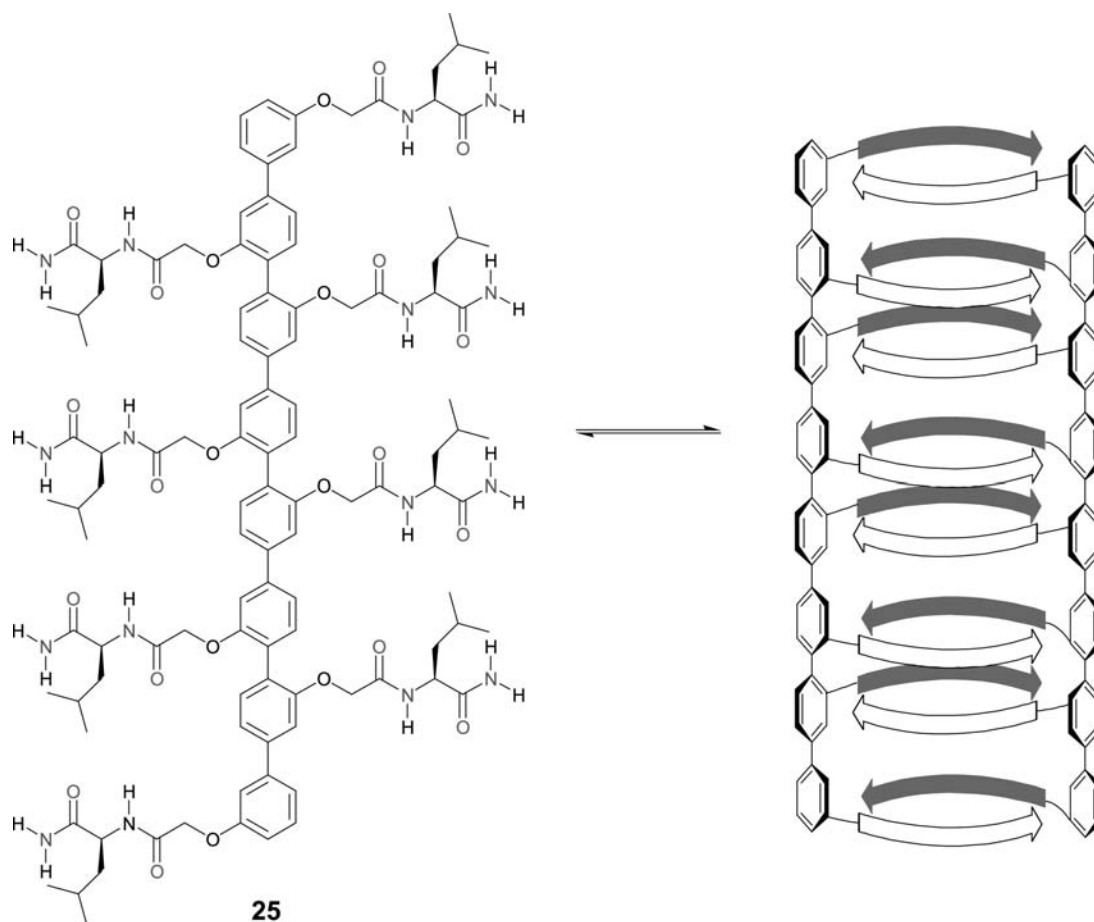


Fig. 16 Self-assembly of  $\beta$ -barrels.



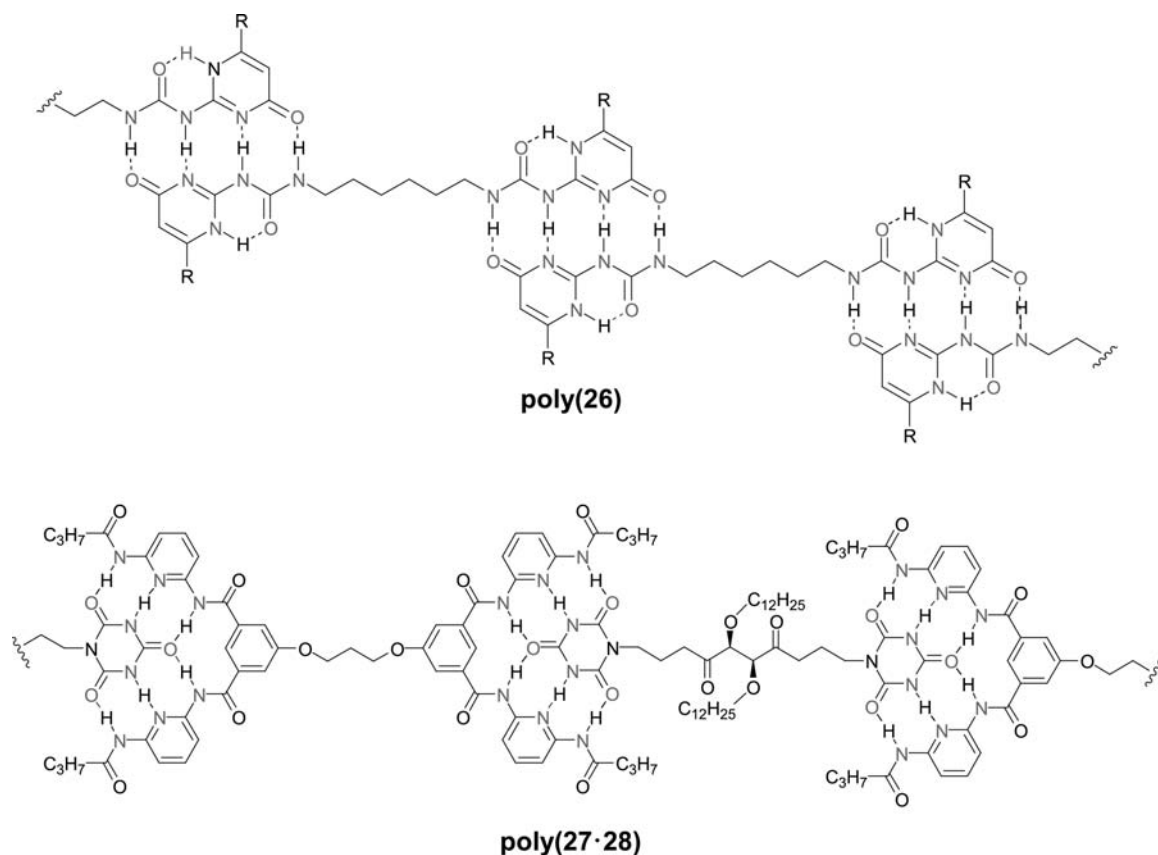


Fig. 17 Self-assembled hydrogen-bonded polymers.

Nanotubes composed of either cyclic D,L  $\alpha$ -peptides or cyclic  $\beta$ -peptides have been found to act as transmembrane ion channels, transporting small ions, e.g., K<sup>+</sup> and Na<sup>+</sup>, or, in the case of nanotubes with larger internal diameters, larger molecules, e.g., glucose and glutamate, across lipid bilayers.<sup>[63–65]</sup> More recently, it has been found that nanotubes of cyclic D,L  $\alpha$ -peptides act as selective antibacterial agents by increasing cell membrane permeability.<sup>[66]</sup>

Sakai, Majumadar, and Matile<sup>[67]</sup> have found that suitably functionalized peptide chains attached to rigid *p*-oligophenyl scaffolds **25** self-assemble to form cylindrical “barrels” as a result of intermolecular hydrogen bonding between the NH and carbonyl functionalities of interdigitating peptide strands (Fig. 16). These artificial  $\beta$ -barrels have a fixed length and may be designed to have either a hydrophilic interior and hydrophobic exterior surface or vice versa. The internal diameter of the barrel is flexible, and can be increased by either increasing the steric demands of the interior amino acid side chains or by using electrostatic repulsion between charged side chains on the interior surface.<sup>[68]</sup>

Artificial  $\beta$ -barrels having a hydrophobic interior have been found to encapsulate carotenoids,<sup>[69]</sup> while those with a hydrophilic interior were found to exhibit

substantial ion channel, esterase, RNAase, and fibrillogenetic activity.<sup>[70–72]</sup>

## HYDROGEN-BONDED POLYMERS

The self-assembly of multiple components can lead either to the formation of discrete aggregates, as described above, or to the formation of “supramolecular polymers.” Hydrogen-bonded polymers have been prepared using many of the recognition motifs described above and the field has been recently reviewed.<sup>[73–75]</sup> Recent examples include the reversible polymerization of self-complementary bisureidopyrimidones **26**<sup>[76]</sup> and the copolymerization of biscyanurate **27** and bisdiaminopyridine **28** monomers (Fig. 17).<sup>[77]</sup>

## CONCLUSION

Hydrogen bonds of the type N–H...O have been utilized for the construction of a wide range of supramolecular architectures. These hydrogen bonds are individually weak, but often a number of such bonds

will act in unison, or cooperatively with other intermolecular interactions (e.g., NH–N hydrogen bonds,  $\pi$ – $\pi$  stacking, or ionic interactions), resulting in, overall, strong attraction between the individual molecular components of an assembly. In this entry, we have presented a selection of representative examples of the large number of such assemblies now reported.<sup>[1,7,78–80]</sup>

## ACKNOWLEDGMENT

We thank the Australian Research Council for support.

## REFERENCES

- Lindoy, L.F.; Atkinson, I.M. *Self-Assembly in Supramolecular Chemistry*; Royal Society for Chemistry: Cambridge, UK, 2000; 1–224.
- Lehn, J.-M. Supramolecular chemistry—scope and perspectives. Molecules, supermolecules, and molecular devices (Nobel lecture). *Angew. Chem., Int. Ed. Engl.* **1988**, *27* (1), 89–112.
- Bryant, J.A.; Ericson, J.L.; Cram, D.J. High preorganization of large lipophilic surfaces common to two complexing partners provides high binding free energies that vary dramatically with changes in organic solvent composition. *J. Am. Chem. Soc.* **1990**, *112* (3), 1255–1256.
- Desiraju, G.R. Supramolecular synthons in crystal engineering—a new organic synthesis. *Angew. Chem., Int. Ed. Engl.* **1995**, *34* (21), 2311–2327.
- Steiner, T. The hydrogen bond in the solid state. *Angew. Chem. Int. Ed.* **2002**, *41* (1), 48–76.
- Jeffrey, G.A. *An Introduction to Hydrogen Bonding*; Oxford University Press: Oxford, 1997.
- Prins, L.J.; Reinhoudt, D.N.; Timmerman, P. Noncovalent synthesis using hydrogen bonding. *Angew. Chem., Int. Ed.* **2001**, *40* (13), 2382–2426.
- Pedersen, C.J. Cyclic polyethers and their complexes with metal salts. *J. Am. Chem. Soc.* **1967**, *89* (26), 7017–7036.
- Cram, D.J.; Cram, J.M. Design of complexes between synthetic hosts and organic guests. *Acc. Chem. Res.* **1978**, *11* (1), 8–14.
- Chang, S.-K.; Hamilton, A.D. Molecular recognition of biologically interesting substrates: synthesis of an artificial receptor for barbiturates employing six hydrogen bonds. *J. Am. Chem. Soc.* **1988**, *110* (4), 1318–1319.
- Chang, S.-K.; Van Engen, D.; Fan, E.; Hamilton, A.D. Hydrogen bonding and molecular recognition: synthetic, complexation, and structural studies on barbiturate binding to an artificial receptor. *J. Am. Chem. Soc.* **1991**, *113* (20), 7640–7645.
- Rebek, J., Jr.; Askew, B.; Ballester, P.; Buhr, C.; Jones, S.; Nemeth, D.; Williams, K. Molecular recognition: hydrogen bonding and stacking interactions stabilize a model for nucleic acid structure. *J. Am. Chem. Soc.* **1987**, *109* (16), 5033–5035.
- Askew, B.; Ballester, P.; Buhr, C.; Jeong, K.S.; Jones, S.; Parris, K.; Williams, K.; Rebek, J., Jr. Molecular recognition with convergent functional groups. 6. Synthetic and structural studies with a model receptor for nucleic acid components. *J. Am. Chem. Soc.* **1989**, *111* (3), 1082–1090.
- Williams, K.; Askew, B.; Ballester, P.; Buhr, C.; Jeong, K.S.; Jones, S.; Rebek, J., Jr. Molecular recognition with convergent functional groups. 7. Energetics of adenine binding with model receptors. *J. Am. Chem. Soc.* **1989**, *111* (3), 1090–1094.
- Hamilton, A.D.; Van Engen, D. Induced fit in synthetic receptors: nucleotide base recognition by a “molecular hinge”. *J. Am. Chem. Soc.* **1987**, *109* (16), 5035–5036.
- Ducharme, Y.; Wuest, J.D. Use of hydrogen bonds to control molecular aggregation. Extensive, self-complementary arrays of donors and acceptors. *J. Org. Chem.* **1988**, *53* (24), 5787–5789.
- Gallant, M.; Viet, M.T.P.; Wuest, J.D. Use of hydrogen bonds to control molecular aggregation. Association of dipyrindones joined by flexible spacers. *J. Org. Chem.* **1991**, *56* (7), 2284–2286.
- Schmuck, C.; Weinand, W. Highly stable self-assembly in water: ion pair driven dimerization of a guanidinio-carbonyl pyrrole carboxylate zwitterion. *J. Am. Chem. Soc.* **2003**, *125* (2), 452–459, and references therein.
- Kimura, E.; Fujioka, H.; Kodama, M. A new ditopic receptor molecule for ionic guest molecules. *J. Chem. Soc., Chem. Commun.* **1986**, (15), 1158–1159.
- Herm, M.; Molt, O.; Schrader, T. Towards synthetic adrenaline receptors—shape-selective adrenaline recognition in water. *Angew. Chem., Int. Ed.* **2001**, *40* (17), 3148–3151.
- Herm, M.; Molt, O.; Schrader, T. Towards synthetic adrenaline receptors—shape-selective adrenaline recognition in water. *Chem. Eur. J.* **2002**, *8* (6), 1485–1499.
- Bisson, A.P.; Carver, F.J.; Eggleston, D.S.; Haltiwanger, R.C.; Hunter, C.J.; Livingstone, D.L.; McCabe, J.F.; Rotger, C.; Rowan, A.E. Synthesis and recognition properties of aromatic amide oligomers: molecular zippers. *J. Am. Chem. Soc.* **2000**, *122* (37), 8856–8868, and references therein.
- Zimmerman, S.C.; Duerr, B.F. Controlled molecular aggregation. 1. Cyclic trimerization via hydrogen bonding. *J. Org. Chem.* **1992**, *57* (8), 2215–2217.
- Marsh, A.; Silvestri, M.; Lehn, J.-M. Self-complementary hydrogen bonding heterocycles designed for the enforced self-assembly into supramolecular macrocycles. *Chem. Commun.* **1996**, (13), 1527–1528.
- Mascal, M.; Hext, N.M.; Warmuth, R.; Moore, M.H.; Turkenburg, J.P. Programming a hydrogen-bonding code for the specific generation of a supermacrocycle. *Angew. Chem., Int. Ed.* **1996**, *35* (19), 2204–2206.
- Kolotuchin, S.V.; Zimmerman, S.C. Self-assembly mediated by the donor–donor–acceptor•acceptor–acceptor–donor (DDA•AAD) hydrogen-bonding motif: formation of a robust hexameric aggregate. *J. Am. Chem. Soc.* **1998**, *120* (35), 9092–9093.
- Ma, Y.; Kolotuchin, S.V.; Zimmerman, S.C. Supramolecular polymer chemistry: self-assembling dendrimers using the DDA•AAD (GC-like) hydrogen bonding motif. *J. Am. Chem. Soc.* **2002**, *124* (46), 13,757–13,769.

28. Corbin, P.S.; Lawless, L.J.; Li, Z.; Ma, Y.; Witmer, M.J.; Zimmerman, S.C. Discrete and polymeric self-assembled dendrimers: hydrogen bond mediated assembly with high stability and high fidelity. *Proc. Natl. Acad. Sci. U. S. A.* **2002**, *99* (8), 5099–5104.
29. Ranganathan, A.; Pedireddi, V.R.; Rao, C.N.R. Hydrothermal synthesis of organic channel structures: 1:1 hydrogen-bonded adducts of melamine with cyanuric and trithiocyanuric acids. *J. Am. Chem. Soc.* **1999**, *121* (8), 1752–1753.
30. Whitesides, G.M.; Simanek, E.E.; Mathais, J.P.; Seto, C.T.; Chin, D.N.; Gordon, D.M. Noncovalent synthesis: using physical organic chemistry to make aggregates. *Acc. Chem. Res.* **1995**, *28* (1), 37–44.
31. Simanek, E.E.; Li, X.; Choi, I.S.; Whitesides, G.M. Cyanuric acid and melamine: a platform for the construction of soluble aggregates and crystalline materials. In *Comprehensive Supramolecular Chemistry*; Atwood, J.L., Davies, J.E.D., MacNicol, D.D., Vögtle, F., Lehn, J.-M., Eds.; Elsevier Science Ltd.: Oxford, 1996; Vol. 9, 595–621.
32. Vreekamp, R.H.; van Duynhoven, J.P.M.; Hubert, M.; Verboom, W.; Reinhoudt, D.N. Molecular boxes based on calix[4]arene double rosettes. *Angew. Chem., Int. Ed.* **1996**, *35* (11), 1215–1218.
33. Paraschiv, V.; Crego-Calama, M.; Fokkens, R.H.; Padberg, C.J.; Timmerman, P.; Reinhoudt, D.N. Nanostructures via non-covalent synthesis: 144 hydrogen bonds bring together 27 components. *J. Org. Chem.* **2001**, *66* (25), 8297–8301, and references therein.
34. Prins, L.J.; Huskens, J.; de Jong, F.; Timmerman, P.; Reinhoudt, D.N. Compete asymmetric induction of supramolecular chirality in a hydrogen-bonded assembly. *Nature* **1999**, *398* (6727), 498–502.
35. Prins, L.J.; de Jong, F.; Timmerman, P.; Reinhoudt, D.N. An enantiomerically pure hydrogen-bonded assembly. *Nature* **2000**, *408* (6809), 181–184.
36. Prins, L.J.; Timmerman, P.; Reinhoudt, D.N. Amplification of chirality: the “seargents and soldiers” principle applied to dynamic hydrogen-bonded assemblies. *J. Am. Chem. Soc.* **2001**, *123* (42), 10,153–10,163.
37. Prins, L.J.; Hulst, R.; Timmerman, P.; Reinhoudt, D.N. Diastereoselective noncovalent synthesis of hydrogen-bonded double-rosette assemblies. *Chem. Eur. J.* **2002**, *8* (10), 2288–2301.
38. Prins, L.J.; Verhage, J.J.; de Jong, F.; Timmerman, P.; Reinhoudt, D.N. Enantioselective noncovalent synthesis of hydrogen-bonded double-rosette assemblies. *Chem. Eur. J.* **2002**, *8* (10), 2302–2313.
39. Conn, M.M.; Rebek, J., Jr. Self-assembling capsules. *Chem. Rev.* **1997**, *97* (5), 1647–1668.
40. Shimizu, K.D.; Rebek, J. Jr. Synthesis and assembly of self-complementary calix[4]arenes. *Proc. Natl. Acad. Sci. U. S. A.* **1995**, *92* (26), 12,403–12,407.
41. Schall, O.F.; Gokel, G.W. Molecular boxes derived from crown ethers and nucleotide bases: probes for Hoogsteen vs. Watson–Crick H-bonding and other base–base interactions in self-assembly processes. *J. Am. Chem. Soc.* **1994**, *116* (14), 6089–6100.
42. Clifford, T.; Abushamleh, A.; Busch, D.H. Factors affecting the threading of axle molecules through macrocycles: binding constants for semirotaxane formation. *Proc. Natl. Acad. Sci. U. S. A.* **2002**, *99* (8), 4830–4836.
43. Ashton, P.R.; Ballardini, R.; Balzani, V.; Gomez-Lopez, M.; Lawrence, S.E.; Martinez-Diaz, M.V.; Montalti, M.; Piersanti, A.; Prodi, L.; Stoddart, J.F.; Williams, D.J. Hydrogen-bonded complexes of aromatic crown ethers with (9-anthracenyl)methylammonium derivatives. *Supramolecular photochemistry and photophysics. pH-controllable supramolecular switching.* *J. Am. Chem. Soc.* **1997**, *119* (44), 10,641–10,651.
44. Chiu, S.-H.; Elizarov, A.M.; Glink, P.T.; Stoddart, J.F. Translation isomerism in a [3]catenane and a [3]rotaxane. *Org. Lett.* **2002**, *4* (21), 3561–3564.
45. Ashton, P.R.; Glink, P.T.; Stoddart, J.F.; Menzer, S.; Tasker, P.A.; White, A.J.P.; Williams, D.J. The solid state structures of a [3]rotaxane and its [3]pseudorotaxane precursor. *Tetrahedron Lett.* **1996**, *37* (34), 6217–6220.
46. Hunter, C.A. Synthesis and structure elucidation of a new [2]-catenane. *J. Am. Chem. Soc.* **1992**, *114* (13), 5303–5311.
47. Ottens-Hildebrandt, S.; Nieger, M.; Rissanen, K.; Rouvinen, J.; Meier, S.; Harder, G.; Vögtle, F. Amide-based furano-catenanes: regioselective template synthesis and crystal structure. *J. Chem. Soc., Chem. Commun.* **1995**, (7), 777–778.
48. Johnston, A.G.; Leigh, D.A.; Pritchard, R.J.; Deegan, M.D. Facile synthesis and solid state structure of a benzylic amide. *Angew. Chem., Int. Ed. Engl.* **1995**, *34* (11), 1209–1212.
49. Adams, H.; Carver, F.J.; Hunter, C.A. [2]Catenane or not [2]catenane? *J. Chem. Soc., Chem. Commun.* **1995**, (8), 809–810.
50. Hamuro, Y.; Geib, S.J.; Hamilton, A.D. Novel folding patterns in a family of oligoanthranilamides: non-peptide oligomers that form extended helical secondary structures. *J. Am. Chem. Soc.* **1997**, *119* (44), 10,587–10,593.
51. Hamuro, Y.; Geib, S.J.; Hamilton, A.D. Novel molecular scaffolds: formation of helical secondary structure in a family of oligoanthranilamides. *Angew. Chem., Int. Ed.* **1994**, *33* (4), 446–448.
52. Zhu, J.; Parra, R.D.; Zeng, H.; Skrzypczak-Jankun, E.; Zeng, X.C.; Gong, B. A new class of folding oligomers: crescent oligoamides. *J. Am. Chem. Soc.* **2000**, *122* (17), 4219–4220.
53. Gong, B. Crescent oligoamides: From acyclic “macro-cycles” to folding nanotubes. *Chem. Eur. J.* **2001**, *7* (20), 4337–4342.
54. Gong, B.; Zeng, H.; Zhu, J.; Yuan, L.; Han, Y.; Cheng, S.; Furukawa, M.; Parra, R.D.; Kovalevsky, A.Y.; Mills, J.L.; Skrzypczak-Jankun, E.; Martinovic, S.; Smith, R.D.; Zheng, C.; Szyperski, T.; Zeng, X.C. Creating nanocavities of tunable sizes: hollow helices. *Proc. Nat. Acad. Sci. U. S. A.* **2002**, *99* (18), 11,538–11,588.
55. Berl, V.; Krische, M.J.; Huc, I.; Lehn, J.-M.; Schmutz, M. Template-induced and molecular recognition directed hierarchical generation of supramolecular assemblies from molecular strands. *Chem. Eur. J.* **2000**, *6* (11), 1938–1946.

56. Ghadiri, M.R.; Granja, J.R.; Milligan, R.A.; McRee, D.D.; Khazanovich, N. Self-assembling organic nanotubes based on a cyclic peptide architecture. *Nature* **1993**, *366* (6453), 324–327.
57. Bong, D.T.; Clark, T.D.; Granja, J.R.; Ghadiri, M.R. Self-assembling organic nanotubes. *Angew. Chem., Int. Ed.* **2001**, *40* (6), 988–1011.
58. Hartgerink, J.D.; Clark, T.D.; Ghadiri, M.R. Peptide nanotubes and beyond. *Chem. Eur. J.* **1998**, *4* (8), 1367–1372.
59. Polaskova, M.E.; Ede, N.J.; Lambert, J.N. Synthesis of nanotubule-forming cyclic octapeptides via an Fmoc strategy. *Aust. J. Chem.* **1998**, *51* (7), 535–540.
60. Seebach, D.; Matthews, J.L.; Meden, A.; Wessels, T.; Baerlocher, C.; McCusker, L.B. Cyclo- $\beta$ -peptides: structure and tubular stacking of cyclic tetramers of 3-aminobutanoic acid as determined from powder diffraction data. *Helv. Chim. Acta* **1997**, *80* (1), 173–182.
61. Clark, T.D.; Buehler, L.K.; Ghadiri, M.R. Self-assembling cyclic  $\beta^3$ -peptide nanotubes as artificial transmembrane ion channels. *J. Am. Chem. Soc.* **1998**, *120* (4), 651–656.
62. Ranganathan, D.; Samant, M.P.; Karle, I.L. Self-assembling, cystine derived, fused nanotubes based on spirane architecture: design, synthesis and crystal structure of cystinospiranes. *J. Am. Chem. Soc.* **2001**, *123* (24), 5619–5624, and references therein.
63. Ghadiri, M.R.; Granja, J.R.; Buehler, L.K. Artificial transmembrane ion channels from self-assembling peptide nanotubes. *Nature* **1994**, *369* (6478), 301–304.
64. Sánchez-Quesada, J.; Kim, H.S.; Ghadiri, M.R. A synthetic pore-mediated transmembrane transport of glutamic acid. *Angew. Chem., Int. Ed.* **2001**, *40* (13), 2503–2506.
65. Sánchez-Quesada, J.; Isler, M.P.; Ghadiri, M.R. Modulating ion channel properties of transmembrane peptide nanotubes through heteromeric supramolecular assemblies. *J. Am. Chem. Soc.* **2002**, *124* (34), 10,004–10,005.
66. Fernandez-Lopez, S.; Kim, H.-S.; Choi, E.C.; Delgado, M.; Granja, J.R.; Khasanov, A.; Kraehenbuehl, K.; Long, G.; Weinberger, D.A.; Wilcoxon, K.M.; Ghadiri, M.R. Antibacterial agents based on the cyclic D,L- $\alpha$ -peptide architecture. *Nature* **2001**, *412* (6845), 452–455.
67. Sakai, N.; Majumadar, N.; Matile, S. Self-assembled rigid rod ionophores. *J. Am. Chem. Soc.* **1999**, *121* (17), 4294–4295.
68. Baumeister, B.; Sakai, N.; Matile, S. Giant artificial ion channels formed by self-assembled cationic rigid-rod  $\beta$ -barrels. *Angew. Chem., Int. Ed.* **2000**, *39* (11), 1955–1958.
69. Baumeister, B.; Matile, S. Rigid-rod  $\beta$ -barrels as lipocalin models: probing confined space by carotenoid encapsulation. *Chem. Eur. J.* **2000**, *6* (10), 1739–1749.
70. Som, A.; Matile, S. Rigid-rod  $\beta$ -barrel ion channels with internal “cascade blue” cofactors—catalysis of amide, carbonate and ester hydrolysis. *Eur. J. Org. Chem.* **2002**, (22), 3874–3883.
71. Baumeister, B.; Matile, S. Toward *p*-octophenyl  $\beta$ -barrel Rnases. *Macromolecules* **2002**, *35* (5), 1549–1555.
72. Das, G.; Ouali, L.; Adrian, M.; Baumeister, B.; Wilkinson, K.J.; Matile, S.  $\beta$ -Fibrillogenesis from rigid-rod  $\beta$ -barrels: hierarchical preorganization beyond microns. *Angew. Chem., Int. Ed.* **2001**, *40* (24), 4657–4661.
73. Brunsveld, L.; Folmer, B.J.B.; Meijer, E.W.; Sijbesma, R.P. Supramolecular polymers. *Chem. Rev.* **2001**, *101* (12), 4071–4097.
74. Sherrington, D.C.; Taskinen, K.A. Self-assembly in synthetic macromolecular systems via multiple hydrogen bonding interactions. *Chem. Soc. Rev.* **2001**, *30* (2), 83–93.
75. Cifferi, A.; Ed. *Supramolecular Polymers*; Marcel Dekker: New York, USA, 2000.
76. Brunsveld, L.; Vekemans, J.A.J.M.; Hirschberg, J.H.K.K.; Sijbesma, R.P.; Meijer, E.W. Hierarchical formation of helical supramolecular polymers via stacking of hydrogen-bonded pairs in water. *Proc. Natl. Acad. Sci. U.S.A.* **2002**, *99* (8), 4977–4982.
77. Berl, V.; Schmutz, M.; Krische, M.J.; Houry, R.G.; Lehn, J.-M. Supramolecular polymers generated from heterocomplementary monomers linked through multiple hydrogen-bonding arrays—formation, characterization, and properties. *Chem. Eur. J.* **2002**, *8* (5), 1227–1244.
78. Archer, E.A.; Gong, H.; Krische, M.J. Hydrogen bonding in noncovalent synthesis: selectivity and the directed organisation of molecular strands. *Tetrahedron* **2001**, *57* (7), 1139–1159.
79. Philp, D.; Stoddart, J.F. Self-assembly in natural and unnatural systems. *Angew. Chem., Int. Ed. Engl.* **1996**, *35* (11), 1154–1196.
80. Fredericks, J.R.; Hamilton, A.D. Hydrogen bonding control of molecular self-assembly: recent advances in design, synthesis and analysis. In *Comprehensive Supramolecular Chemistry*; Atwood, J.L., Davies, J.E.D., MacNicol, D.D., Vögtle, F., Lehn, J.-M., Eds.; Elsevier Science Ltd.: Oxford, 1996; Vol. 9, 565–594.

# Self-Formed Quantum Dots: Structural and Optical Characterization

**Shun-ichi Gonda**

*Fukui University of Technology, Fukui, Japan*

**Hajime Asahi**

*Institute of Scientific and Industrial Research,  
Osaka University, Osaka, Japan*

## INTRODUCTION

There are various methods for the fabrication of quantum dots (QD).<sup>[1,2]</sup> Among them, the self-formation method is one of the most useful methods, because it causes little damage, creates dots of high density, and the fabrication process is rather simple. In this entry, two fabrication methods, i.e., the S–K mode growth method and the composition modulation of short-period superlattices, are introduced. For samples fabricated by these methods, structural characterization with atomic force microscopy (AFM), scanning tunneling microscopy/spectroscopy (STM/STS), magnetic force microscopy (MFM), and transmission electron microscopy (TEM) are described. Furthermore, as optical characterization methods, photoluminescence (PL), time-resolved photoluminescence (TRPL), and electroluminescence (EL) are mentioned and the several results are shown.

## FABRICATION METHODS

Prior to the description of the characterization,<sup>[3,4]</sup> we briefly describe the fabrication methods for self-formed QDs. A frequently used method is the so-called “Stranski–Krastanov (S–K) mode growth method.” In this method, a small amount of materials having a lattice constant different from that of the substrate are supplied at appropriate temperatures on a substrate (e.g., GaAs). Because of the difference of surface energy and the strain, projecting dots of supplied materials are formed on the substrate. A characteristic feature of this method is dot formation on the flat surfaces, shown schematically in Fig. 1A. The typical density of dots made by the S–K mode growth is around  $10^9$ – $10^{10}$  cm<sup>-2</sup>. Examples of materials combination are InAs on GaAs, InGaAs on GaAs,<sup>[5–8]</sup> and InGaN on GaN.<sup>[9]</sup>

As an example, our growth process of InAs dots on GaAs using metal organic molecular beam epitaxy

(MOMBE) is as follows:<sup>[10]</sup> After the growth of GaAs buffer layer, triethylgallium (TEGa) and trisdimethylaminoarsenic (TDMAAS) are supplied at an appropriate substrate temperature. The formation of InAs dots can be monitored by observing the reflection high-energy electron diffraction (RHEED) pattern changes from streaky to spotty. Other growth processes are shown in Refs.<sup>[5–9]</sup>

Another method is the “composition modulation of short-period superlattices.” In this method,<sup>[11]</sup> e.g., short-period GaP/InP superlattice layers are grown on GaAs substrate. The state of grown layers depends on the orientation of GaAs substrates. With this method, wire structures are grown on (100) GaAs substrates<sup>[11]</sup> and CuPt-type GaP/InP superlattices are grown on (111) GaAs.<sup>[12]</sup> On (N11) GaAs substrate, dot structures are self-formed.<sup>[12]</sup> In this case, dots are formed in the grown layer. Therefore the surface is flat, as shown in Fig. 1B. The density of dots is around  $10^{11}$  cm<sup>-2</sup>. Examples of material combination are InP/GaP on GaAs and GaAs/InAs on InP.

Here the fabrication procedure of dots by the above method is described in more detail. Two types of superlattices are grown on Si-doped GaAs(311)A substrates by gas source molecular beam epitaxy. One is (GaP)<sub>n</sub>-(InP)<sub>m</sub>, where *n* and *m* represent the number of the monolayer of each compound. (GaP)(InP) means that the GaP layer was grown first on the substrate and the InP layer was grown next. The other type of sample (InP)<sub>n</sub>(GaP)<sub>m</sub> was formed in the reverse order. Elemental Ga, In, Si, and thermally cracked arsine (AsH<sub>3</sub>) and phosphine (PH<sub>3</sub>) were used as sources.

## STRUCTURAL CHARACTERIZATION

Structure of self-formed quantum dots can be characterized by various methods such as atomic force microscopy (AFM), scanning tunneling microscopy (STM), electron microscopy, and electron diffraction.

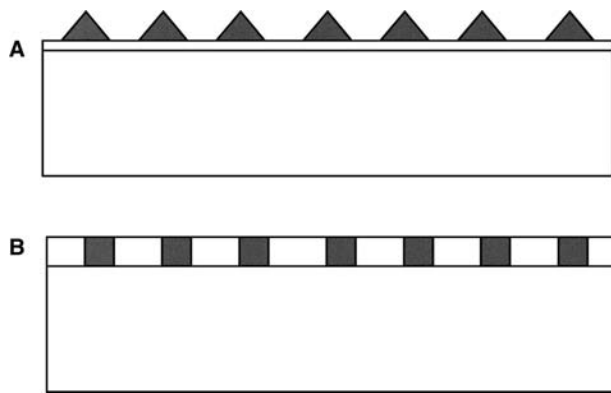


**Fig. 1** Schematic view of (A) QDs fabricated by the S–K mode growth method and (B) QDs fabricated by the composition modulation method.

### AFM, STM, and STS

AFM utilizes the atomic force between a sample surface and a probe.<sup>[13]</sup> Therefore the obtained image is almost independent of the electric properties of

materials. In STM, the height position of the probe is controlled to keep the tunnel current between sample and probe constant, and the variation of probe is displayed.<sup>[14]</sup> Hence the obtained image reflects the electrical properties of materials. In scanning tunneling spectroscopy (STS), the position of the probe is fixed and the current–voltage characteristics are measured. These characteristics reflect the electronic structures of materials.

The shape and position of QDs fabricated by the S–K mode growth method are well characterized by AFM. Fig. 2 shows AFM image for (A) InAs dots as grown and for (B) the surface where smaller dots are eliminated by etching.<sup>[15]</sup> The diameter, height, density, and distribution of dots can be measured. The dependence of dot structures on the growth conditions is investigated via AFM.<sup>[16,17]</sup> On the other hand, in the case of QDs made by composition modulation, AFM shows that the surface is flat, and information on the size and distribution of dots are not obtained.

In some special cases, such as InAs dots including Mn atoms, magnetic force microscopy (MFM) can

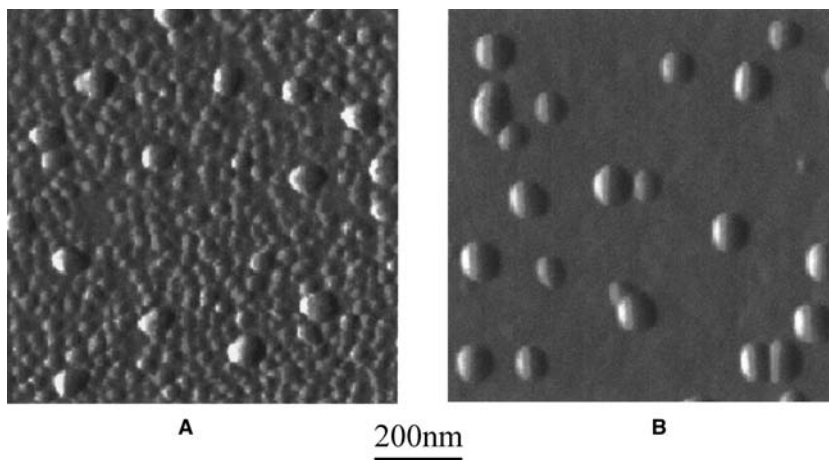


**Fig. 2** AFM images for (A) the InAs dots as grown by S–K mode growth and for (B) the surface where smaller dots are eliminated by etching. *Source:* From Ref.<sup>[15]</sup>.

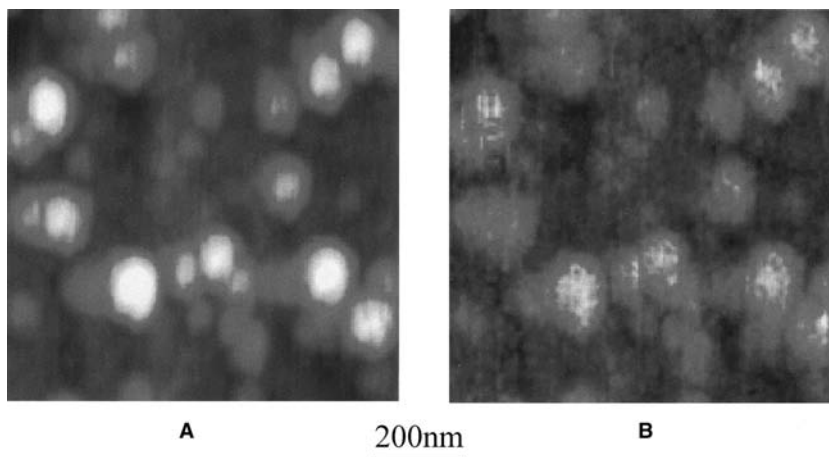


**Fig. 3** (A) AFM and (B) MFM images for the InAs dots including Mn atoms. *Source:* From Ref.<sup>[19]</sup>.



be used.<sup>[18]</sup> For MFM, batch-microfabricated silicon probes were magnetically sensitized by sputter coating with ferromagnetic materials. The tip is scanned tens or hundreds of nanometers above the sample, thus avoiding contact. Magnetic field gradients exert a force on the tip's magnetic moment, and monitoring the tip/cantilever response gives a magnetic force image. Fig. 3 shows AFM and MFM images of the InAs dots including Mn atoms.<sup>[19]</sup>

In the case of QDs by composition modulation, STM is a powerful tool for characterization. The STM image of the sample  $(\text{GaP})_{1.5}(\text{InP})_{1.88}$  on GaAs(311)A substrate is shown in Fig. 4A.<sup>[20]</sup> In the STM image reflecting the electrical properties, shape and distribution can be observed. The self-formed dots are aligned along two perpendicular directions, [0-11] and [233], and distributed side by side. The lateral period (size) of dots (bottom to bottom in the STM image) is about 20 nm ( $\sim 20$  nm along the [0-11] direction,  $\sim 19$  nm along the [233] direction). The distribution (size fluctuation) is about  $\pm 10\%$ . The dot density is of the order  $10^{11} \text{ cm}^{-2}$ . The bright and dark areas correspond to the InP-rich and GaP-rich regions, respectively, based on STS measurement.

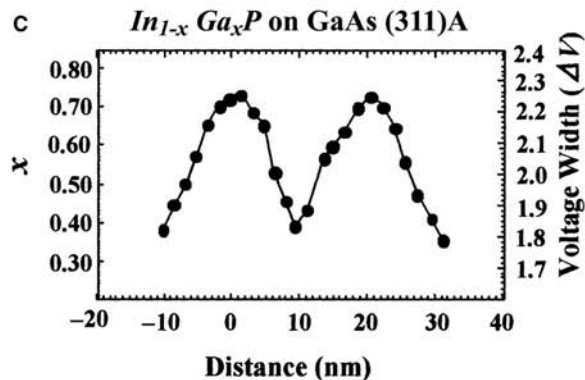
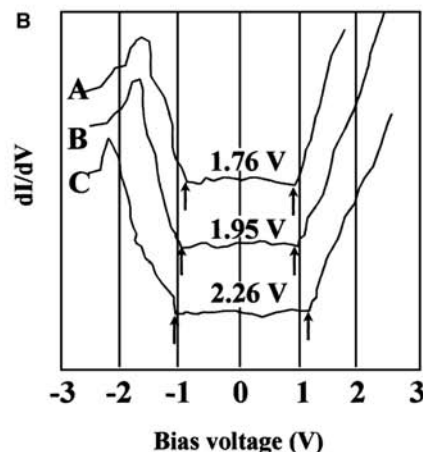
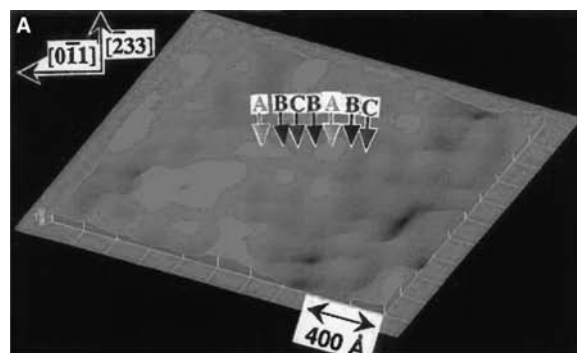
Fig. 4B shows a  $dI/dV$  vs. bias voltage curve at points A, B, and C in the STS measurement. The voltage width for  $dI/dV = 0$  corresponds to the potential change, i.e., the band gap change of the materials. The periodic structure of the voltage width shown in Fig. 4C is not attributable to the geometrical height change, but to the band gap change, because the surface is almost flat as described before.

In the case of the  $(\text{InP})_{1.88}(\text{GaP})_{1.5}$  sample, nearly the same dot structures are observed in the STM measurement. The difference is that the lateral period is about 22 nm ( $\sim 22$  nm along the [0-11] direction,  $\sim 20$  nm along the [233] direction). This is 10% larger than that of the  $(\text{GaP})_{1.5}(\text{InP})_{1.88}$  sample. The size distribution is also about  $\pm 10\%$ , which is nearly the same as  $(\text{GaP})_{1.5}(\text{InP})_{1.88}$  sample. The difference in the lateral period (size) between these two types of QDs was confirmed for several samples.

STM can be also utilized for the characterization of QDs made by the S-K mode growth. (Please see Refs. <sup>[21,22]</sup>.)

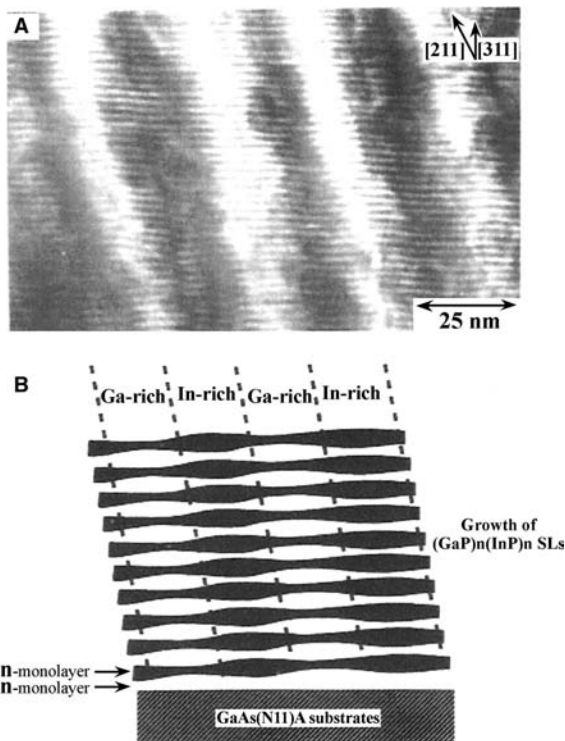
## Electron Microscopy

Inner structures of dots can be observed by using cross-sectional transmission electron microscope (TEM). It is important to carefully prepare specimens without causing damage. First, the sample is sliced or cleaved into bars. The bars, the backside of which is supported with Ti holder, are mounted on glass or metal with carbon epoxy so as to make the cross section



**Fig. 4** (A) STM images for QD structures self-formed  $(\text{GaP})_{1.5}(\text{InP})_{1.88}$  SLs grown on the GaAs (311)A substrate, (B)  $dI/dV$  vs.  $V$  curves at different points, and (C) variation of the voltage width for  $dI/dV = 0$  in (B) along the [0 - 11] direction. The left ordinate is related to  $X$  if the dot mean composition is represented by  $\text{In}_{1-x}\text{Ga}_x\text{P}$ . Source: From Ref.<sup>[20]</sup>.

upside. The bars are thinned by polishing and Ar milling to less than 10 nm. Fig. 5A shows a cross-sectional TEM lattice image of the  $(\text{GaP})_{1.5}(\text{InP})_{1.88}$  sample grown on (311)A GaAs substrate by composition modulation method.<sup>[3]</sup> This shows the lateral periodic thickness undulation, as shown schematically in



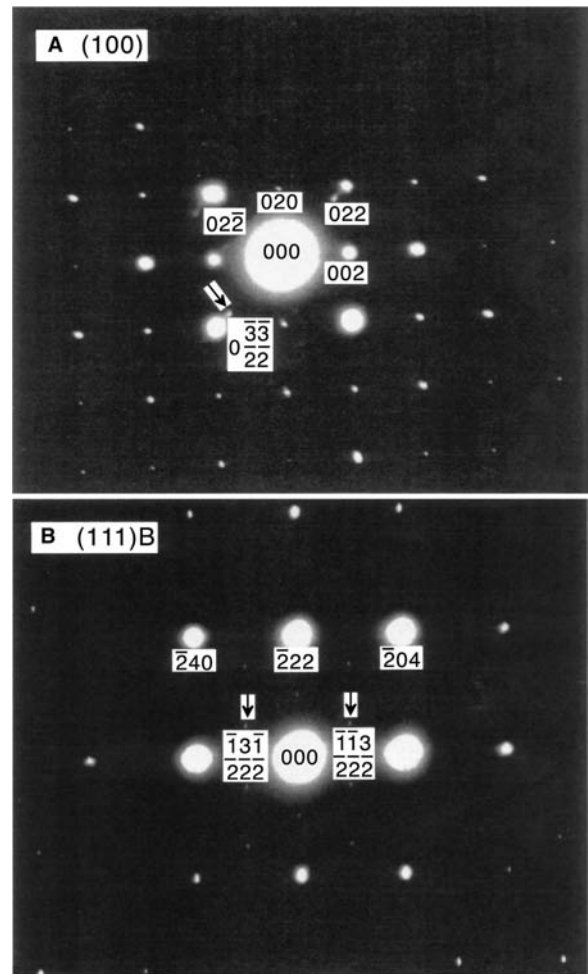
**Fig. 5** (A) Cross-sectional TEM lattice image for the  $(\text{GaP})_{1.5}(\text{InP})_{1.88}$  sample grown on GaAs (311)A substrate, (B) schematic drawing illustrating the lateral composition modulation induced by the lateral thickness modulation. *Source:* From Ref.<sup>[3]</sup>.

Fig. 5B, although GaP/InP superlattice structures are essentially preserved.

Characterizations of QDs made by the S–K mode growth with cross-sectional TEM images are reported.<sup>[23,24]</sup>

### Electron Diffraction

TEM diffraction is also used for the structural characterization. Fig. 6 shows TEM diffraction patterns for the  $(\text{GaP})_1(\text{InP})_1$  superlattices grown on (A) GaAs(100) and (B) GaAs(111)B. Incident electron beam is parallel to the [111] direction in the case of Fig. 6A and to the [211] direction in Fig. 6B.<sup>[25]</sup> The sharp spots  $(0 \ 1/2 \ 1/2)$  and  $(0 \ -1/2 \ -1/2)$  were clearly observed in Fig. 6A. This indicates that the superstructure with a period of twice the usual lattice constant is formed in the  $[0 \ 1 \ 1]$  direction. On the other hand, the sharp superstructure spots  $(1/2 \ 1/2 \ 1/2)$  were observed in Fig. 6B. This indicates that the CuPt-type long-range ordering, i.e.,  $(\text{GaP})_1(\text{InP})_1$  superlattices, is formed in the [111] direction. These observations show that the growth on the (100) and (111) substrates does not form quantum dots by the composition modulation method.



**Fig. 6** TEM diffraction pattern for the  $(\text{GaP})(\text{InP})$  SLs grown on (A) GaAs (100) and (B) GaAs (111)B substrates. *Source:* From Ref.<sup>[25]</sup>.

### X-ray Scattering and Diffraction

Grazing incidence small-angle X-ray scattering<sup>[26]</sup> and grazing incidence X-ray diffraction were used for structural characterization of InAs QDs. The grazing incidence technique probes the crystal surface up to depths of only a few nanometers. This strongly enhances the scattering intensity from the InAs QDs. It is revealed through this method that the lateral distribution of InAs QDs is anisotropic, and the most pronounced ordering of dot distribution is in the [110] direction and that the dot shape is an octagonal-based truncated pyramid with  $\{111\}$  and  $\{101\}$  facet families.<sup>[27]</sup>

### OPTICAL CHARACTERIZATION

In QDs, the electronic structures such as the energy level and the density of state greatly differ from those

of bulk crystal. Therefore it is possible to characterize quantum dots by measuring QDs' optical properties, which reflect the electronic structures.

### Photoluminescence (PL)

Ordinary PL peaks at low temperatures correspond to the energy difference between the lowest energy level in the conduction band of dots and the highest level in the valence band of the dots. Because these levels are a function of the size or radius of the dots, the peak position reflects the size of dots and the peak width reflects the size fluctuation of dots.

Fig. 7 shows an example of room-temperature PL spectra obtained by Songmuang et al.<sup>[28]</sup> for InAs dots fabricated through the S-K mode growth. The peak energy around 1 eV for InAs dots is very high, compared with the energy gap (0.36 eV) for InAs at room temperature. This shows the energy increase between the energy levels by dot formation. In this work, GaAs overgrowth on InAs dots was induced at two different temperatures. One is grown at the same level as the QD growth temperature [500°C; conventionally capped (CC)] and another at a lower temperature [470°C; low-temperature capped (LTC)]. In the lower spectra, the full-width at half maximum (FWHM) of the PL peak of CC dots is 51 meV, and that of LTC dots decreases to 26 meV. This implies that the size

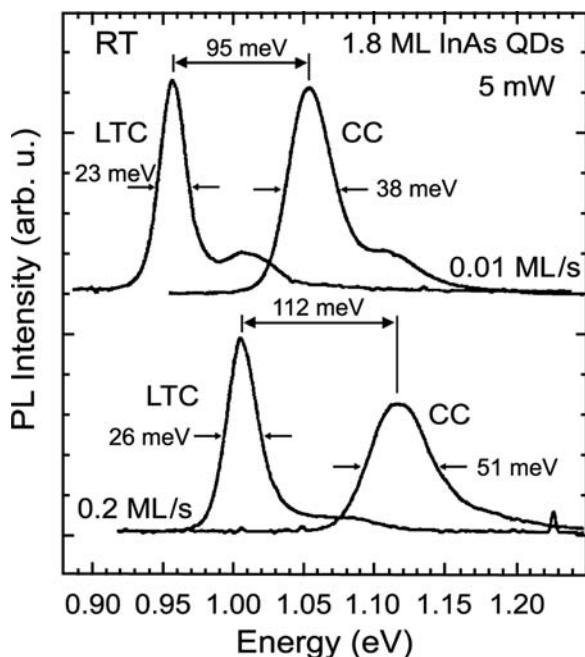


**Fig. 7** PL spectra at room temperature for low-temperature capped (LTC) InAs data and conventionally capped (CC) InAs dots by the S-K mode growth method. *Source:* From Ref.<sup>[28]</sup>.

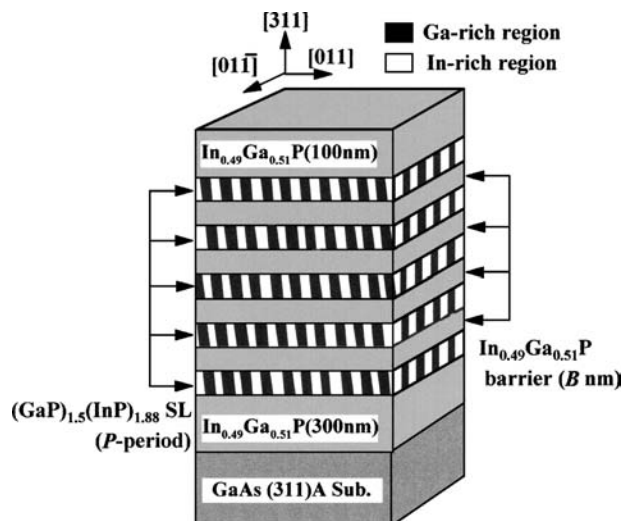


**Fig. 8** Schematic drawing of five cycle multilayer QDs (MQD) formed in the  $(\text{GaP})_n(\text{InP})_m$  SL/InGaP multilayer. *Source:* From Ref.<sup>[29]</sup>.

fluctuations decrease with decreasing overgrowth temperature.

In the PL measurement of QDs fabricated by composition modulation, multilayer QDs, shown in Fig. 8, are used.<sup>[29]</sup> PL spectra at 77 K for  $(\text{InP})_{1.88}(\text{GaP})_{1.5}$  and  $(\text{GaP})_{1.5}(\text{InP})_{1.88}$  samples are shown in Fig. 9.<sup>[3]</sup> PL peak energy of the  $(\text{GaP})_{1.5}(\text{InP})_{1.88}$  sample is higher than that of the  $(\text{InP})_{1.88}(\text{GaP})_{1.5}$  sample by about 10%. This tendency corresponds to the difference in the lateral period of dots of two samples. The FWHM of PL peak of the  $(\text{InP})_{1.88}(\text{GaP})_{1.5}$  sample is wider than that of the  $(\text{GaP})_{1.5}(\text{InP})_{1.88}$  sample by about 10%, as shown in Fig. 9. The FWHM of the  $(\text{InP})_{1.88}(\text{GaP})_{1.5}$  sample decreased nearly monotonically from 100 to 50 meV, when the temperature

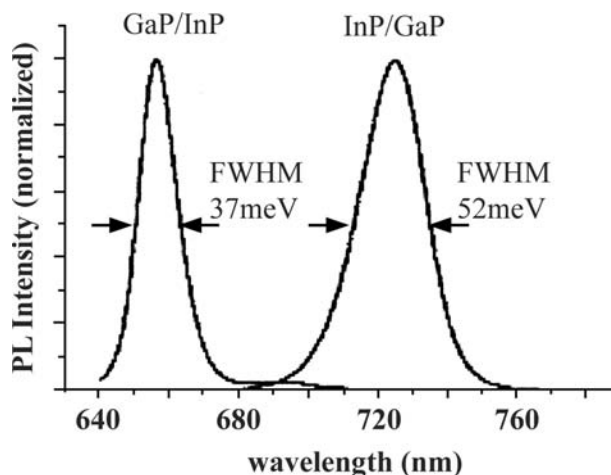


**Fig. 9** PL spectra at 77 K for  $(\text{InP})_{1.5}(\text{GaP})_{1.88}$  and  $(\text{GaP})_{1.5}(\text{InP})_{1.88}$  samples. *Source:* From Ref.<sup>[3]</sup>.

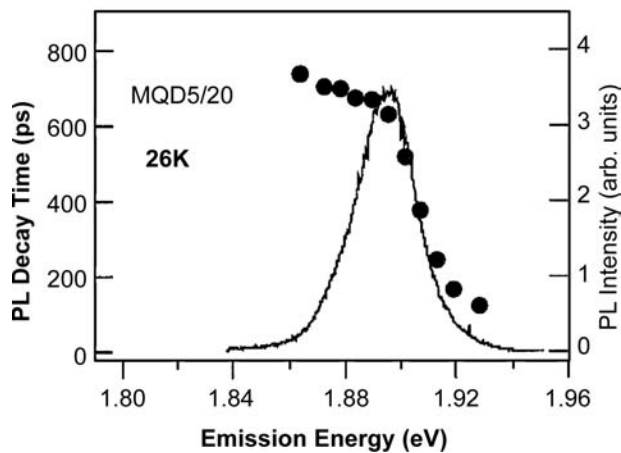


**Fig. 10** Time-integrated PL spectrum and PL decay time as a function of monitored emission energy at 26 K for MQD5/20. *Source:* From Ref.<sup>[29]</sup>.

is lowered from 350 to 10 K. The FWHM of  $(\text{GaP})_{1.5}\text{-(InP)}_{1.88}$  sample also decreases nearly monotonically down to 100 K, but it shows a maximum at  $\sim 50$  K. In this case, fluctuation of dot size is not to be related to the larger FWHM of the  $(\text{InP})_{1.88}(\text{GaP})_{1.5}$  sample, because the deviation of period is nearly the same within the experimental error in both samples. The difference is probably a result of the difference in crystalline quality or the state of strain in the dot layers.

Optical properties of multilayer QDs made by composition modulation are investigated by changing the superlattice period and the InGaP barrier thickness. By decreasing the period, PL peak energy shifts toward higher energy because of the quantum size effect along the growth direction. The PL line width broadening with temperature is reduced by decreasing the period and the barrier thickness. This is attributed to the

reduction of potential distribution among QDs and the enhancement of quantum confinement as a result of the vertical coupling effect between QDs. Very small temperature variation of PL peak energy is observed in multilayer QDs, which is attributed to the existence of the mutual strains in the multilayer QDs. A detailed discussion is given in another work.<sup>[30]</sup>

### Time-Resolved Photoluminescence (TRPL)

TRPL is effective for the investigation of the nature of emission in quantum dots. TRPL measurements are performed with a fast streak camera in conjunction with a monochromator. Pulsed excitation is provided the frequency doubled beam of a mode-locked  $\text{Al}_2\text{O}_3\text{:Ti}$  laser.

An example of the result for multilayer QDs MQD5/20 (5 is the period of  $(\text{GaP})_{1.5}(\text{InP})_{1.88}$  SL and 20 is the barrier thickness in nm) is shown in Fig. 10.<sup>[29]</sup> PL decay time strongly depends on emission energy. Fig. 11 shows the dependence of PL decay time on emission energy and temperature.<sup>[29]</sup> It ranges between 0.1 and 2.5 nsec. The decay time is shorter for higher energies. This dependence implies the existence of a tunneling process between QDs. In QDs, carriers in the higher energy levels of the smaller QDs can transfer to the lower energy levels in the adjacent larger QDs. Because carriers in the higher energy level have a large number of lower energy levels into which they can relax, the decay time becomes shorter for higher energies. Hence Fig. 11 reflects a variety of sizes of QDs and distances between QDs.

TRPL is also used to measure the tunneling time of carriers in coupled QDs. Takeuchi, Kuroda, and Mase<sup>[24]</sup> measured carrier tunneling times between vertically aligned double QDs using TRPL. The vertically

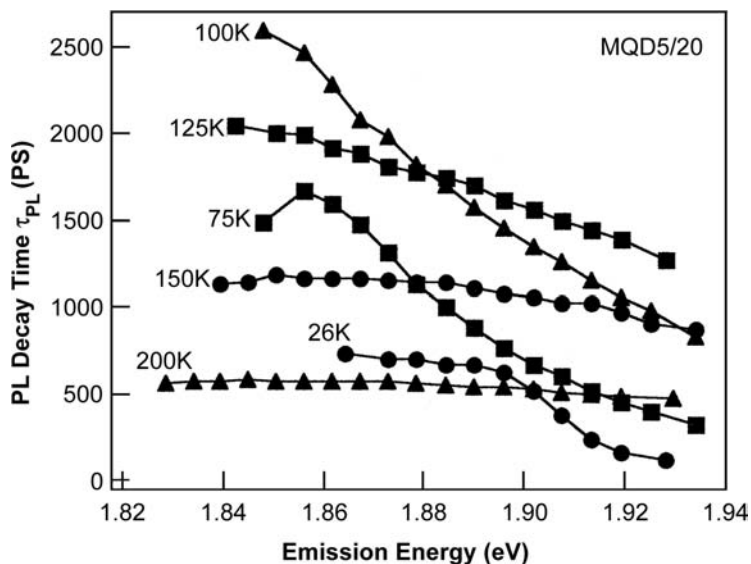


**Fig. 11** Monitored emission energy dependence of PL decay time as a function of measured temperature. *Source:* From Ref.<sup>[29]</sup>.

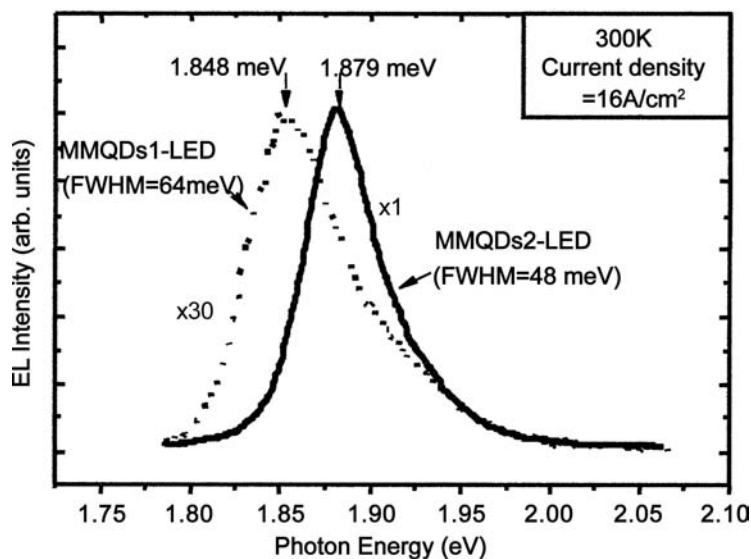


Fig. 12 EL spectra at room temperature. Source: From Ref.<sup>[31]</sup>.

aligned double QD structure consists of  $\text{In}_{0.9}\text{Ga}_{0.1}\text{As}$  QDs, a GaAs barrier layer, and InAs QDs, which is made via the S–K mode growth. They revealed the dependence of the tunneling time on the barrier thickness.

### Electroluminescence (EL)

EL shows another feature of the optical properties of QDs. We fabricated two types of light-emitting diodes (LED) using the composition modulation method. One is the sample MMQDs1, which has  $(\text{InGaP})_{40}(\text{InAlP})_{40}$  cladding layers and  $\text{In}_{0.49}\text{Ga}_{0.51}\text{P}$  barrier layers, and another is the sample MMQDs2, which has  $(\text{InGaP})_5(\text{InAlP})_5$  cladding and  $(\text{InGaP})_4(\text{InAlP})_2$  barrier. EL spectra at room temperature for both samples

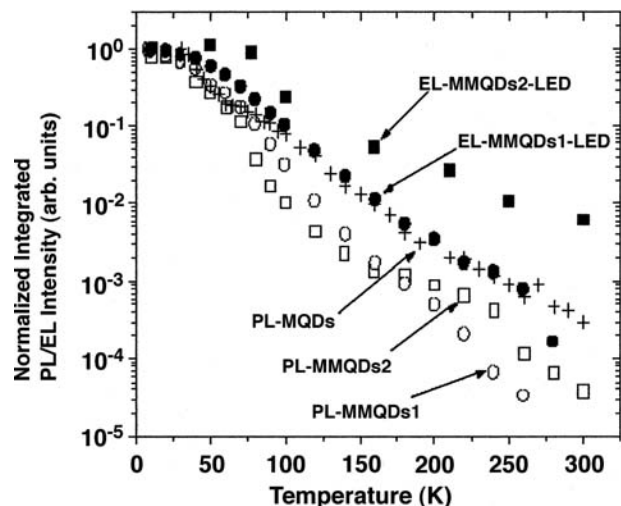


Fig. 13 Temperature variation of normalized EL and PL intensities. Source: From Ref.<sup>[31]</sup>.

are shown in Fig. 12.<sup>[31]</sup> MMQDs2 exhibits a narrower FWHM (48 meV) than that of MMQDs1. The integrated EL intensity of MMQDs2 is about 30 times higher than that of MMQDs1. This improvement results from the introduction of  $(\text{InGaP})_5(\text{InAlP})_5$  as cladding and  $(\text{InGaP})_4(\text{InAlP})_2$  SL as barrier layers. Fig. 13 shows the temperature variations of integrated EL and PL intensities.<sup>[31]</sup> The temperature quenching of EL intensity is smaller for MMQDs2 than for MMQDs1. Because the effective band gap of the  $(\text{InGaP})_5(\text{InAlP})_5$  SL is larger than that of  $(\text{InGaP})_{40}(\text{InAlP})_{40}$  SL, the reason for these temperature variations is considered to be a result of the suppression of carrier flow from the QD region by the use of higher band gap cladding layers.

If the QDs are applied to devices, characterization via device performance is one of the very severe characterizations. The most popular application of self-formed QDs is semiconductor lasers. An example of InAs/InGaAs/GaAs QD lasers is introduced here. Kovsh et al.<sup>[32]</sup> made QDs via the S–K mode growth and fabricated 1.3- $\mu\text{m}$  edge-emitting lasers. They simultaneously obtained threshold current density of  $100 \text{ A/cm}^2$  and differential efficiency of 80% in the same device.

### CONCLUSION

Structural and optical characterization of self-formed quantum dots was described, based mainly from our experience. Structures such as size, position, and distribution are well characterized by AFM, STM, STS, and TEM, and optical characterizations, capable of obtaining information on carriers and their energy states, are well carried out by PL measurements.

Most of the samples treated here were quantum dots fabricated via the composition modulation methods, and samples made by the S–K mode growth method are a little bit smaller in number. There are numerous reports concerning quantum dots produced by the S–K mode growth. For example, reports on In(Ga)As quantum dots are introduced in detail in Ref.<sup>[2]</sup>. For quantum dots of nitrides, the reader is referred to Ref.<sup>[9]</sup>. For further details on quantum dots using SiGe system, CdSe/ZnSe, and PbSe, please see Refs.<sup>[33–35]</sup> respectively.

The above-mentioned methods for structural and optical characterization are very effective and useful for various semiconductor materials.

## REFERENCES

- Bimberg, D.; Grundman, M.; Ledentsov, N.N. *Quantum Dot Heterostructures*; Wiley: New York, 1998.
- Sugawara, S.; Ed. *Self-Assembled InGaAs Quantum Dots, Semimetals and Semiconductors*; Academic Press: New York, 1999; Vol. 60.
- Gonda, S.; Asahi, H.; Mori, J.; Watanabe, D.; Matsuda, S.; Noh, J.H.; Fudeta, M.; Asami, K.; Seki, S.; Matsui, Y.; Tagawa, S. Structural and optical characterization of self-formed quantum dots. *J. Electron. Mater.* **2000**, *29*, 530–534.
- Asahi, H. Self-organized quantum wires and dots in III–V semiconductors. *Adv. Mater.* **1997**, *9* (13), 1019–1026.
- Leonard, D.; Krishnamruthy, M.; Reaves, C.M.; Denbarrs, S.P.; Petroff, P.M. Direct formation of quantum dots from uniform coherent islands of InGaAs on GaAs. *Appl. Phys. Lett.* **1993**, *63* (23), 3203–3205.
- Ahopelto, J.; Yamaguchi, A.A.; Nishi, K.; Usui, A.; Sakaki, H. Nanoscale InP islands for quantum box structures by hydride vapor phase epitaxy. *Jpn. J. Appl. Phys.* **1993**, *32*, L32–L35.
- Nabetani, Y.; Ishikawa, T.; Noda, S.; Sasaki, A. Initial growth stage and optical properties of a three dimensional InAs structure on GaAs. *J. Appl. Phys.* **1994**, *76*, 347–351.
- Moisin, J.M.; Housy, F.; Barthe, F.; Leprince, L.; Andre, E.; Vatel, O. Self-organized growth of regular nanometer-scale InAs dots on GaAs. *Appl. Phys. Lett.* **1994**, *64*, 196–198.
- Tachibana, K.; Someya, T.; Arakawa, Y. Nanometer-scale InGaN self-assembled quantum dots by metalorganic chemical vapor deposition. *Appl. Phys. Lett.* **1999**, *74* (3), 383–385.
- Zhou, Y.K.; Asahi, H.; Asakura, J.; Okumura, J.; Asami, K.; Gonda, S. Magnetic and optical properties of Mn-including InAs dots grown by metalorganic molecular beam epitaxy. *J. Cryst. Growth* **2000**, *221*, 605–610.
- Cheng, K.Y.; Hsieh, K.C.; Baillargeon, J.N. Formation of lateral quantum wells in vertical short-period superlattices by strain-induced lateral-layer ordering process. *Appl. Phys. Lett.* **1992**, *60* (23), 2892–2894.
- Kim, S.J.; Asahi, H.; Takemoto, M.; Asami, K.; Takeuchi, M.; Gonda, S. Self-organized dot/columnar structure and quasi-perfect CuPt type ordering in (GaP)<sub>n</sub>(InP)<sub>n</sub> superlattices grown on GaAs (N11) substrates by gas source molecular beam epitaxy. *Jpn. J. Appl. Phys.* **1996**, *35* (8), 4225–4231. Part 1.
- Binnig, G.; Quate, C.F.; Gerber, Ch. Atomic force microscope. *Phys. Rev. Lett.* **1986**, *56* (9), 930–933.
- Binnig, G.; Rohrer, H.; Gerber, Ch.; Weibel, E.  $7 \times 7$  Reconstruction on Si(111) resolved unreal space. *Phys. Rev. Lett.* **1982**, *50* (2), 120–123.
- Zhou, Y.K.; Asahi, H.; Asakura, J.; Okumura, T.; Tashima, T.; Sato, J.; Asami, K.; Gonda, S. Magnetic and optical properties of Mn-including InAs dots grown by MOMBE. *Physica E* **2000**, *7*, 1001–1005.
- Leonard, D.; Fafard, S.; Pond, K.; Zhang, H.; Merz, J.L.; Petroff, P.M. Structural and optical properties of self-assembled InGaAs quantum dots. *J. Vac. Sci. Technol.* **1994**, *B12*, 2516–2520.
- Ren, H.W.; Nishi, K.; Sugou, S.; Masumoto, Y. Size quantization in InAs/GaAs self-assembled quantum dots grown by gas-source molecular beam epitaxy. *Jpn. J. Appl. Phys.* **1998**, *37*, 1548–1551.
- Martin, Y.; Wickramasinghe, H.K. Magnetic imaging by “force microscopy” with 1000 Å resolution. *Appl. Phys. Lett.* **1987**, *50* (20), 1455–1457.
- Tashima, T.; Asahi, H.; Sato, J.; Asami, K.; Zhou, Y.K.; Gonda, S. Formation of InAs dots including Mn atoms by metalorganic molecular beam epitaxy. *Inst. Phys. Conf. Ser.* **1999**, *162*, 481–486. Chapter 9.
- Noh, J.H.; Asahi, H.; Kim, S.-J.; Gonda, S. Scanning tunneling microscopy study on self-formation process of quantum dot structures by the growth of GaP/InP short-period superlattices on GaAs(311)A substrate. *Jpn. J. Appl. Phys.* **1998**, *37* (6B), 3973–3975. Part 1.
- Hasegawa, S.; Arakawa, K.; Tanaka, M.; Nakashima, H. Scanning tunneling spectroscopy study of InAs islanding on GaAs(001). *J. Cryst. Growth* **2001**, *227–228*, 1029–1033.
- Joyce, P.B.; Krzyzewski, T.J.; Bell, G.R.; Jones, T.S.; Marik, S.; Childs, D.; Murray, R. Growth rate effects on the size, composition and optical properties of InAs/GaAs quantum dots grown by molecular beam epitaxy. *J. Cryst. Growth* **2001**, *227–228*, 1000–1004.
- Ustinov, V.M.; Zhukov, A.E.; Maleev, N.A.; Kovsh, A.R.; Mikhrin, S.S.; Volovik, B.V.; Musikhin, Yu.G.; Shernyyakov, Yu.M.; Maximov, M.V.; Tsatsul'nikov, A.F.; Ledentsov, N.N.; Alferov, Zh.I.; Lott, J.A.; Bimberg, D. 1.3 μm InAs/GaAs quantum dot lasers and VCSELs grown by molecular beam epitaxy. *J. Cryst. Growth* **2001**, *227–228*, 1155–1161.
- Takeuchi, A.; Kuroda; Mase, K. Dynamics of carrier tunneling between vertically aligned double quantum dots. *Phys. Rev.* **2000**, *62*, 1568–1571.
- Kim, S.J.; Asahi, H.; Takahashi, T.; Gonda, S. Substrate orientation dependence of lateral composition modulation in (GaP)<sub>n</sub>(InP)<sub>n</sub> strained short period superlattices grown by gas source MBE. *Inst. Phys. Conf. Ser.* **1995**, *145*, 91–96. Chapter 2.



26. Schmidbauer, M.; Wiebach, Th.; Raidt, H.; Hanke, M.; Kohler, R.; Waura, H. Ordering of self-assembled  $\text{Si}_{1-x}\text{Ge}_x$  islands studied by grazing incidence small-angle scattering and atomic force microscopy. *Phys. Rev.* **1998**, *B58*, 10523–10531.
27. Zhang, K.; Heyn, Ch.; Hansen, W.; Schmid, Th.; Felta, J. Structural characterization of self-assembled InAs quantum dots grown by MBE. *J. Cryst. Growth* **2001**, *227–228*, 1020–1024.
28. Songmuang, R.; Kiravittaya, S.; Sawadsaringkarn, M.; Panyakeow, S.; Schmidt, O.G. Photoluminescence investigation of low-temperature capped self-assembled InAs/GaAs quantum dots. *J. Cryst. Growth* **2003**, *251*, 166–171.
29. Fudeta, M.; Asahi, H.; Asami, K.; Nakamura, Y.; Kawakami, Y.; Noh, J.H.; Mori, J.; Watanabe, D.; Fujita, S.; Gonda, S. Time-resolved photoluminescence study of strain-induced quantum dots self-formed in GaP/InP short-period superlattices. *Jpn. J. Appl. Phys.* **1999**, *38* (9A/B), L1006–L1008. Part 2.
30. Kim, S.J.; Asahi, H.; Asami, K.; Takemoto, M.; Fudeta, M.; Gonda, S. Optical properties of quantum dots self-formed in GaP/InP short period superlattices grown on GaAs(N11) substrates. *Appl. Surf. Sci.* **1998**, *130–132*, 729–736.
31. Watanabe, D.; Asahi, H.; Noh, J.H.; Fudeta, M.; Mori, J.; Matsuda, S.; Asami, K.; Gonda, S. Improvement of optical properties of multilayer quantum dots self-formed in GaP/InP short-period superlattices on GaAs(311)A. *Jpn. J. Appl. Phys.* **2000**, *39* (7B), 4601–4603. Part 1.
32. Kovsh, A.R.; Maleev, N.A.; Zhukov, A.E.; Mikhrin, S.S.; Vasil'ev, A.P.; Semenova, E.A.; Shernyyakov, Yu.M.; Maximov, M.V.; Lifshits, D.A.; Ustinov, V.M.; Ledentsov, N.N.; Bimberg, D.; Alferov, Zh.I. InAs/InGaAs/GaAs quantum dot lasers of 1.3  $\mu\text{m}$  range with enhanced optical gain. *J. Cryst. Growth* **2003**, *251*, 729–736.
33. Jin, G.; Wan, J.; Luo, Y.H.; Liu, J.L.; Wang, K.L. Uniform and ordered self-assembled Ge dots on patterned Si substrates with selectively epitaxial growth technique. *J. Cryst. Growth* **2001**, *227–228*, 1100–1105.
34. Maehashi, K.; Yasui, N.; Ota, T.; Noma, T.; Murase, Y.; Nakashima, H. Structural and optical properties of CdSe/ZnSe self-organized quantum dots. *J. Cryst. Growth* **2001**, *227–228*, 1116–1120.
35. Springhotz, G.; Pinczolit, M.; Bauer, G.; Knag, H.H.; Salamanca-Riba, L. Phase diagram of lateral and vertical ordering in self-organized PbSe quantum dots grown by MBE. *J. Cryst. Growth* **2001**, *227–228*, 1126–1131.

# Self-Organized Superstructures: Molecular Design

Makoto Tadokoro

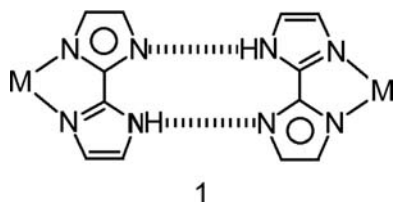
Department of Chemistry, Osaka City University,  
Osaka, Japan

## INTRODUCTION

Molecular arrays with desirable topological networks have recently been realized in crystal by self-organized binding between molecular building blocks with hydrogen-bonding (H-bonding) and metal-coordinating affinities. The coordination bonds and the H-bonds are relatively weak interactions that impart strength, directionality, and complementarity.<sup>[1–6]</sup> Such crystal manipulations, often known as crystal engineering, are performed to yield arrays of controlled superstructures providing new functional molecular solids.<sup>[7,8]</sup> Thus the self-organization of designed molecules containing certain kinds of complementary H-bonding and coordinating units has stimulated new efforts in the material sciences using, for example, controlled molecular arrays adsorbed to a solid surface,<sup>[9–11]</sup> a self-organized molecular assembly with unique cavities,<sup>[12]</sup> and an integrated system of molecular device.<sup>[13]</sup>

## MOLECULAR METAL BUILDING BLOCK

In some molecular systems, it has been possible to control molecular aggregation in the crystal by the di-functional ligands, which bond to metal using coordinate-covalent interactions and to each other using H-bonding interactions.<sup>[14–19]</sup> As 2,2'-biimidazole ( $H_2bim$ ) is a bidentate chelating ligand with multiproton donor sites, it can coordinate to a transition metal with three reversible types of protonated and deprotonated mode: neutral ( $H_2bim$ ), mono-deprotonated (monoanion,  $Hbim^{-1}$ ), and di-deprotonated (dianion,  $bim^{-2}$ ) types.<sup>[20]</sup> The 2,2'-biimidazolate monoanion ( $Hbim^{-1}$ ), recently introduced by us, works as such a di-functional bridging ligand not only to form a stable metal-chelate complex but also a new intermolecular



complementary H-bonding with two sets of NH donors and N acceptors, as shown in Drawing 1.<sup>[21]</sup> Molecular system such as  $Hbim^{-1}$  has not been found in molecular aggregation used for crystal engineering except in our aggregation system.

## CONTROLLED CRYSTAL STRUCTURES WITH ANIONIC $[Ni(Hbim)_3]^{-}$

First of all, we have designed a new anionic building block, a tris-biimidazolate nickel (II) complex ( $[Ni(Hbim)_3]^{-}$ ), where the biimidazolate ligand acts as a strong  $\pi$ -conjugated ligand to form three complementary H-bonding sites, which forms a variety of multidimensional superstructures with long-range ordered arrays. The  $[Ni(Hbim)_3]^{-}$  is constructed from the nickel (II) center coordinated by three bidentate  $Hbim^{-}$  ligands through the lone pairs of the imine nitrogen atoms in the imidazole rings. The  $[Ni(Hbim)_3]^{-}$  has an approximate point group  $D_3$  symmetry, whose  $\Delta$  and  $\Lambda$  isomer are illustrated in Fig. 1. In these cases, the nature of metal anion assembly was affected by the nature and size of the counteranion. Interestingly, synthesis of simple one-pot procedures by mixing the nickel (II) ion,  $Hbim^{-}$ , and counteranion produces four types of H-bonded crystals 1–4 based on the arrangement of  $[Ni(Hbim)_3]^{-}$ .<sup>[22]</sup> The production of the four types of molecular architecture by one-pot molecular self-organization of the  $[Ni(Hbim)_3]^{-}$  evolves from three fundamental factors: 1) three complementary binary H-bonding sites; 2)  $\Delta$  and  $\Lambda$  optical isomers in the chiral coordination mode; and 3) the kind of counteranions. Fig. 2 shows crystal structures of the four patterns of molecular arrangement, respectively: A) a zero-dimensional (0-D) dot structure with no complementary H-bonds of  $Hbim^{-}$ , which are blocked by  $H_2O$  molecules; B) a 1-D H-bonded zigzag ribbon formed from alternative linkages of H-bonds between the  $\Delta$  and  $\Lambda$  optical isomers using two of the three  $Hbim^{-}$  of  $[Ni(Hbim)_3]^{-}$ ; C) a 2-D H-bonded honeycomb sheet self-organized by alternative H-bonds using all three  $Hbim^{-}$  between  $\Delta$  and  $\Lambda$  isomers of  $[Ni(Hbim)_3]^{-}$ ; and D) a 3-D supra cross-catenated network formed from expanded 2-D honeycomb sheets. Each crystal has

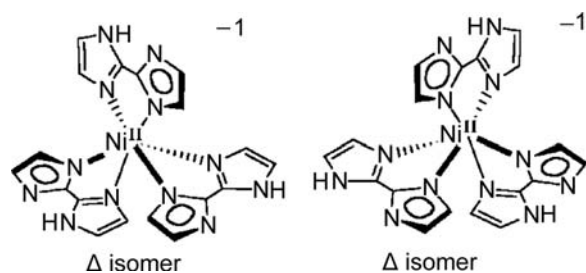


**Fig. 1**  $\Lambda$  and  $\Delta$  isomers of building blocks  $[\text{Ni}(\text{Hbim})_3]^-$ .

a different kind of counteraction, such as alkyl ammonium [a tetramethyl ammonium ( $\text{NMe}_4^+$ ) ions for 1, a tetra-*n*-propyl ammonium ( $\text{N}^n\text{Pr}_4^+$ ) ion for 2, and a tetraethyl ammonium ( $\text{NEt}_4^+$ ) ion for 4] and

a crown ether derivative [a potassium *cis-syn-cis*-dicyclohexano-18-crown-6 ( $[\text{K-DCH}(18\text{-crown-6})]^+$ ) ion for 3]. Therefore our results suggest that the mode of self-organization can be controlled by varying the kind of counteraction, although at this stage the prediction of the cation specificity is difficult. In the present study, we have succeeded systematically in the organization of the  $[\text{Ni}(\text{Hbim})_3]^-$  for the creation of 3 with double channels as included microporous crystals, such as an organic zeolite<sup>[2,3]</sup> and a modified zeolite with MOF<sup>[2,4]</sup> [Fig. 3A], and 4 with double-interlocking chains as polycatenate structures [Fig. 3B]. The 3 is constructed from all three H-bonding sites of  $[\text{Ni}(\text{Hbim})_3]^-$  with the complementary intermolecular H-bonds. Two of the H-bonding sites in it make a 1-D H-bonded zigzag ribbon like 2. Then the 1-D

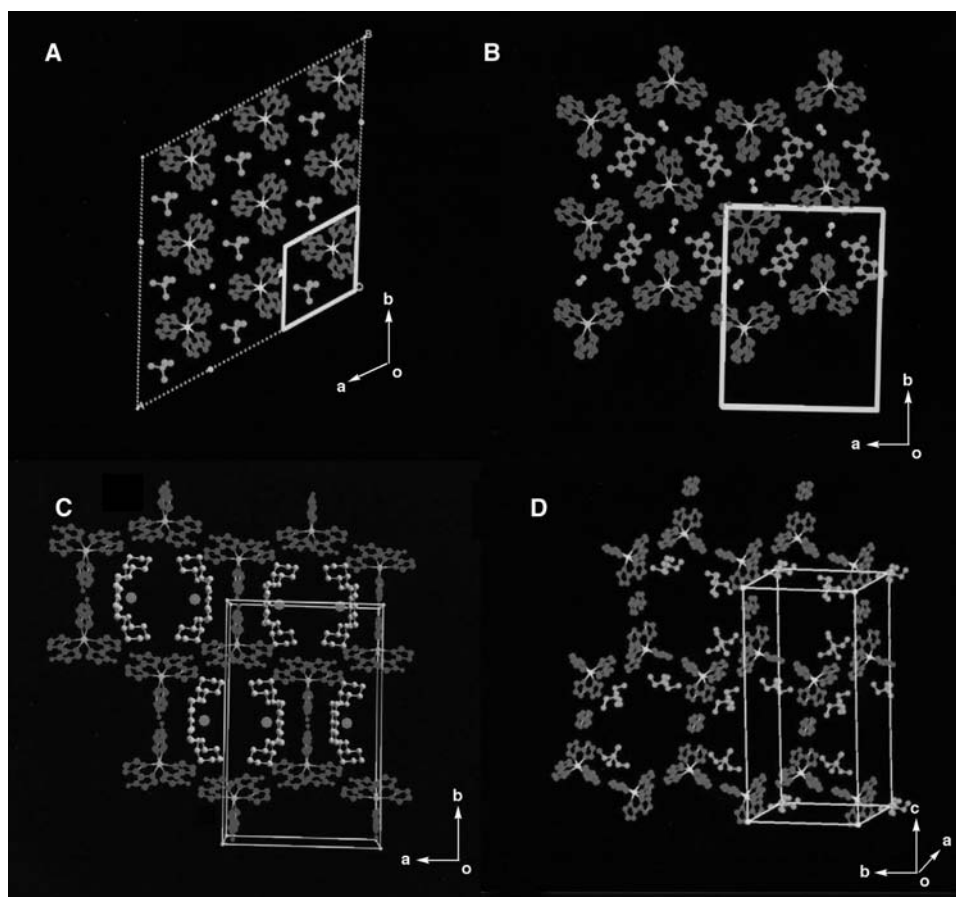


**Fig. 2** The crystal structures of the H-bonded building blocks  $[\text{Ni}(\text{Hbim})_3]^-$ . (A) 0-D Dot structures in 1 formed from  $[\text{Ni}(\text{Hbim})_3]^-$  [ball and stick representation of Hbim<sup>-</sup> ligands (red) and nickel ions (magenta) along the *c* axis]. The orange ball-and-stick lines and the green spheres are shown for the  $\text{NMe}_4^+$  and water molecules, respectively. (B) 1-D Zigzag ribbons in 2 formed from  $[\text{Ni}(\text{Hbim})_3]^-$  along the *c* axis. The orange and the green ball-and-stick lines are shown for the  $\text{N}^n\text{Pr}_4^+$  ions and methanol molecules, respectively. (C) Double channel structures built up by 2-D honeycomb sheets in 3 formed from  $[\text{Ni}(\text{Hbim})_3]^-$ . The inner channels in 3 are constructed by  $\text{K}^+$ -crown ether complexes [the ball-and-stick representations of  $\text{K}^+$  ions (orange spheres) and crown ethers (green ball-and-stick lines) and the outer channels are constructed by  $[\text{Ni}(\text{Hbim})_3]^-$  to form a microporous crystal]. (D) 2-D Expanded honeycomb sheet structure in 4 with  $[\text{Ni}(\text{Hbim})_3]^-$  along the *a* axis. The free neutral  $\text{H}_2\text{bim}$  ligands connect 1-D zigzag-ribbon arrays by complementary H-bonding to form an expanded 2-D sheet structure along the *bc* plane. The orange ball-and-stick lines represent  $\text{NEt}_4^+$  ions.

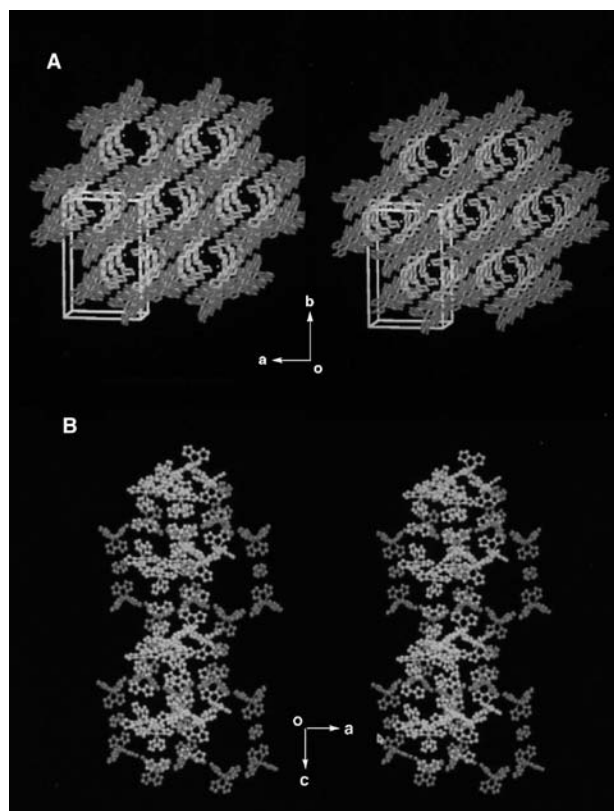


**Fig. 3** (A) A perspective stereo view of a microporous structure with a double channel formed by both  $[\text{Ni}(\text{Hbim})_3]^-$  and  $\text{K}^+$ -crown ether complexes for 3. (B) A portion of the 3-D polycatenate network for 4: red and yellow lines represent the different 2-D expanded honeycomb sheets formed from  $[\text{Ni}(\text{Hbim})_3]^-$ . The stacking honeycomb sheets in red interlock with the other stacking honeycomb sheets with a perpendicular orientation in yellow to generate a double-interlocking polycatenate structure.

zigzag ribbons are connected to each other by the remaining H-bonding site to form the 2-D honeycomb sheets along the  $ab$  plane by the alternate arrangement of  $\Delta$  and  $\Lambda$  optical isomers of the six  $[\text{Ni}(\text{Hbim})_3]^-$ . The 2-D sheet stacks along the  $c$  axis to produce the outer channel structures, which are built up by a sequence of the same optical isomers. While 4 takes an interest in the controlled self-organization of 3-D complicated superstructures for supramolecular chemistry.<sup>[25]</sup> The inner channels are formed by stacking of two  $[\text{K-DCH}(18\text{-crown-6})]^+$  cations facing each other along the  $c$  axis. The channel contains methanol and water molecules with H-bondings. The framework structure of 4 has four structural characteristics. First, this has a 1-D zigzag ribbon structure similar to that with 2. Second, free neutral  $\text{H}_2\text{bim}$  ligands connect 1-D ribbon arrays by complementary H-bondings to form an expanded 2-D honeycomb sheet structure along the  $bc$  plane. Third, the honeycomb sheets interpenetrate the other

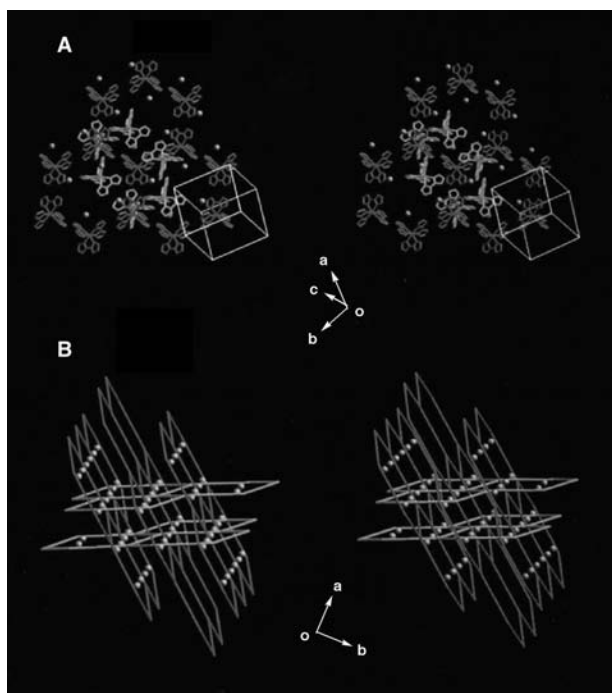
honeycomb sheets having the perpendicular orientation to construct a double interlocking catenate structure. Finally, the catenated structure is arranged in 3-D to form an infinite interlocking cross-catenated structure.

### Toward Complicated Crystal Structure

A major goal of the field of crystal engineering is to control rationally the assembly of 3-D arrays using intermolecular interactions and specific molecular topologies. We have found that the  $\text{Cs}^+$  ion can be used as a new tool to manipulate an H-bonded superstructure built with the  $[\text{Ni}(\text{Hbim})_3]^-$ . Two of the three  $\text{Hbim}^-$  in the  $[\text{Ni}(\text{Hbim})_3]^-$  can be bound to a  $\text{Cs}^+$  ion in crystal 5 by an electrostatic  $\pi$ -bonding interaction, which is not possible for other stable alkali metal ions. Furthermore, a more complicated 3-D superstructure of the double-helical racemate was formed in crystal 6 by cooperative application of an organic cation and the  $\text{Cs}^+$  interaction.

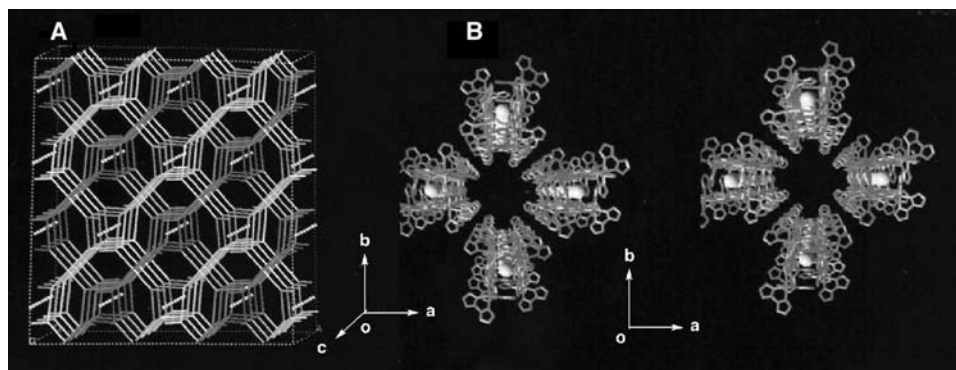
Superstructures with many 3-D frameworks have been created in different crystals by a self-assembly process. Most of the 3-D frameworks were developed by employing various topological building blocks as coordination polymers<sup>[26]</sup> and as H-bonding polymers.<sup>[27]</sup> However, the cooperative construction of 3-D arrays using both the weak H-bonding and coordination interactions has rarely been achieved to date.<sup>[28,29]</sup> We explore the effects of alkali metal ions, as well as organic cations, on superstructures formed by  $[\text{Ni}(\text{Hbim})_3]^-$ . Generally, alkali metal ions with a large polarizability can coordinate to aromatic rings in a multi-haptic mode.<sup>[30]</sup> Of all the stable alkali metal cations (i.e.,  $\text{Li}^+$ ,  $\text{Na}^+$ ,  $\text{K}^+$ ,  $\text{Rb}^+$ , and  $\text{Cs}^+$ ), only the  $\text{Cs}^+$  ion was found to have a rational electrostatic interaction with  $[\text{Ni}(\text{Hbim})_3]^-$ . We have prepared not only a 3-D double interlocking polycatenate superstructure of interpenetrated 2-D honeycomb sheets by using such a  $\text{Cs}^+$  interaction, but also a double-helical 3-D racemate with (10,3)- $a$  nets by using the cooperative interactions between organic cations and  $\text{Cs}^+$ .<sup>[31]</sup>

Fig. 4A shows a fragment structure of  $\{\text{Cs}[\text{Ni}(\text{Hbim})_3]\}_n$  in 5 formed from the interaction of the  $\Delta$  and  $\Lambda$  optical isomers of  $[\text{Ni}(\text{Hbim})_3]^-$  with  $\text{Cs}^+$  as counterions. The three  $\text{Hbim}^-$  ligands in  $[\text{Ni}(\text{Hbim})_3]^-$  are involved in H-bonding interactions forming a 2-D honeycomb sheet with (6,3) nets. Four  $\text{Cs}^+$  ions are located in each hexagonal cavity of the sheet constructed by six  $[\text{Ni}(\text{Hbim})_3]^-$ , and fix the two interpenetrating rods of the other two sheets at an inclination of  $\sim 70^\circ$  to create a 3-D polycatenate superstructure with a double interlocking interpenetration [Fig. 4B]. Electrostatic interaction between  $\text{Cs}^+$  and



**Fig. 4** (A) The stereo view shows two interlocked honeycomb sheets (red and blue) that are linked to each other by Cs<sup>+</sup> ions. The blue and red sheets were built up by alternate linkage between the optical isomers ( $\Lambda$  and  $\Delta$ ) of  $[\text{Ni}(\text{Hbim})_3]^-$ . Four Cs<sup>+</sup> ions (green spots) are present in each hexagon-cavity formed by the six building blocks. (B) The stereo view shows the whole structure of 4 (red and light blue lines) with the shortest Ni–Ni bonds. The green spots represent Cs<sup>+</sup> ions. The main honeycomb sheet framework forms a twofold interpenetration with (6,3) nets, and as a whole they form a double-interlocking polycatenate structure.

the two different optical isomers of  $[\text{Ni}(\text{Hbim})_3]^-$  forms a 1-D alternative coordination polymer with the general formula  $\{(\Delta)\text{-Cs}[\text{Ni}(\text{Hbim})_3]\text{-}(\Lambda)\text{-Cs}[\text{Ni}(\text{Hbim})_3]\}_n$ . Each  $\Delta$  or  $\Lambda$  optical isomer fixed by two Cs<sup>+</sup> ions participates in the formation of a different interpenetrating sheet, respectively. Such a 3-D double interlocking interpenetration based on  $[\text{Ni}(\text{Hbim})_3]^-$  has already been prepared by 4 using an organic  $\text{NEt}_4^+$  ion. Moreover, an organic cation can work cooperatively with Cs<sup>+</sup> to manipulate the new superstructure formed in the crystal. The addition of  $\text{N}''\text{Pr}_4^+$  ion led 6 with the general formula  $\{\text{Cs}[\text{Ni}(\text{Hbim})_3]_2(\text{N}''\text{Pr}_4^+) \cdot \text{MeOH}\}_n$  to form a 3-D double-helical structure of racemate (10,3)-*a* nets having a 1-D column of Cs<sup>+</sup> in the center (Fig. 5A). The columns of Cs<sup>+</sup> in the 4<sub>1</sub> double helices lie along the *c* axis with Cs–Cs distances of 8.60 and 8.14 Å. The networks of 6 are composed of the  $\Delta$ – $\Delta$  and  $\Lambda$ – $\Lambda$  dimers with the same optical isomer of  $[\text{Ni}(\text{Hbim})_3]^-$  linked by one Cs<sup>+</sup> ion. In other words, each 4<sub>1</sub> strand in the helix is formed by using only one optical isomer of  $[\text{Ni}(\text{Hbim})_3]^-$ . Furthermore, each helix is H-bonded to four other identical optical isomers by using the Hbim<sup>−</sup> moiety. The 3-D H-bonded network forms an 8<sub>7</sub> chiral double helix with large cavities (Fig. 5B). The entire racemate structure is created by combining the 4<sub>1</sub> helices into an opposite-handed 8<sub>7</sub> helical structure. The superstructure formation of 6 can be attributed to the cooperative use of  $\text{N}''\text{Pr}_4^+$  and Cs<sup>+</sup> cations. The  $\text{N}''\text{Pr}_4^+$  ions occupy the void spaces created by the interpenetration of each independent chiral 3-D net with  $\Delta$  or  $\Lambda$  isomers of  $[\text{Ni}(\text{Hbim})_3]^-$ . The use of other alkali metals with  $\text{N}''\text{Pr}_4^+$  produces only 1-D zigzag ribbons within 2.



**Fig. 5** (A) A perspective view along the *c* axis showing the whole network with (10,3)-*a* nets of 5. The shortest Ni–Ni distances of  $\Lambda$  isomers (red and yellow) and  $\Delta$  isomers (blue and light blue) of  $[\text{Ni}(\text{Hbim})_3]^-$  are shown. Green spots represent Cs<sup>+</sup> ions. They are constructed from each homochiral trinuclear unit with two  $\Delta$ -isomers or two  $\Lambda$ -isomers of  $[\text{Ni}(\text{Hbim})_3]^-$  bound by Cs (I) ions. (B) The perspective stereo view along the *c* axis is shown for a larger right-handed 8<sub>7</sub> helix constructed from four smaller right-handed 4<sub>1</sub> helices.



The large ionic radius and high polarizability of  $\text{Cs}^+$  ions are important in the formation of this new, more complicated structure. It is believed that the  $\text{Cs}^+$  ion is bound to the deprotonated imidazole site of the  $\text{Hbim}^-$  ligand by using electrostatic  $\pi$ -interactions in both 5 and 6. The binding distances range from 3.188(10) to 3.62(1) Å for the Cs–C bond and 3.323(10) to 3.607(8) Å for the Cs–N bond for 5, and 3.368(6) to 3.565(7) Å (Cs–C) and 3.342(5) to 3.643(6) Å (Cs–N) for 6. It is also believed that the crystal structures presented are the first where the structure was formed from an interaction between a  $\text{Cs}^+$  ion and an imidazole ring. The bond distances found in 5 and 6 are similar to those in different complexes.<sup>[32–34]</sup> This clearly has shown that an electrostatic  $\pi$ -bonding interaction can form between a  $\text{Cs}^+$  ion and an imidazole ring in  $[\text{Ni}(\text{Hbim})_3]^-$ . Furthermore, when  $\text{Cs}^+$  and  $\text{N}^{\text{Pr}}_4^+$  were used at the same time, an intricate 3-D racemate structure with (10,3)-*a* nets was formed by the  $4_1$  double helices wrapping around a 1-D column of  $\text{Cs}^+$  ions. Finally, the current work may possibly be a general route to the formation of 2-D and helical structures by controlling the assembly of only  $D_3$  symmetric building blocks with different optical activity.

## CONTROLLED CRYSTAL STRUCTURES BY NEUTRAL BIIMIDAZOLATE COMPLEX

We have tried to eliminate the counterion and create a new superstructure with an infinite chain without the effect of counterions on the assembly of metal complexes constructed from H-bonding dimer units such as Drawing 1. In this section, four types of self-organizing superstructures with infinite chains are identified by designing four neutral  $\text{Hbim}^-$  complexes with altered metal coordination spheres. As a result, we can systematically produce five types of preprogramming superstructures of a dimer (A), a linear chain (B), a zigzag ribbon (C), a honeycomb sheet (D), and a helical chain (E), respectively, as shown in Fig. 6.<sup>[35]</sup>

Classification of multidimensional superstructures has already been performed in organic compounds assembled by intermolecular H-bonding of carboxylic acid derivatives<sup>[36]</sup> as well as in coordination polymers by bridging ligands such as oxalate.<sup>[37–40]</sup> Carboxylic acid H-bonding- and oxalate coordination polymers have been rationally synthesized in a linear chain and a zigzag ribbon, a honeycomb sheet, and other 3-D superstructures. These superstructures afford the classification of the multiaggregation compounds that

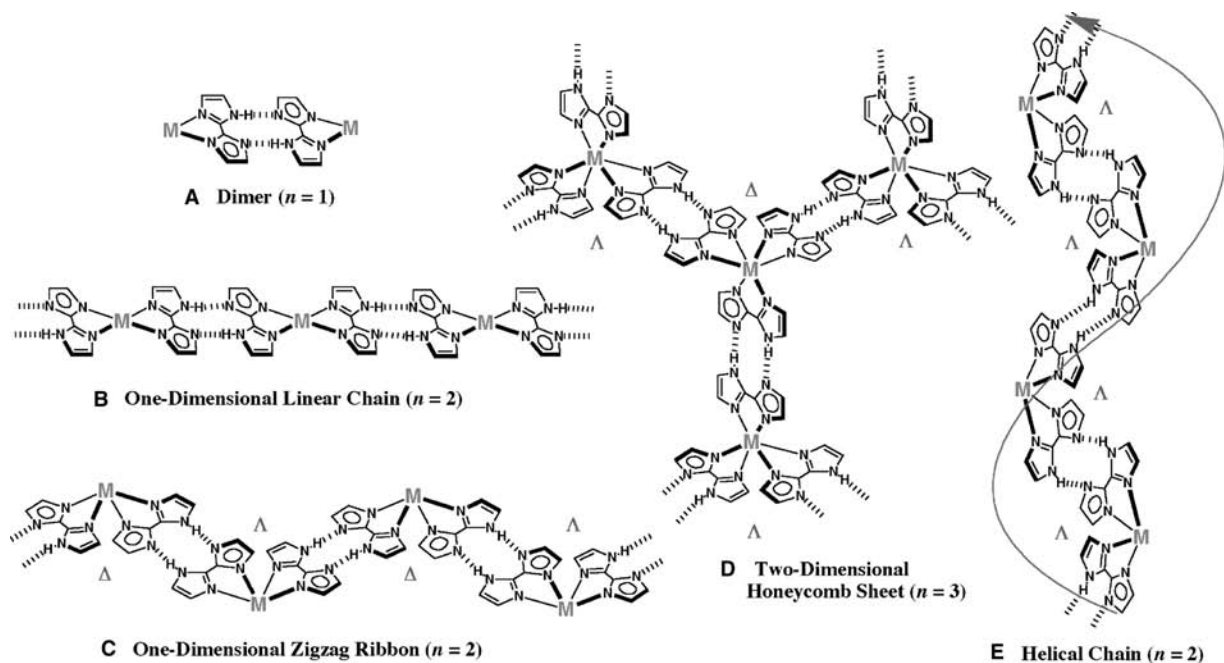


**Fig. 6** Schematic representations of multidimensional assemblies formed by transition-metal complexes with controlled configurations and regulated numbers of  $\text{Hbim}^-$  ligands: (A) “Zero-dimensional dimer” constructed by complementary intermolecular H-bonds between  $\text{Hbim}^-$  in the metal complexes coordinated by only one  $\text{Hbim}^-$  ligand. (B) “One-dimensional linear chain” assembled by the metal complexes with *trans*-configuration coordinated by at least two  $\text{Hbim}^-$  ligands. (C) “One-dimensional zigzag ribbon” assembled by metal complexes with two  $\text{Hbim}^-$  ligands in *cis*-configuration. (D) “Two-dimensional honeycomb sheet” linked by three intermolecular H-bonds between the metal complexes with three  $\text{Hbim}^-$  ligands. The sheet is constructed by H-bonding with alternate linkage between different optical isomers of  $\Delta$  and  $\Lambda$  types. (E) “Helical chain” assembled by intermolecular H-bonding between the same optical isomers of  $\Delta$  or  $\Lambda$  containing at least two  $\text{Hbim}^-$  ligands. The symbol *n* represents the number of  $\text{Hbim}^-$  ligands coordinated to transition metal ions.



consist only of H-bonds or coordination bonds. Here we have established a new categorical classification of the superstructures generated by the simultaneous use of both complementary intermolecular H-bondings and stable coordination bondings.

The H-bonded dimer unit through the  $\text{Hbim}^{-1}$  ligands has been assembled securely and strongly by using neutral complexes containing  $\text{Hbim}^{-1}$  (Drawing 1). For example, the previously reported neutral  $[\text{Cu}^{\text{II}}(\text{Hbim})(\text{SalenNMe}_2)]$  formed an H-bonded dimer of type A. In contrast, the positively charged  $[\text{Cu}^{\text{II}}(\text{Hbim})(\text{taccn})]^+$  formed an intermolecular H-bonding interaction with  $\text{ClO}_4^-$  counteranion in preference to self-complementary  $\text{NH}\cdots\text{N}$  H-bonding interaction between  $\text{Hbim}^{-1}$  ligands.<sup>[41]</sup> It suggests that the counterions, in particular, the anions with strong H-bonding ability in the ionic complexes, interrupt the formation of the dimer unit. Although counteranions such as alkyl ammonium ions in the crystal with the  $[\text{Ni}(\text{Hbim})_3]$  have an effect on the superstructures, they do not perturb the complementary H-bondings. Thus these facts indicate that there is no chance of interruption of self-complementary ligand–ligand interactions because of sterically demanding bulky cations and the preferential H-bonding between  $\text{Hbim}^{-1}$  ligands of anion complexes. From this point, in order to develop the effective self-organization of superstructures, neutral complexes rather than charged ones should be used.

Fig. 7 shows a superstructure with 1-D linear chains of type B in crystal 7 constructed by neutral  $[\text{Ni}^{\text{II}}(\text{Hbim})_2(\text{tBupy})_2]$  ( $\text{tBupy} = 4\text{-tert-butyl pyridine}$ ) with a *trans* configuration. The blue single crystals of it are obtained from a basic methanol solution by simple one-pot self-organization with  $\text{Ni}^{\text{II}}$  ions,  $\text{Hbim}^{-1}$ , and  $\text{tBupy}$ . The chain in the crystal along the *a* axis is composed of infinite links of intermolecular H-bonds of two  $\text{Hbim}^{-1}$  ligands, located in *equatorial* positions on the distorted octahedron (the range of  $\text{NH}\cdots\text{N}$  distances: 2.80–2.82 Å). The two *axial* positions are occupied by two monodentate  $\text{tBupy}$  ligands. Each

chain is piled along the *b* axis to form stacking sheets in the *ac* plane while fitting each  $\text{tBupy}$  group into the space between the chains. On the other hand, formation of the 1-D linear chains can be altered to that of 1-D zigzag ribbons by changing the direction of intermolecular H-bonding sites in the building blocks. Fig. 8 shows the zigzag ribbon of type C in crystal 8 constructed by  $[\text{Ni}^{\text{II}}(\text{Hbim})_2(\text{bpy})]$  with the bpy (= 2,2'-bipyridine) ligand. The pale orange crystals of  $[\text{Ni}^{\text{II}}(\text{Hbim})_2(\text{bpy})]$  are obtained by the same synthetic method of  $[\text{Ni}^{\text{II}}(\text{Hbim})_2(\text{tBupy})_2]$  except for the use of bidentate bpy instead of  $\text{tBupy}$ . The zigzag ribbon consists of 1-D ordered arrays along the *b* axis formed by alternative H-bondings between different optical isomers of  $\Delta$  and  $\Lambda$  of  $[\text{Ni}^{\text{II}}(\text{Hbim})_2(\text{bpy})]$ . Two  $\text{Hbim}^{-1}$  ligands of  $[\text{Ni}^{\text{II}}(\text{Hbim})_2(\text{bpy})]$  are used to form the H-bonded zigzag-ribbon networks, but a coordinated bpy does not participate in the formation of the networks (the range of  $\text{NH}\cdots\text{N}$  distances: 2.78–2.83 Å). Each bpy residue on the zigzag ribbon is aligned standing alternately parallel to each other and perpendicular to the 1-D main chains. Thus we have demonstrated that we can control linear vs. zigzag 1-D networks by using monodentate and bidentate ligands, respectively.

As shown in Fig. 9A, a neutral racemic complex of  $[\text{Ru}^{\text{III}}(\text{Hbim})_3]$  with  $D_3$  symmetry forms a 2-D honeycomb sheet of type D in crystal 9 with (6,3) nets. Compound  $[\text{Ru}^{\text{III}}(\text{Hbim})_3]$  is prepared from the precursor complex  $[\text{Ru}^{\text{II}}(\text{H}_2\text{bim})_3]^{2+}$  and the desired dark blue single crystals are crystallized from a methanol solution.<sup>[42]</sup> All the three  $\text{Hbim}^{-1}$  sites of  $[\text{Ru}^{\text{III}}(\text{Hbim})_3]$  form the complementary intermolecular H-bonds completely. The honeycomb sheet self-organized by  $[\text{Ru}^{\text{III}}(\text{Hbim})_3]$  is constructed by using alternative H-bondings between optical isomers of  $\Delta$  and  $\Lambda$  types of  $[\text{Ru}^{\text{III}}(\text{Hbim})_3]$  (the range of  $\text{NH}\cdots\text{N}$  distances: 2.79–2.80 Å). Each sheet forms an infinite number of identical sheets and passes each hexagonal cavity created by six  $[\text{Ru}^{\text{III}}(\text{Hbim})_3]$  units through the two interpenetrating rods of the other two sheets at

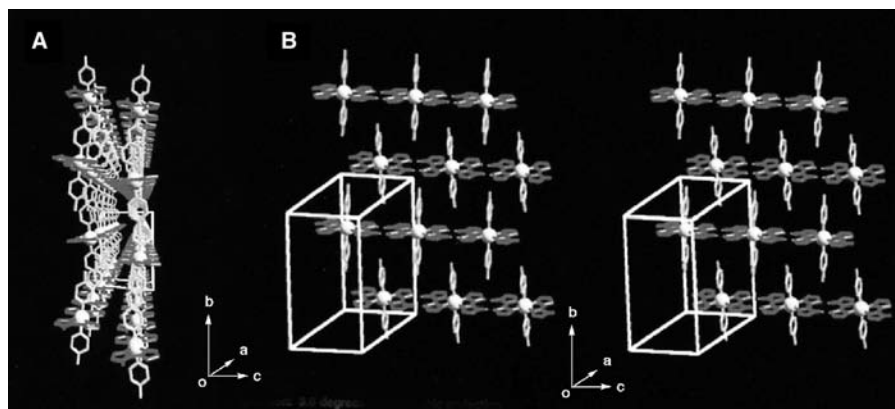


**Fig. 7** Arrangement of one-dimensional linear chains in a crystal formed by 7. Three  $\text{CH}_3$  groups containing  $\text{tBupy}$  are omitted for clarity. (A) A perspective view of one-dimensional linear chains linked along the *a* axis and piled along the *b* axis (color coding:  $\text{Hbim}^{-1}$  is shown in red,  $\text{Ni}^{2+}$  green, and  $\text{tBupy}$  blue). (B) A perspective stereo view of linear chains, as viewed along the *a* axis.

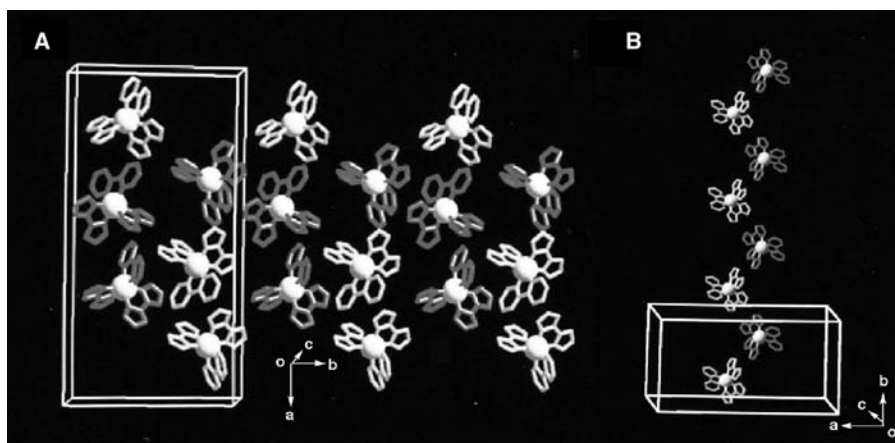


**Fig. 8** Arrangement of one-dimensional zigzag ribbons in a crystal formed by 8. (A) A zigzag ribbon structure is formed by alternate linkage between different optical isomers of  $\Delta$  (red) and  $\Lambda$  (blue) types along the  $b$  axis (nickel ions shown in green). The zigzag ribbons are stacked along the  $a$  axis. (B) A single chain of a one-dimensional zigzag ribbon is represented along the  $b$  axis.

an inclination of  $\sim 70^\circ$  to give a 3-D polycatenate structure with a double interlocking interpenetration in 9 (Fig. 9B). The two chiral building blocks of  $\Lambda$ -[Co<sup>III</sup>(Hbim)<sub>3</sub>] and  $\Delta$ -[Co<sup>III</sup>(Hbim)<sub>3</sub>] form 1-D helical chains of type E with a right-handed (for crystal 10) (Fig. 10A and C represented by red) and a

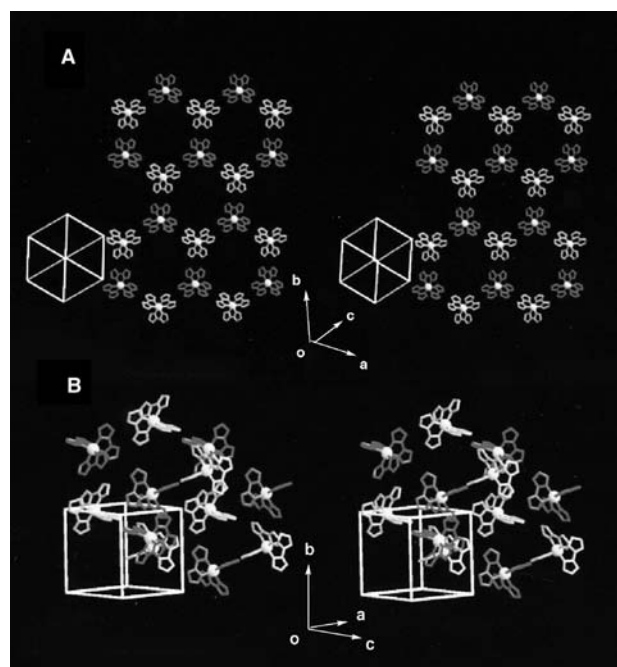


**Fig. 9** Arrangement of two-dimensional honeycomb sheets in a crystal formed by 9 (stereo view). (A) A two-dimensional honeycomb sheet is formed by alternate linkage between different optical isomers of  $\Delta$  (blue) and  $\Lambda$  (red) types (Ru<sup>3+</sup> ions are shown as magenta spheres). The sheet is constructed by complete H-bonds on three Hbim<sup>-1</sup> sites of 9. (B) The crystal structure of the single polycatenate network for the crystal of 9. Double-interlocking interpenetrations with the polycatenate structure are formed by two sets of stacked honeycomb sheets that are nearly perpendicular to each other in three dimensions.

left-handed (for crystal 11) (Fig. 10B and D represented by light blue) orientation, respectively. The red single crystals 10 and 11 of  $\Lambda$ - and  $\Delta$ -[Co<sup>III</sup>(Hbim)<sub>3</sub>] are crystallized from 2-propanol by the deprotonation reaction of the optically resolved  $\Lambda$ - and  $\Delta$ -[Co<sup>III</sup>(H<sub>2</sub>bim)<sub>3</sub>](NO<sub>3</sub>)<sub>3</sub> precursor complexes, respectively.<sup>[43]</sup> Each 1-D helical chain is constructed by employing intermolecular H-bonds between the same optical isomers, which utilize two of three Hbim<sup>-1</sup> sites in  $\Lambda$ - or  $\Delta$ -[Co<sup>III</sup>(Hbim)<sub>3</sub>]. Both helical chains form 4<sub>1</sub> single strands, which have a pitch of ca. 33.4 Å similar to that of the B-DNA double strand. Another residual Hbim<sup>-1</sup> site of  $\Delta$ - and  $\Lambda$ -[Co<sup>III</sup>(Hbim)<sub>3</sub>] is blocked by H-bonds with 2-propanol of crystallization, without using the helical chain construction.

In the case of superstructures on 10 and 11 using all of three sites, a 3-D chiral network with larger porous spaces formed by 8<sub>7</sub> cavities of (10,3)- $a$  nets like 6 would be expected to be constructed as found in the crystal with [Ni(Hbim)<sub>3</sub>]<sup>-1</sup>, which has the structure reinforced by a twofold interpenetration and stable double helical structures. In contrast, 10 and 11 do not have any larger porous networks. It has not been obvious to date why large cavities are not constructed by (10,3)- $a$  single networks, although two factors, solvent effect and the strength of the H-bonds formed, are anticipated. Öhrstrom and Larsson have shown lately the (10,3)- $a$  nets based on single helical H-bonding networks formed from both building blocks of  $\Delta$ - and  $\Lambda$ -[Co<sup>III</sup>(Hbim)<sub>3</sub>] by using a solvent effect with DMF/H<sub>2</sub>O mixed solvent.<sup>[44]</sup> Here the two superstructures of a honeycomb sheet and a helical strand built from tris-2,2'-biimidazolate complexes with  $D_3$  symmetry can be individually prepared by using a racemic compound and an optically resolved ones, respectively.

In summary, we demonstrated the practical structures of A–E in Fig. 6 based on the relationships between specified molecular arrays and molecular building blocks, and identified the four types of new

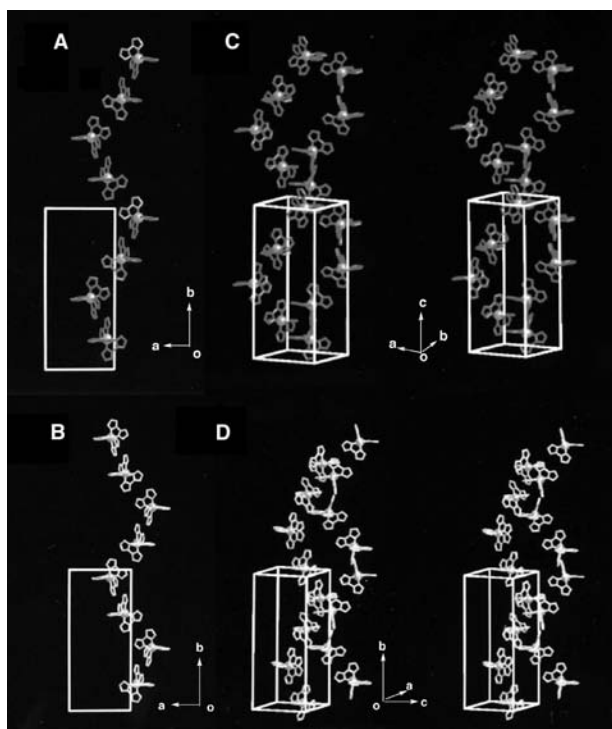


**Fig. 10** Arrangement of helical chains in a crystal formed by 10 or 11 ( $\text{Co}^{3+}$  ions are shown as yellow spheres): (A) and (B) View of each helical chain is represented by the right-handed helix formed by  $\Lambda$ -isomers of 10 in red and the left-handed helix by  $\Delta$ -isomers of 11 in light-blue along the  $c$  axis. (C) Stereo view of two right-handed single helices made up of  $\Lambda$ -isomers 10 (red). The two single helices do not intersect each other and do not form a double helix. (D) Stereo view of two left-handed single helices made up of  $\Delta$ -isomers of 11 (light blue).

superstructures, B–E, by X-ray analysis. The knowledge from structural data should help provide the preprogramming of new superstructures built from the “neutral”  $\text{Hbim}^{-1}$  complexes. Thus we have recently found that the neutral complexes with some  $\text{Hbim}^{-1}$  ligands can control the preprogramming superstructures in multidimensionality by using configurations around the coordination sphere, as there is no chance of interruption of self-complementary ligand–ligand interactions because of sterically demanding bulky cations and the preferential H-bonding between  $\text{Hbim}^{-1}$  ligands of anion complexes.

## CONCLUSION

Crystal engineering techniques using those functionalized molecular building blocks will be utilized in future studies for the creation of new solid-state materials. Thus the building blocks in Fig. 6 would produce the functionalized preprogramming superstructures

by introducing additive ligands with physical properties such as magnetic and photoactive ones to other coordination sites on the arrays of A, B, C, and E. We are now attempting to develop functional solid-state materials using these techniques. Our further study will be aimed at finding the mutual relationship between H-bonded superstructures of  $[\text{Ni}(\text{Hbim})_3]^-$  and the kinds or shapes of their component counter-cations. Thus cations play an important role in predicting the crystal structures and rationalizing the crystal structure engineering in these systems. In addition, the introduction of paramagnetic metal ions and transition metal chromophores into the system of the H-bonding extended arrays may lead to the creation of a new material with interesting magnetic and electronic properties.

## ACKNOWLEDGMENTS

This work was supported by a Grant-in-Aid for Scientific Research (Nos. 13440201 and 10146103) on Priority Areas from the Ministry of Education, Science, and Culture, Japan. The authors thank the Analytical Center in Osaka City University, for use of a single-crystal X-ray diffractometer and elemental analyses. I would like to thank Prof. Kazuhiro Nakasuji of the Graduate School of Science of Osaka University for the useful discussion of this manuscript.

## REFERENCES

1. Batten, S.R.; Robson, R. Interpenetrating nets: Ordered, periodic entanglement. *Angew. Chem., Int. Ed. Engl.* **1998**, *37*, 1460.
2. Zaworotko, M.J. Superstructural diversity in two dimensions: Crystal engineering of laminated solids. *Chem. Commun.* **2001**, 1.
3. Va idhyathan, R.; Natarajan, S.; Rao, C.N. Synthesis of a hierarchy of zinc oxalate structures from amine oxalates. *Dalton* **2001**, 699.
4. Kitagawa, S.; Kondo, M. Functional micropore chemistry of crystalline metal complex-assembled compound. *Bull. Chem. Soc. Jpn.* **1998**, *71*, 1739.
5. Holman, K.T.; Pivovar, A.M.; Swift, J.A.; Ward, M.D. Metric engineering of soft molecular host frameworks. *Acc. Chem. Res.* **2001**, *34*, 107.
6. Sherrington, D.C.; Taskinen, K.A. Self-assembly in synthetic macromolecular synthons via multiple hydrogen bonding interactions. *Chem. Soc. Rev.* **2001**, *30*, 83.
7. Desiraju, G.R. Supramolecular synthons in crystal engineering—A new organic synthesis. *Angew. Chem., Int. Ed. Engl.* **1995**, *34*, 2311.
8. Desiraju, G.R. Hydrogen bonds and other intermolecular interactions in organometallic crystals. *Dalton* **2000**, 3745.

9. Oda, R.; Huc, I.; Schmutz, M.; Candau, S.J.; MacKintosh, F.C. Tuning bilayer twist using chiral counterions. *Nature* **1999**, *399*, 566.
10. Cai, C.; Müller, B.; Weckesser, J.; Barth, J.V.; Tao, Y.; Bösch, M.M.; Kündig, A.; Bosshard, C.; Biaggio, I.; Günter, P. Model for in-plane directional ordering of organic thin films by oblique incidence organic molecular beam deposition. *Adv. Mater.* **1999**, *11*, 750.
11. Höger, S.; Bonrad, K.; Mourran, A.; Beginn, U.; Möller, M. Synthesis, aggregation, and adsorption phenomena of shape-persistent macrocycles with extra-annular polyalkyl substituents. *J. Am. Chem. Soc.* **2001**, *123*, 5651.
12. Fujita, M.; Umemoto, K.; Yoshizawa, M.; Fujita, N.; Kusakawa, T.; Biradha, K. Molecular paneling via coordination. *Chem. Commun.* **2001**, 509.
13. Joachim, C.; Gimzewski, J.K.; Aviram, A. Electronics using hybrid-molecular and mono-molecular devices. *Nature* **2000**, *408*, 541.
14. Burrows, A.D.; Chan, C.-W.; Chowdhry, M.M.; McGrady, J.E.; Mingos, D.M.P. Multi-dimensional crystal engineering of bifunctional metal complexes containing complementary triple hydrogen bonds. *Chem. Soc. Rev.* **1995**, *138*, 329.
15. Mitsumi, M.; Toyoda, J.; Nakasuji, K. Metal-pteridine complexes having three-dimensional hydrogen-bonded networks. *Inorg. Chem.* **1995**, *34*, 3367.
16. Wilton-Ely, J.D.E.T.; Schier, A.; Mitzel, N.W.; Schmidbaur, H. Structural diversity in gold(I) complexes of 4-sulfanylbenzoic acid. *Dalton* **2001**, 1058.
17. Yang, G.; Zhu, H.-G.; Ling, B.-H.; Chen, X.-M. Syntheses and crystal structures of four metal-organic co-ordination networks constructed from cadmium(II) thiocyanate and nicotinic acid derivatives with hydrogen bonds. *Dalton* **2001**, 580.
18. MacDonald, J.C.; Dorrestein, P.C.; Pilly, M.M.; Foote, M.M.; Lundburg, J.L.; Henning, R.W.; Schuitz, A.J.; Manson, J.L. Design of layered crystalline materials using coordination chemistry and hydrogen bonds. *J. Am. Chem. Soc.* **2000**, *122*, 11692.
19. Beatty, A.M. Hydrogen bonded networks of coordination complexes. *CrystEngComm* **2001**, *1*, 243.
20. Kaiser, S.W.; Saillant, R.B.; Butler, W.M.; Rasmussen, P.G. Rhodium and iridium complexes of biimidazole: 1. Mononuclear and dinuclear species. *Inorg. Chem.* **1976**, *15*, 2681.
21. Tadokoro, M.; Toyoda, J.; Isobe, K.; Itoh, T.; Miyazaki, A.; Enoki, T.; Nakasuji, K. Dimeric hydrogen-bonded transition metal complex containing bidentate mono-deprotonated 2,2'-biimidazole ligand. *Chem. Lett.* **1995**, 613.
22. Tadokoro, M.; Isobe, K.; Uekusa, H.; Ohashi, Y.; Toyoda, J.; Tashiro, K.; Nakasuji, K. Cation-dependent formation of superstructures by one-pot self-organization of hydrogen-bonded nickel complexes. *Angew. Chem. Int. Ed.* **1999**, *38*, 95.
23. Moore, J.S.; Lee, S. Molecular craft. *Chem. Ind.* **1994**, 556.
24. Rosi, N.L.; Eddaoudi, M.; Kim, J.; O'Keeffe, M.; Yaghi, O.M. Advances in the chemistry of metal-organic frameworks. *CrystEngComm* **2002**, *4*, 401.
25. Carlucci, L.; Ciani, G.; Proserpio, D.M.; Sironi, A.A. 1-, 2-, and 3-dimensional polymeric frames in the coordination chemistry of AgBF<sub>4</sub> with pyrazine. The first example of three interpenetrating 3-dimensional triconnected nets. *J. Am. Chem. Soc.* **1995**, *117*, 4562.
26. Munakata, M.; Wu, L.P.; Kuroda-Sowa, T. Toward the construction of functional solid-state supramolecular metal complexes containing copper(I) and silver(I). *Adv. Inorg. Chem.* **1999**, *46*, 173.
27. Aakeröy, C.B.; Seddon, K.R. The hydrogen bond and crystal engineering. *Chem. Soc. Rev.* **1993**, *26*, 397.
28. Chowdhry, M.M.; Mingos, D.M.P.; White, A.J.P.; Williams, D.J. Supramolecular self-assembly of a transition-metal-organo network based on simultaneous coordinate- and hydrogen bond interactions. *Chem. Commun.* **1996**, 899.
29. Munakata, M.; Wu, L.P.; Yamamoto, M.; Kuroda-Sowa, T.; Maekawa, M. Construction of three-dimensional supramolecular coordination copper(I) compounds with channel structures hosting a variety of anions by changing the hydrogen-bonding mode and distances. *J. Am. Chem. Soc.* **1996**, *118*, 3117.
30. Lambert, C.; Kaupp, M. "Inverted" sodium-lithium electronegativity: Polarity and metalation energies of organic and inorganic alkali-metal compounds. *Organometallics* **1993**, *12*, 853.
31. Tadokoro, M.; Shiomi, T.; Isobe, K.; Nakasuji, K. Caesium(I) mediated 3-D super-structures by one-pot self-organization of hydrogen-bonded nickel complexes. *Inorg. Chem.* **2001**, *40*, 5476.
32. Gregory, K.; Bremer, M.; Schleyer, P.R.; Klusener, P.A.A.; Brandsma, L. *N*-Cesio-carbazole·pmdta and *N*-potassio-carbazole·pmda (PMDA = *N,N,N',N',N''*-pentamethyl-diethylenetriamine). Cation size and multi-hapto bonding. *Angew. Chem., Int. Ed. Engl.* **1989**, *28*, 1224.
33. Harder, S.; Prosen, M.H. The heaviest alkali metallo-cene: Structure of an anionic cesocene triple-decker. *Angew. Chem., Int. Ed. Engl.* **1996**, *35*, 97.
34. Harrowfield, J.M.; Ogden, M.I.; Richmond, W.R.; White, A.H. Calixarene-cupped caesium: A coordination conundrum. *Chem. Commun.* **1991**, 1159.
35. Tadokoro, M.; Kanno, H.; Kitajima, T.; Umemoto, H.S.; Nakanishi, N.; Isobe, K.; Nakasuji, K. Self-organizing super-structures formed from hydrogen-bonded biimidazole metal complexes. *Proc. Natl. Acad. Sci. U. S. A.* **2002**, *99*, 4950.
36. Desiraju, G.R. Chemistry beyond the molecule. *Nature* **2001**, *412*, 397.
37. Coronado, E.; Galán-Mascarós, J.R.; Gomez-García, C.J.; Laukhin, V. Coexistence of ferromagnetism and metallic conductivity in a molecule-based layered compound. *Nature* **2000**, *408*, 447.
38. Bénard, S.; Yu, P.; Audié, J.P.; Rivière, E.; Clément, R.; Guilhem, J.; Tchertanov, L.; Nakatani, K. Structure and NLO properties of layered bimetallic oxalate-bridged ferromagnetic networks containing stilbazolium shaped chromophores. *J. Am. Chem. Soc.* **2000**, *122*, 9444.
39. Andrés, R.; Brissard, M.; Gruselle, M.; Train, C.; Vaissermann, J.; Malezieux, B.; Jamet, J.-P.; Verdager, M.

- Rational design of three-dimensional (3D) optically active molecule-based magnets: Synthesis, structure, optical and magnetic properties of  $\{[\text{Ru}(\text{bpy})_3]^{2+}, \text{ClO}_4^-, [\text{Mn}^{\text{II}}\Delta\text{Cr}^{\text{III}}(\text{ox})_3]^{-}\}_n$  and  $\{[\text{Ru}(\text{bpy})_2\text{ppy}]^+, [\text{Mn}^{\text{II}}\text{Cr}^{\text{III}}(\text{ox})_3]^{-}\}_n$ , with  $\text{M}^{\text{II}} = \text{Mn}^{\text{II}}, \text{Ni}^{\text{II}}$ . X-ray structure of  $\{[\Delta\text{Ru}(\text{bpy})_3]^{2+}, \text{ClO}_4^-, [\Delta(\text{Mn}^{\text{II}}\Delta\text{Cr}^{\text{III}}(\text{ox})_3)]^{-}\}_n$  and  $\{[\Delta\text{Ru}(\text{bpy})_2\text{ppy}]^+, [\Delta(\text{Mn}^{\text{II}}\Lambda^{\text{III}}(\text{ox})_3)]^{-}\}_n$ . *Inorg. Chem.* **2001**, *40*, 4633.
40. Decurtins, S.; Ferlay, S.; Pellax, R.; Gross, M.; Schmalte, H.; Veciana, N. *Supramolecular Engineering of Synthetic Metallic Materials—Conductors and Magnets*; Rovira, C., Amabilino, J.D., Eds.; B. Kluwer Academic Pub., 1999; 175 pp.
  41. Tadokoro, M.; Nakasuji, K. Hydrogen bonded 2,2'-biimidazolate transition metal complexes as a tool of crystal engineering. *Coord. Chem. Rev.* **2000**, *198*, 205.
  42. Rillema, P.; Sahai, R.; Matthews, P.; Edwards, A.K.; Shaver, R.J. Multimetallic ruthenium(II) complexes based on biimidazole and bibenzimidazole: Effect of dianionic bridging on redox and spectral properties. *Inorg. Chem.* **1990**, *29*, 167.
  43. Kanno, H.; Manriki, S.; Yamazaki, E.; Utsuno, S.; Fujita, J. Preparation and resolution of a series of cobalt(III) complexes containing 2,2'-biimidazole and ethylenediamine. *Bull. Chem. Soc. Jpn.* **1996**, *69*, 1981.
  44. Öhrstrom, L.; Larsson, K.; Borg, S.; Norberg, S.T. Crucial influence of solvent and chirality—The formation of helices and three-dimensional nets by hydrogen-bonded biimidazolate complexes. *Chem. Eur. J.* **2001**, *7*, 4805.



# Semiconductor Nanowires: Macroelectronics Applications

**Yugang Sun**

*Department of Materials Science and Engineering, University of Illinois at Urbana-Champaign, Urbana, Illinois, U.S.A.*

**John A. Rogers**

*Department of Materials Science and Engineering and Beckman Institute, University of Illinois at Urbana-Champaign, Urbana, Illinois, U.S.A.*

## INTRODUCTION

This entry briefly reviews preparation and assembly of inorganic semiconductor nanowires and their potential applications in macroelectronics. It is organized into four sections. The first summarizes approaches to generate semiconductor nanowires with controlled dimension, purity, crystallinity, and uniformity. The synthetic, “bottom-up” methods (i.e., growth of nanowires through assembly and crystallization of atoms of precursors) are compared with the complementary “top-down” processes (i.e., preparation of small objects on the nanometer scale by carving, slicing, or etching macroscale material sources). The second section outlines strategies for the formation of ensembles of aligned nanowires, including manipulation of nanowires in solutions with various external forces, in situ growth of aligned nanowires from patterned catalysts, and dry transfer printing of nanowire arrays generated from “top-down” processes. The third section discusses schemes for fabricating high-performance thin-film transistors (TFTs) on plastic substrates using thin films of aligned nanowires. Several examples of devices and their characteristics demonstrate the current state of the technology. The last section concludes with perspectives on the trends for future work related to flexible macroelectronics.

## BACKGROUND

Macroelectronics systems represent a new class of electronics that consist of integrated circuits on flexible substrates that have sizes much larger than those of conventional semiconductor wafers. The most closely related existing electronic technology is based on TFTs on large-area glass substrates of the type that are used to provide power, switching, computation, and communication for large-area displays (e.g., liquid-crystal-based devices), medical X-ray sensors,

and other systems.<sup>[1]</sup> Recent research developments in active sensory skin and electronic textiles, foldable and expandable antennas for military and space applications, etc., require flexible, lightweight, and low-cost substrates to support the associated electronics.<sup>[2]</sup> Polymeric plastics represent ideal classes of materials for these substrates: they are lightweight, rugged, low in cost, and can be processed in the form of continuous rolls. It is extremely challenging, however, to fabricate high-performance transistors using inorganic semiconductor materials on these unusual electronic substrates because they degrade at the high-temperature steps that are present in traditional microelectronics fabrication sequences. One solution of this problem is to perform high-temperature processing (e.g., preparation of semiconductor materials, annealing, implant activation, etc.) on platforms that can withstand high temperatures and then to do subsequent integration with the final plastic device substrates. For example, crystalline Si nanoparticles and quantum dots synthesized from solution-phase reactions at elevated temperatures can be spin cast on plastic sheets to form thin films that can then be used as semiconductor layers for TFTs patterned using traditional photolithography at relatively low temperatures.<sup>[3]</sup> The performance of transistors using nanoparticle-derived films as transport components, however, is relatively low in terms of carrier mobility due to high resistance boundaries between individual nanoparticles. On the other hand, one-dimensional semiconductor nanowires represent potential building blocks in which the transport from source electrode to drain electrode can occur without interruption through the crystalline semiconductor.<sup>[4]</sup> Furthermore, thin films composed of nanowires can survive relatively high strain (i.e., they are mechanically flexible) because of their small thicknesses.<sup>[5]</sup> Conceptually, carbon nanotubes fall into this class of nanowire-based macroelectronics. These materials, which are beginning to show considerable promise for these applications,<sup>[6–9]</sup> will not be covered here.



## PREPARATION OF SEMICONDUCTOR NANOWIRES

Nanowires made of inorganic semiconducting materials are of considerable interest due to their unique properties and potential applications.<sup>[10,11]</sup> For instance, semiconductor nanowires with lateral dimensions less than 15 nm exhibit band gaps in the ultraviolet (UV) and visible regions of light.<sup>[12]</sup> In addition, nanowires of single-crystalline inorganic semiconductors show excellent transport properties of electrons and holes.<sup>[4,13]</sup> As a result, they offer great promise for electronic and optoelectronic devices with interesting properties. A range of approaches have been developed to generate nanowires of various materials (e.g., Si, Ge, III–V compounds, II–VI compounds, and oxides). The techniques can be classified into two general categories, i.e., “bottom-up” and “top-down” approaches.

### “Bottom-Up” Approaches

Atoms of semiconductor materials can crystallize and grow into nanowires in both gaseous and liquid media by controlling reaction conditions. Because a large number of publications have reviewed these techniques for semiconductor materials,<sup>[14–17]</sup> this entry only summarizes the principles of some of these approaches. Among all vapor-based methods, the vapor–liquid–solid (VLS) process, originally developed by Wagner and Ellis, seems to be the most successful and widely used method for generating single crystal nanowires in large quantities.<sup>[18]</sup> The results demonstrated by Lieber, Yang, and many other research groups confirm that the VLS process starts with the dissolution of vapors of target materials into nanosized liquid droplets of a metal catalyst (e.g., Au), followed by nucleation and growth of single-crystalline wires. The liquid droplets are generated from metal nanoparticles at elevated temperatures; their size determines the diameter of wires. The vapor, which can be generated by laser ablation<sup>[19]</sup> or thermal decomposition of organometallic compounds,<sup>[20]</sup> determines the composition of the wires. In a typical setup, target materials (e.g., InP, CdS, and Si) and silicon substrates covered with gold nanoparticles (serving as catalysts) lie at the upstream end and central part of a tube furnace, respectively. The substrate is heated to high temperature of 600–1200°C while the temperature of target material remains room temperature. A pulsed laser ablates the target to generate a vapor, which transports, through a flow of argon, to the surface of the substrate. This vapor dissolves in the droplets of catalyst until the catalyst is supersaturated with material from the target. At this point, the vapor condenses into nanowires through the VLS process.<sup>[21]</sup> This method

has, in principle, the ability to synthesize nanowires of most semiconductor materials that can be evaporated by tuning the parameters (e.g., power, wavelength and pulse width) of the laser. The size of the catalyst droplets controls the diameter of nanowires. The growth time and ablation conditions control the length of the nanowires.<sup>[22]</sup>

By combining nanoparticles of metals (e.g., In, Ga, or Bi) with low melting points as catalysts with thermal decomposition of organometallic precursors, an analog of VLS process can be extended to liquid phase. This process, so-called solution–liquid–solid process, or SLS, has been pioneered by Buhro and coworkers to synthesize nanowires made of III–V compounds.<sup>[23,24]</sup> For example, nanowires of GaAs and InP with small diameters (e.g., 3–17 nm) and relatively narrow diameter distributions were synthesized by refluxing 1,3-diisopropylbenzene solutions of corresponding precursors (i.e.,  $(^t\text{Bu})_3\text{Ga}$  and  $\text{As}(\text{SiMe}_3)_3$  for GaAs, and  $[\text{Me}_2\text{InP}(\text{SiMe}_3)_2]_2$  for InP) in the presence of In nanoparticles. The SLS process is mainly limited by the availability of suitable organometallic precursors. Also, nanowires synthesized via “bottom-up” approaches always have broad distributions in both lateral and longitudinal dimensions. Furthermore, lengths greater than 100  $\mu\text{m}$  are difficult to achieve. Their surface properties, compositional purity, doping uniformity, and concentration, which all strongly influence their electrical properties, are less well defined than those of the single-crystalline wafers used in the semiconductor industry.

### “Top-Down” Approaches

Microwires and nanowires can be fabricated from bulk wafers via “top-down” approaches. These types of nanowires have well-controlled doping levels, dimensions and crystallinity, which, in turn, give them excellent electrical properties for applications in high-performance electronics. The critical step involved in “top-down” approaches is to generate patterned mask lines on the nanometer scale, using simple lithographic techniques such as phase-shift photolithography with soft-phase masks made of poly(dimethylsiloxane) (PDMS) or nanoimprinting.<sup>[25–27]</sup> For example, Si nanowires have been fabricated from multi-layered wafers (i.e., silicon-on-insulator, or SOI wafers) through the near-field optical lithography.<sup>[28]</sup> In this case, exposing photoresist on an SOI wafer through an elastomeric phase mask, which forms a conformal contact with the layer of photoresist, generates patterned lines with widths ranging from 50 to 300 nm. The features patterned in the photoresist film can be transferred onto the underlying wafer using reactive-ion etching or wet-etching of the top Si layer. After

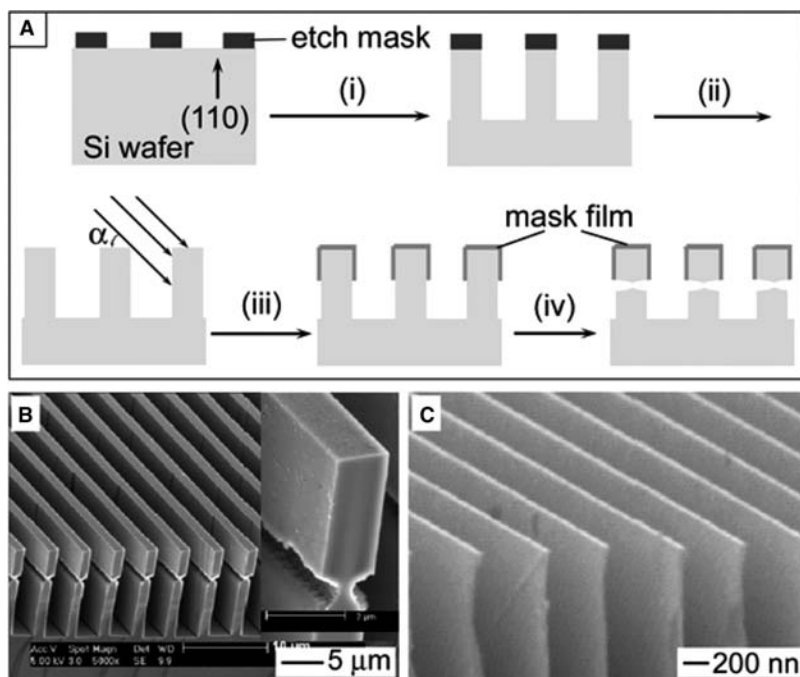


**Fig. 1** Formation of Si wires from a (110) Si wafer. (A) Steps of the fabrication process: (i) anisotropic chemical etching of Si in hot KOH solution using nitride or oxide mask stripes; (ii) removal of mask stripes; (iii) shadow deposition of new mask material on the top and side surfaces of each vertical wall; (iv) isotropic etching to lift off Si wires. (B) SEM image of Si walls with width of  $\sim 1.5 \mu\text{m}$  before lift off. (C) SEM image of Si walls with top surface width of  $\sim 100 \text{ nm}$ .

the buried  $\text{SiO}_2$  layer is selectively dissolved with HF solution, Si nanowires are released from the mother wafer. The resulting wires can be further thinned through oxidation and selective etching of the outer  $\text{SiO}_2$  layer. For many applications, this approach is unsuitable due to the relatively high cost of these kinds of multilayered wafers (e.g.,  $\sim \$500$  for each 6-in. SOI wafer versus  $\sim \$5$  for each 6-in. Si wafer). Developing convenient methods for generating nanowires from inexpensive wafers is therefore crucial to commercialize electronics with large areas, i.e., macroelectronics.

Anisotropic chemical etching of single-crystalline wafers provides a route to fabricate nanowires from inexpensive wafers with uniform compositions. For example, anisotropic etching of a (110) Si wafer with patterned mask lines in a hot aqueous KOH solution can generate trenches with vertical profiles (see Fig. 1A, step i).<sup>[29]</sup> The top surface and partial side surfaces of each wall can be covered with a thin film of inert materials (e.g., Ti/Au and Pd), which can withstand the etchant, through shadow evaporation (step iii).<sup>[30]</sup> Isotropic etching in  $\text{HF-HNO}_3\text{-H}_2\text{O}$  can cut the walls at the edges of mask films on side surfaces to release free-standing wires (step iv). Fig. 1B gives a scanning electron microscopy (SEM) image of the sample before Si wires are released. The width of the top surface of each wall is  $1.5 \mu\text{m}$ ; this dimension can easily be reduced to the nanometer scale by using phase-shift photolithography<sup>[31]</sup> or nanoimprinting.<sup>[32]</sup> Fig. 1C shows an SEM image of the vertical walls with width of  $100 \text{ nm}$  fabricated by phase-shift photolithography. The height of each wire can be easily tuned

by controlling the incident angle ( $\alpha$ ) of the evaporated material. Many other related approaches can generate similar structures.

Anisotropic etching of semiconductor wafer that leads to the formation of reverse mesas (i.e., structures with newly formed sidewalls with an acute angle relative to the original surface of wafer) can be exploited to generate nanowires using only a single etching step. Compound semiconductor materials made of group III and V elements are usually crystallized in the form of zinc blende face-centered cubic (f.c.c.) lattice, whose  $\{111\}$  planes are the most stable.<sup>[33]</sup> The  $\{111\}$  surface terminated by the group III atoms, also called  $\{111\}\text{A}$ , is deficient in electron density compared with the  $\{111\}$  surface terminated by the group V atoms, or  $\{111\}\text{B}$ . This difference makes the  $\{111\}\text{A}$  surface resistant to chemical oxidation and generally difficult to etch. As a result, sidewalls with an acute angle (rather than obtuse angle) relative to top surface can be generated by controlling the orientation of stripes of etching mask. As shown in Fig. 2A, anisotropic etching of (100) wafer patterned with parallel mask lines along  $(0\bar{1}1)$  crystallographic direction in appropriate etchant (e.g.,  $\text{H}_2\text{O}_2\text{-H}_3\text{PO}_4\text{-H}_2\text{O}$  for GaAs and  $\text{Br}_2\text{-methanol}$  for InP) generates reverse mesas with side surfaces terminated by  $(\bar{1}11)\text{A}$  and  $(\bar{1}\bar{1}1)\text{A}$  planes, respectively (step i).<sup>[34,35]</sup> With long etching times, the two side walls of each reverse mesa connect to release a wire with triangular cross section (step ii). Pure wires with single crystallinity, uniform doping concentrations, and well-defined crystalline surfaces are collected after removal of the etching mask (step iii).

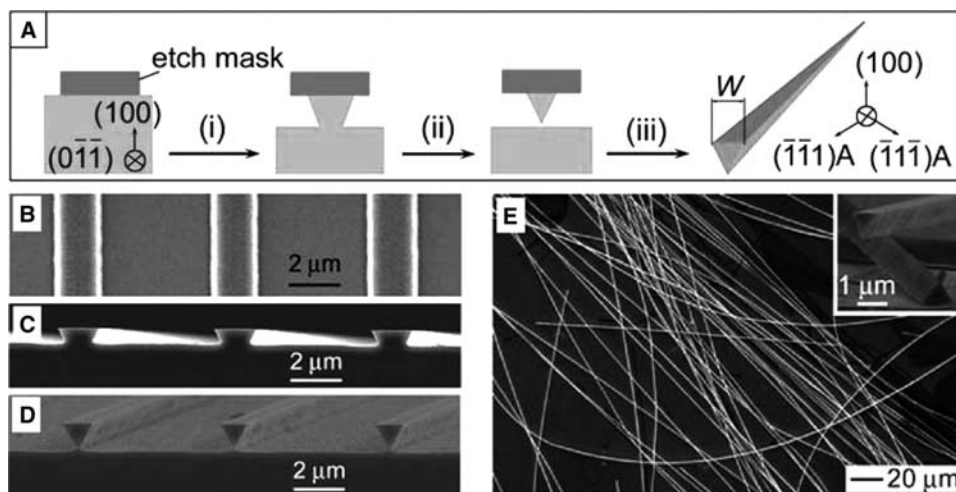


**Fig. 2** Fabrication of wires by anisotropic chemical etching of a III-V semiconductor wafer with top surface of (100) plane. (A) Schematic illustration of the steps: (i) anisotropic etching using mask stripes oriented along  $(0\bar{1}\bar{1})$  direction; (ii) continuous etching and release of wire; (iii) removal of etch mask and generation of free-standing, clean wire. (B–E) SEM images of the samples formed by etching a GaAs wafer patterned with photoresist (PR) stripes in an aqueous solution consisting of  $1\text{H}_3\text{PO}_4$  (85 wt.%)– $13\text{H}_2\text{O}_2$  (30 wt.%)– $12\text{H}_2\text{O}$  (v/v/v) at different etching times. (B) PR stripes on GaAs wafer before etching. (C and D) Cross section of reverse mesas. (E) A random assembly of clean GaAs wires. Etching processes were performed in ice-water bath and ambient environment.

Panels B–E of Fig. 2 show a series of SEM images of samples obtained at different etching times. Fig. 2B presents an SEM image of  $2\ \mu\text{m}$  wide photoresist (Shipley® 1805) lines on a (100) GaAs wafer, clearly showing the straight and uniform width along the longitudinal axis. The SEM images shown in Panels C and D display reverse mesas formed at short and long etching times. Comparison of the lateral dimension between reverse mesas and photoresist lines reveals lateral undercutting along with the vertical etching. Fig. 2E shows an SEM image of free-standing GaAs wires randomly assembled on a GaAs substrate. The wires exhibit uniform widths ( $W$ ) of  $840\ \text{nm}$  along their longitudinal axis. The SEM image shown in the inset displays the triangular cross section of each wire, the roughness of the side walls, and the flatness of the top surface. The roughness of the side walls originates mainly from the edge roughness of the mask lines. The formation of curved structures indicates that the wires are flexible. The bendability increases with decreasing lateral dimensions. Wires with widths of  $\sim 400\ \text{nm}$  can form arc shapes with radii as small as  $\sim 20\ \mu\text{m}$ .<sup>[34]</sup> The excellent flexibility of the nanowires allows them to serve as active components in flexible macroelectronic devices.

It is worth noting that the etching generates undercutting and maintains high anisotropy after the wires lift off the substrate.<sup>[34]</sup> As a result, the lateral dimensions of the wires can be easily decreased to tens of nanometers by controlling the etching time even when the mask lines have widths in the micrometer scale.

Figure 3A–D shows SEM images of individual wires obtained by etching a GaAs wafer patterned with  $2\ \mu\text{m}$  wide mask lines. The wires become thinner with increasing etching time, but the triangular cross sections of the wires are preserved. The dependence of wire width ( $W$ ) on etching time is plotted in Fig. 3E, which indicates that GaAs wires with widths down to  $50\ \text{nm}$  can be obtained in this fashion. The minimum width is determined by the roughness on the side walls. The lengths of the GaAs wires can also be easily tuned by controlling the length of mask stripes. Fig. 3F and G shows SEM images of GaAs rods with average lengths of  $6.4$  and  $15.5\ \mu\text{m}$ , respectively. In principle, wires with lengths as long as tens of centimeters, i.e., the diameter of original wafer, can be fabricated. Fig. 4 gives a composition of several SEM images of long GaAs nanowires with lengths of  $1\ \text{cm}$ , which indicates that most wires are continuous in the observed regions.

The physical parameters of nanowires fabricated via “top-down” approaches exhibit good uniformity (comparable to the high-quality wafer precursors) and enable easy control over the processing. The cost of the wires can be greatly decreased if the resultant mother wafers are polished and reused to generate more wires.<sup>[34]</sup> A disadvantage of the “top-down” approach is that the composition of the wires is limited to materials (e.g., Si, Ge, GaAs, InP, etc.) that are already available in wafer or thin film forms. We have demonstrated this approach with Si, GaAs, InP, and GaN.<sup>[34–37]</sup>

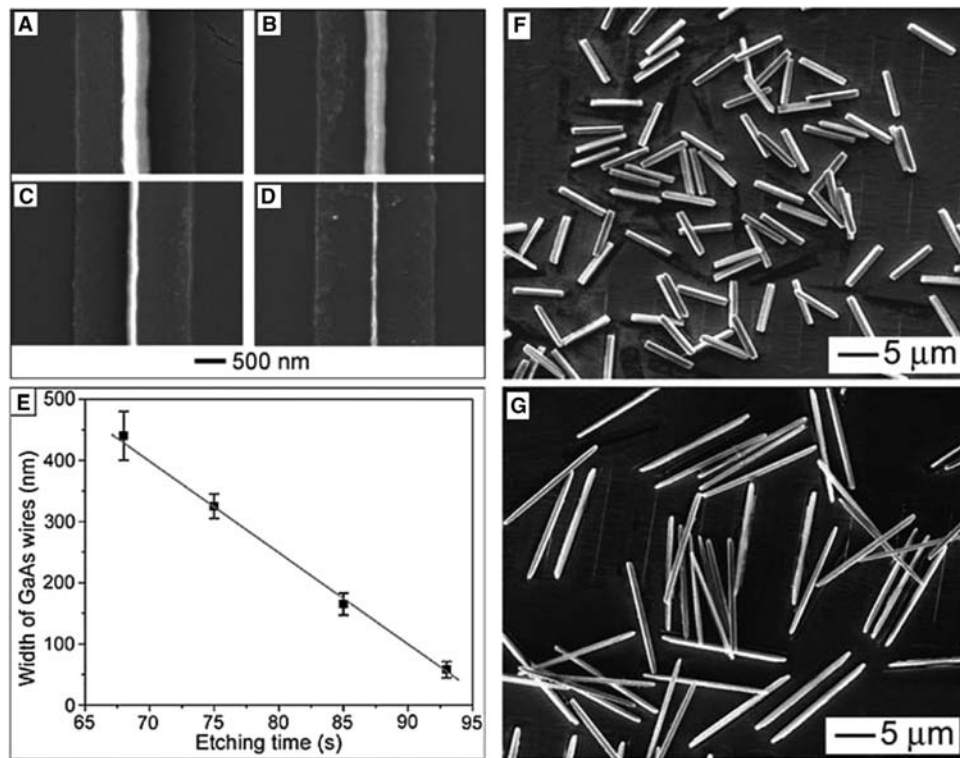


**Fig. 3** (A–D) SEM images of GaAs wires that were generated by etching a GaAs wafer patterned with 2 μm wide SiO<sub>2</sub> stripes at different times: (A) 68, (B) 75, (C) 85, and (D) 93 sec. (E) Plot of the dependence of the average width of GaAs wires with etching time. (F and G) SEM images of GaAs rods obtained by etching GaAs wafers patterned with PR stripes of different lengths: (F) 10 and (G) 20 μm. Etching conditions were similar to that of Fig. 2.

### GENERATION OF ARRAYS OF ALIGNED NANOWIRES

Hierarchical assembly of nanowires into well-defined architectures is the cornerstone for fabrication of functional devices. In particular, monolayers of aligned nanowires with high density and uniform end-to-end registry are critical to build high-performance TFTs

for macroelectronics. A number of approaches have been demonstrated to organize nanowires dispersed in solutions into parallel arrays by applying various external forces (e.g., microfluidic shear force, electric field, surface compression, and magnetic field) to overcome Brownian motion.<sup>[38–43]</sup> In the VLS process, arrays of aligned nanowires can be in situ grown from metal nanoparticles (i.e., catalysts) patterned on

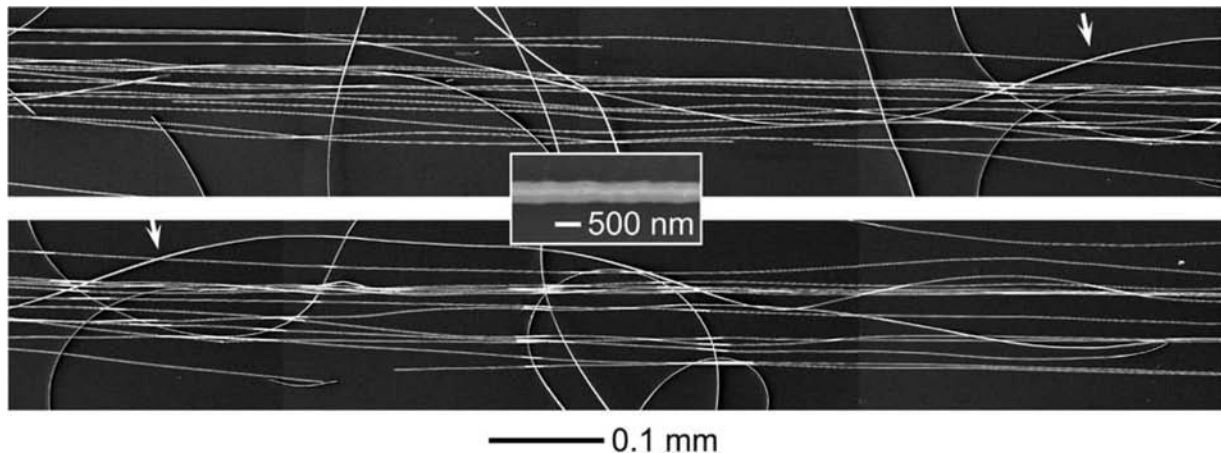


**Fig. 4** SEM images of long GaAs wires. The arrows indicate the same position of the sample.

substrates with specific crystallographic planes.<sup>[44–49]</sup> Nanowires fabricated using “top-down” approaches can be designed to maintain the order defined by lithographic process. The resultant wire arrays can be transfer printed onto any desired substrates including plastic sheets.<sup>[34–37]</sup>

### Assembly of Solution-Based Nanowires Using External Forces

Nanowires synthesized through “bottom-up” approaches are often dispersed in solvents and then deposited onto substrates for further applications. Generating organized arrays, which have relatively low entropy, requires external forces to manipulate the nanowires. For example, flow of a nanowire suspension through microfluidic channels formed between a PDMS stamp and substrate has been demonstrated by Lieber and coworkers to align nanowires of various materials.<sup>[38]</sup> In this case, a shear flow formed near the surface of substrate provides a force ( $F_c$ ) to orient the wires parallel to the flow direction before they are immobilized on the substrate (see Fig. 5A). The degree of alignment, which is represented by the angle ( $\theta$ ) of nanowires with respect to the flow direction, can be controlled by the flow rate. Meanwhile, the spacing between individual aligned nanowires can be narrowed by increasing the time for deposition. A disadvantage of this approach is that it is difficult to produce uniform coverage (i.e., the number of tubes per unit area

tends to be largest near the place where the nanowire suspension is introduced into the channel). In another approach, nanowires in suspension can be induced to generate polarization when they are exposed to an electric field. The interaction between induced wire polarization and electric field aligns the wires parallel to the field direction (Fig. 5B).<sup>[39,40]</sup> It is difficult, however, with either of these approaches to generate uniform films of aligned nanowires with high-density coverage over large areas.

Langmuir–Blodgett (LB) type techniques can push nanowires floating on the water–air interface into nematic liquid-crystal structures.<sup>[41,42]</sup> In this case, the surfaces of the nanowires are first modified with surfactant molecules that have hydrophobic heads facing the water. The repulsive interaction between these hydrophobic groups and the water molecules lifts the nanowires to the water–air interface. Increasing surface pressure ( $P$ ) forces nanowires to rotate perpendicular to the pressure direction (Fig. 5C) in the LB trough. In this manner, a monolayer of aligned nanowires forms on the surface of the water. These wire arrays can be transferred onto other substrates. The advantage of this approach is that it can achieve high density and large area coverage, both of which are critical requirements for fabrication of high-performance macroelectronics. Nevertheless, the surfactant modification on the surfaces of nanowires can affect their electrical properties and thus their performance in applications. The resultant nanowire arrays also have relatively poor end-to-end registry. Finally, the alignment process can

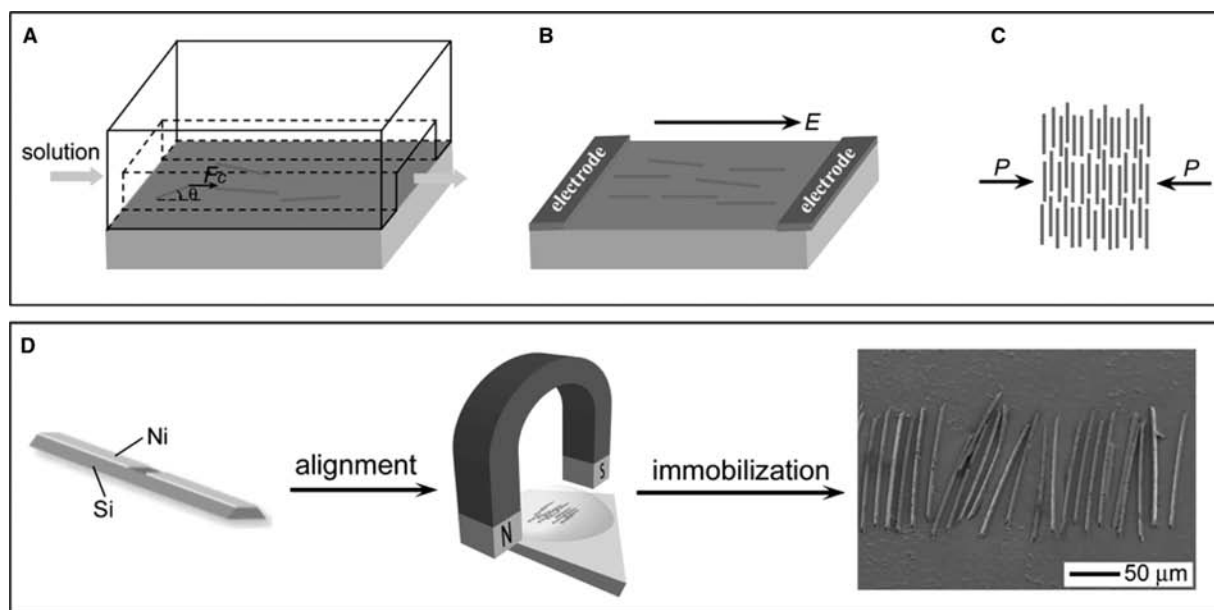


**Fig. 5** Strategies for assembly of as-synthesized nanowires dispersed in solvents through different external forces: (A) shear flow force formed in microfluidic channels; (B) electric field; (C) surface pressure generated through the Langmuir–Blodgett technique; and (D) magnetic field. The wire array demonstrated in (D) consists of Si wires with Ni stripes sitting on the surface of a thin layer of cured polyurethane spin cast on a glass slide.



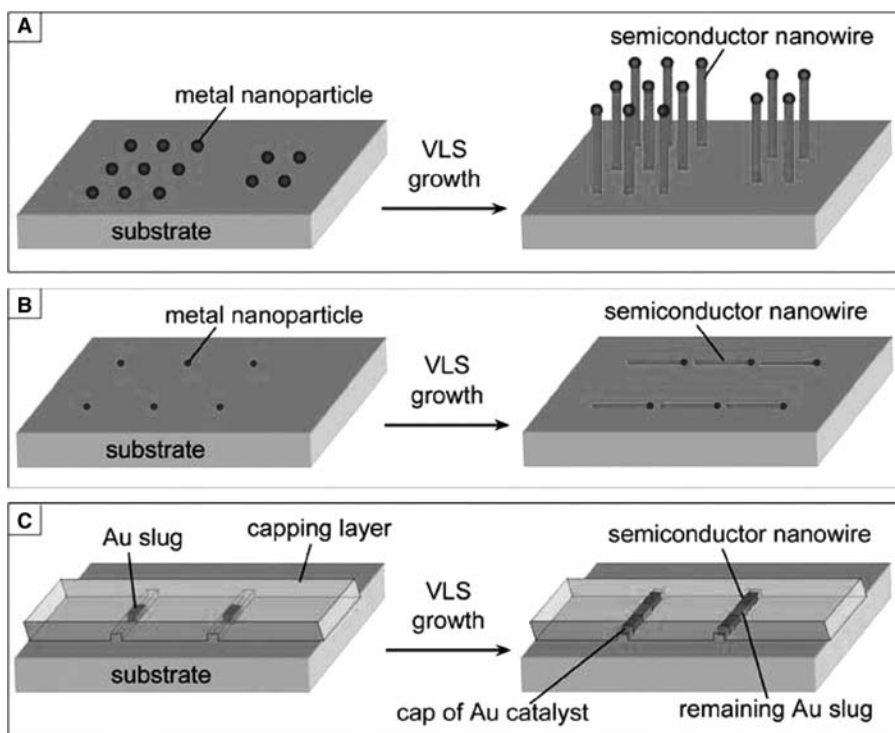


**Fig. 6** In situ growth of nanowire arrays on substrates via the VLS process: (A) wire array perpendicular to surface of substrate; (B) wire array in the plane of substrate; (C) wire array grown on substrate in nanochannels.

be slow, and the transfer mechanism can be inconvenient for many applications.

A different approach exploits magnetism to generate, in a high speed and effective manner, concentrated and aligned arrays.<sup>[43]</sup> Here, ribbons or wires are coated with a ferromagnetic material such as Ni. An external magnetic field applied to a solution suspension of such elements aligns and concentrates them in controlled ways. As shown in Fig. 5D, the interaction between a magnetic field and ferromagnetic Ni coatings induces the ribbons to align parallel to the magnetic field. The aligned ribbons can be fixed such that they maintain their order during the drying process by bonding them to the surface of a photo-cured layer of polyurethane (PU) film (see a typical SEM image in Fig. 5D). This method can precisely position nanostructures by controlling the magnetic field. It is possible to integrate this approach with printing technologies to generate patterns over large areas. In addition, the Ni stripes can serve as electrodes in the further TFT fabrication because Ni can form a silicide with Si to generate ohmic contacts.<sup>[50]</sup>

### In Situ Growth of Aligned Nanowires via VLS Process

Nanowires can epitaxially grow vertically to surfaces of appropriate substrates when reaction conditions are precisely controlled. As a result, patterning metal nanoparticle catalysts on a substrate with specific

crystallographic orientation can direct the in situ growth of aligned nanowire arrays via the VLS process (see Fig. 6A).<sup>[44–47]</sup> For example, an array of Si nanowires perpendicular to a (111) Si wafer can grow through catalysis of Au nanoparticles (>20 nm) deposited on the surface of Si wafer because the Si wires prefer to grow along the  $\langle 111 \rangle$  direction.<sup>[44]</sup> ZnO nanowire arrays can vertically grow on an *a*-plane (110) sapphire substrate although ZnO nanowires tend to grow along the  $\langle 001 \rangle$  direction. The epitaxial growth of ZnO nanowires on the (110) plane of sapphire is attributed to the fact that the *a*-axis of wurzite ZnO and the *c*-axis of sapphire are related by a factor of four (i.e.,  $a_{\text{ZnO}} = 3.24 \text{ \AA}$  vs.  $c_{\text{sapphire}} = 12.99 \text{ \AA}$ ) with mismatching less than 0.08% at room temperature.<sup>[45]</sup> Locations of nanowire arrays grown in this way can be easily controlled by precisely manipulating the positions of Au nanoparticles through various lithographic techniques including, for example, soft lithography, e-beam lithography, photolithography, and microcontact printing. It is apparent that the density of wire arrays is determined by the density of Au nanoparticles on substrate. Arrays formed using this method are highly dense and well aligned on the mother substrate, but they might be difficult to transfer to plastic sheets while preserving their order.

Most recently, Stranick et al. reported that the growth orientation of ZnO nanowires on sapphire surface could be altered by controlling the size and spacing of Au nanoparticles.<sup>[48]</sup> The results indicate it is necessary to have Au nanodroplet catalysts with



diameters smaller than 20 nm and spacings larger than 100 nm to achieve horizontal growth in the surface plane of substrate (Fig. 6B). Au nanoparticles larger than 20 nm always yield nanowires with off-surface orientations regardless of the interparticle spacing. Aligned ZnO nanowires with diameters less than 10 nm have been grown on the surface of *a*-plane (1120) sapphire substrates through VLS process combined with pre patterning of thin Au lines of very narrow widths. These kinds of wire arrays are suitable for transfer onto plastic substrates for TFTs, but it is difficult to increase the wire density due to relatively large spacing between Au nanoparticles.

The “grow-in-place” approach developed by Fonash and coworkers demonstrates the ability to produce self-assembled, crystalline Si nanowires by combining the VLS growth mechanism with lithographically fabricated nanochannels as growth templates.<sup>[49]</sup> As shown in Fig. 6C, Au lines that have heights and widths on the nanometer scale are first generated on an insulating substrate through e-beam lithography, deposition of metal and lift-off. A capping layer (e.g., silicon nitride) is then deposited over the substrate, followed by photolithographic patterning and selective dry etching. The Au lines under the capping layer are shortened to slugs with lengths of several micrometers by wet etching. In this configuration, the remaining Au in the center of channels serves as

catalyst for the growth of semiconductor nanowires (i.e., Si), while the nanochannels act as templates to confine the dimensions of nanowires. When the Au slug is longer than 10  $\mu\text{m}$ , the silicon cannot saturate the whole slug, but instead locally saturates the ends. The nanodroplet of Au–Si alloy at each end induces the growth of one wire by continuous transfer of  $\text{SiH}_4\text{--H}_2$  gas. As a result, two Si nanowires separated by the remaining Au slug form in the nanochannel. These two wires join together to form a continuous wire when the Au slug is short enough (e.g.,  $<2\ \mu\text{m}$ ). The resultant wires have well-controlled size, shape, orientation, and positioning. On the other hand, the use of e-beam lithography makes it expensive to generate wire arrays with large area.

### “Dry Transfer Printing” of Wire Arrays Formed via “Top-Down” Approaches

Nanowires fabricated via “top-down” approaches can inherit the order of the lithographic patterns used to produce them. Ordered nanowires produced in this manner can be transfer printed onto any desired substrates, such as plastic sheets. For example, Fig. 7A summarizes the steps for generating and transferring nanowire arrays of GaAs to a plastic substrate, i.e., poly(ethylene terephthalate) (PET) sheet.<sup>[34]</sup>

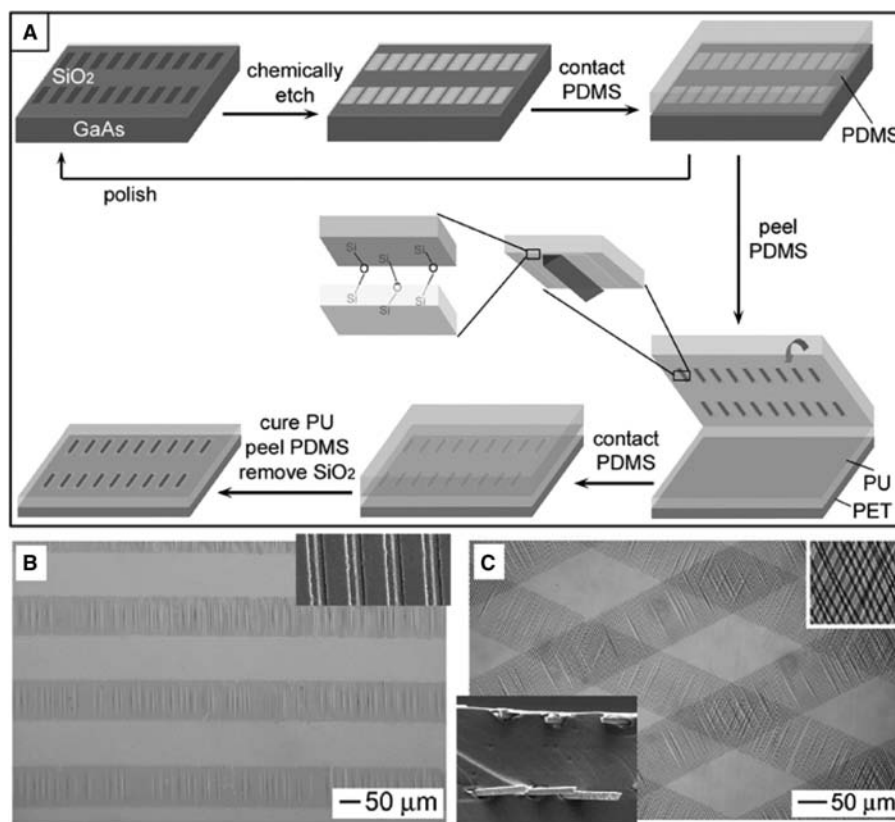


**Fig. 7** Transfer printing wire arrays formed via “top-down” approaches: (A) schematic illustration of steps for transfer printing GaAs wire arrays generated by anisotropic etching; (B and C) optical microscopic images of (B) single and (C) double layers of GaAs wire arrays transfer printed on PET substrates.

If patterned SiO<sub>2</sub> lines (etch masks) surrounded by bulk SiO<sub>2</sub> film are defined on the surface of a (100) wafer, both ends of each GaAs wire generated from anisotropic chemical etching connect to the mother wafer. This connection confines the wires and preserves the spatial orientation defined by the pattern of SiO<sub>2</sub>. GaAs wire arrays can be transfer printed to plastic sheets with retention of their orientation and relative position using a PDMS stamp. In the transfer printing process, the PDMS stamp is slightly oxidized to generate a hydrophilic surface by exposing it to a weak oxygen plasma or ozone. Contacting the oxidized PDMS stamp with SiO<sub>2</sub>-covered GaAs wafer generates strong chemical bonding due to the formation of covalent siloxane (Si–O–Si) linkages between PDMS and SiO<sub>2</sub> via a condensation reaction. This bonding is strong enough to break the crystalline connections at the ends of wires. Peeling the PDMS stamp away from the GaAs substrate transfers all of the wires to the stamp. The remaining GaAs wafer after this transfer step can be polished to regenerate a flat surface for fabrication of more wires. The combination of wafer polishing with wire fabrication has the capability to generate a huge number of GaAs wires from a single piece of wafer, thus significantly decreasing the cost per wire.

In the next step, a photocurable polymer, such as PU, is used as a glue to bind the GaAs wires to a PET substrate. Placing the PDMS stamp (with GaAs wires) against a PET sheet coated with a thin layer of PU (thickness between one and tens of micrometers, determined by spin speed) forms conformal contact by pushing the surfaces of the wires into the liquid PU. Illuminating the sample with a UV lamp crosslinks and solidifies the PU layer, resulting in the formation of a strong bond between the cured PU and the GaAs wires and the underlying PET substrate. Peeling off the PDMS stamp and dissolving the SiO<sub>2</sub> stripes leave the GaAs wire arrays embedded in the matrix of cured PU with order and crystallographic orientation similar to those of the wires prior to transfer. The top flat surfaces of the wires are facing up, and can be exploited for subsequent device fabrication steps.

Fig. 7B gives an optical image of a PU/PET substrate with GaAs wire arrays, indicating that all of GaAs wires were transfer printed onto the PET substrate with preservation of order and spatial orientation. The inset shows an SEM image taken from the same sample, clearly showing that the GaAs wires were well embedded in the cured PU. The flat top surface of each wire is exposed for further applications. The transfer printing process can be repeated to generate multiple layers of GaAs wire arrays on the same PET substrate. Fig. 7C presents an optical image of a sample with two layers of wire arrays formed by rotating the second layer with ~45° relative to the first layer. The bottom left inset is an SEM image of the cross

section of this sample, indicating that the two individual layers of GaAs wire arrays are well separated by the cured PU. These PU layers can electrically insulate circuits or devices built on different layers of GaAs wire arrays.

This “dry transfer printing” process combined with the “top-down” fabrication approach is promising for applications related to high-performance macroelectronics. It controls well the crystallographic orientation of transferred wires, with the top (100) surfaces facing up to provide an extremely flat surface (similar to that of original wafer) for device fabrication. The use of SiO<sub>2</sub> stripes as etch mask and buffer layer for the transfer prevents the (100) surfaces of the GaAs wires from becoming contaminated by organics used in the processing. In addition, conformal contact between PDMS stamp and liquid PU generates GaAs wires conformally bound to, and embedded in cured PU, which prevents the wires from moving, especially when the plastic substrates are bent or twisted.

Circuits for macroelectronics are fabricated on substrates with sizes much larger than semiconductor wafers. Active semiconductor films usually occupy only 10–20% area of the whole substrate, and the remaining regions are used to build interconnection between individual device units (e.g., transistors). Therefore, wire arrays generated on a mother wafer can be selectively transferred from certain regions rather than the whole surface, thus further decreasing the cost of fabrication. Fig. 8A shows a diagram for printing nanowire arrays generated from a single wafer over large areas on a plastic substrate. This process uses a PDMS stamp with patterned posts. Placing the stamp against the wafer and peeling it off picks up only the wires that contact with the surface of extrusive posts. The printing process can transfer patches of wire arrays onto plastic substrates. Repeating the steps over the remaining wires on the mother wafer can yield organized arrays of wires over large areas on a plastic substrate. Fig. 8B gives an optical image of patches consisting of GaAs wire arrays that were transfer printed on a PU/PET substrate. The image with relatively high magnification (as shown in Fig. 8C) shows that the wires of each patch are well aligned and have good end-to-end registry. This transfer printing process can be extended to wire arrays of other materials (e.g., InP, Si, etc.) fabricated via “top-down” approaches.<sup>[34,36,51]</sup> For instance, Fig. 8D shows a 5" × 5" PET sheet with patterned patches of Si ribbons.

## MACROELECTRONICS APPLICATIONS

Monolayer films of nanowires with aligned orientation on plastic substrates can be used to produce flexible

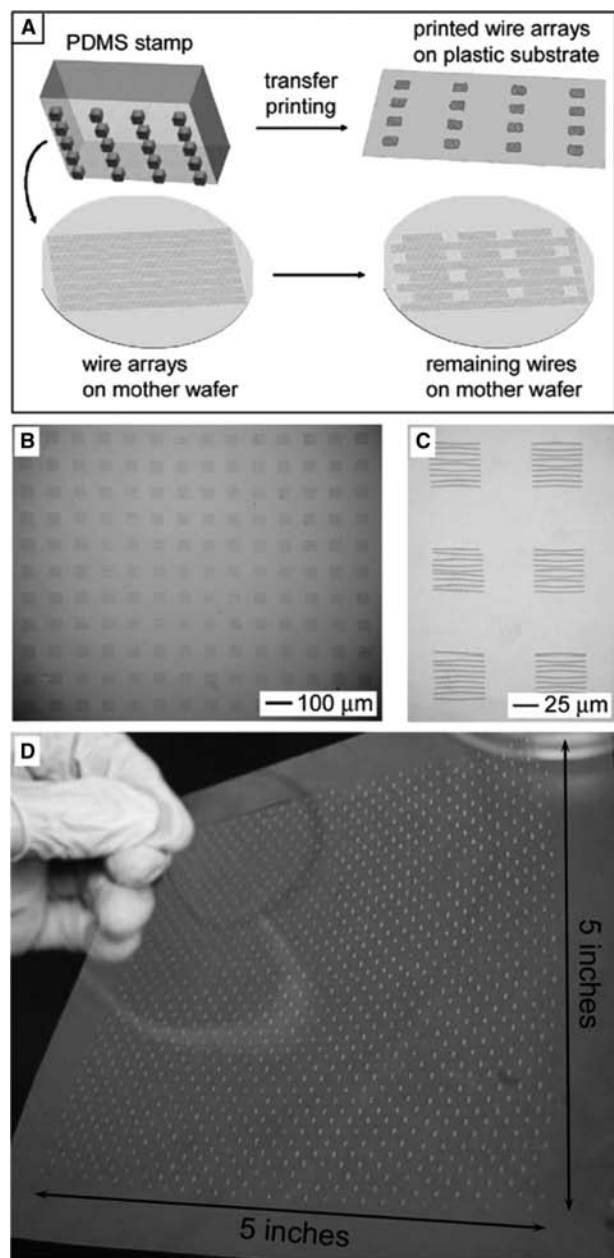


**Fig. 8** Transfer printing patches of wire arrays on plastic substrates using PDMS stamps with patterned posts: (A) schematic illustration of this process; (B and C) optical images of patches of arrays of 50  $\mu\text{m}$  long GaAs wires; (D) a large-area sample with transfer printed Si ribbons on a PET substrate.

TFTs by traditional lithographic processing steps. Fig. 9A depicts the geometric construction of a typical back-gate TFT using an aligned nanowire array as the semiconductor. A thin conductive layer of metal (e.g., Au) or oxide (e.g., indium-tin-oxide, or ITO) and a thin dielectric layer (e.g., aluminum oxide,  $\text{SiO}_2$ , resin epoxy, etc.) are sequentially deposited on the surface of a plastic sheet. Aligned nanowire films formed using

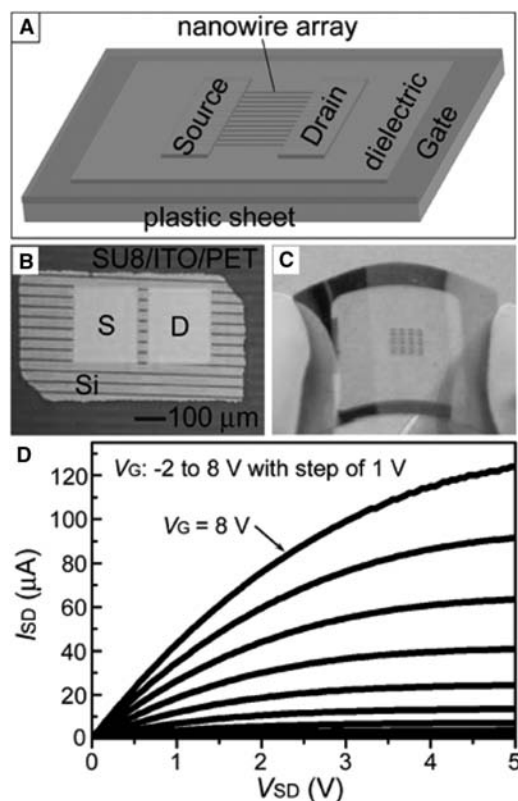


**Fig. 9** (A) Geometry of a thin film transistor (TFT) fabricated on a plastic substrate using aligned wires as a semiconductor film. (B) Optical image of an individual TFT built using aligned Si ribbons on a 530 nm thick cured SU8 epoxy layer spin cast on an ITO-coated PET sheet. (C) Photograph of a piece of a PET sheet with an array of TFTs, indicating their mechanical flexibility. (D) Typical current–voltage characteristics of a Si ribbon transistor on a PET substrate. From bottom to top,  $V_G$  varies from  $-2$  to  $8$  V with steps of  $1$  V.

the approaches described in the previous section are transferred onto the multilayered plastic substrate with controlled positioning and orientation. Finally, large-area lithographic techniques are used to define the pattern of source–drain electrodes over the thin film of oriented nanowires.<sup>[52]</sup>

Duan and coworkers assembled Si nanowires that were synthesized via the laser-assisted VLS process on a polyetheretherketone (PEEK) sheet (with thickness of  $125 \mu\text{m}$ ) by passing a nanowire suspension through microfluidic channels (detailed description referred to in a previous section).<sup>[53]</sup> Before assembly of nanowires, thin strips of Cr/Au (10/30 nm) and a 30 nm layer of aluminum oxide were deposited on the PEEK sheet to serve as gate electrodes and dielectric. Ti/Au (60/80 nm) patches were defined as source and drain electrodes. The resultant devices show a threshold voltage of  $\sim 3.0$  V, an on-off ratio higher than  $10^5$ , and a subthreshold swing of 500–800 mV per decade. The performance of devices did not significantly

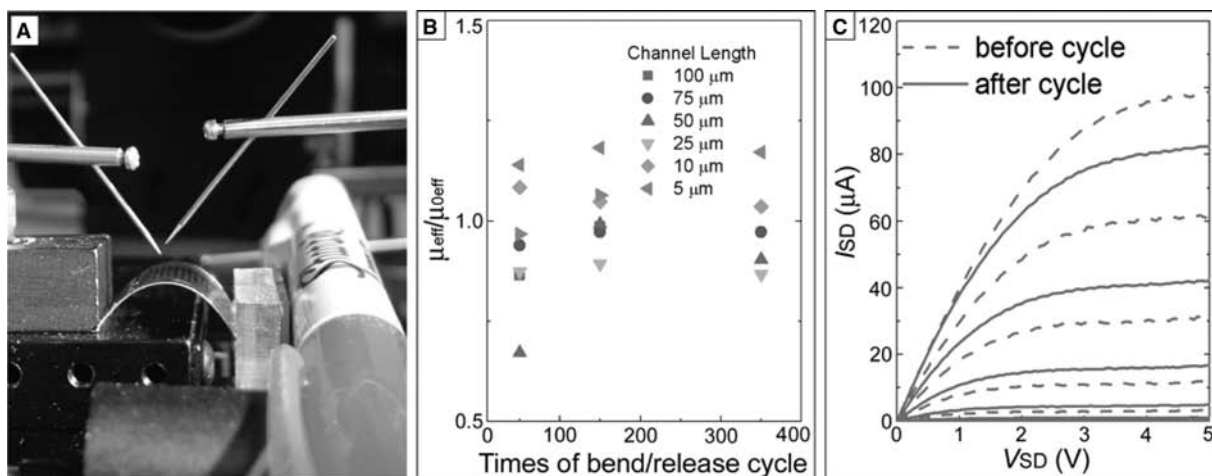


**Fig. 10** Fatigue testing of Si ribbon transistors on a PET substrate: (A) setup for bending test; (B) variation of electron mobility of Si ribbon transistors with different channel lengths after repeated bend/release cycles; (C) comparison of current–voltage curves before and after 350 bending cycles.

change even when the bend radius was  $\sim 55$  mm. In spite of the relatively high per wire mobility ( $\sim 150$  cm<sup>2</sup>/V sec), the device mobilities are low ( $\sim 3$  cm<sup>2</sup>/V sec) due to the low density of these arrays and their random end-to-end registry.

Rogers and coworkers have recently developed a parallel route for fabricating TFTs with high performance on plastic substrates.<sup>[36,51,54]</sup> In their demonstration, Si stripes with thicknesses of 20–100 nm and widths of 1–100  $\mu$ m were fabricated from high-quality SOI wafers via the “top-down” approach. (Note: although the width of Si stripes can be reduced down to 50 nm using phase-shift photolithography, this narrowing is not necessary for macroelectronics applications.) These Si structures, with good order and orientation, were then transferred onto an ITO (100 nm) coated PET (175  $\mu$ m) substrate through the dry transfer printing technique depicted in Figs. 7 and 8A. In this case, a polymeric resin of SU-8 photoresist was used as glue to bind Si film and PET substrate together. This same film served as a gate dielectric. Patterns of 70 nm thick Ti films formed the source and drain electrodes. Fig. 9B shows an optical image of an individual transistor with channel length of 20  $\mu$ m and channel width of 250  $\mu$ m. Fig. 9D presents the  $I$ – $V$  curves of a device at various gate voltages. The electron mobility extracted from the transfer curve is  $\sim 230$  cm<sup>2</sup>/V sec, evaluated in the linear regime. This technique can be easily extended to nanowires of other materials (e.g., GaAs, InP, GaN, Ge, etc.) fabricated from bulk wafers. For example, GaAs nanowire arrays transfer printed onto PET substrates (as shown in Figs. 7 and 8) can serve as active channel for MESFET devices if ohmic contacts are deposited before wires are transferred onto plastic substrates.<sup>[55]</sup>

Because of the flexibility of the thin PET sheet and the nanowires,<sup>[5]</sup> the devices exhibit excellent mechanical bendability. As shown in Fig. 9C, the PET sheet with TFTs can be bent to form curved structures without substantial changes in the electrical properties. The precise degree of flexibility and the fatigue properties have been evaluated using the setup shown in Fig. 10A. The strain generated in the Si ribbons can be determined measuring the geometric parameters of substrate. The data indicate that the electrical properties do not change with 350 bend/release cycles to strains of 0.98%, i.e., bend radii of  $\sim 9$  mm. Fig. 10B shows the variation of the mobilities of transistors with different channel lengths after hundreds of bend/release cycles. Fig. 10C compares the  $I$ – $V$  curves of a device before and after 350 times of bending operation, indicating that this transistor still works well, although with a current drop of  $\sim 25\%$ . These results indicate that the combination of “top-down” fabrication and “dry transfer printing” provides an efficient route to generate substrates for fabrication of large-area, high-performance macroelectronic devices.

## REMARKS AND PERSPECTIVES

Two different paradigms have been demonstrated to have capability for the fabrication of TFTs on plastics using thin film of aligned semiconductor nanowires. In the first strategy, nanowires synthesized via “bottom-up” approaches form aligned arrays through either postassembly or in situ catalyst-positioning growth (i.e., nanowires grow from patterned catalyst nanoparticles into aligned arrays). Chemically synthetic “bottom-up” approaches can produce nanowires with a wide range of materials by controlling

reaction conditions and precursors. The versatility of compositions provides a flexibility to choose suitable nanowires to meet specific applications. However, the moderate quality of nanowires (in terms of dimensional uniformity, purity, dopant concentration, doping uniformity, and surface crystallography) and assembled nanowire film (in terms of density, orientation, and end-to-end registry) might make it difficult to build large arrays of high-performance devices with them. The current lack of effective approaches for assembling high-quality nanowire thin films represents the main challenge for successful technology applications of these systems. In the second strategy, nanowires fabricated from high-quality, single-crystal, bulk wafers via “top-down” approaches adopt the organization and orientation defined by the pattern of mask. The resultant nanowire arrays can be transferred onto plastic substrates through the “dry transfer printing” technique. A drawback of this approach is that it is limited to materials that currently exist in bulk wafer or thin film form.

Although high performance is important, reliable, robust operation of macroelectronic devices is crucial for many of their envisioned applications. In particular, the nature of the interfaces between the plastic sheet (or plastic sheet covered with cured polymer) and the semiconductor, and between the metal and semiconductor are critical from both electronics and mechanical points of view. Appropriate adhesive layer between a semiconductor nanowire film and a plastic sheet is critical for the formation of conformal contact especially when the substrate is bent and relaxed. The long-term reliability of low-temperature dielectrics is also a topic that must be investigated. In spite of these challenges, we believe that printable inorganic semiconductor nanowires represent the most promising approach to building these and other classes of large-area electronic devices.

## ACKNOWLEDGMENTS

This work was supported by DARPA-funded AFRL-managed Macroelectronics Program (FA8650-04-C-7101). Funding is also partially provided by the U.S. Department of Energy under grant DEFG02-91-ER45439. The authors thank Dr. Z.-T. Zhu, E. Menard, K. Lee, Dr. J.-H. An, M.A. Meitl and S. Mack for providing some original images and curves.

## REFERENCES

- Ucjkoga, S. Low-temperature polycrystalline silicon thin-film transistor technologies for system-on-glass displays. *MRS Bull.* **2002**, *27*, 881–886.
- Rogers, J.A.; Bao, Z.; Baldwin, K.; Dodabalapur, A.; Crone, B.; Raju, V.R.; Kuck, V.; Katz, H.; Amundson, K.; Ewing, J.; Drzaic, P. Paper-like electronic displays: large-area rubber-stamped plastic sheets of electronics and microencapsulated electrophoretic inks. *Proc. Natl. Acad. Sci. USA* **2001**, *98*, 4835–4840.
- Ridley, B.A.; Nivi, B.; Jacobson, J.M. All-inorganic field effect transistors fabricated by printing. *Science* **1999**, *286*, 746–749.
- Cui, Y.; Zhong, Z.; Wang, D.; Wang, W.; Lieber, C.M. High performance silicon nanowire field effect transistors. *Nano Lett.* **2003**, *3*, 149–152.
- Isono, Y.; Namazu, T.; Tanaka, T. AFM bending testing of nanometric single crystal silicon wire at intermediate temperatures for MEMS, The 14th IEEE International Conference on MEMS, 2001, 135–138.
- Zhou, Y.; Gaur, A.; Hur, S.-H.; Kocabas, C.; Meitl, M.A.; Shim, A.; Rogers, J.A. p-channel, n-channel thin film transistors and p–n diodes based on single wall carbon nanotube networks. *Nano Lett.* **2004**, *4*, 2031–2035.
- Hur, S.-H.; Khang, D.-Y.; Kocabas, C.; Rogers, J.A. Nanotransfer printing by use of noncovalent surface forces: applications to thin-film transistors that use single-walled carbon nanotube networks and semiconducting polymers. *Appl. Phys. Lett.* **2004**, *85*, 5730–5732.
- Snow, E.S.; Novak, J.P.; Campbell, P.M.; Park, D. Random networks of carbon nanotubes as an electronic material. *Appl. Phys. Lett.* **2003**, *82*, 2145–2147.
- Bradley, K.; Gabriel, J.-C.P.; Grüner, G. Flexible nanotube electronics. *Nano Lett.* **2003**, *3*, 1353–1355.
- Huynh, W.U.; Dittmer, J.J.; Alivisatos, A.P. Hybrid nanorod-polymer solar cells. *Science* **2002**, *295*, 2425–2427.
- Law, M.; Sirbuly, D.J.; Johnson, J.C.; Goldberger, J.; Saykally, R.J.; Yang, P. Nanoribbon waveguides for subwavelength photonics integration. *Science* **2004**, *305*, 1269–1273.
- Yoffe, A.D. Semiconductor quantum dots and related systems: electronic, optical, luminescence and related properties of low dimensional systems. *Adv. Phys.* **2001**, *50*, 1–208.
- Zheng, G.; Lu, W.; Jin, S.; Lieber, C.M. Synthesis and fabrication of high-performance n-type silicon nanowire transistors. *Adv. Mater.* **2004**, *16*, 1890–1893.
- Xia, Y.; Yang, P.; Sun, Y.; Wu, Y.; Mayers, B.; Gates, B.; Yin, Y.; Kim, F.; Yan, H. One-dimensional nanostructures: synthesis, characterization, and applications. *Adv. Mater.* **2003**, *15*, 353–389.
- Lieber, C.M. One-dimensional nanostructures: chemistry, physics & applications. *Solid State Commun.* **1998**, *107*, 607–616.
- Law, M.; Goldberger, J.; Yang, P. Semiconductor nanowires and nanotubes. *Ann. Rev. Mater. Res.* **2004**, *34*, 83–122.
- Wang, Z.L., Ed.; *Nanowires and Nanobelts: Materials, Properties and Devices*; Kluwer Academic Publishers: Boston, 2003, Vols. I and II.
- Wagner, R.S.; Ellis, W.C. Vapor–liquid–solid mechanism of single crystal growth. *Appl. Phys. Lett.* **1964**, *4*, 89–90.



19. Morales, A.M.; Lieber, C.M. A laser ablation method for the synthesis of crystalline semiconductor nanowires. *Science* **1998**, *279*, 208–211.
20. Hiruma, K.; Yazawa, M.; Katsuyama, T.; Ogawa, K.; Haraguchi, K.; Koguchi, M.; Kakabayashi, H. Growth and optical properties of nanometer-scale GaAs and InAs whiskers. *J. Appl. Phys.* **1995**, *77*, 447–462.
21. Duan, X.; Lieber, C.M. General synthesis of compound semiconductor nanowires. *Adv. Mater.* **2000**, *12*, 298–302.
22. Gudiksen, M.S.; Wang, J.; Lieber, C.M. Synthetic control of the diameter and length of single crystal semiconductor nanowires. *J. Phys. Chem. B* **2001**, *105*, 4062–4064.
23. Trentler, T.J.; Hickman, K.M.; Goel, S.C.; Viano, A.M.; Gibbons, P.C.; Buhro, W.E. Solution–liquid–solid growth of crystalline III–V semiconductors: an analogy to vapor–liquid–solid growth. *Science* **1995**, *270*, 1791–1794.
24. Yu, H.; Buhro, W.E. Solution–liquid–solid growth of soluble GaAs nanowires. *Adv. Mater.* **2003**, *15*, 416–419.
25. Rogers, J.A.; Paul, K.E.; Jackman, R.J.; Whitesides, G.M. Using an elastomeric phase mask for sub-100 nm photolithography in the optical near field. *Appl. Phys. Lett.* **1997**, *70*, 2658–2660.
26. Irvine, A.C.; Durrani, Z.A.K.; Ahmed, H.; Biesemans, S. Single-electron effects in heavily doped polycrystalline silicon nanowires. *Appl. Phys. Lett.* **1998**, *73*, 1113–1115.
27. Hua, F.; Sun, Y.; Gaur, A.; Meitl, M.A.; Bilhaut, L.; Rotkina, L.; Wang, J.; Geil, P.; Shim, M.; Rogers, J.A. Polymer imprint lithography with molecular-scale resolution. *Nano Lett.* **2004**, *4*, 2467–2471.
28. Yin, Y.; Gates, B.; Xia, Y. A soft lithography approach to the fabrication of nanostructures of single crystalline silicon with well-defined dimensions and shapes. *Adv. Mater.* **2000**, *12*, 1426–1430.
29. Lee, S.C.; Brueck, S.R.J. Nanoscale two-dimensional patterning on Si (001) by large-area interferometric lithography and anisotropic wet etching. *J. Vac. Sci. Technol. B* **2004**, *22*, 1949–1952.
30. Xia, Y.; Whitesides, G.M. Shadowed sputtering of gold on V-shaped microtrenches etched in silicon and applications in microfabrication. *Adv. Mater.* **1996**, *8*, 765–768.
31. Jeon, S.; Menard, E.; Park, J.-U.; Maria, J.; Meitl, M.; Zaumseil, J.; Rogers, J.A. Three-dimensional nanofabrication with rubber stamps and conformable photo-masks. *Adv. Mater.* **2004**, *16*, 1369–1373.
32. Chou, S.Y.; Keimel, C.; Gu, J. Ultrafast and direct imprint of nanostructures in silicon. *Nature* **2002**, *417*, 835–837.
33. Wang, Z.L. Transmission electron microscopy of shape-controlled nanocrystals and their assemblies. *J. Phys. Chem. B* **2000**, *104*, 1153–1175.
34. Sun, Y.; Rogers, J.A. Fabricating semiconductor nano/microwires and transfer printing ordered arrays of them onto plastic substrates. *Nano Lett.* **2004**, *4*, 1953–1959.
35. Sun, Y.; Khang, D.-Y.; Hua, F.; Hurley, K.; Nuzzo, R.G.; Rogers, J.A. Photolithographic route to the fabrication of micro/nanowires of III–V semiconductors. *Adv. Funct. Mater.* **2005**, *15*, 30–40.
36. Menard, E.; Lee, K.J.; Khang, D.-Y.; Nuzzo, R.Z.; Rogers, J.A. A printable form of silicon for high performance thin film transistors on plastic substrates. *Appl. Phys. Lett.* **2004**, *84*, 5398–5400.
37. Lee, K.J.; Lee, J.S.; Hwang, H.; Davis, R.F.; Rogers, J.A.; Nuzzo, R.G. A printable form of single crystal gallium nitride for flexible optoelectronic systems. **2005**, submitted.
38. Huang, Y.; Duan, X.; Wei, Q.; Lieber, C.M. Directed assembly of one-dimensional nanostructures into functional networks. *Science* **2001**, *291*, 630–633.
39. Smith, P.A.; Nordquist, C.D.; Jackson, T.N.; Mayer, T.S.; Martin, B.R.; Mbindyo, J.; Mallouk, T.E. Electric-field assisted assembly and alignment of metallic nanowires. *Appl. Phys. Lett.* **2000**, *77*, 1399–1401.
40. Duan, X.; Huang, Y.; Cui, Y.; Wang, J.; Lieber, C.M. Indium phosphide nanowires as building blocks for nanoscale electronic and optoelectronic devices. *Nature* **2001**, *409*, 66–69.
41. Whang, D.; Jin, S.; Wu, Y.; Lieber, C.M. Large-scale hierarchical organization of nanowire arrays for integrated nanosystems. *Nano Lett.* **2003**, *3*, 1255–1259.
42. Tao, A.; Kim, F.; Hess, C.; Goldberger, J.; He, R.; Sun, Y.; Xia, Y.; Yang, P. Langmuir–Blodgett silver nanowire monolayers for molecular sensing using surface-enhanced Raman spectroscopy. *Nano Lett.* **2003**, *3*, 1229–1233.
43. An, J.-H.; Meitl, M.; Mack, S. unpublished material.
44. Wu, Y.; Yan, H.; Huang, M.; Messer, B.; Song, J.H.; Yang, P. Inorganic semiconductor nanowires: rational growth, assembly, and novel properties. *Chem. Eur. J.* **2002**, *8*, 1261–1268.
45. Huang, M.H.; Mao, S.; Feick, H.; Yan, H.; Wu, Y.; Kind, H.; Weber, E.; Russo, R.; Yang, P. Room-temperature ultraviolet nanowire nanolasers. *Science* **2001**, *292*, 1897–1899.
46. Bhunia, S.; Kawamura, T.; Fujikawa, S.; Tokushima, K.; Watanabe, Y. Free-standing and vertically aligned InP nanowires grown by metalorganic vapor phase epitaxy. *Physica E* **2004**, *21*, 583–587.
47. Wu, Z.H.; Mei, X.Y.; Kim, D.; Blumin, M.; Ruda, H.E. Growth of Au-catalyzed ordered GaAs nanowire arrays by molecular-beam epitaxy. *Appl. Phys. Lett.* **2002**, *81*, 5177–5179.
48. Nikoobakht, B.; Michael, C.A.; Stranick, S.J.; Vaudin, M.D. Horizontal growth and in situ assembly of oriented zinc oxide nanowires. *Appl. Phys. Lett.* **2004**, *85*, 3244–3246.
49. Shan, Y.; Kalkan, K.; Peng, C.-Y.; Fonash, S.J. From Si source gas directly to positioned, electrically contacted Si nanowires: the self-assembling



- “grow-in-place” approach. *Nano Lett.* **2004**, *4*, 2085–2089.
50. Wu, Y.; Xinag, J.; Yang, C.; Lu, W.; Lieber, C.M. Single-crystal metallic nanowires and metal/semiconductor nanowires heterostructures. *Nature* **2004**, *430*, 61–65.
  51. Menard, E.; Nuzzo, R.G.; Rogers, J.A. Bendable single crystal silicon thin film transistors formed by printing on plastic substrates. *Appl. Phys. Lett.* **2005**, *86* (093507), 1–3.
  52. Kagan, C.R.; Andry, P.; Eds.; *Thin Film Transistors*; Dekker: New York, 2003.
  53. Duan, X.; Niu, C.; Sahi, V.; Chen, J.; Parce, J.W.; Empedocles, S.; Goldman, J.L. High-performance thin-film transistors using semiconductor nanowires and nanoribbons. *Nature* **2003**, *425*, 274–278.
  54. Zhu, Z.; Menard, E.; Hurley, K.; Nuzzo, R.G.; Rogers, J.A. Spin on dopants for high performance single crystalline silicon transistor on flexible plastic substrates. *Appl. Phys. Lett.* **2005**, *86* (133507), 1–3.
  55. Sun, Y.; Kim, S.; Adesida, I.; Rogers, J.A. Bendable GaAs metal-semiconductor field effect transistors formed with printed GaAs wire arrays on plastic substrate. **2005**.

# Semiconductor Nanowires: Nanoscale Electronics and Optoelectronics

**Yu Huang**

*Massachusetts Institute of Technology, Cambridge, Massachusetts, U.S.A.*

**Xiangfeng Duan**

*Advanced Research Center, Nanosys Inc., Palo Alto, California, U.S.A.*

**Charles M. Lieber**

*Department of Chemistry and Chemical Biology, Harvard University, Cambridge, Massachusetts, U.S.A.*

## INTRODUCTION

A bottom-up approach, in which functional systems are assembled from chemically synthesized, well-defined nanoscale building blocks, has the potential to go far beyond of the limits of top-down technology by defining key nanometer scale metrics through synthesis and subsequent assembly—not by lithography. One-dimensional (1D) nanostructures represent the smallest dimension structure that can efficiently transport electrical carriers and can play an important role as both interconnect and functional device elements in integrated nanosystems. Here, we review recent advances in bottom-up assembly of nanoscale electronics and optoelectronics using semiconductor nanowire (NW) as building blocks. First, we review electrical transport studies on individual NWs, and moreover, examine nanoscale electronic and optoelectronic devices assembled using individual NWs as building blocks. Next, we present approaches for the hierarchical assembly of NWs into well-defined arrays with controlled orientation and spatial location. Third, we address critical issues for integration and demonstrate the assembly of integrated nanoscale devices with logic and computation circuits. Lastly, we describe a unique application enabled by nanoscale NW devices: highly sensitive and selective chemical and biological sensing. We conclude with a brief summary and perspective on future opportunities.

## BACKGROUND

### Top-Down Technology: The Limitations

The rapid miniaturization of electronics to the submicron scale has led to remarkable advances in computing power while at the same time reducing costs. These advances have been made possible by many

scientific and technological innovations associated with “top-down” manufacturing, in which small features are patterned in bulk semiconductor materials by lithography, deposition, and other processing to form functional devices. This now remarkable trend in miniaturization was first pointed out by Gordon Moore, and is now universally referred to as Moore’s Law, which dictates that the number of transistors per chip doubles every 18–24 months (Fig. 1).<sup>[1,2]</sup> The magnitude of what has been accomplished can be recognized by the fact that it is now possible to fabricate a 100 million transistors on a chip of the same size as a single transistor when it was first invented a half century ago. However, as the microelectronic industry advances towards ever smaller devices, it is believed that physical and economic limits of current top-down silicon technology will be soon reached. First, photolithography-based top-down strategies will soon reach a fundamental resolution limit of ca. 70 nm that will limit further reduction in feature sizes using relatively conventional optical sources, although solutions such as extreme ultraviolet lithography are being explored to overcome this limit. Second, the exponentially increasing cost to construct each new generation of fabrication line may limit further miniaturization on the basis of economics alone. These and other limitations of current top-down technology have motivated efforts worldwide to search for new strategies to meet the expected demand for increased computational power as well as for integrating low-cost and flexible computing in unconventional environments in the future.<sup>[3–5]</sup>

### Bottom-Up Technology: Requirements and Promises

To go beyond the fundamental and economic limitations of top-down technologies will require new

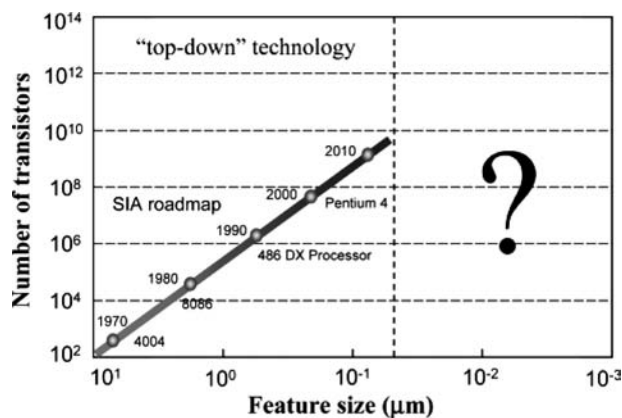


**Fig. 1** Illustration of device scaling in conventional electronics—Moore's law.

methods. A bottom-up approach, in which functional electronic structures are assembled from chemically synthesized, well-defined nanoscale building blocks, much like the way nature uses proteins and other macromolecules to construct complex biological systems, represents a flexible alternative to conventional top-down methods,<sup>[4,6,7]</sup> and moreover, the bottom-up approach has the potential to go far beyond the limits of top-down technology by defining key nanometer scale metrics through synthesis and subsequent assembly—not by lithography.

To enable this bottom-up pathway requires that three key problems, which are at the heart of devices and integration in the broadest terms, be addressed (Fig. 2). First, the bottom-up approach requires nanoscale building blocks with precisely controlled and tunable chemical composition, structure, morphology, and size, since these characteristics determine their corresponding electronic and optical properties. To meet this goal necessitates developing methods that enable rational design and predictable synthesis of the building blocks. Second, it is essential to develop

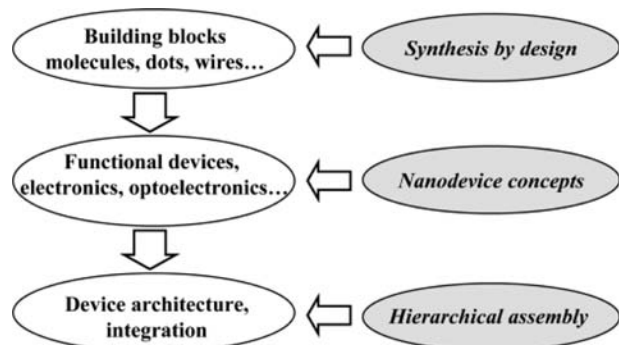


**Fig. 2** Schematic outlining key challenges (open ellipses) and specific research areas (shaded ellipses) required to enable the bottom-up approach to nanoelectronic systems.

and explore the limits of functional devices based on these building blocks. Nanodevices may behave in ways similar to current electronic and optoelectronic devices, although it is also expected that new and potentially revolutionary device concepts will emerge from these building blocks, for example, due to quantum properties. Third and central to the bottom-up concept is the development of device architectures that enable high-density integration with desired function, and the development of hierarchical assembly methods that can organize building blocks into these architectures.

Addressing and overcoming the hurdles in these three major areas of the bottom-up approach could revolutionize fabrication and manufacturing, make a quantum jump in miniaturization, and lead to reduced power consumption and increased speed in next generation electronics and photonics. Moreover, it is very likely that the bottom-up approach could enable entirely new device concepts and new systems. For example, it is possible to combine seamlessly chemically distinct nanoscale building blocks, which could not be integrated together in top-down processing, into the same device architecture and thereby obtain unique function and/or combinations of function in an integrated system. Small and highly perfect building blocks may also lead to quantum electronic or quantum optical devices that enable quantum computing in an architecture that has many common features with digital systems.

## Nanoscale Building Blocks

Individual molecules<sup>[8–12]</sup> and quantum dots,<sup>[13–15]</sup> which can be classified as zero-dimensional (0D) structures, have been proposed as building blocks for bottom-up assembly of nanoscale electronics. These 0D structures have been intensively pursued over the past decade since they represent the smallest building blocks with corresponding high potential for massive integration. However, the use of individual molecules or quantum dots in nanoelectronics has been limited by challenges in establishing reliable electrical contacts needed to study their fundamental properties and interconnect them. It has thus been difficult to elucidate and understand the intrinsic properties of individual devices, and moreover, to develop and demonstrate realistic schemes for scalable interconnection and integration of 0D devices into functional architectures.

One-dimensional nanostructures have also been the focus of extensive studies worldwide due to their unique physical properties and potential to revolutionize broad areas of nanotechnology. First, 1D nanostructures represent the smallest dimension structure that can efficiently transport electrical carriers, and thus are ideally suited to the critical and ubiquitous

task of moving and routing charges (information) in nanoscale electronics and optoelectronics. Second, 1D nanostructures can also exhibit device function, and thus can be exploited as both the wiring and device elements in architectures for functional nanosystems.<sup>[4,16]</sup> In this regard, two material classes, carbon nanotubes (NTs)<sup>[16–27]</sup> and semiconductor NWs,<sup>[28–35]</sup> have shown particular promise.

Single-walled carbon NTs can exhibit either metallic or semiconducting behavior depending on diameter and helicity.<sup>[17]</sup> The unique electronic properties of NTs open up the possibility of creating a number of different devices that could have potential in nanoelectronics.<sup>[16,18–20]</sup> For example, single-walled NTs have been used to fabricate room-temperature field effect transistors (FETs),<sup>[21,22]</sup> diodes<sup>[23,24]</sup> and recently, logic circuits.<sup>[25,26]</sup> However, the inability to control whether NT building blocks are semiconducting or metallic makes specific device fabrication largely a random event. Hence, moving beyond proof-of-concept single device elements to the integrated arrays required for nanoelectronics poses a serious issue for NT-based approaches. A creative solution to the problem of coexisting metallic and semiconducting NTs involves selective destruction of metallic tubes,<sup>[27]</sup> although such an approach requires extensive top-down lithography and subsequent processing to implement and may not be practical for highly integrated nanoelectronics systems.

Semiconductor NWs<sup>[4,28,29]</sup> represent another important type of nanometer scale wire structure. In contrast to NTs, however, semiconductor NWs can be rationally and predictably synthesized in single crystal form with all key parameters controlled, including chemical composition, diameter and length, and doping/electronic properties.<sup>[30–32]</sup> Semiconductor NWs thus represent one of best-defined and controlled class of nanoscale building blocks, which correspondingly have enabled a wide range of devices and integration strategies to be pursued. For example, semiconductor NWs have been assembled into nanometer scale FETs,<sup>[32,33]</sup> p–n diodes,<sup>[33,34]</sup> light emitting diodes (LEDs),<sup>[33]</sup> bipolar junction transistors,<sup>[34]</sup> complementary inverters,<sup>[34]</sup> complex logic gates, and even computational circuits that have been used to carry out basic digital calculations.<sup>[35]</sup> In contrast to NTs, NW devices can be assembled in a rational and predictable manner because the size, interfacial properties, and electronic properties of the NWs can be precisely controlled during synthesis, and moreover, reliable methods exist for their parallel assembly.<sup>[36]</sup> In addition, it is possible to combine distinct NW building blocks in ways not possible in conventional electronics and to leverage the knowledge base that exists for the chemical modification of inorganic surfaces<sup>[37,38]</sup> to produce semiconductor NW devices that achieve new function and correspondingly could lead to unexpected device and system concepts.

## Overview

In this entry, we describe a broad range of studies addressing nanoelectronics and nanophotonics assembled from semiconducting NW building blocks. First, we review electrical transport studies of individual NWs, and moreover, examine nanoscale electronic and optoelectronic devices assembled using individual NWs as building blocks. Next, we present approaches for the hierarchical assembly of NWs into well-defined arrays with controlled orientation and spatial location. Third, we address critical issues for integration and demonstrate the assembly of integrated nanoscale devices with logic and computation circuits. Lastly, we describe an application enabled today by nanoscale NW devices: highly sensitive and selective chemical and biological sensing. We conclude with a brief summary and perspective on future opportunities.

## NANOWIRE ELECTRONIC DEVICE ELEMENTS

In a previous entry, we have reviewed the rational synthesis of semiconductor NWs. The availability of a wide range of NW materials with controlled chemical composition, physical size, and electronic properties opens up many exciting opportunities ranging from fundamental studies of the role of dimensionality on physical properties to a range of potential applications in areas such as nanoscale electronics and optoelectronics. In the section, we focus on fabrication and electrical transport properties of basic nanoscale device elements fashioned from these NW building blocks, including 1) single NW-FETs, 2) crossed NW p–n diodes, intra-NW p–n diode, 3) bipolar transistors, 4) crossed NW-FETs, and 5) NW quantum interference devices.

### Nanowire Field Effect Transistors

#### Device structure and underlying principles

The basic FET structure fabricated from single semiconducting NWs is illustrated in Fig. 3. The FET is supported on an oxidized silicon substrate with the underlying conducting silicon used as a global back gate electrode to vary the electrostatic potential of the NW. In a typical NW-FET device (Fig. 3, inset), two metal contacts, which correspond to source and drain electrodes, are defined by electron beam lithography followed by evaporation of suitable metal contacts. Current ( $I$ ) vs. source–drain voltage ( $V_{sd}$ ) and  $I$  vs. gate voltage ( $V_g$ ) is then recorded for a NW-FET to characterize its electrical properties.

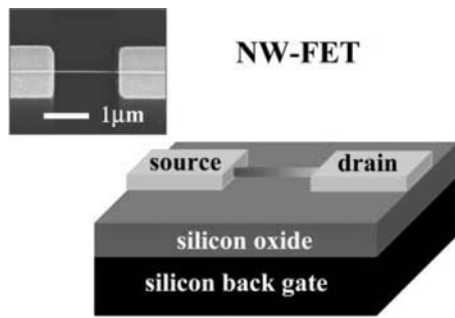


**Fig. 3** Schematic of a NW-FET. Inset: SEM image of a NW-FET; two metal electrodes, which correspond to source and drain, are visible at the left and right sides of the image.

Variation of  $V_g$  during characterization of the NW-FET enables important qualitative and quantitative properties to be elucidated. For example, changes in  $V_g$  produce variations in the electrostatic potential of the NW, and hence change the carrier concentration and conductance of the NW. As shown in Fig. 4, p- and n-type semiconductor NWs, which are contacted at both ends to metal electrodes, respond in opposite ways to the applied gate. When a positive  $V_g$  is applied, the bands are lowered, which depletes the holes and suppresses conductivity in p-NWs, but leads to an accumulation of electrons and an enhancement in conductivity in n-NWs. Conversely, a negative  $V_g$  will increase the conductivity of p-type NWs and decrease the conductivity of the n-type NWs.

### p-Channel nanowire transistors

Typical  $I$  vs.  $V_{sd}$  data obtained from a single boron-doped Si NW-FET at different  $V_g$ s are shown in Fig. 5. The two-terminal  $I$ - $V_{sd}$  curves are linear, which indicates that the metal electrodes make ohmic contacts to the NW, and moreover, the gate response demonstrates that the NW is p-type; that is, the conductance of the p-Si NW decreases (increases) with increasingly positive (negative)  $V_g$ . The transfer characteristics,  $I$ - $V_g$ , of p-Si NW devices (Fig. 5, inset) exhibit behavior typical of p-channel metal-oxide-semiconductor FETs (MOSFETs).<sup>[39]</sup> Significantly, the conductance modulation of the p-Si NW-FET exceeds  $10^3$ , where the  $V_g$  required for switching ( $-10$  to  $10$  V) could be reduced significantly by reducing the thick (600 nm) oxide dielectric layer in these back-gated devices.

Gate-dependent measurements have also been used to estimate the hole concentration in p-channel NW-FETs. The total NW charge can be expressed as  $Q = C \cdot V_{th}$ , where  $C$  is the NW capacitance and  $V_{th}$  the threshold gate voltage required to deplete completely the NW. The capacitance is given by  $C \cong 2\pi\epsilon\epsilon_0L/\ln(2h/r)$ , where  $\epsilon$  is the effective gate

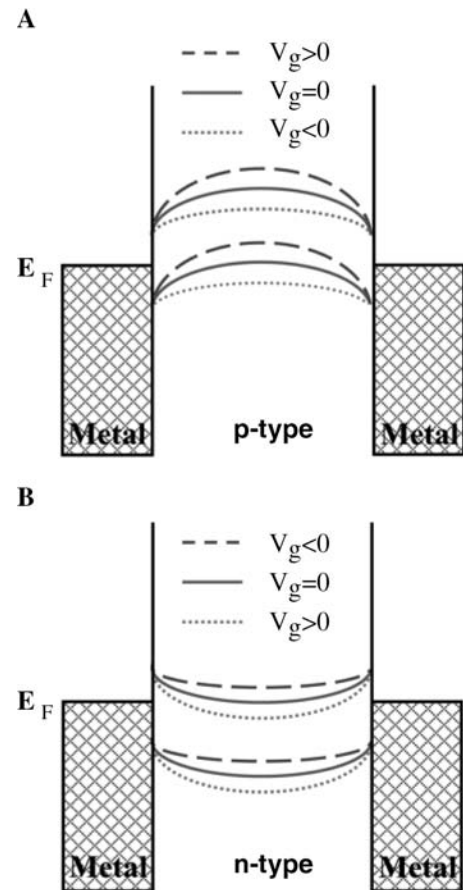


**Fig. 4** (A,B) Band diagrams illustrating the underlying principle for p- and n-channel NW-FETs. When a positive voltage is applied, the bands are lowered, which depletes the holes in p-NWs and suppresses conductivity, but leads to an accumulation of electrons in n-NWs and enhances the conductivity. Conversely, a negative gate voltage will raise the bands and increase the conductivity of p-type NWs and decrease the conductivity of the n-type NWs.

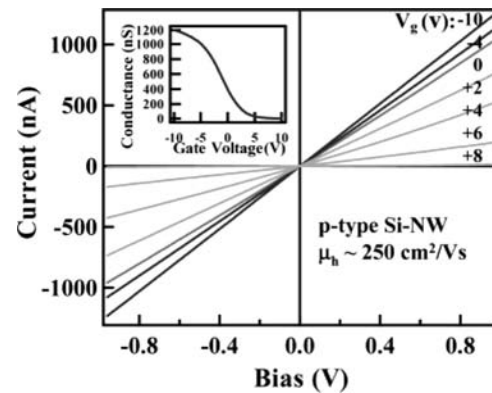


**Fig. 5** Current vs. voltage for a p-type Si NW-FET. The numbers inside the plot indicate the corresponding gate voltages ( $V_g$ ). The inset shows current vs.  $V_g$  for  $V_{sd}$  of 1 V.

oxide dielectric constant,  $h$  is the thickness of the SiO<sub>2</sub> layer on the substrate,  $L$  is the NW length, and  $r$  is the NW radius. The hole density,  $n_h = Q/(e \cdot \pi r^2 L)$ , is estimated to be  $\sim 10^{18}/\text{cm}^3$  for the device shown in Fig. 5. In addition, it is possible to estimate the carrier mobility of the NW-FETs from the transconductance  $dI/dV_g = \mu(C/L^2) V_{sd}$ , where  $\mu$  is the carrier mobility. Plots of  $dI/dV_g$  vs.  $V_{sd}$  are linear for Si NWs, as expected for this model, yield hole mobilities in the range of 50–800 cm<sup>2</sup>/V sec. Significantly, the p-Si NW-FET mobilities are comparable to or larger than the best p-Si planar devices, 100–300 cm<sup>2</sup>/V sec, at comparable hole densities ( $p \sim 10^{17}$ – $10^{18}/\text{cm}^3$ ).<sup>[40]</sup>

### n-Channel nanowire transistors

It is also possible to assemble n-channel NW-FETs in a similar way from n-type NWs. For example, gate-dependent  $I$ – $V_{sd}$  data recorded from an InP NW-FET exhibits increased conductance for positive  $V_g$  and decreased conductance for negative  $V_g$  (Fig. 6), as expected for an n-channel device. The n-InP NW-FET transfer characteristics ( $I$  –  $V_g$ ) show that the current increases rapidly from below 1 nA at  $V_g = -2$  V to above 400 nA at  $V_g = +2$  V (Fig. 6, inset), and tends to saturate at higher voltages, which can be attributed to contact resistance and other factors. Nevertheless, the conductance changes up three orders of magnitude for only a few volts' change in the gate voltage in these unoptimized devices.

The electron concentration and mobility in the n-channel NW-FETs have been estimated as described above for p-channel devices. For the n-InP NW-FET shown in Fig. 6, the electron mobility is 2200 cm<sup>2</sup>/V sec for an electron concentration of  $\sim 10^{18}/\text{cm}^3$ . Studies of a number of different devices yields mobility values from 400 to 3000 cm<sup>2</sup>/V sec, which is comparable to or larger than bulk InP, 1000–2000 cm<sup>2</sup>/V sec, at similar carrier concentrations.<sup>[40]</sup> These mobilities are

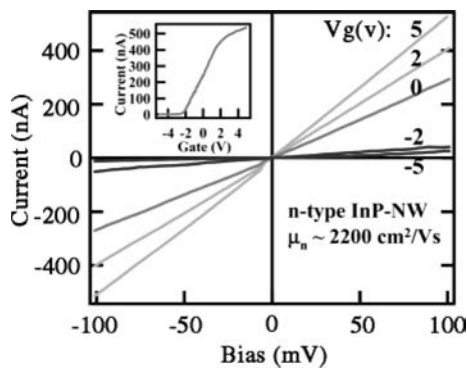


**Fig. 6** Current vs. voltage for an n-type InP NW-FET. The numbers inside the plot indicate the corresponding gate voltages ( $V_g$ ). The inset shows current vs.  $V_g$  for  $V_{sd}$  of 0.1 V.

believed to represent a lower limit in our NW materials since the contact resistance and surface depletion have not been included. Significantly, surface passivation studies suggest that substantially higher carrier mobilities are possible in the NW-FETs. Taken together, these results suggest that the NW-FETs could be essential elements in high performance (e.g., high gain, high speed and low power) nanoelectronics and photonics.

### Crossed Nanowire p–n Diodes

The availability of well-defined n- and p-type NW building blocks opens up the possibility of creating complex functional devices by forming junctions between two or more wires. To explore this exciting opportunity, we have studied the transport behavior of n–n, p–p, and p–n junctions formed by crossing two n-type, two p-type, and one n-type and one p-type NW, respectively (Fig. 7A).<sup>[33]</sup> Significantly, the types of junctions studied in an experiment are reproducible since we can select the specific type of NW used at each of the two stages of device assembly.

First,  $I$ – $V$  data recorded on the individual NWs in n–n and p–p crossed junctions show linear or nearly linear  $I$ – $V$  behavior (Fig. 7B,C), indicating that the metal electrodes used in the experiments make ohmic or nearly ohmic contact to the NWs. This point is

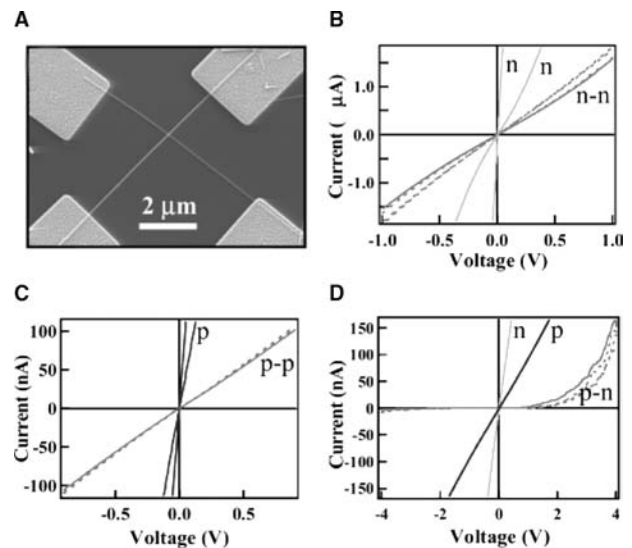


**Fig. 7** Crossed NW junctions. (A) SEM image of a typical crossed InP NW device with four metal electrodes contacted to each of the four arms. (B–D)  $I$ – $V$  behavior of n–n, p–p, and p–n junctions, respectively. The  $I$ – $V$  behavior of individual n- and p-NWs in the junctions is indicated by “n” and “p”, respectively. The  $I$ – $V$  behavior across the junctions is designated by “n–n”, “p–p”, and “p–n”. The solid lines represent transport behavior across one pair of adjacent arms, and the dashed lines represent that of the other three pairs of adjacent arms. *Source:* From Ref.<sup>[33]</sup>.



important since it shows that the NW–metal contacts will not make nonlinear contributions to the  $I$ – $V$  measurements across the nanoscale junctions. In general, transport measurements recorded across the n–n and p–p junctions show linear or nearly linear behavior. These results indicate that interface oxide between individual NWs does not produce a significant tunneling barrier since a tunneling barrier would lead to highly nonlinear  $I$ – $V$  behavior. In addition, the  $I$ – $V$  curves recorded through each pair of adjacent arms show similar current levels, which are smaller than that of the individual NWs themselves, demonstrating that the junction dominates the transport behavior. Taken as a whole, these data show that individual NWs can make good electrical contact with each other, despite the small contact area ( $10^{-12}$ – $10^{-10}$  cm<sup>2</sup>) and simple method of junction fabrication.

Initial studies designed to probe the utility of this new approach for creating functional devices were focused on p–n junctions from crossed p- and n-type NWs. These junctions can be made reproducibly by sequential deposition of dilute solutions of n- and p-type NWs with intermediate drying. Typical  $I$ – $V$  behavior of a crossed InP NW p–n junction is shown in Fig. 20D. The linear  $I$ – $V$  of the individual n- and p-type NWs components indicates ohmic contact between the NWs and metal electrodes, while transport across the p–n junction shows clear current rectification; that is, little current flows in reverse bias, while there is a sharp current onset in forward bias. Significantly, this behavior is similar to conventional semiconductor p–n junctions. In a standard p–n junction, rectification arises from the potential barrier formed at the interface between p- and n-type materials.<sup>[39]</sup> In the case of our crossed NW p–n junctions, this picture is probably modified due to the presence of some interface oxide (Fig. 8), although a thin oxide will not change substantially the overall  $I$ – $V$  response.

The assignment of the observed rectification to the p–n junction formed at the crossing point between p- and n-type InP NWs was further supported by several other pieces of evidence. First, the linear or nearly

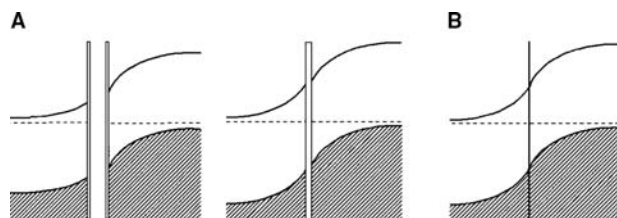


**Fig. 8** Band diagrams of the crossed NW p–n junction. (A) Band bending occurs prior to p–n contact due to surface Fermi level pinning; the bands bend further when the p- and n-type NWs come into contact to achieve equilibrium; (B) band bending in a clean p–n junction structure.

linear  $I$ – $V$  behavior of individual p- and n-type NWs shows that ohmic contacts were been made between the NWs and metal electrodes, and thus exclude the possibility that rectification arises from metal–semiconductor Schottky diodes.<sup>[39]</sup> Second, the  $I$ – $V$  behavior of the junction determined through each pair of adjacent electrodes (Fig. 7D) exhibit similar rectification and current level, which is also much smaller than the current through individual NWs, demonstrating that the junction dominates the  $I$ – $V$  behavior. Third, four-terminal measurements in which current is passed through two adjacent electrodes while the junction voltage drop is measured across the two remaining electrodes exhibit similar  $I$ – $V$  and rectification with only a slightly smaller voltage drop (0.1–0.2 V) compared to two-terminal measurements at the same current level. Fourth, measurements made on over 20 independent InP crossed p–n junctions showed similar rectification in the  $I$ – $V$  data. Lastly, the formation of crossed NW p–n junctions is not by any means restricted to InP NWs, and is general to the wide range of materials. For example, p–n junctions have been assembled from p-Si/n-Si,<sup>[34]</sup> p-Si/n-GaN,<sup>[35]</sup> p-Si/n-InP, p-Si/n-CdS, and p-Si/n-CdSe NWs,<sup>[41]</sup> and transport measurements have demonstrated that all of these crossed p–n junctions show consistent current rectification behavior.

## Bipolar Junction Transistors

Since p–n junctions represent a basic element in many functional electronic devices, including amplifiers and switches, we have explored the possibility of assembling such devices at nanometer scale using the well-defined p- and n-type NW materials. As an example, integrated bipolar transistors,<sup>[34]</sup> which are active devices capable of current gain, have been assembled from three distinct types of Si NWs in the form of two crossed junctions (Fig. 9A). A conventional bipolar transistor requires three distinct material types. For example, in  $n^+$ –p–n structure, a highly doped  $n^+$  layer is used as an emitter (E), a p-type layer for the base (B), and an n-type layer for the collector (C).<sup>[39]</sup> Significantly, this  $n^+$ –p–n basic structure can be easily assembled with Si NWs since NWs with controlled doping type and doping concentration are available (Fig. 9C, inset).<sup>[32]</sup>

To characterize the electrical behavior of assembled NW bipolar transistors, the individual Si NW building blocks and p– $n^+$  and p–n junctions were first tested, and found to exhibit ohmic or nearly ohmic metal contacts and rectification, respectively. The bipolar transistor characteristics were then assessed from measurements of the collector current as a function of C–B voltage (Fig. 9B), while the  $n^+$  Si NW emitter

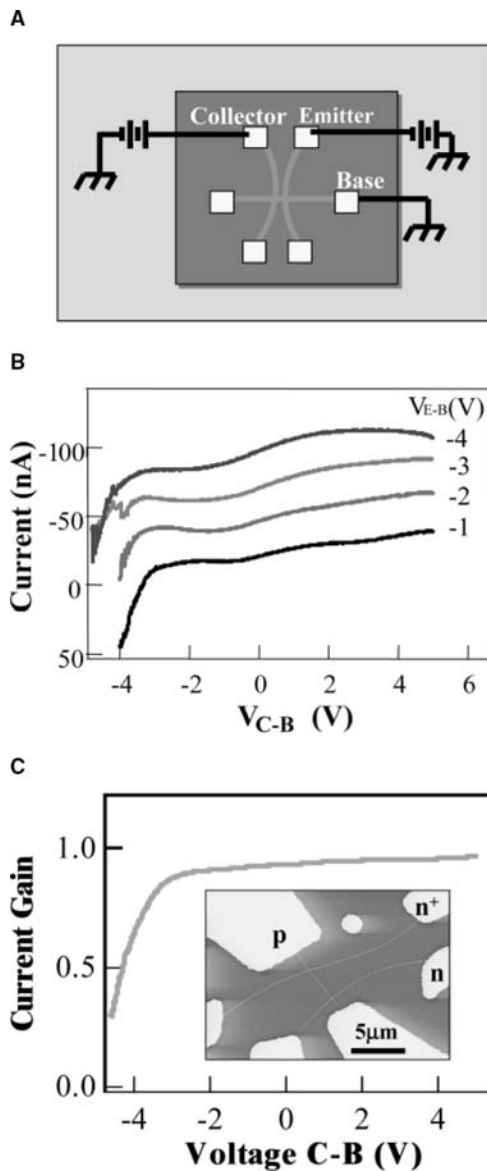


**Fig. 9** Bipolar junction transistors. (A) Schematic illustrating the common base configuration of an  $n^+$ - $p$ - $n$  bipolar transistor built from crossed Si NWs. (B) Collector current vs. collector-base voltage recorded on an  $n^+$ - $p$ - $n$  transistor with emitter and collector Si NWs 15  $\mu\text{m}$  apart. The numbers inside the plot indicate the corresponding emitter-base voltages. (C) The common base current gain vs. collector-base voltage. Inset: Typical SEM image of Si NW bipolar transistors. *Source:* From Ref.<sup>[34]</sup>.

was biased at different values. In general, the collector current is relatively constant (vs. C-B voltage) in the region from 0 to 6 V, which corresponds to the collector in reverse bias with only a very small leakage current, and this current value increases as the emitter forward bias/injected current is increased. The large collector current in reverse bias demonstrates these simple Si NW-based bipolar transistors exhibit behavior similar to that found in standard planar devices,

and moreover, can exhibit very good current gain. The common base current gain, which is defined as the ratio of the collector current to emitter current (Fig. 9C), and the common emitter current gain, which is defined as the ratio of the collector current to base current, were found to be 0.94 and 16, respectively. The relatively large current gain observed in these simple devices suggests several important points. First, the efficiency of electron injection from emitter to base must be quite high, and can be attributed to the controlled NW doping that yields the desired  $n^+$ - $p$  E-B junction. Second, large current gains have been achieved in devices with large (e.g., 15  $\mu\text{m}$ ) base widths. This fact suggests that the mobility of injected electrons can be quite high in the Si NWs and is consistent with the direct mobility studies described above. These observations also indicate clear directions for improving the Si NW bipolar transistors. For example, it will be interesting to study the current gain as a function of base width, because it is easily possible to assemble structures with separations of the  $n^+$  and  $n$ -NWs of the order of 100 nm or less.

### Crossed Nanowire Field Effect Transistors

A major motivation underlying research on nanoscale devices is to achieve integration at densities higher than possible with current technologies. The NW-FETs discussed above represent nanoscale analogs to conventional MOSFETs and have been very useful for testing basic device behavior (e.g., doping type and carrier mobility). However, the basic device structure of the NW-FETs and similar NT FETs<sup>[21,22]</sup> requires lithography to define metallic source-drain electrodes, and use either a global back gate (i.e., the doped silicon substrate) or lithography to define a more local gate. These design and fabrication features pose serious problems for integration. First, lithographically defined metal electrodes (i.e., source, drain, and gate) will limit integration to a level similar to that of conventional silicon technology. Moreover, the use of global back gate electrodes eliminates the possibility of independently addressing individual devices, and thus is incompatible with integration in most architectures.

Direct assembly of highly integrated functional electronic circuits based on NWs requires the development of new device concepts that are amenable to scalable integration. To this end, we recently developed a novel crossed NW-based FET.<sup>[35]</sup> A crossed NW-FET (cNW-FET) is assembled from two NWs where one or both have an oxide coating that serves as the gate dielectric (Fig. 10A,B). This approach is quite flexible since nano-FETs can be readily assembled with  $p$ - or  $n$ -type active channel NWs and the gate NW can also be  $p$ - or  $n$ -type independent of the channel. For

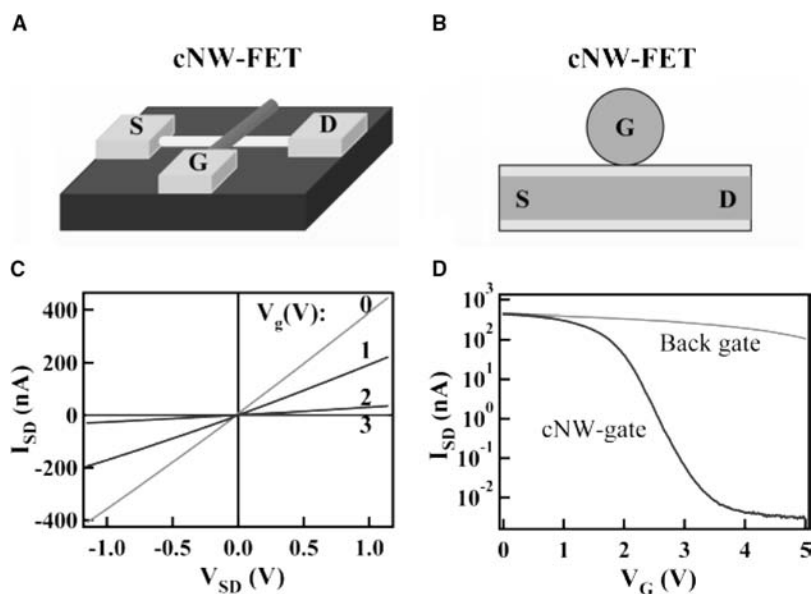


**Fig. 10** Crossed NW-FET (cNW-FET). (A) Schematics illustrating the cNW-FET concept. A nano-FET with both nanoscale conducting channel and nanoscale gate is obtained with one NW used as the gate for the other NW in a crossed configuration. (B) Schematic showing the critical device dimensions of the cNW-FET. Three intrinsic nanometer scale metrics are naturally defined by the structure (see text). (C) Gate-dependent  $I$ - $V_{sd}$  characteristics of a crossed NW-FET. The NW gate voltage for each  $I$ - $V$  curve is indicated (0, 1, 2, and 3 V). (D) The curves showing  $I$  vs.  $V_g$  for n-NW and global back (light gray) gates for  $V_{sd}$  of 1 V. Source: From Ref.<sup>[35]</sup>.

example, using n-type GaN crossed NW as the gate for a p-type Si NW, a p-channel cNW-FET is formed with both a nanoscale channel and a nanoscale gate. Typical  $I$ - $V_{sd}$  data recorded for different NW  $V_g$ s resemble the characteristics of a conventional depletion mode p-channel FET device (Fig. 10C). Notably, the conductance of the Si NW responds very sensitively to the voltage applied to n-NW gate, and can be changed by more than five orders of magnitude with a 1–2 V variation in the NW gate (Fig. 10D). In contrast, the conductance changed less than a factor of 10 for this same device when similar gate voltages were applied to the global back gate (Fig. 23D). The improved sensitivity can be attributed to the intrinsically thin gate dielectric between the two NWs. In addition, there is no leakage current from the n-NW gate when the cNW-FET is operated at low source–drain bias in the depletion mode since the crossed p–n junction is always reverse biased, and in this regard the device is similar to a junction FETs (JFETs).<sup>[39]</sup>

The cNW-FET represents an important new transistor concept for nanoelectronics. With this concept, three critical nanometer scale device metrics are naturally defined in assembled circuits without lithography: 1) a nanoscale channel width determined by the diameter of the active NW; 2) a nanoscale channel length defined by the crossed NW gate diameter; and 3) a nanoscale gate dielectric thickness determined by the NW surface oxide. Significantly, these distinct nanometer scale metrics are determined and can be controlled with near atomic precision during NW synthesis and subsequent assembly, and should enable higher gain, higher speed, and lower power dissipation devices than possible by conventional approaches. Moreover, the cNW-FET concept can be readily

integrated in a parallel manner without lithography, thus enabling one to envision a straightforward way to nanometer scale integrated electronics of the future. Examples of more complex devices—logic gates— assembled from cNW-FET elements are discussed in section “Integrated Nanowire Devices”.

### Summary and Future Directions

Overall, in this section, we have shown that semiconductor NW materials can be doped p- and n-type in a precisely controlled way, and these electronically well-defined NW materials thus enable the assembly of a broad range of nanoscale electronic and optoelectronic devices, including FET, crossed NW p–n diodes, intra-NW p–n diode, bipolar transistors, cNW-FETs. Together, these devices represent a set of critical elements for the bottom-up assembly of more complex electronic circuits. To exploit best, this tool box of elements for building highly integrated electronic circuits will require several issues to be addressed, including: 1) production of device elements in high yield, 2) development of rational methods for assembly of these elements into integrated device arrays, and 3) development of system architectures that best utilize these device element function(s) and assembly capabilities. These important issues are further addressed in sections below.

The availability of electronically well-defined NW building blocks, which have enabled to demonstrate a series of nanoscale electronic devices, opens many exciting opportunities in nanoscale science and technology. For example, the nanoscale electronic devices may enable us to construct functional electronic

circuits with integration density far beyond current technologies. The wide range of electronic applications described above are based primarily upon diffusive motion of electrons as in conventional devices—their uniqueness arises from the small size scale and our ability to obtain unique function from combinations of materials that would be incompatible with conventional fabrication processes. In addition, other effects, such as the quantum mechanical or wave-like nature of carriers, will need to be accounted for for sufficiently small structures,<sup>[15,42]</sup> and at the same time could open up entirely new possibilities for electronic manipulation and devices.<sup>[43]</sup>

The intrinsically nanometer scale devices assembled from NWs or NTs represent ideal systems to probe quantum phenomena and exploit devices exhibiting such phenomena for fundamentally new applications such as quantum computation.<sup>[44,45]</sup> The availability of a wide range of NW materials opens up considerable opportunity for exploring these exciting directions since fundamental properties, such as the Fermi wavelength and number of conduction channels, can be systematically varied through choice of NW material (e.g., InAs vs. Si) and diameter, respectively.

As an example of the potential of NWs to enable behavior not readily accessible with conventional planar devices, we consider recent studies of InAs NWs (Fig. 11A). Significantly, temperature dependent three-terminal transport studies show that the conductance of individual InAs NWs remain essentially unchanged over the temperature range from 300 K down to 1.6 K (Fig. 11B). The temperature independent transport suggests strongly that electrons are not inelastically scattered by either impurities or phonons within the NWs, that is, that the electron transport is ballistic. This important conclusion is supported by several other pieces of data, including 1) most of the InAs NWs exhibit conductance values ranging from one quantum conductance ( $G_0 = 2e^2/h$ ) to  $8G_0$  and 2) the conductance shows little or no dependence on NW length. We have also obtained similar results for clean Si NWs, and thus believe that the ballistic transport phenomena can be considered as a general property to exploit in NW-based nanoelectronics.

Transport studies also suggest that InAs and Si NWs can exhibit coherent phenomena. Specifically, low-temperature gate voltage-dependent conductance measurements exhibit reproducible, quasi-periodic conductance oscillations (Fig. 11C). These oscillations can be interpreted as quantum interference between electron waves reflected by two metallic contacts, much like optical waves interfere within a Fabry–Perot cavity. In our NW electron cavities, the gate-voltage modulates the Fermi level, and hence changes the Fermi wavelength and the interference of the electron waves inside the NW. The observed electron–wave

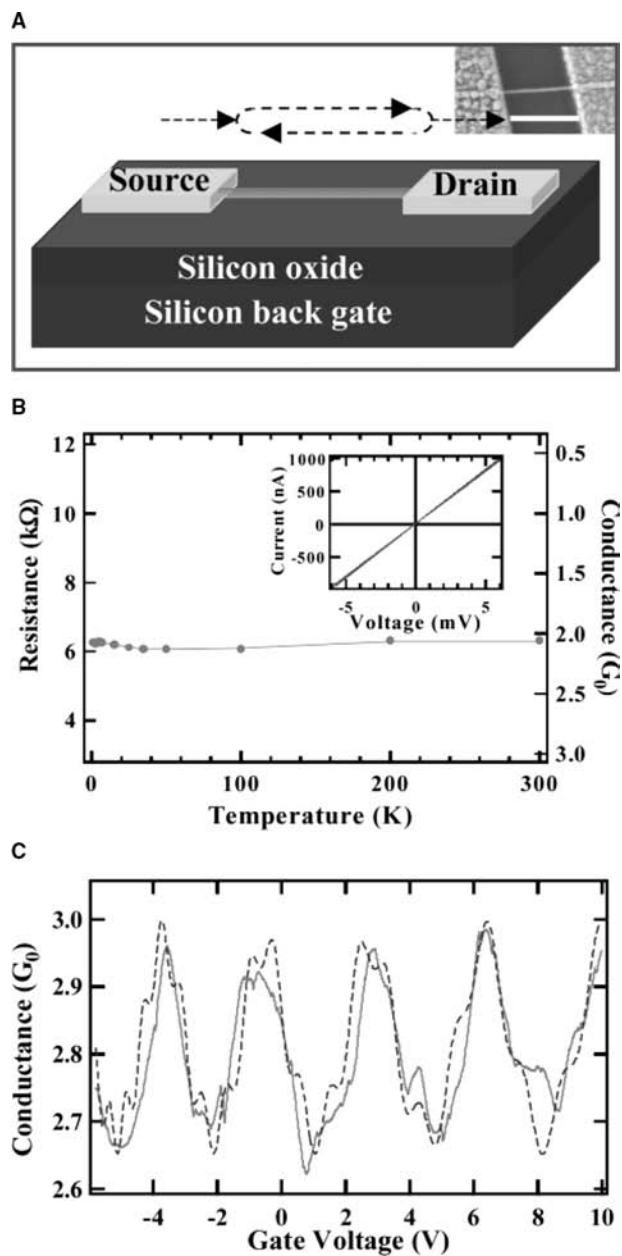


**Fig. 11** Low temperature studies of InAs NWs. (A) Schematic showing an InAs NW device. Electron waves inside the NWs are partially reflected at the two metallic contacts, and the forward and backward reflected waves quantum mechanically interfere with each other. (B) Conductance vs. temperature of an InAs NW device. (C) Conductance vs. gate voltage ( $V_{sd} = 0.5$  mV) at 1.6 K. The dashed line corresponds to a theoretical fit based on multichannel Landauer formalism discussed in the text.

interference has been quantitatively analyzed using a multichannel Landauer formalism,<sup>[42,46]</sup> where the overall conductance is determined from two  $6 \times 6$  scattering matrices representing the NW–metal contacts and one  $6 \times 6$  transmission matrix inside the NWs.<sup>[45]</sup> Significantly, the calculated conductance



behavior accounts for both major and minor oscillatory features in the data, and show that these different features arise from the different sub-band modes of relevance to the InAs NW cavity.

The unique transport properties of these InAs and similar NWs could lead to a number of exciting opportunities for devices and systems integration. For example, ballistic transport will be important to advance interconnects and highly integrated nano-systems since it eliminates power dissipation within the NW. Ballistic and coherent transport should also enable spin-dependent transport and spin-based devices.<sup>[47]</sup> Moreover, the ability of NWs to exhibit coherence over large distances—that is, transmit quantum mechanical information—should also be important in the emerging field of quantum computing.<sup>[44]</sup> In a quantum computer, the usual digital “bits” are replaced by quantum bits (qubits), and these qubits can be manipulated in very different ways by forming superpositions or entangled states, and thereby used to solve computing tasks inaccessible to digital systems. We believe that the availability of high quality NW materials opens up a new pathway for assembling quantum devices and potentially exploiting the potential of quantum computing.

## NANOSCALE OPTOELECTRONICS AND PHOTONICS

In addition to nanoscale electronics, the broad range of optically active III–V and II–VI group compound semiconductor NW materials are attractive as building blocks for miniaturized photonic and optoelectronic devices. In this section, we review exciting progress in this area. First, we discuss results from fundamental photoluminescence (PL) studies of individual NWs. Second, we review assembly and properties of a wide range of photonic devices, including nanoscale LEDs, NW optical cavities, single NW lasers, and photodetectors.

### Photoluminescence Studies of Individual Nanowires

Photoluminescence studies on individual NWs reveal that they exhibit strong PL and can be readily imaged with a liquid nitrogen cooled CCD camera. For example, PL image of an InP NW clearly shows an elongate emission along the wire axis (Fig. 12A). The PL spectrum shows a peak maximum at  $\sim 805$  nm in contrast to bulk value of  $\sim 925$  nm (Fig. 12B). This large blueshift suggests the radial quantum confinement of excitons in the NW, which have been addressed in detail by size-dependence PL studies.<sup>[48]</sup>

In addition to strong quantum confinement caused by the large confining potential for both electrons

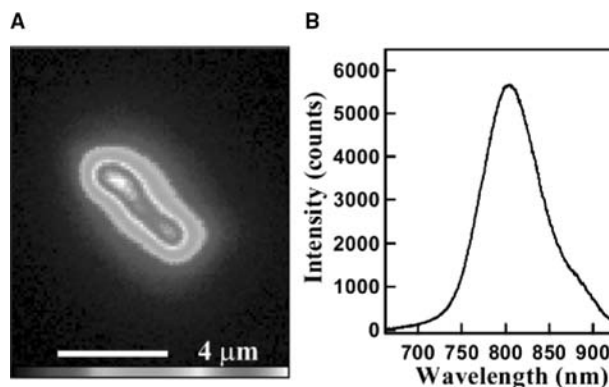


**Fig. 12** Photoluminescence studies of individual NWs. (A) Room-temperature PL image and (B) spectrum from single InP NW.

and holes, another unique feature of free-standing NW structures is the large variation in the dielectric constant between the NW and surrounding (air) medium, which could lead to strikingly new phenomena. For example, PL studies of individual InP NWs show that the PL intensity essentially turns from “on” to “off” as the excitation polarization is rotated from parallel to perpendicular (Fig. 13A,B).<sup>[49]</sup> Integration of the emission intensity as a function of excitation angle shows that the PL intensity exhibits a periodic dependence ( $\cos^2 \theta$ ) on the angle. Photoluminescence spectra recorded from NWs of different diameters ranging from 10 to 50 nm show similar large anisotropy in either excitation (Fig. 13C) or emission polarization (Fig. 13D). In both cases, the ratio of parallel to perpendicular emission is greater than an order of magnitude, with a polarization ratio  $\rho = (I_{\parallel} - I_{\perp}) / (I_{\parallel} + I_{\perp})$  of  $0.91 \pm 0.07$ . This large polarization ratio is significantly larger than previously reported (buried) quantum wire samples, where the polarization anisotropy has been attributed to the mixing of valence bands due to quantum confinement. This quantum mechanical effect yields a much smaller polarization ratio of  $\rho < 0.60$ <sup>[50–52]</sup> and cannot be used to explain the large polarization ratio in the free-standing NWs. Rather, the large and unprecedented polarization anisotropy in the free-standing NWs can be accounted for quantitatively by considering the dielectric contrast between a NW and its air or vacuum surroundings; that is, the perpendicular electric field amplitude is attenuated according to  $E_i = [2\epsilon_0 / (\epsilon + \epsilon_0) E_e]$ , where  $E_i$  is the electric field inside the cylinder,  $E_e$  is the excitation field, and  $\epsilon(\epsilon_0)$  is the dielectric constant of the cylinder (vacuum) (Fig. 13E).<sup>[53]</sup> This model yields a theoretical polarization ratio,  $\rho = 0.96$ , in good agreement with the experimental results for InP NWs.

The strong polarized PL emission from individual NWs allows us to explore them for many exciting

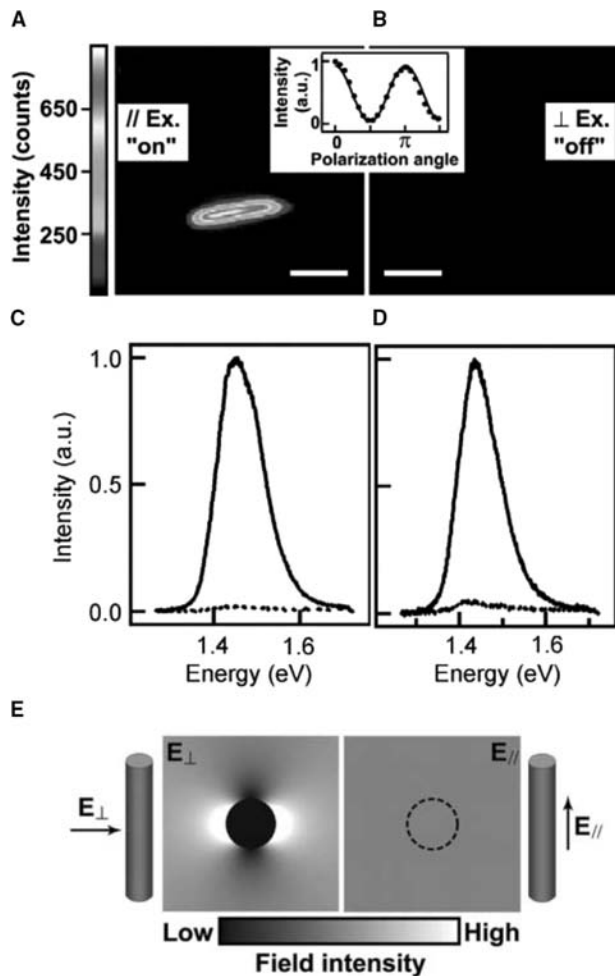


**Fig. 13** Polarized PL excitation and emission from individual NWs. (A) Photoluminescence image of a single 20 nm InP NW with the exciting laser polarized along the wire axis. Scale bar, 3 μm. (B) Photoluminescence image of the same NW as in (A) under perpendicular excitation. Inset: Variation of overall PL intensity as a function of excitation polarization angle with respect to the NW axis. (C) Excitation spectra of a 15 nm diameter InP NW. These spectra were recorded with the polarization of the exciting laser aligned parallel (solid line) and perpendicular (dashed line) to the wire axis. (D) Emission spectra of the same wire as in (C). These spectra were taken with the excitation parallel to the wire, while a polarizer was placed in the detection optics. (E) Dielectric contrast model of polarization anisotropy. Source: From Ref.<sup>[49]</sup>.

application in nanophotonics. For example, the previously described GaAs/GaP NW superlattice structures represent an attractive system for applications such as nanobarcodes because GaAs is a direct band gap semiconductor, while GaP has an indirect gap.<sup>[54]</sup> Indeed, PL imaging of individual NWs from the equally spaced (GaP/GaAs)<sub>3</sub> superlattice sample shows that these NWs exhibit an emission pattern of three spots separated by dark regions (Fig. 14A). This

pattern is consistent with emission originating from the three GaAs regions, separated by dark GaP regions that act as optical “spacers.” Control experiments on individual samples of pure GaAs and GaP NWs confirm that strong luminescence is obtained from GaAs but not GaP, as expected. The GaAs regions also exhibit a strong polarization dependence, emitting when the excitation is polarized parallel (||) to the NW axis and appearing dark when the polarization is perpendicular (⊥) to the NW axis (Fig. 14A, inset).

Such superlattice systems can be further extended to more complicated structures. First, the PL image of an 11-layer superlattice in which the length of the GaP regions was doubled each layer while maintaining a constant GaAs period (Fig. 14B) shows clearly that the separation between emitting GaAs regions is doubling along the length of the NW. Second, the PL image of 21-layer GaP/GaAs superlattices (Fig. 14C) consisting of a short 4-period (GaP/GaAs) repeat, followed by three longer GaP spacer repeats, and ending in a relatively short 4-period (GaAs/GaP) repeat shows consistent PL patterns. We consider that, in their present form, these NW superlattice structures could be exploited as optical nanobarcodes, which could be useful as labels for imaging. Moreover, the wide range of group III–V and II–VI NWs that have been demonstrated previously suggests that it should be possible to encode additional information through variations in the color of the emitting region using multicomponent superlattices. Using materials with a large dielectric contrast might also enable the creation of 1D waveguides with built-in photonic band gaps, or of cavities for NW lasers.

### Crossed Nanowire Light Emitting Diodes

The observation of strong PL from individual NWs has stimulated further interest in exploiting such NWs for optoelectronics. We have previously described a wide range of electronic device assembled from NWs including p–n diodes. In direct band gap semiconductors like InP, the p–n diode also forms the basis for the critical optoelectronics devices, including LED and laser diode. To assess whether our nanoscale devices might behave similarly, we have studied the electroluminescence (EL) from crossed NW p–n junctions. Significantly, EL can be readily observed from these nanoscale junctions in forward bias.<sup>[33]</sup> A three-dimensional (3D) plot of the EL intensity taken from a typical NW p–n diode at forward bias (Fig. 15A) shows the emitted light comes from a point-like source, and moreover, comparison of EL and PL images (Fig. 15A, inset) recorded on the same sample shows that the position of the EL maximum corresponds to the crossing point in the PL image.



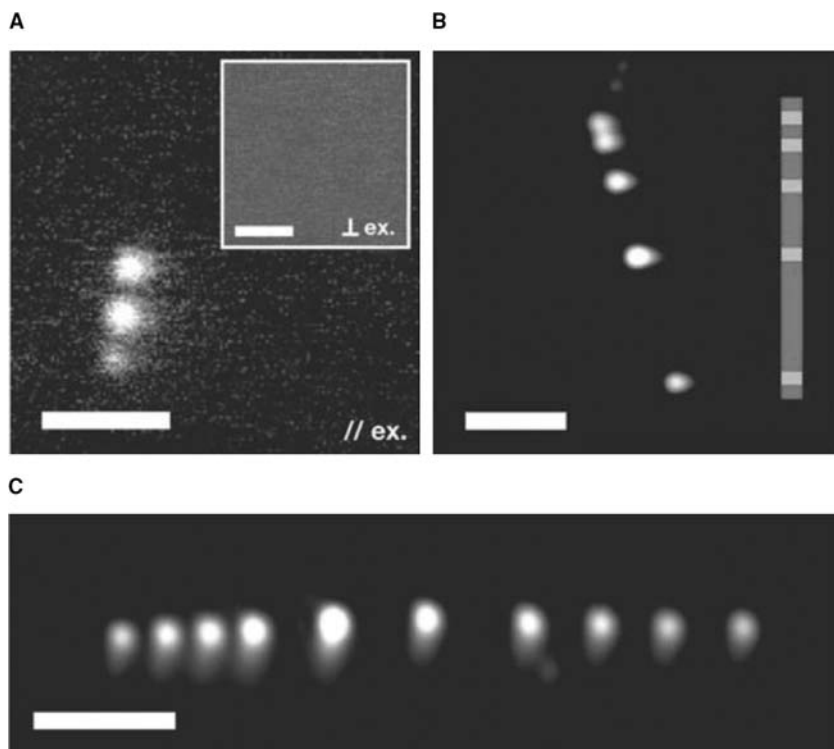


**Fig. 14** Nanowire nanobarcode. (A) Photoluminescence image ( $\parallel$  excitation) of a NW with a  $(\text{GaAs}/\text{GaP})_3$  superlattice structure. The three bright and dark regions correspond to the three GaAs (direct band gap) and GaP (indirect band gap) regions, respectively. Inset: No PL is observed above background for perpendicular excitation. Scale bar, 5 nm. (B) Photoluminescence image of a 40 nm diameter GaP(5)/GaAs(5)/GaP(5)/GaAs(5)/GaP(10)/GaAs(5)/GaP(20)/GaAs(5)/GaP(40)/GaAs(5)/GaP(5) superlattice; the numbers in parentheses correspond to the growth times in seconds for each layer. Inset: Diagram showing the relative lengths of GaAs (blue) and GaP (red) layers. Scale bar, 5 nm. (C) Photoluminescence image of a 21-layer superlattice  $(\text{GaP}/\text{GaAs})_{10}\text{GaP}$ , showing a group of four equally spaced spots on the left, two in the middle with larger gaps, and another set of four with equal spacing on the end. The superlattice is 25 nm in length. *Source:* From Ref.<sup>[54]</sup>.

These data thus demonstrate that the emitted light indeed comes from the crossed NW p-n junction.

Characterization of the EL intensity as a function of forward bias of the junction shows that significant light can be detected with our system at a voltage as low as 1.7 V (Fig. 15B). Further increases in forward bias beyond this “turn-on” voltage produce rapid increase in the EL intensity. In addition, EL spectra recorded from the cNW-LEDs exhibit blueshifts relative to the bulk band gap of InP (925 nm) (Fig. 15C). The blueshifts are due in part to quantum confinement<sup>[55]</sup> of

excitons, although other factors may also contribute. Furthermore, PL studies have demonstrated that the PL peak can be systematically blueshifted as the NW diameter is decreased,<sup>[48]</sup> and thus these results provide a means for controlling the color of the LEDs in a well-defined way. Indeed, EL results recorded from p-n junctions assembled from smaller (and larger) diameter NWs show larger (smaller) blueshifts. In addition, the emission color from nano-LEDs can be further varied by using chemically distinct semiconductor NWs with different band gaps. Considering the wide range of

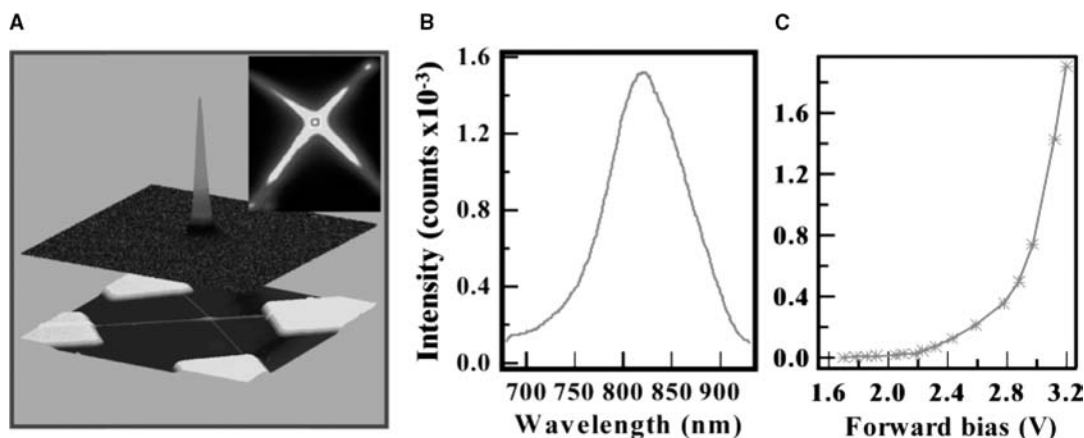


**Fig. 15** Crossed NW LED. (A) (Top) Three-dimensional (3D) plot of light intensity of the EL from a crossed NW LED. Light is only observed around the crossing region. (Bottom) Three-dimensional atomic force microscope image of a crossed NW LED. Inset: PL image of the crossed NW junction. (B) Spectrum of the emission shows a peak at ca. 820 nm. (C) Plot of integrated intensity vs. forward bias voltage. *Source:* From Ref.<sup>[33]</sup>.

group IV, III–V, and II–VI semiconductor NW materials available,<sup>[30]</sup> it is possible to assemble a variety of NW-based nano-LEDs for different spectral regimes.<sup>[41]</sup> The ability to tune color with size as well as composition in these nano-LEDs might be especially useful in future nanophotonic applications. Moreover, the nanoscale light emitting device can be flexibly assembled on virtually any substrate and seamlessly integrated together, and allows us to achieve unique optoelectronic function on many technological important substrates, such as silicon substrate, and can open entirely new opportunities in intra-/interchip optical communication, integrated chemical/biological sensing and medical diagnostics on the chip level.

### Single Nanowire Nanolasers

Semiconductor lasers are finding increasing use in technologies ranging from telecommunications and information storage to medical diagnostics and therapeutics. Free-standing semiconductor NWs are attractive building blocks for creating optically and electrically driven lasers since their defect-free structures exhibit the superior optical and electrical transport properties,<sup>[32–35]</sup> and because a single NW can function as a stand-alone optical cavity and gain medium.<sup>[56–58]</sup> In general, a NW will function as a single mode optical waveguide<sup>[59]</sup> (Fig. 16A) when

$1 \sim (\pi D/\lambda) (n_1^2 - n_0^2)^{0.5} < 2.4$ , where  $D$  is the NW diameter,  $\lambda$  is the wavelength, and  $n_1$  and  $n_0$  are the refractive indices of the NW and surrounding medium, respectively. Taking CdS NWs ( $n_1 = 2.5$ ;  $\lambda = 510$  nm, 300 K) as an example, the minimum diameter needed to support a single mode is of the order of 70 nm. If the ends of the NW are cleaved, they can function as two reflecting mirrors that define a Fabry–Perot optical cavity with modes  $m(\lambda/2n_1) = L$ , where  $m$  is an integer and  $L$  is the length of the cavity. Significantly, CdS NWs typically adopt a [001] direction along the axis and can be easily cleaved using solution phase sonication. Transmission and scanning electron microscopy studies show that the cleaved NW end exhibit flat ends (Fig. 16B) indicative of cleavage perpendicular to the [001] NW axis. A luminescence image of a cleaved CdS NW obtained with a fluorescence microscope under uniform illumination from a mercury lamp shows uniform emission along the entire NW body except the end where greatly enhanced emission is observed (Fig. 16C). The uniform emission from the NW body suggests high quality of the NW materials, and the enhanced emission near the NW end suggests that the NW can function as waveguide.

The optical cavity properties of the CdS NWs, which are central to our use of these nanostructures for lasers, were further characterized by PL measurements at the single NW level using a far-field epifluorescence microscope. A typical room-temperature luminescence image (Fig. 17A) of a CdS NW excited with a tightly focused laser ca. 15  $\mu$ m from the NW end shows strong emission at the excitation locus and also prominent emission near the NW end. Studies of a number of NWs show pronounced emission from the NW end in addition to the excitation region and thus confirms waveguide characteristics of the NWs.

To further probe the NW cavity properties, spectroscopy measurements have been made at different regions as a function of excitation power under uniform illumination. At low power, PL spectra recorded from the body exhibit a broad peak with a maximum at 512 nm and full width at half maximum (FWHM) of 24 nm (Fig. 17B). The peak maximum is consistent with room-temperature band edge emission from CdS, and contrasts the deep level emission around 600 nm that usually dominates epitaxial CdS thin films.<sup>[60]</sup> Spectra recorded from the NW end at low excitation power showed a relatively broad peak that was redshifted ca. 30 nm relative to spectra from the body. The observed spectral redshift is consistent with reabsorption of band edge emission within the CdS NW cavity.

Photoluminescence measurements made at higher excitation powers reveal other important features about the CdS NW cavities (Fig. 17C). First, the NW

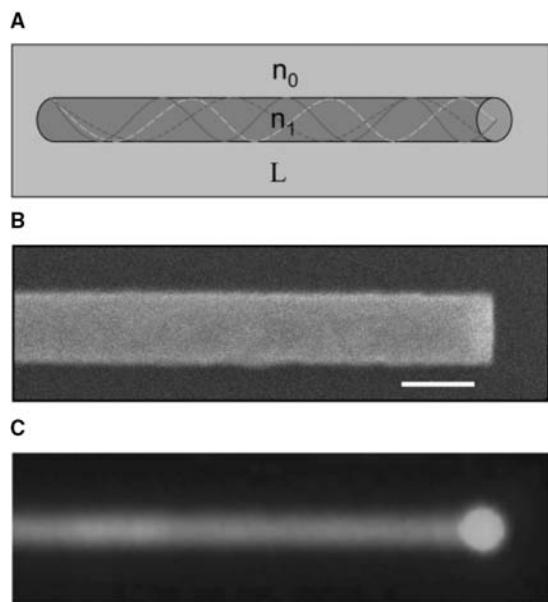


**Fig. 16** Nanowire optical waveguides and cavities. (A) Schematic showing a NW as an optical waveguide; with cleaved ends, it defines a Fabry–Perot cavity. (B) SEM image of a cleaved CdS NW end. Scale bar, 100 nm. (C) Room-temperature PL image of a CdS NW uniformly excited with a mercury lamp. *Source:* From Ref.<sup>[58]</sup>.

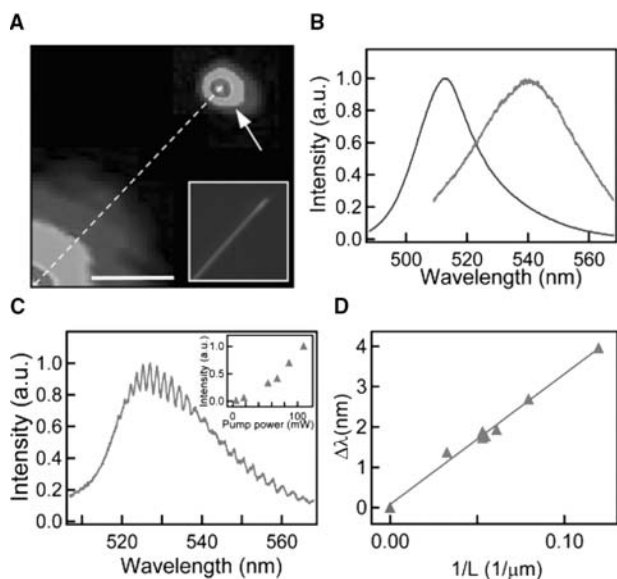


**Fig. 17** Nanowire Fabry–Perot optical cavity. (A) Room-temperature PL image of a CdS NW excited ca. 15 μm away from the NW end. The white arrow and dashed line highlight the NW end and axis, respectively. Scale bar, 5 μm. Inset shows an optical image of the NW obtained with white light illumination. (B) Photoluminescence spectra obtained from the body of the NW (left) and the end of the NW (right) at low pump power. (C) Spectrum from the NW end at higher pump power (80 mW) exhibiting periodic intensity modulation, which corresponds to the Fabry–Perot modes of the NW. Inset shows end emission intensity as a function of pump power. (D) Mode spacing vs. inverse NW length. The triangles are experimental point except the origin (0,0) point that corresponding the extrapolation to infinite length; the line is linear fit to these data. *Source:* From Ref.<sup>[58]</sup>.

end emission blueshifts towards the band edge as the reabsorption is partially saturated with increasing excitation power. Second, the end emission intensity increases superlinearly with excitation power, while emission from the NW body exhibits a slight ca. linear increase. Third, periodic variations in the intensity, which are suggestive of the longitudinal modes of a Fabry–Perot cavity, are observed for excitation powers greater than the changeover from linear to superlinear behavior. For a cavity of length  $L$ , the mode spacing,  $\Delta\lambda$ , is given by  $\lambda^2/2L[n_1 - \lambda(dn_1/d\lambda)]^{-1}$ , where  $dn_1/d\lambda$  is the dispersion relation for the refractive index. This expression provides a good description of the observed spacing when the measured NW length is equated with  $L$ , and moreover, analysis of similar data from NWs of varying length demonstrates that the mode spacing is inversely proportional to the wire length (Fig. 17D) as expected. Together these results show that the CdS NWs form a Fabry–Perot cavity with a cavity quality factor of the order of 600 as estimated from the mode line width.

The observation of sharp modes in the uniform CdS NW gain medium above the superlinear threshold is indicative of amplified spontaneous emission. Significantly, excitation at higher powers, which was possible in low-temperature experiments, leads to preferential gain in a single mode and the onset of lasing (Fig. 18A). At low temperatures, the broad emission peak observed at the NW end rapidly evolved to a sharp single mode with the 0.7 nm line width limited by the resolution of our low-temperature instrument (Fig. 18B). The observed line width exhibits a sudden drop in line width to our instrument resolution at an

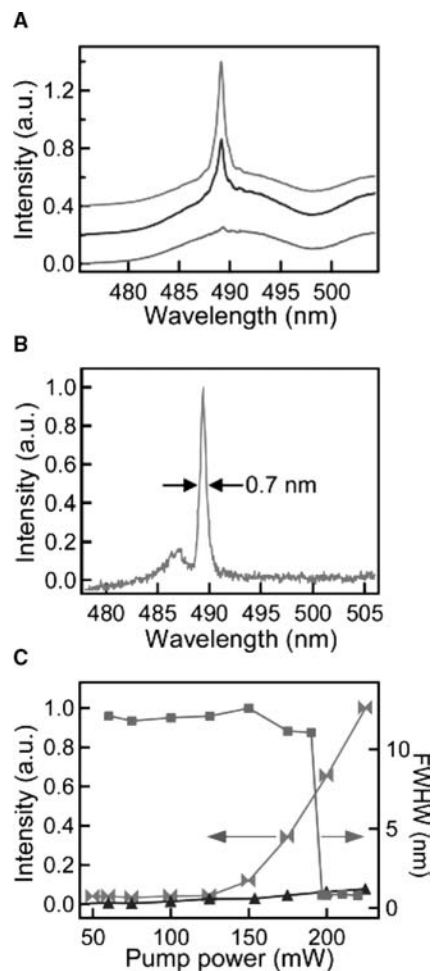


**Fig. 18** Optically pumped NW laser. (A) Emission spectra from a CdS NW end with a pump power of 190, 197, and 200 mW (from bottom up) recorded at 8 K. (B) Laser emission from a CdS NW end at 8 K with instrument resolution limited line width (FWHM ~ 0.7 nm). A second weaker mode is also resolved. (C) Emission intensity and FWHM of emission peaks vs. laser pump power. The FWHM has a nearly constant value of ca. 12 nm at low power, and abruptly narrows to instrumental resolution when the super-linear threshold is exceeded. The solid symbols correspond to experimental data points and lines serve as guides to eye. *Source:* From Ref.<sup>[58]</sup>.

excitation power coincident with the threshold to superlinear dependence for emission (Fig. 18C). In contrast, emission from the NW body is broad and linearly dependent on excitation further demonstrating that the laser emission is due to the cavity along the NW axis. From this superlinear behavior, we estimate the threshold average pump power to be  $40 \text{ kW cm}^{-2}$ , although the threshold varies from NW to NW with the lowest value to date of  $\sim 10 \text{ kW cm}^{-2}$ .

These optical experiments demonstrate that individual NWs can function as Fabry–Perot cavities and support lasing, although without electrical pumping NW lasers would be of limited technological importance. In general, electrically driven lasing requires efficient electron (n-type) and hole (p-type) injection into the cavity region. In the case of planar CdS structures, this has been difficult due to problems in producing high-mobility p-type CdS or combining n-CdS with other high-mobility p-type materials. A clear advantage of NW-based structures is the ability to combine different high quality materials almost at will to achieve desired device function.

Our initial studies of electrical injection into CdS NW cavities were carried out using an n-type CdS and p-type silicon (p-Si) crossed NW structures (Figs. 19A,B). Transport studies of individual CdS NWs show that they are n-type with doping concentrations of the order of  $10^{18}$ – $10^{19}/\text{cm}^3$  and electron mobilities of ca.  $100 \text{ cm}^2/\text{V sec}$ ; the p-type silicon NWs had a doping concentration of ca.  $10^{18}$ – $10^{19}/\text{cm}^3$  and exhibited mobilities of ca.  $50$ – $300 \text{ cm}^2/\text{V sec}$ . Current–voltage ( $I$ – $V$ ) measurements made on a typical n-CdS/p-Si crossed NW structure (Fig. 19C) show current rectification with a sharp forward bias turn-on at about 2 V, consistent with the formation of a p–n diode. In forward bias, these crossed NW structures exhibit strong EL with several important characteristics. Images of the EL (Fig. 19D) show two points of emission: One corresponding to the n-CdS/p-Si NW cross point and the other to the end of the CdS NW. Significantly, the intensity of the end emission is at least two orders of magnitude larger than the cross point emission, thus demonstrating that the CdS NWs can function as excellent waveguides in this relatively simple device configuration.

The EL spectrum recorded from the cross point (Fig. 19E) is a smooth peak with a maximum at 515 nm, which is consistent with band edge emission. In contrast, EL spectra recorded from the CdS NW end exhibit a prominent modulation in the intensity for injection currents greater than ca.  $1.0 \mu\text{A}$  (Fig. 19E). This current (Fig. 19F, inset) corresponds to a changeover from linear to superlinear intensity–current dependence for emission from the NW end. Significantly, the intensity modulation can be assigned to the longitudinal modes of a Fabry–Perot cavity

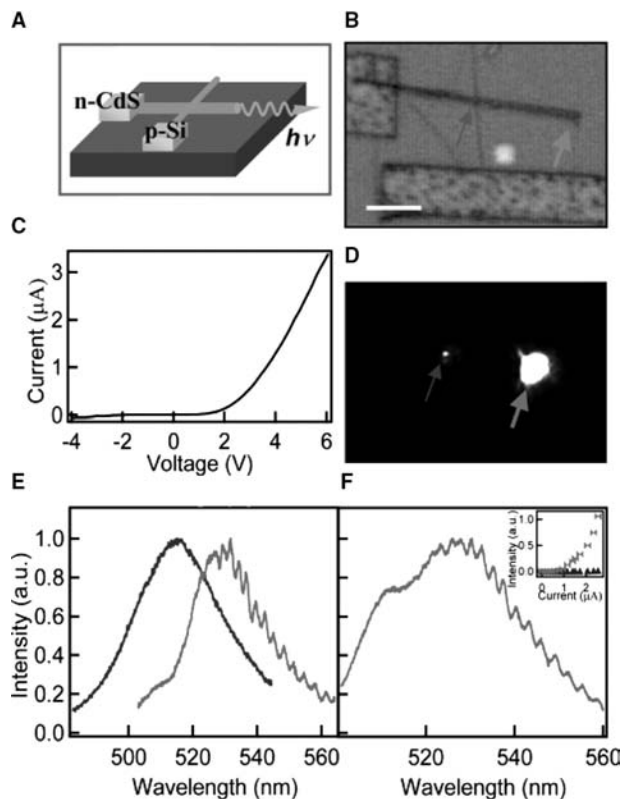


**Fig. 19** Electrical injection in NW Fabry–Perot cavities. (A) Device schematic illustrating a p–n diode formed between p-Si and n-CdS NWs, where the CdS NW forms the cavity and active medium. (B) Optical image of a device. Scale bar,  $5 \mu\text{m}$ . (C) Current–voltage ( $I$ – $V$ ) recorded from the diode in (B). (D) The EL image obtained at room temperature with the device forward biased at 5 V. The two bright spots highlighted by blue and green arrows correspond to the emission from the cross point and end, respectively. (E) Electroluminescence spectra obtained from cross (left) and end (right) of the device at an injection current of ca.  $1.5 \mu\text{A}$ . (F) Emission spectrum from the CdS NW end at an injection current of ca.  $2.4 \mu\text{A}$ . Inset shows emission intensity (linear scale) vs. injection current.

having a length consistent with that measured for the CdS NW in this device. In addition, the EL spectra recorded from the CdS NW end exhibits a redshift relative to emission from the cross point, as expected for reabsorption by the NW cavity. As the injection current is increased in the superlinear regime, the overall spectrum shifts to the blue (Fig. 19F), indicating partial saturation of the reabsorption in the NW. These EL results are thus completely consistent with our optically pumped luminescence data recorded from similar CdS NWs, and suggest that at sufficiently high injection currents lasing should be achieved, although the crossed NW injection devices is clearly not optimal for achieving high-density injection into the whole NW cavity and gain medium.

To enable more uniform injection, we have implemented a hybrid structure (Fig. 20A) in which holes are injected along the length of a CdS NW cavity from a p-Si electrode defined in a heavily doped p-Si layer on a planar substrate. Images of the room-temperature EL produced in forward bias from these structures (Fig. 20B) show strong emission from the exposed CdS NW end. At low injection currents, the spectrum of the end emission (Fig. 20C) shows a broad peak with FWHM  $\sim 18$  nm. Significantly, when the injection current is increased further, we found that the emission intensity increased abruptly, and the spectrum quickly collapsed into a limited number of very sharp peaks with a dominant emission line at 509.6 nm (Fig. 20C). The sharp peaks of this device had an average spacing of ca. 1.8 nm, which is consistent with the Fabry–Perot cavity modes for the length

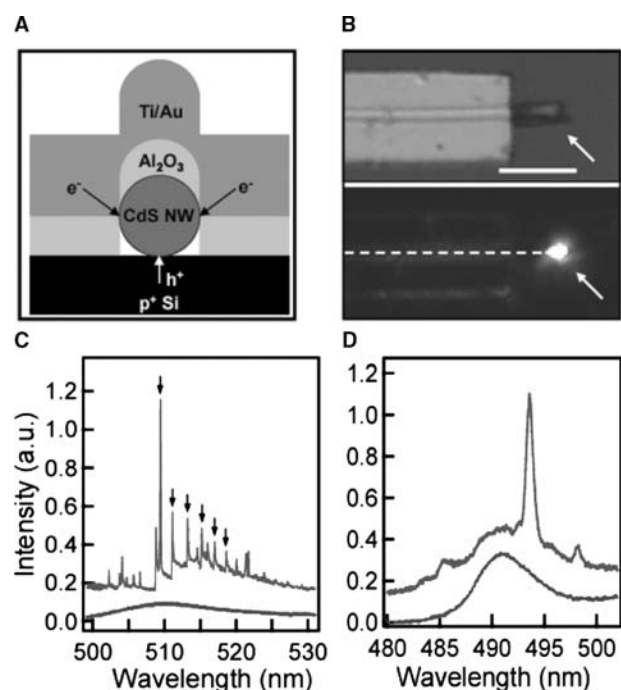


**Fig. 20** Nanowire electrical injection laser. (A) Schematic showing the cross section of the device structure. (B) (Top) Optical image of a device described in (A). The arrow highlights the exposed CdS NW end. Scale bar, 5  $\mu$ m. (Bottom) EL image recorded from this device at room temperature with an injection current of ca. 80  $\mu$ A. The arrow highlights emission from the CdS NW end. The dashed line highlights the NW position. (C) Electroluminescence spectra obtained from the NW end with injection currents of 120  $\mu$ A (lower curve) and 210  $\mu$ A (upper curve). The black arrows highlight Fabry–Perot cavity modes with an average spacing of 1.83 nm. The green spectrum is shifted upward by 0.15 intensity units for clarity. (D) Emission spectra from a CdS NW device with injection currents of 200  $\mu$ A (lower curve) and 280  $\mu$ A (upper curve) recorded at 8 K. The spectra are offset by 0.10 intensity units for clarity. *Source:* From Ref. [58].

of the NW device. Other small, sharp peaks are also observed and their explanation will require more detailed consideration of the NW cavity. Further more, low-temperature measurements (7 K) made on independent CdS injection laser devices. (Fig. 20D) show clearly that the spontaneous emission spectrum can collapse to a single mode, and moreover, these results are very similar to the low-temperature optically pumped results, and thus unambiguously demonstrate the formation of injection NW laser.

Using individual NWs as the laser cavity and gain medium for laser diodes represents a new and powerful approach for producing integrated electrically driven photonic devices. This basic approach, which relies upon bottom-up assembly of the key laser cavity/medium in a single step, can be extended to other materials, such as GaN and InP NWs, to produce nanoscale lasers that not only cover the ultraviolet through near infrared spectral regions but also can be integrated as single or multicolor laser source arrays in silicon microelectronics and lab-on-a-chip devices. There are also scientific and technical challenges that may need to be addressed to realize this potential, including the development of more efficient cavities and injection schemes. Both issues could be addressed at the NW growth stage prior to device assembly by preparing Bragg gratings at the NW ends through axial composition modulation,<sup>[54]</sup> and using core–shell NW structure<sup>[61]</sup> to enable uniform injection into the active medium/cavity, respectively. By addressing these and other issues, such as quantifying contributions to optical losses within the NW cavity, NW lasers could be developed into systems that impact a number of areas where solid state lasers are used today, including telecommunications and data storage, and may enable new applications in highly integrated chemical/biological sensors, near-field optical lithography, a host of scanning probe microscopies, and perhaps even laser-based surgery with unprecedented resolution.

## Photodetectors

In addition to generating photons via carrier recombination in nanoscale NW devices, absorbed photons can produce electrical carriers, which when measured, serve as the basis for Lilliputian photodetectors.<sup>[49]</sup>

The striking PL polarization anisotropy makes these NWs ideally suited for polarization sensitive photonic devices such photodetectors and optically gated switches. For example, a polarization sensitive photodetector can be easily fabricated by making metallic contacts to both ends of individual NWs (Fig. 21A). The conductance ( $G$ ) of individual NWs was found to increase by 2–3 orders of magnitude with increasing laser intensity (Fig. 21B), and these changes



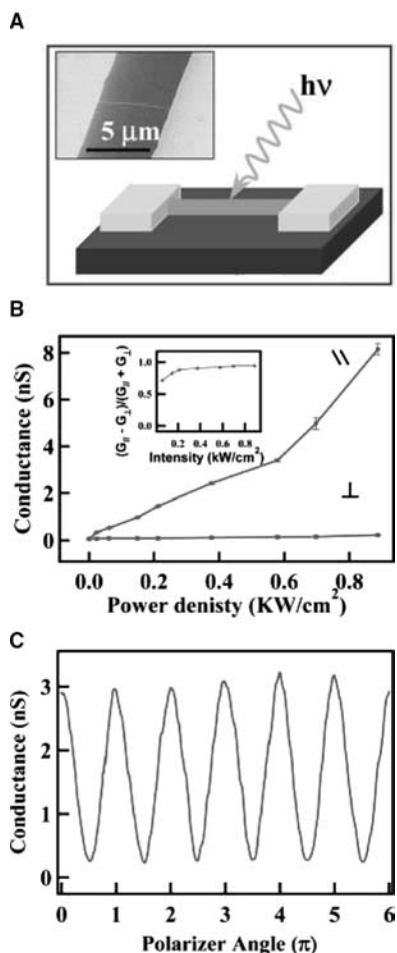


**Fig. 21** Polarized photodetection using individual InP NWs. (A) Schematic depicting the use of a NW as a photodetector. Inset: SEM image of a 20 nm diameter NW and contact electrodes for photoconductivity (PC) measurements. (B) Conductance,  $G$ , vs. excitation power density for excitation light polarized parallel and perpendicular to the NW axis. Inset: PC anisotropy vs. excitation power. (C) Conductance vs. polarization angle as the polarization was manually rotated while measuring the PC. *Source:* From Ref.<sup>[49]</sup>.

were reproducible and reversible, which indicate that the increases in  $G$  are due to direct carrier collection at the NW–metal contacts.

In addition, a large polarization anisotropy was also observed in the photoconductivity (Fig. 21C). The photoconductivity anisotropy,  $\sigma = (G_{||} - G_{\perp}) / (G_{||} + G_{\perp})$ , values were similar to the PL anisotropy and the theoretical predictions described above. The large anisotropy shows that the conductance of devices is essentially switched on and off while the polarization of the incident light is changed. The overall sensitivity of the photodetector can be gauged by the responsivity, which is the ratio of photocurrent vs. absorbed optical power. For the device shown in Fig. 34, the responsivity is about 3000 A/W, which is an impressive number, considering that this device was not optimized.<sup>[62]</sup>

There are several unique features of these NW-based photodetectors that could enable applications. First, the sensitivity and polarization anisotropy is nearly independent of excitation wavelength for energies larger than band gap. In addition, it is easily possible to make a device that simultaneously measures intensity and polarization by using two crossed NWs and measuring their photoconductivity independently. Second, the active device element in the NW-based photodetector is substantially smaller than other polarization sensitive quantum-well based detectors,<sup>[63,64]</sup> which are not smaller than  $50 \times 50 \mu\text{m}$  and usually only sensitive to a very specific wavelength. Lastly, the extremely small size of these devices may open the possibility of creating ultra high-speed detectors.

## Summary

Overall, we have shown that semiconductor NWs can be used to assemble a wide range of photonic and optoelectronic devices, including LEDs, lasers, and photodetectors. The availability of such nanoscale optoelectronic devices can open many exciting opportunities in nanoscale science and technology. Nanoscale light source and detectors may lead to exciting opportunities in photonics. The nanoscale light sources can be used for ultrahigh resolution imaging, sensing, and analysis in lab-on-a-chip systems as well in telecommunications and information storage. For example, nanoscale emitters can be readily used as the excitation source for a variety of materials. Nanowire photodetectors can be exploited as optically gated switches. When nanoscale light sources and photodetectors are combined together, it is possible to create high-density, high-speed interconnects for electronic and/or photonic circuits, where polarization sensitivity can vastly increase the information bandwidth. Considering the wide range of group IV, III–V, and II–VI semiconductor NW materials available, it should be possible to assemble in the future a variety of NW-based light sources and detector arrays for further into infrared spectral regimes, including the  $1.5 \mu\text{m}$  regime that is critical to current optical communications. In addition, the extremely small size of these structures could also lead to fundamentally new types of device such as single photon sources,<sup>[65,66]</sup> which could enable quantum information encryption and possibly optical schemes for quantum computation.

## HIERARCHICAL ASSEMBLY NANOWIRES

A key motivation underlying research on nanoscale devices is the potential to achieve integration at a level not possible in conventional microelectronics. To achieve this goal in future nanosystems will require



the development and implementation of efficient and scalable strategies for assembly of nanoscale building blocks into increasingly complex architectures. First, methods are needed to assemble NWs into highly integrated arrays with controlled orientation and spatial position. Second, approaches must be devised to assemble NWs on multiple length scales and to make interconnects between nano-, micro-, and macroscopic worlds. To address these critical next levels of organization, we have focused significant effort on developing complementary strategies for hierarchical assembly of NWs on surfaces, and describe two promising approaches below.

### Electrical Field Directed Assembly

Applied electric fields (E-fields) can be used effectively to attract and align NWs due to their highly anisotropic structures and large polarizabilities (Fig. 22).<sup>[33]</sup> This underlying idea of E-field directed assembly can be readily seen in images of NW solutions aligned between parallel electrodes (Fig. 22B), which demonstrate that virtually all of the NWs aligned in parallel along the E-field direction. Electric field directed assembly can also be used to position individual NWs at specific positions with controlled directionality. For example, E-field assembly of NWs between an array of electrodes (Fig. 22C) clearly shows that individual NWs can be positioned to bridge pairs

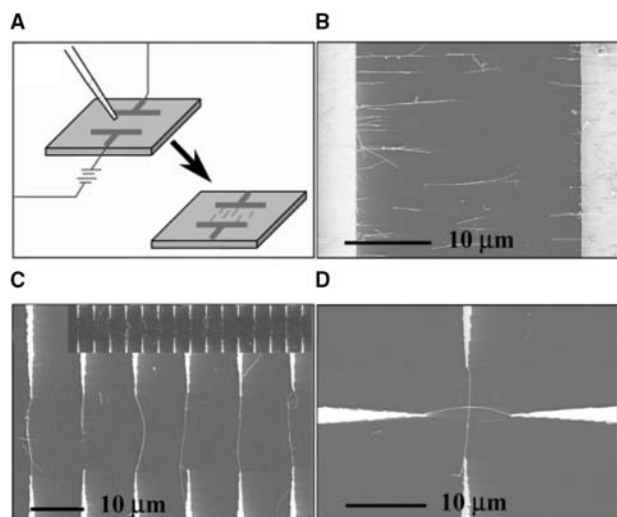


**Fig. 22** E-field directed assembly of NWs. (A) Schematic view of E-field alignment. (B) Parallel array of NWs aligned between two parallel electrodes. (C) Spatially positioned parallel array of NWs obtained following E-field assembly. The top inset shows 15 pairs of parallel electrodes with individual NWs bridging each diametrically opposed electrode pair. (D) Crossed NW junction obtained using layer-by-layer alignment with the E-field applied in orthogonal directions in the two assembly steps. *Source:* From Ref.<sup>[33]</sup>.

of diametrically opposed electrodes and form a parallel array. In addition, by changing the E-field direction with sequential NW solutions, the alignment can be carried out in a layer-by-layer fashion to produce crossed NW junctions (Fig. 22D). These results demonstrate clearly that E-field directed assembly can be used to align and position individual NWs into parallel and crossed arrays, which correspond to two basic geometries for integration, and thus provide one robust approach for rational and parallel assembly of nanoscale device arrays.

### Fluid Flow Directed Assembly

#### Microchannel fluidic device

Electric field directed assembly, which represents the first approach described for assembly of 1D nanostructures, also has limitations, including 1) the need for substantial conventional lithography to pattern micro-electrode arrays used to produce aligning fields, and 2) the deleterious effect of fringing electric fields at the submicron length scales. To achieve a greater flexibility in rational, parallel assembly of 1D nanostructures into nanosystems, we have developed a powerful new approach called fluidic flow directed assembly.<sup>[36]</sup> In this method, NWs (or NTs) can be easily aligned by passing a suspension of NWs through microfluidic channel structures, for example, formed between a poly(dimethylsiloxane) (PDMS) mold<sup>[67]</sup> and a flat substrate (Fig. 23). Parallel and crossed NW arrays

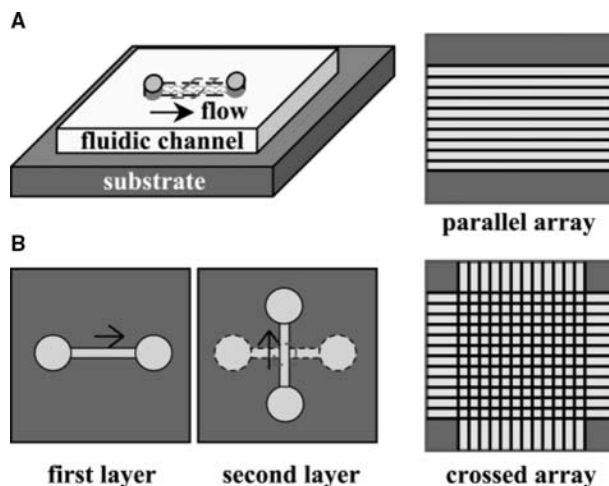


**Fig. 23** Fluid flow directed assembly NWs. (A) A channel is formed when a trench structure is brought in contact with a flat substrate. Nanowire assembly is carried out by flowing a NW suspension through the channel at a controlled rate and for a set duration. Parallel arrays of NWs are observed in the flow direction on the substrate when the trench structure is removed. (B) Crossed NW arrays can be obtained by changing the flow direction sequentially in a layer-by-layer assembly process. *Source:* From Ref.<sup>[36]</sup>.

can be readily created using single (Fig. 23A) and sequential crossed (Fig. 23B) flows, respectively, for the assembly process.

### Parallel assembly of nanowire

Images of NWs assembled on substrate surfaces (Fig. 24A) within microfluidic flows demonstrate that virtually all of the NWs are aligned along the flow direction. This alignment readily extends over hundreds of micrometers (Fig. 24B). Indeed, alignment of the NWs has been found to extend up to millimeter length scales, and is limited only by the size of the fluidic channels used. The alignment of NWs within the channel flow has been explained within the framework of shear flow.<sup>[68,69]</sup> Specifically, the channel flow near the substrate surface resembles a shear flow and aligns the NWs in the flow direction before they are immobilized on the substrate. This idea readily provides the intellectual underpinning needed for controlling the degree of alignment and average separation of the NWs. First, higher flow rates produce larger shear forces and will lead to better alignment, and thus the flow rate can be used to control the degree of alignment. Indeed, the width of the NW angular distribution with respect to the flow direction significantly narrows with increasing flow rate (Fig. 24C). Studies of the distribution widths measured over a range of flow conditions showed that the width decreased

quickly as flow increased to a nearly constant value at  $\sim 10$  mm/sec (where more than 80% of the NWs are aligned within  $\pm 5^\circ$  of the flow direction (Fig. 24C, inset).

Second, these studies<sup>[36]</sup> demonstrated that the average NW density could be controlled by the flow duration (Fig. 24D). Experiments carried out at constant flow rate show that the NW density increases systematically with flow duration, and can, upon extended deposition time, produce NW arrays with spacings of the order of 100 nm or less. The relationship between average separation and flow duration also depends on and can be further controlled by the chemical functionality on the NW and substrate surfaces; that is, strong complementary interactions will facilitate deposition from the flow.

### Crossed nanowire arrays

The fluidic flow assembly approach can be used to organize NWs into more complex crossed structures, which are critical for building dense nanodevice arrays, using a layer-by-layer deposition process (Fig. 23B). The formation of crossed and more complex structures requires that the nanostructure–substrate interaction is sufficiently strong that sequential flow steps do not affect preceding ones: We find that this condition is readily achieved. For example, alternating the flow in orthogonal directions in a two-step assembly process yields crossbar structures in high yield (Figs. 25A,B). These data demonstrate that crossbars extending over 100 s of microns on a substrate with only 100 s of nanometers separation between individual cross points are obtained through a very straightforward, parallel low cost, and fast process.

Fluidic flow directed assembly of multiple crossed NW arrays offers significant advantages over previous efforts. First, it is intrinsically very parallel and scalable with the alignment readily extending over very large length scales. Second, this approach is general for virtually any elongated nanostructure including carbon NTs and DNA molecules. Third, it allows for the directed assembly of geometrically complex structures by simply controlling the angles between flow directions in sequential assembly steps. For example, equilateral triangles (Fig. 25C) were easily assembled in a three-layer deposition sequence using  $60^\circ$  angles between the three flow directions. The method of flow alignment thus provides a flexible way to meet the requirements of many device configurations in the future. An important feature of this layer-by-layer assembly scheme is that each NW layer can be independent of the preceding one(s), and thus a variety of homo- and hetero-junction configurations can be obtained at each crossed point by simply changing the composition of the NW suspension used for each

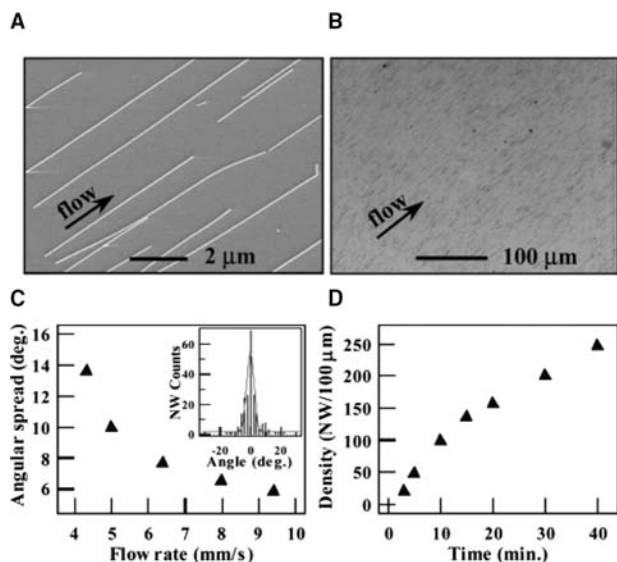


**Fig. 24** Parallel assembly of NW arrays. (A) SEM image of a parallel array of InP NWs aligned by flow. (B) Optical microscope image of a parallel array of InP NWs aligned over very large area. (C) NW angular spread with respect to the flow direction vs. flow rate. The inset shows histogram of NW angular distribution at a flow rate of 9.40 mm/sec. (D) Average density of NWs vs. flow time. Source: From Ref.<sup>[36]</sup>.

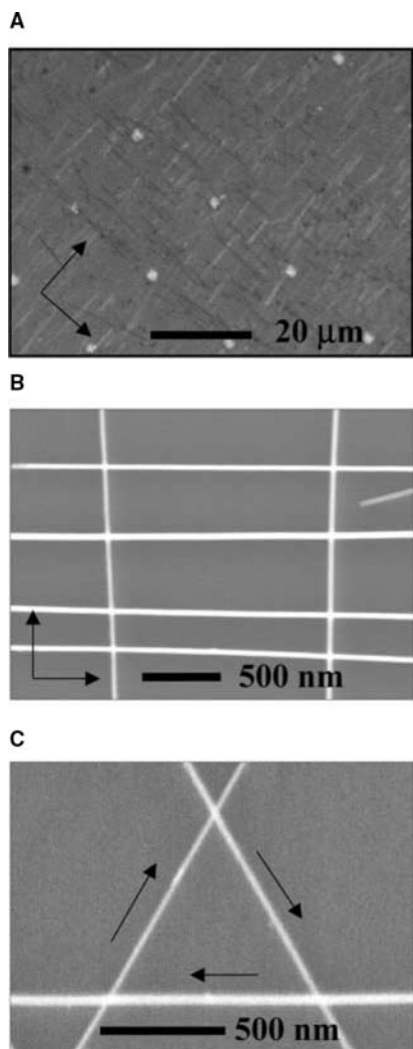


**Fig. 25** Layer-by-layer assembly of crossed NW arrays. (A, B) Typical optical microscope and SEM images of crossed arrays of InP NWs obtained in a two-step assembly process with orthogonal flow directions for the sequential steps. Arrows indicate the two flow directions. (C) An equilateral triangle of GaP NWs obtained in three-step assembly process, with flow directions highlighted by arrows. *Source:* From Ref.<sup>[36]</sup>.

flow step. For example, it should be possible to assemble directly and subsequently address individual nanoscale devices using our approach with n-type and p-type NWs, in which the NWs act as both the wiring and active device elements.

### Control of periodicity

The above results demonstrate clearly the power of the fluidic assembly approach, although to enable systems organization with greatest control requires in many cases that the spatial position also be defined. To realize this additional constraint on the assembly process, we have explored complementary chemical interactions

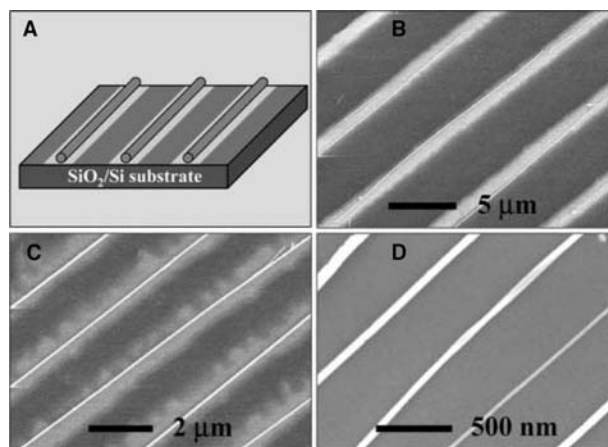


**Fig. 26** Assembly of periodic NW arrays. (A) Schematic view of NW assembly onto a chemically patterned substrate. (B, C) Parallel arrays of GaP NWs aligned on poly(methylmethacrylate) (PMMA) patterned surface with 5 and 2 μm separation. (D) Parallel arrays of GaP NWs with 500 nm separation obtained with a patterned SAM surface. *Source:* From Ref.<sup>[36]</sup>.

between chemically patterned substrates and NWs (Fig. 26A). Substrates for alignment are first patterned with two different functional groups, with one of the functional groups designed to have a strong attractive interaction with the NW surface, and then, following flow alignment, regular, parallel NW arrays with lateral periods the same as those of the surface patterns are produced (Fig. 26D). These data demonstrate that the NWs are preferentially assembled at positions defined by the chemical pattern, and moreover, show that the periodic patterns can organize the NWs into regular superstructures. In addition, periodic crossed NW arrays can also be envisioned using a substrate with a crossed pattern of chemical functionality.

It is important to recognize that the patterned surface alone does not provide good control of the 1D nanostructure organization. Assembly of NTs<sup>[70,71]</sup> and NWs on patterned substrates shows that 1D nanostructures align with bridging and looping structures over the patterned areas and show little directional control. Our use of fluidic flows avoids these significant problems and enables controlled assembly in one or more directions. By combining this approach with other surface patterning methods, such as phase separation in diblock copolymers<sup>[72]</sup> and spontaneous ordering of molecules,<sup>[73]</sup> it should be possible to generate well-ordered NW arrays without the limitations of conventional lithography.

### Future Directions

The above data demonstrate clearly ordering of NW structures over multiple length scales—organization

of nanometer diameter wires with 100 nm to micrometer scale separations over millimeter scale areas. This hierarchical order can readily bridge the microscopic and macroscopic worlds, although eventual device formation still requires conventional lithography to define metallic contact electrodes to the NWs. It is possible to eliminate this step by direct assembly of NWs onto predefined metallic electrode arrays<sup>[74]</sup> that have been deposited by either via conventional or unconventional (e.g., microcontact printing or imprinting methods) lithography techniques. Lastly, it will also be beneficial to develop further these approaches in the future to enable more complex assembly, such as the selective parallel assembly of two or more electronically distinct NWs and/or NWs with different lengths.

## INTEGRATED NANOWIRE DEVICES

The ability to synthesize rationally NWs with controlled electronic properties, to demonstrate individual functional NW devices, and to assemble NWs into regular arrays has enabled us to explore in unprecedented depth the next level of hierarchy in the bottom-up approach to nanoelectronics—that is, integrated device arrays.

### Integrated Cross Nanowire p–n Junctions and Transistors

To achieve integrated functional device arrays requires high yield and high reproducibility of individual devices with controllable functional properties. In order to assess this issue, we have studied a large number of p–n junctions assembled from p-Si NWs and n-GaN NWs (Fig. 27A).<sup>[35]</sup>  $I$ - $V$  measurements made on over 100 of crossed p-Si/n-GaN NW devices show that over 95% of the junctions exhibit current rectification with turn-on voltages of around 1.0 V. Moreover, the turn on voltage of such crossed p–n junction can be controlled naturally and selectively within the framework of bottom-up approach to fabrication. Specifically, high turn-on voltage junctions can be reproducibly formed by increasing the oxide layer thickness at the junctions by either thermal oxidation of the Si NWs prior to assembly or by Joule heating of specific device elements by passing a high current through a junction in air.

Reproducible assembly of crossed NW structures with predictable electrical properties contrasts sharply with results from NT-based device, and has enabled us also to explore the assembly and properties of integrated p–n junction arrays. Significantly, electrical transport measurements made on a typical  $4 \times 1$

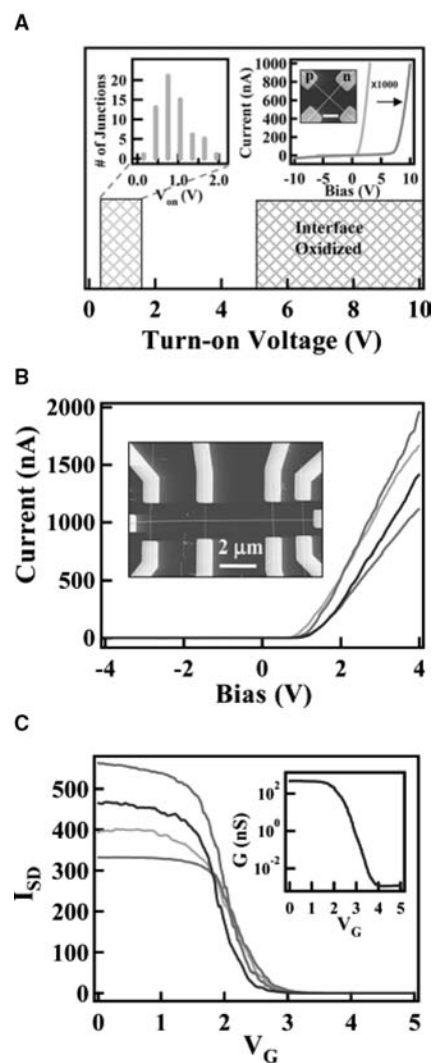


**Fig. 27** Crossed NW nanodevice elements. (A) Turn-on voltage distribution for crossed NW junctions. The top-left inset shows histogram of turn-on voltage for over 70 assembled junctions showing a narrow distribution around 1 V. The top-right inset shows an example  $I$ - $V$  response for low and high turn-on voltage elements. The inset in top-right inset shows a SEM image of a crossed NW device. Scale bar, 1  $\mu$ m. (B)  $I$ - $V$  behavior for a  $4(p) \times 1(n)$  multiple junction array. The four curves represent the  $I$ - $V$  for each of the four junctions and highlight reproducibility of assembled device elements. The inset shows an example of a multiple crossed NW device. (C) Transfer characteristics of four cNW-FET arrays. The inset shows conductance ( $G$ ) vs.  $V_g$  ( $V_{sd} = 1$  V) for one cNW-FET. *Source:* From Ref.<sup>[35]</sup>.

crossed p-Si/n-GaN junction array (Fig. 27B) show that the four nanoscale cross points form independently addressable p–n diodes with clear current rectification and similar turn-on voltages. These data further demonstrate the high yield and reproducibility of our crossed NW p–n devices. In addition, these crossed NW p–n junction arrays can also function as

cNW-FET arrays. The transfer characteristics for an array of four cNW-FETs clearly show that each of these four cNW-FET exhibit highly sensitive gate responses with sharp onset voltages at around 2–3 V (Fig. 27C), where the transfer characteristics can be controlled by varying the doping concentration and other characteristics of the NWs used in the assembly process.

### Nanowire Logic Circuits

The controlled high-yield assembly of crossed NW p–n diodes and cNW-FETs with attractive device characteristics, such as high gain, enables the bottom-up approach to be used for assembly of more complex and functional electronic circuits, such as logic gates. Logic gates are critical blocks of hardware in current computing systems that produce a logic-1 and logic-0 output when the input logic requirements are satisfied. Diodes and transistors represent two basic device elements in logic gates.<sup>[75]</sup> Transistors are more typically used in current computing systems because they can exhibit voltage gain. Diodes do not usually exhibit voltage gain, although they may also be desirable in some cases;<sup>[35,75]</sup> for example, the architecture and constraints on the assembly of nanoelectronics might be simplified using diodes since they are two-terminal devices, in contrast to three-terminal transistors. In addition, by combining the diodes and transistors in logic circuits, it is possible to achieve high voltage gain, while simultaneously maintaining a simplified device architecture. To demonstrate the flexibility of these NW device elements, we have investigated both diode- and FET-based logic.

#### Logic OR gate

A two-input logic OR gate output is HIGH if either or both of the inputs are HIGH. This basic OR gate can be realized using a  $2(p) \times 1(n)$  crossed p–n junction array with the two p-Si NWs as inputs and the n-GaN NW as the output (Fig. 28A). The output–input ( $V_o$ – $V_i$ ) voltage response (Fig. 28B) of a typical device shows that  $V_o$  increases linearly with  $V_i$  when one input is set low (0 V) except for the region near 0 V. This low response region is due to the finite turn-on voltage of the p–n diodes, and produces a logic output typically 0.4–0.2 V less than the input voltage. Small reductions in  $V_o$  do not affect the operation of our logic gates because the low turn-on voltage contributions are reproducible and can be readily accounted for in defining the 0 and 1 states. The  $V_o$ – $V_i$  data also show a nearly constant high output when the second input is set high (5 V). For example, the output voltage vs. four possible logic address levels, which are 00, 10, 01 and

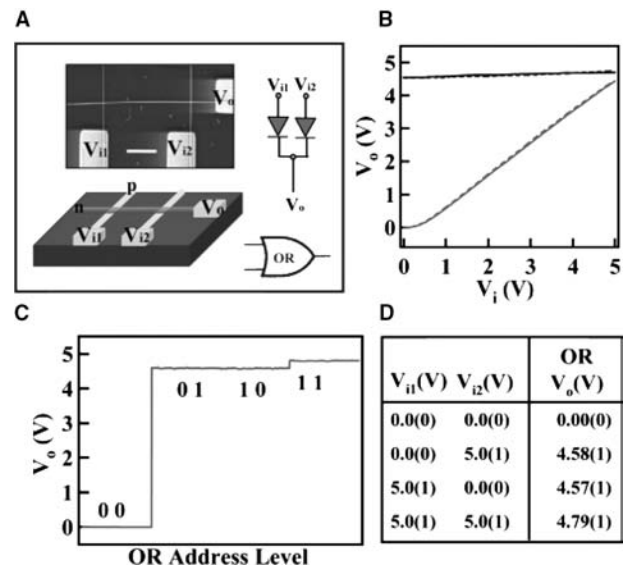


**Fig. 28** Logic OR gate. (A) Schematics of logic OR gate constructed from a  $2 \times 1$  crossed NW p–n junction. The insets show an SEM image of a device (scale bar, 1  $\mu$ m) and the symbolic electronic circuit. (B) Output–input ( $V_o$ – $V_i$ ) relation. (C) The output voltage vs. the four possible logic address level inputs: (0, 0); (0, 1); (1, 0); (1, 1). (D) The experimental truth table for the OR gate. *Source:* From Ref.<sup>[35]</sup>.

11 (Fig. 28C), shows that the output is low (logic-0) when both input voltages are low (0 V), and the output is high (logic-1) when either or both of the input voltages are high (5 V). The experimental truth table for the  $1 \times 2$  crossed NW device (Fig. 28D) summarizes the input–output response and confirms that this NW device behaves as a logic OR gate. We also note that assembly of more p–n diodes would produce in a very straightforward and scalable way multiple input OR gates, that is, a  $1 \times n$  diode array for an  $n$ -input OR gate.

#### Logic AND gate

A two-input logic AND gate output is HIGH only if both inputs are HIGH. We have assembled such two-input AND gates from  $1(p\text{-Si}) \times 3(n\text{-GaN})$  multiple junction arrays (Fig. 29A). In these structures, a p-Si NW is biased at 5 V; two GaN NWs are used as inputs and the third is used as a gate with a constant voltage to create a resistor by depleting a portion of the p-Si NW. The  $V_o$ – $V_i$  data (Fig. 29B) shows constant low  $V_o$  when the other input is low, and nearly linear behavior when the other input is set at high. Correspondingly, logic-0 is observed from this device when either one or both of the inputs are low (Fig. 29C), since  $V_i = 0$  corresponds to a forward biased, low resistance p–n diode that pulls down the output. The logic-1 is observed only when both inputs are high, since this condition corresponds to reverse biased p–n diodes



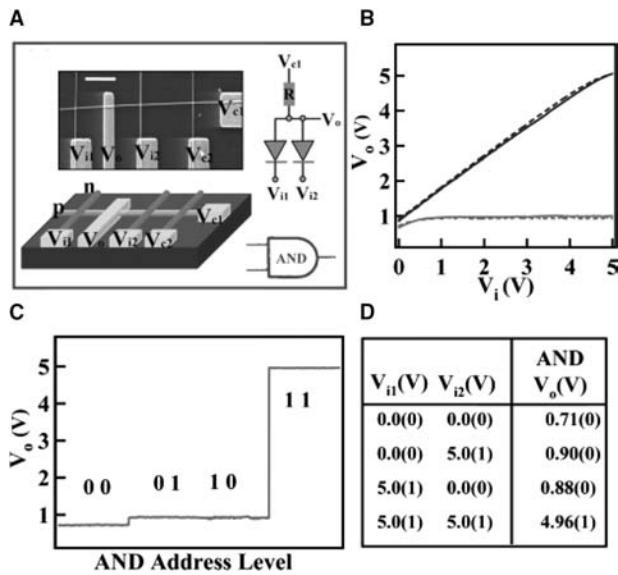


**Fig. 29** Logic AND gate. (A) Schematic of logic AND gate constructed from a  $1 \times 3$  crossed NW junction array. The insets show a typical SEM image (bar,  $1 \mu\text{m}$ ) of the assembled AND gate and symbolic electronic circuit. (B) Output–input ( $V_o$ – $V_i$ ) relation. (C) The output voltage vs. the four possible logic address level inputs: (0, 0); (0, 1); (1, 0); (1, 1). (D) The experimental truth table for the AND gate. *Source:* From Ref.<sup>[35]</sup>.

with resistances much larger than the constant resistor; that is, little voltage drop across the constant resistor and a high voltage is achieved at the output. The experimental truth table for the NW device (Fig. 29D) summarizes the input–output response and confirms that this device functions as a logic AND gate.

### Logic NOR gate

FET-based logic NOR gates have been studied using assembled  $1(\text{p-Si}) \times 3(\text{n-GaN})$  cNW-FET arrays (Fig. 30A). Typically, NOR gates were configured with 2.5 V applied to one cNW-FET to create a constant resistance  $\sim 100$  Mohms, and with the p-Si NW channel biased at 5 V. The two remaining n-GaN NW inputs were used as gates for two cNW-FETs in series. In this way, the output depends on the resistance ratio of the two cNW-FETs and the constant resistor. The  $V_o$ – $V_i$  relation (Fig. 30B) shows constant low  $V_o$  when the other input is high, and a nonlinear response with large change in  $V_o$  when the other input is set low. The logic-0 is observed when either one or both of the inputs is high (Fig. 30C). In this case, one or both of the transistors are off and have resistances much higher than the constant resistor, and thus most of the voltage drops across the transistors. A logic-1 state can only be achieved when both of the transistors are on, that is, both inputs low. Analysis of the  $V_o$ – $V_i$  data demonstrates that these two-input NOR gates

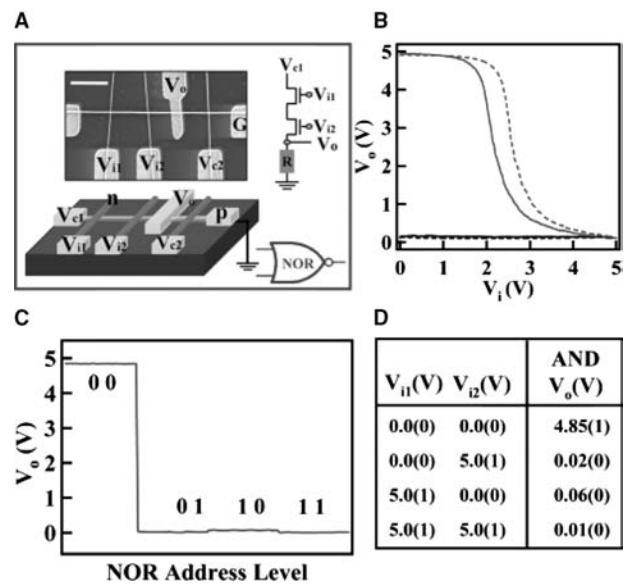


**Fig. 30** Logic NOR gate. (A) Schematic of logic NOR gate constructed from a  $1 \times 3$  crossed NW junction array. The insets show an example SEM image (bar,  $1 \mu\text{m}$ ) and symbolic electronic circuit. (B)  $V_o$ – $V_i$  relation; the slope of the data shows that device voltage gain is larger than 5. (C) The output voltage vs. the four possible logic address level inputs. (D) The measured truth table for the NOR gate. *Source:* From Ref.<sup>[35]</sup>.

routinely exhibit gains in excess of 5, which is substantially larger than the gain reported for complementary inverters based on Si NWs<sup>[34]</sup> and carbon NTs.<sup>[25]</sup> High gain is a critical characteristic of gates since it enables interconnection of arrays of logic gates without signal restoration at each stage. The experimental truth table for this NW device (Fig. 30D) summarizes the  $V_o$ – $V_i$  response and demonstrates that the device behaves as a logic NOR gate. Lastly, these multiple input logic NOR gates can be configured as simple NOT gates (inverters) by eliminating one of the inputs.

### Logic XOR and half adder circuit

Logic OR, AND, and NOR (NOT) gates form a complete set of key logic elements and enable the organization of virtually any logic circuit. To demonstrate the potential for integration of such logic gates, we have interconnected multiple AND and NOR gates to implement basic computation in the form of an XOR gate (Fig. 31A), which corresponds to the binary logic function SUM, and a half adder (Fig. 31B), which corresponds to the addition of two binary bits. The XOR gate is configured by using the output from AND and NOR gates as the input to a second NOR gate, while the logic half adder uses an additional logic AND gate as the CARRY. The truth table for the XOR structure (Fig. 31C) confirms this logic operation. Significantly,



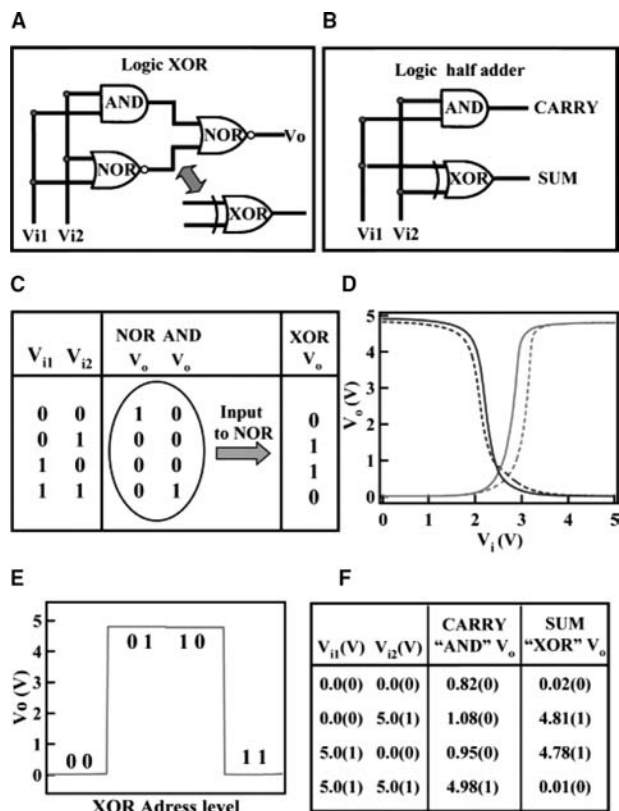


**Fig. 31** Logic XOR gate and half adder. (A) Schematic of logic XOR gate constructed using the output from an AND and NOR as the input to a second NOR gate. (B) Schematic for logic half adder. (C) Truth table for logic XOR gate. (D) XOR output voltage vs. input voltages. The slope of the  $V_o$ - $V_i$  data shows that the gain exceeds 10. The XOR gate was achieved by connecting the output electrodes of an AND and NOR gate to two inputs of another NOR gate. (E) The output voltage vs. the four possible logic address level inputs for the XOR gate. (F) Experimental truth table for the logic half adder. The logic half adder was obtained by using the XOR gate as the SUM and an AND gate as the CARRY. Source: From Ref.<sup>[35]</sup>.

the measured  $V_o$ - $V_i$  transport data for the XOR device (Figs. 31D,E) show 1) that the output is logic-0 or low when the inputs are both low or high, and logic-1 or high when one input is low and the other is high, and 2) that the response is highly nonlinear. The linear response region corresponds to a voltage gain in excess of 10 and is typical of the devices measured to date. We note that this large gain is achieved in an XOR configured from a low gain diode AND gate, and is due to the high gain of the cNW-FET NOR gate. These data are summarized in the experimental truth table (Fig. 31F), which demonstrates that the response is that of the binary logic SUM operation. Significantly, with another AND gate as CARRY, a logic HALF ADDER is formed and can be used to carry out calculations in a manner similar to conventional electronics.

## Summary and Future Directions

In this section, we have demonstrated clearly that our ability to synthesize rationally NWs with controlled electronic properties, to configure them into individual functional NW devices, and to assemble NWs into regular arrays enables the bottom-up approach to move to new levels, including the assembly of devices with an unprecedented level of reproducibility, the integration of these device elements into complex diode and transistor logic gates without resorting to conventional lithography, and the interconnection of logic gates to carry out basic digital computation.

We also note that the OR and AND diode logic gates do not exhibit voltage gain; however, OR and AND logic with substantial gain could be realized if implemented using cNW-FETs. For example, logic OR can be achieved with the NOR gate by reversing the bias and ground connections to the p-Si NW. The AND function could also be implemented using cNW-FETs in parallel (vs. series for OR). In addition, due to finite turn-on voltage of the p-n diodes used in our diode-based OR/AND gates, the overall logic circuits were typically operated at relatively high voltage (5 V). Significantly, it is possible to operate at much lower voltage when all of the logic elements are implemented using cNW-FETs. For example, a logic NOT gate operating at 0.5 V and exhibiting a voltage gain as high as 3 (Fig. 32) was achieved using two cNW-FETs. Such a low operation voltage is a significant improvement over relative high voltage operation of carbon NT circuits (1.5 V) and current commercial circuits (1.2 V), and could be very significant for reducing the power/heat load in highly integrated nanoelectronics logic circuits. In addition, both p- and n-channel transistors could be readily assembled using

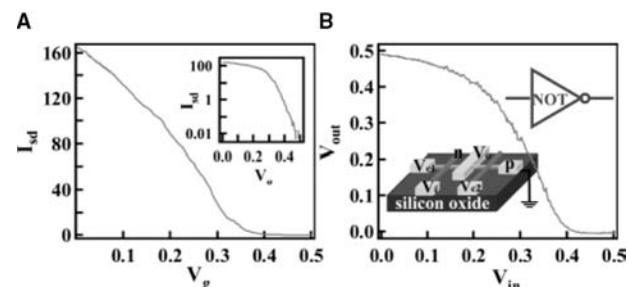


**Fig. 32** Low voltage nanoinverter (logic NOT). (A)  $I$ - $V_g$  behavior of a cNW-FET with onset of  $\sim 0.4$  V. The inset shows that the conductance of the FET can be changed over two orders of magnitude with less than 0.1 V change in the NW gate. The transconductance is  $\sim 500$  nS at  $V_{sd} = 0.5$  V. (B) Output-input ( $V_o$ - $V_i$ ) for a nanoinverter configured from two cNW-FETs. The inverter has an operation voltage of about 0.5 V.

NWs, and would enable further reduction in power dissipation.

The assembly of key logic gates and computation circuits represents a substantial advance compared to previous studies of NTs and molecular systems. First, the controllable electronic characteristics of the NW building blocks and reproducible properties of the devices assembled from these blocks contrasts the much lower control achieved to date with NTs. We believe that predictable and reproducible assembly of device elements and arrays is especially important for integration without resorting to extensive top-down lithography to connect to those few devices that function. Second, the use of crossed NW devices defines all nanoscale device metrics without resorting to top-down lithography. For example, the introduction of the new concept of a cNW-FET incorporates three intrinsic nanometer scale metrics (channel width, length, and gate dielectric thickness) into our devices, and thus can potentially enable the whole circuit architecture to be scaled down to the nanometer level in a straightforward way. This achievement and potential is in stark contrast to NT and molecular devices where the critical device dimension reported to date (length for NTs and area for molecules) have been determined by the same top-down lithography used in conventional electronics. Third, these distinct nanometer scale metrics, which are controlled by synthesis and subsequent assembly, lead to and can potentially lead to significantly improved device characteristics such as high gain, high speed, and low power dissipation, which are especially important to future highly integrated nanoelectronics circuits.

Overall, the predictable and reproducible bench-top assembly of nanoscale crossed p–n diode and cNW-FET elements and arrays reviewed in this section, which have enabled the demonstration of all critical logic gates and basic computation, represent a significant step towards integrated nanoelectronics built from primarily bottom-up vs. top-down approaches. Further improvements can be made by assembling NWs directly onto predefined metal electrode arrays<sup>[74]</sup> and by creating more highly integrated circuit elements by feeding the output from NW to NW. Implementing these approaches could eliminate the conventional lithography used to wire-up devices investigated to date. In addition, in a crossbar array with 5 nm diameter NWs, it may be possible to achieve device densities approaching  $10^{12}/\text{cm}^2$ , which is off the present semiconductor road map for top-down manufacturing. To achieve this goal of bottom-up manufacturing in the future will require substantial work—for example, in developing much greater sophistication in assembly and further improving materials synthesis—but are well within the realm of our current understanding and thus suggest a particularly bright and promising future for this approach to integrated nanoelectronics.

## APPLICATION OF NANOSCALE DEVICES IN CHEMICAL AND BIOLOGICAL SENSING

### Underlying Principle

Developments in nanotechnology will not only lead to improved electronics and make quantum jumps in electronics miniaturization, but could also enable significant advances in medicine and healthcare, which benefit mankind as a whole. For example, nanoscale devices could open up fundamentally new ways to probe single molecule properties, and allow in vivo monitoring of diseases, such as cancer, which could lead to detection at the earliest and most treatable stage.

To this end, NW-based FETs have been exploited for highly sensitive and selective detection of chemical and biological species. Planar semiconductors have been used as the basis for many types of chemical and biological sensors in which detection can be monitored electrically and/or optically. For example, planar FETs can be configured as sensors by modifying the gate oxide with molecular receptors or a selective membrane for the analyte of interest.<sup>[76,77]</sup> Binding of a charged species then results in a depletion or accumulation of carriers within the transistor structures. An attractive feature of such chemically sensitive FETs is that binding can be monitored by a direct change in conductance or related electrical property, although the sensitivity and potential for integration are limited. Our nanoscale sensors are based on a similar framework using NW-based FETs (Fig. 33) but have some obvious advantages compared to planar semiconductor sensors. First, the large surface to volume ratio can dramatically increase the sensitivity. Binding of chemical or biological species to the surface of NWs can lead to depletion or accumulation of carriers in the “bulk” of nanometer diameter structures vs. only the surface region in a planar device, and increase the sensitivity to the single-molecule level. Second, high-density arrays of sensors could be readily prepared owing to the extremely small size of the NWs and the rational assembly techniques discussed in earlier sections of this review. Lastly, the small size of these nanosensors could enable minimally invasive in vivo sensors that could be readily coupled to other device functionality, such as telemetry and drug delivery systems. We have used Si NW-based FETs to demonstrate the principle and potential of such a nanoscale sensor approach.

### Chemical Sensors: The Case of pH

The underlying concept for the NW nanosensor can be illustrated in general for the case of pH sensor

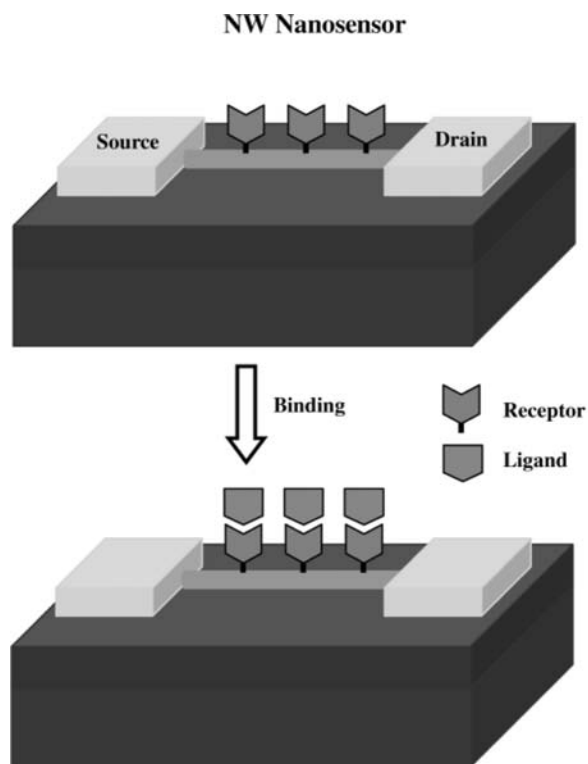


**Fig. 33** Underlying concepts for a nanosensor based on NW-FETs. A solid state NW-FET is transformed into a sensor by modifying the NW surface with molecular receptors. Binding of a charged species (ligand) then results in a depletion or accumulation of carriers within the transistor structures and changes the conductance of the NW-FET.

(Fig. 34).<sup>[78]</sup> Here, a Si NW solid state FET whose conductance is modulated by applied gate, is transformed into a nanosensor by modifying the silicon oxide surface with 3-aminopropyltriethoxysilane (APTES). The APTES provide a surface that can undergo protonation and deprotonation, where changes in surface charge (protonation) chemically gate the Si NW (Fig. 34A). The response of APTES-modified Si NWs to changes in solution pH (Fig. 34B) demonstrate that the NW conductance increases stepwise with discrete changes in pH from 2 to 9 and that the conductance is constant for a given pH. The changes in conductance are also reversible for increasing and/or decreasing pH. A typical plot of the conductance vs. pH (Fig 34C) shows that the pH dependence is linear over the pH 2–9 range and thus suggests that modified Si NWs could function as nanoscale pH sensors.

These results have been explained by considering the mixed surface functionality of the modified Si NWs. Covalently linking APTES to SiNW oxide surface results in a surface terminating in both  $-\text{NH}_2$  and  $-\text{SiOH}$  groups (Fig. 34A), which have different dissociation constants,  $pK_a$ .<sup>[38,79]</sup> At low pH, the  $-\text{NH}_2$  group is protonated to  $-\text{NH}_3^+$  and acts as a

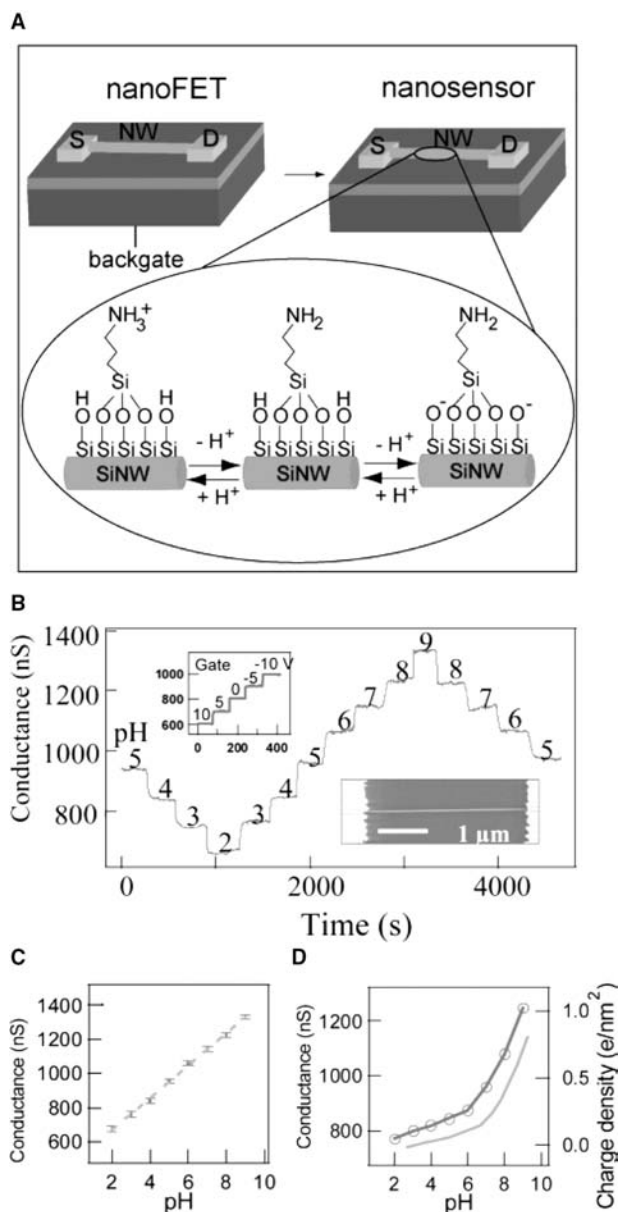


**Fig. 34** NW pH detection. (A) Schematic illustrating the conversion of a NW-FET into a NW pH sensor. (B) Real-time reversible detection of the conductance changes of a modified Si NW as pH is changed from 2 to 9; the pH values are indicated on the conductance plot. Inset: (Top) Plot of the time-dependent conductance of a Si NW-FET as a function of the back-gate voltage. (Bottom) SEM image of a typical device. (C) Plot of the conductance vs. pH; the dashed line is linear fit through this data. (D) The conductance of an unmodified Si NW vs. pH. The dashed curve is a plot of the surface charge density for silica as a function of pH. *Source:* From Ref.<sup>[78]</sup>.

positive gate, which depletes hole carriers in the p-type SiNW and decreases the conductance. At high pH,  $-\text{SiOH}$  is deprotonated to  $-\text{SiO}^-$ , which correspondingly causes an increase in conductance. The observed linear response can be attributed to an approximately

linear change in the total surface charge density (vs. pH) because of the combined acid and base behavior of both surface groups. This point was supported with pH dependent measurements on unmodified (only  $-\text{SiOH}$  functionality) SiNWs, which showed a non-linear pH dependence (Fig. 34D) similar to previous measurements of the pH dependent surface charge density of silica.<sup>[80]</sup>

## Biological Sensors

The above results clearly demonstrate that NW-based FETs can be configured as chemical sensors. Since many biological molecules, such as proteins and DNA, are charged under physiological conditions, it is also possible to detect the binding of these macromolecules to NW surfaces. We have demonstrated detection of biologically relevant species through the detection of proteins, antibodies, and metal ions.<sup>[78]</sup> These critical examples are reviewed briefly below.

Initial investigations of protein detection by Si NW nanosensors were carried out for the well-characterized ligand–receptor binding of biotin–streptavidin (Fig. 35A) using biotin-modified NW surfaces.<sup>[78]</sup> Measurements showed that the conductance of biotin-modified Si NWs increased rapidly to a constant

value upon addition of streptavidin solutions and that this conductance value was unchanged after the addition of pure buffer solution (Fig. 35B). The increase in conductance upon addition of streptavidin is consistent with binding of a negatively charged species to the p-type Si NW surface and the fact that streptavidin ( $pI \sim 5\text{--}6$ )<sup>[81]</sup> is negatively charged at the pH of these measurements. The absence of a conductance decrease with addition of pure buffer also agrees well with the small dissociation constant ( $K_d \sim 10^{-15}$  M) and correspondingly small dissociation rate of biotin–streptavidin.<sup>[81]</sup>

Significantly, the biotin-modified Si NWs nanosensors were also shown to exhibit very high sensitivity. Experiments indicate that it is possible to detect streptavidin binding down to a concentration at least as low as 10 pM (Fig. 35C). This detection level is substantially lower than the nanomolar range demonstrated recently by stochastic sensing of single molecules.<sup>[82]</sup> We note that a time-dependent increase in the conductance can be resolved immediately after streptavidin addition at very low concentrations, which reflects contributions from the forward binding rate and/or diffusion, although future studies will be required to resolve these contributions.

The above studies demonstrate that our NW nanosensors are capable of highly sensitive and selective real-time detection of proteins, although the essentially irreversible biotin–streptavidin binding interaction precludes real-time monitoring of varying protein concentration. To explore this possibility, we studied the reversible binding of monoclonal antibody (m-antibiotin) to biotin.<sup>[83]</sup> Time-dependent conductance measurements made on biotin-modified Si NWs (Fig. 36A) exhibit a well-defined decrease after addition of m-antibiotin solution followed by an increase in the conductance to about the original value upon addition of pure buffer solution. The decrease in conductance upon m-antibiotin addition is consistent with the binding of m-antibiotin, which was positively charged at the pH 7 of these experiments.<sup>[84]</sup> The time scale for the increase in conductance (seconds), which we associate with m-antibiotin dissociation, was also consistent with the reported dissociation rate constant.<sup>[83]</sup>

This reversible, real-time detection of m-antibiotin was further extended to monitor the Si NW sensor conductance as a function of m-antibiotin concentration in these studies.<sup>[78]</sup> These measurements showed a linear change in the conductance as a function of m-antibiotin concentration below  $\sim 10$  nM and saturation at higher values (Fig. 36B) and thus demonstrate several important facts. First, from the linear regime, we estimate that the dissociation constant,  $K_d$ , is of the order of  $10^{-9}$  M, which is in good agreement with the value,  $\sim 10^{-9}$  M, determined previously.<sup>[84]</sup> Second, we can monitor protein concentration in real time,

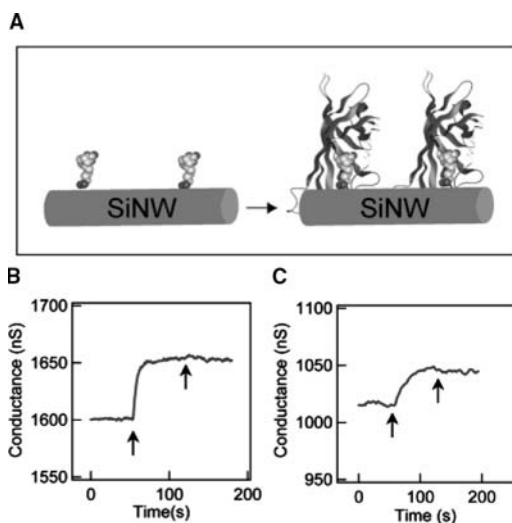


**Fig. 35** Detection of protein binding. (A) Schematic illustrating a biotin-modified Si NW (left) and subsequent binding of streptavidin to the Si NW surface (right). The Si NW and streptavidin are drawn approximately to scale. (B) Plot of conductance vs. time for a biotin-modified Si NW, where first arrow corresponds to the addition of 250 nM streptavidin, and the second arrow corresponds to the addition of pure buffer solution. (C) Conductance vs. time for a biotin-modified Si NW, where the two arrows have the same designation. The streptavidin solution had a concentration of 25 pM. *Source:* From Ref.<sup>[78]</sup>.

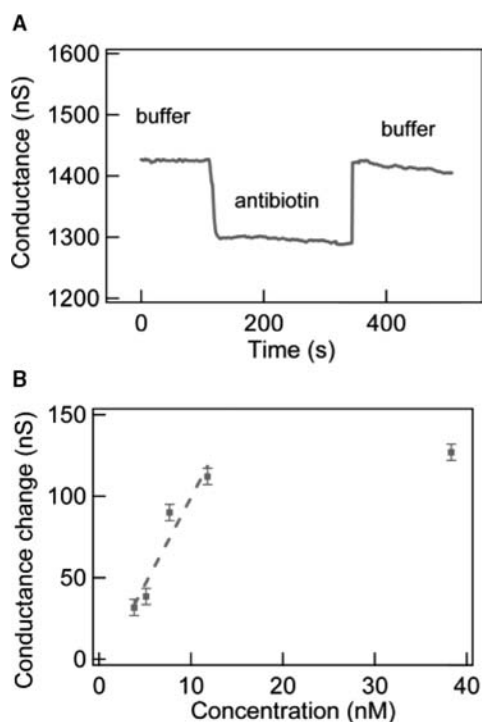


**Fig. 36** Real-time detection of reversible protein binding. (A) Plot of conductance vs. time for a biotin-modified Si NW, where “antibiotin” corresponds to the addition of  $\sim 3 \mu\text{M}$  m-antibiotin. (B) Plot of the conductance change of a biotin modified Si NW vs. m-antibiotin concentration; the dashed line is a linear fit to the four low concentration data points. *Source:* From Ref.<sup>[78]</sup>.

which could have important implications in basic research, for example, in monitoring protein expression, as well as in medical diagnostics. Lastly, preliminary experiments also suggest that the linear response dynamic range can be extended by applying a back gate to the NW, where gating can either increase or decrease the intrinsic binding constant.

The concept of using NW-FETs modified with receptors or ligands for specific detection can be extended in many directions. For example, they can also be used to sense calcium ions ( $\text{Ca}^{2+}$ ), which are important for activating biological processes such as muscle contraction, protein secretion, cell death, and development.<sup>[85]</sup> To this end, a  $\text{Ca}^{2+}$  sensor was fabricated by immobilizing the calcium binding protein calmodulin onto Si NW surfaces. Conductance measurements made with such modified Si NW devices (Fig. 37) showed a drop in the conductance upon addition of a  $25 \mu\text{M}$   $\text{Ca}^{2+}$  solution, and a subsequent increase when a  $\text{Ca}^{2+}$ -free buffer was subsequently flowed through the device. The observed conductance decrease is consistent with expected chemical gating by positive  $\text{Ca}^{2+}$ , and the estimated dissociation constant,  $10^{-5}$ – $10^{-6}$  M, is in good agreement with the reported  $K_d$  for calmodulin.

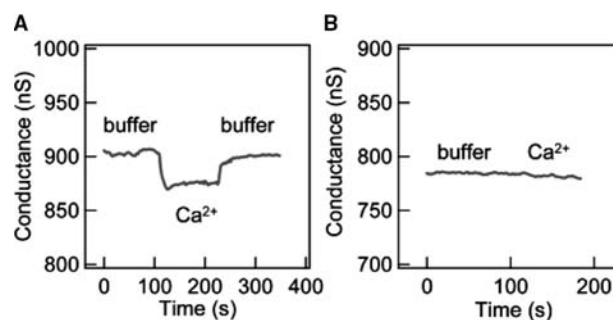


**Fig. 37** Real-time detection of  $\text{Ca}^{2+}$  ions. (A) Plot of conductance vs. time for a calmodulin-terminated Si NW, where “ $\text{Ca}^{2+}$ ” corresponds to the addition of  $25 \mu\text{M}$   $\text{Ca}^{2+}$  solution. (B) Conductance vs. time for an unmodified Si NW. *Source:* From Ref.<sup>[78]</sup>.

### Future Directions

The above studies demonstrate the potential of our NW nanosensors for highly sensitive and selective detection of chemical and biological species. Further development of this new type of nanosensors could also lead to antigen–antibody sensing and/or DNA detection. The availability of NWs with large gate responses should also enable detection down to the single molecule level. More generally, these nanosensors could enable many advances in both basic biological research, such as sensitive detection of many cellular species in real time in an array format to unravel complex signaling pathways, and biotechnology/medicine, where nanosensors might increase the speed of genome sequencing by many orders of magnitude and enable large scale studies designed to unravel the genetic contributions to complex diseases. Moreover, the ability to integrate these electrically monitored nanosensors with other components could facilitate development of multifunctional and minimally invasive implantable devices that enable detection and prevention of diseases at the earliest and most treatable stage.

### SUMMARY AND PERSPECTIVES

In this entry, a brief survey of work drawn primarily from the authors’ laboratory has been presented. Overall, these examples illustrate a series key advances that should ultimately enable nanoelectronics fabrication and manufacturing from the bottom-up. First, we have developed a general approach for the synthesis of NW building blocks with well-controlled chemical compositions, physical dimensions, and electronic properties. Second, we have assembled a wide range of nanoscale electronic and optoelectronic



devices from NW building blocks, and proposed and realized several conceptually new nanodevices, such as crossed NW p–n junctions and cNW-FETs, which are amenable for high-density integration. Third, we have developed methodologies to assemble NWs into integrated device arrays using microchannel fluidics or electrical fields, and have demonstrated integrated functional electronic circuits such as logic gates and carried out basic computations. Lastly, we have developed new types of nanosensors based on NW-FETs that can be used for highly sensitive and selective detection of chemical and biological species.

There is a very bright future for these electronically well-defined NW building blocks both in fundamental science and nanotechnologies. Specifically, we believe that only the very edge of a broad range of ideas has been touched, and that there remain many fascinating fundamental problems in these NW systems, such as the role of finite size and coherent states. Well-defined semiconductor NWs also represent exciting systems to probe fundamental questions about localization or delocalization of electrical carriers and optical excitons in 1D. Further investigations will be not only critical to understanding fundamental issues in 1D systems, but also central to improved device characteristics and possibly conceptually and fundamentally new type of devices, such as single photon emitters and detectors, which could be critical for future quantum communication and computation. Continuing efforts will be required to develop even better control of NW synthesis and more and more sophisticated assembly approaches that can vary device functionality over multilength scales. Lastly, developing new device concepts and integrated architectures will be increasingly essential as we move closer to ultrahigh density integrated nanosystems.

## ACKNOWLEDGMENTS

We thank M. Bockrath, Y. Cui, M.S. Gudixsen, W. Liang, L. Lincoln, H. Park, J. Wang, Q. Wei for helpful discussion and their contributions on the work described in this entry. C.M.L. acknowledges generous support of this work by the Air Force Office of Scientific Research, Defense Advanced Projects Research Agency, National Cancer Institute, National Science Foundation, and Office of Naval Research.

## REFERENCES

1. Moore's Law. <http://www.intel.com/research/silicon/mooreslaw.htm>.
2. The International Technology Roadmap for Semiconductors. <http://www.intel.com/research/silicon/itroadmap.htm>.
3. Meindl, D.J.; Chen, Q.; Davis, J.A. Limits on silicon nanoelectronics for terascale integration. *Science* **2001**, *293*, 2044.
4. Lieber, C.M. The incredible shrinking circuit. *Sci. Am.* **2001**, *285* (3), 58.
5. Polyviou, S.; Levas, M. The future of Moore's Law. <http://www.iis.ee.ic.ac.uk/~frank/surp98/report/sp24>
6. Dagani, R. Building from the bottom up. *Chem. Eng. News* **2000**, *78* (42), 27.
7. Heath, J.R.; Kuekes, P.J.; Snider, G.S.; Williams, R.S. A defect-tolerant computer architecture: opportunities for nanotechnology. *Science* **1998**, *280*, 1716.
8. Reed, M.A.; Tour, J.A. Computing with molecules. *Sci. Am.* **2000**, *282* (6), 86
9. Joachim, C.; Gimzewski, J.K.; Aviram, A. Electronics using hybrid-molecular and mono-molecular devices. *Nature* **2000**, *408*, 541.
10. Collier, C.P.; Wong, E.W.; Belohradsky, M.; Raymo, F.M.; Stoddart, J.F.; Kuekes, P.J.; Williams, R.S.; Heath, J.R. Electronically configurable molecular-based logic gates. *Science* **1999**, *285*, 391.
11. Collier, C.P.; Mattersteig, G.; Wong, E.W.; Luo, Y.; Beverly, K.; Sampaio, J.; Raymo, F.M.; Stoddart, J.F.; Heath, J.R. A [2]catenane-based solid state electronically reconfigurable switch. *Science* **2000**, *289*, 1172.
12. Reed, M.A.; Chen, J.; Rawlett, A.M.; Price, D.W.; Tour, J.M. Molecular random access memory cell. *Appl. Phys. Lett.* **2001**, *78*, 3735.
13. Alivisatos, A.P. Semiconductor clusters, nanocrystals, and quantum dots. *Science* **1996**, *271*, 933.
14. Klein, D.L.; Roth, R.; Lim, A.K.L.; Alivisatos, A.P.; McEuen, P.L. A single-electron transistor made from a cadmium selenide nanocrystal. *Nature* **1997**, *389*, 699.
15. Devoret, M.H.; Schoelkopf, R.J. Amplifying quantum signals with the single-electron transistor. *Nature* **2000**, *406*, 1039.
16. Collins, P.G.; Avouris, P. Nanotubes for electronics. *Sci. Am.* **2000**, *283* (6), 62.
17. Odom, T.W.; Huang, J.-L.; Kim, P.; Lieber, C.M. Atomic structure and electronic properties of single-walled carbon nanotubes. *Nature* **1998**, *391*, 62.
18. Odom, T.W.; Huang, J.; Kim, P.; Lieber, C.M. Structure and electronic properties of carbon nanotubes. *J. Phys. Chem. B* **2000**, *104*, 2794–2809.
19. Dekker, C. Carbon nanotubes as molecular quantum wires. *Phys. Today* **1999**, *52* (5), 22.
20. Dai, H.; Kong, J.; Zhou, C.; Franklin, N.; Tmobler, T.; Cassell, A.; Fan, S.; Chapline, M. Controlled chemical routes to nanotube architectures, physics and devices. *J. Phys. Chem. B* **1999**, *103*, 11,246.
21. Tans, S.J.; Verschueren, R.M.; Dekker, C. Room temperature transistor based on a single carbon nanotube. *Nature* **1998**, *393*, 49.
22. Martel, R.; Schmidt, T.; Shea, H.R.; Hertel, T.; Avouris, P. Single- and multi-wall carbon nanotube field effect transistors. *Appl. Phys. Lett.* **1998**, *73*, 2447.



23. Yao, Z.; Postma, H.W.C.; Balents, L.; Dekker, C. Carbon nanotube intramolecular junctions. *Nature* **1999**, *402*, 273.
24. Fuhrer, M.S.; Nygrad, J.; Shih, L.; Forero, M.; Yoon, Y.G.; Mazzone, M.S.C.; Choi, H.J.; Ihm, J.; Louie, S.G.; Zettl, A.; McEuen, P.L. Crossed nanotube junctions. *Science* **2000**, *288*, 494.
25. Derycke, V.; Martel, R.; Appenzeller, J.; Avouris, P. Carbon nanotube inter- and intramolecular logic gates. *Nano Lett.* **2001**, *1*, 453.
26. Bachtold, A.; Hadley, P.; Nakanishi, T.; Dekker, C. Logic circuits with carbon nanotube transistors. *Science* **2001**, *294*, 1317.
27. Collins, P.G.; Arnold, M.S.; Avouris, P. Engineering carbon nanotubes and nanotube circuits using electrical breakdown. *Science* **2001**, *292*, 706.
28. Lieber, C.M. One-dimensional nanostructures: chemistry, physics and applications. *Solid State Commun.* **1998**, *107*, 106.
29. Hu, J.; Odom, T.W.; Lieber, C.M. Chemistry and physics in one dimension: synthesis and properties of nanowires and nanotubes. *Acc. Chem. Res.* **1999**, *32*, 435.
30. Duan, X.; Lieber, C.M. General synthesis of compound semiconductor nanowires. *Adv. Mater.* **2001**, *12*, 298.
31. Gudixsen, M.S.; Wang, J.; Lieber, C.M. Synthetic control of the diameter and length of single crystal semiconductor nanowires. *J. Phys. Chem. B* **2001**, *105*, 4062–4064.
32. Cui, Y.; Duan, X.; Hu, J.; Lieber, C.M. Doping and electrical transport in silicon nanowires. *J. Phys. Chem. B* **2000**, *104*, 5213.
33. Duan, X.; Huang, Y.; Cui, Y.; Wang, J.; Lieber, C.M. Indium phosphide nanowires as building blocks for nanoscale electronic and optoelectronic devices. *Nature* **2001**, *409*, 66.
34. Cui, Y.; Lieber, C.M. Functional nanoscale electronic devices assembled using silicon nanowire building blocks. *Science* **2001**, *291*, 851.
35. Huang, Y.; Duan, X.; Cui, Y.; Lauhon, L.; Kim, K.; Lieber, C.M. Logic gates and computation from assembled nanowire building blocks. *Science* **2001**, *294*, 1313.
36. Huang, Y.; Duan, X.; Wei, Q.; Lieber, C.M. Directed assembly of one-dimensional nanostructures into functional networks. *Science* **2001**, *291*, 630.
37. Seker, F.; Meeker, K.; Kuech, T.F.; Ellis, A.B. Surface chemistry of prototypical bulk II–VI and III–V semiconductors and implications for chemical sensing. *Chem. Rev.* **2000**, *100*, 2505.
38. Iler, R.K. *The Chemistry of Silica*; Wiley: New York, 1979.
39. Sze, S.M. *Semiconductor Devices, Physics and Technology*; Wiley: New York, 1985.
40. Madelung, O. Semiconductors: intrinsic properties of group IV elements and III–V and II–VI and I–VII compounds. In *Landolt–Bornstein New Series*; Madelung, O., Ed.; Springer: Berlin, Heidelberg, 1987; Vol. III/22a.
41. Huang, Y.; Duan, X.; Lieber, C.M. Nanowires for multi-color photonics. *Small* **2005**, *1*, 142.
42. Datta, S. *Electronics Transport in Mesoscopic Systems*; Cambridge University Press: Cambridge, 1995.
43. Capasso, F.; Datta, S. Quantum electron devices. *Phys. Today* **1990**, *43* (2), 74.
44. Steane, A. Quantum computing. *Rep. Prog. Phys.* **1998**, *61*, 117.
45. Liang, W.; Bockrath, M.; Bozovic, D.; Hafner, H.H.; Tinkham, M.; Park, H. Fabry–Perot interference in a nanotube electron waveguide. *Nature* **2001**, *411*, 665.
46. Buttiker, M.; Imry, Y.; Landauer, R. Generalized many-channel conductance formula with application to small rings. *Phys. Rev. B* **1985**, *31*, 6207.
47. Tsukagoshi, K.; Alphenaar, B.W.; Ago, H. Coherent transport of electron spin in a ferromagnetically contacted carbon nanotube. *Nature* **1999**, *401*, 572.
48. Gudixsen, M.S.; Wang, J.; Lieber, C.M. Size dependent photoluminescence from single indium phosphide nanowires. *J. Phys. Chem B* **2002**, *106*, 4036–4039.
49. Wang, J.; Gudixsen, M.S.; Duan, X.; Cui, Y.; Lieber, C.M. Highly polarized photoluminescence and photo-detection from single indium phosphide nanowires. *Science* **2001**, *293*, 1455.
50. Vouilloz, F. et al. Effect of lateral confinement on valence-band mixing and polarization anisotropy in quantum wires. *Phys. Rev. B* **1998**, *57*, 12,378.
51. Akiyama, H.; Someya, T.; Sakaki, H. Optical anisotropy in 5-nm-scale T-shaped quantum wires fabricated by the cleaved-edge overgrowth method. *Phys. Rev. B* **1996**, *53*, R4229.
52. Ils, P. et al. Linear-polarization of photoluminescence emission and absorption in quantum-well wire structures—experiment and theory. *Phys. Rev. B* **1995**, *51*, 4272.
53. Landau, L.D.; Lifshitz, E.M.; Pitaevskii, L.P. *Electrodynamics of Continuous Media*; Pergamon: Oxford, 1984; 34–42.
54. Gudixsen, M.; Lauhon, L.; Wang, J.; Smith, D.; Lieber, C.M. Growth of nanowire superlattice structures for nanoscale photonics and electronics. *Nature* **2002**, *415*, 617.
55. Micic, O.I.; Sprague, J.; Lu, Z.; Nozik, A.J. Highly efficient band edge emission from InP quantum dots. *Appl. Phys. Lett.* **1996**, *68*, 3150.
56. Huang, M.; Mao, S.; Feick, H.; Yan, H.; Wu, Y.; Kind, H.; Weber, E.; Russo, R.; Yang, P. Room-temperature ultraviolet nanowire nanolasers. *Science* **2001**, *292*, 1897.
57. Johnson, J.; Choi, H.J.; Knutsen, K.P.; Schaller, R.D.; Saykally, R.J.; Yang, P. Single gallium nitride nanowire lasers. *Nat. Mater.* **2002**, *1*, 101.
58. Duan, X.; Huang, Y.; Agarwal, R.; Lieber, C.M. Single nanowire injection laser. *Nature* **2003**, *421*, 241.
59. Chen, C.-L. *Elements of Optoelectronics and Fiber Optics*; Irwin: Chicago, 1996.
60. Bagnall, D.M.; Ullrich, B.; Sakai, H.; Segawa, Y. Microcavity lasing of optically excited CdS thin films at room temperature. *J. Cryst. Growth* **2000**, *214/215*, 1015–1018.
61. Lauhon, L.J.; Gudixsen, M.S.; Wang, D.; Lieber, C.M. Epitaxial core–shell and core–multi-shell nanowire heterostructures. *Nature* **2002**, *420*, 57–61.
62. Bass, M. et al. *Handbook of Optics*; McGraw Hill: New York, 1995; 17.1–17.29.

63. Ura, S.; Sunagawa, H.; Suhara, T.; Nishihara, H. Focusing grating couplers for polarization detection. *J. Lightwave Technol.* **1988**, *6*, 1028.
64. Chen, C.J.; Choi, K.K.; Rokhinson, L.; Chang, W.H.; Tsui, D.C. Corrugated quantum well infrared photodetectors for polarization detection. *Appl. Phys. Lett.* **1999**, *74*, 862.
65. Michler, P.; Kiraz, A.; Becher, C.; Schoenfeld, W.V.; Petroff, P.M.; Hu, L.Z.E.; Imamoglu, A. A quantum dot single-photon turnstile device. *Science* **2000**, *290*, 2282.
66. Kim, J.; Benson, O.; Kan, H.; Yamamoto, Y. A single-photon turnstile device. *Nature* **1999**, *397*, 215–217.
67. Duffy, D.C.; Cooper McDonald, J.; Schueller, O.J.A.; Whitesides, G.M. Rapid prototyping of microfluidic systems in poly(dimethylsiloxane). *Anal. Chem.* **1998**, *70*, 4974.
68. Stover, C.A.; Koch, D.L.; Cohen, C. Observations of fiber orientation in simple shear-flow of semidilute suspensions. *J. Fluid Mech.* **1992**, *238*, 277.
69. Koch, D.L.; Shaqfeh, E.S.G. The average rotation rate of a fiber in the linear flow of a semidilute suspension. *Phys. Fluids A* **1990**, *2*, 2093.
70. Liu, J.; Casavant, M.J.; Cox, M.; Walters, D.A.; Boul, P.; Lu, W.; Rimberg, A.J.; Smith, K.A.; Colbert, D.T.; Smalley, R.E. Controlled deposition of individual single-walled carbon nanotubes on chemically functionalized templates. *Chem. Phys. Lett.* **1999**, *303*, 125.
71. Burghard, M.; Dueberg, G.; Philipp, G.; Muster, J.; Roth, S. Controlled adsorption of carbon nanotubes on chemically modified electrode arrays. *Adv. Mater.* **1998**, *10*, 584.
72. De Rosa, C.; Park, C.; Lotz, B.; Wittmann, J.C.; Fetters, L.J.; Thomas, L.E. Control of molecular and microdomain orientation in a semicrystalline block copolymer thin film by epitaxy. *Macromolecules* **2000**, *33*, 4871.
73. Gleiche, M.; Chi, L.F.; Fuchs, H. Nanoscopic channel lattices with controlled anisotropic wetting. *Nature* **2000**, *403*, 173.
74. Huang, Y.; Duan, X.; Lieber, C.M. unpublished results.
75. Horowitz, P.; Hill, W. *The Art of Electronics*; Cambridge University Press: Cambridge, 1989.
76. Bergveld, P. Development, operation, and application of ion-sensitive field-effect transistor as a tool for electrophysiology. *IEEE Trans. Biomed. Eng.* **1972**, *19*, 342.
77. Blackburn, G.F. *Biosensors: Fundamentals and Applications*; Turner, A.P.F., Karube, I., Wilson, G.S., Eds.; Oxford University Press: Oxford, 1987; 481–530.
78. Cui, Y.; Wei, Q.; Park, H.; Lieber, C.M. Nanowire nanosensors for highly sensitive and selective detection of biological and chemical species. *Science* **2001**, *293*, 1289.
79. Vezenov, D.V.; Noy, A.; Rozsnyai, L.F.; Lieber, C.M. Force titrations and ionization state sensitive imaging of functional groups in aqueous solutions by chemical force microscopy. *J. Am. Chem. Soc.* **1997**, *119*, 2006.
80. Bolt, G.H. Determination of the charge density of silica sols. *J. Phys. Chem.* **1957**, *61*, 1166.
81. Wilchek, M.; Bayer, E.A. Biotin-binding proteins—overview and prospects. *Meth. Enzymol.* **1990**, *184*, 49.
82. Movileanu, L.; Howorka, S.; Braha, O.; Bayley, H. Detecting protein analytes that modulate transmembrane movement of a polymer chain within a single protein pore. *Nat. Biotechnol.* **2000**, *18*, 1091.
83. Blake, R.C., II.; Pavlov, A.R.; Blake, D.A. Automated kinetic exclusion assays to quantify protein binding interactions in homogeneous solution. *Anal. Biochem.* **1999**, *272*, 123.
84. Bagci, H.; Kohen, F.; Kuscuoglu, U.; Bayer, E.A.; Wilchek, M. Monoclonal anti-biotin antibodies simulate avidin in the recognition of biotin. *FEBS Lett.* **1993**, *322*, 47.
85. Klee, C.B.; Vanaman, T.C. Calmodulin. *Adv. Protein Chem.* **1982**, *35*, 213.

## BIBLIOGRAPHY

1. Duan, X.; Lieber, C.M. Semiconductor nanowires: Rational synthesis. In *Dekker Encyclopedia of Nanoscience and Nanotechnology*, 2E; Schwarz, J.A., Contescu, C.I., Putyera, K., Eds.; Taylor & Francis: New York, NY, 2009; Vol. 6, 3941–3953.

# Semiconductor Nanowires: Rational Synthesis

**Xiangfeng Duan**

*Advanced Research Center, Nanosys Inc., Palo Alto, California, U.S.A.*

**Charles M. Lieber**

*Department of Chemistry and Chemical Biology, Harvard University, Cambridge, Massachusetts, U.S.A.*

## INTRODUCTION

Rational design and synthesis of nanoscale materials is critical to work directed towards understanding fundamental properties, creating nanostructured materials, and developing nanotechnologies. One-dimensional (1D) nanostructures [such as nanowire (NW) and nanotubes] have been the focus of considerable interest because they have the potential to answer fundamental questions about role of dimensionality in physical properties and are expected to play a central role in applications ranging from molecular electronics to scanning probe microscopy probes. To explore the diverse and exciting opportunities in 1D system requires materials for which the chemical composition, diameter, length, electronic, and optical properties can be controlled and systematically varied. To meet these requirements, we have focused our efforts on developing a general and predictive approach for the synthesis of 1D structures, much as molecular beam epitaxy has served as an all-purpose method for the growth of two-dimensional (2D) structures. Specifically, it is important to achieve the ability to design and synthesize rationally NWs with predictable control over the key structural, chemical and physical properties, since such control would greatly facilitate studies designed to understand the intrinsic behavior of 1D structures and to explore them as building blocks for nanoscale electronics. Here, in this entry, we review recent advances in rational synthesis of semiconductor NWs. We will first address the key requirement for 1D growth and give a brief overview of various methods towards 1D materials. Subsequently, we will focus our discussion on growth of a broad range of semiconductor NWs via a metal-nanocluster mediated catalytic growth method based on vapor-liquid-solid (VLS) growth mechanism. Next, we further describe growth of NW materials with controlled physical size including diameter and length. Lastly, we discuss growth of NW heterostructures and superlattices with composition/doping modulation along the axial or radial direction.

## SYMMETRY BREAKING: A KEY CONCEPT FOR 1D GROWTH

In general, the growth of 1D nanostructures requires that two dimensions are restricted to the nanometer regime, while the third dimension extends to macroscopic dimensions.<sup>[1-3]</sup> This overall requirement is considerably more difficult to achieve than the corresponding constraints needed for successful growth of 0D and 2D structures.<sup>[4,5]</sup> For example, many important semiconductor materials adopt a cubic zinc-blende (ZB) structure, and thus when growth is stopped at an early stage, the resulting nanoscale structures are nanocrystals with various polyhedron shapes and not 1D NWs (Fig. 1). To achieve 1D growth in systems where atomic bonding is relatively isotropic requires that the growth symmetry be broken rather than simply arresting growth at an early stage.

Over the past decade, considerable effort has been placed on the bulk synthesis of NWs, and various strategies have been developed to break the growth symmetry either “physically” or “chemically.” A common theme in many of these studies has been the use of linear templates, including the edges of surface steps,<sup>[6]</sup> nanofibers,<sup>[7,8]</sup> and porous membranes,<sup>[9]</sup> to direct chemical reactions and material growth in 1D (Fig. 2). This strategy is conceptually simple and has been used to prepare a wide range of NW materials. Despite this simplicity, template-mediated growth is also limited in that the resulting NWs are usually polycrystalline, which could limit their potential for many applications.

Another general strategy that has received increasing focus over that past several years involves exploiting a “catalyst” to confine growth in 1D. Depending on the phases involved in the reaction, this approach is typically defined as VLS,<sup>[10,11]</sup> solution-liquid-solid (SLS),<sup>[12,13]</sup> or vapor-solid (VS)<sup>[14,15]</sup> growth. In VLS growth, a vapor-phase reactant is solubilized by a liquid catalyst particle to form solid wire/rod-like structures. Solution-liquid-solid adopts the same idea with the only change that reactant comes from a

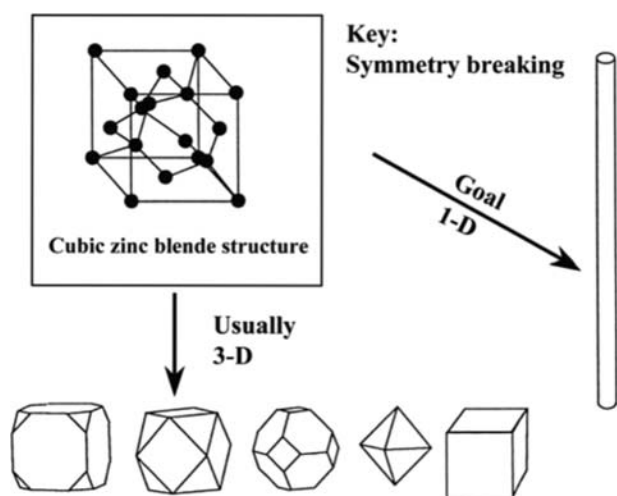


**Fig. 1** Schematic view of key concept for 1D growth. To achieve 1D growth in systems where atomic bonding is relatively isotropic requires that the growth symmetry be broken rather than simply arresting growth at an early stage.

solution rather than vapor phase; in VS, a vapor-phase reactant reacts directly on the solid particle to form a solid wire/tube. Vapor-liquid-solid growth has been used to synthesize a variety of whisker-like structures but with typical diameter much larger than 200 nm.<sup>[10,11]</sup> Solution-liquid-solid has been used to grow NWs of III-V materials but seems to be limited by the availability of low-melting point metal

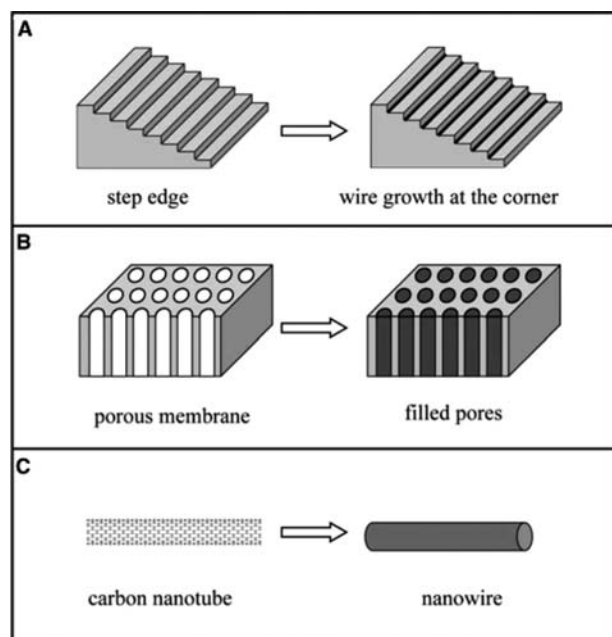


**Fig. 2** Schematic view of growth of NWs by physically confined chemical reaction. Growth of NWs by (A) Step edge deposition; (B) Pore filling; and (C) Deposition on preexisting 1D fibers such as carbon nanotubes.

catalyst.<sup>[12,13]</sup> Vapor-solid growth has been used to grow carbon nanotubes, and a number of different oxide nanorods,<sup>[14,15]</sup> although it seemed to be limited to the growth of only some particular types of materials and the growth mechanism is yet to be understood.

## CATALYTIC GROWTH: CONCEPTS AND SYNTHETIC DESIGN

Catalytic growth, where the catalyst is used to direct 1D growth of single crystal materials via a VLS mechanism (Fig. 3A), is a powerful concept for NW synthesis.<sup>[1-3]</sup> Here, the catalyst is envisioned as a nanocluster or nanodroplet that defines the diameter of and serves as the site that directs preferentially the addition of reactant to the end of a growing NW much like a living polymerization catalyst directs the addition of monomers to a growing polymer chain.

This synthetic concept is especially important since it readily provides the intellectual underpinning needed

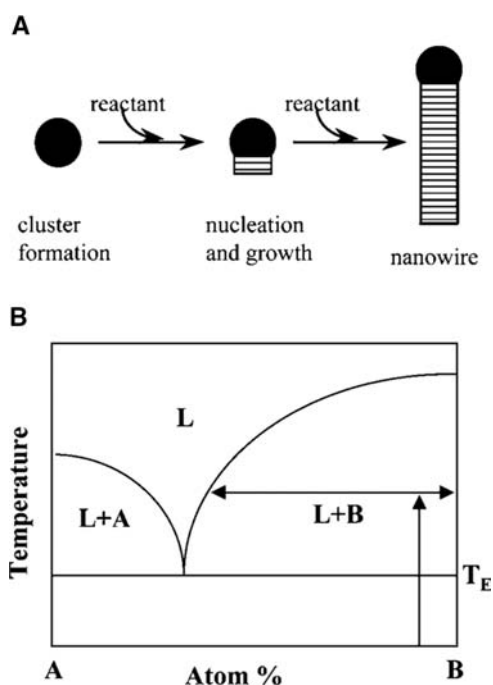


**Fig. 3** Catalytic growth of NWs. (A) Schematics illustrating the underlying concept for catalytic growth of NWs. Liquid catalytic clusters act as the energetically favored site for localized chemical reaction, absorption of vapor-phase reactant, and crystallization of crystalline NWs. (B) Binary A-B phase diagram used as guide for choosing a catalyst for NW growth. The vertical arrow represents a specific composition of catalyst (A) to NW (B) with end point corresponding to the growth temperature. The horizontal arrow defines the composition of the catalyst liquid (L) catalyst-NW (A-B) nanodroplet and shows that pure solid NW (B) is the only solid phase at this temperature.

for the specification of the catalyst and growth conditions required for predictable NW growth. First, equilibrium phase diagrams (Fig. 3B) are used to determine catalyst materials that form a liquid alloy with the NW material of interest. The phase diagram is then used to choose a specific composition and growth temperature such that there is a coexistence of a liquid alloy and solid NW phases. The liquid catalyst alloy cluster serves as the preferential site for absorption of reactant since the sticking coefficient is much higher on liquid vs. solid surfaces and, when supersaturated, the nucleation site for crystallization. Preferential 1D growth occurs in the presence of reactant as long as the catalyst nanodroplet remains in the liquid state. Within this framework, it is straightforward to synthesize NWs with different diameters and composition, if appropriate nanometer scale diameter catalyst clusters are available. Several methods that exploit this general approach are described later with an emphasis on laser-assisted catalytic growth (LCG) and metal-catalyzed chemical vapor deposition (CVD).

## LASER-ASSISTED CATALYTIC GROWTH

A straightforward and general approach for producing the nanometer scale clusters required to nucleate and direct the growth of NWs is laser ablation and condensation.<sup>[16]</sup> In this context, NW growth can be readily achieved by laser ablation of a composite target containing the catalyst and NW material in a heated flow tube (Fig. 4). The background pressure within the flow reactor is used to control condensation of the ablated material and the cluster size, while the temperature is varied to maintain the catalyst cluster in the liquid state. When the laser-generated clusters become supersaturated with the desired NW material, a nucleation event occurs producing a (NW) solid–liquid (NW–catalyst alloy) interface. To minimize the interfacial free energy, subsequent solid growth/crystallization occurs at this initial interface, which thus imposes a highly anisotropic growth constraint that lead to 1D nanoscale wires. We have termed this method “laser-assisted catalytic growth.”<sup>[3]</sup> This approach has proven to be very general for the synthesis of semiconductor NW materials, including group IV elemental,<sup>[17]</sup> group

IV alloys, and group III–V, II–VI, and IV–VI compound semiconductor NW materials.<sup>[3,18–20]</sup> Later we demonstrate the basic principles underlying this approach with the rational and predictable growth of gallium arsenide (GaAs) NWs.

## Laser-Assisted Catalytic Growth of GaAs NWs

A key feature of our catalytic growth approach for NW synthesis is that equilibrium phase diagrams can be used to predict the catalyst material, chemical composition, and growth conditions, thus enabling rational and predictable synthesis of new NW materials. For example, binary phase diagrams have been used to predict the composition and growth temperatures for the synthesis of elemental semiconductor NW materials such as silicon and germanium NWs.<sup>[17]</sup> Predictable catalytic growth of compound NWs is more challenging than that of Si and Ge NWs due to the complexity of ternary and higher order phase diagrams. However, such complexity can be greatly simplified by considering pseudobinary phase diagrams for the catalyst and compound semiconductor of interest. For example, the pseudobinary phase diagram of Au–GaAs (Fig. 5A) shows that Au–Ga–As liquid and GaAs solid are the principle phases above 630°C in the GaAs-rich region of the phase diagram.<sup>[21]</sup> This information implies that Au can serve as a catalyst to grow GaAs NWs by the LCG method, if the target composition and growth temperature are chosen to be within this region of the phase diagram.

Indeed, LCG growth of GaAs NWs using Au as the catalyst produces samples consisting primarily of wire-like structure with diameters on the order of 10 nm, and lengths extending up to tens of micrometers (Fig. 5B). X-ray diffraction (XRD) data from bulk GaAs NW samples can be indexed to the ZB structure with a lattice constant consistent with bulk GaAs, and also show that the material is pure GaAs at least to 1% level. In addition, we note that high yields of GaAs NWs were also obtained using Ag and Cu catalysts. These latter data are consistent with the fact that Ag and Cu exhibit M–Ga–As (M = Ag or Cu) liquid and GaAs solid phases in the GaAs-rich region of the corresponding pseudobinary phase diagrams.<sup>[21]</sup> Taken together, these results demonstrate clearly the power of the LCG approach for predictable NW growth.

Detailed transmission electron microscope (TEM) studies along with electron diffraction (ED) and energy dispersive X-ray (EDX) analysis also revealed important features of the structure and chemical compositions of the produced GaAs NWs. First, diffraction contrast images of individual NWs (Fig. 5C) indicate that NWs are single crystal (uniform contrast) and uniform in diameter. Second, the Ga : As composition

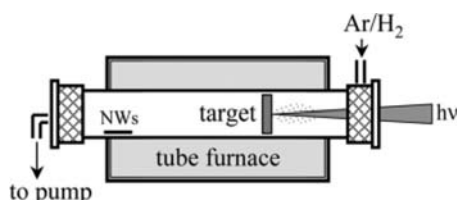
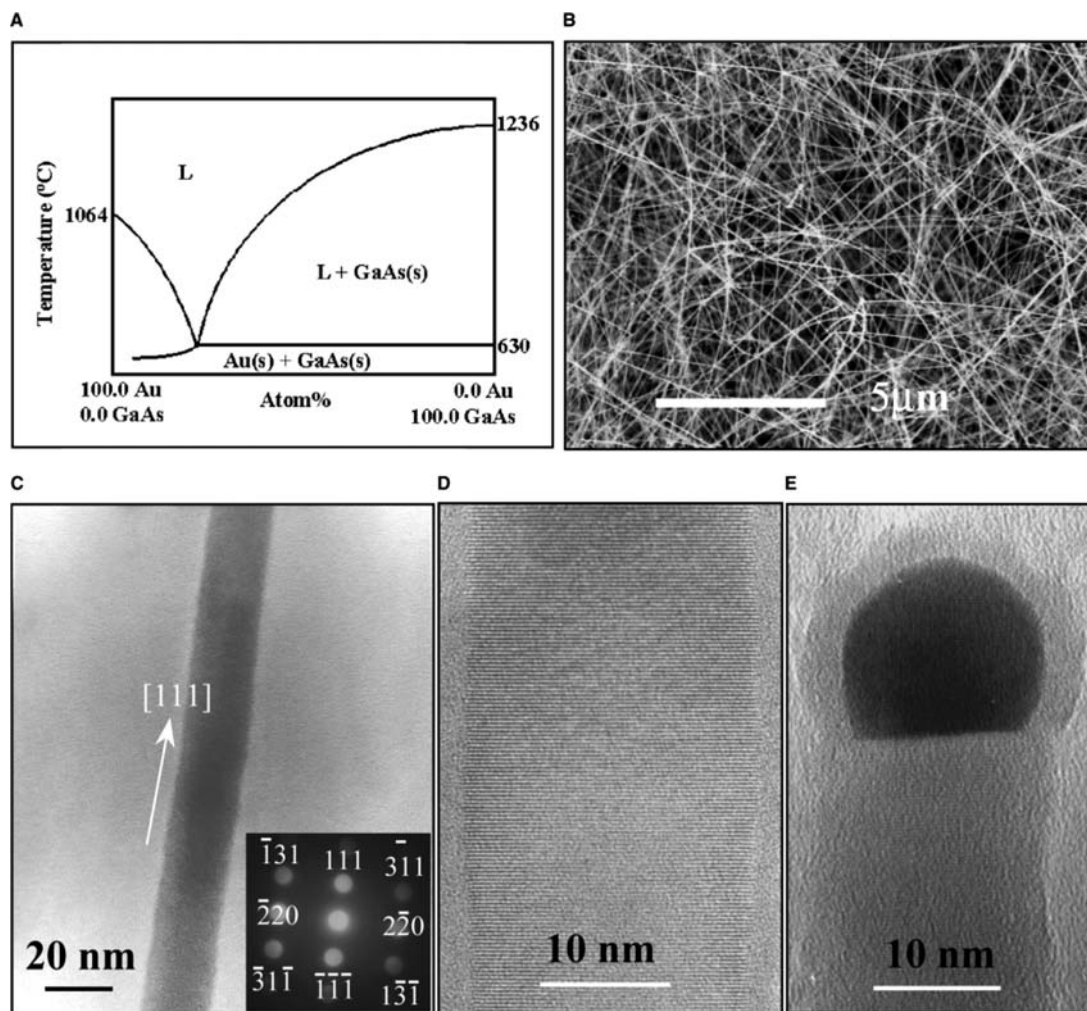


Fig. 4 Schematic of a laser-based NW growth apparatus.



**Fig. 5** Laser-assisted catalytic growth of GaAs NWs. (A) Pseudobinary phase diagram of the GaAs–Au system. (B) Scanning electron microscope (SEM) image of GaAs NWs produced by LCG. (C) Diffraction contrast TEM image of a GaAs NW indicating single crystal structure. The inset shows a convergent beam ED pattern recorded along  $\langle 1\ 1\ 2 \rangle$  zone axis, and demonstrates wire axis (and growth) is along the  $[1\ 1\ 1]$  direction. (D) High-resolution TEM image of the NW. The  $(1\ 1\ 1)$  lattice planes (lattice spacing  $0.32 \pm 0.01$  nm) are clearly seen and perpendicular to the wire axis, further confirming the  $[1\ 1\ 1]$  growth direction. (E) High-resolution TEM image of an NW end showing a catalyst nanocluster. Energy dispersive X-ray analysis indicates that the nanoparticle is composed primarily of Au with trace amounts of Ga and As. *Source:* From Ref.<sup>[3]</sup>.

determined by EDX is consistent with stoichiometric GaAs within limits of instrument sensitivity. Third, the ED pattern recorded perpendicular to the long axis of this NW (Fig. 5C, inset) can be indexed for the  $\langle 1\ 1\ 2 \rangle$  zone axis of the ZB GaAs structure, and thus shows that growth occurs along the  $[1\ 1\ 1]$  direction. Extensive studies of individual GaAs NWs show that growth occurs along the  $\langle 1\ 1\ 1 \rangle$  directions in all cases. This direction and the single crystal structure have been further confirmed by lattice-resolved TEM images (e.g., Fig. 5D) that show clearly the  $(1\ 1\ 1)$  lattice planes perpendicular to the wire axis. Lastly, the TEM studies also revealed that most NWs terminate at one end with a nanoparticle of higher contrast (Fig. 5E). Energy dispersive X-ray analysis indicates that the

nanoparticles are composed largely of Au. The presence of Au nanoparticles at the ends of the NWs is consistent with the pseudobinary phase diagram, and represents strong evidence for a VLS growth mechanism proposed for LCG.

### General Synthesis of Semiconductor Nanowires

The successful synthesis of binary GaAs NWs by LCG is representative of the broad range of binary and more complex NW materials prepared by this method.<sup>[3,18–20]</sup> In a number of cases, phase diagrams could be used to define clearly catalyst, composition and growth



**Table 1** NW materials grown by the LCG approach. All of the NWs were synthesized using gold as the catalyst except for the case of GaN (see text)

Group IV–IV	Group III–V		Group II–VI (Binary)	Group IV–VI (Binary)
	Binary	Ternary		
Si	GaN	Ga(As <sub>(1-x)</sub> P <sub>x</sub> )	ZnS	PbSe
Ge	GaP	In(As <sub>(1-x)</sub> P <sub>x</sub> )	ZnSe	PbTe
Si <sub>(1-x)</sub> Ge <sub>x</sub>	GaAs	(Ga <sub>(1-x)</sub> In <sub>x</sub> )P	CdS	
	InP	(Ga <sub>(1-x)</sub> In <sub>x</sub> )As	CdSe	
	InAs	(Ga <sub>(1-x)</sub> In <sub>x</sub> ) (As <sub>(1-x)</sub> P <sub>x</sub> )		

conditions required for successful NW growth, although appropriate phase diagrams (e.g., pseudobinary and more complex) are not readily available for many compound semiconductor materials and catalytic metals of interest. To extend our synthetic approach to the broadest range of materials, we recognized that catalysts for LCG can be chosen in the absence of detailed phase diagram data by identifying metals in which the NW component elements are soluble in the liquid phase but that do not form solid compounds more stable than the desired NW phase; that is, the ideal metal catalyst should be “physically active” but “chemically stable.” This basic guiding principle suggests that the noble metal Au should represent a good starting point for many semiconductor materials. Indeed, Table 1 summarizes the broad range of NW materials, with different structure types and chemical properties, synthesized as high-quality single crystals using Au as the catalyst. These results demonstrate unambiguously the generality of our approach.

## The Case of GaN Nanowires

Gold nanoclusters are unable to catalyze GaN NW growth due to the low solubility of nitrogen.<sup>[19]</sup> These results are consistent with the basic requirement for a catalyst: physically active and chemically stable. In this context, Au is not physically active. A good catalyst should form a miscible liquid phase with GaN but not lead to a more stable solid phase under the NW growth conditions. This guiding principle suggests that Fe and Ni, which dissolve both gallium and nitrogen, and do not form a more stable compound than GaN, will be good catalysts for GaN NW growth.

Significantly, we found that LCG using either a GaN/Fe or GaN/Ni targets produces a high yield of nanometer diameter wire-like structures.<sup>[19]</sup> Fig. 6A shows a diffraction contrast TEM image of a GaN NW synthesized via an iron catalyst. The uniform contrast of the NW suggests that it has a single crystalline structure. Electron diffraction confirmed that the NWs are single crystals with a wurtzite structure and a [1 0 0] growth direction. Images of the NW ends also exhibited nanoclusters consisting primarily of iron, consistent with a VLS growth mechanism. Lastly, high-resolution TEM images (Fig. 6B,C) confirmed the single crystal structure and growth direction, and moreover, demonstrated that the surfaces of the GaN NWs terminate sharply with only 1–2 atomic layers of amorphous oxide.

## Diameter-, Length-, and Doping-Controlled Synthesis

In the LCG method, laser ablation is used to simultaneously generate nanoscale metal catalyst clusters

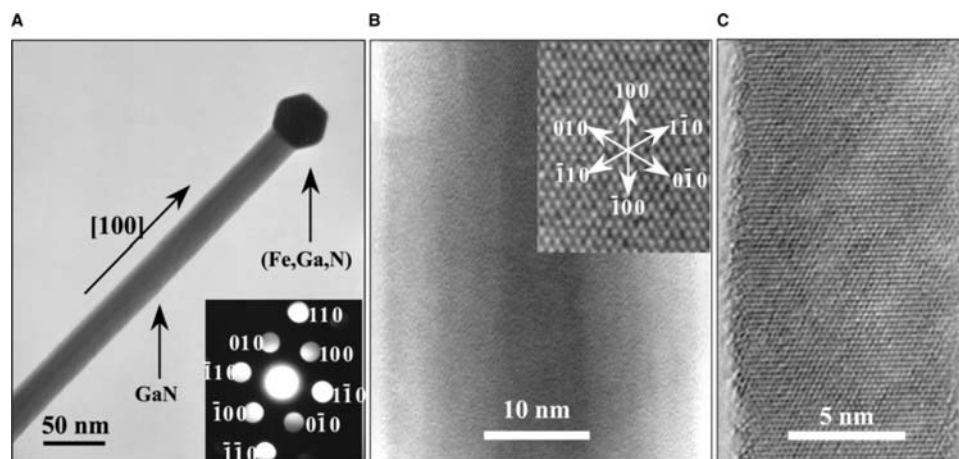


**Fig. 6** Laser-assisted catalytic growth of GaN NWs. (A) Diffraction contrast TEM image of a GaN NW that terminates in a faceted nanoparticle of higher (darker) contrast. (Inset) convergent beam ED (CBED) pattern recorded along  $\langle 0\ 0\ 1 \rangle$  zone axis. (B), (C) Lattice resolved TEM images of GaN NW with diameters of ca. 30 and 10 nm, respectively. The image was taken along  $\langle 0\ 0\ 1 \rangle$  zone axis. Source: From Ref.<sup>[19]</sup>.

and semiconductor reactant that produce NWs via a VLS growth mechanism. A major advantage of this approach is its flexibility and generality since laser ablation can be used to produce nanoclusters of virtually any material, which has enabled the growth of a very wide range of NWs. To fully exploit the potential of these NW materials also requires control of physical dimensions (i.e., diameter and length) and electronic properties (e.g., doping).

Implicit to our catalytic approach to NW growth is the idea that the size of the metal catalysts determine NW diameter, and thus NWs with a narrow size distribution should be obtained from approximately monodisperse nanocluster catalysts. This important idea was verified recently through the demonstration of diameter-controlled growth of GaP,<sup>[22]</sup> InP,<sup>[23]</sup> and Si NWs<sup>[24]</sup> from monodisperse Au nanocluster catalysts. Significantly, the widths of the NW diameter distributions were essentially the same as those of the starting Au nanoclusters, thus demonstrating that NW diameter can be controlled predictably. The use of well-defined catalyst nanoclusters was also used to show that NWs with a given length can be prepared by controlling the growth time.<sup>[23]</sup> Lastly, studies have shown that controlled p- and n-type doping of these semiconductor NWs, which is critical for most nanoelectronic and many photonic applications, can be readily achieved by simply introducing dopant elements into the reactant.<sup>[25,26]</sup>

### CATALYTIC CHEMICAL VAPOR DEPOSITION GROWTH OF NANOWIRES

An alternative to the LCG implementation of catalytic NW growth is nanocluster-catalyzed CVD, in which the reactants and dopants are well-defined gas sources.<sup>[2]</sup> The catalytic CVD method enables the NW size, composition, and doping level to be controlled in a very precise manner.<sup>[24]</sup>

A clear illustration of the potential of this method is the controlled growth of Si NWs using distinct monodisperse diameter Au nanoclusters as the catalyst and silane as the gaseous reactant source (Fig. 7).<sup>[24]</sup> Field emission scanning electron microscope (FE-SEM) images of the Si NWs grown from Au nanoclusters dispersed on SiO<sub>2</sub> planar surfaces showed a comparable NW density to the starting nanocluster density (Fig. 7B). Qualitatively, these images also show that the Si NWs grown from Au nanoclusters are nearly monodisperse with diameters determined by the nanoclusters. This latter point was confirmed from TEM images (Fig. 7B, inset), which show directly that the Au particles at the NW ends are similar to the NW diameters. Histograms summarizing extensive TEM studies of the NW diameters obtained from different

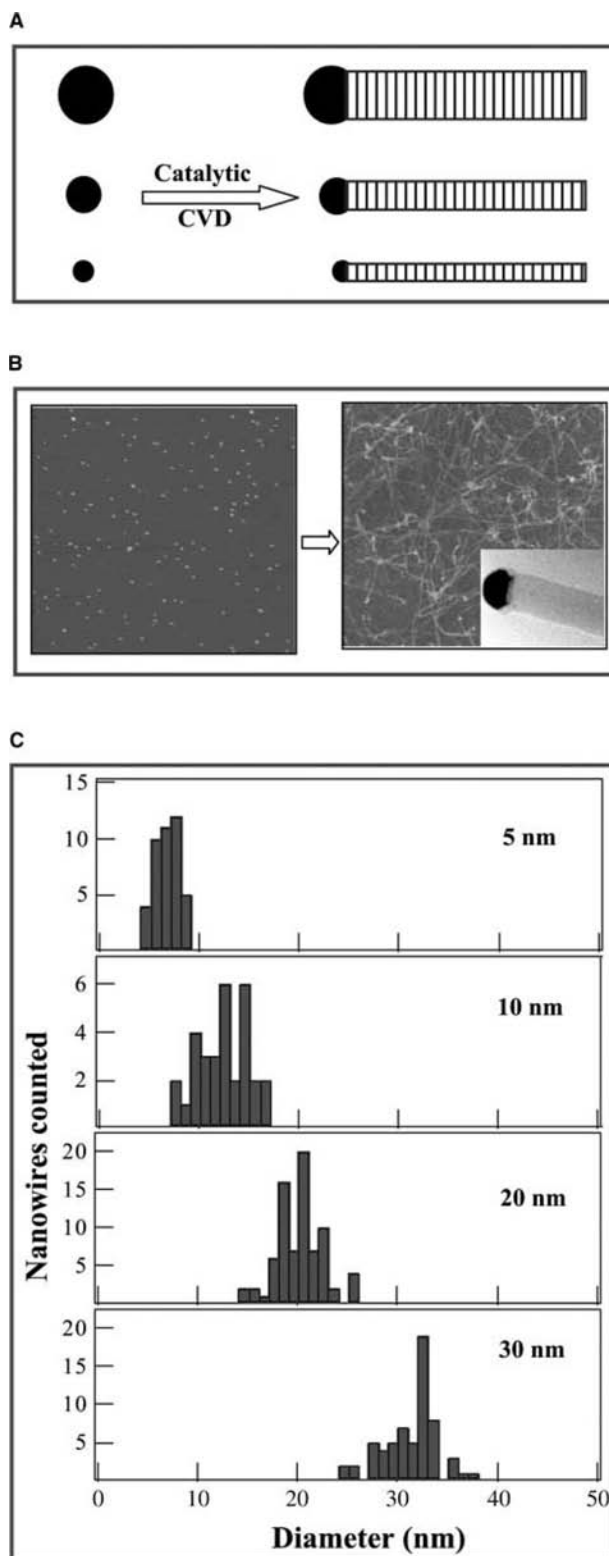


**Fig. 7** Catalytic CVD growth of Si NWs. (A) Schematic of size-controlled NW synthesis using monodisperse Au nanocluster catalysts. (B) Atomic force microscope (AFM) image of Au nanoclusters deposited on a silicon substrate, and the Si NWs grown by CVD. (C) Distributions of NW diameters obtained from 5, 10, 20, and 30 nm diameter nanoclusters. *Source:* From Ref.<sup>[24]</sup>.

diameter nanoclusters also show that Si NWs grown from 5 ( $4.9 \pm 1.0$ ), 10 ( $9.7 \pm 1.5$ ), 20 ( $19.8 \pm 2.0$ ), and 30 nm ( $30.0 \pm 3.0$  nm) Au nanoclusters have average NW diameters of  $6.4 \pm 1.2$ ,  $12.3 \pm 2.5$ ,  $20 \pm 2.3$ , and  $31.1 \pm 2.7$  nm, respectively. Significantly, the dispersion of the Si NW diameters mirrors that of Au catalysts, suggesting that the NW dispersity is limited only by the dispersity of Au nanocluster catalysts.

These studies also showed that the NW diameters were on average 1–2 nm larger than the catalyst sizes. This observation is consistent with the formation of an (Si, Au) alloy prior to the nucleation of NW growth. In addition, postgrowth oxidation of the Si NWs upon exposure to air could increase observed wire diameters. Overall, these results demonstrate the power of our size-controlled growth approach, and also show that it is possible to produce nearly monodisperse Si NWs with specific core diameters ranging from only 2 to more than 30 nm. In addition, the electronic properties of the Si NWs can be precisely controlled by introducing dopant gases during growth. For example, addition of different ratios of diborane or phosphane to silane reactant during growth produces p- or n-type Si NWs, respectively, with dopant concentration varied in a well-controlled way.<sup>[25]</sup>

## SYNTHESIS OF NANOWIRE HETEROSTRUCTURES AND SUPERLATTICES

Modulated nanostructures in which the composition and/or doping are varied on the nanometer scale represent important targets of synthesis since they could enable new and unique function and potential for integration in functional nanosystems. An initial indication of the significance of this idea was the growth of carbon nanotube–Si NW heterojunctions, which created nanometer scale metal–semiconductor junctions showing current rectification.<sup>[27]</sup> In this section, we will describe the synthesis of both longitudinal and radial NW heterostructures.

### Axial Nanowire Heterostructures

Our approach to axial NW heterostructure growth (Fig. 8)<sup>[28]</sup> exploits metal-catalyzed NW synthesis. We introduce vapor-phase semiconductor reactants required for NW growth by either laser ablation of solid targets or vapor-phase molecular species. To create a single junction within the NW, the addition of the first reactant is stopped during growth, and then a second reactant is introduced for the remainder of the synthesis (Fig. 8B); repeated modulation of the reactants during growth produces NW superlattices

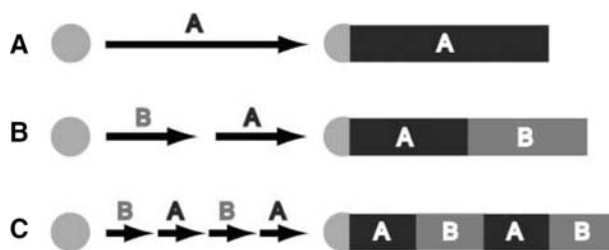


**Fig. 8** Schematics illustrating the synthesis of axial heterostructures: (A) single component NW; (B) heterostructure; and (C) superlattice. *Source:* From Ref.<sup>[28]</sup>.

(Fig. 8C). In principle, this approach can be successfully implemented if a nanocluster catalyst suitable for growth of the different superlattice components under similar conditions is found; our previous studies suggested that Au nanoclusters meet this requirement for a wide range of group III–V and group IV materials.

Gallium arsenide (GaAs) /gallium phosphide (GaP) superlattices have been grown by LCG using GaAs and GaP targets.<sup>[28]</sup> Fig. 9 shows TEM images of the products of this synthesis. It is relatively straightforward to focus on the junction area as the NW lengths can be controlled directly by growth times. High-resolution TEM images of a typical GaAs/GaP junction region (Fig. 9A) exhibit a crystalline NW core without obvious defects, and show that the NW axes lies along the  $\langle 111 \rangle$  direction, in agreement with previous studies of single-component systems. Two-dimensional Fourier transforms calculated from high-resolution images containing the junction region (Fig. 9A, inset) show pairs of reciprocal lattice peaks along the different lattice directions, while such transforms calculated from the regions above and below the junction (not shown) exhibit only single reciprocal lattice peaks. Analysis of these peak data yields lattice constants, indexed to the ZB structures of GaP and GaAs, of  $0.5474 \pm 0.0073$  nm and  $0.5668 \pm 0.0085$  nm, and are in good agreement with the values for both GaP (0.5451 nm) and GaAs (0.5653 nm), respectively.

The TEM structural data suggest that the GaP/GaAs junctions could be abrupt, and thus we have carried out local elemental mapping of the heterojunction by energy dispersive X-ray spectroscopy (EDS) to address composition variation across the junction (Fig. 9E).<sup>[28]</sup> These elemental maps show that Ga is uniformly distributed along the length of the NW, while P (Fig. 9D) and As (Fig. 9E) appear localized in the GaP and GaAs portions of the NW heterostructure, respectively. Quantitative analysis of the P and As composition variation (Fig. 9F) shows, however, that the junction is not atomically abrupt, but rather makes the transition between GaP and GaAs phases over a length scale of 15–20 nm. This length scale is reasonable

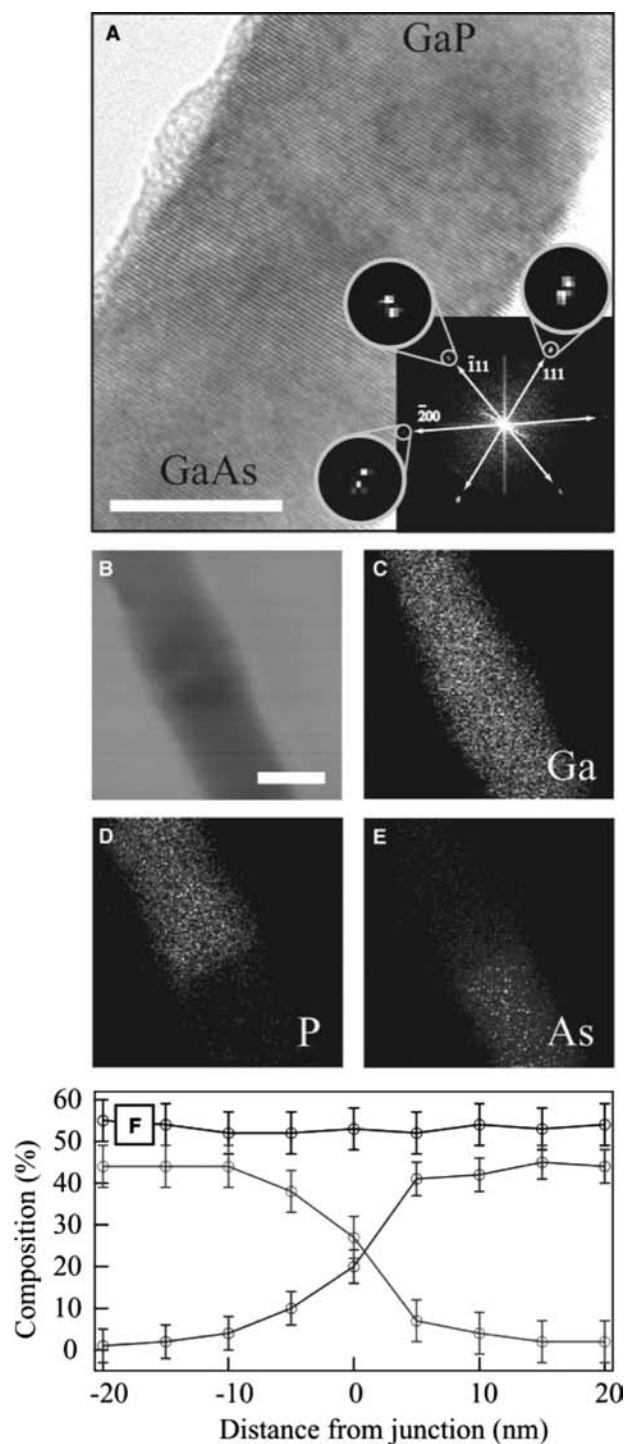


**Fig. 9** GaAs/GaP NW junctions. (A) High-resolution TEM of a GaAs/GaP junction grown from a 20-nm gold nanocluster catalyst. Scale bar, 10 nm. Inset, 2D Fourier transforms show splitting of the reciprocal lattice peaks along the  $\langle 111 \rangle$ ,  $\langle \bar{1}00 \rangle$  and  $\langle 200 \rangle$  lattice directions in the  $[022]$  zone axis. (B) Transmission electron microscope image of another junction. Scale bar, 20 nm. (C)–(E) Elemental mapping of the Ga (shown gray), P (red), and As (blue) content of the junction shown in (B). (F) Line profiles of the composition through the junction region, showing the change in composition as a function of the distance. *Source:* From Ref.<sup>[28]</sup>.

considering that the  $\sim 20$  nm diameter Au catalyst must realloy with GaP after initial GaAs growth. The observed composition variation has several potentially important implications. First, composition variation at the interface can relieve strain, and may enable the defect-free junctions and superlattices that we observe in this system—which has a relatively large lattice mismatch. We note, however, that simple estimates of the length between dislocations suggest that defect-free, atomically abrupt interfaces may be possible in wires of diameter less than 20 nm. Second, there are photonic and electronic applications where abrupt interfaces are important. The observed composition variation can be substantially reduced in smaller-diameter NWs; that is, a 5-nm diameter NW superlattice should have variations of  $< 5$  nm across the junction interfaces. Alternatively, it should be possible to use different nanocluster catalysts or variations in the growth temperature when reactants are switched to obtain sharper interfaces.

We find that this approach can produce compositionally modulated NW superlattices in which the

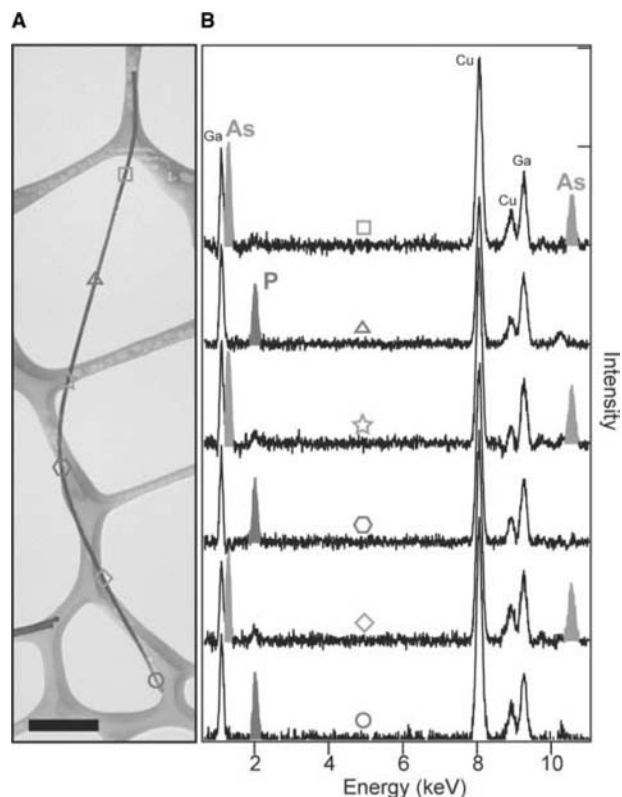


**Fig. 10** Nanowire superlattice structures. (A) Transmission electron microscope image of a  $\sim 20$ -nm diameter  $(\text{GaP}/\text{GaAs})_3$  NW superlattice. Scale bar, 300 nm. (B) Elemental profile of the superlattice along the NW length measured by EDS analysis. The symbols in (A) show the location of each EDS spectrum along the NW and the color of the symbol indicates GaP (red) and GaAs (blue) regions. *Source:* From Ref.<sup>[28]</sup>.

number of periods and repeat spacing can be readily varied during growth.<sup>[28]</sup> Transmission electron microscope images of a six-period structure corresponding to a (GaP/GaAs)<sub>3</sub> superlattice (Fig. 10A) show that the 20 nm diameter NWs are highly uniform over their ~3 μm lengths. Spatially resolved EDS measurements of composition (Fig. 10B) further demonstrate that the P and As regions are distinct from one another, and that there is minimal cross-contamination. Moreover, these data show that each GaP and GaAs NW segment has a length of about 500 nm, and are thus consistent with the equal growth times used for each segment, but also show that growth rates remain relatively constant during the entire NW synthesis.

This methodology for growth of superlattice structures can be generalized in many materials systems. For example, we fabricated p–n junctions within individual Si NWs by Au-nanocluster-catalyzed CVD and dopant modulation.<sup>[28]</sup> Other systems have also demonstrated recently by other groups: Si–Ge<sup>[29]</sup> and InAs–InP.<sup>[30]</sup> These superlattice structures greatly increase the versatility and power of NW building blocks for nanoscale electronic and photonic applications, such as nanobarcodes, injection lasers, and engineered 1D waveguides.

### Radial Nanowire Homo- and Heterostructures

The growth of crystalline overlayers on nanostructure surfaces is important for controlling surface properties

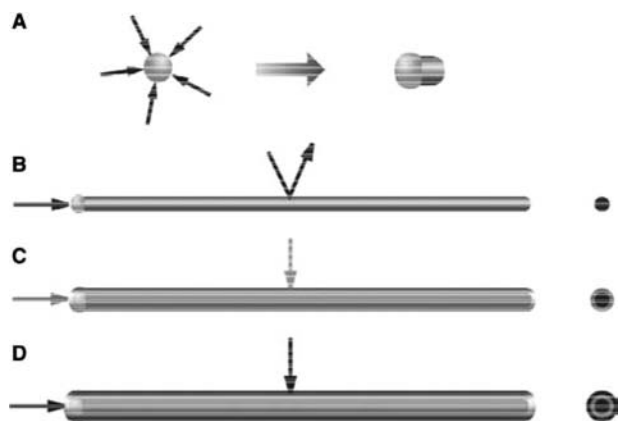


**Fig. 11** Synthesis of core-shell NWs by chemical vapor deposition. (A) Gaseous reactants (red) catalytically decompose on the surface of a gold nanocluster leading to nucleation and axial NW growth. (B) One-dimensional growth is maintained as reactant decomposition on the gold catalyst is strongly preferred. (C) Synthetic conditions are altered to induce homogeneous reactant decomposition on the NW surface, leading to a thin, uniform shell (blue). (D) Multiple shells are grown by repeated modulation of reactants. *Source:* From Ref.<sup>[31]</sup>.

and for enabling new function. We have recently demonstrated this concept with the synthesis of silicon and germanium core-shell and multishell NW homo- and heterostructures using the CVD method applicable to a variety of nanoscale materials.<sup>[31]</sup> The approach to

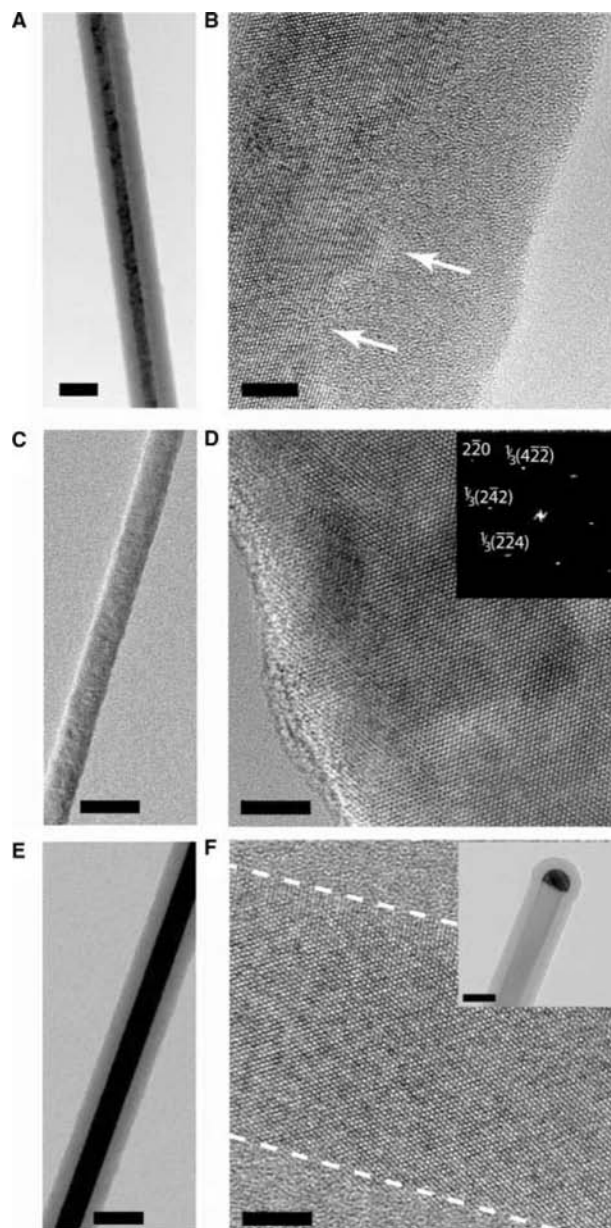


**Fig. 12** Si–Si homoepitaxial core-shell NWs. (A), (B) Diffraction contrast and high-resolution TEM images, respectively, of an unannealed i-Si core and p-Si shell NW. Scale bars are 50 and 5 nm, respectively. (C), (D) Transmission electron microscope images of an i-Si/p-Si core-shell NW annealed at 600°C for 30 min after core-shell growth at 450°C. Inset, 2D Fourier transforms depicting the [1 1 1] zone axis of the single crystal NW. (E), (F) Transmission electron microscope images of an i-Si/SiO<sub>x</sub>/p-Si NW. Inset, TEM image of p-Si coating the NW and the Au nanocluster tip. Scale bar is 50 nm. *Source:* From Ref.<sup>[31]</sup>.



the synthesis of core-shell NW structures is based upon control of radial vs. axial growth (Fig. 11). Axial growth is achieved when reactant activation and addition occurs at the catalyst site and not on the NW surface (Fig. 11B). Correspondingly, it is possible to drive conformal shell growth by altering conditions to favor homogeneous vapor-phase deposition on the NW surface (Fig. 11C). Subsequent introduction of different reactants and/or dopants produces multiple shell structures of nearly arbitrary composition, although epitaxial growth of these shells requires consideration of lattice structures. This approach to core-shell NW heterostructures is elaborated below for the technologically important silicon (Si) and germanium (Ge) systems.

Homoepitaxial Si-Si core-shell NWs were grown by CVD using silane as the silicon reactant (Fig. 12). Intrinsic silicon (i-Si) NW cores were prepared by gold nanocluster directed axial growth, which yields single crystal structures with diameters controlled by the nanocluster diameter, and then boron-doped p-type silicon (p-Si) shells were grown by homogeneous

CVD, where the shell thickness was directly proportional to the growth time. Radial shell growth can be “turned on” by the addition of diborane, which serves both to lower the decomposition temperature of silane and acts as a p-type dopant. Transmission electron microscope images of the i-Si/p-Si product obtained from constant temperature growth shows a uniform core-shell structure consisting of a crystalline Si core and amorphous Si shell (Fig. 12A), where the core diameter, 19 nm, is consistent with the 20 nm nanocluster used in the initial axial growth step. Transmission electron microscope images show reproducible crystalline faceting at the core-shell interface (Fig. 12B). This faceting suggests that the NW surfaces are sufficiently clean following axial growth to nucleate epitaxial shell growth.

To understand and control Si on Si homoepitaxy in core-shell NW structures, we carried out several distinct experiments. First, i-Si/p-Si core-shell NWs prepared as above were annealed in situ at 600°C. Transmission electron microscope images recorded on the annealed samples exhibited no diffraction

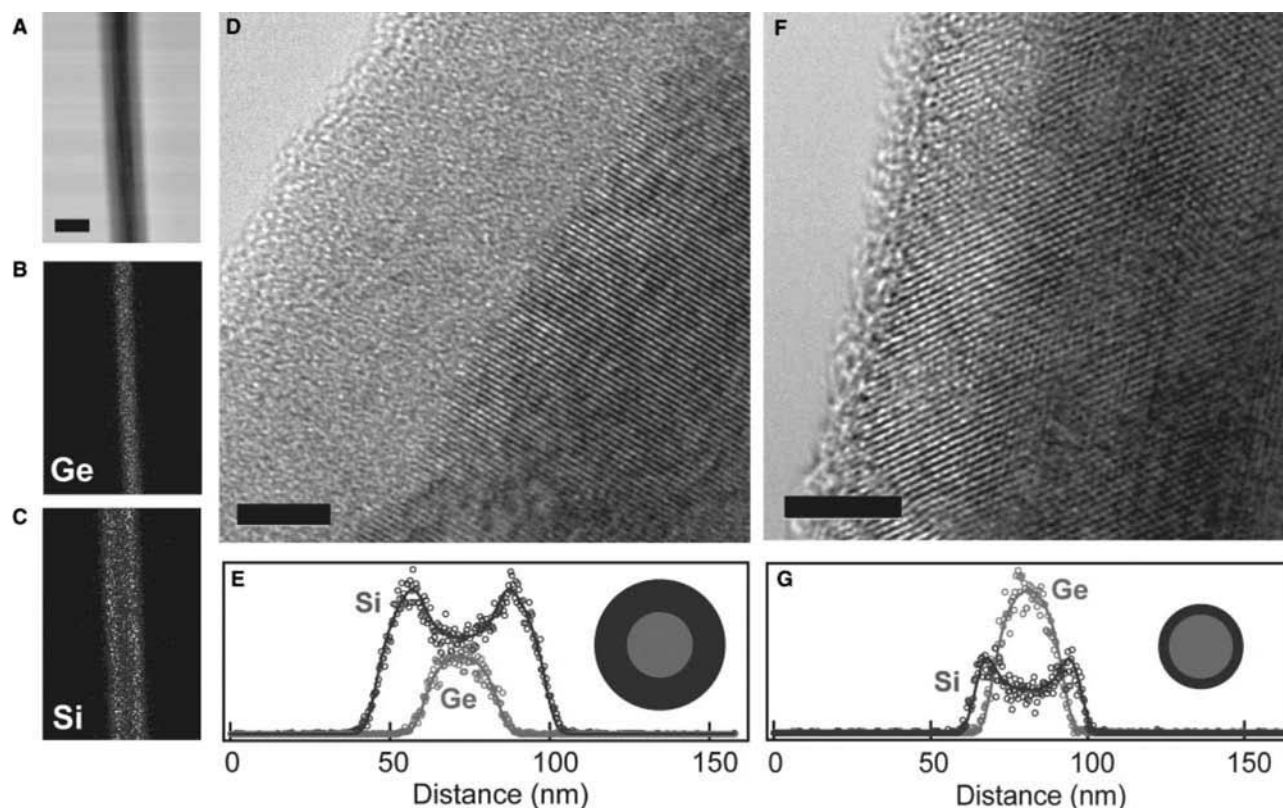


**Fig. 13** Ge-Si core-shell NWs. (A) Bright-field image of an unannealed Ge-Si core-shell NW with an amorphous p-Si shell. Scale bar is 50 nm. (B), (C) Scanning TEM elemental maps of Ge (red) and Si (blue), respectively, in the NW of (A). (D) High-resolution TEM image of an NW similar to those in (A)–(C). Scale bar is 5 nm. (E) Elemental mapping cross-section showing Ge (red circles) and Si (blue circles) concentrations. The solid lines show the theoretical cross-section for a 26-nm diameter core, 15-nm thick shell, and <1 nm interface. (F) High-resolution TEM image of annealed Ge-Si core-shell NW exhibiting a crystalline p-Si shell. Scale bar is 5 nm. (G) Elemental mapping cross-section gives a 5-nm shell thickness with a sharp interface. Source: From Ref.<sup>[31]</sup>.



contrast between the core and shell (Fig. 12C), and lattice resolved images and ED data further show that the shell crystallizes to yield a single crystal structure (Fig. 12D). Second, the importance of the initial nucleation for achieving epitaxy in the shell was probed using in situ oxidation of the silicon core, which produces a thin amorphous silicon oxide layer at the surface of the core, prior to silicon shell growth. Significantly, TEM images of i-Si/SiO<sub>x</sub>/p-Si core-shell-shell structures show a smooth and abrupt interface between the crystalline core and amorphous shell (Fig. 12E,F). The low roughness of the interface is comparable to that observed in NWs after only axial growth, and contrasts sharply with the faceted interface of the low-temperature homoepitaxy (Fig. 12B). These results show that the thin oxide layer completely disrupts homoepitaxy; further annealing and TEM studies show that oxidation inhibits crystallization of the shell under annealing conditions that lead to complete crystallization in samples without the oxide layer.

Radial heteroepitaxy of Si on Ge was also pursued to explore the potential and generality of our approach to core-shell structures in materials of rapidly increasing scientific and technological importance. For example, the energy band offsets in Si-Ge heterostructures produce internal fields that drive charge carrier redistribution, which can enable high mobility devices. Single crystal Ge NWs were defined via gold nanocluster-directed axial growth, and then boron-doped p-Si shells were grown by homogeneous CVD (see “Catalytic Chemical Vapor Deposition Growth of Nanowires”). Bright-field TEM images (Fig. 13A) reveal a core-shell structure that is consistent with Ge-core (dark) and Si-shell (light) structure, and we confirmed this assignment by elemental mapping (Fig. 13B,C), which shows a localized Ge core and Si shell. High-resolution TEM images of i-Ge/p-Si core-shell NWs in which the p-Si shell was deposited at low temperature without annealing show a crystalline Ge core and predominantly amorphous Si shell (Fig. 13D). Analysis of cross-sectional elemental mapping data (Fig. 13E) shows that the Ge core is ~26 nm, the Si shell is ~15 nm, and the Ge-Si interface width is believed to be <1 nm on the basis the electron beam width and modeling.

Significantly, we find that the amorphous Si shell can be completely crystallized following in situ thermal annealing at 600°C.<sup>[31]</sup> Lattice-resolved TEM images of Ge-Si core-shell structures following this thermal treatment exhibit a uniform crystalline Si shell (Fig. 13F), and suggest that thin regions of epitaxially grown Si are present in the unannealed wires. Higher silicon deposition temperatures might make the annealing step unnecessary by improving the surface mobility of adsorbed silicon. Elemental mapping (Fig. 13G) confirms that the contrast in high-resolution TEM

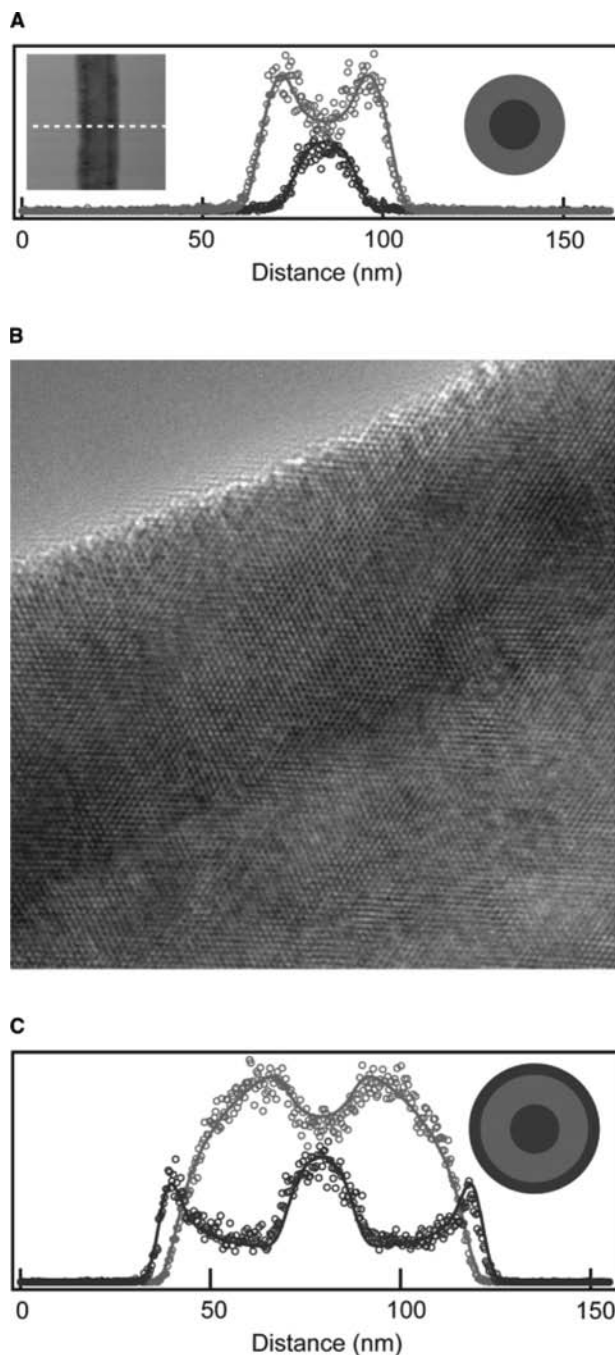


**Fig. 14** Si-Ge and Si-Ge-Si core-shell NWs. (A) Elemental mapping cross-section indicating a 21-nm diameter Si core (blue circles), 10-nm Ge shell (red circles), and <1 nm interface. Inset, TEM image of the Si-Ge core-shell NW. (B) High-resolution TEM image of an NW from the same synthesis as the wire in (A). Scale bar is 5 nm. Inset, 2D Fourier transform of the real-space image. The split lattice reflections perpendicular to the interface can be indexed to the Ge and Si lattice constants (5.657 and 5.431 Å, respectively). (C) Cross-sectional elemental mapping of a double-shell structure with an intrinsic silicon core (diameter, 20 nm), intrinsic germanium inner shell (thickness, 30 nm), and p-type silicon outer shell (4 nm); silicon is blue circles and germanium is red circles. *Source:* From Ref.<sup>[31]</sup>.

images is consistent with an abrupt ( $<1$  nm) Si–Ge interface. Although the present measurements cannot rule out some interface mixing, previous studies of planar growth under similar conditions found no evidence for Si–Ge interdiffusion. Notably, preliminary electrical transport studies of the i-Ge/p-Si core–shell NWs provide good evidence for internal field driven carrier redistribution and we believe these systems will be exciting to investigate in the future.

Synthetic control of Si–Ge core–multishell NW structures could be used to explore a variety of fundamental phenomena and new device concepts, although achieving this goal will require the ability to prepare an essentially arbitrary sequence of Si, Ge, and alloy overlayers on both Si and Ge NW cores. To this end, we also studied Ge deposition on Si NW cores.<sup>[31]</sup> Transmission electron microscope images and composition mapping (Fig. 14A) show the Si–Ge core–shell structure with a sharp ( $<1$  nm) interface, and demonstrate that the Ge shell is fully crystallized for the low-temperature growth (Fig. 14B), presumably due to the higher surface mobility of Ge adatoms. In addition, diffraction data are consistent with coherently strained epitaxial overgrowth (Fig. 14B, inset); that is, a single diffraction peak is observed along the axial direction, which is indicative of compressively strained Ge and tensilely strained Si. Two peaks, which can be indexed to the Ge (5.657 Å) and Si (5.431 Å) lattice constants, are also observed in the radial direction and indicate relaxation normal to the interface. Preliminary transport studies of these structures provide evidence for hole injection from the p-Si core to i-Ge shell as expected from valence band offsets. Finally, we have also explored the growth of more complex multishell structures; composition mapping of a Si–Ge–Si core–double-shell structure (Fig. 14C) demonstrates the ability to make core–multishell structures and suggest that this approach will be viable for introducing complex functionality in the future.

### Summary: Nanocluster Catalyzed NW Growth

To summarize this entry on the controlled and predictable growth of 1D materials, we first review the two crucial points of catalytic NW growth: 1) Nanometer sized catalytic clusters serve as a preferential site for reactant addition and nucleation, and can thereby define the size and direct the growth of crystalline NWs by a VLS mechanism; and (2) equilibrium phase diagrams can be used to predict catalyst material, composition, and growth conditions, and thus enable rational and predictable synthesis of new NW materials. In the absence of detailed phase diagram data, catalysts can be rationally chosen through consideration of the chemical reactivity and physical solubility

of the elements. An ideal catalyst should be physically active—form a miscible liquid phase with elements of the NW—but chemically stable; that is, not form a more stable solid phase than the desired NW phase under the growth conditions.

Two types of catalytic growth method have been developed and have enabled controlled growth of a very wide range of NW materials. First, LCG, where laser ablation is used to produce catalytic nanoclusters and vapor-phase reactants, has been shown to be a general technique for rapidly exploring the growth of new NW materials. Since laser ablation can be used to produce nanoclusters of virtually any material, LCG has perhaps the greatest flexibility and generality for NW synthesis. Second, catalytic CVD, in which gas reactant sources are combined with well-defined nanocluster catalysts, provides exquisite control over NW growth since all of the key parameters, including catalytic nanocluster size, reactant ratios, composition, and doping modulation, can be independently and precisely varied and controlled. In summary, a general approach has been developed for the synthesis of technologically important semiconductor NWs with precisely controlled chemical composition, physical dimension (diameter and length), hierarchical structure (axial or radial heterostructures, superlattices, and core–shell structures), and electronic optical properties. The availability of these broad range of NW materials opens many exciting opportunities in nanoscale science and technology.

### ACKNOWLEDGMENTS

We thank Y. Cui, M.S. Gudixsen, L. Lincoln, J. Wang, Q. Wei for their helpful discussion and contributions on the work described in this entry. C.M.L. acknowledges generous support of this work by the Air Force Office of Scientific Research, Defense Advanced Projects Research Agency, National Cancer Institute, National Science Foundation and Office of Naval Research.

### REFERENCES

1. Lieber, C.M. One-dimensional nanostructures: chemistry, physics and applications. *Solid State Commun.* **1998**, *107*, 106.
2. Hu, J.; Odom, T.W.; Lieber, C.M. Chemistry and physics in one dimension: synthesis and properties of nanowires and nanotubes. *Acc. Chem. Res.* **1999**, *32*, 435.
3. Duan, X.; Lieber, C.M. General synthesis of compound semiconductor nanowires. *Adv. Mater.* **2001**, *12*, 298.
4. Murray, C.B.; Norris, D.J.; Bawendi, M.G. Synthesis and characterization of nearly monodisperse CdE

- (E = S, SE, TE) semiconductor nanocrystallites. *J. Am. Chem. Soc.* **1993**, *115*, 8706–8715.
5. Esaki, L. *Science and Technology for Mesoscopic Structures*; Namba, S., Hamaguchi, C., Ando, T., Eds.; Springer Verlag: Tokyo, 1992.
  6. Himpsel, F.J.; Jung, T.; Kirakosian, A.; Lin, J.L.; Petrovykh, D.Y.; Rausher, H.; Viernow, J. Nanowires by step decoration. *MRS Bull.* **1999**, *24* (8), 20.
  7. Dai, H.; Wong, E.W.; Lu, Y.Z.; Fan, S.; Lieber, C.M. Synthesis and characterization of carbide nanorods. *Nature* **1995**, *375*, 769.
  8. Han, W.; Fan, S.; Li, W.; Hu, Y. Synthesis of gallium nitride nanorods through a carbon nanotube-confined reaction. *Science* **1997**, *277*, 1287.
  9. Martin, C.R. Nanomaterials—a membrane-based synthetic approach. *Science* **1994**, *266*, 1961.
  10. Wagner, R.S.; Ellis, W.C. Vapor–liquid–solid mechanism of single crystal growth. *Appl. Phys. Lett.* **1964**, *4*, 89.
  11. Wagner, R.S. *Whisker Technology*; Levitt, A.P., Ed.; Wiley: New York, 1970.
  12. Trentler, T.J.; Hickman, K.M.; Goel, S.C.; Viano, A.M.; Gibbons, P.C.; Buhro, W.E. Solution–liquid–solid growth of crystalline III–V semiconductor—an analogy to vapor–liquid–solid growth. *Science* **1995**, *270*, 1791.
  13. Trentler, T.J.; Goel, S.C.; Hickman, K.M.; Viano, A.M.; Chiang, M.Y.; Beatty, A.M.; Gibbons, P.C.; Buhro, W.E. Solution–liquid–solid growth of indium phosphide fibers from organometallic precursors: elucidation of molecular and nonmolecular components of the pathway. *J. Am. Chem. Soc.* **1997**, *119*, 2172.
  14. Yang, P.; Lieber, C.M. Nanorod–superconductor composites: a pathway to high critical current density materials. *Science* **1996**, *273*, 1836.
  15. Pan, Z.; Dai, Z.; Wang, Z. Nanobelts of semiconducting oxides. *Science* **2001**, *291*, 1947.
  16. El-Shall, M.S.; Edelstein, A.S. *Nanomaterials: Synthesis, Properties and Applications*; Sedelstein, A.S., Cammarata, R.C., Eds.; Institute of Physics: Philadelphia, 1996.
  17. Morales, A.M.; Lieber, C.M. A laser ablation method for the synthesis of crystalline semiconductor nanowires. *Science* **1998**, *279*, 208.
  18. Duan, X.; Wang, J.; Lieber, C.M. Synthesis and optical properties of gallium arsenide nanowires. *Appl. Phys. Lett.* **2000**, *76*, 1116.
  19. Duan, X.; Lieber, C.M. Laser-assisted catalytic growth of single crystal GaN nanowires. *J. Am. Chem. Soc.* **2000**, *122*, 188.
  20. Wei, Q.; Lieber, C.M. Synthesis of single crystal bismuth-telluride and lead-telluride nanowires for new thermoelectrical materials. *Mater. Res. Soc. Symp. Proc.* **2000**, *581*, 219–223.
  21. Panish, M.B. Ternary phase diagram of GaAs–M (M=Cu, Ag, Au) system. *J. Electrochem. Soc.* **1969**, *114*, 517.
  22. Gudixsen, M.S.; Lieber, C.M. Diameter-selective synthesis of semiconductor nanowires. *J. Am. Chem. Soc.* **2000**, *122*, 8801.
  23. Gudixsen, M.S.; Wang, J.; Lieber, C.M. Synthetic control of the diameter and length of single crystal semiconductor nanowires. *J. Phys. Chem. B* **2001**, *105*, 4062–4064.
  24. Cui, Y.; Lauhon, L.J.; Gudixsen, M.S.; Wang, J.; Lieber, C.M. Diameter-controlled synthesis of single-crystal silicon nanowires. *Appl. Phys. Lett.* **2001**, *78*, 2214.
  25. Cui, Y.; Duan, X.; Hu, J.; Lieber, C.M. Doping and electrical transport in silicon nanowires. *J. Phys. Chem. B* **2000**, *104*, 5213.
  26. Duan, X.; Huang, Y.; Cui, Y.; Wang, J.; Lieber, C.M. Indium phosphide nanowires as building blocks for nanoscale electronic and optoelectronic devices. *Nature* **2001**, *409*, 66.
  27. Hu, J.; Ouyang, M.; Yang, P.; Lieber, C.M. Controlled growth and electrical properties of heterojunctions of carbon nanotubes and silicon nanowires. *Nature* **1999**, *399*, 48–51.
  28. Gudixsen, M.; Lauhon, L.; Wang, J.; Smith, D.; Lieber, C.M. Growth of nanowire superlattice structures for nanoscale photonics and electronics. *Nature* **2002**, *415*, 617.
  29. Wu, Y.; Fan, R.; Yang, P. Block-by-block growth of single-crystalline Si/SiGe superlattice nanowires. *Nano Lett.* **2002**, *2*, 83.
  30. Bjork, M.T. et al. One-dimensional steeplechase for electrons realized. *Nano Lett.* **2002**, *2*, 87.
  31. Lauhon, L.J.; Gudixsen, M.S.; Wang, D.; Lieber, C.M. Epitaxial core–shell and core–multi-shell nanowire heterostructures. *Nature* **2002**, *420*, 57–61.

## BIBLIOGRAPHY

1. Duan, X.; Lieber, C.M. Semiconductor nanowires: nanoscale electronics and optoelectronics. In *Dekker Encyclopedia of Nanoscience and Nanotechnology*, 2E; Schwarz, J.A., Contescu, C.I., Putyera, K., Eds.; Taylor & Francis: New York, NY, 2009; Vol. 4, 3910–3940.

# Semiconductor Quantum Dots: Atomic Ordering over Time

Peter Moeck

Department of Physics, Portland State University, Portland, Oregon, U.S.A.

## INTRODUCTION

This encyclopedia entry consists of two parts. The first part gives a brief overview of epitaxially grown semiconductor quantum dots. This kind of quantum dot is referred to as ordinarily strained random semiconductor alloy quantum dot throughout this review. The objective of the first part is to set the scene for the following part.

The main part of this encyclopedia entry deals with experimental evidence in favor of the existence of long-range atomic order within certain III–V and II–VI compound semiconductor Stranski–Krastanow grown quantum dots a few years after the growth. The objective of the second part of this entry is to review this particular field of inquiry. With necessity, only the most general experimental results can be discussed. A simple thermodynamic model, which, in principle, allows for structural transitions from ordinarily strained random semiconductor alloy quantum dots with the structural prototype of the surrounding matrix to crystallographic superlattices (i.e., long-range atomically ordered quantum dots), is also briefly mentioned in the second part.

## EPITAXIALLY GROWN ORDINARILY STRAINED RANDOM SEMICONDUCTOR ALLOY QUANTUM DOTS

Epitaxial semiconductor quantum dots (QDs) are expected to lead to “paradigm changes in semiconductor physics”.<sup>[1]</sup> As reviewed in recent textbooks,<sup>[2,3]</sup> improved optoelectronic devices (such as lasers<sup>[4,5]</sup> and mid-infrared detectors<sup>[6]</sup>), and novel nanoelectronics concepts which depend on single electron transport, tunneling, or interactions (e.g., quantum cellular automata<sup>[7]</sup>) have either been realized or may be realized as the field matures.

For applications in optoelectronic devices, an entity needs to fulfill three conditions simultaneously to be considered a QD.<sup>[4]</sup> The entity needs to possess an appropriate size in all three dimensions (i) and also needs to be a semiconductor with a smaller band gap that is embedded in a semiconductor matrix with a

larger band gap (ii). No detrimental structural defects (such as dislocations, iii), which lead to non-radiative recombination centers, are allowed to exist in the entity.

Note here that there is no restriction on the structural prototype of the entity. It may either be of the same type as that of the matrix or it may possess a distinctly different structural prototype to that of the matrix. Structural prototypes of an epitaxially grown entity that differ from that of the matrix may be realized over time by atomic rearrangements within the initially more or less random semiconductor alloy entity. In short, atomically ordered entities that may arise from such processes will have to be considered as constituting QDs according to the definition above when conditions i to iii are met simultaneously.

Analogous to the well-known particle in a box model, the simplest quantum mechanical model describes a QD as a three-dimensional (3-D) finite potential-barrier trap for an electron–hole pair. When the size of this trap is in all three dimensions smaller than the bulk exciton Bohr radius (order of magnitude 10 nm), discrete energy levels for the electron and hole arise from the spatial confinement of these particles. The energy separation of the electron levels is, for example, for epitaxially grown (In,Ga)As QDs, of the order of magnitude 100 meV,<sup>[1,8]</sup> i.e., significantly larger than the thermal energy at room temperature ( $kT \approx 26$  meV). It is these discrete energy states of an electron in a QD that are exploited in devices that work at room temperature.

As in the particle in a box model, the spacing of the energy levels in QDs depends sensitively<sup>[8]</sup> on a range of parameters of the matter wave trap. For a QD, these parameters are first and foremost its size, shape, net chemical composition and spatial chemical composition distribution, net lattice mismatch strain and spatial strain distribution, crystallographic phase, and orientation with respect to the surrounding matrix. Because a very large number of QDs are simultaneously employed in optoelectronic devices, it is obvious that variations in the parameters of the individual matter wave traps are to be as small as possible to circumvent undue broadening of the discrete electron energy levels on which the operation of the

devices relies. Although addressing this uniformity issue of QDs by optimized growth and postgrowth annealing processes is still a scientific challenge, optimizations of the basic epitaxial growth processes have been achieved in recent years on the basis of structural and spectroscopic analyses.

Currently most popular with the scientific community are QDs that are grown in the Stranski–Krastanow mode and its variants (such as embedding nominal submonolayers and allowing them to form 3-D entities within a 2-D wetting layer).<sup>a</sup> Either molecular beam epitaxy (MBE) or metal organic chemical vapor deposition (MOCVD) is typically employed.<sup>[2,3]</sup> Because these QDs grow epitaxially, they possess per definition of the term epitaxy the same structural prototype as the employed substrates and surrounding matrices. Epitaxial growth of QDs typically results in a compressive lattice mismatch strain in the QDs of a few percent as the QDs need to have a smaller band gap than the surrounding matrix and smaller band gaps are typically obtained for solid substitutional solutions with larger lattice constants.

The nature of the Stranski–Krastanow 2-D to 3-D transition in (In,Ga)As has recently been identified, and it is believed that QD of other semiconductor systems grows in the same basic manner.<sup>[11–13]</sup> Because of the nature of this transition, the QDs and their predecessor islands are always alloyed, should have a more or less random distribution of the mixed cations and/or anions over their respective sublattices in the structural prototype of the employed substrate, and should have a similar net chemical composition regardless of whether nominally pure substances or substitutional solid solutions are deposited.

Structural studies by numerous investigators employing conventional transmission electron microscopy (TEM), high-resolution phase contrast TEM (HRTEM), and atomic resolution Z-contrast scanning

TEM (Z-STEM) of a wide range of Stranski–Krastanow as-grown III–V and II–VI QD and QD predecessor island samples showed (or at least reported) no evidence of atomic ordering in as-grown structures, e.g., Refs.<sup>[11–21]</sup> and references therein. In addition, it is known that the predecessor islands and QDs have a spatially nonuniform chemical composition distribution with a core that is rich of the component with the smaller band gap (and typically larger lattice constant), i.e., a spatially zonal chemical composition distribution.<sup>[8,14,15]</sup> Significant morphological transformations<sup>[16]</sup> and changes in both the net chemical composition and spatial composition distribution<sup>[14]</sup> of the predecessor island structures take place as a result of the QD embedding process.

Such Stranski–Krastanow mode grown QDs are referred to as “ordinarily strained” in the remainder of this encyclopedia entry because they show pronounced strain fields (either so-called “black-white” or “coffee-bean” contrasts) in conventional diffraction contrast TEM micrographs, e.g., Fig. 1A.<sup>[17–19]</sup> The author of this encyclopedia entry will use the quantifier “random semiconductor alloy” synonymously to refer to ordinarily strained QDs. Occasionally, the author

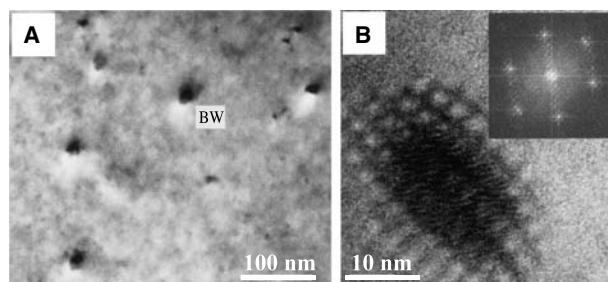


**Fig. 1** (A) Ordinarily strained (In,Ga)Sb quantum dots in GaSb matrix shortly after the growth, showing strain contrast in conventional diffraction contrast TEM images, [001] plan view; the marker “BW” adjacent to a QD stands for “black-white contrast.” (B) (Partly) relaxed (In,Ga)Sb agglomerate in GaSb matrix a few years after the growth, showing  $\pm(002)$  and  $\pm(2\bar{2}0)$  moiré fringes,  $\langle 110 \rangle$  cross-section HRTEM image, Fourier transform power spectrum as insert, modified after Ref.<sup>[27]</sup> and reproduced with permission of the International Society for Optical Engineering (SPIE). The shape of the agglomerate is that of an oblate spheroid/ellipsoid and is believed to result from strain-driven atomic rearrangements in the sphalerite structure. It is well known that if QD predecessor islands grow beyond a certain size/volume limit, the lattice mismatch strain is relaxed to a significant amount by the introduction of misfit dislocation.<sup>[17,18,21]</sup> While the diameter of the quantum dots in (A) is about 10 nm, i.e., below the above-mentioned size limit, the approximate width of the agglomerate in (B) is 47 nm and its height is approximately 28 nm. These latter dimensions result in a volume that is conceivably above the volume limit for lattice mismatch strain relaxation.

<sup>a</sup>What exactly Stranski–Krastanow growth means in semiconductor epitaxy is seldom defined. The classical texts and undergraduate textbooks (e.g., Ref.<sup>[9]</sup>) define this mode simply as one of the three fundamental modes of heteroepitaxial growth (besides the Frank–Van der Merwe and the Volmer–Weber growth mode). Stranski–Krastanow growth is typically described as comprising a sequence in epitaxial growth where first, a 2-D wetting layer is formed, and second, 3-D islands are formed on top of this wetting layer. No particular mechanism is associated with the 2-D to 3-D transition per definition, and the original paper Ref.<sup>[10]</sup> deals only with the energetics of the epitaxial growth of lattice-matched ionic crystals. With explicit mechanisms not being connected to this growth mode, one is free to classify any epitaxial growth where there is a 2-D to 3-D transition of the deposit as Stranski–Krastanow growth. Whether the 3-D entities are formed on top of or within a 2-D wetting layer is thus quite unimportant. Embedding nominal submonolayers of a smaller band gap within a matrix of a larger band gap and allowing them to form 3-D entities within a 2-D wetting layer is therefore just a variant of Stranski–Krastanow growth in semiconductor epitaxy.



will address these QDs with both quantifiers, i.e., as “ordinarily strained random semiconductor alloy QDs,” to emphasize the differences to atomically ordered QDs. Where appropriate, this author will also specify the semiconductor in the general specifier “semiconductor alloy.”

Structural analyses of QDs are mainly performed by transmission electron microscopy and near surface-sensitive X-ray scattering techniques. Only very few of such investigations, however, address the long-term structural and morphological stability of QDs at room temperature over a time period of a few years. Such TEM investigations are therefore reviewed in the second part of this encyclopedia entry.

### ATOMIC ORDER WITHIN EPITAXIAL SEMICONDUCTOR QUANTUM DOTS

As mentioned above, reviewing experimental results on morphological transformations<sup>[21]</sup> and structural transition<sup>[22–32]</sup> in III–V and II–VI compound semiconductor Stranski–Krastanow grown QDs will be the subject of this part of this encyclopedia entry. Because a total of eight original papers are to be reviewed in this part, only the most general result, i.e., the fact that long-range atomic order is present in certain epitaxial compound semiconductor QD systems after the respective samples have been stored at room temperature for a few years, will be discussed in some detail. A variety of TEM images from different QD systems will be shown to demonstrate different kinds of this atomic order. This multitude of TEM images serves the purpose to show the readers (and fellow electron microscopists) the different appearances long-range atomic ordering may take in Stranski–Krastanow grown QDs of different materials systems. Occasionally, the figure captions contain details that complement the text.

The respective structural analyses at the University of Illinois at Chicago, Portland State University, and the University of Oxford, U.K., employed TEM in both the parallel illumination and scanning probe (STEM) mode.<sup>[21–32]</sup> A JEOL JEM-2010F STEM/TEM, a JEOL JEM-3010 TEM, a Philips CM20 TEM/STEM, and a FEI Tecnai G<sup>2</sup> F20 TEM/STEM were used. Parallel illumination TEM utilized conventional diffraction contrast (CTEM), selected area electron diffraction (SAED), and high-resolution phase contrast imaging (HRTEM). Atomic resolution Z-contrast (also known as high-angle annular dark field) imaging in the scanning probe mode (Z-STEM) proved to be especially useful for these investigations because the effects of strain fields in and around QDs and interference effects such as the formation of moiré fringes because of double diffraction are negligible.<sup>[30–32]</sup>

Transmission electron microscopy specimen preparation artifacts were excluded from the analyses by employing both ion milling and chemical thinning to electron transparency. Only those structures that are not an artifact of either of these two physically different specimen preparation processes were likely to be present in both kinds of specimen.<sup>b</sup>

Complementary photoluminescence (PL) spectroscopy analyses were performed at the Physical-technical Federal Institute Braunschweig/Germany on certain II–VI QD structures at a temperature of 6 K. Ar<sup>+</sup> laser light utilizing both the 488-nm line and ultraviolet light of around 350-nm wavelength was used at varying power densities for the excitation of the spectra. The PL emission light was dispersed in a 1-m-long single-grating spectrometer and detected with a cooled (In,Ga)As photomultiplier tube using conventional lock-in techniques.

Although there have been many investigations, there is still some controversy about the actual shape of both the islands that form the QDs when overgrown by a capping layer and of the ordinarily strained QDs themselves. Transmission electron microscopy observations on the shape of ordinarily strained QDs a few years after the growth resulted for a III–V system<sup>[21]</sup> (Fig. 1B) and a II–VI system,<sup>[20,30–32]</sup> in shapes that are oblate spheroids which may have different diameters along  $\pm[110]$  and  $\pm[\bar{1}10]$ , making them, in effect, ellipsoids.<sup>[16]</sup> This shape is known as a possible equilibrium shape of small precipitates that are elastically strained.<sup>[35]</sup> Of each spheroid/ellipsoid, about

<sup>b</sup>The close proximity of three different atomically ordered (Cd,Mn,Zn)Se agglomerates labeled by markers “1,” “2,” and “3” in Fig. 5A can only be interpreted as not being an artifact of the STEM imaging procedure because it is quite incomprehensible how one and the same probing electron beam may have caused three different modes of atomic rearrangements so close to each other. On a similar token, not only atomic ordering, but also phase separation were observed in the same TEM specimen (Fig. 6A–C), and it does not seem likely that the same probing electron beam may have triggered different kinds of atomic rearrangements in the same specimen. On the other hand, thermodynamics allows for the coexistence of atomically ordered and phase-separated entities in many compound semiconductor alloys. Ref.<sup>[33]</sup> Note also the large size of the double period  $\pm(1\bar{1}0)$  agglomerates, i.e., order of magnitude 200 nm (Fig. 4C and D). These entities seem to be by far too large to be caused by the probing electron beam, which had a diameter on the order of magnitude 0.2 nm only. The results of Ref.<sup>[34]</sup> on In agglomeration into QDs within (In,Ga)N quantum wells because of parallel illumination and scanning probe electron beam exposures do not reveal any changes at the structural prototype level. Such structural prototype transitions may, however, have occurred in the sample of Figs. 4C, D, and 5A. One can thus conclude that these entities are definitely not an artifact of the probing electron beam. Because it is quite impossible to produce three different atomically ordered (Cd,Mn,Zn)Se agglomerates in close proximity (Fig. 5A) by means of TEM specimen preparation procedures, such artifacts can also be excluded from the analyses.



one-half was located above the level of the original wetting layer and the other half was located below this level<sup>[20,21,30–32]</sup> (Fig. 1B).

The moiré fringes in Fig. 1B indicate that the (In,Ga)Sb entity possesses its own (partly) relaxed lattice constant, i.e., no longer (fully) strained. Because it must contain dislocations that mediate the relaxed state (i.e., violate the condition iii given in the first part of this entry), it cannot be considered to be a QD and is addressed as an “agglomerate.” The degree of relaxation can only be estimated as the chemical composition of the agglomerate is unknown. This author assumes that the degree of relaxation is less than unity because it is well known that complete relaxation of strained semiconductor structures is rarely achieved. Because numerous STEM and TEM images of QD predecessor islands and QDs by other authors have shown rather different shapes to those oblate spheroids/ellipsoids that were reported in Refs.<sup>[20,21,30–32]</sup>, this author assumes that there are lattice mismatch strain energy-driven morphological transformations over time. As the (In,Ga)Sb agglomerate in Fig. 1B is obviously dislocated but possesses the shape of an oblate spheroid/ellipsoid, even small lattice mismatch strains may have the capacity to cause morphological transformations over time.

Now if one accepts that morphological transformation of QDs may take place over time, the conceptual barrier to accepting that structural transitions in QDs may also take place over a sufficiently long time is lowered. The amount of elastic mismatch strain energy that is stored in ordinarily strained QDs and (partly) relaxed agglomerates may, besides the net chemical composition, be a determining factor for the type of transformation. Either morphological,

structural, or both structural and morphological transformations may thus take place over time. If this strain energy is comparably small (and/or the net chemical composition is unfavorable), as possibly in the case of (partly) relaxed (In,Ga)Sb agglomerates, e.g., Fig. 1B, only morphological transformations may be possible. If, on the other hand, this strain energy is comparably large (and/or the net chemical composition favorable), as possibly in the case of fully strained (In,Ga)Sb QDs, e.g., Fig. 1A, structural transitions may be possible.

Continuing with the (In,Ga)Sb QDs in GaSb matrix system, the results of two CTEM investigations<sup>[18,19]</sup> on the same TEM specimens that were separated by approximately 2 years in time suggest that the number density of ordinarily strained QDs declined over time. This observations could not be explained in 1999, but HRTEM and atomic resolution Z-STEM investigations that were performed on the same specimen about 1 to 2 years later revealed the presence of atomically ordered QDs in these specimen (Fig. 2A–C). If one assumes that ordinarily strained QDs transform structurally into atomically ordered QDs over time while the specimens are stored at room temperature, there seems to be a simple explanation for this inferred decline in the number density of ordinarily strained QDs. In both studies, the ordinarily strained quantum dots were detected by their pronounced strain field contrasts, e.g., Fig. 1A, and only moderate magnifications were employed to cover large specimen areas in a Philips CM 20 (that was not capable of high-resolution phase contrast imaging of medium lattice constant semiconductors). Note here that atomically ordered QDs, e.g., Fig. 2A–C, would, under these experimental conditions,<sup>[18,19]</sup> be

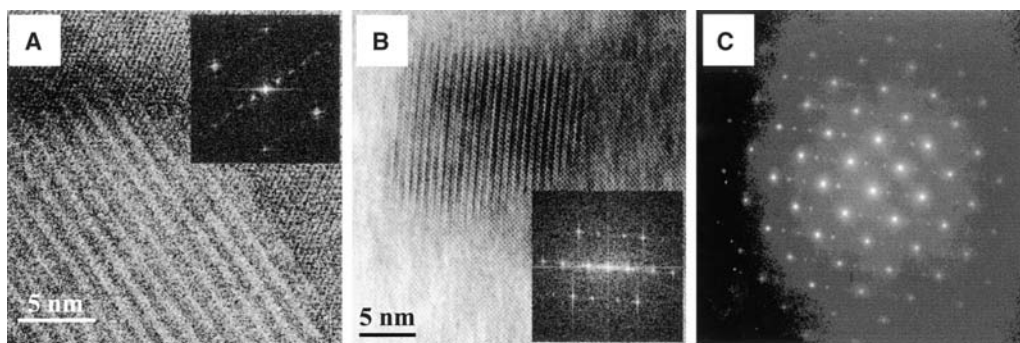


**Fig. 2** Long-range atomically ordered (In,Ga)Sb quantum dots in GaSb matrix a few years after the growth, Fourier transform power spectra as inserts. (A)  $\langle 110 \rangle$  Cross-section Z-contrast STEM image, showing a QD with atomic order in every fourth  $\pm(002)$  plane. (B)  $[001]$  Plan-view HRTEM image which was recorded at 500°C after a thermal treatment in the electron microscope at temperatures of several hundred degrees centigrade for several hours, suggesting that the atomically ordered structure of this QD rather than its original sphalerite prototype structure is thermodynamically stable. (C)  $[001]$  Plan-view SAED pattern to (B) showing the same superlattice spots as the Fourier transform power spectrum insert in (B). This diffraction pattern demonstrates clearly that atomically ordered QDs such as shown in (B) are to be distributed over large areas of the specimen. *Source:* (A) and (B) were modified after Ref.<sup>[27]</sup> and reproduced with permission of SPIE.

effectively undetectable as they are negligibly strained and do not show pronounced strain field contrasts.

It is also noteworthy that short-range order, but no long-range order, was observed in (In,Ga)Sb QDs in GaSb matrix specimen by means of SAED approximately 14 days after the growth.<sup>[17,26]</sup> Similarly to this III–V QD system, both short-range order and beginning long-range atomic order were observed by means of HRTEM in (Cd,Zn)Se QDs in ZnSe matrix samples (Fig. 3A and B) about 3 years after the growth.<sup>[26]</sup> Samples from the same growth run were much earlier analyzed by means of atomic resolution Z-STEM, but no atomic order seemed to have been present at that earlier time.<sup>[20]</sup>

These HRTEM and atomic resolution Z-STEM results from both a III–V and a II–VI system indicate that semiconductor QDs when initially grown are mostly unordered, but during subsequent room temperature storage over a few years (i.e., a long-time low-temperature annealing process), they progressively undergo short-range ordering that eventually goes over into long-range ordering.

Long-range atomically ordered QDs and entities that were probably too large to be considered as a QD (i.e., that probably violated condition i given in the first part of this entry) were also observed in MBE-grown (Cd,Mn,Zn)Se QDs in (Mn,Zn)Se matrix (Figs. 4A–F and 5A).

As the Fourier transform power spectra (Fig. 4E and F) show, the atomic arrangement in the large (Cd,Mn,Zn)Se agglomerate in Fig. 4C and D is a result of atomic ordering of the Cd and (Zn,Mn) cations in every second  $\pm(1\bar{1}0)$  plane. Using the shortest vectors in Fig. 4E as a base (for the sake of coming up with a notation only and assuming that the agglomerate belongs at least to the orthorhombic crystal system),

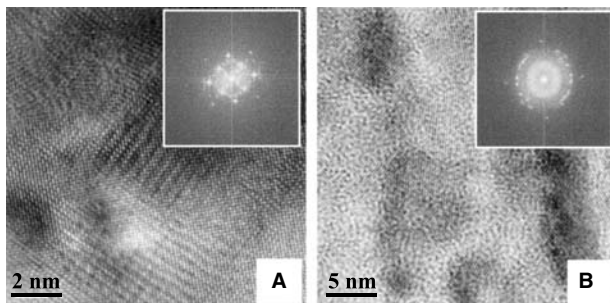


**Fig. 3** High-resolution TEM [001] plan-view images of atomically ordered (Cd,Zn)Se quantum dots in ZnSe matrix a few years after the growth, showing (A) long-range and (B) short-range atomic order in the same TEM specimen. The insert Fourier transforms power spectra show for (A) superlattice spots and for (B) both a diffuse and a spotty ring. None of this atomic order seems to have existed at the time of a much earlier atomic resolution Z-STEM investigation. Source: From Refs.<sup>[20,30–32]</sup>

the orientation relationship between the agglomerate and the (Mn,Zn)Se matrix becomes  $(020)_{(\text{Cd,Mn,Zn})\text{Se}} \parallel (220)_{(\text{Mn,Zn})\text{Se}}$ ,  $(110)_{(\text{Cd,Mn,Zn})\text{Se}} \parallel (1\bar{1}3)_{(\text{Mn,Zn})\text{Se}}$ , and  $[001]_{(\text{Cd,Mn,Zn})\text{Se}} \parallel [110]_{(\text{Mn,Zn})\text{Se}}$  (whereby  $\parallel$  symbolizes that both sets of reciprocal lattice vectors are within the accuracy of the Fourier transform power spectra parallel and of equal length, and that the direct lattice vectors are parallel). This orientation relationship is obviously lattice mismatch strain (and elastic mismatch strain energy) minimizing.

In the same TEM/STEM specimen, there were actually several more large agglomerates which possessed the same lattice mismatch strain energy-minimizing orientation relationship as shown in Fig. 4E and F. From a discussion of the nominal growth condition of this sample,<sup>c</sup> the large size of these agglomerates cannot be explained. Some of these agglomerates had diameters of up to approximately 250 nm and were also free of detrimental structural defects such as dislocations. The author of this encyclopedia entry believes that it is the elastic mismatch strain energy minimization effect of the particular orientation relationship these agglomerates possess with the (Mn,Zn)Se matrix which allows them to be so large while retaining their ideal translational symmetry. Taking the discussion in footnote c into account, the large size of the agglomerates may thus be explained by both the particular elastic mismatch strain energy-minimizing orientation relationship and atomic rearrangements over time. From the thermodynamics of small misfitting precipitates,<sup>[35]</sup> one can simply argue that smaller entities of the same atomically ordered structure and orientation relationship will not contain misfit dislocations either, i.e., will constitute atomically ordered QDs in this materials system.

Having identified large double-period  $\pm(1\bar{1}0)$  ordered (Cd,Mn,Zn)Se agglomerates as by far the dominant kind of structural entity per unit volume of the TEM specimens, it is now interesting to analyze the PL spectra of this sample (Fig. 5B). The ZnSe band gap being at 6 K approximately 2.8 eV, excitation with 350 nm light can be considered as non-resonant above

<sup>c</sup>It is interesting to contrast the large size of these double period  $\pm(1\bar{1}0)$  atomically ordered agglomerates with the nominal as grown sample structure. Starting with a ZnSe/GaAs pseudosubstrate, there should nominally be a multilayer structure of eight sequences of 10 monolayers (2.83 nm) of  $\text{Zn}_{0.9}\text{Mn}_{0.1}\text{Se}$  cladding layer and 0.3 monolayers (0.09 nm) CdSe sheet, capped by a further 10 monolayers of  $\text{Zn}_{0.9}\text{Mn}_{0.1}\text{Se}$  and 50 nm of ZnSe. The agglomerate in Fig. 4C and D being approximately 100 nm thick is thus thicker than the whole nominal epitaxial multiquantum well structure plus the two capping layers. It seems therefore highly improbable that such a large agglomerate could have originated directly during the growth of the QD structure a few years ago. Note that “remains” of this nominal as-grown structure were actually observed by means of HRTEM. Ref.<sup>[23,28]</sup>

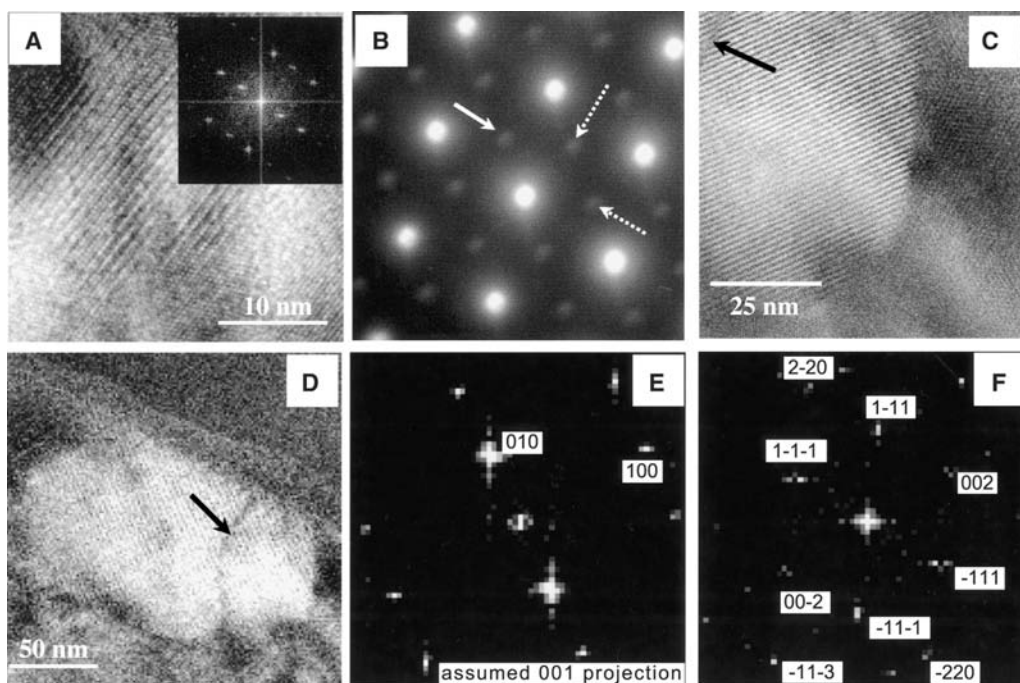


**Fig. 4** TEM/STEM images of long-range atomically ordered (Cd,Mn,Zn)Se quantum dots and agglomerates in (Mn,Zn)Se matrix a few years after the growth; (A), (B), (D), (E), and (F) modified after Ref.<sup>[27]</sup> and reproduced with permission of SPIE. (A)  $\langle 110 \rangle$  Cross-section HRTEM image of a (Cd,Mn,Zn)Se QD in (Mn,Zn)Se matrix, showing cation ordering in every second  $\pm(111)$  plane, i.e., one variant of so-called CuPt-type order, Fourier transform power spectrum as insert. (B)  $\langle 110 \rangle$  Cross-section SAED pattern of (Cd,Mn,Zn)Se QDs in (Mn,Zn)Se matrix, showing  $\pm\frac{1}{3}(2\bar{2}0)$ , full line arrow,  $\pm\frac{1}{3}(\bar{1}13)$ , and  $\pm\frac{1}{3}(1\bar{1}3)$ , broken line arrows, superstructure spots. (C)  $\langle 110 \rangle$  Cross-section atomic resolution Z-STEM image of a part of a large (Cd,Mn,Zn)Se agglomerate in (Mn,Zn)Se matrix, showing atomic order in every second  $\pm(1\bar{1}0)$  plane, the black arrow points to an antiphase boundary. (D) Lower magnification Z-STEM image to (C), the black arrow points to the same antiphase boundary. (E) Fourier transform power spectrum of the large (Cd,Mn,Zn)Se agglomerate in (C). (F) Fourier transform power spectrum of the (Mn,Zn)Se matrix in (C).

this band gap and is expected to reveal most radiatively active structures inside the samples. Light excitation of 488 nm, on the other hand, can be considered as resonant excitation below the ZnSe band gap, is typically of orders of magnitude weaker than non-resonant excitation over the band gap, and is selective of specific structures.

It was suggested that the large and rather broad PL peak at 2 eV in Fig. 5B, which arose when a sample was excited with laser light of approximately 350 nm, is a result of larger and smaller double-period  $\pm(1\bar{1}0)$  agglomerates, as shown in Fig. 4C and D and labeled “1” in Fig. 5A.<sup>[28]</sup> The 2.1-eV PL peak (Fig. 5B), which arose in addition to the 2-eV peak, when the sample was excited with laser light of 488 nm, may be a result of either small double-period  $\pm(1\bar{1}1)$  atomically ordered QDs (Fig. 4A), antiphase boundaries such as marked by an arrow in Fig. 4C and D, or other long-range atomically ordered entities such as labeled “2” and “3” in Fig. 5A.

From Fig. 5B, it can be concluded that the long-range atomically ordered entities must be distributed throughout large regions of the sample because the

PL spectra were collected from areas that were about 6 orders of magnitude larger than the areas that were investigated by means of TEM (Fig. 5A). A brief review of the literature showed that low-energy peaks at approximately 2 and 2.1 eV were also observed in this QD system in comparable nominal structures by several other authors.<sup>[28]</sup> None of these other authors, however, supported their assignment of these PL peaks with structural characterizations.<sup>d</sup>

<sup>d</sup>The high energy PL peaks in Fig. 5B are assigned as follows: 2.78 eV is due to a superposition of the (essentially) 2-D remains of the CdSe submonolayers and the excitonic transition in the ZnSe buffer and capping layers, 2.64 eV is due to a large population of small quasi 2-D CdSe-rich platelets (with sphalerite structure) that act as a first kind of ordinarily strained QD, and 2.25 eV is due to a small population of medium-sized 3-D CdSe-rich QDs (with sphalerite structure) that act as a second kind of ordinarily strained QD Ref.<sup>[28]</sup>. Such a coexistence of small quasi 2-D and medium-sized 3-D ordinarily strained QDs has actually been observed in similar samples of the same QD system Ref.<sup>[23]</sup>. The PL peak at 2.64 eV also shows the typical low-energy tail that is characteristic of a non-uniform Cd distribution in an epitaxial layer that contains small quasi 2-D CdSe-rich platelets Ref.<sup>[36]</sup>.



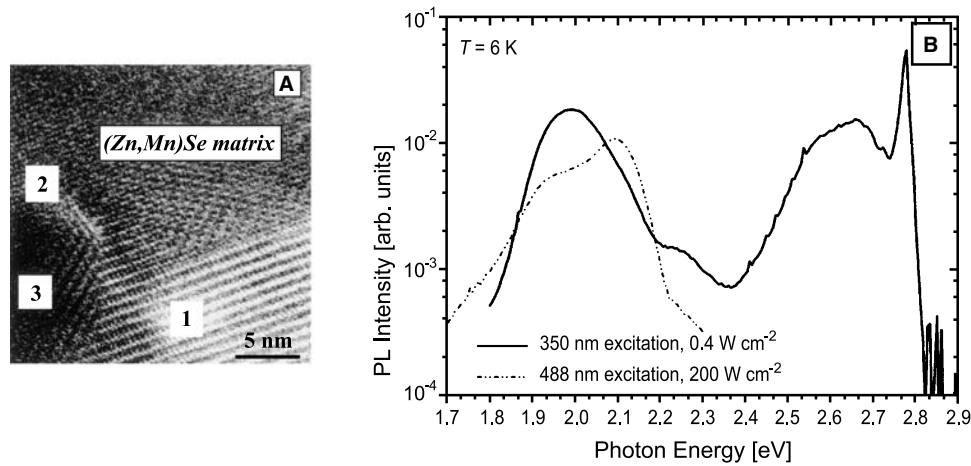


**Fig. 5** (A)  $\langle 110 \rangle$  Cross-section atomic resolution Z-contrast STEM image of (Cd,Mn,Zn)Se entities in a (Mn,Zn)Se matrix, a few years after the growth; modified after Ref.<sup>[27]</sup> and reproduced with permission of SPIE. Note that there are three different long-range atomically ordered entities, labeled as “1,” “2,” and “3” in close proximity; this remarkable fact is discussed in footnote c as proof that the observed atomic order in QDs is not a result of specimen preparation or probing electron beam artifacts. (B) Photoluminescence spectra of the same (Cd,Mn,Zn)Se entities in a (Mn,Zn)Se matrix. While the non-resonant PL is given by a full line, the resonant PL is given by a dotted line. As the area from which the PL spectra were taken is about 6 orders of magnitude larger than the area of a typical TEM image, this figure proves that atomically ordered entities must be present with a larger number density; courtesy of K. Pierz.

The observations on both III–V and II–VI QD systems with mixed cations are thus consistent with the working hypothesis that atomic rearrangements that lead to lower-energy structures take place over a

sufficiently long time. Some growth-induced short-range order may constitute additional “seeds” from which long-range ordered QDs could grow over time. It is interesting that in a III–V quantum dot system

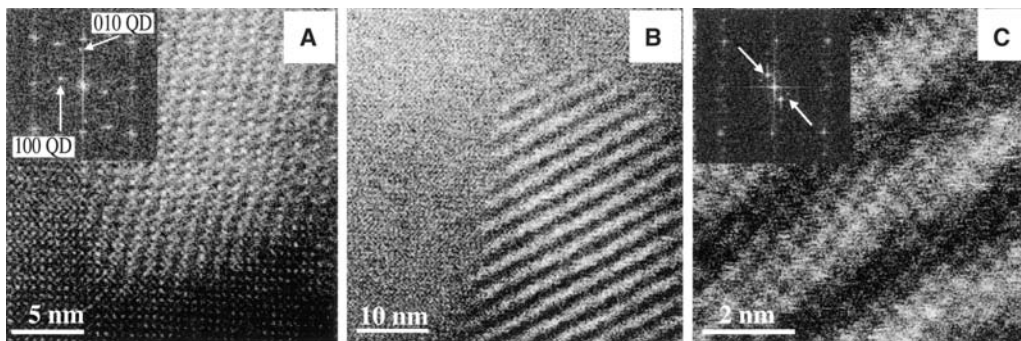


**Fig. 6** [001] Plan view atomic resolution Z-contrast STEM images of long-range atomically ordered and phase-separated In(As,Sb) quantum dots in InAs matrix, a few years after the growth; modified after Ref.<sup>[27]</sup> and reproduced with permission of SPIE. (A) Atomically ordered QD that possesses a lattice mismatch strain energy minimizing orientation relationship with the matrix which can be inferred from the insert Fourier transform power spectrum. (B) Periodic compositional modulation that may have arisen from spinodal decomposition. (C) Same as (B) but in a higher magnification, showing atomic steps in the compositionally modulated entities that are compatible with the two observed additional periodicities in the insert Fourier transform power spectrum. The power spectrum clarifies that the modulation periodicity is not a result of a moiré effect because there are actually two additional periodicities, marked by arrows. These two periodicities add up to a single compositional modulation parallel to  $\pm[110]$  with a periodicity of 0.4 times the length of the vector (110) and may be explained as a lattice mismatch strain response. In addition, Z-contrast imaging in STEM is known to be essentially incoherent so that double diffraction effects are negligible.

with mixed anions, i.e., In(As,Sb) QDs in InAs matrix (Fig. 6A–C), atomically ordered QDs and phase-separated entities were also observed.

Labeling the two shortest vectors in the Fourier transform power spectrum of Fig. 6A as a base of the reciprocal lattice of the atomically ordered In(As,Sb) QD (for the sake of coming up with a notation only), the insert of this figure shows that the  $\pm(210)$  vectors of this QD are almost at the same position in reciprocal space as the  $\pm(110)$  vectors of the InAs matrix. This indicates that this QD possesses a lattice mismatch strain (and elastic mismatch strain energy) minimizing orientation relationship with the matrix, as one would expect it to have if it originated from a structural transition. For this mixed anions III–V QD system, the results of the two already mentioned CTEM investigations<sup>[18,19]</sup> on the same TEM specimen that were separated by approximately 2 years in time also suggested that the number density of ordinarily strained QDs declines over time. Again, a simple explanation of these observations is structural transitions from ordinarily strained QDs to atomically ordered QDs over time.

To summarize the experimental observations, the only commonality of the samples reported upon in the original papers<sup>[21–28]</sup> was that a few years have elapsed between the growth and the TEM/STEM and PL analyses. The weight of the presented TEM/STEM observations (and the careful exclusion of possible specimen preparation and imaging artifacts<sup>b)</sup>) in semiconductor QDs of different materials systems with either mixed cations or mixed anions, grown by different methods, leads this author to the working hypotheses that there are indeed morphological transformations and structural transitions in ordinarily strained random semiconductor alloy QDs over time.

So far, only a few in situ thermal treatments and structural analyses were performed in the electron microscopes under elevated temperatures, e.g., Fig. 2B. When elevated temperatures and annealing times parameter sets are found that in effect correspond to room temperature anneals over a few years, such experiments have the capacity to directly proof that there are structural transitions in ordinarily strained random alloy semiconductor QDs over time. On the other hand, such experiments are quite difficult to set up as atomically ordered QDs may exist only in certain approximate stoichiometries, which uncontrolled mismatch strain energy-driven out-diffusion of atoms from the ordinarily strained QDs during annealing may prevent from occurring. In addition, there must be a certain critical temperature above which randomness in the semiconductor alloy will prevail because of its larger entropy.

Nevertheless, the preliminary results are encouraging and suggest that the atomically ordered QD structure

in Fig. 2B is thermodynamically more stable than the random alloy sphalerite-type structure in which this QD probably had grown a few years ago (Fig. 1A). More such experiments are to be performed in the future because it is expected that this will lead to both irrefutable evidence for the occurrence of the structural transitions that are currently only inferred from TEM/STEM observations<sup>[22–32]</sup> and to information on the operating mechanisms of atomic rearrangements in ordinarily strained random semiconductor alloy QDs.

As one can easily estimate,<sup>[26,29]</sup> there is an essentially hydrostatic pressure in the 1–10 GPa range on epitaxial ordinarily strained random semiconductor alloy QD and an excess Gibbs free energy of approximately 0.1–1 eV (i.e.,  $\gg kT$  at room temperature) for every atom of such a QD associated with the typically encountered lattice mismatch strains.<sup>c</sup> In addition, grown-in and quenched-in vacancies that remained from the cooling down of the QD structure after the growth will, in strain fields, move to the spatial positions of highest compressive strain,<sup>[40]</sup> which are exactly the positions of the Stranski–Krastanow grown QDs. When these vacancies arrive at the position of an ordinarily strained random semiconductor alloy QD, they can facilitate atomic rearrangements there that lead to a reduction of excess Gibbs free energy which results form the compressive stress on these QDs. It is thus not at all inconceivable that thermodynamics-driven morphological transformations and structural transitions should be possible over a long-enough time, even at room temperature.

While it can be seen directly in the TEM and STEM images (Figs. 2B, 3B, 4A, 5A, and 6A) that the size condition i and the condition of absence of detrimental defects (such as dislocations, iii) are fulfilled, atomically ordered semiconductor alloys (i.e., crystallographic superlattices) and phase-separated semiconductor alloys (i.e., chemical superlattices) are known to possess smaller band gaps than the random semiconductor alloys of the same net chemical compositions.<sup>[41]</sup> Combinations of HRTEM and photoluminescence spectroscopy, e.g., Ref.<sup>[28]</sup> or scanning tunneling microscopy-induced luminescence<sup>[42,43]</sup>

<sup>c</sup>For hydrostatic pressure, the product of the bulk modulus (order of magnitude 100 GPa for semiconductors) and the relative elastic volume change is equal to the product of pressure and volume, which is also the excess Gibbs free energy due to lattice mismatch strains. Starting with an unstrained sphere of 10-nm diameter with a lattice constant of 0.5 nm that contains 33510 atoms, one obtains for an elastic volume change of 5% a pressure of 5 GPa and an excess Gibbs free energy of 0.49 eV per atom. Hydrostatic pressures in this range are known to lead to structural transitions in elemental (group IV) and binary III–V compound semiconductors Ref.<sup>[37]</sup>. The usage of this simple formula is justified by studies on the size dependency of elastic properties of nanometer-sized particles, e.g., Refs.<sup>[38,39]</sup>.

investigations demonstrated that smaller band gaps than the random semiconductor alloys of the same net chemical composition are realized for atomically ordered semiconductor entities.

Failure of optoelectronic devices on the timescale of a few years may be explained by structural transitions in ordinarily strained QDs as discussed in this part because devices which employ less severely strained random semiconductor alloy QDs have been found to possess longer lifetimes.<sup>[5]</sup> Growing ordinarily strained, but thermodynamically unstable, random semiconductor alloy QDs that are under compressive stresses in the GPa range, structurally transforming these entities by means of suitable postgrowth thermal treatments, and recovering these novel structures to ambient or device-operating conditions may, on the other hand, become a way to realize Feynman's 1959 vision<sup>[44]</sup> of creating and exploiting atomic arrangements on the nanometer scale that nature does not otherwise provide.

## CONCLUSION

Epitaxial semiconductor quantum dots as grown in the Stranski–Krastanow mode are typically alloyed, possess a more or less random distribution of the cations and/or anions over their respective sublattices, have a spatially nonuniform chemical composition distribution, and are compressively strained to a few percent. The lattice mismatch strains are believed to trigger atomic rearrangements inside quantum dots when the respective samples are stored at room temperature over time periods of a few years. These atomic rearrangements result in long-range atomic order and/or phase separation. While the results suggest that Stranski–Krastanow grown semiconductor quantum dots of certain III–V and II–VI systems are structurally unstable and that devices based on these quantum dots may fail over time, triggering and controlling structural transitions in epitaxial semiconductor quantum dots may also offer an opportunity of creating atomic arrangements that nature does not otherwise provide.

## ACKNOWLEDGMENTS

Collaborations with N.D. Browning, T. Topuria (both from the University of Illinois at Chicago at that time), G.R. Booker, Robin J. Nicholas (both from the University of Oxford/U.K.), Nigel J. Mason (also from the University of Oxford/U.K. at that time), and K. Pierz (Physical-technical Federal Institute, "PTB," Braunschweig/Germany) are kindly acknowledged. Fig. 5B is courtesy of K. Pierz. J.K. Furdyna

and M. Dobrowolska (both from the University of Notre Dame) are thanked for the supply of samples. This research was supported by an award from Research Corporation.

## REFERENCES

1. Bimberg, D. Quantum dots: Paradigm changes in semiconductor physics. *Semiconductors* **1999**, *33*, 951–955.
2. Bimberg, D.; Grundmann, M.; Ledentsov, N.N. *Quantum Dot Heterostructures*; John Wiley & Sons: Chichester, 1999.
3. Pearsall, T.P. *Quantum Semiconductor Devices and Technologies*; Kluwer Academic Publishers: Boston, 2000.
4. Ledentsov, N.N.; Ustinov, V.M.; Shchukin, V.A.; Kop'ev, P.S.; Alferov, Zh.I.; Bimberg, D. Quantum dot heterostructures: Fabrication, properties, lasers (review). *Semiconductors* **1998**, *32*, 343–365.
5. Liu, H.-Y.; Xu, B.; Wei, Y.-Q.; Ding, D.; Han, Q.; Liang, J.-B.; Wang, Z.-G. High-power and long-lifetime InAs/GaAs quantum-dot laser at 1080 nm. *Appl. Phys. Lett.* **2001**, *79*, 2868–2870.
6. Towe, E.; Pan, D. Semiconductor quantum-dot nanostructures: Their application in a new class of infrared photodetectors. *IEEE J. Sel. Top. Quantum Electron.* **2000**, *6*, 408–421.
7. Snider, G.; Orlov, A.O.; Kumamuru, R.K.; Ramasubramaniam, R.; Amlani, I.; Bernstein, G.H.; Lent, C.S. Quantum-dot cellular automata. *Mater. Res. Soc. Symp. Proc.* **2002**, *696*, N7.6.1–N7.6.11.
8. Shumway, J.; Williamson, A.J.; Zunger, A.; Passaseo, A.; DeGiorgi, M.; Cingolani, R.; Catalano, M.; Crozier, P. Electronic structure consequences of In/Ga composition variations in self-assembled In<sub>x</sub>Ga<sub>1-x</sub>As/GaAs alloy quantum dots. *Phys. Rev., B* **2001**, *64*, 125302-1–125302-11.
9. Mahajan, S.; Harsha, K.S. *Principles of Growth and Processing of Semiconductors*; WCB/McGraw-Hill: Boston, 1999.
10. Stranski, I.N.; Krastanow, L. Zur Theorie der orientierten Ausscheidung von Ionenkristallen aufeinander. *Sitzber. Kais. Akad. Wiss., Math.-Nat.wiss. Cl., Abt. IIb* **1938**, *146*, 797–818.
11. Walther, T.; Cullis, A.G.; Norris, D.J.; Hopkinson, M. Nature of the Stranski–Krastanow transition during epitaxy of InGaAs on GaAs. *Phys. Rev. Lett.* **2001**, *86*, 2381–2384.
12. Cullis, A.G.; Norris, D.J.; Walther, T.; Migliorato, M.A.; Hopkinson, M. Stranski–Krastanow transition and epitaxial island growth. *Phys. Rev., B* **2002**, *66*, 81305–81308.
13. Cullis, A.G.; Norris, D.J.; Walther, T.; Migliorato, M.A.; Hopkinson, M. Epitaxial island growth and the Stranski–Krastanow transition. *Mater. Res. Soc. Symp. Proc.* **2002**, *696*, N1.1.1–N1.1.8.
14. Rosenauer, A.; Oberst, W.; Litvinov, D.; Gerthsen, D.; Förster, A.; Schmidt, R. Structural and chemical investigation of In<sub>0.6</sub>Ga<sub>0.4</sub>As Stranski–Krastanow layers



- buried in GaAs by transmission electron microscopy. *Phys. Rev., B* **2000**, *61*, 8276–8288.
15. Kret, S.; Ruterana, P.; Rosenauer, A.; Gerthsen, D. Extracting quantitative information from high resolution electron microscopy. *Phys. Status Solidi, B* **2001**, *227*, 247–295.
  16. García, J.M.; Medeiros-Ribeiro, G.; Schmidt, K.; Ngo, T.; Feng, J.L.; Lorke, A.; Kotthaus, J.; Petroff, P.M. Intermixing and shape changes during the formation of InAs self-assembled quantum dots. *Appl. Phys. Lett.* **1997**, *71*, 2014–2016.
  17. Möck, P.; Booker, G.R.; Mason, N.J.; Alphanđery, E.; Nicholas, R.J. MOVPE grown self-assembled Sb-based quantum dot assessed by means of AFM and TEM. *IEE Proc., Optoelectron.* **2000**, *147*, 209–215.
  18. Möck, P.; Booker, G.R.; Alphanđery, E.; Nicholas, R.J.; Mason, N.J. Self-assembled InSb quantum dots in InAs and GaSb matrices assessed by means of TEM, AFM and PL. *Inst. Phys. Conf. Ser.* **1999**, *164*, 133–136.
  19. Norman, A.G.; Mason, N.J.; Fisher, M.J.; Richardson, J.; Krier, A.; Walker, P.J.; Booker, G.R. Structural and optical characterization of MOVPE self-assembled InSb quantum dots in InAs and GaSb matrices. *Inst. Phys. Conf. Ser.* **1997**, *157*, 353–356.
  20. Kim, C.S.; Kim, M.; Furdyna, J.K.; Dobrowolska, M.; Lee, S.; Rho, H.; Smith, L.M.; Jackson, H.E.; James, E.M.; Xin, Y.; Browning, N.D. Evidence for 2-D precursors and interdiffusion in the evolution of self-assembled CdSe quantum dots on ZnSe. *Phys. Rev. Lett.* **2000**, *85*, 1124–1127.
  21. Möck, P.; Booker, G.R.; Mason, N.J.; Nicholas, R.J.; Alphanđery, E.; Topuria, T.; Browning, N.D. MOVPE grown self-assembled and self-ordered InSb quantum dots in a GaSb matrix assessed by AFM, CTEM, HRTEM and PL. *Mater. Sci. Eng., B* **2001**, *80*, 112–115.
  22. Möck, P.; Topuria, T.; Browning, N.D.; Dobrowolska, M.; Lee, S.; Furdyna, J.K.; Booker, G.R.; Mason, N.J.; Nicholas, R.J. Internal self-ordering in In(Sb,As), (In,Ga)Sb, and (Cd,Zn,Mn)Se nano-agglomerates/quantum dots. *Appl. Phys. Lett.* **2001**, *79*, 946–948.
  23. Möck, P.; Topuria, T.; Browning, N.D.; Titova, L.; Dobrowolska, M.; Lee, S.; Furdyna, J.K. Self-ordered CdSe quantum dots in ZnSe and (Zn,Mn)Se matrices assessed by transmission electron microscopy and photoluminescence spectroscopy. *J. Electron. Mater.* **2001**, *30*, 748–755.
  24. Möck, P.; Topuria, T.; Browning, N.D.; Booker, G.R.; Mason, N.J.; Nicholas, R.J.; Titova, L.V.; Dobrowolska, M.; Lee, S.; Furdyna, J.K. Self-ordering in CdSe/ZnSe, CdSe/(Zn,Mn)Se, InSb/GaSb and InSb/InAs quantum dot structures and a novel type of quantum dot. *Mater. Res. Soc. Symp. Proc.* **2001**, *642*, J6.3.1–J6.3.6.
  25. Topuria, T.; Möck, P.; Browning, N.D.; Titova, L.V.; Dobrowolska, M.; Lee, S.; Furdyna, J.K. Z-contrast transmission electron microscopy on self-assembled CdSe quantum dots in ZnSe and (Zn,Mn)Se matrices. *Mater. Res. Soc. Symp. Proc.* **2001**, *642*, J8.3.1–J8.3.6.
  26. Möck, P.; Topuria, T.; Browning, N.D.; Nicholas, R.J.; Booker, G.R. Atomic self-ordering in heteroepitaxially grown semiconductor quantum dots due to relaxation of external lattice mismatch strains. *Mater. Res. Soc. Symp. Proc.* **2002**, *696*, N8.8.1–N8.8.6.
  27. Möck, P.; Lei, Y.; Topuria, T.; Browning, N.D.; Ragan, R.; Min, K.S.; Atwater, H.A. Structural Transformations in Self-Assembled Semiconductor Quantum Dots as Inferred by Transmission Electron Microscopy. In *Physical Chemistry of Interfaces and Nanomaterials*, Proceedings of the Society of Photo-Optical Instrumentation Engineers, Seattle, WA, July 7–9, 2002; 2002, Vol. 4807.
  28. Möck, P.; Pierz, K.; Topuria, T.; Browning, N.D.; Wu, H.; McCann, P. Atomic ordering in self-assembled epitaxial II–VI and IV–VI compound semiconductor quantum dot systems. *Mater. Res. Soc. Symp. Proc.* **2003**, *749*, W13.5.1–W13.5.6.
  29. Möck, P. Atomic ordering in self-assembled epitaxial and endotaxial compound and element semiconductor quantum dot structures: The first review. *Mater. Res. Soc. Symp. Proc.* **2003**, *776*, Q5.4.1–Q5.4.6.
  30. Browning, N.D.; Arslan, I.; Moeck, P.; Topuria, T. Atomic resolution scanning transmission electron microscopy. *Phys. Status Solidi, B* **2001**, *227* (1), 229–245.
  31. Browning, N.D.; Arslan, I.; James, E.M.; Moeck, P.; Topuria, T.; Xin, Y. Analyzing interfaces and defects in semiconducting materials on the atomic scale. *Inst. Phys. Conf. Ser.* **2001**, *169*, 1–12.
  32. Browning, N.D.; Arslan, I.; Ito, Y.; James, E.M.; Klie, R.; Moeck, P.; Topuria, T.; Xin, Y. Application of atomic scale STEM techniques to the study of interfaces and defects in materials. *J. Electron Microsc.* **2001**, *50* (3), 205–218.
  33. Srivastava, G.P.; Martins, J.L.; Zunger, A. Atomic structure and ordering in semiconductor alloys. *Phys. Rev.* **1985**, *B31*, 2561–2564. *Erratum Phys. Rev.* **1988**, *B38*, 12694.
  34. O'Neill, J.P.; Ross, I.M.; Cullis, A.G.; Wang, T.; Parbrook, P.J. Electron-beam-induced segregation in InGaN/GaN multiple-quantum wells. *Appl. Phys. Lett.* **2003**, *83*, 1965–1967.
  35. Johnson, W.C. Influence of Elastic Stress on Phase Transformations. In *Lectures on the Theory of Phase Transformations*, 2nd Ed.; Aaronson, H.I., Ed.; The Minerals, Metals & Materials Society: Warrendale, 2001; 35–134.
  36. Kim, M.; Furdyna, J.K.; Dobrowolska, M.; Lee, S.; Cheon, M.; Luo, H. Transition form island formation to pseudomorphic growth in the submonolayer CdSe/ZnSe multilayer system. *Appl. Phys. Lett.* **2003**, *83*, 1728–1730.
  37. Ackland, G.J. High-pressure phases of group IV and III–V semiconductors. *Rep. Prog. Phys.* **2001**, *64*, 483–516.
  38. Baker, S.P.; Vinci, R.P.; Arias, T. Elastic and anelastic behavior of materials in small dimensions. *MRS Bull.* **2002**, *27* (1), 26–29.
  39. Miller, R.E.; Shenoy, V.B. Size-dependent elastic properties of nanosized structural elements. *Nanotechnology* **2000**, *11*, 139–147.

40. Girifalco, L.A.; Welch, D.O. *Point Defects and Diffusion in Strained Metals*; Gordon and Breach: New York, 1967.
41. Zunger, A.; Mahajan, S. Atomic Ordering and Phase Separation in Epitaxial III–V Alloys. In *Handbook on Semiconductors*; Completely Revised Ed.; Moss, T.S., Mahajan, S., Eds.; Elsevier Science B.V.: Amsterdam, 1994; Vol. 3, 1399–1514.
42. Håkanson, U.; Sass, T.; Johansson, K.-M.; Pistol, M.-E.; Samuelson, L. Quantum-dot-induced ordering in  $\text{Ga}_x\text{In}_{1-x}\text{P}/\text{InP}$  islands. *Phys. Rev., B* **2002**, *66*, 235308-1–235308-5.
43. Håkanson, U.; Zwiller, V.; Johansson, K.-M.; Sass, T.; Samuelson, L. Luminescence polarization of ordered  $\text{GaInP}/\text{InP}$  islands. *Appl. Phys. Lett.* **2003**, *82*, 627–629.
44. Feynman, R.P. In *There is Plenty of Room at the Bottom*, Lecture at the Annual Meeting of the American Physical Society, December 29, 1959. <http://www.zyvex.com/nanotech/feynman.html>.

# Semiconductor Quantum Dots: Site-Controlled Self-Organization

**S. Kohmoto**

*Femtosecond Technology Research Association (FESTA), Ibaraki, Japan*

**H. Nakamura**

**S. Nishikawa**

*Advanced Technology Research and Development Center, Femtosecond Technology Research Association (FESTA), Ibaraki, Japan*

**T. Yang**

*Nanoelectronics Collaborative Research Center (NCRC), Femtosecond Technology Research Association (FESTA), Ibaraki, Japan*

**K. Asakawa**

*Femtosecond Technology Research Association (FESTA), Ibaraki, Japan*

## INTRODUCTION

The spontaneous formation of nanoscale islands in strained-layer epitaxy, represented by Stranski–Krastanov mode growth, has been widely studied as a simple and efficient method for producing semiconductor quantum dots.<sup>[1–3]</sup> In such a self-organizing approach, quantum dots form randomly on surfaces. If the formation sites of individual quantum dots can be specified, they can be arranged in various configurations, from a single dot to regular, dense, and even coupled dot arrays, and dot placement can be restricted to specific regions, enabling the development of novel electronic and optical devices.

This entry proposes a technique for controlling the self-organization sites of individual quantum dots using scanning tunneling microscope (STM) probe-assisted nanolithography and self-organizing molecular beam epitaxy (MBE).<sup>[4–10]</sup> Two-dimensional (2-D) and three-dimensional (3-D) arrays of InAs site-controlled quantum dots (SCQDs) are successfully fabricated on GaAs substrates with nanoscale pitch and precision. Photoluminescence from the SCQD arrays is investigated at room temperature. The tip repositioning function of the STM system reveals the growth mode of the SCQDs.

## EXPERIMENT

SCQD fabrication was done in situ in an ultrahigh vacuum multichamber system<sup>[6,7,9]</sup> to achieve high-quality structures. As illustrated in Fig. 1, this system consists

of chambers for STM (Large Sample STM, Omicron), solid-source MBE, Auger electron spectroscopy (AES), STM tip cleaning, surface processing, and sample loading, which are connected to each other via a 3-m-long ultrahigh vacuum transfer tunnel. The tungsten (W) probes used for both STM-assisted SCQD fabrication and STM measurements were prepared by electrochemical etching in NaOH solution and cleaned by electron beam heating in the tip-cleaning chamber.

The STM apparatus is specially designed to have a unique tip repositioning function.<sup>[6,7]</sup> This function enables the step-by-step observation of the formation of individual quantum dots. For this purpose, arrays of  $30 \times 30 \mu\text{m}^2$  mesa were patterned on n-GaAs(001) substrates by conventional photolithography and chemical wet etching. After growth of GaAs buffer layers, quantum dot arrays having in-plane array sizes of  $1 \times 1\text{--}2 \times 2 \mu\text{m}^2$  were fabricated at the centers of the mesa top surfaces with a positional accuracy of better than several micrometers. This accuracy was realized by monitoring the approach of the STM probe tip to the mesa top surfaces using a long working distance, high-resolution optical microscope (QM100, Questar; spatial resolution of about  $2 \mu\text{m}$  at a distance of 20 cm) from outside the STM chamber. These dot arrays were easily and repeatedly found in later STM measurements, even when the sample was transferred between the STM and MBE chambers, because of the large scanning area (up to  $15 \times 15 \mu\text{m}^2$ ) of our STM, which enabled detection of the target dot array in a single scan (the typical scan area is  $4 \times 4 \mu\text{m}^2$ ). This technique thus permitted the monitoring of the evolution of an identical quantum dot in the target dot array. STM

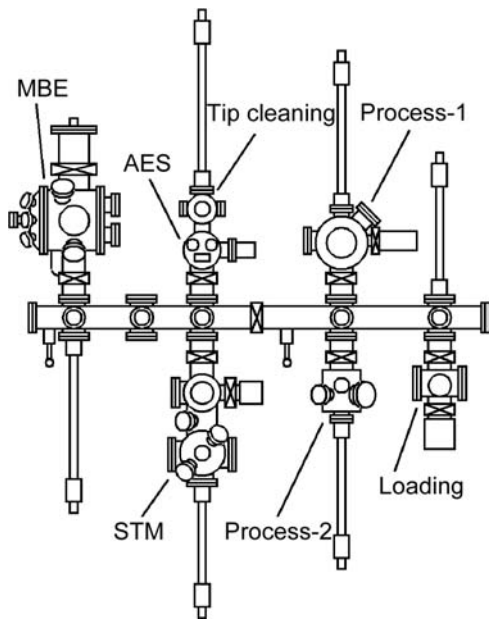


**Fig. 1** Schematic illustration of the ultrahigh vacuum–STM/MBE multichamber system. *Source:* Reprinted with permission from Ref.<sup>[9]</sup>. © 2002, AVS—The Science & Technology Society.

images were taken at sample bias voltages of  $-2.4$  to  $-5.1$  V and tunneling currents of  $0.05$ – $0.49$  nA with constant-current feedback. The optical properties of the quantum dots were investigated by microprobe photoluminescence at room temperature. Photocarriers were generated by He–Ne laser ( $633$  nm) of  $3$ - $\mu\text{m}$  beam diameter, and the photoluminescence signal was detected with a cooled InGaAs photodiode array.

## RESULTS AND DISCUSSION

### Nanoscale Site Control

Fig. 2 schematically illustrates the SCQD fabrication procedure. This procedure comprises in situ deposition and growth, without complex processes such as mask layer formation and pattern etching. First, a flat and clean GaAs(001) surface was prepared by MBE, and the STM W tip was located at a surface target position

with a sample bias voltage of  $-3.2$  V and a tunneling current of  $0.1$  nA. Then, (A) nanoscale deposits were created on a GaAs surface by applying 3–5 pulses of voltage and current ( $+7$  to  $+8$  V and  $10$  nA for  $500$  msec) at intervals of  $10$  msec between the surface and the W probe. The primary composition of the deposit is considered to be a W or a W-containing compound, because the STM probe is composed of W. We confirmed that the deposits remain stable at temperatures up to at least  $610^\circ\text{C}$  under arsenic pressure and act as “nanomasks” on which GaAs does not grow directly. Accordingly, when a thin layer of GaAs or GaAs/Al(Ga)As superlattice was subsequently grown on this surface, (B) the GaAs or superlattice tended to avoid the nanomasks at the initial growth stage, but (C) later covered the nanomasks by lateral growth, leading to the natural formation of nanoholes just above the nanomasks. Finally, (D) the supply of InAs on this surface resulted in self-organization of SCQDs at the nanohole sites.

Fig. 3A, B, and C shows STM images for the fabrication process of an SCQD array corresponding to the steps in Fig. 2A, C, and D, respectively. These are step-by-step images of the identical surface region obtained using the tip repositioning function. As shown in Fig. 3A, a  $2 \times 4$  nanomask array was initially created on the GaAs surface. All nanomasks had a similar size of  $3$  nm in height and  $16$  nm in base diameter. Fig. 3B shows GaAs nanoholes produced by subsequent  $15$ -nm-thick GaAs growth at  $460^\circ\text{C}$ . The holes were elongated in the  $[110]$  direction, because of different incorporation rates of Ga atoms in different surface planes, and had an area of  $27 \times 42$  nm<sup>2</sup> and a depth of  $4$  nm. Comparisons of nanomask height, GaAs layer thickness, and hole depth indicated that the nanomasks were completely covered with the GaAs. Then, as shown in Fig. 3C, a  $2 \times 4$  quantum dot array was self-organized exactly at the nanohole sites by  $1.1$ -ML InAs supply at  $460^\circ\text{C}$ . In this dot growth, a  $0.17$  monolayer [ML;  $1$  ML corresponds to the surface atom density of GaAs(001)] supply per  $4$  sec (occasionally,  $0.087$  ML per  $2$  sec) was repeated with a growth interruption of  $1$  min under a continuous arsenic flux of  $1.3 \times 10^{-5}$  Torr. We observed virtually no undesirable Stranski–Krastanov quantum

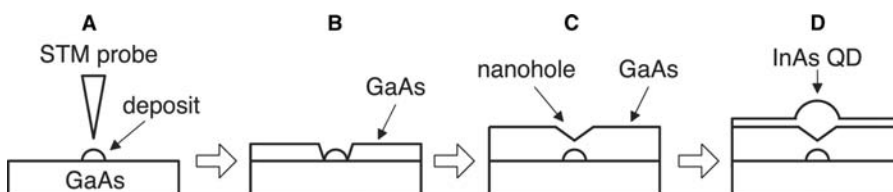


**Fig. 2** Fabrication procedure for InAs SCQDs on GaAs(001) surfaces using STM probe-assisted nanolithography and self-organizing MBE. (A) STM-induced deposits (nanomasks), (B) and (C) GaAs nanoholes, and (D) InAs SCQDs. *Source:* Reprinted with permission from Ref.<sup>[9]</sup>. © 2002, AVS—The Science & Technology Society.

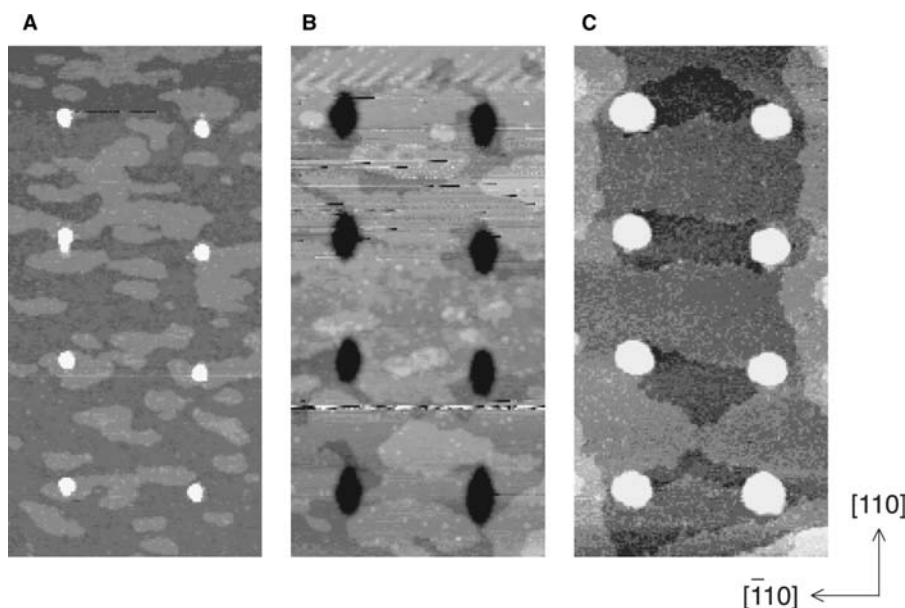


**Fig. 3** Step-by-step STM images for the fabrication process of a  $2 \times 4$  InAs SCQD array on GaAs surfaces corresponding to Fig. 2(A), (C), and (D). (A) STM-induced deposits (nanomasks; height 3 nm, base diameter 16 nm), (B) GaAs nanoholes (depth 4 nm, size  $27 \times 42$  nm), and (C) InAs SCQDs (height 6 nm, base diameter 35 nm). These are images of the identical surface region obtained using the tip repositioning function. Image area:  $200 \times 400$  nm<sup>2</sup>. Source: Reprinted with permission from Ref.<sup>[4]</sup>. © 1999, American Institute of Physics.

dots (SKQDs), the occurrence of which became obvious at 1.3 ML, in the flat surface region. This indicates highly selective SCQD formation. The SCQD was 6 nm in height and about 35 nm in base diameter. A magnified STM image of the SCQD revealed a hexagonal base slightly elongated in the  $[-110]$  direction and a faceted dot surface.

STM-induced nanomasks can be created by this method with nanoscale pitch and precision, and the GaAs nanoholes defined above nanomasks are similar in size to SCQDs. Therefore, the resulting SCQDs can be located in close proximity comparable to the dot

diameter. Fig. 4 demonstrates such close dot positioning, showing three SCQD pairs fabricated by the present site-control method. A 100-nm pitch array of paired SCQDs with 45-nm center-to-center distance and 15-nm bottom-edge spacing was successfully produced.

#### Mechanism of Site-Controlled Self-organization

In previous studies, we used submicron-sized GaAs holes to site-control InAs dots.<sup>[11,12]</sup> In those cases, the dots selectively appeared in the holes at the critical InAs amount for 3-D islanding in Stranski–Krastanov growth mode. The selectivity arose from preferential InAs nucleation at specific planes in the holes, which have a high In incorporation rate. However, in the current study, the SCQDs at the nanohole sites were found to occur in a unique manner, unlike the above case, as described below.

Fig. 5 shows other detailed STM images of the SCQD formation process.<sup>[8]</sup> These are images of the identical surface region obtained using the tip repositioning function. Fig. 5A shows nanoholes produced by growing a 21-nm-thick GaAs/AlGaAs superlattice layer (1.5-nm GaAs/1.5-nm Al<sub>0.3</sub>Ga<sub>0.7</sub>As  $\times$  6, capped with 3-nm GaAs) at 620°C on the surface with the STM probe-induced nanomasks. The holes have an area of  $40 \times 55$  nm<sup>2</sup> and a depth of 10 nm. Also seen in the flat region between the holes are terraces and 2-D islands of a single step height (0.28 nm) elongated in the  $[-110]$  direction. This anisotropic shape occurs because the incorporation probability of Ga and Al atoms at B steps (parallel to  $[110]$ ) is greater than that at A steps (parallel to  $[-110]$ ) during superlattice growth.<sup>[13]</sup> Fig. 5B shows an STM image of the identical surface region after 0.7 ML InAs is supplied. The

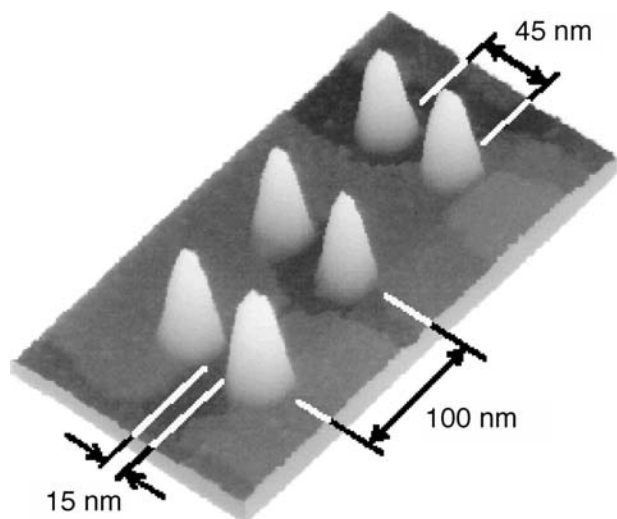


**Fig. 4** STM image of three InAs SCQD pairs on GaAs. Each quantum dot is 6 nm in height and 30 nm in base diameter. Image area:  $155 \times 300$  nm<sup>2</sup>. Source: Reprinted with permission from Ref.<sup>[9]</sup>. © 2002, AVS—The Science & Technology Society.

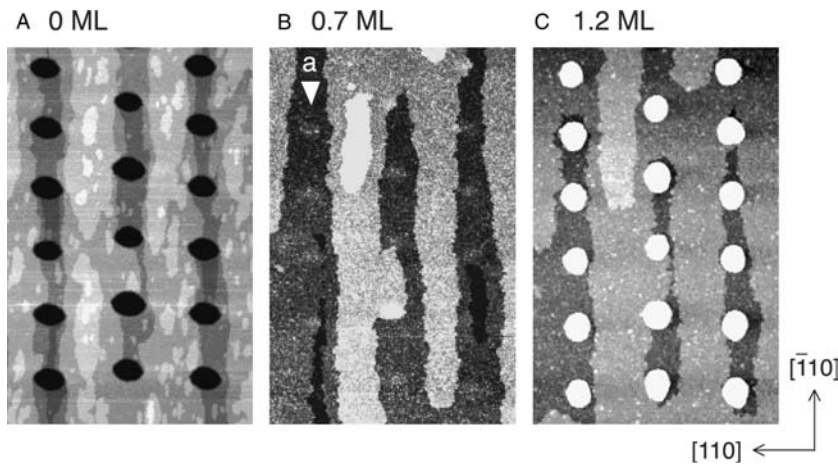


**Fig. 5** STM images showing SCQD and wetting layer evolution with InAs supply. InAs: (A) 0 ML, (B) 0.7 ML, and (C) 1.2 ML. The white arrowhead “a” indicates the position of the original hole. These are images of the identical surface region obtained using the tip repositioning function. Image area:  $380 \times 580 \text{ nm}^2$ . Source: Reprinted from Ref.<sup>[8]</sup>. © 2002, with permission from Elsevier Science.

nanoholes are filled and almost planarized, but the filled parts exhibit slightly bright contrast in the STM image, as indicated, for instance, by arrowhead “a” in Fig. 5B. The area of contrast is elliptical in accordance with the shape of the original holes, and the height corresponding to the contrast is less than that of a single step. Most of the terraces and 2-D islands increased in size, although some of the relatively small 2-D islands disappeared. Consequently, the enlarged terraces and 2-D islands on the same level coalesced into one larger terrace or 2-D island elongated in the  $[-110]$  direction. Some terraces at the lower level disappeared as they were covered by the upper terraces. It should be noted that the extending terraces covered most of the filled hole sites in this process. At 1.2-ML InAs, as shown in Fig. 5C, quantum dots were selectively self-organized at the filled hole sites. In the flat region, terrace size further increased, with the result that only three levels of terraces dominated the surface.

In Fig. 5, we assume that the material filling the nanoholes is InAs or InGaAs and that the observed extension of terraces and 2-D islands indicates the formation of an In(Ga)As wetting layer (WL) that covers the filled hole sites prior to SCQD formation. In this case, since the filling In(Ga)As has a larger lattice constant and lower bandgap energy than the surrounding GaAs, the slightly bright contrast at the filled hole sites in the constant-current STM image shown in Fig. 5B can be explained by upheaval due to compression and/or larger tunneling conductivity at the wetting layer surfaces on the filled holes. Then, the subsequently supplied In atoms for 3-D islanding accumulate at the filled hole sites, because the lattice mismatch of InAs with the wetting layer on the filling In(Ga)As is less than that on the surrounding GaAs, leading to selective self-organization of quantum dots. This growth process can be understood by analogy with vertically aligned SKQDs in close stacking.<sup>[14]</sup> A detailed analysis of the evolution of the SCQD and wetting layer is provided in another publication.<sup>[5]</sup>

In order to form the quantum dots at the nanohole sites, it is important to both cover the nanomasks completely with GaAs (or superlattices) and ensure that the holes are deeper than a certain critical value by selecting suitable GaAs growth conditions and thicknesses. For instance, although 5-nm-thick GaAs growth created  $25 \times 35\text{-nm}^2$ -sized holes, the 1.2-ML InAs supply on this surface did not result in dot formation at the nanohole sites. This is because the top part of the nanomask, on which InAs does not grow directly, was still exposed at the hole bottom because of the thin GaAs layer. On the other hand, even when the nanomasks under certain growth conditions were completely covered with GaAs, dots did not form at nanohole sites when the hole depth was less than about 3 nm. In this case, because the volume of In(Ga)As filling the holes was small, the lattice constant of the wetting layer surface on the filling In(Ga)As was presumably so close to that on the surrounding GaAs surface that In atoms could not selectively accumulate at the nanohole sites.

### Three-Dimensional Site Control

When SKQD layers are stacked with thin spacer layers, the dots align vertically<sup>[14,15]</sup> or obliquely,<sup>[16,17]</sup> depending on elastic anisotropy and the thickness of the spacers, because of strain propagation. It has been predicted that regular strain distribution will gradually develop on the spacer-layer surfaces with increasing stack numbers, leading to increasingly uniform size for the topmost dots.<sup>[14,16–19]</sup> If the stacking is started with regular SCQD arrays in place of random SKQDs, the dots can be site controlled into 3-D quantum dot lattices, and uniform SKQDs array will be obtained more efficiently. In addition, this 3-D site control has the potential to realize novel quantum dot structures such as 3-D quantum dot crystals<sup>[16]</sup> with perfect spatial ordering. In this section, we demonstrate 3-D



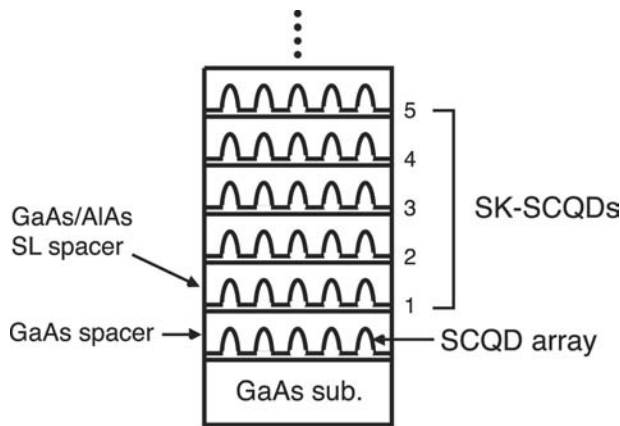


**Fig. 6** Schematic illustration of a 3-D InAs SK-SCQD lattice structure. *Source:* Reprinted with permission from Ref.<sup>[9]</sup>. © 2002, AVS—The Science & Technology Society.

site control of SKQDs based on the site-initiated multistacking approach<sup>[9]</sup> mentioned above.

Fig. 6 illustrates the structure of a 3-D InAs quantum dot lattice. In this structure, an InAs SCQD array of arbitrary configuration was initially prepared on GaAs surfaces by the STM probe-assisted site-control technique described earlier. This array defines the in-plane lattice symmetry and parameters of the 3-D dot lattice. Then, after growth of a 10-nm-thick GaAs spacer layer, InAs was supplied to form SKQDs just above the arrayed SCQDs by strain-induced preferential self-organization. Hereafter, we denote the SKQDs grown above the SCQDs as Stranski–Krastanov mode-grown site-controlled quantum dots (SK-SCQDs). Repeating the spacer layer [GaAs/AlAs superlattice (SL) in case of Fig. 6] and SK-SCQD growth permitted the formation of a 3-D quantum dot lattice with vertically and horizontally aligned dots.

Fig. 7 shows STM images for the vertical stacking process of the SK-SCQDs in the 3-D quantum dot lattice.<sup>[9]</sup> These are images of the identical surface region.

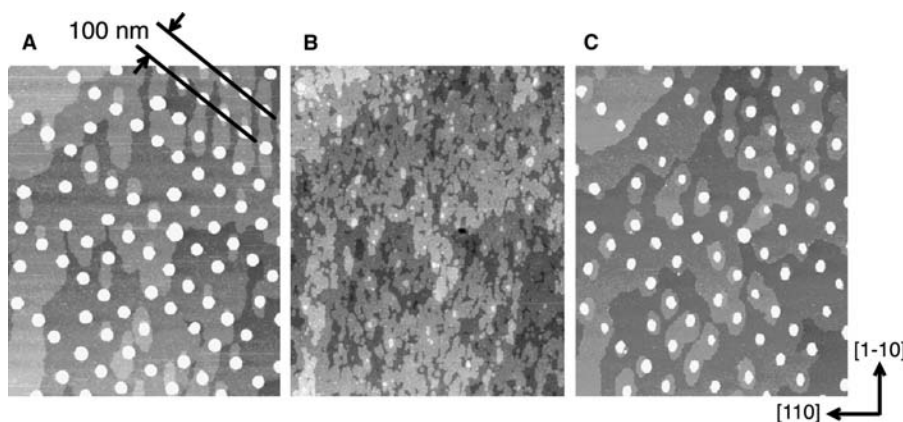


**Fig. 7** STM images for vertical stacking process of InAs SK-SCQDs. (A) the first SK-SCQD layer, (B) spacer layer, and (C) the second SK-SCQD layer. These are images of the identical surface region obtained using the tip repositioning function. Image area:  $1000 \times 1200 \text{ nm}^2$ . *Source:* Reprinted with permission from Ref.<sup>[9]</sup>. © 2002, AVS—The Science & Technology Society.

The first-layer SK-SCQDs shown in Fig. 7A were grown with 0.9 ML InAs supply. This amount is 0.4 ML less than the critical value for the formation of conventional InAs SKQD on unstrained GaAs surfaces, indicating the existing surface strain field on the spacer layer grown over the SCQDs. The SK-SCQD array exhibits a square lattice, although the alignment is not perfect and some dots are missing due to the initial lack of SCQDs. The lattice has unit vectors in the [100] and [010] directions and a lattice parameter of about 100 nm, which are defined by the embedded SCQD strain template. Fig. 7B shows the surface topography of a 20-nm-thick GaAs/AlAs superlattice spacer, terminated with GaAs, grown on the first SK-SCQD layer. The similar positions of surface steps in this image to those in Fig. 7A confirm that these two images are of the identical surface area. The spacer layer surface is almost planarized and dominated by monolayer-high terraces. However, the strain field at this surface, generated by the embedded SK-SCQDs, was visualized when InAs was grown in the next step. Fig. 7C shows an STM image of the second layer SK-SCQDs formed with 1.3 ML InAs supply on the spacer layer. As confirmed by comparing the positions of missing dots between Fig. 7A and C, the square lattice configuration of the first-layer dots is retained in the second-layer dots. The vertical pairing probability of dots between two layers is almost 100%. On the other hand, no dot is observed at interstitial positions. These results indicate that the spatial strain field can be engineered by the site-control technique.

The in-plane lattice symmetry and parameter of the 3-D quantum dot lattice can be arranged arbitrarily, independent of the crystallographic symmetries of the substrates, by designing the SCQD strain template. An example is presented in Fig. 8, where the SK-SCQDs array has a hexagonal-like unit cell with a lattice parameter of 50–60 nm.<sup>[9]</sup> This configuration can achieve area dot densities as high as approximately  $4 \times 10^{10} \text{ cm}^{-2}$ . Close positioning comparable to the dot diameter is realized through the

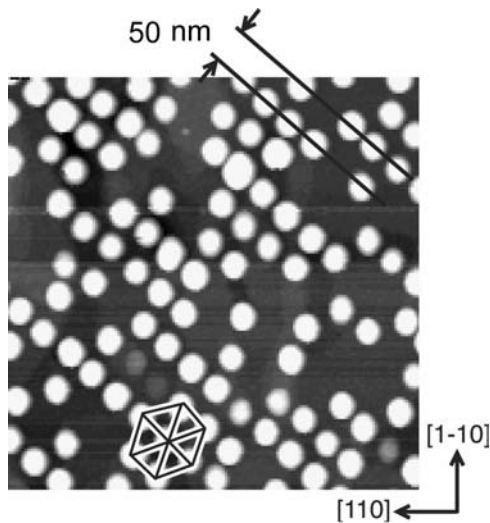


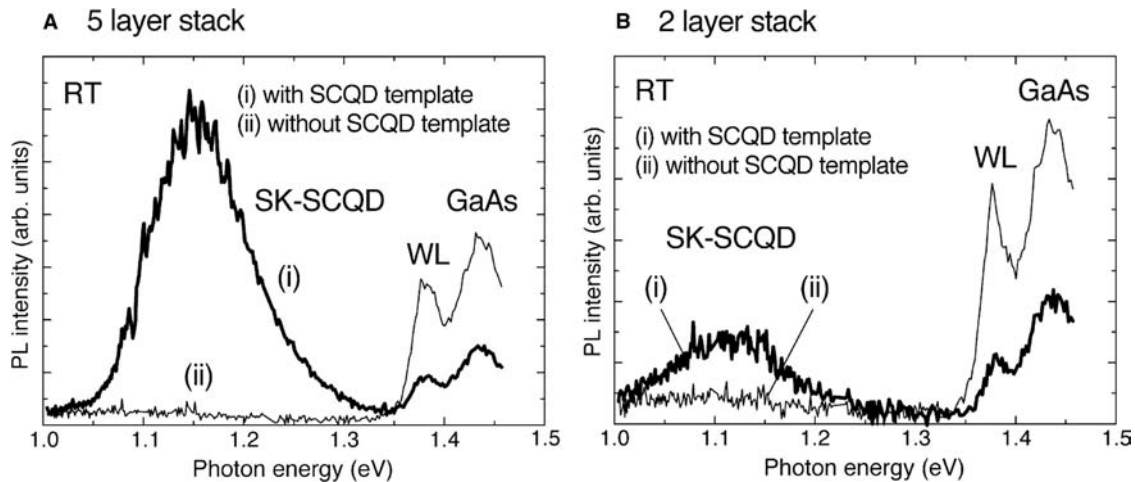
**Fig. 8** STM image of a high-density InAs SK-SCQD array. Hexagonal-like quantum dot configuration is indicated. Image area:  $600 \times 600 \text{ nm}^2$ . *Source:* Reprinted with permission from Ref.<sup>[9]</sup>. © 2002, AVS—The Science & Technology Society.

nanoscale precision of the STM-assisted site-control method.

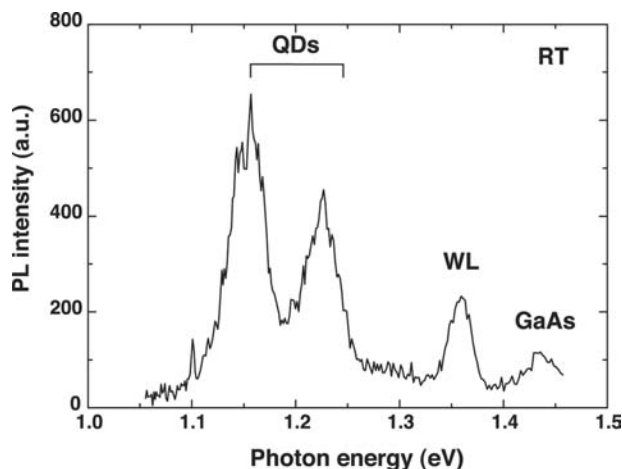
### Optical Properties

Fig. 9A shows the microprobe-photoluminescence spectrum of a 3-D lattice of InAs SK-SCQDs measured at room temperature.<sup>[9]</sup> The sample comprised five SK-SCQD layers stacked in a manner similar to the structures in Fig. 7. The in-plane lattice parameter of the dot layer was about 100 nm. The total number of

SK-SCQDs within the excitation laser beam was estimated to be about 1200 by STM observation of the top SK-SCQD layer before capping layer growth. As shown for the case “with SCQD template” in Fig. 9A, distinct photoluminescence from the 3-D SK-SCQD lattice is observed from 1.05 to 1.30 eV. The different photoluminescence experiments confirmed that the SCQDs of the strain templates exhibit no emission and do not contribute to the photoluminescence spectra of quantum dots in Fig. 9, probably because of the existence of the STM-induced nano-masks at close positions. When a reference area without the initial SCQD strain template on the same sample is excited, no photoluminescence from quantum dots is detected, as shown for the case “without SCQD template” in Fig. 9A. This means that conventional SKQDs are hardly formed in the stacked structure without the SCQD strain template, showing highly selective formation of the 3-D SK-SCQD lattices. The excitation power dependence of the photoluminescence spectral width indicated that the observed quantum dot emission is mainly due to ground state transitions in the SK-SCQDs. Photoluminescence intensity reduction for the WL and the GaAs barrier in the 3-D SK-SCQD lattice suggests that photocarriers were effectively consumed at dots through radiative recombination. Fig. 9B shows the photoluminescence spectrum of a two-layer stacked SK-SCQD sample fabricated in a manner similar to the five-layer sample. Although the number of dots per single layer was increased to some extent in this sample, the total number of measured dots fell to about 600. However, photoluminescence from the SK-SCQDs remains observable at room temperatures, as shown for the case “with SCQD template” in Fig. 9B. These photoluminescence results reveal the good



**Fig. 9** Room temperature photoluminescence (PL) spectra of 3-D InAs SK-SCQD lattices. Samples include (A) five-layer stacked and (B) two-layer stacked SK-SCQDs. *Source:* Reprinted with permission from Ref.<sup>[9]</sup>. © 2002, AVS—The Science & Technology Society.



**Fig. 10** Room temperature photoluminescence (PL) spectrum of a single-layer InAs SK-SCQD lattice with a pitch of 75 nm. The two peaks at lower photon energies are from the ground and first excited states of the InAs SK-SCQDs, respectively. The peak at about 1.36 eV is from the InAs wetting layer (WL). The peak at around 1.44 eV is from the GaAs substrate. *Source:* Reprinted with permission from Ref.<sup>[10]</sup>. © 2003, American Institute of Physics.

crystallographic quality of the SK-SCQD structures, despite the addition of an artificial STM process and STM observation in some fabrication steps. This is because the present 3-D site control is carried out by ultrahigh vacuum in situ processing, which can keep the sample surface clean during the fabrication process,<sup>[20]</sup> using only the crystal growth technique after the initial nanomask deposition.

In Fig. 9, full width at half maximum of the SK-SCQD emissions is more than 100 meV, even in the two-layer stacked structure. This large line width can be attributed to differences in dot size in intradot layers and in interdot layers. For device applications, it is desirable to decrease both kinds of size differences to obtain a narrow line width. Targeting this improvement, we studied the photoluminescence of a single layer of SK-SCQDs.<sup>[10]</sup> A single layer of an InAs SK-SCQD square lattice with a lattice parameter of 75 nm was fabricated above an InAs SCQD strain template. The SK-SCQDs were grown at lower growth rate and lower arsenic pressure and with a greater supply of InAs than applied to the SCQDs during growth. This resulted in the formation of relatively large SK-SCQDs with an average height of about 9 nm and base diameter of about 45 nm. The SK-SCQDs were then buried with GaAs/Al<sub>0.3</sub>Ga<sub>0.7</sub>As/GaAs. Fig. 10 shows a photoluminescence spectrum from the buried structure at room temperature. From excitation spectral measurements, two respective low energy peaks were identified to arise from the ground and first excited states of the SK-SCQDs. The other

two peaks, at about 1.36 and 1.44 eV, are, respectively, attributable to the WL and GaAs substrate. The full width at half maximum of the ground state peak for the SK-SCQDs is about 40 meV, which is fairly good for artificially arranged quantum dot arrays. This is because the SK-SCQDs, like conventional SKQDs, can be made higher under the specific growth conditions described above, and because the energy variation of such higher dots is relatively insensitive to size fluctuations.

## CONCLUSION

We developed a site-controlled self-organization technique for InAs quantum dots on GaAs(001) surfaces using in situ STM probe-assisted nanolithography and self-organizing MBE. We found that it was possible to create nanoscale deposits on a GaAs surface by applying voltage and current pulses between the surface and an STM probe. When the deposits were used as nanomasks for GaAs growth, GaAs nanoholes were formed naturally above the deposits. Subsequently supplied InAs filled and planarized the GaAs nanoholes, providing flat surfaces with modulated strain fields. Consequently, supplying additional InAs on the surfaces led to SCQD formation at the filled-hole sites. Virtually no undesirable SKQDs were observed, indicating highly selective dot formation. This process resulted in successful fabrication of 2-D arrays of InAs SCQDs with nanoscale pitch and precision. 3-D quantum dot lattices were also demonstrated. In-plane dot arrangement of the 3-D dot lattices was initially defined by 2-D arrays of InAs SCQDs. With the SCQD arrays used as strain templates, self-organized InAs quantum dots were vertically aligned by strain-induced multistacking, resulting in 3-D quantum dot lattices. Photoluminescence measurements revealed good crystallographic quality for the 2-D and 3-D SK-SCQD lattices.

The site-control technique demonstrated here enables the location of an isolated single quantum dot at an intended position on the surfaces, which is useful for developing single-photon and electron devices. The high-density dot arrays with small energy dispersion are also technologically significant structures that can be achieved by this site-control approach, because large dots, whose energy variations are relatively insensitive to size fluctuations, can be formed regardless of density. This independent control of dot size and density is a difficult task for conventional crystal growth. Another attractive application of the site-control technique is the formation of dot arrays in limited areas in the devices. For instance, photonic crystal waveguide structures having quantum

dot arrays at specific regions would make it possible to build miniaturized, ultrahigh speed all-optical switches with high switching efficiency.<sup>[21,22]</sup> Such applications will require improvements in the uniformity of the size of SK-SCQDs in the intra- and interlayers. In 3-D site-control processes, it is also important to control lateral strain interaction between neighboring dot sites in vertical stacking, as we pointed out in a recent study.<sup>[10]</sup> Further experimental investigations and theoretical consideration of growth conditions and spatial strain fields will lead to uniform quantum dot size and the realization of novel nanostructure systems.

## ACKNOWLEDGMENTS

This work was supported by the NEDO within the framework of the Femtosecond Technology Project.

## REFERENCES

- Goldstein, L.; Glas, F.; Marzin, J.Y.; Charasse, M.N.; Le Roux, G. Growth by molecular beam epitaxy and characterization of InAs/GaAs strained-layer superlattices. *Appl. Phys. Lett.* **1985**, *47* (10), 1099–1101.
- Leonard, D.; Krishnamurthy, M.; Reaves, C.M.; Denbaars, S.P.; Petroff, P.M. Direct formation of quantum-sized dots from uniform coherent islands of InGaAs on GaAs surfaces. *Appl. Phys. Lett.* **1993**, *63* (23), 3203–3205.
- Bimberg, D.; Grundmann, M.; Ledentsov, N.N. *Quantum Dot Heterostructures*; John Wiley & Sons: New York, 1999, and references therein.
- Kohmoto, S.; Nakamura, H.; Ishikawa, T.; Asakawa, K. Site-controlled self-organization of individual InAs quantum dots by scanning tunneling probe-assisted nanolithography. *Appl. Phys. Lett.* **1999**, *75* (22), 3488–3490.
- Nakamura, H.; Kohmoto, S.; Ishikawa, T.; Asakawa, K. Novel nano-scale site-controlled InAs quantum dot assisted by scanning tunneling microscope probe. *Physica, E* **2000**, *7* (3–4), 331–336.
- Kohmoto, S.; Nakamura, H.; Ishikawa, T.; Asakawa, K. STM probe-assisted site-control of self-organized InAs quantum dots on GaAs surfaces. *J. Electron. Mater.* **2000**, *29* (5), 525–529.
- Kohmoto, S.; Nakamura, H.; Ishikawa, T.; Asakawa, K. STM probe-assisted site-control of self-organized InAs quantum dots on GaAs surfaces. *J. Electron. Mater.* **2000**, *29* (9), 1110
- Kohmoto, S.; Nakamura, H.; Ishikawa, T.; Nishikawa, S.; Nishimura, T.; Asakawa, K. Site-controlled self-organization of InAs quantum dots. *Mater. Sci. Eng., B* **2002**, *88* (2–3), 292–297.
- Kohmoto, S.; Nakamura, H.; Nishikawa, S.; Asakawa, K. Three-dimensional site control of self-organized InAs quantum dots by in situ scanning tunneling probe-assisted nanolithography and molecular beam epitaxy. *J. Vac. Sci. Technol., B* **2002**, *20* (3), 762–765.
- Yang, T.; Kohmoto, S.; Nakamura, H.; Asakawa, K. Effects of lateral quantum dot pitch on the formation of vertically aligned InAs site-controlled quantum dots. *J. Appl. Phys.* **2003**, *93* (2), 1190–1194.
- Ishikawa, T.; Kohmoto, S.; Asakawa, K. Site control of self-organized InAs dots on GaAs substrates by in situ electron-beam lithography and molecular-beam epitaxy. *Appl. Phys. Lett.* **1998**, *73* (12), 1712–1714.
- Kohmoto, S.; Ishikawa, T.; Asakawa, K. InAs-dot/GaAs structures site-controlled by in situ electron-beam lithography and self-organizing molecular beam epitaxy. *Jpn. J. Appl. Phys.* **1999**, *38*, 1075–1077.
- Horikoshi, Y.; Yamaguchi, H.; Briones, F.; Kawashima, M. Growth process of III–V compound semiconductors by migration-enhanced epitaxy. *J. Cryst. Growth* **1990**, *105* (1–4), 326–338.
- Xie, Q.; Madhukar, A.; Chen, P.; Kobayashi, N. Vertically self-organized InAs quantum box islands on GaAs(100). *Phys. Rev. Lett.* **1995**, *75* (13), 2542–2545.
- Solomon, G.S.; Trezza, J.A.; Marshall, A.F.; Harris, J.S., Jr. Vertically aligned and electronically coupled growth induced InAs islands in GaAs. *Phys. Rev. Lett.* **1996**, *76* (6), 952–955.
- Springholz, G.; Holy, V.; Pinczolits, M.; Bauer, G. Self-organized growth of three-dimensional quantum-dot crystals with fcc-like stacking and a tunable lattice constant. *Science* **1998**, *282*, 734–737.
- Pinczolits, M.; Springholz, G.; Bauer, G. Evolution of hexagonal lateral ordering in strain-symmetrized PbSe/Pb<sub>1-x</sub>Eu<sub>x</sub>Te quantum-dot superlattices. *Phys. Rev., B* **1999**, *60* (16), 11524–11529.
- Tersoff, J.; Teichert, C.; Lagally, M.G. Self-organization in growth of quantum dot superlattices. *Phys. Rev. Lett.* **1996**, *76* (10), 1675–1678.
- Solomon, G.S.; Komarov, S.; Harris, J.S., Jr.; Yamamoto, Y. Increased size uniformity through vertical quantum dot columns. *J. Cryst. Growth* **1997**, *175–176*, 707–712.
- Kohmoto, S.; Nambu, Y.; Asakawa, K.; Ishikawa, T. Reduced nonradiative recombination in etched/regrown AlGaAs/GaAs structures fabricated by in situ processing. *J. Vac. Sci. Technol., B* **1996**, *14* (6), 3646–3649.
- Sugimoto, Y.; Ikeda, N.; Carlsson, N.; Asakawa, K.; Kawai, N.; Inoue, K. Fabrication and characterization of different types of two-dimensional AlGaAs photonic crystal slabs. *J. Appl. Phys.* **2002**, *91* (3), 922–929.
- Nakamura, H.; Kanamoto, K.; Nakamura, Y.; Ohkouchi, S.; Ikeda, N.; Tanaka, Y.; Sugimoto, Y.; Ishikawa, H.; Asakawa, K. In *Large Enhancement of Optical Nonlinearity Using Quantum Dots Embedded in a Photonic Crystal Structure for All-optical Switch Applications*, Proceedings of LEOS2002, Glasgow, 2002.



# Sensors Based on Chemicurrents

B. Roldan Cuenya

E. W. McFarland

*Chemical Engineering Department, University of California–Santa Barbara,  
Santa Barbara, California, U.S.A.*

## INTRODUCTION

Selective and non-selective solid-state chemical sensors have been developed for a variety of applications in process control, environmental monitoring, and hazardous substance detection. Most rely on an indirect detection mechanism whereby electronic or electro-optical properties of the device are altered by the substance of interest allowing for a measurable response. Sensors based on analyte–sensor interactions, which modify capacitance, conductivity, and refractive index, operate in this manner.<sup>[1–7]</sup>

Recently, a means of directly monitoring charged carriers produced from gas–surface interactions has been described<sup>[8–18]</sup> whereby “hot” electrons/holes (e–h) from gas–surface reactions are themselves detected using ultrathin film metal–semiconductor (MS) Schottky diodes.<sup>[13]</sup> When an adsorbate binds to the surface with a relatively large adsorption energy, the energy may appear as an energetic e–h pair generated at the metal surface; the excited electron may travel ballistically through the thin metal film and transverse the Schottky barrier (SB) if the film is thin compared with the ballistic mean free path and if the kinetic energy of the electron is larger than the barrier height (Fig. 1A). Once injected into the conduction band of the semiconductor [inverse electron emission, (IEE)], the electron is detected as a “chemicurrent” analogous to the photocurrent in a photodiode.

The energetic charge carriers have a ballistic mean free path of tens of nanometers and thus for small-dimension metal structures, the “hot” charge carriers persist at energies well above the Fermi level. Hot electrons have interesting and unusual reactivity and transport properties which may be taken advantage of in Schottky-barrier metal–semiconductor (MS) and metal–oxide–semiconductor (MOS) diode sensors. Using ultrathin metal films on MS and MOS device structures, we have investigated the “chemielectronic” phenomena associated with a variety of molecular and atomic interactions with transition metal surfaces (Ag, Au, Pt, Pd) and found distinct differences in the

mechanism of signal production between the highly energetic atomic and molecular species and more weakly interacting species such as xenon and hydrocarbons. In this review, the basis for the chemical sensitivity of these diode structures will be addressed, emphasizing the importance of oxide interfacial states in the detection of electronic signals from weakly interacting gases. Experimental evidence linking the surface chemistry to the electronic processes giving rise to signals in MS and MOS diode sensors will be presented.

## BACKGROUND

Gergen et al.<sup>[16,18]</sup> showed that by adding a thin oxide layer between the metal and the semiconductor, the modified metal–oxide–semiconductor (MOS) device had sensitivity to a variety of weakly interacting gas species not detectable on the MS Schottky diode sensor. The original explanation of ballistic charge transport over the Schottky barrier appears valid for species with large adsorption energies including atomic oxygen and atomic hydrogen, O<sub>2</sub>, NO, and NO<sub>2</sub>; however, the mechanism of carrier generation and detection on the same devices for weakly interacting species such as Xe, CO<sub>2</sub>, and hydrocarbons is only now becoming clarified.

Metal–semiconductor and MOS solid-state sensors are used in a variety of sensor applications; however, despite decades of research, there remain controversies regarding a complete description of the detection mechanisms and conduction pathways. The controversy is greatest for devices containing intermediate thin oxides. Formation of a metal–semiconductor junction results in charge redistribution and band bending [Fig. 1A and B, respectively]. The semiconductor barrier height is related to the band bending by  $\Phi_B = \Psi_s + V_n$ , where  $V_n$  is the energy difference between the Fermi level and the majority-carrier band edge and  $\Psi_s$  is the semiconductor work function.

The effect of the intermediate oxide layer is twofold. Primarily, it increases the effective Schottky barrier by enhancing the semiconductor band bending ( $\Psi_s$ ) as a

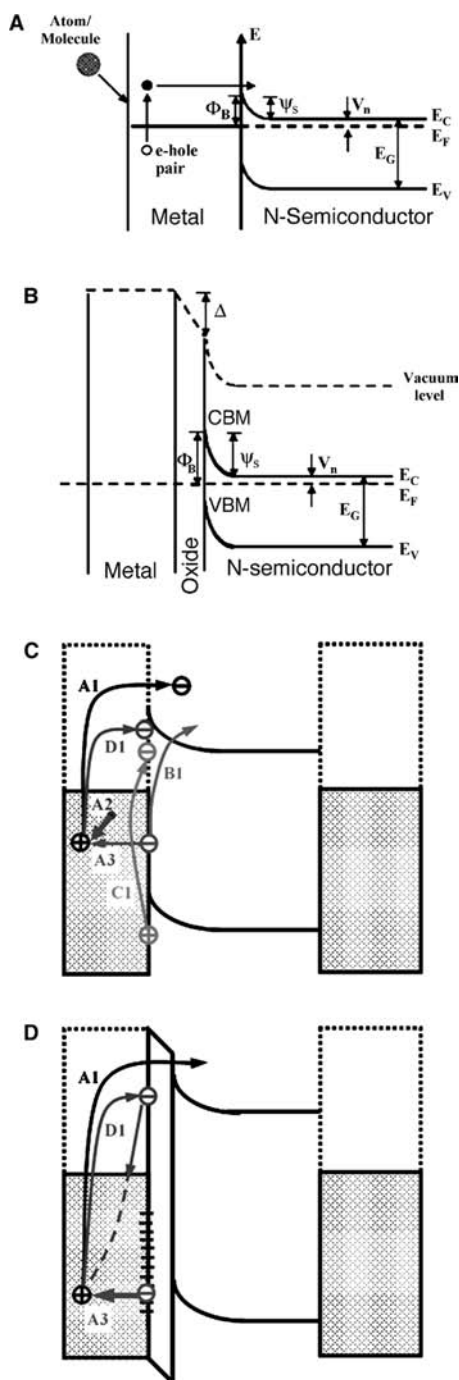


**Fig. 1.** Energy band diagram illustrating (A) ballistic conduction mechanism in an oxide-free Schottky barrier diode. The contact is between a metal and an n-type semiconductor. (B) Thin oxide MOS diode structure. Presence of a negative charge in the oxide causes the barrier height to increase. (C) Conduction pathways in an MS diode. (D) Oxide-trap assisted conduction in a MOS device.

result of additional negative charges trapped in the intermediate region. The Fermi level ( $E_F$ ) of the system will then be nearer in energy to the valence band edge (VBM) than to the conduction band edge (CBM).

In such a structure, current transport may be dominated by the component of current between the metal and the valence band (minority band) in the n-type semiconductor. Minority-carrier current in the semiconductor region will be the sum of the space charge diffusion current and the generation–recombination current associated with the depletion layer. In a “forward current soak,” majority carriers are slowly trapped in the oxide. This increases the barrier resulting in high minority-carrier injection. The opposite behavior is observed in the case of an “avalanche current soak,” where minority carriers are slowly trapped in the oxide layer. This decreases the barrier height resulting in low minority-carrier injection.<sup>[19–21]</sup> Second, the presence of the oxide “unpins” the Fermi level at the surface of the semiconductor allowing the barrier height to reflect the metal-semiconductor work function difference.<sup>[20]</sup>

Photoconduction in MS junctions from photons with energies less than the band gap is generally thought to involve three basic pathways [Fig. 1C]. Inverse electron emission (IEE) may be observed from photon absorption in the metal which produces “hot electrons” with sufficient energy to reach and surmount the Schottky barrier, pathway A1. The deep-hole state may be filled from metal-based electrons, A2, giving rise to reverse bias current, or from electron donor states at the interface, pathway A3. Inverse electron emission may also be observed from electrons excited from electron donor interface states over the barrier, pathway B1, which are refilled by metal-based electrons. An additional conduction path is given when valence electrons in the semiconductor are photoexcited to acceptor interface states, pathway C1, and trapped at the interface. The valence band hole is filled by recombination from donor (dopant) levels at the interface. In an n-type MS device short-circuited through a current monitor, the dominant pathways are A1 and A2, resulting in an observed reverse bias electron current moving through the semiconductor conduction band to the back contact and through the current monitor to the front contact.

In MOS devices [Fig. 1D], because of the relatively large density of interface electron donor states,<sup>[19]</sup> process A3 becomes increasingly important as a source of electrons to the deep photogenerated holes. If the photoelectron energy is too low for transmission over the barrier, depletion of the interface donors will result in a transient discharging of the interface donor states with an apparent forward bias charging current observed. The relative interface state density and effective barrier height will largely determine the relative importance of these various pathways.

Much of the controversy involving MOS chemical sensors involves the understanding of the interface states and their contribution to conduction.<sup>[19,22–26]</sup> The relationships between interfacial charging and



donor or acceptor interface states are indirectly observable in C–V and I–V measurements.<sup>[27–31]</sup> Quantitative characterization of the shifts cannot be performed unambiguously from such measurements because surface states affect the device electrical characteristics in the following manner: 1) surface states trap electrons and holes and 2) surface states act as recombination centers (dynamic effect). As charge traps, the states provide an additional electric field in the insulating layer, and, consequently, the I–V and C–V are shifted by the amount of the increased potential drop across the insulating layer. As recombination centers, the traps provide a current path as a result of surface recombination in addition to other transport pathways such as majority-carrier thermionic-emission current and minority-carrier diffusion current, increasing the total current density.

An electrical response from a chemical interaction with an MS or MOS device may originate from one (or more) fundamentally different mechanism of modifying the interfacial charge. 1) The species can modify the work function (chemical potential) of the conducting metal layer which consequently results in a modification of the space charge layer. 2) The species can introduce dipoles at the metal/semiconductor interface, thereby modifying the charge distribution of the double layer. 3) The species can significantly change the interface state density in the semiconductor interfacial region (pinning or unpinning the Fermi level), thereby changing the charge and barrier in the semiconductor. 4) The species can diffuse into the semiconductor where it may modify its doping density, thereby changing the charge density in the barrier region and, consequently, the barrier. In general, the species to be detected does not need to be the same entity that causes the changes in the metal, semiconductor, or interfacial region. For example, a reaction product generated catalytically at the conductor surface which interacts with the sensor structure may be the species that causes the change.

In our work, we have attempted to separate the device response as a result of chemically induced changes in the electrical characteristics of the MS and MOS junctions from electrical phenomena resulting from charge generation and transport induced directly by the energy transfer associated with surface reactions (direct effects). To this end, we have investigated reactions of several gas species including O<sub>2</sub>, O, H, H<sub>2</sub>, CO<sub>2</sub>, Xe, C<sub>2</sub>H<sub>4</sub>, and several other hydrocarbon gases on Ag-, Au-, Pt-, and Pd-based MS and MOS diodes.

## EXPERIMENTAL

Sensors were formed on (17.5 × 12 mm) rectangles of n-type ⟨111⟩-oriented silicon (phosphorus-doped,

1–10 Ω cm<sup>-2</sup>). All substrates were prepared using a standard RCA cleaning procedure, (NH<sub>4</sub>OH/H<sub>2</sub>O<sub>2</sub>/H<sub>2</sub>O 1/1/4, followed by HCl/H<sub>2</sub>O<sub>2</sub>/H<sub>2</sub>O 1/1/4, both for 10 minutes at 90°C) followed by a 1-min dip in an aqueous solution of buffered-HF and subsequent rinse in DI-water.<sup>[32]</sup> Metal-semiconductor diodes were formed by deposition of metal films on the oxide-free hydrophobic HF-terminated Si surface. The backside of the silicon wafers has been covered by a 1500-Å-thick Ti film (e-beam evaporated at a pressure <1 × 10<sup>-6</sup> Torr), followed by the deposition of 1500-Å gold to achieve an ohmic contact. Metal-oxide-semiconductor junctions were formed by depositing the metal film on a (~10 Å) silicon oxide layer grown on the front side by means of a 5–10 min dip in an aqueous solution of 30% H<sub>2</sub>O<sub>2</sub>.<sup>[16,18]</sup>

Two (3 × 7 mm) Pt films (4000 Å) separated by 7 mm were used as front contacts. The contacts were isolated from the substrate by a 3000-Å-thick SiO<sub>2</sub> film deposited by evaporation. All the processes described above have been performed under clean-room conditions. The sensors were bonded with indium to a molybdenum sample holder for later transfer into the ultrahigh vacuum (UHV) chemical beam chamber. The (10 × 7 mm) active sensor film was deposited between the contact pads by electron-beam evaporation.

The metal films for the Ag-, Au-, and Pt-based sensors were deposited on the sensor substrates at room temperature by electron-beam evaporation under high vacuum conditions (P ~ 10<sup>-7</sup> Torr) and secondarily transferred to an ultrahigh vacuum (UHV) chemical beam chamber. Pd-based sensors were deposited on sensor substrates cooled to ~125 K after transfer into the UHV chamber (P < 5 × 10<sup>-10</sup> Torr) using a wire source electron beam evaporator. Pd films were deposited at low temperature (125 K) and measured immediately after deposition. Using the same sensor after gas exposure, increasing thicknesses were obtained by a subsequent thermal evaporation of Pd under UHV. The metal thickness was measured using a quartz microbalance to calibrate the evaporation rate. Low-temperature deposition was selected to inhibit surface diffusion, which results in a continuous pinhole-free film of a finer-grained morphology at a lower thickness than what would be achieved at higher temperatures.<sup>[33]</sup>

The chemical composition of the Si/SiO<sub>x</sub> surface was investigated prior to metal deposition using X-ray photoelectron spectroscopy (XPS) (AlK<sub>α</sub> radiation, E = 1486.6 eV). The thickness of the intermediate SiO<sub>2</sub> layer (~7 Å) was obtained from exit angle-dependent XPS measurements (data not shown). The roughness of the Si/SiO<sub>2</sub> interface and the growth morphology of the metal films were studied ex situ by scanning tunneling microscopy (STM) and atomic force microscopy (AFM) before and after gas exposure and annealing. A Nanoscope III multimode scanning

probe microscope (Digital Instruments) operating in STM mode and a Dimensions 3100 scanning probe microscope (Digital Instruments) operating in tapping mode were used to obtain STM and AFM micrographs.

The electrical characteristics of the MS and MOS contacts were investigated at room and low temperature (125 K) in UHV using current–voltage (I–V) (not shown) and capacitance–voltage (C–V) measurements at 1 kHz.

Chemically induced electrical signals were measured in an UHV system. Mixed beams of atomic and molecular gas species were produced and delivered by a three-stage differentially pumped atomic beam source.<sup>[8]</sup> Hydrogen and oxygen molecules were dissociated within a microwave plasma at gas pressures between 150 and 800 mTorr. The plasma source was especially designed to extract any photons from the gas beam because the plasma emits intense ultraviolet light with photon energy of 10.2 eV and the Schottky diodes are sensitive photodetectors.

To investigate the diode response to gas exposure, the active sensors were positioned in line to a shuttered collimated gas beam modulated at 4 Hz (50% duty cycle). The room-temperature thermalized beam had a flux that varied between  $2 \times 10^{12}$  and  $5 \times 10^{12}$  atoms  $\text{cm}^{-2}\text{sec}^{-1}$ . The sensors were exposed to molecular and atomic hydrogen and oxygen, several C2, C3, and C4 hydrocarbons, xenon, and carbon dioxide. The detectors were mounted on a manipulator cooled with a flow cryostat. The reaction-induced chemicurrents were detected by the diode connected in series with a current preamplifier (SRS 570). The preamplifier gain was 2 nA/V and its effective impedance was 1 M $\Omega$  at 4 Hz. The preamplifier output was connected either to a lock-in (SR830) or an A-D convertor (Oscilloscope LeCroy 9361). The signals measured by the oscilloscope were averaged over several cycles to minimize the noise present because of 60-Hz pickup. Additionally, all measurements were carried out at low temperature (125 K) to minimize the noise caused by the thermal drift. Other details of the experimental setup are described elsewhere.<sup>[13]</sup>

## RESULTS

Fig. 2A (left) displays a STM image of a 60-Å-thick Pd film deposited at low temperature (125 K) under UHV conditions on a chemically oxidized Si surface ( $d_{\text{SiO}_2} \approx 7 \text{ \AA}$ , determined by XPS). In Fig. 2A, it is observed that Pd does not grow as a uniform flat film as occurred in the case of the Pd films grown on HF-terminated Si wafer (MS devices.<sup>[34]</sup>), but forms hemispheres of  $\approx 5\text{--}8 \text{ nm}$  in diameter. A Volmer–Weber (3-D islands) or Stranski–Krastanov growth

(monolayer plus islands) is expected from thermodynamic considerations because mid-to-late transition metals do not wet oxide substrates in vacuum.<sup>[35]</sup> A similar fine grain film morphology (3–5 nm in size) was discovered by AFM for a 60-Å-thick RT-grown Pt film (Fig. 2B). Room-temperature silver deposition (60 Å), however, leads to large (30–60 nm) and interconnected islands (Fig. 2C). The pictures on the right-hand side of Fig. 2 are 3-D plots obtained from the analysis of the STM and AFM images on the left after taking into account the height information acquired.

Fig. 3 shows  $C^{-2}$  plots obtained from low-temperature (125 K) C–V measurements performed over the reverse bias range at 1 kHz on Au, Pt, Pd/SiO<sub>2</sub>/n-Si(111), and Pd–MS devices before gas exposure. The experimental data are reasonably well described by a linear fit consistent with uniform doping in the semiconductor.<sup>[24,36,37]</sup> The curves are not entirely parallel to one another because of differences in the carrier concentration of the distinct silicon wafers employed as substrate. The donor concentration ( $N_D$ ) and barrier height ( $\Phi_{\text{BO}}$ ) can be obtained from the fits of the data for the different metals on otherwise identical MOS devices (Table 1).<sup>[24,28,38]</sup> For the oxide-free contact (i.e., Pd–MS, open circles, Fig. 3), the intercept on the voltage axis,  $V_i$  (built-in potential), approximately gives the barrier height,  $\Phi_{\text{BO}} = 0.81 \pm 0.01 \text{ eV}$ . The doping concentration calculated from the slope of the  $C^{-2}$ –V plot is  $N_D = (1.72 \pm 0.07) \times 10^{15} \text{ cm}^{-3}$ . In the case of the thin oxide contact (Pd–MOS, full circles, Fig. 3),  $V_i = 0.89 \pm 0.01 \text{ V}$  is not equal to the barrier height, but is the sum of the voltage drop across the oxide layer ( $V_{\text{ox}}$ ) and the semiconductor band bending ( $\Psi_s$ ). At the doping concentration obtained,  $N_D = (1.01 \pm 0.07) \times 10^{16} \text{ cm}^{-3}$ ,  $\Psi_s \approx \Phi_B$ . For the Pd–MOS sample,  $V_i$  is larger than the one obtained for our nearly oxide-free Pd–Si contact. The same trend was observed for the other metals. This suggests a negative oxide charge ( $V_{\text{ox}}$ ) in the n-type contact. Table 1 also lists the diode characteristic parameters obtained from the linear fit of Fig. 3 following the model described in Ref.<sup>[34]</sup>. The values of the semiconductor surface space ( $Q_s$ ) and oxide charge density ( $N_f$ ) calculated must be regarded as order of magnitude because of the change in occupancy of the oxide traps. The occupancy change causes an error in the doping concentration and in the  $V_i$  values obtained from  $C^{-2}$ –V and has not been taken into account here. Nevertheless, we can conclude from Fig. 3 that there is negative oxide charge in the n-type contact which increases the barrier height substantially (0.1–0.15 eV) over the oxide-free contact. Our C–V measurements showed that contrary to a previous literature report,<sup>[16]</sup> a decrease in the Schottky barrier by introducing an ultrathin oxide between a metal/semiconductor contact does not necessarily occur. Tongson et al.<sup>[39]</sup>

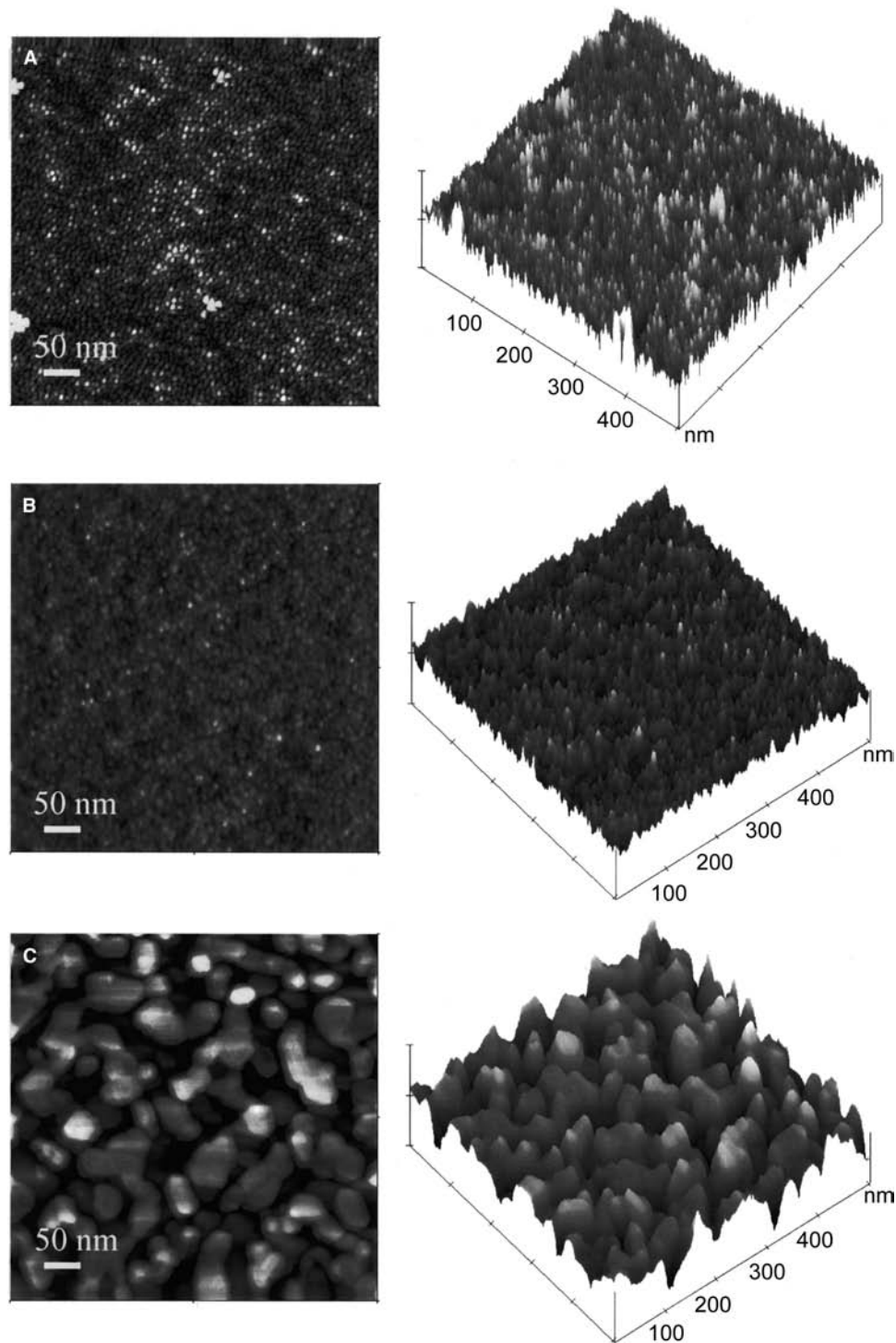


**Fig. 2.** (A) Ex situ STM image ( $z$  range, 3 nm) of a 60-Å-thick Pd film thermally evaporated in UHV at  $T = 125$  K on  $\text{SiO}_2/\text{Si}(111)$ ; (B) ex situ AFM image ( $z$  range, 4 nm) of a RT-deposited 60-Å-thick Pt film grown on  $\text{SiO}_2/\text{Si}(111)$  under high vacuum conditions; (C) ex situ AFM image ( $z$  range, 15 nm) of a RT-deposited 60-Å-thick Pt film grown on  $\text{SiO}_2/\text{Si}(111)$  under high vacuum conditions. The samples were not exposed to any gas after preparation but were imaged under atmospheric pressure.

reported enhancements of the Schottky barrier in Ag and Au MIS devices with respect to MS diodes.

The demodulated lock-in amplifier output from a Pd(60 Å)/n-Si(111) diode during exposure to atomic

oxygen is shown in Fig. 4. In the MS Pd sensor, a large chemicurrent signal was detected upon exposure to energetic oxygen atoms. The initial signal peak of  $\sim 930$  pA corresponds to  $\sim 5.6 \times 10^{-3}$  electrons

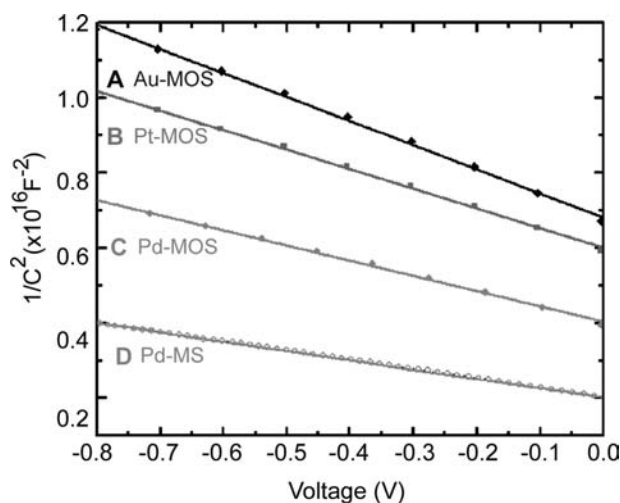


**Fig. 3.**  $C^{-2}$  vs.  $V$  plots of (A) Au(60 Å)/SiO<sub>2</sub>/n-Si(111), (B) Pt(150 Å)/SiO<sub>2</sub>/n-Si(111), (C) Pd(60 Å)/SiO<sub>2</sub>/n-Si(111), and (D) Pd(60 Å)/n-Si(111) measured in UHV at 125 K before any gas exposure.

detected per incident O atom on the initially clean polycrystalline Pd surface. The decay over 500 sec is consistent with formation of an oxide coverage assuming a surface site density of  $1.5 \times 10^{15} \text{ cm}^{-2}$ . Similar behavior has been observed with H atoms, NO, and NO<sub>2</sub>.<sup>[18]</sup> The phase ( $\phi$ ) of the lock-in signal,  $-83^\circ$ , is essentially identical to the photocurrent phase corrected for the difference in beam transit times ( $\sim 0.5$  msec) indicating a reverse bias current analogous to IEE generated by photocurrent. The MS devices are insensitive to hydrocarbons, Xe, CO<sub>2</sub>, or other low adsorption energy species.

Unlike the Pd-MS devices, the Pd-MOS devices were sensitive to a range of gas species (H, O, Xe, C<sub>2</sub>H<sub>4</sub>, CO, etc.), although the amplitude of the signals was lower ( $\sim 29$  pA) compared with the analogous MS devices (Fig. 5A). As with the MS devices, an exponentially decaying chemicurrent is observed in both cases upon exposure to O<sub>2</sub>, O, and H; however, a constant “steady-state” current was observed for C<sub>2</sub>H<sub>4</sub> and CO<sub>2</sub> and other species not observed on MS sensors. The relatively large signal detected upon exposure of the fresh sensor to O<sub>2</sub> is attributed to the atomic

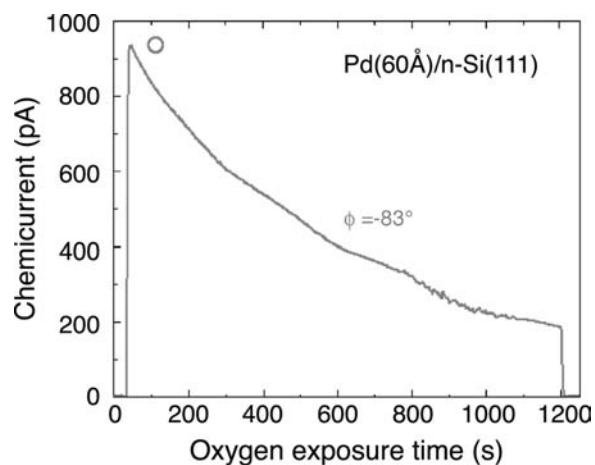


**Fig. 4.** Lock-in detected chemicurrent signal from a nearly oxide-free Pd(60 Å)/n-Si(111) diode as a function of exposure time to atomic oxygen. The signal was modulated at 4 Hz. The gas pressure in the beam chamber during gas exposure was 500 mTorr.

oxygen present at the Pd surface after the dissociative adsorption of molecular oxygen. The phases of the O, H, and O<sub>2</sub> signals measured by lock-in techniques were all similar and consistent with a process analogous to what was described for atomic O on the MS device. For the low-energy species, C<sub>2</sub>H<sub>4</sub> and CO<sub>2</sub> (Fig. 5A), the phase was  $\phi = 95^\circ$  and  $154^\circ$ , respectively, indicating a current direction opposite to that of the energetic high species. From the current transient shown in (Fig. 5B) referenced to the molecular flux, an effective forward bias current moves through the device circuit during the ethylene exposure.

Measurements of the response of both MS and MOS devices to a chopped beam of O, Xe, or ethylene during constant, DC, irradiation with IR or visible light showed no change in the chemicurrent signal (if present) compared with the signal in the absence of irradiation, suggesting that no pulse-to-pulse change in the device electrical characteristics was occurring.

In other experiments, not reported here, we found that the sensitivity to low-energy species was lost after exposure of the Pd sensors to hydrogen atoms or molecules.

**Table 1** Diode characteristic parameters: Capacitance at zero bias ( $C_0$ ), built-in potential ( $V_i$ ), semiconductor surface space charge density at zero bias ( $Q_s$ ), semiconductor surface capacitance per unit area ( $C_s$ ), voltage drop across the oxide layer ( $V_{ox}$ ), and oxide charge density ( $N_f$ ) Obtained from capacitance vs. voltage measurements performed under UHV at 125 K

Sample	$C_0$ (nF/cm <sup>2</sup> )	$V_i$ (eV)	$Q_s$ (nC/cm <sup>2</sup> )	$C_s$ (nF/cm <sup>2</sup> )	$V_{ox}$ (mV)	$N_f$ ( $\times 10^{11}$ cm <sup>-2</sup> )	$\Phi_B$ (eV)
Pt(150 Å)-MOS	12.8	1.08	25.0	12.8	7.9	0.8	$1.07 \pm 0.07$
Au(60 Å)-MOS	23.2	1.00	41.6	23.4	13.0	1.3	$0.99 \pm 0.07$
Pd(60 Å)-MOS	32.0	0.89	50.0	31.0	18.2	4.1	$0.9 \pm 0.2$
Pd(60 Å)-MS	42.7	0.80					$0.807 \pm 0.002$



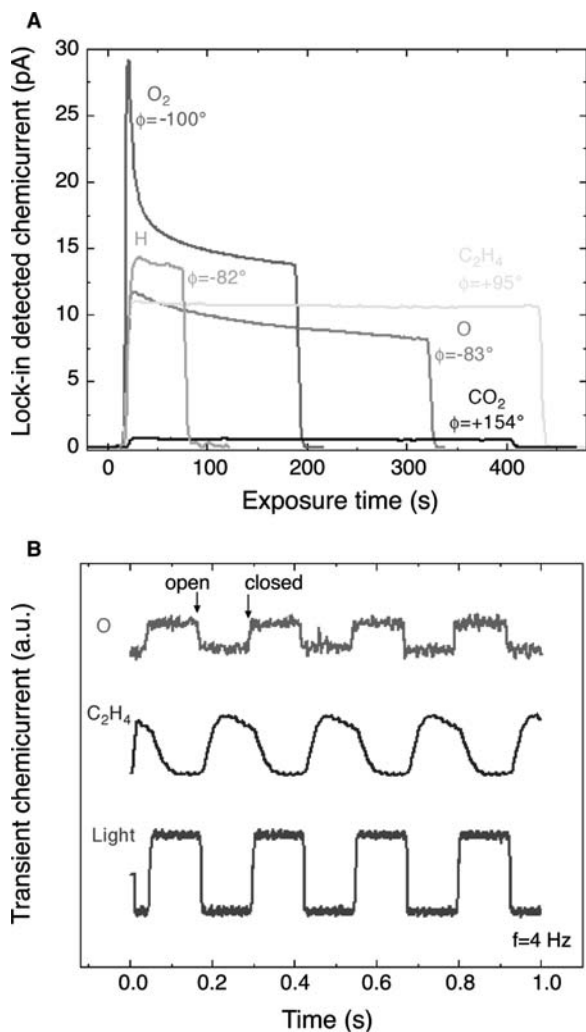


**Fig. 5.** (A) Lock-in detected chemicurrent signals from a Pd(60 Å)/SiO<sub>2</sub>(7 Å)/n-Si(111) diode as a function of exposure time to O<sub>2</sub>, O, H, C<sub>2</sub>H<sub>4</sub>, and CO<sub>2</sub>. (B) Averaged current traces from individual pulses of O, C<sub>2</sub>H<sub>4</sub>, and light (non-monochromatic) measured by an oscilloscope during Pd-MOS exposure. The signals were modulated at 4 Hz. The gas pressure in the beam chamber during gas exposure was 500 mTorr. The current direction of the signal induced by the interaction of C<sub>2</sub>H<sub>4</sub> (same found for CO<sub>2</sub>, Xe, and other hydrocarbons) with the Pd-MOS sensor is contrary to that of the high energetic species studied such as O or H (not shown) and to that of non-monochromatic white light.

The sensor currents measured during exposure of Pd/SiO<sub>2</sub>/n-Si(111) MOS diodes of increasing thickness to several species (O, H, and C<sub>2</sub>H<sub>4</sub>) and to visible (660 nm) and infrared (1550 nm) photons are shown in Fig. 6. The current intensities detected for Pd thicknesses increasing from 40 to 800 Å decreased approximately exponentially for both chemically and photogenerated electrons. Fits of the data to an exponential decay law gave effective attenuation lengths, which are interpreted below. In general, the

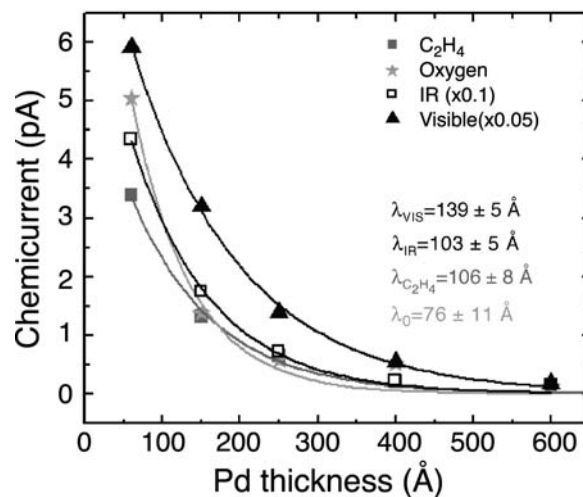


**Fig. 6.** Thickness-dependent chemicurrent after low-temperature Pd evaporation from a Pd(60 Å)/SiO<sub>2</sub>(7 Å)/n-Si(111) structure during C<sub>2</sub>H<sub>4</sub>, O, infrared (1550 nm), and monochromatic visible light (660 nm) exposure. The scales of the IR and visible signals have been reduced by a factor of 0.1 and 0.05, respectively.

energetic gases showed smaller attenuation lengths ( $\lambda_{\text{H}} = 66 \pm 7 \text{ \AA}$  in Pd-MS or  $\lambda_{\text{O}} = 76 \pm 11 \text{ \AA}$  in Pd-MOS) than the ones with low adsorption energies ( $\lambda_{\text{C}_2\text{H}_4} = 106 \pm 8 \text{ \AA}$  in Pd-MOS). These were also smaller than the attenuation lengths measured for visible monochromatic light ( $\lambda_{\text{VIS}} = 139 \pm 5 \text{ \AA}$  in MOS). The values obtained for ethylene and infrared light ( $\lambda_{\text{IR}} = 103 \pm 5 \text{ \AA}$ ) were of the same order. Crowell et al.<sup>[40]</sup> obtained an electron attenuation length of  $170 \pm 30 \text{ \AA}$  from photoemission measurements on Pd/n-Si junctions using photon energies below 1.1 eV (infrared region) which is also on the same order as our data.

Fig. 7 displays the current amplitudes detected at 125 K from exposure to identical fluxes of a variety of C<sub>2</sub>, C<sub>3</sub>, and C<sub>4</sub> hydrocarbons to polycrystalline films of Ag(150 Å), Pt(150 Å), Pd(60 Å), and Au(60 Å) deposited on SiO<sub>2</sub>/n-Si(111) devices. The ordering (left to right) is in approximate increasing order of molecular polarizability (right axis). There is no clear relationship between the polarizability and the relative currents; however, the different sensitivities displayed to different gases by distinct metals suggest that one could fabricate a sensor composed by an array of different metals to selectively detect a wide variety of gases.<sup>[41]</sup>

## DISCUSSION

The signals detected from both MS and MOS devices from the energetic chemisorption of atomic O and H

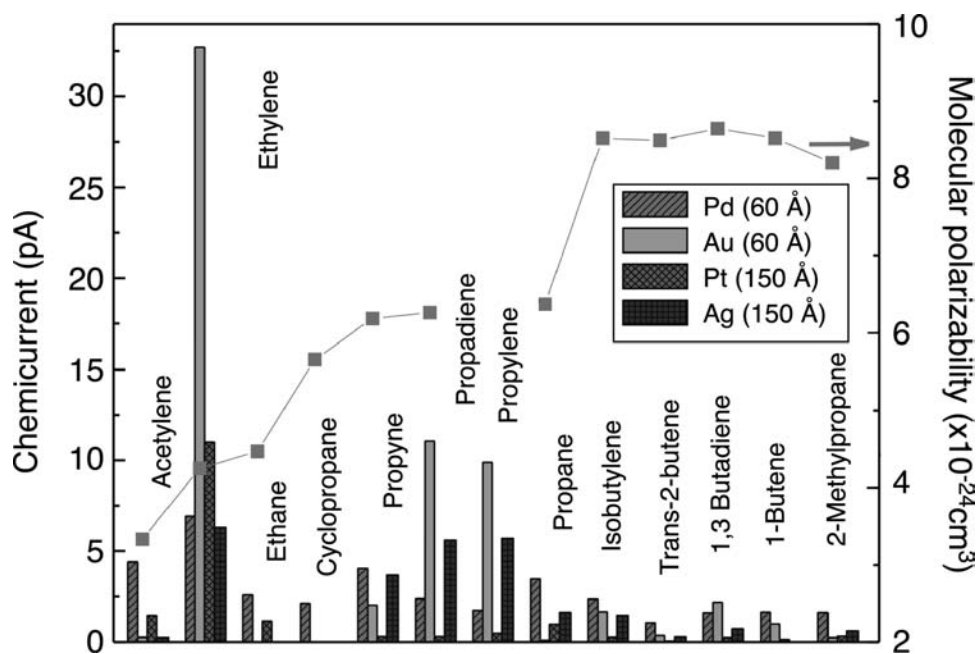


Fig. 7. Current amplitudes detected at 125 K from exposure to identical fluxes ( $P = 1$  Torr in the beam chamber) of C<sub>2</sub>, C<sub>3</sub>, and C<sub>4</sub> hydrocarbons to polycrystalline films of Pd, Au, Pt, and Ag deposited on MOS Si devices. The ordering (left to right) is in approximate increasing order of molecular polarizability (right axis).

and the energetic dissociative chemisorption of O<sub>2</sub> are consistent with hot electron transmission over the Schottky barrier (direct mechanism) as shown in Fig. 1A. The exponential thickness dependence of the signals from these species (Fig. 6) is consistent with attenuation of ballistic, hot electrons generated at the metal surface. The attenuation lengths of  $\sim 100$  Å are consistent with the electron mean free path in the metal film.<sup>[40]</sup> Thus, for energetic adsorption reactions with  $E >$  Schottky barrier, both MS and MOS devices function by the direct chemically induced IEE.

That the MS devices do not show sensitivity to the low-energy species is expected because their adsorption energies are lower than the Schottky barrier height precluding IEE. The requirement of the interfacial oxide in the MOS device for sensitivity to low-energy species and the apparent reversal of the observed current direction requires a new mechanistic explanation of the device function. The chemical signal from surface interactions of the low-energy species in the MOS devices must either be a result of another direct pathway or by a chemically induced indirect change in the device characteristics.

The I–V (not shown) and C–V characterizations indicate that there are clearly electrical differences between the MS and the MOS devices. In particular, the capacitance of the MOS device is nearly twice that of the MS because of the larger band bending from the large interface charge density associated with the oxide and the higher Schottky barrier. The presence of

charge at the interface and trap states is what accounts for the apparent (false) decrease in the SB measured by I–V compared with C–V.

Although the presence of the oxide gives rise to an MOS sensor that has basic electrical characteristics different than the MS device and a surface morphology which is also considerably different, these differences do not, in themselves, explain the dramatically different response of the two devices. The device characteristics as measured by I–V and C–V were insensitive to variations in the metal thickness or short pulses of the adsorbate gases that would result in an exposure equivalent to the pulse-to-pulse beam exposure. It would be very difficult to postulate a mechanism whereby a hundredth of a monolayer of Xe could significantly alter the electrical characteristics of a metal film. Furthermore, the absence of change in the chopped chemicurrent signal during DC photon irradiation compared with the signal in the absence of irradiation suggests that no pulse-to-pulse change in the device electrical characteristics was occurring. The thickness dependence of the adsorption-related signal and experiments using simultaneous DC visible or IR irradiation together with chopped molecular ethylene or Xe showing no modulation in the IEE signal exclude an indirect mechanism whereby the presence of the adsorbate significantly alters the Schottky barrier or device performance on a pulse-to-pulse basis. If the electrons/holes detected undergo a ballistic transport through the metal, the chemicurrent



signals measured should decrease with increasing metal thickness. However, if changes in the surface chemical potential affect the conduction, a nearly constant current should be detected independent of the thickness of the metal that forms the Schottky contact. The thickness dependence displayed in Fig. 6 suggests that one must, in principle, rule out changes in the chemical potential as responsible for the sensor sensitivity. The thickness dependence also suggests that the known coverage-dependent alteration in the surface work function does not give rise to the observed signal because the increased metal thickness from 20 to 40 nm would not have any effect on the surface charge distribution changes associated with the work function change.

The data described above support a direct mechanism for charge generation, transport, and detection in the MOS devices. The measured large surface donor state density has led us to propose the pathway shown in Fig. 1D. As in the case with highly energetic adsorbates, the gas surface reaction gives rise to electron-hole pair excitations albeit at lower energies. The electron is excited above the Fermi level, but below the Schottky barrier. These electrons are not transmitted to the semiconductor. The hole below the Fermi level accepts an electron by resonant charge transfer (and hot electron transport through the metal from the interface) from the donor state at the interface. To balance the change in the interface charge, a forward bias current is required through the external circuit (thus explaining the phase reversal of the lock-in detected signal and the inverted sign of the transient signals). As the rate of depletion of the interface donor states becomes equal to the rate of refilling, the forward bias signal decays to zero at steady state. The lifetime of the donor states may be energy- and field-dependent. Our proposed mechanism is consistent with the observed thickness dependence and unique sensitivity of the MOS devices and with their particularly high interface donor state density.

The details of the electronic behavior of the intermediate oxide layer in MOS device performance are a complex question that has been the subject of great controversy in the past.<sup>[6,23,26,36,37,39,42,43]</sup> In contrast with other experimental groups,<sup>[44]</sup> alteration of surface states is held responsible here for the high sensitivity of the Pd/Si-MOS diodes. In addition to serving as a high-density source of electron donor states, the  $\sim 10 \text{ \AA}$   $\text{SiO}_2$  acts as a diffusion barrier against metal silicide formation which tends to fix the Schottky barrier height in the MS device.<sup>[29]</sup> The larger Schottky barrier in the MOS devices is such that under minimal forward bias, the interface donor states depleted by the charge transfer to metal hole states created by reaction can be refilled on a continuous basis giving rise to large continuous forward bias currents.<sup>[29]</sup> The loss of sensitivity to low energetic gases ( $\text{C}_2\text{H}_4$  and

Xe) following exposure to hydrogen can also be related to the interface donor states. The hydrogen in the Pd sensor diffuses through to the interface and reacts with the site resulting in an electrical charge variation measurable in the IV and CV curves and forming the basis of other, indirect, hydrogen sensors.<sup>[23,26,36,44,45]</sup>

## SUMMARY

We have investigated chemical reaction-induced electronic phenomena on nanometer-scale metal films deposited on semiconductor junctions. We have attempted to identify and separate chemically induced modifications in the device electrical characteristics (indirect effects) from chemically induced charge generation and transport (direct effects) to clarify the mechanism of signal generation in the thin film-covered MS and MOS devices. Chemical reactions on ultrathin metal surfaces give rise to energetic charges which we have shown to give rise to electrically measurable signals observable in MS or MOS device structures when the metal film thickness is less than the ballistic mean free path of the charge carriers generated by the reaction. Ideal metal-Si Schottky diodes are insensitive to reactions with energies lower than the Schottky barrier; however, the presence of an interface oxide between the metal and the semiconductor provides electron donor states at high density which allow charging and discharging of the device interface. This mechanism allows the detection of the electron-hole pairs created during non-adiabatic energy transfer to the metal from low-energy surface reactions.

## ACKNOWLEDGMENTS

The authors are grateful for the technical assistance of Drs. Xi Liu and Brian Gergen and the financial support of the National Science Foundation (CTS-9820134, CHE-9626338) and U.S. Department of Energy (DE-FG03-89ER14048). This work made use of MRL Central Facilities supported by the MRSEC Program of the National Science Foundation under award No. DMR00-80034.

## REFERENCES

1. Lundström, I.; Shivaraman, S.; Svensson, C.; Lundkvist, L. Hydrogen-sensitive MOS field-effect transistor. *Appl. Phys. Lett.* **1975**, *26*, 55–57.
2. Lundström, K.I.; Shivaraman, M.S.; Svensson, C.M. Hydrogen-sensitive Pd-gate MOS-transistor. *J. Appl. Phys.* **1975**, *46*, 3876–3881.

3. Steele, M.C.; Hile, J.W.; Maciver, B.A. Hydrogen-sensitive palladium gate MOS capacitors. *J. Appl. Phys.* **1976**, *47*, 2537–2538.
4. Morrison, R. Semiconductor gas sensors. *Sens. Actuators* **1982**, *2*, 329–340.
5. Filippini, D.; Rosch, M.; Aragon, R.; Weimar, U. Field-effect NO<sub>2</sub> sensors with group IB metal gates. *Sens. Actuators, B, Chem.* **2001**, *81*, 83–87.
6. Fonash, S.J.; Huston, H.; Ashok, S. Conducting MIS diode gas detectors—The Pd/SiO<sub>2</sub>/Si hydrogen sensor. *Sens. Actuators* **1982**, *2*, 363–369.
7. Geistlinger, H.; Eisele, I.; Flietner, B.; Winter, R. Dipole and charge transfer contributions to the work function change of semiconductor thin films: Experiment and theory. *Sens. Actuators, B, Chem.* **1996**, *34*, 499–505.
8. Bergh, H.S.; Gergen, B.; Nienhaus, H.; Majumdar, A.; Weinberg, W.H.; McFarland, E.W. An ultrahigh vacuum system for the fabrication and characterization of ultrathin metal-semiconductor films and sensors. *Rev. Sci. Instrum.* **1999**, *70*, 2087–2094.
9. Nienhaus, H.; Bergh, H.S.; Gergen, B.; Majumdar, A.; Weinberg, W.H.; McFarland, E.W. Ultrathin Cu films on Si(111): Schottky barrier formation and sensor applications. *J. Vac. Sci. Technol., A, Vac. Surf. Films* **1999**, *17*, 1683–1687.
10. Nienhaus, H.; Bergh, H.S.; Gergen, B.; Majumdar, A.; Weinberg, W.H.; McFarland, E.W. Selective H atom sensors using ultrathin Ag Si Schottky diodes. *Appl. Phys. Lett.* **1999**, *74*, 4046–4048.
11. Nienhaus, H.; Bergh, H.S.; Gergen, B.; Majumdar, A.; Weinberg, W.H.; McFarland, E.W. Electron-hole pair creation at Ag and Cu surfaces by adsorption of atomic hydrogen and deuterium. *Phys. Rev. Lett.* **1999**, *82*, 446–449.
12. Nienhaus, H.; Bergh, H.S.; Gergen, B.; Majumdar, A.; Weinberg, W.H.; McFarland, E.W. Direct detection of electron-hole pairs generated by chemical reactions on metal surfaces. *Surf. Sci.* **2000**, *445*, 335–342.
13. Nienhaus, H. Electronic excitations by chemical reactions on metal surfaces. *Surf. Sci. Rep.* **2002**, *45*, 3–78.
14. Nienhaus, H.; Gergen, B.; Weinberg, W.H.; McFarland, E.W. Detection of chemically induced hot charge carriers with ultrathin metal film Schottky contacts. *Surf. Sci.* **2002**, *514*, 172–181.
15. Gergen, B.; Nienhaus, H.; Weinberg, W.H.; McFarland, E.M. Morphological investigation of ultrathin Ag and Ti films grown on hydrogen terminated Si(111). *J. Vac. Sci. Technol., B* **2000**, *18*, 2401–2405.
16. Gergen, B.; Nienhaus, H.; Weinberg, W.H.; McFarland, E.W. Chemically induced electronic excitations at metal surfaces. *Science* **2001**, *294*, 2521–2523.
17. Gergen, B.; Weyers, S.J.; Nienhaus, H.; Weinberg, W.H.; McFarland, E.W. Observation of excited electrons from non-adiabatic molecular reactions of NO and O<sub>2</sub> on polycrystalline Ag. *Surf. Sci.* **2001**, *488*, 123–132.
18. Gergen, B. Observation of Electronic Excitations in Gas–Metal Interactions. Ph.D. Dissertation; University of California: Santa Barbara, 2001.
19. Nicollian, E.H.; Schwartz, B.; Coleman, D.J.; Ryder, R.M.; Brews, J.R. Influence of a thin oxide layer between metal and semiconductor on Schottky diode behavior. *J. Vac. Sci. Technol.* **1976**, *13*, 1047–1055.
20. Childs, R.B.; Ruths, J.M.; Sullivan, T.E.; Fonash, S.J. Effects of ultrathin oxides in conducting Mis structures on GaAs. *J. Vac. Sci. Technol.* **1978**, *15*, 1397–1401.
21. Green, M.A.; King, F.D.; Shewchun, J. Minority-carrier Mis tunnel-diodes and their application to electron-voltaic and photo-voltaic energy-conversion. 1. Theory. *Solid-State Electron.* **1974**, *17*, 551–561.
22. Barret, C. Study of metal-semiconductor interface states using Schottky capacitance spectroscopy. *J. Phys., C, Solid State Phys.* **1983**, *16*, 2421–2438.
23. Keramati, B.; Zemel, J.N. Pd-thin–SiO<sub>2</sub>–Si diode. 1. Isothermal variation of H<sub>2</sub>-induced interfacial trapping states. *J. Appl. Phys.* **1982**, *53*, 1091–1099.
24. Hudait, M.K.; Krupanidhi, S.B. Effects of thin oxide in metal-semiconductor and metal-insulator-semiconductor epi-GaAs Schottky diodes. *Solid-State Electron.* **2000**, *44*, 1089–1097.
25. Poteat, T.L.; Lalevic, B.; Kuliyeve, B.; Yousuf, M.; Chen, M. MOS and Schottky diode gas sensors using transition-metal electrodes. *J. Electron. Mater.* **1983**, *12*, 181–214.
26. Petty, M.C. Conduction mechanisms in Pd/SiO<sub>2</sub>/n-Si Schottky diode hydrogen detectors. *Solid-State Electron.* **1986**, *29*, 89–97.
27. Temple, V.; Shewchun, J. Exact frequency-dependent complex admittance of MOS diode including surface states, Shockley–Read–Hall (Srh) impurity effects, and low-temperature dopant impurity response. *J. Solid-State Electron.* **1973**, *16*, 93–113.
28. Card, H.C.; Rhoderick, E.H. Studies of tunnel Mos diodes. 1. Interface effects in silicon Schottky diodes. *J. Phys., D, Appl. Phys.* **1971**, *4*, 1589–1601.
29. Card, H.C.; Rhoderick, E.H. Effect of an interfacial layer on minority-carrier injection in forward-biased silicon Schottky diodes. *Solid-State Electron.* **1973**, *16*, 365–374.
30. Clarke, R.A.; Shewchun, J. Non-equilibrium effects on metal-oxide-semiconductor tunnel currents. *J. Solid-State Electron.* **1971**, *14*, 957.
31. Berglund, C.N. Surface states at steam-grown silicon–silicon dioxide interfaces. *IEEE Trans. Electron Devices* **1966**, *ED13*, 701.
32. Kern, W.; Puotinen, D.A. Cleaning solutions based on hydrogen peroxide for use in silicon semiconductor technology. *RCA Rev.* **1970**, *31*, 187.
33. Ludeke, R.; Schenk, A. Energy-dependent conduction band mass of SiO<sub>2</sub> determined by ballistic electron emission microscopy. *J. Vac. Sci. Technol., B* **1999**, *17*, 1823–1830.
34. Roldan Cuenya, B.; Nienhaus, H.; McFarland, E.W. Chemically induced charge carrier production and transport in Pd/SiO<sub>2</sub>/n-Si(111) MOS Schottky diodes. *Phys. Rev. B* **2003**. Submitted for publication.
35. Campbell, C.T. Ultrathin metal films and particles on oxide surfaces: Structural, electronic and chemisorptive properties. *Surf. Sci. Rep.* **1997**, *27*, 1–111.
36. Diligenti, A.; Stagi, M.; Ciuti, V. Pd–Si Schottky diodes as hydrogen sensing devices—Capacitance–voltage characteristics. *Solid State Commun.* **1983**, *45*, 347–350.

37. Ashok, S.; Borrego, J.M.; Gutmann, R.J. Electrical characteristics of GaAs MIS Schottky diode. *Solid-State Electron.* **1979**, *22*, 621–631.
38. Vanmeirhaeghe, R.L.; Lafere, W.H.; Cardon, F. Influence of defect passivation by hydrogen on the Schottky-barrier height of GaAs and InP contacts. *J. Appl. Phys.* **1994**, *76*, 403–406.
39. Tongson, L.L.; Knox, B.E.; Sullivan, T.E.; Fonash, S.J. Comparative-study of chemical and polarization characteristics of Pd–Si and Pd–SiO<sub>2</sub>–Si Schottky-barrier-type devices. *J. Appl. Phys.* **1979**, *50*, 1535–1537.
40. Crowell, C.R.; Howarth, L.E.; Spitzer, W.G.; Labate, E.E. Attenuation length measurements of hot electrons in metal films. *Phys. Rev.* **1962**, *127*, 2006–2015.
41. Lewis, F.A. *The Palladium Hydrogen System*; Academic: New York, 1967.
42. Keramati, B.; Zemel, J.N. Pd-thin–SiO<sub>2</sub>–Si diode. 2. Theoretical modeling and the H<sub>2</sub> response. *J. Appl. Phys.* **1982**, *53*, 1100–1109.
43. O’Beirn, B.; Casey, V.; Gubbins, M.A.; McMonagle, J.B. Chemisorption and thermal-decomposition of ethylene on Pd(110)-electron-energy loss spectroscopy, low-energy electron-diffraction, and thermal-desorption spectroscopy studies. *Thin Solid Films* **1998**, *329*, 652–654.
44. Ruths, P.F.; Ashok, S.; Fonash, S.J. A study of Pd–Si MIS Schottky-barrier diode hydrogen detector. *IEEE Trans. Electron Devices* **1981**, *28*, 1003–1009.
45. Fang, Y.K.; Hwang, S.B.; Lin, C.Y.; Lee, C.C. Trench Pd/Si metal-oxide-semiconductor Schottky-barrier diode for a high-sensitivity hydrogen gas sensor. *Appl. Phys. Lett.* **1990**, *57*, 2686–2688.

# Silane Self-Assembled Monolayers: Nanoscale Domains by Sequential Adsorption

Nitin Kumar

*Institute of Soldier Nanotechnology, Massachusetts Institute of Technology, Cambridge, Massachusetts, U.S.A.*

## INTRODUCTION

In recent years, the applications and demand for solid surfaces with nanometer to micrometer patterns have increased because of extensive developments in the fields of nanoscience and nanotechnology. Solid surfaces with nanometer- and micrometer-scale patterns have many potential applications in many fields of nanoscience and nanotechnology, such as phase separation of polymer mixtures,<sup>[1–3]</sup> localized crystal growth,<sup>[4]</sup> the arraying and immobilization of proteins,<sup>[5]</sup> cells,<sup>[6,7]</sup> nanoparticles,<sup>[8]</sup> etc. Methods for patterning micrometer features on surfaces are well developed and include microlithography of self-assembled units,<sup>[4,9]</sup> microcontact printing,<sup>[10–12]</sup> photopatterning of self-assembled monolayers (SAMs).<sup>[13–15]</sup> On the other hand, methods for developing nanometer-scale features, such as nanowriting,<sup>[16,17]</sup> phase-separated Langmuir–Blodgett (LB) films,<sup>[18–20]</sup> and block copolymers<sup>[21]</sup> are time consuming and cumbersome.

Self-assembled monolayers consist of amphiphiles, which spontaneously adsorb onto a solid surface from solution to form a densely packed two-dimensional ordered monolayers. Self-assembled monolayers have been extensively used for modification of surface chemistry of solid surfaces. Recently, Fan Maldarelli, and Couzis<sup>[22]</sup> have demonstrated that nanometer-scale domains of different chemical functionality can be obtained by co-adsorption and phase separation of different silane molecules. Sequential adsorption of self-assembling monolayers had been suggested as an alternate and simpler route for making such surfaces.<sup>[23,24]</sup> The island growth mechanism in silane monolayer can be exploited to prepare surface with nanodomains. In this article, we demonstrate the use of sequential adsorption of silanes to prepare domains of various sizes by controlling their self-assembly on solid surfaces.<sup>[25]</sup> We describe a procedure to prepare domains of one chemical functionality, with size from nanometer to micrometer surrounded by another chemical functionality, using sequential adsorption of silane self-assembled monolayers. Partial monolayers

of octadecyltrichlorosilane (OTS) consisting of condensed islands with controlled size are prepared by varying the deposition conditions. The area surrounding the OTS islands is filled by sequential adsorption of 11-bromo undecyltrichlorosilane (BrUTS) or decyltrichlorosilane (DTS) to obtain nanometer- to micrometer-scale domains of OTS in a monolayer of DTS or BrUTS. First, we describe in detail the methodology to form partial OTS monolayers composed of domains of a desired size. Then, we discuss the procedure and optimum conditions for successful backfilling. These monolayers were analyzed by atomic force microscope (AFM) to obtain the topographical and friction images.

## OVERVIEW

In our study we use the silane-based SAMs, which were first studied by Sagiv et al.<sup>[26–30]</sup> Recent studies<sup>[31–34]</sup> suggest that the silane monolayers are formed by the adsorption of the hydrolyzed silanes<sup>[31–33,35]</sup> onto a water layer, which typically exists on a silica surface.<sup>[36–38]</sup> In addition, there is no evidence of direct binding of the adsorbing silanes to the surface silanols of the substrate. Because of this water layer and the lack of direct bonding, the adsorbed molecules are mobile and can diffuse laterally on the surface.<sup>[25,39]</sup> This mobility allows OTS molecules to aggregate into islands, which can be exploited to form nanometer-size domains by sequential adsorption. These islands, which are formed by aggregation, have been imaged by atomic force microscopy<sup>[25,33,40–44]</sup> and have been found to be “fractal”-like in structure. This is the result of an adsorption–surface diffusion–aggregation mechanism,<sup>[45]</sup> in which surface diffusion is rate determining.

The formation of OTS monolayers is affected by a number of factors during the deposition conditions. Below a critical deposition temperature ( $28 \pm 4^\circ\text{C}$ ), the complete monolayers exist as condensed into ordered phases resembling the liquid condensed (LC)

states analogous to Langmuir monolayers.<sup>[33,39–47]</sup> A complete monolayer prepared above this critical temperature showed regions of chain disorder resembling the liquid expanded (LE) state. Increasing the deposition temperature resulted in more disorder, until the monolayers were in a completely LE state. The formation of LE or LC phases is analogous to the phase coexistence region for Langmuir films. The silane monolayers with shorter hydrocarbon chains (e.g., DTS) have lower critical deposition temperature. As a result they do not form LC states at room temperatures.<sup>[39]</sup>

The intermediate stages of the SAM formation have been investigated by studying the structure of partial monolayers. Atomic force microscope measurements of partial monolayers of OTS at room temperature ( $\sim 22^\circ\text{C}$ ) have shown a two-step growth mechanism.<sup>[25,33,41,44]</sup> In the first step, fractal islands of constant height,  $\sim 21 \text{ \AA}$ ,<sup>[25,33,41,44]</sup> relative to the background, appear and grow on the surface. This step is referred to as the primary growth step. The height of OTS islands, which are in the LC state, is approximately  $25 \pm 1 \text{ \AA}$ .<sup>[25,39,48–50]</sup> The AFM images of OTS monolayers during this step show that the height of islands is  $\sim 21 \text{ \AA}$ , implying that the primary fractal islands are in fact LC phases surrounded by a low-density liquid phase. In the second step, the growth of the primary fractal islands stops, and the difference in height between the islands and the background begins to decrease.<sup>[25,41,43,44]</sup> These facts indicate that the surrounding is an LE phase whose density, and therefore height, is increasing. As the concentration of the LE phase increases, the surface diffusion to the primary islands is reduced, thereby arresting the primary growth. Finally, nucleation and growth of smaller islands of the same height (as the primary islands) occur in the regions surrounding the primary fractal islands.<sup>[25]</sup> This second step is referred to as the secondary growth step and it continues until a complete monolayer of uniform height is formed.

The OTS monolayers show a different growth mechanism at deposition temperatures well below room temperature ( $< 16^\circ\text{C}$ ).<sup>[25,33,41,43]</sup> In this case it is observed that the height of the primary island domains does not change over time and remains constant at  $\sim 21 \text{ \AA}$ . This suggests that during growth the surrounding phase is either gaseous (G) (if the deposition temperature is below the triple point as supposed by Carraro et al.)<sup>[41]</sup> or a low-density liquid phase, if the deposition temperature is above the triple point (as suggested by Davidovits et al.).<sup>[43]</sup> Irrespective of whether the surrounding phase is G or LE, the region surrounding the primary islands is less dense at low temperatures. The primary growth continues longer with less inhibition from the surrounding phase. The growth of secondary phase is observed only when the

primary islands are very close to each other.<sup>[25]</sup> Finally, at temperatures exceeding  $40^\circ\text{C}$ , all AFM studies show a uniform monolayer without any islands.<sup>[33,41,43]</sup>

The presence of water in the solvent and on the substrate also affects the monolayer formation. Octadecyltrichlorosilane molecules are hydrolyzed by water present in the solvent.<sup>[51]</sup> Excess water in solvent results in the formation of particle oligomers, which can deposit on the solid surface.<sup>[40,52]</sup> However, these particulates are not strongly adsorbed on the surface and can be removed by sonication or by mechanical methods, such as scanning AFM tip.<sup>[25]</sup> The presence of water on the solid surface is required for the formation of a dense OTS monolayer.<sup>[31,49,50,53]</sup> The water layer on the solid surface allows the adsorbing OTS molecules to diffuse on the surface. This surface diffusion is the cause of the fractal growth of the primary islands. Thus the structure of OTS monolayers can be controlled by varying the amount of water on the surface.

The ability of OTS molecules to form island-like aggregates in partial monolayers offers a route to fabricate nanometer-scale domains of one chemical functionality in a continuous phase of a different functionality by sequential adsorption of two different silanes. Various macroscopic controls, such as temperature, amount of water, etc., can be used to control the size and structure of islands. In the second step, a second silane is deposited via sequential adsorption on the area surrounding the islands. In this entry, we describe this procedure to control the size and structure of OTS islands by controlling the deposition conditions. The process of sequential adsorption is demonstrated using two different silanes with different terminal groups. The monolayers are imaged using AFM to study the structure of the nanometer domains.

## MATERIALS AND EXPERIMENTAL TECHNIQUES USED FOR PREPARATIONS AND CHARACTERIZATIONS OF SILANE SAMs

Decyltrichlorosilane (DTS, 97% purity) and 11-bromo undecyltrichlorosilane (BrUTS, 95% purity) were purchased from Gelest, Inc. Octadecyltrichlorosilane (OTS, 95% purity) was purchased from Sigma Aldrich Company. HPLC grade hexadecane, chloroform, and carbon tetrachloride were obtained from Sigma-Aldrich Co. Nochromix<sup>®</sup> and sulfuric acid (98%) were purchased from Fischer Scientific. All chemicals were used as received without any further purification. Deionized water, with a resistivity of  $18 \text{ M}\Omega \text{ cm}$  from a Millipore<sup>®</sup> system, was used. Double-side, polished (n type,  $\langle 111 \rangle$ ), single-crystal silicon wafers were purchased from Montco Silicon Technologies Ltd.

The control of the domain size was achieved by controlling the deposition conditions. We used a procedure<sup>[31]</sup> in which the amount of water in the solvent is controlled. A solvent mixture containing hexadecane, carbon tetrachloride, and chloroform was used for making the silane solutions. Chloroform was saturated with water by keeping it overnight in contact with water. The amount of water in the solvent mixture was estimated to be 4–6 mM and was verified using Karl-Fisher titration. The silane concentration was in the range of 0.2 to 2 mM.

The polished silicon wafers (with roughness of  $\sim 1 \text{ \AA}$  as measured by AFM) were cleaned by sonicating in a mixture of Nochromix® and 98% sulfuric acid for about 30 min, followed by successive water rinsing. The cleaned substrates were stored under water at room temperature and dried in a stream of dry nitrogen just before use. The substrates should not be cleaned by any means that involved physical contact, such as cleaning with tissue paper or cleaning paper. Also, the region that is imaged by AFM should not be touched when holding the substrates. These substrates are hydrated with a water layer of thickness of a few nanometers.<sup>[36,54–56]</sup> The amount of water on the surface is controlled by heating the surfaces. Partially dehydrated substrates were prepared by heating clean silicon wafers at 100°C and 150°C for an hour and then cooling under vacuum in a desiccator. The vacuum was broken using dry nitrogen immediately before immersing the substrates in silane solution. It is important to take maximum care to prevent the dehydrated substrates from exposure to sources of moisture.

Silane solutions were prepared by adding OTS, DTS, or BrUTS in the required quantities to carbon tetrachloride. The low amount of water in  $\text{CCl}_4$  prevents the polymerization of silanes in the solution. The required amount of silane and  $\text{CCl}_4$  solution was added to hexadecane and chloroform mixture, so that the final volume ratio of hexadecane, carbon tetrachloride, and chloroform was 30:5:3 by volume, respectively. The substrates were immersed in the silane solutions after 30–60 sec. This provided sufficient time for the silanes to hydrolyze by the water present in the solvents. If silane solutions are kept for a longer time, then bulk polymerization occurs. Partial OTS monolayers were prepared by immersing clean the substrates in OTS solution for varying deposition times. The deposition was terminated by rinsing the samples in chloroform for about 15 min. Excess chloroform was dried with a stream of dry nitrogen. All sample preparation procedures are carried out under ambient atmospheric conditions.

The mixed monolayers of OTS and the other silane are prepared in the following manner. First, OTS islands of desired size are formed by immersing a

hydrated or dehydrated substrate, prepared as described above, in a 1 mM OTS solution maintained at 10°C for varying deposition times. The substrates are then removed from the OTS solution and rinsed in chloroform, also maintained at 10°C, for approximately 1 sec. The second silane is deposited on these partial OTS monolayers, immersing the substrate immediately in a 1 mM DTS or BrUTS solution at 10°C for 1 hr followed by rinsing in chloroform at 10°C. The structures of the monolayers were analyzed by AFM.

Atomic force microscopy images of the monolayers are obtained in contact and frictional force mode.<sup>[25]</sup> All AFM images were acquired at room temperatures (22–25°C). For some substrates, tapping mode images were obtained using silicon tips. Water contact angles on the monolayers were measured using a contact angle goniometer (Rame-Hart, Inc.) by placing a 2- $\mu\text{l}$  water drop on the sample. The contact angle values of at least six different locations were averaged.

## CONTROL OF OTS MONOLAYER FORMATION

In this section we show how the structure of partial silane monolayers is affected by varying the deposition conditions. The OTS monolayers are prepared under varying deposition time, OTS concentration in solution, deposition temperature, and amount of water on the surface. The OTS molecules are hydrolyzed by water present in the bulk and on the surface and adsorbed on the surface. If a water layer is present on the surface, the OTS molecules diffuse on the surface and aggregate to form fractal-shape islands by diffusion-limited growth mechanism. The size of the island can be controlled by changing the rate at which the OTS molecules are adsorbed from the solution, the ability of molecules to diffuse on the water layer, and the ability of OTS molecules to form condensed LC phases.

The effect of deposition time on the monolayer structure is shown in the AFM images shown in Fig. 1. Water contact angles, height differences, friction differences, and area coverages are summarized in Table 1. The AFM image of a sample with a 1-sec deposition time is shown in Fig. 1A. It exhibits the onset of the formation of the primary islands. The islands appear diffused with a height of  $\sim 11 \text{ \AA}$  compared to  $\sim 21 \text{ \AA}$ <sup>[41]</sup> for a condensed (LC) island, suggesting that the islands have not yet condensed. In the friction image, the regions covered by OTS exhibit lower friction than the surroundings.<sup>[57,58]</sup> The friction force data show that the region surrounding the islands can be either bare silica or G or a very lean LE phase. As the deposition time is increased, more OTS are



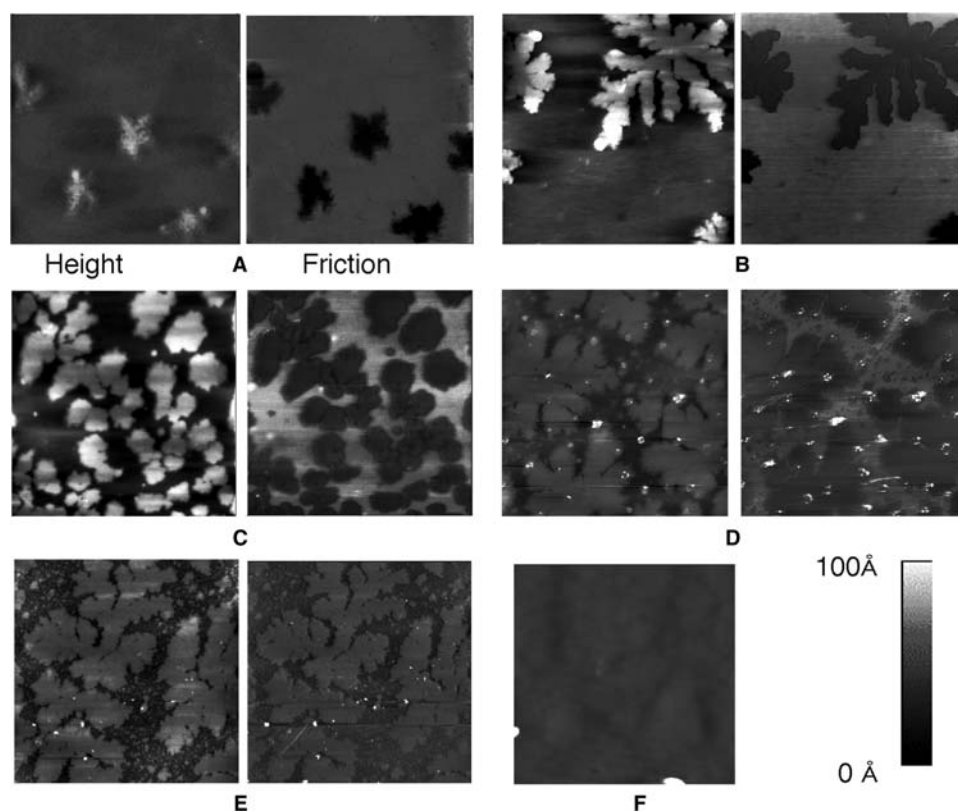


**Fig. 1** Height and friction images of partial OTS monolayers deposited at  $22 \pm 1^\circ\text{C}$  on fully hydrated substrates; image size:  $10 \mu\text{m} \times 10 \mu\text{m}$ ; OTS concentration: 2 mM; deposition times: (A)  $\sim 1$ , (B) 5, (C) 15, (D) 30, (E) 45, (F) 120 sec; in the friction images, brighter regions indicate regions with higher friction. *Source:* From Ref.<sup>[25]</sup>. © 1997, American Chemical Society.

adsorbed on the region surrounding the islands and diffuse toward the primary islands. On reaching the perimeter of an existing island, they become immobilized and aggregate with the island. This leads to the growth of the fractal features. The surface coverage of the primary islands grows rapidly during the primary growth. An image of a sample, with a deposition time of 5 sec, is shown in Fig. 1B. The islands are much larger in size, between 4 and  $8 \mu\text{m}$ , and cover approximately 30% of the surface. The height of these islands is  $\sim 21 \text{ \AA}$ . After 5 sec of OTS deposition, the water contact angle has increased to about  $67^\circ$  compared to  $44^\circ$  for the 1-sec deposition time sample. On increasing the

deposition time further, we observe that the rate of growth of the primary islands is reduced. An image of a sample with a 15-sec deposition time is shown in Fig. 1C. The height and friction difference between the primary island and surrounding area indicate that the phase surrounding the primary islands is becoming denser and starting to increase in height. Surface diffusivity of the OTS molecules in the area surrounding the islands is reduced because of the increase in density of the surrounding phase. The reduction in surface diffusivity reduces the growth of the primary islands.

The images of samples with longer deposition times (Fig. 1D) show that the primary islands cease to grow,

**Table 1** Partial monolayers of OTS on hydrated substrates at  $22 \pm 1^\circ\text{C}$

Deposition time (sec)	$\sim 1$	5	15	30	45	120	300
Height difference ( $\text{\AA}$ ) <sup>a</sup>	11.6	20.9	16.9	15.2	11.4	–	–
Friction difference (V)*	0.76	0.26	0.1	0.03	–0.01	–	–
Area coverage (%)	11.1	30.7	52.1	66.5	65.3	100	100
Water contact angle (deg)	44	67	78	94	97	105	108

<sup>a</sup>Between islands and surrounding region.

*Source:* From Ref.<sup>[25]</sup>. © (1997) American Chemical Society.

but the surrounding liquid phase becomes progressively denser. The height and friction difference between the islands and surrounding phases decrease. The primary islands cover  $\sim 66\%$  of the surface. After 45 sec of deposition, we observe a new growth regime (Fig. 1E). The height difference between the primary islands and the surrounding phase is now reduced to  $11.4 \text{ \AA}$ . Small islands of dimension less than  $0.5 \mu\text{m}$  are observed in the liquid phase surrounding the primary islands. The height of these islands is the same as that of the primary fractal islands. This growth regime is referred to as the secondary nucleation and growth step, in which small, condensed islands nucleate and grow in the surrounding liquid phase. In the friction image, shown in Fig. 1E, the condensed primary and secondary islands exhibit slightly higher friction ( $-0.01 \text{ V}$ ) than the surrounding liquid phase. In all the earlier samples (Fig. 1A–D), the LC primary islands exhibit lower friction than the surrounding phase. This observation suggests that the OTS monolayer in the liquid phase surrounding the islands, as it approaches a “LE–LC phase transition,” has a lower friction than the corresponding denser LC phase. Upon continued adsorption, the secondary condensed islands continue to nucleate and grow from the liquid phase, until all the substrate is covered with a condensed monolayer. An image of a 120-sec deposition time sample (Fig. 1F) shows an almost uniform monolayer. The water contact angle in this sample is approximately  $105^\circ$ , which increases to  $108^\circ$  when the deposition time is increased to 5 min. The primary islands grow rapidly to their fractal-like morphology via adsorption, surface diffusion, and aggregation. On the other hand, the secondary islands grow from the phase surrounding the primary fractal islands as the density of OTS in this phase increases.

The effect of deposition temperature on the primary and secondary growth is shown in Fig. 2, which shows the AFM images of partial monolayer deposited at  $10^\circ\text{C}$ . At this reduced temperature, the primary fractal islands grow at nearly constant height of  $\sim 21 \text{ \AA}$ , until their edges are very close to each other.<sup>[41]</sup> However, at later stages (Fig. 2C), we note the appearance of very small islands in the region between the primary islands (Fig. 2C, inset). These small islands are similar to the secondary islands nucleating in an LE phase as observed at room temperature (Fig. 1E). The height difference between the primary fractal islands and the surrounding phase is  $15\text{--}16 \text{ \AA}$  compared to  $\sim 11.4 \text{ \AA}$  at  $22^\circ\text{C}$  (Fig. 1E). At low temperature, the region surrounding the primary islands is leaner compared to the deposition at higher temperature. As a result, the primary growth continues until the islands are very close to each other. These results show that controlling the deposition time and temperature is an effective way to control the growth of primary islands and the

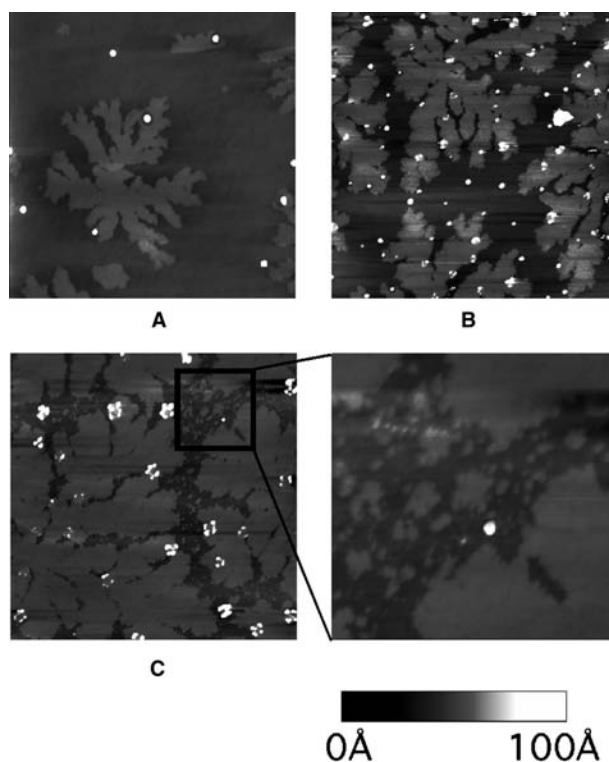


**Fig. 2** Contact mode height images of partial OTS monolayers prepared at  $10^\circ\text{C}$  on hydrated substrates. OTS concentration:  $2 \text{ mM}$ ; image size:  $10 \mu\text{m} \times 10 \mu\text{m}$  image; height scale:  $0\text{--}10 \text{ nm}$ ; deposition times: (A) 5, (B) 10, (C) 30 sec (inset: image size is  $2.75 \mu\text{m} \times 2.75 \mu\text{m}$ ). Source: From Ref.<sup>[25]</sup>. © 1997, American Chemical Society.

density of OTS molecules in the region surrounding the primary islands.

The growth of OTS islands is preceded by the adsorption of OTS from the bulk to the surface. The rate of adsorption is also expected to play a role in the formation of OTS islands. Atomic force microscopy image of a hydrated substrate immersed in a  $0.2 \text{ mM}$  OTS solution for a deposition time of approximately 1 sec is shown in Fig. 3. This concentration is  $1/10\text{th}$  of the concentration used for samples described in Figs. 1 and 2. Very small OTS clusters of about  $50\text{--}100 \text{ nm}$  in diameter and  $15\text{--}20 \text{ \AA}$  in height are distributed almost randomly on the surface. For longer deposition times, the OTS monolayer exhibits various phases (as observed at higher concentrations; Figs. 1 and 2) until a uniform coverage is attained. However, adsorption times to achieve a certain surface coverage are longer at lower concentration. Thus nanometer-scale islands of OTS are obtained when the deposition is carried out at low bulk concentrations.

The presence of water in solvent and on surface plays a very important role in the formation of SAMs. Long deposition times are required when dry solvents

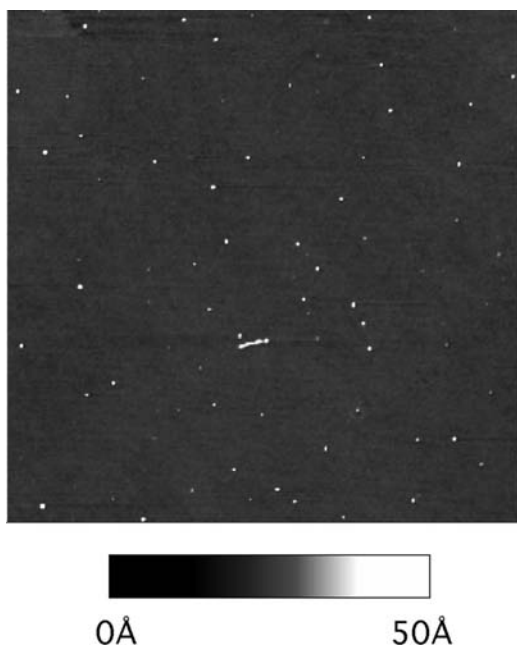


**Fig. 3** Contact mode height image of a hydrated substrate immersed for 1 sec in a 0.2 mM OTS solution at 22°C. Image size: 5  $\mu\text{m}$   $\times$  5  $\mu\text{m}$ ; height scale 0–5 nm. *Source:* From Ref.<sup>[25]</sup>. © 1997, American Chemical Society.

are used.<sup>[51,59]</sup> The possibility of formation of particulate OTS in the bulk increases when the amount of water in solvent is high.<sup>[59,60]</sup> The optimum amount of water in the solvent is maintained as described in the section “Materials and Experimental Techniques Used for Preparations and Characterizations of Silane SAMs.” Good OTS monolayers are not formed on dehydrated substrates.<sup>[33,35,49,50,53,59]</sup> The thickness of the water layer determines the diffusivity of the OTS molecules on the surface, which in turn controls the morphology of the OTS monolayer. This is another

effective way of controlling the structure of OTS monolayers. The preparation of substrates with varying degrees of hydration is described in the section “Materials and Experimental Techniques Used for Preparations and Characterizations of Silane SAMs.” Under ambient conditions, a water layer is present on the native silica surface.<sup>[31,49,50,53,61]</sup> The thickness of this water layer depends on the ambient humidity and can have values of a few nanometers.<sup>[36,54–56]</sup> Upon heating the substrate at 100°C, some of the physisorbed water is removed.<sup>[31,39,49,50,53]</sup> We refer to these surfaces as partially dehydrated. Upon further heating to 150°C, most of the physisorbed water is removed and we refer to these substrates as dehydrated. Partial OTS monolayers are deposited on the fully hydrated, partially dehydrated, and dehydrated substrates by immersing in a 2 mM OTS solution for 30 sec at 22  $\pm$  1°C. An image of the OTS monolayer on a hydrated substrate is shown in Fig. 4A. Primary fractal islands and secondary islands are observed on this surface as expected (Fig. 1). The water contact angle is  $\sim$ 93°. On a partially dehydrated substrate (Fig. 4B), we still observe primary fractal and secondary growth. However, the area occupied by the primary fractal islands is reduced and so is their size, when compared to the hydrated substrate (Fig. 4A). The reduced surface mobility of the OTS molecules on the partially dehydrated substrate reduces the size of the primary islands. The water contact angle is  $\sim$ 90°, which is very close to that of the hydrated substrate. On the dehydrated substrate, the AFM images in contact mode were not stable in successive scans. Therefore the samples were imaged in tapping mode, which overcame this difficulty. Such an image is shown in Fig. 4C. A large number of randomly placed “dots” are observed instead of the primary and secondary islands. These “dots” are about 100 nm in diameter

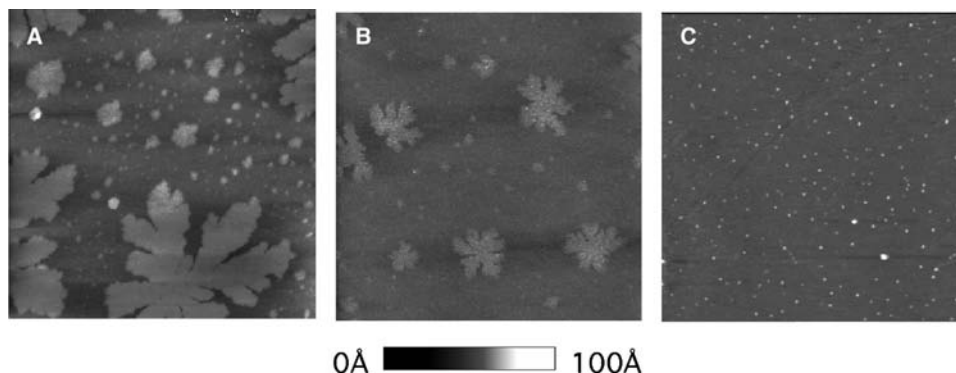


**Fig. 4** Height images of partial OTS monolayers on substrates with different degrees of hydration. Image size: 10  $\mu\text{m}$   $\times$  10  $\mu\text{m}$ ; temperature 22  $\pm$  1°C; OTS concentration: 2 mM; deposition time: 30 sec; height scale: 0–10 nm; (A) fully hydrated substrate (image was acquired in contact mode); (B) partially dehydrated substrate, heated at 100°C (image was acquired in contact mode); (C) dehydrated substrate, heated at 150°C (image was acquired in tapping mode). *Source:* From Ref.<sup>[25]</sup>. © 1997, American Chemical Society.

and 17–18 Å in height. They are clusters of adsorbed OTS molecules, which are unable to form large condensed primary islands because of the negligible surface mobility on the dehydrated substrate. These OTS clusters or “dots” are not strongly adhered to the substrate, and therefore they are swept away by the AFM tip when imaged in contact mode as seen in our experiments. The height of these aggregates is nearly the same as the monolayer height. The water contact angle is only 78° compared to 93° and 90° for a hydrated and partially dehydrated substrate, respectively. This result shows that OTS monolayers do not exhibit the primary and secondary growth on dehydrated surfaces. Much smaller domains of OTS are observed, which are not strongly adhered to the substrate. This result also confirms that the silane molecules do not bind to the surface silanol groups during the monolayer formation process.<sup>[31,49,50,53]</sup> At longer deposition times, the number of random “dots” increases, but no condensed fractal islands are observed. The number of these “dots” continues to grow, until they begin to touch each other to form a disordered monolayer. On a dehydrated substrate, deposition times of about 15 min are required in order to get a monolayer with water at a contact angle of ~105°, compared to a deposition time of 2 min for a hydrated substrate. Similar results are obtained when OTS depositions are carried on dehydrated substrates at 10°C.

These results demonstrate that OTS domains from nanometer to micrometer size can be obtained by proper control of the deposition conditions. The primary and secondary islands are formed during the monolayer formation and are not a result of drying the substrates.<sup>[25]</sup> Primary and secondary growth is controlled by temperature and deposition time. The nanometer-scale OTS domains are obtained by reducing either the adsorption rate of OTS or surface mobility of OTS molecules. The adsorption rate is reduced by reducing the bulk concentration. The surface mobility of OTS molecules is reduced by hydrating the surface. The OTS domains are not strongly adhered to dehydrated surfaces. The density of OTS molecules in the region surrounding the condensed OTS domains is lower at low deposition temperature. For any other silane molecule, the optimum deposition conditions needed to form these domains would be different.

### MIXED MONOLAYERS BY SEQUENTIAL ADSORPTION

The substrates with OTS domains of various sizes and shapes can be used to prepare the mixed monolayers in which the OTS domains are surrounded by other silane

molecules. The surface chemistry of the surrounding region can be changed by varying the terminal group of the second silane. The region surrounding the OTS domains would have a more uniform density of second silane when the OTS density in regions surrounding the OTS domains is low. Thus the OTS domains are prepared at 10°C for the sequential adsorption. The substrates with the desired structure of OTS domains are immersed in the solution of the second silane. We used two different silane molecules for the sequential adsorption. 11-Bromo undecyltrichlorosilane and DTS have bromine and methyl groups at the end of the molecules, as a result they provide different chemical functionality. Both BrUTS and DTS have a low critical temperature (~0°C based on the number of carbons) and as such do not form condensed islands when deposited at 10°C or higher temperatures. The process of the adsorption of second silane in the region surrounding the OTS domains is referred to as backfilling.

Fig. 5 shows the height and friction image of a hydrated substrate that is backfilled with BrUTS after immersing in a 1 mM OTS solution for ~0.5 sec. The AFM image shows small islands with a height of 9 Å and diameter in the range of 30–100 nm. These are OTS islands surrounded by BrUTS. The friction of the OTS islands is lower compared to the region covered by BrUTS. Thus we are able to obtain nanometer-scale islands of methyl functionality surrounded by silanes with bromine functionality. The area covered by the OTS islands is approximately 5.2%. The water contact angle on this sample is ~81°. The lower contact angle is a result of the large fraction of the surface covered by BrUTS. In another

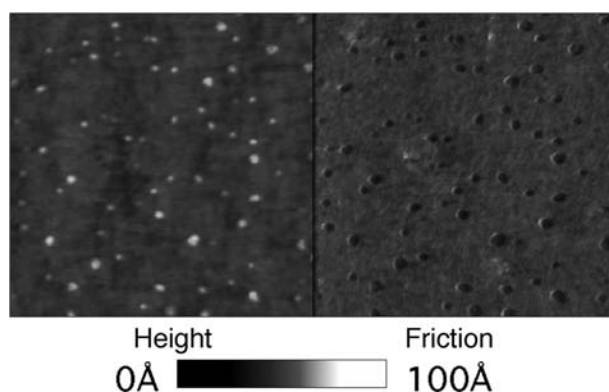


**Fig. 5** Height and friction images of an OTS/BrUTS mixed monolayer showing “nano” islands of OTS surrounded by BrUTS. The procedure is described in the section “Materials and Experimental Techniques Used for Preparations and Characterizations of Silane SAMs.” OTS deposition time ~0.5 sec; hydrated substrate, image size: 2 μm × 2 μm; height scale: 0–10 nm. *Source:* From Ref.<sup>[25]</sup>. © 1997, American Chemical Society.

experiment, larger domains of OTS surrounded by BrUTS are formed as shown in Fig. 6. The larger OTS domains are obtained by increasing the deposition time in 1 mM OTS solution to 3 sec. The fractal islands of OTS are surrounded by BrUTS. No secondary islands of OTS are observed. The height difference between the fractal OTS islands and surrounding BrUTS phase is 12.1 Å. The comparison of heights in the mixed monolayers with the molecular structure suggests that the BrUTS regions are in a disordered state.<sup>[25,39]</sup> Octadecyltrichlorosilane islands on this sample are more condensed than the “nano” islands in Fig. 5. This conclusion is derived from the fact the fractal islands in Fig. 6 are 12.1 Å above the surrounding region, compared to the value of 9 Å for the “nano” islands in Fig. 5. The water contact angle is  $\sim 91^\circ$ , which is a result of the larger surface fraction covered by the OTS regions.

In a similar manner, mixed monolayers of DTS and OTS are also prepared by immersing a hydrated substrate in 1 mM OTS solution for 3 sec and subsequent backfilling with 1 mM DTS solution. Friction and height images of this sample are shown in Fig. 7. As expected, fractal islands of OTS surrounded by DTS are observed. The height difference between the OTS islands and the surrounding phase is 11.4 Å, which suggests that DTS regions are in a disordered state.<sup>[25]</sup> This is expected as complete DTS monolayers have been observed to remain in a disordered state at temperatures above 0°C.<sup>[39]</sup> The water contact angle on this substrate is  $\sim 106^\circ$  compared to  $108^\circ$  on a full OTS monolayer. The similar water contact angles are a result of the same methyl terminal group for DTS and OTS.

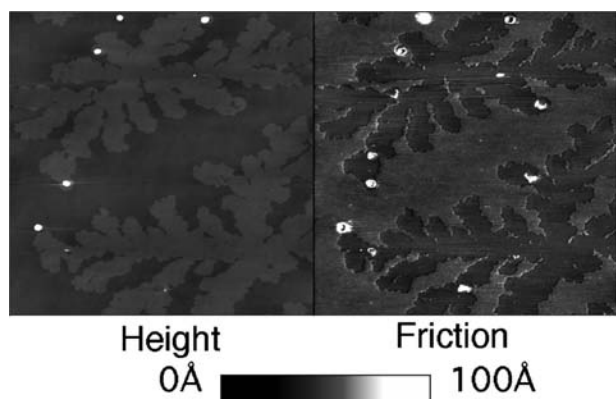


**Fig. 6** Height and friction images of an OTS/BrUTS mixed monolayer showing large condensed fractal islands of OTS surrounded by BrUTS. The procedure is described in the section “Materials and Experimental Techniques Used for Preparations and Characterizations of Silane SAMs.” OTS deposition time: 3 sec; hydrated substrate; image size:  $10\ \mu\text{m} \times 10\ \mu\text{m}$ ; height scale: 0–10 nm. *Source:* From Ref.<sup>[25]</sup>. © 1997, American Chemical Society.

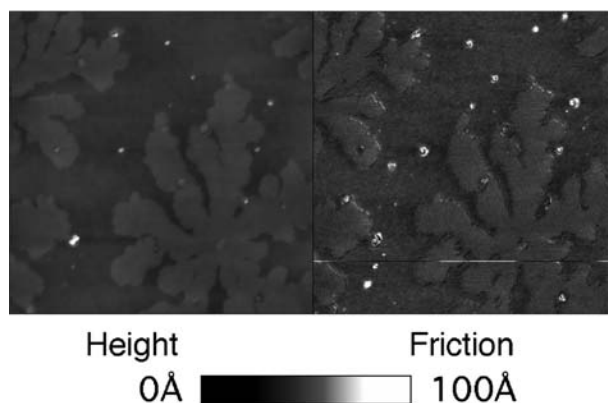


**Fig. 7** Height and friction images of an OTS/DTS mixed monolayer showing large condensed fractal islands of OTS surrounded by DTS. The procedure is described in the section “Materials and Experimental Techniques Used for Preparations and Characterizations of Silane SAMs.” OTS deposition time: 3 sec; hydrated substrate; image size:  $10\ \mu\text{m} \times 10\ \mu\text{m}$ ; height scale: 0–10 nm. *Source:* From Ref.<sup>[25]</sup>. © 1997, American Chemical Society.

The formation of nanometer-scale domains can also be attained by using the dehydrated substrates. Octadecyltrichlorosilane deposits as small “dots” or clusters on a dehydrated substrate as shown in Fig. 4C. In order to explore this method, silicon substrates are dehydrated at  $150^\circ\text{C}$  as described in the section “Materials and Experimental Techniques Used for Preparations and Characterizations of Silane SAMs.” They are then immersed in 1 mM OTS solution for 3 sec and then backfilled with DTS and

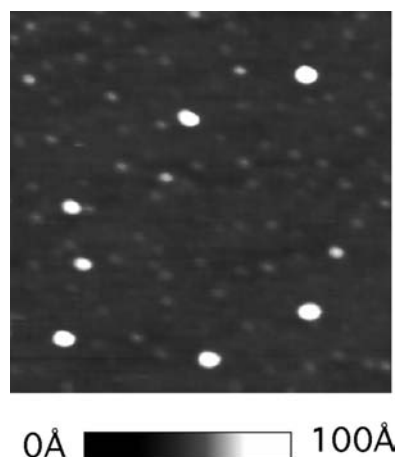


**Fig. 8** Tapping mode image of an OTS/BrUTS mixed monolayer showing “nano” islands of OTS surrounded by BrUTS on a dehydrated substrate. The procedure is described in the section “Materials and Experimental Techniques Used for Preparations and Characterizations of Silane SAMs.” OTS deposition time  $\sim 3$  sec; image size:  $2\ \mu\text{m} \times 2\ \mu\text{m}$ ; height scale: 0–10 nm. *Source:* From Ref.<sup>[25]</sup>. © 1997, American Chemical Society.



BrUTS. Contact mode AFM images do not show any features, but tapping mode images show “nano” islands of OTS surrounded by DTS or BrUTS. Atomic force microscopy image of a BrUTS sample is shown in Fig. 8. The islands of OTS have a height of  $\sim 7.3$  Å. The diameter of the OTS islands is about 50–100 nm. Atomic force microscopy images for the OTS/DTS samples also show similar nanometer-scale islands of OTS with average heights of about 7.6 Å. These mixed monolayers are not strongly adhered to the substrate. The AFM tip in contact mode is able to remove the monolayer from the surface. In conclusion, the dehydrated substrates could be used to produce nanometer domains, but the silane molecules are not strongly adhered to the surface.

## CONCLUSION

The ability of silane molecules to aggregate and form islands during SAM formation can be exploited by controlling the deposition conditions to produce nanometer- and micrometer-scale domains of varying chemical functionality. We have demonstrated this procedure by controlling the assembly of OTS SAMs. Octadecyltrichlorosilane domains of various sizes and shapes are obtained by controlling the temperature, concentration, deposition time, and substrate hydration. Further, the region surrounding these domains can be filled with silane molecules of different chemical functionality. Octadecyltrichlorosilane islands of about 30–100 nm in diameter are obtained on dehydrated surfaces and at low concentrations. Large fractal condensed islands of OTS are prepared by increasing the OTS deposition time. The region surrounding the OTS islands is backfilled by sequential adsorption of DTS and BrUTS to obtain surfaces in which domains of one chemical functionality are surrounded by other chemical functionality.

## ACKNOWLEDGMENTS

The author would like to thank Prof. Charles Maldarelli and Prof. Alexander Couzis of City University of New York; Prof. Robert D. Tilton and Prof. Stephen Garoff of Carnegie Mellon University. The financial support during the preparation of this manuscript was provided by Air Product and Chemicals, Inc.

## REFERENCES

- Seok, C.; Freed, K.F.; Szeleifer, I. Polymer melts and polymer solutions near patterned surfaces. *J. Chem. Phys.* **2000**, *112*, 6443.
- Seok, C.; Freed, K.F.; Szeleifer, I. Polymer blends near patterned surfaces. *J. Chem. Phys.* **2000**, *112*, 6452.
- Peters, R.D.; Yang, X.M.; Nealey, P.F. Morphology of thin films of diblock copolymers on surfaces micropatterned with regions of different interfacial energy. *Macromolecules* **2002**, *35*, 1822–1834.
- Aizenberg, J.; Black, A.J.; Whitesides, G.M. Controlling local disorder in self-assembled monolayers by patterning the topography of their metallic supports. *Nature* **1998**, *394*, 868–871.
- Wadu-Mesthrige, K.; Xu, S.; Amro, N.A.; Liu, G.-Y. Fabrication and imaging of nanometer-sized protein patterns. *Langmuir* **1999**, *15*, 8580.
- Lopez, G.P.; Albers, M.W.; Schreiber, S.L.; Carroll, R.; Peralta, E.; Whitesides, G.M. Convenient method for patterning the adhesion of mammalian cells to surface using self-assembled monolayers of alkanethiolates gold. *J. Am. Chem. Soc.* **1993**, *115*, 5877–5878.
- Levicky, R.; Herne, T.M.; Tarlov, M.J.; Satija, S.K. Using self-assembly to control the structure of DNA monolayers on gold: a neutron reflectivity study. *J. Am. Chem. Soc.* **1998**, *120*, 9787.
- Resch, R.; Meltzer, S.; Vallant, T.; Hoffman, H.; Koel, B.E.; Madhukar, A.; Reqicha, A.A.G.; Will, P. Immobilization of Au nanoparticles on SiO<sub>2</sub> surfaces using octadecylsiloxane monolayers. *Langmuir* **2001**, *17*, 5666–5670.
- Friebel, S.; Aizenberg, J.; Abad, S.; Wiltzius, P. Ultraviolet lithography of self-assembled monolayers for submicron patterned deposition. *Appl. Phys. Lett.* **2000**, *77*, 2406.
- Kumar, A.; Whitesides, G.M. Features of gold having micrometer to centimeter dimensions can be formed through a combination of stamping with an elastomeric stamp and an alkanethiol “ink” followed by chemical etching. *Appl. Phys. Lett.* **1993**, *63*, 2002.
- John, P.M.S.; Craighead, H.G. Microcontact printing and pattern transfer using trichlorosilanes on oxide substrates. *Appl. Phys. Lett.* **1996**, *68*, 1022.
- Xia, Y.; Mrksich, M.; Kim, E.; Whitesides, G.M. Microcontact printing of octadecylsiloxane on the surface of silicon dioxide and its application in microfabrication. *J. Am. Chem. Soc.* **1995**, *117*, 9576–9577.
- Zhao, B.; Moore, J.S.; Beebe, D.J. Pressure sensitive microfluidic gates fabricated by patterning surface free energies inside microchannels. *Langmuir* **2003**, *19*, 1873–1879.
- Haick, H.; Paz, Y. Remote photocatalytic activity as probed by measuring the degradation of self-assembled monolayers anchored near microdomains of titanium oxide. *J. Phys. Chem., B* **2001**, *105*, 3045–3051.
- Kim, H.K.; Lee, J.P.; Park, C.R.; Kwak, H.T.; Sung, M.M. Thermal decomposition of alkylsiloxane self-assembled monolayers in air. *J. Phys. Chem., B* **2003**, *107*, 4348–4351.
- Piner, R.; Zhu, J.; Xu, F.; Hong, S.; Mirkin, C. ‘Dip-pen’ nanolithography. *Science* **1999**, *283*, 661.
- Liu, G.-Y.; Xu, S.; Qian, Y. Nanofabrication of self-assembled monolayers using scanning probe lithography. *Acc. Chem. Res.* **2000**, *33*, 457–466.



18. Kato, T.; Kameyama, M.; Ehara, M.; Iimura, K.-i. Monodisperse two dimensional nanometer size clusters of partially fluorinated long chain acids. *Langmuir* **1998**, *14*, 1786–1798.
19. Fang, J.; Knobler, C.M. Phase-separated two component self-assembled organosilane monolayer and their use in selective adsorption of a protein. *Langmuir* **1996**, *12*, 1368–1374.
20. Kumar, V.; Krishnan, S.; Steiner, C.; Maldarelli, C.; Couzis, A. Measurement of infrared molar adsorptivity of a surfactant onto a solid substrate over a wide range of surface concentration using octadecyltrichlorosilane Langmuir–Blodgett transferred films. *J. Phys. Chem., B* **1998**, *102*, 3152–3159.
21. Thurn-Albrecht, T.; Steiner, R.; DeRouchev, J.; Stafford, C.M.; Huang, E.; Bal, M.; Tuominen, M.; Hawker, C.J.; Russell, T.P. Nanoscopic templates from oriented block copolymer films. *Adv. Mater.* **2000**, *12*, 787–791.
22. Fan, F.; Maldarelli, C.; Couzis, A. Fabrication of surfaces with nanoislands of chemical functionality by phase separation of self-assembling monolayers. *Langmuir* **2003**, *19*, 3254–3265.
23. Fadeev, A.Y.; McCarthy, T. Binary monolayer mixtures: modification of nanopores in silicon-supported tris(trimethylsiloxy)silyl monolayers. *Langmuir* **1999**, *15*, 7238.
24. Mauthauer, K.; Frank, C.W. Binary self-assembled monolayers as prepared by successive adsorption of alkyltrichlorosilanes. *Langmuir* **1993**, *12*, 3446–3451.
25. Kumar, N.; Maldarelli, C.; Steiner, C.; Couzis, A. Formation of nanometer domains of one chemical functionality in a continuous matrix of a second chemical functionality by sequential adsorption of silane self-assembled monolayers. *Langmuir* **2001**, *17*, 7789.
26. Ulman, A. Formation and structure of self-assembled monolayers. *Chem. Rev.* **1996**, *96*, 1533–1554.
27. Sagiv, J. Organized monolayers by adsorption: I. Formation and structure of olephobic mixed monolayers on solid surfaces. *J. Am. Chem. Soc.* **1980**, *102*, 92–98.
28. Netzer, L.; Isovici, R.; Sagiv, J. Adsorbed monolayer versus Langmuir–Blodgett monolayers: why and how: II. Characterization of build-up films constructed by stepwise adsorption of individual monolayers. *Thin Solid Films* **1983**, *100*, 67–76.
29. Maoz, R.; Sagiv, J. On formation and structure of self-assembling monolayers: I. A comparative ATR-wettability study of Langmuir–Blodgett and adsorbed films on flat substrates and glass microbeads. *J. Colloid Interface Sci.* **1984**, *100*, 465–494.
30. Gun, J.; Sagiv, J. On formation and structure of self-assembling monolayers: III. Time of formation, solvent retention and release. *J. Colloid Interface Sci.* **1986**, *112*, 457–472.
31. Silberzan, P.; Leger, L.; Ausserre, D.; Benattar, J.J. Silanization of silica surfaces. A new method of constructing pure or mixed monolayers. *Langmuir* **1991**, *7*, 1647–1651.
32. Tripp, C.P.; Hair, M.L. Direct observation of surface bond between self-assembled monolayers of octadecyltrichlorosilane and silica surface: A low-frequency IR study at the solid/liquid interface. *Langmuir* **1995**, *11*, 1215–1219.
33. Britt, D.W.; Hlady, V. An AFM study of the effect of silanization temperature hydration and annealing on the nucleation and aggregation of condensed OTS domains on mica. *J. Colloid Interface Sci.* **1996**, *178*, 775–784.
34. Zhao, X.; Kopelman, R. Mechanism of organosilane self-assembled monolayer formation on silica studied by second-harmonic generation. *J. Phys. Chem.* **1996**, *100*, 11014–11018.
35. Tripp, C.P.; Hair, M.L. An infrared study of the reaction of octadecyltrichlorosilane with silica. *Langmuir* **1992**, *8*, 1120–1126.
36. Muller, H.J. Extraordinarily thick water films on hydrophilic solids: A result of hydrophobic repulsion. *Langmuir* **1998**, *14*, 6789–6792.
37. Hair, M.L.; Hertl, W. Adsorption on hydroxylated silica surfaces. *J. Phys. Chem.* **1969**, *73*, 4269–4276.
38. Gee, M.L.; Healy, T.W.; White, L.R. Hydrophobicity effects in the condensation of water films on quartz. *J. Colloid Interface Sci.* **1990**, *140*, 450.
39. Parikh, A.N.; Allara, D.; Azouz, I.B.; Rondelz, F. Intrinsic relationship between molecular structure in self-assembled *n*-alkylsiloxane monolayers and deposition temperature. *J. Phys. Chem.* **1994**, *98*, 7577.
40. Schwartz, D.K.; Steinberg, S.; Israelachvili, J.; Zasadzinski, J.A.N. Growth of self-assembled monolayers by fractal aggregation. *Phys. Rev. Lett.* **1992**, *69*, 3354–3357.
41. Carraro, C.; Yauw, O.W.; Sung, M.M.; Maboudian, R. Observation of three growth mechanism in self assembled monolayers. *J. Phys. Chem., B* **1998**, *102*, 4441–4445.
42. Sung, M.M.; Carraro, C.; Yauw, O.W.; Kim, Y.; Maboudian, R. Reversible liquid–liquid transitions in the early stages of monolayer self assembly. *J. Phys. Chem., B* **2000**, *104*, 1556–1559.
43. Davidovits, J.V.; Pho, V.; Silberzan, P.; Goldmann, M. Temperature influence on the formation of silanized monolayers on silica: an atomic force microscope study. *Surf. Sci.* **1996**, 352–354; 369–373.
44. Bierbaum, K.; Grunze, M.; Baski, A.A.; Chi, L.F.; Schrepp, W.; Fuchs, H. Growth of self-assembled *n*-alkyltrichlorosilane films on Si(100) investigated by atomic force microscopy. *Langmuir* **1995**, *11*, 2143–2150.
45. Doudevski, I.; Hayes, W.A.; Schwartz, D.K. Submonolayer island nucleation and growth kinetics during self-assembled monolayer formation. *Phys. Rev. Lett.* **1998**, *81*, 4927–4930.
46. Brzoska, J.B.; Azouz, I.B.; Rondelez, R. Silanization of solid substrates: a step towards reproducibility. *Langmuir* **1994**, *10*, 4367–4373.
47. Rye, R.R. Comments: Transition temperature for *n*-alkyltrichlorosilane monolayers. *Langmuir* **1997**, *13*, 2588–2590.
48. Wasserman, S.R.; Whitesides, G.M.; Tidswell, I.M.; Ocko, B.M.; Pershan, P.S.; Axe, J.D. The structure of self-assembled monolayers of alkylsiloxanes on silicon: a comparison of results from ellipsometry and low angle reflectivity. *J. Am. Chem. Soc.* **1989**, *111*, 5852.

49. Angst, D.L.; Simmons, G.W. Moisture absorption characteristics of organosiloxane self-assembled monolayers. *Langmuir* **1991**, *7*, 2236–2242.
50. LeGrange, J.D.; Markham, J.L.; Kurkijian, C.R. Effect of surface hydration on the deposition of silane monolayers on silica. *Langmuir* **1993**, *9*, 1749–1753.
51. McGovern, M.E.; Kallury, K.M.R.; Thompson, M. Role of solvent on the silanization of glass with octadecyltrichlorosilane. *Langmuir* **1994**, *10*, 3607–3614.
52. Resch, R.; Grasserbauer, M.; Friedbacher, G.; Vallant, T.; Brunner, H.; Mayer, U.; Hoffmann, H. In situ and ex situ AFM investigation of the formation of octadecylsiloxane monolayers. *Appl. Surf. Sci.* **1999**, *140*, 168–175.
53. Opila, R.L.; LeGrange, J.D.; Heyer, G. Effects of surface hydration on the deposition of silane monolayers on silica fiber. *J. Adhes. Sci. Technol.* **1997**, *11*, 1–10.
54. Beaglehole, D. Inadequacy of Lifshitz theory for thin liquid films. *Phys. Rev. Lett.* **1991**, *66*, 2084–2087.
55. Beaglehole, D.; Christenson, H.K. Vapor adsorption on mica and silicon: entropy effects, layering, and surface forces. *J. Phys. Chem.* **1992**, *96*, 3395–4303.
56. Panella, V.; Chiarello, R.; Krim, J. Adequacy of Lifshitz theory for certain thin adsorbed films. *Phys. Rev. Lett.* **1996**, *76*, 3606–3609.
57. Tian, F.; Xiao, X.; Loy, M.M.T.; Wang, C.; Bai, C. Humidity and temperature effects on fractional properties of mica and alkylsilane monolayers. *Langmuir* **1999**, *15*, 244–249.
58. Xiao, X.; Hu, J.; Charych, D.H.; Salmeron, M. Chain length dependence of the frictional properties of alkylsilane molecules self-assembled on mica studied by atomic force microscopy. *Langmuir* **1996**, *12*, 235–237.
59. Wang, Y.; Lieberman, M. Growth of ultrasMOOTH octadecyltrichlorosilane self-assembled monolayers on SiO<sub>2</sub>. *Langmuir* **2003**, *19*, 1159–1167.
60. Foisner, J.; Glaser, A.; Kattner, J.; Hoffman, H.; Friedbacher, G. Atomic force microscopy investigation of the growth of different alkylsiloxane monolayers from highly concentrated solutions. *Langmuir* **2003**, *19*, 3741–3746.
61. Iler, R.K. *The Chemistry of Silica*; A Wiley-Interscience publication: Wiley, New York, 1979.

# Silica Nanotubes: Wetting and Diffusion

Kenji Okamoto  
Karthik Jayaraman  
Sang Jun Son  
Sang Bok Lee  
Douglas S. English

*Department of Chemistry and Biochemistry, University of Maryland,  
College Park, Maryland, U.S.A.*

## INTRODUCTION

Nanoscale porous structures are attracting a great deal of interest due to their significant potential to biological and technological applications, including catalytic supports, biosensors or nanoscale containers. Silica nanotubes, in particular, are promising materials because of their naturally hydrophilic surface, which allows them to form colloidal suspensions in aqueous solvent without aggregation. Furthermore, the use of template-based synthesis methods allows easy production of monodisperse silica nanotubes<sup>[1,2]</sup> and an important technological advantage of this approach is the ability to systematically change both the size and surface chemistry of the nanotube interior.

In order to use nanotubes as chemical nanocontainers, one must understand the transport properties occurring in the nanotube interiors including diffusion and wetting behavior under a variety of conditions. This can be especially important when nanotube cargo is weakly coupled with the tube interior, for example, by adsorption. Diffusion processes occurring on the nanotube interior surface are of fundamental significance for any application of nanotubes. Adsorption, diffusion, and wetting behavior will ultimately determine the success of applications employing template-synthesized silica nanotubes.

This entry discusses several examples that demonstrate some of the valuable applications of silica nanotubes including separations using nanotube-based membranes,<sup>[3]</sup> selective functionalization of nanotube surfaces for the capture and concentration of target solutes<sup>[4]</sup> and investigations of diffusion and wetting phenomena at the interior nanotube surfaces.<sup>[5]</sup>

## SILICA NANOTUBES

In recent decades, various techniques have been demonstrated to manufacture nanoscale tube

structures with silica. Many groups have employed sol-gel synthesis using TEOS (tetraethyl orthosilicate or tetraethoxysilane; Fig. 1A) with various templates of hollow tubular structure, such as supramolecular assemblies,<sup>[6–11]</sup> biological substrates,<sup>[12–17]</sup> organic ammonium carboxylate crystals,<sup>[18–20]</sup> carbon nanotubes,<sup>[21,22]</sup> fiber-like crystals,<sup>[23,24]</sup> or nanoporous membrane materials.<sup>[1,2,25,26]</sup> A method not using TEOS was also introduced in which a silicon nanowire array is fabricated using semiconductor micromachining technology and the surfaces of the wires are oxidized.<sup>[27]</sup>

A common problem with these techniques is controllability of size, shape, and uniformity. Ideally, one desires the ability to arbitrarily change length, diameter, and surface chemistry with a method that is reproducible and simple. Membrane-based template synthesis satisfies these requirements.<sup>[1,2,25,26]</sup> Martin et al.<sup>[1,2]</sup> pioneered this technique, which enables the production of monodisperse nanotubes from a variety of materials, including silica.<sup>[1,2]</sup>

One easily exploited advantage of Martin's method is the ability to independently functionalize the interior and exterior surfaces during synthesis.<sup>[4]</sup> For example, nanotubes simultaneously having a hydrophilic exterior and hydrophobic interior can be produced so that they disperse readily in aqueous solution but have attractive interactions with hydrophobic or amphiphilic molecules. Such nanotubes can provide the ability to capture and concentrate hydrophobic molecules in solution thus serving as nanocontainers, as discussed further.<sup>[4,5]</sup> Surface modifications can be arbitrarily chosen to provide a range of interactions including antigen-antibody interaction<sup>[3,4]</sup> and electrostatic or covalent interactions.

Silica nanotubes possess several important features, which make them ideal for biophysical/biochemical studies:

1. Because of their naturally hydrophilic surfaces, they easily form colloidal suspension in aqueous solvent.

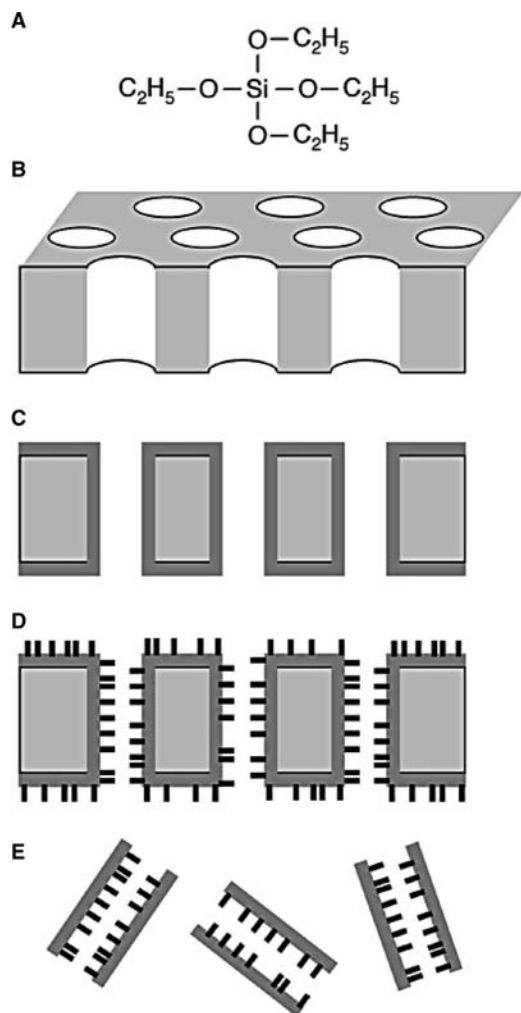


**Fig. 1** Membrane template method using (A) TEOS (tetraethyl orthosilicate or tetraethoxysilane). (B) Nanoporous membrane is used as a template. (C) Silica is coated on surface of template by sol-gel synthesis. (D) Silica surface can be functionalized by silanization. Inner wall of pores become interior surface of nanotubes. (E) Silica nanotubes are liberated by mechanical polish of top and bottom silica layers and dissolution of template.

- Optical transparency allows the use of optical methods to address the interior contents.<sup>[4,5]</sup>
- Silica is robust and innocuous in most physiological environments.
- Surface chemistry is readily modified and silica nanotubes can be differentially functionalized on exterior and interior surfaces.

### NANOPOROUS MEMBRANE TEMPLATE METHOD

Martin's method employs a membrane film with nanoscale cylindrical pores as the template (Fig. 1B).

Commercial alumina membrane are available for this purpose, while membrane with pores having arbitrary size and density can be made by anodic oxidation on alumina films. Additionally, other materials, such as polycarbonate, can be utilized as template materials.

The process is started by immersing the template membrane in a mixture of absolute ethanol, TEOS, and 1 M HCl (50 : 5 : 1 vol/vol) solution. After sonication for 30 min, unbound reagents are removed by vacuum filtration. The sol-gel coated template surface is then cured overnight at 150° (Fig. 1C).

Chemical modification of the sol-gel layer can be achieved by silanization. While still attached to the template membrane, exterior surfaces of nanotubes are not modified because they are in contact with membrane template. For example, C<sub>18</sub> chains can be attached by immersing membranes for 30 min in 5% octadecyltrimethoxysilane solution (vol/vol) in ethanol, pH adjusted to 5.0. After immersion, the membranes are rinsed with ethanol and dried at 150° (Fig. 1D).

To produce liberated nanotubes, the silica layers on membrane surfaces are mechanically polished to expose the alumina template which is subsequently dissolved overnight in H<sub>3</sub>PO<sub>4</sub>. If necessary, the exterior surface of nanotubes can be functionalized at this point. For the purpose of dispersing nanotubes in aqueous solution, the exterior surface can be left bare (Fig. 1E).

Fig. 2 shows transmission electron microscope (TEM) images of liberated nanotubes with diameter of (a) ~200 nm and (b) ~60 nm, respectively. Homogeneity of shape and size can be clearly seen, and wall with 15–20 nm thickness appears highly uniform. Diameter and length of nanotubes can be controlled by pore size and thickness of template membrane, respectively.

### DEMONSTRATION OF SELECTIVE INTERACTION

Here, we give two examples of previous studies illustrating the utility imparted to silica nanotubes through

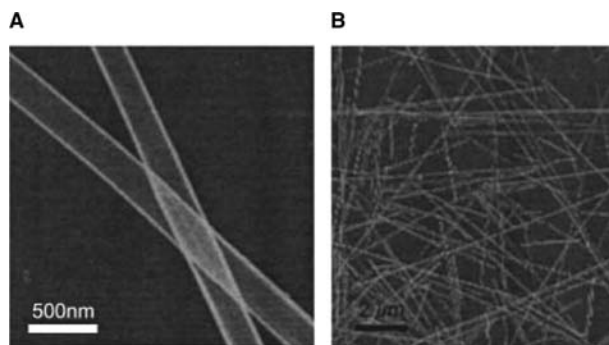


**Fig. 2** TEM image of silica nanotubes with diameter of (A) 200 nm and (B) 60 nm.

selective modification of their exterior and interior surfaces.

The selective functionalization of interior and exterior surfaces was demonstrated by Mitchell et al.<sup>[4]</sup> Two kinds of nanotubes were prepared: one with green fluorescent groups on the interior surface and hydrophobic octadecyl ( $C_{18}$ ) groups on the exterior surface, and the other with blue fluorescent groups on interior surface and the exterior surface was left native (hydrophilic). These nanotubes were added to a mixture of water and the immiscible organic solvent cyclohexane. The two liquids were observed to separate into two distinctly colored phases showing the selective partitioning of the modified nanotubes to their respective solvents.

Another compelling example of chemically tailored selective interactions at a nanotube interface was demonstrated by Lee et al.<sup>[3]</sup> In this example, a silica-coated membrane of nanotubes was used to demonstrate facilitated transport to achieve enantiomeric separation. The nanotube interiors were functionalized with an antibody that selectively binds to one enantiomer of a racemic mixture of a drug molecule. The flux through the membrane was measured for each enantiomer by mounting the antibody modified membrane between the two halves of a U-tube permeation cell. A racemic mixture of two enantiomers (RS and SR) was placed on one side of the U-tube. The anti-RS coated nanotubes showed enhanced transport of their target drug molecule with the RS enantiomer having a flux two to four times that of the SR enantiomer. Interestingly, the anti-RS fragments, which specifically bind the RS stereoisomer, actually promote transport. The separation selectivity was observed to decrease with drug concentration which is in agreement with theories of facilitated transport. By decreasing pore size Lee et al. were able to diminish transport of the non-facilitated enantiomer and reach a maximum selectivity ratio of 4.5. Their results show promise for the use of these materials in highly selective transport of a wide range of molecules.

### DIFFUSION MEASUREMENTS IN SINGLE NANOTUBES

In order to observe the behavior of adsorbed molecules inside nanotubes, fluorescence confocal microscopy and fluorescent dye molecules were used.<sup>[5]</sup> Nanotubes having  $C_{18}$ -modified (hydrophobic) interior surface and native (hydrophilic) exterior surface were used to selectively sequester the fluorescent amphiphilic dye DiI $C_{18}$  (Fig. 3A) in aqueous solutions of varying methanol concentration. The surfactant dye molecule DiI $C_{18}$  was loaded into nanotubes by mixing nanotubes in water and methanol (9:1 vol/vol) solution containing  $10^{-6}$ – $10^{-7}$  M DiI $C_{18}$ . DiI $C_{18}$  is adsorbed

at the interface formed by the hydrophobic interior surface and the dye solution (Fig. 3B).

For microscope observation, nanotubes must be stationary during observation. Silane chemistry was used to immobilize nanotubes on microscope coverslip. To achieve immobilization, the surface of glass coverslips were silanated by briefly sonicating (5 min) in a solution of ethanol, TEOS, and 1 M HCl (40:1:1 vol/vol) after the solution was allowed to sit for 30 min. Coverslips were then rinsed with ethanol and a few drops of solution containing dye-filled nanotubes was spread on the coverslip. The samples were allowed to dry in air at which time covalent bonds formed between the nanotubes and unreacted siloxane groups at the modified coverslip surface, thus immobilizing the nanotubes.

A fluorescence image of a nanotube filled with dye is shown in Fig. 4. The uniform distribution of dyes inside the nanotube can be observed. Diffusion of dyes inside nanotubes can be measured using the fluorescence recovery after photobleach (FRAP) technique. A nanotube image before photobleaching is shown in Fig. 5A. When an intense laser beam irradiates a point on nanotube, dye molecules at that point only are photobleached. In subsequent images taken after photobleaching (Fig. 5B), the bleached point appears as a dark spot (indicated with a circle). If the dye molecules are able to diffuse inside the tube, then the bleached dye molecules exchange position with surrounding unbleached dyes and the fluorescence signal at the bleached point recovers with time. The nanotube image after fluorescence recovery is shown in Fig. 5C. From the recovery rate, the diffusion coefficient of dye molecules can be estimated. For the case, in which dyes diffuse only in one dimension and the bleaching beam has a Gaussian profile, the recovery curve as a function

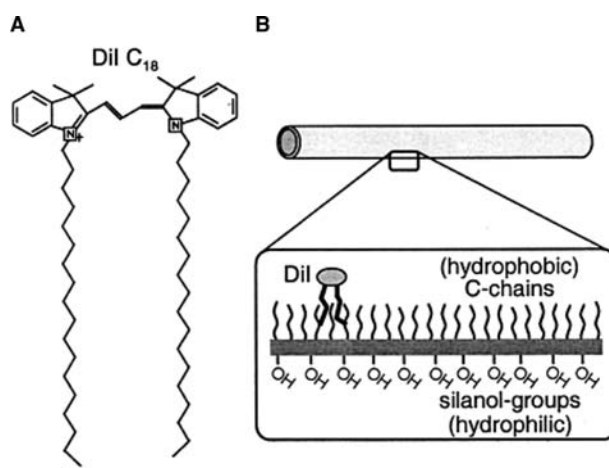


**Fig. 3** (A) Surfactant dye molecule DiI has hydrophilic head and hydrophobic tails, (B) DiI is adsorbed on  $C_{18}$ -attached surface of nanotube interior.

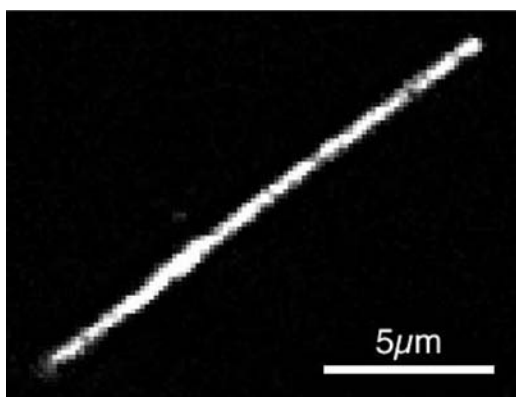


**Fig. 4** Example of fluorescence confocal microscopy image of silica nanotube filled with DiI molecules. The solvent is 0.33 M surfactant (Triton-X-100<sup>®</sup>) solution.

of time  $G(t)$  has the form:<sup>[28]</sup>

$$G(t) = I_{\text{inf}} - \frac{I_0}{1 + 4Dt/s^2}$$

where  $D$  is the diffusion coefficient,  $s$  is the width of Gaussian beam,  $I_{\text{inf}}$  is recovered intensity after infinite time, and  $I_0$  is the bleaching depth.

The diffusion coefficient of DiIC<sub>18</sub> molecules in C<sub>18</sub>-coated nanotube interiors were measured in various solvent environments, including mixtures of water and methanol, and aqueous surfactant solution (0.33 M Triton-X-100<sup>®</sup>). In pure water, diffusion is rarely seen in tubes filled with dyes (Fig. 6A). In pure methanol, dyes are largely extracted from the tube interface and removed to solution (Fig. 6B). At low methanol concentrations and in surfactant solutions, dyes are contained in tubes (Figs. 4 and 5, respectively) and diffusion is often observed.

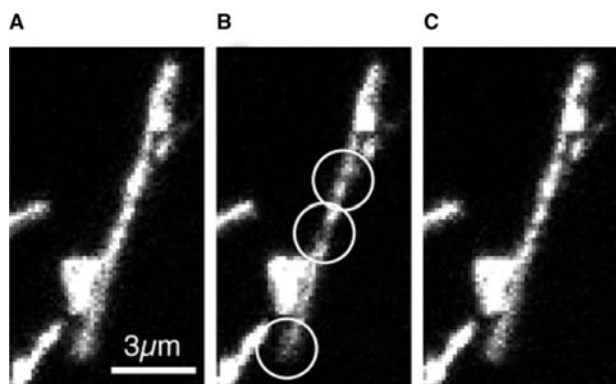


**Fig. 5** Microscopic images of single nanotube filled with fluorescent dye molecules (A) before photobleaching, (B) just after photobleach (the bleached points are indicated with circles), and (C) after recovery. The solvent is water: methanol = 1:1 (vol/vol) mixture.

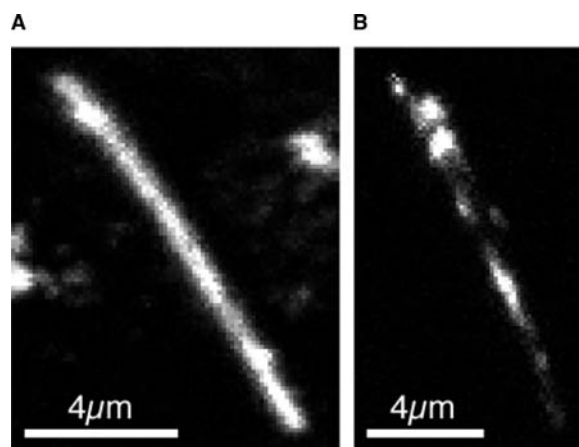


**Fig. 6** Microscopic images of single molecules in (A) pure water, (B) pure methanol.

The diffusion of dye molecules in nanotubes can be classified into the following four types in these experiments:

1. Adsorbed and static.
2. Adsorbed and slowly diffusing ( $D \sim 10^{-12}$ – $10^{-14}$  cm<sup>2</sup>/sec).
3. Adsorbed and rapidly diffusing ( $D \sim 10^{-6}$ – $10^{-8}$  cm<sup>2</sup>/sec).
4. Mostly desorbed with some remaining bright spots.

Type 1 is often seen in pure water and water–methanol mixture with a low methanol fraction. This likely results from a dry nanotube interior. This is due to the high surface tension of pure water and the hydrophobic interior of the tube combining to keep the tube interior dry. If the tube were wet inside, one would expect results similar to the diffusion of DiIC<sub>18</sub> at the planar interface formed by C<sub>18</sub>-modified glass coverslips as observed by Wirth, Swinton, and Ludes.<sup>[29]</sup>

Type 2 is often seen in water–methanol mixtures when the methanol concentration is 50% vol/vol or greater, or in 0.33 M surfactant solution. In these cases, the solvent is believed to have wetted the interior of nanotubes. However, the diffusion coefficient is much smaller than that measured on wet C<sub>18</sub>-modified planar surface.<sup>[29]</sup>

Type 3 is sometimes seen in water–methanol mixture with a high fraction of methanol, but not in pure methanol. The observed diffusion coefficient is comparable with that on wet C<sub>18</sub>-modified planar surface. The inside of nanotubes is considered to be completely wet in this case, since the methanol cosolvent has served to increase the wetting power of the solution to easily enter the hydrophobic tube interior. Types 2 and 3 frequently occur in the same sample



and this may be due to different diffusion processes within individual tubes possessing different degrees of wetting. For instance, slow diffusion could result from two-dimensional diffusion along the nanotube interior surface and faster diffusion could be due to combined surface diffusion and desorption/readsorption processes. This may indicate that in Type 2 tubes, the surface is wet enough for the slower process but not for the latter, while Type 3 is wet enough to allow both.

Type 4 is observed to some degree in all solvents but most notably in 100% methanol. Bright spots are likely due to strongly trapped aggregates at defects on interior surface of nanotubes, comparable to DiI adsorption “hot spots” reported by Wirth, Swinton, and Ludes<sup>[29]</sup> on C<sub>18</sub>-coated fused silica coverslips. In pure methanol or water–methanol mixtures with a high fraction of methanol, this behavior dominates or is more noticeable because the majority of dye has been desorbed and released into solution.

Fig. 7 is a plot describing the probability that the inside of nanotubes are wetted as a function of methanol concentration under the assumption that only wetted tubes show diffusion behavior of Types 2, 3, and 4. The probability is calculated from results of FRAP measurements. It is clear from these results that 200 nm hydrophobic nanotubes qualitatively follow what is expected from macroscopic models of wettability. However, some deviations from the expected behavior is observed.<sup>[5]</sup> For instance, the wetting process is very slow and typically >24 hr is required to reach equilibrium when no mechanical assistance is supplied either by shaking or sonication. Additionally, some tubes appear to never wet and wetting can be reversible, i.e., some tubes are observed to reversibly dry out when the solvent is changed from one of high wettability to pure water.

Several theoretical models have treated the behavior of solvents in nanoscale pores having hydrophobic interior surfaces.<sup>[30–35]</sup> Giaya and Thompson<sup>[35]</sup> have investigated the behavior of fluid in the nanoscale

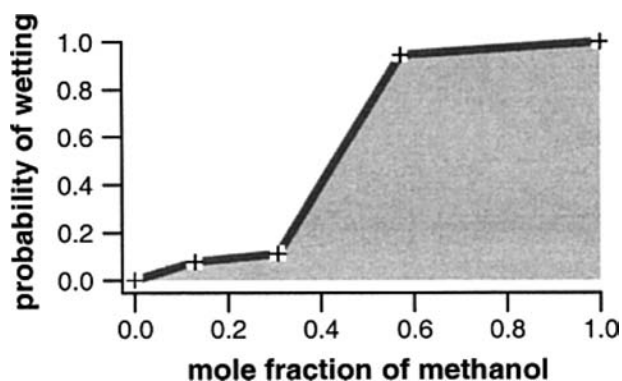


Fig. 7 Probability that inside of nanotube is wet with various fraction of methanol in the mixed solvent.

cylindrical pore. Their results indicate that at room temperature, water behaves as typical bulk water when the pore size is  $\sim 1500$  nm. Below this size, the vapor phase may be more stable if the interaction potential between solvent and wall is zero, i.e., a perfectly hydrophobic wall. Giaya and Thompson also suggested that with stronger fluid–pore–wall interaction, the critical radius at which the fluid phase becomes unstable will decrease. The ability to test theories such as these will be facilitated by using hydrophobically modified tubes in which the tube size and surface hydrophobicity of the nanotube interior can be independently and systematically changed.

## CONCLUSIONS

Silica nanotubes with arbitrary and homogeneous diameter, length, and wall thickness are readily produced by template synthesis and are promising candidates for applications in nanotechnology and bioscience. Their potential applications are far reaching due to the ability to independently functionalize the internal and external surfaces. A variety of applications have already been demonstrated including those discussed above. In addition to technological applications, these materials offer opportunities to systematically examine size and chemical effects on small length scales in well-defined geometries. The distribution and diffusion of dye molecules inside single nanotubes as observed using optical fluorescence confocal microscopy<sup>[5]</sup> has allowed the investigation of wetting of the interior of nanotubes as a function of solvent composition, nanotube surface chemistry, and nanotube size. Further investigation with various materials, surface modification, pore sizes, and solvent will offer unique opportunities to test theories of wettability at extremely small length scales.

## REFERENCES

1. Martin, C.R. Nanomaterials: a membrane-based synthetic approach. *Science* **1994**, *266*, 1961–1966.
2. Lakshmi, B.B.; Patrissi, C.J.; Martin, C.R. Sol–gel template synthesis of semiconductor oxide micro- and nanostructures. *Chem. Mater.* **1997**, *9* (11), 2544–2550.
3. Lee, S.B.; Mitchell, D.T.; Trofin, L.; Nevanen, T.K.; Söderlund, H.; Martin, C.R. Antibody-based bio-nanotube membranes for enantiomeric drug separations. *Science* **2002**, *296*, 2198–2200.
4. Mitchell, D.T.; Lee, S.B.; Trofin, L.; Li, N.; Nevanen, T.K.; Söderlund, H.; Martin, C.R. Smart nanotubes for bioseparations and biocatalysis. *J. Am. Chem. Soc.* **2002**, *124* (40), 11,864–11,865.
5. Okamoto, K.; Shook, C.J.; Bivona, L.; Lee, S.B.; English, D.S. Direct observation of wetting and

- diffusion in the hydrophobic interior of silica nanotubes. *Nano Lett.* **2004**, *4* (2), 233–239.
6. Yang, S.M.; Sokolov, I.; Coombs, N.; Kresge, C.T.; Ozin, G.A. Formation of hollow helicoids in mesoporous silica: supramolecular origami. *Adv. Mater.* **1999**, *11* (17), 1427–1431.
  7. Adachi, M.; Harada, T.; Harada, M. Formation of huge length silica nanotubes by a templating mechanism in the laurylamine/tetraethoxysilane system. *Langmuir* **1999**, *15* (21), 7097–7100.
  8. Jung, J.H.; Ono, Y.; Shinkai, S. Novel silica structures which are prepared by transcription of various superstructures formed in organogels. *Langmuir* **2000**, *16* (4), 1643–1649.
  9. Harada, M.; Adachi, M. Surfactant-mediated fabrication of silica nanotubes. *Adv. Mater.* **2000**, *12* (11), 839–841.
  10. Kleitz, F.; Wilczok, U.; Schiith, F.; Marlow, F. Hollow mesoporous silica fibers: tubules by coils of tubules. *Phys. Chem. Chem. Phys.* **2001**, *3* (17), 3486–3489.
  11. Jang, J.; Yoon, H. Novel fabrication of size-tunable silica nanotubes using a reverse-microemulsion-mediated sol–gel method. *Adv. Mater.* **2004**, *16* (9–10), 799–802.
  12. Baral, S.; Schoen, P. Silica-deposited phospholipid tubules as a precursor to hollow submicron-diameter silica cylinders. *Chem. Mater.* **1993**, *5* (2), 145–147.
  13. Mann, S.; Burkett, S.L.; Davis, S.A.; Fowler, C.E.; Mendelson, N.H.; Sims, S.D.; Walsh, D.; Whilton, N. Sol–gel synthesis of organized matter. *Chem. Mater.* **1997**, *9* (11), 2300–2310.
  14. Ono, Y.; Kanekiyo, Y.; Inoue, K.; Hojo, J.; Nagano, M.; Shinkai, S. Preparation of novel hollow fiber silica using collagen fibers as a template. *Chem. Lett.* **1999**, *28* (6), 475–476.
  15. Shenton, W.; Douglas, T.; Young, M.; Stubbs, G.; Mann, S. Inorganic–organic nanotube composites from template mineralization of tobacco mosaic virus. *Adv. Mater.* **1999**, *11* (3), 253–256.
  16. Jung, J.H.; Shinkai, S.; Shimizu, T. Preparation of mesoscale and macroscale silica nanotubes using a sugar-appended azonaphthol gelator assembly. *Nano Lett.* **2002**, *2* (1), 17–20.
  17. Ji, Q.; Iwaura, R.; Shimizu, T. Controlling wall thickness of silica nanotubes within 4-nm precision. *Chem. Lett.* **2004**, *33* (5), 504–505.
  18. Nakamura, H.; Matsui, Y. Silica gel nanotubes Obtained by the sol–gel method. *J. Am. Chem. Soc.* **1995**, *117* (9), 2651–2652.
  19. Miyaji, F.; Davis, S.A.; Charmant, J.P.H.; Mann, S. Organic crystal templating of hollow silica fibers. *Chem. Mater.* **1999**, *11* (11), 3021–3024.
  20. Wang, L.; Tomura, S.; Ohashi, F.; Maeda, M.; Suzuki, M.; Inukai, K. Synthesis of single silica nanotubes in the presence of citric acid. *J. Mater. Chem.* **2001**, *11* (5), 1465–1468.
  21. Satishkumar, B.C.; Govindaraj, A.; Vogl, E.M.; Basumallick, L.; Rao, C.N.R. Oxide nanotubes prepared using carbon nanotubes as templates. *J. Mater. Res.* **1997**, *12* (3), 604–606.
  22. Fujita, N.; Asai, M.; Yamashita, T.; Shinkai, S. Sol–gel transcription of silica-based hybrid nanostructures using poly(*N*-vinylpyrrolidone)-coated [60]fullerene, single-walled carbon nanotube and block copolymer templates. *J. Mater. Chem.* **2004**, *14* (14), 2106–2114.
  23. Hippe, C.; Wark, M.; Lork, E.; Schulz-Ekloff, G. Platinum-filled oxidic nanotubes. Microporous Mesoporous Mater. **1999**, *31* (3), 235–239.
  24. Zygmunt, J.; Krumeich, F.; Nesper, R. Novel silica nanotubes with a high aspect ratio—synthesis and structural characterization. *Adv. Mater.* **2003**, *15* (18), 1538–1541.
  25. Schlottig, F.; Textor, M.; Georgi, U.; Roewer, G. Template synthesis of SiO<sub>2</sub> nanostructures. *J. Mater. Sci. Lett.* **1999**, *18* (23), 599–601.
  26. Zhang, M.; Bando, Y.; Wada, K.; Kurashima, K. Synthesis of nanotubes and nanowires of silicon oxide. *J. Mater. Sci. Lett.* **1999**, *18* (23), 1911–1913.
  27. Fan, R.; Wu, Y.; Li, D.; Yue, M.; Majumdar, A.; Yang, P. Fabrication of silica nanotube arrays from vertical silicon nanowire templates. *J. Am. Chem. Soc.* **2003**, *125* (18), 5254–5255.
  28. Thompson, J.L.; Burghardt, T.P.; Axelrod, D. Measuring surface dynamics of biomolecules by total internal reflection fluorescence with photobleaching recovery or correlation spectroscopy. *Biophys. J.* **1981**, *33* (3), 435–454.
  29. Wirth, M.J.; Swinton, D.J.; Ludes, M.D. Adsorption and diffusion of single molecules at chromatographic interfaces. *J. Phys. Chem. B* **2003**, *107* (26), 6258–6268.
  30. Kohlmeyer, A.; Hartnig, C.; Spohr, E. Orientational correlations near interfaces. computer simulations of water and electrolyte solutions in confined environments. *J. Mol. Liq.* **1998**, *78* (3), 233–253.
  31. Schoen, M.; Diestler, D. Analytical treatment of a simple fluid adsorbed in a slit-pore. *J. Chem. Phys.* **1998**, *109* (13), 5596–5606.
  32. Lum, K.; Chandler, D.; Weeks, J.D. Hydrophobicity at small and large length scales. *J. Phys. Chem. B* **1999**, *103* (22), 4570–4577.
  33. Truskett, T.M.; Debenedetti, P.G.; Sastry, S.; Torquato, S. A single-bond approach to orientation-dependent interactions and its implications for liquid water. *J. Chem. Phys.* **1999**, *111* (6), 2647–2656.
  34. Truskett, T.M.; Debenedetti, P.G.; Torquato, S. Thermodynamic implications of confinement for a waterlike fluid. *J. Chem. Phys.* **2001**, *117* (7), 2401–2418.
  35. Giaya, A.; Thompson, R.W. Water confined in cylindrical micropores. *J. Chem. Phys.* **2002**, *117* (7), 3464–3475.

# Silica Surfaces Functionalization

V. A. Tertykh

*Institute of Surface Chemistry, National Academy of Sciences of Ukraine, Kiev, Ukraine*

## INTRODUCTION

Imparting desired properties to silica surfaces to obtain functionalized silica surfaces is usually effected in different directions. In some cases, it is necessary to moderate interactions between surrounding molecules and surface sites, while in other cases, such interactions should be enhanced to prepare modified matrices with high specificity and selectivity. Besides, functionalization of silica surfaces is often carried out to immobilize diverse compounds to make them heterogeneous. A description is provided for chemical reactions, which are used to modify surfaces and to produce functionalized silica surfaces. A consideration is given to basic principles that should be adhered to when applying functionalized silica surfaces to various types of chromatographic separation [in such cases as stationary phases in gas and liquid chromatography, reversed and normal phases in high-performance liquid chromatography (HPLC) and affinity chromatography, chiral stationary phases for separating optical isomers]. Examples are presented which are intended to illustrate the production of highly specific and complexing adsorbents based on silicas with functionalized surfaces and their application in solid-phase extraction (SPE) of ions and molecules. A general outline is made of methods for activating surfaces of silica matrices with a view to heterogenize metal complex catalysts, to immobilize enzymes and other biologically active compounds. Also included is a brief analysis of the practical experience acquired in the sphere of application of functionalized silicas in the capacity of chemically active fillers of polymeric compositions and effective thickeners of dispersion media. Some consideration is also given to the state of the art and scope for research into the application of functionalized silica surfaces in formation of nanostructures in various fields of modern materials science (sensitive elements of sensing devices, organically modified silicates, organically modified ceramics, etc.).

## GENERAL NOTIONS

The wide practical use of synthetic silicas (precipitated and pyrogenic silicas, silica gels, and aerogels of silica)

in modern material science and other fields in the capacity of fillers of polymers, thickeners of dispersion media, adsorbents, supports of catalysts, and active compounds is attributable to their chemical, mechanical, and microbiologic stability (silica preparations are resistant to high temperatures, ionizing radiation, oxidizing and reducing agents, solutions of all acids with the exception of the hydrofluoric one; they do not swell in organic solvents and are distinguished for their high mass exchange rate) and to the possible regulation (within certain limits) of their main geometrical characteristics: value of specific surface area, size of particles, diameter, and distribution of pores.<sup>[1]</sup>

The chemical modification of silicas further broadens the opportunities for their effective use because, after deposition or chemical attachment of various functional compounds to the silica surface, the formed functionalized silica surfaces (FSS) retain the major characteristics of starting silica matrices while the attached compounds impart new properties to the support.<sup>[2-4]</sup> Although the modification of silica surface is effected through a thermal treatment (dehydration and dehydroxylation), hydrothermal treatment (hydroxylation and hydration), adsorption of diverse substances (particularly substances with a large molecular weight), and deposition of carbon or metals, the most ample opportunities for a purposeful change of silica properties are provided by the attachment of one chemical compound or another as a result of various chemical reactions with the participation of surface sites. At present, mechanisms of such reactions as well as structures of the formed surface compounds are studied via spectroscopy in infrared (IR), ultraviolet (UV), and visible regions, solid-state  $^{29}\text{Si}$ ,  $^{13}\text{C}$  (and other nuclei) cross-polarization magic-angle spinning nuclear magnetic resonance method (CP-MAS NMR), isotope exchange combined with mass spectrometry, and other contemporary physicochemical techniques.<sup>[3-5]</sup> Under favorable conditions (particularly in nonporous, highly disperse preparations of fumed silicas), infrared spectroscopy enables one to exert a practically direct control over the proceeding of chemical reactions in a surface layer.

The approach employed for imparting desired functional properties to the silica surface depends on the nature of the practical or scientific task in question, and may involve such major methods as weakening of intermolecular interactions of surrounding molecules

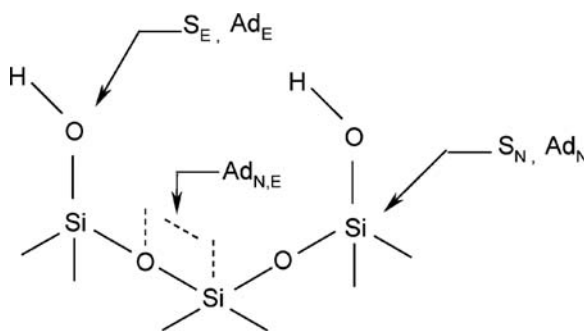
with sites of the surface, enhancement of these interactions with a view to lend specificity and selectivity to the surface, and modification of the silica surface to transfer surface compounds to their heterogeneous state (immobilization of active compounds). Specifically, the substitution of structural silanol groups by methylsilyl groups through reactions with appropriate organosilicon compounds substantially moderates the energy of adsorption of polar adsorbates (one can observe a decrease in values of adsorption and heat of adsorption), and the silica surface acquires stable hydrophobic properties. At the same time, such a chemical modification of surface prevents the aggregation of disperse silica particles and facilitates their more uniform distribution in hydrocarbons and polymeric media. Moreover, attachment of sufficiently long hydrocarbon radicals ( $C_{16}$ – $C_{18}$ ) makes it possible to use such modified silicas as a basis for creation of adsorbents intended to concentrate organic compounds, which is of importance in designing methods of analysis for contents of pesticides and other organic impurities when effecting monitoring of environment.<sup>[6]</sup>

Attachment of a layer of chemically grafted organic radicals with various functional groups ( $-NH_2$ ,  $-COOH$ ,  $-CH=CH_2$ ,  $-CN$ ,  $-SH$ , etc.) that differ in their physico-chemical properties and reactivities enables one to enhance desired characteristics of the silica surface, which offers ample scope and novel potentiality for practical application of FSS. Similar functional silicas find much use in the normal-phase variant of high-performance liquid chromatography. Besides, they may hold considerable promise in the development of chemically active fillers of polymers and in the design of selective adsorbents including highly specific affinity and immune affinity adsorbents for separation and purification of biopolymers.

Furthermore, FSS acquired great importance in the sphere of production of heterogeneous metal complex catalysts and immobilization of enzymes, other biologically active compounds, antibodies, cells, sections of tissues, and microorganisms on an inorganic matrix. This approach holds promise for the development of chemical and biological sensors whose application makes it possible to exert a pulsed or continuous control over corresponding components in a gas phase or liquid medium. For example, chemical modification of the surface of electrodes with functional organosilicon compounds (sol–gel transformations) is rather widely used for the attachment of electroactive compounds in a surface layer (electrochemical sensors). From this standpoint, the most promising technique is the chemical binding of an active compound, because the construction of sensing elements of control systems via polymer encapsulation methods does not provide a perpetual accessibility of an active compound and uniformity of its distribution in a film as well as a necessary strength of bonding with the electrode surface.

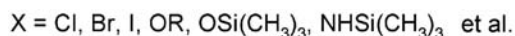
## TYPES OF CHEMICAL REACTIONS USED TO PRODUCE FUNCTIONALIZED SILICA SURFACES

Most of the reactions used to produce FSS are classified among heterolytic processes of electrophilic or nucleophilic substitution ( $S_E$  or  $S_N$ ), addition ( $Ad_E$  or  $Ad_N$ ), and elimination ( $E$ ).<sup>[3,7]</sup> The surface groups are considered as centers of attack whose direction is determined by the character of electron density distribution on the atoms of surface sites participating in a chemical reaction, and by the nature of a corresponding electrophilic or nucleophilic reagent. From this point of view, one can expect that silicon atoms on the silica surface (to be more exact, atoms that are members of groups  $\equiv SiOH$  or  $\equiv SiOSi\equiv$ ) are more preferable for an attack by nucleophilic reagents. In contrast, oxygen atoms as members of the same groups are more preferable for an attack by electrophilic reagents. Possible types of heterolytic reactions involving silica surface sites are represented below:

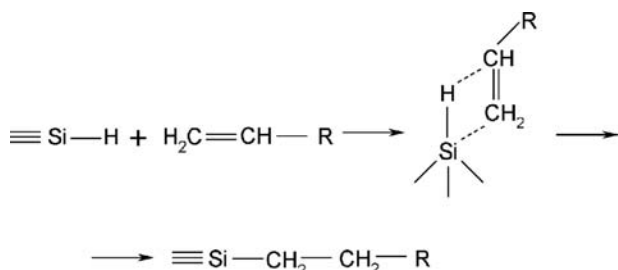


Among the reactions used for chemical modification of a surface, there is a large class of processes where an attack is carried out by an electrophilic reagent through oxygen atoms of silanol groups of the surface. These processes are referred to as reactions of electrophilic substitution of protons ( $S_Ei$ ). They proceed during interactions with various chloro- and alkoxy silanes, organosilazanes, organosiloxanes, numerous organo-elemental compounds, and halogenides of various elements. The class also includes processes of electrophilic addition ( $Ad_E$ ) to groups  $\equiv SiOH$  (for example, in the case of isocyanates or ethylene imine). In particular, the interaction between various trimethylsilylating reagents and silanol groups of the silica surface involves an attack on oxygen atoms and proceeds according to the scheme (see next page top):

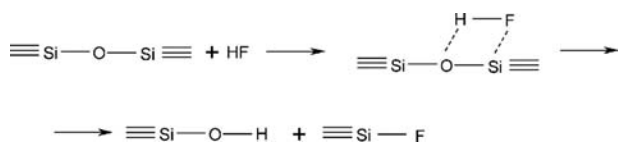
Another class of reactions involves an attack of a nucleophilic reagent on silicon atoms of the silica surface. This class includes processes of nucleophilic substitution ( $S_Ni$ ) (e.g., interactions between silanol groups of the surface and hydrohalogens or alcohols) and processes of nucleophilic addition ( $Ad_N$ ), e.g., reactions of



a solid-phase hydrosilylation of olefins,<sup>[8,9]</sup> with participation of groups  $\equiv\text{SiH}$  attached to the silica surface:



In a number of cases, the function of reactive sites on the silica surface is simultaneously performed by silicon atoms and oxygen atoms of siloxane bonds so that the corresponding processes proceed by mechanism  $Ad_{N,E}$ , for example:



It is also necessary to allow for the possible proceeding of elimination ( $E$ ) and rearrangement processes with participation of chemical surface compounds.<sup>[3,7]</sup>

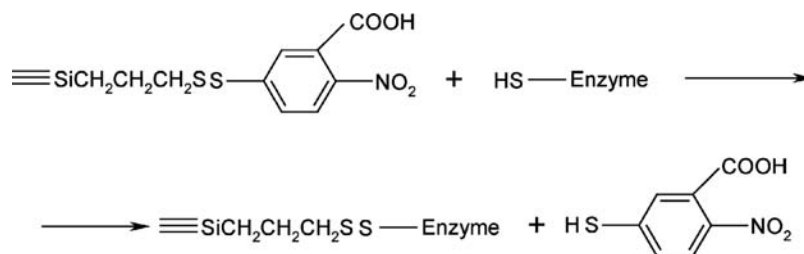
Introduction of new sites (e.g., groups  $\equiv\text{SiR}$ ,  $\equiv\text{SiOR}$ ,  $\equiv\text{SiNH}_2$ ,  $\equiv\text{SiHal}$ ,  $\equiv\text{SiH}$ , etc. where  $R$  is an aliphatic or aromatic radical and  $\text{Hal}$  is a halogen atom) into a surface layer of silica leads to an increase in the number of potential heterolytic transformations with their participation. Grafted organic radicals can also participate in homolytic processes of substitution or addition ( $S_H$  or  $Ad_H$ ). These processes have been the subject of experimental studies, but the amount of experience gained for the present is not large.

## FUNCTIONALIZED SILICA SURFACES IN CHROMATOGRAPHY AND SOLID-PHASE EXTRACTION

Functionalized silica surfaces provide considerable expansion of capabilities of chromatography and sorption techniques, which find much use for separation, purification, and concentration of substances.<sup>[2,10-13]</sup> It is appropriate to mention here that in various types of chromatographic separation [gas-adsorption chromatography, high performance liquid chromatography (HPLC), affinity chromatography],

a surface layer of silica should contain sites that are able to participate in diverse kinds of intermolecular interactions. Thus, gas-adsorption chromatography and reversed-phase HPLC make use of siliceous supports with attached nonspecific methyl, phenyl, octyl, octadecyl groups, while in the case of normal-phase HPLC, it is necessary to use FSS with quaternary ammonium compounds or with aminopropyl, cyanopropyl, carboxyl, propylsulfo, alkyldiol, and other groups capable of participating in donor-acceptor interactions with molecules of compounds which are separated. In affinity chromatography, which depends on the formation of biospecific complexes (enzyme-substrate, enzyme-inhibitor, lectin-glycoprotein, antigen-antibody, etc.), one of the constituents of such a complex should be chemically bonded to the surface of a silica matrix. The function of a biospecific ligand is most often performed by lectins, protein A, certain dyes, polysaccharides, amino acids, monoclonal, and polyclonal antibodies, which are attached to functional silica surface with the help of diverse cross-linking agents. Determination of contents of medicinal preparations in biological fluids containing substantial amounts of albuminous compounds calls for the application of porous FSS of diphilic nature, i.e., there should be a hydrophilic external surface (accessible for proteins) and organophilic internal surface (inaccessible to proteins). Such a structure of FSS makes it possible to retain macromolecules of proteins on the external surface of a sorbent and to effect the separation of medicinal preparation molecules (which have smaller sizes and which interact with the hydrophobic internal surface of pores) via reversed-phase mechanism. It should also be noted that functionalized silica surfaces find use for covalent (chemospecific) chromatography of biopolymers. This chromatography technique is based on reversible chemical reactions between functional groups of modified silica and of a compound, which is separated. It is appropriate to mention here thiol-containing silicas activated with Ellman's reagent,<sup>[14]</sup> which are suitable for the isolation and purification of thiol-containing enzymes, proteins, or peptides with the aid of the following reversible reaction proceeding by the thiol-disulfide exchange mechanism (see next page top).

Functionalized silica surfaces form the basis for designing effective chiral stationary phases for separation of optical isomers. With the view of producing enantioselective sorbents of this kind, the chiral



selectors of various electronic and geometric structures are attached to the silica surface. Such grafted selectors must afford to provide two- or three-point interactions with separated optical isomers.<sup>[15]</sup>

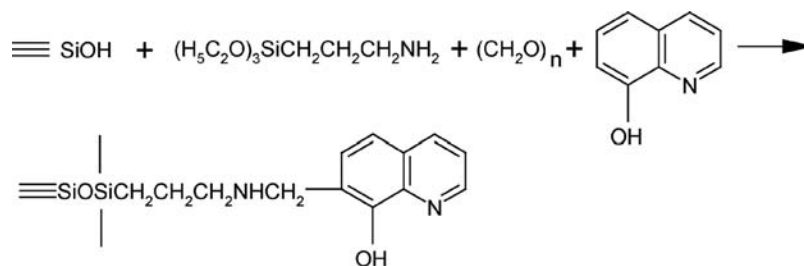
Also significant is the fact that FSS are employed for adsorption concentration of ions and molecules in analytical practice [solid-phase extraction (SPE)].<sup>[6,11–13]</sup> For instance, columns containing FSS with grafted octadecylsilyl groups are used for preconcentration of phenols, pesticides, and herbicides. Octadecylsilica with adsorbed derivatives of dithiocarbamates, crown esters, and other compounds is utilized for SPE of metals. In particular, C<sub>18</sub> columns with adsorbed tri-*n*-octylphosphine oxide are used for extraction and determination of uranium and thorium in water.<sup>[16]</sup> In the case of a repeated use of C<sub>18</sub> cartridges with adsorbed bonding or complexing compounds, there proceeds a gradual elution of such compounds from the surface of a sorbent. Therefore, many researchers put forth their efforts to develop methods for chemical bonding of most important analytical reagents on silica and other appropriate matrices. Such modified silicas with covalently bonded complexing compounds are referred to as complexing silicas. By now, efforts have yielded a number of rather versatile methods suitable for immobilization of a large majority of analytical reagents.<sup>[11]</sup> Characteristically, the researchers of such methods derived benefit from the experience, which was acquired when designing procedures for immobilization of enzymes and other biologically active compounds on inorganic matrices. For example, to attach 4-(2-pyridylazo)resorcinol, 1-(2-pyridylazo)-2-naphthol, and 8-hydroxyquinoline to the silica surface,<sup>[17]</sup> a use was made of the single-stage Mannich reaction (see below).

Although complex-forming adsorbents based on organic polymers possess an increased capacity with respect to extracted compounds in comparison with mineral supports, the developed FSS with grafted analytical reagents do not swell in water and organic solvents. Moreover, they are distinguished for their high rate of mass exchange with a surrounding medium and, hence, for better kinetic characteristics.

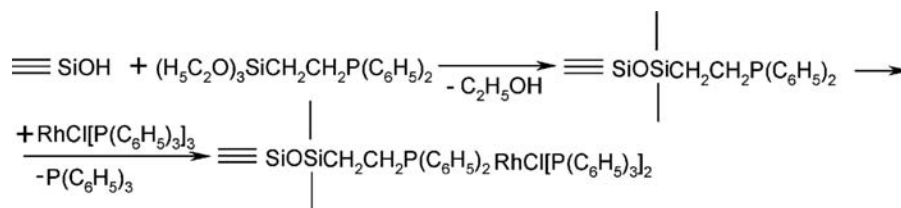
Complexing silicas may be classified according to the nature of an attached functional group (nitrogen-, oxygen-, sulfur-, phosphorus-containing silicas; modified silicas with functional groups involving unsaturated carbon-carbon bonds; polyfunctional silica surfaces)<sup>[3]</sup> or according to the nature of a bond between an ion and a grafted ligand (donor-acceptor bonds, ion exchange, charge-transfer complexes, inclusion complexes of the “host-guest” type).

### METAL COMPLEX CATALYSTS ANCHORED ON SILICAS

It is known that complexes of transition metals are attached to support surfaces (including FSS) for the purpose of producing catalysts that preserve the specificity and selectivity of homogeneous metal complexes and gain technological advantages afforded by heterogeneous contacts.<sup>[18,19]</sup> Attachment of metal complexes to a surface prevents the agglomeration of coordination unsaturated sites and enhances the thermostability of complexes. At the same time, one cannot foretell the possible influence of the surface of a support on the catalytic activity and selectivity of attached complexes. Although production of heterogeneous







metal complex catalysts on siliceous matrices involves adsorption (metal complexes preliminarily prepared by using suitable solvents as well as metal complexes concurrently synthesized in a surface layer with participation of metal ions and of adsorbed ligands) or ion exchange, the most commonly employed methods consist of formation of coordination bonds between metal ions and ligands chemically bonded to surface. In this case, FSS performs the role of a polymeric macroligand. Anchoring of organic ligands on surfaces of silicas is also often accomplished by using functional organoalkoxysilanes whose functional groups, which contain ligands, are bound to surface through hydrolytically stable bonds Si-C, while alkoxy groups and silanol groups form bonds Si-O-Si. For example, anchoring of phosphorus-containing ligands on the silica surface and subsequent formation of metal complexes with rhodium (Wilkinson catalyst), which are active in reactions of hydrogenation of various olefins, can be effected according to the following general scheme (see below).

Introduction of oxygen- and nitrogen-containing ligands and ions of various transition metals makes it possible to obtain heterogeneous metal complex catalysts possessing high activity and selectivity in processes of linear and cyclic oligomerization, hydroformylation, hydrosilylation of olefins, and in some other reactions. Attachment of chiral ligands and complexes on FSS enables the possibility of substantially expanding the potentialities of asymmetric heterogeneous catalysis, which is employed for synthesis of optically active compounds. Also of further interest is the application of metal complexes anchored on FSS in reactions of transfer and activation of oxygen.

## IMMOBILIZED ENZYMES AND FUNCTIONALIZED SILICA SURFACES

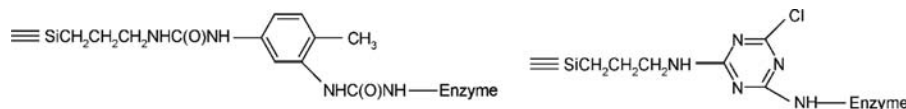
The main aim of immobilization is the production of heterogenized enzymes, which are readily separated from reaction media and which can be repeatedly used under

flow reactor conditions. Immobilization of enzymes on silica matrices is effected by both the adsorption method and method of covalent binding on surface.<sup>[20,21]</sup> Chemical bonding permits one to create more stable immobilized preparations, particularly preparations that are elution-resistant in varying surrounding medium factors (ionic strength, pH, concentration of a substrate, and content of substances which may lead to desorption of enzymes).

At present, the available range of methods for covalent bonding of enzymes with silica surface is rather broad. As a rule, all of them involve a preliminary modification of surface by bifunctional silane and subsequent introduction of active groupings that are able to form covalent bonds with side residues of amino acids of enzymes. The most commonly employed method is a preliminary modification of silica by 3-aminopropyltriethoxysilane and subsequent activation of the surface by various reagents (such as glutaraldehyde, diazonium salts, isothiocyanates, carbodiimides, acylazides, haloalkyls, acid chlorides).<sup>[22]</sup> Good performance is also shown by methods for activating the aminoorganosilica surface with 2,4-toluene diisocyanate (a) and cyanuric chloride (b) (see below).<sup>[14]</sup>

The function of starting organosilicas used for production of activated matrices can be performed not only by aminoderivatives but also by organosilicas with other functional groups (such as  $\equiv\text{SiCH}\equiv\text{CH}_2$ ,  $\equiv\text{SiH}$ ,  $\equiv\text{SiRSH}$ ). In particular, activated silica matrices for immobilization of enzymes were prepared through reactions between grafted vinyl groups and maleic anhydride, addition of acrolein to surface silicon hydride groups, and interaction of grafted sulfhydryl groups with Ellman's reagent.<sup>[14]</sup>

Because the properties of an immobilized enzyme are determined by a package of properties of a biocatalyst and support and are dependent on the method for binding the biocatalyst to the support surface, when carrying out a concrete task it proves useful to test various methods for binding with a view to choose the procedure which is optimal from the standpoint



of activity and stability of products. In porous silica matrices, the geometric characteristics of a support exert a substantial effect on the rate of binding of enzymes, on the capacity of a matrix with respect to a protein, and on the manifestation of activity of immobilized preparations, which is attributable to inside-diffusion retardation. The activity of immobilized preparations is, to a great extent, dependent on the pH of a medium where binding of an enzyme takes place. It has been observed that the maximum degree of binding of a protein to the silica surface is observed at pH values close to the isoelectric point of the protein.

Although the practical application of immobilized enzymes has considerable potential in fine organic synthesis and in various fields of biotechnology, it is in the creation of biosensors that their application is most impressive. In biosensors, a use is made either of flow minireactors with immobilized enzymes or of a biocatalyst that is attached directly to the surface of ion-selective electrodes. In the first case, the function of supports is performed by silica-based materials, which possess a rigid structure and, therefore, set good hydrodynamic conditions in a flow of a buffer and of a solution that is analyzed. Placing an appropriate transducer at the outlet of such a minireactor with an immobilized enzyme makes it possible to create analyzers for a broad spectrum of substances, which are substrates or effectors of the enzyme. The role of transducers is most often played by an oxygen electrode, flow spectrophotometer,  $H^+$ - and other ion-selective electrodes, as well as by a multipurpose enthalpimetric transducer. In the second case, enzymes are directly immobilized on the surface of a sensitive element (such as ion-selective field-effect transistor, piezoelectric quartz element, optical fiber element). So long as the supports used contain silicon dioxide, the chemical attachment of enzymes to their surface should be effected with allowance for the experience acquired in the sphere of immobilization of active compounds on modified silicas.

In recent years, there has been considerable interest in effecting enzyme-catalyzed reactions in non-aqueous solvents with a view to increase yields of products or to carry out novel syntheses. Because of their stability in organic solvent, silica matrices may hold considerable promise in the capacity of supports for appropriate enzymes. For example, it is possible to perform

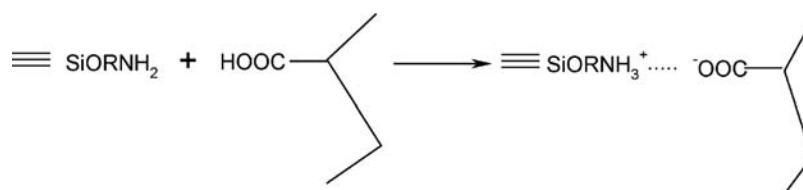
synthesis of various peptides with the help of immobilized proteases and with allowance for reversibility of hydrolysis of peptide bonds.<sup>[14]</sup> In this case, as a consequence of the absence of racemization, the prepared products possess a higher optical purity in comparison with products prepared via the classical peptide synthesis.

## FUNCTIONALIZED SILICA SURFACES IN POLYMERS AND DISPERSION MEDIA

In numerous cases, efficiency of the application of functionalized silica surfaces in polymers and dispersion media is determined by the ratio of hydrophilic sites to hydrophobic sites in a surface layer. This index is of critical importance for thickeners of lubricants and fillers of polymeric materials. Substitution of surface hydroxyl groups by grafted organic radicals favors a better distribution of silica particles in organic media. At the same time, the complete screening of the silica surface (e.g., by alkyl groups) may impair structural and mechanical characteristics of thickened systems, and filling of polymeric materials may worsen their physicochemical properties.

A substantial reinforcement of filled systems can be attained in the situation when active sites of FSS ( $-NH_2$ ,  $-COOH$ ,  $-SH$ ,  $\equiv SiH$ , etc.) are capable of chemical interaction with functional groups of polymeric macromolecules. Such a chemical mechanism of reinforcement was employed for the first time in glass-fiber composites.<sup>[23]</sup> From this standpoint, functionalized silica surfaces containing grafted amine groups may hold considerable promise as chemically active fillers of chlorine- and bromine-containing elastomers and copolymers, epoxy resins, polyurethane rubbers, melamino-formaldehyde and resorcinol-formaldehyde latex and resins, sulfonated ethylene-propylene-diene terpolymers, carboxyl-containing polymer systems. Specifically, in the case of introduction of FSS with amine groups into carboxyl-containing polymers, formation of salt-type cross bonds between the filler and polymer is observed:<sup>[3]</sup>

On the contrary, FSS with carboxyl groups may considerably reinforce butadiene-vinylpyridine copolymer, elastomeric terpolymer of vinylpyridine, styr-



ene, and butadiene, etc. FSS with grafted unsaturated groups can be advantageously employed for reinforcement of a broad range of olefin-containing copolymers and elastomers. Chemisorption of sterically hindered phenols on the surface of highly disperse silicas makes it possible to produce fillers and thickeners having antioxidant properties.<sup>[3]</sup>

Applications of highly disperse silica in varnishes and paints are based on the thixotropic properties of this thickener and on its ability to increase the viscosity of systems and to decrease the sedimentation of pigments of various types. One of the salient features of such systems with siliceous thickeners lies in the fact that, at an infinitely small shearing stress, their behavior is similar to that of solids, and at high shearing stresses, to that of liquid compositions. The thixotropic properties of highly disperse silica are related to the deformation caused by shear, stirring, or shaking, which leads to breaking of bonds at points of contact of particles (of aggregates of particles) or of solvate shells of particles, and to their subsequent restoration at the state of rest. Application of functionalized silica surfaces enables one to exert control over the viscosity of a system and to substantially enhance the water-resisting property of a coating.

## CONCLUSION

Purposeful variation of properties of the surface of silicas is of great importance in carrying out numerous scientific and practical tasks in adsorption, chromatography, catalysis, and chemistry of filled polymers. Presently, functionalized silica surfaces find much use in the production of immobilized reagents, which are successfully employed in synthetic organic chemistry.<sup>[24]</sup> Of particular significance is the ever-growing role of FSS in modern material science and nanodimensional engineering. Also noteworthy is the prevalent use of polysilsesquioxanes produced by the sol-gel method (cohydrolysis of organofunctional trialkoxysilanes and tetraalkoxysilane), organically modified silicates (ormosils) including silicates doped with diverse dyes, and organically modified ceramics (ormocers) for producing novel optical materials and lasers, sensitive elements of sensing devices, biocompatible ceramics.<sup>[25-29]</sup> New vistas in the production of FSS are furnished by chemical modification of surface and core of ordered mesoporous siliceous materials (such as MCM-41 and MCM-48),<sup>[30]</sup> which possess an exceptionally extended surface and unique structure of pores accessible to large molecules. It is not ruled out that such FSS will form the basis for the development of new generation adsorbents and catalysts. Also of significance is the formulation and establishment of principles of mosaic nanodimensional modification of siliceous

supports because, under favorable conditions on the surface of such supports, it is possible to construct models of active centers of multicomponent metal complex catalysts and biological catalysts, as well as to create ultraselective and affinity sorbents. Functionalized silica surfaces are increasingly used in the field of novel dispersion media, polymeric compositions, and modern materials.

## REFERENCES

1. Iler, R.K. *The Chemistry of Silica: Solubility, Polymerization, Colloid and Surface Properties and Biochemistry of Silica*; Wiley: New York, 1979.
2. Unger, K.K. *Porous Silica. Its Properties and Use as a Support in Column Liquid Chromatography*; Elsevier: Amsterdam, 1979.
3. Tertykh, V.A.; Belyakova, L.A. *Chemical Reactions Involving Silica Surface*; Naukova Dumka: Kiev, 1991.
4. Vansant, E.F.; Van Der Voort, P.; Vrancken, K.C. *Characterization and Chemical Modification of the Silica Surface*; Elsevier: Amsterdam, 1995.
5. Legrand, A.P., Ed.; *The Surface Properties of Silicas*; Wiley: New York, 1998.
6. Johnson, W.E.; Fendinger, N.J.; Plimmer, J.R. Solid-phase extraction of pesticides from water—Possible interferences from dissolved organic material. *Anal. Chem.* **1991**, *63* (15), 1510–1513.
7. Tertykh, V.A. Novel Aspects of Chemical Modification of Silica Surface. In *Organosilicon Chemistry III. From Molecules to Materials*; Auner, N., Weis, J., Eds.; VCH: Weinheim, 1998; 670–681.
8. Pesek, J.J.; Sandoval, J.E.; Chu, D.; Jonsson, E. The Synthesis, Characterization and Modification of Hydride Silica Surfaces. In *Chemically Modified Oxide Surfaces*; Mottola, H.A., Steinmetz, J.R., Eds.; Elsevier: Amsterdam, 1992; 57–72.
9. Tertykh, V.A.; Belyakova, L.A. Solid-Phase Hydrosilylation with Participation of Modified Silica Surface. In *Adsorption on New and Modified Inorganic Sorbents*; Dabrowski, A., Tertykh, V.A., Eds.; Elsevier: Amsterdam, 1996; 147–189.
10. Buszewski, B.; Jezierska, M.; Welniak, M.; Berek, D. Survey and trends in the preparation of chemically bonded silica phases for liquid-chromatographic analysis. *HRC. J. High Resolut. Chromatogr.* **1998**, *21* (5), 267–281.
11. Biernat, J.F.; Konieczka, P.; Tarbet, B.J.; Bradshaw, J.S.; Izatt, R.M. Complexing and chelating agents immobilized on silica gel and related materials and their application for sorption of inorganic species separation and purification methods. *Sep. Purif. Methods* **1994**, *23* (2), 77–348.
12. Moors, M.; Massart, D.L.; Mcdowall, R.D. Analyte isolation by solid-phase extraction (SPE) on silica-bonded phases—Classification and recommended practices. *Pure Appl. Chem.* **1994**, *66* (2), 277–304.
13. Stevenson, D. Immunoaffinity solid-phase extraction. *J. Chromatogr., B* **2000**, *745* (1), 39–48.

14. Tertykh, V.A.; Yanishpolskii, V.V. Adsorption and Chemisorption of Enzymes and Other Natural Macromolecules on Silicas. In *Adsorption on Silicas*; Papirer, E., Ed.; Marcel Dekker: New York, 2000; 523–564.
15. Davankov, V.A.; Navratil, J.D.; Walton, H.F. *Ligand Exchange Chromatography*; CRC Press: Boca Raton, FL, 1988.
16. Shamsipur, M.; Yamini, Y.; Ashtari, P.; Khanchi, A.; Ghannadimarageh, M. A rapid method for the extraction and separation of uranium from thorium and other accompanying elements using octadecyl silica membrane disks modified by tri-*n*-octyl phosphine oxide. *Sep. Sci. Technol.* **2000**, *35* (7), 1011–1019.
17. Tertykh, V.A.; Yanishpolskii, V.V.; Panova, O.Yu. Covalent attachment of some phenol derivatives to the silica surface by use of single-stage aminomethylation. *J. Therm. Anal. Calorim.* **2000**, *62* (2), 545–549.
18. Bailar, J.C., Jr. Heterogenized homogeneous catalysts. *Catal. Rev., Sci. Eng.* **1974**, *10* (1), 17–36.
19. Lisichkin, G.V.; Yuffa, A.Ya. *Heterogeneous Metal Complex Catalysts*; Khimiya: Moscow, 1981.
20. Weetall, H.H. Alkaline phosphatase insolubilized by covalent linkage to porous glass. *Nature* **1969**, *223* (5209), 959–960.
21. Weetall, H.H. Trypsin and papain covalently coupled to porous glass: Preparation and characterization. *Science* **1969**, *166* (3905), 615–617.
22. Weetall, H.H. Preparation of immobilized proteins covalently coupled through silane coupling agents to inorganic supports. *Appl. Biochem. Biotechnol.* **1993**, *41* (3), 157–188.
23. Plueddemann, E.P., Broutman, L.J., Krock, R.H., Eds. *Interfaces in Polymer Matrix Composites*; Composite Materials, Academic Press: New York, 1974; Vol. 6.
24. Hodge, P.; Sherrington, D.C., Eds. *Polymer-Supported Reactions in Organic Synthesis*, Wiley: Chichester, 1980.
25. Mackenzie, J.D.; Bescher, E.P. Structures, properties and potential applications of ormosils. *J. Sol-Gel Sci. Technol.* **1998**, *13* (1–3), 371–377.
26. Makote, R.; Collinson, M.M. Organically modified silicate films for stable pH sensors. *Anal. Chim. Acta* **1999**, *394* (2–3), 195–200.
27. Walcarius, A. Analytical applications of silica-modified electrodes—A comprehensive review. *Electroanalysis* **1998**, *10* (18), 1217–1235.
28. Levy, D. Photochromic sol-gel materials. *Chem. Mater.* **1997**, *9* (12), 2666–2670.
29. Haas, K.H. Hybrid inorganic-organic polymers based on organically modified Si-alkoxides. *Adv. Eng. Mater.* **2000**, *2* (9), 571–582.
30. Moller, K.; Bein, T. Inclusion chemistry in periodic mesoporous hosts. *Chem. Mater.* **1998**, *10* (10), 2950–2963.

# Silicon Functionalization for Molecular Electronics

**Gianfranco Cerofolini**

*Post-Silicon Technology, STMicroelectronics, Agrate Brianza, Italy, and Department of Materials Science, University of Milano-Bicocca, Milan, Italy*

**Dario Narducci**

**Elisabetta Romano**

*CNISM and Department of Materials Science, University of Milano-Bicocca, Milan, Italy*

## Abstract

Silicon is the most important material in modern technology; the deep interest in the chemical modification of its surface is due to the trend that is now bringing technology to nanotechnology in various fields, and which makes surface properties prevailing over bulk ones. A promising approach involves the construction of hybrid organic-molecule-silicon devices based on organic molecules covalently grafted onto silicon surface, for applications such as the control of threshold voltage of field-effect transistors (“more Moore”), molecular electronics (“beyond Moore”), sensors and micro-electromechanical systems (“more than Moore”). Silicon is generally considered to have a poor reactivity, so its functionalization with organic moieties is still a critical issue. Synthetic routes in solution and under ultra high vacuum are reviewed and discussed emphasizing the underlying chemistry. Their applicability and process compatibility are also discussed.

## INTRODUCTION

With “silicon functionalization” one usually intends the derivatization of elemental silicon with organic or organometallic species aiming to impart new properties to its surface. The functionalization of silicon may impact the future of electronics in its normal evolution (“more Moore”) or for the preparation of devices with geometry not achievable with standard silicon technology (“beyond Moore”). Furthermore, also the engineering of devices like sensors, actuators, and opto-electrical ones, with new functions with respect to equivalent in the past (“more than Moore”), may be developed.

## MORE MOORE—NON-CONVENTIONAL PROCESSING OF CONVENTIONAL DEVICES

The volume of silicon used in a MOSFET (metal-oxide-semiconductor field effect transistor) at the forefront of the technology (gate length = 0.06  $\mu\text{m}$ ) built on SOI (silicon on insulator) or SON (silicon on nothing) substrate is of about  $10^{-15} \text{ cm}^3$ . For dopant concentration in the range of  $10^{16} \text{ cm}^{-3}$ , the threshold voltage of a MOSFET is thus controlled on the average by a number of atoms of the order of 10. Needless to say, this situation results in an extreme statistical variability of the properties of single devices forming the circuit. In this context, the conduction properties of the device channel are better controlled by modifying its surface potential. That may be

achieved, for instance, derivatizing the surface of the active region with molecules able to impart the desired potential to the channel.<sup>[1]</sup> Of course, in view of the limited thermal stability of organics, this leads to major integration issues. However, in a SON MOSFET the modification is possible by exposing the back-side of the transistor to the functional molecule in the back-end stage of device processing.

## BEYOND MOORE—NON-CONVENTIONAL DEVICES

The scaling down of the MOSFET below a gate length of 0.04  $\mu\text{m}$  seems practically impossible in the frame of the current silicon technology. Below this feature size the crossbar architecture,<sup>[2]</sup> in which the active region is inserted “vertically” in each cross-point formed by the superposition of two perpendicularly oriented conductive-wire arrays, seems producible with methods not involving conventional lithography.<sup>[3–6]</sup>

The first attempt in this direction involved the insertion of reconfigurable conductive molecules between metal arrays:<sup>[7]</sup>



Almost immediately after the original proposal, however, it became evident that the above arrangement was not sufficiently robust to be operated at electric fields useful to produce a sensitive current through

the organic layer (metal electromigration being the weak point).<sup>[8]</sup> Instead, the following arrangement



seems more suitable and consistent with silicon technology,<sup>[5,6]</sup> and can be used to generate a genuine molecular electronics.<sup>[9]</sup>

### MORE THAN MOORE—SENSORS

One of the most prototypical applications of surface functionalization by chemical grafting is chemical sensing.<sup>[10]</sup> A chemical sensor is a device capable of converting in real time chemical information (either qualitative or quantitative) into a physical quantity that can be readily measured, processed, and stored. Surface functionalization has been widely exploited in the field of biosensors, where mainly oxide layers have been used to tailor surface sensitivity to specific analytes.<sup>[11]</sup> Over recent years, silicon surface modifications have proved to be successful also to enhance selectivity and sensitivity toward detection of non-biological targets both in solution<sup>[12]</sup> and in the gas phase.<sup>[13]</sup>

### WHICH CHEMISTRY FOR SILICON DERIVATIZATION?

All the examples considered until here require the ability to bind organic or organometallics (like ferrocenes)<sup>[14]</sup> molecules to silicon surfaces forming an organic layer with assigned electrical properties. Silicon derivatization usually requires a preliminary step leading to an as far as possible homogeneous termination of the surface with species such as halogens, hydrogen, and hydroxyl.

This item is addressed to review the state of the art about the derivatization with organic molecules both of single-crystalline silicon [and especially of its (111) and (100) surfaces, of interest for integrated-circuit processing or molecular electronics] and of porous silicon (of interest not only for sensors, but also for optical devices).

### The Chemistry of Silicon

Even though there are some analogies between the chemistries of carbon and silicon, the differences are prevailing. Similar to carbon, most of the silicon compounds are consistent with  $sp^3$  hybridization of

**Table 1** Some bond dissociation energies and average bond energies

Bond	Bond dissociation energy (eV)	Bond energy (eV)
Si–H	3.6–4.5	
Si–C	3.9–4.1	3.3
Si–Si	3.2–3.4	2.3
Si–F	6.6–7.2	
Si–O	5.3–5.9	4.8
Si–N	4.2–4.7	
H <sub>2</sub> Si=CH <sub>2</sub>	1.6	(of $\pi$ bond only)
H <sub>2</sub> Si=SiH <sub>2</sub>	1.2	(of $\pi$ bond only)
H <sub>2</sub> Si=O	2.6	(of $\pi$ bond only)
H <sub>2</sub> C=CH <sub>2</sub>	2.8	(of $\pi$ bond only)
H <sub>2</sub> C=O	3.25	(of $\pi$ bond only)

outer atomic orbitals of silicon, whose atom in ground state has electronic configuration is  $3s^23p^23d^0$ . Instead, dissimilarly from carbon,

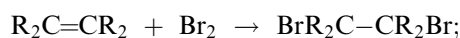
- numerous penta- or hexa-coordinated compounds of silicon are known,
- $sp^2$  and  $sp^1$  hybridizations are observed in very few compounds, and
- silicon has poor tendency toward catenation.

Penta- and hexa-coordinated compounds are usually, but not uniquely, observed when silicon is bonded to very electronegative elements, as in  $[\text{SiF}_6]^{2-}$ . These compounds might easily be explained in terms of lone-electron-pair donation to the empty  $d$  orbital of silicon, but the participation of this orbital in the formation of the bonds is still a matter of debate.<sup>[15]</sup>

The negligible tendency of silicon toward the formation of  $\pi$  bonds is determined by the fact that the stability of the Si=Si double bond is lower than the stability of the Si–Si single bond (see Table 1);<sup>[6]</sup> silenes are thus unstable towards spontaneous decomposition unless the  $\pi$  bonds are protected against internal rearrangements by suitably bulky side groups.<sup>[17]</sup>

Instead, the Si–Si  $\sigma$  bond behaves similarly to the  $\pi$  bond in olefins.<sup>[15]</sup> This analogy is sustained not only by the corresponding bond energies, but also by the following observations:

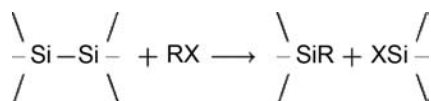
- disilanes undergo electrophilic cleavage by the same reagents that add to olefins by cleavage of the  $\pi$  bond,





- the Si–Si bond forms dative complexes with Lewis acids;
- the Si–Si bond undergoes ionization with formation of a radical ion  $R_3\dot{Si}\cdots\overset{+}{Si}R_3$  where the complex is not destroyed, as it happens for olefins (e.g.,  $H_2\dot{C}-\overset{+}{C}H_2$ ).

The obvious difference is that while the cleavage of the  $\pi$  bond in  $C=C$  does not demolish the molecule (unless the reagent does not add additively to the  $\sigma$  bond too), the cleavage of the  $\sigma$  bond in Si–Si eventually results in the formation of monomers. This process is at the basis of the most important silicon reaction, the Rochow reaction:



with X being a halogen (typically  $X = \text{Cl}$ ) and  $R = \text{H}, \text{CH}_3, \text{C}_2\text{H}_5, \text{C}_6\text{H}_5$ , etc.

This analogy clarifies also the reason why, contrarily to carbon, silicon has poor tendency toward catenation. Although silanes  $\text{Si}_n\text{H}_{2n+2}$  are formally the silicon analogues of alkanes, taking into consideration their chemical properties, they are the analogues of cumulenes, chemical compounds with two or more consecutive double bonds. Long cumulenes are known to be unstable; correspondingly  $\text{Si}_n\text{H}_{2n+2}$  decompose spontaneously to silicon and  $\text{H}_2$  for  $n > 3$ .

From the viewpoint of the ability to catenation, the silicon species more similar to alkanes are siloxanes,

where silicon atoms are linked through oxo bridges  $-\text{O}-$ . In view of the weak dependence of the energy content of the oxo bridge on angle (Si–O–Si), various allotropic forms of silica and siloxo compounds are indeed possible. It is immediately seen that alkane, alkene, and alkyne species have counterparts in siloxo compounds, for which the names *alksoxan*, *alksoxen*, and *alksoxyn* seem the most natural. Table 2 shows the equivalence. In this case, the silicon analogues of cumulenes and polyynes (organic compounds with alternating single and triple bonds) are linear or cyclic  $(\text{SiO}_2\text{SiO}_2)_n$  or  $(\text{SiO}_3\text{SiO})_n$ , which seem to be (or already are) in the reach of the siloxan chemistry even for  $n > 3$ . The major difference is the absence of aromaticity in siloxo compounds. An even more intriguing analogy is discussed in Ref.<sup>[18]</sup>.

### The Role of Surfaces

Before considering in detail the various processes, we intend to address the problem of the role of any solid surface reactivity. Compared with gas- or liquid-phase reactions, the surface introduces several modifications. In fact, imagining of insulating a small portion of the surface separated from the remainder,

1. the reactivity of any group therein toward a reactant in gas or liquid phase is expected to be the same as for the considered group in the considered phase, provided that:
2. the frontier molecular orbitals are replaced by valence and conduction bands (possibly with

**Table 2** Formal analogy between hydrocarbons and siloxo compounds

Name	Formula	Name	Formula
<i>Alkane:</i>		<i>Alksoxan:</i>	
Methane	$\text{CH}_4$	Methsoxan	$\text{Si}(\text{OH})_4$
Ethane	$\text{CH}_3\text{CH}_3$	Ethsoxan	$\text{Si}(\text{OH})_3\text{OSi}(\text{OH})_3$
Propane	$\text{CH}_3\text{CH}_2\text{CH}_3$	Propsoxan	$\text{Si}(\text{OH})_2\text{OSi}(\text{OH})_2\text{OSi}(\text{OH})_3$
Polyethylene	$(\text{CH}_2\text{CH}_2)_n$	Polyethsoxylen	$(\text{Si}(\text{OH})_2\text{OSi}(\text{OH})_2\text{O})_n$
Polypropylene	$(\text{CH}(\text{CH}_3)\text{CH}_2)_n$	Polypropsoxylen	$(\text{Si}(\text{OH})(\text{OSi}(\text{OH})_3)\text{OSi}(\text{OH})_2\text{O})_n$
<i>Alkene:</i>		<i>Alksoxen:</i>	
Ethene	$\text{CH}_2\text{CH}_2$	Ethsoxen	$\text{Si}(\text{OH})_2\text{O}_2\text{Si}(\text{OH})_2$
Propene	$\text{CH}_2\text{CHCH}_3$	Propsoxen	$\text{Si}(\text{OH})_2\text{O}_2\text{Si}(\text{OH})\text{OSi}(\text{OH})_3$
Polyacetylene	$(\text{CH}=\text{CH})_n$	Polyacetsoxylen	$(\text{Si}(\text{OH})\text{O}_2\text{Si}(\text{OH})\text{O})_n$
Cumulene	$(\text{C}=\text{C})_n$	Cumulsoxen	$(\text{SiO}_2\text{SiO}_2)_n$
<i>Alkyne:</i>		<i>Alksoxyn:</i>	
Ethyne	$\text{CHCH}$	Acetsoxyn	$\text{Si}(\text{OH})\text{O}_3\text{Si}(\text{OH})$
Propyne	$\text{CHCCH}_3$	Propsoxyn	$\text{Si}(\text{OH})\text{O}_3\text{SiOSi}(\text{OH})_3$
Polyyne	$(\text{C}\equiv\text{C})_n$	Polysoxyn	$(\text{SiO}_3\text{SiO})_n$

population controlled by doping of the solid), and

- the steric constraint of the surface (which can in turn be considered as an extremely bulky group holding approximately half a space) is considered.

Feature (1) explains how gas-phase chemistry can be imported into surface chemistry to predict on analogical bases the reactivity; features (2) and (3) define the limits of the analogy. Feature (2) is extremely important in redox reactions, where an electron transfer from/to surface occurs and the energy levels involved play a fundamental role. On the contrary, steric constraint plays certainly an important role in any type of on-surface reaction; it forbids free geometrical arrangement of intermediate species and final adduct, and reduces the solvent effect occupying a part of solvation sphere. Of course, steric constraint becomes critical when the reactant has a size comparable with the short-range peak-to-valley roughness of the surface; it is intuitively obvious that an atomically flat surface may be derivatized with a more ordered and dense film than a rough surface.

To understand how strange may be the chemistry at a surface and to rationalize it, consider on one side that silenes in gas phase can only be prepared by protecting the Si=Si double bond with sufficiently bulky unreactive groups, which protect the  $\pi$  bond not only against other molecules but also against internal rearrangements;<sup>[17,19]</sup> their effect is thus progressively destroyed as temperature increases. On another side, observe that the clean,  $2 \times 1$  reconstructed, (100) surface of single crystalline silicon may be seen as a two-dimensional lattice of silene units (for more information on silicon dimers at the  $2 \times 1$  (100)Si<sub>2</sub>, see Ref.<sup>[20]</sup>) stabilized by the underlying entire crystal—an extremely bulky group. Since the silene bonds are accessible to external molecules, they are extremely reactive (and indeed they can be preserved in ultra high vacua only), but they are nonetheless stable at very high temperature too (indeed, they are formed, for instance, by thermal decomposition of silanic bonds at hydrogen-terminated surfaces at temperature higher than approximately 750°C).

## SILICON SURFACES

Silicon wafers are commercially available with various orientations: [111], [100], [110], [113], etc. Of them, only the (100) and (111) surfaces are currently produced and used in semiconductor silicon processing—and the (100) surface alone covers almost all applications.

For many years, the quality of such a surface has been related to

- the polishing procedure, which produces surfaces with prevailing hydrogen terminations, but also containing residual oxo centers (Si–O–Si and Si–O–H);<sup>[21,22]</sup>
- the cleaning process after polishing.

The most widely used cleaning processes were developed by RCA in the mid-1960s. The RCA cleaning employs two steps:

- (SC1) standard cleaning 1, where the wafer is exposed to a hot mixture of H<sub>2</sub>O<sub>2, aq</sub> + NH<sub>3, aq</sub>, aimed at removing organics and particles; and
- (SC2) standard cleaning 2, where the wafer is exposed to a hot mixture of H<sub>2</sub>O<sub>2, aq</sub> + HCl<sub>aq</sub>, designed to remove metals.

The combination of this procedure with “piranha” etching (a concentrated aqueous solution of H<sub>2</sub>SO<sub>4</sub> and H<sub>2</sub>O<sub>2</sub>) before SC1, between SC1 and SC2 or after SC2, leaves the surface oxidized and hydroxylated. The oxo-terminated surfaces exposed to humidity at room temperature undergo further oxidation<sup>[23,24]</sup> and the early stages of oxidation produce a chemically heterogeneous surface region where the silicon oxidation state is distributed between 0 and 4.<sup>[25]</sup> Finally, an etching in HF<sub>aq</sub> followed by a rinsing in de-ionized H<sub>2</sub>O is usually considered an adequate treatment achieving the surface hydrogenation.<sup>[26]</sup> The extent of residual oxidation and hydroxylation depends on HF<sub>aq</sub> concentration, solution pH, concentration of O<sub>2</sub> dissolved in water, air humidity, and duration of exposure. Since these quantities are often known only partially, the state of the surface (the native surface) is generally unknown in a broad distribution of allowed states.

Over the last years, the attention has gradually shifted from the removal of contaminants (organics, metals, particulates) to the chemical termination of the surface after the cleaning process because it affects appreciably the behavior of the Si–SiO<sub>2</sub> interface on gate oxidation in integrated-circuit processing. In the following, we shall describe the methods developed for the preparation of surfaces minimizing the oxo terminations.

## The Surface of Single-Crystalline Silicon

Clean surfaces—reconstructed and highly reactive

**The (111) surface.** There are in principle two (111) surfaces: one is characterized by three unsaturated

dangling bonds per surface atom, and the other is characterized by one dangling bond per atom perpendicularly oriented to the surface. The attention is usually limited to the second case because it occurs at the cleavage plane of silicon.

The clean unreconstructed  $1 \times 1$  (111) surface is unstable and reconstructs first with the formation of  $2 \times 1$  (111) dimers and eventually forming a complex  $7 \times 7$  (111) structure. The passivation of the dangling bonds at the unreconstructed surface produces an almost ideal  $1 \times 1$  (111) SiH surface.<sup>[27]</sup>

**The (100) surface.** The ideal (100) surface is characterized by two dangling bonds per surface atom. This surface is unstable and admits several reconstructions. The most stable one is the  $2 \times 1$  (100) reconstruction, characterized by double-bonded silicon dimers in silene configuration (the bonds being a strained  $\sigma$  bond and a very weak  $\pi$  bond). This surface is formed on heating in an ultra high vacuum (UHV); because of the weakness of the  $\pi$  bond, the  $2 \times 1$  (100)  $\text{Si}_2$  reacts almost immediately with air.<sup>[28]</sup>

#### Hydrogen-terminated surfaces—the search of environmentally stable surfaces

The common belief that defect-free hydrogen-terminated silicon would be indefinitely stable (on the laboratory time scale) in air at room temperature, explains why several methods for the hydrogen termination of (100) silicon have been developed. They include both wet and dry processes:

- the wet etch with  $\text{HF}_{\text{aq}}$  under special  $p\text{H}$  conditions of a sacrificial, thermally grown oxide;
- a two-step process, involving (i) the demolition of the native oxide by heating (at  $T > 850^\circ\text{C}$ ) under UHV with the formation of a clean  $2 \times 1$ -reconstructed surface; and (ii) the subsequent exposure to controlled amounts of atomic hydrogen H;
- the exposure of the native surface to  $\text{H}_2$  at sub-atmospheric pressure (typically in the range  $10^2$ – $10^3$  Pa) and high temperature (typically 800–1100°C).

Hydrogen-terminated surfaces can greatly differ according to the preparation procedure:

**The surface resulting after aqueous HF etching of sacrificially grown  $\text{SiO}_2$ .** The dipping of the native or thermally grown oxide in  $\text{HF}_{\text{aq}}$  results typically in a rough and heterogeneous surface. The quality of the surface is controlled by the  $p\text{H}$  of the etching solution (in turn controlled by  $\text{HF}_{\text{aq}}$  dilution and the presence of

buffering species such as  $\text{NH}_4\text{F}$  or of acids such as HCl), the amount of dissolved  $\text{O}_2$  in the water, and the duration of rinsing. Nonetheless, the following features are usually observed quite irrespective of these details. The (100) surface resulting after  $\text{HF}_{\text{aq}}$  etch displays  $1 \times 1$  reconstruction, and is characterized by a heterogeneous distribution of  $\text{SiH}_3$ ,  $\text{SiH}_2$  (prevalently), and SiH terminations.<sup>[29,30]</sup> Inspected by scanning tunneling microscopy,  $\text{HF}_{\text{aq}}$ -etched surfaces usually display no evidence for regularity; images with atomic resolution, giving evidence for  $1 \times 1$  symmetry, have been obtained only using as etchant a very acidic solution ( $\text{HF}:\text{HCl} = 1:19$ ,  $p\text{H} < 1$ ).<sup>[31]</sup> Almost ideal hydrogen termination of the (111) surface is instead obtained after etching in an HF aqueous solution buffered with  $\text{NH}_4\text{F}$  or  $\text{NH}_3$  at  $p\text{H} > 5$ .<sup>[32]</sup>

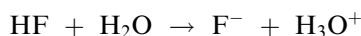
Understanding why the silicon surface after etching in  $\text{HF}_{\text{aq}}$  has prevailing hydrogen, rather than fluorine, termination is not trivial, especially in view of the fact that silicon and fluorine combine to form one of the most stable bonds. The first explanation of this fact was given by Ubara, Imura, and Hiraki in terms of polarization of Si–Si backbonds to Si–F bonds. Assuming that the strength of the Si–F bond derives from an electrostatic reinforcement because of electron transfer from silicon to fluorine, the ionicity of the Si–F bond polarizes the Si–Si backbonds, which allows an easy insertion of HF into the weakened Si–SiF bond. If this bond is cleaved with the addition of fluorine to the SiF site and of hydrogen to the other silicon atom, the ionicity is increased and so is the polarization of the residual backbonds. Reiterating this argument, one obtains that the formation of a  $\text{SiF}_n$  moiety becomes easier the higher is  $n$ , and that the process is concluded with the formation of a volatile molecule,  $\text{SiF}_4$ , and of hydrogen terminations at the silicon surface.<sup>[33]</sup>

This scheme was investigated quantum mechanically on model molecules (such as  $\text{H}_3\text{Si-SiH}_2\text{F}$  or  $\text{H}_3\text{SiF}$ ) by Trucks et al. They showed that the activation energy of the process leading to two fluorine atoms attached to the same silicon atom is 1.0 eV, while the transferring of fluorine to the adjacent silicon atom needs an activation energy of 1.4 eV. Then, the latter process is not favored and the reiterated addition of fluorine on the same SiF site is confirmed. Moreover, they showed that the Si–H bond is spontaneously destroyed by reaction with HF (the reaction being exothermic by 1.3 eV), but an activation energy of 1.2 eV was calculated for this process. The difference between the activation energy for the destruction of the Si–H bond (1.2 eV) and that for the attachment of another fluorine atom to fluorinated silicon (1.0 eV) is of 0.2 eV. Although small, it is sufficient to make the time constant of the former reaction four orders of magnitude higher than that of latter reaction.<sup>[34]</sup> These

calculations support therefore the opinion, first formulated by Ubara, Imura, and Hiraki that the formation of hydrogen-terminated surfaces is kinetically, rather than thermodynamically, controlled.

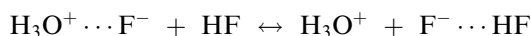
The assumption that undissociated HF is the etching agent is, however, contradicted by the following facts:

1. In diluted aqueous solution, HF is completely dissociated,



Its behavior as a weak acid is a result of the reduction of the  $\text{H}_3\text{O}^+$  activity resulting from tight ion pairing  $\text{H}_3\text{O}^+\cdots\text{F}^-$  between the oxonium and fluoride ions (Ref.<sup>[35]</sup>, Chapter 3).

2. In concentrated aqueous solution, the  $\text{H}_3\text{O}^+$  activity is increased because of the formation of the hydrogen-bonded adduct  $\text{F}^-\cdots\text{HF}$  via the equilibrium



The concentrated aqueous solution does therefore contain undissociated HF, but its binding energy to  $\text{F}^-$  is so high ( $E_b[\text{F}\cdots\text{HF}] = 2.2\text{ eV}$ ; Ref.<sup>[36]</sup>, p. 76) that the adduct  $\text{F}^-\cdots\text{HF}$  is considered a well-defined ion  $\text{HF}_2^-$  (Ref.<sup>[35]</sup>, Chapter 3).

3. In gas phase (where the etching species is undissociated HF), the attack results mainly in fluorine-terminated silicon surfaces.<sup>[37]</sup>

Following the criticism of Ref.<sup>[38]</sup> and using the results of high-level quantum mechanical calculations of the stability of the Si–Si bond in relation to its terminations, Cerofolini thus proposed an ionic route able to account for the observed hydrogen termination resulting after attack by HF-concentrated aqueous solution to thermally oxidized silicon.<sup>[39]</sup> The route is constituted by three cycles each composed by four consecutive steps, the rate-determining one being  $\text{F}^-$  transfer from the etching solution to the coma of  $\text{SiF}_n$  termination.<sup>[40]</sup>

**Hydrogen-terminated silicon via exposure to atomic hydrogen.** The exposure of  $2 \times 1$  (100)  $\text{Si}_2$  to a few langmuirs of atomic hydrogen results in nearly homogeneous surfaces. The obtained surface phase depends on the silicon temperature:<sup>[28]</sup>

- the  $1 \times 1$  dihydride phase,  $1 \times 1$  (100) $\text{SiH}_2$ , is produced at 300 K;

- the  $3 \times 1$  mixed monohydride–dihydride phase,  $3 \times 1$  (100) $\text{SiH}_2(\text{SiH})_2$ , is produced at 400 K; and
- the  $2 \times 1$  monohydride phase,  $2 \times 1$  (100) $(\text{SiH})_2$ , is produced at 600 K.

**Hydrogen-terminated silicon via exposure to molecular hydrogen.** Homogeneously hydrogen-terminated silicon is also obtained after exposing the  $\text{HF}_{\text{aq}}$  etched surface to  $\text{H}_2$  at sub-atmospheric pressure in the temperature interval 800–1100°C. According to the operative conditions, this process results in  $2 \times 1$  (100) $(\text{SiH})_2$ <sup>[29,41]</sup> or  $1 \times 1$  (100) $\text{SiH}_2$ .<sup>[42]</sup> The conditions that allow one phase to prevail on the other are not clear yet.

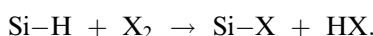
**The evolution in air of hydrogen-terminated silicon.** As already mentioned, an ideally hydrogen-terminated surface is presumed to be indefinitely stable (on the laboratory time scale) in air. The (100) surface resulting after  $\text{HF}_{\text{aq}}$  etching of the overlying oxide, however, not only is formed by a heterogeneous family of mono-, di- and tri-hydride species, but also contains silicon–oxygen centers, their amount depending on the preparation.<sup>[24]</sup> Such oxygen-containing centers are responsible for the environmental instability of these surfaces via the oxidation of the backbonds to Si–O bonds; this process, initiated at oxygen defects and mediated by adsorbed water, proceeds with the growth of an oxide cluster, and is eventually responsible for surface roughening.<sup>[24]</sup>

A microscopic model was proposed by Cerofolini and co-workers in a series of papers in terms of tunneling either of a proton from adsorbed water<sup>[43,44]</sup> or of an electron to adsorbed oxygen.<sup>[45]</sup>

### Halogen-terminated surfaces

The great environmental stability of the Si–H bond is guaranteed more by its modest polarization than by its strength. For instance, the Si–H bond dissociation energy in  $\text{H}_3\text{SiH}$  is  $92\text{ kcal mol}^{-1}$  vs. a Si–F bond dissociation energy of  $157\text{ kcal mol}^{-1}$  in  $\text{H}_3\text{SiF}$  and a Si–Cl bond dissociation energy of  $109\text{ kcal mol}^{-1}$  in  $\text{H}_3\text{SiCl}$ . The Si–H bond dissociation energy is, however, nearly the same as the Si–Br one ( $90\text{ kcal mol}^{-1}$  in  $\text{H}_3\text{SiBr}$ ) and appreciably larger than Si–I one ( $71\text{ kcal mol}^{-1}$  in  $\text{H}_3\text{SiI}$ ).<sup>[16]</sup> The relatively large polarization and length and the weak dissociation energy of the Si–I bond make this an interesting site for the functionalization of the silicon surface.

Halogen-terminated surfaces are prepared by high-temperature treatment of hydrogen-terminated surfaces with the corresponding halogen:



## The Surface of Polycrystalline Silicon

With “poly-silicon,” one intends a variety of materials, typically in the form of ingots, tiles, or films.

*Poly-silicon ingots* are produced via pyrolytic decomposition of  $\text{SiHCl}_3$ ; this material is used (after crushing, melting, and crystallization) as intermediate for the growth in Czochralski pullers of single-crystalline ingots.

*Poly-silicon tiles* are produced by melting in Bridgman furnaces the scraps remaining when the single crystalline ingots are sliced for wafer production. The poly-crystalline silicon grown by the Bridgman technique is formed by large grains (with diameter in the 1–10 cm length scale) and is one of the main materials for photovoltaic applications.

*Poly-silicon films* for microelectronics are generally produced via chemical vapor deposition from  $\text{SiH}_4$ . The typical thickness of these films is in the interval 0.1–1  $\mu\text{m}$ . The large interest of poly-silicon films in nanoelectronics is determined by the fact that in the crossbar structure at least one (but most likely two) wire arrays are formed by poly-silicon. The average grain diameter in poly-silicon films depends on the growth temperature and ranges from the nanometer length scale (for low-temperature deposition, say  $<600^\circ\text{C}$ ) to the whole film thickness (for high-temperature deposition, say  $>800^\circ\text{C}$ ); the grain diameter increases after heat treatments. After sufficiently strong heat treatments, all grains are prevalingly defined by (111) surfaces so that the functionalization of the film surface can be carried out in the same way as for the (111) surface.

## The “Surface” of Porous Silicon

Porous silicon (*por-Si*) is a sponge-like system obtained by dissolution of crystalline silicon on anodization in a solution containing  $\text{HF}$ .<sup>[46–48]</sup> Its internal area can be from  $10^2$  to  $10^3$  times its macroscopic geometrical area.<sup>[49]</sup> Pore diameter, porosity, and porous layer thickness depend sensitively on the electrolyte composition, bulk silicon resistivity, anodization current density, reaction time, and temperature. *Por-Si* is known to be hydrogen-terminated, with spectroscopic evidence<sup>[50]</sup> for  $\text{SiH}_3$ ,  $\text{SiH}_2$ ,  $(\text{SiH})_2$  groups, thus being viewed as a mixture of hydrogenated  $2 \times 1$  (1 0 0)Si and  $1 \times 1$  (1 0 0)Si. Because of its room-temperature photoluminescence,<sup>[51]</sup> *por-Si* attracted the interest of the scientific community as a light emitting material to be used in optoelectronic and photovoltaic devices.<sup>[52,53]</sup> However, owing to its compatibility with the existing silicon-processing technology,<sup>[54]</sup> *por-Si* has also found extensive applications in several other fields, from biorecognition<sup>[55]</sup> to prosthetic systems<sup>[56]</sup>

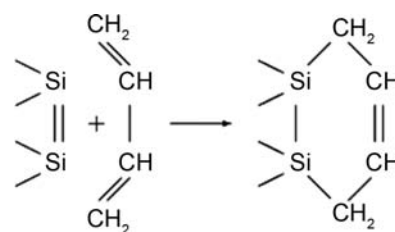
and chemical sensing.<sup>[57]</sup> Whatever the application is, the surface termination plays a crucial role: partial hydroxylation is known to completely suppress *por-Si* photoluminescence,<sup>[58]</sup> while even mild chemical environments (e.g. aqueous solutions at physiological pH) can quickly etch away its surface. Grafted organic functionalities may impart specific tunable properties.

## SILICON DERIVATIZATION

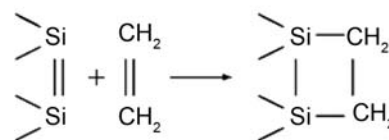
Silicon can be derivatized both via gas-phase chemistry and via wet chemistry.

### Gas-Phase Processing

The most spectacular results come from experiments carried out exposing in UHV the extremely reactive  $2 \times 1$  (100)  $\text{Si}_2$  to an atmosphere of unsaturated species. The extremely weak  $\pi$  bond of the  $2 \times 1$  (100)  $\text{Si}_2$  dimer reacts at room or even lower temperature with the  $\pi$  bond of the organic molecule via cycloaddition (e.g.,  $2 + 2$  or  $2 + 4$ ) forming superficial heterocycles:<sup>[59]</sup>



[4+2] cycloaddition



[2+2] cycloaddition

The practical exploitation of this elegant route meets, however, serious difficulties: In fact, not only does it require ultra high vacua to preserve the highly reactive silicon dimer (that might not be a technological barrier), but also can be applied for volatile reagents only. This second constraint is almost fatal for practical applications because none of the molecules that have been demonstrated as able to impart interesting electronic properties to silicon is volatile. This difficulty suggests focusing the attention on wet chemistry.

## Wet Processing

There is not yet a uniformly accepted classification of organosilicon reactions. A non-exhaustive list includes alkyl/arylation, oxoalkylation, and silanization. Detailed information of the chemistry involved in the organic functionalization of silicon is given in Ref.<sup>[60]</sup>.

### Alkyl/arylation

This reaction includes a large variety of processes and may be carried out exploiting different surface terminations, such as

- halogen-<sup>[61,62]</sup> or hydrogen-terminated<sup>[63,64]</sup> surfaces through organometallic (Grignard or organolithium) reagents,
- hydrogen-terminated surfaces through anodization in Grignard electrolytes,<sup>[65]</sup>
- hydrogen-terminated surfaces through cathodic electrografting of alkynes,<sup>[66]</sup>
- hydrogen-terminated surface through self-<sup>[67]</sup> or electrochemically activated<sup>[68]</sup> diazonium salts and
- hydrogen-terminated surfaces via hydrosilation of unsaturated molecules; this process may occur via one of the following methods:
  - mediated by a metal complex;<sup>[69–72]</sup>
  - initiated by radicals;<sup>[73]</sup>
  - photoexcitation under ultraviolet<sup>[74–76]</sup> or white light<sup>[77,78]</sup> illumination;
  - via anodic electrografting;<sup>[66]</sup>
  - under thermal<sup>[80–85]</sup> or microwave<sup>[79]</sup> excitation.

In most cases, hydrosilation has been demonstrated to occur not only with terminal alkenes and alkynes<sup>[80–83]</sup> but also with aldehydes<sup>[84]</sup> and alcohols.<sup>[85]</sup>

### Oxoalkylation

The oxoalkylation is a well-known process for the functionalization of silica surfaces. For silicon, it can be carried out at

- hydrogen-terminated surfaces through condensation of molecular reactants containing alcoholic groups,<sup>[86]</sup>
- halogen-terminated surface through condensation of alcohols<sup>[87]</sup> or primary amines.<sup>[88]</sup>

### Silanization

Silanization involves the derivation of silicon surface by means of organic groups bonded to chlorosilanes,

alkoxysilanes, or azanes. This reaction has been demonstrated to occur at

- hydroxyl-terminated surfaces<sup>[89,90]</sup> and hydrogen-terminated surfaces<sup>[91]</sup> through reaction with chlorosilanes and elimination of HCl,
- hydroxyl-terminated surfaces<sup>[92]</sup> through reaction with alkoxysilanes and elimination of alcohols, and
- hydrogen-terminated surfaces via reaction with azanes and elimination of NH<sub>3</sub>.<sup>[91]</sup>

## Integration Issues

If the attention is concentrated on the possibility of integrating the derivatization in the back-end stage of integrated circuit processes, one must consider the following constraints:

1. absence of aggressive reaction products (like HCl or HBF<sub>4</sub>),
2. occurrence even in recessed regions (where illumination and electrical bias are impossible),
3. absence of any species (like transition metals, LiCl or MgCl<sub>2</sub>) that may contaminate the silicon circuitry,
4. environmental stability (and thus absence of oxo bridges linking the organic moiety to the silicon),
5. poor dependence of the process on surface orientation and reconstruction.

The combination of all these factors leads to identify the thermally assisted hydrosilation at hydrogen-terminated surfaces of functional molecules with unsaturated terminal(s) as the candidate process for silicon functionalization.

## Hydrosilation

Hydrosilation is a reaction involving hydrogen shift from silicon to a carbon atom involved in the bond and bond formation between the silicon atom and the other carbon atom (Fig. 1). If the number  $n$  of carbon atoms in the alkane chain is small (say,  $n < 8$ ), the alkene hydrosilation occurs only in the presence of a catalyst (e.g., H<sub>2</sub>PtCl<sub>6</sub>) or after activation (radical formation); for long chains (say,  $n > 8$ ), the reaction occurs spontaneously at a temperature of about 200°C.<sup>[93]</sup>

Since hydrosilation involves only one silicon atom, it was mainly studied on the 1 × 1 (111) SiH and only few works have been devoted to study alkene hydrosilation on 1 × 1 (100)H SiH<sub>2</sub>. The hydrosilation of 1-alkenes at 1 × 1(100) SiH<sub>2</sub> is expected to occur according to pathways (I') or (I''), as shown in Fig. 1.



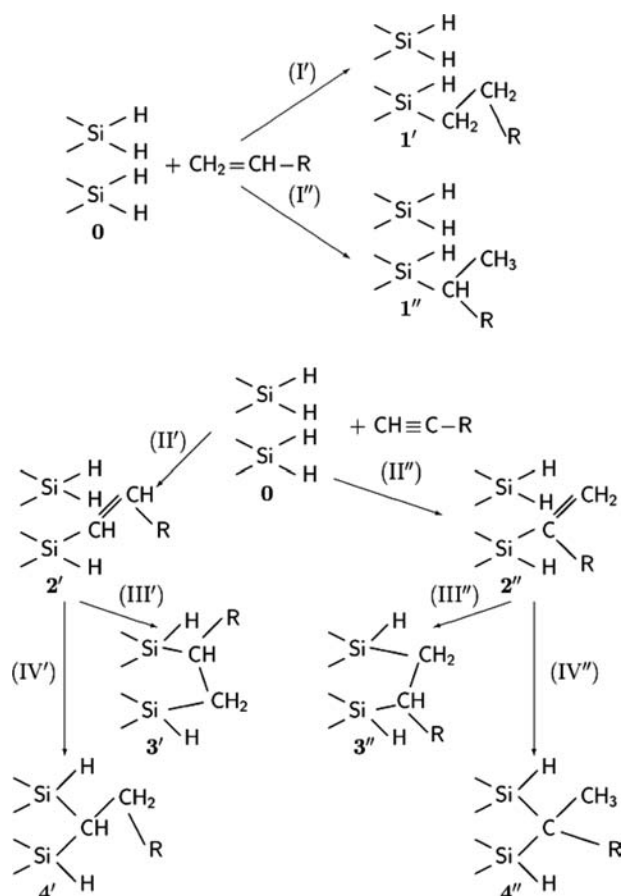


**Fig. 1** Hydrosilylation of 1-alkene [pathway (I)] and 1-alkyne [pathway (II)] at the hydrogen-terminated,  $1 \times 1$ -reconstructed, (100)-oriented, silicon surface; R denotes a suitably terminated alkane chain.

Although the reactivity of 1-alkynes is similar to that of 1-alkenes, there is, however, an important difference: after the first addition (II), the formed species,  $2'$  and  $2''$  contain a double bond in the vicinity of another hydrogen termination of silicon, so that the reaction can, in principle, proceed, via (III) or (IV), with the formation of the species  $3$  or  $4$ . Understanding the nature of the interfacial species is not without interest: for instance, if the reaction stopped after (II), the silicon surface would be equipped with a second reactive group (the C=C group) in addition to the one, if any, carried by R. The persistence of a  $\pi$  bond at the silicon-organic interface might be useful not to destroy the complete  $\pi$  conjugation of  $\pi$ -conjugated molecules grafted to the silicon surface.

## REFERENCES

- He, T.; He, J.; Lu, M.; Chen, B.; Pang, H.; Reus, W.F.; Nolte, W.M.; Nackashi, D.P.; Franzon, P.D.; Tour, J.M. Controlled modulation of conductance in silicon devices by molecular monolayers. *J. Am. Chem. Soc.* **2006**, *128*, 14,537–14,541.
- Heath, J.R.; Kuekes, P.J.; Snider, G.S.; Williams, R.S. A defect-tolerant computer architecture: opportunities for nanotechnology. *Science* **1998**, *280*, 1716–1721.
- Natelson, D.; Willett, R.L.; West, K.W.; Pfeiffer, L.N. Fabrication of extremely narrow metal wires. *Appl. Phys. Lett.* **2000**, *77*, 1991–1993.
- Melosh, N.A.; Boukai, A.; Diana, F.; Gerardot, B.; Badolato, A.; Heath, J.R. Ultrahigh density nanowire lattices and circuits. *Science* **2003**, *300*, 112–115.
- Cerofolini, G.F.; Arena, G.; Camalleri, M.; Galati, C.; Reina, S.; Renna, L.; Mascolo, D.; Nosik, V. Strategies for nanoelectronics. *Microelectr. Eng.* **2005**, *81*, 405–419.
- Cerofolini, G.F.; Arena, G.; Camalleri, M.; Galati, C.; Reina, S.; Renna, L.; Mascolo, D. A hybrid route for molecular electronics. *Nanotechnology* **2005**, *16*, 1040–1047.
- Luo, Y.; Collier, C.P.; Jeppesen, J.O.; Nielsen, K.A.; Delonno, E.; Ho, G.; Perkins, J.; Tseng, H.-R.; Yamamoto, T.; Stoddart, J.F.; Heath, J.R. Electronically configurable molecular-based logic gates. *Chem. Phys. Chem.* **2002**, *3*, 519–525.
- Zhitenev, N.B.; Jiang, W.; Erbe, A.; Bao, Z.; Garfunkel, E.; Tennant, D.M.; Cirelli, R.A. Control of topography, stress and diffusion at molecule-metal interfaces. *Nanotechnology* **2006**, *17*, 1272–1277.
- Cerofolini, G.F.; Mascolo, D. A hybrid micro-nano-molecular route for non-volatile memories. *Semicond. Sci. Technol.* **2006**, *21*, 1315–1325.
- Narducci, D.; Bernardinello, P.; Oldani, M. Investigation of gas-surface interactions at self-assembled silicon surfaces acting as gas sensors. *Appl. Surf. Sci.* **2003**, *212*, 491–496.
- Chen, J.R.; Miao, Y.Q.; He, N.Y.; Wu, X.H.; Li, S.J. Nanotechnology and biosensors. *Biotechnol. Adv.* **2004**, *22*, 505–518.
- Riu, J.; Maroto, A.; Rius, F.X. Nanosensors in environmental analysis. *Talanta* **2006**, *69*, 288–301.
- Oldani, M.; Taffurelli, A.; Narducci, D. Dynamic barrier height modulation analysis of metal-insulator-semiconductor junctions built on silicon surfaces modified by covalent organic monolayers. *Surf. Sci.* **2007**, *601*, 2845–2849.
- Gun'ko, Y.K.; Perova, T.S.; Balakrishnan, S.; Potapova, D.A.; Moore, R.A.; Astrova, E.V. Chemical modification of silicon surfaces with ferrocene functionalities. *Phys. Stat. Sol. (a)* **2003**, *197*, 492–496.
- Barton, T.J.; Boudjouk, P. Organosilicon chemistry. A brief overview. In *Silicon-Based Polymer Science. A Comprehensive Resource*; Zeigler, J.M., Gordon Fearon, F.W., Eds.; Am. Chem. Soc.: Washington, DC, 1990; 3–46.
- Walsh, R. Bond dissociation energy values in silicon-containing compounds and some of their implications. *Acc. Chem. Res.* **1981**, *14*, 246–252.
- West, R.; Fink, M.J.; Michl, J. Tetramesityldisilene, a stable compound containing a silicon-silicon double bond. *Science* **1981**, *214*, 1343–1343.

18. Cerofolini, G.F. Strategies for ultralow- $\kappa$  dielectrics for integrated-circuit interconnects. *Mater. Sci. Semicond. Process.* **2003**, *5*, 265–270.
19. Tsumuraya, T.; Batcheller, S.A.; Masamune, S. Strained-ring and double-bond systems consisting of the group 14 elements Si, Ge, and Sn. *Angew. Chem. Int. Ed.* **1991**, *30*, 902–930.
20. Buehler, E.J.; Boland, J.J. Dimer preparation that mimics the transition state for the adsorption of H<sub>2</sub> on the Si(100)-2 × 1 surface. *Science* **2000**, *290*, 506–509.
21. Pietsch, G.J.; Higashi, G.S.; Chabal, Y.J. Chemo-mechanical polishing of silicon: surface termination and mechanism of removal. *Appl. Phys. Lett.* **1994**, *64*, 3115–3117.
22. Pietsch, G.J.; Chabal, Y.J.; Higashi, G.S. Infrared absorption spectroscopy of Si(100) and Si(111) surfaces after chemomechanical polishing. *J. Appl. Phys.* **1995**, *78*, 1650–1658.
23. Morita, M.; Ohmi, T.; Hasegawa, E.; Kawakami, M.; Ohwada, M. Growth of native oxide on a silicon surface. *J. Appl. Phys.* **1990**, *68*, 1272–1281.
24. Cerofolini, G.F.; La Bruna, G.; Meda, L. Gas-phase room temperature oxidation of (100) silicon. *Appl. Surf. Sci.* **1996**, *93*, 255–266.
25. Himpsel, F.J.; McFeely, F.R.; Taleb Ibrahim, A.; Yarnoff, J.A.; Hollinger, G. Microscopic structure of the SiO<sub>2</sub>/Si interface. *Phys. Rev. B* **1988**, *38*, 6084–6096.
26. Singer, P. Wafer cleaning: Making the transition to surface engineering. *Semicond. Int.* **Oct. 1995**, *18*, 88–92.
27. Desjonquères, M.C.; Spanjard, D. *Concepts in Surface Physics*; Springer: Berlin, 1996; ch. 5, 254–266.
28. Waltenburg, H.N.; Yates, J.T. Surface chemistry of silicon. *Chem. Rev.* **1995**, *95*, 1589–1673.
29. Aoyama, T.; Goto, K.; Yamazaki, T.; Ito, T. Silicon (001) surface after annealing in hydrogen ambient. *J. Vac. Sci. Technol. A* **1996**, *14*, 2909–2915.
30. Terashi, M.; Kuge, J.; Shinohara, M.; Shoji, D.; Niwano, M. Hydrogen adsorption and desorption processes on Si (100). *Appl. Surf. Sci.* **1998**, *130/132*, 260–265.
31. Morita, Y.; Tokumoto, H. Ideal hydrogen termination of Si(001) surface by wet-chemical preparation. *Appl. Phys. Lett.* **1995**, *67*, 2654–2656.
32. Higashi, G.S.; Chabal, Y.J.; Trucks, G.W.; Raghavachari, K. Ideal hydrogen termination of the Si (1 1 1) surface. *Appl. Phys. Lett.* **1990**, *56*, 656–658.
33. Ubara, H.; Imura, T.; Hiraki, A. Formation of Si–H bonds on the surface of microcrystalline silicon covered with SiO<sub>x</sub> by HF treatment. *Solid State Commun.* **1984**, *50*, 673–675.
34. Trucks, G.W.; Raghavachari, K.; Higashi, G.S.; Chabal, Y.J. Mechanism of HF etching of silicon surfaces: a theoretical understanding of hydrogen passivation. *Phys. Rev. Lett.* **1990**, *65*, 504–507.
35. Cotton, F.A.; Wilkinson, G. *Advanced Inorganic Chemistry*, 5th Ed.; Wiley: New York, NY, 1988.
36. March, J. *Advanced Organic Chemistry*, 4th Ed.; Wiley: New York, NY, 1992.
37. Miki, N.; Kikuyama, H.; Kawanabe, I.; Miyashita, M.; Ohmi, T. Gas-phase selective etching of native oxide. *IEEE Trans. Electron Devices* **1990**, *37*, 107–115.
38. Cerofolini, G.F.; Meda, L. Chemistry at silicon crystalline surfaces. *Appl. Surf. Sci.* **1995**, *89*, 351–360.
39. Cerofolini, G.F.; Re, N. Chemical perspectives on growth and properties of ultrathin SiO<sub>2</sub> layers. In *Fundamental Aspects of Ultrathin Dielectrics on Si Based Devices*; Garfunkel, E., Gusev, E., Vul, A., Eds.; Kluwer: Dordrecht, 1998; 117–129.
40. Cerofolini, G.F. A study of the ionic route for hydrogen terminations resulting after SiO<sub>2</sub> etching by concentrated aqueous solutions of HF. *Appl. Surf. Sci.* **1998**, *133*, 108–114.
41. Kumagai, Y.; Namba, K.; Komeda, T.; Nishioka, Y. Formation of periodic step and terrace structure on Si(1 0 0) surface during annealing in hydrogen diluted with inert gas. *J. Vac. Sci. Technol. A* **1998**, *16*, 1775–1778.
42. Cerofolini, G.F.; Galati, C.; Reina, S.; Renna, L.; Spinella, N.; Jones, D.; Palermo, V. Formation of terraced, nearly flat, hydrogen-terminated, (100) Si surfaces after high-temperature treatment in H<sub>2</sub> of single-crystalline silicon. *Phys. Rev. B* **2005**, *72*, 125431.
43. Cerofolini, G.F. Kinetics of tunnel-assisted multilayer chemisorption on homogeneous surfaces. *J. Colloid Interface Sci.* **1994**, *167*, 453–456.
44. Cerofolini, G.F.; Meda, L.; Falster, R. A model for room-temperature wet oxidation of silicon. In *Semiconductor Silicon 1994*; Huff, H.R., Bergholz, W., Sumino, K., Eds.; The Electrochemical Society: Pennington, NJ, 1994; 379–388.
45. Cerofolini, G.F. Room-temperature oxidation of single-crystalline silicon. In *Silicon for the Chemical Industry III*; Oye, H.A., Rong, H.M., Ceccaroli, B., Nygaard, L., Tuset, J.K., Eds.; Tapir: Trondheim, 1996; 117–127.
46. Lehmann, V. Developments in porous silicon research. *Mater. Lett.* **1996**, *28*, 245–249.
47. Thonissen, M.; Berger, M.G.; Arens-Fischer, R.; Gluck, O.; Kruger, M.; Luth, H. Illumination-assisted formation of porous silicon. *Thin Solid Films* **1996**, *276*, 21–24.
48. Janshoff, A.; Dancil, K.P.S.; Steinem, C.; Greiner, D.P.; Lin, V.S.Y.; Gurtner, C.; Moteshare, K.; Sailor, M.J.; Ghadiri, M.R. Macroporous p-type silicon Fabry-Perot layers. Fabrication, characterization, and applications in biosensing. *J. Am. Chem. Soc.* **1998**, *120*, 12,108–12,116.
49. Canham, L.T.; Groszek, A.J. Characterization of microporous Si by flow calorimetry: Comparison with a hydrophobic SiO<sub>2</sub> molecular sieve. *J. Appl. Phys.* **1992**, *72*, 1558–1565.
50. Gupta, P.; Dillon, A.C.; Bracker, A.S.; George, S.M. FTIR studies of H<sub>2</sub>O and D<sub>2</sub>O decomposition on porous silicon surfaces. *Surf. Sci.* **1991**, *245*, 360–372.
51. Canham, L.T. Silicon quantum wire array fabrication by electrochemical and chemical dissolution of wafers. *Appl. Phys. Lett.* **1990**, *57*, 1046–1048.
52. Smestad, G.; Kunst, M.; Vial, C. Photovoltaic response in electrochemically prepared photoluminescent porous

- silicon. *Solar Energy Mater. Solar Cells* **1992**, *26*, 277–283.
53. Duttagupta, S.P.; Fauchet, P.M.; Ribes, A.C.; Tiedje, H.F.; Damaskinos, S.; Dixon, T.E.; Brodie, D.E.; Kurinec, S.K. Photovoltaic device applications of porous microcrystalline silicon. *Solar Energy Materials and Solar Cells* **1998**, *52*, 271–283.
54. Hamilton, B. Porous silicon. *Semicond. Sci. Technol.* **1995**, *10*, 1187–1207.
55. Steinem, C.; Janshoff, A.; Lin, V.S.Y.; Volcker, N.H.; Ghadiri, M.R. DNA hybridization-enhanced porous silicon corrosion: Mechanistic investigations and prospect for optical interferometric biosensing. *Tetrahedron* **2004**, *60*, 11,259–11,267.
56. Canham, L.T. Bioactive silicon structure fabrication through nanoetching techniques. *Adv. Mater.* **1995**, *7*, 1033–1037.
57. Bjorkqvist, M.; Salonen, J.; Laine, E. Humidity behavior of thermally carbonized porous silicon. *Appl. Surf. Sci.* **2004**, *222*, 269–274.
58. Voicu, R.; Boukherroub, R.; Bartzoka, V.; Ward, T.; Wojtyk, J.T.C.; Wayner, D.D.M. Formation, characterization, and chemistry of undecanoic acid-terminated silicon surfaces: patterning and immobilization of DNA. *Langmuir* **2004**, *20*, 11,713–11,720.
59. Bent, S.F. Organic functionalization of group IV semiconductor surfaces: principles, examples, applications, and prospects. *Surf. Sci.* **2002**, *500*, 879–903.
60. Buriak, J. Organometallic chemistry on silicon and germanium surfaces. *Chem. Rev.* **2002**, *102*, 1271–1308.
61. Bansal, A.; Li, X.; Yi, S.I.; Weinberg, W.H.; Lewis, N.S. Spectroscopic studies of the modification of crystalline Si(111) surfaces with covalently-attached alkyl chains using a chlorination/alkylation method. *J. Phys. Chem. B* **2001**, *105*, 10,266–10,277.
62. Nemanick, E.J.; Hurley, P.T.; Brunshwig, B.S.; Lewis, N.S. Chemical and electrical passivation of silicon (111) surfaces through functionalization with sterically hindered alkyl groups. *J. Phys. Chem. B* **2006**, *110*, 14,800–14,808.
63. Kim, N.Y.; Laibinis, P.E. Derivatization of porous silicon by Grignard reagents at room temperature. *J. Am. Chem. Soc.* **1998**, *120*, 4516–4517.
64. Song, J.H.; Sailor, M.J. Functionalization of nanocrystalline porous silicon surfaces with aryllithium reagents: formation of silicon-carbon bonds by cleavage of silicon-silicon bonds. *J. Am. Chem. Soc.* **1998**, *120*, 2376–2381.
65. Teyssot, A.; Fidélis, A.; Fellah, S.; Ozanam, F.; Chazalviel, J.-N. Anodic grafting of organic groups on the silicon surface. *Electrochim. Acta* **2002**, *47*, 2565.
66. Robins, E.G.; Stewart, M.P.; Buriak, J.M. Anodic and cathodic electrografting of alkynes on porous silicon. *J. Chem. Soc. Chem. Commun.* **1999**, 2479–2480.
67. Stewart, M.P.; Maya, F.; Kosynkin, D.V.; Dirk, S.M.; Stapleton, J.J.; McGuinness, C.L.; Allara, D.L.; Tour, J.M. Direct covalent grafting of conjugated molecules onto Si, GaAs, and Pd surfaces from aryldiazonium Salts. *J. Am. Chem. Soc.* **2004**, *126*, 370–378.
68. Henry de Villeneuve, C.; Pinson, J.; Bernard, M.C.; Allongue, P. Electrochemical formation of close-packed phenyl layers on Si(111). *J. Phys. Chem. B* **1997**, *101*, 2415–2420.
69. Buriak, J.M.; Stewart, M.P.; Geders, T.W.; Allen, M.J.; Choi, H.C.; Smith, J.; Raftery, D.; Canham, L.T. Lewis acid mediated hydrosilylation on porous silicon surfaces. *J. Am. Chem. Soc.* **1999**, *121*, 11,491–11,502.
70. Holland, J.M.; Stewart, M.P.; Allen, M.J.; Buriak, J.M. Metal mediated reactions on porous silicon surfaces. *J. Sol. State Chem.* **1999**, *147*, 251–258.
71. Zazzera, L.A.; Evans, J.F.; Deruelle, M.; Tirrell, M.; Kessel, C.R.; Mckeown, P. Bonding organic molecules to hydrogen-terminated silicon wafers. *J. Electrochem. Soc.* **1997**, *144*, 2184–2189.
72. Saghatelian, A.; Buriak, J.M.; Lin, V.S.Y.; Ghadiri, M.R. Transition metal mediated modification of porous silicon. *Tetrahedron* **2001**, *57*, 5131–5136.
73. Linford, M.R.; Fenter, P.; Eisenberger, P.M.; Chidsey, C.E.D. Alkyl monolayers on silicon prepared from 1-alkenes and hydrogen-terminated silicon. *J. Am. Chem. Soc.* **1995**, *117*, 3145–3155.
74. Cicero, R.L.; Linford, M.R.; Chidsey, C.E.D. Photo-reactivity of unsaturated compounds with hydrogen-terminated silicon(111). *Langmuir* **2000**, *16*, 5688–5695.
75. Lie, L.H.; Patole, S.N.; Hart, E.R.; Houlton, A.; Horrocks, B.R. Photochemical reaction of diazomethane with hydrogen-terminated silicon surfaces. *J. Phys. Chem. B* **2002**, *106*, 113–120.
76. Effenberger, F.; Götz, G.; Bidlingmaier, B.; Wezstein, M. Photoactivated preparation and patterning of self-assembled monolayers with 1-alkenes and aldehydes on silicon hydride surfaces. *Angew. Chem. Int. Ed.* **1998**, *37*, 2462–2464.
77. Sun, Q.-Y.; de Smet, L.C.P.M.; van Lagen, B.; Giesbers, M.; Thune, P.C.; van Engelenburg, J.; de Wolf, F.A.; Zuilhof, H.; Sudhölter, E.J.R. Covalently attached monolayers on crystalline hydrogen-terminated silicon: extremely mild attachment by visible light. *J. Am. Chem. Soc.* **2005**, *127*, 2514–2523.
78. Stewart Michael, P.; Buriak Jillian, M. Photopatterned hydrosilylation on porous silicon. *Angew. Chem. Int. Ed.* **1998**, *37*, 3257–3260.
79. Boukherroub, R.; Petit, A.; Loupy, A.; Chazalviel, J.-N.; Ozanam, F. Microwave-assisted chemical functionalization of hydrogen-terminated porous silicon surfaces. *J. Phys. Chem. B* **2003**, *107*, 13,459–13,462.
80. Sieval, A.B.; Vleeming, V.; Zuilhof, H.; Sudhölter, E.J.R. An improved method for the preparation of organic monolayers of 1-alkenes on hydrogen-terminated silicon surfaces. *Langmuir* **1999**, *15*, 8288–8291.
81. Sieval, A.B.; Opitz, R.; Maas, H.P.A.; Schoeman, M.G.; Meijer, G.; Vergeldt, F.J.; Zuilhof, H.; Sudhölter, E.J.R. Monolayers of 1-alkynes on the H-terminated Si(100) surface. *Langmuir* **2000**, *16*, 10,359–10,368.
82. de Smet, L.C.P.M.; Zuilhof, H.; Sudhölter, E.J.R.; Lie, L.H.; Houlton, A.; Horrocks, B.R. Mechanism of the hydrosilylation reaction of alkenes at porous silicon: experimental and computational deuterium labelling studies. *J. Phys. Chem. B* **2005**, *109*, 12,020–12,031.
83. Cerofolini, G.F.; Galati, C.; Reina, S.; Renna, L. Functionalization of the (100) surface of hydrogen

- terminated silicon via hydrosilation of 1-alkyne. *Mater. Sci. Eng. C* **2003**, *23*, 253–257.
84. Boukherroub, R.; Morin, S.; Wayner, D.D.M.; Bensebaa, F.; Sproule, G.I.; Baribeau, J.M.; Lockwood, D.J. Ideal passivation of luminescent porous silicon by thermal, noncatalytic reaction with alkenes and aldehydes. *Chem. Mater.* **2001**, *13*, 2002–2011.
85. Boukherroub, R.; Morin, S.; Sharpe, P.; Wayner, D.D.M. Insights into the formation mechanisms of Si-OR monolayers from the thermal reactions of alcohols and aldehydes with Si(111)-H. *Langmuir* **2000**, *16*, 7429–7434.
86. Cleland, G.; Horrocks, B.R.; Houlton, A. Direct functionalization of silicon via the self-assembly of alcohols. *J. Chem. Soc. Faraday Trans.* **1995**, *91*, 4001–4003.
87. Zhu, X.-Y.; Boiadjev, V.; Mulder, J.A.; Hsung, R.P.; Major, R.C. Molecular assemblies on silicon surfaces via Si-O linkages. *Langmuir* **2000**, *16*, 6766–6772.
88. Bergerson, W.F.; Mulder, J.A.; Hsung, R.P.; Zhu, X.-Y. Assembly of organic molecules on silicon surfaces via the Si-N Linkage. *J. Am. Chem. Soc.* **1999**, *121*, 454–455.
89. Husseini, G.A.; Peacock, J.; Sathyapalan, A.; Zilch, L.W.; Asplund, M.C.; Sevy, E.T.; Linford, M.R. Alkyl monolayers on silica surfaces prepared using heat, heated dimethylmonochlorosilanes with low vapor pressures. *Langmuir* **2003**, *19*, 5169–5171.
90. Allara, D.L.; Parikh, A.N.; Rondelez, F. Evidence for a unique chain organization in long chain silane monolayers deposited on two widely different solid substrates. *Langmuir* **1995**, *11*, 2357–2360.
91. Roth, C.A. Silylation of organic chemicals. *Ind. Eng. Chem. Prod. Res. Develop.* **1972**, *11*, 134–139.
92. Xu, D.; Sun, L.; Li, H.; Zhang, L.; Guo, G.; Zhao, X.; Gui, L. Hydrolysis and silanization of the hydrosilicon surface of freshly prepared porous silicon by an amine catalytic reaction. *New J. Chem.* **2003**, *27*, 300–306.
93. Cerofolini, G.F.; Galati, C.; Reina, S.; Renna, L. Quantitative XPS analysis of hydrosilated 1-alkene and 1-alkyne at terraced, dihydrogen terminated,  $1 \times 1$  (100) silicon. *Surf. Interface Anal.* **2006**, *38*, 126–138.

# Silicon Nanoclusters: Simulations

Aaron Puzder

Lawrence Livermore National Laboratory, Livermore, California, U.S.A.

## INTRODUCTION

The field of research surrounding the optical properties of semiconductor nanoclusters has seen enormous growth over the past decade.<sup>[1–7]</sup> As the dimensions of a semiconductor are reduced below its exciton Bohr radius, quantum confinement causes its bandgap to widen, the electronic states to become discrete, and the oscillator strength of the smallest electronic transitions to increase.<sup>[8,9]</sup> In direct gap II/VI semiconductors such as CdSe, several experiments have reproduced the one-to-one correspondence between the size and the wavelength of absorbed and emitted visible light.<sup>[4,10,11]</sup> The reproducibility and generally straightforward synthesis techniques have made CdSe the cornerstone of emerging technologies such as biological markers<sup>[6,7]</sup> and nanostructure lasers.<sup>[12]</sup> Other semiconductor nanoclusters, specifically those in group IV, are also known to absorb and emit visible light when their size is reduced to the nanometer scale.<sup>[2,5,13–15]</sup> The efficient photoluminescence (PL) observed in porous silicon<sup>[2]</sup> and in freestanding silicon nanoclusters<sup>[5,13,14]</sup> suggests that these structures may serve as an alternative for CdSe in certain applications. One benefit of exploiting the optical properties of silicon nanoclusters is its potential to be integrated within existing silicon technologies to create nanoscale optoelectronic devices. Additionally, the biocompatibility of silicon makes it an ideal candidate for replacing fluorescent dyes as biotags.

Despite the efforts being placed on synthesizing and characterizing silicon nanoclusters, the size dependence of the optical gap has, so far, been difficult to reproduce experimentally. As the physical properties of a material are strongly governed by the surface at the nanometer scale (where surface-to-volume ratios are greatly increased), the interplay of quantum confinement and surface properties is still unclear. Few surface-sensitive probes are available, and distinguishing bulk effects from surface effects is difficult. Theoretical modeling<sup>[16–21]</sup> is challenging within this size regime as a full quantum mechanical description of both the core and the surface atoms are required to provide accurate and predictive data. Developing a thorough understanding of the electronic and optical properties of silicon nanoclusters, in particular

the effect of the surface on their optical properties, is a crucial step toward the utilization of these particles for new technologies. Therefore, theoretical predictions are required to improve our understanding of the influence of the surface on the properties of silicon nanostructures.

The school of thought advocating quantum confinement as the *only* mechanism responsible for PL in silicon would suggest that, regardless of the specific surface chemistry, the same results should be observed as long as all the surface dangling bonds are saturated.<sup>[22–24]</sup> However, recent studies have shown that the surface can affect the optical properties of silicon.<sup>[25–29]</sup> The combination of different passivating surfaces, contaminant atoms, and surface reconstructions are often responsible for disagreement among different experiments and among theories in characterizing the gap dependence on size.

## BACKGROUND

Taking into account the difference between absorption and emission further contributes to experimental and theoretical discrepancies. Experiments generally measure the PL, i.e., the emitted light, whereas theory generally calculates an absorption spectrum, or the lowest absorption gap. In CdSe, this difference between absorption and emission has been attributed to a “dark exciton,”<sup>[30]</sup> a state with zero oscillator strength which will not absorb, but may emit a photon. In silicon, this difference may be due to structural relaxation of the cluster while in its excited state.<sup>[31–38]</sup> Although opinion is divided, evidence exists that this difference can vary by 0.5–1 eV depending on the size of the cluster and the local surface.<sup>[34–38]</sup>

In this entry, we present ab initio calculations of a number of hydrogen-passivated silicon nanoclusters with diameters of up to 2 nm. In our calculations, we replaced one or more of the hydrogen atoms with a number of different passivants including oxygen, sulfur, CH<sub>2</sub>, fluorine, chlorine, and a hydroxyl group (OH). We also reconstructed the silicon surfaces, forming either reconstructed dimers or reconstructed steps. We found that any passivant or reconstruction that distorts the tetrahedral  $sp^3$  network significantly

reduces the gap compared to that of a completely hydrogenated cluster. We found that more than one of these passivants on a single cluster reduces the gap even further, allowing a wide range of gaps to be observed. Conversely, we show that single-bonded passivants have a minimal effect on the optical gap. Finally, we calculated the Stokes shift of different structures by relaxing each cluster in its excited state. Depending on the size and surface, we find that this difference can be as large as 1.2 eV. These results may provide an explanation for the discrepancies found among various experiments with each other<sup>[5,13,22–25,39,40]</sup> and with theory.<sup>[16,17,20,21]</sup>

The rest of this entry is organized as follows: the section “Computational Methods” discusses the theoretical methods we used to perform our calculations, “Effect of Different Surface Passivation” discusses the effect of different surface passivants on silicon nanoclusters, “Surface Reconstructions” discusses the effect of surface reconstructions on silicon nanoclusters, “Emission Gaps Via the Stokes Shift” shows how absorption and emission may generate different results in silicon nanoclusters, and finally the last section offers some concluding remarks.

## COMPUTATIONAL METHODS

Ab initio calculations, capable of covering a range of silicon nanoclusters up to 2 nm in diameter, were performed by using density functional theory (DFT) and quantum Monte Carlo (QMC). Our DFT calculations are based on the local density approximation (LDA) using the Ceperley–Alder exchange–correlation functional and potential<sup>[41]</sup> and the generalized gradient approximation (GGA) using the Perdew–Burke–Ernzerhof (PBE) functional.<sup>[42]</sup> We employed a pseudopotential plane wave approach<sup>[43]</sup> with periodic boundary conditions applied to a supercell having a large enough spacing so that no interactions existed between the periodic replicas. All the clusters were placed in a box with enough vacuum region between clusters for the total charge density to approach zero ( $<10^{-7}$ ) well before the supercell edge. The interactions between the ionic cores and the valence electrons are described by a fully norm conserving, non-local pseudopotential of the Hamann type,<sup>[44]</sup> except for hydrogen in which we used a pseudopotential of the Giannozzi type.<sup>[45]</sup> The Kohn–Sham orbitals are expanded in a plane wave basis set,  $\psi(\mathbf{r}) = \sum_{\mathbf{G}} C_{\mathbf{G}} e^{i\mathbf{G}\cdot\mathbf{r}}$ , where  $C_{\mathbf{G}}$  is the Fourier coefficient,  $\mathbf{G}$  is a three-dimensional reciprocal lattice vector, and  $\mathbf{r}$  is the three-dimensional coordinates in real space. The kinetic energy cutoff used is at least 35 Ry corresponding to about  $10^5$  plane waves in a cell of 41–46 a.u. per side. We found

that a higher cutoff (up to 70 Ry) had a negligible effect (less than 0.3% in all cases) on the difference between eigenvalues of the highest occupied molecular orbital (HOMO) and the lowest unoccupied molecular orbital (LUMO), i.e., the single-particle gap as defined within DFT.

All silicon clusters were initially constructed on a diamond structure lattice with bulk silicon–silicon bond lengths. Dangling bonds were passivated with hydrogen placed along the appropriate tetrahedral direction at the experimental silicon–hydrogen distance in SiH<sub>4</sub>. The structures were then relaxed to zero temperature by using molecular dynamics simulations, with the ions treated classically and the electrons quantum mechanically, until the correct ground state structure was reached. In every case, each atom was relaxed until the residual forces on all atoms were less than  $2 \times 10^{-4}$  eV/Å. GGA calculations on a number of representative clusters, including full geometry reoptimization, tested the effect of gradient corrections in the exchange–correlation potential. Despite slight changes to the structure (e.g., 1.6% longer silicon–silicon bond lengths), the single-particle gaps agree to within 0.05 eV with LDA gaps for all cases tested. Nanoclusters with reconstructed surfaces were generated by first removing a hydrogen atom from each of any neighboring pairs of SiH<sub>2</sub> groups, forming an additional Si–Si bond (dimers). Second, clusters large enough to support a single dihydride bonding with a step ( $\geq 1.8$  nm) were constructed, further reducing the hydrogen coverage of the surface.

Although the LDA HOMO/LUMO gap was shown to qualitatively reproduce the trends of the optical gap, a proper treatment of the self-energy and the exciton binding energy (Coulomb interaction between the excited electron and its resulting hole) requires a more accurate tool to quantitatively calculate optical gaps. For this purpose, we adopted the fixed node, diffusion quantum Monte Carlo (DMC) method,<sup>[46–48]</sup> in which one solves the many-particle, imaginary time Schrödinger equation  $-\partial_{\tau}\Phi(\mathbf{R},\tau) = (\hat{H} - E_{\text{T}})\Phi(\mathbf{R},\tau)$ , where  $\tau$  is imaginary time,  $\mathbf{R} = (r_1, r_2, \dots, r_N)$  is a configuration of electron coordinates in real space,  $\hat{H}$  is the many-body Hamiltonian of the system, and  $E_{\text{T}}$  is a trial energy. Representing the Schrödinger equation in this form allows it to be stochastically sampled when recast in integral form. The true ground state wavefunction is then projected out from a suitably chosen trial wavefunction. Our trial wavefunctions are of the Slater–Jastrow form with one-, two-, and three-body terms expanded as Chebyshev polynomials,<sup>[49]</sup>

$$\Psi = D^{\dagger} D^{\downarrow} \exp \left[ \sum_i^N \chi(r_i) + \sum_{i<j}^N u(r_i, r_j, r_{ij}) \right] \quad (1)$$



We use the recently implemented linear scaling QMC approach<sup>[48]</sup> which constructs the Slater determinants,  $D^\dagger$  and  $D_1$ , from a set of maximally localized Wannier functions.<sup>[50]</sup> The one-body,  $\chi$ , and two- and three-body Jastrow  $u$  functions contain 18–40 variational parameters which are optimized by using the variance minimization approach.<sup>[51]</sup>

Within the QMC approach, the optical gap is defined as  $E^{\text{opt}} = E_N^* - E_N$ , where  $E_N$  is the ground state total energy of the system with  $N$  electrons filling all the occupied states and  $E_N^*$  is the total energy of the system in an excited state. Both the excited electron and the resulting hole introduced into the valence band are present in the system at the same time by exciting an electron from an occupied (valence) orbital to an unoccupied (conduction) orbital. As QMC is a full many-body formalism, gaps calculated within QMC do not suffer from the LDA “band gap problem,” even if the nodal structure for the QMC wavefunction is constructed from LDA orbitals.

The Stokes shift calculations were carried out by considering Frank–Condon-like relaxations for a number of different structures. On absorption of a photon, a cluster undergoes a vertical electronic excitation (Fig. 1). During the excitation, the atoms are instantaneously frozen in their ground state positions. Once in the excited electronic state, the atomic geometry of the cluster relaxes to a lower energy configuration (point 3 in Fig. 1), as the electronic excitation of the cluster has generated new forces on the atoms.<sup>[34,36]</sup>

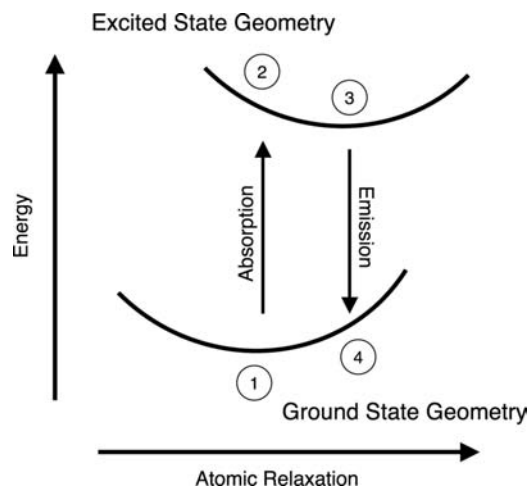


**Fig. 1** Energy states involved in the transitions leading to the Stokes shift. Point 1 is the relaxed ground state structure, point 2 is the forced excited state in the ground state structure, point 3 is the relaxed excited state, and point 4 is the ground state in the excited state relaxed structure. The Stokes shift has been calculated by either a difference between total energies  $(E_2 - E_1) - (E_3 - E_4)$  or the single-particle (optical) gap of the structure in state  $E_1$  and  $E_4$  in LDA (QMC).

We calculated the Stokes shift by performing this relaxation within LDA, i.e.,  $E^{\text{Stokes}} = (E_2 - E_1) - (E_3 - E_4)$ , where  $E_{1-4}$  are the total energies at each of the points in Fig. 1. Within QMC, the Stokes shift was calculated as the difference in the gaps of each configuration. A full detailed description of this method is given in Ref.<sup>[37]</sup>.

## EFFECT OF DIFFERENT SURFACE PASSIVATION

### One Impurity Atom

The effect of different passivants on hydrogenated silicon nanoclusters was initially studied within the LDA on  $\text{Si}_{35}\text{H}_{36}$  clusters (diameter 1.1 nm). Keeping the entire cluster intact, we replaced a single hydrogen with the highly electronegative fluorine atom, which is present in hydrogen fluoride (HF), commonly used for etching porous silicon. Other highly electronegative species, such as chlorine and an OH group, were also considered. In addition to having similar properties to fluorine, chlorine is used often as a precursor in colloidal synthesis of silicon nanoparticles, while OH is a possible passivant of nanoclusters synthesized in a peroxide solution. Fig. 2A shows the density of states (DOS) of each of these systems. The DOS profiles for the clusters with single-bonded passivants (H, F, Cl, OH) are virtually identical, indicating that most single-bonded passivants are likely to generate similar single-particle gaps, regardless of their electronegativity

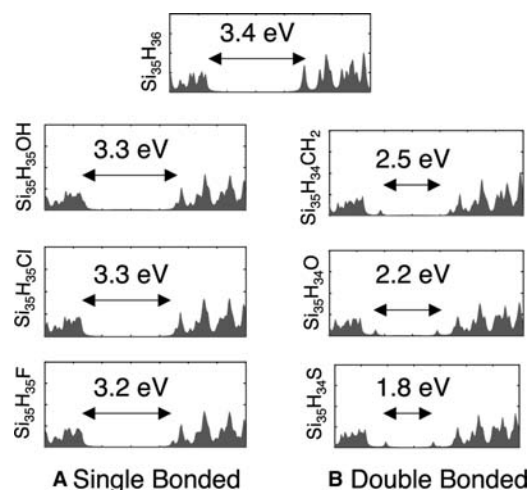


**Fig. 2** Local density approximation calculation of the electron density of states and single-particle gaps of 1.1-nm hydrogenated silicon clusters with A) single-bonded and B) double-bonded passivants. Each curve is Lorentzian broadened by 0.06 eV. The fully hydrogenated (idealized) case is given in the top center.

or individual atomic levels. As shown in Fig. 3A, the probability density of the HOMO and the LUMO of  $\text{Si}_{35}\text{H}_{36}$  are both confined to the core of the cluster. This confinement is similar to that seen in clusters with single-bonded passivants. Using chlorine as an example (Fig. 3B), the HOMO and LUMO densities are only slightly altered with respect to the fully hydrogenated cluster, as the majority of the HOMO and LUMO density remains core-confined.

The second set of passivants considered here are those forming a double bond with a surface silicon atom. In addition to the common contaminant oxygen, we considered sulfur and  $\text{CH}_2$ . The effects of the double-bonded passivants on the HOMO/LUMO gap are profound (Fig. 2B), with the LDA gap decreasing from the completely hydrogenated case by an amount ranging from 0.9 eV (when  $\text{CH}_2$  is added) to 1.6 eV (when sulfur is added). These results offer an explanation of the discrepancies observed in the measured values of the optical gap in silicon nanoclusters. In experiments performed in the presence of oxygen,<sup>[5,22–25]</sup> the actual transition may involve localized oxygen states. Fig. 3C shows that these states in  $\text{Si}_{35}\text{H}_{34}\text{O}$  are indeed localized around the double bond, with little of the core confinement seen in the  $\text{Si}_{35}\text{H}_{35}\text{Cl}$

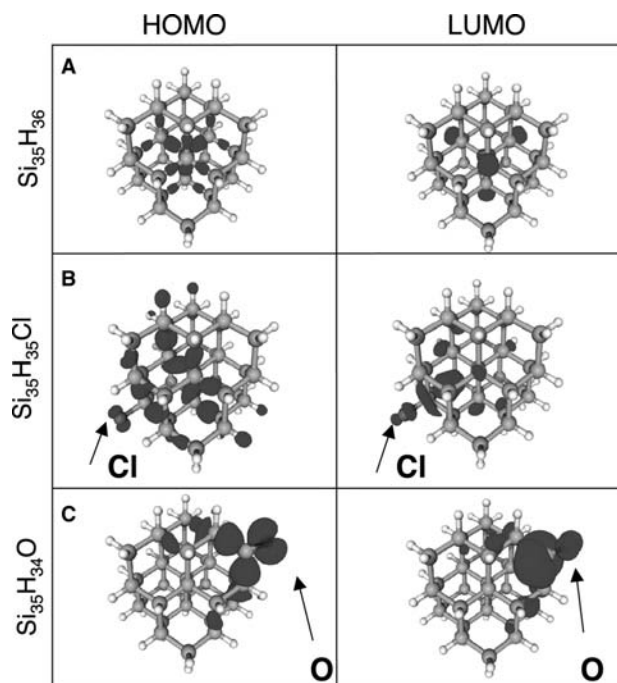


**Fig. 3** The density of the highest occupied molecular orbital (HOMO) and the lowest unoccupied molecular orbital (LUMO) for A)  $\text{Si}_{35}\text{H}_{36}$ , B)  $\text{Si}_{35}\text{H}_{35}\text{Cl}$ , and C)  $\text{Si}_{35}\text{H}_{34}\text{O}$ . The isosurfaces are plotted at 50% the maximum value for A) and B), and at 10% the maximum value for C). In the ball and stick representation, Si is gray, H is white, and O (Cl) is red (pink).

cluster. This localization suggests that these states might be pinned at a fixed energy determined by the oxygen atom and relatively independent of the size of the cluster.

### Size Dependence of the Effects of Oxygen Passivation

The size dependence of the effect of oxygen passivation on the optical properties of hydrogenated silicon nanoclusters was carried out in silicon clusters with a single oxygen atom, double-bonded to the surface. Fig. 4A shows the values of the LDA HOMO–LUMO gap (solid circles and squares) for these clusters, as well as those with pure hydrogen termination as a function of the diameter,  $D = a(3/4\pi N)^{1/3}$ , where  $N$  is the number of silicon atoms and  $a$  is the lattice constant. In clusters without oxygen contamination, the gap

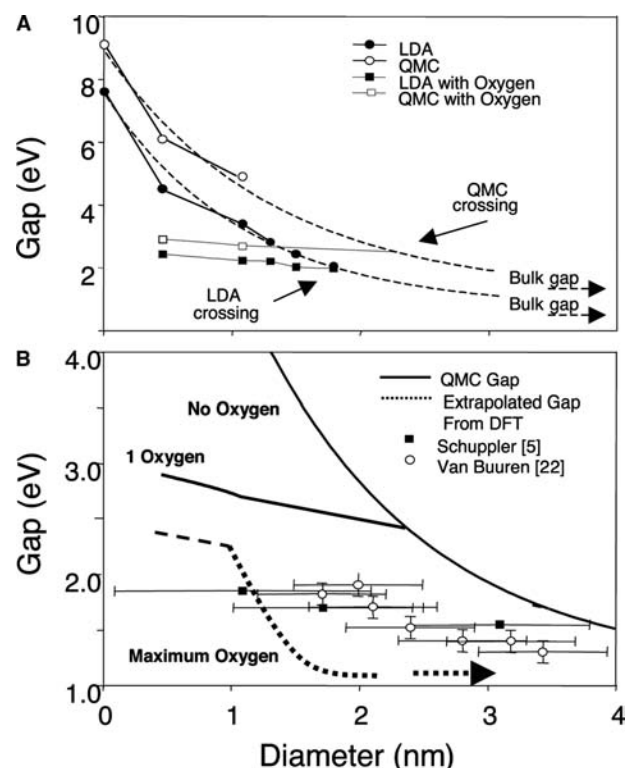


**Fig. 4** A) Local density approximation (LDA) and quantum Monte Carlo (QMC) calculations of the single-particle and optical gaps of hydrogenated Si clusters with and without oxygen as a function of size. The curves are fit to the points and the bulk value, and have been extrapolated to estimate the crossing point beyond which the “oxygen gap” will no longer be observed. B) Comparison of QMC predictions of the optical gap of silicon clusters with and without oxygen to experimental results. The maximum oxygen curve is extrapolated by shifting the LDA calculated curve by an amount equal to the QMC shift in a single oxygen-contaminated cluster.

increases as the size of the cluster decreases, thus demonstrating quantum confinement effects. In clusters with an oxygen contaminant, the “oxygen gap” is smaller than the gap of the purely hydrogenated clusters for clusters smaller than 1.8 nm. As the cluster size increases beyond this critical 1.8-nm diameter, the fundamental HOMO/LUMO gap of pure hydrogenated silicon nanoclusters decreases below this “oxygen gap” and the lowest gap is governed by the core transitions.

Quantum Monte Carlo calculations on several clusters terminated completely with hydrogen, and those including a double-bonded oxygen verify that the LDA trends are well reproduced by QMC (Fig. 4A). The shift in the gap from LDA to QMC in totally hydrogenated clusters is much greater (around 1.5 eV) than in those with oxygen contamination (around 0.6 eV). We believe that the difference in shifts originates from the larger excitonic binding in the oxygen-contaminated clusters, where the oxygen-derived HOMO and LUMO states are more localized than in the absence of such contaminants. Extrapolation of our QMC calculations (dashed line in Fig. 4A) suggests that the critical size beyond which the “oxygen gap” will no longer be observed is between 2 and 2.5 nm, larger than the 1.8 nm size predicted by LDA, yet smaller than the 3.0 nm predicted by empirical tight-binding calculations.<sup>[25]</sup>

### Effect of Multiple Oxygen Termination

In Fig. 4B, we compare our QMC predictions for the optical gap of silicon nanoclusters with two experiments in which oxygen was present. The optical gap predicted by our QMC calculations for clusters passivated with a single oxygen double-bonded to the surface is too large compared with this experimental data.<sup>[5,22]</sup> In addition to the problem of wide experimental size distribution, the effect of multiple oxygen passivation should be considered. The strain introduced by the presence of a single oxygen passivant will not necessarily deter the bonding of additional oxygen passivants, which may also affect the gap. In fact, if the chemical potentials of hydrogen and oxygen is such that it is favorable to replace two surface hydrogen atoms with an oxygen, the oxygenation reaction is likely to continue.<sup>[28]</sup> By shifting our QMC-predicted optical gaps according to the effects of multiple oxygen passivation predicted within LDA, we compare these predictions with the aforementioned experiments (Fig. 4B). The wide range of possible gaps that may be obtained when oxygen contaminates the surface can perhaps explain the wide discrepancy between so many experiments, in which either oxygen was present or the impurities were unknown.

## DISCUSSION

The gaps of silicon clusters containing fluorine, chlorine, and OH indicate that the electronegativity of a passivant does not play a key role in altering the gap. That OH does not alter the gap indicates that lone pair states are not responsible for the reduction observed by the presence of oxygen. This conclusion is further supported by the results obtained for clusters passivated with CH<sub>2</sub>, which has no lone pair when double-bonded to the cluster, yet closes the gap significantly more than all the single-bonded passivants. The presence of a double bond induces a considerable distortion of the tetrahedral *sp*<sup>3</sup> network on the surface and this distortion is possibly responsible for a gap reduction. To support this conclusion, we considered oxygen-bonded in different geometries. In addition to replacing two hydrogen atoms from an SiH<sub>2</sub> surface group to form an Si=O double bond, oxygen may also bond with the surface of a silicon nanocluster in a bridged (Si–O–Si) network, replacing two hydrogen atoms from two separate Si atoms.

Two different silicon nanoclusters were compared, both with a diameter of ≈1 nm (Si<sub>29</sub>H<sub>36</sub> and Si<sub>35</sub>H<sub>36</sub>). In Si<sub>29</sub>H<sub>36</sub>, the proximity of SiH<sub>2</sub> pairs on a (100)-like facet allows oxygen to replace two hydrogens (Si<sub>29</sub>H<sub>34</sub>O) from adjacent SiH<sub>2</sub> groups and to form a bridged bond without significantly distorting the *sp*<sup>3</sup> network. The bond angle between any of the atoms bonded to the silicon and the oxygen is altered by no more than 2° from the initial tetrahedral bonding angle. The resulting LDA single-particle gap is only 0.5 eV lower than the LDA gap in Si<sub>29</sub>H<sub>36</sub> and the QMC gap is also only 0.5 eV lower than the Si<sub>29</sub>H<sub>36</sub> QMC gap. The shift from LDA to QMC is therefore 1.5 eV and *not* 0.6 eV as in the cluster with a double-bonded oxygen. In Si<sub>35</sub>H<sub>34</sub>O, no such aligned dihydrides exists, and so forming an Si–O–Si bridge significantly alters the ideal bond network, with the resulting bond angles distorted by more than 30° from the original *sp*<sup>3</sup> structure. This distortion causes a gap reduction by a significantly greater amount than that of the hydrogenated cluster, over 1 eV in LDA and almost 3 eV in QMC. Therefore any passivation process that significantly distorts the *sp*<sup>3</sup> network will also alter the gap.

## SURFACE RECONSTRUCTIONS

Because the optical gap in silicon nanoclusters will change as a result of bonding networks at the surface and not necessarily because of a specific contaminant atom, surface reconstruction may also affect the optical gap.<sup>[29,52]</sup> Fig. 5 shows the atomic structure of three 1.8-nm clusters: 1) Si<sub>148</sub>H<sub>120</sub>, which has an

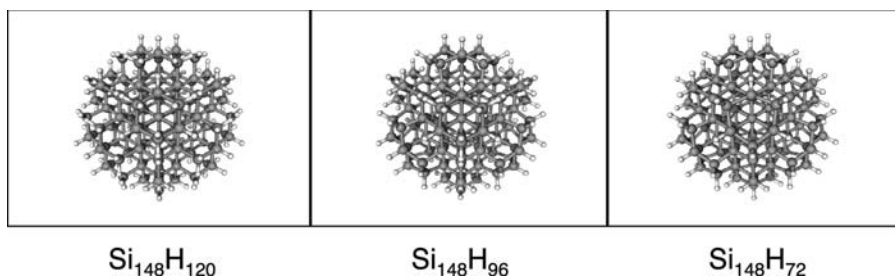


**Fig. 5** Hydrogen-passivated, 1.8-nm-diameter silicon nanocluster A) without a reconstructed surface, B) with reconstructed dimers on the surface, and C) with reconstructed dimers and steps on the surface. In the ball-and-stick model, the Si atoms are gray and the H atoms are white.

unreconstructed surface, 2)  $\text{Si}_{148}\text{H}_{96}$ , which has reconstructed dimers but no reconstructed steps, and 3)  $\text{Si}_{148}\text{H}_{72}$ , which has reconstructed dimers and steps. The Si–Si bond lengths of the reconstructed dimers and the reconstructed steps are similar to those predicted by LDA calculations for flat, hydrogen passivated (100) surfaces<sup>[53]</sup> and reconstructed steps on a (100) surface,<sup>[54]</sup> respectively. The dimer reconstructions are not limited to large clusters with (100)-like facets, but may also occur on clusters with aligned dihydrides, such as  $\text{Si}_{66}\text{H}_{64}$  and  $\text{Si}_{29}\text{H}_{36}$ ,<sup>[55]</sup> although reconstructed steps will not form on clusters smaller than 1.8 nm. That these reconstructions are energetically advantageous in specific situations is demonstrated through the following argument.

The additional energetic advantage from forming dimers on curved silicon surfaces is reflected in the negative formation energy of  $\text{Si}_{148}\text{H}_{120}$  with respect to  $\text{SiH}_4$  and bulk silicon. A negative formation energy is consistent with the formation of nanoscale features in porous silicon formed by HF etching. To predict the relative stabilities of the structures thermodynamically (Fig. 6), we follow a prescription previously used for flat silicon surfaces.<sup>[53]</sup> The relative stability of these nanocluster structures is obtained by the zero temperature formation energy,  $\Omega$ , given by

$$\Omega = E_{\text{Tot}} + E_{\text{ZPE}} - n_{\text{Si}}\mu_{\text{Si}} - n_{\text{H}}\mu_{\text{H}} \quad (2)$$

where  $E_{\text{Tot}}$  is the total energy,  $E_{\text{ZPE}}$  is the zero-point energy,  $n_{\text{Si}}(n_{\text{H}})$  is the number of silicon (hydrogen) atoms, and  $\mu_{\text{Si}}(\mu_{\text{H}})$  is the chemical potential of bulk silicon (hydrogen gas). At  $\mu_{\text{H}} > -0.3$  eV, the structure with the most hydrogen on the surface, and hence no reconstructions ( $\text{Si}_{148}\text{H}_{120}$ ), has the lowest formation energy. As  $\mu_{\text{H}}$  decreases, it becomes energetically favorable to form dimers ( $\text{Si}_{148}\text{H}_{96}$ ). When  $\mu_{\text{H}}$  is decreased even further ( $< -0.7$  eV), reconstructed steps ( $\text{Si}_{148}\text{H}_{72}$ ) become energetically favorable. Fig. 6 demonstrates regions in which each structure is more favorable. Increasing the temperature reduces  $\mu_{\text{H}}$  due to entropic effects; therefore, we predict that nanoclusters synthesized in an  $\text{H}_2$  environment will generally have surfaces with reconstructed dimers and steps, while those formed in higher  $\mu_{\text{H}}$  environments, for

example, in colloidal solutions, may have unreconstructed surfaces.

Reconstructed dimers and steps should affect the electronic and optical properties of silicon nanoclusters as a result of the distortion of the  $sp^3$  bonding network. Fig. 7 shows calculated single-particle gaps within LDA and the optical gap within QMC. Reconstructed dimers demonstrate a relatively flat impurity level at  $\approx 2$  eV (as calculated within the LDA). This flat impurity level is confirmed by QMC calculations, although shifted higher by about 1 eV (the curvature in  $\text{Si}_{29}\text{H}_{24}$  causes the gap in that structure to be slightly larger). The impurity state does not occur in clusters larger than  $\approx 2$  nm and thus reconstructed dimers will not affect larger clusters. However, reconstructed steps generate a separate impurity level at  $\approx 0.7$  eV (as calculated within the LDA). A QMC calculation of this cluster reveals a gap about 0.5 eV higher than the LDA value at  $\approx 1.2$  eV. Because this level is about the same as the bulk gap value of Si, such an impurity level may be seen in clusters as large as 5 nm.

Evidence for the existence of reconstructed surfaces has been observed in porous silicon and in

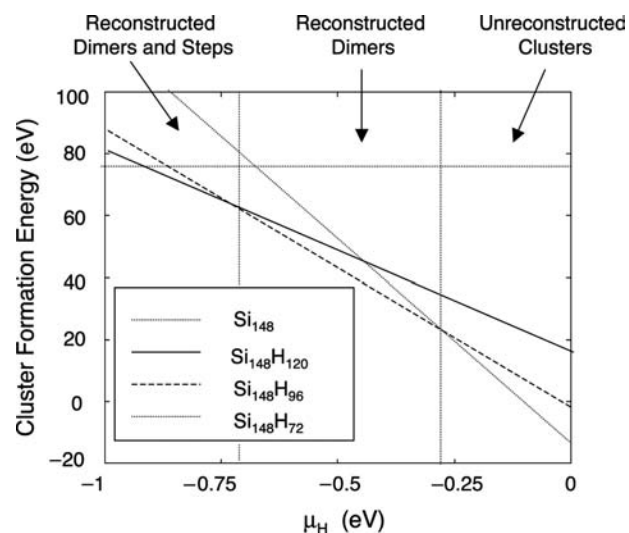


**Fig. 6** Local density approximation formation energy of  $\text{Si}_{148}$  nanoclusters with different surface reconstructions. The origin of  $\mu_{\text{H}}$  is the value at which the formation energy of silane is zero.



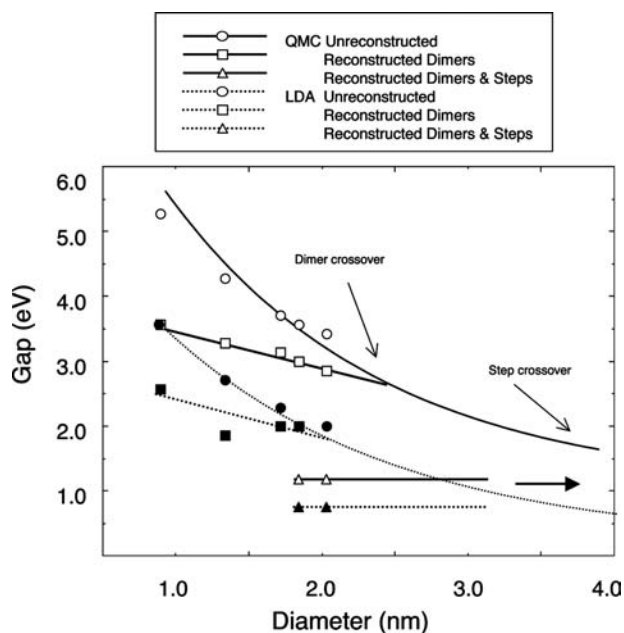


**Fig. 7** Local density approximation (LDA) and quantum Monte Carlo (QMC) gaps of hydrogenated silicon nanocrystals with and without reconstructed dimers and steps. The point at which the impurity levels due to different reconstructions will no longer be observed are indicated by arrows.

nanoclusters about 1.8 nm in diameter. Van Buuren et al.<sup>[56]</sup> used X-ray absorption and valence band photoemission to investigate the shift in the valence and the conduction band edges of porous silicon as a function of thermal annealing. The wavelength of the observed PL suggests that the optical emission in these samples originates from nanoscale features with dimensions and quantum confinement effects similar to the nanoclusters studied here. At an annealing temperature of 500°C, the optical gap is reduced by 1 eV from that at room temperature, consistent with the reduction predicted in Fig. 7 due to reconstruction. Additionally, van Buuren et al. present mass spectrometer measurements showing significant hydrogen evolution during annealing beginning at 400°C, consistent with hydrogen desorption from SiH<sub>4</sub> species. This result is in agreement with our results, demonstrated in Fig. 6, in which structures with reconstructed surfaces and lower hydrogen content are favored as the temperature is increased, that is where  $\mu_{\text{H}}$  is decreased.

Wilcoxon, Samara, and Provencio<sup>[39]</sup> observed two distinct gaps and excitonic lifetimes in similarly sized clusters synthesized using inverse micelles. Our QMC calculations of optical gaps of unreconstructed and reconstructed surfaces of clusters this size are in good agreement with the two gaps measured in that particular work. Therefore, our calculations strongly support the conjecture that the smaller of these two gaps is attributable to surface reconstruction. Therefore in

experiments in which oxygen contamination is controlled, smaller optical gaps than those theoretically predicted may occur, as surface reconstruction is another potential source for disagreement between theory and experiment.

## EMISSION GAPS VIA THE STOKES SHIFT

In addition to the different surface structures affecting the absorption gap from the idealized structure, the difference between the absorption gap and the emission gap is yet another source of discrepancy among experimental results and theoretical calculations. The difference between the two gaps is often referred to as the Stokes shift. Calculating this difference exclusively through relaxation of the excited state, Table 1 summarizes our calculated Stokes shifts for a number of silicon nanoclusters with different surface contaminants and reconstructions. The large difference between absorption and emission gaps could account for further discrepancy among experiment and theory.

Generally, the emission gap is red shifted relative to the absorption gap. The LDA and QMC values of the Stokes shift show that, in a similar manner to optical gaps, the LDA qualitatively predicts correct trends as a function of size and surface structure; however, LDA consistently underestimates the value of the Stokes by 0.2–0.3 eV compared with QMC. As we were able to do many more LDA calculations, we quote those results here. Clusters with unreconstructed hydrogenated surfaces produce values of the Stokes shift that range from 0.3 to 0.8 eV as a function of size. Clusters with oxygen double-bonded (Si–O) to the surface exhibit larger Stokes shifts of 1.2 eV, relatively independent of size. Clusters with reconstructed surfaces and surfaces with bridged oxygen consistently exhibit the smallest Stokes shifts, ranging from 0.1 to 0.3 eV as a function of size.

To gain insight into the large differences in the above Stokes shifts, we examined the nature of the electronic states responsible for absorption and emission, i.e., the band edge HOMO and LUMO. The HOMO and LUMO orbitals of three clusters, all approximately 1 nm in size, are shown in Fig. 8. Fig. 8A shows that in a nanocluster with pure hydrogen passivation and no reconstruction of the surface (e.g., Si<sub>35</sub>H<sub>36</sub>), the HOMO and LUMO densities are delocalized throughout the core of the nanocluster. Fig. 8B shows that the HOMO and LUMO densities are also delocalized in clusters with surface reconstruction, but around the surface. Finally, Fig. 8C shows that the placement of a single oxygen atom in a Si=O double-bonded position on the surface of an otherwise unreconstructed cluster (e.g., Si<sub>35</sub>H<sub>34</sub>O) almost completely localizes both the HOMO and

**Table 1** Local density approximation (LDA) and Quantum Monte Carlo (QMC) calculated absorption gaps and Stokes shifts for a number of silicon nanoclusters with different surface structures

Cluster	Structure	Diameter	Optical gap		Stokes shift		RMS displacement
			LDA	QMC	LDA	QMC	
Si <sub>29</sub> H <sub>36</sub>	Hydrogenated	0.9	3.6	5.3(1)	0.69	1.0(1)	0.31
Si <sub>35</sub> H <sub>36</sub>	Hydrogenated	1.1	3.4	5.0(1)	0.57	0.8(1)	0.25
Si <sub>66</sub> H <sub>64</sub>	Hydrogenated	1.3	2.8	4.7(1)	0.50		0.19
Si <sub>87</sub> H <sub>76</sub>	Hydrogenated	1.5	2.5	4.2(2)	0.22		0.14
Si <sub>148</sub> H <sub>120</sub>	Hydrogenated	1.8	2.1	3.9(3)	0.13		0.11
Si <sub>211</sub> H <sub>140</sub>	Hydrogenated	2.0	2.0		0.06		0.05
Si <sub>29</sub> H <sub>24</sub>	Reconstructed	0.8	2.6	3.6(1)	0.34	0.4(1)	0.13
Si <sub>66</sub> H <sub>40</sub>	Reconstructed	1.3	1.9	3.3(1)	0.16		0.08
Si <sub>29</sub> H <sub>34</sub> O	Si–O–Si	0.9	3.1	4.7(1)	0.27	0.5(1)	
Si <sub>35</sub> H <sub>34</sub> O	Si=O	1.1	2.2	2.5(1)	1.16	1.3(1)	0.30
Si <sub>66</sub> H <sub>62</sub> O	Si=O	1.3	2.2		1.22		0.33
Si <sub>87</sub> H <sub>74</sub> O	Si=O	1.5	2.0		1.13		0.31

All values are quoted in eV and QMC statistical error bars are shown in parenthesis. The RMS displacements are in Å. Structures with bridged oxygen are labeled Si–O–Si and double-bonded oxygen is labeled Si=O.

LUMO densities on the Si=O double bond at the surface of the cluster.

The structural changes resulting from the creation of an exciton in each cluster, expressed as the root

mean squared (RMS) displacement of the atoms, are summarized in Table 1, and more visually expressed in the right-hand column of Fig. 8. The RMS displacement of atoms in the completely hydrogenated structures, e.g., Si<sub>35</sub>H<sub>36</sub>, is  $\approx 0.3$  Å for 1-nm structures and decreases quickly to  $< 0.1$  Å as the cluster size increases to around 2 nm. Because the change in charge density resulting from the HOMO to LUMO excitation is distributed throughout the cluster, all atoms in the cluster experience forces of approximately equal magnitude. The displacements shown in Fig. 8 demonstrate that the excited state structural relaxation of hydrogenated clusters corresponds to a change in shape from a spherical to elliptical geometry, i.e., a global relaxation. As the size of these clusters increases, the relative change in charge density around each atom due to the excitation of a single electron decreases inversely proportionally to the number of atoms in the cluster, and hence the RMS displacements also decrease. The clusters with reconstructed surfaces, e.g., Si<sub>29</sub>H<sub>24</sub> (Fig. 8B) and the clusters with Si–O–Si bridged oxygen on the surface show smaller RMS displacements than the completely hydrogenated clusters. In these clusters, the charge density change associated with the HOMO–LUMO excitation is localized on the surface of the cluster; however, the additional Si–Si or Si–O–Si bonds produced by the reconstruction of the surface restrict the movement of these surface atoms, resulting in significantly lower observed RMS displacements.

In the clusters with oxygen double-bonded to the surface, e.g., Si<sub>35</sub>H<sub>34</sub>O (Fig. 8C), the RMS displacement is slightly larger. However, in this class of clusters, considering the RMS displacement is somewhat

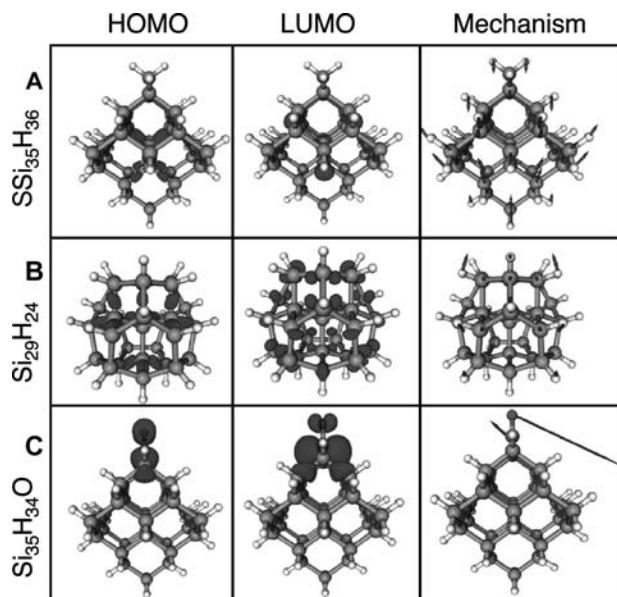


**Fig. 8** Highest occupied molecular orbital (HOMO) and lowest unoccupied molecular orbital (LUMO) density isosurfaces of 1-nm clusters with different surface structures. In the ball-and-stick representation, the Si atoms are gray, the H atoms are white, and the oxygen atom is red. The isosurfaces are chosen at 50% the maximum amplitude in A) and B) and 10% the maximum amplitude in C). The right column shows arrows proportional to the displacement of each atom due to the Stokes shift, magnified by 10 for clarity.



misleading as almost all the atomic relaxation is concentrated on the double-bonded oxygen atom. The displacement vectors plotted in Fig. 8C show that the double-bonded oxygen atom rotates around its attached silicon atom by over  $40^\circ$  when relaxed within its excited state. In these clusters, the Stokes shift is relatively independent of the size of the cluster as the relaxation mechanism is localized on a single bond on the surface.

The above description of the Stokes shift mechanism and calculation of values may be treated through comparison with experiment. A wealth of experimental measurements of the optical absorption and emission wavelengths of silicon nanostructures has been accumulated, much of which appears contradictory.<sup>[14,38,57–64]</sup> However, many apparently conflicting measurements can be explained by considering differences in the sizes and surface properties of the samples.

Fig. 9 combines the results of a number of published values of the Stokes shift plotted as a function of the nanocluster size. For comparison, we include the results of our LDA calculations from Table 1. As a guide to the eye and as a means of extrapolating our results to sizes beyond those currently accessible with first-principles techniques, we fit our results with the dotted lines. Three calculated curves are shown corresponding to the three classes of Stokes shift we have identified. The bulk-derived, hydrogenated nanoclusters are represented by curve (A), which shows Stokes shifts that rapidly decrease from over 2 eV for 0.5-nm clusters to 0.1 eV for 2-nm clusters. The hydrogenated

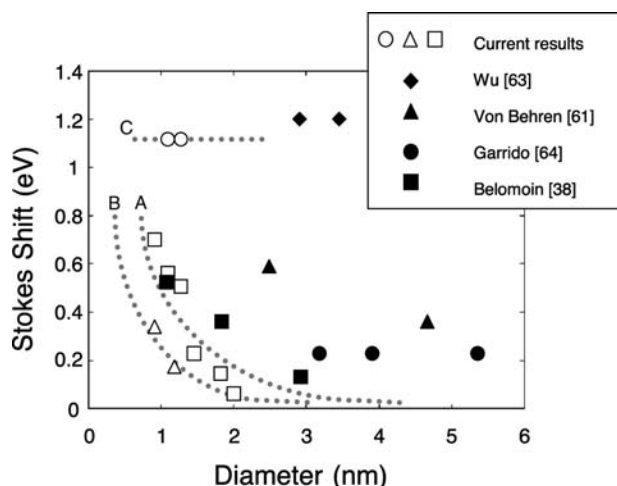


**Fig. 9** A comparison of a number of different experimentally measured values of the Stokes shift (synthesized under different conditions) with local density approximation predicted values. The dotted lines are fit to the A) unreconstructed crystalline structure, B) the reconstructed crystalline structure, and C) the clusters with a double-bonded oxygen on the surface.

nanoclusters with reconstructed surfaces and bridged Si–O–Si oxygen are represented by curve (B), which shows Stokes shifts that are smaller than curve (A) and also decrease to  $<0.1$  eV in 2-nm clusters. The nanoclusters with oxygen double-bonded to the surface are represented by curve (C), which shows Stokes shifts of  $\approx 1.2$  eV, roughly independent of size.

Despite large error bars, the experimental values for the Stokes shift can be broadly divided into three classes that approximately correspond to the three classes of Stokes shift predicted by our calculations. The most striking agreement is between the results of Wu et al.<sup>[63]</sup> and our results for the Stokes shift of clusters with oxygen double-bonded to the surface. Wu et al. found values of the Stokes shift of  $\approx 1.2$  eV that are almost independent of the size of the nanocluster. These measurements agree with our model for the Stokes shift of clusters, where the structural relaxation is focused almost entirely on the silicon oxygen double bond, because of the localization of the HOMO and LUMO charge densities on this bond. The Stokes shifts measured by von Behren et al.<sup>[61]</sup> display a Stokes shift that decreases as the size of the cluster increases. We interpret these particular results as corresponding to the idealized hydrogenated clusters studied here (similar to  $\text{Si}_{35}\text{H}_{36}$ ). The quantitative agreement is even more striking if we consider the 0.2–0.3 corrections due to the LDA error. The Stokes shifts measured by Garrido et al.<sup>[64]</sup> are much smaller over a range of sizes/gaps. These clusters are surrounded by an  $\text{SiO}_2$  matrix and may well contain the bridged Si–O–Si bonds at the surface of the cluster, which we have also shown to significantly suppress the magnitude of the Stokes shift. Likewise, the much smaller clusters characterized by Belomoin, Therrein, and Nayfeh<sup>[38]</sup> which are believed to be reconstructed, show size dependence slightly smaller than that of unreconstructed clusters consistent with our calculated results.

Besides structural changes induced by an exciton, additional phenomena may also contribute to the Stokes shift. A red shift can be introduced by 1) a singlet–triplet splitting of the band edge levels due to the electronic exchange interaction. Light is then absorbed into the higher-energy singlet exciton level and emitted from the lower energy, optically forbidden “dark exciton.” We believe that, in these nanoclusters, the singlet–triplet splitting is negligible and is not included here.<sup>[33,36]</sup> 2) The existence of “surface traps” that exist at energies in the middle of the optical gap of an idealized hydrogenated cluster. An exciton is initially formed in the core of the cluster and then either the electron and/or hole migrate to a lower energy surface localized trap state before recombination and the emission of a photon. Adding such an effect would increase the predicted value of the Stokes shift, but the magnitude is extremely sensitive to the

nature of the trap. 3) A broad size distribution itself can contribute to the Stokes shift. Light is absorbed by clusters with a range of sizes, such that the absorption peak is close to that of the mean size cluster. The excitons then lower their energy by transferring to neighboring larger clusters, before recombination and emission. In this manner, the average measured emission tends to be from the larger clusters of a given size distribution, which, in turn, leads to larger measured Stokes shifts.

In addition to comparing our calculations with measured values of the Stokes shift, we also compared our results with previous calculations.<sup>[31–35]</sup> In general, our results agree with the calculations that have found relatively large ( $\sim 1$  eV) values of Stokes shifts,<sup>[34,35]</sup> and disagree with those predicting significantly smaller (a few meV) Stokes shifts.<sup>[31–33]</sup> In general, we agree with those models that predict large Stokes shifts as a result of structural changes<sup>[35]</sup> and agree with trapped exciton models for the Stokes shift;<sup>[34]</sup> however, we found trapped excitons on double-bonded oxygen, and *not* on reconstructed dimers.<sup>[34]</sup>

The calculated values of the Stokes shift serves two purposes in explaining discrepancies among experimental results. First, the difference between the emission and absorption gaps is not negligible and thus contributes to differences among experiments, especially the ones using different methods to obtain a gap. Second, the difference in observed and calculated Stokes shifts is widely different among nanocrystals with different surface structures. The values are so different that the Stokes shift itself may be used to infer the structure at the surface.

## CONCLUSION

In conclusion, we have demonstrated that quantum confinement is just one mechanism responsible for optical transitions in silicon nanoclusters, and that the specific surface chemistry and the Stokes shift must be considered to interpret experimental results. The interplay between surface and bulk effects requires detailed *ab initio* calculations to properly account for all physical mechanisms contributing to optoelectronic properties. Our calculations show that surface effects due to the different chemistry of single-bonded passivants do not appreciably contribute to optical transitions, even in the case of highly electronegative passivants. We demonstrated that the local distortion of the  $sp^3$  network at the surface significantly affects the energy of photoluminescence. We also discovered that multiple contaminants can further alter the gap, giving a large (over 2.0 eV) range of observed results. Disruption of the  $sp^3$  network also occurs when surfaces are reconstructed, forming dimers or steps. Under

standard synthesis conditions, both unreconstructed and reconstructed surfaces can be thermodynamically stable. Studies of surface reconstructions of clusters with ranges of sizes suggest that even clusters with diameters of up to 5 nm will be sensitive to surface reconstructions, thus increasing the size range by which numerous absorption gaps may be observed.

A further large reduction in gaps may be attributable to differences between absorption and emission, which also varies with respect to the surface structure. Silicon nanostructures exhibit a strong difference between absorption and emission, or Stokes shift. We have determined that the Stokes shift is extremely sensitive to the size, surface structure, and chemistry of the nanocluster. For  $\approx 1$ -nm sized clusters, the Stokes shift ranges from less than 0.1 eV to greater than 1.0 eV, depending on the detailed surface structure and the presence of oxygen in either bridged or double-bonded configurations. Our results enable us to provide explanations for the seemingly contradictory results of a number of experiments. These results demonstrate that combining measurements of the absorption spectrum with measurements of the emission energy provides a powerful tool for optically characterizing both the size and surface structure of semiconductor nanoclusters.

## ACKNOWLEDGMENTS

The body of work included here was performed in collaboration with Andrew J. Williamson, Jeffrey C. Grossman, Giulia Galli, Randolph Q. Hood, and Fernando Reboredo. This work was performed under the auspices of the U.S. Department of Energy at the University of California/Lawrence Livermore National Laboratory under Contract No. W-7405-Eng-48.

## REFERENCES

1. Yoffe, A.D. Semiconductor quantum dots and related systems. *Adv. Phys.* **2001**, *50*, 1 and references therein.
2. Canham, L.T. Silicon quantum wire array fabrication by electrochemical and chemical dissolution of wafers. *Appl. Phys. Lett.* **1990**, *57*, 1046.
3. Bawendi, M.G.; Wilson, W.L.; Rothberg, L.; Carroll, P.J.; Jedju, T.M.; Steigerwalder, M.L.; Brus, L.E. Electronic structure and photoexcited-carrier dynamics in nanometer-size CdSe clusters. *Phys. Rev. Lett.* **1990**, *65*, 1623.
4. Murray, C.B.; Norris, D.J.; Bawendi, M.G. Synthesis and characterization of nearly monodisperse CdE ( $E = S, Se, Te$ ) semiconductor nanocrystallites. *J. Am. Chem. Soc.* **1993**, *115*, 8706.
5. Schuppler, S.; Friedman, S.L.; Marcus, M.A.; Adler, D.L.; Xie, Y.-H.; Ross, F.M.; Harris, T.D.; Brown,

- W.L.; Chabal, Y.J.; Brus, L.E.; Citrin, P.H. Dimensions of luminescent oxidized and porous silicon structures. *Phys. Rev. Lett.* **1994**, *72*, 2648.
- Chen, C.C.; Herhold, A.B.; Johnson, C.S.; Alivisatos, A.P. Size dependence of structural metastability in semiconductor nanocrystals. *Science* **1997**, *276*, 398.
  - Chan, W.C.W.; Nie, S. Quantum dot bioconjugates for ultrasensitive nonisotopic detection. *Science* **1998**, *281*, 2016.
  - Brus, L.E. Electron–electron and electron–hole interactions in small semiconductor crystallites: The size dependence of the lowest excited electronic state. *J. Chem. Phys.* **1984**, *80*, 4403.
  - Lockwood, D.J. Optical properties of porous silicon. *Solid State Commun.* **1994**, *92*, 101.
  - Murray, C.B.; Kagor, C.R.; Bawendi, M.G. Self organization of CdSe nanocrystallites into three dimensional quantum dot superlattices. *Science* **1995**, *270*, 1335.
  - Norris, D.J.; Bawendi, M.G. Structure in the lowest absorption feature of CdSe quantum dots. *J. Chem. Phys.* **1995**, *103*, 5260.
  - Klimov, V.I.; Mikhailovsky, A.A.; Xu, S.; Maiku, A.; Hollingsworth, J.A.; Leatherdale, C.A.; Eigler, H.-J.; Bawendi, M.G. Optical gain and stimulated emission in nanocrystal quantum dots. *Science* **2000**, *290*, 314.
  - Furukawa, S.; Miyasato, T. Quantum size effects on the optical bandgap of microcrystalline Si:H. *Phys. Rev., B* **1988**, *38*, 5726.
  - Holmes, J.D.; Ziegler, K.J.; Doty, R.C.; Pell, L.E.; Johnston, K.P.; Korgel, B.A. Highly luminescent silicon nanocrystals with discrete optical transitions. *J. Am. Chem. Soc.* **2001**, *123*, 3743.
  - Takeoka, S.; Fujii, M.; Hayashi, S.; Yamamoto, K. Size dependent near-infrared photoluminescence from Ge nanocrystals embedded in SiO<sub>2</sub> matrices. *Phys. Rev., B* **1998**, *58*, 7921.
  - Proot, J.P.; Delerue, C.; Allan, G. Electronic structure and optical properties of silicon nanocrystallites: Application to porous silicon. *Appl. Phys. Lett.* **1992**, *61*, 1948.
  - Wang, L.W.; Zunger, A. Electronic structure pseudopotential calculations of large (approximately 1000 atoms) Si quantum dots. *J. Phys. Chem.* **1994**, *98*, 2158.
  - Ogut, S.; Chelikowsky, J.R.; Louie, S.G. Quantum confinement and optical gaps in silicon nanocrystals. *Phys. Rev. Lett.* **1997**, *79*, 1770.
  - Rohlfing, M.; Louie, S.G. Excitonic effects and the optical absorption spectrum of hydrogenated silicon clusters. *Phys. Rev. Lett.* **1998**, *80*, 3320.
  - Vasiliev, I.; Ogut, S.; Chelikowsky, J.R. Ab initio absorption spectra and optical gaps in nanocrystalline silicon. *Phys. Rev. Lett.* **2001**, *86*, 1813.
  - Williamson, A.J.; Grossman, J.C.; Hood, R.Q.; Puzder, A.; Galli, G. Quantum Monte Carlo calculation of nanostructure optical gaps: Application to silicon quantum dots. *Phys. Rev. Lett.* **2002**, *89*, 196803.
  - van Buuren, T.; Dinh, L.N.; Chase, L.L.; Siekhaus, W.J.; Terminello, L.J. Changes in the electronic properties of Si nanocrystals as a function of particle size. *Phys. Rev. Lett.* **1998**, *80*, 3803.
  - Seraphin, A.A.; Ngian, S.T.; Kolenbrander, K.D. Surface control of luminescence in silicon nanoparticles. *J. Appl. Phys.* **1996**, *80*, 6429.
  - Patrone, L.; Nelson, D.; Safarov, V.I. Photoluminescence of silicon nanoclusters with reduced size dispersion produced by laser ablation. *J. Appl. Phys.* **2000**, *87*, 3829.
  - Wolkin, M.V.; Jorne, J.; Fauchet, P.M.; Allan, G.; Delerue, C. Electronic states and luminescence in porous silicon quantum dots: The role of oxygen. *Phys. Rev. Lett.* **1999**, *82*, 197.
  - Puzder, A.; Williamson, A.J.; Grossman, J.C.; Galli, G. Surface chemistry of silicon nanoclusters. *Phys. Rev. Lett.* **2002**, *88*, 097401.
  - Vasiliev, I.; Chelikowsky, J.R.; Martin, R.M. Surface oxidation effects on the optical properties of silicon nanocrystals. *Phys. Rev., B* **2002**, *65*, 121302.
  - Puzder, A.; Williamson, A.J.; Grossman, J.C.; Galli, G. Surface control of optical properties in silicon nanoclusters. *J. Chem. Phys.* **2002**, *117*, 6721.
  - Puzder, A.; Williamson, A.J.; Reboredo, F.A.; Galli, G. Structural stability and optical properties of nanomaterials with reconstructed surfaces. *Phys. Rev. Lett.*, *in press*.
  - Efros, A.L.; Rosen, M.; Kuno, M.; Nirmal, M.; Norris, D.J.; Bawendi, M.G. Band edge exciton in quantum dots of semiconductors with a degenerate valence band: Dark and bright exciton states. *Phys. Rev., B* **1996**, *54*, 4843.
  - Hirao, M.; Uda, T. First principles calculation of the optical properties and stability of hydrogenated silicon clusters. *Int. J. Quan. Chem.* **1993**, *52*, 1113.
  - Martin, E.; Delerue, C.; Allan, G.; Lanoo, M. Theory of excitonic exchange splitting and optical Stokes shift in silicon nanocrystallites: Application to porous silicon. *Phys. Rev., B* **1994**, *50*, 18258.
  - Takagahara, T.; Takeda, K. Excitonic exchange splitting and Stokes shift in silicon nanocrystals and silicon clusters. *Phys. Rev., B* **1996**, *53*, R4205.
  - Allan, G.; Delerue, C.; Lanoo, M. Nature of luminescent surface states of semiconductor nanocrystallites. *Phys. Rev. Lett.* **1996**, *76*, 2961.
  - Filonov, A.B.; Ossicini, S.; Bassani, F.; d'Avitaga, F.A. Oxygen effect on optical properties of nanosize silicon clusters. *Phys. Rev., B* **1998**, *57*, 1394.
  - Wagner, L.; Puzder, A.; Williamson, A.J.; Helmes, Z.; Mitas, L.; Grossman, J.C.; Galli, G.; Nayfeh, M. The structure and Stokes shift of hydrogenated silicon nanoclusters. Submitted.
  - Puzder, A.; Williamson, A.J.; Grossman, J.C.; Galli, G. Computational studies of the optical emission of silicon nanocrystals. *J. Am. Chem. Soc.* **2003**, *125*, 2786–2791.
  - Belomoin, G.; Therrein, J.; Nayfeh, M. Oxide and hydrogen capped ultrasmall blue luminescent Si nanoparticles. *Appl. Phys. Lett.* **2000**, *77*, 779.
  - Wilcoxon, J.P.; Samara, G.A.; Provencio, P.N. Optical and electronic properties of Si nanoclusters synthesized in inverse micelles. *Phys. Rev., B* **1999**, *60*, 2704.
  - Dinh, L.N.; Chase, L.L.; Balooch, M.; Siekhaus, W.J.; Wooten, F. Optical properties of passivated Si

- nanocrystals and  $\text{SiO}_x$  nanostructures. *Phys. Rev.*, B **1996**, *54*, 5029.
41. Ceperley, D.; Alder, B. Ground state of the electron gas by a stochastic method. *Phys. Rev. Lett.* **1980**, *45*, 566.
  42. Perdew, J.P.; Burke, K.; Ernzerhof, M. Generalized gradient approximation made simple. *Phys. Rev. Lett.* **1996**, *77*, 3865.
  43. GP 1.8.0 (F. Gygi, LLNL 1999–2001).
  44. Hamann, D.R. Generalized norm conserving pseudopotentials. *Phys. Rev.*, B **1989**, *40*, 2980.
  45. Giannozzi, P. (Private communication).
  46. Ceperley, D.M.; Alder, B.J. Quantum Monte Carlo. *Science* **1986**, *231*, 555.
  47. Foulkes, W.M.C.; Mitas, L.; Needs, R.J.; Rajagopal, G. Quantum Monte Carlo simulations of solids. *Rev. Mod. Phys.* **2001**, *73*, 33.
  48. Williamson, A.J.; Hood, R.Q.; Grossman, J.C. Linear scaling Quantum Monte Carlo calculations. *Phys. Rev. Lett.* **2001**, *87*, 246406.
  49. Needs, R.J.; Rajagopal, G.; Towler, M.D.; Kent, P.R.C.; Williamson, A.J. *CASINO Version 1.0 User's Manual*; University of Cambridge: Cambridge, 2000.
  50. Marzari, N.; Vanderbilt, D. Maximally localized generalized Wannier functions for composite energy bands. *Phys. Rev.*, B **1997**, *56*, 12847.
  51. Umrigar, C.J.; Wilson, K.G.; Wilkins, J.W. Optimized trial wave functions for quantum Monte Carlo calculations. *Phys. Rev. Lett.* **1988**, *60*, 1719.
  52. Nishida, M. Electronic states and optical properties of silicon nanocrystals terminated by dimers. *Solid State Commun.* **2000**, *116*, 655.
  53. Northrup, J. Structure of  $\text{si}(100)\text{h}$ : Dependence on the chemical potential. *Phys. Rev.*, B **1994**, *44*, 5327.
  54. Reboredo, F.A.; Zhang, S.B.; Zunger, A. Hydrogen induced instability on the flat  $\text{si}[001]$  surface via steric repulsion. *Phys. Rev.*, B **2001**, *63*, 125316.
  55. Mitas, L.; Therrein, J.; Twisten, R.; Belomoin, G.; Nayfeh, M.H. Effect of surface reconstruction on the structural prototypes of ultrasmall ultrabright  $\text{Si}_{29}$  nanoparticles. *Appl. Phys. Lett.* **2001**, *78*, 1918.
  56. van Buuren, T.; Tiedje, T.; Patitsas, S.N.; Weydanz, W. Effect of thermal annealing on the conduction and valence band quantum shifts in porous silicon. *Phys. Rev.*, B **1994**, *50*, 2719.
  57. Wilson, W.L.; Szajowski, P.F.; Brus, L.E. Quantum confinement in size selected, surface oxidized silicon nanocrystals. *Science* **1993**, *262*, 1242.
  58. Zheng, X.Q.; Liu, C.E.; Bao, X.M.; Yan, F.; Yang, H.C.; Chen, H.C.; Zheng, X.L. Midgap localized states and light emission of porous silicon. *Solid State Commun.* **1993**, *87*, 1005.
  59. Hao, P.H.; Hou, X.Y.; Zhang, F.L.; Wang, X. Energy bands line up at the porous silicon/silicon heterointerface measured by electron spectroscopy. *Appl. Phys. Lett.* **1994**, *64*, 3602.
  60. Matsumoto, T.; Arata, G.; Nair, S.V.; Masumoto, Y. Effect of surface termination on the electronic states in nanocrystalline porous silicon. *Jpn. J. Appl. Phys.* **1999**, *38* (1b), 589.
  61. von Behren, J.; van Buuren, T.; Zacharias, M.; Chimowitz, E.H.; Fauchet, P.M. Quantum confinement in nanoscale silicon: The correlation of size with band-gap and luminescence. *Solid State Commun.* **1998**, *105*, 317.
  62. Kanemitsu, Y.; Okamoto, S. Phonon structures and Stokes shifts in resonantly excited luminescence of silicon nanocrystals. *Phys. Rev.*, B **1998**, *58*, 9652.
  63. Wu, X.L.; Xions, S.J.; Fan, D.F.; Gu, Y.; Bao, X.M.; Siu, G.G.; Stokes, M.J. Stabilized electronic states and its luminescence at the surface of oxygen passivated porous silicon. *Phys. Rev.*, B **2000**, *62*, R7759.
  64. Garrido, B.; Lopez, M.; Gonzalez, O.; Perez-Rodriguez, A.; Morante, J.R.; Bonafos, C. Correlation between structural and optical properties of Si nanocrystals embedded in  $\text{SiO}_2$ : The mechanism of visible light emission. *Appl. Phys. Lett.* **2000**, *77*, 3143.

# Silicon Nanocrystals: Quantum Confinement

James R. Chelikowsky

Chemical Engineering and Materials Science, University of Minnesota,  
Minneapolis, Minnesota, U.S.A.

## INTRODUCTION

Silicon is *the* electronic material of choice; it is used for almost all modern electronic devices, e.g., in the manufacture and design of integrated circuits. However, silicon is flawed in one respect. Namely, it is not a particularly good optoelectric material. Laser photodetectors, photocells, and so on are not constructed from elemental silicon. The optical gap of silicon is not amenable for such devices; the gap in silicon is too small to interact effectively with the visible spectrum. In addition, the transitions at the optical threshold in silicon are forbidden unless lattice vibrations are included.<sup>[1]</sup> If the gap could be increased, silicon could be used for virtually any electronic or optical application. Owing to such technological motivation, numerous theoretical methods to predict or simulate the optical properties of silicon nanostructures have been implemented. This section will review some of these methods with an emphasis on atomistic approaches.

## OVERVIEW ON QUANTUM CONFINEMENT

One method to increase the gap size in silicon involves altering the “size of the excitation.” Usually, one alters the properties of matter by changing its chemical composition or its structure. However, it is also possible to change the properties of matter by altering the size of the system. Specifically, the physical properties of matter can have very different behavior at small dimensions. This effect can be illustrated by considering a particle confined by rigid walls to a one-dimensional box of size  $a$ . The lowest energy level of this system is given in elementary textbooks as

$$E = \frac{\pi^2 \hbar^2}{2ma^2} \quad (1)$$

where  $\hbar$  is Planck’s constant divided by  $2\pi$ , and  $m$  is the mass of the particle. If the size of the box is reduced then  $E$  increases. This phenomenon where the energy level increases with reduced dimensionality is called *quantum confinement*. This effect can be readily

understood from the Heisenberg uncertainty principle. The uncertainty principle states that the uncertainty in momentum and position must be such that the product exceeds  $\hbar/2$ :

$$\Delta p \Delta x \geq \hbar/2 \quad (2)$$

where  $\Delta p$  is the uncertainty in the momentum and  $\Delta x$  is the uncertainty in the position of the particle. Consider the energy of a free particle with momentum  $p$ :

$$E = \frac{p^2}{2m} \quad (3)$$

Since the uncertainty in the momentum cannot exceed the momentum itself, one can write  $p > \Delta p$ . Moreover, if the particle is confined to a box of size  $a$ , then

$$E > \frac{\hbar^2}{8ma^2} \quad (4)$$

As one tries to confine the position of a particle, the energy of the particle must increase and diverge as the confining region vanishes.

Although this argument was given for one dimension, it is also true for a particle confined to a box in three dimensions. For example, if a particle is confined within a sphere whose radius is  $R$ , one might expect an energy level to vary with  $R$  according to

$$E(R) = E_\infty + \frac{\alpha}{R^2} \quad (5)$$

where  $\alpha$  is a constant and  $E_\infty$  is the energy as  $R \rightarrow \infty$ .

Suppose we consider an optical gap,  $E_{\text{gap}}$ , as the difference between the highest filled and lowest empty states for a system confined in a sphere of size  $R$ . In the simplest description of the gap we might expect  $E_{\text{gap}}$  scale as

$$E_{\text{gap}}(R) = E_{\text{gap}} + \frac{\beta}{R^2} \quad (6)$$

where  $\beta$  is a constant.

Quantum confinement has been observed experimentally for nanostructures such as silicon *quantum dots* or large clusters. A quantum dot is a *nanocrystal* in which the surface has been passivated. In Fig. 1, an idealized

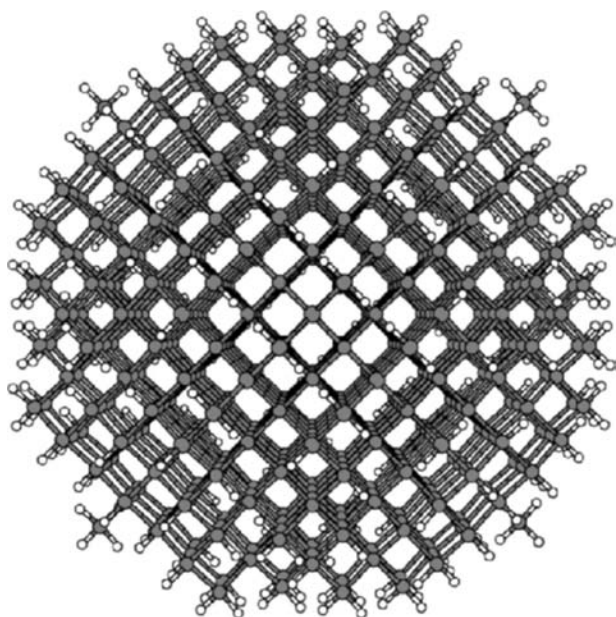


**Fig. 1** Ball and stick model for a quantum dot. The gray dots represent silicon atoms and the white dots, hydrogen. The interior of the dot has the structure of crystalline silicon. The surface of the dot is passivated with hydrogen.

quantum dot of silicon is illustrated. The interior of the dot consists of silicon atoms in the diamond structure; the surface of the dot is hydrogenated. Hydrogen removes any dangling bonds on the surface. As such, all the atoms in the system should be fully coordinated. Unsaturated bonds should not contribute to the electronic properties of the quantum dot. Typically, a quantum dot is a few nanometers to tens of nanometers in size. The smallest dots contain hundreds of atoms, whereas a large dot may contain hundreds of thousands of atoms.

In Fig. 2, one of the first measurements of quantum confinement in silicon nanocrystals is illustrated.<sup>[2]</sup> The nanocrystals measured were about 2–3 nm in diameter. The measured optical gap is between 2.0 and 2.6 eV. This is in contrast to the gap in crystalline silicon, where the gap is known to be about 1.1 eV at room temperature.<sup>[1]</sup> Eq. (6) can be used to fit the data by adjusting the  $\beta$  parameter. Owing to an uncertainty in the nanocrystallite structure and size, there is some scatter in the experimental data, but the overall trend is consistent with what one would expect from quantum confinement. Other experiments have also confirmed the role of quantum confinement in silicon nanostructures. For example, silicon can be so extensively etched as to produce a porous material, which contains nanostructures. Porous silicon is observed to have dramatically altered optical properties; for example, these forms of silicon can exhibit visible photoluminescence at room temperature.<sup>[3]</sup>

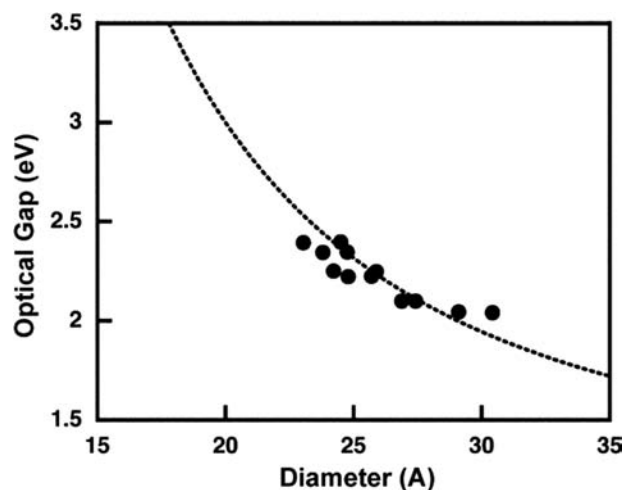


**Fig. 2** The optical gap of hydrogenated silicon quantum dots. The dashed line is a fit to the data using Eq. (6). *Source:* Experimental data from Ref.<sup>[2]</sup>

## COMPUTATIONAL APPROACHES TO EXCITED STATE PROPERTIES IN CONFINED SYSTEMS

Whereas the general concept of quantum confinement has been validated, *quantitative* simulations of the optical properties of nanostructures are difficult. Optical properties require an understanding of both the ground state and excited state for large systems with numerous degrees of freedom. Owing to this situation, several approximate methods have been developed. These methods include empirical descriptions of excitations based on “particle in a box” descriptions to *ab initio* methods based on density functional theory or quantum Monte Carlo methods as described below.

### Empirical Pseudopotential Method

The empirical pseudopotential method is based on several approximations.<sup>[4]</sup> The first approximation concerns the nature of the electronic interactions within matter. It is assumed that these interactions can be accurately replicated by a simple one-electron potential. This approximation can be justified by a Hartree–Fock description of matter in which each electron moves in the average potential of the rest of the electrons. The one-electron approximation results in a Schrödinger equation of the form:

$$\left[ \frac{-\hbar^2 \nabla^2}{2m} + V(\vec{r}) \right] \Psi_n(\vec{r}) = E_n \Psi_n(\vec{r}) \quad (7)$$

where  $V(\vec{r})$  is the electronic potential including electron–nuclear interactions and electron–electron screening,  $E_n$  is the energy level for the  $n$ th state,  $\Psi_n(\vec{r})$ . Another



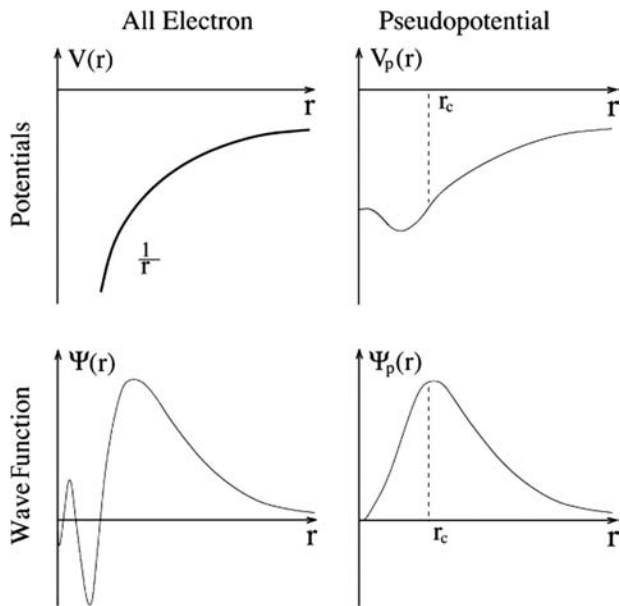


**Fig. 3** Schematic pseudopotential and all-electron potentials. The pseudopotential and pseudo wave function match the all-electron results outside of a core radius given by  $r_c$ .

approximation recognizes the physical content of the periodic table: Electronic properties depend on the valence electron configuration, not the tightly bound core electrons. Consider atoms of silicon ( $1s^2 2s^2 2p^6 3s^2 3p^2$ ) and germanium ( $1s^2 2s^2 2p^6 3s^2 3p^6 3d^{10} 4s^2 4p^2$ ). These atoms have an outer electron, or valence electron, configuration of  $s^2 p^2$  and possess similar electronic and structural properties; that is, they are semiconductors and both occur in the diamond crystal structure. The pseudopotential approximation recognizes this physical content by focusing only on the valence electrons and removing the core electrons from the system.

A schematic atomic pseudopotential is illustrated in Fig. 3. Unlike the “all-electron” potential, which binds both core and valence electrons, the pseudopotential binds only the valence electrons. Within a region around the core ( $r < r_c$ ), the pseudopotential departs strongly from the all-electron potential; for example, the  $1/r$  singularity near the nucleus is removed. The pseudopotential is not only weaker than the all-electron potential; the resulting wave function is nodeless. This transformation between the all-electron potential and the pseudopotential can be made rigorous. Within the empirical pseudopotential approximation, the only requirement is that the pseudopotential be weak and converge rapidly in Fourier space. Typically, one expands the potential in atomic pseudopotentials. For an elemental crystal like silicon (Fig. 4), the pseudopotential for the diamond structure can be written as

$$V_p(\vec{r}) = \sum_{\vec{R}, \vec{\tau}} V_p^a(|\vec{r} - \vec{R} - \vec{\tau}|) \quad (8)$$

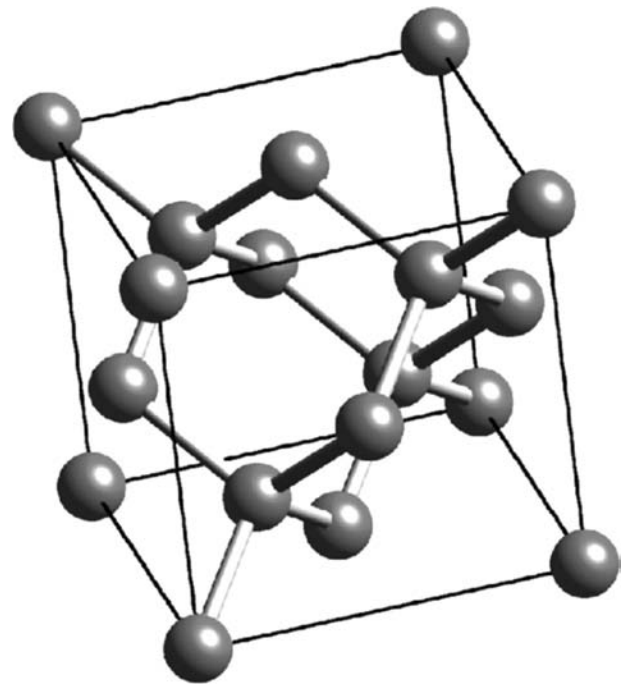


**Fig. 4** Diamond crystal structure for elemental silicon.

where

$$\begin{aligned} \vec{R} &= a(l\hat{x} + m\hat{y} + n\hat{z}) \\ \vec{\tau} &= \pm a(\hat{x} + \hat{y} + \hat{z})/8 \end{aligned}$$

$a$  is the lattice constant, ( $\vec{R}$ ) is a lattice vector and  $\vec{\tau}$  is a basis vector.<sup>[1]</sup> ( $lmn$ ) can take on any integer value. For each atom, one assumes a spherically symmetric pseudopotential,  $V_p^a$ . In Fourier space, Eq. (8) can be rewritten as

$$V_p(\vec{r}) = \sum_{\vec{G}} V_p^a(G) \cos(\vec{G} \cdot \vec{r}) \quad (9)$$

where

$$\vec{G} = \frac{2\pi}{a}(h\hat{x} + j\hat{y} + k\hat{z})$$

( $\vec{G}$ ) is a reciprocal lattice vector. The integers ( $hjk$ ) are constrained to be either all odd or all even.  $V_p^a(G)$  is called a form factor and is defined as

$$V_p^a G = \frac{1}{\Omega_a} \int V_p^a(r) \exp(i\vec{G} \cdot \vec{r}) d^3r \quad (10)$$

where  $\Omega_a$  is the atomic volume. If the pseudopotential converges rapidly in Fourier space, only a few form factors are needed for convergence. These form factors correspond to the smallest  $G$  vectors. This is illustrated in Fig. 5. For crystalline silicon, only three unique form factors are required to define the electronic properties.<sup>[4]</sup> These form factors can be calculated

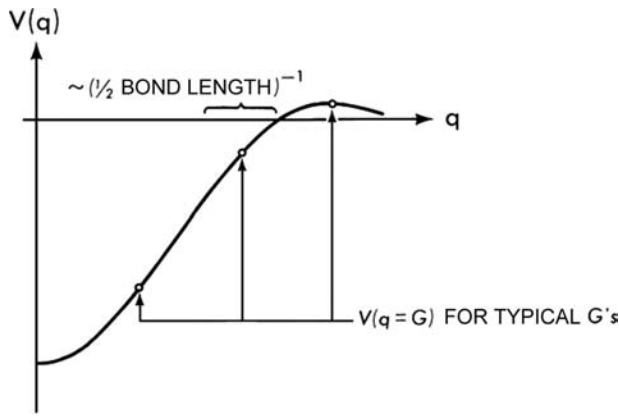


**Fig. 5** Schematic pseudopotential,  $V(q)$  in Fourier space. The values of  $V(q)$  for the lowest reciprocal lattice vectors,  $G$ , are called form factors.

or fit. Within the empirical pseudopotential method, they are commonly fit to experimental data.

Once the potential is defined, the energetic and spatial distribution of electron states can be determined. A common procedure for this task is to define a plane wave basis:

$$\Psi_{n,\vec{k}}(\vec{r}) = \sum_{\vec{G}} \alpha_n(\vec{k}, \vec{G}) \exp(i(\vec{k} + \vec{G}) \cdot \vec{r}) \quad (11)$$

where  $\Psi_{n,\vec{k}}$  is a Bloch function,<sup>[4]</sup>  $n$  is a band index, and  $\vec{k}$  is a wave vector. The wave function and energy bands are determined by solving a secular equation:

$$\det \left( \left( \frac{\hbar^2(\vec{k} + \vec{G})^2}{2m} - E \right) \delta_{\vec{G},\vec{G}'} + V_p^a(|\vec{G} - \vec{G}'|) \times \cos((\vec{G} - \vec{G}') \cdot \vec{\tau}) \right) = 0 \quad (12)$$

This eigenvalue problem gives the values for the energy bands  $E_n(\vec{k})$  and  $\Psi_{n,\vec{k}}$ . Typically, less than 100 plane waves need be considered. Accurate energy bands can be obtained with only three unique form factors. Optical properties of the crystal are used to fit the form factors in this case.

The optical properties of the crystal can be determined by using the imaginary part of the dielectric function,  $\varepsilon_2(\omega)$ , for cubic semiconductors:<sup>[4]</sup>

$$\varepsilon_2(\omega) = \frac{e^2 \hbar}{3\pi m^2 \omega^2} \sum_{\vec{k}, v, c} \delta(\omega_{v,c}(\vec{k}) - \omega) |P_{v,c}(\vec{k})|^2 \quad (13)$$

where

$$\omega_{v,c}(\vec{k}) = (E_c(\vec{k}) - E_v(\vec{k}))/\hbar$$

and

$$\vec{P}_{v,c}(\vec{k}) = \int \Psi_{c,\vec{k}}^*(\vec{r}) \nabla \Psi_{v,\vec{k}}(\vec{r}) d^3r$$

The sum is over occupied valence bands ( $v$ ), empty conduction bands ( $c$ ) and wave vector  $\vec{k}$ .  $\vec{P}_{v,c}(\vec{k})$  is a dipole matrix element. The Dirac delta function in Eq. (13) insures that energy is conserved and the dipole matrix element reflects the allowed symmetry for an optical transition. Once the imaginary part of the dielectric function is known, the real part,  $\varepsilon_1(\omega)$ , can be obtained from the Kramer–Kronig dispersion relation.<sup>[1]</sup> The complex index,  $N$ , is given by

$$N^2 = \varepsilon_1 + i\varepsilon_2 \quad (14)$$

and the normal incident reflectivity is given by

$$R = \left| \frac{N - 1}{N + 1} \right|^2 \quad (15)$$

The reflectivity of a silicon crystal as calculated by the empirical pseudopotential method and as measured<sup>[5]</sup> is illustrated in Fig. 6.

It is possible to apply the empirical pseudopotential method to quantum dots as illustrated in Fig. 1. However, several more approximations must be made. For example, a confined excitation does not possess translational symmetry. Bloch's theorem [Eq. (11)] does not hold; that is, the wave vector  $\vec{k}$  no longer has any physical meaning. One method of overcoming this obstacle is to introduce artificial periodicity into the system by constructing a “supercell.” Each supercell contains a quantum dot surrounded by vacuum. This permits the same formalism to be implemented

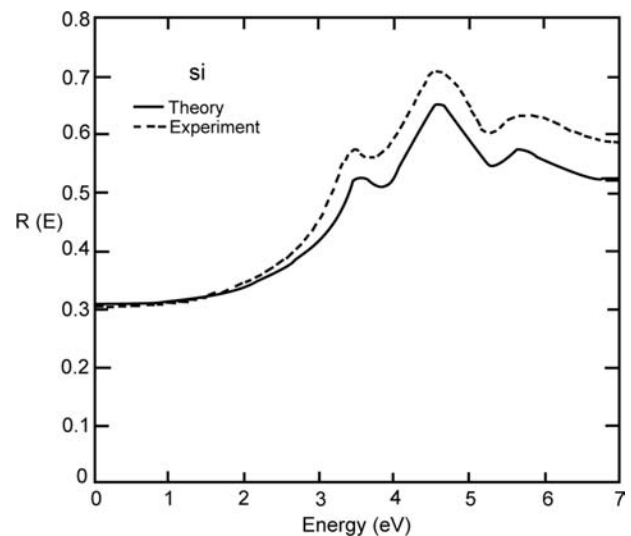


**Fig. 6** Reflectivity for crystalline silicon. Source: From Ref.<sup>[5]</sup>

as for the crystal. Another issue concerns the construction of the form factors. As the supercell grows in size more than just three form factors are required. Effectively, the full curve for  $V_p^a(G)$  must be known. In practice, empirical extrapolations are made from bulk pseudopotentials, often including fits to experimental or theoretical surface properties<sup>[6]</sup> to construct the form factors.

The highest occupied molecular orbital (HOMO) and lowest unoccupied molecular orbital (LUMO) define a HOMO–LUMO gap,  $E_g$ . This gap cannot be directly compared to the optical gaps shown in Fig. 2. Quantum dots physically localize the excited electron and hole such that the Coulombic interactions are enhanced. An empirical and approximate expression for the optical gap,  $E_g^{\text{opt}}$ , is given by

$$E_g^{\text{opt}} \approx E_g - \frac{1.8e^2}{\epsilon R} \quad (16)$$

where  $E_g$  is the HOMO–LUMO gap of the dot,  $\epsilon$  is the dielectric constant of the dot, and  $R$  is the dot radius.<sup>[6,7]</sup> The second term in Eq. (16) represents the electron–hole Coulombic interaction. The scaling of the exciton energy is what one would expect for a particle in a sphere. This expression is quite crude in that it assumes the dielectric properties of the dot can be quantified by a constant value of the dielectric function. For small dots of diameter less than a few nanometers, such approximations will certainly break down.<sup>[8]</sup> Another deficiency of the empirical pseudopotential method concerns the interpretation of the gap,  $E_g$ . For crystalline matter, this gap corresponds to the band gap and includes excitonic interactions, which are small in the crystalline case. However, in the limit of small quantum dots, the gap may be ill defined. It is not clear whether the empirical approach scales many-body interactions correctly.

### Tight Binding Method

Another method for extracting the optical gap of silicon quantum dots is based on tight binding. Within this method a localized basis is taken. For example, one can write the wave function as

$$\Psi_n(\vec{r}) = \sum_{j,k} a_{j,k}^n \Phi_j(\vec{r} - \vec{R}_k) \quad (17)$$

where the sum is over (j,m). These indices label the atomic positions, given by  $\vec{R}_m$ , and a local orbital,  $\Phi_j$ , associated with an (s,p,d, ...) state. The local orbitals,  $\Phi_j$ , can be taken to be atomic orbitals, Gaussians, exponentials, and so on.

Suppose we consider a tight-binding Hamiltonian,  $H_{\text{TB}}$ , and use Eq. (17) as the basis. At this point,  $H_{\text{TB}}$ , need not be specified. Using the basis in Eq. (17), one must solve an eigenvalue problem of the form:

$$H_{lm} \Psi_n = E_n S_{lm} \Psi_n \quad (18)$$

where the Hamiltonian matrix element,  $H_{lm}$ , are given by

$$H_{lm} = \sum_{jj'kk'} a_{j,k}^l a_{j',k'}^m \int \Phi_j^*(\vec{r} - \vec{R}_k) H_{\text{TB}} \Phi_{j'}(\vec{r} - \vec{R}_{k'}) d^3r$$

and the overlap matrix element,  $S_{lm}$ , is given by

$$S_{lm} = \sum_{jj'kk'} a_{j,k}^l a_{j',k'}^m \int \Phi_j^*(\vec{r} - \vec{R}_k) \Phi_{j'}(\vec{r} - \vec{R}_{k'}) d^3r$$

The matrix elements can be computed directly if  $H_{\text{TB}}$  is specified. Otherwise, the matrix elements can be fit to experimental data. Once the matrix elements are specified, the energies and wave functions can be found using standard matrix operation packages.

Tight binding methods have some advantages over the empirical pseudopotential method. Each atom can be represented by a small number of orbitals; for example, one might consider an  $sp^3$  configuration associated with each silicon atom. Instead of having 50–100 plane waves associated with each atom, one might have only four orbitals. The resulting secular equation is correspondingly much smaller. Moreover, one need not have a detailed knowledge of the electronic potentials or the tight-binding Hamiltonian. Usually some rather strong approximations are made in evaluating the Hamiltonian and overlap matrix elements; for example, often the elements are assumed to vanish, save for the first few neighboring atoms. Only matrix elements representing two and three body overlaps are required to solve for the eigenvalues and eigen vectors.<sup>[9–11]</sup> Evaluating accurately the matrix elements is the most difficult aspect of the tight-binding method. Typically, 10–20 elements must be determined. Usually, this task is performed by parameterizing the matrix elements; for example, the parameters are often fit to experimental data or to calculated energy bands. In general, obtaining a robust set of parameters is difficult; however, modeling quantum dots is reasonably straightforward, as one does not need to fit unsaturated bonds or miscoordinated atoms.

Very large dots can be treated within the tight-binding model; dots of several hundred atoms have been examined. The energy levels between the highest and lowest levels can be calculated and the role of

quantum confinement determined in a manner similar to the empirical pseudopotential method.

### Density Functional Methods and Ab Initio Pseudopotentials

One drawback of both empirical pseudopotentials and tight binding concerns the parameterization procedure. In the case of the pseudopotentials, one must transfer bulklike interactions to surfaces or to confined systems where such transfers might be problematic. Likewise, tight-binding methods may involve bases that are too limited to represent the subtleties of charge transfer and hybridization in confined systems. Neither approach allows for screening changes or charge readjustments in a natural way.

Contemporary pseudopotentials are predominantly based on density functional theory.<sup>[12,13]</sup> Within density functional theory, the many-body problem is mapped on to a one-electron Hamiltonian. The effects of exchange and correlation are subsumed to a one-electron potential that depends only on the charge density. This mapping of the many-body problem to a one-body problem is in principle exact, but in practice approximate because the exact functional form for the one-electron exchange-correlation potential is not known. The mapping is usually accomplished via the local density approximation<sup>[13]</sup> in which the exchange-correlation potential is assumed to be that of a homogenous electron gas. Density functional theory, in any of its approximate forms, allows for a great simplification of the one-electron problem. Without this approach, most electronic structure methods would not be feasible for systems of more than a few dozen electrons.

Within the density functional theory approach one can write down a one-electron Hamiltonian and a corresponding one-electron Schrödinger equation, often called the “Kohn–Sham” equation.<sup>[13]</sup> For an atom, the Kohn–Sham equation can be written as:

$$\left[ \frac{-\hbar^2 \nabla^2}{2m} - \frac{Ze^2}{r} + V_H(\vec{r}) + V_{XC}[\rho(\vec{r})] \right] \Psi_n(\vec{r}) = E_n \Psi_n(\vec{r}) \quad (19)$$

where  $Z$  is the atomic number,  $V_H$  is the Hartree or Coulomb potential, and  $V_{XC}$  is the exchange-correlation potential. The Hartree and exchange-correlation potentials can be determined from the electronic charge density,  $\rho$ . The eigenvalue and eigenfunctions,  $E_n, \Psi_n(\vec{r})$ , can be used to determine the total electronic energy of the atom. The charge density is given by

$$\rho(\vec{r}) = -e \sum_{n, \text{occup}} |\Psi(\vec{r})|^2 \quad (20)$$

The summation is over all occupied states. The Hartree potential is determined by

$$\nabla^2 V_H(\vec{r}) = -4\pi e \rho(\vec{r}) \quad (21)$$

This term can be interpreted as the electrostatic interaction of an electron with the charge density of system. The exchange-correlation potential is more problematic. The central tenant of the local density approximation is that the total exchange-correlation energy may be written as

$$E_{XC}[\rho(\vec{r})] = \int \rho(\vec{r}) \varepsilon_{XC}[\rho(\vec{r})] d^3r \quad (22)$$

where  $\varepsilon_{XC}$  is the exchange-correlation energy density (i.e., the exchange correlation energy per electron at a density,  $\rho$ ). The exchange-correlation potential,  $V_{XC}$ , is obtained from the functional derivative:

$$V_{XC}(\vec{r}) = \frac{\delta}{\delta \rho} E_{XC}[\rho(\vec{r})] \quad (23)$$

It is not difficult to solve the Kohn–Sham equation [Eq. (19)] for an atom. The charge density is taken to be spherically symmetric; that is, the problem reduces to solving a one-dimensional problem. The Hartree and exchange-correlation potentials can be iterated to form a self-consistent field.

The atomic solution provides the input to construct a pseudopotential representing the effect of the core electrons and nucleus. This “ion core” pseudopotential,  $V_p^{\text{ion}}$ , can be transferred to other systems such as a silicon quantum dot. One can invert the Kohn–Sham equation to write:

$$V_p^{\text{ion}}(\vec{r}) = E_n - V_H(\vec{r}) - V_{XC}(\vec{r}) + \frac{\hbar^2 \nabla^2 \Psi_n}{2m \Psi_n} \quad (24)$$

If the atomic solution is inserted in Eq. (24) for ( $E_n, \Psi_n$ ), the ionic pseudopotential will reduce to the atomic potential. To construct a pseudopotential, one inserts the all-electron energy level and a modified wave function. For example, consider the 3s state of silicon. The silicon atom is solved so that ( $E_{3s}, \Psi_{3s}$ ) are known. A pseudo wave function,  $\Phi_{3s}$ , is constructed so that the wave function be nodeless and identical to the “all-electron” wave function outside a core region. A typical pseudo wave function,  $\Phi_{3s}$ , is illustrated in Fig. 7. Ion core pseudopotentials formed via Eq. (24) will yield the exact energy level and wave function outside the core region by construction. In principle, the ion core pseudopotential constructed in Eq. (24) is state dependent; for example, the pseudopotential for the 3s and 3p states will be different.

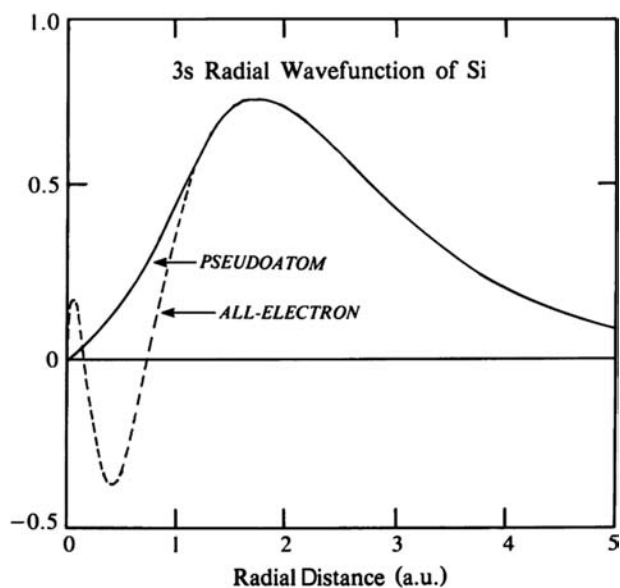


Fig. 7 Wave functions for the Si 3s state from an all-electron potential and from an ab initio pseudopotential.

This state dependency results in an additional complexity: The pseudopotentials are non-local operators. While non-locality complicates the pseudopotential construction, there are straightforward techniques for its implementation. Also, several methods exist for constructing pseudopotentials within density functional theory.<sup>[14]</sup>

Once the pseudopotential has been determined, the resulting eigenvalue problem needs to be solved for the system of interest. Several techniques are available to accomplish this task. For example, one approach is to use a plane wave basis with supercells, as discussed for the empirical pseudopotential method. Another approach is to solve the eigenvalue problem in real space.<sup>[15,16]</sup> The real-space method is highly advantageous over the plane wave method in some respects. Real-space methods do not require supercells and, as a consequence, can examine charged systems without adding artificial compensating backgrounds. Also, no cell-cell interactions exist. Real-space methods for silicon quantum dots have used a three-dimensional cube as shown in Fig. 8. The Kohn–Sham equation can be discretized via a higher-order finite differencing procedure over the grid to yield:

$$\begin{aligned} & \frac{-\hbar^2}{2m} \sum_{n_1 n_2 n_3 = -N}^N C(n_1, n_2, n_3) \Psi_n(x_i + n_1 h, y_j \\ & + n_2 h, z_k + n_3 h) + V_p^{\text{ion}}(x_i, y_j, z_k) \Psi_n(x_i, y_j, z_k) \\ & + V_H(x_i, y_j, z_k) \Psi_n(x_i, y_j, z_k) \\ & + V_{\text{XC}}(x_i, y_j, z_k) \Psi_n(x_i, y_j, z_k) \\ & = E_n \Psi_n(x_i, y_j, z_k) \end{aligned} \quad (25)$$

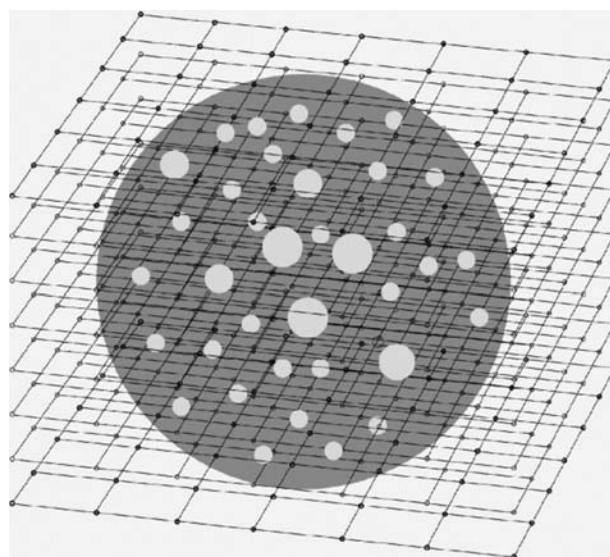


Fig. 8 Example of a grid used for a real-space solution of the Kohn–Sham equation [Eq. (25)].

where  $h$  is the grid spacing,  $C(n_1, n_2, n_3)$  are coefficients for the finite difference, and the summation is over  $N$  neighboring grid points; for example, if  $N = 1$ , then standard finite differencing is used. Real-space methods are easy to implement and have been used for dots up to 1000 atoms in size.

The total electronic energy of the system can be obtained from

$$\begin{aligned} E(N) = & \sum_{n=1}^N E_n - \frac{1}{2} \int V_H(\vec{r}) \rho(\vec{r}) d^3 r + \int [\epsilon_{\text{XC}}(\vec{r}) \\ & - V_{\text{XC}}(\vec{r})] \rho(\vec{r}) d^3 r \end{aligned} \quad (26)$$

where  $N$  is the total number of electrons in the system. The second term in Eq. (26) is required to remove double counting the electrostatic interactions. The last term removes the exchange-correlation potential and replaces it with the exchange-correlation energy density. Eq. (26) allows one to extract the ionization energy,  $I$ , and the electron affinity,  $A$ . In particular, one can then compute gap for elementary excitations involving a “quasiparticle.” (A quasiparticle corresponds to a single-particle excitation in a many-body system. The excitations of the individual particle, in this case an electron, can be modified by interactions between the particle with the electron density). The quasiparticle gap using the definitions of electron affinity and the ionization energy is given by

$$\begin{aligned} E_{\text{gap}}^{\text{qp}} = & I - A = E[N + 1] + E[N - 1] \\ & - 2E[N] \end{aligned} \quad (27)$$



The quasiparticle gap is the energy required to create a non-interacting electron–hole pair. Provided one has a functional for the exchange–correlation energy, this expression can be readily implemented for quantum dots.

However, this gap does not correspond to an optical excitation. Within a quantum dot, the electron and hole interact via Coulombic forces. The Coulombic energy, or exciton energy, can be approximated by

$$E_{\text{Coul}} = -e^2 \iint \frac{|\Psi_e(\vec{r})|^2 |\Psi_h(\vec{r}')|^2}{\epsilon(\vec{r}, \vec{r}') |\vec{r} - \vec{r}'|} d^3r d^3r' \quad (28)$$

where the electron and hole wave functions are given by  $\Psi_e$  and  $\Psi_h$ , respectively.  $\epsilon$  is the full dielectric matrix, which includes any polarization or surface terms. The optical excitation gap,  $E_{\text{gap}}^{\text{opt}}$ , is given by

$$E_{\text{gap}}^{\text{opt}} = E_{\text{gap}}^{\text{qp}} + E_{\text{Coul}} \quad (29)$$

Equation (29) should be compared to the empirical expression [Eq. (16)] where similar terms are considered.

There are a few issues with Eq. (29). The local density approximation, which is commonly used to implement density functional theory, is flawed in the limit of infinite systems.<sup>[17,18]</sup> Namely, the quasiparticle gap as calculated using the local density approximation is about one-half the measured gap.<sup>[19]</sup> The difference, known as a “self-energy correction,” is commonly fixed by the infinite system and transferred without change to finite systems. This transfer is unlikely to be correct, especially for small dots.<sup>[20]</sup>

For small, localized systems, the local density approximation appears to be valid and gives reasonable values for the quasiparticle energies.<sup>[21]</sup> It is not clear how well Eq. (27) holds for larger confined systems, e.g., for dots larger than a few nanometers. Another issue concerns the dielectric function used in Eq. (28). In empirical studies,<sup>[6]</sup> the dielectric function is crudely approximated by a constant. More rigorous attempts have included spatial variations in the dielectric constant.<sup>[10,21]</sup> The full dielectric matrix, which includes the effect of the surface, has not been implemented to date.

An alternative approach using density functional theory is *time-dependent density functional theory*. Just as for “static” density functional theory, it is common to use the local density approximation. In this case, the method is called the *time-dependent local density approximation*. Within the time-dependent local density approximation, the excited state properties are derived as a linear response to an applied periodic (in time) perturbation. The system response is described by a coupling matrix, which can be used to determine the electronic excitations. Within an

adiabatic approximation, this matrix is given by

$$\mathbf{K}_{ij\sigma,kl\tau} = \iint \Psi_{i\sigma}^*(\vec{r}) \Psi_{j\sigma}(\vec{r}) \left( \frac{e^2}{|\vec{r} - \vec{r}'|} + \frac{\delta V_{\text{XC}}^\sigma(\vec{r})}{\delta \rho_\tau(\vec{r}')} \right) \times \Psi_{k\tau}(\vec{r}') \Psi_{l\tau}^*(\vec{r}') d^3r d^3r' \quad (30)$$

The indices ( $ij\sigma$ ) correspond to the occupied state, the unoccupied state, and the spin parameter, respectively. The wave functions for the one-electron wave functions are given by  $\Psi_{j\sigma}$ . The electronic transition energies can be obtained from the solution of the following eigenvalue problem:

$$\left[ E_{ij\sigma}^2 \delta_{ik} \delta_{jl} \delta_{\sigma\tau} + 2\sqrt{f_{ij\sigma} E_{ij\sigma}} \mathbf{K}_{ij\sigma,kl\tau} \sqrt{f_{kl\tau} E_{kl\tau}} \right] \mathbf{F}_n = \epsilon_n^2 \mathbf{F}_n \quad (31)$$

where  $E_{ij\sigma}$  is the transition energy between states ( $ij$ ), i.e., the energy difference between the Kohn–Sham eigenvalues from Eq. (25).  $f_{ij\sigma}$  is the occupation number.  $\epsilon_n$  is the excitation energy and the eigenvectors,  $\mathbf{F}_n$  are related to the oscillator strength.<sup>[22]</sup> Note that if the coupling matrix,  $\mathbf{K}_{ij\sigma,kl\tau}$ , is set equal to zero, the excitation energies would correspond to the standard Kohn–Sham eigenvalues,  $E_{ij\sigma}$ . In general, time-dependent local density methods tend to blue shift the optical gap, which improves agreement with experimental data. Implementations in real time of the time-dependent local density approximation are available.<sup>[23]</sup>

In principle, the time-dependent local density approximation incorporates electron screening and relevant correlation effects for electronic excitations.<sup>[22]</sup> A model screening dielectric function is not required as in Eq. (28) to estimate the screened Coulombic interactions in excitons. It should be noted that in addition to the local density approximation, time-dependent density functional methods almost always assume the adiabatic approximation; that is, the electrons are assumed to follow the external field instantaneously. The validity of this approximation has been questioned and remains an open question.

Time dependent density functional theories have been applied to hydrogenated silicon clusters and quantum dots. Such systems are illustrated in Fig. 9. Optical gaps for the small clusters have been measured and the agreement between the time-dependent local density approximation values for the optical gaps and experiment is quite good.<sup>[23]</sup>

## Hartree–Fock and Configuration Interaction Methods

A rigorous approach to the total energy of a silicon nanocrystal is to use a solution to the many-body



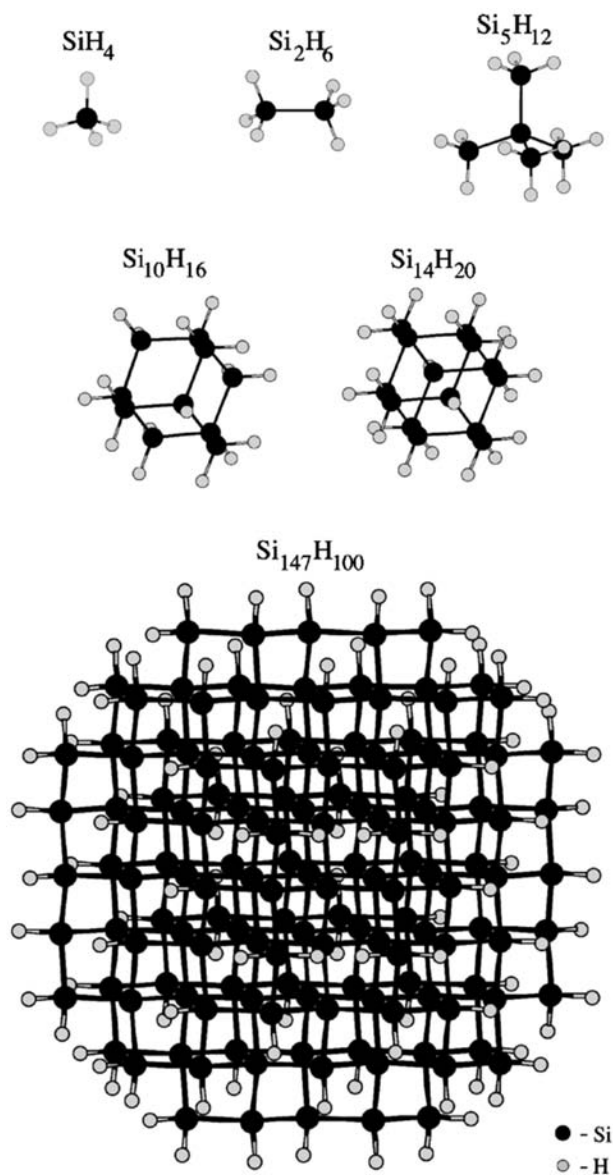


**Fig. 9** Ball and stick models for hydrogenated silicon clusters ( $\text{Si}_n\text{H}_m$ ).

Schrödinger equation. This entails solving a complex problem with numerous degrees of freedom. The electronic part of the Hamiltonian for an  $N$  electron system in its simplest form is given by

$$\left[ -\sum_i \frac{\hbar^2 \nabla_i^2}{2m} - \sum_{im} \frac{Z_m e^2}{|\vec{r}_i - \vec{R}_m|} + \sum_{i > j, i \neq j} \frac{e^2}{|\vec{r}_i - \vec{r}_j|} \right] \Psi(\vec{r}_1, \vec{r}_2, \vec{r}_3, \dots, \vec{r}_N) = E \Psi(\vec{r}_1, \vec{r}_2, \vec{r}_3, \mathbf{K}, \vec{r}_N) \quad (32)$$

The nuclear positions are given by  $\vec{R}_m$  with an atomic number of  $Z_m$ .  $E$  gives the total electronic energy of the system. This difficult problem can be solved, at least approximately, by invoking some approximations.

For example, in the Hartree–Fock approximation the many-body wave function can be written as

$$\Psi(\vec{r}_1 s_1, \vec{r}_2 s_2, \vec{r}_3 s_3, \dots, \vec{r}_N s_N) = \det \begin{vmatrix} \phi_1(\vec{r}_1 s_1) & \phi_1(\vec{r}_2 s_2) & \dots & \phi_1(\vec{r}_N s_N) \\ \phi_2(\vec{r}_1 s_1) & \phi_2(\vec{r}_2 s_2) & \dots & \dots \\ \dots & \dots & \dots & \dots \\ \phi_N(\vec{r}_1 s_1) & \dots & \dots & \phi_N(\vec{r}_N s_N) \end{vmatrix} \quad (33)$$

where the spin coordinate is explicitly written as  $s$ . This form of the wave function is known as a *Slater determinant*.<sup>[24]</sup> It reflects the proper symmetry of the wave function for fermions and incorporates the Pauli principle. If two electrons occupy the same orbital, two rows of the determinant are identical and the wave function will vanish. Likewise, the determinant will vanish if two electrons occupy the same point in space, as two columns of the determinant would be identical.

If one uses a Slater determinant to evaluate the total electronic energy and maintains the orbital normalization, then the orbitals can be obtained from a solution of the Hartree–Fock equation:

$$\begin{aligned} & \left( \frac{-\hbar^2 \nabla^2}{2m} + V_{\text{ion}}(\vec{r}) + \sum_{j=1}^N \int \frac{e^2 |\phi_j(\vec{r}')|^2}{|\vec{r} - \vec{r}'|} d^3 r' \right) \phi_i(\vec{r}) \\ & - \sum_{j=1}^N \left( \int \frac{e^2}{|\vec{r} - \vec{r}'|} \phi_j^*(\vec{r}') \phi_i(\vec{r}') d^3 r' \right) \delta_{s_i, s_j} \phi_j(\vec{r}) \\ & = E_i \phi_i(\vec{r}) \end{aligned} \quad (34)$$

where  $V_{\text{ion}}$  is given by

$$V_{\text{ion}}(\vec{r}) = - \sum_m \frac{Z_m e^2}{|\vec{r} - \vec{R}_m|}$$

This equation is commonly reformulated<sup>[24]</sup> as

$$\begin{aligned} & \left[ \frac{-\hbar^2 \nabla^2}{2m} - V_{\text{ion}}(\vec{r}) + V_{\text{H}}(\vec{r}) + V_x^i(\vec{r}) \right] \phi_i(\vec{r}) \\ & = E_i \phi_i(\vec{r}) \end{aligned} \quad (35)$$

where the Hartree potential is defined as before [Eq. (21)]. This equation is similar to the Kohn–Sham equation [Eq. (19)], save for the presence of an exchange potential given by  $V_x^i(\vec{r})$ . The presence of this potential greatly complicates the solution of the Hartree–Fock problem vis-à-vis the Kohn–Sham potential, as the exchange potential is orbitally

dependent. The exchange potential is given by

$$V_x^i(\vec{r}) = -\frac{1}{\phi_i(\vec{r})} \sum_{j=1}^N \phi_j(\vec{r}) \delta_{s_i, s_j} \times \int \frac{e^2}{|\vec{r} - \vec{r}'|} \phi_j^*(\vec{r}') \phi_i(\vec{r}') d^3 r' \quad (36)$$

Once the Hartree–Fock orbitals,  $\phi_i(\vec{r})$ , are known, the total energy of the system can be evaluated from

$$E(N) = \sum_{n=1}^N E_n - \frac{1}{2} \int V_H(\vec{r}) \rho(\vec{r}) d^3 r - \frac{1}{2} \sum_{i=1}^N \int \phi_i^*(\vec{r}) \phi_i(\vec{r}) V_x^i(\vec{r}) d^3 r \quad (37)$$

By evaluating the total energy with and without an electron, the electron affinity and ionization energy can be determined as in density functional theory [Eqs. (26) and (27)]. This allows one to determine the energy of creating a non-interacting electron–hole pair.

The Hartree–Fock approximation is deficient in that it fails to include *correlation* energies. “Correlation” energies are usually defined as the difference between the exact solution and the Hartree–Fock solution. This can occur because the Slater determinant does not have sufficient flexibility to provide the exact many-body wave function. To overcome this deficiency, one can incorporate determinants containing empty or virtual orbitals. These methods are called “configuration interaction” (CI) methods. Typically only a few dozen electrons can be handled using CI methods and contemporary computational platforms.

## Other Methods

Additional methods have been applied to silicon quantum dots. These methods tend to be computationally intensive and have only recently been applied to silicon quantum dots. These methods are the “GW–Bethe–Salpeter” method<sup>[25–27]</sup> and the “quantum Monte Carlo” method.<sup>[28–30]</sup>

The GW–Bethe–Salpeter method is a many-body method based on a Green function approach that explicitly treats the dynamics of an electron–hole pair in a quantum many-body system. The method proceeds in two steps. In the first step, the energy to create a non-interacting electron and hole pair is considered. This step is analogous to Eq. (27) in which the quasiparticle energy is computed by differencing the electron affinity and ionization energies. This step is referred to as the “GW” part of the calculation. In the second step, the electron and hole are

allowed to interact. In insulators and semiconductors, the electron–hole pair can bind to form localized “excitonic” states. The second step solved the “Bethe–Salpeter” equation. This method has been applied to insulating solids with large excitonic gaps such as silica or magnesium oxide. It has also been applied to hydrogenated silicon clusters. The largest cluster examined to date contained less than 50 atoms.

Solving the full many-body Schrödinger equation can be accomplished using quantum Monte Carlo methods. This approach has only recently been applied to silicon clusters. The method starts with the full Hamiltonian [Eq. (32)] and uses a modified form of the Slater determinant [Eq. (33)] to go beyond the Hartree–Fock approximation and include correlation energies. The quantum Monte Carlo method, as the name implies, is a stochastic technique. One can specify the desired accuracy and perform the Monte Carlo algorithm until the energy criterion is met. Historically, owing to the computational load of quantum Monte Carlo methods, systems with only a few electrons have been examined until recently. Progress in developing new algorithms has made it possible to examine quantum dots with a few hundred electrons.<sup>[28]</sup> Currently, quasiparticle energies can be calculated, but including the oscillator strength is more problematic. As such, optical spectra have not been calculated.

## Predicted Optical Gaps and Spectra for Passivated Silicon Nanocrystals

To expedite the discussion, two size regimes will be considered: small quantum dots and molecular forms of hydrogenated silicon and larger quantum dots. In Fig. 10, predicted optical gaps for dots of diameter of less than 15 Å are shown. The predictions in this figure come from tight-binding, quasiparticle local density approximation, quantum Monte Carlo, time-dependent density functional theory, GW–Bethe–Salpeter, and Hartree–Fock configuration interaction calculations. Despite the variety of theoretical approaches, the six methods agree fairly well in this size regime. One might assume the quantum Monte Carlo and GW–Bethe–Salpeter methods to be the most rigorous and the most accurate. If this is a valid assumption, then the Hartree–Fock configuration interaction results are probably not as accurate as the time-dependent density functional theory, tight-binding, and quasiparticle local density approximation calculations, which are in better agreement with the quantum Monte Carlo and GW–Bethe–Salpeter methods.

As one might expect, the more rigorous methods like quantum Monte Carlo have not considered dots with diameter above 10 Å. Current computational

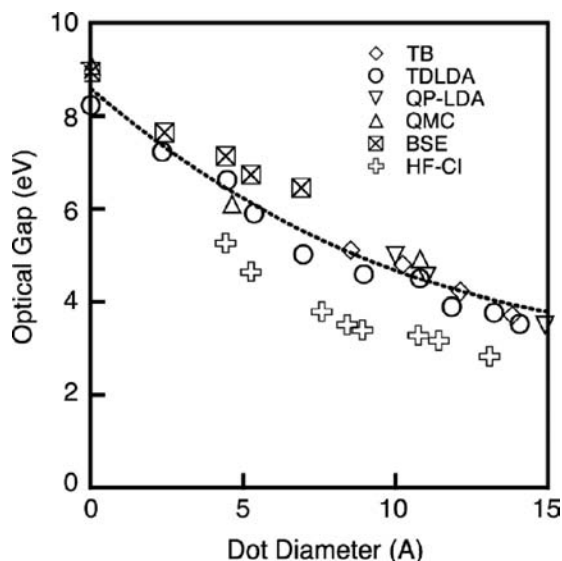


**Fig. 10** Predicted optical gaps for “small” hydrogenated silicon quantum dots. Indicated are predictions from tight-binding (TB),<sup>[11]</sup> time-dependent local density approximation (TDLDA),<sup>[23]</sup> quasiparticle local density approximation (QP-LDA), quantum Monte Carlo (QMC),<sup>[29]</sup> GW–Bethe–Salpeter equation (BSE),<sup>[27]</sup> and Hartree–Fock configuration interaction (HF-CI)<sup>[31]</sup> calculations. The dashed line is a guide to the eye.

platforms are not sufficient to describe systems with more than a few hundred atoms. However, unlike empirical methods, these methods are capable of spanning systems from small molecular species such as silane up to systems with a hundred atoms or so.

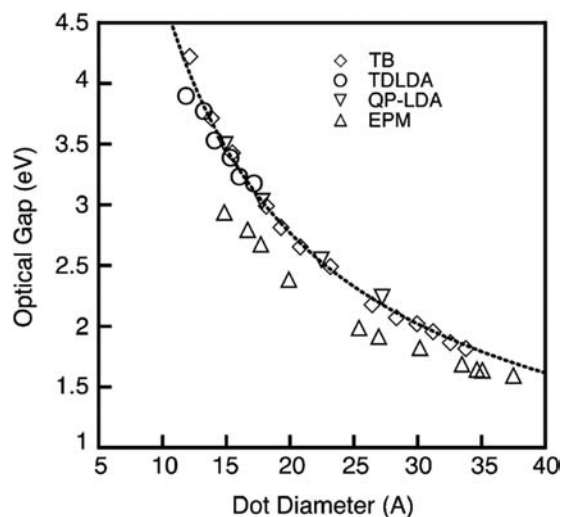


**Fig. 11** Predicted optical gaps for “large” hydrogenated silicon quantum dots. Indicated are predictions from TB,<sup>[11]</sup> TDLDA,<sup>[23]</sup> QP-LDA, and empirical pseudopotential method (EPM)<sup>[32]</sup> calculations. The dashed line is a guide to the eye.

In general, the role of quantum confinement appears to hold down to systems with a few atoms, as the predicted optical gap increases as the size of the dot shrinks. However, one must be careful in this assessment; for example, the ratio of Si–H bonds to Si–Si bonds is larger as the surface to volume ratio is larger for small dots than for large dots. This difference is not reflected in a rigid confinement model, which

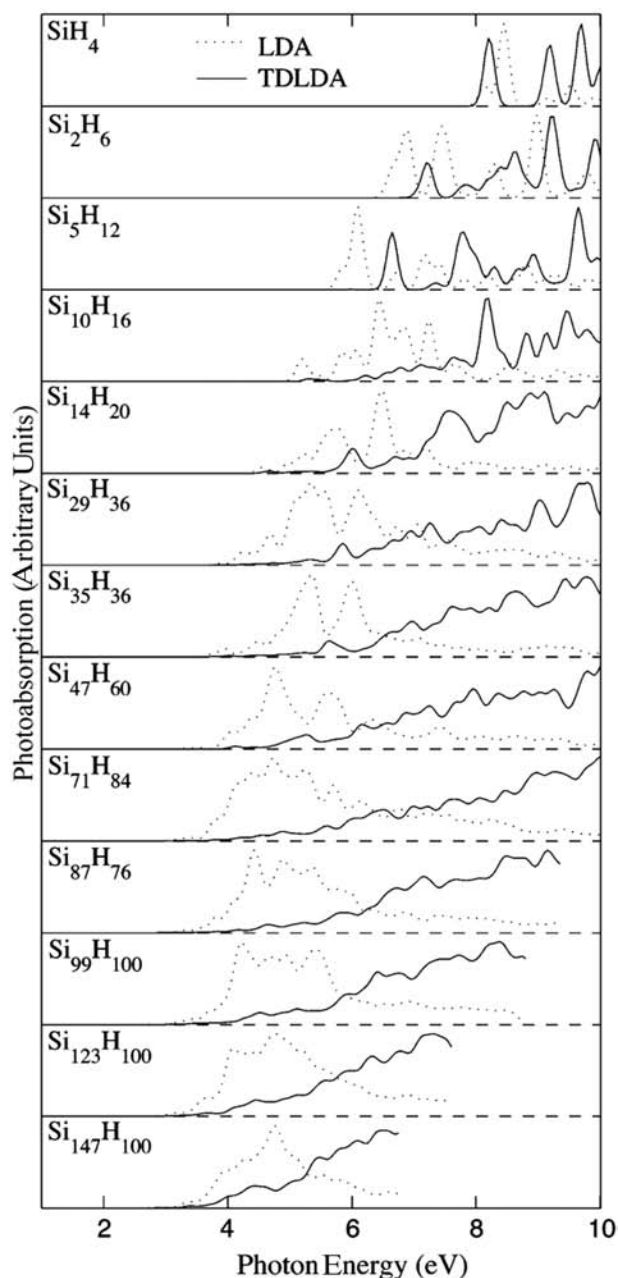


**Fig. 12** Photoabsorption spectra for hydrogenated silicon clusters and quantum dots (as in Fig. 8). The solid line represents spectra calculated using the time-dependent local density approximation. The dotted line represents a static local density approximation.

would predict the gap to diverge as the size of the dot diminished, as in Eq. (6).

In Fig. 11, predicted gaps for dots of diameter from 10 to 40 Å are presented. The predictions are based on time-dependent density functional theory, tight-binding, quasiparticle local density approximation, and empirical pseudopotential method calculations. The general trend of quantum confinement is well reproduced within this size regime. All of the methods, save the empirical pseudopotential method are in surprisingly good accord. The empirical pseudopotential method requires a fitting of the potentials to either experiment or theory as does the tight-binding method. It may be that this particular fitting for the pseudopotential was not as accurate as for the tight-binding method.

In Figs. 10 and 11, only the value for the lowest excitation was presented. Higher excitations were not considered, nor were the oscillator strengths. The latter can be an issue with methods such as quantum Monte Carlo, where higher-order excitations and oscillator strengths have not been explicitly considered. In contrast, methods such as the time-dependent local density approximation include higher excited states and oscillator strengths. In Fig. 12, photoabsorption spectra are presented for hydrogenated silicon clusters as indicated in Fig. 9. Both static and time-dependent local density approximation calculations are illustrated. The static calculations were obtained using Eq. (13), where for clusters the sum is over occupied and empty states, but not wave vector. For small clusters, the spectra tend to have sharp structures as expected for “molecular-like” systems. As the size of the system evolves, the spectra exhibit less structure and resemble the bulklike spectrum of crystalline silicon. Although it may not be apparent in Fig. 11, the oscillator strength for low-lying excitations decreases dramatically with increasing dot size.

## CONCLUSION

Major progress has been achieved within the last decade in simulating optical properties of silicon nanostructures and quantum dots. In particular, traditional approaches such as the empirical pseudopotential method and tight binding have been applied to large quantum dots. In addition, new formalisms and implementation have been developed such a GW–Bethe–Salpeter, quantum Monte Carlo, and time-dependent density functional theory. These new formalisms appear to be consistent for nanocrystals and quantum dots of a few hundred atoms or less and to be in agreement with experimental data, where available. A challenge to workers in this field will be to extend these systems to larger and more complex

systems with no loss of accuracy. Such complex systems will include the role of adsorbates, defects, and passivating media. An additional challenge will be to consider higher excitations and extract the full optical spectra of silicon nanocrystals.

## REFERENCES

1. Kittel, C. *Introduction to Solid State Physics*; John Wiley & Sons: New York, 1996.
2. Furukawa, S.; Miyasato, T. Quantum size effects on the optical band gap of microcrystalline Si:H. *Phys. Rev., B* **1988**, *38* (8), 5726–5729.
3. Canham, L.T. Silicon quantum wire array fabrication by electrochemical and chemical dissolution of wafers. *Appl. Phys. Lett.* **1990**, *57* (10), 1046–1048.
4. Cohen, M.L.; Chelikowsky, J.R. *Electronic Structure and Optical Properties of Semiconductors*, 2nd Ed.; Springer-Verlag: Berlin, Germany, 1989.
5. Philipp, H.R.; Ehrenreich, H. Optical properties of semiconductors. *Phys. Rev.* **1964**, *129*, 1550–1560.
6. Wang, W.L.; Zunger, A. Electronic structure pseudopotential calculations of large (~1000 atom) Si quantum dots. *J. Chem. Phys.* **1994**, *98* (8), 2158–2165.
7. Brus, L. Electronic wave functions in semiconductor clusters: experiment and theory. *J. Phys. Chem.* **1986**, *90* (12), 2555–2560.
8. Pandey, K.C.; Phillips, J.C. Atomic densities near Si (111) surfaces. *Phys. Rev., B* **1976**, *13* (2), 750–760.
9. Kwon, L.; Biswas, R.; Wang, C.Z.; Ho, K.M.; Soukalis, C.M. Transferable tight binding models for silicon. *Phys. Rev.* **1994**, *49* (11), 7242–7250.
10. Hill, N.A.; Whaley, K.B. Size dependence of excitons in silicon nanocrystals. *Phys. Rev. Lett.* **1995**, *75* (6), 1130–1133.
11. Niquet, Y.M.; Delerue, C.; Allan, G.; Lannoo, M. Method for the tight-binding parameterization: application to silicon nanostructures. *Phys. Rev., B* **2000**, *62* (8), 5109–5116.
12. Hohenberg, P.; Kohn, W. Inhomogeneous electron gas. *Phys. Rev., B* **1964**, *136* (3), B864–B871.
13. Kohn, W.; Sham, L. Self-consistent equations including exchange and correlation effects. *Phys. Rev., A* **1965**, *140* (4), A1133–A1138.
14. Chelikowsky, J.R.; Cohen, M.L. Ab initio pseudopotentials for semiconductors. In *Handbook on Semiconductors*; Landsberg, P., Ed.; Elsevier, 1992; Vol. 1, 59–111.
15. Chelikowsky, J.R.; Troullier, N.; Saad, Y. The finite-difference-pseudopotential method: electronic structure calculations without a basis. *Phys. Rev. Lett.* **1994**, *72* (8), 1240–1243.
16. Beck, T.L. Real-space mesh techniques in density-functional theory. *Rev. Mod. Phys.* **2000**, *72* (4), 1041–1080.
17. Perdew, J.P.; Levy, M. Physical content of the exact Kohn–Sham orbital energies: band gaps and derivative discontinuities. *Phys. Rev. Lett.* **1983**, *51* (20), 1884–1887.

18. Sham, L.J.; Schlüter, M. Density functional theory of the energy gap. *Phys. Rev. Lett.* **1983**, *51* (20), 1888–1891.
19. Hybertsen, M.; Louie, S.G. Electron correlation in semiconductors and insulators: band gaps and quasiparticle energies. *Phys. Rev., B* **1986**, *34* (8), 5390–5413.
20. Delerue, C.; Lannoo, M.; Allan, G. Excitonic and quasiparticle gaps in Si nanocrystals. *Phys. Rev. Lett.* **2000**, *84* (11), 2457–2460.
21. Ogut, S.; Chelikowsky, J.R.; Louie, S.G. Quantum confinement and optical gaps in Si nanocrystals. *Phys. Rev. Lett.* **1997**, *79* (9), 1770–1773.
22. Casida, M.E. Time-dependent density functional response theory for molecules. In *Recent Advances in Density-Functional Methods, Part I, Chapter 5*; Chong, D.P., Ed.; World Scientific: Singapore, 1995; 155–196.
23. Vasiliev, I.; Ogut, S.; Chelikowsky, J.R. First principles density functional calculations for optical spectra of clusters and nanocrystals. *Phys. Rev., B* **2002**, *65*, 115416, (1–18).
24. Ashcroft, N.W.; Mermin, N.D. *Solid State Physics*; Harcourt Brace College Publishers: New York, 1976.
25. Alubur, W.G.; Jönsson, L.; Wilkins, J.W. Quasiparticle calculations in solids. *Solid State Phys.* **2000**, *54*, 1–218.
26. Benedict, L.X.; Shirley, E.L.; Bohn, R.B. Optical absorption of insulators and the electron–hole interaction: an ab initio calculation. *Phys. Rev. Lett.* **1998**, *80* (20), 4514–4517.
27. Rohlfing, M.; Louie, S.G. Excitonic effects and the optical absorption spectrum of hydrogenated silicon clusters. *Phys. Rev. Lett.* **1998**, *80* (15), 3320–3323.
28. Hammond, B.L.; Lester, W.A., Jr.; Reynolds, P.J. *Monte Carlo Methods in Ab Initio Quantum Chemistry*; World Scientific: Singapore, 1994.
29. Williamson, A.J.; Hood, R.Q.; Grossman, J.C. Linear scaling quantum Monte Carlo calculations. *Phys. Rev. Lett.* **2001**, *87* (24), 246406, (1–4).
30. Puzder, A.; Williamson, A.J.; Grossman, J.C.; Galli, G. Surface chemistry of silicon nanoclusters. *Phys. Rev. Lett.* **2002**, *88* (9), 097401, (1–4).
31. Baierle, R.J.; Caldas, M.J.; Molinari, E.; Ossicini, S. Optical emission from small silicon particles. *Solid State Commun.* **1997**, *102* (7), 545–549.
32. Reboledo, F.A.; Franceschetti, A.; Zunger, A. Excitonic transitions and exchange splitting in Si quantum dots. *Appl. Phys. Lett.* **1999**, *75* (19), 2972–2974.

# Single-Cell Level Mass Spectrometric Imaging

Sara G. Ostrowski  
Andrew G. Ewing  
Nicholas Winograd

Department of Chemistry, Pennsylvania State University,  
University Park, Pennsylvania, U.S.A.

## INTRODUCTION

Secondary ion mass spectrometry (SIMS) is capable of imaging biological molecules across single cells with several hundred nanometer lateral resolution, and has the potential to examine the functional segregation of lipids in cell membranes. Lipids are believed to play a crucial role in fundamental biological functions, such as intercellular communication.<sup>[1]</sup> For example, high curvature lipids may be concentrated in regions of the lipid bilayer where membrane fusion preferentially occurs, because these lipids allow the bilayer to bend into the high curvature structures that form throughout the membrane fusion process.<sup>[2,3]</sup> Additionally, abnormalities in lipid composition may be involved in a wide range of diseases including Parkinson's disease, Alzheimer's disease, HIV, and atherosclerosis.<sup>[4-6]</sup> Research to better understand the biological role of lipids could help in the development of disease therapies, thus improving the quality and longevity of life. This article will review SIMS as it pertains to biological samples and will address relevant progress in SIMS including fundamental ionization studies of lipids, instrumental developments, and novel applications of SIMS imaging to single-cell analyses.

## SIMS

### Theory and Background

An important goal of SIMS research is to directly image the chemical distribution of small molecules across the surface of biomaterials.<sup>[7-10]</sup> With this method, ionic species that are emitted (or sputtered) from a sample following the impact of an incident, or primary, projectile are detected. More specifically, SIMS analysis uses a pulsed beam of primary ions that is focused onto a sample (Fig. 1).<sup>[11]</sup> Depending on the desired application, a variety of primary projectiles ( $\text{Cs}^+$ ,  $\text{Ar}^+$ ,  $\text{Ga}^+$ ,  $\text{In}^+$ ,  $\text{SF}_5^+$ ,  $\text{Au}_n^+$ ,  $\text{Bi}_n^+$ ,  $\text{C}_{60}^+$ , etc.) may be suitable. The impinging primary particles transfer energy and momentum to the sample, resulting in a

series of complex collisions within the sample. These energetic interactions ultimately cause sample electrons, neutral species, and ions (or secondary species) to be ejected from the sample (Fig. 2).<sup>[12-16]</sup> Secondary ions can form through several routes including electron ejection, protonation, deprotonation, cationization, loss of a functional group, and fragmentation resulting in charged species.<sup>[14]</sup> The secondary ions are then electrostatically collected and directed into a mass analyzer.

Secondary ion mass spectrometry can be divided into two different modes called static SIMS and dynamic SIMS, which are distinguished by the incident dose of primary ions. Secondary ion mass spectrometry is described as static when the primary ion flux is less than 1% of the total number of surface atoms; SIMS is dynamic when the incident dose is greater than this value.<sup>[17]</sup> Dynamic SIMS is marked by extensive beam-induced damage, which destroys molecular information and limits dynamic SIMS to elemental and isotopic studies. Static SIMS is inherently less damaging to the molecular integrity of a sample because of the low primary ion flux (1 nA/cm<sup>2</sup> or less).<sup>[14]</sup> There is minimal chemical damage and spatial perturbation of sample molecules. Therefore, static SIMS is favored for applications where large molecules or molecular fragments are investigated. Another unique aspect of the static regime is that only the top-most sample monolayer is probed, making static SIMS a surface sensitive technique.<sup>[18]</sup> Because of its ability to analyze molecules at surfaces, the static mode of SIMS has been used for examining lipids on tissues and cell membranes.<sup>[9,10]</sup>

## Instrumentation

### Primary ion source

Secondary ion mass spectrometry instruments employ a variety of primary ion source configurations including electron impact ionization-based sources, duoplasmatron sources, and field evaporation-based sources, like the popular liquid metal ion sources (LMIS).<sup>[14]</sup>



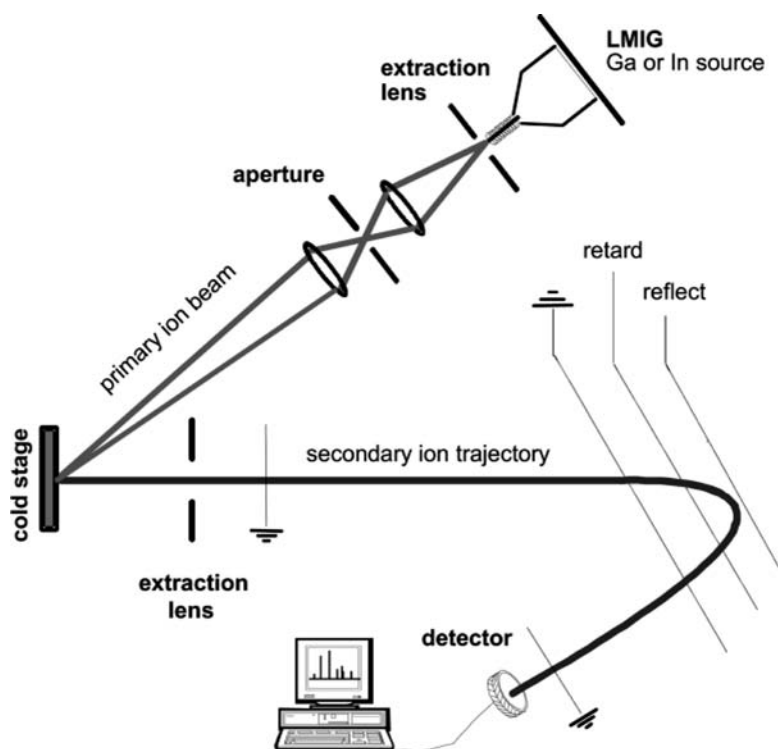


**Fig. 1** Time of flight SIMS (ToF-SIMS) instrumental setup. *Source:* From Ref.<sup>[11]</sup>.

By far, the most commonly used primary ion sources are the LMIS, such as gallium ( $\text{Ga}^+$ ) and indium ( $\text{In}^+$ ), because of their brightness, small spot size, and simplicity. Liquid metal ion sources are mounted on the end of a primary ion gun column adjacent to a negative potential field that initiates primary ion emission from the LMIS.<sup>[14]</sup> The gun column also contains several electrostatic lenses and octupoles to focus the beam down to a 50-nm diameter, and a pair of electrostatic plates that pulse the ion beam for SIMS experiments.

Advances in primary ion beam technology have directed the communities' attention to the benefits of cluster ion primary sources, such as  $\text{Au}_n^+$ ,  $\text{Bi}_n^+$ ,  $\text{SF}_5^+$ , and buckminsterfullerene,  $\text{C}_{60}^+$ .<sup>[19–21]</sup> Experimental results indicate that  $\text{C}_{60}^+$  offers enormous improvements

in secondary ion yield and minimal chemical damage to sample molecules.<sup>[21]</sup> Molecular dynamics simulations suggest that upon surface impact,  $\text{C}_{60}$  cluster projectiles break into individual carbon atoms and disperse the primary projectile energy among the individual atoms.<sup>[15]</sup> This phenomenon allows for a more shallow penetration depth and more surface-localized primary bombardment energy for cluster projectiles, in comparison to their atomic counterparts. The  $\text{C}_{60}^+$  sputtering mechanism allows intact molecules to be gently lifted off the surface, creating higher secondary ion yield, particularly for high mass molecules, and minimal chemical damage.<sup>[21]</sup> Therefore,  $\text{C}_{60}^+$  and other cluster ion sources are attractive alternatives as SIMS primary ion sources for biological applications, where there is a desire to greatly reduce molecular fragmentation of larger-mass target analytes. Additionally, the attributes of  $\text{C}_{60}^+$  suggest that molecular depth-profiling is possible, which will allow 3-D imaging of tissue and cells.<sup>[22–25]</sup>

Secondary ion mass spectrometry images are obtained by scanning the primary ion beam across the sample surface and collecting a unique mass spectrum for every image pixel (Fig. 3).<sup>[26]</sup> The signal sent to the computer contains the location of the primary ion impact and the spectrum collected at that position. The computer uses this information to output a spectrum, called the “total ion spectrum,” which contains the integrated intensities for all the ions at every pixel of the image. Additionally, the computer generates a

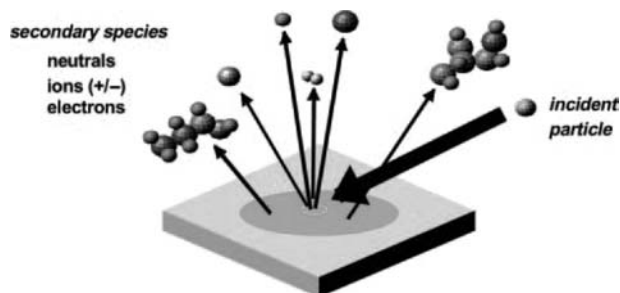


**Fig. 2** Illustration of sputtering and ionization by SIMS. *Source:* From Ref.<sup>[12]</sup>.

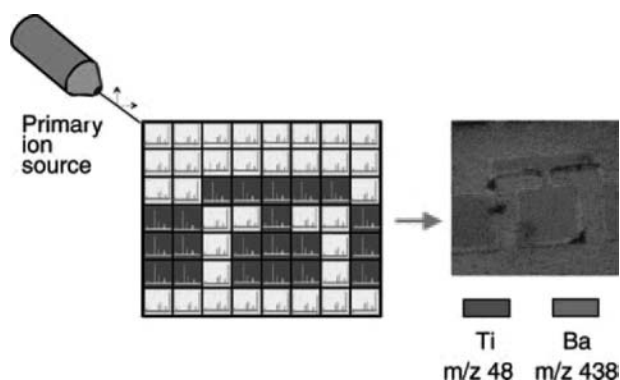


**Fig. 3** Chemical imaging with ToF-SIMS. The primary ion source is rastered across the sample surface and a mass spectrum is collected at each pixel. For every mass range of interest, an intensity plot, which maps the distribution of that signal across the sample, can be generated. The intensity plots can be color coded and overlaid. In this example, an electronic device composed of titanium ( $m/z$  48, green) and barium ( $m/z$  138, blue) is chemically imaged. *Source:* From Ref.<sup>[26]</sup>.

“total ion image,” which is an intensity map for all of the ions in each pixel (Fig. 4). Computer software is then used to extract spatial, chemical-specific information from the “total ion” image and spectrum. In one method of data analysis, the user selects a mass range of interest in the total ion spectrum, and the software creates a 2-D intensity map of the distribution of that signal across the sample (Fig. 4). In an alternative way to analyze the data, the user can select a region of interest in the total ion image, and the computer generates a mass spectrum with integrated intensities for the ions in only the selected pixels.

### Secondary ion extraction

The primary ion source directs the primary ion beam onto the sample, which is mounted on a sample stage

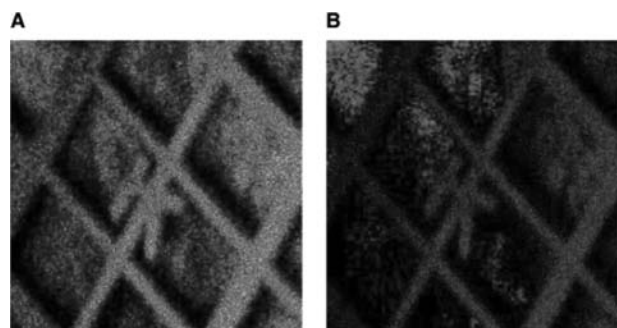


**Fig. 4** Secondary ion mass spectrometry images of a copper London Finder grid. The grid was adhered to a copper sample block with silver paste. (A) Total ion image; (B) chemical image of the distribution of copper (green) and silver (blue).

at  $\pm 2.5$  kV. The stage potential can be pulsed or held constant and repels ions of like charge, which are then collected by an extraction lens oppositely biased at 4.7 kV. For example, if the target analyte is a cation, the sample stage would be positively charged, and the extraction lens would be negatively charged. This mode of operation is called “positive SIMS,” because the positive ions are being analyzed. The instrumental polarities must be switched to generate spectra of negatively charged species.

### Mass analyzers

The extraction lens directs the secondary ions into the mass analyzer, which can be a magnetic sector, quadrupole, or ToF. Of these three mass analyzers, the ToF analyzer is the best equipped for static SIMS imaging, because it detects all ions in parallel, boasts a high transmission, and has a virtually unlimited mass range.<sup>[17]</sup> Additionally, advances in electronic timing systems have allowed ToF analyzers to provide a competitive mass resolution of 10,000.<sup>[14]</sup> The general concept of a ToF analyzer is that the secondary ions are accelerated to a specific kinetic energy and then allowed to travel a defined distance.<sup>[14]</sup> The mass of each secondary ion can be calculated from the time it takes to travel the distance.<sup>[14]</sup> After the secondary ions are separated in the mass analyzer, they impact a detector, such as a multichannel plate detector. The molecules reach the detector sequentially because each molecule has a unique mass, allowing quasi-parallel detection.<sup>[14]</sup>

### Biological Samples: Frozen-Hydrated Sample Preparation for Sims

Maintaining the native chemical distribution in hydrated samples, such as cells, in the ultra-high vacuum environment of a SIM spectrometer is challenging. The low pressures cause rapid sublimation of water, which results in the membranous material and intercellular content of a cell smearing across the sample surface.<sup>[27]</sup> To prevent this phenomenon, a fast-freeze, freeze-fracture sample preparation methodology has been adapted from the electron microscopy community, to preserve biological samples for SIMS analysis (Fig. 5).<sup>[28,29]</sup> A cell sample is delivered onto a clean silicon wafer and a shard of silicon is placed on top of the cells. The sample assembly is then plunged into a cryogen to freeze the cells, while minimizing the ice crystal-induced sample damage.<sup>[30]</sup>

Prior to analysis, the top shard of the fast-frozen sample assembly is removed by a cryogenically cooled knife in a sample preparation vacuum chamber adjoining the SIMS analysis chamber.<sup>[27]</sup> This “freeze-fracture”

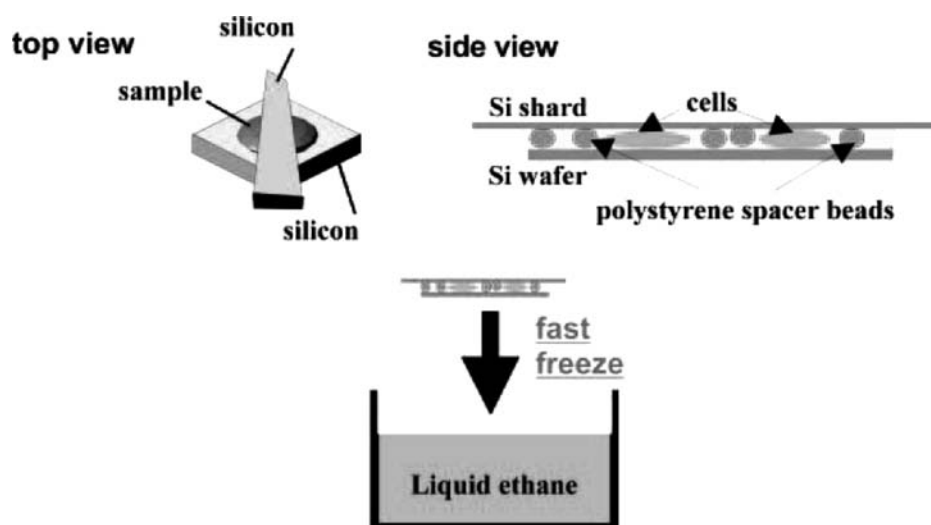


**Fig. 5** Cryogenic preservation of hydrated samples. The sample, containing cells (shown in pink) and polystyrene beads (shown in yellow), is delivered onto a silicon wafer. A silicon shard is placed on top of the sample droplet to create a sandwich assembly. The sandwich assembly is then plunged into a liquid cryogen. *Source:* From Ref.<sup>[27]</sup>.

process results in the exposure of a fresh surface to the vacuum interface. Fracturing is performed at a pressure-dependent sample temperature that equilibrates the condensation and sublimation fluxes of water.<sup>[27]</sup> The sample temperature is controlled throughout the preparation and analysis, by several chamber components that are cryogenically cooled. The details of the freeze-fracture chamber have been described.<sup>[27]</sup>

## OVERVIEW OF ADVANCES IN BIOLOGICAL SIMS

Images of both elemental and molecular analytes have provided a wealth of information, learned using SIMS. For example, dynamic SIMS elemental analysis has allowed Chandra and coworkers<sup>[8]</sup> to assess the efficacy of boron neutron-capture therapy (BNCT) cancer drugs at the single-cell level.<sup>[8]</sup> Images of the subcellular distribution of boron were used to compare the accumulation of two BNCT drugs, *p*-boronophenylalanine (BPA-F) and sodium borocaptate (BSH), in normal and cancerous cocultured cells. *p*-Boronophenylalanine accumulated in both cell types at significantly higher levels than BSH, indicating that BPA-F enters the cell by an active uptake mechanism and not by simple passive diffusion. This research group has been at the forefront of biological dynamic SIMS with many other notable applications including the mapping of elevated concentrations of  $\text{Ca}^{2+}$  in the Golgi apparatus to determine how it is affected by hormone and antigen treatment.<sup>[31]</sup>

Lechene and coworkers<sup>[32–34]</sup> also have worked on an impressive repertoire of mass spectrometric elemental imaging applications. In particular, Lechene utilizes a variation of SIMS called multi-isotope imaging mass spectrometry (MIMS), in which isotopic signals can be

simultaneously monitored, because the instrument has a very high mass resolution. For example, the instrument can distinguish between  $^{12}\text{C}^{15}\text{N}$  ( $m/z = 27.0001$ ) and  $^{13}\text{C}^{14}\text{N}$  [ $m/z = 27.0064$  with a mass resolution ( $m/\Delta m$ ) of 4287].<sup>[32]</sup> One study demonstrated that MIMS is a useful technique to image and quantify isotope ratios in free fatty acids (FFA) on the subcellular scale.<sup>[34]</sup> Adipocytes are cells that sequester FFA from the blood and store them as triacylglycerol in lipid droplets, which are 1  $\mu\text{m}$  sized features within the cells. Adipocytes were incubated in  $^{13}\text{C}$  oleic acid; with MIMS imaging, a higher level of  $^{13}\text{C}$  accumulation was found in the lipid droplets than in the extracellular space or in the remaining intracellular space (Fig. 6). These results illustrated that FFA transport across the cell membrane is protein mediated, because FFA moves against its concentration gradient. In addition to supporting a hypothesis for the controversial FFA transport mechanism, this work was yet another example of the wide range of subcellular, biological questions that isotope ratio quantification with MIMS imaging can answer.

The Levi-Setti research group is renowned for using the elemental imaging capabilities of SIMS for biological applications. In one study, they obtained 50 nm lateral resolution SIMS images of the cation distribution in mammalian interphase cells, mitotic cells, and isolated metaphase chromosomes that supported a role for cations in the regulation of the cell cycle.<sup>[35]</sup> The SIMS images demonstrated that the localization of  $\text{Na}^+$  and  $\text{K}^+$  remained constant during the cell cycle, but  $\text{Mg}^{2+}$  and  $\text{Ca}^{2+}$  changed depending on the stage of the cell cycle: In the interphase these divalent cations were predominately present in the cytosol, whereas during mitosis they were aggregated in the chromatin. Quantification of the SIMS signal revealed that the total intercellular divalent cation concentration

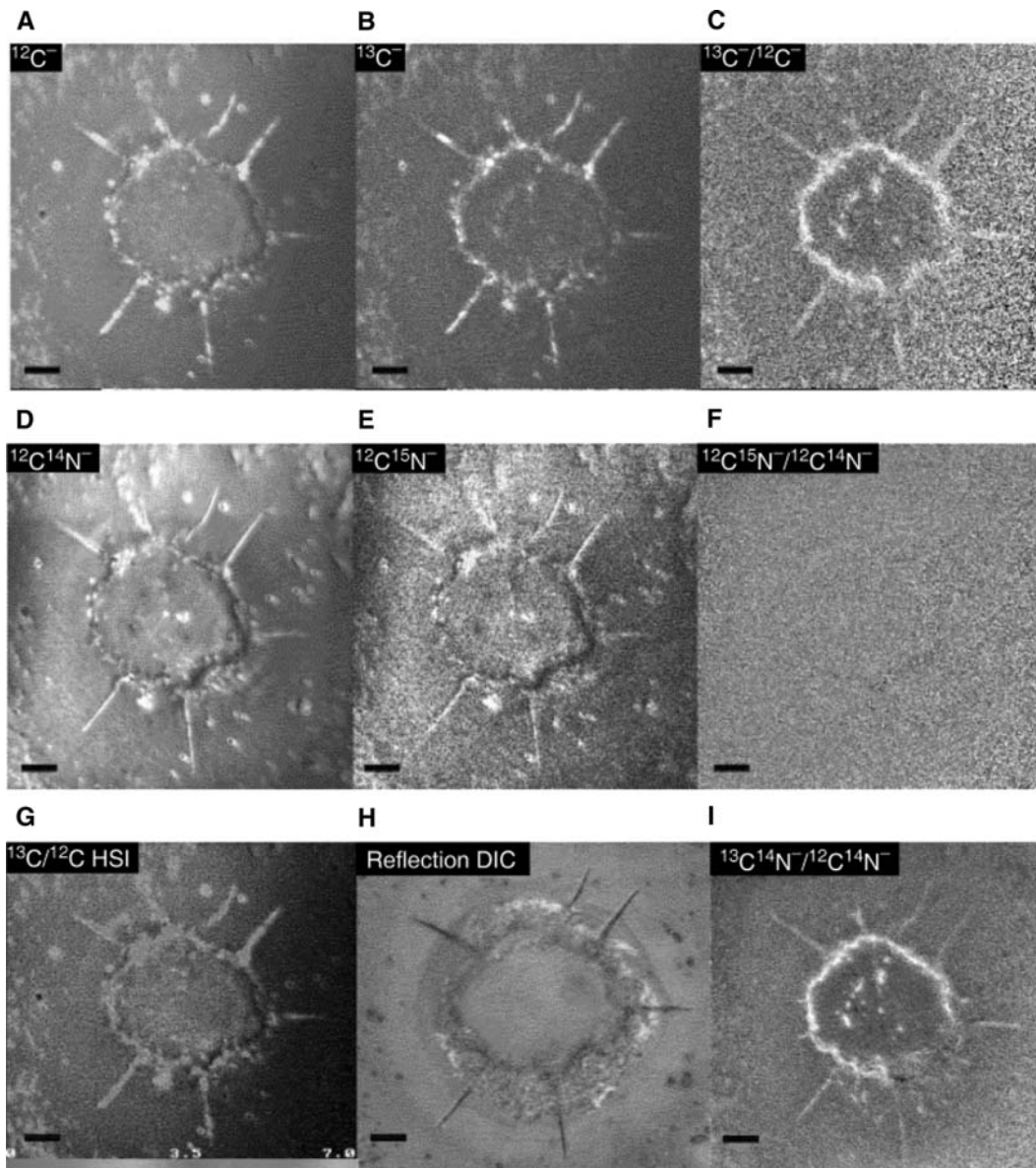


**Fig. 6** Images of unwashed adipocytes treated with  $^{13}\text{C}$  oleate: BSA. The MIMS images of (A)  $^{12}\text{C}^-$  and (B)  $^{13}\text{C}^-$ ; (C) MIMS ratio image of  $^{13}\text{C}/^{12}\text{C}$  showed the enhanced accumulation of isotopically labeled lipid in the lipid droplets. The MIMS images of (D)  $^{12}\text{C}^{14}\text{N}^-$  and (E)  $^{12}\text{C}^{15}\text{N}^-$ ; (F) MIMS ratio image of  $^{12}\text{C}^{15}\text{N}^-/^{12}\text{C}^{14}\text{N}^-$  had no contrast because no exogenous  $^{15}\text{N}$  was added. (G) A hue saturation intensity image of the  $^{13}\text{C}/^{12}\text{C}$  ratio. (H) A reflection differential interference image prior to MIMS analysis. (I) A MIMS ratio image of  $^{13}\text{C}^{14}\text{N}^-/^{12}\text{C}^{14}\text{N}^-$  further demonstrated the accumulation of labeled lipid in the lipid droplets. Scale bar is  $5\ \mu\text{m}$ . Source: From Refs.<sup>[31,34]</sup>

did not change significantly during the cell cycle. From this data, the authors concluded that progression through the cell cycle resulted in a redistribution of divalent cations without a major influx or efflux of the ions. Therefore,  $\text{Mg}^{2+}$  and  $\text{Ca}^{2+}$  likely play a role in chromatin compaction only during the mitotic stage, whereas  $\text{Na}^+$  and  $\text{K}^+$  are involved in compaction throughout the cell cycle. A combination of SIMS imaging and immunofluorescence (IF) have indicated that only  $\text{Ca}^{2+}$  localizes at the chromosome axis with the nonhistone binding protein, topoisomerase II $\alpha$

(Topo II) (Fig. 7). It follows that  $\text{Ca}^{2+}$  probably inhibits the catalytic activity of the protein and plays an important role in stabilizing the chromosomal scaffolding proteins, such as Topo II. When the authors incubated mitotic chromosomes with chelating agents, SIMS and IF images exhibited a loss of Topo II and a decondensed chromosome structure, indicating that  $\text{Ca}^{2+}$  must also be involved in maintaining the chromosome structure during mitosis. This research provided the first evidence, without secondary markers, that cations have specific, functional interactions



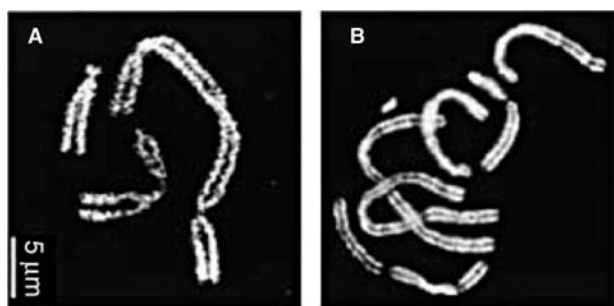


**Fig. 7**  $\text{Ca}^{2+}$  SIMS image (A) and Topo II antibody IF image (B) of metaphase chromosomes. The cation and scaffolding protein antibody colocalize, indicating that  $\text{Ca}^{2+}$  binds to Topo II and mediates its activity. *Source:* From Refs.<sup>[32,35]</sup>.

with chromatin binding proteins, and that cations help control chromosome structure during the cell cycle.

Static SIMS molecular imaging has also been applied to investigations of single cells. The seminal paper in this area presented static SIMS images of molecular species, as well as elemental analytes, on dopant-treated paramecia.<sup>[7]</sup> The cocaine molecular ion, a cocaine fragment ion, dimethyl sulfoxide, and potassium, all colocalized to the treated protozoa. This work demonstrated the capability of SIMS to image molecular analytes across single cells, thus paving the way for single-cell studies of large molecule drugs, and biological molecules such as vitamins and membrane lipids.

Identifying mass spectral peaks from biological molecules in a complex system, such as a cell membrane, is very challenging. Therefore, experiments that associate a peak of a particular mass with a fragment of a biological molecule mark significant advances toward realizing the utility of SIMS for biological applications. Todd and coworkers<sup>[9]</sup> identified abundant high-mass peaks at  $m/z$  184 and  $m/z$  86 observed in several types of tissue as fragment peaks from phosphatidylcholine and sphingomyelin. The identification of mass spectral peaks for lipid fragments presented the option of using SIMS imaging to investigate the lipid distribution in tissue, model membrane systems, and cells.

Experiments with model systems have proven that SIMS imaging of lipid domains is possible, and, therefore, the goal of studying the functionality of lipid domains in cells can be realized. Benninghoven used Langmuir Blodgett (LB) films as lung surfactant model systems to assess lipid involvement in the compression/exhalation and expansion/inhalation of the lung.<sup>[36]</sup> An LB film composed of dipalmitoylphosphatidylcholine (DPPC), dipalmitoylphosphatidylglycerol, and the lung surfactant protein (SP-C) was prepared, and, upon severe compression, a distinctly heterogeneous distribution of the film components

was observed. Specifically, SP-C reorganized into a SP-C-rich phase following film compression, which supported the hypothesis that lung compression causes non-DPPC components to leave the monolayer.<sup>[36]</sup>

Winograd and Ewing have also investigated LB films with static SIMS. In these experiments, LB films of varying amounts of DPPC, dipalmitoylphosphatidylethanolamine (DPPE), and cholesterol were analyzed.<sup>[37]</sup> Micrometer-sized cholesterol domains were observed in LB films of mixtures containing DPPE; however, LB films containing the same percentage of cholesterol and DPPC were homogeneous. The authors explained these results by the interaction strength differences between the three molecules. The DPPE headgroup is known to interact more strongly with other phospholipid headgroups than with cholesterol. Therefore, the phospholipids preferentially aggregated, which excluded cholesterol and resulted in lipid domains. The propensity of cholesterol to induce domain formation implicated a functional role for cholesterol in cell signaling and trafficking.<sup>[37]</sup>

Liposomes are another common artificial model for cell membranes. Molecule-specific images of dynamic membrane events were captured during several stages of fusion between chemically distinct multilamellar liposomes.<sup>[27]</sup> Specifically, liposomes 20  $\mu\text{m}$  in size were prepared that contained cholesterol and either DPPC, dipalmitoylphosphatidyl-*N*-monomethylethanolamine (DPPNME), or dipalmitoylphosphatidyl-dimethylethanolamine (DPDME). The separate batches of liposomes were mixed onto a single substrate, and the samples were frozen after various mixing times.<sup>[27]</sup> Chemical snapshots of three stages of liposome fusion were obtained: liposomes in close proximity, liposomes undergoing initial contact, and liposomes that had fully fused (Fig. 8). Interestingly, during fusion, the liposomes joined at a contact point, where lipid heterogeneity was evident, while fully fused liposomes displayed a completely uniform lipid distribution. These results showed that liposome fusion involves initial lipid domain formation followed by a homogeneous redistribution of lipids throughout the fused liposomes. This publication highlighted liposome model systems as an effective way to investigate membrane dynamics with ToF SIMS.

In addition to imaging lipids in model membrane systems, many research groups have applied SIMS imaging to single-cell membranes. For example, lipids have been localized to single rat pheochromocytoma (PC12) cell membranes, using SIMS imaging.<sup>[10]</sup> Pheochromocytoma cells are an exciting system for neurochemistry applications, because they can be differentiated to have neuronal-like properties when exposed to the nerve growth factor protein.<sup>[38]</sup> Undifferentiated PC12 cells undergo regulated exocytosis and can be used to learn if the lipid composition affects

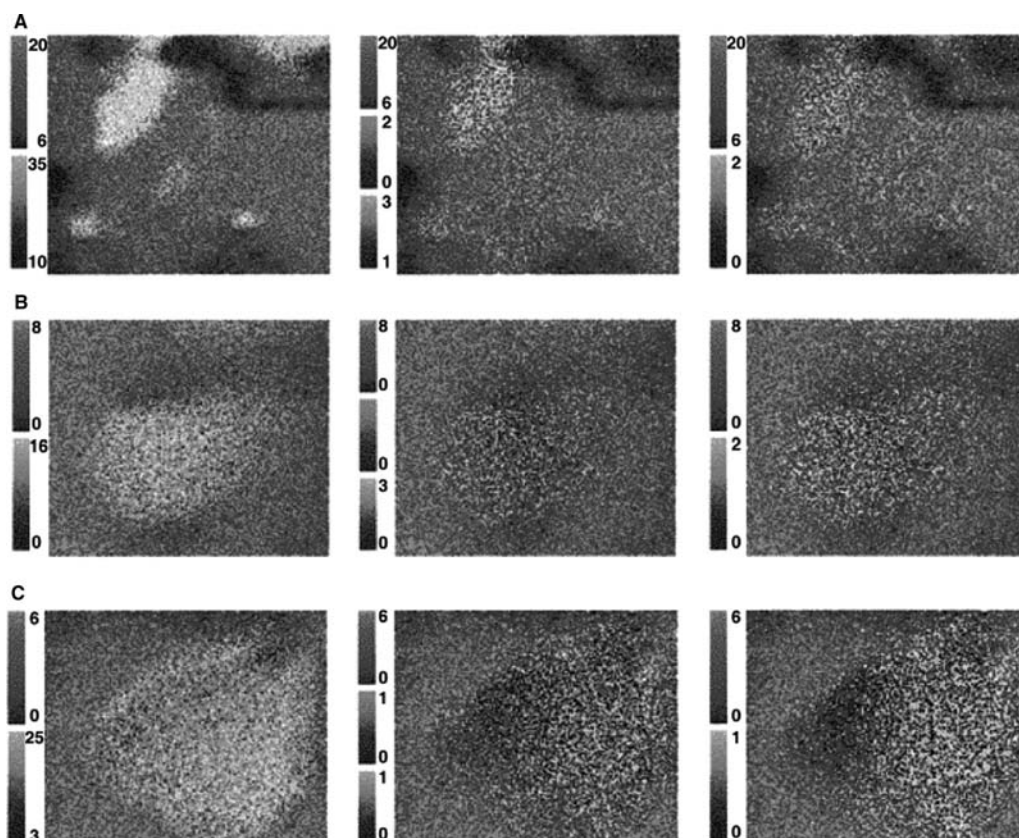


**Fig. 8** Liposomes with distinct lipid compositions: DPPC/cholesterol, DPPNME/cholesterol, and DPPDME/cholesterol, that were mixed together and frozen after different times. In all images, the blue pixels represent water ( $m/z$  17.9–19.1). From left to right, the images are mapped for  $C_3$  hydrocarbons ( $m/z$  40.9–43.3, yellow), two phosphorylated headgroups (various  $m/z$ , yellow and red), and cholesterol ( $m/z$  384.1–387.1, yellow). A DPPC/cholesterol and DPPDME/cholesterol liposomes were mixed and frozen after 30 sec of mixing. The phosphorylated headgroups mapped in the center column were phosphocholine ( $m/z$  183.9–184.3, yellow) and phosphodimethylethanolamine headgroup ( $m/z$  169.9–170.3, red). The two types of liposomes have not yet begun to fuse. B. and C. DPPC/cholesterol and DPPNME/cholesterol liposomes were frozen together after B. 120 sec and C. 60 sec of mixing time. The phosphorylated headgroups mapped in the center column were phosphocholine ( $m/z$  183.9–184.3, yellow) and phospho-*N*-monomethylethanolamine ( $m/z$  155.9–156.3, red). A homogeneous distribution of the two phospholipids was observed after full fusion in B., but a heterogeneous distribution was evident during initial fusion in C. *Source:* From Refs.<sup>[24,27]</sup>

the abnormalities in exocytosis, observed in many neurological diseases. Using SIMS, phosphocholine and cholesterol were imaged across single PC12 cells.<sup>[10]</sup> This study demonstrated the ability of SIMS to detect multiple lipids in biological samples.

In a separate experiment, Ewing and coworkers<sup>[39]</sup> found that freeze-fracture sample preparation can expose different section planes through a cell. Pheochromocytoma cells were dyed with the lipophilic dye, 1,1'-dioctadecyl-3,3,3',3'-tetramethylindocarbocyanine perchlorate (DiI), which is known to incorporate only onto the outer leaflet of the membrane.<sup>[39]</sup> Therefore, the outer leaflet of the cell membrane contained lipid and DiI, the inner leaflet of the cell was composed of lipid and no DiI, and the interior of the cell contained elevated amounts of potassium. Using SIMS imaging of stained PC12 cells, chemical signatures for five

possible cell sections were determined. Two of these cell sections were from exposure of the outer leaflet (top or bottom) of the cell membrane during fracturing. In this scenario, the SIMS images showed colocalization of DiI and phosphocholine, while sodium, potassium (ions present in the freezing medium), and water were depressed at the site of the cell. The top and bottom inner leaflet of the membrane were two other exposed cell sections, and were identified by localization of phosphocholine and potassium to the cell, the absence of DiI signal, and decreased intensities of water and sodium at the area of the cell. Finally, through-cell fractures were characterized by a strong localization of potassium and some phosphocholine from free lipid in the cytoplasm, lipid from organelles, and lipid from the edges of the cell membrane. This cell section contained no DiI signal and showed an inverse



localization of water and sodium. Identifying chemical signatures that define the section of a cell exposed to the surface–vacuum interface was an important advance for the biological SIMS community.

Besides the lipids and steroids discussed above, another important chemical in membrane chemistry is vitamin E, because it affects membrane fluidity and has been implicated in lipid oxidation and, therefore, in numerous neurodegenerative disorders.<sup>[40]</sup> Recently, Sweedler and coworkers<sup>[40]</sup> discovered that a peak at  $m/z$  430 in biological samples arises from vitamin E. Along with this peak identification, the Sweedler group has reported exciting SIMS images that suggest a possible functional role for vitamin E in neuronal membranes.<sup>[40]</sup> Subcellular molecular images of an isolated neuron from *Aplysia californica* revealed that vitamin E ( $m/z$  430 and  $m/z$  165) was strongly localized to the junction between the cell soma and the neurite, compared to the rest of the cell body (Fig. 9). The authors compared a normalized vitamin-E signal

for the soma–neurite junction to the cell body, and found that the junction contained  $165 \pm 11\%$  more vitamin E. These results suggested a possible structural role for vitamin E, in terms of modulating the membrane radius of curvature at the junction, and a possible functional role, in terms of transport mechanisms and neuronal signaling.

Along with mammalian cells, other types of cells have been investigated with SIMS to progress towards the goal of understanding lipid distribution during membrane fusion events. For example, the mating *Tetrahymena thermophila* were imaged with SIMS by Ostrowski et al.<sup>[41]</sup> During mating, two *Tetrahymena* join at their anterior ends and their membranes fuse, creating hundreds of nanometer-sized fusion pores within a well-defined 8- $\mu\text{m}$  region, called the conjugation junction. Secondary ion mass spectrometry images reveal a heterogeneous distribution of signals for specific lipids across the mating cells. Specifically, the total lipid content remained constant across the

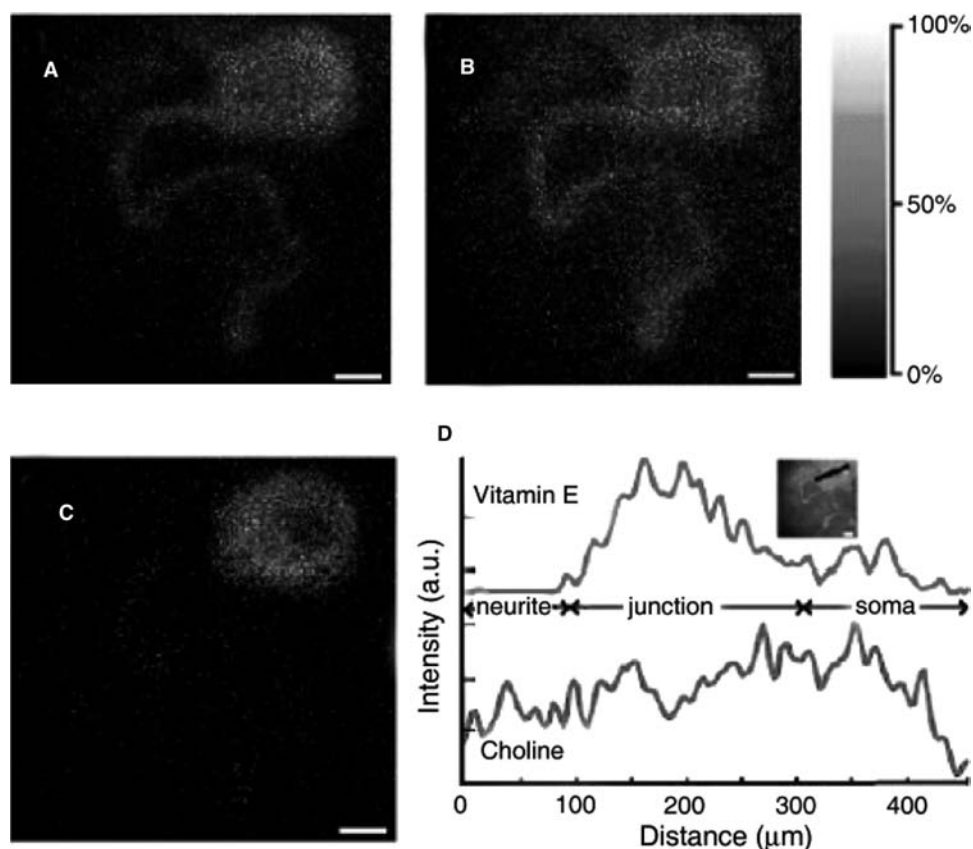


**Fig. 9** Molecule-specific SIMS images and corresponding line scans of an isolated single neuron. (A) SIMS image of choline,  $m/z$  86, a fragment of phosphatidylcholine and a common marker for the cell membrane. (B) SIMS image of a fragment of a lipid acyl chain,  $m/z$  69, another common cell membrane marker. (C) SIMS image of vitamin E,  $m/z$  430, which is strongly localized to the junction between the cell body and the neurite. (D) Line scans for vitamin E (top) and choline (bottom), normalized to  $m/z$  69 and taken along the line indicated in the inset, beginning at the soma. Vitamin E displays a higher signal at the soma–neurite junction than the rest of the cell body, whereas, the choline signal is relatively constant across the distance. *Source:* From Refs.<sup>[37,40]</sup>

mating cells (Fig. 10A and B). However, there was a decreased amount of PC at the conjugation junction, as evidenced by a  $67 \pm 8\%$  decrease in phosphocholine signal at the junction vs. the cell body (Fig. 10C and D). Additionally, statistical analysis of the SIMS images suggests an increase in a cone-shaped lipid, 2-aminoethylphosphonolipid, at the junction. From the observed lipid heterogeneity, it was concluded that *Tetrahymena* synthesize or redistribute lipids to allow the formation of high curvature membrane structures. This work is an elegant example of the capability of molecular SIMS imaging to probe sub-cellular, micrometer-sized membrane regions that contain structures in the nanometer regime.

### Sample Preparation and Instrumental Design Improvements in Biological SIMS

Although all of these application-based advances have been invaluable in promoting SIMS as a bio-analytical technique, instrument and sample preparation developments have also been an important part of the picture. First, epifluorescence microscopy was incorporated into the optical assembly of a SIMS instrument.<sup>[10]</sup> Epifluorescence was a valuable instrumental addition, because it allowed easy location of small, fluorescently labeled cells in ice prior to SIMS analysis. For instance, 15- $\mu\text{m}$  PC12 cells were fluorescently labeled with DiI, located in situ with fluorescence microscopy, and subsequently imaged with SIMS.<sup>[10]</sup>

One notable challenge in SIMS imaging has been that information in the images is limited because of the low secondary ion yield of biomolecules. To circumvent this obstacle and improve signal, different sample preparation protocols and instrumental advances have been developed. Sjovall et al.<sup>[42]</sup> developed an alternate sample-preparation methodology in which cell membranes were imprinted onto Ag foil ex situ. Membranous matter was transferred from cells adhered onto glass to an Ag foil, by placing the foil on the backside of the foil and applying a specific pressure to the backside of the foil. The foil was then transferred into the SIMS analysis chamber. This method was advantageous, because silver cationization enhanced the secondary ion signal from biological fragment ions and molecular ions. In one particular experiment, the distributions of phosphatidylcholine and cholesterol were imaged, with a 500 nm lateral resolution, across blood cell imprints.

A significant instrumental advance that has revitalized biological SIMS has been the advent of cluster primary ion sources, like  $\text{C}_{60}^+$ , as previously discussed.<sup>[19–21]</sup> Vickerman and coworkers have reported impressive secondary ion yields, produced by  $\text{C}_{60}^+$  relative to  $\text{Ga}^+$ . For example, the ion yields for a thin film of DPPC were found to be 158 times higher for  $m/z$  100–200 and 3985 times higher for the molecular ion.<sup>[21]</sup> This signal enhancement will make analyte masses easier to discern from noise in complex biological samples. Also, the contrast between adjacent pixels in images will be improved, because resolution in SIMS

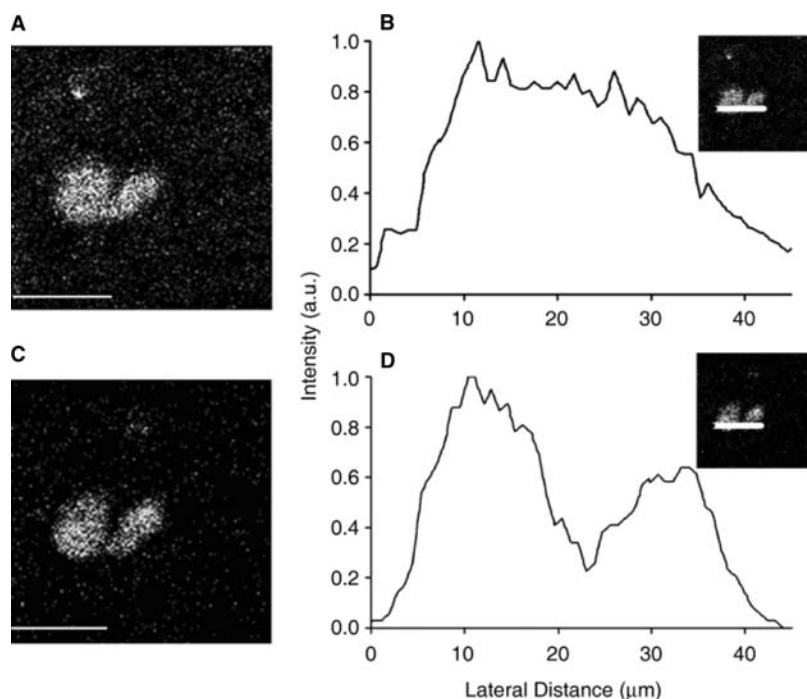


**Fig. 10** Secondary ion mass spectrometry images and line scans of mating *T. thermophila*. (A) SIMS image and (B) line scan for a lipid acyl chain fragment,  $m/z$  69, which is representative of the total lipid distribution. The inset indicates the region of the image selected for the line scan. The total lipid signal is relatively constant across the distance of the mating cells. (C) SIMS image and (D) line scan for phosphocholine,  $m/z$  184. The phosphocholine signal shows a dramatic drop in signal at the junction between the two cells. Scale bars are 50  $\mu\text{m}$ . *Source:* From Refs.<sup>[38,41]</sup>.

images is determined by the number of ions that are collected at each pixel.

## CONCLUSIONS

The abundance of previous SIMS research provides a wealth of examples showcasing the compatibility of this technique and biological applications. Already, SIMS has been used to study the effects of cancer drugs on single cells, to elucidate the role of cations in isolated metaphase chromosomes, and to image large-molecule dopants, vitamins, and lipids across single cells. The ambitious pursuit of challenging applications, coupled with instrumental advances, has set the groundwork for future studies of the cellular functionality of lipid domains.

## ACKNOWLEDGMENTS

The authors gratefully acknowledge the US National Institute of Health, for funding, and the National Science Foundation, for additional instrumentation funding.

## REFERENCES

- Yeagle, P. *The Membranes of Cells*; 2nd Ed.; Academic Press: San Diego, 1993.
- Vance, D.E.; Vance, J.E. *Biochemistry of Lipids, Lipoproteins and Membranes*; 3rd Ed.; Elsevier: Amsterdam, New York, 1996.
- Gruner, S.M. Intrinsic curvature hypothesis for biomembrane lipid composition: a role for nonbilayer lipids. *Proc. Natl. Acad. Sci. U.S.A.* **1985**, *82* (11), 3665–3669.
- Ehehalt, R.; Keller, P.; Haass, C.; Thiele, C.; Simons, K. Amyloidogenic processing of the Alzheimer beta-amyloid precursor protein depends on lipid rafts. *J. Cell Biol.* **2003**, *160* (1), 113–123.
- Simons, K.; Ehehalt, R. Cholesterol, lipid rafts, and disease. *J. Clin. Invest.* **2002**, *110* (5), 597–603.
- Lusis, A.J. Atherosclerosis. *Nature* **2000**, *407* (6801), 233–241.
- Colliver, T.L.; Brummel, C.L.; Pacholski, M.L.; Swaneck, F.D.; Ewing, A.G.; Winograd, N. Atomic and molecular imaging at the single-cell level with ToF-SIMS. *Anal. Chem.* **1997**, *69* (13), 2225–2231.
- Lorey, D.R.; Morrison, G.H.; Chandra, S. Dynamic secondary ion mass spectrometry analysis of boron from boron neutron capture therapy drugs in co-cultures: single-cell imaging of two different cell types within the same ion microscopy field of imaging. *Anal. Chem.* **2001**, *73* (16), 3947–3953.
- McMahon, J.M.; Short, R.T.; McCandlish, C.A.; Brenna, J.T.; Todd, P.J. Identification and mapping of phosphocholine in animal tissue by static secondary ion mass spectrometry and tandem mass spectrometry. *Rapid Commun. Mass Spectrom.* **1996**, *10* (3), 335–340.
- Roddy, T.P.; Cannon, D.M.; Meserole, C.A.; Winograd, N.; Ewing, A.G. Imaging of freeze-fractured cells with in situ fluorescence and time-of-flight secondary ion mass spectrometry. *Anal. Chem.* **2002**, *74* (16), 4011–4019.
- Wood, M.; Zhou, Y.; Brummel, C.L.; Winograd, N. Imaging with ion-beams and laser postionization. *Anal. Chem.* **1994**, *66* (15), 2425–2432.
- Cannon, D.M.; Winograd, N.; Ewing, A.G. Quantitative chemical analysis of single cells. *Ann. Rev. Biophys. Biomol. Struct.* **2000**, *29*, 239–263.
- Benninghoven, A.; Rüdener, F.G.; Werner, H.W. *Secondary Ion Mass Spectrometry: Basic Concepts, Instrumental Aspects, Applications, and Trends*; J. Wiley: New York, 1987.
- Vickerman, J.C.; Briggs, D. *Tof-Sims: Surface Analysis by Mass Spectrometry*; IM Publications and Surface Spectra Ltd: Chichester, West Sussex, 2001.
- Postawa, Z.; Czerwinski, B.; Szewczyk, M.; Smiley, E.J.; Winograd, N.; Garrison, B.J. Enhancement of sputtering yields due to C-60 versus Ga bombardment of Ag{111} as explored by molecular dynamics simulations. *Anal. Chem.* **2003**, *75* (17), 4402–4407.
- Krantzman, K.D.; Postawa, Z.; Garrison, B.J.; Winograd, N.; Stuart, S.J.; Harrison, J.A. Understanding collision cascades in molecular solids. *Nucl. Instrum. Meth. B* **2001**, *180*, 159–163.
- Pacholski, M.L.; Winograd, N. Imaging with mass spectrometry. *Chem. Rev.* **1999**, *99* (10), 2977–3005.
- Benninghoven, A. Surface investigation of solids by statistical method of secondary ion mass spectrometry (SIMS). *Surf. Sci.* **1973**, *35*, 427–457.
- Walker, A.V.; Winograd, N. Prospects for imaging with ToF-Sims using gold liquid metal ion sources. *Appl. Surf. Sci.* **2003**, *203–204*, 198.
- Gillen, G.; Fahey, A. Secondary ion mass spectrometry using cluster primary ion beams. *Appl. Surf. Sci.* **2003**, *203*, 209–213.
- Weibel, D.; Wong, S.; Lockyer, N.; Blenkinsopp, P.; Hill, R.; Vickerman, J.C. A C-60 primary ion beam system for time of flight secondary ion mass spectrometry: its development and secondary ion yield characteristics. *Anal. Chem.* **2003**, *75* (7), 1754–1764.
- Cheng, J.; Winograd, N. Depth profiling of peptide films with ToF-sims and a C-60 probe. *Anal. Chem.* **2005**, *77* (11), 3651–3659.
- Szagal, C.; Sun, S.; Wucher, A.; Winograd, N. C-60 molecular depth profiling of a model polymer. *Appl. Surf. Sci.* **2004**, *231–232*, 183–185.
- Sostarecz, A.G.; Sun, S.; Szagal, C.; Wucher, A.; Winograd, N. Depth profiling studies of multilayer films with a C-60(+) ion source. *Appl. Surf. Sci.* **2004**, *231–232*, 179–182.
- Winograd, N. The magic of cluster sims. *Anal. Chem.* **2005**, *77* (7), 142A–149A.
- Willey, K.F.; Vorsa, V.; Braun, R.M.; Winograd, N. Postionization of molecules desorbed from surfaces by Kev ion bombardment with femtosecond laser pulses.

- Rapid Commun. Mass Spectrom. **1998**, *12* (18), 1253–1260.
27. Cannon, D.M.; Pacholski, M.L.; Winograd, N.; Ewing, A.G. Molecule specific imaging of freeze-fractured, frozen-hydrated model membrane systems using mass spectrometry. *J. Am. Chem. Soc.* **2000**, *122* (4), 603–610.
  28. Pscheid, P.; Schudt, C.; Plattner, H. Cryofixation of monolayer cell cultures for freeze-fracturing without chemical pretreatments. *J. Microsc.* **1981**, *121* (2), 149–167.
  29. Chandra, S.; Morrison, G.H. Sample preparation of animal-tissues and cell-cultures for secondary ion mass-spectrometry (SIMS). *Microscopy. Biol. Cell* **1992**, *74* (1), 31–42.
  30. Severs, N.J.; Shotton, D. *Rapid Freezing, Freeze Fracture, and Deep Etching*; Wiley-Liss: New York, 1995.
  31. Chandra, S.; Smith, D.R.; Morrison, G.H. Subcellular imaging by dynamic SIMS ion microscopy. *Anal. Chem.* **2000**, *72* (3), 104a–114a.
  32. Peteranderl, R.; Lechene, C. Measure of carbon and nitrogen stable isotope ratios in cultured cells. *J. Am. Soc. Mass Spectrom.* **2004**, *15* (4), 478–485.
  33. Hallegot, P.; Peteranderl, R.; Lechene, C. In-situ imaging mass spectrometry analysis of melanin granules in the human hair shaft. *J. Invest. Dermatol.* **2004**, *122* (2), 381–386.
  34. Kleinfeld, A.M.; Kampf, J.P.; Lechene, C. Transport of C-13-oleate in adipocytes measured using multi imaging mass spectrometry. *J. Am. Soc. Mass Spectrom.* **2004**, *15* (11), 1572–1580.
  35. Strick, R.; Strissel, P.L.; Gavrilov, K.; Levi-Setti, R. Cation-chromatin binding as shown by ion microscopy is essential for the structural integrity of chromosomes. *J. Cell Biol.* **2001**, *155* (6), 899–910.
  36. Bourdos, N.; Kollmer, F.; Benninghoven, A.; Ross, M.; Sieber, M.; Galla, H.J. Analysis of lung surfactant model systems with time-of-flight secondary ion mass spectrometry. *Biophys. J.* **2000**, *79* (1), 357–369.
  37. Sostarecz, A.G.; McQuaw, C.M.; Wucher, A.; Winograd, N. Phosphatidylethanolamine induced cholesterol domains chemically identified with mass spectrometric imaging. *J. Am. Chem. Soc.* **2004**, *126*, 2362–2365.
  38. Greene, L.A.; Tischler, A.S. Establishment of a noradrenergic clonal line of rat adrenal pheochromocytoma cells which respond to nerve growth factor. *Proc. Natl. Acad. Sci. U.S.A.* **1976**, *73* (7), 2424–2428.
  39. Roddy, T.P.; Cannon, D.M.; Ostrowski, S.G.; Winograd, N.; Ewing, A.G. Identification of cellular sections with imaging mass spectrometry following freeze fracture. *Anal. Chem.* **2002**, *74* (16), 4020–4026.
  40. Monroe, E.B.; Jurchen, J.C.; Lee, J.; Rubakhin, S.S.; Sweedler, J.V. Vitamin E imaging and localization in the neuronal membrane. *J. Am. Chem. Soc.* **2005**, *127* (35), 12,152–12,153.
  41. Ostrowski, S.G.; Van Bell, C.T.; Winograd, N.; Ewing, A.G. Mass spectrometric imaging of highly curved membranes during *Tetrahymena* mating. *Science* **2004**, *305* (5680), 71–73.
  42. Sjoval, P.L.; Nygren, H.; Carlsson, L.; Malmberg, P. Imaging membrane lipids in single cells by imprint-imaging time-of-flight secondary ion mass spectrometry. *Anal. Chem.* **2003**, *75* (14), 3429–3434.

# Single Molecule Spectroscopy for Nanomaterials Characterization

**Daniel A. Higgins**

*Department of Chemistry, Kansas State University,  
Manhattan, Kansas, U.S.A.*

**Yanwen Hou**

*Kansas State University, Manhattan, Kansas, U.S.A.*

## INTRODUCTION

The optical detection of single molecules in the condensed phase was first demonstrated just over a decade ago by Moerner and Kador,<sup>[1]</sup> Orrit and Bernard,<sup>[2]</sup> and Shera et al.<sup>[3]</sup> Since that time, single molecule spectroscopy has developed into a valuable tool for probing nanoscale heterogeneity in a wide variety of materials.<sup>[4–7]</sup> For such studies, carefully selected dye molecules are doped into samples of interest at low concentrations. The individual molecules are then located and probed one at a time. Their signals are isolated from each other by spectral selection at cryogenic temperatures,<sup>[1,2]</sup> and/or by spatial selection in an optical microscope.<sup>[3,8–11]</sup> Detailed information on the time dependence, wavelength dependence, and polarization dependence of the excitation and emission processes can be obtained. Numerous spectroscopic parameters associated with the excitation and emission events in dye molecules are highly sensitive to the local environment in which each molecule resides. Therefore single molecule spectroscopy can be used as a direct means to assess the chemical and physical properties of the local environments found in almost any sample. The methods associated with the collection and interpretation of optical single molecule spectroscopic data for the purposes of understanding the environmental properties of nanostructured materials is the primary focus of this article.

## Scope

Single molecule spectroscopy is now employed in a wide variety of scientific and engineering disciplines. Hundreds of manuscripts on the subject are published each year. The discussion in this article is limited to methods of direct relevance to the characterization of nanoscale environments in and on condensed-phase materials. Primary emphasis is given to studies performed at room temperature, as these are deemed most broadly applicable. However, no attempt is made

to present a comprehensive review even of this much narrower subject. The interested reader is directed to a number of more comprehensive reviews for more information.<sup>[5–7,12–19]</sup>

## Why Single Molecules?

It is abundantly clear that a large number of chemically distinct nanometer-scale environments exist in virtually all materials. These environments may be comprised of different atoms, molecules, and ions. They may also be physically different, with their constituents organized and oriented in different ways.

In gas- and liquid-phase samples, the atoms, molecules, and ions move at relatively rapid rates. As a result, the local environments are dynamic and rapidly interconvert. Over a short period of time, the components in each region explore the entire range of possible configurations. New chemical species may continuously migrate in and out of each region as well. In time, each local environment possesses the same average properties exhibited by the entire sample. This is the basis for ergodicity.<sup>[5]</sup> One can obtain valuable (and nearly complete) information on the chemical and physical properties of the sample by simply measuring its average (i.e., bulk) properties. Indeed, classic bulk optical spectroscopic methods have long been employed to better understand the static and dynamic properties of a wide variety of samples.<sup>[20]</sup>

In solid samples, the local environments do not rapidly interconvert. Each individual environment may exhibit unique properties over relatively long periods of time. This is especially true in today's nanostructured materials, for which variations in the local sample properties are designed to be especially large. In such materials, it becomes impossible to fully understand the relevant material properties by bulk spectroscopic methods alone. As a result, spectroscopists long ago began seeking methods to probe the properties of individual sample environments. These include methods such as spectral hole burning<sup>[21]</sup> and a variety of

multiresonant non-linear optical spectroscopies (i.e., site-selective spectroscopies).<sup>[22]</sup> While these techniques are extremely powerful, and have their own important advantages, they still probe relatively large numbers of different environments.

With the recent development of single molecule spectroscopic methods,<sup>[1–3,8–10]</sup> means to directly probe the properties of single nanoscale environments now exist. A primary benefit of single molecule methods is that the inhomogeneous distribution in virtually any spectroscopic parameter can be directly visualized,<sup>[4]</sup> without the extensive averaging of bulk spectroscopic experiments. Additional information, inaccessible by bulk techniques, can also be obtained from certain quantum mechanical events that are directly observable by single molecule methods.<sup>[23]</sup>

A dramatic example of the sensitivity of single molecules to their nanoscale environment is shown in Fig. 1. This work, published by the Moerner group,<sup>[4]</sup> depicts a high-resolution fluorescence excitation spectrum for pentacene doped into a *p*-terphenyl matrix maintained at cryogenic temperatures. The individual peaks in the wings of this spectrum are predominantly from excitation of single molecules. While these materials might naively be thought to be homogeneous, clear nanoscale variations in their properties are apparent in the data. Variations in the local properties of these samples arise from the presence of defects, impurities, and resulting lattice strain. The emission

from each individual molecule contains important clues as to the nature of its local environment. Particularly interesting are those molecules having properties far different from the mean. In any sample, such environments are obscured in bulk spectroscopic measurements. However, their presence may be of profound chemical importance. This is especially true in nanostructured materials, for which “minority” sites may control the overall chemical properties of the materials. Single molecule spectroscopic methods represent valuable new means for their identification and characterization.

## Historical Perspective

The optical detection of single molecules labeled with multiple chromophores was first demonstrated in the 1970s and 1980s.<sup>[24–26]</sup> However, the first report describing the actual detection of individual chromophores was published by Moerner and Kador in 1989.<sup>[1]</sup> They used two different double-modulation techniques to record the absorption spectra of single pentacene molecules doped into a *p*-terphenyl host crystal held at cryogenic temperatures (i.e., 1.5 K). A short time later, Orrit and Bernard<sup>[2]</sup> demonstrated the detection of single molecules by fluorescence excitation in the same system. At the same time, Shera et al.<sup>[3]</sup> published a study showing the first detection of single dye molecules in solution, at room temperature.

The spatial location and interrogation of single molecules found at “fixed” positions in room temperature solids was first demonstrated by Betzig and Chichester<sup>[8]</sup> in a paper published in 1993. This work employed near-field scanning optical microscopy (NSOM) methods.<sup>[27]</sup> It was realized shortly thereafter that more conventional far-field (i.e., confocal and wide-field) optical microscopic methods could also be used to detect single molecules,<sup>[9–11]</sup> and that these methods were much more experimentally tractable. Explosive growth in the number of papers published per year began immediately after these initial demonstrations, indicative of the general importance of single molecule methods and the realization that much new knowledge could be uncovered by their implementation.

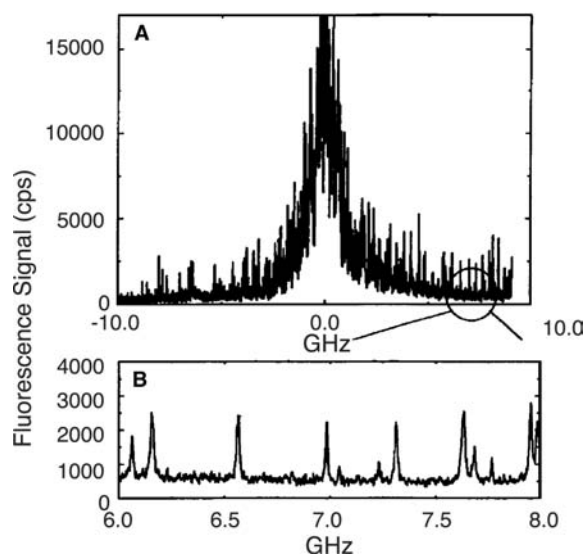


**Fig. 1** Fluorescence excitation spectrum for pentacene in *p*-terphenyl at liquid helium temperatures. (A) Excitation scan across the entire zero phonon line. (B) Expanded region of the spectrum shown in A. The well-separated peaks in the spectrum result from excitation of single molecule fluorescence far out in the wings of the inhomogeneous distribution. Source: From Ref.<sup>[4]</sup>. © 1994, American Association for the Advancement of Science.

## SINGLE MOLECULE DETECTION METHODS

Detection of single molecules requires methods that are both sensitive and selective. The method used must allow for efficient detection of the desired molecule, while effectively eliminating all sources of background. Today, the methods of choice usually involve fluorescence excitation. Fluorescence is emitted into an



inherently “background-free” spectral region, because of the Stokes shift between the excitation and emission wavelengths. The selective detection of one molecule over many others in a sample can be achieved by either one of two methods, or a combination thereof. They involve: (1) spectral selection and (2) spatial selection of the single molecule signals. In both cases, the fluorescence from a single molecule can be usually detected with a signal-to-noise ratio limited only by shot noise.

## Spectral Selection

For spectral selection, dye molecules with rigid molecular structures are doped into crystalline, glassy, or amorphous matrices at low concentrations. The sample is cooled to very low temperatures (i.e., liquid He temperatures).<sup>[1,2]</sup> With proper selection of the dye and matrix, a dramatic reduction in the excitation and emission linewidths can occur. In general, so-called fluorescence line-narrowing<sup>[21]</sup> occurs when the molecules are excited at the electronic origin. That is, the photons employed must have just enough energy to excite the molecules electronically, without exciting vibrations in the molecule and/or its surrounding matrix (i.e., phonons). Under these conditions, the spectral linewidths<sup>[28]</sup> of the molecules are predominantly lifetime-limited.<sup>[2,29]</sup> Individual molecules in the sample can then be selectively excited by the use of a tunable laser with spectrally narrow emission. Often, some form of spatial selection (see below) is employed in these experiments as well.<sup>[1,2,29]</sup> This serves to reduce the probability that more than one molecule will be in resonance with the laser at any given time.

## Spatial Selection

Experiments based on the spatial selection of individual molecules utilize samples doped with very low (i.e., subnanomolar) concentrations of probe dyes. The host system can be a gel<sup>[30]</sup> or solid.<sup>[8]</sup> One of a variety of optical microscopic configurations is then used to spatially resolve the individual molecules in the sample. Spatial selection methods work well at room temperature. Fig. 2 presents a diagram showing some of the possible optical configurations that have been employed; included are both far-field<sup>[3,9,10]</sup> optical and near-field<sup>[8]</sup> optical systems.

### Far-field scanning methods

Far-field microscopic methods are widely used in single molecule detection because of their relative simplicity.<sup>[11,31]</sup> The spatial resolution in all far-field microscopes is limited by diffraction to  $\approx \lambda/2$ .<sup>[32]</sup> This places a lower limit on the spacing between dopant molecules that must be achieved in order to resolve them. A maximum areal density of about 1 molecule/ $\mu\text{m}^2$  is the upper limit. In these methods, the sample is mounted on a “conventional” light microscope. Fluorescence images of the sample can be recorded by sample scanning,<sup>[31,33,34]</sup> beam scanning,<sup>[35,36]</sup> or wide-field illumination.<sup>[10,37]</sup> Each has its own advantages and disadvantages, as discussed below. Oftentimes, the system is operated in an epi-illumination mode, as depicted in Fig. 2A.

In the sample and beam scanning methods, fluorescence images of small sample regions are collected by raster-scanning the sample<sup>[34]</sup> over a focused laser spot, or by scanning a focused laser spot<sup>[36]</sup> over a stationary

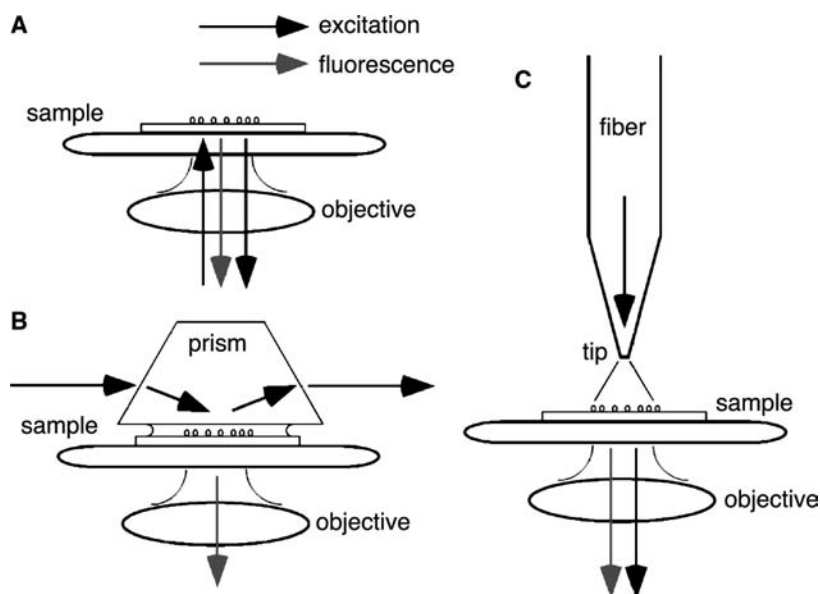


**Fig. 2** Common experimental configurations used for the spatial selection and detection of single molecules. (A) Epi-fluorescence geometry. (B) Total internal reflection geometry. (C) Near-field scanning optical microscopy.

sample. Fig. 3 presents examples of typical images obtained in a sample-scanning system. The appearance of such images provides valuable initial information on the single molecules and their local environmental properties.<sup>[38–40]</sup>

Confocal imaging methods<sup>[35]</sup> are usually employed to achieve extremely low background levels. Modern high numerical aperture (NA) microscope objectives produce focused spot sizes near the theoretical diffraction limit ( $\approx \lambda/2$ ).<sup>[32]</sup> They also have small depths of focus,<sup>[35]</sup> ensuring a small detection volume. Moerner and coworkers<sup>[41,42]</sup> have presented expressions for predicting the signal and background levels in specific optical systems. As background from (relatively high concentration) impurities and Raman scattering by the host matrix are both proportional to the volume of sample illuminated, smaller illumination volumes (at constant incident intensity) result in lower background signals. Consequentially, as a single chromophore is much smaller than the focused excitation spot, its signal remains constant as the focused spot size is reduced (again, for a constant incident intensity). To take full advantage of such signal-to-background enhancement, the single molecule excitation process must not be saturated.<sup>[43,44]</sup>

On the detection side, the high NA objective does an excellent job of efficiently collecting fluorescence

from molecules in all possible molecular orientations.<sup>[45]</sup> Single photon counting avalanche photodiodes (SiAPDs) are most often used for detection of single molecule emission. Microchannel plate photomultiplier tubes (PMTs) are also employed in systems designed for picosecond-resolved single-molecule lifetime measurements, although SiAPDs also work for this purpose.<sup>[11,31,46,47]</sup> Spectrally dispersed fluorescence from single molecules is recorded by using efficient imaging spectrographs and sensitive liquid-N<sub>2</sub>-cooled charge-coupled device (CCD) detectors.

### Wide-field imaging methods

Wide-field illumination<sup>[10,37]</sup> represents an important alternative to sample- and beam-scanning confocal microscopy. In these methods, a relatively large sample area (i.e., several square micrometers) is illuminated. Spatial selection of the fluorescence from individual molecules is accomplished on the emission side alone. To achieve the lowest background levels, such experiments are best performed in a dark-field configuration (Fig. 2B),<sup>[10,24,48–50]</sup> although other configurations also work.<sup>[51,52]</sup> The incident light is brought to the sample surface by using a prism or optical waveguide.<sup>[50]</sup> The angle at which the incident light strikes the working interface is beyond the critical angle. It is the evanescent wave generated by total internal reflection at this interface that excites the single molecules. A microscope objective similar to that described above is then used to collect the single molecule emission. The fluorescence from the sample is imaged onto a liquid-N<sub>2</sub>-cooled CCD, operating in imaging mode. Such multichannel imaging systems have the distinct advantage that images of large sample areas are obtained all at once (i.e., in a short time window). The images can be rapidly acquired and in sequential fashion so that phenomena such as rotational<sup>[49,51]</sup> and translational<sup>[37,53,54]</sup> single molecule motions can be readily followed. However, the recording of single molecule fluorescence spectra is difficult in wide-field systems.

### Near-field optical methods

Near-field optical methods have been used in a number of single molecule experiments.<sup>[8,31,55–62]</sup> Recent reviews cover all the important aspects of NSOM, and its applications in single molecule spectroscopy and other experiments.<sup>[27,63]</sup> Using NSOM, a subdiffraction-limited region of the sample is illuminated by funneling light through a small aperture fabricated at the end of a tapered, metalized fiber-optic probe.<sup>[64]</sup> Figure 2C shows a schematic of how such an aperture-based NSOM system works. At most, an aperture-sized region of the sample (in the transverse plane) is illuminated at any one time, as long as the

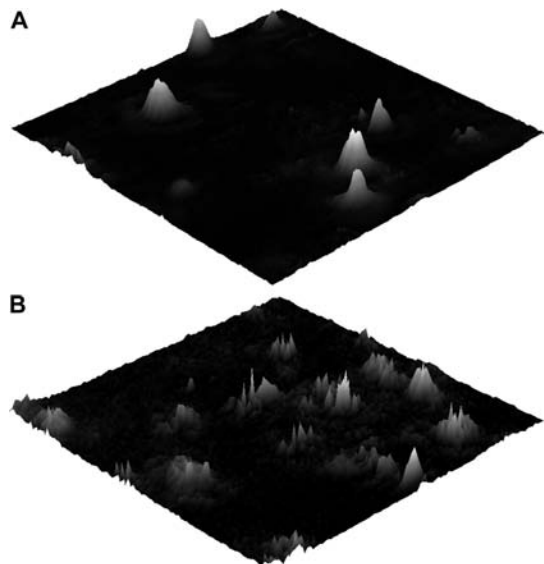


**Fig. 3** Fluorescence images of  $5 \times 5 \mu\text{m}$  regions of thin silicate films prepared by the sol-gel process. The films were doped with Rhodamine B at the nanomolar level. (A) “Fresh” silicate film image. The molecules yield round fluorescent spots of diffraction limited size in this sample. (B) Image of “dried” silicate film. The molecules blink on and off on a time scale similar to the image pixel time (40 msec) in this sample. Source: From Ref.<sup>[39]</sup>. © 2000, American Chemical Society.

distance between the probe and sample is much smaller than the wavelength of the light employed. Fluorescence from a molecule excited by the probe light is then collected by an objective lens, in a manner similar to the far field methods. The same detection systems described above are employed.

Single molecule NSOM methods have several advantages over far-field methods. Because spatial resolution as good as  $\approx \lambda/10$  can be achieved in single molecule NSOM experiments, the areal density of single molecules in the sample can be increased accordingly (i.e., to a few per square micrometer). It is also advantageous that the illumination volume is greatly reduced, often leading to enhanced signal-to-background ratios. In addition, because the tip and sample must be maintained in close proximity, the sample topography must be followed. This is usually accomplished by the so-called tapping mode<sup>[56,65,66]</sup> or shear-force<sup>[67,68]</sup> methods. The availability of topographic information along with the single molecule spectroscopic data makes NSOM methods particularly powerful for characterizing nanostructured materials, because variations in the local sample properties can be correlated with sample morphological features.<sup>[69]</sup> An important final advantage of NSOM-based single molecule detection experiments is that they provide a unique means for “visualizing” the 3-D orientations of single molecules.<sup>[8,55,61,62,70]</sup> However, similar information can now also be gleaned from far-field methods via the use of modified optical systems.<sup>[48,49,51,71]</sup>

The disadvantages of NSOM methods include their comparative difficulty, and the fact that the close proximity of the metalized dielectric probe to the sample can perturb single molecule emission. Several groups have studied probe perturbation effects in detail.<sup>[31,58,62,72]</sup> Theoretical results from Bian, Dunn, and Xie<sup>[58]</sup> are presented in Fig. 4. Their results show that as a molecule is positioned beneath the aluminum coating of the probe, energy is efficiently transferred to the metal, and the rate of non-radiative decay increases. When the molecule is moved nearer to the optical aperture (fused silica), interactions with the probe actually lead to enhanced radiative decay. Position-dependent variations in the emission spectrum are also predicted. Significantly, these perturbations are also shown to depend on the exact orientation of the molecule. Experimental results have provided support for these conclusions, and demonstrated that such perturbations can result in complicated variations in the single molecule emission properties.<sup>[31,57,62]</sup>

## General Experimental Considerations

A number of optical components are common to most forms of single molecule detection. Each uses a light

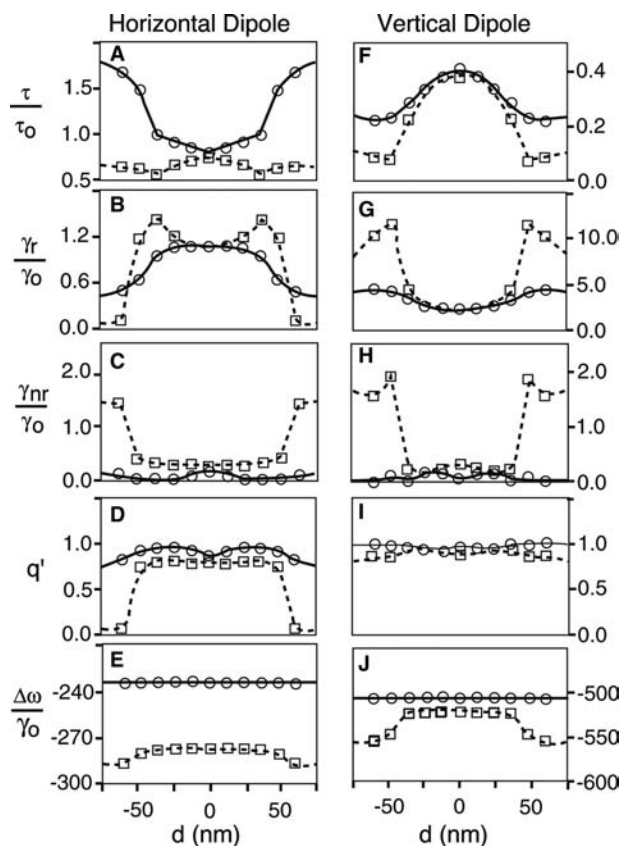


**Fig. 4** Simulations of relevant spectroscopic parameters in near-field optical microscopy studies of single molecules, using a 96-nm-diameter probe aperture. Results are plotted for horizontally oriented transition dipoles (left) and vertically oriented dipoles (right) as a function of lateral tip-molecule displacement. The calculations were performed for two different tip-molecule vertical distances (squares: 6 nm, circles: 24 nm). Shown are the normalized fluorescence lifetime ( $\tau/\tau_0$ ), normalized radiative rate ( $\gamma_r/\gamma_0$ ), normalized nonradiative rate ( $\gamma_{nr}/\gamma_0$ ), quantum yield ( $q'$ ), and spectral shift ( $\Delta\omega/\gamma_0$ ). *Source:* From Ref.<sup>[58]</sup>. © 1995, American Physical Society.

source that allows for resonant excitation of the single molecules by either linear or non-linear<sup>[73–75]</sup> optical methods. Common sources include the green HeNe laser, argon ion and krypton ion systems, Nd:YAG lasers, tunable dye lasers, Ti:sapphire lasers, and other solid-state systems. In addition, all systems rely on the use of appropriate bandpass filters, dichroic mirrors, and notch filters for background rejection and isolation of single molecule emission. Finally, polarization optics are also employed to control the excitation polarization and to select the polarization of the light to be detected.<sup>[76]</sup>

In most experiments, the samples of interest are coated onto commercially available, optically transparent substrates. Glass and fused quartz

microscope coverslips are most often employed. Besides being optically flat, these substrates must be clean and free of fluorescent impurities (i.e., rare earth ions). They can be cleaned either by wet-chemical, plasma etching, or flaming procedures. Undoped samples are often used to verify that any residual fluorescent impurities will not interfere with the single molecule measurements.

### Verification of Single Molecule Detection

Verification that data such as those shown in Figs. 1 and 3 come from single molecules is derived from several observations. First, as a result of changes in the local environment (whether spontaneous or photoinduced),<sup>[4]</sup> single molecule emission peaks often exhibit discrete jumps to new spectral positions (a phenomenon known as “spectral diffusion”).<sup>[16,29,41,77–79]</sup> Second, discrete photobleaching transitions may also be observed. In this case, the signal from a single molecule abruptly drops to the background level. If the signal resulted from multiple molecules, a gradual reduction in the signal would be expected as individual molecules were bleached away.

Observations of photon bunching and antibunching provide additional evidence for single molecule emission.<sup>[2,23,80,81]</sup> Photon antibunching is observed when photon emission from single molecules is detected with high time resolution. As a molecule seldom absorbs additional photons when in an excited state, and only emits a single photon as a result of prior excitation, there is always some finite time (i.e., nanoseconds) between photon emission events for single molecules. This time corresponds to the excited state lifetime. The observation of these short “dead times” provides excellent evidence that a single chromophore has been excited.<sup>[23]</sup> Photon bunching occurs on a longer time scale and is associated with infrequent transitions of the excited molecule to a long-lived “dark” state (usually a triplet). This leads to the observation of relatively long dark periods (i.e., approaching 1 msec) separated by periods where bunches of individual photons are detected as the molecule cycles between the ground and excited states in the singlet manifold.

Additional evidence of single molecule detection may be obtained by verifying that the number of fluorescent spots observed in images (Fig. 3) of a given region scale linearly with the concentration of dye dopant employed. Lastly, the signal levels expected for single molecules can be estimated and compared to that which is observed. Of course, this comparison is relatively crude, because the fluorescence excitation and detection efficiencies vary between molecules for a variety of reasons.

## MATERIALS CHARACTERIZATION

Single molecule spectroscopic methods have the potential to uncover a vast body of new information on the nanoscale properties of a range of materials and surfaces. A number of examples of such experiments are given below. While not all were undertaken for the purpose of understanding nanoscale materials environments, they provide an overview of the types of information that can be obtained. The studies presented are divided into sections based on the type of experiments performed. Wavelength-resolved spectroscopic studies are covered first, followed by those in which the temporal emission characteristics of the molecules are used to assess nanoscale environmental properties.

### Spectroscopic Variability

Bulk optical spectroscopic methods have long been used to probe the average properties of a wide variety of samples.<sup>[20]</sup> In many cases, identical experiments can be performed at the single molecule level. Such single molecule data provides a direct means for observing the inhomogeneous distribution of sites in a sample. Clearly, more information is contained in these distributions than can be gleaned from the average value of a particular spectroscopic parameter alone. For example, the shape of the distribution (i.e., skewed, Gaussian, multimodal, etc.) and the differences between the most common and average environments in a sample can be visualized.<sup>[82]</sup>

### Spectral perturbations by the local environment

One example of the new information that can be obtained when the interactions<sup>[11,31,57,58,62,83]</sup> between dye molecules and their local environment are probed at the single molecule level is shown in Fig. 5. In this work, English, Harbron, and Barbara<sup>[84]</sup> discovered stable (over hours) “rare sites” in poly(methyl methacrylate) (PMMA) films. The authors collected spectra from single sulforhodamine 101 molecules embedded in the films and compared them to those obtained by “bulk” methods. Dramatic molecule-to-molecule variations were observed in the single molecule spectra, reflective of nanoscale variability in the film properties. When the single molecule data were combined to simulate the bulk spectrum of a low concentration sample, a broad fluorescence peak with a prominent vibronic feature was obtained. These features were not observed in bulk spectra at higher concentrations. It was concluded that these single molecule spectra arose from the presence of rare nanoenvironments that were saturated at dye concentrations as low as  $10^{-9}$  M. These sites

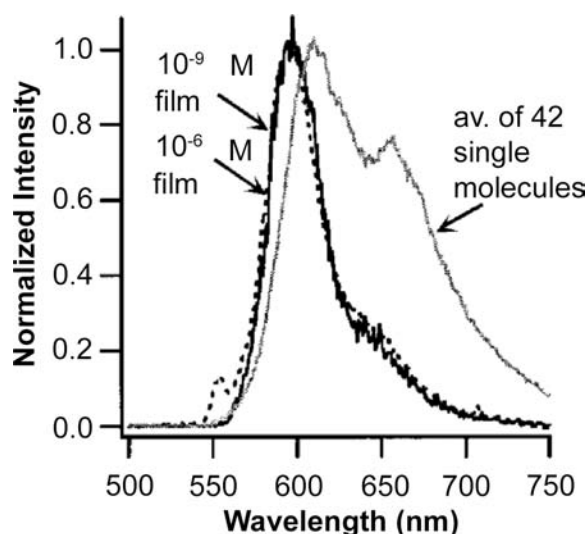


**Fig. 5** Bulk fluorescence spectra of Sulforhodamine 101 in PMMA films (dark solid line and dashed line) and a spectrum obtained by averaging the individual fluorescence spectra from 42 single molecules (light line). *Source:* From Ref.<sup>[84]</sup>. © 2001, American Institute of Physics.

were attributed to the presence of extreme sample heterogeneities or trace impurities, and could reflect the presence of sites differing in matrix rigidity.<sup>[38,85–88]</sup>

The dye molecules employed in such studies must be carefully selected or designed and synthesized to provide information on specific material properties.<sup>[87–89]</sup> Often, such dyes will have pendant functional groups that can undergo conformational changes under certain circumstances. For example, the Meixner group has employed two different aminoperylene derivatives (API and DAPI, as defined in Fig. 6) to probe the local properties of polystyrene thin films. Figure 6 shows data from their experiments.<sup>[87,88]</sup> In these particular molecules, the torsional angle of the pendant amine group, with respect to the aromatic ring structure, is most important in determining the extent to which the amine group is electronically coupled to the  $\pi$ -electronic system. Two (or more) sets of electronic states are possible and two (or more) emission spectra may be observed. Data reflecting the efficiency of amine group rotation and the emission characteristics of each state can yield valuable information on local sample fluidity and polarity.<sup>[38]</sup>

Three different classes of spectra were observed for API single molecules (Fig. 6A), while only two were observed for DAPI (Fig. 6B), in which amine group motions are sterically hindered. Spectra exhibiting pronounced vibronic structure were attributed to emission from a state in which the amine group is decoupled from the  $\pi$ -electronic system. Broad, almost featureless

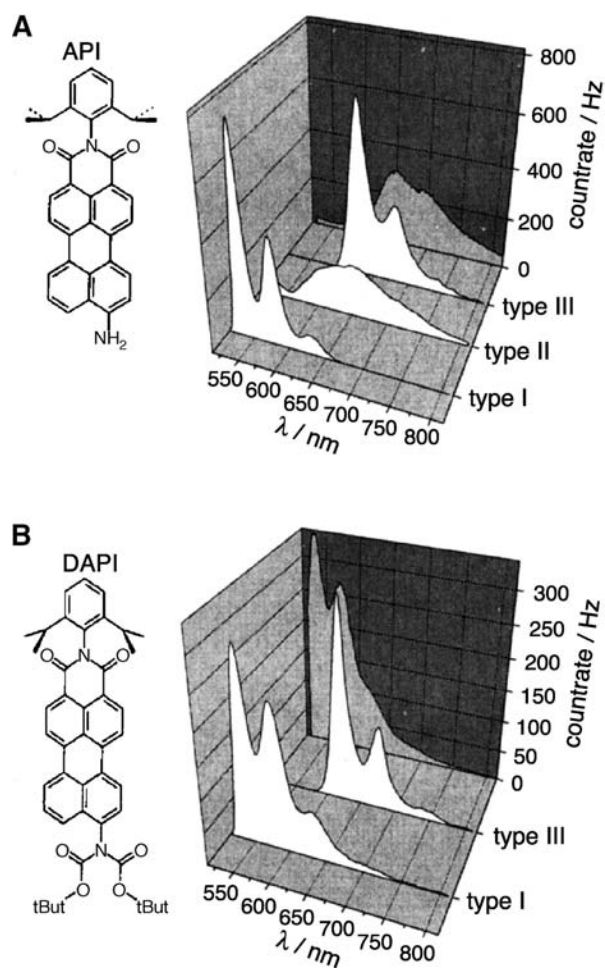


**Fig. 6** (A) and (B) Bulk and single molecule fluorescence spectra for the API and DAPI dyes, respectively. The bulk spectra were recorded in toluene and are displayed at the back of each set. The single molecule spectra were recorded for molecules dispersed in polystyrene. Three characteristic types of single molecule spectra were observed, as designated in the figure. *Source:* From Ref.<sup>[87]</sup>. © 2001, American Chemical Society.

API spectra were attributed to emission from a state in which the amine group is conjugated to the ring structure. The observation of all three types of spectra for API is attributable to the presence of different environments in the polymer films that each favors one conformation over the other.

Meixner and coworkers also made extensive use of these molecules to assess the dynamic properties of the local film environments. While some environments allow rapid conformational changes of the molecule, others do not. They observed the frequency of spectral jumps associated with interconversion of the various forms of these molecules and used the results as a means for evaluating the dynamic fluidity of local regions in their samples.

## Polarity measurements

One common application of organic dyes has been in the determination of solvent polarity by bulk spectroscopic methods.<sup>[90,91]</sup> So-called “solvatochromic”<sup>[91]</sup> dyes exhibiting either hypsochromic or bathochromic spectral shifts with changes in solvent polarity are employed. A number of solvent polarity scales have been developed, based on the spectra obtained.<sup>[20,91]</sup>

Higgins, Collinson, and coworkers have demonstrated the application of similar methods in single molecule studies of organic polymer films<sup>[38]</sup> and sol-gel-derived silicate films.<sup>[39,82,92–94]</sup> Importantly, their results reflect the polarity of the nanoscale environment in which each molecule resides. For these measurements, the highly solvatochromic dye Nile red<sup>[95]</sup> was selected (Fig. 7). Its excitation and emission spectra exhibit a dramatic shift to shorter wavelengths upon transfer from polar to non-polar media.<sup>[96–99]</sup> Unfortunately, its fluorescence quantum yield is also very sensitive to its environment and is appreciably larger in non-polar surroundings.<sup>[96]</sup> This is believed to be a result of the enhanced participation of a non-fluorescent twisted intramolecular charge transfer (TICT) excited state when the dye is dissolved in polar solvents.<sup>[38,99,100]</sup> It must be noted that single molecule results obtained by using dyes such as Nile red can be biased toward environments in which the probe dye is more fluorescent.<sup>[93,94,96]</sup> Care must be taken to ensure the bias is not significant. Bardo, Collinson, and Higgins have evaluated the extent of bias by comparing single molecule results with those of bulk spectroscopic experiments.<sup>[93,94,96]</sup>

In the methods employed by the Higgins group, data reflecting both the static and dynamic nanoscale polarity were obtained by applying a modified form of Marcus theory<sup>[101–104]</sup> for charge transfer transitions to single molecule results. The parameters measured include the shift in the transition energy from that in a vacuum,  $\Delta\Delta G^\circ$ , and the local reorganization energy,  $\lambda$ , associated with the residual environmental and dye motions not frozen upon entrapment of the dye in relatively “rigid” materials environments.<sup>[103]</sup> Several assumptions were required to make use of this model; these were outlined in detail in the original publications.<sup>[38,93,94]</sup>

Figure 7 shows examples of data obtained for Nile red in a poly(methyl methacrylate) (PMMA) thin film.<sup>[38]</sup> Plotted are histograms of the emission maximum,  $\nu_{fl}$ , and full width at half maximum of the highest energy vibronic band,  $\delta\nu_{fl}$ , in each spectrum. Also shown are histograms of the  $\Delta\Delta G^\circ$  and  $\lambda$  values obtained. Bimodal distributions in  $\nu_{fl}$  and  $\delta\nu_{fl}$  lead to a bimodal distribution in  $\lambda$ . A single “Gaussian-shaped” inhomogeneous distribution appears in the  $\Delta\Delta G^\circ$  histogram. These results were attributed to the existence of two

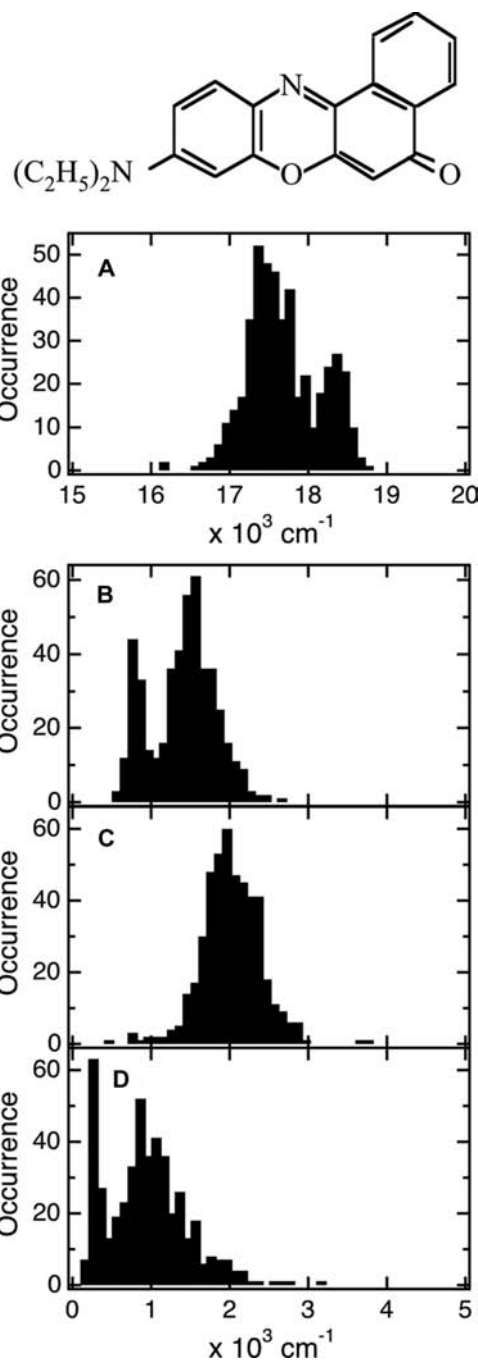


**Fig. 7** Structure of Nile red and single molecule data. (A) Histogram of single molecule emission maxima for Nile red in a poly(methyl methacrylate) thin film. (B) Histogram of the spectral widths (FWHM) for the single molecule spectra. (C) Histogram of single-molecule  $\Delta\Delta G^\circ$  values. (D) Histogram of single-molecule  $\lambda$  values. Source: From Ref.<sup>[38]</sup>. © 2000, American Chemical Society.

classes of environments in the films. The two differ primarily in their dynamic polarity (or local fluidity),<sup>[38]</sup> and likely arise from the presence of relatively rigid “semicrystalline” polymer environments and more fluid “amorphous” regions. These conclusions



are consistent with those of Ishikawa et al.,<sup>[85,86]</sup> who show bimodal distributions in the emission count rates obtained from dye molecules incorporated into PMMA films (see below).

In a collaborative effort, the Higgins and Collinson groups<sup>[82,93,94]</sup> employed the same modified Marcus methods to uncover nanoscale variations in static polarity and environmental rigidity in a series of organically modified sol-gel-derived silicate films. In these studies, films prepared by the hydrolysis and condensation of mixtures containing varying mole percentages of tetraethoxysilane (TEOS) and isobutyltrimethoxysilane (BTMOS), or 3-(triethoxysilyl)propionitrile (CNS) were investigated. Figure 8 shows representative histograms of the  $\Delta\Delta G^\circ$  and  $\lambda$  values obtained.<sup>[82]</sup> The data are presented as a function of the mole percent of organically modified silicate (BTMOS or CNS) used in sample preparation. The authors interpreted this data to reflect gradual changes in local film environments in the CNS series of samples, consistent with molecular mixing of the inorganic and organic precursors. In stark contrast, the samples prepared from mixtures of TEOS and BTMOS showed abrupt changes in environmental polarity and rigidity with increasing BTMOS content, a likely indicator of nanometer (or larger)-scale phase separation of organic- and inorganic-rich domains.

## Acid/base chemistry

Single molecule methods also represent a valuable new means for assessing the nanoscale acid/base properties of a sample, as recently reported by Brasselet and Moerner.<sup>[105]</sup> In their work, the authors describe some of the challenges associated with pH measurements at the single molecule level. Perhaps, most important is the selection of a dye molecule that remains reasonably fluorescent in both its acidic and basic forms. At the same time, the molecule must exhibit a measurable change in its excitation and/or emission spectrum with pH.

Brasselet and Moerner<sup>[105]</sup> employed a dextran-linked seminaphthorhodafluor dye commonly known as SNARF-1 to probe the local acid/base chemistry of agarose gels. The chemical structure of SNARF-1 is shown in Fig. 9; its bulk emission spectrum as a function of solution pH is given in the original work.<sup>[105]</sup> By simultaneously recording single molecule fluorescence in two different wavelength bands, the authors were able to observe pH-dependent variations in the single molecule emission spectra. They constructed histograms of the relative emission observed at the two different wavelengths. Their results are reproduced in Fig. 9. At high and low bulk pH, the single molecule emission results were consistent with the bulk pH

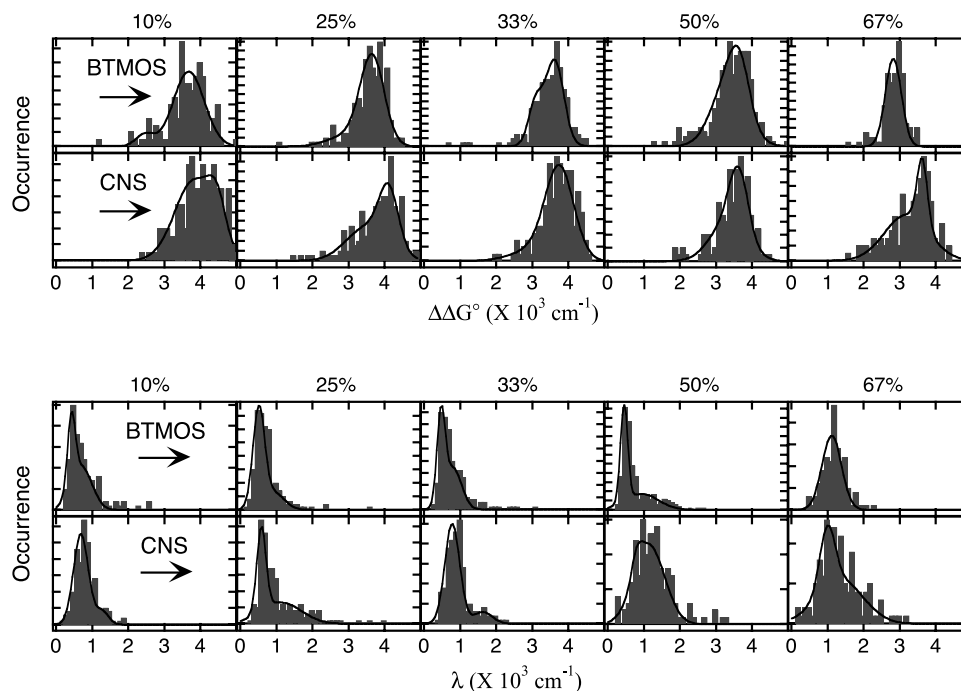


**Fig. 8** Top: Histograms of the  $\Delta\Delta G^\circ$  values for Nile red single molecules doped into organic/inorganic composite silicate thin films. The tick marks denote increments of two molecules. Bottom: Histograms of the single molecule  $\lambda$  values for each film. The tick marks denote increments of five molecules. The organic precursor content of the sol used in the preparation of each film is given at the top. The solid lines represent fits of the data to double Gaussian functions. *Source:* From Ref.<sup>[82]</sup>. © 2000, American Chemical Society.

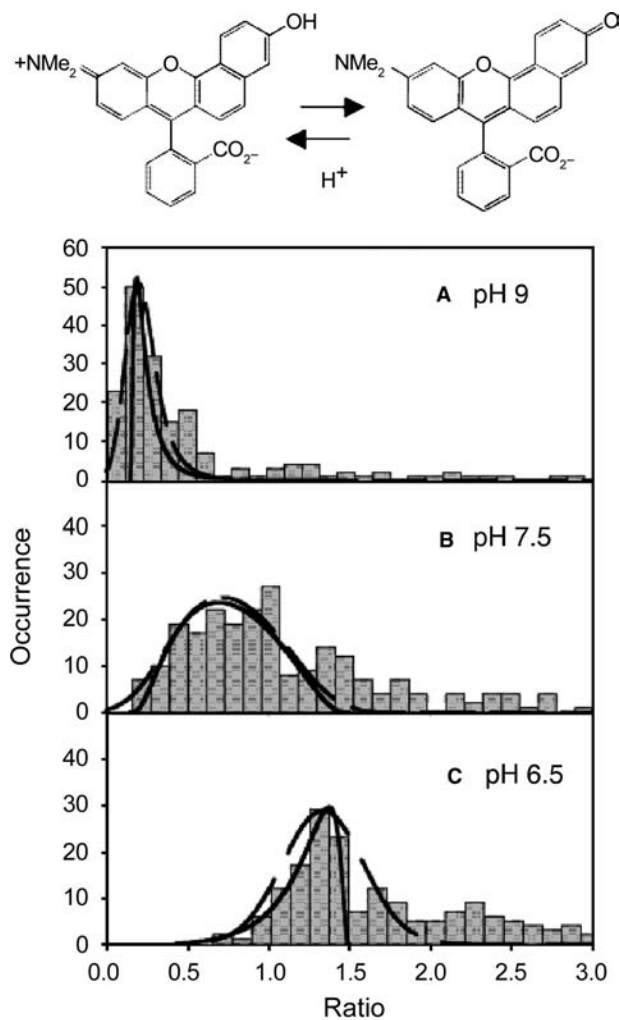


**Fig. 9** Chemical structure of SNARF-1 in its protonated and deprotonated forms and histograms of single molecule emission ratios as a function of bulk pH for SNARF-1-dextran in agarose gels. The emission ratio is defined as the ratio of fluorescence from the protonated (580 nm) and deprotonated (640 nm) forms of SNARF-1. The dashed and solid lines give the distributions expected for  $pK_a$  variations in the sample with and without, respectively, accounting for experimental noise. *Source:* From Ref.<sup>[105]</sup>. © 2000, Wiley-VCH.

dependence of SNARF-1. The widths of the histograms were concluded to be dominated by experimental noise under these pH conditions. However, at intermediate bulk pH, near the dye's  $pK_a$ , a broader distribution was observed. The dynamic equilibrium between the protonated and deprotonated forms of the dye was noted to be too rapid to observe on the time scale of their experiments, as was the rate of proton diffusion through the sample. Therefore the authors attributed the increased histogram breadth (for  $pH \approx pK_a$ ) to variations in the  $pK_a$  of the dye

resulting from local variations in the properties of the gel samples.

### Vibrational information

By far, the most detailed nanoscale information may be obtained by resolving the vibrational structure in single molecule fluorescence spectra obtained at low temperatures.<sup>[7,12,42,106–108]</sup> A number of excellent examples have been published by Tchenio, Myers, and Moerner.<sup>[106,107]</sup> In one series of studies, dramatic variations in the emission spectra of terrylene single molecules in polyethylene were reported. Molecule-to-molecule variations in these spectra were manifested as both variations in the band intensities and band positions, and were attributed to the presence of two distinct nanoenvironments in the samples, one crystalline in nature, and the other amorphous.

While such single molecule resonance Raman experiments<sup>[7]</sup> are possible at low temperatures, single molecule Raman data cannot be obtained at room temperature without substantial signal enhancement. However, room temperature single-molecule/single-particle surface-enhanced Raman scattering (SERS) has been demonstrated.<sup>[109–111]</sup> Single molecules in these experiments were deposited on single silver nanoparticles.<sup>[112]</sup> Extremely large enhancement factors, on the order of  $10^{14}$ – $10^{15}$ , have been reported,<sup>[109,111]</sup> making the Raman cross sections as large as those for fluorescence excitation.<sup>[110]</sup> Such large enhancements are believed to involve both electromagnetic and chemical enhancement mechanisms.<sup>[110,111,113]</sup> If these vibrational methods can be generalized to a wider range of nanostructured materials, they will represent extremely powerful methods for assessing nanoscale environmental properties.

### Temporal Emission Characteristics

The temporal emission characteristics of single molecules can also yield valuable information on the nanoscale environments found in a sample. Significantly, they also yield information on the rate at which the environments interconvert in time. The measurements covered involve a wide range of different experiments. Simple observations of spectrally integrated fluorescence time transients can provide substantial information. These measurements allow for the observation of quantum mechanical and quantum chemical phenomena not directly observable in bulk spectroscopic experiments.<sup>[23,80,114–118]</sup> More complicated methods allow for observation of molecular translational and rotational diffusion.<sup>[40,54,82,93,94,119–123]</sup> The effects of changes in molecular conformation,<sup>[38,85,86,88,115,118,120,124–133]</sup>

electron transfer events,<sup>[134]</sup> and other chemical dynamics<sup>[10,39,129,130,135–138]</sup> can also be observed. Finally, spectrally resolved time transients can be used to observe spectral diffusion phenomena.<sup>[16,29,41,77–79]</sup>

### Survival times and total emission

Photobleaching is observed in virtually all single molecule experiments. Under continuous illumination, single molecules undergo an abrupt and permanent transition to a non-fluorescent form at some point. Again, such behavior has long been used as evidence that single molecules are being probed. However, it has since been demonstrated that multichromophoric species with electronically coupled emitters often exhibit similar signal transitions.<sup>[115,128,139–141]</sup> These permanent signal transitions are attributable to photochemical reactions resulting from excitation of the chromophore. The most common mechanism for photobleaching of dye molecules involves their reaction with singlet dioxygen. Quenching of the triplet state of the dye by triplet dioxygen leads to the initial production of reactive singlet dioxygen. Other proposed mechanisms have included photoinduced conformational changes, especially in multichromophoric species.<sup>[115,128,139,142]</sup>

Wennmalm and Rigler described measurements of the survival time and total emission (i.e., the integrated number of photons) obtained from single molecules, and noted their sensitivity to the molecule's environment.<sup>[143,144]</sup> Measurements of these parameters represent a viable means for uncovering nanoscale materials heterogeneity. Such measurements have recently been used for the characterization of environmental properties in sol–gel-derived silicate films.<sup>[39,120]</sup> Fig. 10 shows representative results from the silicate studies. In these particular experiments, the survival times and total photons obtained from single rhodamine B molecules entrapped in the silicate films were measured as a function of film preparation conditions. The silicate films were characterized: (1) immediately after spin casting, (2) after drying overnight under vacuum, and (3) after drying at 80°C under vacuum for at least 12 hr. The results show an approximately fourfold increase in the survival times of single molecules in the vacuum oven-dried films over those of the fresh films. Simultaneously, a fourfold increase in the total number of photons emitted by the average molecule was also observed for the vacuum oven-dried films. These results are consistent with a dramatic increase in the chemical stability of the dye molecules in the dried materials. Increased dye stability was attributed to a reduced rate of oxygen and/or dye diffusion, as well as a possible reduction in the oxygen concentration of the dried films.

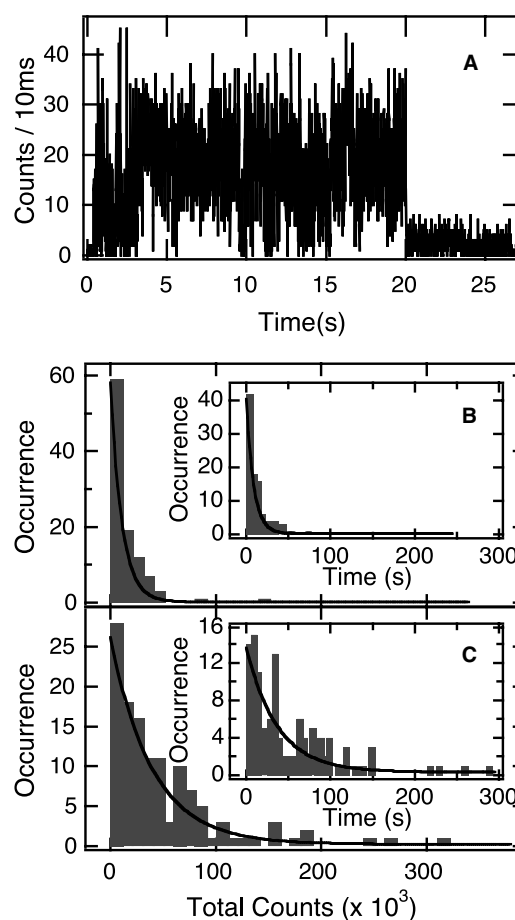


**Fig. 10** (A) Representative fluorescence transient recorded for a single Rhodamine B molecule entrapped in a dried silicate film. This transient exhibits signal fluctuations on a number of different time scales and ends in a discrete and permanent transition to a dark state (presumably a non-fluorescent photoproduct) at approximately 20 sec. The total integrated emission counts and total survival time of each molecule are derived from these transients. (B), (C) Histograms of the total photons detected from a number of single molecules, for fresh and dried silicate samples. The insets show histograms of the total survival time. *Source:* From Ref.<sup>[39]</sup>. © 2000, American Chemical Society.

### Emission intensity and fluorescence lifetimes

The signal levels obtained from single dye molecules can reflect local environmental fluidity. Figure 11 shows data from a study by Ishikawa et al.,<sup>[85,86]</sup> in which crystal violet and Texas red were used to probe the local environments of poly(methyl methacrylate) (PMMA) thin films. A bimodal count distribution was obtained from crystal violet, a flexible molecule, while a single Gaussian distribution was obtained from the more rigid Texas red. The bimodal distribution for crystal violet was attributed to the presence of two general classes of environment in the PMMA materials. One environment was concluded to be less viscous than

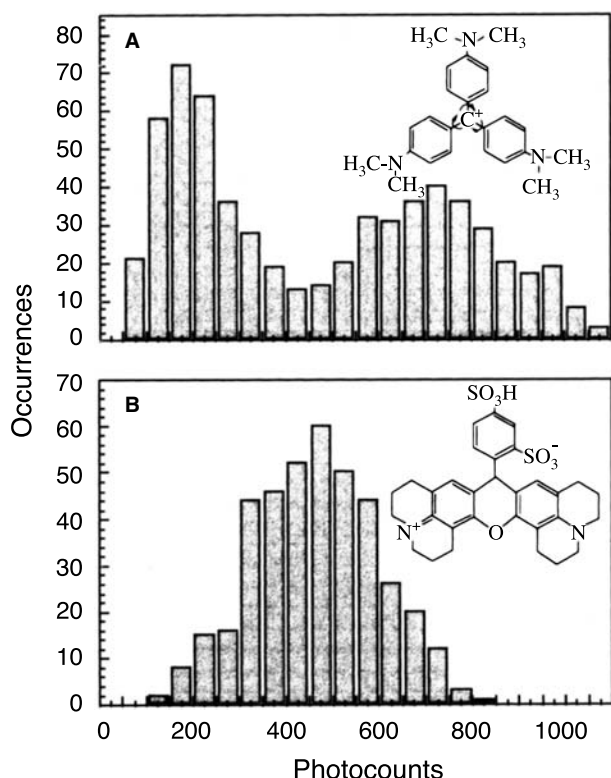


**Fig. 11** (A), (B) Histograms of the fluorescence photocounts obtained from single molecules of crystal violet and Texas red, respectively (structures shown), in poly(methyl methacrylate) films. *Source:* From Ref.<sup>[86]</sup>. © 1999, American Chemical Society.

the other, leading to differences in the rate of non-radiative relaxation of the excited molecules in the two regions. Variations in the viscosity were attributed to local variations in the PMMA side-chain motions.

Measurements of the fluorescence lifetimes of individual molecules provide valuable additional data on the origins of the environmental sensitivity of single molecule emission. In the studies by Ishikawa and coworkers,<sup>[85,86]</sup> the crystal violet molecules exhibited

dramatic molecule-to-molecule variations in their fluorescence lifetimes. In contrast, the Texas red molecules yielded considerably less variable lifetime data. Variations in the crystal violet lifetimes were assigned to environment-dependent variations in the non-radiative relaxation rate of the molecule. Molecules exhibiting relatively large fluorescence signals and long lifetimes were concluded to be entrapped in more viscous film regions. Similarly, less fluorescent molecules were assigned to less viscous film regions.

It is well known that other phenomena can also affect single molecule emission. For example, proximity to a dielectric interface can have a noticeable effect on the emission lifetime of a single molecule. Macklin, et al.<sup>[11]</sup> and Vallee, et al.<sup>[83]</sup> have presented detailed studies of such effects.

### Emission intensity fluctuations

Temporal fluctuations in the emission intensity of single molecules are often attributed to conformational dynamics. Such dynamics may lead to spectral diffusion,<sup>[16,29,41,77–79,87,88,133]</sup> and/or changes in a molecule's fluorescence quantum yield.<sup>[87,115,120,128,142]</sup> To the extent these dynamics are limited by the local environment, the rate of such signal fluctuations may also be reflective of the local environmental properties, or fluctuations therein.<sup>[136,137]</sup>

Table 1 presents results showing the sensitivity of single molecule signal fluctuations to local materials environments. In this work, Talley and Dunn<sup>[131]</sup> studied films of relatively well-controlled properties, namely DiIC<sub>18</sub>-doped lipid films prepared by the Langmuir–Blodgett (LB) technique. The films incorporated phase domains having distinctly different lipid densities. Results for “liquid expanded phase” and “solid condensed phase” regions were obtained. The authors located individual molecules in these different film regions, recorded their emission time transients, and subsequently calculated the signal autocorrelation

**Table 1** Results from autocorrelation analysis of single-molecule fluorescence transients for DiIC<sub>18</sub> in lipid films prepared by the Langmuir–Blodgett technique

Film condition	Subphase	$\tau_1$ (sec)	$\tau_2$ (sec)	<i>N</i>
Liquid expanded phase	10 mM MgCl <sub>2</sub>	0.44 ± 0.10	14.2 ± 3.9	66
Solid condensed phase	10 mM MgCl <sub>2</sub>	1.17 ± 0.27	24.1 ± 5.5	48
Liquid expanded phase	water	0.77 ± 0.22	18.2 ± 6.3	46
Solid condensed phase	water	1.31 ± 0.36	13.1 ± 4.1	37
Bilayer (probe on bottom)	water	2.06 ± 0.50	41.9 ± 12.5	43
Bilayer (probe on top)	water	2.14 ± 0.64	28.9 ± 11.2	32

Listed are the lipid film phase, subphase conditions, time constants ( $\tau_1$  and  $\tau_2$ ) derived from the analysis, and the number of molecules (*N*) employed in the analysis for each case. The error bars give the 90% confidence limits.

*Source:* From Ref.<sup>[131]</sup>. © 1999, American Chemical Society.

function<sup>[79,115,124,131]</sup> for each transient. The autocorrelation functions decayed exponentially in time and could be fit with double exponentials. The fitting procedure provided characteristic signal fluctuation times (i.e., the signal correlation times  $\tau_1$  and  $\tau_2$ ) for each molecule. The signals were observed to fluctuate more rapidly in the liquid expanded phase regions, as evidenced by the smaller value obtained for  $\tau_1$  in these regions (Table 1). Conformational dynamics of the dye, which in turn resulted in time-dependent variations in the dye's emission yield, were concluded to be the source of the fluctuations. The results reflect the much greater fluidity of the liquid expanded phase, in comparison to the solid condensed phase regions and lipid bilayers also described in this study.<sup>[131]</sup>

### Triplet lifetimes and quantum yields

Triplet blinking is the quantum mechanical phenomenon to which repeated, power-dependent signal fluctuations to and from the background level are often assigned.<sup>[114]</sup> When a molecule crosses from its singlet excited state to a long-lived triplet excited state, it usually cannot be excited further and does not emit. Both the rate of intersystem crossing and the rate of triplet relaxation can be obtained for single molecules. These data are obtained either by autocorrelation procedures or by directly measuring the “off times” (or “dark times”) and photon yields between dark periods.<sup>[79,115,124,131]</sup> Photoinduced processes occurring from the triplet state have also been monitored.<sup>[145]</sup> All such phenomena are influenced by the molecule's local environment.<sup>[116,117]</sup> For example, because triplet dioxygen often quenches triplet excited states, the lifetime of a molecule's triplet state may reflect the local concentration of oxygen molecules and/or their mobility.<sup>[39,117,118,146,147]</sup> The singlet–triplet gap and intersystem crossing rate are also expected to depend on the properties (i.e., polarity) of the local environment.<sup>[118]</sup>

### Spectral diffusion

So-called spectral diffusion phenomena,<sup>[16,29,41,77–79,148]</sup> in which the fluorescence excitation and emission spectra for a molecule change in time, are also reflective of dynamic fluctuations in local sample environments.<sup>[136,137]</sup> In studies of DiC<sub>12</sub> on glass surfaces,<sup>[127]</sup> Weston et al. observed that spectral jumps and changes in the appearance of single molecule emission transients are frequently correlated. They also observed these signal variations to be coupled with a change in the appearance of the vibronic structure in the single molecule spectra. The authors attributed those spectra exhibiting resolved vibronic structure to molecules present in highly restricted environments. Broad,

featureless spectra were attributed to environments in which the molecules were free to move. Abrupt conversions between these two classes of behavior are attributable to changes in the environment, the molecule itself, and/or its interactions with the environment.

### Translational diffusion and adsorption phenomena

Observation of the translational motions of single molecules in materials and on their surfaces represents an obvious means of detecting and assessing nanoscale materials heterogeneity. The extent to which such motions occur is highly dependent on the fluidity of the matrix and the prevalence and strength of molecule–matrix interactions. Such molecular translational motions can be observed by single-point illumination methods,<sup>[3,9,122]</sup> or by sample scanning,<sup>[60]</sup> beam scanning,<sup>[36]</sup> or wide-field microscopies.<sup>[37,53,120,149]</sup> The latter three allow for the recording of diffusional trajectories in which the actual motions of the molecules may be directly followed.

Recently, Wirth et al.<sup>[122,123,150]</sup> have been using single molecule methods to uncover nanoscale heterogeneity at chromatographically important interfaces by observing single molecule diffusion and adsorption events. In this work, they studied silicate glass surfaces derivatized with alkylsilanes and submerged in water. The experiments were performed in a single-point illumination mode similar to that used in other solution-phase single molecule experiments.<sup>[3,9]</sup> The fluorescence signal obtained from individual DiI molecules by illuminating a small ( $\approx 80 \mu\text{m}^2$ ) sample region was recorded in time and subsequently analyzed by autocorrelation methods. Information on the rate of single molecule diffusion through the detection volume was obtained. Figure 12 shows an example of their data. In most instances, brief flashes of light were observed from the molecules as they passed through the illuminated spot. For these molecules, (near-surface) diffusion rates could be obtained. However, in certain cases, relatively stable fluorescence signals were also obtained. These signals remained stable for relatively long periods of time (i.e., seconds). The authors attributed these events to adsorption of individual dye molecules at specific sites on the sample surface. It was proposed that these sites were regions of the glass surface left underivatized during the surface silanization procedure. Their observations are reflective of nanoscale variations in the chemical properties of chromatographic surfaces and point to the origins of peak tailing in many forms of column chromatography.

Detailed information on the paths taken by single molecules as they diffuse through materials and across their surfaces has been obtained in a number of experiments. Such single molecule diffusional trajectories have been recorded by near-field<sup>[60,151]</sup> and far-field

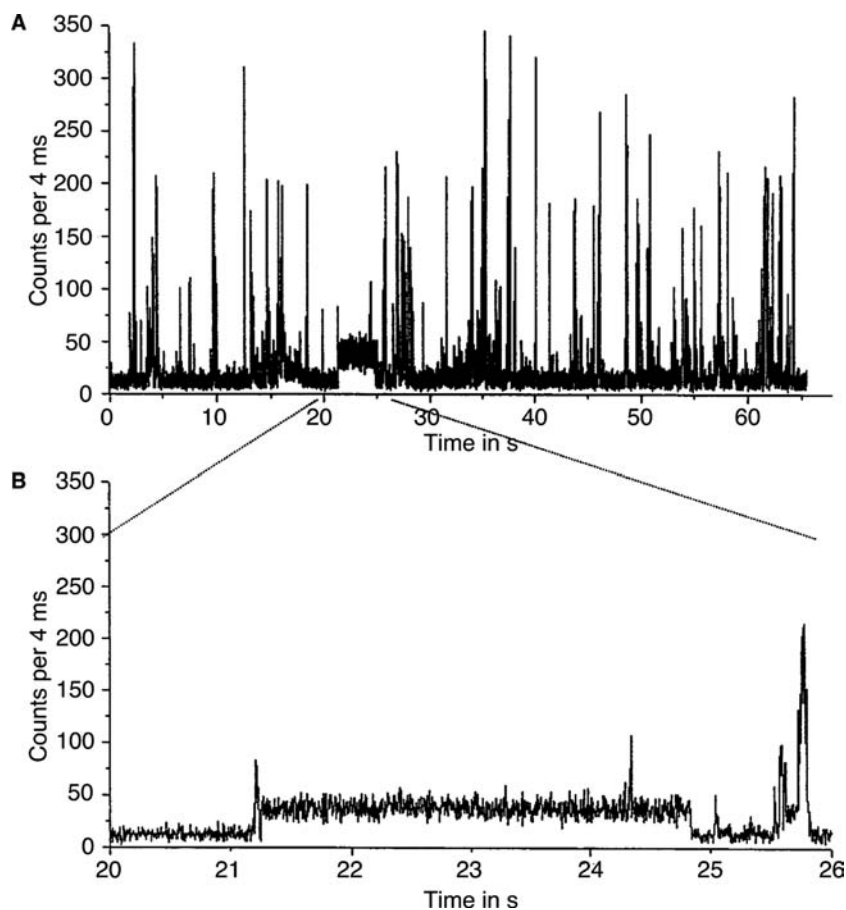


**Fig. 12** (A) Fluorescence transient from the interface between water and a dimethyloctadecylsilane derivatized glass surface in the presence of dilute DiI. The sharp signal spikes represent fluorescence from single DiI molecules diffusing rapidly through the detection volume. A specific adsorption event occurs at about 21.2 sec into the transient, as depicted by the relatively stable fluorescence observed beginning at this time. (B) Expanded section of this transient, showing the stable fluorescence signal from a single molecule. *Source:* From Ref.<sup>[122]</sup>. © 1998, American Chemical Society.

confocal imaging methods.<sup>[36,37,53,54,149,152]</sup> Diffusional trajectories have been obtained in two<sup>[36,37,53,60,152]</sup> and three<sup>[30]</sup> dimensions. Sample scanning methods are best suited to observation of relatively slow molecular

motions having diffusion coefficients in the  $10^{-12}$ – $10^{-13}$   $\text{cm}^2/\text{s}$  range.<sup>[60,120]</sup> Much faster diffusional processes, with diffusion coefficients approaching  $10^{-7}$ – $10^{-8}$   $\text{cm}^2/\text{s}$ , are readily studied by wide-field

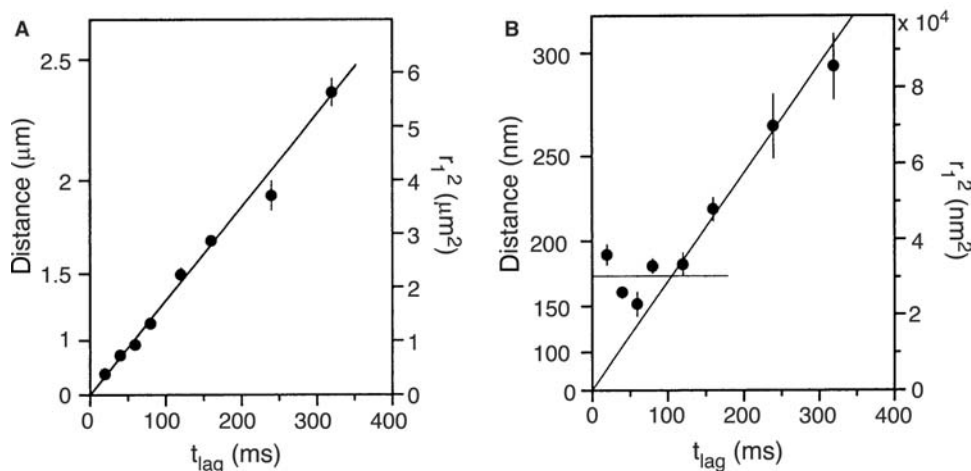


**Fig. 13** Diffusion data for dye-labeled phospholipids in a fluid-supported phospholipid membrane. Diffusion is observed to occur on two different time scales. (A) Expectation value for the squared displacements (right axis) resulting from the fast diffusional component. The data show a linear trend in time. (B) Expectation value for the squared displacements (right axis) resulting from the slow diffusional component. The data show a linear trend in time for  $t_{\text{lag}} > 100$  msec. *Source:* From Ref.<sup>[149]</sup>. © 1997, Biophysical Society.



illumination methods.<sup>[149]</sup> While the resolution of far field methods most commonly employed in such studies is limited, it is important to note that the locations of the single molecules in each image can be determined to relatively high precision (i.e.,  $\pm 30$  nm in far-field imaging<sup>[53]</sup> and  $\pm 1$  nm by near-field methods<sup>[60]</sup>. Such high precision is obtained by curve fitting the Gaussian intensity profiles obtained from the single molecule emission spots in the images. Under appropriate circumstances, the precision to which the position of a molecule can be determined is primarily limited by the signal-to-noise ratio.<sup>[53]</sup>

These methods have tremendous potential for uncovering nanoscale heterogeneity in a wide variety of materials systems. As an example, Schmidt et al.<sup>[37,53,149]</sup> have uncovered anomalous diffusion in fluid- and polymer-supported phospholipid membranes, by using a tetramethylrhodamine-labeled phospholipid as the probe. Data from their studies on fluid-supported membranes are shown in Fig. 13.<sup>[149]</sup> Their results show that diffusion occurs on two different time scales in the fluid-supported samples, yielding diffusion coefficients of  $4.4 \times 10^{-8}$  and  $7 \times 10^{-10}$  cm<sup>2</sup>/s. The more mobile molecules exhibited a linear increase in square displacement in time ( $t_{\text{lag}}$  being the time between consecutive images), as expected for Brownian motion. The less mobile molecules also exhibited such behavior for time scales longer than 100 msec. However, at shorter times, the square displacements for these less mobile molecules were found to be independent of time, suggestive of diffusion confined to small “corrals.” Diffusion restricted to small (140 nm) “corrals” was also observed for polymer-supported lipid films.<sup>[149]</sup>

### Reorientation dynamics

The orientations of single molecules can be determined in the laboratory reference frame via the use of polarization-dependent excitation and emission methods.<sup>[76]</sup> A wide variety of methods for measuring the orientations of single molecules have been demonstrated to date. These include direct polarization-dependent methods,<sup>[30,40,45,71,76,119,121,141,152–154]</sup> in which polarization control optics are used to set the excitation polarization and/or to determine the emission polarization. Elegant polarization-dependent imaging methods using aberrated far-field optical systems<sup>[48,49,51]</sup> and near-field optics<sup>[8,55,61,62,70]</sup> have also been demonstrated. Time-dependent changes in the molecular orientation can also be accurately followed and orientational “trajectories” recorded.<sup>[40,49,51,119,121,152]</sup> Such motions reflect the mobility of the dye molecules within their local environments.<sup>[40,119,121]</sup> Hence the results provide physical evidence of the nanoscale fluidity of each sample.

An excellent example of the information that may be obtained is provided by recent work of Deschenes and Vanden Bout.<sup>[40,119]</sup> In their studies, orientation-sensitive single molecule methods were used to monitor temperature-dependent reorientation dynamics in

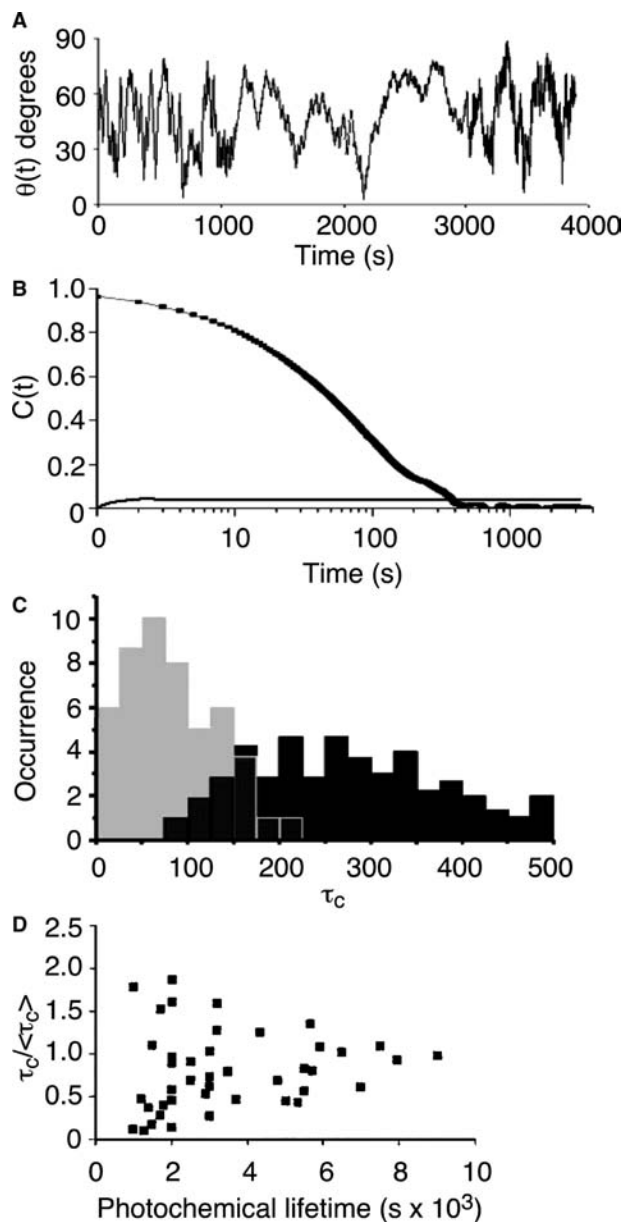


**Fig. 14** (A) In-plane first-quadrant orientation angle for a single rhodamine 6G molecule in poly(methyl acrylate) at  $T_g + 10$  K in time. (B) Autocorrelation of the transient shown in panel A. The data is fit to a stretched exponential (solid line). (C) Histograms of the single molecule rotational correlation times measured for rhodamine 6G molecules in poly(methyl acrylate) (gray) and poly(n-butyl methacrylate) (black). (D) Single-molecule rotational correlation times relative to the ensemble average correlation time as a function of survival time. *Source:* From Ref.<sup>[119]</sup>. © 2001, American Chemical Society.

organic polymer films held near their glass transition temperatures ( $T_g$ ).<sup>[40,119]</sup> A better understanding of the spatial and temporal heterogeneity in molecular motions was sought. New information on the local time scales for molecular reorientation was obtained, along with information on the rate at which the single molecule dynamics approached those of the bulk. This work builds on extensive previous bulk studies.<sup>[155]</sup> Figure 14 depicts representative results from single molecule studies of poly(methyl acrylate) ( $T_g = 281$  K) and poly(*n*-butyl methacrylate) ( $T_g = 285$  K), using rhodamine 6G as the probe molecule.<sup>[119]</sup>

In these studies, the in-plane first-quadrant angle  $\theta$  between the molecular transition dipole and an arbitrarily defined laboratory “*x* axis” was obtained as a function of time, by detecting the fluorescence emitted into two orthogonal polarizations. The angle  $\theta$  is readily calculated from the ratio of these two signals,<sup>[119]</sup> and is plotted in Figure 14A. Clearly apparent in the data are temporal variations in the in-plane orientation of the molecule. Temporal variations in the rate of molecular reorientation are also observed. Figure 14B shows the autocorrelation function derived from this data. By fitting the autocorrelation data to stretched exponentials, the authors obtained parameters that allowed them to determine a weighted average for the rotational correlation time of each molecule. Histograms of these average rotational correlation times are shown in Figure 14C. These data show that the rotational correlation times are larger on average and substantially more variable for molecules in poly(*n*-butyl methacrylate) samples than for those in poly(methyl acrylate).

Deschenes and Vanden Bout<sup>[40,119]</sup> also sought information on the temperature-dependent environmental exchange times. Figure 14D shows results for poly(methyl acrylate) at  $T_g + 10$  K. In these experiments, they determined the (averaged) rotational correlation times for a number of single molecules having different survival times. They found that the rotational correlation times for the longest-lived single molecules most closely approached those of the ensemble average. The rate of decay to the ensemble average value yielded information on how rapidly the reorientation dynamics changed in a particular nanoscale region.

## CONCLUSION

Although new single molecule methods continue to be developed and a complete understanding of all single molecule photophysical phenomena has not yet been obtained, the methods and experiments described above represent important initial steps toward a better understanding of nanoscale phenomena by single molecule methods. The methods themselves represent

powerful means for characterizing the static and dynamic properties of a broad range of materials spanning a range of disciplines. The main advantages of such methods over more conventional bulk methods arise from their ability to probe chemical and physical phenomena at the single molecule level, thereby retaining the information obscured by averaging in bulk methods. As all chemistry occurs on the single molecule level and in single nanoscale environments, information obtained by single molecule methods will be important to the future development of nanoscale materials with tailored physical/chemical properties.

## ACKNOWLEDGMENT

The authors gratefully acknowledge the support of the National Science Foundation (CHE-9701509 and CHE-0092225), the Army Research Office (DEPSCoR), 3M Company, and Kansas State University in the preparation of this article. Prof. M. M. Collinson and the members of the Higgins group are thanked for their comments on early versions of this manuscript.

## REFERENCES

1. Moerner, W.E.; Kador, L. Optical detection and spectroscopy of single molecules in solids. *Phys. Rev. Lett.* **1989**, *62* (21), 2535–2538.
2. Orrit, M.; Bernard, J. Single pentacene molecules detected by fluorescence excitation in a p-terphenyl crystal. *Phys. Rev. Lett.* **1990**, *65* (21), 2716–2719.
3. Shera, E.B.; Seitzinger, N.K.; Davis, L.M.; Keller, R.A.; Soper, S.A. Detection of single fluorescent molecules. *Chem. Phys. Lett.* **1990**, *174* (6), 553–557.
4. Moerner, W.E. Examining nanoenvironments in solids on the scale of a single, isolated impurity molecule. *Science* **1994**, *265* (5168), 46–53.
5. Kelley, A.M. Single-Molecule Spectroscopy. In *Encyclopedia of Chemical Physics and Physical Chemistry*; Moore, J.H., Spencer, N.D., Eds.; Institute of Physics Publishing: Bristol, UK, 2001; 3, 2199–2228.
6. Kelley, A.M.; Michalet, X.; Weiss, S. Single-molecule spectroscopy comes of age. *Science* **2001**, *292* (5522), 1671–1672.
7. Moerner, W.E. A dozen years of single-molecule spectroscopy in physics, chemistry, and biophysics. *J. Phys. Chem., B* **2002**, *106* (5), 910–927.
8. Betzig, E.; Chichester, R.J. Single molecules observed by near-field scanning optical microscopy. *Science* **1993**, *262* (5138), 1422–1425.
9. Nie, S.; Chiu, D.T.; Zare, R.N. Probing individual molecules with confocal fluorescence microscopy. *Science* **1994**, *266* (5187), 1018–1021.
10. Funatsu, T.; Harada, Y.; Tokunaga, M.; Saito, K.; Yanagida, T. Imaging of single fluorescent molecules and individual ATP turnovers by single myosin

- molecules in aqueous solution. *Nature* **1995**, *374* (6522), 555–559.
11. Macklin, J.J.; Trautman, J.K.; Harris, T.D.; Brus, L.E. Imaging and time-resolved spectroscopy of single molecules at an interface. *Science* **1996**, *272* (5259), 255–258.
  12. Moerner, W.E. High-resolution optical spectroscopy of single molecules in solids. *Acc. Chem. Res.* **1996**, *29* (12), 563–571.
  13. Moerner, W.E.; Orrit, M. Illuminating single molecules in condensed matter. *Science* **1999**, *283* (5408), 1670–1676.
  14. Tamarat, P.; Maali, A.; Lounis, B.; Orrit, M. Ten years of single-molecule spectroscopy. *J. Phys. Chem., A* **2000**, *104* (1), 1–16.
  15. Xie, X.S. Single-molecule spectroscopy and dynamics at room temperature. *Acc. Chem. Res.* **1996**, *29* (12), 598–606.
  16. Geva, E.; Reilly, P.D.; Skinner, J.L. Spectral dynamics of individual molecules in glasses and crystals. *Acc. Chem. Res.* **1996**, *29* (12), 579–584.
  17. Plakhotnik, T.; Donley, E.A.; Wild, U.P. Single-molecule spectroscopy. *Annu. Rev. Phys. Chem.* **1997**, *48*, 181–212.
  18. Weiss, S. Fluorescence spectroscopy of single biomolecules. *Science* **1999**, *283* (5408), 1676–1683.
  19. Garcia-Parajo, M.F.; Veerman, J.-A.; Bouwuis, R.; Vallee, R.; van Hulst, N.F. Optical probing of single fluorescent molecules and proteins. *Chem. Phys. Chem.* **2001**, *2* (6), 347–360.
  20. Lakowicz, J.R. *Principles of Fluorescence Spectroscopy*, 2nd Ed.; Plenum: New York, 1999; 698 pp.
  21. Orrit, M.; Bernard, J.; Personov, R.I. High-resolution spectroscopy of organic molecules in solids: from fluorescence line narrowing and hole burning to single molecule spectroscopy. *J. Phys. Chem.* **1993**, *97* (40), 10,256–10,268.
  22. Carlson, R.J.; Wright, J.C. Enhanced selectivity for spectrochemical measurement by mode selection with fully resonant nonlinear mixing. *Anal. Chem.* **1991**, *63* (14), 1449–1451.
  23. Basche, T.; Moerner, W.E.; Orrit, M.; Talon, H. Photon antibunching in the fluorescence of a single dye molecule trapped in a solid. *Phys. Rev. Lett.* **1992**, *69* (10), 1516–1519.
  24. Hirschfeld, T. Optical microscopic observation of single small molecules. *Appl. Opt.* **1976**, *15* (12), 2965–2966.
  25. Nguyen, D.C.; Keller, R.A.; Jett, J.H.; Martin, J.C. Detection of single molecules of phycoerythrin in hydrodynamically focused flows by laser-induced fluorescence. *Anal. Chem.* **1987**, *59* (17), 2158–2161.
  26. Peck, K.; Stryer, L.; Glazer, A.N.; Mathies, R.A. Single-molecule fluorescence detection: Autocorrelation criterion and experimental realization with phycoerythrin. *Proc. Nat. Acad. Sci. U.S.A.* **1989**, *86* (11), 4087–4091.
  27. Dunn, R.C. Near-field scanning optical microscopy. *Chem. Rev.* **1999**, *99* (10), 2891–2928.
  28. Geva, E.; Skinner, J.L. Theory of single-molecule optical line-shape distributions in low-temperature glasses. *J. Phys. Chem., B* **1997**, *101* (44), 8920–8932.
  29. Ambrose, W.P.; Moerner, W.E. Fluorescence spectroscopy and spectral diffusion of single impurity molecules in a crystal. *Nature* **1991**, *349* (6306), 225–227.
  30. Dickson, R.M.; Norris, D.J.; Tzeng, Y.-L.; Moerner, W.E. Three-dimensional imaging of single molecules solvated in pores of poly(acrylamide) gels. *Science* **1996**, *274* (5289), 966–969.
  31. Trautman, J.K.; Macklin, J.J. Time-resolved spectroscopy of single molecules using near-field and far-field optics. *Chem. Phys.* **1996**, *205* (1,2), 221–229.
  32. Abbe, E. Beiträge zur Theorie des Mikroskops und der Mikroskopischen Wahrnehmung. *Arch. Mikrosk. Anat.* **1873**, *9*, 413.
  33. Betzig, E.; Trautman, J.K. Near-field optics: microscopy, spectroscopy, and surface modification beyond the diffraction limit. *Science* **1992**, *257* (5067), 189–195.
  34. Ha, T.; Chemla, D.S.; Enderle, T.; Weiss, S. Single molecule spectroscopy with automated positioning. *Appl. Phys. Lett.* **1997**, *70* (6), 782–784.
  35. Wilson, T.; Sheppard, C. *Theory and Practice of Scanning Optical Microscopy*; Academic Press, Inc.: Orlando, 1984; 213 pp.
  36. Enderlein, J. Position and temporal accuracy of single molecule tracking. *Single Mol.* **2000**, *1* (3), 225–230.
  37. Schmidt, T.; Schütz, G.J.; Baumgartner, W.; Gruber, H.J.; Schindler, H. Characterization of photophysics and mobility of single molecules in a fluid lipid membrane. *J. Phys. Chem.* **1995**, *99* (49), 17,662–17,668.
  38. Hou, Y.; Bardo, A.M.; Martinez, C.; Higgins, D.A. Characterization of molecular scale environments in polymer films by single molecule spectroscopy. *J. Phys. Chem., B* **2000**, *104* (2), 212–219.
  39. Mei, E.; Bardo, A.M.; Collinson, M.M.; Higgins, D.A. Single-molecule studies of sol-gel-derived silicate films. Microenvironments and film-drying conditions. *J. Phys. Chem., B* **2000**, *104* (43), 9973–9980.
  40. Deschenes, L.A.; Vanden Bout, D.A. Single-molecule studies of heterogeneous dynamics in polymer melts near the glass transition. *Science* **2001**, *292* (5515), 255–258.
  41. Basche, T.; Ambrose, W.P.; Moerner, W.E. Optical spectra and kinetics of single impurity molecules in a polymer: spectral diffusion and persistent hole burning. *J. Opt. Soc. Am., B* **1992**, *9* (5), 829–836.
  42. Myers, A.B.; Tchenio, P.; Zgierski, M.Z.; Moerner, W.E. Vibronic spectroscopy of individual molecules in solids. *J. Phys. Chem.* **1994**, *98* (41), 10,377–10,390.
  43. Ambrose, W.P.; Basche, T.; Moerner, W.E. Detection and spectroscopy of single pentacene molecules in a *p*-terphenyl crystal by means of fluorescence excitation. *J. Chem. Phys.* **1991**, *95* (10), 7150–7163.
  44. Plakhotnik, T.; Moerner, W.E.; Palm, V.; Wild, U.P. Single molecule spectroscopy: maximum emission rate and saturation intensity. *Opt. Commun.* **1995**, *114* (1,2), 83–88.
  45. Fourkas, J.T. Rapid determination of the three-dimensional orientation of single molecules. *Opt. Lett.* **2001**, *26* (4), 211–213.
  46. Dunn, R.C.; Holtom, G.R.; Mets, L.; Xie, X.S. Near-field fluorescence imaging and fluorescence

- lifetime measurement of light harvesting complexes in intact photosynthetic membranes. *J. Phys. Chem.* **1994**, *98* (12), 3094–3098.
47. Reid, P.J.; Higgins, D.A.; Barbara, P.F. Environment dependent photophysics of polymer bound J-aggregates determined by time-resolved fluorescence spectroscopy and time-resolved near-field scanning optical microscopy. *J. Phys. Chem.* **1996**, *100* (10), 3892–3899.
  48. Dickson, R.M.; Norris, D.J.; Moerner, W.E. Simultaneous imaging of individual molecules aligned both parallel and perpendicular to the optic axis. *Phys. Rev. Lett.* **1998**, *81* (24), 5322–5325.
  49. Bartko, A.P.; Dickson, R.M. Three-dimensional orientations of polymer-bound single molecules. *J. Phys. Chem., B* **1999**, *103* (16), 3053–3056.
  50. Fang, X.; Tan, W. Imaging single fluorescent molecules at the interface of an optical fiber probe by evanescent wave excitation. *Anal. Chem.* **1999**, *71* (15), 3101–3105.
  51. Bartko, A.P.; Dickson, R.M. Imaging three-dimensional single molecule orientations. *J. Phys. Chem., B* **1999**, *103* (51), 11,237–11,241.
  52. Paige, M.F.; Bjerneld, E.J.; Moerner, W.E. A comparison of through-the-objective total internal reflection microscopy and epi-fluorescence microscopy for single molecule fluorescence imaging. *Single Mol.* **2001**, *2* (3), 191–201.
  53. Schmidt, T.; Schütz, G.J.; Baumgartner, W.; Gruber, H.J.; Schindler, H. Imaging of single molecule diffusion. *Proc. Natl. Acad. Sci.* **1996**, *93* (7), 2926–2929.
  54. Quirin, J.C.; Bartko, A.P.; Dickson, R.M.; Torkelson, J.M. Signature of nanoscale dynamic heterogeneity in polymers near the glass transition: non-gaussian displacement distribution from single-molecule probe diffusion studies. *Polymer Preprints.* **2001**, *42* (2), 174–175.
  55. Hollars, C.W.; Dunn, R.C. Probing single molecule orientations in model lipid membranes with near-field scanning optical microscopy. *J. Chem. Phys.* **2000**, *112* (18), 7822–7830.
  56. Talley, C.E.; Cooksey, G.A.; Dunn, R.C. High resolution fluorescence imaging with cantilevered near-field fiber optic probes. *Appl. Phys. Lett.* **1996**, *69* (25), 3809–3811.
  57. Xie, X.S.; Dunn, R.C. Probing single molecule dynamics. *Science* **1994**, *265* (5170), 361–364.
  58. Bian, R.X.; Dunn, R.C.; Xie, X.S. Single molecule emission characteristics in near-field microscopy. *Phys. Rev. Lett.* **1995**, *75* (26), 4772–4775.
  59. Trautman, J.K.; Macklin, J.J.; Brus, L.E.; Betzig, E. Near-field spectroscopy of single molecules at room temperature. *Nature* **1994**, *369* (6475), 40–42.
  60. Ruiters, A.G.T.; Veerman, J.A.; Garcia-Parajo, M.F.; van Hulst, N.F. Single molecule rotational and translational diffusion observed by near-field scanning optical microscopy. *J. Phys. Chem., A* **1997**, *101* (40), 7318–7323.
  61. Veerman, J.A.; Garcia-Parajo, M.F.; Kuipers, L.; van Hulst, N.F. Single molecule mapping of the optical field distribution of probes for near-field microscopy. *J. Microsc.* **1999**, *194* (2,3), 477–482.
  62. Gersen, H.; Garcia-Parajo, M.F.; Novotny, L.; Veerman, J.A.; Kuipers, L.; van Hulst, N.F. Influencing the angular emission of a single molecule. *Phys. Rev. Lett.* **2000**, *85* (25), 5312–5315.
  63. Higgins, D.A.; Mei, E. Near-Field Scanning Optical Microscopy. In *Scanning Probe Microscopy and Spectroscopy*, 2nd Ed.; Bonnell, D.M., Ed.; Wiley: New York, 2001.
  64. Betzig, E.; Trautman, J.K.; Harris, T.D.; Weiner, J.S.; Kostelak, R.L. Breaking the diffraction barrier: optical microscopy on a nanometric scale. *Science* **1991**, *251* (5000), 1468–1470.
  65. Muramatsu, H.; Chiba, N.; Homma, K.; Nakajima, K.; Ataka, T.; Ohta, S.; Kusumi, A.; Fujihira, M. Near-field optical microscopy in liquids. *Appl. Phys. Lett.* **1995**, *66* (24), 3245–3247.
  66. Hollars, C.W.; Dunn, R.C. Submicron fluorescence, topology, and compliance measurements of phase-separated lipid monolayers using tapping-mode near-field scanning optical microscopy. *J. Phys. Chem., B* **1997**, *101* (33), 6313–6317.
  67. Betzig, E.; Finn, P.L.; Weiner, J.S. Combined shear force and near-field scanning optical microscopy. *Appl. Phys. Lett.* **1992**, *60* (20), 2484–2486.
  68. Toledo-Crow, R.; Yang, P.C.; Chen, Y.; Vaez-Iravani, M. Near-field differential scanning optical microscope with atomic force regulation. *Appl. Phys. Lett.* **1992**, *60* (24), 2957–2959.
  69. Paesler, M.A.; Moyer, P.J. *Near-Field Optics: Theory, Instrumentation, and Applications*; Wiley-Interscience: New York, 1996; 355 pp.
  70. van Hulst, N.F.; Veerman, J.A.; Garcia-Parajo, M.F.; Kuipers, L. Analysis of individual (macro)molecules and proteins using near-field optics. *J. Chem. Phys.* **2000**, *112* (18), 7799–7810.
  71. Sick, B.; Hecht, B.; Wild, U.P.; Novotny, L. Probing confined fields with single molecules and vice versa. *J. Microsc.* **2001**, *202* (2), 365–373.
  72. Kramer, A.; Trabesinger, W.; Hecht, B.; Wild, U.P. Optical near-field enhancement at a metal tip probed by a single fluorophore. *Appl. Phys. Lett.* **2002**, *80* (9), 1652–1654.
  73. Mertz, J.; Xu, C.; Webb, W.W. Single-molecule detection by two-photon-excited fluorescence. *Opt. Lett.* **1995**, *20* (24), 2532–2534.
  74. Plakhotnik, T.; Walser, D.; Pirotta, M.; Renn, A.; Wild, U.P. Nonlinear spectroscopy on a single quantum system: two-photon absorption of a single molecule. *Science* **1996**, *271* (5256), 1703–1705.
  75. Sanchez, E.J.; Novotny, L.; Holtom, G.R.; Xie, X.S. Room-temperature fluorescence imaging and spectroscopy of single molecules by two-photon excitation. *J. Phys. Chem., A* **1997**, *101* (38), 7019–7023.
  76. Ha, T.; Laurence, T.A.; Chemla, D.S.; Weiss, S. Polarization spectroscopy of single fluorescent molecules. *J. Phys. Chem., B* **1999**, *103* (33), 6839–6850.
  77. Reilly, P.D.; Skinner, J.L. Spectral diffusion of single molecule fluorescence: a probe of low-frequency localized excitations in disordered crystals. *Phys. Rev. Lett.* **1993**, *71* (25), 4257–4260.

78. Kettner, R.; Tittel, J.; Basche, T.; Bräuchle, C. Optical spectroscopy and spectral diffusion of single dye molecules in amorphous spin-coated polymer films. *J. Phys. Chem.* **1994**, *98* (27), 6671–6674.
79. Lu, H.P.; Xie, X.S. Single-molecule spectral fluctuations at room temperature. *Nature* **1997**, *385* (6612), 143–146.
80. Bernard, J.; Fleury, L.; Talon, H.; Orrit, M. Photon bunching in the fluorescence from single molecules: a probe for intersystem crossing. *J. Chem. Phys.* **1993**, *98* (2), 850–859.
81. Fleury, L.; Segura, J.-M.; Zumofen, G.; Hecht, B.; Wild, U.P. Nonclassical photon statistics in single-molecule fluorescence at room temperature. *Phys. Rev. Lett.* **2000**, *84* (6), 1148–1151.
82. Higgins, D.A.; Collinson, M.M.; Saroja, G.; Bardo, A.M. Single molecule spectroscopic studies of nanoscale heterogeneity in organically-modified silicate thin films. *Chem. Mater* **2002**, *14* (9), 3734–3744.
83. Vallee, R.; Tomczak, N.; Gersen, H.; van Dijk, E.M.H.P.; Garcia-Parajo, M.F.; Vansco, G.J.; van Hulst, N.F. On the role of electromagnetic boundary conditions in single molecule fluorescence lifetime studies of dyes embedded in thin films. *Chem. Phys. Lett.* **2001**, *348* (3,4), 161–167.
84. English, D.S.; Harbron, E.J.; Barbara, P.F. Role of rare sites in single molecule spectroscopy measurements of spectral diffusion. *J. Chem. Phys.* **2001**, *114* (23), 10,479–10,485.
85. Ye, J.Y.; Ishikawa, M.; Yogi, O.T.O.; Maruyama, Y. Bimodal site distribution of a polymer film revealed by flexible single-molecule probes. *Chem. Phys. Lett.* **1998**, *288* (5,6), 885–890.
86. Ishikawa, M.; Ye, J.Y.; Maruyama, Y.; Nakatsuka, H. Triphenylmethane dyes revealing heterogeneity of their nanoenvironment: Femtosecond, picosecond, and single-molecule studies. *J. Phys. Chem., A* **1999**, *103* (22), 4319–4331.
87. Blum, C.; Stracke, F.; Becker, S.; Müller, K.; Meixner, A.J. Discrimination and interpretation of spectral phenomena by room-temperature single-molecule spectroscopy. *J. Phys. Chem., A* **2001**, *105* (29), 6983–6990.
88. Stracke, F.; Blum, C.; Becker, S.; Müller, K.; Meixner, A.J. Intrinsic conformer jumps observed by single molecule spectroscopy in real time. *Chem. Phys. Lett.* **2000**, *325* (1–3), 196–202.
89. Bowden, N.B.; Willets, K.A.; Moerner, W.E.; Waymouth, R.M. The synthesis of fluorescently-labeled polymers and their use in single-molecule imaging. *Macromolecules* **2002**, *35* (21), 8122–8125.
90. Reichardt, C. *Solvent Effects in Organic Chemistry*; VCH: Weinheim, 1988.
91. Reichardt, C. Solvatochromic dyes as solvent polarity indicators. *Chem. Rev.* **1994**, *94* (8), 2319–2358.
92. Wang, H.; Bardo, A.M.; Collinson, M.M.; Higgins, D.A. Microheterogeneity in dye-doped silicate and polymer films. *J. Phys. Chem., B* **1998**, *102* (37), 7231–7237.
93. Bardo, A.M.; Collinson, M.M.; Higgins, D.A. Nanoscale properties and matrix-dopant interactions in dye-doped organically modified silicate thin films. *Chem. Mater.* **2001**, *13* (8), 2713–2721.
94. Bardo, A.M.; Collinson, M.M.; Higgins, D.A. Nanoscale properties and matrix-dopant interactions in dye-doped organically modified silicate thin films. *Chem. Mater.* **2001**, *13* (9), 3058.
95. Deye, J.F.; Berger, T.A.; Anderson, A.G. Nile red as a solvatochromic dye for measuring solvent strength in normal liquids and mixtures of normal liquids with supercritical and near critical fluids. *Anal. Chem.* **1990**, *62* (6), 615–622.
96. Dutta, A.K.; Kamada, K.; Ohta, K. Spectroscopic studies of nile red in organic solvents and polymers. *J. Photochem. Photobiol. A* **1996**, *93* (1), 57–64.
97. Golini, C.M.; Williams, B.W.; Foresman, J.B. Further solvatochromic, thermochromic, and theoretical studies on nile red. *J. Fluoresc.* **1998**, *8* (4), 395–404.
98. Krishna, M.M.G. Excited state kinetics of the hydrophobic probe nile red in membranes and micelles. *J. Phys. Chem., A* **1999**, *103* (19), 3589–3595.
99. Sarkar, N.; Das, K.; Nath, D.N.; Bhattacharyya, K. Twisted charge transfer process of nile red in homogeneous solution and in faujasite zeolite. *Langmuir* **1994**, *10* (1), 326–329.
100. Rettig, W. Charge separation in excited states of decoupled systems—TICT compounds and implications regarding the development of new laser dyes and the primary processes of vision and photosynthesis. *Angew. Chem. Int. Ed. Engl.* **1986**, *25* (11), 971–988.
101. Marcus, R.A. On the theory of shifts and broadening of electronic spectra of polar solutes in polar media. *J. Chem. Phys.* **1965**, *43* (4), 1261–1274.
102. Marcus, R.A. Relation between charge transfer absorption and fluorescence spectra and the inverted region. *J. Phys. Chem.* **1989**, *93* (8), 3078–3086.
103. Marcus, R.A. Theory of charge-transfer spectra in frozen media. *J. Phys. Chem.* **1990**, *94* (12), 4963–4966.
104. Brunschwig, B.S.; Ehrenson, S.; Sutin, N. Solvent reorganization in optical and thermal electron-transfer processes: solvatochromism and intramolecular electron-transfer barriers in spheroidal molecules. *J. Phys. Chem.* **1987**, *91* (18), 4714–4723.
105. Brasselet, S.; Moerner, W.E. Fluorescence behavior of single molecule pH sensors. *Single Mol.* **2000**, *1* (1), 17–23.
106. Tchenio, P.; Myers, A.B.; Moerner, W.E. Vibrational analysis of the dispersed fluorescence from single molecules of terylene in polyethylene. *Chem. Phys. Lett.* **1993**, *213* (3,4), 325–332.
107. Myers, A.B.; Tchenio, P.; Moerner, W.E. Vibronic spectroscopy of single molecules: exploring electronic-vibrational frequency correlations within an inhomogeneous distribution. *J. Lumin.* **1994**, *58* (1–6), 161–167.
108. Bach, H.; Renn, A.; Wild, U.P. Spectral imaging of single molecules. *Single Mol.* **2000**, *1* (1), 73–77.
109. Nie, S.M.; Emery, S.R. Probing single molecules and single nanoparticles by surface-enhanced Raman scattering. *Science* **1997**, *275* (5303), 1102–1106.
110. Kneipp, K.; Wang, Y.; Kneipp, H.; Perelman, L.T.; Itzkan, I.; Dasari, R.R.; Feld, M.S. Single molecule

- detection using surface-enhanced Raman scattering (SERS). *Phys. Rev. Lett.* **1997**, *78* (9), 1667–1670.
111. Michaels, A.M.; Nirmal, M.; Brus, L.E. Surface enhanced Raman spectroscopy of individual rhodamine 6g molecules on large Ag nanocrystals. *J. Am. Chem. Soc.* **1999**, *121* (43), 9932–9939.
  112. Lee, P.C.; Meisel, D. Adsorption and surface-enhanced Raman of dyes on silver and gold sols. *J. Phys. Chem.* **1982**, *86* (17), 3391–3395.
  113. Doering, W.E.; Nie, S. Single-molecule and single-nanoparticle SERS: examining the roles of surface active sites and chemical enhancement. *J. Phys. Chem., B* **2002**, *106* (2), 311–317.
  114. Ha, T.; Enderle, T.; Chemla, D.S.; Selvin, P.R.; Weiss, S. Quantum jumps of single molecules at room temperature. *Chem. Phys. Lett.* **1997**, *271* (1–3), 1–5.
  115. Yip, W.-T.; Hu, D.; Yu, J.; Vanden Bout, D.A.; Barbara, P.F. Classifying the photophysical dynamics of single- and multiple-chromophoric molecules by single molecule spectroscopy. *J. Phys. Chem., A* **1998**, *102* (39), 7564–7575.
  116. Veerman, J.A.; Garcia-Parajo, M.F.; Kuipers, L.; van Hulst, N.F. Time-varying triplet state lifetimes of single molecules. *Phys. Rev. Lett.* **1999**, *83* (11), 2155–2158.
  117. Hübner, C.G.; Renn, A.; Renge, I.; Wild, U.P. Direct observation of the triplet lifetime quenching of single dye molecules by molecular oxygen. *J. Chem. Phys.* **2001**, *115* (21), 9619–9622.
  118. Köhn, F.; Hofkens, J.; Gronheid, R.; Van der Auweraer, M.; De Schryver, F. Parameters influencing the on- and off-times in the fluorescence intensity traces of single cyanine dye molecules. *J. Phys. Chem. A* **2002**, *106* (19), 4808–4814.
  119. Deschenes, L.A.; Vanden Bout, D.A. Molecular motions in polymer films near the glass transition: a single molecule study of rotational dynamics. *J. Phys. Chem., B* **2001**, *105* (48), 11,978–11,985.
  120. Hou, Y.; Higgins, D.A. Single molecule studies of dynamics in polymer thin films and at surfaces: effect of ambient relative humidity. *J. Phys. Chem., B* **2002**, *106* (40), 10,306–10,315.
  121. Weston, K.D.; Goldner, L.S. Orientation imaging and reorientation dynamics of single dye molecules. *J. Phys. Chem., B* **2001**, *105*, 3453–3462.
  122. Wirth, M.J.; Swinton, D.J. Single-molecule probing of mixed-mode adsorption at a chromatographic interface. *Anal. Chem.* **1998**, *70* (24), 5264–5271.
  123. Wirth, M.J.; Romero, S. Single-molecule spectroscopy of a cationic dye in a 10-nm film of sulfonated polystyrene. *Spectroscopy* **2001**, *16* (7), 20–22.
  124. Dickson, R.M.; Cubitt, A.B.; Tsien, R.Y.; Moerner, W.E. On/off blinking and switching behavior of single molecules of green fluorescent protein. *Nature* **1997**, *388* (6640), 355–358.
  125. Garcia-Parajo, M.F.; Segers-Nolten, G.M.J.; Veerman, J.A.; Greve, J.; van Hulst, N.F. Real-time light-driven dynamics of the fluorescence emission in single green fluorescent protein molecules. *Proc. Nat. Acad. Sci. U.S.A.* **2000**, *97* (13), 7237–7242.
  126. Weston, K.D.; Buratto, S.K. Millisecond intensity fluctuations of single molecules at room temperature. *J. Phys. Chem., A* **1998**, *102* (21), 3635–3638.
  127. Weston, K.D.; Carson, P.J.; Metiu, H.; Buratto, S.K. Room-temperature fluorescence characteristics of single dye molecules adsorbed on a glass surface. *J. Chem. Phys.* **1998**, *109* (17), 7474–7485.
  128. Vanden Bout, D.A.; Yip, W.-T.; Hu, D.; Fu, D.-K.; Swager, T.M.; Barbara, P.F. Discrete intensity jumps and intramolecular electronic energy transfer in the spectroscopy of single conjugated polymer molecules. *Science* **1997**, *277* (5329), 1074–1077.
  129. Ha, T.; Enderle, T.; Ogletree, D.F.; Chemla, D.S.; Selvin, P.R.; Weiss, S. Probing the interaction between two single molecules: fluorescence resonance energy transfer between a single donor and a single acceptor. *Proc. Natl. Acad. Sci. U.S.A.* **1996**, *93* (13), 6264–6268.
  130. Ha, T.; Ting, A.Y.; Liang, J.; Deniz, A.A.; Chemla, D.S.; Schultz, P.G.; Weiss, S. Temporal fluctuations of fluorescence resonance energy transfer between two dyes conjugated to a single protein. *Chem. Phys.* **1999**, *247* (1), 107–118.
  131. Talley, C.E.; Dunn, R.C. Single molecules as probes of lipid membrane microenvironments. *J. Phys. Chem., B* **1999**, *103* (46), 1,0214–10,220.
  132. Cognet, L.; Harms, G.S.; Blab, G.A.; Lommerse, P.H.M.; Schmidt, T. Simultaneous dual-color and dual-polarization imaging of single molecules. *Appl. Phys. Lett.* **2000**, *77* (24), 4052–4054.
  133. Hofkens, J.; Vosch, T.; Maus, M.; Köhn, F.; Cotlet, M.; Weil, T.; Herrmann, A.; Müllen, K.; De Schryver, F. Conformational rearrangements in and twisting of a single molecule. *Chem. Phys. Lett.* **2001**, *333* (3,4), 255–263.
  134. Lu, H.P.; Xie, X.S. Single-molecule kinetics of interfacial electron transfer. *J. Phys. Chem., B* **1997**, *101* (15), 2753–2757.
  135. Lu, H.P.; Xun, L.; Xie, X.S. Single-molecule enzymatic dynamics. *Science* **1998**, *282* (5395), 1877–1882.
  136. Wolynes, P.; Wang, J. Intermittency of single-molecule reaction dynamics in fluctuating environments. *Phys. Rev. Lett.* **1995**, *74* (21), 4317–4320.
  137. Wang, J.; Wolynes, P. Intermittency of activated events in single molecules: the reaction diffusion description. *J. Chem. Phys.* **1999**, *110* (10), 4812–4819.
  138. Brasselet, S.; Peterman, E.J.G.; Miyawaki, A.; Moerner, W.E. Single-molecule fluorescence resonant energy transfer in calcium concentration dependent chameleon. *J. Phys. Chem., B* **2000**, *104* (15), 3676–3682.
  139. Hu, D.; Yu, J.; Barbara, P.F. Single-molecule spectroscopy of the conjugated polymer MEH-PPV. *J. Am. Chem. Soc.* **1999**, *121* (29), 6936–6937.
  140. Hofkens, J.; Maus, M.; Gensch, T.; Vosch, T.; Cotlet, M.; Köhn, F.; Herrmann, A.; Müllen, K.; De Schryver, F. Probing photophysical processes in individual multichromophoric dendrimers by single-molecule spectroscopy. *J. Am. Chem. Soc.* **2000**, *122* (38), 9278–9288.



141. Trabesinger, W.; Renn, A.; Hecht, B.; Wild, U.P.; Montali, A.; Smith, P.; Weder, C. Single-molecule imaging revealing the deformation-induced formation of a molecular polymer blend. *J. Phys. Chem., B* **2000**, *104* (22), 5221–5224.
142. Yu, J.; Hu, D.; Barbara, P.F. Unmasking electronic energy transfer of conjugated polymers by suppression of O<sub>2</sub> quenching. *Science* **2000**, *289* (5483), 1327–1330.
143. Eggeling, C.; Widengren, J.; Rigler, R.; Seidel, C.A.M. Photobleaching of fluorescent dyes under conditions used for single-molecule detection: evidence of two-step photolysis. *Anal. Chem.* **1998**, *70* (13), 2651–2659.
144. Wennmalm, S.; Rigler, R. On death numbers and survival times of single dye molecules. *J. Phys. Chem., B* **1999**, *103* (13), 2516–2519.
145. English, D.S.; Harbron, E.J.; Barbara, P.F. Probing photoinduced intersystem crossing by two-color, double resonance single molecule spectroscopy. *J. Phys. Chem., A* **2000**, *104* (40), 9057–9061.
146. English, D.S.; Furube, A.; Barbara, P.F. Single-molecule spectroscopy in oxygen-depleted polymer films. *Chem. Phys. Lett.* **2000**, *324* (1–3), 15–19.
147. Weston, K.D.; Carson, P.J.; DeAro, J.A.; Buratto, S.K. Single-molecule detection fluorescence of surface-bound species in vacuum. *Chem. Phys. Lett.* **1999**, *308* (1,2), 58–64.
148. Meixner, A.J.; Weber, M.A. Single molecule spectral dynamics at room temperature. *J. Lumin.* **2000**, *86* (3,4), 181–187.
149. Schütz, G.J.; Schindler, H.; Schmidt, T. Single-molecule microscopy on model membranes reveals anomalous diffusion. *Biophys. J.* **1997**, *73* (2), 1073–1080.
150. Wirth, M.J.; Ludes, M.D.; Swinton, D.J. Analytic solution to the autocorrelation function for lateral diffusion and rare strong adsorption. *Appl. Spectrosc.* **2001**, *55* (6), 663–669.
151. Bopp, M.A.; Meixner, A.J.; Tarrach, G.; Zschokke-Gränacher, I.; Novotny, L. Direct imaging single molecule diffusion in a solid polymer host. *Chem. Phys. Lett.* **1996**, *263* (6), 721–726.
152. Harms, G.S.; Sonnleitner, M.; Schütz, G.J.; Gruber, H.J.; Schmidt, T. Single-molecule anisotropy imaging. *Biophys. J.* **1999**, *77* (5), 2864–2870.
153. Ha, T.; Enderle, T.; Chemla, D.S.; Selvin, P.R.; Weiss, S. Single molecule dynamics by polarization modulation. *Phys. Rev. Lett.* **1996**, *77* (19), 3979–3982.
154. Ha, T.; Glass, J.; Enderle, T.; Chemla, D.S.; Weiss, S. Hindered rotational diffusion and rotational jumps of single molecules. *Phys. Rev. Lett.* **1998**, *80* (10), 2093–2096.
155. Ediger, M.D. Spatially heterogeneous dynamics in supercooled liquids. *Annu. Rev. Phys. Chem.* **2000**, *51*, 99–128.

# Single-Walled Carbon Nanotubes: Field Emission Properties

Xiaofeng F. Duan  
Brahim Akdim  
Ruth Pachter

Materials and Manufacturing Directorate, Air Force Research Laboratory,  
Wright-Patterson Air Force Base, Ohio, U.S.A.

## INTRODUCTION

Ongoing developments in the production and characterization of carbon nanotubes, as previously summarized,<sup>[1]</sup> have opened up new fields in science and technology in the last few years. These materials are shown to be versatile building blocks because of their unique electronic,<sup>[2,3]</sup> optical,<sup>[4,5]</sup> and mechanical<sup>[6,7]</sup> properties; for example, most recently, carbon nanotubes were found to act as ballistic field-effect transistors (FET),<sup>[8]</sup> were fabricated as FETs with multiple, individually addressable gate segments,<sup>[9]</sup> were applied in composites,<sup>[10]</sup> and were shown to be photoconductive.<sup>[11]</sup>

Furthermore, because carbon nanotubes emit high currents (up to 1 A/cm<sup>2</sup>) at low field ( $\sim 5$  V/ $\mu$ m),<sup>[12]</sup> and significant advances have been attained in the production of well-aligned tubes, the applicability for field emission previously recognized by de Heer, Chatelain, and Ugarte.<sup>[13]</sup> has now been widely acknowledged,<sup>[14]</sup> and a prototype of a flat panel with color display was achieved.<sup>[15]</sup> Most recently, different production procedures and treatments of nanotubes were shown to result in varying degrees of field emission.<sup>[16–25]</sup>

Despite these technological developments, there are still unanswered questions regarding the field emission mechanism, as it was observed that the  $I$ - $V$  characteristics of Single-Wall Carbon NanoTubes (SWCNTs) could deviate from Fowler–Nordheim’s (FN) theory,<sup>[26]</sup> which assumes the emission to occur by a tunneling mechanism. A range of experimental and theoretical studies were reported to explain this behavior, e.g., by Saito et al., suggesting that the deviation may occur because of the non-metallic behavior of SWCNTs at the tip,<sup>[27]</sup> while Bonard et al. attributed the nonlinearity to tube interactions,<sup>[28]</sup> and others<sup>[29–31]</sup> observed that the exposure of SWCNT samples to

gas adsorption alters their emission properties. Although the effects of gas adsorption, in particular O<sub>2</sub>, were previously reported experimentally,<sup>[32,33]</sup> the detailed chemistry at the adsorption sites under an external field and the resulting field emission properties are still not fully understood. Theoretically, much attention has been devoted thus far to the study of O<sub>2</sub> adsorption at SWCNT tips,<sup>[34–41]</sup> and their effects on field emission, including our recent systematic examination of the adsorption at capped and uncapped tips, performed under a local field to mimic the emission environment.<sup>[42]</sup>

In this review, we outline some of the findings of our previous work,<sup>[42]</sup> and in addition, report preliminary results on the effects of ozonation on SWCNTs. Indeed, although ozonation of carbon nanotubes enhances the propensity for functionalization,<sup>[43]</sup> and alters the field emission properties, e.g., an enhancement in the first 3 min upon exposure to O<sub>3</sub> has been observed,<sup>[32]</sup> Thus far the effects of O<sub>3</sub> have not been extensively explored theoretically. While a mixed quantum mechanics/molecular mechanics (ONIOM) study of O<sub>3</sub> adsorption at the sidewall of a SWCNT, assuming only a 16-atom model at a high level of accuracy, has been recently reported,<sup>[44]</sup> we carried out all-electron Linear Combination of Atomic Orbitals (LCAO) Density Functional Theory (DFT)<sup>[45]</sup> calculations in our preliminary investigation, previously also applied to extended SWCNT systems.<sup>[46]</sup> We identify possible reaction sites for ozonation, which could play a role in the experimentally observed field emission enhancement. Such comprehensive studies, reiterated in this review for O<sub>2</sub> adsorption, and including our new results for the ozonation at the tips, provide an outline for our ongoing interest in gaining insight into the effects of adsorbates on field emission characteristics in these materials, e.g., enhancement by Cs intercalation or deposition.<sup>[47–51]</sup>

## RESULTS AND DISCUSSION

### Computational Details

The Perdew–Burke–Ernzerhof (PBE) exchange–correlation ( $x$ -c) functional<sup>[52]</sup> within the generalized gradient approximation was employed to reduce the overbinding effects caused by the local density approximation, also known to adequately predict the density of states as compared to experiment,<sup>[53]</sup> using a double numerical polarized basis set. As we have previously pointed out, it is important to emphasize that, to accurately discern long-range dispersion effects using DFT, recently assessed for weakly bound test problems,<sup>[54]</sup> theoretical studies have to be systematically carried out with an appropriate ( $x$ -c) functional. Improvements suggested to take into account dynamical correlations, including semiempirical methods,<sup>[55]</sup> hybrid approaches, improved correlation functionals,<sup>[56]</sup> or time-dependent DFT calculations,<sup>[57]</sup> could enable more accurate calculations in the future.

We studied C(5,5) capped and open-ended (uncapped) SWCNT tips (for comprehensive details, see Ref.<sup>[42]</sup>); three-unit cell C(5,5) tubes, terminated with a half C<sub>60</sub> molecule or open-ended, on one end, respectively, and saturated with hydrogen atoms at the other end, were used. As the emission in these systems involves the topmost layers, only adsorption at the tip was taken into account. A uniform external field directed from the top toward the tube tip was applied to simulate the emission environment. Under an applied electric field, the stems of the tubes were fixed to simulate an attached nanotube to a substrate. Geometries were optimized in the absence and presence of an electric field. Transition state geometries were evaluated.<sup>[42]</sup> Note that Kim et al.<sup>[58]</sup> have previously calculated O<sub>2</sub> adsorption for an uncapped SWCNT, also with an applied field; however, an analysis for C(10,0) was primarily emphasized. The work function<sup>[59]</sup> is approximated by the first ionization potential (IP), not dependent on the tube length,<sup>[42]</sup> as compared to the Highest Occupied Molecular Orbital (HOMO)–Lowest Unoccupied molecular Orbital (LUMO) gap, adopted by Kim and Kim.<sup>[60]</sup> The adsorption energy ( $E_{\text{ad}}$ ) was defined as:  $E_{\text{ad}} = E(\text{SWCNT} + \text{O}_2) - E(\text{SWCNT}) - E(\text{O}_2)$ ; a positive or a negative change in  $E_{\text{ad}}$  refers to an endothermic, or exothermic reaction, respectively.

### O<sub>2</sub> Adsorption

Reaction paths of O<sub>2</sub> interacting at the (h–h) and (p–h) sites of a capped tube, for configs.-(a) and -(c), respectively, are summarized in Fig. 1. The initial adsorption process at the (h–h) site forms weak single O–O and O–C bonds, changing the C–C double bond to a single bond. In the absence of an electric field, the reaction is

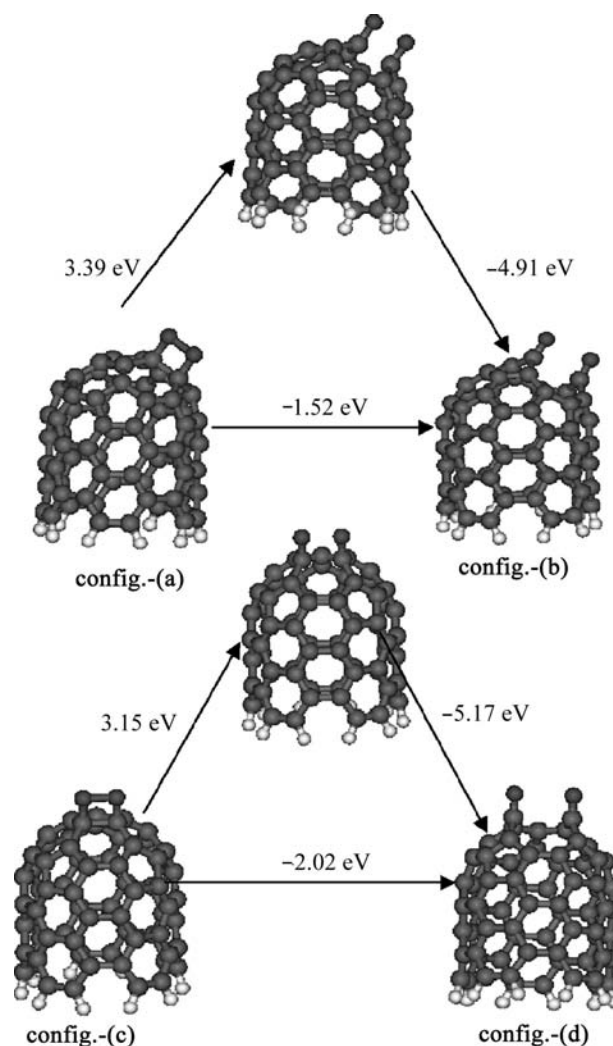


**Fig. 1** O<sub>2</sub> adsorption on a capped tube. Top: At the hexagon–hexagon (h–h) site represented by config.-(a), leading to config.-(b) through an etched transition state. Bottom: O<sub>2</sub> adsorption at the hexagon–pentagon (p–h) site as shown by config.-(c), leading to the etched config.-(d). The transition states were confirmed by vibrational frequency calculations, obtaining one imaginary frequency in each case: 274 and 396 cm<sup>-1</sup> for the transition states leading to configs. -(b) and -(d), respectively. *Source:* From Ref.<sup>[42]</sup>.

endothermic with an adsorption energy of 0.11 eV (Table 1 in Ref.<sup>[42]</sup>), suggesting that the reaction is not favorable; however, if the conditions for chemisorption exist, the O<sub>2</sub> molecule can further react to etch the tube. During etching, structures with a partial double C=O bond are formed after the dissociation of the O–O bond, lowering the energy by about 1.5 eV with respect to the initial structure. However, a large energy barrier of 3.4 eV needs to be overcome for the etching to occur; this result is larger than a previously estimated value (1.02 eV), using a self-consistent tight-binding method.<sup>[35]</sup>

In comparing the energetics and structural parameters for the adsorption at the (p-h) and (h-h) sites, we note that the O<sub>2</sub> adsorption at the (p-h) site has a higher energy (0.85 eV) (Table 1 in Ref.<sup>[42]</sup>). The etching process takes place by overcoming an energy barrier of about 3.2 eV, slightly lower than that at the (h-h) site, but larger than a previously reported value of 0.9 eV. The formation of the O-C bonds in the etched configurations stabilizes the structure by lowering the energy by ca. 2 eV, through an exothermic reaction.

The reaction path of a physisorbed O<sub>2</sub> configuration toward chemisorption on the (p-h) site, shown in Fig. 2, finds an energy barrier of 0.77 eV, which is lower than the energy barrier needed to etch the tube, suggesting that the transition from physisorption to chemisorption could occur if the thermodynamic conditions exist to trigger it. Even in the absence of an electric field, we found physisorption to be exothermic, with no structural changes, and an adsorption energy of -0.12 eV at a distance of 3.3 Å from the tip. Interestingly, the adsorption energy is comparable to H<sub>2</sub> physisorption (-0.1 eV).<sup>[61]</sup> Although the adsorption energy compares well with that reported by Peng and Cho<sup>[62]</sup> for O<sub>2</sub> physisorbed on the sidewall of a (10,0) nanotube (-0.1 eV), the adsorption distance was smaller (2.7 Å). A larger value was obtained at 2.7 Å (-0.25 eV), by applying DFT to model sidewall adsorption.<sup>[34]</sup> Note that our results are consistent with recent MP2 calculations on the interaction of O<sub>2</sub> with a (9,0) carbon nanotube.<sup>[63]</sup>

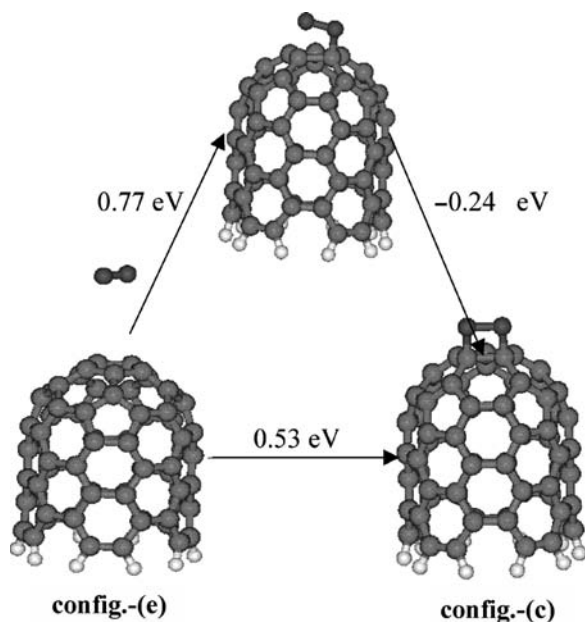


**Fig. 2** The reaction path from an O<sub>2</sub> physisorption configuration to a chemisorbed configuration in the (p-h) site on a capped SWCNT. *Source:* From Ref.<sup>[42]</sup>.

O<sub>2</sub> chemisorption is more favorable (negative adsorption energies for uncapped tip configurations) in the open-ended tip. Fig. 3 shows an O<sub>2</sub> molecule reacting with the open-ended tip (config.-f), as well as the adsorption of O<sub>2</sub> on top of the arm site of the tip (config.-g), forming two O-C bonds with bond lengths of 1.23 Å, and an O-O distance of 2.8 Å (Table 1 in Ref.<sup>[42]</sup>). We studied part of the reaction path to config.-h, which is the most stable state in this case. A slight increase in the O-O bond length drives the structure to config.-h, overcoming a small energy barrier of 0.23 eV, and gaining about 0.5 eV through an exothermic reaction.

In addition, we investigated the effects of O<sub>2</sub> adsorption for fully saturated tips [configs.-i) and -(j) for C(5,5), and configs.-k) and -(l) for C(10,0); Fig. 4]. Config.-i) is a metastable state with an adsorption energy of -2.73 (eV/O<sub>2</sub>) and an IP of 6.17 eV (Table 2 in Ref.<sup>[42]</sup>). These values are comparable to

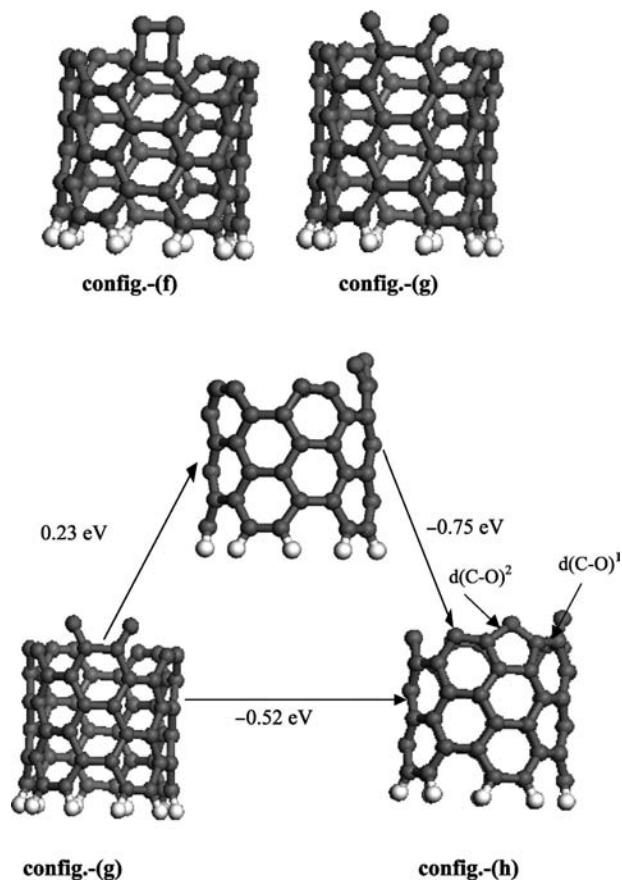


**Fig. 3** O<sub>2</sub> adsorption on an uncapped tube. Top: Intermediate states, shown by config.-f) and config.-g). Bottom: A partial reaction path of O<sub>2</sub> adsorbed on an uncapped tube represented by config.-g); an increase of O-O distance leads to config.-h), where one of the oxygens is bonded with two carbons. The transition state was also confirmed in this case, with a 196 cm<sup>-1</sup> imaginary frequency. *Source:* From Ref.<sup>[42]</sup>.

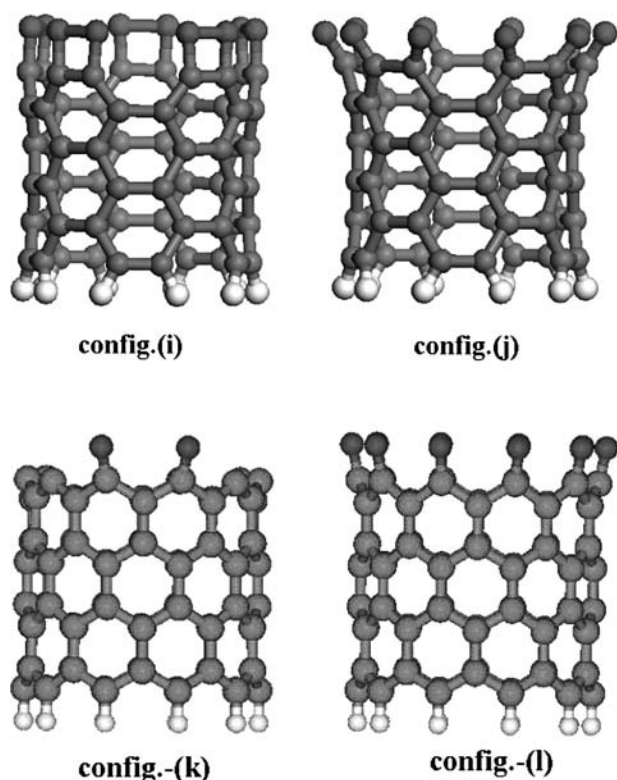


**Fig. 4** Effects of saturating uncapped SWCNT tips by  $O_2$  adsorption are shown for: (Top)  $O_2$  adsorption on the C(5,5) armchair tube—configs.-(i) and -(j). (Bottom)  $O_2$  adsorption on the C(10,0) zigzag tube—config.-(k) shows an  $O_2$  adsorption and config.-(l) represents a saturated tip. Source: From Ref.<sup>[42]</sup>.

those of config.-(f), suggesting that the saturation at the tip in this case has a small effect on field emission properties. On the other hand, the IP in config.-(j) increased by 9% and the tip opening stretched out by about 4% compared to the pristine nanotube, because of the formation of a C=O double bond, and repulsion of neighboring oxygens.

In the initial adsorption process, characterized by configs.-(a) and -(c) for the capped tubes (Fig. 1), values of the adsorption energies decrease smoothly as a function of field strength. This suggests that an applied voltage lowers the adsorption energy, thus setting the conditions for a chemisorption process to take place, which in turn, leads to etching. A  $2\text{ eV/\AA}$  increase in the field significantly alters the structural parameters, resulting in a lower energy barrier for an etching process to occur. Indeed, a  $2\text{ eV/\AA}$  applied field has desorbed the oxygen from the tip in config.-(c), whereas in the final adsorption process [configs.-(b) and -(d)], it is difficult to achieve desorption without disintegrating the nanotube tip. In our study, the C(5,5) open-ended tip was examined, and although the adsorption energies for configs.-(f), -(g), and -(h) are systematically up-shifted by about  $1.4\text{ eV}$ , as

compared to previous self-consistent tight-binding calculations,<sup>[35]</sup> the relative values between intermediate configurations are comparable. Furthermore, we found that under a  $1\text{ eV/\AA}$  field, config.-(f) converges to config.-(g), by forming a double bond (structural results in Table 1 of Ref.<sup>[42]</sup>). Stronger adsorption under a  $1\text{ eV/\AA}$  field is shown, as has been observed for capped tubes. In configs.-(g) and -(h), we note small structural changes, suggesting no desorption at  $1\text{ eV/\AA}$  field strength; however, longer O–C bonds were observed at a higher field ( $2\text{ eV/\AA}$ ).

Overall, our results show that  $O_2$  chemisorption is endothermic on a capped tip, with the (h–h) adsorption site being energetically more favorable than the (p–h) site. If the thermodynamic conditions exist for chemisorption to occur, an energy barrier larger than  $3\text{ eV}$  is required to etch the tube. The application of an electric field sets the conditions for the chemisorption to take place. In open-ended tips, the examined interactions were exothermic with lower adsorption energies. This suggests that the observed current suppression on exposure to  $O_2$  can be rationalized in terms of the presence of a high percentage of open-ended tips or tubes with structural defects.

Under a zero electric field, a small increase of about 2% in the IP was noted for capped tubes, suggesting that  $O_2$  adsorption plays a role in the current suppression observed experimentally (Table 2 in Ref.<sup>[42]</sup>). An applied field exacerbates this current suppression, as shown by the notable increase of the IP, ranging from 2% to 6% for config.-(c), and 8% for config.-(d). While in config.-(a) a small change of the IP has been observed with an applied field, config.-(b) shows a much higher IP, with an increase of about 46%, which could be explained by the specific geometry at the adsorption site. As expected, charge transfer occurs upon adsorption from carbon to oxygen (cf. Fig. 5 in Ref.<sup>[42]</sup>). We also note that an applied field appears to increase the negative partial atomic charge on the oxygen atom.

Upon  $O_2$  adsorption in the absence of an electric field in uncapped tubes, no significant effect on the IP is observed in config.-(f) with respect to pristine C(5,5); however, an increase of 2% is shown for the intermediate and final configs.-(g) and -(h), respectively. The corresponding HOMO energies are consistent with the IP's trend ( $-4.81$ ,  $-4.82$ ,  $-4.96$ , and  $-4.93\text{ eV}$ , for a pristine tube and configs.-(f), -(g), and -(h), respectively). However, under a  $1\text{ eV/\AA}$  applied field, the IPs increase to about 5% in configs.-(f) and -(g), and 9% in config.-(h), respectively. Once again, this implies that the current suppression is exacerbated by an applied field, accompanied by an increase in the charge transfer from carbon to oxygen. We note that the IPs of the pristine capped and uncapped tubes, under zero electric field, are

comparable. However, under a  $1 \text{ eV/\AA}$  field strength, the IP of the uncapped tip is 6% higher than that of a capped tube. As for the  $\text{O}_2$  adsorbed tips, different values were obtained depending on the adsorption sites. The effects of  $\text{O}_2$  adsorption on the field emission properties is, in general, more pronounced in the C(10,0) than in the C(5,5) tip, with an IP increase of 13% and 30% in configs.-(k) and -(l), respectively, compared to the pristine C(10,0) tube. The increase in the IPs for the saturated tip models is also in agreement with experimental results, where a decrease in the output current as a function of the  $\text{O}_2$  exposure time was observed.

### $\text{O}_3$ Adsorption

An enhancement of the field emission current in the first 3 min upon ozonation of carbon nanotubes has been experimentally observed<sup>[32]</sup> although decaying is observed as exposure time increases, indicating the beginning of the tubes' degradation by etching.

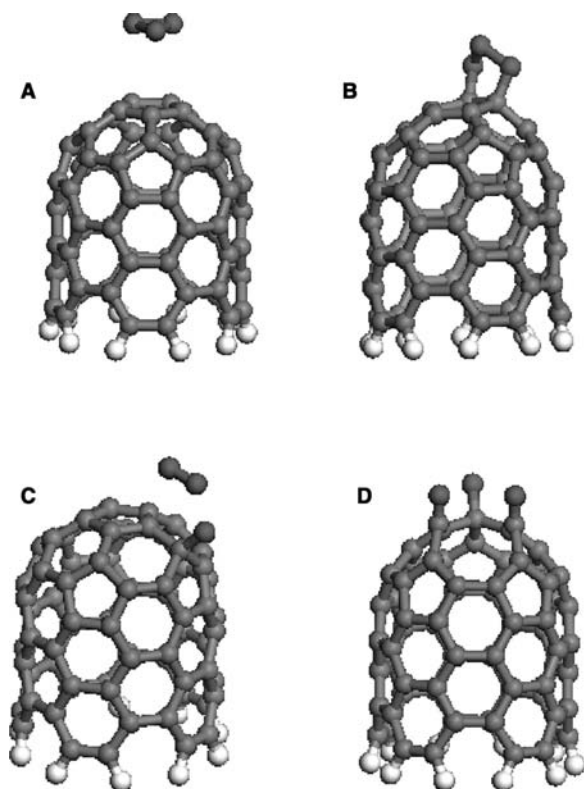


**Fig. 5**  $\text{O}_3$  adsorption on a capped tube: A) physisorption:  $d(\text{O}-\text{C}) = 3.31 \text{ \AA}$  and  $d(\text{O}-\text{O}) = 1.450 \text{ \AA}$ ; B) chemisorption at the p-h site:  $d(\text{O}-\text{C}) = 1.44 \text{ \AA}$  and  $d(\text{O}-\text{O}) = 1.47 \text{ \AA}$ ; C) chemisorption at the p-h site:  $d(\text{O}-\text{C}) = 1.40 \text{ \AA}$ ,  $d(\text{O}-\text{O}) = 1.23 \text{ \AA}$ , and  $d(\text{OO}-\text{OC}) = 1.82 \text{ \AA}$ ; D) etching at the p-h site with the front two O-C bonds at  $d(\text{O}-\text{C}) = 1.22 \text{ \AA}$  and one back O-C bond at  $d(\text{O}-\text{C}') = 1.35 \text{ \AA}$ .

**Table 1** IPs and adsorption energies for  $\text{O}_3$  adsorbed at capped tips

Config.	5a	5b	5c	5d
IP (eV)	6.14	6.28	5.84	6.91
$E_{\text{ad}}$ (eV/ $\text{\AA}$ )	0.62	-1.71	-1.02	-2.34

Fig. 5 shows the optimized structures of  $\text{O}_3$  adsorption on a capped SWCNT. Config.-(5A) represents  $\text{O}_3$  physisorption on a capped tip; the reaction was found to be slightly endothermic, contrary to  $\text{O}_2$  adsorption, where such a reaction was calculated to be exothermic. Config.-(5B) depicts a chemisorption of  $\text{O}_3$  at the p-h site, and as noted from the calculated adsorption energy (cf. Table 1), it is more exothermic than with  $\text{O}_2$ . This configuration may further lead to etching, such that the middle O atom will form the third C=O bond at the tip, and therefore break it. Interestingly, our results are consistent with the binding energies calculated for sidewall ozonation.<sup>[44]</sup>

Although for the (p-h) capped tip site adsorption, the calculation of the vertical IP reveals a suppression of current, it is interesting to note that for config.-(5C), where the ozone reaction takes place at an h-h site, our preliminary calculations predict an enhancement of the current, depicted by a reduction of ca. 5% in the IP compared to the pristine nanotube. In this case, a five-member ring-like structure at the p-h site cannot form, but instead an  $\text{O}_2$  molecule and an O=C double bond are formed. Mulliken analyses reveal that  $\text{O}_2$  acts as charge donor to the O=C structure, hence reducing the work function of the system, which could serve as a possible explanation of the experimentally observed emission enhancement.<sup>[32]</sup> Following  $\text{O}_3$  chemisorption at the p-h site, etching may occur, as shown in config.-(5D), where the two O atoms are double-bonded to the tip, while the other O-C forms a partial double bond. The larger IP of the structure shows suppression of field emission, which is, once again, consistent with experiment, as the field emission decays if the carbon nanotubes are exposed to  $\text{O}_3$  for a longer time. Preliminary calculations of ozonation at uncapped tubes reveal that the ozone strongly reacts with the tube.

### CONCLUSION

In conclusion, the review of our comprehensive examination of the adsorption mechanisms on capped and uncapped SWCNT tip geometries provided insight into the chemistry upon exposure of SWCNTs to  $\text{O}_2$  and  $\text{O}_3$ , in comparison with other studies. We showed that  $\text{O}_2$  adsorbs through a physisorption mechanism, whereas  $\text{O}_3$  prefers to chemisorb on capped tips. However, on uncapped tips, both  $\text{O}_2$  and  $\text{O}_3$  adsorb chemically at the tip apex.



The desorption mechanism of O<sub>2</sub> was examined under an applied field, revealing that once O<sub>2</sub> dissociates and attaches to the tip, it becomes difficult for desorption to take place. Indeed, the inclusion of an electric field provided a more realistic emission environment, showing that the field exacerbates current suppression upon O<sub>2</sub> adsorption by lowering the adsorption energy at the capped tip, thus setting the conditions for an etching process to occur. Our adsorption energies and first IPs clearly illustrate the sites involved in current suppression, and the increase in IP for saturated open-ended tubes is in agreement with experimental results. Further studies on O<sub>3</sub> adsorption under an applied field are being carried out.

## ACKNOWLEDGMENTS

We thank the ASC/MSRC for their excellent support in carrying out the calculations.

## REFERENCES

- Baugham, R.H.; Zakhidov, A.A.; de Heer, W.A. Carbon nanotubes—the route toward applications. *Science* **2002**, *297*, 787.
- Mintmire, J.W.; Dunlap, B.I.; White, C.T. Are fullerene tubules metallic? *Phys. Rev. Lett.* **1992**, *68*, 631.
- Hamada, N.; Sawada, S.-I.; Oshiyama, A. New one-dimensional conductors: graphitic microtubules. *Phys. Rev. Lett.* **1992**, *68*, 1579.
- Charlier, J.-C.; Limbin, Ph. Electronic structure of carbon nanotubes with chiral symmetry. *Phys. Rev., B* **1998**, *57*, 15037.
- Kral, P.; Shapiro, M. Nanotube electron drag in flowing liquids. *Phys. Rev. Lett.* **2001**, *86*, 131.
- Demczyk, B.G.; Wang, Y.M.; Cumings, J.; Hetman, M.; Han, M.; Zettl, A.; Ritchie, R.O. Direct mechanical measurement of the tensile strength and elastic modulus of multiwalled carbon nanotubes. *Mater. Sci. Eng., A* **2002**, *334*, 173.
- Yakobson, B.I.; Avouris, P. *Carbon Nanotubes: Synthesis, Structure, Properties, Applications*; Dresselhaus, M.S., Dresselhaus, G., Avouris, Ph., Eds.; Springer-Verlag: Berlin, 2000; 391 pp.
- Javey, A.; Guo, J.; Wang, Q.; Lundstrom, M.; Dai, H. Ballistic carbon nanotube field-effect transistors. *Nature* **2003**, *424*, 654.
- Wind, S.J.; Appenzeller, J.; Avouris, Ph. Lateral scaling in carbon-nanotube field-effect transistors. *Phys. Rev. Lett.* **2003**, *91*, 058301/1–058301/4.
- Zhang, X.; Liu, T.; Sreekumar, T.V.; Kumar, S.; Moore, V.C.; Hauge, R.H.; Smalley, R.E. Poly(vinyl alcohol)/SWNT composite film. *Nano Lett.* **2003**, *3*, 1285.
- Freitag, M.; Martin, Y.; Misewich, J.A.; Martel, R.; Avouris, Ph. Photoconductivity of single carbon nanotubes. *Nano Lett.* **2003**, *3*, 1067.
- Bonard, J.-M.; Croci, M.; Klinke, C.; Kurt, R.; Noury, O.; Weiss, N. Carbon nanotube films as electron field emitters. *Carbon* **2002**, *40*, 1715–1728.
- de Heer, W.A.; Chatelain, A.; Ugarte, D. A carbon nanotube field-emission electron source. *Science* **1995**, *270*, 1179.
- Lin, M.C.-C.; Lai, H.J.; Yang, M.H.; Li, A.K. Characteristic of field emission from carbon nanotubes synthesized from different sources. *Mater. Phys. Mech.* **2001**, *4*, 138.
- Choi, W.B.; Chung, D.S.; Kang, J.H.; Kim, H.Y.; Jin, Y.W.; Han, I.T.; Lee, Y.H.; Jung, J.E.; Lee, N.S.; Park, G.S.; Kim, J.M. Fully sealed, high-brightness carbon-nanotube field-emission display. *Appl. Phys. Lett.* **1999**, *75*, 3129.
- Zhao, W.J.; Kawakami, N.; Sawada, A.; Takai, M. Field emission from screen-printed carbon nanotubes irradiated by tunable ultraviolet laser in different atmospheres. *J. Vac. Sci. Technol., B* **2003**, *21*, 1734.
- Poa, C.H.P.; Smith, R.C.; Silva, S.R.P.; Watts, P.C.P.; Hsu, W.K.; Kroto, H.W.; Walton, D.R. Field emission from nonaligned carbon nanotube-polymer matrix cathodes. *J. Vac. Sci. Technol., B* **2003**, *21*, 1715.
- Oshima, C.; Matsuda, K.; Kona, T.; Mogami, Y.; Yamashita, T.; Saito, Y.; Hata, K.; Takakura, A. Energy spectra of field emission electrons from multiwalled carbon nanotubes. *J. Vac. Sci. Technol., B* **2003**, *21*, 1700.
- Lin, I.-N.; Teng, M.-Y.; Liu, K.-S.; Hsu, T.; H., J.-H.; Tsai, C.-H.; Cheng, H.-F. Electron field emission properties of carbon nanotubes converted from nanodiamonds. *J. Vac. Sci. Technol., B* **2003**, *21*, 1688.
- Woo, Y.S.; Jeon, D.Y.; Han, I.T.; Park, Y.J.; Kim, H.J.; Jung, J.E.; Kim, J.M.; Lee, N.S. Field emission characteristics of multiwalled carbon nanotubes grown at low temperatures using electron cyclotron resonance chemical vapor deposition. *J. Vac. Sci. Technol., B* **2003**, *21*, 1660.
- Huang, J.H.; Chuang, C.C.; Tsai, C.H.; Chen, W. Excellent field emission from carbon nanotubes grown by microwave-heated chemical vapor deposition. *J. Vac. Sci. Technol., B* **2003**, *21*, 1655.
- Cheng, H.-F.; Tsau, Y.-M.; C., Y.-C.; Hsieh, Y.-S.; Lin, I.-N. Electron field emission properties of carbon nanotubes grown on nickel caps. *J. Vac. Sci. Technol., B* **2003**, *21*, 1640.
- Lee, J.H.; Heo, J.N.; Yi, W.K.; Jeong, T.W.; Yu, S.G.; Lee, C.S.; Kim, W.S.; Yoo, J.-B.; Han, H.S.; Kim, J.M. Field emission characteristics of self-assembled carbon nanotubes on the gold surface. *J. Vac. Sci. Technol., B* **2003**, *21*, 358.
- Rupasinghe, N.L.; Chhowalla, M.; Teo, K.B.K.; Amaratunga, G.A. Field emission vacuum power switch using vertically aligned carbon nanotubes. *J. Vac. Sci. Technol., B* **2003**, *21*, 338.
- Jo, S.H.; Tu, Y.; Huang, Z.P.; Carnahan, D.L.; Wang, D.Z.; Ren, Z.F. Effect of length and spacing of vertically aligned carbon nanotubes on field emission properties. *App. Phys. Lett.* **2003**, *82*, 3520.
- Fowler, R.H.; Nordheim, L. Electron emission in intense electric fields. *Proc. R. Soc. Lond., A* **1928**, *119*, 173.
- Saito, Y.; Hamaguchi, K.; Nishino, T.; Hata, K.; Tohji, K.; Kasuya, A.; Nishina, Y. Field emission patterns

- from single-walled carbon nanotubes. *J. Appl. Phys., Part 2* **1997**, *36*, L1340.
28. Bonard, J.-M.; Salvétat, J.-P.; Stockli, T.; de Heer, W.A.; Forro, L.; Chatelain, A. Field emission from single-wall carbon nanotube films. *Appl. Phys. Lett.* **1998**, *73*, 918.
  29. Lim, S.C.; Choi, Y.C.; Jeong, H.J.; Shin, Y.M.; An, K.H.; Bae, D.J.; Lee, Y.H.; Lee, N.S.; Kim, J.M. Effect of gas exposure on field emission properties of carbon nanotube arrays. *Adv. Mater.* **2001**, *13*, 1563.
  30. Dong, C.; Gupta, M.C. Influences of the surface reactions on the field emission from multiwall carbon nanotubes. *Appl. Phys. Lett.* **2003**, *83*, 159.
  31. Collazo, R.; Schlessler, R.; Sitar, Z. Role of adsorbates in field emission from nanotubes. *Diamond Related Mater.* **2002**, *11*, 769.
  32. Kung, S.-C.; Hwang, K.C.; Lin, N. Oxygen and ozone oxidation-enhanced field emission of carbon nanotubes. *Appl. Phys. Lett.* **2002**, *80*, 4819.
  33. Ulbricht, H.; Moos, G.; Hertel, T. Physisorption of molecular oxygen on single-wall carbon nanotube bundles and graphite. *Phys. Rev., B* **2002**, *66*, 075404.
  34. Jhi, S.-H.; Louie, S.G.; Cohen, M.L. Electronic properties of oxidized carbon nanotubes. *Phys. Rev. Lett.* **2000**, *85*, 1710.
  35. Zhu, X.Y.; Lee, S.M.; Lee, Y.H.; Frauenheim, Th. Adsorption and desorption of an O<sub>2</sub> molecule on carbon nanotubes. *Phys. Rev. Lett.* **2000**, *85*, 2757.
  36. Park, N.; Han, S.; Ihm, J. Effects of oxygen adsorption on carbon nanotube field emitters. *J. Phys. Rev., B* **2001**, *64*, 125401.
  37. Sorescu, D.C.; Jordan, K.D.; Avouris, P.J. Effects of oxygen adsorption on carbon nanotube field emitters. *Phys. Chem., B* **2001**, *105*, 11227.
  38. Moon, C.-Y.; Kim, Y.-S.; Lee, E.-C.; Jin, Y.-G.; Chang, K.J. Mechanism for oxidative etching in carbon nanotubes. *Phys. Rev., B* **2002**, *65*, 155401.
  39. Steckel, J.A.; Jordan, K.D.; Avouris, P. Oxygen atom reactions with circumtrindene and related molecules: analogues for the oxidation of nanotube caps. *J. Phys. Chem., A* **2002**, *106*, 2572.
  40. Grujicic, M.; Cao, G.; Gresten, B. Enhancement of field emission in carbon nanotubes through adsorption of polar molecules. *Appl. Surf. Sci.* **2003**, *206*, 167.
  41. Ricca, A.; Bauschlicher, C.W.; Maiti, A. Comparison of the reactivity of O<sub>2</sub> with a (10,0) and a (9,0) carbon nanotube. *Phys. Rev., B* **2003**, *68*, 035433.
  42. Akdim, B.; Duan, X.; Pachter, R. The effects of O<sub>2</sub> adsorbates on field emission properties of single-wall carbon nanotubes: a density functional theory study. *Nano Lett.* **2003**, *3*, 1209.
  43. Cai, L.; Bahr, J.L.; Yxing, Y.; Tour, J.M.J. Ozonation of single-walled carbon nanotubes and their assemblies on rigid self-assembled monolayers. *Chem. Mater.* **2002**, *14*, 4235.
  44. Lu, X.; Zhang, L.; Xu, X.; Wang, N.; Zhang, Q. Can the sidewalls of single-wall carbon nanotubes be ozonized? *J. Phys. Chem., B* **2002**, *106*, 2136.
  45. Delley, B. From molecules to solids with the DMol<sup>3</sup> approach. *J. Chem. Phys.* **2000**, *113*, 7756.
  46. Akdim, B.; Duan, X.; Adams, W.W.; Pachter, R. Comparative theoretical study of single-wall carbon and boron-nitride nanotubes. *Phys. Rev., B* **2003**, *67*, 245404.
  47. Wadhawan, A.; Stallcup, R.E.; Perez, J.M. Effects of Cs deposition on the field-emission properties of single-walled carbon-nanotube bundles. *Appl. Phys. Lett.* **2001**, *78*, 108.
  48. Suzuki, S.; Bower, C.; Kiyokura, T.; Nath, K.G.; Watanabe, Y.; Zhou, O. Spectroscopy of single-walled carbon nanotube bundles. *Electron Spectrosc.* **2001**, *114*, 225.
  49. Akdim, B.; Duan, X.; Pachter, R., manuscript in preparation.
  50. Jeong, G.-H.; Farajian, A.A.; Hatakeyama, R.; Hirata, T.; Yaguchi, T.; Tohji, K.; Mizuseki, H.; Kawazoe, Y. Cesium encapsulation in single-walled carbon nanotubes via plasma ion irradiation: Application to junction formation and ab initio investigation. *Phys. Rev., B* **2003**, *68*, 075410.
  51. Jeong, G.H.; Farajian, A.A.; Hirata, T.; Hatakeyama, R.; Tohji, K.; Briere, T.M.; Mizuseki, H.; Kawazoe, Y. Encapsulation of cesium inside single-walled carbon nanotubes by plasma-ion irradiation method. *Thin Solid Films* **2003**, *435*, 307.
  52. Perdew, J.P.; Burke, K.; Ernzerhof, M. Generalized gradient approximation made simple. *Phys. Rev. Lett.* **1996**, *77*, 3865.
  53. Avramov, P.V.; Kudin, K.N.; Scuseria, G.E. Single wall carbon nanotubes density of states: comparison of experiment and theory. *Chem. Phys. Lett.* **2003**, *370*, 597.
  54. Wu, X.; Vargas, M.C.; Nayak, S.; Lotrich, V.C.; Scoles, G. Towards extending the applicability of density functional theory to weakly bound systems. *J. Chem. Phys.* **2001**, *115*, 8748.
  55. Allen, M.J.; Tozer, D.J. Helium dimer dispersion forces and correlation potentials in density functional theory. *J. Chem. Phys.* **2002**, *117*, 11113.
  56. Elstner, M.; Frauenheim, Th.; Kaxiras, E.; Seifert, G.; Suhai, S. A self-consistent charge density-functional based tight-binding scheme for large biomolecules. *Phys. Status Solidi, B* **2000**, *217*, 357.
  57. Heselmann, A.; Jansen, G. Intermolecular dispersion energies from time-dependent density functional theory. *Chem. Phys. Lett.* **2003**, *367*, 778.
  58. Kim, C.; Choi, Y.S.; Lee, S.M.; Park, J.T.; Kim, B.; Lee, Y.H. The effect of gas adsorption on the field emission mechanism of carbon nanotubes. *J. Am. Chem. Soc.* **2002**, *124*, 9906.
  59. Sun, J.P.; Zhang, Z.X.; Hou, S.M.; Zhang, G.M.; Gu, Z.N.; Zhao, X.Y.; Liu, W.M.; Xue, Z. Work function of single-walled carbon nanotubes determined by field emission microscopy. *Appl. Phys., A* **2002**, *75*, 479.
  60. Kim, C.; Kim, B. Electronic structures of capped carbon nanotubes under electric fields. *Phys. Rev., B* **2002**, *65*, 165418.
  61. Maiti, A.; Andzelm, J.; Tanpipat, N.; Allen, P.V. Effect of adsorbates on field emission from carbon nanotubes. *Phys. Rev. Lett.* **2001**, *87*, 155502.
  62. Peng, S.; Cho, K. Chemical control of nanotube electronics. *Nanotechnology* **2002**, *11*, 57.
  63. Ricca, A.; Drocco, J.A. Interaction of O<sub>2</sub> with a (9,0) carbon nanotube. *Chem. Phys. Lett.* **2002**, *362*, 217.

# Single-Walled Carbon Nanotubes: Geometries, Electronic Properties, and Actuation

Guangyu Sun  
Marc Nicklaus

National Cancer Institute, National Institutes of Health (NIH), Frederick, Maryland, U.S.A.

Miklos Kertesz

Department of Chemistry, Georgetown University, Washington, District of Columbia, U.S.A.

## INTRODUCTION

Carbon nanotubes were discovered<sup>[1]</sup> in 1991 by means of transmission electron microscopy in the multiwalled form that consists of concentric shells of seamless cylinders of graphene (a layer of graphite). The quasi one-dimensional structure, large mechanical strength, and the conjugated electronic structure are among the most commonly mentioned properties of carbon nanotubes. Current and potential applications of carbon nanotubes include the probing tip in scanning tunneling microscopy,<sup>[2]</sup> artificial “muscle”,<sup>[3]</sup> units of electronic memory storage,<sup>[4]</sup> to name just a few. The fascinating properties and potential uses have attracted much research interest in the carbon nanotubes.

The geometries, electronic properties and actuation of single-walled carbon nanotubes (SWNTs) obtained from high-level quantum mechanical calculations are presented in this entry. The commonly used quantum mechanical methods are first reviewed, then the behaviors of small to medium SWNTs with different structures are discussed and comparison with experimental results is made when possible. The behaviors of different groups of SWNTs are attributed to their electronic band structures.

## OVERVIEW

Shortly after the discovery of carbon nanotubes, the geometries and electronic band structures of these quasi one-dimensional extended systems were described in general terms.<sup>[5,6]</sup> Idealized single-walled carbon nanotubes can be viewed as formed by rolling up a graphene sheet along the chiral vector  $(n,m)$ , where  $n$  and  $m$  are numbers of the two lattice vectors ( $a_1$  and  $a_2$ ) of graphene needed to construct the chiral vector. The translational vector is perpendicular to the chiral vector, thus parallel to the tube axis. Fig. 1 shows the chiral vector of a (5,3) chiral SWNT.

Because of the two-dimensional symmetry of graphene,  $(n,m)$  is the same as  $(m,n)$ , therefore by convention  $n$  is larger than or equal to  $m$ . Depending on the values of  $n$  and  $m$ , SWNTs can be achiral or chiral:  $(n,n)$  armchair and  $(n,0)$  zigzag nanotubes are achiral, whereas general  $(n > m > 0)$  nanotubes are chiral. For a detailed discussion of the general aspects of the geometrical and electronic structures of SWNTs, see other related entries in this encyclopedia. The characteristic behavior of SWNTs shows significant deviations from the behavior of graphene, mostly because the finite dimension perpendicular to the tube axis introduces quantization of the energy levels leading to subgroups of “metallic” and “semiconducting” tubes. The importance of the remainder of the  $(n - m)/3$  division has been discovered by applying a simple tight binding theory to the electronic structure of SWNTs. This simplification leads to results that we refer to as “ideal” in this entry. The remainder of  $(n - m)/3$  is related to the mapping of the highest occupied and lowest unoccupied levels of SWNTs to the energy levels of graphene that are closest to the Fermi energy, and this leads to the broad categories of “metallic” ( $n - m = 3i$ ,  $i$  is an integer) and “semiconducting” ( $n - m = 3i + 1$  and  $3i + 2$ ) SWNTs.<sup>[5,6]</sup>

The observed SWNTs<sup>[7,8]</sup> have diameters from a half to a few nanometers and lengths up to several micrometers, hence the name. In both graphite and nanotubes, the carbon atoms are in an  $sp^2$  hybridized form with one p atomic orbital perpendicular to the surface of graphene or the tube left to form the  $\pi$  molecular orbitals. The planarity of the graphite layer ensures that the overlap between the p atomic orbitals of adjacent carbon atoms is maximal, thus the strongest possible in-plane bond is formed in graphite. In the cylindrical nanotubes, the orbital overlap is reduced because of the curvature. When the diameters are large, the reduction in the bond strength should be minimal, therefore the properties of large nanotubes are expected to mostly follow that of graphene. On

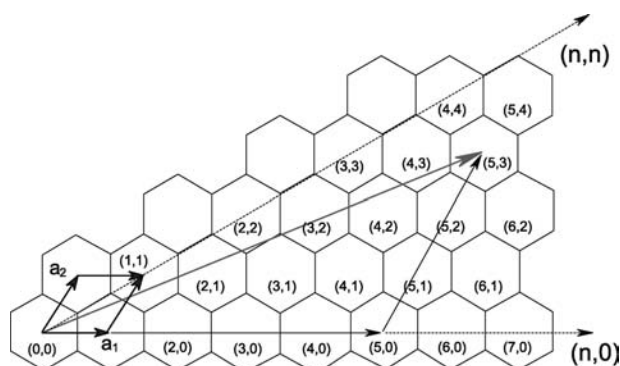


**Fig. 1** The chiral vector of the (5,3) single-walled carbon nanotube. Rolling up the graphene sheet along this chiral vector forms the chiral (5,3) nanotube. The translational vector is perpendicular to the chiral vector. The two lattice vectors of graphene,  $a_1$  and  $a_2$ , are also shown. The achiral nanotubes  $(n,n)$  and  $(n,0)$  are commonly referred to as armchair and zigzag nanotubes, respectively.

the other hand, small diameters introduce large curvatures, thus large changes in both geometrical and electronic properties should occur for small diameter nanotubes. While it was largely ignored early on, recent theoretical and experimental studies have shown that the curvature effect introduces noticeable deviations for the small diameter nanotubes from the “ideal” behaviors expected from that of the idealized SWNTs.

Experimentally, SWNTs are usually formed in bundles where each bundle consists of many intertwined nanotubes. The interaction between the individual tubes in a bundle is small but sometimes noticeable.<sup>[9,10]</sup> Such influences include the observed pseudogap of  $\sim 0.1$  eV (a dip of the density-of-states, DOS, curve at  $E_F$ ) for the bundled (8,8) armchair SWNT instead of the smooth DOS curve at  $E_F$  for the isolated nanotube.<sup>[9]</sup> In this entry, we focus on the intrinsic geometries and electronic band gaps of isolated SWNTs.

This entry reviews the latest understanding of the unique features of small to medium nanotubes based on theoretical studies employing quantum mechanical calculations. First, the commonly used computational methods are reviewed. Second, in groups of different chiralities, we look at the geometrical parameters and the electronic band gaps of neutral nanotubes. The  $(n,n)$  armchair nanotubes and three subgroups of  $(n,0)$  zigzag nanotubes with  $n = 3i$ ,  $3i + 1$ , and  $3i + 2$  show unique trends in these properties. Third, following a brief discussion of the dimensional change in the in-plane lattice of graphite intercalation compounds, we discuss the actuation of isolated SWNTs upon charge injection. Finally, all the unique geometrical and electronic properties of small to medium SWNTs are attributed to the allowed states in the reciprocal  $k$ -space, i.e., their band structures.

## COMMONLY USED COMPUTATIONAL METHODS

The length-to-diameter ratio for SWNTs is on the order of thousand, making them suitable for the application of periodic boundary conditions. Inclusion of one unit cell under periodic boundary conditions has been used by many authors and will therefore be the emphasis of this entry. An oligomer approach, on the other hand, must include at least several unit cells and thus requires a few hundred atoms even for the simplest SWNTs, which becomes computationally expensive when combined with high-level quantum mechanical theory. The oligomer approach is useful in studying the end effect of finite-length SWNTs and several studies have appeared in the literature.<sup>[11–13]</sup>

Quantum mechanical calculations are needed in order to predict reliable geometrical and electronic data for SWNTs. Moreover, the conjugated nature of their electronic structures requires accurate treatment of the electron correlation effects, which calls for post-Hartree–Fock (post-HF) ab initio methods such as the second-order Møller–Plesset perturbation theory (MP2).<sup>[14]</sup> However, the computational cost for the traditional post-HF ab initio methods would be prohibitively expensive. The general need to correctly treat electron correlation effects within reasonable computation time has made density functional theory (DFT)<sup>[15]</sup> a commonly used alternative. Within the framework of DFT, local density approximation (LDA) and generalized gradient approximation (GGA) have both found application for isolated SWNTs. LDA calculations were first carried out by Blasé et al.<sup>[16]</sup> for  $(n,0)$  zigzag nanotubes with  $n = 6–9$ . Kanamitsu and Saito<sup>[17]</sup> used the Ceperley–Alder LDA functional,<sup>[18]</sup> while Kürti et al.<sup>[19,20]</sup> used the Perdew and Zunger LDA functional.<sup>[21]</sup> Sun et al.<sup>[22–24]</sup> used the Perdew–Wang 91 (PW91) GGA functional,<sup>[25]</sup> which has been shown<sup>[26]</sup> to give better bond lengths than LDA functionals for, among others, *trans*-polyacetylene when experimental data. The PW91 functional was also used by Liu and Chan<sup>[27]</sup> for SWNTs with 4 Å diameter and by Gülseren, Yildirim, and Ciraci<sup>[28]</sup> for zigzag SWNTs. Plane-wave basis sets were used in these studies, in combination with either pseudopotentials in the forms of Kleinman–Bylander,<sup>[29]</sup> Vanderbilt,<sup>[30,31]</sup> or in combination with projector augmented-wave methods.<sup>[32,33]</sup> To minimize the effect of neighboring nanotubes, intertube distances were normally set to substantial values, ranging from 6 Å up to 11 Å.

Mintmire and coworkers used a first-principles, all-electron, self-consistent local-density functional (LDF) method and Gaussian-type orbitals in their studies.<sup>[34–36]</sup> This approach specifically takes advantage of the helical symmetry of the SWNTs. The geometry, elastic

properties, and vibrations of selected SWNTs were studied by Ordejón and coworkers<sup>[37–39]</sup> with the Perdew–Zunger LDA functional and the minimum pseudoatomic orbitals<sup>[40]</sup> within the linear combination of atomic orbitals (LCAO) approximation.

A new functionality utilizing periodic boundary conditions<sup>[41]</sup> has been introduced in the newly released Gaussian 03 program package.<sup>[42]</sup> This functionality uses Gaussian-type basis sets and can perform calculations with HF and DFT Hamiltonians. A few applications using this feature have been reported in the literature, including the geometries<sup>[41,43]</sup> of isolated armchair SWNTs using the Perdew, Burke, and Ernzerhof (PBE) functional.<sup>[44,45]</sup> It was also shown<sup>[46]</sup> that the PBE functional gives good results for metallic tubes, whereas the PBE0 hybrid functional<sup>[47,48]</sup> gives good results for semiconducting tubes. More results on SWNTs are expected soon partly because of the availability of many functionals in Gaussian 03 that appear to give good results on geometries and other properties.

## GEOMETRY OF SINGLE-WALLED CARBON NANOTUBES

Each carbon atom in graphite is  $sp^2$  hybridized and has three bonds connecting with its neighbors. These three bonds are symmetrically related and have identical length of 1.42 Å.<sup>[49]</sup> Upon rolling-up to form a SWNT, the equality along the in-plane lattice vectors  $a_1$  and  $a_2$  of graphite is lost, resulting in two types of C–C bonds in achiral nanotubes and three types in chiral nanotubes. We refer to the bonds oriented mainly around the circumference in achiral nanotubes as b1 and the bonds mainly along the tube axis as b2. Two and three types of bond angles also result for achiral and chiral nanotubes, respectively. In the following, results for these parameters from quantum chemical calculations are reviewed. We will also look at the diameters and the lengths of the translational vectors along the tube axis as they describe the overall geometry of the isolated SWNTs.

### Armchair SWNTs

The structures of  $(n,n)$  armchair SWNTs with  $n = 5–16$  were studied by Sun et al.<sup>[24]</sup> using the PW91 GGA functional. The bond lengths (1.419–1.427 Å) for both b1 and b2 are very close to the calculated bond length of graphene, 1.419 Å Fig. 2(A). The larger bond lengths are predicted for b1 in the smallest nanotubes, while the lengths of both b1 and b2 approach that of graphene in medium diameter nanotubes. Both types of bond angles are slightly smaller than the graphene value of 120°. As a result, the diameters are larger than

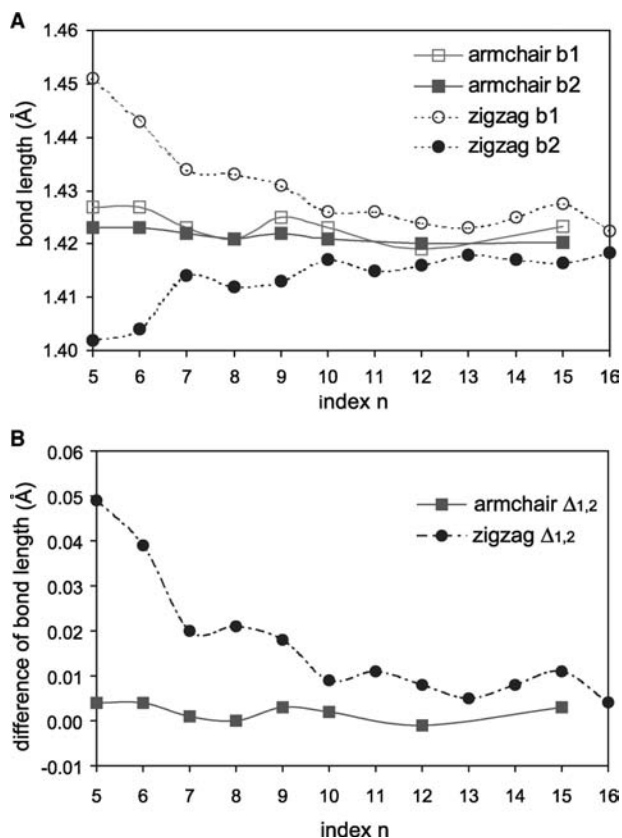


**Fig. 2** The predicted (A) bond lengths and (B) bond length differences between b1 and b2 for armchair and zigzag nanotubes. Lines connecting the calculated points are provided to show trends. Source: From Ref.<sup>[24]</sup>. © 2003, The American Chemical Society.

the values expected from a perfect roll-up of graphene by as much as 0.10 Å, while the lengths of the translational vectors are shorter than the ideal corresponding value by up to 0.03 Å. The structure of the (3,3) armchair SWNT was studied by Liu and Chan using the PW91 functional, where b1 was found to be 0.01 Å longer than b2.<sup>[27]</sup> This is consistent with the results of Sun et al. in that the difference between b1 and b2 should increase from 0.004 Å for (5,5) with decreasing diameter. A similar increase of the diameters for armchair nanotubes was also obtained from LDA calculations by Kürti et al.<sup>[19]</sup>

Bettinger, Kudin, and Scuseria<sup>[43]</sup> calculated the geometries of armchair nanotubes with  $n = 3–10$  and 12 at the PBE/3-21G level of theory. The basis set is probably too small for the accurate absolute bond length values, but the trends appear reliable. The bond lengths of b1 and b2 are in the range of 1.43–1.45 Å with the longer bonds occurring in the small diameter nanotubes. These bond lengths are longer than the abovementioned results, but are consistent with the slightly longer bond length in graphene (1.431 Å) by the same method. Similar results for

$n = 5-6, 8,$  and  $10$  were obtained earlier from LDA-LCAO calculations by Sanchez-Portal et al.<sup>[37]</sup>

### Zigzag SWNTs

The isolated  $(n,0)$  zigzag SWNTs so far are the most intensely studied nanotubes by theory, because they not only have smaller unit cells than armchair and chiral nanotubes with similar diameters, but also display more features in their geometrical and electronic structures. Employing an LDA method, Kanamitsu and Saito showed<sup>[17]</sup> that b1 bonds in zigzag nanotubes with  $n = 5-12$  are elongated relative to graphene, whereas b2 bonds are shortened. The deviations of b1 and b2 from the ideal value of graphene are roughly proportional to  $1/D^2$ , where  $D$  is the diameter of the nanotube. The angle between a b1 bond and a b2 bond remains close to  $120^\circ$  for all zigzag nanotubes studied. In contrast, the angle between two b1 bonds is predicted to be as small as  $111^\circ$  for  $(5,0)$  and increases toward  $120^\circ$  proportionally to  $1/D^2$ . A similar behavior of the bond lengths and bond angles was reported in GGA calculations by Gülseren, Yildirim, Ciraci.<sup>[28]</sup>

The earlier LDA and GGA results were largely confirmed by Sun et al. using PW91 GGA method.<sup>[24]</sup> An interesting trend emerged in the GGA results shown in Fig. 2(A), but was not seen in the earlier results. The bond lengths of the 12 nanotubes form four groups, encompassing from  $n = 5-7, 8-10, 11-13, 14-16$ , respectively. Within each group, the smallest nanotube has the longest b1 and shortest b2, and vice versa. The difference within each group diminishes with increasing  $n$ , i.e., when the diameter increases. This trend is amplified in Fig. 2(B) where the bond length differences between b1 and b2 are shown. This behavior is a direct consequence of the triad periodic feature of the electronic band structures of the zigzag SWNTs, which will be discussed below.

The translational vectors in small zigzag SWNTs are slightly shorter than the values expected from graphene [by  $0.015 \text{ \AA}$  for  $(5,0)$ ], and with larger index  $n$ , the translational vectors approach the graphene value of  $4.257 \text{ \AA}$ .<sup>[24]</sup> Following the trend of bond lengths, a similar triad behavior is seen for the predicted lengths of the translational vectors for zigzag nanotubes. All the calculated diameters are longer than the ideal values by as much as  $0.17 \text{ \AA}$  ( $4.1\%$ ) for  $(5,0)$  and a triad periodicity is also seen.<sup>[50]</sup>

### Chiral SWNTs

Because the repeat units of chiral nanotubes are much larger than those of achiral ones of similar diameters, high-level quantum mechanical results were only recently reported by Kürti et al.<sup>[19,20]</sup> Employing an

LDA functional, these authors studied SWNTs with diameters up to  $8 \text{ \AA}$  for chiral nanotubes and up to  $16 \text{ \AA}$  for achiral ones. For most of the chiral nanotubes, two of the three bonds elongate, whereas the third bond that forms the smallest angle with the tube axis shortens. The shortening of the third bond is consistent with the shortening of bond b2 in zigzag nanotubes. Two chiral nanotubes  $(3,2)$  and  $(4,3)$  have quite different bond lengths from the others. In contrast to other chiral tubes, the third bond in these two nanotubes elongate by up to  $1\%$ . These two tubes have  $(n - m) = 1$ , and this may be the cause of their unusual bond lengths. The lengths of the translational vectors of most chiral tubes are all shorter than the idealized values by up to  $1.3\%$ , except those of  $(3,2)$  and  $(4,3)$ , which are longer. Similar to the achiral tubes, the diameters of the chiral tubes are predicted to be larger than the idealized values, and the change is larger for small nanotubes. The bond angles are all smaller than  $120^\circ$  in chiral nanotubes, and the magnitude of the deviation depends on the particular angle and the  $(n,m)$  index of the nanotube.

## ELECTRONIC PROPERTIES OF SWNTs

The band structures of SWNTs have been the subject of many theoretical studies. Earlier works<sup>[5,6,34,51]</sup> showed that  $1/3$  of the nanotubes with  $(n - m) = 3i$  ( $i$  is an integer) are one-dimensional metals, whereas the remaining  $2/3$  of the nanotubes with  $(n - m) = 3i + 1$  and  $3i + 2$  are semiconductors. This conclusion, based on the tight-binding theory, is valid for nanotubes that have relatively large diameters. For small isolated SWNTs, the curvature effect substantially changes their electronic structures and the deviation from the tight-binding results has been observed in density functional theory calculations.

### Armchair SWNTs

Armchair  $(n,n)$  nanotubes are all metallic as there is a level crossing at  $k = \pm 2\pi/(3c)$  in the tight-binding theory. The recent GGA calculations<sup>[24]</sup> confirmed the tight-binding prediction. Indeed, the level crossing at the Fermi level is predicted to be very close to the above position and all armchair nanotubes with  $n = 5-10, 12,$  and  $15$  have very similar band structures. A similar result was also reported for  $(3,3)$  SWNT.<sup>[27,36]</sup>

### Zigzag SWNTs

The band gaps of zigzag  $(n,0)$  nanotubes occur at  $k = 0$  in the tight-binding theory. They are confirmed by both LDA and GGA calculations as being the gaps



between  $\pi$  and  $\pi^*$  bands.<sup>[16,17,24,28,36]</sup> These  $\pi$ - $\pi^*$  gaps are the overall band gaps for zigzag tubes with large diameters. But for small diameter zigzag tubes, the overall band gaps are the gaps between the doubly degenerate  $\pi$  bands and a non-degenerate band. The non-degenerate band is lower than the doubly degenerate  $\pi^*$  bands and this is the result of the strong  $\sigma^*$ - $\pi^*$  hybridization in small nanotubes.<sup>[16]</sup> In the band structure of (6,0), the non-degenerate band is lower than the doubly degenerate highest occupied  $\pi$  bands at  $k = 0$ , thus a level crossing occurs at a generic  $k$ -point at  $k = \sim 0.16\pi/c$ . As a result, the band gap for (6,0) is zero instead of the small nonzero  $\pi$ - $\pi^*$  gap. This is also true for (4,0) and (5,0) SWNTs.<sup>[17,24,28,36]</sup> For (7,0) and (8,0) SWNTs, the non-degenerate band lies between the  $\pi$  and  $\pi^*$  bands at  $k = 0$ , resulting in overall band gaps that are smaller than the  $\pi$ - $\pi^*$  gaps. For (9,0) and larger nanotubes, the non-degenerate band is above the  $\pi^*$  bands at  $k = 0$ , making the  $\pi$ - $\pi^*$  gap the overall band gap. Both LDA and GGA give similar results for the band gaps of small zigzag nanotubes. Subtle differences include the values of the band gaps and whether the (7,0) tube is metallic<sup>[17]</sup> or semiconducting.<sup>[16,24,28,36]</sup>

According to their band gaps, the zigzag nanotubes can be divided into three subgroups:<sup>[24]</sup>  $n = 3i$ ,  $3i + 1$ , and  $3i + 2$  following the pattern given by the remainder of  $(n - m)/3$ . The zigzag nanotubes with  $n = 3i$  have very small gaps, those with  $n = 3i + 1$  have large gaps and those with  $n = 3i + 2$  have even larger gaps than  $n = 3i + 1$ . These three subgroups are related to the triad periodicity in the bond length and are caused by the allowed states in the  $k$ -space, which will be discussed in the last section in detail.

Gülseren, Yildirim, and Ciraci.<sup>[28]</sup> further addressed the band gaps of zigzag SWNTs. While the energies of the non-degenerate band, the highest occupied  $\pi$  bands, and the lowest unoccupied  $\pi^*$  bands all rise with increasing diameter, the non-degenerate band rises much faster than the others, as shown in Fig. 3(A). The non-degenerate band crosses the highest occupied  $\pi$  bands before (7,0) and further becomes higher than the lowest unoccupied  $\pi^*$  bands at  $n = 9$ , thus all  $n < 7$  zigzag nanotubes are metallic whereas the  $\pi$ - $\pi^*$  separations are the band gaps for  $n \geq 9$ . Consequently, the band gaps of medium zigzag nanotubes ( $n \geq 9$ ) closely follow the  $1/R$  relationship, while the  $(n,m)$  index also plays an important role. The equations earlier derived from tight-binding theory were able to account for the band gaps of medium to large zigzag nanotubes.<sup>[52-54]</sup> Fig. 3(B) illustrates the agreement between the GGA band gaps and the curves obtained from Eq. (1):<sup>[28]</sup>

$$E_g = V_{pp\pi} \frac{d_0}{R} \left[ 1 + (-1)^p \gamma \cos(3\theta) \frac{d_0}{R} \right] \quad (1)$$

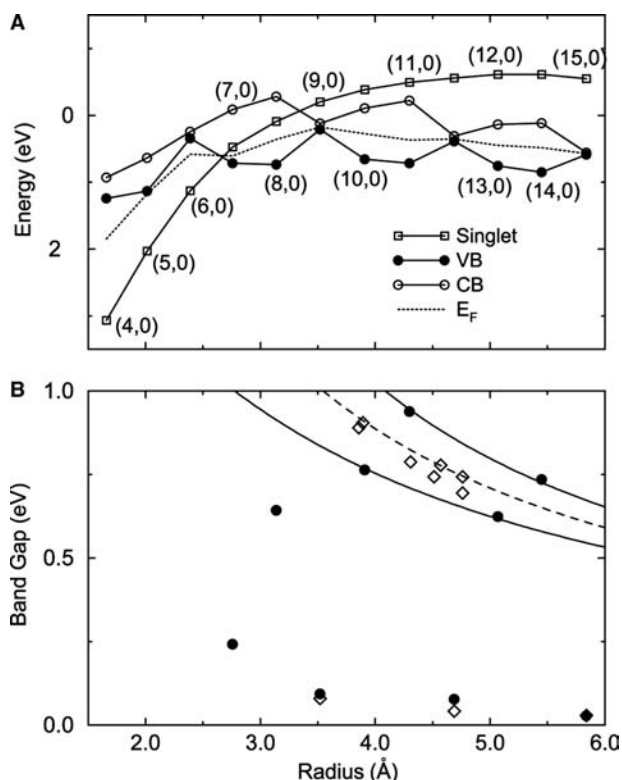


**Fig. 3** (A) Energies of the doubly degenerate  $\pi$  states (VB), the doubly degenerate  $\pi^*$  states (CB), and the non-degenerate  $\pi^*$  state as a function of nanotube radius. Each data point corresponds to  $n$  ranging from 4 to 15 consecutively. (B) The calculated band gaps as a function of the tube radius shown by filled symbols. Solid (dashed) lines are the plots of Eq. (3) [Eq. (2)] in Ref.<sup>[53]</sup>. The experimental data are shown by open diamonds (Refs.<sup>[9,55,56]</sup>). Source: From Ref.<sup>[28]</sup>. © 2002, The American Physical Society.

where  $V_{pp\pi} = 2.53$  eV is the hopping matrix element and parameter  $\gamma$  has a value of 0.43. Other parameters are the bond length  $d_0$  in graphene, the tube radius  $R$ , the chiral angle  $\theta$ , and the index  $p$  defined as  $n - m = 3i + p$ . [Note that this definition is for the  $(n,m)$  notation where  $n \geq m$  instead of  $n \geq 2m$  in Ref.<sup>[53]</sup>.] Good agreement between the GGA results and experimental data<sup>[9,55,56]</sup> is also seen in Fig. 3(B). Note that comparing the DFT predictions with experimental gaps usually requires systematic empirical corrections, for instance scaling. The trends among the calculated gaps are more reliable than the absolute values.

### Chiral SWNTs

Limited quantum mechanical results are available in the literature for the electronic properties of chiral SWNTs. A much-reduced indirect band gap of about 0.2 eV was reported for the (4,2) chiral nanotube.<sup>[27]</sup> In contrast to the symmetric DOS predictions by tight-binding theory, the predicted DOS curve for the

(4,2) nanotube is asymmetric, highlighting the need for high-level quantum mechanical treatment. The asymmetric DOS curve is a consequence of the curvature effect in small nanotubes. Mintmire and White predicted a direct band gap of 0.9 eV for (9,2) SWNT occurring at about one-third of the way from  $k = 0$  to  $\pi$ .<sup>[35]</sup> Mintmire and coworkers<sup>[36]</sup> also studied the band gaps of five other chiral SWNTs. The (4,2) tube is predicted to have an indirect band gap of 0.34 eV, in qualitative agreement with Liu and Chan.<sup>[27]</sup> The (4,3) tube has a gap of 1.28 eV, implying it as the largest band gap among all possible SWNTs. The band gaps for other chiral tubes are 0.46 eV for (3,2) and 0.00 eV for (5,1), respectively, whereas the (4,1) tube is metallic. The analysis of additional chiral SWNTs is certainly desirable and is currently in progress.

## ACTUATION OF SWNTS UPON CHARGE INJECTION

### Graphite Intercalation Compounds

It has long been known that the C–C bonds in *trans*-polyacetylene<sup>[57]</sup> and graphite<sup>[49]</sup> elongate/shorten when doped with electron donors/acceptors. The recent discovery of electrochemical actuation of SWNTs<sup>[3]</sup> has brought renewed attention to these two systems. This asymmetric strain response upon charge injection has recently been reproduced by DFT calculations for both doped *trans*-polyacetylene<sup>[58]</sup> and graphite intercalation compounds.<sup>[59]</sup> Here we briefly summarize the results for the latter as a way of introducing the subject for SWNTs. The geometries of a series of graphite intercalation compounds were optimized by Sun et al.<sup>[59]</sup> using the PW91 GGA functional and pseudopotential plane-wave basis sets. Good agreement was obtained between the calculated interlayer distances and experimental values. The strain–charge relationship (strain is percentage change in the in-plane lattice) for  $\text{LiC}_6$ ,  $\text{KC}_6$ ,  $\text{CaC}_6$ ,  $\text{BaC}_6$ ,  $\text{C}_{18}\text{PF}_6$ , and  $\text{C}_{24}\text{AsF}_6$  agrees well with experimental values,<sup>[60–64]</sup> as shown in Fig. 4. The charge transfers between graphene and dopants are calculated to be complete for  $\text{LiC}_6$ ,  $\text{KC}_6$ ,  $\text{C}_{18}\text{PF}_6$ , and  $\text{C}_{24}\text{AsF}_6$ , whereas they are 85% and 81% for  $\text{CaC}_6$  and  $\text{BaC}_6$ , respectively. Numerical experiments show that the charge value in a hypothetical graphite intercalation compound  $\text{KC}_6$  decreases with increasing interlayer distance, resulting in reduced strain response [Fig. 4B]. This behavior is comparable to the measured low strain values at low doping levels, where the charge transfer from each dopant is complete, but the large carbon-to-dopant ratio makes the per carbon charge small. The generic strain of the carbon network was obtained from calculations that include only the carbon atoms whereas the

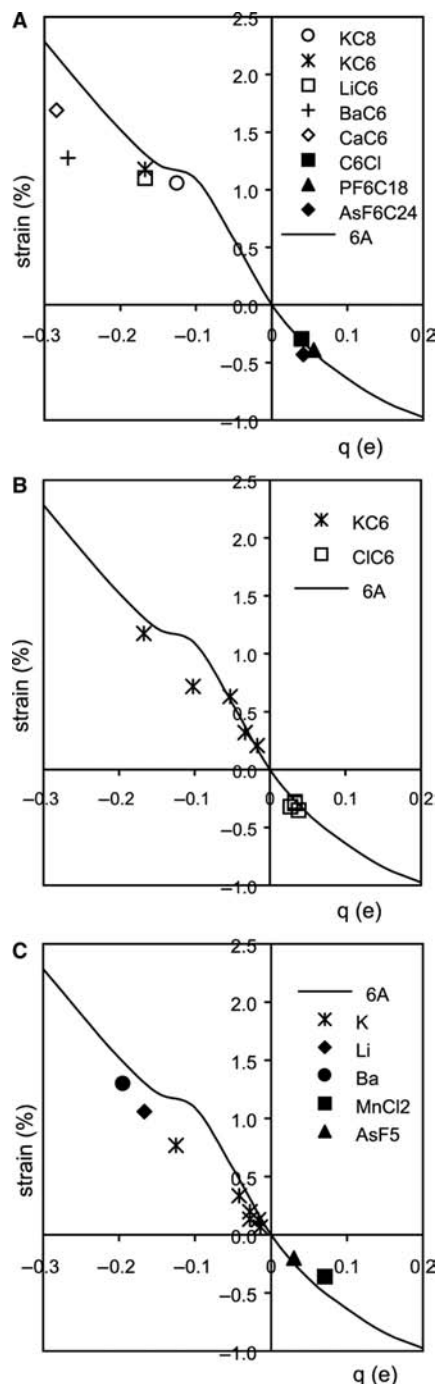


**Fig. 4** Strain in graphite intercalation compounds and charged graphene as calculated by density functional theory and compared with experiment. The continuous curve corresponds to the jellium calculations at  $d = 6 \text{ \AA}$  in all three panels,  $q$  is the per carbon charge. (A) Theoretical results using the relaxed counterion model and the jellium model. (B) The predicted strain in  $\text{KC}_6$  (five different interlayer distances) and  $\text{C}_6\text{Cl}$  (four different interlayer distances) by the fixed counterion model. (C) The strain predicted by the jellium model is compared with experimental data. References: K (Ref.<sup>[60]</sup>), Li (Ref.<sup>[61]</sup>), Ba (Ref.<sup>[62]</sup>),  $\text{MnCl}_2$  (Ref.<sup>[63]</sup>),  $\text{AsF}_5$  (Ref.<sup>[64]</sup>). Source: From Ref.<sup>[59]</sup>. © 2003, The American Physical Society.

dopants are represented by a uniform background charge (jellium model). When negative charges are injected, the in-plane lattice of graphite increases, whereas positive charges cause the in-plane lattice to decrease. As illustrated in Fig. 4C, the generic strain value calculated using an interlayer distance of 6 Å is in good agreement with results from both full calculations and experimental measurements. Earlier studies have predicted larger strain values by Pietronero and Strässler,<sup>[65]</sup> and smaller strain values by Kertesz, Vonderviszt, and Hoffmann<sup>[66]</sup> and Chan et al.<sup>[67]</sup>

Similar results were also obtained for the strain–charge relationship in doped *trans*-polyacetylene using the same theoretical method.<sup>[58]</sup> The different behavior for electron and hole injections in these systems has been tied to the breaking of the electron-hole symmetry due to second neighbor interactions in PA, graphene, and in SWNTs as well.<sup>[68]</sup>

### Isolated SWNTs

Sheets of SWNTs were shown recently to actuate in electrochemical cell upon charge injection, which may find many important applications.<sup>[3]</sup> As no dopant intercalation is required, the electrochemical actuation of SWNTs is considered superior to those techniques that do require it. Quantum chemical and double-layer electrostatic effects were postulated as the cause of the expansion upon electron injection and the contraction upon hole injection. Sun et al. studied the generic strain response of isolated achiral SWNTs using PW91 GGA functional in the DFT calculations.<sup>[22–24]</sup> Different strains were predicted for the  $(n,n)$  armchair nanotubes and the  $(n,0)$  zigzag nanotubes with different  $(n/3)$  values. The armchair nanotubes all have strain–charge curves similar to that of graphene. Generally, this similarity is more pronounced for the larger diameter tubes, as expected. The zigzag nanotubes with  $n = 3i$  also have strain values similar to that of graphene at any given charge transfer value, except for the small  $(6,0)$  tube which shows reduced strain on the negative charge side. For zigzag nanotubes with  $n = 3i + 1$ , the strain curves initially take a deep dive on the positive side, then turn back to approach the graphene curve. This dive is deeper for small tubes than for large tubes. Large deviations from the strain of graphene were predicted for the  $3i + 2$  series. The strain for  $(5,0)$  is positive for small positive charges and negative for small negative charges, in contrast to the graphene curve. At large charges, the strain for  $(5,0)$  resumes the usual asymmetric shape but the magnitude is much smaller than for graphene. The deviation from the graphene curve decreases from  $(5,0)$  to  $(8,0)$  and  $(11,0)$  before eventually vanishing for  $(14,0)$ .

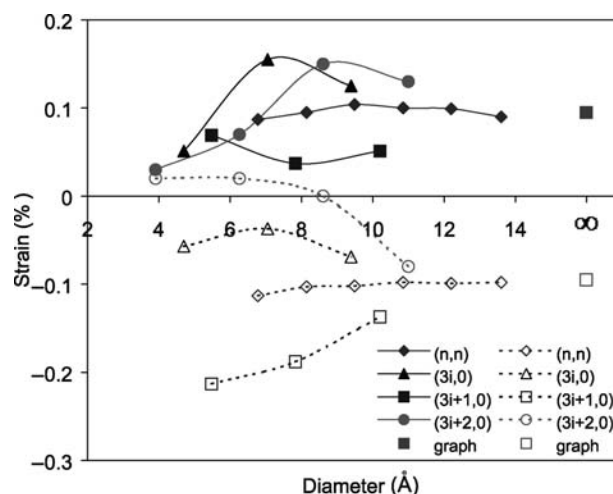


**Fig. 5** Calculated strain as a function of SWNT diameter ( $D$ ) for the four types of achiral nanotubes. Strain is calculated with respect to the neutral tubes at  $q = \pm 0.01 e/\text{carbon}$  charge injection level. Solid marks and lines refer to  $q = -0.01 e$ , and empty marks and dashed lines refer to  $q = +0.01 e$  charge injection. The limiting values calculated for graphene (“graph”) are also shown. Strain is defined as percentage change of the translational vector. *Source:* From Ref.<sup>[24]</sup>. © 2003, The American Chemical Society.

The strain–charge behavior of the achiral SWNTs seems complicated, but a much clearer picture emerges in Fig. 5 when the strains for a given charge are plotted against the tube diameters.<sup>[24]</sup> The four types of achiral tubes show different trends. The strains for armchair nanotubes are similar to that of graphene for both  $+0.01 e$  and  $-0.01 e$  charges, even for the ones as small as  $(5,5)$ . For the zigzag nanotubes, the three subgroups have strain values for small diameters that are different from that of graphene, but all three series approach the strain of graphene with increasing diameters.

### ALLOWED STATES IN THE K-SPACE FOR SWNTS

We have shown above that there are four types of achiral nanotubes:  $(n,n)$  armchair nanotubes plus  $(n,0)$  zigzag nanotubes with  $n = 3i$ ,  $3i + 1$ , and  $3i + 2$ . The bond length, length and diameter of the tube, band gap and strain response upon charge injection all have different behavior for each type. The difference in their properties arises from the different electronic structures for each type. As the electronic structures of SWNTs can be obtained, to the first-order approximation, from the allowed states in  $k$ -space,<sup>[5,6]</sup> we relate the observed trends to the allowed  $k$  states. The allowed  $k$  states for  $(6,0)$  are shown as vertical line segments in Fig. 6(A), where the hexagons represent the first Brillouin zone for graphene. The K point is

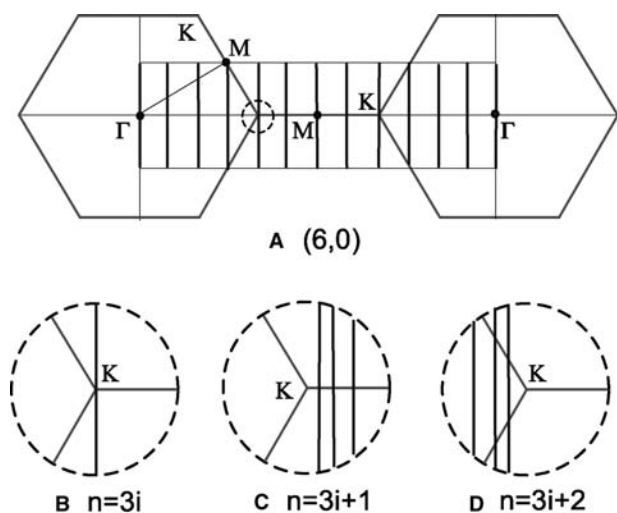


**Fig. 6** (A) The allowed  $k$ -points for (6,0) zigzag SWNT shown in the Brillouin zone of graphene, and the allowed  $k$ -points closest to the K point for ( $n,0$ ) zigzag SWNTs with (B)  $n = 3i$ , (C)  $n = 3i + 1$  for three consecutive  $i$  values and (D)  $n = 3i + 2$  for three consecutive  $i$  values. Larger tubes have the allowed  $k$ -points closer to the K point.

where the highest occupied  $\pi$  band and the lowest unoccupied  $\pi^*$  band of graphene meet to form its zero band gap. For SWNTs, the allowed  $k$ -point that is closest to the K point gives the corresponding  $\pi$  bands, thus the  $\pi$ - $\pi^*$  gaps of nanotubes are determined by how close to K the closest allowed  $k$ -point can be. For armchair and zigzag nanotubes with  $n = 3i$ , the K point is always allowed, the latter being illustrated in Fig. 6(B), therefore the band gaps for these nanotubes are zero in simple tight-binding theory. For the zigzag nanotubes with  $n = 3i + 1$ , the allowed  $k$ -point closest to the K point is located on the MK line and moves closer to the K point with increasing diameter. In Fig. 6(C) three segments are shown representing the closest  $k$ -points for three different zigzag nanotubes with  $n = 3i + 1$ . As the  $\pi$ - $\pi^*$  separation is smaller when closer to the K point, the  $\pi$ - $\pi^*$  gap in this type of SWNTs decreases with increasing diameter. The  $k$ -point closest to K for  $n = 3i + 2$  is located on the  $\Gamma$ K line and approaches the K point with increasing diameter, as shown in Fig. 6(D). As the  $\pi$ - $\pi^*$  separation is larger along the  $\Gamma$ K line than along the MK line, the  $\pi$ - $\pi^*$  gap for  $n = 3i + 2$  is larger than that for  $n = 3i + 1$ .

This analysis holds true for medium to large zigzag nanotubes where the  $\pi$ - $\pi^*$  gaps are the real band gaps. For small nanotubes, the  $\sigma^*$ - $\pi^*$  hybridization needs to be taken into account, resulting in the reduced band gaps for (7,0) and (8,0), the level crossing in the (6,0) and smaller tubes, and the narrow gaps for (9,0), (12,0), and (15,0) tubes. For chiral nanotubes, general trends cannot be drawn from the limited data available

in the literature. However, electronic behaviors similar to the ones discussed above are expected for chiral nanotubes because, after all, it is the electronic structure that determines the other properties.

## CONCLUSION

Density functional theory in various forms of implementations has been applied to study the geometries, electronic band gaps, and strain-charge response for the isolated single-walled carbon nanotubes by a number of research groups. General consensus on the properties of achiral SWNTs has been reached based on both LDA and GGA calculations. The geometries of the ( $n,n$ ) armchair SWNTs closely follow that of graphene and all armchair SWNTs are metallic, which is consistent with early tight-binding predictions. Large deviations from the tight-binding predictions are shown for small diameter ( $n,0$ ) zigzag nanotubes and for small diameter chiral tubes. Zigzag SWNTs belong to different subgroups corresponding to  $n = 3i$ ,  $3i + 1$ , and  $3i + 2$ . This is related to the remainder of  $(n - m)/3$  values and is a consequence of the  $k$ -space mapping of the graphene and nanotube energy levels closest to the Fermi level. Narrow band gaps are predicted for  $n = 3i$  series having medium diameters, in good agreement with experimental data. Medium band gaps are predicted for medium and large nanotubes with  $n = 3i + 1$  and  $3i + 2$  with the latter having slightly larger band gaps than the former. The geometries of zigzag nanotubes show a triad periodicity similar to their band gaps. All small zigzag nanotubes are metallic because of the strong  $\sigma^*$ - $\pi^*$  hybridization caused by the large curvature. Upon charge injection, the length of large diameter nanotubes changes in a way similar to graphene, whereas significant deviations are again observed for small diameter nanotubes.

Unlike the achiral SWNTs, relatively little *ab initio* work has been done on chiral nanotubes, mostly because of their large repeating units. More studies are needed, especially using *ab initio* quantum mechanical methods, which show results deviating from the ideal tight-binding behavior, e.g., the zero band gaps for small zigzag nanotubes and the much-reduced indirect band gap of (4,2) instead of the large direct band gap predicted by tight-binding theory. More chiral nanotubes need to be included to see if any trend that is similar to those of zigzag nanotubes exists. It would also be interesting to see detailed geometrical analysis for additional chiral nanotubes.

It is worth noting that none of the applied theoretical methods was able to correctly reproduce the bond length alternation in *trans*-polyacetylene, an important parameter in extended conjugated systems.<sup>[26,69]</sup>

Employing methods that give better results for this parameter is desirable in future work for SWNTs. Such methods include post-HF methods such as MP2 and hybrid DFT functionals such as B3LYP.<sup>[70,71]</sup>

The effects of the termini and defects in SWNTs have been studied in the literature, although are not discussed here. However, as these effects have important implications for the electronic properties of SWNTs, more high-level theoretical studies are called for.

## ACKNOWLEDGMENTS

We thank Dr. Jenő Kürti for insightful discussions. G.S. thanks the National Cancer Institute at Frederick for a Visiting Fellowship Award. Financial support from the National Science Foundation (Grant CHEM-9802300) and from the Defense Advanced Research Projects Agency (Grants N00173-99-2000 and MDA 972-02-C-0005) is gratefully acknowledged.

## REFERENCES

- Iijima, S. Helical microtubules of graphitic carbon. *Nature* **1991**, *354*, 56–58.
- Dai, H.J.; Hafner, J.H.; Rinzler, A.G.; Colbert, D.T.; Smalley, R.E. Nanotubes as nanoprobe in scanning probe microscopy. *Nature* **1996**, *384*, 147–150.
- Baughman, R.H.; Cui, C.X.; Zakhidov, A.A.; Iqbal, Z.; Barisci, J.N.; Spinks, G.M.; Wallace, G.G.; Mazzoldi, A.; De Rossi, D.; Rinzler, A.G.; Jaschinski, O.; Roth, S.; Kertesz, M. Carbon nanotube actuators. *Science* **1999**, *284*, 1340–1344.
- Rueckes, T.; Kim, K.; Joselevich, E.; Tseng, G.Y.; Cheung, C.L.; Lieber, C.M. Carbon nanotube-based nonvolatile random access memory for molecular computing. *Science* **2000**, *289*, 94–97.
- Hamada, N.; Sawada, S.; Oshiyama, A. New one-dimensional conductors—Graphitic microtubules. *Phys. Rev. Lett.* **1992**, *68*, 1579–1581.
- Saito, R.; Fujita, M.; Dresselhaus, G.; Dresselhaus, M.S. Electronic-structure of chiral graphene tubules. *Appl. Phys. Lett.* **1992**, *60*, 2204–2206.
- Iijima, S.; Ichihashi, T. Single-shell carbon nanotubes of 1-nm diameter. *Nature* **1993**, *363*, 603–605.
- Bethune, D.S.; Kiang, C.H.; Devries, M.S.; Gorman, G.; Savoy, R.; Vazquez, J.; Beyers, R. Cobalt-catalyzed growth of carbon nanotubes with single-atomic-layer-walls. *Nature* **1993**, *363*, 605–607.
- Ouyang, M.; Huang, J.L.; Cheung, C.L.; Lieber, C.M. Energy gaps in “metallic” single-walled carbon nanotubes. *Science* **2001**, *292*, 702–705.
- Delaney, P.; Choi, H.J.; Ihm, J.; Louie, S.G.; Cohen, M.L. Broken symmetry and pseudogaps in ropes of carbon nanotubes. *Nature* **1998**, *391*, 466–468.
- Liang, W.Z.; Yokojima, S.; Ng, M.F.; Chen, G.H.; He, G.Z. Optical properties of single-walled 4 angstrom carbon nanotubes. *J. Am. Chem. Soc.* **2001**, *123*, 9830–9836.
- Cioslowski, J.; Rao, N.; Moncrieff, D. Electronic structures and energetics of (5,5) and (9,0) single-walled carbon nanotubes. *J. Am. Chem. Soc.* **2002**, *124*, 8485–8489.
- Matsuo, Y.; Tahara, K.; Nakamura, E. Theoretical studies on structures and aromaticity of finite-length armchair carbon nanotubes. *Org. Lett.* **2003**, *5*, 3181–3184.
- Møller, C.; Plesset, M.S. Note on an approximation treatment for many-electron systems. *Phys. Rev.* **1934**, *46*, 618–622.
- Kohn, W.; Sham, L.J. Self-consistent equations including exchange and correlation effects. *Phys. Rev.* **1965**, *140*, A1133–A1138.
- Blase, X.; Benedict, L.X.; Shirley, E.L.; Louie, S.G. Hybridization effects and metallicity in small radius carbon nanotubes. *Phys. Rev. Lett.* **1994**, *72*, 1878–1881.
- Kanamitsu, K.; Saito, S. Geometries, electronic properties, and energetics of isolated single walled carbon nanotubes. *J. Phys. Soc. Jpn.* **2002**, *71*, 483–486.
- Ceperley, D.M.; Alder, B.J. Ground-state of the electron-gas by a stochastic method. *Phys. Rev. Lett.* **1980**, *45*, 566–569.
- Kürti, J.; Zólyomi, V.; Kertesz, M.; Sun, G.Y. The geometry and the radial breathing mode of carbon nanotubes: Beyond the ideal behaviour. *New J. Phys.* **2003**, *5*, 125.1–125.21.
- Kürti, J.; Zólyomi, V.; Kertesz, M.; Sun, G.Y.; Baughman, R.H.; Kuzmany, H. Individualities and average behavior in the physical properties of small diameter single-walled carbon nanotubes. *Carbon* **2004**, *42*, 971 pp.
- Perdew, J.P.; Zunger, A. Self-interaction correction to density-functional approximations for many-electron systems. *Phys. Rev., B* **1981**, *23*, 5048–5079.
- Sun, G.Y.; Kurti, J.; Kertesz, M.; Baughman, R.H. Dimensional changes as a function of charge injection in single-walled carbon nanotubes. *J. Am. Chem. Soc.* **2002**, *124*, 15076–15080.
- Sun, G.Y.; Kertesz, M.; Kürti, J.; Baughman, R.H. Dimensional changes as a function of charge transfer in doped trans-polyacetylene: A density functional study. *Polym. Mater. Sci. Eng.* **2000**, *83*, 519–520.
- Sun, G.Y.; Kurti, J.; Kertesz, M.; Baughman, R.H. Variations of the geometries and band gaps of single-walled carbon nanotubes and the effect of charge injection. *J. Phys. Chem., B* **2003**, *107*, 6924–6931.
- Perdew, J.P.; Wang, Y. Accurate and simple analytic representation of the electron-gas correlation-energy. *Phys. Rev., B* **1992**, *45*, 13244–13249.
- Sun, G.Y.; Kurti, J.; Rajczy, P.; Kertesz, M.; Hafner, J.; Kresse, G. Performance of the Vienna ab initio simulation package (VASP) in chemical applications. *Theochem-J. Mol. Struct.* **2003**, *624*, 37–45.
- Liu, H.J.; Chan, C.T. Properties of 4 angstrom carbon nanotubes from first-principles calculations. *Phys. Rev., B* **2002**, *66*. Art. no.-115416.
- Gülseren, O.; Yildirim, T.; Ciraci, S. Systematic ab initio study of curvature effects in carbon nanotubes. *Phys. Rev., B* **2002**, *65*. Art. no.-153405.

29. Kleinman, L.; Bylander, D.M. Efficacious form for model pseudopotentials. *Phys. Rev. Lett.* **1982**, *48*, 1425–1428.
30. Vanderbilt, D. Soft self-consistent pseudopotentials in a generalized eigenvalue formalism. *Phys. Rev., B* **1990**, *41*, 7892–7895.
31. Payne, M.C.; Teter, M.P.; Allan, D.C.; Arias, T.A.; Joannopoulos, J.D. Iterative minimization techniques for ab initio total-energy calculations—Molecular-dynamics and conjugate gradients. *Rev. Mod. Phys.* **1992**, *64*, 1045–1097.
32. Blochl, P.E. Projector augmented-wave method. *Phys. Rev., B* **1994**, *50*, 17953–17979.
33. Kresse, G.; Joubert, D. From ultrasoft pseudopotentials to the projector augmented-wave method. *Phys. Rev., B* **1999**, *59*, 1758–1775.
34. Mintmire, J.W.; Dunlap, B.I.; White, C.T. Are fullerene tubules metallic? *Phys. Rev. Lett.* **1992**, *68*, 631–634.
35. Mintmire, J.W.; White, C.T. Electronic and structural-properties of carbon nanotubes. *Carbon* **1995**, *33*, 893–902.
36. Cabria, I.; Mintmire, J.W.; White, C.T. Metallic and semiconducting narrow carbon nanotubes. *Phys. Rev., B* **2003**, *67*. Art. no.-121406.
37. Sanchez-Portal, D.; Artacho, E.; Solar, J.M.; Rubio, A.; Ordejon, P. Ab initio structural, elastic, and vibrational properties of carbon nanotubes. *Phys. Rev., B* **1999**, *59*, 12678–12688.
38. Reich, S.; Thomsen, C.; Ordejon, P. Electronic band structure of isolated and bundled carbon nanotubes. *Phys. Rev., B* **2002**, *65*. Art. no.-155411.
39. Machon, M.; Reich, S.; Thomsen, C.; Sanchez-Portal, D.; Ordejon, P. Ab initio calculations of the optical properties of 4-angstrom-diameter single-walled nanotubes. *Phys. Rev., B* **2002**, *66*. Art. no.-155410.
40. Ordejon, P.; Artacho, E.; Soler, J.M. Self-consistent order-N density-functional calculations for very large systems. *Phys. Rev., B* **1996**, *53*, 10441–10444.
41. Kudin, K.N.; Scuseria, G.E. Linear-scaling density-functional theory with Gaussian orbitals and periodic boundary conditions: Efficient evaluation of energy and forces via the fast multipole method. *Phys. Rev., B* **2000**, *61*, 16440–16453.
42. Frisch, M.J.; Trucks, G.W.; Schlegel, H.B.; Scuseria, G.E.; Robb, M.A.; Cheeseman, J.R.; Montgomery, J.A., Jr.; Vreven, T.; Kudin, K.N.; Burant, J.C.; Millam, J.M.; Iyengar, S.S.; Tomasi, J.; Barone, V.; Mennucci, B.; Cossi, M.; Scalmani, G.; Rega, N.; Petersson, G.A.; Nakatsuji, H.; Hada, M.; Ehara, M.; Toyota, K.; Fukuda, R.; Hasegawa, J.; Ishida, M.; Nakajima, T.; Honda, Y.; Kitao, O.; Nakai, H.; Klene, M.; Li, X.; Knox, J.E.; Hratchian, H.P.; Cross, J.B.; Adamo, C.; Jaramillo, J.; Gomperts, R.; Stratmann, R.E.; Yazyev, O.; Austin, A.J.; Cammi, R.; Pomelli, C.; Ochterski, J.W.; Ayala, P.Y.; Morokuma, K.; Voth, G.A.; Salvador, P.; Dannenberg, J.J.; Zakrzewski, V.G.; Dapprich, S.; Daniels, A.D.; Strain, M.C.; Farkas, O.; Malick, D.K.; Rabuck, A.D.; Raghavachari, K.; Foresman, J.B.; Ortiz, J.V.; Cui, Q.; Baboul, A.G.; Clifford, S.; Cioslowski, J.; Stefanov, B.B.; Liu, G.; Liashenko, A.; Piskorz, P.; Komaromi, I.; Martin, R.L.; Fox, D.J.; Keith, T.; Al-Laham, M.A.; Peng, C.Y.; Nanayakkara, A.; Challacombe, M.; Gill, P.M.W.; Johnson, B.; Chen, W.; Wong, M.W.; Gonzalez, C.; Pople, J.A. *Gaussian 03*; Gaussian, Inc.: Pittsburgh, PA, 2003.
43. Bettinger, H.F.; Kudin, K.N.; Scuseria, G.E. Thermochemistry of fluorinated single wall carbon nanotubes. *J. Am. Chem. Soc.* **2001**, *123*, 12849–12856.
44. Perdew, J.P.; Burke, K.; Ernzerhof, M. Generalized gradient approximation made simple. *Phys. Rev. Lett.* **1996**, *77*, 3865–3868.
45. Perdew, J.P.; Burke, K.; Ernzerhof, M. Generalized gradient approximation made simple. *Phys. Rev. Lett.* **1997**, *78*, 1396. (Vol. 77, p. 3865, 1996).
46. Avramov, P.V.; Kudin, K.N.; Scuseria, G.E. Single wall carbon nanotubes density of states: Comparison of experiment and theory. *Chem. Phys. Lett.* **2003**, *370*, 597–601.
47. Ernzerhof, M.; Scuseria, G.E. Assessment of the Perdew–Burke–Ernzerhof exchange–correlation functional. *J. Chem. Phys.* **1999**, *110*, 5029–5036.
48. Adamo, C.; Barone, V. Toward reliable density functional methods without adjustable parameters: The PBE0 model. *J. Chem. Phys.* **1999**, *110*, 6158–6170.
49. Dresselhaus, M.S.; Dresselhaus, G. Intercalation compounds of graphite. *Adv. Phys.* **2002**, *51*, 1–186.
50. Sun, G.Y.; Kertesz, M., unpublished results.
51. Saito, R.; Fujita, M.; Dresselhaus, G.; Dresselhaus, M.S. Electronic-structure of graphene tubules based on C-60. *Phys. Rev., B* **1992**, *46*, 1804–1811.
52. White, C.T.; Robertson, D.H.; Mintmire, J.W. Helical and rotational symmetries of nanoscale graphitic tubules. *Phys. Rev., B* **1993**, *47*, 5485–5488.
53. Yorikawa, H.; Muramatsu, S. Energy gaps of semiconducting nanotubes. *Phys. Rev., B* **1995**, *52*, 2723–2727.
54. Yorikawa, H.; Muramatsu, S. Chirality-dependence of energy gaps of semiconducting nanotubes. *Solid State Commun.* **1995**, *94*, 435–437.
55. Odom, T.W.; Huang, J.L.; Kim, P.; Lieber, C.M. Atomic structure and electronic properties of single-walled carbon nanotubes. *Nature* **1998**, *391*, 62–64.
56. Odom, T.W.; Huang, J.L.; Kim, P.; Lieber, C.M. Structure and electronic properties of carbon nanotubes. *J. Phys. Chem., B* **2000**, *104*, 2794–2809.
57. Wada, Y. Doping and Disorder in Conducting Polymers. In *New Horizons in Low-Dimensional Electron Systems, Physics and Chemistry of Material with Low-Dimensional Structures*; Aoki, H., Tsukada, M., Schlüter, M., Lévy, F., Eds.; Kluwer Academic Publishers: Boston, 1991; 415–432.
58. Sun, G.Y.; Kurti, J.; Kertesz, M.; Baughman, R.H. Dimensional changes as a function of charge injection for *trans*-polyacetylene: A density functional theory study. *J. Chem. Phys.* **2002**, *117*, 7691–7697.
59. Sun, G.Y.; Kertesz, M.; Kürti, J.; Baughman, R.H. Dimensional change as a function of charge injection in graphite intercalation compounds: A density functional theory study. *Phys. Rev., B* **2003**, *68*. Art. no.-125411.
60. Nixon, D.E.; Parry, G.S. Expansion of the carbon-carbon bond length in potassium graphites. *Proc. Phys. Soc., London (Solid State Phys.)* **1969**, *2*, 1732.



61. Preil, M.E.; Fischer, J.E.; Dicenzo, S.B.; Wertheim, G.K. Barium intra-atomic reconfiguration in  $\text{BaC}_6$ . *Phys. Rev., B* **1984**, *30*, 3536–3538.
62. Fischer, J.E.; Kim, H.J.; Cajipe, V.B. Neutron-diffraction studies of  $\text{BaC}_6$ -C-axis compressibility, carbon carbon bond length, and charge-transfer. *Phys. Rev., B* **1987**, *36*, 4449–4451.
63. Baron, F.; Flandrois, S.; Hauw, C.; Gaultier, J. Charge-transfer and islands in metal-halides graphite-intercalation compounds—New evidence from X-ray-diffraction of intercalated  $\text{MnC}_{12}$ . *Solid State Commun.* **1982**, *42*, 759–762.
64. Markiewicz, R.S.; Kasper, J.S.; Interrante, L.V. Single-crystal structure studies of  $\text{C}_{16}\text{AsF}_5$ . *Synth. Met.* **1980**, *2*, 363–370.
65. Pietronero, L.; Strassler, S. Bond-length change as a tool to determine charge-transfer and electron-phonon coupling in graphite-intercalation compounds. *Phys. Rev. Lett.* **1981**, *47*, 593–596.
66. Kertesz, M.; Vonderviszt, F.; Hoffmann, R. *Change of Carbon-Carbon Bond Length in Layers of Graphite upon Charge Transfer*; Mater. Res. Soc. Symp. Proc. (Intercalated Graphites); Dresselhaus, M.S., Dresselhaus, G., Fischer, J.E., Moran, M.J., Eds.; Elsevier: Amsterdam, 1983; 141–143.
67. Chan, C.T.; Kamitakahara, W.A.; Ho, K.M.; Eklund, P.C. Charge-transfer effects in graphite intercalates—Ab initio calculations and neutron-diffraction experiment. *Phys. Rev. Lett.* **1987**, *58*, 1528–1531.
68. Kertesz, M. Changes of lattice geometries upon charge-transfer. *Mol. Cryst. Liq. Cryst.* **1985**, *126*, 103–110.
69. Choi, C.H.; Kertesz, M.; Karpfen, A. The effects of electron correlation on the degree of bond alternation and electronic structure of oligomers of polyacetylene. *J. Chem. Phys.* **1997**, *107*, 6712–6721.
70. Becke, A.D. Density-functional thermochemistry: 3. The role of exact exchange. *J. Chem. Phys.* **1993**, *98*, 5648–5652.
71. Lee, C.T.; Yang, W.T.; Parr, R.G. Development of the Colle-Salvetti correlation-energy formula into a functional of the electron-density. *Phys. Rev., B* **1988**, *37*, 785–789.

# Single-Walled Carbon Nanotubes: Separation Using Capillary Electrophoresis

Stephen K. Doorn

Chemistry Division, Los Alamos National Laboratory, Los Alamos, New Mexico, U.S.A.

## INTRODUCTION

Fulfilling the promise that carbon nanotubes hold for new lightweight, high-performance materials and nanoscale electronics<sup>[1]</sup> and sensors,<sup>[2]</sup> among other areas, will require production of bulk quantities of pure material. Much progress has been made in production, including electric-arc,<sup>[3]</sup> laser ablation,<sup>[4]</sup> and catalytic gas-phase growth methods,<sup>[5]</sup> which are beginning to prove themselves for large-scale production of raw nanotube material. Initial purification work has focused on breaking up the carbon mat resulting from production and elimination of amorphous carbon and catalyst material from the end product.<sup>[6–15]</sup>

With the increasing availability of relatively pure product, it is becoming feasible to pursue geometry selective separations of carbon nanotubes. Structure-based purification for isolation of specific properties will be an important tool for advancing nanotube science. For example, differences in the geometrical parameters ( $n$ ,  $m$ ) will determine whether the nanotubes are conducting or semiconducting.<sup>[16]</sup> Changes in ( $n$ ,  $m$ ) also result in differences in diameter. A (10, 6) tube will be semiconducting and have diameter of 1.11 nm, while a (10, 10) tube is conducting, with diameter of 1.32 nm. Thus the ability to separate tubes based on geometry will also ultimately provide a degree of selectivity over electronic properties. Field-flow fractionation<sup>[17]</sup> (FFF) and size-exclusion chromatography<sup>[18,19]</sup> have demonstrated some success at length-based separations, but result in fractions with broad length distributions. However, recent work using flow field-flow fractionation demonstrates progress in producing narrower distributions.<sup>[20]</sup> Electrophoretic separations may also be promising. Bulk electrophoresis has been used for alignment of nanotubes and is capable of separating nanotubes from particulate impurities.<sup>[21]</sup> Gel electrophoresis has produced fractions with similar length distributions as found for FFF separations.<sup>[22]</sup>

Capillary electrophoresis (CE) has only been recently investigated for purification of carbon nanotubes. The high-resolution separations available with this method are intrinsically dependent on solute

geometry and may prove valuable in the separation of nanotubes by geometric specification. The first reported use on electric arc produced nanotubes demonstrated its ability to separate nanotubes according to length.<sup>[23]</sup> More recent work has shown that this approach may be capable of producing diameter-specific separations as well.<sup>[24]</sup> These recent studies are described in this entry.

## CAPILLARY ELECTROPHORESIS

Capillary electrophoresis (CE) is a rapid, high-resolution chemical separation method that has found widespread use in applications ranging from DNA separation to chemical speciation. Depending on analyte and separation parameters, typical elution times range from 1 to 20 min.<sup>[25]</sup> CE separations are based on charge- and size-dependent mobility of solution phase species under the influence of an applied electric field. A brief description of the method as applied to separation/purification of carbon nanotubes is given here. More comprehensive treatments can be found in a variety of sources.<sup>[25,26]</sup>

A schematic of a simple CE apparatus is shown in Fig. 1. CE is performed in narrow bore glass capillaries [typically 50–100  $\mu\text{m}$  inner diameter (i.d.)] that are filled with electrolyte/buffer solution. The capillary ends are immersed in electrolyte reservoirs. Separations are driven by a high voltage applied across the capillary after the introduction of sample at one end. For the single-wall carbon nanotube (SWNT) separations described here, a positive potential is applied at the sample inlet, while the effluent end is held at ground. Detection of separated species is performed at some point downstream through a window in the capillary coating. Separations are influenced by two main factors: the electrophoretic and electroosmotic flows (EOF).

## Electrophoretic Basis for Separations

Separation of different species in CE is a result of differences in their electrophoretic mobilities ( $\mu_{\text{ep}}$ ) under

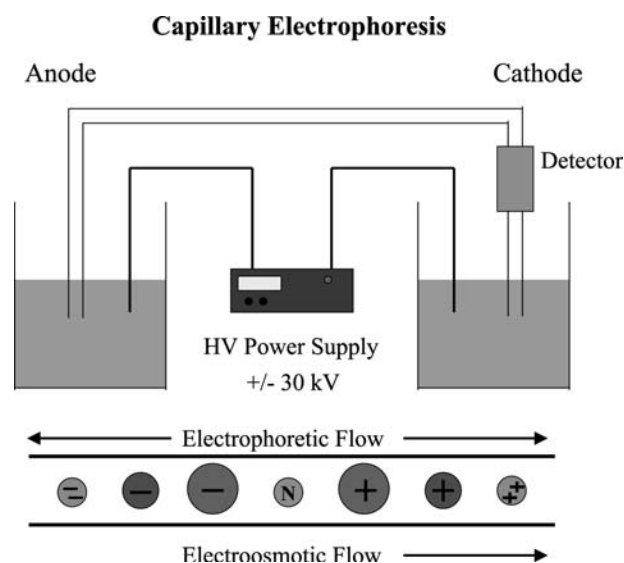


**Fig. 1** Simple schematic of apparatus for performing capillary electrophoresis.

the influence of an applied electric field ( $E$ ). Resultant velocities ( $V_{ep}$ ) are a product of the two [Eq. (1)]:

$$V_{ep} = \mu_{ep}E \quad (1)$$

$$\mu_{ep} = q/6\eta\pi r \quad (2)$$

Mobilities are [Eq. (2)] dependent on the species charge ( $q$ ), solution viscosity ( $\eta$ ), and, for the simplest (spherical) case, species radius ( $r$ ). For more complex geometries, mobility is more correctly determined by overall charge density of the species. Small, highly charged species will be more mobile under the influence of the applied field than large, weakly charged species. This strong dependence on geometric factors makes CE potentially attractive for length- and diameter-based separations of carbon nanotubes.

A number of experimentally controllable factors can influence  $V_{ep}$  through effects on species charge and geometry, as well as on viscosity. Electrolyte pH will influence total charge on a species and may affect geometry through pH-induced conformational changes. Buffer concentration also affects viscosity, as will changes in temperature.

### Electroosmotic Flow

Silica capillaries used in CE are commonly conditioned with NaOH prior to use to convert surface silanol groups (Si-OH) to the negatively charged silanate (Si-O<sup>-</sup>). Introduction of electrolyte subsequently produces a diffuse double layer of buffer cations attracted to the silanate groups. The outer layer is loosely bound

and is mobile in the presence of an applied electric field ( $E$ ). The mobile outer layer moves toward the cathode and effectively drags the bulk solution with it, giving rise to the electroosmotic flow ( $V_{eof}$ ). Electroosmotic flow (EOF) produces a plug flow (rather than hydrodynamic flow) of fractions through the capillary. Plug flow yields sharp narrow fractions. EOF is also largely responsible for the rapid separations available with CE. Finally, EOF makes possible separations of anions, neutrals, and cations in one process.

EOF depends [Eq. (3)] on the zeta potential ( $\zeta$ , proportional to the double layer thickness), applied field ( $E$ ), and buffer viscosity ( $\eta$ ):

$$V_{eof} = \varepsilon\zeta E/4\pi\eta \quad (3)$$

As with  $V_{ep}$ , experimentally controllable parameters have a large effect on  $V_{eof}$ . Changes in buffer concentration and temperature affect the solution viscosity in the same manner as for  $V_{ep}$ . The zeta potential is also directly linked to the buffer concentration: lowering the concentration lowers  $\zeta$ , thus decreasing  $V_{eof}$ . Because  $\zeta$  is proportional to the charge on the capillary wall, pH can also have a significant effect on  $V_{eof}$ . At high pH, most of the silanol groups will be converted to the silanate, resulting in a high charge and  $\zeta$ . Thus  $V_{eof}$  increases as pH is increased. Because pH can also affect  $V_{ep}$  through its influence on the degree of species ionization, pH is generally adjusted to give the best separation, with secondary consideration given to flow velocity.

### CE as Applied to Carbon Nanotubes

The total species velocity ( $V_{tot}$ ) is the sum of  $V_{eof}$  and  $V_{ep}$  [Eq. (4)]. It is possible, as in the case of separations of anions, for these two terms to have opposite signs. As long as the magnitude of

$$V_{tot} = V_{eof} + V_{ep} \quad (4)$$

$V_{eof}$  is greater than  $V_{ep}$  in anionic separations, there will still be net transport of analytes to the cathode, or effluent, end of the capillary. This is an important consideration for nanotube separations, as the solubilized nanotubes are negatively charged. In the absence of an electroosmotic flow, a positive applied voltage (as used in these studies) would simply result in the nanotubes being redeposited at the anode buffer vial. Instead, the EOF results in the passage of nanotubes through the capillary and may be adjusted to optimize separations.

The nanotubes are negatively charged as a result of their dissolution through sonication in aqueous solutions of 0.5% sodium dodecyl sulfate (SDS). This is

slightly above the critical micelle concentration (CMC) for SDS (0.24%), and has been shown to efficiently suspend carbon nanotubes while minimizing their aggregation.<sup>[8,27]</sup> SDS was shown to provide the basis for separation of other carbon materials (fullerenes) in micellar electrokinetic chromatography (MEKC).<sup>[28]</sup> However, for SWNT separations, the use of a micellar medium such as SDS does not have the same significance as in an MEKC application. MEKC relies on partitioning of a neutral solute into the micelle.<sup>[25]</sup> The SWNTs are too large to reside in the spherical intramicellar region. Instead, the hydrophobic SDS tails are expected to specifically interact with the nanotube surface, providing it with a negative charge through the anionic sulfate head groups.<sup>[27]</sup> Modeling of these interactions suggests the resultant geometry to be a nanotube encapsulated in a cylindrical micelle.<sup>[29]</sup> The resultant electrostatic repulsion between encapsulated tubes stabilizes them against van der Waals attraction. Investigations into the phase behavior of the SDS/SWNT/water system show that, for the relative concentration of SDS and SWNTs used here, a stable single phase dispersion of nanotubes results.<sup>[27]</sup>

Typical separation parameters for the studies described here use run buffers of 50 mM Trizma base in 0.5% SDS solution. Separations are carried out in 75  $\mu\text{m}$  i.d., 75- to 100-cm-long glass capillaries. Capillaries are conditioned for 2 min using 0.2–1 M NaOH, followed by flushing with deionized water and buffer solution. Samples are pressure-loaded at 100–500 mbar before applying the separation voltage. The buffer pH of 9 results in relatively rapid separations. Lowering the pH will result in closer matching of  $V_{\text{eof}}$  and  $V_{\text{ep}}$ , which may improve the resolution of the separations, but at the cost of increased separation times. Lowering pH to acidic values may result in decreased charge on the nanotubes through protonation of SDS head-groups. Applied voltage was typically +15 kV in these studies. Higher voltages would result in faster separations but may introduce joule heating that would change buffer viscosity and could induce roping of the nanotubes. The voltages used were kept within the linear range of a voltage-vs.-current plot to minimize joule heating effects.

### Detection Methods

The simplest method of detection used in these studies is ultraviolet/visible (UV/Vis) absorbance at 360 nm. However, this method is limited, in that it is unable to indicate whether a detected fraction is carbon nanotubes, fullerenes, amorphous carbon, or other non-nanotube material. Raman spectroscopic detection has been used to overcome this drawback. The Raman spectra for carbon nanotubes are entirely distinct

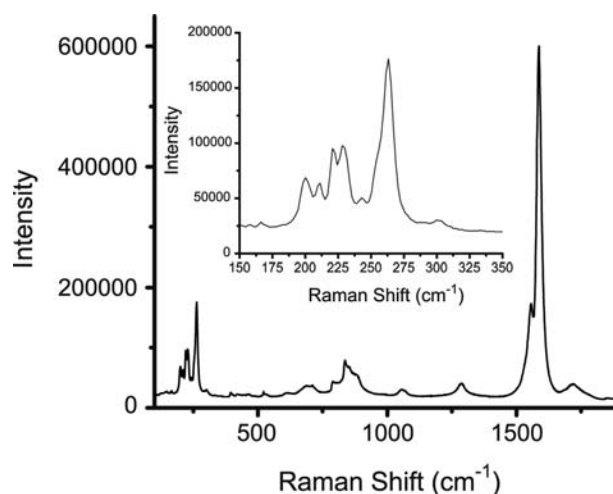


**Fig. 2** Raman spectrum (785 nm excitation, 20 mW, 1 sec integration) of bulk solid HiPco produced nanotubes. Inset: Radial breathing mode region of bulk solid.

(Fig. 2). The two major regions of interest are vibrational modes around  $1590\text{ cm}^{-1}$ , as a result of in-plane carbon–carbon bond deformations, and those at low frequency in the range of  $150\text{--}375\text{ cm}^{-1}$ , which are as a result of the nanotube radial breathing modes (RBM). The frequencies of the RBMs are strongly dependent on nanotube diameter.<sup>[30]</sup>

The key to identification of fractions as nanotubes is the ability to collect Raman spectra in real-time as the separations progress. This is accomplished through the use of high-throughput spectrographs coupled to efficient collection optics and detectors. Excitation at 514.5 or 785 nm is focused onto the sample through a microscope objective [ $20\times$ , 0.5 numerical aperture (NA)]. Scattered light is recollected through the objective and passed (via a confocal microscope or through a fiber optic probehead) through a Kaiser Optical HoloSpec  $f/1.8$  imaging spectrograph. Detection is carried out with a charge-couple device (CCD) camera (red sensitive for the 785-nm excitation case) using 1-sec integration times.

### CE ON ELECTRIC-ARC PRODUCED CARBON NANOTUBES

The first demonstration of CE separations on carbon nanotubes was on single-walled nanotubes prepared using the modified electric-arc method.<sup>[23]</sup> In a typical CE separation using absorbance detection (Fig. 3A), fractions begin to appear around 8 min into the run. From run-to-run, an initial strong sharp peak on top of a broad background followed by a series of sharp (1–2 sec wide) baseline separated peaks is consistently observed. Elution times compare well with what can

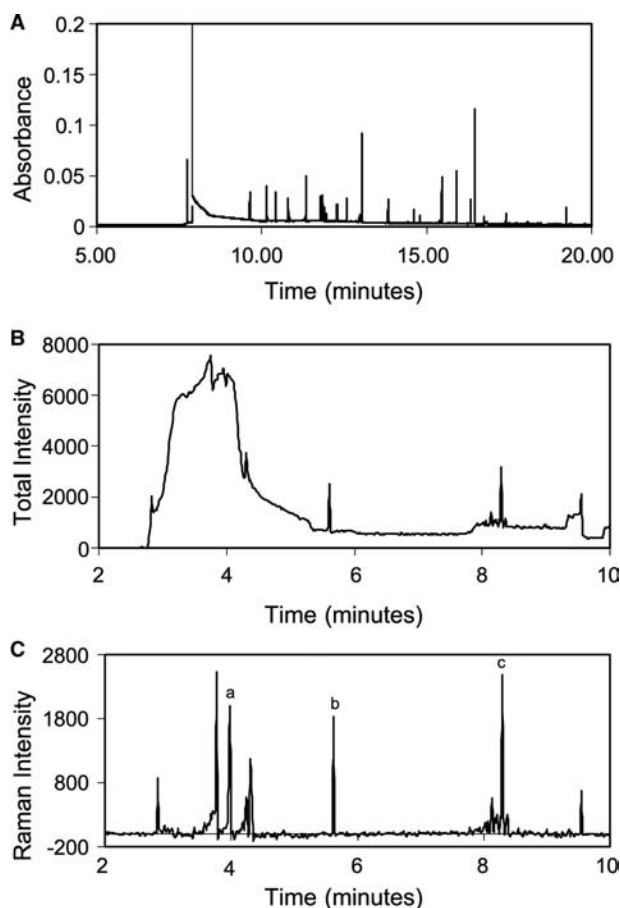


**Fig. 3** Capillary electropherograms (+15 kV in 0.5% SDS/50 mM trizma base buffer) of single-walled carbon nanotubes using A) absorbance detection at 360 nm, and capillary electropherograms of single-walled carbon nanotubes using Raman detection (514.5 nm excitation, 5 mW, 1 sec integration). B) Electropherogram showing total intensity (background fluorescence plus Raman scattering) collected at 560.37 nm. C) Electropherogram showing scattered Raman intensity at  $1591\text{ cm}^{-1}$ . *Source:* From Ref.<sup>[23]</sup>.

be obtained for CE on other types of analytes. The sharp peaks in the electropherogram were assigned to nanotube fractions. However, because of the potential presence of other material (such as fullerenes and graphite), unambiguous identification of these peaks requires Raman detection.

A Raman/CE run showing total detected intensity at 560.37 nm (corresponding to the strong nanotube Raman band at  $1591\text{ cm}^{-1}$ ) displays (Fig. 3B) a similar pattern to that seen in the absorbance data.<sup>a</sup> Initial

<sup>a</sup>Although the electropherograms obtained with Raman detection are presented for only one wavelength, it should be emphasized that each point in the electropherogram actually represents a complete Raman spectrum for that segment of sample flowing through the capillary.

sharp bands appear superimposed on a broad fluorescence background, followed by a series of trailing peaks. Subtraction of the background intensity from the peak intensity at  $1591\text{ cm}^{-1}$  results in an electropherogram displaying only the carbon nanotube fractions (Fig. 3C). No Raman bands are associated with the broad fluorescence feature, nor are any observed for any other point in the electropherogram except at the location of the sharp bands. Strong Raman bands, characteristic of carbon nanotubes, are observed for all the sharp features in the electropherogram giving positive identification of these fractions as containing nanotubes.

Raman spectra of three individual fractions (highlighted in Fig. 3C) are compared in Fig. 4. Raman frequencies are identical for all fractions, indicating that each fraction contains tubes of equivalent diameter. The RBM frequency of  $169\text{ cm}^{-1}$  indicates this diameter to be 1.32 nm.<sup>[31]</sup> The arc method primarily produces nanotubes with diameters near 1.3 nm,<sup>[32,33]</sup> so it is not surprising to find that all fractions in the electropherograms consist of tubes of similar diameter.

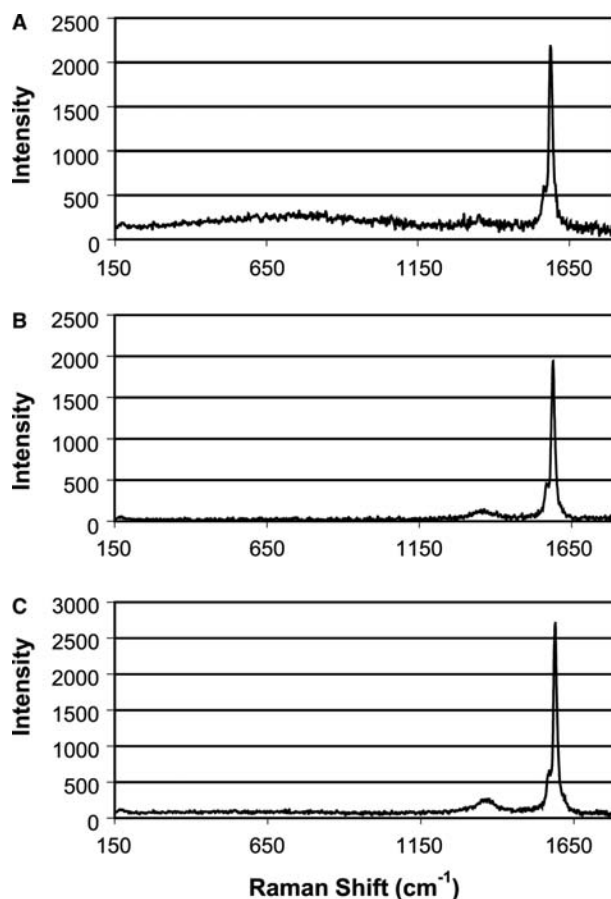


**Fig. 4** Raman spectra of labeled fractions from capillary electropherogram shown in Fig. 3C. A) 3.98 min fraction, B) 5.62 min fraction, C) 8.30 min fraction. *Source:* From Ref.<sup>[23]</sup>.

This suggests that the difference in mobility between fractions is a result of differences in nanotube lengths.

Further evidence for length-based separation was obtained from atomic force microscopic (AFM) images of composited fractions. Composites were collected by turning off the separation voltage, followed by sectioning the capillary, and then depositing and drying the section contents onto a mica AFM substrate. Each capillary section is composed of a series of individual nanotube fractions occurring progressively later in time. The first composite encompassed sample that included the initial spikes and broad peak (Fig. 3). The second composite included the next 2 min of eluting fractions. Subsequent composites were obtained at approximately 5-min intervals. AFM images (Fig. 5) show the first composite consists of nanotubes ranging in length ranging from 0.2 to 1.2  $\mu\text{m}$ . Amorphous non-nanotube material was found only in the first composite. The second composite consists of longer nanotubes (0.5–2.5  $\mu\text{m}$  in length) with no amorphous material being present. This amorphous material is responsible for the broad background observed at early times in both the Raman and absorbance detection runs. Later composites encompass timeframes that do not show this fluorescence background; nor do they contain amorphous particulates.

The trend toward longer nanotubes continues in composites collected at later times. Some degree of overlap in length range between sequential composites is observed. The significance of the overlap can be evaluated by measuring the distribution of lengths present in each composite (Fig. 6). The length range in which overlap occurs between composites contains a relatively small number of nanotubes compared to the length range into which the majority of tubes in each composite falls. This suggests that length range

overlaps between composites results from a diffusion of nanotubes between composites.

In the latest composites, lengths of up to 10  $\mu\text{m}$  are observed, although tubes longer than 2  $\mu\text{m}$  were not observed in the raw nanotube sample. Bundling of individual tubes can result in the existence of longer structures. Although large-scale aggregation is prevented by the presence of SDS, small bundles are known to occur in these solutions. In addition to providing a pathway for producing longer tubes, bundling may also result in short aggregates with effectively larger diameter than individual tubes. The existence of tubes as short as 2–3  $\mu\text{m}$  in composite 4, although possibly present as a result of diffusion from composite 3, instead may be attributable to bundling of short tubes. Tube bundles of identical length to individual tubes will be expected to elute later because of their larger diameter (see later discussion).

The AFM results on composite fractions demonstrate a length-based separation mechanism that leads to elution of short tubes first, followed by progressively longer tubes. The following mechanism for separation of nanotube fractions was proposed.<sup>[23]</sup> In the case of comparing elution times between individual tubes and tube bundles of the same length, the bundled tubes are expected to have a higher charge per unit length because of their greater diameter. The resultant higher electrophoretic mobility for the bundles is expected to translate to a later elution time than for an individual tube of identical length. However, for the case of nanotubes with uniform diameter, charge-density differences are not expected to be significant and forces other than electrophoretic are responsible for separations.

Under the influence of an electrostatic field ( $E$ ), nanotubes will experience an induced dipole moment ( $p_x$ ). The resultant torque on the nanotubes ( $p_x \times E$ ) aligns the tubes along  $E$ .<sup>[34]</sup> For perfectly aligned tubes

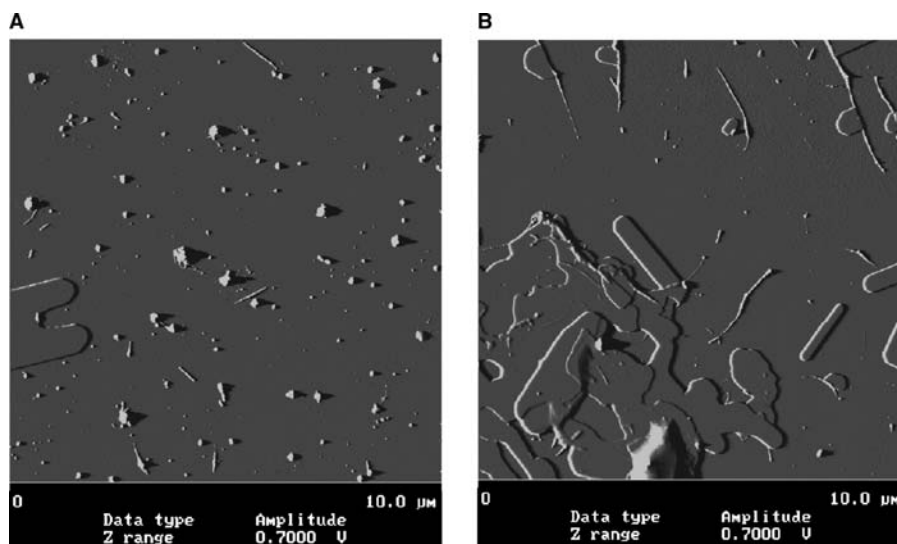


**Fig. 5** A) AFM image (tapping mode on mica substrate) of first (early time) composite of nanotube fractions. B) AFM image of second composite of nanotube fractions. Source: From Ref.<sup>[23]</sup>.



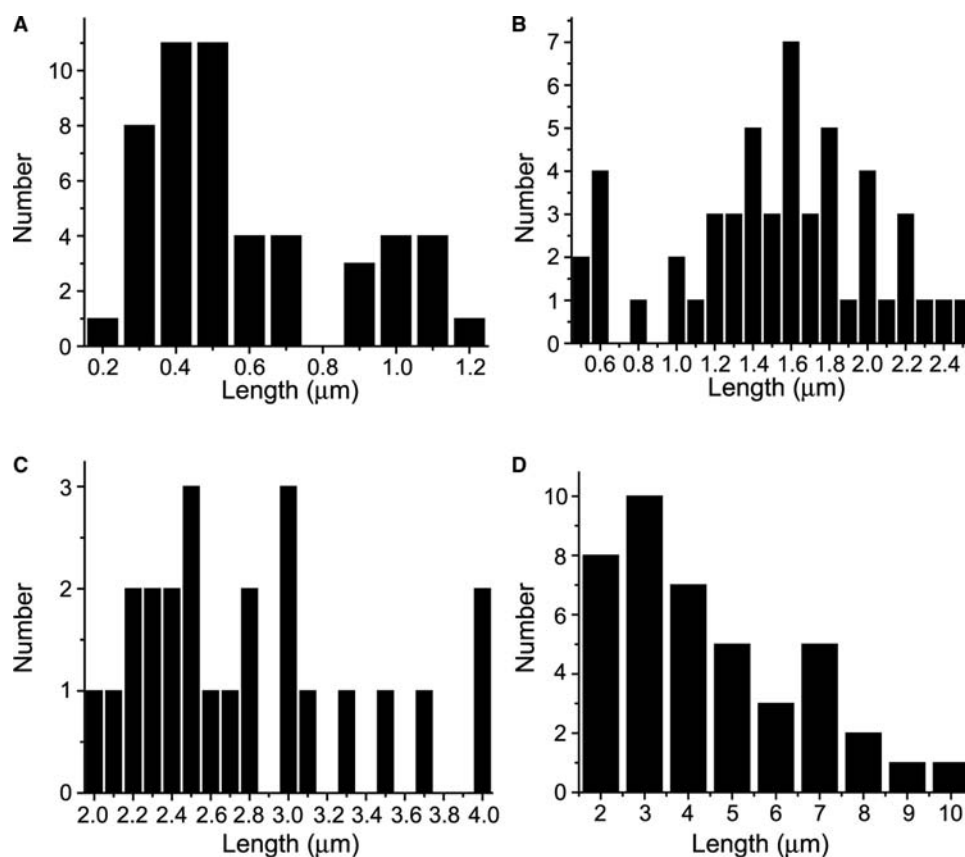


**Fig. 6** Distribution of nanotube lengths observed in each composite as determined from AFM images: (A) composite 1, (B) composite 2, (C) composite 3, (D) composite 4. *Source:* From Ref.<sup>[23]</sup>.

of equal diameter, charge density along  $E$  will be the same, independent of length. However, it has been observed in bulk electrophoresis alignment experiments<sup>[21]</sup> that shorter tubes display a larger deviation from perfect alignment than is observed for longer tubes. This behavior is predicted to occur as a result of opposition to alignment caused by Brownian motion or thermal agitation.<sup>[34]</sup> Shorter tubes are predicted to have a greater deviation from alignment along  $E$ . The resultant “wobble” is expected to effectively create a hydrodynamic resistance to the electrophoretic flow that will increase as tube length decreases. Under a positive applied potential, the negatively charged tubes will be attracted to the anode, or capillary intake, with longer tubes being most strongly attracted because of decreased hydrodynamic resistance resulting from their greater alignment along the applied electric field. EOF produces a net flow toward the capillary outlet (cathode) for all species with shorter tubes eluting first.

### CE ON HIPCO-PRODUCED CARBON NANOTUBES

The separation mechanism described above suggests that, in addition to providing length-based separations,

CE may be capable of producing diameter-dependent separations. However, diameter selectivity in the arc-produced nanotube separations was not apparent because of the limited diameter range present. As seen in Fig. 1, HiPco-produced nanotubes<sup>[5]</sup> have a broad range of observable diameters, making them attractive for investigating the potential of CE for diameter selectivity. RBM frequencies ranging from 169 to 373  $\text{cm}^{-1}$  translate to a diameter distribution of 0.6–1.3 nm for these samples, with the most intense bands corresponding to diameters of 0.88–1.15 nm.

### Behavior of PVP-Stabilized HiPco Nanotubes

Initial investigations into HiPco separations were performed on nanotubes stabilized with polyvinyl pyrrolidone (PVP).<sup>[22]</sup> These samples contain nanotube bundles with a distribution of composition and bundle size. A representative electropherogram from a separation of PVP suspended sample is shown in Fig. 7A. Nanotubes first appear around 17 min into a separation. The electropherogram is dominated by primarily broad, incompletely resolved fractions. This is in contrast to the behavior observed for the SDS suspensions of arc-produced nanotubes. The presence of

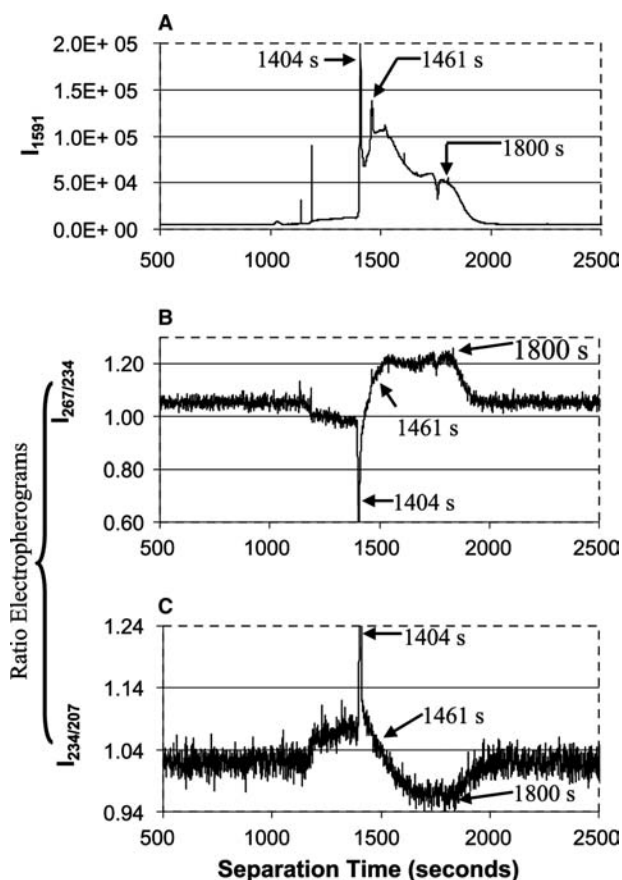


**Fig. 7** Electropherograms of PVP-stabilized nanotubes (+15 kV in 0.5% SDS/50 mM trizma base buffer, 785 nm excitation, 20 mW, 1 sec integration). (A) Monitoring 1591  $\text{cm}^{-1}$  mode intensity, (B) monitoring intensity ratio of 267/234  $\text{cm}^{-1}$  mode, (C) monitoring intensity ratio of 234/207  $\text{cm}^{-1}$  mode.

distinct bands in the electropherogram indicates that some separation process is occurring. Whether this is due only to the previously observed length-based mechanism or combines a diameter-based process requires further analysis of the Raman spectra to determine.

Closer inspection of how the RBM region of the Raman spectra changes over the course of a separation will provide information on whether or not diameter-selective separations are occurring superimposed on the length-based mechanism. Electropherograms showing changes in the most prominent bands are shown in Fig. 7B and C. These plots indicate that at early times (1200–1450 sec), the band at 234  $\text{cm}^{-1}$  is the most prominent in this region, with a significant increase in intensity occurring at 1404 sec. At intermediate times, the 267  $\text{cm}^{-1}$  band is strongest. Finally, from around 1600 sec to the end of the separation, the 234  $\text{cm}^{-1}$  mode diminishes in intensity. Representative spectra for selected times in these regions are shown in Fig. 8.

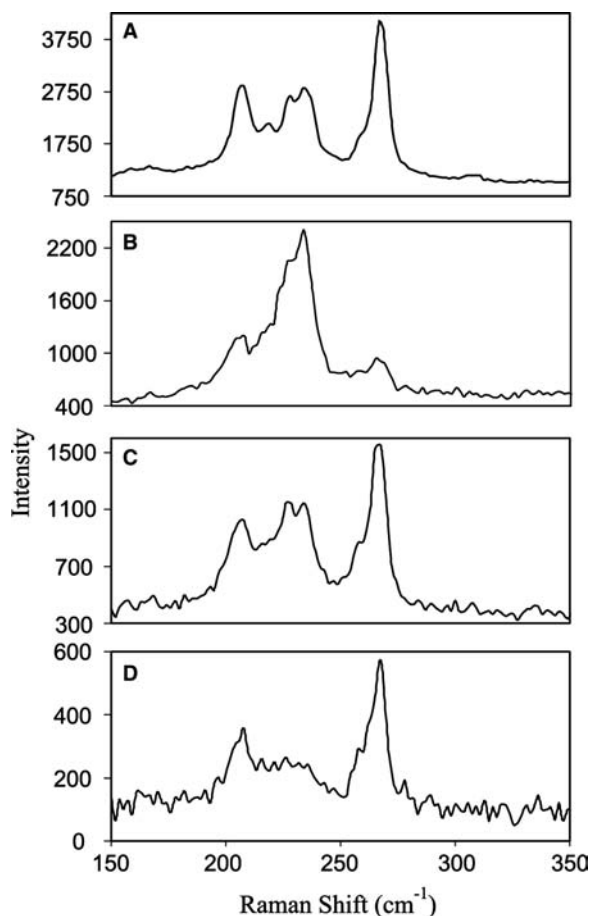


**Fig. 8** (A) Radial breathing mode Raman spectrum of bulk, unseparated PVP-stabilized nanotube solution. Selected Raman spectra from separation shown in Fig. 7: (B) spectrum at 1404 sec, (C) spectrum at 1461 sec, (D) spectrum at 1800 sec.

### Behavior of SDS Suspended HiPco Nanotubes

CE on HiPco SDS suspensions were also investigated for better comparison to the separations on arc-produced samples. A typical electropherogram for the SDS suspended sample is shown in Fig. 9. A series of baseline separated, sharp, and intense spikes are observed throughout the early part of the separation (Fig. 9A). These results are similar to those found for the arc-produced nanotubes. Closer inspection of the electropherogram reveals that the sharp spikes are on top of a broad background (Fig. 9B) that more resembles the results obtained for the PVP suspended tubes.

As seen in the ratio electropherogram of 267  $\text{cm}^{-1}$  intensity divided by 234  $\text{cm}^{-1}$  intensity (Fig. 9C), the behavior of the radial breathing modes undergoes large changes over the course of the separation. Three distinct regions of behavior are observed. In the first, ranging from the first appearance of nanotubes to about 500 sec, ratios for both the spikes and broad envelope are seen to be greater than the baseline ratio observed

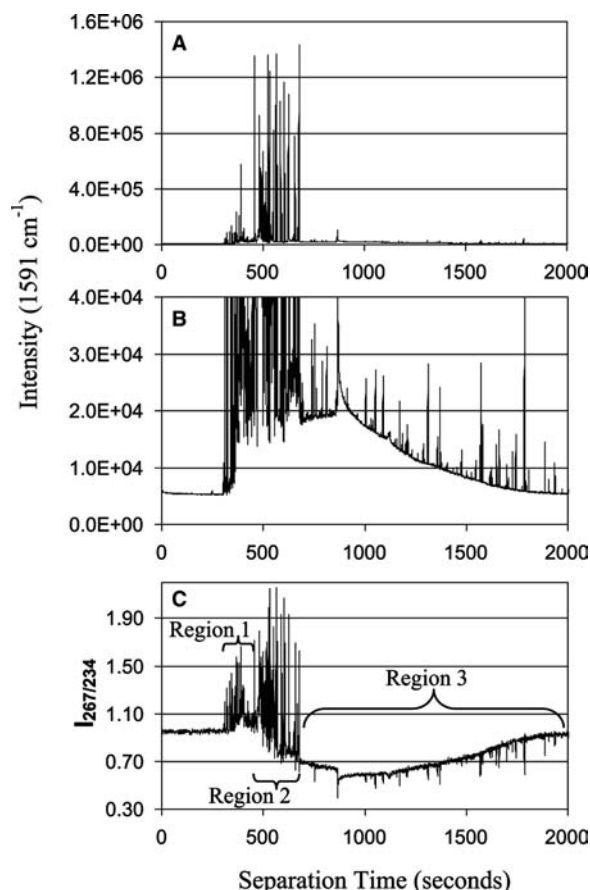


**Fig. 9** (A) Electropherogram of SDS suspended nanotubes, monitoring  $1591\text{ cm}^{-1}$  intensity (+15 kV in 0.5% SDS/50 mM trizma base buffer, 785 nm excitation, 20 mW, 1 sec integration). (B) Electropherogram showing expansion of y axis. (C) Electropherogram monitoring intensity ratio of  $267/234\text{ cm}^{-1}$  mode.

before appearance of nanotubes. At intermediate times (region 2, 500–677 sec), the intense spikes are still positive going, but the broad envelope begins to trend to values less than the baseline. At longer times (region 3, 678 sec to end), the intense spikes disappear and the broad envelope remains in the region below baseline. This later time region is dominated by the  $234\text{ cm}^{-1}$  mode throughout the broad envelope, as well as for the weak spikes observed in this region.

Representative spectra for these three regions are compared to the bulk solution spectrum in Fig. 10. The spectrum at 482 sec (Fig. 10B) is identical to all spikes observed in the first two regions of the electropherogram, except for variations in intensity. The broad background envelope spectra in this region are also identical to this spike-observed frequencies and relative intensities remain the same. In the second electropherogram region (500–677 sec), the spike spectra also display the same frequencies and relative intensities as are observed in the first region. However, the

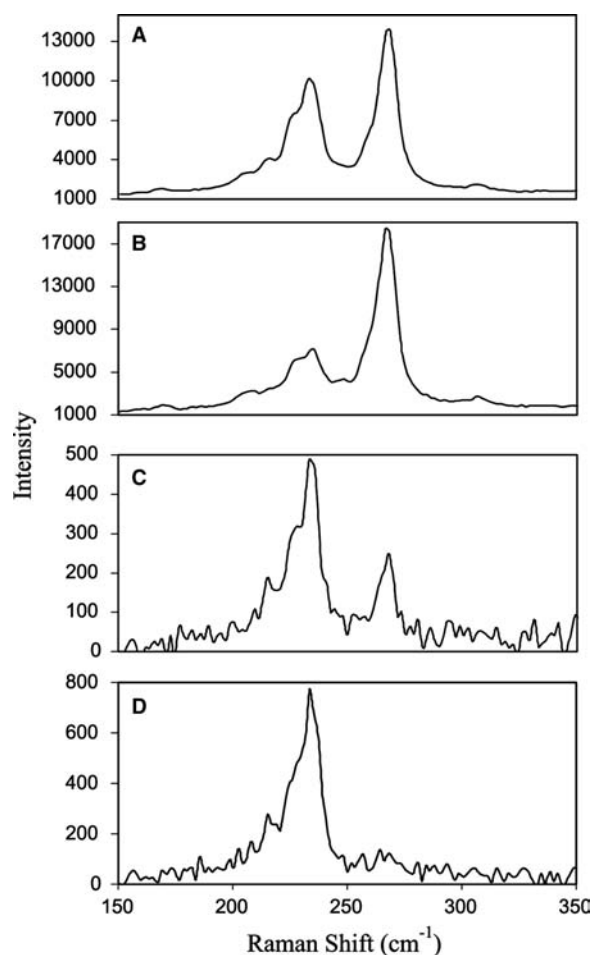


**Fig. 10** (A) Radial breathing mode Raman spectrum of bulk unseparated SDS suspended nanotubes. Selected Raman spectra from separation shown in Fig. 9: (B) spectrum at 482 sec, (C) spectrum at 633 sec, (D) spectrum at 918 sec.

background envelope now shifts to spectra that are dominant in the  $234\text{ cm}^{-1}$  mode (Fig. 10C). A further dramatic shift in relative intensities is seen on going into the third region. Here nearly all the RBM intensity is now in the  $234\text{ cm}^{-1}$  mode, (Fig. 10D). Spectra in this region are similar to those observed in the fraction at 1404 sec in the PVP separations (Fig. 8B).

## DISCUSSION

Variations in RBM intensities indicate that diameter-dependent spectral changes occur during a separation. It is tempting to directly relate these intensity changes to changes in relative population of the corresponding diameter tube. However, there are a number of complicating factors that make the analysis more difficult. The PVP samples are known to be bundles that vary in size and composition. Thus the observed behavior is not that for separations of isolated, individual

nanotubes. Furthermore, Raman spectra for nanotubes display strongly diameter-dependent resonance enhancement effects. Spectra for nanotubes of differing diameter will be enhanced to varying degrees for a fixed excitation wavelength. Only radial breathing modes for nanotubes with a van Hove singularity near the 785 nm excitation energy will be significantly enhanced.

These enhancement effects are further perturbed in the PVP samples because of the strong interaction expected among nanotubes in a given bundle, which results in a change in energy spacing of the van Hove singularities.<sup>[35,36]</sup> For semiconducting nanotubes, the absorption maxima are broadened and shifted to lower energy.<sup>[29,36]</sup> This is a particularly strong effect for the  $267\text{ cm}^{-1}$  mode, which can be used as an indicator of the degree of roping. For large enough bundles, the electronic resonance for this mode strongly overlaps the 785-nm excitation energy. As the bundle size decreases, the resonance energy shifts to shorter wavelengths. This shift will result in a decrease in resonance Raman intensity at  $267\text{ cm}^{-1}$  to a minimum when overlap is minimized between the 785-nm excitation energy and the electronic resonance for an individual nanotube. Conversely, the  $234\text{ cm}^{-1}$  mode gains in intensity on going from a roped sample to isolated individuals. Thus enhancement effects and perturbations may result in spectra that do not accurately indicate the dominant nanotube type in a given population, but may be useful in indicating relative nanotube bundle size.

The bundle size/cross section for a collection of nanotubes is defined by the number of nanotubes present and by their individual diameters. The results for the PVP samples demonstrate that they can be separated into fractions of differing composition that exhibit differing electronic resonance behavior. The majority of PVP-stabilized bundles will contain a random distribution of the available tube diameters. Therefore, spectra observed over the course of a separation might be expected to be similar to that observed for the bulk solution. This is observed at intermediate times (Fig. 8C). The dominance of the  $267\text{ cm}^{-1}$  mode for intermediate to late-time spectra (Fig. 8C,D) also suggest that these fractions consist of the largest bundles. Stronger intensity in the  $234\text{ cm}^{-1}$  mode at early times, and especially for the 1404 sec fraction (Figs. 7 and 8B), suggests these fractions consist of much smaller bundles.

The degree to which bundles of different composition exist in a fraction is indicated by its relative intensity and width. The broad fractions observed in Fig. 7A suggests that there is a relatively continuous change in composition for PVP-bundled samples. In addition to broadening from variation in cross section or size distributions, all fractions will be further

broadened because of the superposition of separations based on length differences. This will also cause some overlap of bands that might otherwise represent “pure” compositions. Thus observed spectra will not be pure indicators of composition.

Significant changes in radial breathing mode spectra over the course of a separation are also observed for the SDS suspended samples (Figs. 9C and 10). The presence of three different regions of spectral behavior in these separations demonstrates that nanotube fractions of at least three different electronic behavior are being separated. However, as with the PVP samples, the shift in relative intensities for the different RBMs may not be attributable to a change in absolute population of different diameter nanotubes. Changes in resonance enhancement conditions and interaction effects are also likely.

Changes in relative intensities of the  $267$  and  $234\text{ cm}^{-1}$  modes throughout the separation are likely because of the same effects observed and discussed for the PVP suspended systems. The spectra observed in the first region (Figs. 9C and 10) are likely because of large aggregates/ropes of nanotubes, as the spectra are dominated by the  $267\text{ cm}^{-1}$  “roping” mode. The weaker intensity observed for this mode in the second region (Fig. 10C) suggests that these aggregates are significantly smaller. Finally, near loss of intensity of this mode in the third region (Fig. 10D) suggests that nanotubes present at these times are aggregates of minimum size or are individual, isolated nanotubes exhibiting minimum interaction with other tubes in solution. The Raman intensity observed from the spikes (in some cases, as high as 100 times that observed for the isolated tubes) also supports the conclusion that they are attributable to aggregates. Strong signals may result from a significant number of tubes being present per aggregate. Weaker intensities observed in the second and third separation regions are consistent with these nanotubes being smaller aggregates and individual nanotubes.

Additional evidence for these assignments is found in the complete spectra for the fractions. A comparison of spectra for the three regions (Fig. 11) shows that the late-time spectra (Fig. 10C,D) contain fluorescence features that are absent in the earlier regions. These fluorescence bands occur on either side of the  $1591\text{ cm}^{-1}$  band, with absolute wavelengths for emission of 878 and 915 nm. These emission bands have only recently been discovered for SWNTs and have been assigned as band-gap emission from the first van Hove transitions occurring in semiconducting tubes.<sup>[29]</sup> Emission is only observed for individual, isolated nanotubes as aggregation of tubes quenches fluorescence due to the presence of increased energy decay pathways or through direct interaction with metallic tubes in a given bundle. Fluorescence is not observed at any



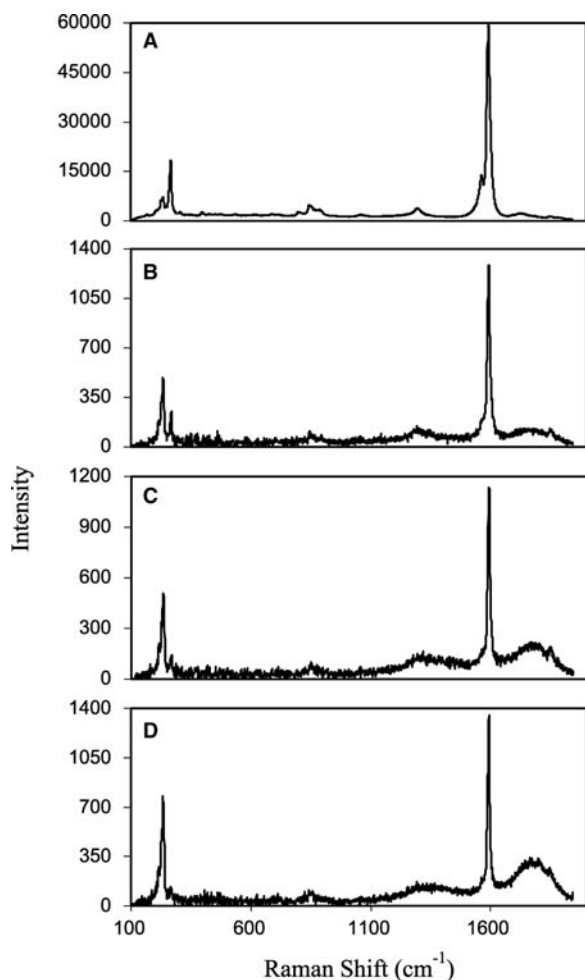


**Fig. 11** Full Raman spectra from separation shown in Fig. 9. (A) Spectrum at 482 sec, (B) spectrum at 633 sec, (C) spectrum at 809 sec, (D) spectrum at 918 sec.

point in the separation of the PVP samples, consistent with the above findings that it can only be observed in isolated tubes.

These findings strongly suggest that spectra observed for early-to-intermediate times in Fig. 9 (first two separation regions), particularly in the strong spikes, are from aggregated nanotubes. This suggests that the strong spikes observed for arc-produced tubes are also attributable to aggregates. Observation of fluorescence in the third separation region indicates that it is dominated by isolated individual nanotubes. Spikes observed in this region, although still dominant in the  $234\text{ cm}^{-1}$  RBM, do not contain the fluorescence bands and are therefore assigned as small aggregates. The large number of aggregate fractions observed in the SDS separations is likely a result of the relatively mild sonication conditions used for sample preparation (10 min at 80 W).

The separations observed in the SDS system build on the PVP results. Not only are separate fractions

observed with differing electronic behaviors, but fractions can also be obtained that differ in large-scale geometry. The SDS results demonstrate that bundles of different cross-sectional area can be separated from each other, and also that bundles can be separated from individual isolated nanotubes. However, the fact that the fraction of isolated nanotubes in the SDS separations contains a wide range of diameters suggests that the separations may not strictly be a function of nanotube diameter or bundle cross section. Instead, molecular weight of the species in a fraction may be the important mechanistic factor for separations, although molecular weight will ultimately be dependent on bundle cross section or individual diameter. That separations are dependent on a number of factors is evident in the overlap observed between the three regions in the SDS separations. Large aggregate spikes continue to be observed in the region containing primarily small- to moderate-sized aggregates, while these smaller aggregates continue to appear as spikes throughout the region primarily containing isolated individual nanotubes. The potential for such overlapping behaviors was also recognized in CE of arc-produced nanotubes, and will be an important problem to overcome in future CE work on carbon nanotubes.

## CONCLUSION

These results represent the first applications of CE to purification and geometry-based separations of carbon nanotubes. CE was shown to be effective at separating nanotubes according to length, and also capable of removing nonnanotube material. CE on HiPco-produced nanotubes demonstrated the ability to produce fractions of differing electronic property. Its ability to separate large aggregates from smaller bundles and to produce a relatively pure fraction of individual isolated nanotubes was also demonstrated. These separations may be based on differences in cross section/diameter or diameter-dependent molecular weight.

This initial work has demonstrated that CE may be a promising approach to geometry-dependent separations of carbon nanotubes. However, there is clearly much work yet to be carried out to reach the goal of selectively separating nanotubes by desired electronic or material property. The full potential of CE for diameter-selective separations may best be reached through working with samples of fully isolated individual tubes. Bulk production of these samples is just now becoming feasible.<sup>[29]</sup> A better understanding of the mechanism for separations will also be essential toward reaching this goal.

Geometry-based separations will be important not only for producing samples with a narrow range of geometrical and electronic properties, but will also

make possible the study of pure nanotube properties on isolated individuals without the need to go to the single nanotube level. This capability will be critical to gaining a more complete understanding of nanotube properties and exploiting their unique behavior in real-world applications.

## ACKNOWLEDGMENTS

These studies could not have been accomplished without the contributions of collaborators at Los Alamos National Lab (Robert Fields and Vahid Majidi), University of Kentucky (Prof. John Selegue), University of California Riverside (Hui Hu, Mark Hamon, Prof. Robert Haddon), and Rice University (Michael Strano, Michael O'Connell, Erik Haroz, Kristy Rialon, Robert Hauge, and Prof. Richard Smalley).

## REFERENCES

1. Yakobson, B.I.; Smalley, R.E. Fullerene nanotubes: C-1000000 and beyond. *Am. Sci.* **1997**, *85* (4), 324–337.
2. Kong, J.; Franklin, N.R.; Zhou, C.; Chapline, M.G.; Peng, S.; Cho, K.; Dai, H. Nanotube molecular wires as chemical sensors. *Science* **2000**, *287* (5453), 622–625.
3. Journet, C.; Maser, W.K.; Bernier, P.; Loiseau, A.; Lamy de la Chapelle, M.; Lefrant, S.; Deniard, P.; Lee, R.; Fischer, J.E. Large-scale production of single-walled carbon nanotubes by the electric-arc technique. *Nature* **1997**, *388* (6644), 756–758.
4. Thess, A.; Lee, R.; Nikolaev, P.; Dai, H.; Petit, P.; Robert, J.; Xu, C.; Lee, Y.H.; Kim, S.G.; Rinzler, A.G.; Colbert, D.T.; Scuseria, G.E.; Tomanek, D.; Fischer, J.E.; Smalley, R.E. Crystalline ropes of metallic carbon nanotubes. *Science* **1996**, *273* (5274), 483–487.
5. Nikolaev, P.; Bronikowski, M.J.; Bradley, R.K.; Rohmund, F.; Colbert, D.T.; Smith, K.A.; Smalley, R.E. Gas-phase catalytic growth of single-walled carbon nanotubes from carbon monoxide. *Chem. Phys. Lett.* **1999**, *313* (1–2), 91–97.
6. Bandow, S.; Rao, A.M.; Williams, K.A.; Thess, A.; Smalley, R.E.; Ecklund, P.C. Purification of single-wall carbon nanotubes by microfiltration. *J. Phys. Chem., B* **1997**, *101* (44), 8839–8842.
7. Tohji, K.; Takahashi, H.; Shinoda, Y.; Shimizu, N.; Jeyadevan, B.; Matsuoka, I.; Saito, Y.; Kasuya, A.; Ito, S.; Nishina, Y. Purification procedure for single-walled nanotubes. *J. Phys. Chem., B* **1997**, *101* (11), 1974–1978.
8. Bonard, J.-M.; Stora, T.; Salvétat, J.-P.; Maier, F.; Stockli, T.; Duschl, C.; Forro, L.; deHeer, W.A.; Chatelain, A. Purification and size-selection of carbon nanotubes. *Adv. Mater.* **1997**, *9* (10), 827–831.
9. Rinzler, A.G.; Liu, J.; Dai, H.; Nikolaev, P.; Huffman, C.B.; Rodriguez-Macias, F.J.; Boul, P.J.; Lu, A.H.; Heymann, D.; Colbert, D.T.; Lee, R.S.; Fischer, J.E.; Rao, A.M.; Ecklund, P.C.; Smalley, R.E. Large-scale purification of single-wall carbon nanotubes: Process, product, and characterization. *Appl. Phys., A Mater. Sci. Process.* **1998**, *67* (1), 29–37.
10. Dillon, A.C.; Gennett, T.; Jones, K.M.; Alleman, J.L.; Parilla, P.A.; Heben, M.J. A simple and complete purification of single-walled carbon nanotube materials. *Adv. Mater.* **1999**, *11* (16), 1354–1358.
11. Li, F.; Cheng, H.M.; Xing, Y.T.; Tan, P.H.; Su, G. Purification of single-walled carbon nanotubes synthesized by the catalytic decomposition of hydrocarbons. *Carbon* **2000**, *38* (14), 2041–2045.
12. Yudasaka, M.; Zhang, M.; Jabs, C.; Iijima, S. Effect of an organic polymer in purification and cutting of single-wall carbon nanotubes. *Appl. Phys., A Mater. Sci. Process.* **2000**, *71* (4), 449–451.
13. Coleman, J.N.; Dalton, A.B.; Curran, S.; Rubio, A.; Davey, A.P.; Drury, A.; McCarthy, B.; Lahr, B.; Ajayan, P.M.; Roth, S.; Barklie, R.C.; Blau, W.J. Phase separation of carbon nanotubes and turbostratic graphite using a functional organic polymer. *Adv. Mater.* **2000**, *12* (3), 213–216.
14. Holzinger, M.; Hirsch, A.; Bernier, P.; Duesberg, G.S.; Burghard, M. A new purification method for single-wall carbon nanotubes (SWNTs). *Appl. Phys., A Mater. Sci. Process.* **2000**, *70* (5), 599–602.
15. Niyogi, S.; Hu, H.; Hamon, M.A.; Bhomik, P.; Zhao, B.; Rozenzhak, S.M.; Chen, J.; Itkis, M.E.; Meier, M.S.; Haddon, R.C. Chromatographic purification of soluble single-walled carbon nanotubes (s-SWNTs). *J. Am. Chem. Soc.* **2001**, *123* (4), 733–734.
16. Dresselhaus, M.S.; Dresselhaus, G.; Pimenta, M. The remarkable properties of carbon nanotubes as nanoclusters. *Eur. Phys. J., D* **1999**, *9* (1–4), 69–75.
17. Liu, J.; Rinzler, A.G.; Dai, H.; Hafner, J.H.; Bradley, R.K.; Boul, P.J.; Lu, A.; Iverson, T.; Shelimov, K.; Huffman, C.B.; Rodriguez-Macias, F.; Shon, Y.-S.; Lee, T.R.; Colbert, D.T.; Smalley, R.E. Fullerene pipes. *Science* **1998**, *280* (5367), 1253–1256.
18. Duesberg, G.S.; Muster, J.; Krstic, V.; Burghard, M.; Roth, S. Chromatographic size separation of single-wall carbon nanotubes. *Appl. Phys., A Mater. Sci. Process.* **1998**, *67* (1), 117–119.
19. Duesberg, G.S.; Blau, W.; Byrne, H.J.; Muster, J.; Burghard, M.; Roth, S. Chromatography of carbon nanotubes. *Synth. Met.* **1999**, *103* (1–3), 2484–2485.
20. Chen, B.; Selegue, J.P. Separation and characterization of single-walled and multiwalled carbon nanotubes by using flow field-flow fractionation. *Anal. Chem.* **2002**, *74* (18), 4774–4780.
21. Yamamoto, K.; Akita, S.; Nakayama, Y. Orientation and purification of carbon nanotubes using ac electrophoresis. *J. Phys., D, Appl. Phys. Anal. Chem.* **1998**, *31* (8), 34–36.
22. O'Connell, M.J.; Boul, P.; Ericson, L.M.; Huffman, C.; Wang, Y.; Haroz, E.; Kuper, C.; Tour, J.; Ausman, K.D.; Smalley, R.E. Reversible water-solubilization of single-walled carbon nanotubes by polymer wrapping. *Chem. Phys. Lett.* **2001**, *342* (3–4), 265–271.
23. Doorn, S.K.; Fields, R.E., III; Hu, H.; Hamon, M.A.; Haddon, R.C.; Selegue, J.P.; Majidi, V. High resolution



- capillary electrophoresis of carbon nanotubes. *J. Am. Chem. Soc.* **2002**, *124* (12), 3169–3174.
24. Doorn, S.K.; Strano, M.S.; O'Connell, M.J.; Haroz, E.H.; Rialon, K.L.; Hauge, R.H.; Smalley, R.E. Capillary electrophoresis separations of bundled and individual carbon nanotubes. *J. Phys. Chem., B* **2003**, *107* (25), 6063–6069.
  25. Weinberger, R. *Practical Capillary Electrophoresis*; Academic Press: San Diego, 2000.
  26. Camilleri, P. *Capillary Electrophoresis. Theory and Practice*; CRC Press: Boca Raton, 1993.
  27. Vigolo, B.; Penicaud, A.; Coulon, C.; Sauder, C.; Pailler, R.; Journet, C.; Bernier, P.; Poulin, P. Macroscopic fibers and ribbons of oriented carbon nanotubes. *Science* **2000**, *290* (5495), 1331–1334.
  28. Treubig, J.M., Jr.; Brown, P.R. Novel approach to the analysis and use of fullerenes in capillary electrophoresis. *J. Chromatogr., A* **2000**, *873* (2), 257–267.
  29. O'Connell, M.J.; Bachilo, S.M.; Huffman, C.B.; Moore, V.C.; Strano, M.S.; Haroz, E.H.; Rialon, K.L.; Boul, P.J.; Noon, W.H.; Kittrell, C.; Ma, J.; Hauge, R.H.; Weisman, R.B.; Smalley, R.E. Band gap fluorescence from individual single-walled carbon nanotubes. *Science* **2002**, *297* (5581), 593–596.
  30. Rao, A.M.; Richter, E.; Bandow, S.; Chase, B.; Eklund, P.C.; Williams, K.A.; Fang, S.; Subbaswamy, K.R.; Menon, M.; Thess, A.; Smalley, R.E.; Dresselhaus, G.; Dresselhaus, M.S. Diameter-selective Raman scattering from vibrational modes in carbon nanotubes. *Science* **1997**, *275* (5297), 187–191.
  31. Bandow, S.; Asaka, S.; Saito, Y.; Rao, A.M.; Grigorian, L.; Richter, E.; Eklund, P.C. Effect of the growth temperature on the diameter distribution and chirality of single-wall carbon nanotubes. *Phys. Rev. Lett.* **1998**, *80* (17), 3779–3782.
  32. Bethune, D.S.; Kiang, C.H.; deVries, M.S.; Gorman, G.; Savoy, R.; Vazquez, J.; Beyers, R. Cobalt-catalyzed growth of carbon nanotubes with single-atomic-layer walls. *Nature* **1993**, *363* (6430), 605–607.
  33. Chen, J.; Hamon, M.A.; Hu, H.; Chen, Y.; Rao, A.M.; Eklund, P.C.; Haddon, R.C. Solution properties of single-walled carbon nanotubes. *Science* **1998**, *282* (5386), 95–98.
  34. Fishbine, B.H. Carbon nanotube alignment and manipulation using electrostatic fields. *Fuller. Sci. Technol.* **1996**, *4* (1), 87–100.
  35. Rao, A.M.; Chen, J.; Richter, E.; Schlecht, U.; Eklund, P.C.; Haddon, R.C.; Venkateswaran, U.D.; Kwon, Y.-K.; Tomanek, D. Effect of van der Waals interactions on the Raman modes in single walled carbon nanotubes. *Phys. Rev. Lett.* **2001**, *86* (17), 3895–3898.
  36. Reich, S.; Thomsen, C.; Ordejon, P. Electronic band structure of isolated and bundled carbon nanotubes. *Phys. Rev., B* **2002**, *65* (15), 5411–5421.

# Single-Walled Carbon Nanotubes: Structures and Symmetries

Carter T. White

Naval Research Laboratory, Washington,  
District of Columbia, U.S.A.

John W. Mintmire

Department of Physics, Oklahoma State University,  
Stillwater, Oklahoma, U.S.A.

## INTRODUCTION

Single-walled carbon nanotubes (SWNTs) represent a novel class of low-dimensional materials exhibiting exceptional electronic properties.<sup>[1-9]</sup> Many of these properties were predicted by theory,<sup>[10-16]</sup> and then confirmed by experiment<sup>[1-3,5-7]</sup> after the successful synthesis of single-walled carbon nanotubes.<sup>[17-19]</sup> In this work, we provide an introduction to the structure and symmetries of SWNTs with emphasis on the use of their helical symmetry. We start by showing how all extended SWNTs can be envisioned by rolling up a single sheet of graphite.<sup>[20]</sup> We then show that all such SWNTs have translational symmetry along the nanotube axis, but often with hundreds, if not thousands, of atoms in the translational unit cell. Next, we show how all SWNTs defined by rolling up a single sheet of graphite have both rotational and helical symmetries that can be used to reduce the number of atoms necessary to generate any SWNT to two.<sup>[15]</sup> (A Fortran program that may be used to calculate the  $x$ ,  $y$ ,  $z$  coordinates for any SWNT defined by rolling up the graphene sheet is provided in Appendix A. This program is based on the helical and rotational symmetries of SWNTs.) We then illustrate some of the uses of helical and rotational symmetries in the calculation of the band structures of SWNTs. Finally, we conclude with brief comments.

## STRUCTURES FROM GRAPHENE

All extended SWNTs can be visualized as a conformal mapping of 2-D graphite (termed graphene) onto the surface of a cylinder. Thus the proper boundary conditions around the cylinder can only be satisfied if the circumference of the cylinder maps onto one of

the Bravais lattice vectors of the graphene sheet.<sup>[11-13]</sup> In addition, each Bravais lattice vector,  $\mathbf{R}$ , can be defined in terms of the two primitive lattice vectors,  $\mathbf{R}_1$  and  $\mathbf{R}_2$ , for graphene depicted in Fig. 1 and a pair of integers, so that

$$\mathbf{R} = n_1 \mathbf{R}_1 + n_2 \mathbf{R}_2. \quad (1)$$

(Note that, if the  $x$  axis in a right-hand coordinate system is oriented along  $\mathbf{R}_1$ , then  $\mathbf{R}_1$  and  $\mathbf{R}_2$  are given by:

$$\mathbf{R}_1 = a \hat{\mathbf{x}} \text{ and } \mathbf{R}_2 = \frac{a}{2} \hat{\mathbf{x}} + \frac{a\sqrt{3}}{2} \hat{\mathbf{y}}, \quad (2)$$

where  $a = \sqrt{3}d$  is the graphene lattice spacing with  $d$  the C-C bond distance, and  $\hat{\mathbf{x}}$  and  $\hat{\mathbf{y}}$  denote the usual unit vectors along the  $x$  and  $y$  axes, respectively.) Thus all unrelaxed SWNTs can be constructed by rolling up a single graphene sheet along one of its 2-D lattice vectors  $\mathbf{R}$  given by Eq. (1) to define an  $[n_1, n_2]$  nanotube with radius,

$$r = \frac{|\mathbf{R}|}{2\pi} = \frac{a}{2\pi} \sqrt{n_1^2 + n_2^2 + n_1 n_2}. \quad (3)$$

The point-group symmetry of the graphene lattice will render many of the SWNTs defined by  $\mathbf{R}$  equivalent. Indeed, this symmetry allows  $\mathbf{R}$  to be restricted to the irreducible wedge of the graphene lattice depicted in Fig. 1, without loss of generality.<sup>[11-13,21]</sup> Each  $\mathbf{R}$  within this wedge defines a different SWNT and all unique SWNTs defined by rolling up the graphene sheet can be generated by this set of  $\mathbf{R}$ 's. Also, within this wedge, only a finite number of SWNTs can be constructed with radii below a given value.

The angle,  $\Theta$ , measured counterclockwise from  $\mathbf{R}_1$  to the roll-up vector,  $\mathbf{R}$ , is usually referred to as the

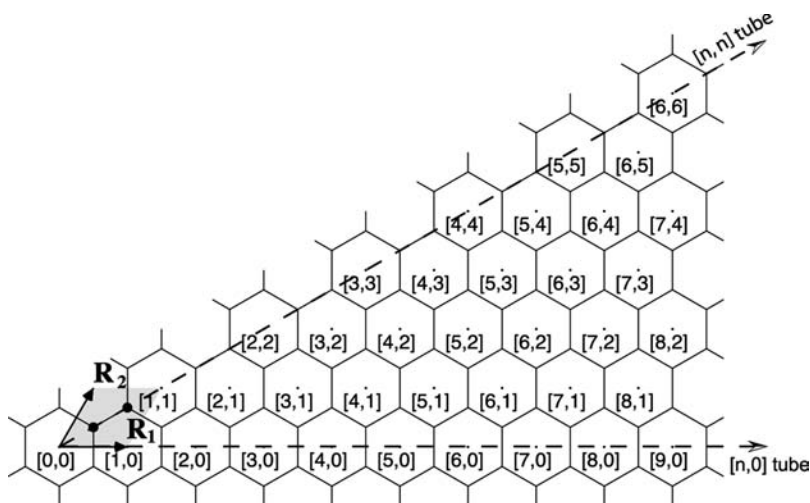


**Fig. 1** Irreducible wedge of the graphene lattice. Primitive lattice vectors  $\mathbf{R}_1$  and  $\mathbf{R}_2$  are shown and the  $[0,0]$  unit cell at the origin is highlighted in gray. Armchair nanotubes are defined by rollup vectors  $\mathbf{R}$  along the  $[n,n]$  direction corresponding to a chiral angle of  $\pi/6$ . Zigzag SWNTs are defined by rollup vectors  $\mathbf{R}$  along the  $[n,0]$  direction corresponding to chiral angle of 0. Source: From Ref.<sup>[15]</sup>.

chiral angle for the SWNT. In terms of  $n_1$  and  $n_2$ ,  $\Theta$  is given by:

$$\Theta = \arccos\left(\frac{2n_1 + n_2}{2\sqrt{n_1^2 + n_2^2 + n_1n_2}}\right) \quad (4)$$

$$= \arctan\left(\frac{\sqrt{3}n_2}{2n_1 + n_2}\right)$$

for tubes defined based on the irreducible wedge of Fig. 1. The set of possible tubes defined by  $\mathbf{R}$  can be completely decomposed into independent families (subsets) with each family member sharing the same orientation of hexagons with respect to the tube axis and, hence, the same  $\Theta$ . Thus, rather than labeling the SWNTs by  $[n_1, n_2]$ , they could have just as well been labeled by  $M[q_1, q_2]$ , where  $[q_1, q_2]$  denotes the family to which  $[n_1, n_2]$  belongs, and  $N$  is the largest common divisor of  $[n_1, n_2]$ .<sup>[12]</sup> Unless otherwise specified, we will use the  $[n_1, n_2]$  notation to label SWNTs.

The construction of the tubule from a conformal mapping of the graphite sheet shows that each tubule can have up to three inequivalent (by point group symmetry) helical operations derived from the primitive lattice vectors of the graphite sheet. Thus while *all* SWNTs have a helical structure, the two families of tubules defined by rollup vectors with chiral angles  $\Theta = 0^\circ$  or  $30^\circ$  in Fig. 1 (which correspond to lattice translation indices of the form  $[n,0]$  and  $[n,n]$ , respectively) will possess a reflection plane. These high-symmetry SWNTs will therefore be achiral. For convenience, these special structures are given family names based on the shapes made by the most direct continuous path of C–C bonds around the circumference of the tubule. Specifically, the  $[n,0]$ -type structures are referred to as zigzag,<sup>[13]</sup> or sawtooth<sup>[21]</sup> tubes, to reflect the path highlighted in gray for the

$[9,0]$  tube at the top of Fig. 2, and the  $[n,n]$ -type structures are referred to as armchair,<sup>[13]</sup> or serpentine,<sup>[21]</sup> tubes to reflect the path highlighted in gray for the  $[5,5]$  tube at the bottom of Fig. 2. For other values of  $\Theta$ , the tubules are chiral.

## TRANSLATIONAL SYMMETRIES

Regardless of whether they are chiral or achiral, all SWNTs defined by  $\mathbf{R}$  in the graphene lattice have translational symmetry along the tube axis<sup>[11]</sup> with a repeat length given by  $\sqrt{3}|\mathbf{R}|$ , as can be seen by inscribing a hexagon with a side coinciding with  $\mathbf{R}$  in the

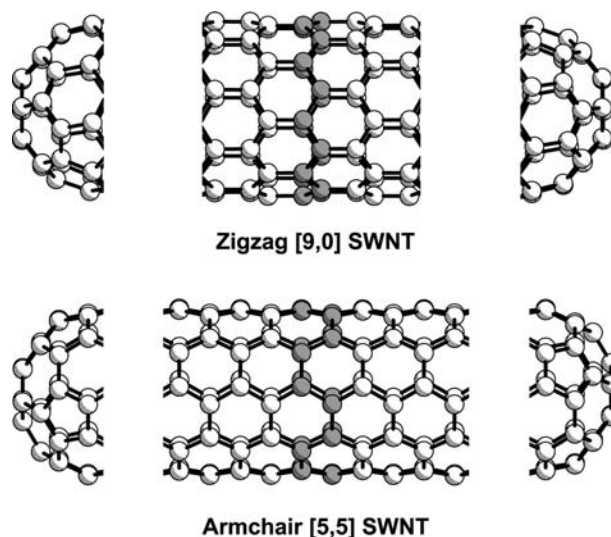


**Fig. 2** Sample achiral zigzag (sawtooth) and armchair (serpentine) SWNTs. Highlighted in gray is the most direct continuous path along C–C bonds around the tube. The shape of this path gives these structures their family names. These two examples can be capped with a hemisphere of  $C_{60}$ . Source: From Ref.<sup>[28]</sup>.

lattice prior to rolling up the sheet. An example is given in Fig. 3 for the [4,2] tube. It might be possible that  $\sqrt{3}|\mathbf{R}|$  is not the minimum translational repeat length. Indeed, by constructing a vector

$$\mathbf{T} = -(2n_2 + n_1)\mathbf{R}_1 + (2n_1 + n_2)\mathbf{R}_2 \quad (5)$$

perpendicular to  $\mathbf{R}$  but lying in the honeycomb lattice, it is immediately obvious that the minimum translational repeat length is given by  $\sqrt{3}|\mathbf{R}|/L$ , where  $L$  is the largest common divisor of  $[2n_2 + n_1]$  and  $[2n_1 + n_2]$ . Hence,  $L = N$ , unless there exists an integer  $m$  such that  $(n_1 - n_2)/N = 3m$ , in which case  $L = 3N$ .<sup>[15]</sup>

Although all SWNTs defined by rolling up the graphene sheet have translational symmetry, the minimum number of atoms in a translational unit cell can be large.<sup>[15]</sup> To see this, first note that the unit cell in graphene contains two atoms and has area given by

$$A_g = |\mathbf{R}_1 \times \mathbf{R}_2| = \frac{\sqrt{3}}{2}a^2 \quad (6)$$

Next, note that the area of the strip that is rolled up to form the minimum-sized translational unit cell of the tube is given by:

$$A_T = \frac{\sqrt{3}|\mathbf{R}|^2}{L} = \frac{\sqrt{3}a^2(n_1^2 + n_2^2 + n_1n_2)}{L}. \quad (7)$$

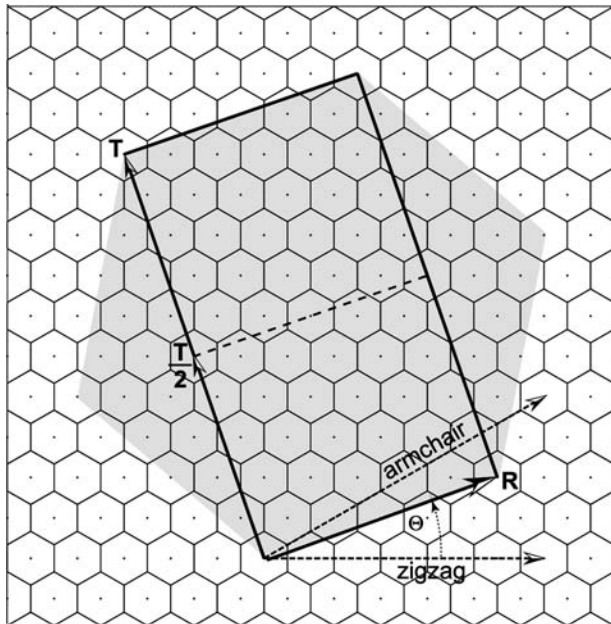


**Fig. 3** The rollup vector  $\mathbf{R}$ , translation vector  $\mathbf{T}$ , and chiral angle  $\theta$  for the [4,2] SWNT. The hexagon highlighted in gray shows that this tube has translational symmetry along the tube axis. For the [4,2],  $L = 2$ , hence the minimum translational repeat length is given by  $|\mathbf{T}|/2$ , which from the properties of the hexagon equals  $\sqrt{3}|\mathbf{R}|/2$ . Source: From Ref.<sup>[28]</sup>.

Hence, the translational unit cell of the SWNT contains  $N_A$  carbon atoms given by:

$$N_A = 2 \frac{A_T}{A_g} = 4 \frac{(n_1^2 + n_2^2 + n_1n_2)}{L}, \quad (8)$$

where

$$L = \begin{cases} 3N & \text{if } (n_1 - n_2)/N = 3m, \text{ with } m \text{ an integer} \\ N & \text{otherwise} \end{cases} \quad (9)$$

and  $N$  is the largest common divisor of  $n_1$  and  $n_2$ . For both the armchair  $[n,n]$  and zigzag  $[n,0]$  tubes, Eq. (9) implies that  $N_A = 4n$ , greatly reducing the number of atoms in the minimum translational unit cell. In these two special cases, Eqs. (3) and (8) show that  $N_A$  scales as the radius,  $r$ , of the tube. It is for this reason that calculations relying on translational symmetry are usually restricted to these two special families of SWNTs.<sup>[12,13]</sup> On the other hand,  $L$  is often 1, so that  $N_A$  scales as  $r^2$ , leading to a large number of atoms in the translational unit cell even for moderate diameter SWNTs. For example, if  $n_1 = 10$  and  $n_2 = 9$ , then the radius of the nanotube is less than 0.7 nm, but from Eq. (8), the translational unit cell contains 1084 carbon atoms. The rapid growth in the number of atoms that can occur in the minimum translational unit cell renders recourse to the helical and any higher point group symmetry of these nanotubes practically mandatory in any comprehensive study of their properties as a function of radius and helicity. As we shall see below, these symmetries can be used to reduce to 2 the number of atoms necessary to generate any nanotube.<sup>[15]</sup>

## HELICAL AND ROTATIONAL SYMMETRIES

The rotational and helical symmetries of a SWNT defined by  $\mathbf{R}$  can be seen by using the corresponding symmetry operators to generate the tubule.<sup>[15]</sup> This is carried out by first introducing a cylinder of radius  $|\mathbf{R}|/2\pi$ . The two carbon atoms located at  $\mathbf{d} \equiv (\mathbf{R}_1 + \mathbf{R}_2)/3$  and  $2\mathbf{d}$  in the [0,0] unit cell of Fig. 1 are then mapped to the surface of this cylinder. The first atom is mapped to an arbitrary point on the cylinder surface, which implies that the position of the second be found by rotating this point by

$$\phi' = 2\pi \frac{\mathbf{d} \cdot \mathbf{R}}{|\mathbf{R}|^2} = \frac{(n_1 + n_2)}{(n_1^2 + n_2^2 + n_1n_2)}\pi \quad (10)$$

about the cylinder axis in conjunction with a translation

$$h' = \frac{|\mathbf{d} \times \mathbf{R}|}{|\mathbf{R}|} = \frac{|n_1 - n_2|}{2\sqrt{3}(n_1^2 + n_2^2 + n_1n_2)^{\frac{1}{2}}}a \quad (11)$$

along this axis. Next, note that the cylinder axis must coincide with a  $C_N$  rotational axis for the tubule, where  $N$  is the largest common divisor of  $n_1$  and  $n_2$ . Thus the positions of these first two atoms can be used to locate  $2(N - 1)$  additional atoms on the cylinder surface by  $(N - 1)$  successive  $2\pi/N$  rotations about the cylinder axis. Altogether, these  $2N$  atoms complete the specification of the helical motif that corresponds to an area on the cylinder surface given by:

$$A_M = N|\mathbf{R}_1 \times \mathbf{R}_2| = \frac{\sqrt{3}}{2}Na^2. \quad (12)$$

This helical motif can then be used to tile the remainder of the tubule by repeated operation of a single-screw operation  $S(h, \phi)$  representing a translation  $h$  units along the cylinder axis in conjunction with a rotation  $\phi$  radians about this axis.

To find  $h$  and  $\phi$  and hence determine  $S(h, \phi)$ , first note that there must exist a real lattice vector

$$\mathbf{H} = p_1\mathbf{R}_1 + p_2\mathbf{R}_2 \quad (13)$$

in the honeycomb lattice that maps to  $S(h, \phi)$  when the sheet is rolled up along  $\mathbf{R}$  to form the tube. In terms of  $\mathbf{H}$  and  $\mathbf{R}$ , the area of the helical motif on the cylinder surface  $A_M$  equals  $|\mathbf{H} \times \mathbf{R}|$ . However,  $A_M$  also equals  $N|\mathbf{R}_1 \times \mathbf{R}_2|$ . Therefore,  $|\mathbf{H} \times \mathbf{R}| = N|\mathbf{R}_1 \times \mathbf{R}_2|$ , or equivalently,<sup>[15]</sup>

$$p_2n_1 - p_1n_2 = \pm N \quad (14)$$

There are no other constraints on  $\mathbf{H}$  and hence on  $S(h, \phi)$ . If a set of integers  $\{p_1, p_2\}$  satisfies Eq. (14), then so too will the sets  $\{p_1 \pm mn_1N, p_2 \pm mn_2N | m \in \text{integers}\}$  and  $\{-p_1, -p_2\}$ . These uncertainties arise because  $\phi$  is defined modulo  $2\pi$  and if  $S(h, \phi)$  generates the tubule, then so will  $S(-h, -\phi)$ . Typically,  $\mathbf{R}$  and  $\mathbf{H}$  are restricted to the irreducible wedge of Fig. 1, the plus sign is chosen in Eq. (14), and then the single solution set is found which yields the minimum value of  $|\mathbf{H} \cdot \mathbf{R}|$  for  $h > 0$ . These choices restrict  $S(h, \phi)$  to a right-handed screw operation along the positive tubule axis that yields a minimum twist angle  $\phi$  around this axis. In contrast to the helical twist angle given by:

$$\begin{aligned} \phi &= 2\pi \frac{\mathbf{H} \cdot \mathbf{R}}{|\mathbf{R}|^2} \\ &= \frac{(2p_1 + p_2)n_1 + (2p_2 + p_1)n_2}{(n_1^2 + n_2^2 + n_1n_2)}\pi \end{aligned} \quad (15)$$

the magnitude of helical translation given by:

$$\begin{aligned} |h| &= \frac{|\mathbf{H} \times \mathbf{R}|}{|\mathbf{R}|} = \frac{N|\mathbf{R}_1 \times \mathbf{R}_2|}{|\mathbf{R}|} \\ &= \frac{\sqrt{3}Na}{2\sqrt{n_1^2 + n_2^2 + n_1n_2}} \end{aligned} \quad (16)$$

is independent of the choice of  $\mathbf{H}$ . These results show that every tubule defined by  $\mathbf{R}$  can be generated by first mapping only two atoms onto the surface of a cylinder of radius  $|\mathbf{R}|/2\pi$ , and then using the rotational and helical symmetry operators to determine the remainder of the tubule.

As an example,<sup>[15]</sup> consider the [6,3] tubule defined by  $\mathbf{R} = 6\mathbf{R}_1 + 3\mathbf{R}_2$ . Then from Eqs. (1), (10), and (11), the first atom of this tubule is mapped to an arbitrary point on the surface of a cylinder of radius  $3a\sqrt{7}/2\pi$ , and the position of the second then found by rotating this point  $\pi/7$  radians around the cylinder axis in conjunction with a translation  $a/(2\sqrt{21})$  units along this axis. Because  $N = 3$ , the cylinder axis must coincide with a  $C_3$  axis for the tubule. Thus the positions of these first two atoms can be used to locate four additional atoms on the cylinder surface by two successive  $2\pi/3$  rotations around this axis. Altogether, these six atoms complete the specification of the helical motif for this tubule. To determine  $S(h, \phi)$  used to generate the remainder of the tubule from this motif, Eq. (14) can be solved subject to the constraints above to find the solution set  $\{1, 1\}$ . Hence  $\mathbf{H} = \mathbf{R}_1 + \mathbf{R}_2$ , which in turn, using Eqs. (15) and (16), implies that  $\phi = 3\pi/7$  and  $h = 3/(2\sqrt{21})$ . If this resultant  $S(h, \phi)$  is applied to only the first two atoms mapped to the cylinder surface, then one third of the tubule is generated as illustrated in Fig. 4 (left). However, if the full helical motif is used, then the entire structure is generated as shown in Fig. 4 (right).

Extended 1-D polymers with both helical and translational symmetries are often labeled as  $N_H^*N_M/N_T$  helices with helical step,  $s$ , where  $N_H$  is the number of

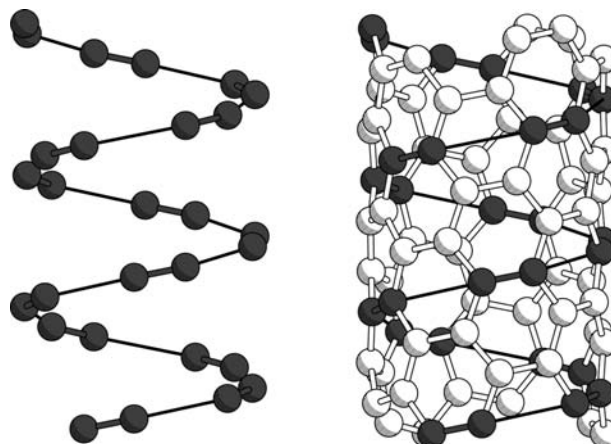


**Fig. 4** Left: One-third of the [6,3] tubule generated by applying  $S(h, \phi)$  with  $\phi = 3\pi/7$  and  $h = 3a/2\sqrt{21}$  to only the first two atoms mapped to the cylinder. Thin dark lines are not bonds but are rather included as a guide to the eye. Right: This same one-third plus the remaining two thirds of the [6,3] tubule generated by applying  $S(h, \phi)$  to the full six-atom helical motif. Source: From Ref.<sup>[15]</sup>.



atoms in the primitive helical motif and  $N_M$  is the number of primitive motifs in the translational unit containing  $N_T$  complete  $2\pi$  helical turns.<sup>[22]</sup> This translational unit need not always correspond to the minimum length translational unit cell because it must contain an integer number of complete helical turns. Also note that the notation  $N_M/N_T$  indicates that any common factors between  $N_M$  and  $N_T$  should be eliminated. Because SWNTs defined by  $\mathbf{R}$  not only have helical, but also translational symmetry, they also can be labeled by using this notation.<sup>[11,15]</sup> In this case,  $N_H = 2N$ ,  $N_M = \sqrt{3}|\mathbf{R}|/|h|$ ,  $N_T = N_M\phi/2\pi$ , and  $s = h$ , where  $N$  is the largest common divisor of  $n_1$  and  $n_2$ , and  $\phi$  and  $h$  are given by Eqs. (15) and (16), respectively. In this notation, for  $h > 0$ , the [6,3] tubule can be labeled as a  $6^*14/3$  helix<sup>[15]</sup> with  $h = 3a/(2\sqrt{21})$ , while the [30,3] tubule can be labeled as a  $6^*222/67$  helix with  $h = \sqrt{3}a/(2\sqrt{111})$ . On the other hand, for  $h < 0$ , the [6,3] tubule can be labeled as a  $6^*42/5$  helix with  $h = -3a/(2\sqrt{21})$ , while the [30,3] tubule can be labeled as a  $6^*222/7$  helix<sup>[11]</sup> with  $h = -\sqrt{3}a/(2\sqrt{111})$ . Assuming  $h > 0$ , the notation is further clarified for the [6,3] tubule in Fig. 5, where the 6 atoms that will form the primitive helical motif ( $\bullet$ ), the 14 successive applications of  $S(h,\phi)$  (represented by  $\mathbf{H}$  in the plane) necessary to generate the translational unit cell (Arabic numerals), and the 3 complete helical turns in this repeat unit (Roman numerals) are all depicted.

Actual SWNTs should relax somewhat from the geometry expected from rolling up a graphene sheet. Indeed, there is no clear reason to assume that after relaxation, they should possess translational symmetry. However, first-principles local density functional

(LDF) calculations have shown that the geometry predicted by rolling up the graphene sheet is quite close to the actual optimized tube geometry for SWNTs that are typically studied experimentally.<sup>[16]</sup> Furthermore, the techniques described below for calculating the electronic structure of an extended SWNT do not rest on the assumption of translational symmetry.

## USE OF HELICAL AND ROTATIONAL SYMMETRIES

The first use of the helical and rotational symmetries of SWNTs is to generate the geometries of an arbitrary  $[n_1, n_2]$  tube defined by rolling up the graphene sheet as a starting point to additional studies. A Fortran computer program that may be used for this purpose is provided in Appendix A. This program implements the procedure outlined in the section ‘‘Helical and Rotational Symmetries’’ and Ref.<sup>[15]</sup> to calculate the  $x, y, z$  coordinates for either a user-defined number of helical motifs or number of translational unit cells in the SWNT. It also returns the tube’s radius,  $r$ , the chiral angle,  $\Theta$ , the number of atoms in the primitive helical motif,  $2N$ , and minimum length translational unit cell,  $N_A$ , and classifies the SWNT as an  $N_H^*N_M/N_T$  helix with helical step  $h$  assumed greater than zero.

The helical and rotational symmetries of SWNTs are, of course, much more broadly useful in studies of their properties. For example, they were used in the earliest band structure calculations of both armchair and chiral SWNTs at both the first-principles LDF<sup>[10,16]</sup> and all-valence tight-binding levels<sup>[11,14,16]</sup> to make these calculations manageable. Here we illustrate how these symmetries can reduce the size of the matrices that have to be diagonalized in a calculation of the nanotube’s electronic structure within a tight-binding approach to one no larger than that encountered in a corresponding electronic structure calculation of graphene.<sup>[15]</sup>

To understand how this is carried out, first assume that each carbon atom in a tubule is described by  $j$  atomic-centered basis functions. Next, let  $(m, \ell)$  denote a cell in the tubule generated by first mapping the [0,0] unit cell of Fig. 1 to the surface of the cylinder, and then translating and rotating this cell by  $m$  applications of the screw operator  $S(h, \phi)$ , followed by  $\ell$  applications of the rotational operator  $C_N$ . Like the helical motif, these cells tile the tubule, but contain 2 instead of  $2N$  carbon atoms. In this notation, a cell labeled by  $(m, \ell)$  in the  $[n_1, n_2]$  tubule corresponds to the unit cell in the graphene plane located at

$$\mathbf{r}_{q_1q_2} = q_1\mathbf{R}_1 + q_2\mathbf{R}_2, \quad (17)$$

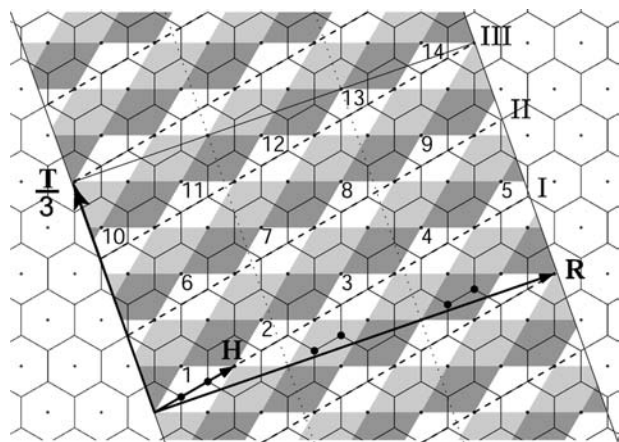


**Fig. 5** Six-atom helical motif ( $\bullet$ ), fourteen helical steps (arabic numerals), and three full twists (roman numerals) used to generate the minimum translational repeat unit for the [6,3] tubule. The light dotted lines illustrate the  $C_3$  axis for this tubule. Source: From Ref.<sup>[15]</sup>.



where from the definitions of  $\mathbf{R}$  and  $\mathbf{H}$  and with the help of Eq. (14),

$$\begin{aligned} m &= (q_2 n_1 - q_1 n_2)/N \text{ and } \ell \\ &= q_1 p_2 - q_2 p_1, \end{aligned} \quad (18)$$

with  $\ell$  defined modulo  $N$ . Now, in a short-hand notation, let  $|m, \ell\rangle$  denote the set of basis functions centered on the two carbon atoms contained in the tubule cell labeled by  $(m, \ell)$ . This set contains  $2j$  elements. Then, because  $S(h, \phi)$  and  $C_N$  commute, symmetry adapted generalized Bloch sums given by:

$$\begin{aligned} |\kappa, n\rangle &= \lim_{M \rightarrow \infty} \frac{1}{\sqrt{2NM}} \\ &\times \sum_{m=-M}^M \sum_{\ell=0}^{N-1} e^{-i\kappa m} e^{-2\pi i n \ell / N} |m, \ell\rangle \end{aligned} \quad (19)$$

can be constructed such that

$$\begin{aligned} C_N |\kappa, n\rangle &= e^{2\pi i n / N} |\kappa, n\rangle \text{ with } n \\ &= 0, \dots, N-1 \end{aligned} \quad (20)$$

and

$$S(h, \phi) |\kappa, n\rangle = e^{i\kappa} |\kappa, n\rangle \text{ with } -\pi < \kappa \leq \pi. \quad (21)$$

Just as  $\mathbf{H}$  maps to  $S(h, \phi)$  when graphene is rolled up along  $\mathbf{R}$  to form the tube, the scalar product  $\mathbf{k} \cdot \mathbf{H}$  maps to  $\kappa$  of the SWNT, where  $\mathbf{k}$  denotes the usual 2-D crystalline momentum of the sheet, i.e.,

$$\kappa = \mathbf{k} \cdot \mathbf{H}. \quad (22)$$

Next, note that the matrix elements of the Hamiltonian,  $H$ , between these generalized Bloch functions must vanish due to symmetry, unless  $n = n'$  and  $\kappa = \kappa'$ , so that  $H$  can be written as

$$H = \sum_k \sum_{n=0}^{N-1} |\kappa, n\rangle \langle \kappa, n | H | \kappa, n \rangle \langle \kappa, n |. \quad (23)$$

where

$$\begin{aligned} \langle \kappa, n | H | \kappa, n \rangle &= \sum_{m=-\infty}^{\infty} \sum_{\ell=0}^{N-1} e^{-i\kappa m} e^{-2\pi i n \ell / N} \langle 0, 0 | H | m, \ell \rangle. \end{aligned} \quad (24)$$

$$\langle \kappa, n | H | \kappa, n \rangle = V_0 \begin{pmatrix} 0 & 1 + e^{\frac{ikn_1 - 2\pi n p_1}{N}} + e^{-\frac{ikn_2 - 2\pi n p_2}{N}} \\ 1 + e^{-\frac{ikn_1 - 2\pi n p_1}{N}} + e^{\frac{ikn_2 - 2\pi n p_2}{N}} & 0 \end{pmatrix}. \quad (25)$$

$$\varepsilon_0(\kappa) = \pm |V_0| \sqrt{3 + 2 \cos n_1 \kappa + 2 \cos n_2 \kappa + 2 \cos(n_1 + n_2) \kappa}, \quad (28)$$

Eqs. (23) and (24) reduce the matrices to be diagonalized in a tubule band structure calculation to a size no larger than those encountered in a corresponding band structure calculation for graphene.<sup>[15]</sup> For example, if we assume an all-valence carbon  $s$  and  $p$  tight-binding model, then the problem is reduced to the diagonalization of an  $8 \times 8$  matrix for each  $\kappa$  and  $\ell$ . In addition, first-principles LDF calculations indicate<sup>[10]</sup> that the highest occupied and lowest unoccupied valence bands of these tubules should be primarily formed from the set of carbon  $p$  orbitals (one per carbon atom) oriented normal to the tubule surface and denoted by  $p_{\perp}$ . Assuming only this set of valence functions, then the right-hand side of Eq. (24) reduces to a  $2 \times 2$  matrix, which within a constant on-site term is given by Eq. (25) below. In obtaining Eq. (25), only matrix elements,  $V_0$ , between nearest-neighboring  $p_{\perp}$  orbitals were retained and small differences in  $V_0$  that arise because of different C-C bonding directions on the tubule surface were neglected. Eq. (18) was also employed to determine that  $S^{(\mp n_1/N)} C_N^{\pm p_1}$  and  $S^{(\pm n_2/N)} C_N^{\mp p_2}$  can be used to locate the four nearest-neighboring cells to  $(0, 0)$  on the SWNT surface. Eq. (25) can then be diagonalized to yield the one-electron dispersion relations for an  $[n_1, n_2]$  SWNT.<sup>[15]</sup>

$$\varepsilon_n(\kappa) = \pm |V_0| \sqrt{3 + A_n(\kappa)}. \quad (26)$$

where

$$\begin{aligned} A_n(\kappa) &= 2 \cos\left(\frac{n_1 \kappa - 2\pi n p_1}{N}\right) \\ &+ 2 \cos\left(\frac{n_2 \kappa - 2\pi n p_2}{N}\right) \\ &+ 2 \cos\left(\frac{(n_1 + n_2) \kappa - 2\pi n (p_1 + p_2)}{N}\right). \end{aligned} \quad (27)$$

$-\pi < \kappa \leq \pi$ ,  $n = 0 \dots N-1$  ( $N$  is the largest common divisor of  $n_1$  and  $n_2$ ), and  $p_1$  and  $p_2$  are given by Eq. (14).

If  $n_1$  and  $n_2$  are relatively prime, then  $N = 1$ , so that Eq. (26) reduces to Eq. (28) below. Thus as a consequence of screw symmetry, a SWNT such as the  $[10, 9]$  has only a single bonding and a single antibonding band as shown in Fig. 6. This is in marked contrast

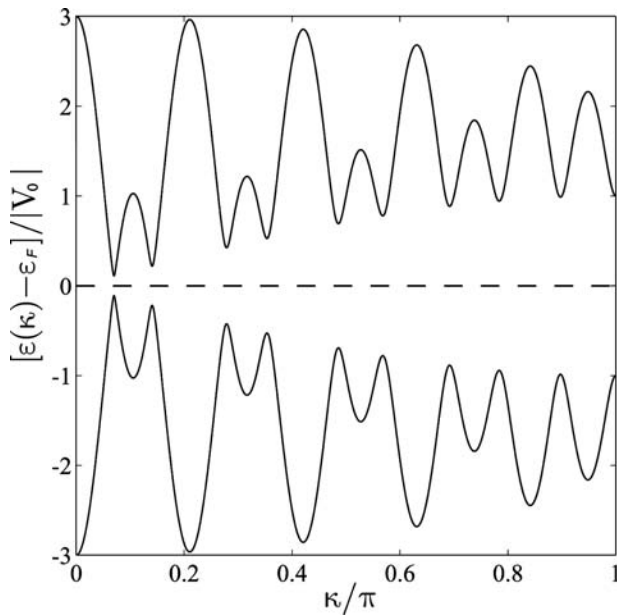


**Fig. 6** Band structures of [10,9] SWNT from Eq. (26) as a function of the helical phase factor  $\kappa$  from 0 to  $\pi$ . The bands at  $-\kappa$  are the same as those at  $\kappa$ . Hence, results are plotted over only half of the central 1-D zone. The Fermi level is shown as a horizontal dashed line. *Source:* From Ref.<sup>[28]</sup>.

to the 1084 bands that would be obtained if translational symmetry were used to obtain the band structure of the [10,9] SWNT within the same model. If  $N \neq 1$ , then  $p_1$  and  $p_2$  must be first obtained from Eq. (14) prior to evaluating Eq. (27). Examples are given for the [5,5] SWNT ( $N = 5$ ) in Fig. 7. Although apparently different, Fig. 7A and B depict equally valid band structures for the [5,5] tube obtained from Eq. (26). The differences arise because a twist angle of  $\phi = \pi/5$  ( $p_2 = 1, p_1 = 0$ ) was assumed in obtaining Fig. 7A, while  $\phi = \pi$  ( $p_2 = 3, p_1 = 2$ ) was assumed

in obtaining Fig. 7B. Either choice is allowed by Eq. (14) for the [5,5] SWNT and will yield identical results for any measurable property. Fewer distinct bands are visible in Fig. 7B because  $\phi = \pi$  also makes the bands eigenstates of the symmetry operations of the  $C_{5v}$  point group which include the doubly degenerate  $e_1$  and  $e_2$  representations.

The neglect of curvature (other than a slight reduction in  $V_0$  from its value in the graphene sheet) and the inclusion of only nearest-neighbor C–C interactions in obtaining Eq. (27) make the model identical to the single-parameter graphene sheet model (GSM) of SWNTs. This GSM, which was proposed in the earliest theoretical paper on the electronic structure of extended SWNTs,<sup>[10]</sup> and now supported by many experiments,<sup>[1–9]</sup> has been used in successfully predicting many of the fundamental properties of carbon nanotubes with diameters similar to or greater than  $I_h C_{60}$ .<sup>[10–16]</sup> These properties include the grouping of SWNTs as either metallic or semiconducting,<sup>[2,3,10,12–16]</sup> the linear dispersion relations of the metallic tubes in the vicinity of the Fermi level,  $\epsilon_F$ ,<sup>[5,6,10,16]</sup> the approximate  $1/r$  dependence of the semiconducting band gaps,<sup>[2,3,12–16]</sup> the stability of the metallic tubes against a Peierls distortion,<sup>[1,10]</sup> and robust ballistic transport through metallic tubes.<sup>[8,9,23]</sup> The graphene sheet model has also been used to successfully explain and relate the positions of the first few divergent van Hove singularities observed both in metallic and semiconducting SWNTs in STM experiments.<sup>[24,25]</sup>

The  $\pi$  bands of graphene are described, within the standard GSM, by a tight-binding Hamiltonian characterized by a single Slater–Koster parameter,  $V_{pp\pi}$ , representing the nearest-neighbor hopping matrix element between carbon  $|p\pi\rangle$  orbitals oriented perpendicular to the graphene sheet. Using translational

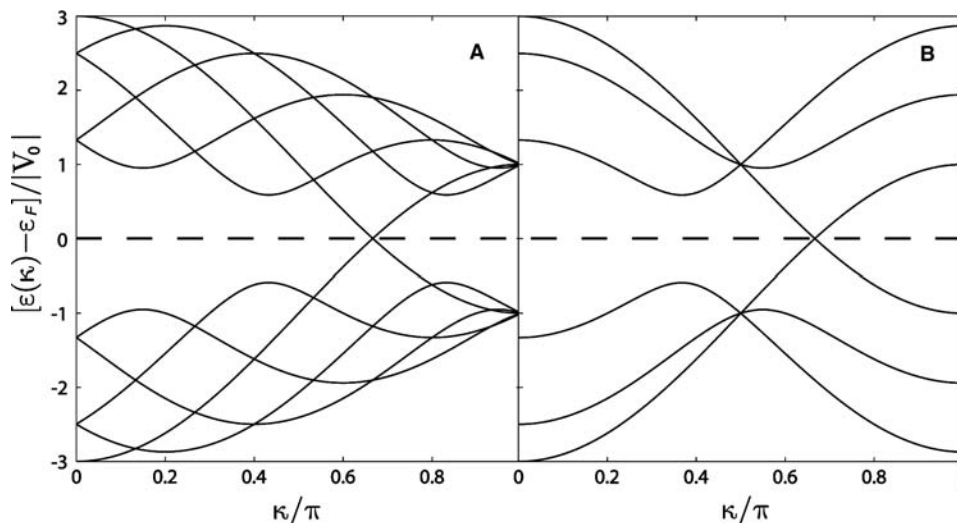


**Fig. 7** Band structures of the [5,5] SWNT from Eq. (26) as a function of the helical phase factor  $\kappa$  from 0 to  $\pi$ . (A) Results obtained by assuming  $\phi = \pi/5$  ( $p_2 = 1, p_1 = 0$ ). (B) Results obtained by assuming  $\phi = \pi$  ( $p_2 = 3, p_1 = 2$ ). The bands at  $-\kappa$  are the same as those at  $\kappa$ . Hence, results are plotted over only half of the central 1-D zone. The Fermi level is shown as a horizontal dashed line.

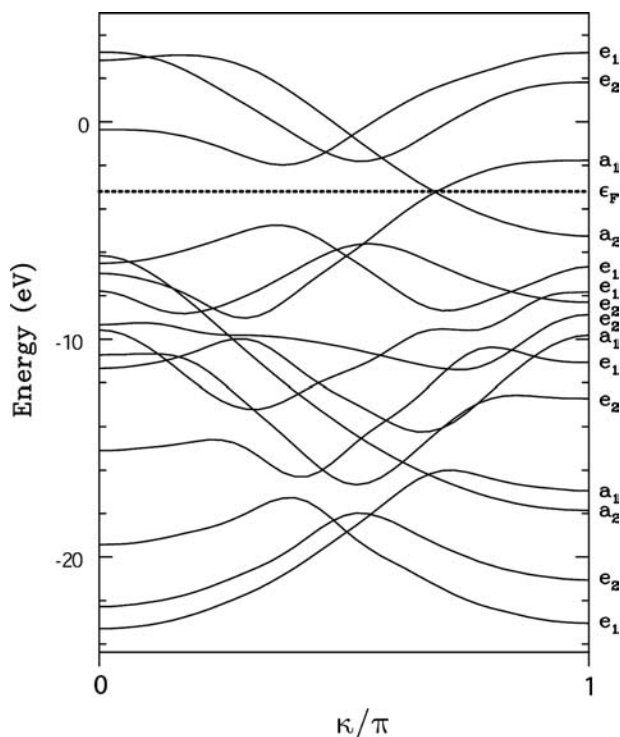


**Fig. 8** First-principles LDF results for the band structure of the [5,5] SWNT obtained by assuming  $\phi = \pi$  ( $p_2 = 3$ ,  $p_1 = 2$ ). These results can be compared to the GSM results of Fig. 7(B). The bands at  $-\kappa$  are the same as those at  $\kappa$ . Hence, results are plotted over only half of the central 1-D zone. The Fermi level is shown as a horizontal dashed line. Source: From Ref.<sup>[10]</sup>.

symmetry, this Hamiltonian reduces to a  $2 \times 2$  matrix, which is easily diagonalized to obtain the one-electron dispersion relations of the graphene sheet given by Eq. (28) below, in terms of the 2-D crystalline momentum  $\mathbf{k}$  and the primitive lattice vectors  $\mathbf{R}_1$  and  $\mathbf{R}_2$ . The band structure of the SWNT defined by  $\mathbf{R}$  is then constructed from Eq. (29) by imposing periodic boundary conditions over the rollup vector  $\mathbf{R}$  so that

$$\mathbf{k} \cdot \mathbf{R} = 2\pi m, \quad (30)$$

where  $m$  is an integer.<sup>[10,12,13]</sup> At this point, the discussion usually proceeds in terms of allowed lines in the 2-D central Brillouin zone of graphene and translational symmetry along the SWNT axis—an approach that can lead to thousands of bands for tubes of experimental interest. However, these complexities

can be avoided by first using Eqs. (1), (13), and (14) to show that

$$\begin{aligned} \mathbf{R}_1 &= \pm(p_2\mathbf{R} - n_2\mathbf{H})/N \text{ and} \\ \mathbf{R}_2 &= \pm(n_1\mathbf{H} - p_1\mathbf{R})/N \end{aligned} \quad (31)$$

and then using these results in Eq. (29), in conjunction with Eqs. (22) and (30) to recover Eq. (26), which takes full advantage of the helical and rotational symmetries. Note that, in Eq. (29), the nearest-neighbor C–C matrix element is written as  $V_{pp\pi}$ , while in Eq. (26), the corresponding quantity is written as  $V_0$ . These differences have been maintained to reflect the observation that, for tubes that are typically studied experimentally,  $V_{pp\pi}$  should be reduced from its value in graphene ( $V_{pp\pi} \approx -2.8$  to  $-3.0$  eV) to a slightly smaller value ( $V_0 \approx -2.5$  to  $-2.8$  eV), consistent with both LDF calculations<sup>[16]</sup> and scanning tunneling microscopy (STM) measurements on SWNTs.<sup>[2,3]</sup> Such a reduction is expected because, in contrast to graphene, the nearest-neighbor  $p_{\perp}$  orbitals are no longer exactly parallel in SWNTs.

Finally, note that screw symmetry has also been extensively employed in all-electron, self-consistent LDF band-structure calculations of SWNTs<sup>[10,16,25]</sup> by using a method originally developed to treat chain polymers<sup>[26]</sup> and especially tailored to take advantage of helical symmetry.<sup>[27]</sup> In this approach, the one-electron wavefunctions are first constructed from linear combinations of helically adapted Bloch functions, which in turn are constructed from linear combinations of nuclear centered products of Gaussians and real solid spherical harmonics, and then these wavefunctions are used in solving the self-consistent LDF equations. A sample LDF band structure obtained by using this approach is shown in Fig. 8.<sup>[10]</sup> These results for the [5,5] SWNT can be compared to the corresponding results for this tube obtained from the GSM (Fig. 7B) for bands in the vicinity of  $\epsilon_F$ .

## CONCLUSION

In this review, we have provided an introduction to the use of helical and rotational symmetries in studying the properties of SWNTs. Attention has been focused on basic electronic properties, but these symmetries are also equally useful in the study of vibrational properties. Furthermore, they are essential if one wishes to study,

$$\epsilon_{\pm}(\mathbf{k}) = \pm|V_{pp\pi}|\sqrt{3 + 2 \cos \mathbf{k} \cdot \mathbf{R}_1 + 2 \cos \mathbf{k} \cdot \mathbf{R}_2 + 2 \cos \mathbf{k} \cdot (\mathbf{R}_1 - \mathbf{R}_2)}. \quad (29)$$

for example, the effects of twists in all but the simplest models of SWNTs.

## ACKNOWLEDGMENTS

This work was supported by the Office of Naval Research both directly and through the Naval Research Laboratory.

## APPENDIX

Program BUILDTUBE<sup>[28]</sup> calculates the  $x$ ,  $y$ ,  $z$  coordinates in Angstroms of an  $[n_1, n_2]$  SWNT for either a user-defined number of helical motifs or primitive translational unit cells using the procedure given in this entry and Ref.<sup>[15]</sup>. Initial input should only be in the form of a couple integers separated by a space. When using this program to generate the coordinates of atoms in a user-specified number of translational unit cells, keep in mind that if  $n_1$  and  $n_2$  are relatively prime, then a single translational unit cell can contain well over a thousand atoms. This is true even for SWNTs with diameters as small as about a nanometer. Output is in the form of two files. Sample output files are given below following the listing of the source code written in Fortran 77.

```

PROGRAM BUILDTUBE
*****
* PROGRAM CALCULATES X,Y,Z COORDINATES OF AN [N1,N2] *
* CARBON NANOTUBE USING THE PROCEDURE OF [C.T.White, *
* D.H.Robertson, and J.W.Mintmire, Phys. Rev. B 47, *
* 5485 (1993)]. *
* INPUTS: N1,N2, AND EITHER NHM OR NUC *
* N1 = FIRST INDEX OF NANOTUBE; N1 > 0. *
* N2 = SECOND INDEX OF NANOTUBE; 0 <= N2 <= N1 *
* NHM = NUMBER OF HELICAL MOTIFS *
* NUC = NUMBER OF TRANSLATIONAL UNIT CELLS *
*****
DIMENSION X(2),Y(2),Z(2)
COMMON/BK1/ PI,DCC,NR,SQRNR
10 WRITE(6,1)
   READ(5,*)N1,N2
   IF(N2.LT.0.OR.N1.LT.0.OR.N1.LT.N2)WRITE(6,2)
   IF(N2.LT.0.OR.N1.LT.0.OR.N1.LT.N2)GOTO 10
30 WRITE(6,7)
   READ(5,*)NCHOICE
   IF(NCHOICE.NE.0.AND.NCHOICE.NE.1)GOTO 30
   IF(NCHOICE.EQ.0)THEN
     WRITE(6,8)
     READ(5,*)NHM
     ELSE
     WRITE(6,9)
     READ(5,*)NUC
     ENDIF
     DCC=1.42
     PI=ACOS(-1.0)
     SQR3=SQR(3.)
     NR=N1**2+N2**2+N1*N2
     SQRNR=SQR(FLOAT(NR))
     CALL LCD(N1,N2,N)
     CALL HELIX(N1,N2,N,NP1,NP2,NM,NT,HS,HA)
     TD=SQR3*SQRNR*DCC/PI
     L=N
     IF(MOD((N1-N2)/N,3).EQ.0)L=3*N
     NA=4*NR/L
     IF(NCHOICE.EQ.1)NHM=NUC*NA/(2*N)
     CHIRALA=ATAN(SQR3*N2/(2*N1+N2))

```

```

WRITE(100,4)N1,N2,NA,TD*.1,180.*CHIRALA/PI,2*N,
5 NP1,NP2,HS*.1,180.*HA/PI
WRITE(100,3)2*N,NM,NT,HS*.1
HA0=PI*(N1+N2)/FLOAT(NR)
HS0=DCC*(N1-N2)/(2.*SQRNR)
CA=COS(HA)
SA=SIN(HA)
X1=TD/2.
Y1=0.
X2=X1*COS(HA0)
Y2=X1*SIN(HA0)
B0=(2.D0*PI)/N
WRITE(200,6) N*2*NHM,DCC,N1,N2,NHM
DO J=0,N-1
  B=J*B0
  CB=COS(B)
  SB=SIN(B)
  X(1)=X1*CB-Y1*SB
  X(2)=X2*CB-Y2*SB
  Y(1)=X1*SB+Y1*CB
  Y(2)=X2*SB+Y2*CB
  Z(1)=0.
  Z(2)=HS0
  WRITE(200,5)X(1),Y(1),Z(1)
  WRITE(200,5)X(2),Y(2),Z(2)
  DO L=1,NHM-1
    DO K=1,2
      XX=X(K)*CA-Y(K)*SA
      Y(K)=X(K)*SA+Y(K)*CA
      Z(K)=Z(K)+HS
      X(K)=XX
      WRITE(200,5)X(K),Y(K),Z(K)
    ENDDO
  ENDDO
  ENDDO
  STOP
1 FORMAT('INPUT: N1 N2')
2 FORMAT('N1 SHOULD BE => N2 => 0')
3 FORMAT('Can be labeled as a',I4,'*',I4,'/',I4,1X,
& 'helix with h =',F8.4,1X,'nm.')
4 FORMAT(['I3,I3,'] SWNT:',///,3X,
& 'Number of atoms in smallest translational unit cell:',
& I6,///,3X,'Diameter (nm):',41X,F8.4,///,3X,
& 'Chiral angle (Degrees):',32X,F8.4,///,
& 3X,'Number of atoms in smallest helical motif:',12X,
& I4,///,3X,'Components of H [p1,p2]:',32X,['I3,I3,']
& ,///,3X,'Helical Twist Step (nm) > 0:',27X,F8.4,///,3X,
& 'Helical Twist angle (Degrees) > 0:',21X,F8.4,///)
5 FORMAT('C ',3(F8.4,3X))
6 FORMAT(I5,/,F8.4,2X,2I4,2X,I5)
7 FORMAT('ENTER 0 TO SPECIFY # OF MOTIFS',/,
& 'ENTER 1 TO SPECIFY # OF TRANSLATIONAL UNIT CELLS')
8 FORMAT('ENTER NUMBER OF HELICAL MOTIFS')
9 FORMAT('ENTER NUMBER OF TRANSLATIONAL UNIT CELLS')
END

SUBROUTINE LCD(N1,N2,MX)
MX = MAX(N1,N2)
MI = MIN(N1,N2)
DO WHILE(MI.NE.0)
  L1 = MI
  MI = MOD(MX,MI)
  MX = L1
ENDDO
RETURN
END

SUBROUTINE HELIX(N1,N2,N,NP1,NP2,NM,NT,HS,HA)
COMMON/BK1/ PI,DCC,NR,SQRNR
NM=2*NR/N
NP1=0
NP2=1
NTEST=NP2*N1-NP1*N2
DO WHILE(NTEST.GT.N)
  NP1=NP1+1
  NTEST=NP2*N1-NP1*N2
ENDDO
IF(NTEST.EQ.N)GOTO 20
NP2=NP2+1
GO TO 10
20 NT=((2*NP1+NP2)*N1+(2*NP2+NP1)*N2)/N
HS=(3.*DCC*N)/(2.*SQRNR)
HA=(DFLOAT(NT)/DFLOAT(NM))*2.*PI
CALL LCD(NM,NT,NMT)
NM=NM/NMT
NT=NT/NMT
RETURN
END

```

Sample output files:

Output file 1:

```
[ 10 9] SWNT:

Number of atoms in smallest translational unit cell: 1084

Diameter (nm):                1.2888

Chiral angle (Degrees):       28.2595

Number of atoms in smallest helical motif: 2

Components of H [p1,p2]:      [ 1 1]

Helical Twist Step (nm) > 0:  0.0129

Helical Twist angle (Degrees) > 0: 37.8598

Can be labeled as a 2* 542/ 57 helix with h = 0.0129 nm.
```

Output file 2: First row: number of atoms treated. Second row: C–C bond distance,  $[n_1, n_2]$  SWNT indices, and number of primitive motifs requested. Following rows:  $x$ ,  $y$ ,  $z$  coordinates of atoms in Angstroms. This file is written out in the standard  $xyz$  format suitable as input to several common molecular graphics programs.

```
20
1.4200 10 9 10
C 6.4440 0.0000 0.0000
C 6.2883 1.4079 0.0431
C 5.0876 3.9549 0.1294
C 4.1006 4.9709 0.1725
C 1.5895 6.2449 0.2588
C 0.1867 6.4413 0.3019
C -2.5777 5.9059 0.3882
C -3.8058 5.2001 0.4313
C -5.6598 3.0808 0.5176
C -6.1962 1.7698 0.5607
C -6.3593 -1.0412 0.6469
C -5.9782 -2.4055 0.6901
C -4.3817 -4.7250 0.7763
C -3.2435 -5.5682 0.8195
C -0.5596 -6.4196 0.9057
C 0.8565 -6.3868 0.9488
C 3.4981 -5.4118 1.0351
C 4.5960 -4.5168 1.0782
C 6.0832 -2.1258 1.1645
C 6.4007 -0.7453 1.2076
```

## REFERENCES

1. Tans, S.J.; Devoret, M.H.; Dai, H.J.; Thess, J.; Smalley, R.E.; Geerligs, L.J.; Dekker, C. Individual single-wall carbon nanotubes as quantum wires. *Nature (Lond.)* **1997**, *386* (6624), 474–477.
2. Wildoer, J.W.G.; Venema, L.C.; Rinzler, A.G.; Smalley, R.E.; Dekker, C. Electronic structure of atomically resolved carbon nanotubes. *Nature (Lond.)* **1998**, *391* (6662), 59–62.
3. Odom, T.W.; Huang, J.L.; Kim, P.; Lieber, C.M. Atomic structure and electronic properties of single-walled carbon nanotubes. *Nature (Lond.)* **1998**, *391* (6662), 62–64.
4. Venema, L.C.; Wildoer, J.W.G.; Janssen, J.W.; Tans, S.J.; Tuinstra, H.L.J.T.; Kouwenhoven, L.P.; Dekker, C. Imaging electron wave functions of quantized energy levels in carbon nanotubes. *Science* **1999**, *283* (5398), 52–55.
5. Lemay, S.G.; Janssen, J.W.; van den Hout, M.; Mooij, M.; Bronikowski, M.J.; Willis, P.A.; Smalley, R.E.; Kouwenhoven, L.P.; Dekker, C. Two-dimensional imaging of electronic wavefunctions in carbon nanotubes. *Nature (Lond.)* **2001**, *412* (6847), 617–620.
6. Ouyang, M.; Huang, J.L.; Lieber, C.M. One-dimensional energy dispersion of single-walled carbon nanotubes by resonant electron scattering. *Phys. Rev. Lett.* **2002**, *88* (6), 066804-1–066804-4.
7. Ouyang, M.; Huang, J.L.; Cheung, C.L.; Lieber, C.M. Energy gaps in “metallic” single-walled carbon nanotubes. *Science* **2001**, *292* (5517), 702–705.
8. Liang, W.J.; Bockrath, M.; Bozovic, D.; Hafner, J.H.; Tinkham, M.; Park, H. Fabry–Perot interference in a nanotube electron waveguide. *Nature* **2001**, *411* (6838), 665–669.
9. McEuen, P.L.; Bockrath, M.; Cobden, D.H.; Yoon, Y.-G.; Louie, S.G. Disorder, pseudospins, and backscattering in carbon nanotubes. *Phys. Rev. Lett.* **1999**, *84* (24), 5098–5101.
10. Mintmire, J.W.; Dunlap, B.I.; White, C.T. Are fullerene tubules metallic? *Phys. Rev. Lett.* **1992**, *68* (5), 631–634.
11. Mintmire, J.W.; Robertson, D.H.; Dunlap, B.I.; Mowrey, R.C.; Brenner, D.W.; White, C.T. Electronic structure of fullerene tubules. In *Electrical, Optical, and Magnetic Properties of Organic Solid State Materials*; MRS Symp. Proc.; Chiang, L.Y., Garito, A.F., Sandman, D.J., Eds.; Materials Research Society: Pittsburgh, 1992; Vol. 247, 339–342.
12. Hamada, N.; Sawada, S.; Oshiyama, A. New one-dimensional conductors: graphitic microtubules. *Phys. Rev. Lett.* **1992**, *68* (10), 1579–1581.
13. Saito, R.; Fujita, A.M.; Dresselhaus, G.; Dresselhaus, M.S. Electronic structure of chiral graphene tubules. *Appl. Phys. Lett.* **1992**, *60* (18), 2204–2206.
14. White, C.T.; Mintmire, J.W.; Mowrey, R.C.; Brenner, D.W.; Robertson, D.H.; Harrison, J.A.; Dunlap, B.I. Predicting properties of fullerenes and their derivatives. In *Buckminsterfullerenes*; Billups, W.E., Ciufolini, M.A., Eds.; VHS Publishers, Inc.: New York, 1993; 125–184.

15. White, C.T.; Robertson, D.H.; Mintmire, J.W. Helical and rotational symmetries of nanoscale graphitic tubules. *Phys. Rev., B* **1993**, *47* (9), 5485–5488.
16. Mintmire, J.W.; Robertson, D.H.; White, C.T. Properties of fullerene nanotubes. *J. Phys. Chem. Solids* **1993**, *54* (12), 1835–1840.
17. Iijima, S.; Ichihashi, T. Single-shell carbon nanotubes of 1-nm diameter. *Nature (Lond.)* **1993**, *363* (6430), 603–605.
18. Bethune, D.S.; Kiang, C.H.; Devries, M.S.; Gorman, G.; Savoy, R.; Vazquez, J.; Beyers, R. Cobalt-catalyzed growth of carbon nanotubes with single-atomic-layer walls. *Nature (Lond.)* **1993**, *363* (6430), 605–607.
19. Thess, A.; Lee, R.; Nikolaev, P.; Dai, H.J.; Petit, P.; Robert, J.; Xu, C.H.; Lee, Y.H.; Kim, S.G.; Rinzler, A.G.; Colbert, D.T.; Scuseria, G.E.; Tomanek, D.; Fischer, J.E.; Smalley, R.E. Crystalline ropes of metallic carbon nanotubes. *Science* **1996**, *273* (5274), 483–487.
20. Iijima, S. Helical microtubules of graphitic carbon. *Nature (Lond.)* **1991**, *354* (6348), 56–58.
21. Robertson, D.H.; Brenner, D.W.; Mintmire, J.W. Energetics of nanoscale graphitic tubules. *Phys. Rev., B* **1992**, *45* (21), 12,592–12,595.
22. Sperling, L.H. *Introduction to Physical Polymer Science*; Wiley: New York, 1986.
23. White, C.T.; Todorov, T.N. Carbon nanotubes as long ballistic conductors. *Nature (Lond.)* **1998**, *393* (6682), 240–242.
24. White, C.T.; Mintmire, J.W. Density of states reflects diameter in nanotubes. *Nature (Lond.)* **1998**, *394* (6688), 29–30.
25. Mintmire, J.W.; White, C.T. Universal density of states for carbon nanotubes. *Phys. Rev. Lett.* **1998**, *81* (12), 2506–2509.
26. Mintmire, J.W.; White, C.T. X-alpha approach for the determination of electronic and geometric structures of polyacetylene and other chain polymers. *Phys. Rev. Lett.* **1983**, *50* (2), 101–105.
27. Mintmire, J.W. Local-density functional electronic structure of helical chain polymers. In *Density Functional Methods in Chemistry*; Labanowski, J.K., Andzelm, J.W., Eds.; Springer-Verlag: New York, 1991; 125–137.
28. White, C.T.; Mintmire, J.W. Fundamental structural and electronic properties of single-walled carbon nanotubes. *J. Phys. Chem.*, submitted.



# Small Amplitude AFM

**Peter M. Hoffmann**

*Department of Physics, Wayne State University,  
Detroit, Michigan, U.S.A.*

## INTRODUCTION

Small-amplitude atomic force microscopy (AFM) is a dynamic AFM technique, in which the AFM cantilever is vibrated at very small amplitudes, typically less than  $\approx 1 \text{ \AA}$  ( $= 10^{-10} \text{ m} = 0.1 \text{ nm}$ ), and the amplitude, phase, and/or resonance frequency of the lever are measured. Small amplitudes serve to *linearize* measurements of tip–surface interactions. Consequently, measurements can be directly related to interaction stiffness (negative if the force gradient) and energy dissipation. Because of the small amplitudes, the measurement is *local*, and interactions can be mapped point by point. This eliminates ambiguities present in large-amplitude techniques.

Historically, scanning tunneling microscopy (STM)<sup>[1]</sup> was the first “easy” technique to reliably provide atomic resolution images of a variety of *conductive* crystalline surfaces. Early on it was realized that forces play an important role in STM measurements.<sup>[2]</sup> This inspired the invention of the atomic force microscope in 1986.<sup>[3]</sup> In terms of applications, it was hoped that AFM would provide atomic resolution on insulators, which was not possible with STM. This goal was finally achieved in 1995, when true atomic resolution imaging was demonstrated by several groups using dynamic, noncontact AFM at *large* amplitudes.<sup>[4–6]</sup> Researchers also realized early on that AFM can be used to measure forces as a function of tip–surface separation in a variety of environments.<sup>[7–10]</sup> However, issues such as drift, mechanical instabilities,<sup>[11]</sup> low sensitivity, and nonlinearities made the direct, local, and linear measurement of force interactions a difficult prospect in many situations.

Small-amplitude AFM techniques were developed to address the issues of nonlinearity and non-locality that continue to plague large amplitude measurements. Moreover, combined with high-sensitivity deflection sensors, such as fiber interferometry, and the use of tailored lever structures, these techniques were able to overcome sensitivity and instability issues as well. In this entry we will discuss the underlying theory of small-amplitude AFM, conditions and limitations for its use, and recent examples of small-amplitude AFM applied to atomic-scale imaging (Fig. 1),

force–distance measurements, atomic-scale dissipation, and force measurements in liquids.

## THEORY AND BACKGROUND

### Limitations of “Standard” AFM Techniques

Commonly used AFM technologies can be categorized into two broad categories: (1) “d.c.” or “contact” AFM and (2) “a.c.” or “dynamic” AFM. Here, dc is meant to signify a *static* technique, while a.c. is meant to signify a *dynamic* technique, involving modulation of the deflection or force. In d.c. AFM the cantilever is static and the equilibrium position of the cantilever in the force field of the sample is measured. The force can then be determined from Hooke’s law. In a.c. AFM the cantilever is vibrated and, typically, two of the observables amplitude, phase, or resonance frequency are measured to determine the tip–sample interaction.

In the following we want to discuss limitations of d.c. and large-amplitude a.c. techniques, which range from drift, mechanical instabilities, and non-linearity to problems of data interpretation.

### Limitations of d.c. and large-amplitude a.c. AFM techniques

d.c. AFM suffers like any d.c. measuring technique from low signal-to-noise and drift. Therefore, d.c. AFM generally utilizes low stiffness levers to increase sensitivity ( $< 1 \text{ N m}^{-1}$ ). Because of the low stiffness of the lever, it is prone to the snap-to-contact instability close to surface.<sup>[11–13]</sup> Consequently, d.c. AFM is generally known as “contact” AFM. This type of AFM is useful in general-purpose imaging at resolutions typically  $> 10 \text{ nm}$ . It is theoretically able to directly yield quantitative force data (via Hooke’s law). However, this is generally hampered by drift and the snap-in instability.

d.c. AFM also has limitations in imaging. Because imaging is generally done in contact, the image resolution is limited to the tip–surface contact radius, which is typically at least several tens of nanometers. In some



**Fig. 1** Atomic resolution image ( $4 \times 2.5$  nm) of the force gradient across a Si(111)-(7  $\times$  7) surface. Round “bumps” correspond to single atoms. Measured with a subresonance AFM at an ultrasmall lever amplitude of 0.25 Å. Feedback was maintained via the tunneling current.

special cases true atomic resolution has been achieved,<sup>[14]</sup> but, typically, apparent “atomic resolution” seen with contact AFM can be attributed to a Moiré-like effect of dragging two well-ordered surfaces (tip and substrate) across each other.<sup>[15,79]</sup> Another disadvantage is the fact that the tip is moved laterally while in contact and that sometimes relatively large forces need to be applied to get a reasonable signal. This can lead to wear and degradation of the sample and tip,<sup>[16]</sup> and is especially detrimental to soft samples.

To overcome some of the disadvantages of d.c. AFM, a.c. AFM techniques were used almost as soon as the AFM was invented.<sup>[8]</sup> There are two major types of a.c. AFM techniques:<sup>[17]</sup> 1) amplitude-modulated (AM) AFM, which includes “tapping mode” AFM, some types of noncontact AFM, and subresonance AFM, and 2) frequency-modulated (FM) AFM, or frequency-shift AFM, also often confusingly called noncontact AFM.

In AM AFM the lever is vibrated at a *constant* frequency, and the amplitude and/or phase are measured. This is typically done with a lock-in amplifier. In tapping mode AFM,<sup>[18]</sup> the cantilever is brought close to the surface while it is vibrated at (or close to) the free resonance frequency of the lever. As the tip approaches the surface, the resonance frequency shifts due to the interaction force gradients. Because the lever is still vibrated at the free resonance frequency, both the phase and the amplitude of the cantilever decrease and can be used as feedback parameters (slope detection).

Tapping mode AFM typically uses large amplitudes of 10–100 nm. As the tip moves through the non-linear force field close to the surface, the motion of the lever becomes highly non-linear. Typically, the system is bistable, and jumps between a low-amplitude and high-amplitude mode are inherent to the system.<sup>[17,19–22]</sup> In addition, relatively low stiffness cantilevers are

typically used (of the order of a few 10 N/m) to boost sensitivity. As a result, the tip is unstable close to the surface and starts “tapping” the surface, hence the name of the technique. This could be avoided by using stiffer cantilevers,<sup>[23]</sup> but that would reduce the signal unduly. Because of the intermittent contact with the surface, the resolution of this technique is comparable to contact AFM. However, because the tip is not dragged across the surface as in contact AFM, the damage to a fragile sample can be much less than in contact AFM.<sup>[18]</sup> In addition, the phase data contain information about sample-mediated damping and can provide additional information about the mechanical properties of the sample. However, although attempts have been made to interpret the results in a quantitative fashion, it is very difficult to completely reconstruct the force field and the distance-dependent loss processes experienced by the tip, and higher resonance modes need to be considered.<sup>[24,25]</sup>

Noncontact AM AFM<sup>[8]</sup> is essentially the same as tapping mode AFM, with the only difference being that the tip is lifted off the surface far enough to avoid contact. Noncontact AM AFM is typically used to measure long-range forces such as electrostatic forces [electrostatic force microscopy (EFM)] or magnetic forces [magnetic force microscopy (MFM)].

In FM AFM the lever is vibrated at its (shifting) resonance at all times. Typically, (but not always) a feedback loop is used to keep the amplitude constant. The lever is maintained at its resonance frequency by using the lever itself as the frequency-determining element in an oscillator circuit. This is achieved by phase shifting the deflection signal and feeding it back to the dither piezo that oscillates the cantilever. The resonance frequency is then measured by an FM demodulator circuit.<sup>[26]</sup> The resonance frequency can be measured very accurately for high quality factor ( $Q$ ) cantilevers, providing improved signal-to-noise (S/N) ratios. Because a high  $Q$  ( $\approx 10^3$ – $10^4$ ) is needed, FM AFM is most often used in ultrahigh vacuum (UHV). The improved S/N ratio allows for the use of higher stiffness levers of typically about  $50 \text{ N m}^{-1}$ . The use of stiffer levers combined with large amplitudes<sup>[27,28]</sup> avoids the snap-to-contact instability and noncontact operation very close to the surface becomes possible. Indeed, it was this technique that yielded the first true atomic resolution AFM images in 1994<sup>[4]</sup> and 1995.<sup>[5,6]</sup> The problems with this technique are the very involved data interpretation when using large amplitudes,<sup>[24,29,30]</sup> the difficulties in measuring local events (because of the large amplitudes), and the almost complete confinement of this technique to ultrahigh vacuum conditions (because of the need for high  $Q$ ). Recently, using an electronic feedback circuit, attempts have been made to increase the low quality factor ( $Q \approx 2$ – $3$ ) of nc-AFM in water to  $Q \approx 30$ – $40$ .<sup>[31]</sup>

However, these low  $Q$  values are still too low to achieve atomic resolution in liquids, and the used techniques raise additional interpretation issues.

### Theory of Small-Amplitude AFM

Small-amplitude AFM is any dynamic AFM technique in which particular attention is paid to vibrating the cantilever at small amplitudes. This means in practice that amplitudes should be small compared to the range of the measured interaction. How small the amplitude has to be to justifiably speak of *linear* measurements can be explored by solving the equation of motion of the oscillating cantilever in the force field of the sample. In addition, by solving the equation of motion, we can distinguish between several conceivable ways of operating a small-amplitude AFM. These include:

1. On-resonance AM operation (“tapping mode”): AM AFM where we drive the cantilever at small amplitudes at a constant frequency close to or at the free resonance frequency. Amplitude and phase are measured and can, in principle, be related directly to the force gradient and damping coefficient.
2. Subresonance operation: AFM is deliberately operated at a constant frequency well below the first resonance. This eliminates dynamic terms in the equation of motion, and makes it easier to keep the AFM in the small-amplitude regime. Measured amplitude and phase relate directly to the force gradient and damping.
3. Frequency shift (FM) operation: Same as regular FM AFM, but using ultrasmall amplitudes. In this case, the frequency shift can be directly related to the force gradient (see below). The cantilever amplitude (or the excitation amplitude if amplitude is kept constant) can be related to the damping coefficient or quality factor.
4. Force-controlled or force modulation AFM: AFM in which a force rather than a displacement is imposed on the cantilever. Typically, a d.c. and a.c. force are applied, and force and stiffness are measured simultaneously. Often used in the subresonance regime.

Actual examples of these different techniques will be discussed toward the end of the chapter.

#### Small-amplitude AFM

The general equation of motion of AFM is given by:

$$m^*\ddot{z} + C\dot{z} + k_L z = k_L A_0 \exp(i\omega t) + F_{ts}(z + d) \quad (1)$$

Here,  $m^*$  is the effective vibrating mass of cantilever and tip,  $z$  is the cantilever deflection,  $d$  is the average tip-surface separation,  $C$  is the damping coefficient,  $k_L$  is the lever stiffness, and  $A_0$  is the applied amplitude (which is equal to the free amplitude in the off-resonance case). If the AFM is operated in the force-modulated mode, the equation is modified by replacing  $k_L A_0$  on the right-hand side by  $F_0$ , the modulated force.

$F_{ts}$  is the sum of forces acting between the tip and the surface.  $F_{ts}$  generally consists of several forces with different interaction ranges. In vacuum, the forces present include chemical bonding, van der Waals forces, electrostatic forces, or magnetic forces. In liquids, we also encounter forces associated with the medium such as solvation forces and hydrophilic/hydrophobic interactions.<sup>[32]</sup> In ambient, capillary forces can be very important. When writing expressions for  $F_{ts}$ , we also need to be careful that forces act on different portions of the tip depending on their range. Long-range forces, such as electrostatic forces in the presence of an applied voltage, might act on the entire vibrating cantilever, while short-range forces, such as chemical bonding forces act on the outermost atoms of the tip only. Finally, we have to take into account that the tip and surface are not infinitely rigid, but instead deform under the influence of the force field. This leads to a rescaling of the tip-surface separation  $z$ .<sup>[13,33]</sup> However, to simplify the discussion, we will ignore these effects for the time being.

In Eq. (1) the cantilever is being treated as a linear spring, which is a very good approximation for the small amplitudes involved.<sup>[34]</sup> We also assumed that the damping coefficient,  $C$ , is independent of tip position. This is in general not true, but again is a good local approximation if small amplitudes are used.

Generally, because of the nonlinear nature of the force field,  $F_{sr}$ , Eq. (1) can only be solved numerically. In some special cases, analytic solutions can be found. A very special case occurs when the AFM is operated at amplitudes over which the force law can be approximately considered linear. We can then write  $F_{ts} = F_{ts,0} - k_{ts}z$ . For convenience, we rescale the displacement  $z$  to account for the equilibrium position of the cantilever  $z_0 = F_{ts,0}/k_L$ , according to  $z - z_0 \rightarrow z$ . By doing this,  $z$  becomes a measure for the *deviation* from the equilibrium position due to the imposed oscillation. The new *linearized* equation of motion becomes:

$$m^*\ddot{z} + C\dot{z} + (k_L + k_{ts})z = k_L A_0 \exp(i\omega t) \quad (2)$$

Note that the interaction stiffness,  $k_{ts}$ , is the negative of the force gradient,  $\partial F/\partial z$ . The steady-state solution of Eq. (2) is  $z(t) = A \exp(i\omega t)$ , where  $A$  is a complex number that includes the phase information.  $A$  is

given by:

$$A = \frac{k_L A_0}{k_L + k_{ts} - \omega^2 m^* + i\omega C} \quad (3)$$

The resonance frequency in the linear regime is given by  $\omega_0 = \sqrt{(k_L + k_{ts})/m^*}$ . Using this we can find for the absolute value of the amplitude:

$$|A| = \frac{k_L A_0}{\sqrt{(k_L + k_{ts})^2 (1 - (\omega^2/\omega_0^2))^2 + (C\omega)^2}} \quad (4)$$

and the phase angle between the  $A_0$  (the drive) and  $A$  (the cantilever):

$$\tan \phi = -\frac{\omega C}{(k_L + k_{ts})(1 - (\omega^2/\omega_0^2))} \quad (5)$$

### Small-amplitude tapping mode AFM

In the case of tapping mode AFM, the system is driven at or near the free resonance. Because the drive frequency is kept constant, the amplitude and/or phase are measured and used as possible feedback signals. When the lever is driven at the free resonance frequency,  $\omega = \omega_{of} = \sqrt{k_L/m^*}$ , the absolute value of the amplitude is given by [Eqs. (4), (5)]:

$$|A| = \frac{k_L A_0}{k_{ts}} \cos \phi \quad (6)$$

The phase angle is given by:

$$\tan \phi = -\frac{\omega_{of} C}{k_{ts}} \quad (7)$$

It is straightforward to solve these equations for  $k_{ts}$  and  $C$ , and thus, at least in principle, a measurement of the amplitude and the phase are sufficient to determine the interaction stiffness and the damping.

This is to be contrasted from the usually used *large* amplitudes. In this case, the interaction and damping are very difficult to reconstruct from the amplitude and phase, because these are the result of an *integral* over the *entire* motion of the cantilever. Thus, for large amplitudes we are not mapping two observables (amplitude and phase) to two unknowns (the local stiffness and damping coefficient), but instead we are trying to map our two observables to *all* values of interaction stiffness and damping coefficient the tip encounters during its trajectory. This is—without additional information—in principle impossible.

Additional information might come from amplitudes and phases of higher vibration modes<sup>[24,25]</sup> or from multiple measurements at different separations and amplitudes. The interpretation, if not impossible in principle, becomes very involved.

### Subresonance AFM

Combining Eqs. (4) and (5), we find that the measured interaction stiffness,  $k_{ts}$ , can be determined directly from the measured amplitude and phase via:

$$k_{ts} = k_L \left( \frac{A_0 \cos \phi}{|A|(1 - (\omega^2/\omega_0^2))} - 1 \right) \quad (8)$$

If we keep the drive frequency,  $\omega$ , well below the first resonance we can use this equation to find the following simple expression for the interaction stiffness:

$$k_{ts} = k_L \left( \frac{A_0}{|A|} \cos \phi - 1 \right) \quad (9)$$

If the AFM is operated reasonably far below the resonance, the phase angle typically is very small, and the  $\cos \phi$  term can in many cases be replaced by unity, resulting in:

$$k_{ts} = k_L \left( \frac{A_0}{|A|} - 1 \right) \quad (10)$$

The same result can be obtained if we realize that by operating the AFM in the subresonance regime, the measurement becomes *quasi-static*. Close to the surface, the cantilever and interaction stiffnesses can be considered as two “springs” in series. Thus the forces in each spring are identical and we can write:  $F = k_{ts}|A| = k_L(A_0 - |A|)$ , which leads to the same result [Eq. (10)].

The damping coefficient can be calculated from:

$$C = \frac{k_L A_0}{|A|\omega} \sin \phi \quad (11)$$

Thus again a measurement of the amplitude and phase are sufficient to determine both the interaction stiffness and the damping coefficient.

### Frequency shift AFM

In frequency shift AFM, the excitation frequency of the cantilever is altered to keep the lever at its resonance at all times. Therefore the frequency becomes an observable in the measurement. At very small

amplitudes,<sup>[35]</sup> the resonance frequency is directly related to  $k_{ts}$ , since  $\omega_0 = \sqrt{(k_L + k_{ts})/m^*}$  (see Eq. (2) and Ref.<sup>[26]</sup>). In terms of the *free* resonance frequency,  $\omega_{0f}$ , the interaction stiffness can be found from:

$$k_{ts} = k_L \left( \frac{\omega_0^2}{\omega_{0f}^2} - 1 \right) \quad (12)$$

This can be approximately written in terms of the frequency shift,  $\Delta f = 1/2\pi (\omega_0 - \omega_{0f})$  as:

$$k_{ts} = 2k_L \frac{\Delta f}{f_{0f}} \quad (13)$$

The amplitude can be calculated from Eq. (4). Introducing the quality factor  $Q = \omega_{0f}m^*/C$ , we find<sup>[36]</sup>

$$|A| = \frac{QA_0}{\sqrt{(k_L + k_{ts})/k_L}} \approx QA_0 \left( 1 - \frac{k_{ts}}{2k_L} \right) \quad (14)$$

In FM AFM, the amplitude is often held constant by a feedback loop, and the excitation amplitude needed to keep a certain constant lever amplitude is measured and related to the damping.<sup>[37]</sup>

In conclusion, by measuring the amplitude and the *frequency*, the interaction stiffness and the damping coefficient (or quality factor) can be determined. At larger amplitudes, the frequency shift is determined by an integral over the entire tip trajectory, and interpretation of the frequency shift data becomes much more involved.<sup>[24,27–30]</sup>

### Force modulation AFM

In the case of force modulation AFM, Eqs. (4) and (5) still hold if we replace  $k_L A_0$  by the modulated force  $F_0$ .<sup>[15]</sup> If a small *subresonance* force modulation is applied to the cantilever and the displacement response is measured, these equations simplify to:

$$k_{ts} = \frac{F_0}{|A|} - k_L \quad (15)$$

which for small phase angles is simply an expression of Hooke's law; that is, the total effective stiffness  $k_{ts} + k_L$  is given by  $F_0/|A|$ . Note that in the case of force-modulated AFM, the cantilever and interaction stiffnesses are to be considered *in parallel*, whereas in "usual" displacement-modulated AFM, they are to be taken to be *in series*. The reason is that in force-modulated AFM, both the sample and the

cantilever base are held fixed, and thus the *amplitudes* of the base–tip and tip–surface separations are identical, while the forces are different. In "usual" AFM it is the *forces* between base and tip and tip and surface that are identical, while the amplitudes are different ( $A_0$  vs.  $|A|$ ).

The damping coefficient in force-modulated AFM can be found from:

$$C = -\frac{F_0}{|A|\omega} \sin \phi \quad (16)$$

### Practical considerations

As we have seen above, the interpretation of the data becomes greatly simplified if amplitudes are small enough to consider the force field to be linear over the range of motion of the cantilever. In all four cases (tapping mode, off-resonance AM AFM, FM AFM, and force modulation AFM), both the interaction stiffness and the damping can in principle be directly measured. In all cases, two parameters are needed: In AM and force-modulated AFM we need amplitude and phase, and in FM AFM amplitude and frequency shift.

In reality, quantitative small amplitude measurements have been used quite frequently in off-resonance measurements (both displacement and force modulated), less frequently in FM AFM, and hardly in tapping mode experiments. The main reasons for this are problems of phase and amplitude stability in tapping mode. Because the drive frequency enters the equations, but is not explicitly measured as in FM AFM, a shift in the drive frequency can greatly affect the obtained results. Indeed a shift to higher or lower frequency than the free amplitude can lead to a bistable behavior of the oscillator if the amplitude is not small enough. Keeping the amplitude small enough, on the other hand, is difficult if the cantilever is operated near its resonance. In subresonance AFM, this problem is avoided by staying far below the resonance, and, as a result, the frequency does not enter into the equations and the amplitude can be kept low.

In FM AFM the lever is deliberately run at resonance, and the frequency should be quite stable if the  $Q$  of the lever is sufficiently high. The needed high  $Q$ , however, results in larger amplitudes, thus violating the small-amplitude condition. If the amplitudes are deliberately kept small, thermal noise can greatly influence the measurements because most of the thermal vibration energy is centered around the lever resonance. For a lever of 40 N/m stiffness, which is typical for FM AFM, the thermal vibration amplitude is of the order of  $\sqrt{k_B T/k_L} = 0.1 \text{ \AA}$ , which is of the same order as the amplitude needed to linearize

measurements of atomic bonding forces. This particular problem can be alleviated by increasing the lever stiffness and sensitivity of the system as recently demonstrated by Giessibl.<sup>[38]</sup>

### Operating Conditions of Small-Amplitude AFM

Limits of linearity or how small is small enough?

As shown above, the linearized equation of motion [Eq. (2)] can be solved in a variety of situations and leads to the simple relation [Eq. (9)] for the interaction stiffness in the case of an AFM operated at small amplitudes and subresonance frequencies, and to Eq. (13) in the case of a small amplitude, frequency shift AFM. However, an important question remains unanswered: Under what circumstances can the system be regarded linear? Or, in other words: When is the amplitude small enough?

This question cannot be answered in general because it strongly depends on the nature of the force law that the tip encounters. Long-range forces, such as electrostatic, magnetic, and van der Waals forces can generally be explored with somewhat larger amplitudes. Short-range forces, such as chemical bonding and solvation forces associated with small molecules, require significantly smaller amplitudes. We might also expect that it depends on the particular AFM technique used, but, at least as a rule of thumb, the results seem to be quite similar for different a.c. AFM techniques.

In the case of frequency shift (FM) AFM and short-range forces, Hölcher, Schwarz, and Wiesendanger<sup>[35]</sup> showed that the frequency shift is determined by the force gradient only if the amplitudes used are in the sub-Angstrom range, typically of the order of a few tenths of an Angstrom. Similar results can be obtained for subresonance AM AFM.<sup>[33]</sup> In a recent simulation<sup>[33]</sup> of a vibrating lever in a short-range force field (with a decay parameter of 0.54 Å), it was found that the error of the measurement was negligible for a lever amplitude of 0.1 Å, very small for an amplitude of 0.25 Å, and about 10% for an amplitude of 0.5 Å, i.e., for an amplitude of the order of the decay parameter. For large amplitudes, e.g., 1 Å, the error was quite significant. This is shown in Fig. 2. For comparison, typical lever amplitudes in tapping mode are of the order of 100–1000 Å, and in FM AFM of the order of 10–100 Å. In the case of subresonance AFM, we also have the added question of the influence of the frequency, i.e., how far below the resonance we need to be to avoid resonance enhancement of the amplitude. It was found that very clean subresonance operation could be achieved up to about one-eighth of the resonance frequency, but acceptable error rates (<10%) could be achieved up to frequencies of one-third of

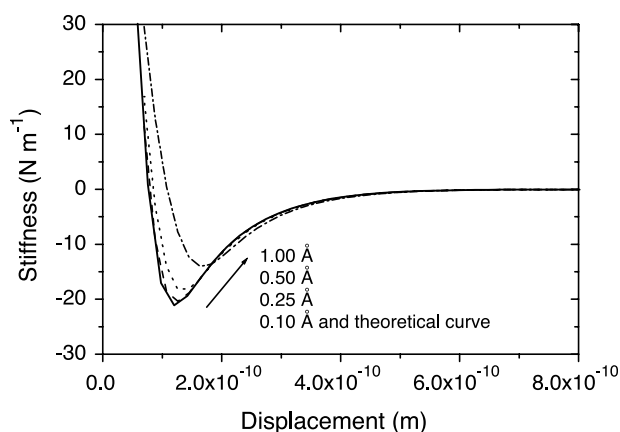


**Fig. 2** Simulation of the measured interaction stiffness–displacement curve for different cantilever amplitudes in a subresonance AM AFM. For  $A_0 = 0.1$  Å the measurement does not visibly deviate from the theoretical curve, at 0.25 Å there is a small error around the minimum, at 0.5 Å this error is about 10%, while at an amplitude of 1.0 Å the error has become quite large. *Source:* From Ref.<sup>[33]</sup>.

the free resonance. Beyond these values, the amplitude has a tendency to become too large because of resonance enhancement, complicating the interpretation of the data.

### Limits of stability

Even if small drive amplitudes are used, there is no guarantee that the actual lever amplitude remains small. One reason for this is resonance enhancement, as discussed above. The other reason is the use of low-stiffness cantilevers. Low-stiffness cantilevers not only exhibit larger deflections in an attractive force field than higher stiffness ones, but, moreover, they can become unstable and “snap” to the surface (“snap-to-contact”).<sup>[11]</sup>

In d.c. AFM there is a straightforward criterion that must be satisfied if snap-to-contact is to be avoided. As long as the *effective* stiffness of the cantilever is positive, no snap-in occurs:

$$k_L + k_{ts} > 0 \quad (17)$$

This means that snap-in occurs when the interaction stiffness is negative (“attractive”) and its absolute value exceeds the lever stiffness.

In a.c. AFM snap-in can still be avoided *even* if condition (17) is violated. The reason is that in order for snap-in to occur the total force (cantilever + interaction) must be negative (attractive).<sup>[27]</sup> In a.c. AFM, the cantilever deflects beyond its equilibrium point and therefore the restoring force can overwhelm



the attractive force between the tip and the surface. The second criterion for snap-in to be avoided can thus be written as:

$$k_L A + F_{ts} > 0 \quad (18)$$

This is one of the reasons for the stability of large-amplitude FM AFM. In these techniques relatively low stiffness cantilevers can be used, which boost sensitivity, but because of the large amplitudes the snap-in instability can be avoided. In small-amplitude methods, we need to mostly rely on criterion (17) and thus high-stiffness cantilevers need to be used. This necessitates high-sensitivity deflection sensing as discussed in the next subsection.

### Sensitivity

Small-amplitude AFM requires higher sensitivity of the deflection sensor than regular AFM. The reason is not only that small amplitudes are more difficult to measure, but also, as we have seen above, the stability criterion demands that high-stiffness levers are used, which reduce the signals even further. There are many ways of sensing the deflection of the cantilever,<sup>[39]</sup> from tunneling as used in the original AFM<sup>[3]</sup> to the now most commonly used optical techniques. For each of these methods, a theoretical sensitivity limit can be calculated.<sup>[40]</sup> However, in reality the experimental sensitivity is typically lower due to nonideal experimental conditions.

Because small-amplitude AM AFM needs to operate preferably at amplitudes of a few tenths of an Angstrom, the deflection sensor needs to be able to sense changes in the amplitude of the order of 0.01 Å (i.e., 1 pm) or better. This is difficult to achieve with commonly used laser-deflection systems. Theoretically, highly optimized laser-deflection systems might be able reach similar sensitivity than interferometer-based systems,<sup>[41]</sup> however, in practice, most cannot sense changes in amplitude much smaller than 0.1 Å. Experimentally, it has been demonstrated that fiber interferometers<sup>[42]</sup> can have at least 10–20 times higher sensitivity than laser-deflection systems and are thus the method of choice in small-amplitude AM AFM.

In FM AFM, when high-stiffness cantilevers are used, the frequency shift is reduced and a high sensitivity frequency measurement becomes essential. A very high  $Q$  cantilever is needed to achieve the needed sensitivity. High  $Q$ , however, leads to increased resonance enhancement of the amplitude, and thus drive amplitudes need to be extremely small. Fortunately, high-stiffness cantilevers also help to reduce the thermal noise at resonance, and measurements at sub-Angstrom lever amplitudes can be achieved.

### Thermal noise

When we deal with cantilever amplitudes of the order of 0.1 Å, we immediately face the question of how this compares with the average amplitude of the thermal excitation of the cantilever. It can be shown<sup>[43]</sup> that the power spectral density of the oscillator amplitude due to thermal excitation is given by:

$$\langle P^2(\omega) \rangle = \frac{4k_B T C}{(k_L + k_{ts} - m\omega^2)^2 + C^2\omega^2} \quad (19)$$

Note that  $\langle P^2 \rangle$  has units of  $\text{m}^2 \text{Hz}^{-1}$ , i.e., it needs to be multiplied with the measurement bandwidth,  $B$ , to calculate the rms amplitude due to the thermal motion of the cantilever. The rms amplitude is given by  $\delta x_{\text{rms}} = \sqrt{B \langle P^2 \rangle}$ . At the resonance frequency, i.e., in FM AFM, the power spectral density reduces to:

$$\langle P^2 \rangle = \frac{4k_B T}{C\omega_0^2} \approx Q \frac{4k_B T}{k_L \omega_{0f}} \quad (20)$$

where we used  $Q = \omega_{0f} m / C$  as the quality factor of the free cantilever, and assumed  $k_{ts} \ll k_L$  and  $\omega_0 \approx \omega_{0f}$  to obtain the approximate result on the right-hand side.

In subresonance AM AFM, the formula (19) instead reduces to:

$$\langle P^2 \rangle = \frac{4k_B T C}{(k_L + k_{ts})^2} \approx \frac{1}{Q} \frac{4k_B T}{k_L \omega_{0f}} \quad (21)$$

Comparing the approximate results [Eqs. (20) and (21)], the thermal noise *increases* with increasing quality factor  $Q$  if the lever is driven at its resonance (as in FM AFM), and *decreases* in the case of subresonance AFM. What does this mean in practice? In order to reliably measure the frequency or amplitude of a cantilever with a 0.1 Å = 10 pm free amplitude, the rms amplitude of the thermal noise needs to be less than 1 pm. At room temperature, for a lever with a  $Q$  of 1000, a resonance frequency of  $\omega_{0f} = 2\pi \times 200$  kHz, kHz, and a measurement bandwidth of 100 Hz, the cantilever stiffness would need to be about 1300 N/m in the case of FM AFM, and  $1.3 \times 10^{-3}$  N/m in the case of subresonance AM AFM. A cantilever of 1300 N/m would provide a frequency shift of 7.7 Hz for an interaction stiffness of 0.1 N/m. The thermal frequency noise can be calculated from:<sup>[26,44]</sup>

$$\delta f_{\text{rms}} = \sqrt{\frac{k_B T B f_{0f}}{k_L A_0^2 \pi Q}} \quad (22)$$

This gives a thermal frequency noise of 14 Hz for a lever of 1300 N/m. The lever amplitude therefore

would need to be somewhat increased beyond this value to get a force gradient sensitivity of 0.1 N/m. A cantilever of such high stiffness may sound difficult to implement, but a lever stiffness of 1800 N/m has recently been used by Giessibl to achieve unprecedented high resolution on Si  $7 \times 7$  surfaces.<sup>[38,45]</sup>

In the case of subresonance AM AFM, the lever stiffness would have to be increased far beyond the thermal noise limit of  $1.3 \times 10^{-3}$  N/m to about 100 N/m to avoid snap-to-contact. In this case, the rms amplitude of the thermal noise would reduce to 3.6 fm, which is more than sufficient for even the most stringent requirements. At a lever stiffness of 100 N/m, a force gradient of 0.1 N/m would result in a change of the lever amplitude of about 10 fm assuming a free lever amplitude of 0.1 Å = 10 pm; that is, the signal would be a factor of three above the thermal noise limit. Of course, measuring 10 fm even with an interferometric sensor is not an easy task. Measurements of this order have been demonstrated recently.<sup>[42,46,47]</sup> Theoretically, much higher sensitivity is possible if more elaborate interferometric methods are used (see, e.g., in gravitational wave detection: Ref.<sup>[48]</sup>).

Thermal noise can of course also be reduced by lowering the temperature of the instrument.<sup>[49]</sup> However, the rms amplitude only scales with the square root of the temperature, and thus the expected reduction in thermal noise is “only” of the order of about 10. On the other hand, there are many additional advantages of low-temperature operation, such as limiting drift and surface diffusion, and low-temperature operation can provide a significant advantage over room-temperature methods.

## A SHORT HISTORY OF SMALL-AMPLITUDE AFM

### Nanoindentation and Force-Controlled AFM

Nanoindentation<sup>[50]</sup> is a technique to measure contact-mechanical properties on the nanoscale. It essentially operates by indenting a very sharp diamond tip into a surface while monitoring the displacement and the applied load. In 1987, Pethica and Oliver<sup>[15]</sup> improved this technique by additionally applying a force modulation. This force modulation was small enough ( $\approx 10^{-8}$  N) such that, at the observed contact stiffnesses, sub-Angstrom tip amplitudes were generated. Such small amplitudes allowed the simultaneous linear measurement of the contact stiffness in addition to the load–displacement curve. From the contact stiffness the size of the contact area could be determined. In their paper, the authors also suggested to operate an AFM in a similar fashion, by applying a small a.c. force to the cantilever via a magnetic transducer.

In 1993, Jarvis et al. demonstrated a force-controlled AFM<sup>[51]</sup> that used a cantilever with an attached magnet and an electromagnet to apply a d.c. and small subresonance a.c. force to the cantilever. The small, applied a.c. force resulted in a very small amplitude ( $\approx 0.3$  Å) of the cantilever, giving a direct measure of the stiffness of the cantilever–surface system via Eq. (9). The amplitude was measured with a heterodyne interferometer. The AFM was able to detect a negative stiffness region under ambient condition, which is difficult to achieve with conventional AFM because of the snap-in instability. This device was subsequently implemented in ultrahigh vacuum,<sup>[52]</sup> resulting in the first direct measurement of the interaction stiffness between clean surfaces.<sup>[53]</sup> Imaging with the force-controlled AFM was also demonstrated.<sup>[54]</sup> This technique was also used in liquids, where O’Shea et al. have successfully used the force-controlled AFM to measure solvation forces<sup>[55,56]</sup> in several organic solvents. They used amplitudes of a few Angstroms, which were appropriate for the relatively large molecules they studied.

### On-Resonance AM AFM

In usual AM or tapping mode AFM, a displacement rather than a force is applied to the cantilever. If the applied displacement is small enough, the at-resonance amplitude of the lever can be kept in the Angstrom regime, depending on the  $Q$  and  $k_L$  of the lever (see our discussion of thermal noise above).

Olsson, Wigren, and Erlandsson demonstrated an on-resonance AM AFM technique<sup>[57]</sup> with small free amplitudes of  $< 10$  Å. The needed sensitivity was provided by the use of a fiber interferometer.<sup>[58]</sup> During imaging the amplitude was reduced by 20–90% of the free value due to the shift of the resonance frequency. Using this technique, true atomic resolution on silicon (111)-(7 × 7) surfaces<sup>[59]</sup> was achieved. However, because of the use of an on-resonance technique and the still relatively large amplitudes, the interpretation of the amplitude data proved difficult.<sup>[60]</sup>

### FM AFM

In FM AFM, cantilever stiffnesses of 10–50 N/m and large amplitudes of 10–50 nm<sup>[44]</sup> are generally used. The large amplitudes provide good stability and signal-to-noise and are thus preferred when imaging with atomic resolution.<sup>[28]</sup> There are rather few examples of FM AFM experiments that utilized amplitudes less than 10 nm. Kitamura and Iwatsuki have used amplitudes as low as 1.5 nm to image Si(111).<sup>[61]</sup> Recently, Eguchi and Hasegawa used amplitudes of 2.8 nm to also image Si(111) and were able to resolve

rest atoms.<sup>[62]</sup> The main reason for the low number of small-amplitude experiments is the use of low-stiffness cantilevers, which require large amplitudes to avoid the snap-in instability [see Eq. (18)].

Stable small-amplitude operation at resonance requires very stiff levers in order to avoid the snap-in instability and to reduce thermal noise. Recently, Giessibl designed a novel force sensor based on a quartz tuning fork.<sup>[38]</sup> This sensor has a very high stiffness of 1300–1800 N/m. Using this new device, he was able to achieve very stable atomic resolution imaging at amplitudes of 4 Å, which is very small for FM AFM.

Using the same setup, Giessibl et al. recently achieved subatomic (orbital) resolution of the tip and the Si substrate.<sup>[45,63]</sup> Better-than-atomic resolution had previously been observed only in STM measurements. A tuning-fork-based sensor was found to also provide atomic resolution and atomic-scale friction measurements in a small-amplitude (3 Å) *lateral* mode.<sup>[64]</sup>

Giessibl et al. have argued that in FM AFM measurements, small amplitudes and large cantilever stiffnesses should be able to *improve* signal-to-noise.<sup>[44]</sup> This depends on the exact nature and magnitude of any dissipative processes. Despite the presence of energy dissipation, the advantages of small amplitudes and stiff cantilevers in FM AFM have been experimentally confirmed.<sup>[38,45,63]</sup> A possible reason for the improved S/N of small-amplitude techniques is that the tip will spend most of its time in the regime of *short-range* forces when small amplitudes are used close to the surface.<sup>[65]</sup> These forces are ultimately responsible for atomic resolution imaging. Large-amplitude techniques are more affected by long-range forces (e.g., van der Waals), thus degrading sensitivity to short-range bonding forces. The same reasoning has recently been applied to the room-temperature observation of rest atoms in Si(111)-(7 × 7) at reduced amplitudes of 2.8 nm.<sup>[62]</sup>

### Subresonance AM AFM

Thermal noise and limits of sensitivity are the most important obstacles in reducing the vibration amplitude of the cantilever into the linear regime of a few 0.1 Å. There are essentially two ways to limit thermal noise: high-stiffness cantilevers and subresonance operation. Sensitivity can be improved by using new detection schemes, such as tuning forks for FM detection<sup>[63]</sup> and fiber interferometers for AM detection.<sup>[58]</sup>

Recently, Oral et al.<sup>[66]</sup> constructed a fiber interferometer-based AFM, which was optimized to operate at ultrasmall amplitudes of < 0.25 Å. This instrument has since been successfully used to obtain atomic resolution maps of the force gradient on Si(111)<sup>[46]</sup> and Si(100),<sup>[67,68]</sup> to measure atomic bonding

forces between a W tip and a clean Si(111) surface,<sup>[42]</sup> and to observe atomic-scale energy dissipation at amplitudes as low as 0.13 Å on Cu(100)<sup>[47]</sup> and with slightly larger amplitudes on Si(100).<sup>[67,68]</sup>

Subresonance detection can also be used in liquids. Although the thermal noise increases somewhat because of the decrease in  $Q$  [see Eq. (21)], subresonance AM detection is better suited for liquid-based measurements because there is no need to measure the resonance frequency under low- $Q$  conditions. Recently, subresonance AFM has been used at an amplitude of 0.35 Å for the first *direct* AFM measurement<sup>[69]</sup> of the molecular stiffness variations of confined water layers.<sup>[32]</sup>

### Force gradients of chemical bonds

Few methods allow the direct measurement of the distance-dependent interactions between single atoms. Recently, large-amplitude dynamic AFM has been used to achieve this goal.<sup>[49,70]</sup> However, there are a few remaining questions, especially the difference of the observed interaction length range measured in low-temperature<sup>[49]</sup> vs. room-temperature<sup>[70]</sup> measurements. Part of the problem might be the dissipative interactions that are not always accounted for in the deconvolution schemes used in large amplitude measurements.

Unambiguous measurements of conservative and dissipative interactions can be achieved by low amplitude measurements. Recently, subresonance, ultrasmall ( $\approx 0.2$ – $0.25$  Å) amplitude AFM has been applied to measure atomic interactions between a tungsten tip and a clean Si(111)-(7 × 7) surface at room temperature<sup>[42]</sup> (Fig. 3). No temperature-related broadening of the interaction was observed in contrast to some large amplitude measurements.<sup>[70]</sup> The measured interaction parameters were in agreement with reported theoretical values.<sup>[71]</sup> Atomic bonding stiffnesses have also been measured on Cu(100)<sup>[47]</sup> and Si(100) surfaces.<sup>[67,68]</sup>

### Force gradient atomic resolution imaging

One problem of subresonance, ultrasmall-amplitude AFM is that signals are exceedingly small, whereas the drive frequency can be quite low. This necessitates long integration times for the lock-in detection of the amplitude or phase, which in turn makes it very difficult to use the lock-in signal for feedback during imaging. Imaging has so far been achieved by using the tunneling current for the feedback, while independently imaging the force gradient signal. Using this approach, atomic resolution images of the force gradient have been achieved on Si(111) (Fig. 1),<sup>[46]</sup> Si(100),<sup>[67,68]</sup> and Cu(100).<sup>[80]</sup> The force gradient images showed atomic contrast independent of the

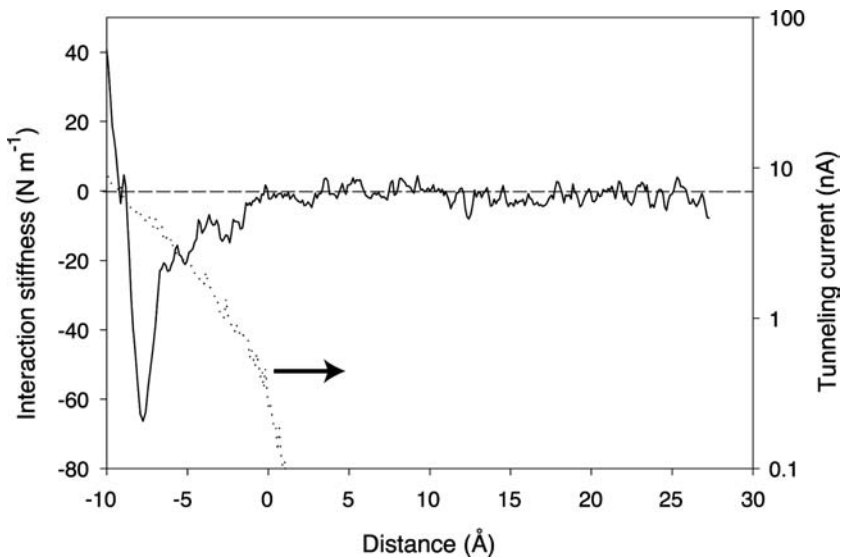


**Fig. 3** Directly measured stiffness of an atomic bond between a tungsten tip and a clean Si(111) surface in UHV.<sup>[42]</sup> The measurement amplitude was 0.24 Å. In addition to the stiffness of the bond, data also include the longer-range van der Waals interaction between the tip and the surface. Long- and short-range forces can be separated by using a suitable fitting procedure.<sup>[42,70]</sup> Also shown is the simultaneously acquired tunneling current.

contrast in the tunneling channel. In the case of Cu(100), atomic contrast was seen in the force gradient image even when no atomic contrast was visible in the tunneling image.

Force gradient feedback is possible by using FM detection<sup>[38]</sup> or by increasing the drive frequency of the lever. The latter can be achieved by increasing the natural resonance frequency of the lever. A higher resonance frequency allows for a higher drive frequency, making imaging possible.

#### Atomic dissipation

A topic of significant interest is the measurement of atomic-scale dissipation in AFM. It has been observed in both large<sup>[37,72,73]</sup> and small-amplitude<sup>[47]</sup> UHV-based AFM that the cantilever loses a few millielectron volts to electron volts of kinetic energy per cycle when it is near the surface. A consensus seems to be that the observed dissipation is related to “slow” stochastic motion of atoms at the tip or the sample surface.<sup>[47,74]</sup>

Small-amplitude AFM is expected to be more sensitive to short-range forces,<sup>[65]</sup> and thus to atomic-scale dissipation.<sup>[75]</sup> Small-amplitude, subresonance AFM is ideally suited to explore dissipation phenomena because any phase difference between drive and lever can be directly related to energy dissipation if the lever is operated in the linear regime far from resonance. Large-amplitude techniques can exhibit phase differences merely because of the inherent nonlinearities of the system.<sup>[76,77]</sup> Recently, subresonance, ultrasmall-amplitude AFM ( $A_0 = 0.13$  Å) has been used to measure atomic dissipation on a Cu(100) surface<sup>[47]</sup> (Fig. 4). It was found that the observed dissipation of a few 10 meV per cycle could be explained by the coupling of the tip motion to the stochastic motion of a

surface atom or defect encountering an energy barrier of the order of 0.5 eV, i.e., of the order of typical surface diffusion barriers.

#### Solvation forces—subresonance AFM in liquids

Subresonance AFM has the distinct advantage of not relying on a measurement of the resonance frequency, which can be exceedingly difficult if the AFM is operated in a highly damping medium, such as water. Exploiting this fact, it was recently shown that subresonance AFM is capable of directly measuring the stiffness oscillations associated with the molecular ordering of water confined between the tip and a flat surface (Fig. 5).<sup>[69]</sup> The advantage of the technique was the unambiguous interpretation of the data and

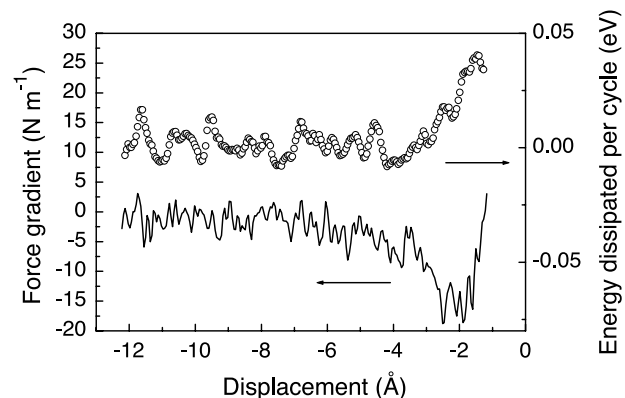


**Fig. 4** Simultaneously measured interaction stiffness and atomic-scale energy dissipation measured with a tip vibrating with an amplitude of 0.13 Å close to a clean Cu(100) surface in UHV. Note that this measurement was performed close to the noise limit of this particular instrument. *Source:* From Ref.<sup>[47]</sup>

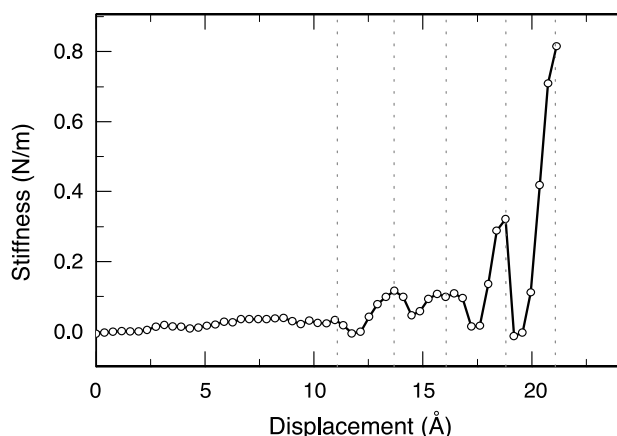


**Fig. 5** Stiffness of a confined water layer measured with a subresonance AFM at a free amplitude of  $0.35 \text{ \AA}$ . Note the regular spacing of higher-stiffness regions, corresponding to positions of the tip that allow the confined water to attain a solidlike structure. Intermediate positions are not commensurate with the molecule size of water, and thus result in a low-stiffness, disordered layer.

the easy separability of conservative and dissipative terms. This was not possible in earlier large-amplitude AFM measurements of the same phenomenon.<sup>[78]</sup>

## CONCLUSION AND OUTLOOK

Small-amplitude AFM offers distinctive advantages over large-amplitude techniques. These include:

1. Linear measurements.
2. Easy data interpretation.
3. Point-by-point, local measurements.
4. Higher sensitivity to short-range forces and potentially better S/N.
5. Easy separation of conservative and dissipative forces, especially when subresonance methods are used.
6. Easier transfer to different environments, especially liquids.

The downside of the techniques is the inherently low signals that need to be measured. However, as we have seen, high-stiffness cantilevers can reduce thermal noise and high-sensitivity displacement sensors are now available that can push amplitude sensitivity into the femtometer regime.

The two most significant developments in this field are the use of subresonance techniques and small-amplitude FM detection schemes. The subresonance techniques offer simple data interpretation, low thermal noise, the possibility of using lower-stiffness levers (as long as the snap-in is avoided), and the easy

transfer of the technique into liquid environments. Recent experiments using FM detection at small amplitudes are also very encouraging, as they combine the advantages of small amplitudes with the high signal-to-noise of FM detection. The very high stiffness levers used in the technique can keep  $Q$  values high even in liquids. This opens up the use of FM detection in liquid environments without the need of  $Q$  control techniques, which raise additional interpretation issues.

In the future, it is anticipated that small-amplitude techniques will play an ever-increasing role in *quantitative* AFM measurements. As they operate in virtually *any* environment, the impact on diverse fields, from atomic and molecular manipulation to the nanomechanics of biomolecules, could be enormous. If the widely heralded nanotechnology industry is to become a reality, methods that can reliably measure forces, stiffnesses, and dissipation at the nanoscale will be essential. Small-amplitude AFM might well be the technique of choice to put hard numbers on the workings of the molecular machinery of future nanodevices.

## REFERENCES

1. Binnig, G.; Rohrer, H.; Gerber, Ch.; Weibel, E. Surface studies by scanning tunneling microscopy. *Phys. Rev. Lett.* **1982**, *49* (1), 57–61.
2. Coombs, J.H.; Pethica, J.B. Properties of vacuum tunneling currents—anomalous barrier heights. *IBM J. Res. Develop.* **1986**, *30* (5), 455–459.
3. Binnig, G.; Quate, C.F.; Gerber, Ch. Atomic force microscope. *Phys. Rev. Lett.* **1986**, *56* (9), 930–933.
4. Giessibl, F.J. Atomic resolution of the silicon (111)-(7 × 7) surface by atomic force microscopy. *Science* **1995**, *267* (5194), 68–71.
5. Kitamura, S.; Iwatsaku, M. Observation of  $7 \times 7$  reconstructed structure on the silicon (111) surface using ultrahigh vacuum noncontact atomic force microscopy. *Jpn. J. Appl. Phys., Part 2* **1995**, *34* (1B), L145–L148.
6. Ueyama, H.; Ohta, M.; Sugawara, Y.; Morita, S. Atomically resolved InP(110) surface observed with noncontact ultrahigh vacuum atomic force microscope. *Jpn. J. Appl. Phys., Part 2* **1995**, *34* (8B), L1086–L1088.
7. Dürig, U.; Gimzewski, J.K.; Pohl, D.W. Experimental observation of forces acting during scanning tunneling microscopy. *Phys. Rev. Lett.* **1986**, *57* (19), 2403–2406.
8. Martin, Y.; Williams, C.C.; Wickramasinghe, H.K. Atomic force microscope—force mapping and profiling on a sub  $100\text{-\AA}$  scale. *J. Appl. Phys.* **1987**, *61* (10), 4723–4729.
9. Meyer, E.; Heinzlmann, H.; Grutter, P.; Jung, T.; Weisskopf, T.; Hidber, H.R.; Lapka, R.; Rudin, H.; Güntherodt, H.J. Comparative study of lithium-fluoride and graphite by atomic force microscopy (AFM). *J. Microsc. (Oxford)* **1988**, *152*, 269–280.
10. Yamada, H.; Fujii, T.; Nakayama, K. Experimental study of forces between a tunnel tip and the graphite surface. *J. Vac. Soc., A* **1988**, *6* (2), 293–295.

11. Cappella, B.; Dietler, G. Force–distance curves by atomic force microscopy. *Surf. Sci. Rep.* **1999**, *34*, 1–104.
12. Burnham, N.A.; Colton, R.J. Measuring the nanomechanical properties and surface forces of materials using an atomic force microscope. *J. Vac. Soc., A* **1989**, *7* (4), 2906–2913.
13. Burnham, N.A. Accounting for the stiffness of the probe and sample in scanning probe microscopy. *J. Vac. Sci. Technol., B* **1994**, *12* (3), 2219–2221.
14. Ohnesorge, F.; Binnig, G. True atomic-resolution by atomic force microscopy through repulsive and attractive forces. *Science* **1993**, *260* (5113), 1451–1456.
15. Pethica, J.B.; Oliver, W.C. Tip surface interaction in STM and AFM. *Phys. Scr.* **1987**, *T19*, 61–66.
16. Pethica, J.B.; Sutton, A.P. On the stability of a tip and flat at very small separations. *J. Vac. Sci. Technol., A* **1988**, *6* (4), 2490–2494.
17. García, R.; Pérez, R. Dynamic atomic force microscopy methods. *Surf. Sci. Rep.* **2002**, *47*, 197–301.
18. Zhong, Q.; Inniss, D.; Kjoller, K.; Elings, V.B. Fractured polymer/silica fiber surface studied by tapping mode atomic force microscopy. *Surf. Sci. Lett.* **1993**, *290*, L688–L692.
19. Gleyzes, P.; Kuo, P.K.; Boccara, A.C. Bistable behavior of a vibrating tip near a solid surface. *Appl. Phys. Lett.* **1990**, *59* (25), 2989–2991.
20. Tsukada, M.; Sasaki, N.; Yamura, R.; Sato, N.; Abe, K. Features of cantilever motion in dynamic-mode AFM. *Surf. Sci.* **1998**, *401* (3), 355–363.
21. Anczykowski, B.; Krüger, D.; Fuchs, H. Cantilever dynamics in quasiconnact force microscopy: spectroscopic aspects. *Phys. Rev., B* **1996**, *53* (23), 15,485–15,488.
22. García, R.; San Paulo, A. Dynamics of a vibrating tip near or in intermittent contact with a surface. *Phys. Rev., B* **2000**, *61* (20), R13381–R13385.
23. Chen, X.; Davies, M.C.; Roberts, C.J.; Tendler, S.J.B.; Williams, P.M.; Burnham, N.A. Optimizing phase imaging via dynamic force curves. *Surf. Sci.* **2000**, *460*, 292–300.
24. Dürig, U. Interaction sensing in dynamic force microscopy. *New J. Phys.* **2000**, *2*, 5.1–5.12.
25. Stark, M.; Stark, R.W.; Heckl, W.M.; Guckenberger, R. Inverting dynamic force microscopy: From signals to time-resolved interaction forces. *Proc. Natl. Acad. Sci. U. S. A.* **2002**, *99* (13), 8473–8478.
26. Albrecht, T.R.; Grütter, P.; Horne, D.; Rugar, D. Frequency modulation detection using high-*Q* cantilevers for enhanced force microscopy sensitivity. *J. Appl. Phys.* **1991**, *69* (2), 668–673.
27. Giessibl, F.J. Forces and frequency shifts in atomic-resolution dynamic force microscopy. *Phys. Rev., B* **1997**, *56* (24), 16010–16015.
28. Schwarz, U.D.; Hölscher, H.; Wiesendanger, R. Atomic resolution in scanning force microscopy: concepts, requirements, contrast mechanisms, and image interpretation. *Phys. Rev., B* **2000**, *62* (19), 13,089–13,097.
29. Ke, S.H.; Uda, T.; Terakura, K. Quantity measured in frequency-shift-mode atomic-force microscopy: an analysis with a numerical model. *Phys. Rev., B* **1999**, *59* (20), 13,267–13,272.
30. Giessibl, F.J. A direct method to calculate tip–sample interaction forces from frequency shifts in frequency-modulation atomic force microscopy. *Appl. Phys. Lett.* **2001**, *78* (1), 123–125.
31. Tamayo, J.; Humphris, A.D.L.; Miles, M.J. Piconewton regime dynamic force microscopy in liquids. *Appl. Phys. Lett.* **2000**, *77* (4), 582–584.
32. Israelachvili, J. *Intermolecular and Surface Forces*; Academic Press: London, 1992.
33. Hoffmann, P.M. Dynamics of small amplitude, off-resonance AFM. *Appl. Surf. Sci.* **2003**, *210*, 140–145.
34. Rabe, U.; Janser, K.; Arnold, W. Vibrations of free and surface-coupled atomic force microscope cantilevers: theory and experiment. *Rev. Sci. Instrum.* **1996**, *67* (9), 3281–3293.
35. Hölscher, H.; Schwarz, U.D.; Wiesendanger, R. Calculation of the frequency shift in dynamic force microscopy. *Appl. Surf. Sci.* **1999**, *140*, 344–351.
36. Chen, G.Y.; Warmack, R.J.; Huang, A.; Thundat, T. Harmonic response of near-contact scanning force microscopy. *J. Appl. Phys.* **1995**, *78* (3), 1465–1469.
37. Gotsmann, B.; Seidel, C.; Anczykowski, B.; Fuchs, H. Conservative and dissipative tip–sample interaction forces probed with dynamic AFM. *Phys. Rev., B* **1999**, *60* (15), 11,051–11,060.
38. Giessibl, F.J. Atomic resolution on Si(111)-(7 × 7) by noncontact atomic force microscopy with a force sensor based on a quartz tuning fork. *Appl. Phys. Lett.* **2000**, *76* (11), 1470–1472.
39. Sarid, D.; Elings, V. Review of scanning force microscopy. *J. Vac. Sci. Technol., B* **1991**, *9* (2), 431–437.
40. Sarid, D. *Scanning Force Microscopy*; Oxford Univ. Press: Oxford, 1994.
41. Gustafsson, M.G.L.; Clarke, J. Scanning force microscope springs optimized for optical-beam deflection and with tips made by controlled fracture. *J. Appl. Phys.* **1994**, *76*, 172–181.
42. Hoffmann, P.M.; Oral, A.; Grimble, R.A.; Özer, H.Ö.; Jeffery, S.; Pethica, J.B. Direct measurement of interatomic force gradients using an ultralow-amplitude atomic force microscope. *Proc. R. Soc. Lond., A* **2001**, *457*, 1161–1174.
43. Saulson, P.R. Thermal noise in mechanical experiments. *Phys. Rev., D* **1990**, *42* (8), 2437–2445.
44. Giessibl, F.J.; Bielefeldt, H.; Hembacher, S.; Mannhart, J. Calculation of the optimal imaging parameters for frequency modulation atomic force microscopy. *Appl. Surf. Sci.* **1999**, *140*, 257–352.
45. Giessibl, F.J.; Bielefeldt, H.; Hembacher, S.; Mannhart, J. Imaging of atomic orbitals with the atomic force microscope—Experiments and simulations. *Ann. Phys.* **2001**, *10* (11–12), 887–910.
46. Oral, A.; Grimble, R.A.; Özer, H.Ö.; Hoffmann, P.M.; Pethica, J.B. Quantitative atom-resolved force gradient imaging using noncontact atomic force microscopy. *Appl. Phys. Lett.* **2001**, *79* (12), 1915–1917.
47. Hoffmann, P.M.; Jeffery, S.; Pethica, J.B.; Özer, H.Ö.; Oral, A. Energy dissipation in atomic force microscopy and atomic loss processes. *Phys. Rev. Lett.* **2001**, *87* (26), 265502, (1–4)
48. Ju, L.; Blair, D.G.; Zhao, C. Detection of gravitational waves. *Rep. Prog. Phys.* **2000**, *63* (9), 1317–1427.
49. Lantz, M.A.; Hug, H.J.; van Schendel, P.J.A.; Hoffmann, R.; Martin, S.; Baratoff, A.; Abdurixit, A.;



- Güntherodt, H.-J.; Gerber, Ch. Low temperature scanning force microscopy of the Si(111)-(7 × 7) surface. *Phys. Rev. Lett.* **2000**, *84* (12), 2642–2645.
50. Pethica, J.B.; Hutchings, R.; Oliver, W.C. Hardness measurement at penetration depths as small as 20 nm. *Philos. Mag., A* **1983**, *48* (4), 593–606.
  51. Jarvis, S.P.; Oral, A.; Weihs, T.P.; Pethica, J.B. A novel force microscope and point contact probe. *Rev. Sci. Instrum.* **1993**, *64* (12), 3515–3520.
  52. Jarvis, S.P.; Yamada, H.; Yamamoto, S.-I.; Tokumoto, H. A new force controlled atomic force microscope for use in ultrahigh vacuum. *Rev. Sci. Instrum.* **1996**, *67* (6), 2281–2285.
  53. Jarvis, S.P.; Yamada, H.; Yamamoto, S.-I.; Tokumoto, H.; Pethica, J.B. Direct mechanical measurement of interatomic potentials. *Nature* **1996**, *384*, 247–249.
  54. Jarvis, S.P.; Lantz, M.A.; Dürig, U.; Tokumoto, H. Off resonance ac mode force spectroscopy and imaging with an atomic force microscope. *Appl. Surf. Sci.* **1999**, *140*, 309–313.
  55. O'Shea, S.J.; Welland, M.E.; Pethica, J.B. Atomic force microscopy of local compliance at solid–liquid interfaces. *Chem. Phys. Lett.* **1994**, *223*, 336–340.
  56. O'Shea, S.J.; Welland, M.E. Atomic force microscopy at solid–liquid interfaces. *Langmuir* **1998**, *14*, 4186–4197.
  57. Olsson, L.; Wigren, R.; Erlandsson, R. Ultrahigh vacuum scanning force/scanning tunneling microscope: application to high resolution imaging of Si(111)7 × 7. *Rev. Sci. Instrum.* **1996**, *67* (6), 2289–2296.
  58. Rugar, D.; Mamin, H.J.; Erlandsson, R.; Stern, J.E.; Terris, B.D. Force microscope using a fiber-optic displacement sensor. *Rev. Sci. Instrum.* **1988**, *59* (11), 2337–2340.
  59. Erlandsson, R.; Olsson, L.; Mårtensson, P. Inequivalent atoms and imaging mechanisms in ac-mode atomic-force microscopy of Si(111)7 × 7. *Phys. Rev., B* **1996**, *54* (12), R8309–R8312.
  60. Erlandsson, R.; Olsson, L. Force interaction in low-amplitude ac-mode atomic force microscopy: Cantilever simulations and comparison with data from Si(111)7 × 7. *Appl. Phys., A* **1998**, *66*, S879–S883.
  61. Kitamura, S.; Iwatsuki, M. Observation of silicon surfaces using ultrahigh-vacuum noncontact atomic force microscopy. *Jpn. J. Appl. Phys., Part 2* **1996**, *35* (5B), L668–L671.
  62. Eguchi, T.; Hasegawa, Y. High resolution atomic force microscopic imaging of the Si(111)-(7 × 7) surface: contribution of short-range forces to the images. *Phys. Rev. Lett.* **2002**, *89* (26), 266105, (1–4)
  63. Giessibl, F.J.; Hembacher, S.; Bielefeldt, H.; Mannhart, J. Subatomic features on the Si(111)-(7 × 7) surface observed by atomic force microscopy. *Science* **2000**, *289* (5478), 422–425.
  64. Giessibl, F.J.; Herz, M.; Mannhart, J. Friction traced to the single atom. *Proc. Natl. Acad. Sci. U. S. A.* **2002**, *99* (19), 12,006–12,010.
  65. Giessibl, F.J.; Bielefeldt, H. Physical interpretation of frequency-modulation atomic force microscopy. *Phys. Rev., B* **2000**, *61* (15), 9968–9971.
  66. Oral, A.; Grimble, R.A.; Özer, H.Ö.; Pethica, J.B. High-sensitivity noncontact atomic force microscope/scanning tunneling microscope (nc AFM/STM) operating at subangstrom oscillation amplitudes for atomic resolution imaging and force spectroscopy. *Rev. Sci. Instrum.* **2003**, *74* (8), 3656–3662.
  67. Özer, H.Ö.; Mehrdad, A.; Oral, A. Ultra-small oscillation amplitude nc-AFM/STM imaging, force and dissipation spectroscopy of Si(100)(2 × 1). *Solid State Commun.* **2002**, *124* (12), 469–472.
  68. Özer, H.Ö.; Mehrdad, A.; Oral, A. Measurement of energy dissipation between tungsten tip and Si(100)-(2 × 1) using sub-Ångström oscillation amplitude non-contact atomic force microscope. *Appl. Surf. Sci.* **2003**, *210*, 12–17.
  69. Hoffmann, P.M.; Jeffery, S.; Oral, A.; Grimble, R.A.; Özer, H.Ö.; Pethica, J.B. Nanomechanics using an ultra-small amplitude AFM. *Mater. Res. Soc. Symp. Proc.* **2001**, *649*, Q9.2.1–Q9.2.6.
  70. Guggisberg, M.; Bammerlin, M.; Loppacher, C.; Pfeiffer, O.; Abdurixit, A.; Barwich, V.; Bennewitz, R.; Baratoff, A.; Meyer, E.; Guntherodt, H.J. Separation of interactions by noncontact force microscopy. *Phys. Rev., B* **2000**, *61* (16), 11,151–11,155.
  71. Pérez, R.; Štich, I.; Payne, M.C.; Terakura, K. Surface-tip interactions in noncontact atomic-force microscopy on reactive surfaces: Si(111). *Phys. Rev., B* **1998**, *58* (16), 10,835–10,849.
  72. Loppacher, C.; Bennewitz, R.; Pfeiffer, O.; Guggisberg, M.; Bammerlin, M.; Schär, S.; Barwich, V.; Baratoff, A.; Meyer, E. Experimental aspects of dissipation force microscopy. *Phys. Rev., B* **2000**, *62* (20), 13,674–13,679.
  73. Gotsmann, B.; Fuchs, H. Dynamic force spectroscopy of conservative and dissipative forces in an Al–Au(111) tip–sample system. *Phys. Rev. Lett.* **2001**, *86* (12), 2597–2600.
  74. Sasaki, N.; Tsukada, M. Effect of microscopic nonconservative process on noncontact atomic force microscopy. *Jpn. J. Appl. Phys., Part 2* **2000**, *39* (12B), L1334–L1337.
  75. Gauthier, M.; Tsukada, M. A theoretical study on mass sensitive surface analysis and subsurface imaging with dynamic force microscopy. *Surf. Sci.* **2001**, *495* (3), 204–210.
  76. Gauthier, M.; Tsukada, M. Damping mechanism in dynamic force microscopy. *Phys. Rev. Lett.* **2000**, *85* (25), 5348–5351.
  77. Gauthier, M.; Pérez, R.; Arai, T.; Tomitori, M.; Tsukada, M. Interplay between nonlinearity, scan speed, damping, and electronics in frequency modulation atomic-force microscopy. *Phys. Rev. Lett.* **2002**, *89* (14), 146104.
  78. Jarvis, S.P.; Uchihashi, T.; Ishida, T.; Tokumoto, H.; Nakayama, Y. Local solvation shell measurement in water using a carbon nanotube probe. *J. Phys. Chem., B* **2000**, *104* (26), 6091–6094.
  79. Giessibl, F.J. Atomic force microscopy in ultrahigh vacuum. *Jpn. J. Appl. Phys., Part 1* **1994**, *33* (6B), 3726–3734.
  80. Özer, H.Ö.; Oral, A.; Hoffmann, P.M.; Pethica, J.B. Nanotechnology, *to be published February 2004*.

# Smallest Size Regime: Control of Ultrafast Dynamics

Stefan Vajda

*Chemical Sciences and Engineering Division, Center for Nanoscale Materials, Argonne National Laboratory, Argonne, Illinois, U.S.A., and Department of Chemical Engineering, Yale University, New Haven, Connecticut, U.S.A.*

Ludger Wöste

*Institut für Experimentalphysik, Freie Universität Berlin, Berlin, Germany*

## Abstract

It is well known that nanoparticles are not rigid structures and may undergo structural/shape changes when exposed to elevated temperatures, reaction environment, or after the absorption of photons. For example, a catalytic active site may change its structure to form a transition state to accommodate the reactant molecules and reaction intermediates. On the other hand, the absorption of light photons may trigger selective vibrations or transient structural changes, affecting the reactivity. Consequently, selective optical excitation of the nanoparticles or nanoparticle–molecule complexes with laser pulses optimized in both time and wavelength domain opens entirely new ways of control of mode-selective photophysics and photochemistry.

Since surface reactions occur on active sites consisting of a handful of atoms only, small metal clusters and organometallic molecules are ideal models for studies of the basic phenomena governing chemical and photochemical processes. In this entry, we explore various schemes to manipulate photoinduced dynamics in the smallest size regime by using tailor-made ultrafast laser pulses. The efficacy of the implemented control approaches will be illustrated on several examples: 1) manipulation of the population of the bound B and X states of the sodium trimer by using linearly chirped laser pulses; 2) control of the ionization and fragmentation pathways of the photoexcited NaK and Na<sub>2</sub>K clusters by shaped laser pulses; and 3) control of branching the photodissociation in CpMn(CO)<sub>3</sub>. The optimum pulse shapes navigating the molecular dynamics are found by employing a feedback loop algorithm based on evolutionary strategies. These pulse shapes contain rich and detailed information about the involved molecular processes.

## INTRODUCTION

With the discovery of the lasers almost half a century ago, an old dream of chemists seemed to get into reach: selective bond breaking and making, which would allow an ultimate control over the outcome of a chemical reaction by using photons with energies corresponding, for example, to the vibration frequencies of the targeted bond. However, it soon became evident that this approach did not bring the highly expected results due to the fast and efficient energy dissipation in the targeted molecules via internal vibrational redistribution (IVR). The advent of tunable femtosecond laser sources, however, has re-opened this fascinating perspective since it allows one to obtain an insight into elementary intramolecular processes like bond shaking, breaking, and making<sup>[1]</sup> and getting ahead of IVR.<sup>[2–8]</sup> Using transient pump&probe spectroscopy, such processes can now be analyzed in real time<sup>[9,10]</sup> and described theoretically.<sup>[11,12]</sup> Also, considerable theoretical effort has been made in various control scenarios to be performed in the time or wavelength domain that would drive the chemical reaction to the desired product state.<sup>[13–33]</sup> The

feasibility of the theoretical models was first verified experimentally on small particles consisting of only a few atoms like monomers, dimers, and trimers.<sup>[1,16,34–36]</sup> In the case of larger and more complex systems, the adaptive laser pulse control strategy has become very attractive.<sup>[37]</sup> The advantage of this method is that it does not require an a priori knowledge of the potential energy surfaces involved in the differently branching reaction pathways. Instead, the employed optimization algorithm “teaches” the light field to maximize the yield of the selected product. This is achieved in an iterative closed-loop experiment in which the genetic algorithm creates an optimal laser pulse that prepares the desired target. Coherent control on larger molecular systems was first confirmed experimentally in a photophysical experiment, where the fluorescence of the iodine molecule was optimized with phase-modulated (chirped) laser pulses.<sup>[38]</sup> Later, it was employed for manipulating a large variety of photophysical and photochemical processes in more complex molecules and nanoparticles: selective fragmentation of the CpFe(CO)<sub>2</sub>Cl molecule,<sup>[39]</sup> selective excitation of solvated dye molecules,<sup>[40]</sup> control of the photodissociation process in CsCl,<sup>[41]</sup> strong-field control of reactivity channels in organic molecules<sup>[42,43]</sup>

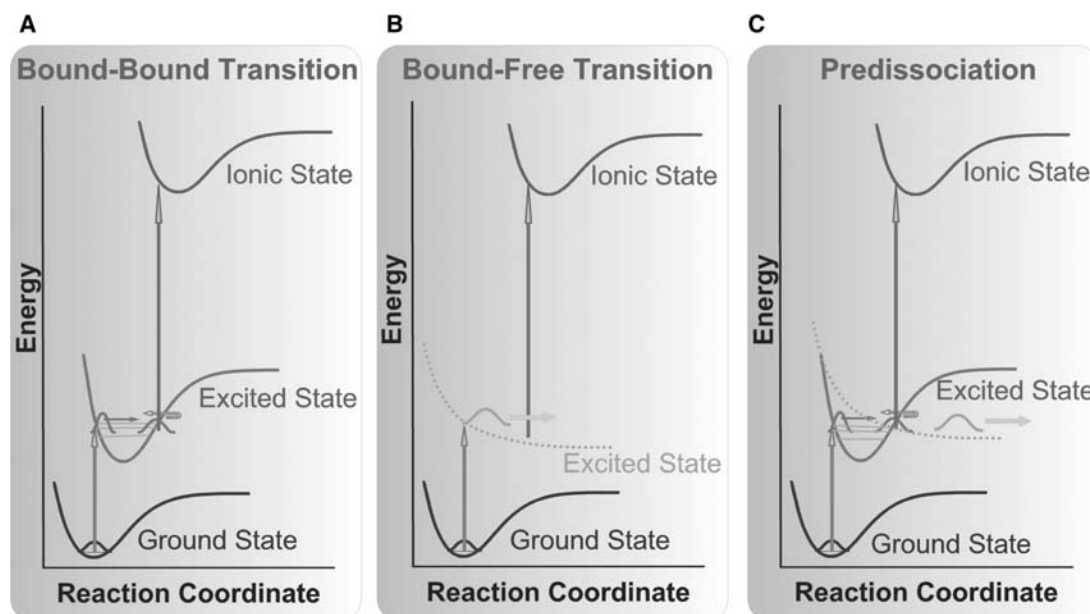


**Fig. 1** The principle of pump&probe spectroscopy illustrated in the example of transient two-photon ionization: The first femtosecond laser pulse (pump) electronically excites the particle into an ensemble of vibrational states, creating a wavepacket in the excited state. The temporal evolution of the wavepacket is probed by a second (probe) pulse, which ionizes the excited particle as a function of the time-dependent Franck Condon-window. (A) Shows the scheme for a bound–bound transition, where an oscillatory behavior of the wavepacket reflecting the vibrations in the excited molecule will appear. (B) Illustrates the pump&probe principle for monitoring a bound-free transition exhibiting an exponential decay. (C) Cartoon of the process of predissociation, when a fraction of the oscillating wavepacket leaks into the repulsive state at every passage through the curve-crossing region.

and liquids,<sup>[44]</sup> control of vibrational motion in room temperature molecular gases,<sup>[45]</sup> control of vibrational Raman scattering in liquids,<sup>[46]</sup> control of wavepacket dynamics, population of electronic states, and fragmentation processes,<sup>[47]</sup> control of non-linear processes in liquids by multi-photon intrapulse interference,<sup>[48]</sup> control of photoisomerization in solutions,<sup>[49]</sup> control of the ground-state vibrational dynamics via a Raman process is demonstrated in polydiacetylene,<sup>[50]</sup> control in biological systems,<sup>[51,52]</sup> quantum control of energy flow in light harvesting systems,<sup>[53]</sup> control of ionization processes in aligned  $I_2$  molecule by optimally polarized femtosecond pulses,<sup>[54]</sup> local field enhancement of electron emission from nanoparticles,<sup>[55]</sup> optical control of ground-state atomic orbital alignment in the chlorine atom for orientation-dependent collision studies,<sup>[56]</sup> control of the population transfer in complex solvated molecules,<sup>[57]</sup> weak-field coherent control of retinal isomerization in bacteriorhodopsin,<sup>[58]</sup> control of electronic energy redistribution pathways in molecules by coupling of molecular electronic states with tunable surface plasmon resonances,<sup>[59]</sup> just to name a few.

This entry is not an exhaustive and detailed overview of the field of laser-controlled chemistry and physics but aims to give basic insight into this exciting and rapidly developing area. We will explain the fundamentals of optical control using ultrashort laser pulses, followed by a discussion of the applied

optimal control scenario. We will then explore various schemes to manipulate photoinduced molecular dynamics, and show several examples. This entry presents selected results of the research performed at the Freie Universität Berlin on the control of light-induced processes by employing optimally shaped laser pulses on systems with well-known dynamics from time-resolved pump&probe experiments and from theoretical calculations. The systems and processes addressed are different in many aspects, but there is a common line unifying them throughout this work, namely the particle size, which determines their basic chemical and photophysical properties. The change in the cluster size gives rise to a large variety of ultrafast photoinduced processes like bound–bound transitions, dissociation, and predissociation. The coupling of various electronic states and excitation of different vibrational modes can lead to extensive structural rearrangements and, thus, create substantial changes in chemical reactivity by means of passages through conical intersections<sup>[60–63]</sup> or as an effect of internal vibrational redistribution.<sup>[64–67]</sup> By the proper choice of the size and composition of the molecular system, the type and number of photoinduced processes evolving from rather different pathways and leaking into different product channels can be systematically varied. The time-evolution of the photoexcited system can be monitored in real time by using ultrafast

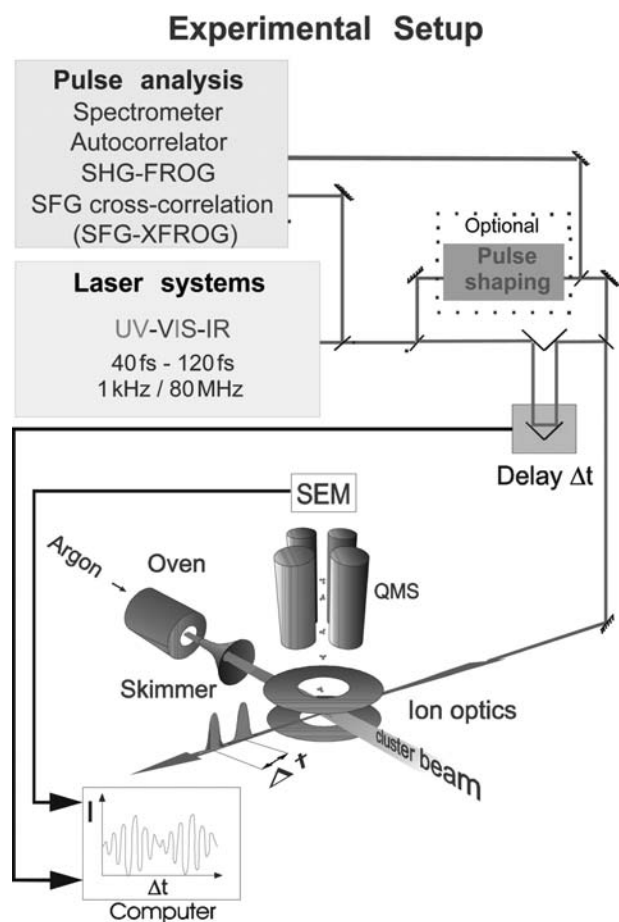


**Fig. 2** Schematic of the experimental setup consisting of a molecular beam machine, laser systems, and laser pulse characterization equipment.

spectroscopy (Fig. 1). Moreover, the molecular dynamics can be manipulated as well when employing a control experiment searching for an optimally shaped laser pulse, which navigates the evolution of the molecular system on the involved potential energy surface(s) towards the desired product channel. The most important output of the optimization experiments is the very rich information content coded in the obtained pulse shapes. In a joint effort with theoretical calculations and pump&probe experiments, system-specific information about the involved electronic states and reaction pathways can be withdrawn.

Metal clusters are excellent model systems for time-resolved investigations and control scenarios: They exhibit pronounced absorption bands, which are located within the tuning range of the commercially available femtosecond laser sources; their photoionization energies are also well within their reach, and the vibrational frequencies can well be resolved in the time domain with the available sub-100 fs pulses. Further, the influence of internal vibrational redistribution

processes, which depend on the amount of internal degrees of freedom, can simply be adapted to the experimental requirements by the right choice of cluster size and its temperature. For this reason, we have first performed extensive systematic pump&probe experiments on alkaline dimers, trimers, etc. to study the evolution of wavepacket dynamics, vibronic coupling, geometrical rearrangement, fragmentation, etc., as a function of cluster size and excitation energy. Later, we extended our investigations to more complex systems, including organometallic molecules.

## EXPERIMENTAL

The experimental setup (Fig. 2), consisting of molecular beam apparatus, has been described in details elsewhere<sup>[68]</sup> and only its brief description is given here. The beam of clusters or molecules is generated in the first vacuum chamber, by an adiabatic coexpansion of a carrier gas and alkali metal vapor or sublimated molecular substances from a heated oven through a 70–100  $\mu\text{m}$  nozzle into vacuum. The emerging beam is collimated by using a skimmer of 1 mm orifice, which enters into the second differentially pumped vacuum chamber. There, the beam passes between the electrical lenses of a quadrupole mass spectrometer (Pfeiffer Balzers QMG 420). The lenses of the quadrupole are oriented perpendicularly to both the molecular beam and the laser beam(s) to extract the produced photoions for mass analysis.

The femtosecond laser pulses covering the ultraviolet, visible, and infrared wavelength regions were generated by using four different laser setups. In the  $\text{Na}_3$  experiments, a Ti:Sa-OPO laser system (Spectra Physics Tsunami 3960 and OPO, pumped by a 15 W argon ion laser) was used, which produced 100–120 fs laser pulses centered at 620 nm after frequency doubling. In the NaK/Na<sub>2</sub>K experiments, a Nd:YLF laser pumped Ti:Sa laser was used (Spectra Physics Millennia X and Tsunami 3960), which produced pulses of about 80 fs duration at a central wavelength of 770 nm. In the experiments on  $\text{CpMn}(\text{CO})_3$ , two Ti:Sa amplifier systems were used. The first consisted of a Ti:Sa Spectra Physics Tsunami seed laser, which was pumped by a Nd:YLF Millennia V laser and produced 70 fs seed pulses at 800 nm central wavelength for a Quantronix multi-pass regenerative amplifier. The amplifier produced 87 fs pulses of up to 1.5 mJ pulse energy at a repetition rate of 1 kHz. The second Ti:Sa amplifier system consisted of a Kapteyn–Murnane oscillator, which was pumped by a 5 W Coherent Verdi laser and produced sub-40 fs seed pulses for the multi-pass amplifier (Quantronix Odin). This amplifier produced sub-40 fs pulses at the central wavelength of 805 nm and repetition rate of 1 kHz.

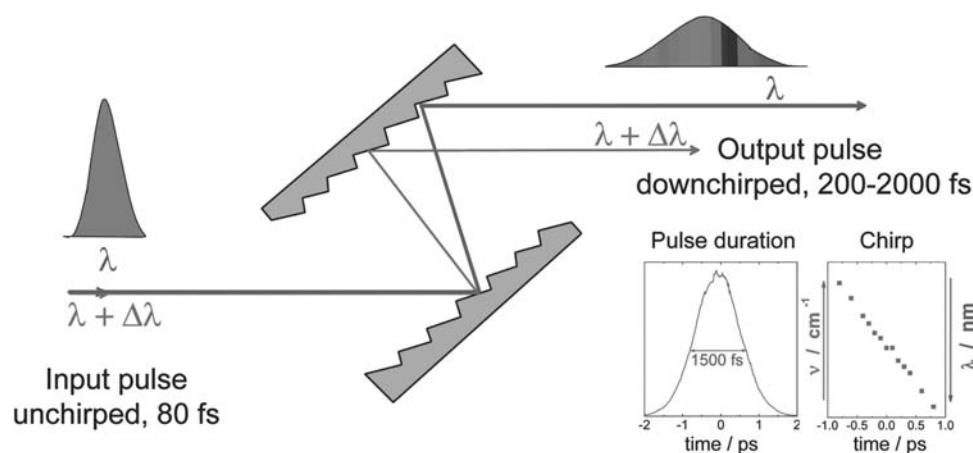


**Fig. 3** Scheme of the experimental setup for generating linearly chirped pulses. The transform limited input pulse passes through the grating pair. On the output, the shorter wavelength spectral components of the pulse are followed by the longer spectral components. The relative time shift of the spectral components and the related duration of the generated pulse can be tuned by changing the separation between the gratings. The insert shows the intensity and wavelength/frequency profile of a typical output pulse as a function of time.

In the control experiments on the sodium trimer, the pulses were shaped with a grating pair with manually adjustable separation between the two gratings, generating linearly chirped laser pulses. When an unchirped input pulse of 120 fs duration with a central wavelength of 620 nm was employed, chirped pulses of 200 fs to 2000 fs duration could be routinely generated (Fig. 3).

For an effective control of multi-photon driven processes, rather complex pulse forms are needed. Such pulse forms were generated by applying voltages to the individual pixels of a liquid crystal spatial light modulator,<sup>[69]</sup> allowing phase and amplitude modulation. We used a double-mask modulator of Cambridge Research Instruments with  $2 \times 128$  pixels positioned between two gratings and two lenses in a 4f arrangement (Fig. 4).<sup>[70]</sup> By computer control, arbitrary pulse forms, such as linearly chirped pulses or pulse trains can be generated, as illustrated in the inserts of Fig. 4. However, the design of such large sets of arbitrary tailored pulses is not straightforward for applications on real molecular systems when pulse forms cannot be predicted by theory or when detailed experimental knowledge of the involved electronic states and the underlying dynamics is not available. In such cases, the optimal pulse shape, which will navigate the molecular system into the desired product channel, can be found in a self-learning closed-loop experiment consisting of a laser, pulse shaper, detector of reaction products and a computer executing an iterative optimization algorithm.<sup>[37]</sup> In the experiments described here, the modulated pulse is focused on the molecular beam and the desired product ion current is monitored on a mass spectrometer and is taken as reference feedback signal for the optimization algorithm. The algorithm, which is based on evolutionary strategies, iteratively

alters the settings on the pulse-shaper until the maximum yield of the selected product ions is achieved. The closed-loop experiment is shown schematically in Fig. 5.

The laser pulses were characterized in both time and wavelength domain by using a Jobin–Yvon monochromator, Spectra Physics autocorrelators for Ti:Sa oscillators, autocorrelator for OPO built by Harald Ruppe,<sup>[71]</sup> single-shot autocorrelator for sub-40 fs pulse characterization constructed by Marcel Krenz,<sup>[72]</sup> second harmonic generation frequency-resolved optical gating (SHG-FROG, Polytec Femtos) and time- and wavelength-resolved sum-frequency cross-correlation (SFG-CC) built by Patrick Wetzel.<sup>[73]</sup>

## RESULTS AND DISCUSSION

### Homogeneous Clusters: Bound–Bound Transitions in $\text{Na}_3$

The time-resolved spectrum of the sodium trimer reflects the vibrations in its bound B-state when excited with a femtosecond pulse with a central wavelength of 620 nm (Fig. 6). In this experiment, a wavepacket in the B-state is populated via one-photon excitation (pump) and the time evolution of the excited state is monitored by one-photon ionization (probe). The observed vibration period of 320 fs is in excellent agreement with the data previously reported in the literature.<sup>[74,75]</sup> Gerber and coworkers<sup>[76]</sup> used amplified laser pulses to study the dynamics in  $\text{Na}_3$  and, in addition to the  $\text{Na}_3$  B-state dynamics, they resolved an additional vibrational component in their pump&probe spectra, which reflected the propagation of the wavepacket in the ground state of  $\text{Na}_3$  as well.

## Laser Pulse Modulation

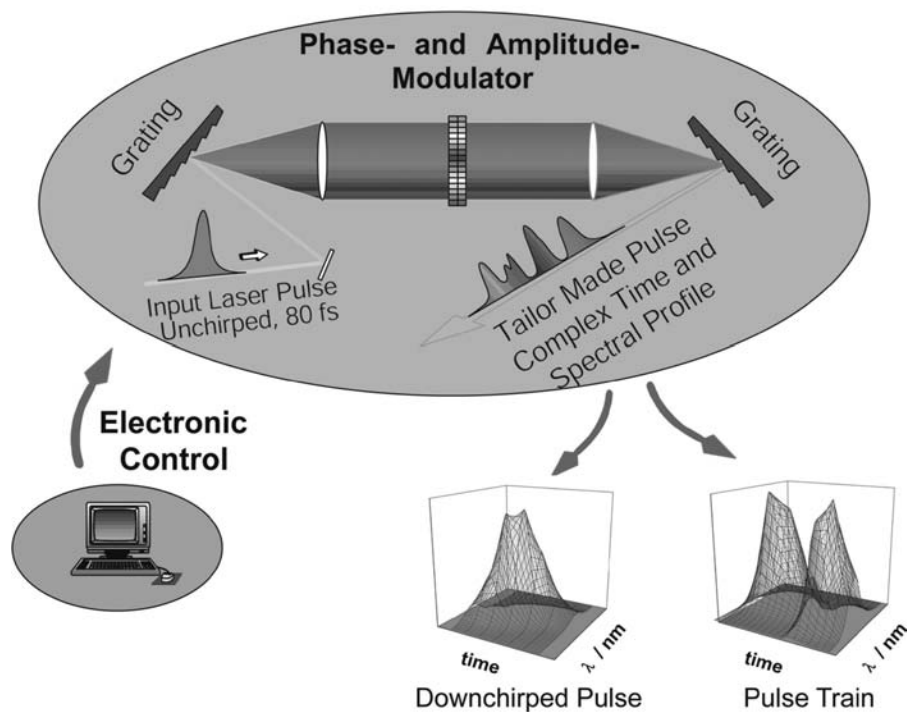


**Fig. 4** Scheme of the setup for generation of phase- and amplitude-modulated pulses. The description of the setup is given in the main text. Shown are two tailor-made pulse forms generated from a 120 fs laser pulse ( $\lambda = 620$  nm) and characterized by time and spectrally resolved cross-correlation technique employing an 80 fs reference pulse ( $\lambda_{\text{ref}} = 775$  nm): a linearly chirped pulse of 300 fs duration and a double-pulse (pulse train).

To achieve control of population of different bound electronic states of the sodium trimer ( $\text{Na}_3\text{-B}$  and  $\text{Na}_3\text{-X}$ ), a series of experiments employing linearly chirped pump&control pulses and an unchirped 120 fs probe pulse was performed. The chirped pulses were characterized by employing SFG-CC using an unchirped 80 fs laser pulse with a central wavelength of 775 nm as reference pulse. When applying down-chirped pulses of

up to 350 fs duration (FWHM, full width at half maximum), the feature of the transient  $\text{Na}_3^+$  signal remained unchanged—reflecting the 320 fs vibration period of the B-state. However, the pump&probe signal changed dramatically when a down-chirped pump&control pulse of 400 fs duration was employed: the period of the oscillatory signal changed abruptly to 230 fs with the pump&control pulse arriving first

## Control of the Fragmentation of Small Clusters & Molecules

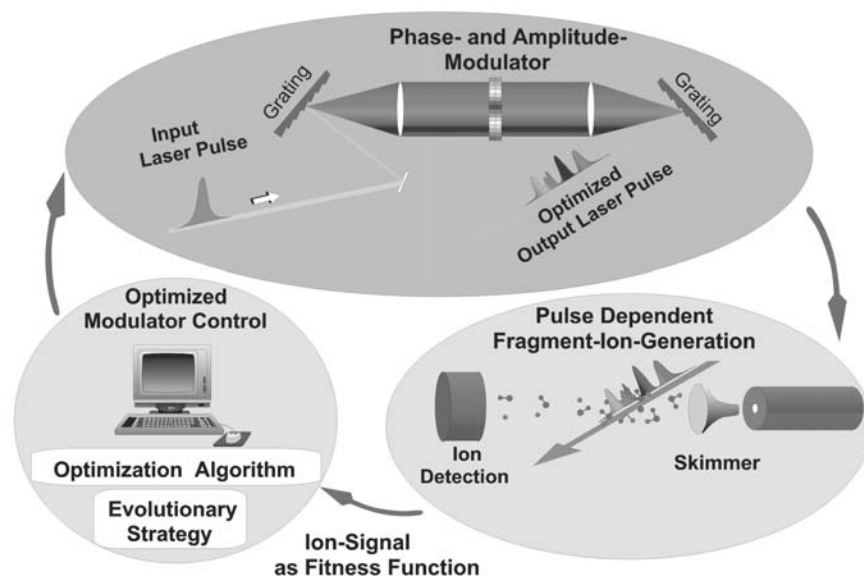


**Fig. 5** Schematic cartoon of the self-learning optimization setup searching for optimal pulse shape, which produces the highest ion yield of the desired ionic product in a multi-step multi-photon process. The description of the setup is given in the main text. *Source:* Reprinted with permission from Ref.<sup>[42]</sup>.



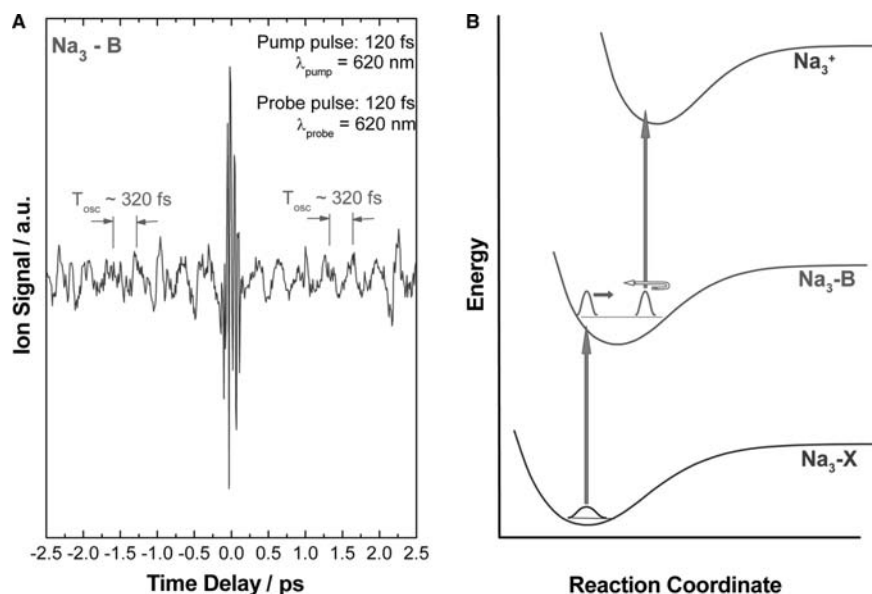


**Fig. 6** Transient two-photon ionization spectrum of  $\text{Na}_3$  recorded with transform-limited 120 fs pulses with a central wavelength of 620 nm (A). The progression exhibits oscillations with a period of 320 fs reflecting the symmetric stretch mode of the electronically excited B-state ( $\text{Na}_3\text{-B}$ ). (B) Illustrates the involved one-photon pump, one-photon probe scheme. Part (A) is compiled with permission from Ref.<sup>[42]</sup>.

(Fig. 7A). This vibrational period reflects the propagation of the wavepacket created in the ground state of  $\text{Na}_3$ . The action of the pump&control pulse is illustrated in Fig. 7B: the initial shorter wavelength components of this pulse first create a wavepacket in the electronically excited B-state of  $\text{Na}_3$ . Then, the evolving wavepacket is transferred into the vibrationally excited, electronic ground state of the trimer (X-state) by the following longer wavelength components of the same pulse. The vibrational dynamics of the ground state is then monitored by two-photon ionization with the unchirped probe pulse. At negative delay times (when the unchirped pulse precedes the chirped pulse), the transient signal still reflects the vibrations in the B-state, thus providing a direct proof of the suggested control scheme.

### Heterogeneous Dimers and Trimers: Bound NaK and Photofragmenting $\text{Na}_2\text{K}$

The vibration dynamics of the electronically excited NaK dimer has been described in detail in several studies,<sup>[77,78]</sup> revealing the 440 fs vibration period of the  $A(2) \ ^1\Sigma^+$  state.<sup>[79]</sup> Pump&probe experiments performed on  $\text{Na}_n\text{K}_m$  ( $n = 0\text{--}2$ ,  $m = 1\text{--}3$ ,  $n + m = 3$ ) trimers with variable laser wavelength in the 730–840 nm region<sup>[80]</sup> revealed strongly wavelength-dependent fragmentation times, as well as NaK fragments emerging from  $\text{Na}_2\text{K}$  on excitation. When employing laser pulses with a central wavelength of 770 nm (Fig. 8), not only the decay time of the fragmenting  $\text{Na}_2\text{K}^*$  trimer and its vibration dynamics

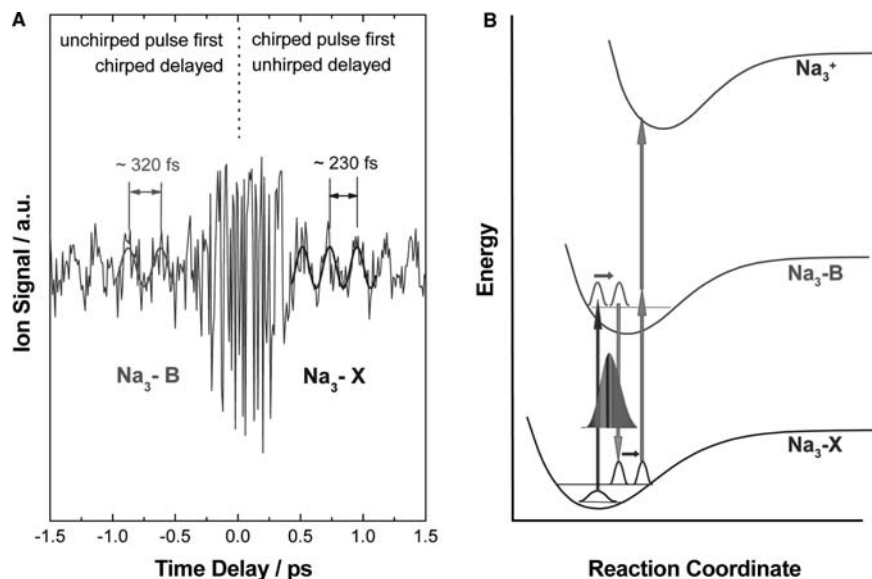


**Fig. 7** (A) Pump&probe spectrum of  $\text{Na}_3$  obtained under identical experimental conditions, as in Fig. 6 with the only exception that the employed pump pulse was a linearly down-chirped 400 fs one. The resulting oscillation time of 230 fs corresponds to the symmetric stretch vibration of the electronic ground state of  $\text{Na}_3$  ( $\text{Na}_3\text{-X}$ ). (B) Schematic of the pump-control-probe scheme. Source: Compiled with permission from Ref.<sup>[42]</sup>.

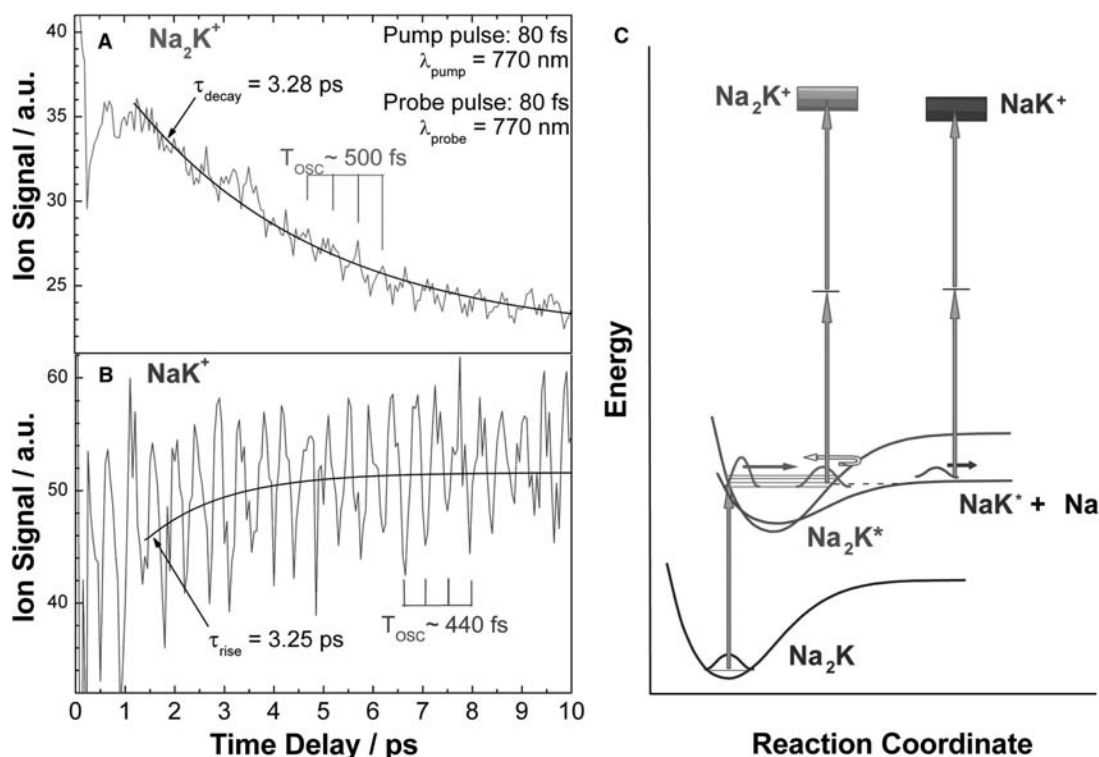


**Fig. 8** Temporal evolution of a transient three-photon ionization signal of the decaying  $\text{Na}_2\text{K}$  (A) and its fragment  $\text{NaK}$  (B). The decay time of the fragmenting trimer matches well with the rise time of its diatomic fragment. The superposed oscillations indicate wavepacket oscillations in the coherently excited system. (C) Shows the schematic view of the investigated three-photon fragmentation and ionization process. *Source:* Figure (A) and (B) compiled with permission from Ref.<sup>[42]</sup>.

with a vibration period of 500 fs could be clearly resolved, but also the identical rise time of the emerging  $\text{NaK}$  fragment exhibiting the distinct vibrational dynamics of the  $\text{NaK}$  dimer. Most importantly, these experiments helped to identify the first suitable candidates for coherent control experiments, namely the fragmenting  $\text{Na}_2\text{K}$  trimer and its fragment dimer  $\text{NaK}$ ; the dynamics of both species observable with the scheme experimental scheme involving one-photon excitation and two-photon ionization at identical laser wavelength.

The results of three optimal control experiments on the  $\text{NaK}/\text{Na}_2\text{K}$  system will be presented in this section, namely the optimization for the maximum yield of  $\text{NaK}^+$  in a cluster beam without trimers and larger aggregates (aimed to optimize the excitation and ionization step in  $\text{NaK}$  only); for the maximum yield of  $\text{NaK}^+$  in the presence of  $\text{Na}_2\text{K}$  and  $\text{NaK}$  in the cluster beam (with the goal to enhance fragmentation of  $\text{Na}_2\text{K}$ ); and optimization for the maximum ion yield of  $\text{Na}_2\text{K}^+$  (with the goal to suppress fragmentation). The focus will be on the interpretation of the optimal pulse shapes with regard to the controlled molecular dynamics.

The optimal pulse producing the highest  $\text{NaK}^+$  yield via optimization of the excitation and ionization

step is shown in Fig. 9A. The enhancement of the ion yield with respect to an unchirped 80 fs pulse of the same energy was about 60%.<sup>[81]</sup> The optimal pulse consists of three subpulses, with time separations  $\sim 650$  fs ( $\sim 1.5 T_{\text{OSC}}^{\text{NaK}}$ ) and  $\sim 220$  fs ( $\sim 0.5 T_{\text{OSC}}^{\text{NaK}}$ ). The explanation of this optimal pulse form can be given based on known transient behavior of the  $\text{NaK}$  dimer.<sup>[78,82]</sup> The first subpulse act as a probe pulse in a one-photon transition and prepares a wavepacket in the  $A(2) \ ^1\Sigma^+$  state (see Fig. 9B). The generated wavepacket evolves and as it reaches the optimal Franck–Condon window for ionization at the outer turning point on the potential surface, it will be ionized with the second subpulse.<sup>[81,83,84]</sup> The high intensity of the second subpulse reflects the two-photon ionization step. The third subpulse serves as an additional ionization pulse via resonant ionization involving most probably the  $B(3) \ ^1\Pi$  state. The up-chirp superimposed on the second subpulse can be understood as it provides a compensation for a defocused wavepacket.

The pulse form producing the highest yield of  $\text{NaK}^+$  in the presence of  $\text{Na}_2\text{K}$  is depicted in Fig. 9C. The increase in the ion yield was about 80% in comparison with the ion yield achieved by a single unchirped 80 fs pulse of the same energy, thus to a

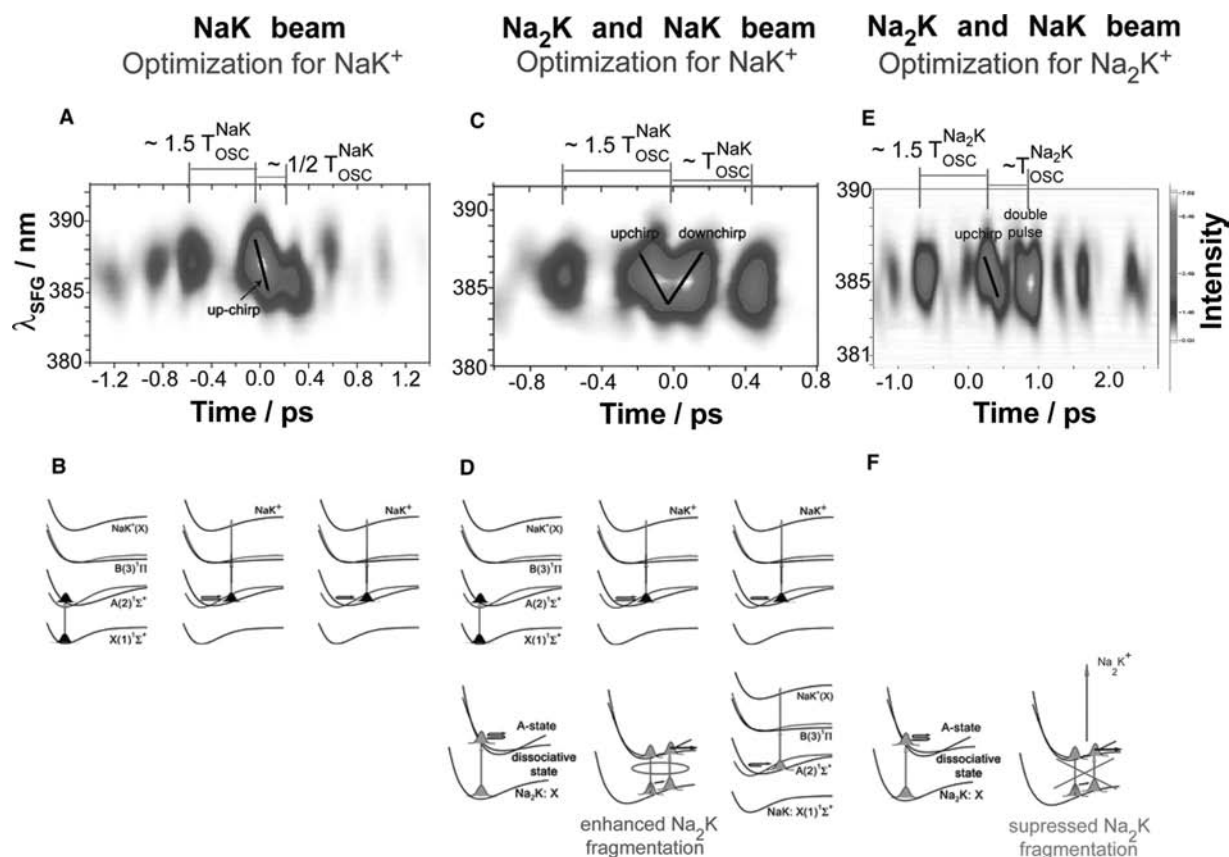


**Fig. 9** SFG-CC traces of the acquired optimal pulse shapes and cartoons of the involved processes for producing maximum yield of NaK<sup>+</sup> in a pure excitation and ionization optimization experiment of the NaK dimer (A, B); maximum ion yield of NaK<sup>+</sup> in the presence of the fragmenting Na<sub>2</sub>K<sup>+</sup> trimer (C, D) maximum ion yield of Na<sub>2</sub>K<sup>+</sup> (E, F). *Source:* Compiled by permissions from Refs.<sup>[25,36]</sup>

20% higher value than in the case of pure NaK ionization.<sup>[47,83]</sup> The optimal pulse shape consists again of three subpulses. The scheme of the control mechanism is shown in Fig. 9D, and first we will focus on the enhancement of the Na<sub>2</sub>K fragmentation by the optimal pulse. The time delay between the first and second subpulse ( $\sim 660$  fs) is the same as in the NaK ionization experiment; however, its structure is different, showing a double-pulse with the opposite chirp superimposed. In this experiment, the first subpulse prepares a propagating wavepacket in the excited trimer. The role of the second up- and then down-chirped subpulse can be explained in the following way. The frontal red-shifted part of the central subpulse stimulates the propagating wavepacket down to the ground state of the trimer, similar to the Na<sub>3</sub> case. The wavepacket continues to move in the same direction in the vibrationally excited electronic ground. The trailing part of the central subpulse then lifts this wavepacket onto the dissociative state leading to NaK\*. In other words, the central pulse navigates the evolving wavepacket into a dissociative channel while avoiding the bottleneck of the conical intersection. Finally, the third subpulse ionizes the

emerging NaK fragments. The excitation and ionization mechanism for NaK dimers already present in the molecular beam can be explained as follows. The first subpulse prepares a wavepacket in the excited state of NaK; the central part of the second subpulse ionizes the NaK\* after 660 fs ( $\sim 1.5 T_{\text{OSC}}^{\text{NaK}}$ ) and the third pulse improves the ionization efficiency after 440 fs ( $\sim 1 T_{\text{OSC}}^{\text{NaK}}$ ). In summary, the 20% rise in the NaK<sup>+</sup> yield when compared with the pure NaK ionization corresponds to NaK<sup>+</sup> gain through enhanced fragmentation of the parent Na<sub>2</sub>K trimer.

The optimal pulse generating the highest yield of Na<sub>2</sub>K<sup>+</sup> is plotted in Fig. 9E and it produced  $\sim 150\%$  increase in the Na<sub>2</sub>K<sup>+</sup> yield when compared with the ion yield gained by an unchirped 80 fs pulse of the same energy.<sup>[47,83]</sup> The timing between the subpulses matches exactly the “internal vibrational clock”—the vibrational period of the excited trimer. The individual subpulses exhibit different wavelengths and chirp structure again: the first two subpulses are red-shifted with respect to the third pulse. The short and unchirped (excitation) subpulse is followed by the second intense up-chirped subpulse arriving after

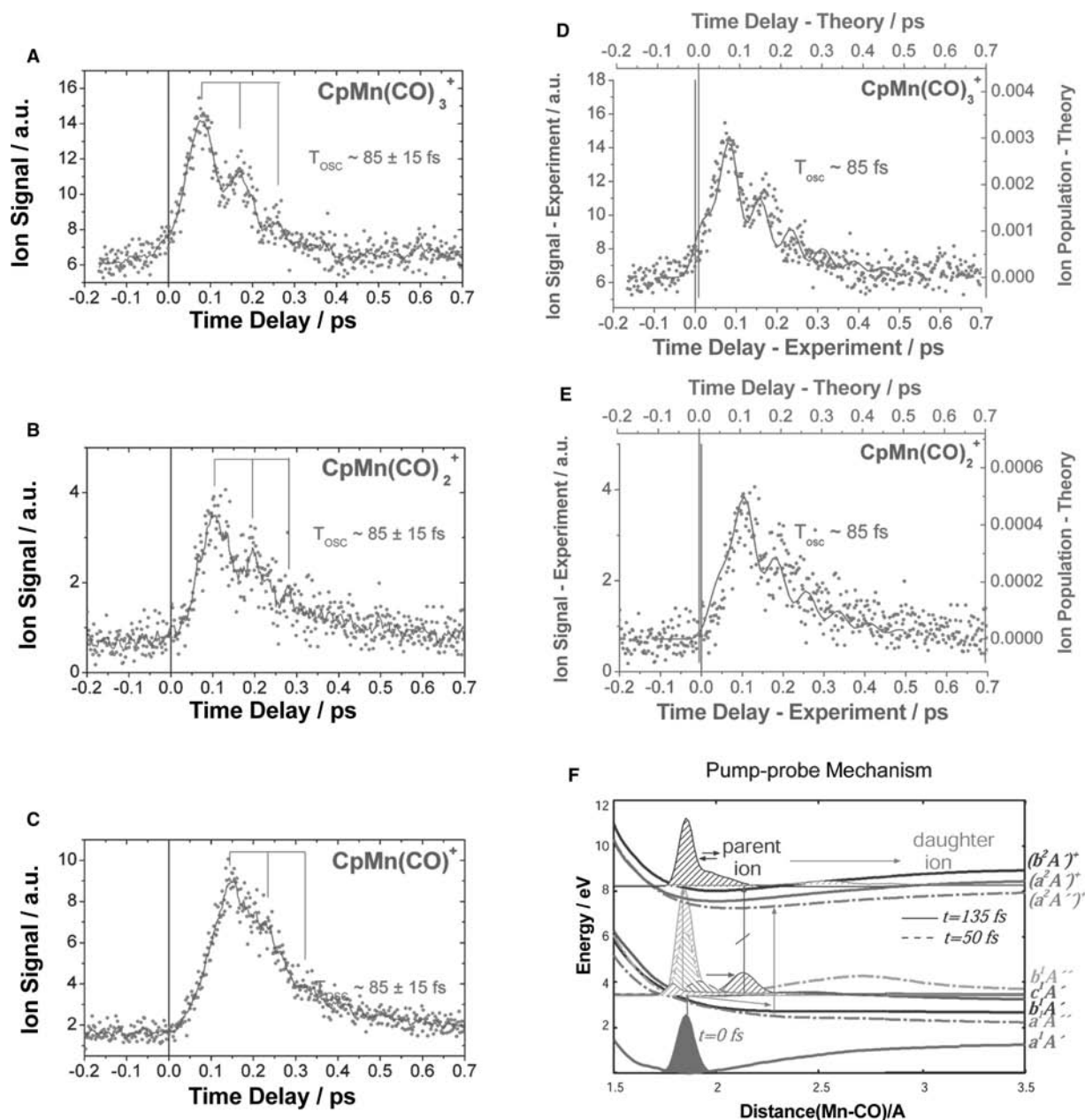


**Fig. 10** Pump&probe trace of CpMn(CO)<sub>3</sub><sup>+</sup> (A) and its fragment ions CpMn(CO)<sub>2</sub><sup>+</sup> (B) and CpMn(CO)<sup>+</sup> (C). Oscillations in the parent molecule signal with a period of ca. 85 fs and the fingerprints of these oscillations in the daughter ion signals are indicated in the plots. The employed wavelengths were 402.5 nm (pump) and 805 nm (probe). Experimental (dots) and theoretical (solid line) femtosecond pump&probe transient spectra for CpMn(CO)<sub>3</sub><sup>+</sup> (D) and for the fragment, CpMn(CO)<sub>2</sub><sup>+</sup> (E). (F) The complex competing pathways leading to the formation of both parent and daughter ions produced in the pump&probe experiment. Source: Compiled by permissions from Refs.<sup>[36,40]</sup>

$\sim 750$  fs ( $\sim 1.5 T_{OSC}^{Na_2K}$ ) delay, which ionizes Na<sub>2</sub>K\* via two photons. The third subpulse delayed by additional 500 fs ( $\sim 1 T_{OSC}^{Na_2K}$ ) ionizes the remaining fraction of excited trimers. In this experiment, the second subpulse suppresses the leakage of the wavepacket into the repulsive state of the excited trimer, which leads to a considerable increase in the final Na<sub>2</sub>K<sup>+</sup> yield. Similar ion yield was achieved by a double-pulse sequence as well, with pulse separation of  $1.5 T_{OSC}^{Na_2K}$ <sup>[70]</sup>.

### Organometallic Molecules: Controlled Photolysis of CpMn(CO)<sub>3</sub>

The ultrafast photoinduced fragmentation dynamics of CpMn(CO)<sub>3</sub> was studied in detail in a two-color experiment by employing a 45 fs pump and 35 fs probe pulse with laser wavelengths centered at 402.5 nm and 805 nm, respectively.<sup>[85]</sup> The molecule is first excited by the pump pulse in a one-photon transition, followed

by a delayed probe pulse, which ionizes  $\text{CpMn}(\text{CO})_3^*$  by three photons. The transient spectra of the mother ion  $\text{CpMn}(\text{CO})_3^+$  and its fragments  $\text{CpMn}(\text{CO})_2^+$  and  $\text{CpMn}(\text{CO})^+$  are shown in Fig. 10A–C, respectively. Oscillations with a period of ca. 85 fs are superimposed on the ultrafast decay of the parent ion signal (Fig. 10A). The transients of the emerging fragment ions carry the fingerprints of the parent molecule vibrations as well (Fig. 10B and C). Theoretical studies on these systems were performed by Manz et al.<sup>[86]</sup> These results lead to the  $\text{CpMn}(\text{CO})_3^+$  and  $\text{CpMn}(\text{CO})_2^+$  transients, which are plotted in Fig. 10D and E together with the corresponding experimental pump&probe spectra; both curves show an excellent agreement. The underlying dynamics can be explained by the simultaneous population of two excited states  $b^1A''$  and  $c^1A'$  during the pump step (Fig. 10F). The wavepacket in the  $b^1A''$  state oscillates with an 80 fs period. A fraction of the oscillating wavepacket in the  $b^1A''$  state leaks non-adiabatically into the  $a^1A''$  state every time it passes the point of near-coincidence of the  $b^1A''$  and  $a^1A'$  potential energy surfaces. Both parent and daughter fragments can be probed with the same ionization pulse. In the pump&probe experiment, the wavepacket in the  $c^1A'$  state does not contribute to the ion signal because of off-resonant probe wavelength. (Note: The vibrational dynamics could not be resolved in the first experiments when laser pulses of about 90 fs duration were employed.<sup>[87–89]</sup> The deciphering of the high-resolution pump&probe traces made the detailed understanding of the results of the previous control experiments employed<sup>[87–89]</sup> on  $\text{CpMn}(\text{CO})_3$  with optimized laser fields possible as well.<sup>[86]</sup> First, the optimization experiments will be described, followed by the interpretation of the optimal pulse forms producing the highest ion yield.

In the optimization experiments, an 80 fs laser pulse centered at a wavelength of 800 nm passed through the optimization cycle with the goal to maximize the ion yield of the parent ion  $\text{CpMn}(\text{CO})_3^+$  or the yield of the daughter ion  $\text{CpMn}(\text{CO})^+$ . The relative ion yield  $\text{CpMn}(\text{CO})_3^+ : \text{CpMn}(\text{CO})^+$  gained by employing an 80 fs unchirped pulse was 1 : 13 as determined from the mass spectrum of the ionic products. The optimization for the maximum  $\text{CpMn}(\text{CO})_3^+$  or  $\text{CpMn}(\text{CO})^+$  yield led to 1 : 16 and 1 : 6 product ratios, respectively, to a significant increase in the desired product ion yield. The SHG-FROG traces of the optimal pulses are shown in Fig. 11A and C, the time profiles of the corresponding pulse shapes retrieved from FROG analysis are depicted in Fig. 11B and D. The pulse sequence that produced the highest  $\text{CpMn}(\text{CO})_3^+ : \text{CpMn}(\text{CO})^+$  product ratio consists of three subpulses of 36–40 fs duration shifted by 70–100 fs. The effective duration of the two dominant pulses is about 100 fs, reflecting a prompt ionization after ionization, which

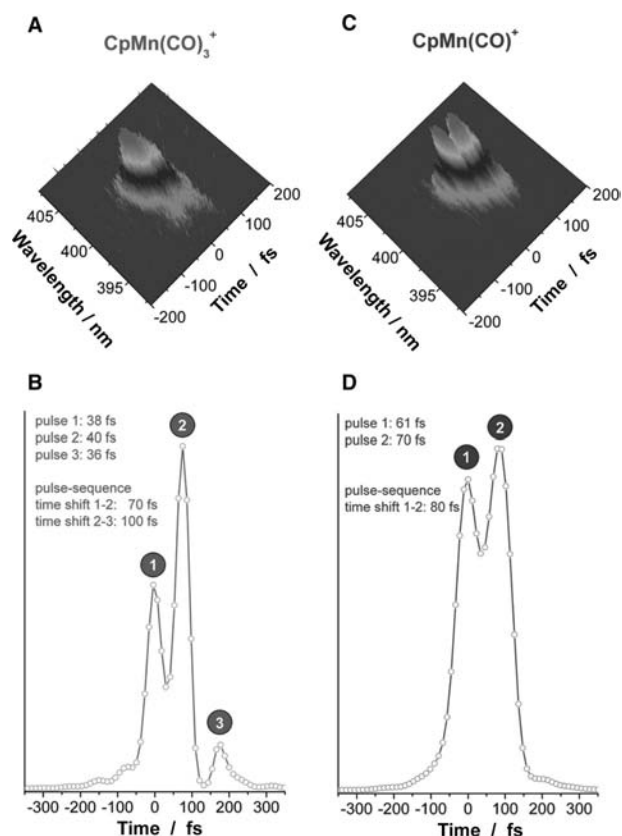


**Fig. 11** SHG-FROG traces of the optimized pulses acquired from the feedback optimization experiment for  $\text{CpMn}(\text{CO})_3^+$  (A) and the  $\text{CpMn}(\text{CO})^+$  (C). Optimized pulse shapes resulting from the analysis of the FROG traces shown in (A) and (C) for the maximum yield of  $\text{CpMn}(\text{CO})_3^+$  (B) and the  $\text{CpMn}(\text{CO})^+$  (D), respectively. Source: Compiled with permission from Ref.<sup>[42]</sup>.

prevents excessive fragmentation of the excited parent molecule. Moreover, the two-photon excitation and three-photon ionization is reflected in the relative intensities of the first two subpulses. The double-pulse producing the highest  $\text{CpMn}(\text{CO})^+ : \text{CpMn}(\text{CO})_3^+$  consists of longer pulses of 60–70 fs duration shifted by 80 fs. The effective duration of the double pulse is about 150 fs, which reflects the time-window of the maximal  $\text{CpMn}(\text{CO})^*$  population—the time needed for the excited parent molecule to lose two CO ligands. But, is it only the timing and duration of the subpulses that determine the outcome of the controlled reaction? Theoretical investigations show that in the case of  $\text{CpMn}(\text{CO})_3^+$ , the phase change between the two subpulses causing a blue shift (Fig. 12A) plays a decisive role.<sup>[86]</sup> The first subpulse has to increase the  $\text{CpMn}(\text{CO})_3^+$  signal, and the solution is demonstrated in Fig. 12B.<sup>[86]</sup> To maximize the  $\text{CpMn}(\text{CO})_3^+$  product formation, the first subpulse must avoid the population of the predissociative  $b^1A''$  state, which would at the end lead to the production of both parent and



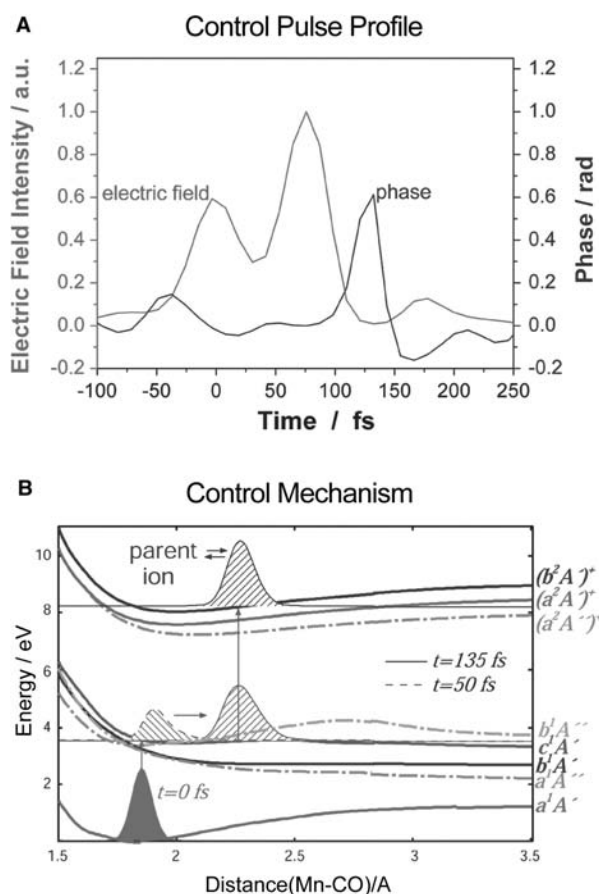


**Fig. 12** Intensity and phase profiles of the optimal pulse that maximizes the ion yield of  $\text{CpMn}(\text{CO})_3^+$  (A). The pathway selected by the optimal control field (B). Detailed description is given in the main text. *Source:* Compiled by permission from Ref.<sup>[40]</sup>, Science, AAAS.

daughter ions during ionization by the second pulse. Instead, the first subpulse should preferentially populate the bound  $c^1A'$  state, which lies slightly above the predissociative  $b^1A''$  state. This is achieved by the wavelength components of the first subpulse centered at 798.7 nm. The second subpulse (800.09 nm) can readily transfer the population of the neutral  $c^1A'$  into the parent ion. In addition to pure ionization, the second subpulse can excite a fraction of molecules into the neutral  $c^1A'$  state as well, which will be ionized by the third subpulse (801.12 nm).

Follow-up studies on sodium–potassium clusters clearly showed that even in the case of the smallest particles consisting of two or three atoms only, because of the large number of electronic states, there are various pathways (thus various pulse forms), which can lead to comparable product yields. The optimal pulse shapes were dominantly consisting of a sequence of subpulses variably delayed with respect to the first subpulse, possessing various peak intensities, time duration, and central wavelength, as well as chirp superimposed

to them. Thus, several ways opened in simplifying the search process for the optimum pulse shape by, for example, limiting the search for pulse sequences consisting of subpulses with equidistant time separation.<sup>[90]</sup> The optimization results obtained with such periodic pulse structures—pulse trains—lead to comparable product yields as in the case of fully optimized pulses; however, now at considerably faster convergence.<sup>[81,91]</sup> An additional chirp superimposed on the pulse trains could lead to further improved product yields.<sup>[81,92]</sup> As shown earlier, in the case of the sodium–potassium aggregates, the interpretation of the obtained optimal pulse shapes was often possible in terms of the molecular dynamics known from pump&probe experiments and theoretical calculations.<sup>[79]</sup> The robustness of the optimization algorithm was demonstrated in the case of mixtures containing  $\text{Na}_m\text{K}_n$  of various particle compositions, when highly complex non-intuitive pulse forms were needed to maximize the yield of the desired photodissociation products.<sup>[83,93]</sup>

The high fidelity of the feedback pulse optimization was illustrated on the isotope selective fragmentation of  $^{39,39}\text{K}_2$  vs.  $^{39,41}\text{K}_2$ ,<sup>[94]</sup> isotope selective separation of  $\text{NaK}$  ( $^{23}\text{Na}^{39}\text{K}$  vs.  $^{23}\text{Na}^{41}\text{K}$ ),<sup>[95,96]</sup> and isotopomer-selective ionization in  $^{124}\text{KRb}/^{126}\text{KRb}$ .<sup>[97]</sup>

Several optimization experiments led to comparable ionic yields even with non-intuitive pulse forms, underlining the role of the phase and increasing demand for detailed theoretical calculations.<sup>[82,98,99]</sup> The obtained control pulses are very rich in information in the time and wavelength domain; they reflect the wavepacket propagation or transient consecutive propagation of states during a multi-step process, as well as the cross-sections of the multi-photon processes.

## CONCLUSION

The results summarized in this entry demonstrate the capability of a feedback optimization loop to actively control the branching between different pathways of the involved photoinduced processes. By employing an evolutionary algorithm for tailoring the applied laser field in the amplitude and phase domain, the yield of the desired products could be controlled with very high selectivity, thus opening new ways of controlling bond-specific chemistry at the nanoscale.

## ACKNOWLEDGMENTS

The authors thank Prof. Herschel Rabitz, Dr. Werner Fuß, and Dr. Sergei Trushin for stimulating discussions, Prof. Thomas Feurer and Prof. Thomas Leisner



for their assistance and advises in the early stages of setting up the pulse shaper experiments. The continuous theoretical support of Prof. Vlasta Bonačić-Koutecký and her group members, Dr. Michael Hartmann, Dr. Roland Mitrić, Dr. Jiří Pittner, and Boris Schäfer-Bung, as well as the cooperation with Dr. Chantal Daniel, Prof. Jörn Manz, and his coworkers, Dr. Leticia González, Dr. Jürgen Full, and Dr. Marcus Oppel, is greatly appreciated. This work would not have been accomplished without the enthusiasm of the post-docs, graduate, and undergraduate students involved in the experiments: Dr. Andreas Bartelt, Dr. Porfirio Rosendo-Francisco, Dr. Cosmin Lupulescu, Dr. Albrecht Lindinger, Dr. Shinichirou Minemoto, Dr. Sören Rutz, Bernd Baptist, Filip Budzyn, Jens Heufelder, Cristina Kaposta, Marcel Krenz, Andrea Merli, Harald Ruppe, and Patrick Wetzel. The financial support of this work by the Deutsche Forschungsgemeinschaft within the Sonderforschungsbereich 450 project is gratefully acknowledged.

## REFERENCES

1. Zewail, A.H. Femtochemistry. Atomic-scale dynamics of the chemical bond using ultrafast lasers. Prix Nobel **2000**, 110–203. Nobel Lecture, December 8, 1999.
2. Bloembergen, N.; Zewail, A.H. Energy redistribution in isolated molecules and the question of mode-selective laser chemistry revisited. New experiments on the dynamics of collisionless energy redistribution in molecules possibilities for laser-selective chemistry with subpicosecond pulses. *J. Phys. Chem.* **1984**, *88* (23), 5459–5465.
3. Zewail, A.H. IVR: Its coherent and incoherent dynamics. *Ber. Bunsen-Ges. Phys. Chem.* **1985**, *89* (3), 264–270.
4. Scherer, N.F.; Perry, J.W.; Doany, F.E.; Zewail, A.H. Ultrafast molecular relaxation of isolated stilbene: measurements by picosecond pump-probe techniques. *J. Phys. Chem.* **1985**, *89* (6), 894–896.
5. Shapiro, M.; Brumer, P. On the origin of pulse shaping control of molecular dynamics. *J. Phys. Chem. A* **2001**, *105* (12), 2897–2902.
6. Windhorn, L.; Yeston, J.S.; Witte, T.; Fuss, W.; Motzkus, M.; Proch, D.; Kompa, K.-L.; Moore, C.B. Getting ahead of IVR: a demonstration of mid-infrared induced molecular dissociation on a sub-statistical time scale. *J. Chem. Phys.* **2003**, *119* (2), 641–645.
7. Mitrić, R.; Werner, U.; Bürgel, C.; Bonačić-Koutecký, V. Dynamical aspects and the role of IVR for the reactivity of noble metal clusters towards molecular oxygen. *Eur. Phys. J. D* **2007**, *43* (1–3), 201–204.
8. Windhorn, L.; Witte, T.; Yeston, J.S.; Proch, D.; Motzkus, M.; Kompa, K.L.; Fuss, W. Breaking bonds with mid IR pulses: femtosecond photolysis of gas-phase metal carbonyls. *Springer Ser. Chem. Phys.* **2003**, *71* (Ultrafast Phenomena XIII), 94–96.
9. Scherer, N.F.; Jonas, D.M.; Fleming, G.R. Femtosecond wave packet and chemical reaction dynamics of iodine in solution: tunable-probe study of motion along the reaction coordinate. *J. Chem. Phys.* **1993**, *99* (1), 153–168.
10. Zewail, A.H. Femtochemistry: concepts and applications. *Femtosecond Chem.* **1995**, *1*, 15–128.
11. Bonačić-Koutecký, V.; Hartmann, M.; Pittner, J. Theoretical exploration of ultrafast spectroscopy of small clusters. *Eur. Phys. J. D* **2001**, *16* (1–3), 133–138.
12. Bonačić-Koutecký, V.; Hartmann, M.; Pittner, J.; Van Dam, H. Theoretical exploration of ultrafast spectroscopy of small clusters. *Int. J. Quantum Chem.* **2001**, *84* (6), 714–739.
13. Rice, S.A. New ideas for guiding the evolution of a quantum system. *Science* (Washington, D.C.) **1992**, *258*, 412–413.
14. Warren, W.S.; Rabitz, H.; Dahleh, M.A. Coherent control of quantum dynamics—the dream is alive. *Science* **1993**, *259*, 1581–1589.
15. Zare, R.N. Laser control of chemical reactions. *Science* **1998**, *279* (5358), 1875–1879.
16. Gordon, R.J.; Zhu, L.; Seideman, T. Coherent control of chemical reactions. *Acc. Chem. Res.* **1999**, *32* (12), 1007–1016.
17. Rabitz, H.; De Vivie-Riedle, R.; Motzkus, M.; Kompa, K.L. Whither the future of controlling quantum phenomena? *Science* **2000**, *288* (5467), 824–828.
18. Paramonov, G.K.; Savva, V.A. Effect of selective excitation of some vibrational states of an isolated molecule by picosecond pulsed laser IR radiation. *Izv. Akad. Nauk SSSR, Ser. Fiz.* **1984**, *48* (3), 449–452.
19. Tannor, D.J.; Rice, S.A. Control of selectivity of chemical reaction via control of wave packet evolution. *J. Chem. Phys.* **1985**, *83* (10), 5013–5018.
20. Shapiro, M. Laser catalysis and control of chemical reactions. *NATO ASI Ser., Ser. B Physics* **1988**, *171*, (At. Mol. Processes Short Intense Laser Pulses), 377–387.
21. Gaubatz, U.; Rudecki, P.; Schiemann, S.; Bergmann, K. Population transfer between molecular vibrational levels by stimulated Raman scattering with partially overlapping laser fields. A new concept and experimental results. *J. Chem. Phys.* **1990**, *92* (9), 5363–5376.
22. Peirce, A.P.; Dahleh, M.A.; Rabitz, H. Optimal control of quantum molecular systems. *IEE Conf. Publ.* **1988**, *285*, (Int. Conf. Control 88, 1988), 351–355.
23. Bergmann, K.; Theuer, H.; Shore, B.W. Coherent population transfer among quantum states of atoms and molecules. *Rev. Mod. Phys.* **1998**, *70* (3), 1003–1025.
24. Rice, S.A. Molecular dynamics: Optical control of reactions. *Nature* **2000**, *403* (6769), 496–497.
25. Rice Stuart, A.; Zhao, M. *Optical Control of Molecular Dynamics*; Wiley, 2000.
26. Brumer, P.; Shapiro, M. Laser control of chemical reactions. *Sci. Am.* **1995**, *272* (3), 56–57, 60–63.
27. Shapiro, M.; Brumer, P. Quantum control of bound and continuum state dynamics. *Phys. Rep.* **2006**, *425* (4), 195–264.
28. Elghobashi, N.; González, L.; Manz, J. Quantum model simulations of symmetry breaking and control of bond selective dissociation of FHF- using IR + UV laser pulses. *J. Chem. Phys.* **2004**, *120* (17), 8002–8014.

29. Bonačić-Koutecký, V.; Mitrić, R. Theoretical exploration of ultrafast dynamics in atomic clusters: analysis and control. *Chem. Rev.* **2005**, *105* (1), 11–65.
30. Bonačić-Koutecký, V.; Mitrić, R.; Werner, U.; Wöste, L.; Berry, R.S. Ultrafast dynamics in atomic clusters: analysis and control. *Proc. Natl. Acad. Sci. U.S.A.* **2006**, *103* (28), 10,594–10,599.
31. Bonačić-Koutecký, V.; Brauer, B.; Burmeister, F.; Eberhardt, W.; Gerber, R.B.; González, L.; von Helden, G.; Kamrath, A.; Kim, S.K.; Manz, J.; Meijer, G.; Mitrić, R.; Neeb, M.; Neumark, D.M.; Schultz, T.; Stanzel, J. Complex systems in the gas phase. Springer Ser. Chem. Phys. **2007**, *87*, (Analysis and Control of Ultrafast Photo-induced Reactions), 153–256.
32. Wang, L.; Meyer, H.-D.; May, V. Femtosecond laser pulse control of multidimensional vibrational dynamics: computational studies on the pyrazine molecule. *J. Chem. Phys.* **2006**, *125* (1), 014102/1–014102/12.
33. Werschnik, J.; Gross, E.K.U. Quantum optimal control theory. *J. Phys. B: At. Mol. Opt. Phys.* **2007**, *40* (18), R175–R211.
34. Zewail, A.H. Femtochemistry: Atomic-scale dynamics of the chemical bond using ultrafast lasers (Nobel lecture). *Angew. Chem., Int. Ed.* **2000**, *39* (15), 2586–2631.
35. Baumert, T.; Thalweiser, R.; Weiss, V.; Gerber, G. Femtosecond time-resolved photochemistry of molecules and metal clusters. *Femtosecond Chem.* **1995**, *2*, 397–432.
36. Meshulach, D.; Silberberg, Y. Coherent quantum control of multiphoton transitions by shaped ultrashort optical pulses. *Phys. Rev. A* **1999**, *60* (2), 1287–1292.
37. Judson, R.S.; Rabitz, H. Teaching lasers to control molecules. *Phys. Rev. Lett.* **1992**, *68* (10), 1500–1503.
38. Kohler, B.; Yakovlev, V.V.; Che, J.; Krause, J.L.; Messina, M.; Wilson, K.R.; Schwentner, N.; Whitnell, R.M.; Yan, Y. Quantum control of wave packet evolution with tailored femtosecond pulses. *Phys. Rev. Lett.* **1995**, *74* (17), 3360–3363.
39. Assion, A.; Baumert, T.; Bergt, M.; Brixner, T.; Kiefer, B.; Seyfried, V.; Strehle, M.; Gerber, G. Control of chemical reactions by feedback-optimized phase-shaped femtosecond laser pulses. *Science* **1998**, *282* (5390), 919–922.
40. Brixner, T.; Damrauer, N.H.; Niklaus, P.; Gerber, G. Photosensitive adaptive femtosecond quantum control in the liquid phase. *Nature (London)* **2001**, *414* (6859), 57–60.
41. Feuerer, T.; Glass, A.; Rozgonyi, T.; Sauerbrey, R.; Szabo, G. Control of the photodissociation process of CsCl using a feedback-controlled self-learning fs-laser system. *Chem. Phys.* **2001**, *267* (1–3), 223–229.
42. Levis, R.J.; Menkir, G.M.; Rabitz, H. Selective bond dissociation and rearrangement with optimally tailored, strong-field laser pulses. *Science* **2001**, *292* (5517), 709–713.
43. Schulz, C.P.; Burnus, T.; Castro, A.; Gross, E.K.U.; Heidenreich, A.; Hertel, I.V.; Jortner, J.; Laarmann, T.; Last, I.; Levis, R.J.; Marques, M.A.L.; Romanov, D.A.; Saenz, A. Molecules and clusters in strong laser fields. Springer Ser. Chem. Phys. **2007**, *87*, (Analysis and Control of Ultrafast Photoinduced Reactions), 485–617.
44. Weinacht, T.C.; White, J.L.; Bucksbaum, P.H. Toward strong field mode-selective chemistry. *J. Phys. Chem. A* **1999**, *103* (49), 10,166–10,168.
45. Weinacht, T.C.; Bartels, R.; Backus, S.; Bucksbaum, P.H.; Pearson, B.; Geremia, J.M.; Rabitz, H.; Kapteyn, H.C.; Murnane, M.M. Coherent learning control of vibrational motion in room temperature molecular gases. *Chem. Phys. Lett.* **2001**, *344* (3,4), 333–338.
46. Pearson, B.J.; Morris, D.S.; Bucksbaum, P.H.; Weinacht, T.C. Strong field coherent control in molecules. *Femtochem. Femtobiol.: Ultrafast Dyn. Mol. Sci.* **2002**, 399–408.
47. Vajda, S.; Lupulescu, C.; Bartelt, A.; Budzyn, F.; Rosendo-Francisco, P.; Wöste, L. Controlling the vibration and dissociation dynamics in triatomic alkaline clusters. In *Femtochemistry and Femtobiology: Ultrafast Dynamics in Molecular Science*; Douhal, A., Santamaria, J., Eds.; World Scientific Publishing, Singapore, 2002; 481–493, ISBN: 981-02-4866-0; 472–480. <http://www.worldscibook.com/chemistry/4892.html>
48. Pastirk, I.; Lozovoy, V.; Dela Cruz, J.; Senekerimyan, V.; Walowicz, K.; Dantus, M. Control of multiphoton excitation in condensed phases based on multiphoton intrapulse interference. *Trends Opt. Photonics* **2003**, *895* (Quantum Electronics and Laser Science (QELS)).
49. Vogt, G.; Krampert, G.; Niklaus, P.; Nuernberger, P.; Gerber, G. Optimal control of photoisomerization. *Phys. Rev. Lett.* **2005**, *94* (6), 068305/1–068305/4.
50. Zeidler, D.; Frey, S.; Wohlleben, W.; Motzkus, M.; Busch, F.; Chen, T.; Kiefer, W.; Materny, A. Control of ground state dynamics in polymers with shaped pulses. Springer Ser. Chem. Phys. **2003**, *71*, (Ultrafast Phenomena XIII), 520–522.
51. Wohlleben, W.; Buckup, T.; Herek, J.L.; Motzkus, M. Coherent control for spectroscopy and manipulation of biological dynamics. *Chem. Phys. Chem.* **2005**, *6* (5), 850–857.
52. Buckup, T.; Lebold, T.; Weigel, A.; Wohlleben, W.; Motzkus, M. Multiphoton quantum control spectroscopy of b-carotene. Springer Ser. Chem. Phys. **2007**, *88*, 483–485.
53. Herek, J.L.; Wohlleben, W.; Cogdell, R.J.; Zeidler, D.; Motzkus, M. Quantum control of energy flow in light harvesting. *Nature* **2002**, *417* (6888), 533–535.
54. Suzuki, T.; Minemoto, S.; Kanai, T.; Sakai, H. Control of multiphoton ionization processes in aligned I2 molecules by optimizing time-dependent polarization of femtosecond pulses. Springer Ser. Chem. Phys. **2005**, *79*, (Ultrafast Phenomena XIV), 161–163.
55. Aeschlimann, M.; Bauer, M.; Bayer, D.; Brixner, T.; Garcia de Abajo, F.J.; Pfeiffer, W.; Rohmer, M.; Spindler, C.; Steeb, F. Adaptive subwavelength control of nano-optical fields. *Nature* **2007**, *446* (7133), 301–304.
56. Sofikitis, D.; Rubio-Lago, L.; Martin, M.R.; Ankeny Brown, D.J.; Bartlett, N.C.M.; Alexander, A.J.; Zare, R.N.; Rakitzis, T.P. Optical control of ground-state atomic orbital alignment: Cl(2P<sub>3/2</sub>) atoms from

- HCl( $v = 2, J = 1$ ) photodissociation. *J. Chem. Phys.* **2007**, *127* (14), 144307/1–144307/7.
57. Prokhorenko, V.I.; Nagy, A.M.; Miller, R.J.D. Coherent control of the population transfer in complex solvated molecules at weak excitation. An experimental study. *J. Chem. Phys.* **2005**, *122* (18), 184502/1–184502/11.
58. Prokhorenko, V.I.; Nagy, A.M.; Brown, L.S.; Dwayne Miller, R.J. On the mechanism of weak-field coherent control of retinal isomerization in bacteriorhodopsin. *Chem. Phys.* **2007**, *341* (1–3), 296–309.
59. Wiederrecht Gary, P.; Hall Jeffrey, E.; Bouhelier, A. Control of molecular energy redistribution pathways via surface plasmon gating. *Phys. Rev. Lett.* **2007**, *98* (8), 083001.
60. De Vivie-Riedle, R.; Hornung, T.; Hofmann, A.; Tesch, C. Adapting optimal control theory to a variety of molecular applications. *Femtochem. Femtobiol.: Ultrafast Dyn. Mol. Sci.* **2002**, 505–513.
61. Mitrić, R.; Hartmann, M.; Pittner, J.; Bonačić-Koutecký, V. New strategy for optimal control of femtosecond pump-dump processes applicable to systems of moderate complexity. *Eur. Phys. J. D* **2003**, *24* (1–3), 177–180.
62. Rozgonyi, T.; González, L. On the location of conical intersections in CH<sub>2</sub>BrCl using MS-CASPT2 methods. *J. Phys. Chem. A* **2006**, *110* (34), 10,251–10,259.
63. Abe, M.; Ohtsuki, Y.; Fujimura, Y.; Domcke, W. Optimal control of femtosecond photoisomerization of retinal in rhodopsin: effects of conical intersections. *Springer Ser. Chem. Phys.* **2005**, *79*, Ultrafast Phenomena XIV, 613–615.
64. Ohtsuki, Y.; Nakagami, K.; Fujimura, Y.; Zhu, W.; Rabitz, H. Quantum optimal control of multiple targets: development of a monotonically convergent algorithm and application to intramolecular vibrational energy redistribution control. *J. Chem. Phys.* **2001**, *114* (20), 8867–8876.
65. Lippert, H.; Manz, J.; Oppel, M.; Paramonov, G.K.; Radloff, W.; Ritze, H.H.; Stert, V. Control of breaking strong versus weak bonds of BaFCH<sub>3</sub> by femtosecond IR + VIS laser pulses: theory and experiment. *Phys. Chem. Chem. Phys.* **2004**, *6* (17), 4283–4295.
66. Bonačić-Koutecký, V.; Mitrić, R.; Bürgel, C.; Schäfer-Bung, B. Cluster properties in the regime in which each atom counts. *Comput. Mater. Sci.* **2006**, *35* (3), 151–157.
67. Gerbasi, D.; Sanz, A.S.; Christopher, P.S.; Shapiro, M.; Brumer, P. Overlapping resonances in the control of intramolecular vibrational redistribution. *J. Chem. Phys.* **2007**, *126* (12), 124307/1–124307/9.
68. Vajda, S.; Rutz, S.; Heufelder, J.; Rosendo, P.; Ruppe, H.; Wetzel, P.; Wöste, L. Observation of predissociated excited states in mixed alkali trimer clusters Na<sub>2</sub>K and K<sub>2</sub>Na: time-resolved spectroscopy of bound-free transitions. *J. Phys. Chem. A* **1998**, *102* (23), 4066–4068.
69. Weiner, A.M.; Leaird, D.E.; Patel, J.S.; Wullert, J.R. Programmable femtosecond pulse shaping by use of a multielement liquid-crystal phase modulator. *Opt. Lett.* **1990**, *15* (6), 326–328.
70. Vajda, S.; Bartelt, A.; Kaposta, E.C.; Leisner, T.; Lupulescu, C.; Minemoto, S.; Rosendo-Francisco, P.; Wöste, L. Feedback optimization of shaped femtosecond laser pulses for controlling the wavepacket dynamics and reactivity of mixed alkaline clusters. *Chem. Phys.* **2001**, *267* (1–3), 231–239.
71. Ruppe, H. Diploma, Freie Universität Berlin, Berlin, Germany, 1994.
72. Krenz, M. Aufbau eines sub-30 fs Ti:Saphir Oszillators und dessen Erweiterung um ein Multipass-Verstärkersystem mit nachgeschalteten TOPAS & Pulscharakterisierung mittels eines eigenkonstruierten Photodioden-Autokorrelators. Diploma, Freie Universität Berlin, Berlin, Germany, 2001.
73. Wetzel, P. Fragmentation heteronuklearer Cluster und Schritte zu Pump & Control. Diploma, Freie Universität Berlin, Berlin, Germany, 1998.
74. De Vivie-Riedle, R.; Gaus, J.; Bonačić-Koutecký, V.; Manz, J.; Reischl, B.; Rutz, S.; Schreiber, E.; Wöste, L. Pulse width controlled molecular dynamics: symmetric stretch versus pseudorotations in Na<sub>3</sub>(B). *Femtochemistry: Ultrafast Chem. Phys. Processes Mol. Syst.* **1996**, 319–325.
75. Rosendo-Francisco, P. Analyse und Steuerung Photoinduzierter Molekulardynamik in kleinen Clustern und Molekülen. PhD, Berlin, Germany, 2000.
76. Baumert, T.; Thalweiser, R.; Gerber, G.; Baumert, T.; Thalweiser, R.; Gerber, G. Femtosecond two-photon ionization spectroscopy of the B state of Na<sub>3</sub> clusters. *Chem. Phys. Lett.* **1993**, *209*, 29–34.
77. Rutz, S. Femtosekundenspektroskopie zur Wellenpaketdynamik in Alkalidimeren und-trimeren. PhD, Freie Universität Berlin, 1996.
78. Heufelder, J. Langzeitdynamik der Femtosekunden-Wellenpaketpropagation im A-Zustand von NaK.-Diploma, Freie Universität Berlin, Berlin, Germany, 1996.
79. Schäfer-Bung, B.; Mitrić, R.; Bonačić-Koutecký, V.; Bartelt, A.; Lupulescu, C.; Lindinger, A.; Vajda, S.; Weber, S.M.; Wöste, L. Optimal control of ionization processes in NaK: comparison between theory and experiment. *J. Phys. Chem. A* **2004**, *108* (19), 4175–4179.
80. Rosendo-Francisco, P.; Lupulescu, C.; Baptist, B.; Vajda, S. Ultrafast fragmentation and vibrational dynamics of triatomic hetero- and homonuclear alkali metal clusters. *J. Chin. Chem. Soc. (Taipei)* **2000**, *47* (4A), 705–708.
81. Bartelt, A.; Lindinger, A.; Lupulescu, C.; Vajda, S.; Wöste, L. One parameter fs-pulse form control on NaK and Na<sub>2</sub>K. *Phys. Chem. Chem. Phys.* **2003**, *5* (17), 3610–3615.
82. Bartelt, A. Steuerung der Wellenpaketdynamik in kleinen Alkaliclustern mit optimierten Femtosekundenpulsen. PhD, Freie Universität Berlin, Berlin, Germany, 2002.
83. Bartelt, A.; Lindinger, A.; Lupulescu, C.; Vajda, S.; Wöste, L. Optimal control of multiphoton dissociation and ionization processes in small Na<sub>m</sub>K<sub>n</sub> clusters. *Phys. Chem. Chem. Phys.* **2004**, *6* (8), 1679–1686.
84. Heufelder, J.; Ruppe, H.; Rutz, S.; Schreiber, E.; Wöste, L. Fractional revivals of vibrational wave packets in the NaK A1S + state. *Chem. Phys. Lett.* **1997**, *269* (1,2), 1–8.

85. Lupulescu, C.; Vajda, S.; Lindinger, A.; Merli, A.; Wöste, L. Femtosecond investigations on the ultrafast photodissociation dynamics of  $\text{CpMn}(\text{CO})_3$  and its fragment ions. *Phys. Chem. Chem. Phys.* **2004**, *6* (13), 3420–3425.
86. Daniel, C.; Full, J.; González, L.; Lupulescu, C.; Manz, J.; Merli, A.; Vajda, S.; Wöste, L. Deciphering the reaction dynamics underlying optimal control laser fields. *Science* **2003**, *299* (5606), 536–539.
87. Daniel, C.; Full, J.; González, L.; Kaposta, C.; Krenz, M.; Lupulescu, C.; Manz, J.; Minemoto, S.; Oppel, M.; Rosendo-Francisco, P.; Vajda, S.; Wöste, L. Analysis and control of laser induced fragmentation processes in  $\text{CpMn}(\text{CO})_3$ . *Chem. Phys.* **2001**, *267* (1–3), 247–260.
88. Vajda, S.; Wöste, L. Controlling the vibration and dissociation dynamics in small molecules and clusters. In *Femtochemistry*; De Schryver, F.C., De Feyter, S., Schweitzer, G., Eds.; Wiley-VCH: Weinheim, New York, 2001; 199–216, ISBNs: 3-527-30259-X (Hardback); 3-527-60018-3 (Electronic).
89. Vajda, S.; Rosendo-Francisco, P.; Kaposta, C.; Krenz, M.; Lupulescu, C.; Wöste, L. Analysis and control of ultrafast photodissociation processes in organometallic molecules. *Eur. Phys. J. D* **2001**, *16* (1–3), 161–164.
90. Bartelt, A.F.; Feurer, T.; Wöste, L. Understanding optimal control results by reducing the complexity. *Chem. Phys.* **2005**, *318* (3), 207–216.
91. Bartelt, A.; Lupulescu, C.; Vajda, S.; Wöste, L. Feedback control of alkali dimers with sinusoidal phase modulated fs-pulses: can we learn from the acquired pulse shapes? In *Femtochemistry and Femtobiology: Ultrafast Dynamics in Molecular Science*; Douhal, A., Santamaria, J., Eds.; World Scientific Publishing: Singapore, 2002; 481–493, ISBN: 981-02-4866-0.
92. Weber, S.M.; Lindinger, A.; Vetter, F.; Plewicky, M.; Merli, A.; Wöste, L. Application of parametric time and frequency domain shaping. *Eur. Phys. J. D* **2005**, *33* (1), 39–42.
93. Lindinger, A.; Lupulescu, C.; Le Roux, J.; Bartelt, A.; Vajda, S.; Wöste, L. Coherent control of the fragmentation of alkali metal clusters. *J. Phys. IV* **2004**, *119* (COLOQ 8), 57–71.
94. Lindinger, A.; Merli, A.; Plewicky, M.; Vetter, F.; Weber, S.M.; Wöste, L. Optimal control of isotope selective fragmentation. *Chem. Phys. Lett.* **2005**, *413* (4–6), 315–320.
95. Vetter, F.; Plewicky, M.; Lindinger, A.; Merli, A.; Weber, S.M.; Wöste, L. Optimized isotope-selective ionization of  $^{23}\text{Na}^{39}\text{K}$  and  $^{23}\text{Na}^{41}\text{K}$  by applying evolutionary strategies. *Phys. Chem. Chem. Phys.* **2005**, *7* (6), 1151–1156.
96. Lindinger, A.; Lupulescu, C.; Vetter, F.; Plewicky, M.; Weber, S.M.; Merli, A.; Wöste, L. Learning from the acquired optimized pulse shapes about the isotope selective ionization of potassium dimers. *J. Chem. Phys.* **2005**, *122* (2), 024312/1–024312/9.
97. Sauer, F.; Merli, A.; Wöste, L.; Lindinger, A. High resolution coherent control measurements on KRb. *Chem. Phys.* **2007**, *334* (1–3), 138–143.
98. Vajda, S. Reactivity and ultrafast dynamics of small clusters and molecules: From analysis to control. Habilitation, Freie Universität Berlin, Berlin, Germany, 2002.
99. Lupulescu, C. Femtosecond analysis and feedback control of molecular processes in organometallic and alkaline systems. PhD, Freie Universität Berlin, Berlin, Germany, 2004.

# Smart Nanotubes for Biotechnology and Biocatalysis

Charles R. Martin

Punit Kohli

*Department of Chemistry, University of Florida,  
Gainesville, Florida, U.S.A.*

## INTRODUCTION

Nanoscience is one of the most important research and development frontiers in modern science.<sup>[1]</sup> Nano is a Greek word meaning dwarf, and the nanometer (nm,  $10^{-9}$  m) defines the length scale that is used to measure systems being studied in nanoscience. In the most simplistic sense, nanoscience is the science of small particles of materials. Such small particles are of interest from a fundamental viewpoint because all properties of a material (e.g., melting point, electronic properties, and optical properties) change when the size of the particles that make up the material becomes nanoscopic. With new properties comes new opportunities for technological and commercial development, and the applications of nanoparticles have been demonstrated or proposed in areas as diverse as microelectronics, coatings and paints, and biotechnology.

For example, one application that is currently in the commercial marketplace entails using gold nanoparticles as visual indicators in over-the-counter medical diagnostic kits.<sup>[2]</sup> This application illustrates nicely how the unique properties of a nanoparticle can lead to technological opportunities. Macroscopic samples of pure gold have only one color—gold—but nanoparticles of gold can show essentially all the colors of the rainbow, depending on the size and the shape of the nanoparticle.<sup>[3]</sup> Furthermore, the intensity of the optical absorption of gold nanoparticles is extraordinarily strong, which means that when suspended in a solution or deposited on a surface, the naked eye can detect a very small quantity of these particles. These properties make gold nanoparticles ideally suited as visual indicators.

Other applications of microparticles and nanoparticles in the biomedical sciences and biotechnology include the use as vehicles for enzyme encapsulation,<sup>[4]</sup> DNA transfection,<sup>[5–7]</sup> biosensors,<sup>[8–10]</sup> and drug delivery.<sup>[11–13]</sup> For example, drugs can be incorporated into nanospheres composed of a biodegradable polymer, and this allows for timed release of the drug as the nanospheres degrade.<sup>[11,12]</sup> The circumstances that cause the particle to degrade can be adjusted by varying the nature of the chemical bonding within

the particle. For example, when acid-labile bonds are used, the particles degrade in acidic microenvironments such as would-be extant in tumor cells or around a site of inflammation.<sup>[13]</sup> This allows for site-specific drug delivery. In another recent study, polymeric nanoparticles were labeled on their outer surfaces with a viral peptide sequence that promotes permeation of substances through cell membranes.<sup>[14]</sup> These peptide-derivatized nanoparticles passed through cell membranes, and got incorporated into living cells, at much higher levels than nanoparticles without the surface-bound peptide.

## OVERVIEW

Surface functionalized nanoparticles can also be used to deliver genetic material into living cells, a process called transfection. For example, silica nanospheres labeled on their outer surfaces with cationic ammonium groups were found to bind DNA—a polyanion—via electrostatic interactions.<sup>[5]</sup> These nanoparticles were then used to deliver the surface-bound DNA into cells. That transfection was successful was proven by showing that the cells produced the protein encoded by the DNA. There is also a tremendous interest in using cationic lipid-based nanospheres—liposomes—as DNA transfection agents.<sup>[6,7]</sup> Finally, the gold nanoparticles introduced above have been used extensively in the development of new types of gene sensors.<sup>[8–10]</sup>

Spherical nanoparticles are typically used in such applications, but this only reflects the fact that spheres are easier to make than other shapes. Microtubes and nanotubes—structures that resemble tiny drinking straws (Fig. 1)—are alternatives to spherical nanoparticles. Examples include organosilicon polymer nanotubes,<sup>[15]</sup> self-assembling lipid microtubes,<sup>[16–20]</sup> fullerene carbon nanotubes,<sup>[21–24]</sup> template-synthesized nanotubes,<sup>[25–28]</sup> and peptide nanotubes.<sup>[29–32]</sup> Nanotubes offer some interesting advantages relative to spherical nanoparticles for biotechnological applications. For example, nanotubes have large inner volumes (relative to the dimensions of the tube), which can be filled with any desired chemical or biochemical

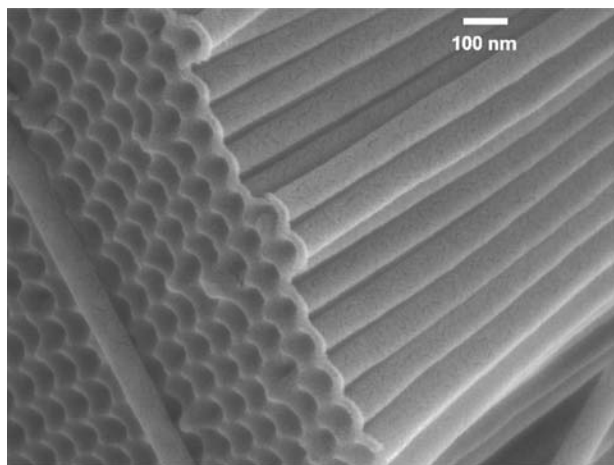


**Fig. 1** Scanning electron micrograph of an array of template-synthesized carbon nanotubes. These nanotubes are composed of disordered graphitic carbon.

species ranging in size from proteins to small molecules.<sup>[25,26]</sup> In addition, nanotubes have distinct inner and outer surfaces, which can be differentially chemically or biochemically functionalized.<sup>[25]</sup> This creates the possibility, for example, of loading the inside of a nanotube with a particular biochemical payload but imparting chemical features to the outer surface that render it biocompatible. Finally, nanotubes have open mouths, which makes the inner surface accessible and the incorporation of species within the tubes particularly easy.

We review here some emergent technologies for preparing microtubes and nanotubes, and we give examples of recent biotechnological applications of these tubular systems. This review is not intended to be all encompassing; instead, it discusses recent trends and emphasizes some particularly promising technologies. Systems reviewed include self-assembling lipid microtubes, fullerene carbon nanotubes, cyclic peptide nanotubes, and template-synthesized nanotubes.

## NOMENCLATURE

In the literature, the tubular structures of interest to this review are called by various names including microtubules, microtubes, nanotubules, and nanotubes. This nomenclature can be simplified by noting that in this context, there is no difference between a tube and a tubule; in this entry, we use only the name tube. Nano vs. micro is a more difficult issue because there is no universally accepted dimension scale above which a particle is micro, and below which it is nano. In our research group, we have agreed that if a tube has at least one dimension that is 100 nm or less, it is called a nanotube.

## SELF-ASSEMBLING LIPID MICROTUBES

In 1984, Yager and Schoen<sup>[16]</sup> of the U.S. Naval Research Laboratory showed that chiral lipid molecules of the type shown in Fig. 2 self-assemble in solution to form microtubes. When diacetylenic lipids (Fig. 2) are used, the resulting microtubes have diameters on the order of 500 nm, lengths varying from about 50 to several hundreds of micrometers, and wall thicknesses from 10 to 60 nm or more.<sup>[17]</sup> The theory of this self-assembly process has been discussed by Selinger, Spector, and Schnur<sup>[18]</sup> In the most simplistic interpretation, the lipids self-assemble in solution to form planar bilayer sheets, which then curl up to make microtubes.

One proposed application of lipid microtubes is as vehicles for controlled drug release. For example, Price and Patchan<sup>[19]</sup> coated such tubes with metallic copper (to improve their mechanical strength) and then loaded antibiotics used to prevent marine fouling into these

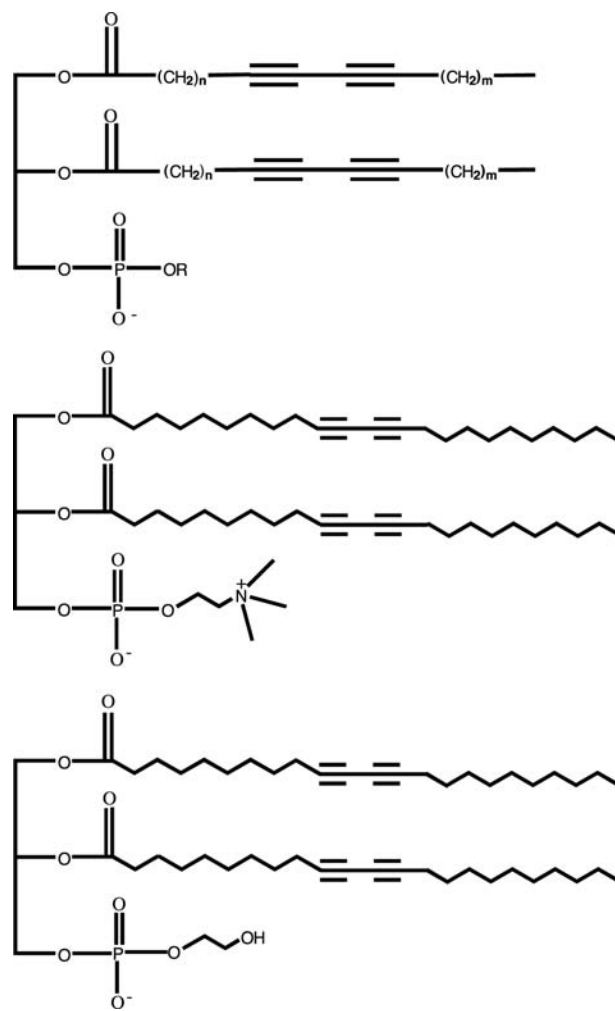


**Fig. 2** Typical lipids used to make self-assembling lipid microtubes.



tubes. The tubes were then incorporated into a paint, which was applied to fiberglass rods. This microtube-based paint successfully inhibited marine fouling during 6 months testing of these rods in ocean water. Microtubes of this type have also been used for the controlled release of testosterone in living rats.<sup>[20]</sup> While these applications provide proof-of-concept, lipid microtubes are mechanically weak and, as indicated above, must be coated before use. In addition, because the ability to form tubes is connected with the unique chemistry and chirality of the lipids used, it would be difficult to use this approach to make tubes with any desired set of chemical, biochemical, or physical properties.

### FULLERENE CARBON NANOTUBES

In 1985, Kroto et al.<sup>[33]</sup> at Rice University discovered a new form of carbon—buckminsterfullerene or  $C_{60}$ —and this work ultimately led to the awarding of the 1996 Nobel Prize in chemistry to Smalley, Kroto, and Curl. Fullerene molecules of this type can be prepared by a carbon arc discharge method, and, in 1991, Iijima<sup>[21]</sup> discovered nanotubes in the products obtained from such a reactor (Fig. 3). These tubes are, in essence, rolled-up, highly ordered graphene sheets, and they may be single-walled or multiwalled.

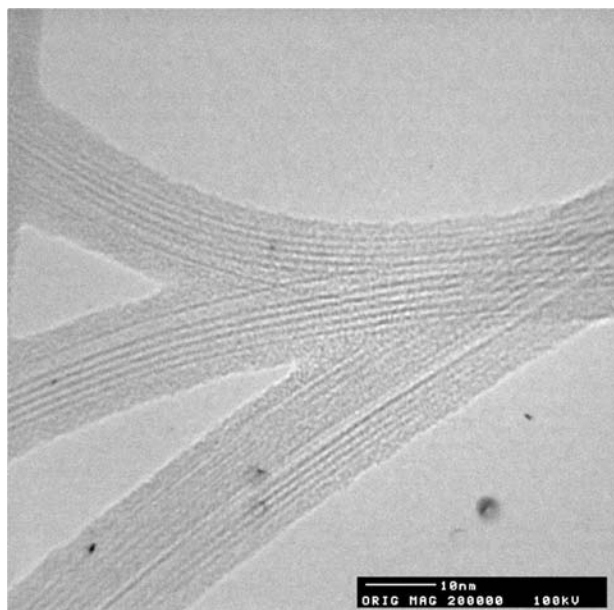


**Fig. 3** Transmission electron micrograph of fullerene carbon nanotubes. The three converging objects are each a small bundle (“rope”) of hexagonally close-packed single-wall carbon nanotubes. These ropes are a little more than 10 nm in diameter and so contain ~50–100 nanotubes, each approximately 1.35 nm in diameter. *Source:* From Prof. Andrew Rinzler, University of Florida.

They are typically referred to in the literature as simply carbon nanotubes; however, because there are examples of nanotubes composed of more disordered forms of carbon (Fig. 1),<sup>[34]</sup> the more precise name, fullerene carbon nanotubes, is used here. Diameters for these nanotubes range from 1 to tens of nanometers, and lengths can be from microns to hundreds of microns.<sup>[22]</sup> Since their discovery, there has been a massive international research effort aimed at understanding the properties of fullerene carbon nanotubes and at developing applications for these nanotubes; a number of authoritative reviews have recently appeared.<sup>[22–24]</sup>

One proposed nonbiomedical application is in the area of microelectronics, where the ultimate objective is to make electronic circuit elements that are composed of these nanoscopic carbon tubes.<sup>[24,35–37]</sup> This research effort is driven by the need to further miniaturize electronic circuits so that increasing numbers of circuits can be accommodated on a chip. It is widely believed that the current silicon-based lithographic technology will reach its limit during the next decade. Fullerene nanotubes are interesting alternatives not only because they are small, but also because depending on the way they are rolled up, they can have electronic properties similar to both metals and semiconductors.<sup>[23,35,36]</sup> A number of groups have demonstrated that fullerene nanotubes can be used as components of electronic circuit elements.<sup>[24,36,37]</sup>

There have been a number of recent reports of putting biomolecules onto and into fullerene carbon nanotubes.<sup>[38–42]</sup> For example, Chen et al.<sup>[38]</sup> used a simple non-covalent route to attach a reactive molecule to the sidewalls of single-walled fullerene nanotubes. This reactive molecule could then be used to attach proteins to the walls of these nanotubes. This and related work is of interest to the development of biosensors based on fullerene nanotubes.<sup>[39]</sup>

Lieber et al.’s group<sup>[42,43]</sup> has pioneered the use of single-walled carbon nanotubes (SWNTs) as probe tips for atomic force microscopy (AFM) imaging of biomacromolecules such as antibodies, DNA, and amyloid  $\beta$  protofibrils (a constituent of the amyloid plaques characteristic of Alzheimer’s disease). As discussed in their recent review,<sup>[43]</sup> AFM is a scanning probe microscopy technique that has molecular-level resolution capabilities. They have shown that SWNTs are ideal probe tips for AFM because of their small diameter (which maximizes resolution), high aspect ratio, excellent chemical and mechanical robustness, and extraordinary stiffness.<sup>[43]</sup> In addition, Lieber’s group has attached biomolecules to SWNTs and used them as “molecular-recognition” AFM tips.<sup>[42]</sup> This approach is used to study the chemical forces that exist between molecules. For example, the molecule biotin was attached to a SWNT, and this tip was used to

explore the binding interaction between biotin and the protein streptavidin.<sup>[42]</sup>

## PEPTIDE NANOTUBES

In 1993, Ghadiri et al.<sup>[29]</sup> at the Scripps Research Institute described a fascinating class of nanotubes based on cyclic peptide molecules that consists of an even number of alternating D- and L-amino acids (Fig. 4). They showed that these molecules self-assemble via hydrogen-bonding interactions into nanotubes, which, in turn, self-assemble into ordered parallel arrays of these nanotubes. The number of amino acid residues in the ring determines the inside diameter of the nanotubes obtained; as an example, a 12-amino-acid ring gave nanotubes with an inside diameter of 1.3 nm.<sup>[30]</sup> The chemical functional groups on the outside of the walls of these nanotubes can be varied by varying the amino acid composition of the ring.

Ghadiri et al. have demonstrated a number of biomedical/biotechnological applications for these nanotubes. Perhaps the most interesting is as a new class of antibiotics against bacterial pathogens.<sup>[31]</sup> They showed that 6 and 8 amino-acid residue cyclic peptides act preferentially on both Gram-positive and Gram-negative bacterial membranes relative to mammalian cells.<sup>[31]</sup> The data suggest that nanotubes formed from these peptides insert into the cell wall of the bacterium resulting in rapid cell death. They have also shown that these nanotubes can function as artificial ion channels in lipid bilayer membranes by self-assembling across the membrane.<sup>[32]</sup> Ion transport rates comparable to those of naturally occurring ion channels were observed.

These cyclic peptides have also been used as components in stochastic sensors—an elegant new chemical and biochemical sensing technology developed by Bayley et al.'s<sup>[44,45]</sup> group at Texas A&M University. This example raises an interesting fundamental point—*Mother Nature has evolved and routinely uses*

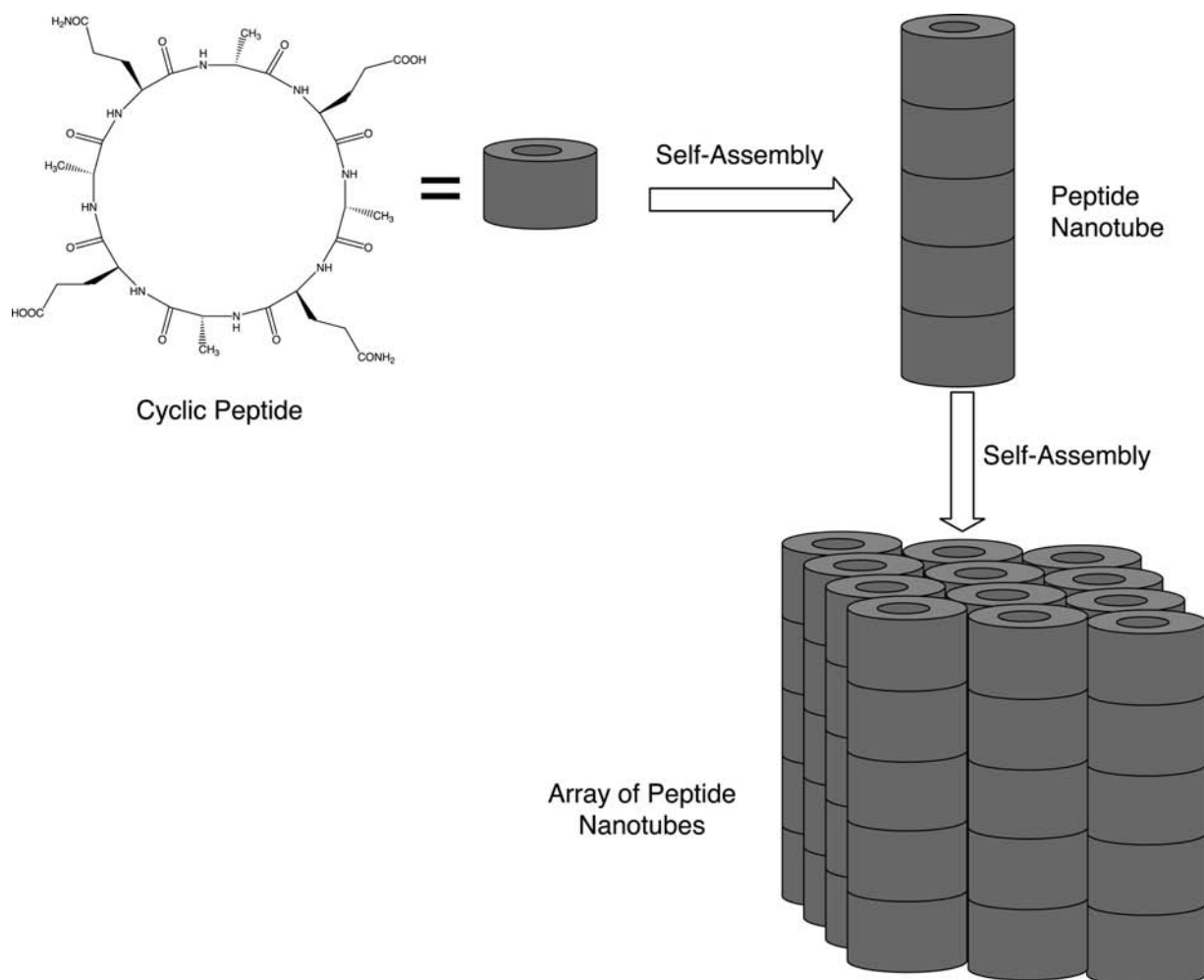


**Fig. 4** Cyclic peptide nanotubes. A typical chemical structure for a cyclic peptide and schematic illustrations of the self-assembly of such peptides into nanotubes and nanotube arrays.

her own brand of nanotubes, called protein channels. The most prevalent examples are the ligand-gated and voltage-gated ion channels that are used for electrical signaling in our brains, nerves, and muscles.<sup>[46]</sup> Another type of protein channel, the  $\alpha$ -hemolysin channel ( $\alpha$ HL) (Fig. 5A), is used as the sensing element in stochastic sensors. In these devices, a lipid bilayer membrane containing a single  $\alpha$ HL channel is mounted between two electrolyte solutions, a constant transmembrane potential is applied, and the resulting transmembrane current is measured. This current is associated with the transport of ions through the  $\alpha$ HL channel.<sup>[44,45]</sup>

In simplest terms, when the chemical species to be sensed (the “analyte”) enters the channel, it acts as a cork and blocks the pathway for ionic conduction through the channel. This results in a transient decrease, or downward pulse, in the measured transmembrane ion current. The term “stochastic” (associated with randomness) is used because the analyte enters and leaves the channel by diffusion,

i.e., a random walk.<sup>[47]</sup> The number of such current pulses is related to the concentration of the analyte, and the duration of the pulse provides clues as to the identity of the analyte. Analytes detected in this way include metal ions, DNA chains, and small organic molecules.<sup>[44,45]</sup>

However, small organic molecules by themselves cannot appreciably block the ion current, and so a larger “molecular adapter” that binds such analytes must be used. Sanchez-Quesada et al.<sup>[44]</sup> demonstrated that cyclic peptides can be used as molecular adapters. In this case, the cyclic peptide gets transiently lodged within the lumen of the channel [Eq. (1), Fig. 5B], and this can be detected as a pulse in the transmembrane ion current. The analyte can, in turn, get transiently bound within the annulus of the cyclic peptide [Eq. (2), Fig. 5B], and these binding/unbinding events produce a second set of current pulses. This is an interesting case where a smaller tube, the cyclic peptide, gets inserted into a larger tube, the  $\alpha$ HL channel.

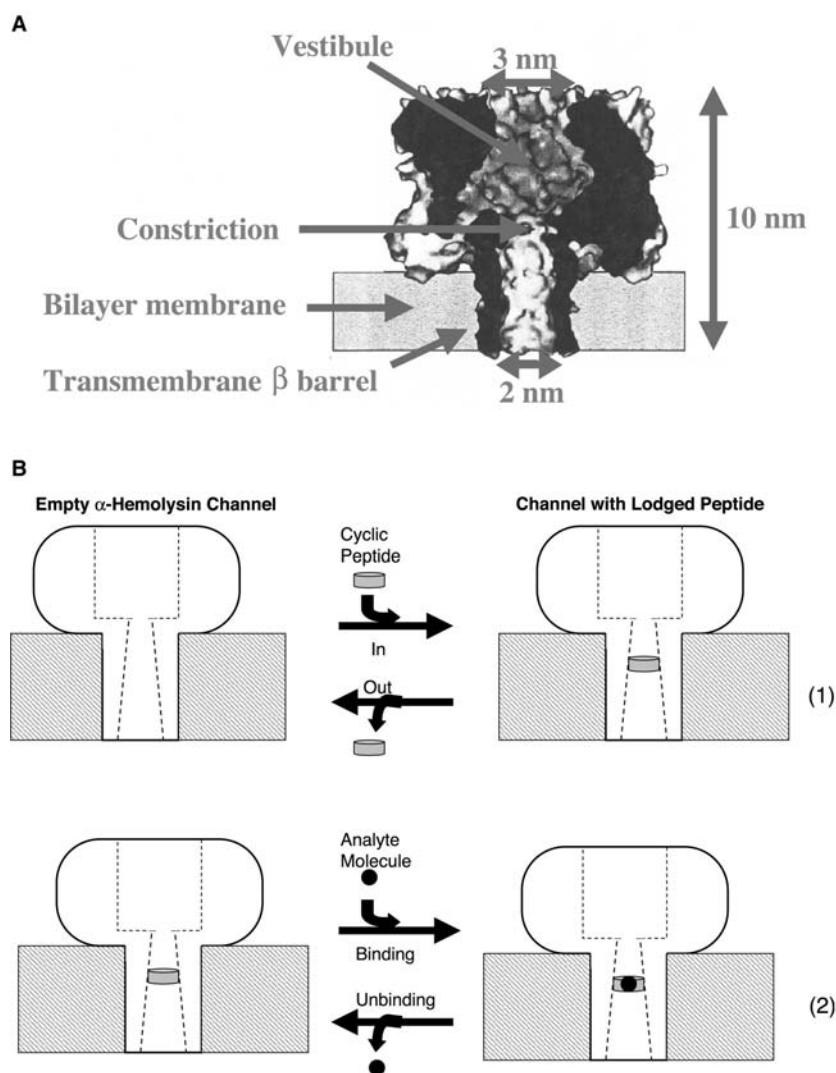


**Fig. 5** The  $\alpha$ -hemolysin protein channel, an example of Mother Nature’s nanotubes. (A) Structure (based on a figure from Prof. Hagan Bayley, Texas A&M University). (B) Schematic representation of the use of a cyclic peptide as a “molecular adapter” for stochastic sensing with the  $\alpha$ -hemolysin channel.

## TEMPLATE-SYNTHESIZED NANOTUBES

The template method is a general approach for preparing nanomaterials that entails synthesis or deposition of the desired material within the cylindrical and monodisperse pores of a nanopore membrane or other solid (see, e.g., Fig. 6A).<sup>[3,48]</sup> Cylindrical nanostructures with monodisperse diameters and lengths are obtained, and depending on the membrane and synthetic method used, these may be solid nanowires or hollow nanotubes. This method has been used to prepare nanowires and tubes composed of many different types of materials including metals, polymers, semiconductors, and carbons.<sup>[3,48]</sup> In addition, the template method can be used to prepare composite nanostructures, both concentric tubular composites<sup>[49]</sup> and segmented composite nanowires.<sup>[50]</sup>

How one makes nanotubes within the pores of a template membrane can be illustrated by the carbon nanotubes shown in Fig. 1.<sup>[34]</sup> An alumina template (Fig. 6A) was heated to 670°C, and ethylene gas was passed through the membrane. This causes the ethylene to decompose on the pore walls to yield graphitic carbon nanotubes within the pores. The alumina template membrane can then be dissolved away and the carbon nanotubes can be collected by filtration. These tubes have monodisperse outside diameters determined by the diameter of the pores in the template. The inside diameter is determined by the carbon deposition time. Other synthetic methods we have used include in-pore polymerization to make polymeric nanotubes, electrodeless deposition to make metal nanotubes, and sol-gel chemistry to make nanotubes composed of silica and other inorganic materials.<sup>[3,48]</sup> Templated silica nanotubes<sup>[25,26]</sup> are shown in Fig. 6B. All these nanotubes are of the same length, which is determined by the thickness of the template membrane.

We have used these silica nanotubes as test vehicles to illustrate the power of the template method for preparing nanotubes for biotechnological applications.<sup>[25,26]</sup> Silica nanotubes are ideal for such proof-of-concept experiments because they are easy to make, readily suspendable in aqueous solution, and because silica surfaces can be derivatized with an enormous variety of different chemical functional groups using simple silane chemistry with commercially available reagents.<sup>[25,26]</sup>

### Attaching Different Functional Groups to the Inside vs. Outside Surfaces

As noted above, one of the most important attributes of a nanotube is that it has distinct inner and outer surfaces that can be differentially chemically and biochemically functionalized. The template method

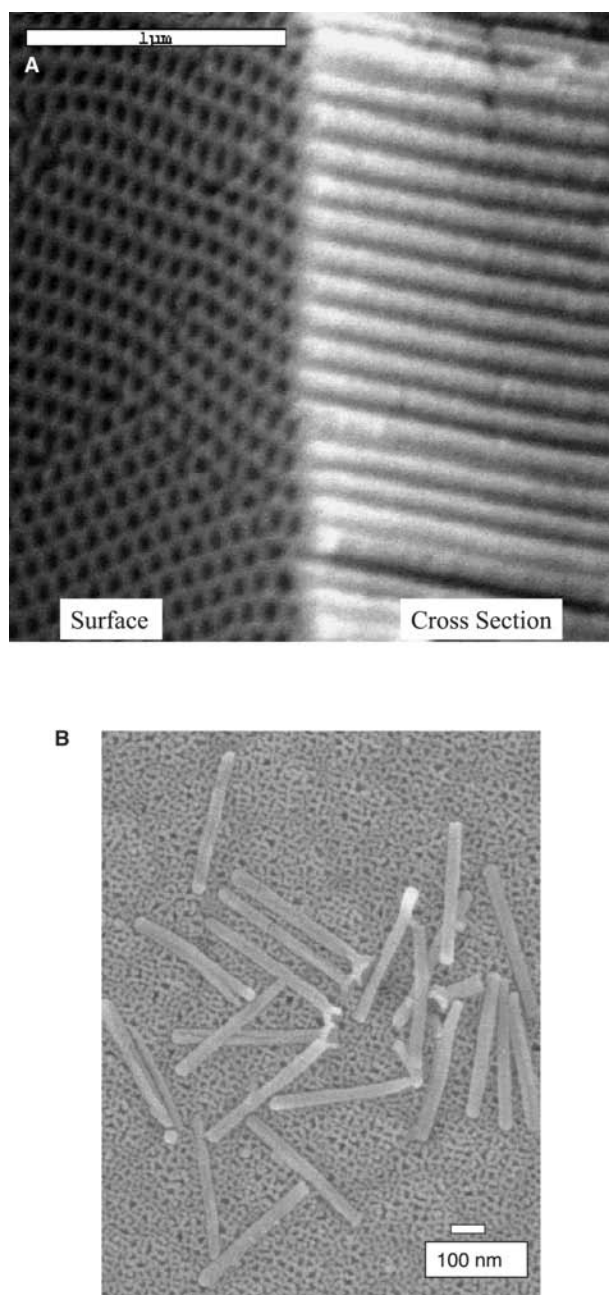


**Fig. 6** Scanning electron micrographs. (A) The surface and cross section of a typical nanopore alumina template membrane prepared in the authors' laboratory. Pores with monodisperse diameters that run like tunnels through the thickness of the membrane are obtained. (B) Silica nanotubes prepared by sol-gel template synthesis within the pores of a template like that shown in (A). After sol-gel synthesis of the nanotubes, the template was dissolved and the nanotubes were collected by filtration.

provides a particularly easy route to accomplish this differential functionalization.<sup>[25]</sup> The silica nanotubes were synthesized within the pores of nanopore alumina template membranes (Fig. 6B) using a sol-gel method described previously.<sup>[25,26]</sup> Templates with pore

diameters of either 60 or 200 nm were used for these studies.<sup>[25,26]</sup>

We have developed the following simple procedure for applying different functional groups to the inner vs. outer surfaces of these nanotubes. Fig. 7A represents schematically a cross section of the alumina template membrane (Fig. 6A) showing two pores. Fig. 7B shows this membrane after sol-gel template synthesis of the silica nanotubes within the pores (blue color). Note that the surfaces of the membrane are coated with thin silica films, which are removed by a brief mechanical polish.<sup>[25]</sup> While still embedded within the pores of the template membrane, the inner nanotube surfaces are reacted with a silane reagent that contains the functional group to be attached to the inner surfaces (green in Fig. 7C). This silane cannot attach to the outer nanotube surfaces because the outer surfaces are in contact with the pore wall and are thus masked. The template is then dissolved to liberate the nanotubes, which unmask the outer nanotube surfaces (Fig. 7D).<sup>[25]</sup> The liberated nanotubes are then exposed to a second silane that contains the functional group to be attached to the outer nanotube surfaces (pink in Fig. 7E).

To demonstrate the concept of differential chemistries inside and outside of the nanotubes, we have used immobilized two different chromophores (green and blue) inside of the nanotubes and making the outside of the nanotubes either lipophilic or lipophobic. A set of nanotubes was prepared with the green fluorescent silane *N*-(triethoxysilylpropyl)dansylamide attached to their inner surfaces and the hydrophobic octadecyl silane (C<sub>18</sub>) attached to their outer surfaces. These nanotubes were added to a vial containing water and the immiscible organic solvent cyclohexane, which were mixed and allowed to separate. Because these nanotubes are hydrophobic on their outer surfaces, they partition into the (upper) cyclohexane phase (Fig. 8B). This may be contrasted to nanotubes that were labeled

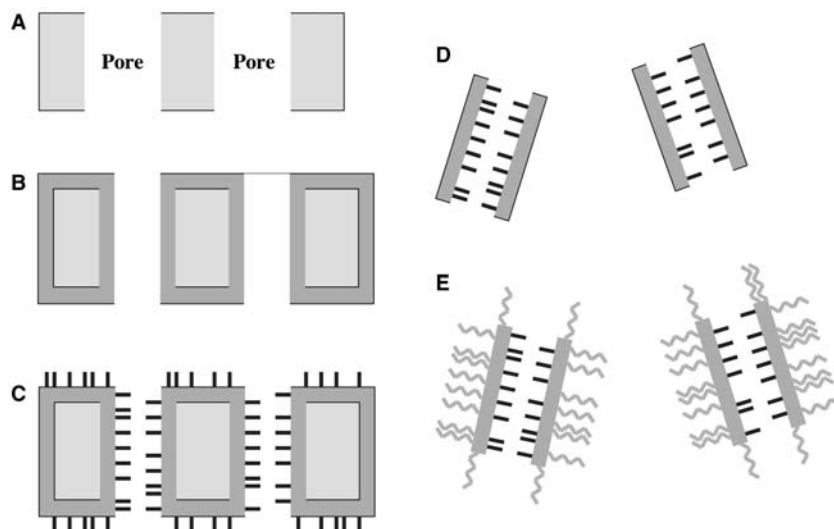


**Fig. 7** Schematic of procedure used to attach different chemical functional groups to the inner vs. outer surfaces of template-synthesized nanotubes. (A) Cross section of the template membrane. (B) Membrane after template synthesis of nanotubes within the pores (blue). (C) After attachment of the first functional group (green) to the inner nanotube surfaces. (D) Liberated nanotubes after dissolution of the template membrane. (E) After attachment of the second functional group to the outer nanotube surfaces (pink).

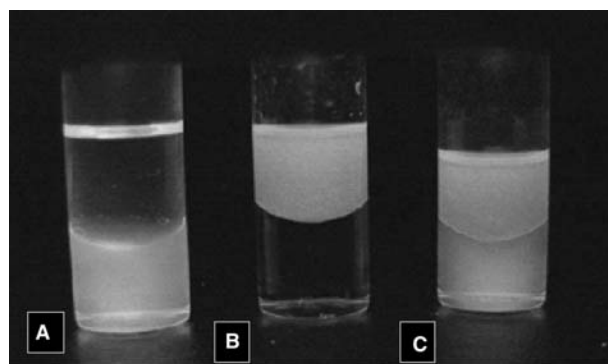


**Fig. 8** Photographs of vials containing nanotubes modified with two different fluorophores in two different solvent medium. (A) Cyclohexane (upper) and water (lower) under UV light excitation after the addition of 10 mg of nanotubes with dansylamide on inner and C<sub>18</sub> on outer surfaces. (B) Quinineurethan on inner and no silane on outer surfaces. (C) Ten milligrams of both A and B nanotubes. Nanotubes, 200 nm in diameter, were used.

on their inner surfaces with the blue fluorescent silane triethoxysilylpropylquinineurethan, but were not labeled with any silane on their outer surfaces. When the same experiment is carried out with these nanotubes, the quinineurethan fluorescence is seen only from the aqueous phase (Fig. 8A). When both sets of nanotubes are added to the solvent mixture in the same vial, the tubes with the C<sub>18</sub> outer surface chemistry go to the cyclohexane and the tubes with the silica outer surface chemistry go to the aqueous phase (Fig. 8C).

### Nanotubes for Chemical and Bioextraction and Biocatalysis

One application for such differentially functionalized nanotubes is as smart nanophase extractors to remove specific molecules from solution.<sup>[25]</sup> Nanotubes with

hydrophilic chemistry on their outer surfaces and hydrophobic chemistry on their inner surfaces are ideal for extracting lipophilic molecules from aqueous solution. The hydrophobic molecule 7,8-benzoquinoline (BQ), which has an octanol/water partition coefficient of  $10^{3.8}$ , was used as a model compound for such nanophase solvent extraction experiments. Five milligrams of the silica-outer/ $C_{18}$ -inner nanotubes was suspended into 5 mL of  $1.0 \times 10^{-5}$  M aqueous BQ. The suspension was stirred for 5 min and then filtered to remove the nanotubes. Ultraviolet spectroscopy showed that 82% of the BQ was removed from the solution. When a second 5-mg batch of these nanotubes was added to the filtrate, >90% of the original amount of BQ was removed from the solution. Control nanotubes that did not contain the hydrophobic  $C_{18}$  inner surface chemistry extracted less than 10% of the BQ.

Nanotubes with the  $C_{18}$  inside will, in principle, extract any lipophilic molecule. This ability to sequester lipophilic molecules can be viewed as a generic type of extraction selectivity, which might be useful in some applications. However, nanotubes that have molecular-recognition capability and extract only one particular molecule from solution might also be useful. We have shown that antibody-functionalized nanotubes can provide the ultimate in extraction selectivity—the extraction of one enantiomer of a chiral drug molecule.

In collaboration with Prof. Hans Soderlund of VTT Biotechnology in Finland, we have been investigating an antibody that selectively binds one enantiomer of the drug FTB (Fig. 9A), an inhibitor of aromatase enzyme activity.<sup>[51]</sup> This molecule has two chiral centers and thus four stereoisomers—RR, SS, SR, and RS. Prof. Soderlund supplied us with the Fab fragment<sup>[52]</sup> of an antibody that selectively binds the RS relative to the SR enantiomer. The antibody was produced against the drug 4-[3-(4-fluorophenyl)-2-hydroxy-1-[1,2,4]triazol-1-yl-propyl]-benzimidazole (FTB, Fig. 9A). The antibody used selectively binds the RS enantiomer, and Fab fragments of this antibody were immobilized to both the inner and outer surfaces of the silica nanotubes. This was accomplished by dissolving the template membrane, collecting the nanotubes, and then dispersing them into a solution of the aldehyde-terminated silane trimethoxysilylbutanal. The nanotubes were then dispersed into a solution of the Fab fragments, which resulted in the attachment of the Fab to the nanotubes via Schiff base reaction between free amino groups on the protein and the surface-bound aldehyde.

The Fab-functionalized nanotubes were added to racemic mixtures of the SR and RS enantiomers of FTB. The tubes were then collected by filtration and the filtrate was assayed for the presence of the two enantiomers using a chiral HPLC method (Fig. 9B).

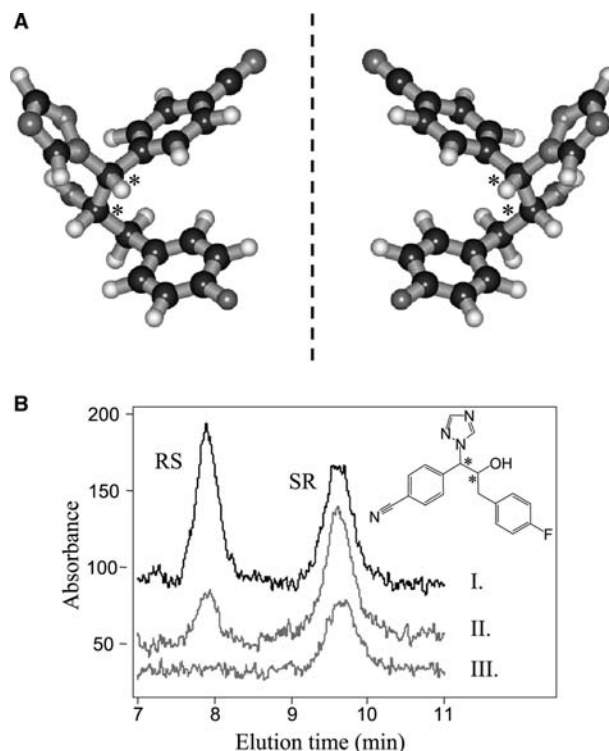


**Fig. 9** Enantioseparations. (A) 3-D structures of the RS enantiomer (left) and the SR enantiomer (right) of the drug FTB. The black, white, blue, red, and yellow balls are carbon, hydrogen, nitrogen, oxygen, and fluorine, respectively, and \* denotes the chiral centers. The geometry optimization was done by ab initio calculation with minimal basis set in HyperChem 6.03. The drug is in clinical trials by Hormos Medical Corp., Turku, Finland. (B) Chiral HPLC chromatograms for racemic mixtures of FTB before (I) and after (II, III) extraction with 18 mg/mL of 200-nm Fab-containing nanotubes. Solutions were 5% dimethylsulfoxide in sodium phosphate buffer, pH 8.5.

Chromatogram I is from a solution that was  $20 \mu\text{M}$  in both enantiomers, and chromatogram II was obtained for the same solution after exposure to the Fab-functionalized nanotubes; 75% of the RS enantiomer and none of the SR enantiomer was removed by the nanotubes. When the concentration of the racemic mixture was dropped to  $10 \mu\text{M}$ , all of the RS enantiomer was removed (chromatogram III). Nanotubes containing no Fab did not extract measurable quantities of either enantiomer from the  $20\text{-}\mu\text{M}$  solution.

We have also developed a chemistry that allows us to attach the Fab to only the inner surfaces of the nanotubes. While still within the pores of the template membrane, the inner surfaces were treated with amino-propyltrimethoxysilane. The template membrane was then dissolved and the amino sites on the inner surfaces were coupled to free amino groups on the Fab fragment using the well-known glutaraldehyde coupling reaction.<sup>[25]</sup> When 18 mg of these interior-only



Fab-modified nanotubes was incubated with 1 mL of a 10- $\mu$ M racemic mixture of the drug, 80% of the RS (and none of the SR) enantiomer was extracted. This corresponds to 0.44 nmol RS enantiomer/mg tubes, whereas almost double that amount, 0.80 nmol/mg, was extracted by the nanotubes with Fab on both their inner and outer surfaces.

Another example concerns the immobilization of a biocatalyst—the enzyme glucose oxidase (GOD)—to the silica nanotubes.<sup>[25]</sup> Glucose oxidase was immobilized, on both the inside and outside surfaces, via the aldehyde silane route. These GOD nanotubes (60-nm diameter) were dispersed into a solution that was 90 mM in glucose and also contained the components of the standard dianisidine-based assay for GOD activity. A GOD activity of  $0.5 \pm 0.2$  U/mg of nanotubes was obtained. These studies also showed that protein immobilized via the Schiff-base route is not leached from the nanotubes, in that all GOD activity ceased when the nanotubes were filtered from the solution.

### Nanotube Membranes for Bioseparations

In all of the examples cited above, the template membrane was dissolved away and the liberated nanotubes were collected by filtration. The nanotubes may also be left embedded within the pores of the template to yield a freestanding nanotube-containing membrane. We have shown that the nanotubes can act as conduits for highly selective transport of molecules and ions between solutions present on either side of the membrane.<sup>[26–28]</sup> For example, membranes containing gold nanotubes with inside diameters of molecular dimensions (<1 nm) cleanly separate small molecules on the basis of molecular size.<sup>[28]</sup> Gold nanotubes with larger inside diameters (20 to 45 nm) can be used to separate proteins, and here again, rendering the nanotubes biocompatible is essential to prevent protein adsorption.<sup>[53]</sup> Generic chemical transport selectivity (lipophilic vs. hydrophilic) can also be imparted to these gold nanotube membranes.<sup>[55]</sup>

More recently, we have shown that membranes containing the silica nanotubes and the enantioselective FTB antibody Fab fragment discussed above can be used to make membranes for chiral separations.<sup>[26]</sup> In this case, the nanotube membrane separates a feed half-cell containing a racemic mixture of the RS and SR enantiomers of FTB and a permeate half-cell that initially contains only buffer solution. The time course of permeation of the two enantiomers across the membrane was determined by periodically assaying the permeate solution.<sup>[26]</sup> Results for a membrane containing ~15-nm diameter silica nanotubes are shown in Fig. 10 as plots of mole enantiomer transported vs.

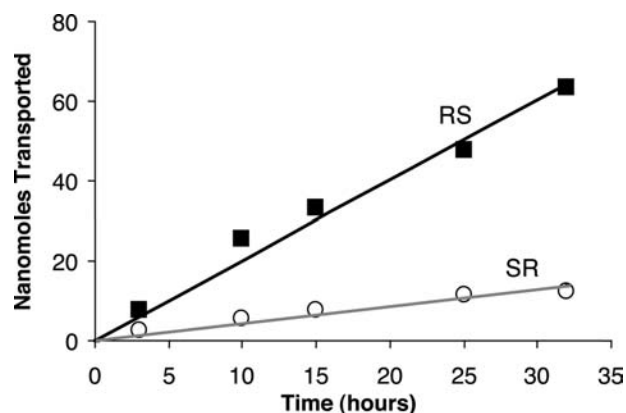


**Fig. 10** Enantioseparations using antibody-immobilized membranes. Plots of moles of each enantiomer transported vs. time for a silica nanotube membrane containing the enantioselective antibody Fab fragment. The inside diameter of the nanotubes was ~15 nm.

permeation time. We see that the flux of the RS enantiomer, the one bound by the antibody, is 5 times higher than the flux of the SR enantiomer. Because, in principle, antibodies can be obtained that selectively bind to any desired molecule or enantiomer, this concept might provide a general approach for obtaining selectively permeable membranes for a host of enantio-separations and bioseparations.

Finally, biocompatibility is an important issue for possible *in vivo* applications of nanotube technology. It is well known that materials can be made biocompatible, as evidenced by decreased protein adsorption, by attaching poly(ethylene glycol) (PEG) chains to their surfaces.<sup>[53]</sup> We have shown that when a PEG silane is attached to the silica nanotubes, adsorption of IgG immunoproteins is strongly suppressed relative to nanotubes that did not contain the attached PEG.<sup>[54]</sup>

### CONCLUSION

We believe that nanotubes offer some important advantages for biotechnological applications of nanoparticles. Because of its tremendous versatility in terms of materials that can be used, sizes that can be obtained, and chemistry and biochemistry that can be applied, the template method might prove to be a particularly advantageous approach for preparing nanotubes for such applications. However, this field of nanotube biotechnology is in its infancy, and there is much work to be performed before products based on this technology are brought to the market place. For example, in our applications to date, we have incorporated the payload into the nanotubes by either covalent bonding or other chemical interactions. However, in some applications, it might be useful to simply

fill the nanotube with a payload and then apply caps to the nanotube ends to keep the payload encapsulated. Furthermore, it might be useful to have these caps fall off, thus spilling the payload, when a particular chemical or biochemical signal is detected. We are currently exploring routes for preparing such capped nanotubes. The issues of cost of production and mass production of nanotubes must also be addressed.

Finally, the synthetic nanotubes discussed here can be thought of as mimics of naturally occurring nanotubes—protein channels;<sup>[46]</sup> indeed, the cyclic peptide nanotubes have been used as artificial ion channels.<sup>[32]</sup> Ion channels open and close in response to chemical and electrical stimuli. We are developing synthetic nanotubes with similar voltage<sup>[27,56]</sup> and chemical<sup>[57]</sup> gating characteristics. These nanotubes can be used in smart membranes whose transport properties change in response to an electrical stimulus<sup>[27,56]</sup> and in sensing devices where a chemical stimulus turns on a current that can be measured in an external circuit.<sup>[57]</sup>

## ACKNOWLEDGMENTS

This work was supported by the National Science Foundation (NIRT for Biomedical Nanotube Technology), the Office of Naval Research, and the UF Engineering Research Center for Particle Science and Technology. We gratefully acknowledge our collaborator Prof. Hans Soderlund for contributions to the antibody research projects.

## REFERENCES

1. Klabunde, K.J. *Nanoscale Materials in Chemistry*; Wiley-Interscience: New York, 2001.
2. Martin, C.R.; Mitchell, D.T. Nanomaterials in analytical chemistry. *Anal. Chem.* **1998**, *70*, 322A–327A.
3. Martin, C.R. Nanomaterials—a membrane-based synthetic approach. *Science* **1994**, *266*, 1961–1966.
4. Chang, T.M.S.; Prakash, S. Procedures for microencapsulation of enzymes, cells and genetically engineered microorganisms. *Mol. Biotechnol.* **2001**, *17*, 249–260.
5. Kneuer, C.; Sameti, M.; Bakowsky, U.; Schiestel, T.; Schirra, H.; Schmidt, H.; Lehr, C.-M. A nonviral DNA delivery system based on surface modified silica-nanoparticles can efficiently transfect cells in vitro. *Bioconjug. Chem.* **2000**, *11*, 926–932.
6. Radler, J.; Koltover, I.; Salditt, T.; Safinya, C.R. Structure of DNA–cationic liposome complexes: DNA intercalation in multilamellar membranes in distinct interhelical packing regimes. *Science* **1997**, *275*, 810–814.
7. Koltover, I.; Salditt, T.; Radler, J.O.; Safinya, C.R. An inverted hexagonal phase of cationic liposome–DNA complexes related to DNA release and delivery. *Science* **1998**, *281*, 78–81.
8. Cao, Y.W.C.; Jin, R.C.; Mirkin, C.A. Nanoparticles with Raman spectroscopic fingerprints for DNA and RNA detection. *Science* **2002**, *297*, 1536–1540.
9. Demers, L.M.; Ginger, D.S.; Park, S.J.; Li, Z.; Chung, S.W.; Mirkin, C.A. Direct patterning of modified oligonucleotides on metals and insulators by dip-pen nanolithography. *Science* **2002**, *296*, 1836–1838.
10. Park, S.J.; Taton, T.A.; Mirkin, C.A. Array-based electrical detection with nanoparticles probes. *Science* **2002**, *295*, 1503–1506.
11. Ulrich, K.E.; Cannizzaro, S.M.; Langer, R.S.; Shakeshelf, K.M. Polymeric systems for controlled drug release. *Chem. Rev.* **1999**, *99*, 3181–3198.
12. Lee, K.E.; Kim, B.K.; Yuk, S.H. Biodegradable polymeric nanospheres formed by temperature-induced phase transition in a mixture of poly(lactide-co-glycolide) and poly(ethylene oxide)-poly(propylene oxide)-poly(ethylene oxide) triblock copolymer. *Biomacromolecules* **2002**, *3*, 1115–1119.
13. Murthy, N.; Thng, Y.X.; Schuck, S.; Xu, M.C.; Frechet, J.M.J. A novel strategy for encapsulation and release of proteins: hydrogels and microgels with acid-labile acetal cross-linkers. *J. Am. Chem. Soc.* **2002**, *124*, 12,398–12,399.
14. Lewin, M.; Carlesso, N.; Tung, C.; Tang, X.-W.; Cory, D.; Scadden, D.T.; Weissleder, R. Tat peptide-derivatized magnetic nanoparticles allow in vivo tracking and recovery of progenitor cells. *Nat. Biotechnol.* **2000**, *18*, 410–414.
15. Linsky, J.P.; Paul, T.R.; Kenny, M.E. Planar organosilicon polymers. *J. Polym. Sci.* **1971**, *A-2 9*, 143–160.
16. Yager, P.; Schoen, P. Formation of tubules by a polymerizable surfactant. *Mol. Cryst. Liq. Cryst.* **1984**, *106*, 371–381.
17. Schnur, J.M. Lipid tubules—a paradigm for molecularly engineered structures. *Science* **1993**, *262*, 1669–1676.
18. Selinger, J.V.; Spector, M.S.; Schnur, J.M. Theory of self-assembled tubules and helical ribbons. *J. Phys. Chem., B* **2001**, *105*, 7157–7169.
19. Price, R.; Patchan, M. Controlled release from cylindrical macrostructures. *J. Microencapsul* **1991**, *8*, 301–306.
20. Goldstein, A.S. et al. Testosterone delivery using glutamide-based complex high axial ratio microstructures. *Bioorg. Med. Chem.* **2001**, *9*, 2819–2825.
21. Iijima, S. Helical microtubules of graphitic carbon. *Nature* **1991**, *354*, 56–58.
22. Ajayan, P.M. *Carbon Nanotubes: Preparation and Properties*; Ebbesen, T.W., Ed.; CRC Press: Cleveland, OH, 1997.
23. Ajayan, P.M. Nanotubes from carbon. *Chem. Rev.* **1999**, *99*, 1787–1800.
24. Dai, H.; Kong, J.; Zhou, C.; Franklin, N.; Tomblor, T.; Cassell, A.; Fan, S.; Chapline, M. Controlled chemical routes to nanotube architectures, physics, and devices. *J. Phys. Chem., B* **1999**, *103*, 11,246–11,255.
25. Mitchell, D.T.; Lee, S.B.; Trofin, L.; Li, N.; Nevanen, T.K.; Söderlund, H.; Martin, C.R. Smart nanotubes for bioseparations and biocatalysis. *J. Am. Chem. Soc.* **2002**, *124*, 11,864–11,865.

26. Lee, S.B.; Mitchell, D.T.; Trofin, L.; Li, N.; Nevanen, T.K.; Söderlund, H.; Martin, C.R. Antibody-based bio/nanotube membranes for enantiomeric drug separations. *Science* **2002**, *296*, 2198–2200.
27. Nishizawa, M.; Menon, V.P.; Martin, C.R. Metal nanotubule membranes with electrochemically switchable ion-transport selectivity. *Science* **1995**, *268*, 700–702.
28. Jirage, K.B.; Hulteen, J.C.; Martin, C.R. Nanotubule-based molecular-filtration membranes. *Science* **1997**, *278*, 655–658.
29. Ghadiri, M.R.; Granja, J.R.; Milligan, R.A.; McRee, D.; Khazanovich, N. Self-assembled organic nanotubes based on a cyclic peptide. *Nature* **1993**, *366*, 324–327.
30. Khazanovich, N.; Granja, J.R.; McRee, D.E.; Milligan, R.A.; Ghadiri, M.R. Nanoscale tubular ensembles with specified internal diameters. Design of a self-assembled nanotube with a 13 angstrom pore. *J. Am. Chem. Soc.* **1994**, *116*, 6011–6012.
31. Fernandez-Lopez, S.; Kim, H.S.; Choi, E.C.; Delgado, M.; Granja, J.R.; Khasanov, A.; Kraehenbuehl, K.; Long, G.; Weinberger, D.A.; Wilcoxon, K.M.; Ghadiri, M.R. Antibacterial agents based on the cyclic D,L-alpha-peptide architecture. *Nature* **2001**, *412*, 452–455.
32. Ghadiri, M.R.; Granja, J.R.; Buehler, L.K. Artificial transmembrane ion channels from self-assembling peptide nanotubes. *Nature* **1994**, *369*, 301–304.
33. Kroto, H.W.; Heath, J.R.; O'Brien, S.C.; Curl, R.F.; Smalley, R.E. C-60-Buckminsterfullerene. *Nature* **1985**, *318*, 162–163.
34. Miller, S.A.; Young, V.Y.; Martin, C.R. Electroosmotic flow in template-prepared carbon nanotube membranes. *J. Am. Chem. Soc.* **2001**, *123*, 12,335–12,342.
35. Jacoby, M. Nanoscale electronics. *Chem. Eng. News* **2002**, *80*, 38–43.
36. Rueckes, T.; Kim, K.; Joselevich, E.; Tseng, G.Y.; Cheung, C.-L.; Lieber, C.M. Carbon nanotube-based nonvolatile random access memory for molecular computing. *Science* **2000**, *289*, 94–97.
37. Bachtold, A.; Hadley, P.; Nakanishi, T.; Dekker, C. Logic circuits with carbon nanotube transistors. *Science* **2001**, *294*, 1317–1320.
38. Chen, R.J.; Zhang, Y.; Wang, D.; Dai, H. Noncovalent sidewall functionalization of single-walled carbon nanotubes for protein immobilization. *J. Am. Chem. Soc.* **2001**, *123*, 3838–3839.
39. Azamian, B.R.; Davis, J.J.; Coleman, K.S.; Bagshaw, C.B.; Green, M.L.H. Biochemical single-walled carbon nanotubes. *J. Am. Chem. Soc.* **2002**, *124*, 12,664–12,665.
40. Erlanger, B.F.; Chen, B.-X.; Zhu, M.; Brus, L. Binding of anti-fullerene IgG monoclonal antibody to single wall carbon nanotubes. *Nano Lett.* **2001**, *1*, 465–467.
41. Shim, M.; Kam, N.W.S.; Chen, R.J.; Li, Y.; Dai, H. Functionalization of carbon nanotubes for biocompatibility and biomolecular recognition. *Nano Lett.* **2002**, *2*, 285–288.
42. Wong, S.S.; Joselevich, E.; Woolley, A.T.; Cheung, C.L.; Lieber, C.M. Covalently functionalized nanotubes as nanometer-size probes in chemistry and biology. *Nature* **1998**, *394*, 52–55.
43. Hafner, J.H.; Cheung, C.-L.; Woolley, A.T.; Lieber, C.M. Structural and functional imaging with carbon nanotube AFM probes. *Prog. Biophys. Mol. Biol.* **2001**, *77*, 73–110.
44. Sanchez-Quesada, J.; Ghadiri, M.R.; Bayley, H.; Braha, O. Cyclic peptides as molecular adapters for a pore-forming protein. *J. Am. Chem. Soc.* **2000**, *122*, 11,757–11,766.
45. Bayley, H.; Martin, C.R. Resistive-pulse sensing from microbes to molecules. *Chem. Rev.* **2000**, *100*, 2575–2594.
46. Hille, B. *Ion Channels of Excitable Membranes*; Sinauer: Sunderland, MA, 2001.
47. Bard, A.J.; Faulkner, L.R. *Electrochemical Methods*; Wiley: New York, 2001.
48. Hulteen, J.C.; Martin, C.R. A general template-based method for the preparation of nanomaterials. *J. Mater. Chem.* **1997**, *7*, 1075–1087.
49. Cepak, V.M.; Hulteen, J.C.; Che, G.; Jirage, K.B.; Lakshmi, B.B.; Fisher, E.R.; Martin, C.R. Fabrication and characterization of concentric tubular composite micro- and nanostructures using the template synthesis method. *J. Mater. Res.* **1998**, *13*, 3070–3080.
50. Nicewarner-Pena, S.R.; Griffith, F.R.; Reiss, B.D.; He, L.; Pena, D.J.; Walton, I.D.; Cromer, R.; Keating, C.D.; Natan, M.J. Submicrometer metallic barcodes. *Science* **2001**, *294*, 137–141.
51. Nevanen, T.K.; Soderholm, L.; Kukkonen, K.; Suortti, T.; Teerinen, T.; Linder, M.; Soderlund, H.; Teeri, T.T. Efficient enantioselective separation of drug enantiomers by immobilized antibody fragments. *J. Chromatogr., A* **2001**, *925*, 89–97.
52. Stryer, L. *Biochemistry*; Freeman: New York, 1988; pp. 392, 893.
53. Yu, S.; Lee, S.B.; Kang, M.; Martin, C.R. Size-based protein separations in poly(ethylene glycol)-derivatized gold nanotubule membranes. *Nano Lett.* **2001**, *1*, 495–498.
54. Lee, S.B.; Martin, C.R. *Unpublished Result*; University of Florida: Gainesville, FL, June, 2002.
55. Jirage, K.B.; Hulteen, J.C.; Martin, C.R. Effect of thiol chemisorption on the transport properties of gold nanotubule membranes. *Anal. Chem.* **1999**, *71*, 4913–4918.
56. Kang, M.; Martin, C.R. Investigations of potential-dependent fluxes of ionic permeates in gold nanotubule membranes prepared via the template method. *Langmuir* **2001**, *17*, 2753–2759.
57. Steinle, E.D.; Mitchell, D.T.; Wirtz, M.; Lee, S.B.; Young, V.Y.; Martin, C.R. Ion channel mimetic micropore and nanotube membrane sensors. *Anal. Chem.* **2002**, *74*, 2122–2416.

# Soft Materials: AFM Investigations and Nanophysics

J. P. Aimé  
R. Boisgard  
S. Marsaudon  
G. Couturier

Centre de Physique Moléculaire Optique et Hertzienne (CPMOH),  
Université Bordeaux I, Talence, France

## INTRODUCTION

Currently, the dynamical modes of atomic force microscopes (AFM) are commonly used to investigate a large variety of molecular systems and samples. The concept of dynamical modes is based on the oscillation of a tip-cantilever system at or near the resonance frequency where the oscillating behavior changes as the tip is moved toward the surface.<sup>[1–5]</sup>

Dynamical modes were first conceived to minimize the contact between the tip apex and the surface. Thus, images can be recorded with only a slight intermittent contact over a cycle of oscillation or with no contact at all. Therefore, if not totally removed, the shear forces are significantly reduced. The merging of dynamical modes can be seen as a significant breakthrough because its ability to probe minute forces has opened avenues in the imaging of reproducibly soft materials<sup>[5–16]</sup> and in routinely obtaining atomic resolution in ultra-high vacuum conditions.<sup>[17–22]</sup>

This review briefly spans selected experimental images recorded on soft and hard materials and focuses on the capability to discriminate between topographical information and mechanical properties at both nanometer and atomic scales. The manuscript is organized as follows: a short technical introduction giving the basic concepts required to understand the main topics; two sections focusing on the study of soft materials and the procedures to obtain either topographical or mechanical information at the nanometer scale; and a final section dedicated to damping images recorded with contrast at the atomic scale.

## TECHNICAL BACKGROUND

Two modes of operation are used to record the change of the oscillating behavior when the tip interacts with a surface:

1. The amplitude modulation mode (AM),<sup>[1,3,4]</sup> often called *tapping mode* as a commercial name, where the tip-cantilever system is excited

at a fixed-driven frequency and a fixed-amplitude excitation. The main advantage is its ability to image polymers without producing the severe damage caused by contact mode.<sup>[3]</sup> Many works have been dedicated to studies on very soft samples<sup>[5–16]</sup> but, although the AM mode provides a convenient and easy way to image soft materials, quantitative analysis of the experimental data remains uneasy.<sup>[17–36]</sup>

2. The frequency modulation technique (FM), often called non-contact resonant mode.<sup>[2]</sup> The FM mode was first used experimentally under ultra-high vacuum conditions to image semiconductor surfaces. The concept is to use a negative resonant frequency shift at constant oscillation amplitude as the error signal to control the distance between the tip and the surface. The interaction between the tip and the surface remains attractive so that the tip never touches the surface. The key experimental achievement was the demonstration that the FM mode was able to obtain images with contrast at the atomic scale.<sup>[17,18]</sup> The experimental data that depend on the interaction between the tip and the surface are the resonance frequency variation and the damping signal extracted from the energy per cycle needed to supply in order to keep the oscillation amplitude constant. The frequency shift is related only to conservative interaction and the additional damping signal should be uniquely governed by the dissipative interaction.<sup>[21,35]</sup>

## Conservative Interaction

In the harmonic oscillator theory, any variation of the resonant frequency shift corresponds either to a change of the mass of the oscillator or to a change of an effective spring constant. For an AFM oscillator, a mass transfer is not expected; therefore, an effective spring constant taking into account the variation of the force interaction is responsible for the frequency shift. A

very general expression to describe the resonant frequency shift is:<sup>[28,33,36]</sup>

$$\Delta\nu = \nu_0 \left( \sqrt{1 + \frac{k_{\text{int}}^{\text{eff}}}{k_c}} - 1 \right), \quad (1)$$

where  $\nu_0$  is the resonant frequency without any interaction,  $k_{\text{int}}^{\text{eff}}$  is an effective spring constant describing change of the force interaction between the tip and the surface over a cycle, and  $\nu_0$  and  $k_c$  are the resonant frequency and cantilever spring constant respectively. The high sensitivity of commercially available electronics allows easy measurement of a weak effective spring constant. For example, with a cantilever spring constant  $k_c = 10 \text{ N m}^{-1}$ , effective spring constants less than  $k_{\text{int}}^{\text{eff}} \sim 10^{-3} \text{ N m}^{-1}$  can be readily measured.<sup>[4,24,31,36,37,38]</sup>

Only a few analyses were dedicated to the study of interaction when the tip goes inside the materials. This case is significantly more difficult to solve. It is primarily encountered in experimental situations where significant indentation depths occur, particularly studies on soft materials.<sup>[4,16,26,27,30,32,37]</sup>

### Dissipative Interaction: A Straightforward Result for Soft Materials with FM-Mode

In addition to conservative forces of the tip-sample interaction, dissipative interactions must also be considered, giving rise to additional energy losses during each oscillation period. Dissipation manifests itself as a hysteresis of force versus displacement curve. Dissipation mechanisms may involve electrical losses, time delays in viscoelastic materials,<sup>[16,28,33,38]</sup> or mechanical instabilities due to adhesion.<sup>[33,39]</sup>

The total damping coefficient writes:<sup>[25]</sup>

$$\gamma_{\text{tot}} = \gamma_0 + \gamma_{\text{int}}, \quad (2)$$

where  $\gamma_0 = m\omega_0/Q$  is the damping coefficient of the AFM oscillator without interaction between the tip and the surface,  $m$  is the effective mass of the oscillator, and  $Q$  is the quality factor. Typically, in vacuum,  $\gamma_0 = 2.10^{-9} \text{ N s m}^{-1}$ , with a cantilever stiffness  $k_c = 20 \text{ N m}^{-1}$ ,  $\omega_0/2\pi = 175 \text{ kHz}$ , and  $Q = 20,000$ . For an oscillation amplitude,  $A$ , of 10 nm the corresponding dissipated energy per period without interaction is  $\langle E_{\text{diss}}^0 \rangle = k_c \pi A^2 / Q \simeq 10^{-19} \text{ J}$ . In air,  $Q = 500$  and the dissipated energy becomes  $\langle E_{\text{diss}}^0 \rangle = k_c \pi A^2 / Q \approx 10^{-17} \text{ J}$ .

Writing  $\gamma_{\text{int}}/\gamma_0 = \langle E_{\text{diss}}^{\text{int}} \rangle_T / \langle E_{\text{diss}}^0 \rangle_T$ , the additional damping coefficient  $\gamma_{\text{int}}$  can be converted into the power dissipated. Thus, in ambient conditions, a damping increase of about  $10^{-19} \text{ J}$  can be measured

while, in vacuum at room temperature, it can be as low as  $k_B T$ .

### Imaging Soft Materials and the Influence of the Quality Factor

A key objective of the AFM is focused on the capability to record reliable topographic images of soft materials. In that part, we will show that such a goal could be achieved with a high-quality factor of the oscillating cantilever.

At the maximum of the oscillator sensitivity, the rate of the oscillation amplitude is proportional to the quality factor:

$$\frac{dA}{d\omega} \propto Q. \quad (3)$$

Therefore, when the mode with the amplitude variation is used, the sensitivity may simply be proportional to the quality factor. At this stage, it is useful to compare the static and dynamic mode.

In the static mode, when the microcantilever is brought to the surface, the slope of the deflection is (see Fig. 1):

$$p(\delta_c) = \frac{1}{1 + \frac{k_c}{k_s}}, \quad (4)$$

where  $k_s$  is the contact stiffness of the sample. For null-contact stiffness corresponding to a usual liquid, the denominator is infinite and, as expected when the sample does not have a mechanical response, the deflection slope is zero. When the surface is infinitely hard, the slope equals one and the cantilever deflection is strictly equals to the vertical motion. In this case, the image

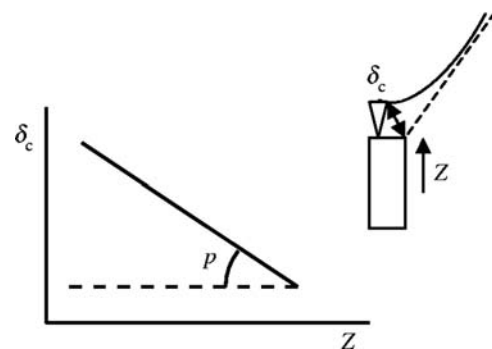


**Fig. 1** Scheme of the cantilever deflection  $\delta_c$  as a function of the vertical displacement,  $Z$ , of the surface. For dynamic mode the deflection  $\delta_c$  is replaced by the oscillation amplitude,  $A$ , and the slope  $p$  is different (see equation 4 and text below).

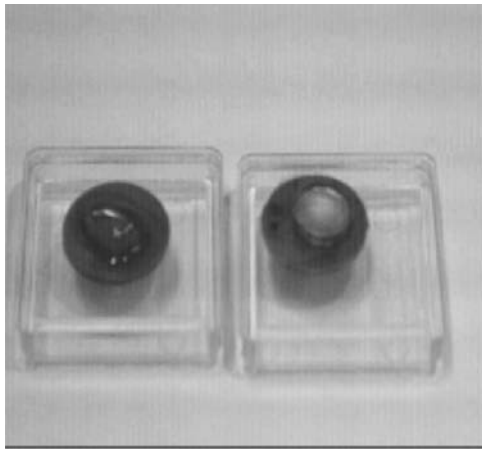


**Fig. 2** Drops of poly-isoprene melt deposited on an AFM sample holder. The left drop is a polymer of molecular weight  $M_w = 3.10^6$  Dalton. The right sample corresponds to a molecular weight  $M_w = 5.10^5$  Dalton. The relative low molecular weight has a repetition time sufficiently small that a small basin is required to prevent the flow of the sample.

corresponds to a true topography without containing any mechanical information.

For a soft sample, an evaluation of the sample contact stiffness is readily obtained as the product of the diameter of the contact area,  $\phi$ , between the tip and the sample and the elastic Young's modulus,  $G$ :  $k_s = G\phi$ . With a typical value for soft polymer,  $G = 1$ , MPa =  $10^6$  N m $^{-2}$ , and a contact diameter,  $\phi = 10^{-9}$  m,  $k_s = 10^{-3}$  N m $^{-1}$ . Usual stiffness values of microcantilever used in dynamic mode are

few tens of Newton per meter and, therefore, four orders of magnitude larger than that of a soft contact. This huge difference makes soft materials behave nearly like liquids.

In contrast, imaging soft materials becomes possible when the dynamic mode is used. One reason for this is that the contact sample stiffness is replaced by the product  $Qk_s$  instead of the contact stiffness  $k_s$  alone. The ratio in the denominator of the equation becomes  $k_c/(Qk_s)$ . Thus, for high-value quality factors, the ratio might be close to one and topographical images become easy to record. The quality factor enhances the influence of the repulsive interaction leading to an apparent and much larger contact stiffness. The slope of the variation of the oscillation amplitude  $p(A) = \delta A/\delta D$  becomes close to one, so that the amplitude modulation technique leads to an image of surface topography of a very soft sample.<sup>[15,27]</sup>

The investigation of a polymer melt, poly-isoprene, is a good experimental result showing the influence of the quality factor. Poly-isoprene behaves as a liquid at room temperature (Fig. 2); however, in vacuum, ( $10^{-7}$  Torr) where the contribution of the fluid viscosity goes to zero, giving a large quality factor,  $Q = 23,000$ , the apparent contact stiffness becomes sufficiently high that the soft surface of the polymer appears as hard as a silica surface.<sup>[15]</sup>

In Fig. 3, several approach curves displayed give the variation of the oscillation amplitude as a function of the vertical displacement of the surface. The experiments are made as follows: for a given oscillation

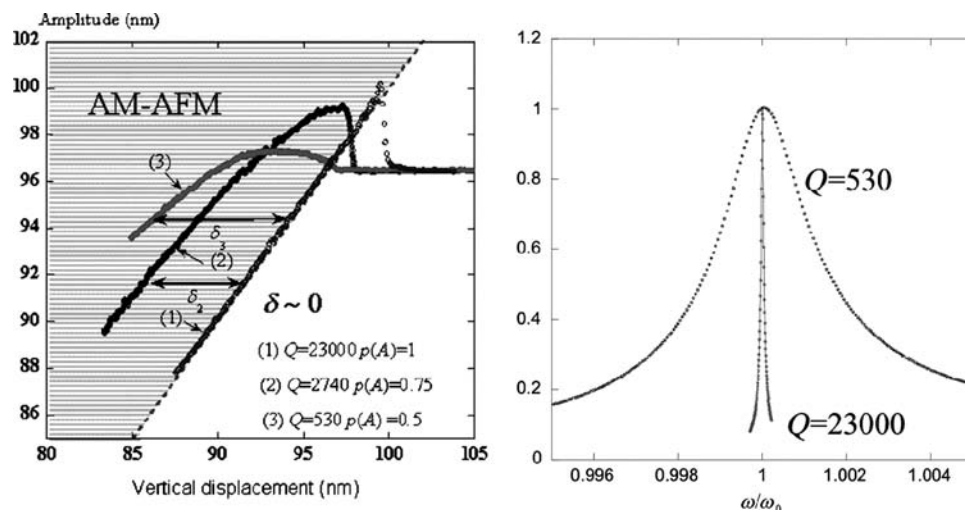


**Fig. 3** Approach curves showing the variation of the amplitude oscillation in AM-AFM as a function of the sample vertical location on a polymer melt: polyisoprene. At atmospheric pressure,  $Q = 530$ ; at 10 mbar (7.5 Torr),  $Q = 2740$ ; and at  $2 \times 10^{-7}$  Torr,  $Q = 23,000$ . The dash line is the location of the surface. The values,  $p(A)$ , are the slopes of the straight sections of the curves. Arrows show a maximum of indentation depth of  $\delta_3 = 8$  and  $\delta_3 = 6$  nm for  $Q = 530$  and  $Q = 2740$ , respectively. The resonance curve at atmospheric pressure and  $2 \times 10^{-7}$  Torr are shown in the right picture. Source: Adapted from EDP Sciences (see Ref.<sup>[15]</sup>).



amplitude, we record an approach curve at a fixed  $(X, Y)$  location on the surface. The approach curve is obtained by moving the sample along the vertical axis,  $Z$ , with a vertical displacement varying between 20 and 40 nm. In Fig. 3, the frontier domain between the polymer and vacuum or air is marked with a red dotted line. The blue part corresponds to the polymer melt domain. When the quality factor is very high ( $Q = 23,000$ ), the slope is equal to one, the tip is unable to penetrate the melt, and the indentation depth,  $\delta_s$ , is close to zero. As a consequence, whatever the reduction of the oscillation amplitude, the true topography of the polymer surface is recorded without any difficulty.

This very important point was the origin of the development of image on soft polymers. For example, among the first works was an investigation showing the surface reconstruction of copolymers.<sup>[5]</sup> In that work, Stocker et al. investigated the surface morphology of a symmetric poly(styrene-*block*-butadiene-*block* methyl methacrylate) triblock copolymer (PS-*b*-PB-*b*-PMMA). The tapping images are compared to the bulk morphology as determined by transmission electron microscopy (TEM). Fig. 4A shows the TEM image of the triblock copolymer. The triblock forms a lamellar morphology with a spatial period of  $42.7 \pm 0.5$  nm. The AFM experiments also show a lamellar morphology but with a spatial period of  $85 \pm 5$  nm, that is a period twice that found in the bulk (Fig. 4B). The AFM image mostly reveals topography information showing a surface reconstruction of the copolymer.

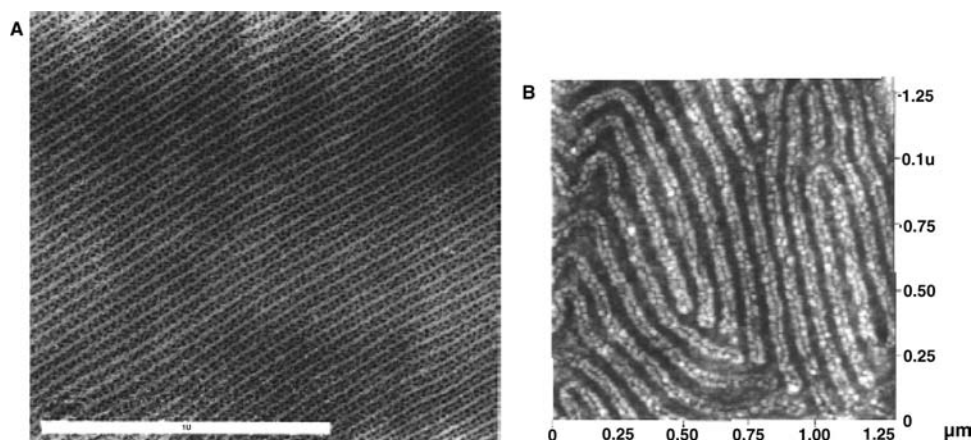


**Fig. 4** (A) Transmission electron micrograph of a triblock copolymer. The system forms a lamellar morphology. The polybutadiene (PB) spheres appear dark in TEM, while the polystyrene (PS) lamellae (gray) show a weak contrast with respect to PMMA lamellae (bright). The long period of the lamellar structure is  $42.7 \pm 0.5$  nm. The diameter of the PB spheres is 9 nm. Adapted from *Macromolecules*. 1996; 29: 7502–7507.<sup>[5]</sup> (B) AM-AFM image of solution cast films of the triblock copolymer. The image of  $1.3 \times 1.3 \mu\text{m}^2$  area shows the lamellar spherical morphology ( $z$  scale 7 nm). Comparison with the bulk morphology (Fig. 4A) illustrates that the surface morphology observed by AFM shows a long period that is doubled from  $42.7 \pm 0.5$  nm in the bulk to  $85 \pm 5$  nm at the surface. *Source*: Adapted from American Chemical Society (see Ref.<sup>[5]</sup>).

Also, dynamic modes were used extensively to investigate crystallization and melting processes.<sup>[13]</sup> In Fig. 5, Reiter et al. took advantage of the huge change of the viscoelastic properties during crystallization and melting of polyethylenoxide in 12 nm spheres of a block copolymer mesophase. The samples are annealed at a high temperature. These annealed samples did not crystallize at ambient conditions. Phase images are recorded for different times at  $-23^\circ\text{C}$ , where the melting happens at the temperature  $+40^\circ\text{C}$ . The phase images show that all the polymer spheres do not crystallize at the same time. The different times needed to develop crystalline spheres indicate that they do not have all the degree of polymer arrangement inside the sphere. In addition not all spheres melted at the same temperature. Therefore, these AFM experiments show that confined crystals have behavior different from those in bulk.

## NANO-RHEOLOGY: EXPERIENCE ON POLYMER MELT AND COPOLYMER

### Polymer Melt

Typical variations of the normalized damping signal versus the tip indentation are shown in Fig. 6A. Note that contrary to AM mode (Fig. 3), the FM mode, under the same vacuum conditions, allows an indentation depth of several nanometers. When the tip dips into the melt, the damping coefficient,  $\gamma_{\text{tot}}$ , becomes the sum of the intrinsic damping coefficient,  $\gamma_0$ , and of the

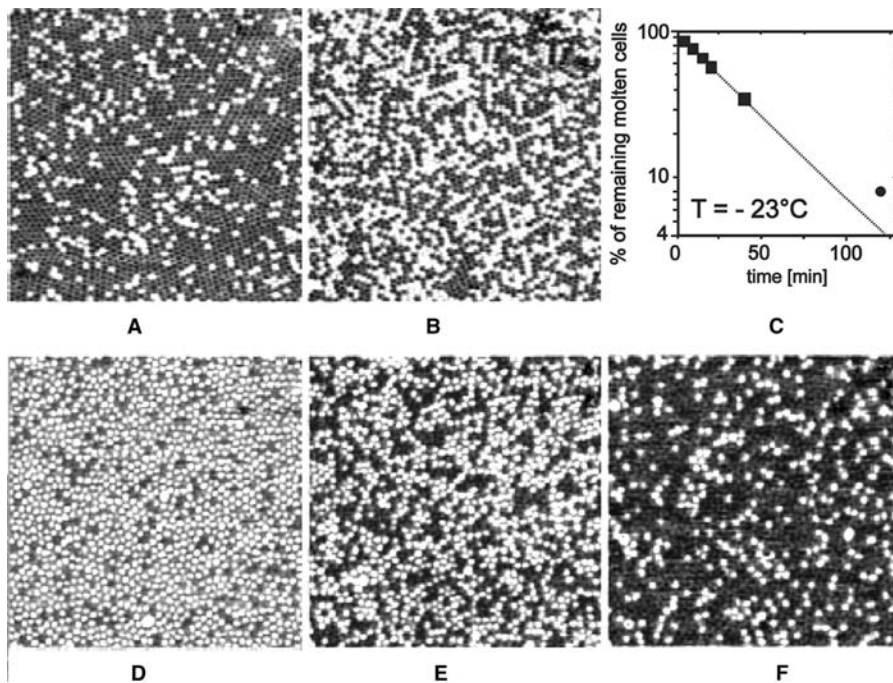


**Fig. 5** AM-AFM phase images ( $1 \times 1 \mu\text{m}^2$ ) showing the variation in the number and distribution of crystalline cells after crystallization of polyethyleneoxide at  $-23^\circ\text{C}$  for (A) 5 mn and (B) 15 mn. The inset (C) shows, on semilogarithmic scales, the percentage of remaining molten cells as a function of time. The line represents a fit of equation  $n = n_\infty[1 - \exp(-\tau)]$  yielding  $\tau = 35$  min. The sample after 120 min at  $-23^\circ\text{C}$  (D) was split into several pieces that were separately annealed for 2 min at  $39^\circ\text{C}$ , (E)  $42^\circ\text{C}$ , and (F)  $44^\circ\text{C}$ . Source: Adapted from American Physical Society (see Ref.<sup>[13]</sup>).

damping coefficient,  $\gamma_{\text{int}}$ , related to the additional dissipation. The damping coefficient,  $\gamma_{\text{int}}$ , is an explicit function of the indentation depth  $\delta$ ,  $\gamma_{\text{int}} = \gamma_{\text{int}}(\delta)$ . The damping curves show three domains (Fig. 6A). At a small indentation depth, the dissipation shows a smooth increase and then abruptly increases within a few Angströms variation. At a larger indentation depth, the last part of the curve again increases smoothly or exhibits a plateau-like behavior. A qualitative explanation of this irregular behavior is that the lower part of the curve corresponds to dissipation processes that involve only motion of segment chains with lengths smaller than the entanglement length. Then, the abrupt increase corresponds to an indentation that involves entanglements, and the last section includes contributions due to significant di-entanglements of the network.

A simple way to evaluate the time scale of the sample characteristic relaxation time is obtained by multiplying the experimental data by the power laws dependence,  $A^{3/2}$  and  $A^{5/2}$ .<sup>[16]</sup> The results are shown in Fig. 6B and C. When the experimental data are multiplied by  $A^{3/2}$ , the low parts of the curves, corresponding to the small indentations, gather together, showing that the relaxation times of the processes induced in the network are much faster than those of the contact times. When the experimental data are multiplied by  $A^{5/2}$ , all the abrupt increases of the dissipation align. Thus, by increasing the indentation depth a fraction of a nanometer, the relaxation processes switch from fast to slow relaxation times. At large indentation depths, the slow relaxation processes governed by the network prevail.

### Triblock Copolymers

The triblock copolymer is composed of two identical thermoplastic sequences of poly(methyl methacrylate), PMMA, attached to a central sequence of low  $T_g$  poly(isooctylacrylate). Spherical, cylindrical, and lamellar morphologies have been observed for block copolymers of increasing PMMA contents.<sup>[8]</sup> These systems exhibit phase-separation at the nanometer scale with a soft central part.<sup>[5,6,8,10]</sup>

The height image recorded in non-contact (Fig. 7A), or nearly non-contact situations, shows a perfect flat surface, according to previous tapping studies.<sup>[10]</sup> Therefore, the contrast observed on the damping image (Fig. 7B) corresponds only to different rheological properties between the two sequences of block forming the copolymer.

Typical resonance frequency shift and damping variations are reported in Fig. 8A and B.

In Fig. 8C, the variation of the dissipation contrast is shown as a function of the strength of the tip-sample interaction. The strength of the tip-sample interaction is monitored with the magnitude of the resonance frequency shift (Fig. 8A). The higher the frequency shift, the higher the damping contrast on the image.

### DAMPING IMAGES AT ATOMIC SCALE

In addition to the height and damping images of soft materials, the AFM dynamic modes were also able to produce dissipation maps with contrast at the atomic scale (Fig. 9). Measurements are usually recorded with

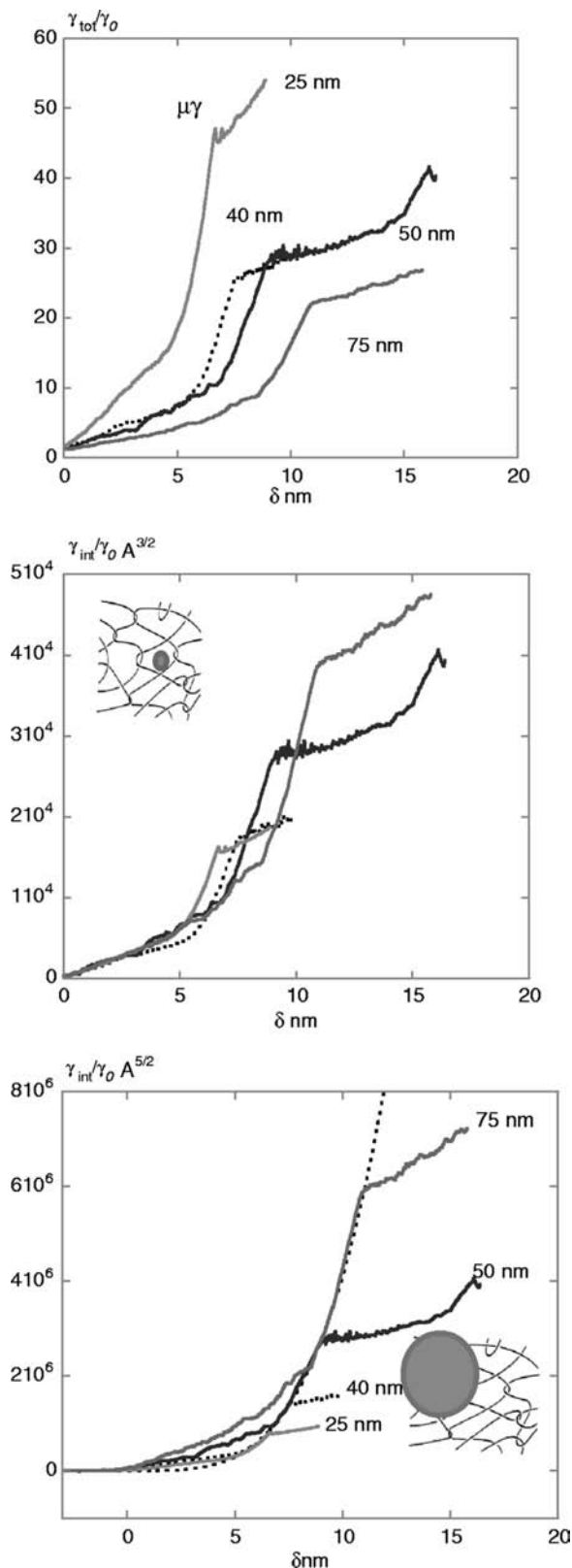


**Fig. 6** FM-AFM curves on a polymer melt. (A) Several damping curves recorded at different locations in the  $(X, Y)$  plane for four oscillation amplitudes 25, 40, 50, and 75 nm. In few cases, the curves show a dispersed behavior at the values of the indentation depth where the transition

cantilevers of resonance frequency between 150–300 kHz. Consequently, the experimental time when the oscillating tip interacts with the surface, about a microsecond, is much larger than the characteristic relaxation times expected at the atomic scale. To explain a possible slowing down of the dynamics at such small scales, numerous approaches were considered, such as stochastic resonance, dispersive soft mode of second-order phase transition, adhesion hysteresis, as well as exhaustive analysis of the stability of the AFM oscillator. At this moment, none of these analyses are sufficiently decisive to explain the atomic contrast of a dissipation image.

Leaving aside the numerous works and discussions concerning the experimental results showing damping image with contrast at the atomic scale in UHV conditions,<sup>[20]</sup> the FM mode should be the most convenient way to extract physical quantities. However, because of the use of a feedback loop to keep constant the oscillation amplitude, spurious effects are possible that may affect the damping contrast at the atomic scale or nanometer scale for soft materials.<sup>[10,41]</sup> In order to evaluate the instrumental contributions, two simple equations can be used to evaluate artifact damping and frequency variation. Eq. (5) gives the damping due to an abrupt change of the resonance frequency:

$$D_a \simeq \frac{1}{\omega_0} \left[ \frac{\omega}{Q} + \frac{1}{\omega_0} \frac{d\omega}{dt} \right]. \quad (5)$$

Eq. (5) gives the contribution of the machine to the damping coefficient without the need of the existence of dissipation processes when the tip interacts with the surface. The first term means that the damping coefficient, scaling as  $1/Q$ , is slightly modified because of the frequency shift. Typical relative variation of the frequency shift is  $10^{-4}$  and can be safely ignored. The second term rises when images, or approach retract curves, are nonadiabatically recorded. The damping signal is averaged over a time  $1/B$ , where  $B$  is the bandwidth of the electronic loop.<sup>[10,41]</sup>  $B$  is typically the kilohertz so that, with  $B\Delta t \sim 1$ , the contribution to the damping scales may be written as  $QB\Delta\omega/\omega_0^2$ . Assuming  $\omega_0 = 10^6 \text{ rd s}^{-1}$ , and  $Q = 10^4$ , gives a contribution

between the different regimes occurs. Whatever the location, the general features remains the same. At a given indentation depth, the variation of the oscillation amplitude induces change of the residence time into the polymer. A consequence is that the transition between the two regimes occurs at different indentation depths. (B) Same data as those shown in Fig. 6A with the y-axis multiplied by the power law  $A^{3/2}$ . (C) Same data as those shown in Fig. 6A with the y-axis multiplied by the power law  $A^{5/2}$ . Source: Adapted from *J. Phys.: Condens. Matter.* 2003; 15: 6167–6177. Ref.<sup>[16]</sup>

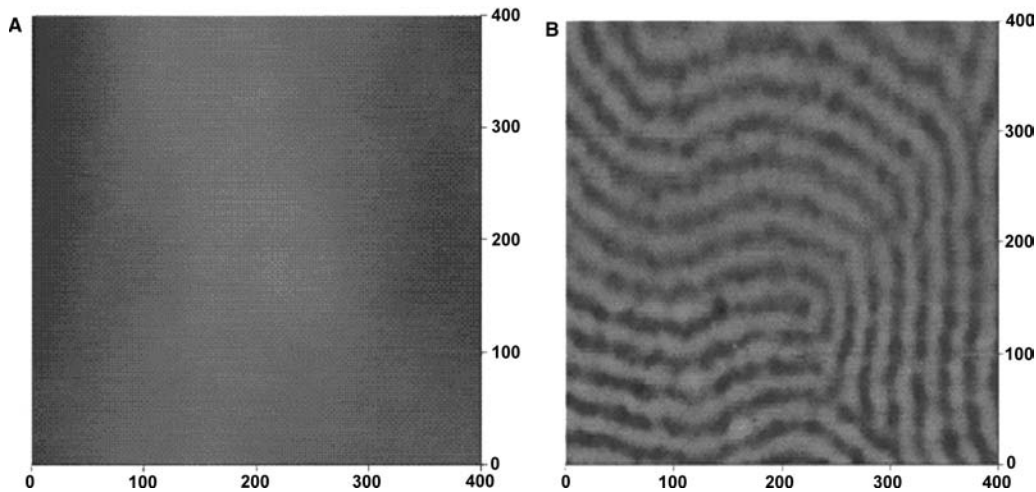


**Fig. 7** (A) FM-AFM height image recorded on a triblock copolymer composed of a central sequence of polymer melt and two sequences of glassy polymer. The image is recorded with a negative frequency shift.<sup>[10]</sup> (B) Corresponding damping image recorded simultaneously with the height image (Fig. 7A). The damping image shows the nanophase segregation.

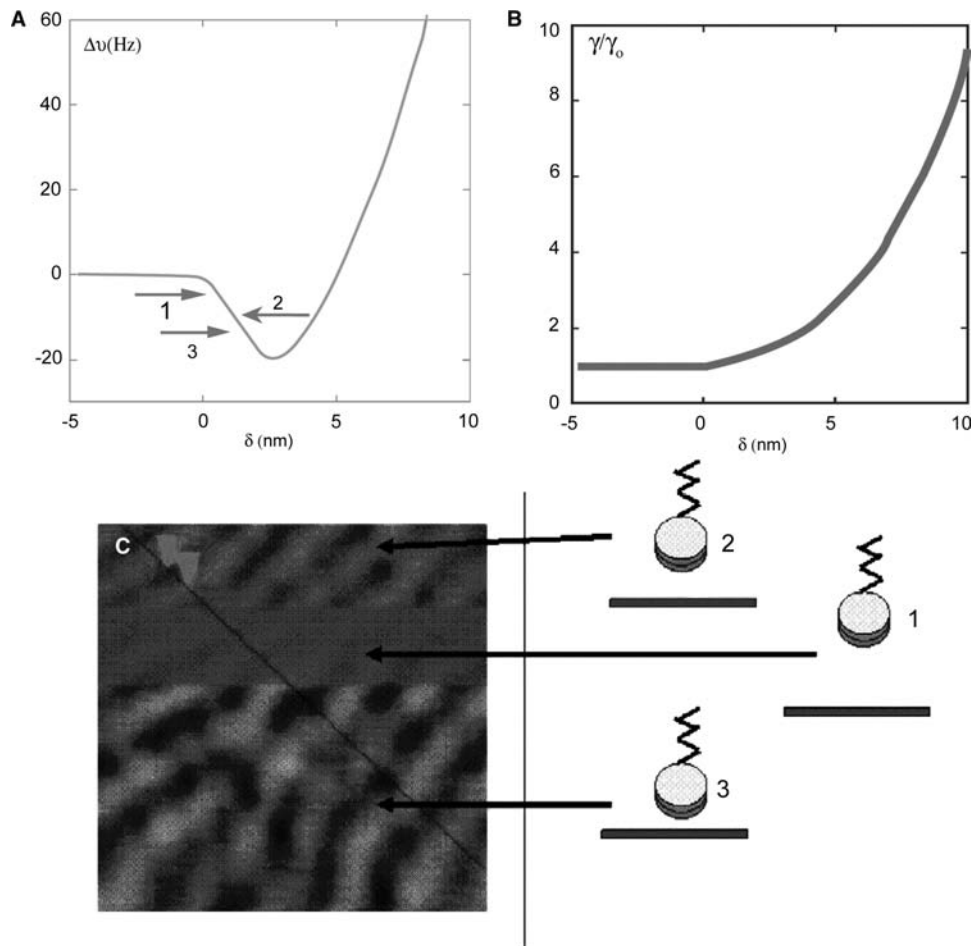


**Fig. 8** Frequency modulation data on triblock copolymers. (A and B) Resonance frequency shift (A) and damping (B) curves as a function of the tip indentation depth. The shift of the resonance frequency comes from a pure conservative interaction. The damping should only be issued from dissipative interaction (see paragraph III). The arrows indicate the different level of frequency shifts used to record the damping image in Fig. 8C. (C) Variation of the contrast on a damping image. The numbers refer to the magnitude of the resonance frequency shift shown in Fig. 8A. The larger the frequency shift, the smaller the distance between the tip and the surface. The interaction between the tip and the surface is strongly enhanced by increasing the amount of dissipated energy.



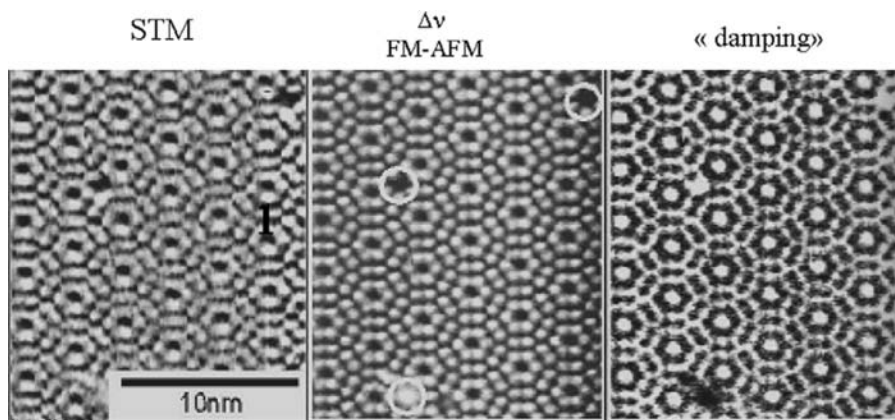


**Fig. 9** Height images of the reconstructed surface  $7 \times 7$  on silicon obtained with STM and FM-AFM apparatus. The third image is the damping image recorded simultaneously with height FM image. <http://www.physik.unibas.ch/>.

$10^{-5} \Delta\omega$ . Therefore, Eq. (5) says that instrumental contributions should always be negligible, provided the FM mode is perfectly set at the resonance frequency. However, as shown recently,<sup>[40]</sup> in a narrow domain of frequencies, the feedback electronic loop can induce unstable behavior. This unstable behavior leads to a strong enhancement of the damping signal, but such an instrumental contribution can be easily removed by varying the scan frequency.

Eq. (6) gives the frequency shift induced by the machine:

$$\frac{\omega - \omega_0}{\omega_0} = \frac{1}{2Q\omega_0} \frac{d \log A}{dt}. \quad (6)$$

Relative fast change of the oscillation amplitude only occurs over the bandwidth  $\omega_0/Q$ . Thus, a typical time interval is  $Q/\omega_0$  and we have  $\omega_0 dt \sim Q$ . In that time interval the relative change of the oscillation amplitude is approximately a few percent and, with  $\Delta\omega/\omega_0 - \Delta A/AQ^2$  for large  $Q$  values, the induced frequency shift remains negligible.

To summarize this section, despite the complexity of the machine, simple expressions are available that provide an unambiguous way to discriminate between contributions from the sample physical properties at the nanometer, or atomic scale, and those rising from the use of the feedback electronic loop.

## SUMMARY

When soft materials are investigated, despite a difference of several orders of magnitude between the sample contact stiffness and the cantilever stiffness, images with a true topography can be recorded with the amplitude modulation technique (tapping mode) and a high-quality factor. Using a high-quality factor is time consuming. Thus, an accurate knowledge of the true topography will always be obtained at the expense of time. However, when the FM mode is used with the same quality factor, the oscillating tip can

deeply penetrate the soft material. Therefore, the FM mode allows study of the mechanical response of the soft material, but is unable to provide accurate information on the topography.

Triblock copolymers provide good samples to illustrate the physical origin of the contrast in height and damping images. Despite the machine's complexity, simple equations are derived extracting the contribution of the AFM electronic so that contrasts at the local scale caused by the mechanical properties are qualitatively understood. However, a more quantitative analysis depends upon the difficult task of obtaining accurate knowledge of the tip size and shape that, in the field of the local probe method, are often poorly known at the nanometer scale.

## REFERENCES

1. Gleyzes, P.; Kuo, P.K.; Boccard, A.C. Bistable behavior of a vibrating tip near a solid surface. *Appl. Phys. Lett.* **1991**, *58* (25), 2989–2991.
2. Albrecht, T.R.; Grütter, P.; Horne, D.; Rugard, D. Frequency modulation detection using high- $Q$  cantilevers for enhanced force microscope sensitivity. *J. Appl. Phys.* **1991**, *69* (2), 668–673.
3. Zhong, Q.D.; Inniss, K.; Kjoller, K.; Elings, V.B. Fractured polymer/silica fiber surface studied by tapping mode atomic force microscopy. *Surf. Sci.* **1993**, *290*, L688–L692.
4. Garcia, R.; Perez, R. Dynamic atomic force microscopy methods. *Surf. Sci. Rep.* **2002**, *47*, 197–301.
5. Stocker, W.; Beckmann, J.; Stadler, R.; Rabe, J.P. Surface reconstruction of the lamellar morphology in a symmetric poly(styrene-block-butadiene-block-methyl methacrylate) triblock copolymer: A tapping mode scanning force microscope study. *Macromolecules* **1996**, *29*, 7502–7507.
6. Leclère, P.; Lazzaroni, R.; Brédas, J.L.; Yu, J.M.; Dubois, P.; Jérôme, R. Microdomain morphology analysis of block copolymers by atomic force microscopy with phase detection imaging. *Langmuir* **1996**, *12*, 4317–4320.
7. Magonov, S.N.; Elings, V.; Wangbo, M.H. Tapping-mode atomic force microscopy study of the near-surface composition of a styrene-butadiene-styrene triblock copolymer film. *Surf. Sci.* **1997**, *389*, 201–211.

8. Leclère, P.; Moineau, G.; Minet, M.; Dubois, P.; Jérôme, R.; Brédas, J.L.; Lazzaroni, R. Direct observation of microdomain morphology in “all-acrylic” thermoplastic elastomers synthesized via living radical polymerization. *Langmuir* **1999**, *15*, 3915–3919.
9. Konrad, M.; Knoll, A.; Krausch, G.; Magerle, R. Volume imaging of an ultrathin SBS triblock copolymer film. *Macromolecules* **2000**, *33*, 5518–5523.
10. Kopp-Marsaudon, S.; Leclère, P.; Dubourg, F.; Lazzaroni, R.; Aimé, J.P. Quantitative measurement of the mechanical contribution to tapping mode atomic force microscopy images of soft materials. *Langmuir* **2000**, *16*, 8432–8437.
11. Knoll, A.; Magerle, R.; Krausch, G. Tapping mode atomic force microscopy on polymers: Where is the true sample surface? *Macromolecules* **2001**, *34*, 4159–4165.
12. Dubourg, F.; Kopp-Marsaudon, S.; Leclère, P.; Lazzaroni, R.; Aimé, J.P. *Eur. Phys. J.E.* **2001**, *6*, 387–395.
13. Reiter, G.; Castelein, G.; Sommer, J.U.; Röttle, A.; Thurn-Albrecht, T. Direct visualization of random crystallization and melting in arrays of nanometer-size polymer crystals. *Phys. Rev. Lett.* **2001**, *87*, 226101–226104.
14. Nony, L.R.; Boisgard, R.; Aimé, J.P. DNA properties investigated by dynamic force microscopy. *Biomacromolecules* **2001**, *2*, 827–835.
15. Dubourg, F.; Aimé, J.P.; Couturier, G.; Salardenne, J. Apparent hardening of soft samples through Q factor change in AFM. *Europhys. Lett.* **2003**, *62* (5), 671–676.
16. Dubourg, F.; Aimé, J.P.; Marsaudon, S.; et al. Probing the relationship between the scales of space and time in an entangled polymer network with an oscillating nanotip. *J. Phys.: Condens. Matter* **2003**, *15*, 6167–6177.
17. Giessibl, F.J. Atomic resolution of the silicon (111)-(7 × 7) surface by atomic force microscopy. *Science* **1995**, *267*, 68–71.
18. Sugawara, Y.; Ohta, M.; Ueyama, H.; Morita, S. Defect motion on an InP (110) surface observed with non contact atomic force microscopy. *Science* **1995**, *270*, 1646–1648.
19. Kitamura, S.; Iwatsuki, M. Observation of 7 × 7 reconstructed structure on the silicon (111) surface using ultrahigh vacuum noncontact atomic force microscopy. *Jpn. J. Appl. Phys., Part 2* **1995**, *34*, L145–L148.
20. Lüthi, R.; Meyer, E.; Bammerlin, M.; et al. *Surf. Rev. Lett.* **1997**, *4*, 1025.
21. Lantz, M.A.; Hug, H.J.; van Schendel, P.J.A.; et al. Low temperature scanning force microscopy of the Si(111)-(7 × 7) surface. *Phys. Rev. Lett.* **2000**, *84*, 2642–2645.
22. Schwarz, A.; Allers, A.; Schwarz, U.D.; Wiesendanger, R. Dynamic-mode scanning force microscopy study of *n*-InAs(110)-(1 × 1) at low temperatures. *Phys. Rev. B: Condens. Matter Mater. Phys.* **2000**, *61*, 2837–2845.
23. Anczykowski, B.; Krüger, D.; Fuchs, H. Cantilever dynamics in quasicontract force microscopy: spectroscopic aspects. *Phys. Rev. B: Condens. Matter Mater. Phys.* **1996**, *53*, 15,485–15,488.
24. Boisgard, R.D.; Michel, D.; Aimé, J.P. Hysteresis generated by attractive interaction: oscillating behavior of a vibrating tip-microlever. *Surf. Sci.* **1998**, *401*, 199–205.
25. Cleveland, J.P.; Anczykowski, B.; Schmid, A.E.; Elings, V.B. Energy dissipation in tapping-mode atomic force microscopy. *Appl. Phys. Lett.* **1998**, *72*, 2613–2615.
26. Wang, L. Analytical descriptions of the tapping-mode atomic force microscopy response. *Appl. Phys. Lett.* **1998**, *73*, 3781–3783.
27. Nony, L.; Boisgard, R.; Aimé, J.P. Non linear dynamical properties of an oscillating tip-cantilever system in the tapping mode. *J. Chem. Phys.* **1999**, *111* (4), 1615–1627.
28. Dürig, U. Conservative and dissipative interactions in dynamic force microscopy. *Surf. Interface. Anal.* **1999**, *27*, 467–473.
29. Garcia, R.; San Paulo, A. Attractive and repulsive tip-sample interaction regimes in tapping-mode atomic force microscopy. *Phys. Rev. B: Condens. Matter Mater. Phys.* **1999**, *60*, 4961–4967.
30. Wang, L. The role of damping in phase imaging in tapping mode atomic force microscopy. *Surf. Sci.* **1999**, *429*, 178–185.
31. Aimé, J.P.; Boisgard, R.; Nony, L.; Couturier, G. Non-linear dynamic behavior of an oscillating tip-microlever system and the contrast at the atomic scale. *Phys. Rev. Lett.* **1999**, *82* (17), 3388–3391.
32. San Paulo, A.; Garcia, R. Tip-surface forces, amplitude, and energy dissipation in amplitude-modulation (tapping mode) force microscopy. *Phys. Rev. B: Condens. Matter Mater. Phys.* **2001**, *64*, 193411–193414.
33. Dürig, U. Interaction sensing in dynamic force microscopy. *New J. Phys.* **2000**, *2*, 5.1–5.12.
34. Stark, M.; Möller, C.; Müller, D.J.; Guckenberger, R. From images to interactions: High-resolution phase imaging in tapping-mode atomic force microscopy. *Biophys. J.* **2001**, *80*, 3009–3018.
35. Hölscher, H.; Schwarz, A.; Allers, W.; et al. Quantitative analysis of dynamic-force-spectroscopy data on graphite (0001) in the contact and noncontact regimes. *Phys. Rev. B: Condens. Matter Mater. Phys.* **2000**, *61*, 12678–12681.
36. Giessibl, F.J. Forces and frequency shifts in atomic-resolution dynamic-force microscopy. *Phys. Rev. B: Condens. Matter Mater. Phys.* **1997**, *56*, 16010–16015.
37. Boisgard, R.; Aimé, J.P. Surface mechanical instabilities and dissipation under the action of the oscillating tip. *Surf. Sci.* **2002**, *511*, 171–182.
38. Dietzel, D.; Marsaudon, S.; Aimé, J.P.; et al. Mechanical properties of a carbon nanotube fixed at a tip apex: A frequency-modulated atomic force microscopy study. *Phys. Rev. B: Condens. Matter Mater. Phys.* **2005**, *72*, 035445–035460.
39. Ferry, J.D. Apple pie. In *Viscoelastic Properties of Polymer*; Sriggant, D., Ed.; Wiley: New York, 19803rd ed..
40. Couturier, G.; Boisgard, R.; Dietzel, D.; Aimé, J.P. Damping and instability in non-contact AFM: contribution of the instrument. *Nanotechnology* **2005**, *16*, 1346–1353.
41. Gauthier, M.; Pérez, R.; Arai, T.; et al. Interplay between nonlinearity, scan speed, damping, and electronics in frequency modulation atomic-force microscopy. *Phys. Rev. Lett.* **2002**, *89*, 146104–146107.



# Stability of Nanostructures on Surfaces

**Karsten Pohl**

*Department of Physics, University of New Hampshire,  
Durham, New Hampshire, U.S.A.*

## INTRODUCTION

Self-assembly of ordered structures, a few nanometers wide, has been observed on many interfaces critical to new nanotechnologies. They are thought to arise because of a delicate balance between long-range strain field interactions and short-range chemical forces that stabilizes these structures. However, a detailed understanding of the driving forces does not exist. In this article, I will show how to identify and control these interactions that have the potential to surpass standard patterning technologies and thus, to lead the way to higher density magnetic storage, more selective catalytic materials, higher sensitivity chemical sensors, and perhaps, quantum computers. Well-ordered networks of misfit dislocations that form in monolayer-high strained metal films can be used as templates to grow two-dimensional nano-arrays of large-scale order and size uniformity in thermal equilibrium. Unique real-time measurements of the dynamics of self-assembled nano-arrays grown on silver and copper films on Ru(0001) and other metal surfaces using a variable-temperature scanning tunneling microscope (STM) will be presented. The results will guide the development of new dynamic models to describe the evolution of nanoscale structures on surfaces.

In particular, vacancy islands formed during room-temperature (RT) exposure to sulfur of a submonolayer Ag film on Ru(0001) order spontaneously to form a triangular lattice at an island area fraction just above 20%. A normal mode decomposition of the thermal vibrations of this vacancy island crystal, measured with time-resolved scanning tunneling microscopy, obtains Lamé coefficients in the range of  $10^8$  (N/m<sup>2</sup>). I will show that these estimates are consistent with stabilizing forces derived from long-range elastic interactions between the islands.

## BACKGROUND

Many observations of self-organized structures at surfaces with well-defined periodicities of 1–10 nm have recently been reported.<sup>[1–10]</sup> Self-assembly of nano-clusters has been seen in a wide variety of systems,

including surface dislocation arrays, surface alloys, metal oxides surfaces, and semiconductor quantum dots and wires. It is expected that these structures find application in higher density magnetic storage,<sup>[11–13]</sup> more selective catalysis and higher-sensitivity chemical sensors,<sup>[14]</sup> and, perhaps, nanoscale computing. It is commonly accepted that a delicate balance between long-range strain field interactions and short-range chemical forces stabilizes these structures. However, an understanding of the fundamental mechanism of self-assembly that is necessary to control the formation and stability of nanostructures does not exist. Novel experiments to identify the ordering forces of self-assembly in strained metal films to advance our basic understanding of this fascinating phenomenon have recently been performed. One particular example is the phonon analysis of the thermal vibrations in nano-arrays that is able to reveal the nanoscale interactions, just as neutron scattering is being used to measure the atomic interactions.

The technological quest for ever smaller, faster, brighter, and longer-lived in the development of electronic, magnetic, and photonic devices imposes increasingly stringent requirements on the quality of heterostructures used in commercial applications. All of these objectives are more or less directly related to an overall device miniaturization, resulting in a growing importance of surfaces, interfaces, and thin films as surface-to-volume ratios increase. Key to the advancement toward new materials is the ability to control atomic-scale growth processes precisely enough to achieve atomically smooth interfaces between dissimilar (mismatched) materials. Lattice and chemical mismatch produces stressed interfaces, significantly altering the growth properties of thin films, causing defect formation at the interface and ultimately, rough growth. Stress is also of central importance in fabricating ordered interface structures. All of this led to an immense amount of information being collected about epitaxial growth over the past decades.<sup>[15,16]</sup> Until recently, the experimental observations of surface dynamics lagged far behind the theoretical understanding. However, the arrival of new microscopes, especially scanning tunneling microscopy (STM) and low-energy electron microscopy (LEEM), which

provide the ability to observe the evolution of individual atoms and nanoscale structures in real-time, finally allowed most of the classical theories to be tested.

The physical and chemical properties of low-dimensional structures depend on their size and shape, and are in general very different from those of bulk matter. If, at least, one dimension of such structures is small enough that quantum-mechanical effects become important, their electronic, magnetic, and catalytic behavior is particularly fascinating and of great technological interest.<sup>[17]</sup> Examples of such nanoscale structures, which lie in size between atoms and solids, are clusters, ultrathin films, macromolecules, and polymers. Most of these structures are grown on crystalline surfaces. However, the controlled fabrication of such nano-arrays with reproducible properties is a serious challenge, and surface physics has to play a key role in the understanding of their formation and their characterization.

Nanofabrication efforts involving mechanical means such as lithography or standard deposition techniques have been consistently inferior to what is typically desired for most applications. Intense interest has been directed toward nanostructures that can fabricate themselves, i.e., self-assemble. There is compelling evidence that natural processes, such as the formation of regular strain-relief structures at surfaces, can be exploited to yield nanostructure arrays of unprecedented regularity. High-technology methods used in reduction of feature sizes may thus be supplanted by simple and elegant patterning techniques.<sup>[18–22]</sup> One illustrative example is the spontaneous organization of three-dimensional (3-D)  $\text{Si}_{0.25}\text{Ge}_{0.75}$  islands on a strained  $\text{Si}(001)$  surface. By observing island nucleation on  $\text{Si}(001)$ , in which  $\text{SiGe}$  islands were imbedded, Tersoff, Teichert, and Lagally<sup>[8]</sup> found strong evidence that the subsequent formation of islands at the surface is determined by the strain due to these buried islands, with nucleation occurring at each local minimum in misfit, i.e., the imbedded islands act as a template for additional island nucleation. In general, growth of a thin film on a dissimilar substrate results in a strained interface as a result of the lattice mismatch between the two materials. The strain is often partially relieved through the formation of well-ordered networks of misfit dislocations. These dislocations networks typically self-assemble into arrays with a 3-to 25-nm spacing.<sup>[23,24]</sup> The herringbone reconstruction of  $\text{Au}(111)$  is an example of how an ordered misfit dislocation network can also form on a clean surface: terminating a  $\text{Au}$  crystal in a  $(111)$  surface leaves the top layer in compression by 4% with respect to the layers below, resulting in this well-known reconstruction.<sup>[25–27]</sup> The  $(111)$  surface of platinum exhibits a similar reconstruction.<sup>[28,29]</sup> Reconstructed surfaces or lattice mismatch systems can serve

as templates for the growth of mesoscopic-scale structures of large-scale order and size uniformity.

In our study on such naturally strained silver films on the  $(0001)$  surface of ruthenium at Sandia National Laboratories, we showed how to combine interfacial stress and corrosion to create a self-ordered nanolattice of unprecedented size and regularity.<sup>[30,31]</sup> A perfectly ordered triangular 2-D lattice of vacancy islands, 25 Å across and 53 Å apart, was formed when a single monolayer of  $\text{Ag}$  on  $\text{Ru}(0001)$  is exposed to

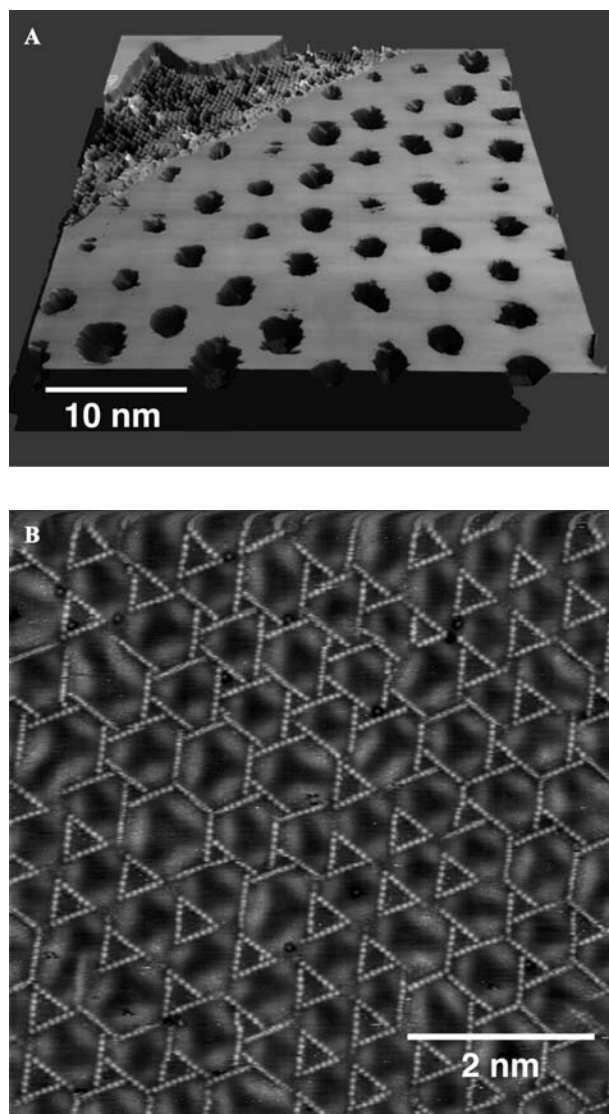


**Fig. 1** Nanoscale self-assembly: (A) STM image of the vacancy island lattice that forms when a monolayer of  $\text{Ag}$  on  $\text{Ru}(0001)$  is exposed to sulfur. (B)  $73 \times 69 \text{ \AA}^2$  STM image of a dislocation array that forms when a strained, two-atom high  $\text{Cu}$  film (dark) on  $\text{Ru}(0001)$  is exposed to sulfur. The individual sulfur atoms appear bright in the image. The Shockley partial dislocations (bright curved regions) form in areas where the  $\text{Cu}$  film is not in registry with the  $\text{Ru}$  substrate.

sulfur at room temperature in ultrahigh vacuum (UHV) Fig. 1A. Another example of our recent work is the formation of self-organized structures of adsorbed sulfur on a dynamically responding strained copper layer, 2 atoms thick, on Ru(0001), shown in Fig. 1B. Highly regular hexagons and equilateral triangles composed of 18 sulfur adatoms are self-assembling at room temperature.<sup>[32]</sup> In both ordered nanosystems, we observed large thermal fluctuations in the arrays from one STM image to the next, taken 1 min apart, which led to the assumption that these structures are in thermodynamic equilibrium.<sup>[31]</sup> For movies of the data, please visit <http://www.nano.unh.edu>.

The great potential of this template approach is that the feature sizes should be tunable according to a basic model for the elastic interaction between vacancy islands. It is generally believed that these structures arise from a balance between short-range attractive forces and long-range repulsive forces.<sup>[33–39]</sup> On surfaces, the short-range chemical interatomic attraction between near neighbors counterbalances the long-range, substrate-mediated elastic repulsion between steps. According to these recent theories, a very important prediction is that the free energy of a surface that is composed of two separate phases can always be lowered by assembling into such patterns. The structure of the pattern depends on the surface area fraction of each phase. We have considered a simple model that can account for the spontaneous formation of the Ag island array and provide a direct connection between the magnitude of the forces and the elastic constants.<sup>[37,38]</sup>

The model has two basic ingredients: 1) The line tension  $\gamma_b$ , i.e., the energy per unit length of the vacancy island edges, expressing the cost of reducing the local coordination of edge atoms. It favors the formation of few large islands. For vacancy islands on Ag(111), one obtains  $\gamma_b \approx 0.1 \text{ eV}/\text{\AA}$ .<sup>[40]</sup> 2) An effective repulsive interaction,  $\gamma_d$ , between neighboring island edges, driven by elastic relaxations in the Ag adlayer and in the Ru substrate. It favors the formation of many small islands. At low area fraction of single vacancies, the lowest energy structure in this model is a hexagonal crystal of near-circular vacancy islands of sharply distributed radius,  $R$ , and repeat distance,  $b$ . These predictions agree qualitatively with our observations. For that model, one readily arrives at the relation

$$\gamma_d = \sqrt{3}(\lambda + \mu)b^2/(\pi R) \quad (1)$$

by assuming that an energy increase due to an isotropic expansion of the lattice unit cell is stored as elastic energy.  $\mu$  and  $\lambda$  are the Lamé constants of the lattice

( $\mu + \lambda$  is the bulk modulus and  $\mu$  is the shear modulus). The complete phase diagram for this model has been analyzed.<sup>[38]</sup> In particular, it predicts the existence of a critical area fraction,  $f_c \approx 0.29$ , at which the hexagonal array of round islands converts to a regular arrangement of parallel stripes and, at  $f_c \approx 0.72$ , transforms back to a hexagonal array but of inverted islands. A beautiful observation of this predicted phase sequence has been recently reported by Plass, Bartelt, and Keliogg<sup>[41]</sup> in a LEEM study of Pb on Cu(111) at elevated temperatures. To assess the feasibility of elastic forces as the root of stable self-organized behavior, one can employ continuum elasticity considerations<sup>[42]</sup> and relate  $\gamma_d$  directly to the stress field around each island as determined by the elastic constants of the substrate and the difference in the surface stress between Ag and Ru regions, ( $\sigma_{\text{Ag}} - \sigma_{\text{Ru}}$ ):

$$\gamma_d \approx (1 - \nu)(\sigma_{\text{Ag}} - \sigma_{\text{Ru}})^2/(2\pi\varepsilon) \quad (2)$$

where  $\nu$  and  $\varepsilon$  are Poisson's ratio and the bulk or Young modulus of the substrate, respectively.

Measurement of the Lamé constants of a 2-D lattice and its feature size and repeat distance yields the strength of the elastic interaction  $\gamma_d$  governing its ordering, by Eq. (1). From this estimate, one can derive the difference in surface stress between the adlayer and the substrate by using Eq. (2), and compare them to independent estimates for other surfaces.<sup>[42]</sup> Therefore, the formation of self-organized pattern could also be used to measure surface stresses.

A main objective of this report is to put these theories to a test, by identifying the forces that form and stabilize self-assembling nanostructures. The experiments described in the following section are designed to measure the dynamics of 2-D nanostructures grown at lattice-mismatched interfaces under various stress conditions. In the next section, I will briefly review the original dynamic approach of determining the Lamé constants of a nano-array by measuring the thermal vibrations of the 2-D lattice of vacancy islands, which allow us to identify the elastic long-range interactions responsible for the observed self-assembly. I will apply this approach to other strained heteroepitaxial interfaces, which may serve as natural templates in the formation of self-assembled nanostructures.

## EXPERIMENTAL APPROACH

The experiments outlined probe the fundamental mechanism of self-assembly of Ag vacancy islands on Ru(0001) by relating the dynamics of the observed

structures to the ordering forces of the ordered nanoscale structure. The approach is unique in the way it uses a combination of *real-time imaging techniques* to study the *elastic properties* of these low-dimensional features, which are otherwise inaccessible.

A clean Ru(0001) surface was prepared in UHV after an initial brief argon sputtering, by repeated oxygen adsorption and flash desorption at 1800 K, and monitored by Auger electron spectroscopy and a room-temperature STM. Micron-wide terraces, separated by monatomic steps, can be typically obtained on this Ru surface. Slightly less than 1 monolayer ( $\sim 0.8$  ML) of Ag was deposited at RT on the prepared Ru surface by evaporation from a resistively heated tungsten basket, at a rate of about  $10^{-2}$  ML/sec as estimated from Auger Electron Spectroscopy (AES) and inspection of STM images. Subsequent flash annealing to 750 K produces a single atomic height film of Ag with the highly ordered equilibrium dislocation pattern shown in Fig. 2A. This structure consists of a network of surface edge dislocations that relieve the local strain induced by the 6.6% lattice mismatch between Ag and Ru.<sup>[43]</sup> In the darker regions in Fig. 2A, Ag atoms reside at bridge sites. These regions nest a pair of surface edge dislocations, the cores of which form a near-square array with a unit cell of about  $40 \times 60 \text{ \AA}$ . In the bright regions, the Ag adlayer is pseudomorphic with the Ru substrate, and thus considerably strained. Presumably, both dark and bright regions are locally highly reactive. We exposed this strained Ag film to sulfur at RT. Sulfur is evaporated from a solid-state electrochemical doser.<sup>[44]</sup> The typical dosing rate was about  $5 \times 10^{-3}$  ML/sec at a background pressure of  $5 \times 10^{-10}$  Torr. Sulfur exposure estimates were based on partial pressure measurements, and S coverages were estimated from Auger spectroscopy and STM images.

In the first stages of the reaction, sulfur etches the region around the cores of the dislocations in the Ag film, forming highly mobile, isolated vacancy islands of monatomic depth, about  $34 \text{ \AA}$  ( $\pm 11 \text{ \AA}$ ) in diameter Fig. 2B. While isolated, these islands are significantly more mobile than has been observed for diffusion of homoepitaxial vacancy islands of similar size on metal(111) surfaces.<sup>[45]</sup> Hopping seems to occur between nearest-neighbor (NN) grid positions defined by the dislocation network, corresponding to an effective island hop rate of about  $0.1 \text{ sec}^{-1}$  at RT. When islands meet, they often form stable clusters of two or more islands, about  $50 \text{ \AA}$  apart, which eventually dissociate, as illustrated in Fig. 2B. Strong short-range repulsions between islands in a cluster seem to prevent them from coalescing. This high mobility suggests that the surface configuration is equilibrated. Atomic resolution images of the islands reveal ordered 2-D sulfur clusters coating the exposed Ru. The sulfur adatoms

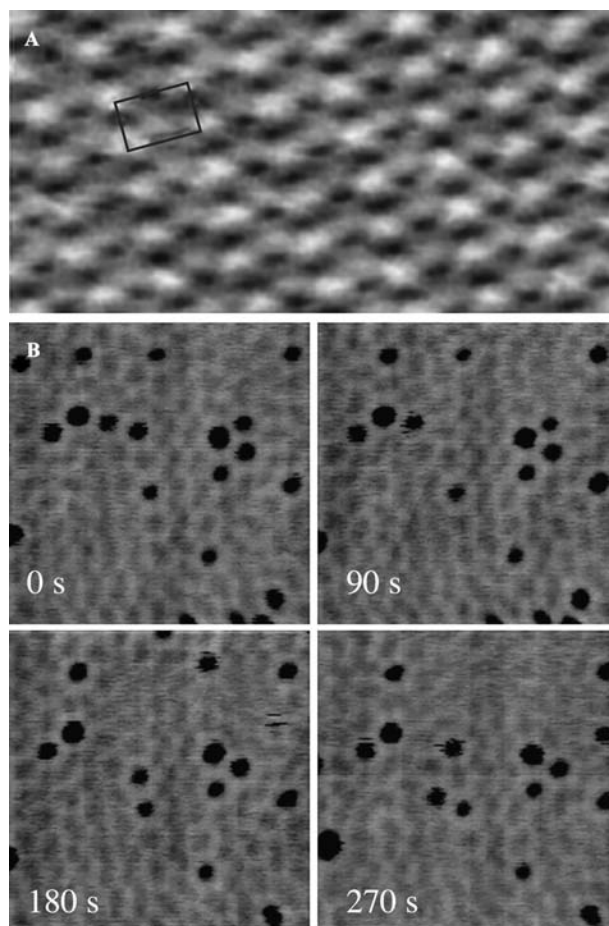


**Fig. 2** Dilute gas of vacancy islands: (A)  $400 \times 200 \text{ \AA}^2$  STM image of the misfit dislocation structure of the annealed submonolayer Ag/Ru(0001) film. (B) Sequence of STM images of the same  $500 \times 500 \text{ \AA}^2$  area after exposure to 0.04 ML of sulfur at RT. Dark depressions are 1-atom deep vacancy islands in the Ag film.

form a  $p(2 \times 2)$  structure, as observed in previous sulfur-on-Ru(0001) adsorption experiments. The presence of sulfur covering the Ru regions is not surprising because it lowers their surface free energy and forms a strong S–Ru bond.

With increasing sulfur coverage, the densities of vacancy islands, and self-assembled clusters of islands, increase and the average size of individual islands decreases slightly (to  $2R \approx 24 \text{ \AA}$  average diameter). For sulfur coverages close to 0.1 ML, a highly ordered triangular lattice of vacancy islands forms, with period of  $b \approx 53 \text{ \AA}$  and a feature density of  $10^{14} \text{ cm}^{-2}$  (Fig. 3). The Fourier transform of this 2-D crystal obtains a sharp sixfold diffraction pattern. The distribution of island sizes is also extremely narrow. The width of the distribution of island diameters,  $\pm 4 \text{ \AA}$  (assuming near-circular islands), is comparable to the imaged width of the island edges. We find a few defects in



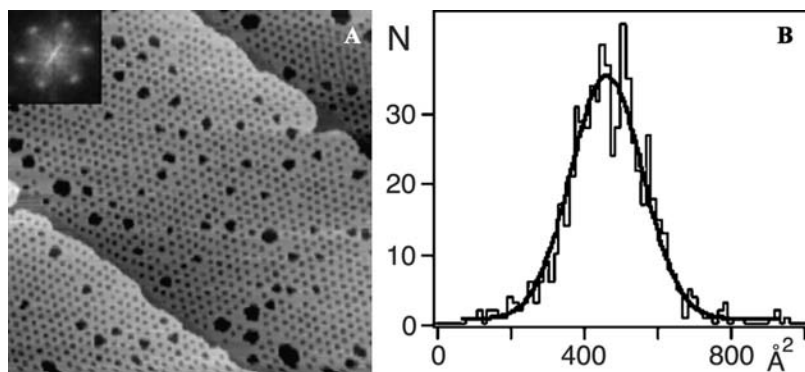


**Fig. 3** Triangular vacancy island lattice: (A)  $2000 \times 2000 \text{ \AA}^2$  STM image of the 2-D vacancy island crystal. Three ruthenium terraces are shown; again, the holes appear dark. The high order of the lattice can be seen in the sharp diffraction pattern of the image, shown in the inset. (B) Size distribution of the vacancy islands:  $N$  is the number of islands and the solid line is the gaussian fit. The average area is  $(462 \pm 117) \text{ \AA}^2$ .

the crystal, mostly larger vacancy islands ( $\sim 50 \text{ \AA}$  in diameter and density of  $\sim 2 \times 10^{-5}$  islands/ $\text{\AA}^2$ ), which we observed to form by accretion of two or more individual islands during larger amplitude vibrations. The range of perfect ordering is only limited by the terrace width.

Fig. 4(A) and (B) shows another STM image of the vacancy island lattice in Ag film on Ru. Taking a sequence of images 20 sec apart revealed that the holes

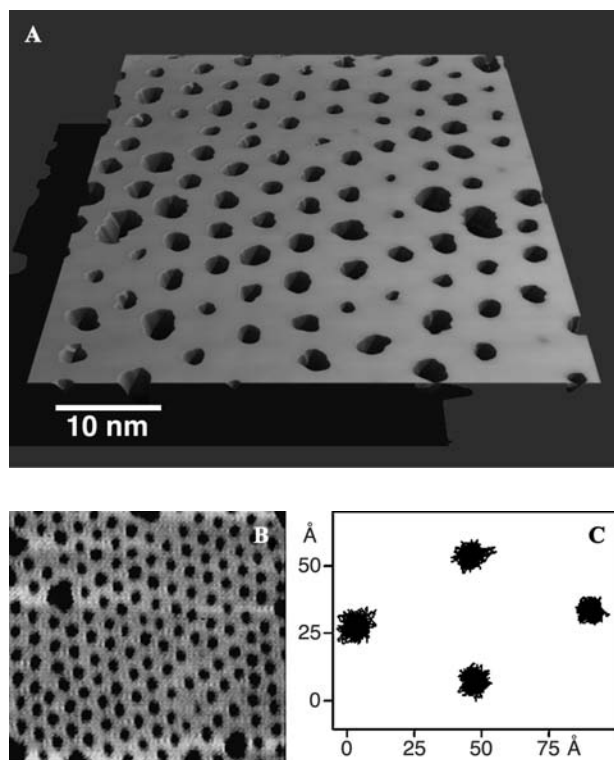


**Fig. 4** Thermal vibrations of 2-D nano-array: (A) and (B)  $700 \times 640 \text{ \AA}^2$  STM image of the 2-D vacancy island lattice. (C)  $x$ - and  $y$ -components of the center-of-mass trajectory of four nearest neighbor islands, taken from a sequence of 690 frames, 20 sec apart. About 80 islands were simultaneously tracked.

are moving collectively at room temperature. The trajectories of four hole centers are shown in Fig. 4C. The thermal motion of the holes is clearly correlated and caused by random Ag atom diffusion. These islands vibrate around their equilibrium positions in a manner similar to atomic vibrations, or phonons, in a harmonic crystal. The amplitude of the harmonic hole motion is determined by the force between the holes holding the 2-D lattice together. One can think of the nano-lattice as an elastic solid with a shear and a bulk modulus. These elastic constants of the 2-D lattice can be determined from a normal mode analysis of the  $\mathbf{q}$ -dependence of the vibrations in the same way as performed for bulk phonons for decades. We determined the amplitude of the longitudinal and transversal phonon modes of the 2-D lattice, by thermally averaging the Fourier transform of many images. Nelson and Halperin<sup>[46]</sup> and Huse<sup>[47]</sup> give the expressions that relates these amplitudes to the Lamé constants  $\mu$  and  $\lambda$  :

$$\begin{aligned} \text{longitudinal mode } \langle u_L(q)u_L(-q) \rangle / A &= \frac{k_B T}{q^2 \mu} \\ &\times \left( 1 - \frac{\mu + \lambda}{2\mu + \lambda} \right) \end{aligned} \quad (3)$$

$$\text{transversal mode } \langle u_T(q)u_T(-q) \rangle / A = \frac{k_B T}{q^2 \mu}$$

$u(q)$  is the Fourier transform of the center-of-mass displacements of the vacancy islands that are directly taken from STM movies,  $\langle \dots \rangle$  denotes an ensemble average,  $A$  is the system area,  $T$  is the temperature, and  $k_B$  is the Boltzmann constant. The data showing the thermal vibrations of the Ag/Ru nano-lattice are available electronically at <http://www.nano.unh.edu>.

For a perfectly ordered  $6 \times 6$  vacancy island cell, and the smallest nonzero  $q = 4\pi/(10\sqrt{3}b) \approx 0.14 \text{ nm}^{-1}$ , we estimate  $\lambda/c \approx \mu/c \approx 10^8 \text{ (N/m}^2\text{)}$ . Here,  $c \approx 4 \text{ \AA}$  is the vertical lattice spacing of the Ag/Ru(0001) film, and is introduced to facilitate comparison with bulk values (notwithstanding major

differences in the physics underlying phonon behavior in a crystal of atoms and thermal fluctuations in our island crystal). Typically, one finds significantly larger values for the bulk quantities,  $\lambda_{\text{bulk}} \approx 10^{11}$  (N/m<sup>2</sup>) and  $\mu_{\text{bulk}} \approx 10^{10}$  (N/m<sup>2</sup>), reflecting the fact that the long-ranged ordering forces of the vacancy island lattice are much weaker than the forces ordering atomic crystals (which is no surprise!).

We found that these estimates were consistent with stabilizing forces derived from long-range elastic interactions between islands.<sup>[42]</sup> Putting the just-measured values for  $\mu$  and  $\lambda$  as well as  $b \approx 53$  Å and  $R \approx 12$  Å in Eq. (1), we obtain  $\gamma_d \approx 0.2$  eV/Å. Assuming  $\nu_{\text{Ru}} \approx 0.5$  and  $\varepsilon_{\text{Ru}} \approx 10^{10}$  N/m<sup>2</sup>, similar to those of other elemental metals, the estimate of  $\gamma_d$  according to Eq. (2) implies  $(\sigma_{\text{Ag}} - \sigma_{\text{Ru}}) \approx 0.4$  eV/Å<sup>2</sup>. This is within the range of  $\sigma$  values reported for unreconstructed metal(111) surfaces,<sup>[42]</sup> providing confidence in our central estimate of  $\gamma_d$ . In summary, we were able to quantify the influence of the individual units of the array on each other's positions to probe the strength and physical origin of the underlying interactions and ultimately describe the equation of motion of a self-organized nano-array.

## OUTLOOK

So far, this powerful method has only been applied to this particular system, and we are currently attacking the problem of self-assembly by systematically measuring the phonon spectra in a variety of self-organizing nanostructures and determine their ordering forces. Performing these experiments at various temperatures will enable us to probe the stability and the thermodynamic properties of the 2-D arrays in a way that has not before been achieved.

A just-completed custom-designed, variable-temperature STM is able to operate in a temperature range between 25 and 500 K. In this design, the operator has the unique ability to go back to exactly the same spot on the surface, even after the sample has been removed to another in situ or even ex situ analysis, or modification tool. To operate the STM, the sample is attached to a thermally well-shielded 6-kg aluminum block that serves as the cooling and heating reservoir. The Al mass that is precooled or preheated guarantees a very high temperature stability of the STM. During our measurements, the change in sample temperature is only about 1°/hr, which makes it possible to take very fast image sequences of images over many hours without significant thermal drift of neither tip nor sample. Through improvements to the thermal shielding of our new STM, the sample can

now be imaged down to 25 K by precooling of the Al reservoir via liquid helium transfer.

We are currently growing 2-D lattices on strained interfaces between a bimetallic atomic layer of catalytic active metals such as Cu, Ag, Au, and Co of varying composition and a single-crystal Ru(0001) substrate in ultrahigh vacuum. The amount of interfacial strain will depend on the lattice mismatch and alloy composition. Exposing these strained metal films to sulfur, oxygen, or hydrogen gases is expected to result in the formation of highly ordered vacancy island structures of specific feature densities, as we have previously observed in the Ag/Ru and Cu/Ru system. We will also grow nanostructures on the reconstructed surfaces of Au(111) and Pt(111) by using the network of misfit dislocation as a template. Novel real-time measurements of the lattice dynamics of these nanometer-sized arrays will enable us to study the thermodynamics and kinetics of the formation of these self-assembled nanostructures. The approach is unique in the way it uses a combination of *real-time imaging techniques* to study the *elastic properties* of these low-dimensional features, that would otherwise be inaccessible.

By increasing the sample temperature, we can determine the melting temperature  $T_m$  of the 2-D equilibrium structure and test the theoretical predictions for the conventional melting transition in two dimensions via dislocation unbinding.<sup>[48]</sup> According to Kosterlitz and Thouless,<sup>[49]</sup> the melting temperature should depend on the elastic lattice properties as

$$T_m = (b^2/4\pi)\mu(\mu + \lambda)/(2\mu + \lambda) \quad (4)$$

The nano-array's elastic constants  $\mu$  and  $\lambda$  and the lattice constant  $b$  are now directly measurable through our original experimental approach, outlined above. However, we expect other mechanisms, e.g., an increase in the density of large clusters of coalesced vacancy islands (corresponding to formation of many-fold disclinations), to play a significant role in the melting behavior of our 2-D crystal.

The melting temperature seems to be within the accessible temperature range of the STM, because according to the phenomenological Lindemann criterion, a crystal is expected to melt when the root-mean-square (rms) fluctuations of the constituent particles about their equilibrium positions exceeds approximately 20% of the interparticle separation. At room temperature, we measured vibrational amplitudes of the thermally excited hole oscillations as large as 10 Å, one-fifth of the average separation between nearest-neighbor islands Fig. 4C.



Armed with an understanding of the mechanisms responsible for the creation of these hole lattices, we will be able to predict new nanostructures and tune their elastic properties by employing new materials. The first attempt in growing new test structures is to vary the film stress in the Ag layer by adding a second metal that will not phase-separate from the Ag nor absorb into the substrate. It has been shown that monolayer films of Ag and Cu alloy on Ru(0001), although all three metals are immiscible in their bulk form.<sup>[43]</sup> Small amounts of Cu added to the Ag film mix upon deposition at room temperature. After annealing to 500°C, it was observed that the smaller Cu atoms preferentially occupy regions in between the corrugation maxima of the Ag dislocation network. The dispersion of Cu in the Ag film had changed the strain-relief pattern and we can expect that the exposure of this alloy film to sulfur will result in a vacancy island array with different dimensions and elastic properties. Measuring the lattice constant  $b^*$ , the Lamé coefficients  $\mu^*$  and  $\lambda^*$ , and the melting temperature  $T_m^*$  as a function of concentration ratio of Cu to Ag will give insight into the ordering forces that drive self-assembly in these strained metal systems.

A variety of other metals such as Au, Co, and Cu display well-ordered characteristic dislocation network when deposited in the monolayer regime on Ru(0001). We are currently studying their reaction as well as their bimetallic combination with etching agents such as sulfur, oxygen, and hydrogen in the second phase of the experiments. A detailed exploration of the phase diagram will reveal important insight in the ability to tune such nanostructures. In addition, once the feature size and spacing in the array is calibrated, it can be used to measure surface stress in strained metal films, according to Eqs. (1) and (2).

We will use the connection between elastic constants and lattice phonons to discuss self-assembly in nanostructures grown on reconstructed surfaces, such as Au(111) and Pt(111), by depositing metals such as Ag, Cu, Co, Fe, or Ni. These measurements will reveal the balance between the short-ranged atomic forces that stabilize the dislocation cores and the long-ranged elastic interactions between the misfit dislocations that make up the reconstruction of the Au(111) and Pt(111) surface.

## CONCLUSION

We have shown that it is possible to grow self-assembled nano-arrays on strained metal films with large-scale ordering and great size uniformity. In particular, we have identified and measured the ordering

forces of a nearly perfect triangular lattice of nanometer-size vacancy islands which forms when a single atomic layer of Ag on Ru(0001) is exposed to sulfur at room temperature. We applied time-resolved scanning tunneling microscopy (STM) to monitor the thermal fluctuations of the centers-of-mass of the vacancy islands around their final positions in the lattice. From analysis of this island motion, we obtained the elastic constants of the lattice,  $\lambda \approx \mu \approx 0.02\text{--}0.04$  (N/m), which shows that, although weak, the forces responsible for the stability of this two-dimensional island crystal can be confidently measured. Our results are consistent with general theories of strain-mediated interactions between surface defects in strained films.

Future studies of the thermodynamics of these equilibrated two-dimensional nanostructures will lead to a refined understanding of the nature of phase transitions in two dimensions, e.g., surface melting. A variety of two-dimensional nano-arrays in thermal equilibrium of large-scale order and size uniformity will be grown on strained interfaces between a bimetallic atomic layer and a dissimilar substrate in ultrahigh vacuum. Combining the structural information (from unique real-time variable-temperature STM measurements) with quantum-size effects in the electronic structure (from high-resolution UV photoemission) will guide the development of new dynamic models to describe the evolution and properties of nanoscale structures on surfaces.

## ACKNOWLEDGMENTS

I am very grateful to Maria C. Bartelt, Norman C. Bartelt, Juan de la Figuera, Jan Hrbek, and Robert Q. Hwang for their support in the original experiments at Sandia National Laboratories in California.

## REFERENCES

1. Seul, M.; Andelman, D. Domain shapes and patterns: The phenomenology of modulated phases. *Science* **1995**, *267*, 476–483.
2. Itano, W.M.; Bollinger, J.J.; Tan, J.N.; Jelenkovic, B.; Huang, X.-P.; Wineland, D.J. Bragg diffraction from crystallized ion plasmas. *Science* **1998**, *279*, 686–689.
3. Evans, J.H. Observations of a regular void array in high purity molybdenum irradiated with 2 MeV nitrogen atoms. *Nature* **1971**, *229*, 403–404.
4. Asai, M.; Ueba, H.; Tatsuyama, C. Heteroepitaxial growth of Ge films on the Si(100)-2 × 1 surface. *J. Appl. Phys.* **1985**, *58*, 2577–2583.
5. Kern, K.; Niehus, H.; Schatz, A.; Zeppenfeld, P.; George, J.; Comsa, G. Long-range spatial self-organization in the adsorbate-induced restructuring of

- surfaces: Cu{110}-(2 × 1)O. *Phys. Rev. Lett.* **1991**, *67*, 855–858.
6. Hörnis, H.; West, J.R.; Conrad, E.H.; Ellialtioglu, R. Island ordering on clean Pd(110). *Phys. Rev.*, **B 1993**, *47*, 13055–13058.
  7. Zeppenfeld, P.; Krzyzowski, M.A.; Romainczyk, C.; David, R.; Comsa, G. Stability of disk and stripe patterns of nanostructures at surfaces. *Surf. Sci.* **1995**, *342*, L1131–L1136.
  8. Tersoff, J.; Teichert, C.; Lagally, M.G. Self-organization in growth of quantum dot superlattices. *Phys. Rev. Lett.* **1996**, *76*, 1675–1678.
  9. Parker, T.M.; Wilson, L.K.; Gordon, N.G.; Leibsle, F.M. Epitaxy controlled by self-assembled nanometer-scale structures. *Phys. Rev.*, **B 1997**, *56*, 6458–6461.
  10. Springholz, G.; Holy, V.; Pinczolis, M.; Bauer, G. Self-organized growth of three-dimensional quantum-dot crystals with fcc-like stacking and a tunable lattice constant. *Science* **1998**, *282*, 734–737.
  11. Tober, E.D.; Farrow, R.F.C.; Marks, R.F.; Witte, G.; Kalki, K.; Chambliss, D.D. Self-assembled lateral multilayers from thin film alloys of immiscible metals. *Phys. Rev. Lett.* **1998**, *81*, 1897–1900.
  12. Tober, E.D.; Marks, R.F.; Chambliss, D.D.; Roche, K.P.; Toney, M.F.; Kellock, A.J.; Farrow, R.F.C. Magnetoresistance of self-assembled lateral multilayers. *Appl. Phys. Lett.* **2000**, *77*, 2728–2730.
  13. Padovani, S.; Chado, I.; Scheurer, F.; Bucher, J.P. Transition from zero-dimensional superparamagnetism to two-dimensional ferromagnetism of Co clusters on Au(111). *Phys. Rev.*, **B 1999**, *59*, 11887–11891.
  14. Valden, M.; Lai, X.; Goodman, D.W. Onset of catalytic activity of gold clusters on titania with the appearance of nonmetallic properties. *Science* **1998**, *281*, 1647–1650.
  15. Pimpinelli, A.; Villain, J. *Physics of Crystal Growth*; Cambridge University Press: Cambridge, 1998.
  16. Venables, J.A. *Introduction to Surface and Thin Film Processes*; Cambridge University Press: Cambridge, 2000.
  17. Timp, G. *Nanotechnology*; Springer Verlag: New York, 1998.
  18. Chambliss, D.D.; Wilson, R.J.; Chiang, S. Nucleation of ordered Ni island arrays on Au(111) by surface-lattice dislocations. *Phys. Rev. Lett.* **1991**, *66*, 1721–1724.
  19. Voigtländer, B.; Meyer, G.; Amer, N.M. Epitaxial growth of thin magnetic cobalt films on Au(111) studied by scanning tunneling microscopy. *Phys. Rev.*, **B 1991**, *44*, 10354–10357.
  20. Voigtländer, B.; Meyer, G.; Amer, N.M. Epitaxial growth of Fe on Au(111): A scanning tunneling microscopy investigation. *Surf. Sci.* **1991**, *255*, L529–L535.
  21. Brune, H.; Giovannini, M.; Bromann, K.; Kern, K. Self-organized growth of nanostructure arrays on strain-relief patterns. *Nature* **1998**, *394*, 451–453.
  22. Helveg, S.; Lauritsen, J.V.; Laegsgaard, E.; Stensgaard, I.; Nørskov, J.K.; Clausen, B.S.; Tøpsøe, H.; Besenbacher, F. Atomic-scale structure of single-layer MoS<sub>2</sub> nano-clusters. *Phys. Rev. Lett.* **2000**, *84*, 951–954.
  23. Günther, C.; Vrijmoeth, J.; Hwang, R.Q.; Behm, R.J. Strain relaxation in hexagonally close-packed metal–metal interfaces. *Phys. Rev. Lett.* **1995**, *74*, 754–757.
  24. Hwang, R.Q.; Hamilton, J.C.; Stevens, J.L.; Foiles, S.M. Near-surface buckling in strained metal overlayer systems. *Phys. Rev. Lett.* **1995**, *75*, 4242–4245.
  25. Barth, J.V.; Brune, H.; Ertl, G.; Behm, R.J. Scanning tunneling microscopy observations on the reconstructed Au(111) surface: Atomic structure, long-range superstructure, rotational domains, and surface defects. *Phys. Rev.*, **B 1990**, *42*, 9307–9318.
  26. Sandy, A.R.; Mochrie, S.G.J.; Zehner, D.M.; Huang, K.G.; Gibbs, D. Structure and phases of the Au(111) surface: X-ray-scattering measurements. *Phys. Rev.*, **B 1991**, *43*, 4667–4687.
  27. Narasimhan, S.; Vanderbilt, D. Elastic stress domains and the herringbone reconstruction on Au(111). *Phys. Rev. Lett.* **1992**, *69*, 1564–1567.
  28. Sandy, A.R.; Mochrie, S.G.J.; Zehner, D.M.; Grubel, G.; Huang, K.G.; Gibbs, D. Reconstruction of the Pt(111) surface. *Phys. Rev. Lett.* **1992**, *68*, 2192–2195.
  29. Bott, M.; Hohage, M.; Michely, T.; Comsa, G. Pt(111) reconstruction induced by enhanced Pt gas-phase chemical potential. *Phys. Rev. Lett.* **1993**, *70*, 1489–1492.
  30. Pohl, K.; Bartelt, M.C.; Figuera, J.d.l.; Bartelt, N.C.; Hrbek, J.; Hwang, R.Q. Identifying the forces responsible for self-organization of nanostructures at crystal surfaces. *Nature* **1999**, *397*, 238–241.
  31. Pohl, K.; Figuera, J.d.l.; Bartelt, M.C.; Bartelt, N.C.; Hrbek, J.; Hwang, R.Q. Thermal vibrations of a two-dimensional vacancy island crystal in a strained metal film. *Surf. Sci.* **1999**, *433–435*, 506–511.
  32. Hrbek, J.; Figuera, J.d.l.; Pohl, K.; Jirsak, T.; Rodriguez, J.A.; Schmid, A.K.; Bartelt, N.C.; Hwang, R.Q. A prelude to surface chemical reactions: Imaging the induction period of sulfur interaction with a strained Cu layer. *J. Phys. Chem.*, **B 1999**, *103*, 10557–10561.
  33. Alerhand, O.L.; Vanderbilt, D.; Meade, R.D.; Joannopoulos, R.D. Spontaneous formation of stress domains on crystal surfaces. *Phys. Rev. Lett.* **1988**, *61*, 1973–1976.
  34. Kashuba, A.B.; Pokrovsky, V.L. Stripe domain structures in a thin ferromagnetic film. *Phys. Rev.*, **B 1993**, *48*, 10335–10344.
  35. Langer, S.A.; Goldstein, R.E.; Jackson, D.P. Dynamics of labyrinthine pattern formation in magnetic fluids. *Phys. Rev.*, **A 1992**, *46*, 4894–4904.
  36. Marchenko, V.I. On the domain structure of two-dimensional ferromagnets. *Sov. Phys. JETP* **1986**, *63*, 1315–1318.
  37. Vanderbilt, D. Phase segregation and work-function variations on metal surfaces: Spontaneous formation of periodic domain structures. *Surf. Sci.* **1992**, *268*, L300–L304.
  38. Ng, K.-O.; Vanderbilt, D. Stability of periodic structures in a two-dimensional dipolar model. *Phys. Rev.*, **B 1995**, *52*, 2177–2183.

39. Stoycheva, A.D.; Singer, S.J. Stripe melting in a two-dimensional system with competing interactions. *Phys. Rev. Lett.* **2000**, *84*, 4657–4660.
40. Morgenstern, K.; Rosenfeld, G.; Comsa, G. Decay of two-dimensional Ag islands on Ag(111). *Phys. Rev. Lett.* **1996**, *76*, 2113–2116.
41. Plass, R.; Bartelt, N.C.; Kellogg, G.L. Dynamic observations of nanoscale self-assembly on solid surfaces. *J. Phys., Condens. Matter* **2002**, *14*, 4227–4240.
42. Ibach, H. The role of surface stress in reconstruction, epitaxial growth and stabilization of mesoscopic structures. *Surf. Sci. Rep.* **1997**, *29*, 193–263.
43. Stevens, J.L.; Hwang, R.Q. Strain stabilized alloying of immiscible metals in thin films. *Phys. Rev. Lett.* **1995**, *74*, 2078–2081.
44. Wagner, C. Investigations on silver sulfite. *J. Chem. Phys.* **1953**, *21*, 1819–1827.
45. Morgenstern, K.; Rosenfeld, G.; Poelsema, B.; Comsa, G. Brownian motion of vacancy island on Ag(111). *Phys. Rev. Lett.* **1995**, *74*, 2058–2061.
46. Nelson, D.R.; Halperin, B.I. Dislocation-mediated melting in two dimensions. *Phys. Rev., B* **1979**, *19*, 2457–2484.
47. Huse, D.A. Shape of diffraction peaks of a two-dimensional solid. *Phys. Rev., B* **1983**, *28*, 6110–6111.
48. Strandburg, K.J. Two-dimensional melting. *Rev. Mod. Phys.* **1988**, *60*, 161–207.
49. Kosterlitz, J.M.; Thouless, D.J. Ordering, metastability and phase transitions in two-dimensional systems. *J. Phys., C* **1973**, *6*, 1181–1203.

# STEM of Chiral Pair Self-Assembled Monolayers

Yuguang Cai

Steven L. Bernasek

Department of Chemistry, Princeton University,  
Princeton, New Jersey, U.S.A.

## INTRODUCTION

Long-chain alkanes [ $\text{CH}_3(\text{CH}_2)_n\text{CH}_3$ ,  $n > 8$ ] and their derivatives such as alkenes, alkanols, ethers, and carboxylic acids physisorb on highly oriented pyrolytic graphite (HOPG) surfaces to form very stable self-assembled monolayers (SAMs). These monolayer structures, with nanometer dimensions, form an entire class of nanoscale objects whose properties are of considerable interest. These nanoscale objects provide important models that are relevant to the understanding of molecular electronic devices, biological recognition chips, tribology, and corrosion inhibition systems. These very interesting nanoscale structures have been extensively studied in recent years.<sup>[1–18]</sup> Unlike the close packed self-assembled monolayer in the alkanethiol/Au(111) system, where the alkane chain stands up from the surface, in the alkane derivative/HOPG SAMs, the alkane chain adsorbs parallel to the graphite basal plane. The alkane molecule adsorbs in an *all-gauche* conformation, which has the lowest energy. In this conformation, the carbon–carbon backbone of the molecule has a zigzag shape. Theoretical and experimental results indicate that in the long-chain alkane self-assembled monolayer on HOPG, the zigzag is parallel to the HOPG basal plane.<sup>[4,6]</sup> Under such packing conditions, the distance between the hydrogens of the neighboring methylene units in the alkane chain is 2.52 Å and the distance between six-fold hollows of HOPG is 2.46 Å. Fig. 1 is a model showing the actual dimensions for an alkane molecule adsorbed on the HOPG surface. This good match between the substrate lattice and the organic molecule adsorbate dimension results in a relatively strong interaction between the substrate and the adsorbate. Such interaction is the basis for formation of a stable monolayer on the HOPG surface. The van der Waals interactions between the long-chain alkane

molecules provide the basis for the self-assembly process.

Sometimes these stable self-assembled monolayers exhibit chirality, or handedness. This can result from the segregation of chiral molecules into chiral domains on the surface, from the distortion of achiral molecules to form an overall chiral structure, or from the pairing or self-assembly within the unit cell to make a chiral structure from an enantiomeric mixture. This entry discusses several examples of self-assembled monolayers formed on HOPG that exhibit chirality. These nanoscaled materials may have interesting applications in chirally selective catalysis and separations, and certainly help us to understand the interactions between molecules and the substrate that govern the self-assembly process. In the following entry, the structures of three separate racemic mixtures of iodine substituted octadecanol and octadecanoic acids adsorbed on the (0001) plane of HOPG are examined. Chiral pairs are formed and the pairs form ordered monolayers, in which different faces of the same molecule are exposed and imaged. These examples illustrate the formation of chiral nanostructured monolayers in this self-assembly process.

## CHIRAL MONOLAYERS

Certain chiral molecules have been observed to spontaneously separate during crystallization in three dimensions, as Louis Pasteur discovered in 1848 for sodium ammonium tartrate. Most racemic mixtures do not spontaneously separate upon crystallization. Lattice structures of these crystals formed by heterochiral enantiomers can be solved by X-ray single crystal diffraction as long as the heterochiral single crystal can be obtained. In the two-dimensional realm, diffraction methods such as grazing incidence X-ray

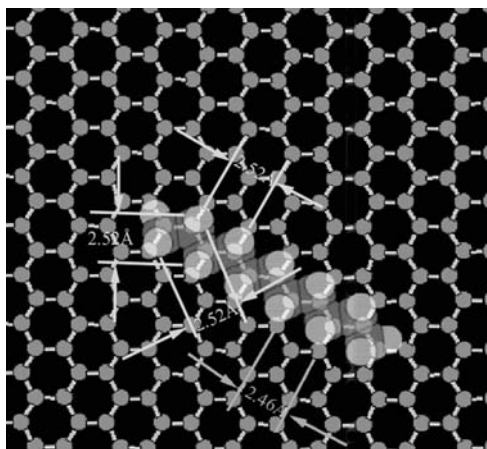


**Fig. 1** Model of alkane molecule on HOPG. For an alkane molecule adsorbed on HOPG, the alkane zigzag chain is parallel to the basal plane. The distance between the neighboring hydrogen atoms is 2.52 Å. The graphite lattice unit is 2.46 Å.

diffraction (GIXD) and helium diffraction provide structural information for well-ordered domains. This information reflects the overall order. To obtain atomic-level structural information inside the unit cell by diffraction methods is still very difficult. However, scanning probe microscopy offers a local, microscopic view of the structure on the surface and is ideal for probing the structure of two-dimensional crystals. Chiral organic molecules adsorbed on the HOPG surface are particularly interesting because of the potential applications in biologically active chiral molecule recognition and separation, as well as in the design of chirally selective catalysts. Some chiral long-chain alkane derivatives form crystalline monolayers on the basal plane of HOPG. Different optical isomers have been observed to spontaneously separate, each forming a chiral domain on the HOPG surface. With the help of scanning tunneling microscopy (STM), these enantiomers have been identified either by the chiral shape of the domains,<sup>[16,19–21]</sup> or in the case of very high resolution images, by directly identifying the chiral center.<sup>[18]</sup> Studies of racemic mixtures that are not observed to form separate chiral domains on the surface are still quite rare, partly because of the lack of very high resolution techniques that would allow direct identification of the chiral center of the molecule.<sup>[18]</sup>

Scanning tunneling microscopy is widely used in characterizing these long-chain alkane and substituted alkane SAMs. Because of the strong adsorbate/substrate and adsorbate/adsorbate interactions, atomic resolution can generally be achieved. Depending on the structure of a monolayer, different aspects of the same molecule can be imaged. For example, in the case of the striped phase of self-assembled alkanethiol monolayers on Au(111), the molecule is imaged with the

chain parallel to the substrate. In contrast, in the  $\sqrt{3} \times \sqrt{3} R30$  phase, the alkanethiol is imaged with the chain standing up. Relatively flat chiral molecules, with no mirror symmetry, can expose two different “faces.” When such molecules adsorb on a surface, usually only one “face” is exposed. The overall adsorption energy of the system will normally favor a specific molecular orientation upon adsorption.

## EXPERIMENTAL SECTION

The STM used in these experiments is a laboratory-built, ultrahigh vacuum, variable temperature STM. The microscope is mounted in an ultrahigh vacuum chamber on a 10-in. diameter ConFlat flange. The suspension stage hangs by four springs enclosed in spring houses attached to the 10-in. flange. Eddy current damping is used for vibrational isolation of the suspension stage. An InchWorm motor is horizontally mounted on the suspension stage. A single tube scanner and tip are mounted on the head of the InchWorm. The tip used for scanning is cut from 0.01-in. diameter platinum iridium wire (Pt/Ir = 90:10) from Good-fellow. Samples are positively biased and all scans were carried out under ambient condition at the liquid/solid interface.

Oleyl alcohol, oleic acid, elaidic acid, phenyloctane, and iodine were purchased from Sigma-Aldrich and used without further purification. Highly oriented pyrolytic graphite is from Union Carbide, ZYA grade.

One drop of iodine-saturated  $\text{CCl}_4$  solution was added to 1 mL of oleyl alcohol to halogenate the alcohol. Halogenation of the central double bond in the oleyl alcohol results in a solution that is a mixture of oleyl alcohol, (9*R*,10*R*)-9,10-diiodooctadecan-1-ol, (9*S*,10*S*)-9,10-diiodooctadecan-1-ol, and  $\text{CCl}_4$ . Composition of the solution following iodination was confirmed by [<sup>1</sup>H]NMR and mass spectrometry. One drop of the resulting solution is directly applied onto a newly cleaved HOPG surface, and this surface is imaged.

Saturated solutions of oleic acid and elaidic acid in phenyloctane were used for imaging. One drop of iodine-saturated  $\text{CCl}_4$  solution was added to 1 mL of these solutions for iodination of these molecules.

Scanning tunneling microscopy studies of pure oleyl alcohol and pure carbon tetrachloride applied to the HOPG surface were also performed. Neither oleyl alcohol nor carbon tetrachloride can be seen by STM to form stable-ordered structures on HOPG. For oleic acid, after iodination, there are mixtures of oleic acid, racemic (9*R*,10*R*)-9,10-diiodooctadecanoic acid/(9*S*,10*S*)-9,10-diiodooctadecanoic acid, and  $\text{CCl}_4$ . Oleic acid does not form a stable structure on HOPG.

For elaidic acid, after iodination, there are mixtures of elaidic acid, racemic (9*R*,10*S*)-9,10-diiodooctadecanoic acid/(9*S*,10*R*)-9,10-diiodooctadecanoic acid, and CCl<sub>4</sub> in the solution. Although elaidic acid does form a stable self-assembled monolayer on HOPG, the appearance of the elaidic acid SAM is different from the (9*R*,10*S*)-9,10-diiodooctadecanoic acid/(9*S*,10*R*)-9,10-diiodooctadecanoic acid SAM. The structures observed by STM and described here are the structures of the corresponding iodination products.

All images were calibrated using the bare HOPG hexagonal lattice. Scanning tunneling microscopy images of the mixture solutions are taken under various tunneling conditions ( $V_b = 0.3\text{--}1.2$  V, tunneling current = 0.4–1.2 nA). Several different tips and HOPG samples were used to ensure reproducibility.

## RESULTS AND DISCUSSION

### Monolayer of Oleyl Alcohol Iodination Products

When alkanols are adsorbed on HOPG, the molecules self-assemble into parallel rows.<sup>[4,5,9,10]</sup> Inside each row, the molecules pack side by side. The molecule chain has a 60° angle to the row boundary. The molecules in adjacent rows have a 120° angle to satisfy the geometric requirement of hydrogen bonding between the two alkanol molecules in these rows. The oxygen atoms at one side of the row boundary appear as a straight dark line in the STM, which bisects the 120° herringbone angle. Fig. 2 is a molecular resolution image of the diiodooctadecanol adsorbate structure.<sup>[22]</sup> The herringbone angle is measured to be  $124 \pm 2^\circ$  in this image. The length of the molecule is  $22.5 \pm 0.3$  Å, which is very close to the length calculated from an extended model of the iodinated oleyl alcohol molecule (22.4 Å).<sup>[22]</sup> Structural features different from those seen with the parent alkanol (1-octadecanol) can be identified.

1. The apparent heights of the neighboring rows of the diiodooctadecanols are different. The diiodooctadecanol rows form a high/low/high/low pattern as seen from the profile scan in Fig. 2.
2. At the center of each row, there is a dark trough.
3. The dark troughs in the lower rows are darker than the troughs in the higher rows.
4. For each row of diiodooctadecanol, the left half of the molecule is brighter (higher) than the right half.

To help explain this fine structure, a model study of diiodooctadecanol using Spartan<sup>[23]</sup> was carried out.

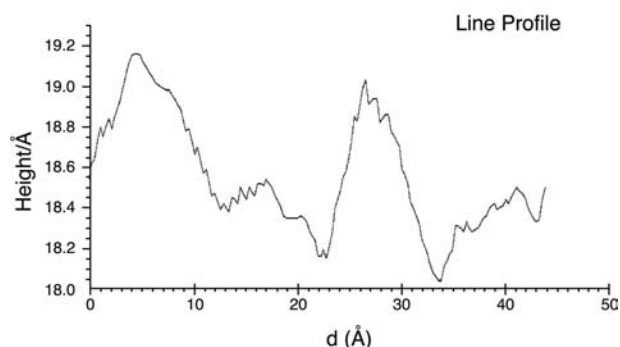
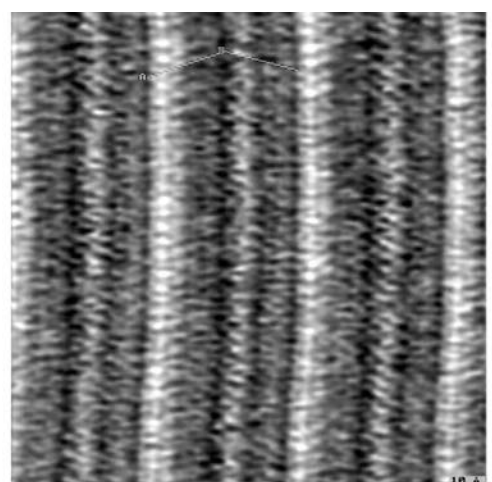


**Fig. 2** High-resolution image of 9,10-diiodooctadecanol on HOPG. Scan size is  $135 \times 135$  Å.  $V_b = 0.99$  V, tunneling current  $I = 1.03$  nA. The image is low pass filtered to remove noise. The angle between each pair is  $124 \pm 2^\circ$ . The length of the molecule measured from this image is  $22.5 \pm 0.2$  Å. Line profile (A–B–C) is along the axis of one molecule pair. Source: From Ref.<sup>[22]</sup>.

The molecule must twist at the C9–C10 bond to provide space for the two bulky iodine atoms. It is very clear from the model that the two iodine atoms must be on the same side of the backbone chain. It is well known that the good match between the H–H distance on the alkane chain and the HOPG unit cell distance leads to well-ordered adsorption of long-chain alkane molecules on the HOPG basal plane. For diiodooctadecan-1-ol, the zigzag of the hydrocarbon backbone chain must adsorb parallel to the HOPG basal plane. In this case, the two iodine atoms have only two possible positions: facing up, above the alkane chain, and facing down, buried underneath the alkane chain. Flipping the molecule over converts one orientation into the other. This suggests an explanation for the high/low/high/low height modulation of the neighboring rows of the diiodooctadecanols. If the two iodine atoms are buried under the alkane chain, the diiodooctadecanol molecule will be a “high” molecule; if the two iodine atoms are facing up, above the alkane



chain, the diiodooctadecanol will be a “low” molecule. In Fig. 2, row A is a row of “high” molecules packed together and the neighboring row B is a row of “low” molecules packed together. This packing model can be verified by examining the depth of the center trough in each row. Because the iodine atoms are at the center of the 9,10-diiodooctadecanol molecule, it is natural to assign the center trough as the positions of these marker atoms.<sup>[17]</sup> In the high row, the iodine atoms are blocked by alkane chains, while in the low row, the iodine atoms are exposed. Exposed iodine atoms appear darker than the alkane-chain-blocked iodine atoms in the high rows. The high/low/high/low height modulation of the neighboring rows suggest that two opposite faces of the same molecule are being imaged.

The model calculated using PM3 suggests that the dihedral angle of I1–C9–C10–I2 is  $89^\circ$  instead of the  $63^\circ$  dihedral angle of H–C9–C10–H. As a result of this rotation, half of the molecular backbone is twisted with respect to the other half. The hydrogen atoms on one half move to a higher position, making half of the molecule brighter (higher) than the other half.

Fig. 3 shows a high-resolution image of the adsorbed layer. The racemic mixture of (9*S*,10*S*)-9,10-diiodooctadecan-1-ol (*S*) and (9*R*,10*R*)-9,10-diiodooctadecan-1-ol (*R*) has been imaged. Long-chain *n*-alkanols adsorbed on HOPG typically form a herringbone structure. Between the rows, the alkanol molecules are packed head to head, with the OH groups close enough to form strong hydrogen bonds. Within each row, the long chain of the molecule is packed side by side. This structure is governed by the requirements of hydrogen bonding.<sup>[6]</sup> Because the angle between the molecular axis and the trough

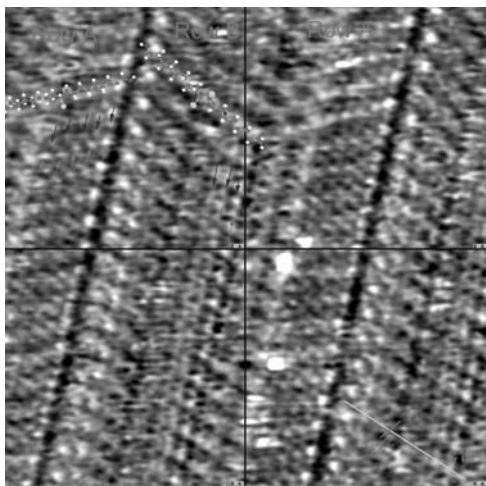


**Fig. 3** Very high resolution image of 9,10-diiodooctadecanol adsorbed on HOPG. Scan size is  $76 \times 76 \text{ \AA}$ ,  $V_b = 0.31 \text{ V}$ , tunneling current  $I = 1.0 \text{ nA}$ . Source: From Ref.<sup>[22]</sup>.

(row boundary) is  $61^\circ$ , inside the row, each alkanol molecule can only shift one methylene unit ( $2.52 \text{ \AA}$ ) while packing.

In Fig. 3, it is seen that in each row, the angle between the molecular axis and the trough (row boundary) is about  $61^\circ$ , and the angle between the hydrogen-bonded pair is around  $122^\circ$ , which is the same as in the *n*-alkanol case. In row A of Fig. 3, the row is entirely composed of “high”-type molecules, and in row B, the row is entirely composed of “low”-type molecules. If within the row, the molecules are a mixture of *R* and *S* types, only *RR* (or *SS*) packed side by side could satisfy the single methylene unit shift (the angle of  $60^\circ$  between the molecular axis and the trough) and maintain the correct registry with the graphite lattice. From the STM image, it is clear that all molecules within a row are either all high (two iodine atoms facing down) or all low molecules (two iodine atoms facing up). If *R* and *S* are packed side by side, they could not form a  $60^\circ$  angle between the molecular axis and trough because only half-integer ( $1/2, 3/2, 5/2, \dots$ , etc.) methylene unit shifts along the neighboring molecule are allowed. Thus each row must be composed of one type of optical isomer, either *R* or *S*, but cannot be composed of both.

A line profile across several rows identifies the position of the OH group because in the line profile, the groove where two oxygen atoms from adjacent molecules meet must be deeper than where two methyl groups meet. After locating the OH position in Figs. 2 and 3, it can be seen that in the high row, the C18 side is higher; in the low row, the C1 side is higher.

This implies only four possible structural combinations, which satisfy the packing constraints described above:

- High-type *R*, C18 part high and low-type *R*, C1 part high (*RR*).
- High-type *R*, C18 part high and low-type *S*, C1 part high (*RS*).
- High-type *S*, C18 part high and low-type *R*, C1 part high (*S'R'*).
- High-type *S*, C18 part high and low-type *S*, C1 part high (*S'S'*).

From the very high resolution image of this adsorbate structure shown in Fig. 3, several points can be noted:

1. For each row, the higher half has only molecular resolution, i.e., only the overall alkane chain is visible, while the lower half shows submolecule resolution, i.e., the individual atoms inside the chain can also be seen.
2. Along the oxygen trough direction, in the lower part, there are five pairs of small raised features

in the high row (row A) while only three pairs are visible in low row (row B).

3. In the low row (row B), in the center of the molecule, the central dark band now appears as a set of discrete dark spots. Each chain has two spots, one on each side. If the upper and the lower iodines are labeled as I1 and I2, the I1–I2 molecular chain cross point is Z, and the angle C18–Z–I1 is an acute angle.

Only the *RS* packing described above can explain all the observations. Hence the high row (row A) is directly identified as (*9R,10R*)-9,10-diiodooctadecan-1-ol (iodines up) and the lower row (row B) as (*9S,10S*)-9,10-diiodooctadecan-1-ol (iodines down). Interestingly, because of the HOPG substrate, although (*9R,10R*)-9,10-diiodooctadecan-1-ol in the high row and (*9S,10S*)-9,10-diiodooctadecan-1-ol in the low row are enantiomers in solution, on the surface the mirror image of the *R* type is not superimposable on the *S* type, and vice versa. The entire domain formed by alternating chirally pure *R* rows and *S* rows is also a chiral structure. Thus an achiral racemic mixture is observed to form a chiral structure on an achiral surface in the regions examined here, because of the chiral pairing across the unit cell.

### Monolayer of Iodination Products of Oleic Acid and Elaidic Acid

Most long-chain carboxylic acid self-assembled monolayers on the HOPG surface pack in the same way: Molecules self-assemble into parallel rows. Inside each row, the molecule chain is perpendicular to the row boundary. The molecules pack antiparallel inside the row, i.e., side by side and head to tail. When a carboxylic head group meets another carboxylic head group from another molecule in a neighboring row, the two carboxylic head groups hydrogen bond to form a hexagonal ring. The ring appears as a dark hole in the STM image. This packing arrangement has two characteristics:

1. At both ends of a row of molecules, there are dark holes.
2. The distance between the dark holes along the row boundary direction corresponds to twice the molecule width (8.8 Å in the long-chain carboxylic acid case).

The iodination of oleic acid generates a racemic mixture of enantiomers: (*9R,10R*)-9,10-diiodooctadecanoic acid and (*9S,10S*)-9,10-diiodooctadecanoic acid. The diiodooctadecanoic acid forms an ordered

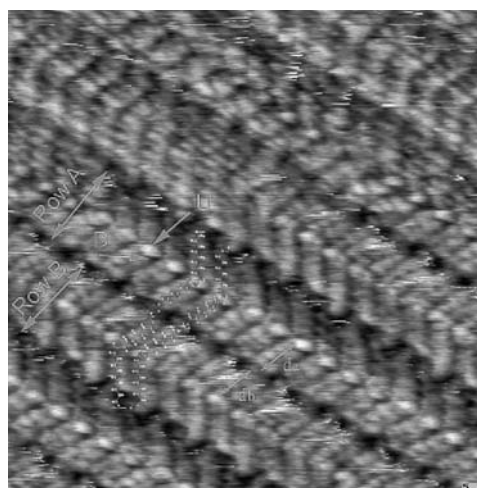


**Fig. 4** Submolecular resolution image of (*9R,10R*)-9,10-diiodooctadecanoic acid/(*9S,10S*)-9,10-diiodooctadecanoic acid SAM. Scan size is  $91 \times 91$  Å,  $V_b = 1.00$  V, tunneling current  $I = 0.73$  nA.

self-assembled monolayer on the HOPG surface in phenyloctane solution.

Fig. 4 is a high-resolution STM image of the diiodooctadecanoic acid SAM. The acid molecules self-assemble into parallel rows. At both sides of the row, there are dark holes at the row boundary. The distance between the dark holes along the row boundary direction seems to be only one molecule wide, which suggests that the acid molecules might pack in parallel style, i.e., side by side and head to tail. Careful study of the image reveals more details: There are two types of dark holes, one type is a plain hole, the other type has many white spikes around it. This implies a different chemical nature for the two features. Thus the periodicity along the row boundary direction is still the expected two-molecule width. Such structure characteristics fit the description of the general packing style of the carboxylic acid. This means that the diiodooctadecanoic acid is also packed antiparallel inside the row.

Several interesting features are seen in this image as well. There are two types of rows. They are labeled in the image as row A and row B. Each molecule inside the row is bent, in a V shape. At the center of the row, where the molecule bends, a bright bump (point U, in Fig. 4) is visible. In row A, it is especially clear that there is also a small dark pit (D, in Fig. 4) beside every white bump. Previous STM studies show that the halogen atom in long-chain alkanes appears as a bright spot when it points upward and as dark when it points downward in phenyloctane solution.<sup>[24]</sup> Considering the position of this bright/dark spot pair, the bright spot is assigned to the iodine atom pointing upward

and the dark spot is assigned to the iodine atom pointing downward.

All molecules in row A appear identical except for the terminal part, i.e., the relative position of the upward and downward iodine atoms are also the same for all molecules in row A. The bending direction is the same for all molecules. It is also clear that molecules in the row pack antiparallel. To satisfy the above two observations, there is only one conclusion: All molecules in row A are one optical isomer. Specifically in Fig. 4, the downward iodine is at the lower side of the upward iodine. Thus the molecule in row A is directly identified as the *R* acid [(9*R*,10*R*)-9,10-diiodooctadecanoic acid].

For row B, the structure characteristics are similar as for row A: All molecules look identical except for the terminal part, and the molecules pack antiparallel. The result is the same, row B is composed of entirely one type of optical isomer, either *R* acid or *S* acid. In row B, the structural details at the center of the molecule are different from row A. The bright spot is visible; unfortunately, the dark spot is not very clear. It is difficult to determine the relative position of the bright spot and dark spot. Hence the identity of the molecules in row B could not be directly identified as in row A. However, a length measurement from the bright spot to the row boundary provides the assignment. If molecules in row B are also *R* type, the whole structure would be centrosymmetric. The distances from bright spot to row boundary in row A and row B would be identical. The ratio  $d_a/d_b$  would be 1. If

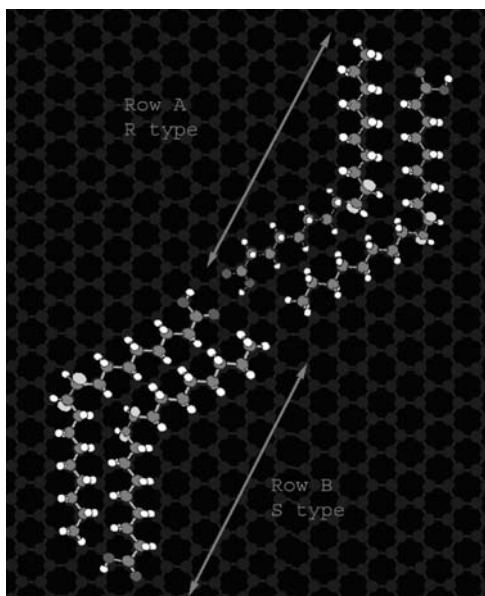


**Fig. 5** Proposed unit cell structure corresponding to the SAM in Fig. 4. *R*-type acid: (9*R*,10*R*)-9,10-diiodooctadecanoic acid. *S*-type acid: (9*S*,10*S*)-9,10-diiodooctadecanoic acid.

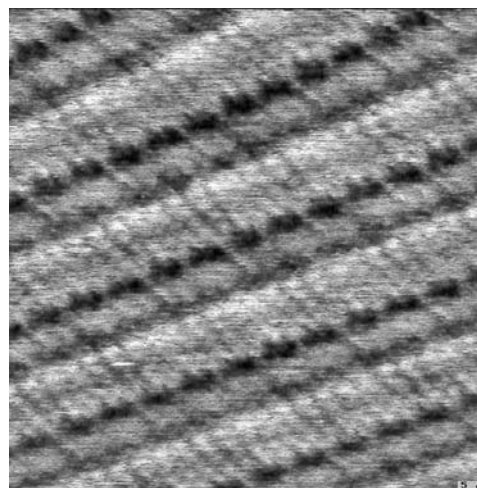


**Fig. 6** Scanning tunneling microscopy image of (9*R*,10*R*)-9,10-diiodooctadecanoic acid/(9*S*,10*S*)-9,10-diiodooctadecanoic acid (elaidic acid iodination products) SAM. Scan size is  $79 \times 79 \text{ \AA}$ ,  $V_b = 0.71 \text{ V}$ , tunneling current  $I = 0.82 \text{ nA}$ .

the molecules in row B are *S* type, the distance from the bright spot to the row boundary would be 4 methylene units (1 methylene unit =  $2.5 \text{ \AA}$ ), while in row A, this distance would be 4.5 methylene units. The ratio of  $d_a/d_b$  would be 1.125. The actual ratio measured from Fig. 4 is  $d_a/d_b = 1.13 \pm 0.04$ , which clearly indicates that all molecules in row B are *S* acid [(9*S*,10*S*)-9,10-diiodooctadecanoic acid].

Fig. 5 is a model of the derived unit cell structure of the observed diiodooctadecanoic acid SAM. Each unit cell is composed of four molecules, two are *R* type,

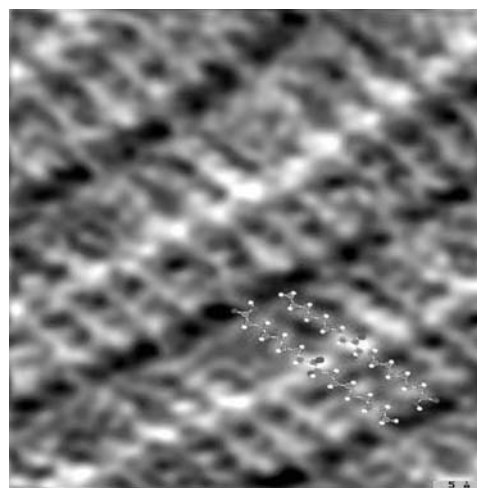


**Fig. 7** Scanning tunneling microscopy image of (9*R*,10*S*)-9,10-diiodooctadecanoic acid/(9*S*,10*R*)-9,10-diiodooctadecanoic acid (elaidic acid iodination products) SAM at higher resolution. Scan size is  $44 \times 44 \text{ \AA}$ ,  $V_b = 0.33 \text{ V}$ , tunneling current  $I = 1.22 \text{ nA}$ .

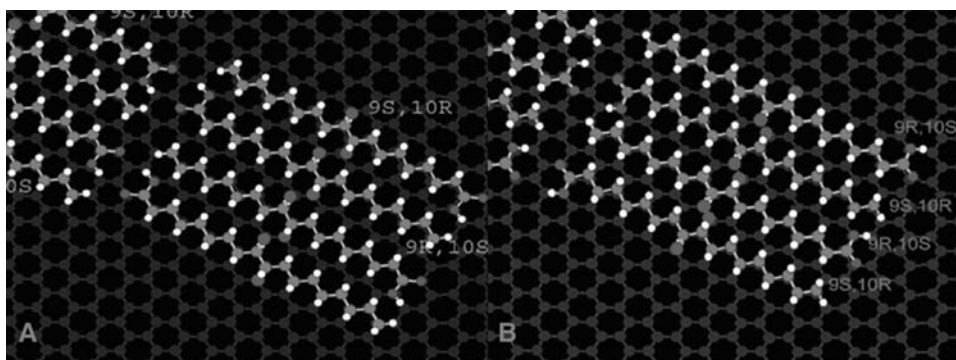


**Fig. 8** Two possible unit cell structures that could explain all observed features in the STM image of (9*R*,10*S*)-9,10-diiodooctadecanoic acid/(9*S*,10*R*)-9,10-diiodooctadecanoic acid (elaidic acid iodination products).

two are *S* type. The molecules in the same row are not identical; they expose different faces upon adsorption on the surface. A  $C_2$  rotation (flipping) along the row direction at the center of the row converts one into the other. This unit cell is composed of a racemic mixture of two optical isomers, and is still a chiral structure. The mirror image structure is also observed by STM in other domains on the graphite surface.

The iodination of elaidic acid also generates a racemic mixture of enantiomers: (9*R*,10*S*)-9,10-diiodooctadecanoic acid and (9*S*,10*R*)-9,10-diiodooctadecanoic acid. The diiodooctadecanoic acids are observed to form ordered self-assembled monolayers on the HOPG surface in phenyloctane solution by STM. Fig. 6 is an STM image of the self-assembled monolayer formed by (9*R*,10*S*)-9,10-diiodooctadecanoic acid and (9*S*,10*R*)-9,10-diiodooctadecanoic acid. The molecules self-assemble into parallel rows. Unlike the SAMs discussed above, each row looks identical. At both sides of the row, dark holes are clear. The distance between the holes along the row boundary corresponds to the two-molecule width. These features fit very well with the general long-chain carboxylic acid SAM structure that is described above. Hence in Fig. 6, the molecules inside a row pack antiparallel as well.

However, there are some features different from the parent carboxylic acid (stearic acid) structure. In the center of a row, there is a bright band. There is also a dark band beside the bright band. Fig. 7 is an STM image of the same type SAM at another domain with higher resolution. In this image, the bright line and dark line inside a row become discrete bright and dark spots. The bright spots are always on the alkane chain; the dark spots are always at the same side of the bright spot and always between the chains. The distance between the bright spots is one alkane chain width (4.8 Å), which is also the distance between the dark spots. The positions of these spots are at the center of the molecule, where the iodine atoms should be. It is natural to assign the bright spot as the iodine

atom pointing upward and the dark spot as the iodine atom pointing downward.

To derive the packing model, three observations must be considered:

1. The unit cell structure must be inside the same row because all rows in the (9*R*,10*S*)-9,10-diiodooctadecanoic acid/(9*S*,10*R*)-9,10-diiodooctadecanoic acid SAM look identical.
2. The molecules pack antiparallel.
3. The upward/downward iodine atom has a single-molecule-width periodicity.

The only possible solution to these requirements is for the two enantiomers to pack in a side by side and head to tail arrangement inside the row. The unit cell is composed of a heterochiral pair of enantiomers of diiodooctadecanoic acid molecules. Although the pair is composed of enantiomers, it is still a chiral structure on the surface. There are two possible arrangements to satisfy the observed requirements, which are shown in Fig. 8A and B, respectively. These two packing arrangements are mirror images of one another. At this time, the STM resolution is not sufficient to determine which of the two possible structures is the actual structure in the image.

## CONCLUSION

The self-assembled monolayers of racemic mixtures of (9*R*,10*R*)-9,10-diiodooctadecanol/(9*S*,10*S*)-9,10-diiodooctadecanol, (9*R*,10*R*)-9,10-diiodooctadecanoic acid/(9*S*,10*S*)-9,10-diiodooctadecanoic acid, (9*R*,10*S*)-9,10-diiodooctadecanoic acid/(9*S*,10*R*)-9,10-diiodooctadecanoic acid have been examined by STM. Each mixture exhibits an interesting chiral grouping upon adsorption, forming a nanoscale surface structure.

In the case of the (9*R*,10*R*)-9,10-diiodooctadecanol/(9*S*,10*S*)-9,10-diiodooctadecanol SAM on HOPG,



the ordered monolayer exhibits a periodic surface height modulation within the monolayer. Analysis of the STM images shows that the molecules are found to pack in alternately high and low rows. As a result of the unique molecular geometry, opposite faces of the molecule are imaged. High-resolution STM images show that the high/low rows correspond to different optical isomers. The enantiomers spontaneously separate into different rows, and inside each row, chirally pure molecules assemble together. The unit cell is a herringbone-shaped heterochiral pair with different molecular faces exposed. Although the molecules in the pair are enantiomers, because of the adsorption exposing different molecular faces, the mirror image of one molecule cannot superimpose on the other.

In the case of the (9*R*,10*R*)-9,10-diiodooctadecanoic acid/(9*S*,10*S*)-9,10-diiodooctadecanoic acid SAM, each type of enantiomer also self-assembles into homochiral rows. Each unit cell is composed of four molecules in the neighboring rows. The same type of isomer in the same row adsorbs exposing opposite faces.

In the case of the (9*R*,10*S*)-9,10-diiodooctadecanoic acid/(9*S*,10*R*)-9,10-diiodooctadecanoic acid SAM, this quasi phase separation does not occur. The two enantiomers pack antiparallel inside the row, still forming a chiral structure.

These SAMs formed by chiral molecules do not spontaneously separate into homochiral domains. Their unit cell structures are revealed by high-resolution STM studies. The unit cells are composed of an equal number of enantiomers. Although the structure of the unit cells are different in these three self-assembled monolayer examples, the unit cell itself is also chiral. In all three cases, an achiral racemic mixture is observed to form chiral domains on an achiral surface. Such a structure is in contrast to the more common instance of chiral molecules that spontaneously separate into pure chiral domains at a surface.

## ACKNOWLEDGMENT

This work was partially supported by the Chemistry Division of the National Science Foundation.

## REFERENCES

1. Spong, J.K.; Minzes, H.A.; Lacombe, L.J.; Dovek, M.M.; Frommer, J.E.; Foster, J.S. Contact mechanism for resolving organic-molecules with tunneling microscopy. *Nature* **1989**, *338*, 137–139.
2. Smith, D.P.E.; Horber, H.; Gerber, C.; Binnig, G. Smectic liquid-crystal monolayers on graphite observed by scanning tunneling microscopy. *Science* **1989**, *245*, 43–45.
3. Smith, D.P.E. Defects in alkylcyanobiphenyl molecular crystals studied by scanning tunneling microscopy. *J. Vac. Sci. Technol.* **1991**, *B(9)* (2), 1119–1125.
4. Claypool, C.L.; Faglioni, F.; Goddard, W.A.; Gray, H.B.; Lewis, N.S.; Marcus, R.A. Source of image contrast in STM images of functionalized alkanes on graphite: A systematic functional group approach. *J. Phys. Chem., B* **1997**, *101*, 5978–5995.
5. Lei, S.; Xu, B.; Wang, C.; Xu, Q.; Bai, C. Scanning tunneling microscopy characterization of aromatic molecules stabilized by a buffer layer of alkane derivatives. *Jpn. J. Appl. Phys.* **2001**, *40*, 4273–4276.
6. Yin, S.; Wang, C.; Xu, Q.; Lei, S.; Bai, C. Studies of the effects of hydrogen bonding on monolayer structures of C<sub>18</sub>H<sub>37</sub>X (X = OH, SH) on HOPG. *Chem. Phys. Lett.* **2001**, *348*, 321–328.
7. Rabe, J.P.; Buchholtz, S. Commensurability and mobility in two-dimensional molecular patterns on graphite. *Science* **1991**, *253*, 424–427.
8. Rabe, J.P.; Buchholtz, S. Molecular imaging of alkanol monolayers on graphite. *Angew. Chem., Int. Ed. Engl.* **1992**, *31* (2), 189–191.
9. Yeo, Y.H.; McGonigal, G.C.; Thomson, D.J. Structure phase transition of a 1-dodecanol monolayer physisorbed at the liquid/graphite interface by scanning tunneling microscopy. Observation of highly ordered, two-dimensional *n*-alkane and *n*-alkanol structures on graphite. *Langmuir* **1993**, *9*, 649–651.
10. McGonigal, G.C.; Yeo, Y.H.; Bernhardt, R.H.; Thomson, D.J. Observation of highly ordered, two-dimensional *n*-alkane and *n*-alkanol structures on graphite. *J. Vac. Sci. Technol., B* **1991**, *9* (2), 1107–1110.
11. Nishino, T.; Buhlmann, P.; Ito, T.; Umezawa, Y. Scanning tunneling microscopy with chemically modified tips: Orientation-sensitive observation of ether oxygens. *Surf. Sci.* **2001**, *490*, L579–584.
12. Lee, H.S.; Musselman, I.H. Identification of halogen atoms in scanning tunneling microscopy images of substituted phenyl octadecyl ethers. *Anal. Chem.* **2001**, *73*, 5532–5538.
13. Okawa, Y.; Aono, M. Materials science-nanoscale control of chain polymerization. *Nature* **2001**, *409*, 683–684.
14. Hibino, M.; Sumi, A.; Hatta, I. Molecular arrangement of fatty-acids cholesterol at liquid graphite interface observed by scanning-tunneling-microscopy. *Jpn. J. Appl. Phys.* **1995**, *34*, 3354–3359.
15. Hibino, M.; Sumi, A.; Hatta, I. Atomic images of saturated and unsaturated fatty acids at liquid/graphite interface and difference of tunneling currents between them observed by scanning-tunneling-microscopy. *Jpn. J. Appl. Phys.* **1995**, *341* (2A), 610–614.
16. Charra, F.; Cousty, J. Surface-induced chirality in a self-assembled monolayer of discotic liquid crystal. *Phys. Rev. Lett.* **1998**, *80* (8), 1682–1685.
17. Fang, H.; Giancarlo, L.C.; Flynn, G.W. Direct determination of the chirality of organic molecules by scanning tunneling microscopy. *J. Phys. Chem., B* **1998**, *102*, 7311–7315.

18. Poulennec, C.L.; Cousty, J.; Xie, Z.X.; Mioskowski, M. Self-organization of physisorbed secondary alcohol molecules on a graphite surface. *Surf. Sci.* **2000**, *448*, 93–100.
19. Stevens, F.; Dyer, D.J.; Walba, D.M. Direct observation of enantiomorphous monolayer crystals from enantiomers by scanning tunneling microscopy. *Angew. Chem., Int. Ed. Engl.* **1996**, *35* (8), 900–901.
20. Eckhardt, C.J.; Peachey, N.M.; Swanson, D.R.; Takacs, J.M.; Khan, M.A.; Gong, X.; Kim, J.H.; Wang, J.; Uphaus, R.A. Separation of chiral phases in monolayer crystals of racemic amphiphiles. *Nature* **1993**, *362*, 614–616.
21. Viswanathan, R.; Zasadzinski, J.A.; Schwartz, D.K. Spontaneous chiral symmetry breaking by achiral molecules in a Langmuir–Blodgett film. *Nature* **1994**, *368*, 440–443.
22. Cai, Y.; Bernasek, S.L. Chiral pair monolayer adsorption of iodine substituted octadecanol molecules on graphite. *J. Am. Chem. Soc.* **2003**, (125), 1655–1659.
23. *Spartan for Silicon Graphics V5.0.1*; Wavefunction, Inc.: Irvine, CA.
24. Yablon, D.G.; Guo, J.; Knapp, D.; Fang, H.; Flynn, G.W. Scanning tunneling microscopy investigation of a chirally pure molecule at the liquid–solid interface: Unambiguous topographic markers. *J. Phys. Chem., B* **2001**, *105*, 4313–4316.



# STEM: Self-Assembly on Graphite

Thomas Müller

Veeco Metrology Group, Santa Barbara, California, U.S.A.

## INTRODUCTION

The two-dimensional self-organization of molecules on surfaces and at interfaces is at the center of vigorous research activity. Thin interfacial films have numerous longstanding technological applications; however, the interest in a fundamental understanding of the self-assembly process has surged in recent years due to the central role envisioned for the controlled bottom-up assembly in future nanoscale molecular engineering. Monolayers physisorbed on the basal plane of graphite can serve as ideal model systems for such studies.

Highly ordered adsorbate monolayers have been generated on graphite substrates for a broad range of molecular species and experimental conditions. On this inert substrate, the dominant dispersion and electrostatic interactions often afford sufficient adsorbate mobility to aid in the self-assembly of thermodynamically favored monolayer structures. A combination of theoretical and experimental approaches, including proximal probes, diffraction-based techniques, and thermal desorption, has been employed to interrogate adsorbate structures and dynamics, and ultimately unravel the delicate balance of forces driving the self-assembly process.

Among experimental techniques, scanning tunneling microscopy (STM) plays a prominent role in elucidating the spatial orientation and conformation of individual adsorbate molecules. The present entry focuses mainly on STM studies addressing the role of interactions associated with functional groups and with saturated hydrocarbon chains in driving self-assembly on the basal plane of graphite. The structure and dynamics of the observed ordered, lamellar monolayers are seen to result from a set of competing geometric requirements. In addition, a brief discussion of STM image contrast is included, highlighting the ability of STM to provide information about the role of individual adsorbate electronic states in mediating electron transport. The final section of this entry is concerned with recent studies exploiting both geometric and electronic contributions to STM image

contrast to address molecular device properties in carefully tailored model systems self-assembled on graphite.

## MONOLAYER GENERATION AND INTERROGATION

Self-assembled, physisorbed monolayers on graphite have been generated at the liquid–solid interface, at the air–graphite interface, and in ultra-high vacuum (UHV).<sup>[1–10]</sup> Structural information has been obtained through both diffraction techniques and scanning probe microscopies (SPMs).<sup>[1,11–17]</sup> Structural data obtained for sets of related compounds and for different experimental conditions in conjunction with thermal desorption data and results from theoretical studies have given insight into the interactions driving the self-assembly process.<sup>[1,12,18–25]</sup>

As STM can provide high resolution locally (i.e., true atomic as opposed to lattice resolution) on a flat, conductive substrate, it has been the most prominent SPM utilized for the study of self-assembly on graphite.<sup>[26]</sup> As shown by Tersoff and Hamann, the tunneling current between a metallic tip and a metallic surface (note that graphite is a semimetal) is proportional to the surface local density of states (LDOS) at the Fermi level,  $E_F$ , evaluated at the location of the tip.<sup>[27,28]</sup> While this simple result is subject to approximations (e.g., small bias, low temperature, and spherical tip represented by an  $s$ -wave function), the interpretation of STM images in terms of the surface LDOS at (or near)  $E_F$  has met with overwhelming success. In general, the LDOS near  $E_F$  at the location of the tip is sensitive to the electronic structure of any molecular adsorbate present in the tunneling junction. For molecules with moderate ionization potentials and moderate gaps between the highest occupied molecular orbital (HOMO) and the lowest unoccupied molecular orbital (LUMO), frontier orbitals can play an important role in mediating the electron tunneling process. Therefore, STM images of molecules with extended

$\pi$ -electron systems or functional groups contain an “electronic” component and can reflect the electron density distribution associated with individual molecular orbitals.<sup>[1,8,29,30]</sup> In contrast, STM images of unsubstituted saturated hydrocarbons are dominated by “geometric” effects and provide a topographic map. Here, the topmost atoms dominate the LDOS near  $E_F$  at the location of the tip.<sup>[30,31]</sup> In addition, the electronic structure of the underlying graphite substrate is often found to contribute to the image contrast, allowing STM images to address questions of substrate commensurability.<sup>[32]</sup>

Numerous studies have addressed self-assembly on graphite by utilizing STM to interrogate ordered monolayers formed by substituted alkanes at the interface between an organic solution and the basal plane of graphite.<sup>[26,31–34]</sup> Aside from monolayer structures, these studies have elucidated dynamics associated with the self-assembly process by probing two-component systems, domain boundaries, temperature-dependence, and the response to external perturbations.<sup>[21,35–39]</sup> In addition, the structure and dynamics of monolayer formation have been examined in light of the requirements for topochemical transformations.<sup>[4,5,40–42]</sup> The success of interrogations of substituted alkanes at the liquid–solid interface has led to extensions of this approach to codeposition of several solutes and monolayers serving as templates for organizing other molecules and nanoparticles, and to ring systems (e.g., porphyrins) with alkyl chains or functional groups at their periphery facilitating self-assembly.<sup>[7,10,43–49]</sup> In contrast, the ambient self-assembly of ring systems without alkyl chains or functional groups at their periphery has been reported less frequently.<sup>[50,51]</sup> Substituted alkanes and hydrogen-bonded systems have also been investigated at the air–graphite interface upon generating monolayers through evaporation of the organic or aqueous solvent or by Langmuir–Blodgett deposition from aqueous solution.<sup>[2–5,45,52,53]</sup>

To address self-assembly on graphite under UHV conditions, vapor-deposited monolayers have been probed using STM and diffraction techniques.<sup>[6–11,14,54]</sup> Ultra-high vacuum studies of self-assembly on graphite have served to extend the scope of self-assembled monolayers to include those not stable under ambient conditions, to assess the influence of solvent by interrogating monolayers analogous to those that do exist at the liquid–solid interface, to study monolayer dynamics (including melting and desorption) over a wide temperature range, and to provide ideal conditions for direct comparisons with theoretical results.<sup>[10–14,18–20,23,25]</sup> Vapor deposition has allowed the generation of ordered monolayers on graphite substrates for hydrocarbon chains as well as ring systems, irrespective of the presence of functional groups.<sup>[6,8,10,14,25,54]</sup> The most important factor limiting

the applicability of this approach might be the need for the species of interest to survive vaporization in a vacuum.

## MONOLAYER STRUCTURE AND DRIVING FORCES FOR SELF-ASSEMBLY

### Substituted Alkanes

Substituted alkanes form weakly physisorbed monolayers on graphite.<sup>[1,26]</sup> Dispersion interactions between alkyl chains and the graphite substrates provide adsorption energies of  $\sim 1$ – $3$  kcal/mol per methylene group, depending on chain length and functionalization, making desorption barriers substantially higher for monolayer than for multilayer adsorption sites.<sup>[18–20]</sup> Substituted alkanes form stable monolayers (i.e., as opposed to three-dimensional island growth) on graphite in a vacuum although no directed chemical bonds are formed between adsorbate molecules and individual carbon atoms of the graphite substrate. Consistent with the absence of covalent adsorbate–substrate bonds, the adsorption energies are accompanied by comparatively smaller barriers to lateral motion. High lateral mobility enables the annealing of monolayers to form minimum energy structures in a vacuum, while solution exchange may provide an alternate path at the liquid–solid interface where ordered monolayers exist in equilibrium with a supernatant solution or melt.<sup>[1,26,55]</sup> Thus, conditions can often be found both in vacuum and in liquid–solid interface for probing such ordered monolayers unimpeded by any formation of additional ordered adsorbate layers.

In self-assembled monolayers of substituted alkanes on graphite, the alkyl chains assume an extended, all-*trans* conformation. In contrast to the dense self-assembled monolayers formed by alkane thiols on gold substrates, the backbone axis is parallel to the surface plane bringing the entire alkyl chain into contact with the graphite substrate.<sup>[1,56–59]</sup> In general, a lamellar structure is formed where the lamella–backbone angle depends on alkane functionalization. In the case of long linear alkanes without any functional group, a lamella–backbone angle of  $90^\circ$  is found. In the all-*trans* conformation of alkanes, all carbon atoms lie in a plane and form a zigzag pattern. As STM images of alkanes on graphite provide a map of the topmost hydrogen atoms, they can reveal the orientation of the carbon backbone plane with respect to the substrate surface plane.<sup>[31]</sup> Fig. 1 shows STM images of hexatriacontane at the interface of a 1-phenyloctane solution and the basal plane of graphite.<sup>[31]</sup> As expected, a rectangular, lamellar structure can be discerned with the lamella width equal to one molecular

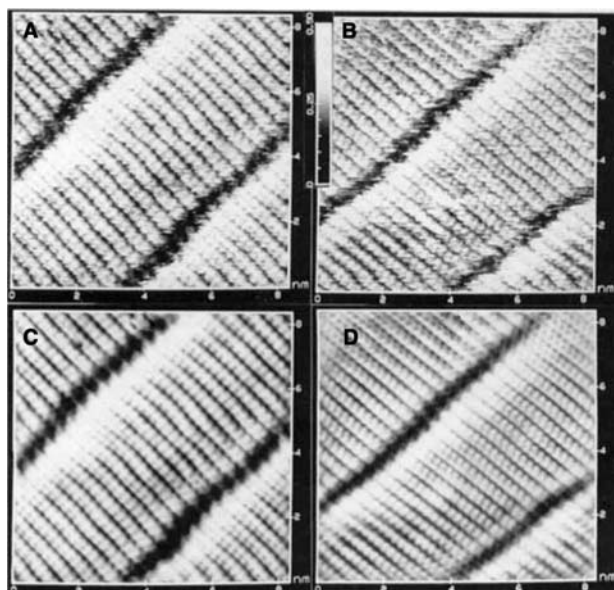


**Fig. 1** Constant current STM image (sample bias—168 mV, 300 pA tunneling current) of hexatriacontane at the interface between a dodecane solution and the basal plane of graphite. Raw data of two successive scans are shown in (A) and (B). Filtered versions of the images in (A) and (B) are shown in (C) and (D), respectively. *Source:* Used with permission from Ref.<sup>[31]</sup>. © 1993 VCH Verlagsgesellschaft mbH, Weinheim.

length,  $\approx 4.5$  nm for  $C_{36}H_{74}$  in its all-*trans* conformation. However, the STM images shown in panels (A) and (B) exhibit different spot patterns within each molecule, even though they represent subsequent scans of the same area. While panel (A) [and the filtered image in (C)] shows the double-spot pattern expected for a vertical orientation of the carbon backbone plane (i.e., perpendicular to the substrate surface), the zigzag pattern in panel (B) [and the filtered image in (D)] is consistent with a horizontal orientation (i.e., parallel to the substrate surface). Apparently, both orientations can (co) exist at the liquid–solid interface.

The spatial requirements of individual alkane molecules may depend on the angle assumed by the carbon backbone plane. In three-dimensional alkane crystals, lateral nearest neighbor spacings of  $\sim 4.8$  and  $\sim 4.2$  Å are found parallel and perpendicular to the molecular carbon planes, respectively.<sup>[60]</sup> In STM studies of long-chain alkane monolayers at the liquid–solid interface, lateral spacings have been found to be closer to 4.2 Å.<sup>[32]</sup> If the molecular backbone axis is aligned with one of the high-symmetry directions of the underlying graphite substrate, a spacing of 4.26 Å is required for each alkane molecule to occupy an equivalent surface site. Such a commensurate monolayer structure is consistent with the absence of moiré patterns in STM images of alkanes at the interface between an organic solution and the basal plane of graphite.<sup>[32]</sup> At first it

may appear to be inconsistent with the substantially larger spacings reported by Herwig et al. based on diffraction studies of vapor-deposited monolayers composed of similarly long alkanes (i.e.,  $C_{32}H_{66}$ ).<sup>[14]</sup> However, Herwig et al. found that the presence of “solvent” (i.e., heptane adsorbed atop a monolayer formed by dotriacontane) leads to a contraction of the monolayer structure accompanied by a change in the distribution of angles assumed by the molecular backbone plane.<sup>[14]</sup> The observed shifts in diffraction maxima are consistent with a commensurate monolayer in the limiting case of full solvent coverage.<sup>[14]</sup> The sensitivity of alkane monolayer structures to the presence of additional alkane layers may also explain the existence of ordered alkane monolayers substantially above the bulk melting temperature in the presence of bulk alkane melt, while essentially no increased melting temperature (i.e., when compared to the bulk melting point) is found for analogous vapor-deposited alkane monolayers in vacuum.<sup>[13,55]</sup> Further variations in alkane monolayer structures exist as a function of alkane chain length.<sup>[11,15,16]</sup> Diffraction studies of short alkanes on graphite have revealed the existence of a herringbone structure for monolayers composed of some short alkanes with an even number of carbon atoms with the transition to a rectangular structure depending on coverage and temperature.<sup>[16]</sup>

Like alkanes, alkanic acids form monolayers at the interface between an organic solution and the basal plane of graphite. As shown in Fig. 2, STM images reveal a lamellar monolayer structure where the molecular backbone axis is perpendicular to the lamellar axis, just as with alkane monolayers.<sup>[32]</sup> Close inspection of Fig. 2 reveals the formation of acid dimers and a zigzag spot pattern associated with each alkyl chain. Introduction of the carboxylic head group has not changed the lamella–backbone angle but has forced

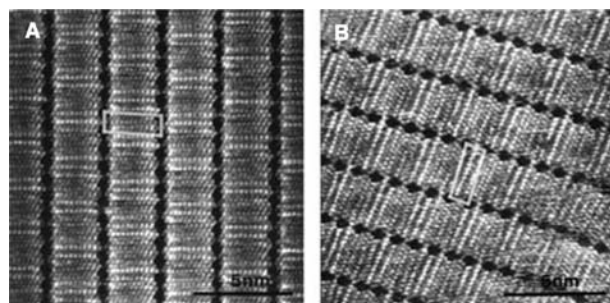


**Fig. 2** Constant current STM images (sample bias—1.3 V, 800 pA tunneling current) of behenic acid at the interface between a 1-phenyloctane solution and the basal plane of graphite. The arrangement of molecules in (A) is the mirror image of that observed in (B). Parallelograms represent the unit cell of the monolayer. *Source:* Reprinted with permission from Ref.<sup>[61]</sup>. © 1998 American Chemical Society.

the entire molecular backbone plane into a “flat” orientation (parallel to the substrate surface). Lateral intermolecular spacings are expanded to  $\sim 4.8$  Å, and STM images of alkanolic acid monolayers often show moiré effects due to the lack of commensurability.<sup>[32]</sup>

The monolayer domains displayed in Fig. 2 are enantiomorphous, although alkanolic acids are achiral in three-dimensional space.<sup>[61]</sup> Due to the symmetry break at the interface and lack of free molecular rotation, individual adsorbed alkanolic acid molecules (and their dimers) can exist in two non-superimposable states that constitute mirror images of each other (i.e., they are prochiral or enantiomorphous). For alkanolic acids with an even number of carbon atoms, each self-assembled domain is constituted of adsorbed molecules in only one of the two enantiomorphous states, making the whole domain enantiomorphous. In contrast, both enantiomers are present in a given domain for an odd number of carbon atoms.<sup>[61]</sup> Thus, the presence of one additional methylene group in an (achiral) alkanolic acid molecule alters the chirality of self-assembled domains at the liquid–solid interface while having no analogous influence in three-dimensional space.

The expression of chirality in two dimensions has been interrogated in more complex situations, where several solutes are codeposited in self-assembled domains at the liquid–solid interface.<sup>[62]</sup> The enantiomorphous domains formed by achiral alkanolic acids with an even number of carbon atoms can be used to induce chiral segregation among codeposited chiral cosolutes.<sup>[46]</sup> As shown in Fig. 3, only one enantiomer of the chiral 2-bromohexadecanoic acid is present in a given enantiomorphous domain formed by the achiral hexadecanoic acid.<sup>[46]</sup> The mixed self-assembly of chiral and achiral species can also lead to the opposite effect, where the chiral component induces the achiral species to be adsorbed in a prochiral state and chirally segregated. De Feyter et al. have shown that the chiral 5-[10-(2-methylbutoxy)-decyloxy]isophthalic acid dissolved in heptanol forms enantiomorphous domains at the liquid–solid interface incorporating heptanol in a prochiral state.<sup>[44]</sup>

Alkanes and alkanolic acids exemplify limiting cases regarding (hindered) molecular rotation about the backbone axis in self-assembled monolayers of substituted alkanes. The structural variations for unsubstituted alkanes point to a shallow potential along several degrees of freedom (as long as a close-packed structure is maintained). In contrast, the carboxylic acid head group apparently forces the entire molecular backbone plane of alkanolic acids into a flat configuration. Terminal halogen substituents represent an intermediate case.<sup>[25]</sup> In general, alkane functionalization affects such structural parameters as the backbone plane rotation angle, backbone–lamella angle, lateral nearest

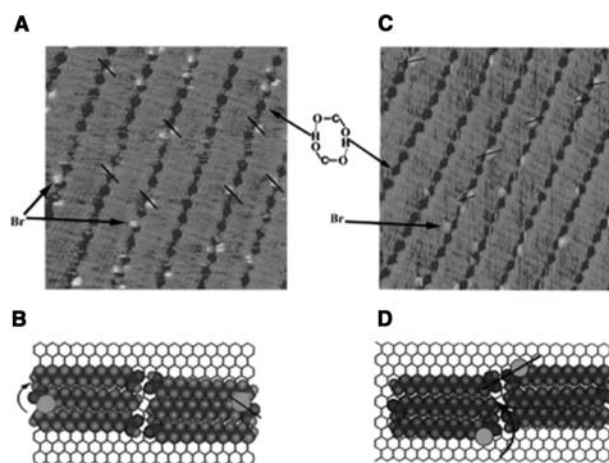


**Fig. 3** (A) Constant current STM image ( $15 \times 15$  nm, sample bias—1.5 V, 300 pA tunneling current) of a hexadecanoic acid domain interspersed with (*R*)-2-Br-hexadecanoic acid. The blue bar represents one molecular length. (B) Corresponding molecular model. The bromine substituent (bright marker) lies in a fixed orientation to the carboxyl group (dark marker) as indicated by the black bars in (A) and (B). The curved arrow in (B) identifies the brominated molecule as *R* enantiomer. (C) Constant current STM image ( $18 \times 18$  nm, sample bias—1.5 V, 300 pA tunneling current) of a hexadecanoic acid domain interspersed with (*S*)-2-Br-hexadecanoic acid. The blue bar represents one molecular length. (D) Corresponding molecular model. Again the bromine substituent (bright marker) lies in a fixed orientation to the carboxyl group (dark marker) as indicated by the black bars in (C) and (D). The curved arrow in (D) identifies the brominated molecule as *S* enantiomer. *Source*: Reprinted with permission from Ref.<sup>[46]</sup>. © 2001 American Chemical Society.

neighbor spacing, and substrate commensurability as functional group interactions can exhibit a pronounced angular dependence (in addition to steric requirements) compared to the more isotropic alkane–alkane and alkane–graphite dispersion forces. Interactions between terminal functional groups and the graphite substrate are not overwhelming in magnitude, even for substituted alkanes of moderate chain length (i.e.,  $C_nH_{2n+1}X$  with  $n = 6$ ).<sup>[25]</sup> In analogy to alkane thiols on Au(111), one might expect overwhelming head group–substrate interactions to be associated with a high-density monolayer structure, where only the terminal functional groups are in direct contact with the substrate.<sup>[56–59]</sup> With the possible exception of 1-fluorohexane this has not been observed.<sup>[25]</sup> The competing geometric requirements associated with functional group and alkyl chain interactions lead to energetic trade-offs that are apparent in the chain length dependence of monolayer desorption energies.<sup>[20]</sup> In the case of alkanes and 1-bromoalkanes, solvent interactions can shift the resulting balance of interactions.<sup>[14,25]</sup>



## Ring Systems

The success in the formation and interrogation of ordered monolayers for a wide range of substituted alkanes suggests strategies for the self-assembly of monolayers composed of ring systems. Large cycloalkanes have been found to self-assemble at the liquid–solid interface forming structures analogous to those of unsubstituted *n*-alkanes.<sup>[63]</sup> In the case of more rigid, planar ring systems with extended  $\pi$ -electron systems, alkyl chains, functional groups, or both have been attached at their periphery to mediate self-assembly on the basal plane of graphite. Reports of self-assembled monolayers composed of such tailored ring systems include polyphenylenes, phthalocyanines, and porphyrins.<sup>[3,53,64]</sup> Fig. 4 shows a high-resolution STM image of 21,23-dihydro-5,10,15,20-tetrakis[4-(tetradecyloxy) phenyl] porphyrin (TPPP) at the air–graphite interface.<sup>[53]</sup> Clearly, an ordered monolayer structure is observed, presumably stabilized by the interdigitization of the 14-carbon long alkyl chains attached to each porphyrin. Consistent with this hypothesis, shorter-chain analogs were found to produce less ordered monolayer structures.<sup>[53]</sup> Ring systems such as trimesic acid and DNA bases lack alkyl chains at their periphery. Here, the formation of intermolecular hydrogen bonds drive the formation of ordered monolayers at the basal plane of graphite.<sup>[2,7,54]</sup> The ability to form intermolecular

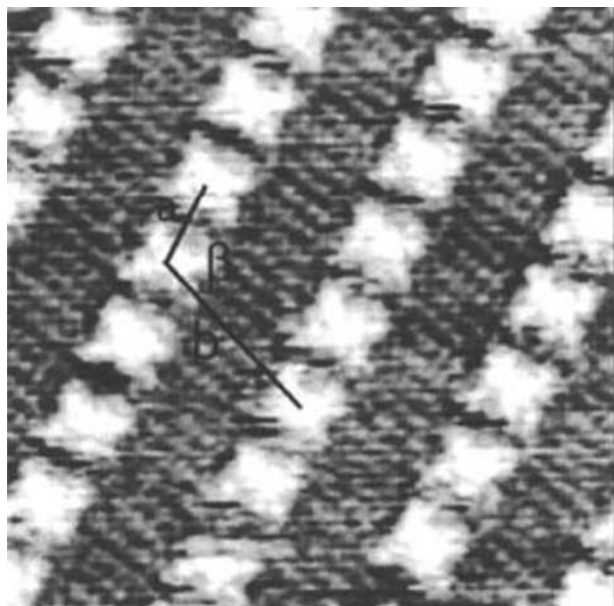


**Fig. 4** High-resolution STM image ( $15 \times 15$  nm, sample bias—752 mV, 1.032 nA tunneling current) of TPPP on graphite. Rows of bright porphyrin cores are interspersed with ordered, interdigitated alkyl chains. *Source:* Reproduced with permission from Ref.<sup>[24]</sup>. © 2001 John Wiley & Sons Limited.

hydrogen bonds is essential to the biological function of DNA bases. It has been suggested that the stabilization of self-assembled monolayers (composed of DNA bases) by intermolecular hydrogen bonding may have played an equally important role in the emergence of life.<sup>[65]</sup>

Monolayers formed by ring systems lacking both alkyl chains and functional groups at their periphery have been studied on a variety of substrates under UHV conditions. Fig. 5 shows an STM image of a naphthalocyanine monolayer that was vapor-deposited onto graphite.<sup>[8]</sup> All molecules are adsorbed with their ring plane parallel to the surface plane. An individual vacancy can be seen which aids in determining the azimuthal orientation of individual adsorbate molecules. The overlaid molecular models in panel (B) reveal the seamless monolayer packing, apparently maximizing the number density of adsorbed molecules. However, substrate commensurability is maintained, indicating that the periodic corrugation of adsorbate–substrate interactions plays a significant role in the formation of this monolayer structure.<sup>[8]</sup> Commensurable monolayer structures have been observed also for other planar ring systems with delocalized  $\pi$ -electron systems, even when intermolecular hydrogen bonds are present.<sup>[2]</sup>

In some cases, the monolayers formed by ring systems without alkyl chains or functional groups have been interrogated under ambient conditions. Both very large polycyclic aromatic hydrocarbons and porphyrins form ordered monolayers at the liquid–solid interface, where the molecular ring plane is either parallel or slightly tilted with respect to the surface plane.<sup>[50,51]</sup> However, in the presence of a supernatant solution such monolayers often coexist with a significant number density of  $\pi$ -stacked aggregates and adsorbate multilayers suggesting at most a weak selective stabilization of the adsorbate monolayer.<sup>[1,50,51]</sup> This may not impede the interrogation of vapor-deposited monolayers composed of the same species under UHV conditions, where the different adsorption procedure and the absence of a supernatant solution change both energies and kinetics. For ring systems that form stable monolayers both in UHV and at the liquid–solid interface, the presence of solvent can have subtle effects such as changing the phase relation with respect to the substrate.<sup>[10]</sup>

## MODEL SYSTEMS FOR MOLECULAR ELECTRONICS

Recently, STM studies of self-assembly on graphite have included molecules specifically tailored both to facilitate both two-dimensional self-assembly and as model systems for molecular electronics. Following

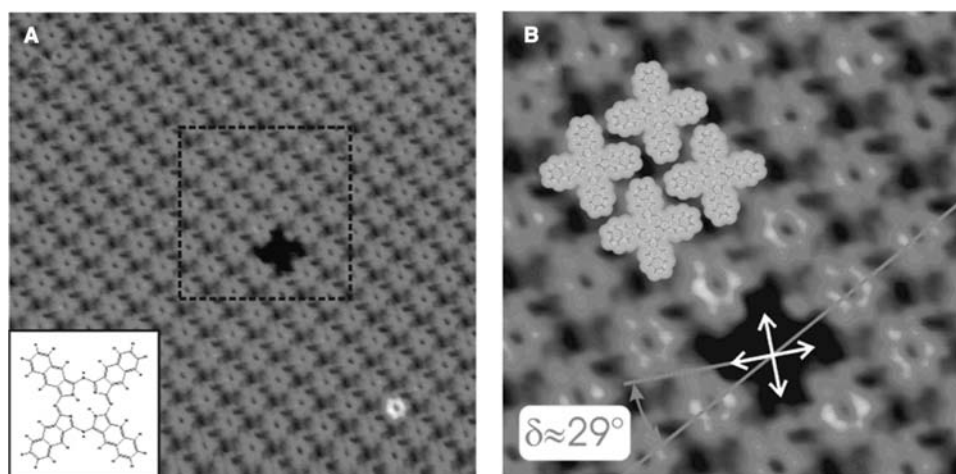


**Fig. 5** (A) Constant current STM image ( $25 \times 25$  nm, sample bias—1.83 V, 83 pA tunneling current) of naphthalocyanine on graphite at a surface temperature of 50 K. The close-packed monolayer contains a single vacancy, allowing the azimuthal orientation of individual molecules to be determined. The inset shows the chemical structure of naphthalocyanine. (B) Expanded section (mean filtered,  $9 \times 9$  nm) as marked in (A). The measured azimuthal angle was applied to the overlaid molecular model. *Source:* Reprinted with permission from Ref.<sup>[8]</sup>. © 2004 American Chemical Society.

early suggestions by Aviram and Ratner, molecular analogs for current rectifiers (diodes) and transistors are being investigated where electron donors (D) and acceptors (A) are linked covalently.<sup>[66]</sup> In addition to providing high spatial resolution, the STM tunneling junction is a probe of charge transport at the nanoscale. Scanning tunneling microscopy studies of molecules adsorbed on surfaces intrinsically address the mediation of charge transport by molecular states and their coupling to one of the electrodes (i.e., the conducting substrate supporting the molecule).

Miura et al. have investigated a large, symmetric D–A–D system composed of oligo-*p*-phenylene vinylene D-units and a perylenediimide A-core as shown in Fig. 6(A).<sup>[48]</sup> The STM images shown in Figs. 6(B), (C), and (E) reveal the formation of ordered monolayer domains at the interface of a 1-phenyloctane solution and the basal plane of graphite. As illustrated in Fig. 6(D), the monolayer structure is stabilized by interdigitated dodecyloxy chains. The ordered monolayer structure observed in STM images of this large molecule permits the identification of D and A subunits within each molecule so that their relative image contrast can be examined as a function of bias voltage. As shown in Fig. 6(E), the D moieties are brighter (i.e., give rise to higher tunneling current) at negative sample bias, while the A moieties are brighter at positive sample bias. Miura et al. have proposed an explanation relating the observed bias dependent charge transmission to the electronic structure of the D–A–D system.<sup>[48]</sup> Among all molecular states, the HOMOs of D-subunits have a dominant influence on the surface LDOS just below the Fermi level, as they are the highest filled states of the D–A–D molecule. Thus,

the D-moieties support a higher tunneling current at negative sample bias, where filled surface states are being probed. Conversely, the LUMOs of A-subunits dominate the density of empty surface states just above the Fermi level, making the A-moieties more transmissive at positive sample bias. Thus, a simple physical picture emerges where the bias dependent charge transmission through this molecular device analog can be understood in terms of resonantly enhanced electron tunneling dominated by individual electronic states associated with molecular subunits.<sup>[48]</sup>

Jäckel et al. have reported STM studies of a prototypical single-molecule chemical-field-effect transistor, where nanometer-sized charge transfer (CT) complexes control current rectification through a covalently linked ring system.<sup>[67]</sup> An electron-rich (or electron donor, D) hexa-peri-hexabenzocoronene (HBC) core, surrounded by six electron-poor (or electron acceptor, A) anthraquinone (AQ) subunits is at the center of these studies.<sup>[67,68]</sup> Again, STM images reveal the formation of an ordered monolayer at the liquid–solid interface, where the high degree of order and large molecular size permits the identification of the covalently linked D and A subunits.<sup>[67]</sup> And once more, the consideration of frontier orbitals associated with the D and A subunits suggests that the bias polarity dependent tunneling probability can be understood in terms of resonantly enhanced electron tunneling. Addition of the electron-rich 9,10-dimethoxyanthracene (DMA) to the solution leads to the formation of DMA–AQ–CT complexes. Self-assembled domains with and without CT complexes coexist and are easily distinguished in STM images and interrogated individually. Current–voltage curves obtained atop the



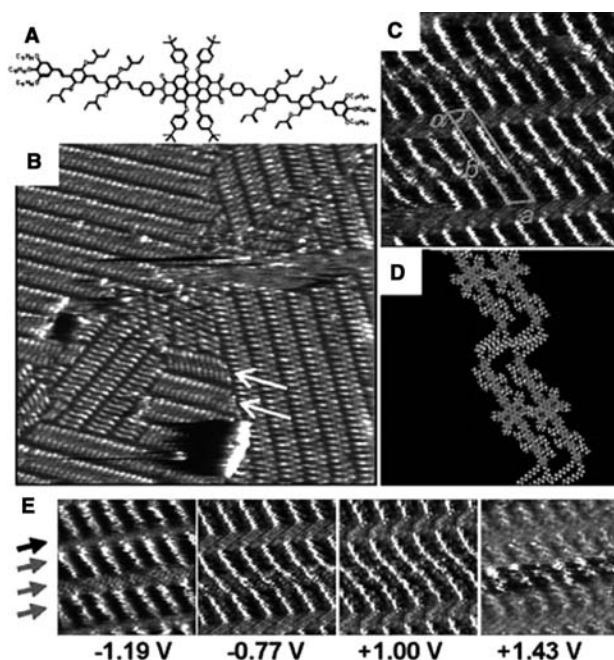


**Fig. 6** (A) Chemical structure of the D–A–D triad. (B) Constant height STM image ( $70.2 \times 70.2$  nm, sample bias— $0.96$  V,  $150$  pA tunneling current) of a D–A–D monolayer at the interface between a 1-phenyloctane solution and the basal plane of graphite. Arrows indicate mirror-image type packing. (C) High-resolution STM image ( $15.5 \times 15.5$  nm, sample bias— $0.70$  V,  $400$  pA tunneling current) with overlaid parallelogram indicating a monolayer unit cell. (D) Proposed molecular model reflecting the ordering in (C). (E) Bias-dependent imaging of the D–A–D triad ( $10.1 \times 10.1$  nm,  $400$  pA tunneling current; sample bias indicated below each image). In order from top to bottom, the arrows on the left refer to alkyl chains, donor units, acceptor units, and donor units. *Source:* Reprinted with permission from Ref.<sup>[48]</sup>. © 2003 American Chemical Society.

HBC cores are asymmetric (rectifying) with the degree of asymmetry controlled by the presence (or absence) of the DMA–AQ–CT complex.<sup>[67]</sup> Jäckel et al. have proposed that the interfacial dipole associated with formation of the CT complex causes a relative shift between the adsorbate's electronic states and the Fermi level of the substrate.<sup>[67]</sup> Thus, current transmission through a single molecule is controlled by a field effect of chemical origin.<sup>[67]</sup>

The STM studies discussed in this section have combined self-assembly on graphite with detailed single-molecule conductance measurements by using specifically tailored molecules synthesized prior to deposition on the graphite substrate. On the other hand, the post-assembly modification of self-assembled monolayers (e.g., topochemical polymerization of diacetylene derivatives) on graphite has been demonstrated.<sup>[4,5,40,42]</sup> Furthermore, self-assembled monolayers of substituted alkanes on graphite have been used as templates for

organizing nanoparticles.<sup>[47]</sup> Based on combinations of these ingredients one could envision powerful recipes for the targeted creation of nanostructures and complex model systems for molecular devices with self-assembly on graphite playing a central role.

## CONCLUSIONS

A wide range of molecular species has been shown to form highly ordered monolayers physisorbed on the basal plane of graphite in vacuum and under ambient conditions. Experimental approaches including proximal probes, diffraction, and thermal desorption have been used in concert with theoretical predictions to interrogate structures and dynamics and unravel the driving forces of the self-assembly process. A large fraction of studies have employed STM and have focused on substituted alkanes self-assembled at the liquid–solid interface. In general, lamellar monolayer structures are observed with structural parameters depending on the balance of interactions associated with the alkyl chains and the functional group. In ambient studies of planar ring systems, monolayer formation is often driven by alkyl chains or functional group interactions. In contrast, UHV studies have been less dependent on substituents at the periphery of ring systems facilitating monolayer stabilization through specific intermolecular interactions.

Aside from providing information about monolayer structure and dynamics, STM studies of self-assembly on graphite can address the mediation of charge transport by individual molecular states. Recent years have witnessed a synthesis where STM studies have combined both aspects to interrogate model systems for molecular devices. Future studies can be envisioned, where the power of this approach is augmented further through combination with postassembly modification and coassembly of multiple nanoscale components, thus allowing self-assembly on graphite to play an even more important role in nanoscience.

## ACKNOWLEDGMENTS

The author is indebted to many colleagues in the scientific community and at Veeco Metrology Group for help, encouragement, and for communicating results. Special thanks go to Professor George W. Flynn for his advice and support.

## REFERENCES

1. Giancarlo, L.C.; Flynn, G.W. Scanning tunneling and atomic force microscopy probes of self-assembled,

- physisorbed monolayers: peeking at the peaks. *Annu. Rev. Phys. Chem.* **1998**, *49*, 297–336.
- Freund, J.E.; Edelwirth, M.; Kröbel, P.; Heckl, W.M. Structure determination of two-dimensional adenine crystals on graphite. *Phys. Rev. B* **1997**, *55* (8), 5394–5397.
  - Qiu, X.; Wang, C.; Zeng, Q.; Xu, B.; Yin, S.; Wang, H.; Xu, S.; Bai, C.L. Alkane-assisted adsorption and assembly of phthalocyanines and porphyrins. *J. Am. Chem. Soc.* **2000**, *122* (23), 5550–5556.
  - Okawa, Y.; Aono, M. Linear chain polymerization initiated by a scanning tunneling microscope tip at designated positions. *J. Chem. Phys.* **2001**, *115* (5), 2317–2322.
  - Okawa, Y.; Aono, M. Nanoscale control of chain polymerization. *Nature* **2001**, *409* (6821), 683–684.
  - Lackinger, M.; Griessl, S.; Heckl, W.M.; Hietschold, M. STM and STS of coronene on HOPG (0001) in UHV—adsorption of the smallest possible graphite flakes on graphite. *Anal. Bioanal. Chem.* **2002**, *374* (4), 685–687.
  - Lackinger, M.; Griessl, S.; Heckl, W.M.; Hietschold, M.; Flynn, G.W. Self-assembly of trimesic acid at the liquid–solid interface—a study of solvent-induced polymorphism. *Langmuir* **2005**, *21* (11), 4984–4988.
  - Lackinger, M.; Müller, T.; Gopakumar, T.G.; Müller, F.; Hietschold, M.; Flynn, G.W. Tunneling voltage polarity dependent submolecular contrast of naphthalocyanine on graphite. A STM study of close-packed monolayers under ultrahigh-vacuum conditions. *J. Phys. Chem. B* **2004**, *108* (7), 2279–2284.
  - Walzer, K.; Hietschold, M. STM and STS investigation of ultrathin tin phthalocyanine layers adsorbed on HOPG(0001) and Au(111). *Surf. Sci.* **2001**, *471* (1–3), 1–10.
  - Stecher, R.; Drewnick, F.; Gompf, B. Influence of preparation conditions on the monolayer structure: bi- and terthiophenes in solution and UHV. *Langmuir* **1999**, *15* (19), 6490–6494.
  - Krim, J.; Suzanne, J.; Shechter, H.; Wang, R.; Taub, H. A LEED and neutron diffraction study of hexane adsorbed on graphite in the monolayer range: uniaxial commensurate incommensurate transition. *Surf. Sci.* **1985**, *162*, 446–451.
  - Hansen, F.Y.; Taub, H. Melting mechanism in monolayers of flexible rod-shaped molecules. *Phys. Rev. Lett.* **1992**, *69* (4), 652–655.
  - Hansen, F.Y.; Herwig, K.W.; Matthies, B.; Taub, H. Intramolecular and lattice melting in *n*-alkane monolayers: an analog of melting in lipid bilayers. *Phys. Rev. Lett.* **1999**, *83* (12), 2362–2365.
  - Herwig, K.W.; Matthies, B.; Taub, H. Solvent effects on the monolayer structure of long *n*-alkane molecules adsorbed on graphite. *Phys. Rev. Lett.* **1995**, *75* (17), 3154–3157.
  - Arnold, T.; Dong, C.C.; Thomas, R.K.; Castro, M.A.; Perdigon, A.; Clarke, S.M.; Inaba, A. The crystalline structures of the odd alkanes pentane, heptane, nonane, undecane, tridecane, and pentadecane monolayers adsorbed on graphite at submonolayer coverages and from the liquid. *Phys. Chem. Chem. Phys.* **2002**, *4*, 3430–3435.
  - Arnold, T.; Thomas, R.K.; Castro, M.A.; Clarke, S.M.; Messe, L.; Inaba, A. The crystalline structures of the even alkanes hexane, octane, decane, dodecane, and tetradecane monolayers adsorbed on graphite at submonolayer coverages. *Phys. Chem. Chem. Phys.* **2002**, *4*, 345–351.
  - Morishige, K.; Takami, Y.; Yokota, Y. Structures of alkanes and alkanols adsorbed on graphite in solution: comparison with scanning-tunneling-microscopy images. *Phys. Rev. B* **1993**, *48* (11), 8277–8281.
  - Paserba, K.R.; Gellman, A.J. Kinetics and energetics of oligomer desorption from surfaces. *Phys. Rev. Lett.* **2001**, *86* (19), 4338–4341.
  - Paserba, K.R.; Gellman, A.J. Effects of conformational isomerism on the desorption kinetics of *n*-alkanes from graphite. *J. Chem. Phys.* **2001**, *115* (14), 6737–6751.
  - Müller, T.; Flynn, G.W.; Mathauser, A.T.; Teplyakov, A.V. Temperature-programmed desorption studies of *n*-alkane derivatives on graphite: desorption energetics and the influence of functional groups on adsorbate self-assembly. *Langmuir* **2003**, *19* (7), 2812–2821.
  - Askadskaya, L.; Rabe, J.P. Anisotropic molecular dynamics in the vicinity of order–disorder transitions in organic monolayers. *Phys. Rev. Lett.* **1992**, *69* (9), 1395–1398.
  - Hentschke, R.; Schürmann, B.L.; Rabe, J.P. Molecular-dynamics simulations of ordered alkane chains physisorbed on graphite. *J. Chem. Phys.* **1992**, *96* (8), 6213–6221.
  - Hansen, F.Y.; Newton, J.C.; Taub, H. Molecular dynamics studies of the melting of butane and hexane monolayers adsorbed on the basal-plane surface of graphite. *J. Chem. Phys.* **1993**, *98* (5), 4128–4141.
  - Yin, S.; Wang, C.; Xiaohui, Q.; Xu, B.; Bai, C.L. Theoretical study of the effects of intermolecular interactions in self-assembled long-chain alkanes adsorbed on graphite surface. *Surf. Interface Anal.* **2001**, *32* (1), 248–252.
  - Müller, T.; Werblowsky, T.L.; Florio, G.M.; Berne, B.J.; Flynn, G.W. Ultra-high vacuum scanning tunneling microscopy and theoretical studies of 1-halohexane monolayers on graphite: functional group interactions, self-assembly, and image contrast. *Proc. Natl. Acad. Sci. USA* **2005**, *102* (15), 5312–5322.
  - De Feyter, S.; Gesquiere, A.; Abdel-Mottaleb, M.M.S.; Grim, P.C.M.; De Schryver, F.C. Scanning tunneling microscopy: a unique tool in the study of chirality, dynamics, and reactivity in physisorbed organic monolayers. *Acc. Chem. Res.* **2000**, *33* (8), 520–531.
  - Tersoff, J.; Hamann, D.R. Theory of the scanning tunneling microscope. *Phys. Rev. B* **1985**, *31* (2), 805–813.
  - Tersoff, J.; Hamann, D.R. Theory and application for the scanning tunneling microscope. *Phys. Rev. Lett.* **1983**, *50* (25), 1998–2001.
  - Giancarlo, L.C.; Flynn, G.W. Raising flags: applications of chemical marker groups to study self-assembly, chirality, and orientation of interfacial films by scanning tunneling microscopy. *Acc. Chem. Res.* **2000**, *33* (7), 491–501.

30. Claypool, C.L.; Faglioni, F.; Goddard, W.A., III.; Gray, H.B.; Lewis, N.S.; Marcus, R.A. Source of image contrast in STM images of functionalized alkanes on graphite: a systematic functional group approach. *J. Phys. Chem. B* **1997**, *101* (31), 5978–5995.
31. Liang, W.; Whangbo, M.H.; Wawkuszewski, A.; Cantow, H.J.; Magonov, S.N. Electronic origin of scanning tunneling microscopy images and carbon skeleton orientations of normal alkanes adsorbed on graphite. *Adv. Mater.* **1993**, *5* (11), 817–821.
32. Rabe, J.P.; Buchholz, S. Commensurability and mobility in 2-dimensional molecular patterns on graphite. *Science* **1991**, *253* (5018), 424–427.
33. McGonical, G.C.; Bernhardt, R.H.; Thomson, D.J. Imaging alkane layers at the liquid graphite interface with the scanning tunneling microscope. *Appl. Phys. Lett.* **1990**, *57* (1), 28–30.
34. Hibino, M.; Hatta, I. Atomic images of saturated and unsaturated fatty acids at liquid/graphite interface and difference of tunneling currents between them observed by scanning tunneling microscopy. *Jpn. J. Appl. Phys.* **1995**, *34* (2A), 610–614.
35. Padowitz, D.F.; Sada, D.M.; Kemer, E.L.; Dougan, M.L.; Xue, W.A. Molecular tracer dynamics in crystalline organic films at the liquid–solid interface. *J. Phys. Chem. B* **2001**, *106* (3), 593–598.
36. Venkataraman, B.; Breen, J.J.; Flynn, G.W. Scanning tunneling microscopy studies of solvent effects on the adsorption and mobility of triacontane triacontanol molecules adsorbed on graphite. *J. Phys. Chem.* **1995**, *99* (17), 6608–6619.
37. Hibino, M.; Sumi, A.; Hatta, I. Molecular motion at domain boundaries in fatty acid monolayers on graphite observed by scanning tunneling microscopy. *Thin Solid Films* **1996**, *273* (1–2), 272–278.
38. Bucher, J.P.; Roeder, H.; Kern, K. Thermally-induced disorder and conformational defects of alkane monolayers on graphite. *Surf. Sci.* **1993**, *289* (3), 370–380.
39. Grim, P.C.M.; Vanoppen, P.; De Feyter, S.; Valiyaveetil, S.; Moessner, G.; Müllen, K.; De Schryver, F.C. Molecular organization of azobenzene derivatives at the liquid/graphite interface observed with scanning tunneling microscopy. *J. Vac. Sci. Technol. B* **1997**, *15* (4), 1419–1424.
40. Grim, P.C.M.; De Feyter, S.; Gesquiere, A.; Vanoppen, P.; Rucker, M.; Valiyaveetil, S.; Moessner, G.; Müllen, K.; De Schryver, F.C. Submolecularly resolved polymerization of diacetylene molecules on the graphite surface observed with scanning tunneling microscopy. *Angew. Chem. Int. Ed. Engl.* **1997**, *36* (23), 2601–2603.
41. Abdel-Mottaleb, M.M.S.; De Feyter, S.; Gesquiere, A.; Sieffert, M.; Klapper, M.; Müllen, K.; De Schryver, F.C. Photodimerization of cinnamate derivatives studied by STM. *Nano Lett.* **2001**, *1* (7), 353–359.
42. Qiao, Y.-H.; Zeng, Q.; Tan, Z.-Y.; Xu, S.; Wang, D.; Wang, C.; Wan, L.-J.; Bai, C.L. Photoinduced organic nanowires from self-assembled monolayers. *J. Vac. Sci. Technol. B* **2002**, *20* (6), 2466–2469.
43. Yablon, D.G.; Giancarlo, L.C.; Flynn, G.W. Manipulating self-assembly with achiral molecules: an STM study of chiral segregation by achiral adsorbates. *J. Phys. Chem. B* **2000**, *104* (32), 7627–7635.
44. De Feyter, S.; Grim, P.C.M.; Rucker, M.; Vanoppen, P.; Meiners, C.; Sieffert, M.; Valiyaveetil, S.; Müllen, K.; De Schryver, F.C. Expression of chirality by achiral coadsorbed molecules in chiral monolayers observed by STM. *Angew. Chem. Int. Ed. Engl.* **1998**, *37* (3), 1223–1226.
45. Lei, S.B.; Yin, C.W.; Wan, L.-J.; Bai, C.L. Modular assembly of alkyl-substituted phthalocyanines with 1-iodooctadecane. *Chem. Mater.* **2002**, *14*, 2837–2838.
46. Yablon, D.G.; Jinsong, G.; Knapp, D.; Fang, H.; Flynn, G.W. Scanning tunneling microscopy investigation of a chirally pure molecule at the liquid–solid interface. unambiguous topographic markers. *J. Phys. Chem. B* **2001**, *105* (19), 4313–4316.
47. Hoeppe, S.; Chi, L.; Fuchs, H. Formation of Au<sub>55</sub> strands on a molecular template at the solid–liquid interface. *Nano Lett.* **2002**, *2* (5), 459–463.
48. Miura, A.; Chen, Z.; Hiroshi, U.; De Feyter, S.; Zdanowska, M.; Jonkheijm, P.; Schenning, A.P.H.J.; Meijer, E.W.; Würthner, F.; De Schryver, F.C. Bias-dependent visualization of electron donor (D) and electron acceptor (A) moieties in a chiral DAD triad molecule. *J. Am. Chem. Soc.* **2003**, *125* (49), 14,968–14,969.
49. Gesquiere, A.; Abdel-Mottaleb, M.M.S.; De Feyter, S.; De Schryver, F.C.; Schoonbeck, F.; Van Esch, J.; Kellogg, R.M.; Feringa, B.L.; Calderone, A.; Lazzaroni, R.; Bredas, J.L. Molecular organization of bis-urea substituted thiophene derivatives at the liquid/solid interface studied by scanning tunneling microscopy. *Langmuir* **2000**, *16* (26), 10,385–10,391.
50. Tao, N.J.; Cardenas, G.; Cunha, F.; Shi, Z. In situ STM and AFM study of protoporphyrin and iron(III) and zinc(II) protoporphyrins adsorbed on graphite in aqueous solutions. *Langmuir* **1995**, *11* (11), 4445–4448.
51. Samori, P.; Severin, N.; Simpson, C.D.; Müllen, K.; Rabe, J.P. Epitaxial composite layers of electron donors and acceptors from very large polycyclic aromatic hydrocarbons. *J. Am. Chem. Soc.* **2002**, *124* (32), 9454–9457.
52. Lei, S.B.; Wang, C.; Yin, S.X.; Wang, H.N.; Xi, F.; Liu, H. W.; Xu, B.; Wan, L.-J.; Bai, C.L. Surface stabilized porphyrin and phthalocyanine two-dimensional network connected by hydrogen bonds. *J. Phys. Chem. B* **2001**, *105* (44), 10,838–10,841.
53. Wang, H.; Wang, C.; Zeng, Q.; Xu, S.; Yin, S.; Xu, B.; Bai, C.L. Chain-length-adjusted assembly of substituted porphyrins on graphite. *Surf. Interface Anal.* **2001**, *32*, 266–270.
54. Griessl, S.; Lackinger, M.; Edelwirth, M.; Hietschold, M.; Heckl, W.M. Self-assembled two-dimensional molecular host–guest architectures from trimesic acid. *Single Mol.* **2002**, *3* (1), 25–31.
55. Magonov, S.N.; Yerina, N.A. High-temperature atomic force microscopy of normal alkane C<sub>60</sub>H<sub>122</sub> films on graphite. *Langmuir* **2003**, *19* (3), 500–504.
56. Schwartz, P.; Schreiber, F.; Eisenberger, P.; Scoles, G. Growth kinetics of decanethiol monolayers self-assembled on Au(111) by molecular beam deposition: an atomic

- beam diffraction study. *Surf. Sci.* **1999**, *423* (2–3), 208–224.
57. Poirier, G.E.; Pylant, E.D. The self-assembly mechanism of alkanethiols on Au(111). *Science* **1996**, *272* (5265), 1145–1148.
58. Everhart, D.S. Self-assembling monolayers. Alkane thiols on gold. *Handbook of Appl. Surf. Colloid Chem.* **2002**, *2*, 99–116.
59. Bain, C.D.; Troughton, E.B.; Tao, Y.T.; Evall, J.; Whitesides, G.M.; Nuzzo, R.G. Formation of monolayer films by the spontaneous assembly of organic thiols from solution onto gold. *J. Am. Chem. Soc.* **1989**, *111* (1), 321–335.
60. Small, D.M. *The Physical Chemistry of Lipids: From Alkanes to Phospholipids*; Plenum: New York, 1986.
61. Hibino, M.; Sunni, A.; Tsuchiya, H.; Hatta, I. Microscopic origin of the odd–even effect in monolayer of fatty acids formed on a graphite surface by scanning tunneling microscopy. *J. Phys. Chem. B* **1998**, *102* (23), 4544–4547.
62. Yablon, D.G. Self-assembly and chirality of molecules at interfaces. In *Dekker Encyclopedia of Nanoscience and Nanotechnology*, 2E; Schwarz, J.A., Contescu, C.I., Putyera, K., Eds.; Taylor & Francis: New York, NY, 2009; Vol. 6, 3840–3847.
63. Wawkuszewski, A.; Cantow, H.J.; Magonov, S.N.; Möller, M.; Liang, W.; Whangbo, M.H. STM study of molecular order and defects in the layers of cycloalkanes (CH<sub>2</sub>)<sub>48</sub> and (CH<sub>2</sub>)<sub>72</sub> adsorbed on graphite. *Adv. Mater.* **1993**, *5* (11), 821–826.
64. Wu, P.; Zeng, Q.; Xu, S.; Wang, C.; Yin, S.; Bai, C.L. Molecular superlattices induced by alkyl substitutions in self-assembled triphenylene monolayers. *Chem. Phys. Chem.* **2001**, *2* (12), 750–754.
65. Sowerby, S.J.; Heckl, W.M.; Petersen, G.B. Chiral symmetry breaking during the self-assembly of monolayers from achiral purine molecules. *J. Mol. Evol.* **1996**, *43* (5), 419–424.
66. Aviram, A.; Ratner, M.A. Molecular rectifiers. *Chem. Phys. Lett.* **1974**, *29* (2), 277–283.
67. Jäckel, F.; Watson, M.D.; Müllen, K.; Rabe, J.P. Prototypical single-molecule chemical-field-effect transistor with nanometer-sized gates. *Phys. Rev. Lett.* **2004**, *92* (18), 188, 303.
68. Samori, P.; Yin, X.; Tchegotareva, N.; Wang, Z.; Pakula, T.; Jäckel, F.; Watson, M.D.; Venturini, A.; Müllen, K.; Rabe, J.P. Self-assembly of electron donor-acceptor dyads into ordered architectures in two and three dimensions: surface patterning and columnar “double cables.” *J. Am. Chem. Soc.* **2004**, *126* (11), 3567–3575.

# Structural Color

Pete Vukusic

*School of Physics, Exeter University, Exeter, U.K.*

## INTRODUCTION

Modern technology is increasingly interested in attaining the ability to carefully mold and control the flow of light. The interest in this is underpinned by the drive toward the use of all-optical signals, rather than electrical ones, for a variety of purposes. Among the more interesting and potentially revolutionary are those associated with high-bandwidth communication and with the miniaturization of digital processing. There is currently a huge research investment dedicated to reaching goals in these areas. As a result, technologists have discovered something nature has been exploiting for a very long time, namely, that the careful design of the structural shape and form of a material will allow it to manipulate the way specific colors propagate within or along it. In this way, the issue of structural color has arisen in physics and engineering, and the subject is predicted to affect our future lives in a fundamental way. As an introduction to the associated optics, this article will principally describe the physical mechanisms associated with structural color, presenting natural examples that offer inspiration and design protocols to current technologists.

## STRUCTURAL COLOR

Color may be defined as the property associated with an elicited physiological perception when light of a certain wavelength impinges on the photoreceptors in a visual system. In human vision, such color is said to comprise the range of wavelengths from red, at around 700 nm, to violet, at around 400 nm.

Colored light can be produced through one of 15 possible mechanisms,<sup>[1]</sup> each of which is independent of the visual system or device that detects it. The more common mechanisms are those associated with optically induced electronic transitions in atomic or molecular orbitals; energy-band effects in metals, alloys, and semiconductors; the vibrations and atomic excitations associated with incandescence; and the geometrical and physical optics involved in the interaction of light with periodicity. All mechanisms may, broadly speaking, be categorized into two groups: color resulting from the transition of electrons between specific

energy levels (such as with pigments or dyes) or color resulting from the interaction of light with the physical structure of a system. The latter group is commonly referred to as structural color and is the subject of this entry.

Structural color first proliferated in the animate natural world in the Cambrian period (515 million years ago) and even earlier with inanimate systems. Many examples are well known, but the color of rainbows and of certain invertebrates and vertebrates have always been both fascinating and intriguing. Much serious scientific research has taken place for many centuries. Through such examples as the investigative work of Theodoric<sup>[2]</sup> in the 13th century examining refraction in a rainbow, to that of Hooke in the 17th century on the color of silverfish,<sup>[3]</sup> to Newton's thesis in the 18th century on the iridescent color of peacock feathers,<sup>[4]</sup> even to modern-day scientists discovering photonic crystals in lepidopteran wing scales,<sup>[5]</sup> the principles of physical optics that underpin natural structural color have become well understood.

Four mechanisms govern such natural structural color: refraction, interference, diffraction, and scattering. These mechanisms also underpin all artificially produced incidences of structural color used by, or associated with, modern technological systems. Fundamentally, color is produced because of the existence of either nonparallel interfaces between media of different refractive index or of a distribution of centers of high or low refractive index, the 1-D, 2-D, or 3-D periodicity of which is similar in spatial dimension to that of visible light. The brevity of such a terse summary may be misleading, however. Each one of the four structural color mechanisms is distinctive enough to merit its own detailed description and discussion of examples. In each case, owing to the length constraints of this article and the existence of eminent and fully detailed explanations elsewhere in the literature, descriptions of these mechanisms in this entry will be condensed and centered on paradigmatic examples.

## Structural Color from Refraction

The rainbow is among the best known natural examples of color by refraction.<sup>[6]</sup> Other examples include atmospheric phenomena known as arcs, glories,

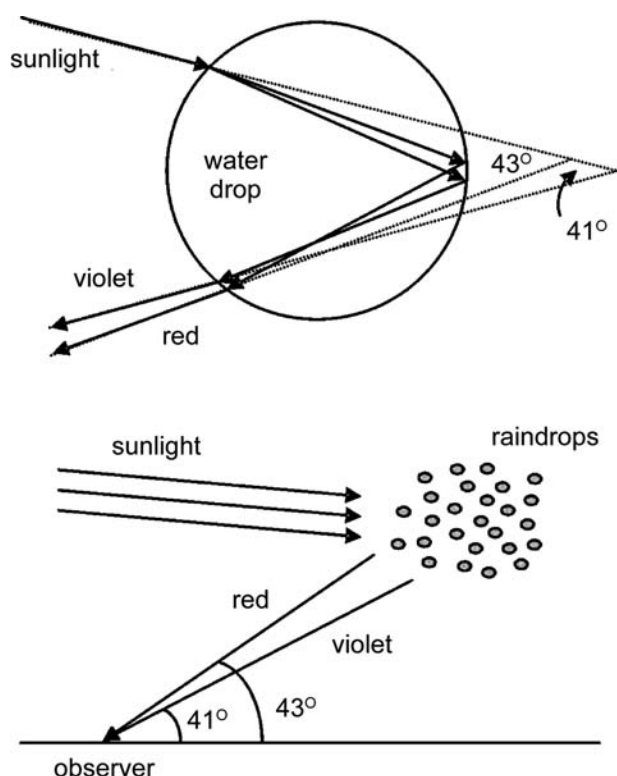


**Fig. 1** The formation of a rainbow is caused by the refraction of sunlight by raindrops. The primary bow is produced by a single reflection within a drop (top image) combined with the dispersion of light associated with the variation of refractive index with wavelength. To observe a rainbow (bottom image), sunlight must come from behind the observer; the red portion forms a bow of  $43^\circ$  cone angle, the violet, a  $41^\circ$  cone angle.

columns, parhelia, and sun and moon haloes produced by refraction and reflection in airborne hexagonal ice crystals.<sup>[7]</sup> One rarely observed yet spectacular phenomenon is the green flash, produced for just a few seconds at sunset under the right circumstances, where the density gradient of the atmosphere acts as a refractive medium to produce distinctive green coloration.<sup>[8]</sup> However, there are no known examples whereby refraction produces significant structural color in animate systems.

Among the most frequently encountered examples of structural color due to refraction are those associated with shaped transparent glass, the best example being a high-index glass prism. Even the incidence of sunlight through a window and onto a glass ornament or the beveled edge of a wall mirror will produce the characteristic spectrum of colors associated with refraction.

Many studies discuss the spectral colors produced in this way through a glass prism.<sup>[9]</sup> The underlying principle is the dispersion of light through glass—the index of refraction of glass increases as the wavelength

decreases. Consequently, blue light refracts through a larger angle than red light at a glass–air (or water–air) interface (with intermediate wavelengths falling between these limits). Parallel front and rear interfaces, such as with a plain rectangular glass block, prevent the production of a spectrum. However, the non-parallel faces of a glass prism bring about and retain an angular displacement between the paths of differently colored light, producing individual colors beyond the prism. The refraction of white light by raindrops is responsible for rainbows.<sup>[6]</sup> They form when sunlight from behind an observer refracts on entering and exiting a raindrop (Fig. 1).

Light forming a primary rainbow will have internally reflected once within each drop (assigning a distinct polarization to the spectral color), whereas light forming a secondary rainbow will have internally reflected twice.<sup>[10]</sup> The formation of supernumerary bows, existing on the inside of primary and secondary arcs and rather rarely observed, involves the additional mechanism of optical interference rather than solely refraction.<sup>[6]</sup>

### Structural Color from Interference

Interference is by far the most common mechanism by which structural color is produced, both naturally and artificially. To describe it, we consider white light incident on a series of overlapping thin films of alternating high and low refractive index. Colored light may be strongly reflected by constructive interference between reflections from the individual interfaces forming this stack of films.<sup>[11]</sup> For this to occur, the resultant reflections from each interface must emerge from the stack with identical phases, i.e., the optical path differences between them must be an integral number of whole wavelengths. This condition is satisfied only by a specific color, or selection of colors, and is additionally influenced by the angle at which the light is incident and reflectivity is observed. The critical variables that determine which color is brightly reflected are the refractive indices of the films in the stack, their individual thicknesses, and the angle of incidence or observation. Any imposed variations on these variables alter the optical conditions that create the interference, thereby producing a reflection and transmission of a different color. The hue from such interference is clearly angle dependent, a property that is implicit in the definition of iridescent color produced by this mechanism. The most favorable narrow-band reflection condition is produced when the optical thickness of each layer in the stack corresponds to a quarter of the wavelength required for optimal reflectivity.<sup>[12]</sup> For a large number of such layers of high refractive index contrast, the reflectivity will be bright, saturated,



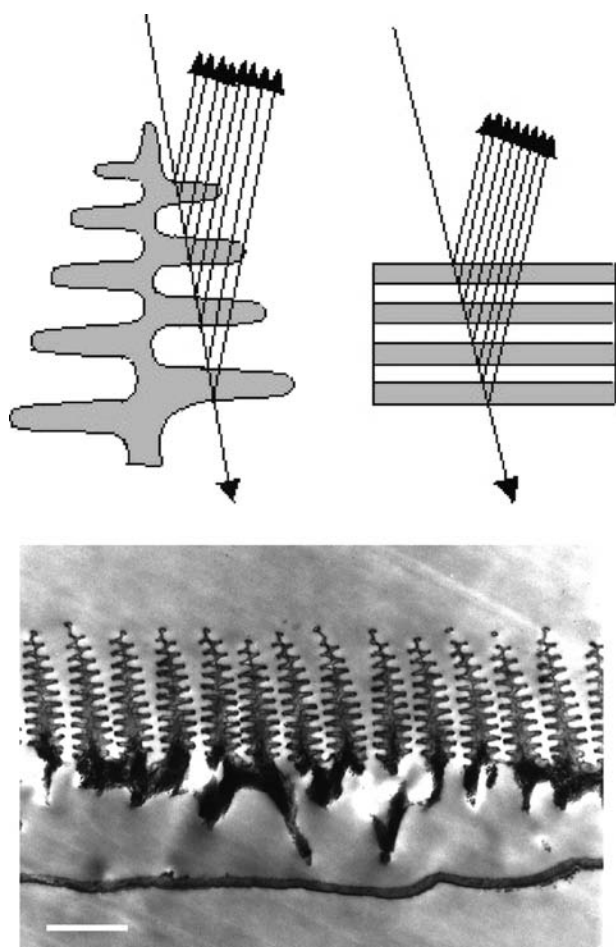


**Fig. 2** The top image is a schematic diagram that illustrates the multiple reflections associated with two types of multilayer structure; the left one is that of a *Morpho* butterfly iridescent scale while the right one represents more conventional flat and continuous layering. The bottom image shows a transmission electron micrograph of a cross section through a *Morpho* iridescent scale. (Scale bar: 700 nm).

and of a narrow spectral band. The brightness of this reflectivity will increase with the number of layers:<sup>[12]</sup> if the dimensions or indices of the system deviate from the quarter-wave condition (something that is common in natural systems), the reflected intensity may be proportionally reduced and the reflected wavelength band will adopt a more complex form.<sup>[13]</sup>

Among the innumerable examples of interference color in nature, those that are most vivid and spectrally pure tend to catch the eye most readily. An excellent example of such stunning structural color is the iridescence associated with several of the male *Morpho* butterflies that are indigenous to South and Central America.<sup>[14]</sup> The striking deep blue color of their dorsal wing surfaces is produced without the aid of any blue pigmentation, generated instead by optical interference within nano-sized laminations in the wing scales<sup>[15]</sup> (Fig. 2).

There is a profound complexity associated with this *Morpho* multilayer system. Whereas conventional technological multilayer systems generally comprise continuous layering over what is often a substantial area, the *Morpho* laminations are distinctly discreet in character, comprising assemblies of up to 10 layers of high-index material called cuticle, separated by intervals of air. This high number of layers yields up to 85% blue light reflectivity despite the presence of some inherent optical absorption because of the presence of melanin pigmentation within the scale structure.<sup>[15]</sup> The laminations are built into long and near-parallel ridge structures that run the length of each iridescent scale and have a spatial periodicity of between 700 and 1200 nm. Analysis of the optics of such *Morpho* structure confirms that the observed layers of thickness approximately 80 nm, separated by “layers” of approximately 100 nm of air, produce blue coloration at normal incidence through interference. The laminations appear to be embedded into the scale ridging to reflect the interference-produced blue light over a much broader angle than would be possible with flat or even curved continuous multilayers.<sup>[15]</sup> Variations in the design of this type of discrete multilayering in other butterfly species lead to more specific, angular-dependent reflection properties.<sup>[16]</sup>

In the case of butterfly systems, one finds that a more complex structure (such as the sculpting of an otherwise continuous multilayer) may produce surprising effects. The butterfly *Papilio palinurus* exhibits structural color that is green to human vision. Close examination of the structure of its wing scales reveals a continuous multilayer that is shaped into juxtaposed concavities<sup>[17]</sup> (Fig. 3).

The multilayers follow the profile of these concavities in such a way that the physical dimensions of each layer remain approximately constant regardless of position across each concavity. This creates the effect of a curved multilayer with uniform layer dimensions, rather than a patterned multilayer of variable dimensions. This particular sculpting simultaneously produces two structural colors, namely, blue and yellow, which combine additively to give the stimulus of a third color, the green that we observe.<sup>[17]</sup>

On close optical inspection (a color image of this detail is included in the on-line version of this entry), a yellow color is produced at or near normal incidence via reflection from the flat center of each concavity, whereas a blue annulus is produced via a double reflection across each opposite side of the concavity. This is possible only because each angled side combines with the surface that is orthogonal to itself on the opposite side of each concavity. The blue annulus pattern is produced in this way: normally incident blue light reflected from one 45°-inclined surface is directed across the concavity to the opposite orthogonal surface from

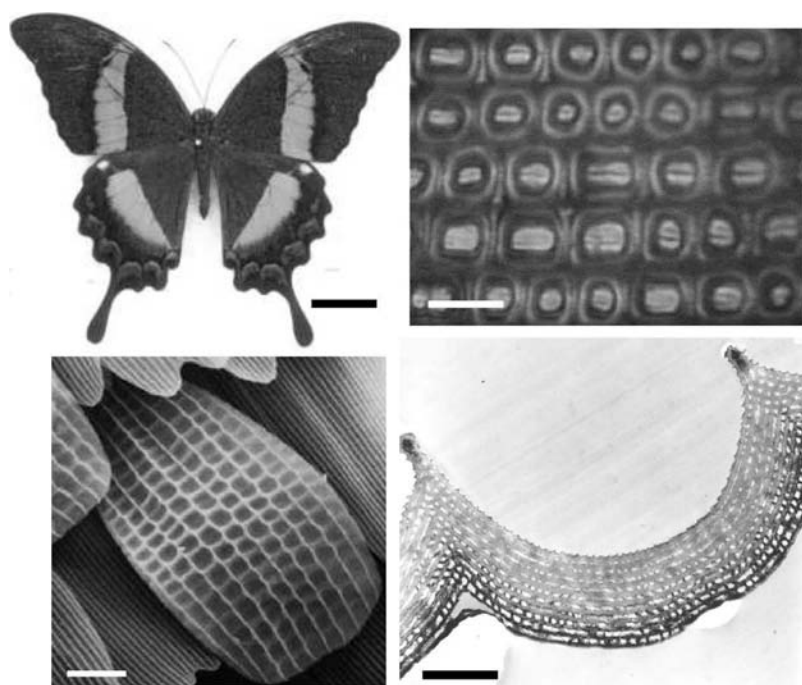


**Fig. 3** Optical images showing the structural color (top left) and scale patterning (top right) of a *P. palinurus* butterfly, together with electron micrographs of one of its iridescent scales (bottom left) and the cross section through one of the concavities (bottom right) of such a scale. The green coloration of *P. palinurus* is produced through color mixing of juxtaposed yellow and blue regions (top right), both colors of which are produced from the same multilayer profile. (The on-line version of this figure is in color.) (Scale bars: top left, 1 cm; bottom right, 6  $\mu\text{m}$ ; bottom left, 10  $\mu\text{m}$ ; bottom right, 1  $\mu\text{m}$ ). Source: From Ref. [18] © 2001.

where it returns parallel to the incident direction. These pairs of inclined surfaces comprise nearly identical multilayering and are both inclined at approximately  $45^\circ$  to the direction of normally incident light on the scale surface. Accordingly, their spectral reflectivity characteristics are closely matched. Furthermore, through a double reflection from the opposite sides of each concavity, the polarization of only one of the colors may be rotated by  $90^\circ$ , a property that is thought to have evolved due to selection pressures associated with both cryptic and conspecific signaling.<sup>[18]</sup>

The examples of *Morpho* and *P. palinurus* are very advanced and complex multilayer systems. Similarly complex multilayer systems have been shown to exist in many different animal taxa, both terrestrial and aquatic.<sup>[19,20]</sup> For instance, the reflecting properties of some scarabaeid beetles are not based on periodicities in refractive index, but rather result from the helicoidal ordering of chitin microfibrils in planes that make up the insect integument.<sup>[21]</sup> Such cuticle is composed of laminar planes of chitin fibers, the axes of which are systematically rotated by a small amount with each consecutive plane. After a certain number of layers through the system corresponding to a specific distance perpendicular to the planes, the fiber axis is rotated  $180^\circ$  and is once again parallel to that of the first layer. In this way, two corresponding planes of cuticle occur over a distance that corresponds to half the helical pitch of the system. The consequent optical effect is that of constructive interference associated with consecutive planes that have unidirectional chitin axes

and which are separated by half the helical pitch. Thus the system may be treated as a multilayer reflector, which reflects a band of wavelength of unpolarized polychromatic light in an analogous way to cholesteric liquid crystals. As a further consequence of the helical arrangement of chitin fibers, optical reflection from these taxa of beetles is circularly polarized. This is not due to any optical rotation arising at a molecular level owing to the L-amino acids of the cuticle protein and the D-amino sugar of the chitin. It instead arises at the supermolecular level and has been termed *form optical rotation*,<sup>[12]</sup> in contrast to the optical rotation exhibited by cholesteric liquid crystals. It should be noted, however, that similar helicoidal structure, found in many other iridescent insect and plant taxa,<sup>[22]</sup> is not responsible for their strong coloration and does not produce anomalous optical properties such as optical activity. For these species, inherent refractive index periodicity within the species' exocuticle is responsible for the iridescence. For optically active beetles, the sub-wavelength pitch of the helical order is responsible for the observed form of optical activity and iridescent color.

Whereas the natural multilayer systems described so far are designed for rather narrow-band reflectivity, modifications to this design can produce broad-band color reflectivity, creating the appearance of gold or silver coloration. Three variations of multilayer design can generate this effect (Fig. 4).

The first of the three variations is known as a *chirped* system, in which the dimensions of the high- and low-refractive-index layers within the stack

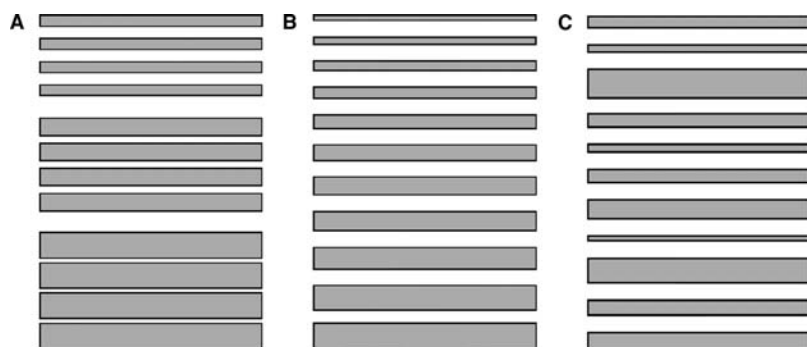


**Fig. 4** Schematic diagrams to illustrate three arrangements of multilayer systems that can produce broad band reflectance: (A) a system comprising three overlapping quarter-wave filters tuned for different portions of the overall reflection band, (B) a chirped system comprising gradually changing layer thicknesses, and (C) a chaotic system in which there is little order in the arrangement of layer thicknesses.

systematically increase or decrease through the system.<sup>[23]</sup> A variation on this, described as a chaotic reflector, produces a similar effect by randomly varying the thicknesses of high- and low-index material. In both of these systems, the range of layer dimensions developed by the specimen, combined with layer refractive index, determine the position and width of the reflected wavelength band and the quality of the silver or goldlike mirror on its surface.<sup>[24]</sup> The third type of layered system incorporates a composite of three overlapping but regular multilayer systems, each tuned to a different wavelength band.<sup>[25]</sup>

There are many applications for artificially manufactured multilayer films, ranging from antireflection coatings on optical instruments such as spectacles, binoculars, and telescopes to specific-band optical filters for transmission or reflection for wavelengths ranging from infrared to X-ray. Their design is based on production of constructive or destructive interference in alternating layers of high- and low-refractive-index dielectric materials deposited onto surfaces. Other multilayer devices that additionally facilitate polarized beam splitting accompany interference by Brewster angle reflection.<sup>[26]</sup>

### Structural Color by Diffraction

Diffraction can produce structural color when white light is incident on the edge of an object or on a medium that comprises a periodicity in structure or refractive index. Such a medium may be called a diffraction grating and may function in reflection or in transmission, depending on its geometry. A high periodicity is generally required for bright structural color, the spatial dimension of which can range from a few thousand to a few hundred nanometers.<sup>[27]</sup>

Consider white light incident on a medium bearing a sinusoidally periodic surface profile of approximately 1- $\mu\text{m}$  pitch. Owing to the presence of the periodicity on the surface, the incident planar wave fronts of all wavelengths comprising the white light are diffracted to form a large number of series of circular wave fronts

for each wavelength. These series of reflected circular wave fronts then interfere strongly with each other, constructively in certain specific directions and destructively in others. Accordingly, diffraction, especially that associated with surface periodicities, manifests itself by the production of colored bands of light in reflection or transmission at different angles from the periodic surface onto which white light is incident.

The use of diffraction gratings is widespread. Measurements of signals are frequently based on the analysis of wavelength content in an incoming light beam.<sup>[27]</sup> Such analysis requires a diffraction grating to discriminate between constituent wavelength components. Within optical devices such as interferometers, laser systems, multiplexers, and microphotonic components (integral in most modern optical communication and instrumentation systems) such as gratings perform an essential function. Structural color produced from diffraction is often observed from objects such as CD or vinyl record surfaces that incorporate micron-sized periodicity. When incident white light diffracts from the periodic data tracks and grooves on their surfaces, color spectra are observed. The production of such color, however, is a side effect. One must look to natural systems for diffractive structural color that is produced for specific purposes.

Until recently, the occurrence of diffractive systems in the natural world was believed to be rather rare.<sup>[28]</sup> They are now known to be fairly common, especially in certain invertebrate phyla. In the phylum Mollusca, iridescence is observed on the outer surfaces of many mollusk shells. The surface of the shell of *Pinctada margaritifera* exhibits bright iridescence that results from diffraction of approximately 3.4- $\mu\text{m}$  pitch from a series of shallow parallel grooves on the shell surface.<sup>[29]</sup> This iridescence is distinctly different from the “milky” opalescence or pearlescence observed in many mother-of-pearl shells, where thick flat  $\text{CaCO}_3$  crystals cemented together with layers of protein yield interference of several colors simultaneously.<sup>[12]</sup>

Series of parallel narrow surface grooves are extensively found on the elytra of scarabaeid beetles, some of which are known to produce structural color

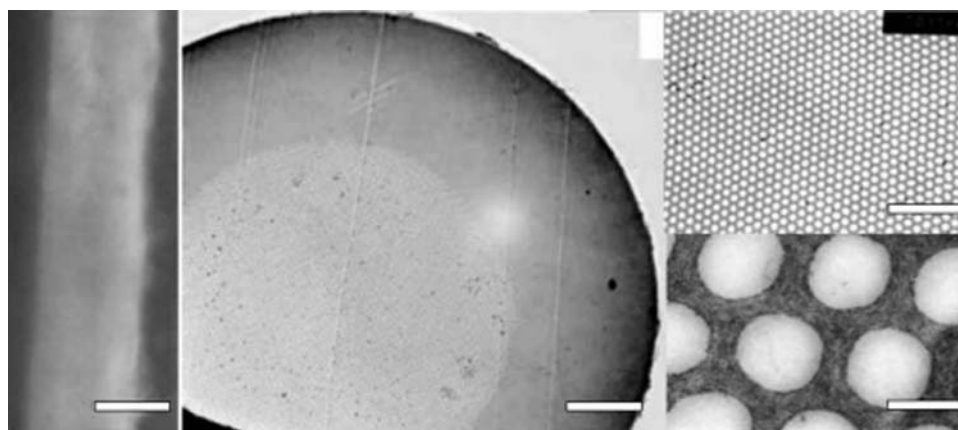


**Fig. 5** A single setae from the polychaete worm *Pherusa*, viewed by optical microscopy (left) and in cross section by electron microscopy showing increasing magnifications of transverse sections through the setae. Structural color effects are visible in the optical image (the on-line version of this figure is in color), produced from highly periodic microstructure derived through the longitudinal stacking of hollow cylinders within each seta. The images on the right show magnified regions of the central portion of the middle image. (Scale bars: left, 0.25 mm; middle, 60  $\mu\text{m}$ ; top right, 4  $\mu\text{m}$ ; bottom right, 250 nm.)

through diffraction.<sup>[30]</sup> For instance, many of the members of the Phalacridae family of scarabs exhibit surface gratings of approximately 1  $\mu\text{m}$  pitch, resulting in several bands of colored reflection. The intensity of these reflected color bands is relatively low, however, because of the heavily melanized cuticular integument that has a relatively low reflection coefficient.

The setae (hairs) of many Crustacea comprise series of juxtaposed rings having walls that are circular in cross section with a pitch of approximately 700 nm. Bright diffracted colors are visible to the eye when the specimen is tilted at an angle under a fixed light source.<sup>[28]</sup>

An interesting example of structural color caused by 2-D periodicity is that exhibited by certain taxa of marine polychaete worm. One of these, *Aphrodita*, a genus of polychaete worm commonly known as the sea mouse, has a short segmented body that is covered with hairlike structures called setae. These setae, extruded by epidermal cells, are exceptional because of their strong iridescence. They are composed of bundles of thin-walled cylinders of chitin held together by sclerotized protein to form fine and threadlike hairs. The diameter of the cylinder centers varies between approximately 100 and 360 nm in *Aphrodita*,<sup>[31]</sup> in another polychaete species, *Pherusa*, optically similar setae exhibit a greater number of cylinder periodicities with a more uniform diameter of approximately 220–270 nm<sup>[32]</sup> (Fig. 5).

The iridescent color in these setae (shown in color in the on-line version of this article) is produced through diffraction from the periodicity of the cylinder elements. Detailed optical analysis associated with the structure of *Aphrodita* is presented elsewhere.<sup>[33]</sup>

A variation of the structure found in iridescently colored polychaete setae is also found in the tapeta

of the eyes of cats. However, whereas polychaete setae consist of bundles of hollow cylinders, the tapeta of cats' eyes consist of bundles of solid cylinders or rods made of cuticular material. Within each bundle, rods of diameter 200–350 nm are spaced 300–500 nm apart and are arranged in a mutually parallel geometry that yields hexagonal symmetry in transverse cross section (Fig. 6).

Strong diffraction, specifically Bragg diffraction, arising as a result of the periodicity of these rods produces the colored eye shine normally observed with cats' eyes.<sup>[34]</sup> This mechanism is similar to the Bragg diffraction of X-rays from a crystalline material,<sup>[35]</sup> except that the difference of scale means the effect is seen for ordinary light. Its physiological function, similar to that of tapeta in certain arthropods, is believed to be optimization of photoreception in the cats' visual system.

In certain Lepidoptera, rather than 2-D periodicity such as that just described for polychaete worm setae, a remarkable 3-D periodicity exists. Such 3-D structures are sometimes referred to as volume diffraction gratings or photonic solids. It is, in principle, possible for photonic solids to expel light of certain frequencies in all directions; this implies that light of these frequencies will simply not propagate in the material and that all of it will be reflected from the surface of the solid. When this occurs, the material is said to exhibit a *photonic band gap*, which is analogous to the familiar electronic band gap of solid-state physics, except that it applies to photons instead of electrons.<sup>[36]</sup> However, for a photonic solid of specific symmetry to exhibit a full photonic band gap, there must be a minimum refractive index contrast between the two media that make up the periodic solid. Natural structures that exhibit these photonic solids are generally composed



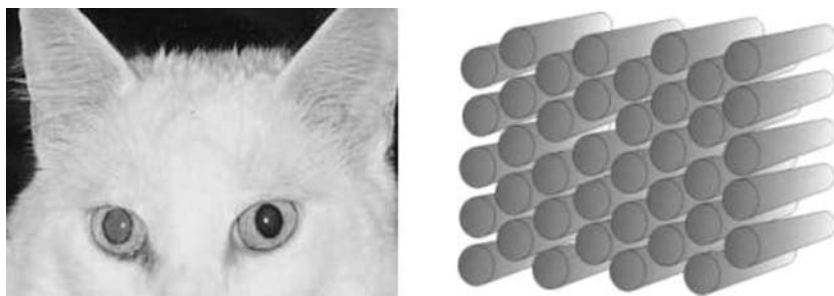


**Fig. 6** Curious color effects and nocturnal eye shine in cats is produced by domains of ordered 2-D lattices of rodlet bundles in the tapetum lucidum of their eyes. Each rodlet is approximately 200 nm in mean diameter.

of cuticle and air or cuticle and water, both refractive index combinations of which are insufficient to create a full photonic band gap. However, their combination and structural symmetry can be enough to produce considerable reflectivities over a significant range of angles and over a relatively small wavelength band. The selective advantage of color production using this manner of microstructure rather than a surface grating or a multilayer system, excluding physiological considerations, is that it can sometimes be incorporated into multiple neighboring grains, each oriented slightly differently, to produce a macroscopic, completely angle-independent, structural color. This effect is found in several butterflies, e.g., *Parides sesostris*, and is shown in color in the on-line version of this entry<sup>[37]</sup> (Fig. 7).

### Structural Color by Scattering

The final category of structural color exists in addition to those that cause refraction, interference, and diffraction, producing wavelength-selective optical scattering.

The phenomenon of blue scatter is fairly widespread in nature. This color effect, associated with the selective scattering of shorter-wavelength light by small

particles, can be observed in the laboratory by using white light to illuminate droplets suspended in liquids (such as water containing small concentrations of milk). When it is viewed from the side, the suspension appears rather blue. Many other inanimate systems offer strong scattering in the laboratory such as highly dispersed systems of elementary sulfur or silver halides in aqueous media. In each case the exact hue and intensity of the scattered color depends on the degree of fineness of small particles in the suspension and on the magnitude of mismatch between the refractive index of the particles and their surrounding medium. Generally, particles that are sufficiently small yield deeply violet scattered color of striking intensity and purity: as particle size is increased, the scattered color passes from deep blue to pale blue. Increasing the particle size beyond approximately 1  $\mu\text{m}$  results in most visible wavelengths being scattered with sufficient intensity to produce the appearance of white.<sup>[20]</sup>

The mechanism that supports these laboratory examples of color by scattering also leads to the blue color of the sky; in this case, however, the scattering centers are the atmospheric molecules themselves rather than suspended solid particles.<sup>[38]</sup>

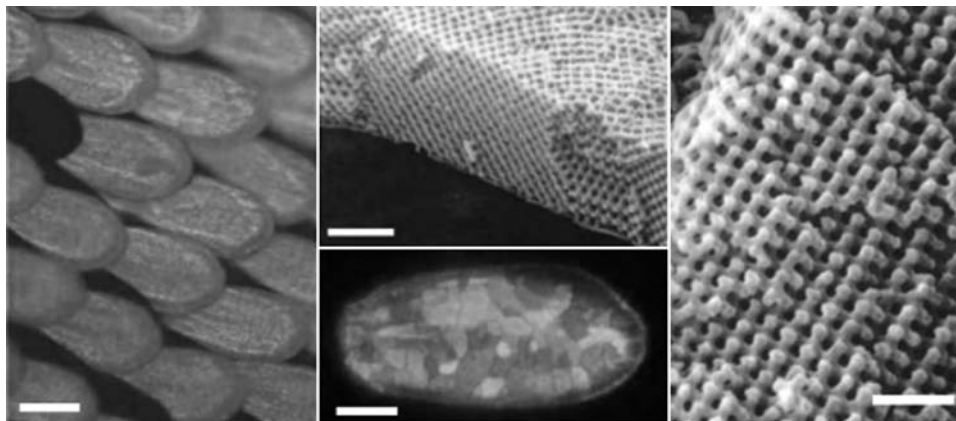


**Fig. 7** Optical micrographs showing *P. sesostris* scales in reflection under normal illumination (left) and a single *P. sesostris* scale viewed in reflection with linearly polarized white light illumination (bottom middle) with the image captured through a crossed linear analyzer. Top center and right images are electron micrographs of a fractured transverse section of a *P. sesostris* iridescent scale (the 3-D periodic lattice of cuticle is clearly visible). (Scale bars: left 90  $\mu\text{m}$ ; bottom middle 50  $\mu\text{m}$ ; top middle 3  $\mu\text{m}$ ; right 1  $\mu\text{m}$ .)

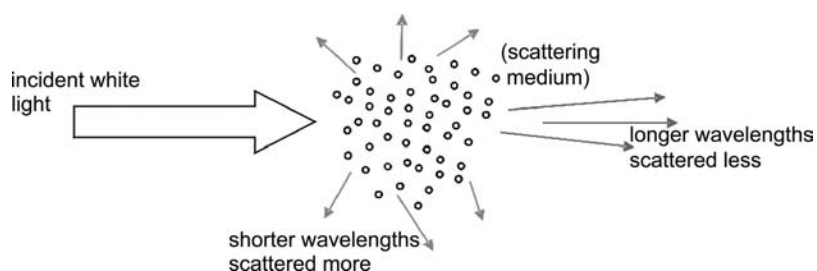


**Fig. 8** A schematic diagram illustrating the scattering of white light by a medium comprising small particles. Shorter wavelengths are preferentially scattered through larger angles according to the Rayleigh law of scattering. In this way, light directly transmitted through such a medium predominately comprises longer-wavelength radiation, whereas shorter wavelengths dominate when the medium is observed from any other perspective.

Scientists working with light scattering use several terms to evoke theories associated with different classes of scattering particles. Authors that detail scattering in animate specimens<sup>[20,39]</sup> have consistently used the terms Tyndall scattering, Tyndall effect, etc. to refer in the broad sense to colors produced through selective scattering of shorter wavelengths by small particles or optical heterogeneities when pigmentation and other structural phenomena are not predominant. In certain studies, Tyndall scattering is equated to Rayleigh scattering by particles that are small compared to the wavelength,<sup>[40]</sup> in others it applies to particles that are the same size or larger than the wavelength.<sup>[41]</sup> Tyndall's original experiments<sup>[38]</sup> embraced both groups of particle size and the expression is usefully retained by many biologists to describe scattering in animate objects. Physicists unfamiliar with such works on natural scattering systems tend to refer to the process as Rayleigh scattering if the sizes of the fluctuations or particles are very small compared to the wavelength of light, or Mie scattering if they become somewhat larger than those associated with Rayleigh scattering.

It is well known that the scattering of light in gases or fluids can involve certain quantum processes more normally associated with pigmentary color. However, in neutral nonabsorbing media a classical oscillator analysis<sup>[41]</sup> describes the relationship between scattered light intensity and wavelength for a specifically sized system of particles. This relationship is the well-known Rayleigh law of scattering, which states that scattered intensity is inversely dependent on the fourth power of wavelength. Physically, this implies that shorter-wavelength colors such as violet and blue are scattered much more strongly through greater angles than longer wavelengths such as red (Fig. 8).

This relationship can also apply to the scattering of light in transparent solid media, where the scattering centers are formed by irregularities in density or structure rather than by individual atoms or molecules. An important technological example lies in the transmission of light down long glass fibers. For this, the highest transmission can be largely limited by Rayleigh

scattering from small irregularities in the glass. Generally, to overcome this loss problem the longest wavelengths for existing and available light sources and detectors are used (but avoiding hydroxyl ion and other material-specific absorption resonances).

Tyndall scattering is believed to be the cause of the non-iridescent blue coloration in mammalian and reptilian integument and of much of the blue of both avian integument and feathers.<sup>[20]</sup> It is additionally attributed to some blues found in certain lower-class phyla such as Odonata and Lepidoptera.

The most conspicuous examples are found in certain mammals, particularly monkeys such as male baboons and mandrills. In these creatures, hairless patches may be deep violet or blue because of Tyndall scattering associated with strata of discrete black melanocytes arranged in an otherwise transparent layer within the epidermis.<sup>[20]</sup> Purple regions on these creatures correspond to areas where Tyndall blues color-mix with red pigmentation associated with blood corpuscles close to the surface: a color effect perhaps more commonly observed as port-wine birthmarks in some humans.<sup>[42]</sup>

Whereas Tyndall blue in mammals is caused by disperse systems of solid-in-solid where the melanin granules have a different refractive index to the surrounding epidermis, non-iridescent avian feathers generally achieve blue scatter using air-in-solid systems. In such feathers, air-filled subwavelength cavities within the keratin of the feather barbs act as the scattering centers from which Tyndall blues are produced. More often than not, the green color in avian feathers is the product of the superposition of yellow reflection from additional carotenoid pigmentation in the feathers with the underlying blue from Tyndall scattering.<sup>[20,39]</sup> Green and sometimes purple coloration in many other taxa, e.g., certain snakes, frogs, lizards, and fish, are produced by similar effects, namely, Tyndall scattering superposed with the effect of colored pigment.<sup>[20,39]</sup>

The bluish tinge on the chin of dark-haired men seen a few hours after shaving is attributed to Tyndall scattering. Without the dark roots of the hair, however, as



an absorbing background, the low-intensity scattered blue tinge would be unsaturated with back reflection from the epidermal surface and would not be seen.

The blue color of mammalian eyes is certainly structural in nature and has been attributed to Tyndall scattering. Early studies of the human eye<sup>[43]</sup> found that the colored portion is composed of a thin membrane bearing unstriped muscular fibers, nerves, and capillaries, all incorporated in a fine delicate reticulum of fibrous tissue. Small protein particles in this region preferentially scatter blue light away from the eye while the remainder enters the eye and is generally absorbed by a curtain layer of brown and black melanin at the back of the reticulum. This prevents back reflections out of the eye from reducing the saturation of the Tyndall blue color. Brown eyes possess an additional layer of some yellow pigmentation with significantly sized brown melanin granules among the interior fibrous structures. These produce a brown coloration through the natural color of the melanin. The transformation from initially blue colored eyes to brown eyes in babies and children is attributed to the gradual appearance and increase in size of melanin granules in the first few months and years.

There are several examples of Tyndall blue coloration in Lepidoptera. The wings of these species have been shown to be composed of scales that are colored through Tyndall scattering from subwavelength-sized nanostructures.<sup>[44]</sup> These structures extend from between series of ridges on the surface of the scales down into the body of the scale. In the butterfly *Papilio zalmoxis*, the scattering structures are in the form of air-filled alveoli approximately 2  $\mu\text{m}$  long and around 220 nm in internal diameter. The simultaneous presence within the alveoli of a UV-absorbing but blue-fluorescing pigment enhances the blue coloration.<sup>[44]</sup> A melanized underlayer of black scales acts as an absorbing background, preventing the reflection of other wavelengths.

## CONCLUSION

There are striking differences between the hues of objects or materials colored through structural means and those colored through pigmentary or other non-structural means. Depending on structure type and the color mechanism it facilitates, the optical properties of these structurally colored surfaces may manifest themselves through one or several properties: angle-dependent or angle-limited color; narrow or very broad spectral bandwidths; ultrahigh reflectivities or transmissivities; strong polarization effects including polarization rotation on reflection or circularly polarized reflection; bicolor production and subsequent

color mixing; and complementary coloration in reflection and transmission.

In modern technological systems, refraction and scattering are rarely used for the purpose of producing color. In the natural world too, relatively few separate examples exist whereby refraction and scattering in either animate or inanimate systems are the cause of color. True diffraction also occupies a place of relatively minor importance in the production of iridescence in natural systems, although a good number of examples are known to exist. By far the most common mechanism by which color is produced structurally in modern systems and those of the natural world is through interference in multilayered systems. Modern physics has an excellent understanding of both the optical properties of most materials and of the physics of multilayer systems; more importantly, the techniques by which such materials are deposited onto surfaces have been refined and advanced to such an extent that highly specialized systems can now be manufactured at reasonable cost for a variety of optical purposes. In nature too, we see evidence of highly specialized multilayer-based structural color. In most of such natural systems, millions of years of selection pressures have shaped and developed them for a variety of purposes, from that of crypsis to that of specialized conspecific signaling. It is rarely an accident that such complex architecture develops in animate systems without the structural color it produces being designated for a specific use or having a definite biological significance. We now find technology is, for its own purposes, increasingly taking lessons from the design protocols nature has created.

## REFERENCES

1. Nassau, K. *The Physics and Chemistry of Color: The Fifteen Causes of Color*; John Wiley & Sons, 1983.
2. Kramer, S. *Theodoric's Rainbow*; W. H. Freeman & Co., 1995.
3. Hooke, R. *Micrographia*; Martyn and Allestry: London, 1665.
4. Newton, I. *Opticks*, 4th Ed.; Dover: New York, 1730. reprinted.
5. Vukusic, P.; Sambles, J.R.; Ghiradella, H. Optical classification of microstructure in butterfly wing-scales. *Photonics Sci. News* **2000**, *6*, 61–66.
6. Nussenzweig, H.M. The theory of the rainbow. *Sci. Am.* **1977**, *236*, 116–127.
7. McCarntey, E.J. *Optics of the Atmosphere*; John Wiley & Sons: New York, 1976.
8. Young, A.T. Green flashes and mirages. *Optics Photonics News* **1999**, *10* (3), 31–36.
9. Smith, F.G.; King, T.A. *Optics and Photonics: An Introduction*; John Wiley & Sons: New York, 2000.
10. Walker, J.D. Multiple rainbows from a single drop of water and other liquids. *Am. J. Phys.* **1976**, *44*, 421–433.

11. Young, H.D.; Freedman, R.A. *University Physics*, 10th Ed.; Addison-Wesley, 2000.
12. Land, M.F. The physics and biology of animal reflectors. *Prog. Biophys. Mol. Biol.* **1972**, *24*, 75–106.
13. Vašiček, A. *Optics of Thin Films*; North-Holland: Amsterdam, 1960.
14. Blandin, P. *The Genus Morpho*; Sciences Nat: France, 1988.
15. Vukusic, P.; Sambles, J.R.; Lawrence, C.R.; Wootton, R.J. Quantified interference and diffraction in single *Morpho* butterfly scales. *Proc. R. Soc. Lond., B* **1999**, *266*, 1403–1411.
16. Vukusic, P.; Sambles, J.R.; Lawrence, C.R.; Wootton, R.J. Limited-view iridescence in the butterfly *Ancyluris meliboeus*. *Proc. R. Soc. Lond., B* **2002**, *269*, 7–14.
17. Vukusic, P.; Sambles, J.R.; Lawrence, C.R. Structural colour: Colour mixing in wing scales of a butterfly. *Nature* **2000**, *404*, 457.
18. Vukusic, P.; Sambles, J.R.; Lawrence, C.R.; Wakely, G. Sculpted-multilayer optical effects in two species of *Papilio* butterfly. *Appl. Opt.* **2001**, *40*, 1116–1125.
19. Herring, P.J. Reflective systems in aquatic animals. *Comp. Biochem. Physiol., A* **1994**, *109*, 513–546.
20. Fox, D.L. *Animal Biochromes and Structural Colours*; University of California Press: Berkeley, 1976.
21. Neville, A.C.; Caveney, S. Scarabeid beetle exocuticle as an optical analogue of cholesteric liquid crystals. *Biol. Rev.* **1969**, *44*, 531–562.
22. Graham, R.M.; Lee, D.W.; Norstog, K. Physical and ultrastructural basis of blue leaf iridescence in two neotropical ferns. *Am. J. Bot.* **1993**, *80*, 198–203.
23. Neville, A.C. Metallic gold and silver colours in some insect cuticles. *J. Insect Physiol.* **1977**, *23*, 1267–1274.
24. McKenzie, D.R.; Yin, Y.; McFall, W.D. Silvery fish skin as an example of a chaotic reflector. *Proc. R. Soc. Lond., A* **1995**, *451*, 579–584.
25. Denton, E.J.; Land, M.F. Mechanism of reflection in silvery layers of fish and cephalopods. *Proc. R. Soc., B* **1971**, *178*, 43–61.
26. McLeod, H.A. *Thin Film Optical Filters*; Adam Hilger: London, 1969.
27. Hutley, M.C. *Diffraction Gratings*; Academic Press: London, 1982.
28. Parker, A.R. 515 million years of structural colour. *J. Opt. A, Pure Appl. Opt.* **2000**, *2*, R15–R28.
29. Liu, Y.; Shigley, J.E. Iridescence colour of a shell of the mollusk *Pinctada Margaritifera* caused by diffraction. *Opt. Express* **1999**, *4*, 177–182.
30. Hinton, H.E.; Gibbs, D.F. Diffraction gratings in phalacrid beetles. *Nature* **1969**, *221*, 953–954.
31. Parker, A.R.; McPhedran, R.C.; Botten, L.C.; Nicorovici, N. Aphrodite's iridescence. *Nature* **2001**, *409*, 36–37.
32. Vukusic, P.; Sambles, J.R. Unpublished.
33. McPhedran, R.C.; Nicorovici, N.; McKenzie, D.L.; Botten, L.C.; Parker, A.R.; Rouse, G.W. The sea mouse and the photonic crystal. *Aust. J. Chem.* **2001**, *54*, 241–244.
34. Pedler, C. The fine structure of the tapetum cellulosum. *Exp. Eye Res.* **1963**, *2*, 189–195.
35. Guinier, A. *X-ray Diffraction*; WH Freeman & Company: San Francisco, 1963.
36. Joannopoulos, J.D.; Meade, R.D.; Winn, J. *Photonic Crystals: Molding the Flow of Light*; Princeton University Press: Princeton, 1995.
37. Vukusic, P.; Sambles, J.R.; Ghiradella, H. Optical classification of microstructure in butterfly wing scales. *Photonics Sci. News* **2000**, *6*, 61–66.
38. Tyndall, J. On the blue colour of the sky, the polarisation of skylight and on the polarisation of light by cloudy matter generally. *Lond. Edin. Dubl. Phil. Mag.* **1869**, *37*, 384–394.
39. Fox, H.M.; Vevers, G. *The Nature of Animal Colours*; Sidgwick & Jackson: London, 1960.
40. Longhurst, R.S. *Geometrical and Physical Optics*, 2nd Ed.; Longman: London, 1967.
41. Ditchburn, R.W. *Light*, 2nd Ed.; Blackie: London, 1963.
42. Verne, J.; Leyani, F. Les dyschromies (in French). *Traité Dermatol. (Paris)* **1938**, *2*, 745–811.
43. Roberts, C. In the report of the anthropometric committee. *Br. Assoc. Adv. Sci. Rep.* **1880**, *50*, 135–136.
44. Huxley, J. The coloration of *Papilio zalmoxis* and *P. antimachus* and the discovery of Tyndall blue in butterflies. *Proc. R. Soc., B* **1976**, *193*, 441–453.

# Structural Nanomaterials

Joanna R. Groza

Jeffrey C. Gibeling

*Department of Chemical Engineering and Materials Science,  
University of California–Davis, Davis, California, U.S.A.*

## INTRODUCTION

By definition, structural materials are used for mechanical strength at room and elevated temperatures, to withstand cyclical loading and for wear and fracture resistance. Structural nanomaterials (with grain sizes less than 100 nm) are distinguished by unusually high strength, hardness, and wear resistance as well as good fatigue resistance, fracture toughness, and extensive high-temperature formability. However, commercial applications have only begun to tap the potential of high-strength parts (e.g., nearly 1 GPa in nano-Al alloys, known as GIGAS,<sup>[1]</sup> and high-strength nano-SiC springs). More commonly, they are used as thermal barrier coatings, or in friction-resistant and wear-resistant rotating parts (e.g., sleeves or bearings).

Nanomaterials used for structural applications may have nanometer size in one dimension (1D), two dimensions (2D), or three dimensions (3D). Generally, 1D nanomaterials are wires, 2D refers to coatings and films, and 3D solids are used to make bulk parts. In this entry, bulk or 3D materials are emphasized, but some 1D and 2D nanomaterials used for their mechanical properties are also presented.

## FABRICATION OF NANOSTRUCTURED MATERIALS

### Processing

The primary challenge in producing bulk nanostructures is to create and to maintain grain sizes less than 100 nm in defect-free, sizable, reproducible, and reliable parts. To date, the processing of raw nanomaterials (powders and thin films) has progressed farther than the formation of bulk parts. Nanosize powders of metals, ceramics, polymers, and composites are now available, sometimes in tonnage quantities. All of these nanostructured powders may be used for processing 2D and 3D parts.

The most common techniques to produce 2D parts are thermal spraying and electrodeposition (ED). The former includes arc, flame, plasma, detonation gun, and high-velocity oxyfuel spraying to produce metal, alloy, ceramic, and composite coatings.<sup>[2]</sup> In the spraying process, the fine microstructure develops when molten or semimolten particles rapidly solidify as they are deposited onto a substrate. Electrodeposition techniques include both electroplating and electroforming, and are typically applied to a limited number of metals, although some ceramics and composites have been also obtained.<sup>[3]</sup> Although electroplating is typically used for coatings, electroforming is a cost-effective method for free-standing ultrathin foils or thick structures, wires, plates, and complex shapes. Grain size is controlled by enhanced nucleation by charge transfer at the electrode surface, high deposition rates, and the inhibition of grain growth by using additives. Electrodeposition can be used to control grain boundary type and to achieve nanocrystalline structures with a relatively narrow grain size distribution and with few pores. Electrodeposition and sputtering also may be used to produce nanolayered materials.

Generally, the processing methods for bulk nanomaterials involve one or two steps. The more commonly used two-step methods consist of producing nanomaterials in a powder form and subsequently consolidating them to a final 3D part. These methods offer the greatest versatility in the shape, size, and weight of the final bulk parts. All powder processing methods have been applied to sinter nanostructured powders and many of them have achieved final grain sizes less than 100 nm.<sup>[4]</sup> The challenge is to fully densify nanopowders without losing the initial metastable features (nanoscale grain size and, sometimes, metastable phases). The consolidation methods use a full range of temperature and pressure conditions from conventional pressureless sintering to high pressure and shock consolidation. Inert gas condensation (IGC) of powders followed by densification has been a widely used technique to process bulk nanocrystalline materials.

Most of these methods leave processing flaws, including incomplete densification, poor interparticle bonding, cracks, or trapped gases.

The one-step methods include severe plastic deformation (SPD), crystallization of amorphous bulk parts, and ED. Severe plastic deformation comprises variants such as equal-channel angular forming and high-pressure torsion straining. Generally, SPD results in grain sizes greater than 100 nm, which are known as ultrafine-grained structures. However, smaller grain sizes (down to 20 nm) have occasionally been achieved.<sup>[5]</sup> Intense plastic deformation has also been used to produce in situ fiber or lamellar composites. A novel intense deformation process based on ball milling with in situ densification (BMID) was recently reported by Koch.<sup>[6]</sup>

The crystallization of bulk amorphous alloys to form nanophases occurs on controlled thermal processing.<sup>[7]</sup> The most challenging step is the formation of bulk amorphous precursors using slow cooling rates similar to conventional casting processes, to enable the fabrication of sizeable parts. This has been achieved in a few metal-based systems (Zr, Mg, and, partially, Al). Next, controlled direct or stepwise devitrification takes place at temperatures within the supercooled liquid region, or close to the onset of crystallization. The resultant structures are typically multiphase alloys formed by the precipitation of nanoscale metastable (metal-based or quasi-crystalline) or stable (intermetallic) phases in an amorphous matrix. The type and the size of nanocrystalline components vary with alloy chemistry and processing conditions.

### Dependence of Properties on Processing

Most processing methods result in some imperfections in the final bulk part. In conventional materials, well-established standards control flaw size and distribution, resulting in a negligible effect on mechanical properties. However, such flaws have a more critical effect on the mechanical properties of nanomaterials, and are different in nature and size than in conventional materials. The most common imperfections in nanocrystalline bulk materials are pores, trapped gases, impurity contamination, cracks, imperfect bonding, surface defects, residual stresses, and texture. Although some defects are common to several techniques (e.g., contamination, surface defects, or pores), texture is typical in ED, residual stresses are most severe in SPD, and incomplete bonding and densification are observed in powder consolidation and thermal spraying. Defect characterization in nanomaterials is a relatively new field, and appropriate guidelines are definitely required.

The most detailed defect characterization has been carried out for the flaws specific to the two-step powder consolidation methods, particularly pores that result from incomplete densification.<sup>[8,9]</sup> At small grain sizes (less than 10 nm), a density shortfall may also originate from the high volume of low-density grain boundaries. Van Swygenhoven, Spaczet, and Caro.<sup>[10]</sup> calculated densities of 97% for a 10- to 12-nm grain size Ni and 95.2% for a 3.4-nm grain size Ni. Experiments confirmed a 97.6% density value measured by a high-precision Archimedes method in 10-nm grain size samples produced by IGC.<sup>[11]</sup>

Processing flaws in nanomaterials have an adverse effect on mechanical properties. The modulus of elasticity or Young's modulus  $E$  is a reflection of interatomic bonding and is largely dependent on defects. The low experimental  $E$  values reported in early studies of nanocrystalline materials have been unquestionably attributed to defects such as pores, poor grain-to-grain bonding, or deficiencies in measuring techniques.<sup>[9,12]</sup> More recent experimental measurements on low-defect nanomaterials demonstrate that grain size has a negligible effect on Young's modulus.<sup>[13]</sup> Simulations also showed no variation in Young's modulus down to a grain size of 10 nm.<sup>[14]</sup> Below this limit, when the slightly lower-density grain boundary volume becomes predominant, the modulus decreases with decreasing grain size. Some calculated values are as low as about 75% of the modulus of bulk metals at 3–6 nm grain size.<sup>[14,15]</sup>

All other mechanical properties, including strength, hardness, and ductility, are sensitive to microstructure and are even more adversely affected by defects. Ample evidence exists for inferior strength and ductility values, particularly in tensile testing, because of pores and trapped gases, cracks, imperfect bonding, and surface defects. Agnew et al.<sup>[8]</sup> Sanders, Youngdahl, and Weertman.<sup>[9]</sup> Legros et al.<sup>[13]</sup> and Nieman, Weertman, and Siegel.<sup>[16]</sup> carefully documented the dependence of strength and ductility on processing flaws in metals. He and Ma<sup>[17]</sup> characterized the variation of hardness with porosity in the Fe<sub>3</sub>Al intermetallics. Hardness values were reported to double by processing improvements to produce dense metals.<sup>[9]</sup> The reduction of the surface imperfections has been shown to increase the tensile strength by up to a factor 4 by preventing premature fracture.<sup>[16]</sup> Consequently, reduced size specimens (e.g., micro and miniature tensile and bend specimens) have been used to lower the defect probability.<sup>[13,18,19]</sup> The elimination of some defects by annealing can also increase the strength of metals<sup>[20,21]</sup> and intermetallics<sup>[20–23]</sup> by decreasing porosity, relaxing the grain boundary structure toward equilibrium, or reducing internal stresses.

As is detailed in "Strength and Ductility," ductility is the property most affected by processing flaws. The

lack of good interparticle bonding is the major cause of brittle failure in consolidated samples tested in tension or bending.<sup>[9,24,25]</sup> As an example, 80-nm Fe<sub>3</sub>Al produced by shock wave consolidation of mechanically alloyed powders displayed brittle behavior in tension but a large plastic strain in compression (true plastic strain of 1.4).<sup>[26]</sup> Similar to strength, an improvement in ductility was reported after annealing at low temperatures without altering the grain size (e.g., an increase from 2 to 7.3% in 30-nm Cu) because of grain boundary relaxation.<sup>[27]</sup> Electrodeposition yields better ductilities than powder consolidation because of reduced porosity and good interparticle bonding. However, some ductility problems have been noted when using grain growth inhibitors, or because of texture development. Throughout this entry, an effort has been made to exclude materials with significant processing deficiencies, when these are reported.

In conventional materials, it is acceptable to use average grain size to characterize mechanical properties. This approach is not appropriate in nanomaterials because of the size dependence of the deformation behavior. For instance, some large recrystallized 1–5 μm size grains enabled larger ductility values in nano-Cu vs. nano-Ni, which had fewer such recrystallized grains and was consequently brittle.<sup>[13]</sup> All processing methods result in a distribution of grain sizes. In nanomaterials, grain size measurements are commonly carried out by X-ray diffraction (XRD) and transmission electron microscopy (TEM). Transmission electron microscopy enables a direct measurement of grain sizes and grain size distribution. In contrast, XRD techniques provide only an average grain size, the value of which also depends on the specific method used [e.g., Scherrer, Warren–Averbach (W–A), or Williamson–Hall].<sup>[28]</sup> Average TEM grain size and X-ray results are in good agreement when the grain size distribution is narrow and XRD corrections are made (Fig. 1A). Log-normal distributions of grain sizes are usually used. When grain size distribution is described by volume fractions, the peak value may be quite different from the TEM number fraction and XRD values (Fig. 1A). Volume fractions more realistically reflect the effect of large grains, which may be predominant on mechanical properties.<sup>[21]</sup> The standard deviation of the volume fraction also affects the grain size distribution (Fig. 1B) and, consequently, the mechanical properties (Fig. 1C).

## STRENGTH AND DUCTILITY

The general description of the mechanical behavior in tension is given in Fig. 2.<sup>[29]</sup> Brittle materials are characterized by a linear elastic stress ( $\sigma$ )–strain ( $\epsilon$ )

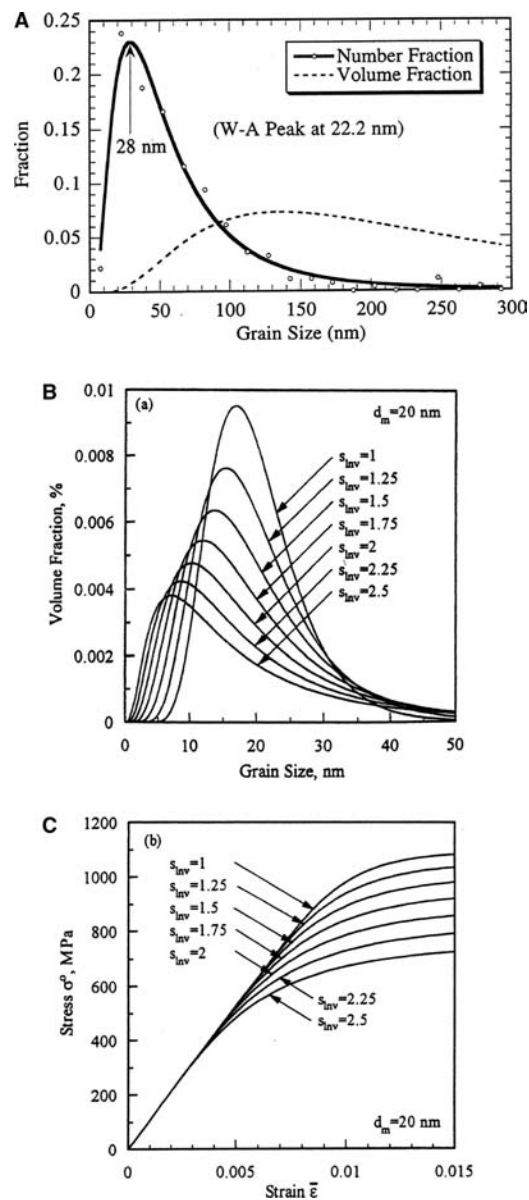


**Fig. 1** Effects of grain size distributions on mechanical properties. *Source:* From Refs.<sup>[14,21]</sup> (A) Comparison of grain size values given by TEM and XRD in IGC copper. The open circles are the relative number of grains in a given size range. The solid and dotted lines indicate the log-normal fits of the data points as number–fraction and volume–fraction curves, respectively. (B) Effects of the standard deviation size  $S_{inv}$  on the grain size distribution and (C) on stress–strain curves for the same average grain size ( $d = 20$  nm). The IGC Cu is heavily twinned and the “grain size” value actually refers to the twin size. *Source:* *MRS Bulletin* and J. R. Weertman.

response and fracture with no plastic deformation (Fig. 2A). Ductile materials yield beyond the elastic region and then fracture after a certain elongation (Fig. 2B). Fig. 2B defines the yield strength ( $\sigma_y$ ), tensile strength ( $\sigma_{UTS}$ ), and elongation to fracture ( $\epsilon_f$ ). In the

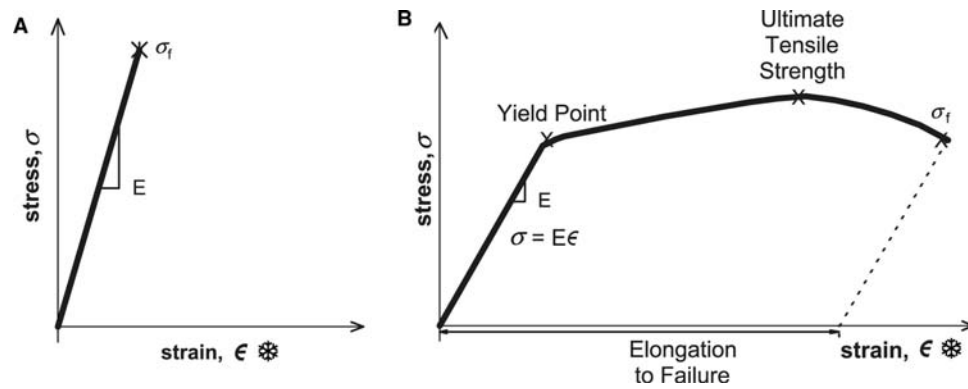


**Fig. 2** Stress–strain curves for brittle (A) and ductile (B) materials. The slope of the linear portion of the  $\sigma$ – $\epsilon$  plot defines the elastic modulus by the Hooke's law ( $\sigma = E\epsilon$ ).

plastic region, work hardening is expressed using a true strain value  $\epsilon$  by:

$$\sigma = K \epsilon^n \quad (1)$$

where  $K$  is a constant and  $n$  is the strain hardening exponent. Strain or work hardening is attributed to the generation and interaction of the dislocations. It controls the amount of uniform elongation at stresses larger than yield strength  $\sigma_y$ . A dimensional instability in tension, or necking, typically starts to develop at maximum load.

Grain size refinement results in the classical grain boundary strengthening (expressed in terms of yield strength  $\sigma_y$  but also valid for  $\sigma_{UTS}$  or hardness  $H$ ), which is described by the Hall–Petch (H–P) relationship:<sup>[29]</sup>

$$\sigma_y = \sigma_0 + k d^{-1/2} \quad (2)$$

where  $\sigma_0$  is the friction stress to move dislocations,  $k$  is a material-dependent and temperature-dependent constant, and  $d$  is grain size.

The H–P relationship can be rationalized by two basic dislocation descriptions: 1) the dislocation pile-up model, in which yielding occurs as a result of stress concentrations caused by pileups (Fig. 3A); and 2) the dislocation network model, in which the slip is because

of dislocations emitted by grain boundaries (Fig. 3B). A third model developed by Meyers and Ashworth<sup>[29]</sup> is a variant of the dislocation emission model with localized plastic flow at a work-hardened grain boundary layer (Fig. 3C). Plastic deformation occurs when the applied stress exceeds the higher-flow stress of the grain boundary region. The resulting grain size dependence of the yield strength is the sum of  $d^{-1/2}$  and  $d^{-1}$  dependencies:

$$\sigma_y = \sigma_0 + k d^{1/2} + k' d^{-1} \quad (3)$$

where  $k'$  is a different constant from  $k$ . The second term is dominant at large grain sizes, whereas the third term becomes important at small grain sizes. All models assume conventional dislocation generation and mobility.

### Strength of Nanostructured Materials

By extrapolating the grain size to the nanometer range, both strengthening and an increase in ductility were predicted.<sup>[30]</sup> Experimentally, this prediction has been observed for a number of materials (Fig. 4).

According to the H–P relationship, a 1000-fold reduction in grain size from microns to nanometers yields more than a 30-fold increase in strength, provided that the same dislocation mechanisms are

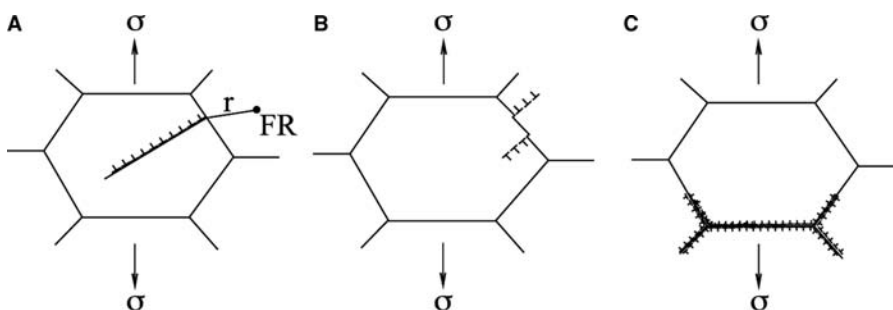


**Fig. 3** Dislocations models to explain the H–P behavior developed by: (A) Cottrell (dislocation pile-up); (B) Li (dislocations generated at ledges in grain boundaries); and (C) Meyers and Ashworth. Source: From Ref.<sup>[21]</sup>.



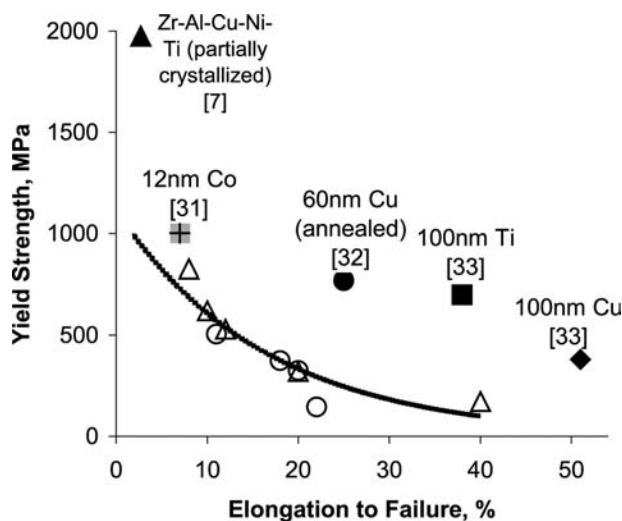


**Fig. 4** Strength–ductility values of nanostructured materials (filled symbols) compared to conventional counterparts (open symbols: circles—dispersion-strengthened Al alloys; triangles—cold-worked steels).

operational. Experimentally, strength or hardness was found to increase by a factor of 5–10 by reducing the grain size from microns down to the 30- to 50-nm level.<sup>[9,25,31]</sup> Similar high-strength values for nanocrystalline metals and alloys were observed in compression, or by hardness measurements, in which processing defects are less detrimental than in tension. Yield strengths greater than 1 GPa were found in Pd (40–50 nm), and yield strengths close to 1 GPa were found in Cu (20 nm).<sup>[9]</sup> Ball-milled and densified Fe (24 nm) had a true compressive strength of approximately 3 GPa,<sup>[24]</sup> whereas IGC-processed 21-nm Ni failed in compression at more than 2.1 GPa.<sup>[21]</sup>

Often the spread of experimental data is quite large, but reasonable H–P correlations at the smallest grain sizes have been revealed (i.e., stronger materials at smaller grain size) (Fig. 5). Deviations from H–P strengthening, where the slope decreases or the curve flattens, also have been reported, usually at grain sizes smaller than about 30 nm (Fig. 5B and C).<sup>[24,32]</sup> An inverse H–P effect, in which strength decreases at the smallest grain sizes, has been reported in alloys such as Ni–P.<sup>[33]</sup> This effect was most often reported in specimens annealed to increase the initial small grain size in metals or intermetallics.<sup>[20,22]</sup> Generally, these results must be treated with caution because either processing artifacts may not have been completely eliminated, or other processes (e.g., precipitation of a second phase in Ni–P alloys or in mechanically alloyed Fe) may have interfered with the measurements.<sup>[24,33]</sup>

Various mechanisms have been proposed to rationalize the deviations from H–P strengthening, such as the breakdown of dislocation pileups, lack of

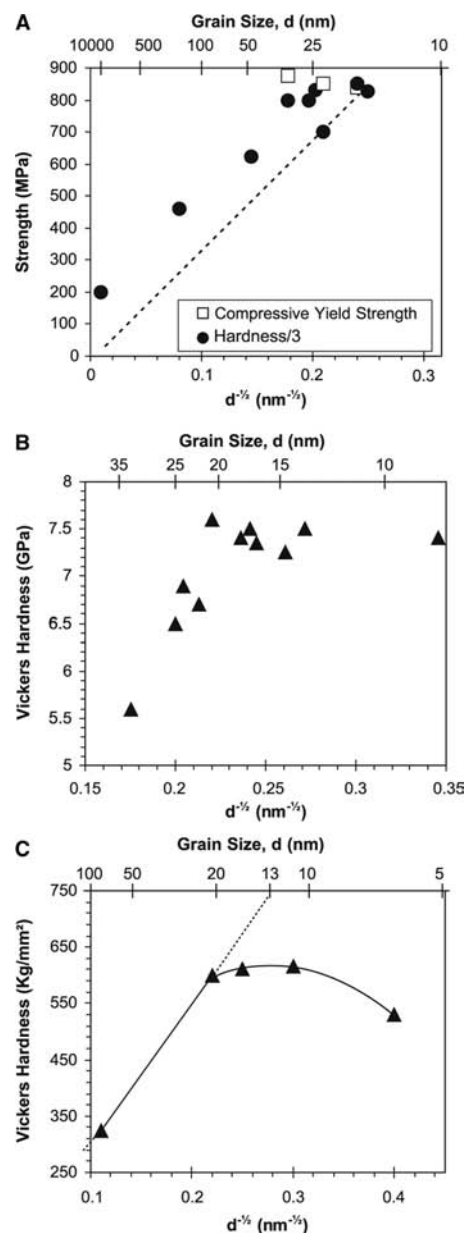


**Fig. 5** Grain size dependence of mechanical properties in nanocrystalline metals: (A) Cu (IGC) Source: From Refs.<sup>[9,21,31]</sup>; (B) Fe (ball-milled/densified) Source: From Ref.<sup>[24]</sup>; and (C) Ni (electrodeposited) Source: From Ref.<sup>[32]</sup>. The dotted lines are the H–P extrapolations of coarse grain data Source: *Materials and Metallurgical Transactions* and J. R. Weertman.

dislocation activity, and increased contributions from diffusional deformation mechanisms (creep and grain boundary sliding).<sup>[14,21,34,35]</sup> Cheng, Spencer, and Milligan<sup>[34]</sup> proposed a deformation mechanism map showing the transition from the dislocation mechanisms to intergranular processes. Transmission electron microscopy studies have confirmed the lack of dislocation structure below a critical grain size of 10–30 nm.<sup>[13,34]</sup>

To explain the H–P behavior, a model based on dislocation generation from grain boundary sources was recently proposed by Cheng, Spencer, and Milligan.<sup>[34]</sup> The model also predicts the observed tension/compression asymmetry based on the pressure dependence of dislocation self-energy during bowout. Composite models considered grain interior and grain boundary properties, and, sometimes, triple junction lines and quadruple nodes.<sup>[21]</sup> The width of grain boundary or adjacent area is still under debate, but the maximum yield strength was found at similar grain size value (about 10 nm). Composite models that are more consistent with microstructural results by accounting for a dispersion in grain sizes have been developed.<sup>[28,35]</sup> These models combine deformation mechanisms that are active in various grain size ranges. Masumara, Hazzledine, and Pande<sup>[35]</sup> considered a combination of dislocation glide for grains larger than a critical size  $d^*$  and Coble creep below  $d^*$ . In the model developed by Mitra et al.<sup>[28]</sup> the critical grain size  $d^*$  differentiates grains that undergo plastic deformation ( $d > d^*$ ) from grains that remain elastic ( $d < d^*$ ).<sup>[21]</sup> The overall calculation was based on the plastic deformation of grains in an elastic matrix that used the mechanics of non-deformable inclusions. The average grain size was given by a volume averaging of the grains, similar to previous work.<sup>[35]</sup> For the same average grain size, the volume fractions are shown to be greatly influenced by the standard deviation (Fig. 1B). In turn, a larger standard deviation (with more small-size grains deformed by creep) results in softer behavior (Fig. 1C).

### Two-phase alloys and nanocomposites

The addition of a second phase produces greater mechanical strength in nanomaterials just as in conventional materials. Bulk materials made of quasi-crystalline or icosahedral phases (less than 50 nm) in an Al matrix (5–10 nm; Al–Cr or Mn–Ln, e.g.,  $\text{Al}_{93}\text{Mn}_5\text{Co}_2$ ) exhibited strength values of 550–850 MPa with 5–25% elongations.<sup>[1]</sup> High strength and high ductilities also have been found in the case of nanoparticles reinforcing amorphous matrices in Mg-based, Al-based, and Zr-based alloys.<sup>[7]</sup> The nanosize particles prevent fracture because of improved interfacial bonding, which favors load transmission from one phase to the other.

Tensile strength doubled in ED Ni–SiC composites by reducing matrix grain size to 10–15 nm. SiC particles (400 nm) up to about 2 vol.% changed the fracture from brittle to nanocrystalline Ni to ductile ( $\epsilon > 2\%$ ) in Ni–SiC composites.<sup>[36]</sup> However, only a modest increase in hardness was observed by the addition of 5 vol.%  $\text{SiO}_2$  particles (20 nm) to 60 nm of SPD copper (microhardness of 2800 vs. 2600).<sup>[37]</sup> The hardness

increase in mechanically alloyed  $\text{Zr}_{55}\text{Al}_{10}\text{Cu}_{30}\text{Ni}_5$  reinforced with 35-nm W particles obeyed the rule of mixtures.<sup>[38]</sup> In contrast, fiber and lamellar composites (multilayers) display hardness values far in excess of the rule of mixture values because of the restriction of dislocation propagation by the second layer.<sup>[39]</sup>

### Ductility of Nanostructured Materials

Ductility is defined as the ability to plastically deform prior to fracture. Therefore it is a critical property for both the performance and the manufacturing of nanostructured materials.<sup>[18]</sup> Ductility is measured by percent elongation before failure (e.g., elongation to failure  $\epsilon_f$  in Fig. 2B), or percent reduction of area after necking in tension.

With the decrease of grain size to nanometer levels, increases in ductility have been predicted.<sup>[18,29,30]</sup> According to Coble's theory, the significantly larger interfacial area enhances deformation by diffusional transport and grain boundary sliding. This enhanced sliding at the more numerous grain boundaries should result in an increased deformation in metals even at room temperature. The most dramatic change of ductility was predicted for normally brittle materials such as intermetallic compounds.<sup>[18]</sup> The prediction is based on conventional material behavior, in which a fine grain size decreases the stress required to nucleate microcracks as compared with that required to propagate them. If crack propagation occurs only at high stress values, the fine-grained materials may undergo plastic strain and work hardening before failure. In other words, in tension testing (Fig. 2B), a material displays ductile behavior if plastic deformation occurs without the onset of catastrophic failure. Chan<sup>[40]</sup> calculated a critical grain size (e.g., 2.8  $\mu\text{m}$  in NiAl) below which crack growth occurs in a stable manner to render the intermetallics ductile. Experimentally, such behavior was observed in the now-classical results for NiAl alloys, which become ductile at a grain sizes below 20  $\mu\text{m}$ . A high ductility (e.g., greater than 11.5% in compression) was reported in NiAl with sub-micron grain size.<sup>[41]</sup> Ductility of more than 5% in compression was reported by Kimura<sup>[42]</sup> in TiAl (grain size less than 22 nm) crystallized from an amorphous precursor. However, this behavior was not reproduced in other intermetallics.

In metals and alloys, ductilities lower than in conventional materials have been reported.<sup>[18,43]</sup> Despite the efforts to improve the processing and testing, it is difficult to differentiate intrinsic from flaw-limited ductilities. When the grain size is reduced to less than 25 nm, ductility values in tension or bending decrease from about 50% in conventional materials to 1–2%.<sup>[18]</sup>

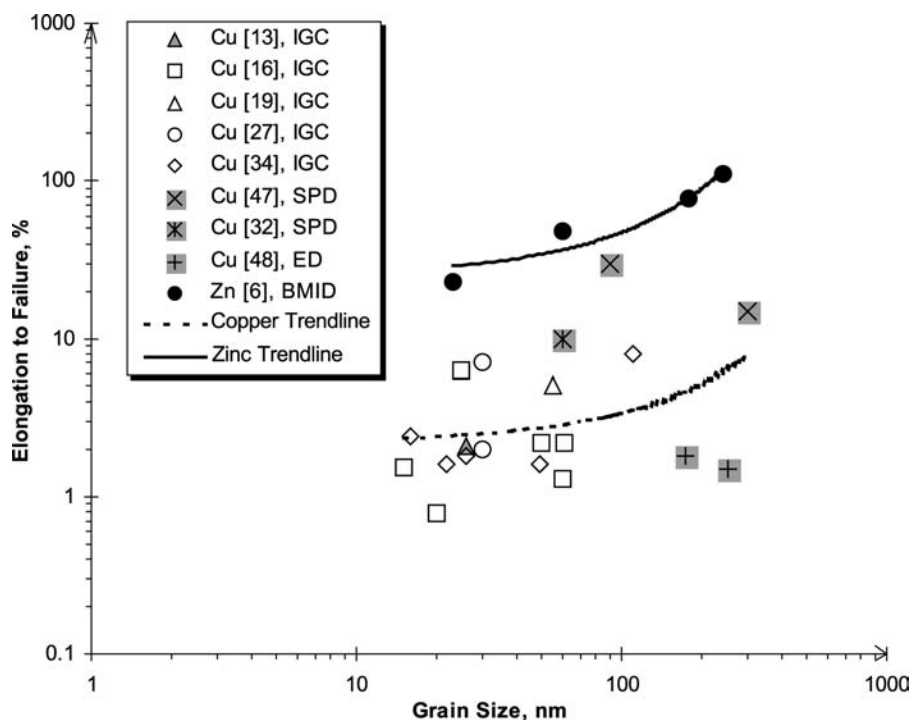


**Fig. 6** Tensile elongation vs. grain size in nanocrystalline Zn and Cu. Source: C. C. Koch.

Little tensile ductility (less than 2%), or completely brittle behavior is commonly reported in metals even after careful processing (e.g., in IGC-processed 28-nm Ni,<sup>[13]</sup> ED-processed 27.5- to 30-nm Ni,<sup>[44]</sup> and IGC-processed 27-nm Cu,<sup>[19]</sup>). An illustration of the variation of ductility with grain size is provided in Fig. 6 for two nanocrystalline metals. It is noteworthy that higher ductility is observed in the hcp metal (Zn) rather than fcc (Cu), which is contrary to the dislocation-based plastic behavior at conventional grain sizes. A few truly ductile nanomaterials ( $\epsilon_f > 5\%$ , as a structural design criterion) are shown in Figs. 4 and 6.

If the dislocation generation and interactions are similar to the coarse-grained materials, strain hardening can be expected in nanosize materials. Strain hardening controls the amount of uniform elongation at stresses larger than yield strength. Generally, hardening was observed, sometimes, to be of a significant value and at a large plastic strain such as in a 60-nm SPD Cu<sup>[37]</sup> or in tension or compression in other metals.<sup>[43]</sup> However, a different behavior with little or no strain hardening and shear banding has also been reported in nanomaterials, mostly bcc metals and alloys (Fe, Fe-Cu, and Ta), but also in fcc and hcp and intermetallics.<sup>[25,43,45]</sup> Perfectly plastic behavior with no strain hardening is typical for materials in which initial plastic flow is difficult (e.g., amorphous or highly strained metals). In nanomaterials, one assumption is that the grain boundaries introduce sufficient defects similar to amorphous materials such that unstable plastic flow is initiated as soon as the yield

strength is reached at a local stress concentration.<sup>[9]</sup> Crack growth will occur, resulting in failure without prior macroscopic ductility.<sup>[24]</sup> Brittleness may be observed if the stress to activate surface cracks is lower than the stress to activate Frank-Read dislocation sources and no crack blunting mechanism is in operation.<sup>[31]</sup> Calculations show that tensile stresses at which brittle fracture occurs indeed correspond to the stresses required for brittle fracture in materials with micron-size flaws.

The other source of low ductility may be the absence of effective mechanisms for plastic deformation, mainly the lack of dislocation activity in grains below a size of about 30 nm.<sup>[13,34]</sup> The lack of noticeable dislocations is consistent with the brittle fracture exhibited by a 28-nm Ni specimen.<sup>[13]</sup> Zimmerman et al.<sup>[36]</sup> also reported higher ductilities in 40- vs. 14-nm grain size ED Ni.

Grain boundary sliding and grain rotation were shown to be the deformation mechanisms in some nanomaterials that exhibited ductile behavior such as electrodeposited Ni or 10-nm sputtered gold films.<sup>[45,46]</sup> Indirect evidence of grain boundary sliding is provided by the strain rate increase as the grain size becomes smaller and there is no change in the total amount of grain boundary deformation.<sup>[14]</sup> Strain rate shows no grain size dependence at larger grain sizes (greater than 10 nm). Molecular dynamics simulations showed grain boundary sliding responsible for inverse H-P behavior even at low temperature and without any porosity.<sup>[14,15]</sup>

## Two-phase nanomaterials

Second-phase particles increase the flow stress on local shear planes, thus resulting in more uniform deformation and higher elongation. High elongations (5–25%) are exhibited by Al-based alloys with nano-scale icosahedral quasi-crystalline phases in a ductile fcc Al matrix (obtained by extrusion).<sup>[1,7]</sup> A homogeneous dispersion of nanosize crystalline particles in an amorphous matrix is able to suppress local shear deformation in Mg-based and Zr-based alloys.<sup>[7]</sup> In some Zr-based or Al-based alloys, the precipitation of nanoscale particles induces considerable strengthening but decreases ductility, as compared with a fully amorphous alloy.<sup>[7]</sup> When the precipitate amount is greater than 50%, the alloys become brittle. However, second-phase particles in metal-based alloys seem to have a different effect in nanosize matrices than in conventional dispersion-strengthened alloys. For instance, an addition of 0.7 vol.% SiC to a nano-Ni matrix increased the ductility to 3.4% as compared with 0.2% in pure 14-nm Ni.<sup>[36]</sup>

## FRACTURE AND FAILURE

Fracture toughness ( $K_c$ ) is defined as the value of a stress intensity factor at a crack tip to induce crack propagation and failure as given by:<sup>[29]</sup>

$$K_c = Y\sigma_f\sqrt{a} \quad (4)$$

where  $Y$  is a dimensionless geometry factor,  $\sigma_f$  is the applied stress at fracture, and  $a$  is the crack length. Usually, a high fracture toughness value is an indication of ductile behavior because work is needed to produce local plastic strain at the crack tip. There is some expectation that decreasing grain size would also result in increased  $K_c$ . This effect was expected to be particularly beneficial for normally brittle materials such as intermetallic compounds. However, Armstrong<sup>[47]</sup> showed that there is a limit when the crack tip plastic zone size is approximately equal to the grain size, below which the toughness should decrease as the grain size decreases.

Only limited measurements of fracture toughness of nanomaterials are available in the literature, owing in part to the stringent specimen size requirements.<sup>[29]</sup> The available data suggest that, in general, the anticipated improvement in fracture toughness with decreasing grain size has not been realized. Rather, experiments and modeling indicate that the fracture resistance in both metals and intermetallics appears to be limited by the nucleation of nanovoids at grain boundaries and intergranular crack propagation.<sup>[48–50]</sup>

Fracture toughness was found to decrease with a reduction in grain size below 1  $\mu\text{m}$  in TiAl, whereas it remained constant down at 12 MPa  $\text{m}^{1/2}$  to  $\sim 40\text{ nm}$ , and then decreased to about 5 MPa  $\text{m}^{1/2}$  in FeAl.<sup>[23,51]</sup> Similarly, very low values of fracture toughness (2 MPa  $\text{m}^{1/2}$ ) were reported in Fe–45% Al and Al<sub>3</sub>Ti.<sup>[52]</sup> Because grain boundary diffusion and sliding can occur in nanocrystalline solids at room temperature, these processes may control toughness at low crack propagation rates. This suggestion is supported by the observation of Mirshams et al.<sup>[53]</sup> of the  $R$ -curve fracture behavior in nanocrystalline nickel produced by ED, in which  $K_c$  increases with the growth of a crack in a slow, stable manner. As with other mechanical properties, these differences in behavior may be partially attributable to the different defect densities associated with the various processing techniques. Additional data are needed to more fully distinguish between intrinsic grain size effects and the influence of processing on fracture toughness.

## FATIGUE PROPERTIES

The study of fatigue is normally divided into two important aspects: 1) deformation under cyclical loading conditions leading to crack initiation; and 2) the rate of growth of a preexisting flaw or crack. Only a few studies of fatigue of nanocrystalline or ultrafine-grained materials, dealing mainly with cyclical deformation, have been published to date. As with other mechanical properties, these studies suggest that the processing method is important.

Nanocrystalline copper prepared by IGC and compaction revealed no cyclical hardening or softening during tension–tension loading.<sup>[54]</sup> However, some creep strain superimposed on the cyclical response was evident. Of particular note is the observation of shear bands extending over many grain diameters on the surface of the fatigued specimens. In addition, the material was observed to protrude from the surface much like the extrusions observed in conventional copper alloys. This finding suggests that some mechanism of strain localization on a scale larger than the grain size is operating. Similar surface observations were reported for SPD-processed ultrafine-grained copper.<sup>[55]</sup> On a strain–life basis, this ultrafine-grained copper was less fatigue-resistant than conventional materials. However, the mechanical response of this material reveals a decreasing stress amplitude with an increasing number of cycles or cyclical softening, as expected for a predeformed metal. A similar material was more fatigue-resistant than conventional copper when compared on a stress–life or S–N basis.<sup>[56]</sup> Surface markings have also been observed in a yttria-stabilized zirconia ceramic, although in this case the strain localization is most likely

because of diffusional deformation processes rather than dislocation processes.<sup>[57]</sup>

It is not yet clear whether any of our understanding of fatigue in conventional materials can be extended to the nanometer grain size level. However, it is important to recognize that the features observed in fatigue are normally on the order of 1  $\mu\text{m}$  in scale, hence are clearly coarser than the nanocrystalline grain size. Additional fundamental studies are needed.

## WEAR

The processes involved in tribological conditions are heavy local deformation, work hardening, cyclical loading, and fracture, collectively resulting in material removal. Nanocrystalline materials have been used for wear resistance in bulk (e.g., cutting tools), or for surface applications (coatings) because of their high hardness. The materials for cutting tools are carbides ( $\text{WC}$  or  $(\text{Fe}, \text{Mo}, \text{Cr}, \text{V})_x\text{C}$ ) in soft matrices ( $\text{Co}$ ,  $\text{Fe}$ , or intermetallics), but most materials used commercially have grain sizes in the submicron range. Wear resistance has been shown to scale with hardness in metal ( $\text{Ni}$  and  $\text{Ni-P}$ ), composites ( $\text{Ni-SiC}$ ), and lamellar coatings (e.g.,  $\text{Cu-Ni}$ ).<sup>[25]</sup> The friction coefficient in sliding and rubbing wear was found to decrease by a factor of 2–3 by decreasing grain size (e.g., in sputtered  $\text{Al}$  layers).<sup>[3,25]</sup> The scratch indentation of 10 wt.%  $\text{TiO}_2$  (32 nm) in an epoxy matrix was 33% smaller than for pure epoxy.<sup>[58]</sup>

## ELEVATED TEMPERATURE BEHAVIOR

At elevated temperatures, creep deformation under sustained loads is of importance in structural materials. Whereas a fine grain size is beneficial in promoting high strength at low temperatures, creep resistance normally becomes worse as the grain size decreases. Rather than deforming by dislocation motion, the principle mechanisms of creep deformation in nanomaterials involve diffusional processes because of enhanced high diffusivity at grain boundary and triple junction paths.

Specific creep mechanisms are characterized by the dependence of creep rate on stress, temperature, and grain size. Temperature dependence is expressed through the activation energy for the diffusion of vacancies. For nanocrystalline materials, the most commonly reported mechanisms involve vacancy transport along grain boundaries. This process is known as Coble creep, and the strain rate is represented by an equation of the form:<sup>[29]</sup>

$$\dot{\epsilon} = A_C \frac{\delta D_b G b}{kT} \left(\frac{b}{d}\right)^3 \frac{\sigma}{G} \quad (5)$$

where  $A_C$  is a constant,  $\sigma$  is the stress,  $G$  is the shear modulus,  $b$  is the Burgers vector,  $\delta$  is the grain boundary thickness,  $D_b$  is the grain boundary diffusivity,  $k$  is the Boltzmann's constant, and  $T$  is the temperature. The Coble mechanism is favored at high stresses and low temperatures, even down to room temperatures in nanocrystalline materials. An alternative deformation mechanism involves grain boundary sliding, accommodated by the diffusion of vacancies in the grain boundaries, and is described by a similar equation:<sup>[29]</sup>

$$\dot{\epsilon} = A_{\text{GBS}} \frac{\delta D_b G b}{kT} \left(\frac{b}{d}\right)^3 \frac{\sigma^2}{G} \quad (6)$$

Grain boundary sliding is the mechanism to control superplastic deformation, in which fine-grained materials exhibit extended ductilities of up to several thousands of percent. One key question is whether nanocrystalline solids exhibit superplasticity at low temperatures and high strain rates. If so, this would enable these materials, especially otherwise brittle ceramics and intermetallics, to be formed readily into near-net shapes. Finally, we note that the above two equations differ primarily in the dependence of strain rate on grain size and stress. Thus by measuring these two dependencies, it is possible to distinguish which mechanism controls the creep deformation.

A variety of pure metallic, intermetallic, and ceramic materials have been creep-tested in nanocrystalline form.<sup>[59]</sup> In addition to the usual processing problems (porosity and suitably large specimens), the interpretation of the creep results is hampered by possible grain growth during testing, testing under constant load rather than constant stress, and often limited amounts of creep strain that may not represent a steady state to which the above equations apply. In spite of these difficulties, a number of common ideas have emerged from the available data. Tests of nanocrystalline pure copper and nickel produced by ED appear to demonstrate Coble creep, even at room temperature.<sup>[60–62]</sup> However, there is some evidence that grain boundary sliding controls the deformation of  $\text{Ni}$  with the finest grain sizes (6 nm).<sup>[61]</sup> In addition, when the grain boundaries are of low angle rather than of high angle as in materials prepared by IGC,<sup>[63]</sup> the creep rates are orders of magnitude slower than those predicted by the Coble creep equation. The creep of nanophase  $\text{Ni-P}$  and  $\text{Fe-B-Si}$  alloys (approximately 25 nm in grain size) produced by crystallizing amorphous alloy ribbons also follows the Coble creep equation, although absolute comparisons cannot be made in the former case because of a lack of diffusivity data.<sup>[64,65]</sup>

In a similar manner, nanocrystalline ceramics such as monoclinical zirconia and yttria-stabilized zirconia

exhibit creep deformation at elevated temperatures with stress dependencies of 1.7 and 1.4, respectively.<sup>[66,67]</sup> These values are difficult to interpret, but the grain size dependence in the former case clearly suggests that Coble creep is the operating mechanism.

Superplastic-like behavior has been observed in nanocrystalline nickel<sup>[68]</sup> and copper,<sup>[69]</sup> which exhibited strains up to 5100% during cold rolling of 28-nm grain size material at room temperature. The intermetallic Ni<sub>3</sub>Al has also been shown to undergo superplastic deformation, with a stable grain structure because of the ordered nature of this material.<sup>[70]</sup> Perhaps the greatest interest is in the potential of nanocrystalline ceramics to deform superplastically. An evidence of such behavior has been presented by a number of authors for TiO<sub>2</sub>, yttria-stabilized zirconia, and MgO–Al<sub>2</sub>O<sub>3</sub> spinels.<sup>[71]</sup> At elevated temperatures, grain growth inevitably occurs and may even contribute to achieving high elongations.

## Two-Phase Nanomaterials

Current experimental evidence suggests that multiphase nanocrystalline materials may exhibit superior ductility, especially at elevated temperatures. For example, Al alloys with nanoscale quasi-crystalline icosahedral (I) phases retain their good mechanical strength up to high temperatures (350 MPa at 473 K and 200 MPa at 573 K).<sup>[72]</sup> This high strength is stable on long exposure to elevated temperatures (1000 hr at 573 K) because of the high microstructural stability of the I phase. In Mg-based alloys (e.g., Mg–Al–Ga), ductility increases with temperature, and superplastic behavior was reported.<sup>[73]</sup> However, much like the ceramic materials, the microstructure had coarsened.

## CONCLUSION

The production and study of structural nanomaterials have challenged the conventional description of microstructural features and mechanical properties. New demands have surfaced to carefully monitor grain sizes and distributions, dislocation structures, as well as other defects (pores, cracks, impurities, and surface and internal stresses). The full characterization of the property dependence on processing is yet to be performed. The fabrication of sizable, reproducible, and reliable parts is an additional challenge driven by the high strength values achieved so far.

The conventional dislocation-based strengthening and yielding mechanisms show limitations, which have fostered an exploration of new mechanisms specific to the nanoscale. The inherently large fractions of atoms in non-equilibrium positions (at grain boundaries)

enhance the interface processes to contribute to plasticity. A better understanding of the deformation mechanisms as a function of crystal structure, stacking fault energy, grain size, and distribution is yet to be developed. Additional data are needed to more fully distinguish between intrinsic grain size effects and the influence of processing on mechanical properties. Simulations of deformation behavior at larger grain sizes, in bcc, hcp, or complex crystal structures, are desirable.

A wider application of structural nanomaterials requires a more reliable mechanical property characterization and a more aggressive shift from the concept to the design and fabrication of optimum parts with unique properties at low cost.

## ACKNOWLEDGMENTS

NSF and ARO support for the work on nanomaterials is gratefully acknowledged. We are grateful to colleagues who provided their preprints and to Crystal Merrill for her help with figures.

## REFERENCES

1. Inoue, A.; Kimura, M. Development of high-strength Al-based alloys by synthesis of new multi-component quasicrystals. *MRS Symp. Proc.* **1999**, 553, 495–506.
2. Lau, M.L.; Lavernia, E.J. Thermal Spray Processing of Nanocrystalline Materials. In *Nanostructured Materials*; Koch, C.C., Ed.; Noyes Publications: Norwich, NY, 2002; 51–72.
3. Erb, U.; Aust, K.T.; Palumbo, G. Electrodeposited Nanocrystalline Materials. In *Nanostructured Materials*; Koch, C.C., Ed.; Noyes Publications: Norwich, NY, 2002; 179–222.
4. Groza, J.R. Nanocrystalline Powder Consolidation Methods. In *Nanostructured Materials*; Koch, C.C., Ed.; Noyes Publications: Norwich, NY, 2002; 115–178.
5. Valiev, R.S. Structure and mechanical properties of ultrafine-grained metals. *Mater. Sci. Eng., A Struct. Mater.: Prop. Microstruct. Process.* **1997**, 234–236, 59–66.
6. Zhang, X.; Wang, H.; Scattergood, R.O.; Narayan, J.; Koch, C.C.; Sergueeva, A.V.; Mukherjee, A.K. Tensile elongation (110%) observed in ultrafine-grained Zn at room temperature. *Appl. Phys. Lett.* **2002**, 81, 823–825.
7. Eckert, J. Structure Formation and Mechanical Behavior of Two-Phase Nanostructured Materials. In *Nanostructured Materials*; Koch, C.C., Ed.; Noyes Publications: Norwich, NY, 2002; 423–526.
8. Agnew, S.R.; Elliott, B.R.; Youngdahl, C.J.; Hemker, K.J.; Weertman, J.R. Microstructure and mechanical



- behavior of nanocrystalline metals. *Mater. Sci. Eng., A Struct. Mater.: Prop. Microstruct. Process.* **2000**, *285*, 391–396.
9. Sanders, P.G.; Youngdahl, C.J.; Weertman, J.R. The strength of nanocrystalline metals with and without flaws. *Mater. Sci. Eng., A Struct. Mater.: Prop. Microstruct. Process.* **1997**, *234–236*, 77–82.
  10. Van Swygenhoven, H.; Spaczer, M.; Caro, A. Characterization of the microstructure of nanophase Ni: A molecular dynamics simulation study. *Nanostruct. Mater.* **1999**, *12*, 629–632.
  11. Sanders, P.G.; Eastman, J.A.; Weertman, J.R. Pore distribution in nanocrystalline metals by small-angle neutron scattering. *Acta Mater.* **1998**, *46*, 4195–4202.
  12. Krstic, V.; Erb, U.; Palumbo, G. Effect of porosity on Young's modulus of nanocrystalline materials. *Scr. Mater.* **1993**, *29*, 1501–1504.
  13. Legros, M.; Elliott, B.R.; Rittner, M.N.; Weertman, J.R.; Hemker, K.J. Microsample tensile testing of nanocrystalline metals. *Philos. Mag., A* **2000**, *80*, 1017–1026.
  14. Weertman, J.R.; Farkas, D.; Hemker, K.; Kung, H.; Mayo, M.; Mitra, R.; Van Swygenhoven, H. Structure and mechanical behavior of bulk nanocrystalline materials. *MRS Bull.* **1999**, *24* (2), 44–50.
  15. Schiøtz, J.; Di Tolla, F.D.; Jacobsen, K.W. Softening of nanocrystalline metals at very small grain sizes. *Nature* **1998**, *391*, 561–563.
  16. Nieman, G.W.; Weertman, J.R.; Siegel, R.W. Mechanical behavior of nanocrystalline Cu and Pd. *J. Mater. Res.* **1991**, *6*, 1012–1027.
  17. He, L.; Ma, E. Full-density nanocrystalline Fe–29Al–2Cr intermetallic from mechanically milled powders. *J. Mater. Res.* **1996**, *11*, 72–80.
  18. Koch, C.C.; Morris, D.G.; Lu, K.; Inoue, A. Ductility of nanostructured materials. *MRS Bull.* **1999**, *24* (2), 54–58.
  19. Gertsman, V.Y.; Hoffmann, M.; Gleiter, H.; Birringer, R. The study of grain size dependence of yield stress of Cu for a wide grain size range. *Acta Mater.* **1994**, *42*, 3539–3544.
  20. Chokshi, A.H.; Rosen, A.; Karch, J.; Gleiter, H. On the validity of the Hall–Petch relationship in nanocrystalline materials. *Scr. Metall.* **1989**, *23*, 1679–1684.
  21. Weertman, J.R. *Mechanical Behavior of Nanocrystalline Metals*. In *Nanostructured Materials*; Koch, C.C., Ed.; Noyes Publications: Norwich, NY, 2002; 397–421.
  22. Chang, H.; Alstetter, C.J.; Averbach, R.S. Characteristics of nanophase TiAl produced by inert gas condensation. *J. Mater. Res.* **1992**, *7*, 2962–2970.
  23. Morris-Munoz, M.A.; Dodge, A.; Morris, D.G. Structure, strength and toughness of nanocrystalline FeAl. *Nanostruct. Mater.* **1999**, *11*, 873–885.
  24. Malow, T.R.; Koch, C.C. Mechanical properties, ductility, and grain size of nanocrystalline iron produced by mechanical attrition. *Metall. Mater. Trans.* **1998**, *29A*, 2285–2295.
  25. Morris, D.G. *Mechanical Behavior of Nanostructured Materials*; Trans. Tech. Publ. Ltd.: Zürich, 1998.
  26. Jain, M.; Christman, T. Synthesis, processing, and deformation of bulk nanophase Fe–28Al–2Cr intermetallic. *Acta Metall. Mater.* **1994**, *42*, 1901–1911.
  27. Gunther, B.; Baalman, A.; Weiss, H. Preparation and mechanical properties of ultrafine grained metals. *MRS Symp. Proc.* **1990**, *195*, 611–615.
  28. Mitra, R.; Ungar, T.; Morita, T.; Sanders, P.G.; Weertman, J.R. Assessment of Grain Size Distributions in Nanocrystalline Cu and Their Effect on Mechanical Behavior. In *Advanced Materials for the 21st Century*; Chung, Y.-W., Dunand, D.C., Liaw, P.K., Olson, G.B., Eds.; TMS: Warrendale, 1999; 553–564.
  29. Meyers, M.A.; Chawla, K.K. *Mechanical Behavior of Materials*; Prentice Hall: Upper Saddle River, NJ, 1999.
  30. Gleiter, H. Nanocrystalline materials. *Prog. Mater. Sci.* **1989**, *33*, 224–315.
  31. Sanders, P.G.; Eastman, J.A.; Weertman, J.R. Elastic and tensile behavior of nanocrystalline copper and palladium. *Acta Mater.* **1997**, *45*, 4019–4025.
  32. Erb, U. Electrodeposited nanocrystals. *Nanostruct. Mater.* **1995**, *6*, 533–538.
  33. Lu, K.; Wei, W.D.; Wang, J.T. Microhardness and fracture properties of nanocrystalline Ni–P alloy. *Scr. Metall. Mater.* **1990**, *24*, 2319–2323.
  34. Cheng, S.; Spencer, J.A.; Milligan, W.W. Strength and tension/compression asymmetry in nanostructured and ultrafine-grained materials. *Acta Mater.* **2002**, submitted for publication.
  35. Masumara, R.A.; Hazzledine, P.M.; Pande, C.S. Yield stress of fine grained materials. *Acta Mater.* **1998**, *46*, 4527–4534.
  36. Zimmerman, A.F.; Palumbo, G.; Aust, K.T.; Erb, U. Mechanical properties of nickel silicon carbide nanocomposites. *Mater. Sci. Eng., A Struct. Mater.: Prop. Microstruct. Process.* **2002**, *328*, 137–146.
  37. Alexandrov, I.V.; Zhu, Y.T.; Lowe, T.C.; Islamgaliev, R.K.; Valiev, R.Z. Microstructures and properties of nanocomposites obtained through SPTS consolidation of powders. *Metall. Mater. Trans.* **1998**, *29A*, 2252–2260.
  38. Eckert, J.; Kubler, A.; Schultz, L. Mechanically alloyed  $Zr_{55}Al_{10}Cu_{30}Ni_5$  metallic glass composites containing nanocrystalline W particles. *J. Appl. Phys.* **1999**, *85*, 7112–7119.
  39. Baker, S.; Nix, W.D. Mechanical properties of compositionally modulated Au–Ni thin films—Nanoindentation and microcantilever deflection experiments. *J. Mater. Res.* **1994**, *9*, 3131–3145.
  40. Chan, K.S. Theoretical analysis of grain size effects on tensile ductility. *Scr. Metall. Mater.* **1990**, *24*, 1725–1730.
  41. Dymek, S.; Dollar, M.; Hwang, S.J.; Nash, P. Deformation mechanisms and ductility of mechanically alloyed NiAl. *Mater. Sci. Eng., A Struct. Mater.: Prop. Microstruct. Process.* **1992**, *152*, 160–165.
  42. Kimura, H. High-strength intermetallic TiAl synthesized via high-temperature crystallization of an amorphous alloy. *Philos. Mag., A* **1996**, *73*, 723–737.
  43. Koch, C.C. Ductility in nanostructured and ultra fine-grained materials: Recent evidence for optimism. *J. Metastable Nanocryst. Mater.* **2003**, *18*, 9.
  44. Ebrahimi, F.; Ahmed, Z.; Morgan, K. Effect of grain size distribution on tensile properties of electrodeposited nanocrystalline nickel. *MRS Symp. Proc.* **2001**, *634*, B2.7.1–B2.7.6.

45. Wang, N.; Wang, Z.; Aust, K.T.; Erb, U. Room temperature creep behavior of nanocrystalline nickel produced by an electrodeposition technique. *Mater. Sci. Eng., A Struct. Mater.: Prop. Microstruct. Process.* **1997**, *237*, 150–158.
46. Ke, M.; Hackney, S.A.; Milligan, W.W.; Aifantis, E.C. Observation and measurement of grain rotation and plastic strain in nanostructured metal thin film. *Nanostruct. Mater.* **1995**, *5*, 689–697.
47. Armstrong, R.W. The (cleavage) strength of pre-cracked polycrystals. *Eng. Fract. Mech.* **1987**, *28*, 529–538.
48. Farkas, D.; Van Swygenhoven, H.; Derlet, P.M. Intergranular fracture in nanocrystalline metals. *Phys. Rev., B* **2002**, *6606*, 101
49. Xiao, C.H.; Mirshams, R.A.; Whang, S.H.; Yin, W.M. Tensile behavior and fracture in nickel and carbon doped nanocrystalline nickel. *Mater. Sci. Eng., A Struct. Mater.: Prop. Microstruct. Process.* **2001**, *301*, 35–43.
50. Gan, Y.; Zhou, B.L. Effect of grain size on the fracture toughness of nanocrystalline FeMoSiB. *Scr. Mater.* **2001**, *45*, 625–630.
51. Morris, M.A.; Leboeuf, M. Grain-size refinement of gamma-Ti–Al alloys—Effect on mechanical properties. *Mater. Sci. Eng.* **1997**, *224*, 1–11.
52. Varin, R.A.; Zbronic, L.; Czujko, T.; Song, Y.K. Fracture toughness of intermetallic compacts consolidated from nanocrystalline powders. *Mater. Sci. Eng., A Struct. Mater.: Prop. Microstruct. Process.* **2001**, *300*, 1–11.
53. Mirshams, R.A.; Mao, C.H.; Whang, S.H.; Yin, W.M. *R*-curve characterization of the fracture toughness of nanocrystalline nickel thin sheets. *Mater. Sci. Eng., A Struct. Mater.: Prop. Microstruct. Process.* **2001**, *315*, 21–27.
54. Whitney, A.B.; Sanders, P.G.; Weertman, J.R.; Eastman, J.A. Fatigue of nanocrystalline copper. *Scr. Metall. Mater.* **1995**, *33*, 2025–2030.
55. Agnew, S.R.; Weertman, J.R. Cyclic softening of ultrafine grain copper. *Mater. Sci. Eng., A Struct. Mater.: Prop. Microstruct. Process.* **1998**, *244*, 145–153.
56. Agnew, S.R.; Vinogradov, A.Y.; Hashimoto, S.; Weertman, J.R. Overview of fatigue performance of Cu processed by severe plastic deformation. *J. Electron. Mater.* **1999**, *28*, 1038–1044.
57. Yan, D.S.; Zheng, Y.S.; Gao, L.; Zhu, C.F.; Wang, X.W.; Bai, C.L.; Xu, L.; Li, M.Q. Localized superplastic deformation of nanocrystalline 3Y-TZP ceramics under cyclic tensile fatigue at ambient temperature. *J. Mater. Sci.* **1998**, *33*, 2719–2723.
58. Ng, C.B.; Schadler, L.S.; Siegel, R.W. Synthesis and mechanical properties of TiO<sub>2</sub>–epoxy nanocomposites. *Nanostruct. Mater.* **1999**, *12*, 507–510.
59. Mohamed, F.A.; Li, Y. Creep and superplasticity in nanocrystalline materials: current understanding and future prospects. *Mater. Sci. Eng.* **2001**, *298*, 1–15.
60. Cai, B.; Kong, Q.P.; Lu, K.; Lu, L. Low temperature creep of nanocrystalline pure copper. *Mater. Sci. Eng.* **2000**, *286*, 188–192.
61. Wang, N.; Wang, Z.R.; Aust, K.T.; Erb, U. Room temperature creep behavior of nanocrystalline nickel produced by an electrodeposition technique. *Mater. Sci. Eng.* **1997**, *237*, 150–158.
62. Yin, W.M.; Whang, S.H.; Mirshams, R.; Xiao, C.H. Creep behavior of nanocrystalline nickel at 290 and 373 K. *Mater. Sci. Eng.* **2001**, *301*, 18–22.
63. Sanders, P.; Rittner, G.M.; Kiedaisch, E.; Weertman, J.R.; Kung, H.; Lu, Y.C. Creep of nanocrystalline Cu, Pd, and Al–Zr. *Nanostruct. Mater.* **1997**, *9*, 433–440.
64. Xiao, M.L.; Kong, Q.P. Creep behaviour of a nanocrystalline Fe–B–Si alloy. *Scr. Mater.* **1997**, *36*, 299–303.
65. Kong, Q.P.; Cai, B.; Xiao, M.L. High temperature creep of two nanocrystalline alloys. *Mater. Sci. Eng.* **1997**, *234*, 91–93.
66. Roddy, M.J.; Cannon, W.R.; Skandan, G.; Hahn, H. Creep behavior of nanocrystalline monoclinic ZrO<sub>2</sub>. *J. Eur. Ceram. Soc.* **2002**, *22*, 2657–2662.
67. Gutierrez-Mora, F.; Dominguez-Rodriguez, A.; Jimenez-Melendo, M.; Chaim, R.; Hefetz, M. Creep of nanocrystalline Y-SZP ceramics. *Nanostruct. Mater.* **1999**, *11*, 531–537.
68. McFadden, S.X.; Zhiyaev, A.P.; Mishra, R.S.; Mukherjee, A.K. Observations of low-temperature superplasticity in electrodeposited ultrafine grained nickel. *Mater. Lett.* **2000**, *45*, 345–349.
69. Lu, L.; Sui, M.L.; Lu, K. Superplasticity extensibility and deformation mechanism of a nanocrystalline copper sample. *Adv. Eng. Mater.* **2001**, *3*, 663–667.
70. McFadden, S.X.; Valiev, R.Z.; Mukherjee, A.K. Superplasticity in nanocrystalline Ni<sub>3</sub>Al. *Mater. Sci. Eng., A Struct. Mater.: Prop. Microstruct. Process.* **2001**, *319*, 849–853.
71. Mayo, M.J. High and low temperature superplasticity in nanocrystalline materials. *Nanostruct. Mater.* **1997**, *9*, 717–726.
72. Inoue, A.; Kimura, H.M.; Kita, K. *New Horizons in Quasicrystals*; Goldman, A.I., Sordelet, D.J., Thiel, P.A., Dubois, J.M., Eds.; World Scientific: Singapore, 1997; 256 pp.
73. Uoya, A.; Shibata, T.; Higashi, K.; Inoue, A.; Masumoto, T. Superplastic deformation characteristics and constitution equation in rapidly solidified Mg–Al–Ga alloy. *J. Mater. Res.* **1996**, *11*, 2731–2737.

## BIBLIOGRAPHY

1. Ebrahimi, F.; Zhai, Q.; Kong, D. Deformation and fracture of electrodeposited copper. *Scr. Mater.* **1998**, *39*, 315–321.
2. Karimpoor, A.A.; Erb, U.; Aust, K.T.; Wang, Z.; Palumbo, G. Tensile properties of bulk nanocrystalline hexagonal Co electrodeposits. *Mater. Sci. Forum* **2002**, *386–388*, 415–420.
3. Valiev, R.Z.; Alexandrov, I.V.; Zhu, Y.Y.; Lowe, T.C. Paradox of strength and ductility in metals processed by severe plastic deformation. *J. Mater. Res.* **2002**, *17*, 5–8.
4. Wang, Y.M.; Ma, E.; Chen, M.W. Enhanced tensile ductility and toughness in nanostructured Cu. *Appl. Phys. Lett.* **2002**, *80*, 2395–2397.

# Structural Transitions in Thin Films

Rajarshi Banerjee  
Gregory B. Thompson  
Hamish L. Fraser

Department of Materials Science and Engineering, Ohio State University,  
Columbus, Ohio, U.S.A.

## INTRODUCTION

When thin films are deposited on suitable substrate surfaces, they can exhibit crystal structures that would be metastable for the same materials in bulk form (in this entry, the terms *stable* and *metastable* refer to bulk forms). The non-equilibrium crystal structure may arise when the lattice constant or symmetry of film and substrate material are different. An example of such a situation is the pseudomorphic growth. When we start depositing a thin film on a substrate, in the initial stages, the film tends to adopt the crystal structure of the substrate. When the energy gain from the lattice fit becomes smaller than the increase in the volume energy of the strained film, pseudomorphic growth breaks down and the layer usually grows in its natural crystal structure with misfit dislocations at the interface accommodating the strain. Therefore such structures which are metastable in the bulk form of a material can be grown by epitaxial growth techniques on different substrates as well as in the form of multilayers, provided the thickness of the layers is sufficiently small, typically in the nanometer or subnanometer regime. In general, metastable pseudomorphic deposits transform to their bulk-stable polymorphs upon thickening, and the transition thickness is on the order of nanometers.

With the continuing thrust toward thinner films in devices and the potential of exploiting novel properties of such dimensionally constrained systems, it is increasingly evident that such pseudomorphic phases will be continually encountered. Furthermore, because the properties of interest, electronic, magnetic, optical, and structural, are intimately linked to the crystal structure of these nanolayered films, it is important to rationalize the formation of pseudomorphic phases and, if possible, even predict their formation. Such metastable structures have been documented for many systems in the literature, including metal/metal (e.g., Refs.<sup>[1,2]</sup>) and metal/semiconductor systems (e.g., Refs.<sup>[3,4]</sup>). Experimental observations on multilayers include ones where either one (e.g., Refs.<sup>[5-7]</sup>) or even both layers<sup>[8]</sup> can exist in metastable structures. The objective of this

entry is twofold: first, to briefly review the reports in the published literature of stabilization of pseudomorphic phases in nanolayered thin films, and second, to attempt rationalizing these observations based on a simple classical thermodynamic model. This model is a generic one which aids in the understanding of phase stability and structural transitions and leads to the development of a phase stability diagram for multilayered thin films.

## SUMMARY OF STRUCTURAL TRANSFORMATIONS OBSERVED IN NANOLAYERED THIN FILMS

### Titanium/Silver Multilayers

For the motivation of producing a one-dimensional diffraction grating to be used as a soft X-ray monochromator, Zheng, Ketterson, and Felcher<sup>[9]</sup> deposited layered films of Ti/Ag using electron-beam vaporization techniques.<sup>[9]</sup> Ti and Ag exhibit hexagonal close-packed (*hcp*) and face-centered cubic (*fcc*) structures in their bulk equilibrium forms at standard temperature and pressure (STP), respectively. The substrate used was mica and the rate of growth was about 0.8 nm/sec. Epitaxial growth was achieved by first depositing 80 nm of silver on virgin mica held at 250°C. Following the deposition of Ag, alternate layers of Ag and Ti were deposited with a bilayer thickness ( $\lambda$ ) or compositionally modulated wavelength (CMW) of 1.9 nm. The bilayer thickness is the sum of the thicknesses of a single Ti and single Ag layer that forms the repeat period of the multilayer. The films were deposited at a series of different substrate temperatures. Structural characterization of the films was performed using X-ray Laue diffraction in the transmission mode. The Ti/Ag multilayers normally develop a preferred growth texture arising from the layering of close-packed planes. Coherent stacking was observed for the {111} *fcc* planes of Ag and {0001} *hcp* planes of Ti for thicker films, suggesting that both Ti and Ag retained their bulk equilibrium

structures. However, for bilayer thicknesses below 1.9 nm, a single *fcc* structure was observed in these multilayers, suggesting the structural transition from *hcp* Ti to *fcc* Ti in the Ti layers of this multilayer.

### Niobium/Zirconium Multilayers

Nb/Zr multilayers were deposited by the process of magnetron sputtering for studying the effect of structure on the superconductivity in these multilayers.<sup>[10]</sup> Bulk Nb exhibits a body-centered cubic (*bcc*) structure, while bulk Zr exhibits the *hcp* structure at STP. The samples had  $\lambda$  values ranging from 20 down to 0.4 nm with equal Nb and Zr layer thickness. These multilayers were characterized by X-ray diffraction experiments (both high-angle as well as low-angle or grazing incidence). The composition profile, which was calculated from the low-angle X-ray diffraction profile, was not square, but rather the Zr component had partially diffused into the Nb layer. For  $\lambda > 10.9$  nm, the structure of the Zr layer was purely hexagonal with lattice constants of  $a = 0.324$  nm and  $c = 0.521$  nm. Within the region of modulation wavelengths,  $10.9 \text{ nm} > \lambda > 5.1$  nm, the Zr lattice undergoes a gradual phase transition from *hcp* to *bcc*. For  $\lambda < 3.1$  nm, the Zr layer is purely *bcc* and forms a coherent interface with the *bcc* Nb layer. Once the multilayer becomes fully coherent and exhibits a *bcc* structure, the superconducting transition temperature increases sharply with decreasing  $\lambda$ .<sup>[10]</sup>

### Nanolayered Cobalt on Gallium Arsenide

Bulk Co exhibits the *hcp* structure at STP.<sup>[4]</sup> A *bcc* form of Co was stabilized in nanolayered Co deposited epitaxially on GaAs substrates by molecular beam epitaxy (MBE), reported by Prinz<sup>[4]</sup> in 1985. The idea which leads to this discovery was a well-known property of the  $\text{Fe}_x\text{Co}_{1-x}$  alloy system which forms a *bcc* phase over the range  $1 > x > 0.25$ . By a simple linear extrapolation of the lattice constant from the *bcc* phase in these alloys, one obtains a predicted value for the lattice constant of metastable *bcc* Co to be 0.2819 nm. Prinz<sup>[4]</sup> found that by depositing Co on GaAs, it is possible to epitaxially grow Co with the desired lattice parameter and thereby form *bcc* Co.<sup>[4]</sup> Experimentally, epitaxial Co films were grown on GaAs by molecular beam epitaxy (MBE). The substrate used was (110) oriented single crystalline GaAs. Auger spectra of the as-deposited films showed small ( $\approx 2\%$ ) traces of carbon and oxygen on the surface. The films were characterized by reflection high-energy electron diffraction (RHEED). The Co diffraction patterns seem to have the same symmetry as that of *bcc* Fe and the same spacing in all the three principal

crystallographic directions on the (110) face. The film thickness of the Co film was 35.7 nm. X-ray diffraction studies showed that thicker films yield both cubic and hexagonal peaks. Very thick films showed the presence of only *hcp* Co. The critical thickness at which the Co film starts transforming from a *bcc* structure to an *hcp* structure depends on the growth conditions. In the report cited here, the authors found the 35.7-nm film to be the most thick *bcc* film without any bifurcation into *bcc* + *hcp* structures occurring. This is another case of stabilization of a metastable in bulk phase (*bcc* Co) because of epitaxial growth on (110) GaAs substrates.

### Iron/Ruthenium Multilayers

Bulk Fe exhibits the *bcc* structure at STP.<sup>[11]</sup> Fe grows in a hexagonal form in Fe/Ru superlattices. These multilayers were grown on freshly cleaved mica substrates or (11 $\bar{2}$ 0) sapphire substrates by MBE. On the basis of RHEED characterization, the authors conclude that during the initial stages of growth, the Fe layers stack pseudomorphically on the (0001) Ru planes. Around 6 to 7 monolayers of Fe, the structure of the Fe layer deteriorates as evidenced by the appearance of diffuse scattering in the RHEED patterns. The authors have attributed this to the loss of complete coherency between the Fe and Ru layers leading to the introduction of misfit dislocations at the interface. The structure of the Fe layer, however, still remains hexagonal. X-ray diffraction does not reveal any dramatic structural modification in multilayers which have 2.1 nm Fe/4.2 nm Ru. A hexagonal symmetry still persists in both the Fe and Ru layers. The authors have not reported a critical thickness at which Fe reverts back to its bulk stable *bcc* structure.<sup>[11]</sup>

### Cobalt/Copper Multilayers

Continuing on structural transitions in Co, metastable *fcc* Co was reported in Co/Cu multilayers by Lamelas et al.<sup>[12]</sup> Co and Cu are interesting candidates for superlattice studies because both elements have a close-packed structure in the bulk with a 2% mismatch within close-packed planes.<sup>[12]</sup> The Co/Cu superlattices were deposited by MBE on annealed GaAs substrates. The Co layer thicknesses investigated were 0.5, 1.0, 1.5, 2.0, 3.0, and 4.0 nm alternating with Cu layers which were maintained at a constant thickness of 2.5 nm. The total superlattice thickness was  $\sim 150$  nm. In all the cases, the authors report the formation of *fcc* Co. They have used RHEED characterization to determine the structure of the films, but conclude that it is not possible to distinguish between (111) *fcc* growth and (0001) *hcp* growth with the

RHEED technique.<sup>[12]</sup> Therefore they have used complementary X-ray diffraction results to confirm the *fcc* structure in the Co layers. Another interesting finding is that the *fcc* stacking coherence increases dramatically for Co layers <2 nm thick. The issue of *fcc* stabilization is addressed to a certain extent. The authors claim that whereas it is possible to understand the stabilization of *fcc* Co on (001) Cu substrates because of the cubic symmetry of the Cu,<sup>[13]</sup> it is not clear as to why the (111) Cu substrate should lead to an *fcc* stacking sequence in the Co layers especially since the in-plane projected symmetry is the same for both (111) *fcc* and (0001) *hcp*. A possible explanation may be related to the change in d-band occupation which takes place across a transition series in the periodic table. The bulk equilibrium structures of *bcc-hcp-fcc* exhibited by Fe-Co-Ni have been accounted for in this way based on calculations by Skriver.<sup>[14]</sup> In addition, the authors have also attributed the large elastic strains in Co/Cu multilayers (1–1.3%) to possibly stabilizing the *fcc* Co phase. Charge transfer across the interface of two dissimilar metals may also be playing a part in this transition. Finally, the authors comment on the Redfield-Zangwill model for bimetallic superlattices based on oscillatory interlayer potentials arising from the interfaces.<sup>[15]</sup> When the modulation period in a superlattice is reduced, the overlap of Friedel-like potentials of stacking faults close to the interface can lead to the formation of periodic stacking faults in the layer transforming an *fcc* layer into *hcp* or vice versa.

### Cobalt/Manganese Multilayers

A more recent study on Co/Mn superlattices<sup>[8]</sup> reports stabilization of metastable forms of both *fcc* Co and *fcc* Mn for very thin layer thicknesses.<sup>[8]</sup> Mn exhibits four different allotropic forms in its bulk form,  $\alpha$  and  $\beta$  Mn, which have complex structures with 58 and 20 atoms per unit cell, respectively, and the  $\gamma$  and  $\delta$  phases, which are *fcc* and *bcc*, respectively. Up to 6 Mn monolayers, the Mn layers being highly strained, Co and Mn are stabilized in out-of-equilibrium close-packed structures (*fcc* stacking). The thin Mn layer (even for 2 monolayers) acts as an *fcc* template for the deposition of *fcc* Co. The stabilization of a metastable structure, such as the *fcc* Co at room temperature, arises through chemical and elastic interactions between Co and substrate atoms. The authors report that the *fcc* Co in-plane lattice parameter is initially strained by the thin Mn layer, but the value returns to that of bulk *fcc* Co within 7 monolayers. This indicates that elastic interactions are probably not the predominant factor in the stabilization of *fcc* Co on thin layers of *fcc* Mn. To consider the chemical

interactions, the authors considered the difference in binding energies between two types of sites on an (111) *fcc* surface: the normal sites which, when occupied, continue the *fcc* stacking sequence, and the fault sites, which, when occupied, lead to the formation of stacking faults. The binding energy of these two types of sites depends on the nature of the adatom. They contend that the experimental observations suggest that the binding energy of the normal sites is larger, and so both Co and Mn reduce their total energies by allowing the Co atoms to continue the *fcc* stacking sequence. As the thickness of the layers is increased, for Mn thicker than 6 monolayers, the dislocation density is maximum at the interfaces with very little strains in either layer. The increase in dislocation density is matched by an increase in the occurrence of stacking faults in the Co layer which eventually lead to the transformation into *hcp* Co.

### Iron/Nickel Multilayers

Unlike Co/Mn multilayers which are a ferromagnetic/paramagnetic pair, Fe/Ni multilayers have ferromagnetic components for both the layers.<sup>[16]</sup> They are also interesting because of their interesting magnetic properties. Molecular beam epitaxy was employed to grow Fe/Ni superlattices on 500-nm-thick Ag silver buffer layers. The layer thicknesses employed were very small, of the order of a few monolayers (ML). While Fe is *bcc* in its bulk equilibrium form, Ni is *fcc* in bulk at STP. Using a 2-ML Fe layer as a template, up to 8 ML of Ni could be grown pseudomorphically with the *bcc* structure. The orientation relationship was Fe (110)//Ni (110). All the growths were carried out under UHV with the substrate at 180°C. The structural characterization was carried out using RHEED, and X-ray fluorescence was used to determine the Ni density.

### Platinum/Cobalt Multilayers

Pt/Co multilayers are a new candidate for a magneto-optical (MO) rewritable, recording medium.<sup>[17]</sup> For Co layer thicknesses less than 1.2 nm, they have perpendicular magnetic anisotropy, which is a requirement in MO recording. The Pt/Co multilayers were deposited using d.c. magnetron sputtering using Ne, Ar, Kr, or Xe gas at pressures less than 10 mTorr. Substrates used were glass and Si. While Pt is *fcc* in its bulk form at STP, Co is *hcp*. The as-deposited specimens were characterized by cross-section transmission electron microscopy (TEM) and high-resolution electron microscopy (HREM). For about 0.4-nm-thick Co, the authors report that the structure was single-phase *fcc* with (111) texture, characterized

by a lattice spacing  $\approx 0.22$  nm along the direction of chemical modulation of film growth. This value corresponds to the average of the Co (111) and Pt (111) *fcc* d-spacings. When Co thickness was increased to 0.9 nm, in addition to the diffraction from the 0.22-nm superlattice spacing, faint diffraction spots appeared at a position corresponding to a lattice spacing of about 0.2 nm. For Co layers 1 nm thick, the large difference in Pt and Co lattice constants ( $\approx 10\%$ ) hindered pseudomorphic growth of Co on Pt and there were many misfit defects visible throughout the structure.

### Ruthenium/Iridium Multilayers

Ru exhibits the *hcp* structure and Ir exhibits the *fcc* structure in their bulk forms at STP.<sup>[18]</sup> Ru/Ir superlattices exhibited an *hcp* stacking sequence for very thin Ir layers. The Ru/Ir superlattices were deposited by MBE. The two samples investigated had wavelengths of  $\lambda = 4.1$  and 6.2 nm (bilayer thicknesses). The Ru layers were 2.4 nm thick, whereas the Ir layers were 8 and 15 atomic layers thick, respectively. While the 4.1-nm multilayer exhibited an *hcp* Ru/*hcp* Ir structure, the 6.2-nm multilayer exhibited an *hcp* Ru/*fcc* Ir structure. Thus the two thicknesses of the Ir layers are on either sides of the crossover thickness for *hcp*–*fcc* transition.

### Nanolayered Copper and Palladium Thin Films on Tungsten Substrate

Bulk Cu and Pd both exhibit the *fcc* structure at STP.<sup>[2]</sup> One of the most recent observations of structural transitions is the formation of *hcp* Cu and Pd films on W (100) substrates.<sup>[2]</sup> The interesting feature in this case is the stabilization of *hcp* phase of Cu and Pd on a *bcc* W substrate. The prismatic plane of *hcp* (11 $\bar{2}$ 0) has a 2-D unit cell that is almost square, the difference between the two orthogonal axes being determined by the length of the *c*-axis. The square *fcc* (100) unit cell of the same material differs from it by at least 25%. The *hcp* structure can be stabilized on the (100) *bcc* square substrate if the misfit is sufficiently small. The authors calculate the misfit as a function of ratio of the overlay atom to the W atom and find that it is almost zero between [1 $\bar{1}$ 00] of *hcp* Cu and W <011> axes. Similarly, the misfit is very small between the [0001] of *hcp* Pd and W <011>. This accounts for the pseudomorphic stabilization of the *hcp* phases of Cu and Pd on *bcc* W (100) substrates.

### Titanium Nitride/Aluminum Nitride Multilayers

Although Ti exhibits a bulk *hcp* structure, TiN has the B1 (rock salt) *fcc*-based structure in its bulk stable

form at STP.<sup>[19]</sup> AlN crystallizes in a hexagonal wurtzite phase at ambient temperature and pressure. At high pressures in AlN, a B1 rock-salt-type structure with a lattice parameter of  $a \sim 0.406$  nm and a zinc-blende-type structure with  $a \sim 0.437$  nm can form. A recent paper<sup>[19]</sup> reported the epitaxial stabilization of the high-pressure B1 phase of AlN in TiN/AlN superlattices grown on MgO (001) substrates. The superlattices were grown in a UHV magnetron sputtering chamber. The bilayer thicknesses ( $\lambda$ ) varied from 1.8 to 8.0 nm. There is a good lattice match between TiN and the cubic (B1) form of AlN which promotes the stabilization of the cubic structure in AlN. The authors have confirmed the epitaxial growth of the multilayers by low-energy electron diffraction and high-resolution electron microscopy. They have reported a critical thickness of 2 nm at which the AlN layer transforms from its epitaxially stabilized cubic structure to its bulk stable hexagonal form.

### Cobalt/Chromium Multilayers

Co/Cr multilayered thin films have been extensively studied because their perpendicular magnetic anisotropy makes them potential candidates for perpendicular magnetic recording.<sup>[20–22]</sup> In their bulk forms, Co and Cr exhibit the *hcp* and *bcc* structures at STP, respectively. Pseudomorphic *bcc*-Co was stabilized on (110) GaAs for the first time by Prinz.<sup>[4]</sup> Subsequently, there have been numerous reports of pseudomorphic phases in Co/Cr multilayers<sup>[20–22]</sup> wherein either Co transformed from its bulk stable *hcp* to *bcc* or Cr transformed from its bulk stable *bcc* to *hcp*. Boher et al.<sup>[20]</sup> reported that in Co/Cr multilayers, involving equally thick Co and Cr layers, with decreasing bilayer thickness, the Co layers transformed from *hcp* to *bcc*. In an independent study, Vavra et al.<sup>[21]</sup> reported that in multilayers with a constant Co layer thickness, with reducing Cr layer thickness, there is a transformation in the structure of the Cr layers from *bcc* to *hcp*. It should be noted that the multilayer deposition technique used by the two groups was also different: Boher et al.<sup>[20]</sup> used radiofrequency (RF) sputter deposition, while Vavra et al.<sup>[21]</sup> used molecular beam epitaxy. Based on these results, in a more recent paper, Metoki, Donner, and Zabel<sup>[22]</sup> suggest that the situation concerning Co/Cr multilayers is *controversial* because of reports of phase transitions in the Co layers in some cases and in the Cr layers in other cases. This apparent controversy between the experimental results of different groups has arisen because of the lack of a framework for understanding phase stabilities in multilayered thin films, which will be addressed later in this entry.



## Niobium/Titanium Multilayers

While Ti exhibits the *hcp* structure ( $\alpha$ -Ti) at STP, it undergoes an allotropic transformation at 880°C from *hcp* to *bcc*.<sup>[23]</sup> The high-temperature equilibrium *bcc* phase of Ti is referred to as  $\beta$ -Ti. Similar to Zr in Nb/Zr multilayers,<sup>[10]</sup> the Ti layers in Nb/Ti multilayers exhibit a transformation from *hcp* to *bcc* on reduction in layer thickness.<sup>[23]</sup> It should be noted that this *bcc* phase adopted by Ti in Nb/Ti multilayers is a pseudomorphic phase and not in equilibrium. An X-ray diffraction pattern in the Bragg reflection geometry from a relatively thicker Nb/Ti multilayer is shown in Fig. 1A. The distinctly split peak in this diffraction pattern can be indexed as a combination of the  $\{0002\}$  *hcp* Ti peak and the  $\{011\}$  *bcc* Nb peak. This observation in conjunction with additional electron diffraction evidence<sup>[23]</sup> clearly indicates the presence of *hcp* Ti and *bcc* Nb in this multilayer. When

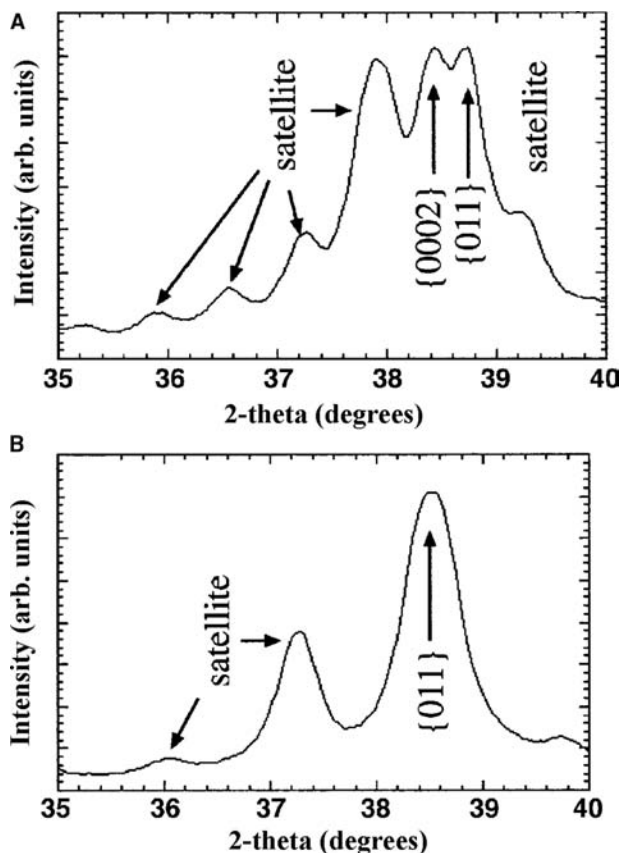


**Fig. 1** (A) X-ray diffraction pattern in the reflection Bragg geometry from a thicker Nb/Ti multilayer showing two distinct peaks (part of the split peak) corresponding to  $\{0002\}$  *hcp* Ti and  $\{011\}$  *bcc* Nb. (B) X-ray diffraction pattern from a thinner Nb/Ti multilayer containing the same volume fraction of Nb as in (A) showing a single  $\{011\}$  *bcc* peak due to the transformation of the Ti layers from *hcp* to *bcc* on reduction in layer thickness.

the layer thickness is reduced, for a Nb/Ti multilayer containing the same volume fraction of Nb, the X-ray diffraction pattern changes and is shown in Fig. 1B. Instead of a split peak, only a single peak visible in this pattern can be consistently indexed as the  $\{011\}$  *bcc* peak. Electron diffraction results<sup>[23]</sup> are in agreement with this observation and indicate that in this multilayer, the Ti layers have transformed to a *bcc* structure. Thus the stacking in the thinner multilayer is *bcc* Nb/*bcc* Ti. The *bcc* Ti layers adopt the same lattice parameter as that of the high-temperature  $\beta$ -Ti equilibrium phase. The high-temperature  $\beta$ -Ti phase exhibits a lattice parameter that is nearly identical to that of Nb (0.33 nm). This allows the *bcc* Ti layers to maintain a coherent interface with the *bcc* Nb layers.

Based on TEM diffraction patterns of the Nb/Ti multilayers, it was determined that for thicker layers, the *hcp*/*bcc* interface has a Burgers or near-Burgers orientation relationship given as

$$\{0001\} \text{ hcp } // \{011\} \text{ bcc}$$

$$\langle 11\bar{2}0 \rangle \text{ hcp } // \langle 111 \rangle \text{ bcc}$$

Upon transformation to a *bcc* / *bcc* interface for thinner Nb/Ti multilayers, the orientation relationship is

$$\{011\} \text{ bcc } // \{011\} \text{ bcc}$$

$$\langle 111 \rangle \text{ bcc } // \langle 111 \rangle \text{ bcc}$$

## Titanium/*fcc* Metal Multilayers

As indicated earlier, bulk Ti is *hcp* at STP. The first report of a structural transition in Ti was by Wawner and Lawless,<sup>[24]</sup> who reported the formation of *fcc* Ti on single crystal NaCl substrates. The *fcc* Ti transformed to its bulk *hcp* structure when the film was between 35 and 300 nm thick (the value varied depending upon the orientation of the NaCl single crystal). There have been a few other reports of *fcc* Ti in epitaxial thin films on substrates.<sup>[25,26]</sup> However, the most recent studies dealing with structural transitions in Ti thin films and multilayers have been carried out by Jankowski and Wall,<sup>[7]</sup> Shechtman, Van Heerden, and Josell,<sup>[27]</sup> Josell, Shechtman, and Van Heerden,<sup>[28]</sup> Van Heerden, Josell, and Shechtman,<sup>[29]</sup> Ahuja and Fraser,<sup>[5]</sup> and Banerjee et al.<sup>[6,30,31]</sup>

Jankowski and Wall<sup>[7]</sup> studied Ti thin films deposited on Ni single crystals and also Ni/Ti multilayers. The multilayers were sputter-deposited with bilayer thicknesses of 26, 8.3, and 1.3 nm with the ratio of Ni to the bilayer thickness being 0.45, 0.46,

and 0.67, respectively. The multilayers were characterized by X-ray diffraction as well as cross-section TEM and HREM studies. Jankowski and Wall<sup>[7]</sup> reported the presence of *fcc* Ti in all the multilayers. Selected area diffraction (SAD) patterns from the multilayers in the cross-section geometry could be indexed on the basis of an *fcc* Ti phase with a lattice parameter of 0.440 nm. The measured d-spacings (from the ring diffraction pattern) for the 8.3- and 26-nm multilayers poorly fit the (1120) reflection of *hcp* Ti. Furthermore, both diffraction patterns did not contain the critical (0002) reflection which is essential for the *hcp* structure. The HREM studies coupled with image simulations also confirmed the *fcc* stacking sequence in the Ti layers of these multilayers. The SAD pattern from the 1.3-nm multilayer was found to fit a single *fcc* structure. There is no evidence of *hcp* Ti in this multilayer. Jankowski and Wall<sup>[7]</sup> also deposited a monolithic 1- $\mu\text{m}$ -thick Ti film on a Ni single crystal substrate. They also found *fcc* Ti in these films in HREM images of the cross-section geometry.

Van Heerden, Josell, and Shechtman,<sup>[29]</sup> Josell, Shechtman, and Van Heerden,<sup>[28]</sup> and Shechtman, Van Heerden, and Josell,<sup>[27]</sup> have also observed the formation of *fcc* Ti in both Ni/Ti as well as Al/Ti multilayers and have attributed the transformation as an artifact of sample preparation during cold-stage ion milling in the cross-section geometry. Their studies on Al/Ti multilayers have involved layer thicknesses of 45/45, 45/180, 45/300, and 45/750 Al/Ti (all in units of nm). An additional multilayer with 90/45 Al/Ti has also been studied. They have used glass substrates and evaporation at rates between 0.3 and 0.8 nm/sec. The authors have characterized their multilayers by X-ray diffraction and TEM/HREM studies. A typical X-ray pattern from the 90/45 multilayer in the Bragg geometry did not show any peak corresponding to (111) *fcc* Ti which should occur at a  $2\theta$  angle of  $35.14^\circ$  (calculated based on the lattice parameter measured for *fcc* Ti = 0.442 nm in cross-section TEM specimens). The authors complemented their X-ray diffraction results in the Bragg geometry with X-ray transmission diffraction studies in which they also found that all the peaks could be indexed on the basis of *fcc* Al and *hcp* Ti. There were no peaks corresponding to *fcc* Ti in any of the X-ray diffraction patterns. This evidence clearly supports the authors' contention that the Ti deposits in an *hcp* form and transform to *fcc* on cold-stage ion milling of the cross section. It should be noted at this point that all the X-ray diffraction results are for the 90/45 multilayer in which the Ti layer is 45 nm thick. This is quite a thick layer and epitaxial stabilization of an *fcc* structure from the Al substrate may not be feasible for such a thick layer. At this point, it is also important to point out that the same authors have reported an evidence for *fcc* Ti based

on X-ray diffraction studies in a Ni/Ti multilayer with composition wavelength of 5.5 nm<sup>[28]</sup> in which they find the absence of a (0002) *hcp* Ti peak. On thinning all these multilayers in cross section, TEM diffraction indicates the formation of *fcc* Ti in all these multilayers, including the one in which the Ti layer thickness is 750 nm.

Ahuja and Fraser<sup>[5]</sup> and Banerjee, Ahuja, and Fraser<sup>[6]</sup> reported a series of novel structural transitions in Ti/Al thin-film multilayers based on the results of TEM observations in the cross-section geometry. These transitions are dimensionally induced in the multilayers as the bilayer thickness was varied. The bilayer thicknesses for the multilayers that have been studied are 108, 21, 9.8, and 5.2 nm. In the first multilayer with  $\lambda = 108$  nm, both Ti and Al retain their bulk stable crystal structures resulting in a stacking sequence of *hcp* Ti/*fcc* Al. Transmission electron microscopy investigations have revealed that the Ti and Al layers grow with a {0001} and {111} texture parallel to the substrate, respectively. For  $\lambda = 9.8$  nm, nm, the stacking sequence is *fcc* Ti/*fcc* Al. A further reduction of the bilayer thickness to  $\lambda = 5.2$  nm results in a stacking sequence of *hcp* Ti/*hcp* Al. It should be noted that in both these papers, the phase stability observations were based on cross-section TEM specimens. The *fcc* Ti phase reported in these papers is  $a = 0.44$  nm, similar to the value reported by Jankowski and Wall<sup>[7]</sup> and Van Heerden, Josell, Shechtman.<sup>[29]</sup> The critical transition thickness for Ti (to transform from *hcp* to *fcc*) is less than 10 nm. Effects of interfacial stabilization are likely to play a much more significant role in these structural transitions than can be expected in the "thick" 750-nm *fcc* Ti layers observed by Van Heerden, Josell, Shechtman.<sup>[29]</sup> Furthermore, it should be noted that in the case of the study by Ahuja and Fraser, for Ti layer thicknesses  $>20$  nm, the structure as observed in ion-milled cross sections of the multilayer is *hcp*, in contrast to the observation of Van Heerden, Josell, Shechtman<sup>[29]</sup> wherein the structure transformed to *fcc* even when 750-nm-thick Ti layers were thinned in cross section.

While Ahuja and Fraser<sup>[5]</sup> studied Ti/Al multilayers in which both Ti and Al layers were equally thick (volume fraction of Ti = 0.5), in more recent investigations, Banerjee et al.<sup>[30,31]</sup> have studied Ti/Al multilayers in which the volume fractions of the components have been varied. For example, the structure of the Ti and Al layers in a 10.5-nm Ti/26-nm Al multilayer is visible in the cross-section high-resolution transmission electron micrograph shown in Fig. 2A. In the cross-section geometry, the planes of atoms parallel to the Ti/Al interface correspond to the close-packed planes in each layer.<sup>[30,31]</sup> From the *ababa*... stacking of the close-packed {0001} planes in Ti layer and the *abcabca*... stacking of {111} planes in the Al layer, it is

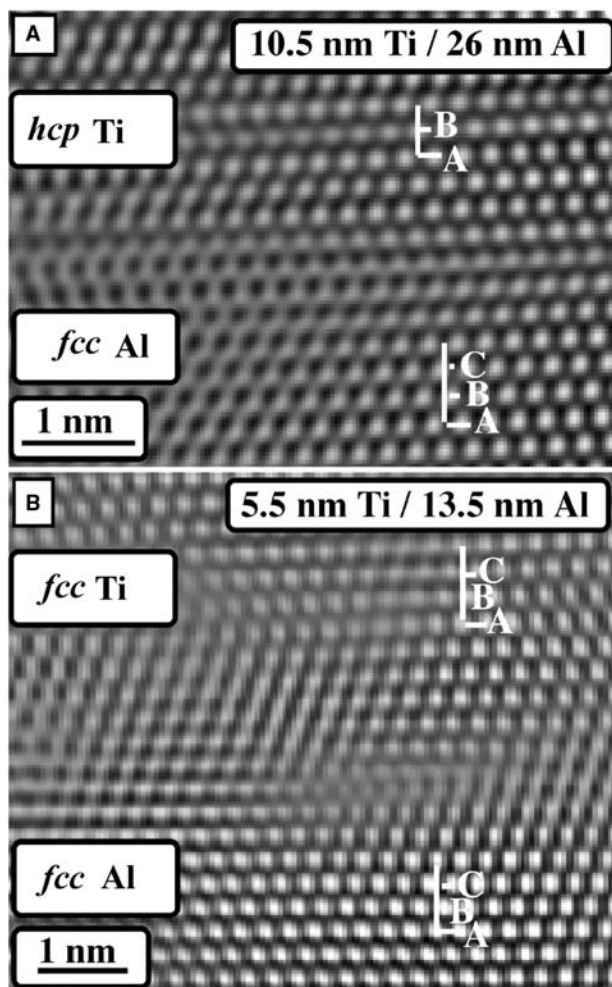


**Fig. 2** (A) High-resolution TEM micrograph from a 10.5-nm Ti/26-nm Al multilayer in the cross-section geometry. The stacking of close-packed planes in the Ti layer is *ababa* . . . , which is characteristic of the *hcp* structure, while the stacking in the Al layer is *abcabca* . . . , which is characteristic of the *fcc* structure. (B) Cross-section high-resolution TEM micrograph from a 5.5-nm Ti/13.5-nm Al multilayer, exhibiting an *abcabca* . . . stacking of close-packed layers in the Ti layer, indicative of a transformation from *hcp* to *fcc* in the thinner Ti layers.

apparent that the Ti layers exhibit an *hcp* structure while the Al layers exhibit an *fcc* structure. When the layer thickness in these multilayers is reduced to 5.5-nm Ti/13.5-nm Al, the structure of the Ti layers changes to *fcc*. This is clearly visible in the *abcabca* . . . stacking sequence of close-packed layers in the Ti layers, characteristic of the *fcc* structure, shown in Fig. 2B. Furthermore, Banerjee, Dregia, and Fraser<sup>[30]</sup> have studied the influence of thinning geometry (cross section vs. plan view) on the crystal structure exhibited by the Ti layer. Based on these results, it appears that the formation of an *fcc* Ti phase with a lattice parameter of  $a = 0.44$  nm is likely to be a consequence of hydrogen stabilization during cross-section ion-beam

thinning, and therefore a sample preparation artifact.<sup>[30]</sup> The diffusivity of hydrogen in Ti is considerably more than the diffusivity of hydrogen in Al.<sup>[32]</sup> Cross-section thinning would actually open up a large number of parallel short-circuit diffusion paths (Ti layers) through the multilayer, whereas in the plan-view specimens, the diffusion of hydrogen is rate-limited through the Al layers before they can reach the Ti layers. Furthermore, there are two titanium hydrides which have *fcc* structures with lattice parameters similar to the one observed for *fcc* Ti in the multilayers: TiH<sub>2</sub> which is *fcc* with  $a = 0.44$  nm and TiH which is *fcc* with  $c/a = 1.09$  and  $a = 0.42$  nm.<sup>[33]</sup> However, pseudomorphic stabilization of an *fcc* Ti phase, unrelated to specimen preparation, occurs in Ti/Al multilayers for substantially thinner Ti layers when sandwiched in between much thicker Al layers. This has been clearly established by Banerjee, Dregia, and Fraser<sup>[30]</sup> Unlike the hydrogen-stabilized *fcc* Ti phase, the pseudomorphic *fcc* Ti phase adopts a lattice parameter  $a = 0.403$  nm, which is similar to that of *fcc* Al.

#### MODELING OF PHASE STABILITY IN NANOLAYERED THIN FILMS

Previous descriptions of phase stability in nanolayered thin films and multilayers can be categorized into three groups based on either classical thermodynamics, the effect of coherency strains, or interface-induced modulations in the stacking fault potential in close-packed structures. In thermodynamic analyses of thin films, the competition between interfacial (area) and bulk (volume) contributions to the free energy defines a thermodynamic critical thickness for structural transitions such as the coherent-incoherent transition in epitaxy, as well as polymorphic transitions in thin surface films.<sup>[34,35]</sup> In this view,<sup>[34]</sup> a metastable structure is stabilized in a deposit as a result of lowering the (surface and) interfacial energy. Thus the metastable structure itself is not necessarily dictated by coherency strains or any other influence of the substrate. However, in models based on coherency strains (e.g., Ref.<sup>[35]</sup>), the metastable structure is considered to result from the natural response of the deposit to large coherency strains induced by the substrate. Both types of thermodynamic models were strictly developed for the case of a thin deposit on a thick substrate, with a single degree of freedom corresponding to film thickness. However, in a multilayer, the need to treat both components in this way adds another degree of freedom. Therefore it is important to expand on the thermodynamic model when it is applied to multilayers, where the total energy of the “unit system,” defined as two layers and *two interfaces*, is minimized (as described below).

In the third type of model proposed by Redfield and Zangwill<sup>[15]</sup> the metastable phase is formed because of the stabilization of stacking faults in a close-packed structure. The lowering of the stacking fault potential results from the superposition of interface-induced modulations in this potential. This model only applies to multilayered systems which involve only close-packed structures, and it is unable to predict phase stability when volume fractions of the two components are varied. Because of these limitations of previous models, recently, a new model based on classical thermodynamics has been developed, *specifically* for rationalizing phase stability in thin-film multilayers.<sup>[30,31,36]</sup>

To expand on the *classical view*, consider as reference a unit bilayer of two metals, A and B, in their strain-free, stable crystal structures. Let the component layer thicknesses be  $h_A$  and  $h_B$ , so that the thickness of the reference bilayer  $\lambda = h_A + h_B$ . The free energy of the reference bilayer is thus:

$$G = N_A\mu_A + N_B\mu_B + 2\gamma S \quad (1)$$

where  $N_i$  is the number of atoms of species  $i$ ,  $\mu_i$  is its chemical potential,  $\gamma$  is the interfacial free energy, and  $S$  is the area of the interface. Note that other terms, for example, describing the interfacial defect content and/or elemental intermixing across interfaces, can be included in Eq. (1), but for simplicity, these are considered to be included in the interfacial energy term. Suppose this reference bilayer is transformed to a candidate state where at least one of the members exists in a metastable structure. The free energy after transformation is given by:

$$G' = N_A\mu'_A + N_B\mu'_B + 2\gamma'S \quad (2)$$

where the prime refers to the candidate state. Note that the  $N_i$ 's are constant in the closed system, and both the lamellar morphology and interfacial area  $S$  are fixed in the variation of state. Whereas the density of both layers is allowed to change on transformation, the constraint of constant area is necessary. Clearly, if the interfacial area was allowed to vary, the thermodynamic problem would include a search for the equilibrium shape, and therefore it would be ill-posed and intractable without some factors opposing the reshaping of the multilayer by an endless decrease in the interfacial area. Thus it is recognized that the proper thermodynamic potential for the problem at hand must be normalized by the interfacial area.

The specific free energy of formation of the candidate bilayer,  $\Delta g$ , is given as follows:

$$\Delta g = 2\Delta\gamma + [\Delta G_A(1 - f_B) + \Delta G_B f_B]\lambda \quad (3)$$

where  $\Delta g$  is normalized by the area of the interface,  $\Delta\gamma$  is the change in interfacial free energy,  $\Delta G_i$  is the allotropic free energy change per *unit volume* of reference

phase for metal  $i$ , and  $f_B$  is the volume fraction of metal B in the reference bilayer. Note that the product  $f_i\lambda$  gives the layer thickness for metal  $i$  in the reference bilayer. It is recognized that there may be several contributions to the terms  $\Delta\gamma$  and  $\Delta G_i$ , including, for example, impurity effects, local elemental intermixing, alloying in miscible systems, interface strain, and defect interactions. However, while these effects may modify the values of interfacial and bulk energies, providing the composition and interfacial area do not change during the given phase transition, such contributions to the energy terms do not invalidate the current thermodynamic analysis. Of course, these various contributions must be taken into account when determining values for these various parameters by, for example, first principles calculations.

To illustrate how the thermodynamics contained in Eq. (3) applies to phase stability in multilayers, consider a multilayered system in which below a critical value of  $\lambda = \lambda^*$ , the crystal structure of component

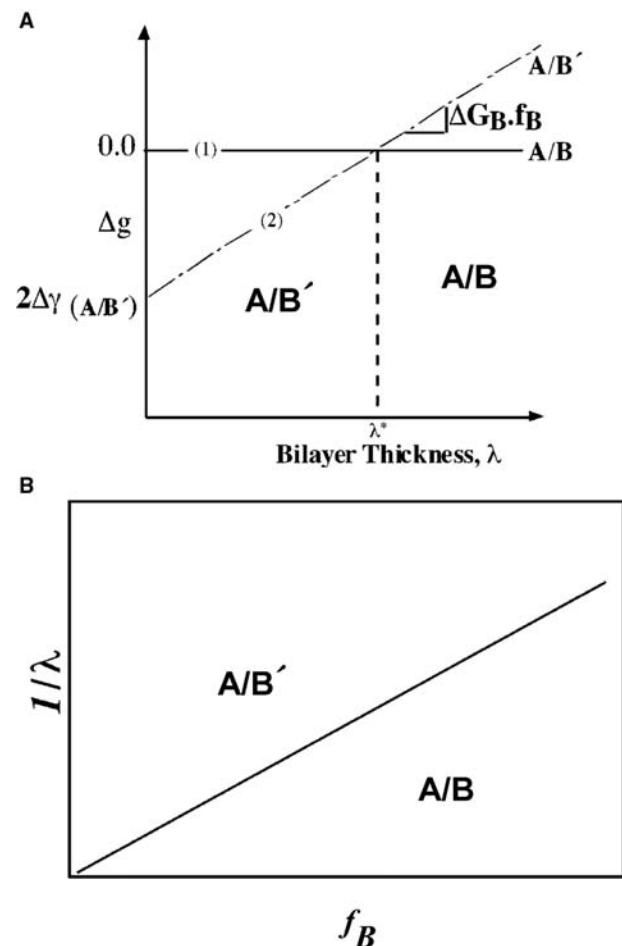


**Fig. 3** (A) A constant volume-fraction cut of the  $\Delta g(\lambda, f)$  surface showing the stabilization of the metastable B' phase by the reduction in interfacial energy ( $\Delta\gamma$ ). (B) A biphasic diagram for A/B multilayers.

B undergoes a transition to a metastable form B'. This situation can be depicted conveniently by a constant volume-fraction cut of the  $\Delta g(\lambda, f)$  surface, i.e., by a plot of  $\Delta g$  vs.  $\lambda$ , as shown in Fig. 3A. As the scale of the multilayer is reduced from an arbitrarily large value of  $\lambda$ , the lowest free energy corresponds to the components adopting their bulk stable forms. However, below the critical value,  $\lambda^*$ , the energy of the system is minimized by transforming component B to its metastable form. As noted above, in the present model, the transition is driven by the reduction in interfacial energy, which is represented in Fig. 3A by the negative intercept  $2\Delta\gamma_{A/B'}$ . There are several factors which influence interfacial energy, and these are conveniently grouped under chemical and structural contributions.

Eq. (3) describes a thermodynamic potential surface that varies as a function of two independent variables,  $f$  and  $\lambda$ . Formally, the thermodynamics is similar to that of phase equilibria in a one-component system under varying temperature and pressure. Here each "biphase" (i.e., one phase for each of the two layers) is represented by a surface in  $f$ - $\lambda$  space, and the equilibrium multilayer structure is the one with the lowest specific free energy of formation  $\Delta g$ . Conditions for coexistence of biphases are determined by the intersection of  $\Delta g$  surfaces, and a variety of biphase diagrams can be constructed, e.g.,  $h_A$ - $h_B$ ,  $\lambda$ - $f$ , and  $(1/\lambda)$ - $f$  diagrams. For example, Fig. 3B is the biphase diagram corresponding to the multilayers of Fig. 3A. For this hypothetical system, only two biphase fields appear on the diagram—one for the biphase composed of the two bulk-stable phases, A/B, and the other field is for the A/B' biphase, where component B is present in a metastable structure. The slope of line (1) in Fig. 3B is given by  $-\Delta G_B/2\Delta\gamma_{A/B'}$ , and because the metastable structure is stabilized by the lowering of the interfacial energy, this slope is positive (i.e.,  $\Delta\gamma$  is negative with respect to the reference state; see Fig. 3A). In a system where metastable forms can be stabilized in both layers, there may be three biphase fields meeting at a triple point. As in the case of conventional pressure-temperature phase diagrams, at the triple point, all phases coexist in equilibrium.

Equilibrium predictions of phase stability are realized experimentally only by permission of kinetics. For example, because of kinetic constraints, multiple biphases may be observed in the same multilayer, especially under experimental conditions near a boundary on the biphase diagram. Of course, it should also be noted that for systems represented by the terminal fractions ( $f_B = 0$  and 1), because there are no interfaces, then  $\Delta\gamma = 0$ , and the coexistence curves become undefined.

The biphase boundaries such as in Fig. 3B are linear because  $\Delta G$  and  $\Delta\gamma$  are assumed to be independent of  $\lambda$  and  $f$ . However, this simple result would not be

obtained in coherently strained multilayers, where the equilibrium coherency strain in each layer is inversely proportional to its thickness.<sup>[37]</sup> If the coherency strain energy was included in the thermodynamics, the resulting  $\Delta g$  would depend non-linearly on volume fraction, and this would ultimately lead to curved boundaries on the  $1/\lambda$ - $f$  biphase diagram. In the present analysis, coherency effects are ignored because they are not necessary for illustrating the basic principles underlying the biphase diagram.

As an example, the concept of the biphase diagram has been applied for rationalizing the experimental trends reported for Co/Cr multilayers. The results reported in the literature may be used to produce a preliminary biphase diagram for these multilayers, which is shown in Fig. 2. Included in this diagram are the results from Boher et al.<sup>[20]</sup> as well as the results from Vavra et al.<sup>[21]</sup> The biphase boundaries marked (1) and (3) in Fig. 4 have been drawn with the data as a guide. The triple point is constrained to be drawn at a value of  $f_{Cr} \approx 0.3$ . The slopes of biphase boundaries (1) and (3) are given by  $-\Delta G_{Cr}/2\Delta\gamma_{hcp/hcp}$  (i.e., positive slope) and  $\Delta G_{Co}/2\Delta\gamma_{bcc/bcc}$  (i.e., negative slope), respectively. From the measured slope of line (1),  $1.45 \times 10^9 \text{ m}^{-1}$ , and the literature value of  $\Delta G_{Cr} = 7.45 \text{ kJ mol}^{-1}$ ,<sup>[38]</sup> one calculates a value of  $\Delta\gamma_{hcp/hcp} = -356 \text{ mJ m}^{-2}$ . Similarly, using the slope of line (3) in Fig. 2 ( $-5.9 \times 10^8 \text{ m}^{-1}$ ) and  $\Delta G_{Co} = 4.2 \text{ kJ mol}^{-1}$ ,<sup>[38]</sup> one obtains  $\Delta\gamma_{bcc/bcc} = -537 \text{ mJ m}^{-2}$ . The  $\Delta\gamma$ 's obtained from lines (1) and (3) were used in conjunction with the available  $\Delta G$ 's to determine the slope of line (2) in Fig. 4 [given by  $(\Delta G_{Co} + \Delta G_{Cr})/2(\Delta\gamma_{bcc/bcc} - \Delta\gamma_{hcp/hcp})$ ]. Note that the resulting line (2) completes the biphase diagram self-consistently, i.e., without violating the phase rule and without conflicting with the experimental data.

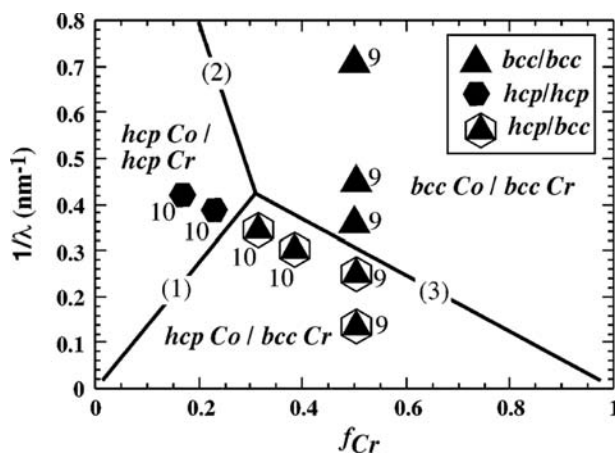


Fig. 4 A biphase diagram for Co/Cr multilayers.<sup>[36]</sup> This diagram has been constructed on the basis of the experimental results from Boher et al.<sup>[20]</sup> and Vavra et al.<sup>[21]</sup>



With the aid of the biphasic diagram, it has been possible to present the various “confusing” experimental results, as noted by Metoki, Donner, and Zabel,<sup>[22]</sup> on a comprehensive, rational basis. In addition, the diagram was used to obtain reasonable values for the model parameters  $\Delta\gamma_{\text{hcp/hcp}} = -356 \text{ mJ m}^{-2}$  and  $\Delta\gamma_{\text{bcc/bcc}} = -537 \text{ mJ m}^{-2}$ . The absolute values of  $\Delta\gamma$  are similar to typical values of interfacial energy for incoherent solid/solid interfaces<sup>[39]</sup> and are significantly less than the value of about  $3 \text{ J m}^{-2}$  deduced from experiments on AlN/TiN multilayers.<sup>[19]</sup> It should be noted that these deduced values of interfacial energy differences, while being influenced by the accuracies of the  $\Delta G$ 's used [i.e., here based on the calculation of alloy phase diagrams (CALPHAD) technique], refer to the experimental samples studied in the referenced works. Hence these multilayers may be characterized to various degrees by elastic strains, defects in the bulk and at interfaces, elemental intermixing across interfaces, and impurities (among other factors). These types of factors will influence the *actual* values of  $\Delta G$ 's and  $\Delta\gamma$ 's and therefore the slopes of the lines in the biphasic diagrams. Therefore it is important to consider these factors when interpreting the values of, for example,  $\Delta\gamma$ 's deduced from biphasic diagrams. The results of applying the model to Co/Cr are encouraging and lend credence to the use of the biphasic diagram as a predictive tool for phase stabilities in the multilayers. Interestingly, one prediction afforded by the biphasic diagram shown in Fig. 4 is the possibility of observing a double transition in one of the metals, as  $\lambda$  is increased at a fixed volume fraction. For Co/Cr multilayers with  $f_{\text{Cr}}$  below the triple-point fraction, e.g.,  $f_{\text{Cr}} \approx 0.25$ , and as a function of increasing  $\lambda$ , the Co is predicted to transform once, from metastable *bcc* to stable *hcp*, but the Cr should transform twice, from stable *bcc* to metastable *hcp*, then back to *bcc*.

## CONCLUSION

Structural transitions often occur in nanolayered thin films and multilayers when the layer thickness is reduced to the nanometer scale. These transitions are usually observed when there is a difference between the bulk equilibrium crystal structures of the film and the substrate or the two layers comprising the multilayer and lead to the stabilization of pseudomorphic phases in these nanolayers. A new model has been presented to account for structural stability in thin-film multilayers, based on classical thermodynamics of the competition between bulk and interfacial free energies in nanolayers. The reduction in interfacial energy is considered to be the main driving force behind the stabilization of pseudomorphic phases in thin-film

multilayers. The thermodynamic analysis permits a new type of phase diagram to be derived for multilayers, the *biphase* stability diagram, in which phase stability is depicted as a function of *size scale* (a natural state variable associated with thin multilayered materials). While the thermodynamic model and the concept of the *biphase* stability diagram are quite simple, their applicability is quite generic.

## ACKNOWLEDGMENTS

The authors would like to thank Professor Suliman A. Dregia for many useful discussions on the subject matter of this article. Financial support for part of this work from the Center for the Accelerated Maturation of Materials at the Ohio State University is also gratefully acknowledged.

## REFERENCES

- Jesser, W.A.; Matthews, J.W. Evidence for pseudomorphic growth of iron on copper. *Philos. Mag.* **1967**, *15*, 1097.
- Wormeester, H.; Huger, E.; Bauer, E. hcp and bcc Cu and Pd films. *Phys. Rev. Lett.* **1996**, *77* (8), 1540.
- Wilson, L.; Bienenstock, A. *Mater. Res. Soc. Symp. Proc.* **1988**, *103*, 69.
- Prinz, G.A. Stabilization of bcc Co via epitaxial growth on GaAs. *Phys. Rev. Lett.* **1985**, *54*, 1051.
- Ahuja, R.; Fraser, H.L. Microstructural transitions in titanium–aluminum thin film multilayers. *J. Electr. Mater.* **1994**, *23* (10), 1027.
- Banerjee, R.; Ahuja, R.; Fraser, H.L. Dimensionally induced structural transformations in titanium–aluminum multilayers. *Phys. Rev. Lett.* **1996**, *76*, 3778.
- Jankowski, A.F.; Wall, M.A. Formation of face-centered cubic titanium on a nickel single crystal and Ni/Ti multilayers. *J. Mater. Res.* **1994**, *9*, 31.
- Ounadjela, K.; Vennegues, P.; Henry, Y.; Michel, A.; Pierron-Bohnes, V.; Arabski, J. Structural changes in metastable epitaxial Co/Mn superlattices. *Phys. Rev., B* **1994**, *49* (13), 8561.
- Zheng, J.Q.; Ketterson, J.B.; Felcher, G.P. Synthesis of layered crystals of titanium–silver. *J. Appl. Phys.* **1982**, *53* (5), 3624.
- Lowe, W.P.; Geballe, T.H. Niobium–zirconium multilayers I. Structure and superconductivity. *Phys. Rev., B* **1984**, *29* (9), 4961.
- Maurer, M.; Piecuch, M.; Ravet, M.F.; Ousset, J.C.; Sanchez, J.P.; Aaron, C.; Dekoster, J.; Raoux, D.; De Andres, A.; De Santis, M.; Fontaine, A.; Baudelet, F.; Rouviere, J.L.; Dieny, B. Magnetism and structure in hexagonal Fe/Ru superlattices with short periodicities. *J. Magn. Magn. Mater.* **1991**, *93*, 15.
- Lamelas, F.J.; Lee, C.H.; Hui, H.; Varva, W.; Clarke, R. Coherent fcc stacking in epitaxial Co/Cu superlattices. *Phys. Rev., B* **1989**, *40* (8), 5837.



13. Jesser, W.A.; Matthews, J.W. Pseudomorphic deposits of cobalt on copper. *Philos. Mag.* **1968**, *17*, 461.
14. Skriver, H.L. Crystal structure from one-electron theory. *Phys. Rev.*, **B 1985**, *31*, 1909.
15. Redfield, A.C.; Zangwill, A.M. Stacking sequences in close-packed metallic superlattices. *Phys. Rev.*, **B 1986**, *34*, 1378.
16. Wiczorek, M.D.; Keavney, D.J.; Storm, D.F.; Walker, J.C. Growth of Fe(110)/bcc Ni(110) superlattices by molecular beam epitaxy. *J. Magn. Magn. Mater.* **1993**, *121*, 34.
17. Li, Z.G.; Garcia, P.F.; Cheng, Y. Co thickness dependence of the microstructure of Pt/Co multilayers. *J. Appl. Phys.* **1993**, *73* (5), 2433.
18. Clarke, R.; Lamelas, F.; Uher, C.; Flynn, C.P.; Cunningham, J.E. Stacking structure and superconductivity in ruthenium-iridium bicrystal superlattices. *Phys. Rev.*, **B 1986**, *34* (3), 202.
19. Madan, A.; Kim, I.W.; Cheng, S.C.; Yashar, P.; Dravid, V.P.; Barnett, S.A. Stabilization of cubic AlN in epitaxial AlN/TiN superlattices. *Phys. Rev. Lett.* **1997**, *78* (9), 1743.
20. Boher, P.; Giron, F.; Houdy, Ph.; Beauvillain, P.; Chappert, C.; Veillet, P. Structure and magnetic properties of diode radio frequency sputtered Cr/Co multilayers. *J. Appl. Phys.* **1991**, *70* (10), 5507.
21. Vavra, W.; Barlett, D.; Egaloz, S.; Uher, C.; Clarke, R. Structural transition in epitaxial Co/Cr superlattices. *Phys. Rev.*, **B 1993**, *47*, 5500.
22. Metoki, N.; Donner, W.; Zabel, H. Grazing incidence X-ray scattering study of (001) oriented high quality epitaxial Co/Cr superlattices. *Phys. Rev.*, **B 1994**, *49*, 17,351.
23. Thompson, G.B.; Banerjee, R.; Fraser, H.L. A comparison of pseudomorphic bcc phase formation in Zr/Nb and Ti/Nb thin film multilayers. **2002**, *in press*.
24. Wawner, F.E., Jr.; Lawless, K.R. Epitaxial growth of titanium thin films. *J. Vac. Sci. Technol.* **1969**, *6*, 588.
25. Yamada, Y.; Yoshida, K. Growth and structure of titanium evaporated films. *Appl. Surf. Sci.* **1988**, *33/34*, 465.
26. Yue, L.P.; Yao, W.G.; Qi, Z.Z.; He, Y.Z. Microstructure of nanometer crystalline films prepared by ion-beam sputtering. *J. Mater. Sci. Lett.* **1994**, *13* (18), 1311.
27. Shechtman, D.; Van Heerden, D.; Josell, D. fcc titanium in Ti-Al multilayers. *Mater. Lett.* **1994**, *20*, 329.
28. Josell, D.; Shechtman, D.; Van Heerden, D. fcc titanium in Ti/Ni multilayers. *Mater. Lett.* **1995**, *22*, 275.
29. Van Heerden, D.; Josell, D.; Shechtman, D. Formation of fcc titanium in titanium/aluminum multilayers. *Acta Mater.* **1996**, *44* (1), 297.
30. Banerjee, R.; Dregia, S.A.; Fraser, H.L. Stability of fcc Ti in Ti / Al multilayers. *Acta Mater.* **1999**, *47* (15), 4225.
31. Banerjee, R.; Zhang, X.D.; Dregia, S.A.; Fraser, H.L. Phase stability In Al/Ti multilayers. *Acta Mater.* **1999**, *47* (4), 1153.
32. Brandes, E.A. *Smithells Metals Reference Book*, 6th Ed.; Butterworths and Co. Ltd.: London, 1983.
33. Numakura, H.; Koiwa, M. Hydride precipitation in titanium. *Acta Metall.* **1984**, *32*, 1799.
34. Machlin, E.S. *An Introduction to Aspects of Thermodynamics and Kinetics Relevant to Materials Science*; Giro Press: Croton-on-Hudson, NY, 1991; 131-133.
35. Bruinsma, R.; Zangwill, A.M. Structural transitions in epitaxial overlayers. *J. Physique (Paris)* **1986**, *47*, 2055.
36. Dregia, S.A.; Banerjee, R.; Fraser, H.L. Polymorphic phase stability in thin multilayers. *Scr. Mater.* **1998**, *39* (2), 217.
37. Dregia, S.A.; Hirth, J.P. A rebound mechanism for Lomer dislocation formation in strained layer structures. *J. Appl. Phys.* **1991**, *69*, 2169.
38. Saunders, N.; Miodownik, A.P.; Dinsdale, A.T. Metastable lattice stabilities for the elements. *Calphad* **1988**, *12*, 351.
39. Schaffer, J. *The Science and Design of Engineering Materials*; Irwin: Chicago, 1995.

# Superconductor Nanowires: Templated by Single Molecules

Alexey Bezryadin

*Department of Physics, University of Illinois at Urbana–Champaign,  
Urbana, Illinois, U.S.A.*

Anthony Bollinger

David Hopkins

Michael Murphey

Mikas Remeika

Andrey Rogachev

*University of Illinois at Urbana–Champaign, Urbana, Illinois, U.S.A.*

## INTRODUCTION

Ultrathin superconducting nanowires (SNWs) can be classified as “weak superconducting links”.<sup>[1]</sup> They have properties in many ways similar to Josephson junctions. Thus, SNWs can find possible applications in superconducting information processing devices: either classical<sup>[2,3]</sup> or quantum.<sup>[4–7]</sup> Nanowires can also be used as detectors and mixers of microwave radiation.<sup>[8,9]</sup> Fundamentally, the SNW is a model system for understanding coherence and decoherence effects, quantum phase transitions, and macroscopic quantum tunneling phenomena in one-dimensional (1-D) superfluids.<sup>[10–21]</sup>

Because of the strong thermal fluctuations in 1-D, the resistance of a nanowire cannot be zero at any finite temperature. The limit of zero temperature is governed by quantum fluctuations, which are not well understood. Therefore, SNWs can fall into one of three different categories: 1) truly superconducting, i.e., with zero resistance in the limit of zero temperature, 2) resistive or normal, with a non-zero but finite resistance ( $R$ ) at zero temperature ( $T$ ), and 3) insulating, with  $R \rightarrow \infty$  as  $T \rightarrow 0$ . On general grounds, it is expected that extremely thin nanowires should lose their ability to carry a supercurrent. General conditions under which this happens are not known. Many experiments show that nanowires having their normal state resistance,  $R_N$ , lower than the superconducting quantum resistance,  $R_Q = h/(2e)^2 \approx 6.5 \text{ k}\Omega$ , obey the predictions of the Langer, Ambegaokar, McCumber, and Halperin (LAMH) theory of thermally activated phase slips (TAPS). Such wires can be considered true superconductors because this theory predicts zero resistance at zero temperature. On the other hand, SNWs with  $R_N > R_Q$  frequently show deviations from LAMH or even an insulating behavior.<sup>[11]</sup> In some cases, these deviations can be explained by the effect of quantum phase slips (QPS).<sup>[12]</sup>

Here we focus on superconducting nanowires produced by sputter-coating single linear molecules (carbon nanotubes, DNA) with thin metallic films. Such molecular templating technique<sup>[11]</sup> results in nanowires that are thinner than 10 nm in diameter. Continuous SNWs were produced with the following two materials:<sup>[11,12,22]</sup> 1) amorphous alloy of MoGe, which is usually used for making extremely thin (down to  $\sim 1.5 \text{ nm}$ ) and homogeneous films,<sup>[23–25]</sup> and 2) Nb metal, which finds applications in superconducting electronic circuits. Although Nb wires are polycrystalline,<sup>[22]</sup> the critical current density in them is  $\sim 10^7 \text{ A/cm}^2$ , i.e., is similar to bulk practical superconductors (Ref.<sup>[26]</sup>, p. 372).

## PROPERTIES OF SUPERCONDUCTING NANOWIRES

### Thermally Activated Phase Slips

The physics of superconducting nanowires is extremely rich and many puzzles remain unresolved. Perhaps the most striking property of SNWs is their inability to reach zero resistance at any nonzero temperature.<sup>[27]</sup> This property agrees with the Mermin–Wagner theorem,<sup>[28]</sup> which prohibits thermodynamic phase transitions in 1-D systems.<sup>a</sup> In particular, a thin 1-D wire made of a superconducting metal cannot undergo a phase transition into a fully superconducting state, i.e., a state with  $R = 0$  at any non-zero temperature. The mechanism of acquiring a non-zero resistance is known as phase slippage (PS) process. It is due to strong thermal (or possibly quantum) fluctuations in 1-D wires.<sup>[29]</sup> The theory of thermally activated phase

<sup>a</sup>A superconducting nanowire is considered 1-D if the diameter of the wire is the same as the superconducting coherence length or smaller.

slips (TAPS) was developed by Langer, Ambegaokar, McCumber, and Halperin (LAMH).<sup>[30,31]</sup> Thermally activated phase slips have been studied since the 70s and are quite well understood. Early experiments on 0.5- $\mu\text{m}$ -diameter tin whiskers confirmed the LAMH theory.<sup>[32,33]</sup>

Each TAPS is a strong and short-lasting thermodynamic fluctuation occurring in a short segment of length,  $\sim 2\xi(T)$ , somewhere along the wire. The order parameter,  $\psi = |\psi|e^{i\varphi}$ , is zero [ $\psi(x,t) = 0$ ] at the center of the TAPS and, correspondingly, the phase,  $\varphi(x,t)$ , is indeterminate at this point. So, with each TAPS the phase difference  $\Delta\varphi = \varphi(L) - \varphi(0)$  along the wire changes by  $\pm 2\pi$ . Here  $x$  is the position along the wire and  $L$  is the wire length. In the absence of phase slips, a state of constant supercurrent,  $\psi(x) = |\psi|e^{ikx}$ , is realized. The wave vector,  $k$ , is proportional to the supercurrent,  $I_S$ . The amplitude,  $|\psi|$ , is constant along the wire if  $I_S = \text{constant}$ . A convenient presentation of  $\psi(x)$  is given in Fig. 1. Here two axes correspond to the real and imaginary parts of  $\psi(x)$ , and the third axis is the space coordinate  $x$ . In this representation a spiral of a constant radius represents a state with  $I_S = \text{constant}$ . The number of turns in the spiral is proportional to  $I_S$ . Thus, if the winding number does not change then the current remains constant. On the other hand, if a phase slip occurs, the order parameter goes to zero at one point and the spiral loses one loop, so the supercurrent diminishes. A phase slip (PS) event is shown in Fig. 1. An antiphase slip (APS) is a similar fluctuation that

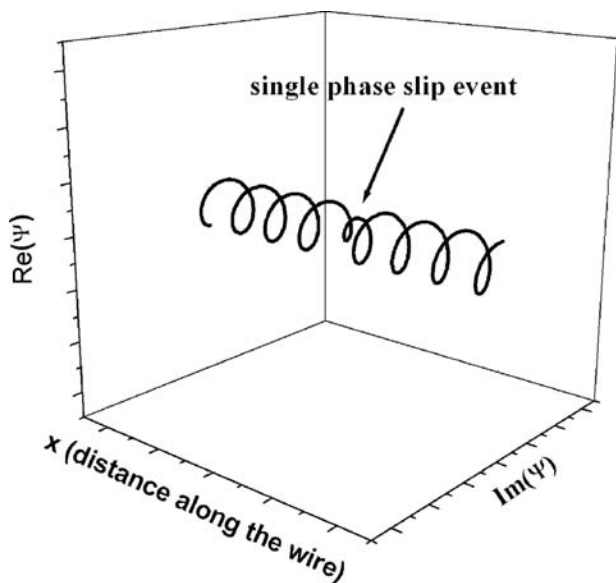


**Fig. 1** Superconducting order parameter of a thin wire with a phase slip (PS) in the center. The PS is a short-lived event ( $\sim 10^{-12}$  sec) during which the order parameter goes to zero at one point. During the PS, the spiral loses one loop and the supercurrent becomes smaller.

increases the winding number by one. Thus, the phase difference between the ends of the wire changes by  $-2\pi$  for each PS and by  $+2\pi$  for each APS.

The problem of calculating the resistance reduces to finding the rate at which phase slips occur in the nanowire. The voltage on the wire (at a fixed small bias current,  $I$ ) is given by the Josephson relation  $2eV = \hbar(d\varphi/dt) = 2\pi(n_+ - n_-)\hbar \equiv 2\pi\hbar\Delta n$ , where  $n_+$  and  $n_-$  are the rates of PS and APS, respectively. The predicted volume of the phase slip is  $V_{\text{PS}} \approx 3.77\xi A$ , where  $A$  is the cross section area of the wire.<sup>[30]</sup> The free energy of a PS is  $\Delta F(T) = [H_C^2(T)/8\pi]V_{\text{PS}}$ , where  $H_C(T)$  is the thermodynamic critical field. At zero bias current,  $I = 0$ , the rates of PS and APS are equal:  $n_+ - n_- = n = \Omega \exp[-\Delta F(T)/k_B T]$ , where  $\Omega = [8k_B(T_C - T)/\pi\hbar][L/\xi(T)]\sqrt{\Delta F/k_B T}$  is the so-called attempt frequency,  $k_B$  the Boltzmann constant,  $\hbar$  Planck's constant,  $T$  the temperature, and  $T_C$  the critical temperature. At  $I > 0$  the barrier corresponding to PS is lower than the APS one, leading to a net phase flow,  $n_+ > n_-$ . We have  $n_{\pm} = \Omega \exp[-(\Delta F(T) \pm \delta F)/k_B T]$  and  $\Delta n = 2\Omega \exp[-\Delta F(T)/k_B T] \sinh(\delta F/k_B T)$ , where  $\delta F = \pi\hbar I/2e$  is half of the free energy difference between PS and APS. Using the relation  $R = dV/dI = (\pi\hbar/e)d(\Delta n)/dI$  one gets the following resistance vs. temperature dependence (here  $t = T/T_C$ ):

$$R_{\text{LAMH}}(T) = Dt^{-3/2}(1-t)^{9/4} \times \exp\left[\frac{-c}{t}(1-t)^{3/2}\right] \quad (1)$$

Because of the normal quasiparticles present in the wire close to  $T_C$ ,<sup>[27]</sup> the final expression for the wire's resistance,  $R(T)$ , is:

$$R^{-1} = R_{\text{LAMH}}^{-1} + R_N^{-1} \quad (1a)$$

where  $R_N$  is the normal-state resistance of the wire. The LAMH defines the constants  $D$  and  $c$  as follows:<sup>[12]</sup>

$$c \equiv \frac{\Delta F(0)}{kT_C} = \frac{1.76\sqrt{2}}{3} \frac{R_Q}{R_N} \frac{L}{\xi(0)} \quad (2)$$

and

$$D = (8/\pi)[L/\xi(0)]R_Q\sqrt{c} \quad (3)$$

where  $\xi(0)$  is zero temperature coherence length [ $\xi(0) \approx 7$  nm for MoGe samples].

## Quantum Phase Slips

Two types of phase slips are usually distinguished: TAPS, discussed above, and QPS. The QPS can be

observed only in very thin wires, about 10 nm in diameter or less.<sup>[14]</sup> Such nanowires can be made using the technique of suspended molecular templates (SMT).<sup>[11]</sup> The SMT method is unique because it results in nanowires that are not only very thin (down to ~3 nm) but also can be made very short, less than 100 nm if necessary. This length is comparable to or shorter than the electronic inelastic mean free path  $L_i = \sqrt{D\tau_i} \simeq 100\text{--}1000$  nm (here  $D = lv_F/3 \sim 10^{-3}\text{--}10^{-4}$  m<sup>2</sup> sec is the diffusion constant and  $\tau_i \sim 10^{-9}\text{--}10^{-10}$  sec is the inelastic scattering time). The electrons in such short SNWs can diffuse through the entire wire without undergoing inelastic collision, and so they are able to preserve quantum phase information.

The possibility of quantum tunneling of phase slips attracts much attention because QPS can be regarded as a macroscopic quantum phenomenon. On general grounds, it is expected that the probability of quantum phase slips should be proportional to  $\exp[-\Delta F(0)/\hbar\omega_S]$ , where  $\hbar$  is the Planck's constant and  $\omega_S$  is some characteristic frequency of quantum fluctuations of the superconducting order parameter. A semiquantitative model of quantum phase slips was suggested by Giordano.<sup>[10]</sup> Recent experiments on MoGe wires showed good agreement with Giordano's model<sup>[12]</sup> (see discussion below). The QPS contribution is explained in detail in Ref.<sup>[12]</sup>. The expression for the resistance in the case of QPS is similar to Eq. (1a) but an additional term is added that represents the contribution of the macroscopic quantum tunneling (MQT) of the phase slips (i.e., the contribution of QPS):

$$R^{-1} = (R_{\text{MQT}} + R_{\text{LAMH}})^{-1} + R_{\text{N}}^{-1} \quad (4)$$

Here  $R_{\text{MQT}} = \rho_{\text{QC}}R_{\text{LAMH}}$  and  $\rho_{\text{QC}} = B[\pi t/8(1-t)]^{3/2} \exp[c\sqrt{1-t}((1-t)/t - a\pi/8)]$ . The coefficients  $a$  and  $B$  are the two fitting parameters. These formulas are equivalent to those used in Ref.<sup>[12]</sup>. Here we explicitly introduce the temperature-dependent ratio  $\rho_{\text{QC}} \equiv R_{\text{MQT}}/R_{\text{LAMH}}$ . By using the formulas from Ref.<sup>[12]</sup>, it can be shown that the  $\rho_{\text{QC}}$  ratio is larger than unity (meaning that quantum tunneling of phase slips occurs with a higher rate than the thermal activation) if the temperature is  $T < 0.7T_C$ . This ratio of the quantum and thermal contributions (i.e.,  $\rho_{\text{QC}}$ ) is plotted in Fig. 8 (inset).

QPS and TAPS have different implications. If only TAPS is present, then the wire is classified as "truly superconducting" in the sense that its resistance approaches zero as the temperature approaches zero. If QPS is also present, the resistance stays above zero even in the limit of zero temperature so the wire remains resistive or normal. Thus, TAPS is responsible for breaking superconductivity at finite temperature and QPS destroys superconductivity in the limit of

zero temperature. The existence of QPS is regarded as a limiting factor for miniaturization of superconducting devices.<sup>[34]</sup> Under certain conditions, a proliferation of QPS can suppress superconductivity and can cause a superconductor-insulator (SI) quantum transition.<sup>[11,14-16]</sup>

## FABRICATION OF SUPERCONDUCTING NANOWIRES

### Molecular Templating with Nanotubes

The suspended molecular templates (SMT) method<sup>[11]</sup> uses suspended, linear rigid molecules as templates for metal coating. Three types of molecules have been tested: 1) ordinary single-wall carbon nanotubes,<sup>[11,12]</sup> fluorinated carbon nanotubes,<sup>[35,36]</sup> which are 100% insulating, and DNA molecules (see below). Because these molecules are very thin, 1–3 nm in diameter, the resulting nanowires can be made thinner than 10 nm. It was found that MoGe wires made on insulating fluorotubes have similar properties to those made on regular nanotubes. Thus the nanotube does not contribute significantly to the total conductance of the wire. Note that suspended nanotubes can also be used for the fabrication of magnetic nanowires.<sup>[37]</sup>

The SMT technique is described in detail in Ref.<sup>[11]</sup>. The fabrication process starts with an Si(100) wafer covered with a layer of 500-nm-thick SiO<sub>2</sub> and 60-nm-thick film of low-stress SiN.<sup>[38]</sup> A narrow and very long trench is then defined in the SiN film using e-beam lithography and reactive ion etching in SF<sub>6</sub> plasma. The resulting trench (Fig. 2) has a width of ~100 nm and length of ~5 mm. An undercut is then formed by placing the sample in HF for 10 sec.

Fluorinated nanotubes are deposited from a solution in isopropyl alcohol. After drying, the sample is sputter-coated with the desired superconducting metal, typically ~4–8 nm of Mo<sub>79</sub>Ge<sub>21</sub> (Fig. 2A). After sputtering, each nanotube suspended over the trench becomes decorated with metal and thus forms a metallic nanowire. A nanowire of desired width is then selected under scanning electron microscopy (SEM) (Fig. 2B) and photolithography is used for making the electrodes and etching all nanowires except the selected one (Fig. 2C).

### Molecular Templating with DNA

The DNA molecule is of course not as rigid as a carbon nanotube. Nevertheless, it is observed that when being suspended, the DNA stretches itself. Thus, DNA provides an excellent molecular template for metal deposition. For example, the micrograph in

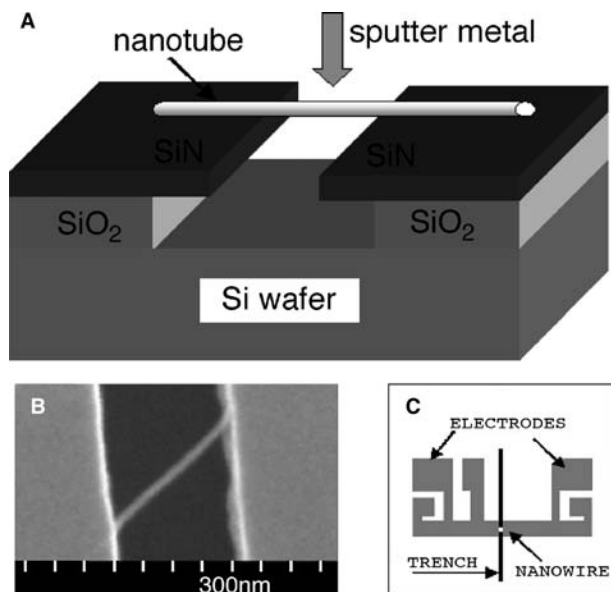


**Fig. 2** The sample schematics. (A) The nanotubes are deposited over a trench, and a superconducting metal (Nb or MoGe) is sputtered over the entire surface of the Si chip. Thus the electrodes are formed on the banks of the trench and, at the same time, suspended nanowires form with nanotubes in their cores. Because the sample is sputtered only once, the wires have the same thickness as the electrodes. In addition, the wires are seamlessly connected to the electrodes, without any unwanted contact barrier. Photolithography and reactive ion etching are subsequently used to define the shape of the electrodes and destroy all wires but one. The d.c. sputtering is done in an argon atmosphere, in a sputtering chamber equipped with a cryogenic liquid nitrogen trap. (B) A scanning electron micrograph of a nanowire (gray line) suspended over a trench (black) and connecting to two MoGe electrodes (gray areas). (C) Schematic top view of the sample. The size of the Si chip is  $5 \times 5$  mm.

Fig. 3A shows six metal-coated DNA wires, which are visible as thin gray lines of length  $\sim 150$  nm. The tests were done on the same type of Si/SiO<sub>2</sub>/SiN substrate with trenches made as described earlier. The  $\lambda$ -DNA molecules have been deposited over the oxygen-plasma-cleaned SiN surface from a buffer solution with a 40  $\mu\text{g}/\text{mL}$  concentration. The samples were then dried and metal coated. Two important conclusions can be drawn from these experiments: 1) Because of some intrinsic mechanism, the suspended DNA molecules become stretched and appear very straight. 2) Many metals, such as Os, Cr, and MoGe, showed good adhesion to the DNA surface and produced visibly homogeneous wires. A coating of DNA with a thin ( $\sim 3$  nm) AuPd film produced granular wires (Fig. 3B). The fact that DNA appears so straight is somewhat unexpected because DNA is not nearly as rigid as carbon nanotubes. A possible explanation is that DNA interacts attractively with the substrate due to the

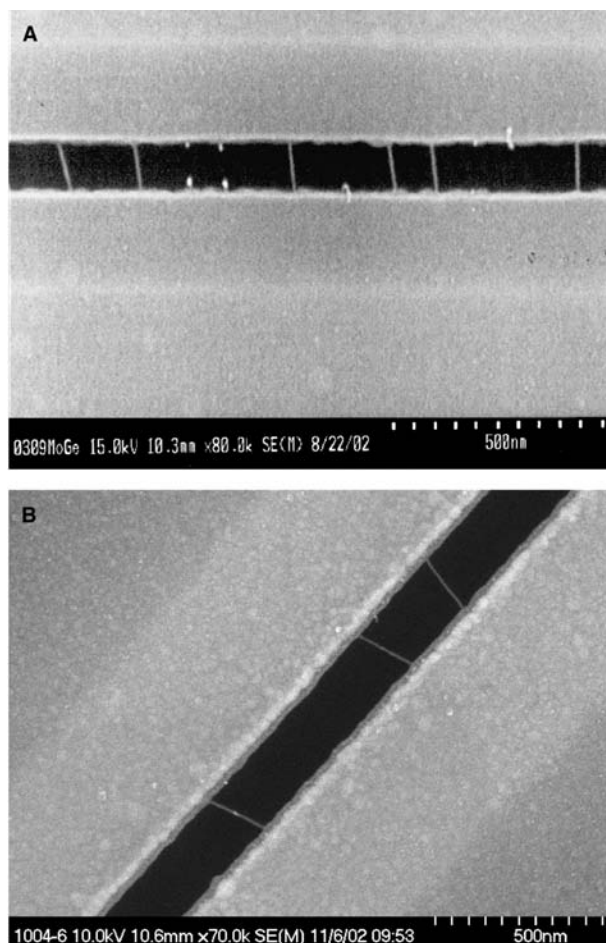


**Fig. 3** Metal decoration of suspended DNA molecules. The black region is the trench with an undercut. Nanowires appear as thin gray lines crossing the trench. The sample (A) has six surviving nanowires.  $\lambda$ -DNA molecules were deposited from a buffer dilute solution, dried, and sputter-coated with 4 nm of MoGe and 3 nm of SiO<sub>2</sub>. (B) Nanowires of gold-palladium templated by DNA. The trench was cut into SiN film using a focused ion beam. A 50-nm-thick gold film was deposited before the application of DNA. After the  $\lambda$ -DNA deposition, the sample was sputter-coated with gold-palladium.

van der Waals force. Thus, it is energetically favorable for the molecule to minimize the length of the freely suspended section. So, the suspended part becomes strained and perfectly straight.

### Morphology of Nb and MoGe Nanowires

The morphology of nanowires was determined using transmission electron microscopy (TEM).<sup>[22]</sup> The wires for these studies were prepared on a TEM grid. Typical micrographs of Nb nanowires are shown in Fig. 4A and B. It is clear from Fig. 4A that Nb wire is polycrystalline. It consists of randomly oriented 3- to 7-nm



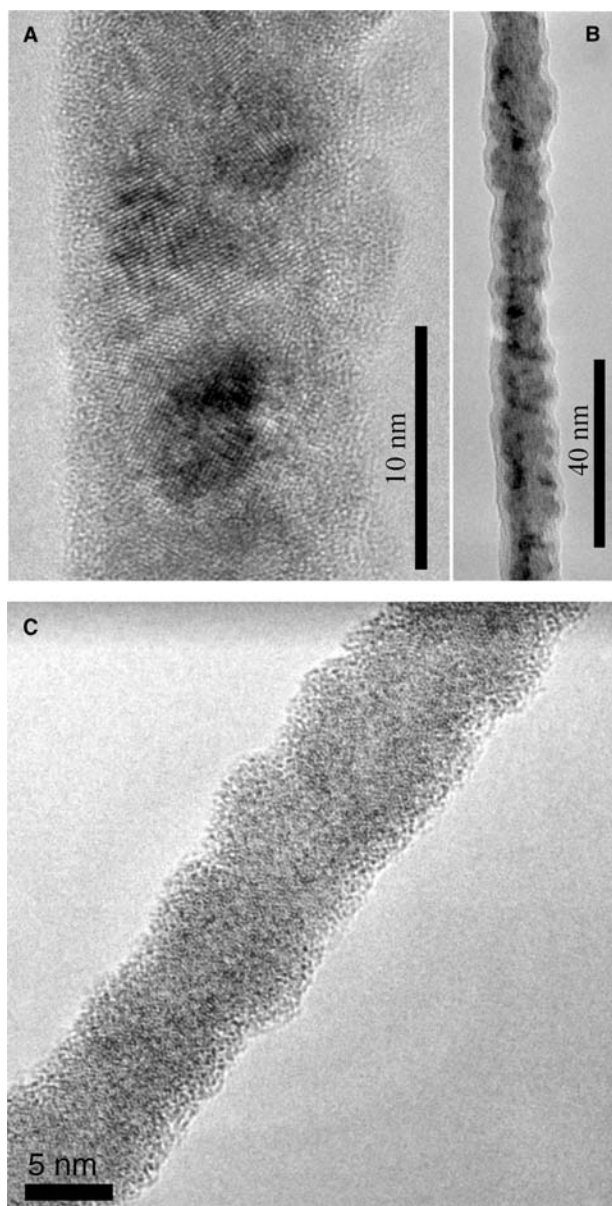


**Fig. 4** (A) A high-resolution TEM (JEOL 2010) image of a Nb nanowire fabricated by sputter deposition of a 6-nm Nb film over a carbon nanotube. (B) Image of a Nb nanowire (4 nm of Nb) covered with a protective layer of Si (2 nm). (C) A TEM (JEOL 2010F) micrograph of an amorphous MoGe wire produced by sputter deposition of 7-nm MoGe film (with no Si) over a fluorinated carbon nanotube. The scale bar is 5 nm. The surface ( $\sim 1.5$  nm) of the wire appears oxidized but the core is intact.

grains. Lattice fringes have a spacing of  $\sim 0.24$  nm, which corresponds to the (111) lattice planes of Nb.

A thin,  $\sim 2$ -nm layer near the edges of the wire does not show any crystalline structure. This layer is probably an amorphous oxide formed on the surface because the wire was exposed to the atmosphere. To prevent Nb oxidation, all samples used for transport

measurements were sputter-coated with a 2-nm-thick Si film. The image of such a wire, protected with Si, is shown in Fig. 4B. The layer of Si (light layer at the surface) produces a uniform coverage of the Nb core (darker center). A typical micrograph of a MoGe nanowire is shown in Fig. 4C. The wire appears amorphous. The width variation of Nb wires (3 nm) appears larger and it has a longer characteristic length scale (along the wire) compared to MoGe wires.

## TRANSPORT MEASUREMENTS

### Setup and Resistance Measurements

In order to measure voltage vs. current,  $V(I)$ , curves of a nanowire, a sinusoidal a.c. current (at 12.7 Hz frequency and 1–10 nA amplitude) is injected through a pair of outer electrodes (Fig. 2C) and the voltage is measured on the inner electrodes, using a low-noise PAR 113 amplifier. The current is taken from the high-precision-function generator (Stanford Research Systems, DS 360) connected in series with a 1-M $\Omega$  resistor. The fifth electrode (Fig. 2C) is used to measure the resistance of the film electrodes, without involving the wire. The zero-bias resistance is determined from the slope of the best linear fit to the  $V(I)$  curves measured at low currents (1–10 nA). The temperature is measured using a Lakeshore calibrated thermometer, Cernox<sup>®</sup>. The leads connecting the sample to the room temperature amplifiers were made from a Teflon-coated resistive alloy wire, Stablohm 800, produced by California Fine Wire Co. Before reaching the sample, the wire is rolled over a cold Cu rod and coated with a layer of a conducting silver paste. Such an environment helps to thermalize the signal leads and acts as an external, microwave radiation filter (which helps to suppress the room temperature blackbody radiation propagating through signal leads). All electrical leads coming to the sample are additionally filtered with room temperature pi filters (BLP-1.9 from <http://www.minicircuits.com>). The measurements were done in an He-3 cryostat or in a pumped He-4 Dewar.

An example of a resistance vs. temperature,  $R(T)$ , curve is shown in Fig. 5. Because the wire is connected in series with some sections of the electrodes (Fig. 2C), two resistive transitions are observed. The first one (at  $\sim 6$  K) is due to the electrodes and the second transition (at  $\sim 3.5$  K) is due to the nanowire itself. Thus, the critical temperature of the nanowire is suppressed<sup>[39]</sup> compared to the film of the same thickness (i.e., the electrodes). The normal-state resistance of the wire,  $R_N$ , is determined right below the superconducting transition of the leads, as shown by an arrow in Fig. 5.



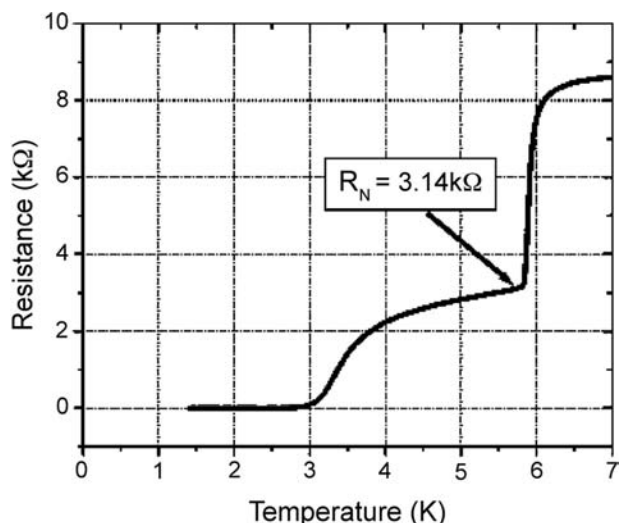


**Fig. 5** A typical resistance vs. temperature curve for a MoGe nanowire. The first resistance drop is due to the electrodes and the second, broadened, transition is due to the nanowire. The normal-state resistance of the wire is measured at a temperature slightly lower than the critical temperature of the electrodes, as shown by the arrow.

### Resistivity of Metallic Nanowires

It is important to determine the resistivity of the metal forming the nanowire and compare this to the known bulk values. The resistivity of the wire and its normal resistance should satisfy the following relation:

$$wt = \rho(L/R_N) + A_0 \quad (5)$$

Here  $R_N$  is the normal resistance of the nanowire,  $L$  is the length measured with SEM,  $t$  is the known thickness of the sputtered film,  $w$  is the apparent width of the wire measured in SEM, and  $A_0$  is the expected area of the insulating material on the surface of the wire, including an oxidized layer and/or protective Si or Ge layers, if any. It is necessary to include the “dead layer” area,  $A_0$ , in Eq. 5 because the width,  $w$ , is not the width of the conducting core of the wire, but is the total width, which is observed in SEM. In Fig. 6, we plot the total area of the nanowire,  $wt$ , vs. the unit length conductance,  $L/R_N$ . Three groups of points correspond to Nb wires (filled squares), unprotected MoGe wires (open circles) and Ge-coated MoGe wires (filled circles). The dependence is linear for each group of samples. The resistivities estimated from the best linear fits (Fig. 6) are  $\rho = 4.2 \times 10^{-7} \Omega \text{ m}$  for Nb wires,  $\rho = 2.35 \times 10^{-6} \Omega \text{ m}$  for unprotected MoGe wires, and  $\rho = 2.46 \times 10^{-6} \Omega \text{ m}$  for protected MoGe wires. This should be compared to bulk resistivity of MoGe,  $\rho_{\text{MoGe,BULK}} = 1.6 \times 10^{-6} \Omega \text{ m}$ <sup>[25]</sup> and to thin film resistivity for

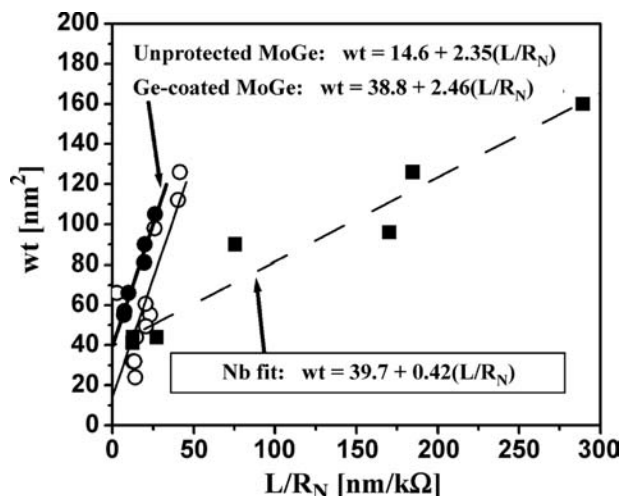


**Fig. 6** Cross-section area of the wire,  $wt$ , is plotted vs. the unit length conductance,  $L/R_N$ . Here  $w$  is the width of the nanowire measured under SEM and  $t$  is the nominal thickness of the sputtered film. Each data point corresponds to a different sample. Filled squares represent Nb wires, open circles, unprotected MoGe wires, and filled circles, MoGe wire protected with a 1.5-nm Ge film. The best linear fits are shown and the parameters of the fits are indicated on the graph: dashed line for Nb, thick solid line for MoGe wires covered with 1.5 nm of Ge, and thin solid line for plain MoGe nanowires.

Nb:  $\rho_{\text{Nb,THINFILM}} = 2.4 \times 10^{-7} \Omega \text{ m}$ .<sup>[40]</sup> The resistivity of wires is slightly larger but of the same order of magnitude.

This indicates that the wires are continuous and contain no breaks or tunnel barrier between grains. The effective “dead area” is  $A_0 \approx 14.6 \text{ nm}^2$  for unprotected MoGe wires,  $A_0 \approx 38.8 \text{ nm}^2$  for Ge-protected MoGe wires, and  $A_0 \approx 40 \text{ nm}^2$  for Nb samples. Protected MoGe samples show a larger  $A_0$  because Ge on their surface contributes to the total width,  $w$ . It appears that such protection is not really necessary because the unprotected wires show a lower resistivity and thinner dead layer. In general, the following factors may contribute to large  $A_0$  values: 1) oxidation, 2) presence of a protective layer, 3) wire morphology, presence of grains on the surface, fluctuations of the wire width, and thickness, and 4) a limited resolution of SEM causing some smearing of the images.

### Superconductivity in MoGe Nanowires

Parameters of studied amorphous  $\text{Mo}_{79}\text{Ge}_{21}$  nanowires of short length ( $L = 100\text{--}150 \text{ nm}$ ) and various diameters are given in Table 1.

Resistance vs. temperature plots (Fig. 7A) show two different types of behavior: superconducting and insulating. Samples A through F and sample X show

**Table 1** Parameters of unprotected MoGe wires deposited over fluorinated single-wall carbon nanotubes

Sample	$L$ (nm)	$w$ (nm)	$D_{\text{CALC}}$ (nm)	$t$ (nm)	$R_N$ (k $\Omega$ )
A	99 $\pm$ 10	21 $\pm$ 3	11.1	8.5	2.39
B	127 $\pm$ 10	19 $\pm$ 3	11	8.5	3.14
C	93 $\pm$ 10	17 $\pm$ 2	8.8	8.5	3.59
D	109 $\pm$ 12	13 $\pm$ 3	8.3	7.0	4.73
E	116 $\pm$ 12	12 $\pm$ 4	7.9	7.0	5.61
F	125 $\pm$ 7	14 $\pm$ 4	7.8	7.0	6.09
G	105 $\pm$ 8	11 $\pm$ 2	6.2	5.5	8.22
H	121 $\pm$ 14	9 $\pm$ 2	6.5	5.5	8.67
I	140 $\pm$ 9	11 $\pm$ 2	6.6	5.5	9.67
J	86 $\pm$ 15	14 $\pm$ 3	3.1	7.5	26.17

The length of the wire,  $L$ , and the width,  $w$ , are measured under SEM. The parameter  $R_N$  is the normal state resistance,  $t$  is the thickness of the sputtered film, and the diameter  $D_{\text{CALC}}$  is calculated from  $R_N$  and  $L$  as  $D \equiv \sqrt{(4/\pi)(\rho L/R_N)}$ , with  $\rho = 2.35 \times 10^{-6} \Omega \text{ m}$ .

a superconducting behavior, i.e., their resistance decreases with temperature. Samples G through J exhibit an increasing resistance (with cooling) and thus considered insulating. Such dichotomy is an indication of an SI quantum transition.<sup>[35]</sup> The insulating samples not only show a slight increase of their resistance with cooling but also, unlike superconducting wires, they exhibit a maximum of the differential resistance at zero bias current (not shown). The SI transition happens when the normal resistance of the nanowire reaches the quantum resistance  $R_Q = h/4e^2 \approx 6.5 \text{ k}\Omega$ . Fig. 7A and the inset clearly show that all wires with  $R_N < 6.5 \text{ k}\Omega$  are superconducting, whereas all others are insulating. This same behavior was found in similar MoGe wires in Ref.<sup>[11]</sup>, in which case the wires were grown on regular (not fluorinated) nanotubes and were

protected with 1.5 nm of Ge. Note again that only  $\sim 100$ -nm-long wires are being considered.

An SI transition was also observed in Ref.<sup>[19]</sup>, but in that work the transition has been seen when the film square resistance (defined as  $R_W = \rho/d$ , with  $\rho$  being the resistivity of the metal and  $d$  the film thickness) reached a critical value close to  $R_Q$ . On the contrary, in our case the film square resistance at the SI transition is much lower than  $R_Q$  because  $R_W \approx R_N(w - \sqrt{A_0})/L \approx 600 \Omega \ll R_Q$ . The total resistance (or perhaps the wire diameter) appears to be a more plausible control parameters driving the transition. Fig. 7B presents all  $\sim 100$ -nm-long samples, including those of Ref.<sup>[11]</sup>. Here the resistance divided by the length of the wire is plotted vs. the temperature normalized by the critical temperature of the film electrodes of each sample. A clear dichotomy confirms the existence of a superconductor–insulator transition.

Now we compare the  $R(T)$  curves of superconducting MoGe samples with the LAMH theory. Fig. 8 shows  $R(T)$  plots for samples A, B, and C (From Fig. 7A) together with the LAMH fits computed using Eq. (1a). The fits show nearly perfect agreement with the experiment (except very near  $T_C$  where the LAMH theory does not work:<sup>[27]</sup>). The experimental fitting constants  $c_{\text{Exp}}$  and  $D_{\text{Exp}}$  are in good agreement with Eqs. (2) and (3). Thus, the wires act as homogenous 1-D superconductors, well described by the LAMH, without including QPS.

Experiments with considerably longer wires (up to 1000 nm) give significantly different results.<sup>[12]</sup> The dichotomy representing the superconductor–insulator transition was not observed in these longer wires. On the contrary, a smooth crossover from strongly superconducting to weakly superconducting wires has been seen (Fig. 9). It was possible to fit the entire series of  $R(T)$  curves of Fig. 9 using only two fitting parameters. The fitting procedure is explained in detail in Ref.<sup>[12]</sup>.

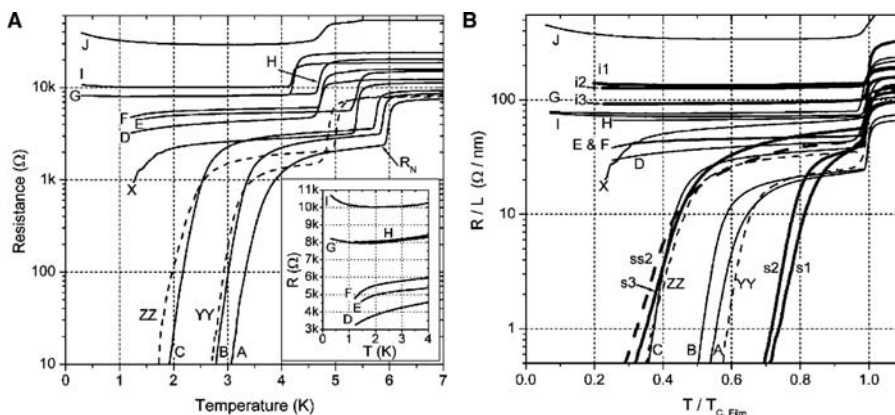


**Fig. 7** Resistance vs. temperature of MoGe nanowires. Each curve represents a different sample. (A) Log-linear plots of zero bias resistance vs. temperature. The dashed curves represent double-wire structures. (Inset) The same  $R(T)$  data magnified near  $R_Q$ . (B) Resistance divided by the length is plotted vs. the temperature normalized by the critical temperature of the film. This combined plot includes all samples listed in Table 1 and the samples from Ref.<sup>[11]</sup> (thicker lines). The sample X, with  $L \approx 50 \text{ nm}$ , is twice shorter than others. A pronounced dichotomy is observed.

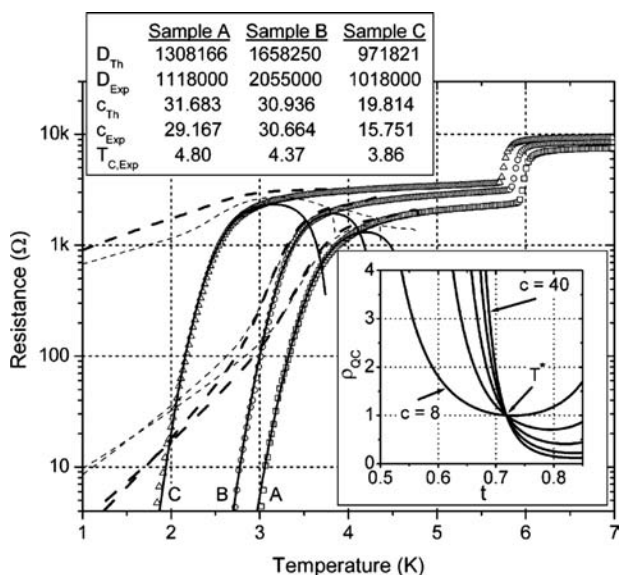


**Fig. 8**  $R(T)$  data (open symbols) for samples A, B, and C compared to the LAMH theory of TAPS (continuous lines). The table shows the best LAMH fitting parameters  $c_{Exp}$ ,  $D_{Exp}$ , and  $T_C$  and compares them to the parameters ( $c_{Th}$  and  $D_{Th}$ ) computed from Eqs. (2) and (3). The dashed lines show the predictions of the Giordano model (Ref.<sup>[12]</sup>) that includes quantum phase slips (heavy dashed lines:  $a = 1.3$ ,  $B = 7.2$ ; light dashed lines:  $a = 1$ ,  $B = 1$ ). The coefficients  $a$  and  $B$  are defined in Ref.<sup>[12]</sup> and determine the ratio of attempt frequencies and the energy barriers for QPS and TAPS. (Inset) Computed plots of  $\rho_{QC} \equiv R_{MQT}/R_{LAMH}$  vs.  $t \equiv T/T_C$  for  $c = 8, 16, 24, 32,$  and  $40$  (assuming  $a = 1$  and  $B = 1$ ). The temperature  $T^* = 0.718T_C$  is a universal temperature below which the Giordano model predicts a higher QPS rate compared to TAPS.

The fits (dashed lines in Fig. 9B) are made using Eq. (4). The coefficients  $a$  and  $B$  are unknown and were used as free fitting parameters. The coefficient  $c$  is defined in Eq. (2). It represents the height of the barrier for the phase slips and it is the same parameter for TAPS as well as for QPS.

The same fitting procedure was applied to short MoGe wires with  $R_N < R_Q$  (Fig. 8). The fits, computed using Eq. (4), are shown by dashed lines in Fig. 8. They deviate from the experimental points considerably. Thus we conclude that in short wires with low enough normal state resistance (possibly defined as  $R_N < R_Q$ ) a new regime is realized. This regime can be called “true” superconductivity because the QPS rate is strongly suppressed and the LAMH theory gives correct predictions. This theory predicts that resistance should be zero at zero temperature. On the contrary, the wires that show finite contribution of QPS (such as those shown in Fig. 9) should have a non-zero resistance even at zero temperature.

The reason for different behavior in short and long wires is not well understood. Nevertheless, it might be significant that all long wires (Fig. 9) had their normal resistance above  $R_Q$ , whereas the superconducting wires (Figs. 7 and 8) have their normal resistance lower than  $R_Q$ . Thus, the above-mentioned short and long wires could simply be on different sides of the SI transition. In general, we find that the low-resistance wires show good agreement with the LAMH theory, whereas the highly resistive wires (i.e., those with  $R_N > R_Q$ ) show a considerable deviations from the LAMH (Fig. 9) or even act as insulators (samples G–J, Fig. 7A), possibly due to QPS.

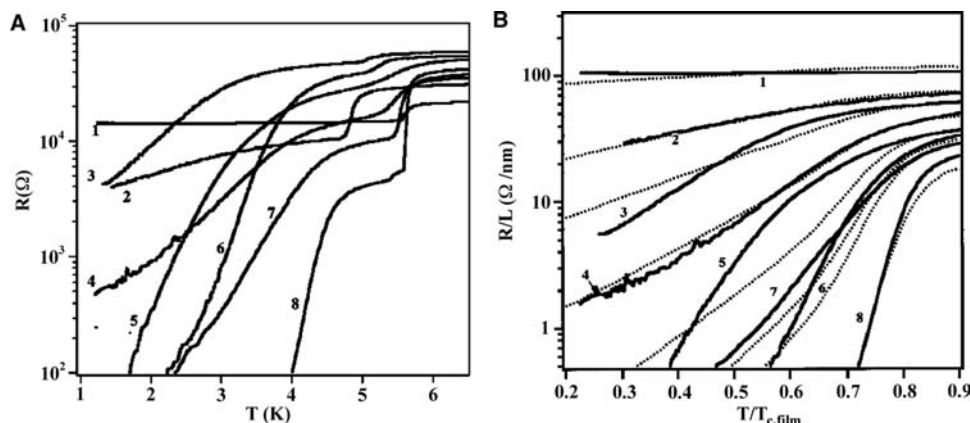


**Fig. 9** (A) Resistances vs. temperature for longer (up to 1000 nm) MoGe wires reproduced from Ref.<sup>[12]</sup>. The wire’s normal-state resistances and lengths are 1: 14.8 kΩ, 135 nm; 2: 10.7 kΩ, 135 nm; 3: 47 kΩ, 745 nm; 4: 17.3 kΩ, 310 nm; 5: 32 kΩ, 730 nm; 6: 40 kΩ, 1050 nm; 7: 10 kΩ, 310 nm; 8: 4.5 kΩ, 165 nm. (B) Resistance divided by the length plotted vs. temperature, normalized by the critical temperature of the film electrodes. The solid lines represent the data. The dotted lines are calculated using the model of quantum phase slips (see Eq. (4) and Eq. (3) of Ref.<sup>[12]</sup>). The two fitting parameters that produced the best agreement with the experiment curves are  $a = 1.3$  and  $B = 7.2$  used for the entire family of experimental curves.

## Superconductivity in Nb Nanowires

Nanowires of Nb, grown on fluorinated carbon nanotubes, have properties similar to MoGe nanowires. Parameters of Nb samples are given in Table 2. All Nb wires were protected with a 2-nm Si film. As in MoGe samples, the resistance vs. temperature curves show two transitions (Fig. 10). The first one is due to the Nb film electrodes. Expectedly, this film transition temperature is lower for thinner films.<sup>[39]</sup> The resistance measured slightly lower than the film transition is taken to be the normal-state resistance of the wire,  $R_N$ . The second resistive transition is due to the nanowire itself. The LAMH theory fits, made using Eq. (1a) (Fig. 10, continuous lines), demonstrate very good agreement with the data (open circles). The dashed curves in Fig. 10 represent the Giordano model and include the QPS effect, calculated with Eq. (5).

They deviate from the experimental points. The effect of quantum phase slips is negligibly low, i.e., much lower than the Giordano model predicts. Thus, similar to MoGe wires,  $\sim 100$ -nm-long Nb wires show very strong suppression of QPS and good agreement with LAMH. The coherence length, extracted from the LAMH fitting procedure, is  $\xi(0) \approx 8$  nm for samples Nb2 and Nb3. This is comparable to  $\xi(0) \approx 7$  nm found in sputtered Nb thin films. It also agrees well with the estimate  $\xi(0) \approx (\xi_0 l)^{1/2} = 6.9$  nm, where  $\xi_0 = 40$  nm is the coherence length for clean Nb, and  $l \approx 1.2$  nm is the mean free path. For higher resistance samples  $\xi(0) \approx 15 \div 20$  nm, probably due to the suppression of the critical temperature.

Interestingly, all Nb wires that show good agreement with LAMH satisfy the condition  $R_N < R_Q$ . The only wire that deviates from LAMH (sample Nb6) satisfies  $R_N > R_Q$ . Thus, again, the quantum resistance appears as a critical point. Examples of SI transitions with a critical point at  $R_{ENV} = R_Q$  have

**Table 2** Parameters of Nb nanowires

Sample	$R_N$ ( $\Omega$ )	$L$ (nm)	$t$ (nm)	$w$ (nm)	$T_C$ (K)	$\xi(0)$ (nm)
Nb1	470	137	8	20	5.8	8.5
Nb2	650	120	7	18	5.6	8.1
Nb3	1610	172	6	16	2.65	18.1
Nb4	2350	177	6	15		
Nb5	4250	110	4	11.5	2.6	16.5
Nb6	9500	113	4	10.3	1.9	16.05
Nb7	15700	196	4	11		
Nb8	47500	235	4	11		

Parameters include the length,  $L$  (measured under SEM), the sputtered film thickness,  $t$ , the apparent width,  $w$  (measured under SEM), and the normal-state wire resistance,  $R_N$ . The critical temperature,  $T_C$ , and the coherence length,  $\xi(0)$ , are obtained from the LAMH best fits.

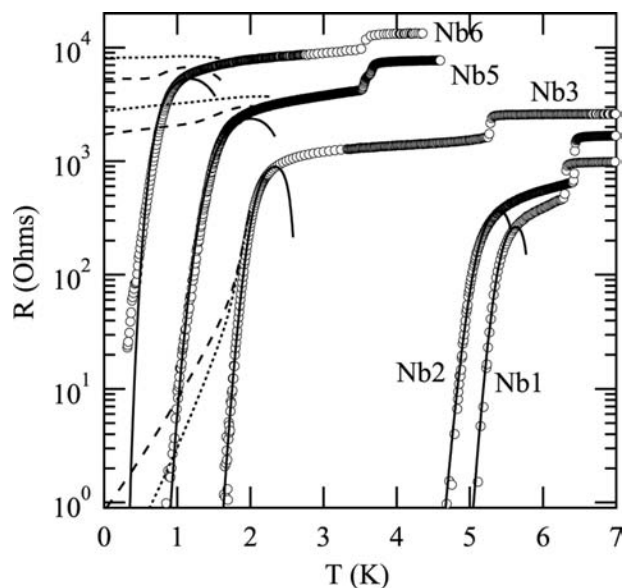


**Fig. 10** Temperature dependence of the resistance of Nb nanowires. The experimental points are given by open circles. The solid lines show the fits to the LAMH theory of thermally activated phase slips. These fits are made without including the quantum phase slips. The fitting parameters,  $\xi(0)$  and  $T_C$ , are indicated in Table 2. The dotted and dashed curves show the fits calculated under the assumption that quantum phase slips do occur. The dashed curves are calculated using generic fitting constants  $a = 1$  and  $B = 1$ , using Eq. (4). The dotted lines represent the constant obtained in Ref.<sup>[12]</sup>, i.e.,  $a = 1.3$  and  $B = 7.2$ . The other parameters are the same as obtained from LAMH fits.

been studied previously in different systems.<sup>[41,42]</sup> Such transitions are called dissipative phase transitions (DPT) and are controlled by the resistance of the environment. Typically, a transition into an insulating state takes place when the resistance of the environment (e.g., a shunting resistance) reaches  $\sim R_Q = 6.5$  k $\Omega$ . In short MoGe and Nb nanowires there are certain similarities to the DPT, in particular the fact that deviations from LAMH occur when the normal resistance approaches 6.5 k $\Omega$ . The dissipative environment for the nanowires could be the bath of normal electrons generated by phase slips in the nanowire itself. Thus, our preliminary conclusion is that such suppression of QPS is due to a quantum dissipation effect, i.e., the DPT. This question certainly requires further investigation.

## High-Bias Current Phenomena in Nanowires

Voltage vs. current measurements,  $V(I)$ , are presented below for a typical Nb nanowire, Nb2. With decreasing temperature, the  $V(I)$  undergoes the following transformations. Slightly below  $T_C$  and at high-bias



currents, the  $V(I)$  follows the exponential dependence predicted by the LAMH theory,  $V(I) \sim \exp(I/I_0)$  (Fig. 11A). The experimental value of the coefficient  $I_0 \approx 0.09 \mu\text{A}$  is close to the theoretical (Ref.<sup>[27]</sup>, p. 291) value,  $I_0 = 2ek_B T/\pi h = 0.06 \mu\text{A}$ . At lower  $T$ , the resistance becomes immeasurably low until the critical current is reached. At the critical current, the sample shows a few voltage steps (Fig. 11B) and then, at higher bias currents, enters a resistive (or dissipative) regime with a linear  $V(I)$ . Each new step in the  $V(I)$  curve is probably due to an appearance of a new phase slip center (PSC) in the wire.<sup>[27]</sup>

The multistep  $V(I)$  curves indicate that the dissipative size of a single PSC is less than the length of the wire. When temperature decreases further, the steps merge, possibly due to a synchronization of PSCs.<sup>[43]</sup> At low temperatures, only one large step is present at the critical current and the hysteresis is always observed (Fig. 11C). The hysteresis can be explained either by heating<sup>[44]</sup> or by the finite relaxation time of the order parameter.<sup>[43,45]</sup> The heating should not be

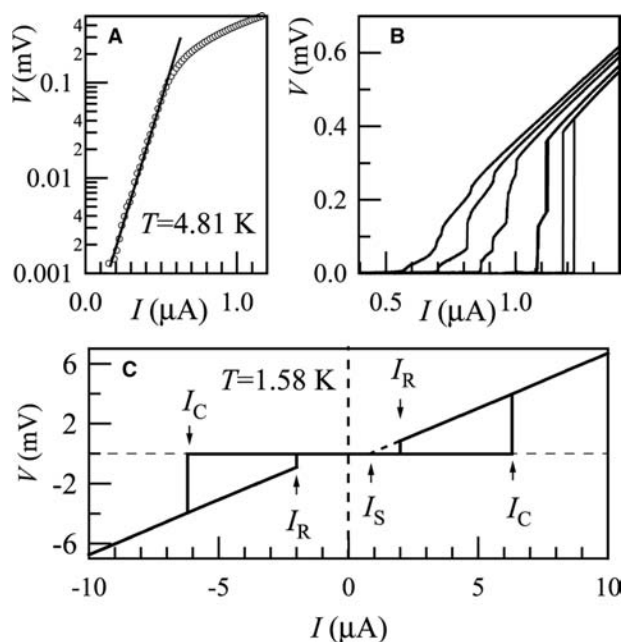


**Fig. 11** Voltage vs. current curves measured on one Nb nanowire, Nb2. (A) A  $V(I)$  dependence measured at  $T = 4.8 \text{ K}$  (open circles) in a log-linear representation. The straight solid line is a guide to the eye. (B) A family of  $V(I)$  curves measured at different temperatures, close to  $T_C = 5.6 \text{ K}$ . From the left to the right, the temperatures are:  $4.76 \text{ K}$ ,  $4.69 \text{ K}$ ,  $4.58 \text{ K}$ ,  $4.45 \text{ K}$ , and  $4.35 \text{ K}$ . Stepwise behavior corresponds to nucleation of phase slip centers. The other tested Nb samples showed similar steps. (None of the MoGe samples showed such steps.) (C) Hysteretic  $V(I)$  variation at the lowest temperature,  $T = 1.58 \text{ K}$ . The critical current,  $I_C$ , the “retrapping” current,  $I_R$ , and the offset current,  $I_S$ , are indicated by arrows.

the dominant effect because the  $V(I)$  curves in the dissipative state are linear and parallel to the normal-state dependence,  $V = R_N I$ , but shifted downward. In other words, they show a non-zero offset current,  $I_S$ , meaning that the linear part of the  $V(I)$  dependence, observed above the critical current, does not extrapolate to zero current, but rather to a positive offset current,  $I_S$ . The  $I_S$  represents a non-zero average supercurrent existing even at  $I > I_C$ . This fact suggests that superconductivity survives in some form in the resistive state.

The critical current for the sample Nb2 extrapolated to  $T = 0 \text{ K}$  is  $I_C(0) = 8 \mu\text{A}$ . This is close to the depairing critical current calculated as  $I_{DP} = (92 \mu\Omega) L T_C / R_N \xi(0)$ ,<sup>[34]</sup> using the parameters extracted from the LAMH fit. This expression gives  $I_{DP} = 12 \mu\Omega$ , reasonably close to experimental value, thus confirming the consistency of the  $I_C(T)$  and  $R(T)$  measurements. Because the measured values of  $I_C(T)$  fluctuate slightly ( $\sim 100 \text{ nA}$ ) from measurement to measurement, it is reasonable to assume that the critical current is suppressed below the expected depairing current due to the premature switching effect.<sup>[27]</sup>

Examples of  $V(I)$  curves of MoGe wires are shown in Fig. 12. They are similar to Nb, but they never show multiple steps as in Fig. 11B. This is an indication of a better homogeneity of amorphous MoGe wires or,

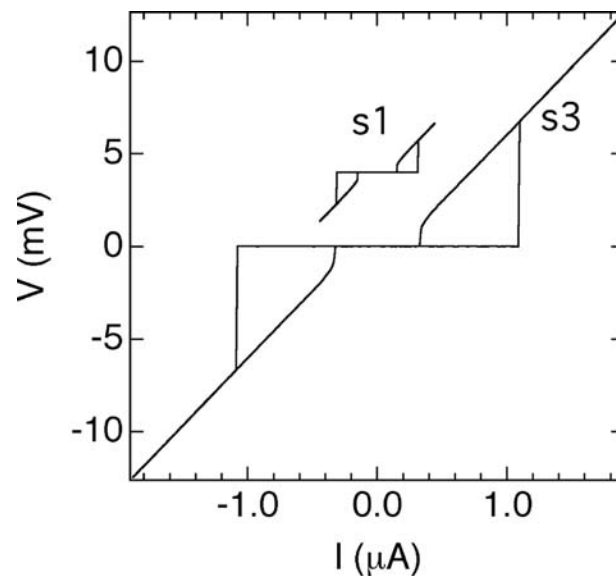


**Fig. 12** Voltage vs. current curves for the MoGe samples s1 and s3 (same samples as presented in Ref.<sup>[11]</sup>). The  $R-T$  curves for these samples are plotted in Fig. 8B. The measurement is done at  $1.5 \text{ K}$ . The sample s1 had a lower critical temperature and higher normal resistance, and was close to the SI transition. Correspondingly, the critical current for s1 is also lower. Yet, the general shape of both curves is similar. Note that the  $V(I)$  curve of this sample is shifted vertically for clarity (but not rescaled). Both curves show a non-zero offset current.

possibly the larger dissipative size of the phase slip centers in MoGe. This conclusion is confirmed by the observation that the differential resistance measured on the resistive part of the  $I(V)$  curve (i.e., above the critical current) coincides with the wire's normal resistance. Therefore, the dissipative size of the phase slip center is equal to the wire's length of  $\sim 100$  nm. The measured critical current of MoGe wires is close to the estimated depairing current and it diminishes with the wire's approaching the SI transition (Fig. 12). Some suppression of the critical current due to premature switching has also been observed.

## CONCLUSION

Suspended molecular templates have been used for the fabrication of sub-10-nm nanowires. This allowed an extensive research of 1-D superconductivity. The main results are: 1) The LAMH theory is tested in a wide range of temperatures and showed very good agreement with measurements carried on short wires ( $\sim 100$  nm), with  $R_N < R_Q$ . These wires behave as "true superconductors" and should approach zero resistance at zero temperature. 2) Deviations from the LAMH are observed on wires with  $R_N > R_Q$ . The Giordano model, involving quantum tunneling of phase slips, provides good fits for such wires. These wires should have a finite resistance at zero temperature. An insulating behavior is also observed in samples, which are short and satisfy the condition  $R_N > R_Q$ . Future work will address such issues as the origin of the superconductor-insulator transition and the nature of the insulating state.

## ACKNOWLEDGMENTS

This work was supported by NSF carrier grant DMR-01-34770. Part of the work was done in the Center for Microanalysis of Materials, University of Illinois, which is partially supported by the U.S. Department of Energy under grant DEFG02-91-ER45439.

## REFERENCES

- Likharev, K.K. Superconducting weak links. *Rev. Mod. Phys.* **1979**, *51*, 101–160.
- Likharev, K.K. *Dynamics of Josephson Junctions and Circuits*; Gordon and Breach: New York, 1986.
- Chen, W.; Rylyakov, A.V.; Patel, V.; Lukens, J.E.; Likharev, K.K. Rapid single flux quantum T-flip flop operating up to 770 GHz. *IEEE Trans. Appl. Supercond.* **1999**, *9*, 3212–3215.
- Makhlin, Yu.; Schön, G.; Shnirman, A. Quantum state engineering with Josephson-junction devices. *Rev. Mod. Phys.* **2001**, *73*, 357–400.
- Averin, D.V. Adiabatic quantum computation with Cooper pairs. *Solid State Commun.* **1998**, *105*, 659–664.
- Nakamura, Y.; Pashkin, Y.A.; Tsai, J.S. Coherent control of macroscopic quantum states in a single-Cooper-pair box. *Nature* **1999**, *398*, 786–788.
- Orlando, T.P.; Mooij, J.E.; Tian, L.; Van der Wal, C.H.; Levitov, L.; Lloyd, S.; Mazo, J.J. A superconducting vortex qubit. *Phys. Rev., B* **1999**, *60*, 15,398–15,413.
- Orlando, T.P.; Delin, K.A. *Foundation of Applied Superconductivity*; Addison-Wesley: Reading, MA, 1991.
- Skalare, A.; McGrath, W.R.; Bumble, B.; LeDuc, H.G.; Burke, P.J.; Verheijen, A.A.; Schoelkopf, R.J.; Prober, D.E. Large bandwidth and low noise in a diffusion-cooled hot-electron bolometer mixer. *Appl. Phys. Lett.* **1996**, *68*, 1558–1560.
- Giordano, N. Evidence of macroscopic quantum tunneling in one-dimensional superconductors. *Phys. Rev. Lett.* **1988**, *61*, 2137–2140.
- Bezryadin, A.; Lau, C.N.; Tinkham, M. Quantum suppression of superconductivity in ultrathin nanowires. *Nature* **2000**, *404*, 971–974.
- Lau, C.N.; Markovic, N.; Bockrath, M.; Bezryadin, A.; Tinkham, M. Quantum phase slips in superconducting nanowires. *Phys. Rev. Lett.* **2001**, *87*, 217003-1–217003-4.
- Matveev, K.A.; Larkin, A.I.; Glazman, L.I. Persistent current in superconducting nanorings. *Phys. Rev. Lett.* **2002**, *89*, 096802-1–096802-4.
- Zaikin, A.D.; Golubev, D.S.; van Otterlo, A.; Zimányi, G.T. Quantum phase slips and transport in ultrathin superconducting wires. *Phys. Rev. Lett.* **1997**, *78*, 1552–1555.
- Rafael, G.; Demler, E.; Oreg, Y.; Fisher, D.S. cond-mat/0302498. <http://xxx.lanl.gov>.
- Büchler, H.P.; Geshkenbein, V.B.; Blatter, G. Quantum fluctuations in thin superconducting wires of finite length cond-mat/0306617. <http://xxx.lanl.gov>.
- Kociak, M.; Kasumov, A.Yu.; Gueron, S.; Reulet, B.; Khodos, I.I.; Gorbatov, Yu.B.; Volkov, V.T.; Vaccarini, L.; Bouchiat, H. Superconductivity in ropes of single-walled carbon nanotubes. *Phys. Rev. Lett.* **2001**, *86*, 2416–2419.
- Smith, R.A.; Handy, B.S.; Ambegaokar, V. Width and magnetic-field dependence of the transition temperature in ultranarrow superconducting wires. *Phys. Rev., B* **2001**, *63*, 094513-1–094513-12.
- Xiong, P.; Herzog, A.V.; Dynes, R.C. Negative magnetoresistance in homogeneous amorphous superconducting Pb wires. *Phys. Rev. Lett.* **1997**, *78*, 927–930.
- Xiong, P.; Herzog, A.V.; Dynes, R.C. Negative magnetoresistance in homogeneous amorphous superconducting Pb wires. *Phys. Rev. Lett.* **1998**, *78*, 927–930.
- Miyazaki, H.; Takahide, H.Y.; Kanda, A.; Ootuka, Y. Quantum phase transition in one-dimensional arrays of resistively shunted small Josephson junctions. *Phys. Rev. Lett.* **2002**, *89*, 197001-1–197001-4.
- Rogachev, A.; Bezryadin, A. Superconducting properties of polycrystalline Nb nanowires templated



- by carbon nanotubes. *Appl. Phys. Lett.* **2003**, *83*, 512–514.
23. Graybeal, G.M.; Beasley, M.R. Localization and interaction effects in ultrathin amorphous superconducting films. *Phys. Rev., B* **1984**, *29*, 4167–4169.
  24. Yazdani, A.; Kapitulnik, A. Superconductor–insulator transition in two-dimensional a-MoGe thin films. *Phys. Rev. Lett.* **1995**, *74*, 3037–3040.
  25. Graybeal, J.M. *Ph.D. Thesis*; Stanford University: Stanford, CA, 1985.
  26. Orlando, T.P.; Delin, K.A. *Foundation of Applied Superconductivity*; Addison-Wesley: Reading, MA, 1991.
  27. Tinkham, M. *Introduction to Superconductivity*, 2nd Ed.; McGraw-Hill: New York, 1996.
  28. Mermin, N.D.; Wagner, H. Absence of ferromagnetism or antiferromagnetism in one- or two-dimensional isotropic Heisenberg models. *Phys. Rev. Lett.* **1966**, *17*, 1133–1136.
  29. Little, W.A. Decay of persistent currents in small superconductors. *Phys. Rev.* **1967**, *156*, 396–403.
  30. Langer, J.S.; Ambegaokar, V. Intrinsic resistive transition in narrow superconducting channels. *Phys. Rev.* **1967**, *164*, 498–510.
  31. McCumber, D.E.; Halperin, B.I. Time scale of intrinsic resistive fluctuations in thin superconducting wires. *Phys. Rev., B* **1970**, *1*, 1054–1070.
  32. Lukens, J.E.; Warburton, R.J.; Webb, W.W. Onset of quantized thermal fluctuations in “one-dimensional” superconductors. *Phys. Rev. Lett.* **1970**, *25*, 1180–1183.
  33. Newbower, R.S.; Beasley, M.R.; Tinkham, M. Fluctuation effects on the superconducting transition of tin whisker crystals. *Phys. Rev., B* **1972**, *5*, 864–868.
  34. Tinkham, M.; Lau, C.N. Quantum limit to phase coherence in thin superconducting wires. *Appl. Phys. Lett.* **2002**, *80*, 2946–2948.
  35. Bollinger, A.T.; Bezryadin, A.; Rogachev, A.; Remeika, M. The effect of morphology on the superconductor-insulator transition in 1-D nanowires. *in press*.
  36. Kelly, K.F.; Chiang, I.W.; Michelson, E.T.; Hauge, R.H.; Margrave, J.L.; Wang, X.; Scuseria, G.E.; Radoff, C.; Halas, N.J. Insight into the mechanism of sidewall functionalization of single-walled nanotubes: an STM study. *Chem. Phys. Lett.* **1999**, *313*, 445–450.
  37. Zhang, Y.; Dai, H. Formation of metal nanowires on suspended single-walled carbon nanotubes. *Appl. Phys. Lett.* **2000**, *77*, 3015–3017.
  38. Bezryadin, A.; Dekker, C. Nanofabrication of electrodes with sub-5 nm spacing for transport experiments on single molecules and metal clusters. *J. Vac. Sci. Technol., B* **1997**, *15*, 793–799.
  39. Oreg, Y.; Finkelstein, A.M. Suppression of  $T_c$  in superconducting amorphous wires. *Phys. Rev. Lett.* **1999**, *83*, 191–194.
  40. Park, S.I.; Geballe, T.H. Superconducting tunneling in ultrathin Nb films. *Phys. Rev. Lett.* **1986**, *57*, 901–904.
  41. Penttilä, J.S.; Parts, Ü.; Hakonen, P.J.; Paalanen, M.A.; Sonin, E.B. Superconductor–insulator transition in a single Josephson junction. *Phys. Rev. Lett.* **1999**, *82*, 1004–1007.
  42. Miyazaki, H.; Takahide, Ya.; Kanda, A.; Ootuka, Yo. Quantum phase transition in one-dimensional arrays of resistively shunted small Josephson junctions. *Phys. Rev. Lett.* **2002**, *89*, 197001-1–197001-4.
  43. Tidecks, R. *Current-Induced Nonequilibrium Phenomena in Quasi-One-Dimensional Superconductors*; Springer: Berlin, 1990; 138 pp.
  44. Tinkelman, M.; Free, J.U.; Lau, C.N.; Markovic, N. Mysteretic I-V curves of superconducting nanowires. *Phys. Rev. B* **2003**, *68*, 134515-1–134515-7.
  45. Song, Y. Origin of capacitance in superconducting microbridges. *J. Appl. Phys.* **1976**, *47*, 2651–2655.

# Supramolecular Networks Synthesized in Nanoparticle–Polymer Mixtures

Anna C. Balazs

Gavin A. Buxton

*Department of Chemical Engineering, University of Pittsburgh,  
Pittsburgh, Pennsylvania, U.S.A.*

## INTRODUCTION

The dispersion of solid nanoparticles within a polymeric matrix can dramatically improve the mechanical, thermal, or electrical properties of the material.<sup>[1]</sup> One of the challenges in fabricating such composites is controlling the distribution of the particles in the polymer. However, in multicomponent mixtures that involve blends of different polymers and the nanoparticles, one can exploit the polymer–polymer and polymer–particle interactions to direct the distribution of nanoparticles within the mixture. For example, consider the case where the polymer matrix is composed of a binary blend of A and B homopolymers. Most polymer pairs are immiscible and thus these blends usually undergo phase separation. Typically, one of the polymers in the blend preferentially absorbs onto, or wets, the particles; in particular, coating the particles with A-like chains provides a mechanism for obtaining the preferential wetting interaction between the particles and the A polymers. Now the interplay between the A/B phase separation and the polymer–particle wetting interactions controls the structure of the composite.<sup>[2]</sup> In particular, the A-like particles localize in the A domains, and depending on the composition of the AB blend, these solids can form a continuous network throughout the material or segregate into A domains that are dispersed in the B matrix.<sup>[3]</sup> The former case is of particular importance because particles that have percolated into an interconnected network can enhance the electrical or mechanical integrity of the system.

In a previous study,<sup>[4]</sup> we used computer simulations to determine the behavior of nanoscale rods that are immersed in a binary, phase-separating blend. The situation becomes even more complicated than the scenario described above because the rods can form liquid crystalline phases. Here the interplay among three phenomena—phase separation, wetting, and anisotropic interparticle interactions—controls the morphology of the material. We found that such

cooperative effects drive the rods to form a percolating structure at very low volume fractions of the nanoparticles. In effect, the rods form a supramolecular network that extends throughout the polymer matrix. These studies revealed that the synergistic interactions among the components provide a means of manipulating the motion of the nanoscopic objects and directing their association into extensive structures.

In addition to harnessing the phase separation of polymer blends, one can exploit the microphase separation of diblock copolymers to control the dispersion of nanoparticles.<sup>[5]</sup> Diblock copolymers are composed of an A chain that is chemically linked to a B chain. Although the A and B chains are incompatible, the diblocks cannot undergo macroscopic phase separation because of the chemical linkage between the two blocks. Instead, at a critical temperature, the diblocks microphase separate into spatially periodic structures that can exhibit spherical, cylindrical, lamellar, and other more complex geometries. Adding particles that are preferentially wetted by one of the blocks can yield spatially ordered hybrid materials. For example, adding particles to the cylindrical phase of the diblocks can result in the formation of solid “nanowires” that extend throughout the material.<sup>[6,7]</sup> If these nanoparticles are metals or semiconductors, the composite can exhibit the unique electrical, optical, or magnetic properties of the inorganics and the flexibility and processibility of the polymers. In addition, the “columns” of particles provide significant reinforcement of the polymer matrix and thus improve the mechanical properties of the material.

## OVERVIEW

Recently, there has been considerable interest in blending nanoparticles and diblock copolymers to create flexible batteries, photonic band gap devices, nanoelectrode arrays, and polymer/clay nanocomposites with significant mechanical strength and toughness.<sup>[5]</sup>

A major challenge in designing such complex materials is predicting the macroscopic behavior of the composite based upon such constituent characteristics as the diblock composition and the nanoparticle surface chemistry. By addressing this challenge, researchers could ultimately understand how choices made in the initial design stage affect the final material's performance and facilitate the efficient fabrication of composites with the desired properties.

In this entry, we describe a means of tackling this challenge by integrating two different computational approaches and thereby relating the polymer architecture, the wetting interactions between the polymer and particles, the structure of the mixture, and the mechanical behavior of the resulting material.<sup>[8]</sup> In particular, we use a hybrid method<sup>[5,8]</sup> that combines a Cahn–Hilliard (CH) model for the diblocks and a Brownian dynamics (BD) simulation for the particles to determine the structural evolution of the particle-filled copolymer melt. As we detail further below, the approach allows us to specify the architecture of the chains and the nature of the polymer–particle interactions. In this entry, we will refer to this hybrid method as the CH/BD model. In recent computational studies that involve this CH/BD model,<sup>[5]</sup> we showed that in the presence of the AB diblocks, A-like particles form a percolated network at a significantly lower volume fraction (essentially half) than would be required in a homogeneous material (i.e., homopolymer melt). In this study, one of our aims is to determine how these percolating networks act to reinforce the copolymer matrix.

To accomplish the above aim, we use the output of the CH/BD simulation as the input to the Lattice Spring Model (LSM), a micromechanical model that captures the elastic properties and mechanical response of the composite. By combining the CH/BD and LSM models, we can determine how the structural evolution, or the history of the material, affects the mechanical response.<sup>[9]</sup> Furthermore, we do not have to make ad hoc assumptions about the distribution of particles in the system; this distribution evolves naturally from the self-assembling interactions between the different components. Through the LSM, we can carry out three-dimensional simulations that include as many as 1564 particles.<sup>[8]</sup> The results allow us to determine how changes in the nature of the components influence the macroscopic properties of the composite.

In the section below, we provide a brief description of the simulation techniques for modeling the structural evolution of diblock/particle mixtures and the micromechanics of solid polymeric composites. In “Results and Discussion,” we investigate the effects of varying the diblock copolymer architecture and particle volume fraction on the morphological and mechanical behavior. The effects of size and polydispersity in the particle systems are also investigated.

In the final section, a summary of results is provided and conclusions are drawn.

## THE MODELS

### Determining the Morphology of Diblock/Particle Mixtures

The system consists of an AB diblock copolymer melt and mobile nanoparticles. We simulate the behavior of this mixture on a three-dimensional cubic lattice, which is  $64^3$  sites in size and has periodic boundary conditions in all three directions. The copolymer melt is characterized by the scalar-order parameter,  $\psi(\mathbf{r}) = \phi_A(\mathbf{r}) - \phi_B(\mathbf{r})$ , which describes the local concentration difference between the A and B components. Note that  $\psi(\mathbf{r}) = -1$  (1) corresponds to the equilibrium order parameter for A-rich (B-rich) phase. In this version of the model, the particles in the system are “soft” or penetrable because we neglect excluded volume interactions between the particles and the fluid. (Excluded volume interactions can be explicitly included in the model;<sup>[5]</sup> for corresponding systems, both the “hard” and “soft” fillers yield similar results for the particle distributions.) The particles have an affinity for the A block. This affinity is introduced via a polymer–particle coupling term in the free energy (as described below). Thus the microphase separation of the diblocks can affect the spatial distribution of the particles, and the particles can influence the size and morphology of the polymer domains.

The Cahn–Hilliard (CH) equation<sup>[10,11]</sup> describes the phase separation of a binary mixture by spinodal decomposition in the absence of hydrodynamics. The dynamics of microphase segregation for a diblock copolymer melt is described by the traditional CH equation with the addition of the term  $-\Gamma(\psi - f)$ , where  $\Gamma$  determines the thickness of the domain structure and  $f$  describes the asymmetry of the diblock.<sup>[12]</sup> The case of  $f = 0$  describes a 50:50 symmetric diblock. The kinetic equation for the order parameter for this system is:

$$\partial\psi/\partial t = M\nabla^2(\partial F\{\psi\}/\partial\psi) - \Gamma(\psi - f) + \xi \quad (1)$$

where  $M$  is the kinetic coefficient (mobility) of the order parameter field and  $\xi$  is the noise field (which is presently set to 0).  $F$  is the local energy term and is given by  $F = F_d + F_{\text{cpl}}$ . In the current study,  $F_d$  is given by

$$F_d = \int [-A \log(\cosh(\psi)) + \psi^2/2 + D(\nabla\psi)^2/2] \partial r \quad (2)$$

where  $A$  and  $D$  are material-specific parameters and the integration is over the volume of the system.

The nanoparticles are introduced through the coupling free energy,  $F_{\text{cpl}}$ . This free energy describes the interaction between the “soft” particles and the polymer and ensures that the forces on the particle as a result of the presence of the polymer induce equal and opposite forces within the polymer. The coupling free energy is of the form

$$F_{\text{cpl}}\{\psi\} = \int \sum_i U(r - x_i)(\psi(r) - \psi_s)^2 \partial r \quad (3)$$

where  $x_i$  is the position of the  $i$ th particle and  $\psi_s$  is the desired value of the order parameter at the particle surface. To model the fact that the particles have an affinity for the A phase, we set  $\psi_s = -1$ . The potential  $U(r - x_i)$  is non-linear and is given by

$$U(r - x_i) = \begin{cases} C \exp(-(r - x_i - R)/r_0) & \text{for } (r - x_i) > R \\ C & \text{for } (r - x_i) < R \end{cases} \quad (4)$$

where  $C$  captures the strength of the wetting interaction,  $r_0$  sets the range of this interaction, and  $R$  is the radius of the particle.

The motion of the particles is dictated by the Langevin equation

$$\partial x_i / \partial t = -M_p (\partial F_{\text{cpl}} / \partial x_i) + \eta \quad (5)$$

where  $M_p$  is the particle mobility and  $\eta$  is a Gaussian white noise term. There is an effective excluded volume interaction between the particles; if a given particle moves to a position that is already occupied by a particle, the move is rejected. Through the coupled Eqs. (1) and (5), the ordering dynamics of the diblock copolymers is integrated with the diffusive motion of the nanoparticles.

A Cell Dynamical Systems (CDS), or Cellular Automaton, methodology is used to evolve the order parameter field for the microphase-separating copolymer melt.<sup>[13,14]</sup> The use of CDS [rather than a conventional discretization of Eq. (1)] significantly reduces the computational expense of the simulations.

### Determining the Micromechanical Behavior of Solid Polymeric Composites

A Lattice Spring Model (LSM) enables the micromechanical investigation of a solid polymer to be undertaken.<sup>[8,9,15,16]</sup> Through the model, the continuum elastic behavior of a given material is discretized and mapped onto a simple cubic lattice. This lattice consists of a network of nearest and next-nearest neighbor interactions, which are harmonic in nature. These

harmonic interactions (springs) result in linear forces between lattice sites (nodes), which enable the emergence of linear elastic behavior. The energy associated with a site or node  $m$  in the lattice is taken to be of the form

$$E_n = (1/2) \sum_m (\mathbf{u}_m - \mathbf{u}_n) \cdot \mathbf{M}_{mn} \cdot (\mathbf{u}_m - \mathbf{u}_n) \quad (6)$$

where the summation is over all the neighboring nodes,  $n$ , connected to  $m$  by a spring. The term  $\mathbf{u}_m$  is the displacement of node  $m$  from its original position, and  $\mathbf{M}_{mn}$  is a symmetric matrix that introduces the elastic properties of the springs, through  $k$  and  $c$ , the central and noncentral force constants, respectively.

It has been shown that this system of springs obeys, to first order in the displacement, the equations of continuum elasticity theory for an isotropic elastic medium, whose elastic constants can be determined in terms of the elements of the matrices  $\mathbf{M}_{mn}$ .<sup>[15]</sup> These elastic constants are the Young's modulus,  $E$ , and Poisson's ratio,  $\nu$ , which are of the form.<sup>[15]</sup>

$$\begin{aligned} E &= (5k(2k + 3c))/(4k + c) \\ \nu &= -(k - c)/(c + 4k) \end{aligned} \quad (7)$$

The force constants are initially assigned to the nodes. Nodes that exist within the boundaries of the inclusions are assigned different force constants than nodes that exist within the matrix. The force constants for the bonds are averaged from the nodes that they connect.

The harmonic form of the energy results in forces that are linearly dependent upon the displacement of the nodes. If forces are applied to the nodes, and the spring constants are specified, then the nodal displacements can be obtained through a set of sparse linear equations. These equations are solved using a conjugate gradient method to find the equilibrium configuration that corresponds to no net force at each node.<sup>[15]</sup>

To present relevant deformation fields, the stress and strain tensors are calculated from these forces and displacements. The strain tensor can be obtained through a finite difference approximation of the displacement field. A central difference approximation can be used

$$\begin{aligned} \delta_x u_{(i,j,k)} &= (-u_{(i+2,j,k)} + 8u_{(i+1,j,k)} - 8u_{(i-1,j,k)} \\ &\quad + u_{(i-2,j,k)})/12h \end{aligned} \quad (8)$$

where  $u_{(i,j,k)}$  is the displacement field at coordinates  $i$ ,  $j$ , and  $k$  and  $h$  is the initial distance between adjacent nodes; alternatively, forward or backward approximations are considered at system boundaries. The stress tensor is directly obtainable from the forces acting on

a node (the center of a cubic unit cell),<sup>[17]</sup>

$$\sigma_{ij} = \sum_m F_m \cdot \mathbf{n}_{ij}^m / A \quad (9)$$

Here  $\sum$  represents a sum over the cube surfaces,  $F_m$  is the force<sup>m</sup> on any surface  $m$  of the cubic cell, while  $\mathbf{n}_{ij}^m$  is a unit vector either normal or parallel to the surface  $m$ , and  $A$  is the surface area. The scalar stress and strain values quoted here correspond to the normal stress and strain components in the tensile direction.

To assess the effective reinforcement provided by the particles within the composite, we determine the relative quantities  $(F - F_0)/F_0$ , where  $F$  is the field in question and  $F_0$  is the homogeneous response of the unreinforced polymeric matrix. The average strain in the system can be determined through the average nodal displacements at the system boundaries, in the tensile direction. The average strain and the applied stress can then be used to calculate the Young's modulus (stress of a material divided by its strain). This allows the global stiffness of this locally heterogeneous material to be determined.

As noted above, the elastic properties of the springs within a LSM simulation are assigned values depending upon whether the node is situated within a particle or the polymer matrix, as dictated by the results of the CH/BD calculation. To accurately capture the deformation fields in the vicinity of the particles within the LSM, the system size is doubled from that of the CH/BD simulation. A LSM consisting of  $148^3$  nodes is utilized; the central  $128^3$  nodes are assigned elastic properties as a function of the particle and polymer positions in the CH/BD calculation. The system is extended by 10 unit lengths in all directions, taking values from the periodicity of the CH/BD simulation, therefore ensuring that all areas of the CH/BD model are represented by bulk nodes in the LSM simulation.

## RESULTS AND DISCUSSION

### Uniform Particle Size

We initially consider the effects of diblock copolymer architecture and volume fraction of monodisperse particles (that is, the particles are uniform in size) on the morphological and mechanical characteristics of the resultant composite. In the following simulations, the parameters  $M$  and  $M_p$  (in Eqs. (1) and (5), respectively) are set equal to 1. Three different diblock copolymers are considered, corresponding to the following parameters: 1)  $\Gamma = 0.004$  and  $f = 0.0$ , 2)  $\Gamma = 0.016$  and  $f = 0.0$ , and 3)  $\Gamma = 0.004$  and  $f = 0.2$  [see Eq. (1)]. The parameter  $\Gamma$  is inversely proportional to  $N^2$ , where  $N$  is the degree of polymerization of the

copolymer. Thus an increase in  $\Gamma$  corresponds to a decrease in the domain size. Varying  $f$  from 0.0 to 0.2 changes the A:B composition from 50:50 to 60:40. Hence by altering  $\Gamma$  and  $f$ , we can model the respective effects of varying the domain size and composition of the diblocks. A range of particle volume fractions, varying from 5% to 25%, is also considered, where the particle radius is 3 unit lengths (6 unit lengths in the LSM). This range in particle volume fraction corresponds to a variation in the number of particles from 116 to 580 in the simulations.

The morphology of a filled diblock copolymer system at late times ( $t = 50,000$ ) is presented in Fig. 1. The parameters of the diblock copolymer are  $\Gamma = 0.004$  and  $f = 0.0$ , and the volume fraction of particles is 20%. The isosurface of the diblock copolymer at an order parameter of zero (midway between phase A and phase B) is colored red, while the regions where a positive order parameter intersects the system boundaries (termed isocaps) are colored blue. In other words, the red regions mark the edge of the B phase and the transparent regions indicate the A phase. The system shows elements of lamellar ordering on a short scale; however, the lamellae are interconnected, and the overall morphology is closer to a bicontinuous structure. While the system will tend toward the thermodynamic limit of a perfect lamellar phase, the timescales for reaching this state through a dynamic model are prohibitively large. In experimental systems, similar morphologies are found because again, it takes long times to reach perfectly ordered phases and the system can get kinetically trapped.

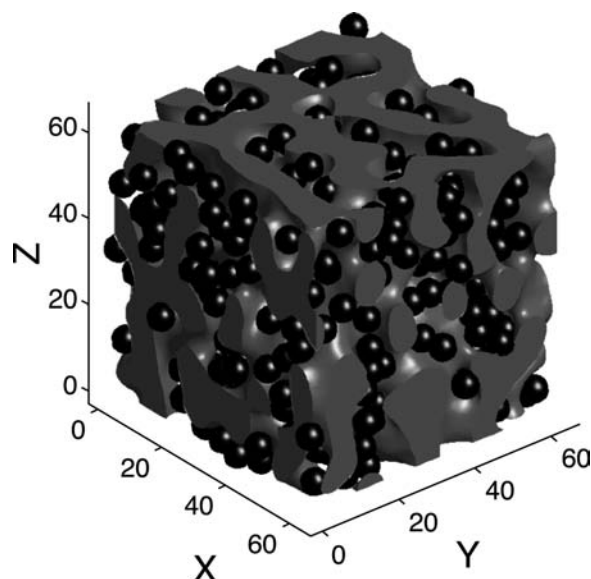


**Fig. 1** Three-dimensional morphology of a filled diblock copolymer system. An isosurface in between the A and B components is colored red, isocaps are colored blue, and the particles are colored black.

The black spheres in Fig. 1 are the particles, which are clearly confined within the transparent A phase of the diblock. The particles appear to form a continuous network within the polymer matrix. In effect, the interplay between the microphase separation of the diblocks and the particle–block wetting interactions has influenced the distribution of the solids within the system.

To quantify the confinement of the nanoparticles within the diblock copolymer domains, we calculate the particle correlation function. The particle correlation function adopted in this study is defined as  $V \sum_i \sum_{j \neq i} \delta(r - r_{ij}) / (4\pi r^2 N_p^2)$ , where  $V$  is the volume of the system and  $N_p$  is the number of particles. The results are averaged over three independent runs and plotted in Fig. 2. For clarity, only two diblock copolymer systems are shown ( $\Gamma = 0.004$  and  $\Gamma = 0.016$  at  $f = 0.0$ ) as the third exhibited similar results. There is only one discernible peak at a distance of 6 unit lengths, which corresponds to the diameter of the particles. This reveals that the system of particles exhibits strong short-range order, but does not display long-range order. The particles are forced to lie within close proximity of each other because of the confinement within the diblock copolymer, but long-range order is suppressed because of the tortuous structure of the diblock domains. For comparison, the particle correlation function for an equivalent number of randomly dispersed particles, which exhibit no such confinement, is also presented. As can be seen, there is no local ordering of the particle positions, and the peaks observed in the diblock copolymer systems are no longer present.

It is the clustering of the diblock-confined particles that is of primary interest in this study. To characterize

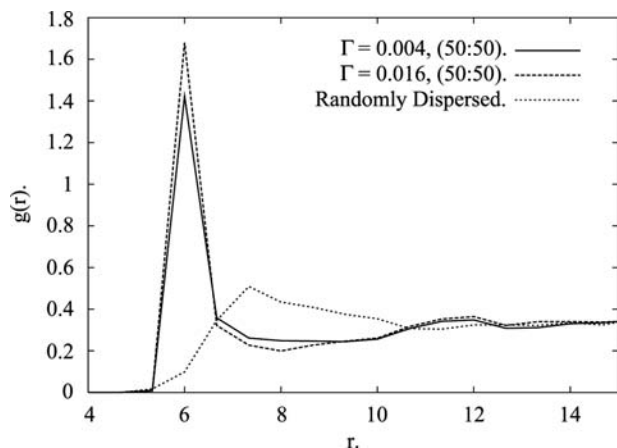


**Fig. 2** The pair correlation function [defined as  $g(r) = V \sum_i \sum_{j \neq i} \delta(r - r_{ij}) / (4\pi r^2 N_p^2)$ ] for particles confined in two diblock copolymer systems and for randomly dispersed particles.

the particle clusters, and determine whether or not geometric percolation occurs when the volume fraction of particles is 20%, we define particles that are closer than a certain distance to be part of the same cluster. Here we adopt a unit length in the LSM simulations as this characteristic distance. Using this definition, we find that the particles confined within the diblocks do in fact form a percolating cluster. (We note that Ginzburg, Qui, and Balazs<sup>[5]</sup> found the percolation threshold for particles confined in a similar diblock matrix to be approximately 10%.) At 20%, however, the randomly dispersed particles do not form such a supramolecular network. (The site percolation threshold for the simple cubic lattice is equal to 31%.<sup>[5]</sup>)

To assess the consequences of such morphological variations upon the resultant mechanical properties of the macroscopic material, we now use the output from our hybrid CH and Langevin dynamics simulations as the input for the LSM. The elastic deformation of the structures is undertaken, with both the force constants of the A and B phases being set to unity, while the particles are assigned a force constant of 100. Thus the effects of particle distribution are of primary interest in the current investigations, and the parameters are consistent with experimental values for filled polymers.<sup>[18]</sup>

The local relative strain field, as a result of the application of a constant stress at the simulation boundaries, for a system where the particles are confined within the domains of a diblock copolymer ( $\Gamma = 0.004$  and  $f = 0.0$ ) is depicted in Fig. 3A. The corresponding relative strain field for a system consisting of randomly dispersed particles is presented in Fig. 3B. The three-dimensional strain fields are displayed as orthogonal contours through the simulation. In both systems, the volume fraction of particles is 20%. The particles are clearly apparent as the dark regions of low strain. In particular, the strain values within the particles are significantly lower than that of the matrix because of the large disparity in elastic constants. The inability of stiff particles to deform to the same extent as the neighboring matrix results in strain concentrations at the particle–matrix interface. These strain concentrations lie along the tensile direction and emanate from the center of a particle. Perpendicular to the tensile direction, the lower deformations within the particle inhibit the deformation of the matrix and results in lower strain fields.

It is apparent from Fig. 3A that the diblock-confined particles are clustered together, forming a percolating network, while the particles in Fig. 3B are more randomly dispersed. The percolating structure inhibits the deformation of the entire material and results in significant reductions in the strain fields, as can be seen by the presence of the dark red domains in Fig. 3A. Alternatively, the randomly dispersed



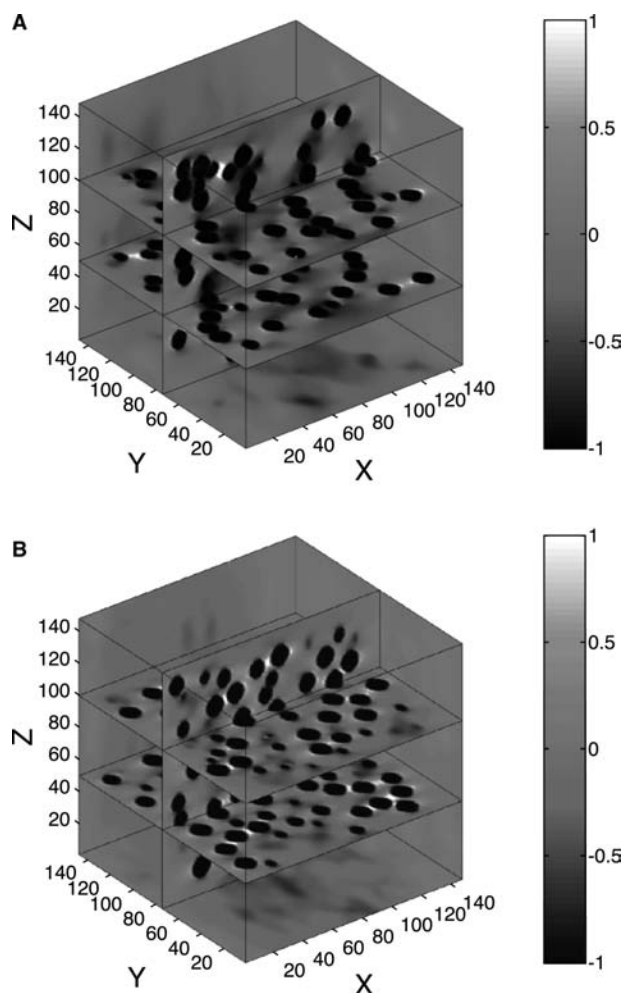


**Fig. 3** The relative strain fields [defined as  $(F - F_0)/F_0$ , where  $F_0$  is the response of the unreinforced polymeric matrix] for (A) a system where the particles are confined within the domains of a diblock copolymer and (B) a system consisting of randomly dispersed particles.

system shows isolated regions of strain relaxation within the particles, but the inhibition of the neighboring matrix is less dramatic than in Fig. 3A. Consequently, the strain concentrations (shown in yellow and white) within the matrix of the randomly dispersed system are also more pronounced as regions within the matrix attempt to deform to the same extent as domains that neighbor the scattered particles. Such areas of strain concentration are less apparent in Fig. 3A. These plots indicate that the confinement of nanoparticles within one of the domains of the bicontinuous structure leads to a continuous network of stiff material, which reduces the overall strain field within the system.

To quantify the deformation of the above confined and randomly dispersed particle systems, the cumulative distribution functions of the local strain fields are plotted in Fig. 4. The cumulative distribution function

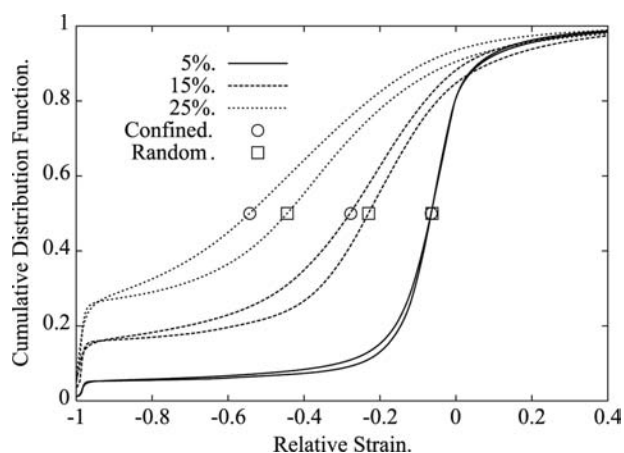


**Fig. 4** The cumulative distribution function of the relative local strain field for systems consisting of randomly dispersed particles and systems where the particles are confined within the domains of a diblock copolymer.

is defined as the probability that the field in the system takes a value less than or equal to a specific amount. A comparison between confined and randomly dispersed particle systems is made for particle volume fractions varying from 5% to 25%. The lower strains are invariably associated with the stiffer particles, while the regions of higher strains correspond to the matrix. At 5%, there would appear to be little difference between the two systems because the confined particles do not percolate at such a low value. At higher particle volume fractions, the disparity between the two systems becomes more apparent, with the confined particle systems possessing significantly lower strain fields. As noted above, the geometric percolation

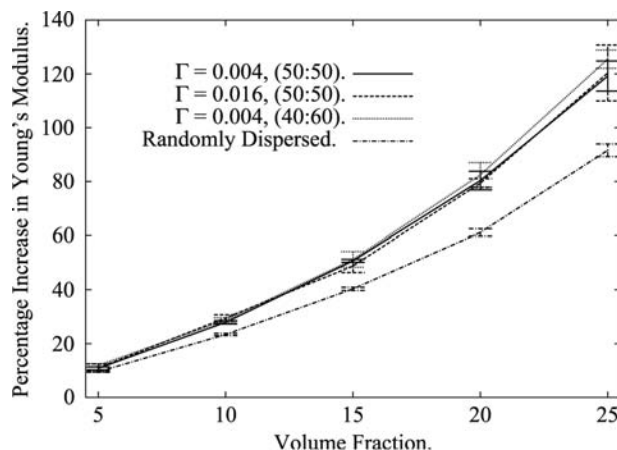


**Fig. 5** The percentage increase in Young's modulus as a function of particle volume fraction. Systems containing particles confined within the domains of various diblock copolymers are compared with a system consisting of randomly dispersed particles.

inhibits the local strain fields and therefore stiffens the composite material.

In Fig. 5, we plot the percentage increase in the Young's modulus relative to the unreinforced polymer for the various systems described above. This parameter is a measure of the macroscopic mechanical properties of these composites. The results are averaged over three independent runs, with the error bars indicating the standard deviation. The three cases involving particles confined within the domains of diblock copolymers are significantly stiffer than the system containing randomly dispersed particles. There is no clear difference between the three confined particle systems, with the error bars showing a clear overlap. For the systems studied here, it is not possible to distinguish effects that diblock copolymer architecture or composition may have on the reinforcement efficiency of the nanoparticle fillers. There is, however, a significant benefit to confining the particles within the diblock copolymer domains.

### Binary Particle Systems

We also investigate the effects of adding a binary particle mixture to the copolymer matrix. The particles in the binary mixture are chemically identical (that is, they both favor the A phase) but differ in size. The smaller particles have a radius of 2, and the larger particles have a radius of 3 unit lengths. The total volume fraction of particles is held fixed at 20%. Note that at a fixed particle volume fraction, decreasing the size of the particles results in an increase in the total number of particles. The ratio of small to large fillers is varied between the limiting cases of all small (1564 particles) and all large (464 particles). These studies provide insight into the role that polydispersity in particle size plays in the distribution of particles within the matrix and, consequently, the mechanical properties of the composite. In these studies, the parameters that characterize the diblock copolymers are fixed at  $\Gamma = 0.004$  and  $f = 0.0$ .

Fig. 6 shows the morphology for a system containing 10% of large and 10% of small particles. The particles are again clearly confined within the A domains of the diblock copolymer. It is also clear from Fig. 6 that the small particles can readily penetrate and localize in regions between the large particles. We can characterize this arrangement quantitatively by measuring  $P$ , the fraction of particles that are a part of the largest cluster. When  $P$  is close to 1, almost all the particles belong to one cluster; when  $P$  is close to 0, the particles form many small clusters. In Fig. 7, we plot  $P$  as a function of the volume fraction of small particles. The results are averaged over three runs, with the error bars corresponding with the standard deviation.

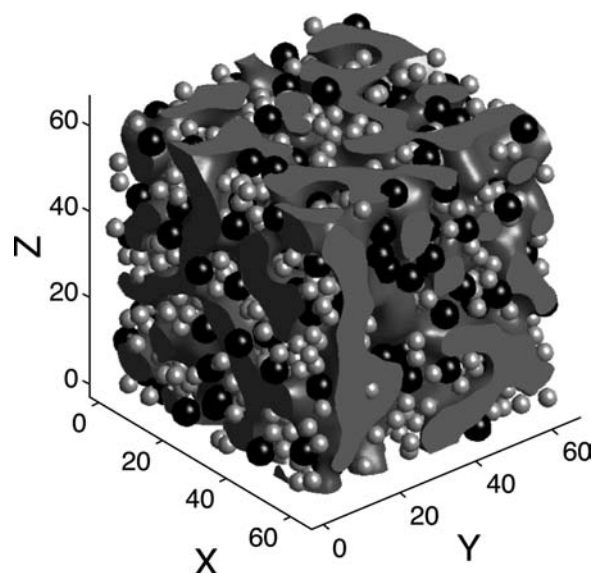


**Fig. 6** Three-dimensional morphology of a filled diblock copolymer system. An isosurface in between the A and B components is colored red, isocaps are colored blue, and the small and large particles are colored black and gray, respectively.

Geometric percolation occurred in all systems. Because at a fixed volume fraction there are a greater number of small particles than large ones, these fillers would be expected to cluster to a greater extent than the larger species (as the characteristic distance used to indicate clustering is not radius-dependent, but is fixed at one unit in our studies). This is in fact the case, with the fraction of particles in the main cluster approaching 1 with increasing number of small particles.

The introduction of a relative fraction of small particle also results in an effective increase in the

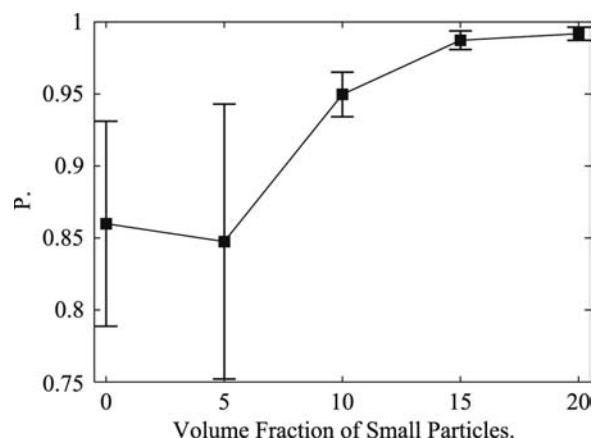


**Fig. 7** The fraction of particles that are a part of the largest cluster as a function of the volume fraction of small particles. The overall volume fraction of small and large particles is maintained at 20%.

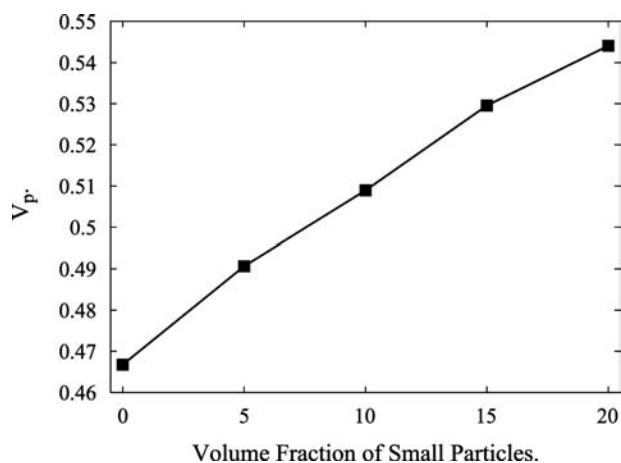


**Fig. 8** The volume fraction of polymeric material that is within a given distance (a unit length) of any particles,  $V_p$ , as a function of the volume fraction of small particles.

particulate surface area (because of the increase in the total number of particles). Consequently, there is a greater surface area available for possible polymer–particle interactions. To illustrate this point, we define  $V_p$  as the volume fraction of polymeric material (A and B) that is within a given distance (a unit length) of any particles and plot  $V_p$  as a function of the volume fraction of small particles (Fig. 8). The results are averaged over three runs and the standard deviations were found to be negligible. As the volume fraction of small particles is increased, the particles come in contact with and affect a greater volume of the matrix. This behavior, as well as the increase in clustering in the bidisperse system, is expected to translate through to the mechanical properties.

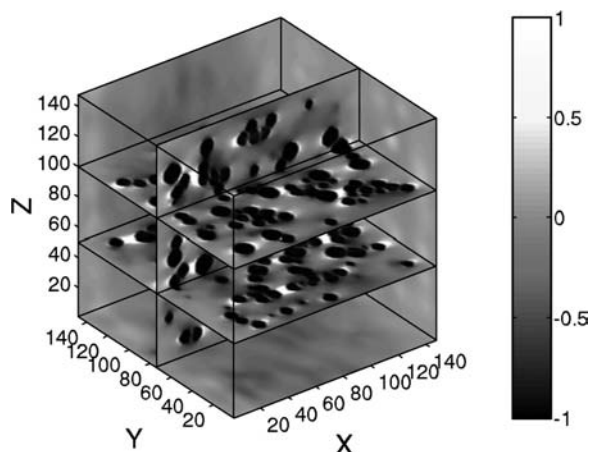


**Fig. 9** The relative strain fields [defined as  $(F - F_0)/F_0$ , where  $F_0$  is the response of the unreinforced polymeric matrix] for a system containing a 10% volume fraction of small and a 10% volume fraction of large particles, confined within the domains of a diblock copolymer.

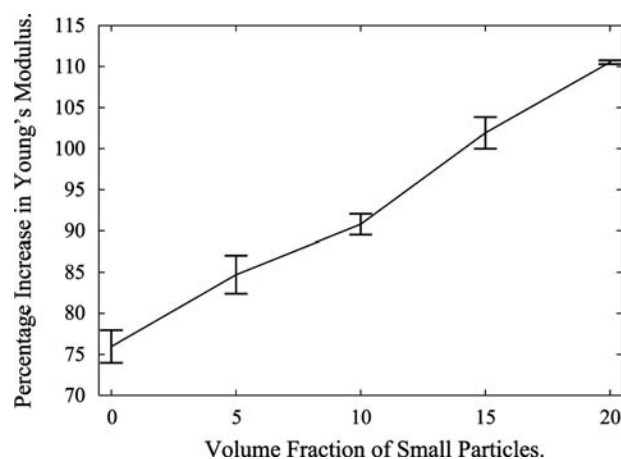


**Fig. 10** The percentage increase in Young's modulus as a function of small particle volume fraction. The overall volume fraction of small and large particles is maintained at 20%.

Fig. 9 reveals the relative strain field for a system containing 10% large particles and 10% small particles. The regions of low strain, corresponding to the stiffer particles, are clearly observed as before. Now, however, the clustering of particles is more apparent than that in Fig. 3A. A significant difference between the cases in Figs. 3A and 9 is the area over which these particles cluster. The smaller particles spread out over a greater volume of the material and inhibit the deformation of the matrix to a greater degree than in the system containing just large particles. Effectively, a larger volume of polymer matrix is trapped or surrounded by the particles and therefore less capable of deforming.

The lower strain fields as a result of the decrease in particle size have a direct impact on the Young's modulus of the macroscopic material. The percentage increase in Young's modulus is plotted in Fig. 10, as a function of the volume fraction of small particles. The data are averaged over three runs, where the error bars represent the standard deviations. An increase in Young's modulus of over 30% is observed as the particle size is altered from all large to all small. This is attributable to an increase in the total particle surface area, a greater degree of clustering, and an increase in the volume of polymeric material that is effectively trapped by the particles. These effects result in lower strains throughout the system and hence an increase in the global Young's modulus.

## CONCLUSION

Through a combination of numerical techniques, we were able to interrelate the structure and micro-mechanical behavior of the copolymer/nanoparticle

composites. Through the CH/BD calculations, we could determine the effects of the microphase separation of the diblocks on the spatial distribution of the mobile particles. Through the LSM, we could capture the elastic deformation of the resultant hybrid material. Furthermore, we could investigate the behavior of systems that contain up to 1564 particles. For randomly dispersed fillers, simulations involving a relatively low number of particles can be sufficient to describe the overall stiffness of the material and thus be large enough to encompass a Representative Volume Element (RVE) of the composite. However, the tortuous spatial arrangement of particles confined in diblock copolymers introduces an additional length scale, that of the domain size. To determine the mechanical behavior of such complex materials, it is important to consider the morphology of a sufficiently large system that captures both the unique structural characteristics of the copolymer domains and the particles' spatial arrangement, which is, in part, templated by these diblock domains. The LSM has proven to be ideally suited for simulating the micromechanics of such large systems. While the utility of the LSM in analyzing two-dimensional RVEs has recently been reported,<sup>[19]</sup> it would appear that this technique might also prove useful in similar three-dimensional analyses.

Through the selective incorporation of nanoparticles into the domains of a diblock copolymer, three-dimensional bicontinuous nanoparticle structures were formed. As the volume fraction of particles was increased, geometric percolation of the particles occurred, and the particles effectively formed a rigid network throughout the system. The deformations within the polymer matrix are significantly suppressed by the presence of this rigid nanostructural network, and the global stiffness of the material is notably increased. It is worth noting that for materials containing randomly dispersed spheres, rods, and platelets, the rods and platelets offer superior reinforcement over the spheres.<sup>[16]</sup> Therefore the mechanical properties of diblock copolymers filled with such high aspect ratio particles may prove to be of particular interest.

Varying the size of the monodisperse particles and introducing bidispersity in the particle size were shown to exert an appreciable influence over both the morphology of the diblock copolymer and the resultant mechanical properties of the solid material. Systems containing small fillers exhibited a greater degree of clustering between the particles. This behavior could explain the increased stiffness that was observed in the corresponding macroscopic material. Also, of considerable consequence is the volume of polymeric material that is effectively trapped between neighboring nanoparticles. For a fixed volume fraction of particles, as the particle size is decreased, the number

of particles increases. Consequently, the volume of material in which the particles are dispersed increases, and the deformation of a greater volume of interparticle polymeric material is inhibited.

We conclude that the inclusion of nanoparticles into a bicontinuous diblock copolymer structure results in a significant increase in the reinforcement efficiency of the fillers. As polymeric nanocomposites become increasingly important, such confinement effects will play a dominant role in optimizing their mechanical behavior and result in an expansion of potential applications to which such novel materials could be employed.

## ACKNOWLEDGMENTS

A.C.B. gratefully acknowledges financial support from the DOE and NSF.

## REFERENCES

1. Karim, A.; Douglas, J.F.; Nisato, G.; Lui, D.W.; Amis, E.J. Transient target patterns in phase separating filled polymer blends. *Macromolecules* **1999**, *32* (18), 5917–5924.
2. Tanaka, H.; Lovinger, A.J.; Davis, D.D. Pattern evolution caused by dynamic coupling between wetting and phase-separation in binary-liquid mixture containing glass particles. *Phys. Rev. Lett.* **1994**, *72* (16), 2581–2584.
3. Balazs, A.J.; Ginzburg, V.V.; Qui, F.; Peng, G.W.; Jasnow, D. Multi-scale model for binary mixtures containing nanoscopic particles. *Phys. Chem., B* **2000**, *104* (15), 3411–3422.
4. Peng, G.W.; Qiu, F.; Ginzburg, V.V.; Jasnow, D.; Balazs, A.C. Forming supramolecular networks from nanoscale rods in binary, phase-separating mixtures. *Science* **2000**, *288* (5472), 1802–1804.
5. Ginzburg, V.V.; Qui, F.; Balazs, A.C. Three-dimensional simulations of diblock copolymer/particle composites. *Polymer* **2002**, *43* (2), 461–466.
6. Thompson, R.B.; Ginzburg, V.V.; Matsen, M.W.; Balazs, A.C. Predicting the mesophases of copolymer–nanoparticle composites. *Science* **2001**, *292* (5526), 2469–2472.
7. Thompson, R.B.; Ginzburg, V.V.; Matsen, M.W.; Balazs, A.C. Block copolymer-directed assembly of nanoparticles: forming mesoscopically ordered hybrid materials. *Macromolecules* **2002**, *35* (3), 1060–1071.
8. Buxton, G.A.; Balazs, A.C. Simulating the morphology and mechanical properties of filled diblock copolymers. *Phys. Rev., E* **2003**, *67*, 031802–031814.
9. Buxton, G.A.; Balazs, A.C. Predicting the mechanical properties of binary blends of immiscible polymers. *Interface Sci.* **2003**, *11*, 175–186.

10. Cahn, J.W.; Hilliard, J.E. Free energy of a nonuniform system. I. Interfacial free energy. *J. Chem. Phys.* **1958**, *28* (2), 258–267.
11. Cahn, J.W. Phase separation by spinodal decomposition in isotropic systems. *J. Chem. Phys.* **1965**, *42*, 93–99.
12. Oono, Y.; Bahiana, M. 2/3-Power law for copolymer lamellar thickness implies a 1/3-power law for spinodal decomposition. *Phys. Rev. Lett.* **1988**, *61* (9), 1109–1111.
13. Onno, Y.; Puri, S. Computationally efficient modeling of ordering of quenched phases. *Phys. Rev. Lett.* **1987**, *58* (8), 836–839.
14. Oono, Y.; Puri, S. Study of phase-separation dynamics by use of cell dynamical systems. I. Modeling. *Phys. Rev. A* **1988**, *38* (1), 434–453.
15. Buxton, G.A.; Care, C.M.; Cleaver, D.J. A lattice spring model of heterogeneous materials with plasticity. *Model. Simul. Mater. Sci. Eng.* **2001**, *9* (6), 47–65.
16. Buxton, G.A.; Balazs, A.C. Lattice spring model of filled polymers and nanocomposites. *J. Chem. Phys.* **2002**, *117* (16), 7649–7658.
17. Monette, L.; Anderson, M.P. Elastic and fracture properties of the 2-dimensional triangular and square lattices. *Model. Simul. Mater. Sci. Eng.* **1994**, *2* (1), 53–66.
18. McCrum, N.G.; Buckley, C.P.; Brucknall, C.B. *Principles of Polymer Engineering*; Oxford University Press, 1997.
19. Jiang, M.; Alzebdeh, K.; Jasiuk, I.; Ostoja-Starzewski, M. Scale and boundary conditions effects in elastic properties of random composites. *Acta Mech.* **2001**, *148*, 63–78.

# Surface-Enhanced Raman Scattering

Adam M. Schwartzberg

Jin Z. Zhang

Department of Chemistry and Biochemistry, University of California–Santa Cruz,  
Santa Cruz, California, U.S.A.

## INTRODUCTION

Surface-enhanced Raman scattering (SERS) is a process by which normal Raman scattering (RS) can be amplified by many orders of magnitude. The utility of this lies in the rich molecular structural information attainable from RS. It is possible to capitalize on the advantages of RS through this manifold increase in scattering intensity, while mitigating its major limitation, a very small cross-section.

Because of the great potential of this technique for practical applications, a significant amount of work has been performed over the last 30 years. This entry will outline the progression of SERS as an analytical technique, from its discovery to recent work. This will include new understanding of the fundamental principles of SERS, advances in experimental techniques, and current applications in various areas including materials and biological sciences.

## BACKGROUND

### RS

In 1928, a landmark spectroscopic phenomenon was discovered by C. V. Raman and K. S. Krishnan in which light, scattered off a molecule following photo-excitation, induces a change in molecular polarization.<sup>[1]</sup> The energy difference between the scattered and incident light is equal to one of many vibrational frequencies of the molecule (Fig. 1).<sup>[2–4]</sup> Therefore, RS, similar to infrared spectroscopy (IR), can provide structural “finger print” information about molecules, because each molecule has a unique set of vibrational frequencies. Because Raman is a zero-background measurement and the signal detected is usually in the visible region, it is much more sensitive than the non-zero background IR experiment, which is based on absorption. In the last several decades, RS spectroscopy has become a routine and powerful analytical technique in academic research and industry.

Even though Raman is molecule specific, it does have one major limitation: a small scattering cross-section

$\sim 10^{-30}$  cm<sup>2</sup>/molecule. Thus, the Raman signal is difficult to detect.<sup>[5]</sup> Fortunately, several techniques have been developed to significantly enhance the Raman signal while preserving the molecular specificity. These include both resonance and surface enhancements. Resonance Raman occurs when the excitation light is in resonance with an electronic transition of the molecule,<sup>[2–4]</sup> resulting in an enhancement factor of  $10^2$ – $10^4$  (Fig. 1). This has been used in the study of a variety of molecules including biological samples such as viruses and cells. However, resonance Raman requires excitation light at a shorter wavelength than that used for standard Raman. This can cause degradation of the sample and sometimes result in fluorescence interference.

Another method of enhancement is SERS.<sup>[6]</sup> In SERS, a molecule is adsorbed onto a noble metal surface with nanoscale features. When the surface plasmon absorption mode is excited by light, a local field enhancement on the surface is created that enhances RS of molecules on or near the surface.<sup>[5,6]</sup> For SERS on roughened metal films, the enhancement is in the order of  $10^3$ – $10^5$ . While isolated metal nanoparticles (NPs), primarily silver, have shown an enhancement of  $\sim 10^6$ , NP aggregates have shown even stronger enhancement of  $\sim 10^7$ – $10^9$ .<sup>[7]</sup> This large increase in Raman cross-section for aggregates is believed to be due to stronger field enhancement at the junctions between NPs.<sup>[8]</sup> Even larger SERS enhancement factors on the order of  $10^{15}$  have been reported for “single,” so called “hot” NPs or aggregates.<sup>[9–11]</sup> These SERS enhancement studies suggest that NP aggregates are better for SERS than isolated NPs and that the Raman signal can be very large and easily detected.

The local field enhancement is only one requirement necessary for SERS. Surface chemistry of metal NPs is another important factor.<sup>[12]</sup> Many studies have determined the first decay length (the length at which the enhancement decreases by half) to be  $\sim 1.5$  nm, virtually requiring that the analyte molecule be adsorbed or very close to the surface for detection.<sup>[13–15]</sup>

There have been several excellent review entries on SERS published previously; therefore this entry will focus on some of the latest developments in SERS.<sup>[5,6,16–18]</sup> These will include new understanding



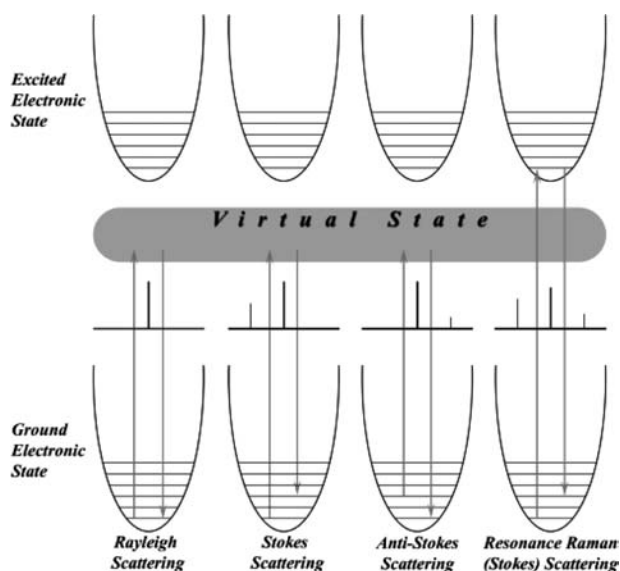


**Fig. 1** Energy diagram of four different scattering schemes: Rayleigh, Stokes, anti-Stokes, and resonance Raman (Stokes) scattering. It should be noted that resonance Raman can also take place by either the Stokes or the anti-Stokes mechanism.

of the fundamental principles of SERS, advances in experimental techniques, and current applications in various areas including materials and biological sciences. In addition, SERS techniques based on optical fibers and single NPs or aggregates will also be highlighted.

## SERS

In 1977, SERS was discovered simultaneously by Jeanmaire and Van Duyne and Albrecht and Creighton.<sup>[19,20]</sup> In their experiments, they observed an unusually intense RS signal from pyridine adsorbed onto an electrochemically roughened silver electrode. Previous studies had observed an enhanced signal; however, the effect was assumed to be because of the increase in electrode surface area.<sup>[21]</sup> Van Duyne and Creighton were the first to realize that some other effect was taking place. Nevertheless, it was Moskovits who made the first correct interpretation of the data.<sup>[22,23]</sup> They surmised that the roughened electrode was essentially a 2-D array of silver NPs, and that these NPs possessed what was called, at that time, an “optical conduction resonance,” or surface plasmon as it is known today.

## Surface Plasmons

The surface plasmon is the collective oscillation of electrons within a metal NP, activated by an incident electromagnetic field.<sup>[24–26]</sup> Fig. 2 is a schematic of

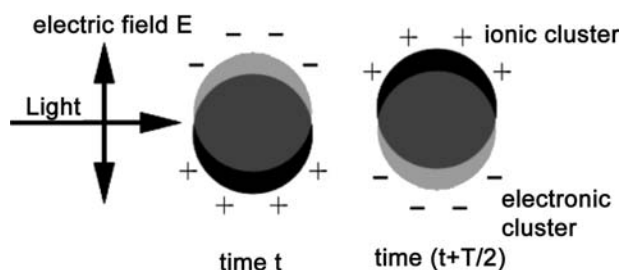


**Fig. 2** Illustration of plasmon activation in metal NPs. Light interacts with the particle and at time  $t$  causes a polarization of the electrons into an electronic cluster. At a later time  $t + T/2$ , where  $T$  is the lifetime of the oscillation, the electronic cluster will have oscillated to the other side of the particle.

the surface plasmon mechanism. An incident field polarizes the NP, shifting the electrons collectively to one side of the system. This is only possible in metal particles with high electron mobility in the lattice such as gold, silver, copper, and, to some extent, platinum. After their initial perturbation, the electrons will oscillate, confined by the surface of the nanocrystal. The frequency of this oscillation corresponds to the energy at which photons will be most strongly absorbed. Because of this, the surface plasmon absorption is strongly dependent on the nature of the NP material and its structure including size and shape, and interparticle interaction (Fig. 3).

By changing the shape or size of the NP or interparticle separation, it is possible to change the resonance

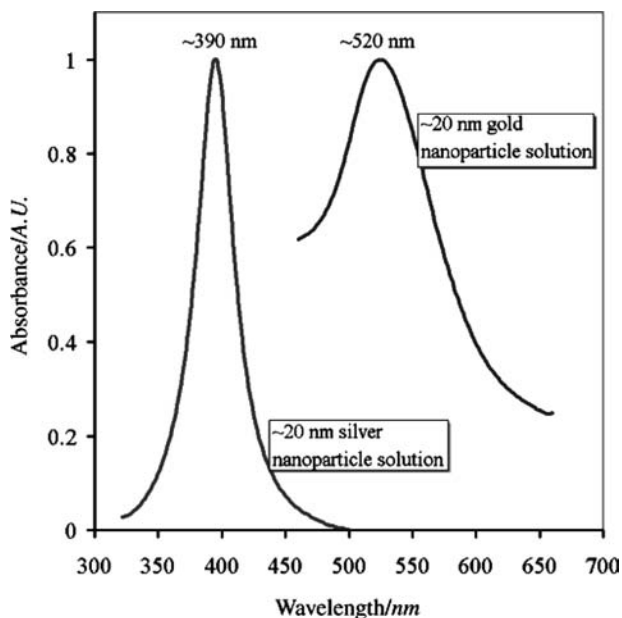


**Fig. 3** Surface plasmon absorption of 20-nm silver and gold particles. The optical properties of the nanoparticle are strongly tied to the material they are made of.

energy of the plasmon mode. For example, by elongating the NP into a nanorod, two directions now exist along which the electrons may resonate—the so-called transverse (short axis) and longitudinal (long axis) axes. Any deviation from the spherical geometry will induce multiple resonances, including nanoshells,<sup>[27–30]</sup> and NP aggregates.<sup>[31–38]</sup> In fact, based on optical absorption alone, it is impossible to discern between nanoshells, nanorods, and NP aggregates.<sup>[39]</sup> This will be discussed in greater detail later.

## SERS ENHANCEMENT MECHANISM

### Electromagnetic and Chemical Enhancement

Two mechanisms are responsible for the SERS effect, the so-called electromagnetic and chemical. While the majority of observed enhancement can be explained in the electromagnetic regime, where NP-molecule contact is not required, there is a portion that seems to require physical contact. The chemical mechanism accounts for enhancement of ~10–100 and requires that the molecule be adsorbed directly to the metal surface. There have been several theories put forward, many of which have been discounted. The most widely referenced mechanism to date is the so-called dynamical charge transfer. For a complete discussion of this, please see the fine review article by Otto et al.<sup>[18]</sup> Briefly, on adsorption, a molecule-metal complex is formed, creating a new low-energy absorption band (assuming the molecular energy levels are spaced symmetrically about the Fermi level of the metal) representing a transition from the Fermi level of the metal to the lowest unoccupied molecular orbital (LUMO) of the molecule. This new electronic transition in the visible region can then behave similar to resonance Raman, at the proper excitation frequency. The steps of the charge transfer are as follows: First, a photon is absorbed, exciting an electron from the metal conduction band to the LUMO of the molecule. Second, if the LUMO is an antibonding or bonding molecular orbital, a change in bond length, a vibration, will take place. Third, charge is transferred back to its original state and a Stokes-shifted photon is released. The more important electromagnetic mechanism does not involve charge transfer but rather energy transfer, and is responsible for the majority of the enhancement.

In normal RS, the intensity of the signal ( $P^{RS}$ ) is directly related to the number of molecules in the probed volume ( $N$ ), the scattering cross-section of the molecule ( $\sigma$ ), and the intensity of the excitation laser ( $I$ ).

$$P^{RS} = N\sigma I \quad (1)$$

SERS intensity ( $P^{SERS}$ ) is dictated by a similar relation, with the addition of field enhancement factors relating to the laser ( $A^L$ ) and Stokes frequencies ( $A^S$ ).  $A^L$  is the enhancement of the laser by the SERS substrate,  $A^S$  is the enhancement of the scattered light. In addition, the increased RS cross-section of the molecule (chemical enhancement) is accounted for in the  $\sigma^{SERS}$  term.

$$P^{SERS} = N^{SERS}\sigma^{SERS}I|A^L|^2|A^S|^2 \quad (2)$$

$N^{SERS}$  is the number of molecules involved in SERS, which is not necessarily the same as the number of molecules in the laser volume. These enhancement factors are complicated functions, which depend on several parameters including the distance of the molecule from the surface and the properties of the molecule and the substrate.

The electromagnetic and chemical enhancements are directly related to the electron oscillations induced by plasmon excitation (Fig. 4). On excitation of the plasmon, the electron oscillations in the NP induce a strong electromagnetic field, or an evanescent wave at the surface, which is related to the  $A^L$  term discussed above. This field will transfer energy to molecules in close proximity to the surface, in the form of a dipole-dipole interaction. Once the energy transfer has taken place, the molecule is induced into a new vibrational state and transfers its energy, slightly changed by the vibration, back into the particle or released directly from the molecule with energy  $h\nu_{scattered}$ . This photon can then be reabsorbed and further enhanced. The  $A^S$  term takes this into account. Like normal RS, the emitted photon energy is related to the vibrations of the molecule by Eq. (3).

$$h\nu_{scattered} = h\nu_{incident} \pm h\nu_{vibration} \quad (3)$$

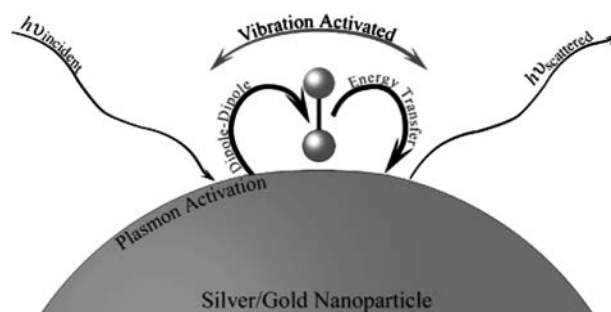


**Fig. 4** A diagram of the SERS electromagnetic mechanism. Incident light,  $h\nu_{incident}$ , is absorbed by the NP activating the plasmon mode; energy is transferred by means of dipole-dipole interaction to the molecule. A vibration is activated in the molecule, and energy is transferred back into the particle. The particle then emits a photon with new energy  $h\nu_{scattered}$ .

The requirement of the molecule to be in close proximity to the substrate is important for understanding the mechanism and application of SERS. Although not related to the chemical enhancement per se, this is a chemical concern. If the molecule in question does not bind or adsorb favorably onto the surface of the SERS substrate, or to something attached to the substrate, no enhancement will be seen. This notion has guided the direction of much of current SERS research.

## Current Applications

Some of the best work being done today in trace molecule detection is in the field of SERS. From biomolecules to chemical warfare agent detection, there are virtually endless possibilities for this technology. There is, however, a major hurdle, which has hindered wider practical SERS applications, till date. The NP-analyte collocation requirement mentioned earlier causes many difficulties. For molecules that bind strongly onto silver and gold surfaces, SERS detection is simple and straightforward; these include amine- and thiol-containing compounds. However, to devise a detection device for a wide variety of analytes, this limitation must be overcome.

For example, one of the most desired molecules for detection is glucose, owing to the prevalence of diabetes. Millions of people suffer from this disease, yet

little advancement has been made in terms of accurate glucose detection using SERS. Blood must still be drawn, and for serious cases this can be required multiple times per day; this leads to an inconvenient and painful lifestyle. The development of an in vitro, implantable, glucose-detection device could revolutionize the lives of millions.

To this end, there has been steady progress in the field of SERS glucose detection. The first work to demonstrate the possibility of glucose detection did so by utilizing a kind of sandwich method. A layer of glucose is dried between two layers of silver NPs, effectively forcing the glucose inside a silver aggregate inducing strong SERS.<sup>[40]</sup> This is not practical for building devices, as it is not stable or usable for real time detection.

More recently, Van Duyne et al. have shown significant progress in practical SERS detection of glucose.<sup>[41,42]</sup> This is achieved by first producing a stable silver substrate on silica, by using latex nanospheres as a template. The substrate is then covered with a self-assembled monolayer (SAM), which acts as a partition between the free solution and the silver. Fig. 5 shows a diagram of this configuration as well as the RS signal achieved. In this configuration, glucose can be detected within the biological range with reasonable accuracy. This is because of the glucose settling into the SAM, close enough to the surface to feel enhancement. This substrate could practically be used in device applications, being robust and simple to reproduce consistently by nanotemplating.

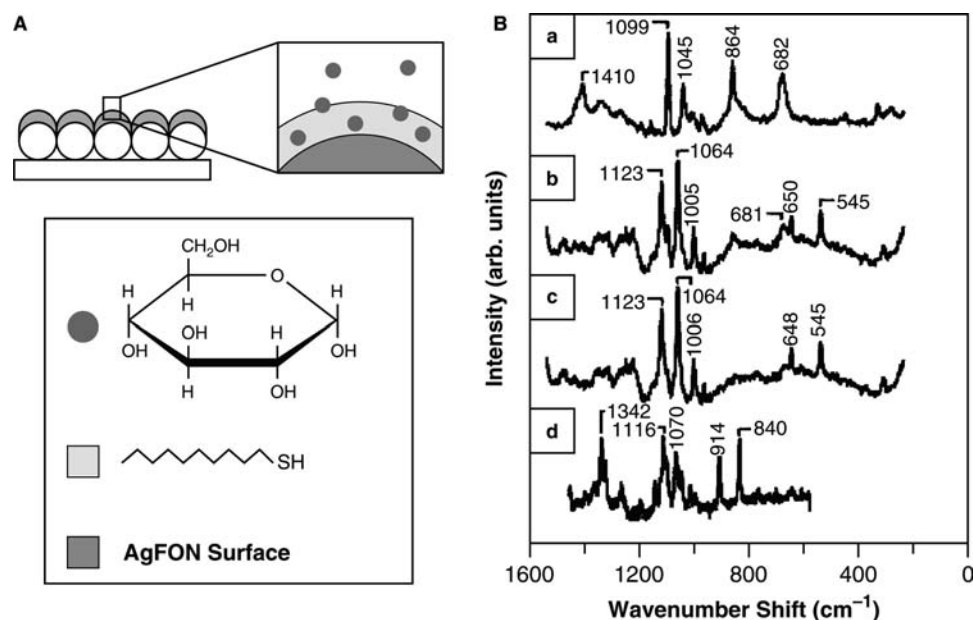


**Fig. 5** (A) Schematic showing hypothetical glucose concentration gradient created by 1-decanethiol (1-DT) partition layer and (B) spectra used in quantitative analysis: (a) 1-DT monolayer on AgFON substrate, (b) mixture of 1-DT monolayer and glucose partitioned from a 100 mM solution, (c) residual glucose spectrum produced by subtracting (a) from (b), (d) normal Raman spectrum of crystalline glucose for comparison. *Source:* From Ref.<sup>[41,42]</sup>.

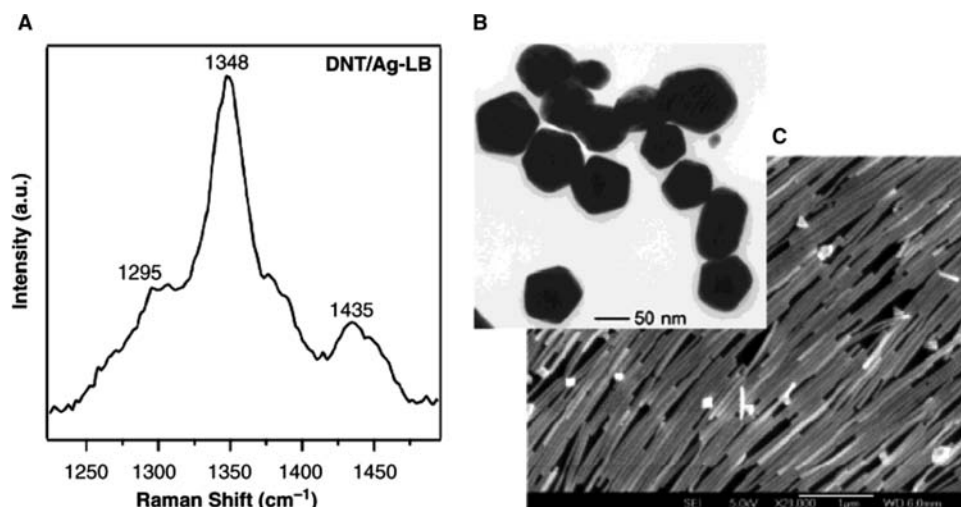


**Fig. 6** (A) SERS spectrum of 2,4-DNT on the thiol-capped Ag nanowire monolayers; (B) transmission electron microscope image of nanowires cross-section; and (C) scanning electron microscope image of nanowires film. *Source:* From Ref.<sup>[44]</sup>.

Another important application is explosive compound recognition, which requires large enhancements from a technique like SERS to detect trace molecules. Surface-enhanced Raman scattering also has much higher molecular specificity than other current detection techniques; molecules similar to enantiomers can be differentiated by SERS. This is important when searching for explosives owing to their structural similarity to many other compounds, namely nitrate fertilizers, and can lead to false positive results. Several studies using varying techniques have attempted to detect trinitrotoluene (TNT) and similar compounds. The first study was done using electrochemically roughened gold films in which TNT at concentrations in vapor as low as 5 ppb were detected.<sup>[43]</sup> By blowing a vaporized sample over the film and monitoring the SERS via a RS fiber probe, this low detection limit was possible. Nevertheless, a significant amount of postacquisition work was still required to extract the signal from the data. A more recent study utilized oriented arrays of pyramidal tipped silver nanowires to detect the explosive 2,4-dinitrotoluene (DNT). Fig. 6 shows the enhanced RS of DNT on the nanowire substrate as well as electron microscope images showing the cross-section of the wires and how they are aligned. While they do not report a detection limit, they do report an enhancement of five orders of magnitude, enough for low-concentration detection.<sup>[44]</sup> It is theorized that the enhancement is increased by the pointed tips of the wires that concentrate the electric field strongly. Both studies show that detection of explosives with SERS is a viable technique and allows the detection of low concentrations of explosives with high spectral resolution.

The major problems that must be overcome for SERS to be a practical technique for detecting in vivo

or explosive and warfare agents are portability, mobility, and ruggedness of the substrate. Currently, most SERS studies are done with a tabletop RS instrument in a laboratory with colloidal solution or one-time use films. There are portable RS instruments; however, a SERS substrate that is portable, reusable, and sensitive has not been available. Recently, Vo-Dinh et al. have demonstrated a reusable fiber optic tip SERS substrate.<sup>[45,46]</sup> With this they are able to obtain SERS spectra from the fiber by merely making it touch a dry surface. Fig. 7 shows the Raman signal of a surface coated with the dye cresyl blue, before and after contact with the SERS fiber tip. It is clear that there is a large enhancement by mere contact. This is achieved by tapering the fiber and depositing silver island films on the surface. This configuration lends itself well to localized, non-destructive experiments, while maintaining a high spatial resolution owing to the small size of the fiber tip. Also, the ability to detect SERS through dry contact is a major advantage over any other currently known system. This type of a device could be used as a sensing probe for SERS detection in a wide variety of situations, whether in the body or in the field.

Many of these fiber-detection applications have extremely low sample volume, and commensurate low signal. Recently, in our lab, we have built a new detection system utilizing a D-shaped, high-surface-area fiber SERS sensor. By polishing down one side of the fiber to the core, light can be coupled into metal particles on the surface and activate SERS. This represents an increase in active SERS surface area of approximately 2800 times from end polished sensors, greatly increasing the total intensity.<sup>[47]</sup>

The studies presented above represent very few of the myriad works being done today. In biological

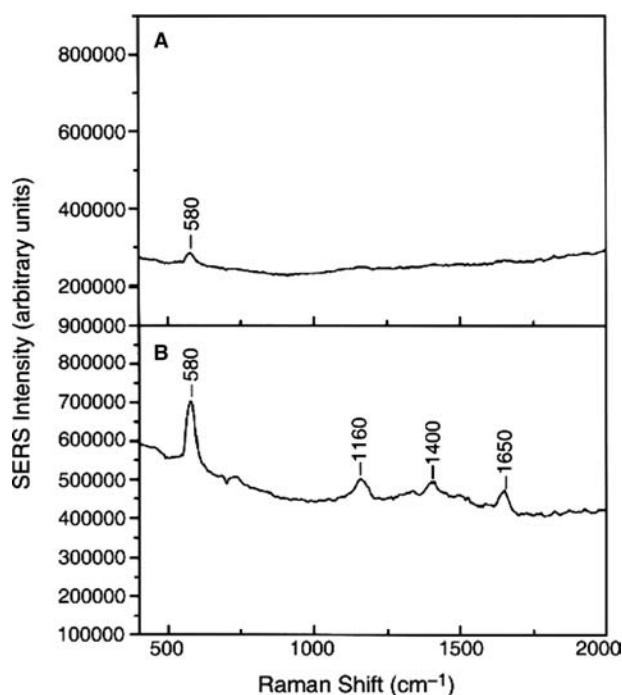


**Fig. 7** Raman spectra of a dry benzocyclobutene sample distributed on a glass slide, acquired A) before and B) after contact with the SERS-inducing nanoprobe. *Source:* From Ref.<sup>[46]</sup>.

detection, significant advances have been made in detection of cancer,<sup>[48–54]</sup> HIV,<sup>[55]</sup> insulin,<sup>[56,57]</sup> and many other exciting areas including amino acids, drugs, and vitamins in human samples.<sup>[58–63]</sup> Also the detection of pollution in sea water has been explored, important for rapid monitoring of environmental conditions.<sup>[64,65]</sup> Even illicit drugs and uranyl ions have been detected via SERS.<sup>[66–68]</sup> This speaks of the vast potential of SERS detection and what can be looked forward to in the future.

### Single Molecule SERS

The first researchers to report the detection of single molecules utilizing SERS were Nie and Emery, however, shortly thereafter Brus and coworkers and Kneipp et al. reported similar results.<sup>[9–11]</sup> This was made possible through the use of the confocal microscope, shown schematically in Fig. 8. The advantage of this system is that very small focal volumes may be probed, and stray light not within the focal volume is excluded by the pinhole. This allows for extremely high spatial resolution in three dimensions. By depositing silver NPs with rhodamine 6G on the surface of a glass slide, single particles can be observed, and by carefully controlling the concentration of the dye, it is possible to maintain a ratio of dye to particle, no

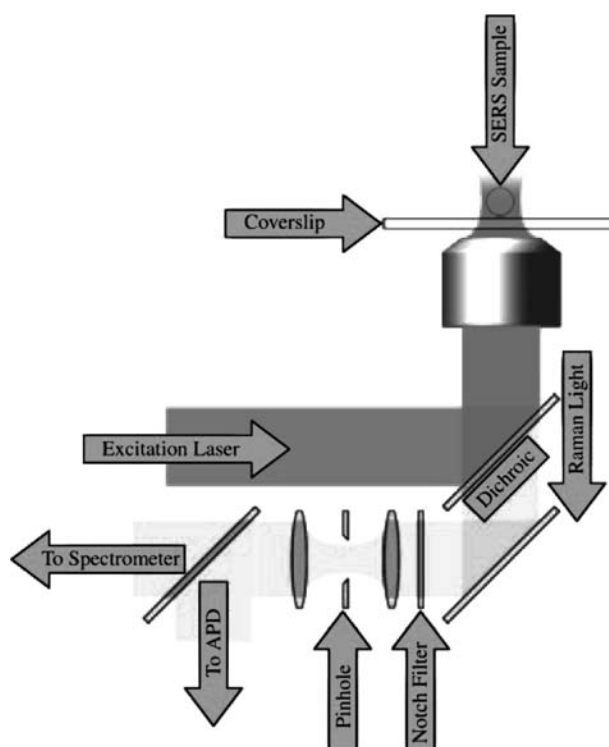


**Fig. 8** Schematic diagram of the confocal microscope setup. The excitation laser is coupled into the microscope through a dichroic into a high numerical aperture objective, which focuses it tightly onto the SERS sample that has been placed on a glass coverslip. The Raman scattered light then passes back through the objective used for excitation and is focused through a pinhole, excluding any scattered light not within the focal volume. This light can then be sent either to an avalanche photodiode (APD) to image the surface of the coverslip, or to a spectrometer to take the spectrum of the Raman scattered light.

greater than 1:1. To observe a signal at this concentration, the enhancement must be very large, and indeed, Nie and Emery report factors as large as  $10^{16}$ . Fig. 9 shows the spectra of a single rhodamine 6G molecule attached to, as Nie claims, a single silver NP. This is an impressive claim; however, there is disagreement in the literature as to whether a single spherical NP can produce this much enhancement.

As the enhancement is because of an electromagnetic field at the surface, it is strongly related to the shape of the particle. In a spherical particle, the charge is distributed evenly over the entire surface. However, if dislocations or points are present, the field will accumulate leading to regions of greater field strength.<sup>[69–71]</sup> Another source of increased fields is aggregation. Two or more particles approaching the enhanced fields will overlap, resulting in regions of high intensity between the particles.<sup>[8,37,72,73]</sup> This has led some to believe that to see SERS from a single

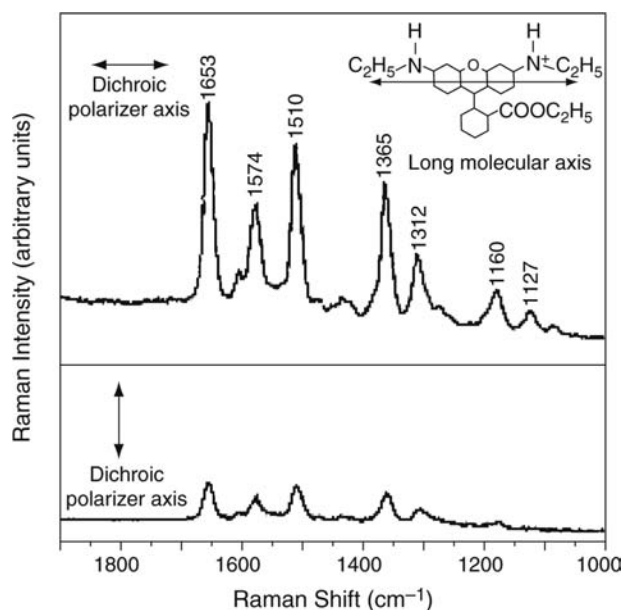


**Fig. 9** Emission-polarized surface-enhanced Raman signals of rhodamine 6G observed from a single silver NP with a polarization-scrambled confocal laser beam. A dichroic sheet polarizer was rotated  $90^\circ$  to select RS signals polarized parallel (upper spectrum) or perpendicular (lower spectrum) to the long molecular axis of rhodamine 6G. *Inset*: Structure of rhodamine 6G, the electronic transition dipole (along the long axis when excited at 514 nm), and the dichroic polarizer orientations. <http://www.sciencemag.org>. Source: From Ref.<sup>[9]</sup>.

molecule there must be aggregation.<sup>[74–76]</sup> However, Nie and Emery have continued producing results to confirm that they are indeed probing single NPs.<sup>[12]</sup> Regardless of the exact nature of enhancement, the power of single or near single molecule detection is clear and has brought about a new field of spectroscopic techniques.<sup>[77–82]</sup>

### Aggregation vs. Core Shell

Core/shell structures are creating a significant stir in SERS research today owing to their excellent optical and SERS properties.<sup>[30]</sup> Optically they are advantageous because of the near IR (NIR) absorption, which is highly desirable for in vivo studies as tissue absorbs weakly in this region.<sup>[16]</sup> Because SERS requires excitation resonance with NP absorption, purely spherical NPs of gold or silver will not absorb in the NIR region, making nanoshells a unique substrate for biological applications. Their SERS properties are also interesting. While they do not have excessively large enhancements, they are highly uniform, which is advantageous for single molecule or single particle studies.<sup>[83]</sup> Often in single particle SERS,

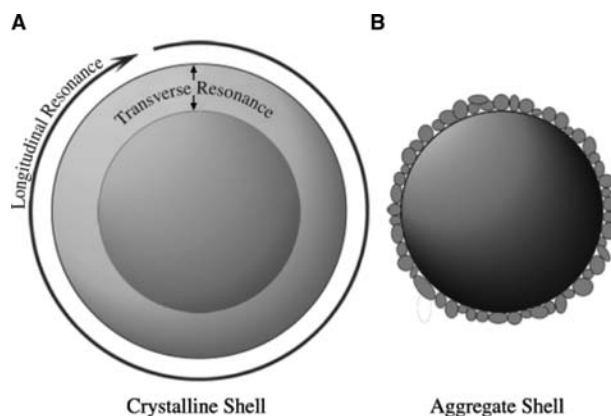


**Fig. 10** Diagram of the (A) crystalline shell and (B) aggregate shell core-shell structures. A shows schematically the path that the longitudinal and transverse resonances take.

one would want reproducible signals from particle to particle; however, most substrates that are aggregated have random shapes and sizes, leading to slight variations. Although in theory, core/shell systems could provide a solution to this problem, there are several complications.

The first major problem with this type of system is determining if core/shell particles are present at all. As stated earlier, a core/shell system can have very similar optical absorption as an aggregated system.<sup>[39]</sup> Therefore, without significant analytical work, it is difficult to prove whether a synthesis is producing aggregates or core/shell particles. The other complicating factor is that even with proper analytical techniques like high-resolution transmission electron microscopy, it may still be difficult to determine if the shell is a single crystal (Fig. 10A) or merely a conglomeration of small NPs on the surface of the core (Fig. 10B).<sup>[31–33]</sup> While this may not seem like a big distinction, the photophysics and SERS properties of the system are entirely dependent on this.

In a core/shell particle with a single crystal shell, the NIR or longitudinal absorption is because of resonance around the particle, as shown in Fig. 6A. However, if the shell is made up of aggregated particles, the transverse band originates in the individual particles, while the longitudinal mode is because of aggregation of the NPs. This is essentially a NP aggregate system and will not have the same properties or advantages as a true core-shell particle. While many report the synthesis of core-shell NPs, few are truly able to show conclusively that this is the case.<sup>[39]</sup>

### CONCLUSIONS

SERS is a powerful technique with great potential for research and analytical detection. In this entry, the



background and basic fundamentals of SERS have been briefly explained, and a quick overview of current research has been given. The importance of the structure of the SERS substrate and its implications in SERS activities has been discussed with core/shell and aggregate structures as examples. The future of SERS is dependent on the development and careful characterization of novel substrates with unique structures as well as on new techniques, to provide reproducible and accurate results for emerging technological applications in areas including biomedicine detection and advanced material characterization.

## REFERENCES

- Raman, C.V.; Krishnan, K.S. A new type of secondary radiation. *Nature* **1928**, *121*, 501.
- Schrader, B.; Bougeard, D. *Infrared and Raman spectroscopy: methods and applications*; VCH: Weinheim, New York, 1995.
- Ferraro, J.R.; Nakamoto, K. *Introductory Raman spectroscopy*; Academic Press: Boston, 1994.
- Grasselli, J.G.; Bulkin, B.J. *Analytical Raman spectroscopy*; Wiley: New York, 1991.
- Kneipp, K.; Kneipp, H.; Itzkan, I.; Dasari, R.R.; Feld, M.S. Ultrasensitive chemical analysis by Raman spectroscopy. *Chem. Rev.* **1999**, *99* (10), 2957–2975.
- Moskovits, M. Surface-enhanced spectroscopy. *Rev. Mod. Phys.* **1985**, *57* (3), 783–826.
- Creighton, J.A. Metal colloids. Surface enhanced Raman scattering **1982**, 315–338.
- Quinten, M. Local fields close to the surface of nanoparticles and aggregates of nanoparticles. *Appl. Phys. B-Lasers Opt.* **2001**, *73* (3), 245–255.
- Nie, S.M.; Emery, S.R. Probing single molecules and single nanoparticles by surface-enhanced Raman scattering. *Science* **1997**, *275* (5303), 1102–1106.
- Michaels, A.M.; Nirmal, M.; Brus, L.E. Surface enhanced Raman spectroscopy of individual rhodamine 6G molecules on large Ag nanocrystals. *J. Am. Chem. Soc.* **1999**, *121* (43), 9932–9939.
- Kneipp, K.; Wang, Y.; Kneipp, H.; Perelman, L.T.; Itzkan, I.; Dasari, R.; Feld, M.S. Single molecule detection using surface-enhanced Raman scattering (SERS). *Phys. Rev. Lett.* **1997**, *78* (9), 1667–1670.
- Doering, W.E.; Nie, S.M. Single-molecule and single-nanoparticle SERS: examining the roles of surface active sites and chemical enhancement. *J. Phys. Chem. B* **2002**, *106* (2), 311–317.
- Kennedy, B.J.; Spaeth, S.; Dickey, M.; Carron, K.T. Determination of the distance dependence and experimental effects for modified SERS substrates based on self-assembled monolayers formed using alkanethiols. *J. Phys. Chem. B* **1999**, *103* (18), 3640–3646.
- Murray, C.A.; Allara, D.L.; Hebard, A.F.; Padden, F.J. Determination of sample morphology of multilayered structures used in surface enhanced Raman-scattering experiments. *Surf. Sci.* **1982**, *119* (2–3), 449–478.
- Ye, Q.; Fang, J.X.; Sun, L. Surface-enhanced Raman scattering from functionalized self-assembled monolayers. 2. Distance dependence of enhanced Raman scattering from an azobenzene terminal group. *J. Phys. Chem. B* **1997**, *101* (41), 8221–8224.
- Kneipp, K.; Kneipp, H.; Itzkan, I.; Dasari, R.R.; Feld, M.S. Surface-enhanced Raman scattering and biophysics. *J. Phys. Condens. Matter* **2002**, *14* (18), R597–R624.
- Campion, A.; Kambhampati, P. Surface-enhanced Raman scattering. *Chem. Soc. Rev.* **1998**, *27* (4), 241–250.
- Otto, A.; Mrozek, I.; Grabhorn, H.; Akemann, W. Surface-enhanced Raman-scattering. *J. Phys. Condens. Matter* **1992**, *4* (5), 1143–1212.
- Albrecht, M.G.; Creighton, J.A. Anomalously intense Raman-spectra of pyridine at a silver electrode. *J. Am. Chem. Soc.* **1977**, *99* (15), 5215–5217.
- Jeanmaire, D.L.; Van duyn, R.P. Surface Raman spectroelectrochemistry. 1. Heterocyclic, aromatic, and aliphatic-amines adsorbed on anodized silver electrode. *J. Electroanal. Chem.* **1977**, *84* (1), 1–20.
- Fleischman, M.; Hendra, P.J.; McQuillan, A.J. Raman spectra of pyridine adsorbed at a silver electrode. *Chem. Phys. Lett.* **1974**, *26*, 123.
- Moskovits, M. Surface-roughness and enhanced intensity of Raman-scattering by molecules adsorbed on metals. *J. Chem. Phys.* **1978**, *69* (9), 4159–4161.
- Moskovits, M. Enhanced Raman-scattering by molecules adsorbed on electrodes—theoretical-model. *Solid State Commun.* **1979**, *32* (1), 59–62.
- Quinten, M.; Pack, A.; Wannemacher, R. Scattering and extinction of evanescent waves by small particles. *Appl. Phys. B-Lasers Opt.* **1999**, *68* (1), 87–92.
- Quinten, M. The color of finely dispersed nanoparticles. *Appl. Phys. B-Lasers Opt.* **2001**, *73* (4), 317–326.
- Kreibig, U. *Optical properties of metal clusters*; Springer: Berlin, New York, 1995; 25 pp.
- Prodan, E.; Nordlander, P.; Halas, N.J. Electronic structure and optical properties of gold nanoshells. *Nano Lett.* **2003**, *3* (10), 1411–1415.
- Nehl, C.L.; Grady, N.K.; Goodrich, G.P.; Tam, F.; Halas, N.J.; Hafner, J.H. Scattering spectra of single gold nanoshells. *Nano Lett.* **2004**, *4* (12), 2355–2359.
- LizMarzan, L.M.; Giersig, M.; Mulvaney, P. Synthesis of nanosized gold-silica core-shell particles. *Langmuir* **1996**, *12* (18), 4329–4335.
- Halas, N. The remarkable optical properties of gold nanoshells. *Gold Bull.* **2004**, *37* (1–2), 137–137.
- Norman, T.J.; Grant, C.D.; Magana, D.; Zhang, J.Z.; Liu, J.; Cao, D.L.; Bridges, F.; Van Buuren, A. Near infrared optical absorption of gold nanoparticle aggregates. *J. Phys. Chem. B* **2002**, *106* (28), 7005–7012.
- Norman, T.J.; Grant, C.; Magana, D.; Anderson, R.; Zhang, J.Z.; Cao, D.; Bridges, F.; Liu, J.; Van Buuren, A. Longitudinal plasma resonance shifts in gold nanoparticles aggregates. *SPIE Proc.* **2002**, *4807*, 51–58.
- Norman, T.J.; Grant, C.D.; Schwartzberg, A.M.; Zhang, J.Z. Structural correlations with shifts in the extended plasma resonance of gold nanoparticle aggregates. *Optical Materials* **2005**, *27*, 1197–1203.

34. Nikoobakht, B.; El-Sayed, M.A. Surface-enhanced Raman scattering studies on aggregated gold nanorods. *J. Phys. Chem. A* **2003**, *107* (18), 3372–3378.
35. Quinten, M.; Stier, J. Absorption of scattered-light in colloidal systems of aggregated particles. *Colloid Polym. Sci.* **1995**, *273* (3), 233–241.
36. Quinten, M.; Leitner, A.; Krenn, J.R.; Aussenegg, F.R. Electromagnetic energy transport via linear chains of silver nanoparticles. *Opt. Lett.* **1998**, *23* (17), 1331–1333.
37. Quinten, M.; Kreibig, U. Absorption and elastic-scattering of light by particle aggregates. *Appl. Opt.* **1993**, *32* (30), 6173–6182.
38. Quinten, M. Evanescent wave scattering by aggregates of clusters—application to optical near-field microscopy. *Appl. Phys. B-Lasers Opt.* **2000**, *70* (4), 579–586.
39. Zhang, J.Z.; Schwartzberg, A.M.; Norman, T.J.; Grant, C.D.; Liu, J.; Bridges, F.; van Buuren, T. Comment on “Gold nanoshells improve single nanoparticle molecular sensors.” *Nano Lett.* **2005**, *5*, 809–810.
40. Mrozek, M.F.; Weaver, M.J. Detection and identification of aqueous saccharides by using surface-enhanced Raman spectroscopy. *Anal. Chem.* **2002**, *74* (16), 4069–4075.
41. Shafer-Peltier, K.E.; Haynes, C.L.; Glucksberg, M.R.; Van Duyne, R.P. Toward a glucose biosensor based on surface-enhanced Raman scattering. *J. Am. Chem. Soc.* **2003**, *125* (2), 588–593.
42. Yonzon, C.R.; Haynes, C.L.; Zhang, X.Y.; Walsh, J.T.; Van Duyne, R.P. A glucose biosensor based on surface-enhanced Raman scattering: improved partition layer, temporal stability, reversibility, and resistance to serum protein interference. *Anal. Chem.* **2004**, *76* (1), 78–85.
43. Sylvia, J.M.; Janni, J.A.; Klein, J.D.; Spencer, K.M. Surface-enhanced Raman detection of 1,4-dinitrotoluene impurity vapor as a marker to locate landmines. *Anal. Chem.* **2000**, *72* (23), 5834–5840.
44. Tao, A.; Kim, F.; Hess, C.; Goldberger, J.; He, R.R.; Sun, Y.G.; Xia, Y.N.; Yang, P.D. Langmuir–Blodgett silver nanowire monolayers for molecular sensing using surface-enhanced Raman spectroscopy. *Nano Lett.* **2003**, *3* (9), 1229–1233.
45. Stokes, D.L.; Vo-Dinh, T. Development of an integrated single-fiber SERS sensor. *Sens. Actuators B-Chem.* **2000**, *69* (1–2), 28–36.
46. Stokes, D.L.; Chi, Z.H.; Vo-Dinh, T. Surface-enhanced-Raman-scattering-inducing nanoprobe for spectrochemical analysis. *Appl. Spectrosc.* **2004**, *58* (3), 292–298.
47. Zhang, Y.; Gu, C.; Schwartzberg, A.M.; Zhang, J.Z. Surface-enhanced Raman scattering sensor based on D-shaped fiber. *Appl. Phys. Lett.* **2005**, *87*.
48. Allain, L.R.; Vo-Dinh, T. Surface-enhanced Raman scattering detection of the breast cancer susceptibility gene BRCA1 using a silver-coated microarray platform. *Anal. Chim. Acta* **2002**, *469* (1), 149–154.
49. Culha, M.; Stokes, D.; Vo-Dinh, T. Surface-enhanced Raman scattering for cancer diagnostics: detection of the BCIL2 gene. *Expert Rev. Mol. Diagn.* **2003**, *3* (5), 669–675.
50. Morjani, H.; Riou, J.F.; Nabiev, I.; Lavelle, F.; Manfait, M. Molecular and cellular interactions between intopicine, DNA, and topoisomerase-I studied by surface-enhanced Raman-scattering spectroscopy. *Cancer Res.* **1993**, *53* (20), 4784–4790.
51. Nabiev, I.R.; Morjani, H.; Manfait, M. Selective analysis of antitumor drug-interaction with living cancer-cells as probed by surface-enhanced Raman-spectroscopy. *Eur. Biophys. J.* **1991**, *19* (6), 311–316.
52. Sokolov, K.; Aaron, J.; Hsu, B.; Nida, D.; Gillenwater, A.; Follen, M.; MacAulay, C.; Adler-Storthz, K.; Korgel, B.; Descour, M.; Pasqualini, R.; Arap, W.; Lam, W.; Richards-Kortum, R. Optical systems for in vivo molecular imaging of cancer. *Technol. Cancer Res. Treat.* **2003**, *2* (6), 491–504.
53. Vo-Dinh, T.; Allain, L.R.; Stokes, D.L. Cancer gene detection using surface-enhanced Raman scattering (SERS). *J. Raman Spectrosc.* **2002**, *33* (7), 511–516.
54. Grubisha, D.S.; Lipert, R.J.; Park, H.Y.; Driskell, J.; Porter, M.D. Femtomolar detection of prostate-specific antigen: an immunoassay based on surface-enhanced Raman scattering and immunogold labels. *Anal. Chem.* **2003**, *75* (21), 5936–5943.
55. Isola, N.R.; Stokes, D.L.; Vo-Dinh, T. Surface enhanced Raman gene probe for HIV detection. *Anal. Chem.* **1998**, *70* (7), 1352–1356.
56. Ortiz, C.; Zhang, D.M.; Xie, Y.; Davisson, V.J.; Ben-Amotz, D. Identification of insulin variants using Raman spectroscopy. *Anal. Biochem.* **2004**, *332* (2), 245–252.
57. Drachev, V.P.; Thoreson, M.D.; Khaliullin, E.N.; Davisson, V.J.; Shalaev, V.M. Surface-enhanced Raman difference between human insulin and insulin lispro detected with adaptive nanostructures. *J. Phys. Chem. B* **2004**, *108* (46), 18,046–18,052.
58. Du, Y.X.; Yin, G.S.; Yin, Y.F.; Gao, Y.; Mo, Y.J. A study of vitamin K-3 by surface enhanced Raman scattering. *Spectrosc. Spectra. Anal.* **2003**, *23* (4), 718–720.
59. O’Neal, P.D.; Cote, G.L.; Motamedi, M.; Chen, J.; Lin, W.C. Feasibility study using surface-enhanced Raman spectroscopy for the quantitative detection of excitatory amino acids. *J. Biomed. Opt.* **2003**, *8* (1), 33–39.
60. Wang, Y.; Li, Y.S.; Zhang, Z.X.; An, D.Q. Surface-enhanced Raman scattering of some water insoluble drugs in silver hydrosols. *Spectrochim. Acta Part A-Mol. Biomol. Spectrosc.* **2003**, *59* (3), 589–594.
61. Premasiri, W.R.; Moir, D.T.; Klempner, M.S.; Krieger, N.; Jones, G.; Ziegler, L.D. Characterization of the surface enhanced Raman scattering (SERS) of bacteria. *J. Phys. Chem. B* **2005**, *109* (1), 312–320.
62. Wang, Y.; Li, Y.S.; Zhang, Z.X.; An, D.Q. SERS spectra of vitamin A acid in silver solution. *Spectrosc. Spectra. Anal.* **2004**, *24* (11), 1376–1378.
63. Koo, T.W.; Chan, S.; Sun, L.; Su, X.; Zhang, J.W.; Berlin, A.A. Specific chemical effects on surface-enhanced Raman spectroscopy for ultra-sensitive detection of biological molecules. *Appl. Spectrosc.* **2004**, *58* (12), 1401–1407.
64. Schmidt, H.; Ha, N.B.; Pfannkuche, J.; Amann, H.; Kronfeldt, H.D.; Kowalewska, G. Detection of PAHs

- in seawater using surface-enhanced Raman scattering (SERS). *Mar. Pollut. Bull.* **2004**, *49* (3), 229–234.
65. Gu, B.H.; Tio, J.; Wang, W.; Ku, Y.K.; Dai, S. Raman spectroscopic detection for perchlorate at low concentrations. *Appl. Spectrosc.* **2004**, *58* (6), 741–744.
  66. Sagmuller, B.; Schwarze, B.; Brehm, G.; Trachta, G.; Schneider, S. Identification of illicit drugs by a combination of liquid chromatography and surface-enhanced Raman scattering spectroscopy. *J. Mol. Struct.* **2003**, *661*, 279–290.
  67. Bao, L.L.; Mahurin, S.M.; Haire, R.G.; Dai, S. Silver-doped sol-gel film as a surface-enhanced Raman scattering substrate for detection of uranyl and neptunyl ions. *Anal. Chem.* **2003**, *75* (23), 6614–6620.
  68. Bao, L.; Mahurin, S.M.; Dai, S. Silver-doped sol-gel films as a surface-enhanced Raman scattering (SERS) substrate for sensitive detection of uranyl ions. *Abstr. Pap. Am. Chem. Soc.* **2003**, 226, U106–U106.
  69. Kottmann, J.P.; Martin, O.J.F.; Smith, D.R.; Schultz, S. Plasmon resonances of silver nanowires with a non-regular cross section. *Phys. Rev. B* **2001**, *64* (23).
  70. Kottmann, J.P.; Martin, O.J.F.; Smith, D.R.; Schultz, S. Spectral response of plasmon resonant nanoparticles with a non-regular shape. *Opt. Express* **2000**, *6* (11), 213–219.
  71. Kottmann, J.P.; Martin, O.J.F.; Smith, D.R.; Schultz, S. Non-regularly shaped plasmon resonant nanoparticle as localized light source for near-field microscopy. *J. Microsc. Oxford* **2001**, *202*, 60–65.
  72. Blatchford, C.G.; Campbell, J.R.; Creighton, J.A. Plasma resonance—enhanced Raman scattering by absorbates on gold colloids: the effects of aggregation. *Surf. Sci.* **1982**, *120* (2 SU-), 435–455.
  73. Kahlau, T.; Quinten, M.; Kreibig, U. Extinction and angle-resolved light scattering from aggregated metal clusters. *Appl. Phys. A-Mater. Sci. Process.* **1996**, *62* (1), 19–27.
  74. Michaels, A.M.; Jiang, J.; Brus, L. Ag nanocrystal junctions as the site for surface-enhanced Raman scattering of single Rhodamine 6G molecules. *J. Phys. Chem. B* **2000**, *104* (50), 11,965–11,971.
  75. Jiang, J.; Bosnick, K.; Maillard, M.; Brus, L. Single molecule Raman spectroscopy at the junctions of large Ag nanocrystals. *J. Phys. Chem. B* **2003**, *107* (37), 9964–9972.
  76. Brus, L. Raman spectra of single R6G molecules on Ag nanocrystal aggregates. *Abstr. Pap. Am. Chem. Soc.* **2001**, 221112–PHYS.
  77. Habuchi, S.; Cotlet, M.; Gronheid, R.; Dirix, G.; Michiels, J.; Vanderleyden, J.; De Schryver, F.C.; Hofkens, J. Single-molecule surface enhanced resonance Raman spectroscopy of the enhanced green fluorescent protein. *J. Am. Chem. Soc.* **2003**, *125* (28), 8446–8447.
  78. Esposito, A.P.; Talley, C.E.; Huser, T.; Hollars, C.W.; Schaldach, C.M.; Lane, S.M. Analysis of single bacterial spores by micro-Raman spectroscopy. *Appl. Spectrosc.* **2003**, *57* (7), 868–871.
  79. Delfino, I.; Bizzarri, A.R.; Cannistraro, S. Single-molecule detection of yeast cytochrome c by surface-enhanced Raman spectroscopy. *Biophys. Chem.* **2005**, *113* (1), 41–51.
  80. Tolaieb, B.; Constantino, C.J.L.; Aroca, R.F. Surface-enhanced resonance Raman scattering as an analytical tool for single molecule detection. *Analyst* **2004**, *129* (4), 337–341.
  81. Kneipp, K.; Harrison, G.R.; Emory, S.R.; Nie, S.M. Single-molecule Raman spectroscopy—Fact or fiction? *Chimia* **1999**, *53* (1–2), 35–37.
  82. Kneipp, K.; Haka, A.S.; Kneipp, H.; Badizadegan, K.; Yoshizawa, N.; Boone, C.; Shafer-Peltier, K.E.; Motz, J.T.; Dasari, R.R.; Feld, M.S. Surface-enhanced Raman Spectroscopy in single living cells using gold nanoparticles. *Appl. Spectrosc.* **2002**, *56* (2), 150–154.
  83. Jackson, J.B.; Westcott, S.L.; Hirsch, L.R.; West, J.L.; Halas, N.J. Controlling the surface enhanced Raman effect via the nanoshell geometry. *Appl. Phys. Lett.* **2003**, *82* (2), 257–259.

# Surface Forces on Nanoparticles Determined by Direct Measurement

Jeong-Min Cho

Georgios Pyrgiotakis

Wolfgang M. Sigmund

*Materials Science and Engineering Department, University of Florida,  
Gainesville, Florida, U.S.A.*

## INTRODUCTION

Interaction forces between two colloidal size bodies have been studied for several decades. They are known to originate from the interatomic forces acting between all of the atoms of those bodies, as well as the atoms of any intervening medium.<sup>[1]</sup> Surface forces especially play a role in many particulate systems, where they control powder flow, viscosity of ink and paint pigments, adhesion, coating, and interactions of biological molecules.<sup>[2,3]</sup> Surface properties of material can dominate bulk properties when the size is smaller than about 100  $\mu\text{m}$ . This is especially important as modern technologies require smaller dimensions and higher performance in application.

Understanding of surface forces is a matter of great importance for colloid science, where the stability and rheology of the colloidal suspension depend on the interaction forces between particles suspended in a liquid medium. The development of both theoretical and experimental approaches that can give qualitative and quantitative results has widely been performed for particles of varying sizes, ranging from several millimeters to several micrometers, and they fit each other well. However, the scalability of those theories down to the nanometer size range is questionable because the premises that were required to develop the current theories directly exclude nano size. For instance, the Derjarguin approximation, which translates from the interaction energy between two flat surfaces into other shapes, such as sphere–sphere and sphere–plane, is only valid when the radius of the particle is much greater than the separation distance between two particles.<sup>[4]</sup> Besides, only a few novel force measurement techniques are capable of directly measuring the surface forces of nanoparticles.

This entry will briefly describe the types of surface forces that are used to describe forces in colloidal suspensions, explaining the mechanisms and parameters attributing to those forces as well as the limitations

to nanoparticles. Then, the colloidal surface force measurement techniques will be reviewed, followed by new development of the direct force measurement for nanoparticles.

## SURFACE FORCES

With the development of the quantum theory, it was established that all surface forces are electrostatic and electrodynamic in origin. For colloidal particles suspending in the medium, complex fluctuating charge distribution takes place around the atom. Even in that case, once the Schrödinger equation solves the distribution of electron clouds of the given system, interaction forces between molecules can be calculated. However, it is not easy to obtain the exact solutions of the Schrödinger equation, even for a simple case such as two hydrogen atoms in vacuum. Thus surface forces are normally classified as short-range and long-range forces. For example, electrostatic force is a long-range force and van der Waals (vdW) force is considered as short-range on a macroscopic scale but long-range on an atomic scale. Surface forces on macroscopic scale will be discussed in the following sections.

### van der Waals

The van der Waals (vdW) force arises from the interaction between atomic and/or molecular dipoles. Those dipoles may exist, by the structure of the molecule, or they may be transient or induced by the molecule–molecule interaction. According to the origin of the dipoles, they are classified in three main categories.

1. Keesom interaction: The dipoles are permanent and are created by the structure of the molecule,

such as water. The dipole creates a finite electric field and this field can orient the neighbor dipoles so they are attracted to the first one.

2. Debye interaction: A permanent dipole can induce a dipole in a polarizable atom or molecule. The new induced dipole is oriented again in a way that it is attracted to the first one.
3. London or dispersion interaction: In this case, it is just the interaction between two polarizable atoms or molecules. The fluctuation of the electron distribution around the nucleus induces dipoles among the surroundings atoms or molecules and those induced dipoles are attracted to each other.

When molecules are close together, polarization is nearly instantaneous relative to relaxation time. At larger separation distances ( $>5$  nm), the synchronicity between instantaneous dipoles becomes less efficient and thus vdW attraction is less, decreasing as  $d^{-8}$ , which is known as retardation.

One way to calculate the vdW force is through the Hamaker approximation, which is based on a pairwise summation over all the atoms in the interacting bodies.<sup>[5]</sup> Hamaker showed that the non-retarded vdW interaction energy of two spheres of radius  $a$  is dependent on the center-center distance  $r$  as:

$$V_{\text{vdW}}(r) = -\frac{A}{6} \left[ \frac{2a^2}{r^2 - 4a^2} + 2\frac{a^2}{r^2} + \ln \left( 1 - 2\frac{a^2}{r^2} \right) \right] \quad (1)$$

and if  $a \gg r$ , this energy can be simply expressed with the separation distance  $D$ :

$$F(D) = -\frac{AR_S}{12D^2}, \quad (A = \pi^2 C \rho_1 \rho_2) \quad (2)$$

where  $A$  is the Hamaker constant and depends on the polarizability and the number of atoms per unit volume in the two interacting bodies ( $\rho$ ), and  $R_S$  is the radius of the sphere.

Because of a large number of body effects, by which an electric field of one given atom is induced not only by the closest atom but also by the other atoms in the vicinity, Lifshitz proposed to consider the bodies as continuum with certain dielectric properties.<sup>[6]</sup> The advantage of the Lifshitz theory is that accurate prediction of vdW force is possible if complete optical data are available. Spectral optical properties over very wide energy ranges can be obtained from optical reflectivity, valence electron energy loss spectroscopy

(VEELS), or band structure calculations.<sup>[7]</sup> The accuracy of the optical properties are critical to the accuracy of the calculated Hamaker constant, but simple index approximation method developed by Tabor–Winterton can be used when extensive data are not available.<sup>[8]</sup> Because the strongest contribution were found to be the high-frequency dielectric responses, the Hamaker constant between materials 1 in the medium 3 can be simplified as:<sup>[9]</sup>

$$A_{131} = \frac{3kT}{4} \left( \frac{\epsilon_1(0) - \epsilon_3(0)}{\epsilon_1(0) + \epsilon_3(0)} \right)^2 + \frac{3h\omega_e}{16\sqrt{2}} \frac{(n_1^2 - n_3^2)^2}{(n_1^2 + n_3^2)^{3/2}} \quad (3)$$

where  $\epsilon$  is the dielectric constant,  $\omega$  is the plasma frequency, and  $n$  is the index of refraction in the visible range.

However, for nano-size particles, it is very difficult to obtain accurate dielectric spectral parameters over the entire frequency range because quantum effects would influence the dielectric data of the given materials. In addition, local dielectric constant of the solvent may be changed because the mobility of the solvent molecules around small ions or particles is restricted in the solvation zone.<sup>[10]</sup>

## Electrostatic Forces

When particles are immersed in a polar liquid such as water, the surfaces are electrically charged. The main sources of this charge are the direct ionization of surface groups, specific ion adsorption, differential ion solubility, and substitution of surface atoms.<sup>[11]</sup> The charge induces an electrostatic potential, which has a certain value at the surface  $\Psi_0$ . Ions of opposite charge, the so-called counterions, dissolved in the polar liquid start to be attracted to the surface of the charged particles. There will be a local excess of counterions around the particles and the result is the development of two layers of different charges. This is known as the electric double layer (EDL), which is composed of the Stern layer and the diffuse layer, as illustrated in Fig. 1. In the Stern layer, counterions are strongly adsorbed and they lower the electric potential at points adjacent to the particle surface. The electrical potential at any point in the diffuse layer can be obtained from the Poisson–Boltzmann (PB) equation:

$$\nabla^2 \psi = \frac{-2nZe}{\epsilon_r \epsilon_0} \sinh \left( \frac{Ze\psi}{2kT} \right) \quad (4)$$

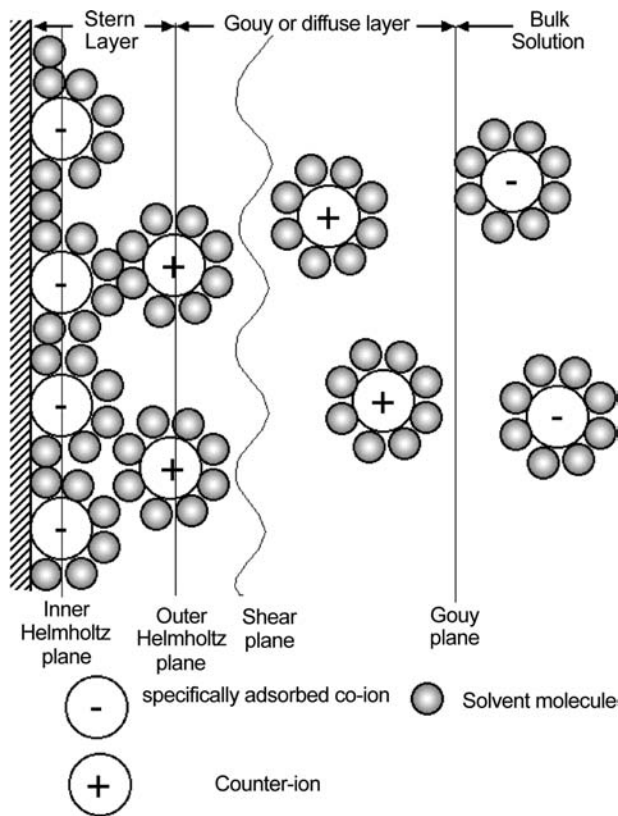


**Fig. 1** Schematic representation of the electric double layer (EDL). The surface due to the presence of charge has a potential  $\Psi_0$ . The outer Helmholtz plane (OHP) marks the closest distance that counterions can come to the surface. Next are the shear plane and the value of the potential at the point called  $\zeta$ -potential ( $\Psi_\zeta$ ).

where  $e$  is the electron charge,  $Z$  is the valence,  $n$  is electrolyte concentration,  $\epsilon_0$  is the dielectric permittivity of vacuum, and  $\epsilon_r$  is the dielectric constant of the solvent, respectively.

The solution of Eq. (4) can be obtained differently depending on the particle size and surface potential, as shown in the Table 1. If the particle size is large, the double layer can be treated as flat and Cartesian coordinates are applied. The Debye–Hückel length  $\kappa$ , which is the inverse of the Debye constant, gives the

thickness of that layer;

$$\Lambda = \kappa^{-1} = \left( \frac{2nZ^2e^2}{\epsilon_r\epsilon_0kT} \right)^{-\frac{1}{2}} \quad (5)$$

However, for nanoparticles, the double layer must be considered as spherical, and Debye–Hückel length can be expressed as:<sup>[12]</sup>

$$\frac{\sigma_d e}{\epsilon_r\epsilon_0\kappa kT} = 2 \sinh\left(\frac{e\xi}{2kT}\right) \left[ 1 + \frac{2}{\kappa a \cosh^2\left(\frac{e\xi}{kT}\right)} + \frac{8 \ln\left[\cosh\left(\frac{e\xi}{4kT}\right)\right]}{\kappa^2 a^2 \sinh^2\left(\frac{e\xi}{2kT}\right)} \right]^{\frac{1}{2}} \quad (6)$$

where  $\sigma_d$  is the diffuse layer charge,  $\xi$  is the potential at shear plane (i.e., zeta potential).

When particles of the same charge interact with each other, the repulsive interaction can be analyzed by considering the free energy change and the osmotic pressure generated by the accumulation of ions between the particles. The complete solution for this interaction is complicated, but simple expression for the electrostatic repulsive energy between two approaching spheres of radius  $a$ , with low surface potential  $\Psi_0$  in a medium of Debye length  $\kappa^{-1}$  is given by:

$$V_{\text{rep}}(r) = \frac{4\pi\epsilon_r\epsilon_0\psi_0^2 a^2}{r} \exp\left[-\kappa a\left(\frac{r}{a} - 2\right)\right] \quad (7)$$

### Derjaguin–Landau–Verwey–Overbeek (DLVO) Theory

van der Waals and EDL forces are the main forces that particles suspended in a solution can experience. Thus the summation of those forces to interaction should give a very good prediction about the interparticle forces. That concept was developed by Derjaguin–Landau–Verwey–Overbeek and is known as the DLVO theory.<sup>[13,14]</sup> The total energy in a particle system can be expressed by the summation of

**Table 1** Solution to the PB equation for high and low surface potentials in a symmetric electrolyte for high and low surface curvature

	$\kappa a \gg 1$	$\kappa a \ll 1$
$\psi_s < 25 \text{ mV}$	$\psi(x) = \psi_1 \exp(-\kappa x)$	$\psi(r) = \frac{a\psi_1}{r} \exp(-\kappa(r - a))$
$\psi_s > 25 \text{ mV}$	$\tanh\left(\frac{y}{4}\right) = \tanh\left(\frac{y_0}{4}\right) \exp(-\kappa x)$ where $y = \frac{ze\psi}{kT}$ and $\kappa = \left(\frac{2Z^2e^2n^\infty}{\epsilon_r\epsilon_0kT}\right)$	$\nabla^2\psi = \frac{d^2\psi}{dr^2} + \frac{2}{r} \frac{d\psi}{dr} = \frac{2ze}{\epsilon_r\epsilon_0} \sinh\left(\frac{e\psi}{kT}\right)$



vdW and EDL energies:

$$V_{\text{total}} = V_{\text{vdW}} + V_{\text{EDL}} \quad (8)$$

The normal criterion is that a barrier of  $25 kT$  is sufficient to achieve stability. The vdW (Eq. (1)), electrostatic (Eq. (7)), and total interaction energy (Eq. (8)) are

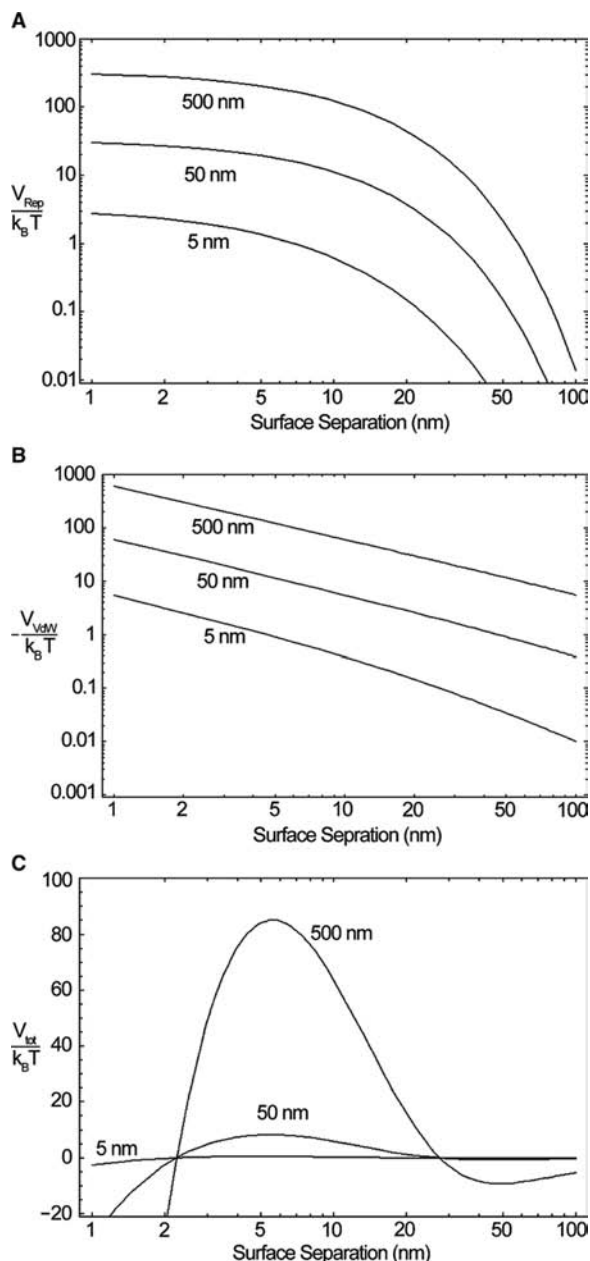


**Fig. 2** The calculated interaction energy between colloid particles as a function of the surface separation from micrometer- to nanometer-size regime of diameter. (A) The repulsive energy calculated from Eq. (7) and the parameters used are  $\Psi_0 = 25 \text{ mV}$ ,  $\kappa^{-1} = 100 \text{ \AA}$ , (B) the non-retarded vdW attractive energy calculated from Eq. (1) and Hamaker constant  $A = 6 \times 10^{-20} \text{ J}$ , (C) the total interaction energy due to both repulsive and attractive forces.

plotted as a function of particle size in Fig. 2. It clearly shows the dependence of the interaction energy on the particle size. The interaction energy increases with particle radius, and the barrier height of the colloidal stability consequently increases as the particle size increases. In other words, as particle size decreases, a greater Stern potential is needed to prevent coagulation. However, the primary and secondary minimum associated with particle coalescence also become deeper as the particle size increases. Thus the range and magnitude of the total interparticle forces is essential in controlling the stability of the given particles. If the relatively large particles coalesce in solution, they will not be separated again because their thermal energy will be insufficient to allow them out of the primary minimum. Nano-sized particles are theoretically easy to decoagulate because of the small primary minimum, although the repulsive barrier is small for nanoparticles. However, kinetics of decoagulation is more important in the practical application of nanoparticles.<sup>[15]</sup> If it is slow, the temporary agglomerate of nanoparticles behaves like a large particle and the vdW interaction energy will gradually increase, and they are difficult to disperse. From this theoretical calculation, it is clear that stabilization by small molecules such as adsorbed polymer or surfactant is much more efficacious than for larger colloidal particles. However, the effect of the repulsive layer thickness on the packing density of nanoparticles has to be considered. A thick repulsive layer is better for the stabilization of particles but it will reduce the achievable packing density.<sup>[16]</sup> Thus, to achieve stable high solids loading slurries, optimal thickness has to be just sufficient to prevent aggregation and minimize the occupied volume.

### Steric and Non-DLVO Forces

Polymeric dispersant molecules have been widely used for stability control in many industries such as ceramic processing, paper, and cosmetics.<sup>[17]</sup> When the polymers are added, they start to adsorb on the surface to minimize the total energy. When particles come close and the chains try to penetrate each other, the entropy is dramatically reduced. Consequently, this effect, known as steric force, prevents particles from coming in distance less than the gyration radius of the polymer. The interaction features of particles are dependent on the concentration of the added polymer. When the concentration is low and not sufficient to cover the surfaces of particles, polymer bridging may occur, where one polymer chain adsorbed on one surface attaches to another particle. The result will be the flocculation of particles. If the polymer concentration keeps increasing beyond full surface coverage, then another effect takes place. When the excess polymer exist in the solution

and the fully coated particles approach closer (i.e.,  $<$  radius of gyration), the non-adsorbed free polymers between them start to be excluded as a result of entropic effects. Eventually, the local concentration becomes lower than the surrounding level. The concentration difference creates osmotic pressure difference that attracts two particles. This is known as the depletion flocculation. If the concentration increases even more then, the polymer actually becomes the solvent and the depletion effect is reversed. The particles are pushed apart and the system is stabilized. This effect is known as depletion stabilization.

In further detail, the conformation of the polymer is important in determining the interactions between them. The conformation of polymers adsorbed to the surface of the particles depends on a number of parameters in the system, such as the solvency of the solution, relative charge of polymer and particles, as well as pH and ionic strength.<sup>[18]</sup> In addition, the relative size of the polymer and colloidal particle may affect the conformation of the polymer. When polymer molecules interact with the nanoparticles, which have a relatively similar size to the polymer molecules, different conformation features are expected. According to molecular dynamics (MD) simulations for the interaction of polyethylene oxide (PEO) with colloidal silica, polymers adopt a flat conformation on the surface when polymer molecules are much larger than the particles. In contrast, when the particle size increases, polymer adopts an extended conformation consisting of loops and tails.<sup>[19]</sup> The expected polymer conformation, depending on the particle size, is illustrated in Fig. 3.

Although the DLVO theory is universal and is mostly accepted to describe the macroscopic colloidal behavior, there are a number of cases where it does not adequately interpret the measured interaction profiles. Because DLVO is based on a continuum

approach, neglecting solvent effects such as ion–solvent interactions, surface–solvent interactions, and ion–ion correlation, non-DLVO forces occur when the property (e.g., density and mobility) and the molecular structure of solvent near surfaces of particles are different from the bulk property.<sup>[20]</sup> The existence of these forces to explain the stability of the fine powders was confirmed with the development of surface force measurement techniques. For example, it was first observed by Horn that oscillatory solvation (or hydration in water) forces occur between smooth surfaces such as mica at very short separation distances because of the overlap of two solvated surfaces, which arise from the specific solute–solvent and modified solvent–solvent interactions.<sup>[21]</sup> Alternatively, attractive hydrophobic forces may occur because of the unfavorable structure of water (i.e., rearrangement of H-bond) near an interface.<sup>[10]</sup> However, interpretation of these forces is not obvious when a radius of curvature of particle is of the order of a few nanometers. This will be further discussed later.

## SURFACE FORCE MEASUREMENT TECHNIQUES

The colloidal behavior of a particular system can be investigated in several ways such as turbidity,<sup>[22,23]</sup> sedimentation,<sup>[24,25]</sup> electrokinetics,<sup>[26]</sup> viscosity,<sup>[27,28]</sup> etc. Among them, surface force measurement techniques have been a useful method to directly characterize the interaction between particles. While the principal idea of direct force measurement is straightforward, which makes use of Hook's law, the challenge arises in measuring very weak forces at very small surface separations. Several different techniques for measuring interaction forces between macro- and microscopic surfaces have been developed including surface force apparatus (SFA), total internal reflection microscopy (TIRM), and atomic force microscopy (AFM). In this section, the fundamentals of operation of each technique will be described. Furthermore, a few modified techniques and the resultant interaction force measurements for nanoparticles will be introduced.

### Surface Force Apparatus (SFA)

Surface force apparatus (SFA) was first developed by Tabor and Winterton,<sup>[8]</sup> and further refined by Israelachvili and Tabor.<sup>[29]</sup> The principles of this technique are depicted schematically in Fig. 4. SFA is composed of two crossed cylinders, one of which is mounted on a spring and the other on a piezoelectric tube. The separation distance between the two surfaces is monitored through the use of optical

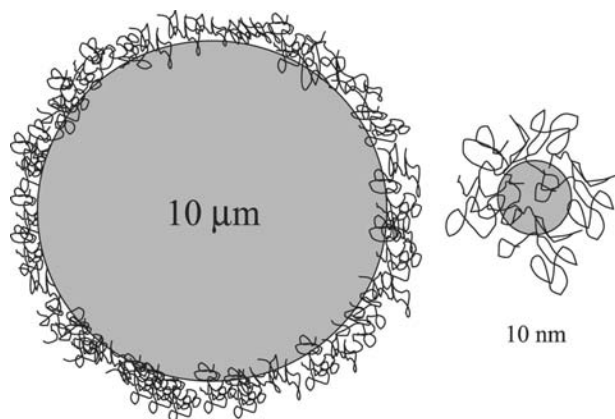


**Fig. 3** Expected polymer conformation with extremely large and small particle sizes.

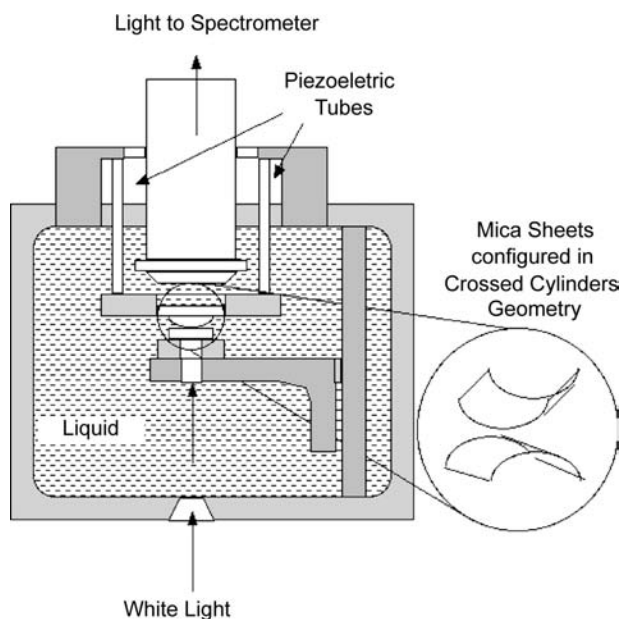


**Fig. 4** A schematic diagram of the surface force apparatus (SFA) for directly measuring the surface forces between surfaces in liquid.

interferometry—fringes of equal chromatic order (FECO). Interaction force is determined by the difference in the applied and measured separation distances multiplied by the spring constant. The distance resolution is approximately 0.1 nm and the force sensitivity is about  $10^{-8}$  N. The advantages of this technique are: 1) true zero separation distance can be known; 2) large range of accessible forces; 3) refractive index of the medium may be simultaneously measured. However, the drawback of this technique is that available samples are limited because surfaces must be optically

transparent and atomically smooth, not to mention the long time-scale experiment.

### Total Internal Reflection Microscopy (TIRM)

This technique measures the change in intensity of an evanescent wave being refracted through the particle for determining the distance between a free particle and a flat surface.<sup>[30]</sup> Mean potential  $\phi(h)$  at separation distance  $h$  is determined by the Boltzmann distribution describing the Brownian motion:

$$p(h) = A \exp(\phi(h)/kT) \quad (9)$$

where  $p(h)$  is proportional to the probability of finding the particle at  $h$ . Force curve is produced by allowing the particle to oscillate in a potential minimum. This technique has an excellent sensitivity in the pN range, which makes it possible to measure the secondary minimum. However, the particles must be spherical, optically transparent, and homogeneous to refract light in a regular manner.

### Atomic Force Microscopy (AFM)

Atomic force microscopy (AFM) was developed as an imaging tool of surfaces in the atomic scale in the late 1980s.<sup>[31]</sup> The use of AFM in surface force measurement has been popular since Ducker introduced the colloidal probe technique, where a well-defined single colloidal particle was attached to the cantilever.<sup>[32]</sup> Force is calculated by the deflection of the cantilever multiplied by its spring constant. Separation distance determined by the constant compliance, which is the region that both cantilever and substrate move

**Table 2** Comparison of SFA, TIRM, and AFM techniques

	SFA	TIRM	AFM
Advantages	True zero separation distance is known Large range of accessible forces Forces measured at equilibrium	High force sensitivity Rotational movement of particle is not hindered	Any materials can be measured Changing solution is relatively easy Approach rate is variable
Disadvantages	Very sensitive to particle contamination Long time scale for experiments Surfaces must be optically transparent and molecularly smooth	True zero separation distance is unknown Particle must be spherical, optically transparent, and homogeneous Maximum force range is limited	True zero separation distance is unknown Sensitive to electrical noise
Sample size	1–2 cm	5–35 $\mu\text{m}$	1–50 $\mu\text{m}$
Force sensitivity	$10^{-7}$ N	$10^{-14}$ N	$10^{-12}$ N

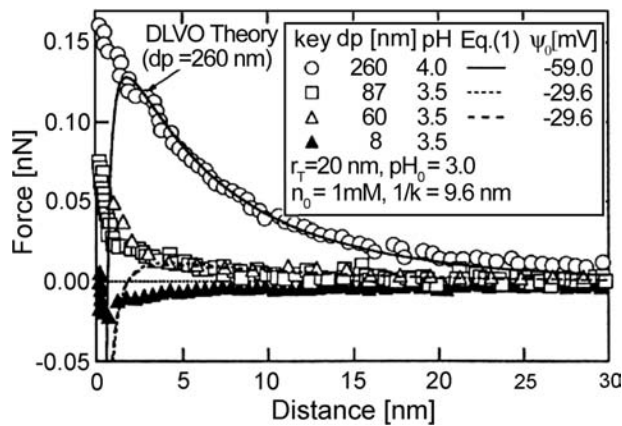


**Fig. 5** Effect of the silica particle diameter ( $d_p$ ) on the force measured via AFM. Solid and broken lines are theoretical fits to the DLVO theory for a constant surface potential. *Source:* From Ref.<sup>[34]</sup>. © 2002 American Ceramic Society.

together after contact. Because the interaction surface area is smaller than SFA, this technique is less sensitive to the surface contamination, and another advantage is that almost all materials can be investigated, including hydrophilic and hydrophobic surfaces, and biological molecules. However, true separation distance is unknown because zero separation is assumed from the constant compliance. Force sensitivity is about  $10^{-12}$  N and distance resolution is 0.1 nm. Some

essential features of three techniques are summarized in Table 2.

### Surface Force Measurement for Nanoparticles

Although the techniques explained above have been powerful tools to measure the interaction force between particles, the size of the sample is limited to micrometers. In AFM, for instance, the attachable colloidal particle is normally a few tens of micrometers and the direct use of AFM tip in many studies have raised some controversy regarding measurement. For example, Cleveland, Schaffer, and Hansma<sup>[33]</sup> measured oscillatory hydration potential on calcite ( $\text{CaCO}_3$ ) and barite ( $\text{BaSO}_4$ ) by using thermal-mechanical noise of cantilever. On the other hand, Kamiya et al.<sup>[34]</sup> utilized the  $\text{Si}_3\text{N}_4$  AFM tip over one primary silica particle after imaging the silica compacts in water to study the effect of the particle size on the formation of hydration layer around the surface. They observed, with FTIR and force measurement, that no hydration force was found for nanoparticles with a diameter of less than about 30 nm (Fig. 5), and a different silanol structure on the surface of  $\text{SiO}_2$  was suggested, depending on the radius of curvature of the particle.

Normally, the typical AFM tip is of pyramidal or cone shape. In a much-sharpened tip, the radius of curvature is about few nanometers in size, but the

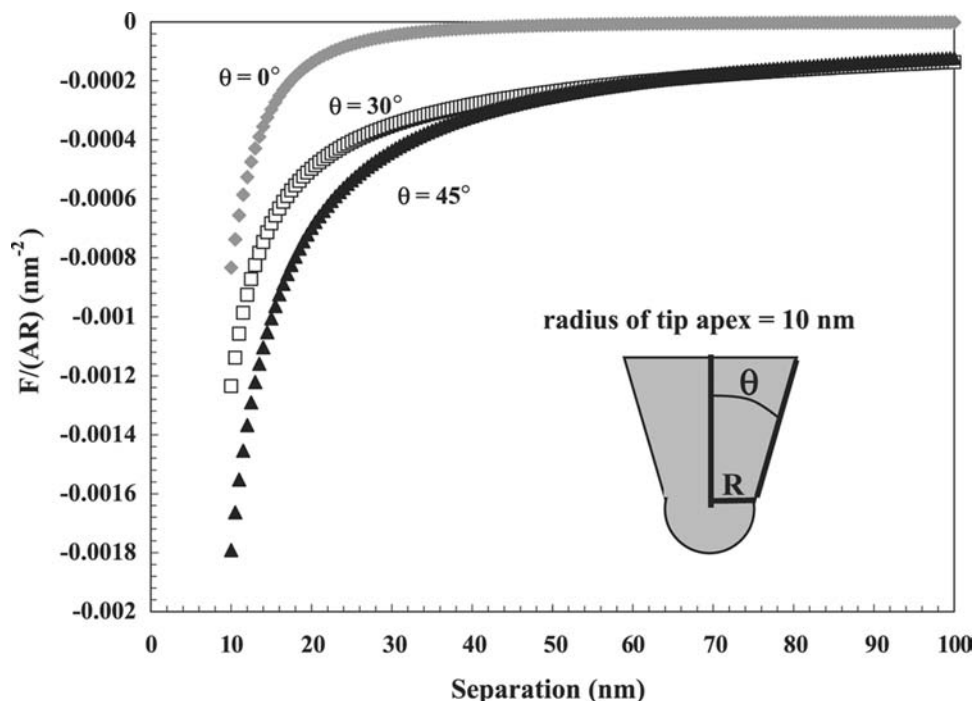


**Fig. 6** Calculated van der Waals interaction force between a cone-shaped AFM tip and a flat plate depending on the angle  $\theta$ .

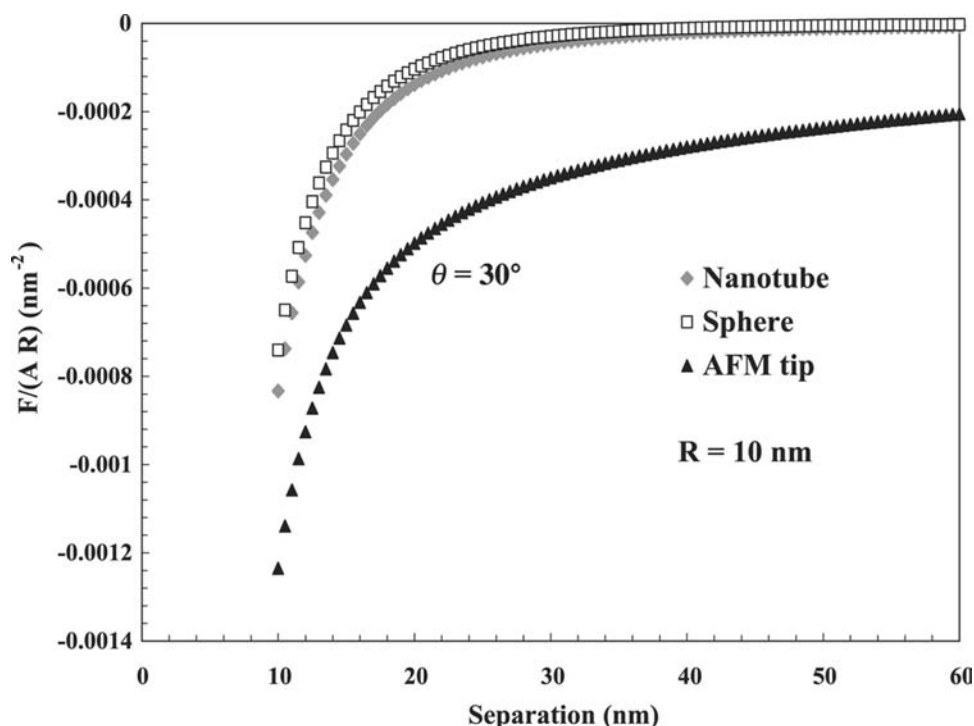


Fig. 7 The calculated van der Waals interaction force of cone-shaped AFM tip, nanosphere, and nanotube tip with a flat plate.

effect from the side wall cannot be neglected in force measurement. Fig. 6 shows how interaction force is affected by the tip angle. The wider the tip, the larger is the expected contribution from the side. Although it is ideal to mount the single nanoparticle on the cantilever, handling and attaching it to the right position is empirically infeasible. To overcome the side effect from the AFM, the carbon nanotube attached tip, so called, the nano colloidal probe technique was recently presented.<sup>[35,36]</sup> Carbon nanotube has extraordinary electrical and mechanical properties such as high resilience. The possible use of the nanotube as an alternative to the single nanoparticle to investigate the interaction force of nanoparticles can be validated with a theoretical calculation as shown in Fig. 7. The calculated force with a conventional AFM tip is much deviated from the force of nanoparticle. On the other hand, the nanotube tip, which has a high aspect ratio, can well represent the interacting behaviors of the nanoparticles as a result of the minimum effect from the side wall. The schematic operation feature of the nanotube-attached AFM tip in force measurement is well described by Cho and Sigmund.<sup>[36]</sup> Unlike the typical deflection signal vs. separation distance, where only one constant compliance exists, two constant compliance regions are observed with a nanotube tip. One is from the contact between the nanotube and substrate, and the other from the consecutive contact between the AFM tip and substrate after bending of the nanotube.

Jarvis et al.<sup>[35]</sup> presented the structural force measurement using the nanotube AFM tip, and found out the scalability of the structural forces to nanoscale and observed the solvation shell on the non-rigid

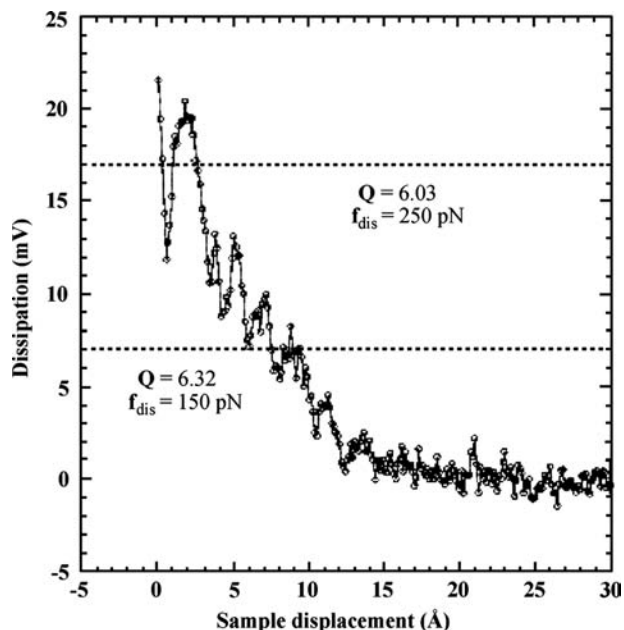
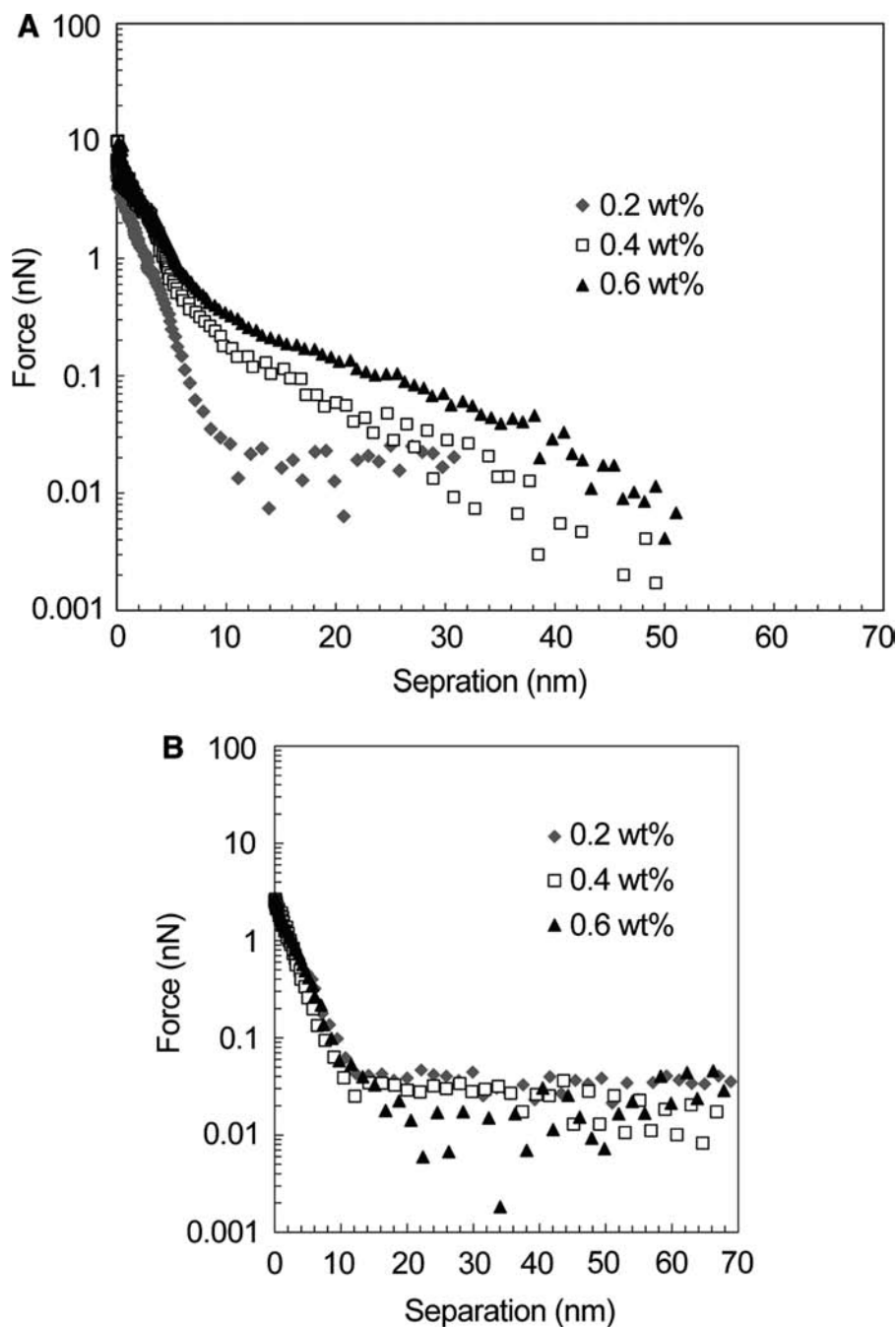


Fig. 8 Measurement of solvation shell between the carbon nanotube and hydrophilic self-assembled monolayer of  $\text{COOH}(\text{CH}_2)_{10}\text{-SH}$  on flat Au surface. Source: From Ref.<sup>[35]</sup>. © 2002 American Chemical Society.



**Fig. 9** (A) Force vs. separation plot between a bare Si tip and SiO<sub>2</sub> substrate (pH 10, 0.01 M NaCl). (B) Force vs. separation plot between a Multiwalled carbon nanotube (MWNT) probe and SiO<sub>2</sub> substrate. Measured forces were independent of the concentration of Polyethyleneimine (PEI) (pH 10, 0.01 M NaCl).

surface, as shown in Fig. 8. Curves showed a periodicity corresponding to the diameter of water molecule and an increase of dissipation at smaller separation due to layering of water. Interaction forces between the nanoparticles in the presence of polymer measured using the nanotube tip shows the different interaction force from one having a bare AFM tip. As shown in Fig. 9, while the forces between the silicon AFM tip and SiO<sub>2</sub> substrate increases with the concentration of polymer, the forces of nanotube tip are independent of the concentration of the polymer. The magnitude and range of the interaction force is

obviously small. This can be explained that, as the concentration of polymer increases, the more packing of the polymer is induced and the thickness of the incompressible layer increases, consequently the resultant interaction layer is also increased. However, the nanotube tip may penetrate into the layer of polymer up to a certain point irrespective of the polymer concentration.

The other application of force measurements using the carbon nanotube probe is to sense and manipulate the biological samples at the molecular level. Wong et al.<sup>[37]</sup> demonstrated the titration of



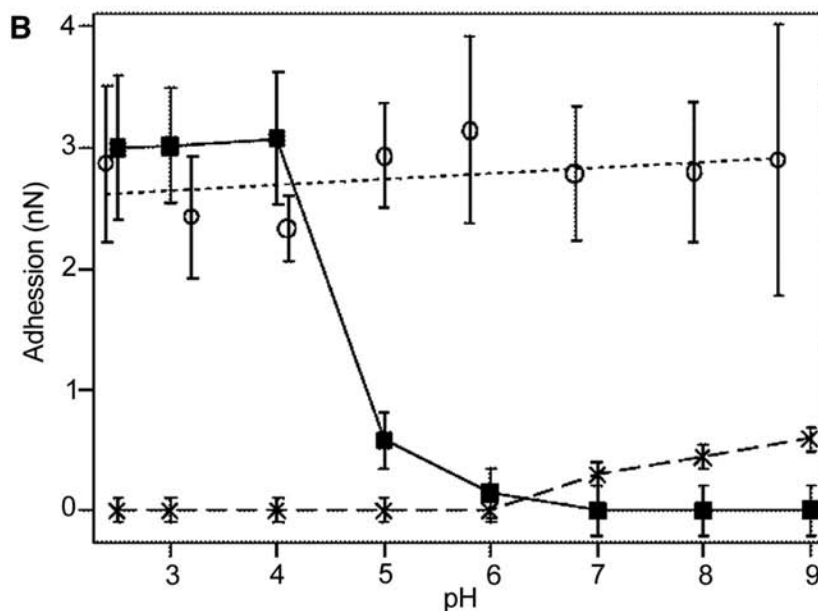
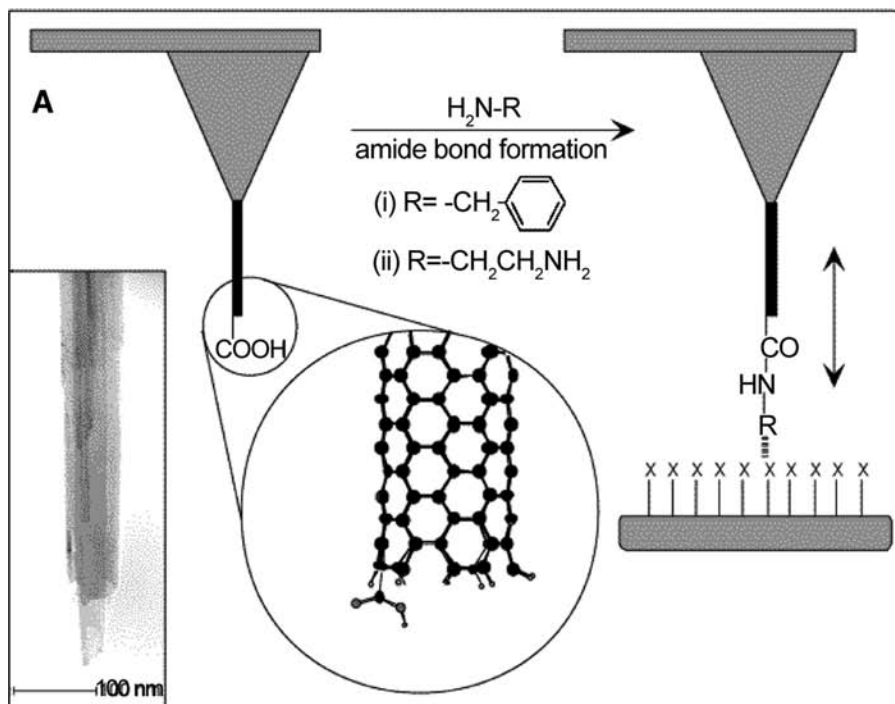


**Fig. 10** (A) Diagram illustrating the modification of carbon nanotube by coupling an amine to a pendant carboxyl group. (B) Adhesion force as a function of pH between hydroxy-terminated SAM. Filled squares: carboxyl (unmodified); open circles: phenyl (modified with benzylamine); crosses: amine (modified with ethylenediamine). *Source:* From Ref.<sup>[37]</sup>. © 2002 Macmillan Magazines Limited.

carboxyl-terminated nanotube by measuring the adhesion force (Fig. 10) and the possibility of detecting the binding force between single protein–ligand pairs.<sup>[37]</sup>

## CONCLUSION

Understanding of the fundamentals of the interacting forces between two objects has been an important issue in colloidal processing, chemistry, biology, etc. The classes and origins of the surface forces including

van der Waals, electrical double layer, steric, and solvation forces are reviewed. Reasonable theories predicting the forces acting on particles of micron size are available, but questions still remain if we scale them down to nanometer range. Currently available surface force techniques were briefly reviewed and a few of examples of direct measurement of surface forces of nanometer-scale objects were introduced. Nanotube-attached AFM tip will be capable of directly measuring the forces of matters at nano level and answering the questions arising from size effect on surface forces.

## REFERENCES

- Horn, R.G. Surface forces and their action in ceramic materials. *J. Am. Ceram. Soc.* **1990**, *73* (5), 1117–1135.
- Johnson, C.A.; Lenhoff, A.M. Adsorption of charged latex particles on mica studied by atomic force microscopy. *J. Colloid Interface Sci.* **1996**, *179* (2), 587–599.
- Kappl, M.; Butt, H.J. The colloidal probe technique and its application to adhesion force measurements. Part. Part. Syst. Charact. **2002**, *19* (3), 129–143.
- Derjaguin, B.V. Friction and adhesion. IV: The theory of adhesion of small particles. *Kolloid-Z.* **1934**, *69*, 155.
- Hamaker, H.C. The London–van der Waals attraction between spherical particles. *Physica (Amsterdam)* **1937**, *4*, 1058–1072.
- Dzyaloshinskii, I.E.; Lifshitz, E.M.; Pitaevskii, L.P. The general theory of van der Waals forces. *Adv. Phys.* **1961**, *10* (38), 165–209.
- French, R.H. Origins and applications of London dispersion forces and Hamaker constants in ceramics. *J. Am. Ceram. Soc.* **2000**, *83* (9), 2117–2146.
- Tabor, D.; Winterton, Rh. Direct measurement of normal and retarded van der Waals forces. *Proc. R. Soc. Lond., A Math. Phys. Sci.* **1969**, *312* (1511), 435–450.
- Mahanty, J.; Ninham, B.W. *Dispersion Forces*; Academic Press: New York, 1976.
- Israelachvili, J.N. *Intermolecular and Surface Forces*, 2nd Ed.; Academic Press: San Diego, 1991.
- Hunter, R.J. *Foundations of Colloid Science*; Clarendon Press: Oxford, 1989.
- Ohshima, H.; Healy, T.W.; White, L.R. Accurate analytic expressions for the surface-charge density surface–potential relationship and double-layer potential distribution for a spherical colloidal particle. *J. Colloid Interface Sci.* **1982**, *90* (1), 17–26.
- Derjaguin, B.V.; Landau, L.D. Theory stability of highly charged lyophobic sols and adhesion of highly charged particles in solutions electrolytes. *Acta Physicochim. USSR* **1941**, *14*, 633–662.
- Verwey, E.J.W.; Overbeek, T.G. *Theory of Stability of Lyophobic Colloids*; Elsevier: Amsterdam, Netherlands, 1948.
- Mulvaney, P. Zeta Potential and Colloid Reaction Kinetics. In *Nanoparticles and Nanostructured Films*; Fendler, J.H., Ed.; Wiley-VCH: New York, 1998; 275–306.
- Sigmund, W.M.; Bell, N.S.; Bergstrom, L. Novel powder-processing methods for advanced ceramics. *J. Am. Ceram. Soc.* **2000**, *83* (7), 1557–1574.
- Napper, D.H. *Polymeric Stabilisation of Colloidal Dispersions*; Academic Press: London, 1983.
- Russel, W.B.; Saville, D.A.; Schowalter, W.R. *Colloidal Dispersions*; University Press: Cambridge, 1989.
- Cosgrove, T.; Griffiths, P.C.; Lloyd, P.M. Polymer adsorption—the effect of the relative sizes of polymer and particle. *Langmuir* **1995**, *11* (5), 1457–1463.
- Greathouse, J.A.; McQuarrie, D.A. Conventional hypernetted chain force calculations for charged plates with adsorbing counterions. *J. Colloid Interface Sci.* **1996**, *181* (1), 319–325.
- Horn, R.G.; Israelachvili, J.N. Direct measurement of structural forces between 2 surfaces in a non-polar liquid. *J. Chem. Phys.* **1981**, *75* (3), 1400–1411.
- Dedinaite, A.; Claesson, P.M. Interfacial properties of aggregates formed by cationic polyelectrolyte and anionic surfactant. *Langmuir* **2000**, *16* (4), 1951–1959.
- Fielden, M.L.; Claesson, P.M. A comparison of three methods for the convenient determination of sodium dodecyl sulfate in aqueous solutions. *J. Colloid Interface Sci.* **1998**, *198* (2), 261–265.
- Colic, M.; Fisher, M.L.; Franks, G.V. Influence of ion size on short-range repulsive forces between silica surfaces. *Langmuir* **1998**, *14* (21), 6107–6112.
- van der Kooij, F.M.; Philipse, A.P.; Dhont, J.K.G. Sedimentation and diffusion in suspensions of sterically stabilized colloidal platelets. *Langmuir* **2000**, *16* (12), 5317–5323.
- Colic, M.; Fuerstenau, D.W. Influence of the dielectric constant of the media on oxide stability in surfactant solutions. *Langmuir* **1997**, *13* (25), 6644–6649.
- Cho, J.M.; Dogan, F. Colloidal processing of lead lanthanum zirconate titanate ceramics. *J. Mater. Sci.* **2001**, *36* (10), 2397–2403.
- Zaman, A.A.; Bjelopavlic, M.; Moudgil, B.M. Effect of adsorbed polyethylene oxide on the rheology of colloidal silica suspensions. *J. Colloid Interface Sci.* **2000**, *226* (2), 290–298.
- Israelachvili, J.N.; Tabor, D. Measurement of van-der-Waals dispersion forces in range 1.4 to 130 Nm. *Nat., Phys. Sci.* **1972**, *236* (68), 106.
- Prieve, D.C.; Frej, N.A. Total internal-reflection microscopy—a quantitative tool for the measurement of colloidal forces. *Langmuir* **1990**, *6* (2), 396–403.
- Binnig, G.; Quate, C.F.; Gerber, C. Atomic force microscope. *Phys. Rev. Lett.* **1986**, *56* (9), 930–933.
- Ducker, W.A.; Senden, T.J.; Pashley, R.M. Direct measurement of colloidal forces using an atomic force microscope. *Nature* **1991**, *353* (6341), 239–241.
- Cleveland, J.P.; Schaffer, T.E.; Hansma, P.K. Probing oscillatory hydration potentials using thermal–mechanical noise in an atomic-force microscope. *Phys. Rev., B* **1995**, *52* (12), R8692–R8695.
- Kamiya, H.; Mitsui, M.; Takano, H.; Miyazawa, S. Influence of particle diameter on surface silanol structure, hydration forces, and aggregation behavior of alkoxide-derived silica particles. *J. Am. Ceram. Soc.* **2000**, *83* (2), 287–293.
- Jarvis, S.P.; Uchihashi, T.; Ishida, T.; Tokumoto, H.; Nakayama, Y. Local solvation shell measurement in water using a carbon nanotube probe. *J. Phys. Chem., B* **2000**, *104* (26), 6091–6094.
- Cho, J.M.; Sigmund, W.M. Direct surface force measurement in water using a nanosize colloidal probe technique. *J. Colloid Interface Sci.* **2002**, *245* (2), 405–407.
- Wong, S.S.; Joselevich, E.; Woolley, A.T.; Cheung, C.L.; Lieber, C.M. Covalently functionalized nanotubes as nanometre-sized probes in chemistry and biology. *Nature* **1998**, *394* (6688), 52–55.

# Surface Plasmon Spectra of Silver and Gold Nanoparticle Assemblies

**Mondona Zangeneh**

*Department of Chemistry, San Jose State University, San Jose, California, U.S.A.*

**Roger Terrill**

*San Jose State University, San Jose, California, U.S.A.*

## INTRODUCTION

This work is a brief topical review of recent literature reports of the localized surface plasmon spectra of silver and gold nanoparticles (NPs) in various assemblies. The desire for such a review arises from the numerous recent reports of NP assemblies, their optical properties, and the importance of their potential applications. The optical properties can be viewed from the perspective of isolated particles, particles coupled by near-field light interactions (roughly when the interparticle separation is less than particle size), and those coupled by far-field interactions (for well separated particles in arrays or gratings). The NPs reviewed are sized from ca. 20–500 nm in diameter or major axis (except for wires), are of various shapes, e.g., spheres, triangles, cylinders, etc., and are arranged by various means including synthetic molecular linking architectures. The preparation of interesting NP systems builds, in part, on relatively recent NP synthetic strategies that yield NPs of uniform size and often organized 1-, 2- and 3-D NP assemblies. Methods for making NPs fall into two broadly defined categories: those based on physical metal deposition and those based on solution chemistry, the latter including electrodeposition. Physical metal deposition methods encompass electron beam lithography (EBL), nanosphere- and colloidal lithography, metal island films, and cosputtered composite materials. Powerful EBL methods can produce arbitrary NP shapes and arrangements, and sizes of about 50 nm and larger are in the literature. Nanosphere lithography, pioneered by Van Duyne et al. (vide infra), yields arrays of triangular and related particles in the 90–2500 nm range. Simple metal island films, e.g., from 2 to 3 nm mass thickness Au and Ag evaporated directly onto non-wetting oxide substrates, can yield reasonable NP distributions, as can cosputter-deposited composites of metal and oxide matrix (e.g., Ag and SiO<sub>2</sub>). Chemical NP preparations resulting in uniform size distributions (e.g., <10% variability) have been the subject of extensive recent development and are predominantly

from two methods: 1) solution phase synthesis (often with a fractional precipitation step); and 2) templating methods such as electrodeposition into nanoporous Al<sub>2</sub>O<sub>3</sub> membranes.

## Localized Surface Plasmon Resonance in Noble Metal Nanoparticles

Light of appropriate wavelength can excite collective oscillations of the conduction electrons in Au, Ag, and other metal NPs—the theoretical description of which by Mie dates back to the turn of the twentieth century.<sup>[1,2]</sup> This phenomenon is analogous to the surface plasmon polariton that can be excited by evanescent wave irradiation in planar metal surfaces. The plasma oscillation in metal NPs of spherical symmetry is well described by the Mie equations, which are solutions to Maxwell's equations for electromagnetic (EM) radiation interacting with small particles ( $d < \lambda/10$ ). The plasma oscillation is variably referred to as a (localized) surface- or particle-plasmon resonance—we adopt the term *localized* surface plasmon (LSPR) coined by Van Duyne et al. to distinguish the NP phenomenon from the propagating surface plasmon polariton of planar metal surfaces.<sup>[3]</sup> Because of the very high electronic polarizability of noble metal NPs, their LSPR oscillations couple very efficiently with light. Accordingly, extinction of transmitted light by NPs is enormous—equivalent to molecular absorption with a molar extinction coefficient  $10^{11} \text{ M}^{-1} \text{ cm}^{-1}$  in some cases.<sup>[4]a</sup> Similarly, a 100-nm Ag NP scatters light equivalently to the emission of  $10^6$  fluorescein fluorophores.<sup>[5]</sup> The strong extinction band ranges from the blue (e.g., 420 nm for 40 nm Ag spheroids in air<sup>[6]</sup>) throughout the visible and into the infrared (e.g., 6000 nm for 2500-nm Ag triangles<sup>[4]</sup>). In most cases,

<sup>a</sup>The term extinction refers to the aggregate effect of absorption and scattering and differentiates LSPR scattering and absorption from molecular absorption.

the peak wavelength of the LSPR band ( $\lambda_{\text{LSPR}}$ ) will red shift with increasing ambient or substrate dielectric constant ( $\epsilon$ ), increasing particle size, or aggregation.<sup>[7]</sup> The high sensitivity to dielectric constant ( $\Delta\lambda_{\text{LSPR}}/\Delta\epsilon$ ), and the highly localized nature of surface electric fields (projecting out from the NP surface by only a small fraction of the light wavelength in some cases) underpins the utility of NPs as surface-affinity based chemical and biosensors.<sup>[8]</sup> The high intensity of the surface electric fields associated with the LSPR of NPs and NP aggregates also underpin spectral enhancements such as the Raman effect.<sup>[9]</sup> NPs and NP films are also interesting for their potential applications in non-linear optics.<sup>[10,11]</sup> The dynamics of NP LSPR processes occur on the femtosecond time scale, and have been explored by Link and El-Sayed.<sup>[12]</sup>

### Theory and Simulation of Nanoparticle Surface Plasmon Spectra

There are a number of excellent recent papers covering theoretical aspects of the optical response, i.e., extinction, scattering, and electric field strengths, of Au and Ag NPs.<sup>[13–17]</sup> The following is merely an overview intended to elucidate points about: 1) the Mie theory,<sup>[18]</sup> 2) the calculation of the small-particle dielectric constants from the bulk-metal values,<sup>[13–15]</sup> 3) calculations of effective refractive index (RI) for particle aggregates,<sup>[15,19,20]</sup> and 4) computational solutions for arbitrary shapes and arrangements.<sup>[16,17]</sup> Discrete electronic structure is not seen in the LSPR spectra of Au and Ag particles larger than about 2 nm and is not discussed.

Mie theory is a set of exact solutions to Maxwell's equations for light interacting with small spherical particles, and is an excellent model for a wide range of NPs of spherical or nearly spherical symmetry. Typically, Mie theory is used to calculate the extinction cross section ( $\sigma$ ) of NPs, and for particles of less than about 20 nm, only the dipolar solution is important:

$$\sigma = \frac{9V\epsilon_M^{3/2}}{c} \frac{\omega\epsilon'(\omega)}{(\epsilon(\omega)' + 2\epsilon_M)^2 + \epsilon'(\omega)^2}$$

where  $\sigma$  is the scattering cross section,  $V$  is the particle volume,  $\epsilon_M$  is the dielectric constant of the medium, and the complex dielectric constant of the metal is  $\epsilon = \epsilon(\omega)' + i\epsilon(\omega)''$ . For a real and fairly constant  $\epsilon_M$ , resonance condition is fulfilled when  $\epsilon(\omega)' = -2\epsilon_M$  for spheres (or  $\epsilon(\omega)' = -\epsilon_M$  for long rods when the electric field is polarized perpendicular to the long axis). The wavelength dependence of  $\lambda_{\text{LSPR}}$  originates from three places—the wavelength and size dependence of  $\epsilon(\omega)$ , the appearance of quadrupole resonances (higher order Mie solutions) for particles

larger than about 20 nm, and damping when, because the particle is approaching or exceeds the light wavelength, the electric field is no longer homogeneous within the particle. Mie theory can also be used to calculate local field strengths.

Accurate application of Mie theory requires good estimates of the frequency-dependent dielectric [ $\epsilon(\omega)$ ] of the NP. But for smaller NPs, adjustments are needed, especially as the NP radius approaches the bulk metal electron mean free path,  $R_B$ . At this point,  $\epsilon(\omega)$  appears to diverge from that of bulk metal. If one considers the contribution to  $\epsilon(\omega)$  from the free electrons to be distinct from other sources, Drude theory can be applied to the confined conduction electrons, and accurate predictions of LSPR band position and shape can be made. This is accomplished by recalculating the electron damping frequency,  $\omega_D = v_F/R$ , where  $v_F$  is the Fermi velocity, using a reduced mean free path,  $R_{\text{EFF}} = (R_{\text{NP}}^{-1} + R_B^{-1})^{-1}$  that reflects electron scattering from the NP surface.<sup>[14,15]</sup> This adjustment also predicts the rapid broadening of NP LSPR bands into baseline as the radius falls below about 2 nm. Electronic fine structure is just discernible in the derivative spectra of Au particles of 1.4 nm and smaller, but does not substantially impact the overall band shapes.<sup>[14]</sup>

Prodan et al. very recently contributed a theoretical approach to the description of LSPR modes. This model is described as the electromagnetic analog of molecular orbital theory, in that it uses a hybridization approach directly analogous to that describing atomic and molecular electronic structures.<sup>[21]</sup> This approach is supported by successful calculations of nanoshell LSPR modes by Nordlander, who treat the electronic structure of the shell with ab initio electronic structure calculations (time-dependent local density approximation) and within the jellium approximation.<sup>[22]</sup> In this method, the nanostructure LSPR is described as the sum of simpler, interacting ones. Or, in other words, the plasmon modes of the simpler or elementary structures hybridize to form new modes. For example, the LSPR of a Au nanoshell (e.g., an Au-coated SiO<sub>2</sub> sphere) is well known to have two prominent LSPR modes. In the hybridization model, these are clearly seen to arise from the symmetric and antisymmetric combinations of the dipolar plasmons of two, more elementary structures: 1) an Au sphere; and 2) a dielectric cavity in an Au medium. Building on this result, two concentric nanoshells can then be described by the symmetric and antisymmetric sums of the inner and outer shell LSPR modes. Hybridization model spectra of concentric nanoshells are in excellent agreement with experiment.

For NP assemblies where the NP volume fraction is significant, there arises the problem of how to accurately account for NP contributions to the medium

dielectric constant  $\epsilon_M$ . In general, the Maxwell–Garnett (MG) theory seems to be the more successful, established theory, although the Bruggeman theory is also used.<sup>[15,19,20,23]</sup> The MG theory predicts the aggregate (complex) dielectric constant,  $\epsilon_C$ , assuming a composite material made up of a matrix of  $\epsilon_M$  and a volume fraction,  $f_M$ , significantly less than 0.5, of “infinitesimal” particles (i.e., much smaller than  $\lambda$ ) of dielectric  $\epsilon_0$ :

$$\frac{\epsilon_C - \epsilon_0}{\epsilon_C + \kappa\epsilon_0} = f_M \left( \frac{\epsilon_M - \epsilon_0}{\epsilon_M + \kappa\epsilon_0} \right)$$

The factor  $\kappa$  is a shape-dependent factor equal to 2 for spherical particles, and 1 for infinitely long “needles” oriented perpendicularly to the incident EM field. For example, Mulvaney<sup>[24]</sup> applied the MG theory to spherical SiO<sub>2</sub>-coated Au NPs of variable Au volume fraction. In this case, the MG theory was very well able to predict the red shift in  $\lambda_{\text{SPR}}$  for Au volume fractions less than about 0.5, but somewhat underestimated it thereafter. The MG theory was also adapted by Foss et al.<sup>[25]</sup> to apply to nanorods with variable aspect ratios through the incorporation of a wavelength-dependent  $\kappa_{\text{EFF}}$  value. The  $\kappa_{\text{EFF}}$  model, also known as dynamic Maxwell–Garnett theory, successfully predicts shape-dependent trends in  $\lambda_{\text{SPR}}$ , but systematically overestimates them. In contrast, naively applying Mie theory to the same rods leads to systematic underestimation of  $\lambda_{\text{SPR}}$ .

Clearly, a more general approach to the prediction of optical and electrostatic aspects of NPs and NP assemblies is desirable. These approaches are generally in the form of computational solutions to Maxwell’s equations using finite-difference approaches. An excellent example of this approach is the work of Schatz et al.<sup>[16]</sup> on the discrete dipole approximation (DDA), which divides the object of interest into a lattice of polarizable cubes whose individual dipole polarizations are determined self-consistently. According to Schatz et al., appropriately applied DDA calculations yield extinction spectra that are consistently within about 10% of the exact or experimental ones independent of the particle size or shape. Other approaches include the multipole–multipole<sup>[26]</sup> and finite difference time domain<sup>[27–29]</sup> variants.

## NANOPARTICLES AND THEIR ASSEMBLIES

The variety of NP shapes, sizes, architectures, and strategies for organizing and studying NPs inspires this section—hence it moves topically through a cross section of the literature by the dimensionality of the NP assembly in question. Other important themes such

as LSPR coupling and multipolar LSPR modes span various dimensionalities and are noted throughout. Nanoparticles have been studied individually, in random 2- and 3-D arrangements and in lithographically organized assemblies or as determined by molecular architectures. Various studies examine LSPR spectra as a function of particle size, shape, spacing, dielectric medium, polarization, and incident angle of light.

### Single Particles, Dimers, Trimers, and Tetramers

#### Single nanoparticle spectroscopy

Recent spectroscopic reports of single noble metal NPs characterizing roughly spherical and “wire” geometries with attention to their potential application as single-particle sensor platforms include reports by Shultz et al.,<sup>[6,30]</sup> Raschke et al.,<sup>[31]</sup> and McFarland and Van Duyne.<sup>[32]</sup> These studies are akin to single *molecule* spectroscopy, but are technologically easier because of the extremely large Rayleigh scattering efficiency (typically equivalent to 10<sup>5</sup>–10<sup>6</sup> fluorophors) of the surface plasmon peak in an NP.<sup>[5]</sup>

The first of these studies<sup>[30]</sup> examines silver, gold, and nickel nanowires (and various segmented variations) prepared by a combination of electroless and electrochemical deposition steps within the pores of commercial polycarbonate filtration membranes (by Nucleopore) and subsequently released. The nanoscopic pores are produced by high-energy alpha-particle perforation of polycarbonate films and are uniquely suited to the templating of nanoparticles because they are highly uniform in diameter and aspect ratio, the former controlled by the manufacturer by etching the filtration membrane, and the latter by variation of the electrodeposition time. In this case, the pores (and hence nanowires) have nominal dimensions of 15 × 7000 nm. As in the latter studies, the wires were imaged with conventional light microscopy under dark field illumination, and detected by virtue of their intense light scattering cross sections. Spectra were acquired by imaging scattered light onto a single monochromator with charge-couple device (CCD) detector.

In wires, the plasma resonance observed is a transverse (radial), dipolar one. The longitudinal (axial) resonance is not seen because the wires are very long. In these,<sup>[30]</sup> resonances that were evident as peaks in the scattering spectra at ca. 400 nm for Ag and 540 nm for Au–Ni wires did not yield a spectral peak. Mie scattering calculations gave an excellent fit to the observed Au and the featureless Ni spectra, but failed to capture the ca. 400 nm resonance for Ag.

In a subsequent report by Mock, Smith, and Shultz<sup>[6]</sup> the response of the dipole resonance to changes in refractive index for single, 60-nm quasispherical particles was measured by using a series of index matching oils. The observed  $\Delta\lambda_{\text{MAX}}/\Delta n$  was 160 nm—in qualitative agreement with Mie calculations (210 nm) that ignore the SiO<sub>2</sub> substrate half space.

More recently, Raschke et al.<sup>[31]</sup> and McFarland and Van Duyne<sup>[32]</sup> have examined single nanoparticles immobilized on glass in the context of their potential application as chemo- or biosensors with extremely low mass detection limits. Single NP sensors are a tantalizing prospect because of the extreme mass sensitivity and spatial resolution of single NP LSPR. For example, just 60,000 molecules could be detected in a volume smaller than a cellular organelle by single NP scattering, or conversely, a very large number of different assays might be simultaneously conducted in a very small area and volume with an assay based on many uniquely identifiable NPs.<sup>[33]</sup> In the report by McFarland and Van Duyne,<sup>[32]</sup> dark field microscopy/spectroscopy was used to detect alkanethiol adsorption to single Ag nanoparticles prepared by citrate reduction. The bulk refractive index (RI) sensitivity of selected particles,  $\Delta\lambda_{\text{MAX}}/\Delta n = 203$  nm, agreed well with Mie theory predictions. The response to monolayer alkanethiol adsorption was very large, with a hexadecanethiol self-assembled monolayer (SAM) producing an easily detectable 40.7 nm red shift at saturation, and corresponding to only ca. 60,000 molecules detected. The similar report by Raschke et al.<sup>[31]</sup> employed Au NPs derivatized with biotinylated bovine serum albumin and binding diffusing streptavidin. They observed a significant, but small 1.2 nm shift corresponding to saturation—again, just slightly less than that predicted by Mie theory for a  $4\pi$  steradian change in RI. These authors suggest that a rod NP would produce higher sensitivity.

### Nanoparticle dimers, trimers, and tetramers

A number of recent articles have examined the optical response of pairs, dimers, and trimers of NPs. In contrast to the above studies, these systems were studied as ensembles, but the degree of particle homogeneity is high and the results are likely to be representative of the 2-, 3-, or 4-particle systems. Novak and Feldheim<sup>[34]</sup> used rigid molecular linkers of variable lengths in the 2–30 nm range to create bridged NP structures. The thioactyl-terminated phenylacetylene bridges were prepared in three varieties; the first, simply a straight rigid rod-like molecule, and the second and third having a central branching point with three and four branches, respectively. These were reacted with 30-nm-diameter Ag NPs, and the resulting

symmetric dimers, trimers, and tetramers were confirmed with transmission electron microscopy. These important solution-extinction spectroscopy experiments confirmed that as the linker is shortened, the near-field coupling first slightly red-shifts, and then spawns a high-frequency band as the separation approaches about 4 nm.

A more recent paper by Sandrock and Foss<sup>[35]</sup> employs a template analogous to the Nucleopore<sup>TM</sup> ones employed above—transparent and porous Al<sub>2</sub>O<sub>3</sub> membranes to produce varied pairs of NPs within the individual pores and to study them in place, without releasing them from the Al<sub>2</sub>O<sub>3</sub> template. Au and Ag were alternately deposited and Ag later dissolved away to create controlled Au–Au spacing. In this way, sphere–sphere, rod–rod, and rod–sphere near-field interactions could be probed. An important aspect of this motif is that it allows the study of the linear dichroic properties of the NP pairs. For example, because all pores in the Al<sub>2</sub>O<sub>3</sub> support are normal to the surface, it is possible to control the polarization of the incident light such that it is predominantly axial or radial in character. Interparticle interactions were indicated by spectral results that showed splitting under polarization that put an E-field component along the particle–particle axis. A subsequent paper by Gluodenis and Foss<sup>[36]</sup> delves into simulation and theory for side–side and end–end interactions of NP rod pairs.

Subsequent reports by Rechberger et al.<sup>[37]</sup> and Su et al.<sup>[38]</sup> examine ensembles and individual NP pairs (respectively) fabricated by using electron beam lithography. Leitner et al. examined 150-nm disks, that were 17 nm thick and spaced between 150 and 450 nm apart; Zhang et al. studied elliptical particles in the 100–150 nm range. Zhang et al. report a red shift in  $\lambda_{\text{SPR}}$  as the particles are brought into proximity. By examining polarizations both parallel and perpendicular to the interparticle axis, Leitner et al. resolved a strong red shift (+78 nm) and a weaker blue shift (–30 nm) as the 150-nm particles were brought into edge contact. The red shift is attributed to favorable head–tail interparticle electrostatic interactions arising from parallel particle dipoles arranged end to end. The weaker blue shift is attributable to particle dipoles arranged side-by-side. Notably, these interactions did not produce band *splitting* observed for the smaller, chemically synthesized NPs of Novak and Feldheim.<sup>[34]</sup>

### Nanoparticle Chains with Near-Field Coupling

Au and Ag NPs arranged in chains, i.e., in a row, are of interest in the technological arena as “plasmonic light waveguides” for guiding light in subdiffraction spaces



and for the production of electron tunneling electronics such as single electron transistors. Chains have been reported in two predominant contexts: 1) systems such as those fabricated by Atwater et al.<sup>[39–41]</sup> using electron beam lithography for plasmonic waveguide experiments; and 2) smaller NPs templated by naturally faceted surfaces of  $\langle 1010 \rangle$   $\text{Al}_2\text{O}_3$ <sup>[42]</sup> and  $\langle 110 \rangle$   $\text{NaCl}$  (Ref.<sup>[43]</sup>, no optical data). Atwater et al. use sophisticated electron beam lithography to make chains of 50-nm diameter Ag NPs with varying interparticle spacing. For these systems, the *longitudinal* (E-field parallel to NP chain) and *transverse* SP modes slightly red and blue shift, respectively, as the interparticle spacing approaches 75 nm, but do not explore closer spacing. Atwater et al. are also one of the few groups to employ finite difference time domain (FDTD) simulations to simulate the optical responses of these systems. One of the qualities of the FDTD simulation is that in addition to  $E(x,y,z)$ , it gives  $E(t)$ , which is useful for characterizing the properties of NP chains as optical energy waveguides. FDTD simulations of the E-field intensities in these chains agree well with experiments, and are useful for estimating collective properties such as waveguide loss. The  $\text{Al}_2\text{O}_3$  templated Ag NPs are fabricated by pulsed laser deposition, followed by high-temperature (1400°C, 8 hr) annealing, yielding slightly prolate particles broadly distributed about 25 nm in diameter and about 31 nm apart. These chains exhibit a far more pronounced dichroism than those of Atwater et al.:  $\lambda_{\text{TRANSVERSE}} = 455 \text{ nm}$  and  $\lambda_{\text{LONGITUDINAL}} = 550 \text{ nm}$ , reflecting both the smaller particle sizes (ca. 25 nm) and their closer proximity (ca. 31 nm). Theoretical work by Zhao, Kelly, and Schatly<sup>[44]</sup> has also contributed to understanding of chains structures.

Previous examples have been of 1-D NP chains, but individual NP pairs have also been examined. For example, Sandrock and Foss made gold particle pairs by alternately electrodepositing Au and Ag into porous  $\text{Al}_2\text{O}_3$ . In this setting, the electrodeposition time controls the Au and Ag NP lengths, and the pore their widths. Following electrodeposition, Ag sections can be removed with  $\text{HNO}_3$ , leaving voids of controlled size between Au NPs of controlled length.<sup>[35]</sup> Accordingly, paired “spheres” (i.e., unity aspect ratio rods), paired rods, and rod–sphere pairs were studied. For these organized NP pairs, the effects of interparticle spacing and the light polarization and incident angle could be systematically studied. At higher angle of incidence ( $\theta_i$ ), the light E-field falls increasingly along the interparticle axis. For example, for large interparticle spacing (114 nm) between paired spheres,  $\lambda_{\text{SPR}}$  (= 548 nm) is independent of  $\theta_i$ . However, if a smaller interparticle spacing is employed (52 nm),  $\lambda_{\text{SPR}}$  redshifts with an increasing in incidence angle reflecting the favorable near-field coupling of LSPR

dipoles. Rod–sphere pair structures exhibited a long-wavelength shoulder with increasing  $\theta_i$ , similarly indicating near-field interactions. Theoretical models used to evaluate sphere pair systems such as simple quasistatic (i.e., total particle pair size  $\ll \lambda$ ), modified long wavelength approximation (MLWA), and discrete dipole approximation (DDA) models reflected experimental shifts in  $\lambda_{\text{SPR}}$  with  $\theta_i$ , but did not accurately reproduce peak position or shape.

## Two-Dimensional NP Arrays

A rich variety of structures, some highly organized, for example, by intermolecular interactions, have been reported for NPs on surfaces. Also, some of the more intriguing spectral behaviors come from 2-D arrays of optically coupled NPs.

### Two-dimensional NP arrays made by electron beam lithography (EBL)

Aussenegg et al.<sup>[45,46]</sup> have contributed important papers on the optical properties of NP arrays in the far-field coupling regime. The former report employs square arrays (spacing  $\Lambda = 350\text{--}850 \text{ nm}$ ) of circular ( $d = 150 \text{ nm}$ ) gold EBL-fabricated NPs studied by both extinction and femtosecond time resolved luminescence measurements. Interestingly, the arrays exhibited a correlated oscillation in  $\lambda_{\text{SPR}}$  and luminescence lifetime ( $2 \leq \tau_{\text{SPR}} \leq 8 \text{ fsec}$ ), as the particle spacing increased. Specifically, they observed a strong (60 nm) redshift and broadening of the LSPR band for  $\Lambda$  values corresponding first to  $\lambda_{\text{SPR}}/n_{\text{SUBSTRATE}}$ , and then to  $\lambda_{\text{SPR}}$ . This effect, called the “grating” effect, evidently reflects the increased radiative fields existing between particles as the particle spacing produces constructive interparticle interference first in the substrate (where the effective radiated wavelength is  $\lambda/n$ ), and then in the airspace above the gradient.

In the latter work, Aussenegg et al. reported studies of EBL-fabricated Ag nanowires (wire widths  $60 \leq w \leq 200 \text{ nm}$ ) and nanowire gratings (spacing  $290 \leq d \leq 680 \text{ nm}$ ) with extinction spectroscopy.<sup>[46]</sup> Similarly to NP chains, Ag nanowires exhibit strong LSPR bands under transverse magnetic (TM) irradiation—i.e., when the E-field is polarized perpendicularly to the long axis of the wire. For individual wires,  $\lambda_{\text{SPR}}$  was found to be linearly dependent on wire width,  $w$ , between 65 and 90 nm. For wire gratings, they similarly find  $\lambda_{\text{SPR}}$  to be a sensitive function of spacing,  $\Lambda$ .  $\lambda_{\text{SPR}}$  redshifts and broadens when  $\Lambda$  approaches  $\lambda_{\text{SPR}}/n_{\text{SUBSTRATE}}$ , corresponding to a transition between evanescent and radiative character for the light field in the substrate half space. This type

of effect also appears in recent computations by Zhao, Kelly, and Schatz<sup>[16]</sup> who simulated LSPR for arrays of period  $\Lambda$  equal to and greater than the particle size.

Haynes et al.<sup>[47]</sup> have also used EBL to produce silver and gold particle arrays. The arrays comprise triangular (170 nm) and circular (200 nm) particles (trigonal prisms and cylinders considering their 35 nm height) in both square and hexagonal lattices of variable spacing between 230 and 500 nm—smaller distances relative to  $\lambda_{\text{SPR}}$  when compared to the studies by Schider et al.,<sup>[45,46]</sup> but still interacting predominantly in the far field. Van Duyne and Schatz observe a linear red shift with increasing lattice constant (ca. 40 optical nm per 100 nm) that is supported qualitatively by coupled dipole simulations. Theoretical calculations used by Zhao and coworkers<sup>[44]</sup> on particle pairs also support far-field interparticle coupling effects seen for large lattice spacing.

### Two-dimensional NP arrays made by nanosphere lithography (NSL)

Van Duyne and coworkers have performed a large body of work using an NP fabrication method they had developed and dubbed “nanosphere lithography” (NSL). In NSL, a substrate is coated with hexagonally close-packed monolayer of highly monodisperse polymer nanospheres by a simple drop casting procedure. The nanosphere coating, in turn, serves as a mask for the evaporation of Ag or Au into the interstitial hollows where substrate surface is exposed. Metal evaporation at normal (or other) incidence, followed by rinsing away the nanosphere mask, thus produces well-ordered 2-D arrays of triangular metal nanoprisms (or variations thereof) (Fig. 1).<sup>[3]</sup> Nanospheres are commercially available in a wide range of sizes, corresponding to a range of NP sizes that exhibit  $\lambda_{\text{SPR}}$  spanning the entire visible, near, and mid infrared spectral regions (Fig. 2). The NP shape can also be

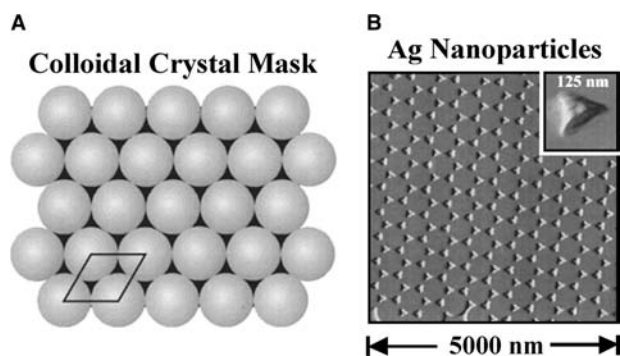


**Fig. 1** AFM image of a Ag nanoparticle array created by nanosphere lithography. *Source:* Reprinted with permission from Ref.<sup>[3]</sup>. © 2003 American Chemical Society.

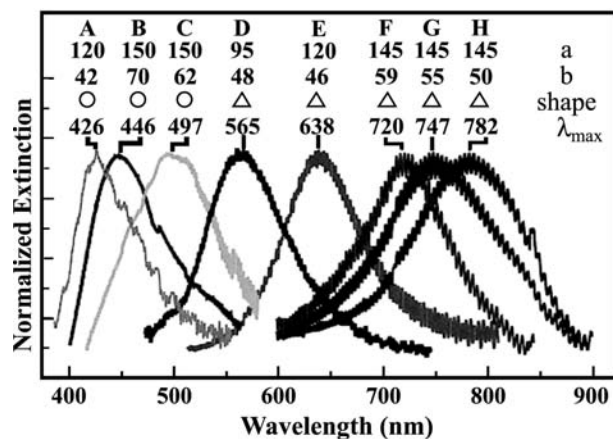


**Fig. 2** Size dependence of the LSPR spectra of Ag NP's fabricated using nanosphere lithography. The dimension “*a*” refers to the NP diameter (for disk particles) or base–apex length (for triangular ones). Dimension “*b*” refers to the NP height. *Source:* Reprinted with permission from Ref.<sup>[3]</sup>. © 2003 American Chemical Society.

altered by evaporating through the nanosphere mask at variable angles—called angle-resolved nanosphere lithography (AR-NSL).<sup>[48]</sup> By sequentially depositing at different angles, AR-NSL can be used to fabricate structures such as “nanoverlaps,” “nanogaps,” and NP chains. Van Duyne et al. have employed NSL–NP arrays in numerous studies focusing on NP size, dielectric environment,<sup>[3]</sup> adsorbate binding (sensor),<sup>[14]</sup> and surface-enhanced Raman activity.<sup>[9]</sup>

The dielectric response of NSL–NP arrays is of considerable interest given the potential utility of these structures in a sensor platform. As is generally observed,  $\lambda_{\text{SPR}}$  increases with ambient dielectric;<sup>[49,50]</sup> however, in the case of a surface (i.e., alkanethiol adsorbate)-induced  $\Delta\epsilon$ , this red shift is larger (3 nm/CH<sub>2</sub>) than predicted for spherical particles of comparable size. This observation is supported (but somewhat overestimated) by discrete dipole approximation (DDA).<sup>[51]</sup> This is a promising property for a surface sensor because, for the most challenging SPR sensing applications, bulk  $\Delta\epsilon$  contributes to noise, whereas surface  $\Delta\epsilon$  reflects the binding of molecular analyte.

### Two-dimensional NP arrays made by colloidal lithography

Hanarp et al.<sup>[52]</sup> report a related “lithographic” preparation yielding disordered arrays of nearly identical nanodisks. As with NSL, this preparation begins with an adsorbed layer of monodisperse polymer nanospheres. However, in this case, the spheres are intentionally deposited such that they are separated

on the surface, and the surface is precoated with Au or Ag. Melting of the spheres creates a removable mask that withstands an ion etch removal of the unmasked metal film, and later, solvent removal of the polymer leaves circular metal NPs. Unlike the observations of Lamprecht et al.,<sup>[45]</sup> Schider et al.,<sup>[46]</sup> and Haynes et al.<sup>[47]</sup> for regular periodic arrays, the average interparticle spacing ( $d$ ) in the  $d \geq d_p$  regime does *not* change the  $\lambda_{\text{SPR}}$  of particles produced via nanosphere lithography, presumably because of the lack of long-range order. Otherwise, the particles' LSPR spectra were fairly well described by a simple oblate spheroid theory,<sup>[53]</sup> and showed the expected red shift in  $\lambda_{\text{SPR}}$  with increasing particle size and ambient dielectric.

### Spontaneously organized 2-D nanoparticle assemblies

The process of 2-D NP self-assembly has been recently reviewed in the context of microelectronics.<sup>[54]</sup>

In many examples in this category, NPs are modified with molecular adsorbates that, in turn, guide the NPs into organized, closely packed assemblies. For example, Tripp and Wei employ an alkane-tailed and “cup-shaped” resorcinarene tetrathiol to decorate 16–170 nm Au NPs. The ligand shell and its alkane tails have a very strong organizing effect leading to hexagonally packed NP arrays on the air–water interface that can be transferred to quartz substrates.<sup>[55]</sup> Kanehara et al.<sup>[56]</sup> find similar results for an amine-terminated disulfide surfactant. In this case, a carboxylic acid adjuvant helps to organize solvent cast NP films.

Stabilized (if not necessarily highly organized) NP assemblies on surfaces have also been made using bidentate ligands—one end of which has affinity for the NP and the other end for the surface of the support. For example, an amino-terminated alkylsilane monolayer on glass will bind mercaptopropionic acid coated NPs by forming covalent (amide) bonds to the surface amino group.<sup>[57]</sup> Similarly, alkanedithiols have been used to tether Au NPs to Au surfaces.<sup>[58]</sup> Single-stranded DNA (ssDNA)-derivatized Au NPs have also been (selectively) bound to Au surfaces by the complementary, surface-bound, DNA oligomers.<sup>[59,60]</sup> This is an important theme, because Au NPs interact strongly with Au film surface plasmon polaritons, and thus amplify the surface sensitivity of analytical surface plasmon polariton spectroscopy.

### Coupled LSPR in 2-D nanoparticle assemblies

Near-field LSPR coupling is evident in some spontaneously organized NP assemblies. This coupling manifests in a band splitting that is sensitive to

polarization, angle, and, as recently shown, interparticle spacing. Observations of this type of mode date back to the work by Ferrell et al. in 1987.<sup>[61,62]</sup> For example, Taleb et al.<sup>[63]</sup> examined arrays of Ag NPs cast from solution and stabilized by dodecanethiol. In these studies, an electrostatic model of coupled dipoles in a 2-D hexagonal array was compared to its experimental counterpart. Both model and experiment yield a high-frequency side band that grows with increasing out-of-plane electric field. In other words, the high-frequency band appeared for higher incident angle and under p-polarization only. Pileni et al. further observed that this mode is more pronounced for more organized assemblies, and appeared for both 4- and 5-nm Ag NPs.

Pileni's observation can be compared to a more recent one by Malynych and Chumanov,<sup>[64]</sup> who found a sharp, high-frequency band that appeared only for smaller interparticle separation of 100 nm Ag NP films. One fascinating aspect of this experiment was that the NP film could be transferred to an elastomer (poly(dimethylsiloxane)) that allowed continuous variation in interparticle spacing simply by stretching the substrate. Fig. 3 shows the resulting normal incidence transmission spectrum and the strong dependence of the sharp, high-frequency band on interparticle

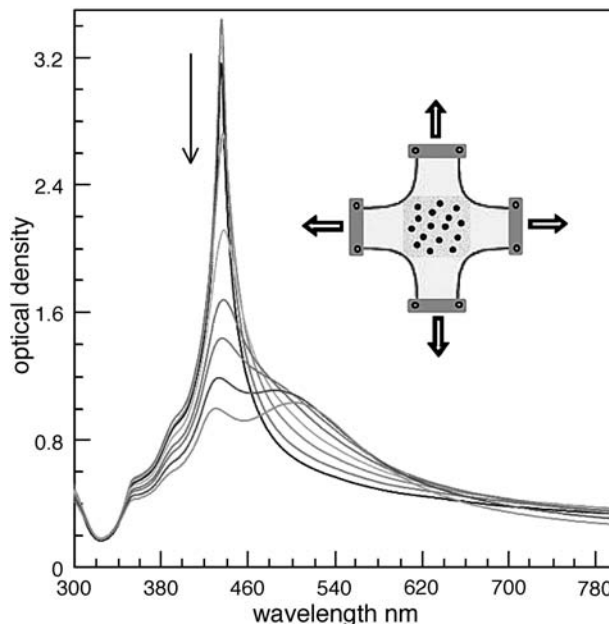


**Fig. 3** LSPR spectrum of a closely spaced 100-nm Ag nanoparticle array on a silicone elastomer support. The collective nature of the sharp band at 420 nm is evident in its hypersensitivity to interparticle spacing. The band at 420 nm disappears as the elastomer is stretched and interparticle spacing decreases (as indicated by the arrow). *Source:* Reprinted with permission from Ref.<sup>[64]</sup>. © 2003 American Chemical Society.

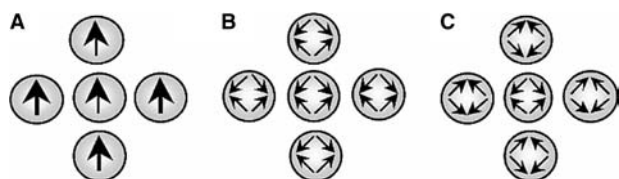


**Fig. 4** Proposed in-plane dipolar and quadrupolar LSPR modes. Interparticle dipolar interactions in A are inequivalent (some dipoles are arranged head–tail and others are side-by-side), but interparticle forces for quadrupolar modes in B and C are all equivalent. *Source:* Reprinted with permission from Ref.<sup>[64]</sup>. © 2003 American Chemical Society.

separation. The mode disappears as the elastomer is stretched, presumably because this spoils the near-field coupling. In contrast to Pileni's observations, this band actually depends on *in-plane* optical fields and *diminishes* under higher incident angles for both p- and s-polarization. Chumanov hypothesizes that this is a result of an in-plane quadrupolar plasmon mode illustrated in Fig. 4. Chumanov argues that, for strong *coherent* interparticle coupling, the quadrupole mode has a more favorable symmetry because all interparticle forces are equivalent. In other words, neighboring particles experience either repulsive (as in Fig. 4B), or attractive (as in Fig. 4C) forces. In contrast, the dipolar excitation of Fig. 4A leads to some attractive interactions (head–tail) and some repulsive ones (side-by-side).

### Three-Dimensional Assemblies of Nanoparticles

A comprehensive discussion of the variety and properties of three-dimensional (3-D) NP assemblies is far beyond the scope of this review. Instead, we present a brief cross section of studies that touch on some important aspects of 3-D NP assemblies. However, one fairly general observation is that LSPR bands tend to broaden and red shift when the component NPs aggregate, or are assembled into a lattice.<sup>[65]</sup>

#### DNA linked 3-D assemblies

Similar to the case for 2-D assemblies, single-stranded (ssDNA) oligomers can be used as a linker in 3-D assemblies of NPs. For example, Taton et al.<sup>[66]</sup> use a strategy for controlled NP film growth wherein a substrate surface and NP's "a" and "b" are derivatized with different, non-complementary ssDNA oligomers, illustrated in Fig. 5. Adding ssDNA oligomers that are the complementary, on opposite ends, to the surface and to NP-a will make a monolayer of NP-a. Further aggregation will *not* take place because the linker

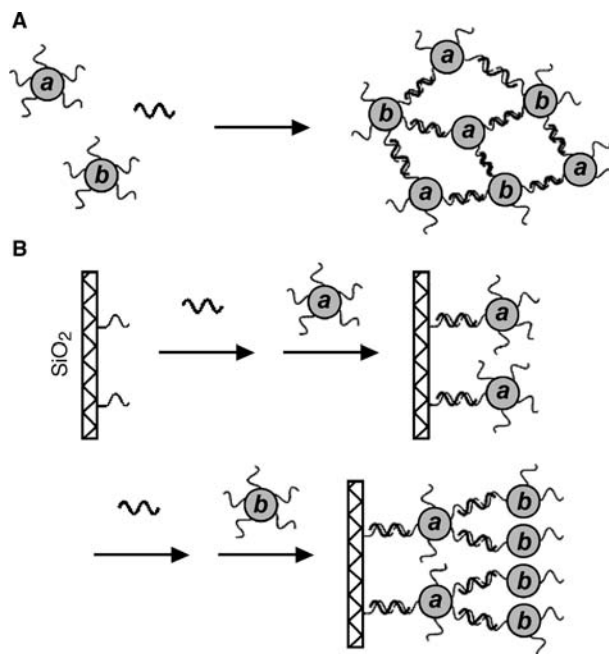


**Fig. 5** Controlled NP aggregate (A) and film (B) growth using "bidentate" single stranded DNA linkers. Linkers are specific to either (SiO<sub>2</sub>)–a, or a–b. *Source:* From Ref.<sup>[66]</sup>. © American Chemical Society, 2003.

ssDNA does not connect "a" to "a" or "a" to "b." Rinsing and subsequent treatment with an "a"–"b" linker will add a layer of NP-b, etc. In addition to 3-D NP architectures, this strategy has been exploited for colorimetric sensing of specific oligonucleotides in solution.<sup>[67]</sup> In this motif, a given target ssDNA strand is detected by a pair of ssDNA derivatized Au NPs, each NP complementary to the opposite half of the target ssDNA. When the target strand is hybridized by both NPs, a large red shift and broadening in the NP LSPR band occurs as a result of near-field coupling. This changes the NP solution from an intense red to a faint purple. Because of the enormous extinction coefficient of the NPs, a target as small as 50 pm could be detected with this simple colorimetric test. Other studies of DNA-linked assemblies are cited in Refs.<sup>[68,69]</sup>

#### Dithiol linked 3-D assemblies

Brust et al.<sup>[70]</sup> have used dithiol linkers to assemble NP films in a controlled layer-by-layer fashion. The oxide substrate was first derivatized with 3-mercaptopropyltriethoxysilane, so that it would present the –SH moiety to solution and bind bare Au, ca. 6 nm NPs from solution. Then, this NP-coated surface was rinsed and treated with an  $\alpha$ - $\omega$  dithiol that, in turn, leaves the NP-coated surface presenting the –SH moiety as a basis for further assembly. Assembly induced

considerable broadening and red shifting in the NP LSPR, but this did not increase after the first few layers.

### Silica encapsulated NPs

Mulvaney et al.<sup>[71]</sup> reviewed the field of silica encapsulation of NPs and noted that these can be assembled into densely packed films. Silica encapsulation is attractive for various technological reasons, i.e., transparency, stability, etc. but also because of the control with which the silica shell can be deposited by using siloxane hydrolysis chemistry, initiated on the NP surface by the S-terminus of 3-mercaptopropyltrialkoxysilane. Particles synthesized in this manner are stabilized by SiO<sub>2</sub>, and the interparticle distance in films made from encapsulated NPs are set by the SiO<sub>2</sub> thickness. Color-tuning in films prepared from SiO<sub>2</sub> encapsulated Au is accurately predicted with the Maxwell–Garnet effective medium theory.<sup>[15]</sup>

### Nanocomposite films

The designation “nanocomposite” is typically applied to materials made from disordered mixtures of Au or Ag NPs at substantial volume fraction in an inert host material. For example, composite films can be prepared by cosputter coating SiO<sub>2</sub>/Ag and thermally annealing the resulting film.<sup>[10]</sup> Similarly, sol–gel methods can be used to prepare Au/BaTiO<sub>3</sub> and other thin film nanocomposites.<sup>[72]</sup> In particular, nanocomposite films appear to be of interest for nonlinear optical applications due in part to the large third-order nonlinear susceptibility lent to these materials by the LSPR active NPs.<sup>[73]</sup> Similarly, nanocomposites are of interest for their potential applications to electronics and as sensors.<sup>[74,75]</sup> Al-Rawashdeh et al.<sup>[23,76]</sup> have prepared ordered polyethylene–Au nanorod composites. The plastic polyethylene matrix provided a means for shear orientation of the nanorods, which, in turn, lend dichroic optical properties to the material.

### CONCLUSION

The localized surface plasmon spectra of silver and gold nanoparticles are interesting in a number of contexts. Spherical NP LSPR spectra are often in good agreement with theory-given adjustments to the metal dielectric function for NPs comparable to, or smaller than, the electron mean free path. However, calculation of the LSPR spectra of nonspherical shapes are still quite challenging because exact electrodynamic solutions such as the Mie theory do not exist, and finite difference simulations, while sometimes quite successful,

are far from routine calculations. However, a recently reported approach based on hybridization of the LSPR modes of more elementary shapes that, in combination, describe others is quite promising.

Basic LSPR spectroscopic phenomena have been the subject of many recent articles. Examples include the observation of multiple LSPR bands for a given NP based on electronic polarization along the different principle axes of the NP, or sometimes for higher-order polarizations in particles with sizes comparable to or greater than  $\lambda$ . Films of NPs often exhibit optical dichroism because of electromagnetic interactions between particles, or, in the case of oriented NPs, because of the optical anisotropy of the particles themselves.

NP LSPR spectroscopy has potential application in numerous technological areas such as subdiffraction light guiding, nonlinear optical applications, Raman enhancement, and chemical sensing. Sensing applications are quite promising given the popularity of the related metal film reflection based surface plasmon sensors. NP sensing can, in theory, detect as few as 60,000 molecules in a volume far smaller than a typical cell.

### REFERENCES

1. Mie, G. Contributions to the optics of turbid media, especially colloidal metal solutions. *Ann. Phys.* **1908**, *25*, 377–445.
2. Ostwald, W. *Theoretical and Applied Colloid Chemistry*; Wiley: New York, 1992; 200 pp.
3. Haynes, C.L.; Van Duyne, R.P. Nanosphere lithography: A versatile nanofabrication tool for studies of size-dependent nanoparticle optics. *J. Phys. Chem., B* **2001**, *105*, 5599–5611, (review).
4. Jensen, T.R.; Malinsky, M.D.; Haynes, C.L.; Van Duyne, R.P. Nanosphere lithography: Tunable localized surface plasmon resonance spectra of silver nanoparticles. *J. Phys. Chem., B* **2000**, *104*, 10549–10556.
5. Yguerabide, J.; Yguerabide, E.E. Light-scattering submicroscopic particles as highly fluorescent analogs and their use as tracer labels in clinical and biological applications: II. Experimental characterization. *Anal. Biochem.* **1998**, *262*, 157–176.
6. Mock, J.R.; Smith, D.R.; Shultz, S. Local refractive index dependence of plasmon resonance spectra from individual nanoparticles. *Nano Lett.* **2003**, *3* (4), 485–491.
7. Kreibig, U.; Vollmer, M. *Optical Properties of Metal Clusters*; Springer-Verlag: New York, 1995; Vol. 25.
8. Riboh, J.C.; Haes, A.J.; McFarland, A.D.; Yonzon, C.R.; Van Duyne, R.P. A nanoscale optical biosensor: Real-time immunoassay in physiological buffer enabled by improved nanoparticle adhesion. *J. Phys. Chem., B* **2003**, *107*, 1772–1780.

9. Haynes, C.L.; Van Duyne, R.P. Plasmon-sampled surface-enhanced Raman excitation spectroscopy. *J. Phys. Chem., B* **2003**, *107*, 7426–7433.
10. Yang, G.; Wang, W.; Zhou, Y.; Lu, H.; Yang, G.; Chen, Z. Linear and nonlinear optical properties of Ag nanocluster/BaTiO<sub>3</sub> composite films. *Appl. Phys. Lett.* **2002**, *81* (21), 3969–3971.
11. Liao, H.B.; Wen, W.; Wong, G.K.L. Preparation and optical characterization of Au/SiO<sub>2</sub> composite films with multilayer structure. *J. Appl. Phys.* **2003**, *93* (8), 4485–4488.
12. Link, S.; El-Sayed, M.A. Spectral properties and relaxation dynamics of surface plasmon electronic oscillations in gold and silver nanodots and nanorods. *J. Phys. Chem., B* **1999**, *103*, 8410–8426.
13. Hovel, H.; Fritz, S.; Hilger, A.; Kreibitz, U.; Vollmer, M. Width of cluster plasmon resonances: Bulk dielectric functions and chemical interface damping. *Phys. Rev., B* **1993**, *48*, 18178–18188.
14. Alvarez, M.M.; Khoury, J.T.; Schaff, G.T.; Shafiqullin, M.N.; Vezmar, I.; Whetten, R.L. Optical absorption spectra of nanocrystal gold molecules. *J. Phys. Chem., B* **1997**, *101*, 3706–3712.
15. Ung, T.; Liz-Marzan, L.M.; Mulvaney, P. Gold nanoparticle thin films. *Colloids Surf., A* **2002**, *202*, 119–126.
16. Zhao, L.L.; Kelly, K.L.; Schatz, G.C. The extinction spectra of silver nanoparticle arrays: Influence of array structure on plasmon resonance wavelength and width. *J. Phys. Chem., B* **2003**, *107*, 7343–7350.
17. Kelly, K.L.; Coronado, E.; Zhao, L.L.; Schatz, G.C. The optical properties of metal nanoparticles: The influence of size, shape, and dielectric environment. *J. Phys. Chem., B* **2003**, *107*, 668–677.
18. Bohren, C.F.; Huffman, D.R. *Absorption and Scattering of Light by Small Particles*; Wiley: New York, 1983.
19. Al-Rawashdeh, N.A.F.; Sandrock, M.L.; Seugling, C.J.; Foss, C.A. Visible region polarization spectroscopic studies of template-synthesized gold nanoparticles oriented in polyethylene. *J. Phys. Chem., B* **1998**, *102*, 361–371.
20. Hornyak, G.L.; Patrissi, C.J.; Martin, C.R. Fabrication, characterization, and optical properties of gold nanoparticle/porous alumina composites: The nonscattering Maxwell–Garnett limit. *J. Phys. Chem., B* **1997**, *101*, 1548–1555.
21. Prodan, E.; Radloff, C.; Halas, N.J.; Nordlander, P. A hybridization model for the plasmon response of complex nanostructures. *Science* **2003**, *302*, 419–422.
22. Prodan, E.; Nordlander, P. Structural tunability of the plasmon resonances in metallic nanoshells. *Nano Lett.* **2003**, *3*, 543–547.
23. Al-Rawashdeh, N.A.F.; Sandrock, M.L.; Seugling, C.J.; Foss, C.A., Jr. Visible region polarization spectroscopic studies of template-synthesized gold nanoparticles oriented in polyethylene. *J. Phys. Chem., B* **1998**, *102*, 361–371.
24. Mulvaney, P. Surface plasmon spectroscopy of nano-sized metal particles. *Langmuir* **1996**, *12*, 788–800.
25. Foss, C.A.; Hornyak, G.L.; Stockert, J.A.; Martin, C.R. Template synthesized nanoscopic gold particles: Optical spectra and the effects of particle size and shape. *J. Phys. Chem.* **1994**, *98*, 2963.
26. Moreno, E.; Ermi, D.; Hafner, C.; Vahldieck, R. Multiple multipole method with automatic multipole setting applied to the simulation of surface plasmons in metallic nanostructures. *J. Opt. Soc., A* **2002**, *19*, 101–111.
27. Krenn, J.R.; Schider, G.; Rechberger, W.; Lamprecht, B.; Leitner, A.; Aussenegg, F.R.; Weeber, J.C. Design of multipolar plasmon excitations in silver nanoparticles. *Appl. Phys. Lett.* **2000**, *77* (21), 3379–3381.
28. Taflove, A. *Computational Electrodynamics: The Finite-Difference Time-Domain Method*; Artech House: Boston, 1995; 599 pp.
29. Maier, S.A.; Kik, P.G.; Atwater, H.A. Observation of coupled plasmon-polariton modes in Au nanoparticle chain waveguides of different lengths: Estimation of waveguide loss. *Appl. Phys. Lett.* **2002**, *81* (9), 1714–1716.
30. Mock, J.J.; Oldenburg, J.S.; Smith, D.R.; Schultz, D.A.; Shultz, S. Composite plasmon resonant nanowires. *Nano Lett.* **2002**, *2* (5), 465–469.
31. Raschke, G.; Kowarik, S.; Franzl, T.; Sonnichsen, C.; Klar, T.A.; Feldmann, J. Biomolecular recognition based on single gold nanoparticle light scattering. *Nano Lett.* **2003**, *3* (7), 935–938.
32. McFarland, A.D.; Van Duyne, R.P. Single silver nanoparticles as real-time optical sensors with zeptomole sensitivity. *Nano Lett.* **2003**, *3* (8), 1057–1062.
33. Nicewarner-Pena, S.R.; Freeman, G.R.; Reiss, B.D.; He, L.; Pena, D.J.; Walton, I.D.; Cromer, R.; Keating, C.D.; Natan, M.J. Submicrometer metallic barcodes. *Science* **2001**, *294*, 137–141.
34. Novak, J.P.; Feldheim, D.L. Assembly of phenylacetylene-bridged silver and gold nanoparticle arrays. *J. Am. Chem. Soc.* **2000**, *122*, 3979–3980.
35. Sandrock, M.L.; Foss, C.A., Jr. Synthesis and linear optical properties of nanoscopic gold particle pair structures. *J. Phys. Chem., B* **1999**, *103*, 11398–11406.
36. Gluodenis, M.; Foss, C.A. The effect of mutual orientation on the spectra of metal nanoparticle rod–rod and rod–sphere pairs. *J. Phys. Chem., B* **2002**, *106*, 9484–9489.
37. Rechberger, W.; Hohenau, A.; Leitner, A.; Krenn, J.R.; Lamprecht, B.; Aussenegg, F.R. Optical properties of two interacting gold nanoparticles. *Opt. Commun.* **2003**, *220*, 137–141.
38. Su, H.-H.; Wei, Q.-H.; Zhang, X.; Mock, J.J.; Xmith, D.R.; Sjulzt, S. Interparticle coupling effects on plasmon resonances of nanogold particles. *Nano Lett.* **2003**, *3* (8), 1087–1090.
39. Maier, S.A.; Brongersma, M.L.; Kik, P.G.; Atwater, H.A. Observation of near-field coupling in metal nanoparticle chains using far-field polarization spectroscopy. *Phys. Rev., B* **2002**, *65*, 193408-1-4.
40. Maier, S.A.; Brongersma, M.L.; Kik, P.G.; Meltzer, S.; Requicha, A.A.G.; Atwater, H.A. Plasmonics—A route to nanoscale optical devices. *Adv. Mater.* **2001**, *13* (19), 1501–1505.



41. Maier, S.A.; Kik, P.G.; Atwater, H.A. Observation of coupled plasmon-polariton modes in Au nanoparticle chain waveguides of different lengths: Estimation of waveguide loss. *Appl. Phys. Lett.* **2002**, *81* (9), 1714–1716.
42. Fort, E.; Ricolleau, C.; Sau-Pueyo, J. Dichroic thin films of silver nanoparticle chain arrays on faceted alumina templates. *Nano Lett.* **2003**, *3*, 65–67.
43. Teranishi, T.; Sugawara, A.; Shimizu, T.; Miyake, M. Planar array of 1D gold nanoparticles on ridge-and-valley structured carbon. *J. Am. Chem. Soc.* **2002**, *124*, 4210–4211.
44. Zhao, L.K.; Kelly, L.; Schatz, G.C. The extinction spectra of silver nanoparticle arrays: Influence of array structure on plasmon resonance wavelength and width. *J. Phys. Chem., B* **2003**, *107*, 7343–7350.
45. Lamprecht, B.; Schider, G.; Lechner, R.T.; Ditlbacher, H.; Krenn, J.R.; Leitner, A.; Aussenegg, F.R. Metal nanoparticle gratings: Influence of dipolar particle interaction on the plasmon resonance. *Phys. Rev. Lett.* **2000**, *84*, 4721–4724.
46. Schider, G.; Krenn, J.R.; Gotschy, W.; Lamprecht, B.; Ditlbacher, H.; Leitner, A.; Aussenegg, F.R. Optical properties of Ag and Au nanowire gratings. *J. Appl. Phys.* **2001**, *90*, 3825–3830.
47. Haynes, C.L.; McFarland, A.D.; Zhao, L.; Van Duyne, R.P.; Schatz, G.C.; Gunnarsson, L.; Prikulis, J.; Kasemo, B.; Kall, M. Nanoparticle optics: The importance of radiative dipole coupling in two-dimensional nanoparticle arrays. *J. Phys. Chem., B* **2003**, *107*, 7337–7342.
48. Haynes, C.L.; Van Duyne, R.P. Dichroic optical properties of extended nanostructures fabricated using angle-resolved nanosphere lithography. *Nano Lett.* **2003**, *3*, 939–943.
49. Malinsky, M.D.; Kelly, K.L.; Schatz, G.C.; Van Duyne, R.P. Nanosphere lithography: Effect of substrate on the localized surface plasmon resonance spectrum of silver nanoparticles. *J. Phys. Chem., B* **2001**, *105*, 2343–2350.
50. Jensen, T.R.; Duval, M.L.; Kelly, K.L.; Lazarides, A.A.; Schatz, G.C.; Van Duyne, R.P. Nanosphere lithography: Effect of the external dielectric medium on the surface plasmon resonance spectrum of a periodic array of silver nanoparticles. *J. Phys. Chem., B* **1999**, *103*, 9846–9853.
51. Malinsky, M.D.; Kelly, K.L.; Schatz, G.C.; Van Duyne, R.P. Chain length dependence and sensing capabilities of the localized surface plasmon resonance of silver nanoparticles chemically modified with alkanethiol self-assembled monolayers. *J. Am. Chem. Soc.* **2001**, *123*, 1471–1482.
52. Hanarp, P.; Kall, M.; Sutherland, D.S. Optical properties of short range ordered arrays of nanometer gold disks prepared by colloidal lithography. *J. Phys. Chem., B* **2003**, *107*, 5768–5772.
53. Bohren, C.F.; Huffman, D.R. *Absorption and Scattering of Light by Small Particles*; John Wiley & Sons: New York, 1983.
54. Fendler, J.H. Chemical self-assembly for electronic applications. *Chem. Mater.* **2001**, *13*, 3196–3210.
55. Kim, B.; Tripp, S.L.; Wei, A. Self-organization of large gold nanoparticle arrays. *J. Am. Chem. Soc.* **2001**, *123*, 7955–7956.
56. Kanehara, M.; Oumi, Y.; Sano, T.; Teranishi, T. Formation of low symmetric 2D superlattices of gold nanoparticles through surface modification by acid–base interaction. *J. Am. Chem. Soc.* **2003**, *125*, 8708–8709.
57. Nath, N.; Chilkoti, A. A colorimetric gold nanoparticle sensor to interrogate biomolecular interactions in real time. *Anal. Chem.* **2002**, *74*, 504–509.
58. Hutter, E.H.; Fendler, J.H.; Roy, D. Surface plasmon resonance studies of gold and silver nanoparticles linked to gold and silver substrates by 2-aminoethanethiol and 1,6-hexanedithiol. *J. Phys. Chem., B* **2001**, *105*, 11159–11168.
59. He, L.; Musick, M.D.; Nicewarner, S.R.; Salinas, F.G.; Benkovic, S.J.; Natan, M.J.; Keating, C.D. Colloidal Au-enhanced surface plasmon resonance for ultrasensitive detection of DNA hybridization. *J. Am. Chem. Soc.* **2000**, *122*, 9071–9077.
60. Hutter, E.; Pileni, M.-P. Detection of DNA hybridization by gold nanoparticle enhanced transmission surface plasmon resonance spectroscopy. *J. Phys. Chem., B* **2003**, *107*, 6497–6499.
61. Royer, P.; Goudonnet, J.P.; Warmack, R.J.; Ferrell, T.L. Substrate effects on surface-plasmon spectra in metal-island films. *Phys. Rev., B* **1987**, *35*, 3753.
62. Kennerly, S.W.; Little, J.W.; Warmack, R.J.; Ferrell, T.L. Optical properties of heated Ag films. *Phys. Rev., B* **1984**, *29*, 2926.
63. Taleb, A.; Russier, V.; Courty, A.; Pileni, M.P. Collective optical properties of silver nanoparticles organized in two-dimensional superlattices. *Phys. Rev., B* **1999**, *59*, 13350–13358.
64. Malynych, S.; Chumanov, G. Light-induced coherent interactions between silver nanoparticles in two-dimensional arrays. *J. Am. Chem. Soc.* **2003**, *125*, 2896–2898.
65. Taleb, A.; Petit, C.; Pileni, M.P. Optical properties of self-assembled 2D and 3D superlattices of silver nanoparticles. *J. Phys. Chem., B* **1998**, *102*, 2214–2220.
66. Taton, T.A.; Mucic, R.C.; Mirkin, C.A.; Letsinger, R.L. The DNA-mediated formation of supramolecular mono- and multilayered nanoparticle structures. *J. Am. Chem. Soc.* **2000**, *122*, 6305–6306.
67. Reynolds, R.A., III; Mirkin, C.A.; Letsinger, R.L. Homogeneous, nanoparticle-based quantitative colorimetric detection of oligonucleotides. *J. Am. Chem. Soc.* **2000**, *122*, 3795–3796.
68. Lazarides, A.A.; Schatz, G.C. DNA-linked metal nanosphere materials: Structural basis for the optical properties. *J. Phys. Chem., B* **2000**, *104*, 460–467.
69. Storhoff, J.J.; Lazarides, A.A.; Mucic, R.C.; Mirkin, C.A.; Letsinger, R.L.; Schatz, G.C. What controls the optical properties of DNA-linked gold nanoparticle assemblies?. *J. Am. Chem. Soc.* **2000**, *122*, 4640–4650.
70. Brust, M.; Bethell, D.; Kiely, C.J.; Schiffrin, D.J. Self-assembled gold nanoparticle thin films with nonmetallic optical and electronic properties. *Langmuir* **1998**, *14*, 5425–5429.

71. Mulvaney, P.; Liz-Marzan, L.M.; Giersig, M.; Ung, T. Silica encapsulation of quantum dots and metal clusters. *J. Mater. Chem.* **2000**, *10*, 1259–1270.
72. Yang, Y.; Shi, J.; Huang, W.; Dai, S.; Wang, L. Preparation and optical properties of barium titanate thin films dispersed with Au nanoparticles. *Mater. Lett.* **2002**, *56*, 1048–1052.
73. Hache, F.; Flytzanis, R.C. Optical nonlinearities of small metal particles: Surface-mediated resonance and quantum size effects. *J. Opt. Soc. Am., B* **1986**, *3* (12), 1647–1655.
74. Feldheim, D.L.; Keating, C.D. Self-assembly of single electron transistors and related devices. *Chem. Soc. Rev.* **1998**, *27*, 1–12.
75. Shipway, A.N.; Willner, I. Nanoparticles as structural and functional units in surface-confined architectures. *Chem. Commun.* **2001**, *20*, 2035–2045.
76. Al-Rawashdeh, N.; Foss, C.A., Jr. UV/visible and infrared spectra of polyethylene/nanoscope gold rod composite films: Effects of gold particle size, shape and orientation. *Nanostruct. Mater.* **1997**, *9*, 383–386.

# Template-Directed Assembly of Dinuclear Triple-Stranded Helicates

Markus Albrecht

RWTH-Aachen, Institut für Organische Chemie, Aachen, Germany

## INTRODUCTION

Helicates are oligonuclear coordination compounds in which linear organic oligodonor ligands wrap around two or more metal centers. The main focus in helicate chemistry is on double-stranded or triple-stranded helicates (for a schematic representation of dinuclear helicates, see Fig. 1), but quadruple-stranded or circular helicates are also well known.<sup>[1,2]</sup>

In dinuclear helicates, both metal complex units possess the same configuration, and a left-handed as well as a right-handed helix can be present. Usually the helicate is formed as a racemic mixture but some examples of enantiomerically pure helicates are known.<sup>[3,4]</sup> If the two metal complex units of a dinuclear complex are oppositely configured, an achiral *meso*-type coordination compound is obtained—the *meso*-helicate (“side-by-side complex,”<sup>[3]</sup> “*meso*-cate”).<sup>[5,6]</sup>

Since the introduction of the term “helicate” by Lehn et al.<sup>[7]</sup> in 1987, the chemistry of helicates has become one of the most intensely studied topics of metallocupramolecular chemistry. This is because of the simplicity of the helicates, which allows the study of fundamental aspects of metal-directed self-assembly such as mechanisms,<sup>[8]</sup> stereochemistry,<sup>[6]</sup> or regiochemistry.<sup>[9]</sup> In this chapter, we will focus on an important mechanistic feature of helicate chemistry—the influence of templates on the formation of triple-stranded dinuclear helicates. This can be observed for several helicates, although templation is not a general requirement for the formation of the complexes. Many helicates that are formed without a template present were observed.<sup>[2]</sup> Here, very often, other stabilizing interactions (e.g., steric constraints) are at work, which support the formation of the helicate.<sup>[10]</sup>

## WHAT IS THE DRIVING FORCE FOR THE SPECIFIC ASSEMBLY OF HELICATES?

Fig. 2 schematically outlines an experiment in which metal ions and appropriate linear ligands with two binding sites for metals are brought to reaction A. If an “undesired” non-specific complex formation takes

place between the metal ions and the ligands, a mixture of oligomers or polymers is obtained by unselective bridging of the organic donors between metal centers, as is shown in reaction B.

Of course, the specific formation of dinuclear triple-stranded helicates (C/D) is the desired reaction path. What will be the driving force to follow this path to obtain helicates and not the oligomers and polymers? To answer this question, it is important to look at the thermodynamics of the reactions. In a thermodynamically controlled self-assembly process, we have an enthalpic ( $\Delta H^\circ$ ) and an entropic term ( $T\Delta S^\circ$ ), which can both influence the reaction path. Looking at this system in a very naive way, the enthalpy change is the same if a polymer or a dinuclear complex is formed. In an ideal system,  $\Delta H^\circ$  only refers to the formation of coordinative bonds between metals and ligands. This happens in cases B and C in a similar way. Therefore entropy favors in our “ideal system” the formation of a maximum number of complexes C over (in extreme) only one polymeric molecule B. However, if no ideal system is present (which usually is the case), the buildup of strain during the complex formation should lead to an enthalpic control of the complex formation. In this case, we usually cannot predict the outcome of a coordination study; the geometry can lead to the formation of either the polymer or the dinuclear complex. However, if we are able to introduce some secondary stabilizing effects, which are in favor for the dinuclear helicate over the polymer, enthalpic forces will direct the complex formation toward the dinuclear complex. As an example, the template-directed assembly of helicates is indicated in Fig. 2D. The binding of a template in the interior of the complex here is the secondary effect that stabilizes the helicate by enthalpic reasons.<sup>[11]</sup> However, there are many possible stabilizing effects other than templating (e.g., in the first paper on helicates in 1987, Lehn et al. already assumed that  $\pi$ -stacking between bipyridine units of different ligand strands of a dinuclear helicate supports the formation of the complex). In this case, a similar stabilizing effect, as in double-stranded DNA, is active in the formation of the simple double-stranded helicate.<sup>[7]</sup> In addition, rigid ligands

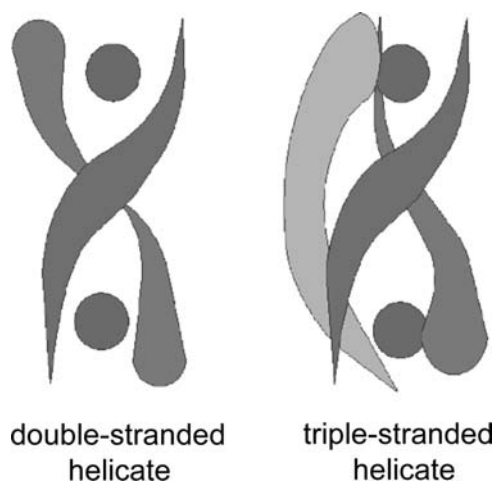


**Fig. 1** Schematic representation of a double-stranded and a triple-stranded helicate.

often favor the discrete helicate enthalpically because of a minimization of the buildup of strain energy.<sup>[12,13]</sup>

### TEMPLATING IN THE FORMATION OF DOUBLE-STRANDED AND CIRCULAR HELICATES

Template-directed formation is not restricted to triple-stranded helicites. The assembly of double-stranded as well as circular helicites sometimes also depends on templates. For example, if a coordination study is performed with the bis(bipyridine) ligand **1** and zinc(II) or copper(I) ions, an undefined mixture of coordination compounds is observed. Without a template, the formation of dinuclear complexes is not favored over the formation of oligomers<sup>[14,15]</sup> (Scheme 1).

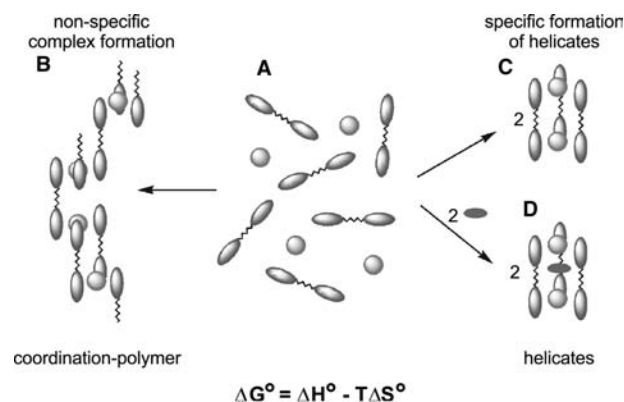
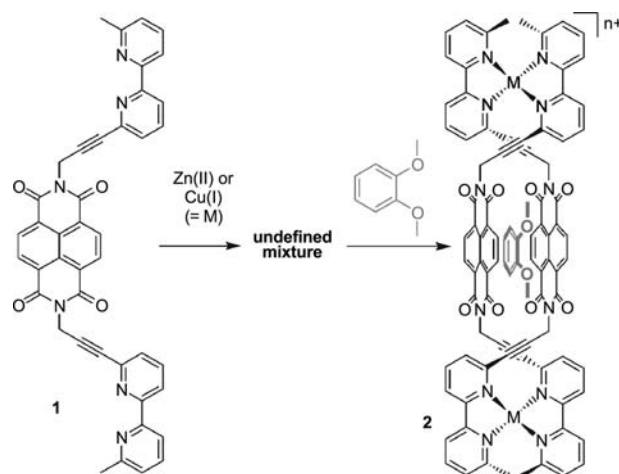


**Fig. 2** Schematic representation of a theoretical coordination study of linear ligands and metal ions (A) leading to a non-specific complex formation of oligomeric or polymeric materials (B) or, specifically, to a spontaneous (C) or template-directed (D) self-assembly process of triple-stranded dinuclear helicites.

### Template-Directed Assembly of Dinuclear Triple-Stranded Helicites



**Scheme 1** Veratrole as a template for the formation of helicate **2**.

However, on addition of veratrole, the undefined mixture transforms into only one defined species, the dinuclear double-stranded complex **2**, in which the electron-rich veratrole is bound between two electron-poor aromatic moieties of the ligand spacer. The veratrole acts as template and, by attractive  $\pi$ - $\pi$  charge transfer interactions, stabilizes the helicate.<sup>[14,15]</sup> This principle impressively was used to prepare catenanes and rotaxanes based on dinuclear metal complexes.<sup>[16]</sup>

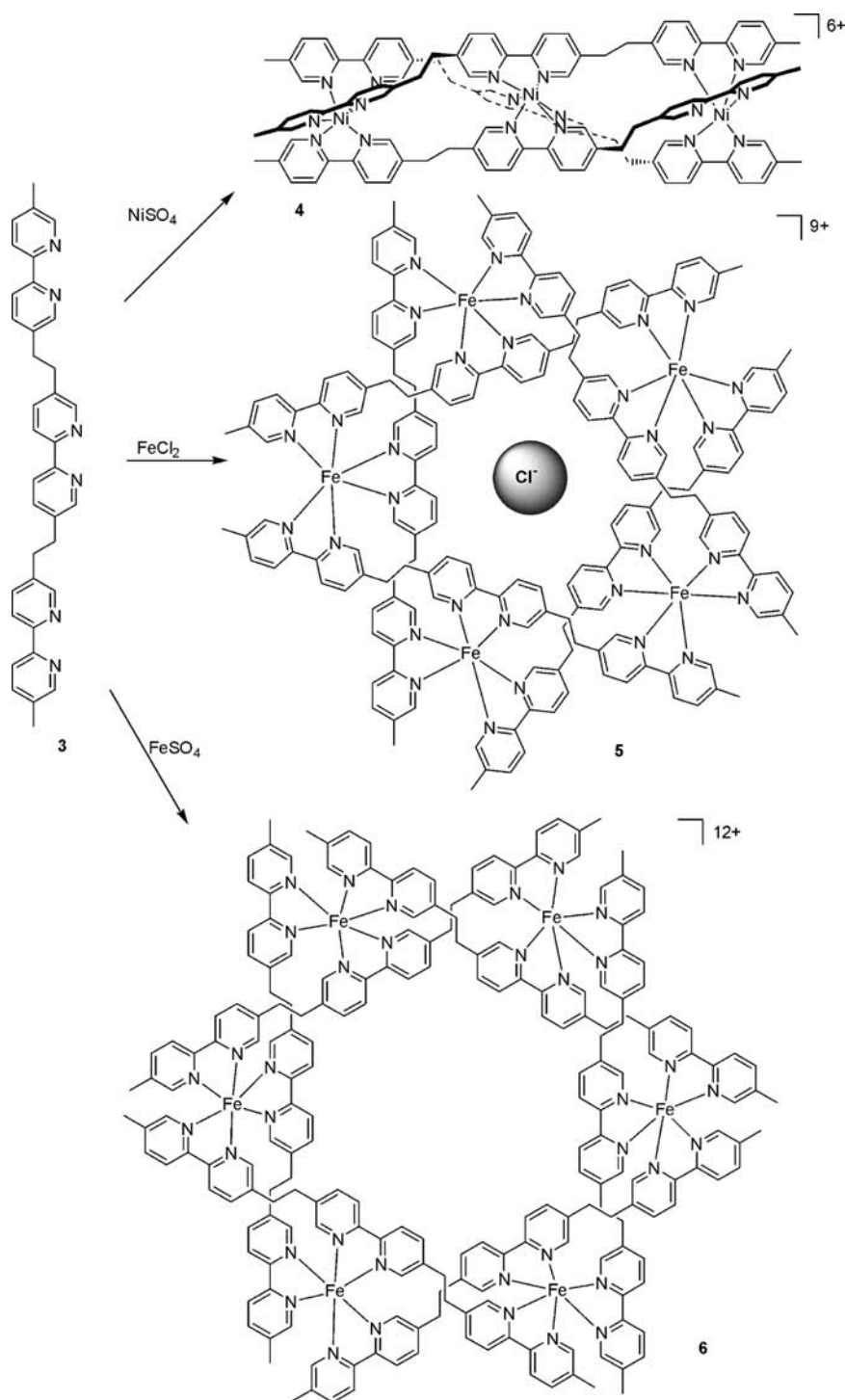
The formation of circular helicites also highly depends on templates that are present during the formation of the complexes (Scheme 2).

The complexation of nickel(II) with the tris(bipyridine) ligand **3** leads to the trinuclear triple-stranded helicate **4**.<sup>[17]</sup> The analogous iron complex also can be observed as a product of the kinetically controlled reaction between **3** and iron(II). However, the outcome of the reaction of **3** with iron(II) ions under thermodynamic reaction control (long reaction times) highly depends on the counterion, which is present. If the small chloride is introduced as a counterion, the pentanuclear circular helicate **5** is obtained, which encapsulates one of the anions in its interior. The larger anions  $\text{BF}_4^-$ ,  $\text{SO}_4^{2-}$ , or  $\text{SiF}_6^{2-}$  favor the formation of the larger hexanuclear circular helicate **6**. The intermediate-sized bromide ion leads to the pentanuclear complex **5** as well as the hexanuclear complex **6**.<sup>[18]</sup>

The example of coordination studies with ligands **1** and **3** shows how effective templating can be in controlling the metal-directed self-assembly of discrete supramolecular species.

### TEMPLATING IN THE FORMATION OF TRIPLE-STRANDED HELICITES

In 1985—2 years before the term helicate was introduced by Lehn et al.—Raymond described a



**Scheme 2** Template directed formation of circular helicates.

triple-stranded dinuclear helicate, which is formed from three bis(hydroxypyridinone) ligands **7** and two iron(III) ions. In the solid state, the helicate binds a water molecule in its interior.<sup>[19]</sup> However, it is not known if this small guest molecule is important for the stabilization of the dinuclear complex. Twelve years later, in 1999, Raymond showed that the related

ligand **8** forms a *meso*-helicate with gallium(III) or aluminum(III) ions if no water is present. However, if water is added, it is encapsulated in the interior of the dinuclear complex and it stabilizes the structure of the corresponding chiral helicate<sup>[5]</sup> (Fig. 3).

A similar structure dependence (helicate vs. *meso*-helicate) based on the presence or absence of a

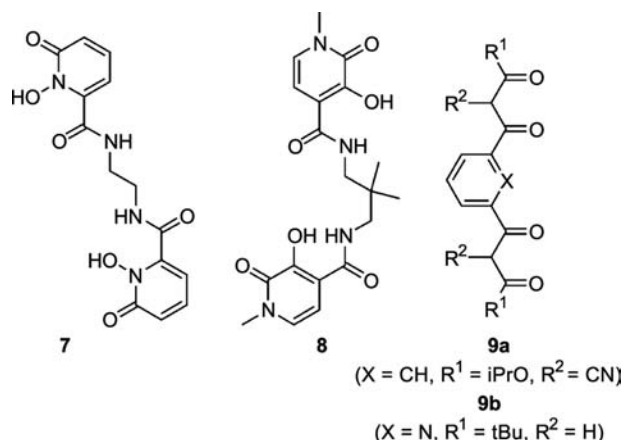


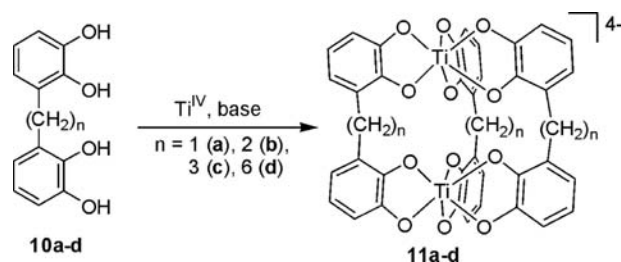
**Fig. 3** Raymond's ligands **7** Source: From Ref.<sup>[19]</sup> and **8** Source: From Ref.<sup>[5]</sup> and Saalfrank et al.'s ligands **9a** and **9b** Source: From Ref.<sup>[20]</sup>, which were introduced for the formation of triple-stranded helicate-type complexes.

template is observed for the complexes of the ligands **9a** and **9b**. Both compounds form triple-stranded complexes with iron(III) ions. However, **9a** is not able to bind a template, and a dinuclear helicate without an encapsulated guest is obtained. In the case of ligand **9b**, the triple-stranded complex with the internal pyridine moieties and oxygen atoms binds potassium as a template in its interior, which stabilizes the structure of an achiral *meso*-helicate.<sup>[20]</sup>

### Dicatechol Ligands as Building Blocks for Helicate-Type Complexes

Alkyl-bridged dicatechol ligands **10a–d** diastereoselectively form either triple-stranded helicates or *meso*-helicates. Diastereoselectivity is controlled by the alkyl chains in the spacer. If an odd number of methylene units is present, the ligand adopts a “C”-type arrangement because of the preferred zigzag conformation of the alkyl chain. Therefore the ligands **10a** and **10c** are predisposed to the formation of the *meso*-helicate. With an even number of methylene units (**10b** and **10d**), an “S”-type arrangement is favored, which leads to the helicate.<sup>[6]</sup> In the case of ligands **10**, the self-assembly process shows a very strong dependence based on the counteranions that are present<sup>[21]</sup> (Scheme 3).

The reaction of the dicatechol ligands **10a–d** with titanium(IV) ions in the presence of base leads to the quantitative formation of dinuclear triple-stranded helicate-type complexes **11a–d**. However, appropriate alkaline metal cations have to be present as counteranions. The X-ray structures of Li-**11a**,<sup>[22]</sup> Li-**11b**,<sup>[23]</sup> Na-**11c**,<sup>[24]</sup> and K-**11d**<sup>[25]</sup> show that in the solid state, cations are bound in the cryptand-type cavity, which is formed by the internal oxygen atoms of the helicate (Fig. 4).



**Scheme 3** Dinuclear helicates from alkyl-bridged dicatechol ligands.

In the case of **11a**, the interior of the complex is too small to encapsulate a counteranion. Therefore in Li-**11a**, three lithium cations bind from the outside to the internal oxygen atoms, and thus “block” the open faces of the self-assembled metallacryptand **11a**.<sup>[22]</sup> On the other hand, in Li-**11b**, the internal cavity is somewhat too big for the small lithium cation, and therefore in addition to Li<sup>+</sup>, two water molecules are observed inside the metallacryptand.<sup>[23]</sup> The bigger sodium cation fits much better into the interior of **11b** and only one cation is found in the interior of Na-**11b** (not shown). In the solid-state structure of Na-**11c**, a sodium cation is encapsulated in the *meso*-helicate and it additionally is

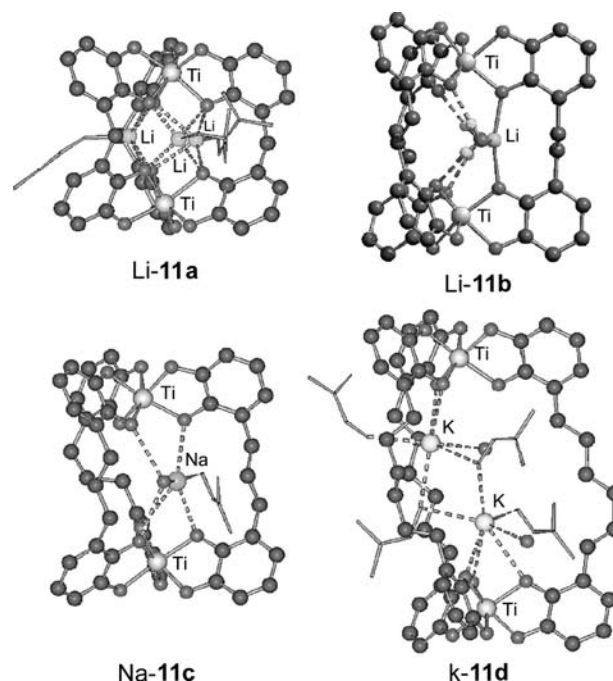
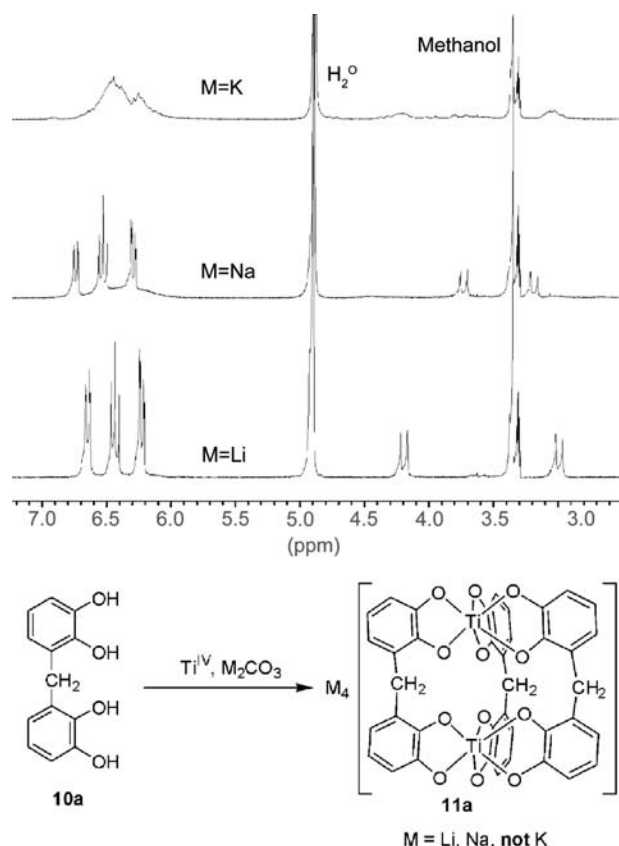


**Fig. 4** Parts of the X-ray structures of Li-**11a** Source: From Ref.<sup>[22]</sup>, Li-**11b** Source: From Ref.<sup>[23]</sup>, Na-**11c** Source: From Ref.<sup>[24]</sup>, and K-**11d** Source: From Ref.<sup>[25]</sup> showing the binding of alkali metal cations to dinuclear triple-stranded helicate-type complexes. DMF molecules are only indicated and only the cations that are bound to the interior of the complexes are shown.





**Scheme 4** NMR spectra of the formation of **11a** in the presence of Li, Na, or K.

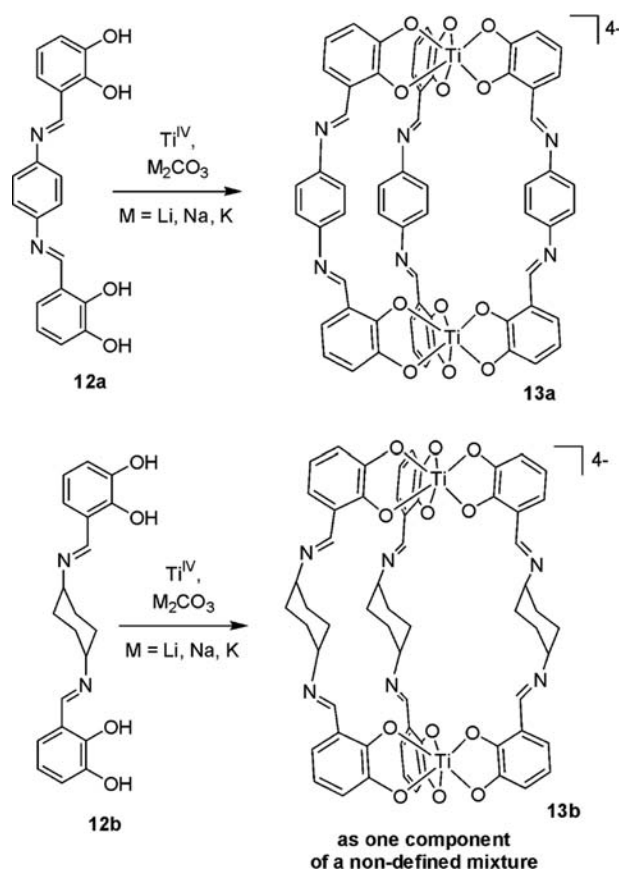
coordinated by one DMF and one water molecule.<sup>[24]</sup> The cavity of **K-11d** is much too big to bind only one potassium cation in its interior. Consequently, in the solid state, two cations are found in the cavity and are additionally complexed by water and DMF.<sup>[25]</sup>

The results of the X-ray structural analyses of **11a-d** show that the counterions are not only innocent spectators but that they are parts of the self-assembled metallocryptand architecture (at least in the solid state). However, to enable templating of the cations, binding to the dinuclear complexes has to be present in solution, too.

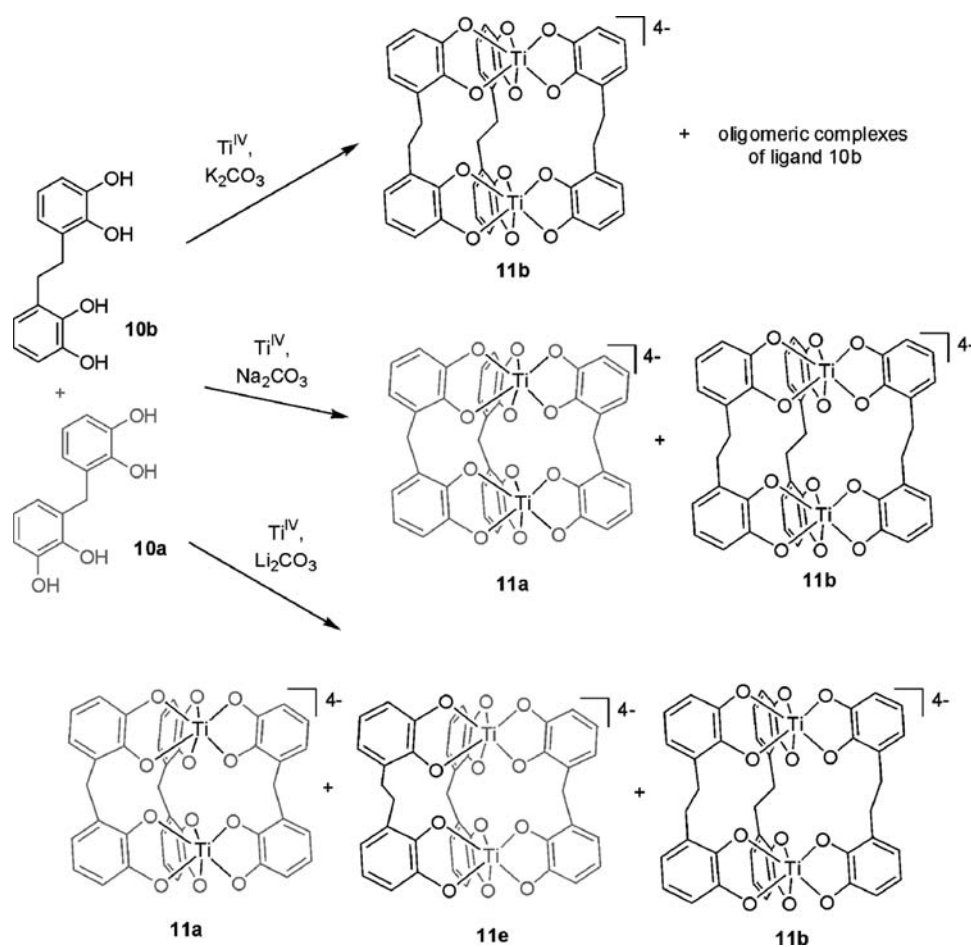
To investigate the cation binding of the tetraanionic self-assembled metallacryptands in solution, heteronuclear nuclear magnetic resonance (NMR) studies were performed (e.g., <sup>7</sup>Li NMR spectroscopy of Li-**11a** in methanol-d<sub>4</sub> at variable temperature reveals that in contrast to the solid-state structure, only two lithium cations bind to the dinuclear complex **11a** in solution).<sup>[26]</sup> <sup>7</sup>Li NMR and <sup>23</sup>Na NMR of the Li salt and Na salt of **11b**, respectively, as well as of Na-**11c** also show binding of the cations. From competition experiments, it is deduced that potassium is encapsulated most effectively by metallacryptands followed by sodium and finally lithium.<sup>[25]</sup>

However, the question remains if the binding of the alkali metal cations in the solid state as well as in solution is really important for the self-assembly of helicate-type complexes (Scheme 4).

If the self-assembly of the small *meso*-helicate **11a** with only short methylene spacers is performed in the presence of potassium carbonate, no defined dinuclear complex is obtained. The <sup>1</sup>H NMR spectrum shows only broad bands that cannot be assigned. Electro-spray ionization mass spectrometry (ESI MS) reveals that a mixture of oligomers is present, with the dinuclear complex being one component of the mixture. However, if the same coordination experiment is performed with sodium or lithium carbonate, complexes **11a** are obtained, which show nicely resolved NMR spectra. Here, the templating influence of the cations is observed directly. The small dinuclear complex **11a** only assembles if small Li cations or Na cations are present, which can stabilize the complex by binding to internal oxygen atoms. The larger potassium cation is not able to bind to **11a** effectively and its presence might even destabilize the dinuclear titanium complex. Therefore a non-defined mixture of oligomers is formed. The addition of lithium or sodium salts as templates to the mixture of oligomeric potassium salts changes the NMR spectrum dramatically. Immediately



**Scheme 5** Imine-bridged dinuclear helicates.



**Scheme 6** Self- and hetero-recognition in the formation of helicates.

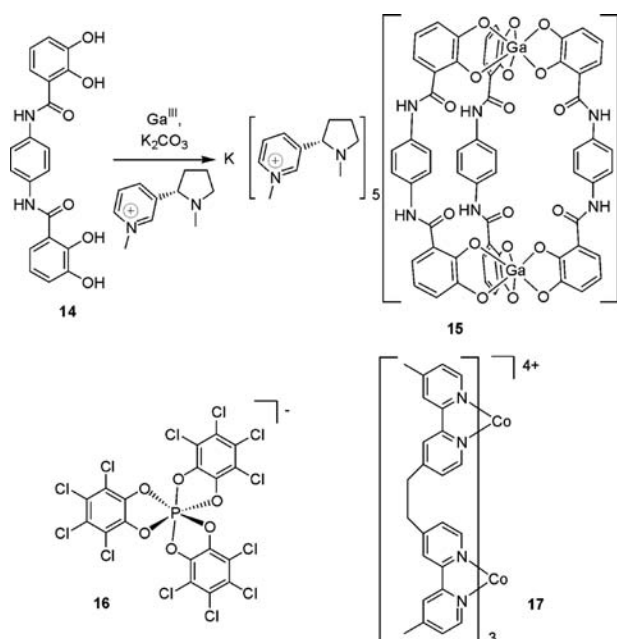
signals start to grow and, after some time, only the resonance of the dinuclear titanium complex **11a** can be observed. Effective templating takes place again.<sup>[22,26]</sup>

To enable the templating by cations in the self-assembly process, the cavities of the helicate-type complexes have to appropriately bind counteranions. Slight variations in the size as well as in the polarity of this cavity can disturb this binding already (Scheme 5).

Use of the two imine-bridged dicatchol ligands **12a** and **12b** leads to different results in a coordination study with titanium(IV) ions. The reaction of **12a** with titanium(IV) and alkali metal carbonate quantitatively leads to the phenyl-bridged dinuclear triple-stranded helicates **13a**. Ligand **12b** with a cyclohexyl spacer reduces the polarity of the cavity of **13b** compared to **13a**. Therefore no encapsulation of cations and no templating can take place. In the reaction of **12b** with titanium(IV) and alkali metal carbonate, only mixtures of oligomers can be observed. Electrospray ionization mass spectrometry shows that the dinuclear complex **13b** is one component of this mixture. But the dinuclear helicate Na-**13b** can be obtained in crystalline form by crystallization from the mixture. Indeed,

comparison of the X-ray structures of K-**13a** and Na-**13b** shows that in the solid state, **13a** binds counteranions in its interior, whereas no cations are encapsulated in **13b**. Only DMF molecules are located in the relatively apolar cavity.<sup>[27]</sup>

The templating of the cations in the formation of the triple-stranded helicate-type complexes **11** can be used for the self-recognition (or heterorecognition) of ligands during the complex formation.<sup>[28]</sup> The use of a 1:1 mixture of ligands **10a** and **10b** for the complex formation theoretically can lead to four different helicate-type complexes: two homoleptic ones with three similar ligands **10a** or **10b** per complex, and two heteroleptic compounds possessing one ligand **10a** and two of **10b**, or vice versa. In addition to this, oligomeric or polymeric material can be formed. However, if the coordination study with a 1:1 mixture of **10a** and **10b** is performed with titanium(IV) ions in the presence of potassium carbonate, only signals of the dinuclear helicate **11b** are observed by NMR on first sight. Having a closer look at the spectrum reveals that broad signals of oligomeric complexes of ligand **10a** are also present. In this experiment, ligand



Scheme 7 Induction of helicity by chiral templates.

self-recognition takes place, leading only to homoleptic complexes. Potassium cations are able to template the formation of complex **11b** but not of **11a**. Therefore the dinuclear complex **11b** is formed from **10b** but only oligomers from **10a**<sup>[29]</sup> (Scheme 6).

With sodium carbonate, a different result is obtained in this self-recognition experiment. Only the homoleptic triple-stranded complexes **11a** and **11b** are formed. Sodium cations are able to stabilize complexes of both ligands. However, because of the different binding modes of the cation to the coordination compounds, a sorting of the ligands takes place on complex formation and solely the homoleptic complexes are obtained.<sup>[29]</sup>

The compounds **11a** and **11b** are also observed in the presence of lithium carbonate as base. However, here, one of the two heteroleptic complexes **11e**,

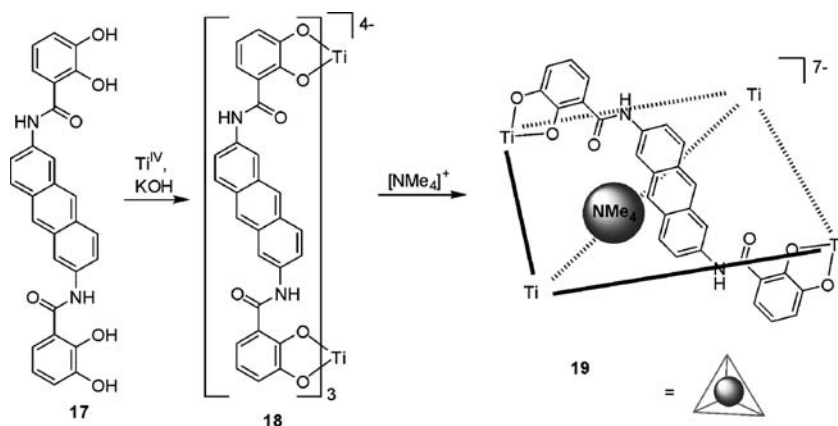
bearing one ligand **10b** and two **10a**, is formed in addition. This is assumed to be because of the reduced size of lithium compared to sodium, which eventually enables a tight encapsulation of a lithium cation in the interior of **11e**.<sup>[29]</sup> (The cavity of **11b** is somewhat too big and the cavity of **11a** is too small for an effective binding of lithium.)

The discussed study on the self-recognition of ligands during complex formation shows how important the influence of the counterions is. The use of three different counteranions leads to three different outcomes in coordination studies. Hereby the templating of the cations strongly controls the assembly and recognition processes.

Further templating effects can be observed by the interaction of counteranions with helicates. If the helicate of ligand **14** is formed in the presence of *S-N*-methylnicotinium cations, an enantiomerically pure triple-stranded helicate **15** is obtained. Here the chiral cation interacts with the helicate and favors one helical twist over the other.<sup>[30]</sup> A similar induction of chirality occurs by addition of Lacour's chiral anion **16** to the triple-stranded dinuclear cobalt(II) helicate **17**<sup>[31,32]</sup> (Scheme 7).

Ligand **17** forms a triple-stranded dinuclear helicate **18** in the presence of potassium cations (Scheme 8). Addition of tetramethylammonium to **18** leads to a destabilizing templating effect, which results in a rearrangement of the dinuclear **18** into the tetranuclear complex **19**. By templating of the cation, the formation of the tetrahedral complex **19** is favored over the helicate **18**.<sup>[33]</sup>

The discussed results show that a strong templating effect is active in the formation of helicates and *meso*-helicates from dicatechol ligands. The investigation of this templating effect should be much easier if neutral helicates are formed without any counterions present. To study systems like this, a ligand unit other than catechol has to be chosen. The charge of the deprotonated catechol unit (2-) is too high to be compensated by a coordinated metal.



Scheme 8 Template-directed transformation of a helicate into a molecular tetrahedron.

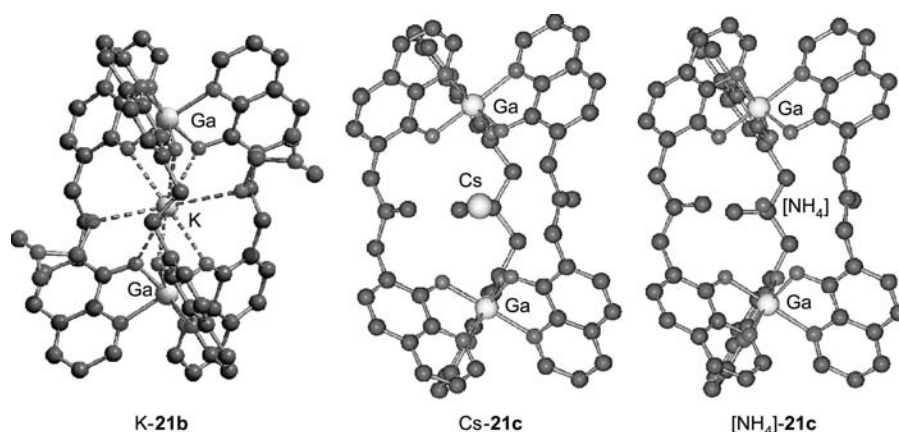


**Fig. 5** Parts of the solid-state structures of **K-21b** Source: From Ref.<sup>[35]</sup>, **Cs-21c**, and **[NH<sub>4</sub>]-21c** Source: From Ref.<sup>[36]</sup>.

### 8-Hydroxyquinoline Ligands as Building Blocks for Helicate-Type Complexes

A ligand moiety, which is geometrically very similar to catechol but possesses only one negative charge (1<sup>-</sup>) in its deprotonated form, is 8-hydroxyquinoline. 8-Hydroxyquinoline forms neutral complexes with metals such as Ga(III), Al(III), Cr(III), or Fe(III).

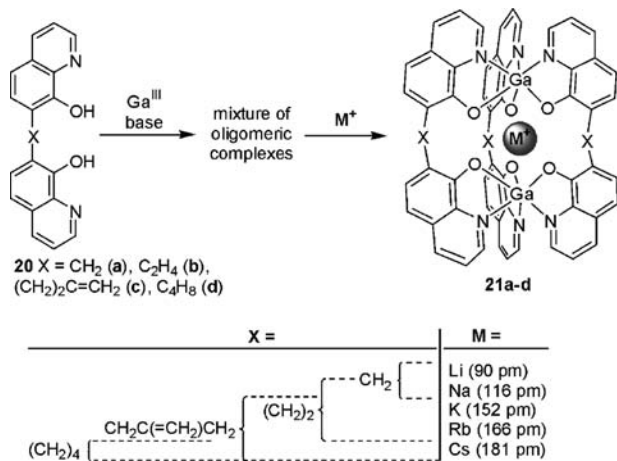
Performing the reaction of the alkyl-bridged di(8-hydroxyquinoline) ligands **20a-d** with gallium nitrate (or aluminum(III) chloride, chromium(III) chloride, or iron(III) chloride) leads to an insoluble material. Elemental analysis shows that this material is composed of ligands and metals in a 3:2 ratio. If long alkyl chains are attached to **20b**, the material becomes soluble in apolar solvents. However, NMR as well as Maldi time-of-flight mass spectrometry (TOF MS) show that not a defined complex but a mixture of oligomers is present.<sup>[34-36]</sup>

Adding alkali metal salts and heating quantitatively transform the mixture of coordination compounds

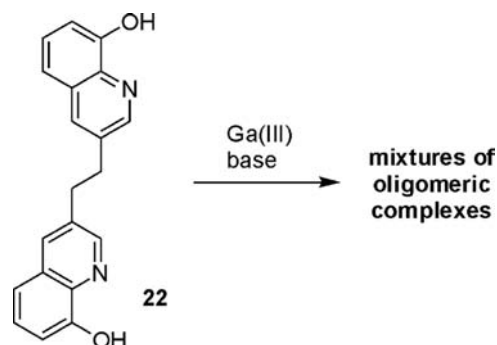
obtained from ligands **20** into the desired dinuclear gallium(III) helicate-type complexes **21a-d** with the alkali metal cation bound in its interior. The same compounds **21a-d** are obtained directly if appropriate alkali metal salts are added during the complex formation of **20a-d** with gallium(III). The helicate-type complexes **21** are formed in a template-directed self-assembly process.<sup>[36]</sup>

Fig. 5 shows parts of the solid-state structures of **K-21b**, **Cs-21c**, and **[NH<sub>4</sub>]-21c**, with the cations encapsulated in the interior of the triple-stranded helicate **21b** or the *meso*-helicate **21c**.<sup>[35,36]</sup> From **[NH<sub>4</sub>]-21c**, it can be seen that ammonium ions also can template the formation of the dinuclear complexes by a combination of electrostatic and hydrogen bonding interactions.<sup>[36]</sup> In one case, it was even possible to show the encapsulation of ammonium in a dinuclear gallium complex by ROESY NMR spectroscopy in solution.<sup>[37]</sup>

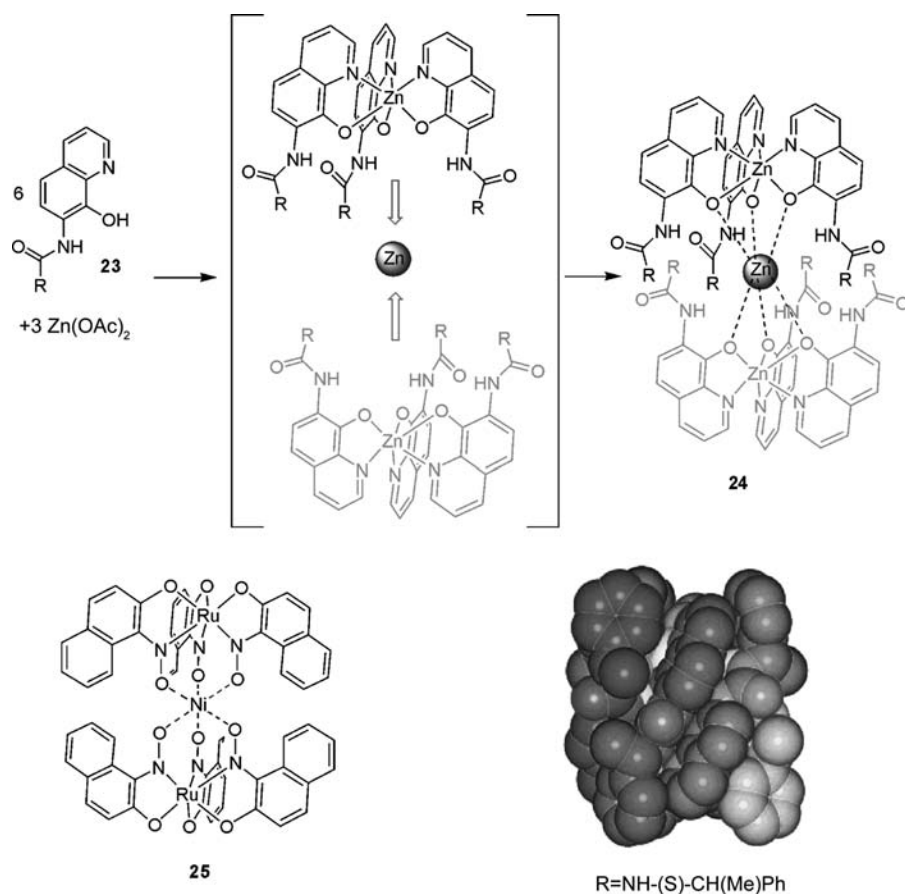
In the formation of the complexes **21a-d**, a strong size dependence between the template and the ligand can be observed (see Scheme 9). The small complex **21a** is only formed in the presence of the small lithium cation. The next bigger complex **21b** is obtained in the presence of sodium cations, potassium cations, and rubidium cations, whereas the compound with C<sub>3</sub>-spacers **21c** is stabilized by potassium, rubidium, and



**Scheme 9** “Size-selectivity” in the template-directed formation of helicates.



**Scheme 10**



**Scheme 11** Template-directed formation of hexa-stranded helical complexes.

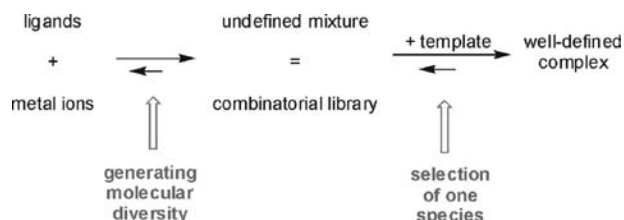
cesium. The biggest complex **21d** assembles only in the presence of the large cesium cation<sup>[36]</sup> (Scheme 10).

For comparison purposes, ligand **22** was synthesized, which does not possess internal oxygen atoms to bind templating cations in the interior of a dinuclear complex. Coordination studies of **22** with gallium again lead to an insoluble material with a correct elemental analysis for a 3:2 ligand/metal ratio. However, on addition of templating cations, no transformation of the mixture into a dinuclear gallium complex takes place.<sup>[34]</sup>

This shows that the stabilization of the helicate-type complexes occurs through binding of the cations to internal oxygen atoms of the complexes. Thus the template, in addition to the ligand spacer, connects the two complex units. The reaction of mono-8-hydroxyquinoline

derivatives **23**, possessing amide or urea moieties in the 7-position of the quinoline, with zinc(II) ions leads to trinuclear “hexa-stranded” complexes **24**. Here templating by the center of the three zinc ions is so strong that a covalent connection of the ligand unit is not necessary to obtain the “hexa”-helical complex **24**. In fact, some hydrogen bonding occurs between the amide or urea moieties and further stabilizes the complexes **24**. The X-ray structural analysis of **24** (R = NH-(S)-CH(CH<sub>3</sub>)Ph) in Scheme 11 reveals the hexa-stranded structure of the trinuclear complex. Because of the chiral substituent, the complex is formed in a stereoselective fashion with only the right-handed helix present.<sup>[38,39]</sup>

Compound **25** represents a very similar trinuclear complex, which is prepared by stepwise introduction of the two different kinds of metals. First, the mononuclear ruthenium(II) complex is formed, which then binds twice to the nickel(II) template to obtain the trinuclear complex **25**.<sup>[40]</sup>



**Scheme 12** The principle of dynamic combinatorial chemistry.

## CONCLUSION

Using the chemistry of dinuclear triple-stranded helicates as an example, it was shown that templating



often is very important in the self-assembly of supramolecular structures. It is an enthalpic driving force for the formation of defined supramolecular complexes. Hereby the templates influence the assembly of defined complexes as well as their structures and stereochemistry. With the discussed results, basic knowledge was gained, which now can be used to understand the formation of bigger, more complex, supramolecular coordination compounds.<sup>[41]</sup>

In the examples presented, very often an undefined mixture of complexes is formed by use of ligands and metal ions. However, because of the non-covalent character of the coordinative bond, the formation of the components of the mixture is reversible and, under appropriate conditions, all the components are in dynamic equilibrium with each other. When a template is added under “equilibration” conditions, it will select and bind the most appropriate compound of the mixture. In an ideal case, this leads to stabilization and the sole formation of the most stable complex-template aggregate<sup>[10]</sup> (Scheme 12).

Hereby, we strictly follow the principle of dynamic combinatorial chemistry<sup>[42]</sup> where, first, a dynamic combinatorial library of compounds is formed from building blocks, which bind to each other by non-covalent or labile covalent interactions. By addition of a template, one derivative is selected from the mixture under equilibration conditions. This method is used to find the most appropriate receptor or substrate of the library for the given template, which can be an ion,<sup>[35]</sup> a small molecular species, or even an enzyme.<sup>[43]</sup>

Templating seems to be even more important in supramolecular chemistry than in “classical” molecular chemistry. In the future, it will help us not only to find more fascinating new helicates, but also to prepare big supramolecular aggregates bearing supramolecular functionalities. It will enable the “bottom-up” approach to nanometer-dimensioned structures starting with simple molecules and using programmed information, which are embedded in the molecular components and which are controlled or “read out” by the template.<sup>[44]</sup>

## REFERENCES

1. Piguet, C.; Bernardinelli, G.; Hopfgartner, G. Helicates as versatile supramolecular complexes. *Chem. Rev.* **1997**, *97*, 2005–2062.
2. Albrecht, M. “Let’s twist again”—Double-stranded, triple-stranded, and circular helicates. *Chem. Rev.* **2001**, *101*, 3457–3498.
3. Zarges, W.; Hall, J.; Lehn, J.-M.; Bolm, C. Helicity induction in helicate self-organization from chiral tris(bipyridine) ligand strands. *Helv. Chim. Acta* **1991**, *74*, 1843–1852.
4. Albrecht, M. Synthesis of a chiral alkyl-bridged bis-(catecholamide) ligand for the self-assembly of enantiomerically pure helicates. *Synlett* **1996**, 565–567.
5. Xu, J.; Parac, T.N.; Raymond, K.N. Coordination number incommensurate cluster formation: Part 10. *Meso* myths: What drives assembly of helical versus *meso*-[M<sub>2</sub>L<sub>3</sub>] clusters? *Angew. Chem., Int. Ed. Engl.* **1999**, *38*, 2878–2882.
6. Albrecht, M. How do they know? Influencing the relative stereochemistry of the complex units of dinuclear triple-stranded helicate-type complexes. *Chem. Eur. J.* **2000**, *6*, 3485–3489.
7. Lehn, J.-M.; Rigault, A.; Siegel, J.; Harrowfield, J.; Chevrier, B.; Moras, D. Spontaneous assembly of double-stranded helicates from oligobipyridine ligands and copper(I) cations: Structure of an inorganic double helix. *Proc. Natl. Acad. Sci. U. S. A.* **1987**, *84*, 2565–2569.
8. Pfeil, A.; Lehn, J.-M. Helicate self-organization: Positive cooperativity in the self-assembly of double-helical metal complexes. *J. Chem. Soc., Chem. Commun.* **1992**, 838–840.
9. Albrecht, M.; Fröhlich, R. Controlling the orientation of sequential ligands in the self-assembly of binuclear coordination compounds. *J. Am. Chem. Soc.* **1997**, *119*, 1656–1661.
10. Albrecht, M. From molecular diversity to template-directed self-assembly—New trends in metallo-supramolecular chemistry. *J. Incl. Phenom. Macrocycl. Chem.* **2000**, *36*, 127–151.
11. Lindsey, J.S. Self-assembly in synthetic routes to molecular devices. Biological principles and chemical perspectives: A review. *New J. Chem.* **1991**, *15*, 153–180.
12. Kersting, B.; Meyer, M.; Powers, R.E.; Raymond, K.N. Dinuclear catecholate helicates: Their inversion mechanism. *J. Am. Chem. Soc.* **1996**, *118*, 7221–7222.
13. Albrecht, M.; Schneider, M.; Fröhlich, R. Self-assembly of a triple-stranded helicate from a rigid di(catechol) ligand and formation of its dimer in the solid state. *New J. Chem.* **1998**, 753–754.
14. Bilyk, A.; Harding, M.M. Guest induced assembly of a chiral [2 + 2] metallomacrocycl. *J. Chem. Soc., Chem. Commun.* **1995**, 1697–1698.
15. Houghton, M.A.; Bilyk, A.; Harding, M.M.; Turner, P.; Hambley, T.W. Effect of guest molecules, metal ions and linker length on the assembly of chiral [2 + 2] metallomacrocycles: Solution studies and crystal structures. *J. Chem. Soc., Dalton Trans.* **1997**, 2725–2733.
16. Try, A.C.; Harding, M.M.; Hamilton, D.G.; Sanders, J.K.M. Reversible five-component assembly of a [2]catenane from a chiral metallomacrocycl and a dinaphthocrown ether. *Chem. Commun.* **1998**, 723–724.
17. Krämer, R.; Lehn, J.-M.; DeCian, A.; Fischer, J. Self-organization, structure and spontaneous racemate cleavage of a trinuclear triple helix complex formed from oligobipyridine ligands and nickel(II) ion. *Angew. Chem., Int. Ed. Engl.* **1993**, *32*, 703–706.



18. Hasenknopf, B.; Lehn, J.-M.; Boumediene, N.; Dupont-Gervais, A.; Van Dorsselaer, A.; Kneisel, B.O.; Fenske, D. Self-assembly of tetra- and hexanuclear circular helicates. *J. Am. Chem. Soc.* **1997**, *119*, 10956–10962.
19. Scarrow, R.C.; White, D.L.; Raymond, K.N. Ferric ion sequestering agents: 14. 1-Hydroxy-2(1*H*)-pyridinone complexes: Properties and structure of a novel Fe–Fe dimer. *J. Am. Chem. Soc.* **1985**, *107*, 6540–6546.
20. Saalfrank, R.W.; Dresel, A.; Seitz, V.; Trummer, S.; Hampel, F.; Teichert, M.; Stalke, D.; Stadler, C.; Daub, J.; Schunemann, V.; Trautwein, A.X. Chelate complexes: 9. Topologic equivalents of coronands, cryptands and their inclusion complexes. Synthesis, structure and properties of {2}-metallacryptands and {2}-metallacryptates. *Chem. Eur. J.* **1997**, *3*, 2058–2062.
21. Albrecht, M. Dicatechol ligands: Novel building-blocks for metallo-supramolecular chemistry. *Chem. Soc. Rev.* **1998**, *27*, 281–288.
22. Albrecht, M.; Kotila, S. Counterion induced self-assembly of a *meso*-helicite type molecular box. *Chem. Commun.* **1996**, 2309–2310.
23. Albrecht, M.; Kotila, S. Stabilization of an unusual coordination geometry at lithium in the interior of a cryptand-type helicate. *Angew. Chem., Int. Ed. Engl.* **1996**, *35*, 1208–1210.
24. Albrecht, M.; Kotila, S. Formation of a “*meso*-Helicate” by self-assembly of three bis(catecholate) ligands and two titanium(IV) ions. *Angew. Chem., Int. Ed. Engl.* **1995**, *34*, 2134–2137.
25. Albrecht, M.; Röttele, H.; Burger, P. Alkali–metal cation binding by self-assembled cryptand-type supermolecules. *Chem. Eur. J.* **1996**, *2*, 1264–1268.
26. Albrecht, M. Self-assembly of dinuclear CH<sub>2</sub>-bridged titanium(IV)/catecholate complexes: Influence of the counterions and of methyl substituents at the ligand. *Chem. Eur. J.* **1997**, *3*, 1466–1471.
27. Albrecht, M.; Janser, I.; Kamptmann, S.; Fröhlich, R. unpublished results.
28. Krämer, R.; Lehn, J.-M.; Marquis-Rigault, A. Self-recognition in helicate self-assembly: Spontaneous formation of helical metal complexes from mixtures of ligands and metal ions. *Proc. Natl. Acad. Sci. U. S. A.* **1993**, *90*, 5394–5398.
29. Albrecht, M.; Schneider, M.; Röttele, H. Template-directed self-recognition of alkyl-bridged di(catechol) ligands in the formation of helicate-type complexes. *Angew. Chem., Int. Ed. Engl.* **1999**, *38*, 557–559.
30. Yeh, R.M.; Ziegler, M.; Johnson, D.W.; Terpin, A.J.; Raymond, K.N. Imposition of chirality in a dinuclear triple-stranded helicate by ion pair formation. *Inorg. Chem.* **2001**, *40*, 2216–2217.
31. Jodry, J.; Lacour, J. Efficient resolution of a dinuclear triple helicate by asymmetric extraction/precipitation with TRISPHAT anions as resolving agents. *Chem. Eur. J.* **2000**, *6*, 4297–4304.
32. Lacour, J.; Jodry, J.; Monchaud, D. Configurational ordering of a cationic dinuclear triple helicate by chiral TRISPHAT anions. *Chem. Commun.* **2001**, 2302–2303.
33. Scherer, M.; Caulder, D.; Johnson, D.W.; Raymond, K.N. Coordination number incommensurate cluster formation: Part 11. Triple helicate–tetrahedral cluster interconversion controlled by host–guest interactions. *Angew. Chem., Int. Ed. Engl.* **1999**, *38*, 1588–1592.
34. Albrecht, M.; Blau, O. Solubilization of a self-assembled metallocryptand by addition of K<sup>+</sup>. *Chem. Commun.* **1997**, 345–346.
35. Albrecht, M.; Blau, O.; Fröhlich, R. An expandable metalla-cryptand as a component of a supramolecular combinatorial library formed from di(8-hydroxyquinoline) ligands and gallium(III)- or zinc(II) ions. *Chem. Eur. J.* **1999**, *5*, 48–56.
36. Albrecht, M.; Blau, O.; Fröhlich, R. “Size-selectivity” in the template directed assembly of dinuclear triple-stranded helicates. *Proc. Natl. Acad. Sci. U. S. A.* **2002**, *99*, 4872–4876.
37. Albrecht, M.; Blau, O.; Zauner, J. Preparation of a highly alkyl-substituted di(8-hydroxyquinoline) derivative and its use for the self-assembly of a lipophilic helicate with an internal binding site for cationic guests. *Eur. J. Org. Chem.* **1999**, 3165–3169.
38. Albrecht, M.; Witt, K.; Röttele, H.; Fröhlich, R. Stereoselective formation of a trinuclear hexa-stranded helicate-type zinc(II) complex. *Chem. Commun.* **2001**, 1330.
39. Albrecht, M.; Witt, K.; Weis, P.; Wegelius, E.; Rissanen, K.; Fröhlich, R. Zinc(II) complexes of amide and urea substituted 8-hydroxyquinoline. *Inorg. Chim. Acta* **2002**, *341*, 25–32.
40. Das, A.K.; Rueda, A.; Falvello, L.R.; Peng, S.-M.; Bhattacharya, S. Tris-1-nitroso-2-naphtholate complex of ruthenium(II): An efficient building unit for polynuclear complexes. *Inorg. Chem.* **1999**, *38*, 4365–4368.
41. Leininger, S.; Olenyuk, B.; Stang, P. Self assembly of discrete cyclic nanostructures mediated by transition metals. *Chem. Rev.* **2000**, *100*, 853–907.
42. Brady, P.A.; Sanders, J.K.M. Selection approach to catalytic systems. *Chem. Soc. Rev.* **1997**, *26*, 327–336.
43. Huc, I.; Lehn, J.M. Virtual combinatorial libraries: Dynamic generation of molecular and supramolecular diversity by self-assembly. *Proc. Natl. Acad. Sci. U. S. A.* **1997**, *94*, 2106–2110.
44. Lehn, J.-M. Programmed chemical systems: Multiple subprograms and multiple processing/expression of molecular information. *Chem. Eur. J.* **2000**, *6*, 2097–2102.

# Templating Aerogels for Tunable Nanoporosity

**Aydin K. Sunol**

*Chemical Engineering Department, University of South Florida,  
Tampa, Florida, U.S.A.*

**Sermin G. Sunol**

*University of South Florida, Tampa, Florida, U.S.A.*

## INTRODUCTION

The engineering of porosity, particularly at the meso-level, is expected to be of great scientific and technological significance in the 21st century where advances in nanoscience and technology are projected to catalyze major breakthroughs in biosciences and materials.

Aerogels are a class of highly porous buoyant materials that find use or show promise in many key products such as catalysts, thermal insulators, chemical adsorbers, sensors, fuel storage, energy absorbers, and aero capacitors. They may be in the form of particles, thin films, fibers, or monoliths. Some of the remarkable properties for the aerogels are high porosity, large pore volume, high surface area, and very good morphological stability during heat treatment at high temperatures. Recent discovery of surfactant-templated pathways enables better control over the properties of the porous materials. The advantages of the templating include high porosity, tunable unimodal or multimodal nanoporosity, and directional control. The new evaporation-induced self-assembly method that enables production of aerogel-like materials using soft chemistry and lower pressures further expands the spate of products that are possible in economically promising fashion. This porous structure can be further functionalized through doping and impregnation to host catalytic sites, conducting phases, or magnetic phases.

This review aims to address the issues of preparation of templated gels, removal of the solvent and template material, and subsequent functionalization of the surfactant-templated aerogels to further tune the porous structures.

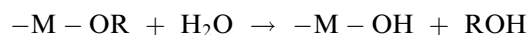
## SOL-GEL SYNTHESIS

Most aerogels involve drying of gels synthesized using sol-gel chemistry. The sol-gel process involves the formation of a sol, which is a liquid suspension of solid particles ranging in size from 1 nm to 1  $\mu$ m. These materials can be obtained by the hydrolysis and partial condensation of a precursor such as a metal alkoxide.

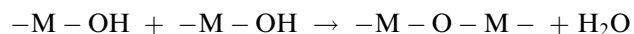
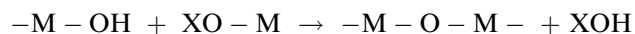
The further condensation of sol particles into a multi-dimensional network produces a gel, which is a solid phase encapsulating a solvent. The gel materials are referred to as aquagel when water is used as the primary solvent and alcogel when alcohol is used instead. The encapsulated liquid can be removed from a gel by either evaporative drying or freeze-drying or processing at supercritical conditions. The resulting solid product is called as either xerogel or aerogel (if synthesized using supercritical processes). The advantages of sol-gel based synthesis of aerogels are their high purity, microstructure, homogeneity at molecular level, and low-temperature preparation.<sup>[1,2]</sup>

Since the introduction of M41S family of solids,<sup>[3]</sup> there has been an explosion of applications for templating applications and pore inducers. Templating is compatible with the sol-gel chemistry. Metal alkoxides have been the most extensively used precursor in sol-gel preparation because they are commercially available in high purity and their solution chemistry is well documented.<sup>[4]</sup> Sol-gel chemistry with metal alkoxides can be described in terms of two classes of reactions:

Hydrolysis reaction:



Condensation reactions:



where X can either be H or R (an alkyl group).

These two kinds of reactions capture the key phenomenon; a two-dimensional or three-dimensional gel network materializes from the condensation of partially hydrolyzed species. Any variables, such as the relative rates of hydrolysis and condensation, that affect either or both of these reactions are thus likely to have impact on the properties of the product. When the condensation reaction rate is relatively higher than the hydrolysis reaction rate, the resulting sol-gel

becomes highly branched and the corresponding primary gel structure is mesoporous. Whereas, if the hydrolysis reaction rate is relatively higher than that of condensation, then the resulting sol-gel is weakly branched and the corresponding gel structure is generally microporous.

Because hydrolysis and condensation are both nucleophilic displacement reactions, the reactivity of metal alkoxides is dependent on the positive partial charge of the metal atom and its coordination number. In general, the longer and bulkier the alkoxide group attached to a particular metal atom, the less reactive that precursor is in hydrolysis and condensation.<sup>[5]</sup> The choice of precursors and/or their concentrations is effective in controlling the hydrolysis and condensation reaction rates. The amount of water used in sol-gel preparation and the rate by which it is added also influence gel characteristics. The former is usually expressed in terms of the hydrolysis ratio  $h$ , defined as the moles of water per mole of metal alkoxide,  $M(OR)_m$ . The tendency of the precursor to condense is small when there is no local excess of water because there are few M-OH groups for cross-linking, gelation, or precipitation. If the hydrolysis ratio is marginally above 1, polymeric gels can form while sufficiently excess water leads to formation of cross-linked polymers, particulate gels, or precipitates. The rate of water addition is usually slow.

Two other important sol-gel parameters are temperature and solvent. Temperature is the most effective way to alter the relative rates of competing reactions and both high and low temperatures are used in practice. The solvent choice can change the nature of an alkoxide through solvent exchange as well as affecting the condensation reaction directly.

The effect of gelation time on gel properties is significant and should be part of the experimental design. Gel time is defined as the time it takes for a solution to undergo a rapid rise in viscosity. This corresponds to solution's transition from a viscous fluid to an elastic gel. At the gel point, there is a continuous solid phase with a structure where particles form and branch as dictated by the specific growth conditions. This particular phase has significant impact on the structural evolution these materials undergo in all subsequent processing steps.

Aging is the time between the formation of a gel network and the removal of solvent from that solid gel network. As long as the pore liquid remains in the matrix, a gel is not static and can undergo many changes. For alkoxide-derived gels, condensations between surface functional groups continue to occur even long after the gel point. This process can actually be desirable because it leads to a more cross-linked network that is mechanically stronger and easier to handle. However, extensive condensation causes a

phenomenon called syneresis, which is the solvent expulsion from the gel as the gel network shrinks. The shrinkage in alcoholic gel systems is attributed to formation of new bonds through condensation reactions, which increase the bridging bonds and cause contraction of the gel network.<sup>[6]</sup> Coarsening or ripening is a physical phenomenon driven by solubility differences associated with surfaces that have different radii of curvature. Coarsening basically involves the dissolution and reprecipitation of particles, resulting in an increase in the average pore size of the gel and a decrease in its specific surface area.

Parameters that affect these aging processes include temperature, time, and pH of the pore liquid. Common approaches to manipulating these parameters are soaking or washing the gel with another liquid, changing the humidity level of the gel environment, heating the gel, and using hydrothermal conditions. Although all these approaches have been demonstrated to change the gel characteristics, an understanding of the cause and effect is at best qualitative at present.

The fields of aerogels and sol-gel chemistry are not limited to metal oxides. Carbon aerogels<sup>[7]</sup> that find use in energetic applications are produced with the aid of sol-gel chemistry through aqueous polycondensation of resorcinol (1,3 dihydroxybenzene) with formaldehyde. This reaction under alkaline conditions proceeds through a sol-gel transition and results in the formation of a highly cross-linked polymer. Other precursors such as the phenol-furfural or melamine-formaldehyde system<sup>[8]</sup> are also possible.

The sol-gel chemistry is well covered in literature including a classic by Ref.<sup>[9]</sup>. The sol-gel gateway in the web provides<sup>[10]</sup> another pathway to vast amount of information.

## TEMPLATE MATERIALS

The chemical modifications aside, selection of the template material is of paramount importance in defining the final porosity, its distribution, orientation, and the surface texture. The general field of surfactant-templated materials and their applications has been the subject of intense work and many reviews.<sup>[11-17]</sup> They are generally classified as direct and mediated paths and involve cationic and anionic surfactants. However, for surfactant-templated aerogel synthesis, nonionic surfactants seem to be the current choice.

The template selection naturally dictates the processes that can be employed for its removal. While the primary removal path is thermal decomposition, extractive processes, particularly supercritical fluid-based ones, offer gentler and environmentally greener avenues, often with superior pore structure retention. Interplay between surfactant and solvent becomes

significant particularly at the drying stage. Question of to what extent the template material should be removed in the supercritical drying stage, along with the solvent, needs to be addressed at the design stage. In instances the surfactant or other templating material is to be removed supercritically, the available options, in decreasing order of desirability, are listed as follows:

- Template is soluble in supercritical carbon dioxide. The most popular supercritical solvent, carbon dioxide, has been used for many years for various applications including drying of aerogels. It is environmentally friendly and minimizes pore structure degradation. Unfortunately, CO<sub>2</sub> is non-polar, has low dielectric constant, and does not engage in van der Waals-type interactions. In other words, CO<sub>2</sub> is a poor solvent for highly polar and high molecular weight material. In the last decade, major strides in the design of CO<sub>2</sub>-philic and amphiphilic surfactants are made. A relevant review will possibly start with a look at the solubility<sup>[18]</sup> of commercial surfactants in carbon dioxide, include McClain et al.'s<sup>[19]</sup> work on design of fluorinated CO<sub>2</sub>-philic hydrocarbon-based surfactants, and focus on CO<sub>2</sub>-philic hydrocarbons composed of only C, H, and O molecules.<sup>[20]</sup> Although the aforementioned CO<sub>2</sub>-philic surfactants were synthesized for other purposes such as metal or protein extraction, cleaning, and polymerization reactions, their teachings will form a solid foundation for CO<sub>2</sub>-philic templating surfactants. The shape, orientation, and access to CO<sub>2</sub>-philic sites of surfactants are important in tuning the pore size distribution of the material synthesized with the aid of such templates.
- Template is soluble in a suitable entrainer plus supercritical carbon dioxide.<sup>[21–23]</sup> The advantages of supercritical fluids can be realized if entrainers (modifiers), such as alcohols, are used to enhance the solubility of the template material. The concern here is the recovery of liquid entrainer that has a tendency to preferentially adsorb within the porous matrix. Naturally, although less significant because of lower corresponding concentrations, the toxicity considerations that exist for liquid solvents are also applicable. If not removed, the indigenous solvent employed in sol-gel synthesis can serve as entrainer or co-solvent. This path for removal of surfactants has been successfully employed in removal of templated material in several applications, particularly nonionic ones.<sup>[21–24]</sup>
- Template soluble in other supercritical systems. In applications where intermediate or higher-temperature template removal is acceptable or desirable, other supercritical solvents may also be employed. The initial aerogel synthesis methods utilized alcohols indigenous within the sol.

The templates and supercritical fluids are two key technologies of self-assembly paths leading to unique materials.<sup>[25,26]</sup> It is also worth mentioning that supercritical fluids can be effectively used in a priori fractionation of surfactants for subsequent extractability.<sup>[27,28]</sup>

In many applications, removal of templating material using thermal means may be inevitable. These thermal operations may lead to sintering, e.g., alumina support. The sol-gel synthesis and template selection do affect the resulting support. This sintering problem can be addressed by adding mixed metal oxides. For example, addition of small concentrations of silica to alumina in the sol-gel formation stage expands the sintering free calcination temperature ranges.<sup>[29–31]</sup> Other attempts to aid preservation of the textural properties include addition of surfactants<sup>[32,33]</sup> and rare earth stabilization.<sup>[34]</sup>

## DRYING METHODS

The pore inducers, templates, and solvents should be removed from the wet gel before further functionalization or end use. The drying and extractive removal of the solvent and the template are discussed here, while thermal treatments and functionalization approaches are subsequently treated. The approaches to drying of wet porous material are evaporation, freeze drying, and supercritical drying. The approaches to drying are summarized in Fig. 1. Although traditionally, materials resulting from non-critical evaporative drying methods are called xerogels, the structural properties of such material are similar to that of aerogels because of recent advances such as use of templates and evaporative film formation through self-assembly.<sup>[35]</sup> Furthermore, evaporative processes inadvertently

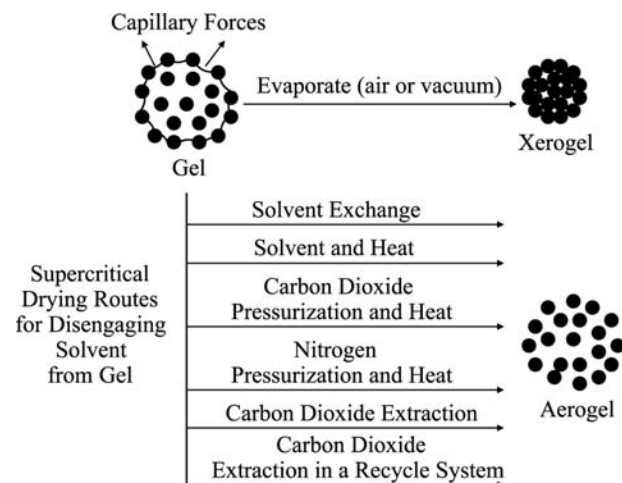


Fig. 1 Drying methods for gels.

become part of even supercritical drying and solvent extraction routes. Therefore evaporative drying is presented before supercritical routes that lead to aerogels are discussed.

### Evaporative Drying

The rate of evaporation,  $V_E$ , is proportional to the difference between vapor pressure of the evaporating fluid and the system pressure. Evaporation continues as long as vapor pressure is greater than bulk fluid pressure, a situation not likely in pressurized environments such as supercritical conditions. The vapor pressure at a surface composed of a large number of very small pores is influenced by the radii of the pores, as shown by the Gibbs–Kelvin equation.

$$\ln\left(\frac{p_s}{p_o}\right) = \frac{B\gamma}{RT} \frac{2}{r_m} \quad (1)$$

where  $p_s$  is the vapor pressure over the meniscus of the pore,  $p_o$  is the vapor over a flat surface (760 Torr),  $B$  is the molar volume of the liquid,  $R$  is the gas constant,  $\gamma$  is the difference between the solid–vapor and liquid–vapor interfacial energies,  $T$  is temperature, and  $r_m$  is the radius of curvature of the meniscus.

Because the pores of gels are generally small, capillary forces are generally dominant during drying and adsorption force and osmotic force are marginal when compared with the capillary forces because capillary force is a direct and strong function in capillary radius as suggested by equation below

$$P = \left(\frac{-2\gamma_{LV}}{r_m}\right) \quad (2)$$

where  $P$  is tension in the liquid inside the pores,  $\gamma_{LV}$  is the liquid–vapor interface energy, and  $r_m$  is radius of the curvature of the meniscus and is related to the cylinder pore radius as in Eq. (3)

$$r_m = \left(\frac{-r}{\cos(\theta)}\right) \quad (3)$$

where  $r$  is the cylindrical pore radius and  $\theta$  is the contact angle between the vapor and the solid gel phase.

Factors other than capillary pressure could affect the gel drying process. Adsorption forces bind solvent and surfactant into an ordered layer, a few molecules thick near a solid surface; the attractive force may drive flow of a film over an exposed solid surface and influence the curvature of the meniscus. However, if there were no capillary force ( $\gamma_{LV}$ ), no compressive force would be exerted on the network as evaporation emptied the pores and no shrinkage would result from

adsorption forces unless in those pores that have initial pore radius in the order of the film thickness of the adsorbed solvent. Removal of this adsorbed liquid can be sometimes difficult and will occur in the last stage of drying after the interparticle space is drained.

Osmotic pressure is also another factor that manifests some controlling effect on the drying process. It induces water to enter the interlayer space in some porous material particles to equalize the concentration of ions in that space and in the surrounding bulk liquid.

The drying behavior of porous solids has been classified into three different stages. The three stages of drying are stage 1, also referred to as constant rate period of drying, stage 2, referred to as first falling rate period, and stage 3, referred to as second falling rate period. The salient features of the rate of drying throughout the three stages are shown in Fig. 2.

This first stage is called “the constant rate period” because the evaporation rate per unit area (mass flux) of the drying surface is independent of time. The gel at the beginning of stage 1 drying has a surface area that is initially largely free liquid, separated by a relatively small area fraction of gel network with a transition zone of bound liquid. As the free liquid evaporates, the solid network contracts because of capillary stresses. The evolution of pore structure from the first stage into the second is depicted in Fig. 2A. During this stage, the decrease in the volume of the gel is equal to the volume of liquid lost by evaporation. The compliant gel network is deformed under the effect of the large capillary forces, which causes shrinkage of the gel and reduction of pore radii during drying. The greatest changes in volume, weight, density, and structure occur during stage 1 drying that ends when shrinkage ceases.

Stage 2, also known as first falling rate period, starts at the critical point as shown in Fig. 2. This stage is characterized with the highest capillary pressure imposed on the gel network during the drying process, hence causing shrinkage to the solid structure and affecting its permanent and final textural and structural properties.

The rate of drying in this stage decreases drastically from the rate of drying in the previous stage, and the temperature of the outer surface rises above the wet-bulb temperature. Liquid is driven to the outer surface by gradients in capillary vapor pressure, where it evaporates because of the ambient vapor pressure being lower than that inside the pores as shown in funicular section of Fig. 2B. The liquid in the pores near the surface remains in the funicular condition, so there are contiguous pathways along which flow can occur. Most of the evaporation is still occurring at the exterior surface, and the surface remains below the ambient temperature, and the rate of evaporation (on

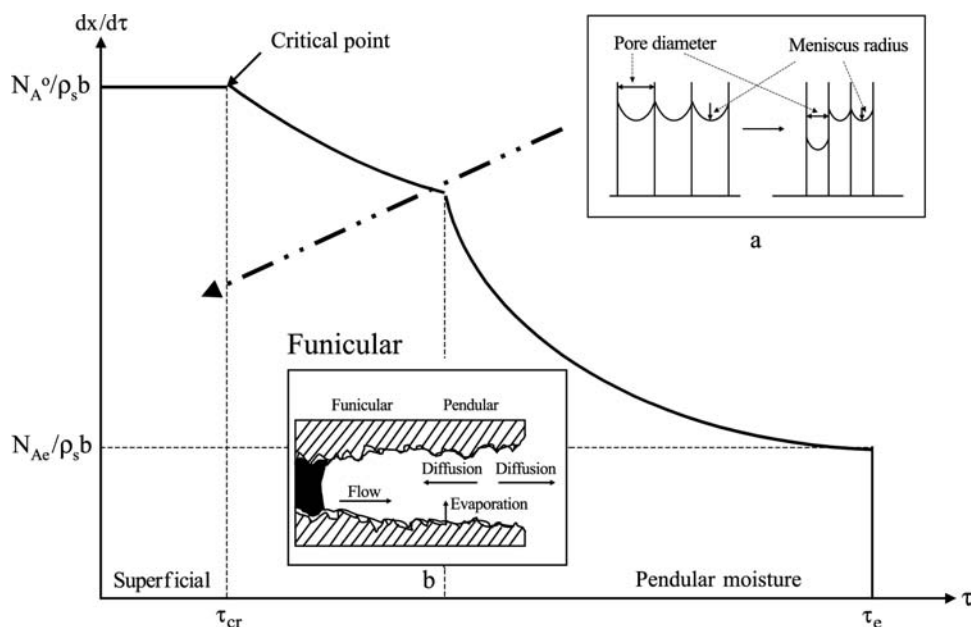


Fig. 2 Stages of evaporative drying.

the outer surface of the gel) is sensitive to the ambient temperature and vapor pressure. At the same time, although some liquid evaporates within the unsaturated pores and the vapor is transported by diffusion, they are negligible when compared with the major liquid flow through the pore walls under capillary and tension forces. Fluid flow in stage 2 is driven by the gradient in capillary stress. Evaporation occurs at the outer surface because the vapor pressure is lower there than inside the humid pores. The vapor pressure gradient through the pores is associated with the capillary stress gradient in the pores. Therefore, the funicular liquid flows toward the exterior surface at all times. Since the vapor pressure and the surface tension are functions of temperature, the temperature affects the gradients in capillary pressure. Both acting forces (capillary and the surface tension) favor flow toward the outer surface. When there is a range of pore sizes in the body, the larger pores will empty first.

As in stage 1, the flow rate may also be influenced by adsorption forces in the same manner as shown in Fig. 2B to keep the surface under a few molecules-thick adsorbed layers of the liquid, and this causes flow of the film. This mechanism is most likely important when the vapor pressure at the surface is very low.

The transition from stage 2 to stage 3 and its inception is associated with a rise in the gel temperature because the temperature of the body is not as strongly suppressed as when evaporation rates were higher. The remaining liquid evaporates within the pores and is removed by diffusion of its vapor to the surface as shown in pendular section of Fig. 2B. This stage of drying is not affected by local changes in temperature,

ambient vapor pressure, or flow rate. At the start of stage 3, the gel is practically dry. It can be removed from the drying chamber and dehydrated under much more severe conditions (high temperature and under near vacuum pressure) without risk of cracking.

### Supercritical Drying

The supercritical drying methods evolved considerably since the pioneering work of Kistler<sup>[36]</sup> where excess alcohol was added to the autoclave and then heat was supplied so that supercritical conditions were reached. Subsequently, supercritical solvent was removed from the autoclave by depressurization above the critical temperature of the solvent.<sup>[36]</sup> These methods all have pressurization, heating, diffusion, and depressurization steps and may be easier to understand using the pressure-temperature (PT) diagram (Fig. 3) of the supercritical fluid. In these methods, the PT path is ABC as shown in Fig. 3. Van Lierop et al.<sup>[37]</sup> modified this method by pressurizing the system using an inert gas prior to heating; the path then corresponds to A'BC. A further improvement was carried out to the second method through the solvent exchange method in which the pore liquid was replaced with carbon dioxide that has a much lower critical temperature than alcohols. Carbon dioxide was then vented out of the system above its critical temperature. In some cases, an intermediate solvent miscible both with the pore liquid and carbon dioxide was pumped to the system to be subsequently replaced with carbon dioxide.<sup>[38]</sup> In yet another method, supercritical carbon



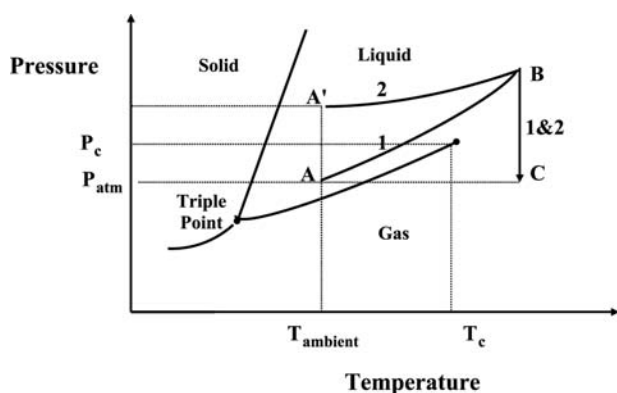


Fig. 3 Pressure–temperature diagram and drying paths.

dioxide was used to extract the pore liquid in a semi-continuous mode.<sup>[39]</sup> In the last method, the system was pressurized with carbon dioxide, and carbon dioxide–alcohol mixture was brought to supercritical conditions and the supercritical fluid was removed from the gel.<sup>[40]</sup>

Supercritical drying allows sustained single fluid phase where drying is free from liquid–vapor interfacial stresses. This facilitates the production of aerogels that have the same morphological properties as their alcogel precursors. On the other hand, production of crack-free monoliths still necessitates selection of best drying technology and the optimization of key processing variables such as heating and depressurization rates. In the heating and depressurization steps, high rates are expected to result in considerable stress formation. During heating, stress develops because of smaller thermal expansion of the solid network in comparison to the pore liquid. In addition, at high temperatures, solid network contracts because of the chemical bonds formed by condensation reactions. If the expanding pore liquid flows out of the body, stress is relieved. However, at high heating rates, limited time restricts the escape of the expanding liquid significantly.<sup>[41]</sup> The same analysis is valid for the depressurization rates. At high depressurization rates, the fluid outside the gel flows out of the reactor at a higher rate than the fluid flowing out of the gel network. Because of differential pressure, the fluid in the gel network expands and stress develops in the gel. Cracking occurs when the stress exceeds the strength of the gel network.<sup>[42]</sup> Scherer modeled the stress development during supercritical drying. The model for a cylindrical geometry with no radial constraint was applied to the heating step of the autoclave drying method assuming elastic behavior, and the analysis was extended to radially constrained viscous gel network for which an analytical solution is also obtained.<sup>[43]</sup>

We analyzed the stress formation in the heating steps of the autoclave drying and the carbon dioxide

exchange (solvent exchange) methods.<sup>[44]</sup> Stress forming in the pore liquid is a function of heating rate, viscosity, and thermal expansion coefficient of the liquid and mechanical properties of the gel network. For the autoclave drying and carbon dioxide exchange methods, the effects of different pore liquids with different thermal expansion coefficients, viscosities, critical temperatures, and critical pressures on the stress development were analyzed. The calculated radial stresses are compared with the modulus of rupture of the gel network to decide whether production of crack-free aerogels is possible as far as the heating steps in both autoclave drying and carbon dioxide exchange methods are concerned. The study showed the superiority of lower-temperature solvent extraction route.

### Removal of Template Material

The removal of the templating surfactant molecules occluded within the mesoporous materials after the synthesis step is often carried out through thermal means under air at temperatures between 500°C and 600°C. Although high-temperature calcinations allow removal of the surfactant completely, the decomposed surfactant cannot be used, the evolving gasses are often noxious, and the pore structures, particularly chemical integrity of the organic groups, are substantially altered.<sup>[45]</sup> At times, calcination is necessary part of the recipe. For example, in synthesis of alumina support, AlOOH is converted to Al<sub>2</sub>O<sub>3</sub> through calcination<sup>[24]</sup> and co-removal of template is feasible.

Alternative means include solvent extraction that allows surfactant removal without decomposition. The liquid extractions are carried under reflux, generate substantial amount of waste that are often toxic, and do require removal of the solvent from the porous matrix. The supercritical fluid extraction that has been used for drying is being increasingly applied to removal of the surfactant. The most popular supercritical solvent, carbon dioxide, has been used for many years for drying of aerogels, is environmentally friendly, and minimizes pore structure degradation.<sup>[24,46–48]</sup> Unfortunately, CO<sub>2</sub> is non-polar, has low dielectric constant, and does not engage in van der Waals-type interactions. In other words, CO<sub>2</sub> is a poor solvent for highly polar and high molecular weight materials.

The advantages of supercritical fluids can be realized if entrainers (modifiers), such as alcohols, are used to enhance the solubility of the template material. The concern here is the recovery of liquid entrainer that has a tendency to preferentially adsorb in the porous matrix.

Synthesis of thermally stable alumina supports has been the subject of intense effort for many years and is an excellent example of how synthesis method and

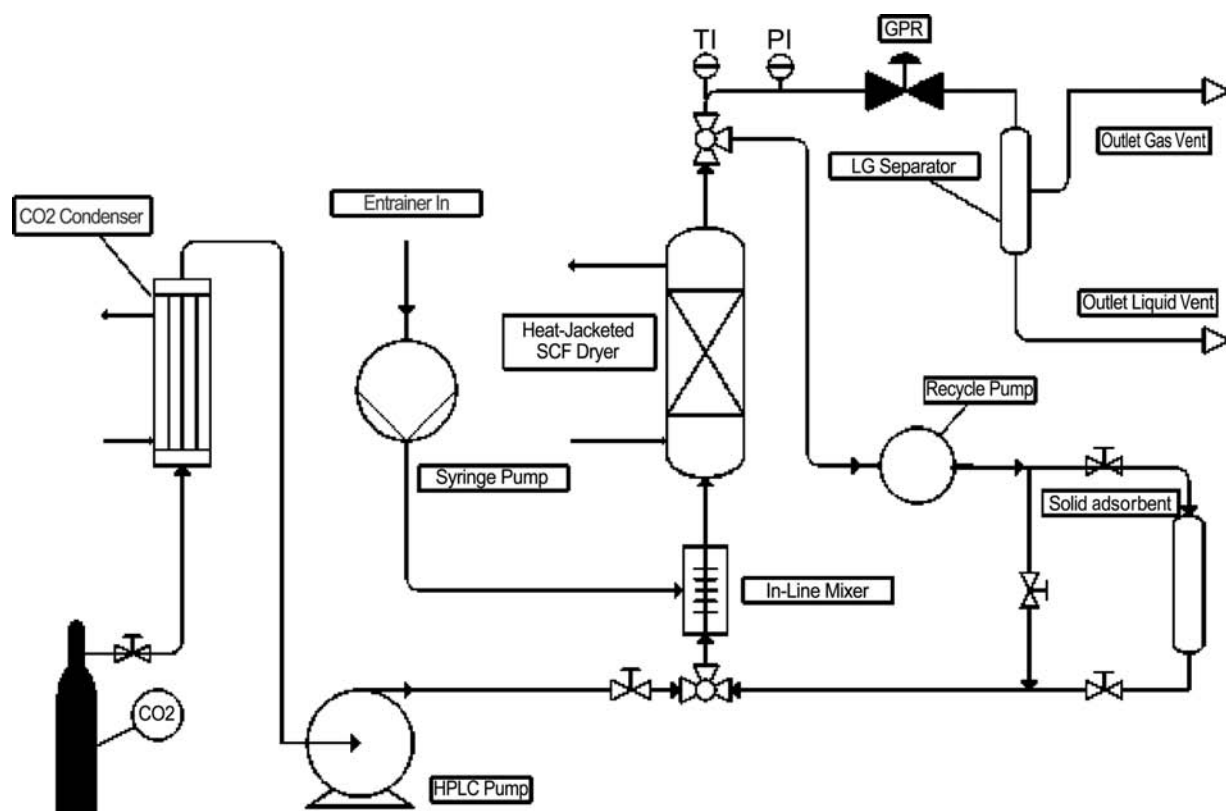


Fig. 4 Pilot plant flow sheet for supercritical drying and impregnation.

template removal technology can affect the pore structure. Fig. 4 shows the multipurpose pilot plant employed in drying as well as surface functionalization. Even after calcination at 773 K, BET pore areas over  $700 \text{ m}^2/\text{g}$  and unimodal pore sizes around 11 nm were achieved through non-ionic surfactant-templated (Triton X-114, a commercial surfactant) synthesis of alumina aerogels. Table 1 summarizes some key results.

## FUNCTIONALIZATION AND TAILORING NANOPOROUS MATERIAL

The approaches to chemical functionalization of porous matrices include impregnation, doping, and

self-assembly in the porous matrix. These approaches not only enable chemical functionalization of the surfaces, but also allow tuning of the surface texture and structure. In liquid-phase functionalizations, the shortcomings discussed in the context of drying, pore size reduction, and collapse are compounded by mass transfer limitations that hinder rate and access to the pores. Furthermore, capillary condensation and multilayer adsorption limit control and tunability. Therefore supercritical fluid-based impregnation and in situ processing offer a major advantage in instances where solubility-related issues are resolved. One of the earliest applications of the technology is simultaneous permeation of diffusion of monomers/polymers into porous wood matrix in the supercritical carbon dioxide

Table 1 Effect of surfactant and drying method on surface area and average pore diameter of alumina gels

Calcination temperature (K)	Without surfactant				With surfactant			
	Surface area ( $\text{m}^2/\text{g}$ )		Pore diameter (nm)		Surface area ( $\text{m}^2/\text{g}$ )		Pore diameter (nm)	
	Xerogel	Aerogel	Xerogel	Aerogel	Xerogel	Aerogel	Xerogel	Aerogel
No calcination	535	763	61	40	714	995	43	109
727	439	503	74	50	484	696	72	129
827	404	455	75	47	474	644	69	112
927	371	373	71	48	426	596	69	122

for synthesis of wood polymer composites.<sup>[49]</sup> The same principle is applied by many for functionalization of mesoporous materials/aerogels.<sup>[50–53]</sup>

Naturally, physical means of functionalization such as etching are possible and widely used, particularly in two-dimensional situations.<sup>[54]</sup>

## CONCLUSION

Porosity of surfactant-templated aerogels can be tuned through judicious selection of sol–gel chemistry, surfactant, drying method employed, and the subsequent functionalization of the surface. The number of steps and manipulated variables are quite a few and are interrelated. The utility of the resulting porous matrix as particles, fiber, films, and monoliths as well as controllability at the nanolevel promise several advances and successful applications in the decades to come. The self-assembly and supercritical fluids are two key technologies that can enable these advances.

## REFERENCES

- Ertl, G.; Knozinger, H.; Weitkamp, J. *Preparation of Solid Catalysts*; Wiley-VCH, 1999.
- Bagwell, R.B.; Messing, G.L. *Key Eng. Mater.* **1996**, *115*, 45–64.
- Beck, J.S.; Vartuli, C.; Roth, W.J.; Leonowicz, M.E.; Kresge, C.T.; Achmitt, K.D.; Chu, C.T.-W.; Olson, D.H.; Sheppard, E.W.; McCullen, S.B.; Higgins, J.B.; Schlenker, J. *J. Am. Chem. Soc.* **1992**, *114*, 10,834.
- Bradley, D.C. *Chem. Rev.* **1989**, *89*, 1317–1322.
- Kistler, S.S. Coherent expanded aerogels. *J. Phys. Chem.* **1932**, *36*, 52–64.
- Yao, N.; Xiong, G.; He, Y.M.; Yang, W. Preparation of novel mesoporous alumina catalysts by the sol–gel method. *Catal. Today* **2001**, *68*, 97–109.
- Schaefer, D.W.; Pekala, R.; Beaucage, G. Origin of porosity in resorcinol-formaldehyde aerogels. *J. Non-Cryst. Solids* **1995**, *186*, 159–167.
- Pekala, R.; Alviso, C.T.; Kong, F.M.; Hulse, S.S. Aerogels derived from multifunctional organic monomers. *J. Non-Cryst. Solids* **1992**, *145*, 90–98.
- Brinker, C.J.; Scherer, G.W. *Sol–Gel Science: The Physics and Chemistry of Sol–Gel Processing*; Academic Press, 1990.
- <http://www.solgel.com> (accessed Nov.15, 2003).
- Oye, G.; Sjoblom, J.; Stocker, M. Synthesis, characterization and potential applications of new materials in the mesoporous range. *Adv. Colloid Interface Sci.* **2001**, *89–90*, 439–466.
- Liu, J.; Kim, A.Y.; Wang, L.Q.; Palmer, B.J.; Chen, Y.L.; Bruinsma, P.; Bunker, B.C.; Exarhos, G.J.; Graff, G.L.; Riefke, P.C.; Fryxell, G.E.; Virden, J.W.; Tarasevich, B.J.; Chick, L.A. Self-assembly in the synthesis of ceramic materials and composites. *Adv. Colloid Interface Sci.* **1996**, *69*, 131–180.
- Ciesla, U.; Schuth, F. Ordered mesoporous materials. *Microporous Mesoporous Mater.* **1999**, *27*, 131–149.
- On, D.T.; Desplandier-Giscard, D.; Kaliaguine, D.S. Perspectives in catalytic applications of mesostructured materials. *Appl. Catal., A Gen.* **2001**, *222*, 299–357.
- Soler-Illia, G.J.A.A.; Sanchez, C.; Lebeau, B.; Patarin, J. Chemical strategies to design textured materials: from microporous and mesoporous oxides to nanonetworks and hierarchical structures. *Chem. Rev.* **2002**, *102*, 4093–4138.
- Corma, A. From microporous to mesoporous molecular sieve materials and their use in Catalysis. *Chem. Rev.* **1997**, *97*, 2373–2419.
- Sayari, A.; Liu, P. Non-silica periodic mesostructured materials: recent progress. *Microporous Mater.* **1997**, *12*, 149–177.
- Consani, K.A.; Smith, R.D. *J. Supercrit. Fluids* **1990**, *3*, 51–65.
- McClain, J.B.; Betts, D.E.; Canelas, D.A.; Samulski, E.T.; DeSimone, J.M.; Londono, J.D.; Cochran, H.D.; Wignall, G.D.; Chillura-Martino, D.; Triolo, R. Design of non-ionic surfactants for supercritical carbon dioxide. *Science* **1996**, *274*, 2049–2052.
- Sarbu, T.; Styranec, T.J.; Beckman, E.J. Design and synthesis of low cost, sustainable CO<sub>2</sub>-philes. *Ind. Eng. Chem. Res.* **2000**, *39*, 4678–4683.
- Liu, J.; Han, B.; Li, G.; Zhang, X.; He, J.; Liu, Z. Investigation of non-ionic surfactant dynol-604 based reverse microemulsions formed in supercritical carbon dioxide. *Langmuir* **2001**, *17*, 8040–8043.
- Liu, J.; Han, B.; Li, G.; Liu, Z.; He, J.; Yang, G. Solubility of the non-ionic surfactant tetraethylene glycol *n*-laurel ether in supercritical CO<sub>2</sub> with *n*-pentanol. *Fluid Phase Equilib.* **2001**, *187–188*, 247–254.
- Liu, J.; Han, B.; Zhang, J.; Mu, T.; Li, G.; Wu, W.; Yang, G. Effect of cosolvent on the phase behavior of non-fluorous Ls-54 surfactant in supercritical CO<sub>2</sub>. *Fluid Phase Equilib.* **2003**, *211*, 265–271.
- Al-Ghamdi, A.; Carvallo, R.; Sunol, S.G.; Sunol, A.K. Supercritical Fluid Aided Synthesis of Surfactant Templated Aerogels, AIChE Annual Meeting, San Francisco, CA, Nov. 16–22, 2003.
- Fan, H.; Bentley, H.R.; Kathan, M.C.; Clem, P.; Lu, Y.; Brinker, C.J. Self-assembled aerogel-like low dielectric constant films. *J. Non-Cryst. Solids* **2001**, *285*, 79–83.
- DeSimone, J.M.; Keiper, J.S. Surfactants and self assembly in carbon dioxide. *Curr. Opin. Solid State Mater. Sci.* **2001**, *5*, 333–341.
- Yilgor, I.; McGarth Novel supercritical fluid technology for polymer fractionation and characterization of functional siloxane oligomers. *Polym. Bull.* **1984**, *12* (6), 491–499.
- Eckert, C.A.; Ekart, M.P.; Knutson, B.L.; Payne, K.P.; Tomasko, D.L.; Liotta, C.L.; Foster, N.R. Supercritical fluid fractionation of a nonionic surfactant. *Ind. Eng. Chem. Res.* **1992**, *31*, 1105–1110.

29. Saliger, R.; Heinrich, T.; Gleissner, T.; Fricke, J. Sintering behavior of alumina modified silica aerogels. *J. Non-Cryst. Solids* **1995**, *186*, 113–117.
30. Miller, J.B.; Ko, E.I. A homogeneously dispersed silica dopant for control of the textural and structural evolution of an alumina aerogel. *Catal. Today* **1998**, *43*, 51–67.
31. Trombetta, M.; Busca, G.; Willey, R.J. Characterization of silica containing aluminum hydroxide and oxide aerogels. *J. Colloid Interface Sci.* **1997**, *190*, 416–426.
32. Gonzalez-Pena, V.; Diaz, I.; Marquez-Alvarez, C.; Sastre, E.; Perez-Pariente, J. Thermally stable mesoporous alumina synthesized with non-ionic surfactants in the presence of amines. *Microporous Mesoporous Mater.* **2001**, *44–45* (203–210), 203–210.
33. Anderson, M.T.; Martin, J.E.; Odinek, J.G.; Newcomer, P.P.; Wilcoxon, J.P. Monolithic periodic mesoporous silica gels. *Microporous Mater.* **1997**, *10* (24), 13–27.
34. Zhang, W.; Pinnavaia, J. *Chem. Commun.* **1998**, 1185–1186.
35. Brinker, C.J.; Anderson, M.T.; Ganguli, R.; Lu, Y. Process to Form Mesostructured Films. US Patent 5,858,457, January 12, 1999.
36. Kistler, S.S. Coherent expanded aerogels and jellies. *Nature* **1931**, *127*, 741.
37. Van Lierop, J.G.; Huizing, A.; Meerman, W.C.P.M.; Mulder, C.A.M. Preparation of dried monolithic SiO<sub>2</sub> gel bodies by an autoclave process. *J. Non-Cryst. Solids* **1986**, *82*, 265.
38. Tewari, P.H.; Hunt, A.J.; Lofftus, K.D. *Aerogels*; Fricke, J., Ed.; Springer: Berlin, 1986; 86 pp.
39. Ayen, R.J.; Iacobucci, P.A. Metal oxide aerogel preparation by supercritical extraction. *Rev. Chem. Eng.* **1988**, *5*, 157–198.
40. Sunol, S.G.; Sunol, A.K.; Keskin, O.; Guney, O. *Innovations in Supercritical Fluids*; Hutchenson, K.W., Foster, N.R., Eds.; ACS Symposium Series: Washington, D.C., 1995; 258 pp.
41. Scherer, G.W.; Hdach, H.; Phalippou, J. Thermal expansion of gels: a novel method for measuring permeability. *J. Non-Cryst. Solids* **1991**, *130*, 157.
42. Scherer, G.W. Stress in aerogel during depressurization of autoclave. *J. Sol-Gel Sci. Technol.* **1994**, *3*, 127.
43. Scherer, G.W. Stress development during supercritical drying. *J. Non-Cryst. Solids* **1992**, *145*, 33.
44. Unlusu, B.; Sunol, S.G.; Sunol, A. Stress formation during heating in supercritical drying. *J. Non-Cryst. Solids* **2001**, *279*, 110–118.
45. Anderson, M.T.; Sawyer, P.S.; Rieker, T. Surfactant-templated silica. *Microporous Mesoporous Mater.* **1998**, *20*, 53–65.
46. Van Grieken, R.; Guillermo, C.; Stucky, G.D.; Melero, J.A.; Garcia, R.A.; Iglesias, J. Supercritical fluid extraction of a nonionic surfactant template from SBA-15 materials and consequences on the porous structure. *Langmuir* **2003**, *19*, 3966–3973.
47. Kawi, S.; Lai, M.W. Supercritical fluid extraction of surfactant template from MCM-41. *Chem. Commun.* **1998**, 1407–1408.
48. Lu, X.B.; Zhang, W.H.; Xiu, J.-H.; He, R.; Chen, L.-G.; Li, X. Removal of template molecules from MCM-41 with supercritical fluid in a flow apparatus. *Ind. Eng. Chem. Res.* **2003**, *42*, 653–656.
49. Sunol, A. Supercritical fluid aided treatment of porous material. US Patent 5,169,687, December 1992.
50. Kluson, P.; Kacer, P.; Cajthami, T.; Kalaji, M. Preparation of titania mesoporous materials using a surfactant-mediated sol-gel method. *J. Mater. Chem.* **2001**, *11*, 644–651.
51. Lu, X.B.; Zhang, W.H.; He, R. Simultaneous removal of surfactant template from MCM-41 and implantation of transition metal complexes into mesopores with supercritical fluid. *Chin. Chem. Lett.* **2002**, *13* (5), 480–483.
52. Tsang, S.C.; Yu, K.M.K.; Steele, A.M.; Zhu, J.; Fu, Q.J. Solid supported micellar catalysis: Some syntheses and characterizations. *Catal. Today* **2003**, *81*, 573–591.
53. Wakayama, H.; Goto, Y.; Fukushima, Y. A novel method for tailoring porous structures of nanoporous materials using supercritical solvents. *Phys. Chem. Chem. Phys.* **2003**, *5*, 3784–3788.
54. Galca, A.C.; Kooij, E.S.; Wormeester, H.; Salm, C.; Leca, V.; Rector, J.H.; Poelsema, B. Structural and optical characterization of porous anodic aluminum oxide. *J. Appl. Phys.* **2003**, *94* (7)1, 4296–4305.

# Templating Polymer Crystal Growth Using Block Copolymers

Yueh-Lin Loo

Department of Chemical Engineering, University of Texas at Austin,  
Austin, Texas, U.S.A.

## INTRODUCTION

Block copolymers<sup>[1,2]</sup> can spontaneously self-assemble<sup>[3,4]</sup> to form periodic arrays of nanoscale domains.<sup>[5]</sup> Incorporating crystallizable moieties within block copolymers can further increase their morphological richness and kinetic complexity. Significant progress has been made in the last decade in understanding polymer crystallization within these semicrystalline materials. For example, we now have a good handle on how crystallization occurs and what the final solid state structures are in these materials. Through a combination of reciprocal space scattering and real space microscopy experiments, we now also understand the requirements for patterning and controlling polymer crystallization using nanoscale periodic domains. This entry will attempt to recount the progress in this field.

Familiarity with the concepts of phase separation in block copolymers will be important in the understanding of the nature of polymer crystallization *within* block copolymers. The section below provides a brief overview of block copolymer phase separation. It is further divided into two subsections for the ease of discussion. Phase separation and its resulting complexities in amorphous systems as well as semicrystalline block copolymers are discussed.

## BLOCK COPOLYMER PHASE SEPARATION—AMORPHOUS SYSTEMS

Block copolymers consist of chemically distinct polymer segments that are covalently strung together. Advances in polymerization techniques over the past four decades have enabled scientists to make model block copolymers of different architectures. Fig. 1 illustrates the architectural differences between a diblock, a triblock, and a starblock copolymer.<sup>[5]</sup> Because of the chemical incompatibility between the unlike polymer segments, block copolymers tend to phase separate; this phenomenon is analogous to oil and water. However, the presence of covalent junctions between the different segments restricts phase separation to a molecular-length scale ( $O \sim \text{nm}$ ). Thus phase separation in block copolymers

is generally known as *microphase separation* (as opposed to macrophase separation in polymer blends, where the domains are at least  $O \sim \mu\text{m}$ ).<sup>[1,2,5,6]</sup>

Minimization of free energy during microphase separation can lead to the formation of various interesting, thermodynamically-stable structures on a nanometer-length scale. With the advent of anionic polymerization, which permits the synthesis of model block copolymers with narrow molecular weight distribution (or narrow chain length distribution), phase separation of block copolymers containing flexible-chain, amorphous blocks has been explored extensively and is presently well understood.<sup>[1,2,5-7]</sup> Fig. 2 illustrates the different equilibrium structures that have been observed: body-centered cubic (BCC) array of spherical domains, hexagonally packed cylinders, cubic bicontinuous gyroid structure, and an alternating lamellar (layered) morphology. Because these structures result from block copolymer microphase separation, they are generally called *microdomains*. This entry focuses on using these microdomains to template or to pattern polymer crystallization. Before we discuss polymer crystallization in nanoscale domains, we should briefly review the phase behavior of amorphous block copolymers.

The equilibrium structure of block copolymers is determined by several factors:<sup>[5,6]</sup> the extent of “dislike” between blocks (or the Flory–Huggins interaction parameter,  $\chi$ ),<sup>[8,9]</sup> the total chain length  $N$  (or molecular weight), and the volume fraction of one block  $f$  (or composition). Fig. 3 contains a phase diagram for model block copolymers.<sup>[10]</sup> When the degree of chemical incompatibility between the dissimilar blocks is small—determined by the product  $\chi N$ <sup>[5]</sup>—the system is homogeneous; that is, microphase separation does not take place. However, if  $\chi N$  is large ( $\gg 10$ ; also known as being *strongly segregated*<sup>[11,12]</sup>), the system spontaneously undergoes microphase separation. The final structure that is adopted by the block copolymer system, e.g., spheres, cylinders, or lamellae, is determined by the block length ratio through  $f$ . Systems with approximately equal lengths of unlike blocks ( $f \approx 0.5$ ) form lamellae, while highly asymmetric systems form BCC spheres, with the short block comprising the

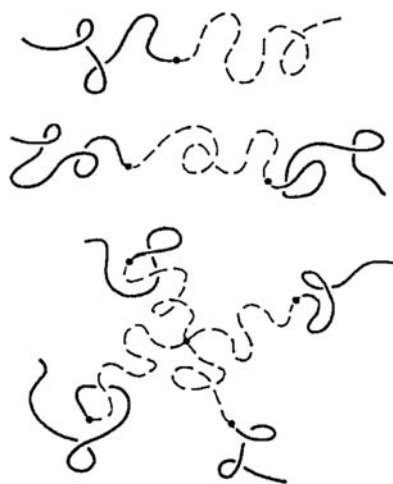


**Fig. 1** Schematic illustration of the architecture of a diblock (top), triblock (middle), and a starblock (bottom) copolymer. *Source:* From Ref.<sup>[5]</sup>, © 1990 Annual Reviews, Inc.

discrete phase. The characteristic spacing,  $d$  (Fig. 2), is determined by  $N$  and scales as<sup>[12]</sup>

$$d \sim N^{2/3} \quad (1)$$

Whether a block copolymer microphase separates, and what structure and microdomain size the block copolymer adopts, can thus easily be tuned during block copolymer synthesis by adjusting  $N$  and  $f$  accordingly.<sup>[5]</sup> Block copolymers with periodic microdomains  $O \sim 20\text{--}50$  nm can be routinely obtained by anionic polymerization.<sup>[13]</sup> The morphological richness and the nanoscale periodicity of block copolymers have been exploited for a variety of applications, ranging from components for car bumpers and shoe soles<sup>[1,2]</sup> to templates for optoelectronics research.<sup>[7,14,15]</sup> From a fundamental standpoint, the periodic nanoscale domains have also been exploited as a means to pattern and control polymer crystallization.<sup>[16]</sup> The latter shall be the focus of this entry.

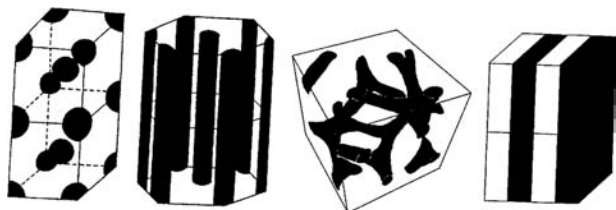


**Fig. 2** Schematic illustration of the different morphologies observed in model diblock copolymers: BCC spheres, hexagonally packed cylinders, bicontinuous cubic gyroid, and alternating lamellae. *Source:* Courtesy of Chiajen Lai.

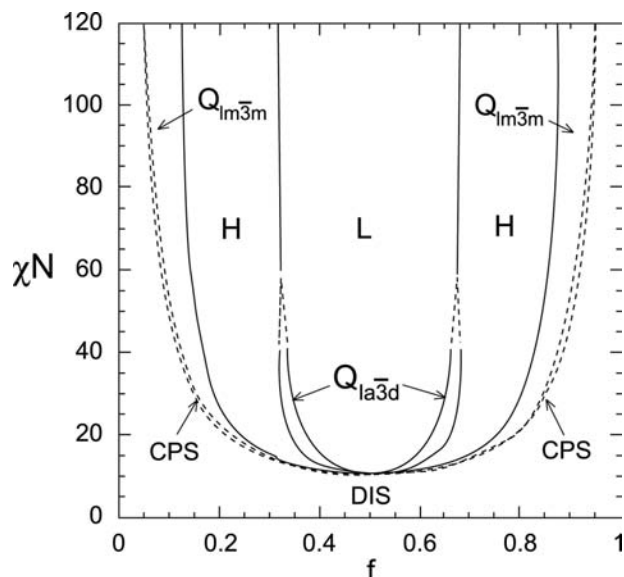


**Fig. 3** Mean-field phase diagram for model block copolymers. Phase are labeled L (lamellar), H (hexagonal cylinders),  $Q_{la3d}$  (bicontinuous cubic gyroid),  $Q_{lm3m}$  (BCC spheres), CPS (close-packed spheres), and DIS (homogeneous). *Source:* From Ref.<sup>[10]</sup>, © 1996 American Chemical Society.

## MICROPHASE SEPARATION IN SEMICRYSTALLINE SYSTEMS

Block copolymers containing one or more crystallizable segments are generally known as *semicrystalline block copolymers*.<sup>[1,16,17]</sup> Aside from microphase separation due to unlike block–block interactions, the incorporation of crystallizable moieties within a block copolymer architecture often lends additional morphological richness to the system. In semicrystalline block copolymers, phase separation can be driven by multiple forces, e.g., microphase separation and crystallization. As a consequence, the final solid-state structures adopted by semicrystalline block copolymers are more complex and, until recently, less predictable.<sup>[1]</sup>

Because our goal in this entry is to describe the phenomenon of templated crystallization in block copolymers, we shall limit our discussion to phase-separated (and not homogeneous) melts. We will examine the consequences of cooling microphase-separated semicrystalline block copolymers below the freezing temperature of the crystallizable block. Energetically, there are two possible outcomes: if microphase separation dominates the structure development process, the nanoscale domains that were created in the melt will remain on crystallization. However, if crystallization is the stronger driving force for phase separation, we expect semicrystalline block copolymers to behave like semicrystalline homopolymers (no amorphous block attached). Cooling from the melt would result in the formation of crystalline alternating lamellae and *spherulitic* superstructures.<sup>[17,18]</sup>



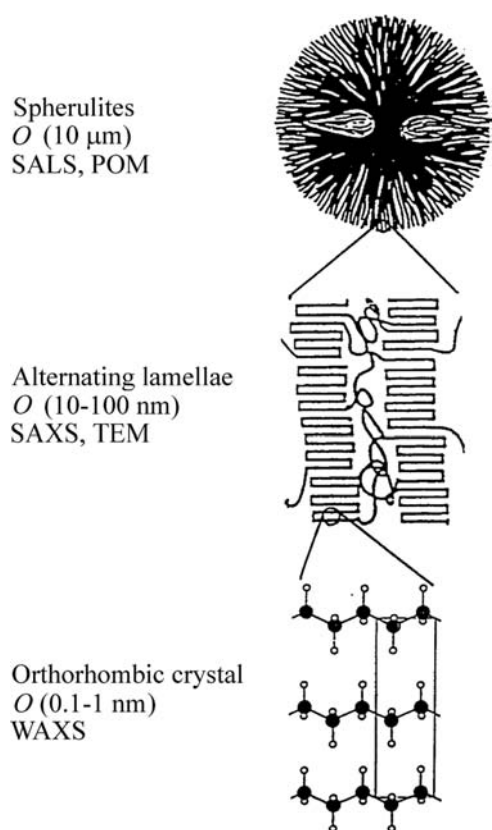


**Fig. 4** Hierarchical structures adopted by a semicrystalline homopolymer on crystallization. *Source:* Courtesy of Pratima Rangarajan and Richard A. Register.

Fig. 4 schematizes the structures that are formed on various length scales when a semicrystalline homopolymer crystallizes. From established calorimetric measurements, the energy associated with crystallization ( $O \sim 100 \text{ J/g}$ )<sup>[18,19]</sup> is much larger than the energy associated with microphase separation ( $O \sim 1 \text{ J/g}$ ).<sup>[20]</sup> Thus crystallization is expected to always dominate the structure development process in these materials; that is, semicrystalline block copolymers would always adopt a crystalline lamellar structure on cooling, regardless of block composition or existing melt structure.<sup>[1]</sup> This prediction also implies enormous structural rearrangement—simultaneous disruption of the melt structure and formation of spherulites—during crystallization. Therefore the final solid state structure of semicrystalline block copolymers would not be too different from that of semicrystalline homopolymers. We shall return to this topic later in this entry.

However, one can *kinetically force* crystallization to occur within the preformed nanoscale microdomains by employing a semicrystalline block copolymer where the amorphous block is *glassy* during crystallization. Vitrification of the amorphous block effectively freezes the microdomain structure in place; subsequent crystallization of the crystallizable block, if it occurs at

all, would have to take place within the prescribed microdomains. The following section examines the impact of crystallization in nanoscale environments in these semicrystalline-glassy systems. Following that, we shall discuss the complex structure development process in semicrystalline-rubbery systems, where the amorphous block remains *fluid* during crystallization.

## CRYSTALLIZATION IN NANOSCALE ENVIRONMENTS—SEMICRYSTALLINE-GLASSY BLOCK COPOLYMERS

Depending on the relative block lengths, the crystallizable component of the semicrystalline-glassy block copolymer can either form *discrete* domains, e.g., spheres and cylinders, or it can form the *continuous* phase, or the *matrix*. For ease of discussion, this section is divided into two subsections: The first subsection examines the crystallization behavior of semicrystalline-poor block copolymer systems where crystallization occurs in the discrete phase while the latter subsection describes how the presence of nanoscale glassy domains impacts crystallization in semicrystalline-rich block copolymers.

The presence of a vitreous component during crystallization strongly impacts the morphological structure of the semicrystalline block copolymer. Because the microphase-separated melt structure is effectively frozen in place, crystallization has to occur *within* the nanoscale domains (semicrystalline-poor systems) or around the nanoscale glassy domains (semicrystalline-rich systems). Not only does this influence the final solid-state structure (resulting in the preservation of the melt structure and preferential crystal orientation in the crystallized domains), it also drastically affects the crystallization kinetics and mechanism.

## SEMICRYSTALLINE-POOR BLOCK COPOLYMERS

In these block copolymers, the glass transition temperature of the amorphous matrix ( $T_{g,a}$ ) exceeds the freezing temperature ( $T_c$ ) of the crystallizable minority block. As the system is cooled from a microphase-separated melt, it first encounters  $T_{g,a}$ . Below  $T_{g,a}$ , the matrix is vitreous so the microphase-separated structure is effectively frozen. Subsequent cooling beyond  $T_c$  induces crystallization of the minor component. Because the melt structure had effectively been captured, crystallization is forced to occur *within* the microdomains prescribed by microphase separation. Thus the melt morphology is faithfully reproduced in the solid state. *Confined crystallization* in semicrystalline-glassy block copolymers was first demonstrated by

Lotz and Kovacs,<sup>[21]</sup> the researchers examined several compositionally asymmetric block copolymers of poly(ethylene oxide)-*b*-polystyrene, EO/S, where  $T_{g,S} > T_{c,EO}$ , and found the spherical melt structure to be preserved even after EO is fully crystallized. Cohen et al.<sup>[22]</sup> subsequently demonstrated the preservation of spherical polyethylene (E) microdomains in the solid state structure of an asymmetric polyethylene-*b*-polystyrene, E/S, diblock. However, if the E/S diblock was cast from a solution, the melt structure would be completely destroyed and a crystalline alternating lamellar morphology would result. This finding implies an important point: *Confined crystallization* in semicrystalline-glassy systems need not correspond to the equilibrium state—the structure with the lowest free energy—as the vitreous matrix kinetically restricts crystallization to occur within these nanoscale domains without substantial rearrangement of the domain structure.

More recently, Weimann et al.<sup>[23]</sup> examined a series of polyethylene-*b*-polyvinylcyclohexane, E/VCH, di- and triblock copolymers of varying compositions (and thus melt structures) and found crystallization to occur within the microdomains prescribed by microphase separation in all cases. Using a unique staining protocol, Loo, Register, and Adamson<sup>[24]</sup> were able to directly visualize these intricate solid state structures, for the first time, using transmission electron microscopy (TEM). Because of the differential uptake of ruthenium tetroxide, RuO<sub>4</sub> (staining agent), in different phases,<sup>[25–27]</sup> the researchers were able to observe individual 5-nm-thick E crystals within block copolymer spherical microdomains that span 16 nm.<sup>[24]</sup> In addition to disk-like crystals within spheres, they had also successfully imaged ribbon- and sheet-like crystals confined within nanoscale cylindrical<sup>[24]</sup> and lamellar<sup>[36]</sup> microdomains, respectively. Fig. 5 contains TEM micrographs reproduced from Ref.<sup>[24]</sup>. Thus a complex “structure-within-structure” type morphology can be routinely obtained in these semicrystalline-glassy systems where crystallization of the minor block is effectively trapped by the vitreous matrix. More recently, Zhu et al.<sup>[28,29]</sup> have demonstrated in a series of papers that crystallization of EO can also be patterned by a metastable perforated lamellar structure in EO/S block copolymers and blends. Block copolymers of various other chemistries, including polytetrahydrofuran-*b*-polystyrene, THF/S;<sup>[30]</sup> poly( $\epsilon$ -caprolactone)-*b*-polystyrene, CL/S;<sup>[31]</sup> as well as triblock copolymers of poly( $\epsilon$ -caprolactone)-*b*-polyethylene-*b*-polystyrene, CL/E/S,<sup>[32]</sup> where both CL and E are crystallizable, have also been examined.

Confining crystallization in an anisotropic environment induces the crystals to grow in a preferential direction. Indeed, Loo, Register, and Adamson<sup>[24]</sup> observed the formation of ribbon- and sheet-like crystals in cylindrical and lamellar domains. To quantify

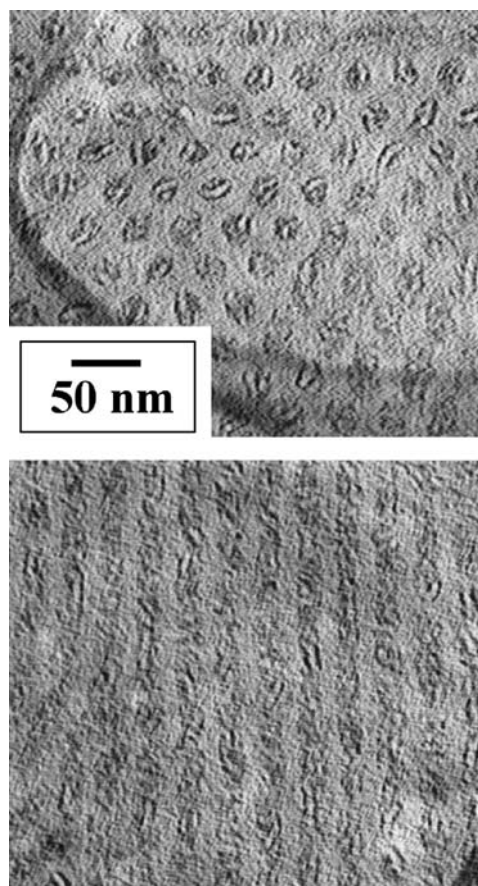


**Fig. 5** Transmission electron micrographs of a fully crystallized E/VCH block copolymer where E comprises the cylindrical domains. The sample was flow aligned; top image reveals a projection along the cylinder axis while the bottom image shows a projection perpendicular to the cylinder axis. Individual ribbon-like crystals can be seen within the cylindrical microdomains. *Source:* From Ref.<sup>[24]</sup>, © 2000 Wiley & Sons, Inc.

the preferential crystal orientation, Hamley et al.<sup>[33]</sup> examined a prealigned lamellar-forming E/VCH diblock copolymer using simultaneous two-dimensional small- and wide-angle X-ray scattering (SAXS/WAXS) techniques. From the solid-state scattering patterns, the researchers inferred that the E crystals were preferentially oriented with their crystal stems *parallel* to the microdomain interface and their fast-growth axis (the *b* axis for polyethylene) randomly oriented in plane. More recently, compositionally asymmetric block copolymers where crystallization is confined within cylinders have also been examined in detail. Quiram<sup>[34]</sup> demonstrated, through simultaneous SAXS/WAXS on fully crystallized flow-aligned samples, that the E chains within cylindrical microdomains crystallize with their stems generally *perpendicular* to the cylinder axis. The preferential crystal orientations adopted by these systems are schematized in Fig. 6.

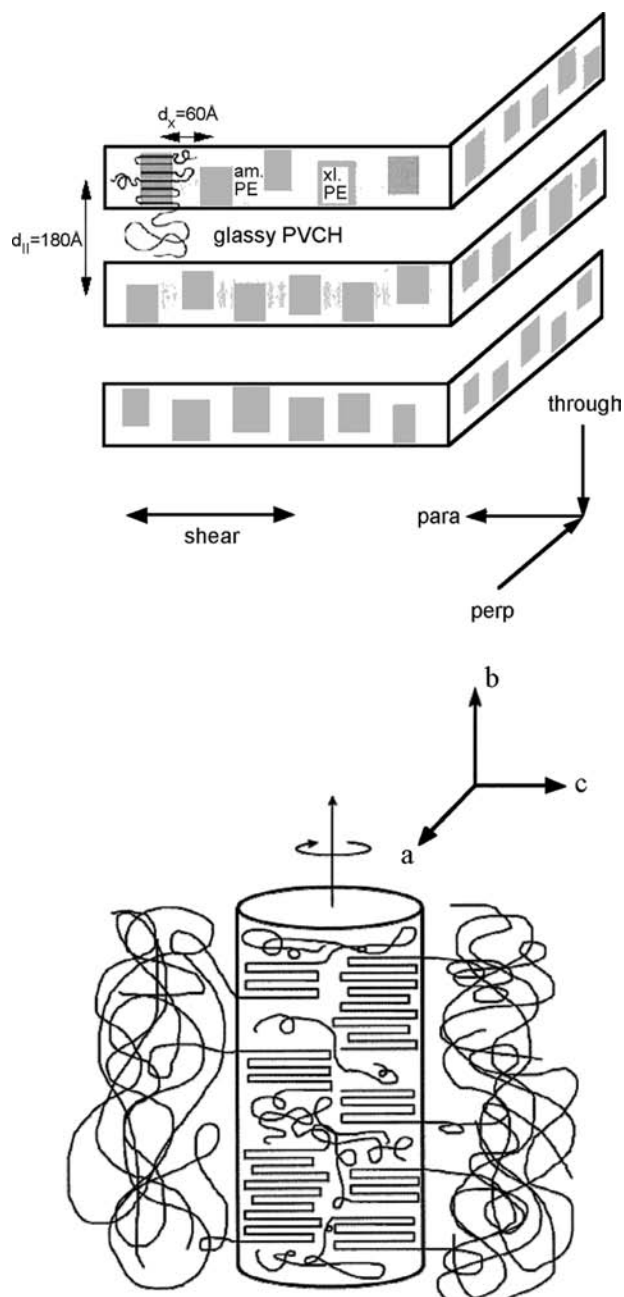


**Fig. 6** Schematic illustration of the orientation of the crystal stems in E-containing semicrystalline lamellar-forming (top) and cylinder-forming (bottom) block copolymers. *Source:* From Refs.<sup>[33]</sup> (top) and<sup>[34]</sup> (bottom), © 1996 (top) and 1998 (bottom) American Chemical Society.

The seemingly disparate orientations obtained in the different systems (and different morphologies) can be understood by noting that all these orientations align the fast growth axes of the crystals with the direction in which the crystals can grow unobstructed. In the lamellar samples, the fast growth axis is in the plane of the lamellae, while in the cylindrical samples, the fast growth axis is along the cylinder axis.

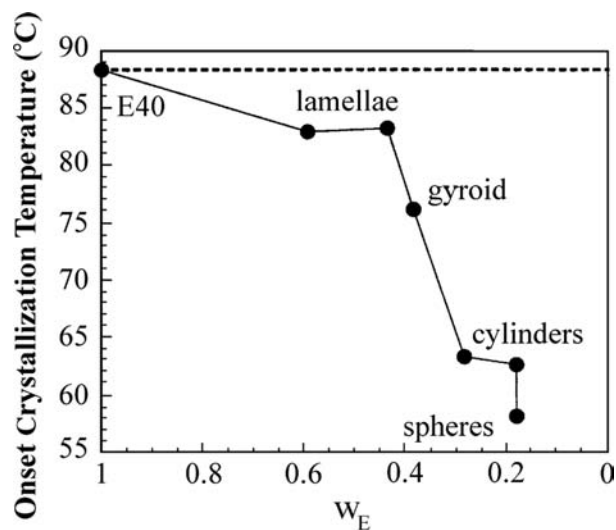


**Fig. 7** Crystallization temperature of E block as a function of block copolymer composition. The crystallization temperature monotonically decreases with E weight fraction. The dashed line represents the crystallization temperature of PE (no amorphous block attached).

Confining crystallization on a nanometer-length scale can also drastically affect the macroscopic properties of the material. For example, restricting crystallization in this manner suppresses spherulite formation so the polymer is optically clear (conventional semicrystalline homopolymers that form spherulites are typically opaque because the spherulites scatter light very intensely).<sup>[35]</sup> Confining crystallization within nanoscale domains also impacts the way by which crystallization occurs. Lotz and his coworkers<sup>[21]</sup> were among the first to notice big differences between the crystallization temperatures of semicrystalline-glassy block copolymers and semicrystalline homopolymers; the addition of an amorphous, glassy block greatly suppressed the crystallization temperatures. This was also observed in a series of E/VCH di- and triblock copolymers of varying compositions.<sup>[23]</sup> More recently, Loo et al.<sup>[36]</sup> found that the onset crystallization temperatures systematically decreased with the weight fraction of the crystallizable block (or as the domains become less connected) (Fig. 7).

In homopolymers, crystallization is typically initiated by *heterogeneous nucleation* on dust particulates or impurities present in the melt; the tendency to form micron-size spherulites suggests that only a small number of nuclei are required to fully crystallize the system.<sup>[17–19]</sup> However, in semicrystalline-glassy block copolymers where crystallization is isolated in nanoscale domains, the domains would need to be individually nucleated to fully crystallize the sample.<sup>[37,38]</sup> Because the number density of microdomains far exceeds the typical impurity density, researchers have

long speculated that *homogeneous nucleation*, a phenomenon not usually observed in bulk semicrystalline homopolymers, is responsible for initiating crystallization in the nanoscale domains of semicrystalline block copolymers. (A large energy barrier is associated with homogeneous nucleation and this is generally reflected by a large crystallization temperature depression.) To examine the mechanistic details of crystallization, high-resolution, time-resolved techniques are required to probe the structural changes that take place. Therefore, it took the development of synchrotron-based, time-resolved simultaneous SAXS/WAXS coupled with in situ differential scanning calorimetry (DSC; capable of excellent temperature control) to investigate the crystallization kinetics in these systems.<sup>[39–42]</sup> In a recent synchrotron study, Loo et al.<sup>[36]</sup> determined both the crystallization temperatures as well as the temperature dependence of the rate of crystallization for a series of E/VCH diblock copolymers of varying block ratios (and thus melt morphology). In sphere and cylinder formers (discrete crystallizable domains), the greatly suppressed crystallization temperature and the steep temperature dependence of crystallization indicated that crystallization in those systems is preceded by *homogeneous nucleation*. This is in stark contrast with bulk homopolymer crystallization where the process is almost always initiated by heterogeneous nucleation on impurities that are present in the system.<sup>[15,16]</sup> In the cubic bicontinuous gyroid-forming diblock, the extensive connection between the crystallizing domains dominated the crystallization kinetics; foreign nuclei that were already present in the melt were able to induce crystallization over large areas because the channels are highly connected. The lamellar samples exhibited peculiar two-step isothermal crystallization kinetics (Fig. 8), leading the researchers to conclude that there were two populations of lamellae within that particular sample: one that is highly interconnected at the grain boundaries so crystallization is preceded by heterogeneous nucleation at a relatively high temperature, and another that contains lamellae that are completely isolated so crystallization has to be induced by homogeneous nucleation.

Semicrystalline-glassy block copolymers remain an interesting subject of research, particularly because they serve as reference samples for studying crystallization behavior in semicrystalline-rubbery systems. This section highlighted recent experimental findings in block copolymers that contain an already-glassy matrix during crystallization. The glassy matrix can effectively preserve the melt structure in the crystalline solid state. This has enabled researchers to examine the impact of crystallization within nanoscale confinements. The following section highlights research on semicrystalline-glassy block copolymers where the semicrystalline block comprises the continuous phase.

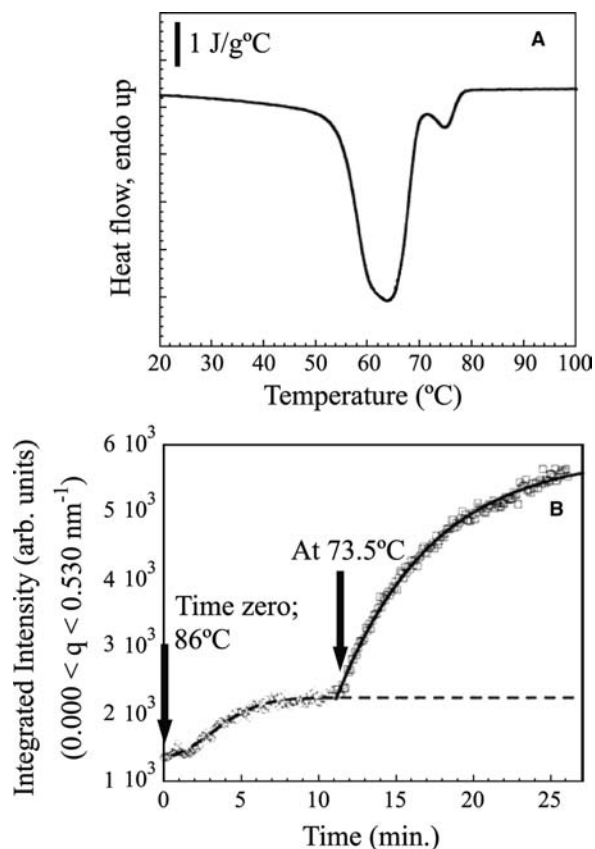


**Fig. 8** Differential scanning calorimetry (top) and SAXS integrated intensity (bottom) indicating peculiar two-step crystallization in a lamellar E/VCH diblock copolymer. The atypical kinetics was attributed to the presence of two distinct populations of lamellar microdomains: one is highly interconnected—these domains are heterogeneously nucleated by dust particles at higher temperatures; the other consists of isolated domains—the individual domains are homogeneously nucleated at lower temperatures. *Source:* From Ref.<sup>[36]</sup>, © 2001, American Chemical Society.

### SEMICRYSTALLINE-RICH BLOCK COPOLYMERS

We previously discussed the possibility of imposing preferential crystal orientation in semicrystalline-glassy diblock copolymers when crystallization occurs within anisotropic nanoscale domains: In both lamellar-<sup>[33]</sup> and cylinder-forming<sup>[34]</sup> block copolymers, the fast growth axis is generally aligned so the crystals can grow unobstructed. As a result, the crystals tend to grow with their stems parallel to the lamellar interface and perpendicular to the cylinder axis in E-containing block copolymers. In semicrystalline-rich block copolymers where the crystallizable component comprises the matrix, we fully expect the presence of glassy anisotropic nanoscale domains to impose a preferential crystal orientation in the surrounding matrix as well. Here,

we highlight some recent work that examined crystal orientation in the continuous phase of semicrystalline-rich block copolymers.

Liu and Chu<sup>[43]</sup> were among the first to examine the possibility of inducing a preferential crystal orientation in the presence of glassy cylinders. The researchers looked at blends of polytetrahydrofuran (THF) with polytetrahydrofuran-*b*-poly(methyl methacrylate), THF/MMA, using synchrotron-based SAXS/WAXS. Despite the preservation of glassy MMA cylinders, the formation of spherulites was observed. This is expected because the crystallizable component comprises the matrix; the spherulites can easily develop around the glassy domains. Based on SAXS peak distortions on crystallization, Liu and Chu speculated that the presence of the cylinders can impart preferential crystal orientation to the matrix. In fact, they hypothesized that, under certain specific conditions, i.e., when the intercylinder spacing is comparable to the crystal long period, preferential packing of the THF crystals should be observed in the plane of the cylinder radii. Unfortunately, Liu and Chu did not directly observe the predicted preferential orientation because they had only examined isotropic samples (samples that were not prealigned). Subsequently, Park et al.<sup>[44]</sup> examined a prealigned polyethylene-*b*-poly(ethylene-propylene)-*b*-polystyrene, E/EP/S, triblock copolymer where crystallizable E comprises the matrix (S forms cylinders). While the preferential orientation of E crystals was observed along the cylinder axis—like crystallization inside cylinders, the crystals tend to grow with the fast growth axis generally aligned along the cylinder axis—preferential orientation was also *not* observed in the plane of the cylinder radii.

More recently, Loo, Register, and Adamson<sup>[45]</sup> examined a prealigned E-rich cylinder-forming semicrystalline block copolymer, E/VCH, using simultaneous two-dimensional SAXS/WAXS and discovered preferential crystal orientation in *two* dimensions. Fig. 9 contains SAXS/WAXS patterns collected with incident X-rays both parallel and perpendicular to the cylinder axis. As expected for unobstructed growth, the crystals are preferentially aligned with their fast growth axis along the cylinder axis. Additionally, preferential crystal orientation that is consistent with that inferred by Liu and Chu was recorded by Loo et al. Using a combination of SAXS and WAXS, the researchers showed that the crystals have their stems preferentially aligned along the (10) planes of the hexagonal microdomain lattice in the plane of the cylinder radii. The preferential orientation observed in the second dimension was subsequently attributed to the commensurability in length scales between the intercylinder spacing and the E crystal long spacing (as was speculated by Liu and Chu). The comparable length scales allow the crystals to

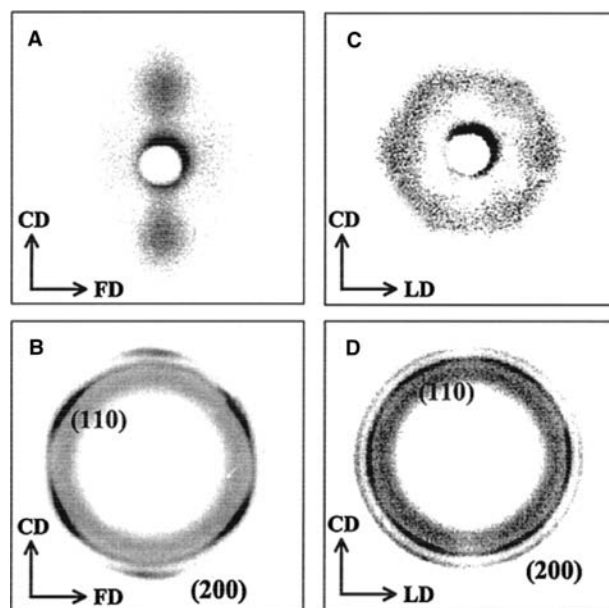


**Fig. 9** Two-dimensional SAXS (A and C) and WAXS (B and D) taken on an aligned, fully crystallized E/VCH diblock copolymer where VCH forms cylinders and E comprises the matrix. Patterns of SAXS and WAXS were simultaneously acquired with the X-ray beam perpendicular (A and B) and along (C and D) the cylinder axis. Preferential crystal orientation (arcs of nonuniform intensities in the WAXS patterns) is observed in both directions. *Source:* From Ref.<sup>[45]</sup>, © 2000 American Chemical Society.

adopt their equilibrium crystal thickness only when they are oriented in a particular direction with respect to the two-dimensional hexagonal microdomain lattice. Such crystal orientation is not observed when crystallization occurs inside cylinders. It was also not observed in the E/EP/S triblock copolymer by Park et al. because the intercylinder spacing was much greater than the E crystal long spacing. Thus the crystals can adopt their equilibrium thickness in any orientation relative to the microdomain lattice, as long as they are parallel to the cylinders.

The presence of glassy cylinders is effective at imparting preferential crystal orientation in the surrounding matrix. At the minimum, the crystals grow in a ribbon-like fashion with their fast growth axis preferentially aligned along the cylinder axis. Such orientation is also observed for crystallization inside cylinders. However, when the intercylinder spacing is comparable to the crystal long spacing, an additional preferential orientation in the plane of the cylinder radii is observed. Such orientation is only observed for crystallization around cylinders and not observed for crystallization inside cylinders. However, crystallization in these systems is almost always initiated by heterogeneous nucleation on impurities that are present in the melt and these crystals subsequently

grow in a three-dimensional fashion to fill space. As a result, micron-size spherulites are formed in the solid state; these materials are frequently opaque in appearance as a result of the presence of spherulites.

## SEMICRYSTALLINE-RUBBERY SYSTEMS

Thus far, we have covered the solid state structure development of semicrystalline-glassy block copolymers. In these materials, the ability to pattern or template crystallization arises purely from the fact that the amorphous component is glassy during crystallization. However, this ability to pattern crystallization becomes less clear when the amorphous block is *rubbery* at the onset of crystallization (recall the energetic argument presented earlier). Indeed, previous experiments conducted on semicrystalline-rubbery block copolymers reveal that the melt structure is typically eradicated on crystallization and a crystalline-alternating lamellar structure is formed. More recently, experiments on more strongly segregated systems have indicated that the melt structure of semicrystalline-rubbery block copolymers can be faithfully reproduced in the solid state.<sup>[37,38]</sup> This section summarizes experimental findings in semicrystalline-rubbery systems.

## MODERATELY-SEGREGATED SYSTEMS

We previously covered the energetics of the phase separation process: When the system is not kinetically frozen in the presence of a vitreous amorphous block, the final solid state structure development is complex and no longer as predictable. The details of the process now depend on the relative strengths of crystallization and microphase separation. In moderately-segregated block copolymers, crystallization generally dominates phase separation, always resulting in the formation of crystalline alternating lamellae (and spherulites) on cooling regardless of the melt structure.<sup>[39,40]</sup>

Many experiments on moderately-segregated block copolymer systems have verified that crystallization can disrupt the preexisting melt morphology on cooling, resulting in a crystalline lamellar structure. Douzinas, Cohen, and Halara<sup>[46]</sup> examined the melt and solid state morphologies of a series of polyethylene-*b*-poly(ethyl ethylene), E/EE, block copolymers of varying composition ( $f_E = 0.37-0.90$ ) using SAXS. Despite the presence of microphase-separated melts, lamellar structures always resulted on crystallization. Similar experiments were also conducted on microphase-separated E/EP diblocks ( $f_E = 0.30-0.70$ )<sup>[47]</sup> and E/EP/E triblocks ( $f_E = 0.30-0.70$ ).<sup>[48]</sup> When fully crystallized, all these materials exhibited alternating lamellar structures, and ultimately spherulites.

The disruption of melt structure (BCC spheres, hexagonally packed cylinders, alternating lamellae) and the simultaneous formation of a crystalline lamellar structure (and perhaps spherulites on a larger length scale) imply significant structural rearrangement during crystallization.<sup>[39,40]</sup> This speculation was verified by time-resolved scattering experiments on a moderately segregated E/EE block copolymer where the E blocks form cylinders in the melt.<sup>[41]</sup> On cooling, the cylindrical morphology is transformed to a lamellar structure with a larger domain spacing. The destruction of the melt morphology on crystallization had also been demonstrated with other block copolymer systems, including poly( $\epsilon$ -caprolactone)-*b*-poly(butadiene), CL/B,<sup>[49]</sup> poly( $\epsilon$ -caprolactone)-*b*-poly(dimethyl siloxane)-*b*-poly( $\epsilon$ -caprolactone), CL/DMS/CL,<sup>[50]</sup> and poly(ethylene oxide)-*b*-poly(butylene oxide), EO/BO.<sup>[51,52]</sup>

The solid-state structure of moderately-segregated semicrystalline-rubbery block copolymers is path dependent. Quiram et al.<sup>[35,53]</sup> examined a series of cylinder-forming polyethylene-*b*-poly(3-methyl-1-butene), E/MB, diblock copolymers and found that the final solid-state structure adopted by the moderately-segregated block copolymers depended on how the materials were crystallized: The cylindrical melt structure appeared to be preserved in the solid state when the sample was quenched in liquid nitrogen from the melt. However, if the diblocks were slowly cooled from the melt, a crystalline lamellar structure always resulted. This was the first demonstration that the melt structure can be *kinetically trapped* in the solid state even in presence of a fluid matrix provided that the cooling rates were sufficiently high. Such effects were also subsequently demonstrated by Loo, Register, and Ryan<sup>[54]</sup> with poly(ethylene)-*b*-poly(styrene-*r*-ethylene-*r*-butene), E/SEB. They were able to directly visualize the extent of structural rearrangement by imaging samples of moderately-segregated E/SEB after they were crystallized under different conditions. Chen et al.<sup>[55]</sup> also reported “crystallization-induced deformation” of the spherical microdomains when blends of EO and EO/B block copolymers were examined. In all these cases, the energetics of crystallization still overwhelms that of microphase separation, but templating crystal growth is achievable with the appropriate kinetic constraints.

The ability for crystallization to disrupt or *break out* of existing melt microdomains also impacts the crystallization kinetics. As expected, the crystallization kinetics are akin to those of semicrystalline homopolymers: The crystals are generally generated by heterogeneous nucleation, on impurities in the melt, and they subsequently grow in a three-dimensional fashion until all the crystallizable material is depleted. Spherulitic growth always results from such a process.

The combination of the energetics argument and well-documented experimental evidence of crystallization-



induced breakout has led researchers to believe that templating polymer crystallization is *not* possible without kinetic constraints in semicrystalline-rubbery systems.<sup>[1]</sup> However, recent experiments on strongly-segregated semicrystalline-rubbery block copolymers<sup>[37,38]</sup> have proven otherwise. By increasing block segregation, researchers have shown that crystallization can be effectively templated by the melt structure, despite the presence of a rubbery matrix at the onset of crystallization. The increase in interblock segregation can be achieved by the following methods: 1) increasing the molecular weight of the polymer ( $N$ ) and 2) tuning the unlike interactions (changing  $\chi$  by going to different chemistries). The section below highlights accomplishments in this area.

### STRONGLY-SEGREGATED SEMICRYSTALLINE-RUBBERY BLOCK COPOLYMERS

The motivation for examining strongly-segregated systems arises from the possibility that microphase separation may dominate over crystallization in the phase separation process. If this were true, the melt structure could be preserved without any kinetic constraints, even when the amorphous block is rubbery during crystallization. Therefore the confinement of crystallization on a nanoscale level would be achieved purely through unlike block segregation. The first evidence of melt structure preservation in a semicrystalline-rubbery block copolymer system was reported by Quiram, Register, and Marchend<sup>[35]</sup> Small-angle X-ray scattering experiments conducted on a high molecular weight (large  $\chi N$ ) E/MB cylinder-forming block copolymer, where  $T_{g,MB} = -17^\circ\text{C}$ , revealed that the melt structure is *generally* preserved on crystallization; that is, the characteristic lattice spacing remained the same even after crystallization. Because crystallization was effectively templated by microphase separation, the researchers may have anticipated the crystallization kinetics to resemble those for cylinder-forming semicrystalline-glassy block copolymers: homogeneous nucleation and instantaneous growth within discrete cylinders. Surprisingly, time-resolved SAXS/WAXS revealed crystallization kinetics that are not markedly different from those of semicrystalline homopolymers.

More recently, Loo, Register, and Ryan<sup>[37]</sup> examined a sphere-forming E/SEB semicrystalline-rubbery diblock and found crystallization of the minority component to be confined within the 25-nm spherical microdomains that are prescribed by microphase separation. Fig. 10 contains a TEM micrograph of the E/SEB sample that had been fully crystallized. Confined crystallization was observed at all cooling conditions, even at extremely slow cooling rates. Time-resolved SAXS/WAXS/DSC experiments conducted on the strongly segregated E/SEB diblock revealed



**Fig. 10** Transmission electron micrograph of a strongly segregated E/SEB diblock copolymer that exhibits *confined crystallization*. The spherical melt microdomains are exactly preserved on crystallization despite the presence of a rubbery matrix. *Source:* From Ref.<sup>[37]</sup>, © 2000 American Physical Society.

first-order crystallization kinetics similar to those observed in semicrystalline-glassy systems, where crystallization occurred in the discrete phase. Such crystallization kinetics are atypical compared to homopolymer crystallization and are indicative of homogeneous nucleation and isolated crystallization within individual spherical domains. Subsequent work on other systems, including EO/B,<sup>[56,57]</sup> have also indicated that the melt structure can be effectively preserved in the solid state without the presence of a glassy amorphous component.

To resolve the apparent disparity between the observed solid-state structure and its crystallization kinetics, Loo et al.<sup>[54]</sup> revisited the E/MB cylinder-forming diblock that had been examined by Quiram, Register, and Marchend<sup>[35]</sup> Using a block staining technique,<sup>[24]</sup> the researchers were able to image the solid state structure of the material. While the microphase-separated cylindrical structure is largely preserved, local distortions due to crystallization were observed. In particular, the crystals were able to traverse from one cylinder to its neighboring microdomain. Despite the general preservation of the melt structure, sigmoidal crystallization kinetics, which reflect the extensive connectivity and growth from a relatively small number of nuclei, was observed. While the E/MB diblock is strongly segregated, the interblock segregation strength during crystallization is

insufficient to effectively isolate crystallization within discrete microdomains. Therefore crystal growth in this material is merely *templated by*, but not *confined in*, nanoscale cylinders. By systematically quantifying the interblock segregation strength at crystallization, the isothermal crystallization kinetics, and the final solid state structures in a series of E-containing semicrystalline-rubbery block copolymers, Loo, Register, and Ryan<sup>[54]</sup> were able to come up with a “classification map” (Fig. 11) for identifying the crystallization modes in semicrystalline block copolymers with rubbery matrices.

The study of structure rearrangement in semicrystalline block copolymers have traditionally been carried out with scattering techniques; two-dimensional X-ray detectors have enabled the examination of preferential crystal orientation in aligned samples while synchrotron-based techniques have allowed us to access the kinetic and mechanistic details of crystallization. More recently, TEM has been employed to examine the melt and final solid state structures of these materials in real space.<sup>[24,54]</sup> With the advent of atomic force microscopy (AFM), direct imaging of the crystallization process is now also possible. For instance, Reiter et al.<sup>[58]</sup> were able to image the individual crystallizing domains in an asymmetric EO/B diblock copolymer during crystallization using AFM. By doing so, the researchers concluded that nanoscale crystallization within discrete domains of block copolymers is

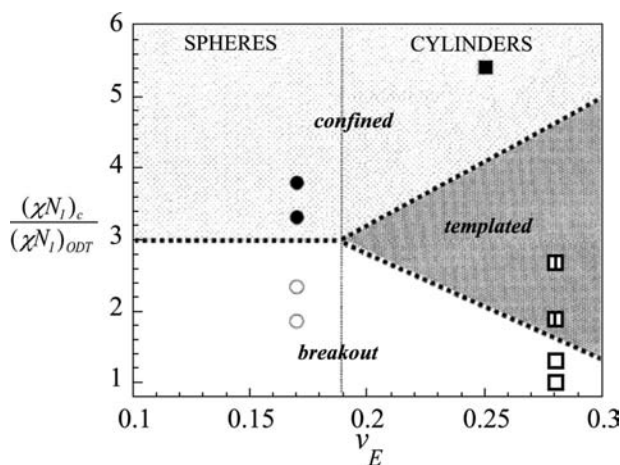


**Fig. 11** Classification map for E-containing semicrystalline block copolymers with rubbery matrices. Three modes of crystallization were observed: “breakout” where the melt structure is completely destroyed on crystallization; “templated” where the melt structure is *generally* but not *faithfully* preserved in the solid state, and where indications of connectivity between crystallizing domains are present in the crystallization kinetics; and “confined” where crystallization occurs within the microdomains prescribed by microphase separation so the nanoscale domains are effectively preserved on cooling. *Source:* From Ref.<sup>[54]</sup>, © 2002 American Chemical Society.

independently stochastic; that is, crystallizing one nanoscale domain does not influence the probability of crystallizing its neighboring domains. By operating an optical microscope in reflection mode, Hong et al.<sup>[59]</sup> were also able to directly image the crystallization of a lamellar-forming EO/B diblock copolymer. In this case, the researchers observed crystallization between neighboring lamellae and attributed extended interdomain crystallization to the presence of defects, such as screw dislocations, in thin films.

## PATTERNING SEMICRYSTALLINE BLOCK COPOLYMERS OVER LARGE AREAS

So far in this entry, we have discussed how the self-assembly of block copolymers can be used to template or pattern polymer crystallization. The ability to control crystallization on a nanometer-length scale has in turn led to complex yet intriguing “structure-within-structure” type morphologies and new understanding of polymer crystallization kinetics and mechanisms. In this last section, we would like to highlight some of the more recent work on patterning semicrystalline block copolymers over large areas.

Block copolymers naturally self-assemble to form periodic nanoscale domains. We have addressed the increased complexity of the structures when block copolymers contain crystallizable segments. From an applications standpoint, the ability to locally pattern polymer crystallization is important, but so is the ability to control the formation of periodic nanoscale domains over large areas (long-range order). However, forming periodic patterns with block copolymers over long range remains a big challenge.<sup>[60]</sup> This is in large part because of the tendency for block copolymers to form micron-size grains. Thus significant research efforts have been dedicated to eliminating grain boundaries and increasing the long-range order in block copolymer thin films. These efforts have primarily relied on the application of external fields, such as electric fields<sup>[15,61]</sup> and temperature gradients,<sup>[62,63]</sup> as well as patterned<sup>[64,65]</sup> and epitaxially matched substrates.<sup>[66]</sup> More recently, De Rosa et al.<sup>[67]</sup> have demonstrated that they can produce large grains that span up to several hundred microns by rapid solidification of a semicrystalline E/S diblock copolymer from a crystallizable solvent. Cocrystallization of the crystallizable block with an epitaxially-matched solvent can effectively induce a preferential orientation of both the microdomains as well as the crystals over large areas.<sup>[67,68]</sup> Reiter et al.<sup>[69]</sup> found that, by combining dewetting with crystallization and microphase separation, the researchers were able to preferentially orient the crystalline lamellae in a poly(ethylene oxide)-*b*-poly(hydrogenated butadiene) diblock

copolymer perpendicular to the substrate over large areas. The ability for a block copolymer to crystallize has imparted an additional mechanism for manipulating long-range order. Furthermore, crystallization can be a fast process; the long-range order that is induced by cocrystallization of a solvent and a crystallizable block or a combination of dewetting and crystallization occurs over much shorter time scales compared to processes that require external fields. Long-range microdomain and crystal order induced by crystallization is straightforward and efficient, thereby making it highly attractive for advanced applications such as the parallel fabrication of quantum dots and memory bits, etc.

## CONCLUSION

Model block copolymers, synthesized by traditional anionic routes and containing only amorphous blocks, are presently considered well understood. Incorporating a crystallizable component in these materials has added morphological richness and kinetic complexity to the systems. We described in this entry the possibility of templating and controlling polymer crystallization in the presence of microphase-separated nanoscale domains. We discussed the crystallization behavior of semicrystalline-glassy block copolymers where the melt structure is exactly preserved as a result of the presence of an already-vitrified component. We also described the solid-state structure development of semicrystalline-rubbery systems; significant progress has been made in the last decade demonstrating that crystallization can also be effectively patterned in the absence of a glassy component. We concluded the entry by describing some recent experiments that pertain to achieving long-range order, both on the nanometer scale as well as on larger length scales. Work in this field continues to be exciting; with the advent of novel synthetic techniques, we are able to revisit and examine fundamental crystallization issues that were previously not addressable with semicrystalline homopolymers alone. Furthermore, with increasing prominence of patterning on a nanometer-length scale, understanding and having the ability to control polymer crystallization over several length scales may prove useful for the development of advanced applications such as lithographic masks, memory storage, as well as parallel fabrication of metal or semiconductor quantum dots.

## REFERENCES

1. Hamley, I.W. *The Physics of Block Copolymers*; Oxford University Press: New York, 1998.
2. Balta Calleja, F.J.; Roslaniec, Z. *Block Copolymers*; Marcel Dekker, Inc.: New York, 2000.
3. Whitesides, G.M.; Grzybowski, B. Self assembly at all scales. *Science* **2002**, *295*, 2418–2421.
4. Whitesides, G.M.; Boncheva, M. Beyond molecules: Self assembly of mesoscopic and macroscopic components. *Proc. Natl. Acad. Sci. U. S. A.* **2002**, *99* (8), 4769–4774.
5. Bates, F.S.; Fredrickson, G.H. Block copolymer thermodynamics—Theory and experiment. *Annu. Rev. Phys. Chem.* **1990**, *41*, 525–557.
6. Bates, F.S.; Fredrickson, G.H. Block copolymers—Designer soft materials. *Phys. Today* **1999**, *52* (2), 32–38.
7. Fasolka, M.J.; Mayes, A.M. Block copolymer thin films—Physics and applications. *Annu. Rev. Mater. Res.* **2001**, *31*, 323–355.
8. Flory, P.J. *Principles of Polymer Chemistry*; Cornell University Press: Ithaca, NY, 1953.
9. deGennes, P.-G. *Scaling Concepts in Polymer Physics*; Cornell University Press: Ithaca, NY, 1979.
10. Matsen, M.W.; Bates, F.S. Unifying weak- and strong-segregation block copolymer theories. *Macromolecules* **1996**, *29* (4), 1091–1098.
11. Helfand, E.; Wasserman, Z.R. *Developments in Block Copolymers-I*; Goodman, I., Ed.; Applied Science: London, 1982.
12. Semenov, A.N. Contribution to the theory of microphase layering in block copolymer melts. *Sov. Phys. JETP* **1985**, *61* (4), 733
13. Rempp, P.; Merrill, E.W. *Polymer Synthesis*, 2nd Ed.; Huthig and Wepf: Heidelberg, 1991; Chap. 5.
14. Park, M.; Harrison, C.; Chaikin, P.M.; Register, R.A.; Adamson, D.H. Block copolymer lithography: Periodic arrays of 1011 holes in one square centimeter. *Science* **1997**, *276* (5317), 1401–1404.
15. Thurn-Albrecht, T.; Steiner, R.; DeRouchey, J.; Stafford, C.M.; Huang, E.; Bal, M.; Tuominen, M.; Hawker, C.J.; Russell, T.P. Nanoscopic templates from oriented block copolymer films. *Adv. Mater.* **2000**, *12* (11), 787–791.
16. Schultz, J.M. *Polymer Crystallization: The Development of Crystalline Order in Thermoplastic Polymers*; American Chemical Society: Washington, DC, 2001.
17. Hamley, I.W. Crystallization in block copolymers. *Adv. Polym. Sci.* **1999**, *148*, 114–137.
18. Mandelkern, L. *Crystallization of Polymers*; McGraw Hill: New York, 1964.
19. Brandrup, J., Immergut, E.H., Eds.; *Polymer Handbook*; Wiley: New York, 1989.
20. Stühn, B. The relation between the microphase separation transition and the glass-transition in diblock copolymers. *J. Polym. Sci., Polym. Phys.* **1992**, *30* (9), 1013–1019.
21. Lotz, B.; Kovacs, A.J. Phase transitions in block-copolymers of polystyrene and polyethylene oxide. *ACS Polym. Prepr.* **1969**, *10* (2), 820–825.
22. Cohen, R.E.; Cheng, P.L.; Douzinas, K.; Kofinas, P.; Berney, C.V. Path-dependent morphologies of a diblock copolymer of polystyrene/hydrogenated polybutadiene. *Macromolecules* **1990**, *23* (1), 324–327.
23. Weimann, P.A.; Hajduk, D.A.; Chu, C.; Chaffin, K.A.; Brodil, J.C.; Bates, F.S. Crystallization of tethered polyethylene in confined geometries. *J. Polym. Sci., Polym. Phys.* **1999**, *37* (16), 2053–2068.

24. Loo, Y.-L.; Register, R.A.; Adamson, D.H. Direct imaging of polyethylene crystallites within block copolymer microdomains. *J. Polym. Sci., Polym. Phys.* **2000**, *38* (19), 2564–2570.
25. Trent, J.S.; Scheinbeim, J.I.; Couchman, P.R. Ruthenium tetroxide staining of polymers for electron microscopy. *Macromolecules* **1983**, *16* (4), 589–598.
26. Trent, J.S. Ruthenium tetroxide staining of polymers: New preparative methods for electron microscopy. *Macromolecules* **1984**, *17* (12), 2930–2931.
27. Sawyer, L.C.; Grubb, D.T. *Polymer Microscopy*, 2nd Ed.; Chapman and Hall: London, 1996.
28. Zhu, L.; Huang, P.; Chen, W.Y.; Ge, Q.; Quirk, R.P.; Cheng, S.Z.D.; Thomas, E.L.; Lotz, B.; Hsiao, B.S.; Yeh, F.J.; Liu, L.Z. Nanotailored crystalline morphology in hexagonally perforated layers of a self assembled PS-*b*-PEO diblock copolymer. *Macromolecules* **2002**, *35* (9), 3553–3562.
29. Zhu, L.; Cheng, S.Z.D.; Huang, P.; Ge, Q.; Quirk, R.P.; Thomas, E.L.; Lotz, B.; Hsiao, B.S.; Yeh, F.; Liu, L.Z. Nanoconfined polymer crystallization in the hexagonally perforated layers of a self-assembled PS-*b*-PEO diblock copolymer. *Adv. Mater.* **2002**, *14* (1), 31–34.
30. Shiomi, T.; Tsukada, H.; Takeshita, H.; Takenaka, K.; Tezuka, Y. Crystallization of semicrystalline block copolymers containing a glassy amorphous component. *Polymer* **2001**, *42* (11), 4997–5004.
31. Nojima, S.; Tanaka, H.; Rohadi, A.; Sasaki, S. The effect of glass transition temperature on the crystallization of  $\epsilon$ -caprolactone-styrene diblock copolymers. *Polymer* **1998**, *39* (8–9), 1727–1734.
32. Balsamo, V.; Muller, A.J.; von Glyndenfeldt, F.; Stadler, R. Ternary ABC block copolymers based on one glassy and two crystallizable blocks: Polystyrene-*b*-polyethylene-*b*-poly( $\epsilon$ -caprolactone). *Macromol. Chem. Phys.* **1998**, *199* (6), 1063–1070.
33. Hamley, I.W.; Fairclough, J.P.A.; Terrill, N.J.; Ryan, A.J.; Lipic, P.M.; Bates, F.S.; Towns-Andrews, E. Crystallization in oriented semicrystalline diblock copolymers. *Macromolecules* **1996**, *29* (27), 8835–8843.
34. Quiram, D.J.; Register, R.A.; Marchand, G.R.; Adamson, D.H. Chain orientation in block copolymers exhibiting cylindrically confined crystallization. *Macromolecules* **1998**, *31* (15), 4891–4898.
35. Quiram, D.J.; Register, R.A.; Marchand, G.R. Crystallization of asymmetric diblock copolymers from microphase-separated melts. *Macromolecules* **1997**, *30* (16), 4551–4558.
36. Loo, Y.-L.; Register, R.A.; Ryan, A.J.; Dee, G.T. Polymer crystallization confined in one, two, or three dimensions. *Macromolecules* **2001**, *34* (26), 8968–8977.
37. Loo, Y.-L.; Register, R.A.; Ryan, A.J. Polymer crystallization in 25-nm spheres. *Phys. Rev. Lett.* **2000**, *84* (18), 4120–4123.
38. Muller, A.J.; Balsamo, V.; Arnal, M.L.; Jakob, T.; Schmalz, H.; Abetz, V. Homogeneous nucleation and fractionated crystallization in block copolymers. *Macromolecules* **2002**, *35* (8), 3048–3058.
39. Rangarajan, P.; Register, R.A.; Fetters, L.J.; Bras, W.; Naylor, S.; Ryan, A.J. Crystallization of a weakly-segregated polyolefin diblock copolymer. *Macromolecules* **1995**, *28* (14), 4932–4938.
40. Rangarajan, P.; Register, R.A.; Adamson, D.H.; Fetters, L.J.; Bras, W.; Naylor, S.; Ryan, A.J. Dynamics of structure formation in crystallizable block copolymers. *Macromolecules* **1995**, *28* (5), 1422–1428.
41. Ryan, A.J.; Hamley, I.W.; Bras, W.; Bates, F.S. Structure development in semicrystalline diblock copolymers crystallizing from the ordered melt. *Macromolecules* **1995**, *28* (11), 3860–3868.
42. Bras, W.; Derbyshire, G.E.; Devine, A.; Clark, S.M.; Cooke, J.; Komanschek, B.E.; Ryan, A.J. The combination of thermal analysis and time-resolved x-ray techniques: A powerful method for materials characterization. *J. Appl. Crystallogr.* **1995**, *28* (1), 26–32.
43. Liu, L.-Z.; Chu, B. Crystalline structure and morphology of microphases in compatible mixtures of poly(tetrahydrofuran-methyl methacrylate) diblock copolymer and polytetrahydrofuran. *J. Polym. Sci., Polym. Phys.* **1999**, *37* (8), 779–792.
44. Park, C.; deRosa, C.; Fetters, L.J.; Thomas, E.L. Influence of an oriented glassy cylindrical microdomain structure on the morphology of crystallizing lamellae in a semicrystalline block terpolymer. *Macromolecules* **2000**, *33* (21), 7931–7938.
45. Loo, Y.-L.; Register, R.A.; Adamson, D.H. Polyethylene crystal orientation induced by block copolymer cylinders. *Macromolecules* **2000**, *33* (22), 8361–8366.
46. Douzinas, K.C.; Cohen, R.E.; Halasa, A.F. Evaluation of domain spacing scaling laws for semicrystalline diblock copolymers. *Macromolecules* **1991**, *24* (15), 4457–4459.
47. Kofinas, P.; Cohen, R.E. Morphology of highly-textured polyethylene/poly(ethylene-propylene) semicrystalline diblock copolymers. *Macromolecules* **1994**, *27* (11), 3002–3008.
48. Kofinas, P.; Cohen, R.E. Melt processing of semicrystalline E/EP/E triblock copolymers near the order-disorder transition. *Macromolecules* **1995**, *28* (1), 336–343.
49. Nojima, S.; Kato, K.; Yamamoto, S.; Ashida, T. Crystallization of block copolymer I. Small-angle x-ray scattering study of  $\epsilon$ -caprolactone/butadiene diblock copolymer. *Macromolecules* **1992**, *25* (8), 2237–2242.
50. Lovinger, A.J.; Han, B.J.; Padden, F.J.; Mirau, P.A. Morphology and properties of polycaprolactone-poly(dimethyl siloxane)-poly(caprolactone) triblock copolymers. *J. Polym. Sci., Polym. Phys.* **1993**, *31* (2), 115–123.
51. Ryan, A.J.; Fairclough, J.P.A.; Hamley, I.W.; Mai, S.-M.; Booth, C. Chain folding in crystallizable block copolymers. *Macromolecules* **1997**, *30* (6), 1723–1727.
52. Mai, S.-M.; Fairclough, J.P.A.; Viras, K.; Gorry, P.A.; Hamley, I.W.; Ryan, A.J.; Booth, C. Chain folding in oxyethylene/oxybutylene diblock copolymers. *Macromolecules* **1997**, *30* (26), 8392–8400.
53. Quiram, D.J.; Register, R.A.; Marchand, G.R.; Ryan, A.J. Dynamics of structure formation and crystallization in asymmetric diblock copolymers. *Macromolecules* **1997**, *30* (26), 8338–8343.
54. Loo, Y.-L.; Register, R.A.; Ryan, A.J. Modes of crystallization in block copolymer microdomains: Breakout, templated and confined. *Macromolecules* **2002**, *35* (6), 2365–2374.

55. Chen, H.L.; Li, H.C.; Huang, Y.Y.; Chiu, F.C. Crystallization-induced deformation of spherical microdomains in block copolymer blends consisting of a soft amorphous phase. *Macromolecules* **2002**, *35* (6), 2417–2422.
56. Chen, H.L.; Wu, J.C.; Lin, T.L.; Lin, J.S. Crystallization kinetics in microphase-separated poly(ethylene oxide)-*b*-poly(1,4-butadiene). *Macromolecules* **2001**, *34* (20), 6936–6944.
57. Chen, H.L.; Hsiao, S.C.; Lin, T.L.; Yamauchi, K.; Hasegawa, H.; Hashimoto, T. Microdomain-tailored crystallization kinetics of block copolymers. *Macromolecules* **2001**, *34* (4), 671–674.
58. Reiter, G.; Castelein, G.; Sommer, J.U.; Rottele, A.; Thurn-Albrecht, T. Direct visualization of random crystallization and melting in arrays of nanometer-size polymer crystals. *Phys. Rev. Lett.* **2001**, *87* (22), art. no. 226101.
59. Hong, S.; MacKnight, W.J.; Russell, T.P.; Gido, S.P. Orientationally registered crystals in thin film crystalline/amorphous block copolymers. *Macromolecules* **2001**, *34* (7), 2389–2390.
60. Garetz, B.A.; Balsara, N.P.; Dai, H.J.; Wang, Z.; Newstein, M.C. Orientation correlations in lamellar block copolymers. *Macromolecules* **1996**, *29* (13), 4675–4679.
61. Thurn-Albrecht, T.; DeRouchey, J.; Russell, T.P.; Jaeger, H.M. Overcoming interfacial interactions with electric fields. *Macromolecules* **2000**, *33* (9), 3250–3253.
62. Bodycomb, J.; Funaki, Y.; Kimishima, K.; Hashimoto, T. Single-grain lamellar microdomain from a diblock copolymer. *Macromolecules* **1999**, *32* (6), 2075–2077.
63. Hashimoto, T.; Bodycomb, J.; Funaki, Y.; Kimishima, K. The effect of temperature gradient on the microdomain orientation of diblock copolymers undergoing an order–disorder transition. *Macromolecules* **1999**, *32* (3), 952–954.
64. Heier, J.; Kramer, E.J.; Groenewold, J.; Fredrickson, G.H. Kinetics of individual block copolymer island formation and disappearance near an absorbing boundary. *Macromolecules* **2000**, *33* (16), 6060–6067.
65. Rockford, L.; Liu, Y.; Mansky, P.; Russell, T.P.; Yoon, M.; Mochrie, S.G.J. Polymers on nanoperiodic, heterogeneous surfaces. *Phys. Rev. Lett.* **1999**, *82* (12), 2602–2605.
66. Segalman, R.A.; Yokoyama, H.; Kramer, E.J. Graphoepitaxy of spherical domain block copolymer films. *Adv. Mater.* **2001**, *13* (15), 1152–1155.
67. De Rosa, C.; Park, C.; Thomas, E.L.; Lotz, B. Microdomain patterns from directional eutectic solidification and epitaxy. *Nature* **2000**, *405* (6785), 433–437.
68. Park, C.; De Rosa, C.; Thomas, E.L. Large-area orientation of block copolymer microdomains in thin films via directional crystallization of a solvent. *Macromolecules* **2001**, *34* (8), 2602–2606.
69. Reiter, G.; Castelein, G.; Hoerner, P.; Riess, G.; Blumen, A.; Sommer, J.-U. Nanometer-scale surface patterns with long-range order created by crystallization of diblock copolymers. *Phys. Rev. Lett.* **1999**, *83* (19), 3844–3847.

# Thermal Effect on the Luminescence Properties of Quantum Dots

X. B. Zhang

R. D. Dupuis

*Microelectronics Research Center, University of Texas at Austin,  
Austin, Texas, U.S.A.*

## INTRODUCTION

Semiconductor quantum dots (QDs) are similar to atoms in having a very sharp density of states distribution. However, what makes QDs such unusual objects are that we can control their shape, size, and hence the detailed characteristics of their energy levels and the number of confined states. The controllable shape, size, spatial distribution, and density of states endow the QDs with many novel properties, which have promising applications in optoelectronic devices. For example, QD-based injection lasers are predicted to have improved performance characteristics, such as a lower threshold current density, higher characteristic temperature, and higher differential gain in comparison with the conventional quantum well lasers.<sup>[1]</sup> The intersubband absorption of QDs can be used to design QD-based photodetectors operated in the mid-infrared spectral region. As compared to quantum wells, the reduced electron–phonon scattering in QDs provides the photoexcited carriers to be swept away as photocurrent before relaxing to the ground state and therefore makes the QDs to be more efficient in detection. Moreover, unlike the quantum-well photodetectors, QD photodetectors are intrinsically sensitive to normal photon incidence due to the breaking of the polarization selection rule.<sup>[2]</sup>

Because of these promising applications, the growth of semiconductor QDs has been extensively investigated in recent years. A major breakthrough in the fabrication of high-quality quantum dots is the growth of self-assembled quantum dots (SAQDs), typically formed by strained-layer epitaxy in systems having a large lattice-mismatch. The growth in such a system is usually through the Stranski–Krastanow (S–K) growth mode or by the Volmer–Weber (V–W) growth mode. For S–K growth, the growth is initially through a layer-by-layer mode, which results in a thin wetting layer; after the wetting layer exceeds a critical thickness, defect-free three-dimensional (3-D) islands nucleate coherently on top of the strained wetting layer. For V–W growth, 3-D islands nucleate directly

on the substrate without the formation of wetting layer. In the past years, laser diodes and photodetectors based on SAQDs with improved operation have been demonstrated. However, many factors, which fundamentally limit the performance of these devices, are still not well understood. Thermal effects have a great influence on the population of carriers in the energy states of QDs, and thus, such effects strongly influence the device performance. In order to realize room-temperature operation of the QD-based devices, the influence of temperature on their emission and absorption properties must be well understood. In this entry, we will review the impact of thermal effects on the optical properties of SAQDs. We first show how thermal excitation affects the optical properties of bulk semiconductors. We believe this knowledge for bulk semiconductors will be helpful for understanding the optical properties of QDs. After that, recent temperature-dependent emission studies of SAQDs are reviewed. In high-quality SAQDs, evidence of thermally excited carrier transfer between QDs is shown. An analytical model based on rate equations is used to interpret the emission properties. Finally, a conclusion and a brief future vision are given.

## THERMAL EFFECTS ON THE OPTICAL PROPERTIES OF BULK SEMICONDUCTORS

The luminescence spectra of high-purity bulk semiconductors at liquid helium temperature are often dominated by the near bandgap bound exciton and free exciton emission. An exciton is the electron–hole pair formed as a result of Coulomb attraction. When the exciton and an impurity atom form a complex, it is called a bound exciton. At low temperatures, electrons and holes are frozen in states associated with donor and acceptor impurities, respectively, and thus form neutral donors and acceptors. An exciton bound to a neutral donor is called a neutral donor-bound exciton, while an exciton bound to a neutral acceptor is called a



neutral acceptor-bound exciton. Sometimes, transitions between donor (or acceptor) and band states, or between donors and acceptors (i.e., donor–acceptor pairs or simply DAPs), are also observed in the emission spectra. The free exciton binding energy,  $E_X$ , depends on the Coulomb interaction between the electron and hole, which form the exciton. The binding energy of a free exciton bound to a neutral donor ( $E_{DX}$ ) or to a neutral acceptor ( $E_{AX}$ ) depends on the ionization energy of the donor ( $E_D$ ) and the acceptor ( $E_A$ ), respectively, and usually follows Hayne's rule:<sup>[3]</sup>

$$E_{DX} = \gamma_1 E_D \text{ and } E_{AX} = \gamma_2 E_A \quad (1)$$

where  $\gamma_1 \sim 0.2$  and  $\gamma_2 \sim 0.1$  were found for shallow donors and acceptors in Si. Similar values were also found in many other semiconductors. With an increase in temperature, the peak energies of the near bandgap emission usually follow the temperature-dependent bandgap and empirically the transition energies follow the Varshni equation:<sup>[4]</sup>

$$E(T) = E(0) - \alpha T^2 / (\beta + T) \quad (2)$$

where  $E(0)$  is emission energy at 0 K,  $\alpha$  and  $\beta$  are Varshni coefficients. The origin of the temperature-dependent bandgap is due to thermal expansion of the lattice and the changes in the electron–phonon interaction. Because of the nature of the electron–phonon interaction, the temperature-dependent bandgap is sometimes described in a Bose–Einstein-type expression:<sup>[4]</sup>

$$E(T) = E(0) - 2\alpha_B / [\exp(\hbar\omega_B/k_B T) - 1] \quad (3)$$

where  $\alpha_B$  represents the exciton–average phonon interaction,  $k_B$  is the Boltzmann constant, and  $\hbar\omega_B$  is the average phonon energy. The quenching of these emissions at high temperature is complicated and depends in detail upon the specific quenching channels involved in the emission. For a bound exciton, usually, each quenching channel is related to a thermal activation of the bound exciton from radiative state into a non-radiative state with a typical activation energy. The dynamic recombination and quenching processes can be described as:

$$\frac{dn}{dt} = -\frac{n}{\tau} - \sum_i \frac{n}{\tau_i} \exp(-\Delta E_i/k_B T) + G \quad (4)$$

where  $n$  is the density of bound exciton,  $\tau$  is the bound exciton radiative recombination lifetime,  $\tau_i$  is the effective scattering time from the radiative state to the  $i$ th non-radiative state,  $\Delta E_i$  is the thermal activation energy and is related to the energy difference between the radiative state and the  $i$ th nonradiative state, and

$G$  is the carrier generation rate. In steady-state conditions (i.e., the generation rate is uniform with time and  $dn/dt = 0$ ), we have:

$$n(T) = \frac{G\tau}{1 + \sum_i \frac{\tau}{\tau_i} \exp(-\Delta E_i/k_B T)} \quad (5)$$

The intensity of the bound exciton emission  $I(T)$  is proportional to  $n(T)$  and thus has the same equation as above. This equation has been widely used to fit the experimental results and gives valuable information related to the nonradiative channels. For example, a neutral acceptor bound exciton  $A^0X$  can be thermally dissociated into:<sup>[5]</sup> 1)  $A^0 + X$ , which has a typical activation energy  $E_{AX}$ ; or 2)  $A^0 + e + h$ , which has a typical activation energy of  $E_{AX} + E_X$ ; or to 3)  $A^-X + h$ , which has an activation energy of  $E_{AX} + E_X - E_{A^0e}$ ; or to 4)  $A^- + h + h + e$ , i.e., fully ionized which has a much larger activation energy. In a temperature-dependent photoluminescence (PL) study of the  $A^0X$  transition in GaAs, through fitting the PL intensity, two non-radiative channels were identified in different temperature regions. For free excitons, the quenching is mainly due to the thermal dissociation of excitons into free carriers. The intensity can be described with single activation energy:

$$I(T) = I(0) / [1 + C \exp(-\Delta E/k_B T)] \quad (6)$$

where  $I(0)$  is intensity at 0 K,  $C$  is related to  $\tau/\tau_n$ , where  $\tau_n$  is non-radiative recombination lifetime,  $\tau$  is radiative recombination lifetime and usually  $\propto T^{3/2}$  for free exciton in bulk materials.<sup>[6]</sup>  $\Delta E$  is the thermal activation energy and is related to the free excitonic binding energy. When both free and bound excitons contribute to the emission spectra, with an increase in temperature, the bound excitons may be dissociated into free excitons, in this case, the density of free excitons will increase and an increase in the intensity of the free exciton emission would be expected. This has been observed in some high-purity semiconductors.<sup>[7]</sup>

The line width of the excitonic emission (or absorption) contains two contributions: the inhomogeneous broadening and the homogeneous broadening.<sup>[8]</sup> This can be described as:

$$\Gamma(T) = \Gamma_0 + \gamma_{ph} T + \Gamma_{LO} N_{LO} \quad (7)$$

where  $\Gamma_0$  is the inhomogeneous line width due to the exciton–exciton, exciton–carrier interaction, and to scattering by defects and impurities, and, in alloy materials, by alloy composition fluctuations. The second term,  $\gamma_{ph} T$ , is due to acoustic phonon scattering. The quantity  $\gamma_{ph}$  represents the exciton–acoustic phonon

coupling strength. The  $T$  in  $\gamma_{\text{ph}}T$  is a result of the linear dependence of the acoustic phonon occupation number on the temperature  $T$ . The third term is the line width due to longitudinal-optical (LO) phonon scattering.  $\Gamma_{\text{LO}}$  is the exciton-LO phonon coupling strength, and  $N_{\text{LO}} = 1/[\exp(\hbar\omega_{\text{LO}}/kT) - 1]$  is the LO phonon occupation number. The values  $\gamma_{\text{ph}}$  and  $\Gamma_{\text{LO}}$  in quantum well or quantum-dot heterostructures are different because of the difference in the exciton-phonon coupling strength.

### THERMAL EFFECTS ON RECOMBINATIONS IN SIMPLE CONFINED SYSTEMS

In contrast to bulk materials, the thermal quenching of the emission in quantum-confined low-dimensional systems is more complicated. A schematic diagram of the emission and thermal activation processes is shown in Fig. 1. Usually, electrons and holes are created mainly in the barriers and are immediately captured into the confined electron and hole states in the quantum dot or quantum well with a large capture rate  $R_c$ . They also have a rate,  $R_1$ , to recombine radiatively, and  $R_n$  to recombine nonradiatively in the barriers. Once the electron and hole are captured in the confined states, they have several ways to recombine: 1) they

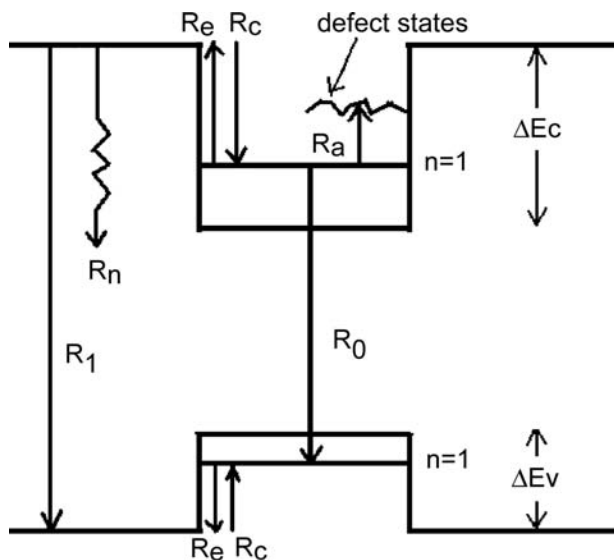


**Fig. 1** Schematic diagram of the emission and thermal activation processes in a single quantum confined system.  $\Delta E_c$  and  $\Delta E_v$  are the conduction and valence band offsets, respectively,  $n = 1$  is the first confined electron or hole states, and  $R_c$  is the electron or hole capture rate.  $R_e$  and  $R_a$  are the rates for thermal activation of carriers from  $n = 1$  confined states into barriers and defect states, respectively.  $R_1$  and  $R_n$  are the radiative and nonradiative recombination rates, respectively, in the barrier.  $R_0$  is the radiative recombination rate in the quantum-confined structure.

have a rate  $R_0$  to recombine radiatively; or 2) they have a rate  $R_e$  to be thermally activated back into barriers; or 3) they have a rate  $R_a$  to be thermally activated into a nonradiative defect state. Generally, Eqs. (4) and (5) can still be used to describe the radiative and non-radiative recombination in such low-dimensional systems. The non-radiative channel through the non-radiative defect states in the confined structures is different from that in bulk materials.<sup>[9]</sup> The reason is that the energy level of these defect states depends on the degree of localization, which is determined through the ratio between the extension of the defect wave function and the size of the confined structures. In case of weak localization, i.e., the extension of the defect wave function is comparable or larger than the size of the confined structures, the energy levels of the defect are quantized and depend on the size of the confined structures and also upon the position of the defect in the confined structures. On the other hand, in the strong localization case, the energetic difference in the conduction and valence bands of the bulk material is unchanged, and, as a consequence, the energetic distance between the defect energy level and the electron and hole subbands becomes a function of the size of confined structure as the quantization of the subbands depends on the size. For the thermal activation of carriers from confined states into the barrier states, two mechanisms have been reported. One is a bipolar activation process,<sup>[10]</sup> where the electron and hole are simultaneously activated into the barriers with a thermal activation energy equal to the energy difference between the emission peak and the barrier bandgap. The other is unipolar activation,<sup>[11]</sup> where the less-confined carrier electron (or hole) is thermally activated into the barrier with an activation energy close to the energy difference between the electron (or hole) confined state and the conduction (or valence) band states in barriers.

### THERMAL EFFECTS ON RECOMBINATIONS IN QUANTUM DOTS

The recombination and the thermal activation processes described above are very simple as the confined structures are isolated and carrier dynamics between ensembles of various-sized confined structures is not considered. Recently, successful fabrication of SAQDs through the S-K growth mode, typically with area density in the range of  $10^9$  to  $10^{11}$   $\text{cm}^{-3}$ , has been widely reported in many III/V, II/VI, and IV/IV semiconductor systems. However, because of the random statistical nature of the nucleation process, the grown QDs have a fluctuation in size. Gaussian distributions, bimodal distributions, or broad size distributions have been reported in different QD systems or under

different growth conditions. Such distributions in size have a great influence on the luminescence properties of QDs and make the carrier recombination in QDs difficult to understand. In the past years, temperature-dependent luminescence of SAQDs has been investigated in many semiconductor systems, such as InAs/AlGaAs,<sup>[12–18]</sup> ZnSe/ZnS,<sup>[19]</sup> CdTe/ZnTe,<sup>[20]</sup> and CdSe/ZnSe,<sup>[21–23]</sup> however, there is still no general agreement upon the thermal effects on the recombination processes in QDs. Generally, three characteristic features are observed in these QD systems: 1) the luminescence peak undergoes a red shift with temperature much faster than that of the bandgap of the bulk material; 2) the peak line width shows an unusual decrease with temperature in an intermediate temperature region; and 3) the luminescence at lower energies quenches much slower than that at higher energies, and in some cases, an enhancement in the luminescence of lower energies with temperature is observed. These features can be clearly seen in a temperature-dependent cathodoluminescence (CL) study of InP/In<sub>0.5</sub>Al<sub>0.5</sub>P QDs grown by low-pressure metal organic chemical vapor deposition (MOCVD).<sup>[24]</sup> The spectra are shown in Fig. 2. Obviously, a decrease in the CL intensity with temperature is observed. The inset of the figure shows an Arrhenius plot of the integrated CL intensity as a function of  $1000/T$ . By using Eq. (6), the thermal quenching at high temperature can be well fitted with an activation energy of  $\sim 150$  meV. This value is much smaller than the energy difference between the bandgap of In<sub>0.5</sub>Al<sub>0.5</sub>P and the CL peak ( $\sim 0.43$  eV) and is

very close to the difference in the conduction band energies, which suggests that unipolar escape of electrons from QDs is a likely mechanism being responsible for the thermal quenching of CL at high temperature.<sup>[11]</sup> Accompanying the quenching of the total CL emission, the CL intensity of the lower-energy tail is, in fact, on the increase with temperature until 200 K. This unusual increase will be discussed later below. Furthermore, the CL peak shows a large red shift and an unusual decrease in CL line width. The CL peak energy and the full width at half maximum vs. temperature are plotted in Fig. 3. The measured red shift amounts to about 160 meV in the temperature range of the experiment, significantly larger than that of bulk InP bandgap (dashed line in the figure). As shown in Fig. 3, the CL line width also shows an unusual behavior. Unlike the usually observed homogeneous broadening described by Eq. (7), the line width decreases first then increases with temperature with a dip around 200 K. These unusual properties were not observed in the temperature-dependent PL study of single QDs,<sup>[25,26]</sup> where the PL of a single QD is very narrow at low temperatures. With an increase in the temperature, the PL peak shifts as the bandgap does, the line width increases and can be described by Eq. (7).

The anomalous temperature-dependent PL was first observed in InAs/GaAs QDs.<sup>[12]</sup> Possibly because of the lower quality of InAs QDs on GaAs, an enhancement in the luminescence of lower energies was not observed in this report. The anomalous PL

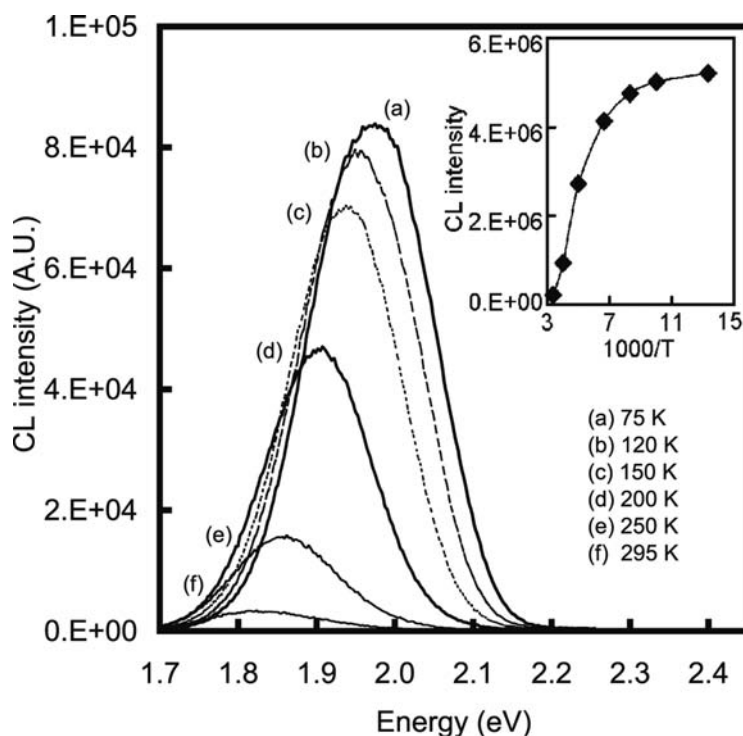


**Fig. 2** Temperature-dependent CL spectra of InP/InAlP QDs. The electron beam current and voltage were 8 kV and 600 pA, respectively. The temperature for each spectrum is indicated in the figure. The inset of the figure shows an Arrhenius plot of the integrated CL intensity as a function of  $1000/T$ , where  $T$  is the temperature.

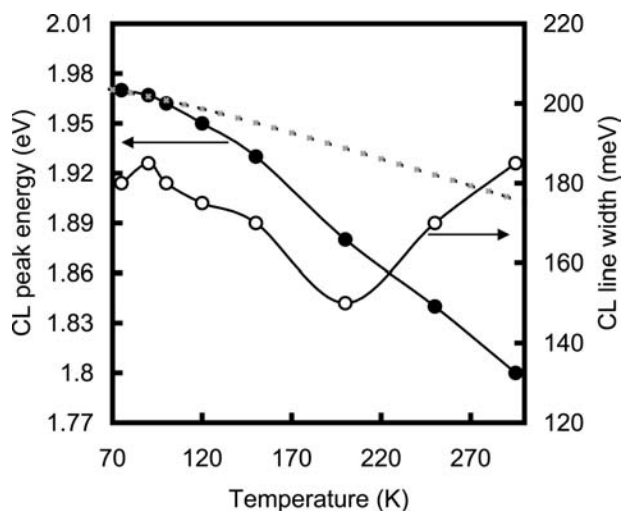


**Fig. 3** The energy and the full width at half maximum (FWHM) of the CL peak of InP/InAlP QDs as a function of temperature. The dashed line shows the temperature dependence of the InP bulk bandgap energy.

was interpreted as carrier tunneling between nearby dots. When the thermal energy becomes comparable to the exciton binding energy, the exciton will be ionized and the free electron and hole in small QDs will tunnel into large QDs very quickly. As a result, a large red shift and a narrowing line width would be expected. However, as the tunneling probability depends on the distance between QDs and the exciton binding energy depends on the QD size, there is no clear evidence to document the QD size and the QD density dependencies. This model was not considered in later studies. Instead of this model, a new model based upon the difference in the thermal activation energy between dots of different sizes was later proposed to interpret similar observations.<sup>[14,19]</sup> In this model, the quenching mechanism was thought to be the thermal activation of electrons and/or holes out of the QDs into barriers, or into the wetting layer (as a result of S-K growth mode), or into upper localized defect states, where they recombine non-radiatively. In this case, the thermal activation energy depends on the confining potential or the energy difference between the QD level and the defect level. With an increase in the temperature, the carriers in the smallest QDs, whose ground-state energies are the closest to that of the barrier or the defect states, would first be ionized. Indeed, this ionization would lead to a line width narrowing and a large red shift of the PL of QDs. In another report, a competition of recombination between the ground- and excited-electron and hole states<sup>[18]</sup> was thought to be the mechanism responsible for the anomalous temperature-dependent PL. In this model, instead of coming from the small QDs, the higher-energy part of the broad PL peak was assumed

to come from the electron- and hole-excited states transition. All these models cannot give rise to an increase in intensity of luminescence of large QDs with an increase in temperature. To account for this, a model of thermally activated carrier transfer from small dots to large ones was proposed.<sup>[15,16,22]</sup> The quenching mechanism is still the thermal activation of electrons and/or holes out of the QDs into barriers or wetting layer. The activation energy is therefore large for large QDs. Because of the high quality of the barrier material, those thermally activated carriers will not all recombine non-radiatively in barriers but have certain chance to be recaptured by the QDs. In an intermediate temperature range, the recapture process would overwhelm the thermal activation process in large QDs and an enhancement in luminescence of large QDs with temperature would be observed.

The fact that the thermal activation of carriers in smaller QDs is easier can be visualized in a temperature-dependent CL imaging study of InP/In<sub>0.5</sub>Al<sub>0.3</sub>Ga<sub>0.2</sub>P QDs grown by MOCVD with a high V/III precursor flow ratio.<sup>[27]</sup> The QDs grown under this condition show a distinct bimodal distribution in size with small QDs of height  $\sim 4$  nm and diameter  $\sim 50$  nm, and large QDs of height  $\sim 9$  nm and diameter  $\sim 70$  nm. The density of small QDs is  $\sim 100 \mu\text{m}^{-2}$  and of large QDs  $\sim 1 \mu\text{m}^{-2}$ . Fig. 4 shows the CL images measured at 75 and 295 K in a scanning electron microscope fitted with

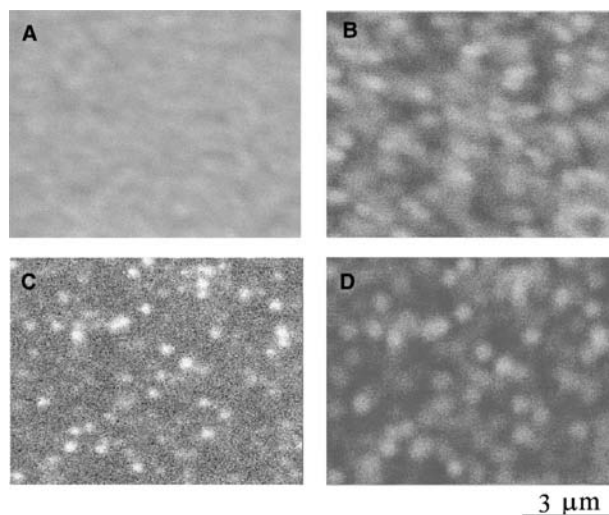


**Fig. 4** Cathodoluminescence images of an InP/InAlGaP QD sample. Images (A) and (B) are monochromatic images measured from the same area at 75 K, monitored at 1.87 and 1.73 eV, respectively. (C) and (D) are panchromatic and monochromatic CL images measured from the same area at 295 K. Image (D) is monitored at the CL peak 1.67 eV. Electron beam voltage was 8 kV and beam currents for images (A)–(D) were 300 pA, 600 pA, 100 pA, and 1 nA, respectively.

a CL system. Fig. 4A and 4B shows monochromatic CL images measured at 75 K, monitored at the CL peak 1.87 and 1.73 eV, respectively. Image (A) is very uniform, suggesting that the CL monitored at the peak comes mainly from the high-density small QDs, which are spatially uniformly distributed. Relatively, image (B) is non-uniform with some bright spots whose density is close to  $1 \mu\text{m}^{-2}$ . This suggests that the CL of lower energy comes from low-density large QDs. With an increase in temperature, the CL of small QDs gets weaker, while relatively, the CL of large QDs gets brighter. This can be clearly seen in a room-temperature panchromatic CL image (C), where the CL of large QDs is much brighter than the surrounding CL coming from high-density small QDs. Fig. 4D is a room-temperature monochromatic CL image, measured from the same area as image (C) and monitored at the peak 1.67 eV. A comparison of images (C) and (D) shows that the bright spots in the two images almost have the same corresponding positions. Therefore the room-temperature CL comes mainly from the low-density large QDs. Because of the large activation energy for these large QDs, the thermal activation of carriers out of the QDs is weak, and relatively, the CL of these large QDs is getting brighter and brighter with an increase in temperature.

## THERMALLY ACTIVATED CARRIERS TRANSFER BETWEEN QUANTUM DOTS

Evidence of thermally excited carrier transfer between QDs of different size comes from the temperature-dependent CL study of a few QDs. Fig. 5A to C shows the spot-mode CL spectra of CdSe QDs grown on ZnSe by MOCVD. The temperature for each spectrum is indicated in the figure. The calculated generation range, using the Kanaya–Okayama model,<sup>[28]</sup> is about  $0.8 \mu\text{m}$  in ZnSe, at the electron beam voltage of 10 kV used. Thus, in the spot-mode CL, the estimated excitation area is only  $0.5 \mu\text{m}^2$ . The number of dots examined by CL is estimated to be about 100. As this is much smaller than in the case of the area scan, the CL spectra are resolved into a series of sharp peaks now. As is labeled as peaks A, B, and C in Fig. 5A, the energies of the three prominent peaks are at roughly 2.20, 2.36, and 2.55 eV, respectively. A spot-to-spot CL measurement shows that the three peaks, A, B, and C, are most probably a result of the transitions in QDs of different sizes, and not of the transitions involving an excited state. An alternative origin of peak C is the CdSe flat islands<sup>[21]</sup> or the CdSe wetting layer<sup>[23]</sup> resulting from the S–K growth mode, as its energy is very close to what is expected.

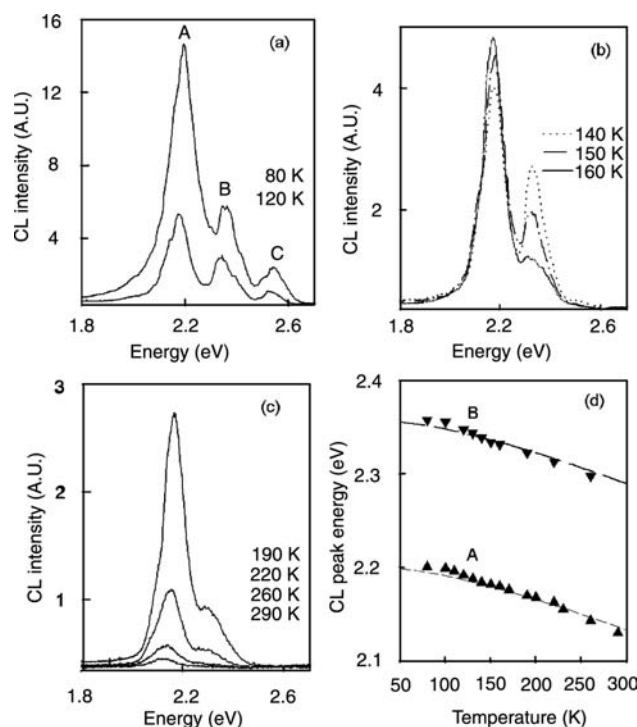


**Fig. 5** (A)–(C) display the spot mode temperature-dependent CL spectra of the CdSe/ZnSe QDs. The temperature at which the spectrum was obtained is indicated in ascending order, corresponding to the top-down sequence of peak B in the spectra presented. The electron beam voltage and beam current were 10 kV and 1 nA, respectively. (D) shows the energies of peaks A and B as a function of temperature. The dash lines are lines that have the same temperature dependence as CdSe bulk band gap. *Source:* From Ref.<sup>[22]</sup>.

The evolution of the CL intensity with temperature can be divided into three characteristic regions. Below 140 K and above 170 K, the three peaks, A, B, and C, decrease in intensity with temperature. Between 140 and 170 K, peak A increases while peaks B and C decrease with temperature. Such an evolution of CL peaks with temperature is evidently responsible for the unusually large red shift and narrowing of the broad CL peak measured from a large area. The CL energies of peaks A and B, as a function of temperature, are shown in Fig. 5D. The two energies now follow the bandgap of bulk CdSe material very well. Peak C becomes too weak to follow, except at very low temperatures, and its energy is not plotted.

The above results strongly suggest that thermally activated carrier transfer between QDs of different sizes is important at intermediate temperatures (140–170 K). Such a transfer results in an increase in the intensity of the lower-energy peaks at the expense of the higher-energy ones. With an increase in the temperature, more and more of the photo-generated carriers in the QDs would be thermally activated into the barriers or the wetting layer. Before they recombine, either radiatively or non-radiatively, some of these activated carriers would be recaptured. A transfer of carrier results when the capturing is by another nearby QD. The difference in activation rates between QDs of different sizes causes a net transfer of carriers from small to large dots and results in a concurrent decrease in the intensities of the higher-energy CL peaks and an increase in those of the lower-energy peaks.

To better understand the carrier dynamics in CdSe QDs, we consider the rate Eq. (4). We assume that the carrier capture rate is large and independent of QD size. Furthermore, as the CL spectra in Fig. 5 are dominated by two peaks, A and B, a bimodal distribution in QD size is assumed here. Including the weaker peak C only adds to the complexity of the equations but does not change the physical outcome of the model. The modified rate equations are then given by:

$$\frac{dn_s}{dt} = N_s G - n_s(R_s + R_{se}) + n_l R_{le} \quad (8)$$

$$\frac{dn_l}{dt} = N_l G - n_l(R_l + R_{le}) + n_s R_{se} \quad (9)$$

where  $G$  is the generation rate,  $N$  the area density of QDs,  $n$  the density of carriers in QDs,  $R$  the recombination rate of carriers in QDs, and  $R_e$  the thermal activation rate of carriers from the QDs. The subscripts  $s$  and  $l$  refer to the small and large QDs, respectively. If we further assume that the carrier recombination rate does not depend on the size of QDs, i.e.,

$R_s = R_l = R$ , then the steady-state carrier density in the QDs becomes:

$$n_{s(l)} = \frac{GN_{s(l)}}{R} \frac{[R + (1 + N_{l(s)}/N_{s(l)})R_{le(se)}]}{R + R_{se} + R_{le}} \quad (10)$$

Although  $R$  is somewhat temperature dependent, especially through the non-radiative recombination processes, the temperature dependence of the carrier density is dominated by that of the activation rates  $R_{se(le)}$ , which can be taken as proportional to  $\text{Exp}(-\Delta E_{s(l)}/kT)$ , where  $\Delta E_s$  and  $\Delta E_l$  are the activation energies of the small and large QDs. Because of the quantum-confinement effect, activation from a state of a small QD would be easier than from a corresponding state of a large QD, so we expect  $\Delta E_s < \Delta E_l$ . The difference  $\Delta E = \Delta E_l - \Delta E_s$  is responsible for the temperature evolution of the CL peak intensities shown in Fig. 5A to C.

At low temperatures, such that  $\Delta E \gg kT$ , the activation rates are small compared to the recombination rate. Moreover, there is negligible transfer of carriers between the QDs of different sizes, and recombination occurs independently, so we have:

$$n_{s(l)} = \frac{GN_{s(l)}}{R} \quad (11)$$

An increase in temperature simply increases the non-radiative recombination rate, which is responsible for the slight decrease in the CL intensities of all peaks [Fig. 5A]. At intermediate temperatures, such that  $\Delta E \approx kT$ , the difference in transfer rates is large and a net transfer of carriers from small QDs to large ones occurs. We have:

$$n_s = \frac{GN_s}{R} \left( 1 - \frac{R_{se}}{R + R_{se}} \right) \text{ and} \\ n_l = \frac{GN_l}{R} \left( 1 + \frac{N_s R_{se}/N_l}{R + R_{se}} \right) \quad (12)$$

which clearly shows that the steady-state carrier density in the large QDs increases at the expense of the small ones. Moreover, the effect of this transfer on the steady-state carrier density depends strongly on the ratio  $R/R_{se}$ . When the activation rate is comparable to the recombination rate, the densities are strongly affected, resulting in an increase in the CL intensity of the low energy peak [Fig. 5B]. In cases where  $R/R_{se}$  are small, the luminescence would be dominated by radiative recombination within the large QDs only. At high temperatures, such that  $\Delta E \ll kT$ , the difference in activation rates is small, there is no net transfer, and we have:

$$n_{s(l)} = \frac{GN_{s(l)}}{R} \quad (13)$$



again. Just as in the low-temperature case, the intensities of the CL peaks from both the large and small QDs decrease as nonradiative recombination becomes increasingly important [Fig 5C].

The above model is very simple but can give a clear picture about thermally activated transfer of excited carriers between quantum dots. In the model, we have neglected the difference in carrier capture rates between the QDs. It has been shown that the strain-induced potential barrier at the QD/host semiconductor interface would slow down the capture of carriers into QDs.<sup>[29]</sup> Larger potential barrier would be expected at the interface of larger QDs.<sup>[30]</sup> The temperature-dependent capture rate  $C_{s(l)}$  may be taken as proportional to  $\text{Exp}(-\Delta E_{bs(b)}/kT)$ , where  $\Delta E_{bs}$  and  $\Delta E_{bl}$  are the potential barriers at the interface of small and large QDs, respectively. Considering the capture rate difference, the first and the last terms on the right side of the rate Eq. (8) should be multiplied by  $C_s$  and  $C_l$ , respectively [reversed in Eq. (9)]. As this potential barrier is found to be very small as compared to the activation energy, it is unimportant at high temperatures. At low temperatures, carriers would have more chance to be captured into the small QDs. In this way, the capture difference is similar to the activation difference at high temperatures.

## CONCLUSION

The growth of self-assembled QDs through the Stranski–Krastanow (S–K) growth mode has been realized in many III/V, IV/IV, and II/VI semiconductor systems, provided there is a large lattice mismatch in the heterostructures. Because of the defect-free nature and the strong 3-D quantum confinement effect, these SAQDs have promising applications in future optoelectronic devices such as laser diodes and photodetectors. However, most of these devices are limited to low-temperature operation. For better performance of these QD-based devices, thermal effects on the emission and absorption processes in QDs must be well understood. Therefore temperature-dependent luminescence studies of QDs have been reported in many semiconductor systems, which, generally, show the following three characteristic features in the luminescence spectra: 1) the luminescence peak undergoes a red shift with temperature much faster than that of the bandgap of bulk material; 2) the peak line width shows an unusual decrease with temperature in an intermediate temperature region; and 3) luminescence of lower energies quenches much slower than that of higher energies, and in some cases, an enhancement in the luminescence of lower energies with temperature is observed. To account for these features, various

models, such as carrier tunneling between nearby dots, difference in thermal activation energy between dots of different sizes, thermally activated carrier transfer between dots of different size, and a competition and redistribution of recombination between the ground- and excited-electron and hole states, have been proposed to interpret the observed anomalous temperature-dependent luminescence. Through the temperature-dependent CL study of high-quality InP/InAlP QDs and the spot-mode CL study of CdSe/ZnSe QDs, it has been shown that only the model of thermally activated carrier transfer between dots of different size can serve to interpret the experimental results well. The results show that with an increase in temperature, carriers in small QDs will be thermally activated into wetting layer (or barriers) first. Before they recombined, either radiatively or non-radiatively in barriers, some of these activated carriers would be recaptured by QDs. As the thermal activation of carriers in large QDs is relatively weak, a net transfer of carriers from small QDs into large ones results, which is eventually responsible for the above three features. The thermal activation process, which results in the large red shift of emission peak, the quenching of emission, and the dominant emission from large QDs at high temperatures, is not desired for device operations. How to suppress these features is very important in future studies. Temperature insensitive emission was reported in InGaAs/GaAs QDs by inserting a thin less-strained  $\text{In}_{0.3}\text{Ga}_{0.7}\text{As}$  layer just between the QDs and the upper GaAs layers.<sup>[31]</sup> The results were thought to be due to the temperature-dependent strain effect. Temperature insensitive emission was also reported in strain-engineered InGaAs quantum wire heterostructures.<sup>[32]</sup> Using strain to engineer the QD heterostructures is a promising way to develop temperature-insensitive QD emission. Recently, we found that the quantum-well and quantum-dot coupled structures, when employing optimized designs, show quite stable emission energy and line width with an increase in temperature.<sup>[33]</sup> Developing novel quantum-well and quantum-dot coupled structures is another way to stabilize the QD emission. Results have shown that the uniformity in QD size and shape is the main reason for the anomalous temperature-dependent luminescence. Obtaining QDs with a high uniformity in size, shape, and spatial distribution is very important in future work. This might be done after the growth is well understood and controlled. Relative to the emission studies, thermal effects on the intersubband absorption of QDs are quite less investigated, although it might have a great influence on the performance of QD-based infrared photodetectors. Carrier transfer between QDs of different size, and the thermal population of carriers in different energy levels in QDs are believed to have some effect on the intersubband

absorption process. This needs to be further explored in future work.

## ACKNOWLEDGMENTS

We thank the National Science Foundation for support of this work under grant DMR-0080630 and Epichem for continued support of our research in MOCVD growth. Additionally, RDD gratefully acknowledges the support of the Judson S. Swearingen Regents Chair in Engineering.

## REFERENCES

- Asada, M.; Miyamoto, Y.; Suematsu, Y. Gain and the threshold of three-dimensional quantum box lasers. *IEEE J. Quantum Electron.* **1986**, *QE-22*, 1915–1921.
- Phillips, J.; Bhattacharya, P.; Kennerly, S.W.; Beekman, D.W.; Dutta, M. Self-assembled InAs–GaAs quantum dot intersubband detectors. *IEEE J. Quantum Electron.* **1999**, *QE-35*, 936–943.
- Haynes, J.R. Experimental proof of the existence of a new electronic complex in silicon. *Phys. Rev. Lett.* **1960**, *4*, 361–363.
- Logothetidis, S.; Cardona, M.; Lautenschlager, P.; Garriga, M. Temperature dependence of the dielectric function and the interband critical points of CdSe. *Phys. Rev., B* **1986**, *34*, 2458–2469.
- Bimberg, D.; Sondergeld, M.; Grobe, E. Thermal dissociation of excitons bounds to neutral acceptors in high-purity GaAs. *Phys. Rev., B* **1971**, *4*, 3451–3455.
- Lasher, G.; Stern, F. Spontaneous and stimulated recombination radiation in semiconductors. *Phys. Rev.* **1964**, *133*, A553–A563.
- Wojdak, M.; Wysmolek, A.; Pakula, K.; Baranowski, J.M. Emission due to exciton scattering by LO-phonons in GaN. *Phys. Status Solidi B* **1999**, *216*, 95–99.
- Zhang, X.B.; Gil, B. Electron phonon interaction in GaN and its low dimensional structures. In *Low Dimensional Nitride Semiconductors*; Gil, B., Ed.; Clarendon Press: Oxford, 2002; 257–286.
- Michler, P.; Forner, T.; Hofsäß, V.; Prins, F.; Zieger, K.; Scholz, F.; Hangleiter, A. Nonradiative recombination via strongly localized defects in quantum wells. *Phys. Rev., B* **1994**, *49*, 16,632–16,636.
- Bacher, G.; Hartmann, C.; Schweizer, H.; Held, T.; Mahler, G.; Nickel, H. Exciton dynamics in In<sub>x</sub>Ga<sub>1-x</sub>As/GaAs quantum-well heterostructures: competition between capture and thermal emission. *Phys. Rev., B* **1993**, *47*, 9545–9555.
- Gurioli, M.; Martinez-Pastor, J.; Colocci, M.; Deparis, C.; Chastaingt, B.; Massies, J. Thermal escape of carriers out of GaAs/Al<sub>x</sub>Ga<sub>1-x</sub>As quantum-well structures. *Phys. Rev., B* **1992**, *46*, 6922–6927.
- Lubyshev, D.I.; Gonzalez-Borrero, P.P.; Marega, E., Jr.; Petitprez, E.; La Scala, N., Jr.; Basmaji, P. Exciton localization and temperature stability in self-organized InAs quantum dots. *Appl. Phys. Lett.* **1996**, *68*, 205–207.
- Dai, Y.; Fan, J.C.; Chen, Y.F.; Lin, R.M.; Lee, S.C.; Lin, H.H. Temperature dependence of photoluminescence spectra in InAs/GaAs quantum dot superlattices with large thicknesses. *J. Appl. Phys.* **1997**, *82*, 4489–4492.
- Lee, U.H.; Lee, D.; Lee, H.G.; Noh, S.K.; Leem, J.Y.; Lee, H.J. Visible photoluminescence from self-assembled InAs quantum dots embedded in AlAs cladding layer. *Appl. Phys. Lett.* **1999**, *74*, 1597–1599.
- Brusaferri, L.; Sanguinetti, S.; Grilli, E.; Guzzi, M.; Bignazzi, A.; Bogani, F.; Carraresi, L.; Colocci, M.; Bosacchi, A.; Frigeri, P.; Franchi, S. Thermally activated carrier transfer and luminescence line shape in self-organized InAs quantum dots. *Appl. Phys. Lett.* **1996**, *69*, 3354–3356.
- Polimeni, A.; Patane, A.; Henini, M.; Eaves, L.; Main, P.C. Temperature dependence of the optical properties of InAs/AlGaAs self-organized quantum dots. *Phys. Rev., B* **1999**, *59*, 5064–5068.
- Sanguinetti, S.; Henini, M.; Alessi, M.G.; Alessi, Capizzi, M.; Frigeri, P.; Franchi, S. Carrier thermal escape and retrapping in self-assembled quantum dots. *Phys. Rev., B* **1999**, *60*, 8276–8283.
- Lee, H.; Lee, W.; Sercel, P. Temperature and excitation dependence of photoluminescence line shape in InAs/GaAs quantum-dot structures. *Phys. Rev., B* **1997**, *55*, 9757–9762.
- Wu, Y.H.; Arai, K.; Yao, T. Temperature dependence of the photoluminescence of ZnSe/ZnS quantum-dot structures. *Phys. Rev., B* **1996**, *53*, R10485–R10488.
- Karczewski, G.; Mackowski, S.; Kutrowski, M.; Wojtowicz, T.; Kossut, J. Photoluminescence study of CdTe/ZnTe self-assembled quantum dots. *Appl. Phys. Lett.* **1999**, *74*, 3011–3013.
- Strassburg, M.; Deniozou, Th.; Hoffmann, A.; Heitz, R.; Pohl, U.W.; Bimberg, D.; Litvinov, D.; Rosenauer, A.; Gerthsen, D.; Schwedhelm, S.; Lischka, K.; Schikora, D. Coexistence of planar and three-dimensional quantum dots in CdSe/ZnSe structures. *Appl. Phys. Lett.* **2000**, *76*, 685–687.
- Zhang, X.B.; Ha, K.L.; Hark, S.K. Evidence of thermally activated transfer of excited carriers between CdSe/ZnSe quantum dots. *J. Electron. Mater.* **2001**, *30*, pp. 10, 1332.
- Xin, S.H.; Wang, P.D.; Yin, A.; Kim, C.; Dobrowolska, M.; Merz, J.L.; Furdyna, J.K. Formation of self-assembling CdSe quantum dots on ZnSe by molecular beam epitaxy. *Appl. Phys. Lett.* **1996**, *69*, 3884–3886.
- Zhang, X.B.; Heller, R.D.; Noh, M.S.; Dupuis, R.D.; Walter, G.; Holonyak, N., Jr. Effect of Si-Delta-doping on the luminescence properties of InP/InAlP quantum dots. *Appl. Phys. Lett.* **2003**, *82*, 4343–4345.
- Matsuda, K.; Ikeda, K.; Saiki, T.; Tsuchiya, H.; Saito, H.; Nishi, K. Homogeneous linewidth broadening in a In<sub>0.5</sub>Ga<sub>0.5</sub>As/GaAs single quantum dot at room temperature investigated using a highly sensitive near-field scanning optical microscope. *Phys. Rev., B* **2001**, *63*, R121304–R121307.

26. Fafard, S.; Raymond, S.; Charbonneau, S.; Wang, G.; Leon, R.; Leonard, D.; Merz, J.L.; Petroff, P.M.; Bowers, J.E. Temperature effects on the radiative recombination in self-assembled quantum dots. *Surf. Sci.* **1996**, *361/362*, 778–782.
27. Zhang, X.B.; Heller, R.D.; Noh, M.S.; Dupuis, R.D. unpublished.
28. Yacobi, B.G.; Holt, D.B. *Cathodoluminescence Microscopy of Inorganic Solids*; Plenum: New York, 1990.
29. Marcinkevicius, S.; Leon, R. Photoexcited carrier transfer in InGaAs quantum dot structures: Dependence on the dot density. *Appl. Phys. Lett.* **2000**, *76*, 2406–2408.
30. Chen, Y.; Washburn, J. Structural transition in large-lattice-mismatch heteroepitaxy. *Phys. Rev. Lett.* **1996**, *77*, 4046–4049.
31. Mukai, K.; Sugawara, M. Suppression of temperature sensitivity of interband emission energy in 1.3- $\mu\text{m}$ -region by an InGaAs overgrowth on self-assembled InGaAs/GaAs quantum dots. *Appl. Phys. Lett.* **1999**, *74*, 3963–3965.
32. Wohlert, D.E.; Chou, S.T.; Chen, A.C.; Cheng, K.Y.; Hsieh, K.C. Observation of temperature-insensitive emission wavelength in GaInAs strained multiple-quantum-wire heterostructures. *Appl. Phys. Lett.* **1996**, *68*, 2386–2388.
33. Zhang, X.B.; Heller, R.D.; Noh, M.S.; Dupuis, R.D.; Walter, G.; Holonyak, N., Jr. Temperature dependent cathodoluminescence study of InP/InAlGaP quantum dots with a coupled InGaP quantum well. *in press*.

# Thermodynamics at the Meso- and Nanoscale

Mikhail A. Anisimov

*Department of Chemical Engineering and Institute for Physical Science and Technology,  
University of Maryland, College Park, Maryland, U.S.A.*

## INTRODUCTION

Thermodynamics is a keystone in engineering and science, bridging the gap between fundamentals and applications. However, when one compares the content of traditional courses in thermodynamics with what engineers often do in practice, one notices a gap and the gap is widening every year. New emerging technologies and products deal with subjects such as biomembrane and gene engineering, microreactor chemistry and microcapsule drug delivery, microfluids and porous media, nanoparticles and nanostructures, supercritical-fluid extraction and artificial organs. Engineers often must design processes for systems where classical thermodynamics (in particular, the Second Law) becomes insufficient, as in the case of strongly fluctuating and nanosize systems, or dissipative systems under conditions far away from equilibrium. Mesoscopic thermodynamics can be defined as a semiphenomenological approach to phenomena in systems where a length—intermediate between the atomistic scale and the macroscopic scale—emerges and where such a length explicitly affects the thermodynamic properties and phase behavior. Finite-size and fluctuation thermodynamics, critical phenomena in fluids and solids as well as in soft-matter materials (such as complex fluids), wetting and interfacial phenomena, self-organized criticality and dissipative structures, thermodynamics of pattern formation and fractals are examples of topics addressed in mesoscopic thermodynamics (equilibrium and non-equilibrium). While conventional methods of statistical mechanics remain the fundamental background of mesoscopic thermodynamics, coarse-grained approaches emphasizing universality rather than microscopic details, such as the Landau–Ginzburg local free-energy functional, can be successfully applied to describe what seem to be very different phenomena on mesoscales: from critical fluctuations to near-surface and interfacial density profiles, from micelles and microemulsions to porous media, from thin layers to nanoparticles. For this purpose, one can utilize a number of powerful theoretical concepts, such as renormalization-group theory, finite-size scaling, percolation theory, and coupling between

different order parameters so as to predict the properties at meso- and nanoscales.

## WHAT IS “MESOSCOPIC THERMODYNAMICS”?

Is traditional (macroscale) thermodynamics sufficient to deal with systems and processes mentioned above? Can one apply without restriction the laws and equations of classical thermodynamics to calculate chemical reaction equilibrium and design a microreactor with reaction space of only 100 nm thick, or describe the solubility of a protein molecule in a cell and its transport through a biomembrane? What is the definition of a phase in such systems? All biological cells are natural microreactors.<sup>[1]</sup> Can we still use the concepts of chemical potential, osmotic pressure, surface tension, etc. for such objects? A microchip can contain only hundreds of atoms. What is the limiting size for which thermodynamics is still applicable? In a microporous medium, not only does the surface energy dominate over the bulk energy, but also the surface itself can be poorly defined. Is still there room for thermodynamics there, beyond trivial mass and energy balances?

Classical thermodynamics is essentially macroscopic. To define thermodynamic states and thermodynamic properties, one needs systems with a huge number of individual particles, such as atoms or molecules. Statistical mechanics defines thermodynamic states and properties only in the so-called “thermodynamic limit”: the volume ( $V$ ) and the number of particles ( $N$ ) must tend to infinity, while the density of the substance,  $\rho = N/V$ , remains finite. Even 1 mm<sup>3</sup> of liquid water (1 mg) contains  $3 \times 10^{19}$  molecules. It is quite sufficient to regard such a small droplet of water as a macroscopic body and neglect surface effects in considering its bulk properties. If the characteristic size of the object is  $L$ , the surface energy is proportional to  $L^2$ , while the bulk energy is proportional to  $L^3$ . This is why one can measure the temperature of steam condensation and the vapor pressure in a small tube and use the data in design of an upscale distillation column that is 100 m high. Macroscopic thermodynamics eliminates

the size of the system by reducing the extensive thermodynamic properties, which depend on size, by the number of particles, number of kilograms, or by volume. Equations of thermodynamics usually operate with intensive properties, such as density, concentration, molar or specific volume, etc. which do not depend on size. The actual length scale is restored only in the stage of engineering design.

*Mesoscopic and nanoscale thermodynamics* is designed to fill the gap between the macroscopic and truly microscopic (atomistic) worlds. This field of science (“mesothermodynamics”) can be defined as a semiphenomenological approach to systems and phenomena in which a length—intermediate between the atomistic scale and the macroscopic scale—emerges and where such a length explicitly affects the thermodynamic properties. This science is still thermodynamics as its objects are still governed by statistical physics but, in contrast to “macrothermodynamics,” it explicitly contains a mesoscopic length scale associated with the structure of materials. It also includes thermal fluctuations, which emerge in the apparent violation of the Second Law. Typical models of mesothermodynamics are coarse-grained models that do not have to account for every detail on the atomic scale.<sup>[2]</sup> Instead, such models emphasize universality. For example, the behavior of many polymer solutions is often determined not by the particular structure of the monomer units, but by the fact that the polymer molecule is a long, flexible curve in three-dimensional space that cannot be crossed by other polymer molecules.

### “THINNER THAN A HAIR”

One can consider a length scale less than  $100\ \mu\text{m}$  as *mesoscopic*.  $100\ \mu\text{m}$  is a thickness of human hair (Fig. 1), and usually a microscope, optical or electronic, is needed to see objects smaller than that. Below  $1\ \mu\text{m}$ , one enters a *submicron* world. Between  $1$  and  $100\ \text{nm}$ , a size can be called *nanoscopic*. Any classification is conditional and approximate: sometimes “thinner-than-a-hair” objects can be treated macroscopically and some properties of larger objects may require a mesoscopic approach. There are three categories of popular objects in mesothermodynamics:

1. Soft condensed-matter materials such as complex fluids (polymer solutions, polymer melts, microemulsions, foams, gels, colloidal dispersions, liquid crystals).<sup>[2–7]</sup> Most food and cosmetics is soft matter. Humans (like other living organisms) are “soft machines.” The common feature of all soft condensed-matter systems is the existence of a (or more than one) *mesoscopic length scale*.

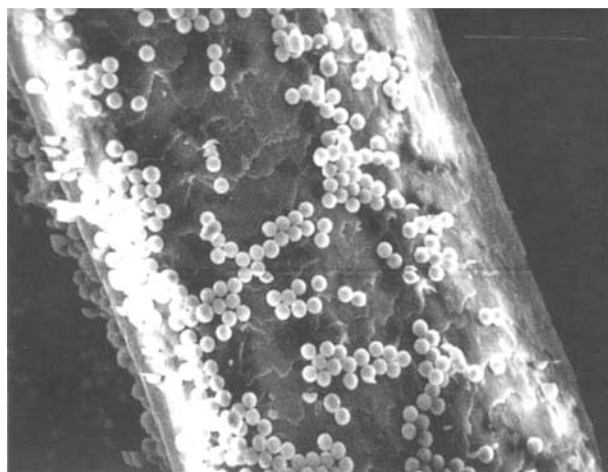


**Fig. 1** Scanning electron microscope (SEM) image of  $3.4\text{-}\mu\text{m}$  polystyrene particles on human hair. *Source:* Courtesy of Spherotech, Inc.

2. Systems that are essentially *finite* (practically speaking, of submicron- or nanosize) at least in one dimension.<sup>[8–10]</sup> Examples include nanoparticles (if the particle is considered as a separate system), pores, films and layers, strings and threads. Sometimes such systems can be truly microscopic (atomistic length scale) in a certain dimension and they can thus be treated as two- or even one-dimensional.
3. Systems in a *near-critical state* (i.e., in the vicinity of critical or second-order phase-transition points).<sup>[11–13]</sup> Such systems are mesoscopically inhomogeneous, i.e., like complex fluids, they possess a mesoscopic length scale, known as the “correlation length,” diverging at the critical point. As this correlation length is associated with spontaneous *thermal fluctuations*, the inhomogeneities are not real particles; they are loose clusters, statistically appearing and disappearing, and so have a finite (but diverging at the critical point) lifetime. As fluctuations exist in violation of the Second Law of thermodynamics, the near-critical state is close to instability and thus very fragile. Spectacular effects associated with diverging critical fluctuations are called “critical phenomena.”

The approach to introduce a mesoscale in thermodynamic properties goes back to van der Waals,<sup>[14]</sup> and is sometimes called “quasi-thermodynamics,” “local thermodynamics,” or “point-thermodynamics.”<sup>[15]</sup> Representation of a microheterogeneous system as an “ensemble” of small open systems was introduced and elaborated by Hill.<sup>[16]</sup> Many ideas and concepts of mesoscopic thermodynamics were developed and explored in colloid and interface science long ago.<sup>[17,18]</sup> However,

only recently has a high degree of *universality* (and thus “simplicity”), originating from the very existence of the mesoscopic length scale, been recognized. Furthermore, such powerful theoretical approaches as finite-size scaling, renormalization-group theory, percolation, and self-organized criticality have now become fully applicable to the variety of phenomena at mesoscales.

## ROLE OF FLUCTUATIONS

An important feature of a mesoscopic object that is commonly neglected in traditional thermodynamics is the effect of thermal fluctuations. Thermodynamics is based on two fundamental laws, the First Law and the Second Law. The First Law is the law of conservation of energy; it is exact and can be equally applied to any system regardless of size. The Second Law is a purely statistical law. It states that the entropy of an isolated system never decreases. The entropy always increases in irreversible processes and reaches its maximum in equilibrium. The asymmetric character of entropy is directly associated with the asymmetric nature of time: the past and the future of an isolated system are different if the entropy values are different. In statistical physics (see, e.g., Refs.<sup>[19,20]</sup>), entropy is defined as

$$S = k_B \ln W \quad (1)$$

where  $k_B = 1.381 \times 10^{-23}$  J/K is Boltzmann’s constant,  $W$  is the statistical weight—the number of possible microscopic states that realize the given macroscopic state (given volume, temperature, concentration, etc.). The larger the number of possible microscopic states—the larger the disorder—the higher the entropy. However, in any thermal (containing a large number of particles) system, the chaotic motion of particles leads to spontaneous deviations of locally defined properties (at any point of the system) from their average equilibrium values. Such deviations are known as *fluctuations*. As the fluctuations mean spontaneous deviations from equilibrium, they lead to local decrease of the entropy and thus exist in apparent violation of the Second Law of thermodynamics. A fluctuation will reduce the total entropy of the system, hence the probability,  $w$ , of fluctuation is

$$w \propto e^{\Delta S/k_B} \quad (2)$$

The mean square fluctuations of a density-like variable (“order parameter”)  $\varphi$  at temperature  $T$  are proportional to a generalized susceptibility  $\chi$ :

$$\langle(\Delta\varphi)^2\rangle = \frac{k_B T}{V} \chi \quad (3)$$

The smaller the volume,  $V$ , under consideration—the larger the fluctuations. In two-dimensional (planar)

systems, fluctuations are stronger. In one-dimensional (linear) systems, fluctuations are so strong that they destroy any long-range order.<sup>[19]</sup> The generalized susceptibility  $\chi$  is the inverse second derivative of the free energy with respect to  $\varphi$ . Depending on the system, it can be the isothermal compressibility (fluids), osmotic compressibility (fluid mixtures), magnetic or electric susceptibility, etc. while the order parameter will be associated with the density, concentration, magnetization, or polarization, respectively, or with another “density-like” variable. For example, the mean-square fluctuations of density,  $\rho$ , is given by

$$\langle(\Delta\rho)^2\rangle = \frac{k_B T}{V} \rho \left( \frac{\partial \rho}{\partial P} \right)_T \quad (4)$$

( $P$  denotes the pressure).

Another example is a fluctuation deviation from verticality in a micropendulum with a mass  $m = V\rho$ . The thermal collisions of the molecules in the medium with the pendulum cause random fluctuations in the angle  $\theta$  of suspension with length  $l$  (the equilibrium value of  $\theta$  is zero).<sup>[19]</sup>

$$\langle\theta^2\rangle = \frac{k_B T}{V\rho g l} \quad (5)$$

with  $g$  being the free-fall acceleration. The mean square fluctuation in the bending angle of the suspension thread is

$$\langle\gamma^2\rangle = \frac{l k_B T}{K} \quad (6)$$

with  $K$  being proportional to the bending elastic constant. In the above two examples, the susceptibilities are  $\chi = 1/(\rho g l)$  and  $\chi = (lV)/K$ , respectively.

## BUILDING A NANOPARTICLE

One of the ways to create a nanosize particle is to use amphiphilic molecules (surfactant) dissolved in water.<sup>[21]</sup> Two simple arrangements allow the tails to be away from the water: spherical *micelles* and a bilayer (Fig. 2). Biological membranes are double layers. A closed surface of a bilayer with the hydrophobic tails screened by the hydrophilic heads is known as a *vesicle*.

Suppose that we are interested in building a mono-disperse population of nanoparticles with a stable aggregation number  $m$ . The equilibrium fraction,  $\phi$ , of amphiphilic molecules in micelles or vesicles<sup>[2,18,22]</sup>

$$\phi = m[(x - \phi)f]^m \quad (7)$$

$$f = \exp\left(\frac{\mu_s(m=1) - \mu_s(m)}{k_B T}\right) \quad (8)$$



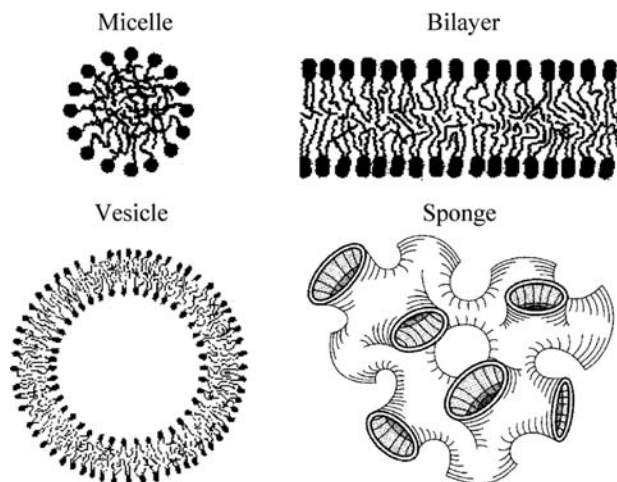


**Fig. 2** Possible arrangements of amphiphilic molecules in aqueous solutions.

(with  $x$  being the total concentration of amphiphilic molecules) assumes that all micelles (or vesicles) have the same (optimal) aggregation number. The fluctuation deviation of the surfactant chemical potential,  $\mu_s$ , from its optimal value may be written as

$$\Delta\mu_s = \mu_s(n) - \mu_s(m) = \frac{1}{2}K(n - m)^2 \quad (9)$$

The coefficient  $K$  is a response function ( $\chi = 1/\rho K$  serves as the susceptibility, similar to the compressibility or elasticity). For large  $m$ , Eq. (9) leads to a Gaussian mean-square fluctuation:

$$\langle (n - m)^2 \rangle = \frac{k_B T}{V} \chi = \frac{k_B T}{mK} \quad (10)$$

The larger the aggregation number—the sharper the micellization and more stable the aggregate. Spontaneously formed nanosize spherical vesicles [like those formed from some two-tailed amphiphilic molecules such as didodecyldimethylammonium bromide (DDAB)]<sup>[23]</sup> are usually more mono-disperse than spherical micelles, because the vesicle aggregation number is larger and the bilayer is less fragile (due to the two-tail structure,  $K$  is larger). At larger concentration of surfactant, aggregates of various shapes can be formed, such as worm-like micelles, onion-like bilayers (Fig. 3), or a bicontinuous “sponge” phase (Fig. 2). In such objects, fluctuations of the shape become important.

## CRITICAL PHENOMENA

Near a critical point of any kind (in fluids and fluid mixtures, near the Curie point in ferromagnetics, near the superfluid transition in liquid helium, near the

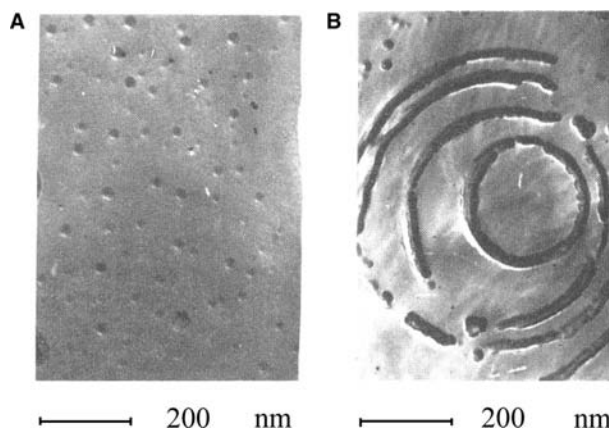


**Fig. 3** SEM micrographs of replicas from DDAB aqueous solutions: (A)  $5 \times 10^{-5}$  mol/L; (B)  $8 \times 10^{-4}$  mol/L. Source: From Ref.<sup>[23]</sup>.

second-order phase transitions in liquid and solid crystals), the fluctuations of the appropriate order parameter become so large and they live so long that they fully determine the macroscopic behavior, both of equilibrium and non-equilibrium properties. In other words, the macroscopic properties can be explained and calculated through the fluctuational mesoscopic length-scale. This is why the thermodynamics of critical phenomena is essentially mesoscopic.

Experimentally, it has been well established that asymptotically close to the critical point, all physical properties obey simple power laws (known as “scaling laws”)<sup>[11–13]</sup> (Fig. 4). The universal powers in these laws are called *critical exponents*. In all fluids and

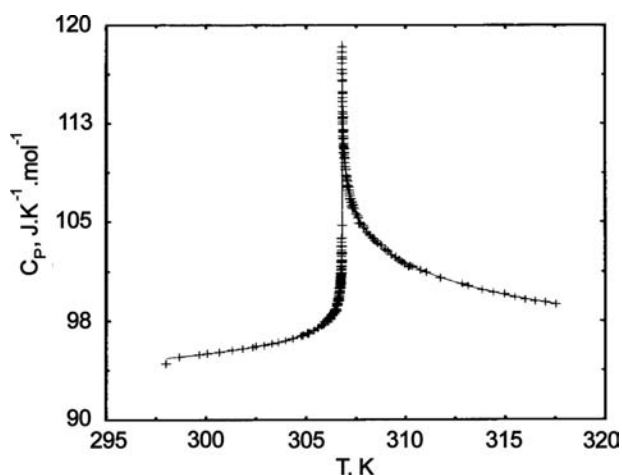


**Fig. 4** Heat capacity at constant pressure,  $C_p$ , near the lower critical consolute point of 2,6-lutidine aqueous solution at the critical composition. (From Ref.<sup>[29]</sup>.) The solid curve corresponds to Eq. (13) with  $\alpha = 0.11$ . Note that in liquid mixtures,  $C_p$  has the same anomaly as  $C_v$  in one-component fluids. (From Ref.<sup>[13]</sup>.)

fluid mixtures, the critical exponents for analogous properties are the same numbers. The theory that explains the power laws is called *scaling theory*. The theory that calculates the universal critical exponents is known as *renormalization-group theory*.<sup>[12]</sup> The physical principle that governs the nature of critical phenomena is called the *critical point universality*. The physical background for the scaling and renormalization-group theory is the divergence of a mesoscopic characteristic length-scale—the size of fluctuations of the order parameter. Accurate scattering experiments have shown that the correlation length of fluctuations diverges at the critical point of a fluid as

$$\xi = \xi_0 \varepsilon^{-\nu} \text{ with } \nu = 0.63 \pm 0.01 \quad (11)$$

Here  $\xi_0$  is the range of intermolecular interactions and  $\varepsilon = (T - T_c)/T_c$ , the temperature distance to the critical temperature,  $T_c$ .

Let us assume that the near-critical state is a “gas” of fluctuational clusters with a mesoscopic size  $\xi$ . Then the fluctuational part of the Helmholtz energy,  $\Delta A$ , and the isochoric heat capacity per unit volume,  $\rho C_v = NC_v/V$ , read:<sup>[13]</sup>

$$\begin{aligned} \Delta A &\sim Nk_B T_c \sim \frac{Vk_B T_c}{\xi^3}, \quad \rho C_v \\ &= -T \left( \frac{\partial^2 (A/V)}{\partial T^2} \right)_V \end{aligned} \quad (12)$$

Along the critical isochore,  $\rho = \rho_c$ :

$$\rho C_v = A_0 \varepsilon^{-\alpha} \sim \frac{\varepsilon^{3\nu-2}}{\xi_0^3} \quad (13)$$

We conclude that the divergence of the correlation length is responsible for the divergence of the heat capacity, and that the critical amplitude of the heat capacity,  $A_0$ , is related to the amplitude of the correlation length (Fig. 4). Note that in the van der Waals theory, the isochoric heat capacity does not diverge at the critical point. The relations between the universal critical exponents for the space of any dimensionality,  $d$ ,

$$\alpha = 2 - d\nu \quad (14)$$

and between the system-dependent amplitudes

$$\rho_c A_0 \xi_0^d = \text{universal constant} \quad (15)$$

are known as *universal scaling relations*.

Another example of a property that can be estimated through the mesoscopic size of fluctuations scaling is the surface tension. As the surface tension vanishes at the critical point (Fig. 5), the interface

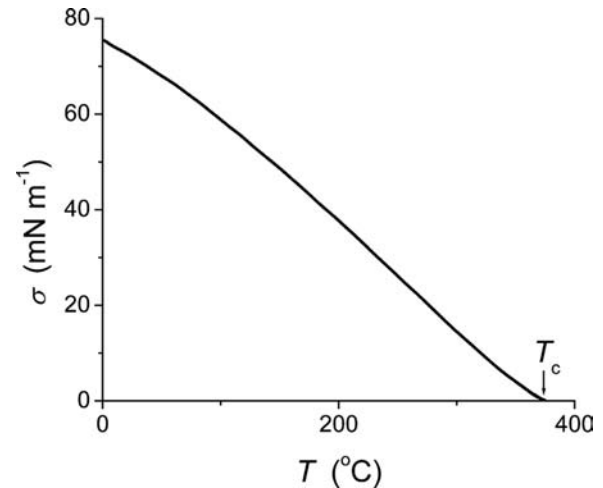


Fig. 5 Vapor–liquid surface tension of water.

becomes smooth and eventually disappears. The surface tension can be estimated as a product of the density of the Helmholtz energy

$$\frac{\Delta A}{V} \propto A_0 |\varepsilon|^{2-\alpha} \quad (16)$$

and the thickness of the interface, assumed to be equal to the correlation length,  $\xi = \xi_0 |\varepsilon|^{-\nu}$ .<sup>[13,15]</sup> Therefore taking into account Eqs. (14) and (15), we obtain

$$\sigma = \sigma_0 |\varepsilon|^{\vartheta} \propto \frac{\Delta A}{V} \xi \propto A_0 \xi_0 |\varepsilon|^{(d-1)\nu} \propto \frac{1}{\xi_0^2} |\varepsilon|^{\vartheta} \quad (17)$$

$$\vartheta = (d-1)\nu = 1.26 (\text{for } d=3) \quad (18)$$

$$\frac{\sigma_0 \xi_0^{d-1}}{k_B T_c} = \text{universal constant} \quad (19)$$

Note that in the van der Waals theory, that neglects fluctuations  $\vartheta = 3/2$ . The relations between other thermodynamic properties and the diverging correlation length can be obtained in a similar fashion.

## LANDAU–GINZBURG MESOSCOPIC FUNCTIONAL

The simplest way to introduce fluctuations or any other smooth heterogeneities in the mesoscopic thermodynamics is to consider a local (coordinate-dependent) density of an appropriate thermodynamic potential.<sup>[19]</sup> To be specific, consider the local density of the fluctuational part of the Helmholtz free energy

of a fluid with the local order parameter

$$\varphi(\vec{r}) = \frac{\rho(\vec{r}) - \rho_c}{\rho_c} \quad (20)$$

which is now spatially dependent on the position  $\vec{r}$ . In fluid binary mixtures, the order parameter will be associated with the partial density (molarity).<sup>[24]</sup> The part of the free-energy density, associated with the order parameter, thus will be defined as

$$\Delta(A/V) = \frac{k_B T}{v_0} \times \int \left[ \frac{1}{2} X[\varphi(\vec{r})]^2 + \frac{1}{2} c_0 (\nabla \varphi)^2 \right] d\vec{r} \quad (21)$$

where  $X$  is related to the inverse susceptibility as

$$\chi^{-1} = X + 2\varphi \frac{\partial X}{\partial \varphi} + \frac{1}{2} \frac{\partial^2 X}{\partial \varphi^2} \varphi^2$$

(inversely proportional to the second derivative of the free energy with respect to the order parameter),  $c_0$  is a constant associated with the range of intermolecular interactions, and  $v_0$  is the molecular volume. The expression

$$f[\varphi(\vec{r})] = \frac{1}{2} X[\varphi(\vec{r})]^2 + \frac{1}{2} c_0 (\nabla \varphi)^2$$

is known as *Landau–Ginzburg functional*. As the energy is scalar, the first non-vanishing gradient term is quadratic. Equation (21) simply states that not only a deviation from the equilibrium value of the order parameter will increase the free energy, but any fluctuational inhomogeneity represented by gradients of the order parameter will also increase the free energy and, thus, will not be thermodynamically favorable.

In mean-field (or van der Waals) approximation (valid for long-range interactions), the susceptibility is given by

$$\chi^{-1} = a_0 \varepsilon + 3u_0 \varphi^2 \quad (22)$$

and the correlation length reads

$$\xi = \sqrt{\frac{c_0}{a_0 \varepsilon}} = \xi_0 \varepsilon^{-1/2} \quad (23)$$

The constants  $a_0$  and  $u_0$  are order of unity. Note that the mean-field result ( $\nu = 0.5$ ) is in disagreement with the experimental fact ( $\nu = 0.63$ ) that is well described by the scaling theory.

## APPLICATIONS OF LANDAU–GINZBURG FUNCTIONAL

The Landau–Ginzburg functional can be used for description of a variety of phenomena on mesoscale such as interfacial phenomena, wetting transitions, near-surface density profile and adsorption, formation of microemulsions and liquid crystalline phases, spinodal decomposition, phase separation in polymer solutions and polymer blends, etc. This approach is more accurate when the local order parameter is not too much different from its macroscopic equilibrium value (smooth heterogeneities). As an example, consider the calculation of a smooth density profile in the fluid–fluid interface with the characteristic thickness  $\xi$ . The interfacial tension

$$\begin{aligned} \sigma &= \frac{d[\Delta(A/V)]}{dx dy} \\ &= \frac{k_B T}{v_0} \int \left[ \chi^{-1} \varphi^2 + \frac{1}{2} c_0 \left( \frac{d\varphi}{dz} \right)^2 \right] dz \\ &= \frac{k_B T}{v_0} \int_{-\infty}^{+\infty} \left[ c_0 \left( \frac{d\varphi}{dz} \right)^2 \right] dz \approx \frac{k_B T}{v_0} \int_{-\xi}^{+\xi} \left[ c_0 \left( \frac{\varphi_0}{\xi} \right)^2 \right] dz \\ &= 2 \frac{k_B T}{v_0} c_0 \frac{\varphi_0^2}{\xi} \end{aligned} \quad (24)$$

In this expression,  $\varphi_0$  is the equilibrium value of the order parameter in the bulk (the difference of densities or concentrations in the coexisting phases). Because of the conservation of mass through the interfacial profile:

$$\chi^{-1} \varphi^2 = \frac{1}{2} c_0 \left( \frac{d\varphi}{dz} \right)^2 \quad (25)$$

Thus in the Landau–Ginzburg functional approximation, also known as the Ornstein–Zernike approximation,

$$\chi \propto \xi^2 \text{ and } \varphi_0^2 \propto \frac{1}{\xi} \quad (26)$$

and we obtain the well-known result for the surface tension in the scaling theory [Eqs. (18) and (19)], which is valid even beyond this approximation.<sup>[15]</sup>

$$\sigma = \sigma_0 t^{\mathfrak{g}} \text{ with } \mathfrak{g} = 2\nu \text{ and } \sigma_0 \propto \frac{1}{\xi_0^2} \quad (27)$$

In the van der Waals approximation, which neglects effects of fluctuations on the macroscopic thermodynamic properties, the susceptibility is described by

Eq. (22). Hence in this approximation

$$\chi \propto \xi^2 \propto \varepsilon^{-1}, \quad \varphi_0 \propto \frac{1}{\xi} \propto \varepsilon^{1/2}, \quad \text{and } \sigma \propto \varepsilon^{3/2} \quad (28)$$

Nevertheless, the interfacial density profile obtained in the van der Waals theory,

$$\varphi(z) = \varphi_0 \tanh\left(\varphi_0 \sqrt{\frac{u_0}{2c_0}} z\right) = \varphi_0 \tanh(z/2\xi), \quad (29)$$

does not specify any particular temperature dependence and thus can serve as a reasonable approximation to describe the actual density profile (which is calculated properly only in the renormalization-group theory: see Fig. 6).

Another example of an application of the Landau–Ginzburg functional is the description of modulated and microheterogeneous phases.<sup>[25,26]</sup> If the coefficient  $c_0$  in the functional changes its sign, the next order term  $d_0(d^2\varphi/dz^2)^2$  must be added and a *modulated phase* (in  $z$  direction) with the wave number of modulation  $q_0 = (-c_0/d_0)^{1/2}$  may become stable. The inverse wave number of modulation serves as a new characteristic mesoscopic length in the system. The point where both  $c_0$  and  $\chi^{-1}$  vanish is known as the Lifshitz point (LP). If the density is “modulated” isotropically in all directions (like in the “sponge”

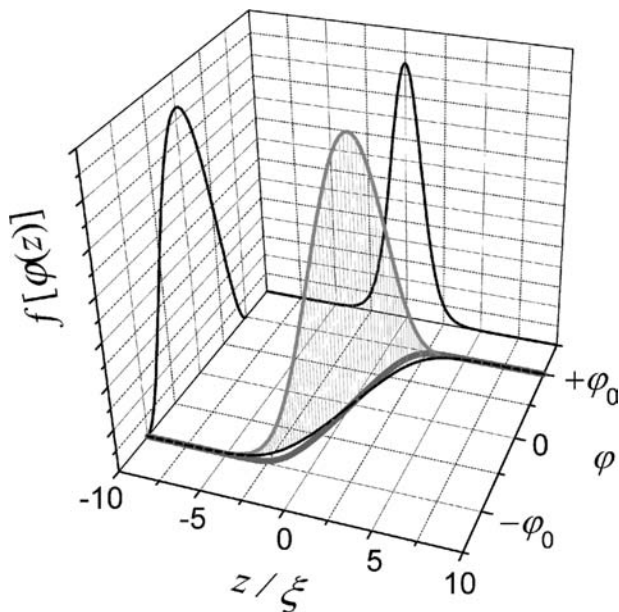


**Fig. 6** Landau–Ginzburg functional and order-parameter profile within the interface in van der Waals approximation. The thicker curve shows the profile calculated in renormalization-group theory. The correction to the classical result given by Eq. (29) reads:  $[1 + 1/2 \operatorname{sech}^2(z/2\xi)]^{-1/2}$ . Source: From Ref.<sup>[15]</sup>.

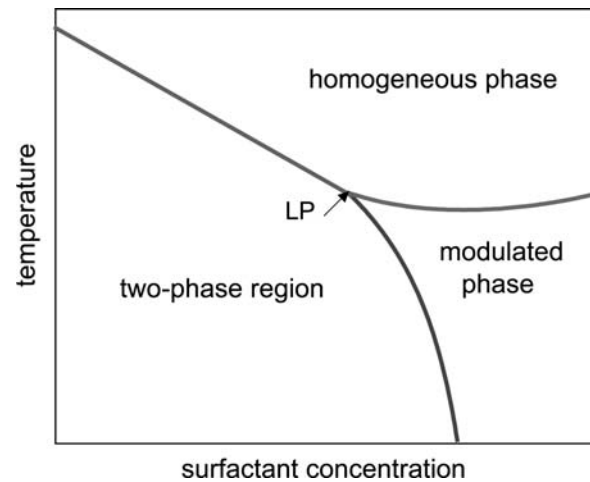


**Fig. 7** A schematic phase diagram of surfactant solution forming a modulated phase. The Lifshitz point (LP) separates the critical line of liquid–liquid phase separation (on the left) and the first-order phase separation (lower curve on the right). The transition between the homogeneous disordered phase and the modulated phase is second order. Source: From Ref.<sup>[27]</sup>.

phase of microemulsions), this point is known as the isotropic Lifshitz point<sup>[26,27]</sup> (Fig. 7).

## MESOSCALE SUSCEPTIBILITY

Mesoscale heterogeneities can be probed by the intensity of electromagnetic or neutron scattering at a selected wave number  $q = [(4\pi n)/\lambda] \sin(\theta/2)$  (where  $\lambda$  is the wave length of radiation,  $n$  is the refractive index, and  $\theta$  is the angle of scattering). With a static light-scattering experiment, one cannot probe inhomogeneities smaller than 30 nm, whereas dynamic light scattering enables one to measure the particle size as small as 3 nm through the diffusion coefficient of the Brownian motion. Neutron scattering can probe scales down to atomistic size.

The wave-number-dependent mesoscale susceptibility,  $\chi_q$ , is the correlation function in momentum space that can be obtained via the Fourier transformation of the coordinate-dependent correlation function. In the Ornstein–Zernike approximation

$$\chi_q = \int C(r) e^{-iqr} dV = \frac{\langle (\Delta\varphi)_q^2 \rangle V}{k_B T} = \frac{\chi}{1 + q^2 \xi^2} \quad (30)$$

In the limit of zero wave number and/or when the length  $\xi$  is small ( $q\xi \ll 1$ ), this formula becomes the usual thermodynamic expression (3) for the mean-square fluctuations. The susceptibility becomes spatially dependent and can diverge only in the zero wave-number limit (thermodynamic limit). It means that, at small scales,

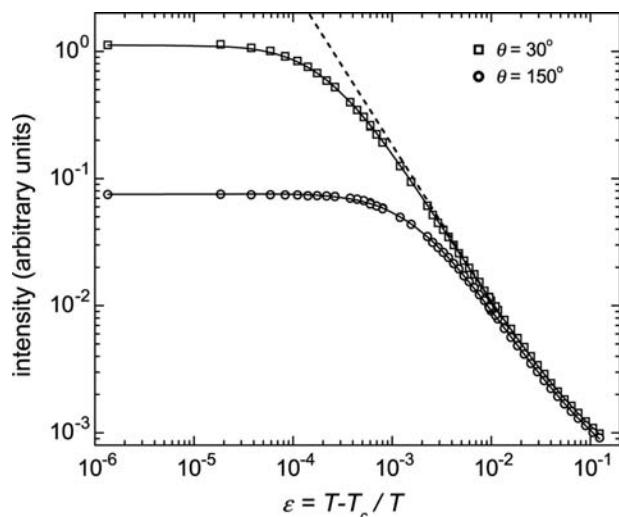


**Fig. 8** Mesoscale osmotic compressibility (intensity of light scattering) measured at two different wave numbers in polystyrene ( $M = 2 \times 10^{-5}$ ) cyclohexane solution. The scattering angle  $150^\circ$  corresponds to the length scale of 36.3 nm. The solid curves are the scaling predictions in accordance with Eq. (30). The dashed curve denotes the osmotic compressibility in the thermodynamic limit (zero wave number). Source: From Ref.<sup>[28]</sup>.

the susceptibility is suppressed. For example, the compressibility of fluids or osmotic compressibility of binary mixtures near the critical point becomes smaller when one goes to shorter length scales (Fig. 8). At  $q\xi \gg 1$ , the mesoscopic susceptibility explicitly depends on the instrumental scale, being proportional to  $q^{-2}$ .

### FINITE-SIZE SCALING

The mesoscopic susceptibility is an example of a property restricted by a finite size (either by the instrumental probe like in a scattering experiment or by the inherent finite nature of the system).<sup>[7,8]</sup> If the isotropic system is restricted in three dimensions by a size  $L$ , the susceptibility

$$\chi(L, \xi) = \chi_\infty(\xi) \Upsilon(\xi/L) \quad (31)$$

The asymptotic behavior of the scaling function  $\Upsilon(\xi/L)$ :

$$\begin{aligned} (\xi/L) \ll 1 \quad \Upsilon(\xi/L) &\rightarrow 1 & \chi &= \chi_\infty(\xi) \sim \xi^{\gamma/\nu} \\ (\xi/L) \gg 1 \quad \Upsilon(\xi/L) &\rightarrow (\xi/L)^{-\gamma/\nu} & \chi &= \chi_L \sim L^{\gamma/\nu} \end{aligned} \quad (32)$$

The correlation length is replaced by the finite size. In a similar fashion, one can estimate the heat capacity near

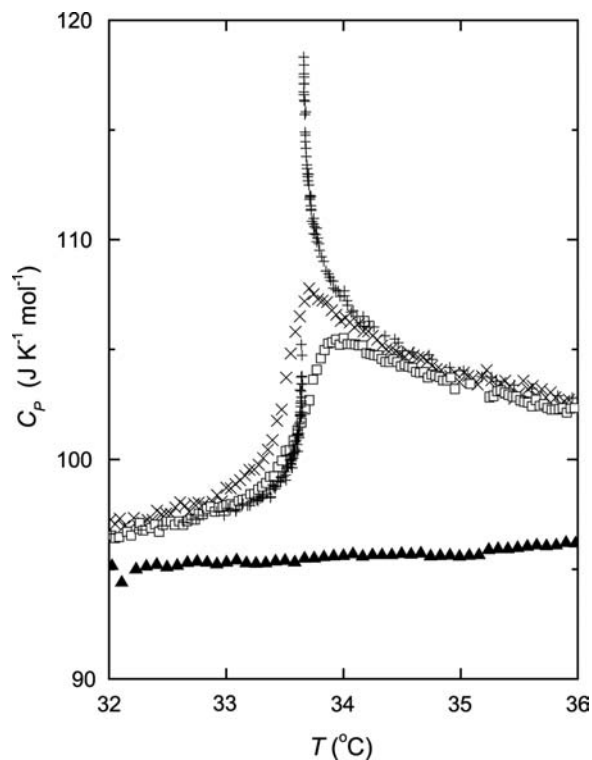


**Fig. 9** Finite-size heat capacity at constant pressure near the lower critical consolute point of 2,6-lutidine aqueous solution at the critical composition. (+) In the bulk, (x) 250 nm porous nickel, (□) 100 nm porous glass, (▲) 10 nm porous glass. Source: From Ref.<sup>[29]</sup>.

the critical point in porous media:

$$C(L, \xi) = C_\infty(\xi) \Psi(\xi/L) \quad (33)$$

$$\begin{aligned} (\xi/L) \ll 1 \quad \Psi(\xi/L) &\rightarrow 1 & C &= C_\infty(\xi) \sim \xi^{\alpha/\nu} \\ (\xi/L) \gg 1 \quad \Psi(\xi/L) &\rightarrow (\xi/L)^{-\alpha/\nu} & C &= C_L \sim L^{\alpha/\nu} \end{aligned} \quad (34)$$

Experiments confirm the predictions of the finite-size scaling (see, e.g., Fig. 9 and Ref.<sup>[29]</sup>). If the size  $L$  is restricted in one dimension, we should expect a crossover from a three-dimensional system to a two-dimensional system and the finite scaling becomes affected by this crossover.

### COMPETITION OF MESOSCALES IN COMPLEX FLUIDS

Finite-size scaling is an example of competition between mesoscales. Another example is a polymer solution near the critical point of phase separation. In such a system, two mesoscopic lengths can be tuned independently: the correlation length of the critical

fluctuations by the proximity to the critical point of demixing and the size of the polymer molecules (radius of gyration,  $R_g$ ) by the molecular weight  $M$ . In dilute polymer solutions, the long polymer chain can exhibit a random walk or a self-avoiding walk. These two regimes are separated by the *theta* point, the limited point of polymer–solvent phase separation in the limit of the infinite degree of polymerization. The random walk is possible when the polymer chain and the solvent form either ideal or quasi-ideal solution. For the random walk, the radius of gyration of a chain (made up of  $N$  links with a length  $a$ ):

$$R_g = \sqrt{\langle R^2 \rangle} = aN^{1/2} \quad (35)$$

Real polymer solutions are not ideal. In the mean-field Flory–Hugging model, the virial expansion of the osmotic pressure,  $\Pi$ , reads:<sup>[30]</sup>

$$\frac{\Pi v_0}{k_B T} = \frac{\phi}{N} + B\phi^2 + C\phi^3 \dots$$

$$\left( \text{with } B = \frac{1}{2} - \frac{w}{k_B T} \text{ and } C = \frac{1}{3} \right) \quad (36)$$

Here  $v_0$  is the solvent molecular volume. The product  $v_0 B$  is called the *excluded volume*. The interaction parameter  $w$  determines the *theta* temperature:

$$w = \frac{k_B \Theta}{2} \quad (37)$$

When  $B > 0$ , the chain monomers repel each other and the chain swells in solution (good solvent). When  $B < 0$ , the chain monomers attract each other (poor solvent) and the chain collapses to form a compact globule. When  $B = 0$ , attractions and repulsions cancel each other and the chain exhibit a random walk (*theta* condition). The *theta* point is defined by the simultaneous vanishing of the first ( $1/N$ ) and second ( $B$ ) virial coefficients.

The fact that in a good solvent, the polymer chain is swollen means that the radius of gyration increases with degree of polymerization faster than in the ideal random-walk conditions. Instead of finding Eq. (35), we should expect in a good solvent

$$R_g = aN^\nu \text{ with } \nu > 1/2 \quad (38)$$

The chain cannot intersect itself; the monomer units have finite volume and two chains cannot be in the same place at the same time. This is a self-avoiding walk problem. Indeed, by minimization of the free energy, one can obtain for the self-avoiding chain

$$R_g = aN^{\frac{3}{d+2}} \text{ so that, } \nu = \frac{3}{d+2} \quad (39)$$

In three dimensions,  $\nu = 3/5$  in close agreement with scattering experiments<sup>[31]</sup> and renormalization group theory.<sup>[32]</sup>

The exponent  $\nu$  is similar to the critical exponent of the correlation length given by Eq. (11). Indeed, the radius of gyration can be regarded as the correlation length of fluctuations of a polymer–chain order parameter. According to de Gennes,<sup>[32]</sup> the polymer chain is characterized by the order parameter associated with the concentration of the chain ends (a probability for the ends to meet each other). This is a “vector” order parameter, while the square of the probability, the volume fraction of polymer, is the observable property. For the infinite chain, the probability tends to zero while the correlation length (radius of gyration) diverges. Such a state in infinite dilution (“self-avoiding walk singularity”) can be regarded as an analogue of a critical-point state. Tuning the second virial coefficient, one can drive this critical state to a first-order transition at which the chain collapses and the collapse is accompanied by phase separation. Such a singular point is known as a tricritical point, and it always originates from a coupling between two different order parameters. Phase separation means the emergence of a new order parameter—concentration. This is why the *theta* point is also a tricritical point.<sup>[32]</sup> A schematic phase diagram of a polymer solution is shown in Fig. 10. The *lambda*-line (vertical, at infinite dilution) is the line of self-avoiding walk singularities (analogous to a second-order transition line). The solid curve is the critical line of demixing. Asymptotically close to the critical point of phase separation, the correlation length of concentration fluctuations,  $\xi$ , eventually dominates, being much larger than the radius of gyration. In this (critical) regime, the polymer solution behaves like an ordinary fluid near its critical point. Close enough to the *theta* point, the radius of gyration

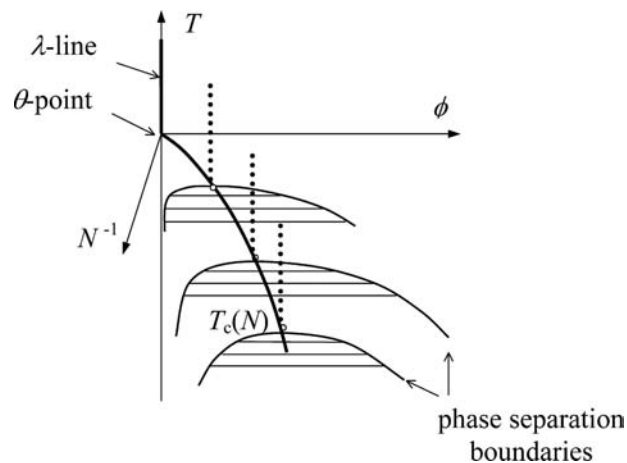


**Fig. 10** A schematic phase diagram of polymer solution. The dotted line shows the paths at critical compositions.



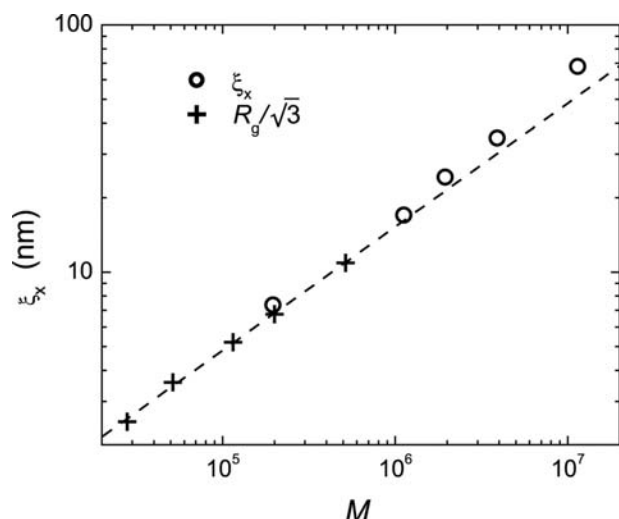


**Fig. 11** Molecular weight dependence of the correlation length in polystyrene-*n*-hexane solutions at the crossover temperature (circles). Crosses denote the normalized radius of gyration  $R_g/\sqrt{3}$ . Source: From Ref.<sup>[33]</sup>. From Ref.<sup>[34]</sup>. Dashed line denotes extrapolation as square root of  $M$ .

eventually dominates. It screens the concentration fluctuations and the polymer solution exhibits the theta-point tricritical (almost mean-field like) behavior. A regime where  $\xi$  and  $R_g$  are comparable is crossover between fluid criticality and theta-point tricriticality (Ref.<sup>[33]</sup> and Fig. 11).

The Landau–Ginzburg functional in the Flory–Huggins approximation reads.<sup>[35]</sup>

$$f(\varphi, N) = \frac{1}{2}\varepsilon\varphi^2 + \frac{1}{12}N^{-1/2}\varphi^4 + \frac{1}{2}N^{1/2}\nu_0^{2/3}(\nabla\varphi)^2 \quad (40)$$

Comparing Eq. (40) with Eqs. (22) and (23), we obtain the amplitude of the correlation length for polymer solutions in this approximation

$$\xi_0 = \nu_0^{1/3}N^{1/4} \quad (41)$$

Hence not only the radius of gyration, but also the effective range of “intermolecular” (including intra-chain) interactions diverge in the limit of infinite degree of polymerization.

## PERCOLATION

Another interesting example of a mesoscale structure is gel. Gel is a material composed of molecules or molecular aggregates that are able to form a macroscopic network with a non-zero shear modulus. The isolated subunits form usual liquid—a sol. Like

liquids, gels are structurally disordered and may contain a considerable fraction of liquid solvent. In a physical gel, heating can break the crosslinks while cooling can restore the links. Therefore the gel can be thermally reversible. Gelatin is an example of a thermo-reversible gel.

The change of macroscopic properties of gelatin solution changes at gelation point discontinuously, while the number of bonds changes continuously. It is similar to the symmetry break associated with phase transition points. The order parameter is the probability that a randomly chosen subunit belongs to the infinite network. A model, known as the *percolation* model, can describe generic features of the transition from sol to gel.<sup>[36]</sup> The percolation model emphasizes the geometrical features of network formation: the growth of the domain (“cluster”) in which all the subunits are interconnected. The correlation length is defined as the root mean square distance between the pair of sites that belong to the same cluster (proportional to the average size of cluster):

$$\xi = \xi_0|x - x_c|^{-\nu} \quad (42)$$

where  $x$  is the concentration of the bonds and  $x_c$  is the critical concentration (*percolation threshold*). For a simple three-dimensional cubic lattice  $\nu = 0.875$ .<sup>[37]</sup> The percolation model describes gelation as a “geometrical” phase transition and does not contain thermodynamics per se. However, in thermo-reversible gels, the temperature is coupled with geometry, making the configurational entropy and the percolation order parameter to be thermodynamic properties.<sup>[38]</sup>

## CONCLUSION

A variety of phenomena in condensed matter at submicron- and nanoscales, despite their diversity, demonstrate some generic features originating from the existence of a length scale intermediate between the size of atoms and the size one can see without a microscope. Mesoscopic thermodynamics is a semi-phenomenological approach that explicitly introduces this length scale into thermodynamics. The models of mesothermodynamics, such as the Landau–Ginzburg functional, emphasize a high degree of universality associated with a mesostructure and with the importance of fluctuations.

In this entry, only a few examples of mesoscale phenomena and systems have been discussed. Other promising objects of mesothermodynamics include polymer blends and melts, wetting transitions and critical adsorption, thermotropic and lyotropic liquid crystals, surface melting, and colloid crystals.

Meso- and nanoscales in non-equilibrium systems are the subject of non-equilibrium mesothermodynamics, which is still in its earliest stage. In particular, similar to thermodynamic properties, transport coefficients such as the diffusion coefficient or viscosity become spatially dependent at mesoscales (see, e.g., Ref.<sup>[39]</sup>). Moreover, away from equilibrium, generic long-range correlations emerge even in simple molecular fluids, making the famous concept of local equilibrium, at least, questionable.<sup>[40]</sup>

## ACKNOWLEDGMENTS

The author would like to thank J. V. Sengers who read the manuscript and made useful comments and A. F. Kostko for assistance in preparing the figures. A new interdisciplinary course on mesoscopic and nanoscale thermodynamics was supported by the University of Maryland at College Park. Related research was supported by the Division of Chemical Sciences, Geosciences and Biosciences, Office of Basic Energy Sciences, Department of Energy, under Grant No. DE-FG02-95-14509.

## REFERENCES

- Pollack, G.H. *Cells, Gels and the Engines of Life*; Ebner and Sons: Seattle, 2001.
- Jones, R.A.L. *Soft Condensed Matter*; Oxford Univ. Press: Oxford, 2002.
- De Gennes, P.G.; Prost, J. *The Physics of Liquid Crystals*, 2nd Ed. Ed.; Oxford Univ. Press: Oxford, 1993.
- Daud, M.; Williams, C.E.; Eds.; *Soft Matter Physics*; Springer: Berlin, 1999.
- Hamley, I.W. *Introduction to Soft Matter*, 2nd Ed.; J. Willey: Chichester, 2000.
- Kleman, M.; Lavrentovich, M.O.D. *Soft Matter Physics: An Introduction*; Springer: New York, 2003.
- Safran, S. *Statistical Thermodynamics of Surfaces, Interfaces, and Membranes*; Perseus Books: Cambridge, MA, 1994.
- Privman, V.; Ed.; *Finite Size Scaling and Numerical Simulation of Statistical Systems*; World Scientific: Singapore, 1990.
- Brankov, J.G.; Danchev, D.M.; Tonchev, N.S. *Theory of Critical Phenomena in Finite-Size Systems*; Series in Modern Condensed Matter Physics; World Scientific: Singapore, 2000; Vol. 9.
- Fendler, J.H.; Dekany, I.; Ed. *Nanoparticles in Solids and Solutions*; NATO Partnership Sub-Series 3, High Technology; Kluwer Academic Publishers: Dordrecht, 1996; Vol. 18.
- Stanley, H.E. *Introduction to Phase Transitions and Critical Phenomena*; Clarendon Press: Oxford, 1971.
- Fisher, M.E. Scaling, universality, and renormalization group theory. In *Lecture Notes in Physics*; Hahne, F.J.W., Ed.; Springer: Berlin, 1982; Vol. 186, 1 pp.
- Anisimov, M.A. *Critical Phenomena in Liquids and Liquid Crystals*; Gordon and Breach: New York, 1991.
- van der Waals, J.D. The thermodynamic theory of capillarity under the hypothesis of a continuous variation of density. *J. Stat. Phys.* **1979**, *20*, 197 (English transl.).
- Rowlinson, J.S.; Widom, B. *Molecular Theory of Capillarity*; Clarendon: Oxford, 1982.
- Hill, T.L. *Thermodynamics of Small Systems*; Dover: New York, 1994.
- Everett, D.H. *Basic Principles of Colloid Science*; The Royal Society of Chemistry, Thomas Graham House: Cambridge, 1994.
- Israelachvili, J. *Intermolecular and Surface Forces*, 2nd Ed.; Academic Press: London, 1992.
- Landau, L.D.; Lifshitz, E.M. *Statistical Physics*; Pergamon: Reading, 1958.
- Reichl, L.E. *A Modern Course in Statistical Physics*; J. Wiley: New York, 1998.
- Degiorgio, V.; Corti, M.; Eds.; *Physics of Amphiphiles: Micelles, Vesicles, and Microemulsions*; North Holland Publishers: Amsterdam, 1983.
- Anisimov, M.A.; Kurlandsky, A.S.; Kazakova, N.F. Micellization as a phase transition. *Mol. Cryst. Liq. Cryst.* **1988**, *159*, 87.
- Zhuravleva, E.V.; Anisimov, M.A.; Svitova, T.F.; Lobanova, V. Yu. New kind of water/oil interface instability and the nature of ultra-low interfacial tension. In *Physical Chemistry of Colloids and Interfaces in Oil Production*, Proceedings of the 6th IFP Exploration and Production Research Conference, Saint-Raphael, 1991; Toulhoat, H., Lecourtier, J., Eds.; Editions Technip: Paris, 1992, 133–139.
- Anisimov, M.A.; Gorodetskii, E.E.; Kulikov, V.D.; Sengers, J.V. Crossover between vapor-liquid and consolute critical phenomena. *Phys. Rev., E* **1995**, *51*, 1199.
- Hornreich, R.M.; Luban, M.; Shtrikman, S. Critical behavior at the onset of k-space instability on the lambda line. *Phys. Rev. Lett.* **1975**, *35*, 1678.
- Fredrickson, G.H.; Bates, F.S. Design of bicontinuous polymeric microemulsions. *J. Polym. Sci.* **1997**, *35*, 2775.
- Anisimov, M.A.; Gorodetsky, E.E.; Davydov, A.J.; Kurlandsky, A.S. Landau model for self-assembly and liquid crystal formation in surfactant solutions. *Liq. Cryst.* **1992**, *11*, 941.
- Jacob, J.; Anisimov, M.A.; Sengers, J.V.; Dechabo, V.A.; Yudin, I.K. Light scattering and crossover phenomena in polymer solutions. *Appl. Opt.* **2001**, *40*, 4160.
- Voronov, V.P.; Buleiko, V.M. Experimental investigation of the behavior of the specific heat in the finite systems in the vicinity of the critical mixing point. *J. Exp. Theor. Phys.* **1998**, *86*, 586.
- Flory, P.J. *Principles of Polymer Chemistry*; Cornell University Press: Ithaca, NY, 1953.
- Okano, K.; Wada, E.; Taru, Y.; Hiramatsu, H. Small-angle x-ray scattering study on density correlation function of flexible polymers in solutions. 2. Dilute

- solution of polystyrene. Rep. Prog. Polym. Phys. Jpn. **1974**, *17*, 145.
32. De Gennes, P.G. *Scaling Concepts in Polymer Physics*; Cornell University Press: Ithaca, NY, 1979.
  33. Anisimov, M.A.; Kostko, A.F.; Sengers, J.V. Competition of mesoscales and crossover to tricriticality in polymer solutions. Phys. Rev., E **2002**, *65*, 051805.
  34. Melnichenko, Yu. B.; Wignall, G.D. Dimensions of polymer chains in critical semidilute solutions. Phys. Rev. Lett. **1997**, *78*, 686.
  35. Povodyrev, A.A.; Anisimov, M.A.; Sengers, J.V. Crossover Flory model for phase separation in polymer solutions. Physica A **1999**, *264*, 345.
  36. Stauffer, D.; Aharony, A. *Introduction to Percolation Theory*, 2nd Ed.; Taylor and Francis: London, 1994.
  37. Bunde, A.; Havlin, S. Eds.; *Fractals and Disordered Systems* 2nd Ed.; Springer: Berlin, 1996.
  38. Martin, J.E.; Wilconxon, J.; Adolf, D. Critical exponents for the sol-gel transition. Phys. Rev., A **1987**, *36*, 1803.
  39. Kostko, A.F.; Anisimov, M.A.; Sengers, J.V. Dynamic crossover to tricriticality and anomalous slowing down of critical fluctuations by entanglements in polymer solutions. Phys. Rev., E **2002**, *66*, 020803 (R).
  40. Dorfman, J.R.; Kirkpatrick, T.R.; Sengers, J.V. Generic long-range correlations in molecular fluids. Annu. Rev. Phys. Chem. **1994**, *45*, 213.

# Three-Dimensional Nanofabrication Using Multiphoton Absorption

John T. Fourkas  
Tommaso Baldacchini

*Eugene F. Merkert Chemistry Center, Boston College, Chestnut Hill, Massachusetts, U.S.A.*

## INTRODUCTION

One of the major goals of nanotechnology is to be able to fabricate complex, functional nanostructures at will. In recent years, there has been a tremendous effort from many groups to develop microfabrication techniques that can be adapted to the realm of nanostructures.<sup>[1–3]</sup> One driving force for such studies is the desire to break free from the constraints of conventional lithography. Although processes such as photolithography and electron beam lithography have been extremely successful in the production of electronic circuits with ever-decreasing feature sizes,<sup>[4]</sup> these techniques have significant limitations that preclude their use in many other contexts. These techniques are incompatible with many chemical and biological environments, can create sub-100-nm features only with difficulty, are not capable of fabricating structures with complex 3-D shapes, and generally require expensive facilities. Techniques such as nanoimprint lithography,<sup>[5]</sup> proximity probe lithography,<sup>[6]</sup> and soft lithography<sup>[7]</sup> are being developed to overcome these limitations. For instance, replica molding can be used to fabricate and replicate 2-D patterns with a resolution of 30 nm.<sup>[8]</sup> It has also been shown that intricate 3-D structures can be fabricated by soft lithography, although generally with feature sizes of 25  $\mu\text{m}$  or greater.

Microstereolithography allows for 3-D microfabrication with a feature size down to few micrometers.<sup>[9]</sup> UV lasers are focused on a thin layer of a liquid photoresist that undergoes solidification upon absorption of light. A second layer of photoresist is then added and another pattern is imposed over the first one. This process is repeated until the desired structure is completed. A developer solution is then used to wash away the unsolidified material, liberating the freestanding 3-D structure. Prototyping under these conditions is slow. For each layer, fresh resin must be spread flat on the polymerized object, which is the rate-determining step for the entire process. The wavelength of light and the film thickness are the major factors in determining the resolution limit of a few micrometers.

Since the first papers about microstereolithography appeared in 1993, many variations have been proposed

and demonstrated that improve resolution and production time.<sup>[10]</sup> Among these, the one that has allowed the fabrication of the smallest features is two-photon absorption polymerization (TPAP), which was introduced by Strickler and Webb<sup>[11]</sup> in 1991. It was the work of Maruo, Nakamura, and Kawata<sup>[12]</sup> in 1997 that first demonstrated the promise of this method for the fabrication of non-trivial 3-D structures with submicrometer resolution. In this entry, we will describe the basic principles of TPAP, illustrate how it can be applied to the fabrication of small 3-D structures with high accuracy, and discuss new developments that should bring this technique into the realm of nanofabrication.

## TWO-PHOTON ABSORPTION

All materials can be excited by a two-photon process when exposed to intense light. The only requirement is that the sum energy of the photons matches the energy required for the transition. The two-photon absorptivity is proportional to the imaginary part of the third-order susceptibility,  $\chi^{(3)}$ , which is non-zero in all materials.<sup>[13]</sup> Although Göppert-Mayer predicted this phenomenon in 1931,<sup>[14]</sup> the first experimental observation was not made until 1961.<sup>[15]</sup>

Two-photon absorption (TPA) is a rare event. For instance, Denk and Svoboda<sup>[16]</sup> calculated that under sunlight, a molecule of Rhodamine B, a good one- and two-photon absorber, undergoes one-photon excitation once per second, while the two-photon process occurs once every 10 million years. To increase the probability of TPA, intense sources of light (generally lasers) must be used.

The TPA cross sections of most molecules are small, usually on the order of  $10^{-50} \text{ cm}^4 \text{ sec photon}^{-1}$  (now defined as 1 GM in honor of Göppert-Mayer) or less. As a result, high local photon fluxes are needed to promote TPA. Commercially available Ti:sapphire lasers producing pulse durations  $\tau$  shorter than 100 fsec can meet this requirement. Each pulse has a peak power on the order of a kilowatt, while at a typical repetition

rate,  $f_p$ , of 80 MHz, the average power is on the order of hundreds of milliwatts. For comparison, a continuous wave laser must operate at a power  $(\tau f_p)^{-1/2}$  times higher than that required by an ultrafast-pulsed laser to achieve the same two-photon excitation efficiency.<sup>[17]</sup>

It has been shown that the probability  $n_a$  that a molecule will absorb two photons per pulse simultaneously when an objective of numerical aperture NA is used to focus the laser is given by

$$n_a \approx \frac{p_o^2 \delta}{\tau f_p^2} \left( \frac{(NA)^2}{2hc\lambda} \right)^2 \quad (1)$$

where  $p_o$  is the laser average power and  $\delta$  is the two-photon cross section of the molecule at wavelength  $\lambda$ .<sup>[18]</sup>

Because the probability of a TPA event is proportional to the square of the light intensity, excitation can be localized within the focal volume.<sup>[19]</sup> The higher the NA of the objective, the smaller the excitation volume. As shown above, the TPA efficiency falls off as the fourth power of the distance from the focal point.

In TPAP, the ability to excite a photoinitiator selectively within the focal volume allows for a spatial confinement of matter transformation. If upon TPA a liquid resin can be solidified, then with accurate positioning of the focal point, 3-D microstructures can be fabricated with submicron resolution. As long as the solubility properties of the solidified and unsolidified resins are different, the nonpolymerized material can be washed away to leave a freestanding structure.<sup>[20]</sup>

This fabrication process offers a unique combination of advantages. First, subdiffraction-limited resolution can be attained because chemical non-linearity results in a power threshold below which polymerization will not occur. Second, no topological constraints are present in the fabrication of 3-D structures. Third, the optical penetration depth is greatly increased with the use of near-IR light, which allows for the use of higher concentrations of photoinitiator than in one-photon polymerization. Fourth, movable components can easily be created without the use of sacrificial layers. Finally, the carbon-based nature of the materials can be used as a chemical handle to make polymers with tunable physical and chemical properties.

## MATERIALS AND EXPERIMENTAL SETUP

Two-photon absorption polymerization has been applied successfully to radical and cationic polymerization. In both cases, an initiator molecule plays a fundamental role. Its properties, such as the TPA cross section, the initiation efficiency, and the quantum yield, all influence the fabrication process.

Photoinitiators in radical polymerization are divided in two main groups.<sup>[21]</sup> Photoinitiators that

undergo unimolecular reaction are termed Type I. In these initiators, a bond breaks homolitically after excitation to form two radicals, at least one of which initiates the polymerization reaction. Photoinitiators that undergo a bimolecular reaction with a coinitiator to create radicals are termed Type II.

Lucirin TPO-L, Irgacure 369, and Irgacure 184 are all Type I photoinitiators and have been successfully used in TPAP.<sup>[22,23]</sup> Lucirin TPO-L is a member of the acylphosphine oxide photoinitiator family. Its absorption in the UV/visible region of the spectrum results from an  $n \rightarrow \pi^*$  transition that is red-shifted as a result of conjugation between a phosphonyl group and the carbon atom of the adjacent carbonyl group. Upon excitation, the carbon-phosphorus bond is cleaved, forming two radicals. The phosphinoyl radical has a tetrahedral structure with a single electron at one corner, which allows it to attack efficiently many substrates with no steric hindrance. As opposed to most acylphosphine oxide photoinitiators, Lucirin TPO-L is a liquid. The importance of this feature should not be underestimated, as most of the monomers and oligomers used in TPAP are highly viscous, but can form homogeneous solutions with Lucirin TPO-L readily.

Acylphosphine oxides are strongly inhibited by the presence of molecular oxygen. Although this represents a limitation to their use in curing thin films, it is an advantage in TPAP. By quenching the triplet state of the photoinitiator and by scavenging primary radicals efficiently, oxygen contributes to the formation of a threshold laser power below which fabrication is not possible. It is this threshold that allows for breaking of the diffraction limit, permitting fabrication with submicron resolution.

H-Nu 470 and Rose Bengal are Type II photoinitiators. They have been used in TPAP in the presence of a coinitiator, which is generally a bulky tertiary amine.<sup>[24,25]</sup> Upon excitation, the photoinitiator abstracts an  $\alpha$ -hydrogen atom from the amine.

All of the photoinitiators discussed so far are commercially available, and their properties have been optimized only for linear absorption. For this reason, some research groups have chosen a different approach, in which molecules with large two-photon-absorption cross sections are designed rationally and then synthesized.<sup>[26-29]</sup> It has been shown that molecules having electron-donating (D) and electron-withdrawing (A) groups separated by  $\pi$ -conjugated systems have large  $\delta$  values. An example is 4,4'-bis(*N,N*-di-*n*-butylamino)-*E*-stilbene. Starting with this structural motif, Cumpston et al. synthesized molecules with  $\delta$  values as large as 4400 GM, at least 3 orders of magnitude greater than those of most commercially available photoinitiators. Upon excitation by TPA, these molecules go through a large electronic reorganization and can undergo efficient electron

transfer with many substrates to initiate polymerization.<sup>[30]</sup> An appealing characteristic of this approach is the ability to shift the  $\lambda_{\max}$  of the TPA by small modifications in the molecular structure of the photoinitiator. Another structural motif characterized by large  $\delta$  values is a fluorenyl group intercalated between A and D groups. Molecules with this moiety have also successfully initiated radical polymerization induced by TPA.

A binary system consisting of 7-diethylamino-3-(2'-benzimidazolyl)coumarin and an iodonium salt has also been used in TPAP.<sup>[31,32]</sup> In this system, an electron transfer process occurs upon photoexcitation, leading to the formation of active aryl radicals.

Use of designer photoinitiators with TPA has allowed for fabrication with a low power threshold and wide dynamic range (defined as the ratio between the threshold and the damage powers).<sup>[33,34]</sup> Although these are desirable properties in TPAP, the scarce availability of these initiators makes their widespread use difficult.

Because of their high rate of polymerization, acrylates are the monomers and oligomers most widely used in radical TPAP.<sup>[35]</sup> Introducing chemical modifications in the ester group produces materials with different properties while having little effect on the polymerization rate. Because acrylates are used extensively in industry, a large variety of them are available commercially. To give the required stiffness to microstructures fabricated by TPAP, highly branched monomers incorporating cyclic structures are generally used.

Irgacure 369 has been used in the polymerization of an inorganic-organic hybrid material by TPA.<sup>[36]</sup> The organic portion consists of a methacrylate group, while the inorganic portion is an alkoxy- or perfluoroaryl silane whose length can be controlled via a hydrolysis/condensation reaction.<sup>[37]</sup> Changing the ratio between organic and inorganic groups changes the physical and chemical properties of the polymerized material.

Cationic photopolymerization employs initiators that generate strong Brønsted acids, which initiate chain reactions in substrates such as multifunctional epoxide and vinyl ether monomers.<sup>[21]</sup> It is important to note that cationic polymerization is not affected by the presence of molecular oxygen, and so the power threshold in this process is an intrinsic property of the materials used. Commercially available diaryliodonium and triarylsulfonium salts have been used successfully in TPAP.<sup>[29]</sup> In addition, a cationic photoinitiator with a large  $\delta$  value (690 GM at 705 nm) was synthesized by Kuebler et al.<sup>[38]</sup> The molecule, BSB-S<sub>2</sub>, consists of a bis[(diarylamino)styryl]benzene core with covalently attached sulfonium moieties and is an efficient photoacid.

Most of the resins used in TPAP are negative photoresists, in that the regions exposed to light harden, becoming insoluble in a postexposure development solvent. However, it has been shown that BSB-S<sub>2</sub>

can be used as a positive photoresist by inducing an ester-cleavage reaction in a solid polymer.<sup>[39]</sup> The newly formed polar groups make the volume in which they are present soluble in an aqueous base developer. This technique is promising for areas of microfabrication in which empty spaces have to be created, such as in microfluidics.

Microfabrication by TPAP can be performed by either moving the laser beam inside the photocurable resin or by moving the sample around a fixed laser beam. In the first case, a set of galvano mirrors is used to scan the focal spot in the  $x$ - $y$  plane and a piezo stage to move the sample or objective up and down. In the second scheme, the sample is moved in all three dimensions with the aid of a three-axis stage.

### 3-D Spatial Resolution

The ultimate resolution and complexity of 3-D microstructures fabricated by TPAP depend upon the factors influencing the shape and size of the smallest polymerized volume element or voxel. It is the accurate overlapping of these voxels that produces the desired surface topology of the final structure.

The square light intensity (SLI) distribution of the laser at the focal volume is an important determinant of voxel size. In this region, the highest concentration of active species is formed, thus inducing a state modification of the sample. Sun, Tanaka, and Kawata<sup>[40]</sup> have calculated that the near-focus SLI contour has a complicated distribution. Because an intensity threshold is present in TPAP, only the central portion is meaningful for microfabrication. As a consequence, the shape of a voxel resembles an ellipsoid with the two minor axes equal to each other and lying in the geometrical focal plane. The ellipsoid volume is proportional to the cube of the wavelength of the laser. Although shorter wavelengths will form smaller voxels, the choice of the excitation energy is dictated by the photoinitiator efficiency. In general, the working wavelength of choice optimizes the product of the photoinitiator two-photon cross-section ( $\sigma$ ) and quantum yield for radical generation ( $\eta$ ).

An analytical equation for the prediction of the photopolymerized voxel dimensions has been developed recently.<sup>[36]</sup> Assuming a Gaussian distribution of light intensity at the focal volume and a constant photon flux ( $I_0$ ) during the laser pulse, the expressions relating voxel diameter ( $d$ ) and length ( $l$ ) to the experimental parameters are

$$r(I_0, t) = r_0 \left[ \ln \frac{\sigma \eta I_0^2 f_p \tau_p t}{\ln \left( \frac{\rho_0}{\rho_0 - \rho_{th}} \right)} \right]^{\frac{1}{2}} \quad (2)$$



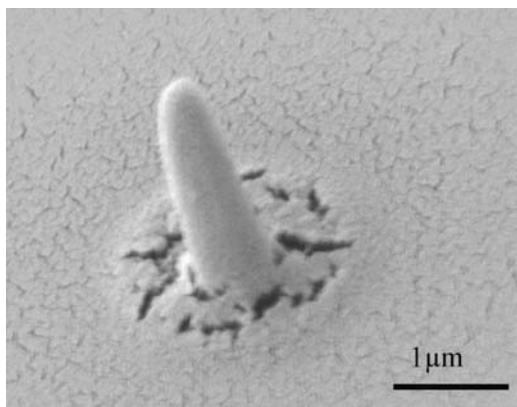


**Fig. 1** Truncated voxel fabricated using a 1.3-NA objective with a power of 2.0 mW at the sample and an exposure time of 500 msec.

and

$$l(I_o, t) = 2z_R \left[ \left( \frac{\sigma \eta I_o^2 f_p \tau_p t}{\ln \left( \frac{\rho_o}{\rho_o - \rho_{th}} \right)} \right)^{\frac{1}{2}} - 1 \right]^{\frac{1}{2}} \quad (3)$$

where  $t$  is the total processing irradiation time and  $\rho_o$  and  $\rho_{th}$  are the photoinitiator concentration and minimum concentration of radicals required to form a voxel, respectively. Thus knowledge of the radial ( $r_o$ ) and axial ( $z_R$ ) resolutions of the objective, which are given by the Abbe relations, is not sufficient to describe the voxel formation and growth in TPAP; correction factors involving the excitation light and the material properties have to be considered as well.

Experimentally, an accurate measurement of a photopolymerized voxel has to take into consideration the truncation effect.<sup>[40]</sup> To observe a single voxel using electron microscopy, it must be attached to a solid support so that it will not be washed away with the unpolymerized resin during the developing step. Consequently, a portion of each voxel is “truncated” by the substrate (Fig. 1), making the measurement of the complete voxel size impossible. An ascending scan technique overcomes this problem. At constant average power and exposure time, a series of voxels is fabricated, increasing the height of the laser beam focal point successively for each voxel starting from inside the solid support. Between voxels that are truncated and ones that are completely free to float away, some are barely attached to the solid support and will lie horizontally after washing. These voxels reveal their entire structure, allowing for the measurement of  $d(I_o, t)$  and  $l(I_o, t)$ .

In TPAP, the voxel size can be tuned by changing either the average power of the excitation light or the irradiation time. In the latter case, different groups

have experimentally confirmed the predictions of Eq. (2).<sup>[36,41]</sup> The lateral voxel dimension is proportional to the square root of the natural logarithm of the exposure time. Kawata et al.<sup>[42]</sup> have reported the best resolution to date in microfabrication by TPAP with a lateral voxel resolution of 120 nm. This value is roughly 4 times smaller than the diffraction limit predicted from the objective numerical aperture and the excitation wavelength. For such resolution, the intensity of the laser light must be set at a value that is just slightly higher than the intensity threshold for polymerization.

When the microfabrication conditions are optimized, the ratio between the axial and lateral dimensions ( $\mu$ ) of a photopolymerized voxel varies between 3 and 5, depending on the average power ( $p_o$ ) or the exposure time. In both cases,  $\mu$  increases with increasing  $p_o$  and  $t$ . This implies that the length of the voxel grows more rapidly than its diameter. This effect results from the fact that the SLI distribution is elongated along the optical axis of the laser beam.

Sun et al.<sup>[41]</sup> have elucidated the scaling laws for voxel growth in TPAP. They have observed that the rate with which  $\mu$  increases depends on whether  $p_o$  or  $t$  is varied. A change in average power produces a larger effect in  $\mu$  than does a change in exposure time. The same work highlighted an interesting phenomenon: at long exposure times,  $\mu$  saturates. Although such behavior is still not fully understood, it is believed that the diffusion of radicals plays an important role.

In microfabrication by TPAP, the most important characteristic of an objective is its numerical aperture. High-NA (1.3 to 1.4) objectives are generally employed because of their ability to reduce the excitation focal volume to a fraction of a femtoliter. When comparing voxels fabricated using different objectives under the same exposure conditions, unexpected results are observed. If the intensity of the laser beam is far from the intensity threshold, low NA objectives (e.g., 0.9) produce slimmer voxels than do high-NA objectives.<sup>[43]</sup> Near the intensity threshold, the smallest voxels are fabricated by high-NA objectives.

It has been suggested that high-NA objectives may break the symmetry of the focal field.<sup>[44]</sup> If this is true, then, when using linearly polarized light in TPAP, a polarization-dependent voxel shape will be observed. Sun et al.<sup>[43]</sup> have observed voxels with an ellipsoidal shape in which the two minor axes are no longer identical. The ratio between the two minor axes is approximately 1.1. This effect was eliminated with the use of circularly polarized light, which is consistent with asymmetry resulting from the high NA of the objective.

During microfabrication, the excitation laser beam has to traverse different interfaces before the sample.

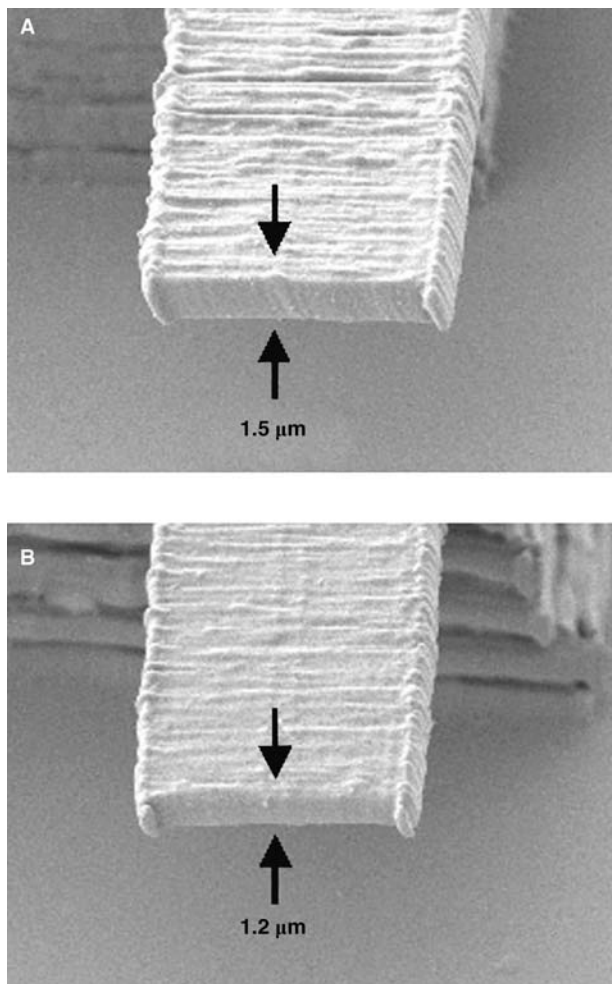


**Fig. 2** Freestanding cantilevers fabricated using a  $40\times$  oil-immersion objective with an NA of 1.3 at a stage velocity of  $20\mu\text{m}/\text{sec}$  and average power of  $3.4\text{mW}$ . The index of refraction of the resin in (A) is 1.4930 while in (B) is 1.5222.

It is well known in TPA microscopy that refractive index mismatches among these interfaces produce aberrations at the focal volume that lead to a decrease in resolution, principally along the optical axis.<sup>[45]</sup> The same effect can be expected in TPAP, where the largest difference in indices of refraction is between the resin and the immersion oil used in combination with high-NA objectives. Scanning electron microscopic (SEM) images of two freestanding cantilevers fabricated by TPAP are shown in Fig. 2. Both structures were fabricated using a  $40\times$  oil-immersion objective (NA = 1.3) with identical stage velocity and power. The index of refraction of the resin used in (A) was lower than the one used in (B). In this second case, the resin was altered to render its refractive index similar to that of the immersion oil. The cantilever thickness in the index-matched system is approximately 20% smaller.

## MICROSTRUCTURES FABRICATED BY TWO-PHOTON ABSORPTION POLYMERIZATION WITH SUBMICRON RESOLUTION

In 1997, Maruo, Nakamura, and Kawata<sup>[12]</sup> first demonstrated that TPAP can be used to create complex 3-D microstructures. A spiral structure  $1.3\mu\text{m}$  wide,  $6.0\mu\text{m}$  in diameter, and  $10.3\mu\text{m}$  in axial pitch was fabricated as the first example of a 3-D microstructure created on such a small scale without employing a complicated layer-by-layer stacking process. Two-photon absorption fabrication techniques have continued to advance since this pioneering work, and it is now possible to create structures with intricate geometries and small dimensions. An example of such a microstructure is the microbull shown in Fig. 3.<sup>[42]</sup> It is interesting to note the fine reproduction of the complex surface topology of this object, the size of which is comparable to that of a human red blood cell. Fabrication of a solid bull required approximately 3 hr with a raster-scanning technique. However, this time was reduced to 13 min when only the exterior of the bull was polymerized using a vector-scanning method. Of course, the vector scan method provides a technical advantage exclusively when the microstructure exterior is self-supporting and when postcuring of the unpolymerized resin in its interior does not produce distortions.

Representative microstructures fabricated by TPAP in our laboratory are presented in Figs. 4–7. These images show 3-D structures that, because of their shape and size, cannot be produced using conventional lithographic techniques. For example, Figs. 5 and 6 show images of microstructures spanned by cables or bridges at different heights.

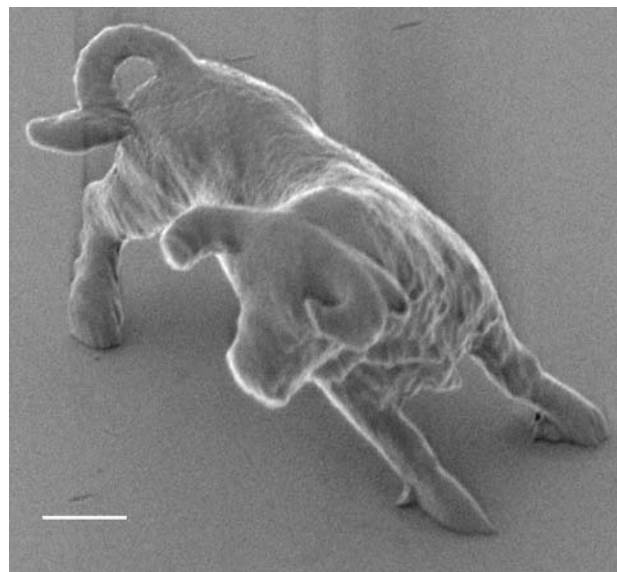


**Fig. 3** Microbull fabricated by TPA photopolymerization. Scale bar,  $2\mu\text{m}$ . Source: Prof. Hong-Bo Sun.

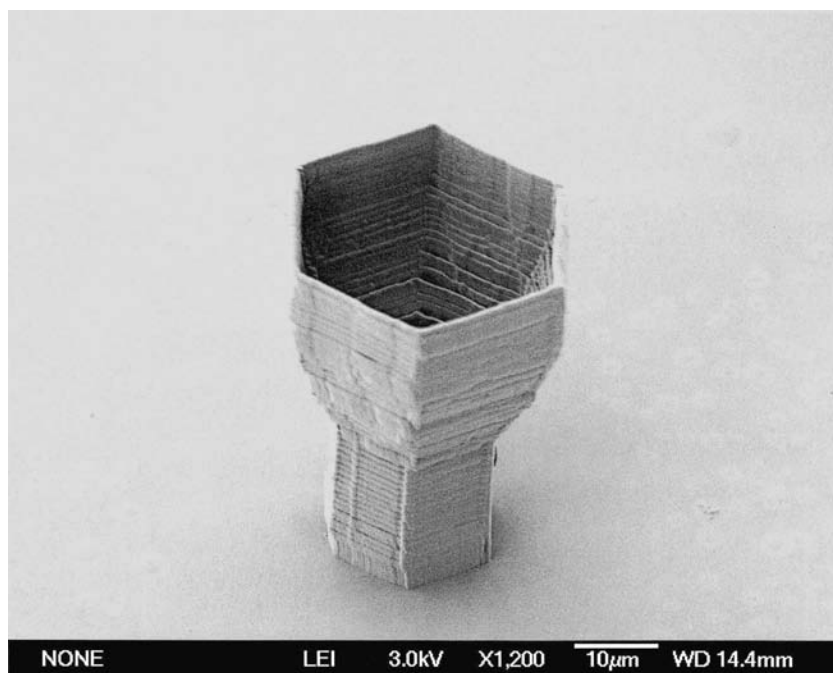


Fig. 4 Microcup with a diameter that increases with height.

The ultimate goal of any microfabrication/nanofabrication technology is the efficient production of devices that can deliver standard and non-standard functionality. Thus the analysis of materials performance on such small scales became of uttermost importance. It is a well-known fact in the world of semiconductor microfabrication that the scaling laws for many physical properties are not linear at small dimensions. Sun, Takada, and Kawata<sup>[46]</sup> have proven this point for a polymerized functional micromachine/

nanomachine as well. They fabricated a microspring with a feature size of 150 nm, a coil radius of 1 µm, and a pitch of 2 µm. One end of the spring was fixed to a polymerized anchor, and the other end had a polymerized bead of 1.5-µm diameter attached to it. The entire assembly was put in ethanol, and the microspring was mechanically activated by trapping the bead with optical tweezers. After being elongated without any elasticity failure, the bead was set free from the optical trap, letting the coil relax to its

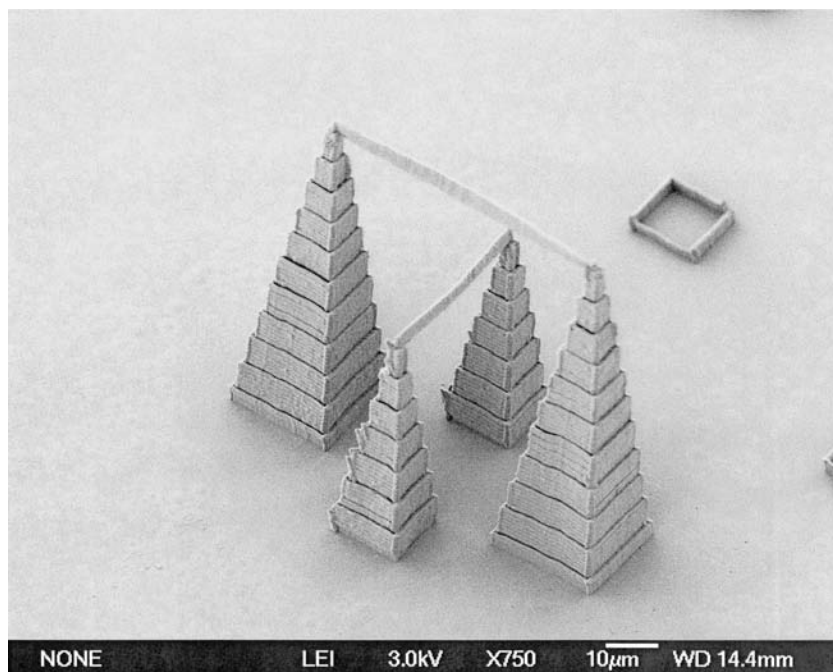
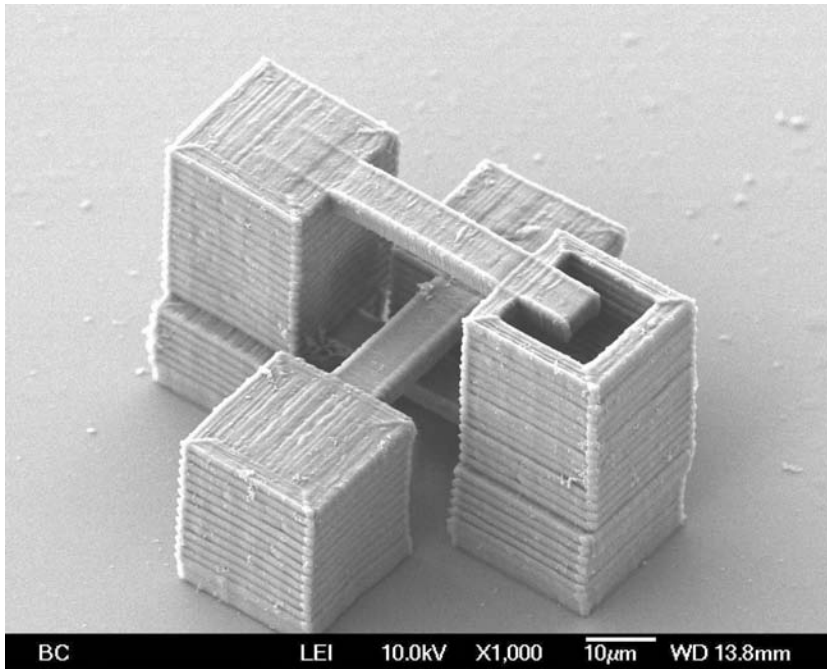


Fig. 5 Pyramids interconnected by microcables at heights of 40 and 60 µm.



**Fig. 6** Overlapping microbridges at heights of 12, 24, and 42  $\mu\text{m}$ .

equilibrium point. The spring movement was overdamped and no oscillations around the equilibrium point was observed. The value of the spring constant was found to be 3 orders of magnitude smaller than that predicted from the bulk physical properties of the material. The main reason for the discrepancy between predicted and experimental values is presumed to be that the mechanical characteristics of the polymer are not the same for macroscopic and microscopic samples. In particular, the polymerization conversion percentage

induced by TPA is not known under the conditions used by the authors, and the Young's modulus depends critically on the degree of cross-linking. It is therefore dangerous to predict performance of microdevices/nanodevices by simply scaling down the properties of their macroscale counterparts.

One of the current trends in optoelectronics is the fabrication of 3-D periodic structures that have the ability to block the propagation of modes in certain region of the frequency spectrum. The geometry most

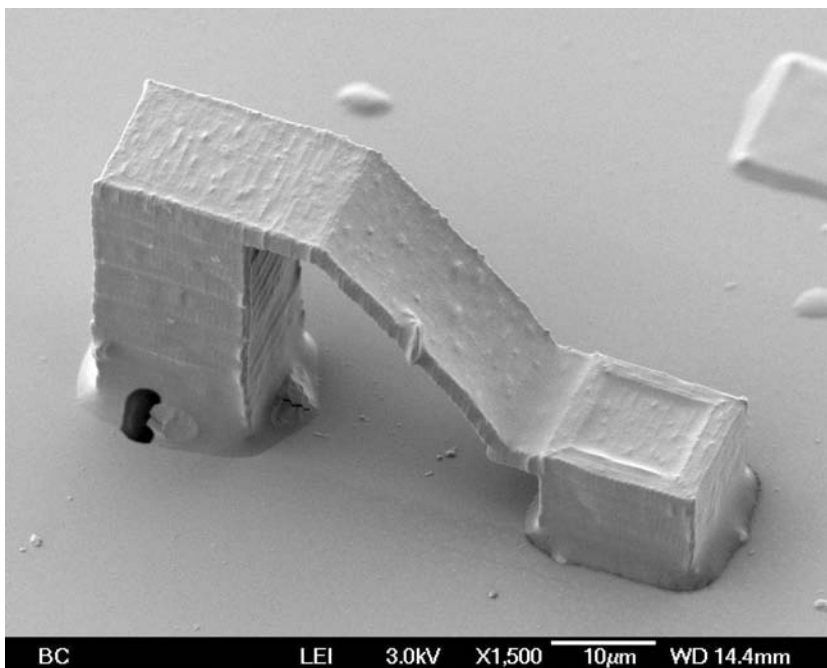


**Fig. 7** Inclined ( $45^\circ$ ) microplane.

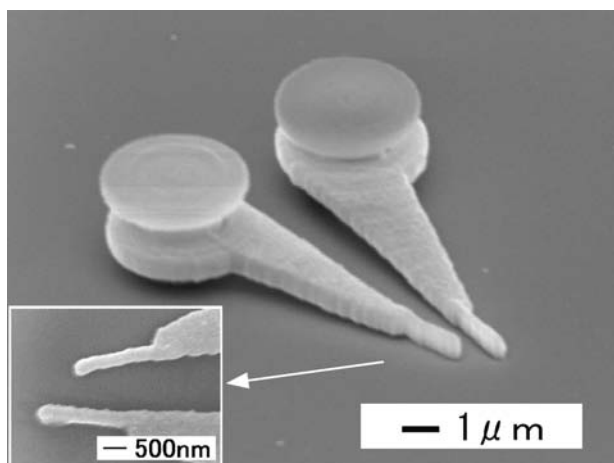


**Fig. 8** Freely movable microtweezers. *Source:* Prof. Shoji Maruo.

commonly used to create this photonic band gap (PBG) effect is a 3-D log-pile structure. It consists of layers of parallel rods in which the rod orientation in each layer is perpendicular to that in the adjoining layers. The center wavelength of the PBG is approximately the spacing between the rods. Thus submicron resolution in fabrication is a requirement for the creation of photonic crystals with PBG properties in the visible and near-IR region of the spectrum. Two-photon absorption polymerization presents an attractive alternative to semiconductor-based microfabrication for such devices, as complex geometries with resolutions reaching a few hundreds of nanometers are achievable. Log-pile microstructures with rod spacings of 1.2, 1.3, and 1.4  $\mu\text{m}$  were fabricated by TPAP, and their PBG properties verified experimentally.<sup>[47]</sup> As expected, the larger spacing created the more red-shifted PBG and the greater dip in transmission. In all three cases, the transmission dips were less than 50%. This limitation is a result of the poor refractive index contrast between polymer and air ( $\approx 0.5$ ), and it represents the main obstacle for applications. The appealing advantage of TPAP in the fabrication of microstructures with periodic modulation of refractive index was recently demonstrated. By connecting polymerized rods and sphere of 580 and 500 nm in diameter, respectively, Kaneko et al.<sup>[48]</sup> have fabricated a diamond-lattice microstructure that presents a strong PBG effect. In the race for the fabrication of 3-D microstructures with band gap at approximately the communication wavelength (1.55  $\mu\text{m}$ ), TPAP is surely a forerunner.

Objects with various other kinds of 3-D geometries have been made by TPA microfabrication. For example, a series of microgears was fabricated by TPAP.<sup>[49]</sup> They were fabricated around a shaft linked to the solid support and thus were able to rotate freely

under the flow of a solvent. With a similar procedure, Maruo, Ikuta, and Kovogi<sup>[50]</sup> have fabricated micro-scale/nanoscale manipulation tools that can be driven by light. An SEM image of a pair of microtweezers with submicron probe tips is shown in Fig. 8. Once in aqueous solution, laser trapping can optically drive the arms of the microtweezers. This type of remote control is promising in the realm of bionanotechnology, where electrostatic types of manipulators cannot be applied.

## CONCLUSION

The basic principles of TPAP have been described in this entry. Its ability to produce structures with any 3-D geometry at submicron resolution introduces a kind of freedom in microfabrication never before possible with other pattern formation techniques. For example, microstructures with curved surfaces and/or interconnected parts at different heights are easily fabricated.

In any fabrication process, resolution plays a fundamental role. In two-photon microfabrication, the achievement of sub-100-nm resolution will bring this technique into the realm of true nanofabrication. There are a number of clear steps that may be taken to achieve this goal. First, one might increase the order of the optical non-linearity. The volume excited by a three-photon absorption is smaller than that excited by a two-photon absorption. Perhaps more attractive, though, is the potential use of stimulated emission depletion (STED).<sup>[51]</sup> It has already been shown in fluorescence microscopy that the diffraction limit resolution can be broken by quenching excited chromophores at the rim of the focal spot through stimulated emission. The combination of the threshold effect and STED in TPAP should produce voxels with sub-100-nm sizes.

Although TPAP has been used to fabricate freely movable microparts and passive optic components, few functional devices have been made to date. To operate as actuators or sensors, microstructures fabricated by TPAP will greatly benefit from the optical, electrical, and magnetic properties of metals. Thus the fabrication of polymer/metal hybrid microstructure holds is a promising future direction of this technique for applications such as microelectrical mechanical systems and micrototal analytical systems.

## ACKNOWLEDGMENTS

The microstructures fabricated in our laboratory were created with support from the National Science Foundation (Grant ECS-0088438).

## REFERENCES

- Xia, Y.N.; Rogers, J.A.; Paul, K.E.; Whitesides, G.M. Unconventional methods for fabricating and patterning nanostructures. *Chem. Rev.* **1999**, *99* (7), 1823–1848.
- Mirkin, C.A.; Rogers, J.A. Emerging methods for micro- and nanofabrication. *MRS Bull.* **2001**, *26* (7), 506–509.
- Chen, Y.; Pepin, A. Nanofabrication: conventional and nonconventional methods. *Electrophoresis* **2001**, *22*, 187–207.
- Levenson, M.D. Deep pockets needed in the photoresist industry. *Solid State Technol.* **1995**, *38* (1), 57–66.
- Chou, S.Y.; Krauss, P.R.; Remstrom, P.J. Imprint of sub-25 nm vias and trenches in polymers. *Appl. Phys. Lett.* **1995**, *67* (21), 3114–3116.
- Marrian, C.R.K.; Snow, E.S. Proximal probe lithography and surface modification. *Microelectron. Eng.* **1996**, *32* (1–4), 173–189.
- Xia, Y.; Whitesides, G.M. Soft lithography. *Angew. Chem., Int. Ed.* **1998**, *37*, 550–575.
- Xia, Y.; Enoch, K.; Zhao, X.M.; Rogers, J.A.; Prentiss, M.G.; Whitesides, G.M. Complex optical surfaces formed by replica molding against elastomeric masters. *Science* **1996**, *273* (5273), 347–349.
- Bertsch, A.; Jiguet, S.; Bernhard, P.; Renaud, P. Microstereolithography: a review. *Mater. Res. Soc. Symp. Proc.* **2003**, *758*, LL1.1.1–LL1.1.13.
- Ikuta, K.; Maruo, S.; Hasegawa, T.; Adachi, T.; Takahashi, A.; Ikeda, K. Biochemical IC chips fabricated by hybrid microstereolithography. *Mater. Res. Soc. Symp. Proc.* **2003**, *758*, LL5.6.1–LL5.6.12.
- Strickler, J.H.; Webb, W.W. Two-photon excitation in laser scanning fluorescence microscopy. *Proc. SPIE* **1991**, *1398*, 107–118 (Can-Am East '90).
- Maruo, S.; Nakamura, O.; Kawata, S. Three-dimensional microfabrication with two-photon-absorbed photopolymerization. *Opt. Lett.* **1997**, *22* (2), 132–134.
- Meyers, F.; Marder, S.R.; Perry, J.W. Introduction to the nonlinear optical properties of organic materials. In *Chemistry of Advanced Materials*; Interrante, L.V., Hampden-Smith, M.J., Eds.; Wiley-VCH: New York, 1998; 207–269.
- Göppert-Mayer, M. Über elementarkette mit zwei quantensprüngen. *Ann. Phys.* **1931**, *9*, 273–295.
- Kaiser, W.; Garrett, C.G.B. Two-photon excitation in CaF<sub>2</sub>:Eu<sup>2+</sup>. *Phys. Rev. Lett.* **1961**, *7* (229–231).
- Denk, W.; Svoboda, K. Photon upmanship: why multiphoton imaging is more than gimmick. *Neuron* **1997**, *18*, 351–357.
- Diaspro, A.; Sheppard, J.R. Two-photon excitation fluorescence microscopy. In *Confocal and Two-Photon Microscopy. Foundations, Applications, and Advances*; Diaspro, A., Ed.; Wiley-Liss: New York, 2002; 39–73.
- Denk, W.; Strickler, J.H.; Webb, W.W. Two-photon laser scanning fluorescence microscopy. *Science* **1990**, *248*, 73–76.
- Soeller, C.; Cannel, M.B. Two-photon microscopy: imaging in scattering samples and three-dimensionally resolved flash photolysis. *Microsc. Res. Tech.* **1999**, *47*, 182–195.
- Sun, H.B.; Kawata, S. Two-photon laser precision microfabrication and its applications to micro-nano devices and systems. *J. Lightwave Technol.* **2003**, *21* (3), 624–633.
- Crivello, J.V.; Dietliker, K. *Photoinitiators for Free Radical, Cationic and Anionic Photopolymerization*, 2nd Ed.; John Wiley and Sons: New York, 1998; Vol. 3.
- Baldacchini, T.; Chen, H.; Farrer, R.A.; Previte, M.J.R.; Moser, J.; Naughton, M.J.; Fourkas, J.T. Multiphoton photopolymerization with a Ti:sapphire oscillator. *Proc. SPIE* **2002**, *4633*, 136–144.
- Kawata, S.; Sun, H.B. Two-photon photopolymerization of functional micro-devices. *J. Photopolym. Sci. Tech.* **2002**, *15* (3), 471–474.
- Belfield, K.D.; Ren, X.B.; Van Stryland, E.W.; Hagan, D.J.; Dubikovskiy, V.; Miesak, E.J. Near-IR two-photon photoinitiated polymerization using a fluorone/amine initiating system. *J. Am. Chem. Soc.* **2000**, *122* (6), 1217–1218.
- Pitts, J.D.; Campagnola, P.J.; Epling, G.A.; Goodman, S.L. Submicron multiphoton free-form fabrication of proteins and polymers: studies of reaction efficiencies and applications in sustained release. *Macromolecules* **2000**, *33* (5), 1514–1523.
- Albota, M.; Beljonne, D.; Bredas, J.L.; Ehrlich, J.E.; Fu, J.Y.; Heikal, A.A.; Hess, S.E.; Kogei, T.; Levin, M.D.; Marder, S.R.; McCord-Maughon, D.; Perry, J.W.; Rockel, H.; Rumi, M.; Subramaniam, G.; Webb, W.W.; Wu, X.L.; Xu, C. Design of organic molecules with large two-photon absorption cross sections. *Science* **1998**, *281*, 1653–1656.
- Rumi, M.; Ehrlich, J.E.; Heikal, A.A.; Perry, J.W.; Barlow, S.; Hu, Z.; McCord-Maughon, D.; Parker, T.C.; Rockel, H.; Thayumanavan, S.; Marder, S.R.; Beljonne, D.; Bredas, J.L. Structure-property relationships for two-photon absorbing chromophores: bis-donor diphenylpolyene and bis(styryl)benzene derivatives. *J. Am. Chem. Soc.* **2000**, *122*, 9500–9510.
- Reianhardt, B.A.; Brott, L.L.; Clarson, S.J.; Dillard, A.G.; Bhatt, J.C.; Kannan, R.; Yuan, L.; He, G.S.; Prasad, P.N. Highly active two-photon dyes: design, synthesis, and characterization toward application. *Chem. Mater.* **1998**, *10*, 1863–1874.
- Belfield, K.D.; Schafer, K.J.; Liu, Y.U.; Liu, J.; Ren, X.B.; Van Stryland, E.W. Multiphoton-absorbing organic materials for microfabrication, emerging optical applications and non-destructive three-dimensional imaging. *J. Phys. Org. Chem.* **2000**, *13* (12), 837–849.
- Cumpston, B.H.; Ananthavel, S.P.; Barlow, S.; Dyer, D.L.; Ehrlich, J.E.; Erskine, L.L.; Heikal, A.A.; Kuebler, S.M.; Lee, I.Y.S.; McCord-Maughon, D.; Qin, J.Q.; Rockel, H.; Rumi, M.; Wu, X.L.; Marder, S.R.; Perry, J.W. Two-photon polymerization initiators for three-dimensional optical data storage and microfabrication. *Nature* **1999**, *398* (6722), 51–54.
- Li, C.D.; Luo, L.; Wang, S.F.; Huang, W.T.; Gong, Q.H.; Yang, Y.Y.; Feng, S.J. Two-photon microstructure-polymerization initiated by a coumarin derivative/iodonium salt system. *Chem. Phys. Lett.* **2001**, *340* (5–6), 444–448.



32. Luo, L.; Li, C.D.; Wang, S.F.; Huang, W.T.; Wu, C.Y.; Yang, H.; Jiang, H.B.; Gong, Q.H.; Yang, Y.Y.; Feng, S.J. Optical microstructures fabricated by femtosecond laser two-photon polymerization. *J. Opt. A, Pure Appl. Opt.* **2001**, *3* (6), 489–492.
33. Kuebler, S.M.; Cumpston, B.H.; Ananthavel, S.; Barlow, S.; Ehrlich, J.E.; Erskine, L.L.; Heikal, A.A.; McCord-Maughon, D.; Qin, J.; Rockel, H.; Rumi, M.; Marder, S.R.; Perry, J.W. Three-dimensional microfabrication using two-photon activated chemistry. *Proc. SPIE* **2000**, *3937*, 97–105.
34. Kuebler, S.M.; Rumi, M.; Watanabe, T.; Braun, K.; Cumpston, B.H.; Heikal, A.A.; Erskine, L.L.; Thayumanavan, S.; Barlow, S.; Marder, S.R.; Perry, J.W. Optimizing two-photon initiators and exposure conditions for three-dimensional lithographic microfabrication. *J. Photopolym. Sci. Tech.* **2001**, *14* (4), 657–668.
35. Decker, C. Recent developments in photoinitiated radical polymerization. *Macromol. Symp.* **1999**, *143*, 45–63.
36. Serbin, J.; Egbert, A.; Ostendorf, A.; Chichkov, B.N.; Houbertz, R.; Domann, G.; Schulz, J.; Cronauer, C.; Frohlich, L.; Popall, M. Femtosecond laser-induced two-photon polymerization of inorganic–organic hybrid materials for applications in photonics. *Opt. Lett.* **2003**, *28* (5), 301–303.
37. Streppel, U.; Dannberg, P.; Wachter, C.; Brauer, A.; Frohlich, L.; Houbertz, R.; Popall, M. New wafer-scale fabrication method for stacked optical waveguide interconnects and 3D micro-optic structures using photoresponsive (inorganic–organic hybrid) polymers. *Opt. Mater.* **2002**, *21*, 475–483.
38. Kuebler, S.M.; Braun, K.L.; Zhou, W.H.; Cammack, J.K.; Yu, T.Y.; Ober, C.K.; Marder, S.R.; Perry, J.W. Design and application of high-sensitivity two-photon initiators for three-dimensional microfabrication. *J. Photochem. Photobiol., A Chem.* **2003**, *158* (2–3), 163–170.
39. Yu, T.; Ober, C.K.; Kuebler, S.M.; Zhou, W.; Marder, S.R.; Perry, J.W. Chemically amplified positive resists for two-photon three-dimensional microfabrication. *Adv. Mater.* **2003**, *15* (6), 517–521.
40. Sun, H.B.; Tanaka, T.; Kawata, S. Three-dimensional focal spots related to two-photon excitation. *Appl. Phys. Lett.* **2002**, *80* (20), 3673–3675.
41. Sun, H.B.; Takada, K.; Kim, M.S.; Lee, K.S.; Kawata, S. Scaling laws of voxels in two-photon photopolymerization nanofabrication. *Appl. Phys. Lett.* **2003**, *83* (6), 1104–1106.
42. Kawata, S.; Sun, H.B.; Tanaka, T.; Takada, K. Finer features for functional microdevices—micromachines can be created with higher resolution using two-photon absorption. *Nature* **2001**, *412* (6848), 697–698.
43. Sun, H.B.; Maeda, M.; Takada, K.; Chon, J.W.M.; Gu, M.; Kawata, S. Experimental investigation of single voxels for laser nanofabrication via two-photon photopolymerization. *Appl. Phys. Lett.* **2003**, *83* (5), 819–821.
44. Dorn, R.; Quabis, S.; Leuchs, G. The focus of light-linear polarization breaks the rotational symmetry of the focal spot. *J. Mod. Opt.* **2003**, *50* (12), 1917–1926.
45. de Grauw, C.J.; Frederix, P.L.T.; Gerritsen, H.C. Aberrations and penetration in in-depth confocal and two-photon-excitation microscopy. In *Confocal and Two-Photon Microscopy. Foundations, Applications, and Advances*; Diaspro, A., Ed.; Wiley-Liss: New York, 2002; 153–169.
46. Sun, H.B.; Takada, K.; Kawata, S. Elastic force analysis of functional polymer submicron oscillators. *Appl. Phys. Lett.* **2001**, *79* (19), 3173–3175.
47. Sun, H.; Matzuo, S.; Misawa, H. Three-dimensional photonic crystal structures achieved with two-photon-absorption photopolymerization of resin. *Appl. Phys. Lett.* **1999**, *74* (6), 786–788.
48. Kaneko, K.; Sun, H.B.; Duan, X.M.; Kawata, S. Submicron diamond-lattice photonic crystals produced by two-photon laser nanofabrication. *Appl. Phys. Lett.* **2003**, *83* (11), 1–4.
49. Maruo, S.; Ikuta, K. Three-dimensional microfabrication by use of single-photon-absorbed polymerization. *Appl. Phys. Lett.* **2000**, *76* (19), 2656–2658.
50. Maruo, S.; Ikuta, K.; Korogi, H. Submicron manipulation tools driven by light in a liquid. *Appl. Phys. Lett.* **2003**, *82* (1), 133–135.
51. Klar, T.A.; Jakobs, S.; Dyba, M.; Egner, A.; Hell, S.H. Fluorescence microscopy with diffraction resolution barrier broken by stimulated emission. *PNAS* **2000**, *97* (15), 8206–8210.

# Titania Coatings on Stainless Steel

Ganesh Balasubramanian  
Dionysios D. Dionysiou  
Makram T. Suidan

*Department of Civil and Environmental Engineering, University of Cincinnati,  
Cincinnati, Ohio, U.S.A.*

## INTRODUCTION

Titanium dioxide ( $\text{TiO}_2$ ) is a photosensitive semiconductor and its valence electrons are excited into the conduction band by high-energy radiation in the ultraviolet (UV) range (200–400 nm).<sup>[1,2]</sup>  $\text{TiO}_2$  has been used for diverse applications in various configurations as pellets, beads, powders, and immobilized films. The most frequently cited applications for  $\text{TiO}_2$  in a film configuration are as self-cleaning materials,<sup>[3,4]</sup> agents for heterogeneous photocatalysis,<sup>[5–7]</sup> solar cells,<sup>[8–10]</sup> gas sensors,<sup>[11,12]</sup> and corrosion-control coatings.<sup>[13–15]</sup>

Pure  $\text{TiO}_2$  pellets or beads tend to be brittle and susceptible to attrition or fragmentation under mild stress and shear forces.  $\text{TiO}_2$  powders are active because they have a high specific surface area, but removing the powder catalyst from the reaction bulk media can be troublesome.

Thus  $\text{TiO}_2$  film coatings have attracted considerable interest in the last decade. Film coatings make available the catalytic properties of  $\text{TiO}_2$  while benefiting from the mechanical properties of the substrate.  $\text{TiO}_2$  films are fabricated onto supporting materials (substrates) by a variety of different methods including the sol-gel method,<sup>[16]</sup> sputtering technique,<sup>[17]</sup> electrochemical process,<sup>[18,19]</sup> chemical vapor deposition (CVD),<sup>[20,21]</sup> and spray pyrolysis.<sup>[22,23]</sup>

## OVERVIEW

The substrate most commonly reported in the literature is quartz glass. This is because quartz glass coupons are easily available in many sizes and in different thickness sizes. In addition, studying the optical properties of the film is easier when the substrate is transparent and with known optical properties. Various other substrate materials used are silicon whiskers, ceramics, and stainless steel.

Stainless steel is an excellent substrate material for many reasons. It retains its structural integrity under

the high temperature required for heat treatment of the  $\text{TiO}_2$  films whereas quartz glass softens and deforms. Stainless steel also is not susceptible to attack during the coating process except under drastic conditions. Quartz and ceramics cannot be used in electrochemical processes because of their dielectric properties. Unlike quartz or ceramics, stainless steel can easily be worked into complex shapes and possesses excellent mechanical properties.

When substrates coated with  $\text{TiO}_2$  films are heat-treated, the ions from the substrate diffuse through the  $\text{TiO}_2$  layer.<sup>[24]</sup> Electron dispersive spectroscopy (EDS) studies show that when glass coated with  $\text{TiO}_2$  films is heat-treated near the melting point of glass (500–600°C), ions such as  $\text{Na}^+$ ,  $\text{Si}^+$ , and  $\text{Ca}^{2+}$  diffuse into the layer.<sup>[25]</sup> These cations act as sinks for the photogenerated electrons and inhibit the activity of the photocatalytic  $\text{TiO}_2$  film. Electron dispersive spectroscopy studies further show that when stainless-steel substrates coated with  $\text{TiO}_2$  are heat-treated,  $\text{Fe}^{3+}$  and  $\text{Cr}^{3+}$  ions diffuse into the  $\text{TiO}_2$  film<sup>[25]</sup> and these ions similarly inhibit the activity. However, the magnitude of diffusion is much smaller for stainless steel when compared with glass and the inhibitory effect is much lesser. Thus  $\text{TiO}_2$  photocatalytic coatings on stainless steel have higher photoactivity than  $\text{TiO}_2$  coatings on glass. For the above reasons, stainless steel is the material of choice for the purposes of fabricating practical process equipment such as  $\text{TiO}_2$  photocatalytic reactors for water and air treatment.

In this article, the first section focuses on the nanoscience of titanium dioxide by describing its crystal atomic structure and phase-transformation behavior and their influence on the observed photocatalytic and photosensitive properties of titanium dioxide. The nanotechnological methods used to fabricate  $\text{TiO}_2$  films on stainless-steel substrates are described with a brief discussion of their relative merits. Sol-gel methods to synthesize  $\text{TiO}_2$  films are discussed in detail because of their significant advantages over many other methods. The concluding section discusses the applications of  $\text{TiO}_2$  films on stainless steel.

## PHASES OF TiO<sub>2</sub> AND THEIR IMPACT ON PHOTOCATALYTIC AND PHOTSENSITIVE PROPERTIES

TiO<sub>2</sub> has an amorphous form and three crystalline phases: anatase, brookite, and rutile. At room temperature, the stable crystal phase is rutile. The anatase and brookite phases are metastable phases that can be converted, under suitable conditions, to the rutile phase. The brookite phase is rare and is rapidly converted to the rutile phase.

Anatase TiO<sub>2</sub> is composed of a tetragonal lattice forming octahedral structures.<sup>[26]</sup> Rutile TiO<sub>2</sub> is a hexagonal close-packed lattice also forming octahedral structures. It is characterized by the presence of the bridging oxygen on the 110 face.<sup>[27]</sup> The band gap for the anatase phase is 3.2–3.3 eV, while the band gap for the rutile phase is 3.0 ~ 3.1 eV. These energy levels correspond to UV radiation of 380–376 and 400 ~ 410 nm for anatase and rutile, respectively. When the surfaces of the crystals are illuminated with UV radiation of appropriate wavelength, electron-hole pairs are generated<sup>[2]</sup> by the excitation of an electron from the valence band to the conduction band. Some of these photogenerated pairs are destroyed by recombination either in the bulk or on the surface of the particle.

Other electron-hole pairs achieve charge separation and diffuse to the surface of the crystal to initiate and catalyze redox reactions with electron donors or acceptors.<sup>[28]</sup> The diffused electrons reduce Ti<sup>4+</sup> sites [Ti(IV)] on the surface of the crystals to Ti<sup>3+</sup> [Ti(III)]. The formation of the reduced Ti<sup>3+</sup> sites serves to lower the rate of recombination allowing the photogenerated holes to diffuse to the surface of the crystal to eventually generate the OH<sup>•</sup> radical that attack the organic compounds.<sup>[29,30]</sup>

For photocatalytic applications in the aqueous media, a number of studies have indicated that an increased fraction of the anatase phase increases the photoactivity.<sup>[31,32]</sup> Other studies<sup>[34,75,77]</sup> suggest that the ideal catalyst is a mixture of anatase and rutile phases. The proposed reason behind the enhanced photocatalytic activity is the transfer of electron between the crystal phases leading to lesser electron-hole recombination in the electron donor phase. Thus the more holes in the electron donor phase can diffuse to the surface of the crystal to take part in the radical generation step.

Some investigators have suggested that the electron transfer takes place from anatase to rutile. The removal of the hydroxyl group is easier from anatase 101 and 001 faces than the rutile 110 crystal face.<sup>[30]</sup> Since the hydroxyl groups are less strongly bound to the anatase phase than to the rutile phase, an increase in the number of holes diffusing to the anatase surface would

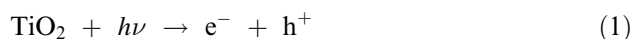
presumably increase the number of relatively easy to remove hydroxyl groups available for radical generation thus increasing the rate of attack on organic compounds.

Other investigators<sup>[75]</sup> have proposed that it is more likely that the electrons are transferred to lower energy anatase electron traps. The rate of generation of electronhole is higher in rutile than in anatase due to the lower band gap energy. However, the anatase is phase traps more electrons than the rutile phase. Hence there is less recombination in the anatase phase than in the rutile phase leading to more holes being available. Hurum et al.<sup>[76]</sup> suggest that the increased activity of the anatase-rutile mixed catalyst is due to transfer of electrons from rutile phase to lower energy anatase electron traps leading to a greater number of rutile originating holes diffusing to the surface and taking part in hydroxyl adsorption followed by radical generation.

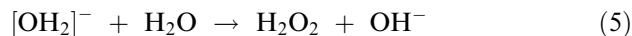
In aqueous media, upon irradiation by UV light, the surface of TiO<sub>2</sub> undergoes a conversion from hydrophobic to hydrophilic state<sup>[29]</sup> by adsorbing hydroxyl groups from the dissociation of water molecules and by forming hydrogen bonds with the OH groups of undissociated water molecules.<sup>[34]</sup>

As suggested above, an ideal catalyst is possibly a mixture of anatase and rutile phases.

The following series of reactions for the photocatalytic pathway in aqueous media have been proposed:<sup>[35]</sup>



The superoxide radical then reacts with water



The final step is the radical generating step



The radicals subsequently react with the radical scavenging species.

## METHODS USED TO FABRICATE TiO<sub>2</sub> FILMS ON STAINLESS STEEL

Numerous methods have been used to fabricate TiO<sub>2</sub> films. Some of the published methods discussed here have been applied to produce films on substrates other

than stainless steel, but the techniques are equally applicable on stainless steel. The most widely used method is the sol-gel method because of its many advantages. It will be discussed in greater detail than the other methods.

Magnetron sputtering<sup>[36,77]</sup> is a process by which the substrate to be coated is placed in a low-pressure chamber. The chamber is evacuated and suitable sputtering gases are introduced. The commonly used gases are oxygen and argon. A source for the TiO<sub>2</sub> (also known as the target) is prepared by either compressing and sintering Ti powder or by using a Ti filament or bar. Magnets are placed on one side of the target. The distance between the target and the substrate is between 10 and 15 cm. A high d.c. voltage, usually in the order of a few thousand volts, is applied between the substrate and the target. A cyclical electromagnetic field (40 kHz–2.45 GHz)<sup>[36,77]</sup> is simultaneously applied to create plasma in the chamber. The Ti ions are transported from the target to the substrate under the effect of the applied potential.

Sputtered films are usually heat-treated at temperatures ranging from 500°C to 1000°C to convert the sputtered films to anatase and rutile phases<sup>[37,38]</sup> and thus improve their photocatalytic activity.

Sputtering is a technique limited to substrates that are small enough and can fit into a vacuum chamber. The coatings produced by sputtering are nonhomogeneous with respect to thickness. A more uniform coating can be produced by moving the target during deposition and by increasing the number of magnets used.<sup>[36]</sup> The roughness of the coatings is directly proportional to the deposition rate, which in turn is proportional to the applied voltage. Reducing the applied voltage results in smoother films. Reducing the O<sub>2</sub> partial pressure also produces smoother coatings.<sup>[39]</sup> Sputtered TiO<sub>2</sub> film catalysts have been used for photocatalysis both in the liquid phase and the gas phase.<sup>[17,38,40]</sup>

Spray pyrolysis is a method in which TiO<sub>2</sub> colloids or precursors are sprayed over a hot substrate using O<sub>2</sub> or air as a carrier gas. Some of the starting materials used for synthesis of the TiO<sub>2</sub> films are TiCl<sub>4</sub>,<sup>[41]</sup> titanium tetraisobutoxide,<sup>[22]</sup> and titanium tetraisopropoxide (TTIP).<sup>[42]</sup> The substrate temperature is maintained at 200–500°C by heating the substrate during the spraying process. Spraying is performed by means of spray guns, which may be computer-controlled to provide uniform spraying.<sup>[40]</sup> After the TiO<sub>2</sub> film is deposited, further heat treatment may be performed at temperatures up to 1050°C to convert TiO<sub>2</sub> into anatase or rutile phases.

Spray pyrolysis is a relatively simple technique that can be used for simple shapes including flat plate-like surfaces and the curved surfaces of tubes.<sup>[43]</sup> A major

advantage is that there is no limitation on the size of the substrate that can be coated by spraying. Thicker films may be obtained by increasing the spraying time or by repeating the spray process after heat treatment. However, precise control of the intrinsic film properties may be difficult to achieve.

Electrodeposition methods produce cathodic TiO<sub>2</sub> films on stainless steel. The source of the titanium can be a sacrificial anode<sup>[44]</sup> or titanium precursor salt such as TiO(SO<sub>4</sub>).<sup>[45]</sup> Titanium precursors are prone to hydrolysis and precipitation of titanium hydroxide gels catalyzed by the presence of very small amounts of water or other hydrolysis catalysts. Therefore acetone or acidic solvents are used as the bulk media.<sup>[44,46]</sup> A drawback of the electrodeposition method is the limitation on the thickness of the films that can be obtained as a result of backvoltage. Oxidation of the titanium metal to the oxide can occur in situ in the presence of water.<sup>[44]</sup> Alternatively, the deposited Ti films can be converted to the oxidized state by heat treatment in the presence of air. Heat treatment or annealing may also be performed to obtain phase transformation to the crystalline anatase or rutile phases. Electrodeposited TiO<sub>2</sub> films on stainless steel have been shown to have photocatalytic properties.<sup>[44]</sup>

Chemical vapor deposition (CVD) is a film synthesis process that utilizes a carrier gas to transport TiO<sub>2</sub> precursors onto a heated substrate. The typical precursor used is titanium tetraisopropoxide.<sup>[47]</sup> The substrate to be coated is placed in a closed chamber, which is then pumped out to a low pressure via vacuum pumps. The substrate is heated in this chamber at temperatures varying from 150°C to 750°C.<sup>[48–50]</sup> The carrier gas, usually N<sub>2</sub>, is bubbled through the precursor and transported into the chamber. The gases are adsorbed onto the heated substrate and deposition of the precursor takes place followed by oxidation. The coated substrate may be subsequently heat-treated to obtain crystalline TiO<sub>2</sub> films.<sup>[51]</sup> A variation of the basic CVD method is the laser-assisted CVD<sup>[47,52]</sup> in which a laser is used to provide the energy to convert the precursor to TiO<sub>2</sub>, thereby rendering the use of lower temperatures for the film coating and phase transformation process. The CVD process is subject to the same limitation as the sputtering process; the substrate must be small enough to be placed in the vacuum chamber. Furthermore, this technique is mainly useful for depositing very thin layers on smooth substrates. Precise control of film properties such as particle size and porosity is not achievable by this method.

Other methods of synthesizing TiO<sub>2</sub> films are through the use of binders to immobilize TiO<sub>2</sub> powder,<sup>[53,54]</sup> dip coating in reverse micellar<sup>[55]</sup> gels, and the hot wall technique.<sup>[56]</sup>

## SOL-GEL PROCESSES TO SYNTHESIZE TiO<sub>2</sub> FILMS ON STAINLESS-STEEL SUBSTRATES

Sol-gel processes are the most widely used methods to prepare TiO<sub>2</sub> photocatalytic films on substrates. A sol consisting of TiO<sub>2</sub> precursors is prepared and placed in a suitable container. The substrate to be coated is cleaned and placed in a lifting device. The substrate is then dipped into the sol container and pulled out (dip coating method). The obtained film is dried and heat-treated. The process can be repeated as desired to obtain thicker coatings.

A variety of titanium alkoxides have been used as starting materials for the sol. These include titanium tetraisopropoxide (TTIP),<sup>[16]</sup> titanium tetrabutoxide,<sup>[57]</sup> and titanium ethoxide.<sup>[58]</sup> The alkoxides are usually dissolved in ethanol, isopropanol, or 2-butanol.

Dip-coating produces uniform coats on substrates. However, to obtain uniform coats, the withdrawal speed of the substrate from the sol must be kept constant. Furthermore, the sol container must be large enough that the removal of the substrate causes negligible changes in liquid level. The thickness of the coating is directly dependent on the withdrawal speed up to a point.<sup>[66]</sup> The constant rate of removal is achieved by means of a simple lifting apparatus fitted with a variable speed controller. Removal of the substrate by hand is not recommended.

It is important to note the effect of solvent on the properties of the film derived from TTIP sols by dip coating. It has been reported that isopropyl alcohol is preferable than ethanol as a solvent for TTIP.<sup>[59]</sup> When ethanol is used as a solvent, oligomeric complexes of TTIP are formed. These oligomeric complexes are more slowly hydrolyzed because of steric hindrance. The lower rates of hydrolysis and condensation result in smaller particles of sol and produce a smooth surface.<sup>[59]</sup>

Formation of oligomeric complexes of TTIP is lesser when isopropyl alcohol is used as a solvent instead of ethanol.<sup>[59]</sup> The larger proportion of monomers of TTIP that remain in solution undergo hydrolysis and condensation faster and thus form larger particles. These larger particles of sol also produce a higher viscosity.<sup>[59]</sup> All other factors being constant, the film thickness is controlled by the viscosity. These larger particles produce a rough film. The use of isopropyl alcohol as solvent promotes crystallization of the anatase phase at a lower temperature than when ethanol is used as the solvent. Higher concentration of Ti<sup>3+</sup> sites is also obtained when isopropyl alcohol is used as the solvent. It is known that Ti<sup>3+</sup> sites are active sites for water decomposition during the photocatalytic process.<sup>[29,30]</sup>

Drying the dip-coated film on a substrate is essential prior to heat treatment. When the dip-coated liquid

film is heated, the rise in temperature decreases the viscosity. A simultaneous increase in viscosity occurs because of the loss of the solvent phase and the formation of cross-linked networks of polymers from the monomers. If the heating is rapid, the overall viscosity may decrease, leading to gravitational collapse of the dip-coated film. Drying at the same temperature as the dip-coating process allows for gradual loss of solvent and networking of the precursor monomers preventing a collapse of the film upon heat treatment.

Because the photocatalytic activity is intrinsically bound with the grain size and crystal phase fractions, controlling these parameters is essential to fabricate useful photocatalytic TiO<sub>2</sub> films. Grain size has an important effect on the transformation of anatase to rutile. It has been demonstrated for a system with water as the hydrolysis catalyst that pure anatase is formed between 225°C and 550°C.<sup>[60]</sup> At 550°C, the first peaks of rutile are observed. Above 800°C, anatase is entirely transformed into rutile. The phase transformation is accompanied by a grain-growth process.<sup>[60]</sup> The increase in grain size leads to a decrease in surface area. Phase transformation is a surface process as nucleation occurs on the surface and the decrease in surface area limits the number of available nucleation sites, thus tending to inhibit the transformation process. Grain growth is also driven by the surface energy. The decrease in surface area with the increase in grain size further slows down the growth of the grains. Smaller grains undergo the phase transformation from anatase to rutile easier than larger grains, which are more likely to be of mixed phase.

Diethanolamine (DEA)<sup>[61]</sup> may be added to stabilize the sol and increase the viscosity. It also promotes crystallization and increases the viscosity of the sol. Hydrolysis catalysts such as water or HCl are also added to the sol to facilitate the hydrolysis of the precursors. It has been demonstrated that the ratio of water/Ti alkoxide (denoted by  $w$ ) is crucial in determining the crystallization rate, the crystal structure of the crystals formed, the size of the crystal grains, and the phase-transformation temperatures.<sup>[61]</sup>

Water hydrolyzes titanium alkoxides and the extent of hydrolysis is directly dependent on the molecular ratio  $w$ . A  $w$  of 4 or above is needed for the complete hydrolysis of the alkoxide. The hydrolysis is followed by the polycondensation step. Gels with a lower  $w$  form linear polymer molecules in a weakly cross-linked network. This weakly cross-linked network allows for the relatively easy elimination of the organic components during heat treatment. Hence sols with a lower  $w$  form smaller anatase grains at a lower temperature and undergo phase transformation from anatase to rutile at a lower temperature. Gels with a higher  $w$  form a nonlinear three-dimensional polymer that is highly cross-linked. During heat treatment, the high

degree of cross-linking makes it relatively more difficult to eliminate the organic and water components.<sup>[61]</sup> The temperature of crystallization is observed to be higher and larger grains of anatase crystals are formed under the same conditions.<sup>[61]</sup> Because the stability of crystallites increases with grain size,<sup>[60]</sup> the larger grains formed also transform from anatase to rutile at a higher temperature.

The sols may be further modified by addition of components such as polyethylene glycol (PEG)<sup>[62]</sup> as discussed below. The objective is to improve the porosity of the anatase film obtained by the alkoxide sol-gel methods. An increase in porosity has a twofold effect on photocatalytic activity. Increased porosity means increased surface area for reaction and mass transfer. Pores of an optimum size also aid in capturing the incident radiation. It has been found that the porosity increases with an increase in the amount of polyethylene glycol. The pores are uniformly distributed over the surface of the film. The pore diameter also increases with an increase in the amount of polyethylene glycol. It has been demonstrated<sup>[61]</sup> that pores whose diameters are one-third to  $\frac{1}{2}$  the wavelength of the incident radiation are the most effective in capturing the incident radiation. For capturing radiation in the 200–400 nm range, intermediate pore sizes in the 100–150 nm range are the most effective.<sup>[61]</sup> When films were synthesized with pore sizes in the range 200–350 nm, they displayed a lower activity than films with 100–150-nm pore size.<sup>[61]</sup>

Another approach to increase the porosity is to use fine-powdered activated carbon as an additive to the sol.<sup>[63]</sup> Upon heat treatment, the carbon is eliminated, leading to the formation of very porous non-homogenous TiO<sub>2</sub> aggregates. Films formed by this technique, while exhibiting increased porosity, may be susceptible to mechanical problems such as flaking or fracture.

TiO<sub>2</sub> sol-gel-derived films also lend themselves to be easily doped by various materials to enhance their photocatalytic activity. Silicon has been used as a dopant for TiO<sub>2</sub> films.<sup>[64]</sup> Silicon in the form of silica (SiO<sub>2</sub>) suppresses the growth of crystal grain while also inhibiting the phase transformation from anatase to rutile. The surface area of the TiO<sub>2</sub> film increases with the increase in silica content, with mesopores being observed when the content was greater than 30%.<sup>[64]</sup> The crystal grain size does not increase after the silica content is greater than 10% by weight.<sup>[64]</sup> The resulting smaller grain size results in a large surface area. The surface area continues to increase with the increase in silica content even after the crystal-size increase tapers off as a result of the formation of mesopores and surface structures. It has been suggested<sup>[64]</sup> that while smaller pores may be more effective in absorption of light, larger pores may allow for better mass transfer,

and thus TiO<sub>2</sub> films with larger pores may be more effective as photocatalysts.

Platinum and iron have also been investigated as possible dopants for TiO<sub>2</sub> films.<sup>[65]</sup> TiO<sub>2</sub> doped with Pt displays about a third more photocatalytic activity than undoped TiO<sub>2</sub> films. Fe<sup>3+</sup> decreases the activity of the TiO<sub>2</sub> films possibly by acting as charge recombination site.

The sol-gel route of synthesis of TiO<sub>2</sub> films is the method of choice in many cases for several reasons: The sol-gel method does not need any special equipment other than a furnace for heat treatment. Dip-coating techniques for sol-gel methods allow complex-shaped substrates to be uniformly coated. Large substrates can be easily coated. The film properties can be precisely determined by controlling sol preparation parameters such as concentration and nature of precursors,<sup>[66]</sup> viscosity,<sup>[16]</sup> dipping temperature,<sup>[67]</sup> withdrawal speed,<sup>[16,68]</sup> and temperature and duration of heat treatment. The film thickness in sol-gel methods can be increased by repeating the dip-coating/drying/heat treatment cycle.<sup>[16,62,68]</sup>

## APPLICATIONS OF TiO<sub>2</sub> COATINGS ON STAINLESS STEEL

Most of the initial work in the area of TiO<sub>2</sub> photocatalysis focused on the use of TiO<sub>2</sub> powder slurries, pure beads, and pellets despite their obvious disadvantages as discussed earlier. With the realization that the photocatalytic activity is confined to a relatively shallow surface layer, the focus has shifted to the use of supported films of TiO<sub>2</sub>. The improvement and refinement of different techniques to support TiO<sub>2</sub> films on stainless steel and other substrates has resulted in a growing list of applications for TiO<sub>2</sub> photocatalytic films.

One of the primary areas of interest in TiO<sub>2</sub> photocatalysis is the destruction of organic contaminants in contaminated water and air. Supported TiO<sub>2</sub> films are illuminated by UV radiation of the appropriate wavelength. The contaminant to be destroyed is contacted with the catalyst surface either by immersion in the bulk phase or by a thin-film flow. Reaction takes place on the surface with the mass transfer of reactants occurring across the diffusive layer on the surface. The controlling step in TiO<sub>2</sub> photocatalysis is either the photogeneration of electrons-hole pairs via light absorption or the diffusion of reactants and products across the diffusive layer.

Plate photoreactors<sup>[69,70]</sup> utilize illuminated TiO<sub>2</sub> films on plates to degrade target compounds. Another type of photoreactor that has been used for degradation of organic pollutants is a rotating disk reactor.<sup>[71,72]</sup> The stainless-steel rotating disk is dip-coated with



titanium dioxide by a sol-gel process followed by heat treatment to obtain a mixed phase anatase-rutile film. As the disk rotates out of the aqueous phase, it carries up a thin layer of liquid on the surface. Several UV lamps mounted perpendicular to the surface provide UV illumination to the catalyst surface. Oxygen from the gas phase diffuses through the thin film to the catalyst surface and destruction of the contaminants takes place in the thin layer. A variation of this type of photoreactor is the use of a rotating cylinder instead of a rotating disk to enable the use of solar radiation instead of UV lamps.

## CONCLUSIONS

TiO<sub>2</sub> photocatalytic films immobilized on stainless steel show potential for use as anticorrosion agents.<sup>[13,73,74]</sup> The films exhibit self-cleaning properties against corrosive organic compounds.<sup>[15]</sup> Conventional paint and other anticorrosion coatings are passive agents. Photocatalytic TiO<sub>2</sub> films function as active agents, mineralizing organic deposits over time and thus cleaning themselves. This is a significant parameter for the reduction of maintenance costs. The same principle is used in the production of easily cleaned surgical tools for use in battlefield situations where the stainless-steel surgical tools coated with titanium dioxide are sterilized by UV irradiation in the presence of air.

Other emerging applications of TiO<sub>2</sub> films include solar-powered photoelectric cells, gas sensors for use in automobiles, and protective nonporous coatings for in vivo biomaterials.

## ACKNOWLEDGMENTS

Dr. Dionysiou is grateful to the National Aeronautics and Space Administration (NASA) for financial support (Grant Number 02-OBPR-01-083) on the development of high-performance TiO<sub>2</sub> photocatalytic coatings.

## REFERENCES

1. Blake, D.M.; Webb, J.; Turchi, C.; Magrini, K. Kinetic and mechanistic overview of TiO<sub>2</sub>-photocatalyzed oxidation reactions in aqueous solution. *Sol. Energy Mater.* **1991**, *24* (1-4), 584-593.
2. Ollis, D.F.; Pelizzetti, E.; Serpone, N. Photocatalyzed destruction of water contaminants. *Environ. Sci. Technol.* **1991**, *25* (9), 1522-1529.
3. Wolfrum, E.J.; Huang, J.; Blake, D.M.; Maness, P.-C.; Huang, Z.; Fiest, J.; Jacoby, W.A. Photocatalytic oxidation of bacteria, bacterial and fungal spores, and model biofilm components to carbon dioxide on titanium dioxide-coated surfaces. *Environ. Sci. Technol.* **2002**, *36* (15), 3412-3419.
4. Paz, Y.; Luo, Z.; Rabenberg, L.; Heller, A. Photooxidative self-cleaning transparent titanium dioxide films on glass. *J. Mater. Res.* **1995**, *10* (11), 2842-2848.
5. Chemseddine, A.; Boehm, H.P. Study of the primary step in the photochemical degradation of acetic acid and chloroacetic acids on a TiO<sub>2</sub> photocatalyst. *J. Mol. Catal.* **1990**, *60* (3), 295-311.
6. Loddo, V.; Marci, G.; Martin, C.; Palmisano, L.; Rives, V.; Sclafani, A. Preparation and characterization of TiO<sub>2</sub> (anatase) supported on TiO<sub>2</sub> (rutile) catalysts employed for 4-nitrophenol photodegradation in aqueous medium and comparison with TiO<sub>2</sub> (anatase) supported on Al<sub>2</sub>O<sub>3</sub>. *Appl. Catal., B Environ.* **1999**, *20* (1), 29-45.
7. Grzechulska, J.; Morawski, A.W. Photocatalytic decomposition of azo-dye acid black 1 in water over modified titanium dioxide. *Appl. Catal., B Environ.* **2002**, *36* (1), 45-51.
8. O'Regan, B.; Graetzel, M. Low-cost, high-efficiency solar cell based on dye-sensitized colloidal TiO<sub>2</sub> films. *Nature* **1991**, *353* (6346), 737.
9. Thelakkat, M.; Schmitz, C.; Schmidt, H.-W. Fully vapor-deposited thin-layer titanium dioxide solar cells. *Adv. Mater.* **2002**, *14* (8), 577-581.
10. Gratzel, M. Sol-gel processed TiO<sub>2</sub> films for photovoltaic applications. *J. Sol-Gel Sci. Technol.* **2001**, *22* (1-2), 7-13.
11. Demarne, V.; Balkanova, S.; Grisel, A. Integrated gas sensor for oxygen detection. *Sens. Actuators, B, Chem.* **1993**, *B14* (1-3), 497-498. Part 2.
12. Huusko, J.; Lantto, V.; Torvela, H. TiO<sub>2</sub> thick-film gas sensors and their suitability for NO<sub>x</sub> monitoring. *Sens. Actuators, B, Chem.* **1993**, *B16* (1-3), 245-248. Part 2.
13. Atik, M.; Zarzycki, J. Protective TiO<sub>2</sub>-SiO<sub>2</sub> coatings on stainless steel sheets prepared by dip-coating. *J. Mater. Sci. Lett.* **1994**, *13* (17), 1301-1304.
14. Trzaskoma-Paulette, P.P.; Nazeri, A. Effects of sol-gel coatings on the localized corrosion behavior of 304 stainless steel. *J. Electrochem. Soc.* **1997**, *144* (4), 1307-1310.
15. Ohko, Y.; Saitoh, S.; Tatsuma, T.; Fujishima, A. Photoelectrochemical anticorrosion and self-cleaning effects of a TiO<sub>2</sub> coating for type 304 stainless steel. *J. Electrochem. Soc.* **2001**, *148* (1), B24-B28.
16. Takahashi, Y.; Matsuoka, Y. Dip-coating of TiO<sub>2</sub> films using a sol derived from Ti(O-i-pr)<sub>4</sub>-diethanolamine-H<sub>2</sub>O-i-proh system. *J. Mater. Sci.* **1988**, *23* (6), 2259-2266.
17. Weinberger, B.R.; Garber, R.B. Titanium dioxide photocatalysts produced by reactive magnetron sputtering. *Appl. Phys. Lett.* **1995**, *66* (18), 2409-2411.
18. Natarajan, C.; Nogami, G. Cathodic electrodeposition of nanocrystalline titanium dioxide thin films. *J. Electrochem. Soc.* **1996**, *143* (5), 1547-1550.
19. Kamada, K.; Mukai, M.; Matsumoto, Y. Electrodeposition of titanium(IV) oxide film from sacrificial titanium anode in I<sub>2</sub>-added acetone bath. *Electrochim. Acta* **2002**, *47* (20), 3309-3313.

20. Maruyama, T.; Arai, S. Titanium dioxide thin films prepared by chemical vapor deposition. *Sol. Energy Mater. Sol. Cells* **1992**, *26* (4), 323–329.
21. Rausch, N.; Burte, E.P. Thin TiO<sub>2</sub> films prepared by low pressure chemical vapor deposition. *J. Electrochem. Soc.* **1993**, *140* (1), 145–149.
22. Abou-Helal, M.O.; Seeber, W.T. Preparation of TiO<sub>2</sub> thin films by spray pyrolysis to be used as a photocatalyst. *Appl. Surf. Sci.* **2002**, *195* (1–4), 53–62.
23. Blesic, M.Dj.; Saponjic, Z.V.; Nedeljkovic, J.M.; Uskokovic, D.P. TiO<sub>2</sub> films prepared by ultrasonic spray pyrolysis of nanosize precursor. *Mater. Lett.* **2002**, *54* (4), 298–302.
24. Fernández, A.; Lassaletta, G.; Jiménez, V.M.; Justo, A.; González-Elipe, A.R.; Herrmann, J.-M.; Tahiri, H.; Ait-Ichou, Y. Preparation and characterization of TiO<sub>2</sub> photocatalysts supported on various rigid supports (glass, quartz and stainless steel). Comparative studies of photocatalytic activity in water purification. *Appl. Catal., B Environ.* **1995**, *7*, 43–49.
25. Balasubramanian, G.; Dionysiou, D.D.; Suidan, M.T.; Subramanian, V.; Baudin, I.; Laine, J.M. Titania powder modified sol gel process for photocatalytic applications. *J. Mater. Sci.* February 15, **2003**, *38* (4), 823–831.
26. Gonzalez, R.J.; Zallen, R.; Berger, H. Infrared reflectivity and lattice fundamentals in anatase TiO<sub>2</sub>. *Phys. Rev., B, Condens. Matter* **1997**, *55* (11), 7014–7017.
27. Paxton, A.T.; Thien-Nga, L. Electronic structure of reduced titanium dioxide. *Phys. Rev., B, Condens. Matter* **1998**, *57* (3), 1579–1584.
28. Hoffmann, M.R.; Choi, W.; Martin, S.T. Environmental applications of semiconductor photocatalysis. *Chem. Rev.* **Jan./Feb.** **1995**, *95*, 69–96.
29. Wang, R.; Hashimoto, K.; Fujishima, A.; Chikuni, M.; Kitamura, A.; Shimohigoshi, M.; Watanabe, T. Light-induced amphiphilic surfaces. *Nature* **1997**, *388*, 431.
30. Sakai, N.; Wang, R.; Fujishima, A.; Watanabe, T.; Hashimoto, K. Effect of ultrasonic treatment on highly hydrophilic TiO<sub>2</sub> surfaces. *Langmuir* **1998**, *14*, 5918–5920.
31. Yu, J.; Zhao, X.; Zhao, Q. Photocatalytic activity of nanometer TiO<sub>2</sub> thin films prepared by the sol-gel method. *Mater. Chem. Phys.* **2001**, *69* (1–3), 25–29.
32. Wang, T.; Wang, H.; Xu, P.; Zhao, X.; Liu, Y.; Chao, S. Effect of properties of semiconductor oxide thin films on photocatalytic decomposition of dyeing waste water. *Thin Solid Films* **1998**, *334* (1–2), 103–108.
33. Balasubramanian, G.; Dionysios, D.D.; Suidan, M.T.; Laine, J.M.; Baudin, I. *Appl. Catal., B Environ* **2003**. Accepted for publication.
34. Vittadini, A.; Selloni, A.; Rotzinger, F.P.; Gratzel, M. Structure and energetics of water adsorbed at TiO<sub>2</sub> anatase (101) and (001) surfaces. *Phys. Rev. Lett.* **1998**, *81* (14), 2954–2957.
35. Gerischer, H. Photocatalysis in aqueous solution with small TiO<sub>2</sub> particles and the dependence of the quantum yield on particle size and light intensity. *Electrochim. Acta* **1995**, *40* (10), 1277–1281.
36. Honbo, E.; Miyata, M.; Ueno, T.; Kato, Y.; Ishii, S. Preparation of TiO<sub>2</sub> thin films by sputtering applying electron cyclotron resonance plasma produced in arched magnetic mirrors. *Vacuum* **2002**, *66* (3–4), 263–267.
37. Ting, C.-C.; Chen, S.-Y.; Liu, D.-M. Preferential growth of thin rutile TiO<sub>2</sub> films upon thermal oxidation of sputtered Ti films. *Thin Solid Films* **2002**, *402* (1–2), 290–295.
38. Zheng, S.K.; Wang, T.M.; Xiang, G.; Wang, C. Photocatalytic activity of nanostructured TiO<sub>2</sub> thin films prepared by dc magnetron sputtering method. *Vacuum* **2001**, *62* (4), 361–366.
39. Szczyrbowski, J.; Braeuer, G.; Ruske, M.; Bartella, J.; Schroeder, J.; Zmelty, A. Some properties of TiO<sub>2</sub> layers prepared by medium frequency reactive sputtering. *Surf. Coat. Technol.* **1999**, *112* (1), 261–266.
40. Dumitriu, D.; Bally, A.R.; Ballif, C.; Hones, P.; Schmid, P.E.; Sanjines, R.; Levy, F.; Parvulescu, V.I. Photocatalytic degradation of phenol by TiO<sub>2</sub> thin films prepared by sputtering. *Appl. Catal., B Environ.* **2000**, *25* (2), 83–92.
41. Okuya, M.; Prokudina, N.A.; Mushika, K.; Kaneko, S. TiO<sub>2</sub> thin films synthesized by the spray pyrolysis deposition (SPD) technique. *J. Eur. Ceram. Soc.* **1999**, *19* (6–7), 903–906.
42. Chen, C.H.; Kelder, E.M.; Schoonman, J. Electrostatic sol-spray deposition (ESSD) and characterization of nanostructured TiO<sub>2</sub> thin films. *Thin Solid Films* **1999**, *342* (1), 35–41.
43. Miki-Yoshida, M.; Collins-Martinez, V.; Amezaga-Madrid, P.; Aguilar-Elguezabal, A. Thin films of photocatalytic TiO<sub>2</sub> and ZnO deposited inside a tubing by spray pyrolysis. *Thin Solid Films* **2002**, *419* (1–2), 60–64.
44. Kamada, K.; Mukai, M.; Matsumoto, Y. Electrodeposition of titanium(IV) oxide film from sacrificial titanium anode in I<sub>2</sub>-added acetone bath. *Electrochim. Acta* **2002**, *47* (20), 3309–3313.
45. Natarajan, C.; Nogami, G. Cathodic electrodeposition of nanocrystalline titanium dioxide thin films. *J. Electrochem. Soc.* **1996**, *143* (5), 1547–1550.
46. Zhitomirsky, I.; Petric, A. Electrolytic and electrophoretic deposition of CeO<sub>2</sub> films. *Mater. Lett.* **1999**, *40* (6), 263–268.
47. Watanabe, A.; Imai, Y. KrF laser CVD of titanium oxide from titanium tetraisopropoxide. *Thin Solid Films* **1999**, *348* (1), 63–68.
48. Furman, P.; Gluszek, J.; Masalski, J. Titanium dioxide film obtained using the MOCVD method on 316L steel. *J. Mater. Sci. Lett.* **1997**, *16* (6), 471–472.
49. Leistner, T.; Leimbacher, K.; Harter, P.; Schmidt, C.; Bauer, A.J.; Frey, L.; Rysse, H. MOCVD of titanium dioxide on the basis of new precursors. *J. Non-Cryst. Solids* **2002**, *303* (1), 64–68.
50. Babelon, P.; Dequiedt, A.S.; Mostefa-Sba, H.; Bourgeois, S.; Sibillot, P.; Sacilotti, M. SEM and XPS studies of titanium dioxide thin films grown by MOCVD. *Thin Solid Films* **Jun 8 1998**, *322* (1–2), 63–67.
51. Wang, D.; Wang, M.; Xu, X.H.; Hou, Y.; Wang, H.; Han, H. Characteristics of titanium dioxide films deposited by metalorganic chemical vapor deposition. *J. Mater. Sci. Lett.* **2002**, *21* (8), 635–637.
52. Halary, E.; Benvenuti, G.; Wagner, F.; Hoffmann, P. Light induced chemical vapor deposition of titanium

- oxide thin films at room temperature. *Appl. Surf. Sci.* **2000**, *154*, 146–151.
53. Kochev, K.D. Preparation and photoelectrochemical properties of TiO<sub>2</sub> thin binder layers. *Sol. Energy Mater.* **1985**, *12* (4), 249–256.
  54. Sopyan, I.; Watanabe, M.; Murasawa, S.; Hashimoto, K.; Fujishima, A. Film-type photocatalyst incorporating highly active TiO<sub>2</sub> powder and fluoro-resin binder: Photocatalytic activity and long-term stability. *J. Electroanal. Chem.* **1996**, *415* (1–2), 183–186.
  55. Stathatos, E.; Tsiourvas, D.; Lianos, P. Titanium dioxide films made from reverse micelles and their use for the photocatalytic degradation of adsorbed dyes. *Colloids Surf., A Physicochem. Eng. Asp.* **1999**, *149* (1), 49–56.
  56. Nakamura, T.; Asai, H.; Akiyama, M.; Azuma, N.; Takahashi, N.; Ishino, K.; Fujiyasu, H.; Yoshioka, M. Preparation of titanium dioxide thin films by means of a hot wall technique. *Appl. Surf. Sci.* **1999**, *142* (1), 182–187.
  57. Imai, H.; Hirashima, H. Preparation of porous anatase coating from sol-gel-derived titanium dioxide and titanium dioxide-silica by water-vapor exposure. *J. Am. Ceram. Soc.* **1999**, *82* (9), 2301–2304.
  58. Nagpal, V.J.; Davis, R.M.; Desu, S.B. Novel thin films of titanium dioxide particles synthesized by a sol-gel process. *J. Mater. Res.* **1995**, *10* (12), 3068–3078.
  59. Hu, L.; Yoko, T.; Kozuka, H.; Sakka, S. Effects of solvent on properties of sol-gel-derived TiO<sub>2</sub> coating films. *Thin Solid Films* **1992**, *219* (1–2), 18–23.
  60. Ding, X.-Z.; Liu, X.-H.; He, Y.-Z. Grain size dependence of anatase-to-rutile structural transformation in gel-derived nanocrystalline titania powders. *J. Mater. Sci. Lett.* **1996**, *15* (20), 1789–1791.
  61. Ding, X.-Z.; Qi, Z.-Z.; He, Y.-Z. Effect of hydrolysis water on the preparation of nano-crystalline titania powders via a sol-gel process. *J. Mater. Sci. Lett.* **1995**, *14* (1), 21–22.
  62. Kato, K.; Tsuzuki, A.; Torii, Y.; Taoda, H.; Kato, T.; Butsugan, Y. Morphology of thin anatase coatings prepared from alkoxide solutions containing organic polymer, affecting the photocatalytic decomposition of aqueous acetic acid. *J. Mater. Sci.* **1995**, *30* (3), 837–841.
  63. Colon, G.; Hidalgo, M.C.; Navio, J.A. A novel preparation of high surface area TiO<sub>2</sub> nanoparticles from alkoxide precursor and using active carbon as additive. *Catal. Today* **2002**, *76* (2–4), 91–101.
  64. Jung, K.Y.; Park, S.B. Enhanced photoactivity of silica-embedded titania particles prepared by sol-gel process for the decomposition of trichloroethylene. *Appl. Catal., B Environ.* **2000**, *25* (4), 249–256.
  65. Sawunyama, P.; Yasumori, A.; Okada, K. Nature of multilayered TiO<sub>2</sub>-based photocatalytic films prepared by a sol-gel process. *Mater. Res. Bull.* **1998**, *33* (5), 795–801.
  66. Kajihara, K.; Yao, T. Macroporous morphology of the titania films prepared by a sol-gel dip-coating method from the system containing poly(ethylene glycol). II. Effect of solution composition. *J. Sol-Gel Sci. Technol.* **1998**, *12* (3), 193–201.
  67. Kajihara, K.; Yao, T. Macroporous morphology of the titania films prepared by a sol-gel dip-coating method from the system containing poly(ethylene glycol): Effects of molecular weight and dipping temperature. *J. Sol-Gel Sci. Technol.* **2000**, *19* (1–3), 219–222.
  68. Kajihara, K.; Yao, T. Macroporous morphology of the titania films prepared by a sol-gel dip-coating method from the system containing poly(ethylene glycol). IV. General principle of morphology formation and effect of heat treatment. *J. Sol-Gel Sci. Technol.* **2000**, *17* (2), 173–184.
  69. Deguchi, T.; Imai, K.; Iwasaki, M.; Tada, H.; Ito, S. Photocatalytically highly active nanocomposite films consisting of TiO<sub>2</sub> particles and ZnO whiskers formed on steel plates. *J. Electrochem. Soc.* **2000**, *147* (6), 2263–2267.
  70. Krysa, J.; Jirkovsky, J. Electrochemically assisted photocatalytic degradation of oxalic acid on particulate TiO<sub>2</sub> film in a batch mode plate photoreactor. *J. Appl. Electrochem.* **2002**, *32* (6), 591–596.
  71. Dionysiou, D.D.; Balasubramanian, G.; Suidan, M.T.; Khodadoust, A.P.; Baudin, I.; Laine, J.-M. Rotating disk photocatalytic reactor: Development, characterization, and evaluation for the destruction of organic pollutants in water. *Water Res.* **2000**, *34* (11), 2927–2940.
  72. Dionysiou, D.D.; Burbano, A.A.; Suidan, M.T.; Baudin, I.; Laine, J.-M. Effect of oxygen in a thin-film rotating disk photocatalytic reactor. *Environ. Sci. Technol.* **2002**, *36* (17), 3834–3843.
  73. Huang, J.; Shinohara, T.; Tsujikawa, S. Protection of carbon steel from atmospheric corrosion by TiO<sub>2</sub> coating. *Zairyo to Kankyo/Corros. Eng.* **1999**, *48* (9), 575–582.
  74. Nishimura, R.; Yamakawa, K.; Ishiga, J.; Matsumoto, Y.; Nagano, H. Highly corrosion resistant stainless steel with Si implanted/deposited phase. *Mater. Chem. Phys.* **1998**, *54* (1–3), 289–292.
  75. Loddo, V.; Marci, G.; Martin, C.; Palmisano, L.; Rives, V.; Sclafani, A. Preparation and characterization of TiO<sub>2</sub> (anatase) supported on TiO<sub>2</sub> (rutile) catalysts employed for 4-nitrophenol photodegradation in aqueous medium and comparison with TiO<sub>2</sub> (anatase) supported on Al<sub>2</sub>O<sub>3</sub>. *Appl. Catal., B Environ.* **1999**, *20* (1), 29–45.
  76. Hurum, D.C.; Agrios, A.G.; Gray, K.A.; Rajh, T.; Thurnauer, M.C. Explaining the enhanced photocatalytic activity of Degussa P25 mixed-phase TiO<sub>2</sub> using EPR. *J. Phys. Chem., B* **2003**, *107* (19), 4545–4549.
  77. Weinberger, B.R.; Garber, R.B. Titanium dioxide photocatalysts produced by reactive magnetron sputtering. *Appl. Phys. Lett.* **1995**, *66* (18), 2409–2411.

# Titania Nanoparticles: Photocatalytic Properties

**Scott Buzby**

*Department of Materials Science and Engineering, University of Delaware, Newark, Delaware, U.S.A.*

**S. Ismat Shah**

*Department of Materials Science and Engineering, Department of Physics and Astronomy, University of Delaware, Newark, Delaware, U.S.A.*

## INTRODUCTION

Nanoparticles, arbitrarily defined as particles having particle sizes between 1 nm and 100 nm, have attracted significant interest due to their unique properties and are used in several revolutionary and important technological applications such as photocatalysis, sensors, solar cells, and memory devices. Nanosized semiconductors have become increasingly important in the world. Most organic pollutants consist of harmful constituent chemicals. Semiconductor photocatalysis uses light to activate nanoparticle catalysts in order to break down these chemicals. Photocatalysis works on the principle that positive charge carriers (holes) and negative charge carriers (electrons) are created when a semiconductor with an appropriate band gap, or energy difference between the conduction and the valance bands, is exposed to light. These carriers may then be used to initiate reactions at the catalyst surface. Electrons may be used for reducing metal ions ( $\text{As}^{+3}$ ,  $\text{Cr}^{+6}$ , etc.) while the positively charged holes can be used for the oxidation of organic chemicals (2-chlorophenol, trichloroethylene, etc.). However, several competing effects inherently limit the efficiency of a photocatalyst. The holes and electrons tend, by nature, to recombine through the emission of a photon (light) or a phonon (heat), yielding a neutral state. This recombination can occur in the bulk of the particle via volumetric recombination, as well as on the catalyst surface via surface recombination. Nanoparticles with a size of 20–30 nm provide the optimal balance between these effects and are thus best suited for photocatalysis.

Titanium dioxide is the most promising compound for photocatalysis applications.  $\text{TiO}_2$  is stable in aqueous media and is tolerant of both acidic and alkaline solutions. It is inexpensive, recyclable, reusable, and is relatively simple to produce. Most importantly its band gap is appropriate to initiate a variety of organic reactions as the redox potential of  $\text{H}_2\text{O}/\text{OH}\cdot$  lies within the bandgap.

The large bandgap of  $\text{TiO}_2$ ,  $\sim 3.2$  eV, lies in the UV range of the electromagnetic spectrum. This allows only 5–8% of sunlight that has the required energy to be useable for photocatalysis. Therefore, a visible-light activated catalyst would be much more efficient and effective. There are several known ways to increase the efficiency of a photocatalyst. Tailoring the bandgap of  $\text{TiO}_2$  to allow for visible light photocatalysis may be accomplished by reducing the particle size,<sup>[1]</sup> metal ion doping,<sup>[2–4]</sup> or electronegative atom doping.<sup>[5,6]</sup>

In 1972, Fujishima and Honda discovered the photocatalytic splitting of water on  $\text{TiO}_2$  electrodes<sup>[7]</sup> marking the beginning of heterogeneous photocatalysis. Since then, extensive research has been carried out to understand the fundamental processes and to enhance the photocatalytic efficiency of  $\text{TiO}_2$ . One of the most active areas of study for heterogeneous photocatalysis has been environmental cleanup applications owing to the fact that  $\text{TiO}_2$ -based photocatalysts cause total destruction of organic pollutants in wastewater.<sup>[8–14]</sup>

## EXCITON GENERATION AND RECOMBINATION

The first step in heterogeneous photocatalysis by semiconductors is the generation of electron-hole pairs in the semiconductor particles. Unlike metals, semiconductors possess an energy region where there are no electron energy levels. This region extends from the highest occupied molecular orbital (HOMO) of the filled valence band, to the lowest unoccupied molecular orbital (LUMO) of the vacant conduction band, and is called the band gap of the semiconductor. When a semiconductor absorbs light with energy equal to, or greater than its band gap, an electron is excited from the valance band to the conduction band leaving a hole in the valance band, thereby creating an electron-hole pair, as shown in Fig. 1. After excitation, the electrons

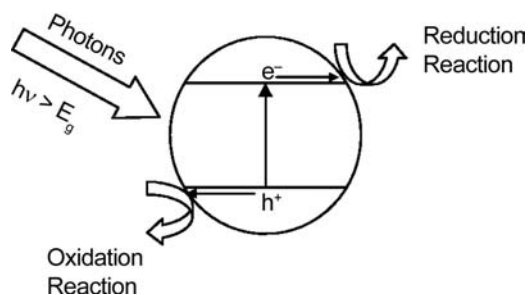


**Fig. 1** - Exciton generation by electron promotion from valance band to conduction band in semiconductors.

and holes generated can follow several pathways, as shown in Fig. 2. The migration of electrons and holes to the semiconductor surface allows for electron and/or holes to be transferred to the adsorbed organic or inorganic species. The semiconductor can donate electrons to reduce an electron acceptor (photocatalytic reduction).<sup>[15,16]</sup> Alternatively, when holes migrate to the surface and interact with an electron donor, oxidation of the donor (photocatalytic oxidation) occurs.<sup>[8-13]</sup> In competition with charge transfer to adsorbed species is electron/hole recombination. Excitons (electron/hole pairs generated in pure/bulk semiconductors) have a very short lifetime (nanoseconds) because of charge recombination.<sup>[17]</sup> Recombination of the separated electron and hole can occur in the volume of the semiconductor or on the surface, resulting in the emission of a photon (light) or phonon (heat). In order to reduce volume recombination, it is necessary to minimize the volume of the particle through the use of nanoparticles. However, nanoparticles have a very high surface to volume ratio. Therefore, surface recombination becomes more probable, offsetting the decrease in volumetric recombination. Therefore, the particle size must be optimized to minimize both surface and volume recombinations. Doping with metal ions (Nd, Pd, Co, Pt, etc.) or electronegative atoms (C, N, S, F, P, etc.) of TiO<sub>2</sub> offers a way to trap charge carriers and extend the lifetime of one or both of the charge carriers, enhancing the efficiency of the photocatalyst.<sup>[18-21]</sup>

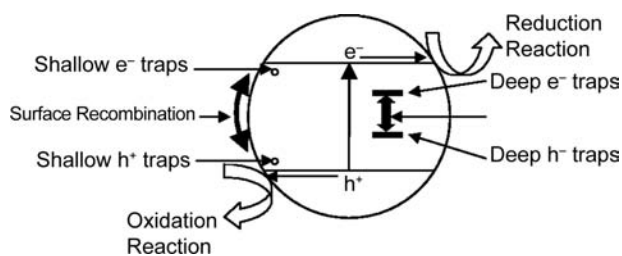


**Fig. 2** Exciton recombination.

## PHOTOCATALYSIS ON NANOPARTICLES

### Photocatalyst Selection

When selecting a photocatalyst there are several characteristics that should be considered. It should be stable, inexpensive, non-toxic, highly photoactive and, for organic compound degradation, the redox potential of H<sub>2</sub>O/ $\cdot$ OH couple ( $\text{OH}^- \rightarrow \cdot\text{OH} + \text{e}^-$ ;  $E_0 = -2.8 \text{ eV}$ ) should be within the bandgap of the semiconductor. Table 1 shows a partial list of semiconductors that could be used as photocatalysts. However, only TiO<sub>2</sub> exhibits all of the factors listed above. It is chemically and biologically inert and it is found in such everyday products as paper, paint, sunscreen, food additives, etc. In addition, titanium dioxide is inexpensive (\$0.93/pound for micron size particles) and easy to produce in large amounts. The worldwide capacity for production of TiO<sub>2</sub> is estimated at 5,000,000 metric tons per year in over 16 countries.<sup>[22]</sup> Most importantly, the redox potential of H<sub>2</sub>O/ $\cdot$ OH ( $E_0 = -2.8 \text{ eV}$ ) falls within the bandgap of TiO<sub>2</sub> ( $E_g = 3.2 \text{ eV}$ ).

### CRYSTAL STRUCTURE OF TiO<sub>2</sub>

The two crystal structures of TiO<sub>2</sub> that are commonly used in photocatalysis are rutile and anatase. The structures of both rutile and anatase are tetrahedral differing in the number of atoms in the unit cell and the lattice constants  $a_0$  and  $c_0$ . A rutile unit cell contains six atoms, with lattice constants of  $a_0 = 4.593 \text{ \AA}$  and  $c_0 = 2.958 \text{ \AA}$ .<sup>[23]</sup> An anatase unit cell contains twelve atoms per unit cell with lattice parameters  $a_0 = 3.785 \text{ \AA}$  and  $c_0 = 9.511 \text{ \AA}$ .<sup>[24]</sup> Of the two phases, anatase shows relatively greater photocatalytic activity and is used more frequently for photocatalytic oxidation reactions.<sup>[25]</sup> However, the large band gap of anatase ( $E_g = 3.2 \text{ eV}$ ) only allows absorption of the UV portion of the solar spectrum. It would be desirable to alter the bandgap so that it could absorb in the visible range of the spectrum to increase the photocatalytic efficiency. Absorption in the visible range can

**Table 1** Band gap of some semiconductor photocatalysts

Semiconductor	Band Gap (eV)
TiO <sub>2</sub>	3.2
ZnO	3.2
ZnS	3.6
$\alpha$ -Fe <sub>2</sub> O <sub>3</sub>	2.8
WO <sub>3</sub>	2.8
SrTiO <sub>3</sub>	3.2

be improved by doping,<sup>[1–5]</sup> sensitization by surface modification,<sup>[26,27]</sup> and particle size modification.<sup>[28,29]</sup>

## PHOTOCATALYST SYNTHESIS

Currently, a variety of synthesis methods are being used for the preparation of semiconductor nanoparticles for photocatalytic uses. Ideally, the synthesis methods employed should form nanoparticles with a narrow size distribution and should allow easy control of particle properties (e.g., size, surface, doping, etc.). As will be seen later, these requirements are useful for the improvement of the photocatalytic properties of the semiconductor nanoparticles.

### Chemical Synthesis Methods

These methods utilize chemical precursors and/or chemical reactions to produce nanoparticles. They include chemical vapor deposition (CVD), sol-gel synthesis, chemical impregnation, co-precipitation, hydrothermal methods, and flame synthesis. There are several good review papers describing these techniques.<sup>[30–32]</sup> In the following sections, the two most commonly used techniques for nanoparticle synthesis, metallo-organic chemical vapor deposition (MOCVD) and sol-gel synthesis will be described.

### METALLO-ORGANIC CHEMICAL VAPOR DEPOSITION

The basic idea in MOCVD is that the chemical reactions among precursors occur at a certain temperature in a hot wall chamber so that no post-synthesis processes, like calcination, are required for crystallization or particle refinement. The size distribution of the particles can be achieved by controlling the temperature of the reactor or the flow rate of the precursors. Dopants can also be easily introduced into the reactor through a solid source, separated from the other liquid-precursor, or mixed in with the precursor. The formation of oxide nanoparticles is basically divided into four steps:

1. Introduction of precursor vapor (with carrier gas) and O<sub>2</sub> into the reactor.
2. Production of oxide monomers from the reaction of the precursor and O<sub>2</sub>.
3. Condensation of monomers to form larger oxide clusters by homogeneous nucleation in the gas phase based on a collision mechanism.
4. Formation of nanoparticles in the gas phase and on the substrates after attachment of large clusters to the substrate.

The reaction and condensation phases are two crucial steps in the formation of semiconductor nanoparticles by MOCVD as these determine the size and composition of the nanoparticles. Depending on the experimental conditions used (e.g., temperature, gas flow rates, and pressure) either thin films or free-standing nanoparticles can be created.

### SOL-GEL SYNTHESIS

The main advantage of this process is the ease of preparing nanocomposite materials such as organic-coated nanoparticles and nanoparticles in an organic network. The process starts by mixing a precursor solution and a solvent. The solvent is usually an alcohol such which has a low boiling point, such as ethanol. For the purpose of surface modification or doping, organic material or dopant precursor solutions can be mixed with the initial solution. The chemical reactions are carried out by dip-coating desired substrates in the precursor solution, usually at room temperature. The samples are required to rest with ventilation for enough time for gas-phase by-products to dissipate and to remove excess solvent. The as-grown nanoparticles are amorphous, and a calcination process is needed to form crystals. Thus, the sol-gel process is normally followed by heat treatment for crystallization.

## PHOTOCATALYST ENHANCEMENT

### Doping of Photocatalysts

The effects of doping semiconductors to increase the photocatalytic activity have been extensively studied.<sup>[1–5]</sup> Doping of semiconductors increases the efficiency of photocatalysts in two ways. First, doping of the TiO<sub>2</sub> solid with non-isovalent ions adds electron deficient sites (hole provider) or electron abundant sites (electron provider). These sites decrease recombination by trapping electrons or holes during their transportation from the interior of the particle to the surface. The trapping of electrons and holes at these sites effectively increase their lifetime and the probability that they will participate in the desired photocatalysis reaction at the surface.<sup>[3]</sup> Doping may also increase the efficiency by extending the absorption edge into the visible range. If the electronic coupling effect between dopant and semiconductor is strong enough to change the band structure, band gap narrowing becomes possible. The band gap narrowing can cause a small reduction of the photoredox potential energy of TiO<sub>2</sub>, but the increased photon absorption efficiency can compensate for this negative effect and overall greatly enhance photoreactivity of the



semiconductor. New molecular orbitals may form as a result of doping, effectively narrowing the band gap and lowering the absorption edge into the visible-light region.<sup>[2,4]</sup> Doping with various metal ions has been attempted in order to improve the photocatalytic activity and optical absorption of TiO<sub>2</sub>.<sup>[1-5,33,34]</sup> However, only in a few cases has doping led to noticeable absorption of visible light, such as in, Ti<sub>1-x</sub>Nd<sub>x</sub>O<sub>2</sub> (2), TiO<sub>2-x</sub>N<sub>x</sub> (4), TiO<sub>2-x</sub>S<sub>x</sub> (4) and Ti<sub>1-x</sub>Cr<sub>x</sub>O<sub>2</sub> (31). The effect of metal ion doping can be seen in Fig. 3.

### Sensitization by Surface Modification

A second semiconductor with a smaller band gap or other sensitizer is used to compensate the deficient charge generation of host semiconductor TiO<sub>2</sub>.<sup>[26,27]</sup> The photosensitization process expands the excitation wavelength range of the semiconductor through excitation of the sensitizer followed by charge transfer to the semiconductor. If the energy level of the excited state of the sensitizer is more negative than the conduction band energy level of the semiconductor, then the sensitizer molecule can transfer the electron to the conduction band of the semiconductor.<sup>[35]</sup> There are some problems associated with this method including the instability of the organic sensitizers, change of the selectivity of the host semiconductor, and the complexity of materials synthesis.

### Particle Size Modification

The quantum confinement effect was first proposed by Efros and Efros in 1982<sup>[36]</sup> based on the experimental findings by Ekimov and Onushchenko<sup>[37]</sup> of the size

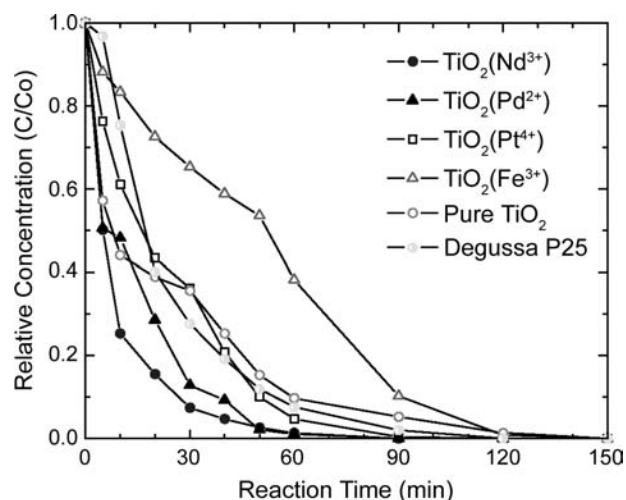
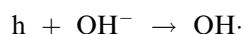


**Fig. 3** Effect of dopants on the photocatalytic degradation of 2-chlorophenol.

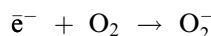
effect on the blue shift in the main exciton absorption of CuCl (30 Å) nanocrystallites. The model was further modified by Lois Brus.<sup>[38]</sup> It has been shown that the bandgap of a semiconductor nanoparticle increases as the particle size decreases below the Bohr radius. The exciton Bohr radius for TiO<sub>2</sub> is about 10 nm.<sup>[33]</sup> It has been shown for TiO<sub>2</sub> nanoparticles that the band gap reduces between 23 nm and 10 nm.<sup>[28,29,33]</sup> At particles sizes smaller than the Bohr radius there is a sharp increase in the bandgap due to quantum confinement effect (Fig. 4).

### Photocatalytic Oxidation on TiO<sub>2</sub> Catalysts

When the charge carriers migrate to the surface of the catalyst the electrons may act as reducing agents while the holes act as oxidizing agents. The holes now located on the catalyst surface may react with adsorbed hydroxyl (OH<sup>-</sup>) groups to produce hydroxyl radicals (OH·) which are strong oxidizing agents.



The trapped electrons react with adsorbed molecular oxygen to produce the oxygen radicals, O<sub>2</sub><sup>-</sup> and O<sub>2</sub><sup>-2</sup>.<sup>[39]</sup>



Any organic species (R-H) present will either react directly with the holes at the surface<sup>[40]</sup> or with the hydroxyl radicals<sup>[41]</sup> and get oxidized. The possibility of the reaction of organic molecules with freely diffusing hydroxyl radicals has also been studied.<sup>[42]</sup>

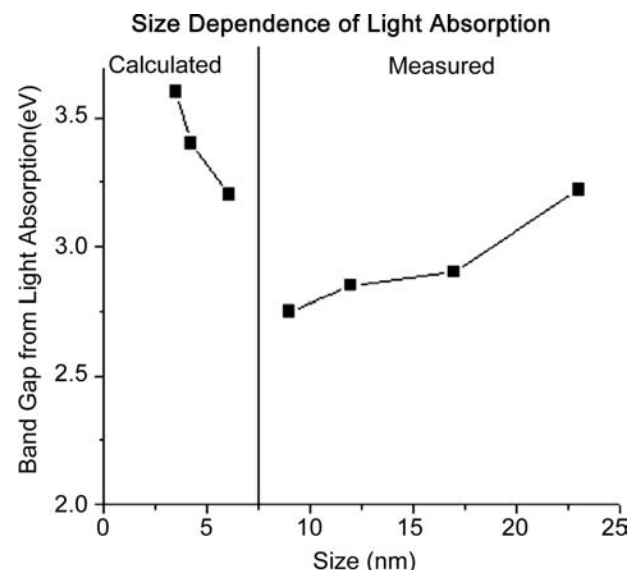
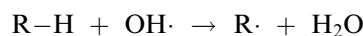
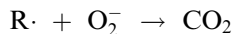


**Fig. 4** Effect of particle size on a semiconductor band gap.

As long as an excess of oxygen is present and the reaction is allowed to continue (i.e., by exposing it to light), complete oxidation (mineralization) of the organic species will be achieved.<sup>[39]</sup>



Studies have shown that oxygen plays a more significant role during photocatalytic oxidation than simply scavenging the trapped electrons. It was found that degradation of 4-chlorophenol occurs at much lower rates, 20%, in the presence of an alternative electron acceptors or in oxygen depleted environments as compared to complete mineralization when the system is completely oxygen saturated.<sup>[43,44]</sup> It has also been shown that photocatalytic oxidation rates of organic compounds increase as the oxygen concentration is increased.<sup>[45]</sup>

### Photocatalytic Sterilization

Semiconductor photocatalysts may be used to kill bacteria. This allows for the creation of self-sterilizing surfaces. The first work of this type was carried out with *E. Coli* suspensions.<sup>[46,47]</sup> *E. Coli* suspensions exposed to UV illuminated TiO<sub>2</sub>-coated plates showed no surviving cells after only one hour of exposure. Suspensions exposed to UV light with no TiO<sub>2</sub> present showed that only 50% of the cells had been killed. Direct contact with the semiconductor is not a requirement for the cell destruction as it has been reported that when the cells and the TiO<sub>2</sub> were separated by a 50 μm PTFE film with 0.4 μm pores, all cells were destroyed when illuminated for four hours.<sup>[46]</sup> Photocatalysis has also been shown to be effective in the destruction of endotoxins such as O-157<sup>[47]</sup> that was the cause of a 1996 food poisoning outbreak in Japan.<sup>[48]</sup> After two hours of UV illumination most of the endotoxin was decomposed, with complete decomposition occurring in four hours.<sup>[46]</sup>

### Cancer Treatment Using Photocatalysis

In 1986, illuminated TiO<sub>2</sub> was used to kill tumor cells. TiO<sub>2</sub> film electrodes and colloidal suspensions were found to be effective in killing HeLa cells.<sup>[49]</sup> Various experimental conditions were studied including the effect of superoxide dismutase, that was found to enhance the effect due to the production of peroxide.<sup>[50–52]</sup> By using a UV illuminated TiO<sub>2</sub> microelectrode it was found possible to selectively kill a single cancer cell.<sup>[53]</sup> Animal experiments were carried out in a joint research between the University of Tokyo and the Yokohama City University School of Medicine where cancer cells were implanted under the skin

of mice to cause the formation of tumors. When the tumors grew to a size of 0.5 cm a titanium dioxide solution was injected. After a few days the skin was cut open exposing the tumor, that was subsequently irradiated with UV light. Thirteen days later the titanium dioxide treatment was repeated and a marked antineoplastic effect was observed.<sup>[54]</sup>

### CONCLUSION

When an aqueous suspension of a semiconductor, such as TiO<sub>2</sub>, is irradiated with light that has energy greater than the band gap of the semiconductor, an electron is promoted from the valance band to the conduction band. The holes generated in the semiconductor along with the radical species produced (i.e., OH·) and the activated oxygen species created by electron trapping (O<sub>2</sub><sup>-</sup> and O<sub>2</sub><sup>-2</sup>) are all strong oxidation agents for organic compounds. The oxidizing species generated have large enough oxidizing potential to completely transform any organic species to CO<sub>2</sub>, water, and mineral acids. The non-selective property of the system for complete oxidation/reduction has been applied to water purification for the photodegradation of organic and reduction of heavy metal pollutants.

### REFERENCES

1. Li, W.; Shah, S.I. Semiconductor nanoparticles for photocatalysis. In *Encyclopedia of Nanoscience and Nanotechnology*; Nalwa, H.S., Ed.; American Scientific Publishers: Stevenson Ranch, CA, 2004; Vol. 9, 669–695.
2. Barakat, M.A.; Schaeffer, H.; Hayes, G.; Shah, S.I. Photocatalytic degradation of 2-chlorophenol by Co-doped TiO<sub>2</sub> nanoparticles. *Appl. Catal. B* **2004**, *57*, 23.
3. Li, W.; Wang, Y.; Lin, H. et al. Bandgap tailoring of Nd<sup>3+</sup>-doped TiO<sub>2</sub> nanoparticles. *Appl. Phys. Lett.* **2003**, *83*, 4143.
4. Shah, S.I.; Li, W.; Huang, C.P.; Jung, O.; Ni, C. Study of Nd<sup>3+</sup>, Pt<sup>4+</sup>, Pd<sup>2+</sup>, and Fe<sup>3+</sup> dopant effect on the photoreactivity of TiO<sub>2</sub> nanoparticles. *Proc. Natl Acad. Sci. U.S.A.* **2002**, *99*, 6482.
5. Asahi, R.; Morikawa, T.; Ohwaki, T.; Aoki, K.; Taga, Y. Visible-light photocatalysis in nitrogen-doped titanium oxides. *Science* **2001**, *293*, 269.
6. Suda, Y.; Kawasaki, H.; Ueda, T.; Ohshima, T. Preparation of high quality nitrogen doped TiO<sub>2</sub> thin film as a photocatalyst using a pulsed laser deposition method. *Thin Solid Films* **2004**, *162*, 453–454.
7. Fujishima, A.; Honda, K. Electrochemical photolysis of water at a semiconductor electrode. *Nature* **1972**, *37*, 238.
8. Bahnemann, D. Photocatalytic detoxification of polluted waters. In *Environmental Photochemistry*; Boule, P., Ed.; Springer: Berlin, 1999; Vol. 2, 285–351.

9. Bahnemann, D.; Cunningham, J.; Fox, M.A.; Pelizzetti, E.; Pichat, P.; Serpone, N. Photocatalytic treatment of waters. In *Aquatic and Surface Photochemistry*; Helz, G.R., Zepp, R.G., Crosby, D.G., Eds.; Lewis: Boca Raton, FL, 1994; 261–316.
10. Carey, J.H. An introduction to advanced oxidation processes (AOP) for destruction of organics in wastewater, paper no. 1, *Proceedings Symposium on Advanced Oxidation Processes for the Treatment of Contaminated Water and Air*, Wastewater Technology Centre, Burlington, Ontario, 1990.
11. Fujishima, A. Water treatment using TiO<sub>2</sub> photocatalyst. Shigen Kankyo Taisaku **1997**, *33* (3), 241–245.
12. Fujishima, A.; Fujita, S. TiO<sub>2</sub> photocatalyst for water treatment. *J. Adv. Sci.* **1997**, *9* (3–4), 192–195.
13. Halmann, M.M. *Photodegradation of Water Pollutants*; CRC Press, Inc.: Boca Raton, FL, 1996.
14. Fujishima, A.; Rao, T.N.; Tryk, D.A. Titanium dioxide photocatalysis. *J. Photochem. Photobiol. C: Photochem. Rev.* **2000**, *1*, 1–21.
15. Khalil, L.B.; Mourad, W.E.; Rophael, M.W. Photocatalytic reduction of environmental pollutant Cr(VI) over some semiconductors under UV/visible light illumination. *Appl. Catal. B* **1998**, *17* (3), 267–273.
16. Lee, H.; Choi, W. Photocatalytic oxidation of arsenite in TiO<sub>2</sub> suspension: kinetics and mechanisms. *Environ. Sci. Technol.* **2002**, *36*, 3872–3878.
17. Martin, S.T.; Morrison, C.L.; Hoffman, M.R. Photochemical mechanism of size-quantized vanadium-doped TiO<sub>2</sub> particles. *J. Phys. Chem.* **1994**, *98*, 13,695–13,704.
18. Rideh, L.; Wehrer, A.; Ronze, D.; Zoulalian, A. Photocatalytic degradation of 2-chlorophenol in TiO<sub>2</sub> aqueous suspension: modeling of reaction rate. *Ind. Eng. Chem. Res.* **1997**, *36*, 4712–4718.
19. Chen, J.N.; Chan, Y.C.; Lu, M.C. Photocatalytic oxidation of chlorophenols in the presence of manganese ions. *Water Sci. Technol.* **1999**, *39* (10–11), 225–230.
20. Doong, R.A.; Maithreepala, R.A.; Chang, S.M. Heterogeneous and homogeneous photocatalytic degradation of chlorophenols in aqueous titanium dioxide and ferrous ion. *Water Sci. Technol.* **2000**, *42* (7–8), 253–260.
21. Chen, X.; Yongbing, L.; Samia, A.; Burda, C.; Gole, J. Formation of oxynitride as the photocatalytic enhancing site in nitrogen-doped titania nanocatalysts: comparison to commercial nanopowder. *Adv. Funct. Mater.* **2005**, *15* (1), 41–49.
22. Gambogi, J. *Titanium and Titanium Dioxide*; U.S. Geological Survey, Mineral Commodity Summaries; U.S. Department of Interior: Washington DC, January 2005; 178–179.
23. Stizzaumainis, M.E.; Ejima, T.; James, W.J. The TiO<sub>2</sub> phase explored by the lattice constant and density method. *Acta Crystallogr.* **1961**, *14*, 493–497.
24. Arlt, T.; Bermejo, M.; Blanco, M.A. et al. High-pressure polymorphs of anatase TiO<sub>2</sub>. *Phys. Rev. B* **2000**, *61* (21), 14,414–14,419.
25. Sclafani, A.; Palmisano, L.; Davi, E. Photocatalytic degradation of phenol in aqueous polycrystalline TiO<sub>2</sub> dispersions—the influence of Fe<sup>3+</sup>, Fe<sup>2+</sup>, and Ag<sup>+</sup> on the reaction rate. *Photochem. Photobiol. A* **1991**, *56*, 113.
26. Tennakone, K.; Kumara, G.; Kumarasinghe, A.; Wijayantha, K.; Sirimanne, P. A dye-sensitized nanoporous solid-state photovoltaic cell. *Semicond. Sci. Technol.* **1995**, *10* (12), 1689–1693.
27. Kocher, M.; Daubler, T.K.; Harth, E.; Scherf, U.; Gugel, A.; Neher, D. Photoconductivity of an inorganic/organic composite containing dye-sensitized nanocrystalline titanium dioxide. *Appl. Phys. Lett.* **1998**, *72* (6), 650–652.
28. Jang, H.D.; Kim, S.-K.; Kim, S.-J. Effect of particle size and phase composition of titanium dioxide nanoparticles on the photocatalytic properties. *J. Nanoparticle Res.* **2001**, *3* (2–3), 141–147.
29. Xu, N.; Shi, Z.; Fan, Y.; Dong, J.; Shi, J.; Hu, M.Z.-C. Effects of particle size of TiO<sub>2</sub> on photocatalytic degradation of methylene blue in aqueous suspensions. *Ind. Eng. Chem. Res.* **1999**, *38*, 373–379.
30. Howe-Grant, M., Ed.; *Kirk-Othmer Encyclopedia of Chemical Technology*; Wiley: New York, 1997; Vol. 24, 225 pp.
31. Trindade, T.; O'Brien, P.; Pickett, N.L. Nanocrystalline semiconductors: synthesis, properties, and perspectives. *Chem. Mater.* **2001**, *13*, 3843.
32. Rajeshwar, K.; de Tacconi, N.R.; Chenthamarakshan, C.R. Semiconductor-Based composite materials: preparation, properties, and performance. *Chem. Mater.* **2001**, *13*, 2765.
33. Hoffmann, M.R.; Martin, S.T.; Choi, W.; Bahnemann, D.W. Environmental applications of semiconductor photocatalysis. *Chem. Rev.* **1995**, *95* (1), 69–96.
34. Takeuchi, M.; Yamashita, H.; Matsuoka, M. et al. Photocatalytic decomposition of NO under visible light irradiation on the Cr-ion-implanted TiO<sub>2</sub> thin film photocatalyst. *Catal. Lett.* **2000**, *67* (2–4), 135–137.
35. Cho, Y.; Choi, W.; Lee, C.H.; Hyeon, T.; Lee, H.I. Visible light-induced degradation of carbon tetrachloride on dye-sensitized TiO<sub>2</sub>. *Environ. Sci. Technol.* **2001**, *35* (5), 966–970.
36. Efros, A.L.; Efros, A.L. Interband absorption of light in a semiconductor sphere. *Sov. Phys. Semicond.* **1982**, *16*, 772–775.
37. Ekimov, A.I.; Onushchenko, A.A. Quantum size effect in three-dimensional microscopic semiconductor crystals. *JETP Lett.* **1981**, *34* (6), 345–349.
38. Brus, L. Electronic wave functions in semiconductor clusters: experiment and theory. *J. Phys. Chem.* **1986**, *90* (12), 2555–2560.
39. Matthews, R.W. Photocatalytic oxidation of organic contaminants in water: an aid to environmental preservation. *Pure Appl. Chem.* **1992**, *64* (9), 1285–1290.
40. Draper, R.B.; Fox, M.A. Titanium dioxide photosensitized reactions studied by diffuse reflectance flash photolysis in aqueous suspensions of TiO<sub>2</sub> powder. *Langmuir* **1990**, *6* (8), 1396–1402.
41. Turchi, C.S.; Ollis, D.F. Mixed reactant photocatalysis: intermediates and mutual rate inhibition. *J. Catal.* **1989**, *119* (2), 483–496.
42. Turchi, C.S.; Ollis, D.F. Photocatalytic degradation of organic water contaminants: mechanisms involving hydroxyl radical attack. *J. Catal.* **1990**, *122* (1), 178–192.

43. Stafford, U.; Gray, K.A.; Kamat, P.V.; Varma, A. An in situ diffuse reflectance FTIR investigation of photocatalytic degradation of 4-chlorophenol on a TiO<sub>2</sub> powder surface. *Chem. Phys. Lett.* **1993**, *205* (1), 55–61.
44. Fonseca, S.M.; Barker, A.L.; Ahmed, S.; Kemp, T.J.; Unwin, P.R. Direct observation of oxygen depletion and product formation during photocatalysis at a TiO<sub>2</sub> surface using scanning electrochemical microscopy. *Chem. Commun.* **2003**, *21* (8), 1002–1003.
45. Xu, W.; Raftery, D.; Francisco, J.S. Effect of irradiation and oxygen concentration on the photocatalytic oxidation of 2-propanol and acetone studied by in situ FTIR. *J. Phys. Chem. B* **2004**, *107*, 4537–4544.
46. Kikuchi, Y.; Sunada, K.; Iyoda, T.; Hashimoto, K.; Fujishima, A. Photocatalytic bactericidal effect of TiO<sub>2</sub> thin films: dynamic view of the active oxygen species responsible for the effect. *J. Photochem. Photobiol. A: Chem.* **1997**, *106*, 51–56.
47. Sunada, K.; Kikuchi, Y.; Hashimoto, K.; Fujishima, A. Bactericidal and detoxification effects of TiO<sub>2</sub> thin film photocatalysts. *Environ. Sci. Technol.* **1998**, *32*, 726–728.
48. Fujishima, A.; Honda, K.; Kikuchi, S. Photosensitized electrolytic oxidation on semiconducting *n*-type TiO<sub>2</sub> electrode. *Kogyo Kagaku Zasshi* **1969**, *72*, 108–113.
49. Fujishima, A.; Ohtsuki, J.; Yamashita, T.; Hayakawa, S. Behavior of tumor cells on photoexcited semiconductor surface. *Photomed. Photobiol.* **1986**, *8*, 45–46.
50. Cai, R.; Hashimoto, K.; Itoh, K.; Kubota, Y.; Fujishima, A. Photokilling of malignant cells with ultra-fine TiO<sub>2</sub> powder. *Bull. Chem. Soc. Jpn* **1991**, *64*, 1268–1273.
51. Cai, R.; Hashimoto, K.; Kubota, Y.; Fujishima, A. Increment of photocatalytic killing of cancer cells using TiO<sub>2</sub> with the aid of superoxide dismutase. *Chem. Lett.* **1992**, 427–430.
52. Cai, R.; Sakai, H.; Hashimoto, K.; Kubota, Y.; Fujishima, A. Phagocytosis of titanium dioxide particles chemically modified by hematoporphyrin. *Denki Kagaku* **1992**, *60*, 314–321.
53. Sakai, H.; Baba, R.; Hashimoto, K.; Kubota, Y.; Fujishima, A. Selective killing of a single cancerous T24 cell with TiO<sub>2</sub> semiconducting microelectrode under irradiation. *Chem. Lett.* **1995**, 185–186.
54. Cai, R.; Kubota, Y.; Shuin, T.; Sakai, H.; Hashimoto, K.; Fujishima, A. Induction of cytotoxicity by photoexcited TiO<sub>2</sub> particles. *Cancer Res.* **1992**, *52*, 2346–2348.

# Toxicological Effects and Screening of Engineered Nanoparticles

**Paul Borm**

*Centre of Expertise in Life Sciences, Zuyd University, Heerlen, The Netherlands*

**Ken Donaldson**

*Queens Medical Research Institute, University of Edinburgh, Edinburgh, Midlothian, U.K.*

## INTRODUCTION

Recent years have witnessed an unprecedented growth in research in the area of nanoscience and nanotechnology. The applications of nanotechnology will affect and improve almost every aspect of our lives from information technology to fabrics, finishes and materials generally. Most of these involve nanotechnological applications where there is no tangible direct health risk from exposure to the nanomaterial during manufacture or use. For instance, there is an increasing optimism that use of nanoparticles (NPs) in medicine will bring significant advances in the diagnosis and treatment of major diseases such as cancer and cardiovascular (CV) diseases.<sup>[1,2]</sup> Anticipated applications include use of NP (particles <100 nm in diameter) for drug delivery and diagnosis, and in nutraceuticals and production of biocompatible materials. The reason why NPs are attractive for such purposes is based on important and unique features, such as their surface-to-mass ratio, which are much larger than that of other particles, their quantum properties, and their ability to adsorb and carry other compounds. NPs have a large (functional) surface, which is able to bind, adsorb, and carry other compounds such as drugs, probes, and proteins.

Engineered NPs are important tools to realize a number of these applications in nanotechnology but may have the potential to get airborne resulting in human exposure or spread into the environment. As little is known about the hazards of these new materials, the emergence of nanotechnology has also initiated the debate on how these materials should be classified, tested, and used. The specific challenge for toxicologists is to understand the hazards associated with NP exposure and use this to determine and manage the risk to individuals who are exposed, to minimize adverse effects on health.

This entry first concentrates on the health hazards of NPs upon different exposure routes (lung, skin, and oral). Subsequently, it anticipates to translate the

know-how on effects of combustion-derived NPs (CDNPs) in ambient atmosphere to testing strategies that may be used for engineered NPs.

## DESCRIPTION OF RELEVANT PARTICLES

### Particle Definitions

Particle toxicology has developed along the lines of industrial development and has experience with particles down to the NP size range.<sup>[3]</sup> As shown in [Table 1](#), there have been decades of human exposure to NPs in the form of diesel soot and bulk NPs from industrial processes. Toxicological research has produced a database that is quite extensive for certain NPs, like diesel soot and carbon black, but less so for others such as fumed silica and alumina. The similarity or differences of these “traditional” NP to the new engineered NP is important since we have some concept of the hazard that these provide and so they may act as “benchmarks.” This database on CDNP [previously ultrafine particles (UFP)] demonstrates that exposure to these particles is associated with pulmonary inflammation,<sup>[4]</sup> immune adjuvant effects<sup>[5]</sup> and adverse systemic effects including blood coagulation and CV effects.<sup>[6,7]</sup> The meeting of the worlds of Nanoscience, with its engineered NP, and that of toxicology, with its know-how of ultrafines, has led to an impressive series of workshops and meetings over the past several years. However, so far little exchange of methods and concepts has occurred although both disciplines are expected to benefit from an exchange of methods and know-how.

Previously NPs were referred to by the toxicology community as UFPs, which are denominated as the fraction of ambient particulate matter (PM), which is smaller than 100 nm. Nowadays the denomination of the term NP is more frequent, and in this entry, we use the term NP for particles being intentionally produced with the same cutoff size of 100 nm.

**Table 1** Nomenclature of NPs: each class of NPs is described by source, exemplar particle, target exposure group, and toxicological knowledge at the time of writing

Nomenclature	Source	Example	Who is exposed?	Toxicological knowledge
CDNPs (ultrafine)	Combustion	Diesel soot	Everyone	+++
Bulk-manufactured NP (ultrafine)	Combustion	Carbon black	Occupational	++
	Synthesis	Amorphous silica	Occupational	+
Engineered NP	Geological/synthesis	Alumina	Occupational	-/+
	Nanotubes	Combustion	Occupational	-/+
	Q-dots	Synthesis	Patients	-/+

+++ = substantial toxicology database; ++ = some toxicology data available; + = limited toxicology database; -/+ = virtually no data available on toxicology.

NPs therefore include both bulk products such as carbon blacks and titanium dioxide (TiO<sub>2</sub>), but also particles that are engineered and produced in low quantities such as quantum dots and polymer carriers for imaging and drug delivery. This terminology is also illustrated in Fig. 1, which shows the different particles, their sources, and the evidence for potential health effects. In Table 2, a brief summary of the above definitions is given. Some specific groups of NP are described in the paragraphs below and concern CDNPs, bulk-manufactured NPs, and nanotubes.

### PM<sub>10</sub> and CDNPs

CDNPs are a component of environmental PM, which is measured by mass-based sampling conventions such as PM<sub>10</sub> and PM<sub>2.5</sub>. CDNPs are a small mass fraction of total anthropogenic particulate emissions but constitute a very large proportion of the particle number in the urban cloud. CDNPs are primary particles or agglomerates with a diameter smaller than 100 nm, although they tend to aggregate further with time and enter the accumulation mode of fine particles. The impact of PM on health has been extensively addressed in epidemiological studies across the globe; increased participation of PM in chronic and acute scenarios is associated with deaths and adverse health

effects in susceptible groups. These susceptible groups comprise patients with chronic lung disease and CV disease. From these studies, it is estimated that a 10 µg/m<sup>3</sup> increase in the concentration of PM<sub>2.5</sub> causes an overall mortality increase of 0.9%, while deaths from specific respiratory diseases can increase by as much as 2.7%. Epidemiological studies do not readily allow associations of adverse effects with subcomponents of PM, dependent as they usually are on mass measures of PM. However, several epidemiological studies have been able to identify combustion-derived particles as an important component in driving adverse effects of PM.<sup>[8]</sup> Toxicology can more easily study the components of PM, and there has been considerable amount of research on the combustion-derived particles component.

### Bulk-manufactured NPs

Most of the experimental, toxicological insights and hazards of NP have been explored with a small set of CDNP and bulk-manufactured NPs. Bulk-manufactured NPs have been used in industry for some decades and are produced in many tons/year; in 2004, the largest production volumes were recorded for colloidal silica, TiO<sub>2</sub>, and various iron oxides. All these bulk NPs were previously considered to be so-called nuisance dusts until it was observed that upon prolonged exposure in rats inflammation and lung tumors (Fig. 3) can occur.<sup>[4,6,7,9]</sup> In summary, these findings (Table 3) set the stage for the current discussion on risks of NPs illustrated in Fig. 1. A key question is whether the different pieces of toxicological and epidemiological evidence on different NP can be mutually used or whether a more sophisticated approach is necessary.

### Nanotubes

Carbon nanotubes (CNTs) comprise entirely carbon; they can be viewed as formed by rolling a single sheet

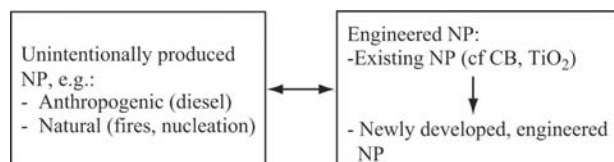


**Fig. 1** Illustration of the different sources and applications of NP. Epidemiology and toxicology have demonstrated acute effects of anthropogenic NP in humans, as well chronic effects of existing, manufactured NP in animals. It remains an open issue whether the hazards and risks found with those types of NP can be extrapolated to newly developed, engineered NP.



**Table 2** Definitions of particles in relation to their sources and application

Particle type	Description
PM <sub>10</sub> , PM <sub>2.5</sub>	Particle mass fraction in ambient air with a mean diameter of 10 or 2.5 μm, respectively. Basis of current standards for ambient particles in Europe and U.S.A.
Coarse particles	The mass fraction of PM <sub>10</sub> , which is bigger than 2.5 μm
UFP (PM <sub>0.1</sub> )	The fraction of PM <sub>10</sub> with a size cutoff at 0.1 μm. Contains primary particles and agglomerates smaller than 100 nm
PSP	Poorly soluble particles with low specific toxicity. Terminology used in relation to bulk synthetic UFP
NPs	Primary particles of intentionally produced material smaller than 100 nm
Liposomes	Particles, not strictly NP, consisting of fatty acids and derivatives
Carriers conjugates	Polymer-protein or polymer-drug conjugates with a size below 100 nm used in drug delivery

of graphite into a seamless cylinder. There are two classes of CNTs: single-walled and multiwalled. Multiwalled nanotubes are larger and consist of many single-walled tubes stacked one inside the other. Single-walled tubes can be as much as 10 times as strong as steel and 1.2 times as stiff as diamond, so they find many applications in the industry for reinforcing materials. They have a needle-like shape and are commonly a few nanometers wide but can be several millimeters in length. They therefore have some commonality with asbestos and other fibers used in industry. The harmful effects of fibers are driven by three properties: by length, thinness and biopersistence (i.e., resistance to breakdown in the lungs). A typical long, thin, biopersistent fiber that causes lung disease is amphibole asbestos. The experience with asbestos-related lung disease suggests that CNTs should be treated as a special case, and that their toxicity testing and possibly their regulation should be benchmarked against asbestos and not conventional NPs. Another reason to specifically address this group is the anticipated increase in production and use in the next few years.<sup>[10]</sup>

## TOXICOLOGICAL EFFECTS OF NPs

### Lung Exposure

The largest database on the potential toxicity of NPs has originated from the PM<sub>10</sub> literature, where the “NP hypothesis” has proved to be a powerful force for research. Therefore we consider it relevant to discuss this evidence in the expectation that it will shed light on the toxicity of engineered NP. The idea that CDNPs are an important component that drives the adverse effects of environmental particulate air pollution or PM<sub>10</sub> comes from several sources:

1. Much of the mass of PM<sub>10</sub> is considered to be non-toxic and so there has arisen the idea that there is a component(s) of PM<sub>10</sub> that actually drives the proinflammatory effects and CDNPs seem a likely candidate.
2. CDNPs are the dominant particle type by number suggesting that they may be important and their small size means that they have a large

**Table 3** Important findings on the biological activity in the toxicity of NPs between 1990 and now

Description of finding
NP TiO <sub>2</sub> causes pulmonary inflammation. Later studies show that inflammation is mediated by surface-area dose
NPs cause more lung tumors than fine particles in rat chronic studies. Effect is surface-area mediated
NPs inhibit macrophage phagocytosis, mobility, and killing
NPs affect immune response to common allergens
NPs are related to lung function decline in asthmatics
NPs cause oxidative stress in vivo and in vitro, by inflammatory action and generation of surface radicals
NP exposure adversely affects cardiac function and vascular homeostasis
NPs have access to systemic circulation upon inhalation and instillation
NPs interfere with Ca-transport and cause increased binding of proinflammatory transcription factor nuclear factor (NF)-κB
NPs cause progression of plaque formation
NPs can affect mitochondrial function
NPs can translocate to the brain from the nose
NPs do affect rolling in hepatic tissue

surface area/unit mass. Particle toxicology suggests that, in general, for toxic particles, more particle surface equals more toxicity.

3. Substantial toxicological data and limited data from epidemiological sources support the contention that NPs in PM<sub>10</sub> are important drivers of adverse effects.

Toxicological studies with inhaled NP have suggested several major mechanisms by which this CDNP component of PM may cause responses that explain mortality in those with existing pulmonary and CV diseases.<sup>[11,12]</sup>

1. First, inhalation exposure to NP can invoke bronchoalveolar inflammation in susceptible individuals and exacerbate existing airways disease such as COPD leading to death.<sup>[12]</sup>
2. Bronchoalveolar inflammation may also cause the release of inflammatory mediators that can trigger systemic hypercoagulability of the blood thereby increasing the risk for CV events such as those observed when PM levels increase.<sup>[13]</sup>
3. A second mechanism is the progression and destabilization of atheromatous plaques by inhalation of PM.<sup>[14]</sup> NP properties are likely to promote plaque destabilization through their documented effects such as inflammation and oxidative stress causing LDL oxidation and lipid peroxidation.
4. A third mechanism is provided by recent observations that NP upon inhalation deposits to a large extent in the nose, and may pass through the olfactory epithelium in the upper nose and reach the brain.<sup>[15]</sup> Little is known about the effects of the uptake, but one could imagine disturbance in the central nervous system (CNS) control of the autonomic nervous system as a possible consequence.
5. Finally, NP may translocate from various deposition sites [lung, gastrointestinal (GI) tract, and dermis] to the systemic circulation and distribute to secondary organs (vascular wall, heart, liver, and spleen) and affect organ function directly. However, quantitative estimates of translocation range between 50% of lung-deposited <sup>13</sup>C NP (26 nm size) within 24 hr in a rat model to less than 1% using 18 nm Iridium particles in vivo or in isolated perfused lung; further research in this area is clearly warranted.

A large series of molecular epidemiological studies in combination with animal studies have supported aspects of the plausibility of the above mechanisms. A multinational trial on CV risks (MONICA), performed between 1984 and 1988, reported a higher

blood viscosity and C-reactive protein (CRP)<sup>[16]</sup> during an air pollution episode in 1985. Recent studies from the same research group in Erfurt (Germany) have identified combustion NP as an important variable explaining cardiac deaths owing to increased ambient particle exposure. In fact, the association became stronger with smaller particles, and individuals with CV diseases were more likely to die than others. Clearly further research is needed, but the research reported to date has direct relevance to public-health policy, because both coal-burning and traffic emissions continue to be major sources of NP exposure worldwide. Recent studies in the Netherlands and Ireland have demonstrated the importance of regulating combustion-derived particle emissions.<sup>[17,18]</sup>

### Intravenous Exposure

Studies on effects of injected engineered NP have been performed with particles developed for therapeutic purposes such as polymers, liposomes, and engineered inorganic NPs. For intravenous (IV) administration, the choice of an appropriate NP is crucial with regard to many chemical and biological properties that determine biocompatibility. The toxicology of NPs that are used in drug delivery is now well understood thanks to extensive studies on cytotoxicity, hemotoxicity, complement activation, and cellular or humoral immunogenicity of many candidate NP.<sup>[19]</sup> Polycationic particles are in general cytotoxic, hemolytic, and can activate complement. On the other hand, polyanionic particles are less cytotoxic, but can cause procoagulant activity, and can also stimulate cytokine release from lymphocytes and mononuclear cells. Polymeric macromolecules (including polyaminoacids or polysaccharides) can elicit a humoral response characterized by increased total or specific immunoglobulin E (IgE) or immunoglobulin M (IgM) levels. All biological responses seem to be molecular-weight dependent for polymers and also depend on size when considering (in)organic NP. It has to be realized that the potential biological interactions of the NP can change when drugs or complementary antibodies are attached.

Toxicokinetics, usually described as absorption, distribution, metabolism and excretion (ADME), can change when new chemical entities are attached or other properties are modified. Ideally, the NP or the skeleton should be biodegradable or soluble. If the skeleton is not degradable at all, the molecular weight of the copolymers should be limited to <40,000 Da to ensure renal elimination as a backup for clearance. All these elements and toxicological concepts are developed and demonstrated in the use of surface-engineered iron oxide NPs, which have been used to pioneer the biocompatibility of nanomaterials.

Magnetite, because of its strong magnetic properties, was used first in biology and then in medicine for cell separation and magnetic guidance of particles for site-specific drug delivery. Nowadays, a whole series of compounds is known [e.g., polyethylene glycol (PEG)] that can be used for coating of iron oxide particles to allow drug delivery applications.

### GI Uptake and Effects of NP

NPs (<0.1  $\mu\text{m}$ ) and microparticles (0.1–3  $\mu\text{m}$ ) are ingested at high levels/person/day, and it is estimated that  $10^{12}$ – $10^{14}$  particles, mainly silicates and  $\text{TiO}_2$ , are ingested/person/day in the Western world.<sup>[20]</sup> After entering the GI tract, NPs are scavenged by M-cells overlying the Peyer's patches lymphoid follicles and in this way circumvent active uptake by intestinal epithelium. Some studies have shown that NPs ( $\text{TiO}_2$  and silicates) can accumulate locally in the GI tract in the Peyer's patches and have suggested that this may be related to exacerbation of inflammation in Crohn's disease, but the evidence is weak.

Translocation of ingested NP from the GI tract to the blood is suggested by studies in rats and humans, which have shown that ingested  $\text{TiO}_2$  particles (150–500 nm) can translocate to the blood and accumulate in liver and spleen.<sup>[21]</sup> Earlier studies described a mechanism of "persorption" by GI tract epithelial cells, whereby even larger particles are taken up into lymphatic and blood circulation and translocated to the liver and other organs.<sup>[22]</sup> Recently, nanocrystals have become the subject of intense investigation for oral administration of drugs and functional food components. Nanocrystals of drugs or food constituents, produced by precipitation or other processes, are 100% pure. As they are very efficiently taken up in vivo, and easy to produce, their production for oral application is expected to increase considerably. Interestingly, studies with ultrafine metal particles did not show a significant translocation to the blood circulation from the GI tract and thereby to other organs.<sup>[23]</sup> In the latter study after esophageal administration of 18 nm  $^{192}\text{Ir}$  particles in suspension, virtually the whole of the  $^{192}\text{Ir}$  dose was found in fecal excretion within 2–3 days. During the six-day observation period, no detectable  $^{192}\text{Ir}$  was observed in urine. Six days after administration, there was no detectable  $^{192}\text{Ir}$  in any organ or tissue of the body. Hence, it was concluded that for these particles, there was no uptake and/or absorption from the GI tract.

### Dermal Uptake and Effects of NP

The skin is one of the major exposure routes to NPs because of its large surface (well over  $2\text{m}^2$ ) and

Administration	Surface	Secondary targets
INTRAVENOUS		All organs
SKIN	$2\text{m}^2$	Liver
GI-Tract	$40\text{m}^2$	
<u>Respiratory tract</u>		
• Olfactory epithelium	$5\text{cm}^2$	Brain
• Bronchial epithelium		Heart
• Alveolar epithelium	$90\text{m}^2$	Circulation
		Liver

**Fig. 2** NP uptake routes and secondary target organs. The primary route of exposure to NP is determined by the type of exposure and preventive actions. However, upon uptake, the secondary target of NP differs substantially between routes of uptake. For example, uptake of NP through the small epithelial surface ( $5\text{cm}^2$ ) maybe a small quantitative route, but on the other hand, the target organ brain is directly accessed.

frequent application of consumer products that contain NP (Fig. 2). Particles with a size of approximately 50–500 nm are widely used in cosmetic products, to improve the homogeneity of the formulations applied to the skin surface, or to act as a UV filter against sun radiation. In the latter case, the

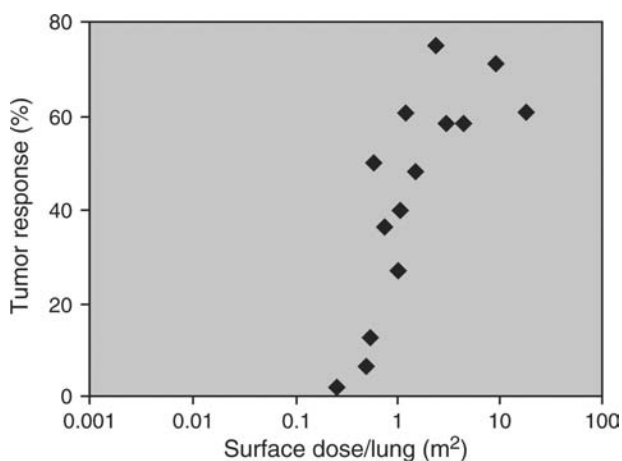


**Fig. 3** Relationship between lung tumor responses and particle surface area. Various poorly soluble low toxicity particles including nanoparticles have been shown to cause inflammation and lung tumors after intratracheal administration in rats. Fine and UFP were administered by intratracheal instillation in rats, and lung tumors were evaluated after 129 weeks. In both cases, straight line is obtained with a threshold between 0.2 and  $0.3\text{m}^2$  for lung cancer and  $200\text{cm}^2$  for inflammation in the rat. Source: Reproduced with permission from Ref.<sup>[9]</sup>.

smallest particles act as “nanomirrors” on the skin and partly reflect the sunlight. Because of their scattering properties, they increase the optical pathway of UV photons entering the upper part of the horny layer, and energy is absorbed by the stratum corneum and by the other organic components of the sunblock. Paradoxically, TiO<sub>2</sub>, one of the mostly prevalent NP found in cosmetics, has considerable photocatalytic activity. To prevent potential adverse effects caused by this property, the TiO<sub>2</sub> used in cosmetic preparations is often coated. The usual concentration of the NPs in the formulations is usually less than 3%. Sunscreens are usually applied to the skin at a concentration of 2 mg/cm<sup>2</sup>, which means that if 1 m<sup>2</sup> of skin is treated, the total external amount of NP applied is ~600 mg of NP. There is considerable discussion about the uptake of NP through the skin. In principle, there are three possible penetration pathways of topically applied substances through the skin: intercellular penetration, intracellular penetration, and follicular penetration. In the past, the penetration was described as a diffusion process through the lipid layers of the stratum corneum. Liposomes with a diameter between 20 nm and 200 nm have been found to be active carriers of topically applied drugs into the living epidermis via the intercellular penetration route.<sup>[24]</sup>

The penetration of native and coated TiO<sub>2</sub> NP into the stratum corneum of living human skin has been investigated by tape stripping and biopsy in combination with spectroscopic measurements. Penetration of NPs through the horny layer could not be detected by x-ray fluorescence in sections of the biopsy.<sup>[25]</sup> These data also confirmed the results of earlier work, which detected no percutaneous absorption of particles in skin samples from humans treated with a microfine titanium oxide-containing sunscreen. A more recent study on the percutaneous penetration of micronized TiO<sub>2</sub> preparations in sunscreens used two different samples, one containing primary particles of 10 to 15 nm present as aggregates of approximately 100 nm, and another sample with primary particles of approximately 100 nm. Both of these particle types remained on the surface of the stratum corneum, and did not penetrate into the stratum corneum or living compartments of the skin.<sup>[26]</sup> It cannot be excluded that some physical properties of NP may enhance the absorption/penetration of certain substances applied to the skin such as reported for methanol or octanol. However, the results of available studies suggest that, although small particles may be deposited on the follicle orifice, they do not penetrate the skin via the follicle. This was confirmed by the results of a recent study, which showed that polystyrene NP (20 to 200 nm) accumulated in the

follicle orifices but did not penetrate into the skin or the follicle.<sup>[27]</sup>

### Effects of NP in the CNS

NPs might gain access to the brain by two different mechanisms:

- Trans-synaptic transport after deposition on the olfactory epithelium
- Uptake from the blood through the blood–brain barrier (BBB)

The first pathway has been studied primarily with model particles such as carbon, Au, and MnO<sub>2</sub> in experimental inhalation models.<sup>[15]</sup> The second pathway has been the result of extensive research and particle surface manipulation in drug delivery, as an approach to try to deliver drugs to the brain.<sup>[28]</sup> The latter studies suggest that the physiological obstacle that the BBB provides may limit the distribution of some proteins and viral particles after transvascular delivery to the brain, suggesting that the healthy BBB contains defense mechanisms protecting it from being breached by blood-borne NPs. A number of pathologies, including hypertension and allergic encephalomyelitis, however have been associated with experimental increases in permeability of the BBB to NPs. Conversely, the NP surface charge has been shown to alter the blood–brain integrity<sup>[29]</sup> and so warrant consideration for brain toxicity and brain distribution profiles.

Paramagnetic NPs have been used for magnetic resonance imaging (MRI) of different cell types within neural tissue. This has proved efficacious, and it has been suggested that this might be useful in humans for tracking the development of stem cell grafts used to treat neurodegenerative diseases. However, the potential impact of NPs on human neuronal tissue has not yet been investigated in detail. NPs have, however, been shown to induce the production of reactive oxygen species (ROS) and oxidative stress. Oxidative stress has been implicated in the pathogenesis of neurodegenerative diseases such as Parkinson’s and Alzheimer’s.<sup>[30]</sup> Therefore it is conceivable that the long-term effects of NP exposure might include a decrease in cognitive function. Evidence for such effects is presented by studies in biopsies from city dwellers and Alzheimer’s-like pathology have demonstrated increased markers of inflammation and AB42-accumulation in frontal cortex and hippocampus in association with the presence of NPs. Chronic (four months) exposure to concentrated airborne particles caused degeneration in dopaminergic neurons in a specific area of brains of mice.<sup>[31]</sup>

## SCREENING-ENGINEERED NP FOR TOXICOLOGICAL HAZARDS

From the above it is clear that a range of end points should be considered for the testing of NP for potential hazards. Some engineered NP, which becomes airborne, may pose inhalation hazards, but cosmetics containing NP normally provide only dermal exposures. Therefore hazards should be tested appropriately, to their mode of exposure and portal of entry. Other engineered NPs are being used as devices to target drugs to specific tissues, to increase their biological half-time, or for imaging purposes such as extravasation and tumor treatment. The testing of engineered NP for these purposes follows guidelines such as defined in European union (EU) or Food and Drug Administration (FDA) medical device regulations, which are based on their biocompatibility as measured by platelet adhesion and activation, neutrophil attachment, angiogenesis, and cell spreading.<sup>[19]</sup> However regulatory bodies start to realize that current guidelines or classification may not be valid. In addition, important questions remain such as the following:

Which components should be tested?

The following should all be considered: Native particle, native particle with surface modification, stability of the surface coating, effects of the NP and surface coating, and materials used for synthesis of NP.

What type of tests should be used? A range of in vitro and in vivo tests should provide information that can contribute to hazard assessment. Both classical tests and newer models reflecting current insights into the mechanisms of NP toxicity should be employed.

### Relevant Particle Properties and Mechanisms

The present data indicate that apart from particle size, particle surface chemistry and particle surface charge are important parameters determining NP toxicity, translocation and subsequent effects. Apart from particle characteristics, the permeability of several cellular barriers is considered to play a role.<sup>[32]</sup> Toxicological studies have shown that oxidative stress is a central mechanism that may be responsible for the inflammatory effects of PM and NP causing pulmonary responses.<sup>[6,33]</sup> On the other hand, inflammation is known to amplify the burden of ROS to the lung, and thereby causes a persistent oxidative stress. For several reasons, NPs are particularly able to generate oxidative stress when the particles deposit on the epithelium of the respiratory tract:

1. NP surface area: The surface area of particles is known to be a major factor in driving inflammation<sup>[6,34]</sup> as well as lung carcinogenicity in

experimental systems (Fig. 3).<sup>[9]</sup> NPs of low-toxicity, low-solubility materials have a very high surface area/unit mass. They are also highly inflammogenic by virtue of this high surface area and oxidative stress, generated through mechanisms that are not well understood. NPs typically form aggregates both in the air and upon deposition, which are aerodynamically larger than the classical definition of a NP, i.e., they can be larger than 100 nm. However, these NPs in aggregates still express toxicity consistent with their geometric surface area and not in relation to their surface area as deduced from their aerodynamic diameter as an aggregate.

2. Carrier function: NPs may contain or adsorb components that have the ability to generate free radicals and cause oxidative stress. These components include polycyclic aromatic hydrocarbons (PAHs), *n*-alkanes, nitro-PAHs and quinones formed by combustion or derived from unburnt fuel. Interaction of these organics with enzyme systems can result in oxidative stress via the production of oxidants such as superoxide anion. Absorbed or soluble metals can typically generate ROS in acellular and cellular systems<sup>[35]</sup> and is related to the inflammatory response to NPs in vivo.<sup>[36]</sup>
3. Surface modification and coatings: Whatever test will be used or developed, it needs to be appreciated that most suppliers apply postproduction strategies to modify NPs to prevent aggregation or stimulate disaggregation. In both industrial and life sciences applications, different coatings are employed (Table 4). There is now a body of evidence from the drug delivery and toxicological literature that surface modification as well as surface charge can have major impacts on biological response to particles, including phagocytosis, genotoxicity, and inflammation. Particle coating with PEG or dextran is commonly used to prevent recognition by the reticuloendothelial system and increase the half-life of particle-conjugated drugs.<sup>[37]</sup> A clear example, albeit not in NP, demonstrating the crucial role of particle surface comes from work with respirable, quartz samples. Coating with aluminum lactate or the polymer polyvinyl-pyridine-*N*-oxide (PVNO) has a dramatic impact on the various adverse effects of the native quartz, including phagocytosis/endocytosis, oxidative deoxy ribonucleic acid (DNA) damage, and inflammation following instillation into rat lung.<sup>[38]</sup> In sunscreens, NP TiO<sub>2</sub> is often used as “nanomirrors” to partly reflect the sunlight from the skin. To reduce potential photocatalytic adverse effects,

**Table 4** Surface modifications of NP used for technical (polysynthetic route) and drug delivery applications. Whereas most coatings for medical applications have been designed or tested to prevent adverse effects, most industrial coatings serve technological purposes

Postsynthetic modification or coating of NP	Specific properties
<i>Industrial applications</i>	<i>Dispersable in</i>
4-Dimethylaminopyridine	Water
Mercaptoundecane acid	Water
Thiols (e.g., Dodecanethiol)	Non-polar solvents like hexane, toluene, chloroform, acetone
Fluoroalkanes	Non-polar solvents like hexane, toluene, chloroform, acetone
Trialkoxysilanes and derivatives thereof	Water, alcohol
Phosphorous-containing substances like $\text{Ph}_2\text{PC}_6\text{H}_4\text{SO}_3\text{Na}$	pH dependent in water or non-polar solvents
Aminoalkanes and derivatives	Dependent on functionalization in non-polar solvents or alcohol
<i>Medical applications (ferrofluids)<sup>a</sup></i>	<i>Biological/physical properties</i>
PEG	Improves biocompatibility
Dextran	Enhances blood circulation time
Fatty acids	Colloidal stability
Polyvinyl alcohol (PVA)	Monodisperse particles
Polyacrylic acid	Helps bioadhesion, improves stability
Poly (D,L-lactide)	Biocompatible, low cytotoxicity
Phosphorylcholine	Prevents complement activation
Chitosan	Natural biocompatible, hydrophilic and widely employed on agricultural, cosmetics, foods and medicine
Gelatin	Hydrophilic emulsifier, natural

<sup>a</sup>Modified from Gupta & Gupta (2005) as applied to iron oxide particles.

the  $\text{TiO}_2$  is often coated. Surface modified  $\text{TiO}_2$  has been the subject of considerable toxicological investigation and has shown that the hydrophobic coatings usually tend to lower the inflammatory response after inhalation or instillation. However, one study reported very substantial acute toxicity after instillation of doses around 1 mg/rat. It is crucial to know-how the surface modification has been achieved and if this can be released from the NP in biological media (e.g., low pH in macrophages). In the case of sunscreen-grade coated titanium oxide NPs, the stability of the coating was investigated by laser-induced plasma spectroscopy. No changes in the mechanical stability of the coated micro-particles could be detected during the manufacturing of the sunscreen.

### Tests for Toxicity of Engineered NP

Considering the large amount of research on effects and mechanisms of CDNP, it is surprising to note that little has been done to screen engineered NP for potential adverse health effects. There are different opinions as to whether existing tests may pick up all of the

hazards. Existing tests detecting toxicological hazards of NP may not be sensitive enough, or may not look in the correct place, e.g., blood or brain. Lessons can be learned from animal research with CDNP failing to reproduce the effects of PM seen in epidemiological studies. Although the reasons for this are somewhat understood (e.g., poor models of susceptibility and variability in exposure), this underscores the need to develop and validate new test models as well as to evaluate and validate existing methods for testing of engineered NP.<sup>[39]</sup>

Currently there is no alternative to the approach used in the pharmaceutical industry, i.e., a case-by-case approach. There is a clear need to develop concepts of testing, which can be achieved through bridging studies with appropriate regard to dosimetry. The dosimetry should be related to the anticipated application of the nanostructured materials and to the metric, which is chosen or investigated. Another reason for the right dosimetry is that often only small amounts of nanomaterials are available, and for instance, inhalation studies are virtually impossible. With regard to testing of the toxicity of engineered NPs, a variety of tests may be used that were applied to particles of highly contrasting size and dimension such as asbestos and man-made fibers, quartz and coal mine dust, fly ashes,



and diesel exhaust particles. In response to the “NP hypothesis,” a number of *in vitro* and *in vivo* tests have been introduced for comparative toxicity testing at equal mass of commercial particles of fine vs. ultrafine size (e.g., carbon black and TiO<sub>2</sub>). Tests for NP toxicity can be arbitrarily subdivided into four levels:

1. Testing of the (re)activity of NP in acellular or subcellular systems (e.g., dissolution, radical generation, protein/DNA oxidation, lipid peroxidation enzyme inactivation/immobilization, and action on isolated mitochondria).
2. Testing of NP *in vitro*, using intact cells or cell systems (e.g., lung epithelial cells, skin cells, gut cells, vascular endothelium, and macrophages).
3. Testing of NP in isolated organ culture systems (e.g., intact skin models, whole blood, isolated perfused lung, and heart).
4. *In vivo* testing.

#### Short-term tests for reactivity and toxicity

Very rapid and basic acellular approaches that have been used to predict particle reactivity include testing of plasmid DNA unwinding or oxidation of calf thymus DNA. Electron paramagnetic resonance (EPR) combined with a spin trap has been used to determine the radical generation properties of particulate materials well above the nanosize range such as quartz and asbestos in relation to (surface) modification, as well as of ambient PM. With a few exceptions, these EPR studies showed positive associations with toxicity *in vitro* and/or *in vivo*.

#### Cellular tests

Cellular tests are very common in particle toxicology because little material is required, they have short-term readouts, and microscopical techniques are easy to apply concomitantly. A classic test is the hemolysis assay, which is based on properties of reactive constituents to elicit hemoglobin leakage upon red blood cell membrane damage. Nowadays, toxicity testing of particles *in vitro* mainly uses primary cells and/or immortalized cell lines. End points for toxicity include membrane-damaging properties (e.g., LDH leakage) or changes in mitochondria-associated metabolic competence [e.g., MTT assay and adenosine triphosphate (ATP)], reflecting necrosis and/or apoptosis. Various cell types can be tested, with due regard to the route of entry and/or target tissue or organ of concern (e.g., pulmonary type II cells, colon cells, keratinocytes, and endothelial cells). Notably, alveolar epithelial cells are often used to screen for markers of proinflammatory pathways and or toxicity of inhaled NP, but other assays can be chosen based on the application of the NP. Differential cell adhesion and toxicity (fibroblast) are often used as a screening test to optimize surface modification in NP for drug delivery of coatings of biocompatible materials.

#### Isolated organ and *in-vivo* testing

**CV Effects.** Patients with CV diseases are the principal vulnerable group with respect to effects of inhaled CDNP. Therefore it is recommended that *in vivo* screening of engineered NP will concentrate on CV end points using appropriate animal models. An overview of end points and models that can be used is given in Table 5.

**Table 5** Test methods and models that can be used to explore potential hazards of NP particles for the CV system

Test System	End point	Interpretation
<i>Cardiomyocytes</i>		
Primary	Beating frequency, Ca <sup>2+</sup> -response Ca-dependent channels, cytoskeletal behaviour	Basic effects on cardiac metabolism
Cell lines	Ca <sup>2+</sup> -response, ATP response, apoptosis	
<i>Aorta rings (in vitro)</i>	Contraction-relaxation with epinephrine-carbachol	Autonomic innervation
Langendorf perfusion ( <i>ex vivo</i> )	Coronary flow, left ventricular developing pressure, heart rate	Heart function
<i>Telemetry (whole animal)</i>	Heart rate variability, ECG, blood pressure, vessel diameter	Cardiac and vascular function
Biomarkers in plasma/blood	Fibrinogen, CRP	Acute phase response
	Factor VII	Blood coagulation
	Viscosity, clotting time	
	Plasminogen activator inhibitor	
	Endothelin, angiotensin converting enzyme (ACE)	Endothelial damage/activation

Broadly the CV effects of NPs that need to be considered include the following:

1. Effects on clotting homeostasis: Several toxicological studies have demonstrated that CDNPs and model NPs can gain access to the blood following inhalation or instillation. There is also evidence that NP introduced into the bloodstream or lung can enhance experimental thrombosis.<sup>[40]</sup>
2. Effects on neural control of CV function: Humans, dogs, rats, and mice have been used to study heart rate variability after inhalation of combustion NP and significant effects seen.<sup>[31]</sup>
3. Effects in models of coronary artery disease: Progression/worsening of plaques has been demonstrated in animal models of coronary artery disease. In Watanabe hyperlipidemic rabbits, instilled PM caused both development and activity in the plaques compared with controls. In ApoE mice, which spontaneously develop atheromatous plaques, chronically inhaled CAPS also caused worsening of the plaques.
4. Effects on vascular function: Both in vivo and ex-vivo experiments have been conducted after pulmonary exposure to NP. For example, arterial diameters decreased and blood pressure increased when measured in vivo. Isolated aorta rings or hearts can also be used to study autonomic innervation and function of the heart and vascular tissue<sup>[41]</sup> but show outcomes

physiologically different from in vivo findings. Telemetric procedures can be applied in most animals to measure cardiac function and vascular function.

**Uptake and Effects in the CNS.** It has been recently reported that inhaled UFPs translocate into the CNS via the olfactory epithelium nerve,<sup>[15]</sup> and NP drugs have been shown to cross the BBB under certain conditions.<sup>[28]</sup> Routine tests of uptake into the CNS by various NPs, as well as assays to predict their possible adverse consequences for this organ, need to be developed. For such tests, one may consider neuroimaging techniques in exposed animals, in vitro tests with glial cells and astrocytes, and the use of non-invasive quantitative electroencephalogram (QEEG).

## CONCLUSIONS

Building on data on the known behavior and toxicity of CDNPs and the few data that exist on other NP, the potential fate and adverse effects of engineered NPs is shown diagrammatically in Fig. 4. Presently, it is unknown whether the hazard, the specificity to vulnerable groups, the translocation, or the mechanism of adverse effects induced by CDNP in epidemiological studies can be extrapolated to hazard and risk estimation of the immense variety of engineered NP. In addition, we are unsure whether inhalation studies with bulk NP (carbon black and TiO<sub>2</sub>) can be used

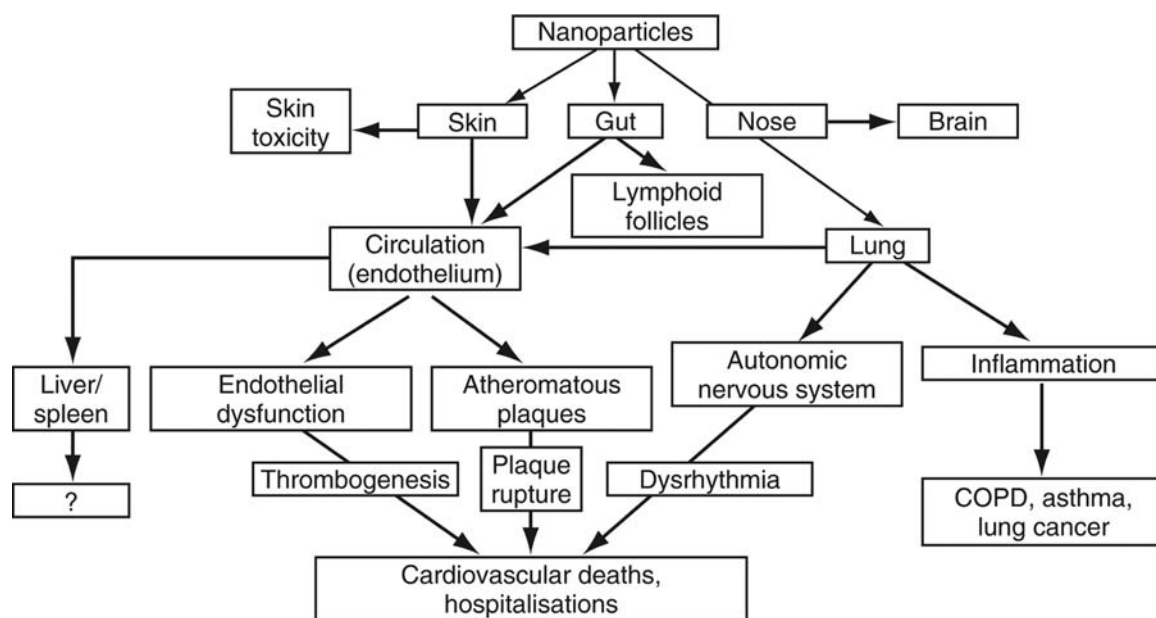


**Fig. 4** The potential fate and adverse effects of engineered NPs is diagrammatically illustrated. NPs may use different uptake routes (gut, nose, skin, and lung) and exert different toxicity or reach different secondary targets after uptake or deposition. The major known health effects (of UFP) affect patients with pulmonary and cardiovascular diseases.

for direct comparison with engineered NP (Fig. 1). Paradoxically, whereas toxicology is trying to understand the mechanisms of NP translocation and how these minute amounts of NP might invoke response, pharmacology involves the injection of large numbers of NP into the blood for the systemic delivery of drugs or for imaging and therapy. Clearly these different concepts need to be reconciled. In this review, we have indicated what effects of NP toxicologists have found, and how this know-how could be used to develop new screening procedures for safe NP for industrial and nanomedical purposes.

Where possible, we have tried to indicate where nanoscience and toxicology should connect, communicate, and exchange methods. An even more favorable approach is to include toxicological testing in early phase of development, as has been generated for man-made mineral fibers to prevent a repeat of the asbestos experience. In producing numerous engineered NPs at low volume, a conceptual understanding of biological actions of materials is an obligatory. Such a conceptual understanding would provide an umbrella to protect society and consumers against low amounts of potentially toxic materials.

## ACKNOWLEDGMENTS

The authors are indebted to many collaborators in the development of their know-how in this area. In particular, collaboration with Roel Schins (IUF), Wolfgang Kreyling (GSF), Lang Tran (IOM), Vicki Stone (Napier University), and Detleff Müller-Schulte (Magnamedics GmbH) has generated a lot of the thinking that is included in this article. In addition, the authors thank Catrin Albrecht, Doris Hoehr, and Welf Mahlke for the use of their work on lung microscopy.

## REFERENCES

- Buxton, D.B.; Lee, S.C.; Wickline, S.A.; Ferrari, M. National heart, lung, and blood institute nanotechnology working group. Recommendations of the national heart, lung, and blood institute nanotechnology working group. *Circulation* **2003**, *108* (22), 2737–2742.
- Ferrari, M. Cancer nanotechnology: opportunities and challenges. *Nat. Rev.* **2005**, *5* (March 2005), 464–474.
- Borm, P.J.A. Particle toxicology: from coal mining to nanotechnology. *Inhal. Toxicol.* **2002**, *14*, 311–324.
- Donaldson, K.; Brown, D.; Clouter, A.; Duffin, R.; MacNee, W.; Renwick, L.; Stone, V. The pulmonary toxicology of ultrafine particles. *J. Aerosol Med.* **2002**, *15*, 213–220.
- Granum, B.; Lovik, M. The effect of particles on allergic immune responses. *Toxicol. Sciences* **2002**, *65*, 7–17.
- Oberdörster, G. Pulmonary effects of ultrafine particles. *Int. Arch. Occup. Environ. Health* **2001**, *74*, 1–8.
- Borm, P.J.A.; Kreyling, W. Toxicological hazards of inhaled nanoparticles—potential implications for drug delivery. *J. Nanosci. Nanotechnol.* **2004**, *4*, 521–531.
- Laden, F.; Neas, L.M.; Dockery, D.W.; Schwartz, J. Association of fine particulate matter from different sources with daily mortality in six U.S. cities. *Environ. Health Perspect.* **2000**, *108*, 941–947.
- Borm, P.J.A.; Schins, R.P.F.; Albrecht, C.A. Inhaled particles and lung cancer. Part B: paradigms and risk assessment. *Int. J. Cancer.* **2004**, *110* (1), 3–14.
- The Royal Academy of Sciences & Royal Society of Engineering. In *Nanoscience and Nanotechnologies: Opportunities and Uncertainties*; Royal Academy of Sciences: London, July 2004.
- Dockery, D.W.; Pope, C.A., 3rd; Xu, X.; Spengler, J.D.; Ware, J.H.; Fay, M.E.; Ferris, B.G., Jr; Speizer, F.E. An association between air pollution and mortality in six U.S. cities. *N. Engl. J. Med.* **1993**, *329*, 1753–1759.
- Pope, C.A., 3rd; Burnett, R.T.; Thurston, G.D.; Thun, M.J.; Calle, E.E.; Krewski, D.; Godleski, J.J. Cardiovascular mortality and long-term exposure to particulate air pollution: epidemiological evidence of general pathophysiological pathways of disease. *Circulation* **2004**, *109* (1), 71–77.
- Seaton, A.; MacNee, W.; Donaldson, K.; Godden, D. Particulate air pollution and acute health effects. *Lancet* **1995**, *345*, 176–178.
- Kuenzli, N.; Jerrett, M.; Mack, W.J.; Beckerman, B.; LaBree, L.; Gilliland, F.; Thomas, D.; Peters, J.; Hodis, H.N. Ambient air pollution and atherosclerosis in Los Angeles. *Env. Health Persp.* **2004**, doi:10.1289/ehp.7523. Available at: <http://dx.doi.org/>, 22 November 2004.
- Oberdorster, G.; Sharp, Z.; Atudorei, V.; Elder, A.; Gelein, R.; Kreyling, W.; Cox, C. Translocation of inhaled ultrafine particles to the brain. *Inhal. Toxicol.* **2004**, *16* (6–7), 437–445.
- Peters, A.E.; Wichmann, H.E.; Tuch, T.; Heinrich, J.; Heyder, J. Respiratory effects are associated with the number of ultrafine particles. *Am. J. Respir. Crit. Care Med.* **1997**, *155*, 1376–1383.
- Hoek, G.; Brunekreef, B.; Goldbohm, S.; Fischer, P.; van den Brandt, P.A. Association between mortality and indicators of traffic-related air pollution in the Netherlands: a cohort study. *Lancet* **2002**, *360* (9341), 1203–1209.
- Clancy, L.; Goodman, P.; Sinclair, H.; Dockery, D.W. Effect of air-pollution control on death rates in Dublin, Ireland: an intervention study. *Lancet* **2002**, *360* (9341), 1210–1214.
- Rihova, B. Biocompatibility of biomaterials: haemocompatibility, immuno compatibility and biocompatibility of solid polymeric materials and soluble targetable polymeric carriers. *Adv. Drug Delivery Rev.* **1996**, *21*, 157–176.
- Lomer, M.C.; Hutchinson, C.; Volkert, S.; Greenfield, S.M.; Catterall, A.; Thompson, R.P.; Powell, J.J. Dietary sources of inorganic microparticles and their intake in healthy subjects and patients with Crohn's disease. *Br. J. Nutr.* **2004**, *92* (6), 947–955.

21. Jani, P.U.; McCarthy, D.E.; Florence, A.T. Titanium dioxide (rutile) particles uptake from the rat GI tract and translocation to systemic organs after oral administration. In *J. Pharm.* **1994**, *105*, 157–168.
22. Volkheimer, L. Passage of particles through the wall of the gastrointestinal tract. *Environ. Health Perspect.* **1974**, *9*, 215–225.
23. Semmler, M.; Seitz, J.; Erbe, F.; Mayer, P.; Heyder, J.; Oberdorster, G.; Kreyling, W.G. Long-term clearance kinetics of inhaled ultrafine insoluble iridium particles from the rat lung, including transient translocation into secondary organs. *Inhal. Toxicol.* **2004**, *16*, 453–459.
24. Egbaria, K.; Weiner, N. Liposomes as a topical drug delivery system. *Adv. Drug Del. Rev.* **1990**, *5*, 287–300.
25. Lademann, J.; Weigmann, H.J.; Rickmeyer, C.; Barthelmes, H.; Schaefer, H.; Müller, G.; Sterry, W. Penetration of titanium dioxide microparticles in a sunscreen formulation into the horny layer and the follicular orifice. *Skin Pharm. Appl. Skin. Phys.* **1999**, *12*, 247–256.
26. Pflücker, F.; Wendel, V.; Hohenberg, H.; Gärtner, E.; Will, T.; Pfeiffer, S.; Wepf, R.; Gers-Barlag, H. The human stratum corneum layer: an effective barrier against dermal uptake of different forms of topically applied micronised titanium dioxide. *Skin Pharmacol. Appl. Skin Physiol.* **2001**, *14* (Suppl 1), 92–97.
27. Alvarez-Roman, R.; Naik, A.; Kalia, Y.N.; Guy, R.H.; Fessi, H. Skin penetration and distribution of polymeric nanoparticles. *J. Control Release* **2004**, *99* (1), 53–62.
28. Kreuter, J.; Shamenkov, D.; Petrov, V.; Ramge, P.; Cychutek, K.; Koch-Brandt, C.; Alyautdin, R. Apolipoprotein-mediated transport of nanoparticle-bound drugs across the blood-brain barrier. *J. Drug Target.* **2002**, *10* (4), 317–325.
29. Lockman, P.R.; Koziara, J.M.; Mumper, R.J.; Allen, D.D. Nanoparticle surface charges alter blood-brain barrier integrity and permeability. *J. Drug Target* **2004**, *12*, 635–641.
30. Calderon-Garciduenas, L.; Reed, W.; Maronpot, R.R.; Henriquez-Roldan, C.; Delgado-Chavez, R.; Calderon-Garciduenas, A.; Dragustinovis, I.; Franco-Lira, M.; Aragon-Flores, M.; Solt, A.C.; Altenburg, M.; Torres-Jardon, R.; Swenberg, J.A. Brain inflammation and Alzheimer's-like pathology in individuals exposed to severe air pollution. *Toxicol. Pathol.* **2004**, *32* (6), 650–658.
31. Veronesi, B.; Makwana, O.; Pooler, M.; Chen, L.C. Effects of subchronic exposures to concentrated ambient particles. VII. Degeneration of dopaminergic neurons in Apo E<sup>-/-</sup> mice. *Inhal. Toxicol.* **2005**, *17*, 235–241.
32. Meiring, J.J.; Borm, P.J.A.; Bagate, K.; Semmler, M.; Seitz, J.; Takenaka, S.; Kreyling, W. The role of endothelial permeability in translocation of nanoparticles in the isolated perfused rat lung. Part. *Fibre Toxicol.* **2005**, *2* (27 June), 3.
33. Donaldson, K.; Stone, V.; Borm, P.J.A.; Jimenez, L.A.; Gilmour, P.S.; Schins, R.P.F.; Knaapen, A.M.; Rahman, I.; Faux, S.P.; Brown, D.M.; MacNee, W. Oxidative stress and calcium signalling in the adverse effects of environmental particles (PM<sub>10</sub>). *Free Radic. Biol. Med.* **2002**, *34*, 1369–1382.
34. Tran, C.L.; Buchanan, D.; Cullen, R.T.; Searl, A.; Jones, A.D.; Donaldson, K. Inhalation of poorly soluble particles. II. Influence of particle surface area on inflammation and clearance. *Inhal. Toxicol.* **2000**, *12* (12), 1113–1126.
35. Shi, T.; Schins, R.P.F.; Knaapen, A.M.; Kuhlbusch, T.; Pitz, M.; Heinrich, J.; Borm, P.J.A. Hydroxyl radical generation by electron spin resonance as a new method to monitor ambient particulate matter composition. *J. Environ. Monit.* **2003**, *5*, 550–556.
36. Schaumann, F.; Borm, P.J.A.; Herbrich, A.; Knoch, J.; Pitz, M.; Schins, R.P.F.; Luetti, B.; Hohlfeld, J.J.; Heinrich, J.; Krug, N. Metal rich particles (PM<sub>2.5</sub>) causes airway inflammation in healthy subjects. *Am. J. Resp. Crit. Care Med.* **2004**, *170*, 898–903.
37. Gupta, A.K.; Gupta, M. Synthesis and surface engineering of iron oxide nanoparticles for biomedical applications. *Biomaterials* **2005**, *26*, 3995–4021.
38. Knaapen, A.M.; Albrecht, C.; Becker, A.; Höhr, D.; Winzer, A.; Haenen, G.R.; Borm, P.J.A.; Schins, R.P.F. DNA damage in lung epithelial cells isolated from rats exposed to quartz: role of surface reactivity and neutrophilic inflammation. *Carcinogenesis* **2002**, *23*, 1111–1120.
39. Fubini, B.; Aust, A.E.; Bolton, R.E.; Borm, P.J.A.; Bruch, J.; Ciapetti, G.; Donaldson, K.; Elias, Z.; Gold, J.; Jaurand, M.C.; Kane, A.B.; Lison, D.; Muhle, H. Non-animal tests for evaluating the toxicity of solid xenobiotics. ECVAM Workshop report 30; ATLA **1998**, *26*, 579–617.
40. Nemmar, A.; Hoylaerts, M.F.; Hoet, P.H.; Vermeylen, J.; Nemery, B. Size effect of intratracheally instilled particles on pulmonary inflammation and vascular thrombosis. *Toxicol. Appl. Pharmacol.* **2003**, *186* (1), 38–45.
41. Bagate, K.; Meiring, J.J.; Gerlofs-Nijland, M.E.; Vincent, R.; Cassee, F.R.; Borm, P.J. Vascular effects of ambient particulate matter instillation in spontaneous hypertensive rats. *Toxicol Appl. Pharmacol.* **2004**, *197* (1), 29–39.

# Tribology of Inorganic Nanoparticles

Lev Rapoport

*Tribology Laboratory, Holon Academic Institute of Technology,  
Holon, Israel*

## INTRODUCTION

One of the main tribological properties of rubbed pairs is self-lubrication. The key to self-lubricating materials is the rapid and easy shear and transfer of thin films from one surface to another. The solid lubricants assure a “self-lubrication” of oils, greases, coatings, polymer composites, bearing powder materials, etc.

In the present work, a novel brand of nanomaterials—inorganic fullerene (IF)-like solid lubricant nanoparticles of  $WS_2$  and  $MoS_2$  (IF)—is considered. Friction and wear properties of IF nanoparticles are compared with commercially available layered  $WS_2$  and  $MoS_2$  solid lubricants. IF solid lubricant nanoparticles were added to oil, grease, and impregnated into the pores of powdered materials. Polymer nanocomposite with IF nanoparticles and alumina covered by thin IF film showed superior tribological properties in comparison to the reference materials. The mechanisms of IF self-lubrication are discussed.

## INORGANIC FULLERENE-LIKE SOLID LUBRICANT MATERIALS

Inorganic layered compounds are abundant, in particular, among the transition-metal chalcogenides (sulfides, selenides, and tellurides), halides (chlorides, bromides, and iodides), oxides (hydroxides), and numerous ternary and quaternary compounds. Layered materials such as graphite,  $MoS_2$  and  $WS_2$  (platelets of the 2H polytype) are used both as solid lubricants<sup>[1,2]</sup> and as additives in liquid lubricants.<sup>[3,4]</sup> Minimum tangential resistance is commonly associated with shearing of the weak interlayer (typically van der Waals) bonds in these materials.<sup>[5,6]</sup> Unfortunately, the 2H platelets tend to stick to the mating metal pieces through the reactive dangling bonds on the prismatic edges (10 $\bar{1}0$ ), which lead to their rapid annihilation through burnishing and oxidation. The friction coefficient of  $MoS_2$  solid lubricant particles is more than 0.1 at humid and oxygen-containing environments.

Recently, the tribological properties of  $C_{60}$  and  $C_{70}$  fullerenes were described.<sup>[7–9]</sup> It was speculated that the nearly spherical fullerenes might behave as nanoscale

ball bearings. Intuitively, fullerene molecules are thought to be too small to separate between asperities of the mating metal surfaces and, therefore, they tend to enter into crevices or valleys. Experiments by Campbell et al.<sup>[10]</sup> with  $C_{60}$  molecules dissolved in dry toluene tend to substantiate this hypothesis, but comparison of this result with macroscopic friction measurements does not yield a conclusive outcome. Further work of this group has demonstrated that, whereas the adhesion energy of smooth  $C_{60}$  films is very low, the friction coefficient is rather high in this case. The tendency of the fullerene powders to clump and compress into a high shear strength layer was demonstrated to be a main cause of the high friction coefficient.<sup>[11]</sup>

Using a reasoning similar to that of carbon fullerenes<sup>[12]</sup> and carbon nanotubes,<sup>[13]</sup> several groups proposed<sup>[14–16]</sup> that their formation is not unique to carbon and is, in fact, a genuine property of 2-D (layered) compounds, such as  $WS_2$  and  $MoS_2$ . However, in contrast to graphite, each molecular sheet consists of multiple layers of different atoms chemically bonded to each other. The initial discovery of IF materials elicited a substantial effort of many groups, which has been recently reviewed by a number of authors.<sup>[17,18]</sup> These nanomaterials were termed under the generic name inorganic fullerene-like (IF) materials. The results of a detailed study of inorganic fullerene-like nanomaterials are considered in this book, in a separate chapter.<sup>[19]</sup>

The analysis of IF nanoparticles showed that the most, if not all, nanoparticles were closed and hollow, and their shape was found to be irregular with a small fraction of the particles (<10%) having nearly spherical shape. The hollow cage structure of the IF imparts a high elasticity, which augments their resilience in a specific loading range.<sup>[20]</sup> Dislocations, which have deleterious influence on the chemical stability and the tribological behavior, were abundant in these nanoparticles. A typical assortment of such nanoparticles is shown in Fig. 1. The tilting of the samples in the TEM suggests that the IF- $WS_2$  nanoparticles have a spherical shape. Atomic force microscopic (AFM) image of an IF- $WS_2$  nanoparticle, confirming a spherical shape, is presented in Fig. 2. The average size of

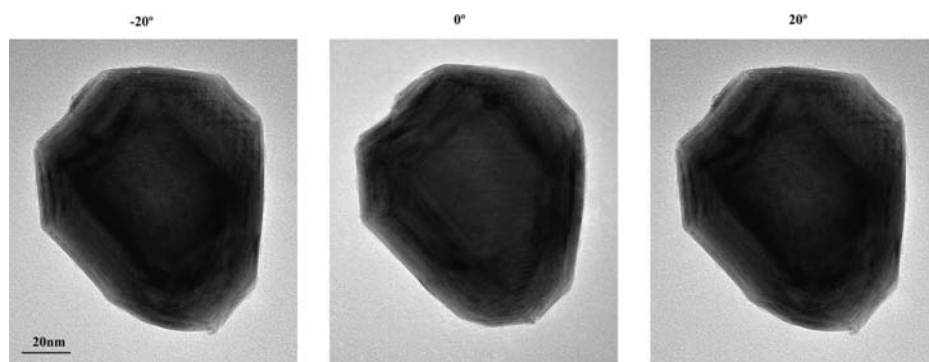


**Fig. 1** Transmission electron microscopic (TEM) image of typical IF-WS<sub>2</sub> nanoparticles at different tilt angles. Results demonstrate the spherical shape of these nanoparticles.

the IF-WS<sub>2</sub> particles was close to 120 nm, while it was about 50 nm for IF-MoS<sub>2</sub>. High elasticity of the IF-WS<sub>2</sub> nanoparticles was confirmed by the analysis of the IF-WS<sub>2</sub> nanoparticle ensemble under hydrostatic compression.<sup>[21]</sup> This experiment was performed to evaluate the behavior of IF solid lubricant nanoparticles as a self-lubricating medium. It was found that these nanoparticles are capable of withstanding a severe hydrostatic pressure, caused by compression. Detailed structural studies revealed that no phase changes were observed during compression. With increasing load, some IF-WS<sub>2</sub> nanoparticles were found to be damaged (Fig. 3). Frequently observed defects can be associated with the breakout of the outer shells of the nanoparticles. The layer-to-layer distance of 0.62 nm was preserved in the broken sheets. The inner layers of these nanoparticles seem to remain intact. The broken outer layers are expected to be transferred to friction surfaces, providing superior tribological properties of rubbed surfaces. The 2H-WS<sub>2</sub> particles with platelet shape suffered severe damage under the same loading conditions.

The behavior of the IF nanoparticles has been compared with layered 2H-WS<sub>2</sub> and 2H-MoS<sub>2</sub>. Preliminary friction experiments showed that IF added to oil possess lubricating properties superior to those of 2H platelets in a definite range of operating conditions.<sup>[22]</sup> The weak van der Waals forces operating between the

layers leading to easy shear of the films likely cannot control the tribological properties of spherical IF-WS<sub>2</sub> nanoparticles. We attributed the recently reported outstanding tribological behavior of IF-WS<sub>2</sub> to its chemical inertness and to the hollow cage structure, which leads to high elasticity and allows the particles to roll, rather than slide (rolling friction), in appropriate loading regimes. It was realized that the addition of small amounts of quasi-spherical WS<sub>2</sub> or MoS<sub>2</sub> nanoparticles with fullerene-like structure to various kinds of lubricant greatly improves their tribological characteristics. Thus a systematic study of the tribological behavior of such nanoparticles under different contact conditions was undertaken. Based on this study, some applications for these nanoparticles are offered. Hereinafter, some recent highlights of this progress will be delineated.

### THE EFFECT OF THE IF NANOPARTICLES IN OIL

Ring-block test of a steel pair at sliding velocities  $V = 0.22$ – $1$  m/sec and loads of 150–1200 N was performed.<sup>[23]</sup> To simulate typical industrial conditions,

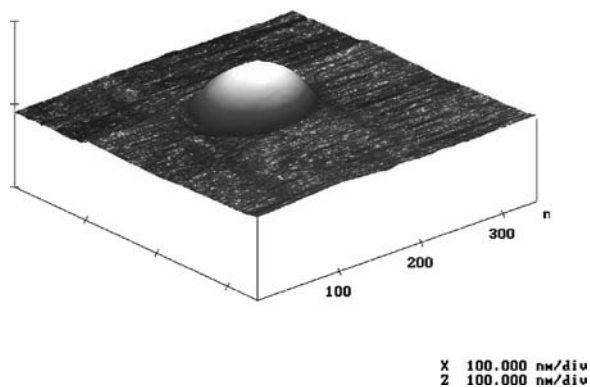


**Fig. 2** AFM image of spherical IF-WS<sub>2</sub> nanoparticles.

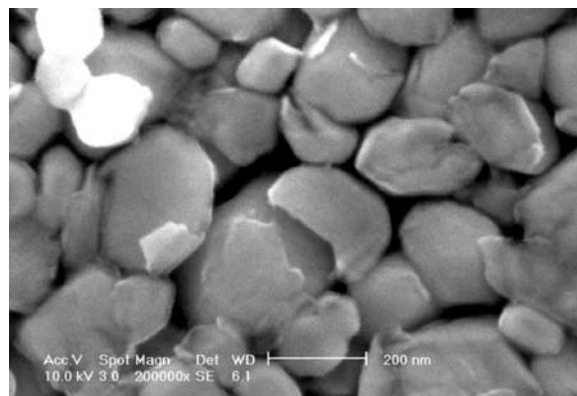


**Fig. 3** Scanning electron microscopic (SEM) micrograph of ensemble of the IF-WS<sub>2</sub> nanoparticles after compression with a pressure of 500 MPa.



only 5 wt.% of the solid lubricants (IF or 2H-WS<sub>2</sub>) were dispersed in oil. It was observed that IF showed superior friction and wear properties under relatively low values of the loads and sliding velocities. Analysis of the solid lubricant particles showed that a substantial number of the 2H platelets were destroyed, whereas IF particles were found to remain undamaged under these conditions. With increasing load, three mechanisms of IF particle damage could be discerned: plastic deformation of the quasi-spherical nanoparticles into ovoid shape; peeling-off of external sheaths; and splitting.<sup>[23]</sup> The quantity of damaged particles increased with increasing load. The amount of the oxide was found to be substantially larger on the surface of the wear track in contact with the 2H-WS<sub>2</sub> platelets compared to IF nanoparticles. The chemical reactions that are relevant to the wear of platelet materials occurred predominantly at the prismatic edges, where reactive dangling bonds exist. The presence of unsaturated or dangling bonds in metal dichalcogenides led to oxidation of the surface in the surrounding environment, especially at elevated temperatures which may occur as a result of friction. For instance, a switch from an environment of dry nitrogen to humid air led to an increase of the friction coefficient of 2H-WS<sub>2</sub> from 0.03–0.04 to 0.15–0.20, and a decrease in its resistance to oxidation by several orders of magnitude.<sup>[24]</sup> Therefore, the absence of dangling bonds may be one of the prime advantages of IF nanoparticles over the crystalline platelet (2H) particles for reduction of friction and wear.

Mixed lubrication is an extremely important regime of liquid lubrication when both fluid film and boundary lubrication take place.<sup>[25]</sup> Mixed lubrication region is the transition to scuffing and seizure. The behavior of IF-WS<sub>2</sub> solid lubricant in oil has been compared with pure oil.<sup>[26]</sup> The kinetic of the friction force change between two feedings of lubricants has been analyzed. Based on this analysis, it was concluded that the addition of IF nanoparticles to oil induces protection for the contact surface, decreases the fraction of straight asperity contact, and thus improves the tribological properties of pin-on-disk contact pair under mixed lubrication. It was found that the wear of the pin rubbed with oil + IF lubricant is lower in comparison to the pin lubricated by a pure oil. This effect grows with increasing load, suggesting that the favorable role of the IF increases with the load. Damage and destruction of IF-WS<sub>2</sub> was usually observed over a pressure of 0.5 GPa. The main damage incurred to the IF nanoparticles was the exfoliation (delamination) of external sheets (Fig. 4). Thin nanosheets of delaminated IF are also observed. Usually, only a few external molecular sheets of the IF are damaged. Appreciable damage occurred for the small number of fullerene-like nanoparticles. The surface of the pin

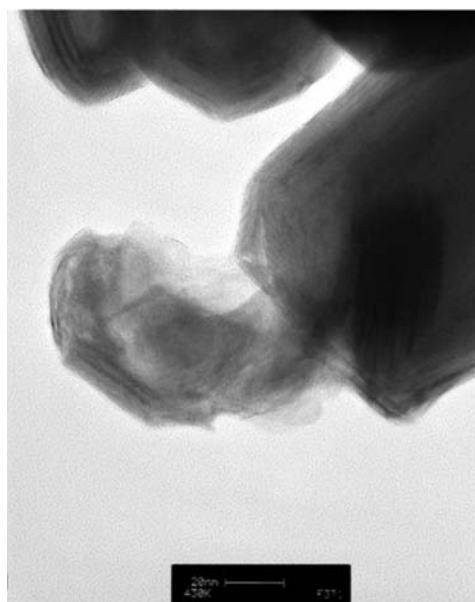


**Fig. 4** TEM image of the IF nanoparticles after the pin-on-disk test.

rubbed with oil + IF was found to be covered by a film. X-ray photoelectron spectroscopy (XPS) analysis revealed that this film consisted of WS<sub>2</sub>.

IF agglomerates are compressed and penetrate into the surface layers of the soft pin (Fig. 5). As a result of this effect, the surfaces rubbed with oil + IF were rougher compared to the surfaces lubricated with a pure oil. The main friction mechanism for IF nanoparticles in the range of mixed lubrication is the transfer of exfoliated thin sheets to the contact surface. The transfer is probably responsible for the self-lubrication of the IF solid lubricant nanoparticles in the mixed range of lubrication.

After the friction test, the loaded pin was etched lightly with 3% HNO<sub>3</sub> in alcohol, which dissolved the wear debris impregnated onto the metal surface and

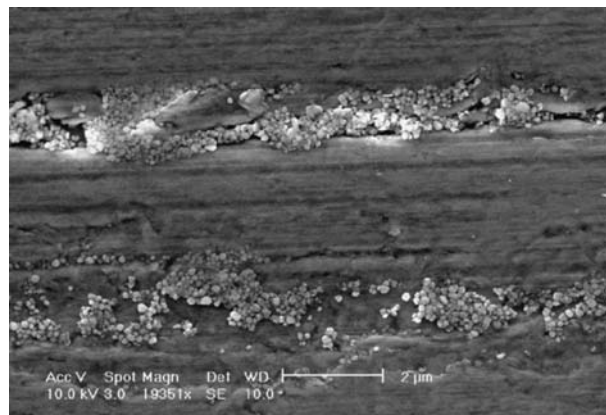


**Fig. 5** Penetration of the IF nanoparticles and their agglomerates into the surface layers of hard disk.

revealed the wear damage. SEM analysis of the etched surface showed that, while the oil-lubricated surface was heavily damaged with deep scratches and grooves occurring, the surface of the metallic pin lubricated with oil + IF remained almost unchanged.

The thickness of the lubricant film depends on contact conditions (viscosity of lubricant, load, and sliding velocity). Using the analysis of mixed lubrication for the surface with a real roughness,<sup>[25]</sup> the mean film thickness was found to be smaller than the size of IF nanoparticles. When film thickness is smaller than the size of nanoparticles, IF-WS<sub>2</sub> have to delaminate or, they can be preserved in the valleys of the roughened surfaces, or the two processes can occur together. Identification of WS<sub>2</sub> on the contact surface (XPS and etching), preservation of the full shape of IF nanoparticles (TEM analysis), and the formation of a rough surface under steady friction prove that a part of the IF-WS<sub>2</sub> is preserved in valleys of the contact surface while another portion of the IF nanoparticles is delaminated and transferred to the rubbed surfaces.

IF nanoparticles in the valleys and delaminated transferred nanosheets on the surface decrease the straight asperity contact under mixed lubrication. Thus the IF-WS<sub>2</sub> film protects the contact surface and enhances the wear resistance of contact surfaces. We suppose that sliding/rolling of the IF nanoparticles in the interface between rubbed surfaces is the main friction mechanism under loads, when the shape of nanoparticle is preserved. It was found that the efficacy of IF nanoparticles was increased with the load. It may be expected that, under friction with very high loads (>1 GPa), a considerable number of nanoparticles will be delaminated and consequently, transfer of thin nanosheets a few nanometers in size may be a dominant friction mechanism. Recent results confirm this assumption.<sup>[27]</sup> Also, this study underscores the importance of size control for the IF nanoparticles.

Using the surface force apparatus, the friction behavior of IF nanoparticles was investigated in detail.<sup>[28–30]</sup> It was revealed that IF nanoparticles are gradually exfoliated, leaving molecular sheets of WS<sub>2</sub> on the mica surface, thereby reducing the shear resistance of the matting pairs in tetradecane suspension. Therefore the interplay between the rolling/sliding of the nanoparticles and their slow exfoliation seem to play an important role in the self-lubricating of mating tribological surfaces with IF. In contrast, 2H-WS<sub>2</sub> particles did not show favorable tribological properties.<sup>[30]</sup>

## IMPREGNATION OF IF NANOPARTICLES INTO POWDER MATERIALS

Modern powder metallurgy (PM) technologies are used to produce low-cost, high-quality bearings and

gears with long-term performance and reliability in critical applications (high loads and sliding velocities). Interconnected system of pores renders the supply of oil impregnated throughout the entire metal piece, thereby providing self-lubrication of these bearings. The lubricating fluid flows through the porous structure and is furnished to the metal surface. However, the addition of oil is prohibitive for various applications, such as aerospace, vacuum systems, and electrical motors. The impregnation of solid lubricants platelets, such as powders of WS<sub>2</sub> and MoS<sub>2</sub>, into the powder matrix allows for an increased loading of the bearings. Unfortunately, the friction coefficients encountered in bearings stuffed with solid lubricants are invariably higher (0.1–0.3) than in oil-impregnated bearings.

For most applications, the porosity of self-lubricating bearings lie between 25% and 35%. It is clear that such high porosity diminishes the mechanical properties of the porous material. On the other hand, reducing the porosity to increase the strength of the matrix would restrict the permeation of the solid lubricant into the pores. It was hypothesized that IF-WS<sub>2</sub> nanoparticles will benefit self-lubricating bearing technology in a number of ways. First, being small (0.005–0.2 μm), they could be easily impregnated into bearings of substantially smaller porosity. Such bearings will have appreciably higher mechanical strength combined with an improved tribological behavior, especially under extreme loads and velocities. Second, their seamless character and spherical shape will allow their facile impregnation throughout the entire bearing matrix. Also, being stocked in microscopic pores, these slippery nanoparticles would not be removed at once from the contact area. Instead, a slow release of the nanoparticles from the matrix pores will provide steady flux of lubricants and easy shearing of the metal–metal interface, even under extreme loads. It was also expected that the spherical shape of IF nanoparticles impregnated inside a porous solid matrix will lead to an easy flow from the pores to the contact surface, thus alleviating both friction losses and wear. The continuous supply of solid lubricant nanoparticles to the sliding contact is of great importance in this case. Therefore, it is expected that impregnation of spherical nanoparticles into the densified powder matrix will lead to a nanocomposite with superior mechanical and self-lubricating properties. Porous metal pieces, which are similar in size and shape to commercially available sliding bearings, were manufactured according to a standard PM procedure. The details of preparation PM parts were described in Ref.<sup>[31]</sup> Bronze, iron, and iron–nickel matrices were been used in this work. Subsequently, impregnation of oil–2H-WS<sub>2</sub> and oil–IF-WS<sub>2</sub> (10 wt.%) suspensions into the porous metal parts was carried out under low vacuum. IF-WS<sub>2</sub>

nanoparticles and layered platelets 2H-WS<sub>2</sub> with size close to 4 μm were used as solid lubricants. The density of IF nanoparticles is about 15–20% smaller than that of the bulk (2H) particles. Afterward, the samples were dried at 150°C (2 hr), under a vacuum of 10<sup>-2</sup> Torr, in order to release the fluid lubricant from the porous metal piece. The hollow IF nanoparticles were 5 wt.% of the powder bronze, compared with 6% for the 2H-WS<sub>2</sub>.

Fig. 6A shows SEM micrographs of the virgin bronze surfaces after impregnation of the 2H-WS<sub>2</sub> platelets has taken place. As shown by the micrograph, the surface of the metal matrix is non-uniform, and the 2H-WS<sub>2</sub> platelets are “glued” edge-on onto the metal surface through their reactive prismatic (10 $\bar{1}$ 0) faces (Fig. 6B). This orientation is unfavorable for the tribological action of this lubricant, and is, in fact, expected to “glue” the asperities of the two mating metal surfaces. Contrarily, the IF-WS<sub>2</sub> nanoparticles are scattered quite randomly on the porous metal matrix surface. Spherical agglomerates of the IF nanoparticles, which are trapped in the cavities on the metal

block surface, are discernible. The SEM image of the powder nanocomposite showed that the penetration of IF-WS<sub>2</sub> nanoparticles is close to 150–250 μm, and it depends on the matrix density.

The study of friction and wear was performed by using a ring-block tester at wide range of sliding velocities and load.<sup>[32]</sup> Samples that were oil-impregnated and dried (hereafter designated as reference) were studied first. It was established that the surface pores of this sample are rapidly filled with agglomerated wear particles already under the low load. The agglomeration and compaction of the wear particles in the pores led to a formation of smooth surfaces. With increasing load, severe plastic deformation of the surface layers was obtained. In this case, delamination of thin surface plates was observed. The fast agglomeration and compaction of the wear particles within the pores and the severe plastic deformation of the surface layers led to an increase of the friction coefficient, contact temperature, and wear rate. With increased loading, the pores became completely closed, and a smooth surface of the densified powdered block is obtained. Upon transition to seizure, the wear particles adhere to the contact surface, leading to the formation of a rough surface. The friction coefficient and temperature increase abruptly, which finally leads to seizure of the matting surfaces.

The friction coefficient and temperature for bronze part impregnated with oil + IF and reference sample were very low ( $\mu = 0.006$ ) over a large range of contact conditions, while it was higher ( $\mu = 0.06$ ) for reference sample. In this case, a lot of small pores were preserved on the surface of powdered bronze impregnated with IF under steady friction conditions. With increasing load the detached and trapped wear particles fill the pores, but a fraction of the pores nevertheless remained opened. Friction and wear of the samples impregnated with IF nanoparticles associated with their release from the interconnected system of pores in the metal matrix and a furnishing to the contact interface. Supply of the solid lubricant from the pores to the surface requires the preservation of an open porosity at the surface. Furthermore, IF nanoparticles facilitate the dislodging of the agglomerated wear particles from the pores and thus preserve the porosity and the supply of IF nanoparticles to contact surfaces. Thus the impregnation of IF nanoparticles into the pores enables the improvement of the self-lubricating properties of powder materials, thereby considerably decreasing the friction coefficient and wear rate. Diminution of the friction coefficient with the IF nanoparticles can be attributed to the following effects:<sup>[33–36]</sup>

1. The slow release and furnishing of nanoparticles from the open pores to the contact surface prevent the direct contact between the first bodies.

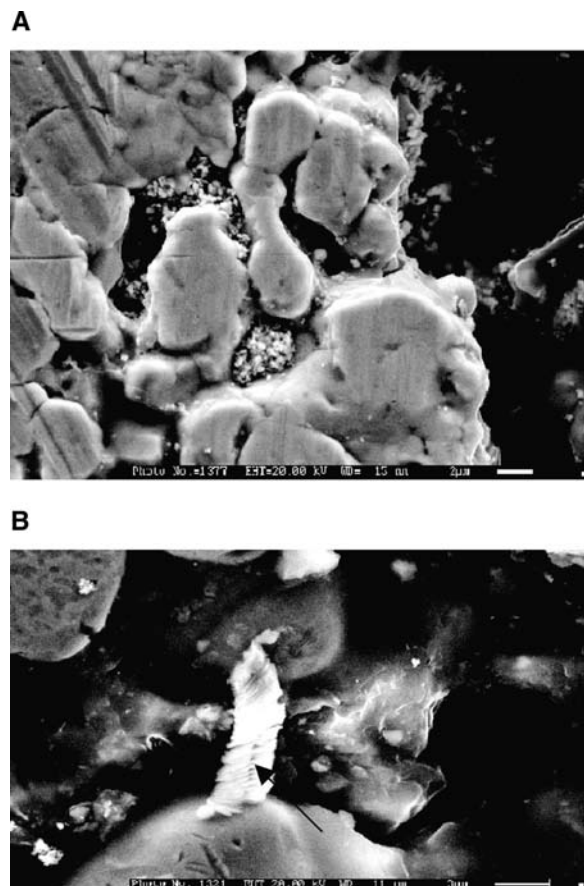


**Fig. 6** SEM micrographs of the virgin bronze surfaces after the impregnation of the solid lubricant particles: A) IF-WS<sub>2</sub> nanoparticles distributed in the pores; B) 2H particles glued onto the metal surface (noted by arrow).

2. The sliding/rolling of IF nanoparticles in the boundary of the first bodies and in between the wear particles (third body) facilitate the shear of the lubrication film.
3. The adhesion of IF nanoparticles to the agglomerated wear particles facilitates their dislodging from the pores, keeping the pores to remain open during loading.

It was shown that 2H particles are “glued” edge-on to the underlying metal surface through their reactive prismatic faces (10 $\bar{1}$ 0).<sup>[32]</sup> The sticking (“gluing”) of the prismatic edges of the 2H platelets to the metal surface averts their permeation deep into the metal piece and leads to their accumulation at the metal surface. The accumulation of 2H particles in the superficial pores leads to the formation of a thin WS<sub>2</sub> film on the surface of the sample. Under low load, this film provides the low friction coefficient and a reduced wear rate. However, with increasing load, the WS<sub>2</sub> film is cracked and its favorable tribological properties are diminished. The transition to seizure occurs under a load much lower than with IF nanoparticles.

The supply of solid lubricant from the pores to the surface requires the preservation of an open porosity at the surface. In the case of powdered materials impregnated with 2H-WS<sub>2</sub>, the large delaminated wear debris filled the pores. This effect led to smoothing of the rubbed surface and clogging of the pores. In contrast, the IF-WS<sub>2</sub> nanoparticles, which are dispersed throughout the entire porous metal reservoir, are forced to proceed gradually to the metal surface, and some of them are even picked up by the disk.

The efficacy of the IF is considerably increased when an oil film is supplied to the interface. The application of oil allowed the considerable increase in the load-bearing capacity of powdered bearing samples impregnated with oil + IF nanoparticles.<sup>[34]</sup> It is likely that the release and furnishing of the solid lubricant from the interconnected system of pores to the contact surface is also facilitated by the oil.

#### ADDITION OF THE IF NANOPARTICLES INTO THE GREASE

The effect of IF nanoparticles added to a heavy-duty (lithium-based) grease was studied by using a ring-block tester.<sup>[37]</sup> Here, the friction behavior of the base grease (containing 5 wt.% IF-WS<sub>2</sub> nanoparticles) and a commercial grease [containing 5 wt.% 2H-MoS<sub>2</sub> particles (platelets) as additives] were compared. SEM examination of the tested grease shows that IF nanoparticles remained intact, but partially agglomerated. The fibrelous structure of the grease is preserved after the tribological experiments with the added IF

nanoparticles, suggesting that grease does not decompose, or react, with either the nanoparticles or the metal surfaces, even under the heavy loads employed in the present experiment (Fig. 7A). The delamination of thin layers is observed on the surface of the 2H-MoS<sub>2</sub> (Fig. 7B). The friction and wear behavior of the base grease, the same state-of-the-art grease formulated with 2H MoS<sub>2</sub> platelets, and the grease formulated with IF tungsten disulphide nanosphere material were compared. Notably, the addition of only a small amount (5 wt.%) of the IF-WS<sub>2</sub> nanoparticles to the grease leads to very low friction coefficient under very high loads, largely surpassing the critical loads for seizure of the pristine grease, or the grease with 5 wt.% 2H-MoS<sub>2</sub>, added. While the temperature of the grease with 2H-MoS<sub>2</sub> particles rises to 75°C under high load of 2700 N load, it does not

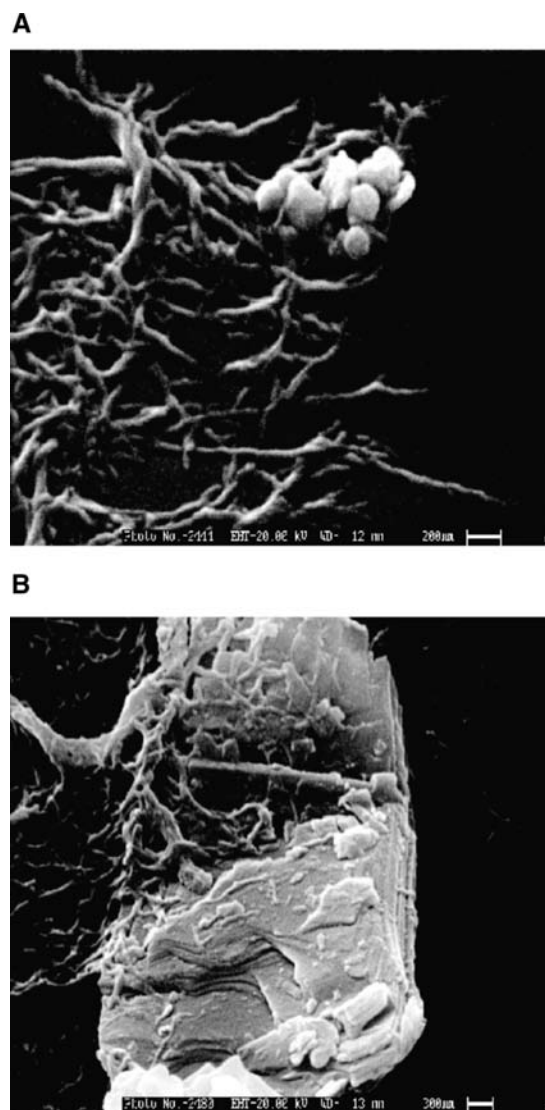


Fig. 7 SEM micrograph showing the thickener fibers with IF A) and 2H B) particles of solid lubricant.

exceed 55°C under 3300 N for the grease with added IF nanoparticles. The effect of IF nanoparticles in greases on the friction, wear, and the temperature of powdered iron samples was studied. Under low loads, friction coefficients for greases with IF and 2H were close. However, with increasing load, the IF became more effective. Under load of 2700 N, a transition to seizure occurred with 2H particles, while the test with IF was continued up to the maximum possible load of the tester (3300 N). It was found that, in analogy to the friction coefficient, the effect of IF increases with the load. Thus it may be concluded that all the tribological parameters studied were considerably improved for the grease with IF nanoparticles in comparison to commercially available grease with 2H-MoS<sub>2</sub> particles. A large part of the pores was preserved on the surface of the powdered sample lubricated with grease + IF, while most of the pores were found to be clogged on the surface of the sample rubbed with a virgin grease. The study of friction and wear of powdered materials with greases showed high efficacy of the IF in comparison to commercial grease with 2H-MoS<sub>2</sub> particles and the base grease. IF nanoparticles were transferred from the grease to the contact surface. Energy-dispersive X-ray (EDS) and XPS analyses demonstrated that IF nanoparticles are confined in the pores of powdered matrix and are released to the interface even over high contact conditions.

### NEW APPLICATIONS OF IF SOLID LUBRICANT NANOPARTICLES

Thin films of IF nanoparticles were deposited on metal substrates, either in the pure form or embedded in electroless coatings,<sup>[30,38,39]</sup> and were found to confer low friction and wear to the substrate, even under very high loads, ultrahigh vacuum (UHV), and in a humid atmosphere. It was shown that the frictional and wear properties of MoS<sub>2</sub> thin films deposited by ablating a solid MoS<sub>2</sub> target can be improved by the incorporation of fullerene-like nanoparticles.<sup>[38]</sup> IF-MoS<sub>2</sub> nanoparticles were tested under boundary lubrication and ultrahigh vacuum (UHV) and were found to yield an ultralow friction coefficient in both cases compared to hexagonal 2H-MoS<sub>2</sub> material.<sup>[30]</sup> The friction coefficient under high pressure (maximum pressure above 1.1 GPa in oil and 400 MPa in high vacuum) and slow sliding velocities (1.7 mm/sec in oil test and 1 mm/sec in high vacuum), and decreased and stabilized at about 0.04 for 800 cycles in both cases. It was found that 2H-MoS<sub>2</sub> particles are flattened and then break because of the contact pressure. The lamellar structure discovered in wear particles, MoS<sub>2</sub>, leads to ultralow friction.

Ceramic materials are very ionic and consequently, are rather tough and brittle, notoriously known for

exhibiting very poor tribological behavior. This poor behavior can be also attributed to the high surface roughness of ceramic materials. When rubbed against another surface, asperities of the rough ceramic surface detach and small wear particles are formed, which scratch and damage the mating surface, leading to its rapid deterioration. The surface of an alumina wafer was coated with a thin dry layer of IF-WS<sub>2</sub> nanoparticles, which was stressed under pressure applied by the reciprocating action of a ceramic ball. The added IF nanoparticles were found to decorate the irregularities and scratches on the surface of ceramic materials. Fig. 8A shows the results of a tribological experiment with Si<sub>3</sub>N<sub>4</sub> ball and a flat alumina wafer. Here a 1 order-of-magnitude reduction of the friction coefficient is obtained by adding IF-WS<sub>2</sub> to the interface in comparison to a dry friction test. Furthermore, severe wear damage occurs to the surface of the ceramic ball rubbed against alumina (a) in Fig. 8B. Contrarily, almost no wear was incurred to the ceramic ball that was rubbed against the alumina surface coated with IF film (b) in Fig. 8B. This remarkable behavior could potentially be very useful for machine parts in the textile, food, and microelectronic industries, where ceramic components take part in the manufacturing processes. Under very high pressure (>1 GPa), nanoparticles suffer a severe plastic deformation and they gradually exfoliate, producing a continuous film 3–5 nm thick on the underlying surface, which has been studied by AFM.<sup>[36]</sup> This film is expected to provide easy shear of thin exfoliated sheets of IF nanoparticles under such extreme circumstances. This observation was, in fact, preceded by a theoretical calculation, which predicted that IF nanoparticles 60 nm in diameter will plastically deform under pressures exceeding 1 GPa.<sup>[39]</sup>

A polymer-fullerene-like-WS<sub>2</sub> nanocomposite was developed by impregnating the epoxy resin with IF-WS<sub>2</sub> nanoparticles. Polymer pin-steel disk test has been performed to evaluate the self-lubricating properties of this composite.<sup>[40]</sup> The friction coefficient of a disk-pin impregnated with IF-WS<sub>2</sub> is shown to be three times lower than for a pair: epoxy resin-steel disk. The wear rate of the polymer nanocomposite is found to be 10 times lower than for the virgin polymer. It is shown that polymer nanocomposites are transferred to the hard metal surface, releasing slowly the IF nanoparticles, which provides easy shear for the mating surfaces. Analysis of the contact surfaces of the steel disk rubbed with the polymer nanocomposite identified a transferred black film on the surface. To prepare the samples for TEM analysis, the transferred film was carefully delaminated from the surface of the disk. Using EDS analysis, it was observed that, apart from the epoxy matrix, the delaminated particles contain WS<sub>2</sub>. It is likely that increasing the strength of

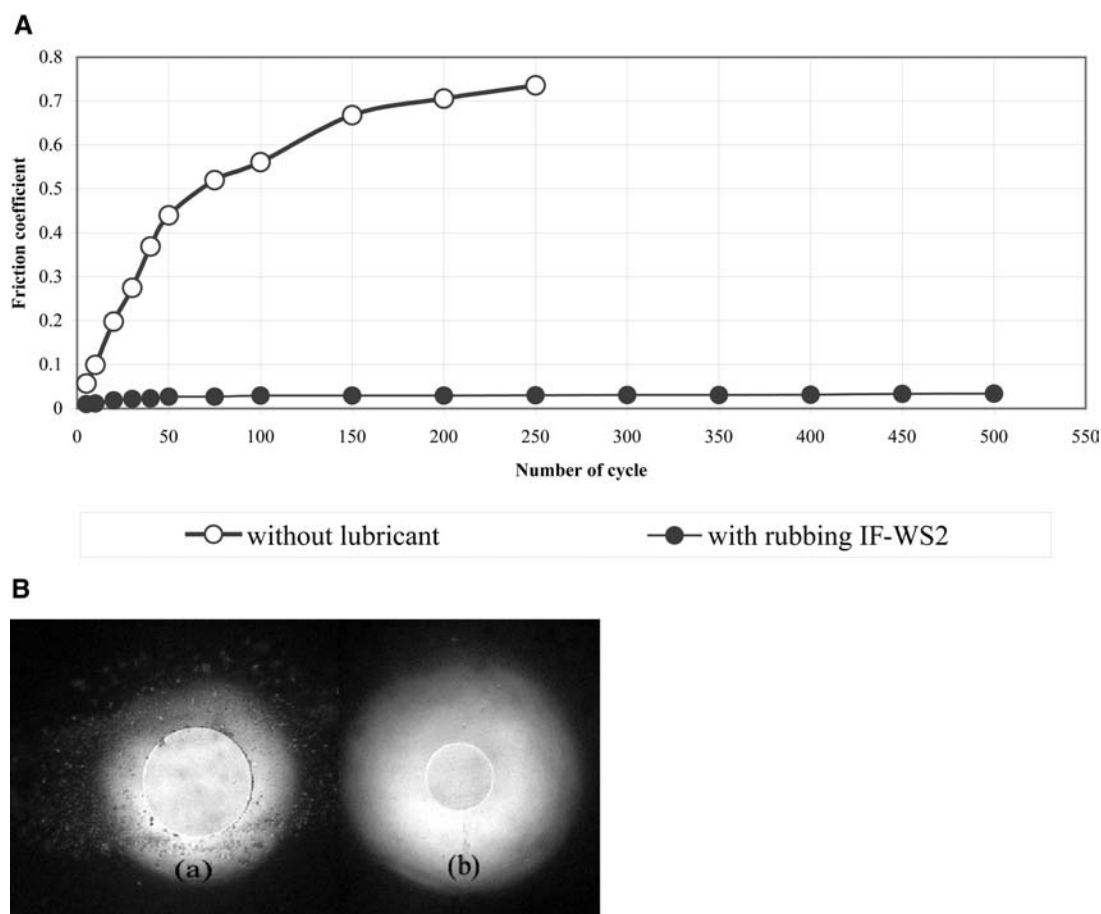


**Fig. 8** A) The friction coefficient of a  $\text{Si}_3\text{N}_4$  ball loaded against  $\text{Al}_2\text{O}_3$  flat wafer; B) micrographs demonstrating the wear damage on the surface of the balls loaded against alumina wafer: a) without IF film and b) with thin film of IF nanoparticles.

nanocomposite, as a result of impregnation of stiff and elastic spherical particles and the formation of the transfer films containing the IF solid lubricant nanoparticles, are the main factors leading to lowering of the friction of the nanocomposite with solid lubricant nanoparticles. The wear coefficient,  $K_w$ , for nanocomposites was  $0.5 \times 10^{-11}$  vs.  $4.6 \times 10^{-11} \text{ mm}^3/\text{mmN}$  for the epoxy samples.<sup>[40]</sup>

## CONCLUSION

This description shows a plethora of somewhat unrelated tests and disparate set of data, whereby different interfaces lubricated with IF nanoparticles exhibited invariably significantly better tribological behavior compared with the reference systems, especially under heavy loads. It suggests that the beneficial self-lubricating properties of IF nanoparticles cannot be attributed to a single mechanism alone. Under low loads, the film thickness is close to the size of nanoparticles. In this case, the shape of the nanoparticles is preserved and sliding/rolling of the spherical IF

nanoparticles at the interface seems to be the dominant friction mechanism. The agility of IF nanoparticles in the contact region also depends on their shape and size, underscoring the importance of their synthesis. The quasi-spherical shaped nanoparticles produced by the fluidized bed reactor are very suitable in this respect. When the film thickness is smaller than the size of the solid lubricant nanopowder (high contact pressures), deformation and destruction of IF nanoparticles leads to the exfoliation of thin external sheets. The self-lubricating behavior of IF solid lubricant nanoparticles is probably provided by shear of the thin transfer film. Note, that the distorted IF nanoparticles were found to be both in the valleys of contact surface and as transferred sheets at the summits of the asperities. The IF- $\text{WS}_2$  film serves to protect the contact surface and thus enhances the wear resistance of contact surfaces. Nanoparticles confined in the surface irregularities are unable to slide freely away from the contact area and are gradually released from the grooves and furnished to the mating surface, providing easy shearing, temporarily, until they are trapped again in another groove. This mechanism explains the



beneficial role of surface roughness on the performance of the IF nanoparticles in tribological contacts. Self-lubricating properties of the powder materials impregnated with IF solid lubricant nanoparticles are explained by their easy furnishing and slow release to the contact surface. Stiffness of IF nanoparticles and their self-lubricating properties impart superior tribological properties to ceramic surfaces coated by IF and polymer nanocomposites with embedded solid lubricant nanoparticles.

## ACKNOWLEDGMENTS

I am grateful to Prof. V. Leshchinsky, Prof. Ya. Soifer, Dr. M. Lvovsky, Dr. O. Nepomnyashchy, Dr. Yu. Volovik, Dr. I. Lapsker, Dr. A. Verdyan all from Holon Academic Institute of Technology; Prof. R. Tenne, Dr. R. Rosentsveig, Dr. Y. Feldman, Dr. R. Popovitz-Biro, all from the Weizmann Institute of Science. Support of the Israeli Ministry of Science (Tashtiot) and Bi-National Science Foundation (BSF) are greatly acknowledged. I am grateful to NanoMaterials, Ltd., Israel ([www.apnano.com](http://www.apnano.com)) for their cooperation and assistance in developments regarding the inorganic fullerene-like materials.

## REFERENCES

- Bowden, F.P.; Tabor, D. *The Friction and Lubrication of Solids, Part II*; Oxford University Press: London, 1964.
- Bhushan, B.; Gupta, B.K. *Handbook of Tribology*; McGraw Hill, Inc.: New York, 1991.
- Black, A.L.; Dunster, R.W.; Sanders, J.V. Comparative study of deposits and behavior of MoS<sub>2</sub> particles and molybdenum dialkyl-dithio-phosphate. *Wear* **1969**, *13*, 119–132.
- Gansheimerand, J.; Holinsky, R. A study of solid lubricants and oils and greases under boundary conditions. *Wear* **1972**, *19*, 439–449.
- Bowden, F.P.; Tabor, D. *Friction: An Introduction to Tribology 91*; Anchor: Garden City, NY, 1973.
- Singer, I.L. *Fundamentals of Friction: Macroscopic and Microscopic Processes*; Singer, I.L., Pollock, H.M., Eds.; Kluwer: Dordrecht, 1992.
- Bhushan, B.; Gupta, B.K.; Van Cleef, G.W.; Capp, C.; Coe, J.V. Sublimed C<sub>60</sub> films for tribology. *Appl. Phys. Lett.* **1993**, *62*, 3253–3255.
- Bhushan, B.; Gupta, B.K.; Van Cleef, G.W.; Capp, C.; Coe, J.V. Fullerene (C<sub>60</sub>) films for solid lubrication. *Tribol. Trans.* **1993**, *36*, 573–580.
- Schwarz, U.D.; Allers, W.; Gensterblum, G.; Wiesendanger, R. Low-load friction behavior of epitaxial C<sub>60</sub> monolayers under Hertzian contact. *Phys. Rev., B* **1995**, *52*, 14976–14984.
- Campbell, S.E.; Luengo, G.; Srdanov, V.I.; Wudi, F.; Israelachvili, J.N. Very low viscosity at the solid-liquid interface by adsorbed C<sub>60</sub> monolayers. *Nature* **1996**, *382*, 520–522.
- Blau, P.J.; Haberlin, C.E. An investigation of the microfrictional behavior of C<sub>60</sub> particle layers on aluminum. *Thin Solid Films* **1992**, *219*, 129–134.
- Kroto, H.W.; Heath, J.R.; O'Brein, S.C.; Curl, R.F.; Smalley, R.E. C<sub>60</sub>: Buckminsterfullerene. *Nature* **1985**, *318*, 162.
- Iijima, S. Helical microtubules of graphitic carbon. *Nature* **1991**, *354*, 56.
- Tenne, R.; Margulis, L.; Genut, M.; Hodes, G. Polyhedral and cylindrical structures of WS<sub>2</sub>. *Nature* **1992**, *360*, 444–445.
- Margulis, L.; Salitra, G.; Tenne, R.; Talianker, M. Nested fullerene-like structures. *Nature* **1993**, *365*, 113–114.
- Feldman, Y.; Wasserman, E.; Srolovitz, D.J.; Tenne, R. Nested inorganic fullerenes and nanotubes. *Science* **1995**, *267*, 222–225.
- Tenne, R. *Progress in Inorganic Chemistry*; Karlin, K.D., Ed.; John Wiley & Sons: New York, 2001; Vol. 50, 269–315.
- Nath, M.; Rao, C.N.R. Inorganic nanotubes. *Dalton Trans.* **2003**, *1*, 1–25.
- Tenne, R. Inorganic nanotubes. In *Dekker Encyclopedia of Nanoscience and Nanotechnology, 2E*; Schwarz, J.A., Contescu, C.I., Putyera, K., Eds.; Taylor & Francis: New York, NY, 2009; Vol. 3, 1598–1605.
- Srolovitz, D.J.; Safran, S.A.; Homyonfer, M.; Tenne, R. Relaxed curvature elasticity and morphology of nested fullerenes. *Phys. Rev. Lett.* **1995**, *74*, 1779–1881.
- Leshchinsky, V.; Popovitz-Biro, R.; Soifer, Ya.; Gartsman, K.; Rosenberg, Yu.; Tenne, R.; Rapoport, L. Behavior of solid lubricant nanoparticles under compression. *J. Mat. Sci.* **2004**, *39*, 4119–4129.
- Rapoport, L.; Bilik, Yu.; Homyonfer, M.; Cohen, S.R.; Tenne, R. Hollow nanoparticles of WS<sub>2</sub> as potential solid lubricants. *Nature* **1997**, *387*, 791–793.
- Rapoport, L.; Feldman, Y.; Homyonfer, M.; Cohen, H.; Sloan, J.; Hutchison, J.L.; Tenne, R. Inorganic fullerene-like material as additives to lubricants: Structure–function relationship. *Wear* **1999**, *225–229*, 975–982.
- Prasad, S.V.; Zabinski, J.S. Tribology of tungsten disulfide (WS<sub>2</sub>): Characterization of wear-induced transfer films. *J. Mater. Sci. Lett.* **1993**, *11*, 1413–1415.
- Spikes, H.A.; Olver, A.V. *Lubricants, Materials, and Lubrication Engineering: Proceedings of the 13th International Colloquium Tribology*; Bartz, W.J., Ed.; 2002; Vol. 1, 19–30. Ostfildern.
- Rapoport, L.; Leshchinsky, V.; Lapsker, I.; Volovik, Yu.; Nepomnyashchy, O.; Lvovsky, M.; Popovitz-Biro, R.; Feldman, Y.; Tenne, R. Tribological properties of WS<sub>2</sub> nanoparticles under mixed lubrication. *Wear* **2003**, *255*, 785–793.
- Cizaire, L.; Vacher, B.; Le-Mogne, T.; Martin, J.M.; Rapoport, L.; Margolin, A.; Tenne, R. Mechanisms of ultra-low friction by hollow inorganic fullerene-like MoS<sub>2</sub> nanoparticles. *Surf. Coat. Technol.* **2002**, *160*, 282–287.

28. Golan, Y.; Drummond, C.; Homyonfer, M.; Feldman, Y.; Tenne, R.; Israelachvili, J. Microtribology and direct force measurement of WS<sub>2</sub> nested fullerene-like nanostructures. *Adv. Mater.* **1999**, *11*, 934–937.
29. Golan, Y.; Drummond, C.; Israelashvili, J.; Tenne, R. In situ imaging of shearing contacts in the surface forces apparatus. *Wear* **2000**, *245*, 190.
30. Drummond, C.; Alcantar, N.A.; Israelachvili, J.; Tenne, R.; Golan, Y. Microtribology and friction-induced material transfer in WS<sub>2</sub>. *Adv. Funct. Mater.* **2001**, *11*, 348–354.
31. Leshchinsky, V.; Aloyshina, E.; Lvovsky, M.; Volovik, Y.; Lapsker, I.; Tenne, R.; Rapoport, L. Inorganic nanoparticle impregnation of self lubricated materials. *Int. J. Powder Metall.* **2002**, *38*, 50–57.
32. Rapoport, L.; Lvovsky, M.; Lapsker, I.; Leshchinsky, W.; Volovik, Yu.; Feldman, Y.; Tenne, R. Friction and wear of bronze powder composites including fullerene-like WS<sub>2</sub> nanoparticles. *Wear* **2001**, *249*, 149–156.
33. Rapoport, L.; Lovovsky, M.; Lapsker, I.; Leshchinsky, V.; Volovik, Yu.; Feldman, Y.; Tenne, R. Slow release of fullerene-like WS<sub>2</sub> nanoparticles from Fe–Ni–graphite matrix: A self-lubricating nanocomposite. *Nano Lett.* **2001**, *1*, 137–140.
34. Rapoport, L.; Leshchinsky, V.; Lvovsky, M.; Lapsker, I.; Volovik, Yu.; Tenne, R. Load bearing capacity of bronze, iron and iron–nickel powder composites containing fullerene-like WS<sub>2</sub> nanoparticles. *Tribol. Int.* **2002**, *35*, 47–53.
35. Rapoport, L.; Leshchinsky, V.; Lvovsky, M.; Nepomnyashchy, O.; Volovik, Yu.; Tenne, R. Friction and wear of powdered composites impregnated with WS<sub>2</sub> inorganic fullerene-like nanoparticles. *Wear* **2002**, *252*, 518–527.
36. Rapoport, L.; Leshchinsky, V.; Lvovsky, M.; Lapsker, I.; Volovik, Yu.; Feldman, Y.; Popovitz-Biro, R.; Tenne, R. Superior tribological properties of powder materials with slid lubricant nanoparticles. *Wear* **2003**, *255*, 794–800.
37. Rapoport, L.; Leshchinsky, V.; Volovik, Yu.; Lvovsky, M.; Nepomnyashchy, O.; Feldman, Y.; Popovitz-Biro, R.; Tenne, R. Modification of contact surfaces by fullerene-like solid lubricant nanoparticles. *Surf. Coat. Technol.* **2003**, *163–164*, 405–412.
38. Chowalla, M.; Amaratunga, G.A.J. Ultra low friction and wear MoS<sub>2</sub> nanoparticle thin films. *Nature* **2000**, *407*, 164–166.
39. Schwarz, U.S.; Komura, S.; Safran, S.A. Deformation and tribology of multi-walled hollow nanoparticles. *Europhys. Lett.* **2000**, *50*, 762–768.
40. Rapoport, L.; Leshchinsky, V.; Popovitz-Biro, R.M.; Nepomnyashchy, O.; Volovik, Yu.; Itah, B.; Tenne, R. Non-published results.

# Tribology at the Nanoscale

**Peter T. Cummings**

*Department of Chemical Engineering, Vanderbilt University, Nashville, Tennessee, U.S.A., and Chemical Sciences Division, Oak Ridge National Laboratory, Oak Ridge, Tennessee, U.S.A.*

**Clare McCabe**

*Colorado School of Mines, Golden, Colorado, U.S.A.*

## INTRODUCTION

The moving contact of two solid surfaces results in friction and wear. Annually, friction and wear are estimated to cost the United States 6% of the gross national product,<sup>[1]</sup> or over half a billion dollars per year. Friction is a familiar concept that many people assume is well understood. Students often learn in high school or introductory college physics that friction can be described by a simple expression  $-F_f = \mu F_N$ , where  $F_f$  is the magnitude of frictional force,  $\mu$  is the (constant) coefficient of friction, and  $F_N$  is the magnitude of the normal force between two surfaces—and that there is a different coefficient of friction for initial motion (i.e., beginning at rest) and for two surfaces already moving (sliding friction), with tabulations of the coefficients of friction available for various pairs of surfaces. However, these relatively simple concepts—which often fail in practice, because the phenomenological coefficient of friction turns out to be a function of the details of the preparation of the two surfaces in contact, the operating conditions, the sliding velocity, and so on—hide the fact that friction is a very complicated phenomenon, little understood fundamentally, and dependent on processes taking place at the nanoscale.

Lubrication—defined by Webster's dictionary as the "application of a substance capable of reducing friction, heat, and wear when introduced as a film between solid surfaces"—is necessary to reduce damage to the moving surfaces and to enable reliable operation. Fundamentally, the phenomena of friction, wear, and lubrication involve molecular mechanisms occurring on a nanometer scale, and hence a good understanding of lubricant behavior on this scale is critical to developing new technologies for reduction of loss due to friction. Practical examples are many and range from applications at the leading edge of lubrication technology [microelectromechanical systems (MEMS) and next generation magnetic disk drives] to the

superficially more mundane area of automotive lubrication (where the distances between asperities in moving metal surfaces can be in the range of nanometers or less).

In recent years, the goal of understanding lubrication at the nanoscale, and the related concepts of friction and wear, has resulted in the emergence of the field of nanotribology as both an experimental and a theoretical discipline. Experimentally, the development of versions of the surface force apparatus that permitted the controlled oscillatory sliding motion of two surfaces (typically mica) at measurable gaps of the order of nanometers opened up the possibility of studying friction and lubrication at the nanoscale.<sup>[2–4]</sup> Similarly, around the same time, the ever-increasing availability of computing power made it possible to perform molecular-level simulations of the tribology of nanoconfined systems.<sup>[5,6]</sup> For more details, several recent reviews of various aspects are available.<sup>[7–12]</sup> In this entry, we will focus on a relatively small set of nanotribological experiments and related theoretical calculations. However, before doing so, we briefly comment on some applications of nanotribology to provide some perspective on the range of situations encountered.

## POTENTIAL APPLICATIONS

Nanoscale lubrication is ubiquitous in lubrication scenarios, even in such apparently large-scale applications as automotive lubrication. As a result of the asperities on the moving surfaces in an automobile engine and gears, extreme shear rates in excess of  $10^7 \text{ sec}^{-1}$  are found,<sup>[13]</sup> when gears come together in automotive lubrication, extreme pressures can result in elastohydrodynamic lubrication (EHL), in which the surfaces deform elastically with a thin lubricant film trapped between them. EHL is not necessarily associated with high strain rates, and is, in fact, usually an issue when

two rolling curved surfaces come together; however, the distances between the surfaces can be in the nanometer range (e.g., 25 nm for some ball bearings). The usual phenomenological explanation for EHL behavior is that, under extreme pressures, the confined lubricant undergoes a transition to a solid or glassy state. Other examples of nanoscale lubrication include magnetic disk drive lubrication, the operation of which relies on the relative motion of the magnetic head and the recording media with a spacing on the scale of nanometers,<sup>[14]</sup> producing shear in the fluid between the surfaces. Current air-bearing designs have a spacing of about 10 nm,<sup>[15]</sup> to achieve higher linear recording density and thus high data storage, this spacing needs to be reduced even further. With an ultrathin lubricant film (composed of fluorinated compounds) of  $L = 10$  nm and an operation speed  $V = 10$  m sec<sup>-1</sup> (typical for 30-mm disk drive), the shear rate  $\dot{\gamma} = V/L$  when the slider comes into contact with the lubricant would be  $\approx 10^9$  sec<sup>-1</sup> and higher. Similar nanoscale lubrication considerations arise in many microelectromechanical systems (MEMS), including micromotors. Finally, the nascent field of nanobiotribology<sup>[16]</sup> seeks to understand the nanoscale processes involved in lubrication in biological systems (e.g., the lubricants in joints are predominantly water), as well as utilize the principles of biological lubrication to engineer biomimetic lubricants.

### Experimental Characterization of Nanotribological Behavior

Much of the recent progress in experimental characterization of nanotribology has been made possible by the relatively recent development of instruments capable of maintaining two surfaces at fixed nanometer-scale spacing while applying a lateral force to move the surfaces with respect to each other. The instruments used most frequently are the atomic force microscope (AFM) and its frictional counterpart, the lateral force microscope (LFM),<sup>[8,17,18]</sup> the surface forces apparatus (SFA),<sup>[7,19]</sup> and the closely related surface force balance (SFB).<sup>[20–22]</sup> In the AFM, a cantilever tip (radius of about 30 nm, corresponding to a contact area of  $\sim 10^{-15}$  m<sup>2</sup>) is passed over the surface of interest; by measuring the deflection of the tip in both the horizontal and vertical directions, the surface morphology and the friction can be simultaneously measured.

Much of what we know about the rheology of nanoconfined liquids comes from the laboratories of Granick and Klein, and we briefly describe them here. In Granick et al.'s SFA experiments,<sup>[23,24]</sup> the lubricant of interest is confined between atomically smooth, step free single crystals of muscovite mica. Changes in the surface separation are measured by optical

interferometry. Surface forces are applied and the resulting motion detected using piezoelectric bimorphs. The contact region results from two crossed curved surfaces; hence, the contact region is circular with a diameter on the order of 100  $\mu$ m (corresponding to a contact area of  $\sim 10^{-8}$  m<sup>2</sup>). The diameter is measured by viewing flattened interference fringes through an optical microscope. In Klein and Kumacheva's SFB,<sup>[20–22]</sup> the contact region is also formed by crossed mica cylinders with a contact area of  $\sim 10^{-10}$  m<sup>2</sup>. The normal and lateral (or shear) forces between the two curved mica sheets are measured by monitoring the bending of two orthogonal sets of leaf springs.

We now briefly review the findings from Granick's and Klein's experimental studies. For non-polar fluids, such as short alkanes and octamethylcyclotetrasiloxane (OMCTS), which is approximately spherical with diameter  $\sim 9$  Å, the low-shear-rate (i.e., Newtonian) viscosity is many orders of magnitude greater than that of the same fluid in the bulk. Moreover, the fluid makes the transition to non-Newtonian shear thinning behavior at strain rates that are orders of magnitude lower than those of the corresponding bulk fluid. A case in point is dodecane, shown in Fig. 1A. The experimental results are from Granick's group<sup>[19]</sup> and correspond to six layers of dodecane confined between mica sheets. Note that the Newtonian viscosity is 6 orders of magnitude greater than bulk dodecane at the same temperature and pressure, and that transition to non-Newtonian shear thinning is observed for a strain rates of  $\sim 10^3$  sec<sup>-1</sup>, compared with  $\sim 10^{10}$  sec<sup>-1</sup> for bulk dodecane (derived from simulations) at the same temperature and at a pressure equal to the normal pressure in the confined experiment. As the transition to non-Newtonian behavior takes place at strain rates approximately equal to the inverse of the slowest relaxation time in the system, these results suggest that under nano-confinement, relaxation times are increasing by many orders of magnitude, perhaps indicating the onset of an ordered or glassy state. A stronger conclusion is made by Klein, who, for nano-confined OMCTS, finds a transition from fluid-like behavior (when the distance between the confining surfaces accommodates seven layers or more of OMCTS) to solid-like behavior for six layers or less. "Solid-like" behavior, in this context, means the existence of a measurable yield stress, the stress below which no sliding motion takes place. A liquid has zero yield stress, as the application of any amount of stress causes flow. The measured yield stress in Klein's experiment is less than that of a typical bulk solid, suggesting the formation of a "soft" solid (or certainly one with a different structure than a bulk).

However, for nano-confined water, strikingly different results are found.<sup>[25]</sup> Klein's experiments show no dramatic increase in viscosity under nanoconfinement—the

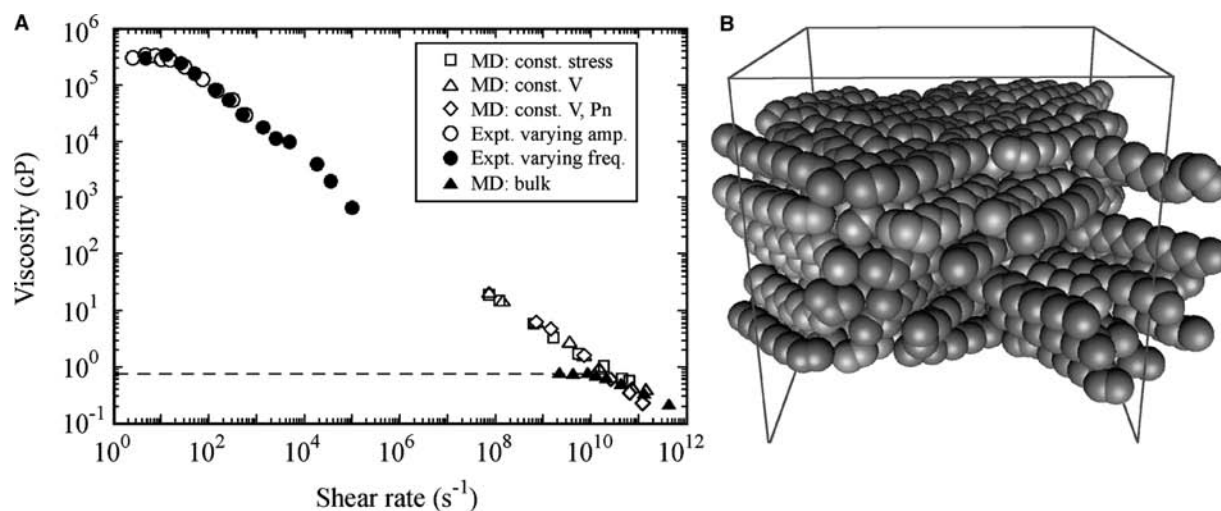


**Fig. 1** (A) Log–log plot of viscosity as a function of shear rate for six layers of dodecane confined between mica sheets. The open and filled circles are experimental results; the open square, triangle, and diamond are molecular dynamics (MD) simulations of this system performed in different ways (constant applied stress, constant applied sliding velocity and the latter at fixed normal pressure); the filled triangles show non-equilibrium MD results for dodecane in the bulk at the same temperature and pressure. Note that there is quite good agreement between experiment and simulation, although there remains a gap between the highest strain rate in experiment and the lowest addressable by straightforward MD. (B) Structure of six-layer dodecane system in the absence of shear. The structure evolves from a disordered structure over a period of nanoseconds, and exhibits a nonzero yield stress. *Source:* From Ref.<sup>[29]</sup>. From Ref.<sup>[27]</sup>.

increase in viscosity is not directly measurable, but can be shown to increase by less than a factor of 3. Even at extreme nanoconfinement (three water layers), water does not exhibit many orders of magnitude increase in viscosity nor does it exhibit properties associated with an ordered solid-like phase (such as sustaining a yield stress).

As we shall see below, computer simulations of nanotribological behavior exhibit many of the features of the above experiments, and there has been general satisfaction that discrepancies between experimental measurements (or their interpretation) would be resolved over time. However, at the time of writing this entry (2003), a controversy has arisen over the impact of surface impurities on the measured rheological responses of nanoconfined fluids. Christenson and coworkers<sup>[26,27]</sup> have shown that cleaved mica sheets cut with a white-hot platinum wire (as used in surface force apparatus experiments) are contaminated by platinum nanoparticles. Their explanation for the strikingly different behavior of water and non-polar fluids is as follows: in the presence of water, they assert that platinum particles leave the surface, while in the presence of non-polar fluids, the platinum particles remain on surface. This raises the possibility that some of the reported experiments may be producing artifacts resulting from platinum surface contamination. Granick has responded with a careful analysis of his own experiment, confirming the presence of platinum

nanoparticles<sup>[28]</sup> in the usually employed procedures. He has followed up with experiments using a protocol that eliminates Pt nanoparticle contamination.<sup>[29]</sup> These new experiments reproduced much of the behavior reported previously by Granick's group, but adds a new twist: the viscosity of the confined fluid is found to be dependent on the speed at which the two surfaces are brought together. In the case of so-called "rapid quenches" (surfaces brought together at speeds of the order of nm/sec), the viscosity of nanoconfined OMCTS is orders of magnitude above the bulk; in the case of "quasistatic quenches" (surfaces brought together at speeds of  $<10^{-2}$  nm/sec), the degree of viscosity enhancement is experimentally unresolvable, but is certainly not in the many-orders-of-magnitude range. Given that the rapid-quench Pt-nanoparticle-free experiments confirm his earlier results, Granick concludes that the Pt nanoparticles do not play a dominant role in determining the rheology of the nanoconfined system. Granick also reasserts the absence of an order–disorder transition in the nanoconfined fluid, similar to his previous findings. As of the writing of this entry, Klein has not responded in print to the issues raised by Christenson et al. However, from discussions with Klein and members of his group, it appears that, long before any questions were raised about Pt nanoparticle contamination, the Klein group adopted experimental protocols to minimize the presence of Pt nanoparticles on their mica surfaces.

## Computer Simulations of Nanotribological Behavior

The existence of experimental data (such as that reviewed above) and the importance of nanotribology have inspired many molecular simulation studies of nanotribological systems. The simulations have attempted to model both the AFM and SFA/SFB experiments; in the former case, it is reasonable to simulate the experiment fully because the size of the AFM tip is small enough to be accessible to simulation. Simulations of the SFA/SFB experiments have usually involved treating the contact surface as essentially infinite in two dimensions and nanoscopic in the direction of confinement. The brevity of this entry does not permit a thorough discussion of the molecular simulations; instead, we refer the interested reader to several overview papers.<sup>[9,30–34]</sup>

Rather, we focus our discussion here on computer simulations<sup>[35–37]</sup> directly relevant to the experimental measurements described above. In these simulations, nanoconfined mica was studied by classical molecular dynamics using standard united-atom alkane force fields and an approximation to the mica surface consisting of a Lennard–Jones (LJ) solid with the LJ energy determined by experimental values for the surface energy of mica. The nanoconfined systems were prepared by beginning with an equilibrated bulk system of dodecane (i.e., in periodic boundary conditions); the mica-like surfaces were then introduced into the simulations (thus eliminating periodic boundary conditions in one direction) and slowly (on simulation time scales) brought together until the normal pressure was of the same order of magnitude as the normal pressure in the experiment, resulting in compression of the nanoconfined dodecane. [Note that according to the definition introduced by Zhu and Granick,<sup>[29]</sup> this corresponds to a rapid quench.] The major conclusions from this work are as follows: first, although we are currently unable to simulate down to the strain rates at which experiments can be performed because of the very long relaxation times in the system, the sliding behavior of nanoconfined dodecane (as can be seen in Fig. 1A) is similar to that measured experimentally by Granick and coworkers.<sup>[37]</sup> Second, a transition from disordered fluid (for seven or more layers of confined dodecane) to an ordered solid-like phase (for six layers or less, see Fig. 1B), in agreement with the findings of Klein and Kumacheva<sup>[21,38]</sup> for similar non-polar fluids. For wall–fluid interactions that are attractive, the density of the confined fluid increases above the bulk density at the same density and pressure. The transition to a solid-like phase occurs when the confined density exceeds the bulk solidification density.<sup>[35]</sup> For branched alkanes, we observe an enhancement in the confined density, but

it is insufficient to exceed the solidification density for the branched alkane, and so no solidification is observed.<sup>[36]</sup> This insight between the densification of the confined fluid and the conditions under which a transition can take place to an ordered phase was used by Klein and coworkers in understanding the striking difference between the behavior of water under nanoconfinement<sup>[25]</sup> and non-polar fluids such as alkanes noted above. Klein and Kumachera attributed this to the fact that the expected densification on nanoconfinement, when interpreted in terms of bulk behavior, pushes water *away* from the bulk solidification density (owing to the density maximum in water).

## CONCLUSION

Nanotribology and nanoscale lubrication are fields that are still at an early stage, with ongoing experimental and theoretical controversies. The importance of nanoscale lubrication in fields as diverse as automobiles, hard disk drives, and biology, as well as the difficulty of simulating and performing experiments on these systems, will ensure that it will continue to be a very active area of research in the years to come.

## REFERENCES

1. Bhushan, B. *Handbook of Micro/Nanotribology*, 2nd Ed.; CRC Press: Boca Raton, FL, 1998.
2. Israelachvili, J.N.; McGuiggan, P.M.; Homola, A.M. Dynamic properties of molecularly thin liquid films. *Science* **1988**, *240*, 189–191.
3. van Alsten, J.; Granick, S. Molecular tribometry of ultrathin liquid-films. *Phys. Rev. Lett.* **1988**, *59*, 1942.
4. Israelachvili, J.N.; McGuiggan, P.; Gee, M.; Homola, A.; Robbins, M.; Thompson, P. Liquid dynamics in molecularly thin-films. *J. Phys., Condens. Matter* **1990**, *2*, SA89–SA98.
5. Schoen, M.; Rhykerd, C.L.; Diestler, D.J.; Cushman, J.H. Shear forces in molecularly thin-films. *Science* **1989**, *245*, 1223–1225.
6. Thompson, P.A.; Robbins, M.O. Origin of stick–slip motion in boundary lubrication. *Science* **1990**, *250*, 792.
7. Hu, Y.Z.; Granick, S. Microscopic study of thin film lubrication and its contributions to macroscopic tribology. *Tribol. Lett.* **1998**, *5*, 81–88.
8. Feldman, K.; Fritz, M.; Hahner, G.; Marti, A.; Spencer, N.D. Surface forces, surface chemistry and tribology. *Tribol. Int.* **1998**, *31*, 99–105.
9. Gao, J.P.; Luedtke, W.D.; Landman, U. Structures, solvation forces and shear of molecular films in a rough nanoconfinement. *Tribol. Lett.* **2000**, *9*, 3–13.
10. Czichos, H. Tribology and its many facets: from macroscopic to microscopic and nano-scale phenomena. *Meccanica* **2001**, *36*, 605–615.



11. Blau, P.J. The significance and use of the friction coefficient. *Tribol. Int.* **2001**, *34*, 585–591.
12. Adams, J.B.; Hector, L.G.; Siegel, D.J.; Yu, H.L.; Zhong, J. Adhesion, lubrication and wear on the atomic scale. *Surf. Interface Anal.* **2001**, *31*, 619–626.
13. Chynoweth, S.; Klomp, U.C.; Scales, L.E. Simulation of organic liquids using pseudo-pairwise interatomic forces on a toroidal transputer array. *Comp. Phys.* **1991**, *62*, 297–306.
14. Bhushan, B.; Israelachvili, J.; Landman, U. Nanotribology: friction, wear and lubrication at the atomic scale. *Nature* **1995**, *374*, 607–616. Review Article.
15. *Head Disk Interface/Head-to-Disk Interaction*. <http://almel.almaden.ibm.com/sst/storage/hdi/interaction.shtml>.
16. Luginbühl, R.; Overney, R.M.; Ratner, B.D. Nanotribology at the confined biomaterial interface. In *Interfacial Properties on the Submicrometer Scale*; Frommer, J., Overney, R.M., Eds.; Oxford University Press: Washington, DC, 2001; 178–196.
17. Johnson, K.L.; Woodhouse, J. Stick–slip motion in the atomic force microscope. *Tribol. Lett.* **1998**, *5*, 155–160.
18. Tani, H. Observation of PFPE lubricant film on magnetic disk surface by atomic force microscopy. *IEEE Trans. Magn.* **1999**, *35*, 2397–2399.
19. Hu, H.W.; Carson, G.A.; Granick, S. Relaxation-time of confined liquids under shear. *Phys. Rev. Lett.* **1991**, *66*, 2758–2761.
20. Klein, J.; Kumacheva, E. Simple liquids confined to molecularly thin layers. I. Confinement-induced liquid-to-solid phase transitions. *J. Chem. Phys.* **1998**, *108*, 6996–7009.
21. Kumacheva, E.; Klein, J. Simple liquids confined to molecularly thin layers. II. Shear and frictional behavior of solidified films. *J. Chem. Phys.* **1998**, *108*, 7010–7022.
22. Klein, J.; Kumacheva, E. Confinement-induced phase-transitions in simple liquids. *Science* **1995**, *269*, 816–819.
23. Peachey, J.; Vanalsten, J.; Granick, S. Design of an apparatus to measure the shear response of ultrathin liquid-films. *Rev. Sci. Instrum.* **1991**, *62*, 463–473.
24. Granick, S.; Carson, G.; Hu, H.W.; Peanasky, J.; Cai, L.J. Molecular tribology of fluids and additives. *Abstr. Pap. Am. Chem. Soc.* **1992**, *203*, 287-COLL.
25. Raviv, U.; Laurat, P.; Klein, J. Fluidity of water confined to subnanometre films. *Nature* **2001**, *413*, 51–54.
26. Ohnishi, S.; Hato, M.; Tamada, K.; Christenson, H.K. Presence of particles on melt-cut mica sheets. *Langmuir* **1999**, *15*, 3312–3316.
27. Kohonen, M.M.; Meldrum, F.C.; Christenson, H.K. Particles on melt-cut mica sheets are platinum. *Langmuir* **2003**, *19*, 975–976.
28. Lin, Z.; Granick, S. Platinum nanoparticles at mica surfaces. *Langmuir* **2003**, *19*.
29. Zhu, Y.; Granick, S. Reassessment of solidification in fluids confined between mica sheets. *Langmuir* **2003**, *19*, 8148–8151.
30. Bhushan, B.; Israelachvili, J.N.; Landman, U. Nanotribology—friction, wear and lubrication at the atomic-scale. *Nature* **1995**, *374*, 607–616.
31. Grest, G.S. Computer simulations of shear and friction between polymer brushes. *Curr. Opin. Colloid Interface Sci.* **1997**, *2*, 271–277.
32. Landman, U. On nanotribological interactions: hard and soft interfacial junctions. *Solid State Commun.* **1998**, *107*, 693–708.
33. Grest, G.S. Normal and shear forces between polymer brushes. In *Polymers in Confined Environments*; 1999; 149–183.
34. He, G.; Muser, M.H.; Robbins, M.O. Adsorbed layers and the origin of static friction. *Science* **1999**, *284*, 1650–1652.
35. Cui, S.T.; Cummings, P.T.; Cochran, H.D. Molecular simulation of the transition from fluid-like to solid-like behavior in complex fluids confined to nanoscale gaps. *J. Chem. Phys.* **2001**, *114*, 7189–7195.
36. Cui, S.T.; Cummings, P.T.; Cochran, H.D. Effect of branches on the structure of narrowly confined alkane fluids: *n*-Hexadecane and 2,6,11,15-tetramethylhexadecane. *J. Chem. Phys.* **2001**, *114*, 6464–6471.
37. Cui, S.T.; McCabe, C.; Cummings, P.T.; Cochran, H.D. Molecular dynamics study of the nano-rheology of *n*-dodecane confined between planar surfaces. *J. Chem. Phys.* **2003**, *118*, 8941–8944.
38. Klein, J.; Kumacheva, E. Confinement-induced phase-transitions in simple liquids. *Science* **1995**, *269*, 816.

# Tungsten Carbide–Cobalt Nanocomposites

**Purnesh Seegopaul**

*Technology and Business Development, Umicore USA Inc., Hillsborough, New Jersey, U.S.A.*

**Zhigang Zak Fang**

*Department of Metallurgical Engineering, University of Utah, Salt Lake City, Utah, U.S.A.*

## INTRODUCTION

Over the past decade, substantial research efforts have been directed toward the synthesis of nanostructured powders and thin films, which raise the prospects of advanced materials with dramatically improved properties based on nanoscale grain structure. It would be particularly advantageous to exploit these improved properties to extend the lifetime and robustness of tungsten carbide tools. As a result of this industrial significance, intensive efforts are being made to produce these tungsten carbide-based materials with finer and nanoscale grain size.

Many differing process technologies have been introduced to produce both nanostructured tungsten carbide and tungsten carbide–cobalt composite powders. Process technologies range from improvements to the conventional solid-state synthesis to more radical techniques such as spray conversion and vapor deposition methods.

For many applications, nanocrystalline powders have to be consolidated and sintered to make *bulk* materials and engineering components. However, most nanostructured powders lose their nanoscale characteristics after sintering because of extremely rapid rate of grain growth during sintering. Controlling grain growth during sintering and producing bulk nanocrystalline hard materials remain a critical technology challenge.

For those materials, especially metallic structural materials, the inability to achieve nanoscale grain sizes at sintered state also hinders efforts to characterize and understand their mechanical behavior as nanostructured materials. Cemented tungsten carbide is one of those materials. There are strong indications of dramatic shift in the mechanical behavior when the grain sizes of tungsten carbide cobalt (WC–Co) become progressively finer. But the potential of fully consolidated cemented tungsten carbide with true nanoscale grain sizes (<30 nm) remains unexplored.

## PRODUCTION TECHNOLOGY

The potential benefits of such finer grain size materials sparked keen interest in toolmakers, and work in this area was initiated as early as 1929.<sup>[1]</sup> While numerous techniques to produce nanostructured tungsten carbide (WC) and WC–Co powders have been developed, only a few have been proven capable at the industrial level. Production challenges include economic considerations, powder properties, powder handling, and processability. These preparation techniques cover a diverse array of processes as evident from the discussion below.

Thermochemical processing, involving spray conversion technology, was first introduced in the early 1990s for the production of these WC–Co powders and subsequently scaled up to produce the powders at an industrial level. This is a simple three-step process involving aqueous solution formation, spray drying to form an amorphous powder, and gas-phase carburization with carbon containing gases to form phase pure WC–Co powders.<sup>[2,3]</sup> The dissolution of soluble salts of tungsten, cobalt, and other additives allows uniform mixing at the molecular level. This phase uniformity is maintained in the spray drying process that yields large, porous, and flowable precursor powder particles. These particle features facilitate a uniform and complete gas phase conversion to the WC–Co cermet. The process has been demonstrated at the industrial level and is also amenable to the incorporation of grain growth inhibitors, such as vanadium carbide and chromium carbide, while facilitating recycling capabilities. As shown in Figs. 1 and 2, each large micron-sized particle contains millions of nanograin WC particles distributed in the binder matrix. The large particles reduce both powder-handling difficulties and reactivity as the discrete nanograin particles are all contained in a larger body in a type of hierarchical structure. The powders have been processed and consolidated into finished tooling parts, and significant improvements in printed circuit board drills were reported by

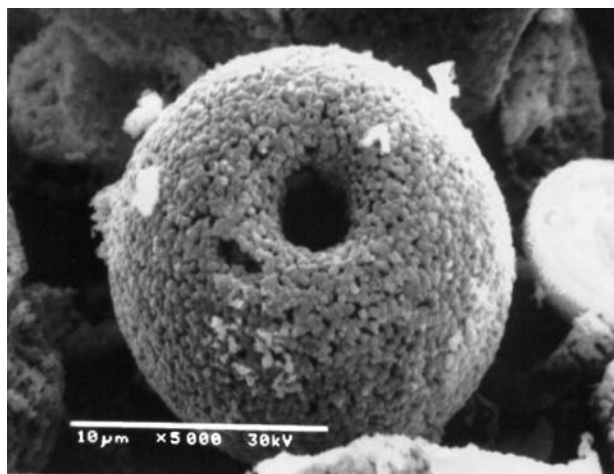


**Fig. 1** Etched nanocomposite WC–Co particle, showing the substructure containing WC nanograins.

Eason et al.<sup>[4]</sup> Dramatic changes in the properties of sintered parts prepared from these nanostructured WC–Co powders have also been demonstrated, as evident from the scratch test data shown in Fig. 3.

Gao, Kear, and Seegopaul<sup>[5]</sup> have reported a direct gas phase process to produce nanophase WC from the tungsten precursor, ammonium metatungstate. It is felt that the carbide formation is possible at low temperatures through a substitution of carbon for oxygen in the matrix. The authors have also demonstrated a recycling process in which spent carbide tools of various compositions and grain sizes are recycled into nanostructured tungsten–carbide–cobalt composite powders.<sup>[6]</sup>

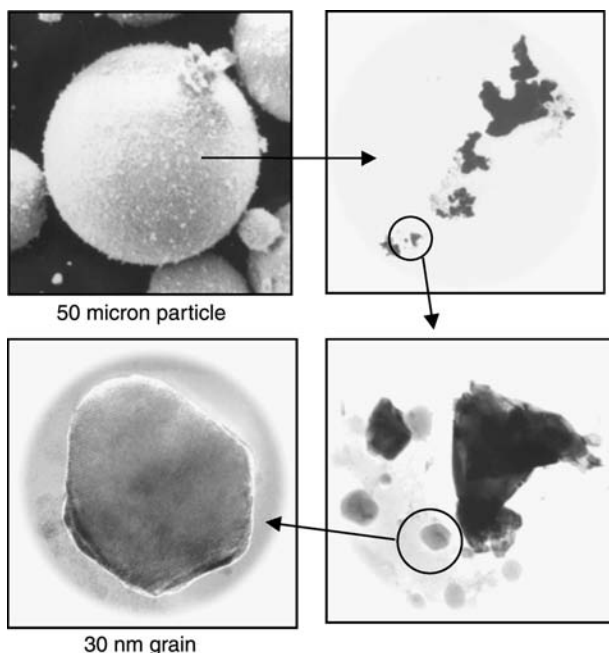
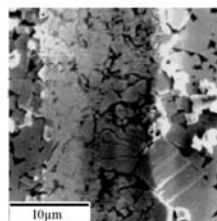


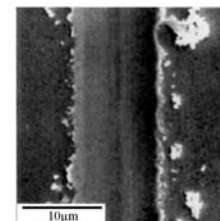
**Fig. 2** Nanocomposite hierarchical structure of WC–Co particles as produced by the spray conversion process.

Comparison with conventional WC–Co @ 100g load



Conventional

HV = 1220 Kg/mm<sup>2</sup>  
Deformed/Fractured WC Grains  
Loose WC Grains



Nanostructured

HV = 2260 Kg/mm<sup>2</sup>  
Purely Ductile Deformation  
(Not seen before at this hardness)

**Fig. 3** Surface scratch test comparison of sintered WC–Co from nanocomposite powder against coarse grain WC–Co cermet.

Kim et al.<sup>[7,8]</sup> varied the thermochemical process by introducing a mechanical milling treatment of the spray-dried powder that contained added carbon to assist in the carburization phase. The milled powder is then converted to nanophase composite powder by gas phase reduction and carburization. It was also shown that grain growth inhibitors could be incorporated into the composite powders to assure a uniform dispersion for improved grain growth control.

Another variation of the spray conversion process involves the coprecipitation of cobalt with salts of tungsten, such as ammonium paratungstate.<sup>[9]</sup> As in the spray conversion process, the hardmetal constituents are mixed at the atomic level. Low-temperature hydrogen reduction together with the catalytic activity of cobalt facilitated the production of the nanostructured powders. W–Co powders (20–50 nm) were also produced by a similar process.<sup>[10]</sup>

High-energy milling has been shown to possess the capability to produce nanoscale WC and WC–Co nanocomposites.<sup>[11]</sup> In one such example, the synthesis of the WC–Co composite is completed by the process of mechanical alloying driven principally by the interdiffusion reactions and the high densities of defects and interfaces. Tan and Wu<sup>[12]</sup> varied the classical high-energy milling process by using magnesium-containing graphite mixtures. The graphite provided the carbon for carbide formation, while the magnesium facilitated the reactive synthesis. Acid dissolution is required for the magnesium removal from the 4–20 nm sized tungsten carbide product.

Vapor phase techniques have also been reported to prepare these nanocarbides, but scale-up to industrial levels would be problematic. Direct-current arc plasma was used to synthesize 40-nm WC–Co powders from a cobalt tungstate precursor, using ethylene as a carbon source.<sup>[13]</sup>

Another approach, termed integrated mechanical and thermal activation (IMTA) process, was reported by Ban and Shaw.<sup>[14]</sup> Nanoscale WC–Co powders were prepared from mixtures of cobalt, tungsten oxides, and graphite. Use of a polymer precursor as an in situ carbon source was also shown to produce phase pure WC–Co nanocomposites.<sup>[15]</sup>

## SINTERING OF NANOCRYSTALLINE WC–CO CERMETS

Cemented tungsten carbide is usually sintered via liquid phase sintering (LPS) under vacuum, or the so-called sinter hot isostatic pressing (HIP), where a low-pressure HIP is applied following vacuum sintering. Hot pressing and standard HIP can also be used to consolidate WC–Co, but they are normally not used unless there are special needs. Typical pressures for HIP and HIP are 10–70 and 100–350 MPa, respectively.

The consolidation of nanostructured WC–Co powder has been studied using a variety of means including the standard liquid phase sintering (LPS),<sup>[16–24]</sup> hot isostatic pressing (HIP),<sup>[25]</sup> and unconventional processes such as microwave<sup>[26]</sup> and spark plasma sintering (SPS).<sup>[27]</sup> In all cases of high-temperature conditions during sintering, grains grow rapidly. The finest grain size of sintered WC–Co reported in the literature to date, using nanostructured powders, is approximately 100 nm; grain size of 70 nm<sup>[42,43]</sup> was also reported by measuring the same group of samples as in Ref.<sup>[16]</sup>

Studies of the grain growth behavior have found that grain growth occurs extremely rapidly during the early stages of sintering. Fang and Eason<sup>[16]</sup> documented the densification and grain size vs. the LPS time and temperature. It was found that at the first data point ( $t = 5$  min), the grain sizes of the samples were already dramatically increased from their initial nanometer sizes, as shown in the Fig. 4. McCandlish, Kear, and Kim<sup>[9]</sup> observed that the WC grain size in a WC–10 wt.% Co alloy sintered using nanostructured WC–Co powder manufactured by Nanodyne, Inc. was 200 nm after 30 sec at 1400°C, and it became 2  $\mu$ m (2000 nm) after additional 30 sec of sintering.

Schubert<sup>[28]</sup> pointed out that grain growth started during heating up to the temperature, which is attributed to the high degree of “metastability” of the powder. Specifically, it was reported<sup>[28]</sup> that up to 85% of densification is accomplished below 1280°C when grain sizes are <0.3  $\mu$ m, while up to 70% of densification is accomplished at the same temperature when grain size is 0.7  $\mu$ m, which suggests that the onset of sintering is a function of the temperature. Experimental evidence of the sintering and grain growth at solid state provided by Goren-Muginstein<sup>[29]</sup> and Porat, Berger, and Rosen<sup>[23]</sup> indicated that large amount of grain growth

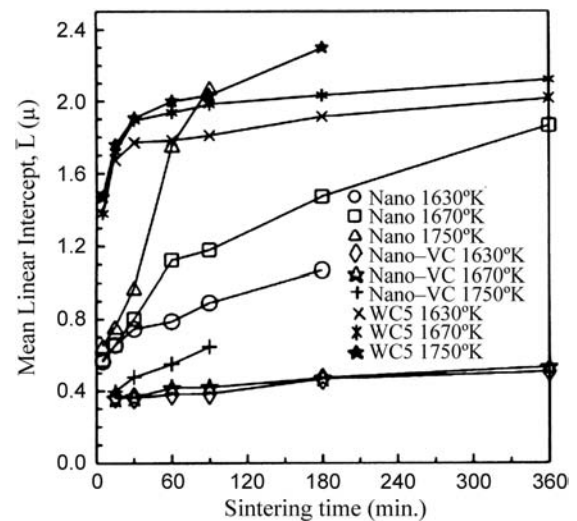


**Fig. 4** Grain size vs. sintering time comparing WC–Co materials made from nanocrystalline powders to those from conventional fine grain powders and the effects of VC grain growth inhibitor.

is already widespread at 1200°C, while liquid phase is not expected to form until 1280°C. In summary, when grain sizes of WC powder are <100 nm, significant sintering and densification will occur at solid state.

## Grain Growth Inhibitors

Grain growth inhibitors have been used to mitigate grain growth during sintering. It was found that 100–150 nm grain sizes at full density could be obtained with the addition of 1.5 wt.% vanadium carbide via standard LPS.<sup>[16,22,30]</sup> In the same study, 100–200 nm grain sizes were achieved without grain growth inhibitors at 99% relative density by employing a plasma-activated sintering (PAS) technique. The use of grain growth inhibitors is widely practiced for sintering fine grain and ultrafine grain WC–Co materials in the industry. Commonly used grain inhibitors include chromium carbide ( $\text{Cr}_3\text{C}_2$ ), tantalum carbide (TaC), and vanadium carbide (VC). Their relative effectiveness in mitigating grain growth can be ranked in the order  $\text{VC} > \text{Cr}_3\text{C}_2 > \text{NbC} > \text{TaC}$ , although other considerations such as corrosion resistance and hot hardness may also affect the choice of grain growth inhibitors.

The mechanisms of growth inhibition are the subject of many research reports.<sup>[31]</sup> Sadangi<sup>[32]</sup> carried out an in-depth study on the effects of VC addition on grain growth in WC–Co, which suggested that VC or  $\text{Cr}_3\text{C}_2$  are more effective in inhibiting grain growth because they have higher solubility and diffusivity in cobalt binder phase. The dissolution of VC and  $\text{Cr}_3\text{C}_2$  in the binder phase mitigates the solution–reprecipitation of

tungsten carbide, which is the mechanism of grain growth during sintering of WC–Co materials. Based on this theory of mechanism, grain growth inhibitors are incorporated in a solid solution of cobalt phase. These solid solution grain growth inhibitors form low melting point ternary liquids(s) at temperatures in the range of 1200–1250°C. Because these low melting point solid solutions are saturated with grain growth-inhibiting elements, the dissolution of W and C in the binder phase is prevented and grain growth is minimized.

### Pressure-Assisted Sintering

Pressure-assisted sintering is another approach for controlling grain growth. Published microstructures showed WC grains to be ~200 to 500 nm after HIP.<sup>[17,25]</sup> In particular, Azcona et al.<sup>[25]</sup> investigated the sintering of nanostructured WC–Co powder by conducting HIP at solid state. But even when grain growth inhibitors were used in combination with HIP at solid state, the final sintered grain sizes were reported to be between 200 and 600 nm.

In particular, it has been demonstrated that nanoscale grain sizes after sintering can be achieved with ultrahigh-pressure processes such as hot pressing using ultrahigh-pressure cells with >1 GPa pressure,<sup>[33]</sup> explosive compaction,<sup>[34]</sup> or severe plastic deformation methods.<sup>[35]</sup> However, all current high-pressure processes (>1 GPa) are laboratory techniques that are not suitable for mass production.

A fundamental reason for using external pressure during sintering is to promote densification. Externally applied pressure adds a driving force for densification. It is a particularly important factor for sintering nanostructured powder because it does not directly contribute to the driving force for grain growth. The effects of pressure are constrained by the pores and any gases in the pores. With conventional pressure-assisted sintering techniques, such as hot pressing and HIP, a longer holding time is required to allow diffusion and creep flow-controlled mechanisms to contribute to the final densification. The longer holding time, however, leads to significant grain growth. Higher pressures are capable of collapsing pore structures and inducing plastic flow and rapid bonding in powder compacts at elevated temperatures. This eliminates the need for long holding times at high temperatures and hence prevents grain growth to occur.

Mechanisms of grain growth during the sintering of nanoscale powders are of great interest. It is reasonable to assume that there are new mechanisms that are unique to nanocrystalline particles. There have been numerous suggestions that the grain growth occurs by coalescence of grains. Coalescence is initiated by

contact between particles. It can occur via several mechanisms including grain rotation. Another mechanism is the faceted WC crystal growth along preferential orientations, which could happen in solid state because of localized chemical inhomogeneity.<sup>[36]</sup> To date, however, there is no experimental confirmation of such mechanisms nor is there any method for controlling coalescence.

The behavior of nanocrystalline WC–Co powder during sintering is consistent with published research on sintering of other nanocrystalline powders. An excellent review on the consolidation of nanostructured powders was presented by Groza and Dowding.<sup>[37]</sup> Based on many sintering studies of mostly ceramic powders, the following viewpoints are summarized. The onset of sintering is reported to be consistently and significantly lower in nanoparticulates compared with conventional materials. Sintering of both metal and ceramic nanoparticles was found to start at temperatures of 0.2–0.4 T<sub>m</sub> compared with 0.5–0.8 T<sub>m</sub> for conventional powders. Oxides densify without significant grain growth until the density reaches approximately 90% of the bulk density. Then the grain growth becomes very rapid.<sup>[38,39]</sup> This phenomenon is attributed to the effects of pores on grain growth. There are unique and different mechanisms operating during the sintering of nanopowders because of the low apparent activation energy for early-stage sintering of nanopowders. When nanosizes are approached, atomic mechanisms become more obvious. For example, the rotation and alignment of nanosized grains may be easier. Although these possibilities have not been experimentally proved, a simple scaling down of the conventional sintering equations is not applicable.

In summary, the published data show that no true nanocrystalline (<50 nm) *bulk* WC–Co materials have been produced to date. Grain growth occurs extremely rapidly during the early stages of sintering. Grains grow significantly in solid state during sintering of nanocrystalline powders. The extreme rapid rate of grain growth cannot be explained by the mechanisms of densification and grain growth known for the sintering of micron- or submicron-sized particles. Mechanisms for grain growth in solid state may include coalescence by grain rotation. Experimental observations suggest that ~100 nm is the low limit of grain size refinement for WC–Co materials given the currently available knowledge and technologies. The need to fully densify the material and limit grain growth at the same time causes opposing considerations in process design. However, there is little published research that focuses on the interactions between densification and grain growth during sintering.

Finally, it is noted that sintered grain sizes between 0.6 and 0.9 μm can be, and are being, manufactured commercially by using conventional ultrafine tungsten

carbide powders. The initial grain size of commercial ultrafine WC powder ranges between 0.3 and 0.5  $\mu\text{m}$ . Recently, Gille et al.<sup>[30]</sup> reported a new grade of sintered hardmetal with a 100-nm mean linear intercept length using 1% total of a VC/Cr<sub>3</sub>C<sub>2</sub> additive.

## MECHANICAL PROPERTIES OF BULK NANOCRYSTALLINE WC–Co

Cemented tungsten carbide, consisting of large volume fractions of WC particles in a cobalt metal matrix, is a cermet composite material. It is well understood that the hardness of cermet materials is inversely proportional to its grain size and that the fracture toughness is inversely proportional to the hardness. Therefore finer grain size usually results in lower fracture toughness. But for nanostructured metal alloys and ceramics, it has been noted that the mechanisms of strengthening are different because of the large volume fractions of grain boundaries. The deformation mechanisms depend on grain boundary sliding and diffusion-controlled processes.<sup>[40,41]</sup> Grain boundaries in polycrystalline metals also impede the motion of cracks, which contributes to better fracture toughness. Therefore it is hypothesized that the fracture toughness of WC–Co composite will improve when WC grain sizes reach nanoscale.

### Hardness and Fracture Toughness

Hardness and fracture toughness are the two most important mechanical properties of cemented tungsten carbide and other cermets. Other mechanical properties, such as flexural strength, wear resistance, and impact resistance, are fundamentally dependent on the hardness and fracture toughness and their relationship.

The mechanical properties of nanostructured WC–Co composites were reported in several studies.<sup>[16,17,42–44]</sup> As expected, very high hardness was achieved with the ultrafine-grained microstructure. Data show that the fracture toughness of the sintered WC–Co using nanostructured powder decreases as the hardness increases. Denseley and Hirth<sup>[43]</sup> studied the fracture toughness of sintered WC–Co with an average grain size of 70–100 nm and 6.7% of cobalt using modified compact tension method. They suggested that the mode I and mode I/III fracture toughness of nanoscale tungsten carbide grains (70 nm) in cobalt was less than the toughness of mesoscale WC–6.7%Co alloys with similar cobalt volume fractions. Although this is consistent with the general trend for the conventional WC–Co, it was disappointing for many in the field because the toughness

improvement is much more highly needed than the increase in hardness.

However, several other reported data in literature indicate that the mechanical behavior of bulk WC–Co deviates significantly from its coarser grain counterpart when the grain sizes approach 100 nm. Fang and Eason<sup>[16]</sup> showed that the surface crack resistance of sintered bulk WC–Co using nanostructured powder by the Palmquist method is higher than that using conventional fine powder when they are compared at the same hardness level, as shown in Fig. 5.

Jia, Fisher, and Gallers<sup>[42]</sup> further showed that the reduction in toughness vs. hardness levels off when grain size reaches nanoscale as shown in Fig. 6. It was suggested that the toughness decreases with increasing hardness in conventional composites, but the increase of hardness in nanostructured composites does not decrease their bulk fracture toughness. The difference between the fracture toughness of WC–Co using nanostructured powder and that using conventional ultrafine powder has also been shown to depend on the cobalt contents (Fang, unpublished). For example, when a sample was sintered using nanostructured WC–10%Co powder, the sintered hardness was  $R_a = 92.0$  and the fracture toughness  $K_{Ic}$  was  $12.0 \text{ MPa} \cdot \text{m}^{1/2}$ , while the fracture toughness of the conventional WC–Co is approximately  $9.0 \text{ MPa} \cdot \text{m}^{1/2}$  when  $R_a = 92.0$ . This indicates over 30% increase in the fracture toughness.

A similar result is reported by Bartha et al.<sup>[17]</sup> as shown in Fig. 7. It shows an isolated case in which the fracture toughness is higher for samples made from

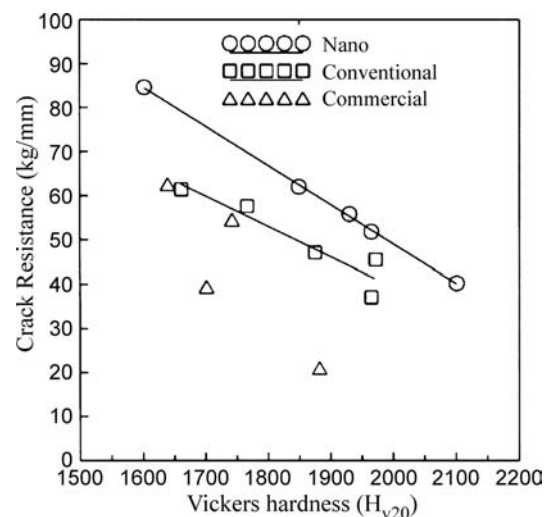


**Fig. 5** Surface crack resistance vs. hardness comparing WC–Co materials made from nanocrystalline powders with those from conventional fine grain powders and commercial products.



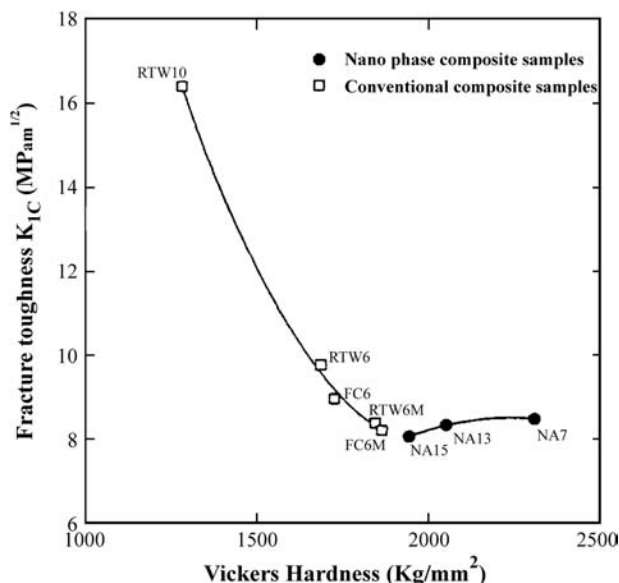


**Fig. 6** Fracture toughness vs. hardness of WC–Co materials comparing nanophase composite samples to conventional composite samples.

nanocrystalline powders than those from conventional powders when compared at a similar hardness level.

Based on these data, it is clear that the mechanical behavior deviates from the normal trend for hardness vs. toughness for *bulk* WC–Co when grain sizes approach nanoscale. In addition, the trend of deviation is toward the improvement of hardness vs. toughness relationship. Because all these data are based on samples that have submicron grain sizes at sintered state, the mechanical behavior of WC–Co with truly nanoscale grain sizes (<30 nm) remains unexplored. A breakthrough in sintering technologies based on in-depth research is needed to enable one to manufacture *bulk* materials with nanoscale grain structure

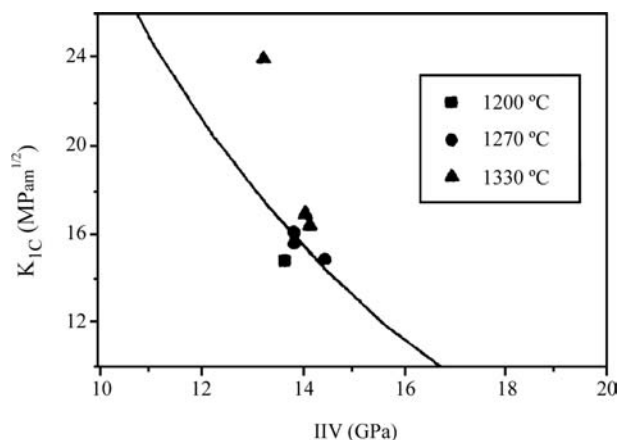


**Fig. 7** Fracture toughness vs. hardness of WC–Co sintered from nanocrystalline powders at various temperatures.

before the true mechanical behavior of nanoscale WC–Co can be studied.

There are three categories of possibilities by which the mechanical properties of WC–Co with nanoscale grain sizes may be improved over those of the conventional WC–Co materials. The first is based on the effects of flaws. It is expected that the flaw sizes, for example, pore sizes, in the sintered material starting with nanocrystalline WC–Co powder are drastically reduced when compared with that in the conventional *bulk* WC–Co. If the grain size is preserved at < 30 nm, the flaw size will then be a few nanometers or less. This is beneficial for the fracture toughness, independent of the hardness of the material.

The second possibility is based on the effects of interfaces. At the nanoscale level, there will be a tremendous increase in the amount of interfaces between the WC grains and the Co binder compared with coarser-grained counterparts. The partition of the crack path through binder/carbide (B/C) interfaces as opposed to other interfaces or transgranular cracks will increase dramatically in nanocrystalline WC–Co. It has been shown<sup>[45]</sup> that the crack does not advance exactly along the interface but proceeds in the binder, forming closely spaced shallow dimples in conventional WC–Co. There is an appreciable amount of plastic deformation of the binder involved in fracturing through B/C. The increase in the fractions of crack path through B/C will contribute a significant amount of fracture energy to the process, which would in turn enhance the overall toughness of the material.

The third possibility is also related to the effects of interfaces involving the deformation mechanisms. As pointed out by Gleiter<sup>[40]</sup> and Siegel,<sup>[41]</sup> the conventional dislocation generation and migration become increasingly difficult as the scale is reduced into the nanometer range. The more likely mechanisms for deformation will be grain boundary sliding and short-range, diffusion-assisted events such as grain rotation and grain shape accommodation. Both of the above interface-dependent mechanisms will be possible particularly at a relatively high cobalt content when the nano-WC particles are enclosed by the cobalt phase, the grain size of which is also at a nanoscale. When the nanocrystalline cobalt becomes the controlling phase, the behavior of the composite will also change.

It should be noted that for conventional bulk WC–Co, the fracture toughness is a function of mean free path (MFP) between the WC grains. It is dependent on the plastic deformation and tearing of cobalt metal binder. A finer grain size results in a smaller MFP at a given constant volume fraction of cobalt and a smaller plastic zone and therefore lower fracture toughness. For nanocrystalline WC–Co, the effect of

the plastic mechanisms of Co will no doubt be reduced from the viewpoint of MFP. Therefore all the possible grain boundary mechanisms including sliding and rotation are critical for its toughness. The question is whether the fracture energy through grain boundaries will be enough to compensate the loss of plastic deformation of binder phase, and what would be the final relationship between the hardness and the fracture toughness. The answers to these questions will have far-reaching scientific significance not only with respect to WC–Co cermet materials, but also many other material systems including other metal matrix composites (MMCs).

### Wear Resistance and Performance

The sliding wear resistance of nanostructured WC–Co materials was studied in detail by Jia and Fisher<sup>[46]</sup> using a carefully constructed pin-on-disc method without lubricant at room temperature. A series of grades of WC–Co with varying grain sizes and cobalt contents were made into pins with polished hemispherical shape, with the radius of the tip being about 3.5 mm. During the tests, the pins slid under modest load (9.8 N) on commercially ground silicon nitride plates. The results showed that the wear resistance of nanostructure WC–Co is higher than that of conventional cermets in proportion to their hardness as shown in Fig. 8. The sliding wear of the conventional and nanostructured WC–Co composites is, in first approximation, expressed by a Blok–Archard equation with

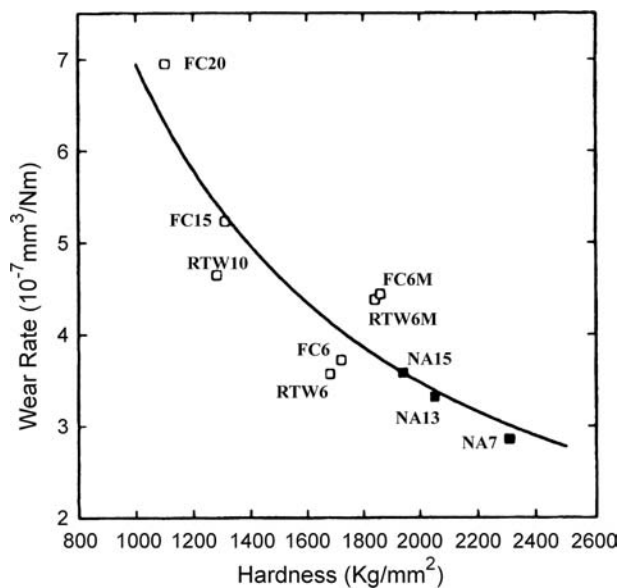


**Fig. 8** The dependence of wear rate of WC–Co composites sliding against silicon nitride at 9.8-N applied load and 31.4 mm/s sliding speed.

wear coefficient  $k = 6.9 \times 10^{-6}$ . The Blok–Archard equation is given as follows.

$$V = kPs/H$$

where  $k$  is the wear coefficient,  $H$  is the hardness,  $P$  is the load, and  $s$  is the sliding distance. However, a more detailed analysis found that the wear coefficient  $k$  as functions of grains sizes and cobalt content does not follow the same trend as that of conventional WC–Co composites as shown in Fig. 9, which suggests that the general trend of increasing wear with decreasing WC grain size does not extend to nanostructured materials.

The wear resistance of WC–Co materials is a functional property that depends on the hardness and fracture toughness of the material and the wear environment/mechanisms. It is particularly important to note the effects of wear mechanisms. Different wear applications, i.e., wear environment, have different mechanisms of wear. The ranking of the wear resistance of WC–Co materials and the effects of grain size and cobalt content differ depending on specific applications. Therefore the results obtained from sliding wear tests may not be directly applied to sand abrasion or cutting tool applications. To the best knowledge of the authors, to date, there are no studies on the wear resistance of nanostructured WC–Co materials in machining or sand abrasion applications that are available in public literature.

Applications of nanostructured cemented tungsten carbide include all areas where conventional WC–Co materials are used. However, industrial interests have been focused on the manufacturing of printed circuit board (PCB) drills. Printed circuit board drills can have drill tip as fine as 40  $\mu\text{m}$  as shown in Fig. 10. The grain size of the material that the drills are made of becomes a significant portion of the tip. Extremely fine grain sizes are required to achieve long and reliable tool life. Fig. 11

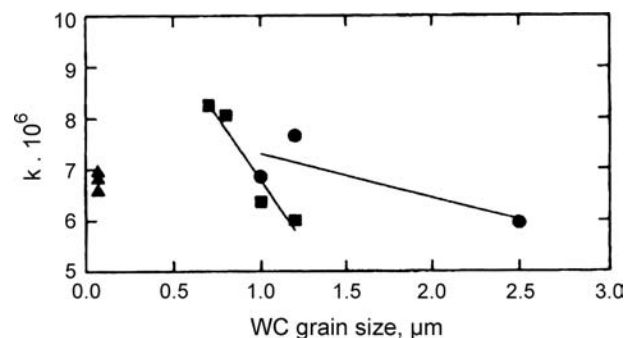


**Fig. 9** The variation of wear coefficient  $k$  with the carbide grain size in WC–Co composites sliding against silicon nitride at 9.8-N applied load and 31.4 mm/s sliding speed. Triangles: nanocomposites; squares: cermets with 6%Co; circles: other commercial grades of WC–Co with 10%Co, 15%Co, and 20%Co respectively.

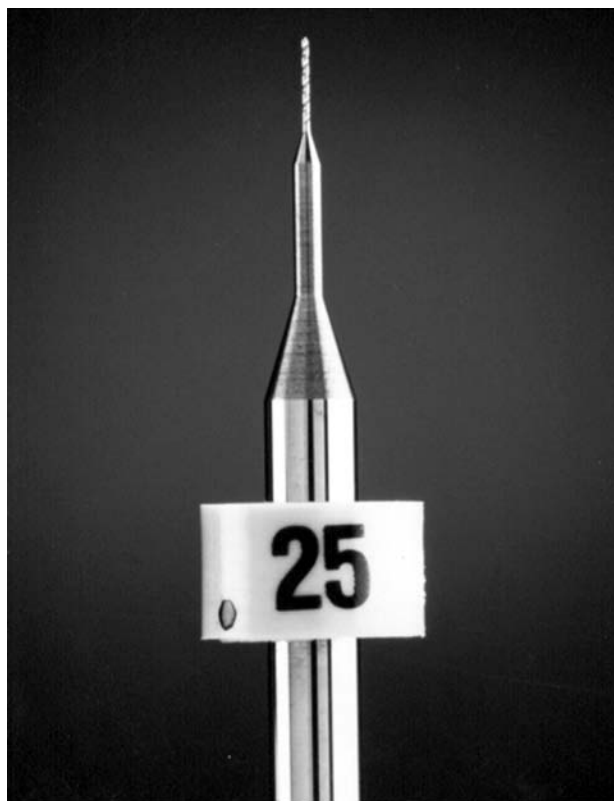


**Fig. 10** A printed circuit board drill with a tip diameter of 0.25 mm.

compares the tool life of a PCB drill made of nanocrystalline powders with that of conventional powders. The result is consistent with the higher hardness of the nanocrystalline WC–Co composites. But it also demonstrates the effectiveness of using nanocrystalline powder in preventing premature tool failures.

Another area of application for nanocrystalline WC–Co powder that attracted active research interests

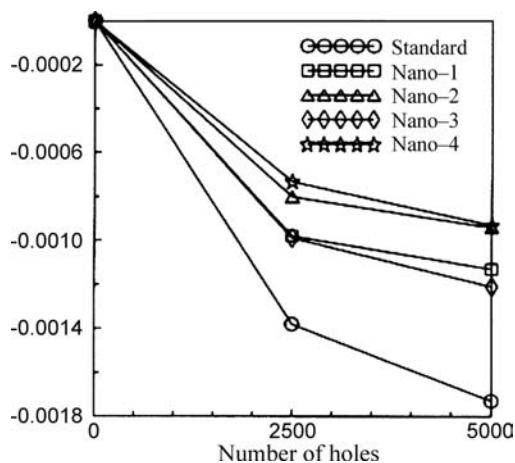


**Fig. 11** The primary wear of printed circuit board drills vs. the number of holes drilled.

is the use of nanocrystalline WC–Co powders for thermal spray coatings. The availability of nanostructured WC–Co composites sparked interest in preparing nanostructured coatings to exploit enhanced hardness, toughness, abrasion, and corrosion properties. While extensive efforts have been made to produce WC–Co hard coatings by use of conventional thermal spray techniques and despite the maturity of thermal spray technology, difficulties were still encountered in preparing dense non-porous coatings, with limited decarburization.<sup>[47]</sup> As a result, the expected increases in the hardness of the coatings were not obtained. The authors recommended that improvements in the powder feedstock or better thermal spray conditions be required to achieve the advanced properties. Skandan et al.<sup>[48]</sup> reported a unique approach to limit the decarburization during thermal spray. The nanophase WC–Co powders were mixed with larger grain size tungsten carbide to create a multimodal coating that yielded improved wear resistance in the absence of decarburization. Improvements were expected by the use of lower-temperature cold spray process, and Lima et al.<sup>[49]</sup> have reported such improved properties by using the cold spray process to prepare nanostructured WC–Co coatings.

## CONCLUSION

The advent of nanotechnology has been heralded as the “new industrial revolution.” Nanostructured materials, a subset of nanotechnology, are expected to have major impact across all industries, improving our everyday lives. The cutting tool industry has already seen the benefits of fine grain tungsten carbide cobalt cermets, and significant improvements over the existing performance are expected from finished tools with a nanograin structure.

Many powder production technologies have been developed over the years, with a few of these reaching commercial-scale levels. More work is needed, however, both to improve the processability of the powders and attain acceptable production economics. As these powders are then consolidated into tooling parts, the major challenge involves the retention of the nanograin structures after the required sintering of the parts made from the nanoscale powders. Many sintering processes have been presented, but in all cases, the basic grain growth mechanism becomes the limiting factor in attaining a true nanograin WC–Co tool.

## REFERENCES

1. Spriggs, G.E. A history of fine grained materials. *Int. J. Refract. Met. Hard Mater.* **1995**, *13*, 241–255.

2. McCandlish, L.E.; Kear, B.H.; Bhatia, S.J. Spray Conversion Process for the Production of Nanophase Composite Powders. US Patent 5352269, 1994.
3. McCandlish, L.E.; Seegopaul, P. Development and Applications of Nanostructured Tungsten Carbide/Cobalt Powders. In *Proceedings of the 1996 European Conference on Advances in Hard Materials*; Stockholm, 1996; 93–100.
4. Eason, J.W.; Reed, J.M.; Tindle, S.E.; Fang, Z. The application of nano-structured WC–Co composite in the manufacturing of PWB drills. *CircuitTree* February 1994, 7 (2), 34–36.
5. Gao, L.; Kear, B.; Seegopaul, P. Method of Forming Tungsten Particles. US Patent 5919428, 1999
6. Seegopaul, P.; Gao, L. Method of Forming Nanograin Tungsten Carbide and Recycling Tungsten Carbide. US Patent 6524366, 2003
7. Lee, G.-G.; Ha, G.-H.; Kim, B.-K. Synthesis of nanostructured W base composite powders by chemical processes. *J. Korean Inst. Met. Mater.* 1999, 37 (10), 1233–1237.
8. Kim, B.-K.; Ha, G.-G.; Woo, Y. Method of Production WC/Co Cemented Carbide Using Grain Growth Inhibitor. US Patent 6511551, 2003
9. Zhang, Z.; Wahlberg, S.; Wang, M.; Muhammed, M. Processing of nanostructured WC–Co powder from precursor obtained by co-precipitation. *Nanostruct. Mater.* 1999, 12, 163–166.
10. Zongyin, Z.; Yu, Z.; Mamoun, M. The reduction of cobalt doped ammonium paratungstate to nanostructured W–Co powder. *Int. J. Refract. Met. Hard Mater.* 2002, 20, 227–233.
11. Ma, X.; Ji, G.; Zhao, L.; Dong, Y. Investigation of nanostructured WC–Co alloy prepared by mechanical alloying. *Rare Met.* 1998, 17, 88–93.
12. Tan, G.-L.; Wu, X.-J. Mechanochemical synthesis of nanocrystalline tungsten carbide powders. *Powder Metall.* 1998, 41, 300–302.
13. Fan, Y.; Fu, L.; Xiao, J.; Yang, J. Preparation of nano-size WC–Co composite powders by plasma. *J. Mater. Sci. Lett.* 1996, 15, 2184–2187.
14. Ban, Z.-G.; Shaw, L.L. Synthesis and processing of nanostructured WC–Co materials. *J. Mater. Sci.* 2002, 37, 3397–3403.
15. Manthiram, A.; Zhu, Y.T. *Synthesis of WC–Co Nanocomposites Using Polymer as Carbon Source*; MRS Symp. Proc.; Materials Research Society: San Francisco, 1994; 346, 463–468.
16. Fang, Z.; Eason, J.W. Study of Nanostructured WC–Co Composites. In *Proc. 13th Int. Plansee Seminar*; Bildstein, H., Eck, R., Eds.; Metallwerk Plansee: Reutte, 1993; Vol. 3, 625–638.
17. Bartha, L.; Atato, P.; Toth, A.L.; Porat, R.; Berger, S.; Rosen, A. Investigation of HIP-sintering of nanocrystalline WC/Co powder. *J. Adv. Mater.* July 2000, 32 (3).
18. Fang, Z. *Powder Processing, Sintering, and Fracture Toughness of Sintered WC–Co Using Nanocarb Powder by Nanodyne*; 1994. Unpublished data.
19. McCandlish, L.E.; Kear, B.H.; Kim, B.K. Processing and properties of nanostructured WC–Co. *Nanostruct. Mater.* 1992, 1, 119–124.
20. McCandlish, L.E.; Seegopaul, P.; Sadangi, R.K. The inhibition of WC grain growth during sintering of nanostructured WC–Co powder compacts. *Adv. Powder Metall. Part. Mat.* 1995, 3, 13/17–13/23.
21. Wu, L. Grain Growth Inhibition in Sintering of Nanostructured WC–Co Alloys. In *Proc. 13th Int. Plansee Seminar*; Bildstein, H., Eck, R., Eds.; Metallwerk Plansee: Reutte, 1993; 3, 667–669.
22. Zhang, L.; Madey, T.E. Initial stages of sintering of nanostructured WC7wt%Co. *Nanostruct. Mater.* 1993, 2, 487–493.
23. Porat, R.; Berger, S.; Rosen, A. Dilatometric study of the sintering mechanism of nanocrystalline cemented carbide. *Nanostruct. Mater.* 1996, 7, 429–436.
24. Carroll, D.F. Processing and Properties of ultrafine WC/Co hard materials. *Int. J. Refract. Met. Hard Mater.* 1999, 17, 123–133.
25. Azcona, I.; Ordonez, A.; Dominguez, L.; Sanchez, J.M.; Castro, F. Hot Isostatic Pressing of Nanosized WC–Co Hardmetals. In *Proceedings of the 15th International Plansee Seminar*; Kneringer, G., Rodhammer, P., Wildner, H., Eds.; Plansee Holding AG: Reutte, 2001; 2, 35–49.
26. Cheng, J.P.; Agrawal, D.K.; Komarneni, S.; Mathis, M.; Roy, R. Microwave processing of WC–Co composites and ferrotic titanates. *Mater. Res. Innov.* 1997, 1, 44
27. Groza, J.R.; Risbud, S.H.; Yamazaki, K. Plasma activated sintering of additives-free ALN powders to near-theoretical density in 5 minutes. *J. Mater. Res.* 1992, 7 (10), 2643–2645.
28. Schubert, W.D. In *2000 Conf. On Tungsten, Hard Metals, and Refractory Alloys*, Annapolis, MD, USA, September, 2000.
29. Goren-Muginstein, G.R.; Berger, S.; Rosen, A. Sintering study of nanocrystalline tungsten carbide powders. *Nanostruct. Mater.* 1998, 10 (5), 795–804.
30. Gille, G.; Szesny, B.; Dreyer, K.; van den Berg, H.; Schmidt, J.; Gestrich, T.; Leitner, G. Submicron and Ultrafine Grained Hardmetals for Microdrills and Metal Cutting Systems. In *15th Int. Plansee Seminar*; Kneringer, G., Rodhammer, P., Wildner, H., Eds.; Plansee Holding AG: Reutte, 2001; Vol. 2, 782–816.
31. Bock, A.; Schubert, W.D.; Lux, B. Inhibition of grain growth on submicron cemented carbide. *PMI* 1992, 24 (1), 20–26.
32. Sadangi, R.K. Grain growth inhibition in liquid phase sintered nanophase WC/Co alloys. *Int. J. Powder Metall.* 1999, 35 (1), 27
33. Gonzalez, E.J.; Piermarini, G.J. Low-Temperature Compaction of Nanosize Powders. In *Handbook of Nanostructured Materials and Nanotechnology*; Nalwa, H.S., Ed.; Synthesis and Processing, 1993; Vol. 1.
34. Prummer, R.; Weimar, P. Explosive consolidation of nanopowders. *Int. Ceram. Rev.* November 2002, 51 (6), 394–398.
35. Yavari, A.R.; Botta Filho, W.J.; Rodrigues, C.A.D.; Cardoso, C.; Valiev, R.Z. Nanostructured bulk Al90Fe5Nd5 prepared by cold consolidation of gas atomized powder using severe plastic deformation. *Scr. Mater.* 2002, 46 (10), 711–716.

36. Schubert, W.D.; Bock, A.; Lux, B. General aspects and limits of conventional WC powder manufacture and hard metal production. *Int. J. Refract. Met. Hard Mater.* **1995**, *13*, 281–296.
37. Groza, J.R.; Dowding, R.J. Nanoparticulate materials densification. *Nanostruct. Mater.* **1996**, *7* (7), 749–768.
38. Averback, R.S.; Hofler, H.J.; Hahn, H.; Logas, J.C. Sintering and grain growth in nanocrystalline ceramics. *Nanostruct. Mater.* **1992**, *1*, 173–178.
39. Owen, D.M.; Chokshi, A.H. An evaluation of the densification characteristics of nanocrystalline materials. *Nanostruct. Mater.* **1993**, *2*, 181–187.
40. Gleiter, H. Materials with ultrafine microstructure: Retrospectives and perspectives. *Nanostruct. Mater.* **1992**, *11*, 1–19.
41. Siegel, R.W. Synthesis, Structure and Properties of Nanostructured Materials. In *Fundamental Properties of Nanostructured Materials*, Fiorani, D., Sberveglieri, G., Eds.; Rimini, Italy, Sept., 20–25, 1993; World Scientific: 3–19.
42. Jia, K.; Fisher, T.E.; Gallois, B. Microstructure, hardness, and toughness of nanostructure and conventional WC–Co composites. *Nanostruct. Mater.* **1998**, *10* (5), 875–889.
43. Densley, J.M.; Hirth, J.P. Fracture toughness of a nanoscale WC–Co tool steel. *Scr. Mater.* **1998**, *38* (2), 239–244.
44. Richter, V.; Rutherdorf, M.v. On hardness and toughness of ultrafine and nanocrystalline hard materials. *Int. J. Refract. Met. Hard Mater.* **1999**, *17*, 141–152.
45. Sigl, L.S.; Exner, H.E. Experimental study of mechanics of fracture of WC–Co alloys. *Metall. Trans., A* July **1987**, *18A*, 1299–1308.
46. Jia, K.; Fisher, T.E. Sliding wear of conventional and nanostructured cemented carbides. *Wear* **1997**, *203–204*, 310–318.
47. Voyer, J.; Marple, B.R. *Proceedings of the First International Thermal; Spray Conference*; Berndt, C.C., Ed.; ASM International, 2000; 895–904. Montreal.
48. Skandan, G.; Jain, M.; Fischer, T.E.; Kear, B.H.; Rigney, W.R.; Shropshire, R.; Brunhouse, S. *Proceedings of the First International Thermal; Spray Conference*; Berndt, C.C., Ed.; ASM International, 2000; 971–976. Montreal.
49. Lima, R.S.; Karthikeyan, J.; Kay, C.M.; Lindemann, J.; Berndt, C.C. Microstructural characteristics of cold sprayed nanostructured WC–Co coatings. *Thin Solid Films* **2002**, *416* (1–2), 129–135.

# Ultrathin Polymer Films: Nanoparticle Nucleation

Pieter Stroeve

Department of Chemical Engineering and Materials Science, University of California–Davis, Davis, California, U.S.A.

## INTRODUCTION

In recent years, the fabrication of nanostructured materials and exploration of their properties have attracted the attention of physicists, chemists, biologists, and engineers.<sup>[1–4]</sup> Interest in such systems arises from the fact that the mechanical, chemical, electrical, optical, magnetic, electrooptical, and magneto-optical properties of these particles are different from their bulk properties and depend on the particle size.<sup>[5–9]</sup> There are numerous areas where nanoparticulate systems are of scientific and technological interest. To produce these systems in appropriate matrices is a significant challenge. This entry considers nanoparticles in nanofilms of polyelectrolyte. First, we will briefly review some key areas of applications of nanoparticle systems, with an emphasis on nanoparticles in matrices, and then we will address the area of layer-by-layer deposition of polyelectrolytes. Finally, nucleation and growth of nanoparticles in nanofilms of polyelectrolytes will be discussed.

## OVERVIEW

### Semiconducting Nanoparticles

Nanoparticulate systems are deemed technologically important in the design of miniaturized, ultrahigh density integrated circuits and information storage devices of the future and in some sense an alternate route to overcoming the 100-nm barrier in conventional electronics and develop nanodimensional molecular electronic devices.<sup>[10–13]</sup>

Owing to their semiconducting properties, group II–VI and IV–VI compounds have been intensively examined by various authors.<sup>[14]</sup> The size-dependent optoelectronic properties of nanoparticles (diameter 1–100 nm) are attributed to quantum confinement effects.<sup>[1–13]</sup> Briefly, electronic excitation in semiconductors arises from an exciton (an electron and hole bound pair) localized in a potential well. Theoretical calculations<sup>[6–13]</sup> have demonstrated that when particle sizes corresponding to the De Broglie wavelength of the free charge carriers are approached, quantum

confinement effects become dominant. One manifestation of such an effect is an increase in the optical band gap energy with decreasing particle size that is readily manifested as sharp changes in color visible to the naked eye. Depending on the particle size, the color of CdS colloids may vary from blue to red, whereas PbS nanoparticles may appear pale yellow, orange, red, or black.

Nanoparticles has been studied in micelles,<sup>[15–17]</sup> vesicles,<sup>[18,19]</sup> sol–gel glasses,<sup>[20,21]</sup> zeolites,<sup>[22,23]</sup> Langmuir–Blodgett (LB) films,<sup>[24,25]</sup> and polymers.<sup>[26,27]</sup> In most cases the clusters have poorly defined surfaces and a broad distribution of particle sizes. Empedocles et al.<sup>[28]</sup> have demonstrated control in preparing monodisperse CdSe clusters using a synthesis medium consisting of trioctylphosphine and its oxide. While size exclusion chromatography permits a narrow size distribution of particle sizes, only minute quantities of the materials are obtained, which is unsuitable for any large-scale applications. On the contrary, the synthetic route used by Empedocles, Norris, and Bawendi<sup>[28]</sup> permits the production of gram quantities of nanoparticulate solids. Chemical reactions initiated within the microscopic cavities of zeolites, glasses, polymers, and micelles provide another process of preparing nanoparticles. The shape and sizes of the nanoparticles in these “microreactors” are largely controlled by the restricted geometry of the cavities in which nucleation and growth of these particles occur. Thermodynamic and entropic requirements also play a crucial role in determining the size of these clusters.

### Iron Oxide Nanoparticles

In the attempt to improve magnetic recording technology, great effort has been made for obtaining high-density recording media. For this purpose, the production of nanoparticles that are uniform, highly dispersible, and oriented in a matrix is essential. Controlled coercivity (between 500 and 1500 Oe) and high saturation magnetization are important tasks. Increasing the coercivity to an applicable level has been fulfilled by doping or coating the maghemite particles with Co.<sup>[29]</sup> The production of nanoparticles has been



achieved on the basis of a mimetic approach, i.e., with the utilization of an organic support that plays an essential role in crystal nucleation and in its growth control.

Nguyen and Diaz reported a simple synthesis of bulk poly(pyrrole-*N*-propylsulfonate) polymer composites containing nanosized magnetite ( $\gamma$ -Fe<sub>2</sub>O<sub>3</sub>) particles.<sup>[30]</sup> Using FeCl<sub>3</sub>, they polymerized pyrrole-*N*-propylsulfonate, resulting in a black polymeric powder. Using sulfonate groups as nucleation sites for the growth of nanoparticles was a new technique introduced by Ziolo et al.<sup>[31,32]</sup> when they reported a matrix-mediated synthesis of maghemite ( $\gamma$ -Fe<sub>2</sub>O<sub>3</sub>). The bulk magnetic material that they synthesized, a  $\gamma$ -Fe<sub>2</sub>O<sub>3</sub>/polymer nanocomposite, was optically active at room temperature. Using FeCl<sub>3</sub> and FeCl<sub>2</sub> they ion-exchanged sulfonated polystyrene cross-linked with divinylbenzene which yielded a polymer with iron cations ionically bonded to sulfonate groups. Washing with NaOH, then heating to 60°C, while adding aqueous H<sub>2</sub>O<sub>2</sub> solution, oxidized the iron to  $\gamma$ -Fe<sub>2</sub>O<sub>3</sub>. Ziolo et al. proposed that the sulfonate groups of the polymer matrix provide spatially located sites for the growth of  $\gamma$ -Fe<sub>2</sub>O<sub>3</sub>, while the void volume in the cross-linked resin imposes a limit on the maximum size of the crystals grown, thereby minimizing aggregation of the iron oxide particles. Particles ranged in size from 5 to 10 nm, as determined by transmission electron microscopy (TEM).

A similar technique was used to prepare a superparamagnetic form of goethite in pores of sulfonated, highly cross-linked poly(divinylbenzene) microspheres.<sup>[33]</sup> The synthesized iron oxide had a calculated magnetic susceptibility, which was about 3 orders of magnitude larger than bulk goethite. Chemically, ferrous ion oxidation reaction leads to the formation of  $\gamma$ -Fe<sub>2</sub>O<sub>3</sub>/polymer composites, using a commercial ion exchange resin consisting of sulfonated, lightly cross-linked polystyrene. The use of polymers with different pore diameters and grade of cross-linkage lead to the oxidation of ferrous chloride to different iron oxides. In this behavior it could be shown that organic matrices have a dramatic influence on the crystallization product.

## Biom mineralization

Biom mineralization occurs naturally in many biological systems including bacteria.<sup>[4]</sup> In the presence of a supersaturated solution, minerals may form on the surface of a living organism. The formed structures are characterized by a high degree of regularity and the supramolecular architectures are finely controlled. Although biom mineralization had been widely

studied,<sup>[4,34–36]</sup> the mechanisms of growth are not always understood. The supramolecular organization of the organic support seems to have an essential role in the process; these organized architectures (such as vesicles, micelles, polymeric networks) provide functionalized surfaces that act as templates and assist in the interfacial molecular recognition. In many cases the organic matrix provides precise sites for oriented nucleation.

## LAYER-BY-LAYER DEPOSITION

The layer-by-layer deposition technique of building supramolecular multilayers on solid substrates by adsorbing polyelectrolytes has emerged as a simple means of producing templates of controlled thickness. Decher<sup>[37,38]</sup> has established that such multilayers may be reproducibly built and the resultant structure is mechanically and thermally stable. Such films have been utilized in the preparation of electroluminescent devices, zener diodes, and the possibility of their use in flat screen displays has been suggested.<sup>[13]</sup> The porous and supramolecular structure of these films provides opportunities for studying chemical reactions in the nanoscale regime. Fig. 1 shows pictorially an example of the layer-by-layer deposition technique for sequential deposition of a polyanion followed by a polycation on a positively charged surface.

The procedure of layer-by-layer deposition is simple. For example, poly(diallyldimethylammoniumchloride) (PDDA), a polycation, and poly(styrene-sulfonate) (PSS), a polyanion, can be deposited sequentially on a negatively charged surface as follows. The polyionic solutions of PDDA and PSS can be prepared separately in 20-mM concentrations: the former is dissolved in deionized water, whereas the latter is dissolved in a 0.1-M NaOH solution, and then adjusted to a pH of 4.5 by drop wise addition of 0.1 M HCl. All concentrations are calculated based on the monomer molecular weights. Polymer films can be assembled on negatively charged substrates if one starts with PDDA. A PDDA/PSS deposition cycle is termed the deposition of one layer-pair. For nanoparticle nucleation, deposition is preferably ended with the first half of a layer-pair in order to terminate the film with a PDDA layer, as will be discussed later. The deposition of the layer-by-layer films can be followed by UV-visible spectroscopy as shown in Fig. 2, and the absorbance is linear with the number of layer-pairs deposited. For the above conditions each layer-pair is approximately 4–5 nm thick, so that a 10.5-layer-pair-thick nanofilm is about 50 nm in total thickness.

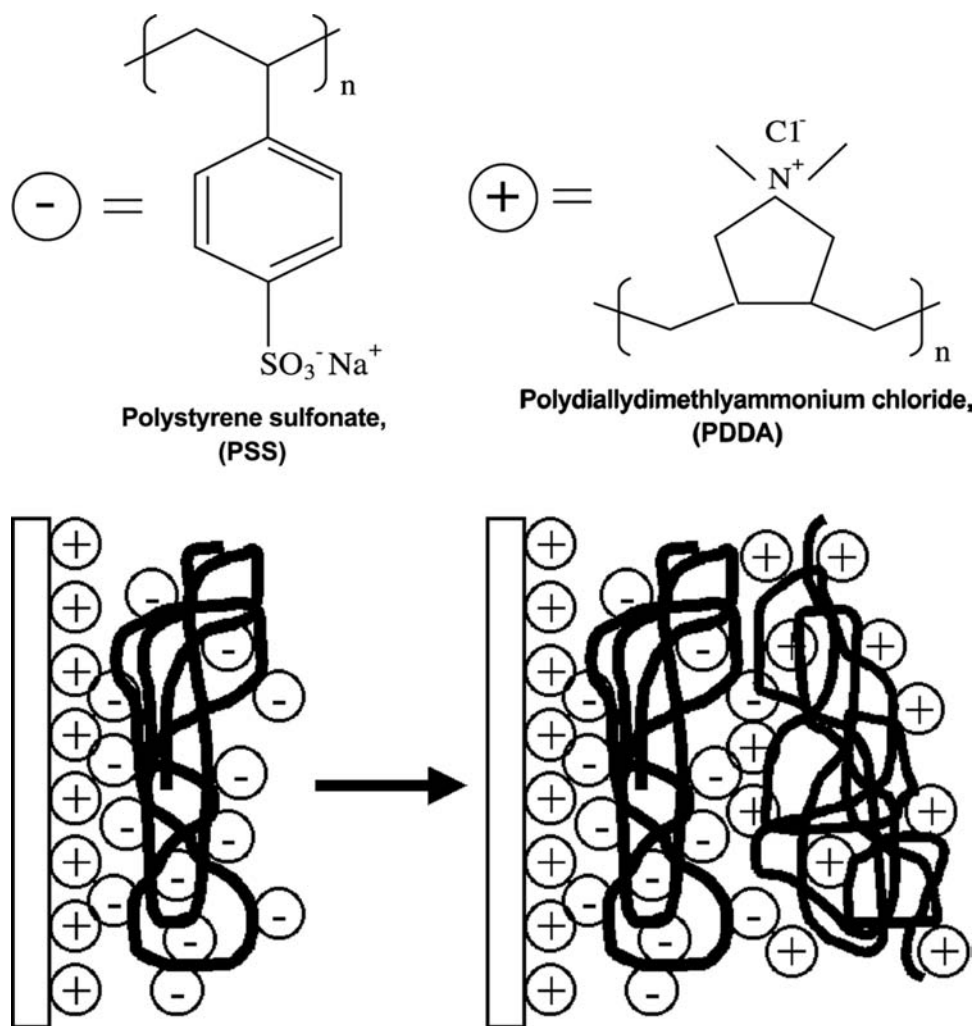
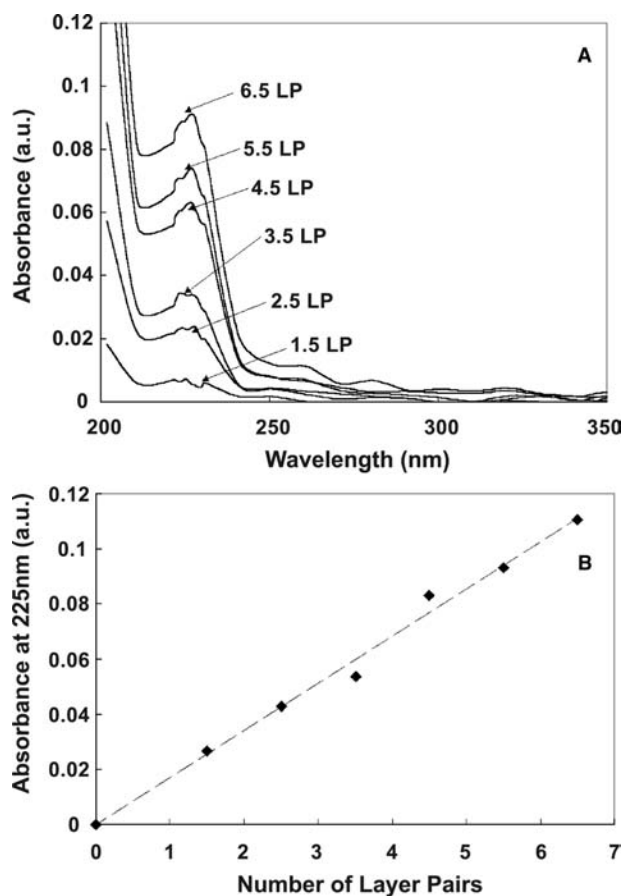


Fig. 1 Schematic representation of layer-by-layer deposition for a positively charged surface.

### NUCLEATION OF NANOPARTICLES IN NANOFILMS OF POLYELECTROLYTES

It has been demonstrated by Stroeve and coworkers<sup>[39–43]</sup> that divalent and trivalent ions can bind to the negatively charged sulfonate groups in layer-by-layer polyelectrolyte nanofilms and that the absorbed ions can be oxidized to form nanoparticles of oxides, or reduced to form nanoparticles or other compounds. For example, nucleation of metal oxide nanoparticles within a nanofilm of polyelectrolyte occurs by cycling the polymer-coated substrates first in  $\text{M}^{2+}$  and then in  $\text{NaOH}$  or  $\text{NH}_4\text{OH}$  solutions (absorption–oxidation cycles or oxidative hydrolysis cycles). The  $\text{M}^{2+}$  solutions can be prepared in concentrations of 4–40 mM by dissolving a  $\text{M}^{2+}$  salt [e.g.,  $\text{MCl}_2$  or  $\text{M}(\text{NO}_3)_2$ ] in purified water. The solutions of 0.1–1.0 M base are made using purified water. Before cycling, all solutions are vigorously sparged for 45 min with nitrogen gas to remove any

dissolved oxygen in solution. In Schlenken tubes, under nitrogen gas, the polymer nanofilm on a substrate can be exposed to the  $\text{M}^{2+}$  solution for a few minutes. Typical substrates can be quartz, silicon wafers, ZnSe wafers, membranes, or more complex-shaped substrates such as catalytic particles. The substrates are rinsed with degassed and purified water to remove excess ions absorbed in the film, and then exposed to  $\text{NaOH}$  or  $\text{NH}_4\text{OH}$  solution for several minutes. Substrates are then rinsed with degassed and purified water and dried completely before the absorption–oxidation cycle is repeated. Fig. 3 shows that the process of oxidative nucleation and growth can be followed by UV–visible spectroscopy.<sup>[39]</sup> Fig. 3B shows that the nucleation of nickel hydroxide nanoparticles with the number of oxidative hydrolysis cycles is linear. The resulting nickel hydroxide nanoparticles after  $x$  cycles is shown in Fig. 4. Each oxidative hydrolysis cycle nucleates new nanoparticles, while nanoparticles from previous cycles grow in size.



**Fig. 2** A) UV-visible absorption for a number of layer-pair (LP) deposition (without absorption-oxidation cycles); B) absorbance at 225 nm with respect to the number of layer-pairs deposited. *Source:* From Fojas et al. [Ref.<sup>[39]</sup>], with permission.

Dante et al.<sup>[40]</sup> demonstrated the formation of akaganéite ( $\beta$ -FeOOH) in multilayered, polymer films of PDDA and PSS produced by the layer-by-layer technique. Ferrous chloride was used as the starting metal ion solution. Uniform, needlelike nanoparticles of  $\beta$ -FeOOH were obtained inside the nanofilm. Transmission electron microscopy showed uniform needles with a diameter of 10 nm and a length of 100 nm. Deposition of the nanofilms had to be terminated with the last layer being PDDA. In the case that the last layer was PSS, two types of nanoparticles were obtained:  $\beta$ -FeOOH and  $\gamma$ -Fe<sub>2</sub>O<sub>3</sub>. The  $\gamma$ -Fe<sub>2</sub>O<sub>3</sub> nanoparticles were spherical and 10 nm in size. Presumably, the mechanism of oxidation of iron ions on the outermost PSS surface layer was different from the oxidation of the iron ions bound to the inner PSS layers.

Dutta et al.<sup>[41]</sup> studied the nucleation and growth of lepidocrocite ( $\gamma$ -FeOOH) crystals in a nanofilm generated as a result of a layer-by-layer adsorption of PDDA and PSS. Interest in lepidocrocite stems from the fact that it is paramagnetic at room temperature having a low Neel temperature of 77 K and is easily

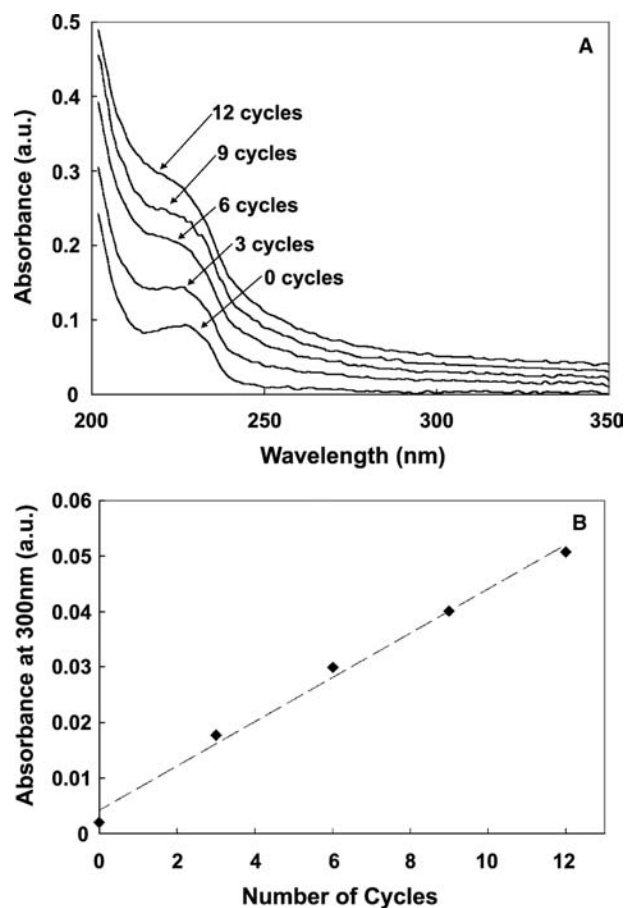


**Fig. 3** A) UV-visible absorption spectra for 6.5 layer-pairs cycled in a 40-mM NiCl<sub>2</sub>·6H<sub>2</sub>O solution and in 1.0 M NaOH solution; B) absorbance at 300 nm with respect to number of oxidative cycles. *Source:* From Fojas et al. [Ref.<sup>[39]</sup>], with permission.

converted into other industrially important magnetic oxides, namely, maghemite and hematite upon heating. Nanofilm films were formed by the layer-by-layer deposition technique on a quartz substrate. Nucleation of nanoparticles in the nanofilm of polyion was initiated by adsorbing ferric nitrate and its subsequent hydrolysis with ammonium hydroxide. Repeating the above process resulted in an increase in the density of the nanoparticles initially formed followed by the appearance of crystallites that grow in dimensions with the number of adsorption and hydrolysis cycles. The size of the crystals can be controlled by the number of cycles used. Analysis of the steady-state UV-visible absorption spectra of the films revealed the formation of lepidocrocites, which was confirmed by FTIR and selected area electron diffraction (SAED) studies. An important feature of this work was that lepidocrocite ( $\gamma$ -FeOOH) is formed instead of akaganéite, which was generated when ferrous chloride was used as the starting material as reported in the work of Dante et al.<sup>[40]</sup> It therefore appears likely that the initial

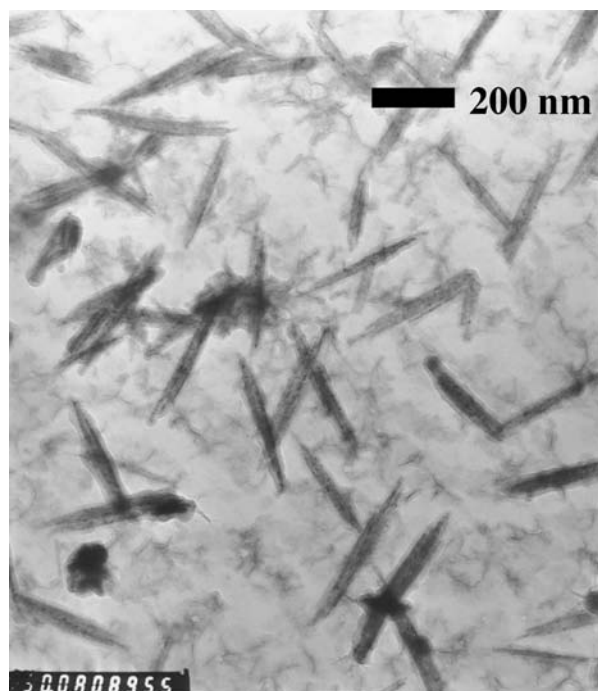


**Fig. 4** TEM image of 2.5 layer-pairs with eight oxidative hydrolysis cycles using 4 mM  $\text{NiCl}_2 \cdot 6\text{H}_2\text{O}$  and ammonia base ( $50 \text{ K} \times$  magnification). The smaller particles are about 50 nm in length, while the larger particles are about 300 nm in length. The smaller nanoparticles are generated with each cycle, whereas existing particles continue to grow in size with each cycle. *Source:* From Fojas et al. [Ref.<sup>[39]</sup>], with permission.

starting material plays a key role in determining the structural and morphological characteristics of iron oxyhydroxides although their chemical compositions are the same.

Nucleation and growth of lead sulfide (PbS) nanoparticles in a PDDA–PSS film produced by the layer-by-layer deposition technique has been studied by Dutta et al.<sup>[42]</sup> Interest in PbS arises from the fact that it is a semiconductor having a small band gap (0.41 eV) and large exciton diameter (18 nm) that permits size-quantization effects to be observable even for large-sized particles or crystallites. Moreover, the non-linear optical (NLO) properties of PbS nanoparticles show large differences in their optical limiting behavior below and above the absorption edge, suggesting that such systems may be utilized in high-speed switching.<sup>[43]</sup> Chemical reaction within the polymer film was initiated by Dutta et al.<sup>[42]</sup> by absorbing  $\text{Pb}^{2+}$  from an aqueous solution of  $\text{Pb}(\text{NO}_3)_2$  followed by exposing the film to  $\text{H}_2\text{S}$  gas. Electron microscopic examination of the films revealed that while nanoparticles are formed in films that were subject to one or two reaction cycles, large crystallites were formed when these films were exposed to a large number<sup>[10]</sup> of reaction cycles. In the latter case a broad distribution of particle sizes is observed and may

perhaps be attributed to a form of Ostwald ripening. Detailed studies show the nucleation and growth of the PbS nanoparticles into larger crystallites. UV–visible absorption studies reveal that the absorption spectral profiles of the films are dependent on the size of the PbS crystallites. The broadened absorption spectral profile observed for films subject to a large number of reaction cycles may be attributed to the superposition of the spectral profiles of the small clusters that tend to be blue shifted due to quantum confinement effects and the large clusters that are red shifted. Crystal size can be controlled by the number of cycles. Essentially, a single cycle only gives nanoparticles that continue to grow in size with more cycles. Instead of using a reducing reaction, it was also possible to oxidize the Pb ions to make  $\text{PbSO}_4$  particles.<sup>[42]</sup>

Zhang et al.<sup>[44]</sup> reported the oxidative hydrolysis of  $\text{Co}^{2+}$  ions absorbed in organized, multilayered, polymer films to form cobalt hydroxide nanocrystals. It was found in this study that using more polymer layer-pairs result in more crystal growth. Hydrolysis of the  $\text{Co}^{2+}$  ions in a nitrogen-rich environment gave rise to mainly needlelike crystallites of  $\alpha\text{-Co}(\text{OH})_2$  that were initially about 100 nm in length and then increased in size with the number of absorption–hydrolysis cycles. However, in an oxygen-rich micro-environment, hexagonal crystallites were found to be predominant. X-ray diffraction (SAED) and TEM studies revealed that these hexagonal crystallites are mainly that of  $\beta\text{-Co}(\text{OH})_2$ . Fig. 5 shows the transition from the alpha to the beta form as observed by TEM. These studies suggest that by varying the nitrogen-to-oxygen ratio the formation of  $\alpha\text{-Co}(\text{OH})_2$  and  $\beta\text{-Co}(\text{OH})_2$  may be controlled.

Rubner and colleagues<sup>[45,46]</sup> have further improved the method of Dante et al.<sup>[40]</sup> by using weak polyelectrolytes, such as poly(acrylic acid) (PAA), instead of a strong polyelectrolyte such as PSS. The advantage of their technique is that the linear charge density can be varied with pH. Thus it is possible to control the charge density of the adsorbing polyelectrolyte and the charge of the previously adsorbed polymer. This technique allows the control of the thickness of the nanofilm, the composition, surface properties, and the level of polymer interpenetration. Rubner and colleagues synthesized layer-by-layer nanofilms containing silver nanoparticles and semiconductor nanoparticles. They showed that it was possible to stratify the nanofilm in layers with nanoparticles and layers without nanoparticles. Dai and Bruening used postreduction of metal ions to obtain layer-by-layer films of catalytic metal nanoparticles with a size range of 4 to 30 nm.<sup>[47]</sup> Recently, Rubner and colleagues nucleated palladium nanoparticles as catalytic seeds for further growth of electroless nickel on the nanoparticle seeds.<sup>[48]</sup> The size of the seeded nickel nanoparticles could be controlled

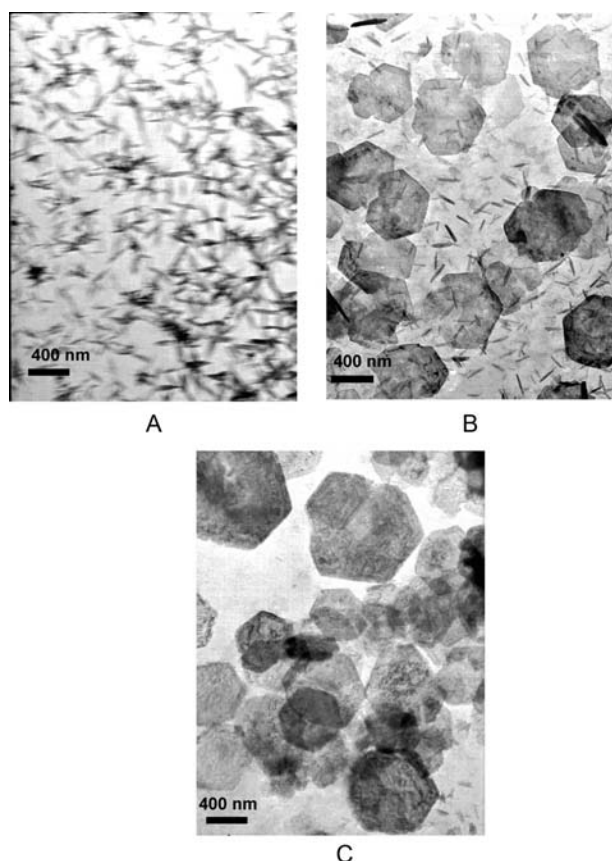


**Fig. 5** TEM micrographs of a 3.5 layer pairs of PDDA-PSS films at different stages of the absorption-hydrolysis process in a nitrogen-enriched environment: (A) two cycles, and in an oxygen-enriched microenvironment panels; (B) four cycles; (C) eight cycles. The concentrations of cobalt chloride and sodium hydroxide solutions were 4 and 10 mM, respectively. Source: From Zhang et al. [Ref.<sup>[44]</sup>], with permission.

and up to 14-nm-diameter nanoparticles were obtained inside the nanofilms.

## CONCLUSION

The layer-by-layer technique of depositing polyions on substrates to build nanofilms of specific thickness, composition, and surface charge can be used to carry out nanoreaction inside the films to form nanoparticle-polymer complexes. Nanofilms of nanoparticle-polymer are useful in coatings, catalysis, electrical, optical, magnetic, electrooptical, and magneto-optical applications. Manipulation of film type and reaction conditions allows for control of the nanoparticle product, distribution, and size inside the polymer matrix.

## REFERENCES

- Nirmal, M.; Brus, L. Luminescence photophysics in semiconductor nanocrystals. *Acc. Chem. Res.* **1999**, *32*, 407.
- Alivisatos, A.P. Semiconductor clusters, nanocrystals, and quantum dots. *Science* **1996**, *271*, 933.
- Chan, W.C.W.; Nie, S. Quantum dot bioconjugates for ultrasensitive nonisotopic detection. *Science* **1998**, *281*, 2016.
- Dujardin, E.; Mann, S. Bio-inspired materials chemistry. *Adv. Mater.* **2002**, *11*, 775-788.
- Brus, L.E. Luminescence of direct and indirect gap quantum semiconductor crystallites. *MRS Symp. Ser.* **1992**, *272*, 215.
- Wang, Y. Nonlinear optical properties of nanometer-sized semiconductor clusters. *Acc. Chem. Res.* **1991**, *24*, 133.
- Steigerwald, M.L.; Brus, L.E. Semiconductor crystallites: A class of large molecules. *Acc. Chem. Res.* **1990**, *23*, 183.
- Norris, D.J.; Bawendi, M.G.; Brus, L.E. Optical Properties of Semiconductor Nanocrystals (Quantum Dots). In *Molecular Electronics*; Jortner, J., Ratner, M., Eds.; Blackwell: Oxford, U.K., 1997.
- Weller, H. Quantized semiconductor particles—A novel state of matter for materials science. *Adv. Mater.* **1993**, *5*, 88.
- Koyama, H.; Araki, M.; Yamamoto, Y.; Koshida, N. Visible photoluminescence of porous silicon and related optical properties. *Jpn. J. Appl. Phys.* **1991**, *30*, 3606.
- Dabbousi, B.O.; Bawendi, M.G.; Onitsuka, O.; Rubner, M.F. Electroluminescence from CdSe quantum-dot/polymer composites. *Appl. Phys. Lett.* **1995**, *66*, 1316.
- Nirmal, M.; Dabbousi, B.O.; Bawendi, M.G.; Macklin, J.J.; Trautman, J.K.; Harris, T.D.; Brus, L.E. Fluorescence intermittency in single cadmium selenide nanocrystals. *Nature* **1996**, *383*, 802.
- Cassagneau, T.; Mallouk, T.E.; Fendler, J.H. Layer-by-layer assembly of thin film zener diodes from conducting polymers and CdSe nanoparticles. *J. Am. Chem. Soc.* **1998**, *120*, 7848.
- Kamat, P.V., Meisel, D., Eds.; *Semiconductor Nanoclusters—Physical, Chemical and Catalytic Aspects*; Elsevier: Amsterdam, 1997.
- Pileni, M.P. *Structure and Reactivity in Reverse Micelles*; Elsevier: Amsterdam, 1989.
- Petit, C.; Lixon, P.; Pileni, M.P. Synthesis of cadmium sulfide in situ in reverse micelles: 2. Influence of the interface on the growth of the particles. *J. Phys. Chem.* **1990**, *94*, 1598.
- Fendler, J.H. Atomic and molecular clusters in membrane mimetic chemistry. *Chem. Rev.* **1987**, *87*, 877.
- Youn, H.C.; Baral, S.; Fendler, J.H. Dihexadecyl phosphate, vesicle-stabilized and in situ generated mixed cadmium sulfide and zinc sulfide semiconductor particles: Preparation and utilization for photosensitized charge separation and hydrogen generation. *J. Phys. Chem.* **1998**, *92*, 6320.
- Kennedy, M.T.; Korgel, B.A.; Montbouquette, H.G.; Zasadinski, J.A. Cryo-transmission electron microscopy confirms controlled synthesis of cadmium sulfide nanocrystals within lecithin vesicles. *Chem. Mater.* **1998**, *10*, 2116.
- Rajh, T.; Micic, O.I.; Lawless, D.; Serpone, N. Semiconductor photophysics: 7. Photoluminescence and picosecond charge carrier dynamics in cadmium sulfide quantum dots confined in a silicate glass. *J. Phys. Chem.* **1992**, *96*, 4633.



21. Minti, H.; Eyal, M.; Reisfeld, R.M.; Berkovic, G. *Chem. Phys. Lett.* **1991**, *183*, 277.
22. Wang, Y.; Herron, N. Photoluminescence and relaxation dynamics of cadmium sulfide superclusters in zeolites. *J. Phys. Chem.* **1988**, *92*, 4988.
23. Ozin, G.A.; Steele, M.R.; Holmes, A.J. Intrazeolite topotactic MOCVD. 3-Dimensional structure-controlled synthesis of II–VI semiconductor nanoclusters. *Chem. Mater.* **1994**, *6*, 999.
24. Yang, J.; Meldrum, F.C.; Fendler, J.H. Epitaxial growth of size-quantized cadmium sulfide crystals under arachidic acid monolayers. *J. Phys. Chem.* **1995**, *99*, 5500.
25. Yang, J.; Fendler, J.H. Morphology control of PbS nanocrystallites, epitaxially grown under mixed monolayers. *J. Phys. Chem.* **1995**, *99*, 5505.
26. Tassoni, R.; Schrock, R.R. Synthesis of PbS nanoclusters within microphase-separated diblock copolymer films. *Chem. Mater.* **1994**, *6*, 744.
27. Kane, R.S.; Cohen, R.E.; Silby, R.J. Synthesis of PbS nanoclusters within block copolymer nanoreactors. *Chem. Mater.* **1996**, *8*, 1919.
28. Empedocles, S.A.; Norris, D.J.; Bawendi, M.G. Photoluminescence spectroscopy of single CdSe nanocrystallite quantum dots. *Phys. Rev. Lett.* **1996**, *77*, 3873.
29. Saito, S. *Fine Ceramics*; Elsevier: New York, 1988.
30. Nguyen, M.T.; Diaz, A.F. A novel method for the preparation of magnetic nanoparticles in a polypyrrole powder. *Adv. Mater.* **1994**, *6* (11), 858–860.
31. Ziolo, R.F.; Giannelis, E.P.; Weinstein, B.A.; O'Horo, M.P.; Ganguly, B.N.; Mehrotra, V.; Russell, M.W.; Huffman, D.R. Matrix-mediated synthesis of nanocrystalline  $\gamma$ -ferric oxide: A new optically transparent magnetic material. *Science* **1992**, *257*, 219–223.
32. Vassiliou, J.K.; Mehrotra, V.; Russell, M.W.; Giannelis, E.P.; McMichael, R.D.; Shull, R.D.; Ziolo, R.F. Magnetic and optical properties of  $\gamma$ -Fe<sub>2</sub>O<sub>3</sub> nanocrystals. *J. Appl. Phys.* **1993**, *73* (10), 5109–5115.
33. Winnik, F.M.; Morneau, A.; Ziolo, R.F.; Stoeber, H.D.H.; Li, W.H. Template-controlled synthesis of superparamagnetic goethite within macroporous polymeric microspheres. *Langmuir* **1995**, *11*, 3660–3666.
34. Tarasevich, B.J.; Rieke, P.C.; Liu, J. Nucleation and growth of oriented ceramic films onto organic interfaces. *Chem. Mater.* **1996**, *8*, 292–300.
35. Lowenstam, H.A.; Weiner, S. *On Biomineralization*; Oxford University Press: Oxford, 1989.
36. Mann, S.; Webb, J.; Williams, R.J.P. *Biomineralization: Chemical and Biochemical Perspectives*; VCH: Weinheim, 1989.
37. Decher, G. *Comprehensive Supramolecular Chemistry*; Sauvage, J.P., Ed.; Pergamon Press: New York, 1996.
38. Decher, G. Fuzzy nanoassemblies: Toward layered polymeric multicomposites. *Science* **1997**, *277*, 1232.
39. Fojas, A.M.; Murphy, E.; Stroeve, P. Layer-by-layer polymeric supramolecular structures containing nickel hydroxide nanoparticles and microcrystallites. *Ind. Eng. Chem. Res.* **2002**, *41*, 2662–2667.
40. Dante, S.; Hou, Z.; Risbud, S.; Stroeve, P. Nucleation of iron oxy-hydroxide nanoparticles by layer-by-layer polyionic assemblies. *Langmuir* **1999**, *15*, 2176.
41. Dutta, A.; Jarero, G.; Zhang, L.; Stroeve, P. In-situ nucleation and growth of  $\gamma$ -FeOOH nanocrystallites in polymeric supramolecular assemblies. *Chem. Mater.* **2000**, *12*, 176.
42. Dutta, A.; Ho, T.; Zhang, L.; Stroeve, P. Nucleation and growth of lead sulfide nano- and microcrystallites in supramolecular polymer assemblies. *Chem. Mater.* **2000**, *12*, 1042.
43. Colvin, V.L.; Schlamp, M.C.; Alivisatos, A.P. Light-emitting diodes made from cadmium selenide nanocrystals and a semiconducting polymer. *Nature* **1994**, *370*, 354.
44. Zhang, L.; Dutta, A.; Jarero, G.; Stroeve, P. Nucleation and growth of cobalt hydroxide crystallites in organized polymeric multilayers. *Langmuir* **2000**, *16*, 7095.
45. Joly, S.; Kane, R.; Radzilowski, T.; Wang, A.; Cohen, R.E.; Thomas, E.L.; Rubner, M.F. Multilayer nanoreactors for metallic and semiconducting particles. *Langmuir* **2000**, *16*, 1354–1359.
46. Wang, T.C.; Rubner, M.F.; Cohen, R.E. Polyelectrolyte multilayer nanoreactors for preparing silver nanoparticle composites: Controlling metal concentration and nanoparticle size. *Langmuir* **2002**, *18*, 3370–3375.
47. Dai, J.; Bruening, M.L. Catalytic nanoparticles formed by reduction of metal ions in multilayered polyelectrolyte films. *Nano Lett.* **2002**, *2*, 497–500.
48. Wang, T.C.; Rubner, M.F.; Cohen, R.E. Manipulating nanoparticle size within polyelectrolyte multilayers via electroless nickel deposition. *Chem. Mater.* **2003**, *15*, 299–304.



# Virus Nanoparticles: Adsorption and Organization on Substrates

Jiyu Fang

*Advanced Materials Processing and Analysis Center, University of Central Florida,  
Orlando, Florida, U.S.A.*

## INTRODUCTION

Virus particles are supramolecular structures containing a nucleic acid [either deoxyribonucleic acid (DNA) or ribonucleic acid (RNA)] core surrounded by a protein layer, known as the capsid. They are important entities in biological systems and useful templates for the synthesis of inorganic nanocrystals. Recently, studies regarding the interfacial behavior of virus particles have begun to emerge from the understanding of two-dimensional (2-D) protein crystallization, the immobilization for studying their structures with atomic force microscopy (AFM) and the preparation of scaffolds for assembling mesoscale materials. The adsorption and organization of virus particles on surfaces are the topic of this entry.

## BACKGROUND

Adsorption and self-organization of biological molecules on surfaces have attracted considerable interest because of their biological implications and potential applications. Viruses are architectural biological assemblies containing two basic units:<sup>[1]</sup> a core of nucleic acid plus a capsid. The viral capsid consists of a large number of protein subunits. Highly monodispersed virus particles with specific shapes are useful templates for the synthesis of inorganic materials. For example, Shenton et al.<sup>[2]</sup> demonstrated that the external surface of tobacco mosaic virus (TMV) particles, consisting of repeated patterns of charged amino acid residues, could be used as nucleation sites for surface-controlled deposition of inorganic materials. The TMV-templated sol-gel condensation of tetraethoxysilane led to the formation of SiO<sub>2</sub> rods. Douglas and Young<sup>[3]</sup> synthesized inorganic nanoparticles within the spherical cage of the well-defined cowpea chlorotic mottle virus (CCMV), devoid of nucleic acid. In this system, the positively charged inner compartment provided a suitable interface for inorganic crystal nucleation. The resulting nanoparticles of paratungstate and decavanadate showed a uniform size

distribution, which is determined by the dimensions of the viral cage. Mao et al.<sup>[4]</sup> genetically engineered M13 particles by binding specific peptides to the particle surfaces. They found that the modified M13 particles could be used to directly synthesize magnetic and semiconducting nanowires. We expect that the organization of these virus templates on substrates will lead to the ordered arrays of the dots and nanowires, which are essential for the next generation of nanodevices. The immobilization of virus particles on substrates will provide an opportunity for us to study their structures with AFM. However, the interfacial behaviors of virus particles are poorly understood due to their complicated structures, variegated electrostatic surfaces, and conformational dynamics. The goal of this entry is to highlight studies on the adsorption and organization of virus particles on substrate surfaces.

## ADSORPTION OF VIRUS NANOPARTICLES ON SUBSTRATES

Recently, a number of methods have been developed to control the adsorption of virus particles on substrates and immobilize them on the substrate surfaces with the goal of studying their structures with AFM. Kuznetsov et al.<sup>[5]</sup> studied the adsorption of several virus particles on substrates using AFM. They found that brome mosaic virus (BMV) and cauliflower mosaic virus (CaMV) adhered well to mica and were stable to repeated AFM scanning. The appearance and organization of capsomere structures on the surface of single BMV particles are clearly visible in the AFM image shown in Fig. 1A. The capsomere consists of either five or six protein capsid subunits. Each has a depression at the center. The capsomeric units on the CaMV surface organize into a hexameric lattice with a spacing ranging from 10 to 12 nm (Fig. 1B).

Knez et al.<sup>[6]</sup> studied the adsorption of TMV on chemically modified substrates with AFM. They found that the TMV particles adsorbed on hydrophobic graphite surfaces showed a cylindrical shape with a height of 18 nm. While on the chemically modified,

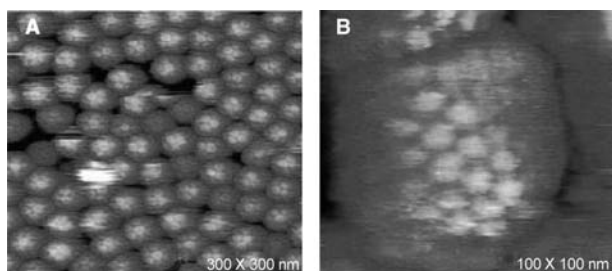


**Fig. 1** AFM images of A) bromo mosaic virus and B) cauliflower mosaic virus immobilized mica. Capsid substructures are clearly visible. *Source:* From Ref.<sup>[4]</sup>.

hydrophilic surfaces, the TMV particles were flattened to a height of 15 nm. The conformation change was suggested to be a result of the strong hydrogen binding of the carboxylate or acyl chloride termini of the hydrophilic surfaces with the TMV particles.

We reported the selective adsorption of bacteriophage T4 and its tail on a patterned organosilane monolayer consisting of  $\text{CH}_3$ -terminated islands surrounded by a  $\text{CF}_3$ -terminated continuous phase.<sup>[7]</sup> As can be seen from the AFM image, which is shown in Fig. 2A, the tail tubes are preferentially adsorbed on the  $\text{CF}_3$ -terminated surface. The strong affinity of the tubes for the  $\text{CF}_3$ -terminated continuous phase allows detailed imaging by AFM. It is known that T4 tubes are 9.8 nm wide and 98 nm long. The average width of the tubes measured in the AFM image is  $43 \pm 2$  nm. Much of the difference in the widths is

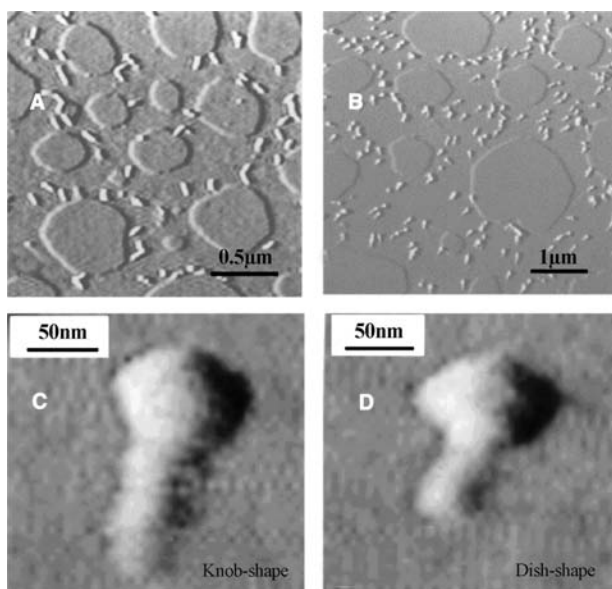
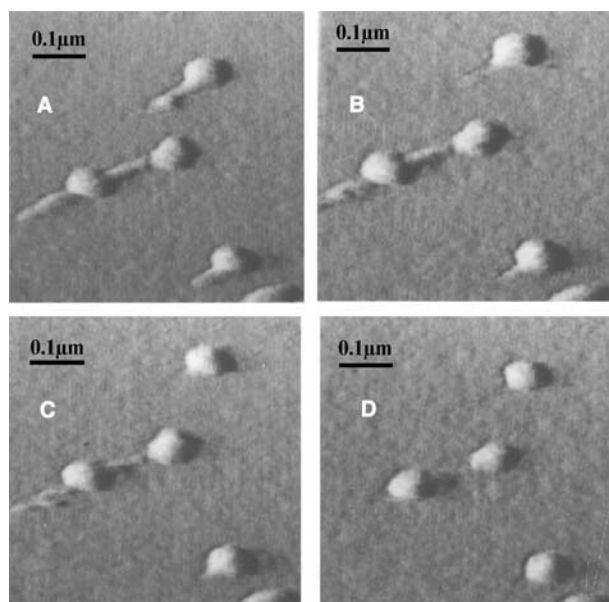


**Fig. 2** AFM images of tail tubes and tube baseplates adsorbed on a patterned silane monolayer consisting  $\text{CH}_3$ -terminated islands surrounded by a  $\text{CF}_3$ -terminated continuous phase.

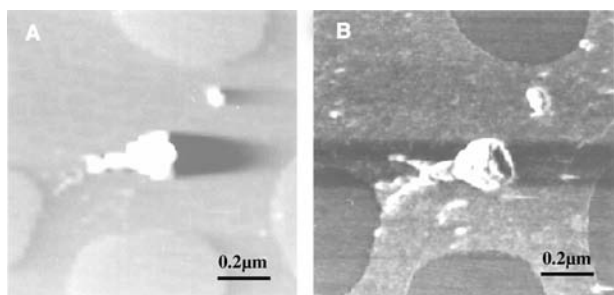
attributed to the geometrical effect of the AFM tip. The measured height of the tube is unaffected by the tip size, and we find that it ranges from 9.4 to 10.3 nm. Although broadening by the AFM tip affects the image resolution, there is an evidence of the final bulge, an increase of the radius by about 4 nm on one end of the tubes. Tube dimers, which are formed by linking two fibers that project from one end of the tubes, are also clearly visible. The angle between the tubes in a dimer varies from  $80^\circ$  to  $180^\circ$ .

Fig. 2B shows the adsorption of T4 tail tubes with baseplates on patterned organosilane monolayers. The characteristic T-shaped tube baseplates selectively adsorb on the  $\text{CF}_3$ -terminated surface. The baseplates are flexible. For example, baseplates are negatively stained baseplates can undergo a transition from a dish shape to a knob-shaped configuration under the influence. We find that most of the baseplates adsorbed on the  $\text{CF}_3$ -terminated surface exhibit a knob configuration (Fig. 2C), but dish-shaped baseplates are also observed (Fig. 2D). Tail tubes joined to baseplates are stable when the loading force applied on the tip is  $<4$  nN; however, if the force is  $>5$  nN, the tubes can be gradually removed from the baseplates during repeated scans although the baseplates are not displaced (Fig. 3). In this situation, the AFM tip acts like a knife to cut the tube from the baseplate.

An AFM image of a complete T4 is shown in Fig. 4A. The  $\text{CH}_3$ -terminated surface resists T4 adsorption. The T4 adsorbed on  $\text{CF}_3$ -terminated continuous phase can be repeatedly imaged if the loading



**Fig. 3** AFM images of tube baseplates adsorbed on the  $\text{CF}_3$ -terminated surface. The images were taken after A) 2, B) 4, C) 6, and D) 10 scans.



**Fig. 4** A) AFM and B) FFM images of individual T4 on a patterned silane monolayer consisting  $\text{CH}_3$ -terminated islands surrounded by a  $\text{CF}_3$ -terminated continuous phase. The two images were taken simultaneously during scanning.

force is  $<4\text{ nN}$ . The head, tail, and probably three fibers of the phage are observed in the AFM image. The head height measured from the cross-sectional profile is about 71 nm, which is close to the known value of 75 nm. Fig. 4B is a frictional force microscopy (FFM) image of the T4 that was taken simultaneously with the AFM image shown in Fig. 4A. The resolution in the FFM image of the T4 is better than that of the AFM image. Although the apparent dimensions of the head (120-nm length and 100-nm width) are affected by tip broadening, the ratio of the head length to width is close to the expected value. The tail structures (neck and baseplate), which are not detected by the AFM, are better resolved by the FFM. The better resolution may be attributed to the high sensitivity of the frictional force to the chemical nature of the T4 surface. Occasionally, the leaking of DNA from the T4 tail is observed. This can be seen

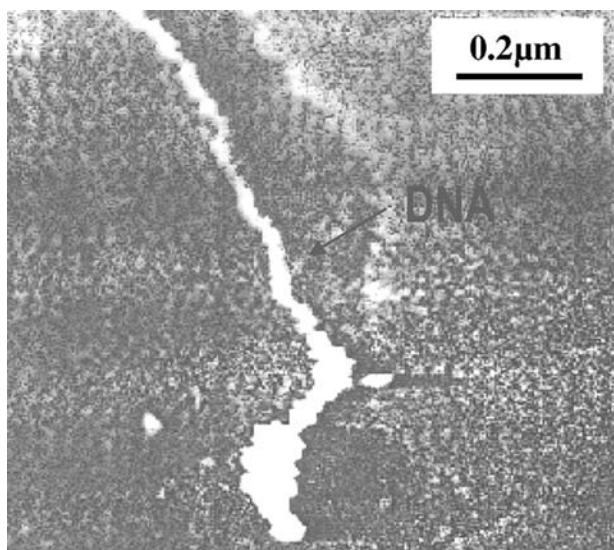


**Fig. 5** AFM image of a collapsed T4 with the ejected DNA on the  $\text{CF}_3$ -terminated surface.

from the AFM image shown in Fig. 5 in which the empty head collapses. The measured height of the collapsed head is about 43 nm. The leaked DNA spreads onto the  $\text{CF}_3$ -terminated surface.

Fig. 6A shows a FFM image of a giant T4 (a T4 phage with a normal tail but an elongated head), immobilized on the  $\text{CF}_3$ -terminated surface. The giant head is 250 nm long and is flatter than a normal head. It is known that the sheath around the tail tubes consists of the 144 copies of gp18 protein arranged in 24 annuli of six subunits each. These sheath annuli are visible on the tail surface (Fig. 6A). The measured spacing of the annuli from the high-resolution FFM image (Fig. 6B) is about 8.9 nm, which from transition electron microscopy is expected to be 4.1 nm. The doubling of the periodicity may perhaps be explained by a pairing of the annuli as a result of drying. A higher-resolution image of the head surface is shown in Fig. 6C. The characteristic hexagonal capsid lattice of the head is evident. The lattice spacing from the FFM image is about 15.8 nm. This value agrees with the known lattice.

High-resolution AFM images of individual virus particles can be obtained when the particles are strongly immobilized on substrates. This allows us to study their structures in great details. For the T4 particles immobilized on the  $\text{CF}_3$ -terminated surface, structural features, such as head, neck, tail, baseplate, and fibers, as well as detailed organization on a scale smaller than 8 nm have been resolved by AFM. Now we know how to use genetic and chemical approaches to bind functional groups to the specific sites of the virus surfaces.<sup>[8,9]</sup> Anisotropic immobilization of the virus particles on surfaces will open up new avenues for the structural investigation of the selected sites.

## ORGANIZATION OF VIRUS NANOPARTICLES ON SUBSTRATES

Virus particles are highly monodispersed in size and well defined in shape. Their ability of self-assembly on substrates has attracted considerable interest in forming organized structures and patterned surfaces. Maeda<sup>[10]</sup> studied the organization of TMV particles on a glass substrate. The TMV particles were found to organize into birefringent crack and zigzag patterns during the drying of 50 mg/mL suspension on the glass substrate (Fig. 7). In the ordered region of the crack pattern, TMV particles appear as a hard rod and are uniaxially oriented. While in the zigzag pattern, TMV particles act as a semiflexible rod rather than a hard rod and were bent by  $60^\circ$ . Wadu-Mesthrige et al.<sup>[11]</sup> showed that the drying of 75  $\mu\text{g/mL}$  suspension on mica substrate could lead to the formation of 2-D



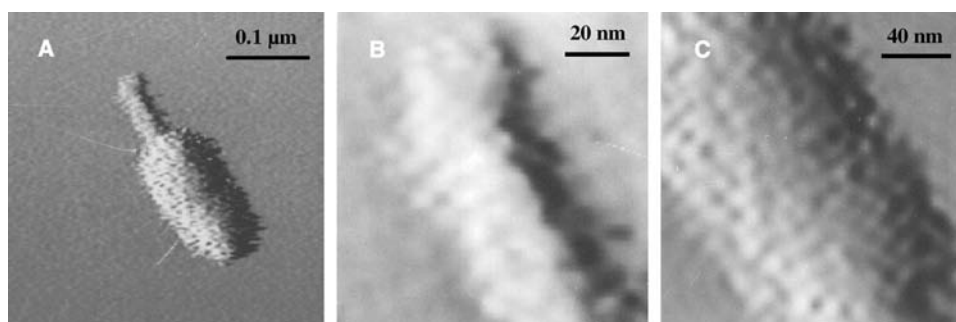


**Fig. 6** A) FFM image of a giant T4 on the  $\text{CF}_3$ -terminated surface, B) FFM image of the tail sheath, and C) FFM image of the head lattice.

spindle patterns, in which TMV particles branch and fuse to form a 2-D networks (Fig. 8A). They also demonstrated that the 2-D organization of the TMV particles could be controlled by adding bovin serum albumin (BSA) in the suspension. In this system, the attachment of BSA proteins on TMV particles changes the interparticle interactions and eliminates the organization of TMV particles on mica (Fig. 8B).

Nam et al.<sup>[12]</sup> reported the genetically driven assembly of M13 virus. The M13 virus is a rodlike particle, which is coated by 2700 copies of polypeptides that cover the interior single-stranded, circular DNA, giving the virion with a length of 880 nm and a diameter of 6.6 nm.<sup>[13]</sup> In this system, M13 particles were genetically modified by binding an anti-streptavidin peptide at one end of the M13 and a hexahistidine peptide at the other end. A nanoring could be assembled using the streptavidin–NiNTA molecule as a link to bridge both ends of the M13 particle. Li et al.<sup>[14]</sup> reported the self-assembly of ZnS-nanocrystal modified M13 particles on substrates during the drying of 30 mg/mL suspension; the modified M13 particles were found to organize into a smectic structure, in which the M13 particles orient parallel to the substrate surface and share a long-range positional order. The ZnS nanocrystals, which link at one end of the M13 particles, showed an ordered array within the self-assembled

smectic structure. The ordered films of nanocrystal functionalized M13 particles are expected to have potential applications in photonic bandgap materials and microelectronics.

Work carried out in my laboratory showed the drying-induced 2-D organization of M13 particles on substrates. Fig. 9A shows a typical AFM image of a self-organized structure of M13 particles on mica by the drying of 0.1 mg/mL suspension. The morphologies of the organized structures are reminiscent of the dewetting process and thought to be dried droplets. A higher-resolution AFM image (Fig. 9B) shows that the dried droplets contain a 2-D lateral condensation of the M13 particles. They are slightly bent and gradually change their orientation to form singular points at which the M13 particles gather.

We also studied the organization of icosahedral cowpea mosaic virus (CPMV) particles on substrates.<sup>[15]</sup> The CPMV particle has a picornalike  $T = 1$  protein shell with an asymmetric unit containing three  $\beta$ -sandwich folds formed by two polypeptides.<sup>[16]</sup> When a droplet of 0.08 mg/mL suspension is dried on mica, the CPMV particles organize into a 2-D hexagonal array that has some degree of crystalline order (Fig. 10). The measured height, and therefore the diameter of the CPMV particles, is about 28 nm, consistent

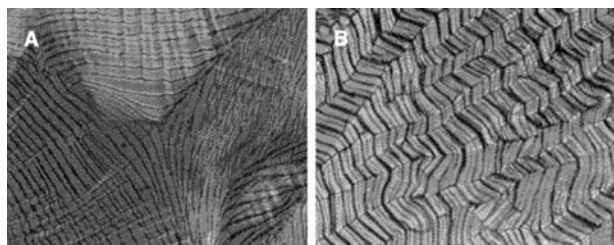


**Fig. 7** Polarizing microscopy images of dried TMV assemblies on glass substrates: A) crack and B) zigzag patterns. Source: From Ref.<sup>[7]</sup>. ©1997 American Chemical Society.

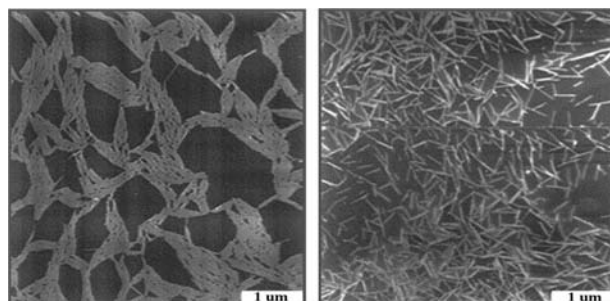


**Fig. 8** AFM images of TMV particles organized on mica without (left) and with (right) the presence of BSA in solution. Source: From Ref.<sup>[8]</sup>.

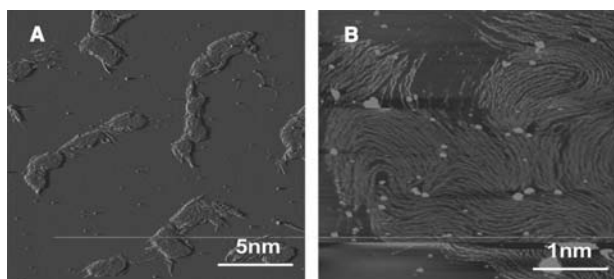


**Fig. 9** A) Low and B) high resolution tapping AFM images of dried droplets of 0.1 mg/mL M13 solution on mica.

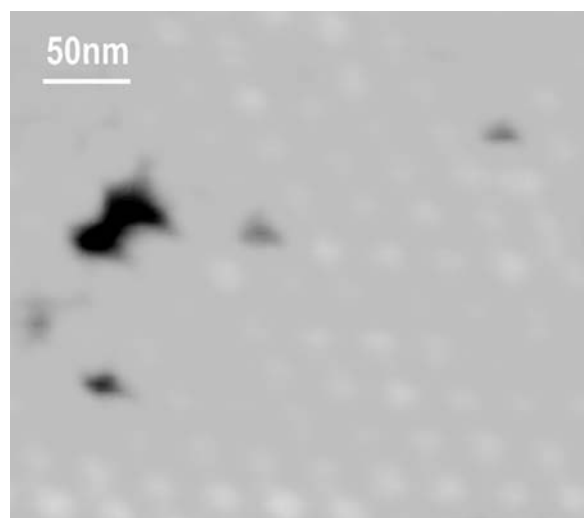


**Fig. 10** Tapping AFM image of 2-D ordered structures of CPMV particles on mica. *Source:* From Fang, J.Y., Soto, C.M., Ratna, B., Lin, T., Johnson, J.E., unpublished data.

with data from X-ray crystallography. This suggests that the CPMV particles are not distorted by drying. The center-to-center distance along the nearest neighbor direction is about 29 nm. Voids are also visible within this hexagonal lattice. The 2-D organization

process of the CPMV particles, which is visualized here, can be speculated as thus: When the solvent evaporates from a droplet of the virus solution, the solubility limit exceeded and a lattice of viruses nucleates on the mica surface due to the particle–particle and particle–substrate interactions.

As the concentration of the CPMV particles increases, we can expect that the virus–virus interactions become strong. The CPMV particles are found to organize into parallel and orthogonal lines as a droplet of 0.15 mg/mL suspension is dried on mica in air (Fig. 11A). More details of the self-organized lines can be seen from the AFM image shown in Fig. 11B. There is slight distortion in the width of the lines near the connections. The height profile along the lines drawn in Fig. 11B shows that these parallel lines have almost the same height, 250 nm, which is closed to nine virus layers. The average width of the lines is about  $600 \pm 40$  nm. The typical distance between the parallel lines is about  $7 \mu\text{m}$ . It is important to point out that the Tris buffer used in our experiments does not show line formation in the absence of CPMV particles. The parallel and orthogonal lines are only observed by drying a droplet of CPMV-containing solution on mica. Fig. 11C shows a fluorescence microscopy image of the organized structures of the CPMV particles, in which the RNA was labeled with SYTO 13. This dye fluoresces only when it is bound to RNA. This confirms that the parallel and orthogonal lines are indeed a result of the self-organization of the CPMV particles.

Recently, a new approach based on the combination of genetic engineering and chemical modification has been developed to organize and pattern virus particles on substrates. For example, Smith et al.<sup>[17]</sup> used dip-pen nanolithography to write self-assembled monolayers (SAMs) into nanoscale patterns presenting functional maleimide groups. They found that the genetically engineered CPMV particles with cysteine (Cys) inserted at the specific locations selectively adsorb on the patterned SAMs through the specific

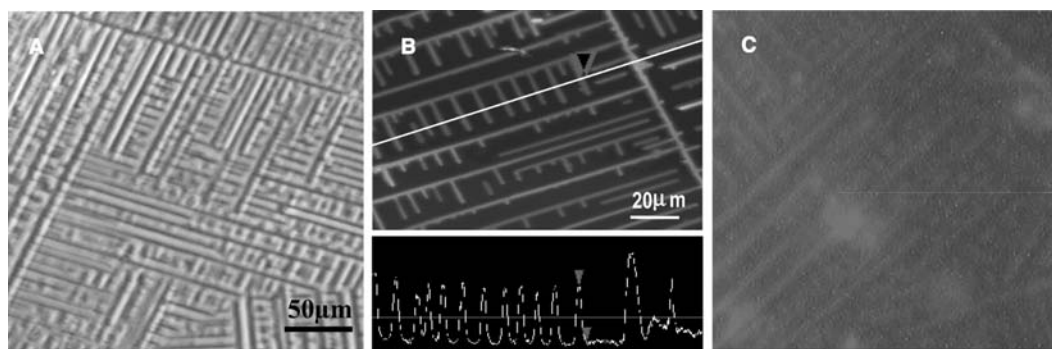


**Fig. 11** A) Optical microscopy, B) tapping AFM, and C) fluorescence microscopy images of self-organized CPMV patterns on mica. RNA within the CPMV shown in Fig. 8C was labeled with a probe.

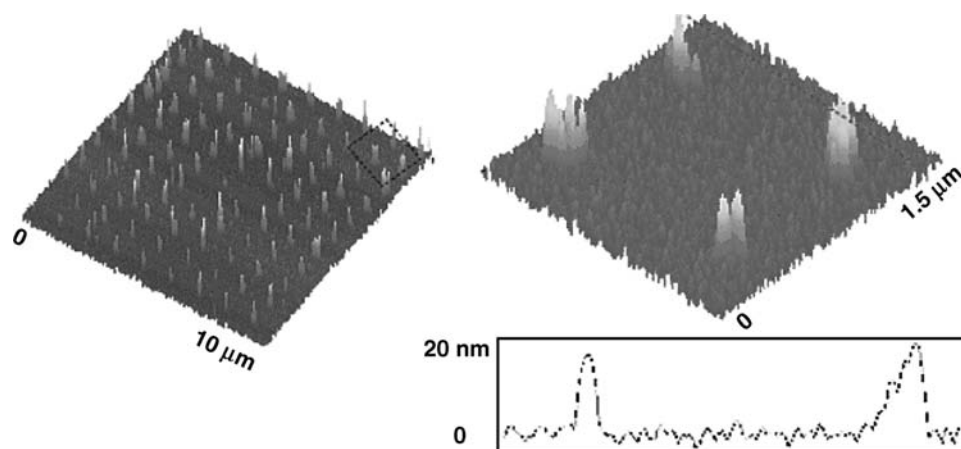


**Fig. 12** Tapping-mode AFM images and high profile of a wt-VCP nanoarray. *Source:* From Ref.<sup>[14]</sup> ©2003 American Chemical Society.

binding between the maleimide and cysteine groups (Fig. 12). In order to prevent interparticle cross-linking via disulfide bond formation during the adsorption process, Klem et al.<sup>[18]</sup> used a solid-phase synthetic approach to break the symmetry of the genetically engineered cysteine-rich CCMP particles. The CCMP particles with asymmetric functional groups were found to form a 2-D array on Au surfaces.

## CONCLUSION

The immobilization of virus particles on substrates allows detailed imaging by scanning force microscopy in air and solution. Structural features and surface lattices of single virus particles (T4 and BMV) immobilized on substrates can be resolved at the nanometer scale. Future directions involve the site-specific immobilization of virus particles for presenting selected sites for structural investigation.

Self-organization of virus particles from a concentrated suspension onto substrates can lead to the formation of complex ordered structures over a large area, providing not only new insights regarding a variety of complex biological structures at interfaces but also new prospects in the field of patterning on surfaces. Recently, there has been a growing interest in the use of virus particles as templates to synthesize inorganic nanocrystals on the outer surface or in the inner surface of the capsids.<sup>[2–4,19–21]</sup> Future efforts include exploring the self-assembly capability of nanocrystal-modified viruses to organize the resulting nanocrystals into ordered arrays, which are essential for the next generation of nanodevices. Undoubtedly, the development of virus building blocks that can self-assemble into well-ordered structures will stimulate our interest in nanotechnology.

## REFERENCES

1. Chiu, W., Burnett, R.M., Garcea, R., Eds. *Structural Biology of Viruses*; Oxford University Press: New York, 1997.
2. Shenton, W.; Douglas, T.; Young, M.; Stubbs, G.; Mann, S. Inorganic–organic nanotube composites from template mineralization of tobacco mosaic virus. *Adv. Mater.* **1999**, *11*, 253.
3. Douglas, T.; Young, M. Host–guest encapsulation of materials by assembled virus protein cages. *Nature* **1998**, *393*, 152.
4. Mao, C.; Solis, D.J.; Reiss, B.D.; Kottmann, S.T.; Sweeney, R.Y.; Hayhurst, A.; Georgiou, G.; Iverson, B.; Belcher, A.M. Virus-based toolkit for the directed synthesis of magnetic and semiconducting nanowires. *Science* **2003**, *303*, 213.
5. Kuznetsov, Yu.G.; Malkin, A.J.; Lucas, R.W.; Plomp, M.; McPherson, A. Imaging of virus by atomic force microscopy. *J. Gen. Virol.* **2001**, *82*, 2025.
6. Knez, M.; Sumser, M.P.; Bittner, A.M.; Wege, C.; Jeske, H.; Hoffmann, D.M.P.; Kuhnke, K.; Kern, K. Binging the tobacco mosaic virus to inorganic surfaces. *Langmuir* **2004**, *20*, 441.
7. Fang, J.Y.; Knobler, C.M.; Gingery, M.; Eiserling, F.A. Imaging bacteriophage T4 adsorbed on patterned self-assembled monolayers of organosilanes by scanning force microscopy. *J. Phys. Chem., B* **1997**, *101*, 8692.
8. Wang, Q.; Lin, T.; Tang, L.; Johnson, J.E.; Finn, M.G. Icosahedral virus particles as addressable nanoscale building blocks. *Angew. Chem., Int. Ed.* **2002**, *41*, 459.
9. Wang, Q.; Lin, T.; Johnson, J.E.; Finn, M.G. Natural supramolecular building blocks: Cysteine-added mutants of cowpea mosaic virus. *Chem. Biol.* **2002**, 813.
10. Maeda, H. An atomic force microscopy study for the assembly structures of tobacco mosaic virus and their size evaluation. *Langmuir* **1997**, *13*, 4150.
11. Wadu-Mesthrige, K.; Pati, B.; McClain, M.; Liu, G.Y. Disaggregation of tobacco mosaic virus by bovine serum albumin. *Langmuir* **1996**, *12*, 3511.



12. Nam, K.T.; Peelle, B.R.; Lee, S.W.; Belcher, A.M. Genetically driven assembly of nanorings based on the M13 virus. *Nano Lett.* **2004**, *4*, 23.
13. Model, P.; Russel, M. Filamentous Bacteriophage. In *The Bacteriophages*; Calender, R., Ed.; Plenum Publishing: New York, 1988; 375–456.
14. Li, J.P.; Lee, S.W.; White, J.M.; Belcher, A.M. Molecular orientation of a ZnS-nanocrystal modified M13 virus on silicon substrates. *J. Polym. Sci., Polym. Phys. Ed.* **2004**, *42*, 629.
15. Fang, J.Y.; Soto, C.M.; Lin, T.; Johnson, J.E.; Ratna, B. Complex pattern formation by cowpea mosaic virus nanoparticles. *Langmuir* **2002**, *18*, 308.
16. Lin, T.; Chen, Z.; Usha, R.; Stauffacher, C.V.; Dai, J.B.; Schmidt, T.; Johnson, J.E. The refined crystal structure of cowpea mosaic virus at 2.8 Angstrom resolution. *Virology* **1999**, *265*, 20.
17. Smith, J.C.; Lee, K.B.; Wang, Q.; Finn, M.G.; Johnson, J.E.; Mrksich, M.; Mirkin, C.A. Nanopatterning the chemospecific immobilization of cowpea mosaic virus capsid. *Nano Lett.* **2003**, *3*, 883.
18. Klem, M.T.; Willits, D.; Young, M.; Douglas, T. 2-D array formation of genetically engineered viral cages on Au surfaces and imaging by atomic force microscopy. *J. Am. Chem. Soc.* **2003**, *125*, 10806.
19. Dujardin, E.; Peet, C.; Stubbs, G.; Culver, J.N.; Mann, S. Organization of metallic nanoparticles using tobacco mosaic virus templates. *Nano Lett.* **2003**, *3*, 413.
20. Allen, M.; Willits, D.; Mosolf, J.; Young, M.; Douglas, T. Protein cage constrained synthesis of ferromagnetic iron oxide nanoparticles. *Adv. Mater.* **2002**, *14*, 1562.
21. Lee, S.W.; Lee, S.W.; Belcher, A.M. Virus-based alignment of inorganic, organic, and biological nanosized materials. *Adv. Mater.* **2003**, *15*, 689.

# Yttria-Tetragonally Stabilized Zirconia

R. Allen Kimel

Materials Science and Engineering Department, Pennsylvania State University,  
University Park, Pennsylvania, U.S.A.

## INTRODUCTION

In the field of structural ceramics, yttria-tetragonally stabilized zirconia (Y-TZP) is of great interest because of its high strength and toughness and good wear resistance.<sup>[1-3]</sup> Previous studies have demonstrated that wet processing routes provide the best possible mechanism for obtaining “bulk” nanocrystalline ceramics because wet processing does not call for extremely high pressures for consolidation as are needed with conventional dry forming techniques.<sup>[4-6]</sup> The chief problem with wet processing is aqueous attack on Y-TZP.<sup>[7-21]</sup> Aqueous degradation can lead to processing dilemmas as the dissolution of yttrium ions from the surface of the powder changes the surface chemistry of the powder while leading to a lack of control over suspension pH values. Furthermore, dissolution of the yttrium-stabilizing agent can lead to catastrophic degradation of the ceramic in service as a result of the tetragonal to monoclinic phase change which leads to spallation of the ceramic because of stresses produced by the 5–6 vol.% expansion associated with the phase change. It is the aim of this review to summarize the current scientific understanding about the aqueous chemistry of Y-TZP and the implications toward synthesis, dispersion, and processing of nanosized Y-TZP. After reviewing the wealth of knowledge in the literature, elucidation of the techniques that will allow for the aqueous synthesis and processing of nanosized Y-TZP will be apparent. Improvement and utilization of these techniques will lead to the accomplishment of a universal goal in structural ceramics which is the production of bulk ceramics from nanosized ceramic powders.

## AQUEOUS CHEMISTRY OF YTTRIA-TETRAGONALLY STABILIZED ZIRCONIA

Several research groups have investigated aqueous attack of Y-TZP ceramics.<sup>[7-21]</sup> There are two major theories for the reaction of Y-TZP in water. The first theory comes from work performed by Lange,

Dunlop, and Davis<sup>[7]</sup> They performed a study on sintered, polycrystalline Y-TZP with yttrium content ranging from 2 to 6 mol%. The aging experiments in this study were performed at 250°C in a tube furnace in a humid environment. From this study, Lange, Dunlop, and Davis concluded that water attacks a tetragonal grain on the surface of the ceramic. Lange, Dunlop, and Davis hypothesized that during aqueous attack, water leaches a sufficient amount of yttrium such that the surface tetragonal grain transforms into the monoclinic phase. Further depletion of yttrium causes the monoclinic structure to grow until a critical size is reached. At this critical size, the monoclinic structure will grow spontaneously until the entire grain is transformed to the monoclinic phase. If this new monoclinic grain is greater than a critical size, then microcracks will form exposing more virgin surface from which yttrium can be leached. Lange, Dunlop, and Davis further showed that transformation of tetragonal phase to monoclinic phase decreases with increasing yttrium content. Conclusions by Lange, Dunlop, and Davis were reached through the use of high-resolution transmission electron microscopy (HRTEM) and X-ray diffraction (XRD), but no solution analysis or kinetic studies were performed. Therefore no direct measurement of yttrium in solution was made nor was the rate at which the proposed leaching mechanism took place measured. Yoshimura et al.<sup>[8]</sup> have also performed studies on the aqueous attack of sintered, polycrystalline Y-TZP. The aging experiments in this study were performed over a range of temperatures from 250°C to 800°C under hydrothermal conditions. It was concluded by Yoshimura et al. that water chemically adsorbs to the surface of the ceramic. Then hydroxide groups migrate through the oxygen vacancies in the Y-TZP lattice leading to the formation of zirconium and yttrium hydroxides. The increase in the size of the hydroxide groups with respect to the oxygen vacancy gives rise to stressed sites at the oxygen vacancies within the lattice. The stressed site defect, in turn, acts as a site for the nucleation of the monoclinic phase. The transformation of tetragonal to monoclinic then

leads to microcracking and macrocracking. The major difference between the mechanisms proposed by Lange, Dunlop, and Davis and Yoshimura et al. is that in the Yoshimura et al. model, hydroxide transport into the material, not yttrium leaching, contributes to the failure of the ceramic seen in aqueous environments. Studies on oxygen diffusion in Y-TZP and the effect of oxygen on the tetragonal to monoclinic transformation pose problems for the Yoshimura et al. theory in the temperature range at which Yoshimura et al. conducted aging experiments.<sup>[22,23]</sup> Research has demonstrated that as the yttrium content increases, oxygen diffusion rates increase.<sup>[22]</sup> Thus one might expect that OH<sup>-</sup> diffusion rates would also increase which would lead to the presence of many stressed sites in the ceramic according to the degradation model proposed by Yoshimura et al. These stressed sites, which would lead to degradation of properties in the ceramic, have not been observed in other studies. Research has also been shown that simply replacing <sup>16</sup>O in Y-TZP with <sup>18</sup>O leads to a decrease in the amount of tetragonal to monoclinic transformation.<sup>[23]</sup> If such a small mass change leads to such a significant change in transformation, it is reasonable to expect that replacing <sup>16</sup>O with OH<sup>-</sup> would have a similar effect, but such has not been observed in the literature.

Beyond these two aforementioned studies, a recent publication has shown that at room temperature, a diffusion-controlled leaching model is supported by data from kinetic studies of the aqueous degradation of 3 mole percent yttria tetragonally stabilized zirconia (3Y-TZP).<sup>[21]</sup> Experiments performed by Kimel and Adair allowed for leaching kinetics of yttrium to be measured and the effects of the aqueous degradation to be established. Interestingly, it was shown that the leaching of yttrium from 3Y-TZP did not have an adverse effect on the crystal structure of the 3Y-TZP powder within the sensitivity of XRD. However, it was also shown that yttrium leaching has significant effects on the surface chemistry of 3Y-TZP powder which can have a deleterious effect on the stability of 3Y-TZP aqueous suspensions.

In addition to characterizing the mechanism behind the aqueous degradation of 3Y-TZP, the work by Kimel and Adair showed that the addition of a surface passivation agent could trivialize the effects of aqueous degradation. It was determined that the addition of oxalic acid to the aqueous suspension of 3Y-TZP led to the formation of a passivation layer, suspected to be yttrium oxalate, that reduced yttrium ions in solution beyond detection. Furthermore, the formation of the passivation layer led to the development of significant surface charge that could be used to facilitate dispersion of the 3Y-TZP powder in aqueous suspension.

## SYNTHESIS METHODS FOR YTTRIA-TETRAGONALLY STABILIZED ZIRCONIA

There are a variety of ways to produce nanosized Y-TZP powder including, but not limited to, polymerization/sol-gel, coprecipitation, and hydrothermal synthesis.<sup>[24-42]</sup> Synthesis by polymerization or sol-gel methods typically takes on a procedure similar to that of Pechini.<sup>[24]</sup> In the Pechini process, a complexing agent, such as citric acid, chelates cationic precursors. This suspension is then reacted with a glycol to form organic ester monomers, which polymerize with the addition of heat to form a sol of homogeneously distributed metal ions in an organic matrix. This sol is further heated to produce a resin, which is further heated to remove organic residuals producing the desired stoichiometric oxide powder. Coprecipitation involves the precipitation of individual amorphous metal hydroxides from solutions of metal salts in a solvent. Precipitation is typically achieved by changing the suspension pH or by the addition of heat to evaporate solvent which leads to a supersaturated environment that facilitates precipitation. The metal hydroxides are then calcined to form the desired stoichiometric metal oxide. Hydrothermal synthesis is precipitation with the addition of heat in excess of the boiling point of the solvent in a pressure vessel.

In some instances, precipitation occurs out of a homogeneous solution.<sup>[31,34,43,44]</sup> The homogeneous solution is produced by keeping the participating metal ions in solution by some complexation chemistry. Precipitation takes place when the complex is broken and large amounts of nuclei are dumped into solution. The complex is usually broken by the addition of a reagent, a change in the solution pH, or heat is added to the homogeneous solution causing a physical breaking of the complex as opposed to the chemical breaking that occurs with the addition of a reagent. The method of precipitation by the addition of heat takes advantage of nucleation/growth ideas to produce ultrafine particles. With the addition of a complexing agent, the critical limit of supersaturation is increased. When the complex is broken, the time available for self-nucleation is increased. After the complex is broken at temperature, the temperature is decreased. When the suspension temperature reaches the point at which the complex is stable again, any metal ions present in solution are recomplexed and thus not available for growth after self-nucleation. As a consequence, no growth occurs because of the decrease in the time available for growth and the resulting particles are ultrafine in size.

The choice of complexing agent is made based on several considerations. First, the complexing agent needs to form a stable complex with the metal ions

over a wide range of pH values. Second, a complexing agent is chosen such that it will impart some sort of surface passivation to the precipitated particles to prevent aggregation of the as-synthesized particles. The surface passivation or colloid protection of the particles by the complexing agent can be accomplished by electrostatic repulsion, steric repulsion, or both occurring simultaneously. Beyond those two considerations, a complexing agent with simple chemistry (i.e., requiring least amount of reagents, time for formation of homogeneous solution, lowest cost, etc.) is desirable for ease in preparing solutions and for future processing steps. Complexing agents have been studied in detail for many years.<sup>[45–49]</sup> Intorre and Martell<sup>[45–47]</sup> had a series of papers in which they studied complexes for zirconium in aqueous solution. The complexing agents were based on structures having multidentate ligands.

Recent research has been performed on the aqueous synthesis of sub-10-nm Y-TZP using a metal ligand approach.<sup>[42]</sup> In this study by Kimel, sub-10-nm 1.7 mole percent yttria tetragonally stabilized zirconia (1.7Y-TZP) powder was produced hydrothermally by precipitation from homogeneous solution. Bicine was used as the metal ligand complexing agent. The powder was precipitated after hydrothermal treatment of the homogeneous solution at 200°C for 8 hr. This treatment yielded 2-wt.% solids with a nominal particle size of 7–8 nm. The as-precipitated powder was crystalline and did not require further calcinations. In addition, it was found that the bicine provided a form of surface protection that would allow for dispersion of the as-precipitated powder.

## WET PROCESSING OF NANOSIZED PARTICLES

To pursue wet processing techniques for the fabrication of bulk ceramics from nanoparticles, obtaining well-dispersed nanoparticles suspensions is essential. However, obtaining well-dispersed nanoparticle suspensions proves to be a mountainous challenge. This challenge is primarily because of the fact that as particle size decreases, surface area increases. In nature, a system will evolve to the lowest energy state, so too it is with nanoparticles. With an increase in surface area generally comes an increase in surface energy, thus nature will try to lower the energy of a nanoparticles system in a way that will be detrimental to developing a well-dispersed suspension for wet processing.

The detrimental result of lowering the energy of a nanoparticle system will be agglomeration, which effectively increases the particle size and lowers the surface area. Generally, agglomeration will occur by the collision of two particles in suspension. Particles

collide via random motion caused by thermal energy present in the system. Upon collision, two scenarios can occur—the particles can stick together or the particles can repel each other. Which scenario occurs depends on the interaction energy between the two particles. The theory of the interaction energy between two-particle double layers is described by Derjaguin, Landau, Verwey, and Overbeek (DLVO).<sup>[50,51]</sup> The DLVO theory predicts the interaction of two-particle double layers by accounting for the repulsive forces present. The presence of repulsive forces leads to colloidal stability as these forces prevent particles from sticking together.

In terms of colloidal stability, there are generally three ways in which a colloid can be stabilized.<sup>[52,53]</sup> The three general types of colloid stability are known as steric, electrostatic, and electrosteric. The third type of stability, electrosteric, is a combination of both electrostatic and steric stabilization. In the realm of polymeric stabilization of colloids, electrosteric stabilization is also associated with the term protective or association colloid. The coinage of the term of “protective colloid” is given to Zsigmondy, who conducted experiments with gold colloids and gelatin around the turn of the 20th century.<sup>[54]</sup> The idea of protective or association colloid has been discussed thoroughly in the literature.<sup>[54–63]</sup> Some of the benefits of this type of protection are insensitivity to electrolyte concentration, applicability in both aqueous and nonaqueous systems, and effectiveness in a large range of solid loading. In a research by Kimel,<sup>[64]</sup> it was found that complexing agent, bicine, formed a protective colloid around the as-precipitated 1.7Y-TZP powder. The 1.7Y-TZP powder was dispersed, recovered, and concentrated to a 50-wt.% (14 vol.%) aqueous suspension by centrifugation and ultracentrifugation. The bicine was found to flocculate the powder but prevents particle to particle contact. The flocculation was reversed by displacing the bicine on the surface of the 1.7Y-TZP powder with the oxalate anion by washing the suspension in an oxalic acid solution using centrifugation. Centrifugation then allowed for concentration of the aqueous suspension by forming a pellet, followed by redispersion in a smaller volume of an oxalic acid solution.

Once a well-dispersed suspension is in place, a forming technique needs to be chosen. A majority of ceramic components made from powders containing a nominal particle size of 1 μm or greater are generally formed using dry-pressing techniques such as uniaxial or isostatic compression. However, use of these techniques with nanosized powders is inherently difficult because of consolidation and energy issues.<sup>[4,65–67]</sup> Nanosized powders are significantly affected by hydration forces which lead to aggregation which, in turn, can lead to the problems of poor powder flow

and poor packing of the powder particles in the die. The high surface area associated with nanosized powders can lead to friction problems along the die and also lead to poor flow and powder packing. These problems also contribute to the need for forces larger than the capabilities of most conventional presses and also greatly inhibit the ability to make large bulk samples.

Wet processing techniques avoid the problems of dry forming techniques by keeping the powder in a suspension. Using a well-dispersed suspension circumvents the issues of powder flow and powder packing, leaving only the problem of consolidation to overcome. Consolidation during wet processing can be addressed by drying techniques and/or the application of a load.

Drying without application of a load is a technique used in evaporation, sol-gel drying, and slip casting. Evaporation has problems as applied to nanoparticles because of agglomeration and phase separation while driving off solvent with the application of heat.<sup>[68,69]</sup> Evaporation without stringent control of heating can also lead to the development of drying stresses in the body which can result in internal defects and cracking. Sol-gel drying is similar to evaporation in terms of producing drying stresses because of the large amount of solvent that has to be removed for consolidation.<sup>[70]</sup> As a consequence, sol-gel drying is typically only applied to bodies that are thin and have low dimensionality such as thin films and fibers.

Slip casting is performed by placing a suspension into a porous mold, where drying and consolidation then take place by water being removed from the suspension into the porous mold via capillarity forces resulting from the mold having a finer pore structure than the suspension body.<sup>[52,53]</sup> However, suspensions of well-dispersed nanosized particles will have nanosized pore structures which will result in capillarity forces much greater than those found in a typical mold material. Thus there will be no driving force for drying of the nanosize particle body, and as a result, poor consolidation and low green densities will be obtained.

Wet processing techniques using the application of force for consolidation include centrifugation and filter pressing. Centrifugation uses centrifugal forces to pack powder particles by pulling them out of suspension. Submicron alumina powders have been consolidated in this manner as well as being used in this research for recovery of the well-dispersed as-synthesized Y-TZP powder.<sup>[70]</sup> However, a wide particle size distribution can lead to mass separation in the final compact and conventionally, centrifuge tubes are limited in size, thus limiting the size of the bulk body to be made.

Filter pressing consolidates the powder by pressing the suspension into the bottom of a die where a membrane is located. The membrane allows the water to pass through leaving behind a consolidated powder

compact. Because the powder is in suspension, friction between the die walls and the powder is negated and as such, much lower pressures are needed for compaction as compared with dry pressing. Most studies on filter pressing in literature were performed on alumina powders.<sup>[65,68,69,71-74]</sup> While many of these studies resulted in well-packed green bodies, none of the studies was performed with nanosized powders on the order of 20 nm or less as is the case with this thesis work. Also, while the use of zirconia was discussed, there is a lack of literature on drying and sintering of such as-pressed pellets. Furthermore, cracking issues associated with drying filter-pressed pellets have not been satisfactorily addressed. Despite the lack of literature and the drying issues, filter pressing provides an excellent opportunity for forming bulk bodies from nanosized particles.<sup>[75]</sup> Transparent pellets of 1.7Y-TZP with a nominal thickness of 2-3 mm were produced by filter pressing by Kimel.<sup>[76]</sup> The green pellets were found to have a 48% theoretical density and average grain size of 18 nm after drying to 120°C.

## CONCLUSION

A goal of aqueous processing of nanosized Y-TZP powders is the production of bulk Y-TZP ceramics. To accomplish this goal, several issues will be addressed. First is determining the nature of aqueous degradation of Y-TZP and finding a method for the controlling degradation such that it becomes a non-issue. Surface passivation provides a mechanism by which such control can be found. However, as particle sizes decrease below 10 nm, conventional dispersants will need to be replaced by much smaller organic molecules. Once familiarity with the degradation issues is gained, a suitable synthesis technique to produce nanosized particles and allow for future aqueous processing of the nanosized particles must be developed. From the literature review, precipitation from homogeneous solution is a promising technique that provides for control over particle size as well as the surface chemistry of the particles. Upon the production of nanosized Y-TZP, recovery and dispersion of the powder must take place. From the literature review of processing techniques, the production of a well-dispersed suspension is imperative for the use of wet processing techniques to consolidate the nanosized Y-TZP powder into a bulk Y-TZP ceramic body.

## REFERENCES

1. Garvie, R.C.; Hannink, R.H.J.; Pascoe, R.T. Ceramic steel? *Nature* **1975**, 258 (5537), 703-704.

2. Porter, D.L.; Heuer, A.H. Mechanism of toughening partially stabilized zirconia ceramics (PSZ). *J. Am. Ceram. Soc.* **1977**, *60* (3–4), 183–184.
3. Lange, F.F. Transformation toughening. *J. Mater. Sci.* **1982**, *17* (1), 225–239.
4. Mayo, M.J. Nanocrystalline ceramics for structural applications: processing and properties. In *Nanostructured Materials: Science and Technology*; Chow, G.-M., Ed.; Kluwer: Dordrecht, The Netherlands, 1998; Chap. 18.
5. Boschi, A.O.; Gilbert, E. Wet forming processes as a potential solution to agglomeration problems. In *Advanced Ceramic Processing and Technology I*; Binner, J.G.P., Ed.; Noyes Publications: Park Ridge, NJ, 1990; 73–93.
6. Nienburg, H.; Harbach, F. Pressure filtration of fine ceramic suspensions. In *Ceramic Powder Science IV*; Hirano, S., Messing, G.L., Hausner, H., Eds.; American Ceramic Society: Westerville, OH, 1991; 321–327.
7. Lange, F.; Dunlop, G.; Davis, B. Degradation during aging of transformation-toughened  $ZrO_2$ - $Y_2O_3$  materials at 250°C. *J. Am. Ceram. Soc.* **1986**, *69* (3), 237–240.
8. Yoshimura, M.; Noma, T.; Kawabata, K.; Somiya, S. Role of  $H_2O$  on the degradation process of Y-TZP. *J. Mater. Sci. Lett.* **1987**, *6*, 465–467.
9. Sato, T.; Shimada, M. Control of the tetragonal-to-monoclinic phase transformation of yttria partially stabilized zirconia in hot water. *J. Mater. Sci.* **1985**, *20*, 3988–3992.
10. Standard, O.C.; Schindhelm, K.; Milthorpe, B.K.; Sorrell, C.C. In-vitro aging of tetragonal zirconia polycrystal (TZP) ceramics. *J. Aust. Ceram. Soc.* **1993**, *29* (1/2), 111–123.
11. Drummond, J.L. In vitro aging of yttria-stabilized zirconia. *J. Am. Ceram. Soc.* **1989**, *72* (4), 675–676.
12. Lawson, S. A new technique for monitoring aging in yttria-tetragonal zirconia polycrystals. *J. Am. Ceram. Soc.* **1993**, *76* (12), 3170–3172.
13. Sato, T.; Shimada, M. Transformation of yttria-doped tetragonal  $ZrO_2$  polycrystals by annealing in water. *J. Am. Ceram. Soc.* **1985**, *68* (6), 356–359.
14. Hirano, M. Inhibition of low temperature degradation of tetragonal zirconia ceramics—a review. *Br. Ceram., Trans. J.* **1992**, *91*, 139–147.
15. Kim, Y.S.; Kwon, S.C. Crystallization and degradation of zirconium oxide in various pH solutions. *J. Nucl. Mater.* **1999**, *270*, 165–173.
16. Koh, Y.-H.; Kong, Y.-M.; Kim, S.; Kim, H.-E. Improved low-temperature environmental degradation of yttria-stabilized tetragonal zirconia polycrystals by surface encapsulation. *J. Am. Ceram. Soc.* **1999**, *82* (6), 1456–1458.
17. Li, J.-F.; Watanabe, R.; Zhang, B.-P.; Asami, K.; Hashimoto, K. X-ray photoelectron spectroscopy investigation on the low-temperature degradation of 2 mol%  $Y_2O_3$ - $ZrO_2$  ceramics. *J. Am. Ceram. Soc.* **1996**, *79* (12), 3109–3112.
18. Li, J.-F.; Watanabe, R. Phase transformation in  $Y_2O_3$ -partially-stabilized  $ZrO_2$  polycrystals of various grain sizes during low-temperature aging in water. *J. Am. Ceram. Soc.* **1998**, *81* (10), 2687–2691.
19. Chevalier, J.; Cales, B.; Drouin, J.M. Low-temperature aging of Y-TZP ceramics. *J. Am. Ceram. Soc.* **1999**, *82* (8), 2150–2154.
20. Guo, X. On the degradation of zirconia ceramics during low-temperature annealing in water or water vapor. *J. Phys. Chem. Solids* **1999**, *60*, 539–546.
21. Kimel, R.A.; Adair, J.H. Aqueous degradation and chemical passivation of yttria tetragonally stabilized zirconia at 25°C. *J. Am. Ceram. Soc.* **2002**, *85* (6), 1403–1408.
22. Ikuma, Y.; Tsubaki, Y.; Masaki, T. Oxygen diffusion in  $Y_2O_3$ -containing tetragonal zirconia polycrystals with different grain sizes. *J. Ceram. Soc. Jpn.* **1990**, *99*, 99–101.
23. Kim, B.; Hamaguchi, H. Role of oxygen phonons in the martensitic phase transformation of yttria stabilized tetragonal zirconia polycrystals. *J. Mater. Sci. Lett.* **1997**, *16*, 645–647.
24. Pechini, M. U.S. Patent No. 3,330,697, July 1967
25. Laberty-Robert, Ch.; Ansart, F.; Deloget, C.; Gaudon, M.; Rousset, A. Powder synthesis of nanocrystalline  $ZrO_2$ -8%  $Y_2O_3$  via a polymerization route. *Mater. Res. Bull.* **2001**, *36*, 2083–2101.
26. Wang, J.A.; Valenzuela, M.A.; Salmones, J.; Vazquez, A.; Garcia-Ruiz, A.; Bokhimi, X. Comparative study of nanocrystalline zirconia prepared by precipitation and sol-gel methods. *Catal. Today* **2001**, *68*, 21–30.
27. Oliveira, A.P.; Torem, M.L. The influence of precipitation variables on zirconia powder synthesis. *Powder Technol.* **2001**, *119*, 181–193.
28. Li, M.; Messing, G.L. Preparation of spherical zirconia particles by controlled coagulation in zirconia sols. In *Ceramic Powder Science III*; Ceramic Transactions; Messing, G.L., Fuller, E.R., Jr., Hausner, H., Eds.; The American Ceramic Society: Westerville, OH, 1990; vol. 12, 129–136.
29. Rinn, G.; Schmidt, H. Preparation of monodispersed zirconia powders from solution. In *Ceramic Powder Science III: A*; Ceramic Transactions; Messing, G.L., Fuller, E.R., Jr., Hausner, H., Eds.; The American Ceramic Society: Westerville, OH, 1987; vol. 1, 23–30.
30. Lee, M.H.; Tai, C.Y.; Lu, C.H. Synthesis of spherical zirconia by precipitation between two water/oil emulsions. *J. Eur. Ceram. Soc.* **1999**, *19*, 2593–2603.
31. Li, W.; Gao, L. Nano  $ZrO_2$  ( $Y_2O_3$ ) particles processing by heating of ethanol-aqueous salt solutions. *Ceram. Int.* **2001**, *27*, 543–546.
32. Xia, B.; Duan, L.; Xie, Y.  $ZrO_2$  nanopowders prepared by low-temperature vapor-phase hydrolysis. *J. Am. Ceram. Soc.* **2000**, *83* (5), 1077–1080.
33. Tsukada, T.; Venigalla, S.; Morrone, A.A.; Adair, J.H. Low-temperature hydrothermal synthesis of yttrium-doped zirconia powders. *J. Am. Ceram. Soc.* **1999**, *82* (5), 1169–1174.
34. Stambaugh, E.P.; Adair, J.H.; Sekercioglu, I.; Wills, R.R. Hydrothermal Method for Producing Stabilized Zirconia. U.S. Patent No. 4,619,817, October 28, 1986.
35. Denkwicz, R.P.; TenHuisen, K.S.; Adair, J.H. Hydrothermal crystallization kinetics of *m*- $ZrO_2$  and *t*- $ZrO_2$ . *J. Mater. Res.* **1990**, *5*, 2698–2705.



36. Vesteghem, H.; Charissou, I.; Reveron, H. Hydrothermal synthesis of colloidal zirconia. *Key Eng. Mater.* **1997**, *132–136*, 129–132.
37. Yoshimura, M.; Somiya, S. Fine zirconia powders by hydrothermal processing. In *Report of the Research Laboratory of Engineering Materials*; Tokyo Institute of Technology, 1984; Number 9.
38. Dell'Agli, G.; Mascolo, G. Agglomeration of 3 mol% Y-TZP powders synthesized by hydrothermal treatment. *J. Eur. Ceram. Soc.* **2001**, *21* (1), 29–35.
39. Vasyukiv, O.; Sakka, Y. Hydroxide synthesis, colloidal processing and sintering of nanosized 3Y-TZP powder. *Scr. Mater.* **2001**, *44*, 2219–2223.
40. Piticescu, R.R.; Monty, C.; Taloi, D.; Motoc, A.; Axinte, S. Hydrothermal synthesis of zirconia nanomaterials. *J. Eur. Ceram. Soc.* **2001**, *21*, 2057–2060.
41. Kholam, Y.B.; Deshpande, A.S.; Patil, A.J.; Potdar, H.S.; Deshpande, S.B.; Date, S.K. Synthesis of yttria stabilized cubic zirconia (YSZ) powders by microwave-hydrothermal route. *Mater. Chem. Phys.* **2001**, *71*, 235–241.
42. Kimel, R.A. Solution Chemistry Issues During the Aqueous Synthesis and Processing of Nanosized Yttria Tetragonally Stabilized Zirconia (YTZP). In *Ph.D. Thesis*; The Pennsylvania State University: University Park, PA, August, 2002; Chapter 4.
43. LeMer, V.K.; Dinegar, R.H. Theory, production and mechanism of monodispersed hydrosols. *J. Am. Chem. Soc.* **1950**, *72* (11), 4847–4854.
44. Willard, H.H. Separation by precipitation from homogeneous solution. *Anal. Chem.* **1950**, *22*, 1372–1374.
45. Intorre, B.I.; Martell, A.E. Zirconium complexes in aqueous solution. I. Reaction with multidentate ligands. *J. Am. Chem. Soc.* **1960**, *82* (1), 358–364.
46. Intorre, B.I.; Martell, A.E. Zirconium complexes in aqueous solution. II. Mixed chelates. *J. Am. Chem. Soc.* **1961**, *83* (9), 3618–3623.
47. Intorre, B.I.; Martell, A.E. Zirconium complexes in aqueous solution. III. Estimation of formation constants. *Inorg. Chem.* **1964**, *3* (1), 81–87.
48. Adair, J.H.; Kerchner, J.A.; Bell, N.S.; Carasso, M.L. Application of chemical principles in the solution synthesis and processing of ceramic and metal particles. In *Synthesis and Characterization of Advanced Materials (Symposium, Orlando, FL, August 1996)*; Serio, M.A., Gruen, D.M., Malhortra, R., Eds.; American Chemical Society: Washington, DC, 1998; Chap. 9.
49. Chang, H.C.; Healy, T.W.; Matijevic, E. Interactions of metal hydrous oxides with chelating agents. III. Adsorption on spherical colloidal hematite particles. *J. Colloid Interface Sci.* **1983**, *92* (2), 469–478.
50. Hunter, R.J. *Introduction to Modern Colloid Science*; Oxford University Press Inc.: New York, 1993.
51. Israelachvili, J. *Intermolecular and Surface Forces*, 2nd Ed.; Academic Press: New York, 1992.
52. Reed, J.S. *Principles of Ceramic Processing*, 2nd Ed.; John Wiley & Sons Inc.: New York, 1995.
53. Ring, T.A. *Fundamentals of Ceramic Powder Processing and Synthesis*; Academic Press Inc.: New York, 1996.
54. Booi, H.L. Association Colloids. In *Colloid Science II*; Kruyt, H.R., Ed.; Elsevier Publishing Company: New York, 1949; Chapter XIV.
55. Overbeek, J.T.G. Stability of Hydrophobic Colloids and Emulsions. In *Colloid Science I*; Kruyt, H.R., Ed.; Elsevier Publishing Company: New York, 1949; Chapter VIII.
56. Vold, R.D.; Vold, M.J. *Colloid and Interface Chemistry*; Addison-Wesley Publishing Company: Massachusetts, 1983; 275–276.
57. Napper, D.H. *Polymeric Stabilization of Colloidal Dispersions*; Academic Press: New York, 1983; Chapters 2.3–2.5.
58. Caruso, F. Nanoengineering of particles surfaces. *Adv. Mater.* **2001**, *13* (1), 11–22.
59. Chern, C.S.; Lee, C.K.; Tsai, Y.J. Dextran stabilized poly(methyl methacrylate) latex particles and their potential application for affinity purification of lectins. *Colloid Polym. Sci.* **1997**, *275* (9), 841–849.
60. Kimura, H.; Taniguchi, H. Cu/Ni colloidal dispersions stabilized by calcium and barium stearates for the amination of oxo-alcohols. *Catal. Letters* **1996**, *40*, 123–130.
61. Dobashi, T.; Yeh, F.; Ying, Q.; Ichikawa, K.; Chu, B. An experimental investigation on the structure of microcapsules. *Langmuir* **1995**, *11*, 4278–4282.
62. Yonezawa, T.; Gotoh, Y.; Toshima, N. Protecting structure model for nanoscopic platinum clusters protected by non-ionic surfactants: <sup>13</sup>C nuclear magnetic resonance investigation. *React. Polym.* **1994**, *23*, 43–51.
63. Stierhof, Y.D.; Humbel, B.M.; Schwarz, H. Suitability of different silver enhancement methods applied to 1 nm colloidal gold particles: An immunoelectron microscopic study. *J. Electron Microsc. Tech.* **1991**, *17*, 336–343.
64. Kimel, R.A. Solution Chemistry Issues During the Aqueous Synthesis and Processing of Nanosized Yttria Tetragonally Stabilized Zirconia (YTZP). In *Ph.D. Thesis*; The Pennsylvania State University: University Park, PA, August, 2002; Chapter 5.
65. Novich, B.E.; Pyatt, D.H. Consolidation behavior of high-performance ceramic suspensions. *J. Am. Ceram. Soc.* **1990**, *73* (2), 207–212.
66. Skandan, G.; Hahn, H.; Kear, B.H.; Roddy, M.; Cannon, W.R. The effect of applied stress on the densification of nanostructured zirconia during sinter-forging. *Mater. Lett.* **1994**, *20*, 305–309.
67. Sagel-Ransijn, C.D.; Winnubst, A.J.; Kerwijk, B.; Burggraaf, A.J.; Verweij, H. Production of defect-poor nanostructured ceramics of yttria-zirconia. *J. Eur. Ceram. Soc.* **1997**, *17*, 831–841.
68. Velamakanni, B.V.; Lange, F.F. Effect of interparticle potentials and sedimentation on particle packing density of bimodal particle distributions during pressure filtration. *J. Am. Ceram. Soc.* **1991**, *74* (1), 166–172.
69. Lange, F.F.; Miller, K.T. Pressure filtration: consolidation kinetics and mechanics. *Am. Ceram. Soc. Bull.* **1987**, *66* (10), 1498–1504.
70. Aksay, I.A. Molecular and colloidal engineering of ceramics. *Ceram. Int.* **1991**, *17*, 267–274.

71. Shan, H.; Zhang, Z. Slip casting of nanometre sized tetragonal zirconia powder. *Br. Ceram. Trans.* **1996**, *95* (1), 35–38.
72. Pearce, D.H.; Ponton, C.B. Optimization of an alumina slip for pressure filtration. *Ceram. Eng. Sci. Proc.* **1994**, *15* (5), 1076–1083.
73. Greil, P.; Gruber, U.; Travitzky, N.; Kulig, M. Pressure filtration of silicon nitride suspensions with constant filtration rate. *Mater. Sci. Eng.* **1992**, *A151*, 247–254.
74. Miller, K.T.; Melant, R.M.; Zukoski, C.F. Comparison of the compressive yield response of aggregated suspensions: pressure filtration, centrifugation and osmotic consolidation. *J. Am. Ceram. Soc.* **1996**, *79* (10), 2545–2556.
75. Lang, A. The Role of Dissolution in Pressure Filtration of Yttria Stabilized Nanocrystalline Zirconia. In *B.S. Thesis*; The Pennsylvania State University: University Park, December, 1998.
76. Kimel, R.A. Solution Chemistry Issues During the Aqueous Synthesis and Processing of Nanosized Yttria Tetragonally Stabilized Zirconia (YTZP). In *Ph.D. Thesis*; The Pennsylvania State University: University Park, PA, August, 2002; Chapter 6.

# Zeolite Membranes

**Wei Xing**

**João C. Diniz da Costa**

*Nanomaterials Centre, School of Engineering, University of Queensland, Brisbane, Queensland, Australia*

**Gao Qing (Max) Lu**

*Nanomaterials Centre, Department of Chemical Engineering, University of Queensland, Brisbane, Queensland, Australia*

**Z. F. Yan**

*Institute of Catalysis, University of Petroleum, Dongying, China*

## INTRODUCTION

Zeolites are three-dimensional, microporous, crystalline solids with well-defined structures that contain aluminum, silicon, and oxygen in their regular framework. When zeolite crystals are intergrown to form continuous layers, the resulting membranes can separate gas mixtures with high selectivities because their pore sizes are comparable to the molecular dimensions. Separation is possible by molecular sieving, preferential adsorption, or differences in diffusion rates. Zeolitic membranes can be classified as either symmetric membranes (self-supported) or asymmetric membranes (supported). Different from the mesoporous inorganic membranes used in gas diffusion process for uranium isotope separation, zeolite membranes consist of many crystallites packed together without crystallite boundary gap in ideal cases. Different types of membranes have varying crystal structure, pore size, and surface properties, thus exhibiting different separation and/or catalytic properties.

Up to date, some zeolite membranes such as the MFI type have been well developed in the last decade since some early works in this area.<sup>[1,2]</sup> Preparation techniques have been developed and fine-tuned in recent years, which makes it possible to fabricate a large and pinhole-free zeolite membrane. Zeolite-membrane-based separations<sup>[3]</sup> and reactions<sup>[4]</sup> have generated much interest in recent years. They are attractive for a variety of reasons, including steady state operation, tailored selectivity, low energy consumption, compatibility to high-temperature and high-pressure conditions, and potential for effective separation and combined reaction-separation systems. Such merits offer the opportunity to solve problems associated with high production costs. Zeolite

membranes have been the highlight in the separation technology and novel reactor engineering fields, and is widely expected to find commercial applications in the near future. Some excellent reviews on the preparation and application of zeolite membranes have appeared in the last several years.<sup>[5,6]</sup> However, the rapid development of this field necessitates a timely update on this topic, particularly on preparation of zeolite membrane and its application to environmental separation and reactions.

## TYPES OF ZEOLITE MEMBRANES

Zeolite, with its well-defined, nanometer-sized pore structure, is an attractive material for inorganic membrane separation and reactions. Small (i.e., 0.3–0.4 nm with 6- and 8-membered ring), medium (i.e., 0.5–0.6 nm with 10-membered ring), and large pore (i.e., 0.7–0.8 nm with 12-membered ring) zeolites have been successfully made into membranes.

SAPO-34 and NaA, having pore size windows of 0.38 and 0.43 nm, respectively, are examples of small-pore zeolite membranes. SAPO-34 zeolite membranes were reported by Poshusta et al.<sup>[7]</sup> to separate CO<sub>2</sub>/CH<sub>4</sub>, CO<sub>2</sub>/N<sub>2</sub>, N<sub>2</sub>/CH<sub>4</sub>, H<sub>2</sub>/CH<sub>4</sub>, H<sub>2</sub>/CO<sub>2</sub>, and H<sub>2</sub>/N<sub>2</sub> binary mixtures. NaA membrane has been intensively studied for dehydration of solvents and alcohols.<sup>[8]</sup> Their use in hybrid membrane reactor has been demonstrated for esterification reaction.<sup>[9]</sup> Recently, Xu et al.<sup>[10]</sup> and Dong, Xu, and Shi<sup>[11]</sup> used a novel process to synthesize a high-quality NaA membrane from clear solution. Besides, Xu and other researchers<sup>[12,13]</sup> investigated the effects of microwave heating on the synthesis of NaA zeolite membrane. Their results indicated that the microwave

synthesis has the advantages of very short time, small zeolite particle size and narrow particle size distribution, and large permeance. Shah et al.<sup>[14]</sup> applied the NaA zeolite membrane to separate methanol/water, ethanol/water, and dimethylformamide/water mixtures with selectivities of 140, 2140, and 330, respectively.

The MFI structure (i.e., silicalite or its aluminosilicate analog, ZSM-5) has been most intensively investigated experimentally and theoretically and often employed in laboratory membrane devices. Owing to its medium-size (~0.55 nm) pore network, which are close to the dimensions of industrial gases, it has been applied in many areas such as hydrocarbons separation, recycling of valuable gases<sup>[15]</sup> and novel metal complexes,<sup>[16]</sup> natural gas cleaning,<sup>[17]</sup> membrane reactor, and so on. With their three-dimensional pore channel network, MFI zeolites are fairly robust and have been a main subject of research in zeolite membrane. Separations of light gases, close-boiling hydrocarbons, organic-water solution, and butane or xylene isomers have been reported in the literature using MFI zeolite membranes. MFI zeolites have an anisotropic pore structure consisting of straight channels along the 010 crystallographic orientation intersected by sinusoidal channels along the 100 direction. This structural anisotropy is expected to influence the transport properties along the different zeolite crystallographic orientations. Foreign atoms can be easily substituted for Si in the MFI zeolite framework.<sup>[18]</sup> These include aluminum for ZSM-5, titanium for TS-1, and vanadium for VS-1.<sup>[19]</sup> This renders MFI zeolites a wider range of chemical and catalytic properties as compared to other zeolite families. Silicon-rich silicalite membrane is inert and hydrophobic, whereas the addition of Al in ZSM-5 transforms the zeolite into acidic catalyst with hydrophilic property. Similarly, the incorporation of titanium and vanadium in TS-1 and VS-1 impart the zeolites with unique catalytic properties. Besides modifying the zeolite chemistry, the presence of these foreign atoms in the framework also perturbs the size and shape of the zeolite pores affecting the transport of molecules through the channel. It also alters the chemical interaction between the diffusing molecule and the zeolite pore wall. The unsaturated charges caused by the insertion of foreign atoms are balanced by counterions, whose presence can further physically restrict and chemically modify the pore channels. Ge,<sup>[20]</sup> B,<sup>[21]</sup> V,<sup>[22]</sup> and Fe<sup>[23]</sup> atoms have been incorporated into the framework of MFI zeolite membrane with interesting properties exhibited.

Faujasite zeolites including zeolite NaY and NaX are representatives of large-pore zeolite (0.74 nm) membranes. Hence it can be used in applications involving larger molecules. Depending on their Si/Al

ratios, faujasites are categorized into X (Si/Al  $\approx$  1–1.5) and Y (Si/Al  $>$  2) although they both have topologically the same framework. Furthermore, modification of the faujasite crystals, either by ion exchange or by dealumination, can be used to control the adsorption or intracrystalline diffusion properties, providing a way of tailoring the membranes to specific applications. Hasegawa et al.<sup>[24]</sup> prepared ion-exchanged faujasite membranes that can separate CO<sub>2</sub>/N<sub>2</sub> with a separation factor of 40. They also synthesized an NaY-type zeolite membrane on the inner surface of a porous  $\alpha$ -alumina support tube by a hydrothermal technique. The synthesized Y-type zeolite membranes were stable at temperatures up to 400°C. Kita et al.<sup>[25]</sup> employed an NaY pervaporation membrane for the separation of methanol and methyl-*tert*-butyl ether (MTBE) mixtures. Nikolakis et al.<sup>[26]</sup> applied faujasite zeolite membrane to successfully separate benzene/cyclohexane, benzene/*n*-hexane, toluene/*n*-heptane, propylene/propane, and ethylene/methane with the separation factors of 160, 144, 45, 6.2, and 8.4, respectively. Lassinantti, Hedlund, and Sterte<sup>[27]</sup> described the preparation of FAU zeolite membrane on polished, seeded alumina wafers. The film thickness was found to be a linear function of synthesis duration up to a certain point. Further treatment reduced the film thickness. Continuous and crack-free films with thicknesses in the range 210–2670 nm were synthesized in their work. Jeong et al.<sup>[28]</sup> and Kobayashi et al.<sup>[29]</sup> studied the application of the NaY-type zeolite membrane to separate C<sub>6</sub> hydrocarbon mixtures both experimentally and theoretically. Another large-pore zeolite, mordenite,<sup>[30–32]</sup> has also been used for H<sub>2</sub>/N<sub>2</sub> and water/alcohol separation. Mordenite's unidimensional, straight pore channels provide easy access and transport through the membrane, but make it more susceptible to fouling.

## PREPARATION OF ZEOLITE MEMBRANES

In general, there are two categories of zeolite membranes mainly related to their preparation processes, i.e., self-supported membranes and composite membranes. The first type of membrane is constituted by a pure zeolitic phase, while a zeolitic thin film formed on a support is the composite type. The preparation of self-supported zeolitic films easily introduces some drawbacks in terms of lack of homogeneous thickness and mechanical instability. So far, zeolitic films have been synthesized in the presence of momentary support (therefore removed after the preparation) or permanent support (to form zeolite composite membranes). A momentary support can be a poly(tetrafluoroethylene) slab, a Teflon sleeve, a Vycor frit, a silver, nickel, or stainless-steel plate. A permanent support can be

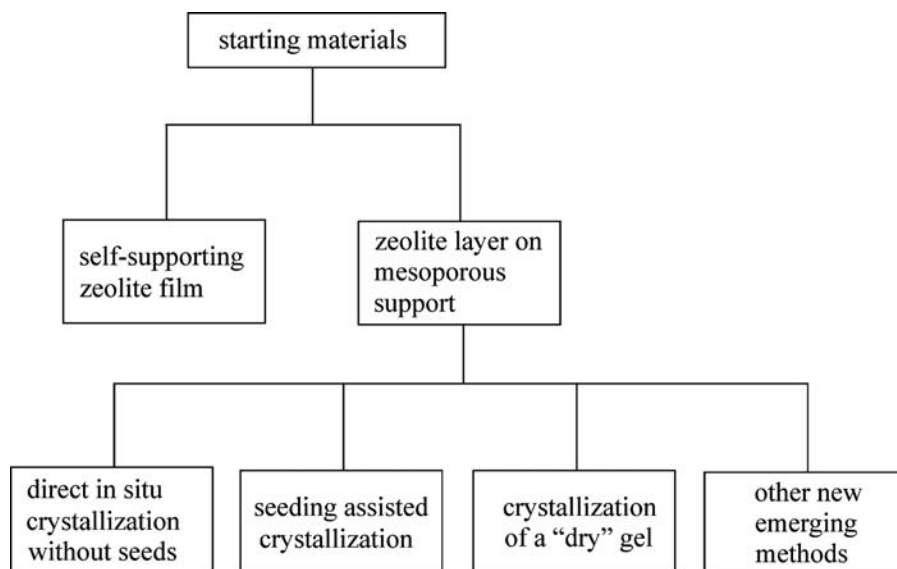


**Fig. 1** Preparation strategy for zeolite membrane.

any of the numerous available materials such as amorphous silica, silicon wafers, glass, aluminum platelets, stainless steel, porous ceramics, or porous  $\alpha$ -Al<sub>2</sub>O<sub>3</sub>,  $\gamma$ -Al<sub>2</sub>O<sub>3</sub> membranes.

Freestanding zeolite layers larger than a few square centimeters are difficult to form, and the resulting structures are fragile. Therefore zeolite membranes are typically deposited on mechanically robust porous supports (alumina, stainless steel, etc.). The technical challenge developing supported zeolitic membranes lies in how to decrease the large thickness (typically 50  $\mu$ m) of the membrane required to obtain defect-free samples, because defects are easily presented in very thin layers. Several methods have been reported to grow zeolite films on porous supports by the in situ approach. Among the different strategies for the preparation of zeolite membranes, as shown in Fig. 1, the preparation of the so-called composite membranes seems to be the most frequently used and most promising technique.

The thin zeolite top layer can be hydrothermally crystallized in one step on the top of the support or inside the pores of the support, which can be called "direct in situ crystallization." The essence of the in situ approach is to bring the surface of a porous support in contact with a zeolite synthesis solution (sol or gel) and keep the system under controlled conditions so zeolite can nucleate and grow to a continuous film on the support surface. If the zeolite layer is formed in several steps using seed crystals that grow together to a continuous supported zeolite layer in a subsequent hydrothermal synthesis, the process is referred to as "seeding supported crystallization." In addition to the hydrothermal crystallization as the main technique to prepare supported zeolite layers, defect-free zeolite layers can be synthesized by a vapor-phase method

called "dry synthesis." An amorphous dry gel can be crystallized on a porous alumina support by a vapor-phase transport method. Other new preparation concepts, such as pulsed-laser deposition,<sup>[33,34]</sup> microwave assisting synthesis,<sup>[12,13]</sup> and substrate heating method,<sup>[35]</sup> have been proposed in recent years.

## ZEOLITIC MEMBRANES USED IN ENVIRONMENTAL SEPARATION

Zeolites have been conventionally used as catalysts, ion exchangers, and adsorbents. Molecules with different sizes and shapes can be discriminated or separated by zeolites through their channels. Generally, separation or purification of gases by zeolites is carried out by pressure swing adsorption. High capital costs and energy consumption characterizes the limitations of such process, and continuous operation is not easily realized. In a membrane configuration, both equipment and operation costs can be dramatically reduced, and continuous operation is possible. Since the 1990s, much research effort has been devoted to the synthesis of zeolite membrane. The potential of using zeolitic materials for membrane-based separations has been realized only in recent years. Uses of zeolite membranes in environment-friendly separations such as the production of clean fuel and energy-efficient processes are emerging. Among them, H<sub>2</sub> separation from light gas mixtures and alcohol from aqueous solutions have received increasing attention. Some researchers have also studied other environment-relating separations. For example, Turlan et al.<sup>[16]</sup> applied silicalite membrane to recover a palladium homogeneous catalyst from its mixture with solvent and product. Piera et al.<sup>[36]</sup> used MFI-type zeolite membranes to

separate CO/air at very low CO concentrations (160 ppbv). At 245 K, a CO/air separation factor of 3.14 was achieved, which shows that it is possible to use zeolite membranes for the removal of pollutants from air, especially where these gases are present in trace concentrations. This is the first work in the open literature dealing with gas separations at trace concentration levels using zeolite membranes.

## H<sub>2</sub> Separation from Gas Mixtures

Hydrogen as a clean energy carrier has attracted increasing attention worldwide because of their higher energy content, environmental advantages, and potential market. The greatest potential use for hydrogen is as an energy carrier for fuel cell vehicles. Moreover, the use of hydrogen presents a totally clean energy use without any emissions of NO<sub>x</sub>, CO, and CO<sub>2</sub>. However, H<sub>2</sub> usually coexists with other light gases when it is produced from industrial processes such as gasification reactions and steam reforming reactions. Therefore it is highly desirable to separate hydrogen from other gases from hydrogen-rich gas streams. Membrane separation has been demonstrated to be superior than the present PSA technology. Studies in separation of H<sub>2</sub> from light gases have been performed by many groups in recent years. Some key findings related to hydrogen separation are summarized in Table 1.

Smaller-pore zeolites such as zeolite A (0.38-nm pore diameter) and SAPO-34 (about 0.43-nm pore diameter) have the potential to improve light gas separation by exploiting differences in size between light gases. Several research groups<sup>[7,37,42]</sup> have explored the synthesis of small-pore zeolite membranes for the separation of light gas mixtures. They reported that H<sub>2</sub>/CH<sub>4</sub> mixture was separated primarily by differences in molecular size, and the selectivity was about 4–25. Aoki, Kusakabe, and Morooka<sup>[38]</sup> reported that H<sub>2</sub>/N<sub>2</sub> selectivities through NaA zeolite membranes were 3.7. Masuda et al.<sup>[39]</sup> develop a silane-cracking

method to modify the pore size of MFI-type membrane, which was applied to H<sub>2</sub> separation from mixture gases containing H<sub>2</sub> and N<sub>2</sub> or O<sub>2</sub> in a flow system. The permeances of N<sub>2</sub> and O<sub>2</sub> of the modified membrane were markedly reduced to about 1/500 of those of a fresh membrane, whereas the permeance of H<sub>2</sub> decreased to only 1/10 of that of a fresh membrane. Consequently, the separation factor of H<sub>2</sub>, which is 1.5–4.5 for a fresh membrane, could be enhanced to about 100. Illgen et al.<sup>[40]</sup> fabricated H<sub>2</sub>-selective MFI zeolite membranes on a porous ceramic tube. At 500°C, this membrane separate H<sub>2</sub> from isobutane with separation factors of 70 and H<sub>2</sub> permeances of ca. 1 m<sup>3</sup> (STP)/m<sup>2</sup> hbar. The high temperature is applied to eliminate the adsorption effects on the permeation. Lai and Gavalas<sup>[41]</sup> prepared the supported ZSM-5 membranes using a TPA-free synthesis gel on asymmetric  $\alpha$ -Al<sub>2</sub>O<sub>3</sub> tubular supports. The membranes have Si/Al ratio much greater than the membranes prepared using TPA<sup>+</sup> in the synthesis gel. Gas permeation measurements yielded high selectivities based on the molecular size. At room temperature, the selectivities of H<sub>2</sub> over N<sub>2</sub>, CH<sub>4</sub>, and *n*-butane were 38, 61, and 10<sup>4</sup>, respectively.

## Membranes for Energy-Efficient Alcohol/Water Separations

Alcohol/water separations are conventionally achieved by distillation, which is apparently inferior to membrane separation both in operating costs and energy consumption. Besides, membrane separation between alcohol and water usually exhibits quite high selectivities because of the strong affinity between zeolites and water. Fruitful results in this area have been achieved in recent years and are summarized in Table 2.

Mitsui Engineering and Ship-Building Co. first installed a commercial plant using 16 zeolite A tubular membrane modules and produced 600 L/hr of dehydrated solvents (ethanol, 2-propanol, acetone, etc.)

**Table 1** H<sub>2</sub> separation data from gas mixtures

Gases	Membrane type	Permeance [10 <sup>-8</sup> mol/(m <sup>2</sup> s Pa)]	Selectivity	Reference
H <sub>2</sub> /CH <sub>4</sub>	SAPO-34	5.0–17/0.48–3.8	4.5–13.5	[7]
H <sub>2</sub> /CH <sub>4</sub>	SAPO-34	3.2/0.13	24.6	[37]
H <sub>2</sub> /N <sub>2</sub>	A type	5.0/1.3	3.7	[38]
H <sub>2</sub> /N <sub>2</sub>	Modified MFI	~2.5/~0.025	90–140	[39]
H <sub>2</sub> /O <sub>2</sub>	Modified MFI	–	110–120	[39]
H <sub>2</sub> / <i>i</i> -C <sub>4</sub> H <sub>10</sub>	MFI	12.4/–	70	[40]
H <sub>2</sub> /N <sub>2</sub>	MFI	2.6/0.068	38	[41]
H <sub>2</sub> /CH <sub>4</sub>	MFI	3.3/0.054	61	[41]
H <sub>2</sub> / <i>n</i> -C <sub>4</sub> H <sub>10</sub>	MFI	–	10 <sup>4</sup>	[41]



**Table 2** Data for alcohol/water separations

Gases	Membrane type	Total flux of the permeate (kg/m <sup>2</sup> ·h)	Selectivity	Reference
Ethanol/water	A type	1.10–4.53	>10,000	[8]
Ethanol/water	Faujasite	0.89–1.59	130–360	[8]
Methanol/water	A type	0.57–3.50	2,100–5,700	[8]
2-Propanol/water	A type	1.76	10,000	[8]
Ethanol/water	A type	2.1	2,140	[14]
Methanol/water	A type	1.8	140	[14]
Methanol/water	Silicalite	0.12	12	[43]
Methanol/water	ZSM-5	0.10–0.30	13–49	[43]
Ethanol/water	ZSM-5	0.05–0.11	2.1–29	[43]
<i>i</i> -Propanol/water	ZSM-5	0.03–0.06	0.9–16	[43]
<i>t</i> -BuOH/water	Silicalite	3.5	144	[44]
<i>t</i> -BuOH/water	A type	1.5	16,000	[44]
<i>t</i> -BuOH/water	Polymeric	0.5	3,615	[44]

containing less than 0.2% of water from feeds at 120°C containing 10% of water.<sup>[8]</sup> Shah et al.<sup>[14]</sup> explored the commercial zeolite NaA membranes for the pervaporation separation of binary solvent/water systems in a broad range of concentrations and temperatures. Tuan et al.<sup>[43]</sup> separated liquid mixtures by pervaporation using metal ion-substituted ZSM-5 zeolite membranes. Their results indicate that substituted ZSM-5 membranes had higher methanol/water separation factors than silicalite-1. The B-ZSM-5 membrane had a methanol/water separation factor of 49. The separation factors and fluxes in pervaporation through substituted ZSM-5 membranes (except Ge-ZSM-5) were in the order methanol > ethanol > propanol. Gallego-Lizon et al.<sup>[44]</sup> compared the commercially available polymeric, microporous silica and zeolite (NaA type) membranes by pervaporation with respect to the dehydration of binary mixtures of *t*-butanol and water. They showed that the microporous silica membrane resulted in the highest flux (3.5 kg m<sup>-2</sup> h<sup>-1</sup>) and the NaA zeolite membrane exhibited the highest selectivity (16,000).

## ZEOLITIC MEMBRANES FOR MEMBRANE REACTORS

Zeolite membranes are thermally stable and well adapted to high-temperature applications because they can be used as separators only and/or as active contactors if they are catalytically active. The use of zeolite membranes in reactors has many advantages in terms of the several unique functions: to separate the products formed, to remove inhibitors, or to add reactants in a variety of reaction scenarios. In addition, the zeolite materials that constitute the membranes often

have intrinsic catalytic properties, which makes it possible to conceive reactors where the membrane itself performs the reaction and separation functions. Integration of reaction and separation at the microscopic level has numerous potential advantages in applications, such as the increase of selectivity in situations where a short-lived valuable intermediate product is generated. It has demonstrated an increase in conversion of the reactants and, in some situations, increase in selectivities. Membrane reactors are now widely used in reaction processes.

Generally, there are two configurations in the membrane reactor. The first is that the membrane performs the exclusive separating function, and does not take part in the reactions. The other is an integrated system with the membrane simultaneously performing the functions of separation and catalysis in the reaction. In the former case, the products formed on the catalyst must desorb, diffuse to the membrane surface, and transport to the opposite side. Obviously, this introduces a supplementary transport resistance compared to the case where reaction and separation are carried out in the absence of catalytic materials other than the membrane itself.

## Membrane Reactors with Separation Functions

In this case, zeolite membranes are used as separation membranes and not as catalytic membranes. The use of zeolite membranes for the dehydrogenation of hydrocarbons is a typical example for this configuration. Ciavarella et al.<sup>[45]</sup> showed that the isobutene yields were increased to four times higher than that observed in a conventional reactor. The possibility of using membrane reactors to increase the removal of hydrogen in dehydrogenation reactions or in other processes

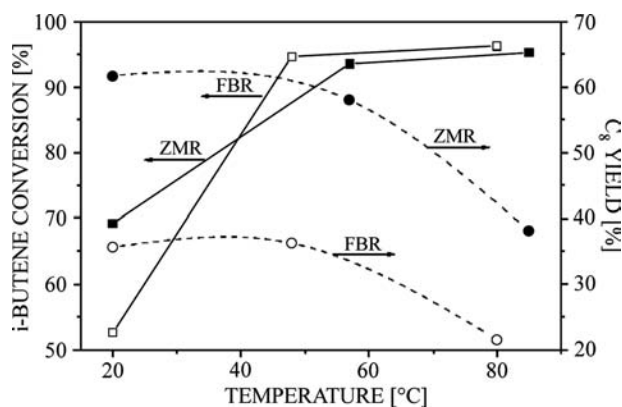


**Fig. 2** Comparison of ZMR (zeolite membrane reactor) and FBR (fixed-bed reactor) performances. The *i*-octene yield as a function of temperature. *Source:* From Ref.<sup>[46]</sup>.

producing hydrogen, such as decomposition ( $H_2S$ ,  $H_2O$ ) and synthesis gas production, will significantly promote the conversion of reactants. Illgen et al.<sup>[40]</sup> fabricated  $H_2$ -selective, MFI zeolite membranes on a porous ceramic tube, which was used to support the packed bed inside. The conversion of isobutane dehydrogenation was increased by almost a factor of 2.

Piera et al.<sup>[46]</sup> investigated the use of an MFI (silicalite) zeolite membrane reactor (ZMR) in the liquid-phase oligomerization of *i*-butene. The membrane was used for the selective removal of *i*-octene from the reaction environment, thus reducing the formation of unwanted  $C_{12}$  and  $C_{16}$  hydrocarbons. Reaction experiments were then carried out over an acid resin catalyst bed located on the membrane tube side. Seen from Fig. 2, the ZMR (zeolite membrane reactor) produced a very significant increase in the selectivity, and as a consequence also in the yield of *i*-octenes (intermediate product in the oligomerization of *i*-butene), compared to a conventional fixed-bed reactor (FBR), while maintaining the similar *i*-butene conversion.

Salomon et al.<sup>[47]</sup> employed some different hydrophilic membranes (mordenite or NaA zeolite) to selectively remove water from the reaction atmosphere during the gas-phase synthesis of methyl-*tert*-butyl ether (MTBE) from *tert*-butanol and methanol. This reaction was carried out over a bed of catalyst packed on the inside of this zeolite tubular membrane. Their results indicate that MTBE yields were obviously higher than the traditional fixed-bed reactor. Farrusseng, Julbe, and Guizard<sup>[48]</sup> applied three different porous ceramic membranes (microporous MFI zeolite, mesoporous  $SiO_2$ , and meso-macroporous  $AlPO_4$  membranes) to distribute  $O_2$  for the partial oxidation of  $C_3H_8$  in an inert membrane reactor. The performance of the three membranes as  $O_2$  distributors were evaluated by their ability 1) to control the  $O_2$  partial pressure in the tube side and 2) to limit the back-diffusion of

$C_3H_8$  to the shell side by application of a transmembrane pressure. The  $AlPO_4$  membrane was shown to be the most efficient membrane as a porous  $O_2$  distributor. Jafar, Budd, and Hughes<sup>[9]</sup> applied zeolite A membranes to the esterification of lactic acid with ethanol to give ethyl lactate. Experimental results demonstrated the removal of water by pervaporation or vapor permeation enhanced the yields of ethyl lactate by about 20%. Liu, Gao, and Au<sup>[49]</sup> applied the NaA membrane in a membrane reactor ( $NiO/La_2O_3-\gamma-Al_2O_3$  as catalyst) for  $CH_4/CO_2$  reforming.  $CH_4$  and  $CO_2$  conversions, and  $CO$  and  $H_2$  selectivities were significantly higher than the values observed over a traditional fixed-bed reactor by more than 10%, especially for the increase of  $CO_2$  conversion by 30%.

### Membrane Reactors with Combined Separation and Catalytic Functions

Zeolite membrane, with its intrinsic or incorporated catalytic properties, can be applied in zeolite membrane reactors, combining the reaction and separation functionalities at the same time. Oxidative dehydrogenation of alkanes is a good case in point. The potential use of catalytic membrane reactors in this case appears to be of particular interest for 1) controlling the oxygen feeding to limit the highly exothermic total combustion and 2) improving the contact between the reactant and the catalytic sites. Immobilizing transition metal ions in zeolites by ion exchange or by incorporation into the lattice leads to stable, isolated, and well-defined, redox-active catalytic sites. Julbe et al.<sup>[22]</sup> tested the oxidative dehydrogenation of propane on V-free MFI membranes and V-MFI zeolite membranes. Both MFI and V-MFI membranes were found to produce propene with about 40% selectivity but with higher  $O_2$  and  $C_3H_8$  conversions for the V-MFI. Hasegawa et al.<sup>[50,51]</sup> applied noble metal-impregnated Y-type zeolite membranes for the selective oxidation of  $CO$ , which was present at concentrations of several 100 ppm in a stream of hydrogen. Ciavarella et al.<sup>[52]</sup> separated  $H_2$  and isobutene mixture using composite alumina-MFI-zeolite with a separation factor of 25 at 723 K, a typical temperature of the isobutane dehydrogenation in membrane reactor, which indicates a good commercial prospect. Takata et al.<sup>[53]</sup> applied the ion-exchanged H-type MFI zeolite membranes to the alkylation of toluene with methanol. A *p*-xylene selectivity of 80% were attained using H-MFI zeolite membranes at 450–500°C, as illustrated in Fig. 3, providing the possible application of an MFI zeolite membrane for use in a catalytic membrane reactor (CMR).

Bernal et al.<sup>[54]</sup> used a catalytically active zeolite membrane to shift the reaction equilibrium by selective water permeation during ethanol esterification.

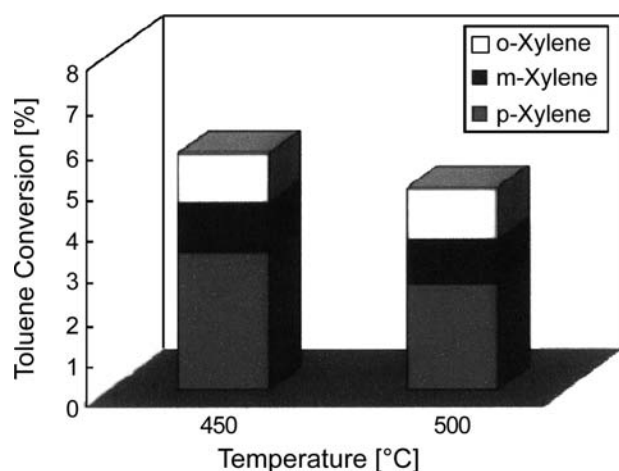


Fig. 3 Toluene conversion Source: From Ref.<sup>[53]</sup>.

The H-ZSM-5 membrane used in their work had sufficient catalytic activity to carry out the esterification of ethanol with acetic acid, and at the same time was selective for water permeation. As a consequence, the reaction and separation functions could be very efficiently coupled, and the conversion obtained (63.1%) at the same feed rate and catalyst loading was greater than in conventional fixed-bed reactors (49.4%), or in reactors where the zeolite membrane was kept separated from the catalyst (56.9%). Zhang et al.<sup>[23]</sup> fabricated the crack-free Fe-MFI zeolite that was used for the conversion of ethylbenzene to styrene and obtained 15% of conversion increase over the conventional fixed-bed reactor.

## CONCLUSION

Successful synthesis of high-quality microporous zeolite membranes has opened up new fields of membrane applications in environmental separation and reactions. Some separation applications such as  $H_2$  from mixtures and water/alcohol separation have great commercial potential. Zeolite membranes permit the integration of reaction and effective separation in a single stage. Some reactions have been tested in zeolitic membrane reactors and showed promising results. Extending the catalytic zeolite membrane to more reactions is currently the focus of many industrial and research groups around the world.

However, many challenges exist in zeolite membranes. A typical example is the low flux through the zeolite membrane because of the fact that relatively thick zeolite layers on the order of a few micrometers to 50  $\mu\text{m}$  are necessary to ensure a pinhole-free and crack-free zeolite layer. Decreasing the membrane thickness while keeping its compactness will dramatically

increase its flux, thus resulting to more throughputs in practical applications. Some researchers have reported some significant advances in increasing the gas flux through the membrane by reducing the membrane thickness or by fabricating the membrane with higher surface area. However, reproducibility for thick zeolite membrane fabrication is always a challenge. In this regard, the search for optimal zeolite membrane materials and novel synthesis methods for improved chemical and structural stability will require continuing efforts of researchers.

Many catalytic processes of industrial importance involve the combination of high-temperature and chemically harsh environments, two factors that strongly favor zeolite membranes. They can be integrated in broad arrays of membranes in membrane reactors for separation and reaction applications, ranging from biochemical through environmental to petrochemical applications. The zeolite membranes can be employed for the permeation of the products to shift equilibrium limitations or the distribution of reactants for the control of concentration of selected species, or to carry out catalysis and separation at the same time. Hence conversion enhancement can be significantly achieved in several reaction processes such as hydrogenation, dehydrogenation, and esterification. Therefore the employment of zeolite membrane reactors for several industrial applications is envisioned. However, scale-up problems are still the main limitations of this technology, in particular that large, crack-free zeolite membrane surface areas are required for membrane reactors in industrial application. This area requires major research and development efforts to take the technology to the industrial application stage.

## ACKNOWLEDGMENTS

Financial support from the Australian research council is gratefully acknowledged and thanks are also due to Prof. Feng-shou Xiao, Jilin University, China, for some useful discussions and suggestions.

## REFERENCES

1. Geus, E.R.; Den Exter, M.J.; Van Bakkum, H. Synthesis and characterization of zeolite (MFI) membranes on porous ceramic supports. *J. Chem. Soc., Faraday Trans.* **1992**, *88* (20), 3101–3109.
2. Yan, Y.; Tsapatsis, M.; Gavalas, G.R.; Davis, M.E. Zeolite ZSM-5 membranes grown on porous  $\alpha\text{-Al}_2\text{O}_3$ . *J. Chem. Soc., Chem. Commun.* **1995**, (2), 227–228.
3. Ishikawa, A.; Chiang, T.H.; Toda, F. Separation of water–alcohol mixtures by permeation through a zeolite

- membrane on porous glass. *J. Chem. Soc., Chem. Commun.* **1989**, (12), 764–765.
4. Jansen, J.C.; Koegler, J.H.; Van Bekkum, H.; Calis, H.P.A.; Van Den Bleek, C.M.; Kapteijn, F.; Moulijn, J.A.; Geus, E.R.; Van Der Puil, N. Zeolitic coatings and their potential use in catalysis. *Microporous Mesoporous Mater.* **1998**, *21* (4–6), 213–226.
  5. Tavolaro, A.; Drioli, E. Zeolite membranes. *Adv. Mater. (Weinheim, Germany)* **1999**, *11* (12), 975–996.
  6. Lin, Y.S. Microporous and dense inorganic membranes: current status and prospective. *Sep. Purif. Technol.* **2001**, *25* (1–3), 39–55.
  7. Poshusta, J.C.; Tuan, V.A.; Falconer, J.L.; Noble, R.D. Synthesis and permeation properties of SAPO-34 tubular membranes. *Ind. Eng. Chem. Res.* **1998**, *37* (10), 3924–3929.
  8. Kondo, M.; Komori, M.; Kita, H.; Okamoto, K.-I. Tubular-type pervaporation module with zeolite NaA membrane. *J. Membr. Sci.* **1997**, *133* (1), 133–141.
  9. Jafar, J.J.; Budd, P.M.; Hughes, R. Enhancement of esterification reaction yield using zeolite A vapor permeation membrane. *J. Membr. Sci.* **2002**, *199* (1–2), 117–123.
  10. Xu, X.; Yang, W.; Liu, J.; Lin, L. Synthesis of NaA zeolite membranes from clear solution. *Microporous Mesoporous Mater.* **2001**, *43* (3), 299–311.
  11. Dong, Q.; Xu, N.; Shi, J. Study on synthesis of NaA type zeolite membrane in clear aluminosilicate solution. *Guisuanyan Tongbao* **2002**, *21* (1), 54–57.
  12. Han, Y.; Ma, H.; Qiu, S.; Xiao, F.-S. Preparation of zeolite A membranes by microwave heating. *Microporous Mesoporous Mater.* **1999**, *30* (2–3), 321–326.
  13. Xu, X.; Yang, W.; Liu, J.; Lin, L. Synthesis of NaA zeolite membrane by microwave heating. *Sep. Purif. Technol.* **2001**, *25* (1–3), 241–249.
  14. Shah, D.; Kissick, K.; Ghorpade, A.; Hannah, R.; Bhattacharyya, D. Pervaporation of alcohol–water and dimethylformamide–water mixtures using hydrophilic zeolite NaA membranes: mechanisms and experimental results. *J. Membr. Sci.* **2000**, *179* (1–2), 185–205.
  15. Chao, K.J.; Kao, C.H.; Chiu, Y.W.; Lin, X.R.; Tan, C.S. Regeneration of supercritical carbon dioxide by alumina-supported MFI zeolite and mesoporous silica membranes. *Stud. Surf. Sci. Catal.* **2001**, *135*, 3168–3174. *Zeolites and Mesoporous Materials at the Dawn of the 21st Century*.
  16. Turlan, D.; Urriolabeitia, E.P.; Navarro, R.; Royo, C.; Menendez, M.; Santamaria, J. Separation of Pd complexes from a homogeneous solution using zeolite membranes. *Chem. Commun. (Cambridge, United Kingdom)* **2001**, (24), 2608–2609.
  17. Arruebo, M.; Coronas, J.; Menendez, M.; Santamaria, J. Separation of hydrocarbons from natural gas using silicalite membranes. *Sep. Purif. Technol.* **2001**, *25* (1–3), 275–286.
  18. Aoki, K.; Tuan, V.A.; Falconer, J.L.; Noble, R.D. Gas permeation properties of ion-exchanged ZSM-5 zeolite membranes. *Microporous Mesoporous Mater.* **2000**, *39* (3), 485–492.
  19. Au, L.T.Y.; Chau, J.L.H.; Ariso, C.T.; Yeung, K.L. Preparation of supported Sil-1, TS-1 and VS-1 membranes. Effects of Ti and V metal ions on the membrane synthesis and permeation properties. *J. Membr. Sci.* **2001**, *183* (2), 269–291.
  20. Li, S.; Tuan, V.A.; Noble, R.D.; Falconer, J.L. A Ge-substituted ZSM-5 zeolite membrane for the separation of acetic acid from water. *Ind. Eng. Chem. Res.* **2001**, *40* (26), 6165–6171.
  21. Tuan, V.A.; Noble, R.D.; Falconer, J.L. Boron-substituted ZSM-5 membranes: Preparation and separation performance. *AIChE J.* **2000**, *46* (6), 1201–1208.
  22. Julbe, A.; Farrusseng, D.; Jalibert, J.C.; Mirodatos, C.; Guizard, C. Characteristics and performance in the oxidative dehydrogenation of propane of MFI and V-MFI zeolite membranes. *Catal. Today* **2000**, *56* (1–3), 199–209.
  23. Zhang, X.; Li, Y.; Wang, J.; Tong, H.; Liu, C. Synthesis and characterization of Fe-MFI zeolite membrane on a porous  $\alpha$ -Al<sub>2</sub>O<sub>3</sub> tube. *Separation and Purification Technology* **2001**, *25* (1–3), 269–274.
  24. Hasegawa, Y.; Tanaka, T.; Watanabe, K.; Jeong, B.-H.; Kusakabe, K.; Morooka, S. Separation of CO<sub>2</sub>–CH<sub>4</sub> and CO<sub>2</sub>–N<sub>2</sub> systems using ion-exchanged FAU-type zeolite membranes with different Si/Al ratios. *Korean J. Chem. Eng.* **2002**, *19* (2), 309–313.
  25. Kita, H.; Fuchida, K.; Horita, T.; Asamura, H.; Okamoto, K. Preparation of faujasite membranes and their permeation properties. *Sep. Purif. Technol.* **2001**, *25* (1–3), 261–268.
  26. Nikolakis, V.; Xomeritakis, G.; Abibi, A.; Dickson, M.; Tsapatsis, M.; Vlachos, D.G. Growth of a faujasite-type zeolite membrane and its application in the separation of saturated/unsaturated hydrocarbon mixtures. *J. Membr. Sci.* **2001**, *184* (2), 209–219.
  27. Lassinantti, M.; Hedlund, J.; Sterte, J. Faujasite-type films synthesized by seeding. *Microporous Mesoporous Mater.* **2000**, *38* (1), 25–34.
  28. Jeong, B.-H.; Hasegawa, Y.; Sotowa, K.-I.; Kusakabe, K.; Morooka, S. Vapor permeation properties of an NaY-type zeolite membrane for normal and branched hexanes. *Ind. Eng. Chem. Res.* **2002**, *41* (7), 1768–1773.
  29. Kobayashi, Y.; Takami, S.; Kubo, M.; Miyamoto, A. Computational chemical study on separation of benzene and cyclohexane by a NaY zeolite membrane. *Desalination* **2002**, *147* (1–3), 339–344.
  30. Zhang, Y.; Xu, Z.; Chen, Q. Synthesis of small crystal polycrystalline mordenite membrane. *J. Membr. Sci.* **2002**, *210* (2), 361–368.
  31. Navajas, A.; Mallada, R.; Tellez, C.; Coronas, J.; Menendez, M.; Santamaria, J. Preparation of mordenite membranes for pervaporation of water–ethanol mixtures. *Desalination* **2002**, *148* (1–3), 25–29.
  32. Lin, X.; Kikuchi, E.; Matsukata, M. Preparation of mordenite membranes on  $\alpha$ -alumina tubular supports for pervaporation of water–isopropyl alcohol mixtures. *Chem. Commun. (Cambridge)* **2000**, (11), 957–958.
  33. Munoz, T.; Balkus, K.J. Preparation of oriented zeolite UTD-1 membranes via pulsed laser ablation. *J. Am. Chem. Soc.* **1999**, *121* (1), 139–146.
  34. Balkus, K.J.; Gbery, G.; Deng, Z. Preparation of partially oriented zeolite MCM-22 membranes via pulsed laser deposition. *Microporous Mesoporous Mater.* **2002**, *52* (3), 141–150.

35. Erdem-Senatalar, A.; Tatlier, M.; Urgan, M. Preparation of zeolite coatings by direct heating of the substrates. *Microporous Mesoporous Mater.* **1999**, *32* (3), 331–343.
36. Piera, E.; Brenninkmeijer, C.A.M.; Santamaria, J.; Coronas, J. Separation of traces of CO from air using MFI-type zeolite membranes. *J. Membr. Sci.* **2002**, *201* (1–2), 229–232.
37. Poshusta, J.C.; Tuan, V.A.; Falconer, J.L.; Noble, R.D. Synthesis and permeation properties of SAPO-34 tubular membranes. *Ind. Eng. Chem. Res.* **1998**, *37* (10), 3924–3929.
38. Aoki, K.; Kusakabe, K.; Morooka, S. Gas permeation properties of A-type zeolite membrane formed on porous substrate by hydrothermal synthesis. *J. Membr. Sci.* **1998**, *141* (2), 197–205.
39. Masuda, T.; Fukumoto, N.; Kitamura, M.; Mukai, S.R.; Hashimoto, K.; Tanaka, T.; Funabiki, T. Modification of pore size of MFI-type zeolite by catalytic cracking of silane and application to preparation of H<sub>2</sub>-separating zeolite membrane. *Microporous Mesoporous Mater.* **2001**, *48* (1–3), 239–245.
40. Illgen, U.; Schafer, R.; Noack, M.; Kolsch, P.; Kuhnle, A.; Caro, J. Membrane supported catalytic dehydrogenation of iso-butane using an MFI zeolite membrane reactor. *Catal. Commun.* **2001**, *2* (11–12), 339–345.
41. Lai, R.; Gavalas, G.R. ZSM-5 membrane synthesis with organic-free mixtures. *Microporous Mesoporous Mater.* **2000**, *38* (2–3), 239–245.
42. Poshusta, J.C.; Tuan, V.A.; Pape, E.A.; Noble, R.D.; Falconer, J.L. Separation of light gas mixtures using SAPO-34 membranes. *AIChE J.* **2000**, *46* (4), 779–789.
43. Tuan, V.A.; Li, S.; Falconer, J.L.; Noble, R.D. Separating organics from water by pervaporation with isomorphously-substituted MFI zeolite membranes. *J. Membr. Sci.* **2002**, *196* (1), 111–123.
44. Gallego-Lizon, T.; Edwards, E.; Lobiundo, G.; Freitas dos Santos, L. Dehydration of water/*t*-butanol mixtures by pervaporation: comparative study of commercially available polymeric, microporous silica and zeolite membranes. *J. Membr. Sci.* **2002**, *197* (1–2), 309–319.
45. Ciavarella, P.; Casanave, D.; Moueddeb, H.; Miachon, S.; Fiaty, K.; Dalmon, J.A. Isobutane dehydrogenation in a membrane reactor influence of the operating conditions on the performance. *Catal. Today* **2001**, *67* (1–3), 177–184.
46. Piera, E.; Tellez, C.; Coronas, J.; Menendez, M.; SaIntamaria, J. Use of zeolite membrane reactors for selectivity enhancement: application to the liquid-phase oligomerization of isobutene. *Catal. Today* **2001**, *67* (1–3), 127–138.
47. Salomon, M.A.; Coronas, J.; Menendez, M.; Santamaria, J. Synthesis of MTBE in zeolite membrane reactors. *Appl. Catal., A Gen.* **2000**, *200* (1–2), 201–210.
48. Farrusseng, D.; Julbe, A.; Guizard, C. Evaluation of porous ceramic membranes as O<sub>2</sub> distributors for the partial oxidation of alkanes in inert membrane reactors. *Sep. Purif. Technol.* **2001**, *25* (1–3), 137–149.
49. Liu, B.S.; Gao, L.Z.; Au, C.T. Preparation, characterization and application of a catalytic NaA membrane for CH<sub>4</sub>/CO<sub>2</sub> reforming to syngas. *Appl. Catal., A Gen.* **2002**, *235* (1–2), 193–206.
50. Sotowa, K.-I.; Hasegawa, Y.; Kusakabe, K.; Morooka, S. Enhancement of CO oxidation by use of H<sub>2</sub>-selective membranes impregnated with noble-metal catalysts. *Int. J. Hydrogen Energy* **2002**, *27* (3), 339–346.
51. Hasegawa, Y.; Ueda, A.; Kusakabe, K.; Morooka, S. Oxidation of CO in hydrogen-rich gas using a novel membrane combined with a microporous SiO<sub>2</sub> layer and a metal-loaded  $\gamma$ -Al<sub>2</sub>O<sub>3</sub> layer. *Appl. Catal., A Gen.* **2002**, *225* (1–2), 109–115.
52. Ciavarella, P.; Moueddeb, H.; Miachon, S.; Fiaty, K.; Dalmon, J.A. Experimental study and numerical simulation of hydrogen/isobutane permeation and separation using MFI-zeolite membrane reactor. *Catal. Today* **2000**, *56* (1–3), 253–264.
53. Takata, Y.; Tsuru, T.; Yoshioka, T.; Asaeda, M. Gas permeation properties of MFI zeolite membranes prepared by the secondary growth of colloidal silicalite and application to the methylation of toluene. *Microporous Mesoporous Mater.* **2002**, *54* (3), 257–268.
54. Bernal, M.P.; Coronas, J.; Menendez, M.; Santamaria, J. Coupling of reaction and separation at the microscopic level: esterification processes in a H-ZSM-5 membrane reactor. *Chem. Eng. Sci.* **2002**, *57* (9), 1557–1562.